EuroSun2022

25 - 29 September 2022
Kassel, Germany

Proceedings

ISES and IEA SHC International Conference
on Solar Energy for Buildings and Industry

Conference of

ISES International Solar Energy Society

SHC SOLAR HEATING & COOLING PROGRAMME INTERNATIONAL ENERGY AGENCY

SOLAR. UNI-KASSEL.DE

Proceedings

Proceedings of EuroSun 2022 - ISES and IEA SHC International Conference on Solar Energy for Buildings and Industry

Copyright © 2023 by the International Solar Energy Society and
the Authors

International Solar Energy Society
Wiesentalstr 50
79115 Freiburg
Germany

Tel + 49 761 45906 – 0
Fax + 49 761 45906 – 99
Email hq@ises.org
http://www.ises.org

ISBN 978-3-982 0408-8-2

All rights reserved. No part of the publication may be reproduced, transmitted, in any form or by any means, electronic, mechanical, photocopying, recording or otherwise, without permission of the publisher, except in the case of brief quotations embodied in critical articles and review or where prior rights are preserved.
Produced by International Solar Energy Society

Notice

The International Solar Energy Society, the IEA SHC, the University of Kassel (Department of Solar and Systems Engineering) nor any one of the supporters or sponsors of the EuroSun 2022 conference make any warranty, expressed or implied, or accepts legal liability or responsibility for the accuracy, completenessor usefulness of any information, apparatus, product or process disclosed, or represents that its use would not infringe privately on rights of others. The contents of articles express the opinion of the authors and are not necessarily endorsed by the International Solar Energy Society, the IEA SHC, the University of Kassel (Department of Solar and Systems Engineering) or supporters or sponsors of the conference. The International Solar Energy Society, the IEA SHC, the University of Kassel (Department of Solar and Systems Engineering) or any one of the supporters or sponsors of the EuroSun 2022 conference do not necessarily condone the politics, political affiliation and opinions of the authors or their sponsors.

Disclaimer

We cannot assume any liability for the content of external pages. The operators of those linked pages are solely responsible for their content. We make every reasonable effort to ensure that the content of this web site is kept up to date, and that it is accurate and complete. Nevertheless, the possibility of errors cannot be entirely ruled out. We do not give any warranty regarding the timeliness, accuracy or completeness of material published on this web site and disclaim all liability for (material or non-material) loss or damage incurred by third parties arising from the use of content obtained from the website.

EuroSun 2022 Proceedings Editorial

By the EuroSun 2022 Organizing Team

From 25 - 29 September, ISES together with the IEA Solar Heating & Cooling Programme, welcomed almost 500 scientists from 54 countries to Kassel for EuroSun 2022, the International Conference on Solar Energy for Buildings and Industry.

After four conference days with contributions by 16 invited speakers from leading European and global institutions, almost 300 expert oral and poster presentations, five workshops, as well as two excursions to solar industry and research institutions, it is clear that a sustainable and crisis-proof heat and energy supply with renewable energies is possible. Critical pillars for this include especially heat pumps, solar energy and district heating based on local heat management plans.

Spread over 20 conference themes, the latest research results, trends and technology developments covering components, applications and cross-cutting topics such as solar resources & energy meteorology, strategies, scenarios, financing and policies were presented. Special focal areas were thermal storage as well as digitalization and artificial intelligence, whereby the conference emphasis on heat supply especially for buildings and industry, could not have been more timely.

A particular focus of the EuroSun 2022 organizers was to promote the exchange between young and experienced experts. Several events were held especially for young researchers including a Masters Course in Solar Energy, a Solar Speed Dating session and a special Young ISES Party. 75 students were also given free admission to the conference as well as the option of private accommodation offered by local researchers during the conference days. The enthusiasm of young and emerging experts was omnipresent during the conference and the conference was enhanced by the exchange and the shared motivation to establish renewable energies as the solution to current and future supply problems.

Prof. Klaus Vajen, together with Tomas Olejniczak Chair of the EuroSun 2022 conference, was very satisfied with the event: "Both in terms of security of supply and for climate protection, the long-neglected heat supply is of crucial importance. Many technical solutions using renewable energies have already been developed, are produce in Europe and can be used immediately."

Committees

Conference Chairs

Conference Chair: Prof. Klaus Vajen | University of Kassel & ISES President

Conference Co-Chair: Tomas Olejniczak | RVO Netherlands & IEA SHC Chair

International Organizing Committee

Tomas Olejniczak | RVO (Chair)
Prof. Ulrike Jordan | University of Kassel (Co-Chair)
Prof. Klaus Vajen | University of Kassel
Prof. Bulent Yesilata | Ankara Yildirim Beyazit University, Turkey
Prof. Andreas Häberle | Eastern Switzerland University of Applied Science
Ken Guthrie | IEA Solar Heating and Cooling Programme
Ms Pam Murphy | IEA Solar Heating and Cooling Programme
Ms Jennifer McIntosh | International Solar Energy Society
Ms Arabella Liehr | International Solar Energy Society
Ms Melina Hanhart | International Solar Energy Society

Scientific Committee

Chairs:

Prof. Bulent Yesilata | Ankara Yildirim Beyazit University, Turkey

Prof. Klaus Vajen | University of Kassel, Germany

Scientific Program Theme Chairs:

Applications

Solar and Efficient Buildings Prof. Monika Woloszyn, University Savoie Mont Blanc; Dr. Harald Drück, University of Stuttgart

Energetic Renovation of Buildings Prof. Dr. Alexandra Troi, Eurac

Daylighting Prof. Barbara Szybinska Matusiak, Norwegian University of Science and Technology; Dr. Jan de Boer, Fraunhofer Institute for Building Physics

Solar Domestic Hot Water and Space Heating Dr. Rosie Christodoulaki, Centre for Renewable Energy Sources and Saving (CRES); Dr. Mathias Ehrenwirth, Institute of new Energy Systems InES at Technische Hochschule Ingolstadt

Innovative District Heating and Cooling Dr. Karin Rühling, Technical University of Dresden; Dr. Daniel Muschick, Bioenergy and Sustainable Technologies - BEST

Innovative Industrial Process Heat Felix Pag, University of Kassel, DI Jürgen Fluch, AEE Intec

Solar Air Conditioning and Refrigeration Dr. Salvatore Vasta, Institute for Advanced Energy Technologies "Nicola Giordano" ITAE; Prof. Dr. Uli Jakob, HFT Stuttgart

PV and PVT Systems for Buildings and Industry Dr. Federico Giovanetti, Institute for Solar Energy Research Hamelin, Dr. Corry de Keizer, TNO Energy Transition

Solar Energy and Heat Pumps Dr. Michel Haller, Eastern Switzerland University of Applied Science, Prof. Chris Bales, Dalarna University

Water Purification through Renewable Energy Dr. Isabelle Oller, PSA Spain; Christoph Brunner, AEE - Institute for Sustainable Technologies

Carbon Neutral University Campus Prof. Dr. Anton Maas, University of Kassel; Prof. Dr. Thomas Bednar, Technical University Vienna

Urban Planning, Solar and Efficient Districts Dr.Georgios Dermentzis, Aristotle University of Thessaloniki; Prof. Dr. Fabian Ochs, University of Innsbruck

Components

Solar Thermal and PVT Collectors and Solar Loop Components Dr. Daniel Zenhäusern, SPF Institute for Solar Technology; Dr. Tomas Matuska, Czech Technical University

Thermal Energy Storage Prof. Dr. Luisa Cabeza, University of Lleida; Dr. Andreas Hauer, ZAE Bayern

Testing, Certification and Monitoring Dr. Vassiliki Drosou, Centre for Renewable Energy Sources and Saving (CRES); Stefan Mehnert, Fraunhofer Institute for Solar Energy Systems ISE

Cross Cutting

Solar Resources and Energy Meteorology Jan Remund, Meteotest; Adam Jensen, Technical University of Denmark

System Modelling, Artificial Intelligence, Digitalization Cedric Paulus, CEA; Dr. Bernd Hafner, Federation of German Heating Industry

Sector Coupling and Grid Stabilization Dr. Richard Hall, UK Department for International Trade; Prof. Dr. Christian Doetsch, Fraunhofer UMSICHT

Renewable Energy Strategies, Scenarios, Financing and Policies Assistant Professor Alexandros Charalambides, Cyprus University of Technology, Pedro Dias, Solar Heat Europe

Renewable Energy Education Prof. Dr. Birgit Steffenhagen, University of Applied Sciences Stralsund; Prof. Frank Späte, OTH – Technical University of Applied Sciences

Scientific Review Committee Members:

Beccali, Marco
Berberich, Magdalena
Burduhos, Bogda-Gabriel
Calderoni, Marco
Carvalho, Maria
Chemisana, Daniel
Chéze, David
Coronas, Alberto
David, Mathieu
De Araujo Passos, Luigi Antonio
Du, Jingtao
Eames, Philip
Fan, Jianhua
Fink, Christian
Fischer, Stephan
Franco, Judith
Frazzica, Andrea
Furbo, Simon
Gari da Silva Fonseca Junior, Joao
Gentile, Niko
Gölles, Markus
Göttsche, Joachim
Häberle, Andreas
Hall, Richard
Heinz, Andreas
Herrando, Maria
Herrera, Daniel
Kazantzidis, Andreas
Kazmerski, Lawrence
Kok Skov, Christian
Lämmle, Manue
Lamnatour, Chrysovalantou
Lazaro, Ana
Lee, Eleanor
Leeb Markus
Leibbrandt, Pascal
Lobaccaro, Gabriele
Lollini, Roberto
Martin, Shawn
Menezo, Christophe

Middleton, Paulette
Moia-Pol, Andreu
Madimi, Maedeh
Nateghi, Roshi
Nielsen, Kristian
Nielsen, Elsabet
Ohnewein, Philip
Orozaliev, Janybek
Pellegrini, Marco
Pischow, Kaj
Polo, Jesus
Raturi, Atul
Reiter, Thomas
Renne, Dave
Rojas, Esther
Russo, Roberto
Rzadkowska, Agnieszka
Sapienza, Alessio
Schabbach, Thomas
Schmidt, Dietrich
Schrag, Tobias
Schweigler, Christian
Serra, Luis
Shahrooz, Mahdi
Sommerfeldt, Nelson
Thebault, Martin
Thür, Alexander
Travasaros, Costas
Valenzuela, Loreto
Weiss, Werner
Wilbert, Stefan

Conference Themes

Applications

1. Solar and Efficient Buildings
2. Energetic Renovation of Buildings
3. Daylighting
4. Solar Domestic Hot Water and Space Heating
5. Innovative District Heating and Cooling
6. Innovative Industrial Process Heat
7. Solar Air Conditioning and Refrigeration
8. PV and PVT Systems for Buildings and Industry
9. Solar Energy and Heat Pumps
10. Water Purification through Renewable Energy
11. Carbon Neutral University Campus
12. Urban Planning, Solar and Efficient Districts

Components

13. Solar Thermal and PVT Collectors and Solar Loop Components
14. Thermal Energy Storage
15. Testing, Certification and Monitoring

Cross Cutting

16. Solar Resources and Energy Meteorology
17. System Modelling, Artificial Intelligence, Digitalization
18. Sector Coupling and Grid Stabilization
19. Renewable Energy Strategies, Scenarios, Financing and Policies
20. Renewable Energy Education

Sponsors

Public Support

Supported by:

Federal Ministry
for Economic Affairs
and Climate Action

on the basis of a decision
by the German Bundestag

UNIKASSEL
VERSITÄT

LEA
HESSEN
LANDES ENERGIE AGENTUR

Gold Sponsor

VIESMANN

Supporting Sponsors

Städtische Werke
Aktiengesellschaft

cdw stiftung

QONCEPT
ENERGY

enersolve

Partners







Scientific Program

A. Solar and Efficient Buildings

Study and Simulation of Low Energy Solar Powered House in Libya
Alkishriwi, N., Elayeb, M. 1

An Energy Trading Model for a Lab-scale PV Microgrid in the Tunisian Context
Alvarado Alvarado, E.E., Belkhodja, I.S., Bennani, A.A., Buitrago Otalora, A.C.,
Ferchichi, S., Khalifa, I., Taimoor, M. 11

Metrics Behind the Implementation of Photovoltaic Solar Energy in Urban Area
Aparecida Oliveira de Sousa, J., BERRAH, L., KUMAR PATEL, M. 20

Solar Decathlon - New Ways of Construction for Decarbonised Buildings
Gerber, A., Frühschütz, L. 30

The Future of Solar Integration: Towards Efficiency in Solar Design through Aesthetics, Optimisation and Customisability
Jaspers, K., Ketelaars, E.W., Kütt, M.L., Roefs, L.H.H.M. 37

Evaluating the Potential of Annual Solar Heat Gains from Manually Operated Shading System
Kumar, S.R., Gentile, N., Hendrix, A. 49

Sustainable Housing Insulation for High-Altitude Kyrgyzstan: A Technical Guide
Mehta, K., Beringer, J., Ehrenwirth, M., Trinkl, C., Zörner, W. 58

Solar Energy Buildings with High Degree of Independence of Energy Supply from Grids
Nielsen, E., Furbo, S. 70

Monitoring Results of the Energy Consumption Behaviour of Two Highly Solar-Powered Apartment Buildings
Oppelt, L., Fieback, T., Gäbler, A., Storch, T. 82

Hidden Colored Building Integrated Photovoltaics: Technology Overview and Design Challenges
Pelle, M., Canosci, E., Luzi, G., Maturi, L. 88

Analysis of Solar Thermal Polygeneration Systems for the Residential-Commercial Sector
Serra, L.M., Lozano, M.A., Lázaro, A., Pina, E.A. 97

Building Energy Efficiency Enhancement through Load Reduction in Air Conditioning System
Sharma, R.K., Kumar, A., Rakshit, D. 98

B. Energetic Renovation of Buildings

Sustainable and Efficient Energy Supply for the Development of Tourist Villages at the Adriatic and Ionian Sea
Bockelmann, F., Dreier, A. **110**

Renovation of a Multi-Family-House with External Wall Heating System
Calabrese, T., Bosshard, I., Haller, M., Neugebauer, M., Philippen, D. **121**

Evaluation of Building Energy Performance: Comparison Before and After Envelope Retrofitting
Derai, A., BERRAH, L., PIOT, A., WOLOSZYN, M. **133**

Renovation Towards NZEB with PV
Haase, M. **145**

Experiences from Local Authorities Stimulating the Adoption of Low-Carbon Technologies by Homeowners
Mlecnik, E. **156**

A Novel Statistical Method to Improve Energy Efficiency of Housing Stock in the Eastern Mediterranean Climate
Ozarisoy, B., Altan, H. **166**

ATLAS-FeliCity: Supporting Energy Retrofit of the Heritage Building Stock Through a Simplified Digital Twin
Polo López, C.S., Curto, I., Exner, D., Haas, F., Khjoa, A., Troi, A. **178**

Participation Potential for Energy-Active Facades in Future Flexibility Markets
Ramschak, T., Gumhalter, M. **190**

D. Solar Domestic Hot Water and Space Heating

100 % Solar Heating with Seasonal Thermal Storage, Solar Thermal Collectors, PV and Heat Pump

Ruesch, F., Ammann, S., Bohara, K., Brauchli, L., Haller, M., Lichtensteiger, F., Villasmil, W., Worlitschek, J. ***202***

Radiant Cooling System without Any Energy Input

Yoo, S., Choi, H.J. ***213***

E. Innovative District Heating and Cooling

Impact of Domestic Hot Water Preparation Systems on District Heating Network Design and Operation
Braas, H., Best, I., Janybek, O., Johannes, Z., Jordan, U., Klaus, V., Weena, B. ... 225

Performance Monitoring of an 800m2 Solar Thermal Plant with Evacuated Flat Plate Collectors coupled to a DHN
Duret, A., Demonchy, G., Jobard, X., Pauletta, S. ... 234

Operability of District Heating Plants Combining a Large-Scale Solar Thermal Field and Condensing Wood Chip Boilers – a Case Study in Switzerland
Jobard, X., Duret, A. ... 243

Solar District Heating versus Renovation of Buildings as Measures for Decarbonization of Heat Supply in Rural Areas
Kelch, J., Kusyy, O., Orozaliev, J., Vajen, K., Zipplies, J. ... 254

Quasi-Dynamic Testing of Thermal Sun Air Collectors and Numerical Simulations of a Cold District Heating Network
Lott, S., Drück, H., Fischer, S., Hafner, B. ... 263

Early-stage Feasibility Study of an Ambient-temperature District Thermal Network: A Case Study in Denmark
Maccarini, A., Afshari, A. ... 275

Software-supported Investment Optimization for District Heating Supply Systems
Panitz, F., Behrends, T., Stange, P. ... 282

Optimisation of a Theoretical 4th Generation District Heating Network located at the town of Loughborough, UK
Pans Castillo, M.A., Eames, P. ... 290

About the Efficiency of District Heating with Flexible Heat and Temperature Distribution
Paulick, S., Boß, V., Felsmann, C. ... 302

Optimized Adsorption Heat Pump for Efficiency Increase of District Heating Networks
Piccoli, E., Civioc, R., Daguenet, X., Duret, A., Galmarini, S., Gantenbein, P., Jobard, X. ... 312

Direct Excess Heat Utilization from a High Performance Computer in an Existing Unrenovated Building: A Case Study
Sauerwein, D., Feike, F. ... 324

Low Temperature District Heating as a Key Technology for a Successful Integration of Renewable Heat Sources in our Energy Systems
Schmidt, D., Lygnerud, K. ... 330

Integration of Different Solar Collectors into District Heating Networks and Floor Space Allocation
Stahlhut, M. ... 340

Development of a Combined Model Predictive and Adaptive Control Strategy for the Operation of a Cold District Heating Network
Ullmann, J., Drück, H., Hafner, B. ... 350

Techno-Economical Assessment of a Solar Regenerated Borehole Heat Exchanger Field with PVT Collectors for District Heating
Weiland, F., Chhugani, B., Kracht, N., Pärisch, P. ***360***

F. Innovative Industrial Process Heat

Non-Tracking Asymmetric Shadeless (NASH) Solar Collectors for Decarbonizing Industrial Process Heat Applications
Bhusal, Y., Abido, M., Brinkley, J., Widyolar, B., Winston, R. **372**

Techno-Economic Comparison of Steam Generation Systems with Industrial Heat Pumps
Dahash, A., Dusek, S., Helminger, F., Riedl, J. **384**

Modeling of a Solar Heat for Industrial Processes (SHIP) System using Fresnel Collectors
David Hernández, M.A., Cazorla-Marín, A., Gonzálvez Macia, J., Paya Herrero, J. **396**

A Novel Method for Assessing the Techno-Economical Compatibility of Solar Thermal Integrations
Gambardella, A., Saini, P. **408**

Using Heat Maps to Assess the Energy Efficiency of Industrial Companies
Holway, S., Pag, F., Vajen, K. **420**

Effect of HTF Flow Direction on Thermal Performance in an Upward Facing Cavity Receiver
Kumar, S., Bapat, S.L. **425**

Scenario based Heating and Cooling Load Profiles in Piglet Production Systems
König, K., Pag, F., Vajen, K. **436**

Design of a Small-scale Maize Dryer
Muusha, P., Mhlanga, S. **441**

How To Combine a Solar Heating Plant and a CHP most Efficiently for Industrial Applications?
Pag, F., Pino, A., Vajen, K. **450**

Comparative Techno-Economic Analysis of High Temperature Heat Pump and Parabolic Trough Collector System for Industrial Steam Generation: Analysis for Europe
Saini, P., Arpagaus, C., Bless, F., Ghasemi, M. **456**

Upgradation of Khoa Production Method in Manchar, India using Solar Thermal System
Tadlimbekar, S., Torio, H. **467**

Energy Savings for Gas Preheating in the Gas Transport Sector with Air Dehumidification and Expansion Turbines
Völker, L., Fleig, D., Jordan, U., Louvet, Y., Pag, F., Vajen, K. **479**

G. Solar Air Conditioning and Refrigeration

Experiments On a Solar Vapour Absorption Refrigeration Cold Storage System
Annamalai, M., Vijayakumar, S. **492**

Adapted Components and Show Cases on Solar Cooling Systems in Sunbelt Region Countries
Beccali, M., Baby, B.A., Bonomolo, M., Vasta, S., Weiss, W. **504**

The Application of Concentrating Solar Thermal Systems in Hospital Buildings
Dimoudi, A., Christodoulaki, R., Drosou, V., Vavalos, P., Zoras, S. **516**

Annual Energy Performance of a Solar/Biomass HVAC System: Experimental Characterization through Concise Cycle Tests
Dongellini, M., Haberl, R., Morini, G.L., Naldi, C., Omlin, L., Varga, S. **528**

Analysis of Constructive Modifications for Enhancing the Performance of Solar Collector/Regenerators for Liquid Desiccant Systems
Gómez Castro, F.M., Eicker, U., Jordan, U. **540**

A New Method for Determining the Nusselt and Sherwood Numbers in Simultaneous Heat and Mass Transfer in Solar Collector/Regenerators
Gómez Castro, F.M., Eicker, U., Jordan, U. **550**

Parabolic Trough Collector (PTC) System for Combined Cooling and Heating Supply for a Factory Building in Izmir, Turkey
Lokurlu, A., Commandeur, L., Ramesh, A. **559**

Energy Analysis Of A Solar-Driven Hybrid Air Conditioning System With An Absorption Heat Pump And A Desiccant Evaporative Cooling System
Prieto, J., Ajona, J.I., Comino, F., Coronas, A., Kotegov, R., Ruiz de Adana, M. **566**

Hybrid Solar Thermal Field (FPC-PTC) Applied for Solar Heating and Cooling Process in the Agroindustry Sector
Rosales-Pérez, J.F., Cardemil, J.M., Escobar, R.A., Gil, J.D., Pérez-Garcia, M., Villarruel-Jaramillo, A. **576**

Covering Energy Demands of Africa with Radiative Cooling and Solar Collection using a Single Device
Vilà, R., Castell, A., Medrano, M., Monterrubio, J., Solé, C. **583**

Optimal Conceptual Design of a Novel Façade-Integrated Adsorption Cooling System
Weber, S.O., Böckmann, O., Greiner, A., Park, S., Schäfer, M. **595**

H. PV and PVT Systems for Buildings and Industry

Decarbonizing Heating Supply Systems in Existing Single-family Houses Through PVT - Heat Pump Systems
Chhugani, B., Giovannetti, F., Pärisch, P. **606**

Simplified Thermal Performance Model for the Design of a PVT Heat Exchanger Dedicated to Solar-assisted Heat Pump
Delachaux, V., Bennacer, R., Brottier, L. **618**

Investigation of Creep-Fatigue Lifetime in Solar Photovoltaic Module Interconnections
Eslami Majd, A., Amini Sedehi, A., Ekere, N.N., Rahmati Darvazi, A., Tchuenbou-Magaia, F. **630**

Energy Performance Investigation of PVT Assisted Heat Pump System for a Net Zero Office Building
Kim, M., Ahn, Y., Han, G., Kim, J. **642**

Fire Protection Requirements and Solutions for the Implementation of BIPV on a High-Rise Residential Building in Frankfurt/Germany
Krause, M., Erban, C., Funtan, P., Müller, R. **645**

Performance of Heat Pump Systems with PVT Collectors with Optimized Finned Heat Exchangers Integrated as Single Heat Source
Lämmle, M., Munz, G. **654**

Failure Risk Analysis of Photovoltaic Systems Based on Literature Review
Mathieu, A., BODDAERT, S., FRAISSE, G., GAILLARD, L., Thebault, M., Thebault, S. **660**

Comparative Analysis of the Performance of Four Different Photovoltaic-Thermal Modules
Mussard, M., Dai, Y., Foss, S.E., Li, Z., Maret, P., Shen, W., Zhao, Y., Zhu, J. **672**

A PVT Driven Direct Expansion Heat Pump Field Operation Results
Sanz, A., Fuente, R., Ibañez, P., Martín, A.J., Pereda, A., Roman, E. **683**

Energy Performance of Four Prototypes of PVT Collectors. A Comparative Study
Simón-Allué, R., Coca-Ortegón, A., Guedea, I., Lara, Y. **690**

Prefabricated Renewable Energy Facades for Cost-effective Buildings (PREFAB)
de Keizer, C., Dörenkämper, M., Villa, S. **702**

I. Solar Energy and Heat Pumps

Modular Refurbishment of Multi-Family Houses with PVT-PCM Heat Pump Systems and Self-Learning Energy Management
Bernard, T., Leibfried, U., Schlosser, F., Stürtz, S., Wallner, S. ***715***

Solar-Thermal Activation of Rear-Ventilated Façades as a Source for Heat Pump Based Heat Supply Systems
Büttner, C. ***727***

The Potential of Combined PV and Air Source Heat Pump Systems in German Residential Buildings
Dabrock, K., Beuth, H., Knosala, K., Kotzur, L., Pflugradt, N., Stolten, D. ***738***

Comparison of a Centralized with Decentralized Heat Pump Systems in a Multy Family Building
Haberl, R., Bohara, K., Haller, M.Y., Zehnder, M. ***748***

Increasing PV Self-Consumption with Heat Pumps – Sense or Non-Sense of additional Electric Heaters
Haller, M.Y., Heinz, A. ***756***

Numerical Study of the Effect of Hybrid Solar Collectors on the Performances of the System Combining PVT With Heat Pumps
Jaafar, M.A., Brottier, L., Chhugani, B. ***768***

Testing a Flexible Configuration of a Solar-Assisted Heat Pump with PVT Collectors for Domestic Hot Water Production
Meramveliotakis, G., Karellas, S., Kosmadakis, G., Pilou, M. ***777***

Emission-Free Heat Supply of Residential Districts with Solar Thermal Energy and a Heat Pump Storage System
Nefodov, D., Richter, M., Urbaneck, T., Xiao, S. ***789***

Analysis of the Electrical Consumption of an Air-Cooled Single Effect Ammonia/Water Chiller
Palacios Lorenzo, M., Marcos del Cano, J.D., marcos del Cano, J.D. ***801***

Experimental Investigation on Solar-Driven GAX-based Absorption Heat pump for Domestic Hot Water production
Phan, H.T., Aste, F., Demasles, H. ***811***

Experimental Investigation of a Novel Hybrid Heat Pump
Reum, T., Ehrenwirth, M., Schrag, T., Summ, T. ***824***

PV Driven Air Heat Pump Using Overheating Effects as Thermal Battery in Single Family Houses
Thür, A., Leu, F., Schett, B. ***833***

J. Water Purification through Renewable Energy

Experimental Studies on Solar Multi - Effect Desalination System
Annamalai, M., Kannappan, T. ***846***

Falling Film Measurements Using High Speed Camera and High Speed Infra-Red Camera
Kannappan, T., Annamalai, M. ***858***

Nexus Energy and Water: Integration Concepts for Solar Energy in Industrial Water and Waste Water Management
Meitz, S., Brunner, C. ***869***

K. Carbon Neutral University Campus

Measures for Energy Optimization for Resource-Saving Consumption Development on a University Campus
Arendt, M., Felsmann, C., Kremonke, A. ***875***

Identification of Waste Heat Potentials and Their Integration Into a District Heating Subgrid
Bergstraesser, W., Orozaliev, J., Vachhani, A., Vajen, K. ***884***

Comparison of the Simulated and Measured Performance of the PV Plant of Austria's Largest (Plus-)Plus-Energy Office Building
David, A., Bednar, T., Sint, S. ***894***

Identification of Temperature Reduction Potentials in Heating Circuits based on Measurements
Fox, S., Knissel, J., Schüler, M. ***906***

Towards a More Sustainable Campus, Proposal of Improvement Through Renewable Energies Implementation
Granados-López, D., García, I., García-Fuente, M., García-Rodríguez, S.,
García-Rodríguez, A., Garrachón-Gómez, E., González-Peña, D. ***918***

SmartPrioGIS - A Concept for Recording, Holding and Evaluating Data as a Contribution to CO2 Reduction for the Kassel University Campus
Klauß, S., Gross, R., Lohse, L., Maas, A. ***926***

Derivation of Heating Load Profiles on the Basis of Demand-Consumption Analyses
Krause, M., Klauß, S., Maas, A., Schellhase, L., Stricker, T. ***934***

Transformation of a University Campus: Comparison of Ranking Methods for Temperature Reduction from Network and Building Perspective
Neusuess, H., Bergstraesser, W., Knissel, J., Orozaliev, J., Vajen, K. ***941***

A Holistic Energetic Transformation Concept for the Heating and Cooling Supply of a University Campus
Stanica, D., Bachmann, M., Friebe, M., Kononenko, N., Kriegel, M., Schumann, F. ***953***

L. Urban Planning, Solar and Efficient Districts

Estimating Rooftops' Suitability for PVs Using Pleiades-1B Satellite Image for Charging Electric Vehicles
Ahmed, S., El-Morsi, M., Serag El Din, M.A. ***965***

Supply Temperature Stabilization of Decentralized Solar Thermal Collectors for Integration into District Heating and Cooling System
Bogdanovics, R., Zajacs, A. ***977***

Integration of Renewable Energies into Cityscape
Boß, V., Felsmann, C., Rühling, K. ***987***

Photovoltaic Panels and Planning in the UK
Brotas, L. ***998***

Towards Net-Zero Neighborhoods in Greece
Dermentzis, G., Papadopoulos, A. ***1010***

Evaluation of Angular Distribution Models to Estimate Sky Diffuse Irradiance on Tilted Planes in Urban Environments
García, I., Alonso Tristán, C., Díez-Mediavilla, M., González-Peña, D., Granados-López, D., Torres, J.L. ***1019***

Comparison of Solar Planning Tools
Haase, M. ***1029***

Case Study of a Positive Energy Community for Renewable Energy Sharing
Kim, M., Kim, H., Kim, J., Kim, D., Lee, D. ***1041***

Modelling and Simulation of Booster Heat Pump for DHW Preparation in a Multi-Family Building Connected to the District Heating
Magni, M., Dermentzis, G., Ochs, F., Venturi, E. ***1046***

Heat Pumps, Photovoltaics and Energy Storage in Buildings –Load Characteristics and Flexibility Options on District Level
Ochs, F., Dermentzis, G., Magni, M., Tosatto, A., Venturi, E. ***1058***

Buried Twin Pipe Model Validation for System Simulations of Ice Storage Tanks in 5GDHC networks
Schubert, M., Birchler, D., Carbonell, D., Neugebauer, M., Ruesch, F. ***1070***

Municipal Heat Planning to Exit from Coal, Oil and Natural Gas in a German Major City
Vaupel, T., Best, I., Braas, H., Jordan, U., Orozaliev, J., Vajen, K. ***1078***

Heat Pumps in Positive Energy Districts
Wemhoener, C., Betzold, C., Bockelmann, F., Ochs, F. ***1085***

M. Solar Thermal and PVT Collectors and Solar Loop Components

Spectral Beam Splitting in Compound Parabolic Collector Based Photovoltaic Thermal System
Barthwal, M., Rakshit, D. **1097**

Empirical Validation of Low-Temperature PVT Collector for Heat Pump Integration
Beltrán, F., Madani, H., Sommerfeldt, N. **1109**

Experimental Testing of a Solar Thermal Collector with composited TIM of Plastic Honeycomb and Silica Aerogel Polyurethane Containers
Castro, J., Febrer, R., Kizildag, D., Zheng, J. **1121**

Numerical modeling and simulation comparisons of a cost efficient novel CPVT Solar Collector
Castro, J., Kizildag, D., Rigola, J., Santos, D. **1128**

Numerical Investigation of the Performance of a Solar Air Heater Equipped with a Packed Bed
Ebadi, H., Cammi, A., Savoldi, L. **1138**

Validation of an Alternative Methodology for Direct Steam Generation Modelling in Parabolic Collectors
Gonzalez-Mora, E., Durán-García, M.D. **1149**

Effects of Atmospheric Gases on the Efficiency of Heating and Cooling Supply Components: **1159**

Collector Efficiency Curves considering an Adapted Calculation Approach for Convective Heat Transfer in Insulating Gas Layers of Solar Collectors
Leibbrandt, P., Giovannetti, F., Jordan, U., Schabbach, T. **1170**

Experimental Investigation on A Novel Flat-Plate Water-Based Photovoltaic-Thermal Module
Liu, W., Yao, J., Zhao, Y. **1176**

Interception on Solar Absorbers: Ray Tracing for Comparison between a Parabolic Reflector and a Compound Parabolic Concentrator
Lwiwa, C., Nydal, O. **1184**

Angel-Dependent Features of MorphoColor TM Solar Collectors: Color Stability, IAM, Yield
Mehnert, S., Bläsi, B., Bueno, B., Höhn, O., Kroyer, T., Kuhn, T., Wilson, H. **1195**

Hardware-in-the-Loop Integration of PVT Models using Internet of Things-enabled Communication
Meiers, J. **1204**

Development and Indoor Testing of a High-Performance PV/thermal (PVT) Panel with Integral Stagnation Control
Mesquita, L., Harrison, S., Indranil, R., Stinson, B. **1215**

A Performance Analysis of a Parabolic Trough Collector using Numerical Computation And Real-Time Parameters
Saini, P., Dhar, A., Kumar, P. **1222**

Modelling and Experimental Verification of an Unglazed Metal Facade Collector Model
Shemelin, V., Matuska, T. **1234**

Agri Solar Thermal Systems: A Brief Study on the Energetic Potential of Bifacial Solar Thermal Systems
Summ, T., Ehrenwirth, M., Trinkl, C., Zörner, W. ***1245***

N. Thermal Energy Storage

Modelling Analysis of Phase Change Materials for Reducing Cold Climate Space Conditioning Loads
Baylis, C., Cruickshank, C.A. 1254

Study of Thermal Degradation of Adipic Acid as PCM under Stress Conditions: A Kinetic Analysis
Bayón, R., García, R.J., Quant, L., Rojas, E. 1265

Comparative Experiments on a Novel CaCl2-Based Composite Material and Zeolite 13X Inside a Sorption Reactor for Solar Heat Storage
Bérut, E., Bois, L., Lange, H., Le Pierrès, N., Ondarts, M., Outin, J. 1275

New Concept for High Temperature Thermal Energy Storage Using a Concrete Tank
Cabeza, L.F., Borri, E., Prieto, C., Vérez, D., Zsembinszki, G. 1285

Load Management for Seasonal Heat Storage Applications based on Sorption Storage Technology
Daborer-Prado, N., Gaisberger, L., Gayaneh, I., Zettl, B. 1295

Increasing Renewable Energy Integration using Advanced Residential Thermal Energy Storage
Djebbar, R., Brdeau, S., McNevin, C. 1304

Numerical Investigation of Energy Absorption in Dual Metal Hydride Bed based Thermo-Chemical Energy Storage System
Dubey, S.K., SRIVASTVA, U., TIWARI, V. 1315

The Experimental Performance Characterisation of a Three Module Phase Change Energy Storage System for Domestic Heating Applications
Eames, P., Fadl, M., Nycz, P. 1327

Demonstration of a Latent Heat Storage Unit Using a Pillow-Plate Heat Exchanger in a Zero Emission Building
Galteland, O., Salgado-Beceiro, J., Sevault, A. 1338

Numerical Investigation of a Large-Scale Water Pit Heat Storage
Gao, M., Furbo, S. 1344

Sorption Test Bench for Zeolite and Salt-Composite Based Thermochemical Storage
Issayan, G., Zettl, B. 1355

Performance Investigation on Cascade Latent Heat Storage for Various Geometric Orientations
Jain, S., Premachandran, B., Rakshit, D., Reddy, K.S. 1362

Characterization of Enhanced Biobased Phase Change Material with Graphene Nanoplatelets
Jesus D'Oliveira, E., Azimov, U., Costa Pereira, S.C., Groulx, D. 1374

Loading Slim Hot Water Tanks with and without Swirl Generation - First Results
Oestreich, F., Urbaneck, T. 1384

Experimental Investigation of a Falling Film Horizontal Tube Bundle Absorber for Thermal Absorption Storage with H2O/LiBr
Pressl, D., Laevemann, E. 1396

Kinetic Analysis of TGA Measurements When Evaporation Is a Degradation Process in PCM
Quant Colón, L., Bayón, R., Diarce, G., García, R., García-Romero, A., Rojas, E. ***1402***

Thermal Performance of Eccentric High-Temperature Latent Heat Storage System: Passive Heat Transfer Enhancement Strategy
Ray, A.K., Gurgenci, H., KUMAR, K.R., Rakshit, D. ***1410***

Development of an Open System for Evaluating Material Charging Characteristics from Industrial Waste Heat
Reynolds, J., Elvins, J., Jewell, E., Searle, J. ***1422***

A Novel Alginate/Expanded Graphite based Composite for use in Solar and Waste Heat Storage
Reynolds, J., Elvins, J., Jewell, E., Ke, X., Searle, J., Williams, R. ***1434***

Thermal Energy Storage Capacity on Mineral Zeolite
Seco Calvo, O., Ferrer Tevar, J.A., López Moreno, H., Olmedo Mezcua, R., Sanchez Egido, M.N., Soutullo Castro, S. ***1445***

Effect of Design Characteristics on Pit Thermal Energy Storage (PTES) Performance
Sifnaios, I., Fan, J., Furbo, S., Jensen, A. ***1457***

Parametric Study of Structured Thermocline Storage Systems
Vera Fernandez, J., Perez Segarra, C.D., Sanmarti, O., Torras, S. ***1464***

Numerical Investigation and Performance Evaluation of Food Grain Drying Unit Integrated with the Thermal Energy Storage System.
Verma, A., Buddhi, D., Kukreja, R., Tangellapalli, S. ***1474***

Development of a Virtual Sensor for State-of-Charge Evaluation of TCM-Energy Storage
Zettl, B., Daborer-Prado, N., Issayan, G., Kirchsteiger, H., Resch, A., Wagner, W. ***1484***

O. Testing, Certification and Monitoring

Accelerated Ageing Test Bench for Advanced Ceramic Slabs under Extreme and Controlled CSP Conditions
Canadas, I., Ballestrín, J., Candelario, V.M., Fernández-Reche, J.,
Galindo, J., Morales, A., Rodríguez, J., San Vicente, G. ***1495***

Accelerated Aging Test and Service Life Time Estimation for Solar Collectors
Fischer, S., Ullmann, J., Weiss, k. ***1503***

DHW Tanks - 40 % Savings by Better Stratification
Haberl, R., Haller, M.Y. ***1515***

Operational Analysis of 5 PVT Heat Pump Systems Based on Field Measurement Data
Helmling, S. ***1526***

Novel Hardware-in-the-Loop Approach for Thermal Systems
Reum, T., Klump, D., Schrag, T. ***1536***

Flow Rate Estimation In Glandless Circulator Pumps - Influence Of Temperature And Water-Glycol Heat-Transfer Fluids
Sauer, C., Georgii, M., Orozaliev, J., Schmelzer, C., Vajen, K. ***1543***

Fault Detection for Solar Thermal Systems: Evaluation and Improvement of Existing Algorithms
Schmelzer, C., Georgii, M., Orozaliev, J., Sauer, C., Vajen, K. ***1553***

Cost-Effective Energy Balancing of Thermal Systems Based on Temperature Measurements Only
Seiz, M.J., Bestenlehner, D., Drueck, H., Lang, X. ***1561***

P. Solar Resources and Energy Meteorology

Assessment of Downward Longwave Radiation Models in Clear-Sky Desert Conditions
Bachour, D., AlHajri, H., Perez-Astudillo, D., sanfilippo, A. ***1574***

A new Framework to Evaluate the Adequation between the Solar Potential and Energy Demand of an Urban-Rural Territory in a Mountainous Area
Ferry, A., Berrah, L., Fueyo, N., Gómez Samper, A., Ménézo, C., Thebault, M. ***1581***

A Comparative Study on Solar Radiation Datasets for Photovoltaic Energy Prediction at High Latitudes
Manni, M., Bellmann, M., Lobaccaro, G., Nocente, A., Skeie, K.S. ***1589***

Quality Assurance Procedure for Solar Radiation at Minute Resolution
Miranda, D., Barboza, L., Costa, A., Filho, J.B., Galdino, J., Gomes, E.,
Jatobá, E., Neto, A., Pereira, A., Petribú, L., Vilela, O., de Medeiros, J. ***1601***

Mapping Radiative Cooling Potential Predictions for Africa
Monterrubio, J., Castell, A., Martorell, I., Rincón, L., Vilà, R. ***1613***

Management and Operation of Qatar's Solar Radiation Monitoring Network
Perez-Astudillo, D., Al-Hajri, H., Bachour, D., Sanfilippo, A. ***1620***

Study on Analysis of Solar Panel Efficiency in Vietnam a Power Comparison Before and Post Cleaning
Rangaraju, S., Bhaumik, A., Phu, V.L. ***1629***

24/365 Firm Solar Power Generation in Switzerland
Remund, J., Perez, R., Perez, M. ***1638***

Dual Axis Optimization of Solar Photovoltaic at Various Sites in Pakistan
Tahir, Z.u.R., Abbas, S., Abdullah, M., Ahmad, S., Asim, M., Atif, M.,
Hassan, A., Irfan, M., Nadeem, A., Raza, H., Saad, M., ud DIn, N. ***1649***

Gap Filling in Solar Radiation Data using Artificial Neural Network for Nine Stations in Pakistan
Tahir, Z.u.R., Abbas, S., Abdullah, M., Adil, M.T., Ahmad, S., Akbar, Z.,
Asim, M., Hadi, A., Hassan, A., Nawaz, I., Raza, A.H., Usman, R., Zafar, U. ***1657***

A Comparison of Eight Transposition Models Applied for Different Orientations Under Different Albedo Scenarios
de Medeiros, J.V.F.F., Barboza, L., Galdino, J., Gomes, E., Jatoba, E.,
Miranda, D., Neto, A., Pereira, A., Vilela, O., de Melo Filho, J.B. ***1666***

Q. System Modelling, Artificial Intelligence, Digitalization

Implementation of Adapted Black Box Models for the Performance Characterization of Commercial Sorption Chillers
Altamirano, A., Maragna, C., Tremeac, B. **1678**

Detection of Tracker Failures for a 2-Axis Photovoltaic System
Barboza, L., Brennand, L.J.d.P., Gomes, E.T.A., Miranda, D., Novaes, G., Vilela, O., de Medeiros, J. **1688**

Data-Driven Approach Utilising Random Forest Regression for PV Performance Monitoring
David, A., Bednar, T., Sint, S. **1699**

Digital Representation of Heating Systems for Fault Detection Purposes
Georgii, M., Orozaliev, J., Sauer, C., Schmelzer, C., Vajen, K. **1711**

A TRNSYS Type for the Simulation of Temperature Limiting Heat Pipe Collectors
Jensen, J., Giovannetti, F., Schiebler, B. **1717**

Data-Based Modeling of High-Resolution Household Load Profiles
Kirchsteiger, H., Gaisberger, L. **1728**

Building Information Modeling for Solar Energy Systems
Mandow, W., Edenhofner, F., Giovannetti, F., Maier, T. **1737**

Efficiency Evaluation and Comparisons of Solar Cell Technologies Based on Measurements from the Arabian Peninsula
Pantazis, Y., Abdullah, M., Gereige, I., Jamal, A., Kalligianaki, E.,
Kamarianakis, Y., Katsaounis, T., Kotsovos, K., Tzavaras, A. **1747**

KNN-Based Ensembles for Day-Ahead Forecasting of Solar Power Outputs
Pantazis, Y., Abdullah, M., Gereige, I., Kalligianaki, E., Kamarianakis, Y.,
Katsaounis, T., Kotsovos, K., Tzavaras, A. **1755**

DHgeN: Automated Generation of District Heating Network Layouts for Feasibility Studies
Peronato, G., Kämpf, J.H. **1767**

A Multistep Optimization Procedure for a Fair Sharing of Profits in Energy Communities
Steinmaurer, G. **1775**

Applying Machine Learning Methods and Outlier Detection to Process and Analyse Incomplete Heat Meter Data
Trabert, U., Orozaliev, J., Pag, F., Vajen, K. **1782**

Data Clustering and Genetic Algorithm for the Design Optimization of a Hybrid Concentrated Solar System for SHIP
Vuillerme, V., Kamerling, S. **1790**

Development of Models for Long-Term Simulations of District Heating Networks at High Temporal and Spatial Resolutions
Zipplies, J., Orozaliev, J., Vajen, K. **1802**

Optimal Control Based on Deep Learning Techniques for a Hybrid Solar-Biomass System for Residential Buildings
Zsembinszki, G., Borri, E., Cabeza, L.F., Fernández, C. **1811**

R. Sector Coupling and Grid Stabilization

Aluminium-Redox-Cycles for the Production of Heat and Electricity in Buildings based on Renewable Energies
Baeuerle, Y.I., Dudita Kauffeld, M., Haller, M. ***1819***

S. Renewable Energy Strategies, Scenarios, Financing and Policies

Impact of Incentives Towards Lowering the Levelized Cost of Electricity of Concentrating Solar Power Plants in India
Aseri, T.K., Kandpal, T.C., Sharma, C. *1827*

Techno-Economics of Central Tower Receiver Power Plants in India: Effect of Heat Transfer fluids/Thermal Storage Media
Aseri, T.K., Kandpal, T.C., Sharma, C. *1838*

What Can PV Self-supply Do for System Integration?
Becker, S., Metzler, K. *1847*

Electric Self-production for LV Subscribers: Is It Better to Have Decentralized or Centralized PV Production?
Chouket, M., Bouden, C., Znouda, E. *1857*

Definitions for Climate Neutrality and their Relevance for the Assessment of Solar Energy based Heating Systems
Drück, H., Bestenlehner, D. *1867*

Efficiency of Electricity Self-Production for Medium Voltage Subscribers in Tunisia
Elmalleh, K., Bouden, C., Chouket, M., Znoudi, E. *1876*

Promotion of Solar Heat in Industrial Processes: Policy and Law Analysis with Focus on Turkey and Germany
Erden Topal, Y., Akdemir, S.D., Artantas, O.C. *1884*

Standardized Economic Evaluation Criteria of Solar Process Heat in Hybrid Systems - Results from IEA SHC Task 64 Subtask E
Fluch, J., Nitz, P., Pag, F., Reiter, J. *1890*

Technical Feasibility Study of Micro-Grid Integration to Electrify Rural Settlements of Sub-Saharan Africa
Lwakatare, B., Ehrenwirth, M., Ileka, H., Katende, J., Kaunda, J.,
Mehta, K., Trinkl, C., Zörner, W. *1897*

Mini-Grid or Grid Extension? The Strategies for Electrification Schemes Concerning Population Density in Sub-Saharan Africa
Mehta, K., Ehrenwirth, M., Ileka, H., Katende, J., Kaunda, J., Lwakatare, B., Trinkl, C., Zörner, W. *1909*

100% of Renewable Energies at Mallorca Hotels
Moià-Pol, A., Canals, V., Martinez-Moll, V. *1921*

Renewable Energy Education: Gendered Design and Innovation in the Context of a Small Island Developing State
POORUN, S.(., ELAHEE, M.K., Juggurnath, D., Khoodaruth, A., Sultan, R. *1929*

T. Renewable Energy Education

Energy Scenarios: Designing the Renewable World of Tomorrow Together
Gothe, T., Schierenbeck, A. ***1942***

Master's Courses at Solar Energy Conferences
Louvet, Y. ***1952***

Solar Decathlon Prototypes and their Use as Post-Competition Living Labs in Higher Education
Masseck, T. ***1961***

Development of a Small-Scale Plant for Electricity and Water Supply in Rural Regions of Côte d'Ivoire as Part of the First Ivorian Dual Study Program with Focus on Renewable Energies
Saars, L., Graßmann, A., Kouakou, A.P., Kre, N.R., Newiadomsky, C. ***1970***

The Life and Death of a Solar Energy Course - Lessons in Challenge Based Learning
Sommerfeldt, N. ***1977***

Renewable Energy and PtX-Technologies in Education
Steffenhagen, B., Gulden, J., Sklarow, A.S., Sommer, R. ***1985***

A. Solar and Efficient Buildings

Study and Simulation of Low Energy Solar Powered House in Libya

Nouri A. Alkishriwi[1] and Mustafa E. Elayeb[2]

[1] Engineering Faculty /University of Tripoli, Tripoli (Libya)

[2] Renewable Energy Centre/Misurata University, Misurata (Libya)

Abstract

This paper was prepared within the program of a national action plan for energy efficiency, where a building code will be prepared within this program in Libya. The goal of this work is to build a simulated environment that can accurately assess the energy consumption of a six-person, one-story family house. The simulation will consider the hot water heating system, the cooling and heating systems and the selection of building materials that help conserve energy. The TRNSYS model is built and programmed to evaluate system performance on an hourly basis throughout the year.

As a result of using an insulating material for the building envelope, the cooling load of the building loads were reduced by 55% compared to the original design of the project. In addition, a hot water solar heater is used to produce around 2546 kWh (with solar fraction of 96%) of hot water yearly. A 15-kW roof top PV system is designed for this house. The total electric energy produced from this system is 25424 kWh. This electrical energy generated by the solar PV system is sufficient to cover the loads of air conditioning, heating, and the auxiliary heating element in the solar water heater. The surplus of electricity generated by PV system can be exported to the public network in non-summer months.

Keywords: Low energy buildings, Solar cooling and heating, Rooftop PV, TRNSYS

1. Introduction

The continued rise in global demand for energy, especially in rapidly growing economies, has turned the issue of energy availability and security into an important geopolitical issue and a key component of all economies more than ever, especially with the Russo-Ukrainian war and the desire of European countries to search for new energy sources, especially from North African countries, instead of Russian oil and gas. Libya is facing a similar situation, as it depends entirely on fossil fuels as the main source of energy, in addition to the increasing consumption of energy against the background of large economic and population growth - all of which put pressure on the country. Also, due to the lack of renewable water resources, Libya depends partly on desalination, but it is expected that the share of desalination to provide water from desalination plants to the population will increase significantly in the near future, which will put additional pressure on the fossil fuels resources. In addition, the need for alternative and renewable energy is of strategic importance for the long-term prosperity and security of Libya's energy supply. In this context, this study was prepared to develop a sustainable sector for alternative and renewable energy in the Libyan state.

The Libyan electricity sector is going through a complex crisis due to aging infrastructure and the aftermath of recent political instability and associated conflict. The most visible and compelling aspect of the crisis is electricity blackouts and load shedding which are both increasing in severity every year. In simplistic terms, blackouts occur when the immediate demand for electricity exceeds the immediate supply. This triggers an unavoidable self-protection response from the generation and grid equipment, that rapidly shuts down the grid. Once offline, it can take hours to restart the grid. Load shedding is the practice of selecting parts of the grid to deliberately blackout, usually for several hours, to reduce the total load on the grid and thereby avoid a national blackout. The past response of the Libyan government to this crisis has been almost exclusively focused on trying to reduce blackouts, by maintaining and recovering the capacity to supply electricity. This translates into plans to overhaul existing power stations and build new stations which is a very expensive and slow process. However,

© 2022. The Authors. Published by International Solar Energy Society
Selection and/or peer review under responsibility of Scientific Committee
doi:10.18086/eurosun.2022.01.01 Available at http://proceedings.ises.org

the government of Libya is now considering other responses in the form of Demand Side Management (DSM), Energy Efficiency (EE) practices, and Renewable Energy (RE) development. Successful energy efficiency interventions will reduce the demand for electricity without reducing the benefits that electricity provides to the population of Libya and can be implemented quickly and cost-effectively. In this paper, we will simulate the use of air-conditioning units with Minimum Energy Performance Standard (MEPS), as well as the use of energy-saving LED lamps instead of the incandescent lamps currently used in buildings.

The built environment in the world accounts for over 55% of delivered energy consumption (Hamilton and Rapf, 2020). In Libya, the residential sector is responsible for almost 39% of final energy consumption (GECOL, 2010), Fig.1, where a huge proportion of electrical energy consumed in buildings is used to run air conditioning equipment. This is because Libya's climate is characterized by high ambient temperatures and high humidity, especially during summer periods. Therefore, there is significant potential to improve energy efficiency with savings in space cooling and water heating.

Libya's per capita electric consumption is consistently above world averages. The current demand for electricity in Libya is about 9000 MW, with a deficit of more than 2,000 MW. The main source of peak demand comes from air conditioning and heating load in summer and winter respectively. Based on monitoring of the energy situation in Libya, the United Nations estimates that air conditioners constitute between 40-70% of the peak electricity demand in the summer, while lighting constitutes about 10-15% of the total demand (UN Support Team in Libya, 2021). In addition, the increase in demand of air-conditioning has significantly increased and become the major of electricity consumption in residential buildings. Therefore, if quick measures are not taken to reduce the large increase in electricity loads, the General Electricity Company in Libya-GECOL, which is responsible for the generation, transmission, and distribution of electricity, will not be able to keep pace with the increasing loads on the one hand, which is now suffering from a generation deficit of more than 2000 megawatts on the other hand.

Energy efficiency involves using less energy to provide the same or an improved level of service to the energy consumer in an economically effective manner. Energy efficiency enhances energy security, stimulates the economy of countries, makes energy more affordable to families and businesses, creates jobs, provides economic benefits (increased productivity, lower costs, net job creation) and improves people's well-being and comfort. Achieving Libya's desired energy efficiency outcomes will require involvement of a broad range of actors. While there are many challenges to overcome in appropriately influencing all involved, consistent and appropriate energy efficiency policies are the foundational element for success.

This paper, directed to the Libyan government to draw its attention to the importance of focusing on initiating energy efficiency initiatives on the one hand and designed for architects and intended to be as direct and practical as possible, summarizes the knowledge needed to integrate energy efficiency principles of active solar technologies in buildings, while dealing with the same time with issues of architectural integration and energy production requirements.

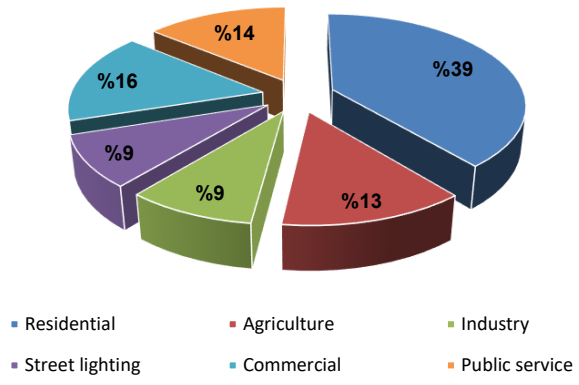

Fig. 1: Distribution of end energy consumption in Libya

2. Analysis Approach

The first step to design the low energy house is to reduce the energy consumption at minimal through passive design (insulation, orientation, natural ventilation, etc.). The next step is to use renewable energies to cover the optimized thermal loads; geothermal heat pumps, small wind turbines and solar energy are common methods to produce the required energy in the house. Flat plate collectors and PV panels offer a practical solution since they can be integrated on the design on the building. Also, a PVT collector system may be used for hot water production and electricity generation for the house. The technical specifications and the analysis of the PVT system is explained in detail by the authors in (Alkishriwi & Elayeb, 2017). The last step is to use conventional resources, e.g., extra energy from the grid as efficient as possible; it has a lot of importance in places where renewable energy resources are limited; however, the goal is to achieve energy neutrality without this last step. In this study, we seek to reduce the need for energy in the house under study as much as possible, while generating enough energy to meet the needs of the house and exporting the surplus to the public network to achieve the principle of a plus-energy building. When designing and constructing residential buildings, some auxiliary rules must be considered in the implementation of systems and specifications that lead to energy savings and reduce the operational cost of buildings to reach economic buildings in operation through the following:

- The use of thermal insulation materials for all external elements such as roofs, walls, bridges, and columns.
- Use double glazing for all external openings.
- Implementation of solar architecture standards to reduce heating and cooling loads.
- Use of solar energy technologies (every possible) to heat and cool the interior spaces of the building.
- Using solar energy to secure hot water for buildings when needed.
- Switch to the use of energy-saving lamps (LED lamps).
- Install photovoltaic cells to generate electricity as much as possible.

3. Building Description

The building is a typical residential building for a family located in Tripoli. The building is made of one-story building, Fig.2. It has a total volume of 594 m^3 and a treated floor area of 198 m^2 per house.



Fig. 2: The typical residential building under study

According to the construction files of building, walls are built as multi-layer to provide high quality of thermal insulation, high soundproofing with overall heat transfer U-Value (0.4-0.5 W/m^2. k). Likewise, the construction of the roof based on multi-layers to provide high quality of thermal insulation, high soundproofing with overall heat transfer U-Value (0.3-0.4 W/m^2. k). The overall U-value for the Floor is ranged between (0.4 to 0.5 W/m^2. k). The criteria to choose the technology is based on that insulation should be located outside. Table 1 shows the properties of selected insulation materials in both cases: Reference Case and Target (Low Energy) Case.

Tab. 1: The properties of selected insulation materials

	Reference Case	Target Case
External walls, W/m^{2}K	2.8	0.5
Floor, W/m^{2}K	0.6	0.5
Roof, W/m^{2}K	2.2	0.4
Average uncontrolled infiltration, ACH	0.5	0.1
Glazing, W/m^{2}K	2.1	1.4

4. The Operative Conditions

Libya is a country in the middle of North Africa, bordering the Mediterranean Sea to form a coast 1900 km long, 1,750,000 km^2 deep in the Sahara, Fig.3. It is exposed to a solar radiation reaches to 2300 kWh/m^2 /year, and sunshine duration is about 3500 h/year (Glaisa et al 2014).

Tripoli is located in the northwest of Libya with the GPS coordinates of 32° 53' 7.2708" N and 13° 10' 48.5796" E. Geographically located at the Mediterranean Sea on a plateau 17 meters above sea-level. Tripoli has relatively hot weather in summer with high humidity. Temperatures average around 33 °C in the mid of this season, although sometime reached 47 °C or above. In the evening the average temperature is around 28 °C due to cool breezes. Winter is a cold season. Rainfall usually starts from October to the end of April. The temperature drops to around 15 to 18°C. In Spring and Fall the weather becomes moderate, and usually there is no need to any cooling or heating system in this time of the year (Mashena and Alkishriwi 2016). The temperature set point is defined for this analysis in 24°C.



Fig. 3. Location of Tripoli, Libya (source: https://www.nationsonline.org/oneworld/map/libya-political-map.htm)

Building insulation was rare until recently in Libya. With the spread of air conditioning and the excessive consumption of electrical energy, interest in thermal insulation began to appear in some buildings in a limited way. This coincided with the authorities' interest in introducing energy efficiency standards and labels for appliances and equipment, where the energy efficiency specifications for air conditioners have been approved, with a minimum energy efficiency ratio (EER) not less than 11 BTU/h/W (Libyan national center of

standardization and metrology, 2022). Domestic water heating is done using electricity in Libya so far, despite the favorable conditions for the use of the solar heater in the country. Figure 4 shows the hot water consumption pattern adopted in this study.

To run the simulation for a whole year, a weather data for Tripoli city was used. These are data for the typical meteorological year (TMY) for the period 1990-2005. This weather data is read by Type 109 TMY2 in TMY2 format which it uses to compute radiation on different surfaces defined by the user. Theses data is also compared with the data downloaded from (Photovoltaic Geographical Information System website). A good agreement was obtained by comparing the two weather data files together.

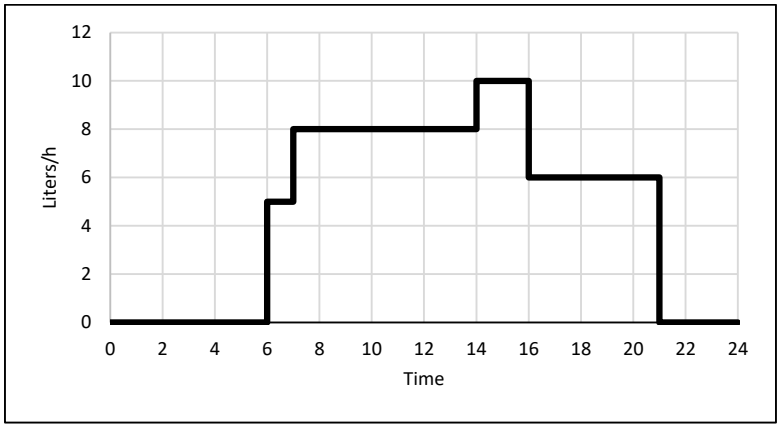

Fig. 4 shows the hot water consumption pattern

5. Model Approach

The dynamic simulation of multizone building, solar heaters, and solar photovoltaic system is carried out using the TRNSYS program (TRNSYS Simul. Platform, Sol., Univ. Wisconsin-Madison). The simulation was conducted for the selected systems over a year and at a time step of 15 minutes. The program chosen to model the residential building in terms of thermal loads (cooling and heating loads) as well as the power supply system of the solar building is TRNSYS. This transient systems simulation software was developed by the Solar Laboratory at the University of Wisconsin. This software supports detailed simulations of multi-zone buildings and their power supply equipment. TRNSYS equipment library includes advanced building models; many components of equipment commonly found in the construction of thermal power systems; Components that facilitate entry of weather data, equipment, and specific schedules; and components that support the output of simulation results.

The objective of this work is to build a simulation environment that can evaluate accurately the energy consumption of a 6 people, one story family house. The simulation will consider hot water heating system, PV system, and selection of construction materials helps in energy conservation. A TRNSYS model was constructed and programmed to evaluate the performance of the system on hourly basis throughout a complete year, Fig.5. The simulation of the residential building aims to calculate the effect of the shape of the building, external and internal walls, lighting, windows, internal loads for individuals, ventilation, roof and floor on thermal loads, in order to calculate the cooling and heating loads over a whole year. From the side of the energy supply to the building, the solar hot water system was simulated, and the building was supplied with electricity by installing a 15-kilowatt photovoltaic system.

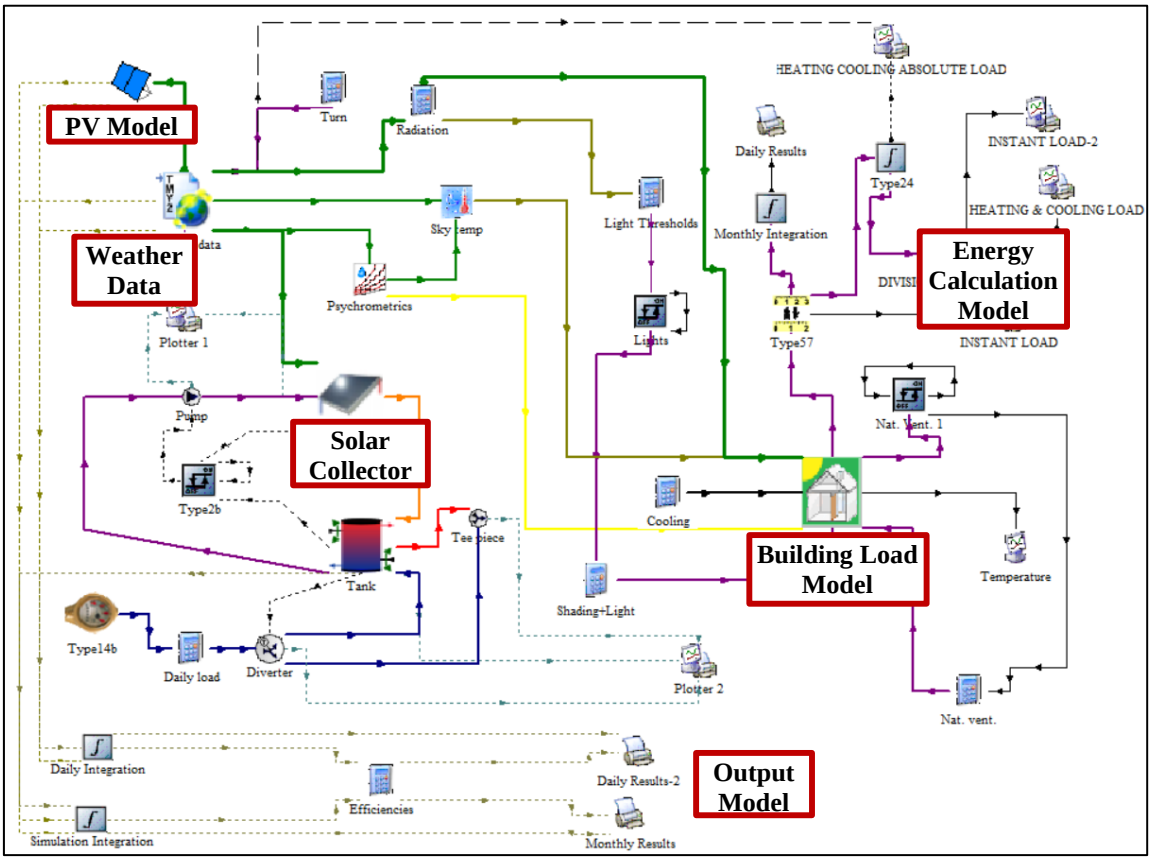

Figure 5. Performance prediction model.

6. The Results

The TRNSYS model is built for cooling, heating, water solar heater and PV system. The simulation was conducted to evaluate system performance on an hourly basis throughout the year. Here a sample of the results will be presented, discussed and some comparisons made.

Figures 6, 7 show the instantaneous cooling and heating loads throughout the year, while Figure 8 shows the accumulated energy required for cooling and heating in both cases: the reference case (business as usual- BAU) and the target case (sustainable-SUS). It is noticed that the cooling loads appear in March and increase steadily until October, when the weather begins to moderate before the heating loads appears in December. It is also noticed that the cooling loads are more important than the heating loads according to the weather of the Tripoli city. Similarly, the possibility of reducing the cooling loads seems more effective and illustrates the feasibility of energy efficiency in buildings in Libya, especially during summer, where the need for air conditioning is greater and the generation deficit in the electrical network increases.

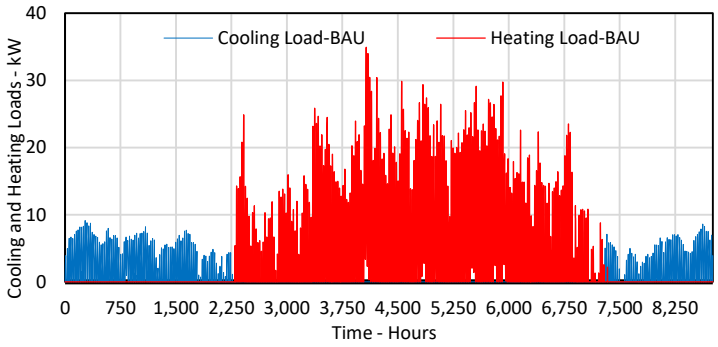

Fig. 6: Cooling and heating load in BAU case.

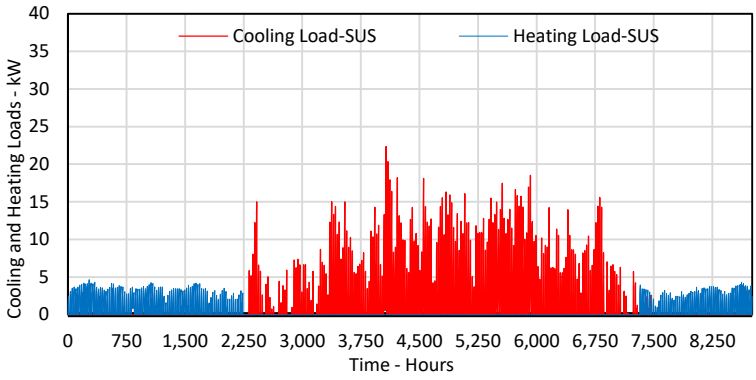

Fig. 7: Cooling and heating load in SUS case.

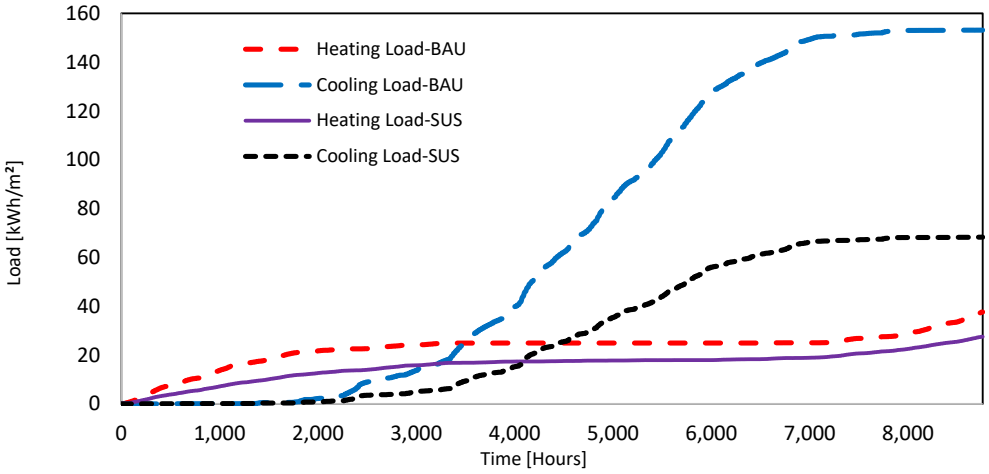

Fig. 8: Accumulated energy for cooling and heating load in BAU case and SUS case.

From the results obtained, it is clear that the annual cooling loads can be reduced from 151 kWh/m2 in the BAU case to 67 kWh/m2 in the SUS case. Figure 9 shows monthly cooling loads in both cases BAU and SUS. It can be seen that the significant impact of building insulation on saving energy wasted in building cooling.

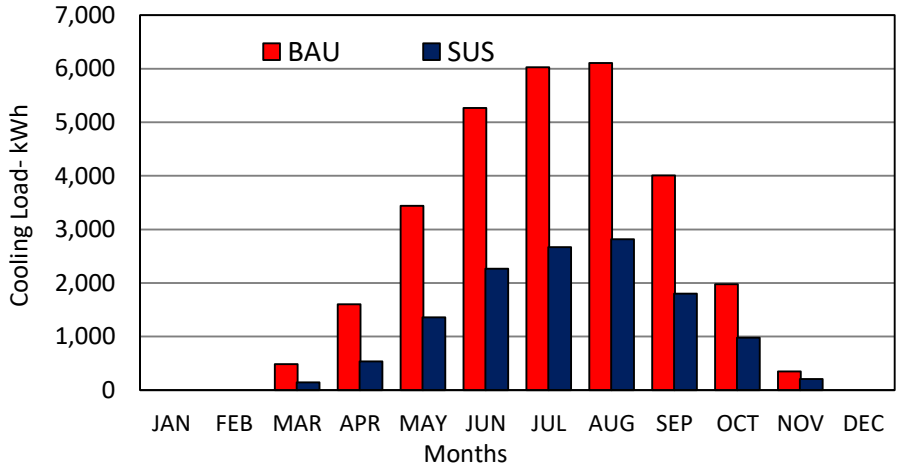

Fig. 9: Cooling load in the building in both cases

A 15-kWp roof top PV system is designed to supply the house with the necessary electrical energy. Figure 10 shows the daily monthly average of the solar irradiance incidence per unit area of the PV panels (the right vertical axis), as well as the monthly energy generated by the solar cells (DC output) and the electrical energy converted by the inverter (AC output) to feed the loads of the house. The total electric energy produced from this system is about 25424 kWh annually.

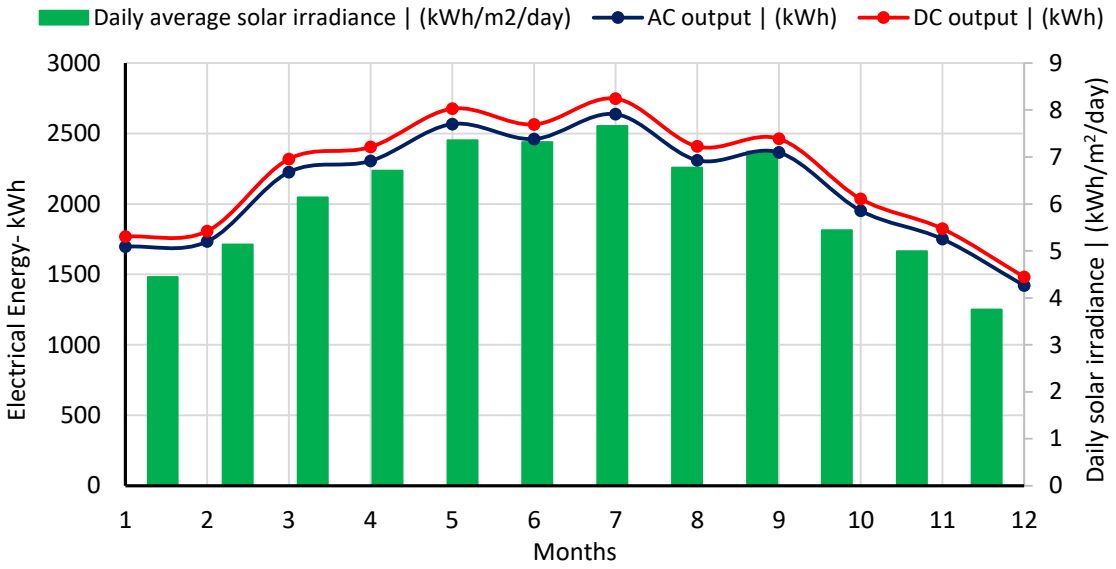

Fig. 10: PV electricity generation during the year on the roof of the house

This amount of energy is sufficient to operate an efficient heating and air conditioning system (4048 kWh when the minimum energy efficiency ratio, EER_{min}=11; according to the Libyan Energy Efficiency Standard for Air Conditioning and Heating Equipment 2022) and the energy consumed by the auxiliary heating unit (about 111 kWh annually), in addition to lighting and other household electrical supplies, Fig.11. The surplus generated energy can be exported to the public grid. In the same Figure, the monthly saving of electrical energy can be observed in the processes of air conditioning, heating and domestic water heating. As the total annual electrical energy savings in these processes is about 8294 kWh. Also, the figure shows the thermal energy used in solar water heating. The annual average of the solar fraction is equal to 96%. It is worth noting that the remaining 4% of water heating was made using solar electricity generated by PV system.

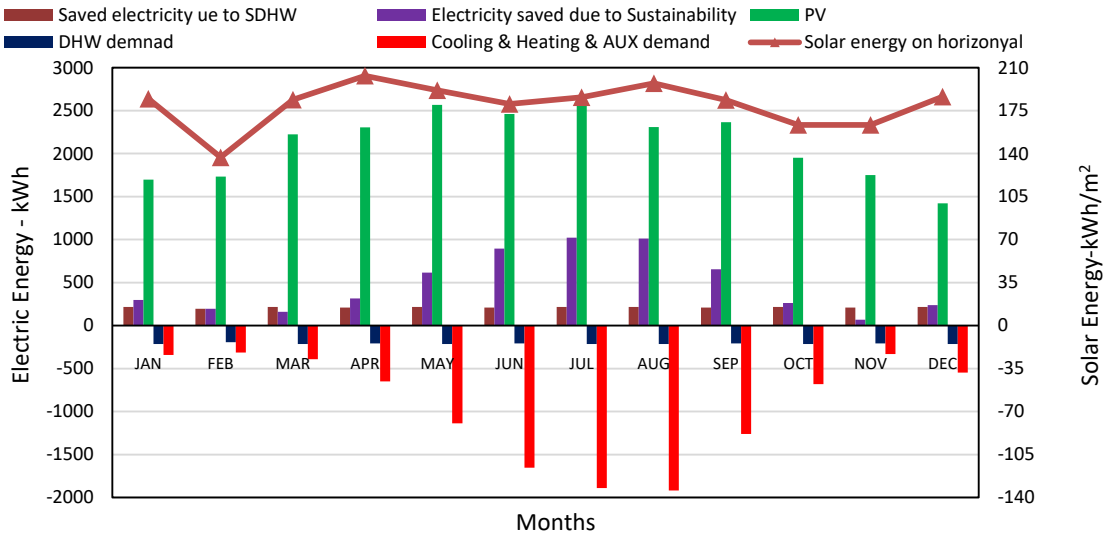

Fig. 11: Energy balance diagram

7. Conclusions

A proper passive design can reduce considerably the amount of energy that has to be consumed to cover the cooling or heating load. Our studies have shown that proper wall and roof insulation alone can save up to 55% of the energy used in MENA (Middle East and North Africa) region, especially in the residential sector. The prevailing climate in Libya, provides a suitable environment for zero-energy and plus-energy buildings. This would save huge amounts of fossil fuels burned daily to generate electricity in Libya, thus reduce the emission of tons of carbon oxides, in addition to contributing to solving the electricity generation deficit, which is a real problem at the present time in Libya. For Example, the average efficiency of the power plants currently operated in the Libyan utility grid in 2016 did not exceed 33.3%. This means that 66.7% of the fuel that was consumed in those stations was wasted, and this lost value represents about 2275 million dinars of the value of the fuel subsidy allocated to the GECOL in the same year, which resulted in the emission of about 23 million tons of carbon dioxide (Eshtaiwi, et al.2022). The authors recommend the local authorities in Libya pay attention to energy efficiency in buildings, and adopt the appropriate specifications for that, especially at this phase that has a shortage of electricity generation and the instability of the public network. Rooftop solar PV systems play an important role in the energy mix of sustainable cities. Currently, the installation of rooftop units can be an important option at this point for grid-connected solar deployment where utility scale PV systems are difficult to install on the ground due to instability in the country. Also, homeowners can reduce their electricity bills by consuming the energy produced by rooftop solar PV systems. In addition, these systems enable owners to export energy to the grid and make financial profits. Thus, this empowerment turns the owners of rooftop solar PV systems into the so-called producers and consumers, which is important now in the face of a significant increase in electricity prices.

8. Acknowledgments

The authors would like to express their sincere gratitude and appreciation to Mr. Mahamoud Aljabou and Ms. Mona Altaweel for their technical and Linguistic support.

9. References

Alkishriwi, N.A., Elayeb, M.E., 2017. Studying the performance of PVT solar collectors under the climatic conditions of Tripoli using the TRNSYS, International Journal of Engineering and Information Technology, volume 03, pp 8-13.

Eshtaiwi, S. et al.2022. Rooftop Systems as a Solution to The Electric Power Shortage in Libya. The 13th Mediterranean Conference on Power Generation, Transmission, Distribution and Energy Conversion (MEDPOWER2022), Valletta, Malta, 07-09 November 2022. In press.

General Electric Company of Libya, 2010. The annual report.

Glaisa, K.A., Elayeb, M.E., Shetwan, M.A., 2014. Potential of Hybrid System Powering School in Libya, Energy Procedia 57,1411 – 1420. https://doi.org/10.1016/j.egypro.2014.10.132.

Hamilton, I., Rapf, O., 2020. Executive Summary of the 2020 Global Status Report for Buildings and Construction, Global Alliance for Buildings and Construction (GlobalABC), UNEP.

Libyan national center of standardization and metrology, 2022. Air Conditioners: Minimum Energy Performance, Label and Test Requirements for Window AC and Split AC (low capacity).

Mashena, M., Alkishriwi, N., 2016.The Economics of Solar Thermal Electricity (STE) in Libya, International Conference on Recent Advances in Electrical Systems ICRAES'2016, Hammamet, Tunisia.

Photovoltaic Geographical Information System Website, https://re.jrc.ec.europa.eu/pvg_tools/en/#TMY. last accessed 11 September 2022.

TRNSYS16, "A Transient Systems Simulation Program," TRNSYS Simul. Platform, Sol. Energy Lab. Univ. Wisconsin-Madison, USA, pp. 1–5, 2015.

United Nations Support Team, 2021. The importance of energy-saving lighting devices in the rationalization of electric energy consumption in Libya, A project proposal submitted to the Libyan government.

An Energy Trading Model for a Lab-Scale PV Microgrid in the Tunisian Context

Erasmo Elias Alvarado Alvarado[1], Muhammad Taimoor[1],Andrea Catalina Buitrago[1], Souha Ferchichi[2], Ines Khalifa[2], Afef Abdelghani Bennani[3], Ilhem Slama Belkhodja[3]

1 Université de Lorraine, Nancy (France)

2 Mediterranean Renewable Energy Centre, Tunis (Tunisia)

3 University of Tunis El Manar, National Engineering School of Tunis, Tunis (Tunisia)

Abstract

The paper proposes an energy trading strategy that emulates residential building electrification through a lab-scale microgrid in Tunisia. A Mid-Market Rate (MMR) model is proposed for a 10kW grid-connected PV microgrid including battery storage and emulated loads. The trading algorithm proposes a uniform trading price for both electricity export and import within the microgrid. Multiple scenarios are formulated with regard to load profile, system sizing, and electricity market conditions. The results are analyzed and a set of Key Performance Indicators (KPIs) are defined to compare the proposed scenarios. The preliminary analysis shows that the proposed algorithm reduces the CO_2 emissions of the microgrid by 24% and improves the self-consumption of the locally generated energy. The model can be scaled up to include local communities effectively.

Keywords: energy trading, energy management strategy, microgrid, mid-market rate, peer-to-peer.

1. Introduction

Microgrids operate in distribution markets, which differ from the wholesale market not only in the size of the bids for energy trading, but also in the source of their energy –mainly from renewable sources with near-zero marginal cost. The transition into smarter and greener energy networks requires the utilization of new technologies and market models, thus, bringing the innovative business model of Peer-to-Peer (P2P) energy trading into context. The main objectives of the use of the P2P energy trading model are the maximization of the benefits of the users and the energy balance of the grid.(Yang et al., 2019)

Many models have been developed in recent years and multiple authors have compared and analyzed the performance of such energy trading mechanisms. Zhang et al. compared three pricing models: Double Auction, MMR, and Supply and Demand Ratio, and proposed a P2P energy trading framework considering a dynamic retail price and a forecasting agent to predict prices and energy production(Zhang et al., 2019). Long et al. compared three different P2P energy trading structures, namely, a Bill Sharing; MMR, and Auction-based Pricing Strategy. The clearing price mechanism of each of these market paradigms is tested in a PV-powered microgrid model with 10 households connected to the grid. The simulation resulted in a substantial reduction in energy prices (Long et al., 2017). Kuruseelan et al. used a Bill Sharing and MMR approach to study the performance of different market structures in P2P energy trading and compared them with a traditional Peer-to-Grid (P2G) scenario. These markets were designed and applied to a microgrid composed of three prosumers with PV generation and one non-PV consumer. The study showed that the income perceived by the prosumers is greater when MMR is used as the clearing-price mechanism (Subburaj and C, 2019).However, these findings cannot be adopted in various cases, given that the simulation is highly dependent on the local context. The present study focuses on adapting MMR algorithm to the Tunisian electricity market conditions while considering local scenarios and constraints.

© 2022. The Authors. Published by International Solar Energy Society
Selection and/or peer review under responsibility of Scientific Committee
doi:10.18086/eurosun.2022.01.02 Available at http://proceedings.ises.org

This paper assesses the performance and techno-economic viability of a lab-scale microgrid system, SMARTNESS (Smart Micro-grid plAtfoRm wiTh an eNergy managEment SyStem), implemented at the National Engineering School of Tunis, El Manar, Tunisia, in the framework of the Euro-Mediterranean project Med-EcoSuRe ("Med-EcoSuRe," n.d.). It explores the feasibility of social cooperation between prosumers within the energy network in establishing their sustainable participation in a P2P energy trading setup. The microgrid is composed of four households with an individual PV installation and a Li-ion battery for one of the houses. Moreover, a central unit, with a PV installation and two battery modules acts as the operator of the microgrid and deals with the energy management and exchange of power with the grid. The microgrid architecture and real photo are demonstrated in Figure 1.

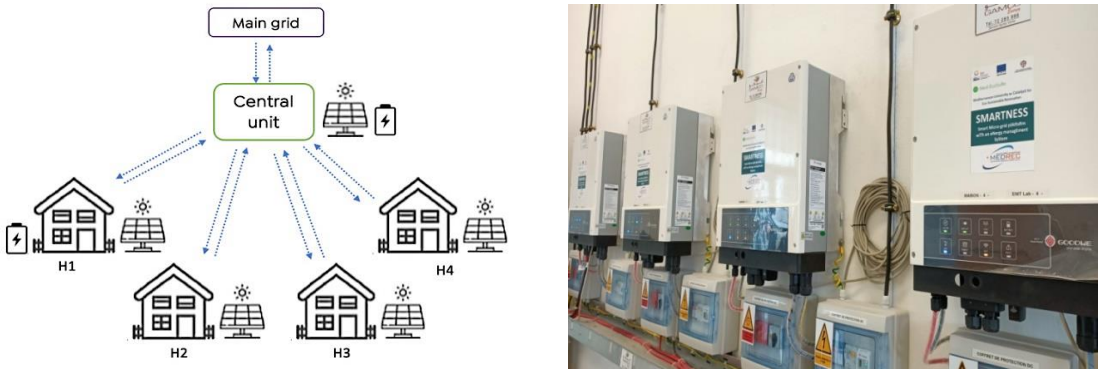

(a) **(b)**

Figure 1: SMARTNESS microgrid. (a) Microgrid architecture. (b) Real photo ("Med-EcoSuRe," n.d.).

2. Methodology

A MMR method was developed based on the economic models proposed by (Long et al., 2017) and (Subburaj and C, 2019). This model consists of setting an internal price of electricity to trade energy inside the microgrid and is defined as the simple average of the retail prices to sell energy to the grid and buy energy from the grid, ensuring that every agent is treated equally. The MMR is developed for the hypothetical case of a Feed-in Tariff (FiT) scheme in the Tunisian electricity market, contrary to the net-metering system currently in place. Moreover, the retail price paid by the consumer is calculated according to a tier tariff scheme based on the amount of electricity consumption as established by the Tunisian Society of Electricity and Gas (STEG) ("STEG: Les tarifs d'électricité," 2019). The electricity tariff as of 2021 can be seen in Table 1.

Table 1. Low voltage electricity tariff in Tunisia. ("STEG: Les tarifs d'électricité," 2019)

Sector	1 – 200 kWh	201 – 300 kWh	301 – 500 kWh	501 or more kWh
Residential (mill/kWh)	176	218	341	414

2.1 Mid-Market Rate Model

The internal price of electricity is computed as per the MMR methodology as follows:

$$C_{P2P} = \frac{C_{BFG} + C_{STG}}{2} \quad \text{(Eq. 1)}$$

Where:
C_{P2P} : Internal Price in P2P Microgrid.
C_{STG}: Retail price of Energy, Sell To Grid (STG).

C_{BFG}: Retail price of Energy, Buy From Grid (BFG).According to the power balance between the load and the power generation, there may exist three different cases which will affect the internal price of energy; an energy balance between generation and demand (scenario 1), an excess of energy generated (scenario 2), or a lack of energy generated (scenario 3) within the microgrid. With each case, the MMR remains the same, but the price to import or export electricity will be determined according to the energy balance in a given timeslot. The model considers one-hour timesteps to perform the power balance of the system and the amount of energy imports and exports, and the change of tier in the tariff scheme, will affect the electricity bill of each prosumer differently.

The power production in the microgrid is considered as the power exported from the houses to either the central battery or the main grid, and the power exported from central PV and central battery to the houses and or grid:

$$P_{prod}(t) = \sum_{n=1}^{N} (P_{PV}^{n}(t)) + P_{CB_to_houses}(t) \quad \text{(Eq. 2)}$$

Where:
$P_{prod}(t)$: Total PV production within the Microgrid in kW at timestep (t)
$P_{PV}^{n}(t)$: PV production of each prosumer "n" in kW for timestep (t)
$P_{CB_to_houses}(t)$: Power exported from the Central battery to the prosumers in kW for timestep (t)

The load in the microgrid will, thus, be the sum of the houses' imports and the local consumption of the central unit plus the power delivered to the central battery. Given that the central battery is considered in the load computation, it is possible to characterize the central battery as a dynamic load balancing the microgrid:

$$L(t) = \sum_{n=1}^{N} L^{n}(t) + L_{CB}(t) \quad \text{(Eq. 3)}$$

Where:
$L(t)$: Total Load within the Microgrid in kW for timestep (t).
$L^{n}(t)$: Load of user "n" (including Central consumption) in kW for timestep (t).
$L_{CB}(t)$: Load of the Central Battery in kW for timestep (t).

The first scenario occurs when the power produced is exactly equal to the load of the microgrid. This may occur when the batteries and loads can absorb the energy exported by all the other agents. In this case, both the import and export prices for each prosumer will be equal to the internal price:

$$C_{im}(t) = C_{P2P} \quad \text{(Eq. 4)}$$

$$C_{ex}(t) = C_{P2P} \quad \text{(Eq. 5)}$$

Where:
$C_{im}(t)$: Price of Imported Energy
$C_{ex}(t)$: Price of Exported Energy

The second scenario occurs when the power production is higher than the demand, the remaining of the power production will be exported to the main grid at the sell-to-grid price, lowering the final price of energy:

$$C_{im}(t) = C_{P2P} \quad \text{(Eq. 6)}$$

$$C_{ex}(t) = \frac{L(t) * C_{P2P} + (P_{prod}(t) - L(t)) * C_{STG}}{P_{prod}(t)} \quad \text{(Eq. 7)}$$

The third and final scenario proceeds when the energy production is lower than the demand, in this case, all the energy produced is consumed by the prosumers, while the remaining of the load is supplied by the main grid, causing the prices of electricity to increase inside the microgrid.

$$C_{ex}(t) = C_{P2P} \quad \text{(Eq. 8)}$$

$$C_{im}(t) = \frac{L(t) * C_{P2P} + (L(t) - P_{prod}(t)) * C_{BFG}}{L(t)} \quad \text{(Eq. 9)}$$

As the prices vary on an hourly basis depending on the ratio of energy imported from or exported to the main grid, the electricity bill for each individual household is calculated by considering the different prices and consumption levels at each timestep as follows:

$$C_j = \sum_{t=0}^{T} (P_{im}^{j}(t) * t * C_{im}(t)) - \sum_{t=0}^{T} (P_{ex}^{j}(t) * t * C_{ex}(t)) \quad \text{(Eq. 10)}$$

Where:

$P_{im}^{j}(t)$: Imported Power of User "j"

$P_{ex}^{j}(t)$: Exported Power of User "j"

The electricity bill for the Central Unit will be calculated differently as it needs to have an overall earning to pay for operation and maintenance expenses, therefore, the central battery is arbitrarily considered to export energy to the prosumers at buy-from-grid price and import energy at the internal price of energy:

$$C_{Central} = \sum_{t=0T} (P_{im}^{Central}(t) * t * C_{im}(t)) - \sum_{t=0T} (P_{PV}^{Central}(t) * t * C_{ex}(t) + (P_{CB_exports}^{Central}(t) * t * C_{STG}) \quad \text{(Eq. 11)}$$

Where:

$P_{im}^{Central}(t)$: Imported Power of Central Unit in kW for timestep (t)

$P_{PV}^{Central}(t)$: Exported PV Power of Central Unit in kW for timestep (t)

$P_{CB_{exports}}^{Central}(t)$: Central Battery exports in kW for timestep (t)

2.2 Microgrid Scenarios

For a comprehensive analysis, multiple scenarios of microgrid configurations are defined to evaluate the trading algorithm. These scenarios evaluate the impact of changing microgrid parameters such as BFG prices, load profiles and PV production on energy trading. Typical load profile values were obtained from OpenEL developed by the US Department of Energy and used for the houses in the microgrid (OpenEI, n.d.). Moreover, the PV generation profile was obtained for the city of Tunis from NREL data (NREL, n.d.).The baseline scenario is designed to be run with STG price of zero and central battery capacity of 4.8 kWh. Other scenarios include increasing the battery capacity, modifying the BFG and STG prices and changing the load profiles of individual prosumers.

Table 2:Analyzed Microgrid Scenarios

Case	Description	Purpose
Baseline	The load profiles are obtained by multiplying the original data (OpenEI, n.d.) by a random factor ranging from 0.75 to 1.25, the PV profiles(NREL, n.d.) are multiplied by 0.9 to 1.1	To serve as a baseline to compare with all the other scenarios. The random choice of the multiplying factors in load and PV profiles is made so that trading between houses is possible.
Optimum PV production (HOMER)	A simulation of microgrid is run in Homer Pro and optimal values for PV production are obtained, PV production is increased for each user to match these optimal values; load profile remains the same	This represents the best possible case with regards to sizing the PV modules. The effect of higher exports levels at optimum PV production were analyzed
Higher battery capacity	The total battery capacity is doubled	To analyze the effect when energy can be stored or sold to central. Increased battery size will allow energy to be traded between the central unit and individual houses.
One high consumer	One of the prosumers has a load profile 4 times higher than the original, allowing it to absorb most of available energy in the microgrid	To analyze the effect of increased trade within the microgrid. When the demand of one prosumer increases, it will obtain more energy from peers and central unit, causing an increase in trading price.
Various STG prices	STG prices are set at 0, 100, and 200 mill as FiT	To evaluate how changing the tariff will impact the earning and whether it causes a major difference in revenues for stakeholders.
Load Profiles shifted by 12 hours for 2 prosumers	The load profiles of 2 houses are shifted by 12 hours to simulate complementary load profiles inside the microgrid	To increase the energy traded among the prosumers. The amount of energy traded increases with different load profiles
Fixed BFG price	BFG price is a fixed value set equal to the highest value in the tariff scheme i.e., 414 mill and no longer depends on the energy consumption	To evaluate earnings in a flat tariff scheme. In the baseline, the consumer is charged according to its consumption. Once we remove it, we can understand the earnings with a flat tariff structure
Fixed BFG price, 3 Low demand Prosumers & 1 High-demand Prosumer	BFG price is a fixed value set equal to the highest value in the tariff scheme i.e., 414 mill, and no longer depends on the energy consumption. One of the prosumers' demand is 4 times higher than the original and the rest have half the original demand	To evaluate earnings in a flat tariff scheme. This will ensure that consumers are not penalized for additional consumption. Besides, one big consumer and 3 small consumers will increase the energy traded inside the P2P market as the bigger consumer will consume all the energy excess generated by rest

3. Results and Discussion

The P2P energy trading model was analyzed for the scenarios described in Table 2, and the total savings were calculated by comparing the electricity bill for a microgrid with and without P2P trading. For this purpose, three main aspects were considered: environmental impact, electrical performance, and economic evaluation.

For analyzing the environmental impact, the reduction in the carbon dioxide emissions was set as key performance indicator (KPI), which calculates the amount of CO_2reduced by implementing energy trading algorithm inside the microgrid. The grid emission factor taken as a reference specifically for Tunisia was 463 g/kWh. This grid emission factor was multiplied by the amount of energy traded inside the microgrid to calculate the amount of reduction. ("IFI Default Grid Factors 2021 v3.1 | UNFCCC," n.d.; IFI TWG, 2020)

For the electrical performance, the self-consumption level (SCL) and the self-sufficiency level (SSL) are considered. The SCL is the ratio between the total local consumption from the houses and the total amount of locally produced energy, in this case with Renewable Energy sources. It includes the surplus injected to the grid, and indicates which percentage of local generation is used to cover the demand. The SSL is the ratio between the consumption covered by local PV production and the total consumption from the houses. It indicates which percentage of the demand is covered by the local generation.

Finally, for the economic evaluation, the net-present value (NPV) and the bill savings were calculated in Tunisian Dinars (TND). The NPV is the difference between the costs the system incurs over its lifetime and the revenue it earns over its lifetime, with the value at present time, with a discount rate of 6.25%based on Tunisian Central bank rate, and a lifetime of 25 years, the typical duration of a PV project (Reuters, 2022).The bill savings indicate the difference between the cost of producing energy locally and making transactions directly with the grid (Business as Usual), and the cost producing energy locally produced and trading in the microgrid. The results from these KPIs are presented below in Table 3 and Figure 2.

The results in Table 3 show that the Homer and higher battery capacity scenario optimize the NPV of the system and leads to a higher self-sufficiency. Both increase the amount of energy available for trading. One high consumer provides the highest savings as more energy trading takes place due to a high demand by the high consumer. Changing the STG prices does not have a significant effect on the KPIs defined. Similarly, shifting the load profile scenario has little impact on KPIs due to the load profile being mostly flat throughout the day. Having a fixed BFG price significantly improves the savings and NPV. In fact, a higher consumption by one of the prosumers causes increased electricity rates for all prosumers in the microgrid due to combined grid imports through one central unit and the tier tariff scheme in force in Tunisia as of 2021. Therefore, a scenario with fixed BFG price is simulated to ensure that the prosumers will not be severely affected by the tier tariff scheme, which resulted into higher savings compared to dynamic BFG price.

The results for SCL show that at least 58.33% of the PV generation is used to cover the demand. These values are in accordance with results presented by other authors (Heilscher et al., 2014). A German study highlights that a PV system producing 1/3 of the annual demand may reach values of self-consumption of 60-90%, which goes in accordance with the scenarios, as for most of the cases the PV generation is almost 1/3 of the annual demand (Heilscher et al., 2014).

From the SSL, it is possible to state that no more than 36% of the demand is locally covered during the year. This means that a major amount of power has to be imported from the Tunisian grid. This can be due to the lack of PV generation during the night which is usually a period of high demand in households, small PV generation in comparison to the load consumption, or lack of sufficient energy storage. A study in Spain shows that the values for self-sufficiency range between 30% and 40% for small consumers like offices and educational buildings (Ordóñez Mendieta and Hernández, 2021). Another study developed in Germany calculated the optimal electrical self-sufficiency for houses which ranges between 30% and up to 70% under specific frameworks (McKenna et al., 2017). The microgrid falls short in most scenarios if it is compared

with the German study. This could be because the PV generation is small compared to the load consumption, therefore, the use of batteries is advised to increase this ratio and to match the PV generation with the demand (Ciocia et al., 2021).

Table 3: Results of KPIs for the analyzed scenarios

Scenario	CO2 emissions avoided by Microgrid (tCO2)	CO2 emissions avoided by Microgrid with P2P (tCO2)	Additional CO2 emissions avoided	SCL	SSL	NPV (TND)	Saving (TND)
1. Baseline case	6.5	8.1	26%	91%	24%	- 48,005	- 1,375
2. Optimum PV production (HOMER)	11.2	12.5	12%	58%	36%	- 42,659	- 1,582
3. Higher battery capacity	11.4	13.3	16%	58%	36%	- 45,672	- 904
4. One high consumer	12.8	17.7	38%	82%	29%	- 1,653	1,702
5. STG=0	6.5	8.1	26%	91%	24%	- 48,005	- 1,375
6. STG=100	6.5	8.1	26%	91%	24%	- 47,576	- 1,340
7. STG=200	6.5	8.1	26%	91%	24%	- 47,148	- 1,306
8. Load Profiles shifted 12 hours for two prosumers	6.2	8.0	28%	89%	23%	- 46,967	- 1,292
9. Fixed BFG price	6.5	8.1	26%	91%	24%	- 11,175	1,575
10. Fixed BFG price, 3 Low demand Prosumers & 1 High-demand Prosumer	11.2	12.5	12%	97%	18%	987	2,549

Regarding the CO_2 emissions avoided in a P2P market, the results show that using photovoltaic energy and batteries contributes significantly in reducing the carbon footprint, especially in countries like Tunisia that rely heavily on natural gas.

From the SSL, it is possible to state that no more than 36% of the demand is locally covered during the year. This means that a major amount of power has to be imported from the Tunisian grid. This can be due to the lack of PV generation during the night which is usually a period of high demand in households, small PV generation in comparison to the load consumption, and lack of sufficient energy storage. A study in Spain shows that the values for self-sufficiency range between 30% and 40% for small consumers like offices and educational buildings (Ordóñez Mendieta and Hernández, 2021). Another study developed in Germany calculated the optimal electrical self-sufficiency for houses which ranges between 30% and up to 70% under specific frameworks (McKenna et al., 2017). The microgrid falls short in most scenarios if it is compared with the German study. This could be because the PV generation is small compared to the load consumption, therefore, the use of batteries is advised to increase this ratio and to match the PV generation with the demand(Ciocia et al., 2021).

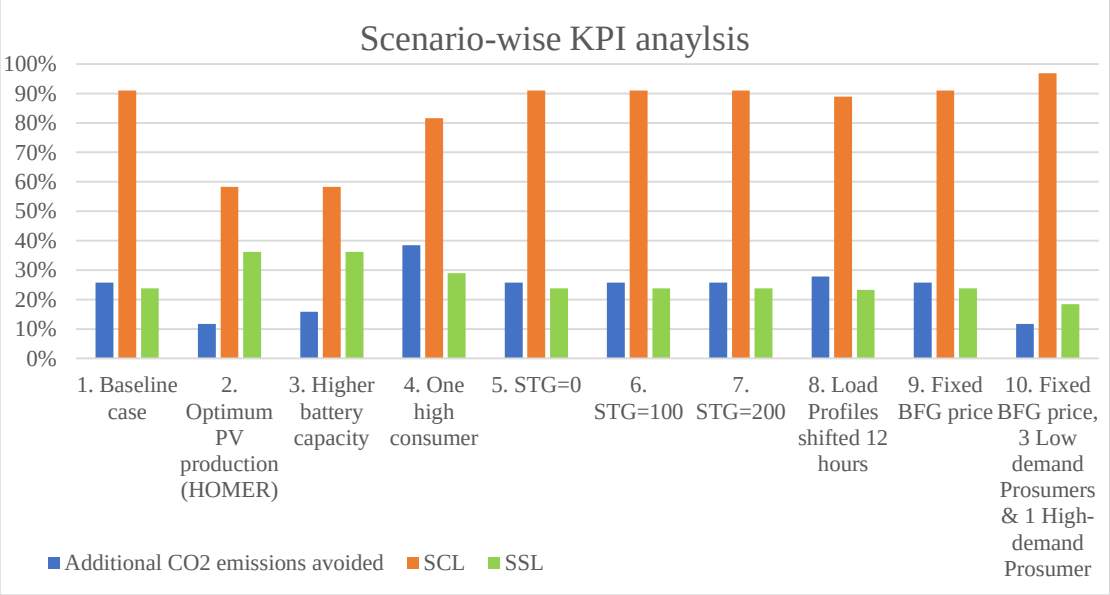

Figure 2: Scenario-wise KPI analysis

Concerning the economic analysis, negative values for NPV and savings represent that the project under those scenario conditions are not financially attractive. The resulting NPVs were mostly influenced by factors as the relatively high cost of investment, the replacement of the inverter every 10 years and the batteries every 15 years, and that the total billing of the microgrid was higher than expected in comparison to an individual configuration. The scenario 10 with one high consumer and fixed BFG price becomes profitable. In fact, under these conditions the prosumers would recover their investment with a small margin of gains, while decreasing their carbon emissions.

In general, it was observed that under a high load profile, there is an overall higher energy import from than export to the grid. This higher import results in increased electricity cost, thus, there is a need to promote self-consumption to increase savings. The savings can be increased when the central battery capacity is expanded, as the central unit can, in this case, store more energy which allows more trading. If one prosumer has a much higher load than the others, there are notable savings in the monthly electricity bill. This is because the excess of energy available during peak sun hours from other prosumers is consumed by the consumer with high load profile.

Implementing the Tunisian tier tariff scheme in the microgrid is challenging as the price of electricity is dependent upon total electricity consumption. A subsidy to the initial investment or a mechanism to promote the trading of the energy inside the microgrid and, hence, increase the savings in the energy billing, would contribute to making the project more economically feasible. Other schemes such as the participation in ancillary services markets could also improve the profitability of a smart microgrid, however, this falls out of the scope of this project.

4. Conclusion

P2P energy trading not only improves the local balance of energy generation and consumption but enable prosumers to move from being passive to active managers of their energy networks. The paper proposes an energy trading algorithm based on a Mid-Market Rate (MMR) for a lab scale microgrid emulating residential buildings in Tunisia. The model is evaluated for multiple scenarios proposed and key performance indicators are calculated for each one of them. The results reveal the environmental benefits of energy trading and highlight the importance of self-consumption. Moreover, the electrical performance of the algorithm is at part with similar projects across the world.

Around 60% of the PV generation is utilized for fulfilling the demand and 36% of the annual demand is covered locally at max. The trading algorithm has a positive environmental impact by reducing the emissions around 6-12% depending upon the scenario. Finally, the economic performance of the project depends upon the exact scenario considered and may or may not be financially lucrative. It is possible to observe a high dependence of revenues and the amount of energy traded inside the microgrid, which is a result of the interaction of the load and PV production profiles chosen for the prosumers. Moreover, a fixed Buy-from-Grid price is favourable for the total savings of the microgrid as it eliminates the negative impact of having consumption-dependant tariffs. A dynamic tariff that depends on time and not on consumption could have also been used and obtained a similar effect. The results can be used as a blueprint for future electricity market legal framework in Tunisia to promote energy trading in local microgrid setups.

5. References

Ciocia, A., Amato, A., Di Leo, P., Fichera, S., Malgaroli, G., Spertino, F., Tzanova, S., 2021. Self-Consumption and Self-Sufficiency in Photovoltaic Systems: Effect of Grid Limitation and Storage Installation. Energies 14, 1591. https://doi.org/10.3390/en14061591

Heilscher, G., Ruf, H., Huld, T., 2014. Self-Consumption of Electricity by Households, Effects of PV System Size and Battery Storage. 29th Eur. Photovolt. Sol. Energy Conf. Exhib. 4014–4017. https://doi.org/10.4229/EUPVSEC20142014-7AV.6.8

IFI Default Grid Factors 2021 v3.1 | UNFCCC [WWW Document], n.d. URL https://unfccc.int/documents/437880 (accessed 9.5.22).

IFI TWG, 2020. Methodological Approach for the Common Default Grid Emission Factor Dataset 1–6.

Long, C., Wu, J., Zhang, C., Thomas, L., Cheng, M., Jenkins, N., 2017. Peer-to-peer energy trading in a community microgrid, in: 2017 IEEE Power Energy Society General Meeting. Presented at the 2017 IEEE Power Energy Society General Meeting, pp. 1–5. https://doi.org/10.1109/PESGM.2017.8274546

McKenna, R., Merkel, E., Fichtner, W., 2017. Energy autonomy in residential buildings: A techno-economic model-based analysis of the scale effects. Appl. Energy 189, 800–815. https://doi.org/10.1016/j.apenergy.2016.03.062

Med-EcoSuRe [WWW Document], n.d. . ENI CBC Med. URL https://www.enicbcmed.eu/tunisia-med-ecosure-sets-stage-energy-generation-and-trading-micro-grid-platform-0 (accessed 4.10.22).

NREL, n.d. PVWatts Calculator [WWW Document]. URL https://pvwatts.nrel.gov/pvwatts.php (accessed 4.3.22).

OpenEI, n.d. Index of Residential Load Data [WWW Document]. URL https://openei.org/datasets/files/961/pub/RESIDENTIAL_LOAD_DATA_E_PLUS_OUTPUT/LOW/ (accessed 4.3.22).

Ordóñez Mendieta, Á.J., Hernández, E.S., 2021. Analysis of PV Self-Consumption in Educational and Office Buildings in Spain. Sustainability 13, 1662. https://doi.org/10.3390/su13041662

Reuters, 2022. Tunisia's central bank keeps key rate unchanged at 6.25%. Reuters.

STEG: Les tarifs d'électricité [WWW Document], 2019. URL https://www.steg.com.tn/fr/clients_res/tarif_electricite.html?tknfv=678B2868NOPQRSTUV01345678989046D (accessed 4.4.22).

Subburaj, K., C, V., 2019. Peer-to-Peer Energy Trading of a Community Connected with an AC and DC Microgrid. Energies 12, 3709. https://doi.org/10.3390/en12193709

Yang, J., Zhao, J., Qiu, J., Wen, F., 2019. A Distribution Market Clearing Mechanism for Renewable Generation Units With Zero Marginal Costs. IEEE Trans. Ind. Inform. 15, 4775–4787. https://doi.org/10.1109/TII.2019.2896346

Zhang, B., Du, Y., Lim, E.G., Jiang, L., Yan, K., 2019. Design and Simulation of Peer-to-Peer Energy Trading Framework with Dynamic Electricity Price. Presented at the 2019 29th Australasian Universities Power Engineering Conference (AUPEC), pp. 1–6. https://doi.org/10.1109/AUPEC48547.2019.211948

Metrics Behind the Implementation of Photovoltaic Solar Energy In Urban Area: A Preliminary Literature Review

Joyce A. O. de Sousa[1,2], Martin Thebault[2], Lamia Berrah[1] and Martin K. Patel[3]

[1] Université Savoie Mont Blanc, LISTIC, Annecy-le-Vieux, France

[2] LOCIE, Université Savoie Mont Blanc, CNRS, Le Bourget du Lac, France

[3] Energy Efficiency Group, Institute for Environmental Sciences and Fore Institute, University of Geneva, Genève, Switzerland

Abstract

The massive implementation of solar energy in urban environment is part of the strategic efforts that aim to diversify the energy matrix of a territory, achieving energy independence from fossil fuels in the medium to long term and mitigating carbon emission impacts. However, even if policies are defined regarding the massive implementation of solar energy in urban areas, there is still a lack of studies on the metrics underlying decision-making enabling such an implementation. The improvement of decision making in the process which is complex calls for an integrated assessment of several metrics. Therefore, this work subscribes to the creating a framework that integrates and classifies the most important metrics indicating drivers and barriers for the implementation of photovoltaic panels in urban areas. The framework is assumed to be built in a systemic way in order to support the climate policy and public authorities aiming to integrate solar energy in their urban planning.

Keywords: decision-making metrics, solar energy, photovoltaic panels, urban planning, solar districts

1. Introduction

Currently, more than 75% of global energy consumption occurs in urban territories (Martins et al., 2016). In relation to this matter, a pressing transition to renewables is requited due to the scarcity of fossil fuel based energy and also its consequent pollution (Paleri, 2022) that can be partially addressed by the implementation of photovoltaic (PV) panels in urban areas (Cergibozan, 2022).

This subject has gained even more notoriety given the necessity to be also energy independent from conflict zones (Ostrowski, 2022). As solar energy is a promising sustainable energy, urban areas may become high-potential electricity producers by deploying photovoltaic systems (Fakhraian et al., 2021).

The growing scarcity of energy resources drives the incorporation of renewable energy sources in urban electrical systems worldwide (Goel et al., 2022). The increased use of solar energy in place of fossil fuel-based electricity can help cities striving to become more independent of highly polluting fossil energy to reach the net zero emissions.

The solar energy will be one of the fastest growing renewable energy sources from now to 2050 worldwide, (Rigo et al., 2022), with a potential forecast of 8.5TW and as solar PVs are present the lowest-cost option for renewable electricity it is expected that investments will be propelled for its massive deployment the coming years, IEA (2021).

To enable the implementation of photovoltaic systems in urban environments, it is important to make use of metrics capable of supporting decision makers, showing them clearly what are the benefits and limitations found in this kind of application.

The decision-making process for the implementation of photovoltaic panels (PVs) in urban areas is multifaceted and it involves different disciplines varying between technical, economic, political, environmental and social ones. Therefore, these different metrics may influence local decision-makers whether to invest or not in the photovoltaic technologies.

© 2022. The Authors. Published by International Solar Energy Society
Selection and/or peer review under responsibility of Scientific Committee
doi:10.18086/eurosun.2022.01.03 Available at http://proceedings.ises.org

In addition, the authorities responsible for renewable energy projects, urban planners and the policy makers come from different backgrounds and need to make decisions accounting for the local conditions and maximizing the socio-economic benefits for their communities (Lobaccaro et al., 2019).

Technological progress and cost reduction have allowed to significantly expand the use of solar energy in urban areas in recent years (Kammen and Sunter, 2016). Nevertheless, there is still a lack of studies to support decision makers in how to conduct a PV project in urban scale taking into account the various criteria that are essential for the implementation of solar energy in urban areas (P. et al., 2019).

Hence, it is necessary to focus on enabling the application of large solar energy systems in cities in such a way that makes energy transition strategies feasible. To address the current need to expand the energy resources through photovoltaics, this article was developed to identify the most used metrics when implementing photovoltaic systems in urban context.

2. Methodology

An extended systematic literature review (SLR) with scientific content produced in between 2002 and 2022 was carried out in three phases as shown in Fig 1. The concepts were formulated in order to answer the central research question of: what quantitative metrics are used to assess PV systems deployment at large urban scales?

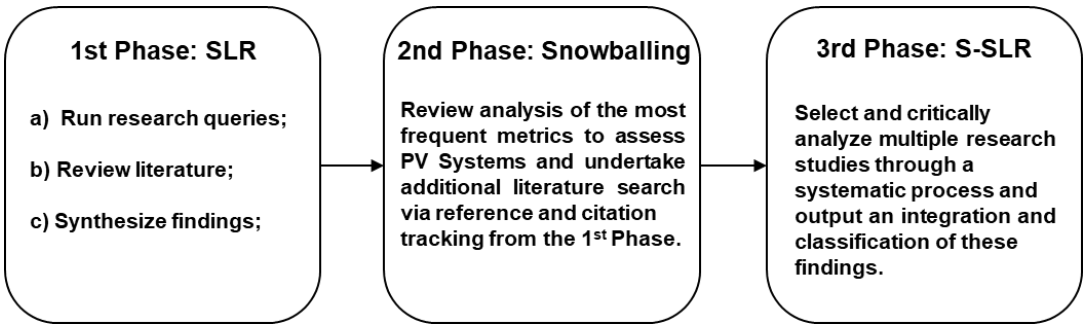

Fig. 1. Extended systematic literature review (SLR) phases inspired from (Rigo et al., 2022)

Firstly, the search criteria focused on identifying scientific literature review papers as these can assist in rapidly identifying the most common metrics present in this research field, as well as the research gaps and approaches in a given scientific field (Lagisz et al., 2022), which allow us to identify the key terms commonly used in this exploratory research.

Secondly, others broader scientific sources such as conference proceedings, grey literature reports, book chapters and thesis were also consulted later to integrate the scope of this research and help us to identify and classify the metrics related to the deployment of photovoltaic panels in urban areas. In total, more than 760 scientific contents were consulted, where 127 of them were selected to support the development of this research. In this paper, we chose to present an extraction of the most frequent metrics found in the literature, eliminate redundancies, define each of them and calculate their usage rate.

The usage rate was calculated for each metric type analyzed in this article by the Equation 1.

$$Usage\ rate\ (\%) = \frac{Number\ of\ Scientific\ Content\ Mentioning\ a\ given\ Metric}{Total\ Number\ of\ Scientific\ Content} \quad \text{(eq. 1)}$$

Finally, the scientific findings were select and critically analyze through a systematic process made by integrating and classifying them in order to answer the central research question.

Tab. 1. Keywords used in this review

	1st Keywords	2nd Keywords	3rd Keywords	4th Keywords	5th Keywords
↑ OR ↓	Solar Energy	Planning Deployment Review Availability Feasibility	Metrics Indicators Requirements Enablers Assessment	Technical Economic Energy	Urban City District Neighborhood Building
			← AND →		

In the Tab. 2., we introduce the combined keywords used to identify the metrics searched on Google Scholar, Springer Link, ACM, Science Direct and IEEE and classified into technical, energy and economic metric types accordingly to the hierarchical approach firstly proposed by VanWijk and Coelingh (van Wijk and Coelingh, 1993) and later applied in different regions (Assouline et al., 2017). In this paper, we have chosen some representative metrics belonging to the technical, economic and energy metric types to discuss.

For the purpose of describing the overall view in research and use of the metrics identified through this article, we have Europe leading the production of content related to these metrics to deploy PV System in urban areas followed by Asia and North America in Fig. 2.

We also have identified the percentage of each type of scientific content selected in this SLR through the Fig. 3, where we can see the majority of chosen content comes from journals (84%) followed by Reviews and PhD Thesis totalizing together 9%.

While the frequency of contents related to the metrics selected for this SLR can be contemplated on Fig. 4 (a) as well as and the frequency of each type of quantitative metrics (Economic Technical or Energy related) approached in this SLR are plotted on the Fig. 4 (b).

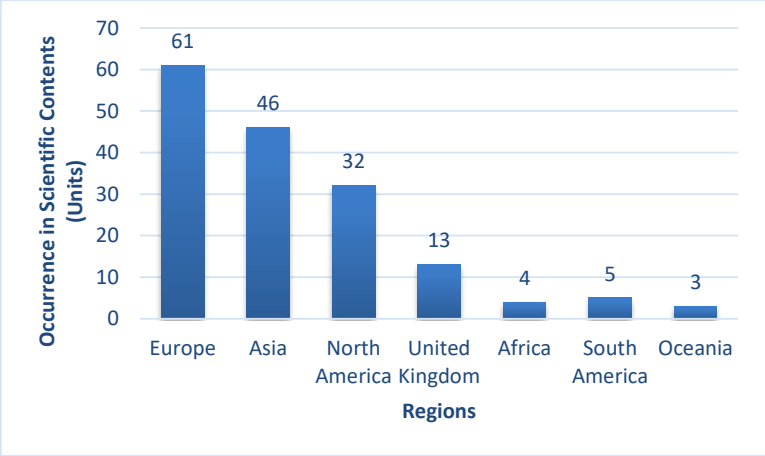

Fig. 2. Occurrence of Scientific Contents per Regions in the conducted SLR.

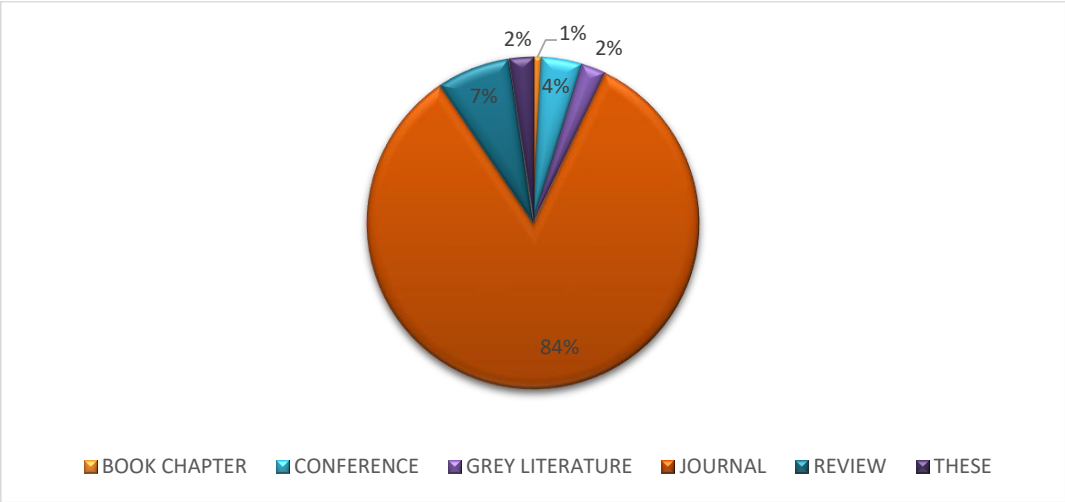

Fig. 3. Percentage of Content selected for this SLR

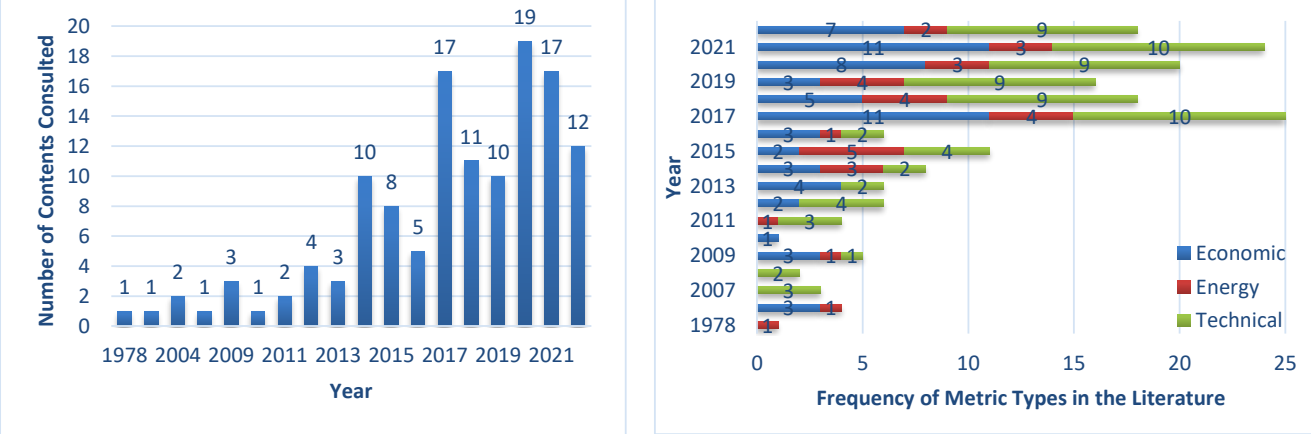

(a) (b)

Fig. 4. a) Frequency of scientific contents related to PV metrics per year. b) Cumulative frequency of scientific contents related to PV metrics per type yearly.

The occurrence of scientific content across regions may suggest where more studies are being developed in this regard. In the meanwhile, the percentage of selected content shows the scientific support to carry out the present SLR.

3. Results

At this stage, 20 technical metrics, 17 economic and 9 energy ones were identified as the most current in scientific contents related to PV Systems deployment.

The findings from this SLR were organized in an extracted version of the results through the tables **Tab. 2**, **Tab. 3** and **Tab. 4**. where the metrics related to the technical, economic and energy aspects were defined, analyzed according to their occurrence in scientific contents and associated to pertinent references.

The technical, economic and energy metrics related to the PV systems are able to betoken us the most used metrics approached for practical assessments and application in urban context.

In the technical overview of metrics, it has been found that the Rooftop Area (13%) suitable and available for PV Systems is the most used factor to determine whether or not is worth to proceed with a PV project as well as the Real efficiency delivered by this systems (13%) and followed by the grid capacity (11%) which is related to the power outputs enabled by the grid.

In this study, it was seen that the reasoning for the adoption or not of PV Systems in urban context is intrinsic related to the Grid-parity which is still a milestone for further PV diffusion (Breyer and Gerlach, 2013).

Tab. 2. Overview extraction of the main technical metrics behind the deployment of solar panels

Metrics	Definition	N. Articles	Usage rate (%)	Refs.
Rooftop Area (m^2)	The surface occupied by the photovoltaic modules and / or the suitable area available for implementation of solar panels on rooftop surfaces.	17	13%	(Hong et al., 2017), (Thebault et al., 2022)
Real efficiency (%)	Efficiency including pre-module losses, module losses, system losses and operation & maintenance downtime	16	13%	(Gupta et al., 2021)
Grid capacity (MWp)	The sum of the maximum power outputs of the generators attached to an electrical grid.	14	11%	(Assouline et al., 2017), (Yassuda Yamashita et al., 2021)
Unshaded ratio (Unitless Ratio)	The proportion of unshaded roof area	11	9%	(Walch et al., 2020)
Lifetime (years)	The duration for which a PV system works close to its nominal performances.	7	6%	(Zhu et al., 2020)

The most present economic metrics found in this scientific literature review are the Net Present Value (10%) and the Return on investment (9%), both responsible for the feasibility of a project in economic terms.

The economic potential analysis need arises because during the development of this SLR some economic models used for PV systems were identified and they make use of several metrics that together will show the economic feasibility of a given photovoltaic project.

Tab. 3. Overview extraction of the main economic metrics behind the deployment of solar panels

Metrics	Definition	N. Articles	Usage rate (%)	Refs.
Net Present Value (Currency)	The difference between the present value of cash inflows and the present	13	10%	(de Souza Dutra et al., 2019)

	value of cash outflows over a given period of time.			
Return on investment (%)	Evaluate the efficiency or profitability of an investment by comparing the amount of return on a particular investment related to the initial investment cost.	11	9%	(Müller and Trutnevyte, 2020)
Levelized Cost of Energy (Currency/ Energy)	A measure of the average net present cost of electricity generation by a certain technology over its lifetime.	10	8%	(Zou et al., 2017)
Simple Payback Time (Years)	The number of years to refund an investment.	8	6%	(Sommerfeldt and Madani, 2017)
Grid reinforcement cost (Currency)	Cost related to the electricity grid infrastructure to receive the photovoltaic panels.	5	4%	(Wang et al., 2022)

The most used energy metrics are Electricity generation (20%) and Insolation (9%) both correlated to the photovoltaic potential of a given region.

The energy analysis of photovoltaic systems is able to show us the capacity that a given case study has to produce electricity according to its characteristics as well as the return on investment in energy terms and it is a complementary evaluation that allow us to measure the viability of a PV project.

Tab. 4. Overview extraction of the main energy metrics behind the deployment of solar panels

Energy Metrics	Definition	N. Articles	Usage rate (%)	Refs.
Electricity generation (kWh/year)	The expected energy output per year (kWh/year)	25	20%	(Assouline et al., 2018)
Insolation (kWh/m²/(day)	The incoming solar radiation on a surface on earth in a given time-period.	12	9%	(Jones et al., 2004)
Energy Payback Time (years)	The required period in which the PV system can produce the same amount of electricity with the energy consumed over its life cycle.	6	5%	(Burg et al., 2017)
Energy Return on Investment (years)	A ratio of the amount of energy (the exergy) delivered from a certain energy resource to the amount of exergy used to obtain that energy resource.	4	3%	(Bhandari et al., 2015)

4. Discussion

After listing the various metrics, it is important to seek the complementary participation of stakeholders and urban experts in the construction of the context of the region that will adopt an energy transition strategy and which aims to focus efforts on the use of photovoltaic panels. Among the questions that may guide the following initiatives to enable decision making in the massive deployment of PV systems in urban scale are:

i) What are the stakeholders involved in the massive adoption of PV systems in urban scale?

ii) What are the level of influence of these stakeholders in the PV system massive deployment?

iii) What are the phases that will enable the massive deployment of panels in urban areas?

iv) What is the photovoltaic potential of the studied urban region?

v) What are the main enablers playing an important role in PV system's implementation in urban territories?

Some of these metrics are only informative or intermediary metrics, whereas others are key performance indicators that are directly related to the decision- making process for some solar asset stakeholders. Due to the complexity of decision making, there are metrics that can be seen as mere measures for some actors but have a high influence on decision making for others.

The discussion about metrics may become overly broad and unfocused because a metric that is considered a simple measure for a solar asset stakeholder may be deemed as an important indicator for an expert throughout a different perspective.

Thus, assessing the metrics behind the deployment of photovoltaic systems in urban areas is a preliminary step before creating a value proposition to aid the interested parties regarding the effective employment of these systems. The identified metrics demonstrate the significance of evaluating the urban photovoltaic potential while simultaneously taking into account technical, economic, and energy factors.

Even though these factors have each been well-covered by other studies, it is crucial to take them into account collectively in order to facilitate decision-making, particularly in the case of urban energy transition projects that aim for the fast pace deployment of photovoltaic energy systems in their territories.

Therefore, the metrics identified and described in this paper can provide answers to questions about technical and economic as well as energy feasibility, allowing investors, urban planners, and public authorities to make more informed decisions.

In practical terms, it has been demonstrated the importance of investigating the metrics underlying the implementation of photovoltaic energy as they serve as the basis for designing decision-making models that take into account the complementarity of various factors to make photovoltaic energy systems viable from a large-scale perspective.

The benefits of making decisions using the metrics identified in this paper include defining realistic spatial and time-based objectives for the urban area aiming to deploy photovoltaic systems, as well as ensuring a return on investment in both financial and energy terms.

By using these metrics, multi-criteria models can be proposed, created and integrated into the urban energy management system in order to respond to project demands in a meaningful, pertinent, and goal-aligned manner.

It is worth to highlight that the study of qualitative metrics may be complementary and also should be explored in order to understand how such factors influence the decision-making process of certain types of stakeholders.

5. Conclusion

This paper aimed to explore the main quantitative metrics behind the decision making process of PV Systems implementation in urban scale by developing an extensive review to lead us to fill the gap between the theoretical and practical application of the most used metrics.

Most of the metrics reviewed not cover in-detail the costs, technical constraints and energy generation production and benefits of PV systems at the same time, we have more often an overview using relatively simple analysis to evaluate the energy potential from a given region.

However, accordingly to the dimensions of the PV project and policies implemented, the simplicity in this assessment might not be enough to evaluate urban PV projects application in terms of techno-economic feasibility. Nonetheless, a simple assess may infer a point of departure to encourage greater initiatives towards a core techno-economic analysis in its viability to overcoming PV grid issues related to its deployment and energy production.

Other primary themes uncovered through this review are needed to complement the understanding of what are the global key-factors that can either enable or not the PV System adoption in urban scale (1) social (2) political commitment and also (3) regulatory aspects.

Acknowledgment

This work has been supported by the French National Research Agency, through the Investments for Future Program (ref. ANR-18-EURE-0016 – Solar Academy). This work is also supported by the CSMB

References

Adrianus Johannes Maria van Wijk and Jan P Coelingh. Wind power potential in the OECD Countries. Department of Science, Technology and Society, Utrecht University, 1993.

Assouline, D., Mohajeri, N., Scartezzini, J.-L., 2018. Large-scale rooftop solar photovoltaic technical potential estimation using Random Forests. Appl. Energy 217, 189–211. https://doi.org/10.1016/j.apenergy.2018.02.118

Assouline, D., Mohajeri, N., Scartezzini, J.-L., 2017. Quantifying rooftop photovoltaic solar energy potential: A machine learning approach. Sol. Energy 141, 278–296. https://doi.org/10.1016/j.solener.2016.11.045

Bhandari, K.P., Collier, J.M., Ellingson, R.J., Apul, D.S., 2015. Energy payback time (EPBT) and energy return on energy invested (EROI) of solar photovoltaic systems: A systematic review and meta-analysis. Renew. Sustain. Energy Rev. 47, 133–141. https://doi.org/10.1016/j.rser.2015.02.057

Burg, B.R., Ruch, P., Paredes, S., Michel, B., 2017. Effects of radiative forcing of building integrated photovoltaic systems in different urban climates. Sol. Energy 147, 399–405. https://doi.org/10.1016/j.solener.2017.03.004

Cergibozan, R., 2022. Renewable energy sources as a solution for energy security risk: Empirical evidence from OECD countries. Renew. Energy 183, 617–626. https://doi.org/10.1016/j.renene.2021.11.056

de Souza Dutra, M.D., Anjos, M.F., Le Digabel, S., 2019. A general framework for customized transition to smart homes. Energy 189, 116138. https://doi.org/10.1016/j.energy.2019.116138

Goel, M., Verma, V.S., Tripathi, N.G., 2022. International Solar Alliance—Toward Clean Energy Transition, in: Goel, M., Verma, V.S., Tripathi, N.G. (Eds.), Solar Energy: Made Simple for a Sustainable Future, Green Energy and Technology. Springer Nature, Singapore, pp. 175–185. https://doi.org/10.1007/978-981-19-2099-8_14

Gupta, R., Pena-Bello, A., Streicher, K.N., Roduner, C., Farhat, Y., Thöni, D., Patel, M.K., Parra, D., 2021. Spatial analysis of distribution grid capacity and costs to enable massive deployment of PV, electric mobility and electric heating. Appl. Energy 287, 116504. https://doi.org/10.1016/j.apenergy.2021.116504

Hong, T., Lee, M., Koo, C., Jeong, K., Kim, J., 2017. Development of a method for estimating the rooftop solar photovoltaic (PV) potential by analyzing the available rooftop area using Hillshade analysis. Appl. Energy 194, 320–332. https://doi.org/10.1016/j.apenergy.2016.07.001

Jones, P.J., Alexander, D., Marsh, A., Burnett, J., 2004. Evaluation of Methods for Modelling Daylight and Sunlight in High Rise Hong Kong Residential Buildings. Indoor Built Environ. 13, 249–258. https://doi.org/10.1177/1420326X04045177

Kammen, D.M., Sunter, D.A., 2016. City-integrated renewable energy for urban sustainability. Science 352, 922–928. https://doi.org/10.1126/science.aad9302

Lagisz, M., Vasilakopoulou, K., Bridge, C., Santamouris, M., Nakagawa, S., 2022. Rapid systematic reviews for synthesizing research on built environment. Environ. Dev. 43, 100730. https://doi.org/10.1016/j.envdev.2022.100730

Lobaccaro, G., Croce, S., Lindkvist, C., Munari Probst, M.C., Scognamiglio, A., Dahlberg, J., Lundgren, M., Wall, M., 2019. A cross-country perspective on solar energy in urban planning: Lessons learned from international case studies. Renew. Sustain. Energy Rev. 108, 209–237. https://doi.org/10.1016/j.rser.2019.03.041

Martins, T.A. de L., Adolphe, L., Bastos, L.E.G., Martins, M.A. de L., 2016. Sensitivity analysis of urban morphology factors regarding solar energy potential of buildings in a Brazilian tropical context. Sol. Energy 137, 11–24. https://doi.org/10.1016/j.solener.2016.07.053

Müller, J., Trutnevyte, E., 2020. Spatial projections of solar PV installations at subnational level: Accuracy testing of regression models. Appl. Energy 265, 114747. https://doi.org/10.1016/j.apenergy.2020.114747

Ostrowski, W., 2022. The Twenty Years' Crisis of European Energy Security: Central and Eastern Europe and the US. Geopolitics 27, 875–897. https://doi.org/10.1080/14650045.2020.1835863

P., R., K., K.M., A., K., 2019. Performance analysis and energy metrics of grid-connected photovoltaic systems. Energy Sustain. Dev. 52, 104–115. https://doi.org/10.1016/j.esd.2019.08.001

Paleri, P., 2022. Energy Security (Energysec) (es2), in: Paleri, P. (Ed.), Revisiting National Security: Prospecting Governance for Human Well-Being. Springer Nature, Singapore, pp. 625–660. https://doi.org/10.1007/978-981-16-8293-3_15

Rigo, P.D., Siluk, J.C.M., Lacerda, D.P., Spellmeier, J.P., 2022. Competitive business model of photovoltaic solar energy installers in Brazil. Renew. Energy 181, 39–50. https://doi.org/10.1016/j.renene.2021.09.031

Sommerfeldt, N., Madani, H., 2017. Revisiting the techno-economic analysis process for building-mounted, grid-connected solar photovoltaic systems: Part one – Review. Renew. Sustain. Energy Rev. 74, 1379–1393. https://doi.org/10.1016/j.rser.2016.11.232

Thebault, M., Desthieux, G., Castello, R., Berrah, L., 2022. Large-scale evaluation of the suitability of buildings for photovoltaic integration: Case study in Greater Geneva. Appl. Energy 316, 119127. https://doi.org/10.1016/j.apenergy.2022.119127

Walch, A., Castello, R., Mohajeri, N., Scartezzini, J.-L., 2020. Big data mining for the estimation of hourly rooftop photovoltaic potential and its uncertainty. Appl. Energy 262, 114404. https://doi.org/10.1016/j.apenergy.2019.114404

Wang, R., Hasanefendic, S., Von Hauff, E., Bossink, B., 2022. The cost of photovoltaics: Re-evaluating grid parity for PV systems in China. Renew. Energy 194, 469–481. https://doi.org/10.1016/j.renene.2022.05.101

Yassuda Yamashita, D., Vechiu, I., Gaubert, J.-P., 2021. Two-level hierarchical model predictive control with an optimised cost function for energy management in building microgrids. Appl. Energy 285, 116420. https://doi.org/10.1016/j.apenergy.2020.116420

Zhu, R., Wong, M.S., You, L., Santi, P., Nichol, J., Ho, H.C., Lu, L., Ratti, C., 2020. The effect of urban morphology on the solar capacity of three-dimensional cities. Renew. Energy 153, 1111–1126. https://doi.org/10.1016/j.renene.2020.02.050

Zou, H., Du, H., Brown, M.A., Mao, G., 2017. Large-scale PV power generation in China: A grid parity and techno-economic analysis. Energy 134, 256–268. https://doi.org/10.1016/j.energy.2017.05.192

Solar Decathlon - New Ways of Construction for Decarbonised Buildings

Andreas Gerber, Lena Frühschütz

Biberach University of Applied Sciences, Biberach (Germany)

Abstract

For the international building competition Solar Decathlon Europe 2021/22, a renovation and extension of an existing building was developed with the aim of sustainable construction and minimal carbon footprint. Prefabricated timber elements are used for the construction, which were developed with the aim of long-term CO_2 sequestration and the separability and recycling of the components. The highly thermally insulated building envelope, passive solar gains and ventilation with heat recovery form the basis for covering the demand for heat and electricity through façade-integrated PVT collectors and a PV system on the roof. A novel storage system, which uses the weighting of the wooden ceilings for impact sound insulation, decouples generation and consumption.

A representative section of the design with a usable area of 60 m² was built for the competition. This article presents the concept, planning and construction of the building.

Keywords: PVT collector, building integration, thermal storage, demonstration, Solar Decathlon

1. Solar Decathlon

Solar Decathlon is an international student competition for architecture and energy (Bergische Universität Wuppertal, 2022). Highly efficient and self-supplied buildings are planned, built, operated and juried. At Solar Decathlon Europe 2021/22 (SDE21/22) the student competition was focused on urban context, for the first time. Sustainable building and living in cities were the aims that 18 teams of eleven countries had to find innovative solutions for. The concept for the developed high energy efficient and autarch operated buildings should then be transferable and replicable to other European cities. The transition of cities is seen as an important step towards a climate-friendly future. A sustainable transition always has to take place on several levels. This is why the contributions give answers to the ten disciplines in the decathlon – from architecture, solar energy, social awareness up to urban mobility.

In this case, sustainable building and living was seen with the eyes of resource saving, energy efficiency and social responsibility. Construction of the building shell was in consideration to the choice of materials, separability, carbon footprint, way of construction as well as to the quality, insulation and air tightness of the building shell. In terms of energy, topics like integrated energy generation, storage concepts, components of the energy system and their interaction and automation were discussed. These architectural and technical topics have then been embedded in a social context. New ways of building integration in its neighborhood, ownership structures and addressed groups of residents gave the social framework for the concept.

The SDE21/22 competition was divided into two parts – a design and a building part. The design challenge contained the renovation and extension of real existing buildings by consideration the mentioned points for sustainable building and living in cities before. Generating living space without sealing additional land was the aim of this challenge. Sustainable redensification of urban areas had to be planned interdisciplinary and integral with all trades involved.

In the building challenge, a demonstrative part, a small excerpt, of the planned residential building was planned as a self-standing unit. This demonstrator (House Demonstration Unit, HDU) could have up to 70 sqm living space and contained all necessary functions of living. This part had then to be constructed, prefabricated and

© 2022. The Authors. Published by International Solar Energy Society
Selection and/or peer review under responsibility of Scientific Committee
doi:10.18086/eurosun.2022.01.04 Available at http://proceedings.ises.org

assembled within only two weeks for the competition final in Wuppertal in June 2022. During three weeks in the final, the demonstration unit was operated and evaluated by a professional jury. Figure 1 and Figure 2 show the constructed demonstration unit (HDU) on site of the team X4S.



Figure 1: Assembled House DemonHDU elevation north-east



Figure 2: Assembled HDU elevation south-west

2. Given Situation and Objectives

As one of the 18 participating teams, the Biberach University of Applied Sciences took part in the SDE21/22 competition as "Team X4S" – the short form for "Extension for Sustainability". By choosing one situation given by the organizers, the team of Biberach planned the renovation and addition of Café Ada – a two storey building from the Gründerzeit that is located in the Mirke quarter in Wuppertal, Germany. The cafés footprint is about 400 sqm and the building is used for cultural activities. Additionally, the adjacent outdoor area was also part of the competition to be included in the planning.

For the renovation and addition of Café Ada, the team X4S developed a holistic concept that also meets economic, social as well as urban integration requirements. The existing building should be renovated moderately (specific heating demand less than 50 kWh/m²) usable floor space) and the public use should remain. On top of these two floors, a four storey extension with roof garden is planned. Living space as well as community and co-working spaces are offered, see also Figure 3 and Figure 4. The roof garden provides also community space for urban farming, is used as rain retention in case of heavy precipitation events and is covered by a PV-roof. The building shell is carried oud in passive house quality. The roof and façade are used for energy generation to supply the whole building.



Figure 3: Modell of café Ada and its planned extention, elevation south-west



Figure 4: Modell of café Ada and its planned extention, elevation north-west

The entire solution excels in terms of sufficiency, efficiency, consistency and resilience. The extension of café Ada acts as a transferable example on how to change the built environment in order to achieve greater

sustainability and address social and economic demands at the same time.

Densification solves urban issues like excessive land use, increased traffic due to spread-out cities or social isolation. The design focuses on residents who are interested in social participation. With different small and flexible floor plans, like it is shown in Figure 5, the building provides living space for one or two-person households as well as for small families.

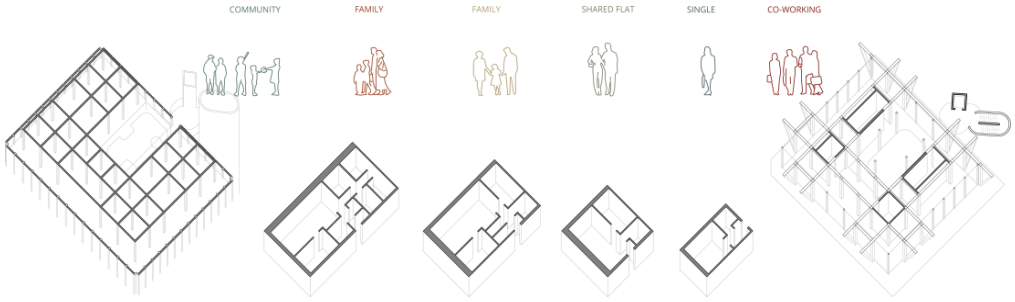

Figure 5: Different flats for different needs are part of the architeture

Cost-effective and fast to build constructions are achieved by solid timber elements which are developed with prefabrication of elements and modules, minimal loads by using solid wood constructions and separability to ensure reuse and recycling of the building materials. Fire protection is achieved with this solid wood construction without additional concrete parts or encapsulation.

The climate neutrality of the building is achieved through the use of renewable raw materials with low a percentage of grey energy, highly thermally insulated building envelope, the energy refurbishment of the existing building, heat recovery from the ventilation system and solar activated façades and roof surfaces. A consistent low-temperature concept and the use of the building's mass as storage increase system efficiency. A grid friendly operation is enabled by storage systems in combination with an intelligent management system.

To make sustainability affordable, we employ existing efficient technologies integrated in a highly efficient and resilient system design. Reduced private in combination with huge communal spaces, multifunctional building elements like integration of ventilation systems or electrical distribution system and less technic but high efficient are just examples for this.

In terms of energy, the objectives are described in detail below:

- Reduction of energy consumption through the highly thermally insulated building envelope and heat recovery from ventilation systems
- Extensive renovation measures of the building envelope of the existing building
- Replacement of fossil fuels with heat pumps that draw their energy from renewable sources
- Use of solar radiation on façade and roof to generate electricity and heat
- Improvement of system efficiency of heat pumps through the use of PVT collectors and the consistent reduction of system temperatures for both heating (panel heating systems) and hot water production (decentralized fresh water stations)
- Thermal storage with minimal additional costs due to the activation of required building component layers.
- An open-source smart home system as an information system for the users of the building and for monitoring and automating the system.

3. Energy Concept and Solar System

In order to minimise the carbon footprint with measures in and on the building, a energy concept was developed that is shown schematically in Figure 6. Building-integrated solar systems for electricity and heat form the basis of the system.

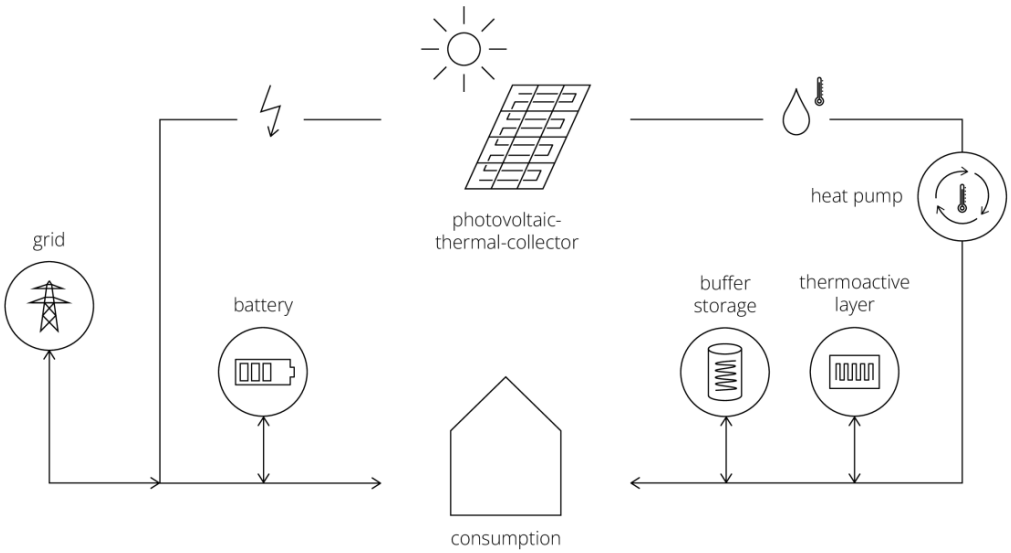

Figure 6: Energy concept with solar systems for both electricity and heat. Load management together with battery and thermal storage enables high solar fraction and grid-friendly operation

Semi-transparent PV modules on the roof are used to generate electricity. For the building design, the extension of café Ada semi-transparent glass-in-glass modules were chosen. In the demonstration unit, newly developed tubular thin-film PV modules were used, see Figure 7 and Figure 8. Due to the distance between the tubes, the tubular modules have a lower yield in relation to the gross area than closed modules. On the other hand, the solar yield is more even and higher in the daily sum due to the more favourable angle of irradiation.

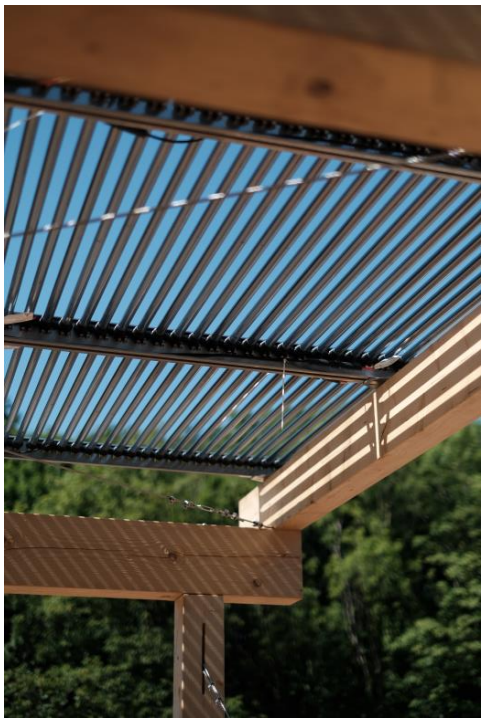

Figure 7: Air- and water-permeable solar roof with solar tubes for energy generation

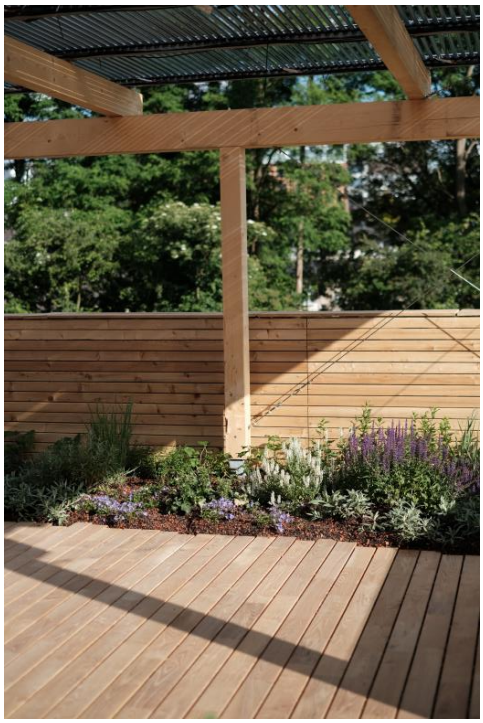

Figure 8: Extensive and intensive greening is possible under the solar roof.

A special feature is that the drainage of the solar module takes place on the underlying retention roof. This relieves the load on the public drainage system during heavy rainfall events.

Since the energy demand of the building increases with the number of storeys, but the roof area is limited, the façade is also used to generate solar energy. As a result, the solar yield scales with increasing floor space.

Vertically installed uncovered PVT collectors are used. A challenge in technical and design terms was the integration of marketable PVT modules into the façade. The solution developed in cooperation between architecture, building physics, timber construction and energy technology is shown in Figure 9 and Figure 10. Important aspects were the rear (passive) ventilation of the modules, the removal of condensation during the heating period and the reduction of penetrations in the façade for a durable construction.



Figure 9: Eastern and southern facade of the HDU are solar activated with PVT modules



Figure 10: The facade integration of the PVT modules has been developed interdisciplinary

The thermal system, see Figure 11 for a schematic representation, uses the PVT collectors in the façade as a heat source for a power-controlled heat pump. The power control is used to adapt the operation to the electrical and thermal solar yield. This improves the COP of the system, especially during the heating season.

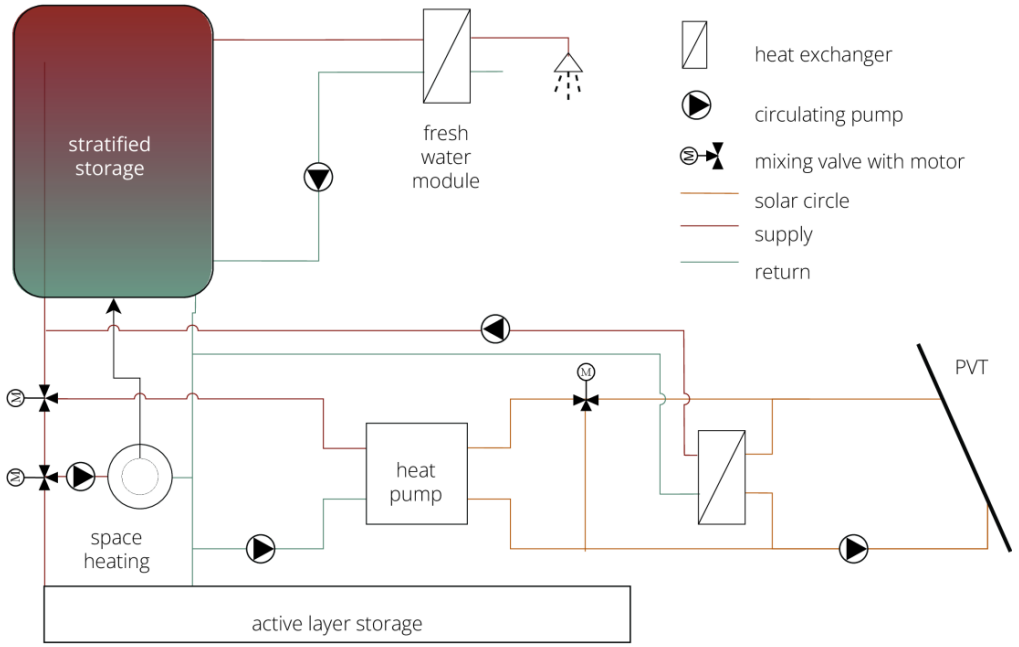

Figure 11: Thermal system with PVT collectors integrated in the facade, heat pump buffer storage and active layer storage.

Two thermal storages help to realise this efficient mode of operation: A buffer storage tank with two thermal zones stores heat for surface heating up to 35°C and for hot water preparation at 50°C. The mass of the impact sound insulation serves as a second storage. This is operated in the temperature range from 20°C to 35°C. Due to its dual use as impact sound insulation and as a thermal storage as well as its simple construction, it can be realised very cost-effectively. Another important feature is that this storage scales with the usable area and thus

with the required heating energy. This combined storage system is the basis for decoupling the heat demand from the solar yield. classic underfloor heating system installed below the flooring is used for the heat output to the room.

Hot water is provided via decentralised fresh water stations installed in all the flats. This achieves hygienic hot water preparation at low temperatures and without hot water circulation. Heat recovery from the shower water can also be integrated very efficiently into this system. The associated device is integrated into the drainage channel of the shower.

The electrical system uses a battery constructed from common Li-ion cells of the type 18650 as storage. These are found in notebooks, e-bikes, etc. The modular concept of the battery allows the use of second-life cells and the exchange of individual cells. Due to the design of the stack, high charging and discharging currents are possible even without welding. This is the basis for separability at cell level.

Battery inverters available on the market have high efficiencies of over 90 % at nominal power. In the partial load range, however, the efficiency drops significantly. Now this load range is the dominant one in buildings. Against this background, an AC-DC hybrid system was developed. Electrical devices that generate heat at high power are supplied with alternating current (AC) via the battery inverter. Appliances with loads up to about 100 W are supplied with direct current (DC) directly from the battery. For this purpose, a component-integrated DC distribution system was realised as a prototype.

4. Student's Team X4S

The creation of sustainable building and living demands the participation of all involved trades from the beginning of the planning. Therefore, the team X4S was an interdisciplinary team with team members of architecture, energy engineering, project management and civil engineering (Hochschule Biberach, 2022). Students and professors contribute with their special expertise. Normally, the collaboration of students from different disciplines is not practiced at university. Therefore, it was a great challenge to develop together an integral and sustainable solution for the competition entry. In joint interdisciplinary meetings, the awareness and understanding for the other disciplines raised slowly. An exciting and exhausting process over more than two years bonded all members to the team X4S. So, it was possible to consider special requirements and boundary conditions of all trades.



Figure 12: Interdisciplinary collaboration of students and professors

A close cooperation between students and professors was also important as it is at small and familiar universities like Biberach. By integration the topics of the SDE into the courses, students could make basic research, evaluation and simulations. At the Biberach University, even new, interdisciplinary courses were created for the preparation of the competition entry in order to enable joint work. With the support of the university administration, study regulations were adapted. So, professors and students could invest more time and energy during their everyday university life to work on the project. One outcome of this process is that team members have gained a deeper understanding of unknown but important aspects from other disciplines. This cross-disciplinary knowledge is necessary for the construction and refurbishment of buildings for a carbon-neutral future.

The implementation of the planning into a real building was achieved with the support of the carpentry training center of Biberach. The team X4S did all executive work, prefabrication and assembly on his own, see also Figure 13 and Figure 14. A large number of the students involved were trained craftsmen. Therefore, there was no need to award contracts to specialist companies for the execution of the planned demonstration unit. This linking of planning and execution supported the learning process in a particular way.



Figure 13: Some difficult connections were solved during prefabrication.



Figure 14: The students did the whole prefabrication and assembly by their own.

5. Conclusions

The international Solar Decathlon competition provides an impulse for the conception and realisation of sustainable buildings with a high proportion of solar coverage by student teams. The example of the team from Biberach University of Applied Sciences shows the importance of interdisciplinary teams for sustainable construction and CO_2-free operation of buildings. Beyond the competition, the buildings can be used for research topics such as active-layer storage and façade-integrated PVT collectors.

The project was supported by the German Federal Ministry for Economic Affairs and Climate Protection, among others, under the funding code 03EGB0030.

6. References

Bergische Universität Wuppertal, F. f. A. u. B., 2022. *Solar Decathlon Europe 21/22 (SDE21/22).* [Online]. https://sde21.eu/de/ [Last access: 15 September 2022].

Hochschule Biberach, I. f. G.-. u. E., 2022. *Team X4S.* [Online]. https://www.team-x4s.de/ [Last access: 15 September 2022].

K**.** Voss, 2022, Solar Decathlon Europe 22 - Experiences and Perspectives of a Student Building Competition by Karsten Voss, Kassel, Eurosun 2022

The Future of Solar Integration: Towards Efficiency in Solar Design through Aesthetics, Optimisation and Customisability

Karim Jaspers[1], Erwin W. Ketelaars[1], Lotte H.H.M. Roefs[1] and Meril Liis Kütt [1]

[1] Team VIRTUe, Eindhoven University of Technology (The Netherlands)

Abstract

The efficient integration of Building Integrated Photovoltaic and Solar Thermal systems (BIPV/T) within an increasingly dense urban fabric requires both technical optimisation and qualitative, formal innovation. However, the latter is often overlooked in technological developments; current BIPV/T systems discourage a widespread implementation by stakeholders as these systems are perceived of having a poor formal quality. The aim of this paper is therefore to provide a new perspective for the development of the solar industry. Following a Research through Design methodology, this approach is examined firstly through the design and construction of a prototype unit, and secondly by a thermal and electrical evaluation of the solar design. The prototype unit, featuring a coloured solar facade with customised photovoltaic and thermal collectors, participated in the Solar Decathlon Europe 21/22 in Wuppertal, Germany.

The key finding is that BIPV/T systems ought to be considered as design elements or architectural building blocks rather than optimised technological systems. This holistic perspective to solar integration resulted from the essential collaboration between architect and engineer. In this way the formal potential of solar design within its production limitations is explored while meeting the technical requirements. Even more, solar design can be used to reach social objectives, as demonstrated in the prototype unit. The full potential of solar integration is, however, to be explored further. The formulated perspective can stimulate an alternative direction for both engineers and designers of the solar industry to work towards a net-zero built environment.

Keywords: Solar Design, Building Integrated Photovoltaic Thermal Systems, Architectural Integration, Energy-Efficiency

1. Introduction

The imperative of climate change demands an accelerated transition towards renewable energy sources. To transit towards a sustainable energy system a mix of different renewable energy sources is needed (IEA, 2021; IPCC, 2022). In this mix solar power plants play an important role as peak load operators (Bhattacharyya, 2011). There used to be a primary focus on substantial solar fields subsidised by governments and companies, however, there is currently a tendency towards decentralisation and smaller, local application of solar energy involving the current building stock (Ng et al., 2022). This resulted from both the competition of rural space necessary for agriculture and natural environments, and an increasing awareness of sustainability combined with policy implementations allowing for a monetary benefit for residents to adopt solar panels (Bahaj & James, 2007; Vasseur & Kemp, 2015). Simultaneously, it is expected that 68% of people worldwide will live in urban areas by 2050 compared to the current 55% (United Nations, 2018) and, therefore, space will become even scarcer, leading to an increased focus on Building Integrated Photovoltaic and Solar Thermal systems (BIPV and BIST; from here on abbreviated as BIPV/T). BIPV/T can be defined as a system which "makes use of the building envelope for solar energy collection to produce both electrical and thermal energy, providing an efficient way of reducing building energy consumption" (Yang & Athienitis, 2016, p. 887). BIPV/T is currently mainly adopted on building roofs even though facades contain larger available surfaces, thus providing a further opportunity for the implementation of solar design. This facade generation is, however, not yet inherently part of the current toolbox for both newly built houses and renovated dwellings. This is among others due to economic difficulties, critical regulatory issues, and problems regarding grid interaction (D'Ambrosio et al., 2021). Current focus lies on the technological and economic optimalisation of solar design, especially on circularity, grid interaction, and efficiency of vertical solar cells.

© 2022. The Authors. Published by International Solar Energy Society
Selection and/or peer review under responsibility of Scientific Committee
doi:10.18086/eurosun.2022.01.05 Available at http://proceedings.ises.org

Parallel to these quantitative advancements, the typo-morphological characteristics and the architectural integrability of BIPV/T are also considered a barrier for a greater rate of adoption (D'Ambrosio et al., 2021; Munari Probst & Roecker, 2007). BIPV/T is increasingly implemented in facade design and require a higher delicacy in formal qualities (Frattolillo et al., 2020). Since the facade of buildings determine the public face of the city, BIPV/T cannot be simply considered as technological additions but should be recognised as integral parts of its urban architecture (Munari Probst et al., 2004). The current BIPV/T catalogues contain only a limited selection of variations available for stakeholders while the building stock consists of a vast diversity of appearances. Residents and architects wish not to be limited by sustainable design and implementation of solar generation, but rather they aim for a perpetual improvement of their environment (Alipour et al., 2021; Heinstein et al., 2013). Therefore, technological advancement is no longer the only issue to increase the rate of adoption of solar design: efficiency in deployment can be intensified through aesthetics, optimalisation and customisability.

However, this pathway of future solar integration through aesthetic improvements should not become an excuse to limit the technological optimalisation of solar energy production. The planetary boundaries demand engineers and architects to fundamentally consider the limited resources, the tremendous carbon footprint of PV production and the risks of grid overload (Finnegan et al., 2018; Kabir et al., 2018). The focus should therefore lie both on architectural integrability and on technological optimalisation through solar orientation, preferred solar angle, peak usage of appliances, and limitations provided by BIPV/T production. The authors consider this holistic perspective as a fundamental priority to reach a net-zero built environment.

Current research around solar power generation is focused mainly on the technological testing and optimising of solar systems, on the reduction of costs and on the possibilities of recycling photovoltaic panels after the end of their lifespan (Yang, 2015). Regarding BIPV/T, Maghrabie et al. (2021) have dedicated initial research to outline the development of BIPV/T products and materials. According to the authors, economic and technological innovation are accompanied by a growing interest in the "increasing possibilities of the aesthetics of the BIPV systems" (Maghrabie et al., 2021, p. 17). Munari Probst & Roecker (2007) have set up a range of guidelines for the optimal integration of solar thermal design through several interviews and an additional survey with engineers and architects to ensure both architectural integrability and energy efficiency. In short, these guidelines illustrate the need for 1) using solar energy systems as construction elements, 2) implementing BIPV/T in the general building concept, 3) the ability to choose colours, materials, module size and shape of BIPV/T panels based on the building's material textures (Munari Probst & Roecker, 2007).

Furthermore, Attoye et al. (2018) focused on defining the barriers of adopting BIPV/T and analysing the necessary market tools to elude these barriers. Similar to Munari Probst & Roecker (2007), they mention the urgent need for collaboration between stakeholders such as architects, engineers and solar system companies. Moreover, the need for demonstration products is mentioned in which BIPV/T is seamlessly integrated and which can be used to educate the general public on environmental issues and energy use. It is also stated that BIPV/T products should allow to be customisable. This connects to the vision of Douglass (2008) on how any sustainable architectural innovation requires the design to be 'universally specific', meaning that every architectural innovation aiming for sustainability should have a universal concept that can be specified to the demands and needs of different geographical situations and local environmental conditions (Douglass, 2008). Lastly, the conventional solar energy peak could be optimised by flattening the peak distribution and combining it with demand side management (Saffari et al., 2018). This can simultaneously enhance the awareness by residents of solar generation and consumption.

To recapitulate, forementioned research mainly focuses on either the optimisation of solar systems or the theoretical integrability of solar designs within architecture. Combining these two aspects into a 'universally specific' physical prototype would allow for a niche area of research around BIPV/T. This can be further complemented by following the guidelines of Munari Probst & Roecker (2007) while simultaneously aiming to decrease the barriers of BIPV/T adoption as indicated by Attoye et al. (2018). In addition, the demand side management is to be researched concurrently. This paper therefore aims to increase the efficiency of an integrated solar design by researching the possibilities in aesthetics, optimisation and customisation in a holistic manner. A mixed methods approach is utilised in which the design and construction of a physical prototype unit is combined with a thermal and electrical evaluation. Subsequently, the architectural integrability and technical potential of BIPV/T are evaluated and improved guidelines for a holistic integrability are outlined to increase the rate of adoption of solar design within the built environment.

2. Methodology

2.1 Context of the project

Adhering to a Research through Design methodology, the approach of the paper is to evaluate integrated solar design through a realised project named 'ripple', which participated in the Solar Decathlon Europe (SDE) competition 21/22 in Wuppertal, Germany. The SDE 21/22 was an international student team competition where fifteen teams from ten countries participated with innovative ideas for energy-efficient, sustainable and socially responsible design (Solar Decathlon Europe, 2022). 'Ripple' is designed by Team VIRTUe, a student team from Eindhoven University of Technology (VIRTUe, 2022). The concept ripple is inspired by the ripple effect, where small actions leads to large effects. Starting in 2019, the project was under development for three years and has been realised with a fully built and operational house prototype unit which is named 'ripple demonstration unit' (RDU). The RDU was firstly constructed at the Eindhoven University of Technology for testing and optimalisation. Later, the prototype was demounted and built for a second time at the SDE Competition in Wuppertal.

A mixed methods approach is used which combines the design and construction of the prototype unit (RDU) with a qualitative and quantitative evaluation. In the RDU a facade with BIPV/T is constructed and tested as a demonstration of future adoption of solar technology. The RDU was a result of a close collaboration between students of engineering and architecture, academics and companies in the context of a multidisciplinary team. These aspects will be evaluated in the paper with a reflection on architectural integrability and potential for an efficient near future adoption. Additionally, measured results from the RDU will be presented to confirm the feasibility of the proposed design and evaluate the performance of the BIPV/T system. Finally, all results are incorporated into a set of guidelines that aim to increase the efficiency of deployment of solar design.

2.2 Architectural design and construction

The RDU is designed as a universal concept that is scalable to cities in similar climates, however, the elements could be adapted to local environmental conditions and different architectural contexts. The RDU is part of a larger design in which the renovation and addition of storeys is applied to an existing commercial building in Wuppertal. The model in figure 1 on the left shows the Building Design of the renovation and addition of storeys in Wuppertal and the picture on the right shows the RDU during test-building.



Fig. 1: The relation between the Building Design and the RDU. On the left, a model of the Building Design in Wuppertal. On the right, a picture of the RDU after test-building.

The challenge of designing in an urban context with limited space resulted into the idea to integrate Photovoltaic (PV) panels in the building envelope through the design of a solar facade. The starting point for the solar concept was to integrate it into the building concept from the first phase of the design to create an architectural unity and a clear logic that is fitting to the building its surroundings. Consequently, the solar facade is treated as an integrated part of the design and not as a technological addition in the final design stage. The building concept is based on a tessellating pattern that can be repeated as it is built up from rotatable and stackable units. By the selection of a distinctive shape a higher degree of diversity and complexity can be achieved in the created spaces in contrast to the conventionally used rectangle. This yields a spatial variety in the design that is more intriguing and generates more specific rooms and atmospheres inside as well as the outside of the building. This building concept resulted in a specific exterior shape to which the solar panel design needs to relate. The approach was to enhance the exterior shape of the building by altering the shape of the solar panels in a logical way that was fitting to the

building concept. Therefore, the solar panel design avoids the accustomed rectangular shape and in contrary consists of glass panels with different angles laminated with PV cells, made possible by the ColourBlast technology (KameleonSolar). The technology allows the creation of coloured solar panels suitable for facade application with a wide-reaching range of available colours.

The placement of the panels along the facade was based on an optimal fit to the building concept in combination with optimisation of the BIPV/T energy generation. The optimal angle for the tilt in PV panels on the roof was identified through simulation study to be 20° for the competition period of June in Wuppertal. The facade, however, presents a 90° surface. Therefore, the optimal combination was found in application of PV panels in the shape of a solar belt that wraps around the roof edge of the facade, where the PV panel angle changes from 90° in the facade to 20° in the roof edge. The detail drawing of the solar belt is presented in figure 2. To prevent shade on these panels, glass railings were selected to minimize the blocking of sunlight by the railing.

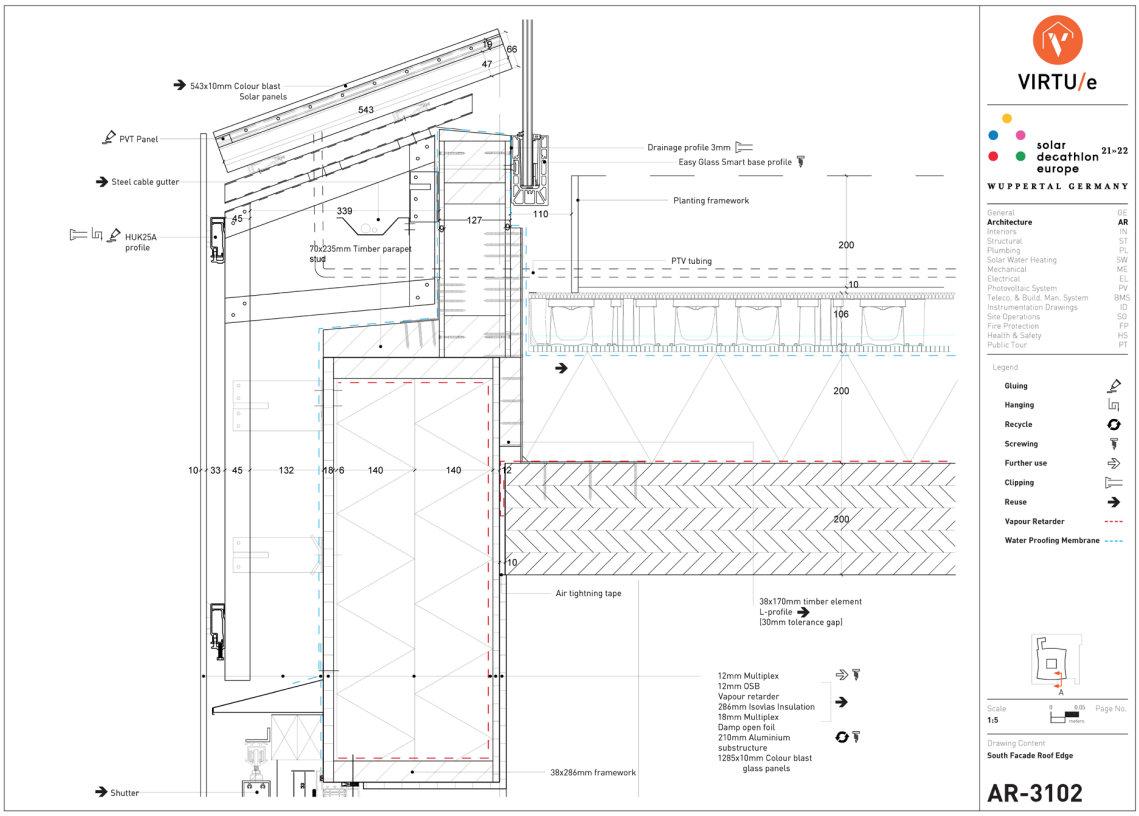

Fig. 2: A detail drawing of the solar belt of the RDU. It shows the tilted PVT panel in the roof edge and the glass railings.

In the facades, the placement of panels was furthermore dependent on the orientation of the facade. The building is built on a -15° orientation. From simulation studies it is found that the west facade would be the most optimal for vertical PV panels, so it was almost fully clad in BIPV/T. The amount of surface area covered by BIPV/T gradually decreased in the design subsequently for the south, east and north facade. The north facade featured no solar panels and the shape of the roof edge was continued with nesting boxes for sparrows and bats made from timber cladding.

2.3 System design

2.3.1 Energy generation

The BIPV/T system of the prototype house is composed of PV modules and a solar collector on the roof, as well as a PVT system integrated into the facade (figure 3). The electrical energy is generated by PV modules integrated in the roof and parts of the facade. In total, seventeen PV modules are installed, and the system has a capacity of approximately 3 kWp, which was the maximum that was allowed by the Rules and Regulations of the SDE competition. Because of this limitation, the position with the highest energy generation potential throughout the day was selected for the equipment of the PV modules. Five conventional crystalline silicon (c-Si) modules, with a capacity of 1825 Wp, are placed on the roof. Twelve coloured PV modules (1152 Wp) are installed along the

solar belt (tilted upper section of the facade), which include microinverters. The average efficiency of the coloured PV cells was measured as 16.7% under standard test conditions. The tilt of the PV modules (20°) was optimised using a simulation study to maximise the energy generation potential in the month of June in Wuppertal, Germany. The intention of placing the PV modules at different orientations was to potentially increase the generation of energy in the late afternoon and create a more balanced profile of energy production throughout the day.

In addition to electrical energy, thermal energy is produced in the prototype house by means of a solar-assisted heat pump to heat water for Domestic Hot Water (DHW) and the floor heating. The coloured PV modules of the solar belt are part of a PVT system, with the thermal loop consisting of tubing behind the PV modules that is connected to the heat pump. In addition, thermal energy is captured using a solar collector (1.6 m2) on the roof. The water heated by the solar collector is stored in a tank that is also connected to the heat pump. Due to the water being preheated by the solar collector and the PVT system, the heat pump would possibly need less power to operate. Additionally, hot-fill appliances have been installed – the washing machine and dishwasher make use of water preheated by the solar thermal systems, potentially decreasing their energy demand.

2.3.2. Energy storage

Two 1.2 kWh batteries are used for electrical energy storage (total size of the storage 2.4 kWh). Thermal storage concerns the solar boiler buffer tank of 120 L and a 176 L water storage integrated in the water/water heat pump.

2.3.3. Demand side management

Demand side management has been incorporated in the design of the RDU. By closely monitoring the energy consumption and production patterns and by managing the energy storage systems, the energy management system can decide when building systems and appliances should be using their energy in order reach the lowest amount of carbon emissions while keeping the energy grid balanced. In order to do this, the system gathers data from the local weather forecasts, PV system, battery and power meters. It then creates an approximation of the buildings' energy production and consumption patterns over the following 48 hours. Every suitable building system and appliance is then scheduled and remotely turned on at a certain timeslot which helps in balancing the energy consumption. A prototype of the software that manages and optimises the energy system, capable of working fully autonomously, was demonstrated in the SDE competition.

The energy management system shares data with a physical interface that enables building occupants to interact with the building's energy system. Through a circular interface which consists of a circular LCD screen and a rotary button, it acts as the central energy hub where data about the building's energy consumption, production and storage levels are visualized (figure 4). This visualization informs inhabitants about the conditions outside of the building but also helps them to reflect on their own energy consumption behaviour inside of the home. The occupants can access their personal schedules where devices and systems are turned on in order to reach an energy pattern with higher self-consumption. An overview of all the schedules is also shown throughout a 24-hour timeline. This timeline visualizes when low-carbon energy is in abundance or when it is not.

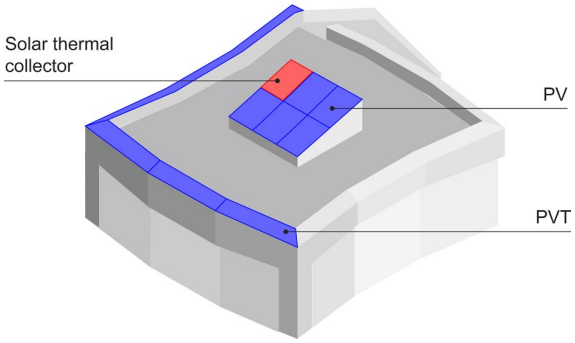

Fig. 3: The BIPV(T) system.



Fig. 4: The interface of the energy management system

2.4 Performance evaluation of the solar design

The performance of the BIPV(T) system with the energy management is evaluated based on the self-consumption index and the overall energy balance. The self-consumption index (eq. 1) describes the proportion of generated energy that is used in the building instead of being fed into the grid:

$$I_{SC} = \frac{E_G - E_F}{E_G} \quad \text{(eq. 1)}$$

in which I_{sc} represents the self-consumption index; E_G is the electrical energy that is generated on site (kWh) and E_F represents the electrical energy which is feed into the electricity grid (kWh) (SDE, 2020).

The measurements were taken during a 10-day period by members of the monitoring team of the SDE, according to the competition rules (SDE, 2020). Various tasks such as running the washing machine or cooking using the oven were performed each day to account for energy consumption.

The energy balance gives an overview of the difference between the total generated and consumed energy during the measurement period. The self-consumption reflects the influence of the solar design, the energy management strategy and the use of solar thermal systems combined with hot-fill appliances for heating water.

3. Results

3.1 Architectural integration

In this chapter, the results from the design and construction of the RDU will be presented in the relation to the BIPV/T design that was created. During the design, the guidelines of Probst et al. (2007) were reflected in the design process. The BIPV/T system has been integrated in a way that it is considered a building element along with the timber cladding, shutters and windows in the facade. By specifying the colour, shape and size of the BIPV/T panels, the solar design has become part of the general building concept of ripple, which will be explained in this chapter.

The shape of the panels was determined by the shape of the building. To make it economically feasible, the choice was made to apply the angle only on one side of the PV panel. The choice for adapting a single angle made it possible to design the strings of PV cells in the same way for each panel, decreasing the production time between different shaped panels as was noted by the manufacturer (KameleonSolar). Therefore, the PV cells are the same for each panel, but the glass shape is different (figure 5), which has no effect on production time hence it is an automized process with 3D laser-cutting technology. Through the scalability concept that is part of ripple in its universal application, the BIPV/T concept can be applied at larger contexts, where different PV panel shapes can be realised without a necessary increase in manufacturing time.

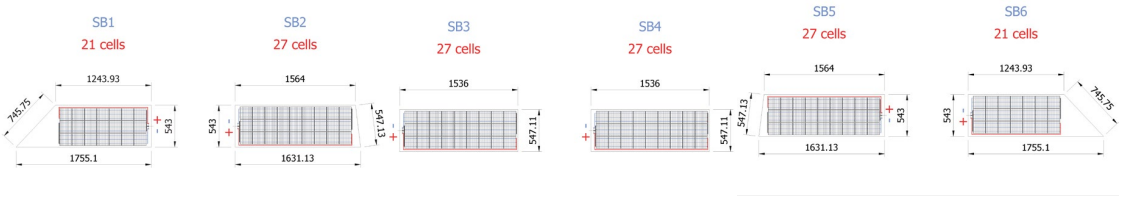

Fig. 5: Example of the BIPV/T panels that were manufactured for the RDU. One side features a different angle for different panels and the opposing rectangular side was used as a reference line to place the PV cells in the same way for all panels.

By rotating the panels corresponding to the design of the facade, the angles could be applied in different directions, allowing the designers to strengthen the building concept with concave and convex facades. In the concave facades (east and west) the solar panels have a tapered shape to become smaller in the middle segment of the facade, where in the convex facades (south and north) the panels have the same shape but become larger instead. The use of both concave and convex facades enhances the visual strength of the effect that is created by the slightly angular walls. When viewed from the corner, as shown in figure 6, this creates a wave-like image that resonates with the overall concept of ripple.



Fig. 6: A picture of the RDU during test-building in July 2021 at the campus of the Eindhoven University of technology.

The coloured PV panels are created by digitally printing a pixelated pattern on the glass, which creates an illusion of a homogenous colour on a distance larger than five metres. The selection of the colour of the panels was made through a careful analysis of the urban context in Wuppertal together with the adjacent material use in the facade. The latter consists of recycled pinewood cladding in two finishings and anodic black powder coated aluminium window frames. The final colour that was selected, a medium taupe colour, was chosen as a fitting colour to be a balance between modesty to fit within the urban context consisting of Gründerzeit dwellings from the 19th century and vivid enough to brighten up the wooden facade which would be subject to turning grey over time due to exposure. The pattern makes it possible to pass-through the light. In the RDU, a 45% colour coverage was chosen for the facade and a 25% coverage for the roof edge, which therefore looked as a slightly darker shade in comparison with the facade. This difference in coverage allows for optimalization of the energy generation of the PV panels where the overall architectural design supports it. Conventionally, a hexagonal pattern is used. However, the patterns are printed by 3D printer and the only constraint for the pattern shape it that it is a tessellating shape, and therefore infinitely repeatable in order to blend uniformly together when viewed from a distance. In the RDU, the shape of the building itself, was therefore used as the tessellation pattern printed on the PV panels as visible in figure 7 on the right.

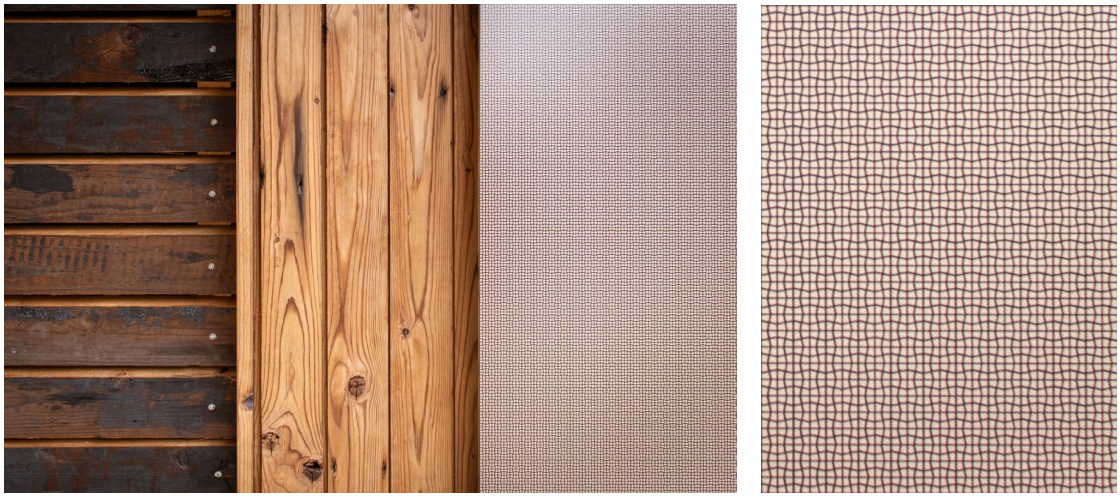

Fig. 7: (right) A detailed facade fragment where the solar panel meets the recycled timber cladding. (left) A more detailed view of the solar panel, where the printed tessellation pattern can be seen that resembles the shape of the building.

Together, all of the customized parts of the facade panels of ripple creates a stronger integration of the BIPV/T system and make it an indispensable part of the overall building concept, which resonates in the materials used. The formal integration of BIPV/T elements makes spatial optimisation possible as it is possible to create the

desired amount of BIPV/T panels in the cladding of each facade and use other building elements where BIPV/T elements are not desirable, such as in the north facade. As was demonstrated in the RDU, this would be different in each facade according to the orientation of the building and the climatic conditions in the specific scenario.

Endless customization can however create an vast increase of elements with different specifications in the project, which could potentially increase manufacturing time. This was prevented through standardization of the most time-intensive tasks in the manufacturing process, which is the implementation of solar cells. The customization of the glass panel shape was used in a restrained way that neutralizes impact on the production process, because each panel had a similar solar cell configuration. This makes it possible to construct a custom solar facade with various shapes within production capabilities.

Lastly, it was found that the implementation of the BIPV/T facade in the RDU allowed for the education of the public on the way that energy can be generated in the buildings shell in a way that enhances the architectural expression of the building. This is, however, only possible through a close collaboration between engineers, designers and manufacturers, as it requires multidisciplinary input.

3.2 Measurement results

The overall energy balance during the measurement period, as well as the data describing the self-consumption is shown in figures 8 to 11. In total, more energy was generated than consumed during the competition period, as shown in figure 8. Figure 9 shows the daily generation and consumption of AC electricity by the BIPV/T system. Figures 10 and 11 describe the self-consumption of the RDU. A self-consumption of 1 indicates that all the generated energy was used and no feed-in occurred. The average self-consumption index is 0.73.

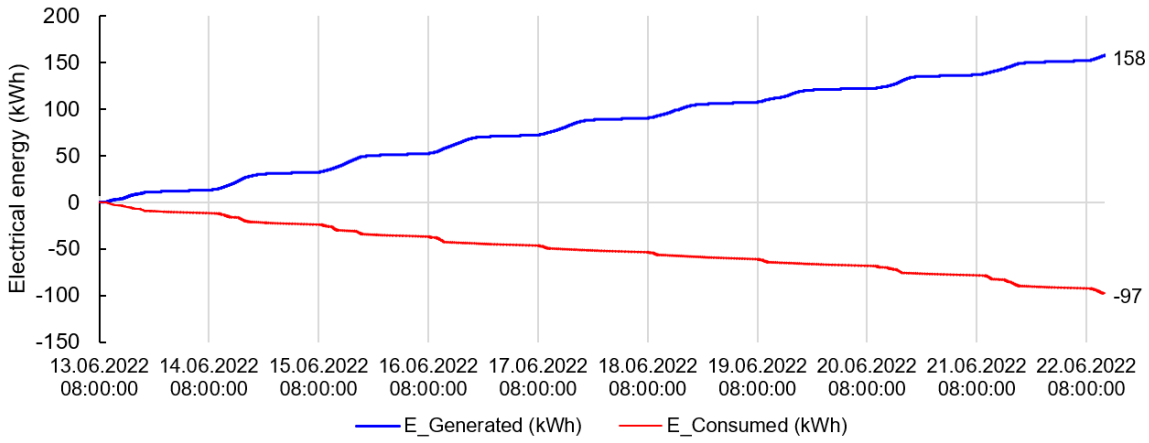

Fig. 8: Cumulative energy balance

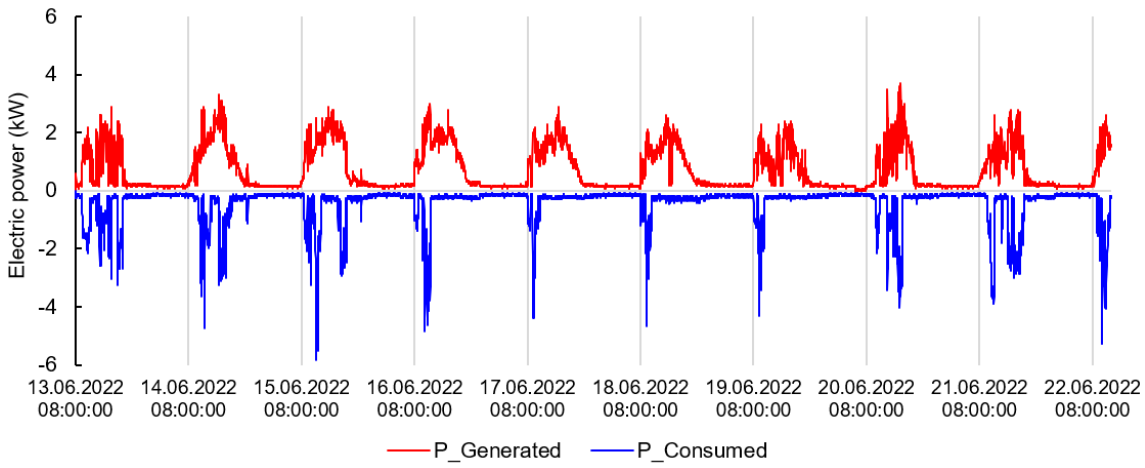

Fig.9: Total AC electricity generated and consumed on site

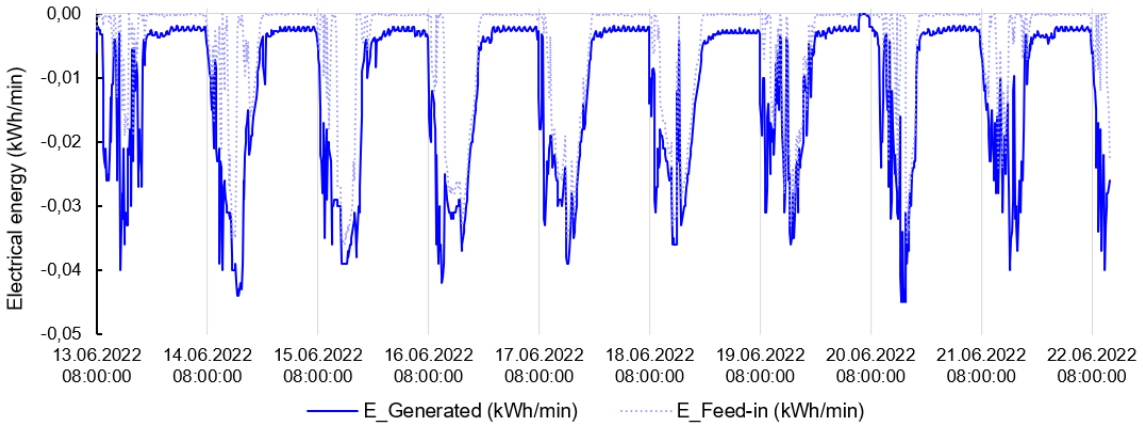

Fig. 10: The electrical energy generated on site or fed into the electricity grid, measured at a 10-minute interval.

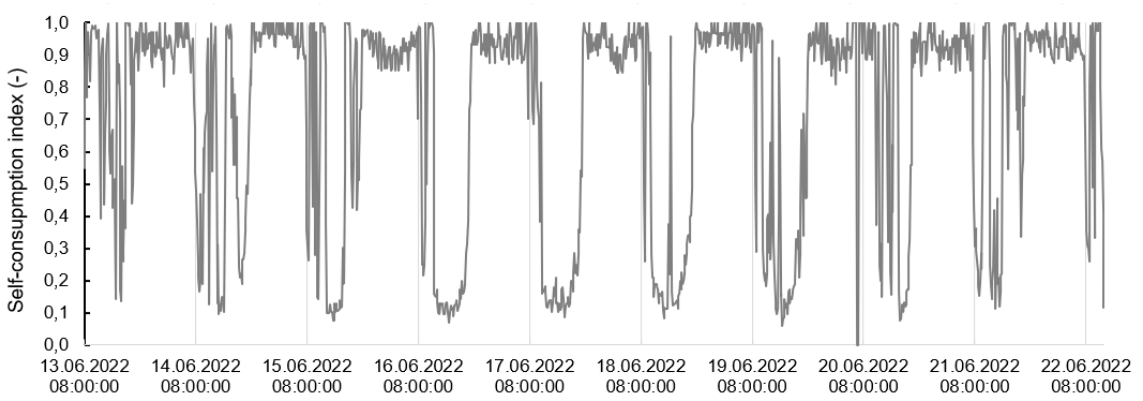

Fig. 11: Self-consumption index, calculated based on the measurements of generated and feed-in electricity

4. Conclusion and discussion

The use of the RDU as a physical prototype to conduct research has given novel insights in the possibilities on optimising, customising and aesthetically integrating solar design to make the use of solar power in buildings more efficient, a before rather neglected area of research (Attoye et al., 2018; Munari Probst & Roecker, 2007).

Firstly, the optimisation of the solar design was researched and evaluated through both a technological and architectural perspective. The optimal tilt of the PV modules along solar belt improves the energy generation potential of the BIPV facade. In addition, the building element can be replaced where it is not needed for other functions such as bird houses for increasing biodiversity. By the implementation of coloured BIPV modules on the East and West façades, a higher energy production is made possible during the morning and evening hours.

Higher-efficiency PV modules were used on the roof to ensure a higher yield from a small area, leaving space for other roof usage such as a green roof and roof terraces. The further optimalization of the solar facade was realized through placement of a higher number of solar panels on the south and west facades in comparison to the east and north facades, with higher-efficiency solar panels at the tilted parts of the solar belt. It additionally brings continuity to the architectural expression of the facade.

Furthermore, the performance of the BIPV/T system in combination with the energy management system was evaluated. During the period in which the energy generation and consumption was measured, it was found that more energy had been generated than consumed. Moreover, the system shows a relatively high self-consumption (average 73%). In comparison, a review of literature (Luthander et al., 2019) indicates that PV systems with a similarly small battery may have an average self-consumption of 60% and systems with demand side management have a self-consumption of 42%. In the RDU, both demand side management and a battery are used, which further helps to increase the self-consumption.

Secondly, the used solar panels allow for customisation and were therefore designed to be fitting to their facade composition and other facade elements. Additionally, the unique shapes of solar panels are standardised in such way that it makes the production process relatively straightforward, while still allowing for a high amount of customisation. This high level within customisation possibilities makes it possible for the solar system to be relatively easily adapted and applied to other buildings within different urban contexts, fitting the principle of universally specific and allowing for application on a large scale.

Lastly, it has been evaluated whether it is possible to integrate BIPV/T in an aesthetically integrated manner from a holistic perspective. By making the solar design an integrated part throughout the entirety of the building design process, it was possible to implement the design guidelines defined by Probst et al. (2007). Due to the close collaboration between students of architecture, engineering and the producer of the PV modules, it has been possible to integrate the solar design in an architectural manner while still having a sufficiently high efficiency due to orientation, placement and colour choice.

By combining the findings on the three different aspects of solar energy efficiency, it was possible to build further on the design guidelines of Probst et al. (2007). The proposed additions are less focused on the aesthetics of integrating BIPV/T and more on the design process to make this integration possible. The following five guidelines are proposed:

1) To make optimal use of the potential for BIPV/T, solar design should be incorporated within the design process from the beginning. As soon as it is conceptualised within the primary design framework, solar design can become an integral part for both the energy system design and architectural building concept. This can greatly benefit rather than limit the overall building concept, the technological performance and its appearance.
2) To foster this integration of solar design into the design process, a multidisciplinary integration between system designers, structural engineers and architects is highly advised. A reciprocal awareness of both aesthetic requirements and technological and production possibilities and limitations of solar systems requires a constant collaboration between producer and designer.
3) Even though novel PV(T) technologies afford many varying and exceptional uses of solar design, it is advised to think about solar integration in a more subtle manner. The aim of BIPV/T is not to create a unique artwork but to embed the renewable technology on a wider scale within its urban context in a delicate matter. This requires nuances in material textures, hues and compositions rather than an expressive exploration of opportunities. As a result, solar technology can visually almost disappear, leading to an enhanced feeling of integration within the urban fabric.
4) In terms of technical performance, integrating solar thermal and photovoltaic installations may be beneficial in residential buildings. In order to achieve a higher self-consumption, energy storage with demand side management could be used.
5) Since the inhabitants may have a significant influence on the energy use of a building, it may be beneficial to have a larger focus on user experience and increasing environmental awareness. Although dependent on the specific user, a physical interface may encourage the occupants to interact with the energy management system.

The findings of the conducted research show how a close collaboration between architect, engineer and solar design company can establish architectural integrability while being realistic about the technical limitations. Moreover, the advantages of improving not only the technological part of the energy system but also its visible appearance is demonstrated. It shows an alternative to the conventional roof PV panels perceived to be a limit in the design of buildings by residents, urban planners and architects. With this, the authors hope that the RDU provides an example of the integration of a solar system in architectural design, it being a start of the systematic implementation of BIPV/T in the design process of buildings. Perceiving BIPV/T as yet another architectural element – such as brick or wood – having its own limitations and opportunities rather than being an unavoidable element to contribute to sustainable housing would increase the immediate implementation of solar systems in buildings. The authors therefore agree with Yang & Athienitis (2016, p. 887): *"*Establishing BIPV/T systems both as a standard architectural concept and as a functional building component replacing conventional claddings, roofing materials, would aid in the widespread use of BIPV/T systems*"*. When applied on a large scale, this could contribute to the acceleration of the global energy system transition.

4.1 Improvements and limitations

This study has taken place in the context of the Solar Decathlon Europe which resulted in certain regulations and limitations to be complied with. Firstly, due to a limit to the capacity of the PV installation (3000 Wp), only the PV modules at the most efficient locations were connected instead of the whole BIPV/T facade and the full energy generation potential of the BIPV/T design could not be tested. Subsequently, the measurement results cannot be used to evaluate the influence of east and west oriented BIPV facades in increasing the energy generation during the morning and evening hours. Additionally, the entire building diverged from the south-west orientation, such that the west facade was slightly oriented towards the South. This likely influenced the energy generation in the evening hours. Finally, the performance of the solar thermal systems could not be evaluated independently since the type of measurements conducted during the contest are not suitable to assess the performance and efficiency of the systems.

The design of the RDU itself also demonstrated certain limitations: due to the combination of an accessible roof and the tilted solar belt, it was necessary to implement a transparent, glass balustrade to transfer sunlight towards the PV cells. This resulted in a considerable carbon footprint due to the excessive amount of glass and aluminium used. Furthermore, the current system of construction led to a significant increase in building time. This was mainly due to a discrepancy between the tessellated solar panels and the conventional substructure design, giving rise to difficulties in placement and levelling. The aesthetic evaluation of residents was neither considered in this study. In addition to these technical and aesthetical limitations, the affordability and viability of the BIPV/T was currently neglected in this study since the aim was to create a functioning prototype.

A consecutive design should consider these wide-ranging issues, and further research is recommended to test the feasibility of flattening the energy peak throughout the day to unite the demand and supply of solar energy. In addition, the BIPV/T implementation and different energy storage options could be studied on a wider scale, such as a neighbourhood. Moreover, to make solar design inherently part of the toolbox for urban architecture, policy changes should accommodate this development. In general, future studies could investigate the optimal balance between aesthetics, customisability and optimisation to develop the rate of adoption of solar design within urban contexts.

5. Acknowledgments

We would like to thank Team VIRTUe (2022) for offering a space where design, building, construction and testing were made possible. Furthermore, we are grateful for the valuable advice of our advisory board (consisting of architectural firms Paul de Ruiter and BiermanHenket, and professors of Eindhoven University of Technology) and the fruitful collaboration with KameleonSolar, Steinfort, AFS Solar, VolkerWessels and Stam + DeKoning.

This research was supported by the Stimuleringsfonds Metropool Regio Eindhoven (proj.nr. ripple), Europees Innovatieprogramma Zuid Nederland (proj.nr. Innovation-space - PROJ.01736), and Impulsregeling S mart E nergy R egios Brabant (proj.nr. ripple) voor innovatie en bedrijvigheid in energie in de gebouwde omgeving voor bedrijven in de provincie Noord-Brabant. Additionally, the research program was subsidised by Eindhoven University of Technology and sponsored by diverse industrial partners.

6. References

Alipour, M., Salim, H., Stewart, R. A., & Sahin, O. (2021). Residential solar photovoltaic adoption behaviour: End-to-end review of theories, methods and approaches. *Renewable Energy*, *170*, 471–486. https://doi.org/10.1016/J.RENENE.2021.01.128

Attoye, D. E., Adekunle, T. O., Aoul, K. A. T., & Ahmed, H. (2018). Building integrated photovoltaic (bipv) adoption: a conceptual communication model for research and market proposals. *ASEE*, 1–7. https://www.researchgate.net/profile/Timothy-Adekunle-3/publication/324809308_Building_Integrated_Photovoltaic_BIPV_Adoption_A_conceptual_Communication_Model_for_Research_and_Market_Proposals/links/5aeb325daca2725dabb692b3/Building-Integrated-Photovoltaic-BIPV-Adoption-A-conceptual-Communication-Model-for-Research-and-Market-Proposals.pdf

Bahaj, A. S., & James, P. A. B. (2007). Urban energy generation: The added value of photovoltaics in social housing. *Renewable and Sustainable Energy Reviews*, *11*(9), 2121–2136. https://doi.org/10.1016/J.RSER.2006.03.007

Bhattacharyya, S. C. (2011). Energy economics: Concepts, issues, markets and governance. In *Energy Economics: Concepts, Issues, Markets and Governance*. Springer London. https://doi.org/10.1007/978-0-85729-268-1/COVER

D'Ambrosio, V., Losasso, M., & Tersigni, E. (2021). Towards the Energy Transition of the Building Stock with BIPV: Innovations, Gaps and Potential Steps for a Widespread Use of Multifunctional PV Components in the Building Envelope. *Sustainability 2021, Vol. 13, Page 12609*, *13*(22), 12609. https://doi.org/10.3390/SU132212609

Douglass, D. B. (2008). *Defining a sustainable aesthetic: a new paradigm for architecture* [University of Southern California]. http://digitallibrary.usc.edu/cdm/ref/collection/p15799coll127/id/52628

Finnegan, S., Jones, C., & Sharples, S. (2018). The embodied CO2e of sustainable energy technologies used in buildings: A review article. *Energy and Buildings*, *181*, 50–61. https://doi.org/10.1016/J.ENBUILD.2018.09.037

Frattolillo, A., Canale, L., Ficco, G., Mastino, C. C., & Dell'Isola, M. (2020). Potential for Building Façade-Integrated Solar Thermal Collectors in a Highly Urbanized Context. *Energies 2020, Vol. 13, Page 5801*, *13*(21), 5801. https://doi.org/10.3390/EN13215801

Heinstein, P., Ballif, C., & Perret-Aebi, L. E. (2013). Building integrated photovoltaics (BIPV): Review, potentials, barriers and myths. *Green*, *3*(2), 125–156. https://doi.org/10.1515/GREEN-2013-0020/MACHINEREADABLECITATION/RIS

IEA. (2021). *Statistics report Key World Energy Statistics 2021*. https://www.iea.org/reports/key-world-energy-statistics-2021

IPCC. (2022). *Climate Change 2022: Mitigation of Climate Change - Summary for Policymakers*.

Kabir, E., Kumar, P., Kumar, S., Adelodun, A. A., & Kim, K. H. (2018). Solar energy: Potential and future prospects. *Renewable and Sustainable Energy Reviews*, *82*, 894–900. https://doi.org/10.1016/J.RSER.2017.09.094

Luthander, R., Nilsson, A. M., Widén, J., & Åberg, M. (2019). Graphical analysis of photovoltaic generation and load matching in buildings: A novel way of studying self-consumption and self-sufficiency. *Applied Energy*, *250*, 748–759. https://doi.org/10.1016/J.APENERGY.2019.05.058

Maghrabie, H. M., Abdelkareem, M. A., Al-Alami, A. H., Ramadan, M., Mushtaha, E., Wilberforce, T., & Olabi, A. G. (2021). State-of-the-Art Technologies for Building-Integrated Photovoltaic Systems. *Buildings 2021, Vol. 11, Page 383*, *11*(9), 383. https://doi.org/10.3390/BUILDINGS11090383

Munari Probst, M. C., & Roecker, C. (2007). Towards an improved architectural quality of building integrated solar thermal systems (BIST). *Solar Energy*, *81*(9), 1104–1116. https://doi.org/10.1016/J.SOLENER.2007.02.009

Munari Probst, M. C., Roecker, C., Schuler, A., & Scartezzini, J. L. (2004). Impact of New Developments on the Integration into Facades of Solar Thermal Collectors. *EuroSun Conference* , 351–357.

Ng, P., Doria, D., Odaibat, B., Fernandez, A., & Karastathi, N. (2022). Decentralised Solar Economy: Unattended and Smart Solar Energy Urban System (UnSSEUS). *Proceedings of the 27th Conference on Computer Aided Architectural Design Research in Asia (CAADRIA) [Volume 2]*, *2*, 759–768. https://doi.org/10.52842/CONF.CAADRIA.2022.2.759

Solar Decathlon Europe. (2022). *Solar Decathlon Europe 21/22*. https://sde21.eu/

United Nations. (2018, May 16). *68% of the world population projected to live in urban areas by 2050, says UN*. https://www.un.org/development/desa/en/news/population/2018-revision-of-world-urbanization-prospects.html

Vasseur, V., & Kemp, R. (2015). The adoption of PV in the Netherlands: A statistical analysis of adoption factors. *Renewable and Sustainable Energy Reviews*, *41*, 483–494. https://doi.org/10.1016/J.RSER.2014.08.020

VIRTUe. (2022). *Team VIRTUe | Eindhoven University of Technology*. https://teamvirtue.nl/

Yang, R. J. (2015). Overcoming technical barriers and risks in the application of building integrated photovoltaics (BIPV): hardware and software strategies. *Automation in Construction*, *51*(C), 92–102. https://doi.org/10.1016/J.AUTCON.2014.12.005

Yang, T., & Athienitis, A. K. (2016). A review of research and developments of building-integrated photovoltaic/thermal (BIPV/T) systems. *Renewable and Sustainable Energy Reviews*, *66*, 886–912. https://doi.org/10.1016/J.RSER.2016.07.011

Evaluating annual solar heat gains from manually operated shading system

Sunil Raghavendher Kumar[1], Niko Gentile[2] and Anton Hendrix[2]

[1] Lund University, Department of Building and Environmental Technologies, Lund (Sweden)

[2] ACC Glas och Fasadkonsult AB, Stockholm (Sweden)

Abstract

Occupant behavior towards manual solar shading systems affects the energy performance of buildings. Behavior depends on several aspects which interact in a nontrivial way. This paper presents a simple prediction model of behavior based on self-reported use of manual shading and a user survey. The specific model is applicable to the case study building, which is an office building in Gothenburg, Sweden, but the approach can be extended to other buildings. The model was tested against a hypothetical automated solar shading system for the same building. The results show that cooling loads increased by at least 25 % with the manual model in respect to the automatic system due to fewer blind movements. The results show that not accounting for occupant behaviour leads to a significative performance gap between predicted and actual building energy use.

Keywords: Occupant behaviour, Shading system, Annual solar heat gains, Prediction model.

1. Introduction

Occupant behavior towards shading systems has a major impact on heating and cooling loads (Hong & Hung-Wen, 2012). Studying behavior towards building systems and their interfaces is not trivial, as it depends on both environmental triggers and psychological processes (Gentile, 2022). While some behavioral models have been proposed for use of shading in respect to environmental triggers, for example LightSwitch-2002 (Reinhart, 2004), occupant actions related to other individual evaluations are not yet fully understood and are currently object of extensive research. As a result, simplified behavioral models are usually adopted by simulation software and a performance gap between simulated and performed energy performance has been often reported (Borgeson and Brager, 2008).

In relation to solar shades, the choice is usually between manual and automatic shading systems. Manual shading systems are often applied because of low installation and maintenance costs; however, it can lead to higher energy use. Automatic shading systems should perform better in respect to energy, but since shadings are generally chosen at late stages of building design (Yao, 2014), integrating shades automation in the building management system is complicated, if not impossible in real projects. In addition, real life projects suggest to to always provide a manual override to automatic shading (Gentile et al., 2022), which increases the uncertainties in real operation performance. Many building simulation programs for dynamic thermal and energy modelling consider the use of manual solar shades deterministically linked to changes in the luminous and/or thermal environment (Newsham, 1994), including incoming radiation on the facade, indoor temperature, glare (Fisekis et al., 2003), or daylight illuminance (Roche, et al, 2000). This approach requires typically the definition of occupancy schedules and set-points for temperature, facade radiation, or indoor lighting (Yao, 2014). Occupant actions on shades, however, are not necessarily completely aligned with the indoor environmental conditions. For example, once shading is lowered, occupants generally do not raise them back even if when the environmental conditions would suggest so (Scorpio et al, 2022). A deterministic approach to occupants' behavior overlooks the complexity of human behavior, which is, in the best of cases, of stochastic nature, see e.g., Reinhart (2004).

In general, occupants act on shading to 1) achieve visual comfort and allow access to view, and to 2) achieve thermal comfort (Katsifaraki, 2019), whereas visual comfort seems to be the main trigger for closing blinds (Van Den Wymelenberg, 2012). In addition, individual factors related to social norms or previous experiences are modulating such actions (Gentile, 2022).

© 2022. The Authors. Published by International Solar Energy Society
Selection and/or peer review under responsibility of Scientific Committee
doi:10.18086/eurosun.2022.01.06 Available at http://proceedings.ises.org

In this article, a model to predict the use of solar shading has been developed. The model uses both environmental information (glare probability, façade radiation) and individual factors to determine the use of shading. Since the individual factors are derived via a survey for a specific case building, the model is applicable as such only to that specific case. However, the approach for deriving the model can be extended to other case study buildings.

The model is then implemented in a simulation software and the energy performance of manual shades is compared to that of an ideal automatic one.

2. Methods

The study consisted of a collection of both technically measured and survey data on the use of shadings for a case study building. The data was used to develop the prediction model. The prediction model was used to test the performance of a daylight and thermal model with a manual shading system, whose operation was based on the prediction model, and an ideal automatic system (Fig. 1).

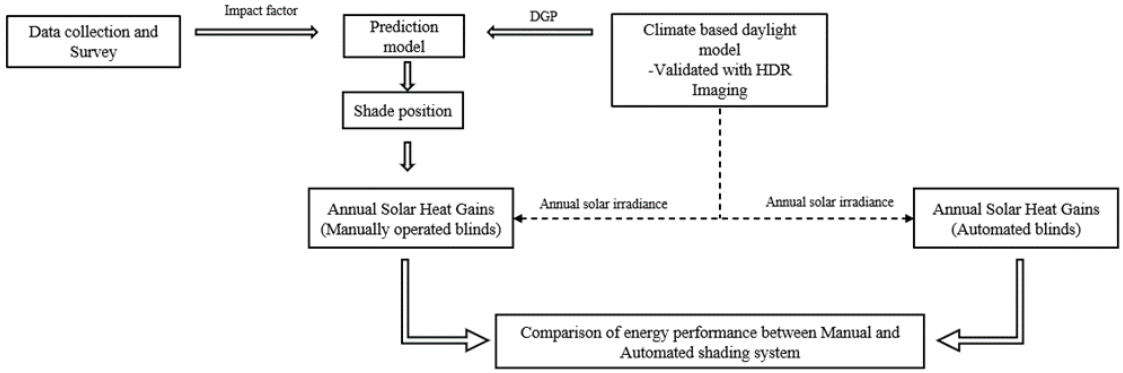

Fig. 1: Sequence of study

2.1 Case study building

The study was carried out on the fourth floor of an office building located located in Gothenburg, Sweden (Fig.2). The building has a window-to-wall ratio of 45 %. The office layout consisted of predominantly landscape offices, and few private offices around the courtyard. All offices are currently equipped with manually operated internal shades. The total heated floor area of the fourth level is 1 916 m^2.

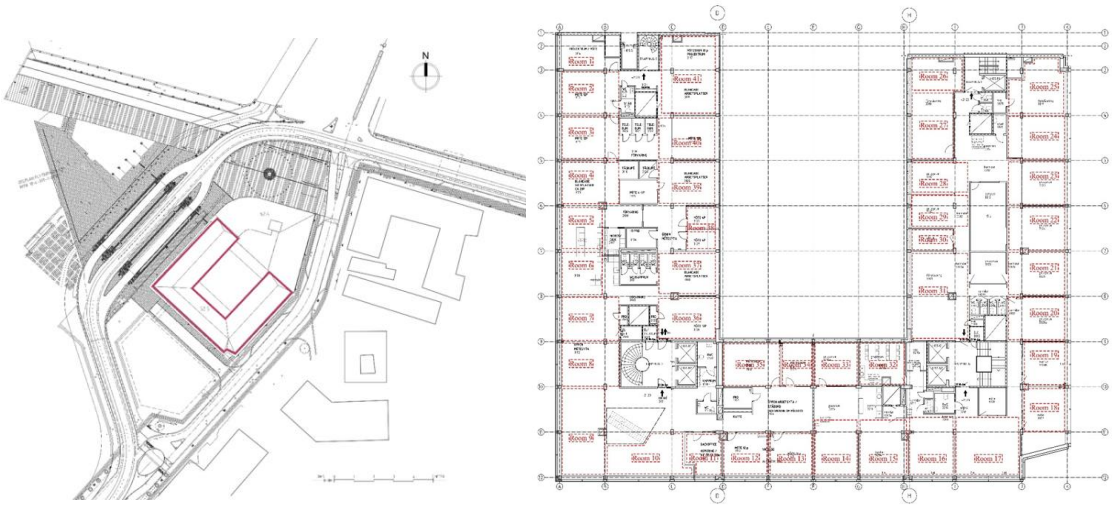

Fig. 2: Map and layout of the case study building

2.2 Existing daylight condition and visual comfort in the office building

A daylight and thermal model were drawn in Rhino. Image based-simulation and both horizontal and vertical illuminance values were validated against the measured data from both HDR images and illuminance meter. Daylight and energy analysis were performed via Honeybee and Ladybug plugins for Grassopper. Grid-based annual lighting simulations without roller blinds and electric lighting were run for the office building.

2.3 Survey and participants

The participants filled in the Lighting-Diary (Maleetipwan-Mattsson et al., 2013), which consist of a self-reported diary where they could log when they operated the solar shades with the approximate position (0% - 25% - 50% - 100% closed). The diary was filled during a week. It gave insights about individual actions on shades that could enrich the usage model based on only environmental predictors (visual and thermal comfort).

Participants were required to fill in a short written longitudinal survey concerning questions about general glare experience at their workplace and their perceived control over the shading system. The survey included open-ended questions and it was administered three times, at the beginning of the months of February, March, and April. On all occasions, there were clear sky conditions in Gothenburg.

2.4 Development and testing of the prediction model

The observations represented the base for the prediction model which is illustrated in Results. The validity of the prediction model was tested by visual documentation of the position of the solar shades in the real building during two specific days, 7th of March and 1st of April 2022, at 09:00, 13:30, and 16:00. The positions recorded in the real building were successfully compared with those predicted by the model.

2.6 Energy performance with the manual and automatic shading systems

2.6.1. Manual solar shading system

The solar shading position of the blinds in the private office rooms and landscape office were determined from the prediction model. Shades in common areas were assumed fully open throughout the year, as this was an outcome from the survey. Solar heat gains were calculated according to equation 1.

$$SHG = I.g.\frac{A_{glass}}{A_{room}} \qquad [W/m^2] \qquad \text{(eq. 1)}$$

Where I is the solar radiation against the glazing system with a solar factor g for the area of glazing A_{glass} in the room of area A_{room}. The g-value considers solar shades. The g-values for intermediate shading states were unknown. In such cases, the solar heat gains were calculated assuming that the shading position is installed on the exterior side of the glazing, reducing the glazed area. Then the solar radiation on the glazing surface was reduced proportionately instead of reducing the g-value of the glazing system with a partially closed shading system.

The Daylight Glare Probability (DGP) was calculated for the different shading states. According to the shading state, annual solar heat gains were later calculated using equation 1. Peak loads were calculated for the hour with the highest solar radiation; in such cases, it was assumed that shades were fully closed.

2.6.2. Automated solar shading system

The automated shading system had a set-point of 150 W/m^2 on the façade, which is a common threshold in northern Europe (Wienold et al, 2011). The automated shading could be either fully open or fully closed. The annual solar heat gains through the automated shading system were calculated based on this control algorithm using equation 1 and later compared with the manual shading system. Peak loads on each room were also calculated based on the same control algorithm.

3. Results

3.1 Daylight and glare analysis

The existing daylight conditions in the building suggest that there is a relative high glare risk in most of perimetral zones of the building. The office area is well daylit, with a DF_{mean} of 4.3 and a DF_{median} of 3.2.

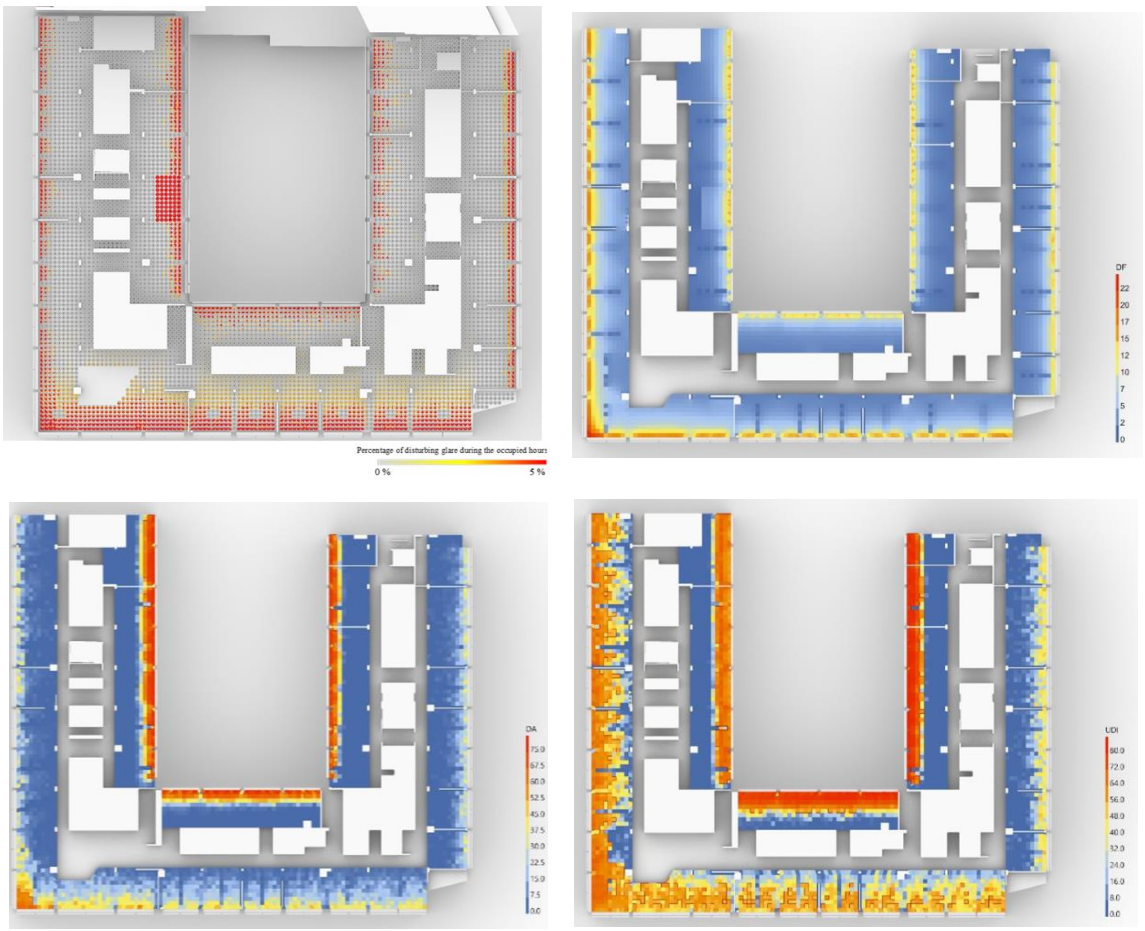

Fig. 3: Top-left to bottom-right: spatial daylight glare probability, daylight factor, daylight autonomy (DA_{300}) and useful daylight illuminance ($UDI_{300\text{-}2000}$) for the fourth floor of the case study building.

3.2 Observations from the survey

A total of 47 employees responded to the survey and filled in the lighting diary, but nine responses were discarded because wrongly filled. All responded were full-time employees who occupied the workspace for at least 30h per week. Among the 38 remaining respondents, 37 % represented employees with sitting desks adjacent to the South-East façade, 34 % to the North-West façade, and the remaining to the South-West façade. 8 % of the respondents had an individual office, 24 % shared the office with a colleague, and the remaining where in the landscape offices. Responded from the individual or two sharing office rooms had windows facing towards the courtyard, while the landscape office had windows facing the exterior. All responded had access to the manual control for at least one window in their workspace.

The survey and diary results confirmed that the occupants control solar shading primarily to avoid glare according (86 % of respondents). When glare was occasional and not persisting, the occupants first tended to adapt to the situation by moving the monitor slightly. Shadings were not operated unless it was impossible to avoid reflections on the screen after reasonable adjustments of its position. If glare persisted for longer periods, then occupants would operate the shading. Only 21 % of the recorded solar shading states included fully closed position, while shading was closed only to the extent that this protected from glare source. According to the survey, the occupants did so to keep high daylight and view out. Most of solar shading movements were recorded at the beginning and end of the day, with solar disc in the field of view for the more East and West oriented façade. Blinds were 50 % to 100% closed during the morning and at the end of a workday for 79 % and 51 % of the respondents, respectively. The shadings were open or at most 25 % closed at other times.

Occupants experiencing glare in the afternoon were likely to leave the shades in the same state until the next day morning. Almost all respondents (91 %) did not change the shading position before leaving the office at the end of a workday. Employees sitting next to the windows were twice as likely to operate the shading than other

employees. Those having control over the shading system were also more satisfied than the other employees in respect to the daylight conditions and solar shading system in the space.

3.3 Development of prediction model

Since glare appeared to be the main driver for shading operation, the prediction model was based entirely on visual comfort. The model includes reflections on screens. The shading state is derived by the information provided by the survey (Fig. 4). Glare is assessed by mean of DGP with threshold DGP ≥ 0.35. Screen reflection is accounted in a simplified way, i.e., if DGP ≥ 0.45 for the field of view opposite to the screen, then there should be a high luminous source which can cause reflection on the screen. The developed prediction model accounts for the reported individual behavior, but it is of deterministic nature.

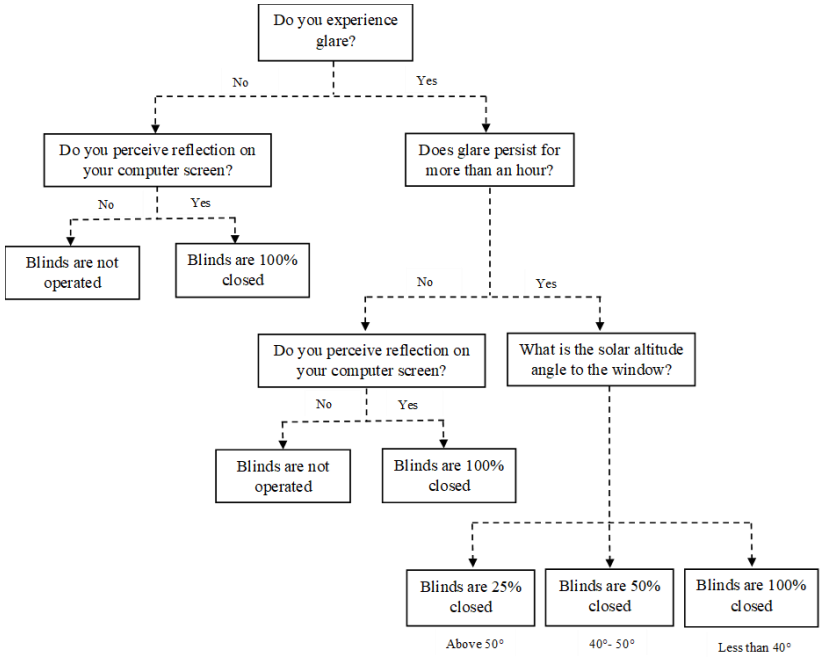

Fig. 4: The prediction model for operation of manual shades for the case study building.

When tested against the actual shade positions, 10 % of the solar shades were in a different state than the predicted position with respect to the total number of solar shades in the fourth level of the building, mainly on the South-West and North-West facades. The South-East façade towards the courtyard and the North-West façade to the exterior showed minimum to no deviation between actual and predicted position. The shading positions recorded at 13:30 had the highest deviation from the prediction model on both test days (17-19 % of difference).

3.5 Blind movements

Blind Use Frequency (BUF) and the Number of Blind Movements (NBM) were used to describe the use of blinds. BUF represents the hours in which at least one blind on the façade of the fourth floor is changed from the previous position to the new position (partly or entirely). BUF does not consider the number of shading devices that are used at a given time. NBM represents the ratio of the total number of blind movements per hour to the total number of blinds moved in the day with respect to an automated shading system.

The automated mode was much more responsive to changes in the weather conditions (Figure 5). Differences are higher during the summertime, mainly due to the irradiation set point since the prediction model is based on visual comfort only. Differences are less marked during the winter, when even the manual mode responds to low sun angles, causing glare and triggering use of shades. Similar considerations apply to NBM (Figure 6).

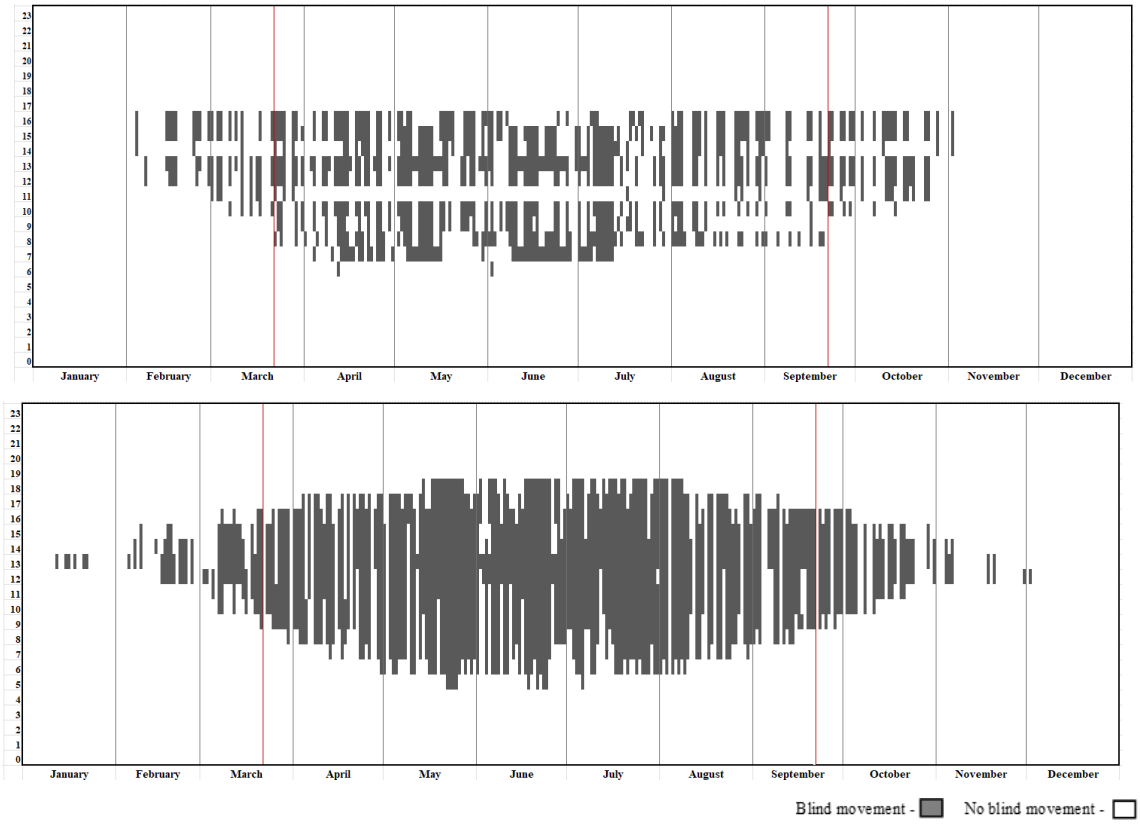

Fig. 5: BUF for the manual (above) and automated (below) modes of the solar shading. The red lines delimit the cooling period, assumed to be between the two equinoxes.

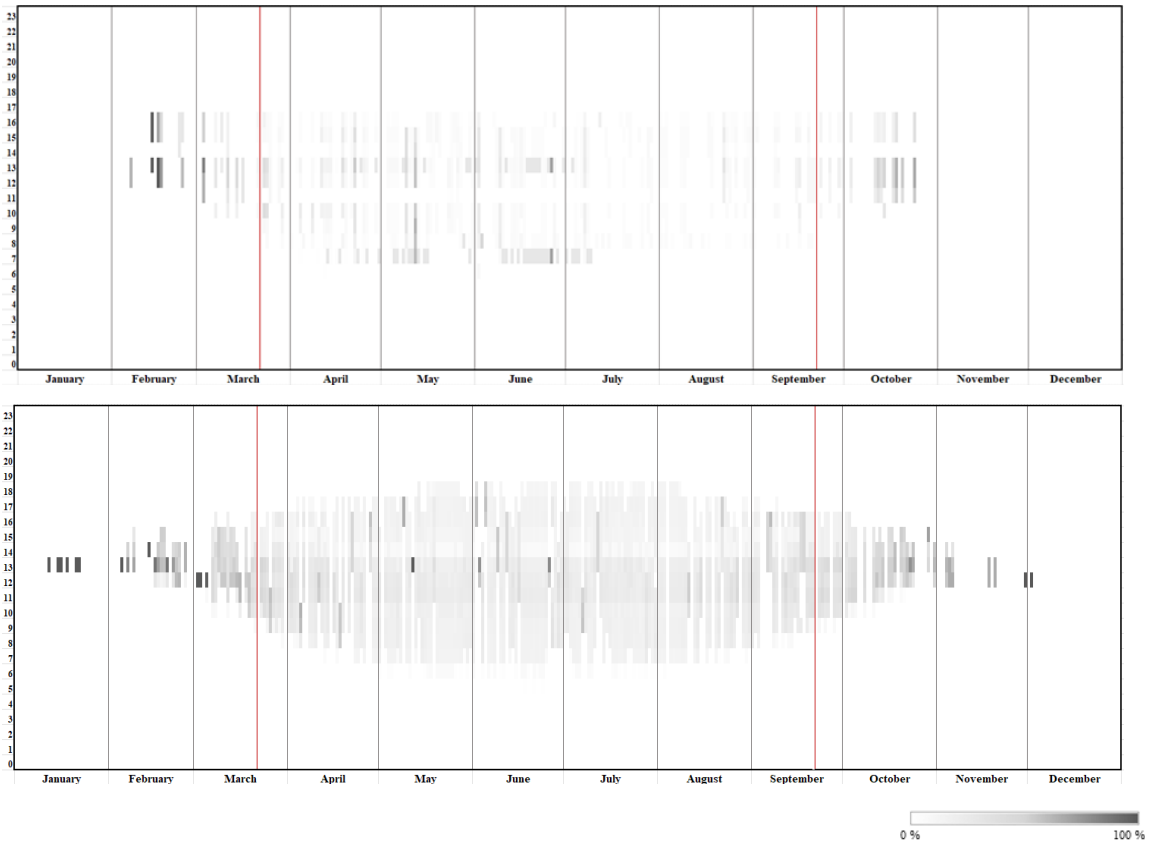

Fig. 6: NBM for the manual (above) and automated (below) modes of the solar shading. The red lines delimit the cooling period, assumed to be between the two equinoxes.

3.6 Annual solar heat gains

The annual solar heat gains for the manually operated shading system as from the prediction model were 22 % higher than that of the automated shading system, accounting for 764 kWh/m^2/year and 626 kWh/m^2/year, respectively. This is mainly explained by the unresponsiveness to solar radiation of the developed model. Winter solar gains were 9 % higher for the manually mode (118 kWh/m^2 vs 108 kWh/m^2), which is positive in energy performance perspective. Summer solar gains were 25 % higher for the manually mode (646 kWh/m^2 and 518 kWh/m^2), which is instead negative in energy performance perspective.

The prediction model failed to reduce peak loads. According to the model, only 17 % the shadings were in fully closed position during peak radiation.

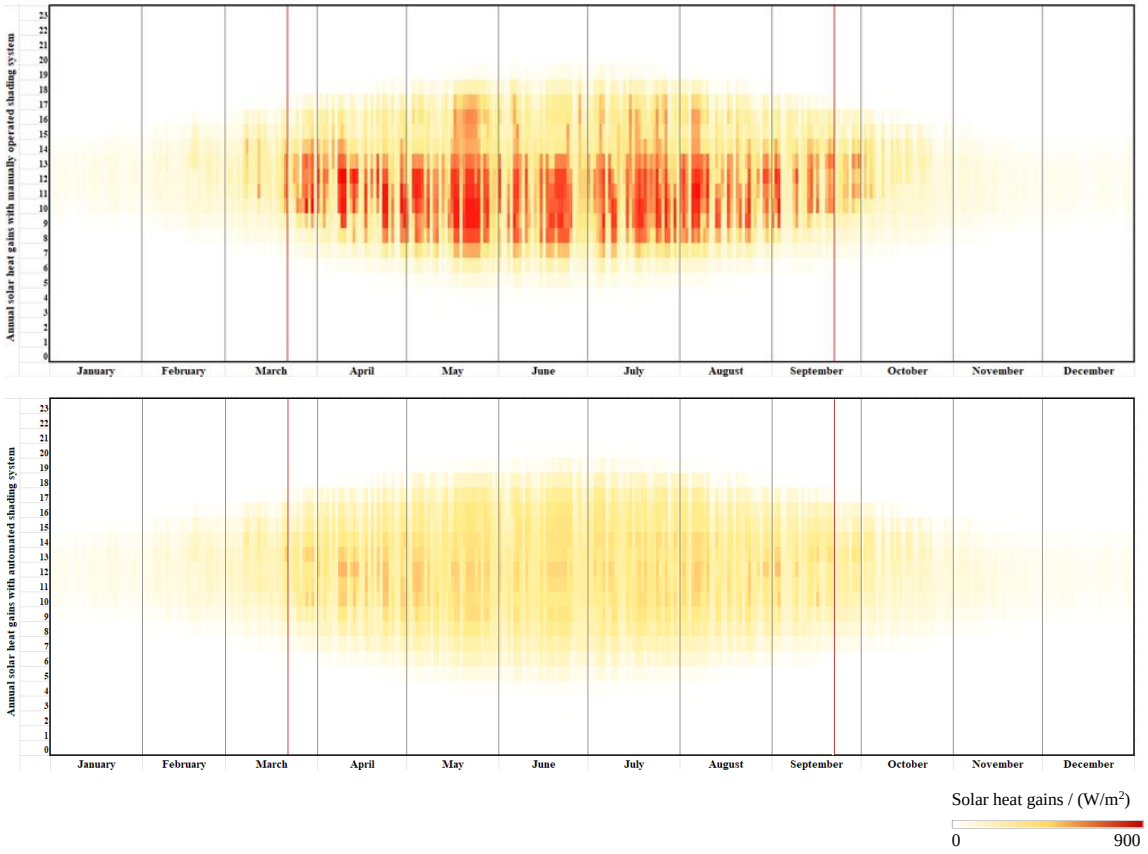

Fig. 7: Annual solar heat gains for the manual (above) and automated (below) modes.

4. Discussion and Limitations

The core of the study, which is the development of the predictive model, showed that behavior towards shading is not trivial. The survey allowed us to understand that, at least for the case study building, action depends largely on visual comfort. However, it is still questionable whether our specific prediction model would be largely or in part applicable to other case study buildings or even to the same case study building during the whole year.

In fact, the observations were carried out during the spring months, when visual discomfort is more likely to occur at north latitudes due to low sun angle, and thermal discomfort is less likely to occur due to weather conditions. Thus, the survey may have led to a model which overweighted visual discomfort and underweighted thermal discomfort. This hypothesis sounds reasonable when looking at the wide differences of BUF and NBM between the model-based manual mode and the automatic one.

During the spring months, however, the model proved reliable. This suggests that the approach for building the model - survey information combined with set-points for environmental cues – can be tested for further and extended to longer periods and situations.

The model led to higher energy use in respect to automatic shades. Such result was expected as automatic systems

are explicitly designed to maximize energy savings. It is however unknown if such automatic systems would be generally appreciated by the occupants; low appreciation may lead to frequent overriding and even sabotage, as shown in other research. Also, the relatively big difference in measured solar heat gains between the two control modes – manual and automatic – might be largely explained by the model construction.

The model comes with further limitations in its current form. Among them, two main issues can be mentioned. First, screen reflection was deemed important for shading operation, but this is yet computed in an extremely simplified way, i.e., via luminance mapping of the field of view in front of the screen. Reflection can also be caused in other instances due to highly reflective material in and around the office or by neighbouring buildings which are difficult. The measure of tolerable and intolerable reflections on the monitor are also very individual. Second, and somewhat linked to the "individuality" of what is tolerable or not, the model is deterministic, since the limited number of subject and the time of observation did not allow to built probability curve that would have been useful to add a stochasticity layer to the model.

5. Conclusion

In this study, a prediction model for shade position was illustrated. The model was based on survey responses, and it used visual comfort as the only predictor for action on shading. The model was found to predict well the actual operation during three test days in spring. The following can be concluded:

- Minimizing visual discomfort was the major driving factor for the occupants to control the shading system.
- Occupants also adapt to the environmental conditions to a certain degree and delay the operation of the shading system.
- Visual discomfort and glare can be reduced significantly even when the solar shading is at a partially open/close state.
- A comparison with automatic mode of shading control revealed a better energy performance of the latter, mainly due to more automatic adjustments of shadings during summertime.
- Blind movements are significantly higher in an automated shading system when compared to a manually operated shading system.
- Occupant behavior on manually operated shading systems causes a negative impact on the building cooling load in comparison to automated shading systems.

The simplifications done in the study method limit the applicability of the results, but they still suggest a relevant impact of occupant behavior on manually operated solar shading devices.

6. Acknowledgments

The authors wish to acknowledge the employees that agreed to be part of the study. The first author acknowledges that ACC Glass and Facades consultants for the support provided during the study.

7. References

Borgeson, S., & Brager, G., 2008. Occupant control of windows: accounting for human behavior in building simulation. A report of Center for the Built Environment (CBE), University of California, Berkeley.

Fisekis, K., Davies, M., Kolokotroni, M., & Langford, P., 2003. Prediction of discomfort glare from windows. Lighting Research & Technology, 35(4), 360-369. https://doi.org/10.1191/1365782803li095oa

Gentile, N., 2022. Improving lighting energy efficiency through user response. Energy and Buildings, vol. 263, 112022. https://doi.org/10.1016/j.enbuild.2022.112022

Gentile, N., Lee, E. S., Osterhaus, W., Altomonte, S., Naves David Amorim, C., Ciampi, G., Garcia-Hansen, V., Maskarenji, M., Scorpio, M., & Sibilio, S., 2022. Evaluation of integrated daylighting and electric lighting design projects: Lessons learned from international case studies. Energy and Buildings, 268, [112191].

https://doi.org/10.1016/j.enbuild.2022.112191

Hong, T., Hung-Wen, L., 2012. Occupant Behavior: impact on energy use of private offices, *ASim 2012 - 1st Asia conference of International Building Performance Simulation Association*, Shangai, China.

Katsifaraki, A., 2019. Development and evaluation of a simulation-based adaptive shading control for complex fenestration systems. PhD Dissertation, Technische Universitaet Berlin (Germany). http://dx.doi.org/10.14279/depositonce-8327

Maleetipwan-Mattsson, P., Laike, T., & Johansson, M., 2013. Self-report diary: A method to measure use of office lighting. Leukos, 9(4), 291-306. https://doi.org/10.1582/LEUKOS.2013.09.04.004

Newsham, G. R., 1994. Manual control of window blinds and electric lighting: implications for comfort and energy consumption. Indoor Environment, 3(3), 135-144. https://doi.org/10.1177/1420326X9400300307

Reinhart, C. F. (2004). Lightswitch-2002: a model for manual and automated control of electric lighting and blinds. Solar energy, 77(1), 15-28. https://doi.org/10.1016/j.solener.2004.04.003

Roche, L., Dewey, E., & Littlefair, P., 2000. Occupant reactions to daylight in offices. Lighting Research and Technology, 32(3), 119-126. https://doi.org/10.1177/096032710003200303

Scorpio, M, Ciampi, G, Gentile, N & Sibilio, S 2022, Effectiveness of low-cost non-invasive solutions for daylight and electric lighting integration to improve energy efficiency in historical buildings, Energy and Buildings, vol. 270. https://doi.org/10.1016/j.enbuild.2022.112281

Van Den Wymelenberg, K., 2012. Patterns of occupant interaction with window blinds: A literature review. Energy and buildings, 51, 165-176. https://doi.org/10.1016/j.enbuild.2012.05.008

Wienold, J., Frontini, F., Herkel, S., & Mende, S., 2011. *Climate based simulation of different shading device systems for comfort and energy demand*. In Proceedings of Building Simulation 2011: 12th Conference of International Building Performance Simulation Association, Sydney, 14-16 November, pp. 2680-2687.

Yao, J., 2014. Determining the energy performance of manually controlled solar shades: A stochastic model based co-simulation analysis. Applied Energy, 127, 64-80. https://doi.org/10.1016/j.apenergy.2014.04.046

Sustainable Housing Insulation for High-altitude Kyrgyzstan: A Technical Guide

Kedar Mehta, Jakob Beringer, Mathias Ehrenwirth, Christoph Trinkl and Wilfried Zörner

Institute of new Energy Systems (InES), Technische Hochschule Ingolstadt, Germany

Abstract

Kyrgyzstan – a high-altitude and cold climatic Central Asian country, suffers from high residential energy consumption, especially in the rural housing sector. Due to the age of the building stock as well as lack of insulation, the energy consumption of Kyrgyz buildings is 3 to 5 times higher compared to European buildings. The implementation of thermal insulation is considered one of the potential measures for energy conservation. However, the local boundary conditions (especially low-income, remote locations, and lack of knowledge and awareness) do not allow local people to consider the insulation measures. There is a lack of scientific knowledge available about sustainable insulation of high-altitude rural Kyrgyz houses. Against this background, the presented research article provides comprehensive scientific information on sustainable housing insulation for high-altitude Kyrgyzstan. The research was carried out on three key dimensions; why (use insulation), which (insulation to use), and how (to use insulation) theoretically and technically. The necessary data was composed of the author's stay on site and literature review. Based on the three main research questions, why, how, and which, the article formulates a complete technical guide for sustainable insulation housing in high-altitude Kyrgyzstan.

Keywords: energy efficient house, high-altitude, sustainable, thermal insulation, cold climate, space heating

1. Introduction

1.1 Setting the scene: high-altitude rural Kyrgyz houses

The residential sector of Kyrgyzstan is considered the highest energy consumption among Central Asian countries. This is due to the existing housing conditions, lack of building insulation, and the age of the building stock. Due to the cold weather conditions, a typical Kyrgyz household spends a high portion (almost half of the income) of its budget on energy expenses (i.e., space heating). Eventually, this results in low thermal comfort and high energy consumption. This situation is very critical for high-altitude rural houses because more than 50% of rural houses were built from earthen materials during the Soviet era more than 30-50 years ago without proper building construction techniques and insulation dimensions (Mehta et al., 2021). These buildings are now in obsolete condition and do not provide minimum hygienic and comfortable living conditions. Fig. 1 represents the total final energy consumption by sectors in Central Asia and the residential buildings construction year to provide a full picture to the reader of the issue. This is expected to remain high unless the need for greater energy efficiency is fully realized and given due consideration during building construction and renovation.

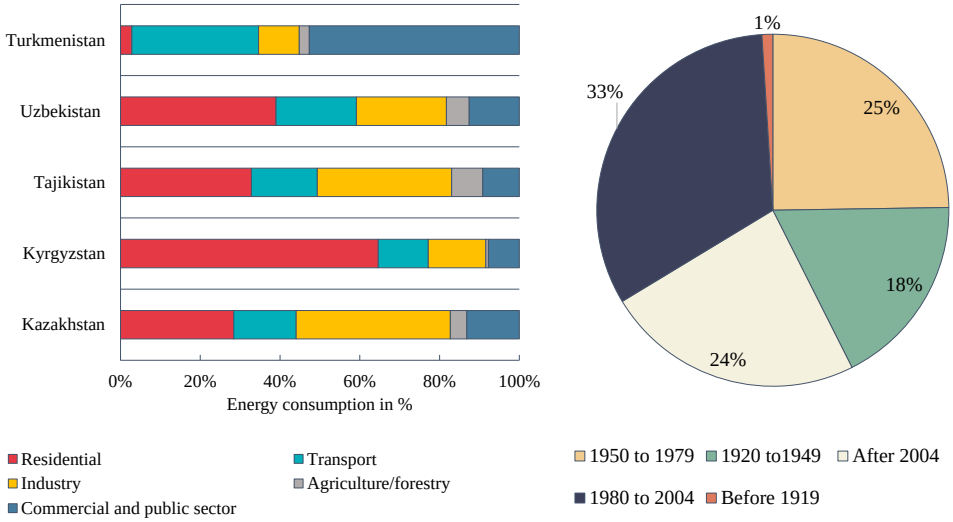

Fig. 1: Total final energy consumption by sectors in Central Asia based on International Energy Agency (left) and Residential buildings construction year in Kyrgyzstan (right) based on International Energy Charter (2018)

© 2022. The Authors. Published by International Solar Energy Society
Selection and/or peer review under responsibility of Scientific Committee
doi:10.18086/eurosun.2022.01.07 Available at http://proceedings.ises.org

From the field visit, it was identified that a typical rural house has natural walls with a thickness of 0.35 m to 0.50 m without any insulation. The uninsulated earthen floor is constructed with wooden beams and floorboard with a total thickness of 0.20 m to 0.40 m. Similar to the floor, the ceiling consists of a wooden beam structure and open space under the roof. Further to this, the installed windows in the houses were mostly cracked and exposed to air leakages. This typical building profile is partially applicable to most rural communities as families assist each other with house construction and transfer knowledge of building styles. Therefore, the housing profile in most rural communities is relatively homogeneous in Kyrgyzstan (Mehta et al., 2020).

The literature review identified that the energy use per square meter of Kyrgyz households is almost 3-5 times higher as compared to European homes. The annual heating energy consumption of Kyrgyz buildings varies between 320 and 690 kWh/m^2/year. Because of the mountainous and high-altitude characteristics, Kyrgyzstan's climate is characterised as sharp continental with a long and harsh winter (-20 to -30 °C in the mountainous areas). The cold and extended winter in the country defines house heating as a primary need for Kyrgyz people. Due to the remote location and low population density, high-altitude rural Kyrgyz houses are generally not connected with modern energy services to meet the primary energy need, which is space heating in this case (Mehta et al., 2020). The absence of modern energy services forced local people to extract their energy needs from the local surroundings. Fig. 2 represents typical high-altitude rural Kyrgyz houses.



Fig. 2: Typical rural residential / family houses in high-altitude Kyrgyzstan (Source: Author)

To maintain thermal comfort, local rural people use traditional heating stoves operated with solid fuels during the winter months. Currently, the thermal comfort in Kyrgyz households is not that high compared to other global regions. Most rural houses in Kyrgyzstan are simple buildings typically constructed with soil, clay-straw, or adobe without any insulation parameters and resulting in low thermal comfort inside the building. The most relevant reason for this high demand is the lack of insulation in most rural Kyrgyz houses (Beringer et al., 2021b). The current buildings in rural Kyrgyzstan are often poorly insulated, which results in a high heat flow rate out of the building (c.f. Fig. 3).



Fig. 3: Thermography of a typical rural house

1.2 Sustainable and environmental challenges

Mehta et al. (2021) identified that the average rural Kyrgyz family needs to employ 2–6 tons of coal (cost ~50–250 €), 1.5–3 m^3 of firewood (cost ~5–30 €), and 1–2 truckloads of cow dung (most of the time self-prepared, but in case they outsource, it costs ~5–10 €) for house heating. The overconsumption of non-sustainable solid fuels significantly contributes to the production of indoor and outdoor air pollution. According to Brakema et al. (2019), the high-altitude rural settlements in Kyrgyzstan are particularly vulnerable to Chronic Obstructive Pulmonary Disease

(COPD) and significantly experience respiratory issues because of the housed air pollution. Also, the available widespread forest cover (i.e., riparian forests) is often exploited to fulfill the energy need of rural people. The burden on local forest cover for wood leads to a negative impact on the riparian forests in Kyrgyzstan. This is an alarming thing as the absence of energy efficiency is directly or indirectly connected with the ecology and climate change in the country (Lauermann et al., 2020).

2. The need of research and research methodology

2.1 The need for sustainable housing insulation

Such high heat demand is expected to remain the same unless the implementation of energy efficiency is fully realized. Hence, the application of insulation is one of the most promising solutions to overcome this problem. The implementation of building energy efficiency can help to reduce the existing residential heat demand by 50-70% (Mehta et al., 2020). However, due to the geographical isolation (i.e. distance from the major economic centres), modern building materials are costly and rarely available for the rural population. This is the same for the insulation materials. Besides availability, affordability is the key concern for the high-altitude rural population. Many rural households, especially in mountainous areas, do not have a permanent source of income because job opportunities are often scarce. Due to unstable income sources and low-income scenario in rural Kyrgyzstan, the application of thermal insulation to their homes is not considered practical for most rural households. Therefore, there is an urgent need to identify insulation solutions that should be sustainable, affordable and locally obtainable by considering the local assessment (especially the different rural house design). To our knowledge, there is no study made available to the scientific community that articulates the thematic and technical knowledge about sustainable insulation for high-altitude Kyrgyz houses.

2.2 Research methodology

To provide a complete guide on sustainable insulation for high-altitude Kyrgyzstan, methodically, the presented research article investigated three key dimensions; why (use insulation), which (insulation to use) and how (to use insulation) theoretically and technically. By these three key pillars, the study provides a comprehensive and comparative analysis of the conventional materials (extruded polystyrene, polyurethane foam), sustainable materials (sheep wool, reed, straw) and concept insulation materials (composites of more than one material, which are currently in development). All types of available materials in Kyrgyzstan were evaluated on their thermal, chemical and physical properties. However, the main aim of the paper is to develop theoretical knowledge and provide scientific knowledge only about available sustainable insulation materials. Fig. 4 shows a graphical representation of the research methodology.

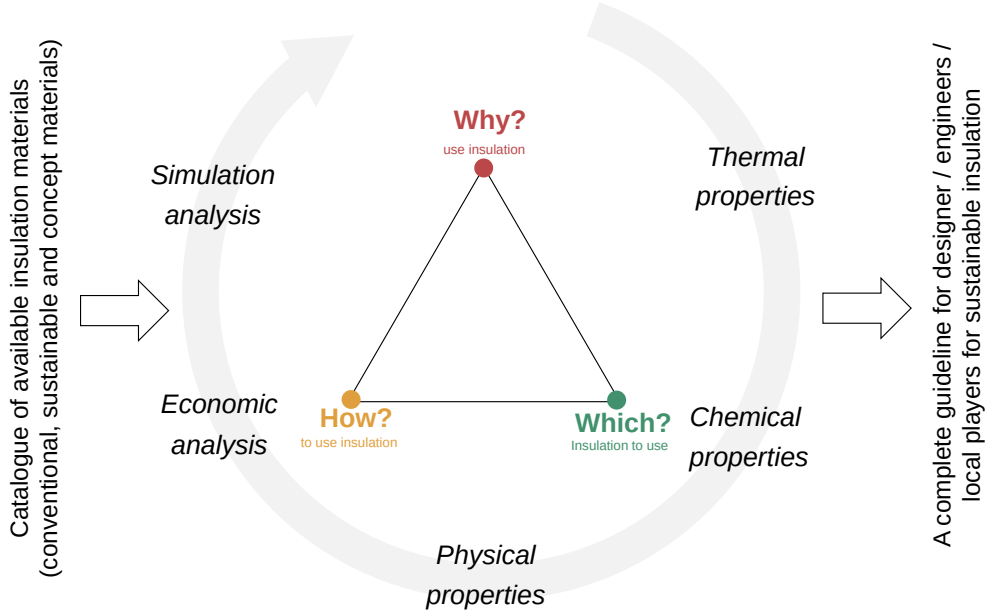

Fig. 4: Research methodology for proposed research article

Therefore, in order to investigate the technical performance and affordability of such sustainable materials, a detailed technical parametric study was performed for the two predominately types of rural Kyrgyz houses. The data / information required for the presented research was collected from the author's visit to the site and the literature review.

3. Catalogue of available insulation materials in Kyrgyzstan

Thermal insulation materials (from now on insulation materials as this study deals only with materials whose main purpose is to reduce heat flux) investigated in this study are divided into three groups. These groups are non-sustainable materials, sustainable materials, and concept materials. Fig. 5 classifies the available insulation materials (as well considered in the presented study) in Kyrgyzstan.

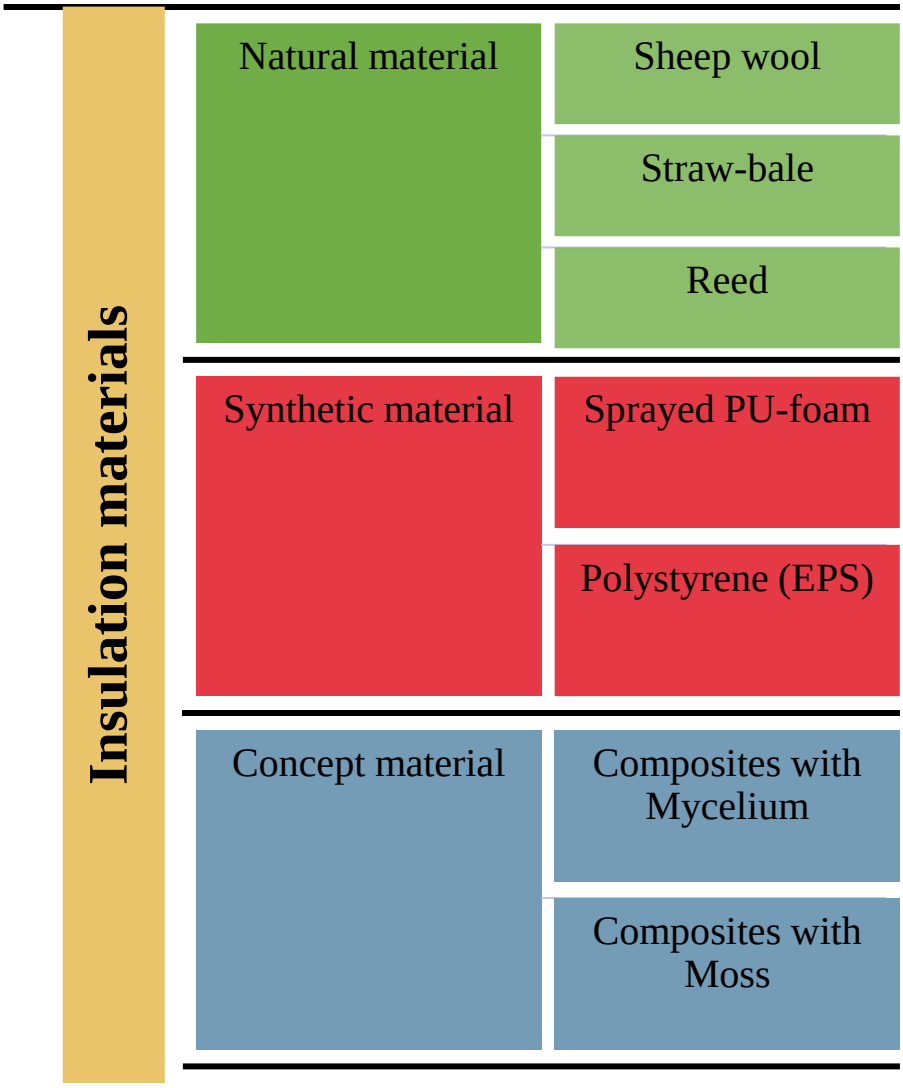

Fig. 5: Classification od insulation materials used in the presented study

To guarantee comparability between the different classes, the parameters used to analyse the materials are always identical. In that need, the presented chapter reports the parameters which are usually relevant when selecting the suitable material for insulation (thermal conductivity, density, specific heat capacity, acoustic properties, typical moisture content, compression strength, fire resistance, costs for raw material, and costs for finished material). Through an extensive literature review and market survey, Tab. 1 offers a comprehensive overview of available materials and their respective properties. It also estimates the material costs, which may vary as the construction and insulation market in Kyrgyzstan is not always stable. Raw material costs, such as those for straw from fields, can sometimes be difficult to evaluate or may not be applicable to non-sustainable materials that rely on crude oil and other chemicals that are only available in their finished form. The cost of finished materials is even more important,

as it indicates the cost of the insulation material used in the house. However, the cost of installation is not included in this estimation, as it was calculated separately in the study. The costs are given in €/kg or €/m^3 (by using density for calculation). This is relevant as different thicknesses cause different quantity requirements.

Tab. 1: Catalogue of available insulation materials in Kyrgyzstan with various properties

	Polystyrene	**Sprayed PU-foam**	**Sheep wool**	**Straw bale**	**Reed**	**Composites with Mycelium**	**Composites with Moss**
Thermal conductivity in W/(m·K)	0.034 (Penoplex Ltd., 2021)	0.022-0.05 (BASF, 2019; Plag, 2022)	0.033-0.049 (Zach et al., 2012; Ruchti and Sägesser, 2021)	0.038-0.2 (Beck et al., 2004; Cascone et al., 2019);	0.045-0.065 (Keskküla et al., 2020; Plag, 2022);	0.078-0.104 (Xing et al., 2018; Dias et al., 2021)	0.044-0.046 (Bakatovich and Gaspar, 2019)
Density in kg/m^3	25-32 (WikiBath, 2020)	70 (Plag, 2022)	20-40 (Zach et al., 2012; Ruchti and Sägesser, 2021; Plag, 2022)	50-150 (Ashour et al., 2011; Cascone et al., 2019)	130-225 (Keskküla et al., 2020)	57-99 (Elsacker et al., 2019)	156-190 (Bakatovich and Gaspar, 2019)
Specific heat capacity in kJ/(kg·K)	1.3-1.7 (Vo et al., 2011)	1.5 (Plag, 2022)	1.7 (Plag, 2022)	0.6-2.1 (Asdrubali et al., 2015; Plag, 2022)	1.2 (Asdrubali et al., 2015)	0.4 (Xing et al., 2018)	N/A
Acoustics -NRC (acc. to Tiuc et al. (2016))	0.26 (Sokol, 2019)	0.28 (Tiuc et al., 2016)	0.45 (Borlea Mureşan et al., 2020)	insufficient (Cascone et al., 2019)	~ 0.4 (Oldham et al., 2011)	N/A	N/A

Moisture content	0.03-9 % (Jones et al., 2020; Penoplex Ltd., 2021)	0.01-72% (Jones et al., 2020)	20-25 % (Zach et al., 2012)	11 % (Ashour et al., 2011; Cascone et al., 2019)	N/A	40-580 % (Jones et al., 2020)	N/A
Compression strength in MPa	0.15 (Penoplex Ltd., 2021)	0.20 (BASF, 2019)	N/A	1.6-6.1 (Musa and Mohammed, 2015)	N/A	0.17-1.1 (Jones et al., 2020);	0.2 (Bakatovich and Gaspar, 2019)
Costs for raw materials in €/kg	N/A	N/A	2.3-3.5 (Tuzcu, 2007; Corscadden et al., 2014)	<< 0.20	0.11 – 0.19 (CEEBA, 2011)	0.06-0.15 (Jones et al., 2020)	N/A
Costs for finished material in €/kg	12.78 (Dom Penoplex LLC, 2021)	1 (Riman company, 2021)	12.46 (Corscadden et al., 2014)	< 0.20 (Kudryavtseva, 2014)	N/A	N/A	N/A
Costs for finished material in €/m^3	358 (Dom Penoplex LLC, 2021)	70 (Riman company, 2021)	436	20	0.45-25 (CEEBA, 2011)	N/A	N/A

4. Calculation of total insulation material cost

The aim of this section is to find the most economically reasonable quantity of sustainable thermal insulation for a rural building in Kyrgyzstan. All prices given in this chapter are aimed for the Kyrgyz market and thus, are not valid for a general statement. One can read the author's previous work Beringer et al. (2021a) to get more details about sustainable insulation materials in rural Kyrgyzstan. It is important to get the overall material cost (including installation cost) to get a full picture of housing insulation. Tab. 1 shows numbers for material cost in m^3 (last column)

without any installation efforts. However, depending on the thickness of the insulation layer, the required material (quantity) will be varied. The calculation is displayed in eq.1.

$$Total\ material\ costs\ (in\ €) = Total\ wall\ area\ (in\ m^2) \times Insulation\ layer\ thickness\ (in\ m)\ x\ cost\ for\ finished\ material (in \frac{€}{m^3}) \quad \text{eq. 1}$$

Installation costs, the second component in economic feasibility calculations, are difficult to evaluate due to their dependence on individual cases, as well as the wide variation in transportation and personnel costs based on settlement location. However, these costs are not heavily influenced by the thickness of the insulation layer, as most processing steps are consistent regardless of thickness **e**q. 2 displays the calculation, and Tab**.** 2 provides generalized installation costs for different materials.

$$Total\ installation\ costs\ (in\ €) = Total\ wall\ area\ (in\ m^2) \times Installation\ costs\ (in \frac{€}{m^2}) \quad \text{eq. 2}$$

Tab. 2: Overview of estimation of the installation costs for insulation in Kyrgyzstan

Material		Installation costs for the wall in €/m²	Installation costs for the ceiling in €/m²	How to install?
Conventional	Extruded polystyrene	8	6	Can easily be glued on a brick structure
	Polyurethane foam	6	5	Can easily be sprayed on brick structure (Riman company, 2021)
Sustainable	Sheep wool	15	6	With spcial construction applicable on wall (i.e. sheep wool, holidg structure)
	Straw bale	12	6	With spcial construction applicable on wall (i.e. straw bale, holidg structure)
	Reed	12	6	Similar to straw bale
Composite	Mushroom and plant	Not applicable as no large-scale installations were performed so far; this does not allow any calculations of break-even point		
	Moss			

5. Special focus on sustainable insulation structure

5.1. Availability of insulation materials to rural Kyrgyz population

This section will provide a detailed explanation about which insulation rural houses should use for better and more affordable energy efficiency. From the literature review, discussion with the construction agency and market survey, it was identified that conventional materials are common and accepted in urban areas (especially in Bishkek). The majority of the conventional material is imported from the neighboring countries to Kyrgyzstan (c.f. Fig 6). That has a huge influence on the cost (c.f. Tab.1). If one needs to order that material to rural areas, that could be even more costly as the price will be increased due to the material transportation to the remote / isolated community location. Hence, conventional materials are rarely used in rural areas.

Additionally, the literature review showed minimal use of composite materials in Kyrgyzstan. Given the limited availability and high cost of conventional insulation materials, rural Kyrgyz households do not usually use them. Hence, this article provides technical and scientific information on affordable insulation materials that are locally available to the rural population.

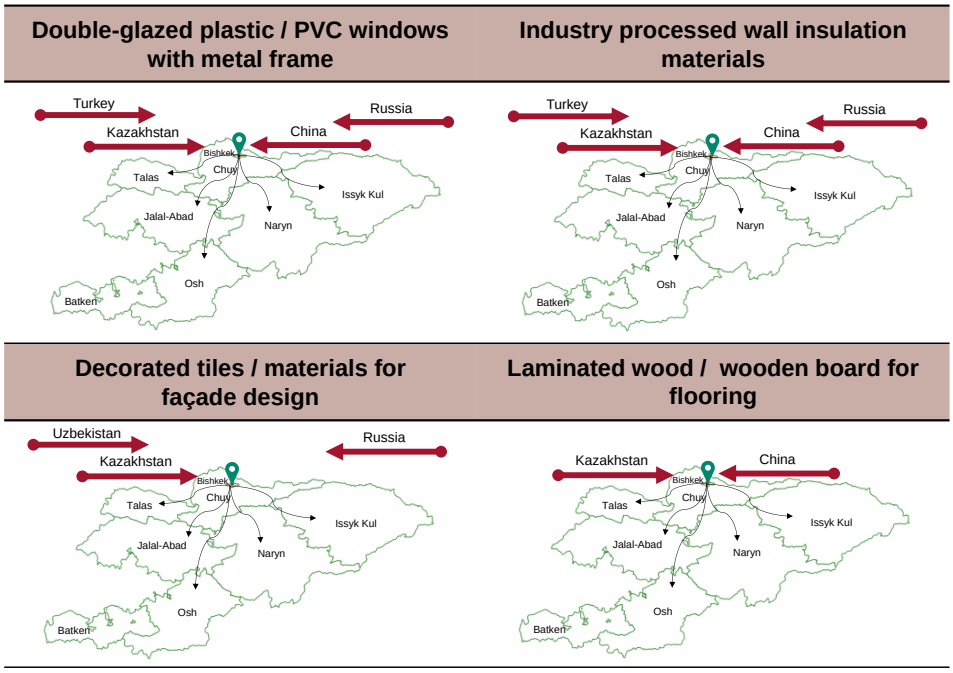

Fig. 6: Supply chain of the conventional insulation materials based on the market survey

5.2 Simulation model development

From the field visit, it was identified that there are two different types of houses available in typical rural Kyrgyz communities; 1) Open roof houses and 2) Closed roof houses.

Open roof house:

Generally, in such houses, the metal roof is placed on the wooden beam ceiling. Mehta et al (2020) mentioned that the open roof house is a very common and predominant practice in rural Kyrgyzstan due to a lack of knowledge and lack of income. The open space induces a considerable amount of heat loss during windy days. Naturally, such a house has a high heat demand.

Closed roof house:

Closed roof houses are similar to open roof houses when it comes to construction work. However, as the name suggested, in these houses, the roof is ideally closed or covered with the help of metal sheets from both ends in order to prevent the wind from passing through it.

Tab. 3: Illustration of two different house models with the range of space heating demand

Open roof house	Closed roof house
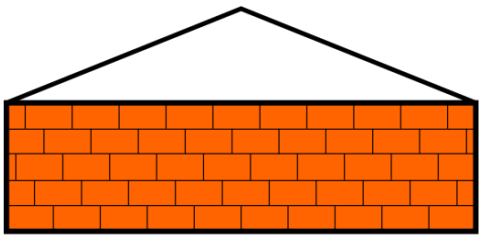	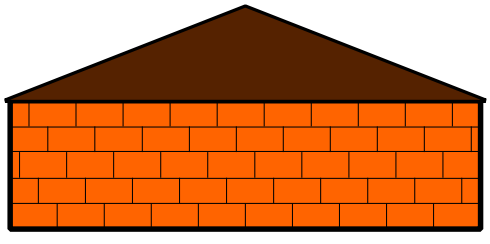
Range of annual specific heat demand 250 – 330 kWh/m^2	Range of annual specific heat demand 210 – 270 kWh/m^2

EnergyPlus employs a heat balance algorithm that integrates DOE-2 and BLAST (Building Loads and System Thermodynamics) simulation engines to compute heat demand of the building which is widely adopted as a reliable method for simulating building energy consumption. The model estimates the heat gain / loss of individual thermal zone by considering various parameters such as heat losses through different building components (i.e., walls, floor

and ceiling), local climate, occupant's behaviour, internal gains, external solar gains etc. The model then calculates temperature changes over time, based on the heat gain or loss in each thermal zone. EnergyPlus predicted heating demand for the building over the course of a year, based on the thermal characteristic of building the outside air temperature. The building simulation models were designed as single thermal zone models as there were no different thermal zones identified. The heating set-point of all the houses was considered as 20 °C to maintain pleasant thermal comfort for all simulated houses as indicated in Botpaev et al. (2012). Simulation models utilised standard settings for natural ventilation in EnergyPlus due to the unavailability of accurate data. One can read the author's previous work to get more explanation about the house construction (open house: Mehta et al. (2020) and closed roof house: Beringer et al. (2021b)), detailed building elements, and the mathematic model of the house used in this simulation study.

6. Results and discussion

6.1 Parametric study and simulation outcomes

The study aimed to assess the effects of sustainable insulation materials on two types of houses using a simulation and parametric analysis conducted with the aid of EnergyPlus and jEPlus, respectively, for wall and ceiling insulation. The parametric study involved manipulating materials and thicknesses to identify the optimal configuration for maximum insulation efficiency.

To achieve this, three insulation materials - sheep wool, straw, and reed - were selected, and their thicknesses were varied from 3 cm to 15 cm in increments of 3 cm. The results were then compared for both types of houses, and Fig. 7 dispays the comparative outcomes.

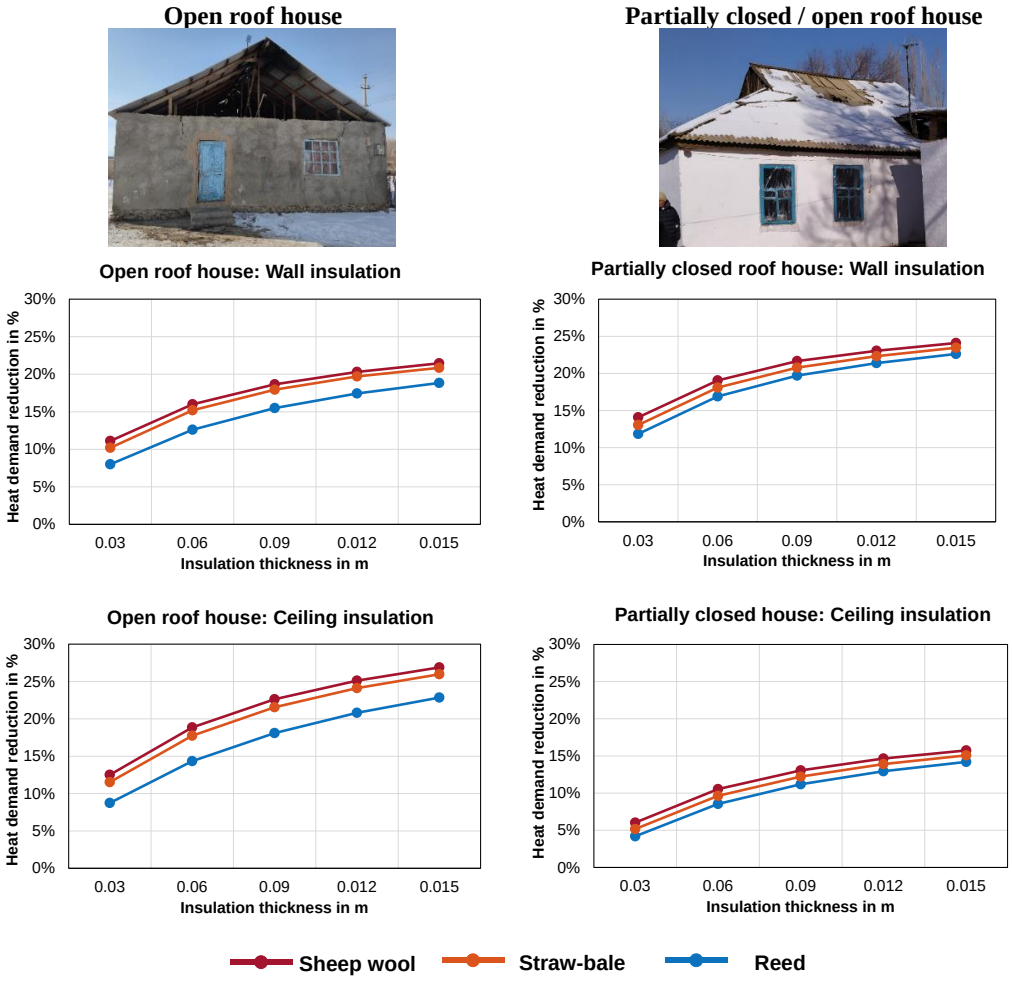

Fig. 7: Graphical representation of the parametric study based on the thickness and its effect on the heat demand reduction in %. The graphical representation provides a comparative overview and impacts of the insulation materials on the open roof house and closed roof house

6.2 Impact of sustainable insulation

Naturally, with the increment of the insulation thickness, there is more potential for heat demand reduction available. In general, wall insulation will help to reduce the heat demand up to 24% depending on the material and thickness. Similar to wall insulation, ceiling insulation also has the potential to reduce the heat demand up to 26%.

The comparative simulation results bring interesting and novel theoretical information. It can be seen from the simulation results that the insulation will be more effective in the case of a closed roof house compared to an open roof house. On the contrary, ceiling insulation is more effective in the case of open roof houses compared to closed roof houses. This finding will lead to the motivation of the sequential thermal modification in rural Kyrgyz houses.

Due to the open roof condition, the wind will pass over the ceiling which will induce a huge amount of heat losses through ceiling. Hence, investing in ceiling insulation should be the priority of the rural Kyrgyz household. This will allow reducing the heat demand more effectively. After the ceiling insulation, one can close the open roof. The author already demonstrated the positive impact of closing the roof and mentioned that "*covering the open sides of the roof raises the opportunity to decrease the specific heat demand by up to 22%.*". Once the ceiling is insulated (average heat demand saving up to 15%) and the roof is closed (heat demand reduction up to 25%), wall insulation can further help to drag down bluing heat demand. A novel information / scientific knowledge about sequential information will help rural people to make building energy efficiency more effective. The recommended thermal modifications allow for gradual investment in energy efficiency, making it financially feasible for low-income rural households in Kyrgyzstan. This contributes to the establishment of sustainable buildings in rural areas.

6.3 Limitations of the study

The study aimed to perform a comparative analysis of available house types and evaluate the impact of sustainable insulation on rural Kyrgyz houses through technical simulations. While the study conducted a parametric evaluation of insulation thickness, it did not provide any specific recommendations. Future scope includes multi-objective optimization considering heat demand reduction, cost, and insulation thickness. Sustainable insulation materials offer advantages such as higher volumetric heat capacities and lower carbon footprint compared to conventional materials. However, they also have disadvantages, including higher combustibility and higher thermal conductivity than state-of-the-art conventional materials. Considering thermal comfort, acoustic and hygroscopic properties, and cost-effectiveness are crucial to select the most suitable insulation material. The latest findings in composite materials aim to eliminate these drawbacks. Successful implementation of green building strategies has been analyzed in several publications, but large-scale experiments such as model houses are necessary for long-term observations of material changes due to weather, climate, and environment.

7. Conclusion

The presented research article carried out an in-depth assessment of available insulation materials in Kyrgyzstan from a technical, economic and sustainable point of view. Based on the three main research questions, why, how, and which, the article formulates a complete technical guide for sustainable insulation housing in high-altitude Kyrgyzstan. This guide shows a comprehensive design on *why* and *how* to build a sustainable and affordable energy-efficient building from *which* materials in high-altitude and cold climatic regions. This is how a detailed catalogue is available through the presented study in order to insulate high-altitude rural Kyrgyz houses sustainably. Therefore, by providing a complete solution for affordable and sustainable energy-efficient buildings, the research paper contributes to the knowledge. When upgrading the thermal shell of the building, material and insulation costs can be considered key parameters. Further to this, the presented study brought novel knowledge and recommended the sequence of the insulation which is not only effective but affordable as well. Unfortunately, all the listed insulation materials in the paper are still not acknowledged as insulation materials in Kyrgyzstan. Hence, it is necessary to make the local residentials aware of the enormous potential of using such materials.

8. Acknowledgement

The work presented in this paper was funded by the Federal Ministry of Education and Research (BMBF) of the Federal Republic of Germany within the CLIENT II funding programme International Partnerships for Sustainable Innovations under the project "ÖkoFlussPlan" (Project ID 01LZ1802A-F). The overall aim of ÖkoFlussPlan is to preserve the alluvial forests along the Naryn river and to implement sustainable energy solutions for the local population.

9. References

Asdrubali, F., D'Alessandro, F., Schiavoni, S., 2015. A review of unconventional sustainable building insulation materials. Sustainable Materials and Technologies 4, 1–17.

Ashour, T., Georg, H., Wu, W., 2011. Performance of straw bale wall: A case of study. Energy and Buildings 43 (8), 1960–1967.

Bakatovich, A., Gaspar, F., 2019. Composite material for thermal insulation based on moss raw material. Construction and Building Materials 228, 1–9.

BASF, 2019. Technical Data Sheet Walltite v.3. Spray Polyurethane Foam Insulation / Air Barrier. https://www.ecocomfort.ca/wp-content/uploads/sites/322/2020/01/WALLTITE-v.3-Technical-Data-Sheet.pdf. Accessed 6 September 2022.

Beck, A., Heinemann, U., Reidinger, M., Fricke, J., 2004. Thermal Transport in Straw Insulation. Journal of Thermal Envelope and Building Science 27 (3), 227–234.

Beringer, J., Mehta, K., Ehrenwirth, M., Trinkl, C., Zörner, W., 2021a. Performance comparison of different types of solar thermal collectors on residential space heating demand in high-altitude cold climatic environment: A simulation-based study, in: Proceedings Solar World Conrgess 2021.

Beringer, J., Mehta, K., Ehrenwirth, M., Zörner, W., 2021b. Sustainable materials for insulating high-altitude rural Kyrgyz residential houses: A parametric economic study, in: Applied Research Conference 2021. Ostbayerische Technische Hochschule Amberg-Weiden, pp. 183–188.

Borlea Mureşan, S.I., Tiuc, A.-E., Nemeş, O., Vermeşan, H., Vasile, O., 2020. Innovative Use of Sheep Wool for Obtaining Materials with Improved Sound-Absorbing Properties. Materials (Basel, Switzerland) 13 (3), 694.

Brakema, E.A., Tabyshova, A., Kasteleyn, M.J., Molendijk, E., van der Kleij, R.M.J.J., van Boven, J.F.M., Emilov, B., Akmatalieva, M., Mademilov, M., Numans, M.E., Williams, S., Sooronbaev, T., Chavannes, N.H., 2019. High COPD prevalence at high altitude: does household air pollution play a role? The European respiratory journal 53 (2).

Cascone, S., Rapisarda, R., Cascone, D., 2019. Physical Properties of Straw Bales as a Construction Material: A Review. Sustainability 11 (12), 1–19.

Corscadden, K.W., Biggs, J.N., Stiles, D.K., 2014. Sheep's wool insulation: A sustainable alternative use for a renewable resource? Resources, Conservation and Recycling 86, 9–15.

Dias, P.P., Jayasinghe, L.B., Waldmann, D., 2021. Investigation of Mycelium-Miscanthus composites as building insulation material. Results in Materials 10, 1–28.

Dom Penoplex LLC, 2021. Penoplex Comfort. https://www.kupi-penoplex.ru/uteplitel-plity-penoplekskomfort. Accessed 8 November 2021.

Elsacker, E., Vandelook, S., Brancart, J., Peeters, E., Laet, L. de, 2019. Mechanical, physical and chemical characterisation of mycelium-based composites with different types of lignocellulosic substrates. PloS one 14 (7).

2011. Info thermohouse insulation. http://www.ceeba.kg/index.php?ln=en&pg=srv. Accessed 3 May 2021, not retrievable since start of November (status of 14 December 2021).

International Energy Charter, 2018. In-Depth Review of the Energy Efficiency Policy of the Kyrgyz Republic, Brussels, Belgium. https://www.energycharter.org/fileadmin/DocumentsMedia/IDEER/IDEER-KyrgyzstanEN2018.pdf.

Jones, M., Mautner, A., Luenco, S., Bismarck, A., John, S., 2020. Engineered mycelium composite construction materials from fungal biorefineries: A critical review. Materials & Design 187, 1–17.

Keskküla, K., Aru, T., Kiviste, M., Miljan, M.-J., 2020. Hygrothermal Analysis of Masonry Wall with Reed Boards as Interior Insulation System. Energies 13 (20), 1–10.

Köbbing, J.F., Thevs, N., Zerbe, S., 2013. The utilisation of reed (Phragmites australis): a review. undefined.

Kudryavtseva, T., 2014. Hay prices in Kyrgyzstan increase by 2 times. https://24.kg/archive/en/economics/171607-news24.html/. Accessed 14 December 2021.

Lauermann, M., Betz, F., Mehta, K., Thevs, N., Ehrenwirth, M., Zörner, W., Cyffka, B., 2020. Preservation of Selected Ecosystem Services in the Floodplains of the Naryn River (Kyrgyzstan): Introducing the ÖkoFlussPlan Project, in: Geographica Augustana, pp. 47–53.

Mehta, K., Ehrenwirth, M., Missall, S., Degembaeva, N., Akmatov, K., Zörner, W., 2021. Energy Profiling of a High-Altitude Kyrgyz Community: Challenges and Motivations to Preserve Floodplain Ecosystems Based on Household Survey. Sustainability 13 (23), 13086.

Mehta, K., Ehrenwirth, M., Trinkl, C., Zörner, W., Greenough, R., 2020. Impact of Locally Available Thermal Insulation Structures on Space Heating Demand of High-altitude Rural Buildings: A Case Study of Kyrgyzstan, in: Proceedings of the ISES EuroSun 2020 Conference – 13th International Conference on Solar Energy for Buildings and Industry. International Solar Energy Society, Freiburg, Germany, pp. 1–12.

Musa, A.H., Mohammed, A., 2015. Compressive strength testing of plastered straw bale.

Oldham, D.J., Egan, C.A., Cookson, R.D., 2011. Sustainable acoustic absorbers from the biomass. Applied Acoustics 72 (6), 350–363.

Penoplex Ltd., 2021. PENOPLEX® WALL. https://penoplex.com/individual-construction/penoplex-wall/. Accessed 8 November 2021.

Plag, R., 2022. U-Wert Rechner ubakus. u-wert.net GmbH.

Riman company, 2021. Утепление пенополиуретаном в Бишкеке. https://riman.kg/. Accessed 16 August 2022.

Ruchti, M.H., Sägesser, N., 2021. Leistungserklärung. gemäß Anhang 3 der Bauprodukteverordnung (EU) Nr. 305/2011. https://www.fisolan.ch/sites/default/files/2021-11/Leistungserkl%C3%A4rung_ab%2020210111_Fisolan%20D%C3%A4mmplatte.pdf. Accessed 1 December 2021.

Sokol, E., 2019. Is Styrofoam Good for Soundproofing? Better Soundproofing.

Tiuc, A.-E., Vermeşan, H., Gabor, T., Vasile, O., 2016. Improved Sound Absorption Properties of Polyurethane Foam Mixed with Textile Waste. Energy Procedia 85, 559–565.

Tuzcu, T.M., 2007. Hygro-thermal properties of sheep wool insulation.

Vo, C.V., Bunge, F., Duffy, J., Hood, L., 2011. Advances in Thermal Insulation of Extruded Polystyrene Foams. Cellular Polymers 30 (3), 137–156.

WikiBath, 2020. Penoplex: technical characteristics, market overview. Do-it-yourself foam insulation. q2. Accessed 16 May 2022.

Xing, Y., Brewer, M., El-Gharabawy, H., Griffith, G., Jones, P., 2018. Growing and testing mycelium bricks as building insulation materials. IOP Conf. Ser.: Earth Environ. Sci. 121 (2), 1–8.

Zach, J., Korjenic, A., Petránek, V., Hroudová, J., Bednar, T., 2012. Performance evaluation and research of alternative thermal insulations based on sheep wool. Energy and Buildings 49, 246–253.

Solar energy buildings with high degree of independence of energy supply from grids

Elsabet Nielsen and Simon Furbo

Department of Civil and Mechanical Engineering, Technical University of Denmark, Kgs. Lyngby, Denmark

Abstract

A 60 m² solar heating/heat pump/42 m² PV system with a large hot water storage and electric battery can cover about 90% of the total yearly energy demand of 9500 kWh for a typical Danish one family house. If the house is connected to the electrical grid, additional 5500 kWh electricity produced by the system can be sold to the electrical grid during the summer months. The energy demand of the house not covered appear in January and February, which in Denmark are windy months with periods with extremely low electricity costs. The energy storages of the system can be charged during these periods and the total energy demand of the house can in this way be covered 100% by renewables.

Further, the hot water storage and the battery can be operated in a smart way in a good interplay with the electrical grid. The energy storages can be charged in periods with low cost electricity and electricity can be sold to the grid in periods with expensive electricity.

Finally, the hot water storage volume for the solar heating system can be strongly reduced due to the charge periods during the winter with limited solar radiation.

It is recommended to develop optimally designed and sized solar heating/heat pump/PV systems with smart control strategies for different one family houses, so that CO_2 is not emitted by the energy systems of the houses.

Keywords: Solar energy buildings, solar heating/heat pump systems, PV systems, large independent ratios

1. Introduction

Due to the rapid man-made climate change and biodiversity crisis there is a need for urgent conversions from fossil fuel based energy systems to energy systems relying totally on renewables. Today about 80% of the World's energy consumption is covered by fossil fuels. Countries around the World have made commitments on reductions on their coming CO_2 emissions. It is expected that the conversion period from relying on fossil fuels to relying on renewables will be long and costly. Further, the war in Ukraine has shown that democratic countries finance non-democratic countries' vicious activities by importing goods from the non-democratic countries. For that reason, there are urgent needs for democratic countries to stop import of goods inclusive fossil fuels and energy components from non-democratic countries, where the goods often are produced cheap with high CO_2 emissions. This will result in further increase of future energy costs. Consequently, it is foreseen that energy, both electricity and thermal energy, will be expensive in a future only relying on renewables.

Worldwide, operation of buildings accounts for about 40 % of our primary energy consumption and approximately 25 % of our greenhouse gas emissions. In Europe, buildings are responsible for 40 % of our energy consumption and 36 % of our CO_2 emissions.

Based on the above mentioned, it is a great wish that buildings outside district heating areas in the future are equipped with "domestic" energy systems covering almost the total yearly heat demand and a high part of the yearly electricity demand. Further, for buildings in district heating areas it would be great if centralized renewables cover the total yearly heat demand of the buildings and if the electricity demand is covered by "domestic" energy systems with a high degree of independence of energy supply from the electrical grid.

In 1975 the so-called zero energy house was built at the campus of the Technical University of Denmark, Esbensen and Korsgaard (1976). A solar heating system with 42 m² vertical solar collectors and a 30 m^3 hot water tank as heat storage could theoretically cover the yearly heat demand of the house in the Danish climate. However, mainly due to larger heat losses from the heat storage than expected, the system could not completely cover the total

© 2022. The Authors. Published by International Solar Energy Society
Selection and/or peer review under responsibility of Scientific Committee
doi:10.18086/eurosun.2022.01.08 Available at http://proceedings.ises.org

yearly heat demand of the house, Esbensen and Korsgaard (1977).

In 1978 the first so called plus energy house was built in Denmark, Fischer (1982). The one family house was equipped with its own wind turbine and electric battery and a solar heating system with 40 m² solar collectors and a 5 m^3 hot water rubber tank. The intension was that all heat demands and electricity demands of the house and of an electric vehicle was covered without any energy supply from outside. Unfortunately, the rubber heat storage leaked after a short period, so the ambitious goal was not reached.

The two above mentioned examples on Danish houses with solar heating systems aiming for 100% yearly solar fractions initiated research activities on solar heating systems and heat storage at the Technical University of Denmark. Most research efforts were focused on assistance to solar collector manufacturers in connection with their efforts to develop attractive solar heating systems and components for solar heating systems for the marked. The manufacturers developed competitive solar domestic hot water systems, solar combi systems and solar heating plants for district heating areas. Almost all the systems were economically attractive but had relatively low solar fractions, relying on different types of auxiliary energy supply systems. Systems with high solar fractions were not prioritized due to economically reasons.

PV systems on buildings allow that a part of the electricity demand can be covered by the PV systems. Further, combinations of PV panels and heat pumps allow that the systems can cover a part of both the electricity and heat demand of the buildings. Recently, differently designed, sized and smartly operated PV/heat pump systems have been investigated by Battaglia et al. (2017), Toradmal et al. (2018), Thür et al. (2018) and Heinz and Rieber (2021). Focus has been on how to achieve the highest possible coverage of the electricity and heat demand of the buildings. Also research with the same focus on PVT/heat pump systems have been carried by Dannemand et al.(2019), Sifnaios et al. (2021) and Chhugani et al. (2023),

During the last decades, there has not been much research on how individual solar heating systems can cover almost all heat demand of buildings. However, in Switzerland the first successful one family solar house with a yearly solar fraction of 100% was built in 1989 by the company Jenni Energietechnik AG, Das Sonnenhaus, 2. Auflage 2009, https://docplayer.org/18236832-Unabhaengig-und-umweltbewusst-wohnen-mit-der-sonne-das-sonnenhaus-2-auflage-2009.html (2009). A large solar heating system with several large hot water stores covered the total heat demand of the house during the first year of operation. Jenni Energietechnik AG is one of a kind company focusing on solar energy systems covering the total yearly energy demand with solar energy.

Recently an IEA (International Energy Agency) SHC Task 66 project Solar Energy Buildings has started, https://task66.iea-shc.org/. The focus of the project is on development of economic and ecologic feasible solar energy supply concepts with high solar fractions for new and existing single buildings and building blocks or communities. The targeted solar thermal and solar electrical fractions depend significantly on the climate zone. For central European climate conditions solar fractions of at least 85% of the heat demand, 100% of the cooling demand and at least 60% of the electricity requirements for households and e-mobility should be achieved.

In this paper preliminary calculations for a house with differently designed and sized solar energy/heat pump systems with high solar fractions are presented. Both solar heating systems and PV systems are considered.

2. House and energy systems

Calculations are carried out with the POLYSUN program, https://www.velasolaris.com/software/ for a 120 m² one family house located in Denmark outside district heating areas. Three different concepts of the energy system of the house are considered: 1) A heat pump system, 2) a heat pump system and a PV system, 3) a solar heating/heat pump system combined with a PV system. The sizes of the systems inclusive heat storages and electric batteries are varied, allowing determining how the degree of independence of energy supply from the electrical grid is influenced by system size.

The yearly heating and electricity demands assumed are given in Table 1. The energy quantities are typical for relatively new Danish one family houses. Hourly weather data from the Danish design reference year, DRY are used in the calculations.

Tab. 1: Assumed yearly energy demands for one family house

Space heating demand	Domestic hot water consumption	Electrical energy demand	Total energy demand
4707 kWh/year	1749 kWh/year	3000 kWh/year	9456 kWh/year

The heating system of the house is a floor heating system based on hot water flowing through heating coils. The flow temperature is 35°C and the return temperature is 30°C under the dimensioning conditions.

Figure 1 shows a schematically illustration of the heat pump/PV system, and Figure 2 shows a schematically illustration of the solar heating/heat pump/PV system taken in calculation.

The efficiency of the PV panels is 20% at 25°C.

Two different solar collectors are taken in calculation, a standard flat plate collector and an evacuated tubular solar collector from Kingspan, MS30-TMO500.

A 5 kW air-to-water heat pump and electrical batteries of different sizes are assumed.

Two hot water tanks are used for the heat pump system, while one hot water storage is used for the solar heating/heat pump system together with an external DHW unit supplied with heat from the heat storage.

The electricity produced by the PV panels cover the electrical energy demand in the house directly, power the heat pump, charge the electrical battery or is sold to the electric grid.

If the required electricity needed to operate the energy and heating systems and to cover the electrical energy demand in the house can not be covered by the PV panels or the battery, electricity is bought from the electrical grid. The calculations are carried out in such a way, that the total energy demand of the house is meet.

Systems with an electrical battery and heat storages can in the future be operated in a smart way in a good interplay with the electrical grid. This possibility is however not considered in this paper.

To compare the different concepts two energy quantities are used for each investigated system: Electricity bought from the electrical grid and Electricity sold to the electrical grid

Further, an independent ratio, defined as Energy savings/Total energy demand = (Total energy demand – electricity bought from the electrical grid)/Total energy demand, is used.

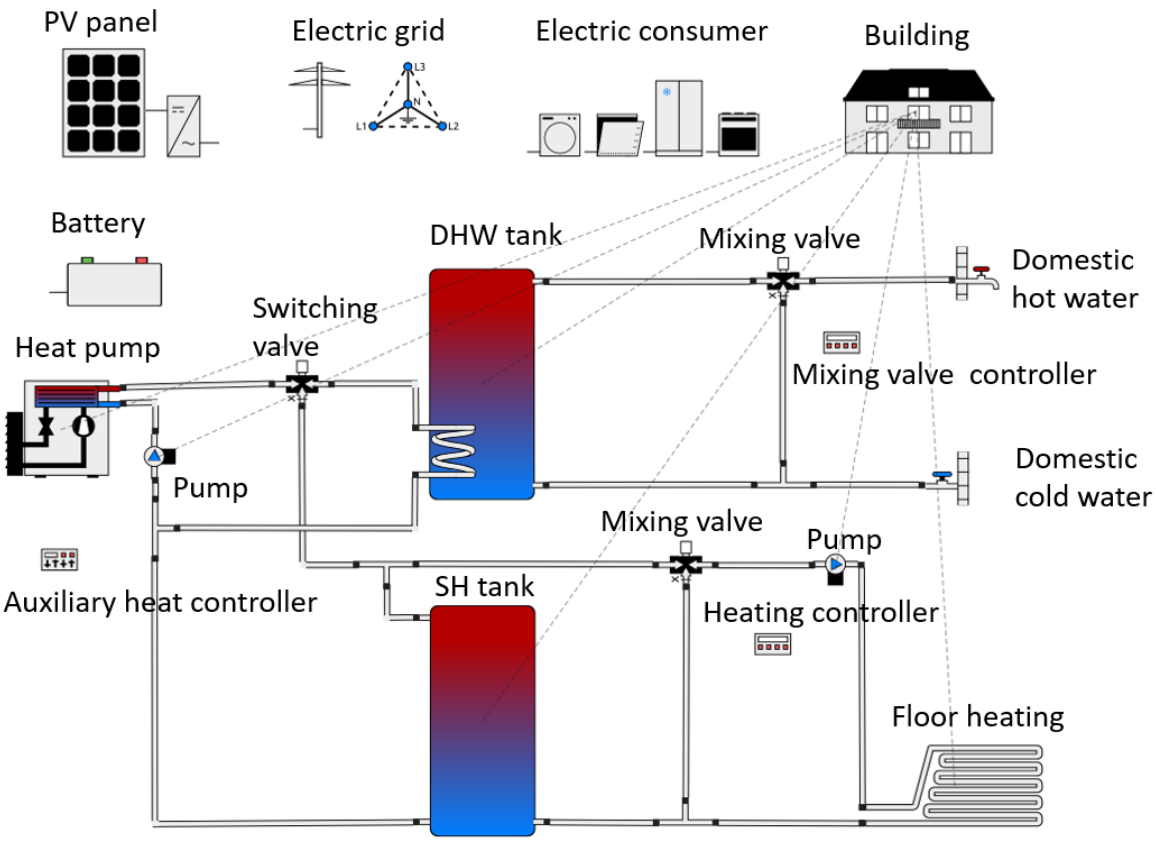

Fig. 1: Schematically illustrations of the heat pump/PV system taken in calculation.

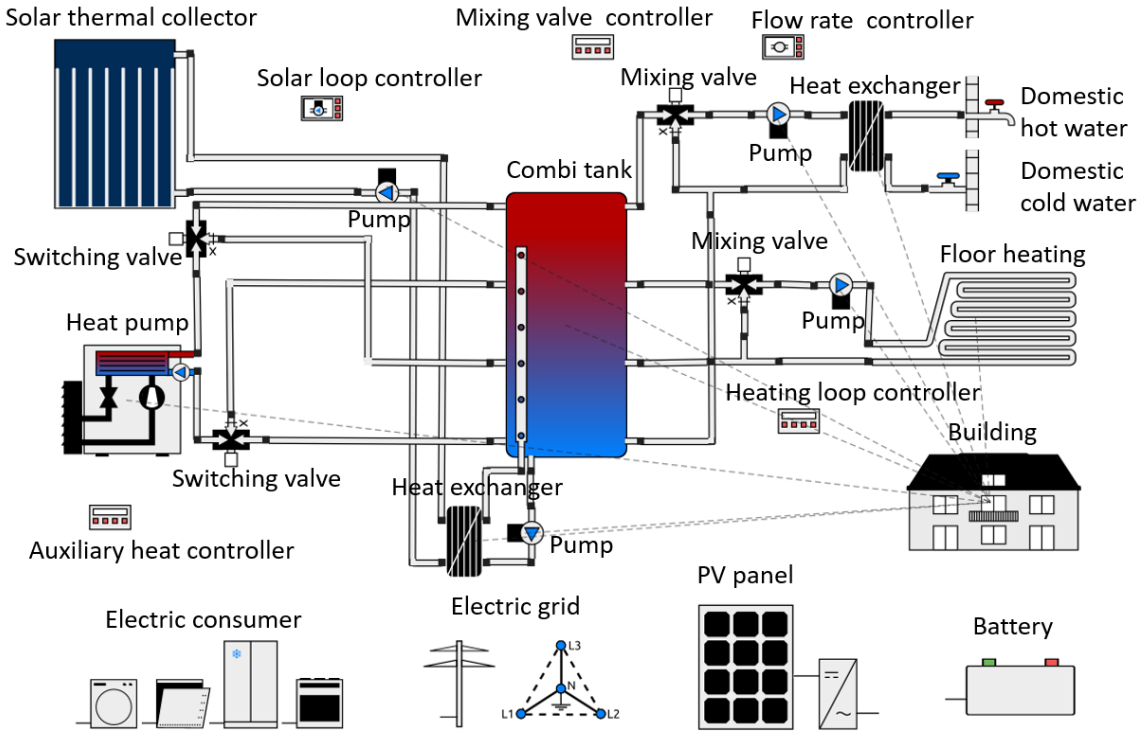

Fig. 2: Schematically illustrations of the solar heating/heat pump/PV system taken in calculation.

3. Calculation results

Calculated results for the heat pump system without PV panels, electrical battery and solar collectors are shown in Figure 3 and Figure 4 for different domestic hot water tank volumes. The hot water tank volume for space heating is 600 L in all the calculations. A small domestic hot water tank results in the highest yearly independent ratio of about 45%, because a reduced tank volume results in a reduced tank heat loss. Additional calculations show that the volume of the hot water tank for space heating not significantly influence the independent ratio of the system.

Calculation results for the heat pump system with PV panels without electrical battery and solar collectors are shown in Figure 5, Figure 6 and Figure 7 for different south facing PV panel tilts. The PV area is 53 m², the domestic hot water tank volume is 300 L and the hot water tank volume for space heating is 600 L. The yearly electricity sold to the grid and the yearly independent ratio peaks, and the electricity bought from the grid is lowest for a PV panel tilt of 40°. The highest yearly independent ratio for the heat pump/PV system is about 69%. Calculations with the same system with PV areas of 28 m² and 14 m² showed that the yearly independent ratio decreased to about 64% and 58%, respectively, see figure 8 and Figure 9. Also for the heat pump/PV system a small domestic hot water tank results in the highest yearly independent ratio, while the volume of the hot water tank for space heating not significantly influence the independent ratio of the system.

Calculations with the heat pump system combined with PV panels with an area of 53 m² and a 30 kWh electrical battery showed that the yearly independent ratio increased to 81%.

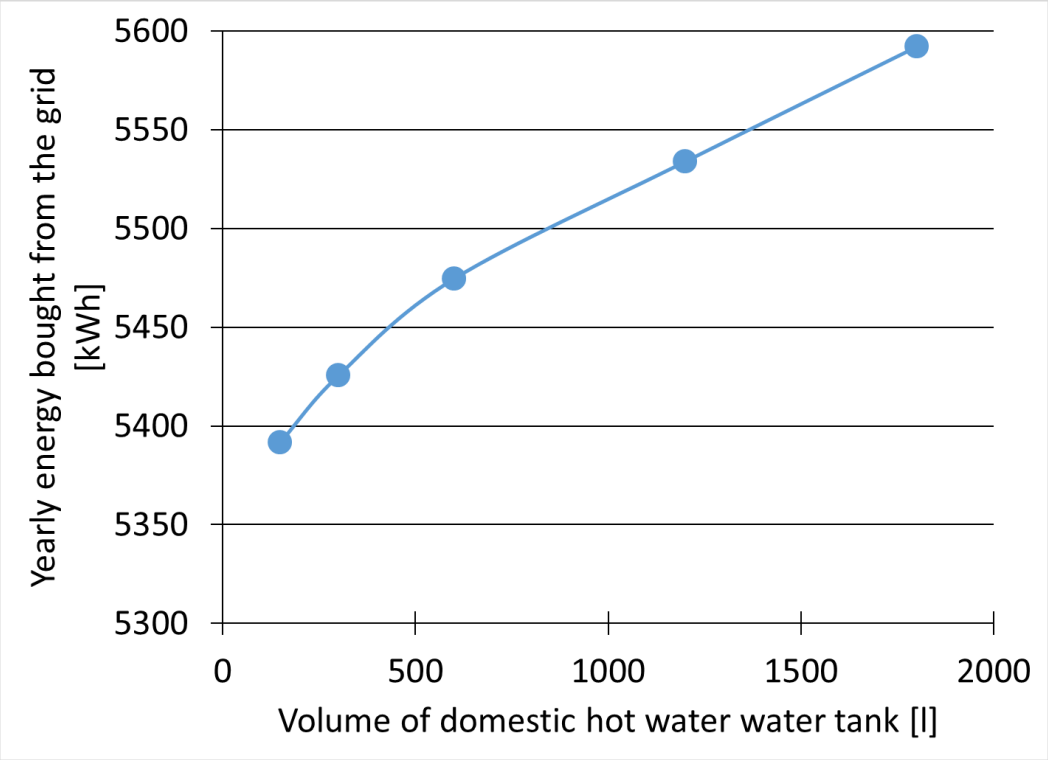

Fig. 3: Yearly electricity bought from the grid as function of the domestic hot water tank volume for the heat pump system.

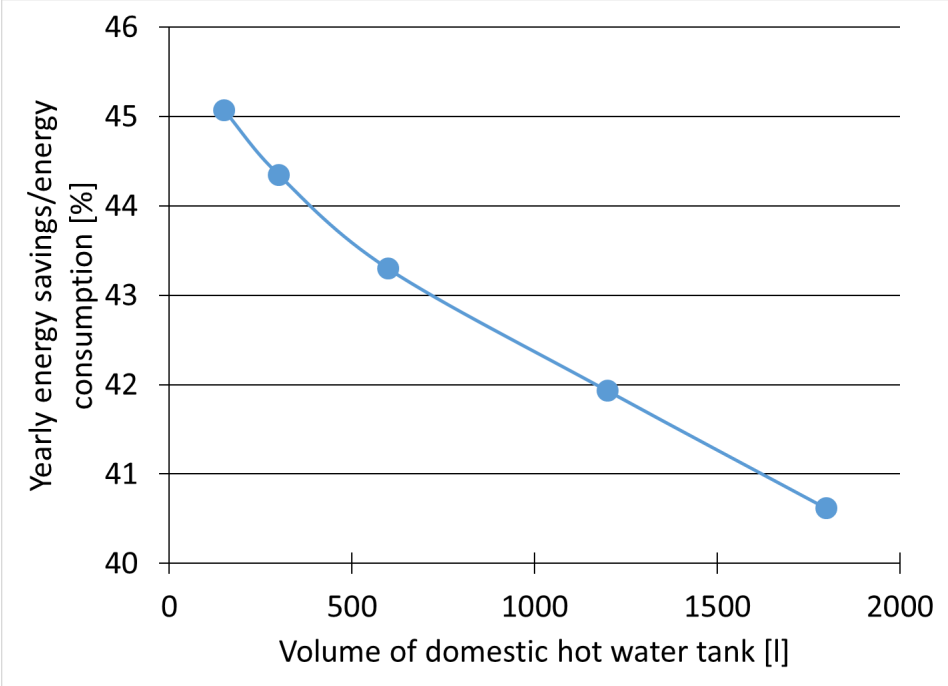

Fig. 4: Yearly independent ratio as function of the domestic hot water tank volume for the heat pump system.

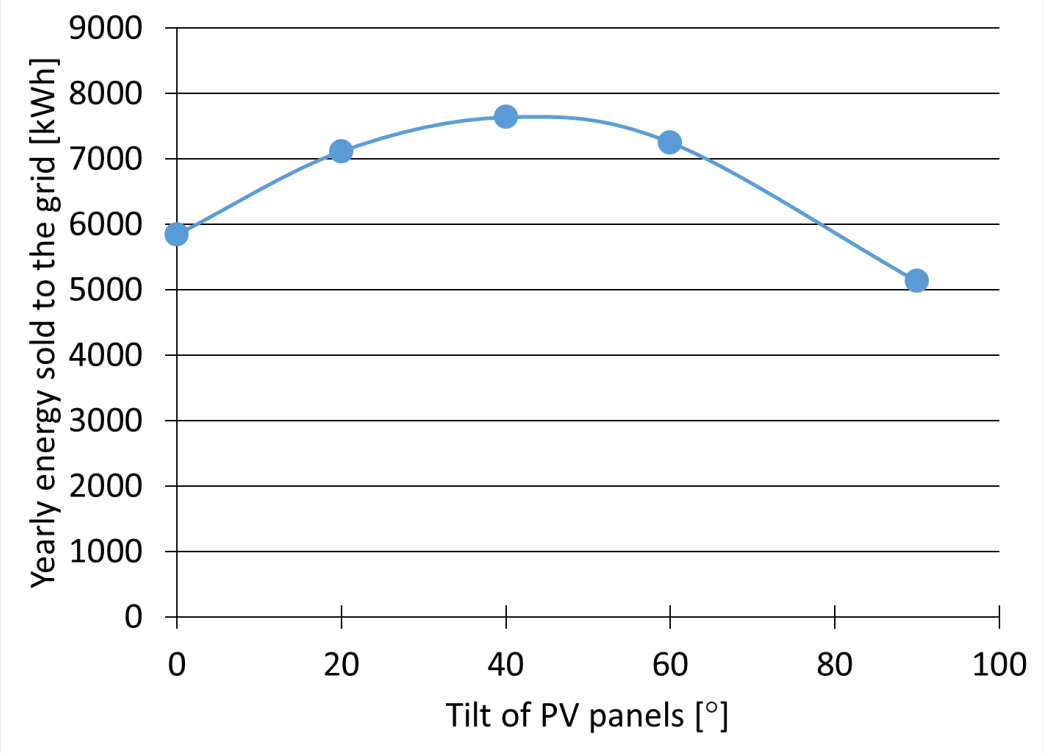

Fig. 5: Yearly electricity sold to the grid as a function of the PV panel tilt for the heat pump/PV system

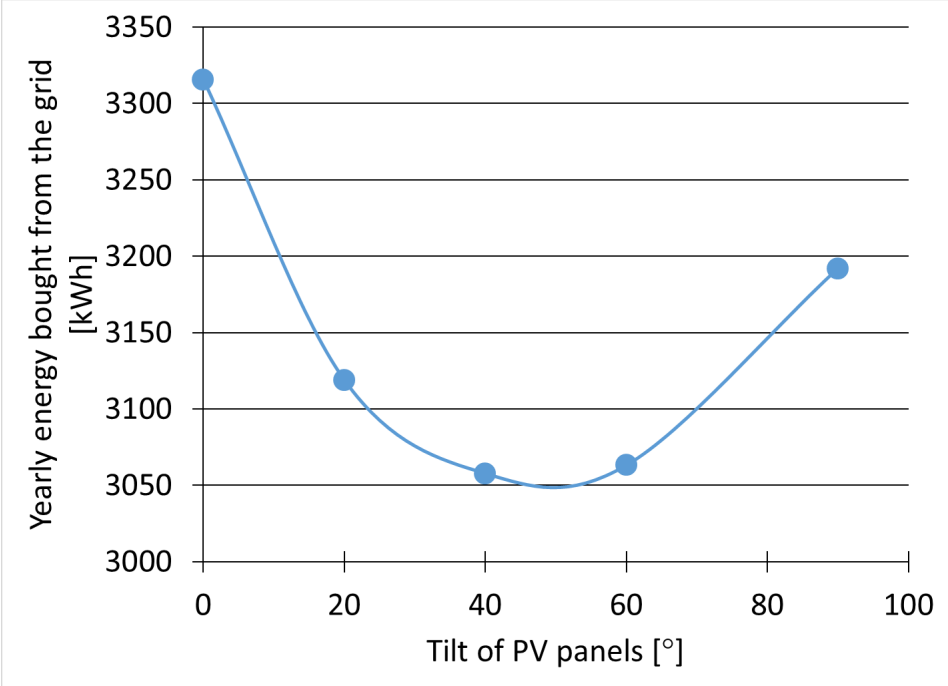

Fig. 6: Yearly electricity bought from the grid as a function of the PV panel tilt for the heat pump/PV system

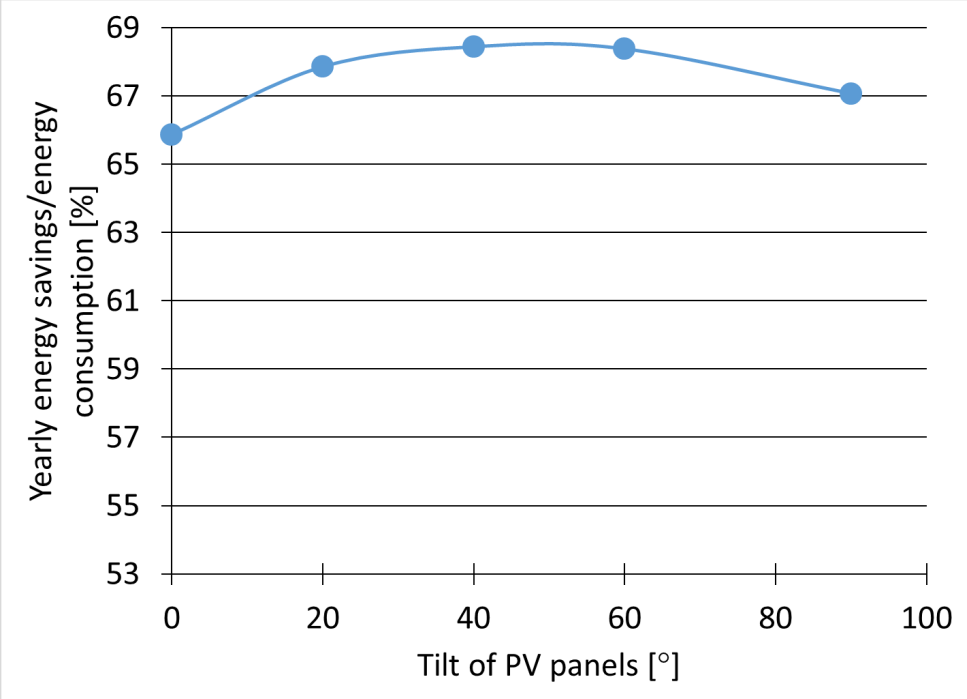

Fig. 7: Yearly independent ratio as a function of the PV panel tilt for the heat pump/PV system. PV area is 53 m²

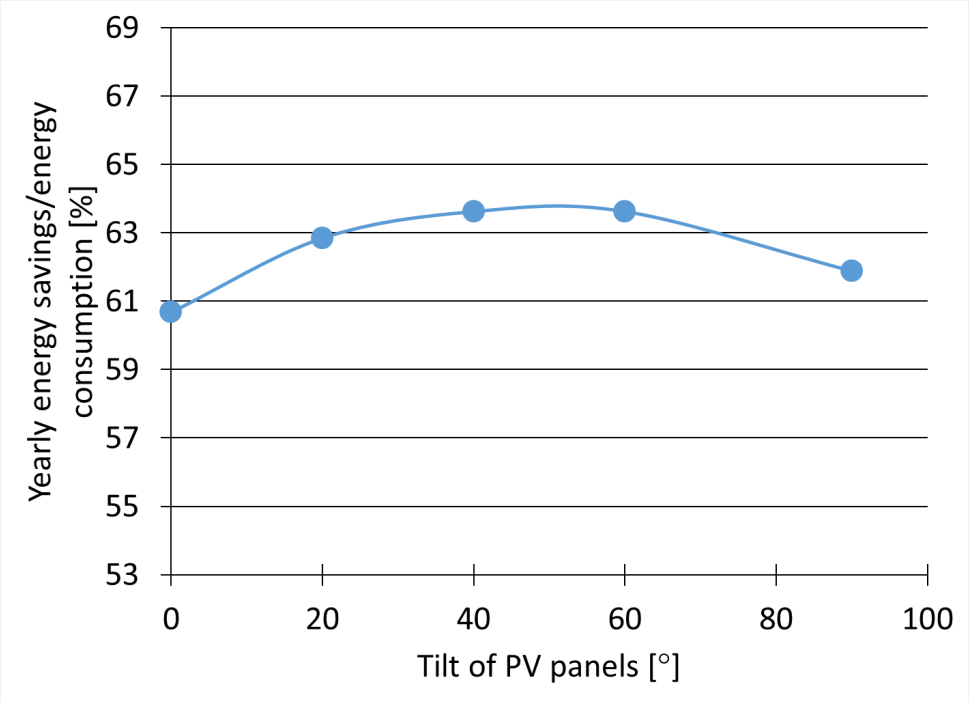

Fig. 8: Yearly independent ratio as a function of the PV panel tilt for the heat pump/PV system. PV area is 27 m^2

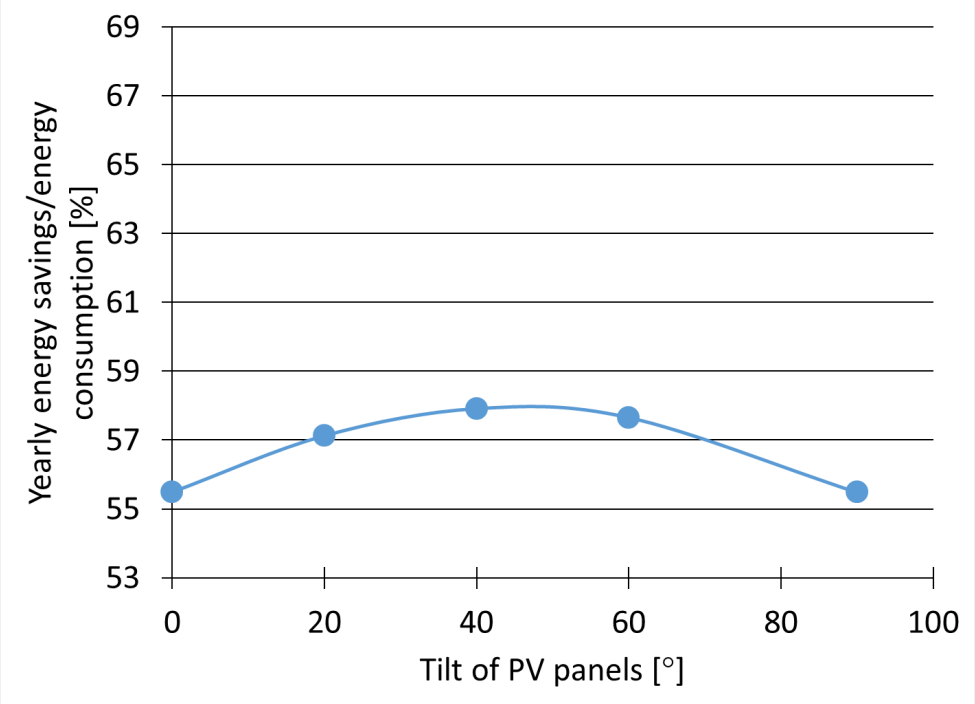

Fig. 9: Yearly independent ratio as a function of the PV panel tilt for the heat pump/PV system. PV area is 14 m²

Calculations show that the yearly independent ratio for the solar heating/heat pump system without PV panels and with 60 m² flat plate solar collectors and a 2500 L heat storage with the upper 208 L reserved for heat supply to the DHW unit is about 57%. The best solar collector tilt is about 75°.

Figure 10, Figure 11 and Figure 12 show the yearly electricity sold to the electrical grid, bought from the electrical grid and the independent ratio for the 60 m² solar heating/heat pump system combined with south facing 40° tilted PV panels as function of the PV panel area. Introduction of PV panels increase the independent ratio. With a PV panel area of 42 m² the independent ratio reach about 67% for the combined solar heating/heat

pump/PV system. By adding an electrical battery of 30 kWh, the yearly independent ratio is further increased to about 72%, 79% and 81% for 14 m², 28 m² and 42 m² PV panels, respectively.

By replacing the flat plate solar collector with the evacuated tubular solar collector the yearly independent ratio is increased to 85% for the 60 m² solar heating/heat pump/42 m² PV system with 30 kWh electrical battery. By using a 90 kWh or a 200 kWh electrical battery, the independent ratio is increased to 86% and 87%, respectively.

For the 60 m² solar heating/heat pump/42 m² PV system with evacuated solar collectors, a 30 kWh electrical battery and a 30 m^3 hot water tank the yearly independent ratio is 87%. For the 60 m² solar heating/heat pump/42 m² PV system with evacuated solar collectors, a 200 kWh electrical battery and a 30 m^3 hot water tank the yearly independent ratio is 91%. 5540 kWh produced by the system can on a yearly basis be sold to the electrical grid. The electricity is sold in the summer months.

The calculations shows that it is not possible without extremely large heat storages and electrical batteries for the solar energy systems to cover the energy demand completely in the house in Denmark. However, the only period of the year where the large systems with large energy storages can not cover the energy demand completely is in January and February. In this period, windy days with extremely cheap electricity are available in Denmark due to the high number of wind turbines. Consequently, during these days the heat storage and the electrical battery can be charged with renewable energy in a cheap way. In this way the energy demand of the house can be completely covered by renewables.

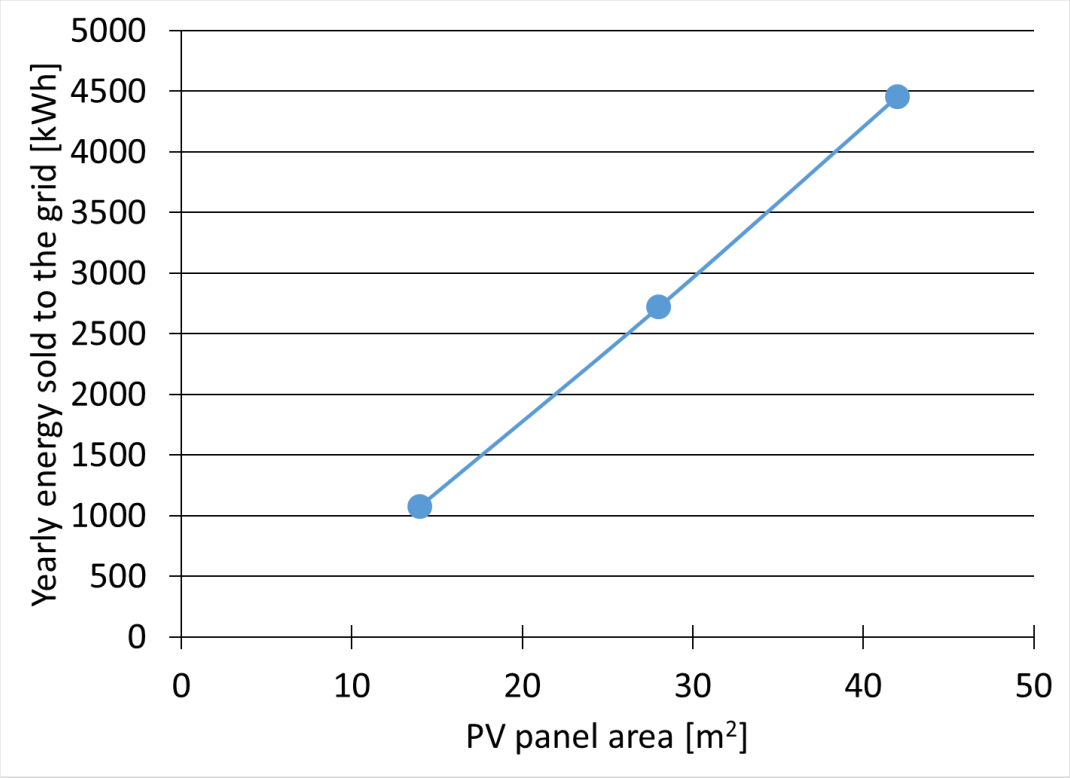

Fig. 10: Yearly electricity sold to the grid for a 60 m² solar heating/heat pump system combined with PV panels with different areas.

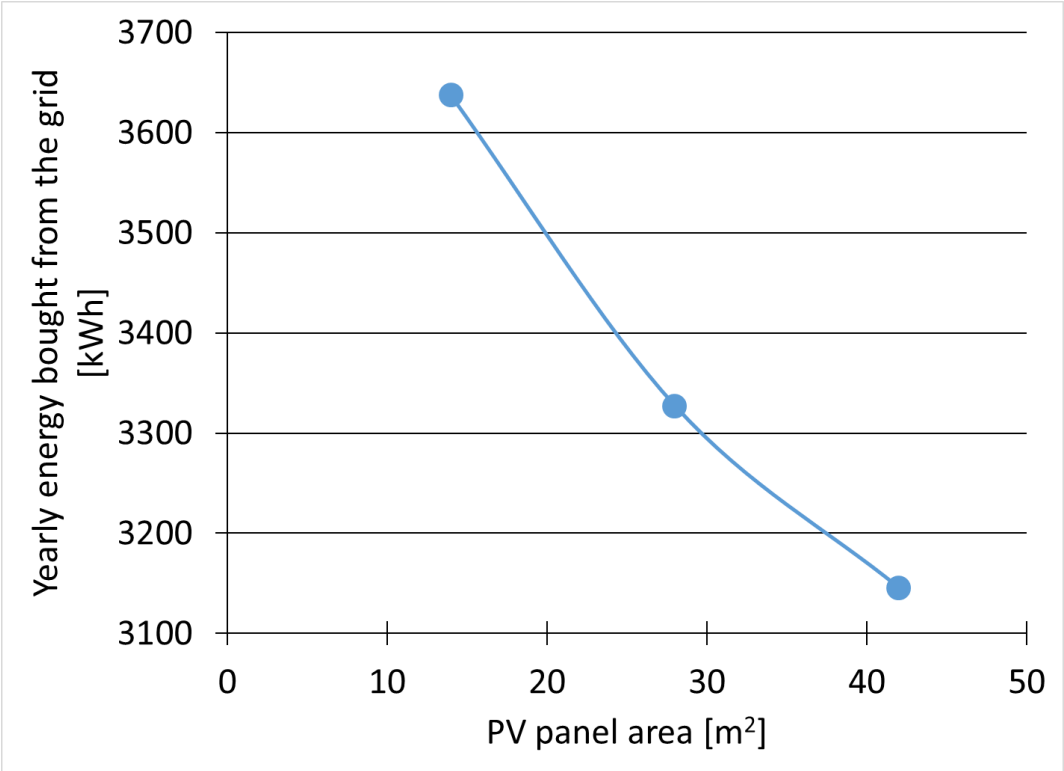

Fig. 11: Yearly electricity bought from the grid for a 60 m² solar heating/heat pump system combined with PV panels with different areas.

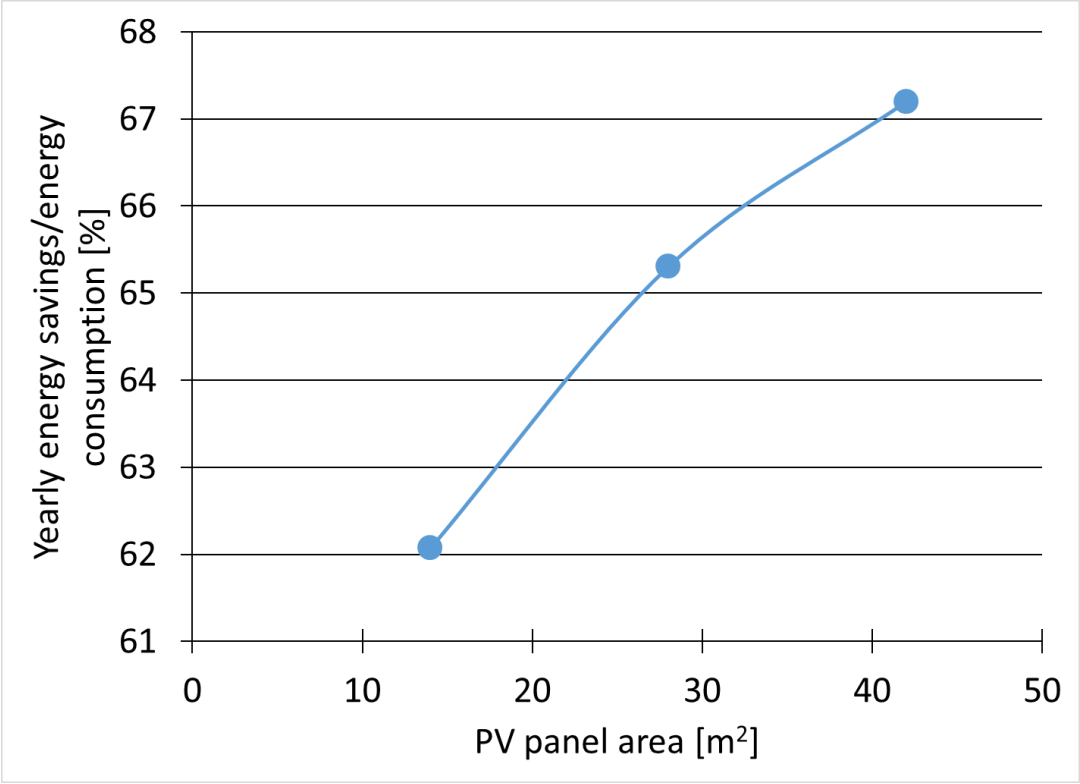

Fig. 12: Yearly independent ratio for a 60 m² solar heating/heat pump system combined with PV panels with different areas.

4. Conclusions

A 60 m² solar heating/heat pump/42 m² PV system with a large hot water storage and battery can cover about 90% of the total yearly energy demand of 9500 kWh for a typical Danish one family house. If the house is connected to the electrical grid, 5500 kWh electricity produced by the system can furthermore be sold to the electrical grid during the summer months. The energy demand of the house not covered appear in January and February, which in Denmark are windy months with periods with extremely low electricity costs. The energy storages of the system can be charged from the electrical grid during these periods and the total energy demand of the house can in this way be covered 100% by renewables.

The optimal tilts for the south facing solar collectors and PV panels are about 75° and 40°, respectively.

Further, the hot water storage and the battery can be operated in a smart way in a good interplay with the electrical grid. The energy storages can be charged in periods with low cost electricity and electricity can be sold to the grid in periods with expensive electricity.

Finally, the hot water storage volume for the solar heating system can be strongly reduced due to the charge periods during the winter with limited solar radiation.

It is recommended to develop optimally designed and sized solar heating/heat pump/PV systems with smart control strategies for different one family houses, so that CO_2 is not emitted by the energy systems of the houses.

5. Acknowledgments

The investigations are financed through the IEA Task 66 project. The Danish Energy Agency supports the Danish participation in the project. This support is greatly appreciated.

6. References

Battaglia, M, Haberl, R., Bamberger, E., Haller. M., 2017. Increased self-consumption and grid flexibility of PV and heat pump systems with thermal and electrical storage. Energy Procedia 135: 358-66.

Chhugani, B., Pärisch, P., Helmling, S., Giovannetti, F., 2023. Comparison of PVT – heat pump systems with reference systems for the energy supply of a single-family house. Solar Energy Advances 3 (2023) 1000031.

Dannemand, M. Sifnaios, I., Tian, Z, Furbo, S., 2019. Simulation and optimization of a hybrid unglazed solar photovoltaic-thermal collector and heat pump system with two storage tanks. Energy Conversion and Management 206.

Esbensen, T.V., Korsgaard, V., 1976. Dimensioning of the solar heating system in the zero energy house in Denmark. Solar Energy, Volume 19, 195-199.

Esbensen, T.V., Korsgaard, V., 1977. Performance of the zero energy house in Denmark, report 64. Thermal Insulation Laboratory, Technical University of Denmark.

Fischer, J., 1982. Plusenergihuset. Borgen.

Heinz, A., Rieberer, R., 2021. Energetic and economic analyses of a PV-assisted air-to-water heat pump system for renovated residential buildings with high-temperature heat emission system. Applied Energy 293: 116953.

Sifnaios, I, Jensen, A.R., Dannemand, M., Dragsted, J., 2021. Demonstration of a domestic photovoltaic-thermal (PVT)-heat pump system, performance simulation, and economic analysis for different climates. Proceedings of SWC 2021: ISES Solar World Congress. International Solar Energy Society, p. 588-599.

Thür, A., Calaqbrese, T., Streicher, W., 2018. Smart grid and PV driven ground heat pump as thermal battery in small buildings for optimized electricity comsumption. Solar Energy 174, pp. 273-285.

Toradmal, A., Kemmler, T., Thomas, B., 2018. Boosting the share of onsite PV-electricity utilization by optimized scheduling of a heat pump using buildings thermal inertia. Applied Thermal Engineering 137, pp. 248-258.

https://www.velasolaris.com/software/

Das Sonnenhaus, 2. Auflage 2009, https://docplayer.org/18236832-Unabhaengig-und-umweltbewusst-wohnen-mit-der-sonne-das-sonnenhaus-2-auflage-2009.html

IEA (International Energy Agency) SHC Task 66 project Solar Energy Buildings, https://task66.iea-shc.org/.

Use of units and symbols: For the use of units and symbols, please see the appendix below.

Monitoring results of the energy consumption behaviour of two highly solar-powered apartment buildings

Lukas Oppelt[1], Thomas Storch[1], Andreas Gäbler[1], Tobias Fieback[1]

[1] Chair of technical thermodynamics, Institute of Thermal Engineering, TU Bergakademie Freiberg, Freiberg, (Germany)

Abstract

The CO_2-neutral self-supply of heat and electric energy is an important objective for new buildings. Two new apartment buildings (7 units each) built in 2018 according to the solar house concept will achieve solar fraction of up to 77% electrically and 65% thermally through solar thermal and photovoltaic systems and thermal and electrical storages. The residents receive all energy services, independent of consumption, financed by a flat-rate rent. Within this article, the first results of two years monitoring with the effects of the user's behaviour on the energy balance of the apartments and building is analyzed. It is clear that users prefer high room temperatures that are up to 5K above the German average. The electricity consumption, on the other hand, is average and the measured consumption matches the results of a residents survey conducted. Nevertheless, different user behaviour in terms of when they purchase electricity leads to a different load on the electricity storage and to a different individual electricity mix.

Keywords: energy efficiency in buildings, solar energy, energy storage, solar fraction, NZEB, measurement

1. Introduction

In the EU the nearly zero-energy building-standard (NZEB) is obligatory for all new buildings by 2021 (Directive 2010/31/EU). Therefore, an improvement of the energy efficiency of buildings and their evolution to new integrated building concepts with solar systems is necessary. Over the past 30 years, various low energy house concepts have been developed with different, mostly regenerative, energy supply systems. Nevertheless, in the literature, there exists a big leakage on detailed scientific measurement data to proof their efficiency under real user behaviors, see also Storch and Wilde 2018. This paper focuses on first measurement results of two identical new solar apartment buildings (see table1) with high solar fraction in electrical and thermal energy.

Table 1: Parameters of one partially self-sufficient apartment building at the Cottbus location (* approx. 2400 kWh/apartment; ** from EnEV-certificate 2013)

effective area / heated house-volume	853.5 m^2 / 2921 m^3
Area of solar thermal- / PV –collector / roof pitch	100 m^2 / 29.6 kW_p (facade & roof)/ 50° (S)
Volume of heat storage tank/ storage battery (Li-Ion)	24.6 m^3 / 52 kWh
Auxiliary heating (gas)	48.2 kW
Solar fraction el./ heat	~ 77% / ~ 65%
Annual demand in electrical energy* / thermal heat**	18,665 kWh/yr / 15.58 kWh/m^2
Annual primary energy consumption**	8.40 kWh/m^2yr

2. Results

The main heat source for the buildings is the solar thermal system. These can be temporarily stored in a hot water tank. In addition, it is possible to use a gas boiler if the heat demand is higher than the yields of the solar thermal system. Table 2 compares the heat demand for heating and hot water for building 1 with the planned values. It is clear that the planned values are significantly exceeded during operation.

© 2022. The Authors. Published by International Solar Energy Society
Selection and/or peer review under responsibility of Scientific Committee
doi:10.18086/eurosun.2022.01.09 Available at http://proceedings.ises.org

Table 2: Comparison of measured values and planning (for 6 residential units) for building 1, Measuring period 2020/21 (Heating consumption and hot water consumption related to effective area, solar thermal yields related to area of solar thermal-collectors)

	Measurement house 1	Compared to planned values
Heating consumption	52,365 kWh / 61.4 kWh/(m²a)	344 %
Hot water consumption	23,425 kWh / 27,4 kWh/(m²a)	234 %
Hot water tap volume	180 m³	82 %
Solar thermal yields	52,365 kWh / 523,6 kWh/(m²/a)	201 %

Various reasons were identified for this strong deviation from the planned values. In addition, it should be noted that the planning was carried out for a building with 6 residential units; the buildings that were finally constructed each comprise 7 residential units.

During the heating period the measurements showed that the room air temperatures of the individual rooms are about 2.5 to 5 K above the average temperatures in living rooms and bedrooms according to Techem 2017 and thus also above the assumptions for the pre-calculation of the EnEV energy certificate. Figure 1 on the left shows an example of the room temperatures of three apartments. In all apartments, the bedroom is kept slightly cooler than the living room, which may be due to more frequent and longer window ventilation in addition to the setting of the room thermostat. In figure 1 (right), the presence of the residents is clearly indicated by the increase in CO_2 and humidity. The continuous drop in room temperature suggests that the window is open throughout the night from 11 p.m. to 6 a.m. This caused a cooling of the bedroom temperature of about 5 K due to a low outside temperature of about 0 °C. This means heat losses from the room with underfloor heating through uncontrolled air exchange and cooling of the walls. By comparing the heat consumption quantities in the respective periods with an apartment without window ventilation, the heat that escapes in this way can be quantified at approx. 27.2 kWh. A nightly regulation of the heating operation alone can thus avoid about half of the additional consumption. A further influence is the reduction of the room set point temperature. However, it cannot be safely concluded that the cause of this behavior is due to the flat-rate energy billing. Ignorance and convenience can also influence user behavior.

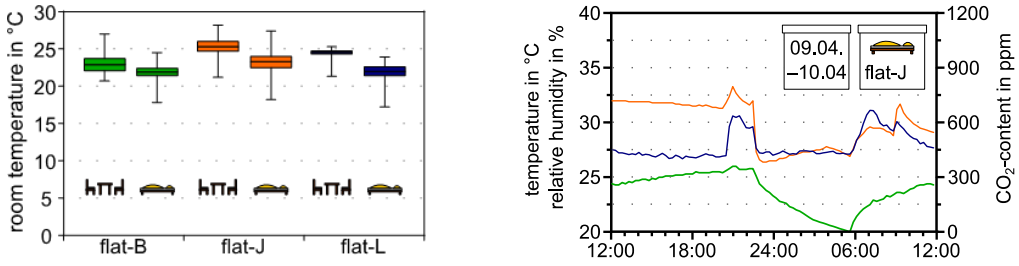

Fig. 1: Left: average room temperatures of apartments (living / bedroom, 19.03. to 14.05.2019); right: air properties of 1 bedroom, with green = temperature; blue = CO_2; orange = humidity (09.04. to 10.04.2019), Oppelt 2019

The hot water consumption is also significantly above the planned values. Here, too, a major cause is that the planned values were prepared for a building with 6 residential units. Figure 2 clearly shows that there is a more or less normal distribution across all residential units. The high and low consumers roughly balance each other out. The averaged hot water consumption in Germany is about 33 – 36 l/ person. There is no particular outlier to be seen, which could indicate possible abusive behaviour. The measured values also fit relatively well with a tenant survey that was conducted with the residents from this building. In this survey, 7 out of 14 units estimated their water consumption as average, 3 estimated it as very high and 4 as very low. Table 2 also showed that the planned hot water volume was undercut. Only the heat quantity for hot water is above the planned values. The reason for this is that the planned hot water temperature of 50 °C was not implemented, but the hot water is provided at 60 °C during operation. In addition, it must be considered that the washing machine and dishwasher have a hot water connection and thus there may be a higher hot water consumption compared to other residential units.

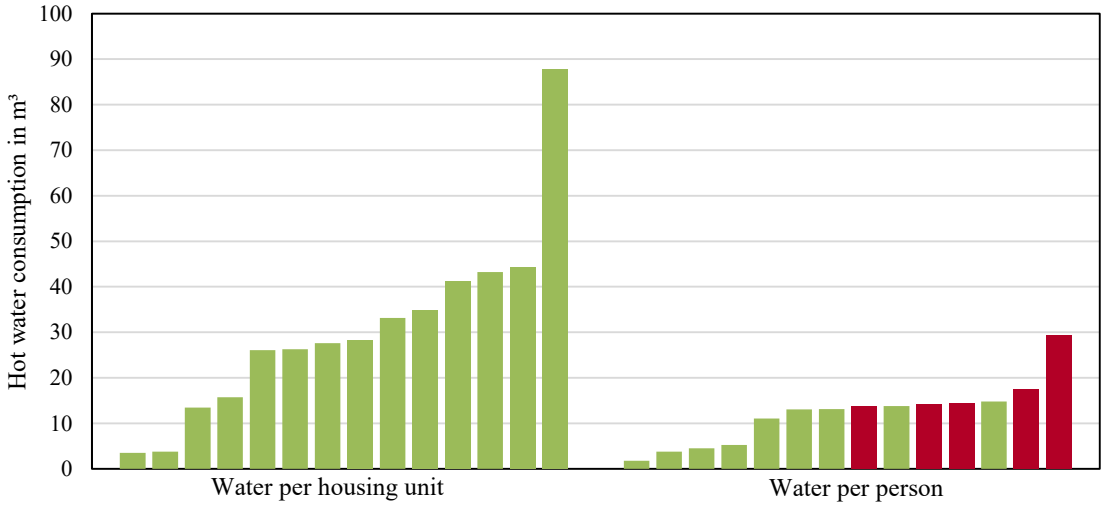

Fig. 2: Individual hot water consumption of the flats of both buildings related to the residential unit and related to one person

The annual electricity consumption under full occupancy is about 2,200 kWh (with 2.4 persons/flat) which is within the same range of 2-person households, see stromspiegel. A comparison of the averaged load profiles of all flats of one house with the standard load profiles of BDEW 2017 (figure 3, left) also shows a typical curve shape with regard to the level of the base load and the time distribution of peak loads. However, a comparison of the individual flats with each other reveals a clear heterogeneity, see figure 3 (right). The average daily load curve shape of the individual flats shows that the peak loads mainly fall during times of maximum coverage by direct photovoltaic (pv) supply. Typical peaks in the evening occur in times of higher coverage by battery supply. There is a fluctuation in the degree of coverage of individual flats through direct pv consumption between approx. 28 % to 41 %. Overall, however, a similarly high degree of solar fraction (pv and battery) of 68 % to 73 % is achieved for all flats. Thus, the electrical energy storage leads to a doubling of the solar fraction.

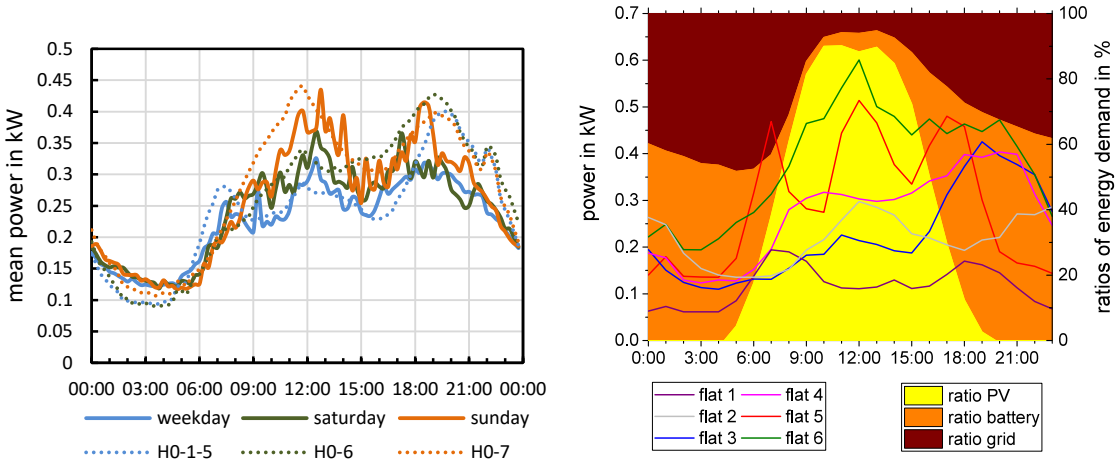

Fig. 3: left: average daily load profile of all apartments with the scaled standard load profile (Germany, H0) according to BDEW; right: day-dependent electricity mix, average values from 15-min. measured values (07/19 to 03/20).

As described in Table 1, both buildings each have electricity storage with a capacity of 52 kWh. Figure 4 shows the battery's state of charge, the PV yield and the current electricity consumption of house 1. As expected, the battery's state of charge is also high in summer when PV yields are high. No seasonal fluctuations can be seen in consumption. Overall, it can be observed that the state of charge hardly drops below 30 % in summer and hardly rises above 50 % in winter. Only in the transitional period is the full capacity utilized. It becomes clear that the accumulator could be significantly smaller without affecting the behaviour of the house. Alternatively, integration into a neighborhood with the surrounding buildings (several apartment buildings and an office building) would reduce the grid feed-in and increases the self-consumption of renewable electricity in the district.

The storage losses of the accumulator are also not negligible. For the measurement period 2020/21, the loss of the accumulator for house 1 was about 2020 kWh, which roughly corresponds to the amount of energy of an additional household. The annual utilization rate was thus around 75.4 %, which also corresponds to the utilization rate observed by Großklos et al. 2016 for other multifamily buildings.

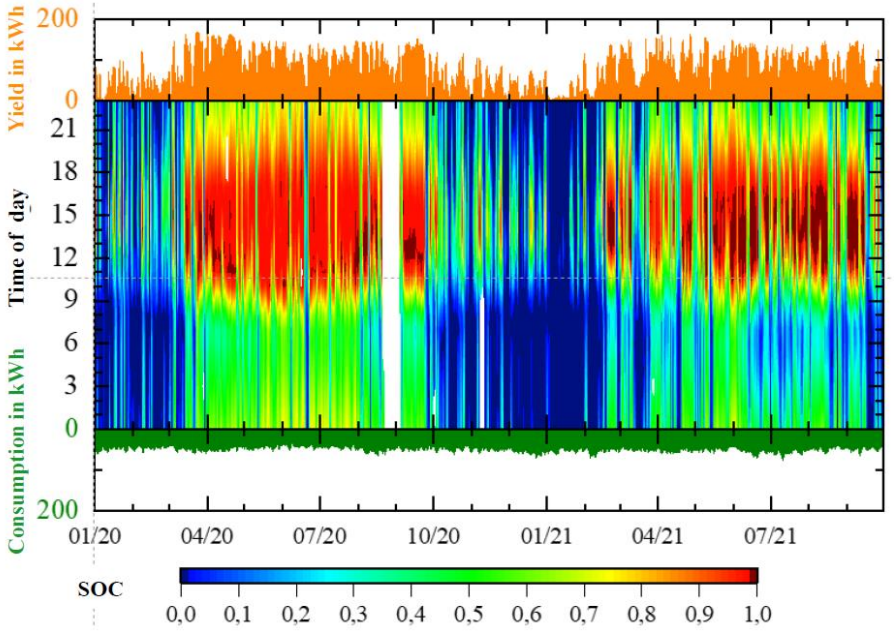

Fig. 4: Yield of PV system, charging status of accumulator, electricity consumption of buildings (house 1)

A detailed look at the consumption of the individual residential units in Figure 5 (left) shows that individual user behaviour has a significant influence on PV use. Residents who are still very active at night (night owls, orange arrow) consume more electricity at night and less in the morning. This means that less PV electricity is consumed directly in these residential units, and more electricity is drawn from the accumulator or the grid at night. This is also shown in Figure 5 (right). The share of PV is lowest for the flat marked with orange arrow, e.g. in April. Due to the accumulator, however, the grid consumption of the flats is almost the same, regardless of user behaviour. The best behaviour for the building is marked in blue: a high share of electricity in the morning (and thus a direct use of PV yields) and a low share at night (and thus a low use of the accumulator).

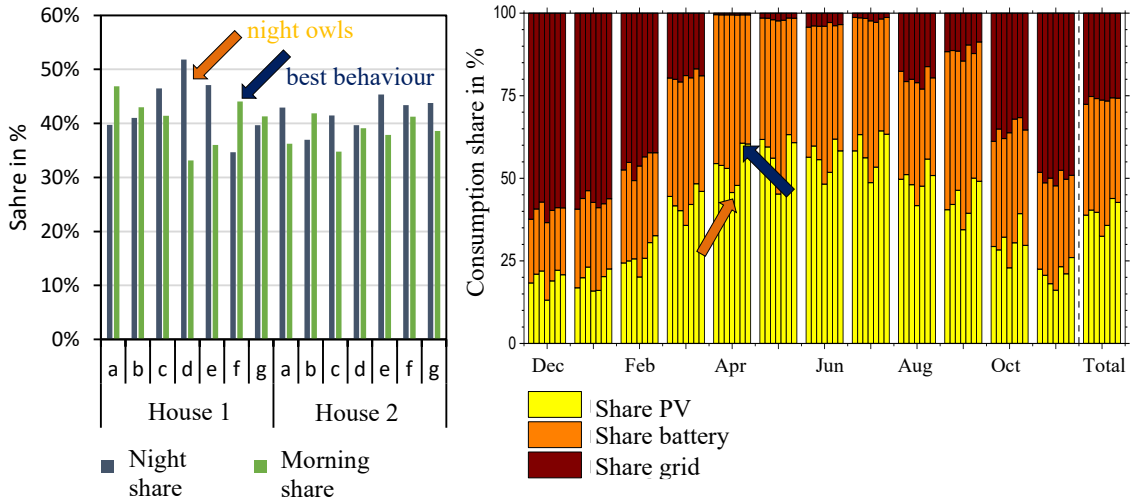

Fig. 5: Left: Electricity consumption by time of day (according to Weniger et al. 2015), Right: User-specific electricity mix, measurement period 12/2019-11/2020

In figure 6 an interpolated detailed temperature distribution inside the hot water storage is presented. Two to three facts are visible:

- a high temperature difference over the height of storage is detectable. Thus, a good layering of different temperatures is achieved.
- In 4-5 month per year the storage is unused
- The storage tank could be decreased for next buildings

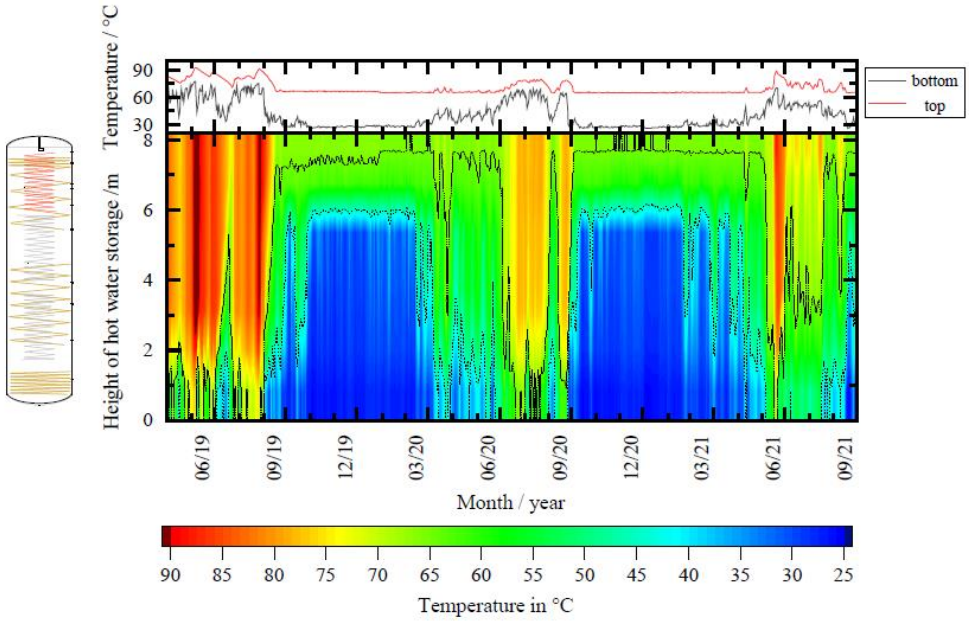

Fig. 6: Storage temperatures of hot water storage (house 1)

3. Conclusion

On the heating side, the first measured values are significantly higher than the planned values, and the user behaviour, among other things, was identified as a possible cause. For example, the users open the windows in the bedroom during the night without turning off the heating mode. Measurement results show that in one night in only one flat, this results in 27 kWh of additional heating demand. In addition, the measured values for room temperatures are between 2.5 and 5 K above the average values for energy demand calculation of living rooms.

The buildings examined in detail achieve the high planned solar fractions for electricity very well due to the generously dimensioned systems. The electricity consumption profile is comparable with literature values and does not show any conspicuous features. In general, it can be stated that a high level of equipment is used sparingly, which corresponds to the sociological tenant profile. In addition to the distribution of typical loads over the time of day, the total consumption of a residential unit can also influence the solar direct consumption share, whereby user behaviour over the time of day has a stronger influence. The installed electric storage tank is only fully used during the transition period between March and October. A smaller capacity would therefore be possible in future buildings with the same concept without restrictions for the residents. Furthermore, the storage tank could be planned some smaller to save valuable space in the building.

In the future, the integration of the buildings into a district will be investigated, e.g. surpluses from the solar thermal system will be passed on to surrounding residential buildings.

4. Acknowledgments

We would like to thank the German Federal Ministry for Economic Affairs and Climate Protection and the Project Management Organisation Jülich for the financial support and supervision of the eversol project (eversol.iwtt.tu-

freiberg.de, funding: 03ETS004). We would also like to thank the house owner eg Wohnen 1902 and all the technicians and students involved.



5. References

BDEW, 2017. Standardlastprofile Strom. https://www.bdew.de/energie/standardlastprofile-strom.

Directive 2010/31/EU of the European Parliament and of the Council of 19. May 2010 on, The energy performance of buildings: OJ L153 of 18.6.2010. English, in: Official Journal of the European Union, Art.9.

Großklos, M., Schaede, M., Hinz, H., 2016. Mehrfamilienhaus mit Energiegewinn, Cordierstraße 4, Frankfurt am Main, Endbericht der Messphase 2014-2016

Oppelt, L., 2019. Energetische Simulation und Evaluierung von zwei teilautarken Mehrfamilienhäusern mit Pauschalmiete. Masterthesis, TU Bergakademie Freiberg.

Storch, T., Wilde, L.-M., 2018. Gebäudestandards und Niedrigenergiehauskonzepte in Deutschland. Gebäudetechnik in Wissenschaft & Praxis – Recknagel Science, issue 3, vol. 139, S. 198-207, ISSN: 2195-643X,

stromspiegel.de. Stromspiegel für Deutschland 2019, accessed on 22.05.2019.

Techem, 2017. Techem Energiekennwerte 2017. Techem Energy Services GmbH, Corporate Communications, Eschborn.

Weniger J., Bergner, J., Tjaden, T., Quaschning, V. 2015. Dezentrale Solarstromspeicher für die Energiewende, Berliner Wissenschafts-Verlag, ISBN 978-3-8305-3548-5 (online: http://pvspeicher.htw-berlin.de

Hidden colored Building Integrated Photovoltaics: technology overview and design challenges

Martina Pelle[1,3], Elena Canosci[2], Gazmend Luzi[2] and Laura Maturi[1]

[1] Institute for Renewable Energy, EURAC Research, Bolzano, Italy

[2] SUNAGE sa, Balerna, Switzerland

[3] Department of Energy, Politecnico di Milano, Milano, Italy

Abstract

Colored building integrated photovoltaics (BIPV) modules can hide the PV cells behind colored patterns which hinder the perception of the cells so that the PV modules appear very similar to standard construction materials. This feature represented a turning point in the social acceptance of BIPV applications and a wide range of colors is currently available on the market. This wide selection enables PV to be easily integrated in architecture, also in traditional roofs, façades, and shading systems. Nevertheless, further R&D activities are needed to improve their performance and reliability. The manufacturing of these modules is predominantly customizable for a specific installation, whereby is essential to balance aesthetic and energy aspects, and this poses challenges in the evaluation of their technical performance. This work aims at presenting the possibilities for integrating PV in the building envelope, focusing on printed, coated or finished front glass to provide additional aesthetic features to the BIPV systems. An overview of technological solutions for introducing colors in BIPV modules is provided and the design challenges for colored BIPV integration in the building stock are discussed, by presenting some exemplary case studies.

Keywords: BIPV; appealing PV; aesthetics; color; component performance; customization; cost-benefit.

1. Introduction

Transforming the building stock into nearly zero or positive energy is a key aspect to meet the decarbonization targets worldwide (United Nation Framework Convention on Climate Change in 21st Conference of the Parties 2015; Chiang et al. 2013; European Parlament 2018). In this context, building integrated photovoltaic (BIPV) technologies stand as a promising solution to harvest solar energy for on-site and diffuse energy production, contributing to the transition from fossil fuels to cleaner energy to be used in buildings (Michas *et al.*, 2019). BIPV systems are multifunctional envelope elements, which can be integrated into the building skin at three different levels: (i) aesthetic, i.e., by meeting the architectural language of the building; (ii) technological/functional, i.e., by fulfilling all the functional requirement of a standard envelope component; (iii) energy, by interacting efficiently with the energy systems of the building, increasing the share of renewables used to cover the building's energy use (Maturi and Adami, 2018). Despite their high potential, the large-scale application of BIPV has been hampered due to the difficulty of traditional photovoltaic modules in meeting the aesthetic features of conventional architectural materials (Saretta, Bonomo and Frontini, 2018). The introduction of colored BIPV modules represented a breakthrough in the spread of BIPV installations and their social acceptance ("PV Accept"; "3ENCULT: Efficient Energy for EU Cultural Heritage"; "BIPV Meets History: Value-Chain Creation for the Building Integrated Photovoltaics in the Energy Retrofit of Transnational Historic Buildings"). The aesthetic improvements of BIPV technologies may unlock the solar potential of a large set of vertical and horizontal envelope surfaces that would not be exploited otherwise, but it requires a very high customization level, concerning colors, shapes, sizes, finishing (Huang *et al.*, 2019; Lovati *et al.*, 2019). Therefore, one of the main challenges in the design of hidden colored BIPV modules is the balance between aesthetic and energy aspects, i.e., the optimization of the technical performance of highly customizable products against the real requirements of the built environment. In particular, there is the need to improve the awareness on colored BIPV technologies with regards to their multifunctional integration features, assessing their performance reliably as envelope components and as well power generation systems (Pelle *et al.*, 2020). This work aims at presenting the technological solutions for integrating PV in the building envelope, focusing on printed, coated or finished front glass used in front of a PV layer, to provide additional aesthetic features to the final product. Firstly, an overview of technological solutions exploiting colored layers to modify BIPV modules' appearance is presented, with a particular focus on the methodologies used to link aesthetic and energy features, i.e., modules' color and

© 2022. The Authors. Published by International Solar Energy Society
Selection and/or peer review under responsibility of Scientific Committee
doi:10.18086/eurosun.2022.01.10 Available at http://proceedings.ises.org

efficiency. Then, the design challenges for the multilevel integration of BIPV systems in the envelope are discussed. Specific focus is given to architectural integration, and detailed discussion on the customization possibility of products is presented, based on specific aesthetic parameters. Finally, exemplary case study collection, using colored BIPV as envelope solution, is provided.

2. Technological solution for hidden colored PV modules

High customizable BIPV technologies guarantee larger aesthetical possibilities, required by architectural applications to ensure flexibility in the design (Pelle *et al.*, 2020). The ability of BIPV products to match the architectural language and composition of buildings, through different shapes, dimensions, colors, and textures represent a clear advantage for BIPV integration in the building envelope (A. Scognamiglio, A. Berni, F. Frontini and Maturi, 2012; Farkas *et al.*, 2012; Franco and Magrini, 2017). Large possibilities for customization constitute on one hand the strength and the uniqueness of BIPV products in the PV scene, but on the other hand, it could also represent a limit for industrial production and cost reduction (Gewohn *et al.*, 2021). Different customization techniques to obtain colored or textured BIPV modules are currently used. They mainly differ from the position and kind of colored layer used for manufacturing (Grobe, Terwilliger and Wittkopf, 2020). Colored layers can be introduced as part of the active layer or added to the module's assembly, as a further component of the module stuck, behind or in front of the active layers (Eder *et al.*, 2019). The introduction of a colored layer behind the active components of the PV module does not interfere with the conversion of solar radiation into electricity, thus it does not affect the energy yield of the system. Whereas, when colored layers are interposed between the active layer and the light source, or it is integrated within the active layer, it modifies the spectral power distribution of the solar radiation available for power conversion, since part of it is reflected, in the visible spectrum, to display colors (Peharz and Ulm, 2018; Halme and Mäkinen, 2019; Røyset, Kolås and Jelle, 2020). Integrating the color in the active layer of PV technologies means that the color is introduced in the manufacturing process of the PV cells, within the active layers. This is possible, for example, by including different dyes in the production of perovskite solar cells, dye-sensitized solar cells (DSSCs) or luminescent solar concentrator (LSC) or employing active materials that exhibit different absorption spectra in semitransparent organic photovoltaic cells (OPVs) (Kuhn *et al.*, 2021). The BIPV modules produced with such a technique present a uniform, semitransparent colored appearance. Another possibility is to optimize the thickness and the refractive index of the passivation or anti-reflection coating (ARC) of silicon or CIGS PV cells (Pascual-San José *et al.*, 2018; Ji *et al.*, 2019). This process results in different colored cells, according to the coating typology and thickness. Interposing a solar layer between the active layer and the light source means that an additional colored layer is added to the modules stuck, during the lamination process, without interfering with the manufacturing of the active layer. The colored layer can be added in interlayers or encapsulant films or through the modification of the front glass, that can be printed, coated or textured, according to the architectural needs. Colored additional layers can be used in the lamination of several BIPV technologies, including crystalline and amorphous silicon, thin-film, perovskite (Kuhn *et al.*, 2021). Among interposed colored layers, some present almost endless customization possibilities, such as BIPV modules with printed, coated or finished front glass, polymeric interlayer or textile additional layers that can be digitally printed. In the following, the focus is given on this kind of technology, which can guarantee a higher level of flexibility in the design choices, while relaying on robust and efficient technology, such as c-Si PV cells as active layer. In particular, the design challenges to be addressed for a correct multilevel integration of BIPV systems in envelope are highlighted, and the possibility for customization presented.

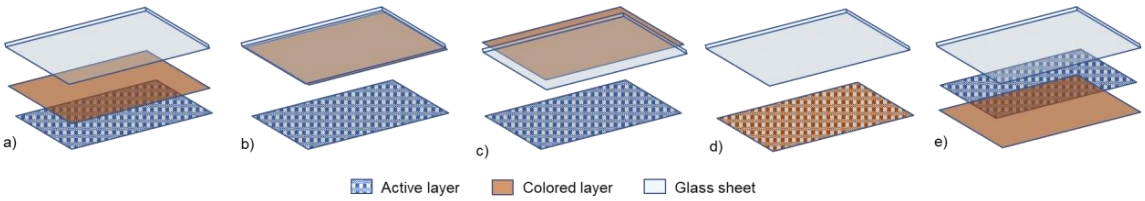

Fig. 1. Schematization of the customization techniques to obtain colored or textured BIPV modules: a) colored interlayer or encapsulant; b) colored coated front glass; c) colored layer on top of the front glass; d) colored or coated active layer; e) colored back sheet.

3. Design challenges for BIPV architectural integration

Aesthetical integration of BIPV is crucial for boosting the spread of BIPV technologies. Highly customizable products allow designers to study and select freely the best integration features of BIPV modules in their projects. But it is always important to keep in mind the multifunctionality of BIPV modules as technological envelope

elements. To guarantee the complete freedom of expression for designers, there must be a sufficient range of modules, colors, and finishing, so that it is possible to design using these elements as traditional building materials, as stone, metal, and glass. Existing BIPV modules can be produced in a wide range of sizes or shapes, but consideration should be given to the required electrical system, consisting of PV cells and electrical connections. Therefore, the architectural and technical design must be addressed simultaneously. To obtain the best results out of BIPV installation, designers must consider the energy generated by the modules as a part of an integrated design process, that includes architectural, technological and energy aspects. Moreover, since every building is different, in terms of shape, landscape context, size, function, etc., the design of BIPV systems should also consider the context in which the PV modules are applied. For example, the integration of BIPV modules with a shining finish on the façade of a building could cause glare problems to the surroundings, and this is particularly critical in dense urban environments and in presence of high traffic streets. Nowadays market provides a wide range of possibilities to customize BIPV installation, but the multifaced available technical solutions could make module selection complex for the designer, who needs proper information to support the design choices on the three integration aspects. In (Pelle *et al.*, 2020), a methodology is provided, for the evaluation and selection of the most suited BIPV technology to be used in a specific project. The study identifies the specific parameters needed to better assess BIPV integration features. From a technological integration point of view, BIPV technologies that provide multifunctionality, i.e., the possibility to be used in different envelope positions by choosing the appropriate mounting system (e.g., as façade rain-screen and as a roof tile) facilitates the standardization of the products manufacturing and the procurement design. From the energy integration point of view, it is always fundamental to consider the efficiency and nominal power of the specific product. The most challenging aspects to be considered are the ones related to aesthetic integration, which, as said, could affect all the design levels. Among these, shape, and dimension, color, which affects the modules' efficiency, and the finishing, which influences the modules' reflectance, are identified as crucial information for the system design. Hereafter, a detailed overview of these design parameters for BIPV technology is provided.

3.1 Dimension

The use of standard single-sized BIPV modules on building facades is prevented by numerous obstacles such as windows, doors, roof pitches, etc. For this reason, the BIPV modules must adapt to the geometry of the façade. Most of BIPV modules can be customized in shape and size. In the case of new buildings, priority is given to making the module size as homogeneous as possible, but this is not always achievable. In the case of renovations, however, the BIPV modules always have to adapt to the geometry of the existing façade. Consideration should be given to the required electrical system consisting of PV cells and electrical connections. Currently, standard BIPV modules based on silicon PV cells use cells of size 156.75 x 156.75 mm or 158.75 x 158.75 mm, although the current market is moving towards larger cells. The modules' electrical components must adhere to specific regulations (IEC 61215, IEC 61730, LU1703) to guarantee optimal functioning and safety. For example, all active elements within the module must be spaced at least 8 mm away from the edge of the glass, and distances of up to 20 mm are possible for safety reasons. As a consequence, if the architectural design requires module dimensions that are too small to accommodate the circuit board with the PV cells while complying with the specific standard (the minimum size for an active module accommodating standard c-SI cells is 360x360 mm), dummy modules, i.e., passive PV modules that are aesthetically identical to active modules but without PV cells must be manufactured, to guarantee chromatic and materic uniformity to the façade. The introduction of passive façade components has an impact also on the energy integration of the BIPV system since it implies a smaller surface available for energy production.

3.2 Finishings

In addition to the dimension, architects and designers can also customize the finish of the front glass. Solar glass, which has a microstructure that allows the best performance of the module in terms of efficiency, is mostly used for roof-integrated modules. Shining glass is mainly used for PV modules that can be integrated into facades or balconies. Nonetheless, the integration with this glass type must be carefully considered because of its high reflectance that may cause glare in the surrounding area. On the contrary, sating glass provide antireflective feature allowing an easier integration into all vertical and horizontal surfaces of the building. One of the latest innovations in the BIPV scene is structured glass. In this case, the front glass sheet of the BIPV module is provided with tridimensional patterns. There are different possibilities for structured glass customization, including vertical and/or horizontal lines or sanding, that allows the BIPV module to better mimic the texture of a traditional building material (Fig. 2).

3.3 Colors and patterns

To provide better integration of PV modules in all environmental contexts and building types, architects and designers have the opportunity to customize the front glass of the BIPV module. The customization can provide

uniform colors and reproduce an image or texture on the front glass (Fig. 3). For example, it is possible to reproduce the pattern or a high-resolution photograph of traditional building materials, so that the modules can be perfectly integrated into the surrounding traditional landscape. In cases of renovation of an existing building, the exact texture of the original material can be replicated on the BIPV modules. This solution is mainly adopted where landscape constraints for the integration of BIPV modules are present. The color shades or the pattern can be chosen from a standard palette, but it is also possible to customize modules design depending on the project requirements. As explained before, each color has a different effect on the efficiency of the PV modules. For standard colors (e.g., traffic white, terracotta, brown, greyish blue, green) the electrical specifications are determined, whereas in customized colors they are usually determined by post-production tests.



Fig. 2. Examples of modules' size customization for adapting the BIPV system to the façade geometry. On the left; Wohnüberbauung Männedorf Project, Männedorf, Switzerland (2020-2021) on the right: Opfikon Project, Opfikon, Switzerland (2018). Images courtesy of SUNAGE sa.

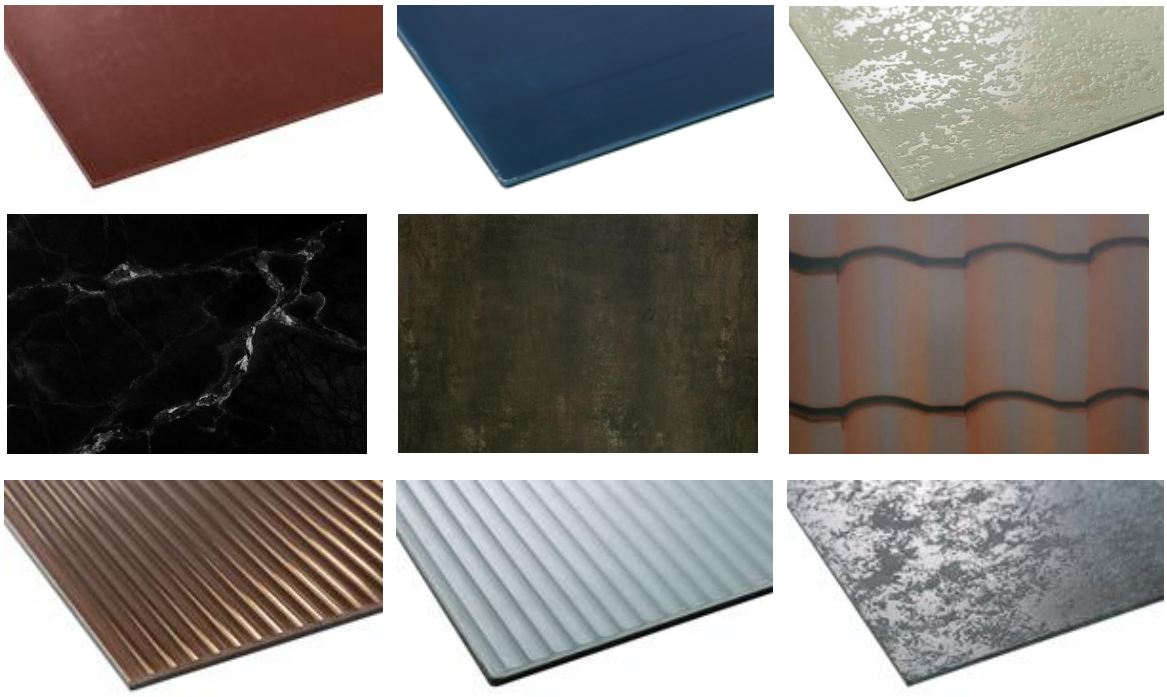

Fig. 3. Examples of customized colors and patterns. From the top left: terracotta color, grayish-blue color, sanded light green, marble pattern, cortex pattern, roof tiles pattern, vertical lines bronze, vertical line grey and sanding. Images courtesy of SUNAGE.

4. Colored BIPV: case study collection

In the following, some exemplary case studies that used colored and/or textured BIPV modules in the envelope (façade and/or roof) are reported and discussed. The peculiarity of each project in terms of design challenges are highlighted, describing the technical solution introduced to address them. Each case study is presented with a short introduction, a technical sheet providing information on the building type, the power installed, the efficiency of the installed BIPV modules, the BIPV installation surface, the number and type of the installed modules, their color and

finishing. Then a short description of the most peculiar design features of the BIPV system are provided and a discussion on the technical solution adopted is presented.

4.1 Multi-functional Centre of Pregassona, Lugano, Switzerland (2020-2021)

Multi-functional "zero energy" building. It currently has the largest BIPV facade in Ticino and hosts:

- a medical residence for elderly people.
- a day-care center for senile dementia patients
- the new headquarters of the Municipal Social Welfare Service (SAS);
- a kindergarten.

This project was commissioned by the municipality of the city of Lugano. The project was determined by a public tender and was initially designed with a traditional white panel façade. After the project was approved and in progress, the architect and the client decided to transform the facades into an active surface by integrating BIPV modules. The building is very complex and consists of 10 different facades with different exposures. As the project was already underway, the BIPV modules had to be adapted to the existing design in terms of shape and color. Minimum efficiency of the PV system on the façade was required by the designers and the client to facilitate the investment. The color required by the architectural design was white, and it could not be changed. White color is very difficult to achieve in c-Si BIPV, as the PV cells underneath the colored layer are black. Therefore, achieving the required efficiency with the already established color was a challenge. The color design required numerous samples and tests, but in the end, the desired result was achieved. Furthermore, the size of the PV modules could not be changed from the original design. For this reason, different sizes were needed and modules up to a size of 0.9 x 2.905 m were produced. For a better energy yield, depending on the exposure of the building, irradiation models were made to study the shadows cast over the building from the surroundings. The results of these analyses have been used to determine the best configuration of the electrical circuit within the PV modules so to reduce the impact of the shadows on the global efficiency of the BIPV system.



- Type of building: Public
- Power installed: 220 kWp
- Efficiency: 13.5%
- Surface: 1'675 sqm
- Number of modules: 806
- Type of modules: Glass / Glass 4+4 mm
- Color: Light grey
- Finishing: Front satin glass

Fig. 4. Pregassona project, Switzerland: overview of the solar façade (left) and BIPV modules' detail (in the center). On the right: project's figures. Images courtesy of SUNAGE

4.2 Project Thalwil, Switzerland (2020)

This project has been developed by Tobler Litscher GmbH firm. The building is characterized by the brown structured glass BIPV modules on the facade, and it also includes a customized grey solar roof made with structured glass BIPV modules. The modules were produced in a uniform brown color to blend in with the surrounding landscape and to match the colors of the window frames. All facades and the roof are covered with the same type of BIPV modules. The glass front is structured in vertical lines with a shining finish. The façade modules were custom-made but are designed to be almost all the same size, to lower the production costs. The roof modules were also custom made and have different shapes to suit the shape of the four-pitch roof.



- Type of building: Residential
- Power installed: 32 kWp
- Efficiency: 12.3%
- Surface: 264 sqm
- Number of modules: 282
- Type of modules: Glass / Glass 4+4 mm
- Color: Brown (façade): Brown (roof)

Finishing: Front structured shining glass type BA with vertical lines

Fig. 5. Thalwil project, Switzerland: overview of the solar façade (left) and BIPV modules' detail (in the center). On the right: project's figures. Images courtesy of SUNAGE

4.3 Solar Living Kloten Kloten, Switzerland (2020)

The Kloten project is a private multi-family building. The BIPV modules were designed with only 2 different sizes and in 3 different colors. The modules combined with different colors give movement to the façade, like a mosaic. The architect's stylistic choice also opted for a structured satin-finished glass with vertical lines to further mark the direction of the modules. The modules do not cover all the available surfaces of the façades, but only some vertical bands. The modules blend into the building façade with other traditional building materials.





- Type of building: Residential
- Power installed: 26.7 kWp
- Efficiency: 14.9%
- Surface: 223 sqm
- Number of modules: 408
- Type of modules: Glass / Glass 4+4 mm
- Color: 3 different shades of green
- Finishing: Front structured satin glass type BA with vertical lines

Fig. 6. Kloten project, Switzerland: overview of the solar façade (left) and BIPV modules' detail (in the center). On the right: project's figures. Images courtesy of SUNAGE

4.4 Erschmatt Project Erschmatt, Switzerlan (2020)

The Erschmatt project is a traditional mountain-dwelling typical of Switzerland's Alpine environment. The traditional tiles roof blends with the terracotta BIPV modules. The architects wanted to intervene on an existing traditional building by applying BIPV modules on a portion of the roof. Because of the valuable surroundings, modules were chosen to be reminiscent, in terms of color and mounting system, of the traditional tile covering which were installed on the other roof surfaces. The photovoltaic modules were applied on both sides of the roof, given the building's excellent exposure. The brown-colored modules reproduce the traditional tile roofing, provide aesthetical integration for the BIPV components into the building and the surrounding landscape.





- Type of building: Residential
- Power installed: 10.64 kWp
- Efficiency: 15.75 %
- Surface: 69.50 sqm
- Number of modules: 70
- Type of modules: Glass / Glass 3.2+3.2 mm
- Color: Terracotta
- Finishing: Front solar glass

Fig. 7. Erschmatt project, Switzerland: overview of the solar façade (left) and BIPV modules' detail (in the center). On the right: project's figures. Images courtesy of SUNAGE

5. Conclusion and future work

On-site production from renewable energy is pivotal for promoting zero energy or positive buildings and building integrating photovoltaics (BIPV) constitute a valuable solution to integrate PV technologies in the building envelope. The introduction of colored BIPV modules represented a breakthrough in spreading BIPV installations and improving their social acceptance, due to the difficulty of traditional photovoltaic modules in meeting the aesthetics features of conventional architectural materials. High customizable BIPV technologies guarantee larger aesthetical possibilities, required by architectural applications to ensure flexibility in the design. The ability of BIPV products to match the architectural language and composition of buildings, through different shapes, dimensions, colors, and textures represents a clear advantage for BIPV integration in the building envelope. Nowadays market provides a wide range of possibilities to customize BIPV installation and different customization techniques to obtain colored or textured BIPV modules are used, even if further R&D is needed to improve their performance and reliability. Among colored technologies, some guarantee a higher level of flexibility in the design choices, allowing almost endless customization possibilities while relying on robust and efficient technology, such as c-Si PV cells. This is the case of BIPV modules with printed, coated, or finished front glass, polymeric interlayer or textile additional layers that can be digitally printed. Nonetheless, architectural and technical design must be addressed simultaneously, considering that BIPV envelope components host an electrical system, consisting of PV cells and electrical connections. Therefore, the modules' energy generation should be addressed as a part of an integrated design process,

that includes architectural, technological and energy aspects, to obtain the best results out of BIPV installation. The most challenging aspects to be considered are related to aesthetic integration, which could affect all the design levels. Among these, modules characteristics that are identified as crucial for a better design are (i) the shape and dimension, (ii) the color, which affects the modules' efficiency, and (iii) the finishing, which influences the modules' reflectance. In this work, these features are investigated in deep, and the challenges that they pose for a correct multilevel integration of BIPV systems in the envelope are highlighted by providing exemplary case studies. Future challenges for colored BIPV systems will deal with balancing industrialization and customization aspects, to make BIPV technologies more competitive and profitable. In fact, the use of colored front glass may result in an extra cost up to + 40%, when compared to standard glass-glass BIPV modules with transparent front glass, while using a colored and structured glass may result in an extra cost up to + 60%. A possible solution to support this process, is the development of tools that allow the prediction of the energy yield for arbitrary chosen colors or patterns. These tools would provide manufacturers with useful information on both the aesthetic appearance and on the energy performance of colored PV modules, avoiding the manufacturing and testing of prototypes for new customized products. These aspects are currently investigated within the Horizon 2020 INFINITE project ("INFINITE Building Renovation").

6. Acknowledgments

The INFINITE project has received funding from the European Union's Horizon 2020 research and innovation programme under grant agreement No 958397. This paper reflects only the author's view, neither the European Commission nor HADEA are responsible for any use that may be made of the information it contains.



Operation co-financed by the European Union, European Regional Development Fund, the Italian Government, the Swiss Confederation and Cantons, as part of the Interreg V-A Italy-Switzerland Cooperation Program, within the context of the BIPV meets History project (grant n. 603882).

7. References

3ENCULT: Efficient Energy for EU Cultural Heritage (no date). Available at: http://www.3encult.eu/en/project/welcome/default.html (Accessed: 5 June 2020).

A. Scognamiglio, A. Berni, F. Frontini, C. S. P. L. and Maturi, L. (2012) 'The Complex Dialogue between Photovoltaics and Pre-Existing: Starting Point for a Discussion', in *27th European Photovoltaic Solar Energy Conference and Exhibition*, pp. 4161–4168. doi: 10.4229/27thEUPVSEC2012-5BV.1.1.

BIPV meets history: Value-chain creation for the building integrated photovoltaics in the energy retrofit of transnational historic buildings (no date). Available at: http://www.bipvmeetshistory.eu (Accessed: 6 June 2020).

Chiang, Y.-F. *et al.* (2013) 'Non-color distortion for visible light transmitted tandem solid state dye-sensitized solar cells', *Renewable Energy*, 59, pp. 136–140. doi: 10.1016/j.renene.2013.03.018.

Eder, G. *et al.* (2019) 'Coloured BIPV-Market, Research and Development', p. 60. Available at: http://www.iea-pvps.org/fileadmin/dam/public/report/technical/IEA-PVPS_15_R07_Coloured_BIPV_report.pdf.

European Parlament (2010) *DIRECTIVE (EU) 2010/31. Energy performance of buildings*. Available at: http://data.europa.eu/eli/dir/2010/31/oj.

European Parlament (2018) *DIRECTIVE (EU) 2018/844. Energy performance of buildings*.

Farkas, K. *et al.* (2012) *International Energy Agency, T.41.A.2: Solar Energy Systems in Architecture - Integration Criteria and Guidelines Subtask A: Criteria for Architectural Integration*. Available at: https://task41.iea-shc.org/Data/Sites/1/publications/T41DA2-Solar-Energy-Systems-in-Architecture-28March2013.pdf.

Franco, G. and Magrini, A. (2017) *Historical Buildings and Energy*. Cham: Springer International Publishing. doi: 10.1007/978-3-319-52615-7.

Gewohn, T. *et al.* (2021) 'Predicting color and short-circuit current of colored BIPV modules', *AIP Advances*, 11(9), p. 095104. doi: 10.1063/5.0063140.

Grobe, L. O., Terwilliger, M. and Wittkopf, S. (2020) 'Designing the colour, pattern and specularity of building integrated photovoltaics', in *Proceedings ATI 2020: Smart Buildings, Smart Cities*. Izmir, pp. 44–53. doi:

10.5281/ZENODO.4049446.

Halme, J. and Mäkinen, P. (2019) 'Theoretical efficiency limits of ideal coloured opaque photovoltaics', *Energy & Environmental Science*, 12(4), pp. 1274–1285. doi: 10.1039/C8EE03161D.

Huang, P. *et al.* (2019) 'Transforming a residential building cluster into electricity prosumers in Sweden: Optimal design of a coupled PV-heat pump-thermal storage-electric vehicle system', *Applied Energy*, 255, p. 113864. doi: 10.1016/j.apenergy.2019.113864.

INFINITE Building Renovation (no date). Available at: https://infinitebuildingrenovation.eu/ (Accessed: 28 February 2022).

Ji, C. *et al.* (2019) 'Vivid-colored silicon solar panels with high efficiency and non-iridescent appearance', *Nanoscale Horizons*, 4(4), pp. 874–880. doi: 10.1039/c8nh00368h.

Kuhn, T. E. *et al.* (2021) 'Review of technological design options for building integrated photovoltaics (BIPV)', *Energy and Buildings*, 231. doi: 10.1016/j.enbuild.2020.110381.

Lovati, M. *et al.* (2019) 'New method for the early design of BIPV with electric storage: A case study in northern Italy', *Sustainable Cities and Society*, 48, p. 101400. doi: 10.1016/j.scs.2018.12.028.

Maturi, L. and Adami, J. (2018) *Building Integrated Photovoltaic (BIPV) in Trentino Alto Adige*. Cham: Springer International Publishing (Green Energy and Technology). doi: 10.1007/978-3-319-74116-1.

Michas, S. *et al.* (2019) 'Identifying Research Priorities for the further development and deployment of Solar Photovoltaics', *International Journal of Sustainable Energy*, 38(3), pp. 276–296. doi: 10.1080/14786451.2018.1495207.

Pascual-San José, E. *et al.* (2018) 'Comparing the potential of different strategies for colour tuning in thin film photovoltaic technologies', *Science and Technology of Advanced Materials*. Taylor & Francis, 19(1), pp. 823–835. doi: 10.1080/14686996.2018.1530050.

Peharz, G. and Ulm, A. (2018) 'Quantifying the influence of colors on the performance of c-Si photovoltaic devices', *Renewable Energy*. Elsevier Ltd, 129, pp. 299–308. doi: 10.1016/j.renene.2018.05.068.

Pelle, M. *et al.* (2020) 'Coloured BIPV Technologies: Methodological and Experimental Assessment for Architecturally Sensitive Areas', *Energies*. MDPI AG, 13(17), p. 4506. doi: 10.3390/en13174506.

PV Accept (no date). Available at: http://www.pvaccept.de (Accessed: 5 June 2020).

Røyset, A., Kolås, T. and Jelle, B. P. (2020) 'Coloured building integrated photovoltaics: Influence on energy efficiency', *Energy and Buildings*, 208. doi: 10.1016/j.enbuild.2019.109623.

Saretta, E., Bonomo, P. and Frontini, F. (2018) 'Active BIPV glass facades: current trends of innovation', in *GPD Glass Performance Days 2017*. Tampere, Finland.

United Nation Framework Convention on Climate Change in 21st Conference of the Parties (2015) *Paris Agreement*. Paris.

EUROSUN 2022
Answer to Reviewers' Comments
Paper: Analysis of Solar Thermal Polygeneration Systems for the Residential-Commercial Sector

We would like to thank the Reviewers for their efforts and insightful contributions to this manuscript.

Reviewer

This study has been well presented with a clear aim and methods. Some interesting results were achieved.

Answer: Thank you very much for your kind comments.

Sone minor parts may need to be clarified:

1. *for the performance simulation, if a commercial package was applied or just the theoretical calculations were used?*

Answer: As it is explained just before the subsection 2.3.1: *"A mixed-integer linear programming (MILP) model in LINGO (Schrage, 2016) has been developed to minimize the total annual cost of each system and to analyze its operation hour by hour throughout the year."*
Therefore, the software used for the calculations is only LINGO. No other commercial package has been used. In order to clarify this aspect, the next sentence has been included in subsections 1.3.1; 1.3.2 and 1.3.3: *"The objective function implemented in the LINGO software minimizes the total annual cost […]"*

2. *How to validate the calculations?*

Answer: The three systems modeled do not exist, therefore it is not possible to use experimental values for the validation. Nevertheless, we have compared the obtained results with those obtained by other authors as it is explained in the paragraph after Fig. 7 and previous to Section 3.2:
"The previous results are consistent and in agreement with those obtained by other authors, as for instance: Roumpedakis et al. (2020) proposed the design optimization of small-scale solar-driven ORC plants in Cyprus, Greece, and Turkey, considering different types of solar thermal collectors (flat plate, evacuated tube, and PTC). The results showed that the PTC presented better economic performance, with the lowest payback periods. Wu et al. (2018) assessed the economic and environmental performances of three solar-biomass hybrid Combined Cooling, Heat and Power (CCHP) systems, and obtained that the solar-ORC configuration had the best economic performance. Petrollese and Cocco (2019) proposed the pre-design of solar-based ORC systems taking into consideration the effects of heat source and heat sink variations. Shirazi et al. (2016) assessed the energy, economic and environmental performances of five solar heating and cooling absorption chillers taking into account the type of chiller and solar collector, as well as different climate conditions. It was observed that RATE with PTC resulted in the most energy-efficient and cost-effective plant configurations for regions with very high Direct Normal Irradiance (DNI) levels. Nevertheless, RADE with EFPC were also good alternatives for most regions."

© 2022. The Authors. Published by International Solar Energy Society
Selection and/or peer review under responsibility of Scientific Committee
doi:10.18086/eurosun.2022.01.11 Available at http://proceedings.ises.org

Building Energy Efficiency Enhancement Through Load Reduction in the Air Conditioning System

Rahul Kumar Sharma[a], Ashish Kumar[a,b] and Dibakar Rakshit[a]

[a]Indian Institute of Technology Delhi, New Delhi (India)

[b]Galgotias University, Greater Noida (India)

Abstract

The humid and hot climate of the Indian Subcontinent steers air conditioning (AC) ownership. These conditions are made worse by global climate change and the "heat island effect". India's energy outlook report predicts growth in electricity consumption for cooling by sixfold to 650 TWh by 2040, more than Germany's total today, and accounts for more than half of all building electricity consumption. Further, with the onset of COVID-19, the health and air-conditioning societies have modified guidelines and suggested incorporating fresh air from ambient conditions to dilute the indoor air and reduce the contaminant level. Phase change materials provide constant temperature operation and store thermal energy. The present study aims to design a shell and tube heat exchanger to reduce a load of an HVAC system by cooling the fresh air from ambient temperature and subsequently mixed with the recirculated air of the AC unit. The fresh air at 315 K flows through the inner tube of the heat exchanger with calcium chloride hexahydrate filled in the annulus. Additionally, the effect of incorporating longitudinal internal fins into the inner tube of the heat exchanger on energy saving is investigated. The designed heat exchanger with no fin, fin of 50 mm height, and 75 mm height led to an average energy saving of 3%, 4.95% and 5.56%, respectively, for 3600 s of operation. The proposed system will provide a guideline to the sustainable solution pertaining to the issue of increasing energy consumption by the HVAC system, hence making buildings energy efficient.

Keywords: HVAC, Building Energy Efficiency, Phase Change Material, Heat Exchanger

1. Introduction

Buildings are an essential and integral part of the human race and account for 20% of the total energy usage in the world(Conti et al., 2016). Almost 60% of this energy demand in tropical regions is required to maintain human thermal comfort (Abu-Hamdeh et al., 2021). India, a developing country lying in the tropical climatic zone of the earth, expects a twofold increase in the building floor area in 2040 compared to the building floor area in 2021(Energy Agency, 2021). Further, the units of air conditioners installed are expected to increase to 1.6 units per household and will increase India's consumption of electricity for cooling to 650 TWh by 2040, which is more than the total electricity consumption of Germany today and accounts for around half of all electricity consumption in buildings (Energy Agency, 2021). Energy efficiency improvements in air conditioners, as well as thermally efficient building design, cool roofs, and the use of alternative more efficient cooling appliances such as desert air coolers, could help to reduce the increase in cooling demand.

Phase change materials (PCM) that work on the principle of latent energy storage have good energy storage capacity, operate at a constant temperature range, and can absorb thermal energy when the temperature is higher than the melting point. At the same time, release the heat when the temperature drops below the melting point temperature. Due to the aforementioned properties, studies have been found with active applications in the preservation of food and pharmaceutical products (Belman-Flores et al., 2015), solar cooling and solar power plants (Aydin et al., 2015), photovoltaic electricity systems (Ma et al., 2015), solar dryers in the agricultural industry (Shalaby et al., 2014) waste heat recovery systems (Fang et al., 2014), domestic hot water (Seddegh et al., 2015), and enhancing the energy performance and thermal comfort in buildings. PCM increases the thermal mass of the building envelope and helps in energy management (Verma et al., 2023). With this technique, the insulating envelope absorbs the heat and releases it when the outdoor temperature drops, leading to a shift and decrease in the peak indoor loads. Over the years, PCM has been used in buildings in different configurations. The application of PCM to ceiling panels effectively reduces energy consumption through active cooling systems (Yahaya & Ahmad, 2011). PCM used in brick walls reduced 24.32% of the cooling load for the PCM wall under summer conditions(Wang et al., 2016). Window glazing with PCM has effectively reduced the cooling load(Fasi & Budaiwi, 2015). PCM-air heat exchangers (PAHX) can provide an efficient and effective solution to the problem of ambient air at a higher temperature. Yanbing et al.(Yanbing et al., 2003) combined the PAHX system with a night ventilation strategy for the moderate climate of Beijing and

© 2022. The Authors. Published by International Solar Energy Society
Selection and/or peer review under responsibility of Scientific Committee
doi:10.18086/eurosun.2022.01.12 Available at http://proceedings.ises.org

achieved a considerable enhancement in indoor thermal performance. Osterman et al.(Osterman et al., 2015) studied system thermal performance for free cooling and heating in Slovenia and observed its heating and cooling potential for different weather conditions.

The onset of COVID-19 affected human lives and the guidelines for cooling and heating the building envelopes. The Indian Society of Heating, Refrigerating and Air Conditioning Engineers (ISHRAE), American Society of Heating, Refrigerating and Air-Conditioning Engineers (ASHRAE) and health societies have suggested the incorporation of fresh air into closed spaces to dilute the air and reduce contamination levels in closed areas (Kapur et al., 2020; Washington State Department of Health, 2020). During the summer, the ambient temperature in Delhi may reach 315 K, as per the observation from the weather station at the Indian Institute of Technology Delhi. In typical air conditioners, the air from the room is recirculated to the air-conditioning unit (AC). However, when fresh air is introduced, a portion of the total air is replaced by the ambient air at ambient conditions, as illustrated in Figure 1. Hence it will further increase the energy consumption of the AC unit and thereby the energy consumed by a building (Kumar Sharma et al., 2022).

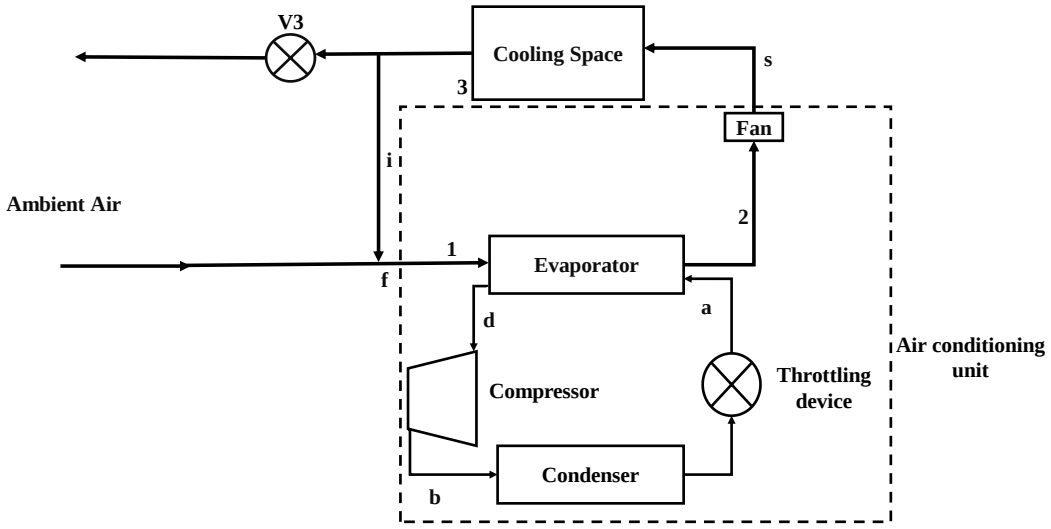

Figure 1 Schematic Layout of a conventional air-conditioning system with fresh air incorporation

The literature review has suggested the PCM capabilities to act as a thermal energy storage system and enhance buildings' energy efficiency via different designs and configurations. However, its application with the HVAC system in buildings is not being explored. The reports by various agencies indicate a steep rise in HVAC systems in the coming decades. The present numerical study uses a PCM-based shell and tube heat exchanger to make an AC system with fresh air incorporation more energy efficient. The heat exchanger is used to cool the fraction of ambient air before mixing it with the recirculation air, reducing the AC unit's cooling load and making it more energy efficient. Further, the effect of enhancing the heat transfer rates using fins is also analysed in the study. So the heat exchanger design is tested for three configurations, unfinned, 75 mm × 5 mm, and 50 mm × 5 mm, with six longitudinal fins.

2. Physical Domain

In the present study, a type of latent heat energy storage system (LHESS) is considered for cooling the air. The system is a simple shell and tube heat exchanger. The tube diameter is 200 mm, made of aluminium with a thickness of 5 mm and a shell diameter of 250 mm, while the heat exchanger length is 1500 mm, as shown in figure 2(a). The PCM considered for the study is calcium chloride hexahydrate, having a melting temperature of 30°C. Air flows through the heat exchanger and releases its thermal energy, which gets stored in the latent heat energy storage medium. Since the thermal diffusivity of air is low, six equidistant longitudinal internal fins are incorporated, which are placed at 60° radial angle with two sets of fin dimensions, one of 50 mm height and 5 mm width, while the other has dimensions of 75 mm in height and 5 mm in width.

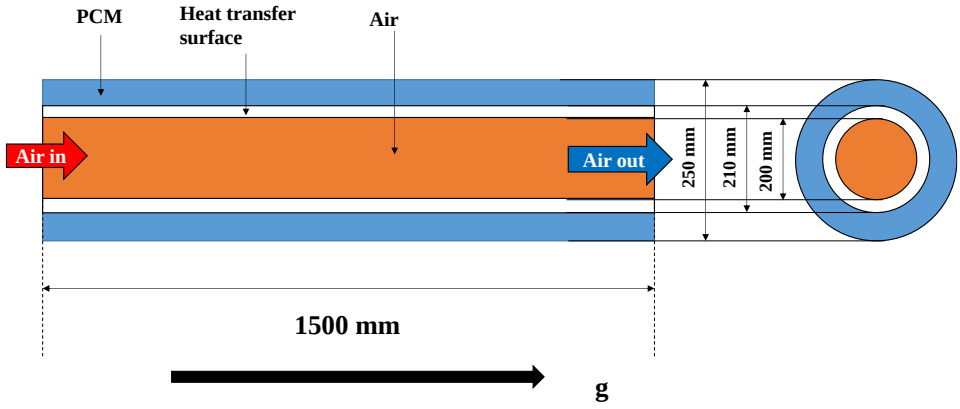

(a)

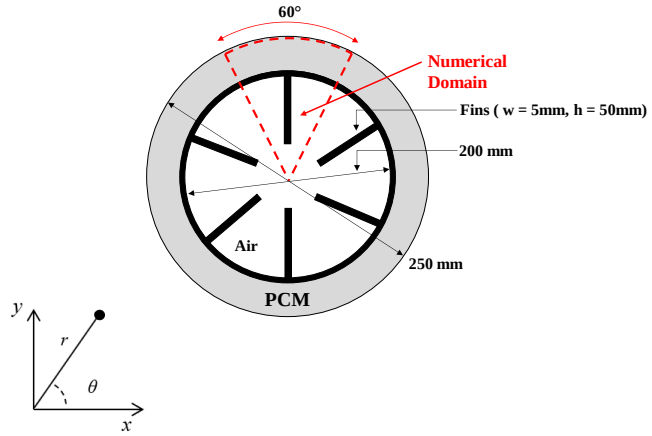

(b)

Figure 2: (a) Schematic of PCM-based shell and tube heat exchanger (b) Physical domain

To reduce the computational time and effort, the analysis is considered by considering one-sixth axisymmetric three-dimensional domain of the LHESS by imposing symmetrical boundary conditions and assuming a constant velocity at the inlet, as shown in figure 2(b). The considered axisymmetric case will replicate the heat transfer and flow phenomenon of the complete shell and tube heat exchanger. The thermophysical properties of calcium chloride hexahydrate, air and aluminium are mentioned in table 1. The velocity of the air inlet is fixed at 6 m/sec. After passing the air through the heat exchanger, the air is mixed with a fraction of recirculation air and fed to the AC unit. The AC unit works on a vapour compression refrigeration cycle with a compression ratio of 5 and maintains the office space at 300 K.

Table 1 Thermophysical properties of PCM, Air and Aluminium

Properties	**$CaCl_2.6H_2O$**(Das et al., 2021)	**Air**	**Aluminium**
c_p (kJ/kg.K)	2.230	1.006	8.710
ρ (kg/m^3)	1538	1.225	2719
k (W/m/K)	0.546	0.242	202.4
μ(kg/m.s)	0.1	1.789×10^{-5}	-
Latent heat(kJ/kg)	170	-	-
β (K^{-1})	0.0005	-	-
T_m (K)	303	-	-

3. Mathematical Modelling

A three-dimensional axisymmetric numerical model is used to solve the transient heat transfer and fluid flow in the shell and tube LHESS. An enthalpy porosity approach based on a fixed grid is used to illustrate the phase change behaviour of PCM. For the development of the numerical model, a few assumptions are made: (a) the phase change of the PCM occurs at a constant temperature, (b) the effect of expansion and contraction during the solidification and melting of PCM is excluded, and (c) the thermophysical properties of PCM, air, and pipe material are isotropic and temperature-invariant, except for the density of PCM in the direction of gravity (z-direction). The conservation equations for the PCM, air, and pipe are written in vector form as follows:

Continuity equation:

$$\frac{\partial(\rho_i)}{\partial t} + \nabla.(\rho_i V_i) = 0 \qquad \text{(eq. 1)}$$

Momentum equation:

$$\frac{\partial(\rho_i V_i)}{\partial t} + V_i \nabla.(\rho_i V_i) = -\nabla P + \nabla^2[\mu V_i] + AV_i + S_z \qquad \text{(eq. 2)}$$

Energy equation:

$$\frac{\partial(\rho_i c_{p,i} V_i)}{\partial t} + V_i \nabla.\left(\rho_i c_{p,i} V_i\right) = \nabla^2[k_i T_i] + S_{TP} \qquad \text{(eq. 3)}$$

Here i represent PCM, and for air, there is no source term and AV_i. In the case of the tube, only the energy equation is solved. The source term in the conservation of momentum equation for PCM represents the Boussinesq approximation in the z-direction, which assumes no change in thermophysical properties other than the fluid's density and can be expressed as :

$$S = \rho g \beta (T_p - T_m) \qquad \text{(eq. 4)}$$

Where β is the thermal expansion coefficient, and T_m is the melting temperature of PCM, while the parameter A can be represented as :

$$S = -A\frac{(1-\beta)^2}{\delta^3 + b} \qquad \text{(eq. 5)}$$

The source term in equation 3 is known as nodal latent heat revolution with time and is a function of temperature. The source term can be represented as :

$$S_{TP} = -\frac{\partial(\rho \Delta E)}{dt} \qquad \text{(eq. 6)}$$

ΔE represents the nodal heat value content, and its value varies from zero to latent heat of fusion.

In the present study, PCM is assumed to have the same solidus and liquidus temperatures. After the energy is transferred from the air to PCM through the aluminium finned/unfinned surface, the air is fed to the AC unit.

Initial and boundary conditions –

To minimise the sensible heating of PCM before melting, the initial temperature condition in the present study is considered relatively lower than the melting point of the PCM. The initial temperature condition can be expressed numerically as:

$$T(r,\theta,z,0) = 315\ K \qquad \text{(eq. 7)}$$

The boundary condition to solve the mass, momentum and energy conservation equation for air and PCM zone are :

(a) For the air domain:

(i) u = 0, at wall

(ii) z = 0, $u_z = u_{in}$ and $T_z = T_{in}(t)$ at inlet

(iii) p = 0 at outlet

(b) For the PCM domain:

(i) u = 0, at wall

(ii) At θ = -30˚ and θ = 30˚, symmetric boundary condition is imposed. i.e. $\frac{\partial \phi}{\partial n}\Big|_{sym} = 0$ and $\phi.\vec{n} = 0$

where, ϕ is either u or T and n is the unit vector normal to the surface.

3.1 Solution procedure

The governing equations (2), (3), (4) are iteratively solved using the Finite Volume Method (FVM), and the SIMPLE scheme is used for pressure-velocity coupling. The spatial discretisation of momentum and energy equations is carried out using power law. Ansys Fluent V2021 is a commercially available software to solve governing equations with suitable initial and boundary conditions. The convergence criteria for momentum and energy equation are set to 10^{-3} and 10^{-6}, respectively.

3.2 Energy content

The energy in the LHESS stored is stored in the form of latent heat and sensible heat, and their estimation is based on the average PCM temperature and the liquid fraction of PCM. Equations 8 and 9 can be used to calculate the total sensible heat and latent heat during the energy storage process :

$$Q_{sensible} = \sum_{t=0}^{t}(T^{t}_{avg,p} - T^{t-1}_{avg,p}) \quad \text{(eq. 8)}$$

$$Q_{sensible} = \sum_{t=0}^{t} mL_{latent}(\epsilon^{t} - \epsilon^{t-1}) \quad \text{(eq. 9)}$$

where m is the mass of PCM in the heat exchanger, t is the total time of operation, $t_{avg,p\ is}$ the average PCM temperature, and ϵ is the liquid fraction of PCM.

3.3 Energy consumption by Air-Conditioning system

The conventional AC system with fresh air incorporation is illustrated in figure 1. The AC system operates on a vapour compression and refrigeration (VCR) system. The temperature of the air inside the office space is managed as per the ISHRAE standards, i.e. 300 K DBT and relative humidity of 50% (Indoor, Quality, and Second 2019; Kapur et al. 2020; Refrigeration and Air Conditioning). The fresh air and the recirculated air mix adiabatically before entering the AC unit (Refrigeration and Air Conditioning;).

The total sensible heat extracted from the space (Qs) is given as :

$$Q_s = \dot{m}_a(1.005 + 1.88\omega)(T_{mix} - T_s) \quad \text{(eq. 10)}$$

Here $\dot{m}_a$ is the total mass of air and calculated as :

$$\dot{m}_a = \dot{m}_{ai} + \dot{m}_{ao} \quad \text{(eq. 11)}$$

The present study supplies a 0.42 kg/s mass to cool the office space.

The enthalpy(h_{mix}) and temperature(T_{mix}) of the mixture of air obtained by :

$$h_{mix} = \frac{\dot{m}_{ai}h_i + \dot{m}_{ao}h_{out}}{\dot{m}_{ai} + \dot{m}_{ao}} \quad \text{(eq. 12)}$$

$$T_{mix} = \frac{\dot{m}_{ai}T_i + \dot{m}_{ao}T_o}{\dot{m}_{ai} + \dot{m}_{ao}} \quad \text{(eq. 13)}$$

The load on the chiller ($Q_{chiller}$) is dependent on the temperature of mixed air, and the supply air temperature is estimated as :

$$Q_{chiller} = \dot{m}_a(h_1 - h_s) \quad \text{(eq. 14)}$$

$Q_{chiller}$ then determines the mass of the refrigerant required to achieve the desired refrigeration effect.

$$\dot{m}_{ref} = \frac{Q_{chiller}}{(h_a - h_d)} \quad \text{(eq. 15)}$$

Since in a VCR system, the compressor is the primary energy-consuming unit, so for the study, we have assumed the total energy consumed by the AC system corresponds to the energy consumed by the compressor in the system. The work required by the compressor is given by :

$$W_{comp} = \dot{m}_{ref}(h_{bs} - h_d) \quad \text{(eq. 16)}$$

The compressor's efficiency is a function of its operating pressures (Barthwal et al., 2021), hence calculating the work required by the AC system :

$$\eta_{comp} = \frac{h_{bs} - h_d}{h_b - h_d} = 0.85 - 0.046667\frac{p_2}{p_1} \quad \text{(eq. 17)}$$

$$W_{ac} = {}^{W_{comp}}/_{\eta_{comp}} \quad \text{(eq. 18)}$$

3.4 Grid Independence Test

A grid independence study for the designed LHESS is conducted to determine an appropriate grid size. To find the most suitable size, a coarse, fine and finer grid with the number of cells rising by a factor of two is studied. The coarse grid contains 354806 cells, whereas the fine and finer grids have 685350 and 1211560 cells, respectively. In the computational domain, the average output air temperature variation with time from the heat exchanger is compared at different mesh sizes. The maximum divergence of average outlet air from heat exchanger temperature during charging is 0.16 K when the number of cells is amplified from 354806 to 685350 and 0.014 K for an increase in the number of cells from 685350 to 1211560. As a consequence of this study, the fine grid can be considered for future investigations. Because the difference in temperature distribution in LHESS becomes minor as the time step is reduced further, the time step is set at 0.1 s.

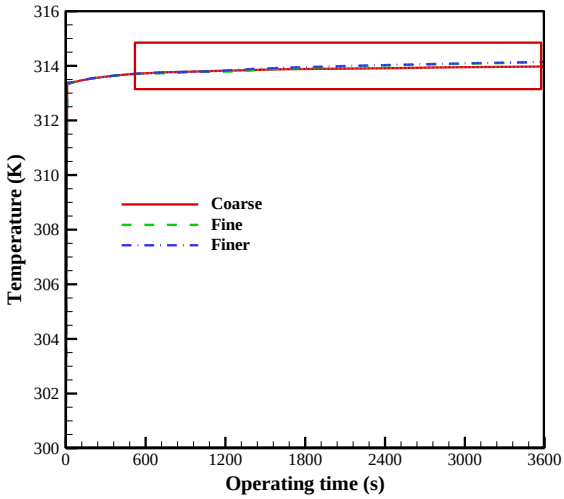

Figure 3: Grid Independence Study

4. Results and Discussion

4.1 Melting Fraction

The heat transfer characteristics of the shell and tube heat exchanger while the charging process is discussed, followed by the energy savings achieved by retrofitting the heat exchanger into an AC system. The fins of height 50 mm and 75 mm are considered in the inner tube of the shell and tube configuration, and the performance is compared with an unfinned tube. The temporal variation of the melting fraction for the three different configurations on the inner tube in the heat exchanger is illustrated in Figure 4. The melting process indicates that the thermal energy from the air gets absorbed into the phase latent energy storage medium in the heat exchanger. It can be observed from the figure that the melting of the PCM starts after 180 s of the charging process for the unfinned inner tube. However, with the addition of six internal fins in the inner tube, the onset time of PCM melting reduces. For six longitudinal fins of a height of 50 mm and width of 5 mm running through the heat exchanger, the start of the melting process is noticed after 122 s of changing process. This is because of an increase in the heat transfer area and consequently the heat transfer rate due to internal fins. The increase in the height of the internal fins to 75 mm while keeping the width and the number of fins constant further reduces the beginning of the melting process of PCM to 80 s. In the charging process, one hour of operation is considered; it is observed that complete melting of PCM is achieved at 2960 s and 2910 s for the cases with 50 mm and 75 mm fin configuration, while some portion of PCM remains unmelted in the heat exchanger with no fin.

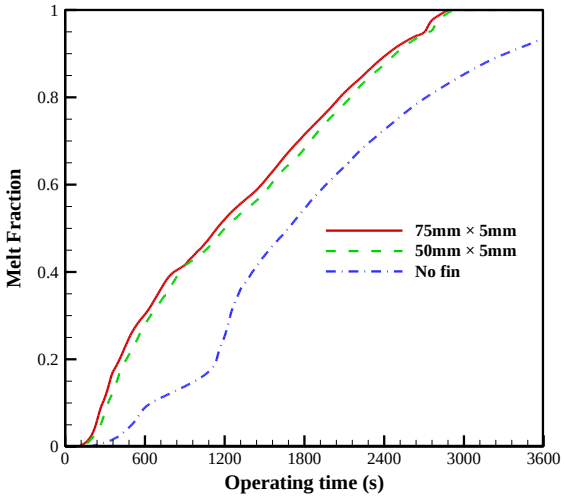

Figure 4: Melt fraction variation with time for different configurations of the heat exchanger

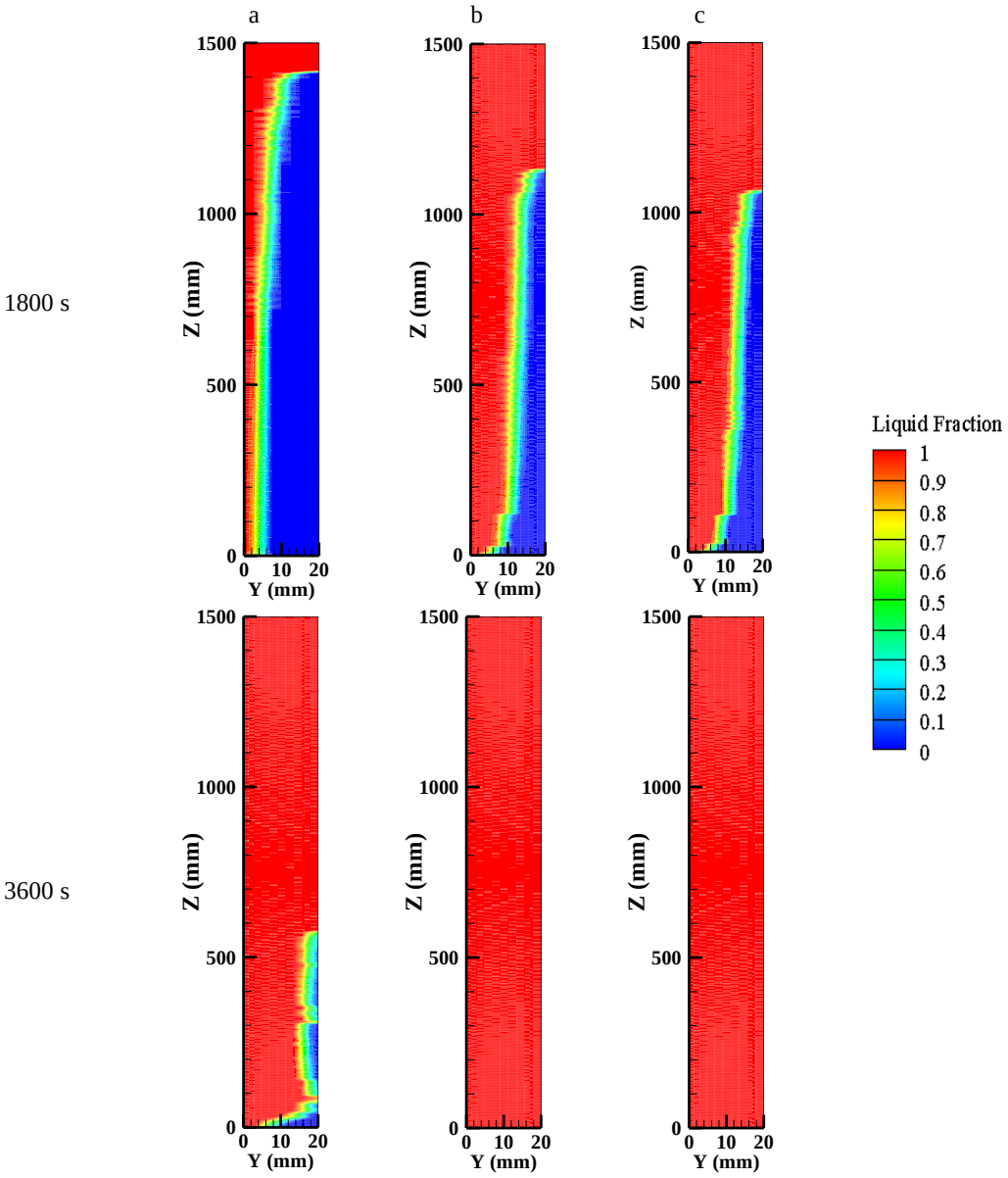

Figure 5: Melting fraction for a) no fin, b) six fins of 50 mm × 5 mm, and c) six fins of 75 mm × 5 mm

Further, the melting profile is observed from the melt front contours at the time instances of 1800 s and 3600 s of charging, as shown in figure 5. From the contour of melted PCM for a heat exchanger without fins, it can be observed that after 1800 s, the melted PCM in the upper portion of the heat exchanger is higher than in the lower part. The behaviour in melting is due to the dominance of conduction in the initial phase of operation. With time the convection currents also enhance the heat transfer within the fluid. Due to the buoyancy effect and temperature difference, the melted PCM rises upwards, and the heat transfer phenomenon occurs due to natural convection. Further, after 3600 s, the melt fraction of the PCM increases from 54.5% after 1800 s to 93.5%.

Figure 5 (b) shows the melt front for 50 mm × 5 mm fin configuration, and it is found that after 1800 s of operation, the PCM melt fraction increases to 68.23% as compared to 54.5% melt fraction in no fin condition. The PCM melts completely after 2960 s; hence, the energy storage in latent heat ceases, and sensible heating dominates afterwards. In the case of 75 mm height of internal fins, it can be observed from figure 5 (c) that after 1800 s, the PCM melt fraction is 71.4%, which is increased to 100% before the end of the charging process. The fins effectively increase the heat transfer rate, which is evident from the melting fraction contours demonstrated in figure 5. When compared to unfinned, six fins of 50 mm height and 5 mm width increase the melting rate and at a time instance of 1800 s, an enhancement of 13.73%, while for the fins of 75 mm height and 5 mm width, the melting is further increased by 16.9%. The increase in melting fraction rate is highest for the heat exchanger with six fins of 75 mm height and 5 mm width and least for the heat exchanger with no fins.

4.2 Air outlet temperature

The air temperature at the outlet temperature varies with operation time and is illustrated in Figure 5. The rate of increase in air temperature is high for the initial 300 s temperature, and after that, it is constant. For the heat exchanger with no fin, the air temperature at the outlet of the heat exchanger has fewer fluctuations, with an average temperature reduction of 1.25 K and 1.09 K for 1800 s and 3600 s, respectively.

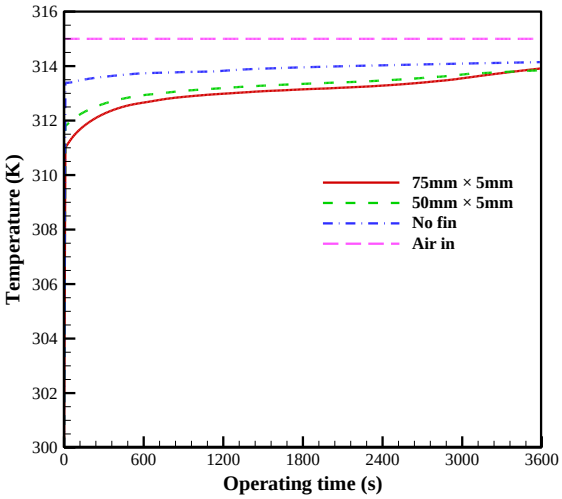

Figure 6: Temporal variation in air temperature at the outlet for different configurations of the heat exchanger

The 50 mm × 5 mm fin configuration achieved a more significant drop in air temperature at the heat exchanger outlet when compared with the unfinned configuration. The reduction in air temperature is 2.03 K and 1.74 K after 1800 s and 3600 s, respectively. The air temperature is reduced by 63.55% and 57.8% compared to the heat exchanger with no fins after 1800 s and 3600 s, respectively. The air temperature profile in figure 6 indicates the air temperature reduction in the proximity of fins.

Further increasing the dimension of the fin to 75 mm × 5 mm, the temperature reduced to 2.31 K and 1.93 K after 1800 s and 3600 s, respectively. Hence, increasing the reduction further by 86.23% and 76.78% for the air temperature with no fins after 1800 s and 3600 s, respectively. While the air temperature drop obtained from 75mm fins is 12% more compared to the fins with 50 mm height.

Time a b c

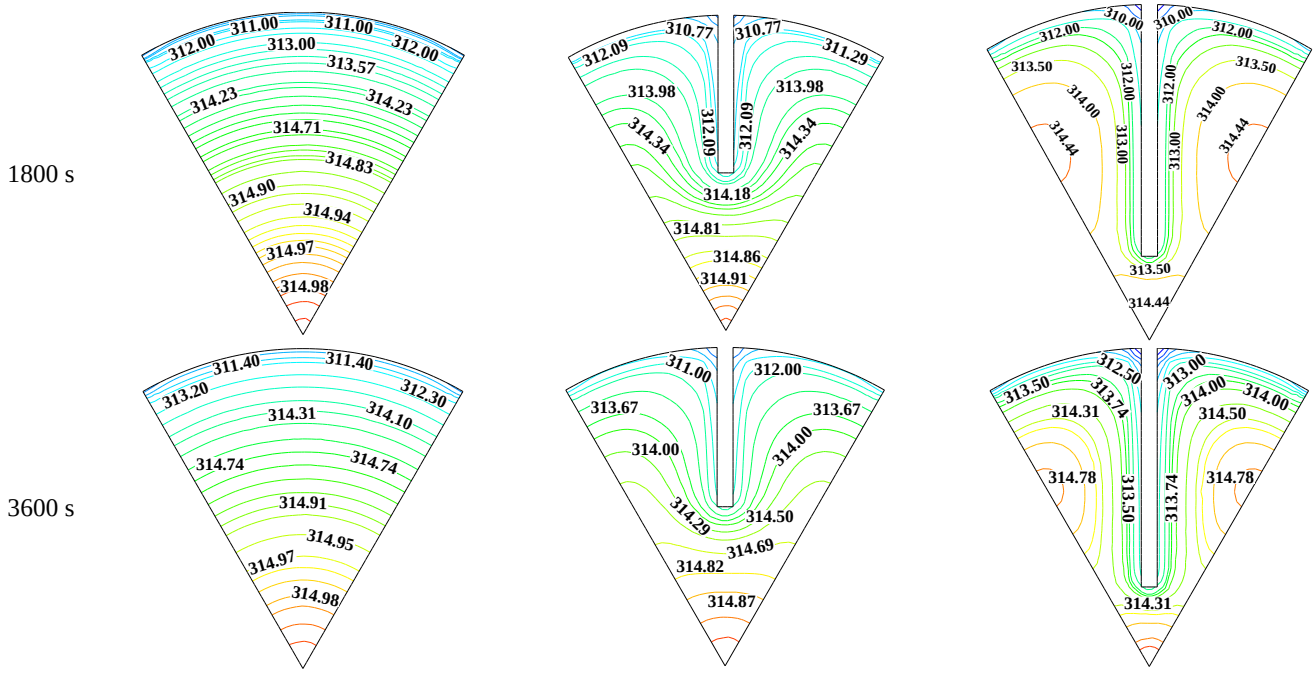

Figure 7: Air temperature at the outlet for a) no fin, b) six fins of 50 mm × 5 mm, and c) six fins of 75 mm × 5 mm

In a VCR cycle compressor is the major energy-consuming component of the system. Hence, the energy saving is estimated through compressor load for the cases with VCR connected to the proposed heat exchanger unit compared to a non-retrofitted AC unit. The temporal variation of energy saved by using the heat exchanger is shown in figure 8. For the first 180 s, 100 s and 90 s in the heat exchangers with no fin, 50 × 5 and 75 × 5 fins, respectively, the energy saving is not estimated because of marginal heat transfer between air and PCM. For an unfinned shell and tube heat exchanger, a maximum energy savings of 3.57% is achieved at 180 s. The energy savings decrease with time, and the system achieves an average energy savings of 2.74% for the operation of 3600 s. The heat exchanger, with six fins of dimension 50 mm × 5 mm, has a maximum and average energy savings of 6.11% and 4.95% for 100 s and 3600 s, respectively. Further a maximum energy saving of 7.11% is achieved for the heat exchanger with six longitudinal fins of 75 mm height and 5 mm width, while the average energy saving is 5.56% for 3600 s. Among the three configurations, the heat exchanger with six fins of 75 mm × 5mm saves maximum energy compared to an AC system without a heat exchanger.

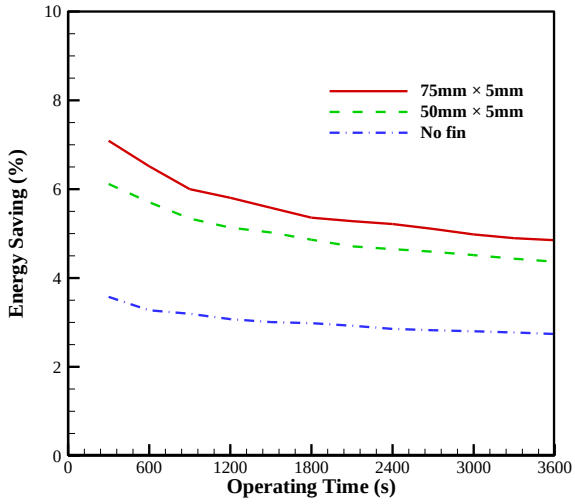

Figure 8: Energy saving by retrofitting air conditioner with different heat exchangers

Conclusions

A strategy to reduce the energy consumption of an AC unit using 50% fresh air per circulation is studied. The AC system is based on the VCR cycle and operates for 3600 s with ambient air supplied at a temperature of 315 K. To reduce the temperature of the fresh air provided at ambient conditions a PCM-based shell and tube heat exchanger with a PCM thickness of 20 mm is designed. The fresh air flows through it, and PCM stores the thermal energy in latent heat. The heat transfer performance of the heat exchanger is analysed, and its effect on energy consumed is studied. It is found that a shell and tube heat exchanger provided an average outlet air temperature reduction of 1.09 K for 3600 s of operation. Incorporating this heat exchanger into a VCR-based AC system leads to a peak and average energy savings of 3.57% and 3%, respectively, for 3600 s. Additionally, the effect of extruding fins on the air side of a heat exchanger is explored. The modified heat exchangers have six longitudinal fins running through the length of the heat exchanger with a width of 5 mm and height of 75 mm and 50 mm. The incorporation of internal fins in the heat exchanger increases the energy saving of the VCR system through further reduction of air outlet temperature. However, it is observed that due to the fast melting rate in the presence of internal fins, sensible heating dominates after the complete melting of PCM. This results in a slight reduction in energy saving with the increase in charging time. It is found that the longitudinal internal fins of a width of 5 mm in the inner pipe of the heat exchanger, attributed to enhancement in the temperature drop by 76.78% and 57.5% for fins of height 75 mm and 50mm, respectively. The proposed system will provide an effective solution to the ever-increasing energy demand for the AC system. The study will serve as a guide in designing a PCM heat exchanger with VCR systems.

Acknowledgments

The authors thank HPC facility at IIT Delhi for computational resources. The second author acknowledges the Institute Postdoctoral fellowship. The author also acknowledges the Department of Science and Technology, Government of India "Different Energy Vector Integration for Storage of Energy" - Grant number- TMD/CERI/MICALL19/2020/03(G). The first author would like to thank IIT Delhi for providing the travel assistance- Grant number- IITD/PGSR/2022/67206.

Nomenclature

List of Acronyms			
AC	Air conditioning	HVAC	Heating Ventilation and Air Conditioning
DBT	Dry bulb temperature	LHESS	Latent Heat Energy Storage System
HTF	Heat Transfer Fluid	VCR	Vapour Compression Refrigeration
PCM	Phase Change Material		

List of Symbols			
A	Contact Area (m^2)	h	Enthalpy per kg (kJ/kg)
Q	Heat Flow Rate (W)	k	Thermal Conductivity (K/W)
T	Temperature (K)	$\dot{m}$	Mass Flow Rate (kg/s)
W	Work Done (W)	p	Pressure (Pa)

List of subscripts			
a	Ambient	mix	Mixed Air
avg	Average	ref	Refrigerant
comp	Compressor	s	Supply Air

Greek Letters			
η	efficiency	μ	Viscosity (kg/m.s)
ρ	density (m3/kg)	β	thermal expansion coefficient (K^{-1})

References

Abu-Hamdeh, N. H., Melaibari, A. A., Alquthami, T. S., Khoshaim, A., Oztop, H. F., & Karimipour, A. (2021). Efficacy of incorporating PCM into the building envelope on the energy saving and AHU power usage in winter. *Sustainable Energy Technologies and Assessments*, *43*, 100969. https://doi.org/10.1016/J.SETA.2020.100969

Aydin, D., Casey, S. P., & Riffat, S. (2015). The latest advancements on thermochemical heat storage systems.

Renewable and Sustainable Energy Reviews, *41*, 356–367. https://doi.org/10.1016/J.RSER.2014.08.054

Belman-Flores, J. M., Barroso-Maldonado, J. M., Rodríguez-Muñoz, A. P., & Camacho-Vázquez, G. (2015). Enhancements in domestic refrigeration, approaching a sustainable refrigerator – A review. *Renewable and Sustainable Energy Reviews*, *51*, 955–968. https://doi.org/10.1016/J.RSER.2015.07.003

Conti, J., Holtberg, P., Diefenderfer, J., LaRose, A., Turnure, J. T., & Westfall, L. (2016). *International Energy Outlook 2016 With Projections to 2040*. https://doi.org/10.2172/1296780

Das, D., Sharma, R. K., Saikia, P., & Rakshit, D. (2021). An integrated entropy-based multi-attribute decision-making model for phase change material selection and passive thermal management. *Decision Analytics Journal*, *1*, 100011. https://doi.org/10.1016/J.DAJOUR.2021.100011

Energy Agency, I. *India Energy Outlook 2021 World Energy Outlook Special Report*. Retrieved September 7, 2022, from www.iea.org/t&c/

Fang, G., Tang, F., & Cao, L. (2014). Preparation, thermal properties and applications of shape-stabilized thermal energy storage materials. *Renewable and Sustainable Energy Reviews*, *40*, 237–259. https://doi.org/10.1016/J.RSER.2014.07.179

Fasi, M. A., & Budaiwi, I. M. (2015). Energy performance of windows in office buildings considering daylight integration and visual comfort in hot climates. *Energy and Buildings*, *108*, 307–316. https://doi.org/10.1016/J.ENBUILD.2015.09.024

Kapur, V., Agarwal, B., Baliga, G., Bhambure, J. M., Garg, V., Mathur, J., Mittal, R., Murthy, V., Rajasekaran, S., Shukla, Y., & Sur, A. (2020). ISHRAE COVID-19 Guidance Document for Air Conditioning and Ventilation. *Indian Society of Heating, Refrigerating & Air Conditioning Engineers*, 15.

Kumar Sharma, R., Yagnamurthy, S., & Rakshit, D. (2022). Energy analysis of a phase change material embedded heat exchanger for air conditioning load reduction in different Indian climatic zones. *Sustainable Energy Technologies and Assessments*, *53*, 102776. https://doi.org/10.1016/J.SETA.2022.102776

Ma, T., Yang, H., Zhang, Y., Lu, L., & Wang, X. (2015). Using phase change materials in photovoltaic systems for thermal regulation and electrical efficiency improvement: A review and outlook. *Renewable and Sustainable Energy Reviews*, *43*, 1273–1284. https://doi.org/10.1016/J.RSER.2014.12.003

Osterman, E., Butala, V., & Stritih, U. (2015). PCM thermal storage system for 'free' heating and cooling of buildings. *Energy and Buildings*, *106*, 125–133. https://doi.org/10.1016/J.ENBUILD.2015.04.012

Seddegh, S., Wang, X., Henderson, A. D., & Xing, Z. (2015). Solar domestic hot water systems using latent heat energy storage medium: A review. *Renewable and Sustainable Energy Reviews*, *49*, 517–533. https://doi.org/10.1016/J.RSER.2015.04.147

Shalaby, S. M., Bek, M. A., & El-Sebaii, A. A. (2014). Solar dryers with PCM as energy storage medium: A review. *Renewable and Sustainable Energy Reviews*, *33*, 110–116. https://doi.org/10.1016/J.RSER.2014.01.073

Verma, R., Kumar, S., Rakshit, D., & Premachandran, B. (2023). Design and Optimization of Energy Consumption for a Low-Rise Building With Seasonal Variations Under Composite Climate of India. *Journal of Solar Energy Engineering*, *145*(1). https://doi.org/10.1115/1.4054831

Wang, X., Yu, H., Li, L., & Zhao, M. (2016). Experimental assessment on the use of phase change materials (PCMs)-bricks in the exterior wall of a full-scale room. *Energy Conversion and Management*, *120*, 81–89. https://doi.org/10.1016/J.ENCONMAN.2016.04.065

Washington State Department of Health. (2020). *Ventilation and Air Quality for Reducing Transmission of COVID-19*. *19*(October 27, 2020), 1–4.

Yahaya, N. A., & Ahmad, H. (2011). Numerical Investigation of Indoor Air Temperature with the Application of PCM Gypsum Board as Ceiling Panels in Buildings. *Procedia Engineering*, *20*, 238–248. https://doi.org/10.1016/J.PROENG.2011.11.161

Yanbing, K., Yi, J., & Yinping, Z. (2003). Modeling and experimental study on an innovative passive cooling system—NVP system. *Energy and Buildings*, *35*(4), 417–425. https://doi.org/10.1016/S0378-7788(02)00141-X

B. Energetic Renovation of Buildings

Sustainable and efficient energy supply for the development of tourist villages at the Adriatic and Ionian Sea

Franziska Bockelmann and Ann-Kathrin Dreier

Steinbeis Innovationszentrum (siz) energieplus, Braunschweig (Germany)

Abstract

The increasing number of tourists in small villages at the Adriatic and Ionian Sea causes problems in view of marine pollution, energy consumption, CO_2 emissions and the accumulation of waste. Aim of the project is the development of an overall sustainable EcoTourism. To reduce energy consumption, the refurbishment of buildings and implementation of renewable energy will be in focus.
Various measures, from thermal renovation to changing the heat and cooling generators, are considered and analyzed. Energy consumption can be reduced up to 10 – 70 % by refurbishment (wall, window, roof). Changing generators can achieve a reduction in energy demand of around 30 %. However, the investment costs or the resulting total annual costs of thermal improvement do not reflect the energy saving results. Here, the measures regarding replacement and renewal of the heat and cooling generators are more economical.

Due to restrictions such as monument protection, not many regenerative concepts can be pursued. However, potential for regenerative generation of heat and electricity is theoretically available. Above all, the use of solar collectors leads to an effective reduction in energy requirements for hot water production, which in any case accounts for the largest share of electricity requirements.

Keywords: renewable energy, energy supply concepts, building refurbishment

1. Introduction

The increasing numbers of tourists in the holiday regions on the Adriatic coast and the Ionian Sea lead to immense seawater pollution, high energy consumption and associated high CO_2 emissions as well as a large amount of waste. Due to the supply and disposal structure that needs improvement, short- and long-term tourists in this region have aggravated the situation in recent years. The landscape and tourism are shaped by the small villages and their hotels, but rehabilitation and necessary measures for environmentally sound and efficient management of the facilities and accommodation have not yet taken place.

The research project "EcoTourism - Regional Development of Tourist Villages of the Adriatic Sea through Energy Efficient and Sustainable Supply and Waste Management" focuses on smaller villages and their hotels and "Bed & Breakfast" facilities, whose supply and waste management are at a comparatively environmentally harmful and inefficient level.
Within the framework of the project, transferable, country-specific concepts in the areas of energy, wastewater and waste for sustainable supply and disposal will be developed as a basis for ecologically sustainable tourism, which will serve as best practice examples and be easily transferable to all villages in the countries under consideration.

> Goal - Energy: Transformation into climate-friendly and energy-efficient tourism. Holistic approach to the economic and ecological optimization of energy supply and reduction of energy consumption (heating, cooling and electricity) of existing buildings as well as use of renewable energy sources.
>
> Goal - waste water: Wastewater solutions and concepts for the greatest possible recycling, taking into account quality standards and energy efficiency. The focus is on sustainable tourism use.
>
> Goal - waste: Reduction of the amount of waste as a causal source of environmental pollution and introduction of an energetic bio-waste utilization for energy generation as well as a material utilization of recyclable packaging.

The concepts and simulations presented below are based on a pilot village in Albania but can be transferred to other

© 2022. The Authors. Published by International Solar Energy Society
Selection and/or peer review under responsibility of Scientific Committee
doi:10.18086/eurosun.2022.02.01 Available at http://proceedings.ises.org

"ideal villages of the Adriatic" in a further step.

So far, holistic, sustainable, and transferable energy concepts for the implementation of climate-friendly and energy-efficient tourism have been developed. Furthermore, the potentials for the use of renewable energies in the neighborhood were determined and the possibility of integration was evaluated in order to present a transferable, implementable, sustainable and energy-efficient supply concept.
The wastewater solutions and concepts will be developed specifically in the direction of the greatest possible recycling (water and nutrients), consideration of quality standards (pollutants and hygiene) and energy efficiency (including the energetic use of wastewater resources), considering the relevant national and international standards on wastewater treatment and water reuse.
With regard to waste management, the current status is examined and placed in the context of current concepts and technologies. Based on this, a sustainable waste management concept will be developed.

2. The pilot project

Dhërmi is a village in the south of Albania in the municipality of Himara. In the region of Sarande and Himare, several villages and areas have been declared UNESCO World Heritage Sites. Thus, the historical core of Dhërmi is also under historical/cultural monument protection. The historical centre of Dhërmi is situated high above the coast of the Ionian Sea and is built into a rock face. Induced by seaside tourism, a second village district developed near the coast. In recent years, the tourist infrastructure of Dhërmi has been steadily expanded and the number of holidaymakers, especially from other parts of Albania, is increasing. Primarily, however, these are bathing tourists. This new core is not subject to monument protection, as it differs greatly from the historical core of Dhërmi in terms of building structure and construction. The subject of the pilot project is the historic old core of the village of Dhërmi.



Fig. 1: View Mountain village of Dhërmi

In the project area under investigation (116 buildings in the centre of Dhermi), three different construction types can be identified for the buildings. Old building, mixed building and new building. It can be assumed that these building types will also be present in other areas under consideration. (Table 1)

The old buildings are characterized by plastered but also unrendered facade made of natural stone, small windows, hipped roofs with a wooden beam construction and clay tiles. The old buildings usually do not have balconies. New buildings, which are based on the architectural style of the historical old buildings, do not differ significantly from the old buildings in terms of the building substance and the building materials as well as the cubature and are treated as such in the further processing. Purely new buildings, on the other hand, have a facade of reinforced concrete skeleton construction with brick infills. In general, these houses have larger windows than the old buildings, balconies primarily on the south and west facades, and flat concrete roofs. The third building style is a combination of old and new construction, or mixed construction. These are either new buildings, which have a reinforced concrete skeleton construction, but have a hipped roof with clay tiles, or mixed buildings as new additions to old buildings. (Figure 2)



Fig. 2: Examples of building stock: old (left), new (middle) and mixed (right) building

Tab. 1: Assumptions of the component structures of the different building types

	New building	Mixed building	Old building
Outside wall (to air)	1 cm gypsum plaster 25 cm vertically perforated brick 2 cm exterior plaster	1 cm gypsum plaster 25 cm vertically perforated brick 2 cm exterior plaster	1 cm gypsum plaster 45 cm natural stone 4 - 5 cm plaster and lime mortar
Outside wall (to ground)	1 cm gypsum plaster 25 cm reinforced concrete	1 cm gypsum plaster 25 cm reinforced concrete	1 cm gypsum plaster 45 cm natural stone
Ground floor	0.5 cm tiles 25 cm normal concrete 30 cm sand and gravel layer	0.5 cm tiles 25 cm normal concrete 30 cm sand and gravel layer	0.5 cm tiles 25 cm normal concrete 30 cm sand and gravel layer
Ceiling	1 cm gypsum plaster 25 cm reinforced concrete 0.5 cm screed	1 cm gypsum plaster 25 cm reinforced concrete 0.5 cm screed	2.5 cm wooden battens (Beech/ Oak) 15 cm clay 2.5 cm wooden battens (Beech/ Oak) Floorboards
Roof	25 cm reinforced concrete	2.5 cm wooden battens (Beech/ Oak) Air layer 3 - 5cm ceramic/ clay tile	2.5 cm wooden battens (Beech/ Oak) Air layer 3 - 5cm ceramic/ clay tile

3. Energy supply concepts and refurbishment

The processing and analysis of possible energy supply concepts base on the facts that

- no or only little renewable energy has been implemented so far.
- there is a high demand for heating and cooling. With respect to thermal insulation buildings have a poor standard and until now have not been refurbished.
- heating and cooling are provided room by room by wood stoves and inefficient split units, respectively.
- listed (heritage) buildings complicate a thermal refurbishment and the implementation of renewable energy in several cases.

Since it has not been possible to carry out a comprehensive review of the current situation of the buildings, the heating and cooling requirements for the three references (old, mixed and new building) has been determined by means of thermal simulation using TRNSYS. The heating and cooling demand is calculated on the basis of an example building with the help of the thermal simulation. The example building is created as a simplified building model for the defined three building styles with a gross floor area of 240 m² and is divided into five residential units (average 48 m²) with an occupancy of 2.6 persons per unit. Furthermore, a distinction was made between summer season with full occupancy and low season and winter season with half season. Care was taken to ensure that the building models of the old, new and mixed buildings corresponded to the description of the respective building types and that the defined component structures were applied.

As a result of the simulations, specific heating and cooling energy requirements are obtained for the three building types. With around 68 kWh/(m²a) and around 17 kWh/(m²a) in relation to the gross floor area, the old building has the lowest heating and cooling energy requirements. With around 103 kWh/(m²a) for heating and 18 kWh/(m²a) for cooling, the mixed building is in the middle. The new building has the highest heating and cooling energy requirements with around 104 kWh/(m²a) and 29 kWh/(m²a). (Figure 2)

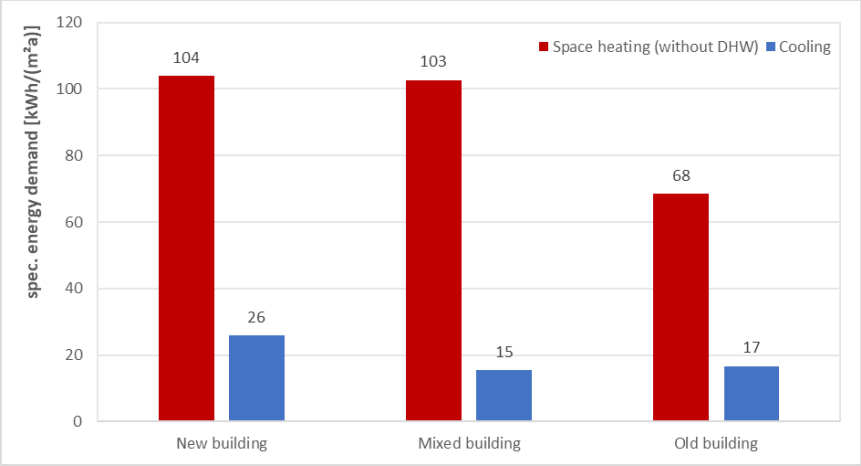

Fig. 2: Specific energy demand of heating and cooling for the three building types

The results are extrapolated to the three building categories and to the entire neighborhood using the data from the survey of the buildings. The energy requirements for the total reference area of 116 buildings (without refurbishment) results to 2,470 MWh/a for space heating and 822 MWh/a for space cooling as well as 2,143 MWh/a for domestic hot water production. (Figure 3)

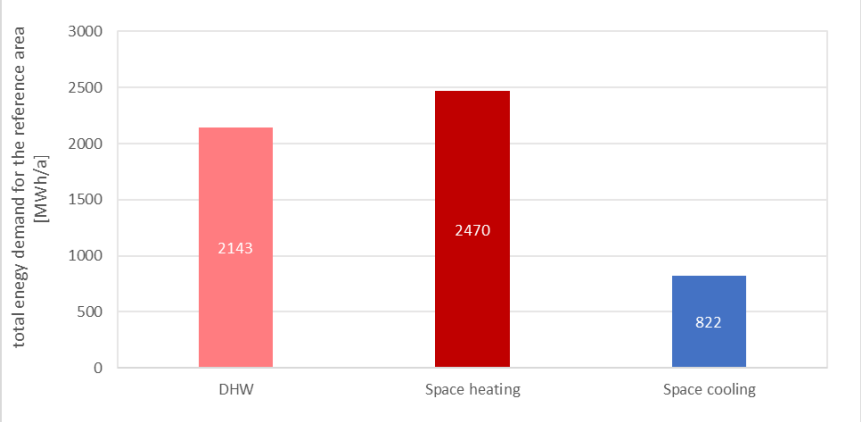

Fig. 3: Heating and cooling demand of the reference area

3.1 Thermal refurbishment

In order to save additional energy in addition to a new efficient heating and cooling supply, thermal refurbishment measures are recommended, which can also be implemented within the framework of an existing listed building. For thermal refurbishment, minor construction measures within the houses and flats are considered. Nevertheless, at the time of refurbishment, the houses can usually not be rented out.

The proposed refurbishment stages differ in terms of the effort required or the building components to be insulated and the insulation thicknesses (Table 2). All renovation stages can be applied equally to all three building. Since the building types differ in their previous construction, the savings potential of the renovation levels depends on the building type. Within each renovation level, differences are made in the renovation of the windows, the walls and the roof.

To reduce the energy consumption of the buildings, six refurbishment levels have been defined. Taking the protection of historical monuments into account, the levels range from low (level 2) to a high effort for refurbishment (level 6).

Tab. 2: Examples of refurbishment levels

Level	Refurbishment measures	Comment
1	Replacement of the windows: 2 panes, sun protection glazing	
2	Level 1 + thermal insulation of the roof (10 cm)	Minimal invasive version
3	Level 1 + thermal insulation of the wall and roof (5 cm)	
4	Level 1 + thermal insulation of the wall and roof (10 cm)	
5	Level 4 + thermal insulation of the base plate (3 cm)	
6	Level 1 + thermal insulation of walls (10 cm) + roof (12 cm) + base plate (5 cm)	Highest effort

3.2 Energy supply refurbishment

The energy supply concepts are analyzed and evaluated on two levels. On the so-called room level, the individual usage zones or rooms within the building are considered. Here, the focus is on the respective heat or cold transfer system in the room. Furthermore, the type of ventilation (window ventilation, mechanical ventilation) plays a decisive role and to what extent the existing systems can influence each other.

The building level, on the other hand, reflects the overall concept (total system) with the corresponding building envelope as the system boundary. Within the framework of the overall system, the generation and distribution of heat and cooling are considered. It should be possible to implement efficient and regenerative producers as well as a possible division of the base and peak load suppliers. The division of base and peak load only makes sense for larger houses.

The supply concepts presented are primarily standard solutions rather than individual solutions, so that the concepts developed can also be applied to a large number of houses. A large variance in the concepts at room and building level can lead to confusing regulations and dependencies of the individual components. The standard solution here is a simple combination of a maximum of two components.

The focus is on the implementation of regenerative-based energy supply concepts and systems for holiday homes / flats under a holistic consideration of heating / cooling and electricity. The consideration also includes the sustainability of the components as well as possible obstacles in the implementation of the different approaches. The six variants developed are based on technologies currently relevant to the market (Table 3).

In addition to decentralized energy supply solutions such as air-conditioning split units, heat pumps and gas boilers, local heating network approaches are also included. The generators must be able to meet the energy demand for both heating and cooling, or a combination of both. The combination of different generators for base and peak load coverage is one possibility. However, for residential buildings and on the scale at hand, it cannot be implemented efficiently and does not make sense. A division into heating and domestic hot water should be considered in order to cover the different temperature levels efficiently.

Table 2 lists the supply concepts being applied. As due to monument protection, photovoltaics and solar thermal collectors may not be installed on individual houses and are not listed, therefore.

In the course of finding the energy supply concept and selecting the possible components for heat/cold and electricity generation as well as heat and cold distribution in the building, approaches were already discarded or excluded in advance.
Components and concepts that require a major refurbishment effort in the existing building stock and cannot be implemented easily include floor heating, concrete core activation, air handling units and for the heat pumps borehole heat exchanger. However, these components could be used in a complete refurbishment and gutting of houses.

Tab. 3: Options for energy supply concepts

	Option	Heat supply	Cold supply	Domestic hot water
Decentral energy supply	As build	Existing split units	Existing split units	Instantaneous water heater
	1	New split units	New split units	Instantaneous water heater
	2	Gas boiler and buffer storage	Compression chiller	Gas boiler and buffer storage
	3	Heat pump and buffer storage	Rev. heat pump and buffer storage	Heat pump and buffer storage
	4	Electrical heater	Compression chiller	Instantaneous water heater
Central energy supply	5	Local heating network (60°C)	Local cooling network (15°C)	Local heating network (60°C)
	6	Local heating network (0°C), heat pump and buffer storage	Local cooling network (15°C)	Local heating network (60°C), heat pump and buffer storage

4. Potentials on energy reduction

In the context of the presentation of the potentials of energy savings through thermal refurbishment as well as through the change of the heat / cooling generator, it is taken into account that there will be an increase in the number of tourists in the holiday resorts. The user behavior and the higher tourist numbers are compiled in the studies within the framework of the heating and cooling profile of the building simulation, the domestic hot water profile, and the electricity demand profile.

4.1 Energy reduction through thermal refurbishment

Based on the defined example buildings and the location in Albania, the heating and cooling demand is determined, and the renovation stages are compared with the demand of the actual state (figure 4). It can already be noted in the actual state that the old building has lower energy requirements (heating and cooling) than the mixed and new buildings. Refurbishment level 2 can already achieve a reduction in energy demand of up to 15%. In total, a reduction in energy demand of up to 70% can be achieved by refurbishing all building components (refurbishment level 6). The renovation of new and mixed buildings has the greatest savings potential, as the buildings already have a higher demand in their current state than the old building.

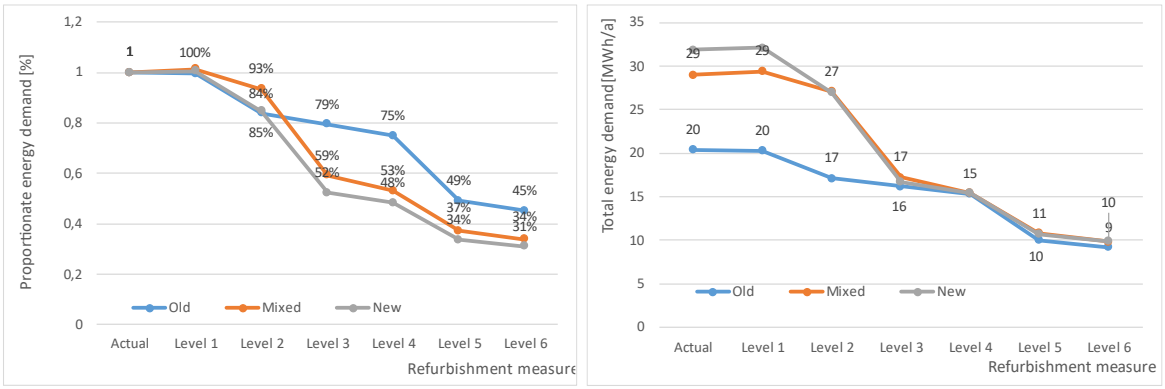

Fig. 4: Energy demand reduction and potentials for the entire reference area and for the different refurbishment stages

4.2 Energy reduction through system technology

Figure 5 shows the first results for different variants of energy supply concepts developed for the project area (116 houses). Based on the results it can be stated that the way of heat and cold generation has much greater influence on the reduction in energy consumption than the refurbishment of the buildings. The energy demand calculated for the reference area includes electricity for households and domestic hot water preparation.

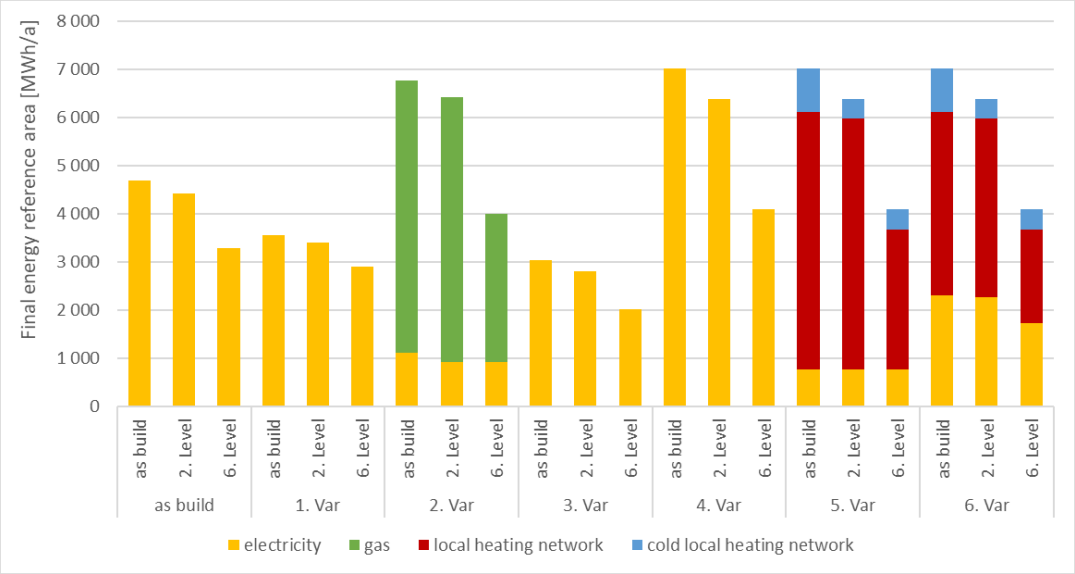

Fig. 5: Energy demand of the reference area depending on the refurbishment level and the energy supply

The fact that the individual heat and cooling generator technologies have different modes of operation also results in different efficiencies. Air-conditioning split units, for example, use a proportion of outdoor air heat or cold to condition the rooms. This means that a lower proportion of electricity or final energy is required here. A gas condensing boiler, for example, does not convert all the thermal energy in the fuel into heat. Due to losses, an efficiency of only 95% can be achieved here. This situation results in different energy requirements for the different variants.

Exclusion criteria for the selection of variants to be implemented result from the outstanding ecological and economic considerations as well as the feasibility of implementation in the reference area. In this project, for example, due to protection of historical monuments and the preservation of the ancient village appearance, the utilization of renewable energy close to buildings is only possible to a very limited extent - although the location is predestined for the installation of photovoltaics and wind power plants. By relocating a small wind farm outside the village and implementing photovoltaics on the flat roofs of new buildings and a public car park, it is nevertheless assumed that 80% of the electricity demand can be covered by renewable energy.

5. Potentials of solar energy use

The current state of implementation and integration of solar thermal and photovoltaic is very limited. In general, there are very few solar thermal systems or solar siphons in the pilot village. In 20 buildings of the 116 considered, solar siphons were visible, which corresponds to 17 % of the considered houses. The installed solar collectors are often installed on the hipped roofs and flat roofs or next to the building in gardens. The collectors are oriented in a south-west direction with an angle of inclination of 10 - 45°. (Figure 6)



Fig. 6: Solar siphons in the garden (left) and on the roof (right)

Photovoltaic systems, on the other hand, are not installed at all. Many of the historical buildings are under monument protection. The installation of solar collectors or photovoltaic systems on the roofs or facades is not permitted due to the preservation of the historic village image.

Within the framework of the research project, it should nevertheless be shown which possible potentials exist for the use of solar energy sources, also in order to transfer the results and concepts to other villages.

5.1 Solar coverage of hot water demand

The personal daily domestic hot water demand is estimated on the basis of typical load profiles and seasonal fluctuations and extrapolated to the entire village area. A domestic hot water heating to 60°C is assumed. The simulation program TRNSYS is used to calculate the possible hourly yields of a flat plate collector. First, all roof surfaces facing east, south and west are assumed as potential collector installation area. Based on the reference building, several scenarios were investigated assuming a southern orientation and an angle of inclination of 30° of the collector: (figure 7)

1. 0.5 m² collector area per person per building: energy reduction for domestic hot water of 48 %.
2. 1.0 m² collector area per person per building: energy reduction for domestic hot water of 72 %.
3. 1.5 m² collector area per person per building: energy reduction for domestic hot water of 80 %.

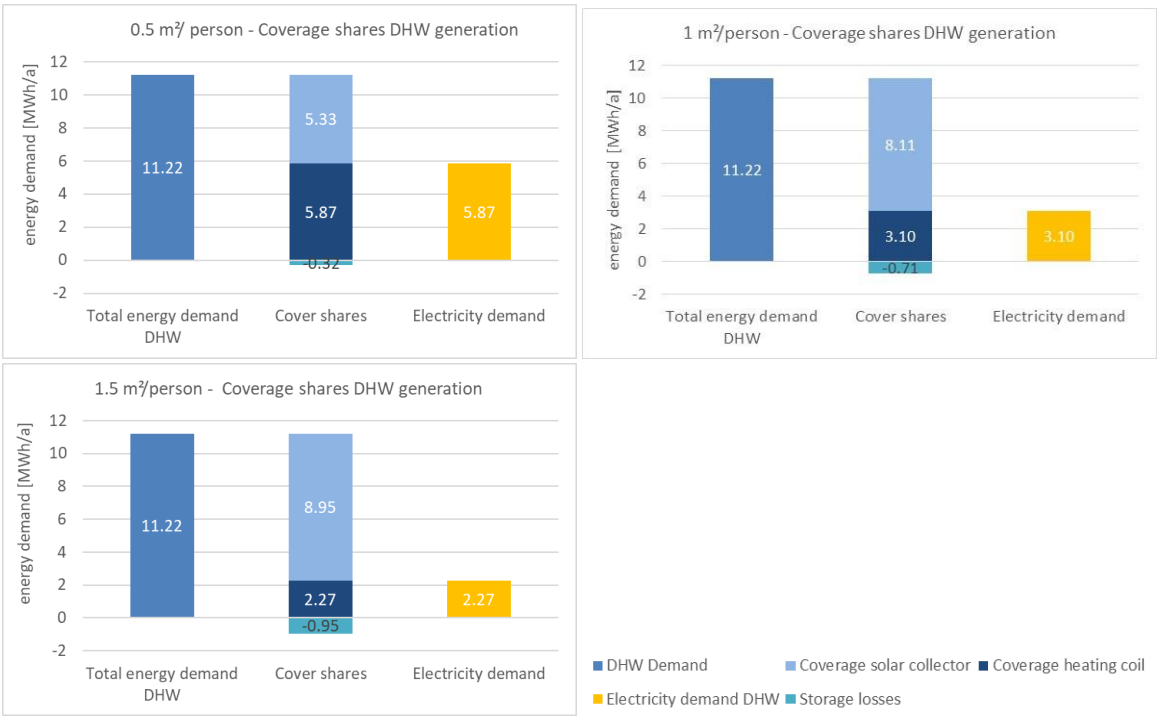

Fig. 7: Coverage shares with solar for the different variants of domestic hot water production for the reference building

For the entire district, an occupancy of 1 m² of collector area per person per building would mean a reduction from 2,143 MWh/a to 600 MWh/a. The additional expenditure for the increase to 1.5 m² per person per building would result in an energy demand reduction of 80 %. However, the additional expense compared to variant 2 does not justify the energy savings here. The recommendation here would be to install 1 m² of collector area per person per building.

5.2 Solar coverage of electricity

A similar study was conducted for the photovoltaic potential. The estimated total electricity demand of the district is 3,770 MWh/a (assumption for Var. 1), which is divided among the different sectors as follows, figure 8. The largest share, 57 %, is accounted for domestic hot water production, with the assumption that this is done electrically.

Two scenarios were examined here. Firstly, the assumption that 75 % of all roof surfaces (also north) and secondly, that 25 % of the roof surfaces (also north) can be covered with PV. An hourly resolved TRNSYS simulation was performed.

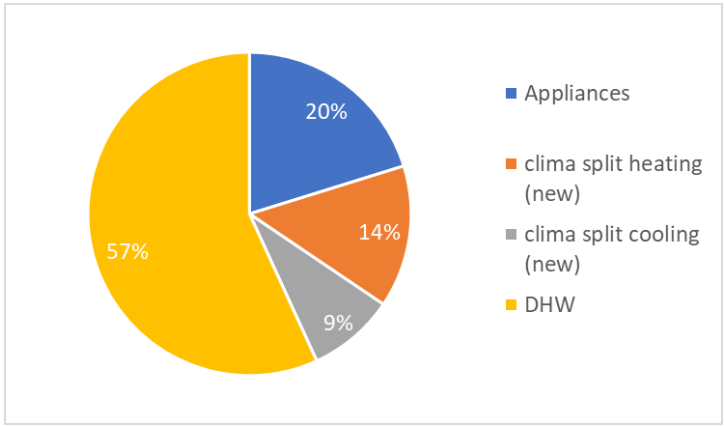

Fig. 8: Shares of electricity demand in the district

In the variant with 75 % occupancy, the energy yield is 1.06 times higher than the energy demand for heating (electric), cooling (electric), domestic hot water, and appliances in the district. Initially, no renovation level was considered in this study. 43 % of the energy demand can be covered by the PV-production itself. 60 % of the yields, on the other hand, are surplus and should have to be fed into the local grid.

In the variant with 25 % occupancy, on the other hand, the yields are 0.29 times lower than the electricity demand of the district. The self-consumption with self-generated electricity is 22 %. However, there is also only 22 % surplus, which can be fed into the grid.

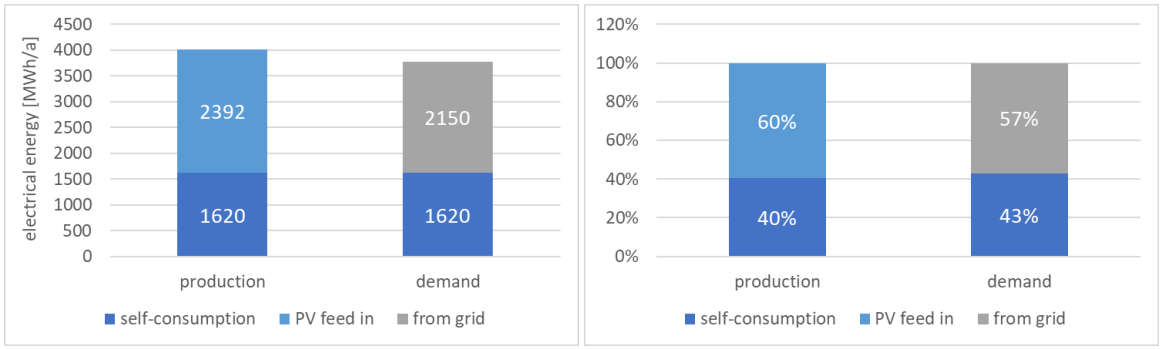

Fig. 9: PV potential for self-consumption, 75 % roof occupancy of the 116 houses

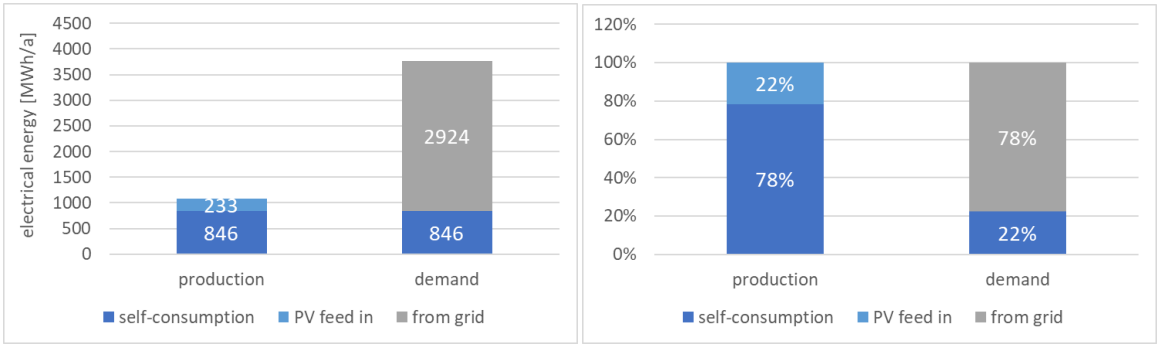

Fig. 10: PV potential for self-consumption, 25 % roof occupancy of the 116 houses

6. Potentials on CO_2 reduction

The potential for CO_2 reduction in Albania cannot be recorded or mapped on the basis of the non-existent CO_2 emissions. In Albania, a CO_2-equivalent of 0 kg/kWh is assumed for biomass (wood), electricity and solar energy. The background is the high production of electricity from hydropower. Only for LPG (Liquefied Petroleum Gas) is a value of 0.227 kg/kWh specified.

7. Economic efficiency

Within the framework of the economic efficiency analysis, the investment costs as well as demand-related and operational costs are taken into account that arise during the purchase and operation of the system components (renovation of the building envelope, heat and cold generators as well as space heating and cooling systems). The economic efficiency is determined using the annuity method (based on the guideline VDI 2067 Part 1 (Economic efficiency of technical building systems) - the total annual costs consist of capital-related, operational (i.e. maintenance and repair costs) and demand-related costs.

The following bases are used in the calculations:

- Costs for planning and contingencies are taken into account at 20 % and 15 % of the investment costs.
- Capital interest rate 5.0 %
- Working price public electricity grid: 0.40 €/kWh (covering 20 % of the demand)
- Energy price for district electricity: 0.24 €/kWh (covers 80 % of demand)
- Energy price increase for electricity is assumed to be 2%.
- CO_2 pricing on electricity not taken into account as well as subsidies

The investment costs are taken from an extensive market research of 03/2022. Since no investment costs from Albania are known and many of the suppliers and installers are supposed to come from Germany, the product and price research is limited to the German market. A cost function was determined depending on the respective performance or dimensioning of the respective component and an average of the entire market was depicted. However, it should be noted that due to the current price increases on the markets, an exact and up-to-date statement is not possible. The economic efficiency analysis merely relates the variants to each other and thus enables a rough economic evaluation.

Figure 11 shows the total annual costs of the variants that could be implemented in Dhermi. It can be seen that variant 4 with electric heating and an additional air-conditioning split unit for cooling the rooms is the most cost-intensive variant, which can lead to additional costs of up to 50 % compared to the current state. By implementing variants 2 and 3, the total annual costs can be reduced by up to 10% compared to the actual state. On the basis of the subdivision into the refurbishment levels, it can be shown that a costly refurbishment of the buildings (Level 6) cannot lead to any cost savings. The heating and cooling generators have the greatest influence on the total annual costs.

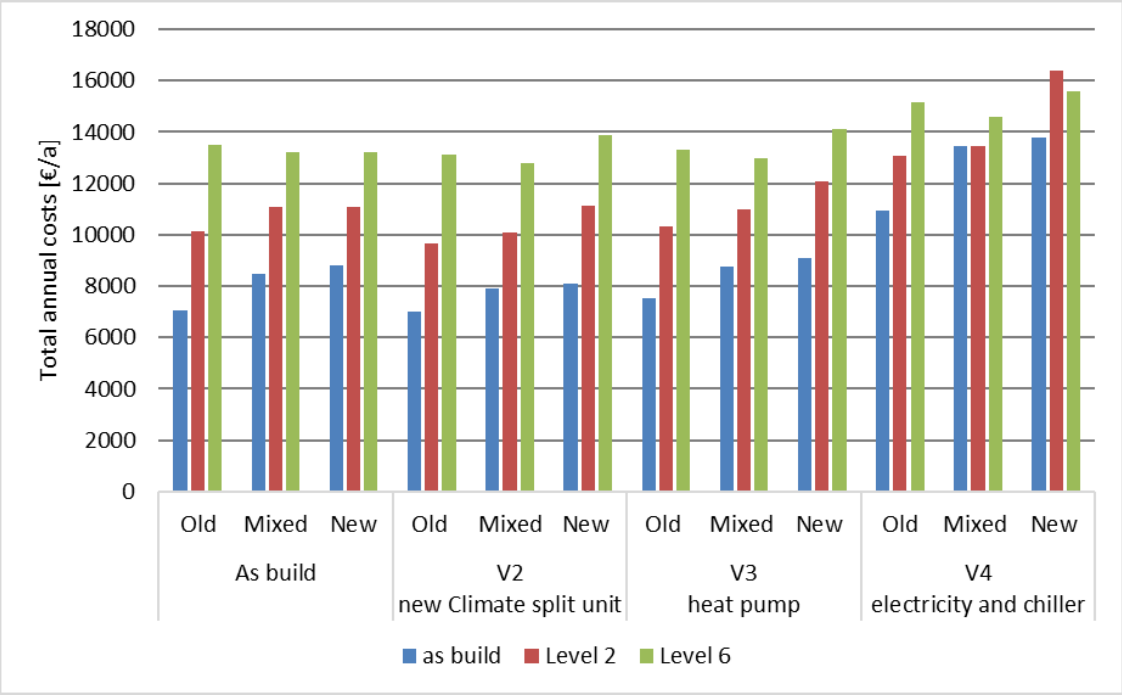

Fig. 11: Total annual costs of possible suppling- and refurbishment-variants of the three building types

8. Summary

The increasing number of tourists in small villages at the Adriatic and Ionian Sea causes problems in view of marine pollution, energy consumption, CO_2 emissions and the accumulation of waste. Aim of the project is the development of an overall sustainable EcoTourism. To reduce energy consumption, the refurbishment of buildings and implementation of renewable energy will be in focus.

The current state of the ongoing project reveals that the development of building standards in foreign countries with different climates is challenging. Demands on the protection of historical monuments require creative solutions, especially in ancient villages. Nevertheless, significant energy saving can be achieved by skillful implementation.

The total energy demand in the reference area of Dhermi is defined as the energy demand for the conditioning of the buildings (heating and cooling) and the appliances. An example building and three building standards were defined and applied to the total number of buildings (116 buildings in the project area). The different periods and occupancies of the buildings are also taken into account. The results show a total heating demand (space heating and domestic hot water) of about 4,610 MWh/a and a demand for cooling of 820 MWh/a for the entire district in Dhermi. In addition to heating and cooling, energy is needed for hot water, for lighting and for all other services in the buildings (cooking, washing, etc.). It is assumed that the entire demand for electricity is covered, the district then needs around 3,700 MWh/a of electricity.

Various measures, from thermal renovation to changing the heat and cooling generators, are considered and analyzed. Energy consumption can be reduced by renovating the building envelope, which can result in a reduction of 10 – 70 %, depending on the building standard and renovation stage. Changing generators to new efficient technology or to a heat pump can achieve a reduction in energy demand of around 30 %. The thermal improvement of the building envelope (windows, roof and walls) is a sensible measure from the point of view of energy saving. However, the investment costs or the resulting total annual costs do not reflect the energy saving results. Here, the measures regarding replacement and renewal of the heat and cooling generators are more economical.

Due to restrictions such as monument protection and the energy sources available at the site, not many regenerative concepts can be pursued. However, potential for regenerative generation of heat and electricity is theoretically available. It can be seen that the utilization of solar energy potentials could lead to a significant reduction in energy requirements in the district. Above all, the use of solar collectors leads to an effective reduction in energy requirements for hot water production, which in any case accounts for the largest share of electricity requirements.
The installation of PV or solar thermal on individual buildings causes difficulties with the appearance and function of the renovated houses (monument protection). A solution for the use of PV is envisaged in the installation of panels on public spaces (e.g. multi-storey car park) and under special conditions (shading) in the project area.

9. Acknowledgments

The research projects “EcoTourism - Regionalentwicklung touristischer Dörfer der Adria durch energieeffiziente und nachhaltige Ver- und Entsorgung” (67EXI4023A_B) were funded by the German Federal Ministry for the Environment, Nature Conservation, Nuclear Safety and Consumer Protection by the Export Initiative Environmental Protection GreenTech „Made in Germany“. We would like to thank all building owner and operator as well as our project partner Goduni for their help and support as well as providing measurement data and information about the buildings and pilot village.

Renovation of a Multi-family-house with External Wall Heating System

Toni Calabrese[1], Daniel Philippen[1], Martin Josef Neugebauer[1], Igor Bosshard[1] and Michel Haller[1]

[1] SPF Institute for Solar Technology / Eastern Switzerland University of Applied Sciences (OST), Rapperswil (Switzerland)

Abstract

A new and cost-effective heating concept integrated in a prefabricated façade for renovation of multi-family-houses was investigated in the framework of the European project PLURAL with the help of dynamic building and system simulations. The concept consists of a prefabricated insulated timber-frame façade containing the heating pipes of a low temperature hydronic distribution system for space heating. After renovation, the building can be heated with these heating pipes through the existing external walls. The simulation results show that such a system can ensure good thermal comfort for the flats and fulfill Nearly Zero Energy Building requirements. An optimized control strategy of the heating system allows to increase the photovoltaic self-consumption and to decrease the net costs for electricity of the building. Under certain conditions, such a system is a beneficial solution for fast and cost-effective renovation of multi-family-houses.

Keywords: renovation of multi-family-houses, external wall heating, prefabricated façade, NZEB, PV self-consumption

1. Introduction and motivation

In the European Union, the building sector is responsible for 40% of the final energy consumption (European Commission, 2021). An important challenge for the building sector concerns the energetic renovation of existing buildings (European Commission, 2016). Currently, the refurbishment rate of existing buildings is below 1% (European Commission, 2021) and, for this reason, it is crucial to overcome obstacles of renovation processes (e.g., high amount of time and investment cost, reallocation of the building's inhabitants, loss of rent, etc.) in order to achieve faster the goals of the energy transition in this sector.

Within the European project PLURAL (PLURAL, 2020), innovative "Plug-and-Use" kits for fast and energy efficient retrofitting are developed to meet Nearly Zero Energy Building (NZEB) targets, but also to ensure minimum disturbance of the inhabitants during the retrofitting phase.

The so-called Conductive External Wall (ConExWall) heating system is one of the solutions developed within the project PLURAL for energy retrofitting, in particular for multi-family houses (MFH). Such a system can be mounted directly on the existing outer walls of a building, providing energy for heating and cooling via a heating layer, thermal insulation, ventilation and, optionally, electricity by means of a photovoltaic (PV) system installed on the façade. Time and cost reduction for retrofitting, versatility, high potential of self-sufficiency, and integration with low temperature heating systems (e.g., heat pumps), make this system ideal for renovating MFHs with the goal of low specific energy demand and conversion from fossil fuels to energy systems with a high share of renewable energy.

2. ConExWall system

The operation principles of the proposed external wall heating concept without prefabrication were suggested and analyzed earlier by Luther et al. (2002) and limits and potential of such a concept were studied within different projects (Schmidt, 2018). Such a system allows the renovation of buildings "from outside" and this represents one of its biggest advantages, since the inhabitants are not forced to leave the building during the renovation period. Another big advantage of this heating concept is the thermal activation of the whole existing façade because the heating layer heats the rooms through the façade. This characteristic allows for using the existing wall as thermal storage. In case of a heating system with heat pump and PV, this enables to run the heat pump longer and to higher temperatures during times of excess electricity gains from the PV system and, on the other hand, to run it shorter during times were electricity has to be purchased from the electric grid.

Such a system presents, on the other side, some disadvantages and a crucial issue is that the potential heating

© 2022. The Authors. Published by International Solar Energy Society
Selection and/or peer review under responsibility of Scientific Committee
doi:10.18086/eurosun.2022.02.02 Available at http://proceedings.ises.org

energy delivered to a room is strongly dependent on the opaque external wall area. This aspect is important because some rooms (e.g. with higher window ratio) could become critical with regard to the thermal comfort. In addition, this system has to be supported by a different heat distribution system in case of internal rooms without external wall area (e.g., the bathroom).

The proposed ConExWall module (see Fig. 1) represents an evolution of the original concept because of two aspects: 1) the heating system is enclosed in a prefabricated timber-based module and 2) the module can be equipped with optional components for ventilation and renewable electricity production. The ConExWall module consists of:

- Timber frame construction with insulation of about 20-30 cm (depending on climate);
- Low temperature external wall heat (and optionally cold) emission system;
- Module-integrated windows with mechanical ventilation system including heat recovery (MVHR) integrated in the frame of the windows or in the new façade;
- Building integrated photovoltaic (BIPV) modules for electricity production.

The feasibility of such a system without extensive prefabrication was already demonstrated by means of a prototype test and simulations within a Swiss project (ProsumerSkin, 2017) where a first MFH located in Bern (Switzerland) has been renovated with this concept.

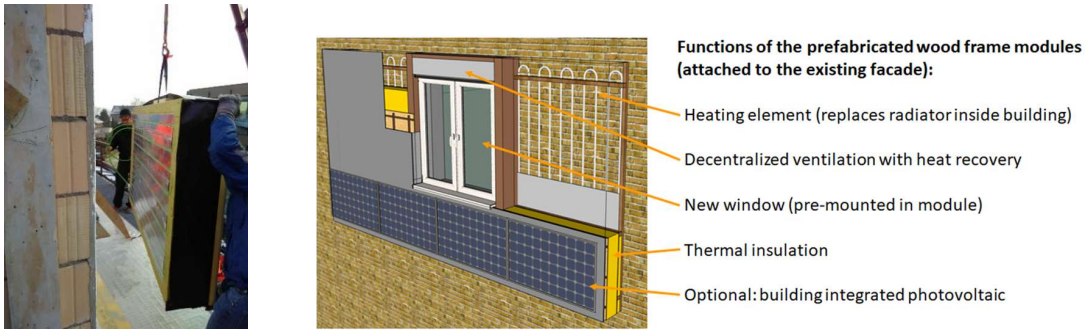

Fig. 1: Mounting of the prefabricated ConExWall on the façade test box (left) and concept visualization of the ConExWall solution (right).

3. Building and system simulation

3.1 Building

In the framework of the project PLURAL, the ConExWall concept will be installed for the renovation of a double dwelling (see Fig. 2) located in Kasava, Czech Republic. The existing building has an Energy Reference Area (ERA) of 196 m^2 and matches to the proposed ConExWall concept because of the high U-value (1.3 W m^{-2} K^{-1}) of the existing walls that allows for a good heat transmission between the ConExWall module and the building through the existing walls.

As detailed information about user behavior is not available (e.g., set point temperature, internal gains, ventilation and infiltration rates, etc.), the existing building was simulated in its pre-renovation state assuming standard boundary conditions. Simulation results showed an annual heating demand (with a set point temperature of 20 °C) of 163 kWh m^{-2}_{ERA} a^{-1}. Simulation results of the building before renovation were validated against real energy consumption, showing a good match (relative deviation of 7%).

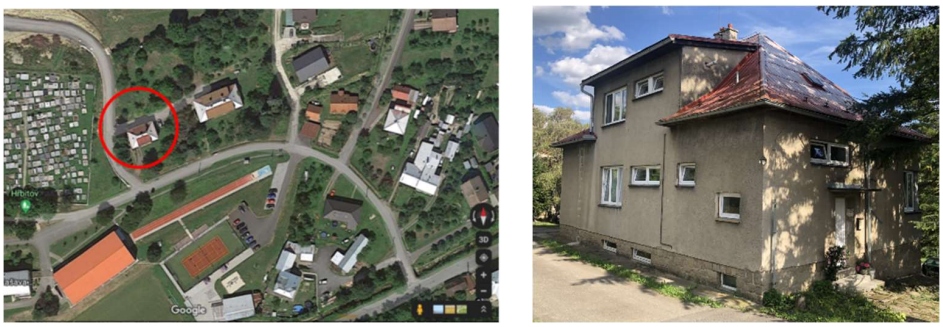

Fig. 2: Location of the building under study (left) and view of the existing building (right).

3.2 Building model and boundary conditions

In order to study the energetic performance of the ConExWall and the thermal comfort of the renovated building, a building model (see Fig. 3) was generated (SketchUp, 2022) and then imported into the simulation tool (i.e. through the use of TRNSYS-Type 56), where the complete heating system was modelled in order to perform the building and heating system simulation (TRNSYS, 2022).

The renovated building (with an ERA of 275 m^2) consists of a cellar (modelled as a single thermal zone) and two floors (i.e. two apartments), with an internal staircase. In order to study the thermal comfort of each room of the building in detail, each room was modelled as a single thermal zone. In total, 17 thermal zones are simulated. Each of the two flats consists of a corridor ("Hall"), a bathroom ("Bath"), a restroom ("Rest"), one kitchen/living room ("Liv") and two resp. three sleeping rooms ("Bed") (see Fig. 5). Each flat has also an external unheated storage room next to the staircase. More living area through a new and higher roof will be created in the first floor with the renovation.

Tab. 1 summarizes the wall and window constructions of the building after renovation. In the table the construction “External wall” represents the existing wall (i.e. the wall on which the ConExWall will be placed) after renovation, while “External $wall_{new}$” represents the new external wall of the first floor that will be necessary in order to extend the second flat. The building will be equipped with triple panes window (filled with Argon) with internal Venetian blinds between two of the panes. Reference shading control strategies were considered for the simulation based on the total irradiation on the window surface and convective temperature of the room.

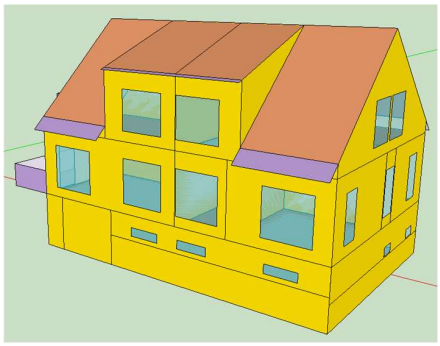

Fig. 3: 3D model in SketchUp of the same building after renovation.

Tab. 1: U- value of wall and window constructions of the building after renovation

Wall / Window construction	U [W m^{-2} K^{-1}]	Note
Basement floor/wall/ceiling	3.43/1.31/0.30	basement ceiling insul. with PUR
Internal ceiling/wall	0.82/2.65	
Internal wall of staircase	0.34	insulated with EPS
Roof	0.10	
External wall	0.13	
External $wall_{new}$	0.14	new ext. walls of the first floor
Window	0.60	frame ratio of 0.2, g = 0.49

In the building model, internal gains due to people, lighting, and appliances were considered. Since hourly profiles for occupancy are not available in the Czech national regulations, standard occupancy profile from Swiss norm SIA 2024 (SIA, 2022) was assumed. A specific internal gain due to people (P) of 2.0 W m^{-2} and humidity source of 80 g h^{-1} P^{-1} were considered. Benchmark numbers of the latest study of Czech Statistical Office (CSU, 2017) show a specific electricity consumption (for lighting, appliances, cooking and other) of 28.6 kWh m^{-2} a^{-1} for dwellings in Single Family House (SFH). To reach this electricity consumption, a specific internal gain (for equipment and lighting) of 5.5 W m^{-2} was set, assuming a typical electric power profile processed statistically by the Czech energy market operator. Internal gains inside staircase, cellar and storage rooms were set to zero.

Fixed infiltration rate of 0.15 $m^3 h^{-1} m^{-2}$ was assumed for all rooms, according to the Swiss norm SIA 2024.

3.3 ConExWall in TRNSYS – Active layer in Type 56

As described in previous sections, the simulation study is performed with the simulation tool TRNSYS and, in particular, "Type 56" is used in order to model the building. Within the Type 56, to model the ConExWall, the sub-model "active layer" was used. This active layer model can be added to a wall, floor, or ceiling in order to model a radiant heating or cooling system. The layer is called "active" because it contains fluid filled pipes that add or remove heat from the building component. For the definition of the "active layer" of the ConExWall in Type 56, distance between the heating pipes was set to 0.13 m and a pipe wall conductivity of 0.4 $W m^{-1} K^{-1}$ was assumed. Pipe outside diameter and pipe wall thickness were set to 0.014 m and 0.002 m, respectively. As it is important to take into account possible imperfections in the thermal coupling of the ConExWall modules to the old façade due to surface roughness, an air gap of 2 mm was assumed in the model between the "active layer" and the existing wall. This air gap reduces the heat transfer from the external wall heating system into the building.

3.4 HVAC system and control strategy

Fig. 4 shows the layout of the heating and domestic hot water (DHW) system. An air to water heat pump (AWHP) with a nominal heating capacity of 11.3 kW is used for space heating (SH) and DHW preparation. A combi thermal energy storage (TES) with 750 l water volume is considered in order to store heat produced by the heat pump (HP). In the SH demand side of the system, each ConExWall was modelled as a separate heating loop (i.e. all the loops are in parallel and with the same supply temperature) and is equipped with a circulation pump in order to control the mass flow rate of each heating loop independently. When realized, the ConExWall loops will be equipped with control valves instead and a central recirculation pump will control the mass flow of the heating water.

Fig. 5 shows the layout of the heat emission system of the building. As described in previous sections, the ConExWall represents the main heating system and almost all the rooms of the building are heated through this concept (see Tab. 2). Since new walls will be built on the first floor, the children room and part of the living room of the first floor will be heated through a standard heating wall system (see orange elements in Fig. 5) located at the inside of the respective walls. Cellar, staircase, and storage rooms are not heated, while electric radiators are considered in the two bathrooms for comfort reasons.

As described, the AWHP will cover the SH as well as the DHW demand. As measurement data of the building for DHW consumption are not available, reference DHW load profiles for SFH were used (IEA SHC Task44). In order to take into account the presence of two apartments, a scale factor of two was assumed for a total energy demand for DHW preparation for the whole building of 4266 $kWh a^{-1}$.

Within the renovation process of the building, decentralized ventilation units integrated in the walls or in the window frame will be installed. In the building model, the cellar, staircase, halls, and storage rooms are not actively ventilated, while the other rooms are equipped with decentralized ventilation units with energy recovery (i.e., heat and humidity). Constant heat recovery (70%) and humidity efficiency (56%) is assumed for the ventilation unit with a control of the airflow rate through step variation as function of the room relative humidity (airflow rate between 10 and 85 $m^3 h^{-1}$ for each ventilation unit). Summer night cooling (i.e., by-pass of heat recovery) is implemented in the model based on the ambient temperature and on the room temperature.

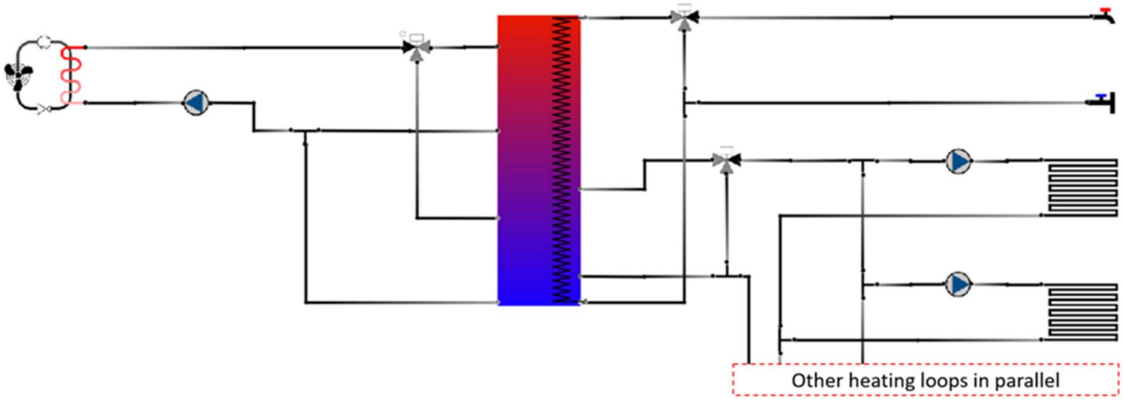

Fig. 4: Layout of the system for space heating and DHW preparation.



Fig. 5: Layout of the heating surfaces of the ground floor (Gf) and first floor (1f) of the building - ConExWall (red), electric radiator (yellow) ad internal wall heating (orange).

Tab. 2: Window ratio (Window area / External wall area) and net heated wall area for all rooms of the building.

Zone	Window ratio [%]	Net heated wall area [m^2]
GfRest	0	6.1
GfHall	21	10.7
GfBath	15	8.0
GfBedN	5	24.4
GfLiv	23	30.1
GfBedS	40	4.6
GfBedE	17	24.3
1fRest	0	3.0
1fHall	19	5.4
1fBath	12	9.3
1fLiv	31	16.7
1fBedS	32	6.1
1fBedE	23	19.7

The reference control strategy of the system is based on "standard" control for the activation of the HP for space heating and DHW preparation. The thermal storage is equipped with four temperature sensors (two sensors in the DHW volume and two sensors in the SH volume) with which the HP is activated to keep the TES volumes to the desired temperatures. In particular, a set point temperature of 50 °C is used for DHW preparation, while for space heating a heating curve as linear function of the average ambient temperature (i.e. supply water temperature of 35 °C at -10 °C and 24 °C at 14 °C) is used. The heat pump gives priority to the DHW preparation (with respect to the SH), while the heating season is defined based on the ambient temperature ($Tamb_{48h}$ < 15 °C). Each circulation pump is activated depending on the room temperature in order to keep a convective temperature of 21 °C in each heated room. Modulation of compressor power or optimization strategies of PV self-consumption are not considered in the reference control strategy.

3.5 PV system

Fig. 6 shows the layout of the PV system that will be installed on the roof of the building during the renovation process. Only the part of the roof oriented to the south (i.e. 16° S-E) will be covered with PV panels for a total photovoltaic surface of approximately 48 m^2 (9.9 kW_p). Each PV subfield will be equipped with an inverter and the system will be connected to the grid.

In the building model, the PV electricity is used firstly to cover the electricity demand for households and ventilation and then, if PV is still available, to cover the electricity demand of the HP (i.e. heating and DHW preparation).

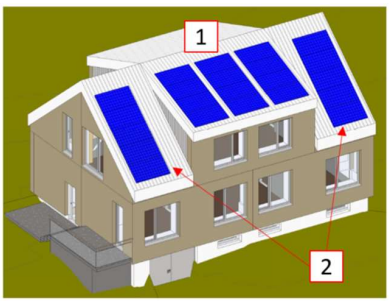

	PV Field 1	PV Field 2
Inclination	20°	40°
Number of PV modules	12	10
PV surface [m^2]	26.1	21.7
PV power [kW_p]	5.4	4.5

Fig. 6: Layout of PV system (left) and information about the two PV subfields (right).

4. Simulation results and discussion

4.1 Overview of the simulation study

The simulation study was performed with the pytrnsys package (Pytrnsys, 2022), a complete python-based framework for TRNSYS simulations developed at the SPF Institute for Solar Technology at the Eastern University of Applied Sciences (OST). Pytrnsys provides a framework to build, simulate, post-process, plot and report TRNSYS simulations. It is designed to give users an extensively automatized way to execute and share building and system simulations performed with TRNSYS.

Energy consumption of the system and thermal comfort of the building was investigated. The simulation study was performed with the reference control strategy (see 3.4) and an optimized control strategy was tested (see 4.4) in order to study the influence on the PV self-consumption and net costs for electricity.

A whole year was simulated considering a time step of five minutes. Climate data from Meteonorm for the location of Kasava (CZ) was used. A set point temperature for the building of 21 °C was considered.

4.2 Energy

Fig. 7 to Fig. 9 show the main simulation results concerning the heating and electricity balance for the whole system. A total space heating demand of 4542 kWh a^{-1} was calculated (i.e. 16.5 kWh m^2_{ERA} a^{-1}) for the whole building. In the summer period from June to September, the HP works only to cover the DHW demand (Fig. 7). 21% of the heating energy delivered by the HP is lost (through HP, pipes and TES).

On the electrical side, Fig. 8 shows that most of the self-consumed electricity from PV (approx. 93%) is used for building demand (i.e., light, equipment and ventilation) and only a small part is used by the HP. A total annual PV production (after inverter) of 11'187 kWh was calculated with a PV self-consumption quota (i.e. PV_{self} / PV) of 30%. Fig. 9 shows that most of the electricity demand of the building is covered by electricity from the grid with an annual grade of autarky (PV_{self} / El_{tot}) of 31%. The HP causes 25% of the total electricity demand of the building.

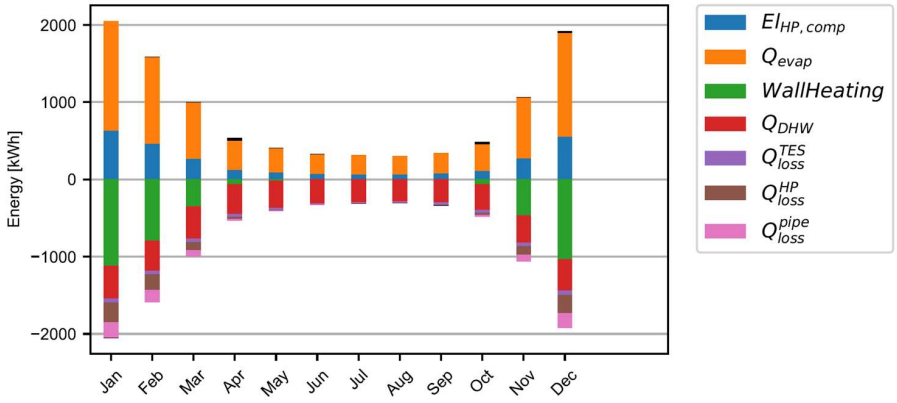

Fig. 7: Monthly heating balance of the system - heat delivered by the heat pump is used to cover heating demand of building ("WallHeating") and DHW.

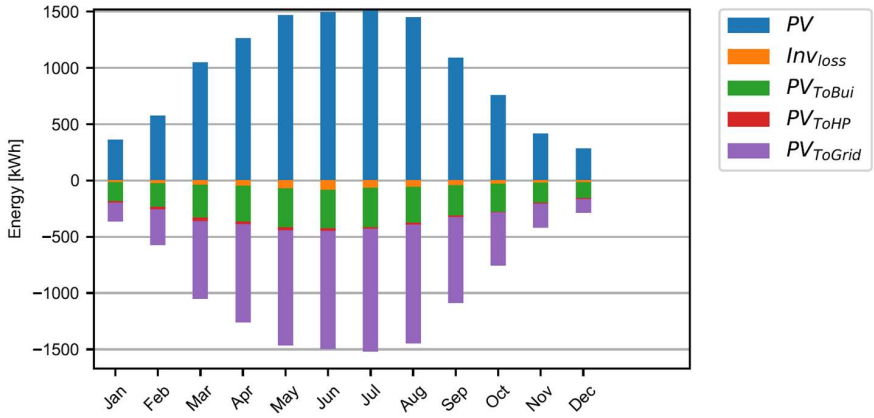

Fig. 8: Monthly balance of PV electricity - "PV_{ToBui}" represents the PV electricity self-consumed by the building (i.e. for households and ventilation), "PV_{ToHP}" represents the PV electricity self-consumed by the HP.

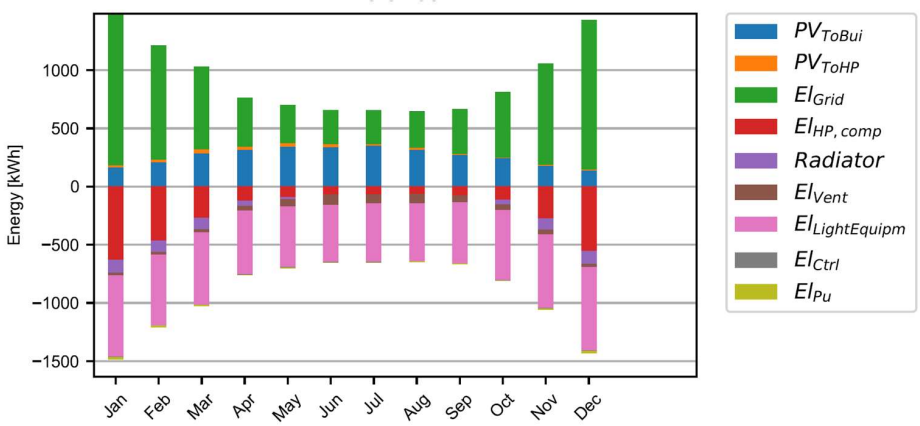

Fig. 9: Monthly electricity balance of the system.

The general behavior of the system for a week during the heating season is given in Fig. 10. It is interesting to note that the heating concept ConExWall is able to keep 21 °C in the room "GfBedN", but the actual reference control strategy leads the heat pump to work especially during the nighttime, when PV electricity is not available and all the electricity demand of the compressor of the heat pump must be purchased from the grid. The plot shows also that there is a good potential to increase PV self-consumption through a control of compressor speed. This strategy could make the heating cycle longer by means of reducing the compressor power in order to avoid peaks in electricity demand and, as consequence, match the actual PV electricity.

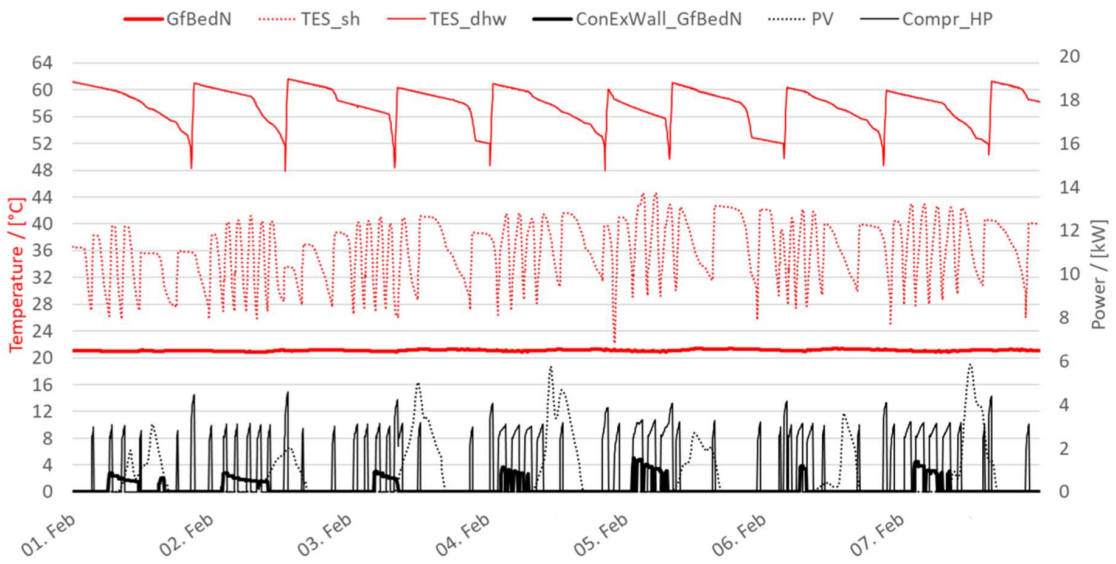

Fig. 10: Behavior of the system for a week during the wintertime. "ConExWall_GfBedN" represents the heating energy delivered to the room (i.e. GfBedN). Temperature in the thermal storage of the two volumes (space heating and domestic hot water) is given.

The building under investigation will be renovated with the goal to achieve NZEB requirements. Simulation results were used to calculate the NZEB energy performance indicators (see Tab. 3) according to the national Czech laws (in particular the "Act. No 406/2000 Coll." and "Decree No. 264/2020 Coll."). The three indicators are defined as follows:

- U_{em} is the U value of the building weighted with the surfaces area;
- Q_{fuel} is the sum of the total electricity demand of the building and the extracted ambient energy from the evaporator of the HP;
- Q_{nPE} is the non-renewable primary energy (PE) demand of the building, assuming that the primary energy factors (f_{PE}) for purchased electricity, electricity to the grid and ambient energy are 2.6, -2.6 and 0, respectively.

Simulation results show that the renovation concept is able to fulfill the NZEB requirements. In particular, the non-renewable primary energy demand (i.e., Q_{nPE}) is negative because of the fact that, on annual basis, the amount of electricity fed into the grid is higher than the electricity purchased from the grid.

Tab. 3: NZEB analysis of the building with the proposed renovation concept.

Energy performance indicators	New building as NZEB (2022)	Simulation results	Fulfilled/Not fulfilled
U_{em} [W m^{-2} K^{-1}]	0.29	0.21	Fulfilled
Q_{fuel} [kWh a^{-1}]	34094	18531	Fulfilled
Q_{nPE} [kWh a^{-1}]	19383	-213	Fulfilled

4.3 Thermal comfort

The standard EN ISO 7730 was followed to define the thermal comfort zone, since there are no special regulations in Czech Republic regarding the definition of thermal comfort for dwellings. Fig. 11 shows the thermal comfort for three rooms of the building exemplarily. It is important to note that in this simulation study a cooling of the building during the summer season was not considered. The thermal comfort plots show that, in general, thermal discomfort during wintertime does not occur and the ConExWall system is able to heat the different rooms of the building sufficiently. If the two bedrooms of the ground floor (i.e., "GfBedS" and "GfBedN") are compared, it can be noted that the heating system is able to keep the set point temperature of 21 °C better in room "GfBedN"

than in room "GfBedS". The reason is due to the larger heated surface of the first room compared to the latter one, which has only a small heated area and a large window. The living room of the first floor ("1fLiv") shows a good thermal comfort, even if overheating during the summer season occurs with a maximum operative temperature of 27.6 °C.

Fig. 12 gives an overview of the thermal comfort for the different rooms of the building when using the Predicted Mean Vote (PMV) factor defined in the standard norm ISO 7730 (ISO, 2022) regarding the thermal comfort for buildings. The norm recommends a PMV between -0.5 and 0.5 (in case of category B), but a small percentage of time (not defined in the norms) outside this interval is accepted in general. To calculate the PMV in Type 56 for the different rooms, a metabolic rate of 1.2 met and a clothing factor of 0.5 in summer and of 1 in winter was assumed. The plot shows that the PMV value goes below the limit of -0.5 for most of rooms of the ground floor. Despite this, detailed analysis of the PMV for the different rooms indicates that the number of hours for which PMV < -0.5 is below 4% for each of the rooms.

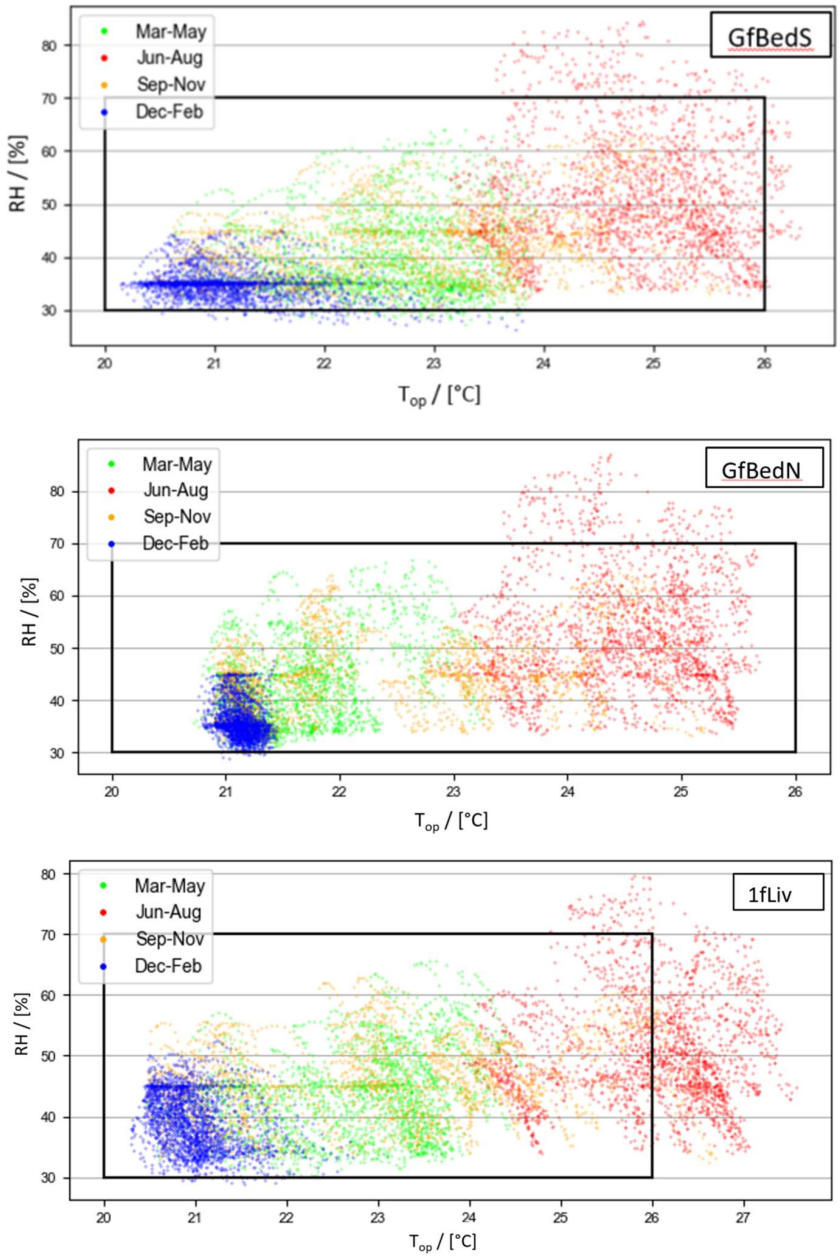

Fig. 11: Thermal comfort (relative humidity vs. operative temperature) for three different rooms of the building (names of the rooms: see Fig. 5). The colors indicate the seasons (see legend).

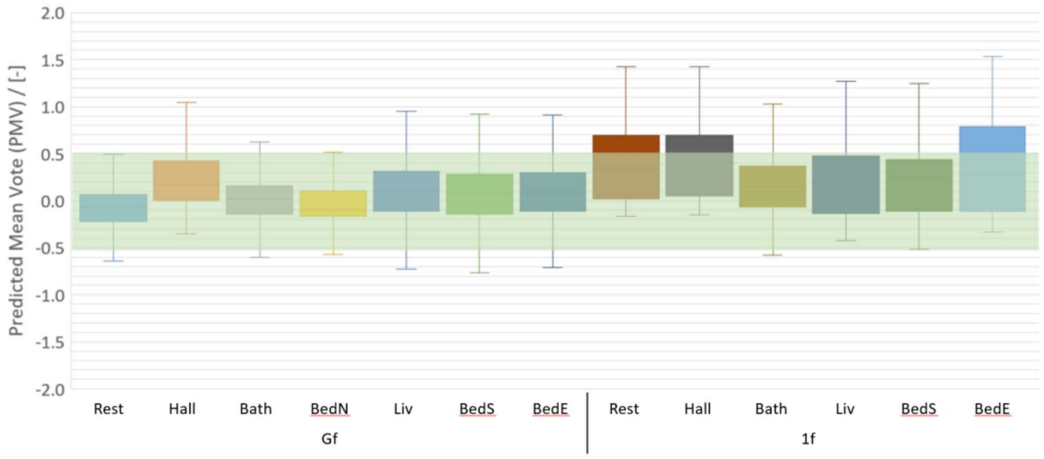

Fig. 12: Predicted Mean Vote (PMV) for the rooms of the building.

4.4 Control strategies – Optimization of PV self-consumption

As described in the previous sections, the standard control strategy neither includes a modulation of compressor speed of the HP nor a coordination between the HP and the PV production in order to increase the PV self-consumption.

To decrease the costs for electricity of the system, an optimized control strategy was implemented and tested (see Fig. 13). The approach is simple and is based on the overheating of the thermal storage (TES) and of the building (using its thermal mass) if PV electricity is still available after subtracting the electricity demand of the building. Through the modulation of the compressor power, remaining electricity coming from PV system (i.e., PV_{forHP}) and compressor power are equalized as much as possible in order to increase PV self-consumption, avoiding peaks in electricity demand for HP. On the other side, when PV electricity is not available for the HP, the control tries to reduce the heating demand of the whole system through the reduction of the set point temperature in the thermal storage and in the building. Following this approach, the goal was to move the heating cycles of the HP as much as possible to the daytime (where PV is available and outside temperature is higher) to decrease net costs of the system during operation phase and to increase the efficiency of the HP.

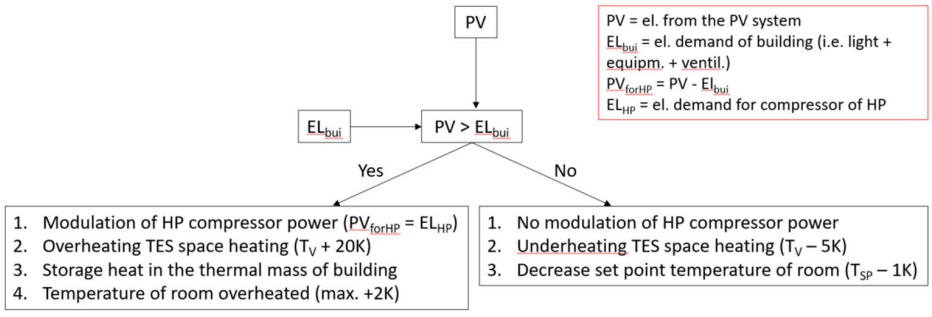

Fig. 13: Block diagram of the optimized control strategy.

Fig. 14 shows how the optimized control strategy works for a typical week during wintertime. It is immediately clear that the control strategy reduces strongly the number of heating cycles of the compressor of the heat pump ("Compr_HP") and, in the meantime, moves them to the day when PV is potentially available for the system ("PV_forHP"). Peaks are reduced and the modulation of compressor speed allows to increase PV self-consumption during the day when, in the meantime, heat is stored in the thermal mass of the building. Overheating of thermal storage is not visible here because of the fact that PV production (and as consequence potentially available for the heat pump) is small in comparison to warmer period like Apr – May.

Tab. 4 shows the comparison of the reference and the optimized control strategy on an annual basis. As expected, due to the fact that the thermal storage and the façade are overheated during the winter season, thermal losses of the storage are higher as well as the heating energy through the ConExWall. Because the heat pump works more during the day (i.e., higher evaporation temperature due to higher ambient temperature), the seasonal performance factor (SPF) of the heat pump is slightly increased (+10%). Tab. 4 shows also the comparison between the control

strategies with regard to the electricity exchange with the grid and net costs (i.e., difference between costs for purchased electricity and profit from PV fed into the grid). The electricity exchange with the grid is decreased (good effect on grid stability) and the optimized control strategy allows to reduce the net costs for electricity of 20% (feed-in tariff for PV of 0.06 €/kWh and tariff for purchased electricity of 0.19 €/kWh were assumed). Considering the optimized control strategy, PV self-consumption is increased to 42% (from 30% of the reference control strategy) and the grade of autarky is increased to 43% (from 31% of the reference case).

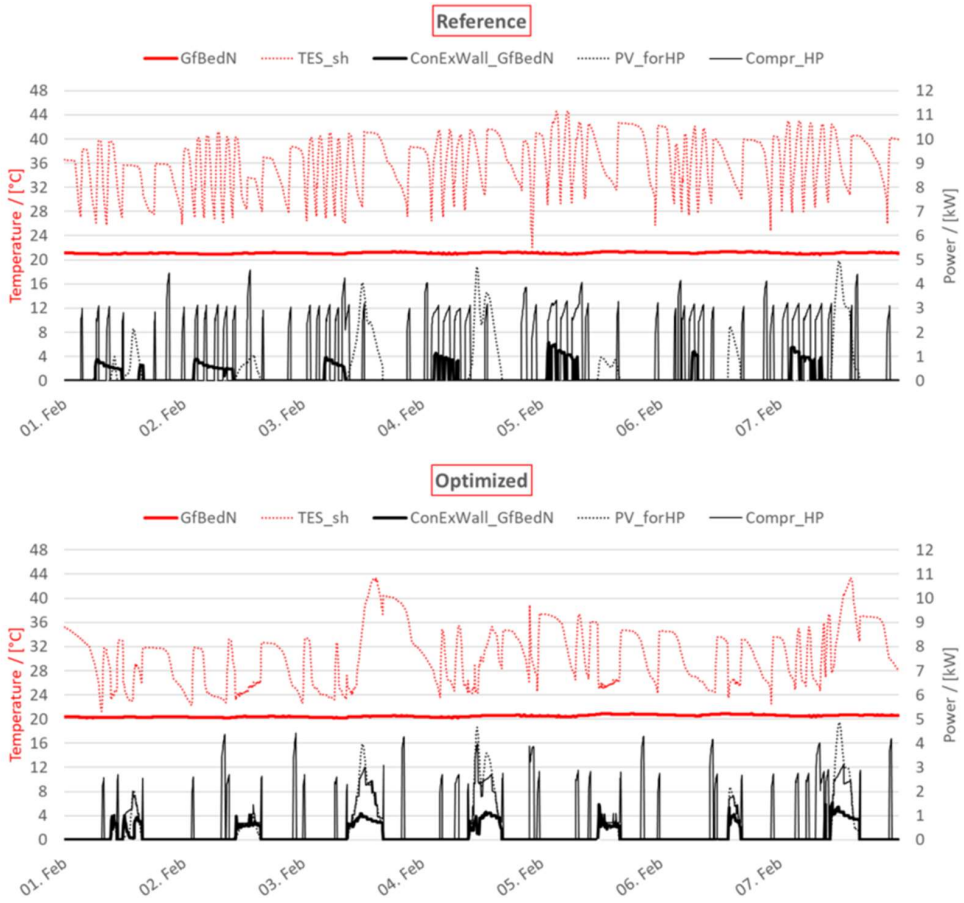

Fig. 14: Behavior of the system during a typical week of the heating season - Comparison between "Reference" and "Optimized" control strategy. "PV_forHP" represents the PV electricity available for the HP (PV electricity for households and ventilation already subtracted).

Tab. 4: General comparison of the reference and optimized control strategy - Feed-in tariff for PV: 0.06 €/kWh, tariff for purchased electricity: 0.19 €/kWh.

	Reference control strategy	Optimized control strategy	Relative deviation [%]
El. from grid [kWh a^{-1}]	7717	6265	-19%
PV to grid [kWh a^{-1}]	7799	6528	-16%
Net costs [€ a^{-1}]	998	799	-20%
TES_{loss} [kWh a^{-1}]	420	471	+12%
Heat of ConExWall [kWh a^{-1}]	3915	4411	+13%
SPF_{HP} [-]	3.3	3.6	+10%

5. Conclusions

The proposed ConExWall heating concept was investigated within the European project PLURAL through building and system simulations. The simulation results show that such a system is able to ensure good thermal comfort in all the rooms of the analyzed building (PMV < -0.5 for less than 4% of the time) and fulfill Czech NZEB energy requirements. The results show some possible critical issue for the rooms with high window ratio or small façade area available for heating. These particular rooms (e.g. the small bedrooms on the south side of the investigated building) might need an additional heat source (like a convector) or an increase of the heating curve in order to ensure good thermal comfort. Through an optimized control strategy of the system, PV self-consumption and grade of autarky are increased to 42% and 43% (from 30% and 31% of the reference case, respectively), while the net costs for electricity decrease by 20%. The ConExWall system can represent, under certain conditions, a valuable solution in case of renovation of multi-family-houses.

6. Acknowledgments

This paper was written in the frame of the EU project PLURAL (funded by the Horizon 2020 programme, Grant Agreement No. 958218).

7. References

European Commission (2021). European Commission: Energy statistical country datasheets.

European Commission (2016). An EU Strategy on Heating and Cooling. Brussels 16.02.2016 COM (2016) 51 Final. https://eur-lex.europa.eu/legal-content/EN/TXT/PDF/?uri=CELEX:52016DC0051&from=EN

PLURAL (2020, August 2022). https://www.plural-renovation.eu/

Luther, G.; Altgeld, H.: Die außenliegende Wandheizung, In: Gesundheitsingenieur 123, 2002 (1), pag. 8–15

Schmidt C.; Altgeld H.; Gross B.; Luther G.; Maas S.; Scholzen F: «Aussenliegende Wandtemperierung», Praktische Umsetzung anhand eines Demonstrationsgebäude und Ermittlung der Systemkosten, 2018, DOI: 10.1002/bapi.201810021. https://core.ac.uk/download/pdf/162022157.pdf

ProsumerSkin (2017, August 2022). https://www.ost.ch/de/forschung-und-dienstleistungen/technik/erneuerbare-energien-und-umwelttechnik/spf-institut-fuer-solartechnik/forschung/projekte/details/prosumerskin-neuartige-renovationsloesung-fuer-mfh-1370

SketchUp (August 2022). https://www.sketchup.com/

TRNSYS (August 2022). https://www.trnsys.com/index.html

SIA (August 2022). http://shop.sia.ch/normenwerk/architekt/sia%202024/d/2015/D/Product

CSU (2017, August 2022). “Spotreba paliv a energii v domacnostech”, Cesky Statisticky Urad. Prague, 2017, 266/2017-51. https://www.czso.cz/documents/10180/50619982/ENERGO_2015.pdf/86331734-a917-438a-b3c2-43a5414083fc?version=1.4

Pytrnsys (August 2022). https://pytrnsys.readthedocs.io

ISO (August 2022). https://www.iso.org/standard/39155.htm

Evaluation Of Building Energy Performance: Comparison Before And After Envelope Retrofitting

Ali Derai[1], Monika WOLOSZYN[1], Amandine PIOT[2] and Lamia BERRAH[3]

[1] Univ. Savoie Mont Blanc, Solar Academy Graduate School, LOCIE, Chambéry, F-73000

[2] Univ. Grenoble Alpes, CEA, Liten, Campus Ines, 73375 Le Bourget du Lac, France

[3] Univ. Savoie Mont Blanc, LISTIC, Annecy-le-Vieux, France

Abstract

Both governments and scientific communities across the world have identified the potential and need for energy efficiency in buildings and have initiated significant efforts in this direction. The energy performance could be improved by adding envelope insulation and exploiting the energy resources that come from the surroundings. To succeed in this process, the evaluation of building performance and energy resource quality is necessary. Different configurations of a single-family house (INCAS Building) will be evaluated and compared in this article. To determine the most effective configuration for optimizing the building envelope, as well as to explore the effect of insulation on the bioclimatic performance of the building. This study examines a building's performance using a new set of indicators developed from earlier research. The results of the analyses will be used to better understand those indicators and improve their use; and finally, this study will serve as the first step toward developing a new building evaluation method.

Keywords: energy efficiency, insulations, solar resources, performance indicators, buildings envelopes.

1. Introduction

Building energy consumption has increased to a level that exceeds that of other key sectors (industry and transportation), due to population growth, improvements in comfort and building services, as well as an increase in the amount of time people spend within buildings. This fact highlights the crucial need for energy savings in buildings. Today, both governments and scientific communities believe that focusing on buildings is essential to reducing energy consumption and carbon emissions. Almost 75% of the EU building stock was built before the introduction of the first building codes in the 1970s. Those existing buildings constitute, therefore, the greatest opportunity for energy efficiency improvements. The buildings we find today are expected to achieve both energy-efficient and environmental-friendly designs. The concept of sustainable buildings includes several challenges relating to environmental pollution, interior and outdoor air quality, energy, water, land, and material conservation. Active or passive energy-efficient measures can be used to increase a building's energy efficiency. HVAC system upgrades, electrical lighting upgrades, etc. may all be considered active techniques, whilst building envelope element upgrades fall under the category of passive strategies. Recently, there has been a renewed interest in passive building energy efficiency techniques. They are considered to be an effective solution to the issues of the energy crisis and environmental pollution (Sadineni et al., 2011). The effort to improve the envelope's energy performance can be divided into two types. The first type consists of thermal insulation to prevent heat exchange with the exterior of the building. The second way is by improving the building capacity to exploit more energy from its surrounding, by applying passive strategies. Such approach is called bioclimatic architecture.

Following this introduction, the next sections of this paper provide a brief literature review on the topic of bioclimatic architecture and passive technologies, followed by a presentation of the various indicators that will be employed in the study. After that comes the methodology, which contains a description of the building and simulation configurations. Then, the next section describes the simulation results and the different indicators graphs. Finally, the paper is closed with the main conclusions of the study presented in Section 6.

© 2022. The Authors. Published by International Solar Energy Society
Selection and/or peer review under responsibility of Scientific Committee
doi:10.18086/eurosun.2022.02.03 Available at http://proceedings.ises.org

2. Brief literature review

The aim of architecture has always been to shelter man from the outer environment, architectural evolutions have happened throughout history and in every region and climate to reach the best comfort levels in interior spaces. In this situation, bioclimatic architecture strives to accomplish human thermal comfort by engaging energetically with the exterior climate (Manzano-Agugliaro et al., 2015). The bioclimatic architecture term refers to the technique of construction that considers local climate conditions. It employs appropriate technologies and design principles based on a reflexive focus on the climate and environment to increase energy efficiency. Passive strategies are constructive technologies integrated within buildings, the main objective and function of these solutions are to contribute to the natural cooling or heating of the building and to minimize the building energy needs. These methods are the oldest way to reduce heating and cooling loads in buildings. When dimensioned correctly, they can significantly reduce a household's energy consumption (Bajcinovci & Jerliu, 2016; Budescu, 2013; Ness, 2017).

Passive strategies could be classified as heating and cooling strategies. Passive heating solutions are built into building structures or housings and can act as collectors and accumulators of incidental solar energy, without using active air conditioning systems. Passive heating disperses heat through natural transfer processes, enhancing interior comfort. Different passive heating solutions can be used, those techniques favor the use of solar energy as it is the essential source of heat. Glazing is the transparent part of the facade, it contributes a significant portion of direct solar gains, and the walls' vast surface area creates a path for thermal transmission, allowing solar radiation to travel through the building in high sunlight. For passive cooling the main bioclimatic design strategies have been focused on reducing solar gains and external heat loads. Resulting in reduced cooling needs, the major techniques for many cities with hot climates are natural ventilation and solar shading for windows (Enteria et al., 2019). Various passive techniques have been described, and each of the above-mentioned strategies can minimize energy use to some amount. A combination of multiple passive approaches is required to obtain a high level of energy performance (Gupta & Tiwari, 2016).

3. Building energy performance indicators

Building energy performance assessment is critical for determining the efficiency of energy use and serves as the foundation for any choice and decision to improve energy efficiency. It can provide building owners and/or occupants with relevant information about how much energy is used and how the performance is compared to benchmarks (Wang et al., 2012). Today, the key indicators used to evaluate building performance are related to energy consumption, but this is a simplified and incomplete evaluation system that does not exploit the full potential of the building structure and cannot guide the user to the optimal improvement. Few authors highlighted the need for new and complete evaluation methods for buildings, and proposed a set of indicators that could be used to better optimize the performance of the existing buildings. The present study is based on indicators proposed by (Chesné et al., 2012), where the authors developed a new set of indicators to assess the building bioclimatic performances. They proposed three type of indicators: the building needs indicators, environmental potential indicators, and building performance indicators. those indicators are introduced in this paper.

First It is possible to negate the impact of an environmental resource (noted as *R*, for example solar radiation) on the building by using dynamic energy simulation. As a result, the needs of the building in the scenario where the influence of environmental resource is removed have been defined as the real needs of the building noted as $b_{Ui-Rj}(t)$, when *U* is the use of the resource (for heating or cooling). The residual need is defined in the typical real-life scenario, where the building could employ those resources $b_{Ui}(t)$.

The second set is the Indicators of potential. As the environmental potential is an important element for the energy of the building, this amount of energy needs to be quantified. The total flux exchanged between the resource *Rj* and the total envelope of the building at all times is defined at each instant as the total potential $ptot_{Rj}(t)$, given by (eq. 1). Thus, the coincident potential $pconc_{Ui;Rj}(t)$ (eq. 2) is equal to the total potential if there are some building energy needs $b_{Ui-Rj}(t)$, or set to zero. The purpose of this indicator is to know if the resource is globally sufficient to cover the energy needs for a given period, the integrated energy needs have to be compared to the integrated coincident potential. Secondly, another indicator is defined. It is called the adjusted potential $paj_{Ui;Rj}$ (t) and is given by equations 4. It is the portion of the coincident potential that perfectly matches the energy needs.

At each time step, it is calculated as the difference between the energy needs and the coincident potential.

Total potential is equal to:

$$Ptot_{Rj}(t) = \int_{Periode} ptot_{Rj}(t)\, dt \qquad \text{(eq. 1)}$$

Coincident potential:

$$pconc_{Ui;Rj}(t) = \begin{cases} ptot_{Rj}(t) & if \quad b_{Ui-Rj}(t) > 0 \\ 0 & \text{Else} \end{cases} \qquad \text{(eq. 2)}$$

The integral of coincident potential over a given period gives the total coincident potential at this period.

$$Pconc_{Ui;Rj}(t) = \int_{Periode} pconc_{Ui;Rj}(t)\, dt \qquad \text{(eq. 3)}$$

Adjusted potential:

$$paj_{Ui;Rj}(t) = \min\left(ptot_{Rj}(t), b_{Ui-Rj}(t)\right) \qquad \text{(eq. 4)}$$

$$Paj_{Ui;Rj}(t) = \int_{Periode} paj_{Ui;Rj}(t)\, dt \qquad \text{(eq. 5)}$$

Indicators of performance are the third set of indicators. After the quantification of the environmental resources, the next step is to evaluate the exploited part of those resources by the building. To do so it is possible to compare the needs of the building in an environment without and with a given resource. The exploited potential $pexp_{Ui;Rj}(t)$ is calculated as the difference between the energy needs in the simulation without and with the resource at each time step using equations 6 and 7. It is defined as the part of the resource which is actually used by the building. The Indicators that are able to resume the performance of the building are: the cover rate, the exploitation rate, and the generation rate. The cover rate $\tau\ couv_{Ui;Rj}$ (eq. 8) expresses the part of the building's real energy needs which are covered by the resource. The exploitation rate $\tau exp_{Ui;Rj}$ (eq. 9) represents the part of the resource energy that is actually used by the building, and the generation rate is part of the resource energy that create needs for the building (cooling or heating needs) when there is an excess of this energy.

The exploited potential:

$$pexp_{Ui;Rj}(t) = b_{Ui-Rj}(t) - b_{Ui}(t) \qquad \text{(eq. 6)}$$

The integral of exploited potential over a given period gives the total exploited potential at this period:

$$Pexp_{Ui;Rj}(t) = \int_{Periode} pexp_{Ui;Rj}(t) \qquad \text{(eq. 7)}$$

The cover rate:

$$\tau\ couv_{Ui;Rj} = \frac{Pexp_{Ui;Rj}(t)}{b_{Ui-Rj}(t)} \qquad \text{(eq. 8)}$$

The exploitation rate:

$$\tau exp_{Ui;Rj} = \frac{Pexp_{Ui;Rj}(t)}{Pconc_{Ui;Rj}(t)} \quad \text{(eq. 9)}$$

4. Methodology

The set of indicators presented above is used to evaluate the performance of INCAS Building: a single-family experimental house, located at INES Chambery, in South-Eastern France. The reason for choosing to work on this building is that all its characteristics is well known. Multiple studies have been done on this building and the modelling results were compared and validated with previous publications (Chesné et al., 2012. Chahwane, 2012). Therefore, the energy modelling can be considered as reliable.

The glazing area ratio per oriented surface is 36% for the South, 15% for the West, 6% for the East and 4% for the North. There is a south-oriented extended overhang above both ground and upper floor windows to prevent direct solar radiation from entering the building in summer. All windows of the insulated building are double glazed with a total U-value (window and frame) of 1.3 W/ (m2 K) and a solar factor of 0.76. The windows of the old building are single-glazed and their total U-value is 5 W/ (m2 K). The solar factor of the windows is 0.86.

Tab. 1: Non-insulated building envelope configuration.

Wall type	Material	Thickness [cm]	Conductivity [W/m.K]	Density [kg/m3]	Specific heat [J/kg·K]
Exterior wall	Plaster	2	1.15	1700	1000
	Concrete blocks	15	0.74	800	648
Ground floor	deck slabs	16	1,23	1300	648
Roof	Light wood	16	0,15	500	1200
Internal floor	solid concrete	22	1,75	2400	880

Tab. 2: Insulated building envelope configuration.

Wall type	Material	Thickness [cm]	Conductivity [W/m.K]	Density [kg/m3]	Specific heat [J/kg·K]
Exterior wall	Glass wool	20	0.035	12	840
	Concrete blocks	15	0.74	800	648
Ground floor	Extruded polystyrene	25	0.029	15	880
	deck slabs	16	1.23	1300	648
	heavy concrete	4	1.75	2400	880
Roof	External Rendering	2.5	0.5	1300	1000
	MW Stone Wool	24.5	0.04	30	840
	Timber Flooring	0.5	0.14	650	1200
Internal floor	solid concrete	22	1,75	2400	880

The heating set-point is 19 C and the cooling set-point is 26 C. In both configurations, night ventilation is planned during summer (from the beginning of June to the end of August) with a ventilation rate of 4 vol/h between 10 pm and 7 am. Otherwise, the ventilation rate is 0.5 vol/h. An occupancy scenario is integrated to the simulation. The air infiltrations are considered equal to 0.04 vol/h. The scenario of total power dissipated by both inhabitants and household appliances is given in table 03

A non-insulated and two insulated versions of the building (insulated from the inside and outside) will be studied and compared. The purpose of this study is to evaluate a set of building performance indicators by applying them to various building configurations, then to evaluate the performance of three different building configurations and select the building that performs best in terms of energy consumption and resource exploitation. Although the indicators used in this study are still in the theoretical stage, using them could provide insight into their limitations and pave the way for future advancements.

The building is modelled in Design Builder, then the simulation is run using EnergyPlus. The adopted model consists of two zones. Each zone is on one per level, and three configurations of the INCAS building are studied.

The first one is a non-insulated building (before retrofitting), then the next two buildings' configurations are different only in insulation type: interior or exterior. The Thermal bridges have not been taken into consideration, the wall compositions for the two versions of the INCAS house are listed in table 1 and table 2.

Tab. 3: Daily scenario of the total power dissipated

Hours	0-6	7	8	9-16	17	18-19	20	21	22	23	24
Power [W]	340	830	730	20	570	730	950	1030	830	810	340

5. Results and Discussion

The simulation's results "from the 19th to the 29th of January in the 3 types of buildings" are expressed as graphs that show the application of earlier indicators in the case study of the INAS building. The three types of indicators will be presented in different graphs to assess the solar potential and building performance, and to draw conclusions about the presented indicators.

5.1 Building energy needs:

The results of the building simulation for the first set of indicators, which describe the building's heating demands, are shown in figure 1, figure 2 and figure 3. The three types of building configurations (Non-insulated building, interior insulation, and exterior insulation) are presented in the same figure. The results show in the three types of buildings, the real heating needs are greater. It is the case where the solar potential is null. That means that the sun covers a part of the building's heating needs, so it reduces the building's energy consumption. By analysing the building heating needs graph, it can be noticed that this value decreases each day to very low values, then go higher, the lowest value is located almost in the middle of each day when the solar potential is in its highest value. Those results highlight that the sun is a source of heating that compensate for the heating energy of the building.

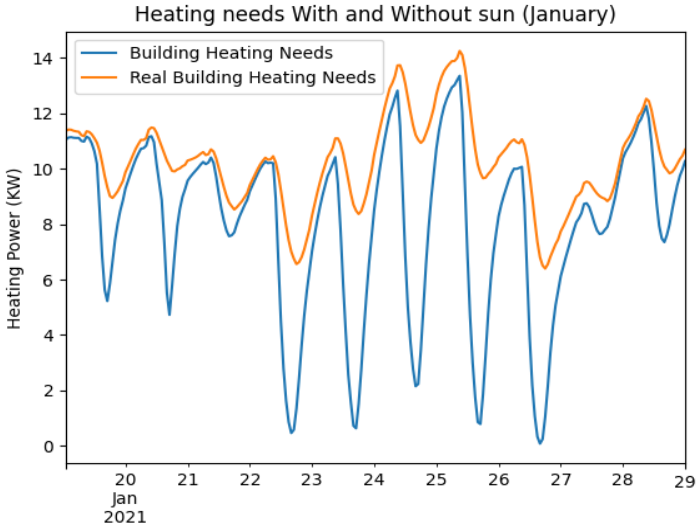

Fig. 1: Need indicators result in Non-Insulated building

When comparing the three configurations, the non-insulated building shows the highest consumption at a maximum of 14kW. The exterior and interior insulation graphs have almost the same shape, while the lowest building consumption is in the exterior insulation building. As the wall's materials compositions are the same in both interior and exterior insulated buildings, both transfer heat in the same way. The thermal bridging is neglected in this simulation, so the only parameter that made a difference is the placement of the insulation. That leads us to a conclusion that the exterior insulation is a better design, this could be due to better use of thermal mass or this configuration improves the building performance on the exploitation of solar energy. More investigation is needed to validate those assumptions using the other type of indicators.

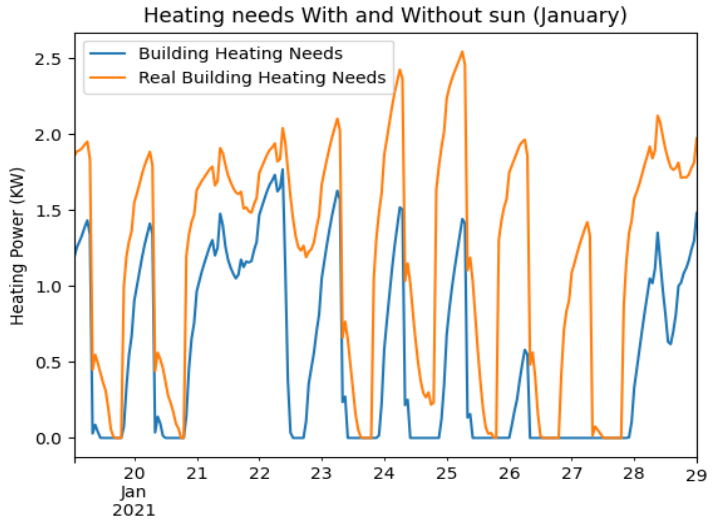

Fig. 2: Need indicators result Interior insulated building

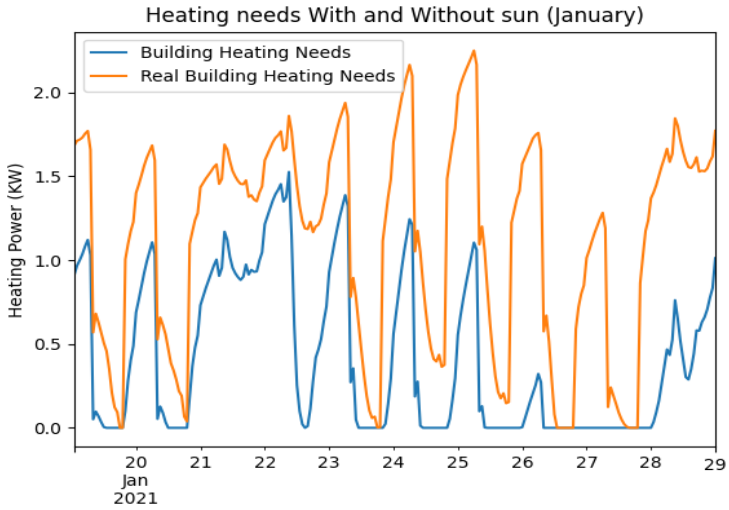

Fig. 3: Need indicators result Exterior insulated building

Need indicators show the capacity of identifying the type of energy source (heat source or heat sink), and compare the performance of the building design. The heating needs is the type of energy consumption indicators that is most used in research, and by removing the influence of one energy source (Sun in this case of study) it will make it a superior indicator that can provide more information about the building and its surrounding. but it is still limited because it doesn't qualify the environment energy potential, and justify the reason for the better performance of a building, and how it can be improved.

5.2 Environmental energy potential:

To assess the available energy in the building surrounding, the potential indicators have been introduced. Figure 3, Figure 4 and Figure 5 present the building's simulation results using potential indicators. The building total solar incident radiation, is the amount of solar energy incident on the total surface of the building envelope. When building needs energy for heating, the coincident potential (concomitant potential) is equal to the total incident solar energy. In the case of a non-insulated building, the graph of both indicators is superposed, which means that there is always heating needs for the building. When in insulated buildings the concomitant potential goes to zero at some hours on days 27 and day 28, which means that no heating energy is required for the building at those hours of the day. In the three buildings the concomitant potential is higher than the building needs during the day

hours, which means that at those hours, theoretically, the building heating needs can be covered completely by the solar energy incident on the envelope of the building.

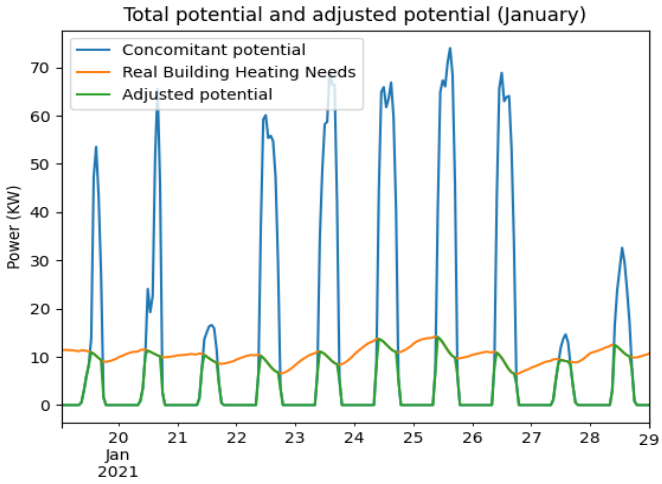

Fig. 4: Potential indicators results for Non-insulated building

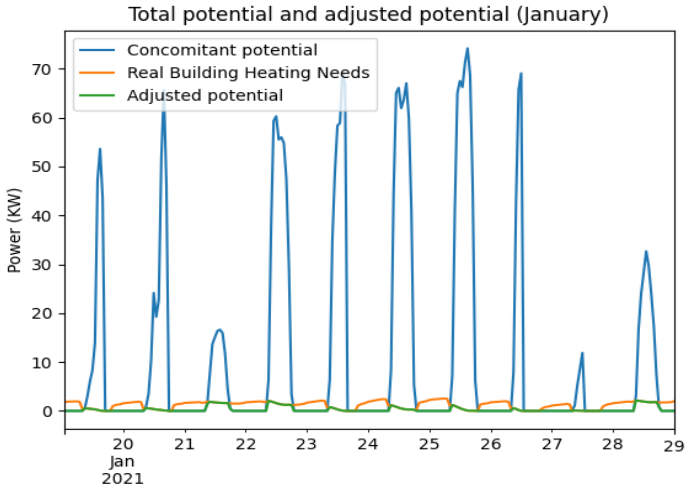

Fig. 5: Potential indicators results for interior insulated building

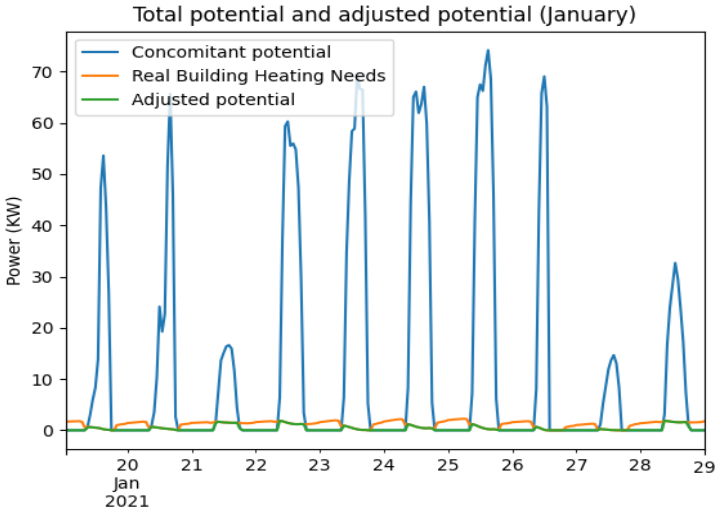

Fig. 6: Potential indicators result for exterior insulated building

The adjusted potential presented by the green graph, is the amount of energy required to use from the concomitant. potential, it goes to zero when there is no solar potential (at night) and is always lower than the building needs, in another word it is the useful part of the resource, that is to say the part that meets the building needs. When comparing the three cases, the concomitant's potentials and adjusted potential are higher in non-insulated building, because there are more heating needs and slightly lower in the building insulated from the inside. After all, there are more hours when the heating needs are null.

The concomitant potential indicator is not an indicator capable of evaluating and comparing the performance of buildings, the purpose of this indicator is to evaluate the environmental energy potential and its capacity to cover the building needs. The indicators also show the intersection between the demand and the energy potential, those kinds of information could be useful for studying thermal storage in the building.

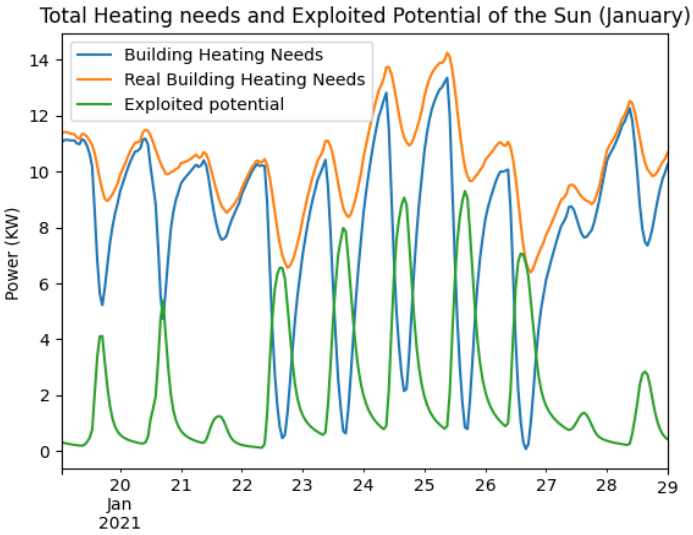

Fig. 7: Sun exploited potential result for non-insulated building

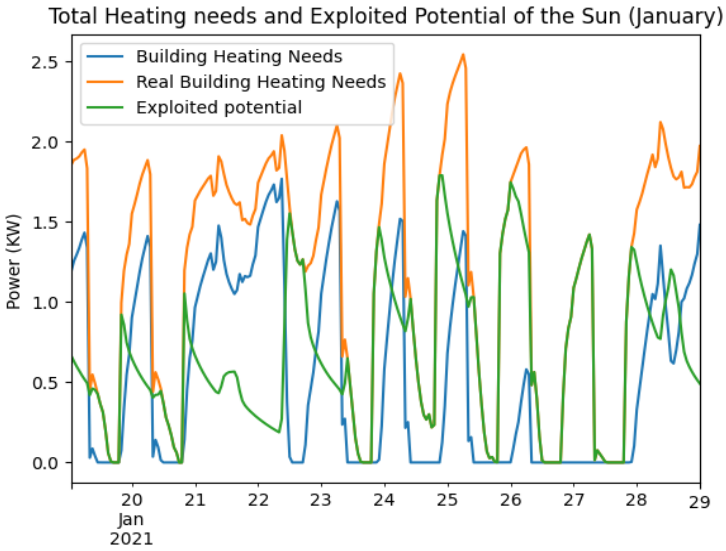

Fig. 8: Sun exploited potential result for interior insulated building

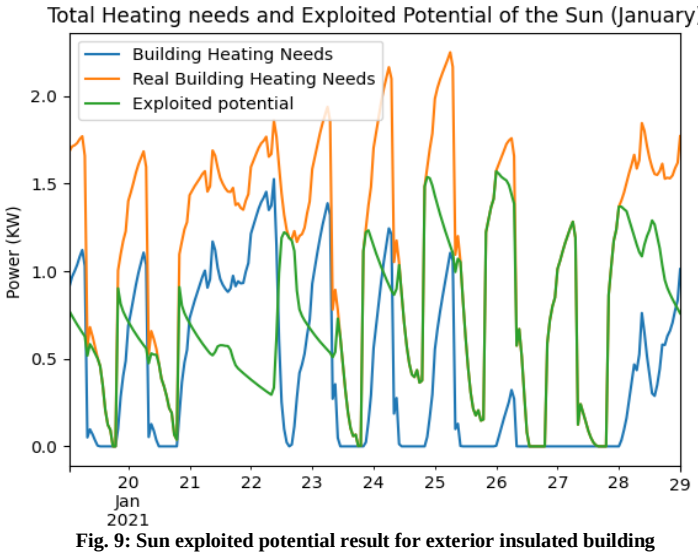

Fig. 9: Sun exploited potential result for exterior insulated building

Another important parameter is presented as exploited potential (figure 03). It is the difference between the residual and the real heating needs of the building, it represents the part of solar energy that is exploited by the building and provides for some of the heating needs. The sun potential is maximal at mid-day, that's why the building heating needs are the lowest and the exploited potential is the highest at that time. At night there is no sun, and by looking at the case of a non-insulated building, the value of exploited potential is almost never zero. that means that the building uses the sun's energy for heating even at night time, the explanation of that is that the energy is stored in building walls by thermal massing, and released gradually at night.

In the case of insulated buildings, the heating needs are considerably lower, the sun could cover the total heating needs of the building, which have been shown in the superposed graphs of real heating needs and exploited potential. The comparison between the performance of both interior and exterior insulation buildings is not so clear in this type of indicator and representation, the exterior insulation building shows a slightly better exploitation performance. The next parts of this study will include the integrated results for the whole period to validate for more conclusions.

The previous potential indicators are a useful tool to evaluate the building capacity of using the environmental energy, it defines the relationship between the building and its environment. This indicator can be used to evaluate the capacity of a building to store energy by thermal mass or to design a thermal storage system that uses that energy during the high consumption hours generally at night in residential buildings, to provide better comfort and less energy consumption.

5.3 Building performance evaluation:

The prior analysis utilizing need and potential indicators were useful in assessing the energy demands of the building and its environment, but it was not sufficient to fully compare the performance of each case study, which is why performance indicators were included. These percentage-based indicators are comparable numbers that summaries each building's performance and identify the most effective design. Figure 4 presents the exploitation and coverage rate for the three types of buildings, when comparing the three cases the coverage rate improved from 2.9% in the non-insulated building to 63% in the exterior insulated building. This is because the energy needs are lower on insulated building cases. The exploitation rate shows a decrease from 17% in Non-insulated buildings to 5% in the case of external insulation. That proves that the thermal insulation separates the building from the exterior environment, and decrease its capacity of exploiting the energy from its surrounding. The building performance and its energy consumption could be improved by applying the proper technics to increase its exploitation rate, on the same side as improving its insulation. The most suitable solution is to find a compromise between those values by applying the fitted passive technics to optimize the energy performance of the building.

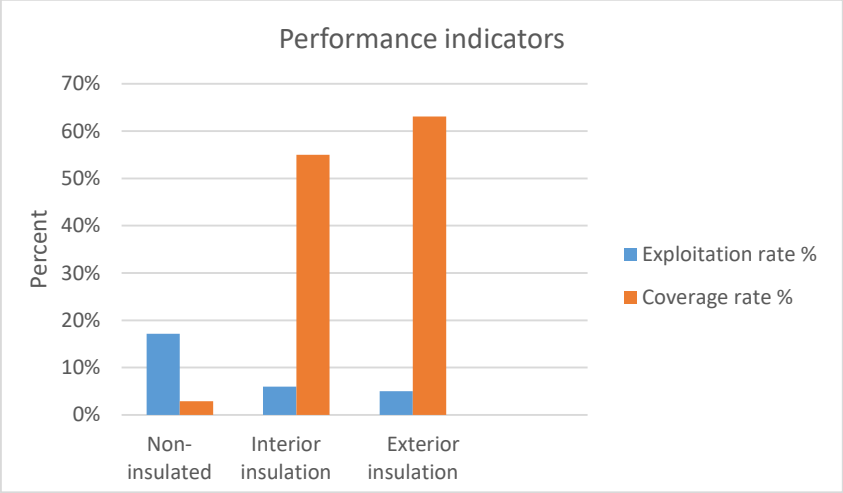

Fig. 10: Performance indicators result of the 3 different configurations of INCAS building.

Table 4 presents a summary of the previously studied indicators, the values in the table are an integral values for the 10-day of study. Those values will be used to come to conclusions regarding the performance of each case study. Passing from a non-insulated building to an insulated building significantly reduces the heating needs, and this is reducing the concomitant potential. The lowest building consumption is in the exterior insulation case, the exploitation rate shows the opposite result because the non-insulated buildings use more solar energy to provide for their heating needs. The comparison of the three buildings makes the exterior insulated building better in performance. It has the lowest heating needs and the highest coverage rate, in the opposite, the exploitation rate is so low, around just 5,8%. According to table 4, the external insulated building's exploited potential value is greater, but the concomitant potential is higher. The value of the exploitation rate is lower because it is the value of exploited potential divided by the concomitant potential that results make it lower.

Tab. 4: Energy performance indicators, result of the 3 different configurations of INCAS building.

	Non-insulated building	**Interior insulation**	**Exterior insulation**
Building Heating Needs [kWh]	1923	129	99
Real Building Heating Needs [kWh]	2462	287	268
Concomitant potential [kWh]	3143	2666	2922
Adjusted potential [kWh]	845	67	68
Exploited potential [kWh]	539	158	169
Exploitation rate %	17,13	5,93	5
Coverage rate %	2,9	55	63,1

By using the previous indicators, we were able to examine the building's performance and determine the most effective configuration. However, this study is incomplete, in terms of envelope evaluation. The indicators were only used to evaluate the building as a whole when those indicators could be adopted to evaluate each part of the building envelope (walls, ceiling and windows). The extensive analysis of the envelope might give more information about the building's principal thermal loss locations and the thermal behavior of each component. Those sets of data could be used to better optimize the envelope performance adapting retrofitting at each part of the building envelope.

This study only considers solar potential as a source of energy for the building, during the period of winter, when all the other natural energy resources should be considered and well evaluated (Air, sky...etc.). Those energy natural potentials could be seen as a source of energy that reduces the building energy consumption, for a period of time. In another period, the same potential could create more needs and increase energy consumption, for example, when studying solar potential, it is the main heating source, it provides heating in winter while in summer it creates cooling needs. So, depending on the season and weather, all-natural energy potentials should be evaluated in terms of how much energy it provides and how much needs it creates.

The generation rate was introduced in this study as this part of the resource energy potential that creates a need for the building, it was not evaluated in this study because the resources potential that generates needs in winter was not evaluated. The importance of evaluating all the potential resources and their contribution to the energy balance of the building is to improve the building capacity to exploit the sources that provide energy and to protect against or eliminate the sources that create more needs for the building, depending on local climates and seasons.

There are various limitations to the indicators employed in this study, the basic idea for those indicators is that the simplest way to value a resource, is to do it instantaneously. The indicators consider only the energy portion of the resource available when there is a need for it, otherwise, when there is no need, the resources are assumed to be zero. Realistically, this is not the case, because the energy resources could never disappear, and the thermal phase shifting of the building must be considered.

Adopting the evaluation process only on the simultaneity of energy resources and building needs, excludes the possibility of optimizing the coverage of resources by thermal storage. At the time steps when there are no building energy needs, the environmental energy potential should be evaluated as an excess of energy that could be stored for later use, as it can create another need for the building and need to be evacuated. Giving example by solar energy in mid-season, the thermal energy could create a need for cooling in the building as it can be stored to be used for night heating.

Another improvement is suggested for the definition of exploitation rate, this indicator is in direct relationship with concomitant potential, as seen in the analysis results, the concomitant potential changes when changing the building envelope, which influences the exploitation rate and makes it a non-comparable parameter. The suggested improvement is to make this indicator depends on the total potential rather than the concomitant potential. Finally, the presented indicators were based on energy simulations of buildings with and without the presence of environmental resources. In our case, the cancellation of the effect of certain environmental energy resources could lead to a dynamic of unrealistic thermal behavior of the building. The investigation of more realistic methods on the same side using the present evaluation method is recommended for the upcoming studies.

6. Conclusion

In this study, we used a comprehensive set of indicators to evaluate and compare the performance of three different single-family house building configurations. Unlike traditional evaluation methods, which focus mainly on the building envelope as a source of energy losses, our approach takes into account the building's ability to harness and exploit energy from its surroundings.

The findings show that exteriorly insulated buildings have the lowest energy requirements when compared to non-insulated and interiorly insulated buildings. It is important to note, however, that this configuration has a low exploitation rate of only 5%. This limitation comes from its ability to restrict heat exchange between the building and the external environment, preventing solar heat absorption by the building envelope from reaching the interior spaces.

While insulation is an effective solution for reducing heating losses in buildings, it also creates a barrier between the building and its surroundings, reducing the structure's bioclimatic performance. Additional investigation is needed to strike a balance between increasing insulation levels and improving the building's ability to exploit solar resources. While insulation is an effective solution for reducing heating losses in buildings, it also creates a barrier between the building and its surroundings, reducing the structure's bioclimatic performance. More research is needed to strike a balance between increasing insulation levels and improving the building's ability to exploit solar resources. Windows play a crucial role in solar radiation transmission, while walls primarily influence heat exchange with the exterior environment. Analysing the performance of each part of the envelope walls individually, taking into account different orientations, will yield valuable insights. To gain a clearer understanding of the overall behaviour of the building it is also important to separately consider the specific effects on windows and walls, a more detailed analysis is needed to differentiate the impact of solar radiation on windows versus walls.

The aforementioned indicators provide a solid foundation for evaluating building performance, comparing various configurations, and determining the most effective approach. These measures will serve as the foundation for the

creation of a new, effective evaluation technique aimed at optimizing building performance and reducing energy consumption. The next steps in this research will be to analyse additional scenarios and building configurations to maximize building performance, as well as to investigate innovative indicators and passive construction techniques. We can improve our understanding and contribute to advancements in sustainable building design and construction practices by doing so.

7. Acknowledgments

This work has been supported by the French National Research Agency, through Investments for Future Program (ref. ANR-18-EURE-0016 – Solar Academy). The research units LOCIE and LISTIC are members of the INES Solar Academy Research Hub.

8. References

Bajcinovci, B., & Jerliu, F. (2016). Achieving Energy Efficiency in Accordance with Bioclimatic Architecture Principles. 18(December), 54–63. https://doi.org/10.1515/rtuect-2016-0013

Budescu, M. (2013). Bioclimatic architecture , a sensible and logical approach towards the future of building development. Lxiii.

Chahwane, L. (2012). Valorisation de l ' inertie thermique pour la performance énergétique des bâtiments To cite this version : HAL Id : tel-00701170 Valorisation de l ' inertie thermique pour la performance énergétique des bâtiments.

Chesné, L., Duforestel, T., Roux, J.-J., & Rusaouën, G. (2012). Energy saving and environmental resources potentials: Toward new methods of building design. Building and Environment, 58, 199–207. https://doi.org/10.1016/j.buildenv.2012.07.013

Enteria, N., Awbi, H., & Santamouris, M. (2019). Building in hot and humid regions: Historical perspective and technological advances. Building in Hot and Humid Regions: Historical Perspective and Technological Advances, 1–219. https://doi.org/10.1007/978-981-13-7519-4

Gupta, N., & Tiwari, G. N. (2016). Review of passive heating/cooling systems of buildings. Energy Science and Engineering, 4(5), 305–333. https://doi.org/10.1002/ese3.129

Manzano-Agugliaro, F., Montoya, F. G., Sabio-Ortega, A., & García-Cruz, A. (2015). Review of bioclimatic architecture strategies for achieving thermal comfort. Renewable and Sustainable Energy Reviews, 49, 736–755. https://doi.org/10.1016/j.rser.2015.04.095

Ness, M. (2017). review and analysis in cold climates – principles and tools for bioclimatic building design - an applied review and analysis in cold climates –. July.

Sadineni, S. B., Madala, S., & Boehm, R. F. (2011). Passive building energy savings: A review of building envelope components. Renewable and Sustainable Energy Reviews, 15(8), 3617–3631. https://doi.org/10.1016/j.rser.2011.07.014

Wang, S., Yan, C., & Xiao, F. (2012). Quantitative energy performance assessment methods for existing buildings. Energy & Buildings, 55, 873–888. https://doi.org/10.1016/j.enbuild.2012.08.037

RENOVATION TOWARDS NZEB WITH PV

Matthias Haase[1]

[1] Institute of Facility Management, ZHAW, Waedenswil (Switzerland)

Abstract

A typical residential building from 1937 located near Wuerzburg, Germany undergone deep energy renovation in 2013. A balanced ventilation system with integrated air-to-water heat pump was installed together with an 8 kW PV system (roof-integrated). The key performance indicators were measured over a period of seven years (2014-2020). Energy production, energy use, self-consumption and exported electricity to the grid were monitored. The results show variations in performance indicators. The self-consumption varied between 16.9% and 25% while the level of autarchy varies between 34.1% (2014) and 45.4% (2020). The robustness of the key performance indicators is discussed and recommendations for designers and planners as well as prosumers are given.

Keywords: Solar PV, heat pump, envelope renovation, ventilation

1. Introduction

Residential use of energy is responsible for 28% of EU energy consumption (EC 2012). The barriers to consumer-related energy saving have been known for more than 30 years but are still present, in particular split incentives (e.g. tenants vs. landlords), lack of information, high initial investment in energy-efficient measures and equipment and energy users behaviors (BPIE 2012). Likewise, while awareness of the existence of renewable energies has improved considerably in the last years, there is still a lack of understanding of how to use and optimize them in practice. As of 2021, all new buildings have to be Nearly-Zero Energy Buildings (NZEBs) as required by the EPBD (EPBD 2010). There are many approaches to this goal and several pilot buildings have been built and extensively measured. The theoretical approach in the NZEB concept is typically based on three pillars. The first one refers to energy saving measures to reduce the heating energy needs. The second pillar is focusing on using energy efficient equipment and appliances. The third pillar is represented by the consumption of renewable energy produced on-site (Satori et al. 2012; Voss and Musall 2011). All measures have been applied in this case study. A residential building from 1937 located near Wuerzburg in Germany was deep retrofitted in 2013 (Haase, 2016). Roof, façade and basement ceiling were highly insulated and thermal bridges were minimized. Existing windows were replaced with triple glazing and wood-aluminium framed windows. A balanced ventilation system with integrated air-to-water heat pump was installed together with an 8 kW PV system (roof-integrated). The ventilation ducts were integrated into the existing chimneys. The residential appliances (white goods) (refrigerator, washing machine, dishwasher) were installed or replaced by A+++ equipment. The cooking equipment was replaced by induction device. The existing lighting fittings were replaced with LED lighting products. The project received funding from the German Bank for Rebuilding (KfW) in the class kfW55 which uses 55% of the energy budget defined in the existing German building code EneV. (KfW 2014; EneV 2014). More ambitious levels (e.g. KfW40 or any type of zero energy buildings) did not exist for refurbishments, only for new constructions. However, there were additional funding schemes for heating systems and FIT for photovoltaics (PV) (EEG 2014). Today, the funding schemes as well as FIT are under revision (Bergner and Quaschning 2021).

A 7.95 kW roof-integrated PV system with a south-west orientation and 50°angle was installed. The PV system consists of 30 modules with 265 W each (see Figure 1).

© 2022. The Authors. Published by International Solar Energy Society
Selection and/or peer review under responsibility of Scientific Committee
doi:10.18086/eurosun.2022.02.04 Available at http://proceedings.ises.org



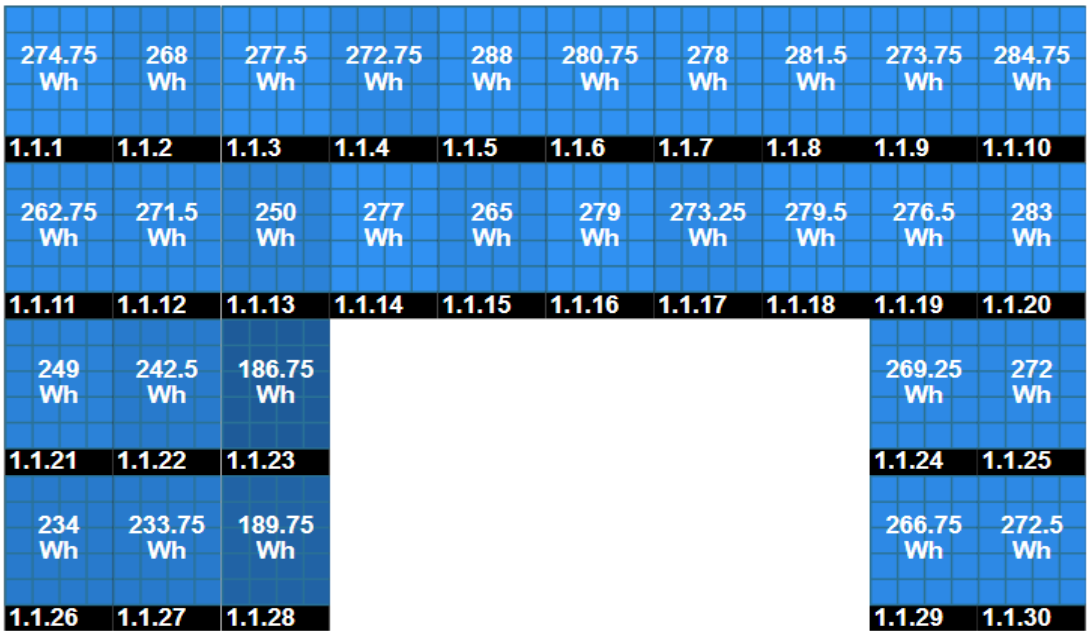

Fig. 1: PV system and layout. south-west orientation (top: photo of the south-west facade; bottom: module layout with monitoring figures for each module (average annual data))

The inverter controls each module separately, ensuring minimized shading effects from the roof obstruction ('Gaube'). The electricity produced by the PV system is primarily used to cover the energy needs of the household and the surplus is exported to the grid. The system was installed in October 2013, thus a rate of 0.1454 €/kWh was given by the local energy provider ('Stadtwerke') for buying (FIT). Although this approach of prosumer is widely used and there exist some experience with new constructions, there is still a lack of knowledge on the long-term performance of buildings based on prosumer models under real conditions. At least the energy produced, purchased from and sold to the grid provide additional performance parameters that define energy performance and related energy costs. Thus, data from seven years of measurements was collected and different performance indicators were calculated in order to analyze how robust these are in practice.

2. Methodology

The monitored key performance indicators (KPI) are:

- Electricity produced by PV
- Electricity exported to the grid
- Electricity purchased from the grid

The electricity exported to the grid is monitored (for obvious tariffs reasons). Based on these measurements measured from 2014 to 2021 energy production, energy use, energy costs, self-consumption and exported electricity to the grid which were monitored it was possible to calculate key performance indicators (KPIs): self-consumption [10], level of autarchy, load matching and grid integration. The following definitions were used:

- Self-consumption: $SC = E_{OC} / E_{PV}$ (eq. 1)
- Level of autarchy: $LA = E_{OC} / E_{total}$ (eq. 2)
- Load matching: $f_{load} = \frac{1}{N} \cdot \sum_{year} \min\left[1, \frac{g(t)}{l(t)}\right]$ (eq. 3)
- Grid interaction: $f_{grid} = STD\left(\frac{ne(t)}{max(|ne(t)|)}\right)$ (eq. 4)

where

E_{CO} is own consumption (household)

E_{PV} is the electricity produced by PV system

E_{total} is the total energy use of household

g(t) is the energy generation at each time step

l(t) is the energy load at each time step

N is the number of samples in the evaluation period

ne(t) is the net export at each time step

3. Results

The difference between the energy produced and the exported energy gives an indication of the renewable energy consumed by the household (self-consumption). When adding the self-consumed component of the PV electricity production, the household energy use was calculated. The monitored key performance indicators (KPI) are:

- Electricity produced by PV (as shown inf Figure 1-3)
- Electricity exported to the grid (shown in Figure 4)
- Electricity purchased from the grid (shown inf Figure 4)

In addition, the KPIs were calculated and are shown inf Figure 5 to 7.

3.1. Electricity produced by PV

Electricity production from PV was monitored. Figure 2 shows the electricity production of each module (P1.1.1 to P1.1.30 according to the layout shown in Fig. 1) for the 1. July 2020 as an example. It can be seen that some modules are producing more and some considerably less (e.g. P1.1.22 P1.1.23, P1.1.27 and P1.1.28). These are left from the obstruction and more shaded than the rest (on that day).

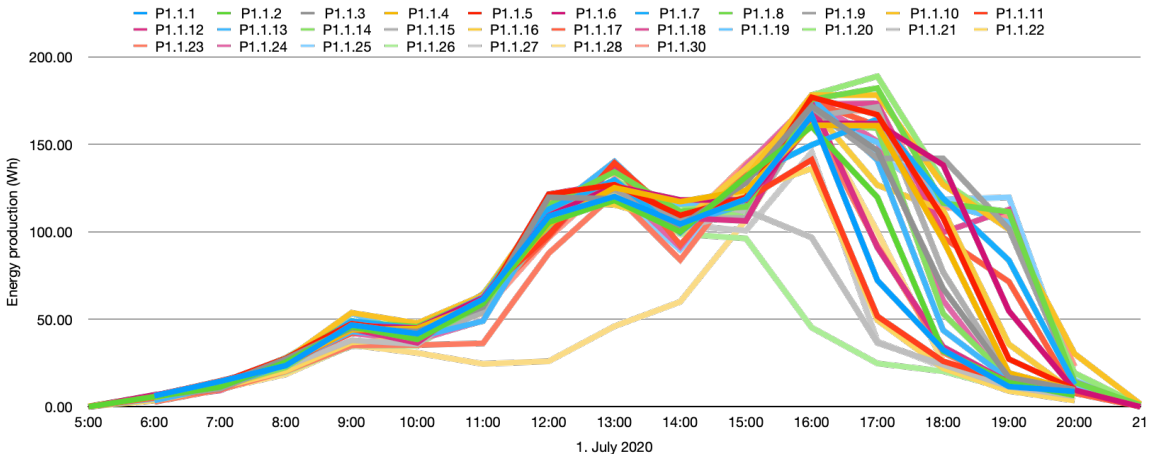

Fig. 2: Electricity produced by PV panels 1-30 on 1. July 2020 at inverter

Fig. 3 gives values of the electricity production of each module (P1.1.1 to P1.1.30 according to the layout shown in Fig. 1) for the 1. January 2020 as another example. Here, it can be seen that modules P1.1.22 P1.1.23, P1.1.27 and P1.1.28 produce considerably less than the rest. This is due to the shading from the obstruction is even more prominent during the winter months with its azimuth angles.

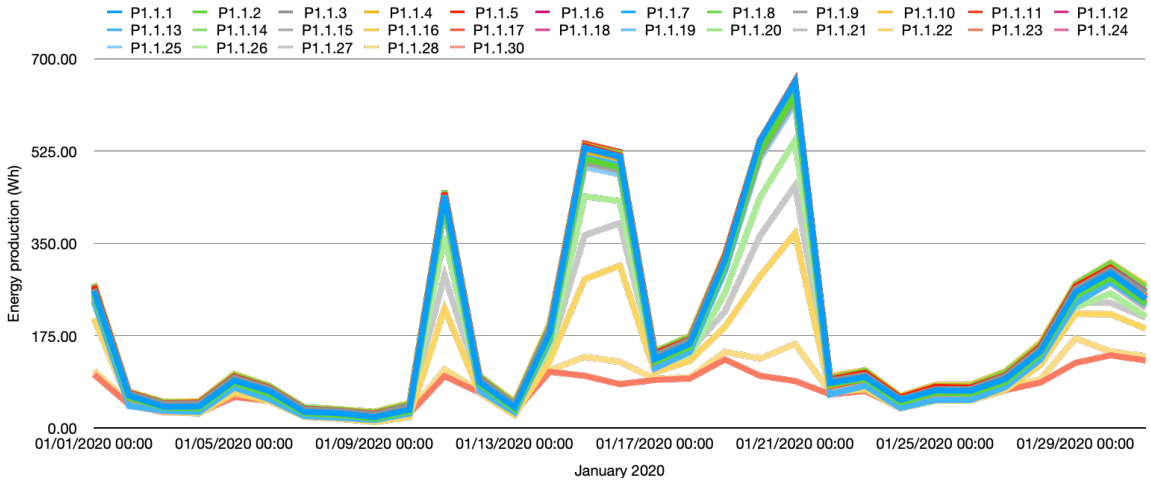

Fig. 3: Electricity produced by PV panels 1-30 on January 2020 at inverter

The electricity production values were monitored for the monitoring period and summarized in daily, weekly and monthly values.

Fig. 4 shows the monthly electricity production which varies over the year with maximum yields in summer months and minimal yields in winter months. The largest (median) values were monitored in July (851 kWh/month), followed by May (802 kWh/month). The lowest (median) values were monitored in December (82 kWh/month), followed by January (136 kWh/month). Figure 4 shows the predicted electricity production (sim_min and sim_max) form the planning phase. Sim_min was based on PVGIS, while sim_max was based on the simulation tool of the PV planner. Both value sets were estimated based on local weather data and not taking into consideration any shading effects of surrounding vegetation. It can be seen that the measurements mostly fall within the bandwidth (sim_min and sim_max) with some months higher (Jan 2017, March 2015, April 2015, April 2020; Sep 2020, Nov 2020, Oct 2018) and some moths with lower values (Jan 2015, Jan 2016, Jan 2018, Jan 2019, Jan 2019, Feb 2014, Feb 2016, Feb 2020, Mar 2018, Apr 207, May 2019, Jun 2014, Jun 2016, Jun 2020, Jul 2017, Aug 2014, Sep 2014, Sep 2017, Oct 2014, Oct 2015, Oct 2016, Nov 2014, Nov 2017, Dec 2014-2020).

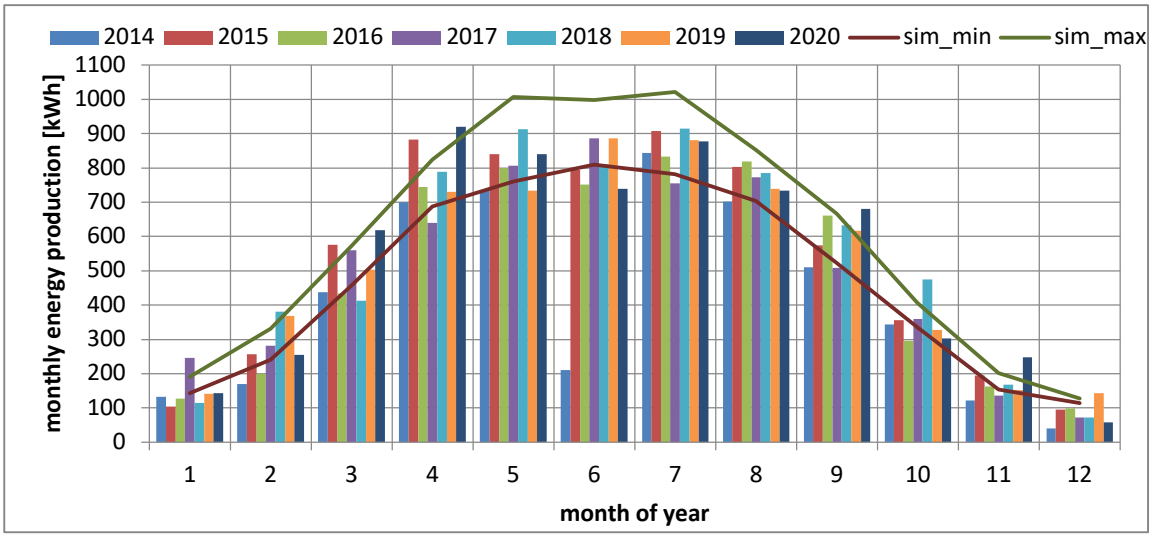

Fig. 4: Electricity produced at inverter for 2014 to 2020

3.3 Electricity purchased from and sold to the grid

Fig. 5 shows annual electricity purchased from and sold to the energy provider (grid). Electricity was purchased for the heat pump and the household (appliances and lighting). It can be seen that electricity purchased as well as electricity sold are varying over the seven years measurement period. The highest amount of electricity sold was in 2018 (5470 kWh) and the lowest amount in 2014 (4198 kWh). The highest amount of electricity purchased was in 2020 (7500 kWh) and the lowest amount in 2014 (5975 kWh).

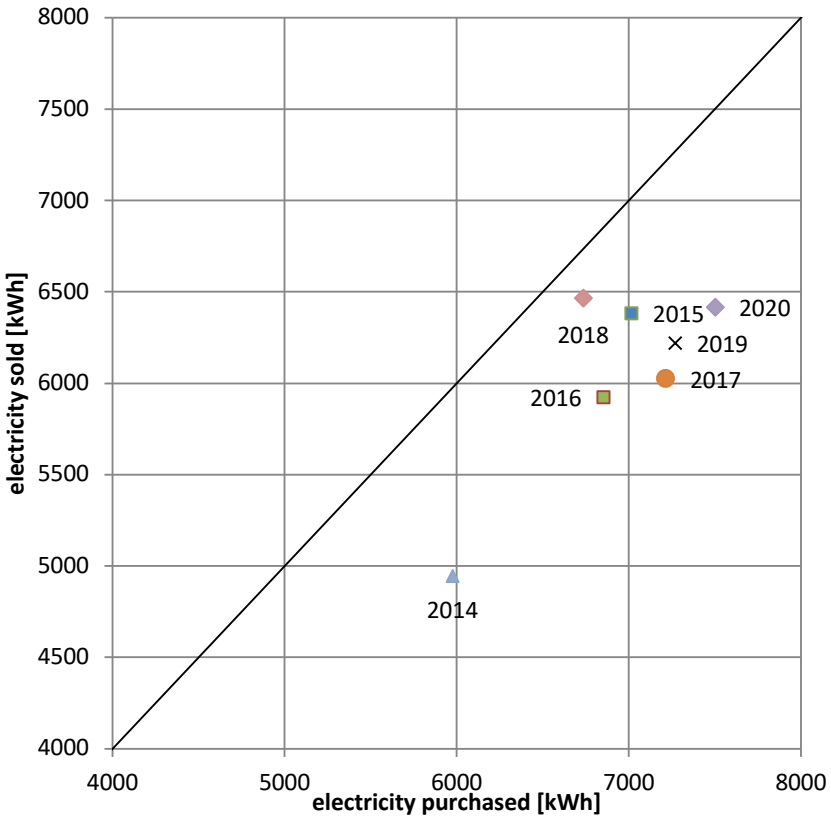

Fig. 5: Electricity sold and purchased, monitored for the period from 2014 to 2020

3.2. Key performance indicators

The purchased electricity was monitored separately for the heat pump and the household. The difference between electricity production from PV and electricity sold was calculated to self-consumption of household energy. Figure 6 illustrates the annual energy balance with electricity purchased (negative values) and electricity sold and self-consumed (positive values). While the balance between PV and household energy is always positive it becomes always negative if the electricity consumption of the heat pump is included. The average mismatch is -883 kWh for the period 2014 until 2020.

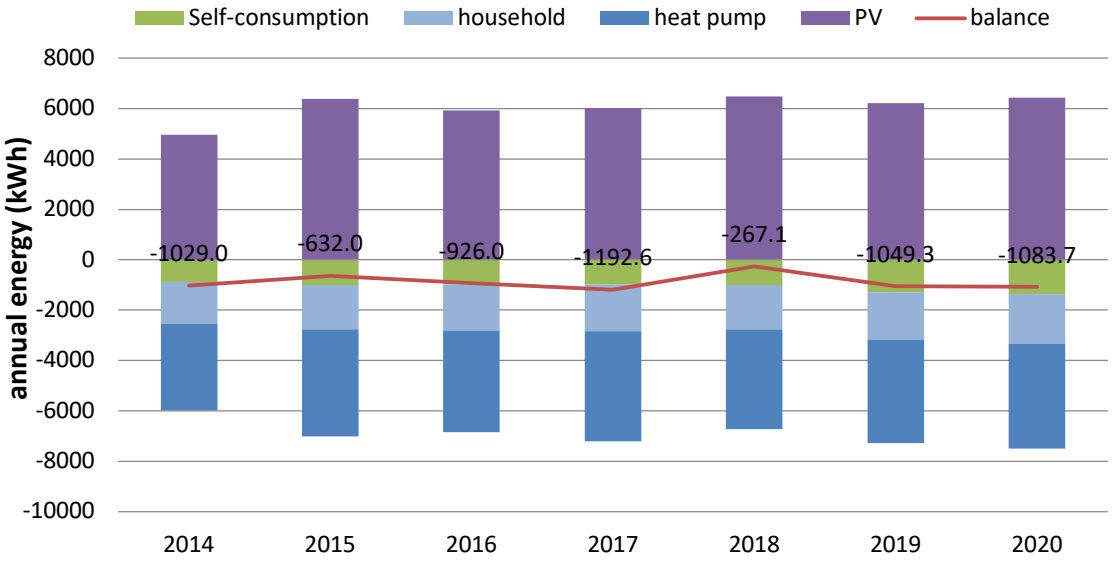

Fig. 6: PV (FIT), Self-consumption and electricity purchased (household and heat pump)

Table 1 shows the figures in specific values (divided by the area of heated floor space). It can be seen that self-consumption increases from 5.45 kWh/(m^2 a) in 2014 to 8.53 kWh/(m^2 a) in 2020. Household electricity use increased from 10.53 kWh/(m^2 a) (2014) to 12.31 kWh/(m^2 a) in the same period. This is due to an increase in appliances (an additional dryer was installed in 2015 and more communication equipment and computers were installed). PV production increased in the same period from 30.91 kWh/(m^2 a) (2014) to 40.11 kWh/(m^2 a) (2020). However, the lower electricity production from PV in 2014 is due to a failure of an inverter part which lead to a maintenance in June without electricity production. The electricity balance varies between 1.67 kWh/(m^2 a) in 2018 and 7.45 kWh/(m^2 a) in 2017.

Tab. 1: Specific electricity use (negative values) for self-consumption (household), household, heat pump, and production (positive values) from PV

(kWh/(m^2 a)	2014	2015	2016	2017	2018	2019	2020
Self-consumption	-5.45	-6.31	-6.15	-6.19	-6.24	-8.13	-8.53
household	-10.53	-11.04	-11.38	-11.55	-11.00	-11.74	-12.31
heat pump	-21.37	-26.49	-25.29	-27.36	-24.85	-25.56	-26.03
PV	30.91	39.89	37.03	37.64	40.42	38.87	40.11
balance	-6.43	-3.95	-5.79	-7.45	-1.67	-6.56	-6.77

The level of autarchy (LA) is shown in Fig. 7. LA was calculated with weekly values and for household energy (in blue) as well as theoretically values including the electricity used for the heat pump. It should be noted that these are not measured values as the heat pump is connected in a separate circuit and does not get electricity from the PV system. It was included here to illustrate the potential for connecting the heat pump and the PV. As shown, the level of autarchy (LA) varies over the year. Obviously, the LA is higher during summer months than during winter months. LA reaches 100% in 23 weeks of 2020 (week 9, 13, 14, 16, 17, 18, 19, 20, 22, 23, 24, 26, 27, 28, 29, 30, 31, 32, 34, 36, 37, 38, and 45). In three weeks, LA reaches 200% (week 17, 22, and 45). The largest LA is observed in week 45 (340%) which is due to a combination of high PV production and very low household energy use (due to absence).

During the winter months, in 21 weeks, LA is below 50% and below 20% in 12 weeks (week 3, 6, 10, 38, 42, 46, 48, 49, 50, 51, 52, and 53). This illustrates that the PV system can deliver only a small fraction of the household electricity use during these weeks. The figures for LA including the electricity use of the heat pump are much lower and do not show potential for an increase of LA by additional batteries.

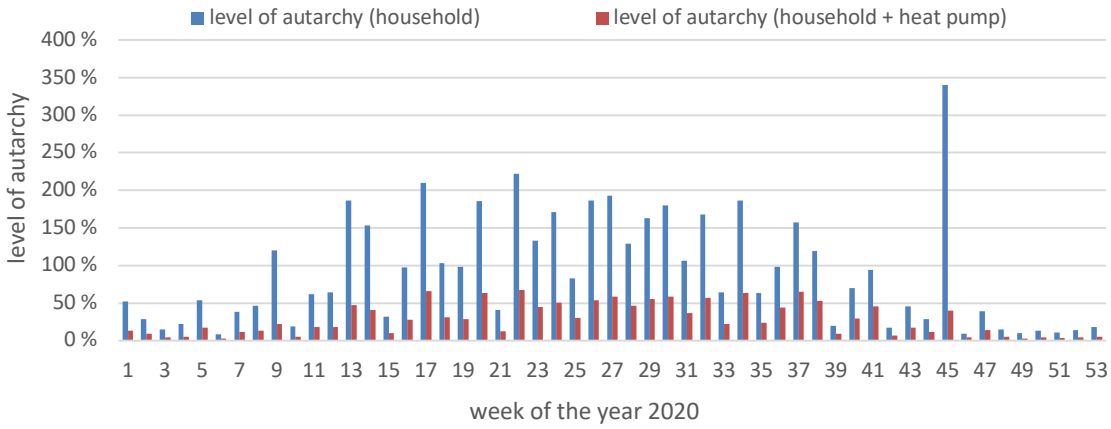

Fig. 7: Weekly level auf autarchy for 2020 (blue: household; red: household + heat pump)

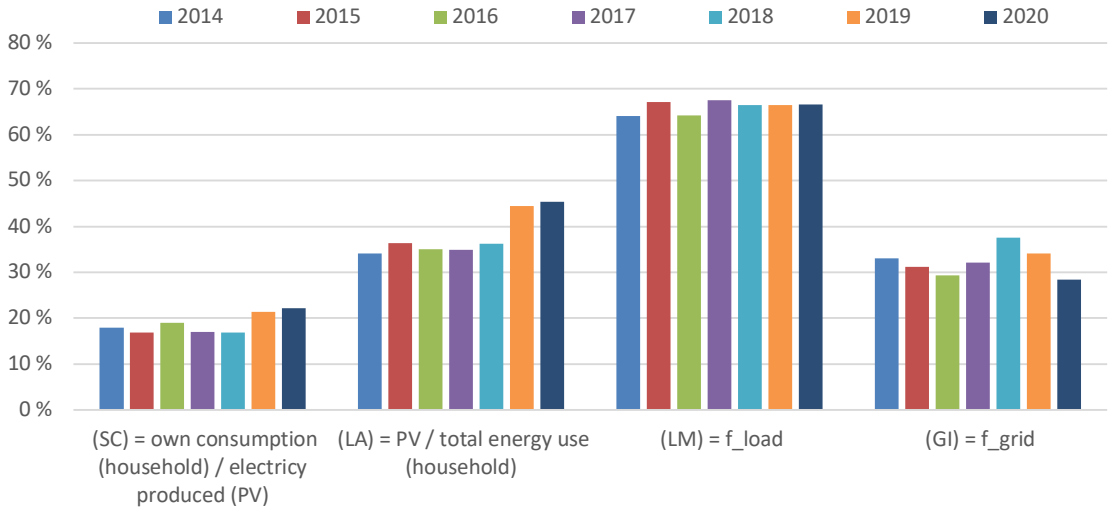

Fig. 8: Key performance indicators SC, LA, LM and GI (eq. 1 – 4)

The other key performance indicators are shown in Fig. 8. Annual self-consumption (SC) varies between 16.9% (2015) and 22% (2020). The level of autarchy (LA) varies between 34.1% (2014) and 45.4% (2020). Load

matching (LM) varies between 64.1% (2014) and 67.5% (2017). Grid interaction (GI) varies between 28.4% (2020) and 37.1% (2019).

4. Conclusions

An energy renovated building was equipped with BIPV on the roof. Energy use was monitored over a period of seven years. The first step of the renovation process was successful as purchased energy was reduced to extremely low levels (6937 kWh on average for the period from 2014 to 2020). In addition, PV produced is on average 6055 kWh in the monitoring period. The electricity balance varies between 1.67 kWh/(m^2 a) (2018) and 7.45 kWh/(m^2 a) (2017). Electricity purchased from and sold to the grid are important measurements that provide robust information about the performance of the building. However, electricity use in the building is thus derived from electricity produced by the PV and the electricity self-consumed in the building. This is a standard prosumer model which will become more and more common. The PV system exporting energy into the grid and delivering electricity to the household can be used to introduce new performance indicators of grid interaction, level of autarchy, self-consumption and load matching. Energy storage based on batteries will in these cases have only a limited effect on LA, as the total electricity produced is not sufficient to cover the household electricity. These new key performance indicators are varying over the monitored period of seven years. This provides valuable information to designers and planners of prosumer models. However, they provide relatively robust indicators of the system. Energy balance can vary over time due to variations in household and heat pump electricity use and variations in electricity production from PV. These should be considered when planning a prosumer model, e.g. by sensitivity analysis of the influencing parameters.

The next step will be to analyze the performance of the systems. This includes the performance of the PV system, the heat pump system, the appliances, and lighting.

Another step must include the detailed study of the weather data. Variations in cloud cover and thus solar radiation influences of course the performance of the PV system and the PV modules.

It will also be interesting to analyze associated costs to the building. Electricity tariffs vary for household, heat pump and PV (feed-in tariff). Thus, the economic performance of a prosumer will be interesting to evaluate.

5. Acknowledgments

This work has been conducted within the strategic project DECARB of ZHAW which is highly acknowledged.

6. References

EEG, Act on the Development of Renewable Energy Sources, Renewable Energy Sources Act RES Act 2014. (in German: Erneuerbare Energien Gesetz). http://www.erneuerbare-energien.de/EE/Redaktion/DE/Gesetze-Verordnungen/eeg_2014_engl.pdf?__blob=publicationFile&v=4. access date: jan 2016

Bergner, J. and Quaschning, V., Sinnvolle Dimensionierung von Photovoltaikanlagen für Prosumer, in German: Meaningful sizing of PV systems for prosumers, Verbraucherzentrale NRW e.V, https://pvspeicher.htw-berlin.de/, access date: 21.12.2021

BPIE 2013. Data Hub for the energy performance of buildings. Source: http://www.buildingsdata.eu/

EC – European Commission, Energy strategy for Europe (2012) *Energy market country report 2011 – Belgium*. European Commission.

Energieeinsparverordnung 2014. (EneV). http://enev-2014.info/. access date Jan 2016

EPBD. 2010. Energy Performance in Buildings Directive 2008/0223. European Commission. Brussels. revised 2010. http://eur-lex.europa.eu/LexUriServ/LexUriServ.do?uri=OJ:L:2010:153:0013:0035:EN:PDF. access date: April 2015

Haase, M., Case study of deep retrofitting of a residential building towards plus energy level, proceedings IEECB&SD conference (IEECB&SD2016), 16-18 March 2016, Frankfurt, Germany,

Kreditanstalt für Wiederaufbau (KfW). Energy efficient refurbishment (in German: Energieeffizientes

Sanieren).updated in 2015. financial support program. https://www.kfw.de/inlandsfoerderung/Privatpersonen/Bestandsimmobilie/Energieeffizient-Sanieren/Das-KfW-Effizienzhaus/; access date: Jan 2016

Sartori. I.. Napolitano. A. and Voss K. (2012). Net zero energy buildings: a consistent definition framework. *Energy and Building*. 48. pp. 220–232. https://doi.org/10.1016/j.enbuild.2012.01.032

Voss. K. and Musall. E. (2011). Net Zero Energy Buildings – International Projects on Carbon Neutrality in Buildings. DETAIL. Munich. ISBN-978-3-0346-0780-3.

Appendix: Units and Symbols

This section provides guidance on the use of units and symbols in your paper. Please follow these guidelines.

1. Units

The use of S.I. (Système International d'unités) in papers is mandatory. The following is a discussion of the various S.I. units relevant to solar energy applications.

Energy
The S.I. unit is the joule ($J \equiv kg\ m^2\ s^{-2}$). The calorie and derivatives, such as the langley (cal cm^{-2}), are not acceptable. No distinction is made between different forms of energy in the S.I. system so that mechanical, electrical and heat energy are all measured in joules. Because the watt-hour is used in many countries for commercial metering of electrical energy, its use is tolerated here as well.

Power
The S.I. unit is the watt ($W \equiv kg\ m^2\ s^{-3} \equiv J\ s^{-1}$). The watt will be used to measure power or energy rate for all forms of energy and should be used wherever instantaneous values of energy flow rate are involved. Thus, energy flux density will be expressed as $W\ m^{-2}$ and heat transfer coefficient as $W\ m^{-2}\ K^{-1}$. Energy rate should not be expressed as $J\ h^{-1}$.
When power is integrated for a time period, the result is energy that should be expressed in joules, e.g. an energy rate of 1.2 kW would produce 1.2 kW x 3600 s = 4.3 MJ if maintained for 1 h. It is preferable to say that

Hourly energy = 4.3 MJ

rather than

Energy=4.3 MJ h^{-1}.

Force
The S.I. unit is the Newton ($N \equiv kg\ m\ s^{-2}$). The kilogram weight is not acceptable.

Pressure
The S.I. unit is the Pascal ($Pa \equiv N\ m^{-2} \equiv k^2\ m^{-1}\ s^{-2}$). The unit kg cm^{-2} should not be used. It is sometimes practical to use 10^5 Pa = 1 bar = 0.1 MPa. The atmosphere (1 atm = 101.325 kPa) and the bar, if used, should be in parenthesis, after the unit has been first expressed in Pascals. e.g. 1.23 x 10^6 Pa (12.3 atm). Manometric pressures in meters or millimeters are acceptable if one is reporting raw experimental results. Otherwise they should be convened to Pa.

Velocity
Velocity is measured in $m\ s^{-1}$. Popular units such as $km\ h^{-1}$ may be in parentheses afterward.

Volume
Volumes are measured in m^3 or litres (1 litre = $10^{-3}\ m^3$). Abbreviations should not be used for the litre.

2. Flow

In S.I. units, flow should be expressed in $kg\ s^{-1}$, $m^3\ s^{-1}$, litre s^{-1}. If non-standard units such as litre min^{-1} or $kg\ h^{-1}$ must be used, they should be in parentheses afterward.

Temperature
The S.I. unit is the degree Kelvin (K). However, it is also permissible to express temperatures in the degree Celsius (°C). Temperature differences are best expressed in Kelvin (K).
When compound units involving temperature are used, they should be expressed in terms of Kelvin, e.g. specific heat $J\ kg^{-1}\ K^{-1}$.

3. Nomenclature and Symbols

Tables 1-5 list recommended symbols for physical quantities. Obviously, historical usage is of considerable importance in the choice of names and symbols and attempts have been made to reflect this fact in the tables. But conflicts do arise between lists that are derived from different disciplines. Generally, a firm recommendation has been made for each quantity, except for radiation where two options are given in Table 5.
In the recommendations for *material properties* (see Table 1), the emission, absorption, reflection, and transmission of radiation by materials have been described in terms of quantities with suffixes 'ance' rather than 'ivity', which is also sometimes used, depending on the discipline. It is recommended that the suffix 'ance' be used for the following four quantities:

$$\text{emittance } \varepsilon = \frac{E}{E_b}\left(or \frac{M_s}{M_{sb}} \right)$$

$$\text{absorptance } \alpha = \frac{\Phi}{\Phi_i}$$

$$\text{reflectance } \rho = \frac{\Phi}{\Phi_i}$$

$$\text{transmittance } \tau = \frac{\Phi}{\Phi_i}$$

where E and ϕ is the radiant flux density that is involved in the particular process. The double use of α for both absorptance and thermal diffusivity is usual, as is the double use of ρ for both reflectance and density. Neither double use should give much concern in practice.

Table 1: Recommended symbols for materials properties

Quantity	Symbol	Unit
Specific heat	c	J kg^{-1} K^{-1}
Thermal conductivity	k	W m^{-1} K^{-1}
Extinction coefficient^{+}	K	m^{-1}
Index of refraction	n	
Absorptance	α	
Thermal diffusivity	α	m^2 s^{-1}
Specific heat ratio	γ	
Emittance	ε	
Reflectance	ρ	
Density	ρ	kg m^{-3}
Transmittance	τ	

$^{+}$ In meteorology, the *extinction coefficient* is the product of K and the path length and is thus dimensionless.

Table 2: Recommended symbols and sign convention for sun and related angles

Quantity	Symbol	Range and sign convention
Altitude	α	0 to ± 90°
Surface tilt	β	0 to ± 90°; toward the equator is +ive
Azimuth (of surface)	γ	0 to 360°; clockwise from North is +ive
Declination	δ	0 to ± 23.45°
Incidence (on surface)	Θ, i	0 to + 90°
Zenith angle	Θ_z	0 to + 90°
Latitude	Φ	0 to ± 90°; North is +ive
Hour angle	ω	-180° to +180°; solar noon is 0°, afternoon is +ive
Reflection (from surface)	r	0 to + 90°

Table 3: Recommended symbols for miscellaneous quantities

Quantity	Symbol	Unit
Area	A	m^2
Heat transfer coefficient	h	W m^{-2} K^{-1}
System mass	m	kg
Air mass (or air mass factor)	M	
Mass flow rate	$\dot{m}$	kg s^{-1}
Heat	Q	J
Heat flow rate	$\dot{Q}$	W
Heat flux	q	W m^{-2}
Temperature	T	K
Overall heat transfer coefficient	U	W m^{-2} K^{-1}
Efficiency	η	
Wavelength	λ	m
Frequency	ν	s^{-1}
Stefan-Boltzmann constant	σ	W m^{-2} K^{-4}
Time	t, τ, Θ	s

Table 4: Recommended subscripts

Quantity	Symbol
Ambient	a
Black-body	b
Beam (direct)	b
Diffuse (scattered)	d
Horizontal	h
Incident	i
Normal	n
Outside atmosphere	o
Reflected	r
Solar	s
Solar constant	sc
Sunrise (sunset)	sr, (ss)
Total of global	t
Thermal	t, th
Useful	u
Spectral	λ

Table 5: Recommended symbols for radiation quantities

	Preferred name	Symbol	Unit
a)	Nonsolar radiation		
	Radiant energy	Q	J
	Radiant flux	Φ	W
	Radiant flux density	Φ	W m^{-2}
	Irradiance	E, H	W m^{-2}
	Radiosity or Radiant exitance	M, J	W m^{-2}
	Radiant emissive power (radiant self-exitance)	Ms, E	W m^{-2}
	Radiant intensity (radiance)	L	W m^{-2} sr^{-1}
	Irradiation or radiant exposure	H	J m^{-2}
b)	Solar radiation		
	Global irradiance or solar flux density	G	W m^{-2}
	Beam irradiance	G_b	W m^{-2}
	Diffuse irradiance	G_d	W m^{-2}
	Global irradiation	H	J m^{-2}
	Beam irradiation	H_b	J m^{-2}
	Diffuse irradiation	H_d	J m^{-2}
c)	Atmospheric radiation		
	Irradiation	$\Phi\downarrow$	W m^{-2}
	Radiosity	$\Phi\uparrow$	W m^{-2}
	Exchange	Φ_N	W m^{-2}

Experiences from Local Authorities Stimulating the Adoption of Low-Carbon Technologies by Homeowners

E. Mlecnik[1]

[1] TU Delft, Faculty of Architecture and the Built Environment, Delft (The Netherlands)

Abstract

To meet carbon reduction goals, local authorities aim to achieve a market acceleration for owner-occupied single-family home renovations by increasing awareness of – and enabling access to – low-carbon technologies for homeowners in target areas. In this framework, this research summarizes and examines project experiences of seven local authorities in Belgium, France, The Netherlands and the UK in the period 2017-2021. These cover the use of different models of demo exemplars and pop-up consultancy centres in target areas, web module developments and the use of Home Energy Monitoring Systems by local authorities. The results show that local authorities can benefit from using an innovation adoption model to develop an integrated mix to support homeowners throughout their whole renovation journey. Depending on their context, local authorities can focus on specific customer segments and target areas to support adopting new technologies, renovation measures at district level, deep renovation, phased retrofits and any combinations thereof. Physical and digital communication can be tailored to (pop-ups in) specific target areas, customer segments and local actors. Local authorities can work more closely together with intermediaries, also to achieve more renovations, group buying actions, specific energy coaching for groups of homeowners and Integrated Home Renovation Services.

Keywords: Renovation, homes, local authorities, innovation adoption, low-carbon technologies, customer journey

1. Introduction

To meet the objectives of the European Green Deal to reduce greenhouse gas emissions by at least 55% by 2030, European authorities need to boost the energy performance of existing buildings (European Commission, 2019). Buildings account for 40% of the EU's total energy consumption and for 36% of its greenhouse gas emissions from energy (European Commission, 2019; European Commission, 2020). At least 40% of buildings floor area in developed economies was built before 1980, when the first thermal regulations came into force (IEA, 2022), 85% of the EU's building stock was built before 2001 (European Commission, 2020), and 85-95% of the buildings that exist today will still be standing in 2050 (European Commission, 2020). Roughly 75% of buildings in the EU is energy inefficient according to current building standards (Filippidou & Jiménez Navarro, 2019).

Building renovations are happening but the rate is too slow: the annual renovation rate of the building stock varies from 0.4 to 1.2% per year in the Member States and this rate will need at least to double to reach the EU's objectives (EU, 2019). An annual deep renovation rate of over 2% is needed from now to 2030 and beyond, and policymakers are urged to retrofit 20% of the existing building to a zero-carbon-ready level by 2030 (IEA, 2022). This implies that building renovations need to happen much faster and with more ambitious energy-saving goals and that consequently low-carbon technologies - such as improved glazing and window frames, thermal insulation, airtightness solutions, energy-efficient HVAC systems, energy-saving lighting and appliances, renewable energy systems - need to be adopted faster and in greater amount by more building owners.

The adoption of such solutions is influenced by building characteristics and a range of personal, contextual and external factors (Ebrahimigharehbaghi, 2022). A key barrier is that the decision to proceed with home energy renovation often belongs to non-professional property owners, who experience home renovation as a huge undertaking (de Vries et al., 2020). Single-family homeowners find a renovation effort too expensive, too complicated, too cumbersome, while their knowledge about processes, solutions, measures, legal aspects and incentives is limited. This suggests the need for de-hassling policy interventions (de Vries et al., 2020).

© 2022. The Authors. Published by International Solar Energy Society
Selection and/or peer review under responsibility of Scientific Committee
doi:10.18086/eurosun.2022.02.05 Available at http://proceedings.ises.org

Local Authorities (LAs) see it as their task to help implement national goals and try to help solve local barriers to speed up single-family home renovations (Mlecnik and Hidalgo-Betanzos, 2022). Besides incentives, local energy planning and control of regulations, they also engage in communication and facilitation of energy renovations. LAs aim to cleverly nudge homeowners to invest in energy renovation measures and renewable energy systems, making best use of local skills and support schemes. In the local context, they provide homeowners and citizens in general with knowledge and services to understanding the home renovation process, evaluating options, managing the process, financing the renovation and delivering an end result, in general: to facilitate their renovation decision processes.

In this context LAs are looking for a mix of policy interventions that can help to create awareness and easy access for low-carbon renovation solutions. LAs have for example developed improved digital interfaces that target homeowners to adopt such solutions (Kwon et al., 2021a) and they have experimented with the development of pop-up consultancy centres in districts where energy advice is given to visiting citizens (Mlecnik et al., 2021; Kwon et al., 2021b). Furthermore, LAs have used demo exemplars to convince homeowners (Baylis et al., 2021). Also, Home Energy Monitoring and Management Systems (HEMS) have been deployed by local authorities to homeowners to nudge homeowners to invest in renovation measures (Kwon et al., 2021c).

To better understand the barriers LAs encounter in such developments, this paper assesses the activities of seven local authorities regarding how they dealt with creating awareness for - and providing easy access to - low-carbon technologies for homeowners, including energy efficiency solutions and renewable energy systems.

2. Research approach

This qualitative study is done using the widely accepted theoretical framework of innovation adoption theory (Rogers, 2003), as also discussed and adapted by various authors for the topic of housing (e.g. Mlecnik, 2013; van Oorschot et al., 2020). It assesses innovation adoption in the framework of the Interreg 2 Seas Triple-A project (2017-2021, www.triple-a-interreg.eu). In this project seven local authorities (LAs: cities of Rotterdam, Breda, Antwerp, and Mechelen; EOS Ostend; SPEE Hauts-de-France; Kent County Council) identified, tested and evaluated new ways of supporting homeowners in local target areas using adapted communication policy approaches involving web portals, pop-up consultancy centres, visits to demonstration exemplars and easy access to Home Energy Monitoring Systems (HEMS). A systemic approach was jointly developed with universities (TU Delft, University of Ghent) and energy distribution net manager Fluvius. This resulted in a model that helps the LAs to identify strategic priorities and activities they can develop to improve single-family homeowner adoption of low-carbon renovation measures (see Figure 1).

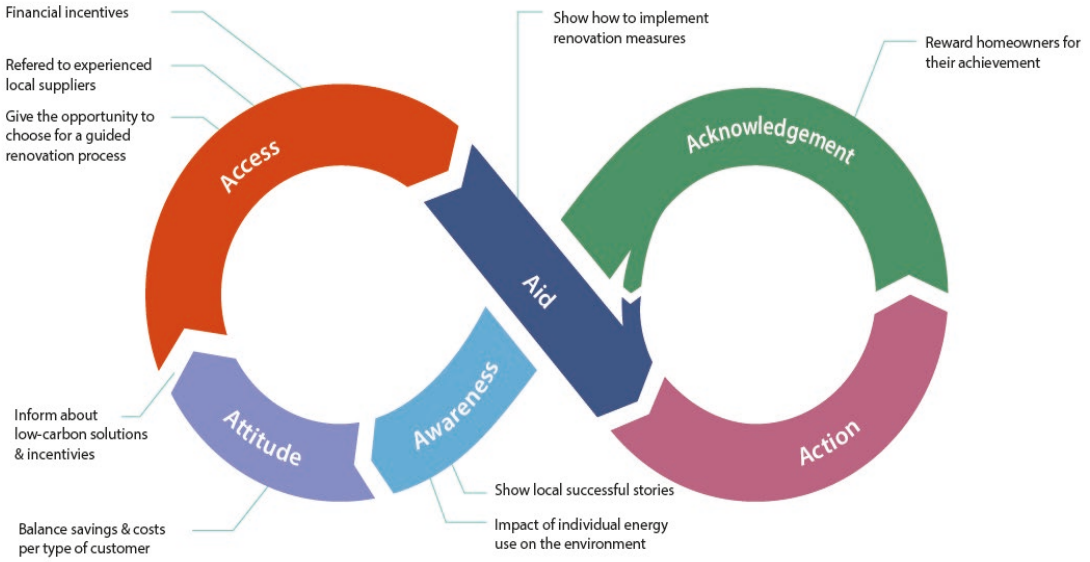

Fig. 1: Model for local authorities for developing operational activities and policy instruments for supporting the adoption of low-carbon technologies by homeowners. Sources: Triple-A (2021); Kwon et al., (2021a).

The LAs used this model for reflecting on available and needed actions and local policies that could be developed either by themselves or with partners and local stakeholders in co-creation. Per type of activity the model was also used to discuss how the activity could lead to creating awareness and changing the homeowners' attitude towards a proposed renovation solution. Furthermore, LAs reflected on how they could facilitate easier access to the solutions and help the homeowners further along the process, for example for contracting executors, for providing help during execution and for checking quality. Hoping that this would lead to speeding up homeowner decisions, LAs further aimed to engage homeowners acknowledging the successful implementation of a solution to help other homeowners, for example by letting them explain their experiences during home visits or online. Specific developments were supported by literature research, questionnaires, interviews, an inventory of low-carbon technologies and financial schemes, jointly organized business modelling and co-creation workshops and local events.

For the LAs the systematic thinking in terms of the homeowner renovation journey was rather new. In this framework LAs aimed to innovate their own working processes and internal arrangements with a specific focus as described in the Triple-A (2021) project. Within this project, the LAs developed both their virtual and physical consultancy for homeowners and an integrated mix of measures to support adoption of low-carbon technologies by homeowners. LAs' existing web portals would be adapted with additional web modules developed by the LAs, using both qualitative and quantitative research as well as co-creation with local stakeholders (Kwon et al., 2021a). The seven LAs also wanted to test local pop-up consultancy centres in target areas, either on a fixed location or in a mobile format (Meijer et al., 2018; Kwon et al., 2021b; Mlecnik et al., 2021). HEMS were used to support convincing homeowners to renovate (Kwon et al., 2021c) and installation of low-carbon technologies was to be tested through demo exemplars (Baylis et al., 2021).

3. Main project results

Main cumulative results achieved by the LAs during four years project activity (until December 2021) are illustrated below. The figures were developed based on obligations from the Interreg 2 Seas Programme Manual to continuously track key performance indicators, which were defined in detail by the project partners. The figures can give an indication of the relative merit of the various actions. Note that all activities are heavily interrelated, so the figures should be interpreted with care.

3.1 Experiences with demo exemplars and target areas

The demonstration exemplars implemented in the LAs ranged in their approaches but were grouped into four different types (Baylis et al., 2021):

- Model A: Utilizing new and innovative technologies: particularly looking at the use of battery storage systems when combined with solar panels to increase their effectiveness.
- Model B: Whole house or nearly-zero carbon retrofit: often included a range of measures to make the house as energy efficient as possible.
- Model C: Large scale or community wide mass retrofit: included group buying schemes or whole district approaches.
- Model D: Longer term phased retrofit: often only one or two resident-led measures depending on the circumstances of the homeowner, aiming to drive renovation and more engagement before the measures were installed.

These models were explored using a structured development approach (Baylis et al., 2021):

- Identifying suitable target areas: 8 local authority regions for single-family home renovations
- Exploring how to engage citizen segments in target areas: young families, empty-nesters, existing adopters, people with major life changes, highly educated financially successful persons, persons receptive to renovation in their district, fuel poor citizens.
- Identifying suitable financial incentives for engaging single-family homeowners: funding and finance including individual subsidies, group subsidies, property tax incentives and added tax incentives
- Testing installation of technologies through demonstration homes
- Evaluating CO_2 reduction of demo exemplars and awareness raising

For developing the demo exemplars LAs used the input from jointly organized workshops, brainstorms, meetings, buddy cooperation, standardized contracts and information about finance, funding and demo models.

Regarding Model A, in total 12 battery storage systems were installed. Experiences were mixed. For example, the Kent County Council could easily convince 10 homeowners to install a battery pack. These households were mainly interested in new technology developments and volunteered to install the system. In Flanders the LAs found it very difficult to select homeowners indiscriminately. Finally, actors were found that engaged in the development of a virtual power plant in a renovated apartment building, supported by European funding. Other partners tried to engage homeowners as well. Available data from Rotterdam show that four storage systems with solar panels in Rotterdam achieved 4,8 tons annual carbon savings.

Regarding Model B, Antwerp offered a consultant for homeowners, but wasn't able to convince citizens to achieve this type of renovation. Also Mechelen struggled to convince citizens due to the needed high investment cost, the administrative burden of building permits and the lack to predict or guarantee the expected energy savings. On the other hand, the Integrated Home Renovation Services (IHRS) offered by SPEE Hauts-de-France led to developing personalized work programs for 61 demo houses achieving annual savings of 227 tons carbon emissions. The Rotterdam door-to-door campaign offering energy scans and further support on request led to 21 installed measures in 5 homes, leading to annual carbon savings of 16.9 tons. This shows that nearly-zero carbon retrofit can be difficult to implement but gives excellent carbon savings results. To achieve deep retrofits there seems to be a need to develop IHRS beyond awareness raising and providing easy access and to include also specific aid and financial solutions for homeowners.

Concerning Model C, SPEE Hauts-de-France successfully used residents to engage other persons in the district: measures in 62 homes led to 250 tons annual carbon savings. Rotterdam successfully used a regional energy consultancy desk as intermediary between supply and demand to organize group purchases, which could target 24 cities at the same time. Through this partnership Rotterdam installed measures in 187 homes in the target areas leading to 172 tons annual carbon savings. EOS successfully organized a group purchase of 363 solar panel installations using dedicated social media, adverts, face-to-face and group meetings, leading to 249 tons annual carbon savings.

For Model D, SPEE Hauts-de-France successfully used their IHRS to install measures for 499 demo homes, achieving 1,901 tons of annual carbon savings. Rotterdam also used its energy consultancy desk to carry out door-to-door actions and energy scans and support until installation on request. In this framework most residents chose 1 or 2 measures, resulting in 1,049 measures in target areas in 435 homes, leading to 624 tons annual carbon saving. Breda developed awareness raising and easy access together with a local citizen energy cooperation, which resulted in 2000 registered interested homeowners, about 500 kitchen table consultancies by energy coaches and 134 financial loans offered in target areas, saving annually 138.9 tons of carbon emissions. The cooperation was also successful in engaging homeowners to tell their adoption story to other homeowners. Mechelen also successfully used motivated citizens as 'ambassador' in the target district. In a street with 50 homes this led to collective action engaging 21 families guided by an energy coach. Mechelen achieved in total 17 installations leading to 8,640 tons of annual carbon savings. This experience led to a broader system of energy coaches that support collective action in Mechelen.

Cumulatively LAs also developed 27 open home events. Demo events attracted 90 visitors. Homeowner engagement during visits ensured language was at the right technical level for non-experts. Events and peer-to-peer communication were effective at engaging new audiences to engage with home retrofit measures. On the other hand, it was also difficult to find volunteers and maintain a good rapport with the homeowners sharing their experience.

LAs also successfully used 1599 thermographic surveys to convince homeowners. Also, process-related homeowner feedback surveys were part of the strategy and 199 surveys were received.

Overall, the seven LAs installed in total 2,542 demo technologies in homes achieving carbon savings of 4,095.7 tons per year (calculated according to national standards). In a wider area 4,215 homeowners were engaged, resulting in annual carbon savings of 2,104 tons. The results per model show mixed experiences per LA, but also the power of more integrated services, collective action and instruments for engaging homeowners to achieve better carbon savings. Due to COVID-19 most demo activities ceased in 2021.

3.2 The use of pop-up consultancy centres

As a key feature related to the success of awareness raising and easy access in target areas, LAs successfully developed and deployed short-term or longer-term renovation consultancy in the target areas using mobile or fixed pop-up consultancy desks and units, which are exemplified in Figure 2.

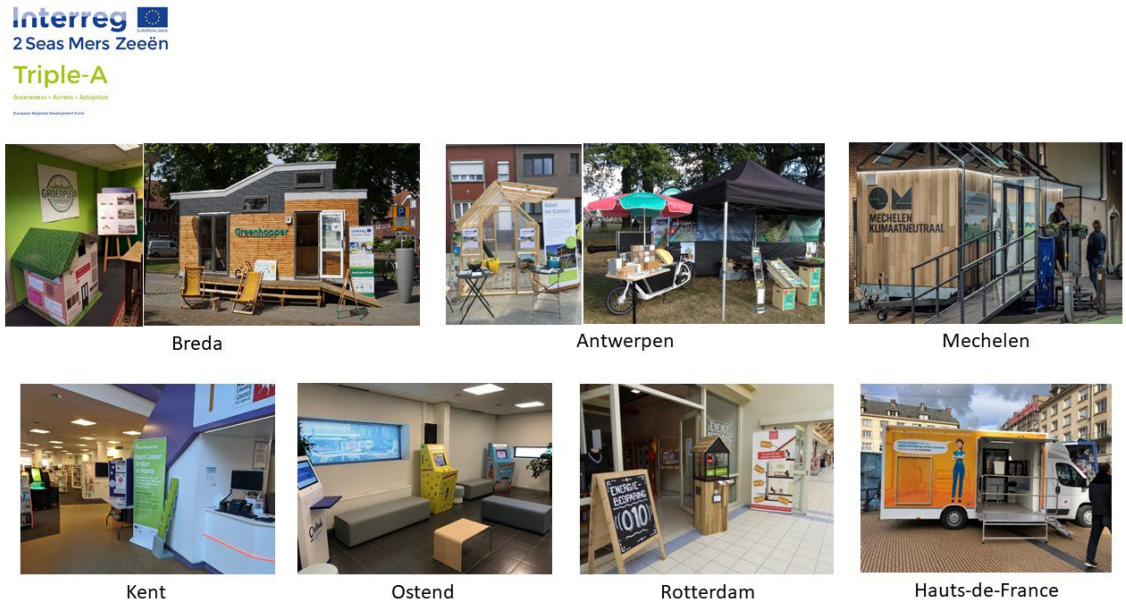

Fig. 2: Different types of pop-up consultancy centres developed and tested within the Triple-A project for stimulating the adoption of low-carbon technologies by homeowners. Source: Triple-A (2021).

Figure 2 shows for example the first unstaffed consultancy booths developed by Breda in libraries (top left). This action attracted far less homeowners compared to the mobile staffed pop-up developed by Breda (second top left). Ostend had a similar experience placing an information booth in a public office and later also developed a mobile unit. Also Mechelen and SPEE Hauts-de-France were inspired by the Breda development and used a mobile unit. Antwerp engaged in more low-cost staffed information stands on events and in target areas. Kent County Council also targeted low-cost unstaffed consultancy booths in libraries and public offices. Rotterdam developed two staffed sustainability consultancy centres in a shopping centre.

The LAs developed 10 pop-up consultancy centres in target areas. for guiding visitors and invested cumulatively €371,355 for developing the centres, involving in total 182 supply-side actors. The operating costs per pop-up varied from €6,435 to €246,310 and the investments varied from €4,065 to €101,790 depending on the planning, the size and format of the pop-up, the location/ mobility, the political framing, the staffing, opening hours, and so on. Cumulatively, 11,545 persons visited the pop-up centres. LAs spent in total 3,677 person-hours staffing the pop-ups. See also Kwon et al. (2021b) for further details and an evaluation of the effectiveness per pop-up.

Not all LAs systematically tracked the number of visitors engaging in follow-up consultancy or adoption of low-carbon technologies, mainly due to a lack of a CRM system or staff. From those who did, LAs counted at least 327 visitors engaged in follow-up consultancy or adoption, and 164 homeowners requested financial measures through the pop-ups. The project experiences show there is no one-size-fits-all approach for developing local pop-ups. Amongst other, the customer segments in the target areas, local policy strategies, political focus and available resources will influence the choice of pop-up. Promotional activities, embedded events, staffing and partnerships with local organizations, consultants and suppliers can highly influence the functional effectiveness of the pop-ups (Kwon et al., 2021b; Mlecnik et al., 2021). Due to COVID-19 most pop-up activities ceased in 2021.

One might speculate that such pop-up development cannot be financed or staffed by smaller LAs. Nevertheless, the pop-up idea was copied by multiple other LAs. Inspired by the seven LAs, pop-ups were for example adopted by Hoogstraten, Meijerijstad, Oosterhout, Gilze-Rijen, Dartford, Sittingbourne, Amiens, South of Aisne, Rotterdam's WoonWijzerWinkel, Woonkantoor Antwerpen, Kamp C, Groene Groei.

3.3 The development of specific web modules

LAs highly rely on operating web portals to communicate with citizens. Therefore digital consultancy is an integral part of any LA action to support adoption of low-carbon technologies for citizens. In this framework, it was observed that LAs are developing strategic plans to improve their web portals. In practice, this often translates into the development of specific web modules that can either operate dependent or independent from the LA main website, depending on what they perceive the best option for homeowners to find and collect reliable information and to get familiar with low-carbon renovation solutions.

LAs found that the activation of customer segments in target areas needs to be supported with specific digital tools that were previously not a part of the LA web portals. These included for example cost-calculation tools or mapping tools for homeowners to search related renovation projects or to search their home on a thermography map. But also low-end modules like registration, referral, appointment and feedback forms, information and consultancy modules on renovation measures and financing, were often still missing. Furthermore, LAs found a need to develop specific modules to be able to find a contractor and to share renovation experiences and adoption success stories.

LAs developed up to 20 modules; some were discarded after evaluation or redevelopment of the main website. For a remaining set of 15 web modules LAs measured cumulatively 52,621 unique number of visitors. See also (Kwon et al., 2021a) for an evaluation per web module. Overall web module visits were highly influenced by events and communication actions that drew attention to these new modules. The registration of web visitors didn't allow a breakdown per target group. Although this could not be tracked for all LAs, cumulatively at least 3,724 requests for information about low-carbon technologies were related to the web modules. 24 financial measures were made available by the LAs via the web modules. Cumulatively 10,942 financial measures were requested by homeowners. LAs also engaged 2 energy consultants and 172 SMEs in further business model development of web modules. Online 'events' proved to be popular.

Some LAs organized feedback from stakeholders to decide on the specific content of web modules. Only a few module developments effectively used co-creation or tried to develop web modules or platforms which cover all home renovation journey stages.

LAs experienced organizational or policy changes during the development of the web modules which led to an increased needed budget and sometimes the need to start again from scratch. For example, Breda's main website was totally redeveloped after an election. LAs were mainly tied by fitting web module development into ongoing web portal development plans and communication campaigns. During the development process, some LAs discovered their web sites lacked modular build-up. The investment and exploitation costs were higher for new websites than for web modules that could be integrated in an existing website. For most LAs basic infrastructure for following up actions, such as a Customer Relationship Management system, was missing. This made it also difficult to understand the success factors related to policy actions and the Triple-A development.

Specific modules also led to specific problems. For example, LAs also needed to carefully take into account Global Data Protection Regulations for developing modules using homeowner experiences. Also, instead of making contractor lists by themselves, LAs finally opted to provide links to third parties (non-profit organisations) that host such lists. Some LAs observed that some web modules would be better hosted at a regional or national level to serve multiple LAs at the same time. Particularly smaller LAs don't have to means to invest in elaborate web modules.

3.4 The deployment and use of HEMS

All LAs investigated the use of Home Energy Monitoring and Management Systems (HEMS) as a means to influence homeowner decisions, and consequently identified promising ways of using, adapting, selecting and procuring HEMS, as well as improved ways to collaborate with local stakeholders. 606 HEMS were installed by the end of 2020. During COVID-19 the installation of HEMS largely ceased. Until the end of 2021, a few additional homeowners were found for implementing the HEMS. Next to the seven LAs engaged in the project also the city of Sint-Niklaas adopted the HEMS Triple-A method.

A good response rate was achieved to questionnaires: 57% of HEMS users answered to questionnaires (Kwon et al., 2021c). 77,2 % of people reported they are at least satisfied with having the HEMS, 56.1% of people reported they are at least satisfied with the use of the HEMS. There was no direct follow-up planned of the number of low-

carbon technologies adopted by HEMS users, but in the second questionnaire 29,3% participants confirmed having invested in energy-saving measures and about 29% of the responding users also adopted energy saving measures.

LAs originally intended to modify HEMS before bringing them into homes and to monitor energy use. In practice this was technically not possible, and later also no longer wished for due to rapid commercial HEMS technology development. Also, the need for data cleaning and correction was underestimated and would require a huge staff effort. Finally, LAs decided to offer commercially available HEMS. In practice,

LAs found it very difficult to offer HEMS to homeowners, even if they were for free, due to privacy regulations and the need for unbiased selection of homeowners and open procurement. Also, compatibility issues and homeowner trust were sometimes factors that formed a barrier. During the project also energy distribution net managers started rolling out digital meters in homes which were perceived as competing or not compatible with the chosen HEMS.

Overall, in the beginning of the project LAs thought HEMS distribution would be a key success factor for the adoption of renovation measures, but in practice it proved to be an added benefit for homeowners. Due to the rapid commercial development, most LAs no longer see the need to offer HEMS as a LA service, unless they are part of a quality assurance system, such as in the SPEE Hauts-de-France IHRS system.

3.5 Dissemination and exploitation of results

Overall, the project could show promising results and strategies worth multiplying. Multiple reports and hands-on recommendations for local authorities were made available (www.triple-a-interreg.eu). A cross-border implementation guideline for local authorities was made available in English, Dutch and French and a “Get started!” page (https://www.triple-a-interreg.eu/get-started) was put online for LAs.

Results were promoted through on-line roadshow sessions and newsletters. For example, a Dutch roadshow communicated strategies and results to 151 project managers of LAs; in total nearly 600 participants were reached.

Overall the Triple-A method was embraced by multiple actors and Triple-A communication activities reached more than 175,000 stakeholders, including 4,479 LAs, 6,042 SMEs, 119,499 homeowners.

Regarding the management of the actions, the COVID situation impacted the need for organizing the project mostly online. The communication was considered the most critical topic, but effective online communication was achieved despite important delays. For example, events were originally developed to take place physically, were postponed and transferred to online events.

4. Discussion and outlook

When diving deeper into the Triple-A experiences of the LAs - see also the Interreg 2 Seas project reports on https://www.triple-a-interreg.eu/project-reports -, recommendations come forward that should be addressed in future developments:

- The success of awareness raising using online or physical homeowner consultancy highly depends on the nature and intensity of communication activities (see above).
- Most local authorities are not (yet) used to think in terms of subsequent needs of homeowners during a customer renovation journey (Triple-A workshop result).
- Communication is needed in carefully identified target areas to reach out to customer segments for upscaling renovation activities (Triple-A workshop result).
- Specific initiatives are needed for vulnerable households (Triple-A workshop result).
- The success of actions in districts highly depends on strengthening a “neighborhood feeling” (see for example Rotterdam).
- Co-creation processes are highly recommended to develop knowledge bases and incite public, private and civic actors (positive experiences Triple-A partners).
- LAs need to attract specific skills, such as specialized IT staff (Kwon et al., 2021a).

- Smaller local authorities usually don't have sufficient budget and need to find a centralized solution, for example a provincial desk or regional support (Triple-A roadshow result).
- Lack of CRM systems and privacy and security issues can hinder follow-up of homeowner activities and thus evaluation of policy targets (see above).
- Most local authorities do not yet have a 'modular' build-up of their online communication (Kwon et al., 2021a).
- Public-private collaboration can be hindered by a reluctance of LAs to engage in collaboration with local supply side or service actors (Triple-A experiences).
- In case of referral to private consultants or suppliers, independent listing is preferred Kwon et al., 2021a).
- To promote deeper retrofits IHRS are needed that also support deeper in the renovation process (Triple-A workshop result).
- Quality control within renovation processes and solutions to support after-care are not yet sufficiently integrated in LA consultancy processes (Triple-A workshop result).
- To reach multiple homeowners and suppliers at the same time it is recommended to work closely together with energy cooperatives (see for example Breda) or non-profit associations that act as intermediaries between supply and demand (see for example Rotterdam)
- Group buying initiatives of for example solar technologies can be highly successful in target areas (see for example Ostend)
- Energy coaches can be deployed for guiding groups of homeowners at the same time (see for example Antwerpen and Mechelen).

Regarding these issues, the Triple-A project also led to a spin-off project proposal on Integrated Home Renovation Services, which was prepared and submitted in the LIFE-CET call HOMERENO. During the Triple-A project it became clear that another strategy to multiply renovation measures would be to engage groups of homeowners at the same time, for example by using citizen-led energy cooperatives or formal assemblies of homeowners. The new project will focus on developing six Integrated Home Renovation Services for Condominium Associations in the Netherlands and Flanders. The new project, entitled 'CondoReno' will also compare LA-driven and market-driven IHRS and develop a digital resource centre for the IHRS in Mechelen and Ostend. It will also explore achieving living-cost neutral deep renovations to engage all target groups.

5. Conclusion

The Interreg 2 Seas Triple-A (2021) project showed multiple new opportunities, successes but also important barriers for Local Authorities (LAs) to further support the Renovation Wave. The project experiences show that LAs can certainly improve awareness raising for homeowners for adopting low-carbon technologies, and make access to carbon-saving renovation solutions easier. LAs can benefit from using a customer renovation journey model to develop more targeted actions. Depending on their context, LAs can focus on specific customer segments and target areas to support adopting new technologies, renovation measures at district level, deep renovation, phased retrofits and any combinations thereof.

Both physical and digital communication and consultancy provided by LAs remain very important and can be tailored to (pop-ups in) specific target areas and customer segments, including tailored information on available funding and clear information in layman's terms. Using demo exemplars, pop-up consultancy centres, specific web modules and HEMS can all have their merit to make homeowners adopt low-carbon technologies, but the relative effectiveness of such actions largely depends on local context and available resources and persons and the way these actions are embedded in LA programs and communication.

While LAs traditionally invest in awareness raising, providing easy access to low-carbon solutions can still be facilitated more. In this framework LAs can work more closely together with for example experienced homeowners, citizen energy cooperatives and non-profit organizations that act as intermediary between renovation measure supply and homeowner demand. To achieve more renovations, facilitating group buying actions and specific energy coaching for groups of homeowners can also be relevant. To achieve more deep renovations it is important to develop services beyond traditional consultancy services including specific aid and

financial solutions embedded in Integrated Home Renovation Services.

While this project mainly focused on single-family homes, a follow-up LIFE-CET project entitled 'CondoReno' will create and multiply Integrated Home Renovation Services for private condominiums in the Netherlands and Flanders.

6. Acknowledgements

The author would like to thank the Triple-A partners City of Antwerp, City of Breda, Kent County Council, City of Mechelen, Public Service for Energy Efficiency (SPEE) Hauts-de-France, City of Rotterdam, AG EOS (Ostend), Ghent University and Fluvius for their valuable input for this work. The Interreg 2 Seas Mers Zeeën project Triple-A (https://www.triple-a-interreg.eu/) was funded by the European Fund for Regional Development (grant number 2S02-029) and the Provinces of South Holland and West Flanders. The integration of Triple-A results in wider policy recommendations is also supported by the IEA EBC Annex 75 Cost-effective Building Renovation at District Level Combining Energy Efficiency & Renewables (http://annex75.iea-ebc.org/) to which the author could contribute thanks to support from the Dutch Enterprise Agency (RVO) and EIT Climate-KIC.

7. References

Baylis, F., Mlecnik, E., Kwon, M., de Snoo, M., Oung, O., Nurali, L., Vos, C., M'Foungoulie, K., Van de Vyver, I., Van Camp, B., Vercruyce, A., 2021. Increasing awareness and adoption of low-carbon technologies through demonstration homes. Report Interreg 2 Seas project 2S02-029 'Triple-A: Stimulating the Adoption of low carbon technologies by homeowners through increased Awareness and easy Access'. https://www.triple-a-interreg.eu/project-reports.

de Vries, G., Rietkerk, M., Kooger, R., 2020. The Hassle Factor as a Psychological Barrier to a Green Home. Journal of Consumer Policy 43, 345–352. https://doi.org/10.1007/s10603-019-09410-7.

Ebrahimigharehbaghi, S., 2022. Understanding the decision-making process in homeowner energy retrofits. PhD Thesis. A+BE 6. Delft: TU Delft. https://doi.org/10.7480/abe.2022.06.6573.

European Commission, 2019. The European Green Deal. Communication from the Commission to the European Parliament, the European Council, the Council, the European Economic and Social Committee and the Committee of the Regions. COM/2019/640 final. https://eur-lex.europa.eu/legal-content/EN/TXT/?qid=1576150542719&uri=COM%3A2019%3A640%3AFIN.

European Commission, 2020. A Renovation Wave for Europe – greening our buildings, creating jobs, improving lives. Communication from the Commission to the European Parliament, the Council, the European Economic and Social Committee and the Committee of the Regions. COM/2020/662 final. https://eur-lex.europa.eu/legal-content/EN/TXT/?qid=1603122220757&uri=CELEX:52020DC0662.

Filippidou, F., Jiménez Navarro, J.P., 2019. Achieving the Cost-Effective Energy Transformation of Europe's Buildings. JRC Technical Report, Luxembourg: Publications Office of the European Union.

IEA, 2022. Technology and innovation pathways for zero-carbon-ready buildings by 2030 – A strategic vision from the IEA Technology Collaboration Programmes, Technology Report, Paris:International Energy Agency. https://www.iea.org/reports/technology-and-innovation-pathways-for-zero-carbon-ready-buildings-by-2030.

Kwon, M., Mlecnik, E, 2021a. Modular Web Portal Approach for Stimulating Home Renovation: Lessons from Local Authority Developments. Energies 14, 1270. https://doi.org/10.3390/en14051270.

Kwon, M., Mlecnik, E., Gruis, V., 2021b. Business Model Development for Temporary Home Renovation Consultancy Centres: Experiences from European Pop-Ups. Sustainability 13, 8450. https://doi.org/10.3390/su13158450.

Kwon, M., Hudders, L., Mlecnik, E., M'Foungoulie, K., 2021c. Evaluation of the use of Home Energy Monitoring and Management Systems (HEMS) to support adoption of renovation measures. Report Interreg 2 Seas project 2S02-029 'Triple-A: Stimulating the Adoption of low carbon technologies by homeowners through increased Awareness and easy Access'. https://www.triple-a-interreg.eu/project-reports.

Meijer, F., Straub, A., Mlecnik, E., 2018. Consultancy Centres and Pop-Ups as Local Authority Policy Instruments to Stimulate Adoption of Energy Efficiency by Homeowners. Sustainability 10, 2734. https://doi.org/10.3390/su10082734.

Milin, C., Bullier, A., 2021. Towards large-scale roll out of "integrated home renovation services" in Europe, ECEEE 2021 Digital Summer Study, online, 7-11 June, 817-826.

Mlecnik, E., 2013. Innovation development for highly energy-efficient housing. Amsterdam:IOS Press. http://resolver.tudelft.nl/uuid:ea0215ed-30b9-47aa-a7ef-a1e426c1aade.

Mlecnik, E., Oung, O., Lelieveld, A., de Snoo, M., Vos, C., 2021. Neighbourhood consultancy centres for the adoption of low-carbon technologies by homeowners: experiences from Dutch initiatives. Energy Evaluation Europe 2021 conference, online, 10-16 March.

Mlecnik, E., Hidalgo-Betanzos, J.M., 2022. Policy instruments for energy-efficient renovations at district level. Proceedings of the SBE2022 conference, Delft: TU Delft, 11-13 October, accepted for publication. https://sbe22delft.com/.

Rogers, E.M., 2003. Diffusion of innovations (5th ed.). New York: Free Press.

Triple-A, 2021. Encouraging energy-efficient home renovation. Interreg 2 Seas project. https://www.triple-a-interreg.eu/.

Van Oorschot, J., Halman, J.I.M., Hofman, E., 2020. Getting innovations adopted in the housing sector. Construction Innovation, 20 (2), 285-318. https://doi.org/10.1108/CI-11-2018-0095.

A Novel Statistical Method to Improve Energy Efficiency of Housing Stock in the Eastern Mediterranean Climate

Bertug Ozarisoy[1] and Hasim Altan[2]

1 Sustainable Environment and Energy Systems (SEES) Graduate Program, Middle East Technical University, Northern Cyprus Campus, Kalkanli, Guzelyurt, North Cyprus, via Mersin 10, Turkey

2 Department of Architecture, College of Architecture and Design, Prince Mohammad bin Fahd University, Khobar, Dhahran, Saudi Arabia

Abstract

This paper presents a novel methodology that was developed according to the *in-situ* measurements of the building-fabric thermal performance to assess as-built energy models of case-study residential tower blocks. It seeks to corroborate the empirical model by integrating the findings from the questionnaire survey and energy-assessment analyses to feed building-energy simulation (BES) procedures. It discusses the uncertain input parameters for the BES that quantitative modelling adopted for the energy assessment of dynamic thermal simulation findings in conjunction with occupants' socio-demographic characteristics, occupancy patterns, household size and environmental conditions recorded. The present study revealed that weekday cooling consumption patterns were significantly and strongly related to the weekend heating consumption patterns (χ^2 = 54,590, p < 0,001, Cramer's V = 0,522). Specifically, longer duration of heating consumption was related to longer duration of cooling consumption. The developed framework provides a scientific background that can be included in the BES platform to serve as a set of guidelines for the European Performance of Buildings Directive scientific committee for energy policy design and retrofitting strategies.

Keywords: Energy efficiency, Energy use, Overheating risk, Energy retrofit, Thermal comfort

1. Introduction

The conventional terminology of energy efficiency gap (EEG) was defined by Jaffe and Stavins as "the energy efficiency gap is described as the gap that exists between the current or expected future energy use of homes and the optimal current or future energy use" (Ozarisoy & Altan, 2022). Jaffe and Stavins then further describe the EEG in order to provide a foundation of theoretical information to guide policymakers in the implementation of energy policy design in the residential sector. However, the starting point of a well-established meaning for EEG dates to the 1970s. A pilot study project entitled "Drivers and Barriers to Improving Energy Efficiency and Reducing CO_2 Emissions in the Private Housing Sector" states that in the UK little action had been taken towards energy conservation through the method of considering existing housing stock that was built in the UK pre-1973 (Altan, 2004). This pilot study demonstrated the relevance of the rapid increase in energy prices in the 1970s. The present study is the first to target and conduct building-energy simulation (BES) procedures on existing Cypriot social-housing stock. A BES analysis was integrated into the implementation of energy performance certificates (EPCs) because of the reliable assumptions thereof to assess the energy performance of case-study residential tower blocks (RTBs). The energy simulation inputs seek to identify the impact of household occupancy patterns and habitual adaptive behaviour on home-energy performance to provide a basis for the information that is needed to properly calibrate the building-energy performance of targeted households. It also envisages demonstrating that occupants' real-life energy-use experiences have had a significant impact on calibrating domestic-energy use to simultaneously identify discrepancies between the actual and predicted energy use on the dynamic energy-simulation platform. As such, the present study was developed according to human-based BES input parameters obtained from the questionnaire survey, *in-situ* measurements, the infrared-radiometer thermography (IRT) survey and environmental monitoring of the project site to demonstrate real data for energy-use policy making decisions. This conceptual framework can be applied to efforts to implement the Energy Performance of Buildings Directives (EPBD) mandates and to demonstrate the exemplar development framework, policy and regulations as it relates to the social-housing stock of the Republic of Cyprus (RoC) and other EU-27 member states.

© 2022. The Authors. Published by International Solar Energy Society
Selection and/or peer review under responsibility of Scientific Committee
doi:10.18086/eurosun.2022.02.06 Available at http://proceedings.ises.org

2. Method

2.1. The Concept of Statistical Representativeness

In order to provide a background analysis for developing the concept of statistical representativeness, this section presents a review of selected theoretical information and exemplar pilot projects and their applicability. Table 1 delineates the original research articles that were reviewed to identify the most appropriate concept of statistical representativeness for the present study.

Tab. 1: Reviewing the concept of representativeness in statistics.

References	Concept(s)	Method(s)	Outcome(s)
Chasalow and Levy (2021)	Law, social and behavioural sciences	- Stratification of population sample size - Generalisability of research findings	Equal representation of each subgroup of the user population was recommended
Hirsch and O'Donnell (2017)	Education, social and behavioural sciences	- A multiple-choice test-based survey was distributed - Descriptive statistics - 4 x 2 chi-square test of independence	A unique set of test questions to identify students who hold common representativeness was developed
Schmill *et al.* (2014)	Global change sciences (i.e., human factors, climate, remote sensing)	- Pearson's chi-square tests - Heat mapping - Histograms - Kullback-Leibler *f*-divergence test - Multivariate analysis	Implementing a variety of methods for making assessments about the representativeness of a collection of case studies across the globe
Schouten *et al.* (2009)	Social and behavioural sciences	- Population R-indicators - Chi-square statistics used to test independence and goodness-of-fit - Logistic regression models	A mathematically rigorous definition and perception of representative response was developed

Ozarisoy & Altan (2021) and Hu and Kohler-Hausmann (2020) highlight the importance of the integration of the STS approach into using the conceptual analysis of sampling size to test associations gathered through various experimental statistical analyses. Chasalow and Levy (2021) discuss the STS approach providing a multidisciplinary integrated conceptual framework that enables both statisticians and engineers to interrogate taken-for-granted terms and categories while developing benchmarks in energy-policy design. These studies indicate that representativeness of sampling size shows differences between one pilot study and another, due to demographic structures, geography and the political conditions of each research context. Chasalow and Levy (2021) explain their own representativeness concerns while developing a novel methodological framework for representativeness in statistics, politics and machine learning. In this theoretical study, these scholars contribute a sense of the variety of meaning and values associated with representativeness in order to prove the validity of chosen sampling sizes. Chasalow and Levy indicate that they did not select a large sampling to develop their own representative study. In their pilot research project, these scholars predominantly focused on sampling in Europe and the United States more than other parts of the world. According to Chasalow and Levy, it is difficult to identify the limitations of their own selected sampling size representativeness because of the geographical extent of their research context. To avoid a research bias and provide a generalisation of their research findings, their study set out to offer reliable and statistically representative sampling criteria that would allow the targeted reader group to understand their research outcomes.

Garett (1942), Jensen (1926), Kurksal and Mosteller (1980) and McNemar (1940) all discuss the issue of how to check a particular sample for representativeness. Kiaer (1976) states that "the representative method can be

applied in several ways". To explain this claim, Kiaer develops two different sample types. His first method is an arbitrary filtering of the variables gathered from the sampling. Kiaer explains that this selection should be done in a "haphazard or random way" to avoid giving preference to subject respondents in certain occupations or belonging to particular social strata. This method of selection highlights that the representativeness of sampling size results from the absence of selective discretion. His second method involves allocating representativeness in a mechanical procedure that can provide a feasible method of design to undertake statistical analysis faster and provide an opportunity to detect discrepancies in the sample.

In previous studies that develop the concept of statistical representativeness of sampling size, one of the main strengths of the selection of a random sampling method is that it enables the use of all available data to ensure a proportionate match on known relevant variables. This was proven by Kiaer in 1976 in a population study that consisted of surveyors in rural areas and used census data to allocate counts per country and then selected districts within the countries to "represent the main industry groups within the country as well as its various geographic conditions" (Kiaer, 1976). This method of design demonstrates that it can be applicable to choose a single geographic domain to develop the concept of statistical analysis by integrating census data and applying outcomes to other geographic domains that have been shown to have similar demographic structures, political assets and cultural norms.

Hirsch and O'Donnell (2001) have developed a scientific method of design that measures the reliability of datasets and the applicability of concepts of statistical design to provide an understanding of conceptual change that can have a long-term impact on conceptual-level analysis. Schmill *et al.* (2014) developed a theory of analytics for assessing global representativeness in social science studies to guide future scholars that was aimed at addressing sampling bias and providing a public domain for similar pilot projects. This pilot study aimed to reduce the gap between local and global researchers in providing analytical methods of design that could help scholars assess the representativeness of a sampling size and assist in correcting any bias for the interpretation of statistical findings. Schmill *et al.* (2014) recommends the chi-square test as the most appropriate statistical method that allows scholars to apply to their own hypothesis testing. In the Schmill study, Pearson's chi-square tests were used for testing the independence of two samples using a model function defined over a contingency table of observed versus expected values. To test the reliability of their statistical analysis, Schouten *et al.* (2007) conducted logistic regression models to predict the type of responses expected. In a further study conducted by Schouten *et al.* (2009), the researchers developed an advanced indicator to identify the concept of statistical representativeness of sample sizes. In this pilot study, the researchers found that the field survey approach gave more accurate results regardless of the limitation of only being able to recruit relatively small sample sizes. As an outcome of this pilot study, Schouten *et al.* (2009) recommend that in multinominal logistic regression models, variables give a significant contribution at the 5% level, and where this cannot be done, these variables should be excluded from the sampling size.

The study adopts the Cohen's statistical convention to identify the significance of occupants' TSVs within *in-situ* recorded environmental parameters. On further questioning the identified 9.46% margin of error, a priori power analysis using G*Power 3.1.9 was conducted to determine the minimum sample size. With the power set at 0.08, alpha level set at 0.05, a moderate effect size of 3.5 (odds ratio) and with the proportion of the control group at 0.5, results indicate that a total of 104 participants would be needed in order to reach an adequate sample size for the study. While this section discusses theoretical information around the concept of statistical representativeness, further exemplary pilot studies are reviewed and discussed in Section 2.2.

2.2. Equation model

Semi- structured interviews and participant feedback were transcribed and translated. The Statistical Package for Social Sciences (SPSS) Version 28.0 software (IBM: Armonk, NY, U.S.) was utilised to conduct the quantitative analysis; and tests-of-associations were conducted between the numeric factors and the questionnaire responses to join the questionnaire results with the statistical analysis. Little and Rubin (2002) suggest that the pattern of missing data is a more important factor than the actual amount of missing data. Missing values that are randomly scattered throughout the data matrix (i.e., data is missing completely at random; MCAR) is a less serious problem than missing values that are not random. If the missing values on a variable are not random but are associated with other variables in the data, this is referred to as missing at random (MAR) and can be alleviated with imputation methods. The three pie charts below summarise the

frequency and percentage of missing data in the dataset by variable, case/observation and individual values. The third pie chart represents the full data matrix and was used to evaluate the 5% threshold of the proportion of missing values in the data matrix that was discussed above. If the missing values on a variable are associated with the variable itself (i.e., missing not at random; MNAR), this has serious implications for inferences, regardless of imputation procedures (Dong *et al*., 2021). Recently, Schouten *et al.* (2009) proposed two definitions of representativeness with respect to survey response: strong (given in Definition 1.1) and weak (given in Definition 1.2). Definition 1.1 (strong). A response subset is representative with respect to the sample if response propensities are the same for all units in the population:

$$\forall_i \; E(R_i) = \rho_i = P(R_i = 1 \mid I_i = 1) = \rho \quad \ldots \quad (1)$$

The response of a unit is independent of the response of all other units, which denotes the response of unit *i* and is an indicator showing whether a unit took part in the survey. Schouten *et al.* (2009) notes that strong representativeness corresponds to the Missing Completely at Random (MCAR) pattern for every target variable *y*. This means that non-response does not cause estimators to be biased. Although this definition is appealing, its validity can never be tested in practice. To solve this problem, a weaker definition of representativeness was introduced by Schouten *et al.* (2009).

$$\bar{\rho}_h = \frac{1}{N_h} \sum_{i=1}^{N_h} \rho_{ih} = \rho, for\ h = 1, 2, \ldots, H, \quad (2)$$

Definition 1.2 (weak). A response subset is representative of categorical variable x with H categories if the average response propensity over the categories is constant, where is the population size of category *h,* is the response propensity of unit i in category *h*, and summation is over all units in this category.

2.3. Assumption tests

A general rule for sample sizes is that group sizes are approximately equal if *n* of the largest group is no more than about twice *n* of the smallest group. Another general rule for sample sizes is at least 10% of the sample should be in each group. Categorical variables with very uneven splits between categories present problems for several multivariate analyses (Tabachnick & Fidell, 2007). The following variables were recoded to reflect the conceptualisation of statistically representative findings in accordance with the research hypotheses, as shown in Table 2.

Tab.2: Coded Variables During the Data Preparation Stage.

Age band	Cooling energy consumption in August 2015	Floor level
Cooling consumption on weekdays	Cooling energy consumption in summer 2015	Health condition
Clothing insulation levels of participants	Heating energy consumption in winter 2015	Occupation
Type of cooling control in home	Cooling energy consumption in August 2016	Heating consumption on the weekend
Ethnicity	Cooling energy consumption in summer 2016	Household density
Thermal preference	Heating energy consumption in winter 2016	Income
Interviewed room condition	Metabolic rates of participants	Length of residency
Orientation	Reasons for thermal discomfort	Space conditioning
Overall thermal satisfaction in summer	Thermal sensation in bedrooms 1, 2, 3 and living room	Type of cooling system
Window closing reasons	Window opening patterns in winter	Type of heating system
Note: Additionally, all categorical variables were recoded in ordinal sequence where possible (e.g., metabolic rate) Variables related to occupants' thermal preferences were recoded from very cold to very hot All variables were recoded from smallest value to largest value All dichotomous variables were recoded to 1 = yes, 0 = no		

Virtually all parametric statistics have an assumption that the data comes from a population that follows a known distribution. This assumption of normality is often erroneously applied, however, because many populations are not normally distributed. Therefore, researchers need to understand what their samples consist of. It is standard practice to assume that the sample mean from a random sample is normal because of the central-limit theorem. However, almost all variables have a slight departure from normality. If researchers have a large enough sample, then any statistical test will reject the null hypothesis. In other words, the data will never be normally distributed if the sample size is large enough.

It was found that the data was missing completely at random (MCAR). After preparing the data for analysis, it was observed that out of 100 recorded cases, 98 cases contained missing data (98.0%) and out of 53 variables, 2 variables contained missing data (2.8%), which amounted to a total of 0.04% missing information in the dataset. To assess whether the pattern of missing values was MCAR, Little's MCAR test (Little, 1988) was conducted. The null hypothesis of Little's MCAR test is that the pattern of the data is MCAR and follows a chi-square distribution. Using an expectation-maximisation algorithm, the MCAR test estimates the univariate means and correlations for each of the variables. The results revealed that the pattern of missing values in the data was MCAR: χ^2 (104) = 121,645, p = 0,114. Even though the proportion of the total missing data is less than 5% and the data is MCAR, the final sample size may still be affected by listwise or pairwise deletion when the analysis is run. Listwise deletion removes a case if a case has any missing value for any of the variables used in an analysis.

To assess normality, skewness and kurtosis statistics are assessed. Skewness refers to the symmetry of the distribution and kurtosis refers to the peakedness. Variables that have distributions that are very asymmetrical, flat, or peaked could bias any test that assumes a normal (i.e., bell-shaped) distribution. Generally, skewness and kurtosis values (converted as z-scores) that fall outside ±4 should be further inspected for potential outlier removal, nonparametric testing, or transformation. However, researchers may have flexibility in larger samples (Field, 2013). Some normality tests are done for sample sizes smaller than 100 (i.e., Shapiro–Wilks and Kolmogrov–Smirnov tests). If these tests are significant beyond $p < 0.001$, these variables should be further inspected (Gamst, Meyers & Guarino, 2008). Graphing methods are also employed for assessing normality. These graphs include histograms, normal quantile–quantile (Q-Q) plots and box plots, as shown in Figures 1 (a)-(d).

Statistics			
Outdoor relative humidity (%)			
N	Valid	100	
	Missing	0	
Mean		59.166	
Median		59	
Std. Deviation		11.76264	
Skewness		-0.853	-3.5394191
Std. Error of Skewness		0.241	
Kurtosis		1.39	2.90794979
Std. Error of Kurtosis		0.478	
Minimum		19.6	
Maximum		78	

(a)

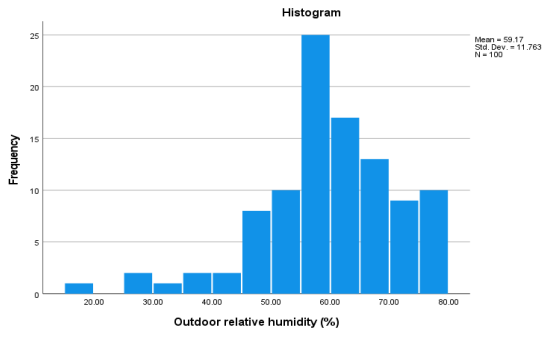

(b)

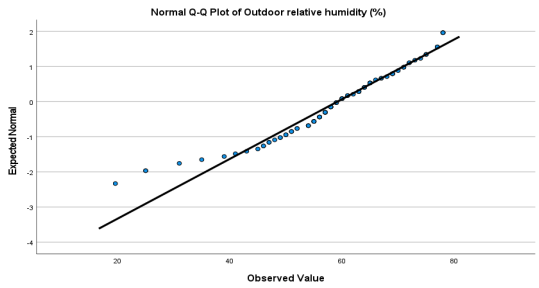

(c)

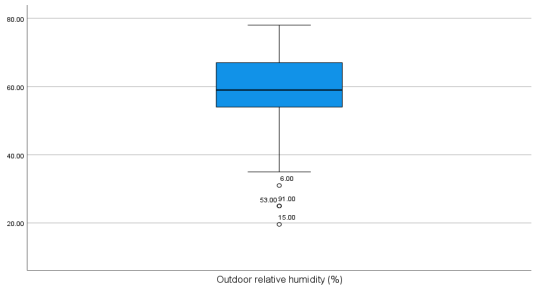

(d)

Fig.1: (a) Skewness and Kurtosis of the *on-site* recorded outdoor relative humidity (RH); (b) Histogram of the outdoor Relative Humidity (RH); (c) Normality analysis of the outdoor RH; (d) Whisker graph of the outdoor RH.

Histograms should look fairly bell-shaped. Q-Q plots should follow a straight line when plotting the expected values against the observed values. Box plots show the overall interquartile range and whether extreme values exist in the variable (see section on outliers below). If the data contains outliers, graphic displays both with and without the outliers should be examined to see how the graphs changed. If a continuous variable has serious deviations from normality, it must be addressed through transformation (log, inverse, Box-Cox, etc.), recoding into an ordinal variable, or assessment for whether nonparametric analysis needs to be conducted. Regardless, researchers should run analysis both with and without outliers to see whether the pattern of results changes. Univariate and multivariate outliers are also known as extreme values and can significantly bias any parametric test. We have checked our variables for univariate outliers. SPSS identifies these values as being three times the interquartile range beyond the 25th and 75th percentile values. In the present study, multivariate outliers were tested before the primary analyses were conducted where appropriate, as shown in Table 3.

Tab.3: Descriptive analysis of the variables related to identification of 'neutral' adaptive thermal comfort thresholds for benchmarking.

Variable Name	Mean	Median	Std. Deviation	Percentiles		
				25th	50th	75th
Overall thermal satisfaction in summer [0 to 6] - Discrete	1.64	2.00	1.453	1.00	2.00	3.00
Overall thermal satisfaction in summer [-3, +3] - Continuous	1.68	2.00	1.36241	1.00	2.00	3.00
Thermal sensation in bedroom 1 [0 to 6] - Discrete	0.52	1.00	1.396	0.00	1.00	2.00
Thermal sensation in bedroom 2 [0 to 6] – Discrete	0.46	1.00	1.290	0.00	1.00	1.00
Thermal sensation in bedroom 3 [0 to 6] – Discrete	0.55	1.00	1.234	0.00	1.00	1.00
Thermal sensation in kitchen [0 to 6] - Discrete	-0.35	-1.00	1.533	-2.00	-1.00	1.00
Thermal sensation in living room [0 to 6] - Discrete	0.20	0.00	1.595	-1.00	0.00	1.75
Thermal sensation in bedroom 1 [-3, +3] - Continuous	0.51	1.00	1.30651	0.00	1.00	2.00
Thermal sensation in bedroom 2 [-3, +3] - Continuous	0.45	1.00	1.23399	0.00	1.00	1.00
Thermal sensation in bedroom 3 [-3, +3] - Continuous	0.53	1.00	1.20147	0.00	1.00	1.00
Thermal sensation in kitchen [-3, +3] - Continuous	-0.42	-1.00	1.39393	-2.00	-1.00	1.00
Thermal preference	1.50	1.00	1.07778	1.00	1.00	3.00

In this study, a dataset related to occupants' thermal sensation votes (TSVs) was designed in accordance with the thermal comfort assessment convention recommended by Wang *et al.* (2018). As presented in Table 3, in accordance with Wang *et al.* (2018), the thermal sensation scale was set out in two conceptual assessment criteria in order to undertake the statistical analysis accurately. First, Wang *et al.* (2018) recommend a 7-point discrete thermal sensation scale that can be applied to assess occupants' TSVs. In this case, the TSV is set as an ordinal variable, thus enabling researchers to undertake Cramér's *V* test for the statistical analysis and apply the statistical findings whenever it is appropriate at the time of developing an evidence-based energy policy design. In the present study, the dataset was coded as follows: 0 = -3, 1 = -2, 2 = -1, 3 = 0, 4 = +1, 5 =+2, 6 = +3. Notably, the [-3, +3] scale band represents the outcome of occupants' thermal sensation as an ordinal measure used to accurately conduct the Cramér's *V* test. This type of coding was applied to determine households' TSVs gathered through a questionnaire survey. In the questionnaire survey, questions related to households' thermal sensation were ranked on a 7-point Likert scale that could be used as an ordinal measure. In this dataset, to provide consistency of the interpretation of households' TSVs [0 to 6], a coding range representation of thermal sensation scale band at [-3, +3] was used, which was developed by Fanger in the 1970s and was commonly used by thermal comfort scholars between 1990 and 2000.

Second, Wang *et al*. (2018) recommend a 7-point continuous thermal sensation scale that can be applied to assess occupants' TSVs. With the TSV set as a continuous variable, researchers are able to undertake Pearson's

correlation analysis. This method of design is commonly applied by thermal comfort researchers to identify "neutral" adaptive thermal comfort thresholds. Using occupants' TSVs as continuous variables is the most well-known method for reporting field survey findings concurrently with *in-situ* measurements or *on-site* environmental monitoring findings. This is an essential method of design that was developed by a team of experts at the University of California at Berkeley to contribute to the ASHRAE Global Thermal Comfort Database II (see at - https://repository.uel.ac.uk/item/89zv1). Further to this on-going method of analysis in thermal comfort studies, in the present study, the dataset was coded as follows: -3 = Cold, -2 = Cool, -1 = Slightly cool, 0 = Comfortable, +1 = Slightly warm, +2 = Warm, +3 = Hot. Notably, the [-3, +3] scale band enables thermal comfort researchers to identify "neutral" adaptive thermal comfort thresholds for benchmarking. In this dataset, to provide consistency of the interpretation of households' TSVs, the [-3, +3] coding range represents the [Cold to Hot] thermal sensation scale, which was recommended by Fanger in the 1970s and further developed by de Dear in 1998 and 2001.

3. Results and Discussions

3.1. Assessing households' socio-demographic characteristics

This section explores the relationships among the household socio-demographic characteristics, energy use and other variables collected from the respondents during the field-study period; and a set of questions developed to undertake statistical tests was utilised to determine the correlations between different socio-demographic characteristics based on the survey findings. The relationships between occupant age, economic status, education level, occupation, income, and health conditions were examined using cross tabulations with chi-square tests, as shown in Table 4.

Tab.4: Relationships Between Age Band, Economic Status, Education, Occupation, Income, and Health Conditions.

Research Questions	Age Band	Economic Status	Education Level	Occupation	Income	Health
Q 1.1: What is your age?	1	0,201	0,114	0,399***	0,213	0,496**
	—	0,447	0,989	0,000	0,324	0,000
Q 1.2: What is your economic status?	0,201	1	0,416**	0,171	0,136	0,178
	0,447	—	0,000	0,763	0,936	0,661
Q 1.3: What is your highest level of education?	0,114	0,416**	1	0,162	0,190	0,288
	0,989	0,000	—	0,648	0,333	0,196
Q 1.4: What is your occupation?	0,399***	0,171	0,162	1	0,275	0,342**
	0,000	0,763	0,648	—	0,092	0,000
Q 29: What is your monthly income?	0,213	0,136	0,190	0,275	1	0,174
	0,324	0,936	0,333	0,092	—	0,480
Q 28: How is your health in general?	0,496**	0,178	0,196	0,342**	0,174	1
	0,000	0,661	0,288	0,000	0,480	—

As shown in Table 4, age bands were significantly related to the health conditions, and this relationship was strong ($\chi^2 = 73{,}739$, $p < 0{,}001$, Cramer's $V = 0{,}496$). Younger age appeared to report better health conditions (good or very good) than older age. Household occupation was significantly related to health conditions, and the relationship was moderate ($\chi^2 = 33{,}071$, $p < 0{,}001$, Cramer's $V = 0{,}342$). A greater proportion of participants with very good condition worked outside the home than those with mediocre health conditions, whereas none of the participants who retired had very good conditions. Household occupations were also significantly associated with age with a moderate-strong relationship ($\chi^2 = 44{,}810$, $p < 0{,}001$, Cramer's $V = 0{,}399$). The results revealed that economic status was significantly related to educational level ($\chi^2 = 48{,}808$, $p < 0{,}001$, Cramer's $V = 0{,}416$). A greater proportion of participants with high school had full time jobs than those with only elementary or secondary school, whereas most participants who were pensioners graduated from elementary or secondary school, and none of undergraduate/postgraduate students were pensioners. Income was not significantly related to any variables.

Tab.4: Relationships Between Age Band, Economic Status, Education, Occupation, Income, and Health Conditions (Continued).

Health condition - Age, χ^2 (12) = 73,74, p = 0,000, *Cramer*'s V = 0,496
Health condition – Employment status, χ^2 (12) = 9,48, p = 0,661, *Cramer*'s V = 0,178
Health condition – Education level, χ^2 (9) = 10,83, p = 0,288, *Cramer*'s V = 0,196
Health condition – Occupation, χ^2 (9) = 33,07, p = 0,000, *Cramer*'s V = 0,342
Health condition – Income, χ^2 (9) = 8,63, p = 0,472, *Cramer*'s V = 0,170
Income - Age, χ^2 (12) = 8,63, p = 0,324, *Cramer*'s V = 0,213
Income – Employment status, χ^2 (12) = 5,58, p = 0,936, *Cramer*'s V = 0,136
Income – Education level, χ^2 (9) = 10,22, p = 0,333, *Cramer*'s V = 0,190
Income – Occupation, χ^2 (9) = 8,55, p = 0,480, *Cramer*'s V = 0,174
Occupation – Age, χ^2 (12) = 44,81, p = 0,000, *Cramer*'s V = 0,399
Occupation – Employment status, χ^2 (12) = 48,81, p = 0,000, *Cramer*'s V = 0,416
Occupation – Education, χ^2 (9) = 6,89, p = 0,648, *Cramer*'s V = 0,162
Age – Education, χ^2 (12) = 3.68, p = 0,989, *Cramer*'s V = 0,114
Age – Employment status, χ^2 (16) = 16.09, p = 0,447, *Cramer*'s V = 0,201
Employment status – Education, χ^2 (12) = 48.81, p = 0,000, *Cramer*'s V = 0,416

As shown in Table 4, feed-forward interviews of the residents of 100 flats revealed that age bands were significantly related to the health conditions, and this relationship was strong (χ^2 = 73,739, p < 0,001, Cramer's V = 0,496). Younger age appeared to report better health conditions (good or very good) than older age. Household occupations were also significantly associated with age with a moderate-strong relationship (χ^2 = 44,810, p < 0,001, Cramer's V = 0,399). Of the surveyed flats, 73% had owner-occupiers whose ages ranged between 55 and 65 or were 65 and older; these age bands were in the high-income group, and the energy consumption of these households was higher than the national average, all of which demonstrates an association between age and level-of-income factors, which suggests that household socio-demographic characteristics should be evaluated before any type of building retrofitting is developed.

3.2. Assessing occupants' thermal comfort

In Table 5 (a) Pearson's correlation analysis was undertaken to assess occupants' TSVs. To provide an accurate conventional method of design in thermal comfort studies, households' TSVs [-3, +3] coding range represents the [Cold to Hot] thermal sensation scale. Wang *et al.* (2018) recommended 7-point continuous thermal sensation scale which allows researchers to conduct Pearson's correlations at the time of identifying 'neutral' adaptive thermal comfort in longitudinal field studies. In Table 5 (b) Cramer's V test was undertaken to demonstrate relationships between households' TSVs, orientation factor of each RTB in the post-war social housing estate and floor level differences of each apartment in the RTB. To provide an accurate conventional method of design in thermal comfort studies, households' TSVs [0 to 6] coding range represents [-3, +3] thermal sensation scale band. Wang *et al.* (2018) recommended 7-point discrete thermal sensation scale could be applied to assess occupants' TSVs. This means that the variables related to occupants' TSVs could be used as ordinal variables to conduct the relevant Cramer's V test. It should be noted that in the questionnaire survey pro-forma, the survey was set on a 7-point Likert scale to assess occupants' TSVs.

In this respect, Cramer's V test was conducted to demonstrate the appropriateness of the chosen statistical analysis. Hence, according to adaptive thermal comfort theory which was developed by Haghighat and Donnini (1998) and Haldi and Robinsion (2008) recommended that [-3, +3] coding should be applied as a continuous variable to conduct Pearson's correlations while interpreting the households' TSVs. These scholars highlighted the interpretation of households' TSVs by selecting these variables which could not have a significant effect on the outcome to identify 'neutral' adaptive thermal comfort thresholds in a field study. In the present study, both Pearson's correlations and Cramer's V test were conducted and only Pearson's correlation findings were reported according to the statistical convention. Additionally, Cramer's V findings were presented to respect the convention in statistics. In this present study, Fisher's exact test was applied before undertaking Cramer's V test to avoid any research bias and demonstrate the statistical representation of this method of design. However, in general many thermal comfort studies recommend Pearson's correlation outputs could provide a reliable guidance to the researchers to measure the effect of households' TSVs.

Tab.5 (a): Relationships Between Occupant TSVs for Each Occupied Space in the Summer: Living Room, Kitchen, Bedroom 1, Bedroom 2, Bedroom 3.

Thermal sensation votes (TSV) for each occupied space		Living Room	Kitchen	Bedroom 1	Bedroom 2	Bedroom 3
Living Room	Pearson's correlation	1	0,462**	0,302**	0,146	0,200*
	Significance	—	< 0,001	0,002	0,147	0,046
Kitchen	Pearson's correlation	0,462**	1	0,133	0,205*	0,220*
	Significance	< 0,001	—	0187	0,041	0,028
Bedroom 1	Pearson's correlation	0,302**	0,133	1	0,763**	0,724**
	Significance	0,002	0187	—	< 0,001	< 0,001
Bedroom 2	Pearson's correlation	0,146	0,205*	0,763**	1	0,829**
	Significance	0,147	0,041	< 0,001	—	< 0,001
Bedroom 3	Pearson's correlation	0,200*	0,220*	0,724**	0,829**	1
	Significance	0,046	0,028	< 0,001	< 0,001	—
** Correlation is significant at the 0,01 level (two-tailed) *Correlation is significant at the 0,05 level (two-tailed)						

As shown in Table 5 (a), several strong and moderate positive correlations related to the occupants' decisions on TSVs in the summer were detected. TSVs in bedroom 1, bedroom 2, and bedroom 3 were strongly and positively correlated with each other (rs= 0,724 - 0,829, ps < 0,001). A moderate positive correlation was noted between the TSVs in the living room and kitchen spaces (r = 0,462, p < 0,001). TSVs in living room was significantly but weakly correlated with TSVs in bedroom 1 (r = 0,302, p = 0,002) and bedroom 3 (r = 0,200, p = 0,046). TSVs in kitchen was significantly but weakly related to TSVs in bedroom 2 (r = 0,205, p = 0,041) and bedroom 3 (r = 0,220, p = 0,028), which indicates that the position of the rooms in the flats should be taken into account to assess the occupants' thermal comfort and provide a basis for an ordinal logistic regression analysis; this is presented in Figures 2 (a)-(d). It is important to know occupants' TSVs in their bedrooms because of the significance of night-time sleep is strongly correlated with the hot and humid climate characteristics of this Eastern-Mediterranean region. Table 5 (b) demonstrates the Fisher's Exact tests if over 25% of cells had less than 5 expected counts that revealed relationships between occupant TSVs for each occupied space in the summer, orientation and floor level.

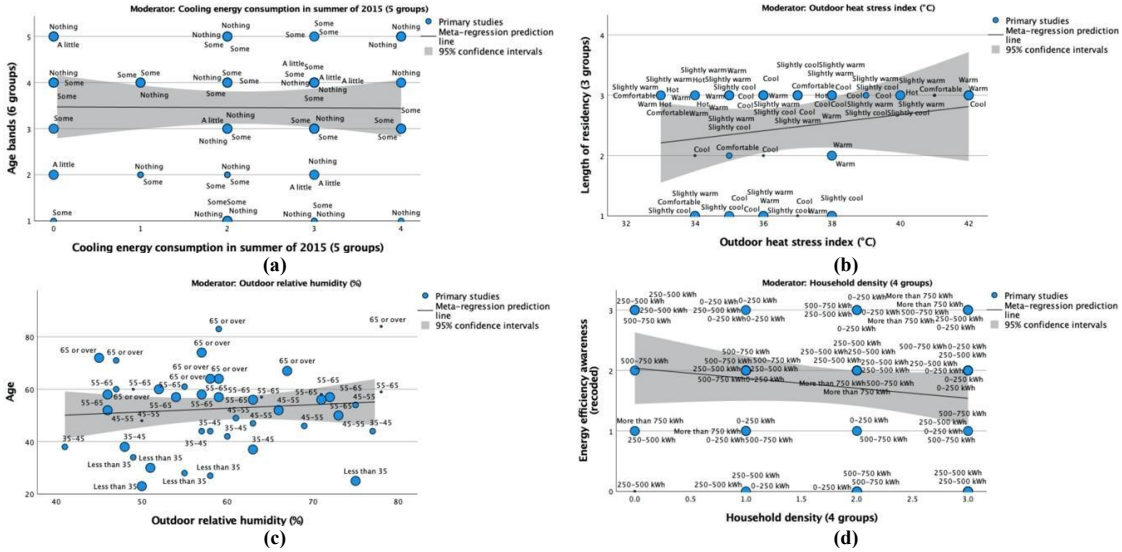

Fig.2: (a) Meta-regression analysis between age bands and cooling consumption in summer by exploring energy efficiency awareness; correlations between households' length of residency and outdoor heat stress index factor by thermal sensation votes integration; (c) regression analysis between households' age and outdoor relative humidity; (d) correlations between households' energy efficiency awareness and households' density by exploring energy consumption.

Tab. 5 (b): Relationships Between Occupant TSVs for Each Occupied Space in the Summer: Living Room, Kitchen, Bedroom 1, Bedroom 2, Bedroom 3, RTB Orientation and Floor Level.

Thermal sensation votes (TSV) for each occupied space		**Orientation**	**Floor Level**
Living Room	Cramer's V	0,226	0,232
	Significance	0,379	0,220
Kitchen	Cramer's V	0,279	0,222
	Significance	0,118	0,384
Bedroom 1	Cramer's V	0,274	0,177
	Significance	0,176	0,952
Bedroom 2	Cramer's V	0,272	0,194
	Significance	0,121	0,891
Bedroom 3	Cramer's V	0,263	0,221
	Significance	0,094	0,489
Orientation	Cramer's V	1	0,197
	Significance	—	0,188
Floor Level	Cramer's V	0,197	1
	Significance	0,188	—
Living room TSV – Orientation, *Fisher's exact* = 15,40, *p* = 0,379, *Cramer*'s *V* = 0,226 Kitchen TSV – Orientation, *Fisher's exact* = 19,72, *p* = 0,118, *Cramer*'s *V* = 0,279 Bedroom 1 TSV – Orientation, *Fisher's exact* =20,81, *p* = 0,176, *Cramer*'s *V* = 0,274 Bedroom 2 TSV – Orientation, *Fisher's exact* = 22,54, *p* = 0,121, *Cramer*'s *V* = 0,272 Bedroom 3 TSV – Orientation, *Fisher's exact* = 20,19, *p* = 0,094, *Cramer*'s *V* = 0,263 Floor level - Orientation, *Fisher's exact* = 12,11, *p* = 0,188, *Cramer*'s *V* = 0,197 Living room TSV – Floor level, *Fisher's exact* = 18,15, *p* = 0,220, *Cramer*'s *V* = 0,232 Kitchen TSV – Floor level, *Fisher's exact* = 15.35, *p* = 0,384, *Cramer*'s *V* = 0,222 Bedroom 1 TSV – Floor level, *Fisher's exact* = 10,23, *p* = 0,952, *Cramer*'s *V* = 0,177 Bedroom 2 TSV – Floor level, *Fisher's exact* = 10,09, *p* = 0,891, *Cramer*'s *V* = 0,194 Bedroom 3 TSV – Floor level, *Fisher's exact* = 13,86, *p* = 0,489, *Cramer*'s *V* = 0,221			
Occupant TSVs for living room, kitchen and bedrooms 1, 2 and 3 in the summer: (0) to (6) RTB orientation: 0 (north-east), 1 (south), 2 (north-west), 3 (south-west) and 4 (south-east) Different floor levels: 0 (ground), 1 (first), 2 (second), 3 (third), 4 (fourth) and 5 (fifth			

The results revealed that orientation and floor level were not significantly related to any TSVs. This was probably due to the small floor area of these spaces, which means the physical condition of the RTBs can lead to thermally uncomfortable indoor-air temperatures due to the poor window design in the interviewed flats. Data related to the occupants' adaptation to slightly warmer indoor-environment conditions and outdoor-air temperatures could be seen as a significant contribution to the ASHRAE Global Thermal Comfort Database II in terms of the delineation of a specific method to conduct a longitudinal field survey in this particular south-eastern Mediterranean climate and the prediction of neutral adaptive thermal comfort levels with the use of an ordinal logistic regression analysis (see at - https://doi.org/10.6078/D1F671). The present study also provides a roadmap to the EN 15251 thermal-comfort assessment criteria in the event that industry-based temperature design criteria are unable to comply with the ASHRAE Global Thermal Comfort Database II because they conflict with the occupants' adaptive comfort temperatures, as shown in Figure 3.

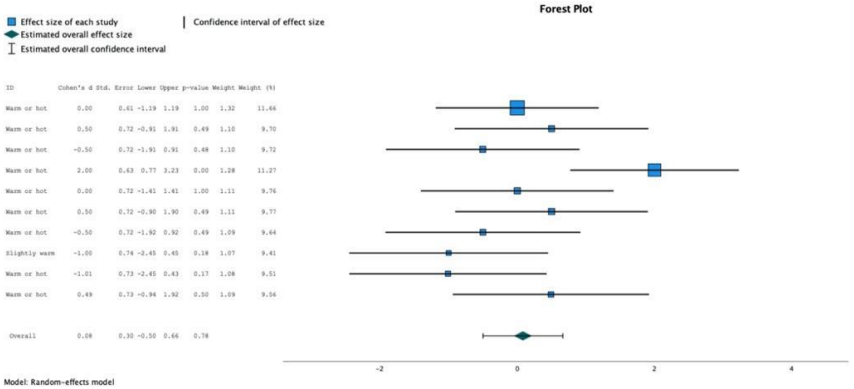

Fig.3: Households' thermal sensation votes by using Forest Plot analysis.

According to Figure 3, the recorded temperatures were above the acceptable benchmark of 25°C that was determined to maintain the occupants' thermal comfort (BSI, 2005; CIBSE, 2017; CEN, 2007). Additionally, the average mean temperatures that were recorded across the indoor measurement results and the outdoor monitoring results were ranged from 30,59–32,12°C, which is above the recommended thermal-comfort level of 23–25°C indicated by the CIBSE TM52 Overheating Task Force. It is worth noting that recorded daily running mean outdoor temperatures reflected the thermal experiences of the occupants more accurately than the monthly mean temperatures, because the outdoor mean temperatures sometimes changed in significantly shorter intervals (Nicol *et al*., 2012). Even though the monthly mean temperature was taken as an average temperature of the month as a whole in the present study, the occupants' TSVs were found to be correlated with their thermal experiences and their ability to adapt their physiological body temperatures to changing summer climate conditions (Ozarisoy & Altan, 2023).

4. Conclusions

The present study detailed a model that can be employed to investigate a range of potential retrofitting interventions related to housing-energy consumption and to address issues associated with overheating risks experienced during the summer; as such, the research design and methodology of the present study aims to enhance policymakers' understandings of the complex nature of energy consumption and occupant thermal comfort. The developed framework provides a scientific background that can be included in the building energy simulation (BES) platform to serve as a set of guidelines for the EPBD scientific committee for energy policy design and retrofitting strategies. The study findings can be extrapolated by current industry benchmarks or assessment criteria as a new European Norm (EN) that can be adopted by other EU countries. The findings of this study enhanced the overall understanding of the complex interrelationships between household socio-demographic characteristics, building thermal properties and occupants' habitual adaptive behaviour related to thermal comfort in heat-vulnerable MFHs. It was found that TSVs in living room was significantly but weakly correlated with TSVs in bedroom 1 (r = 0,302, p = 0,002) and bedroom 3 (r = 0,200, p = 0,046). TSVs in kitchen was significantly but weakly related to TSVs in bedroom 2 (r = 0,205, p = 0,041) and bedroom 3 (r = 0,220, p = 0,028). The present study is the first to follow the recommended methodology laid out in *EN 15251 – Indoor environmental input parameters for design and assessment of energy performance of buildings addressing indoor air quality, thermal environment, lighting and acoustics*. To date, no other studies have focused on the development of this particular *EN 15251* standard; as such, the present study developed a socio-technical-systems (STS) conceptual framework to provide a significant contribution to the body of knowledge related to a novel methodological framework for building performance evaluation studies.

5. Acknowledgments

The authors would like to acknowledge the Graduate School, School of Architecture, Computing & Engineering (ACE), London, United Kingdom. The lead author (Dr. Bertug Ozarisoy) would also like to acknowledge the Sustainable Environment and Energy Systems (SEES) Graduate Program at the Middle East Technical University Northern Cyprus Campus.

Data Access Statement: The datasets generated during and/or analysed during the current study are publicly available at - https://doi.org/10.15123/uel.8q713

6. References

Altan, H. (2004). Energy efficiency in housing: drivers and barriers to improving energy efficiency and reducing carbon dioxide emissions in private sector housing. PhD Thesis. University of Sheffield. ISNI: http://isni.org/isni/0000000134185603 (accessed on 10/05/2019)

Chasalow, K., & Levy, K. (2021). Representativeness in statistics, politics, and machine learning. In *FAccT 2021 - Proceedings of the 2021 ACM Conference on Fairness, Accountability, and Transparency* (pp. 77–89). Association for Computing Machinery, Inc. https://doi.org/10.1145/3442188.3445872

British Standards Institution (BSI). (2007). BS EN 15251: 2007: Indoor Environmental Input Parameters for Design and Assessment of Energy Performance of Buildings Addressing Indoor Air Quality, Thermal Environment, Lighting and Acoustics; BSI: London, UK, 2007.

CEN. (2007). Indoor environmental input parameters for design and assessment of energy performance of buildings addressing indoor air quality, thermal environment, lighting and acoustics. EN 15251. Technical report, European Committee for Standardization, Bruxelles. [accessed on 11/05/2018]

CIBSE. (2017). CIBSE TM59 - Design methodology for the assessment of overheating risk in homes. London: The Chartered Institution of Building Services Engineers.

Dong, B., Liu, Y., Fontenot, H., Ouf, M., Osman, M., Chong, A., … Carlucci, S. (2021). Occupant behavior modeling methods for resilient building design, operation and policy at urban scale: A review. Applied Energy, 293. https://doi.org/10.1016/j.apenergy.2021.116856

Field, A. (2013). Discovering statistics using IBM SPSS statistics (4th ed.). Los Angeles, CA: Sage.

Gamst, G., Meyers, L. S., & Guarino, A. J. (2008). Analysis of variance designs: A conceptual and computational approach with SPSS and SAS. New York: Cambridge University Press.

Garrett., H. E. (1942). The Representativeness of a Sample. The American Journal of Psychology 55, 4 (1942), 580–581. http://www.jstor.org/stable/1417131

Haghighat, F., & Donnini, G. (1999). Impact of psycho-social factors on perception of the indoor air environment studies in 12 office buildings. *Building and Environment*, *34*(4), 479–503. https://doi.org/10.1016/S0360-1323(98)00034-1

Haldi, F., & Robinson, D. (2008). On the behaviour and adaptation of office occupants. *Building and Environment*, *43*(12), 2163–2177. https://doi.org/10.1016/j.buildenv.2008.01.003

Hirsch, L. S., & O'Donnell, A. M. (2001). Representativeness in Statistical Reasoning: Identifying and Assessing Misconceptions. *Journal of Statistics Education*, *9*(2). https://doi.org/10.1080/10691898.2001.11910655

Hu, J. and Kohler-Hausmann, I. (2020). What's Sex Got to Do with Machine Learning?. In Proceedings of the 2020 Conference on Fairness, Accountability, and Transparency (Barcelona, Spain) (FAT* '20). Association for Computing Machinery, New York, NY, USA, 513. https://doi.org/10.1145/3351095.3375674

Jensen., A. (1926). Report on the Representative Method in Statistics. Bulletin de l'Institut international de statistique 22, 1 (1926), 359–438.

Kiaer., A. N. (1976). Den repræsentative undersøgelsesmethode = The representative method of statistical surveys. Oslo: Aschehoug.

Kruskal, W., and Mosteller, F. (1980). Representative Sampling, IV: The History of the Concept in Statistics, 1895-1939. International Statistical Review / Revue Internationale de Statistique 48, 2 (1980), 169–195. http://www. jstor.org/stable/1403151

Little, R. J. A. (1988). A test of missing completely at random for multivariate data with missing values. Journal of the American Statistical Association, 83, 1198–1202.

Little, R. J. A., & Rubin, D. B. (2002). Statistical analysis with missing data (2nd ed.). New York: Wiley.

McNemar, Q. (1940). Sampling in psychological research. Psychological Bulletin 37, 6 (1940), 331–365. https://doi.org/10.1037/h0063476

Nicol F, Humphreys, M. and Roaf, S. (2012). Adaptive Thermal Comfort, Principles and practice, London Routledge.

Ozarisoy, B., & Altan, H. (2021). Developing an evidence-based energy-policy framework to assess robust energy-performance evaluation and certification schemes in the South-eastern Mediterranean countries. *Energy for Sustainable Development*, *64*, 65–102. https://doi.org/10.1016/j.esd.2021.08.001

Ozarisoy, B., & Altan, H. (2022). Significance of occupancy patterns and habitual household adaptive behaviour on home-energy performance of post-war social-housing estate in the South-eastern Mediterranean climate: Energy policy design. *Energy*, *244*. https://doi.org/10.1016/j.energy.2021.122904

Ozarisoy, B., & Altan, H. (2023). Energy Policy Design in the Eastern Mediterranean Basin: A Roadmap to Energy Efficiency, Taylor & Francis Group, Routledge Explorations in Energy Studies, ISBN 9781032493046, https://www.routledge.com/Energy-Policy-Design-in-the-South-Eastern-Mediterranean-Basin-A-Roadmap/Ozarisoy-Altan/p/book/9781032493046

Schmill, M. D., Gordon, L. M., Magliocca, N. R., Ellis, E. C., & Oates, T. (2014). GLOBE: Analytics for assessing global representativeness. In *Proceedings - 5th International Conference on Computing for Geospatial Research and Application, COM.Geo 2014* (pp. 25–32). Institute of Electrical and Electronics Engineers Inc. https://doi.org/10.1109/COM.Geo.2014.21

Schouten, B., Cobben, F., & Bethlehem, J. (2009). Indicators for the representativeness of survey response. *Survey Methodology*, *35*(1), 101–113.

Tabachnick, B. G., & Fidell, L. S. (2007). Using multivariate statistics (5th ed.). Boston, MA: Pearson.

Wang, Z., de Dear, R., Luo, M., Lin, B., He, Y., Ghahramani, A., & Zhu, Y. (2018). Individual difference in thermal comfort: A literature review. Building and Environment. Elsevier Ltd. https://doi.org/10.1016/j.buildenv.2018.04.040

ATLAS-FeliCity: Supporting Energy Retrofit of the Heritage Building Stock Through a Simplified Digital Twin

Cristina S. Polo López[1], Ivan Curto[1], Ahmed Khoja[2], Dagmar E. Exner [3], Franziska Haas[3] and Alexandra Troi[3]

[1] University of Applied Sciences and Arts of Southern Switzerland (SUPSI), Mendrisio (Switzerland)

[2] Munich University of Applied Sciences (MUAS), Munich (Germany)

[3] European Academy Bozen, Bozen (Italy)

Abstract

Retrofitting the heritage buildings (listed or not) is a complex task due to legal, financial and technical barriers. The decision makers often lack a holistic view about the condition of the existing building stock in their jurisdiction, possible renovation options and the impact of the renovation actions on the overall sustainability performance of the building stock. Within the ATLAS research project, the ATLAS-FeliCity online tool was developed. The tool provides a simplified digital twin version of the built environment and allows the user to conduct an energy performance analysis at various spatial scales (single, or portfolio of buildings). The developed tool was tested in different demo sites in the Alpine Space area characterized by similar building types and specially focused on the historic building stock. The tool is designed to be used as basis for the decision-making at municipality level. Municipalities will be supported in developing optimized renovation strategies in terms of reducing the ecological footprint and carbon emissions as well as increasing building´s energy efficiency. This paper presents a summary of the main features of the FeliCity-ATLAS tool and the results achieved during two-demo site testing: Madruzzo/Calavino (Italy) and Locarno (Switzerland).

Keywords: Renovation of building stock, energy retrofit, heritage buildings, digital twin, 3D digital-tool

1. Introduction

Over a quarter of the European building stock is classified as “historic” with vast majority of it concentrated in the rural areas (Troi, 2011). The traditional architecture in the Alps is a key enabler for sustainable development in the social, ecological and economic spheres. In this context, improving the sustainability of the historic buildings can lead to several positive effects on the sustainability of the whole Alpine area. It would promote the use of the existing infrastructure and the local economy thus, limiting the land use changes and the rural depopulation. Moreover, the energy renovating of the traditional historic architecture extend their service life and reduce the ecological footprint and have an overarching socioeconomic impact that goes beyond the environmental or economic benefits (Khoja et al., 2021a)

The retrofitting of historic buildings is a complex task. Very often in the case of historic buildings (HB) specific constraints and restrictions may limit the architects and designers in the application and selection of retrofitting solutions during the design phase (e.g., buildings protected by cultural heritage, legal constraints, technical constraints or financial constraints, etc.). In order to achieve the most effective results, all involved stakeholders must cooperate in a well-coordinated and structured way. This requires a thoughtful methodology that guides the stakeholders through the different phases of the retrofitting project. Local guidelines and the EU standards EN 16883 - 2017-0899 Conservation of cultural heritage - Guidelines for improving the energy performance of historic buildings can give certain recommendations to be followed, but there is a lack of specific tools at operational level to help with this task (Buda et al., 2022). Hence, Within the ATLAS research project (https://www.alpine-space.org/projects/atlas/en/home), a digital twin decision support online tool named ATLAS-FeliCity was developed (Khoja et al., 2021b). The tool is designed to support a holistic energy retrofit of the heritage building stock. The tool supports planners in the complex task of improving the sustainability of the built environment through providing a simplified digital twin of buildings, neighborhoods or cities, which is connected to several analysis and optimization functions (e.g. energy, carbon emissions, renewables, etc.). Moreover, the tool offers a highly flexible and easy to

© 2022. The Authors. Published by International Solar Energy Society
Selection and/or peer review under responsibility of Scientific Committee
doi:10.18086/eurosun.2022.02.07 Available at http://proceedings.ises.org

use plug and play approach, useful for non-expert users to get a quick start in the applications of the tool. During the development, the tool was tested at different municipalities in Italy, Switzerland, Slovenia and Germany. The developed tool is a key enabler of the novel ATLAS integrated decision support methodology (DS-Toolkit) which guides the stakeholder throughout the renovation work of historical buildings in five sequential phases, starting at the initiation phase up to the in-use phase. (Figure 1).

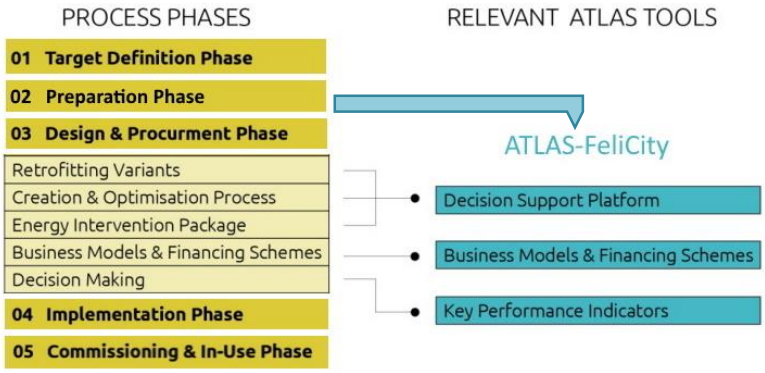

Fig. 1: Main phases in the ATLAS integrated decision support methodology (IDS) to support energy renovation of Historical Buildings (HB). Preparation phase (02) serves as input data for the tool. Source: Khoja et al., 2020a.

2. ATLAS- FeliCity Tool architecture and requirements

The effectiveness of building retrofitting can be increased significantly through district wide, multi scale renovation of the building stock (Khoja et al., 2019). This multi scale renovation enables the planners to exploit energy synergies between the existing buildings, utilize district energy systems and take advantage of the economics of scale (Khoja et al., 2019). However, working beside an own isolated project on multiple scales faces major challenges as the complexity of planning grows exponentially and traditional planning methods and tools do not support such multi scale consideration. Modern digital twin tools can help the sector overcome this barrier by providing the planner with multi scale consideration of their interventions. ATLAS-FeliCity is one of the few advanced planning software tools that are able to address this holistic, multi-layered approach.

ATLAS-Felicity bundles a comprehensive 3D building database with open-source GIS data and connect external webservices. These open sources serve as an extendible basis for real-time hourly thermal simulation and data visualisation. Thus, the user is able via the cloud to import and activate information directly objects from the built environment (building models, streets, landscape objects, public transport stops, etc.) in the tool web-interface without any pre-processing or uploading of data (e.g. GIS). A core part of the default dataset in ATLAS-FeliCity is the building construction database, which includes default parameters for various building types (e.g., residential, school, offices, retail, etc.), several construction periods (since about 1850, until 1900 and after 2010) and heritage protection status (e.g., listed, buildings protected as part of a conservation area, building with historic values but not listed, and without historical values). The database holds all the needed information and parameters to run a single zone hourly energy simulation using the ISO 13790 calculation method. To support the design team in assessing the impact of different renovation scenarios on the heritage buildings, ATLAS-FeliCity provides an advanced Simulation and Design Hub (SDH) which is a convergence of Dynamic Simulation Modelling, Geographic Information Systems (GIS), cloud data storage & analysis supported by key performance indicators (KPIs) and valuable analysis tools. The SDH allows performing various analyses like energy demand, carbon emissions, share of renewables, and payback period of the selected interventions. The objective therefore is to create and optimise the selected intervention measures in terms of energy, heritage compatibility, cost efficiency as well as the overall sustainability.

2.1. The ATLAS-FeliCity Decision Support (DS) Process in the preparation phase

When dealing with retrofitting projects, understanding the current energy performance of the building and its potential for energy demand reduction is an important step in the early decision-making process of the project to set the targets to be achieved during the project (01 Target definition phase, Fig.1). During the preparation phase (phase 02, Fig.1), various stakeholders gather information about the building and its surrounding serving as input for the FeliCity tool. Thus, within the preparation phase, the following three processes take place:

a) *Populating the building model*: intensive data collection to perform a qualified energy assessment of the as-

it-state of the building, the effect of the retrofitting project as well as for its interaction with the environment and local grids. To help the designer in this complex task, the ATLAS DS-Toolkit provides a list of minimum data, which is required to populate the building model. According to this list, also default data are included in the ATLAS-FeliCity tool which can replace unknow values based on the building age class. This allows for having a fairly acceptable result of the energy performance in short modelling time;

b) *Identification of the building weak points*: during the diagnosis the designer need to specify the building components (i.e. envelop, systems, etc.) that are causing the highest amount of energy consumption and can/shall be improved. The ATLAS-FeliCity provide a detailed ranking list of the different energy performance weaknesses of the building. This serves as a basis for selecting and prioritising the most efficient retrofitting solutions and for creating a package of interventions for the building in the next steps;

c) *Identification of the potential solutions*: A core element of the ATLAS project was the collection of good examples on very different levels from historic building typologies and existing guidelines for energy retrofitting, to the use of renewable energy sources (RES) in a regional Alpine Space context documented in Atlas Deliverable D.T3.2.1 (Polo López, et al. 2020, 2021). ATLAS research gathered best-practice examples of how historic buildings can be renovated to achieve high levels of energy efficiency while respecting and protecting its heritage significance. A database of best practice building renovations is available with the HiBERatlas (www.hiberatlas.com) (Haas et al. 2021) and accordingly for technical solutions for energy retrofit with the HiBERtool (www.tool.hiberatlas.com) (Rieser et al., 2021). These tools developed within the Interreg AS ATLAS are strategic elements aiming at establishing transnationally integrated low carbon policy instruments. They are useful information to stakeholders involved in the renovation process of historic buildings, as the ATLAS holistic decision-support (DS) methodology and toolkit, Atlas Deliverable D.T3.4.1 (Khoja et al. 2020a) and Deliverable D.T3.5.1 (Khoja et al. 2021)).

2.2. Design and Procurement phase (phase 03, in Fig.1),

A retrofitting design variant in ATLAS-FeliCity DS is a package of different retrofitting interventions applied on single buildings or a group of buildings, in the whole neighbourhood and its energy related infrastructure, like heat networks or power plants. Thus, each concept may contain several different design variants that on the one hand need to reach the set targets and as well must be in line with the identified constraints and restrictions determined in the Target definition phase (phase 01, Fig. 1). Therefore, all valid variants would then be later assessed in the decision-making step to choose the concept to be developed. In the later decision-making step, the developed design variants within a concept are compared against each other thanks to a Multiple Criteria Decision Analysis (MCDA) value assessment. Retrofitting design variants can include one package of interventions which has been applied to relevant objects (i.e., building or group of buildings) or in urban environments (i.e., energy infrastructure, neighbourhood objects). For example, to promote multi scale renovation approaches as roof sharing strategies, smart grids or energy storage for the neighbourhood. The objective therefore is to create and optimise the selected intervention measures in terms of energy, heritage compatibility, cost efficiency as well as the overall sustainability. The following in figure 1 represent the sequence of applying retrofitting interventions in the iteration steps of the DS that is to be adopted by the "Planners team":

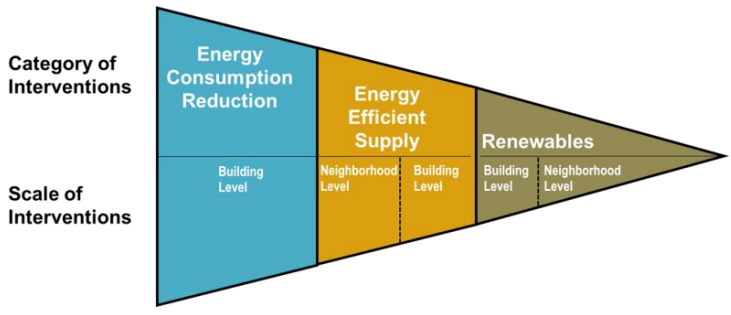

Fig. 2: Sequence of applying retrofitting interventions in the iteration steps of the DS. Source: Khoja et al., 2020a.

While creating a design variant the "Planners team" must consider several aspects like the determined targets, constraints, and restrictions as well as different interactions between the applied interventions and the buildings in the neighbourhood or its energy infrastructure. Moreover, the "Planners team" also needs to involve all relevant project stakeholders like "Managers/Coordinators", "End-Users", "Client/Owners" and others in the design process of variants. To make all these challenges manageable, the ATLAS DS process in the Concept phase contains the following main steps to create design variants which need to be followed by the "Planners team":

1. *Selection and optimisation of energy interventions* on building and neighbourhood level;
2. Addition of *non-simulated interventions*;
3. Inclusion of *business models and financing schemes*;
4. *Approval of design variant*.

First step in the *selection and optimisation of the intervention package* is to identify and exclude all interventions, which may not be suitable to be applied for the building or neighbourhood due to the previously defined constraints, or restrictions. For example, if cultural heritage protection laws restrict the works on the façade of the building the "Planners team" needs to filter out all interventions which cannot be applied. Then, based on the identified weak-points in the preparation phase, "Planners team" can assess the potential for improvements and therefore select most useful retrofitting interventions from the ATLAS-FeliCity technology library datasheet.

Secondly, there may also be *non-quantifiable or non-simulated interventions* on objects which have not been defined in the ATLAS technology library. Such non-quantifiable interventions are introduced in a qualitative way (written text) in a design variant and considered in the design phase by the "Planners". Such non-quantifiable interventions cannot be simulated or calculated with ATLAS tools but can be quantified by the ATLAS KPIs. The ATLAS project has developed based on the CESBA (Common European Sustainable Built Environment Assessment) Alps key performance indicators KPIs, the ATLAS KPIs. The ATLAS KPI are specific for heritage buildings and should help guide the "Planning Team" in establishing the renovation targets in terms of energy, CO_2 savings and payback periods (Khoja et al., 2020b). These KPIs are partially incorporated within the ATLAS-FeliCity tool to aid the decision-making process and monitor the target achievements after renovation works are concluded.

The third step then provides for the *incorporation of business models and financing schemes*. Depending on the site of the project the "Planners Team" must search for the current financing schemes and their specific conditions in the region or site of the project. The results of the ATLAS Task 3.3, Deliverable D3.1/3.3 (Khoja et al. 2020 c) can be used a preliminary starting point for this search. However, due to dynamic nature of national and regional funding schemes, up-to-date research by the "Planners Team" must be done. The ATLAS-FeliCity tool provides an initial estimation of the area and cost of each intervention, however, the specification of the investment cost data for each applied intervention needs to be done based on local price indexes or other external software tools to get accurate investment estimation. Only with having an estimation of the expected total investment costs, it is possible to select useful financing mechanism and business models for the variant. If direct cost benefits from incentives like grants are available, the "Planners Team" needs to calculate the benefits based on the specific conditions of each financing mechanism and intervention. Hence, the final investment cost for the applied interventions may reduce by applying these financing mechanisms depending on the availability in the related country or region of the project. After collecting data on investment costs and all financing mechanisms for the variants, the "Planners Team" can calculate the ROI (Return on Investment) and PP (Payback Period) of the interventions.

At last, fourth step, it is necessary *to approve the design variant*. The design variant finally needs to be matched with the set targets defined in the definition phase and to compare the results of the design variant against the KPIs targets (e.g. Figure 3). Depending on the kind of set targets (Benchmarks) the KPIs can be compared with the current state results in a quantitative way by checking the absolute values of the results (e.g. kWh m^{-2} per year) or using the relative results (20% reduction). "Planners Team" needs to check after each iteration if the targets already have been reached or not by the selected package of measures. All KPIs can be calculated for different variants on each scale of application and are aggregated or averaged. Hence, these comparisons and checks already should have been done for several times after each iteration step. Final matching between the variant results and the set targets is the last step in the optimisation and creation process. If the optimisation is finished and the targets have been reached by the variant, the iteration loops stops and the variant is ready for a presentation and an approval by the relevant project stakeholders (e.g. "Client/Owner" and the "Manager/Coordinator") and the implementation phase can start.

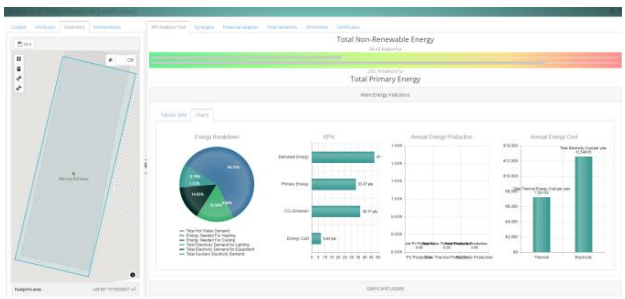

The KPIs available in FeliCity are as follows:

- Delivered and Primary Energy Demand
- Carbon Emissions
- Operational Energy Cost
- Share of renewables on-site
- Self-Sufficiency rate from electricity grid
- Share of own consumption from renewables
- Investment cost for maintenance, repair and retrofitting works
- Return on Investment ROI and Life cycle cost (LCC)

Fig. 3: A screenshot of the ATLAS DS tool showing the KPIs value.

ATLAS-FeliCity DS Tool main features applied to case studies

The ATLAS-FeliCity fully supports the Pareto principle, which allows achieving accuracy in energy and cost results of at least 80 % by only providing around 20% of input data. Hence, minimizing the data collection time and cost effort by the users. ATLAS-FeliCity Data Collection process is based on gathering digital building data, city data and data for the surrounding infrastructure on multiple scales via a simple to use Data Collection wizard. The collected data is stored in a cloud-based webserver for subsequent use through the whole conception and refurbishment process that uses two modes methodology for data capturing on different building data in a multi-scale environment (basic and advanced). This enables working on urban larger scales and multiple buildings (e.g. large building stock portfolios) in an efficient and precise way.

The building construction default dataset in ATLAS-FeliCity includes typical building construction for various building types and construction periods, and also historical status characteristics of the building or urban area. The database holds all the needed information and parameters to run an energy simulation. ATLAS-FeliCity will then be able to set up an energy model of the building by combining the default database with the geometric data from the geometry database. Afterwards, the planning team can start applying various renovation interventions using the ATLAS-FeliCity intervention catalogue. The ATLAS-FeliCity renovation catalogue provides over 300 different kind of retrofitting measures which can be simulated on different scales of application. For each selectable measure the effect in terms of energy efficiency and further KPIs can be simulated and the investment cost of the intervention can be estimated as well as the reduction in the running costs. To run simulations, ATLAS-FeliCity includes the U.S. Department of Energy's DOE dataset of hourly-based climate data, which are automatically assigned by the simulation and planning hub based on the GIS location of the project. All input data from the default database can be displayed and overwritten step-by-step by the user in case more detailed information has been collected. This enables the user to overwrite and input all needed data for the creation of the geometry information model, modelling of building components or systems (HVAC, pipes, etc.), thermal and energy simulation models, and further related models like financial and life-cycle analysis models.

A novelty of the ATLAS-FeliCity tool is its capability to allow planners working with the built environment on a multi-scale level in a flexible and intuitive way by activated on a virtual map and selecting the scale on which the user intends to work. Thus, it is possible to flexibly switch between the scales from the highest level of detail to a lower level of detail on a larger scale, depending on the projects scope and objectives. Enlarging the scale of application implies add further buildings (Figure 4) which it turns allows upscaling to a neighbourhood or even a city scale (Figure 5). FeliCity in this case calculates depending on the metric of interest a weighted average of the required values (e.g. primary energy demand or carbon emissions per m² and year). The cost of each intervention as well as the bill of quantities is estimated based on the 3D building geometries (e.g. wall area, roof area, windows area, floor area, etc.) and statistical methods. Using the estimated bill of quantity, the average cost of the intervention per reference unit and country stored in the FeliCity backend database are applied to estimate the rough renovation cost. Based on the investment cost and savings in operational cost a return of investment and payback period of all applied renovation measures considering the real building geometries, actual climate data and construction costs at the present location is conducted by the tool.

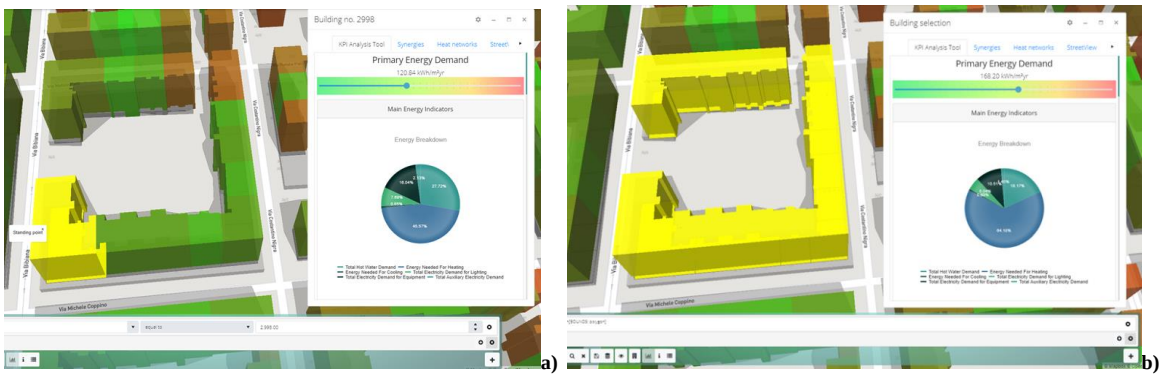

a) b)

Fig. 4: ATLAS-FeliCity example of upscaling from the primary energy demand on a single building (a) to aggregated primary energy demand at building block scale (b,12 buildings). Source: Khoja et al., 2020a.

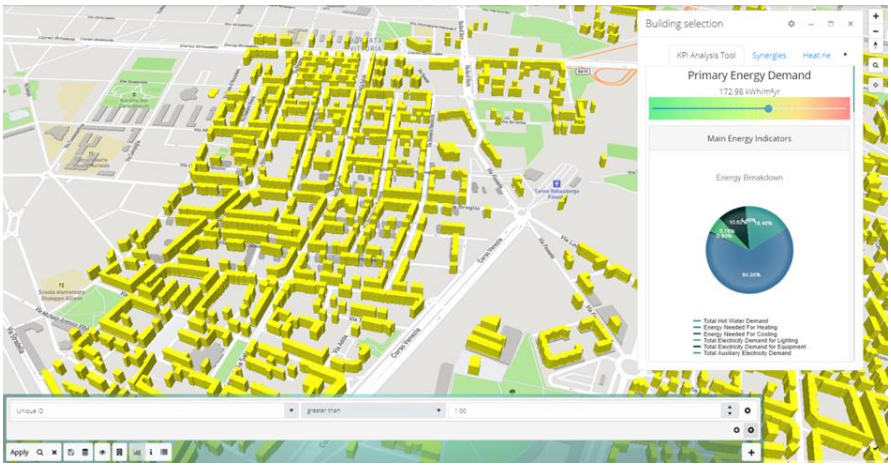

Fig. 5: Aggregated primary energy demand and energy breakdown's on a city scale (3000 buildings). Source: Khoja et al., 2020a.

2.4. Implementing and commissioning & end-use phases

In these phases (04 and 05 phases) as any construction activity whether it is a newly built project or a retrofitting one, the goal is to create a set of drawings, documents and detailed specifications that would allow for implementing the developed retrofitting design on the ground. Depending on the complexity of the project, it might be necessary to engage consultants and moreover, in this phase it is important to engage the local knowledge in the final development of the project. The developed project must reflect the "End User's "requirements defined in concept phase. Furthermore, "planners' team" in cooperation with "Manager/ Coordinator" need to develop a detailed breakdown of the project budget that reflects the project cost estimations and to make sure that the developed design is within the project performance targets previously defined. The 'Planners Team', in coordination with the 'Manager/Coordinator' and 'Builder', must develop methods and strategies to be used in the handover, commissioning and utilisation phase. These could include monitoring and optimisation of energy performance as well as continuous post-occupancy investigation to avoid sub-optimal utilisation, which is indeed crucial in the long-term sustainability of successful retrofit projects.

3. ATLAS-FeliCity Decision Support Tool: Beta testing in Alpine municipalities

Within the ATLAS project, a beta-version of ATLAS-FeliCity Decision Support DS Tool has been tested in four demo sites (Madruzzo/Calavino (Italy), Locarno o Lugano (Switzerland), Tolmin (Slovenia) and Mering (Germany). This paper will discuss the results of the demo site testing for two cases namely (Figure 6): Locarno (Switzerland) and Madruzzo/Calavino (Italy), dicussing the main features of the ATLAS-FeliCity- and its usability and limitation for guiding the decision-makers in renovating their existing stock.

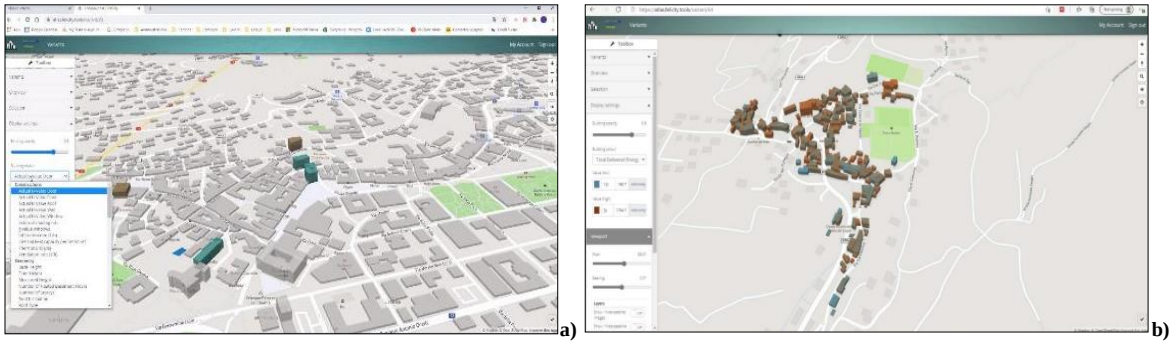

a) b)

Fig. 6: ATLAS-FeliCity Decision Support Tool application to Locarno municipality (Switzerland) and Calavino center (Italy).

3.1 ATLAS-FeliCity DS Tool: Case Study Locarno (Canton of Ticino, Switzerland)

The existing real estate portfolio in Switzerland, but also in Canton of Ticino, consists mainly of "old buildings" (i.e. 45% of the buildings were built before 1960, and almost 70% before 1980.) characterized by high heating consumption due to poor energy efficiency of the building envelope and systems. The technical age of their constructive elements is for the most part higher than their useful life span due to lack of renewal cycles and a lack

of renovation strategy. This situation, in addition to the continued loss of property value, is a serious obstacle to the achievement of the Confederation Energy Strategy 2050 (BFE, 2017; Boulouchos, et al., 2022). In 2019, the City of Locarno commissioned the University of Applied Sciences and Arts of Southern Switzerland, SUPSI to analyse and plan the rehabilitation of its real estate portfolio (Branca et al., 2019). The work has been aimed to find a concrete solution to the management and rehabilitation needs of the building stock of the city of Locarno. The study aimed to allow the property owner, in this case Locarno municipality, planning the interventions at the scale of the real estate portfolio by identifying priorities and sustainability. The real estate park City of Locarno consists of 21 buildings with different uses, mainly composed of school buildings and offices (i.e. 9 schools, 10 offices and 2 apartments, all built before the 1980s, with almost 50% of structures built before 1960). A first diagnosis of each single building was carried out with the PETRA tool, a Web Platform for Energetic and Technological Retrofit in Architecture (Buda et al., 2022; Branca et al., 2012). The tool developed by SUPSI in collaboration with the Swiss Federal Institute of Technology Lausanne (EPFL) and three private companies makes use of a database on sustainable building renovation with constantly updated information taking into account Swiss regulations. Ten historic buildings within the real estate portfolio of Locarno City have been used in the Beta Test of ATLAS-FeliCity tool (Figure 7).

Building City of Locarno	Building Use	Construction Data
01 Palazzo Marcacci	Office	1897
11 P.tta Capitani	Office	1900
30 Casorella	Office	1890
32 Casa rusca	Office	1890
33 Morettini	Office	1900
21 SE Solduno	School	1958
25 SI San Francesco	School	1890
51 Centro Diurno	Apartments	1901
87 Casa Bastoria	Office	1890
91 Casa Cristina	School	1920



Fig. 7: List of 10 historic buildings of Locarno Municipality (CH) and geolocation in ATLAS-FeliCity (e.g. 01. Palazzo Marcacci). Source: SUPSI

The current energy status scenario was defined for the calculation of the heat balance to get a picture of the theoretical energy consumption at historic buildings current state in the city of Locarno real estate park. In order to assess the differences between the initial state in the City of Locarno's building stock in energy terms and the final state, various retrofit intervention scenarios have been defined. First analysis of the distribution of losses and gains, expressed in percentages, for individual building elements during the heating period and the cooling period respectively before energy retrofit measures, shown that walls and windows of buildings are the main dispersing elements on which an effective retrofit strategy would need to be implemented. After identifying the theoretical energy consumption (quantified by 1,993,543 kWh/yr.), a comparison with the results obtained with regard the actual consumption collected in 2019 were possible (total energy consumption of 2,432,347 kWh/yr.). A difference between the actual consumption and theoretical with ATLAS-FeliCity of about 22% is observed (Figure 8). This margin of error is acceptable (+/- 20%) because it allowed evaluating with some precision the savings achieved in the new renovation scenarios simulated after.

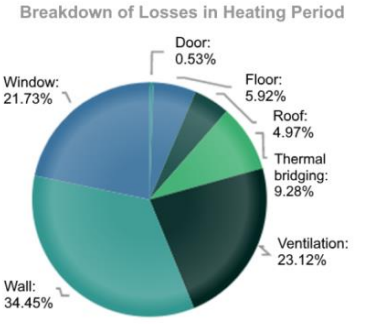

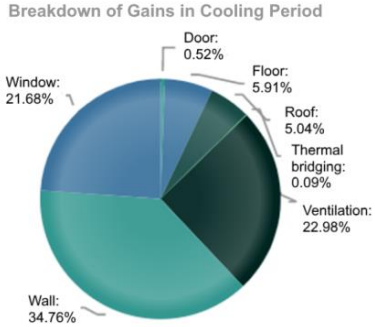

CURRENT ENERGY STATUS SCENARIO

Label	Value	Unit
Total Delivered Energy	138.70	kWh/m²yr
Total Delivered Thermal Energy	105.58	kWh/m²yr
Total Delivered Electricity	33.12	kWh/m²yr
Total Primary Energy	196.27	kWh/m²yr
Total Primary Thermal Energy	113.47	kWh/m²yr
Total Primary Electricity	82.79	kWh/m²yr
Total Delivered Energy	1,993,542.80	kWh/yr
Real consumption	2,432,347.00	kWh/yr
Difference between real and theoretical consumption	438,804.20	kWh/yr ---------> 22 %

Fig. 8: Gains and losses during the heating and cooling period before energy retrofits. Difference between actual and theoretical energy consumption calculated by the ATLAS-FeliCity DS tool for the total buildings analysed.

Based on the results of the current state, five different renovation scenarios were defined and the theoretical energy saving for each retrofit estimated. For each scenario a single renovation measure has been considered. In a second step, the individual scenarios were merged to see how much existing (theoretical) power consumption would be affected when multiple modernization measures are implemented at the same time and the cost of the intervention.

The simulated and assessed scenarios were:

- S1, Roof / Type of intervention: Rehabilitation of 6 roofs;
- S2, Window / Type of intervention: Refurbishment of 6 buildings with new windows;
- S3, Wall / Type of intervention: Façade insulation works on 8 buildings;
- S4, District Heating Network (DHN) / Type of intervention: 10 buildings connected to DHN;
- S5, Photovoltaic (PV) / Type of intervention: Installation of 10 PV plants in buildings.

Based on the results of the status-quo analysis, these five renovation scenarios were defined and the theoretical energy saving and investment need for each renovation were estimated. As the buildings are not listed under the heritage protection law, but on the protected city core ISOS (Federal Inventory of Swiss heritage sites of national importance), the building renovation must adhere, as much as possible, to thermal values defined in the Cantons Regulation on the use of energy (RUEn, 2008). Hence, the follow renovation measures have been assessed (Table 1):

Tab. 1: Case study Locarno (CH) – results of energy savings obtained by combining the individual scenarios.

Scenario, Building element	Status quo	Renovation target	Measures applied	Energy savings	Cost foreseen
S1, Roof	Current U-value of the roofs varies between 0.40 $Wm^{-2} K^{-1}$ and 0.61 $Wm^{-2} K^{-1}$	U value ≤ 0.23 $W m^{-2} K^{-1}$ to achieve an improvement of about 42% to 61%	Greater insulation to reduce the U-value of 6 roofs (restoration scenario applied only to buildings under a threshold U-value > 0.30 $W m^{-2} K^{-1}$).	52,600 kWh per year (ca. 3% of current total primary energy consumption)	232’600 €
S2, Window	Current U-value of the windows varies between 3.59 $Wm^{-2}K^{-1}$ and 2.50 $Wm^{-2} K^{-1}$	U value ≤ 0.80 $W m^{-2} K^{-1}$	New windows have been planned for 6 buildings. A limit U-value of 2.00 $Wm^{-2} K^{-1}$ was considered, as for historic buildings it already assumes a good energy performance.	184,000 kWh per year (ca. 9% of current total primary energy consumption)	93’256 €
S3, Wall	There are 8 buildings with not optimum wall insulation performances (U-value > 0.70 $Wm^{-2}K^{-1}$)	U-value ≤ 0.65 $Wm^{-2} K^{-1}$ with an improvement of about 30% to 57%	A thinner internal insulation layer (i.e. 10 cm internal insulation) was applied to the historic building.	264,000 kWh per year (ca. 13% of total primary energy consumption)	124’197 €
S4, DHN	Locarno City is planning to have a District Heating Network (DHN)	Non-invasive measures to improve the energy performance	The whole real estate park of buildings studied were selected to be connected to DHN.	341,000 kWh per year (ca. 8.5% of current total primary energy consumption)	- Cost cannot be calculated
S5, PV Plants	Under current regulations, PV systems may also be installed in historic buildings (*)	Implementation of renewable energy sources RES (PV). Total nominal power installed: 10 kWp	Installation of PV systems in the roof of all buildings studied. Self-sufficiency rate of about 4%, own consumption rate of about 87%. Total PV energy production is about 70,709.79 kWh per year.	70,700 kWh per year (ca. 14% of energy demand for auxiliary energy, lighting, and equipment; 2% of current primary energy consumption)	301,000 € (ca. 30,000 € each)

(*) Note: Only federal or cantonal listed buildings required the authorisation from the cultural heritage and landscape protection commissions.

As a result of the analysis, and combining the individual scenarios (Table 2), it was possible to observe that by intervening only on the building envelope – energy measures on roofs (S1), plus windows (S2) and walls (S3) – an energy savings of around 25% could be achieved. Through the S1+S2+S3 scenarios, approximately 500,000 kWh per year could be saved. If the connection to a district heating network for all buildings is considered an energy reduction of about 42% could be achieved (842,313 kWh per year). The best retrofit scenario, where scenarios S1+S2+S3+S4+S5 are combined, it is possible to see that the energy reduction is even greater. This result is achieved when a photovoltaic system is implemented on the roofs together with all previous measures that would further reduce the energy consumption of Locarno's building stock until the 46% (912,022 kWh per year).

Tab. 1: Case study Locarno (CH) – results of energy savings obtained by combining the individual scenarios.

	Actual energy status	**S1+S2**	**S1+S2+S3**	**S1+S2+S3+S4**	**S1+S2+S3+S4+S5**
Energy saved (kWh/yr.)		236,507	500,191	841,313	912,022
Total delivered energy (kWh/yr.)	1,993,543	1,757,036	1,493,352	1,152,230	1,081,521
Energy saving rate (%)		**12%**	**25%**	**42%**	**46%**

3.2 ATLAS-FeliCity DS Tool: Case Study Calavino, Madruzzo (Italy)

Calavino, one of the five fractions of the municipality of Madruzzo, is a historical village situated in the Valle dei Laghi in the Province of Trento (Italy). Is characterized by a historic city center with a rather homogeneous appearance, with traditional residential buildings whereof a large majority was built before 1860. Calavino has a high rate of vacant houses and as well as a high rate of non-refurbished buildings. A building stock analysis were already done in a preliminary project (Lucchi, 2018) where a specific datasheet for 220 private and public buildings gathered relevant information (e.g. location; construction period and constructive elements; typological aspects or building use and type, ownership; heritage value and legislation framework; conservation state; energy aspects, etc.). The data were then transferred and integrated into a GIS model software using two digital models (both derived from Light Detection and Ranging, LiDAR data), which were gathered from the GeoBrowser of the Province of Trento. The testing in the ATLAS-FeliCity tool included 216 buildings or building units of the historic centre. Of the buildings included are 84% built before 1860, 79% residential buildings; 75% not subject to conservation related regulations (only 5.7% are listed buildings, 17.2% have historical elements to be preserved); 16% abandoned or not used.

The study with the ATLAS-Feli-City tool aimed to identify these measures for retrofit and to investigate the energy savings potential of the historic building stock of Calavino. A further aspect was to compare the values of the baseline scenario of the FeliCity tool with those of the previous study. The preliminary study serves to input accuracy data on ATLAS-Felicity tool and only a few parameters were filled in automatically with default values. Thus, two baseline models in the Felicity tool were created: Calavino (with default U-values from ATLAS-FeliCity) and Calavino measured (with U-values from the preliminary study) with 216 buildings or building units. When doing a building stock analysis, it were useful to divide the building stock into different building groups or "archetypes" that share similar characteristics or according different attributes (e.g. listed buildings, in a conservation area, not listed, etc.). In case of Calavino the building stock is quite similar in terms of construction method, building age and building use, etc. It was useful distinguish the historic building stock between different intervention categories, in order to be able to tailor interventions to the heritage and conservation requirements (Figure 9). In that way different building groups (archetypes) were created: (I) historic buildings of the inner village of Calavino, (II) all buildings without historic value, (III) all listed historic buildings, (IV) all buildings with historic value and (V) buildings from 1860 and (VI) apartments from 1860. Additionally, a series of single buildings was studied more in detail.

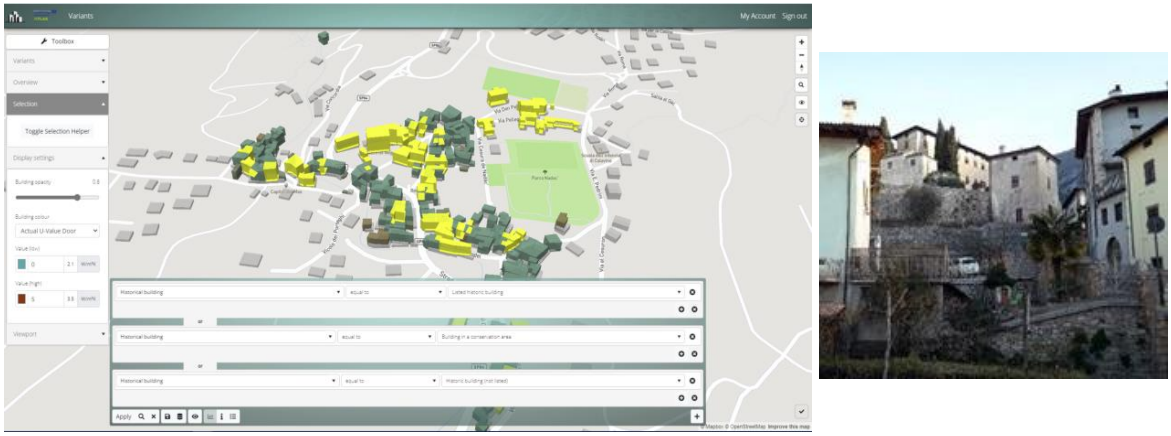

Fig. 9: Screenshot of ATLAS-FeliCity tool of Calavino´s historic center and view of the historical town of Calavino. Source: EURAC.

Figure 10 shows besides the "Absolute Energy Demand Breakdowns" also the share of losses and gains during the heating and cooling period per construction element before energy retrofit (all buildings studied, baseline scenario for 217 buildings). According to these results, the retrofit of the façades, but also of the windows, would have the greatest impact. Additionally, both would improve the airtightness and thus reduce the high ventilation losses. With regard the building services, the installation of a controlled ventilation system with heat recovery would decrease the ventilation losses even more.

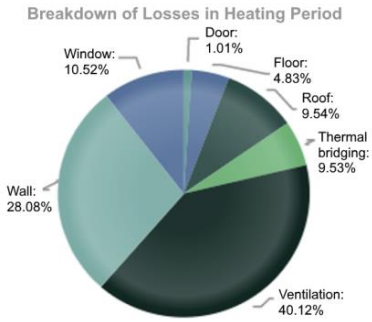

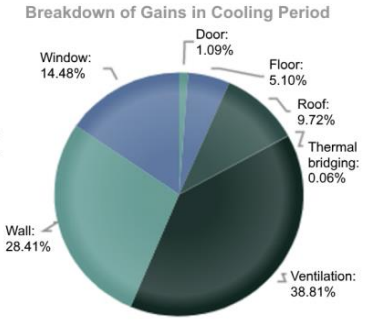

CURRENT ENERGY STATUS SCENARIO

Label	Value	Unit
Total Delivered Energy	389.24	kWh/m²yr
Total Delivered Thermal Energy	365.88	kWh/m²yr
Total Delivered Electricity	23.36	kWh/m²yr
Total Primary Energy	445.94	kWh/m²yr
Total Primary Thermal Energy	387.55	kWh/m²yr
Total Primary Electricity	58.40	kWh/m²yr
Total Delivered Energy	24,372,829.60	kWh/yr
Thermal energy demand (149 buildings)	329.84	kWh/yr
Real primary thermal demand	229.45	kWh/yr
Difference (149 buildings)	---------> 32%	

Fig. 10: Gains and losses during the heating and cooling period before energy retrofits. Difference between actual and theoretical thermal primary energy demand calculated by the ATLAS-FeliCity DS tool for 149 buildings analysed.

Furthermore, the heating energy demand was assessed for 149 selected residential buildings belonging to the biggest building group with the most common characteristics in terms of constructive techniques and materials. For this a stationary calculation method was elaborated using the software Passive House Planning Package (PHPP) version 9. From this calculation, from the 220 total number of buildings, were excluded all non-residential buildings, buildings built after 1860 and a few highly damaged buildings. Then, the energy demand for heating on building level calculated with the beta version of ATLAS-FeliCity, in kWh m^{-2} per year, has been compared with the results from the PHPP calculation for 149 buildings (329.84 kWh m^{-2} per year). The big difference of the preliminary staudy of the Calavina building stock based on PHPP and the results derived from FeliCity (initially 100.21 kWh m^{-2} per year) were assessed. Tendentially the results for energy demand calculated in PHPP are lower.An iterative process was used to identify and reconcile differences in the corresponding input data, for example, weather datasets. The aim was not to produce equivalent absolute values, but to have as sound database enabling the estimation of savings effects for the various measures. With the help of the in-depth analysis and the comparison of the two studies, the FeliCity tool could be significantly improved, especially for the application in the historic building stock.

4. Conclusions, remarks, and lessons learned

Energy Efficiency of Buildings as one of the key actions for the sustainable growth and the historic architecture of the Alpine region is a key factor for sustainable development in the social, ecological and economic sense. FeliCity-ATLAS Decision-Support (DS) tool has been developed and tested for some municipalities within the Interreg Alp ine Space ATLAS research project. That's include capitalizing and optimizing existing best practice solutions for

building refurbishment and regional development to increase number of high value renovations –considering historic and energetic aspects. The FeliCity-ATLAS DS-Toolkit provides a simplified digital twin version of the built environment to perform energy analysis at various spatial scales, that work as a hub for information from other activities developed during the project and will work as interlocking system, empowering municipalities to set the right course for building renovation strategies, balancing ecological, economic and social factors. The toolkit has been applied as pilot offline version to the ATLAS model regions (beta demo version applied to four municipalities), but will serve interface to later web-based 3D and BIM approaches as an offline tool with interface for later online web-based 3D and BIM approaches. This paper has shown results obtained for two demo sites, two historical city cores in the Alpine region: Locarno municipality (Canton Ticino, Switzerland) and Calavino (Madruzzo, Italy). The ATLAS-FeliCity tool has been proved to be very interesting and functional, as well as, easy to handle, in determining the possible renovation scenarios to be applied to the real estate parks studied. Within the tool it was possible to appreciate several very interesting functions such as the geo-localisation of the buildings within a map, or the possibility of filtering the different buildings by entering specific "attributes" (year of construction, U value, etc.) or by "archetypes" that share similar characteristics. Results obtained for the two locations were compared with previously in-depth studies and were possible to verify differences on calculations done with ATLAS-FeliCity DS tool in terms of actual consumption and theoretical delivered energy calculated (total delivered energy for Locarno building stock analysed or thermal primary energy demand, in the case study of Calavino). In the case study of Locarno municipality, it was possible to verify that the calculation of the energy balance in its initial state (before interventions) calculated by ATLAS-FeliCity tool is in line (+/- 20%) with the real energy consumption data (data from 2019) provided by the City of Locarno, which is very interesting. Different scenarios of retrofit at different scales (building or neighbourhood) can be simulated at the same time and key performance indicators (KPIs) were designed to enable the decision maker to assess the impact of the renovation interventions on the sustainability performance of historic buildings. ATLAS KPIs, implemented in ATLAS-FeliCity, that are specific for heritage buildings, shown if targets in terms of energy, CO_2 savings and payback periods are achieved.

5. Acknowledgments

Operation co-financed by the European Union, European Regional Development Fund, as part of the Interreg Alpine Space Programme 2014-2020 for the project "ATLAS, Advanced Tools for Low-carbon, high-value development of historic architecture in the Alpine Space" (ID n. ASP644). Swiss participation in ATLAS project is co-financed within the framework of the NPR (SECO) through the Regional Development Fund and coordinated by the Federal Office for Spatial Development (ARE).

6. References

Troi, A., 2011. Historic buildings and city centres, the potential impact of conservation compatible energy refurbishment on climate protection and living conditions. In: Int. Conf. Energy Management in Cultural Heritage 2011 Apr (Vol.2011)

Khoja, A., Danylenko, O., Polo López, C., Davis, A., and Essig, N., 2021a, *Socioeconomic Reflections on Historic Buildings Renovations: A Portrait of Rural Alpine Municipalities*, in *IOP Conf. Ser.: Earth Environ. Sci*, **863**, no. 1. DOI:10.1088/1755-1315/863/1/012001 (accessed 18.08.22)

EN 16883 - 2017-08 Conservation of cultural heritage - Guidelines for improving the energy performance of historic buildings, Comité Europeen de Normalisation, Brussels, Belgium, 2017.

Buda, A., et al., 2021. Conservation-Compatible Retrofit Solutions in Historic Buildings: An Integrated Approach. Sustainability, **13**, 2927. DOI: https://doi.org/10.3390/su13052927 (accessed 29.03.22)

Khoja, A., Eber, S., Hatt, T., Hass, F., Polo, C., Davis, A., Essig, N., Rieser, A., Kristan, M., 2020a. ATLAS Decision-Support Methodology (DS) for Sustainable Retrofitting of the Heritage Building Stock. Deliverable D.T3.4.1 Development of the ATLAS holistic decision-support methodology | Baseline for decision-support methodology (DS). Technical report ATLAS DOI: 10.13140/RG.2.2.14081.07528 (accessed 29.03.22)

Polo López,C.S., Khoja, A., and Hatt T., 2020. Deliverable D.T3.2.1 Methods for assessment and quantification of local renewable energy sources in the alpine space. Technical report ATLAS [Internet]:t.3.2.1_methods_for_assessment_and_quantification_low2.pdf (accessed 22.08.22)

Polo López, C.S. et al., 2021. *Strategies and tools for potential assessment of Renewables (RES) in Alpine Space*

areas valid for historic buildings and sites, in *IOP Conf. Ser.: Earth Environ. Sci*., **863**, no. 1. DOI: 10.1088/1755-1315/863/1/012007 (accessed 18.08.22)

Haas, F., Exner, D., Herrera-Avellanosa, D., Hüttler, W. and Troi, A., 2021. *Making deep renovation of historic buildings happen learnings from the Historic Buildings Energy Retrofit Atlas*, in *IOP Conf. Ser.: Earth Environ. Sci*. **863**, no. 1. DOI: 10.1088/1755-1315/863/1/012017 (accessed 18.08.22)

Rieser, A., Leonardi, E., Haas, F., and Pfluger, R. 2021. A new decision guidance tool for the adoption of energy retrofit solutions in historic buildings, in *IOP Conf. Ser.: Earth Environ. Sci*., **863**, no. 1. DOI: 10.1088/1755-1315/863/1/012016 (accessed 18.08.22)

Khoja, A., Exner, D., Haas, F., Polo López, C.S., Curto, I., Gerbec, N., Kristan, M., 2021. Deliverable D.T3.5.1 – ATLAS Decision-Support Platform (DSToolkit) performed for model regions. Technical Report ATLAS [Internet]: https://www.alpine-space.org/projects/atlas/deliverables/d.t3.5.1_temp-muas-supsi-prc-eurac-final-version-compr.pdf (accessed 22.08.22)

Khoja, A., Essig, N., Erber, S., Krista, M., Hass, F., Davis, A., 2020b. Assessment Scheme Including KPI for the Assessment and Benchmarking the Sustainability of Historic Buildings. Technical report ATLAS [Internet]: http://rgdoi.net/10.13140/RG.2.2.34213.73445 (accessed 18.08.22).

Khoja, A., Davis, A. and Essig, N. 2020c Deliverable D.T3.1.1 and D.T3.3.1 Inclusive business models, co-benefits and socio-economic value in historic building renovation in the Alpine Space & Report of sustainable revitalization concepts and funding strategies. Technical report ATLAS.

PETRA - Platform for Energetic and Technical Retrofit in Architecture. Available online: http://www.petraweb.ch/ (Italian version, accessed 18.08.22).

BFE (2017) Energy Strategy 2050. https://www.bfe.admin.ch/bfe/en/home/policy/energy-strategy-2050.html

Boulouchos, K., Neu, U. et al., 2022, Swiss Energy System 2050: Pathways to Net Zero CO2 and Security of Supply. Basic report. Swiss Academies Reports 17, Swiss Academies of Arts and Sciences (a+), Bern, Switzerland, p.61, ISSN (online) 2297-1572 DOI: doi.org/10.5281/zenodo.6967084 (accessed 22.08.22).

Branca, G., Curto, I., Maltese, S., Tamborini, D., Mobiglia, M., Pereira Soares, C., 2019. Report Analisi e pianificazione risanamento parco immobiliare comune di Locarno, City of Locarno. Report SUPSI 2019.Buda, A., Gori, V., Jan de Place Hansen, E., Polo López, C.S., Marincioni, V., Giancola, E., Vernimme, N., Egusquiza, A., Haas, F., Herrera-Avellanosa, D., 2022. Existing tools enabling the implementation of EN 16883:2017 Standard to integrate conservation-compatible retrofit solutions in historic buildings, J. Cult. Herit., 57, 34-52, ISSN 1296-2074. DOI: https://doi.org/10.1016/j.culher.2022.07.002.

Branca, G., Colombo, L., Rudel, R., Tamborini, D., Strepparava, D., Ortelli, L., Thalmann, P., Flourentzou, F., Genre, J.L. and Kaehr, P., 2012. *Computer-based Tool PETRA For Decision-Making in Networks About the Maintenance and Renovation of a Mixed Building Estate*, Swissbau – ETH Zürich (Switzerland). Available online: https://repository.supsi.ch/6826/1/BRENET_Branca%20et%20al%20-%20Seite%2060.pdf (accessed 18.08.22).

ISOS, Ticino, Locarnese (Italian version), Republic and Canton Ticino, Volume 3 Locarno (2 volumes) 2010, 402 pages, Federal Office of Culture FOC No. 310. 626.VI. Available online: https://www4.ti.ch/fileadmin/DFE/DR-SL-COMMESSE/4376/F%20-%20ISOS_3965_Locarno.pdf (accessed 18.08.22).

Regulation about use of energy (RUEn, 2008). 740.110 Regolamento sull'utilizzazione dell'energia RUEn (del 16 settembre 2008). *Il Consiglio di Stato. della Repubblica e Cantone Ticino.* Available online (italian version): https://www.lexfind.ch/fe/it/tol/22799/versions/127804/it (accessed 18.08.22).

Lucchi, E., Exner, D., D'Alonzo, V., 2018. *Building-Stock Analysis as a method to assess the heritage value and the energy performance of an Alpine historical urban settlement*, International Conference on Energy Efficiency in Historic Buildings, Visby, 26-27 September 2018.

ISO 13790:2008 Energy performance of buildings — Calculation of energy use for space heating and cooling (revised by ISO 52016-1:2017), International Organization for Standardization ISO, Geneva, Switzerland.

Passive House Planning Package (PHPP), energy balance and planning tool for efficient buildings and refurbishments, http://passivehouse.com/04_phpp/04_phpp.htm (accessed 18.08.22)

PARTICIPATION POTENTIALS FOR ENERGY-ACTIVE FACADES IN FUTURE FLEXIBILITY MARKETS

Thomas Ramschak[1], Michael Gumhalter[1]

1 AEE INTEC, Feldgasse 19, 8200 Gleisdorf, Austria

Abstract

The global pathway to net-zero emissions by 2050 in the building sector requires significantly strengthening and successfully implementing energy and climate policies. Energy efficiency, electrification and flexibility of the stock are three main drivers of decarbonization of this sector. Still, without tackling the existing buildings, the building sector will not be fully decarbonized by 2050. To achieve cost savings and minimize disruption, retrofits need to be comprehensive, one-off, and able to transform buildings into active players in the energy system. A renovation concept based on energy-active façade and elements of flexibility markets (FM) are introduced to provide demand-side flexibility in existing buildings. Moreover, the work shows that the innovative business model, such as energy flexibility as a service, could play an essential role in engaging consumers and energy-related service providers.

Keywords: Energy active Facades, Flexibility Market, Active Demand Response, Sector Coupling

1. Introduction

Electricity systems are characterized by the fact that consumption and generation of electricity must occur simultaneously, and there must always be a steady balance of power. However, both supply and demand for electricity are fluctuating, and until recently, demand fluctuations were the main focus of attention (Villar et al. 2018). This paradigm is now changing because two-thirds of all energy needs must be generated from renewables such as wind, solar, geothermal, and hydropower with fluctuating capacity until 2050. Solar PV has to be increased 20-fold and wind power 11-fold from now (IEA 2021a). The energy generated from volatile renewable sources cannot be dispatched and is subject to significant variation and uncertainties. This has increased the complexity of operating the power system and requires new sources of flexibility as existing sources are no longer sufficient. Reducing global carbon dioxide (CO_2) emissions to net-zero by 2050 is in line with efforts to limit the long-term rise in global temperatures to 1.5 Kelvin. This requires nothing less than a complete transformation of how we will produce and consume energy at an unrivalled speed and scope which brings specific challenges but also opportunities for all energy sectors.

Exceptionally large potential can be found in the building sector, which today accounts for almost one-third of total final energy consumption. Furthermore, according to current building standards, almost 75% of that building stock is inefficient, and 85 % to 95 % of the existing buildings are still in operation in 2050 (European Commission, 2021). In any case, the energy consumption of the building stock needs to be tackled, which means both an increased speed and depth of building renovation. Comprehensive renovation must become the standard approach. Without this, the sector will not be fully decarbonized by 2050. The renovation wave aims to double the renovation rate by 2030 (European Commission 2020). Calculations have shown that the renovation rate must reach 3% per year as soon as possible before 2030 and be maintained until 2050 (Sibileau et al 2021).

Numerous studies have led to the development of new industrialized construction systems for building renovation. Calelgari et al. (2015), Ruud et al. (2016), Malacarne et al. (2016), Sandberg e al. (2016), Pittau et al. (2017) present modular and prefabricated façade elements, made of wood and lightweight components intended for the retrofitting of existing buildings, to improve the energy performance of the building. While the focus of all these studies is only on improving the thermal performance of the building envelope, thereby

© 2022. The Authors. Published by International Solar Energy Society
Selection and/or peer review under responsibility of Scientific Committee
doi:10.18086/eurosun.2022.02.08 Available at http://proceedings.ises.org

mainly reducing the energy demand of the building, other studies propose to have the façades become multifunctional.

Dermentzis et al. and Ochs et al. presents an exhaust air heat pump in combination with a ventilation system with heat recovery, both integrated into a prefabricated timber frame façade. Dugue et al. (2017) and Garay et al. (2017) describe a façade-integrated ventilation concept. Furthermore, Hejtmánek et al. (2017) presented prefabricated insulating panels, and new intelligent HVAC systems for the use of renewable energy sources. Hengel et al. (2020) studied prefabricated thermally activated curtain façades that offer the possibility to upgrade insulation and the heating system in one step, reducing residents´ disturbance during the renovation process. The proposed façade uses an integrated thermal active layer for heating and cooling purposes and can be mounted directly to the existing walls from the outside. Detailed energy analysis shows that the concept of external wall heating is suitable for a wide range of applications with various wall constructions made of concrete, vertical coring brick, or solid brick in typical existing buildings from the 1960s to 1980s. These systems can meet comfort criteria and, moreover, feature a heat dissipation which can be used for flexibility measures in interplay with the thermal mass of the building's walls (Gumhalter et al., 2021).

In a follow-up study, Gumhalter and Ramschak (2022) analyzed the flexibility potential in combination with on-site PV-systems. With a weather-based storage control system the thermal storage capabilities were used to exploit the optimization potential for self-consumption. For this purpose, an Active Demand Response Signal (ADR signal) was introduced, which provides the heat pump and the room temperature control with a charging signal based on the generation of the PV system. This control strategy, in conjunction with the building-integrated PV generator presented, leads to a weather-dependent, daily signal of 6 to 12 hours depending on the season. The study showed that this control strategy can drastically increase the renewable load cover factors for space heating from 25 % up to 77 % renewable energy share for space heating.

In this paper, the approach of active flexibility usage will be further investigated and an additional application field will be presented. This work focuses mainly on the evaluation of the provision of flexibility as a service for flexibility markets (FM). The common concept is to forecast potential constraint violations and the location of the respective congestion points and to determine locationally differentiated grid prices. If the flexibility of the building reacts to these price signals in a FM by changing its load profile, constraint violations can be indirectly avoided. In this case, the change in the load profile is not inevitably accompanied by a change in the behavior of the users. For example, if the building is confronted with a significant increase in the grid price, it will reduce its load and consequently purchase less energy from the grid. In contrast, if the building faces a decrease in the grid price it tries to increase its load by using the active façade to charge the storage capacity of the existing walls while maintaining the thermal comfort. Although the main intention is the provision of flexibility to a Distribution System Operators (DSO) or Transmission System Operator (TSO) in a FM through a uniform price signal, a numerical example provided in this paper illustrates the expected financial impact for the engaged end-user.

The paper is structured as follows. First, based on an energy flexibility quantification framework, the energy flexibility profile of a typical multifamily building studied in Gumhalter and Ramschak (2022) is quantified; secondly, according to the energy flexibility and a yearly day-ahead price curve of the electricity, a simple to implement control strategie is designed, aiming to minimize the end-user's electricity costs. Finally, the expected financial implications are illustrated in a series of numerical examples showing the impact of activating demand side flexibility.

2. Parameters for defining the flexibility of a building

To evaluate the flexibility potential of the active façade system, the sample building and a series of Key Performance Indicators (KPIs) is introduced in this chapter.

2.1. Sample Building

The building used for the experiments is based on a multi-family house in urban areas in Austria which is typical for the construction period between 1960 and 1980 and has already been described in detail in Gumhalter and Ramschak (2022). The experiments were carried out for a single thermal zone representing a 70 m² flat. While in Gumhalter and Ramschak (2022) the four most common building material types for these

unrenovated houses were analyzed, the focus in this study is on the building with reinforced concrete as existing walls with the specific properties summarized in Table 1. The entire building hull is considered to meet the numbers listed in Table 2 which leads to a maximum heating load in the observed dwelling of 1,255 W total, or 17.9 W/m² specific, which is based on the static method described in ÖNORM12831 (2018), a minimum annual ambient temperature of -12,2 °C (ÖNORM8110 2019) and a thermal zone temperature of 22 °C.

Table 1: Material-specific properties for the wall

Wall material	Thickness [m]	Thermal conductivity [W/mK]	Spec. heat capacity [J/kgK]	Density [kg/m³]
Ferro concrete	0.21	2.30	1000	2300

Table 2: Thermal heat transfer values of surfaces and corresponding areas

Envelope part	U-value [W/m²K]	Area in total building [m²]	Area in observed dwelling [m²]
Outside walls	0.15	392.7	49.3
Basement ceiling	0.17	227.4	0
Top floor ceiling	0.11	236.1	0
Windows (panes)	0.6	107.2	9.9
Windows (frame)	2.0	30% of window panes	30% of window panes

2.2. Characteristic load profiles

The characteristics of the heating process are important parameters for the utilization of flexibility. It can be described by two parameters. $Q_h$defined in eq. 1 represents the daily heat capacity transferred to the building via the active façade to maintain thermal comfort. The loading time t represents the duration required for this purpose.

$$Q_h = \int_0^t P_h dt \qquad \text{(eq. 1)}$$

Figure 1 shows heating (left) and cooling curves (right) and the aggregated curves (bold) for the observed dwelling, simulated with the building simulation software IDA ICE featuring a validated model of the active façade setup (EQUA, 2021). The heating and cooling power provided by the active façade system to the thermal zone shows a peak power of approximately 2200 W (≈45 W/m²) for heating and 1500 W (≈25 W/m²) for cooling due to transient behavior caused by the thermal mass (high temperature gradient between the heating/cooling medium and the wall material). The charging of the walls is mainly concentrated in time periods of four hours for the heating and ten hours for the cooling season. This time span should be taken into account when choosing the ADR signal in order to carry out the majority of the loading process within the times with the lowest energy prices.

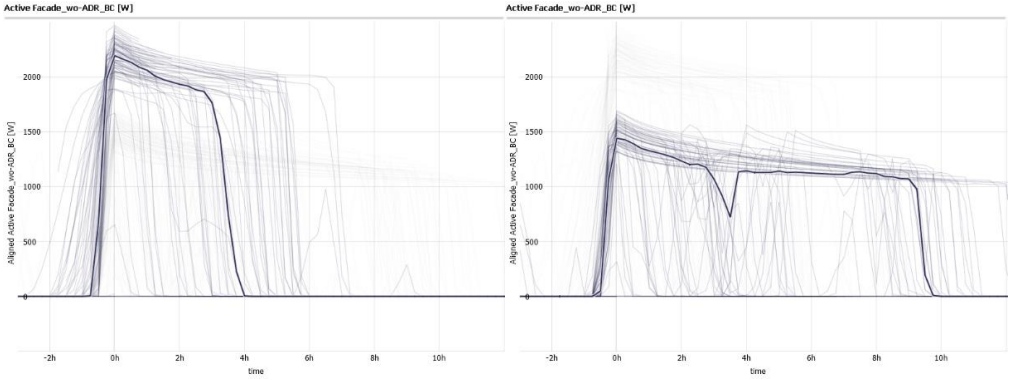

Figure 1: Aggregated heating (left) and cooling (right) curves showing the mean value for the observed dwelling.

2.3 Day-ahead price-based ADR-Signal

Modern building energy management systems, using smart technologies, connectable devices, sensors and smart meters, enable individual households to interact with the electricity grid and the energy market and optimize the operation. Business-model innovations, such as flexibility as a service, could play an important role in engaging consumers and energy-related service providers. For the Building operator, as well as for the end users, smart charging of the building's storage capacity is attractive mainly because it offers economic benefits by allowing controlled charging at times with low prices. This paper assumes that the building energy management system participating in smart charging reacts to prices by a central wholesale market; however, this scenario could also be applied for example to local energy communities with their own electricity market or an independent flexibility market where incentives would come directly from the TSO or DSO to support congestion management in the transmission or distribution grid.

The price information is retrieved exemplary for Austria. The overall day-ahead price on quarter hour values from August 2021 to July 2022 (APG, 2022) is plotted in Figure 2, showing a drastically increased day-ahead price. The statistical distribution in Figure 3 also shows the fact that prices vary significantly on a daily basis from, in average up to 83 €/MWh in August 2021 and 360 €/MWh in July 2022. The analysis of revenues for this business scenario, shown in chapter 3, should be considered as an illustrative exercise rather than a prediction of price trends over time.

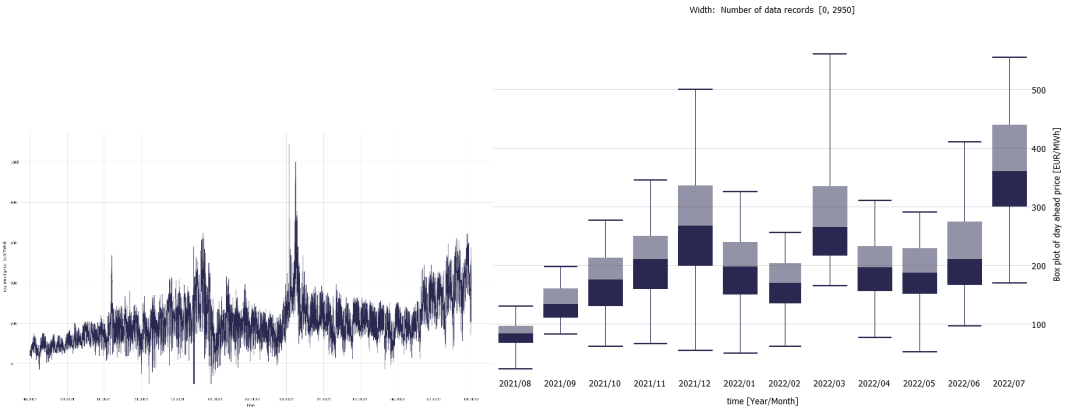

Figure 2: Day-ahead price in €/MWh from 08/2021 – 07/2022 (left), monthly bandwidth of the day-ahead price (max 97.5%, quantile 75%, mean, quantile 25%, min 2.5%) (right)

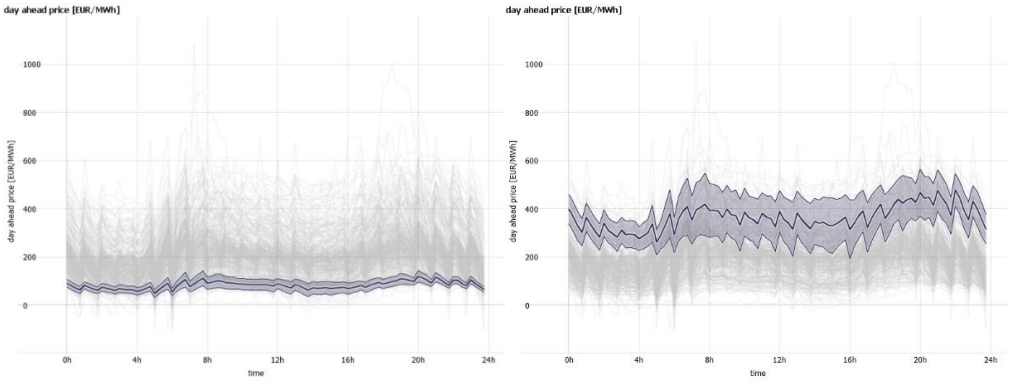

Figure 3:Daily day-ahead price curves for August 2021 (left) and July 2022 (right), the central curves show the aggregated mean curves with the boundaries with a standard deviation of 1.

In order to adapt to price signals on a flexibility market, a simplified mechanism was applied. Scenarios were defined that vary in the way the ADR signal is modified. As already described, the aim is to keep the electricity

costs for heating and cooling as low as possible. Instead of using an elaborate model predictive control, a simplified price based ADR control signal is identified. A charging proposal can be imposed on the smart controlled heating system depending on this ADR signal. To impose such ADR-signals (eq. 2) the quantile value of the mean day-ahead price for the next 24 hours is the basis. The ADR signal ($status_{ADR}$) is triggered if the actual price at actual time is below the 24-hour price quantile.

$$p_t < p_{qi} \rightarrow status_{ADR} = 1 \qquad \text{(eq. 2)}$$

The following four scenarios were defined: The ADR signal is active when the current price is below the value of the 24 h mean 50% quartile, 33% quartile, 25% quartile and 10% quartile based on the day-ahead price. If the ADR-signal is active a signal is passed to the zone controller which raises the room temperature set point by 1 K. This control strategy leads to an active loading of the thermal mass of the building envelope without having to intervene in the higher-level heating controls. Figure 4 shows the time periods and the corresponding day-ahead prices if active loading is forced. Conversely, this does not mean that heating or cooling is prohibited any other time if the comfort conditions are not met.

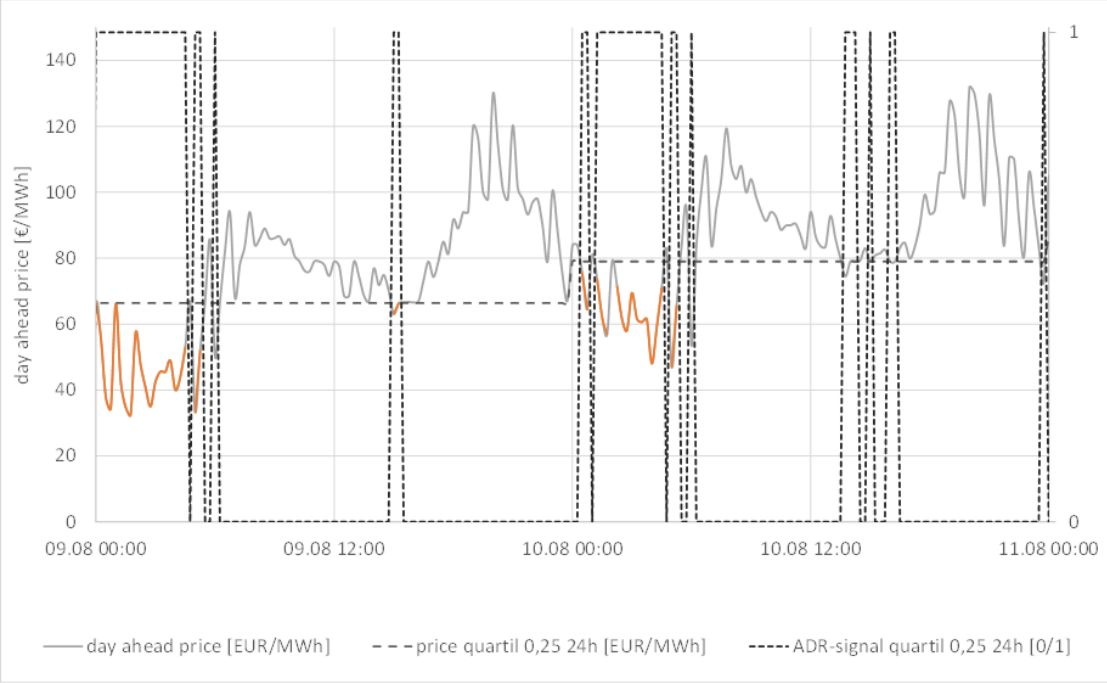

Figure 4: ADR-signal based on the day-ahead 25th empirical quartile

The On/Off ratio of the ADR-signal depends on the threshold values that are permitted, as also shown in Figure 4. While a positive ADR-signal occurs for an average of 12.3 hours per day for the 50 % quantile (q50), this duration is reduced to 8.3 hours for q33, to 6.3 hours for q25 and to 2.4 hours for q10. Comparing the load profile from chapter 2.2 with the average available On-periods of the ADR signal, it can be concluded that with a q50 signal, heating takes place at times with unnecessarily high prices. Similarly, controlling the heating with a q10 ADR signal would not be sufficient to heat only at times with the cheapest prices. Figure 5 shows the daily distribution of the ADR-signals for August 2021.While ADR-signals are distributed throughout the whole day at a quantile of 50 % (q50), the focus of the daily ADR-signals shifts slightly to night hours for smaller quantile ADR-signals. This shift to the night time is particularly pronounced in the winter months.

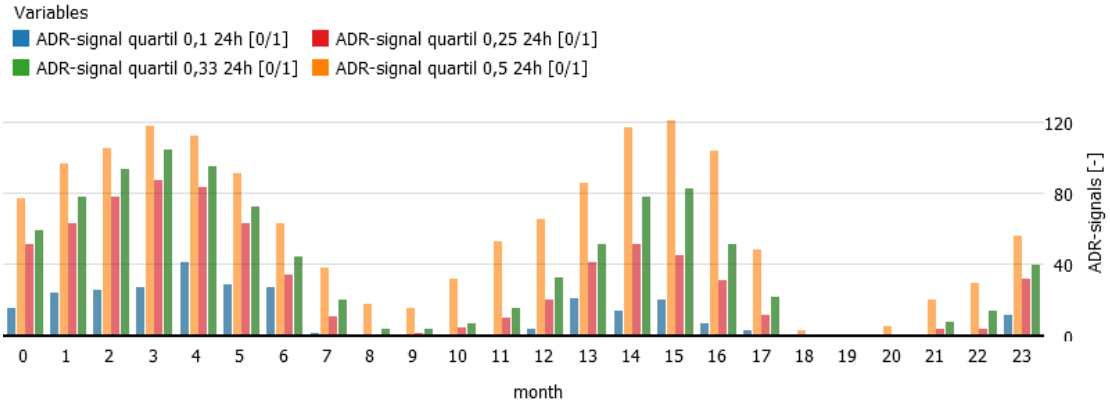

Figure 5 Distribution of ADR-signals over 24 hours

The simulation model provides the results (visualized in Figure 6) as electricity consumption profiles for every 15-min interval. In all scenarios a heat pump system with a constant COP of 3 for heating and cooling is considered. In the plot, the exemplary ADR-signal based on a 25 % quantile is represented by the light blue line, the façade´s energy consumption with standard control (without ADR-signal) by the red line, the façade´s energy consumption with ADR-signal by the green line and the electricity tariffs for the heat pump producing cold in this case as blue line. When comparing the electricity consumption, it becomes apparent how the facades shift their consumption into low price zones in response to the price (ADR) signal. To quantify the cost savings potential, we compare the resulting costs for different scenarios which are described in detail in chapter 3.

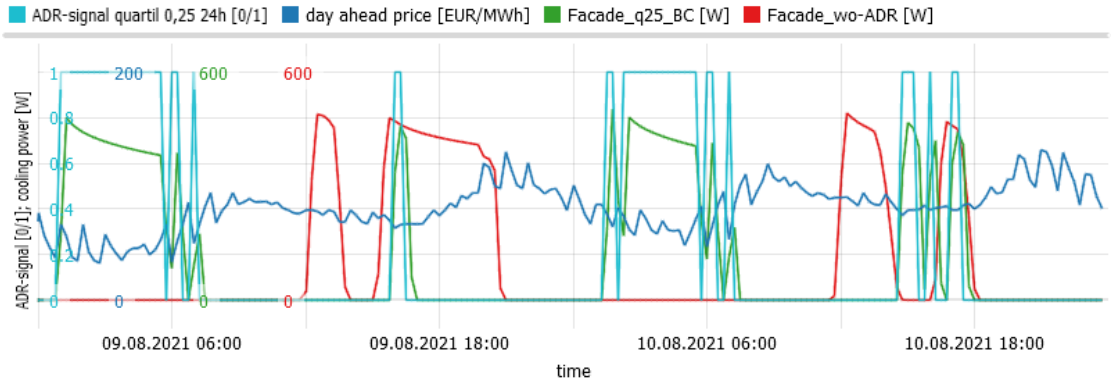

Figure 6: Shifting of cooling loads exemplary for the q25 ADR-signal

2.4 Structure storage capacity

To answer the question targeting the size of the flexibility potential, which could be offered as a service to a flexibility market, the evaluation of the flexibility related indicators is done for the observed dwelling. The structure storage capacity C_{ADR} (eq. 3) represents the amount of additionally stored energy during a positive ADR-signal compared to the reference scenario (with radiator heating system) over the duration t_{ADR}. With $\dot{Q}_{ADR}$ representing the energy flow provided by the energy active façade and $\dot{Q}_{Ref}$ representing the energy flow provided by a reference system. In the presented case the reference heating system is based on radiators for heating which are typically installed in existing buildings in the relevant construction period and a fan coil as fast-reacting cooling system.

$$C_{ADR} = \int_0^{t_{ADR}} (\dot{Q}_{ADR} - \dot{Q}_{ref})dt \qquad \text{(eq. 3)}$$

In Figure 7 the dynamic behavior of the fan coil system without ADR-signal (light blue line) is compared with

an active-façade-based system (orange line) influenced by the ADR-signal (red line) described in section 2.3. The cooling of the active-façade-based system mainly concentrates during the ADR On-periods. In contrast, the fan coil-based system shows a relatively constant behavior with peaks during the noon but without cooling interruptions in the night times. Calculating the daily utilized structure storage capacity according to eq. 3 for the active-façade-based system during the exemplary observation period (August 2021) results in the numbers displayed in Table 3.

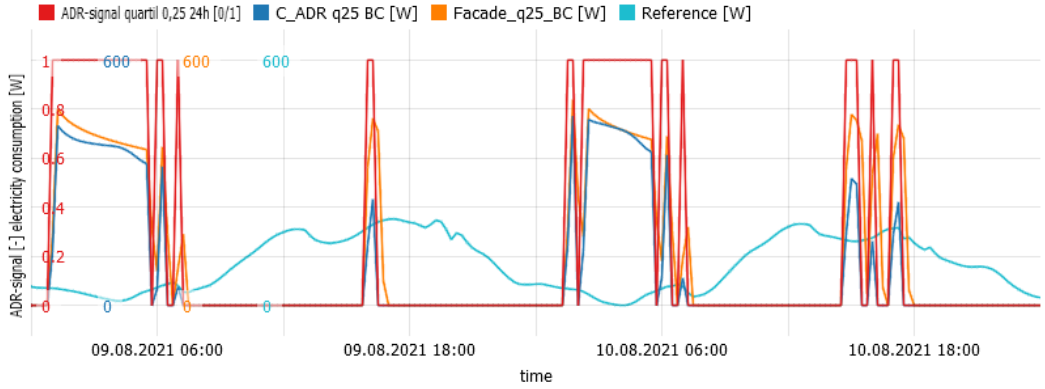

Figure 7: Comparison of space heating demand exemplary for the q25 ADR-signal

Table 3: Comparison of utilized structure storage capacity for cooling in August 2021

Szenario	MAX C_ADR $[Wh_{el}]$	MAX C_ADR $[Wh_{th}]$	Daily mean C_ADR $[Wh_{el}]$	Daily mean C_ADR $[Wh_{th}]$	spec. MAX C_ADR $[Wh_{th}/m^2]$	spec. Daily mean C_ADR $[Wh_{th}/m^2]$
Active façade q10	839	2516	593	1779	51	36
Active façade q25	2502	7507	1529	4588	152	93
Active façade q33	3061	9186	1667	5510	186	102
Active façade q50	3462	10387	2241	6722	210	136

Evaluating the same indicator for the heating in December 2021 reveals a maximum daily amount of stored energy of 5,6 kWh_{el} (16,9 kWh_{th}; 0,34 $kWh_{th,}$/m²wall) for the q50 scenarios. The remaining scenarios results are summarized in Table 4.

Table 4: Comparison of utilized structure storage capacity for heating in December 2021

Szenario	MAX C_ADR $[Wh_{el}]$	MAX C_ADR $[Wh_{th}]$	Daily mean C_ADR $[Wh_{el}]$	Daily mean C_ADR $[Wh_{th}]$	spec. MAX C_ADR $[Wh_{th}/m^2]$	spec. Daily mean C_ADR $[Wh_{th}/m^2]$
Active façade q10	1180	3540	832	2498	72	51
Active façade q25	2840	8520	1879	5638	173	114
Active façade q33	3663	10989	1912	5737	223	116
Active façade q50	5635	16904	2755	8267	343	168

To assess the business case from a technical perspective the aspect of flexibility response time to the trigger, or signal and the availability throughout the day and year can be analyzed. In general, the active façade is independent from the energy generation technology.
In the presented use case, a heat pump system is used, which is highly suitable for providing flexibility as it can be instantaneously switched on and off and can also be power modulated. The availability of flexibility is mainly constrained by the building´s energy demand.

Generally, the large storage capacity and the low heat losses of well-insulated buildings can provide flexibility for several hours throughout the day. Only the room temperature, which can rise during the day without an external energy supply due to passive solar gains, limits the flexibility in times of high irradiation, as the comfort limits may be reached. Power flexibility is higher in winter because of higher energy demand and higher temperature gradient between the heating medium and the external wall. However, the flexibility is also significant for cooling in summer.

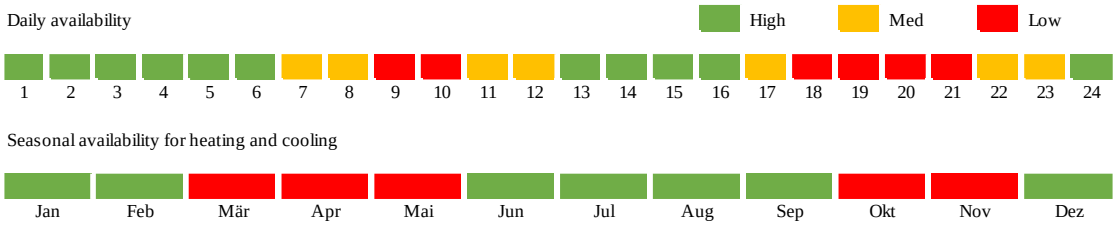

Figure 8: Availability of flexibility from active facades for heating and cooling throughout the day and year

3. Economic assessment

In order to illustrate the monetary benefits that could be gained by consumers in the building with energy active facades, the day-ahead price model has been applied in a set of experiments.

The prices for end customers are made up of different price components. A rough distinction can be made between energy costs, grid costs and taxes and fees. However, network tariffs and taxes are not considered in this study.

The economic scenario 0 represents the Reference (Ref) case with the radiator system and the fan coils, no flexibility deployed. Scenario 1 represents a system based on active facades but without ADR-signal. In scenarios 2 to 5 load shifting with the active façade based on ADR-signals is considered. Table 5 gives an overview of the scenarios. The resulting costs in each of these scenarios are summarized in Table 6 and Table 7 below. First the total electricity consumption for heating and cooling in the observed scenario are compared. Then the electricity cost in € and the savings in % are compared to the Reference case.

Table 5: Scenario overview

Scenario	Day-ahead price tariffs	Load shifting
0 Ref wo-ADR	Yes	No
1 Active façade wo-ADR		
2 Active façade q10		Yes
3 Active façade q25		
4 Active façade q33		
5 Active façade q50		

Table 6: Scenario results

Scenario	electricity consumption ADR_match [kWh]	electricity consumption ADR_mismatch [kWh]	ADR_match [%]	ADR_mismatch [%]	total electricity consumption [kWh]
0 Ref wo-ADR	-	486.31	0%	100%	486.31
1 Active façade wo-ADR	-	522.80	0%	100%	522.80
2 Active façade q10	168.26	342.16	31%	69%	510.43
3 Active façade q25	336.26	181.61	58%	42%	517.87
4 Active façade q33	376.08	144.40	65%	35%	520.47
5 Active façade q50	423.65	99.15	75%	25%	522.79

Table 7: Scenario results (2)

Scenario	electricity cost ADR_match [€]	electricity cost ADR_mismatch [€]	specific costs ADR_match [€/kWh]	specific costs ADR_mismatch [€/kWh]	total electricity costs [€]	Cost savings [%]
0 Ref wo ADR	-	105.0	-	0.22	105.0	-
1 Active façade wo-ADR	-	104.8	-	0.20	104.8	0.2
2 Active façade q10	20.6	73.1	0.12	0.21	93.8	10.7
3 Active façade q25	52.6	41.1	0.16	0.23	93.7	10.7
4 Active façade q33	62.6	33.7	0.17	0.23	96.3	8.3
5 Active façade q50	76.7	24.1	0.18	0.24	100.9	3.9

If a participation in a flexibility marked is assumed the active façade system is able to shift up to three quarters of the buildings heating and cooling demand in time for a q50 ADR-signal. This is reduced to approximately 31% for a q10 ADR-signal.

In the Reference Scenario the total costs sum up to 105.0 € per year. The active façade in the scenarios 1 to 5 reduce the overall cost. However. the profitability of smart charging depends heavily on the spreads of the actively used intraday prices. An ADR-signal making use of the lower 50 % price quantile leads to a very small cost reduction in comparison to the reference system, as the reference system also uses the full range of the lower costs and has a slightly lower total energy demand. But especially in the case of applying a stricter ADR-signal the costs for the end-user are reduced by 8.3 % in q33 Scenario and even by 10.7% in the q25 and q10 scenario.

4. Conclusion

In this paper, a renovation concept based on energy active facades has been proposed to enable the widespread adoption of FM.

The results of the load profile analysis showed, that in comparison to conventional heating system the characteristic is changed dramatically in heating power and daily heating duration due to the dynamic nature of the thermal capacity. Furthermore, the mean amount of thermal mass storage capacity that is utilized in day-to-day use, when applying active façade systems, is up to 0.168 kWh/m²wall, stored within active demand response signal period, which lead to an overall storage capacity of 22 kWh_{el} or 66 kWh_{th} on daily average for the entire building.

The proposed market model based on ADR signals was primarily considered to provide flexibility for the DSO in a FM. The approach is that flexibility is activated by spatial-temporally varying prices with associated ADR signals. A simple mechanism, the setpoint temperature increase, is used, which does not require any intervention from the higher-level energy management system.

A day ahead price was considered for the identification of the ADR signals by gradually using the lower limit values of the price signal for the activation. This is equivalent to prioritisation by the DOS, for example, in order to avoid bottlenecks. However, the general concept is also transferable to a smaller market, such as a renewable energy community that sets its community prices based on locally renewable energy.

Although the focus is on flexibility provision for the DOS, the numerical examples provided in this paper serve to illustrate the expected financial impact on the end user. Concludingly, the main benefit for end-users are cost savings of up to ten percent just from responding to volatile energy price signals. This is especially relevant regarding the latest developments on the energy markets which show even more range of fluctuation in daily business compared to the previous years.

Acknowledgement

The work was carried out as part of the "Sol4City" project and is funded by the BMK - Federal Ministry for Climate Action, Environment, Energy, Mobility, Innovation and Technology. (Project number FO999886948).

References

Austrian Power Grid AG. EXAA spot market prices. day-ahead prices of the AT bidding zone 2021. accessed 19 August 2022. [online] https://www.apg.at/de/markt/Markttransparenz/Uebertragung/EXAA-Spotmarkt

Callegari. G.; Spinelli. A.; Bianco. L.; Serra. V.; Fantucci. (2015) A Solar Timber Façade System for Building Refurbishment: Optimization Process through in Field Measurements. Energy Procedia 2015. 78. 291–296; doi: 10.1016/j.egypro.2015.11.641.

Cruz. M.R.M.; Fitiwi. D.Z.; Santos. S.F.; Catalão. J.P.S. (2018) A comprehensive survey of flexibility options for supporting the low-carbon energy future. Renew. Sustain. Energy Rev. 2018. 97. 338–353; doi: 10.1016/j.rser.2018.08.028.

Dugué, A.; Raji, S.; Bonnamy, P.; Bruneau, D. E2VENT: An Energy Efficient Ventilated Façade Retrofitting System. Presentation of the Embedded LHTES System. Procedia Environ. Sci. 2017, 38, 121–129; doi: 10.1016/j.proenv.2017.03.093

EQUA (2021) IDA ICE simulation software for indoor climate and environment. EQUA Solution AB. Sweden

European Commission (2020). Communication: A Renovation Wave for Europe – greening our buildings. creating jobs. improving lives. p. 3.

European Commission (2021). DIRECTIVE OF THE EUROPEAN PARLIAMENT AND OF THE COUNCIL on the energy performance of buildings (recast)

Garay, R.; Arregi, B.; Elguezabal, P. Experimental Thermal Performance Assessment of a Prefabricated External Insulation System for Building Retrofitting. Procedia Environ. Sci. 2017, 38, 155–161; doi: 10.1016/j.proenv.2017.03.097

Gumhalter M.; Hengel F.; Ramschak T. (2021) Sanierung von Geschoßwohnbauten mit thermisch aktivierten Fassaden – Bestimmung des Flexibilitätspotentials. e.nova 2021/2022 Pinkafeld Tagungsband. ISBN: 978-3-903207-64-6

Gumhalter M.; Ramschak T. (2022) Flexibility Potential of Prefabricated Façade Elements with Integrated Active Layer. ISEC Graz

Hejtmánek, P.; Volf, M.; Sojková, K.; Brandejs, R.; Kabrhel, M.; Bej˘cek, M.; Novák, E.; Lupíšek, A. First Stepping Stones of Alternative Refurbishment Modular System Leading to Zero Energy Buildings. Energy Procedia 2017, 111, 121–130. doi:10.1016/j.egypro.2017.03.014

Hengel F.; Ramschak T.; Gumhalter M.; Venus D. (2020) Showing new concepts with thermal activated prefabricated facades for retrofitting residential buildings. BauSim 2020 Graz. doi: 10.3217/978-3-85125-786-1-01

International Energy Agency. 2021a. Net Zero by 2050 – A Roadmap for the Global Energy Sector

International Energy Agency. 2021b. World Energy Outlook 2021

Ochs. F.; Siegele. D.; Dermentzis. G.; Feist. W. (2015). Prefabricated Timber Frame Façade with Integrated Active Components for Minimal Invasive Renovations. Energy Procedia. 78. Doi: 61-66; 10.1016/j.egypro.2015.11.115

Radl. J.; Fleischhacker. A.; Revheim. F.H.; Lettner. G.; Auer. H. (2020). Comparison of profitability of PV electricity sharing in renewable energy communities in selected European countries. Energies 13 (19). 5007. doi: 10.3390/en13195007

Ruud. S.; Östman. L.; Orädd. P. (2016) Energy Savings for a Wood Based Modular Pre-fabricated Façade Refurbishment System Compared to Other Measures. Energy Procedia 2016. 96. pp. 768–778.

doi: 10.1016/j.egypro.2016.09.139

Malacarne. G.; Monizza. G.P.; Ratajczak. J.; Krause. D.; Benedetti. C.; Matt. D.T. (2016) Prefabricated Timber Façade for the Energy Refurbishment of the Italian Building Stock: The Ri.Fa.Re. Project. Energy Procedia 2016. 96. pp. 788–799. doi: 10.1016/j.egypro.2016.09.141

Sandberg. K.; Orskaug. T.; Andersson. A. (2016) Prefabricated Wood Elements for Sustainable Renovation of Residential Building Façades. Energy Procedia 2016. 96. pp. 756–767. doi: 10.1016/j.egypro.2016.09.138

Österreichs E-Wirtschaft (2021). stromgrosshandel-preisentwicklung-und-wesentliche-einflussfaktoren-update-und-ergaenzung. accessed 01 May 2021. [online] https://oesterreichsenergie.at

Pittau. F.; Malighetti. L.E.; Iannaccone. G.; Masera. G. (2017) Prefabrication as Large-scale Efficient Strategy for the Energy Retrofit of the Housing Stock: An Italian Case Study. Procedia Eng. 2017. pp. 1160–1169. oi: 10.1016/j.proeng.2017.04.276

Sibileau. H.; Broer. R.; Dravecký. L.; Fabbri. M.; Álvarez. X.; Kockat. J.; Jankovic. I. (2021); Deep Renovation: Shifting from Exception to Standard Practice in EU Policy. BPIE (Buildings Performance Institute Europe)

Villar. J.; Bessa. R.; Matos. M. (2018) Flexibility products and markets: Literature review. Electr. Power Syst. Res. 2018. 154. 329–340. doi: 10.1016/j.epsr.2017.09.005

D. Solar Domestic Hot Water and Space Heating

100 % Solar Heating with Seasonal Thermal Storage, Solar Thermal Collectors, PV, and Heat Pump

[1]Florian Ruesch, [1]Fabio Lichtensteiger, [1]Kanchan Bohara, [2]Luca Brauchli, [2]Sebastian Ammann, [2]Willy Villasmil, [2]Jörg Worlitschek and [1]Michel Y. Haller

[1]SPF Institute for Solar Technology, Eastern Switzerland University of Applied Sciences (OST), Rapperswil (Switzerland)

[2]Institute of Building Technology and Energy, Lucerne University of Applied Sciences and Arts (HSLU), Horw (Switzerland)·

Abstract

In this contribution, the concept of 100 % solar-heated multifamily buildings with seasonal water storage is analyzed and optimized. Simulations of the system have been implemented in TRNSYS and were calibrated with measured data from the first winter of a real building with 160 m^2 of solar thermal collectors and a water seasonal thermal energy storage of 110 m^3. In a second step, this system has been complemented with photovoltaics and a heat pump with different heat sources. Parameter variations to optimize sizing of the collector field, the PV area, the storage volume, and the heat pump size were carried out and the corresponding investment costs were estimated. Furthermore, shower heat recovery systems were included in the simulations to estimate their potential to further reduce the size of the storage tank.

The most promising combination of solar thermal collectors, PV-system, heat pump, and shower heat recovery resulted in a 40 % reduction of the required storage volume compared to the original standard system and reduced the investment cost by about 15%. This "combined system" not only covers the heat demand of the building but is also able to cover part of the electricity used by households and feed some excess electricity into the grid.

Replacing all solar thermal collectors by PV and combining the PV and heat pump system with direct electrical heaters was not favorable compared to the combined system described above and was only possible with larger tanks and heat pump sizes. But when increasing the hypothetic solar roof area from 160 m^2 to 210 m^2, PV only systems became attractive. With increased PV sizes combined with heat pumps and direct electrical heaters, the needed storage volume could be further reduced to 33 m^3 and the investment cost to 65.6 % compared to the original standard system. However, contrary to the combined systems, no excess electricity was fed to the grid in the case of 100 % PV system configurations.

Keywords: Seasonal thermal energy storage, thermal autarky, solar thermal, PV, heat pump, shower heat recovery

1. Introduction

The energy strategy 2050 that was issued by the Federal Council of Switzerland requires a tremendous increment in renewable heat and electricity supply to meet the demand of different end-use sectors. The final energy consumption of Switzerland in 2020 was 747.9 PJ of which around 29.3 % was consumed by the private household sector (Bundesamt für Energie, 2022). Out of that total energy consumed by private households, around 80 % of the energy was consumed to meet the demand for space heating and domestic hot water, and almost half of the energy demand in private households (49.6 %) was met by the supply of fossil fuels (mainly heating oil, natural gas, and coal) (Kemmler and Spillmann, 2021). The replacement of these largely fossil-based heat supply systems is a main concern of the energy strategy 2050. Renewable energies, such as solar energy, are considered to have a high potential in this context. However, solar energy shows a pronounced seasonality with a high supply in summer and a low supply in winter. Therefore, the coincidence of low solar energy generation and high heating demand during the winter season leads to the requirement for affordable seasonal thermal energy store (TES) technology.

There are several examples of fully solar heated multifamily buildings MFB in moderate climates, which use solar thermal collectors (STC) only. Contrary to the widely reached net zero electricity concepts, thermal autarky can only be reached with seasonal TES. Large seasonal water storages, the state of the art for such concepts, induce elevated levelized cost of energy storage (LCOES). Additionally, for the concept investigated here, they occupy

© 2022. The Authors. Published by International Solar Energy Society
Selection and/or peer review under responsibility of Scientific Committee
doi:10.18086/eurosun.2022.03.01 Available at http://proceedings.ises.org

valuable space within the building. In such systems, STCs are used to heat the TES to temperatures close to 100 °C in summer. However, the efficiency of thermal collectors in winter is strongly reduced due to low irradiation and cold outdoor temperature. In order to still achieve significant winter heat production, collector fields are usually sized in a way that the TES is already fully charged in spring. This leads to heat rejection or stagnation in summer. On the other hand, PV modules deliver electricity also with low irradiation conditions, profit from cold temperatures in winter, and reach similar area-specific efficiencies for producing heat when combined with heat pumps (HP). Since standard heat pumps are not able to reach elevated temperatures to fully charge the TES in summer, a combination with STC for this purpose is advantageous.

Along with that, energy efficiency measures like the shower or drain water heat recovery (HR) systems result in a significant saving in hot water demand. There is a possibility of reducing the useful energy expenditure for shower water heat by at least 30 % under standardized boundary conditions (Passivhaus Institut, 2020).

This contribution analyzes and optimizes the cost and storage volume of fully solar heated MFB by combining STC, PV, and HP. Furthermore, the potential of HR to optimize these systems is analyzed. Additionally, these combined STC, PV and HP systems are compared to PV systems with HP and direct electrical heating (DEH).

2. Methodology

The analysis was based on a real multifamily solar home, built by Jenni Liegenschaften AG in Huttwil, Switzerland. It consists of four floors with two apartments on each floor (total living area of 1100 m^2), seasonal TES with 110 m^3 volume, and 160 m^2 of roof area used for STC. This building was monitored and served as a reference case for the dynamic simulations.

4.1. Simulations

The simulation software TRNSYS was used to model the building as well as the thermal system. The modelling of the building was done with “Type 56” (SPF-OST, 2021). Some simplifications of the geometry were done by implementing the building (see Fig. 1). In addition, the window opening and shading behavior were taken from the reference building described in detail in (Mojic et al., 2019).

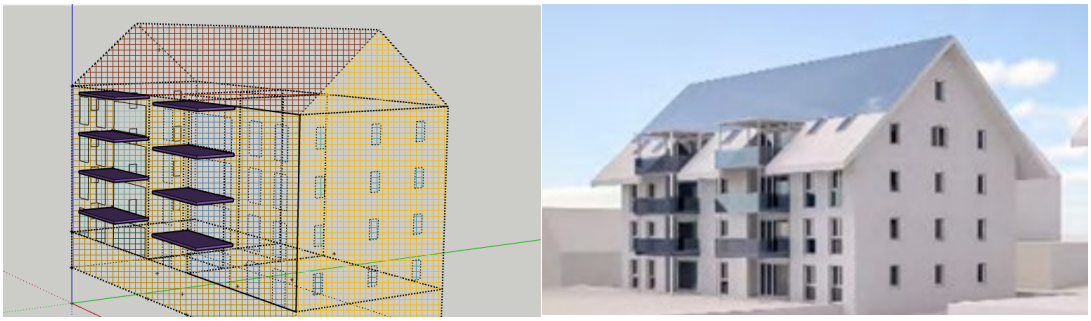

Fig. 1 Simplified building model in TRNSYS3d/Sketchup (left) compared to the detailed architectural representation (right, source: Jenni Liegenschaften AG)

Hot water profiles, household electricity consumption and internal thermal gains were used from the same reference MFB, which was created based on the monitoring data and the results of the ImmoGap project (Mojic et al., 2018). A detailed piping model was simulated with short timesteps in order to estimate the reduced consumption of DHW during showering when a HR system was present. The combination of the real piping sizes of the building and the measured parameters of a good central shower heat recovery unit (Passivhaus Institut, 2020) resulted in a reduction of 23.6 % of the total DHW consumption. Adapted DHW profiles were used to implement this reduced DHW demand into the annual simulations. Weather data from the village of Wynau (the closest SIA weather station near Huttwil) in Switzerland was used in the simulations. These combinations resulted in space heating demand of 10.2 MWh and a DHW demand of 12.9 MWh.

Fig. 2 is based on the hydraulic scheme of the reference MFB in Huttwil with the solar loop (yellow) the DHW preparation (blue) and the floor heating loop (purple). The existing system of Huttwil was complemented for simulation purpose with a heat pump (green). Different sources such as outside air, ground collector, Air PVT

and an activation of the foundation plate of the building were simulated. The hydraulics with the foundation activation is shown in brown color. For the simulation of a simpler system, some of the loops were kept inactive.

The following models were used for the simulation:

- Solar collectors were modelled using an adapted version of the "dynamic collector model by Bengt Perers" (Haller, 2012) with $\eta_0 = 0.825\ [-]$, $a_1 = 3.13\ [W/(m^2K)]$ and $a_2 = 0.0152\ [W/(m^2K^2)]$. Collectors were south oriented with an inclination of 40°.
- A stratified plug flow model by (Haller and Carbonell, 2013) was used to model the TES.
- The energy system was coupled to the building by detailed floor heating model (Battaglia, 2017). The same floor heating type was coupled to a simplified 2D ground model, to model the foundation plate as source for the HP.
- A characteristic curve-based HP model (Haller, 2015) was used and linearly scaled for variable sizes. Parametrization was done based on a real HP with a COP of 4.47 (A0W35) for air source and 4.79 (B0W35) for brine source HPs. In both cases the HP was limited to 60° water supply temperature from the condenser.

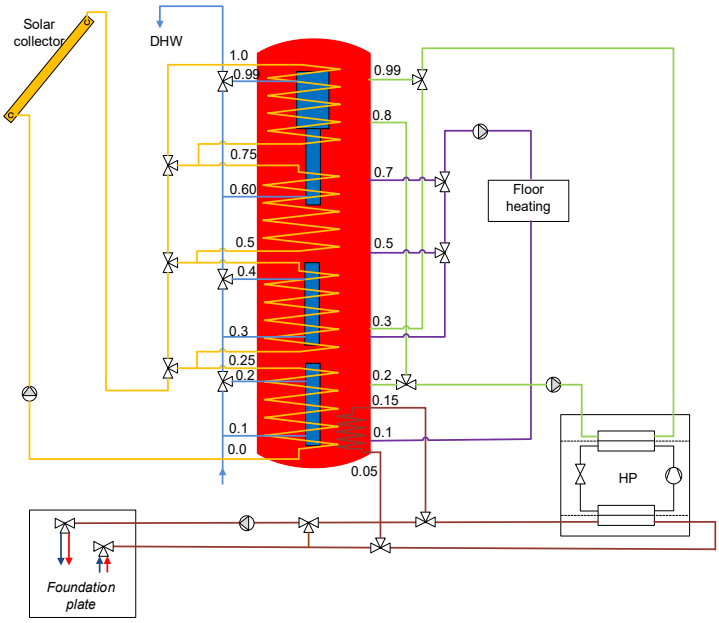

Fig. 2 Hydraulic scheme used for system simulations, a variant with foundation plate as a heat source for brine-to-water HP and as a sink for excess thermal gains in Summer

For the solar charging of the TES, the heat exchanger that is lowest in the tank was used with priority and further exchangers were added in series when the return temperature of the collectors increased over the TES temperature at the according height. In the reference system, an hourly volume flow rate of 43 l/(m²h) was used, respective to the collector area. Because of the increasing pressure drop, when several heat exchangers were operated in series, the flow rate was lowered down to 25 l/(m²h). The heat pump was controlled by the PV production and was only operated with self-produced PV electricity. Therefore, the HP was modulated. Like the STC system a priority was set to the charging of the lower storage volume. Only when the temperature in the top of the TES dropped below 55 °C the HP switched to DHW mode.

3. Results

4.2. Comparison of monitoring and simulation

A monitoring system was installed in the MFB in Huttwil, monitoring the main energy flows and the temperatures in the seasonal storage in detail. In the first year of operation, only one of the eight apartments was inhabited, wherefore the DHW and, to some extent, the heating demand was not yet comparable to the designed use case. Nevertheless, monitoring data of the first year of operation was used to validate the simulations of the seasonal water storage. For this purpose, the measured load for DHW and floor heating and the inputs of the solar collector were integrated into the simulation. By simulating only the TES and the connecting hydraulics, a high agreement of measured and simulated data was confirmed (see Fig. 3).

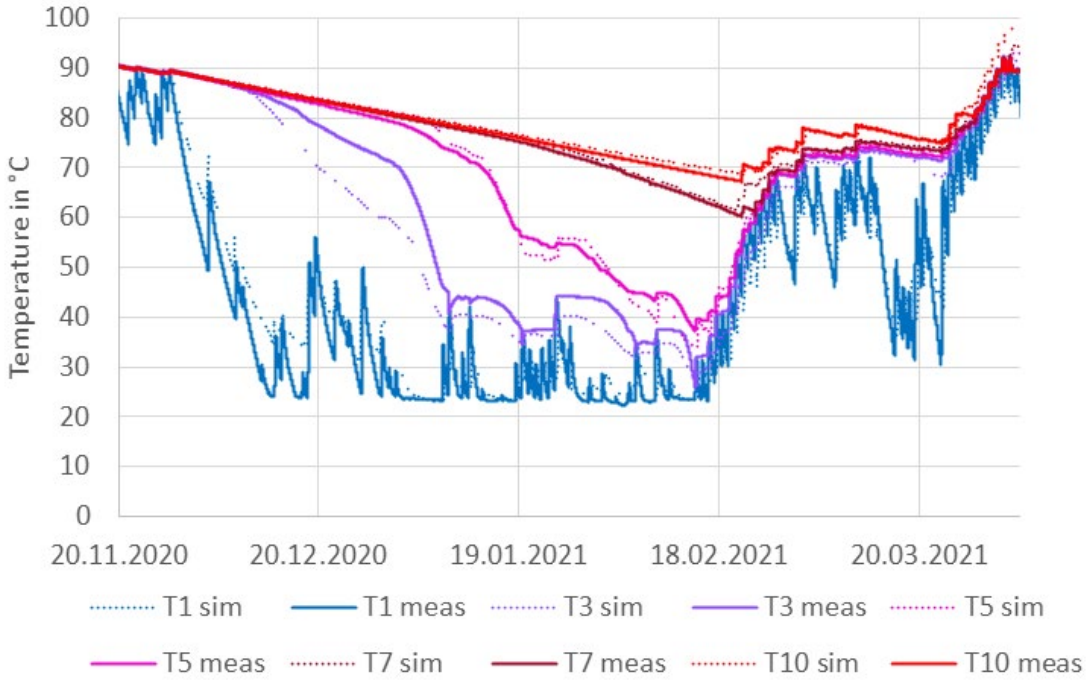

Fig. 3 : Comparison of measurements with a simulation of the TES combined with measured loads. Positions T1 to T10 are equally distributed from the bottom to the top of the tank

4.3. Reference system with only solar thermal

In Fig. 4, the temperature evolution in the seasonal TES is given for the standard system with 160 m^2 STC and a TES volume of 110 m^2. For the selected boundary conditions, in combination with the weather data of the location Wynau the standard system needed an additional (virtual) auxiliary energy input of 135 kWh (<0.5 % of the final energy demand) to fulfill the requirement of always reaching 55 °C DHW temperature (as required by the Swiss standard (SIA 385/1, 2020) at the outlet of the TES. For the evaluation of other system variants, this 99.5 % instead of 100 % solar fraction was taken as a benchmark. When the virtual auxiliary need was lower than this benchmark, the system variant was selected to be equivalent or better than the standard system.

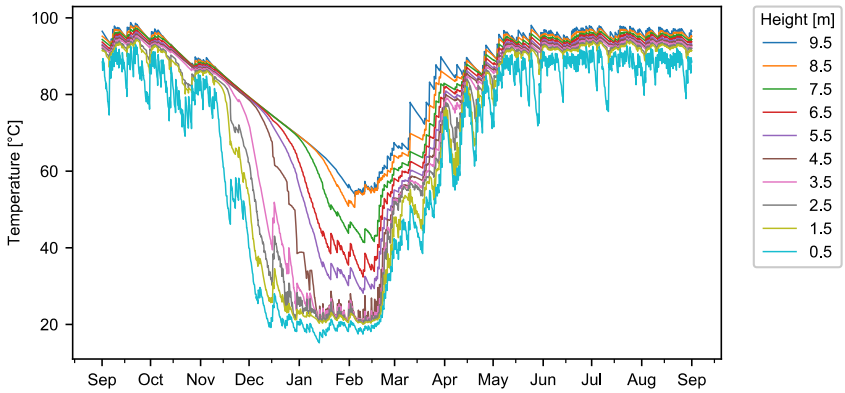

Fig. 4 Temperature evolvement at different heights of the seasonal TES from the simulation of the standard system with solar thermal collectors only

Based on the findings from the OPTISAIS project (Villasmil et al., 2021), a low flow controls (12.5 l/(m^{2}h)) was used to optimize the reference system. With this low volume flow strategy, the storage volume could be reduced to 99 m^3 (-10% compared to reference TES volume). However, permanent low flow control also can cause incomplete loading of the storage during the summer months. Therefore, a combined control strategy was implemented, with high flow in summer, but switching to low-flow when the temperature at the bottom of the TES dropped below 60 °C. With this combined control strategy (a low-flow in winter and a high-flow in summer), the storage volume could be reduced by 20 % (to 88 m^3) without increasing virtual auxiliary demand compared to the reference system (see Fig. 5).

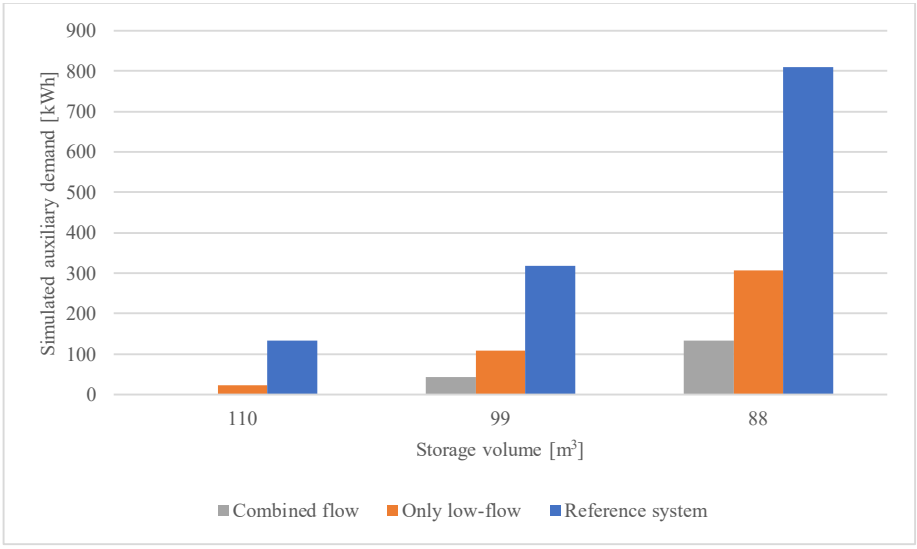

Fig. 5 Comparison of simulated auxiliary demand with different control strategies of the volume flow rate, depending on the storage volume

4.4. Solar thermal, PV, and air-source HP system

Based on the reference system with optimized control, a PV system, coupled to an air-to-water HP, was added to the system and different parametric studies were performed. The constraint on useable roof area of 160 m^2 was kept constant and shared between PV and STC. However, the PV roof area share, different HP sizes and the TES volume were varied. All the systems with virtual auxiliary demand of less than the benchmark of 135 kWh are performing better than the reference system with standard control and are therefore valid alternatives. For the combination with an air-source heat pump, the storage volume could be reduced by a maximum of 30 % (77 m^3) with 40 m^2 PV, 120 m^2 of STC, and 10 kW HP (see Fig. 6). This system not only delivers more than 99.5 % of the heating demand of the building based on local solar resources, but also directly covers around 19% of the household electricity and additionally feeds more than 2 MWh of electric energy to the grid.

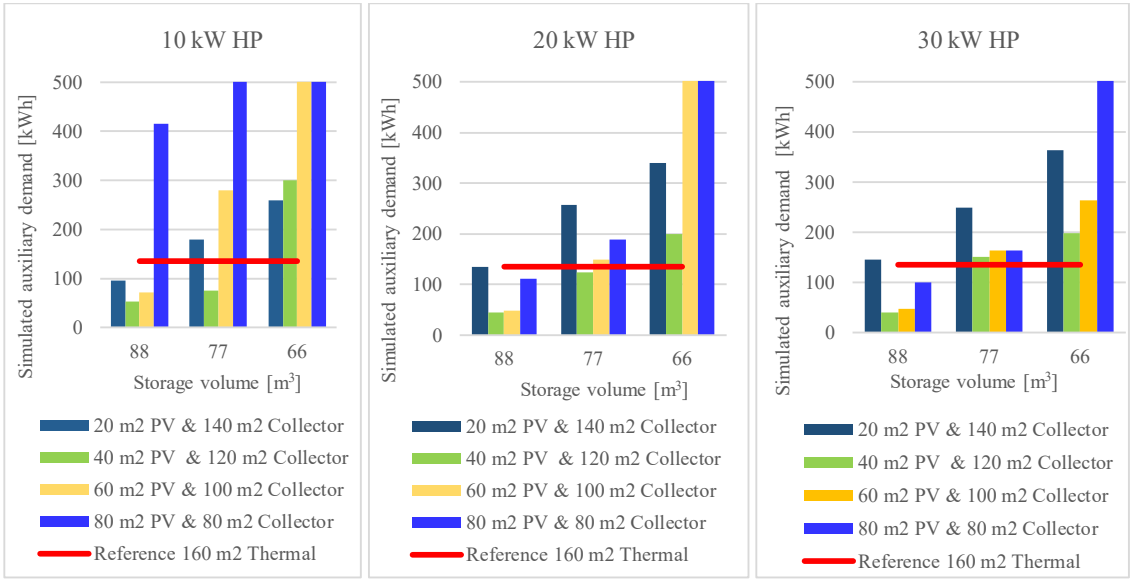

Fig. 6 Simulatedauxiliary demand of the reference system implemented with PV and air-to-water HP with different storage volumes and without HR unit.

4.5. Solar thermal, PV, and HP with foundation plate as a heat source

The combination of the original system with a HP which uses the thermally activated foundation slab of the building as a source was simulated as an alternative to the air-to-water HP system. The foundation plate must be actively regenerated with the unused solar heat during summer months to prevent it from cooling down in the long term. In this case, only systems which achieved a regeneration >100 % were considered as long-term stable system. Systems with less than 100 % of regeneration are likely to face a decrease of their performance under long term operation and were not considered for the comparison.

Fig. 9 shows the maximum possibility of reducing the storage volume as a result of different combinations of PV, STC and HP sizes, when the constraint on the roof area of 160 m^2 is maintained. With brine-to-water HP and foundation slab source, the storage volume could be reduced to 77 m^3 (30 %) using 60 m^2 PV, 100 m^2 STC and a HP of 10 kW. This system covers not only more than 99.5% of the heating demand, but also directly 23 % of the electric household demand, and additionally feeds 4.1 MWh of electrical energy into the grid.

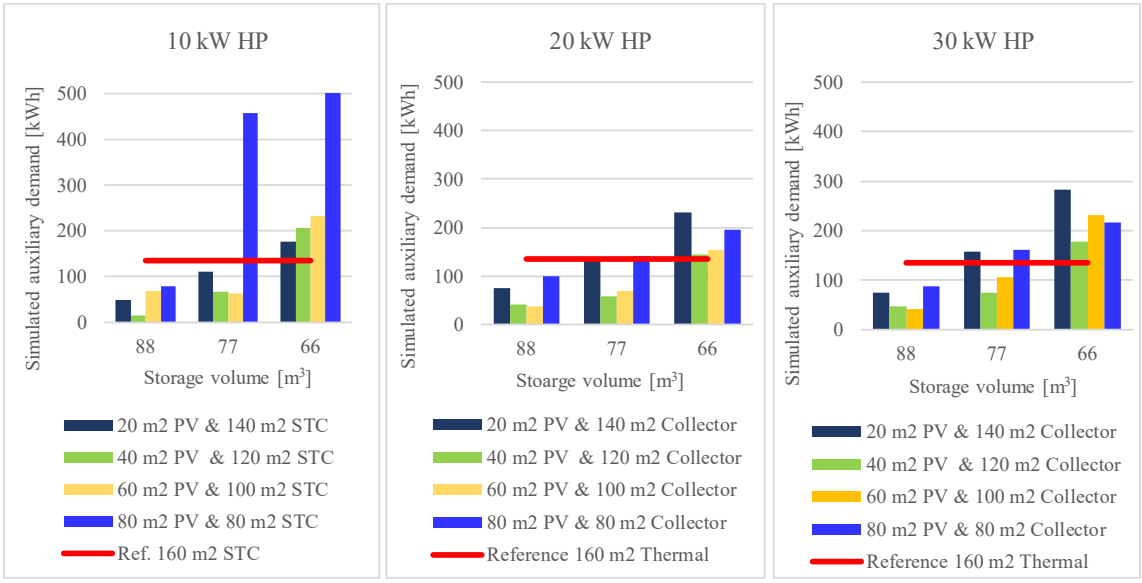

Fig. 7 Simulated auxiliary demand of the reference system implemented with PV and brine-to-water HP with the foundation plate together with different storage volumes, without HR unit.

4.6. Heat recovery

By including a DHW HR unit, the storage size for the combined systems could further be reduced. In the case of a combination with an air source system, a reduction to 66 m^3 was possible only in the case of a 10 kW HP, 40 m^2 of PV and 120 m^2 of STC (see Fig. 8). Similar results were obtained for the system with a HP and the foundation plate as a source. In this case a reduction of the storage size to 66 m^3 was possible for different combinations, where a 20 kW HP, 60 m^2 PV and 100 m^2 STC was the most promising one (these graphs are not shown in this paper).

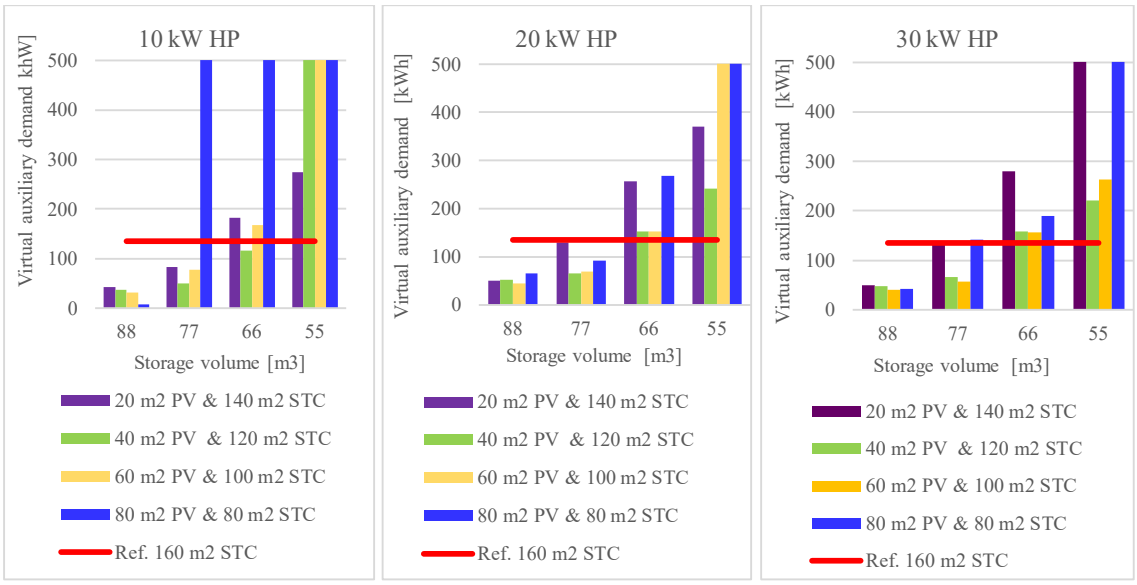

Fig. 8 Simulated auxiliary demand of the reference system implemented with PV and air-to-water HP with different storage volumes, with HR unit.

4.7. PV and direct electrical heating

When the PV roof area is constrained to 160 m^2, the TES volume cannot be reduced as there is always an additionall auxiliary heating demand above the reference benchmark. However, when such a system was implemented with a HR unit and when the size of the air-source HP was further increased to 50 kW, the reference benchmark could just be reached with a storage volume of 99 m^3. Systems with a foundation plate source HP and only PV as solar input reached the benchmark already with smaller HP sizes, but were not able to fully regenerate the ground. Therefore, these systems are not considered for comparison.

4.8. PV and direct electrical heating, increase of building surface used for solar

As the analyzed building has the potential to increase the solar area to about 210 m^2, parameter variations with larger PV fields were carried out. When changing the constraint of the solar area, a direct system comparison is no longer valid. However, systems with large PV installations can drastically reduce the size of the needed TES volume. As shown in Fig. 9, the storage volume can in this case be reduced to 33 m^3 when using 210 m^2 of PV installation and a 40 kW HP.

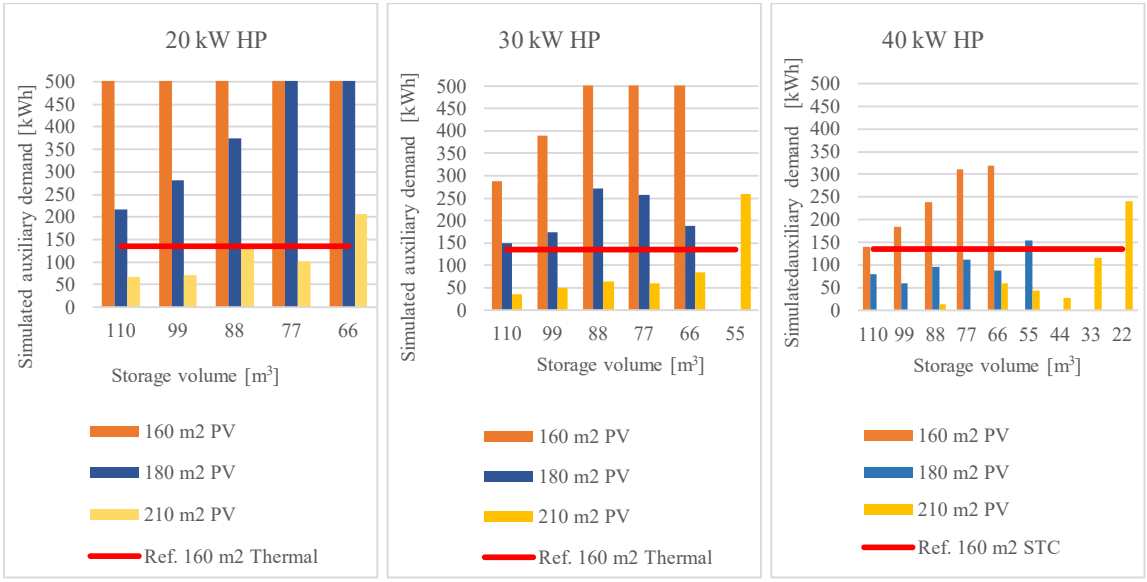

Fig. 9 Aimulated auxiliary demand of the system with only PV, direct electrical heating and air-to-water HP with different storage volumes without HR unit

4.9. Investment cost analysis

The financial analysis was limited to investment cost, as the systems don't use external energy and therefore don't generate external energy cost. Running cost are dominated by capital cost, which depend directly on investment cost. A precise estimation of operational cost, which are for these systems dominated by maintenance cost, is difficult. Simplified maintenance cost estimations are given as percentages of the investment and are again directly dependent on investment cost. Therefore, an estimation of running cost doesn't bring added value for fully solar heated systems.

Based on real cost from the constructed building and further indicative offers of the company Jenni Energietechnik AG, investment cost estimations for different system combinations were carried out. These cost estimates cover investment and installation cost. Planning cost were excluded from the analysis, as standard planning cost cannot be applied for such pilot systems. On the other hand, similar planning cost can be expected for all analyzed systems. Fig. 10 provides a comparison of the investment cost for different system configurations. For all system types, the sizing with the lowest investment cost is chosen for this comparison. As some system configurations can provide part of the household electricity and feed excess PV electricity to the grid, the financial returns from this additional PV production (for a period of 20 years) are also given for comparison in Fig. 10. Electricity cost for Huttwil 2021 (consumption: 0.175 CHF/kWh and feed in: 0.07 CHF/kWh) were used for this analysis. When reducing the storage size, living area in the building is gained. The financial benefit of this effect is difficult to quantify and strongly depends on the location and other parameters. Therefore, the return from the gain of living area is not given precisely but is represented by a bar with a color that is fading out.

It can be seen that the combined systems have lower investment cost than the standard STC system. Especially when the financial gains of the PV production are accounted for, the system with the foundation plate HP is economically most attractive.

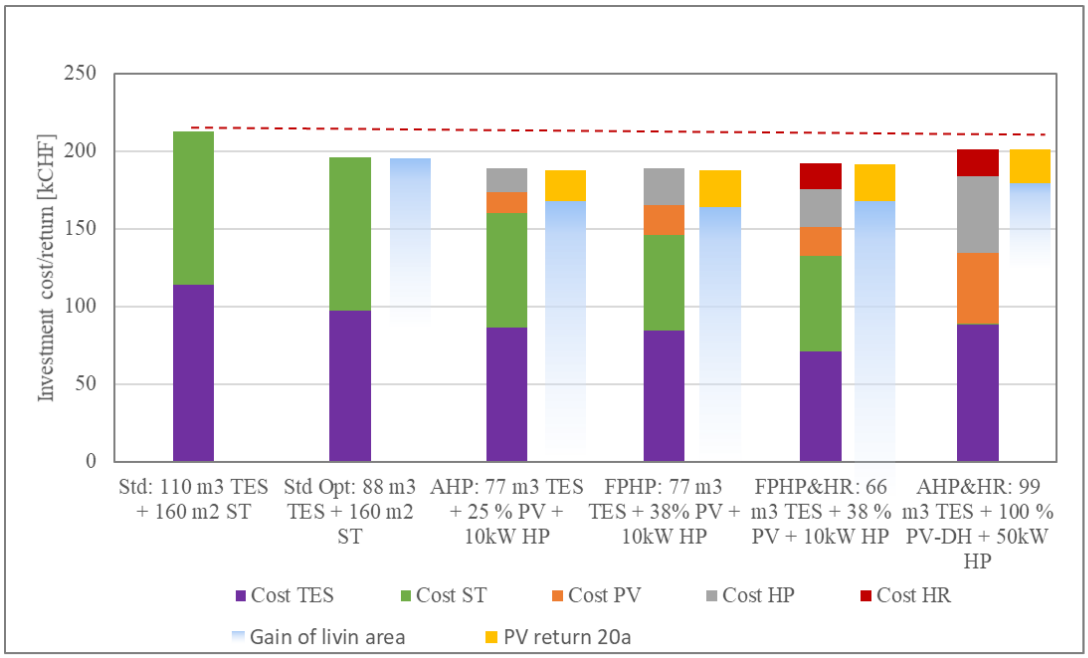

Fig. 10 Investment cost for different system configurations compared to the return from produced PV electricity and the virtual return from the gain of building volume when reducing the size of the TES

By increasing the solar roof area, investment cost increased for the case of the combined systems but decreased in the case of PV only systems on the other hand. This can be seen in Fig. 11 (Annex), where the system with optimized control (standard reference system) and the best combined system with a solar field size of 160 m^2 is compared with various system combination with a solar field of 210 m^2.

4. Conclusion

In comparison to the reference system with only solar thermal, the combined system with PV and HP has both energetic and economic advantages. The additional costs of the HP can be compensated by the savings in the storage tank size and the lower cost of PV compared to STC. Systems without STC but with PV and direct electrical heaters are only possible in combination with a large HP and shower heat recovery. These systems are therefore more expensive than the best combined systems.

With the combined system, almost all the heat demand of the building can be covered and part of the electricity demand of the building can be supplied with the PV electricity. In summer, some systems even feed excess electricity to the grid. Financial benefits of this PV production and benefits from the gain of living area from the size reduction of the TES make the combined systems even more attractive. Using the foundation plate of the building as a source for the HP is economically the most attractive of the analyzed solutions, especially when the gains are accounted for.

5. Acknowledgements

We would like to thank Mr. Josef Jenni from Jenni Energietechnik AG for enabling the measurements on the MFB in Huttwil as for providing technical and economic information's. Further, we would like to thank the Swiss Federal Office of Energy (SFOE) who supported this work within the projects SensOpt and 100%SolarLCA.

6. References

Battaglia, M., 2017. TRNSYS - Type 1792 – Radiant Floor - Version 1.00. SPF-OST, internal document

Bundesamt für Energie, 2022. Schweizerische Gesamtenergie Statistik 2021 (No. Art.-Nr. 805.006.21 / 08.22 /1100 / 860513711). Bundesamt für Energie BFE, Bern, Bern.

Haller, M., 2015. TRNSYS-Type 977-Compression Heat Pump with start losses and defrosting based on CurveFit of COP and condenser heat V4.00.

Haller, M., 2012. TRNSYS Type 832 v5.00 „Dynamic Collector Model by Bengt Perers“ - Updated Input-Output Reference. Institut für Solartechnik SPF, Hochschule für Technik HSR, Rapperswil, Switzerland.

Haller, M., Carbonell, D., 2013. TRNSYS Type 1924 - Stratified Plug Flow Solar Combi-Store Model.

Kemmler, A., Spillmann, T., 2021. Der Energieverbrauch der Privaten Haushalte 2000–2020, Auswertung nach Verwendungszwecken und Ursachen der Veränderungen. Prognos AG.

Mojic, I., Crameri, S., Caflisch, M., Carbonell, D., Haller, M., 2019. Reference Framework for Building and System Simulations: Multifamily Reference Building.

Mojic, I., Luzzatto, M., Haller, M., Lehmann, M., Benz, M., Van Velsen, S., 2018. ImmoGap - Einfluss der Kombination aus Nutzerverhalten und Gebäudetechnik auf den Performance Gap bei Mehrfamilienhäuser (BFE Schlussbericht), BFE Schlussbericht. SPF Institut für Solartechnik, HSR Hochschule für Technik Rapperswil, Rapperswil.

Passivhaus Institut, 2020. Criteria and algorithms for Certified Passive House Components: Drain Water Heat Recovery.

SIA, 2015. Klimadaten für Bauphysik, Energie- und Gebäudetechnik – Korrigenda C1 zu SIA 2028:2010. schweizerischer ingenieur- und architektenverein, Zürich.

SIA 385/1, 2020. Anlagen für Trinkwarmwasser in Gebäuden - Grundlagen und Anforderungen (No. 546385/1).

SPF-OST, Documentation of the pytrnsys framework, https://pytrnsys.readthedocs.io/en/latest/, © Copyright 2021, Institute for Solar Technology (SPF), OST Rapperswil (accessed 12.9.2022)

Villasmil, W., Troxler, M., Hendry, R., Schuetz, P., Worlitschek, J., 2021. Control strategies of solar heating systems coupled with seasonal thermal energy storage in self-sufficient buildings. J. Energy Storage 42. https://doi.org/10.1016/j.est.2021.103069

7. Annex

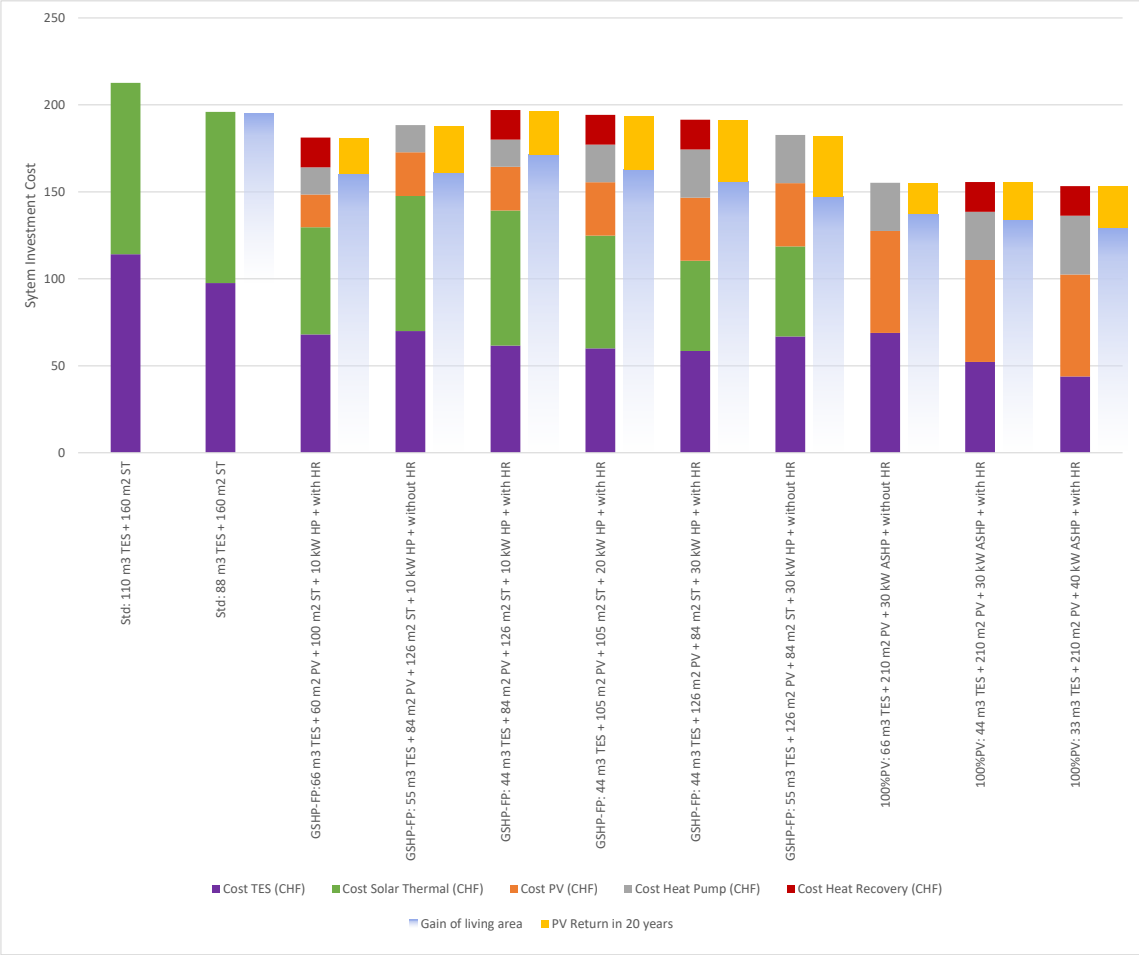

Fig. 11 Investment cost for different system configuration with larger solar areas compared to the return from PV electricity production and the virtual return from the gain of building volume when reducing the size of the TES

Radiant Cooling System without Any Energy Input

Seung-Ho Yoo[1], Hee-Jeong Choi[2]

[1]Solar Architecture Laboratory/Sehan University, Youngam (Republic of Korea),

[2]Department of Biomedical Science, Catholic Kwandong University, Beomil-ro 579 beon-gil, 25601 Gangneung-si, Republic of Korea

Efficient cooling and heating solutions for nearly zero-energy solar dwellings are required to mitigate climate change and to make sustainable dwellings nowadays. The installed pipeline for a radiant heating system, which is used for space heating just during the heating period, can be used also to cool the room just by the enthalpy use of the natural city water without any energy and power input by releasing the natural city water through the embedded pipeline already installed for the radiant heating. The natural city water used for radiant cooling can be used at the necessary places such as toilets flushing, car washing, wash machine, garden water, etc. which are corresponding to approximately 56% of the water we use at home. As a result, the embedded pipe of the radiant heating system can be converted to a radiant cooling system with a minimum added installation and control system without any energy or power input. Thermal comfort and behavior analyses in an enclosure with a radiant cooling system are fulfilled by experiment, mean radiant temperature simulation, and asymmetric radiation calculation. No uncomfortable asymmetric radiations are encountered for the cooling period so that the cooling spaces are well controlled within the comfortable cooling range without any energy and power input. The radiant cooling concepts by the use of natural city water could be a nice solution for comfortable and reasonable zero-energy dwellings. No extra cooling energy and power are required to cool the space just by the use of enthalpy and pressure from the natural city water.

Keywords: Radiant cooling, No energy input, On-dol heating, Mean radiant temperature, Natural water, Thermal comfort, Asymmetric radiation, Enthalpy

1. Introduction

Buildings are critical to the transition to a net-zero future, as they are responsible for about 40% of the global energy consumption and about one-third of global GHG emissions. Energy consumption for space cooling has more than tripled since 1990, especially during peak demand periods and extreme heat events. Over 10% of building energy use is used for air conditioning and indoor thermal comfort in hot seasons. Changing the air conditioning mode is one solution to meet the cooling demand without increasing power consumption and CO_2 emission. Global space cooling demand continued to grow in 2020, driven in part by greater home cooling as more people spent more time at home. Space cooling accounted for nearly 16% of the building sector's final electricity consumption in 2020. Residential AC units for space cooling in operation account for nearly 70% of the total (IEA, 2021).

An environmentally friendly or energy-efficient heating & cooling systems attract great attention, due to energy, environmental problems, and climate change, etc. Especially radiant heating and cooling system are the exact example of these cases. The heat balance of the human body is about 46-50% influenced by radiation exchange in the built environment (Rietschel and Raiss, 1963; Fanger, 1972). Therefore thermal characteristics in a radiant built environment need to be precisely accessed through an efficient evaluation method (Glueck, 1982) (Klima- und Lueftungstechnik). The heat flow density on the floor surface was determined by pipe spacing, thickness,and heat conductivity of the layer above the pipe etc (Konzelmann and Zoellner, 1982). Radiant cooling can be an energy-efficient strategy, thereby reducing both sensible and latent loads in spaces (Teitelbaum et al., 2019).

In Germany, the first reports of the application and experimentation of ceiling systems that are heated in the ceiling in the winter and used for cooling purposes at the same time in the summer appear (GI, 1938). In Switzerland, a thermal active building structure system has been applied for radiant heating and radiant cooling purpose (Koschenz and Lehman 2000).

Almost of Korean dwellings have conventionally used the On-Dol (Warm stone plate) heating system which is a traditional radiant floor heating system. A radiant cooling system attracts also much attention nowadays from the

© 2022. The Authors. Published by International Solar Energy Society
Selection and/or peer review under responsibility of Scientific Committee
doi:10.18086/eurosun.2022.03.02 Available at http://proceedings.ises.org

viewpoint of energy conservation and thermal comfort. Thermal behavior such as comfort characteristics and asymmetric radiation in an enclosure with a radiant cooling without any energy input, and thermal capacity of the system in a dwelling are analyzed by experiment and simulation through an application in a private house.

2. Radiant cooling system without any energy and power input

2.1 Principle of radiant cooling without any energy and power input

The conventional radiant heating system, which is used only for space heating during the heating period, can be used also to cool the room without any waste of city water and power input by releasing the natural city water through the embedded pipeline already installed for the conventional radiant heating system. That is a kind of passive intelligent radiant cooling concept. Even when the outside air temperature is over 36°C during the cooling period, the natural city water temperature is approximately 19-20°C in Korea at the tap water in principle because the city water is supplied at least 90 cm under the earth in Korea. The corresponding city water temperature is respectively 19-20°C in Turkiye, and 10~14°C in Germany and Denmark. Korean water supply facilities should be buried at least under 90cm of earth. The natural city water flows through a pipeline which is embedded in the cooling surface during occupants' water use for toilets, washing machines, cleaning, car washing, garden water, and shower which are corresponding to approximately 56% of the water we use at home (Daniels, 1994). It is a similar one of the multi-purpose principle which the room is automatically heated by the hot exhaust gas that flows into the heating flue after burning the timbers to cook something in a kitchen in a traditional On-dol (Warm stone plate) radiant heating system in Korea (Yoo, 2021). No power and water are requested to cool the room. The enthalpy of the natural city water for the radiant cooling is used to cool the room space and the used water continues to flow at the necessary places such as toilets, washing machines, car washing, cleaning, garden water etc. Fig.1 shows the principles of radiant cooling system without any energy input (Yoo, 2015).

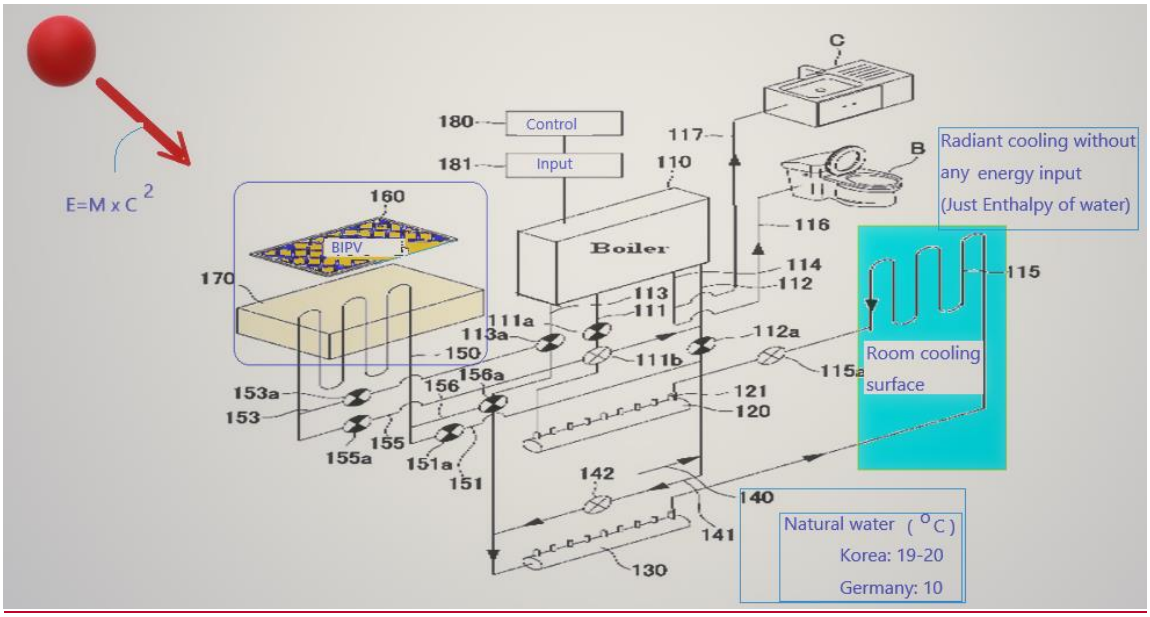

Fig.1: Principles of radiant cooling system without any energy input

2.2 Description of the passive intelligent radiant cooling system

The thermal behavior and capacity of the passive intelligent radiant cooling system is evaluated in the house where is located in Chung-Nam Province, Republic of Korea. The radiant cooling system is composed of two different parts. There are the 1st one converged to a BIPV as a night cooling which is numbered 160 and 170 on the left side and the 2nd one converged to a radiant heating system on the right side of Fig.1. The right side is the target of this study. Figure 2 shows the floor plan of the private house with the attached glass house which the radiant floor heating system is installed.

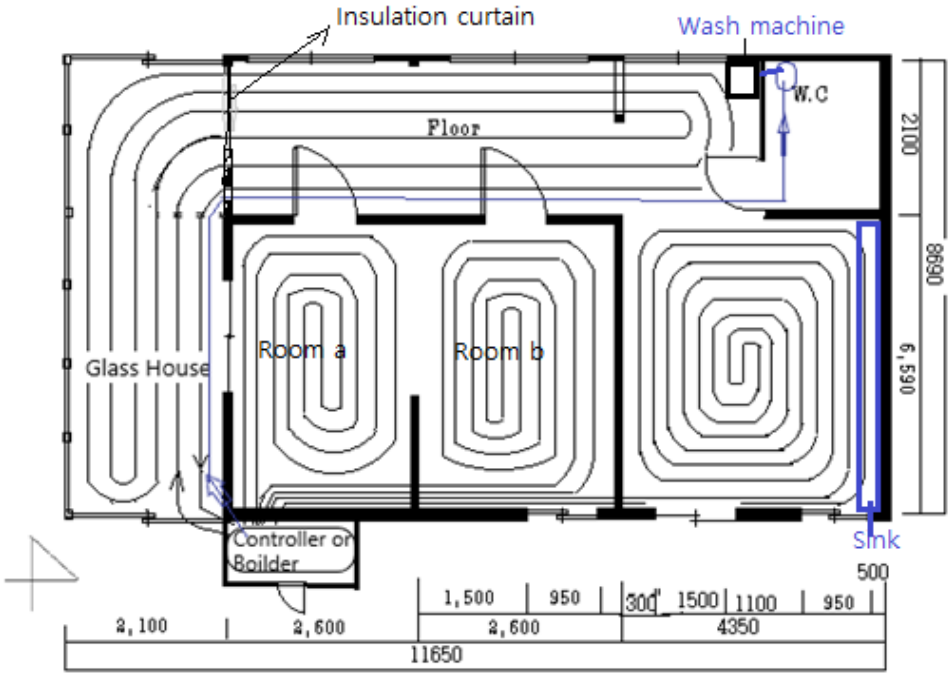

Fig.2: Floor Plan of radiant cooling and heating system with an attached glass house

The total dimension of the house is approximately 11.7 M × 8.7 M × 2.5 M (Horizontal axis×Vertical axis×Height) including the glass house which is attached. The glass is made up of vacuum glazing, and the outer wall has been remodeled with 5 cm thick sandwich paneling, but the interior wall remains the original 10 cm thick traditional earthen wall. But the glass window between the glass house and the room a is 3 mm thick. Figure 3 shows the section of the radiant cooling and heating pipe installation plan.

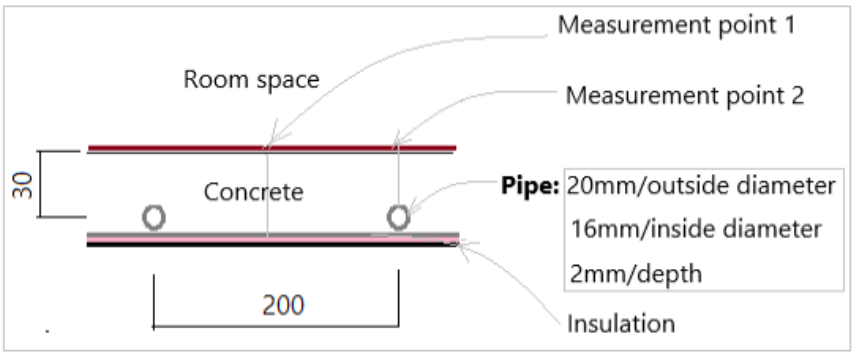

Fig.3: The section of the radiant cooling and heating pipe installation plan

The distance between pipes is 200 mm, and the depth of the concrete from the pipe to the floor surface is 30 mm. The house had been originally constructed by an On-dol (Warm stone plate) radiant heating system heated by the hot gas through timber combustion during cooking in a kitchen approximately since the end of 1800. Then the On-dol radiant heating system has been converted to the present hot water On-dol radiant heating system since early 1980. Namely, almost all such traditional On-dol radiant heating systems have been improved to a radiant heating system heated by the hot water which flows through the pipeline embedded in concrete floor. The hot water is circulated through the embedded pipeline to heat the room in winter by the boiler.

The glass house has been attached since the late 1990. The target radiant cooling system without any energy and power input has been converted to cool the house since 2018.

In summer the natural city water flows to cool the room through a pipeline embedded in the floor surface. No power and no extra water are required to cool the room space. The more people live in the radiant cooling space, the more city water automatically flows to cool the room space by the water pressure of city water because the

people use more water as per the increased number of occupants. The amount of the city water flows approximately 0.112-0.115 kg/s during using the water system such as wash machine, toilet, cleaning, etc. while the occupants stay at home.

2.3 Research methodologies

32 thermal points have been measured by the Data logger per every 30 or 60 minutes the vertical room air, surface temperature of the room, and the other boundary conditions including inlet and outlet water temperature for the room, and outdoor air temperature. Tg means the glass house temperature. Tr means room temperature. The table 1 shows the measurement detail.

Table 1: Measurement detail

Measurement factor (Position)	Method	Accuracy
Outdoor air temperature (1.5 m)	Data logger + T-type Thermo couple	±0.75%
Vertical Air temperature (0.1 m, 0.8 m,2.3 m)		
Inside surface temperature (South wall, south window, west wall, north wall, floor surface 1, 2, 3, 4, Ceiling surface)		
Inside temperature of the glass house -Surface (Floor, south, east, and inclined glass ceiling) -Vertical air (0.1 m, 0.8 m, 2.3 m) - Inlet and outlet water temperature(Pipe surface temp.)		
Glove temperature(Room and Glass house) (0.8 m)	Glove thermometer+ T-type Thermo couple	
Room humidity (0.2 m)	Asman humidity meter	

Some simulations to figure out the thermal behavior of the system are fulfilled by the use of the measurement data such as air temperature, surface temperature, inlet and outlet water temperature to calculate mean radiant temperature, operative temperature, the thermal capacity of the radiant cooling system.

3. Thermal Behavior of the Radiant cooling system

3.1 Evaluation of mean radiant temperature (MRT) and Operative temperature (OT)

A cubic box model which has the same surface area as the human body is used to evaluate the thermal comfort characteristics such as MRT and OT. The human body surface area is calculated according to the following equation (1)(Fanger, 1970).

$$A_{du} = 0.203 \times W^{0.425} \times H^{coef} \quad (1)$$

Herein, the coefficient coef is 0.696 for a sitting person. Weight W of a person is 70 kg, Height H is 110 cm for a sitting person. MRT is calculated by the following equation (2) (ISO7730, 2005).

$$T_{mrt} = \sqrt[4]{\sum_{i=1}^{n}((\Phi_{b,si}) \bullet T_{si}^4)} \quad (2)$$

$Ø_{b,si}$: View factor between human body model and room surface,
T_s^4: Absolute temperature of the surrounding surface s
Operative temperature T_{ot} is calculated by the following equation (3) (ISO7730, 2005).

$$T_{ot} = a \bullet T_{air} + b \bullet T_{mrt} \quad (3)$$

Herein a+b=1, a:0.5, b:0.5.

3.2. Asymmetric radiation

A small cubic box of 1cm^2 on the height of 0.6 m is considered to calculate the asymmetric radiation among the room surfaces including the floor cooling surface. The asymmetric radiation (Asym) is calculated by the following equation (4) (ISO7730, 2005).

$$Asym=|T_{MRTu}-T_{MRTo}| \quad (4)$$

Herein, T_{MRTu} is MRT for the underside, T_{MRTo} is MRT for the opposite side. The simulation program 'COMFORT (Yoo, 2018)" is used to calculate MRT, OT and Asymmetric radiation which can evaluate thermal behavior including thermal comfort characteristics for the target house.

4. Experiment and Simulation results

4.1 Radiant cooling concept and experiment results for the target house

A radiant heating system, which is used only for space heating during the heating period, can be used also to cool the room by releasing the natural city water through the embedded pipeline already installed for the radiant heating system. The city water used for radiant cooling can be used at the necessary places such as toilets flushing, car washing, wash machine, garden water, etc. For this purpose, even when the outside air temperature is maintained over 36ºC during summer, the city water is approximately 19-20ºC in the Republic of Korea, 10ºC (Germany) for tap water, so that the cooling surface flows through a pipeline embedded in the floor, wall, or ceiling where it is not needed to drink water, whenever the occupants use the water system. No power is needed to flow the water. No wastewater results either. The amount of the city water flowed was approximately 0.112-0.115 kg/s. Figure 5 shows the temperature variations during the radiant cooling operation depending on the time-sequential process.

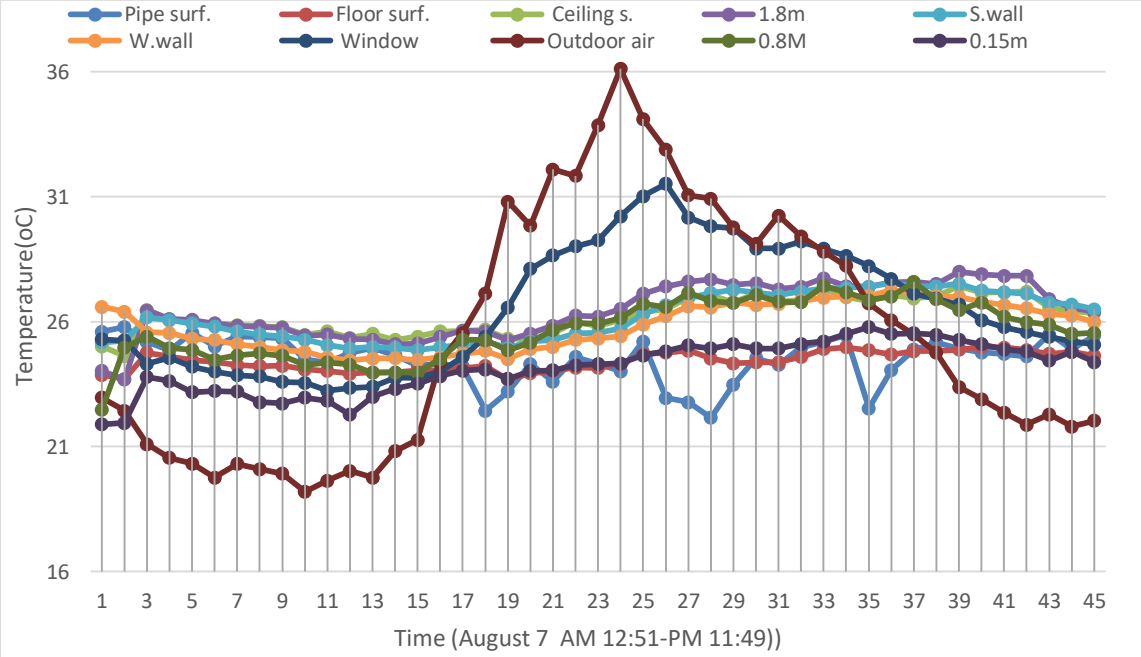

Fig. 5: Temperature variations of the radiant cooling space depending on the time-sequential process

Measurement was made every 30 minutes from 1-45 (am 12:51-pm 11:49) for 24 hours. The highest outdoor air temperature is 36.1ºC at 12:51. The gardening water was supplied from AM 09:30-09:45. The sequential time is corresponding to 17-18 (AM 09:12-09:44) in Fig. 5. A person took a shower from am 11:00-11:12 (21: 11:17:36). The washing machine did the laundry from pm 13:35-15:25 (25: PM 1:22:51, about 75L water consumption per one laundry). The gardening water and car washing were done from 18:05-18:33 (34: pm 6:04:38). A person took a shower from 21:00-21:10 (40: pm 9:12:31). A person usually used to go to WC 8-9 times per day. If the water is used during the shower, the laundry, and the WC usage, etc, the embedded pipe surface temperature automatically goes down, so that the concrete structure that contacts the cooling pipe falls in temperature to cool the corresponding room. This causes to fall the surrounding surface temperature including ceiling, wall, and

window surfaces to increase the thermal comfort for the occupant due to the cold radiation effects. During the laundry, the floor surface temperature is 24.69ºC while the temperature at 0.15m height is 24.64ºC. The ceiling surface temperature is 26.4ºC while the air temperature is 27.1ºC at the near position of the ceiling surface. The west wall surface, south wall surface, south window surface temperature, and air temperature at the 0.8 m height are respectively 26.22ºC, 26.67ºC, 31.51ºC, and 26.71ºC. The temperature difference profile between surface temperature and air temperature at the same height shows a similar distribution to the temperature profile between the floor surface and 0.15m height air temperature due to the cold radiation effect. But the temperature difference profiles near the vertical surfaces and ceiling surface show respectively 0.7ºC (Ceiling: 27.1-26.4), 0.5ºC (West wall: 26.71-26.22), 0.04ºC (South wall: 26.71-26.67), and -4.8ºC (Window: 26.71-31.51). The similar and revered temperature at the South wall and window comes from the poor insulation of the south wall and the window and the high air temperature of the glass house. Figure 6 shows the temperature variations of the radiant cooling space depending on the time-sequential process.

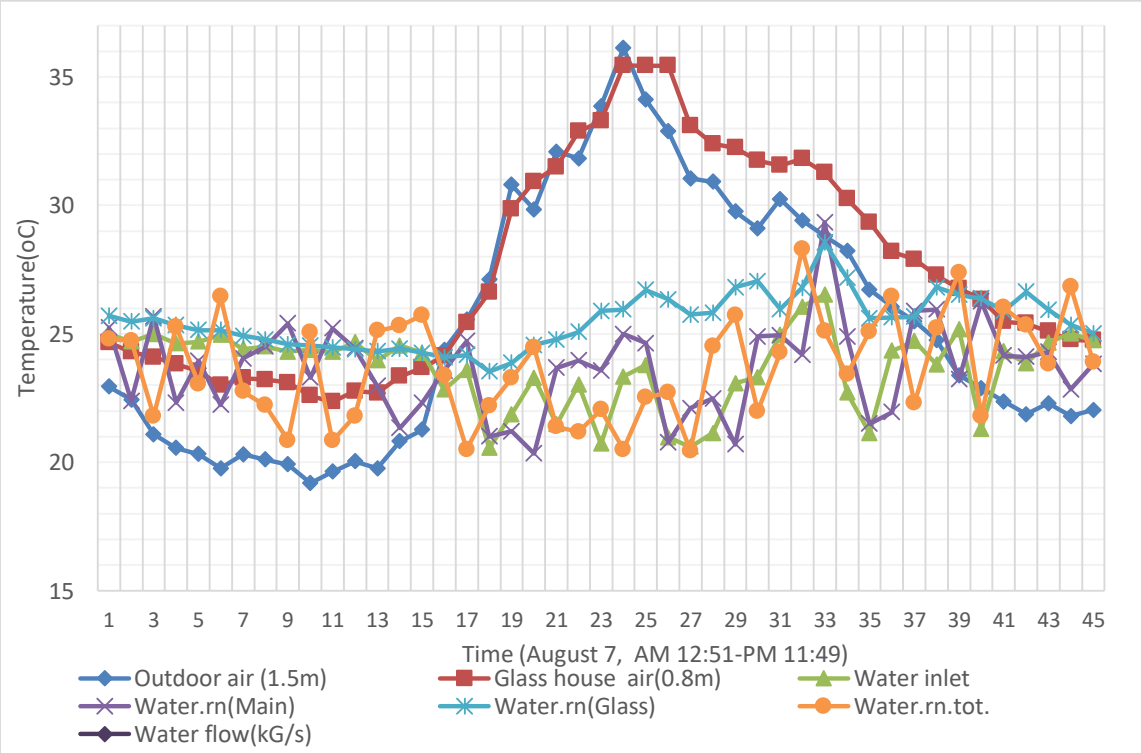

Fig.6: Temperature variations of the radiant cooling room depending on the time-sequential process

The maximum outdoor air temperature was 36.12ºC at pm 12:51. The glasshouse is lasting high for 1 hour 30 minutes from pm 12:51. The returned water was shown to be the highest temperature in the glasshouse. This demonstrates the returned water (26-27ºC) from the glasshouse can be reasonable for taking a shower in Summer. The inlet (City) water temperature was approximately 19-20ºC. Figure 7 shows the average vertical temperature profile for the room for one day.

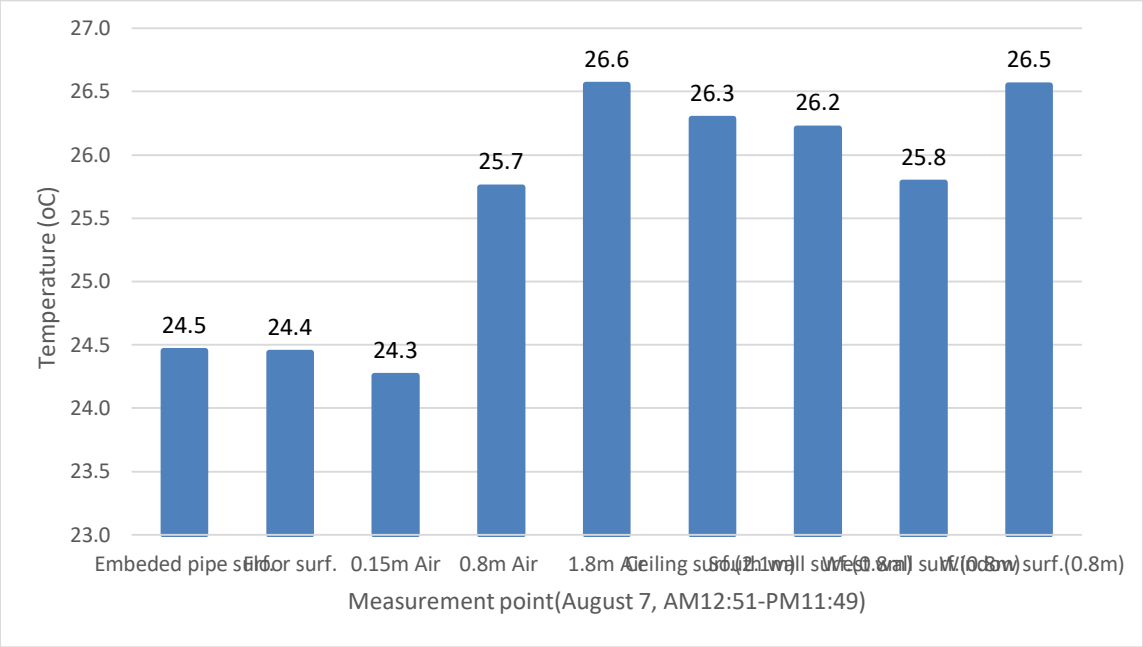

Fig.7: Vertical average temperature profile for the room for one day

The average outdoor air and glass house temperature for one day is respectively 25.4ºC and 27.5ºC. The average room air temperature at 0.15 m height is the lowest one 24.3ºC which could be comfortable for the occupants. The interesting one is the temperature at the 1.8m height which the ceiling surface temperature is 0.3ºC lower than the air temperature near the ceiling due to the cold radiation effect mainly from the floor radiant cooling surface. Figure 8 shows the vertical temperature profile for the room on pm 12:51.

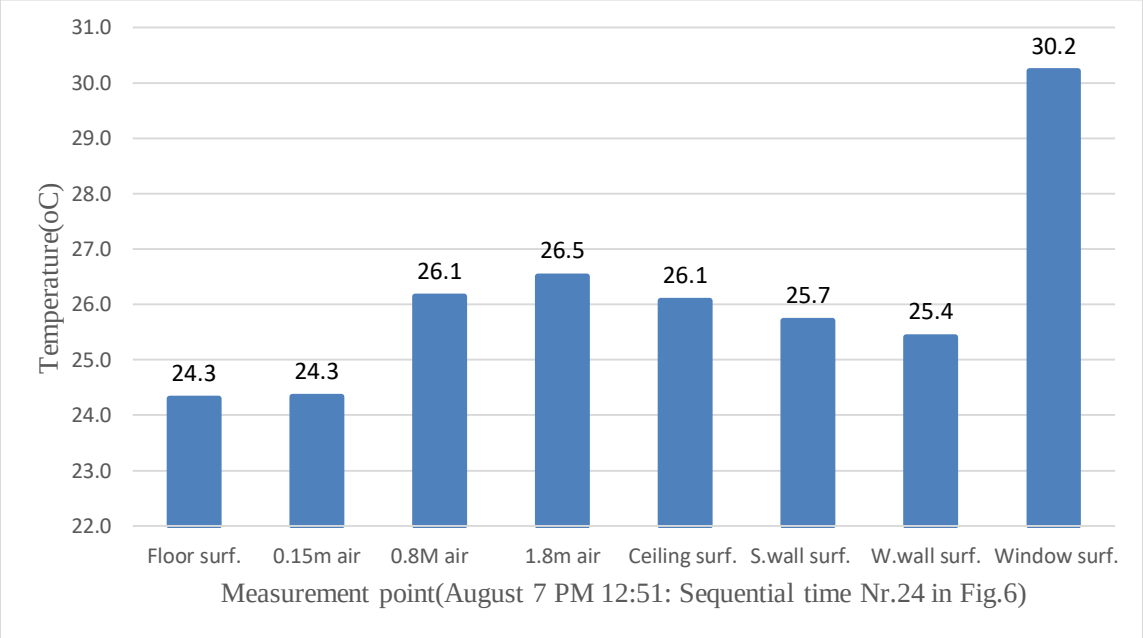

Fig.8: Vertical temperature profile for the room for one instant

At this moment, the radiant cooling floor surface temperature is similar to the air temperature at 0.15 m height (near the floor cooling surface) so there is little convective heat transfer on the floor radiant cooling surface. Alternatively, radiant cooling floor surface radiates to the ceiling surface, south wall surface, west wall surface, and window surface to fall in surface temperature. Therefore the surface temperature of the ceiling and the west wall at 0.8 m height is lower or similar to the air temperature at 0.8 m height. But the inside surface temperature

of the window is 4.1ºC higher than the air temperature at 0.8m height due to the high temperature (35.5ºC) of the adjacent glasshouse.

4.2 Mean radiant temperature (MRT) and Operative temperature (OT) calculation

MRT and OT are calculated by the simulation program COMFORT based on equations (1), (2), and (3). Figure 9 shows the MRT distribution for the radiant floor cooling system for the house.

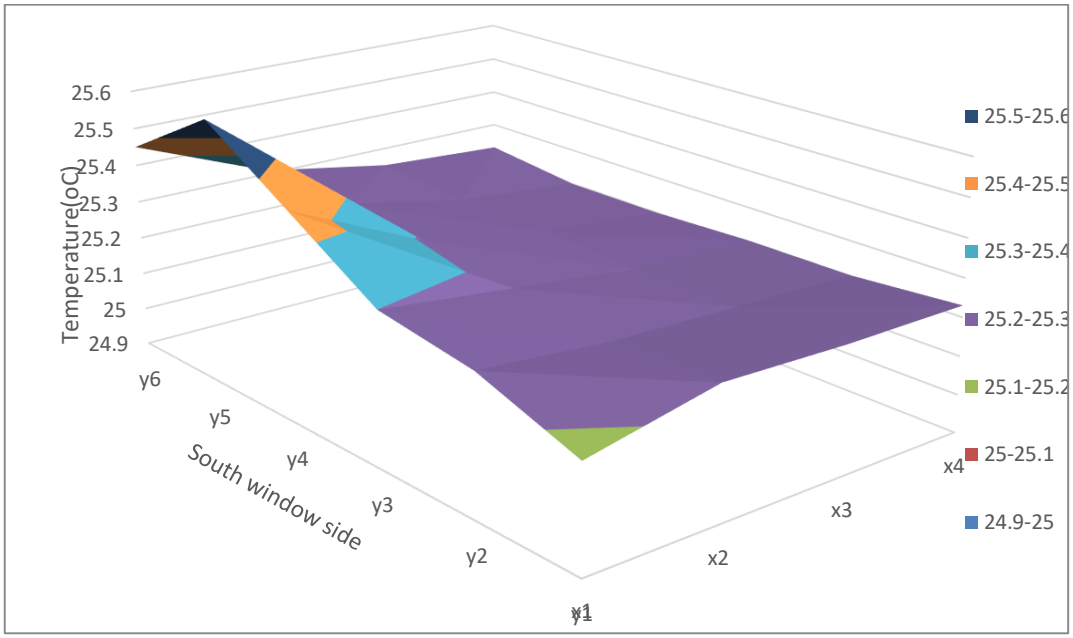

Fig.9: MRT distribution for the radiant floor cooling system for the house (August 7, pm 12:51, Outdoor air temperature: 36.1ºC)

A total of 24 points which keep 1m distance from every 4 different room surface orientations were chosen to simulate the MRT and OT. The average temperature of MRT was 25.27ºC. But the temperature at the window side was relatively higher than the inner side due to the high window surface temperature from the adjacent glass house. But the effect of the floor surface temperature on the MRT is the most influential factor and the average floor surface temperature 24.4ºC is within the lowest percentage dissatisfied range as per the local thermal discomfort caused by warm or cold floors (ISO7730, 2005). Figure 10 shows the operative temperature (OT) distribution for the radiant floor cooling system for the house.

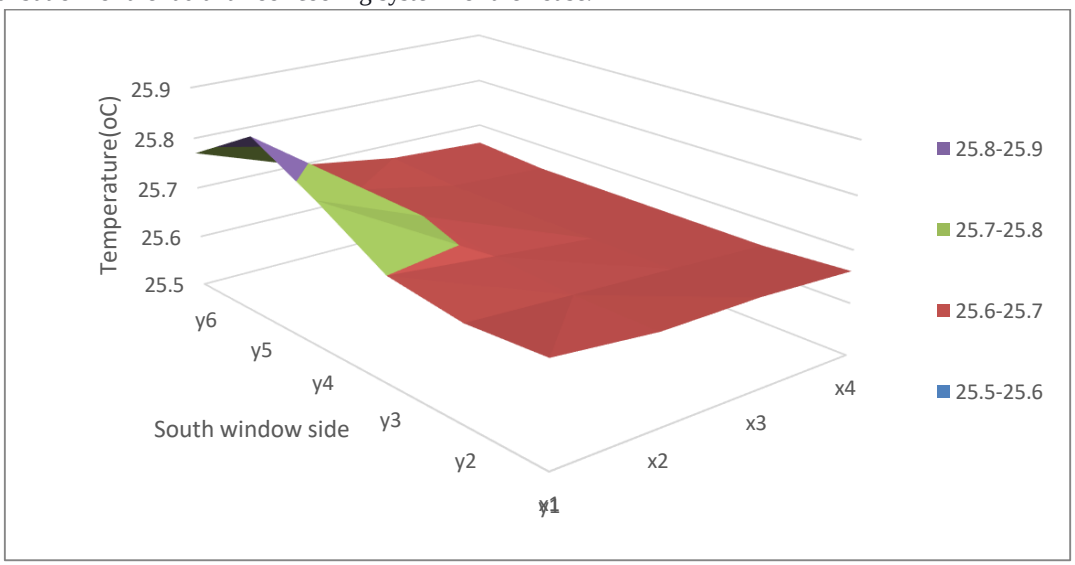

Fig.10: Operative temperature (OT) distribution for the radiant floor cooling system for the house (August 7, pm 12:51, Outdoor air temperature: 36.1ºC)

The average temperature of OT was 25.69ºC which is a comfortable range for the occupants. The room OT range is 25.5~25.8ºC even on the hottest day. But the temperature at the south window side was relatively higher than the inner side due to the higher south window surface temperature.

4.3 Asymmetric radiation simulation

The asymmetric radiation simulation for 6 different positions which keep 1m distance from the south window and wall was fulfilled by the use of the simulation program COMFORT based on the equation (4). The possible biggest temperature difference orientations between two different opposite surfaces were chosen to calculate the radiant asymmetry, namely ceiling and floor surface, south window side and north sidewall surface, east and west wall. Figure 11 shows the calculation results for asymmetric radiation on August 7 PM12:51 (Sequential time Nr.24 in Fig.6)

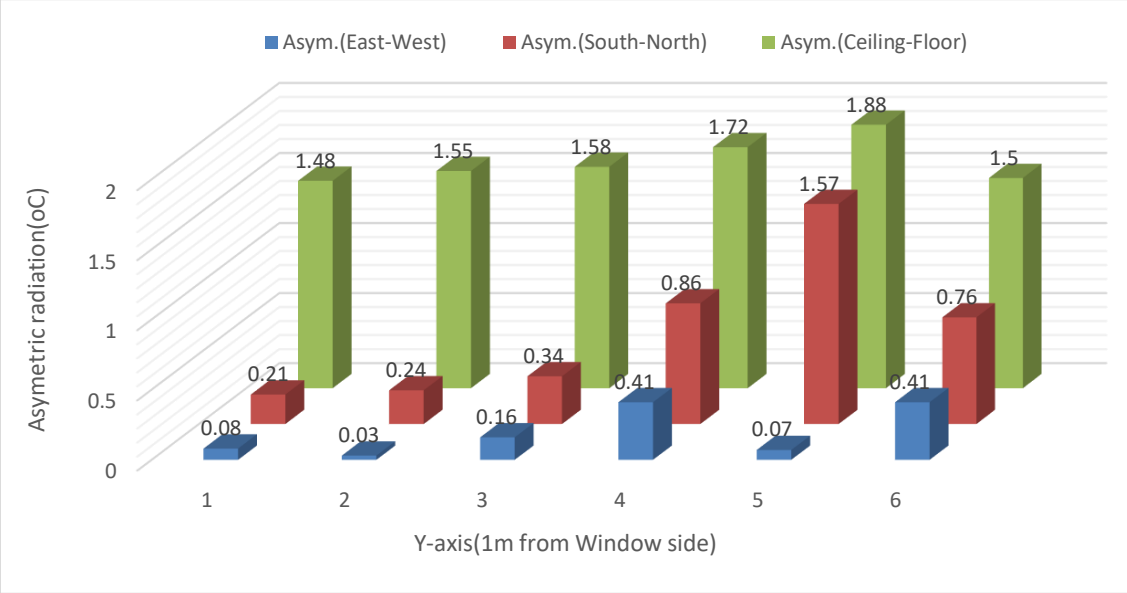

Fig.11: Asymmetric radiation (August 7 pm12:51)

The maximum asymmetric radiation (1.88ºC) is raised at the y5 (Ceiling and floor at the window side). Asymmetric radiation does not happen in this radiant cooling space because the floor radiant cooling radiates to the surrounding surfaces mostly by the radiation. The highest radiant asymmetry is 1.88 ºC near the south window side. This means that the local thermal discomfort is not caused by the radiant cooling system without any energy input in any position of the house (ISO7730, 2005).

4.4 Recommendations for an energy-efficient dwelling with the passive intelligent radiant cooling system without any energy input

The author recommend the following considerations for an energy-efficient dwelling with the passive intelligent radiant cooling system without any energy input. The radiant cooling system could meet the condensation problem on radiant cooling surface depending on the thermal capacity of the system and the room humidity condition. Therefore the outside shading is recommended to reduce the cooling load as possible which can reduce the cooling load by up to 34% to prevent the possible condensation problem in Seoul, Korea (Yoo et al., 2021). The source flow ventilation system is recommended for the radiant cooling system without any energy input to compensate for the system as per the radiant cooling floor surface temperature is similar to the 0.15m height room air temperature so that the source flow ventilation system can be very effective.

5. Conclusion

Efficient cooling and heating solutions for nearly zero-energy solar dwellings are requested to mitigate climate change and to make sustainable dwellings nowadays. The passive intelligent radiant cooling system without any energy input has been converted from the radiant heating system over 3 years in summer. The pipeline embedded for a radiant heating system, which is used for space heating just during the heating period, can be utilized also to cool the room just through the enthalpy use of the natural city water without any energy and power input by releasing the natural city water through the embedded pipeline already installed for the radiant heating. The natural city water used for radiant cooling can be used at the necessary places such as toilets flushing, car washing, wash machine, garden water, etc. which are corresponding to approximately 56% of the water we use at home. As a result, the embedded pipe of the radiant heating system can be converted to a radiant cooling system with a minimum added installation and control system without any energy or power input. Thermal comfort and behavior analyses in an enclosure with a radiant cooling system are fulfilled by experiment, mean radiant temperature simulation, and asymmetric radiation calculation. No uncomfortable asymmetric radiations are encountered for the cooling period so that the cooling spaces are well controlled within the comfortable cooling range without any energy and power input. The radiant cooling concept by the use of natural city water could be a nice solution for comfortable and reasonable zero-energy dwellings. No extra cooling energy and power are requested to cool the space just by the use of enthalpy and pressure from the natural city water.

The radiant cooling floor surface temperature is similar to the air temperature near the floor cooling surface so there is little convective heat transfer on the floor radiant cooling surface. Alternatively, radiant cooling floor surface almost all radiates to the ceiling surface, south wall surface, west wall surface, occupant, and window surface to fall in surface temperature. This passive intelligent radiant floor cooling concept automatically causes to fall in the surrounding surface temperatures including 0.7ºC at the ceiling and 0.5ºC at the west wall against the room air temperature near the corresponding surface to increase the thermal comfort of the occupant just by the radiation from the radiant cooling floor surface. The average OT was 25.69ºC which is a comfortable range for the occupants. The room OT range is maintained at 25.5~25.8ºC even on the hottest day. The house can be cooled very well without any ventilator or air-conditioner all summer just in the aspect of comfort temperature. But the source flow ventilation system is recommended for the passive intelligent radiant cooling system without any energy input to compensate for the system as per the radiant cooling floor surface temperature is similar to the 0.15m height room air temperature so that the source flow ventilation system can be very effective.

In the future the heat flow density on the radiant cooling floor surface will be precisely evaluated in the experimental set-up by pipe spacing, thickness, the heat conductivity of the layer above the pipe, etc.

6. Acknowledgments

This research is supported by Sehan University.

7. References

Daniels, K., 1994. The Technology of Ecological Building, Birkhaeuser Verlag, Basel Boston, Berlin.

Delmastro, C. et al., IEA. 2021. Cooling, Tracking report.

Fanger, 1970. Thermal Comfort, McGraw-Hill Book Company.

Gesundheit-Ingenieur(GI), 9/1938.

Glueck, B., 1982. Strahlungsheizung-Theorie und Paxis, Verlag C.F.Mueller Karlsruhe.

Hongshan, G. et al., 10.2019. Simulation and measurement of air temperatures and mean radiant temperatures in a radiantly heated indoor space, Energy.

IEA, 11 2021. The Role of Energy Efficient Buildings on the Path to Net-Zero - Strategies for policy makers.

IEA, 2021. EBC Annual Report 2020, Energy in buildings and communities programme.

ISO7730, 2005. Ergonomics of the thermal environment — Analytical determination and interpretation of thermal comfort using calculation of the PMV and PPD indices and local thermal comfort criteria.

Konzelmann, M., Zoellner, G., 1982. Waermetechnische Pruefung von Fussbodenheizungen, HLH 33.

Koschenz, M., Lehman, B., 2000. Thermoaktive Bauteilsysteme tabs, EMPA.

Mehmet, F.O., Cihan, T., 2022. A comprehensive comparison and accuracy of different methods to obtain mean radiant temperature in indoor environment, Thermal Science and Engineering Progress.

Rietschel, H., Raiss, W., 1963, Heiz-und Lueftungstechnik, Springer Verlag, Berlin/Goettingen/Heidelberg.
Teitelbaum, E. et al., 2019. The Cold Tube: Membrane assisted radiant cooling for condensation-free outdoor comfort in the tropics. J. Phys.: Conf. Ser. 1343 012080.
Yoo, S.H., Choi, H.J., 2021. Solar architecture integrated bi-facial photovoltaic system as a shade. Processes, https//doi.org/10.3390/pr9091625.
Yoo, S.H., 2021. Radiant colling and heating system for zero energy solar aechitecture, SWC 2021, ISES.
Yoo, S.H., 2015. Warem and cold water cycle structure of boiler, Korean intellectual Property office.
Yoo, S.H., Sohn, J.R., 2014. A Radiant Floor Cooling System for the Use of Natural Energy by Convergence of traditional Ondol and hot water Ondol heating system, KFMA.

E. Innovative District Heating and Cooling

Impact of Domestic Hot Water Preparation Systems on District Heating Network Design and Operation

Hagen Braas[1], Isabelle Best[1], Weena Bergstraesser[1], Johannes Zipplies[1], Janybek Orozaliev[1], Ulrike Jordan[1] and Klaus Vajen[1]

[1]University of Kassel, Institute of Thermal Engineering, Kassel (Germany)

Abstract

With more ambitious energy efficiency standards in newly constructed buildings and increased renovation rates in existing buildings, domestic hot water preparation systems are of increasing importance for the connected heat load, total heat demand, flow temperature requirements and return temperatures of residential buildings. This means, that the design and operation of district heating networks is heavily impacted by the domestic hot water preparation systems of its consumers. In this case study, three domestic hot water preparation systems are investigated regarding their impact on the district heating network design and operation. The investigated systems include instantaneous domestic hot water preparation and hot water storages, both at 60 °C, as well as preparation with buffer storages at 45 °C with heat exchangers on apartment level. Instantaneous preparation results in lower heat demand, distribution heat losses and return temperatures, while yielding similar costs as hot water storages (both at 60 °C). Domestic hot water preparation at 45 °C allows to significantly reduce the district heating network's flow temperature (from 75 to 50 °C) and also yields lower heat demand, distribution heat losses and return temperatures. However, because of high costs for the heat exchangers on apartment level, this system is not economically competitive in the evaluated case.

Keywords: domestic hot water, district heating, simulation study

1. Introduction

Studies such as the *Heat Roadmap Europe* (Persson et al., 2019) show that for the European Union to reach a cost-efficient energy system transformation, in the future a large share of district heating and cooling, especially in urban areas, will be needed. Existing and newly constructed district heating systems must be operated with low temperatures and use excess heat or renewable sources, such as solar thermal, geothermal or ambient heat, to contribute to the reduction of CO_2-equivalent emissions (Lund et al., 2014). Low temperature district heating offers new possibilities for higher energy efficiency and better utilization of renewable energy sources on a system level.

With more ambitious energy efficiency standards in newly constructed buildings and increased renovation rates in existing buildings, domestic hot water (DHW) preparation systems are of increasing importance for the connected heat load, total heat demand, flow temperature requirements and return temperatures of residential buildings. This means, that the design and operation of newly constructed district heating networks (DHN) and the transformation of existing DHN is heavily impacted by the domestic hot water preparation systems of its consumers.

A fundamental distinction of DHW systems is between instantaneous preparation and systems that use storages. There are innovations of the DHW systems' design that include reduced temperature levels e.g., with additional heat exchangers on apartment level or electric temperature boosters (direct electric or via heat pumps) (Østergaard et al., 2022).

In this study, the impact of three DHW preparation systems on the DHN design and operation is investigated regarding total heat demand, heat distribution costs and temperature levels for the case study district called "Sullivan". The Sullivan district is part of a former US-Military base that is being transformed into a residential area and consists of a mix of newly constructed and refurbished buildings as well as single family dwellings, apartment buildings and commercial buildings (Figure 1). It is planned to supply the district's 121 buildings through a subgrid, that is connected to the main district heating network of Mannheim, Germany, but is operated on lower temperatures to achieve a higher efficiency and allow to integrate local renewable energy technologies

© 2022. The Authors. Published by International Solar Energy Society
Selection and/or peer review under responsibility of Scientific Committee
doi:10.18086/eurosun.2022.04.01 Available at http://proceedings.ises.org

such as air source heat pumps or solar thermal systems.

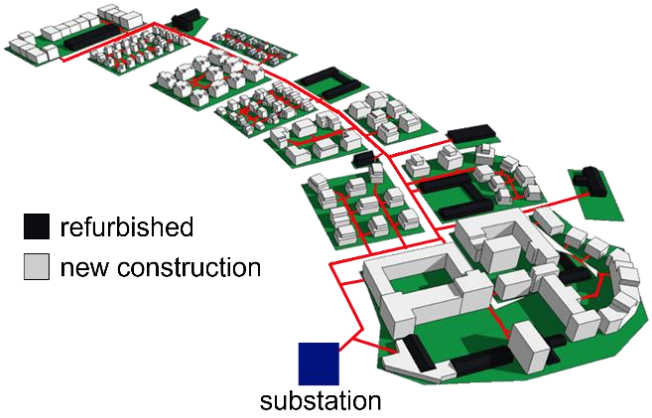

Figure 1: Scheme of the Sullivan district in Mannheim with newly constructed (white) and existing refurbished buildings (black).

2. Consumers

In a past research project, the investor's plans for the Sullivan district have been analyzed and comprehensive thermal simulations of the heat consumers' space heating and DHW demand have been conducted. The resulting design capacities and heat load profiles, including return temperatures, were used to design DHN for three DHW preparation systems (Figure 2):

- DHW preparation in hot water storages at 60 °C
- Instantaneous DHW preparation at 60 °C
- DHW preparation with storages at 45 °C, with heat exchangers on apartment level

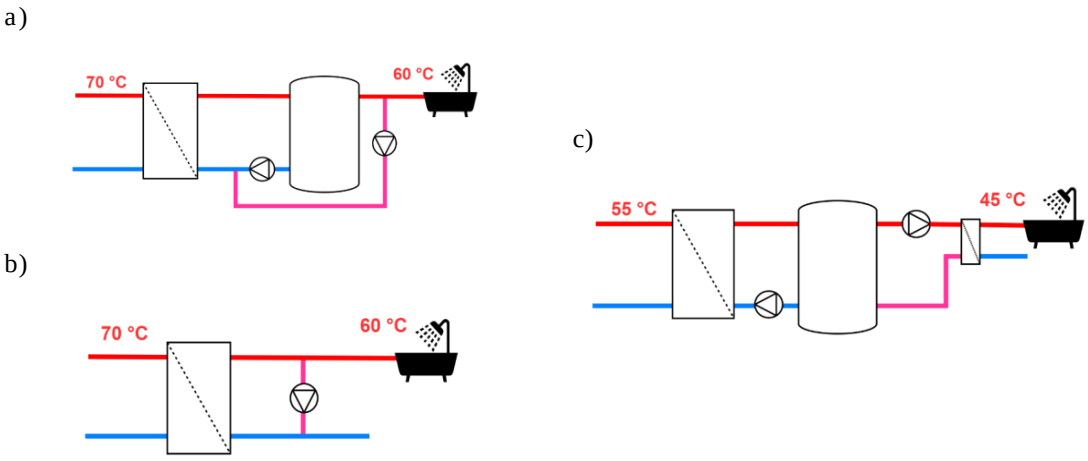

Figure 2: Simplified h*ydraulic schemes of the investigated domestic hot water preparation systems. a) Preparation in a hot water storage at 60 °C. b) Instantaneous preparation at 60 °C. c) Buffer storage at 45 °C with distribution towards heat exchangers at apartment level*

All DHW systems are installed in parallel to the space heating systems, which are using underfloor heating. For hygienic and comfort reasons, circulation systems were assumed for all building types. For DHW preparation at 60 °C a minimum return temperature of 55 °C for the circulation system was assumed. For DHW preparation at 45 °C the circulation return temperature was reduced. The minimum district heating flow temperature (at the consumers) was set to 70 °C for DHW preparation at 60 °C. DHW preparation at 45 °C allows lower minimum flow temperatures of 50 °C.

Figure 3 shows the simulation results aggregated for the whole district as daily mean values. For all DHW preparation systems the return temperatures follow a sine curve, which is proportional to the course of the potable

water temperature. The space heating return temperature is highly dependent on the buildings' energy efficiency standards (newly constructed and refurbished) and their usage schedules (residential and commercial). DHW preparation in storages at 60 °C results in higher return temperatures than instantaneous DHW preparation at 60 °C. By reducing the flow temperature and using buffer storages as well as heat exchangers on apartment level, the return temperature is also reduced, because of the reduced circulation temperatures in the buildings.

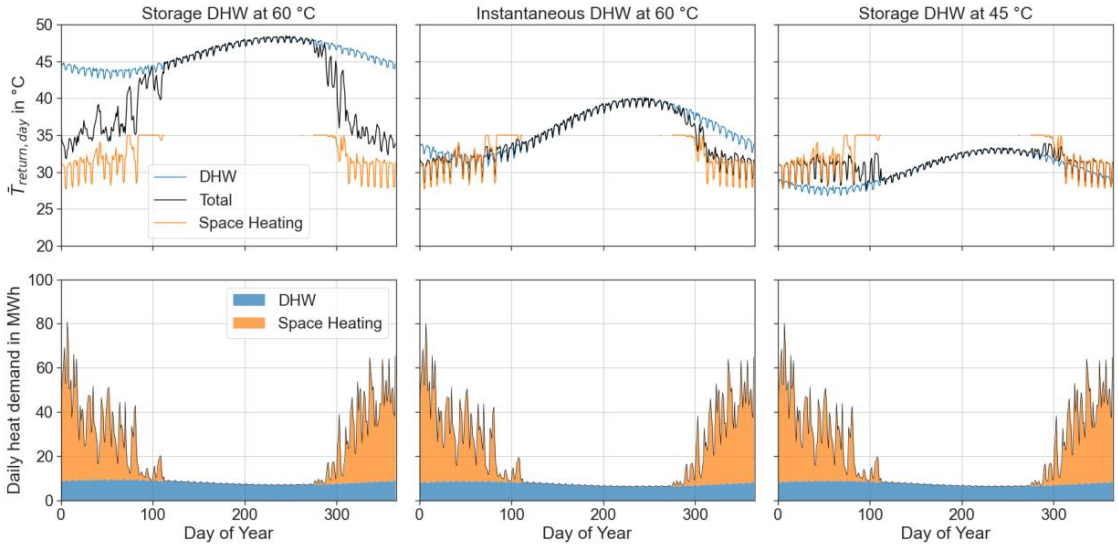

Figure 3: Daily mean values of return temperatures for DHW, space heating and total as well as for the heat demand aggregated for the whole Sullivan district.

The total yearly heat demands as well as the total yearly mass flow weighted average return temperature for all three systems are displayed in Table 1. The space heating demand at 4,554 MWh/a is equal for all systems. Thus, DHW has a share in the total energy consumption of about 40 %. The simulation results show, that instantaneous DHW preparation yields lower total heat demand, because storage heat losses are avoided. By reducing the temperatures in the buffer storage and the DHW distribution pipes, the heat losses are also reduced, which also results in a reduced total heat demand compared to DHW preparation in storages at 60 °C.

Table 1: Simulation results aggregated for all consumers in the Sullivan district

	Total heat demand (space heating and DHW) in MWh/a	Yearly mass flow weighted average return temperature (space heating and DHW) in °C
Storage at 60 °C	7,576	38.7
Instantaneous at 60 °C	7,311	33.0
Storage at 45 °C	7,353	31.1

Additionally, the connected heat loads the consumers were evaluated. The total connected heat loads of the district heating network for the three DHW preparation systems are displayed in Table 2. For instantaneous DHW preparation the individual buildings have much higher connected heat loads, as the maximum DHW demand must be considered. However, the simultaneity is much lower compared to storage systems, which have reduced connected heat loads. This results in a slightly increased total connected heat load (+ 11 %) of instantaneous DHW preparation, when simultaneity is considered.

Table 2: Connected heat loads with and without simultaneity

	Total connected heat load, simultaneity not considered in MW	Total connected heat load, simultaneity considered in MW
Storage at 60 °C	8.1	7.0
Instantaneous at 60 °C	18.4	7.8
Storage at 45 °C	8.1	7.0

3. District Heating Network

A district heating network route is designed to connect all the consumers (see Figure 1). The total route length amounts to 5.1 km. The pipes are dimensioned individually for the three different DHW preparation systems. For all systems the pipes are dimensioned for a maximum specific pressure loss of 300 Pa/m. Simultaneity factors are considered individually for each pipe segment, dependent on the number of consumers supplied through the segment. The design temperatures are set to 75 °C / 40 °C flow and return temperature, respectively, for DHW preparation at 60 °C. For DHW preparation at 45 °C the design temperatures are reduced to 60 °C / 30 °C.

Figure 4 shows the distribution of pipe diameters (DN) for the three DHN as well as an average DN. Because of the higher peak loads for instantaneous systems, the average of the pipe dimensions is larger, especially for lead in pipes. Down the line, in transport pipes, the effect is reduced because of lower simultaneity. For storage systems at 45 °C the design temperature difference between flow and return is lower, which leads to larger pipe dimensions compared to storage systems with DHW preparation at 60 °C.

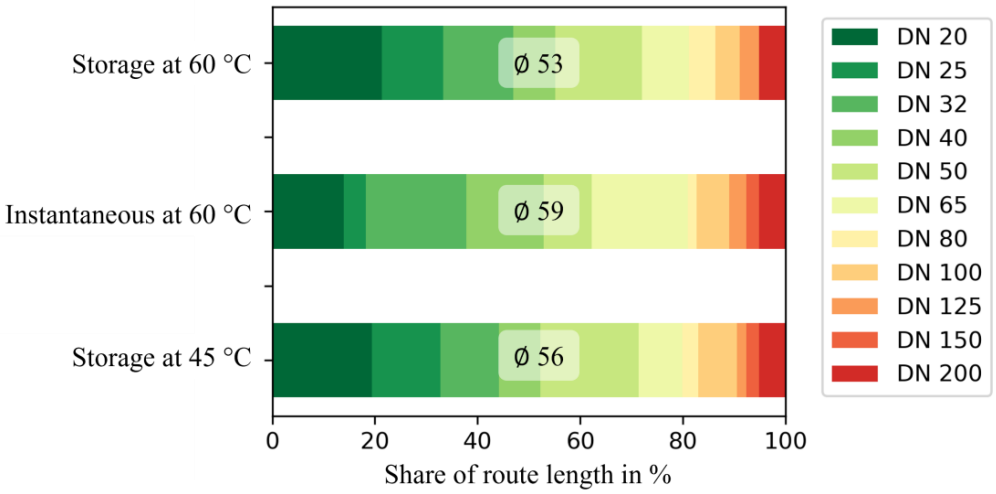

Figure 4: Distribution of pipe diameters for DHN with three different DHW preparation systems. Ø-Numbers indicate the average DN. Total route length: 5.1 km

The thermo-hydraulic DHN model is described by Zipplies et al. (2022). The pipes considered are steel pipes with plastic casing, which are constructed as twin-pipes with the highest insulation standard. Annual simulations are performed, using the previously described load and return temperature profiles as input. For the instantaneous DHW preparation, the simulations yield that the pipes are cooling down during periods without load. To ensure that the consumers' temperature demand can be satisfied all the time, bypasses are considered for the DHN with instantaneous DHW preparation for some of the consumers (marked in Figure 5). The bypasses are controlled so that the flow temperature is always kept above 58 °C. For storage systems this is not necessary because periods without demand occur less frequently and with shorter duration. However, the simulation results show, that the influence of the bypasses on the distribution heat losses (+ 0.8 %) and average return temperatures (+ 0.1 K) is very small.

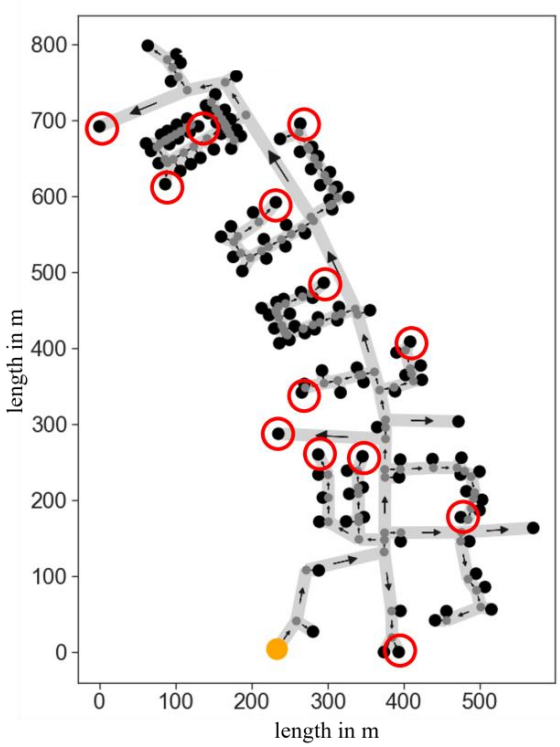

Figure 5: Graphical representation of the district heating network. Red circles indicate substations, where bypasses were considered for instantaneous DHW preparation at 60 °C

The aggregated simulation results are given in Table 3. For all variants, the relative distribution heat losses are very low (around 4 to 5 %). This results from several factors, such as relatively low flow and return temperature levels, a relatively high linear heat density (1.5 MWh/m/a), the usage of the highest insulation standard (DS3), and the usage of twin-pipes. The return temperatures at the heat supply show only little differences to the return temperatures at the consumers (see Table 1). Another interesting indicator is the yearly mass flow weighted average mean temperature (flow and return). This can be used to calculate cost reduction gradients (CRG) which are described in the following chapter. Instantaneous DHW preparation at 60 °C yields slightly (2.9 K) lower mean temperatures (compared to storages at 60 °C), whereas DHW preparation at 45 °C significantly reduces the mean temperatures (-11.4 K). This is of course largely a consequence of the flow temperature reduction.

Table 3: Results of annual simulations

	Storages at 60 °C	Instantaneous at 60 °C	Storages at 45 °C
Heat sold in MWh/a	7,576	7,311	7,353
Distribution heat losses in MWh/a	416	396	309
Distribution heat losses in % related to totally supplied heat	5.2	5.1	4.0
Hydraulic work in MWh/a	25	21	34
Yearly mass flow weighted average return temperature in °C	38.7	32.9	30.9
Yearly average return temperature (over time) in °C	41.9	35.0	31.0
Yearly mass flow weighted average mean temperature (flow and return) in °C	56.9	54.0	45.5

4. Economic evaluation

An economic evaluation is conducted over a period of 30 years, where a discounting interest rate of 3 % is considered. The considered costs include initial and replacement investments, costs for operation and maintenance as well as heat supply costs. The heat supply costs are varied in a range from 30 to 100 €/MWh. All cost assumptions are given in Table 4. For the piping the parameter for ground condition ($f_{condition}$) is assumed as - 25 % (corresponding to "green areas") and the parameter for piping (f_{piping}) is assumed as 0 % (corresponding to "plastic casing").

Table 4: Cost assumptions for economic evaluation

Position	Cost function / Value	Reference
District Heating Network (Piping)		
Investment costs in €/kW	$c(DN) = (270 + 2{,}2 \cdot DN) \cdot (1 + f_{condition}) \cdot (1 + f_{piping})$	Große et al., 2017
Operation and maintenance costs in %/a of initial invest	0,5	Verein Deutscher Ingenieure, 2012
Economic life time in years	30	Große et al., 2017
Network Pump		
Investment costs in €	9.900	wilo, 2017
Operation and maintenance costs in %/a of initial invest	3	Verein Deutscher Ingenieure, 2012
Economic life time in years	10	Verein Deutscher Ingenieure, 2012
Electricity costs in €/MWh	240	
Substations		
Investment costs in €/kW	$c(\dot{Q}) = 0{,}026 \cdot (\dot{Q})^{-0{,}46}$	Große et al., 2017
Operation and maintenance costs in %/a of initial invest	3	Verein Deutscher Ingenieure, 2012
Economic life time in years	30	Große et al., 2017
Storages		
Investment costs in €/l	2,39	Forschungsgesellschaft für Energiewirtschaft mbH, 2017
Operation and maintenance costs in %/a of initial invest	3	Verein Deutscher Ingenieure, 2012
Economic life time in years	30	Verein Deutscher Ingenieure, 2012
Apartment substations		
Investment costs in €/kW	75	Meesenburg et al., 2020
Operation and maintenance costs in %/a of initial invest	3	Verein Deutscher Ingenieure, 2012
Economic life time in years	30	Verein Deutscher Ingenieure, 2012

Figure 6 shows annual full costs corresponding to the three different DHN designs shown in Figure 4, when heat supply costs of 50 €/MWh are assumed. The levelized cost of heat (LCOH, in relation to the heat sold) range from 75 €/MWh (storage at 60 °C) to 100 €/MWh (storage at 45 °C). Instantaneous DHW preparation at 60 °C yields LCOH of 79 €/MWh. From the illustration of the cost distribution, it can be concluded that the differences in costs for heat supply, heat losses, pump energy, piping and substations are rather small. However, the heat exchangers on apartment level add significant costs for the DHW preparation at 45 °C. Because the Sullivan district consists mainly of multi-family houses, more than 1,000 apartments would have to be equipped with heat exchangers. At the assumed rated thermal power of 24 kW per apartment, these would come at a cost of 1,800 € per apartment.

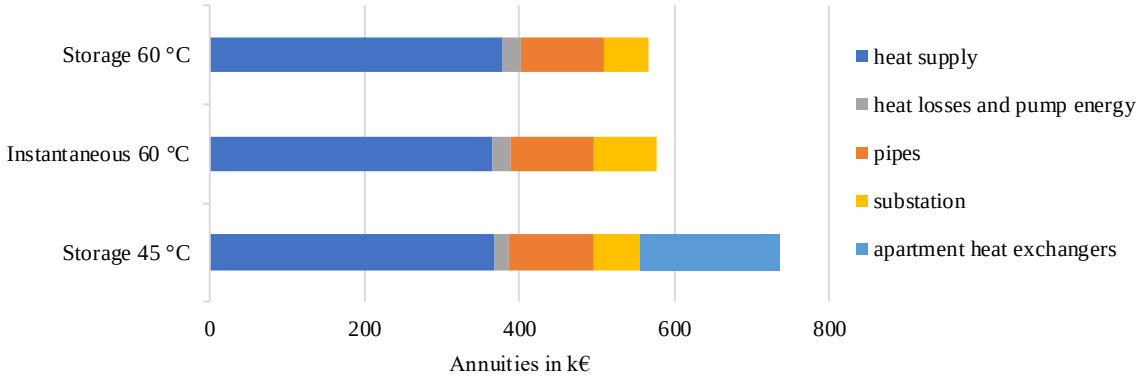

Figure 6: Annual full costs for all three variants for heat supply costs of 50 €/MWh

As mentioned before the heat supply costs are varied in a range from 30 to 100 €/MWh. Because of the reduced heat demand for DHW preparation and heat losses, instantaneous DHW preparation and DHW preparation in storages at 60 °C reach a cost equilibrium at heat supply costs of 90 €/MWh.

The study described so far evaluates the DHN temperature's impact on the heat distribution and consumption. However, the effect on the heat supply is not yet been taken into account. To do this, cost reduction gradients (CRG) are calculated. Geyer et al. (2021) define CRG as the benefit in LCOH of a case with lower temperatures compared to a reference case with higher temperatures, in relation to the temperature reduction (eq. 1).

$$CRG = \frac{LCOH_{Benefit}}{Temperature\ reduction}\left[\frac{€}{MWh \cdot K}\right] \qquad \text{(eq. 1)}$$

For instantaneous DHW preparation at 60 °C and DHW preparation at 45 °C the necessary CRG for reaching a cost equilibrium are calculated, using DHW preparation with storages at 60 °C as the reference case. The values for the CRG are calculated using the yearly mass flow weighted average mean temperature (flow and return, see Table 3). The results are plotted in Figure 7 over the heat supply costs.

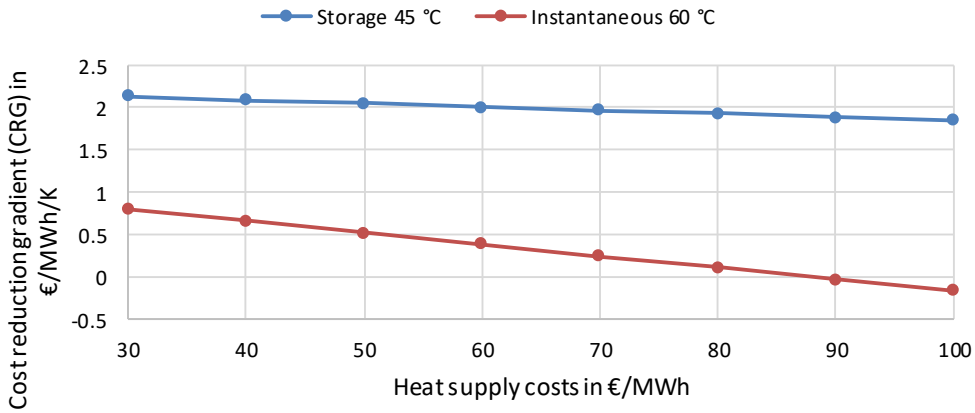

Figure 7: Necessary CRG to reach cost equilibrium with DHW preparation in hot water storages at 60 °C

The results show that for instantaneous DHW preparation at 60 °C the CRG is below 0.8 €/MWh/K and reaches negative values for heat supply costs above 90 €/MWh. For DHW preparation at 45 °C the CRG is between 1.8 and 2.1 €/MWh/K. Geyer et al. (2021) calculated CRG for different heat supply systems. The highest values were calculated for flat plat solar thermal collectors, geothermal heat supply (both: 0.67 €/MWh/K) and heat pumps (0.60 €/MWh/K). However, for geothermal heat supply only return temperature reductions and for heat pumps only flow temperature reductions were considered.

5. Summary

This case study shows that domestic hot water preparation systems have a significant impact on the total heat demand, connected heat load and temperature levels of a district heating network.

Compared to DHW preparation in storages at 60 °C, instantaneous DHW preparation at 60 °C leads to significantly higher connected heat loads for individual buildings, however because of lower simultaneity the total heat load at the heat supply is only about 11 % (7.0 to 7.8 MW) increased. Because storage heat losses are reduced, also the total heat demand is reduced for instantaneous DHW preparation (- 3 %). Another effect are reduced return temperatures, which in turn result in reduced heat losses. On the other hand, instantaneous DHW preparation makes the use of bypasses necessary. These however have low impact on the total DHN efficiency and temperature levels. At low heat supply costs (below 90 €/MWh), the economic evaluation shows slightly higher costs for instantaneous DHW preparation, mainly because of higher costs for substations. Depending on the heat supply system, the cost difference could be compensated for through cost benefits for the heat supply, that are resulting from the return temperature reduction.

DHW preparation with buffer storages and heat exchangers on apartment level also leads to heat demand reductions (- 3 % compared to DHW preparation in storages at 60 °C), because of lower temperature levels and thus heat losses in buildings. A main benefit of this variant is that the DHN supply temperature can be reduced, while the return temperatures are also reduced. However, the economic evaluations show that because of high costs for the heat exchangers on apartment level, DHW preparation at 45 °C is not competitive in this case. This is true even when the cost benefits of the temperature reduction for the heat supply are taken into account.

6. Acknowledgment

The authors acknowledge the financial support of the project by the German Federal Ministry for Economic Affairs and Climate Action (FKZ: 03ET1580C).

7. References

Geyer, R., J. Krail, B. Leitner, R.-R. Schmidt, and P. Leoni, 2021: Energy-economic assessment of reduced district heating system temperatures, Journal Pre-proof. Smart Energy, 2, 100011, https://doi.org/10.1016/j.segy.2021.100011.

Große, R., B. Christopher, W. Stefan, R. Geyer, and S. Robbi, 2017: Long term (2050) projections of techno-economic performance of large-scale heating and cooling in the EU: External study performed by ILF Consulting Engineers Austria GmbH, and AIT Austrian Institute of Technology GmbH for the Joint Research Centre, EUR28859, https://doi.org/10.2760/24422.

Forschungsgesellschaft für Energiewirtschaft mbH (FfE), 2017. Kostenanalyse Wärmespeicher bis 10000 l Speichergröße: Stand Dezember 2016.

Lund, H., S. Werner, R. Wiltshire, S. Svendsen, J. E. Thorsen, F. Hvelplund, and B. V. Mathiesen, 2014: 4th Generation District Heating (4GDH): Integrating smart thermal grids into future sustainable energy systems. Energy, 68, 1–11, https://doi.org/10.1016/j.energy.2014.02.089.

Meesenburg, W., T. Ommen, J. E. Thorsen, and B. Elmegaard, 2020: Economic feasibility of ultra-low temperature district heating systems in newly built areas supplied by renewable energy. Energy, 116496, https://doi.org/10.1016/j.energy.2019.116496.

Østergaard, D. S., K. M. Smith, M. Tunzi, and S. Svendsen, 2022: Low-temperature operation of heating systems to enable 4th generation district heating: A review. Energy, 248, 123529, https://doi.org/10.1016/j.energy.2022.123529#.

Persson, U., E. Wiechers, B. Möller, and S. Werner, 2019: Heat Roadmap Europe: Heat distribution costs. Energy, 176, 604–622, https://doi.org/10.1016/j.energy.2019.03.189.

Verein Deutscher Ingenieure (VDI), 2012: Economic efficiency of building installations: Fundamentals and economic calculation 91.140.01 (2067, Part 1), Beuth Verlag GmbH.

wilo, 2017: high efficiency pumps: Stratos 40/1-16 PN 6/10, Stratos GIGA 50/1-20/1,2, operating mode dp-v.

Zipplies, J., Orozaliev, J., Vajen, K., 2022. Development of Models for Long-Term Simulations of District Heating Networks at High Temporal and Spatial Resolutions. Proc. EuroSun. Kassel, 25.09.-29.09.2022.

Performance Monitoring of an 800m² Solar Thermal Plant with Evacuated Flat Plate Collectors Coupled to a DHN

Alexis Duret[1], Xavier Jobard[1], Gauthier Demonchy[1] and Stefano Pauletta[1]

[1] Laboratory for Solar Energy and Building Physics (LESBAT), School of Management and Engineering Vaud, HES-SO

Abstract

The performances of a 800 m² solar thermal plant coupled to a large District Heating in Geneva has been monitored for more than one year. The solar field is composed of 400 high performance evacuated flat plate collectors manufactured by TVP Solar. It has an average operating temperature above 80°C. This plant has been equipped with sensors to monitor and follow its performances over time. In 2021, the solar plant has injected 536 MWh in the DHN which corresponds to a specific yearly productivity of 684 kWh/m²/y or 45 % of average efficiency. Performances were compared between 2021 and the first half of 2022, with no observed performance degradation. The monitoring will be pursued at least until the end of 2024.

Keywords: solar thermal district heating system, performances monitoring, high vacuum flat plat collector

1. Introduction

The Geneva canton utility company (Service Industriels de Genève or SIG) owns and operates an important portfolio of District Heating Network (DHN). The "CADSIG" DHN is one of the largest and oldest DHN operated by SIG. This DHN built in the 1960's uses a mix of heat produced by natural gas combustion and by a Municipal Waste Incineration Plant (MWI). It has delivered more than 240GWh of heat in 2013/14 to satisfy Space Heating (SH) and Domestic Heat Water (DHW) demand in more than 3 Million m² of housing (Quiquerez and Faessler, 2015). It operates at relatively high temperatures with a forward temperature fluctuating between 115 (winter) and 90°C (summer) and a return temperature around 72°C +/- 2°C all year round. It has average yearly losses of ~10%. The CADSIG DHN energy mix in 2017 is given in the Table 1 below.

Tab. 1: Energy mix of the CADSIG DHN in 2017

Heat producer	Total heat injected
Heat from natural gas boilers (η = 96 %)	204 GWh
Heat from the MWI	125 GWh
Expected solar heat production	0.5 GWh

The use of solar heat in DHN has gained an important interest in the last decade following the successful pioneering large scale applications in Denmark (Perez-Mora et al., 2018). Countries like Germany and Austria (Tschopp et al., 2020) have recently developed subsidy schemes to support the growth of large solar thermal plant. DHN is a very promising application for solar heat for different reasons. Large solar fields can benefit from important economy of scale which drives down the cost of solar heat making it more competitive. In addition, the average efficiency and specific productivity are typically larger than for smaller solar plants mainly because the regulation is more efficient on larger plants (Noussan et al., 2017). The rebound observed in the market of solar thermal collectors in 2018/2019 can partly be explained by the growth of the number of solar thermal plants for DHN and process heat applications.

As the operating temperatures of DHN can be relatively high, it is necessary to find innovative solar thermal technologies able to produce heat at medium to high temperatures with reasonable efficiency and moderate over-costs. This is one of the objectives of the recent IEA-SHC task 68 ("IEA-SHC task 68 - Efficient Solar District Heating Systems," n.d.). Evacuated Flat Plate collectors (EFP) use high vacuum as highly efficient thermal insulation to increase the efficiency and operating temperature range up to 150°C (Benz and Beikircher, 1999). EFP is a very promising technology for operation above 70-80°C. For example, Moss et al (Moss et al., 2018) have recently shown by simulation that, when operated at 85°C, the yearly specific productivity could be double

© 2022. The Authors. Published by International Solar Energy Society
Selection and/or peer review under responsibility of Scientific Committee
doi:10.18086/eurosun.2022.04.02 Available at http://proceedings.ises.org

with EFP than with classical flat plate collectors. The main challenge of this technology is to prove that it can maintain a sufficient level of vacuum inside the collector over its lifetime (20 years or more).

Swiss based company TVP Solar has developed a very efficient EFP mainly for industrial process heat and DHN applications. This collector is one of the first EFP commercially available. The efficiency of their product is particularly superior to alternative technologies above 50K of temperature difference between ambient and solar collector (Beikircher et al., 2015). The TVP Solar collectors are insulated by vacuum (~< 0.1Pa) thus strongly reducing thermal losses due to gas convection and conduction. The vacuum is maintained throughout the life of the collector thanks to a getter pump, which has been designed to absorb gases outgassing from the solar collector components and compensate micro leaks (Benvenuti, 2013).

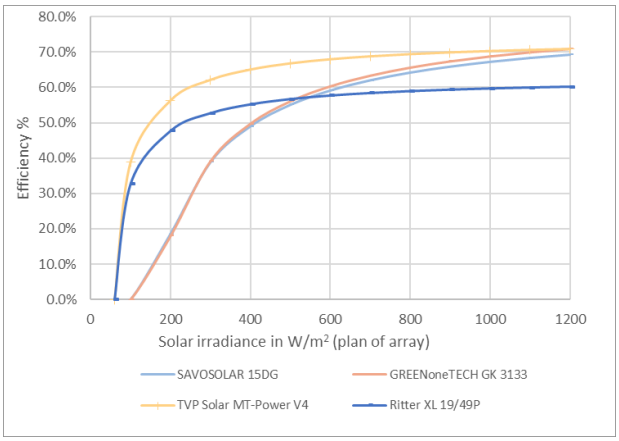

Fig. 1 Efficiency comparison for different solar collectors commercially available established with the Solar Keymark certificates (for an average collector temperature of 70°C and an ambient temperature of 25°C)

Compared to other solar collectors on the market for an average temperature of 70°C (Figure 1), the MT-Power collector from TVP Solar offers the best performance. It should be noted that this collector maintains very good conversion efficiencies at low irradiances (< 500 W/m^2) where competing technologies have lower efficiencies. This characteristic is very interesting for applications in northern Europe where the share of solar energy with irradiances lower than 500W/m^2 is very important. In Geneva, for example, more than 50% of the solar energy corresponds to irradiance lower than 500 W/m^2. Each of the TVP Solar collectors is also equipped with a Spot Check^{TM}, which can be used to check the vacuum quality: when the vacuum integrity of one collector is compromised, the Spot Check^{TM} color will change from pale yellow to transparent white. The high thermal insulation compared to classical solar thermal collector explains the higher performances of TVP collector. The thermal losses are very low allowing to maintain good efficiency with low irradiance of when operating with important temperature difference with ambient.

2. Solar thermal plant characteristics

In 2019, SIG decided to test the performance and reliability of the TVP products in a decentralized large pilot plant called “SOLARCADII” connected to “CADSIG” DHN (see characteristics in Table 2). This large pilot plant is composed of two different parts: (1) the solar thermal plant connected to (2) the heat transfer station by a plate heat exchanger (HEX). The solar thermal plant has total gross area of ~800m^2 and is composed of 400 TVP MT-Power collectors. The solar field has been integrated on a ~1’700m^2 existing metallic structure close to the DHN and is oriented with an azimuth angle of 4° W (see Figure 2). The collectors are arranged in 50 lines separated by 0.8m, composed each of 8 collectors installed with a tilt angle of 17.5°. This solar plant is the first one to use EFP technologies at this scale.

Tab. 2: Main characteristics of the SOLARCAD II solar plant

Solar central name	SOLARCAD II
Owner	Services Industriels de Genève (SIG)
Solar plant engineering company	TVP Solar SA
Solar thermal field	
Solar thermal collector model	EFP MT-POWER v4.3
Total number of collectors	400
Solar thermal field total surface	784 m²
Nominal operating temperature	75-95°C
Peak thermal power at 85°C (T_a=25°C ; G=1000 W/m²)	537 kW
DHN and DHN connection	
CAD auquel est raccordé la centrale	CAD SIG
Type of DHN connection	Decentralized, Return/Return
Inlet temperature at the solar substation	72°C +/- 1.5°C ;

The heat transfer fluid is a 11.1% glycol/water mixture. Two pumps are used to circulate the fluid with a flowrate varying between 5 and 23m^3/hr. In case of emergency, the solar heat is dissipated in a 610kW cooling tower to prevent overheating of the solar field. The HEX has a rated power of 500kW and is used to hydraulically decouple the DHN from the solar plant. The heat transfer station circulates demineralized water from the DHN return pipe at a maximum flowrate of 47m^3/h trough the HEX to be heated by solar heat before being re-injected into the DHN return pipe. Due to the very low yearly solar fraction, it was not necessary to integrate a heat storage (<0.5%).

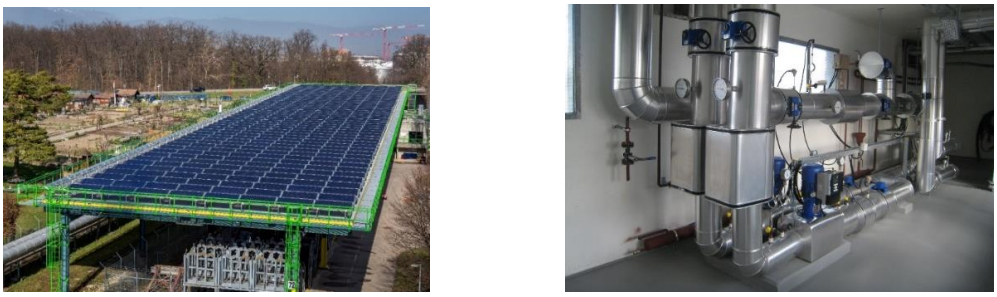

(a) (b)

Fig. 2 Picture of the solar field on the metallic structure (a) and of the heat transfer station (b) (integrated in a room below the metallic structure)

The regulation of the solar plant is done as follow (see Figure 3):

1. **Plant startup:** the fluid is circulated in the solar field once the solar irradiation exceeds 200W/m^2 for more than 5minutes (Loop 1 in Figure 3). The three-way valve is positioned so that the fluid circulates only in the solar field until the outlet solar field temperature reaches 80°C. Then the three-way valve is operated to circulate the fluid in the HEX (Loop 2 in Figure 3). After a 120sec delay, the pump on the DHN side is activated and solar heat is injected in the thermal grid (Loop 3 in Figure 3).

2. **Plant in operation:** in operation, the solar field flowrate is regulated to maintain the outlet solar field temperature at 80°C until reaching the maximum flowrate. The DHN pump is regulated at minimum flowrate when the temperature gain on the DHN side is lower than 3°C. It follows the solar flowrate with a proportional factor above this threshold until the maximum flowrate is reached.

3. **Plant shutdown:** when the irradiance is below 200W/m^2 for 5 minutes, the plant shutdown process is initiated. The flowrate on the solar side is reduced to a minimum and stopped. The pump on the DHN side is stopped when the temperature gain in the HEX is less than 1°C. The plant is then ready to start up again.

In addition, there are routines to protect the plant from freezing (on DHN and solar side) and to dissipate solar heat in the cooling tower in case it is not possible to inject the heat in the DHN.

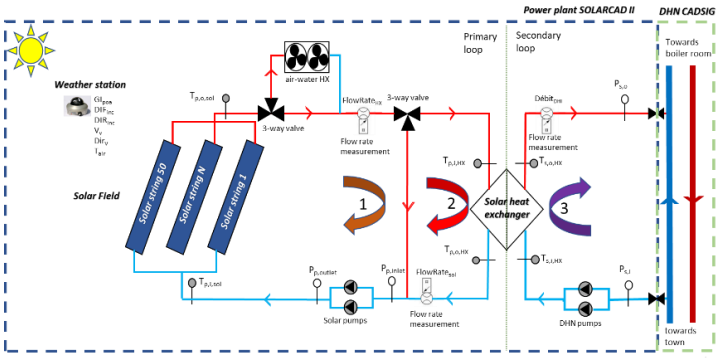

Fig. 3 Hydraulic layout of the "SOLARCADII" plant with the position of each sensor used for performances monitoring

The shading mask has been generated from the middle of the solar field to evaluate the potential irradiation losses due to various shading sources. The Figure 4 presents the shading mask with far shading, close shading (mainly building and chimney) and self-shading. The total losses due to shading represents to less than 1% of the total yearly irradiation.

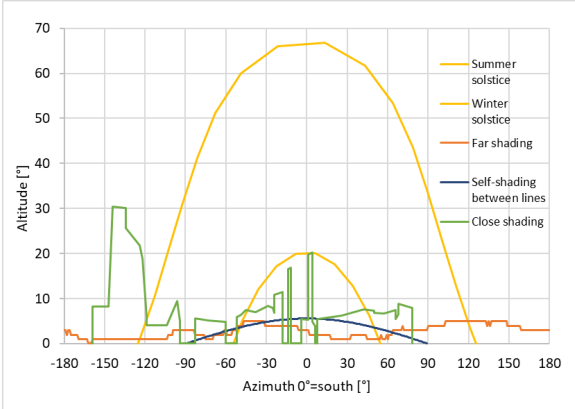

Fig. 4 Shading mask taken in the middle of the solar field

3. Solar thermal plant monitoring

The solar thermal plant performances are monitored since its start up in January 2021. Sensors were installed in order to measure the meteorological conditions and to perform energy balances between the different plant sections. The installed sensors positions are given in the Figure 3.

There are temperature sensors at the inlet and outlet of the solar field and solar exchanger (Endress Hauser TMR31). On the solar side, the flowrate is measured at two points (in the solar loop at the outlet of the solar field and after the HEX) using two Yokogawa DY050 flowmeter. Additionally, a temperature sensor has been installed at the outlet of each line on the solar field. A weather station has been installer close to the middle of the field to measure ambient temperature, humidity, wind speed and direction. The solar irradiance is measured with a pyranometer installed in the plan of array (SPN1 from Delta-T) also located close to the middle of the solar field. This pyranometer measures both the global and diffuse irradiances. The direct irradiance can be deduced by calculation. On the DHN side, the solar heat injected is measured with a heat meter (Calec Energy master coupled with a Krohne flowmeter). The signal of each sensor is acquired at a one-minute sampling rate by the PLC which controls the plant. Measurement data are then sent daily on a server where they are archived in a database for further utilization.

In order to analyze the solar plant performance, various Key Performance Indicators (KPIs) have been used. A definition of each of those KPIs is given below. The total heat produced yearly by the solar field (E_{sol}) corresponds to the total amount of heat produced by the solar field (using inlet and outlet solar field temperature sensors). The total heat produced yearly by the solar plant (E_{DHN}) is calculated by summing the heat injected in the DHN. The solar field efficiency (η_{Sol}) is calculated as follow:

$$\eta_{Sol} = \frac{E_{sol}}{E_{Sol_poa}} \qquad \text{(eq. 1)}$$

where E_{Sol_poa} is the total amount of global solar irradiation received in the plan of array during one year. Similarly, the efficiency of the solar plant (η_{tot}) is calculated using as follows:

$$\eta_{tot} = \frac{E_{DHN}}{E_{Sol_poa}} \qquad \text{(eq. 2)}$$

The yearly specific heat productivity of the solar field $E_{Spec,sol}$ is calculated as the ratio of the heat produced by the solar field (E_{sol}) divided by the solar field gross are (784m^2). Similarly, the specific productivity of the solar plant $E_{Spec,tot}$ is defined as the ratio of the total solar heat injected in the DHN (E_{DHN}) divided by the solar field total gross area (784m^2).

4. Solar plant performances analysis

The solar thermal plant yearly performances have been calculated using the measures realized in 2021. In total, 535MWh were injected into the DHN in 2021 for a global irradiation of 1528kWh/m^2/yr in the plane of array (poa). This corresponds to a yearly specific productivity of 684kWh/m^2/yr and an average conversion efficiency of 45 % for an average solar field operating temperature above 80°C. At the solar field level, a yearly efficiency of 46.4% has been measured which corresponds to a specific productivity of 705kWh/m^2/yr. This high productivity and efficiency demonstrate the interest of the EFP technology for heat production above 80°C, particularly when compared to the typical conversion efficiency of conventional flat plate collectors (between 35 and 40% at 80°C, Furbo et al., 2018). This 10 to 30% difference is explained by the higher conversion efficiency of the EFP from TVP Solar at low irradiance (<500W/m^2).

The yearly electrical coefficient of performance (COP) has also been estimated using the pumps efficiency curve given by the suppliers and the measured flowrates. The COP is defined as the ratio of the heat production to the electricity consumption required to move the heat transfer fluid in the plant and to regulate the plant. For 2021, a COP of 38.5 has been calculated for the plant, while for the solar field only a COP of 53.5 has been found due to significant pressure losses on the solar side. For the solar plant, typical COP reported in the literature are in principle above 100.

A Sankey diagram has been generated to visualize the energy losses for the first year of operation of the plant (see Figure 5). This figure shows that the diffuse radiation represented ~33% of the total yearly irradiation. 10% of the yearly irradiation has been lost because of the 200W/m^2 irradiation threshold. This threshold could certainly be reduced in order to increase the field productivity. The solar HEX losses are negligible.

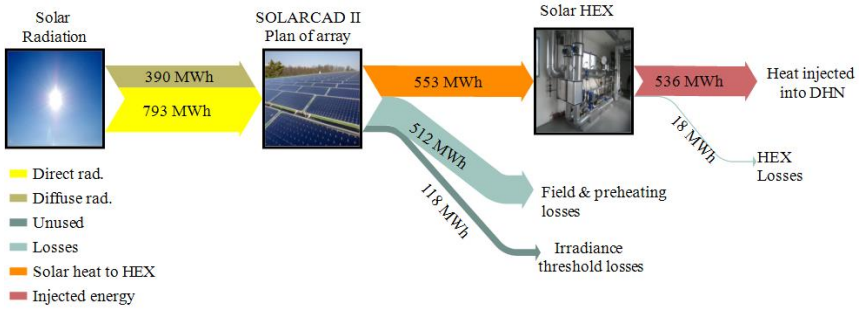

Fig. 5 Sankey diagram representing the main losses of the SOLARCADII installation for year 2021

The Figure 6 shows the temperature and flowrate profile in different section of the installation during a clear sky day (16th of June 2021). The preheating phase is started as soon as the irradiance is above 200W/m^2 for five minutes (05:45). Once the solar field has reached 80°C, the heat starts to be injected first in the solar HEX and then in the DHN (07:00). The flowrate in the solar loop is adjusted in order to regulate the solar operating temperature until the irradiance is too high to maintain the temperature at 80°C (above 450W/m^2). Above this irradiance, the temperature in the solar loop increases up to 95°C when the solar irradiance is maximum (~1'000W/m^2). Then the temperature of the solar field decreases and the injection in the solar HEX is stopped when it is below 80°C (17:00). The solar pump is still operating at reduced flowrate until the irradiance is below 200W/m^2 and the solar field temperature below 75°C.

The relatively high temperature reached in the solar loop when the irradiance is above 450W/m^2 reduced the solar field efficiency. Nevertheless, with the TVP technologies, the efficiency reduction when operating 95°C instead of 80°C is very small (<5%). Thus, it seems not necessary to increase the flowrate in the solar loop to better regulate the operating temperature.

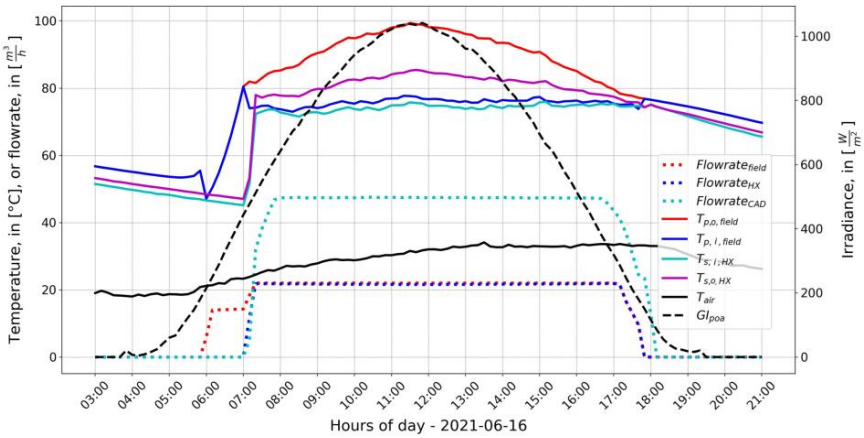

Fig. 6 Clear sky day typical solar plant production profile

5. Solar plant performances stability

As mentioned above, EFP is a very promising technology to increase the specific productivity and to produce heat at temperature above 80°C. The advantages of these technologies could help lower the cost of solar heat and expand their potential applications in solar thermal technology. On the other hand, the high vacuum used as highly efficient thermal insulation has to be guaranteed during the solar collector lifetime (~25 years) in order to maintain high conversion efficiencies. Therefore, several tests have been performed since the startup of the solar plant in order to check that the performance of the solar field and of each of the solar collectors remain stable over time.

The Figure 7 shows the global daily plant production (heat injected into DHN) as a function of the daily global solar irradiation on the plan of array of the solar field for 2021 and 2022. This figure demonstrates that the performance of the solar plant remained unchanged since its startup. This graph also illustrates the ability of EFP to convert solar radiation into heat above 80°C with very high efficiencies from 45 (days with low irradiation) to 60% (days with high irradiation).

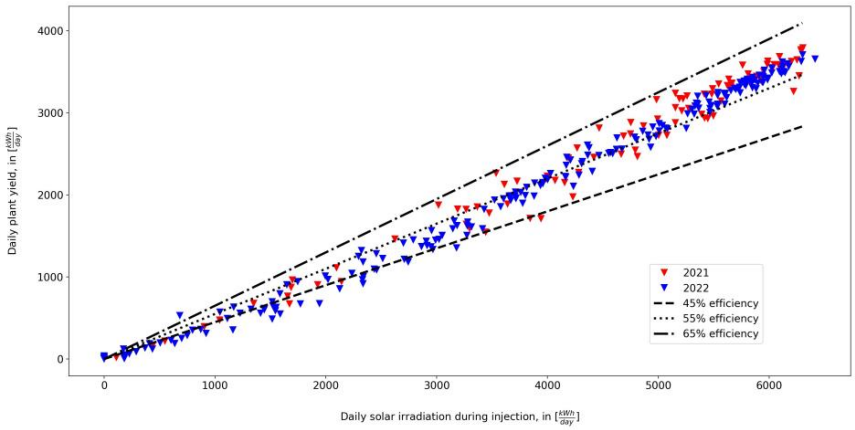

Fig. 7 Total daily heat injected in the DHN as a function of the daily global solar irradiation received by the solar field

In addition, the quality of the thermal insulation of each collector has been evaluated with an IR camera while the plant was in operation (see Figure 8). The objective of this test was to identify the collectors with higher surface temperatures. For each of the collectors with higher surface temperature, surface temperature was measured in the front and the back of the collectors at 11 different points. Two verification campaigns of the collectors were realized: one in January 2021 shortly after the commissioning of the plant and one in February 2022 after a year of operation. Eight collectors with higher surface temperature were identified. For those collectors the surface temperature is higher by 2°C in average compared to the other collectors. At this point of the project, it is not clear if the performances of those collectors have been significantly reduced or not. Additional investigations will be performed in 2023 in order to address this question. A new verification campaign will be repeated at the beginning of 2023 following the same procedure.

Fig. 8 IR Camera picture of the solar field showing one collector with higher surface temperature

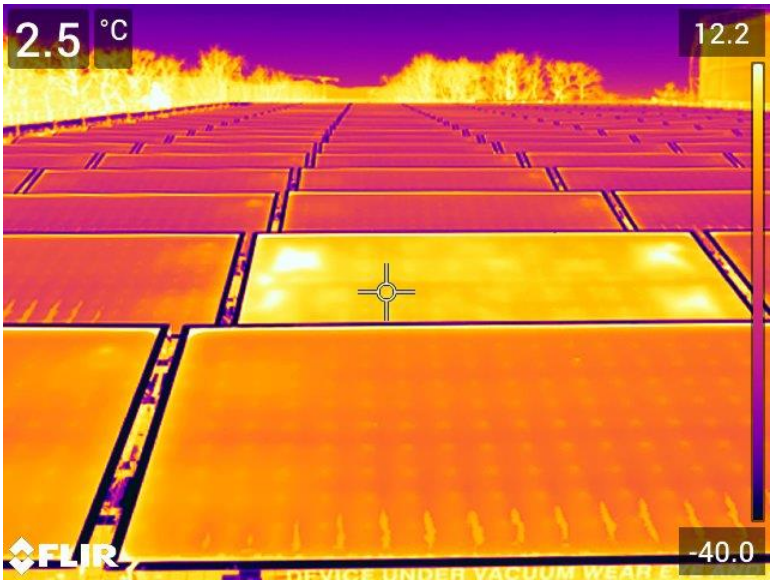

6. Conclusions & perspectives

An 800m^2 solar plant using EFP from TVP Solar has been installed in Geneva and commissioned in January 2021. This plant is connected to the return of a large high temperature DHN. It is operating between 80°C and 90°C. Up to today, this plant is the largest solar plant using EFP technologies connected to a DHN. A monitoring system has been deployed in order to follow the plant performance and its stability over time. During the first year of monitoring, the plant has produced and injected 536MWh of heat in the DHN corresponding to a specific productivity of 684kWh/m^2/yr or 45% of conversion efficiency. This high productivity illustrates the advantage of EFP technology for application above 80°C and with a large share of low irradiance. This productivity is much higher than the state-of-the-art flat plate collector under similar conditions. Electrical COP of 53.5 and 37.5 were estimated for the solar field alone and the plant respectively. This COP could certainly be improved by reducing the pressure losses (tubes with larger diameter) and the pumps operating time.

In addition, the performance stability was studied at the solar field level and for each collector. For the first 18 months of operation, no performance degradation has been found at the solar field and at the collector scale. Nevertheless, 8 collectors with higher surface temperature were identified. At this stage of the project, it is not clear if the performance of those collectors is significantly reduced. Further investigation will be pursued in 2022 on this issue.

The performance monitoring of this plant will continue at least until 2024 with objective to study the stability and reliability of EFP from TVP Solar. In addition, a numerical model of the plant is being developed in Trnsys. This model will be validated using the data collected. The validated model will then be used to evaluate and compare various optimization measures to improve the plant performance (irradiance threshold for plant startup for example).

7. Acknowledgments

This project was funded by the Pilot and Demonstration program from the Swiss Federal Office of Energy (SFOE)

8. References

Beikircher, T., Möckl, M., Osgyan, P., Streib, G., 2015. Advanced solar flat plate collectors with full area absorber, front side film and rear side vacuum super insulation. Sol. Energy Mater. Sol. Cells 141, 398–406. https://doi.org/10.1016/J.SOLMAT.2015.06.019

Benvenuti, C., 2013. The SRB solar thermal panel. Europhys. News 44, 16–18. https://doi.org/10.1051/EPN/2013301

Benz, N., Beikircher, T., 1999. High efficiency evacuated flat-plate solar collector for process steam production. Sol. Energy 65, 111–118. https://doi.org/10.1016/S0038-092X(98)00122-4

IEA-SHC task 68 - Efficient Solar District Heating Systems [WWW Document], n.d. URL https://task68.iea-shc.org/

Moss, R.W., Henshall, P., Arya, F., Shire, G.S.F., Hyde, T., Eames, P.C., 2018. Performance and operational effectiveness of evacuated flat plate solar collectors compared with conventional thermal, PVT and PV panels. Appl. Energy 216, 588–601. https://doi.org/10.1016/J.APENERGY.2018.01.001

Noussan, M., Jarre, M., Degiorgis, L., Poggio, A., 2017. Data Analysis of the Energy Performance of Large Scale Solar Collectors for District Heating. Energy Procedia 134, 61–68. https://doi.org/10.1016/J.EGYPRO.2017.09.619

Perez-Mora, N., Bava, F., Andersen, M., Bales, C., Lennermo, G., Nielsen, C., Furbo, S., Martínez-Moll, V., 2018. Solar district heating and cooling: A review. Int. J. Energy Res. 42, 1419–1441. https://doi.org/10.1002/er.3888

Quiquerez, L., Faessler, J., 2015. Increasing waste heat recovery by connecting existing thermal networks. EuroHeat Power Mag. 12, 22–26.

Tschopp, D., Tian, Z., Berberich, M., Fan, J., Perers, B., Furbo, S., 2020. Large-scale solar thermal systems in leading countries: A review and comparative study of Denmark, China, Germany and Austria. Appl. Energy 270, 114997. https://doi.org/10.1016/J.APENERGY.2020.114997

9. Nomenclature

Abbreviations	Signification
η_{Sol}	Solar field efficiency [%]
η_{Tot}	Solar plant efficiency [%]
DHN	District Heating Network
DHW	Domestic Hot Water
E_{DHN}	Total solar heat injected yearly in the DHN [MWh]
EFP	Evacuated Flat Plate Solar Collector
E_{sol}	Total heat produced yearly by the solar field [MWh]
E_{Sol_poa}	Total solar irradiation received yearly by the solar field on the plan of array [MWh]
HEX	Plate Heat Exchanger
MWI	Municipal Waste Incineration Plant
$Flowrate_{CAD}$	Flowrate in the HEX on the DHN side (secondary) [m^3/h]
$Flowrate_{Field}$	Flowrate in the solar field [m^3/h]
$Flowrate_{HX}$	Flowrate in the HEX on the solar side (primary) [m^3/h]
GI_{poa}	Global Irradiance on the plan of array [W/m^2]
T_{Air}	Ambient air temperature [°C]
$T_{p,i,field}$	Solar field inlet temperature [°C]
$T_{p,o,field}$	Solar field outlet temperature [°C]
$T_{s,i,HX}$	Plate heat exchanger intlet tempreature on DHN side [°C]
$T_{s,o,HX}$	Plate heat exchanger outlet tempreature on DHN side [°C]

Operability of District Heating Plants combining a Large-Scale Solar Thermal Field with Condensing Wood Chip Boilers – A Case Study in Switzerland

Xavier Jobard[1] and Alexis Duret[1]

[1] Laboratory for Solar Energy and Building Physics
School of Management and Engineering Vaud, HES-SO, Yverdon-les-Bains (Switzerland)

Abstract

The subject of this work is the integration and operability of a large-scale solar thermal field with condensing wood chip boilers for district heating application in rural areas. Based on a case study in Switzerland, a large-scale solar field is designed to be coupled with the existing heating plant composed of two wood boilers with external flue gas condensers. The operability of the new central heating plant is then assessed with numerical simulations carried out with TRNSYS. In a first step, two scenarios with two different solar fractions are simulated to analyze the performances of the solar system and the influence of the integration of the solar thermal field on the operation of the wood boilers. The main results are: 1) The specific productivity is between 450 and 500 $kWh.m^{-2}.y^{-1}$ for the considered operating temperatures and solar fractions. 2) The startup cycles are important if the heating needs in summer are not totally covered by the solar system. 3) After optimization of the controls, the startup cycles of the boilers in mid-season are very low.

Keywords: Solar District Heating, Large-scale solar thermal, Wood Chip Boiler, Numerical simulation, operability

1. Introduction

The subject of the proposed article is the integration of large scale solar thermal field with biomass boilers for district heating (DH) application in rural areas. (Lund et al., 2014) identifies this combination as relevant to the principle of 4th Generation DH principles assisting the development of sustainable energy systems. Moreover, (Tschopp et al., 2020) refers to installations on this best practice concept as "Bioenergy Villages" and report on the first demonstration object in Büsingen, DE. There a solar field is coupled with two wood chip boilers backed-up with an oil boiler. The solar field shows good performance with 13% of solar fraction (100% from end of June to mid-August) and with a solar specific productivity of 603 $kWh.m^{-2}.y^{-1}$. Based on this success, five similar plants were commissioned in 2018. However, no information was found on the operability of these plants and the impact on the startup's cycles of the boilers. Only (Ruesch, 2020) through numerical simulation concluded that the starts up cycles of wood boilers can be important in summer and widely reduced with the integration of solar heat production. However, increase of the boiler's startups was also found in mid-season but only marginally higher. In a similar way, this paper proposes to study the operability of central heating plant combining a large-scale solar thermal field and wood chip boilers supplying a DH network. The particularity is that the boilers are equipped with flue gas condensers and induce higher complexity to integrate the solar thermal system.

Base on a case study located in Switzerland with extensive monitoring data, numerical simulations were carried out at a fine timestamp allowing the evaluation of the operability of the system. The modeled central heating plant consists of the actual installed condensing wood chip boilers upgraded with a large scale solar thermal field and thermal energy storage (TES). Firstly, the actual design of the heating plant and the selected solar thermal field integration concept will be described. Secondly, chosen numerical modeling method and models are presented briefly before finally discussing the simulation results.

© 2022. The Authors. Published by International Solar Energy Society
Selection and/or peer review under responsibility of Scientific Committee
doi:10.18086/eurosun.2022.04.03 Available at http://proceedings.ises.org

2. DH plant and integration of solar thermal field with TES

The considered DH network is located in the rural town of Les Ponts-de-Martel, NE, Switzerland and went into operation in September 2007. Initially, 32 buildings were supplied by the network, with a total length of 2.1 km. Ten years later, nearly 80 buildings are connected to the district heating system. The entire district heating network belongs to a cooperative called "Le Marais-rouge". Each consumer (including potential future consumers) of the network can be part of this company. This particular legal status makes "Le Marais-rouge " a completely different DH system than the one managed by utility companies. The involvement of the consumers in a cooperative makes it easier to access the secondary heat distribution circuits for energy efficiency measures, since the heat consumers benefit from them: the price of the energy consumed depends on the overall efficiency of the district heating network. Therefore and thanks to efficient substation design, very low return temperatures are achieved with a yearly mean value in 2019 of 44°C and peak value as low as 28°C were measured in winter. Table 1 presents the main characteristic of the DH network “le Marais-Rouge”.

Tab. 1: Characteristic of the district heating network of “les Marais-Rouge”, values given for the year 2019

Heat supply	5.81	GWh
Linear heat density	1.53	$MWh.kml^{-1}.y^{-1}$
Heat losses	0.76	GWh
Supply temperatures	80 - 70	°C
Mean return temperature	44	°C

The DH network “le Marais-Rouge » makes a good candidate for the integration of solar heat: 1) its rural area provides plenty land space for the solar field, 2) low supply and return temperature allow efficient heat production and 3) main fuel should be spared for use in Winter. Only drawback found is a low heat consumption in summer causing high distribution losses. Figure 1 shows the simplified hydraulic diagram of the central heating plan comprising of 2 wood boilers (1.25 MW and 1 MW) equipped of flue gas condensers installed separately upstream of the boilers on the DH return pipe. Cascading of the boilers is possible in series in winter, while only one boiler is operated in mid-season and summer. The flue gas condensers allow to preheat the water of the network returning to the power plant. This is beneficial since it allows the recovery of energy otherwise lost in the flue gas and limits the recirculation of water in the wood-fired boilers, which must not have inlet temperatures below 65°C.

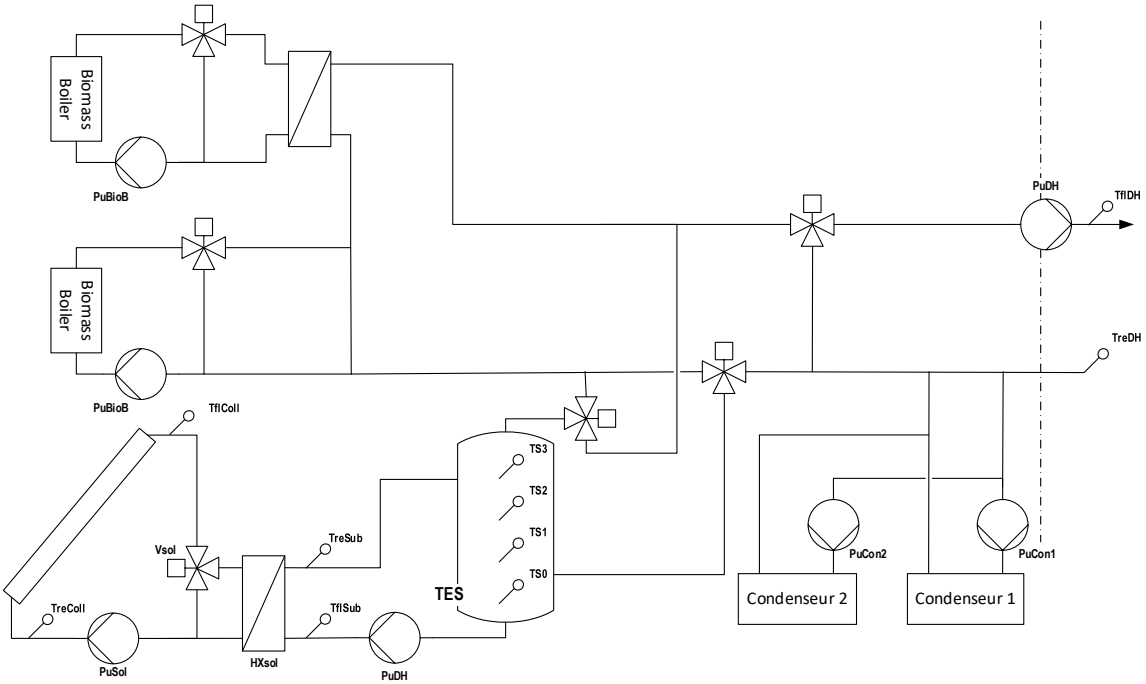

Fig. 1: Simplified hydraulic diagram of the central heating plant of the DH “le Marais-Rouge” upgraded with the integration of a large-scale solar thermal system.

The fact that the condensers need low inlet temperatures to recover effectively the latent heat contained in the flue gas, implies that the solar installation should be integrated after them. In winter and mid-season, the solar field is design to preheat the flow on the return line of the boilers. As the inlet temperature of the wood boiler should be kept above 65°C, the solar thermal system operates thus between the supply temperature of the condensers and 65°C. In summer the solar field is designed to supply, when possible, the total heat demand of the network, if not one boiler is fired-up and takes over. In winter and mid-season, the solar field inject the heat on the return line before the gas In order to guarantee the heat supply even at night or when the weather does not allow the solar installation to fulfill the demand, a hot water tank is installed to store the produced solar energy and to inject it later on the grid. The technology chosen here is insulated steel tanks. These tanks must be highly insulated. As reported (Sveinbjörnsson et al., 2017): In Denmark, those tanks are insulated with between 30 and 45 cm of mineral wool to have acceptable losses at about 2% per week for 500 m3 and 1% per week for 5000 m3 tanks. The tank is integrated in the hydraulic diagram to store exclusively solar heat. This was chosen to simplify the controls.

3. Numerical model of the system

The heating plant modeling was performed with TRNSYS 17 software (Klein and Al., 2014). The wood boilers are modeled with the type 869 developed by (Haller et al., 2011). It is a numerical model to simulate any kind of boiler of different technology and fuel and especially wood chips boilers. The parameters are defined from the data provided by the manufacturer and hourly monitoring data from the heating plant. For simplicity, the condensers are modeled with a simple model derived from the available measurements. Finally, the TES and solar field are modelled with well-known models respectively type 60 and type 832 (Haller et al., 2013). Other components (tubes, controls) are modelled with standard types from the TRNSYS library.

Validation of the models (boiler and condenser) has been conducted by comparing monitoring data with the simulation results and by assessing cvRMSE (eq. 1). Only the heat flow rates were compared with each other.

$$cvRMSE = \frac{\sqrt{\sum(y-\hat{y})^2}}{\bar{y}} \quad \text{(eq. 1)}$$

With: y the monitoring values and $\hat{y}$ the simulated values et $\bar{y}$ the average of the monitoring values.

3.1 Wood chip boiler model

The validation of the simulations gives mitigated results (see figure 2). The comparison shows high cvRMSE values (38% and 39%). The dynamic behavior of the boilers is relatively well represented considering the input data and the noise of the measurements. Indeed, the temperature measured at the boiler outlet deviates strongly from the setpoint temperature given by the water law.

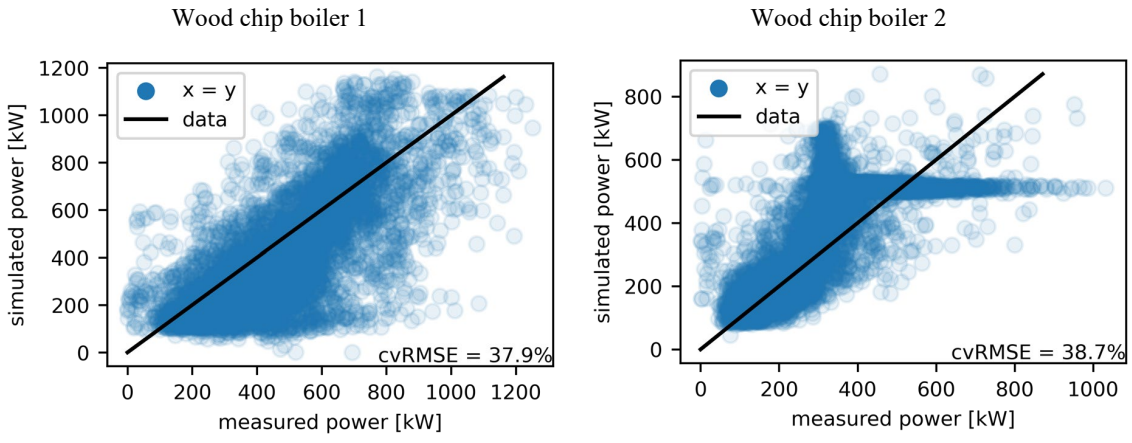

Fig. 1: Comparison of monitoring data and simulations for wood boiler 1 (left) and 2 (right)

This is confirmed by the comparison of the boiler power monotones presented at figure 3 and figure 4. Nevertheless, a reservation can be made for boiler 2 whose model does not allow to reproduce its load rate measured during the cascade operation i.e., in winter period. In fact, and as shown in the figure 4, the simulated load of boiler 2 have a level at 500 kW which does not exist. This point should be further studied to find its causes. Annually, the absolute error on the produced energy is -12% for boiler 1 and 18% for boiler 2.

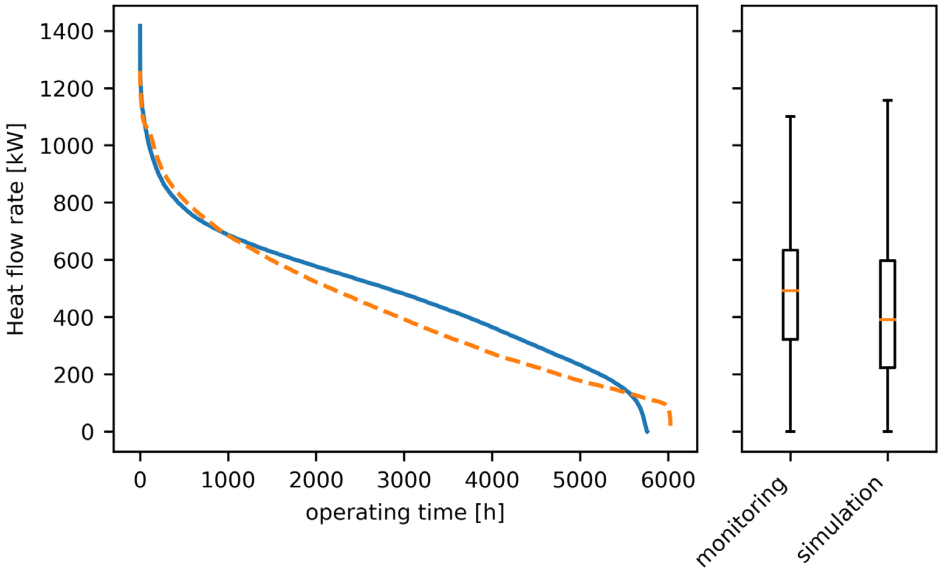

Fig. 2: Comparison of the power monotones of Boiler 1 from monitoring and simulations

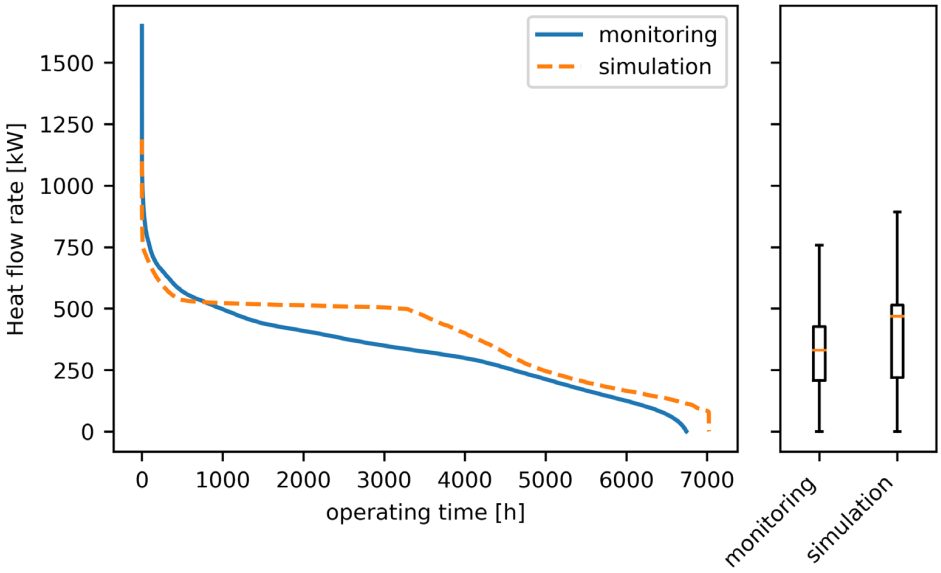

Fig. 3: Comparison of the power monotones of Boiler 2 from monitoring and simulations

3.2 Flue gas condensers

The condensers are modeled very simply by taking constant heat losses and heat recovery efficiency on the fatal heat (latent and sensible) of the flue gas at the exit of the wood boilers. The equation defining this operation is given below in equation 2:

$$\dot{Q}_{con} = \eta_{fg} \cdot (\dot{Q}_{fg} - \dot{Q}_{fg,loss}) \quad \text{(eq. 2)}$$

With :

- η_{fg}: The efficiency of heat recovery from the flue gases
- $\dot{Q}_{fg}$: The latent and sensible heat flow rate in the flue gas, given by the model of the wood boiler and the characteristics of the fuel.
- $\dot{Q}_{fg,loss}$: The sensible heat flow rate lost between the boiler and the condensers

The parameters of the equations η_{fg} and $Q_{fg,loss}$ were identified graphically by comparing the monitoring data and the result of the simulations. The values obtained are given in table 2.

Tab. 2: Parameters for the numerical condenser model

Parameters	Condenser 1	Condenser 2
$\boldsymbol{\eta_{fg}}$	0.90	0.90
$\boldsymbol{\dot{Q}_{fg,loss}}$	90 000 kJ/h	72 000 kJ/h

The figure 5 present a comparison of the results of the numerical model with the monitoring data. The graphs show that the model approximations roughly reproduce the condenser operation with a cvRMSE value of 49% for condenser 1 and 37% for condenser 2. However, the relative deviations of the annual heat production of the condensers are 30% for condenser 1 and 1% for condenser 2. The measured data show a non-linearity between the boiler heat output and the condenser heat output that the model does not reproduce. A variable efficiency and a better identification of the parameters would improve the performance of the model. However, for the purpose of this study, the model is considered satisfactory.

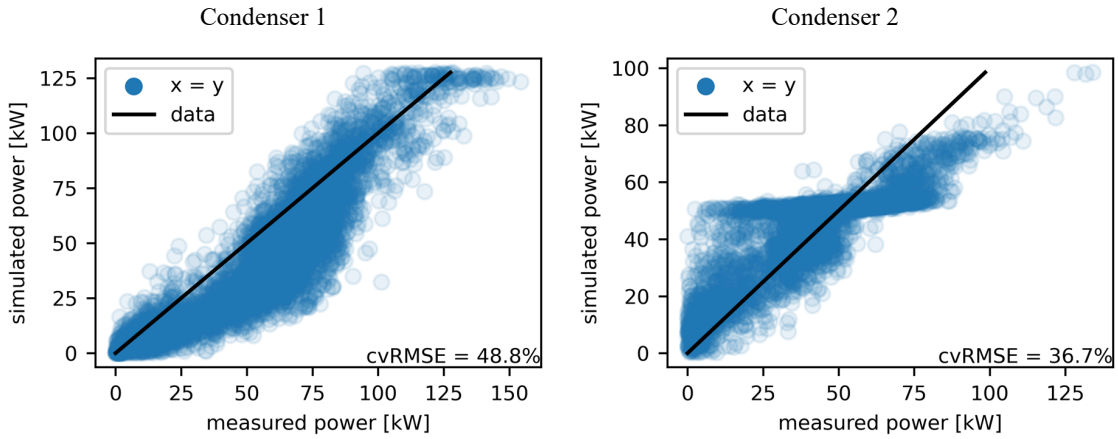

Fig. 5: Comparison of monitoring data and simulations for condenser 1 (left) and 2 (right)

3.3 Thermal Energy Storage (TES)

The hot water tank is modelled with the generic type 60. It is configured to have two double ports, on for charging the tank with solar heat and one to discharge the tank. Type 60 takes as main parameters, the tank's volume VS, height H, and overall heat loss coefficient U. To vary the volume of the tank, height/diameter ratio has been fixed to 2 to ensure compactness while keeping an efficient stratification. The overall heat loss coefficient has been calculated for 5 different volumes [50, 500, 5000, 10000, 15000] m^3. The calculation was carried according to (Bergman and Incropera, 2011) with a outer convection heat transfer coefficient of 10 W/(m^2.K), insulation thickness of 0.45 m, heat conductivity of 0.04 W/(m.K) and assuming constant physical properties of material over the temperature range (20°C – 100°C). The results were regressed to obtain a continuous function given in equation 3 and figure 6:

$$U = 0.11\,.\,(VS - 48)^{-0.02}; r^2 = 0.998 \qquad \text{(eq. 3)}$$

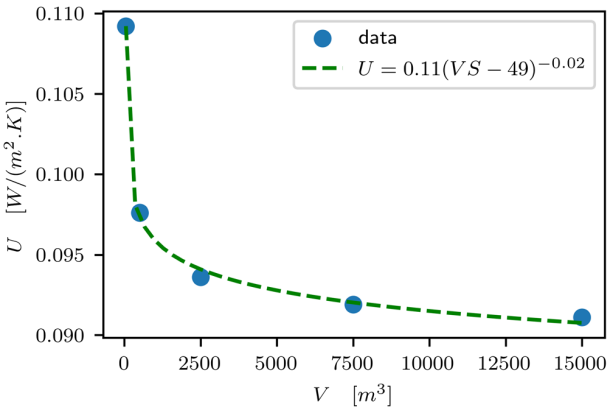

Fig. 4: Evolution of the heat loss coefficient U as a function of the volume of the storage tank with a constant height/diameter ratio of 2.

3.4 Solar collectors

The solar collectors are modelled with a well-known third-party model, type 832. The performance coefficients considered are given in table 3, they were obtained by averaging the coefficients of large flat plate collector on the market these last years from several European manufacturers. Heat capacity and incident angle modifier coefficient for diffuse and direct irradiation are also taken into account.

Tab. 3 : Performance coefficient of an average large scale flat collector

	value	**unit**
$\boldsymbol{\eta_0}$	0.79	-
$\boldsymbol{a_1}$	2.9	W/(m^2.K)
$\boldsymbol{a_2}$	0.0135	W/(m^2.K^2)

4. Results

This section presents the results obtained with the numerical model described in section 3. and their analysis to show the technical potential of integrating solar thermal in wood based and rural DH network. An underlying objective is to give elements on the influence of the solar thermal installation on the operation of the wood chip boilers and to establish if there is an increase of the boiler startup cycles. For this purpose, several scenarios were implemented and sized based on an available pre-feasibility study:

1. Solar fraction less than 15% with 1500 m^2 of solar thermal panels and 75 m^3 of TES (scenario 1)
2. Solar fraction around 30% with 3300 m^2 and 1060 m^3 TES (scenario 2)
3. Optimization of startup cycles for scenario 2 (scenario 3)
4. Sensitivity analysis of the sizing parameters (Gross panel area and TES size)

4.1 Scenario 1: low solar fraction

A first scenario was defined to analyze systems with a low solar fraction (< 15%) and a limited storage volume. The solar heat is injected on the return line before the boilers and downstream of the condensers. The annual results presented in table 4 shows a very satisfactory productivity and efficiency of respectively 516 kWh/(m^2.an) and 33%. The solar heat is thus very well used.

On the one hand, the figure 7 also shows a very good solar coverage above 60% in summer for the months of July and August but insufficient to cover the total needs. On the other hand, the coupling return/return generates important cycle of starting of the wood boiler in summer (figure 8). It starts every time the installation does not allow to cover the needs completely. An optimization is surely possible to reduce them, but it would not allow to totally suppress these cycles. The installation of a larger storage that can be used by the biomass boilers would be beneficial.

Tab. 4: Annual performance of the solar system including storage losses in scenario 1

Solar resource in the collector plane (30°, 0° South)	1558	kWh/(m^2 .a)
Yield	773	MWh
Productivity	516	kWh/(m^2 .a)
Solar efficiency	33	%
Solar fraction	13	%

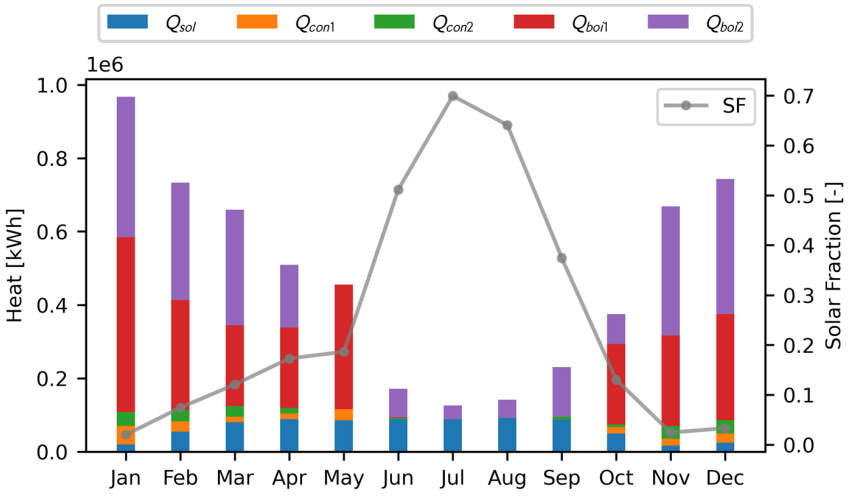

Fig. 7: Monthly heat production per installation and solar fraction for scenario 1

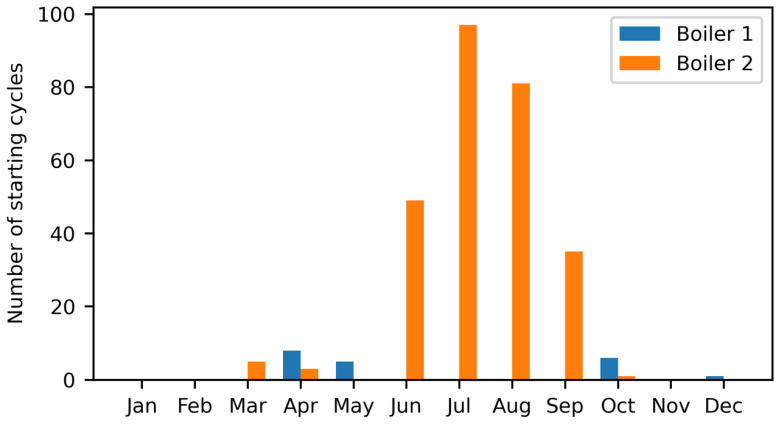

Fig. 8: Number of boiler start-up cycles with injection on the outflow in the off-season and in the summer of scenario 1

4.1 Scenario 2: Solar fraction of about 30%.

The sizing of this variant is intended to turn off the boilers during the summer period. The figure 9 shows a possible boiler shutdown from July to the end of September. The results (table 5) show an interesting productivity higher than 450 kWh/(m^2 .an) including storage loss. The yield is also in the expected range, although slightly lower than in scenario 1. As for the solar fraction, it falls short at 26% compared to the target value of 30%. The monthly results presented in figure 9 show that the fraction reaches 100% of the needs for the months of July, August, and September. In the off-season the solar fraction is also interesting between 30 and 40%. The boiler load is also reduced during these months.

Tab. 1: Annual performance of the solar system including storage losses in scenario 2

Solar resource in the collector plane (30°, 0° South)	1558	kWh/(m² .a)
Yield	1497	MWh
Productivity	454	kWh/(m² .a)
Solar efficiency	29	%
Solar fraction	25.7	%

However, this is only problematic for the month of June, as shown in figure 10. Because the solar system is very close to covering the entire demand of the DH network but does not reach it, boiler 1 presents a high number of starting cycles (n=60). This operation is not satisfactory and can strongly reduce the performance of the boiler. An optimization of the operation of the installation is therefore necessary and has been realized in scenario 3.

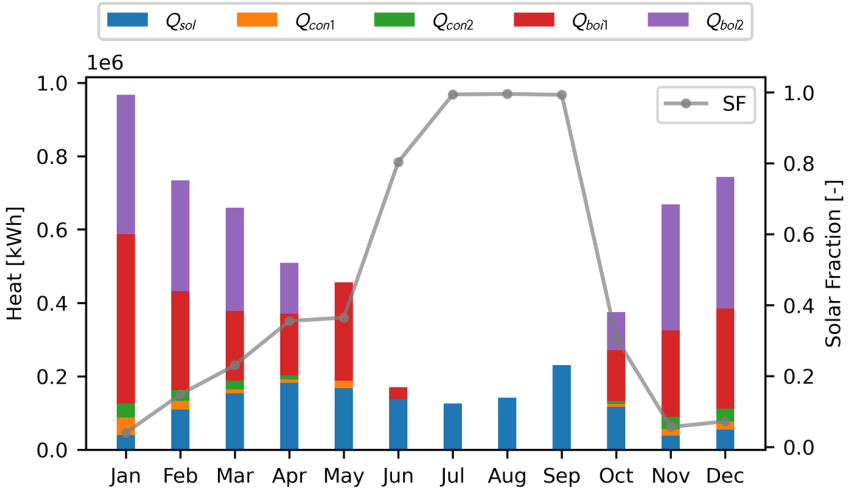

Fig. 9: Monthly heat production per installation and solar fraction for scenario 2

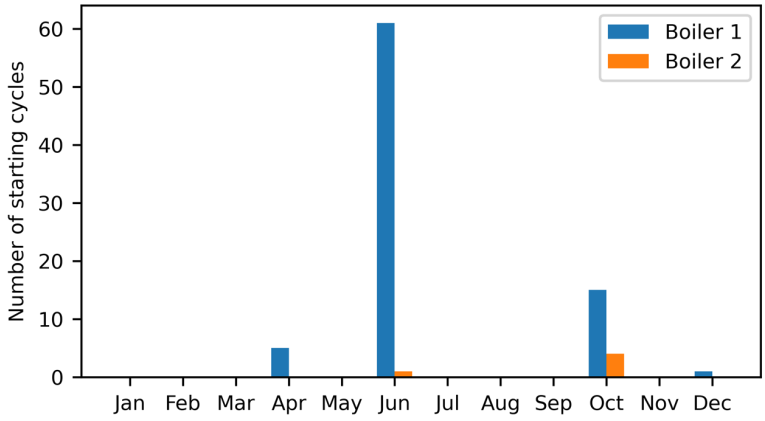

Fig. 10: Number of boiler start-up cycles with injection on the outflow in the off-season and in summer

4.3 Scenario 3: Optimization of boiler start-up cycles in the off-season

In scenario 2, boiler 1 cycles strongly in June. In this scenario, the season changes is optimized in order to shut down the boiler earlier and leave the solar thermal field to fulfill the entire demand sooner. After analyzing the instantaneous powers of the boilers, an advancement of the summer to the hour at 3634 instead of 3967 and an extension of the fall inter season to the hour 7238 instead of 7057 was implemented. The figure 11 shows a clear decrease in boiler start-up cycles.

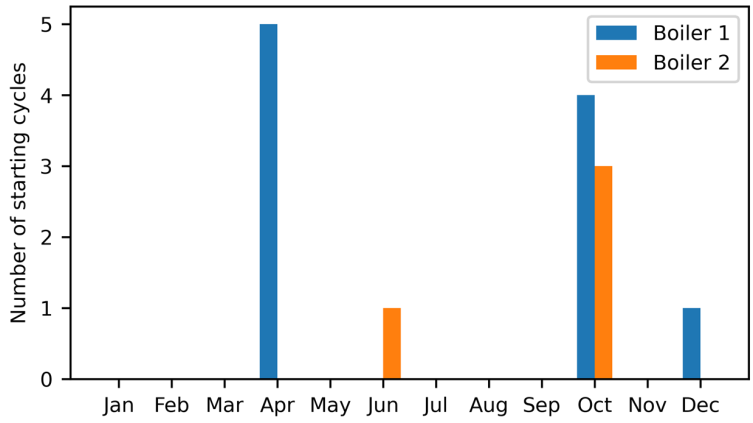

Fig. 11: Number of boiler start-up cycles with injection on the outward journey in the off-season and in the summer after optimization of the dates of the change of season

After this optimization, it also results in a better solar heat production in June and allows to cover the total heat demand of this month, see figure 12.

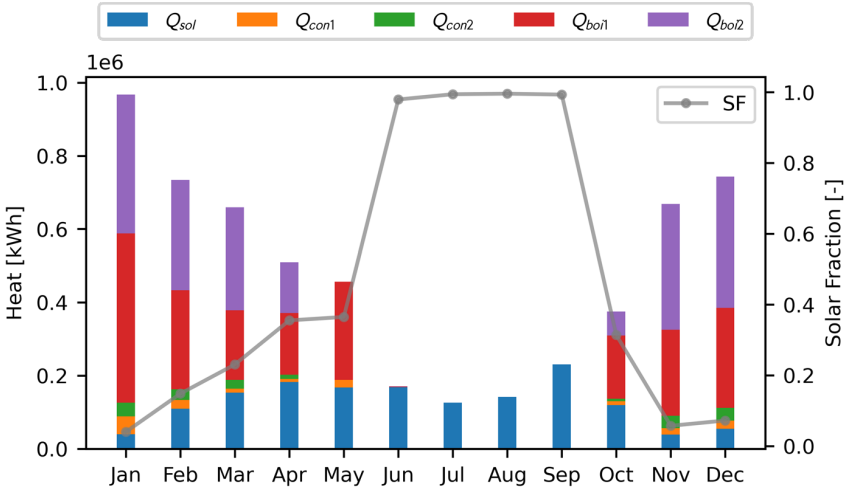

Fig. 12: Monthly heat production per installation and solar fraction for the optimized scenario 2

From the point of view of the annual performances presented in the table 6. A slight improvement is noted with a gain of 2% on the solar yield and one additional efficiency point.

Tab. 6: Annual performance of the solar system including storage losses in optimized scenario 2

Solar resource in the collector plane (30°, 0° South)	1558	kWh/(m2.a)
Yield	1531	MWh
Productivity	464	kWh/(m2.a)
Solar efficiency	30	%
Solar fraction	26.2	%

4.4 Sensitivity analysis

In order to be able to assess the sizing of the solar thermal installation and its storage, 6 sizes of solar field from 1500 m^2 to 4000 m^2 as well as 6 specific storage volumes (VS_{spe}) were simulated with the TRNSYS model described above. Figure 13 presents the results by showing the variation of the solar fraction (solid lines) in parallel with the specific productivity of the solar thermal panels (dashed lines) as a function of the installed solar panel area. Like any solar thermal system, 3 main trends are observed:

- The larger the solar field, the larger is the solar fraction.
- The larger the solar fraction, the lower is the specific productivity of the panels as the system losses increase.
- For a given solar array size, there is an optimal specific storage volume above which there is no increase in the specific productivity of the panels.

It is found that a specific volume of 0.05 [m3 /m2] is not optimal with respect to the specific productivity of the solar field. Taking 1500 m2, the increase of the specific volume from 0.05 to 0.25 [m3 /m2] allows a gain of specific productivity from 535 kWh/(m2 .an) to 600 kWh/(m2 .an) that is to say approximately 12% of increase. Beyond 0.25, the gain is no longer as decisive for this panel surface.

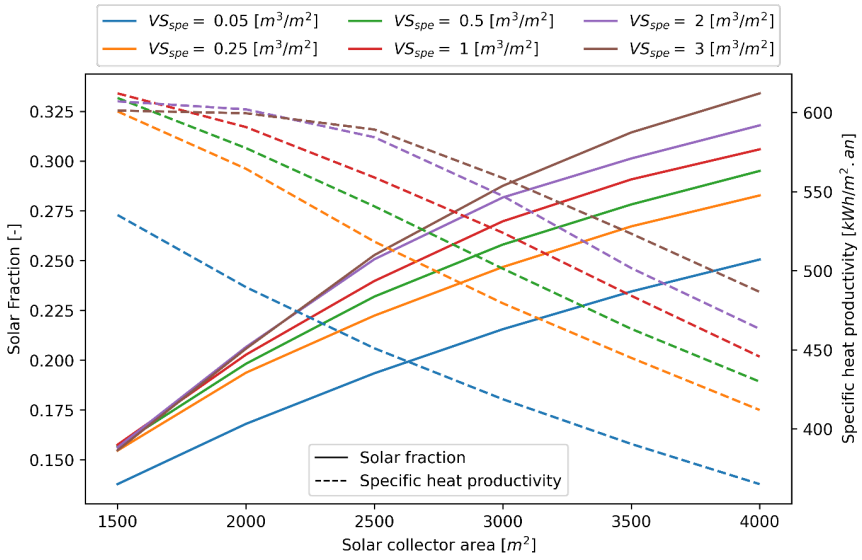

Fig. 5: Solar fraction and specific heat productivity for different surfaces of solar thermal panels connected to the Ponts-de-Martel boiler room obtained from the TRNSYS model results

5. Conclusion

A numerical model of the boiler room of the DH "les Marais-Rouge" integrating a large-scale solar thermal system was developed with the software TRNSYS 17. In a first step, this model allowed to calculate 2 scenarios of solar coverage (< 15% and about 30%) and to analyze the performances of the solar system and the influence of the integration of the solar thermal on the operation of the wood boilers. The main results are:

- The specific solar yield is between 450 and 500 kWh/(m^2 .an) for the operating temperatures and solar coverages considered
- Start-up cycles are important if the summer heat demand is not fully covered by the solar system
- Boiler start-up cycles in mid-season are very low in the scenarios studied

In a second step, a sensitivity study on the size of the field and the specific storage volume was conducted in order to better appreciate the sizing parameters. From the point of view of the specific heat productivity, an optimum storage volume appears between 0.5 m^3/m^2 and 1 m^3/m^2 for a 1500 m^2 surface of solar thermal panels. This optimum increases for larger surfaces (between 2 and 3 m^3/m^2 to 2000 m^2) to reach very large storage volumes (> 5 000 m^3). These applications are generally not very profitable in Switzerland. However, a financial calculation should be made to confirm this trend.

6. Acknowledgments

This work was financially supported, by the Swiss Federal Office of Energy. This work was carried out during the SolCAD project carried out in collaboration with the CREM, KAEMCO and Planair. The authors would also like to thank M. Didier Barth avec the "Marais-Rouge" cooperative for providing the monitoring data and technical information of the heating plant as well as for his availability to answer their questions.

7. References

Bergman, T.L., Incropera, F.P., 2011. Fundamentals of heat and mass transfer. Wiley.

Haller, M., Perers, B., Bales, C., Paavilainen, J., Dalibard, A., Fischer, S., Bertram, E., 2013. TRNSYS Type 832 v5.01 „Dynamic Collector Model by Bengt Perers" - Updated Input-Output Reference. Rapperswil.

Haller, M.Y., Paavilainen, J., Konersmann, L., Haberl, R., Dröscher, A., Frank, E., Bales, C., Streicher, W., 2011. A unified model for the simulation of oil, gas and biomass space heating boilers for energy estimating purposes. Part I: Model development. J. Build. Perform. Simul. 4, 1–18. https://doi.org/10.1080/19401491003671944

Klein, S.A., Al., 2014. TRNSYS 17: A Transient System Simulation Program.

Lund, H., Werner, S., Wiltshire, R., Svendsen, S., Thorsen, J.E., Hvelplund, F., Mathiesen, B.V., 2014. 4th Generation District Heating (4GDH): Integrating smart thermal grids into future sustainable energy systems. Energy 68, 1–11. https://doi.org/10.1016/J.ENERGY.2014.02.089

Ruesch, F., 2020. BioSolFer Integration von Solarwärme in Biomasse Fernwärmenetze.

Sveinbjörnsson, D., Linn Laurberg Jensen, Trier, D., Bava, F., Hassine, I. Ben, Jobard, X., 2017. FLEXYNETS D2.3 - Large Storage Systems for DHC Networks.

Tschopp, D., Tian, Z., Berberich, M., Fan, J., Perers, B., Furbo, S., 2020. Large-scale solar thermal systems in leading countries: A review and comparative study of Denmark, China, Germany and Austria. Appl. Energy 270, 114997. https://doi.org/10.1016/j.apenergy.2020.114997

8. Nomenclature

Abbreviations	Description
DH	District Heating
fg	Flue gas
SF	Solar Fraction
loss	Heat losses

symbol	description	Unit
η	Effiency	-
cvRMSE	Coefficient of variance of RMSE:	-
$\dot{Q}$	Heat flow rate	kW
Q_{sol}	Heat flow supplied by the solar system (storage output)	kWh
Q_{boi}	Heat flow supplied by the wood boiler	kWh
Q_{con}	Heat flow supplied by the flue gas condenser	kWh
U	Overall heat loss coefficient of the storage	$W/(m^2.K)$
VS	Storage volume	m^3
VS_{spe}	Specific storage volume according to the gross area of the solar field	m^3/m^2

Solar District Heating versus Renovation of Buildings as Measures for Decarbonization of Heat Supply in Rural Areas

Jan Kelch, Oleg Kusyy, Johannes Zipplies, Janybek Orozaliev and Klaus Vajen

University of Kassel, Kassel (Germany)

Abstract

In this study two different decarbonization strategies for rural heat supply are compared on the example of 180 buildings located in a german village called Rauschenberg-Bracht. The comparison shows that the erection of a solar district heating system with solar fraction of about 67% leads to similar heating costs as a profound energy efficient renovation followed by installation of decentralized air heat pumps for most buildings. Both concepts aim to achieve a heat supply that is free from the local use of fossil fuels. While the solar district heating system can probably be realized within a few years and therefore achieves the full CO_2e savings promptly, this would take decades for the implementation of energy rehabilitation and heat pumps due to a low renovation rate. To reach climate-neutrality for the heat supply could thus be accelerated significantly by the construction of a solar district heating system. Moreover, the two decarbonization approaches do not appear to be fundamentally exclusive: subsequent steady renovation of connected buildings will either increase the solar share in heat supply or enable the connection of new consumers at a similar solar coverage rate. However, it should be also noted that with solar district heating not the same thermal comfort as with profound energy efficient building renovation is achieved.

Keywords: decarbonization strategy, rural heating, solar district heating, energy efficient renovation

1. Introduction

About 150 million tonnes (BDEW 2021) or about 18% of the total annual CO_2e emissions in Germany are attributed to the heating and cooling of buildings, with heating having the largest share. Especially against the backdrop of the climate crisis, the question arises how the decarbonization of building heat can be achieved as fast as possible and at lowest possible costs. This study focuses on rural areas and develops two different heat supply scenarios for 180 buildings in a German village called Rauschenberg-Bracht as an example. A solar district heating system with 67% solar fraction and basic renovation measures (centralized solution) is compared to profound renovation combined with the installation of air heat pumps for most of the buildings (decentralized solution). The primary target is to achieve a heat supply which is free from the local use of fossil fuels. The annual costs of heat for an average building are used as the key figure. Furthermore, the annual CO_2e emissions for the next three decades are compared.

2. Current state analysis

At present, about two thirds of the village heat is generated by heating oil and one quarter comes from biomass (wood logs, wood chips and pellets). Almost all buildings are single or two-family houses, about 90% were built (some of them in half-timbered construction) before 1980. The village is not connected to the natural gas grid. Inhabitants of Bracht founded a local energy initiative to implement the solar district heating system. According to current information about 180 buildings will be connected to the local heating network. This building stock comprises 156 existing and 24 planned buildings that will be erected in a few years. All 180 buildings are classified in five categories based on construction year and renovation needs:

- renovation sensitive
- before 1980

© 2022. The Authors. Published by International Solar Energy Society
Selection and/or peer review under responsibility of Scientific Committee
doi:10.18086/eurosun.2022.04.04 Available at http://proceedings.ises.org

- 1980 till 2000
- after 2000
- new building

The category “renovation sensitive” includes the buildings erected in a half-timbered construction and additional buildings built before 1919. The underlying assumption of this category is, that the facades of these buildings are worth to preserve or they are even under monumental protection, thus, they can be insulated only internally. Because the region around Bracht is densely forested, short transportation routes are assumed and, thus, a CO_2e emission factor of 0 g_{CO2e}/kWh for wood is chosen. Based on survey database, the current overall heat consumption (4,082 MWh/a), CO_2e emissions (926 t_{CO2e}/a) and wood consumption (1,526 MWh/a) are estimated for the 180 buildings. A second data set based on the results of brief energy consultations conducted by the energy agency of Hessen (LEA), contains detailed information for 27 buildings: firstly, heat transfer coefficient and area for each building component of the thermal building envelope which are later used to estimate the necessary insulation measures for the decentralized renovation, and, secondly, recommended minimum-investment renovation measures like insulation of the top or basement ceiling which are applied when considering solar district heating.

3. Comparability of two scenarios

To ensure comparability, the following framework conditions are defined for both scenarios "solar district heating" and "decentralized renovation":

- Supply of heat (space heating and domestic hot water) for the 180 potential consumers
- Supply of heat without local use of fossil fuels
- No more use of biomass is allowed than in the present

The emission factor of 366 g_{CO2e}/kWh is taken for the consumed electricity at the current state, while, for the scenario period from 2025 until 2044, the estimated average value of the emission factor is 62 g_{CO2e}/kWh based on the Germany’s policy goal of reaching 80% renewable share for power generation in 2030 and emission factors by Luderer et al. 2021.

4. Solar district heating scenario

In this scenario the CO_2e emissions are mainly reduced by the implementation of renewable energies, especially solar thermal energy. Only minimum renovation measures, such as insulation of upper floor and basement ceilings are exploited to reduce the initial investment costs. The potential reduction of heat demand due to these measures is estimated at about 2 % based on detailed recommendations for 27 buildings by the LEA, estimations on the reduction of heat consumption by the method of tabula according to Loge et al. 2015 and following extrapolation on the rest of the 156 existing buildings with account of building category. The total net cost of minimum renovation is about 631 k€. The most important components of the central heating concept are a large solar thermal collector field (12,900 m²) and a seasonal heat storage (26,600 m³), which is designed as a pit storage filled with water, covered with a foil on the ground side and insulated with a floating thermal insulation on the top. An electric heat pump (1,190 kW_{th}) is used to cool the storage in the heating period down to about 30°C. This enables to reduce the storage size and, thus, the investment costs, compared to the direct storage discharge down to the return temperature of the district heating network of about 50°C only. The remaining heating load is covered by two wood chip boilers (150 and 400 kW_{th}), which serve as auxiliary heating to increase the heat pump’s efficiency.

The solar thermal heating system, illustrated in Figure 1, has the following operating states listed in decreasing priority. For simplification in Figure 1 the heat flow of the first operation state is not illustrated seperatly and added to the second operation state.

- Direct heat supply from solar collector
- Direct heat supply from seasonal storage tank

- Simultaneous heat supply from heat pump and wood chip boilers

The heating system is simulated in TRNSYS with the modified type 343 "ICEPIT" as pit storage for 3.5 years. Only the last year when the ground around the storage tank has warmed up and, apart from the temperature changes within the annual cycle, has reached a thermal equilibrium, is used for energetical and economical evaluation. For the optimization TRNSYS is coupled with the GenOpt software (Generic Optimization program) to determine the component sizes that yield minimum levelized costs of heat.

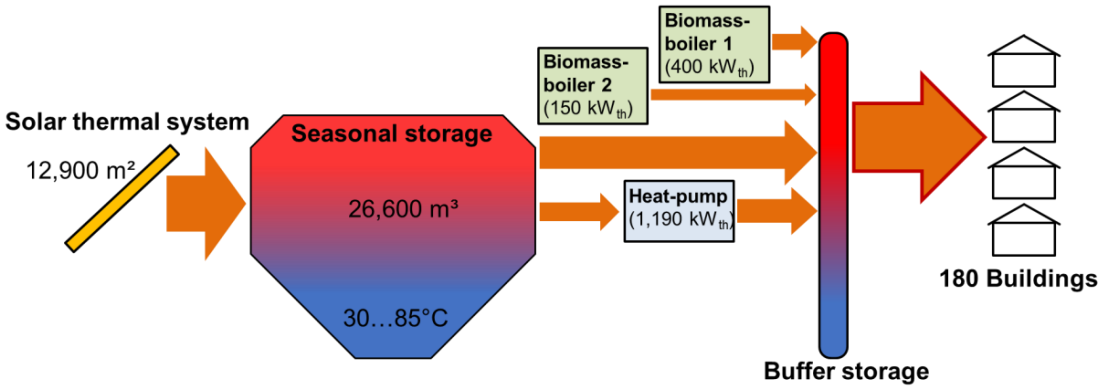

Figure 1: Solar district heating system

The shares of heat supply by different energy sources are shown in Figure 2 for the optimized system. With 67% solar thermal energy has the highest share. The heat pump is working with a SCOP of about 4.7 and the seasonal storage tank is operated in a temperature range of 30 till 85°C. Due to solar district heating the CO_2e emissions are reduced by -98% compared to current state.

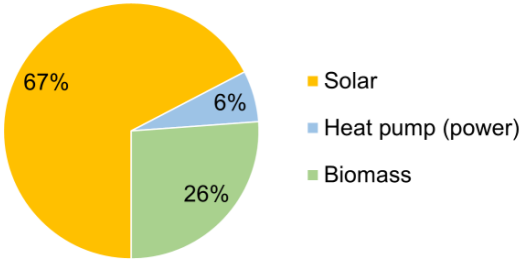

Figure 2: Distribution of heat sources feeding into the district heating network

5. Decentralized renovation scenario

In this scenario the decarbonization is achieved with decentralized measures in the buildings only. The estimation of the measures is based on evaluation of 27 buildings for which detailed data are available. To estimate the extent of the measures the aproach is as described:

- To determine necessary measures for improving the building's thermal envelope, insulation thresholds are defined, which means that all components of the 27 buildings with heat transfer coefficients higher than the chosen thresholds will be insulated.
- It is assumed, that the existing insulation remains and the new insulation is implemented on top (except for windows, which must be replaced).
- If a measure is necessary, it will be dimensioned to reach the minimal heat transfer coefficient required

by federal funding for efficient buildings (BEG) for individual measures (BMWi 2021).

The thresholds and minimum requirements for funding are presented in table 1.

Table 1: Heat transition coefficients for the scenario decentralized renovation

Building component	Assumed thresholds for the existing insulation in $W/m^2 \cdot K$	Minimum requirement of funding if new measures are done in $W/m^2 \cdot K$
roof	0.4	0.14
top ceiling	0.3	0.14
basement ceiling	1.0	0.25
basement wall	0.5	0.25
base plate	1.0	0.25
outer wall (external)	0.4	0.20
outer wall (internal)	0.7	0.65
windows	2.6	0.95

The reduction of heat consumption for each of the 27 buildings is calculated by the method of tabula with considering the rebound effects caused by changing resident's behavior in buildings with increased efficiency. For this a correction factor determined by the Institute for Housing and the Environment (IWU) (Loge et al. 2015) is used.

For the 180 buildings that should be supplied by the district heating network, the estimated distribution by building category is presented in table 2. The building categories are known only for 132 existing and 24 new buildings but not for the remaining 24 existing buildings. For that reason, the categories of existing buildings are scaled up from 132 to 156 resulting in decimal numbers. This distribution serves for the extrapolation of the identified measures as well as specific heat consumption (per m² living area) from 27 to 180 buildings.

Table 2: Estimated distribution of 180 buildings into five building categories

	1	**2**	**3**	**4**	**5**	
	renovation sensitive*	**before 1980**	**1980 till 2000**	**after 2000**	**new building**	**∑**
Number of buildings	50.8	82.7	17.7	4.7	24.0	180

The estimated insulation measures for 180 buildings shown in Figure 3 indicate that insulation of the outer wall and replacement of windows are quite often required for buildings constructed before 2000. It will be shown later that this has a large influence on the total investment costs. It is assumed that architect's services are necessary for buildings for which roof or outer wall are to be insulated and blanket costs for that services are considered later in the economic evaluation.

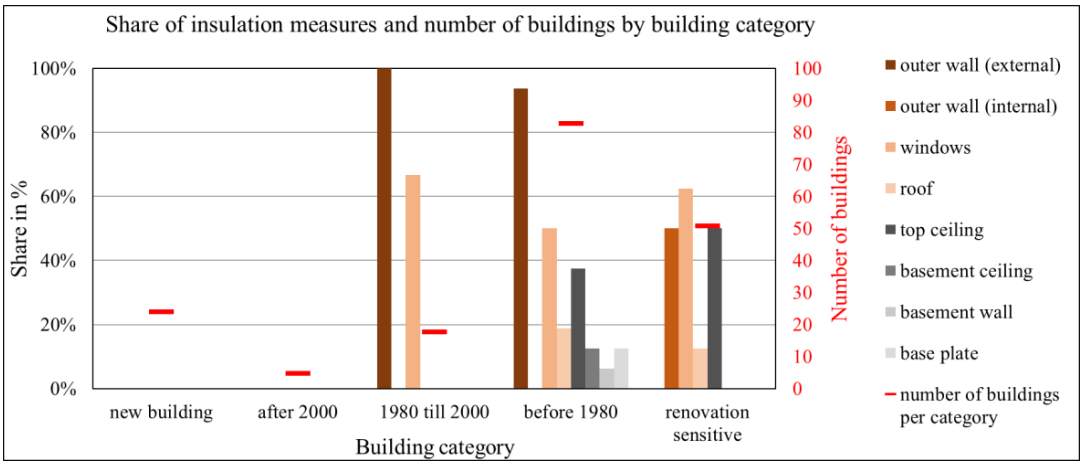

Figure 3: Estimated insulation measures for 180 buildings in decentalized renovation scenario

Figure 4 presents the shares of heat pumps and wood fired boilers by building category. This distribution is a result of the assumptions that new wood fired boilers will be implemented in the buildings with highest specific heat consumption and only either in the renovation sensitive buildings or in the buildings which heat with the wood at present. The wood amount is enough to heat around 55 buildings, while the rest is heated by air heat pumps. To ensure a high SCOP for the buildings heated with air heat pumps the underfloor heating systems are implemented, what is probably not always reasonable (or possible) and could overestimate the investment costs.

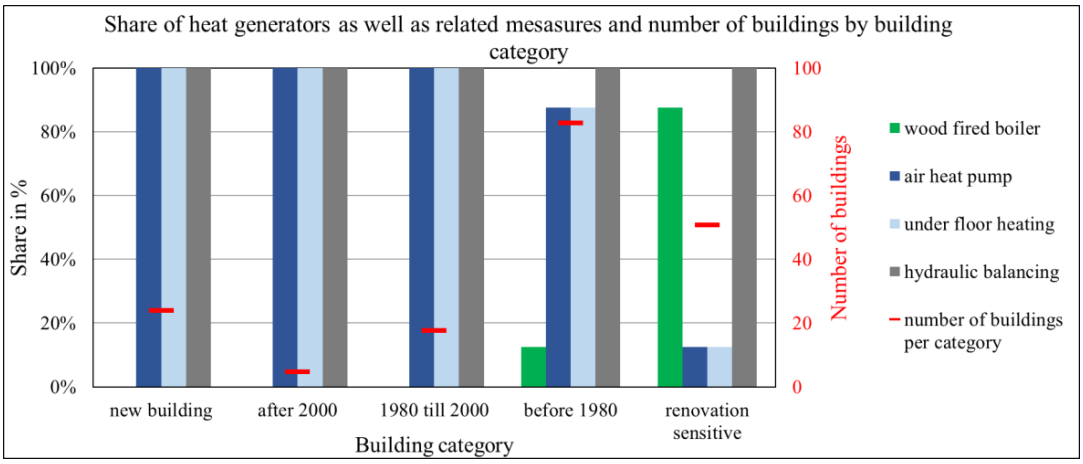

Figure 4: Estimated measures for 180 buildings concerning heat generation and distribution inside the building in decentralized renovation scenario

By the implementation of all measures presented in Figure 3 and Figure 4 the heat consumption decreases by about -14% and the CO_2e emissions by -95% in total for all 180 buildings. The shares of heat supply by air heat pumps and wood fired boilers as well as the reduction of heat consumption are shown in Figure 5.

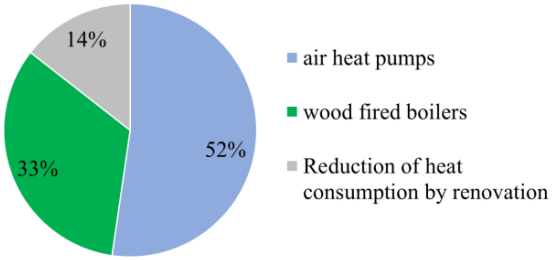

Figure 5: Reduction of heat consumption and shares of heat supply for decentralized renovation

6. Comparison of two scenarios

Figure 6 shows, that the largest investments for solar district heating are the solar thermal system, the heating network and the seasonal storage. The federal funding by the German program KfW EE Premium (BMWK 2022) is around 42% of the total investment. Especially the solar thermal system and seasonal storage gain high subsidies of around 58%.

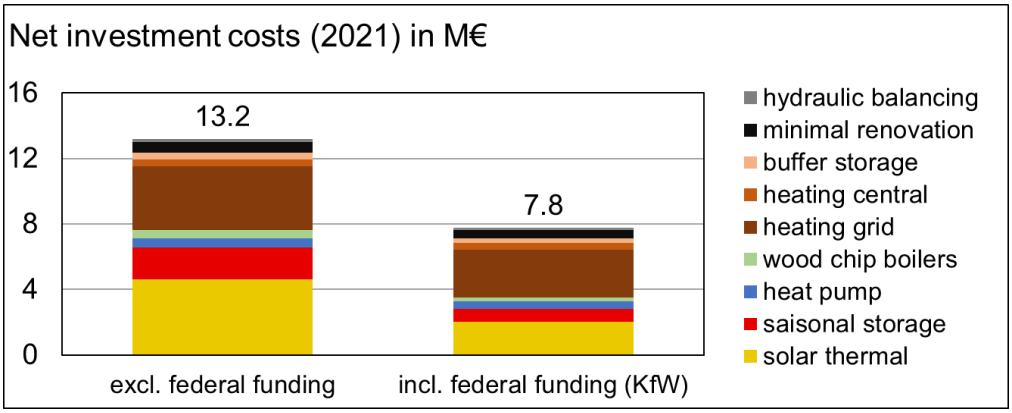

Figure 6: Investment costs for solar district heating

The total investment costs for decentral renovation presented in Figure 7 are very similar to those for solar district heating. The constructional measures with the highest investment costs are outer wall insulations, replacement of windows and underfloor heating systems. Funding by BEG (15. August 2022) is considered (BAFA 2022).

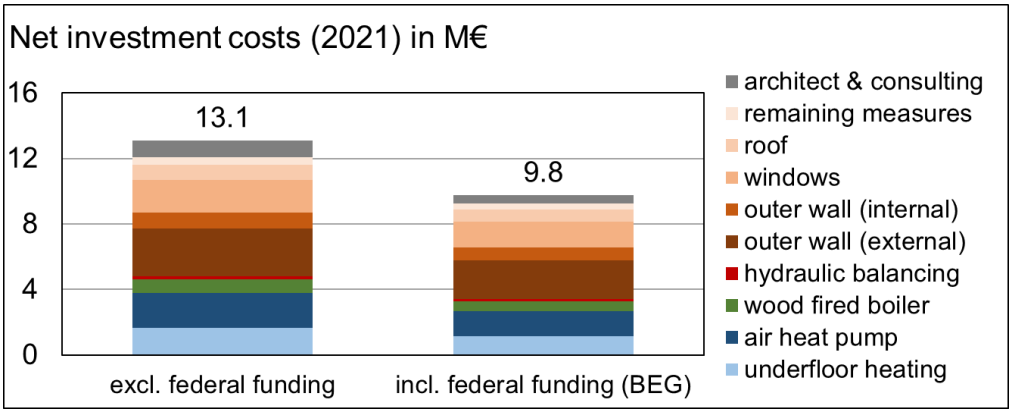

Figure 7: Investment costs for decentralized renovation

The operation costs presented in Figure 8 are similar for both scenarios in total. Differences are the higher maintainance and repairs costs for solar district heating explained by higher investments for components that need to be maintained (heat generators, heating network and storages), and the higher electricity consumption of air heat pumps for decentralized renovation. Although the amount of wood is the same in both scenarios, the costs for biomass differ because of the higher prices for log wood used in decentralized renovation scenario compared to wood chips used in solar district heating scenario (Carmen 2021). Costs for maintenance and repairs of the building's envelope have still to be investigated for both scenarios. In this study these costs have been neglected.

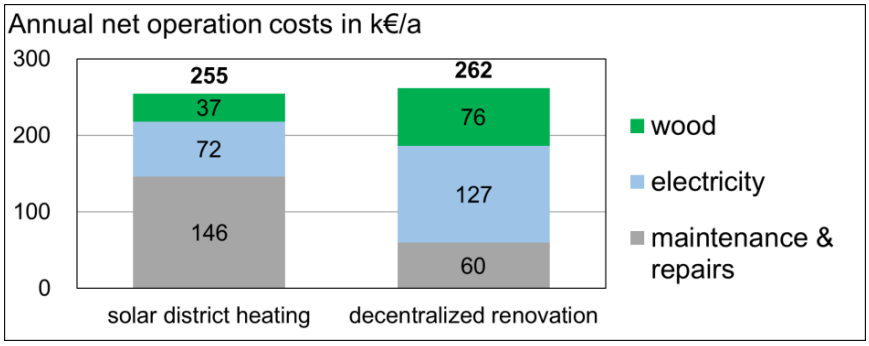

Figure 8: Annual net operation costs of both scenarios (annuity) during observation period of 20 years

A calculation is done with the annuity method under the following assumptions:

- observation period: 2025 until 2044 (20 years)
- interest rate: 3.0 %/a
- inflation rate: 1.8 %/a

Figure 9 shows the comparison of the annual net cost per average building in total. While the costs without federal funding are a bit lower for the decentralized renovation (5,147 €/a) compared to solar district heating (5,421 €/a), this changes after applying the federal funding resulting in solar district heating costs (3,734 €/a) slightly lower than costs for decentralized renovation (4,176 €/a). Considering the calculation accuracy both scenario's costs are on a similar level.

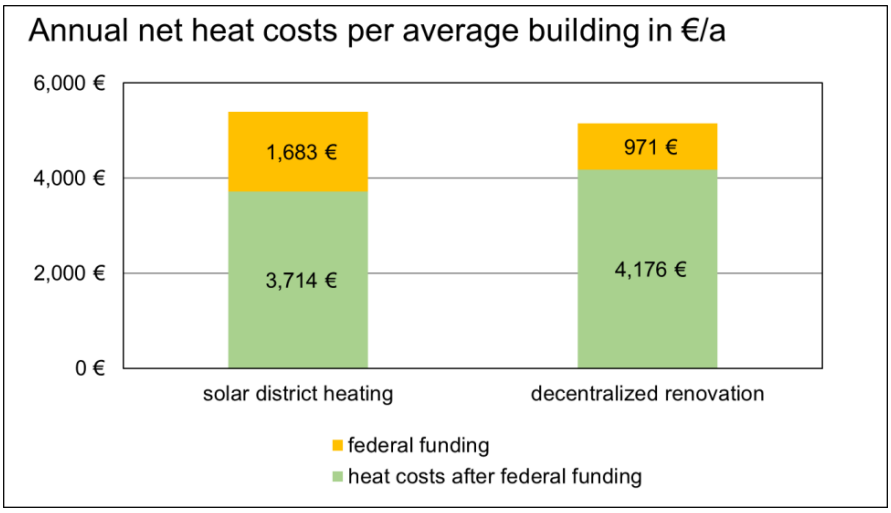

Figure 9: Comparison of annual heat costs per average building for solar district heating and decentralized renovation

The main difference between the two scenarios is illustrated in Figure 10. While solar district heating can reach the full reduction of annual CO_2e emissions already at the start of operation (after a few years of planning and construction), this will take decades for decentralized renovation because of the low renovation rates. The accumulated CO_2e amount for the next three decades would be about 3,318 t_{CO2} with solar district heating and 14,202 t_{CO2} with decentralized renovation, which is an increase of 328%.

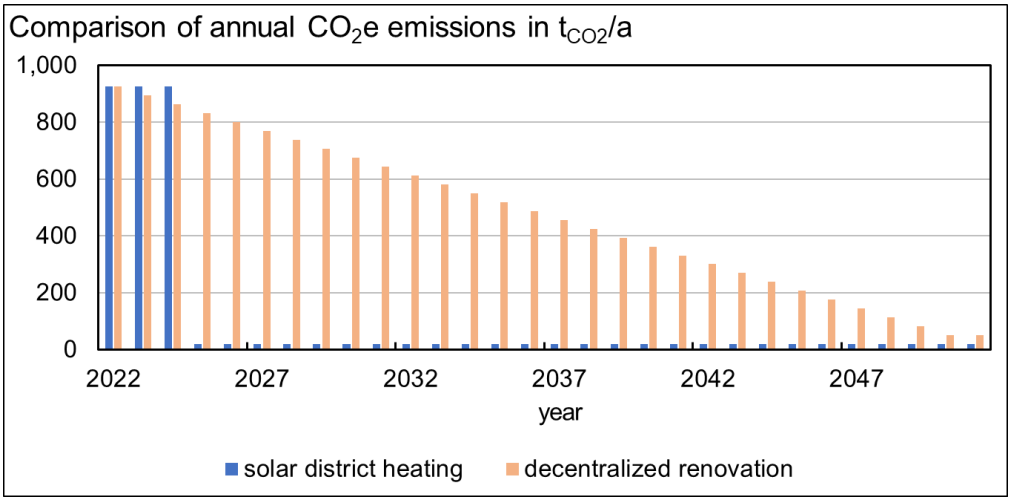

Figure 10: Comparison of the annual CO_2e emissions for both scenarios assuming a renovation rate of 3%/a to implement the measures for decentralized renovation

It should be mentioned that there should be still a cost reduction potential for the decentralized renovation scenario, because an economical optimization was implemented for solar district heating only.

7. Conclusion and Outlook

It is possible to significantly accelerate the decarbonization of heat supply in rural areas with solar district heating systems, while the heating costs are not increased compared to the alternative strategy of profound building renovation and use of heat pumps. The main advantage of profound building renovation on the other hand is higher living comfort (e.g., foot warmth thanks to underfloor heating, more even temperatures and fewer draught). It should be also mentioned that decentralized renovation scenario is not economical optimized. However, synergies between the two decarbonization strategies are possible: renovation of buildings connected to a heating network can still be carried out later, which leads to free capacities concerning heat generation and distribution which could be used for connecting further consumers.

8. Acknowledgment

Many thanks to the financial support of the project by the Hessian Ministry of Economics, Energy, Transport and Housing (funding source: European Regional Development Fund (ERDF)). (FKZ: EF960 0039/2021 20008503)

9. References

BAFA (15.08.2022): Förderübersicht: Bundesförderung für effiziente Gebäude (BEG). Available online at https://www.bafa.de/SharedDocs/Downloads/DE/Energie/beg_em_foerderuebersicht.pdf?__blob=publicationFile&v=5, last accessed 22.09.22.

BDEW 2021. Available online at https://www.bdew.de/presse/presseinformationen/zahl-der-woche-fast-ein-fuenftel-aller-co2-emissionen-in-deutschland/, last accessed 31. March 2022.

BMWi (16.09.2021): Richtlinie für die Bundesförderung für effiziente Gebäude – Einzelmaßnahmen. BEG EM.

Available online at https://www.energiewechsel.de/KAENEF/Redaktion/DE/PDF-Anlagen/BEG/bundesfoerderung-f%C3%BCr-effiziente-gebaeude-einzelmassnahmen-20210916.pdf?__blob=publicationFile&v=4, last accessed 22.09.2022.

BMWK (01.01.2022): Erneuerbare Energien Premium (KfW). Available online at https://www.kfw.de/PDF/Download-Center/F%C3%B6rderprogramme-(Inlandsf%C3%B6rderung)/PDF-Dokumente/6000002410_M_271_281_272_282.pdf, last accessed 22.09.22.

Carmen 2021. Preisvergleich Deutschland. Available online at https://www.carmen-ev.de/service/marktueberblick/marktpreise-energieholz/marktpreisvergleich/, last accessed 22.09.22

Loga, T., Stein, B., Diefenbach, N., Born, R, 2015. Deutsche Wohngebäudetypologie - Beispielhafte Maßnahmen zur Verbesserung der energieeffizienz von typischen Wohngebäuden. 2. Edition. Published by Institut Wohnen und Umwelt (IWU). Darmstadt.

Luderer, G., Kost, Ch., Sörgel, D. 2021: Deutschland auf dem Weg zur Klimaneutralität 2045. Szenarien und Pfade im Modellvergleich. Ariadne-Report. Published by Kopernikus-Projekt Ariadne und PIK.

Quasi-Dynamic Testing of Air-Brine-Collectors and Numerical Simulations of a Cold District Heating Network

Stefanie Lott[1], Stephan Fischer[1], Harald Drück[1] and Bernd Hafner[2]

[1] University of Stuttgart, Institute of Building Energetics, Thermotechnology and Energy Storage (IGTE), Stuttgart (Germany)

[2] Viessmann Climate Solutions SE, Allendorf (Germany)

Abstract

So-called air-brine-collectors increasingly available on the market are mostly uncovered absorbers without thermal insulation. Hence, their thermal performance is significantly affected by ambient conditions such as wind speed, sky and air temperature. In order to model the thermal performance of air-brine-collectors, it is necessary to know how the above-mentioned ambient conditions affect their thermal performance.

For this purpose, the thermal performance of an air-brine-collector available on the market was determined in two variants according to ISO 9806 by means of outdoor testing using the quasi-dynamic test method. The characteristic values resulting from the measurements are then used within an annual system simulation of a typical cold district heating network, also called fifth generation district heating and cooling (5GDHC) network, in the simulation environment TRNSYS. Whereas the air-brine-collectors in combination with an ice store act as heat sources for decentralized heat pumps in the heating and cooling system.

Keywords: air-brine-collector, quasi-dynamic test method, heat pumps, cold district heating, 5GDHC, TRNSYS

1. Introduction

Since the 1970s, research and development has been carried out worldwide on various types of covered and uncovered photovoltaic thermal (PVT) collectors. In addition, heat pumps have been understood for a few years as one of the most promising technologies for future decarbonized energy supply. Therefore, for the last 10 years about, a trend has been developing towards the increased investigation of PVT collectors in system combination with heat pumps (Kumar et al., 2015) (Al-Waeli et al., 2016). Thus, the research, development and commercialization of the so-called air-brine-collectors, which serve as the heat source of the heat pump, has also been intensified. Air-brine-collectors are designed both with and without photovoltaic modules as a cover. The air-brine-collectors with photovoltaic modules as a cover also belong to the PVT collectors.

Air-brine-collectors are heat exchangers that extract heat from the ambient air and also convert solar radiation into usable heat. Thus they also function as solar collectors and are ideally suited as heat sources for heat pumps. Especially in heating and cooling systems based on cold district heating networks, also called fifth generation district heating and cooling (5GDHC) networks, but also in single- or multi-family buildings, air-brine-collectors as a heat source for a heat pump are an important and very cost-effective alternative to conventional air source heat pumps (Giovannetti et al., 2018).

The air-brine-collectors increasingly available on the market are mostly without transparent cover, i.e., uncovered and without thermal insulation, which means that their thermal performance is significantly affected by ambient conditions such as wind speed, sky and air temperature (Giovannetti et al., 2018). In order to characterize the thermal behavior of air-brine-collectors it is necessary to know how the above-mentioned ambient conditions affect their thermal performance (Leibfried et al., 2019).

For this purpose, the thermal performance of an air-brine-collector available on the German market was determined in two variants at the Institute for Building Energetics, Thermotechnology and Energy Storage of the University of Stuttgart (IGTE) following ISO 9806 (ISO, 2013) using the quasi-dynamic outdoor test method. Fig. 1 shows the two variants investigated. The uncovered variant 1 (one) is shown on the left and the covered variant 2 (two) on the right. The covered variant represents the case where photovoltaic modules are attached above the air-brine-collector.

© 2022. The Authors. Published by International Solar Energy Society
Selection and/or peer review under responsibility of Scientific Committee
doi:10.18086/eurosun.2022.04.05 Available at http://proceedings.ises.org



Fig. 1: Illustration of the two variants investigated, left: uncovered (variant 1), right: covered (variant 2)

The characteristic values for the numerical description of the thermal behavior of the air-brine-collectors determined by means of measurements according to ISO 9806 are subsequently used within annual system simulations of a typical 5GDHC network in the simulation environment TRNSYS. Thereby, it was investigated how the thermal performance of the air-brine-collectors influences the performance of the entire heating and cooling system.

The procedure for determining the thermal performance of the air-brine-collectors, the boundary conditions and results of the measurements as well as those of the annual system simulations of the two sun-air-collector variants as heat sources for a cold district heating system are presented in detail in the following.

2. Measurements and characteristic values

The measurements to determine the characteristic values were performed in accordance to ISO 9806. Deviating from the specifications of the standard, measurements without irradiation (nighttime measurement), measurements with an average fluid temperature below the ambient air temperature, and measurements with negative thermal performance, i.e. heat dissipation, were also performed.

The measurements without irradiation and at a mean fluid temperature below the ambient air temperature represent typical operating conditions of air-brine-collectors. The measurements with negative thermal performance are used to determine a set of characteristic values that is also valid within the simulations, if the air-brine-collectors are used for recooling purposes.

Equations (eq. 1) and (eq. 2) show the modeling of the thermal collector performance according to ISO 9806.

$$\frac{\dot{Q}}{A_G} = \eta_{0,b} K_b(\theta_L, \theta_T) G_b + \eta_{0,b} K_d G_d - c_6 u G - c_1(\vartheta_m - \vartheta_a) - c_2(\vartheta_m - \vartheta_a)^2 - c_3 u(\vartheta_m - \vartheta_a) + c_4(E_L - \sigma T_a^4) - c_5 \frac{d\vartheta_m}{dt} \quad \text{(eq. 1)}$$

$$K_b(\theta_L, \theta_T) = K_b(\theta_L, 0) \cdot K_b(0, \theta_T) \quad \text{(eq. 2)}$$

With

A_G	m²	Gross area of collector
c_1	W m^{-2} K^{-1}	Heat transfer coefficient at ($\vartheta_m - \vartheta_a$) = 0
c_2	W m^{-2} K^{-2}	Temperature dependent heat transfer coefficient
c_3	J m^{-3} K^{-1}	Wind speed dependent heat transfer coefficient
c_4	-	Factor for calculating the radiant heat losses in dependency of the sky temperature

c_5	kJ m^{-2} K^{-1}	Effective specific heat capacity of the collector
c_6	s m^{-1}	Coefficient for calculating the wind dependence of the conversion factor
E_L	W m^{-2}	Longwave irradiance ($\lambda > 3$ µm)
$\eta_{0,b}$	-	Conversion factor based on beam irradiance
G_b	W m^{-2}	Beam irradiance
G_d	W m^{-2}	Diffuse irradiance
G	W m^{-2}	Total irradiance ($G_b + G_d$)
$K_b(\theta_L,\theta_T)$	-	Incidence angle modifier (IAM) for beam irradiance
K_d	-	Incidence angle modifier (IAM) for diffuse irradiance
$\dot{Q}$	W	Thermal performance extracted from collector
t	s	Time
T_a	K	Ambient air temperature
u	m s^{-1}	Wind speed
ϑ_a	°C	Ambient air temperature
ϑ_m	°C	Mean temperature of heat transfer fluid
θ	°	Angle of incidence of beam irradiance G_b
σ	W m^{-2} K^{-4}	Stefan-Boltzmann constant $\sigma = 5.67 \times 10^{-8}$ W m^{-2} K^{-4}

Tab. 1 shows the determined characteristic values and Tab. 2 and Tab. 3 the incidence angle modifiers of the two tested air-brine-collector variants. For the investigated north-south orientation of the longitudinal axis of the air-brine-collector variants, the incidence angle modifiers for beam irradiance in the longitudinal direction are used to characterize the influence of the annual season and the associated position of the sun on the thermal performance of the air-brine-collector variants. Since the measurements were performed in only two out of twelve months, the longitudinal incidence angle modifiers were calculated analytically from the geometry. The gross area of the air-brine-collector in both cases is 4 m².

Tab. 1: Characteristic values of the two air-brine-collector variants

Characteristic Value	Unit	Variant 1	Variant 2
$\eta_{0,b}$	-	0.75	0.71
c_1	W m^{-2} K^{-1}	47.30	33.50
c_2	W m^{-2} K^{-2}	0.00	0.00
c_3	J m^{-3} K^{-1}	20.20	32.40
c_4	-	0.75	1.00
c_5	kJ m^{-2} K^{-1}	77.49	91.61
c_6	s m^{-1}	0.09	0.04
K_d	-	1.01	0.95

The conversion factors $\eta_{0,b}$ determined for the beam irradiance G_b appear surprisingly high at a first glance. However, if the fact that it is a volumetric absorber and thus the radiation-absorbing area is a multiple of the reference area (gross area) is taken into account, the conversion factor for variant 1 is realistic. Equation (eq. 1) represents for such air-brine-collectors, consisting of volumetric absorbers with opaque cover, not the physical but only the mathematical description of the thermal performance. Thus, by inserting an almost freely selectable combination of incidence angle modifiers and a related conversion factor into equation (eq. 1), a curve fitting is

performed to fit the measured thermal performances of the air-brine-collectors at different ambient conditions including different angles of incidents. The conversion factor of variant 2 is therefore not directly comparable with conversion factors of other air-brine-collectors. The very high incidence angle modifiers for beam irradiance in the transverse direction for variant 2 result from the very low incidence angle modifiers in the longitudinal direction due to the cover.

Tab. 2: Incidence angle modifiers for beam irradiance (variant 1)

Angle of Incidence θ in °	**0**	**10**	**20**	**30**	**40**	**50**	**60**	**70**	**80**	**90**
$K_b(\theta_L,0)$ in -	1.00	0.99	0.97	0.94	0.92	0.88	0.8	0.66	0.35	0.00
$K_b(0,\theta_T)$ in -	1.00	1.04	1.08	1.11	1.15	1.37	1.42	1.74	2.47	0.00

Tab. 3: Incidence angle modifiers for beam irradiance (variant 2)

Angle of Incidence θ in °	**0**	**10**	**20**	**30**	**40**	**50**	**60**	**70**	**80**	**90**
$K_b(\theta_L,0)$ in -	0.00	0.00	0.00	0.01	0.01	0.01	0.02	0.02	0.02	0.00
$K_b(0,\theta_T)$ in -	0.00	11.00	23.90	28.30	34.50	44.40	83.40	100.00	219.00	0.00

The differences in the heat transfer coefficients c_1 and the wind-dependent heat transfer coefficients c_3 of the two variants can be explained as follows: Due to the cover of variant 2, the upward convection currents are obstructed, resulting in a lower value for c_1. On the other hand, the cover creates a certain tunnel effect which increases the wind speed inside the volumetric absorber compared to the surroundings, resulting in a higher value for c_3 at the same time.

The thermal collector performance is described analytically according to equation (eq. 1), in particular as a function of the temperature difference between the mean fluid temperature and the ambient air temperature. The temperature dependent heat transfer coefficient c_2 is used to account for the nonlinear increase in thermal losses, especially for high temperature differences or high mean fluid temperatures. Due to the low stagnation temperature of approx. 20 K above ambient air temperature air-brine-collectors are operated within a narrow range of temperature difference to the ambient air temperature. For these temperature differences, the behavior of the thermal losses can be described as linear to the temperature differences. Thus, c_2 is set to zero for the air-brine-collectors investigated.

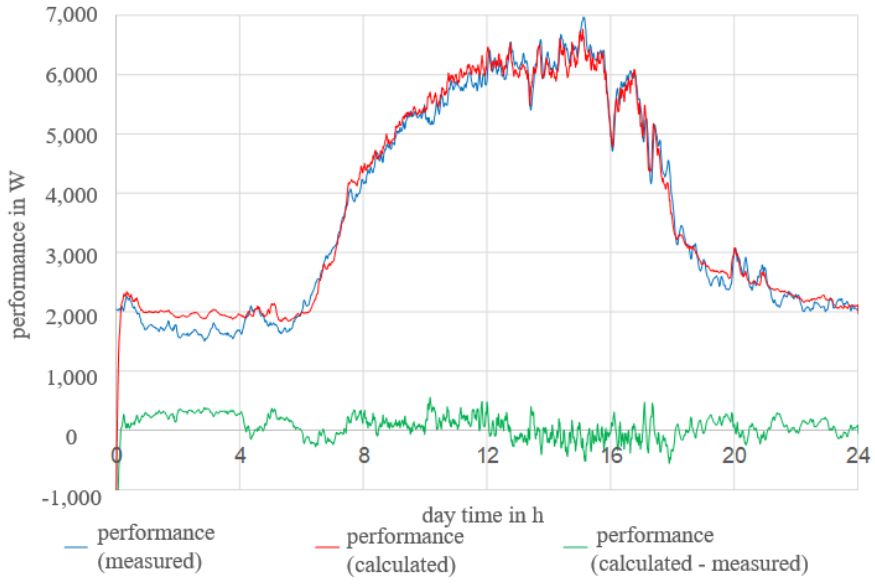

Fig. 2: Measured, calculated and the difference between calculated and measured thermal performance extracted from the air-brine-collector of variant 1 on Aug. 21st, 2020

Fig. 2 shows an example of the measured thermal performance extracted from the air-brine-collector of variant 1 together with the thermal performance calculated using the characteristic values as well as the difference between the calculated and the measured thermal performance for a day used for the evaluation (Aug. 21st, 2020). Fig. 3 shows the irradiance and Fig. 4 shows the wind speed as well as the difference between mean fluid temperature and ambient air temperature for variant 1 on Aug. 21st, 2020.

From Fig. 2, it can be seen that the measured thermal performance extracted from the air-brine-collector can be replicated with good accuracy using the determined characteristic values. However, it should also be mentioned that the heat losses of both variants depend not only on the wind speed, but also on the wind direction, which was not recorded during the measurements and is not taken into account by ISO 9806.

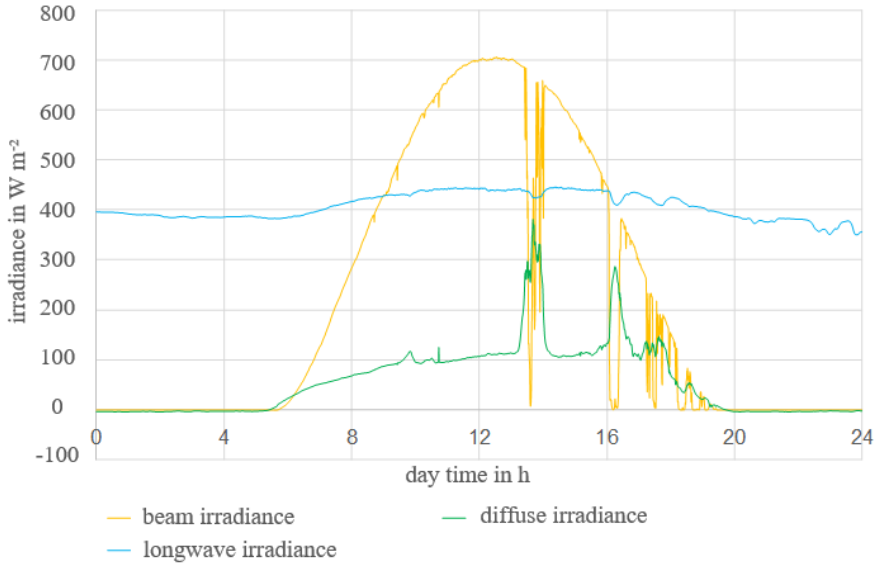

Fig. 3: Irradiance on Aug. 21st, 2020

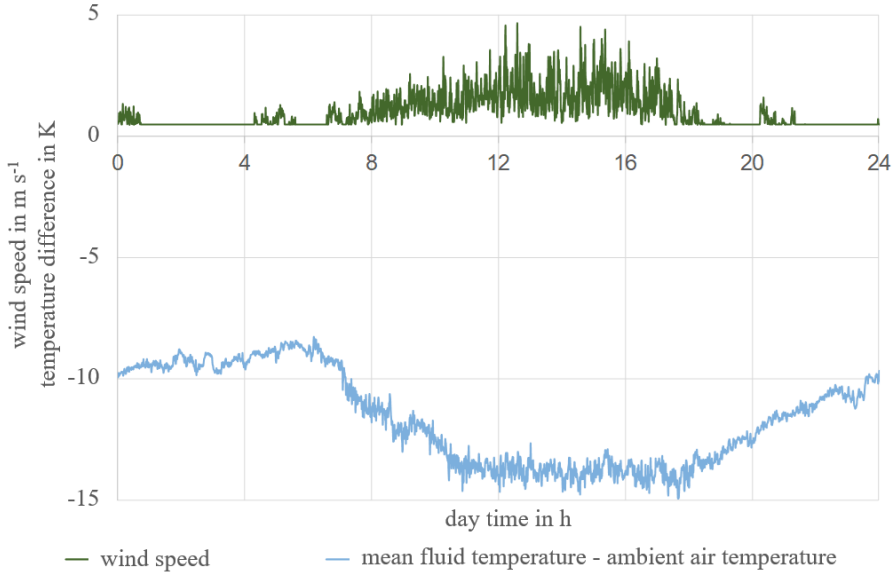

Fig. 4: Wind speed and temperature difference between mean fluid temperature and ambient air temperature for variant 1 on Aug. 21st, 2020

3. System simulations

Using the determined characteristic values, dynamic system simulations with TRNSYS were performed to investigate how the two variants of air-brine-collectors behave in a heating and cooling system and to what extent the two variants differ.

The influence of the two variants on the heating and cooling system is characterized by a comparison of the annual environmental and solar thermal useful heat supplied by the respective air-brine-collectors. The environmental and solar useful heat supplied by the air-brine-collectors depend on the operation of the heating and cooling system, in addition to the characteristic values, the incidence angle modifiers and the ambient conditions. Therefore, the boundary conditions and the control strategy of the heating and cooling system are described in the following.

3.1 Boundary conditions

Use case and location

A typical application for the investigated air-brine-collectors is their use as heat source for heat pumps in 5GDHC networks or so-called anergy networks. Therefore, the heating and cooling system of a new building district in Ludwigsburg, a city in the south of Germany near Stuttgart, is modeled. Within the framework of the project 'Development of integrated solar supply concepts for climate-neutral buildings for the "city of the future" (Sol4City)' the described 5GDHC system is to be investigated, analyzed and optimized.

The new building district comprises nine multi-family buildings and a kindergarten with three residential units above. The buildings are equipped with unheated basements. In total, the district with 107 residential units has a heated usable floor space of 8,567 m². For the design of the system components and the 5GDHC network, a heating demand of 507 MWh a^{-1} and a cooling demand of 166 MWh a^{-1} were assumed.

For the system simulations, a weather data set of the German weather service (DWD) was used for a current average test reference year for the Ludwigsburg site. The annual global radiation sum amounts to 1,048 kWh m^{-2}. The mean ambient air temperature is 10.4 °C and the mean wind speed is 2.9 m s^{-1}.

Heating and cooling concept

The heating and cooling supply of the district is based on a 5GDHC network, which is operated with temperatures between - 10 °C and + 20 °C. A central ice store with a water volume of 770 m³ and a central collector field consisting of air-brine-collectors with a total gross area of 137 m² serve as heat sources and sinks for the decentralized brine-to-water heat pump of each building. The total rated heating capacity of the total of ten heat pumps is 428 kW_{th} at the standard rating conditions according to DIN EN 14511-2 (DIN, 2019). Whereby the standard rating conditions correspond to a brine temperature at the evaporator inlet of 0 °C and a water temperature at the condenser outlet of 35 °C and will be referred to as operating point B0/W35 in the following. The total electrical power consumption of the heat pumps at this operating point is 93 kW_{el}. Each heat pump is hydraulically decoupled from the consumer circuit by a buffer store with a volume of 1.5 m³ each. The cylindrical ice store has two separate heat exchangers - regeneration and discharge heat exchanger - through which a water-glycol mixture is circulated. The storage medium is water.

The heat supply within the buildings is provided by underfloor heating with a constant supply temperature of 35 °C and an assumed constant return temperature of 28 °C. The domestic hot water is generated exclusively by means of electric instantaneous water heaters and is therefore not taken into account in the system simulation.

Additional heat exchangers are also used on a decentralized building-by-building basis to perform building cooling via the 5GDHC network. In the cooling period, the underfloor heating of the buildings serves as the heat source of these decentralized heat exchangers. The buildings are cooled with a constant supply temperature of 17 °C on the consumer side and a corresponding assumed return temperature of 20 °C. In the passive cooling mode, the so-called natural cooling (NC) mode, the ice store represents the heat sink of the 5GDHC network. For the possibility of an active cooling, a second additional heat exchanger, the so-called residual heat exchanger, is installed in the building no.10. An active cooling (AC) mode is achieved by the heat pump in building no. 10 using the air-brine-collectors as heat sink on the condenser side. The cooling energy thus generated on the evaporator side is fed from there into the 5GDHC network. Buildings no. 1 to no. 9 do not have this second additional heat exchanger, but are supplied with additional cooling energy via the 5GDHC network using the

decentralized building-by-building heat exchangers described above. The active cooling mode is used exclusively when the natural cooling mode is insufficient.

For simplification, not all possible operating modes are represented in the system simulations described here. Only the heat supply modes and the natural cooling mode of the new building district in Ludwigsburg are considered. The simplified hydraulic structure of the modeled system as well as the initial values for the annual system simulations can be seen in Fig. 5.

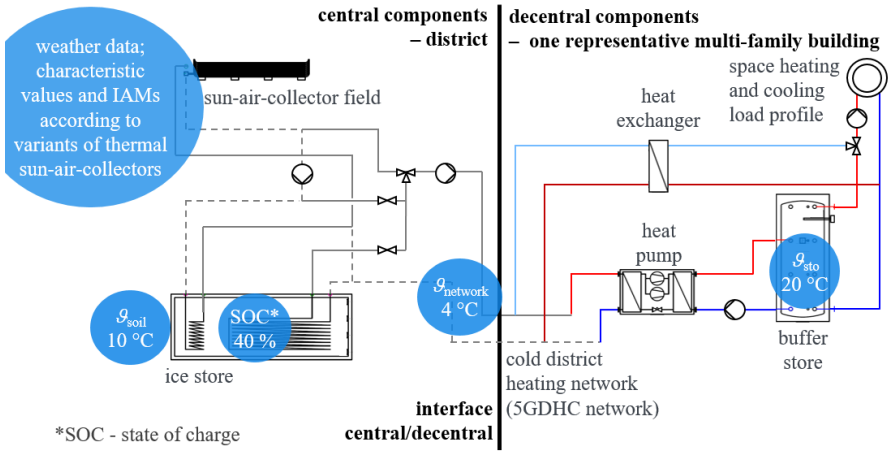

Fig. 5: Simplified hydraulic scheme of the heating and cooling system with initial values for the annual system simulations

Assumptions

To further simplify the simulation model, only one of the ten buildings is modeled. For this purpose, a representative space heating and cooling load profile of one characteristic building of the district is used.

Due to the difference in thermal loads of the building no. 10 with a kindergarten, a non-residential building, and of the residential buildings no. 1 to no. 9, dynamic building simulations in TRNSYS of both one of building no. 10 and one of building no. 1 were performed. Based on target room air temperatures of 20 °C in winter and 26 °C in summer, the hourly heating and cooling capacities that must be supplied to the respective building in order to achieve the target room air temperature were determined. These hourly heating and cooling capacities represent the respective space heating and cooling load profile. To create the representative space heating and cooling load profile, the load profile of building no. 10 with kindergarten was summed with that of nine residential buildings and then divided by the factor of ten for the number of buildings of the district. The factor of ten was chosen because the new building district in Ludwigsburg consists of ten buildings, each with a heating center. In this way, the dynamic thermal behavior of the components decentralized in the respective heating center, such as buffer stores, heat pumps and heat exchangers, can also be investigated. At the "central/decentral" interface (see Fig. 5), the mass flow rate is converted accordingly. Which means that the mass flow rate from the network to the individual building is divided by the factor of ten and from the individual building back to the network is multiplied by the factor of ten. The supply and return temperatures are not changed or converted as all buildings are connected in parallel. Decentralized components are designed for the representative space heating and cooling load profile, centralized components for the entire district.

Simultaneity effects are neglected, since only the heat supply for space heating and not that for domestic hot water is accounted for. Thus, it is assumed that the heat load peaks of the individual buildings always occur at the same time. The heat losses or gains of the pipes of the 5GDHC network are neglected. This can be justified due to an existing thermal insulation and the low network temperatures, respectively the small temperature differences between the fluid in the pipes and the surrounding soil. For the ice store, the heat exchange with the soil is taken into account and for the buffer stores heat losses to the surrounding air are considered.

For both the heating and cooling supply, a variable consumer-side mass flow rate results from the definition of the target temperatures at the consumers, in order to be able to meet the representative space heating and cooling load profile that changes over time. On the network side, a constant mass flow rate is assumed in accordance with the planning. In the 5GDHC network, a water-glycol mixture (33 %) is also assumed as the heat transfer medium. In the consumer circuit, the heat transfer medium is water.

Furthermore, in order to avoid condensate formation, a minimum inlet temperature of 15 °C is aimed for on the network side of the building-by-building heat exchangers during the cooling period. Since the network temperature in natural cooling mode (NC mode) corresponds to the outlet temperature of the ice store, the required heat exchangers inlet temperature in this modeling is often only achieved by mixing the outlet temperature of the ice store with the building-by-building heat exchangers outlet temperature on the network side. If the ice store outlet temperature is too high, the building-by-building heat exchangers inlet temperature is also too high. For this reason, it is assumed that the cooling demand can only be met up to an average ice store temperature of 16 °C. For simplicity, the described possibility of active cooling mode via the residual heat exchanger is not considered at this point.

During the heating period, a controller ensures that the temperature in the decentralized buffer stores is maintained between 40 °C and 46 °C in the upper 60 % of the store. If the buffer store temperature falls below this point, the heat pumps are switched on. If the evaporator temperature exceeds - 10 °C, the set heating supply temperature of 35 °C on the consumer side is reached. If the evaporator temperature falls below - 10 °C and the buffer store temperature falls below the target heating supply temperature of 35 °C, the heating demand can no longer be met in the simulation. In the real heating and cooling system, electrical heating elements are then used as emergency heaters.

The TRNSYS Type 832 is used to model both variants of the air-brine-collectors, covered and uncovered. This Type uses the collector model also used for the quasi-dynamic outdoor measurements according to ISO 9806 (ISO, 2013).

System control

A total of seven operating modes will be available in the new building district in Ludwigsburg. For the sake of simplicity, however, only four of them are modeled here: discharging mode, absorber-direct mode, regeneration mode and natural cooling mode.

It is assumed, that the air-brine-collectors are available for the heat pumps as a heat source in the operating mode **absorber-direct mode** between November 15th and March 15th of each year, when the collector outlet temperature is above - 4 °C. If this temperature is below, the ice store serves as the heat source to the heat pumps during this period until the collector outlet temperature is either above the ice store outlet temperature or the ice store is already consisting to 90 % of ice. During this period of the year, the absorber-direct mode is the prioritized operating mode of the system simulations under consideration. This is to ensure that the heat pumps are supplied with the highest possible evaporator inlet temperature and thus operate as efficient as possible.

Furthermore, the ice store may also be regenerated during this period. For this purpose, heat is transferred from the air-brine-collectors to the ice store when the collector outlet temperature is above the average ice store temperature and the ice store is at least consisting of 50 % ice and no absorber-direct mode is required. This operating mode is named **regeneration mode.**

From March 16th of each year until the start of the cooling period on April 30th the air-brine-collectors are only available as a heat source if no more heat can be extracted from the ice store. This is the case when it is iced up to a maximum of 90 %. During this period, **discharging mode** is prioritized and no regeneration mode may take place. The reason for this is a desired targeted maximum icing of the ice store before the start of the cooling period, in order to provide as much cooling energy as possible by the ice store in the summer months. After the end of the cooling period on September 30th until November 14th the ice store is also initially preferred as a heat source in order to additionally utilize the sensible heat of the completely liquid storage medium of the ice store, which can reach up to 16 °C.

During cooling in the summer months, the extracted space heat of the district is first dissipated into the 5GDHC network via the building-by-building heat exchangers. For building cooling with the **natural cooling mode**, the cold district network is then cooled by using the ice store as a heat sink. As a result, the storage medium melts. Once the ice store has reached a completely liquid state and a temperature of 16 °C, the active cooling mode should theoretically take place. However, as already explained, this mode of operation has not yet been implemented in the simulation. Fig. 6 shows the simplified system control described here schematically in relation to the representative hourly space heating and cooling load profile used.

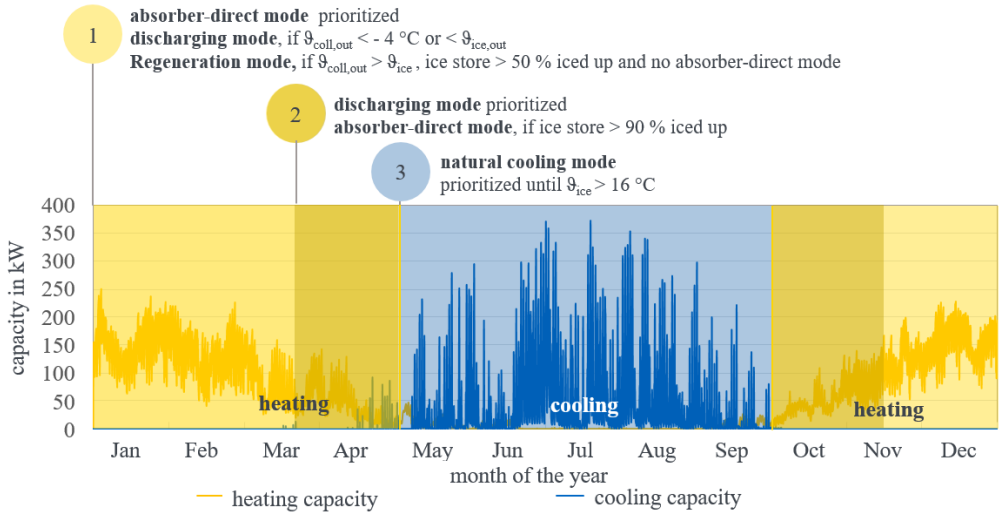

Fig. 6: Schematic representation of the operating modes of the system control with reference to the representative space heating and cooling load profile

The system control is based on so-called “hard switchover points” between heating and cooling operation, i.e. from a fixed date onwards, the system switches between heating and cooling operation. Between May 1st and September 30th, only cooling is possible. During the rest of the year, only heating is possible. It is assumed that heating demands that occur in the cooling period and cooling energy demands that occur in the heating period are negligible. These are therefore not covered by the heating and cooling system. The switching points can vary from year to year depending on the weather data.

3.2 Results

In order to achieve a full coverage of the heating and cooling demand of the district, the cooling demand must be met within the specified summer period and the heating demand must be met within the specified winter period due to the hard switching points. The composition of the monthly supply of thermal energy to meet the monthly heating and cooling demands of the described heating and cooling system and the corresponding monthly heating and cooling demands of the district are shown in Fig. 7 and Fig. 8. The heat losses of the buffer stores are included in the heating demand of the district. The simulations of the heating and cooling system were carried out for variant 1 and variant 2 of the air-brine-collectors (see section 2).

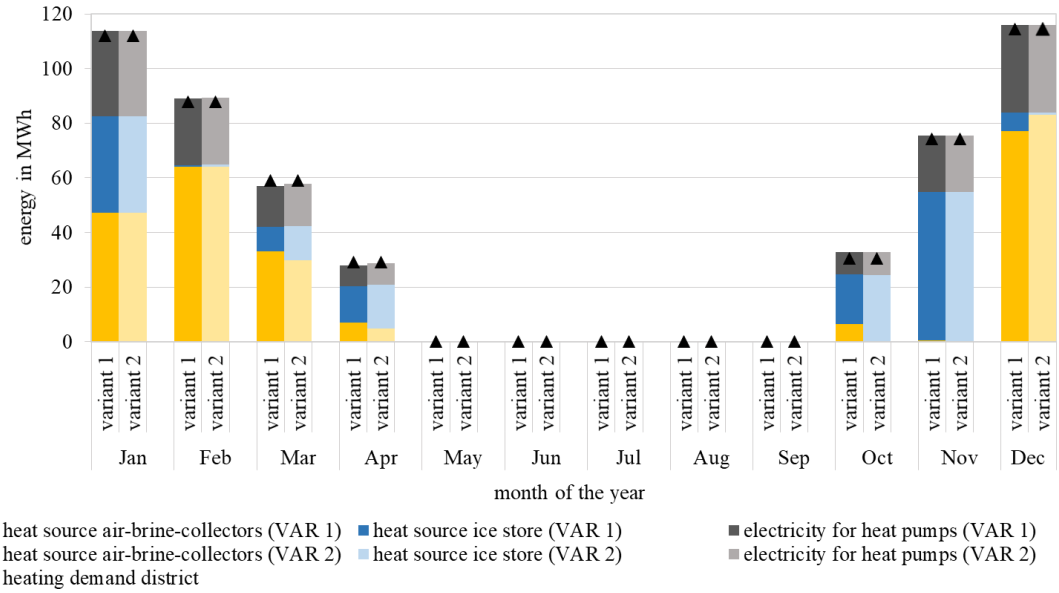

Fig. 7: Monthly heating demand and composition of the heating supply for variants 1 and 2 of the air-brine-collectors

Fig. 7 shows that the heating demand of the district can be completely covered by the previously described heating

and cooling system with an assumed initial icing of the ice store of 40 % and the described system control for both variants of the air-brine-collectors. The annual operation of the 5GDHC system does not mean that the ice store must be 40 % iced again at the end of December. Thus, for both variants of the air-brine collector with the implemented simplified control, a level of icing of 90 % is reached at the end of December. In order to cover the heating demand, the control system would have to be adjusted accordingly in real operation. At low ambient air temperatures and low solar irradiation, the heating and cooling system relies on the heat of the ice store, especially in the month of January, even though the absorber-direct mode is actually prioritized. In February, on the other hand, the collector outlet temperature is predominantly either above a temperature of - 4 °C or above the outlet temperature of the ice store, so that in the majority of time the absorber-direct mode, which is prioritized in this month, can be used. Contrary to the prioritization of the discharging mode in April (cf. Fig. 6), the absorber-direct mode is required in April, as the ice store is already at least consisting of 80 % ice at the beginning of April. This high ice content may be caused by the intensive use of the discharging mode in January. The conditions for the regeneration mode are not reached at any time of the simulations, which is why the ice store is not regenerated by the air-brine-collectors.

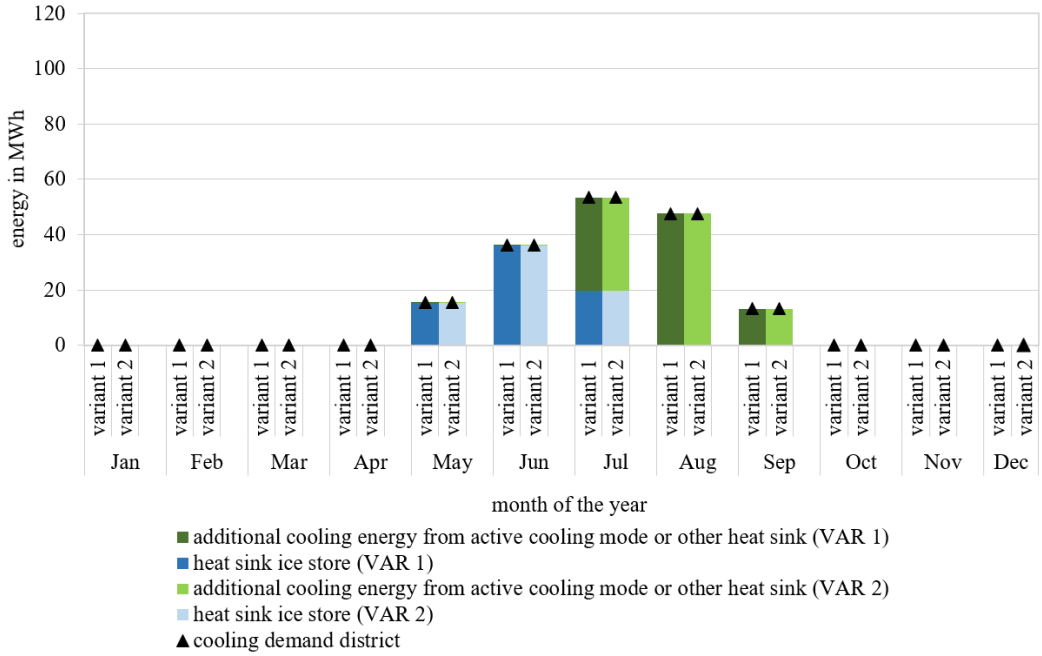

Fig. 8: Monthly cooling demand and composition of cooling supply for variants 1 and 2 of the air-brine-collectors

From Fig. 8, it can be estimated that approx. 43 % of the annual cooling demand for both variants can be met by the natural cooling mode. Thus, for the months of May and June, the ice store provides sufficient thermal energy for cooling the buildings completely. In July, 37 % of the cooling demand can still be covered by the natural cooling mode. In the remaining cooling period, an additional active cooling mode is required, since the ice store is completely liquid from mid-July onwards and has reached an average temperature of 16 °C. As a result, heat is available again from mid-July to cover the heating demand with the discharging mode, but this heat is not required until October 1st. Thus, the ice store remains completely liquid until October 1st and cannot be further used for building cooling.

With variant 2 of the air-brine-collectors 45 % of the annual heating demand is covered by the air-brine-collectors as the heat source of the heat pumps. The ice store supplies 28 % of the annual heating demand. 27 % of the annual heating demand is generated by the electrical energy required for the operation of the heat pumps. It is noticeable that the environmental and solar thermal heat source equipped with variant 1 of the air-brine-collectors, compared to that equipped with variant 2, covers the annual heating demand by 1.2 percentage points more, which means that the ice store heat source is used somewhat less.

If the annual environmental and solar thermal useful heat supplied by variant 2 of the air-brine-collectors is used as a reference, the annual environmental and solar thermal useful heat supplied by variant 1 is only 2.6 % (relative) higher. The deviation in the individual months of the heating period can be either positive or negative, as shown

in Fig. 9. Overall, however, it can be concluded from the simulation results that in the considered application, assumptions and simplifications within the given model and measurement uncertainties, there is no significant difference between the two investigated variants of the air-brine-collectors.

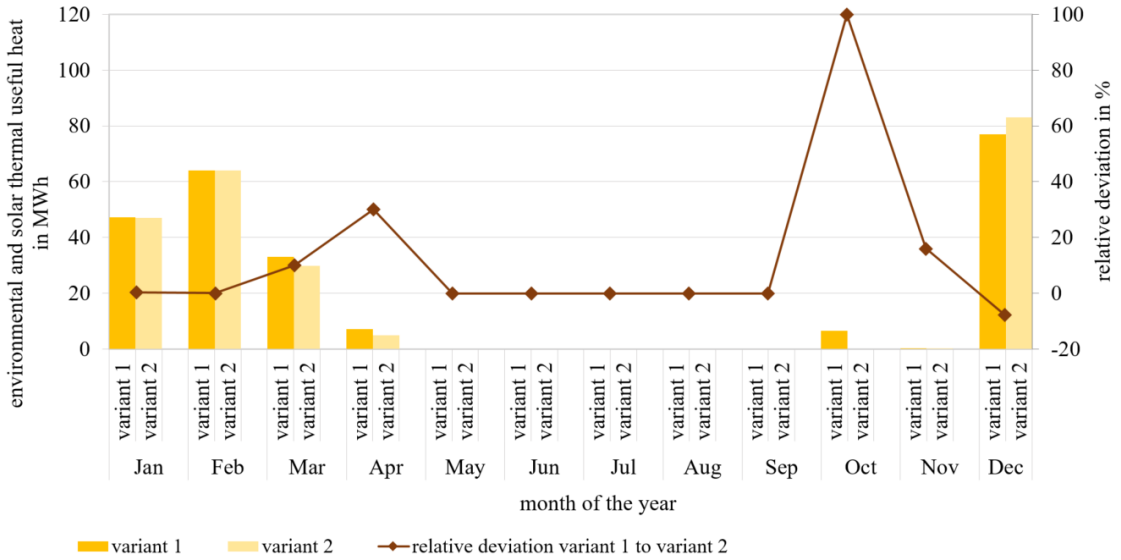

Fig. 9: Monthly environmental and solar thermal useful heat of the two air-brine-collector variants and associated relative deviation

Since the regeneration mode does not occur in the system simulations carried out, the environmental and solar thermal useful heat of the air-brine-collectors shown in Fig. 9 is exclusively the heat used at the evaporator of the heat pumps, which is provided by the air-brine-collectors in the absorber-direct mode. So in this concept, the environmental and solar thermal useful heat of the air-brine-collectors is at such a low temperature level that it cannot be used directly to heat the district.

4. Conclusion and outlook

According to ISO 9806 the characteristic values of two variants of air-brine-collectors were determined by means of outdoor testing using the quasi-dynamic test method. Due to measurements with an average fluid temperature below the ambient air temperature, the two sets of characteristic values are suitable for typical operating conditions of air-brine-collectors in a heating and cooling system combined with an ice store. The resulting characteristic values from the measurements were used for the numerical description of the thermal behavior of the air-brine-collectors within annual system simulations of a heating and cooling system.

The results of the system simulations carried out so far show that for the application studied, almost half of the required heating demand can be provided by the air-brine-collectors as heat source for the evaporator of the heat pumps. The difference in the annual environmental and solar thermal useful heat supplied between the sun-air-collectors of variant 1, i.e. without a cover, and that of variant 2, i.e. with a cover, is less than three percent (relative). The differences of the two variants of the air-brine-collectors related to their thermal performance and thus their influence on the heating and cooling system under consideration are within the given model and measurement uncertainty and thus negligible. This applies especially in this application of the air-brine-collectors in heating and cooling systems based on cold district heating networks, also called fifth generation district heating and cooling (5GDHC) networks, with an ice store and the resulting utilization period of the air-brine-collectors.

With regard to the simulation results it should be noted, that the characteristic values and incidence angle modifiers were determined for a single air-brine-collector under outdoor conditions. Placing multiple air-brine-collectors side by side can further affect both, convective and solar gains. Therefore, in further considerations, system simulations should be performed taking into account the arrangement as a field. The influence of the arrangement of multiple air-brine-collectors as a collector field on the characteristic values required for the system simulations

must be investigated in more detail. It is still unclear whether a measurement of a collector field is necessary to model the effects of field arrangement or whether the effects can be described analytically in connection with a measurement of a single air-brine-collector. Accordingly, it remains to be analyzed whether new measurements are necessary for the modeling of an air-brine-collector field, which would result in new characteristic values, or whether a correction of the characteristic values presented here is possible on the basis of an analytical description of the effects of field arrangement. Further, it can be assumed that the effects of a field arrangement influence the convective and solar gains for the air-brine-collectors with a cover, such as variant 2, more than the convective and solar gains for variant 1 without a cover.

Furthermore, it can be expected that the dimensioning of the central components, i.e. the volume of the ice store as well as the number of air-brine-collectors respectively the total resulting gross area, has a significantly larger influence on the composition of the heating and cooling supply than the difference between the two investigated variants of the air-brine-collectors. Within the framework of the aforementioned project "Sol4City", this assumption will be investigated by means of further system simulations.

Additionally, heating and cooling supply concepts like the one described, but without ice store, represent another typical application area of the investigated air-brine-collectors and hence will be investigated as well.

The influence of other system control strategies on the environmental and solar thermal useful heat in such a system will also be investigated in further system simulations.

The aim of the measurements and system simulations carried out is to derive optimization potentials and improved control strategies for both, the solar heating and cooling system and the individual components, in order to realize the most energy-efficient and cost-effective heating and cooling supply possible.

5. Acknowledgments

The activities of IGTE and Viessmann described in this paper are being supported by the German Federal Ministry for Economic Affairs and Climate Action (BMWK) based on a decision of the German Bundestag by Projektträger Jülich (PtJ) within the project ‘Development of integrated solar supply concepts for climate-neutral buildings for the “city of the future” (Sol4City)’ under grant numbers 03ETW019 A\B. The authors gratefully acknowledge this support and carry the full responsibility for the content of this publication.

6. References

Kumar, A., Baredar, P., Quteshi, U., 2015. Historical and recent development of photovoltaic thermal (PVT) technologies, in: Renewable and Sustainable Energy Reviews Volume 42, February 2015.

Al-Waeli, A., Sopian, K, Kazem, H., Chaichan, M., 2016. Photovoltaic Solar Thermal (PV/T) Collectors Past, Present and Future: A Review, in: International Journal of Applied Engineering Research ISSN 0973-4562 Volume 11 Number 22.

Giovannetti, F., Kastner, O., Lampe, C., Reinike-Koch, R., Park, S., Steinweg, J., 2018. Technologiebericht 1.4 Solare Wärme und Kälte, in: Wuppertal Institut, ISI, IZES (Eds.), Technologien für die Energiewende. Teilbericht 2 an das Bundesministerium für Wirtschaft und Energie (BMWi), Wuppertal, Karlsruhe, Saarbrücken.

ISO, 2013, ISO 9806. Solar energy – Solar thermal collectors – Test methods.

Leibfried, U., Fischer, S., Asenbeck, S., 2019. PVT-Wärmepumpensystem SOLINK – Systemvalidierung und zwei Jahre Praxiserfahrung, in: Tagungsband Symposium Solarthermie und innovative Wärmesysteme, Kloster Banz, Bad Staffelstein.

DIN, 2019, DIN EN 14511-2. Air conditioners, liquid chilling packages and heat pumps for space heating and cooling and process chillers, with electrically driven compressors – Part 2: Test conditions.

Early-Stage Feasibility Study of an Ambient-Temperature District Thermal Network: A Case Study in Denmark

Alessandro Maccarini[1] and Alireza Afshari[1]

1 Aalborg University, Department of the Built Environment, Copenhagen (Denmark)

Abstract

District heating systems have been used for space heating and domestic hot water since the 1880s. Since then, the efficiency of these systems has been improved continuously. The aim of this work is to conduct an early-stage feasibility study to calculate the energy performance of an ambient-temperature district heating and cooling system serving a new urban area located in Denmark. Dynamic energy simulation models of buildings and district network components were developed using Modelica. Results show that the evaluation of the water temperature in the network is critical, as it must be lower than a certain value to enable compressor-less cooling. Furthermore, due to the small temperature difference between supply and return pipes, higher water flow rates are required with respect to a traditional DH network. In terms of primary energy, savings of about 41% can be achieved in comparison to a traditional DH network. This is mainly due to the ability of decentralized heat pumps to adapt the temperature of heat distribution to different uses.

Keywords: District heating and cooling, heat pumps, energy modeling and simulation

1. Introduction

In Europe, heating and cooling demand in the building sector is responsible for a share of about 40% of the overall final energy usage (European Commission, 2016). In most countries, the energy required for heating is larger by far than the energy used for cooling. However, factors such as global warming, proliferation of glass facades, thermal insulation and rising standards in comfort are leading to new scenarios. In fact, it is expected that by 2050 the heating demand will decrease between 20% and 30% and the cooling demand will rise of about three times compared to 2006 values (Joint Research Centre, 2011). This tendency is confirmed by the number of air-conditioning units installed in Europe, which increased with a growth rate of 3% per year since 1990s (Pezzuto et al., 2016).

District heating and cooling (DHC) systems have been acknowledged as a promising solution for the reduction of both primary energy consumptions and CO_2 emissions to cover the heating and cooling demand of buildings. District heating (DH) systems have been used for space heating and domestic hot water since the 1880s. Conventional DH systems consist of centralized plants that feed hot water or steam into pipes to distribute heat in urban areas. Such systems suffer from significant heat losses and low potential for integration of sustainable energy sources. In addition, in traditional DH systems the same piping network is typically not able to provide simultaneously both heating and cooling services to different buildings.

For these reasons, current research focuses on novel systems, which can reach high efficiencies by operating at temperatures close to ambient (Buffa et al., 2019). Such systems, which are also referred to as the 5th generation of district heating and cooling (5GDHC), enable covering both heating and cooling demands of buildings with the same pipeline. The 5GDHC technology is still in early stages of research and development, and few pilot sites and demonstration projects are currently being operated across Europe. Most of the previous studies have focused on the development of simulation models to evaluate the energy performance of 5GDHC systems.

Wirtz et al. (2020) proposed a novel methodology for designing and evaluating bidirectional 5GDHC systems. Based on linear programming, this design approach led to a cost reduction of 42% and caused 56% less CO_2 emissions compared to a reference case based on individual building systems. Calixto et al (2021), modeled an existing 5GDHC network located in Italy using both detailed and simplified modeling approaches. The results showed reasonable agreement between the two models, with the simplified model underestimating the overall electric consumptions by about 15% with respect to the detailed model. Allen et al. (2020) analyzed

© 2022. The Authors. Published by International Solar Energy Society
Selection and/or peer review under responsibility of Scientific Committee
doi:10.18086/eurosun.2022.04.06 Available at http://proceedings.ises.org

the energy performance of 5GDHC systems for a prototypical district located in Denver (USA). Results showed that radiant hydronic systems connected with 5GDHC systems achieved a source energy use intensity that was 49% lower than that of air-based systems and conventional district thermal energy systems.

This paper presents preliminary results from an early-stage feasibility study that aims to calculate the energy performance of a 5GDHC system serving a new urban area located in the municipality of Køge (Denmark).

2. Methodology

2.1 Building energy models

The urban area considered in this work is located in the municipality of Køge (Denmark), and it consists of about 85,000 m^2 floor area of residential buildings and 50,000 m^2 floor area of office buildings. The total annual heating and cooling demand is about 4 GWh and 0.7 GWh, respectively. To calculate hourly heating and cooling demand of the future buildings, four representative building energy models were developed: terraced house (TH), multi-family house (MFH), block apartments (BA) and office buildings (OB).

Hourly demand profiles for space heating, domestic hot water and space cooling, were generated with the Python-based tool BAGEL (Maccarini et al., 2021), which enables an automatic creation of building energy models starting from pre-defined geometries and basic input parameters (e.g. U-values, internal gains, ventilation rates). The energy models developed in BAGEL use a resistance-capacitance method to describe the thermo-physical behavior of buildings, as specified in the ISO 13790 standard (International Standard Organization 2008). Since the urban area is still under development, only little information was available about the characteristics of the buildings. Therefore, most of the input parameters for the models were assumed based on Danish Building Regulation and authors' assumptions. These parameters are shown in Table 1. Note that the three residential building typologies (TH, MFH and BA) only differ in terms of geometry and boundary conditions (e.g., terraced houses have some adiabatic walls).

Buildings were equipped with floor heating systems with supply water temperature of about 35°C. Cooling for office buildings was delivered by chilled beam units with supply water temperature of about 20°C (Maccarini et al., 2020). Cooling demand in residential buildings was not considered. Domestic how water was provided at 60°C.

Tab. 1: Input parameters for typical building typologies

	Residential (TH, MFH, BA)	**Office (OB)**
Total floor area	85,000 m^2	50,000 m^2
U-value (walls/roof/floor/windows)	0.3/0.2/0.2/1.1 W/m^2K	0.3/0.2/0.2/1.1 W/m^2K
Internal heat gains	5 W/m^2 (weekly schedule)	25 W/m^2 (weekly schedule)
Window-to-wall ratio	0.25	0.4
Domestic hot water load	4 W/m^2 (constant profile)	1.5 W/m^2 (constant profile)
Air change per hour	0.4 h^{-1}	1.25 h^{-1}
Heating set-point	20°C	21°C
Cooling set-point	-	24°C

2.2 District network energy models

The schematic layout of the 5GDHC system is illustrated in the Figure 1. The plant consists of a heat exchanger connected to an industrial facility, which provides wastewater at 15°C. Prosumer substations consist of three components (see Fig. 1b): decentralized heat pump for space heating, decentralized heat pump for domestic how water, and heat exchanger for direct cooling (in office buildings). A temperature difference of 4 K was assumed between supply and return pipelines. Pipes were dimensions assuming a pressure drop per pipe length of 250 Pa/m.

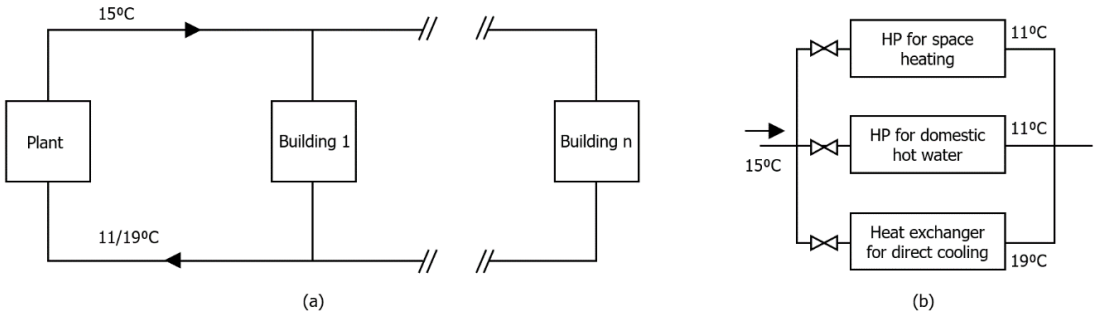

Fig. 1: Schematic of the 5GDHC network (a). Schematic of the prosumer substation (b).

To evaluate the energy performance of the 5GDHC system, a comparative study was conducted in respect to a traditional DH network, which operates with supply water temperature of 80°C. Figure 2 shows the schematic layout of the traditional DH system. Substations consists of two components: heat exchanger for space heating and heat exchanger for domestic hot water. Cooling is provided by stand-alone air-based chillers.

To describe the thermal and hydraulic dynamics of the network simulation models of both system configurations were developed using the open-source, equation-based and object-oriented Modelica language (Mattsson et al., 1998). As demonstrated by previous works (Wetter et al. 2019, Saelens et al., 2019), Modelica represents a useful tool for the modeling and simulation of district heating and cooling networks. Basic models such as pipes, valves, heat exchangers and heat pumps were retrieved from the Modelica Buildings library (Wetter et al., 2014), while more complex models, such as substations and ground heat losses were developed in-house during the project. To reduce modeling efforts and computational time, the buildings were aggregated in five clusters. Table 2 illustrates the distance between each cluster in the network.

Tab. 2: Distance between clusters

Pipe segment	Distance [m]
Plant – Cluster A	170
Cluster A – Cluster B	190
Cluster B- Cluster C	180
Cluster C- Cluster D	220
Cluster D – Cluster E	170
Total	930

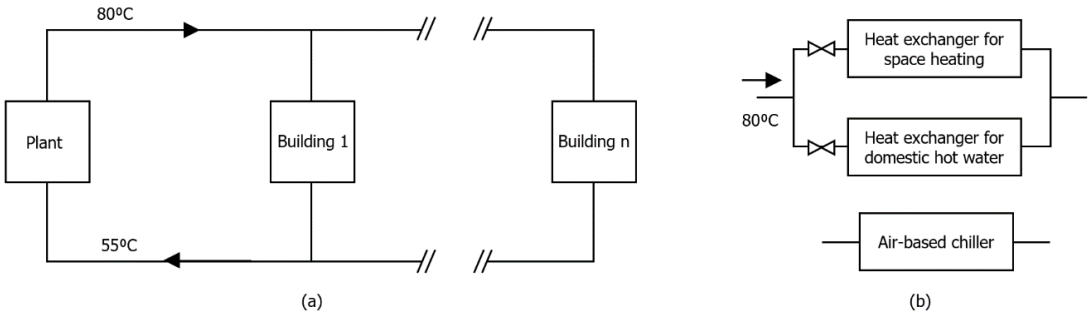

Fig. 2: Schematic of the traditional DH network (a). Schematic of the substation (b).

2.3 Component models

This section describes the physical assumptions made for the main component models. Heat pumps were modelled using an idealized internal control that can track the set-point of the water temperature leaving the condenser. The COP of the heat pump model is calculated as:

$$COP = \eta \frac{T_{con}}{T_{con} - T_{eva}} \quad \text{(eq. 1)}$$

Where T_{con} [K] is the condenser temperature, T_{eva} [K] is the evaporator temperature, and η [-] is the Carnot effectiveness, which was assumed equal to 0.4. Air-based chillers in office buildings were modelled with a similar approach.

The plant was modeled differently for the two system configurations. In the 5GDHC system, the plant was represented by an unlimited source of thermal energy at 15°C, which can deliver a constant water temperature of 15°C in the network at any time. Such energy source can be, for example, a lake, ground water or waste heat/cold from industries. In the traditional DH system, the plant was represented by an ideal heat source, which can raise the temperature in the network from 55°C to 80°C using an amount of thermal power equal to:

$$\dot{Q} = \dot{m} c_p \left(T_{sup} - T_{ret}\right) \quad \text{(eq. 2)}$$

Where ṁ [kg/s] is the water mass flow rate, c_p [J/kg K]is the specific heat capacity, T_{sup} [K] is the supply water temperature, and T_{ret} [K] is the return water temperature.

The pipes were modelled in such as way that the flow resistance is calculated using a fixed flow coefficient, which is computed based on a pre-defined pressure drop at design flow rate. For off-design conditions, the model is capable of calculating the flow friction as a function of the flow rate. Pipes were insulated in the traditional DH system configuration, while they were uninsulated in the 5GDHC system configuration.

The ground surrounding the pipes was set to a pre-calculated value, according to a formula as a function of the time of the year and the depth below the ground surface, which was assumed to be 1 m.

Circulation pumps were modelled by assuming that that the required mass flow rate can be provided at any time by overcoming the pressure drop in the hydraulic circuit. The electric power consumption is determined as a function of the hydraulic and motor efficiency as:

$$P_{ele} = \frac{\dot{V} \Delta P}{\eta_{hyd} \eta_{mot}} \quad \text{(eq. 3)}$$

Where $\dot{V}$ [m^3/s] is the water volumetric flow rate, ΔP [Pa] is the pressure drop, η_{hyd} [-] is the hydraulic efficiency and η_{mot} [-] is the motor efficiency. A constant value of 0.7 was assumed for both the motor efficiency and the hydraulic efficiency.

3. Results and discussion

Figure 3 shows the water temperature entering the substation of Cluster E, which is the farthest substation from the plant. This is the substation where the water temperature is most affected by heat exchange with the ground. Results show that the water temperature in the 5GDHC varies between approximately 5°C in winter and 17°C in summer. This means that, in winter, the water in the circuit rejects heat to the ground, while in summer it absorbs heat. The value of the water temperature entering the substation in summer is particularly critical as it should be sufficiently low for direct cooling (i.e., via heat exchanger). In this specific case, since buildings are equipped with high-temperature cooling systems (about 20°C), a maximum temperature of 17°C may represent a suitable value.

Figure 4 illustrates the water flow rate circulating in the network for both system configurations. For the 5GDHC system, the water flow rate ranges between 10 kg/s and 110 kg/s. For the traditional DH system, the water flow rate is between 1.5 kg/s and 20 kg/s. The larger values obtained for the 5GDHC system are mainly due to the smaller temperature difference between the supply and return pipe, which is 4 K. In comparison, the traditional DH system has a temperature difference of 25 K. It can be also noticed that, in summer, the traditional DH system circulates a small, constant water flow rate, which is required for domestic hot water. Conversely, the 5GDHC system operates large water flow rates, as it provides not only domestic hot water, but also cooling to buildings.

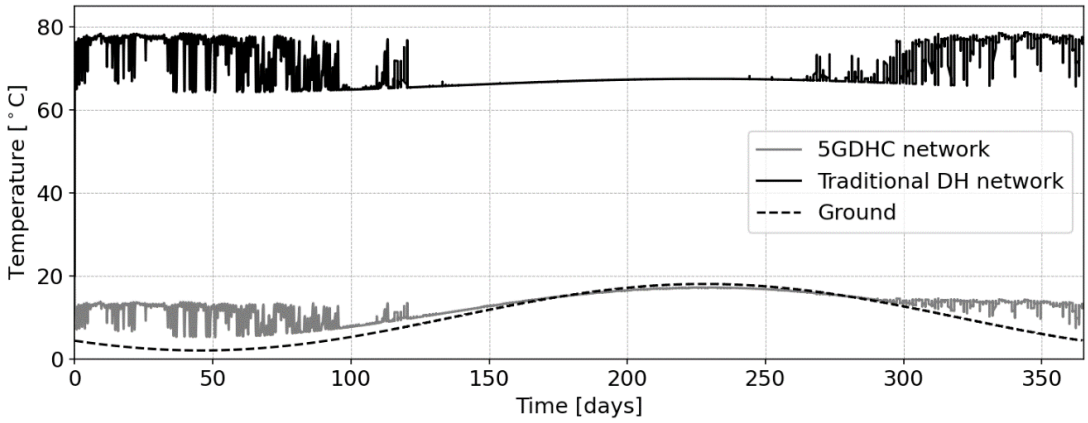

Figure 3: Water temperature entering the substation of Cluster E in comparison to ground temperature

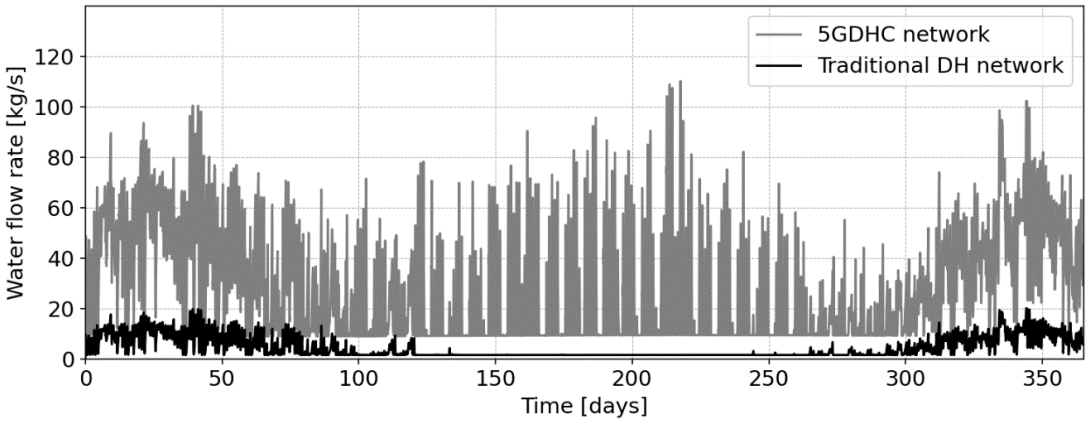

Figure 4: Water flow rates circulating in the network

Figure 5 shows the annual primary energy use of the 5GDHC system in comparison to the traditional DH system. Primary energy factors of 0.8 and 2.5 were used, respectively, for district heat and electricity [6]. Simulation results show that primary energy savings of about 41% can be achieved for the case study considered in this work. This is mainly due to the ability of decentralized heat pumps to adapt the temperature of heat distribution to different uses. This represents a significant advantage, as each machine operates at the best possible ideal COP. In comparison, traditional DH systems are constrained by the worst user in term of heat distribution temperatures. In addition, the 5GDHC network can deliver cooling without any energy input (except for circulation of water).

4. Conclusions

The present work carried out an early-stage feasibility study of an ambient-temperature DHC system located in Denmark. To evaluate the energy performance of the ambient-temperature DHC system, a comparative study was conducted in respect to a traditional DH network. Dynamic energy simulation models were developed using Modelica. Results show that the evaluation of the water temperatures in the 5GDHC network is critical, especially when substations are equipped with compressor-less cooling. Furthermore, due to the small temperature difference between supply and return pipes, higher water flow rates are needed with respect to a traditional DH network. To reduce pressure losses, pipes with large diameters are typically installed. In terms of primary energy use, savings of about 41% can be achieved in comparison to a traditional DH network. This is mainly due the ability of decentralized heat pumps to adapt the temperature of heat distribution to different uses.

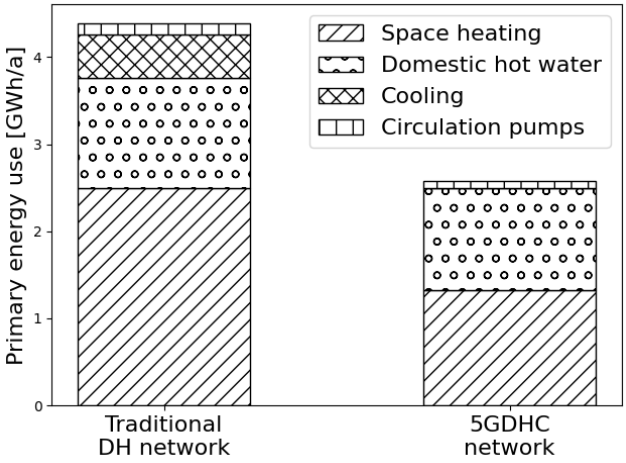

Fig. 5: Primary energy use comparison between traditional DH network and ambient-temperature DHC network

5. Acknowledgments

This work was supported by the Danish Energy Agency, under the Energy Technology Development and Demonstration Program (EUDP), journal no. 64019-0548.

6. References

European Commission, 2016. Towards a smart, efficient and sustainable heating and cooling sector.

Joint Research Centre, Institute for Environment and Sustainability, Mutka, K., Papillon, P., Kalf, R., et al., 2011. 2020-2030-2050, common vision for the renewable heating and cooling sector in Europe: European technology platform on renewable heating and cooling. Publications Office.

Pezzutto, S., Fazeli, R., De Felice, M., Sparber, W., 2016. Future development of the air-conditioning market in Europe: An outlook until 2020. Wiley Interdisciplinary Reviews: Energy and Environment. 5(6), 649-669. https://doi.org/10.1002/wene.210

Buffa, S., Cozzini, M., D'Antoni, M., Baratieri, M., Fedrizzi, R., 2019. 5th generation district heating and cooling systems: A review of existing cases in Europe. Renewable and Sustainable Energy Reviews. 104, 504-522. https://doi.org/10.1016/j.rser.2018.12.059

Wirtz, M., Kivilip, L., Remmen, P., Muller, D., 2020. 5th Generation District Heating: A novel design approach based on mathematical optimization. Applied Energy, 260, 114158. https://doi.org/10.1016/j.apenergy.2019.114158

Calixto, S., Cozzini, M., Manzolini, G., 2021. Modelling of an Existing Neutral Temperature District Heating Network: Detailed and Approximate Approaches. Energies, 14, 379. https://doi.org/10.3390/en14020379

Allen, A., Henze, G., Baker, K., Pavlak, G., 2020. Evaluation of low-exergy heating and cooling systems and topology optimization for deep energy savings at the urban district level. Energy Conversion and Management, 222, 113106. https://doi.org/10.1016/j.enconman.2020.113106

Maccarini, A., Mans, M., Grau CS., Afshari, A., 2021. Towards an automated generator of urban building energy loads from 3D building models. Proceedings of the 14th Modelica Conference, Linköping, Sweden, September 20-24. https://doi.org/10.3384/ecp21181659

International Standard Organization, 2008. ISO 13790:2008 Energy performance of buildings — Calculation of energy use for space heating and cooling.

Maccarini, A., Hultmark, G., Bergsøe, NC., Rupnik, K., Afshari, A., 2020. Field study of a self-regulating active beam system for simultaneous heating and cooling of office buildings. Energy and Buildings, 224, 110223. https://doi.org/10.1016/j.enbuild.2020.110223

Mattsson, SE., Elmqvist, E., Otter, M., 1998. Physical system modeling with Modelica, Control Engineering Practice, 6, 4, 501-510. https://doi.org/10.1016/S0967-0661(98)00047-1

Wetter, M., Van Treeck, C., Helsen, L., Maccarini, A., Saelens, D., Robinson, D., Schweiger, G., 2019. IBPSA Project 1: BIM/GIS and Modelica framework for building and community energy system design and operation - ongoing developments, lessons learned and challenges. IOP Conf. Ser.: Earth Environ. Sci., 323, 012114. https://dx.doi.org/10.1088/1755-1315/323/1/012114

Saelens, D., De Jaeger, I., Bünning, F., Mans, M., Vandermeulen, A., Van der Heijde, B., Garreau, E., Maccarini, A., Rønneseth, Ø., Sartori, I., Helsen, L., 2019. Towards a DESTEST: a District Energy Simulation Test Developed in IBPSA Project 1. Proceedings of the 16th Building Simulation Conference, Rome, Italy, September 2-4. https://doi.org/10.26868/25222708.2019.210806

Wetter, M., Zuo, W., Nouidui, TS., Pang, X., 2014. Modelica Buildings library, Journal of Building Performance Simulation, 7:4, 253-270. https://doi.org/10.1080/19401493.2013.765506

Software-supported investment optimization for district heating supply systems

Felix Panitz, Peter Stange, Tiedo Behrends

Technische Universität Dresden, Chair of Building Energy Systems and Heat Supply, Dresden (Germany)

Abstract

For district heating or cooling systems the optimal supply system fulfilling the supply task has a high importance. Because of the enormous variety of investment options (kind, amount and size of supply units and storages) the process of finding a cost-optimal set-up of the supply system is very complex. An exemplary system focuses on the right investment decision for an available area. Out of 60 specific generation profiles for solar thermal and photovoltaic plants (with different tilt, azimuth and distance between rows) the optimal set-up and size of several photovoltaic and solar thermal plants are calculated. Even size dependent area demand for heat storage is taken in to account.

Python framework flixOpt is introduced. It supports the process for finding optimal investment decisions for complex supply systems. The framework flixOpt is published open source. Set-up options of flixOpt and challenges to solve complex problems are discussed through the exemplary system. Time series aggregation method is used for reducing computing time.

Keywords: optimization of operation, optimal investment decision, mixed-integer linear programming, MILP, district heating, flixOpt, solar plants, solar thermal, photovoltaic

1. Introduction

Investment decisions for the supply of district heating systems with solar fraction have a very high complexity. The optimal solution means: optimal kind, amount and size of heat and electricity generation units and storages. Usually ‘optimal’ means lowest costs, but often aspects of greenhouse gas emissions and primary energy consumption have to be considered as well.

If solar thermal (ST) or photovoltaic (PV) plants are taken into account, optimal configuration for the given system set-up and heat-demand has to be found. Optimal types and configurations of solar plants should be chosen as well as optimal size of the plants or - if area is limited - optimal usage of a given area.

Mathematical optimization can help in the process of finding this optimum. It gives the theoretical exact solution and finds even intuitively unexpected optimal investment decisions out of the pool of defined options and an optimized operation schedule.

Within this paper an exemplary supply system is considered. The optimal investment option for decarbonizing the system shall be calculated out of a pool of investment possibilities with special focus on solar plants.

The python framework flixOpt for modeling complex energy systems and solving the optimization problem was developed and is applied on the example.

2. Framework flixOpt

2.1 General

FlixOpt is a python framework for modeling and optimizing energy systems via solving mixed-integer programming problems (MILP). It is created for networks of energy flows between so called components like sinks, sources, transforming units and storages. It can also be used for material flows, e.g. ash, water, carbon dioxide.

© 2022. The Authors. Published by International Solar Energy Society
Selection and/or peer review under responsibility of Scientific Committee
doi:10.18086/eurosun.2022.04.07 Available at http://proceedings.ises.org

FlixOpt development is based on previously used Matlab framework flixOptMat (FAKS, 2019) and has a few influences from package oemof/solph (Krien et al., 2020). FlixOpt is published under MIT license (flixOpt, 2022).

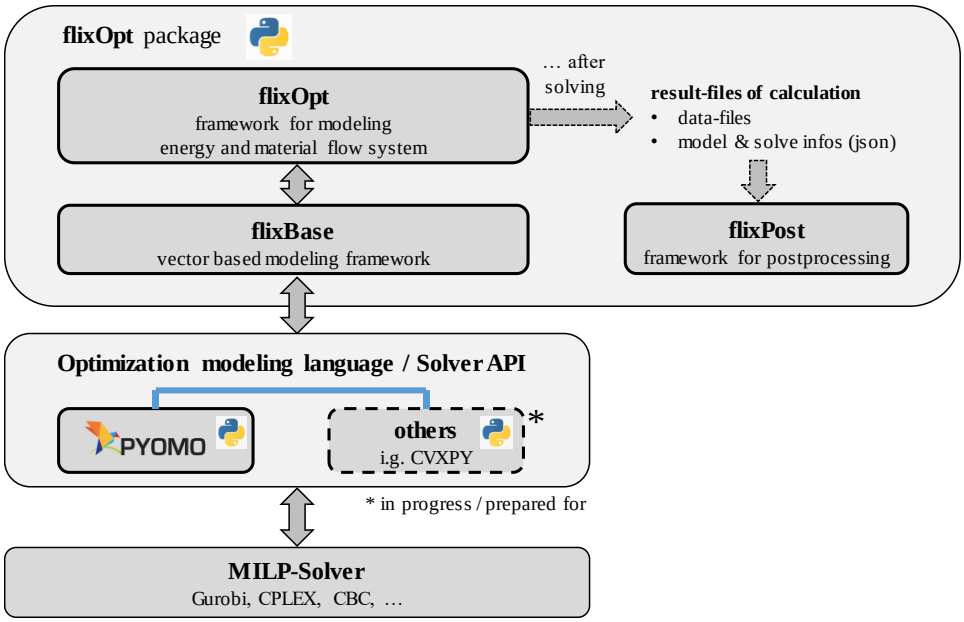

Fig. 1: structure / work flow of flixOpt

It uses pyomo as mathematical optimization modeling language. In preparation for other languages or an own modeling language (as used in flixOptMat) it additionally has a simple intermediate framework flixBase (see Fig. 1). FlixBase actually just provides a vector-variable class and linear equation class for vector based mathematical modeling and transfer to pyomo or to other alternative options.

FlixOpt is developed focusing on fast calculations of energy systems with a high variability in settings like selectable time steps, non-equidistant time steps etc.

A separate python module flixPost provides a simple framework for post-processing of the optimization results.

2.2 Modeling in flixOpt

A flixOpt model consists of buses and components, i.e. transformers, storages, sources and sinks. Each component has input flows and/or output flows. These flows are linked to a node, called ‘bus’, which realizes the flow balance in every time step of all linked flows. Typically, ‘heat’ and ‘electricity’ are common used buses. All details that are relevant for optimization, e.g. costs, efficiency factors, limitations, are implemented as parameters of components and flows.

Boilers, heat pumps, cogeneration units are ‘transformer’ components as one input flow is transformed to one or more output flows. A component of the type transformer can have any number of input and output flows. The (piecewise) linear correlation between the flows is defined within the component.

A component of the type ‘storage’ has one input and one output flow. It can be used to model heat storages as well as batteries, fuel or material storages. It provides several parameters like ‘size of the storage’, ‘fractional loss per hour’, ‘load efficiency’, ‘unload efficiency’ etc.

A component ‘sink’ has only an input flow and can be used to realize demands like a time-resolved heat profile or a feed-in-tariff.

A component of the type ‘source’ has only an output flow and can be used to implement supply tariffs, e.g. for electricity or gas. It is also usable to integrate solar load profiles.

By defining any of the components, the belonging flows have to be defined as well. Flows have many parameters, i.g.

- maximum and minimum load,

- switch-on costs,
- costs per flow-hour (e.g. €/kWh in the case of an electricity tariff),
- maximum full load hours,
- maximum number of switch-on procedures,
- maximum or minimum load factor.

To couple the defined components to a system, every flow has to be linked with the belonging bus.

Usually the optimization target is minimizing the annualized total costs (Stange et al, 2018). But minimizing other aspects like greenhouse gas (GHG) emissions or primary energy consumption must be possible as well.

Costs, emissions etc. are so called 'effects' within the scope of flixOpt and are freely definable in any number. Single shares of the defined effects can be parametrized for any component and flow.

Any effect can be defined as the optimization target. The combined use of several effects as optimization target is possible by internalizing: For example, if the effect 'costs' is used as the main optimization target and another effect 'GHG emissions' is defined, 'specific costs' of GHG emissions coupling both effects.

Another possibility to combine targets is to set boundaries, e.g. maximum of permitted primary energy consumption or a limited GHG budget, while finding a cost optimal invest decision for the energy system is the target of optimization. In the following example the effect 'unbuilt area' will be defined to consider the limited unbuilt area to realize new supply units.

A theoretically global optimal result is calculated on the basis of the relevant, time-dependent data (demand profiles, prediction of prices etc.) within boundaries of the model accuracy. The result includes not only the optimization target value (e.g. operating costs) but also the optimal operation schedule for all components.

Besides the operational parameters, it is also possible to define the investment as a degree of freedom. In this case the optimization result includes the decision whether or not to invest in a component. Additional to the optimal operation schedule the corresponding optimal investment size is given as a result.

2.3 Time series aggregation in flixOpt

A large number of components and especially a large pool of investment decisions significantly increase the computing time.

For dimensioning of heat-supply and storage units, however, the calculation of an exact, time-resolved operation management plays a subordinate role. In this case, minimizing the sum of annualized investment costs and annual operating costs is of primary importance. This allows the use of the python package TSAM (Hofmann et al., 2020). It provides an optional, automatic time series aggregation to reduce the problem size by a sequence of typical periods described by Welder et al. (2018). First the typical periods and their levelized time series are calculated. Afterwards a reduced model is built to represent the original problem as a sequence of linked typical days. Special focus has to be given to correct implementation of the storage and the transition between periods (Behrends, 2021).

In Behrends (2021) the annual operating costs for a given district heating supply system are computed in a very good approximation in a fraction of the time that is required to solve the non-aggregated problem. This computing time reduction can be up to 90% and thus significantly increases the applicability of the mathematical optimization.

In flixOpt the aggregation method is pragmatically implemented. First the full problem, i.e. variables for every time step, is modelled. Hereby the aggregated (levelized) time series data is used. In the following, optimization time series variables are equalized each time when the typical period occurs where they belong to.

This method significantly increases the amount of equations compared to a slim aggregated model containing each typical period once-only. Due to the equalization it has even more equations than the full non-aggregated problem. But after the pre-solving process by the solver, the number of variables and equations is significantly reduced.

As described before, this pragmatical implementation method uses the identical problem formulation compared to the full model. Therefore, the standard modeling algorithm of the full implementation in flixOpt can be used.

Among other advantages, implementation mistakes of inter-periodical equations are avoided in this way. In case of exceeding the maximum number of variables of the used solver, flixBase could be extended by further pre-solving variable reduction routines.

3. Supply system with solar options

3.1 Basics

A district heating system with nominal load of about 5 MW_{th} has been supplied by an oil boiler and a gas boiler so far. A transformation, i.e. decarbonizing strategy, for the system shall be investigated. For a future supply system several investment options exist and are modeled in flixOpt (Fig. 2).

Details of the preselected pool of investment options are described in table 1. There are two buses, heat and electricity, realizing the energy balance. A heat load profile is given as well as the pump power load profile ('sinks'). Auxiliary electricity demand is considered and depends on the operation of the components.

Regarding the given heat load the supply by new biomass boilers is an option as well as a heat pump and a combined heat and power production (CHP) unit ('transformers'). A heat storage is an invest option to store temporarily surplus energy from the heat sources.

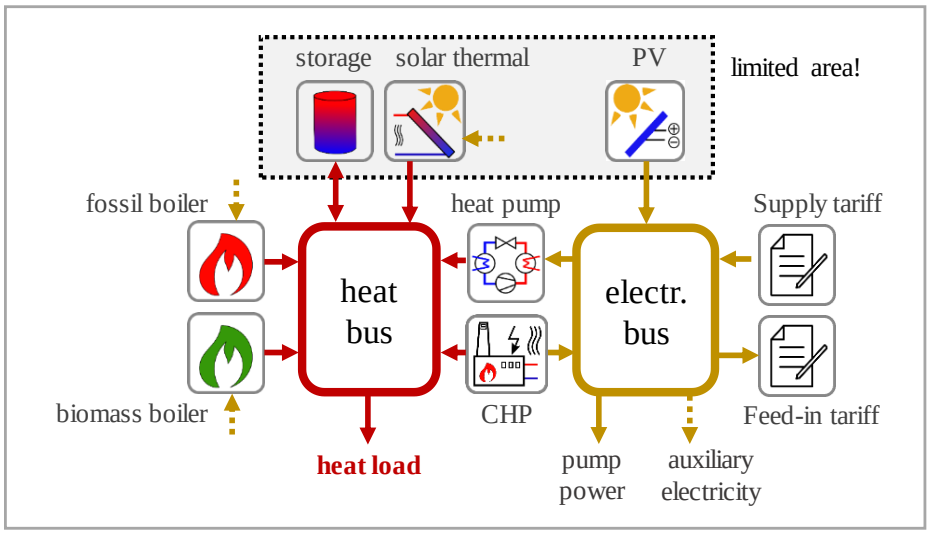

Fig. 2: Exemplary supply system with different invest options of boilers, solar thermal plants and storage

Special focus is given to the usage of a limited unbuilt area, which can be used for the heat storage, solar thermal and photovoltaic plants ('sources').

Besides the effect 'costs' the effect 'unbuilt area' is defined to consider the limited unbuilt area of 20,000 m² in optimization. Consequential specific 'unbuilt area demand' for solar plants and the storage have to be defined. A further effect 'CO_2 emissions' is internalized to the effect 'costs' via the factor of specific costs of CO_2 emissions. The representative investigation period is the year 2019 using hourly time steps.

An extract of the modelled system and used parameters is shown in the following.

Buses and effects:

- buses for electricity and heat
- additional buses for oil, gas and biomass
- 5 effects: costs (optimization target), CO_2 emissions (with specific costs of emissions), unbuilt area (max. 20,000 m²), number of PV plants (max. 3), number of ST plants (max. 3)

Transformers and belonging flows:

- efficiencies, maximal power and minimum partial load for boilers, CHP, heat pump
- switch-on costs for boilers, CHP, heat pump
- specific auxiliary electricity demand for boilers, CHP

Storage:

- specific area demand
- maximal capacity
- fractional loss per hour, efficiency of loading

Sinks/sources and belonging flows:

- relative solar profiles for solar plants
- specific floor area demand for solar plants
- specific auxiliary electricity demand for ST plants
- specific costs and CO_2 emissions for flows of oil, gas, electricity-supply, biomass

Annualized investment costs:

- fixed investment costs for CHP-unit and boilers
- fixed and specific investment costs for solar plants, heat-pump, storage and min./max. of investment size.

Annualized investment costs are used as the calculation period is one year.

Table 1: invest options and results of calculation

	invest options	
	**60 ST plant options/ load profiles**	
	tilt	15°, 30°
	azimuth	±90°, ±45°, 0°
	distance between rows (d.b.r.)	1 m to 4 m (steps of 0.5 m)
	Investment options	
	min size	200 m^2_{coll}
	max no. of plants	3
	**60 PV plant options/ load profiles**	
	tilt	15°, 30°
	azimuth	±90°, ±45°, 0°
	distance between rows	1 m to 4 m (steps of 0.5 m)
	Investment options	
	min size	200 m^2_{coll}
	max no. of plants	3
	**heat storage**	
	size	50 m^3 to 10,000 m^3
	**oil boiler** (existing)	5 MW
	gas boiler (existing)	3 MW
	**biomass boiler 1**	1.5 MW
	biomass boiler 2	2.5 MW
	biomass boiler 3	3.5 MW
	**heat pump**	50 kW to 3,000 kW
	**CHP unit**	68 kW_{el}
	**floor area for storage, ST and PV plants**	
	max Size	20,000 m^2

3.2 Solar Profiles

60 specific load profiles -in kilowatt per m² floor area- for each ST and PV in a given range of tilt, azimuth and distance between rows (see table 1) were pre-calculated. This calculation is based on python algorithms by Narusavicius (2022) and further work by the authors. Diffuse and total irradiance data on horizontal surface (DWD, 2022) is converted to tilted surface. In addition, time-resolved ambient, supply and return temperature of the district heating system are used for the calculation of ST yield.

PV plant yield is calculated with pvlib´s (Holmgren et al., 2018) PVWatts model. Default set-up for loss values

is used. Additional focus was placed on self-shading of the modules. To recognize non-linear shading effects of PV, the model from Ingenhoven et al. (2019) is applied. Annual yield of the profiles varies from 671 to 935 kWh/kW_{peak}.

ST plant yield is calculated according to simplified model in DIN EN ISO 9806 (2017). Additionally, self-shading is considered. Pipe loss and pipe capacity effects will be added in future. Annual yield of the profiles varies from 442 to 663 kWh/m^2_{coll}.

Initially, the yield, the number of module rows and shading loss is calculated for a quadratic floor area of 1,000 m². The yield is transformed to specific yield per m² module area. Floor area demand per module area differs widely and is considered. Finally, the resulting specific values are used within the optimization process.

In order of practical reasons, the maximum number of realized plants is limited to three PV plants and three ST plants. Considering the maximal available unbuilt area each must have any size greater than 200 m² module area. Taking into account that a higher number of plants possibly cause more planning and installation effort a share of fixed cost is added to every plant.

3.3 Results

The problem is modelled and solved in full and in aggregated form of formulation. For the aggregated model the following time series are considered:

- 60 load profiles of ST plant (weight for aggregation 5/60)
- 60 load profiles of PV plant (weight for aggregation 5/60)
- 1 heat load profile (weight 1)
- 1 coefficient of performance profile of heat pump (weight 1)

The aggregation period is 24 hours. Equal weights for each profile would lead to overweighting the solar profiles due to their number. To obtain acceptable representative periods for all load profiles, the weights for the solar profiles are reduced as shown above. Acceptable aggregated load profiles where found by using 35 typical periods.

In table 2 the results of both models are compared. Both are solved by the solver Gurobi using a gap fraction ≤2.5%. FlixBase counts the variables and equations in the vector based manner as they are defined in the flixBase model. That's why their number seems to be quite small.

Table 2: Comparison of full calculation and aggregated calculation

	full		**aggregated**	
computing time	19 h		1.4 h	
number of…	**variables**	**equations**	**variables**	**equations**
flixBase (vector based)	616	616	616	778
single	1.6e6	1.65e6	1.6e6	2.9e6
single, after pre-solving	290e3 50 % bin	360e3	37e3 56 % bin	50e3
total annual costs	828,000 €		927,000 €	
theoretical lower bound	807,000 €		904,000 €	

As described in chapter 2.3, the number of equations increases when using the aggregation method. The additional number of equations corresponds to the number of time series variables. However, although the number of single variables for the aggregated model is equal and the number of single equations is quite higher compared to the full model, after pre-solving the number of variables and equations is significantly lower. As a consequence, the computing time is strongly reduced due to the aggregation.

Regarding the total costs and the optimized investment decisions, the aggregated model overestimates the total costs by about 12 %. Either the chosen number of the typical periods (35) is still too low for the solar time series, or the weights of the time series must be revised. Behrends (2021) had realized a better representation of a supply system by the aggregated model even with a lower number of typical periods. However, in Behrends (2021) solar profiles were not part of the system. Concluding, a greater focus on the suitable mapping of the aggregated solar time series is suggested.

Table 3 shows the optimal investment decisions for the system. The aggregated model results in one ST plant and one larger PV plant while the full model results in only one PV plant. Tilt, azimuth and distance between rows are optimized. The storage size is quite equal in both models. In both variants the fossil boilers are removed. The result of the aggregated model includes a second boiler and a small powered heat pump, whereas the result of the full model has a high powered heat pump and a CHP unit. In both results the available unbuilt area is used completely.

In pre-calculations containing very high storage costs results with two or three ST plants with different tilt and azimuth occurred both for aggregated and complete model (Panitz & Stange, 2022). This is a consequence since the simultaneity of yield and load becomes more important if a big storage is not cost-optimal or available.

Table 3: Investment decision results of optimization

	aggregated model		**full model**	
	ST plant tilt 30°, azimuth 0°, d.b.r 1.5 m	3350 m^2_{coll}	-	
	PV plant tilt 15°, azimuth 0°, d.b.r 1.0 m	2 MWp	PV plant tilt 15°, azimuth 0°, d.b.r 1.0 m	2.8 MWp
	668 m³		694 m³	
	removal of oil boiler removal of gas boiler		removal of oil boiler removal of gas boiler	
	bm boiler 1 bm boiler 2	1.5 MW_{th} 2.5 MW_{th}	bm boiler 1	1.5 MW_{th}
	heat pump	0.56 MW_{th}	heat pump	2.37 MW_{th}
	-		CHP unit	68 kW_{el}
	20,000 m²		20,000 m²	

For avoidance of misinterpretation it has to be checked that the result is not a random result in the bandwidth of the admitted fractional solver gap. It is advisable that one additional calculation with just one single south orientated PV plant or one ST plant with typical parameters of tilt and distance between rows should be made. The resulting costs of the multi-plant solution should be lower, otherwise the simple solution should be chosen.

4. Summary

The Python tool flixOpt is an universal open source tool to model and optimize complex energy systems. It was used to optimize a district heating supply system with 120 options of solar plants (each with variable size) and invest options for several other generation units with heat and electricity flows. The framework already provides a wide range of functionality so that there is no need to implement additional equations to model and solve the demonstrated example. Specific yield profiles of the solar plants were pre-calculated via simulations for a representative quadratic floor area of 1,000 m². Self-shading of ST modules and PV modules is considered.

For optimizing the system two approaches of computation are used: one containing the full model and one containing the aggregated model. Aggregation reduces computing time significantly compared to the full model. However, the aggregation has to be used very carefully in combination with solar profiles because results can significantly differ as shown in the given example.

In summary, mathematical optimization supports the decision maker to evaluate different options of solar plants and to calculate optimized size of plants as shown. In the given example only one type of ST collector and PV module is used. Moreover, decision problems with several types of ST collectors or PV modules with different corresponding invest costs and yield characteristics can be of interest in practical issues and can be implemented likewise.

Acknowledgments

This project was founded by the German Federal Ministry for Economic Affairs and Energy (FKZ: 03KB159B).

References

Behrends, T., 2021. Rechenzeitreduktion der Erzeugereinsatzoptimierung durch Zeitreihenaggregation. (Computational time reduction of generator usage optimization by time series Aggregation). Diploma Thesis. Technische Universität Dresden, 2021.

DIN EN ISO 9806, 2017. Solarenergie - Thermische Sonnenkollektoren – Prüfverfahren. Deutsche Fassung EN ISO 9806:2017. Deutsches Institut für Normung e.V.

DWD, 2022. Data for location Görlitz (Germany). Climate data center. https://opendata.dwd.de/climate_environment/CDC/ (01.06.2022)

Hoffmann, M.; Kotzur, L., Stolten, D., Robinius, M., 2020. A Review on Time Series Aggregation Methods for Energy System Models. In: Energies 13 (2020), nr. 3. – ISSN 1996–1073.

FAkS, 2019. Feldtest Absorptionskälteanlagen für KWKK-Systeme - FAkS. Abschlussbericht, Kapitel 8. Gesamtsystembetrachtung KWKK. Technische Universität Dresden. Project, founded by the German Federal Ministry for Economic Affairs and Energy (FKZ: 03ET1171B). https://doi.org/10.2314/KXP:1666931608.

flixOpt, 2022. URL https://github.com/flixOpt/ (01.11.2022)

Holmgren, W.F., Hansen, C.W., Mikofski, M. A., 2018. pvlib python: a python package for modeling solar energy systems." Journal of Open Source Software, 3(29), 884. https://doi.org/10.21105/joss.00884

Ingenhoven, P., Stein, J.S., Dallapiccola, M., Moser, D., 2018. Simplified method for partial shading losses calculation for series connected pv modules with experimental validation. https://doi.org/10.4229/35thEUPVSEC20182018-6CO.3.1

Krien, U., Schönfeldt, P., Launer, J., Hilpert, S., Kaldemeyer, C; Pleßmann, G, 2020. oemof.solph—A model generator for linear and mixed-integer linear optimisation of energy systems. Software Impacts, Volume 6, 2020, 100028, ISSN 2665-9638, https://doi.org/10.1016/j.simpa.2020.100028

Narusavicius, B. Implementation and validation of a python package for the calculation of time-resolved solar yields. Diploma Thesis. Technische Universität Dresden, 2022.

Panitz, F., Stange, P. 2022. Softwaregestützte Dimensionierung von Erzeugern und Speichern. Poster. 32. Symposium Solarthermie und innovative Wärmesysteme. https://doi.org/10.13140/RG.2.2.31085.87527

Smartbiogrid. Optionen zum Einsatz fester Biomasse in dekarbonisierten Wärmenetzen; Teilvorhaben: Tool zur robusten Optimierung. Technische Universität Dresden 2019-2022. Project, founded by the German Federal Ministry for Economic Affairs and Energy (FKZ: 03KB159B)

Stange, P., Matthees, A., Sander, T., 2018: Operational optimization of energy systems, 25 years – established and promising use cases. Energy Procedia, Volume 149, p. 15-24. ISSN 1876-6102. https://doi.org/10.1016/j.egypro.2018.08.165.

Welder, L., Ryberg D.S., Kotzur, L., Grube, T., Robinius, M., Stolten, D., 2018. Spatio-temporal optimization of a future energy system for power-to-hydrogen applications in Germany. Energy, Volume 158, 2018, Pages 1130-1149, ISSN 0360-5442, https://doi.org/10.1016/j.energy.2018.05.059.

Optimisation of a theoretical 4th generation district heating network located at the town of Loughborough, UK

M. A. Pans[1], and P.C. Eames[1]

[1] Centre for Renewable Energy Systems Technologies (CREST), Wolfson School of Mechanical Electrical and Manufacturing Engineering, Loughborough University, Loughborough (UK)

Abstract

A cost and efficiency optimization for a net zero district heat (DH) network providing hot water and space heating for a specific urban area in the town of Loughborough, UK, was performed using a previously developed model. The model simulates a DH system with heat provided from i) renewable heat sources (RHS), i.e. heat pumps powered by PV and/or Wind and evacuated tube solar thermal collectors (ETSTCs), and ii) stored heat from centralized long duration (namely long-term water tank, LTWT) and decentralized thermal energy storage (TES) systems. Based on hourly weather data, building specifications and occupancies the model calculates a) hourly domestic heat demands for both space and domestic hot water, b) the hourly heat production from the specified RHS and c) losses from TES and pipes. The DH network simulations were performed for an 18-month period from the 01/06/2018 00:00 to 31/12/2019 23:00. The effect of parameters affecting the performance of the decentralized short-term water tanks (STWT) used for heat stores including i) the average volume of the STWT (V_{STWT}) per dwelling and ii) the specified STWT charging temperatures ($T_{charging\ STWT}$), on a) the DH system cost per dwelling and b) the energy efficiency of the DH system (η_{DH}) were assessed. The predictions showed that increasing either the V_{STWT} and/or $T_{charging\ STWT}$ leads to i) an increase in the total cost of the DH system per dwelling, and ii) to a decrease in the η_{DH}. These results are mainly due to a reduced use of the LTWT, which results in a greater required installed Wind generation capacity and number of heat pumps to fully meet heat demands at certain periods of the year and as a consequence greater heat losses and increased amounts of heat being shed in the DH system.

Keywords: district heating; thermal energy storage; modelling; optimization; renewable; simulation

1. Introduction

The green deal recently approved by the European Union aims to reduce the greenhouse gas emission to 50% by 2030 relative to 1990 levels. In order to do this, reductions of greenhouse emissions originating in the residential sector [which was responsible for 26.1% of the final energy consumption of the European Union in 2018 (European Union, 2020)] are crucial. Different paths can be taken to accomplish this target including: i) replacing common fossil fuel heat sources by renewable heat sources, ii) increasing the efficiency of domestic heating systems and iii) implementation in urban areas of highly efficient 4th generation district heating (DH) networks. The recent increase in the costs of fuel together with the energy crisis in Europe resulting from Russia's invasion of Ukraine adds urgency to the transition to in-country local production of renewable energy instead of the importation of fossil fuels.

The 4th generation DH system approach aims to almost fully decarbonize the production of heat for domestic use by predominantly using renewable heat sources (RHS) and low/zero carbon heat sources (Lund et al., 2014). Due to the intermittent nature of renewable heat sources, the inclusion of thermal energy stores (TES) in 4th generation DH seems crucial. TES consist of a storage medium that stores thermal energy (heat or cold) produced at a time when heat production is greater than demand which can be released later when demand exceeds production. TES systems are classified depending on the storage approach used and may be sensible, latent or thermochemical. TES can also be classified based on storage duration: short-term and long-term storage. Short term stores for space heating are usually small devices located near or inside dwellings which are used to alleviate peak domestic heat requirements, whereas long term stores are generally larger stores which are charged during the summer months

© 2022. The Authors. Published by International Solar Energy Society
Selection and/or peer review under responsibility of Scientific Committee
doi:10.18086/eurosun.2022.04.08 Available at http://proceedings.ises.org

and discharged in winter months, providing backup in winter months for renewable heat generation and short-term stores.

One of the key parameters in the design of TES is to determine both the optimum volume and charging temperature that enables all domestic heat loads of dwellings connected to a DH network to be met all year round at minimum cost. Studies of how these parameters affect the cost and energy efficiency of a DH system are scarce, and most of the research publications in this area have focused on dynamic models of selected elements of a DH system rather than undertaking the simulation of a full DH system. The current simulations include i) different RHS available near a given urban area and ii) different short-term and long-term TES options (which include the three main types of TES systems used for storing heat, i.e. sensible, latent and thermochemical).

Allison et al. (Allison et al., 2018) calculated the theoretical maximum heat storage capacity required for different TES options to support load shifting. A hot water storage tank, concrete, high-temperature magnetite blocks, and a phase change material (PCM) (Paraffin C28) were the TES options considered. The results obtained showed that i) with low temperature heat storage, domestic load shifting is feasible over a few days (beyond this timescale, the very large storage volumes required makes integration in dwellings problematic); ii) supporting load shifting over 1–2 weeks is feasible with high temperature storage (retention of heat over periods longer than this is challenging, even with significant levels of insulation); iii) seasonal storage of heat in an encapsulated store appeared impractical in all cases modelled due to the volume of material required. The authors calculated the store heat capacities assuming that the heat load was to be fully met just using the stores with no additional heat input. Long-term large scale heat storage options, such as water tanks for seasonal heat storage and/or thermochemical storage (TCS) systems were not considered. Gaucher-Loksts et al. (Gaucher-Loksts et al., 2022) carried out the simulation of a system composed of air source heat pumps and building-integrated photovoltaic systems located in a solar house. Three different configurations of the system were evaluated, two of them including thermal storage (hot water). The authors determined that the tank volume and solarium size had the highest impact on the flexibility of the system. An optimal size for the store volume of between 300 and 600 L was determined for a house with a floor area of 116 m^2 (no seasonal heat stores were considered in the study). Schuetz et al. (Schuetz et al., 2017) carried a simulation of a system consisting of a combination of heat pumps and thermal storage systems for residential heating. The authors found that a larger heat pump size improves the system's flexibility while the size of the store had little impact. The authors also found also that the store volume, heat pump size, and load significantly impact the length of time the store remains charged and thus the flexibility of a system.

The present research aims to contribute to the development of designs for and future successful implementation of 4th generation DH systems in the UK and similar climates. The main objective of the reported research was to apply a novel model to simulate a theoretical 4th generation district heating system (which is fully described in (Pans et al., 2023) to determine the optimum operating conditions that i) minimises the cost of the DH network per dwelling and ii) maximises the energy efficiency of the network (by minimising heat shed in summer), while completely meeting domestic heat loads for the full simulation period. The proposed DH network modelled was based on the characteristics of two residential areas in Loughborough, UK. The effect of changing key parameters related to the decentralised TES system, [referred to as "short-term water tank" (STWT)], including the store charging temperature ($T_{charging\ STWT}$) and the store volume (V_{STWT}), on a) the total average cost per dwelling and b) energy efficiency of the DH system were assessed.

2. Methodology

2.1. Description of the proposed DH system

A detailed description of the model employed can be found in (Pans et al., 2023). Fig. 1 shows the general components and arrangement proposed for a DH system using only renewable heat sources and TES systems to meet annual hourly heat demands. As can be seen, in the model schematic presented in Fig. 1 the heat to meet domestic heat demands is produced using i) heat pumps (HPs) powered only by electricity produced by solar photovoltaic (PV) and Wind Turbines (it is assumed that there is no connection with the electricity grid) and ii) evacuated tube solar thermal collectors (ETSTCs) located on or very near the dwellings. In scenarios where the heat produced is higher than the heat demand, the extra heat is stored in domestic TES located inside or near the dwellings. In those scenarios where both the heat produced is higher than the demand and the domestic TES have reached their maximum storage capacity, the power not used from PV and Wind is used in another set of

HPs located near a seasonal TES - the long-term water tank (LTWT) - to increase the temperature of the water inside the LTWT to the required charging temperature. The extra heat generated by the ETSTCs not used to meet the domestic heat demands and/or to fill the stores is shed.

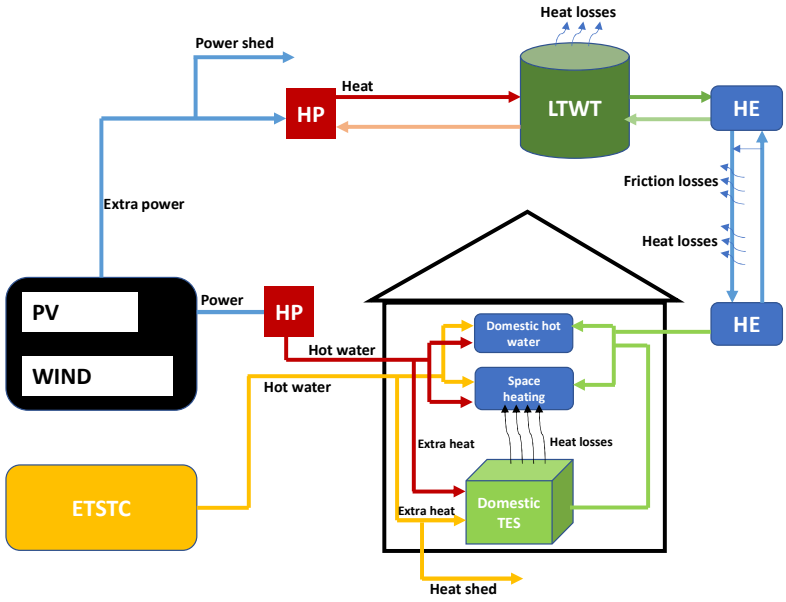

Fig. 1: A schematic diagram illustrating the components and operating mode proposed for a net zero DH network.

2.2. Methodology

The methodology used to carry out the simulation of the DH system described in detail in (Pans et al., 2023), can be split in to two different well-defined stages:

i) Calculation of hourly heat demand profiles for both space heating and domestic hot water by means of a) the number and type of buildings in a specified area and b) location specific hourly weather data. Four different building forms, detached, semi-detached, terraced and flats, were considered in this study. Key characteristics of the buildings such as floor areas, fabric form and U-values, glazing areas, orientation and occupancy were included in the model.

ii) Calculation of hourly energy/heat produced by the employed different RHS types. An online tool created by Pfenninger and Staffell (Pfenninger and Staffell, 2016) was used to estimate the hypothetical hourly capacity factor for both PV and Wind energy sources and the hourly ground-level solar irradiance (needed to calculate the efficiency of the ETSTCs).

Four different thermal storage systems were considered:

a) A centralized large long term heat store (water based, called long-term water tank, LTWT);

b) 3 types of decentralized small scale thermal stores located in the building stock: STWT, PCM-based stores and TCS-based stores.

Heat losses from stores and the distribution network in addition to pumping power requirements were calculated for each hour.

2.3. Application of the model to a residential area in Loughborough, UK

Fig. 2 shows the two urban areas in Loughborough, UK, considered in this simulation study (namely blue and red areas). The total number of dwellings is 262 (173 dwellings in the blue area and 89 in the red area). The two different areas were divided into different sub-areas with an average of ca.10 dwellings per sub-area. Data

regarding the number of dwellings, type of dwelling and household type was exogenously obtained from the official labour market statistics for both residential areas (Pans et al., 2023).

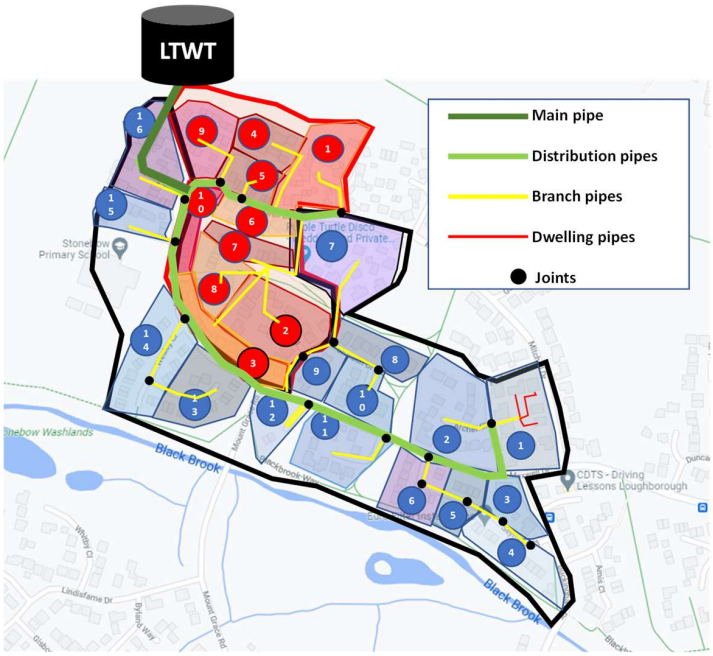

Fig. 2: Residential areas of the town of Loughborough considered for the simulations performed, illustrating the proposed layout of the DH network and the location of the LTWT

The piping network proposed for the DH system located in Loughborough is presented in Fig. 2. The location of the LTWT was assumed to be adjacent to the residential area. Four different types of pipes with different diameters were used: LTWT main (dark green), main distribution (light green), branch (yellow) and dwelling pipes (red). The LTWT main is the pipe that connects the LTWT with the main distribution pipes; the main distribution pipes connect the LTWT with the two different urban areas (red and blue); the branch pipes connect the main pipes to the different sub-areas; and finally, the dwelling pipes connect the branch pipes to the dwellings. The black dots indicate joints between two or more pipes. The distance between joints was calculated using Google maps. The total length of the modelled piping network was 3466 m. The pipes were assumed to be made of polyvinyl chloride with an insulation of foam (Aluflex type). The diameters of the different pipe sections were chosen to avoid maximum velocities of water inside the pipes greater than ca. 1.5 m/s. The thickness of the insulation material for the different pipes was chosen following manufacturers recommendations. The heat losses and friction losses in the piping network were calculated for each hour for every pipe section (sections of the pipe between two joints) based on the flow rate and dimensions of each specific pipe section (Pans et al., 2023). The time-period considered in the simulation of the DH system was from 01/06/2018 00:00 to 31/12/2019 23:00.

2.4. DH system optimization methodology

Tab. 1 shows the values used in the simulations for the main parameters of the DH network. Optimisation was performed by determining the mix of installed capacities of Wind ($Wind_{capacity}$) and solar PV ($PV_{capacity}$) required to fully meet domestic heat demands for the whole time period of the simulation for the minimum cost per dwelling. The model uses the hourly capacity factor for both PV and Wind in the town of Loughborough obtained exogenously from ("Renewables Ninja on-line tool," n.d.), as explained in section 2.2. The Coefficient of Performance (COP) values for the two types of HPs were calculated for each hour in the simulation using the equation and parameters show in (Pans et al., 2023). The total number of heat pumps required to meet the loads was calculated at every hour by dividing i) the hourly power output from the combination of different amounts of PV and Wind (thus assuming that the HPs are not connected to the grid) by ii) the minimum power required to operate a heat pump, which was assumed 5 kW for domestic HPs and 15 kW for HPs used to boost the temperature of the water inside the LTWT. The sizes were chosen according to information regarding typical sizes for domestic

HPs, which range between 5 and 15 kW (Ecoexperts, n.d.; Evergreen energy, n.d.). In this work, a HP size of 5 kW was used to provide heat for dwellings and 15 kW to charge the LTWT, as the amount of extra heat to be stored in the latter is usually much higher than the amount of heat required in individual dwellings to meet demands and/or the amount of heat to be stored in individual domestic TES. Once the minimum number of heat pumps needed in each hour was determined, the minimum number of heat pumps required for to meet loads for the whole time-period considered in a simulation, was the maximum of all hourly minimum-number-of-heat-pump values. For the simulations half of the minimum number of heat pumps required were specified to be air-source heat pumps (ASHPs) and half ground-source heat pumps (GSHPs) (for heat pumps used for boosting the LTWT temperature the acronyms used are ASHP-LTWT and GSHP-LTWT). The mix of heat pump types can be varied based on local conditions. The average area of ETSTC per dwelling was set at 2 m^2. The size of the LTWT was determined taking into consideration the maximum monthly heat demand predicted for the proposed DH system and for the full time-period of the simulation, which in this case corresponds to the heat demands obtained for January 2019 (625875 kWh). A volume of 15000 m^3 was specified for the LTWT to provide sufficient capacity to store/discharge the heat needed to satisfy the heat demands of the DH system in the coldest month of the year (15000 m^3 provides 696666 kWh of heat storage, based on a charging temperature of 60°C and a return temperature of 20°C with a perfectly stratified store).

Tab. 1: Main fixed parameters specified for the simulation

TESsystem main parameters	
Deployment (% of dwellings with stores)	
STWT	50%
PCM	30%
TCS	20%
Charging temperature (°C)	
STWT	Variable (50 – 90°C)
PCM	50
TCS	120
LTWT	60
Volume	
STWT volume per dwelling (m^3)	Variable (0.1 – 0.4)
PCM volume per dwelling (m^3)	0.2
TCS volume per dwelling (m^3)	0.2
LTWT (m^3)	15000

The selected levels of deployment of different decentralised TES systems into dwellings was based on their current technology readiness levels. 0.2 m^3 per dwelling was specified for PCM and TCS systems. The effects of two key parameters in the design of the STWT systems, the volume (V_{STWT}) and charging temperature ($T_{charging\ STWT}$) on a) the average total cost per dwelling and b) energy efficiency of the DH system was assessed.

2.5. Assumed capital costs of the DH system components

Only initial capital costs were considered in this work. The capital costs for the different constituent parts of the simulated DH network obtained from a range of sources are detailed in Tab. 2. The cost of the piping network includes the cost of pipes, installation work, circulation pumps and heat exchangers in dwellings.

Tab. 2: Costs for the different constituent parts of the DH system

Energy and heat sources		Capital cost
Installed PV (£/MW)((STA), n.d.)		1000000
Installed Wind (£/MW)(Briefings for Britain, n.d.)		1290000
ETSTC (£/m²)[1]		170
ASHPs (£/kW)(Staffell et al., 2012)	Capital cost (£/kW_{th})	$\frac{£}{kW_{th}} = 200 + \frac{4750}{kW_{th}^{1.25}}$
	Installation cost (£)	1500
GSHPs (£/unit)(Staffell et al., 2012)	Capital cost (£/kW_{th})	$\frac{£}{kW_{th}} = 200 + \frac{4750}{kW_{th}^{1.25}}$
	Installation cost (£/kW_{th})	800
TES		
TCS (£/kg)(Mahon et al., 2020)		0.2
PCM (£/kg)(Fadl and Eames, 2019)		6
STWT (£/0.2 m³)(Guelpa and Verda, 2019)		200
LTWT (£/m³)(Guelpa and Verda, 2019)		50
Network		
Piping network (£/dwelling) (Energy research partnership, 2016; Energy technologies institute, 2018)		800

[1]Obtained as an average of prices found online for different ETSTCs brands.

3. Results

3.1. Effect of V_{STWT} and $T_{charging\ STWT}$ on the average cost of DH system per dwelling.

The simulations show that for all different studied scenarios the minimum cost is always achieved when no PV is installed at the dwellings to power the domestic HPs and only wind turbines are used to generate power. The reason for this is that in the Loughborough area, the average capacity factor (i.e. the average power output divided by the maximum power capability) of wind turbines for the time-period considered in the simulations is more than double that for PV (as shown in Fig. 3), which results in an average higher cost required to produce the same amount of power when using PV compared to when using Wind turbines.

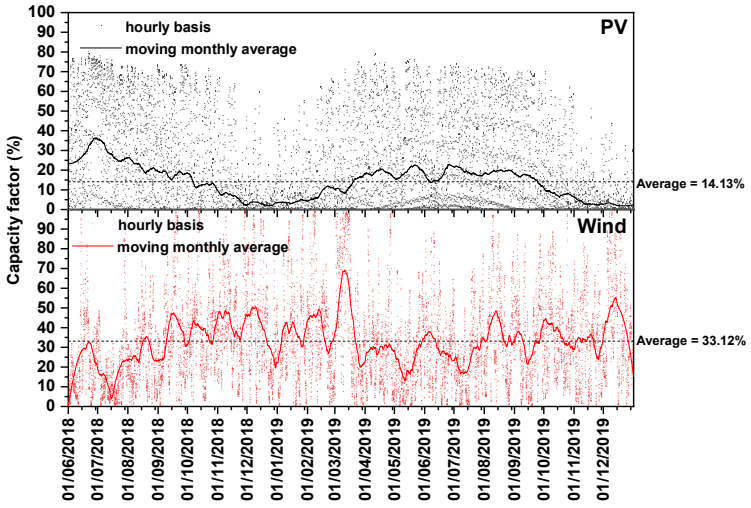

Fig. 3. Capacity factor for solar PV and Wind power generation from 01/06/2018 00:00 to 31/12/2019 23:00 in the Loughborough area. Hourly basis (dots) and moving monthly average (lines). Results obtained using weather date from the online simulation software www.renewables.ninja ("Renewables Ninja on-line tool," n.d.)**.**

Fig. 4 shows the effect of V_{STWT} on the average cost of the DH system per dwelling for different $T_{charging\ STWT}$ values. As can be seen, higher values of V_{STWT} lead to an increase in the cost per dwelling. At $T_{charging\ STWT}$ = 50°C, the increase in the cost with increasing V_{STWT} is mainly due to an increase in the cost of the store, with the cost of the other components of the DH system remaining roughly constant, as can be seen in Fig. 5. As $T_{charging\ STWT}$ increases, the Wind capacity needed and number of HPs increases with $V_{STWT,}$ which leads to a further increase of the cost. This is because with increasing V_{STWT} more heat can be stored in the STWT and as a consequence less heat is stored in the LTWT, which leads to a shortage of available heat from the LTWT at certain times of the year and thus to a higher Wind capacity and, as a consequence, number of HPs needed to meet demands. This can be seen in more detail in Fig. 6, where the hourly heat stored in the LTWT is presented for different V_{STWT} values when operating at $T_{charging\ STWT}$ = 80°C with a set $Wind_{capacity}$ = 0.4277 MW (which is the minimum $Wind_{capacity}$ required in the simulations using the minimum V_{STWT} value used in this work, i.e., 0.1 m^3 per dwelling). As can be seen in Fig. 6, the increase of V_{STWT} reduces the amount of heat available in the LTWT between 15/01/2019 and 15/03/2019, as a consequence the domestic heat demands cannot be met at certain times of this period, as shown in Fig. 7. This results in a higher Wind capacity needed to meet the domestic heat demands for those specific times and dates.

The shortage of available heat from the LTWT when increasing V_{STWT} can be explained by the fact that the rate of heat losses from heat stored in the LTWT are smaller than the heat losses per unit of heat stored in the STWT (due to the greater surface area to volume ratio of the STWT). Thus, at higher V_{STWT} more heat can be stored in STWT, meaning higher heat losses in the system.

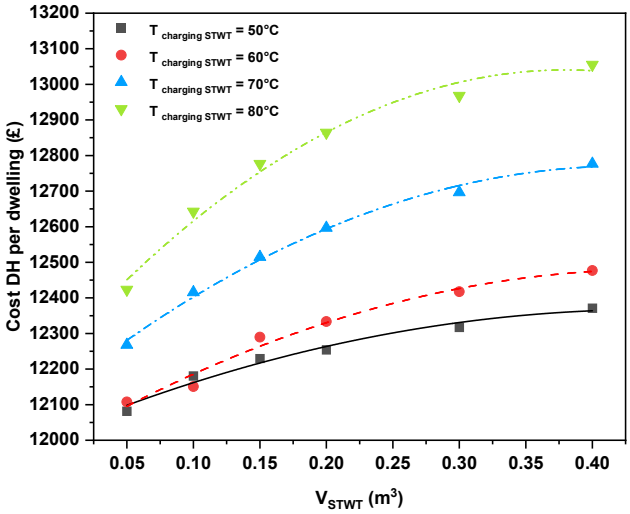

Fig. 4: Effect of V_{STWT} and $T_{charging\ STWT}$ on the average cost of the DH system per dwelling.

As can be seen in Fig. 4, the increase of $T_{charging\ STWT}$, leads to an increase in the cost of the system (for set volumes V_{STWT}) which is again due to the increase in both $Wind_{capacity}$ and minimum number of HPs required to meet fully domestic heat demands, as seen in Fig. 5. Similar explanations of that mentioned above when explained the effect of V_{STWT} on cost can be given here, i.e. the higher $T_{charging\ STWT}$ the higher storage capacity available in STWT which leads to less use of the LTWT and thus to a shortage of the heat stored in the LTWT in winter/autumn months. Further, when $T_{charging\ STWT}$ increases the efficiency of both HPs and ETSTC decreases which leads to less heat produced and stored in the STWT. Due to this, the charging of the STWT store is slower and consequently at certain dates and times higher $Wind_{capacity}$ is required, compared to the $Wind_{capacity}$ needed for simulations with low $T_{charging\ STWT}$ values, to meet the domestic heat demands.

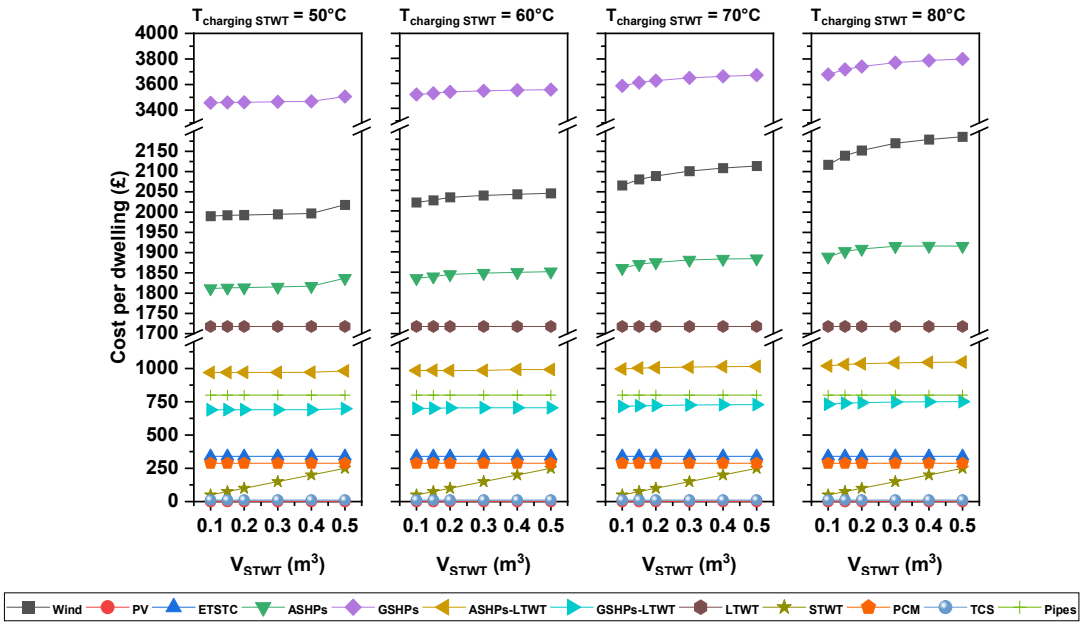

Fig. 5: The effect of V_{STWT} on the cost of the different parts of the DH system when operating at $T_{charging\ STWT}$ values of 50,60,70 and 80 °C.

A minimum cost of £12,103 per dwelling was obtained for V_{STWT} = 0.1 m^3 and $T_{charging\ LTWT}$ = 50°C, which is in the same range of cost obtained for DH networks by different authors (AECOM, 2017; Department of energy and climate change, 2015; Wang, 2018). Unlike these studies, the present study assumes only decentralised renewable heat sources, which it is assumed would result in a much higher costs than that of DH systems using centralized heat sources. However, the cost predicted was similar to those estimated by sources considering centralized heat sources which indicates the benefits of incorporating TES into DH networks supplied using only renewables in terms of cost and efficiency. The predicted average cost per dwelling is also less than the installation cost of a single GSHP and slightly higher than the cost of a single ASHP.

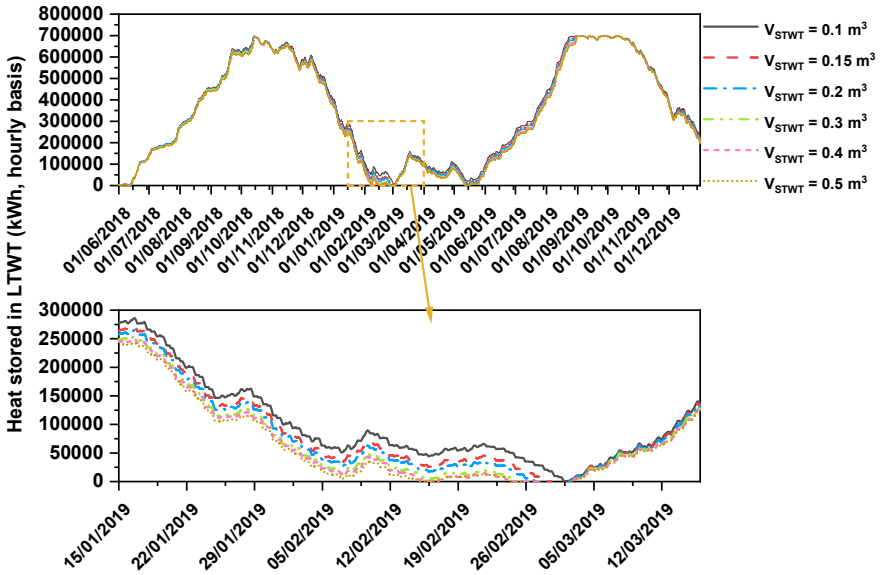

Fig. 6: The effect of V_{STWT} on the heat stored in the LTWT from 01/06/2018 00:00 to 31/12/2019 23:00 when operating at $T_{charging\ STWT}$ = 80°C and $Wind_{capacity}$ = 0.4277 MW.

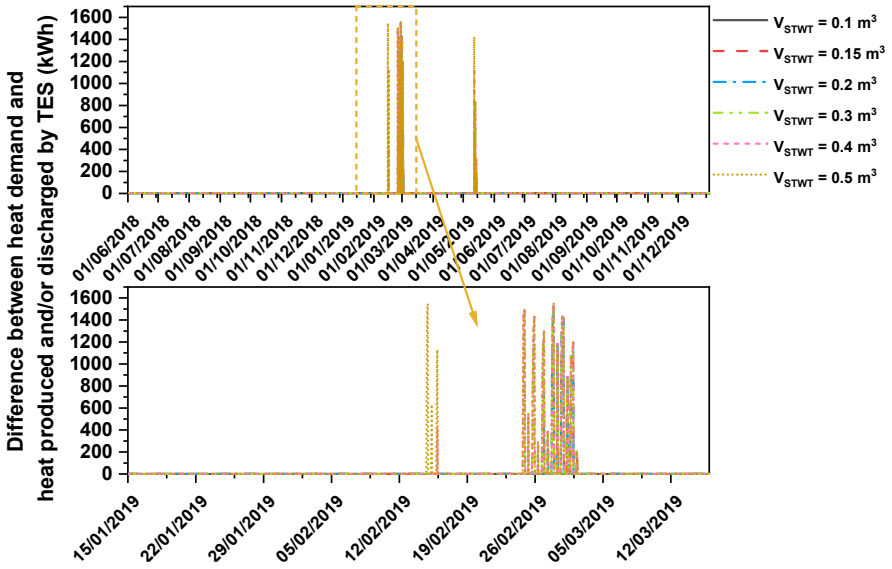

Fig. 7: The effect of V_{STWT} on the difference between i) heat demand and ii) heat produced and/or discharged by TES, from 01/06/2018 00:00 to 31/12/2019 23:00 when operating at $T_{charging\ STWT}$ = 80°C and $Wind_{capacity}$ = 0.4277 MW.

3.2. Effect of V_{STWT} and $T_{charging\ STWT}$ on η_{DH}.

The overall energy efficiency of the DH network (η_{DH}) was calculated using **Eq. 1**:

$$\textbf{Eq. 1}\quad \eta_{DH\,(t)}\,(\%) = \frac{Useful\ hea\ _{(t)}}{Energy\ delivered_{(t)}} \cdot 100$$

Where $Useful\ energy_{(t)}$ is the sum of the heat used in dwellings plus the heat stored in TES, and $Energy\ delivered_{(t)}$ is the sum of the i) heat produced by the different RHS ii) the heat discharged from TES and iii) the heat losses in STWT and PCM stores. The reason behind the inclusion of heat losses from both STWTs and PCM stores is that as these devices were assumed to be located inside the dwellings, the heat losses from these stores can act as heat gains to dwellings and be used to reduce the domestic space heat demand.

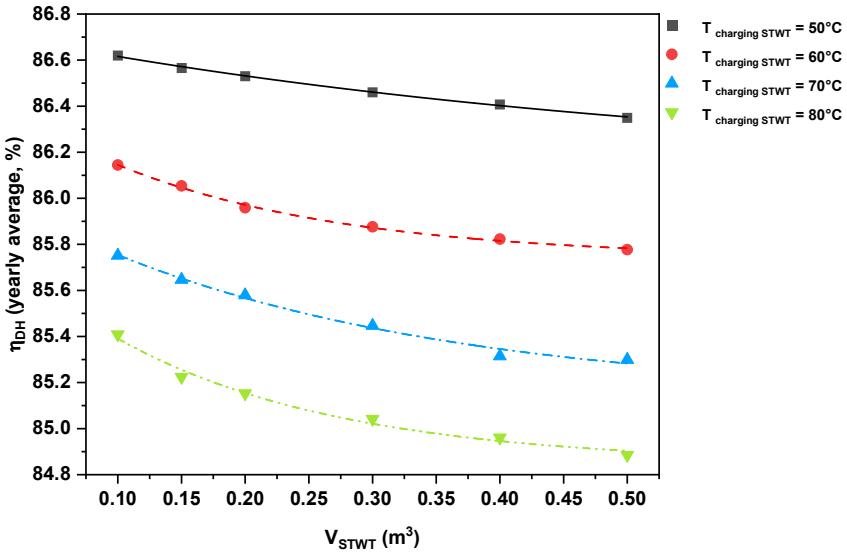

Fig. 8: Effect of V_{STWT} and $T_{charging\ STWT}$ on η_{DH}.

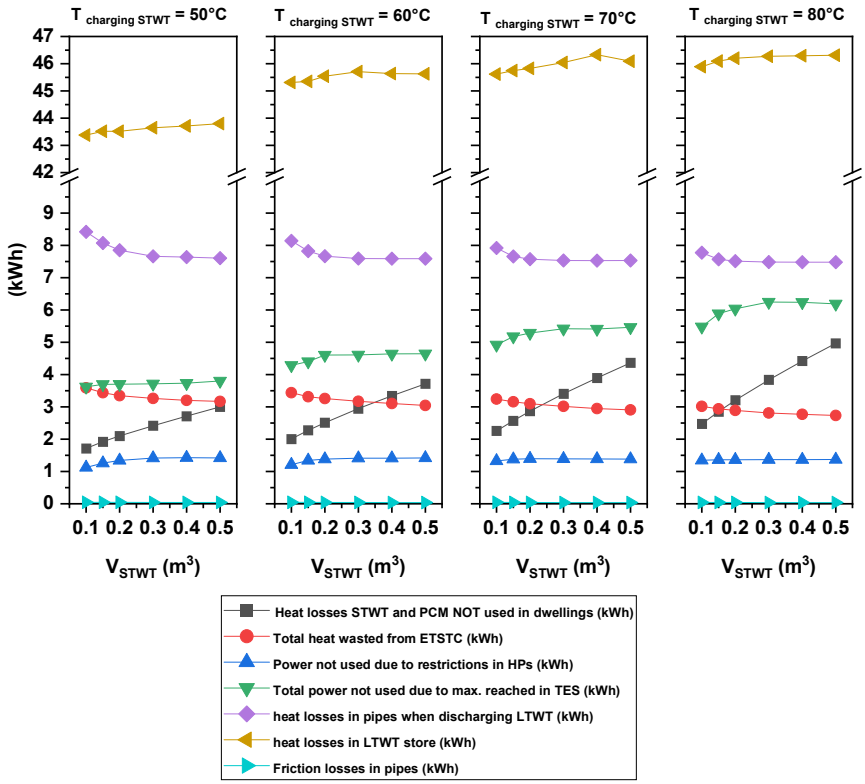

Fig. 9: The effect of V_{STWT} on the heat and power shed and heat losses from different parts of the DH system for different $T_{charging\ STWT}$ values (yearly average).

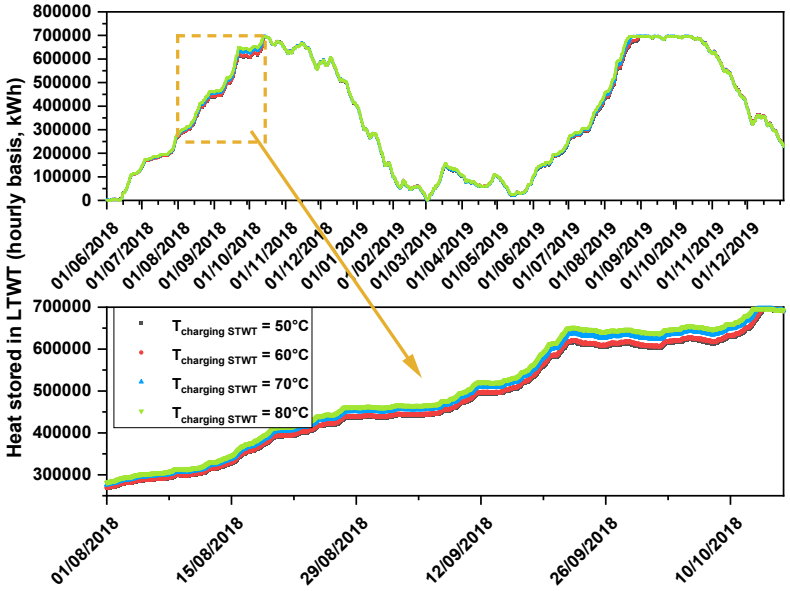

Fig. 10: The effect of $T_{charging\ STWT}$ on the heat stored in the LTWT for V_{STWT} = 0.5 m³.

The predicted effect of both $T_{charging\ STWT}$ and V_{STWT} on the yearly average DH network energy efficiency are presented in Fig. 8. From Fig, 7, it is clear that for the range simulated both V_{STWT} and/or $T_{charging\ STWT}$ have little effect on predicted η_{DH}, with a maximum difference of ca. 1.8 percent between the systems with the highest and lowest η_{DH} value. When V_{STWT} and/or $T_{charging\ STWT}$ increases the overall energy efficiency of the DH system decreases, due mainly to the increase in both the power shed and the heat losses from the STWT devices, as can be seen in Fig. 9. It is important to remark here two aspects: i) first, the heat losses from STWT that affect the energy efficiency are heat losses that cannot be used to alleviate heat loads at certain hours, due to the absence of

heat demands at these hours; the power shed is power not used in HPs, but in real applications this power could be used somewhere else in the buildings or to be sold, so it would not be shed (so the efficiency would be higher).The increase in the power shed with increasing either V_{STWT} and/or $T_{charging\ STWT}$ is due to the increase in the minimum $Wind_{capacity}$ needed to fully meet the domestic heat demands. This means that, at certain times of the year, the amount of power generated that is not used despite the higher STWT storage capacity available and thus shed will be high (at those times when the LTWT is also fully charged). The greater heat losses from the LTWT obtained when increasing $T_{charging\ STWT}$ can be explained again by the higher $Wind_{capacity}$ needed at higher $T_{charging\ STWT}$, which results in higher levels of heat stored in the LTWT at certain times of the year, as can be seen in Fig. 10. The predicted yearly average η_{DH} obtained for the minimum-cost case-scenario, i.e. V_{STWT} = 0.1 m^3 and/or $T_{charging\ STWT}$ = 50°C, was 86.62%, which is in the same range as those obtained in other studies (Li and Svendsen, 2012; Zhang et al., 2021).

4. Conclusions

In the present work, an optimisation study of a simulated DH network for two areas in the town of Loughborough, UK, for the time period from the 01/06/2018 00:00 to 31/12/2019 23:00 was undertaken. This was achieved by a parametric analysis of the effect of operating parameters for the DH network, V_{STWT} and $T_{charging\ STWT}$ on the DH system cost per dwelling and the overall energy efficiency of the DH system. For each simulated case the results were obtained by modifying the installed capacity of both Wind and PV in order to ensure domestic heat loads were met for the whole time-period at the minimum cost. The predictions show that the increase of both V_{STWT} and $T_{charging\ STWT}$ lead to an increase in the total cost per dwelling and a decrease in the overall η_{DH} value, due to the greater amount of heat stored in the STWT which leads to a reduction in heat stored in the LTWT. This results in ii) more heat losses and ii) a shortage of heat from storage in the winter months and thus more $Wind_{capacity}$ needed to meet demands (meaning more power shed).

A predicted minimum cost of £12,103 per dwelling and DH network energy efficiency of 86.62% was obtained at the optimum conditions found.

5. References

(STA), S.T.A., n.d. Solar Trade Association (STA) [WWW Document]. URL https://solarenergyuk.org/

AECOM, 2017. Reducing the capital cost of district heat network infrastructure.

Allison, J., Bell, K., Clarke, J., Cowie, A., Elsayed, A., Flett, G., Oluleye, G., Hawkes, A., Hawker, G., Kelly, N., de Castro, M.M.M., Sharpe, T., Shea, A., Strachan, P., Tuohy, P., 2018. Assessing domestic heat storage requirements for energy flexibility over varying timescales. Appl. Therm. Eng. 136, 602–616. https://doi.org/10.1016/J.APPLTHERMALENG.2018.02.104

Briefings for britain, n.d. No Title [WWW Document]. URL https://briefingsforbritain.co.uk/

Department of energy and climate change, 2015. Assessment of the Costs, Performance, and Characteristics of UK Heat Networks. London, UK.

Ecoexperts, n.d. What Size Air Source Heat Pump Do You Need? [WWW Document]. URL https://www.theecoexperts.co.uk/heat-pumps/air-source-heat-pump-sizing#:~:text=07 Next steps-,How big is an air source heat pump%3F,will need a 10kW machine.

Energy research partnership, 2016. Potential Role of Hydrogen in the UK Energy System.

Energy technologies institute, 2018. DISTRICT HEAT NETWORKS IN THE UK: POTENTIAL, BARRIERS AND OPPORTUNITIES 1–17.

European Union, 2020. EU energy in figures - Statistical pocketbook 2020 [WWW Document].

Evergreen energy, n.d. what size heat pump do I need for my house? [WWW Document]. URL https://www.evergreenenergy.co.uk/heat-pump-guides/size-heat-pump-need-house/

Fadl, M., Eames, P.C., 2019. An experimental investigation of the heat transfer and energy storage characteristics of a compact latent heat thermal energy storage system for domestic hot water applications. Energy 188. https://doi.org/10.1016/j.energy.2019.116083

Gaucher-Loksts, E., Athienits, A., Ouf, M., 2022. Design and energy flexibility analysis for building integrated

photovoltaics-heat pump combinations in a house. Renew. Energy 195, 872–884. https://doi.org/10.1016/J.RENENE.2022.06.028

Guelpa, E., Verda, V., 2019. Thermal energy storage in district heating and cooling systems: A review. Appl. Energy 252, 113474. https://doi.org/10.1016/J.APENERGY.2019.113474

Li, H., Svendsen, S., 2012. Energy and exergy analysis of low temperature district heating network. Energy 45, 237–246. https://doi.org/10.1016/J.ENERGY.2012.03.056

Lund, H., Werner, S., Wiltshire, R., Svendsen, S., Thorsen, J.E., Hvelplund, F., Mathiesen, B.V., 2014. 4th Generation District Heating (4GDH): Integrating smart thermal grids into future sustainable energy systems. Energy 68, 1–11. https://doi.org/10.1016/J.ENERGY.2014.02.089

Mahon, D., Henshall, P., Claudio, G., Eames, P.C., 2020. Feasibility study of MgSO4 + zeolite based composite thermochemical energy stores charged by vacuum flat plate solar thermal collectors for seasonal thermal energy storage. Renew. Energy 145, 1799–1807. https://doi.org/10.1016/J.RENENE.2019.05.135

Pans, M.A., Claudio, G., Eames, P.C., 2023. Modelling of 4th generation district heating systems integrated with different thermal energy storage technologies – Methodology. Energy Convers. Manag. 276, 116545. https://doi.org/10.1016/J.ENCONMAN.2022.116545

Pfenninger, S., Staffell, I., 2016. Long-term patterns of European PV output using 30 years of validated hourly reanalysis and satellite data. Energy 114, 1251–1265. https://doi.org/10.1016/J.ENERGY.2016.08.060

Renewables Ninja on-line tool [WWW Document], n.d.

Schuetz, P., Gwerder, D., Gasser, L., Fischer, L., Worlitschek, J., 2017. Thermal storage improves flexibility of residential heating systems for smart grids.

Staffell, I., Brett, D., Brandon, N., Hawkes, A., 2012. A review of domestic heat pumps. Energy Environ. Sci. 5, 9291. https://doi.org/10.1039/c2ee22653g

Wang, Z., 2018. Heat pumps with district heating for the UK's domestic heating: individual versus district level. Energy Procedia 149, 354–362. https://doi.org/10.1016/J.EGYPRO.2018.08.199

Zhang, Y., Johansson, P., Kalagasidis, A.S., 2021. Applicability of thermal energy storage in future low-temperature district heating systems – Case study using multi-scenario analysis. Energy Convers. Manag. 244, 114518. https://doi.org/10.1016/J.ENCONMAN.2021.114518

About the Efficiency of District Heating with flexible Heat and Temperature Distribution

Sven Paulick[1], Vera Boß[1] and Clemens Felsmann[1]

[1] Technische Universität Dresden, Institute of Power Engineering,

Chair of Building Energy Systems and Heat Supply, 01062 Dresden, Germany

Abstract

Decentralisation of heat supply is one option to transform and decarbonise district heating (DH) networks. However, the volatility and availability of the diversified heat sources also require a much more flexible operation of the heating networks compared to conventional operation. In a German research project "*ZellFlex*" (www.tud.de/mw/zellflex), various methods for network flexibilisation are being investigated in a simulation study. This paper presents latest results of the project with focus on existing district heating networks with higher temperature demand and centralised heat supply, as these kinds of networks are the most common among Germany und Europe.

Keywords: DH network simulation, flexible operation, cell balancing, decentralised feed-in

1. Introduction

The desire and necessity for flexible operation arise for two reasons: on the one hand, limitations and restrictions in the availability of the increasingly used non-adjustable heat sources and, on the other hand, the possibility of increasing efficiency by minimising distribution losses and increasing efficiency of the heat transport. Essential elements are the demand-driven deployment of heat, the shifting or adaptation of heat load requirements to the heat supply on the heat sink side, and the low-loss transport and distribution of thermal energy.

The locally scattered arrangement of decentralised heat sources as well as the different heat and temperature requirements of the heat consumers in parts of the network will increasingly require the evaluation of flexibility measures regarding smaller network sections (*cells*). The balancing of network sections could be conducted within a cellular approach, which is familiar from the electricity sector in the form of balancing groups and the assigned balance responsible parties.

2. Simulation study and flexibility measures

To quantify the effects of different flexibilisation measures, simulations studies have been done. The flexibility measures considered in this paper are (see Fig. 1, a-c):

(a) Pulsating operation (see section 2):

Cyclic operation of cells, especially in off-peak periods, to reduce heat losses

(b) Decentralised and local heat retention (see section 3):

Integration of decentralized heat generators (e.g., solar thermal, waste heat) in combination with heat storage systems to locally und temporally supply a cell

(c) Local and temporal adaption of supply temperature (see section 4):

Local and, if possible, temporary reduction or increase of the network supply temperature in cells with a different demand compared to the main network

© 2022. The Authors. Published by International Solar Energy Society
Selection and/or peer review under responsibility of Scientific Committee
doi:10.18086/eurosun.2022.04.09 Available at http://proceedings.ises.org

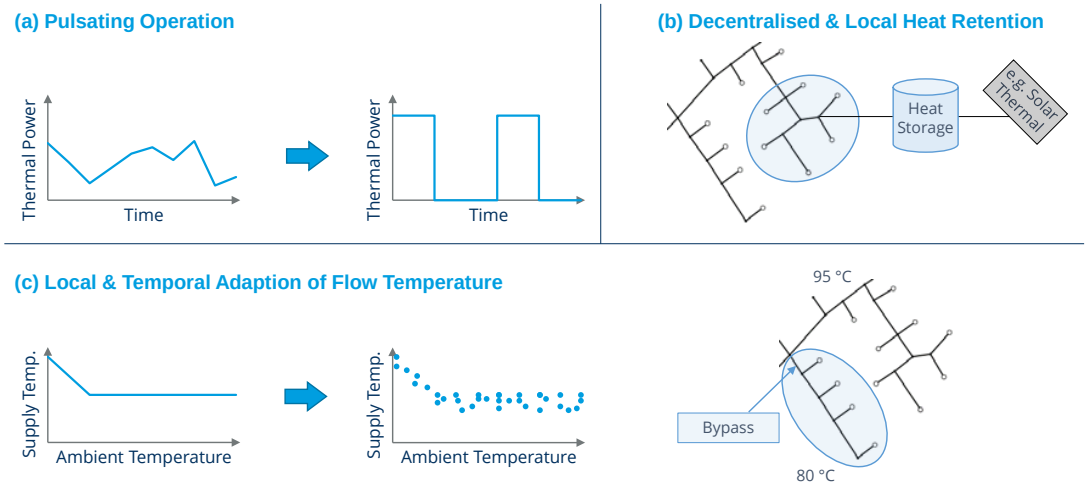

Fig. 1: Flexibility measures considered for selected cells in the DH network

The subject of the investigations is a large heating network with 556 consumer points (Fig. 2), 28.5 MW connected load and approx. 19 % annual heat loss in the district heating network. The network is a 2nd generation, meshed network (following IEA-DHC Annex X Classification). It is a representative real inner-city network in Germany, which was transferred into a simulation model and validated with measurement data. For most of the study, an annual simulation with a time-step of 15 minutes was done with real measurement data for the ambient temperature and solar radiation.

The following flexibility measures were done with a handpicked selection of cells in the heating network, see Fig. 2. The structure, size and number of consumers are different, as well as the distance to the central heat producer. Findings on the selection of a cell area, as well as necessary requirements and challenges, are discussed in section 5.

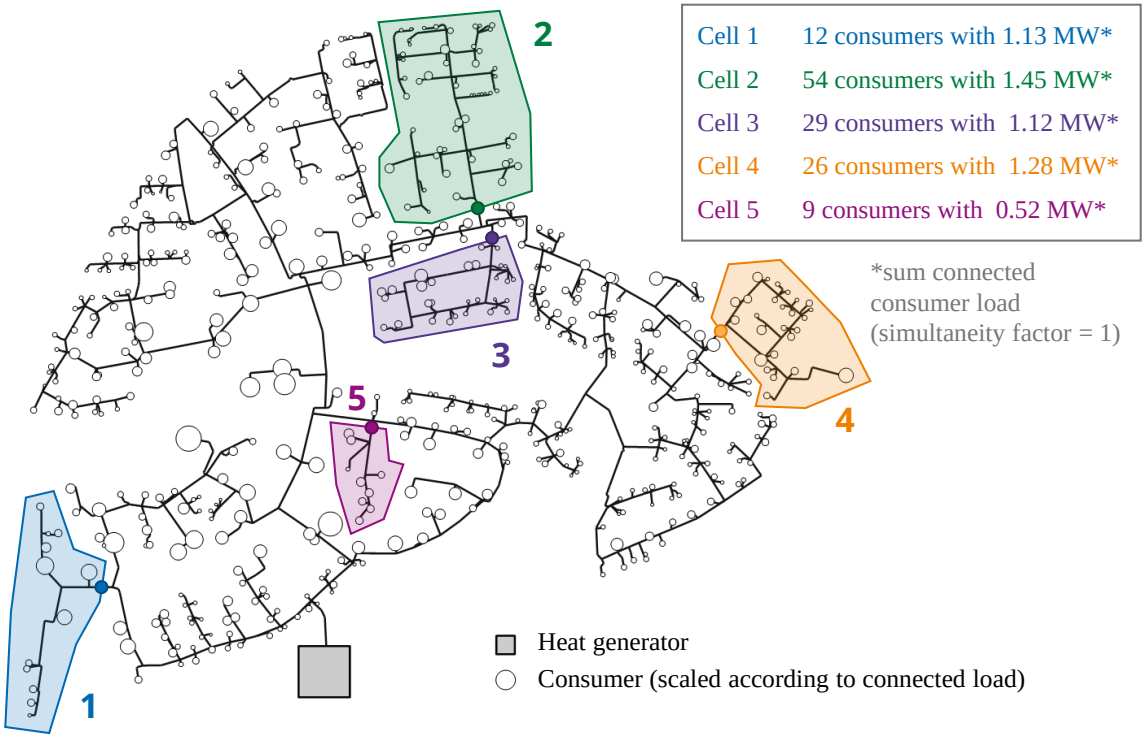

Fig. 2: Structure of the 2nd generation heating network - with central heat producer und the five chosen cells with respective sum of the connected consumer load.

3. Pulsating operation

3.1 Explanation

Especially at off-peak times, the ratio of heat losses to transferred heat output/quantity is particularly unfavourable in heating networks, because as a rule almost the entire network is kept permanently "warm", although the individual consumers have a low heat demand over longer periods of time. Thus, especially in summer and the transition period, the network is permanently in an inefficient partial load range with the consequence of proportionally high network heat losses. This condition could be eliminated by a kind of intermittent operation - here called pulsating operation: a network, respectively a network section (*cell*), is only temporarily flown through and the heat distribution losses can be reduced. However, the heat supplied intermittently (pulsating) must then be stored decentrally and delivered with a time delay without causing further distribution losses. The temporal course of such pulsed operation can be seen as an example in Fig. 3 in comparison with conventional operation (reference).

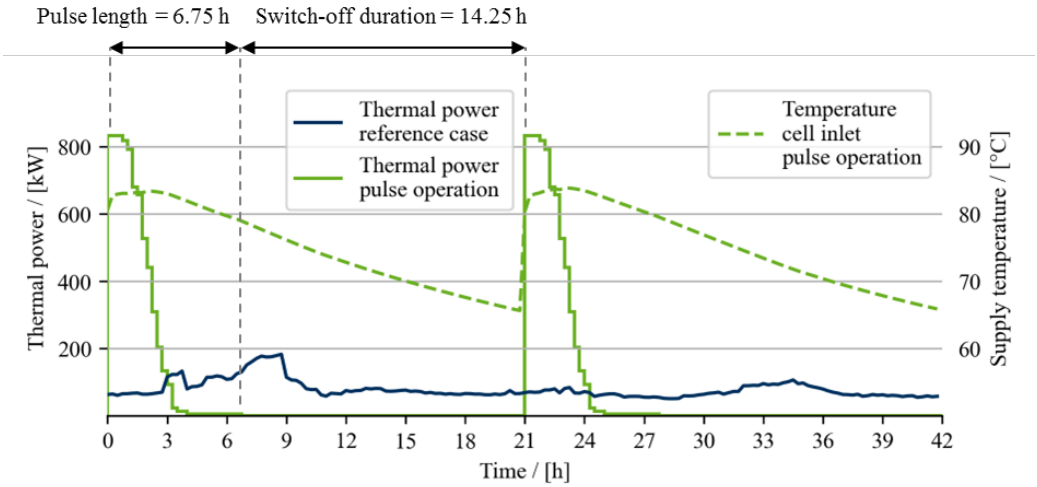

Fig. 3: Pulse operation and reference operation

In pulsating operation, a group of consumers in a cell (defined network area or network section) is considered as a unit and is equipped with decentralized heat storage units (in the building). These are always loaded simultaneously: If one of the heating buffer storages reports a heat demand, all buffer storages within the cell are loaded (pulse - in Fig. 3, for example, from time 0 to 6.75 h). As soon as the last buffer storage is loaded, the cell is "switched off", since for the time being all consumers can cover their heat demand from the heat storage tank assigned to them and thus no heat has to be transported into the cell (switch-off period - in Fig. 3 e.g. from time 6.75 to 21 h). As soon as at least one of the buffer storages in the cell is discharged again, the next pulse starts by fully charging all buffer storages again. The complete shutdown and thus cooling of the cell between the pulses aims at reducing the heat losses. The smaller the pulse length and the longer the switch-off period, the greater is the heat loss reduction.

Enerpipe, a German company that builds innovative local heating networks, has been using this mode of operation for several years, primarily in sparsely populated areas (Euring, 2017, 2020), because pulse operation makes it possible to operate district or local heating networks economically in some cases, even where this would not be possible with conventional operation due to the low density of the heat demand.

3.2 Pulsating Operation in large existing district heating networks

In the German research project “ZellFlex”, this approach is now being applied to a large existing network with urban building density. The aim is to investigate the extent to which pulsating operation in certain cells and at certain times makes heat transport more efficient. The assessment is made with respect to heat distribution losses as well as the hydraulic energy demand of the pump(s), and factors influencing the efficiency of pulsed operation are evaluated.

Five terminal cells in the network were selected, which differ in structure, connected load, location in the network and route length, with the aim of determining influencing factors and restrictions for efficient operation. For an approach to automatic identification of cells, please refer to Mann (2020). In simulation studies, the five cells were each placed in pulsating operation while the rest of the network was in a common operation mode. For a potential analysis, a decentralized heating buffer storage with a volume of 2 m^3 and standby heat losses of 4.5 kWh/d (according to Viessmann (2021)) was assigned to each consumer.

3.3 Heat losses and hydraulic energy

The largest reduction in heat losses in the district heating network was observed in cell 2. The graph in Fig. 4 compares the monthly heat losses for the reference case (without pulse operation) and with pulse operation. The heat losses in pulsed mode are composed of the heat losses of the network and those of the heat storage tanks. The heat losses can be reduced in all months by pulsed operation, whereby the effects are particularly large in summer. In January, 18 % of the network heat losses can be avoided, and up to 52 % in June/July. If the standby heat losses of the distributed storage are added, the relative reduction is still 8 to 36 %.

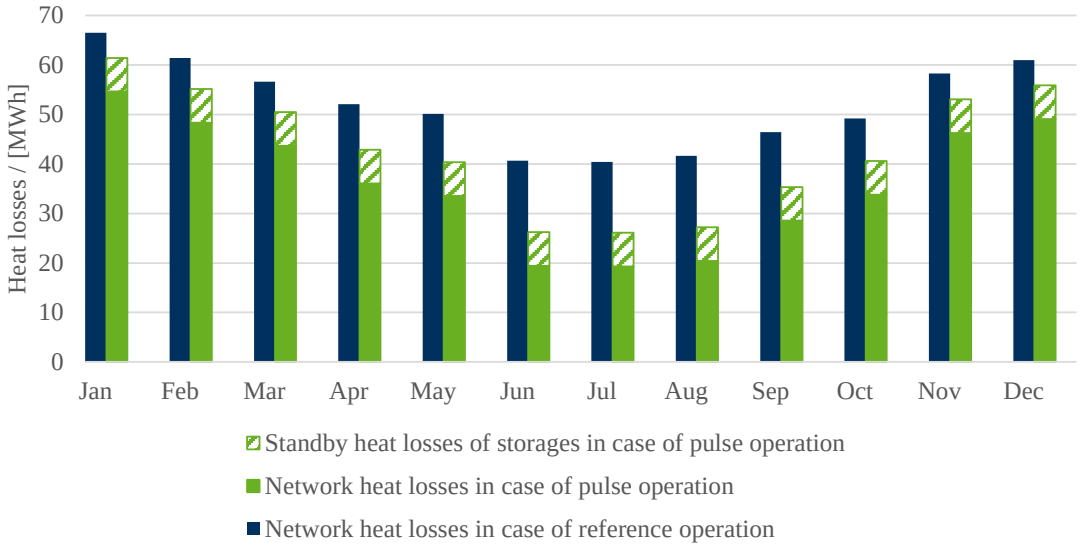

Fig. 4: Heat losses in case of reference and pulse operation for cell 2

This is in line with the expectations that pulsating operation can increase the efficiency of heat transport, especially at off-peak times. This was shown to be true for all cells considered, although to varying degrees. In cell 1, the reduction in network losses is lowest, at 12 to 14 % in summer. This is partly due to the shorter off-time, which is 5 h in summer in cell 1, compared to14.25 h in cell 2 (see Fig. 3). Cell 2 is "switched off" (no heat is supplied) about 68 % of the summertime, compared to 62.5 % in cell 1.

The auxiliary energy demand of the pumps (hydraulic energy) was also considered regarding possible changes due to pulse operation for all periods and cells. A reduction of the hydraulic energy could be determined throughout by the pulse operation, even if to a lesser extent. In all cells, this is in the order of 1 to 2 % in summer.

3.4 Factors influencing the efficiency of pulsating operation

Within the scope of the simulation study, different pulse lengths or switch-off periods were investigated to quantify their influence on the reduction of heat losses. Fig. 5 shows the relative reduction of the network heat losses for each of the five cells in relation to the reference operation for the month of June depending on the length of the switch-off period. (Note: The additional standby heat losses of the storage tanks are not included here). It can be clearly seen that a long interruption of the heat supply (switch-off duration) is advantageous in terms of heat losses. When evaluating the simulations, two factors could be identified that lead to unfavourable switch-off periods and pulse lengths:

- Storage capacity of the decentralised heat storage tank is too low: If the heat demand of the consumer is very high compared to the storage capacity, the storage tank is quickly discharged during the switch-off

period. This means that the storage tank must be loaded again early and the length of the switch-off period is thus reduced.

- Volume flow limitation: If a consumer has a rather high heat demand during a pulse, its volume flow limitation might be (almost) reached. Thus, only an extremely low heat flow remains to load the storage tank. This leads to an exceedingly long loading time of the heat storage tank and thus a long pulse length and a short switch-off period.

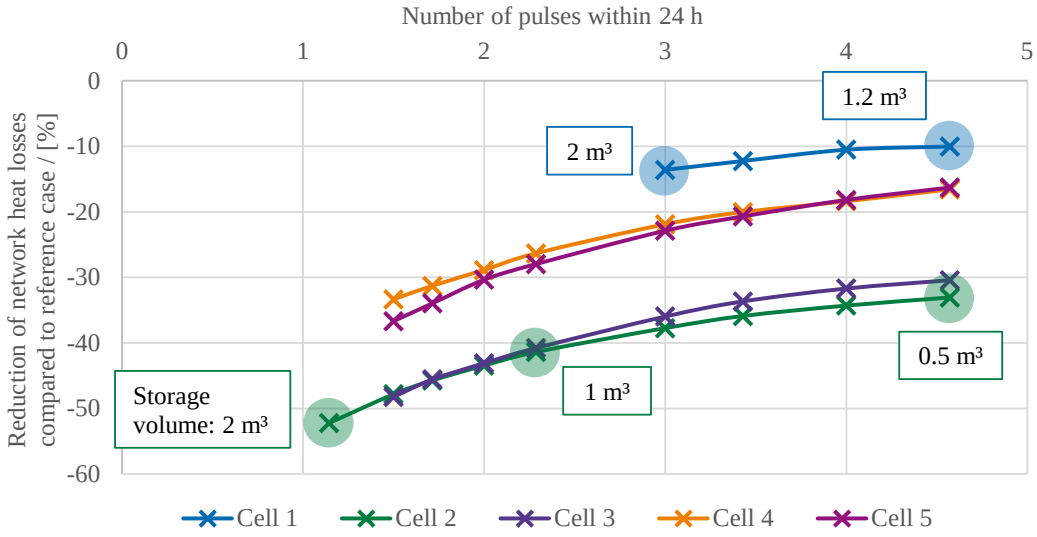

Fig. 5: Reduction of network heat losses compared to reference operation depending on switch-off duration

3.5 Adjustment of the investigated variants

To improve the efficiency of the pulse operation even further, the following measures are now taken - as an example for the month of June in cell 2:

- Measure A: The consumer whose storage is discharged first and thus triggers the start of a new pulse is excluded from the 2 m³ limit, so that it only applies to the other consumers. Therefore, the switch-off time increases from 14.25 to 19.25 hours. The storage volume of the described consumer would have to be increased to 2.50 m^3.
- Measure B: For the consumer, whose storage tank has the longest loading duration, the volume flow limitation is increased by 50 %. This shortens the loading time of the storage tank, and the switch-off period is extended from 14.25 to 17.5 hours.

The original implementation of pulse operation already resulted in a reduction of 52 % of the network heat losses in the month of June in cell 2. With measure A, this value can be increased to 57 %, but with measure B there is almost no improvement. This shows that the switch-off time is only one of several factors that influence the efficiency of pulse operation. In addition, it becomes clear that a significant increase in efficiency can be achieved through relatively simple measures (increasing the size of only one storage unit in the cell). Consequently, the implementation of pulse operation in real DH networks requires careful and extensive planning.

3.6 Summary and outlook – pulsating operation

The results of the simulation study have shown the benefits of pulse operation for certain network areas and under certain conditions. It became apparent that the effects differed greatly for the five cells. Therefore, the development of cell identification characteristics will be taken up again in the further course of the project. In addition, the pipe stress due to the temperature fluctuations caused by the pulsed operation will be investigated. Restrictions could possibly arise here, depending of the type of pipes.

The investigations shown here are only an initial assessment of the potential. For practical implementation, there are some requirements for heating networks that are not (yet) fulfilled everywhere. These include:

- Digitalisation of the house stations (iHAST): It must be possible to control the charge of the storage tanks from a central point (e.g., the control room of the network operator) and track all consumers of a network section (cell). For this purpose, there must be a data connection including write access by the heating netwokr operator to the house side of the house stations (Rapp et. al., 2020).
- Decentralised heat storage: Every consumer participating in pulsed operation needs a sufficiently large heat storage. It is important that this storage also enables buffering of the space heating demand, as otherwise pulsed operation is only possible in times with an exclusive demand for domestic hot water. In the studies shown here, a storage tank size of 2 m^3 was assumed - an optimistic value in practice, which means that the economic efficiency would have to be checked. However, it should be noted that the storage tanks could not only be used for pulsed operation, but also for peak shaving in winter, for decentralised heat retention and for increasing renewable heat shares in the network.

4. Decentralised and local heat retention

Local heat retention is intended to distribute decentrally generated heat locally in a targeted manner. The main objectives are:

- Avoiding hydraulic bottlenecks
- Enable higher decentralised feed-in, if available
- Possible reduction of peak loads in the overall network
- Constant, consumption-dependent supply temperature.

In the case of decentralised heat supply, there is a so-called supply limit. This is the point in the network up to which the heat supply is realised solely by the decentralised feed-in. In Fig. 6, this point is marked by an "X". In conventional operation, the supply limit moves quite strongly in the network depending on the feed-in power and the heat load of the consumers (see Fig. 6, left). Especially at times of high heat feed-in, hydraulic bottlenecks can occur. This is because the pipelines at connection points - especially at the ends of the lines - in existing networks are usually not designed to transmit high heat outputs. This means that a lot of hydraulic energy is needed for heat transport.

Avoiding such hydraulic bottlenecks could be made possible by local heat retention. Here, a decentralised storage is used to keep the supply limit as constant as possible in the heating network (see Fig. 6 right). Demand and local generation combined with the storage capability form a cell.

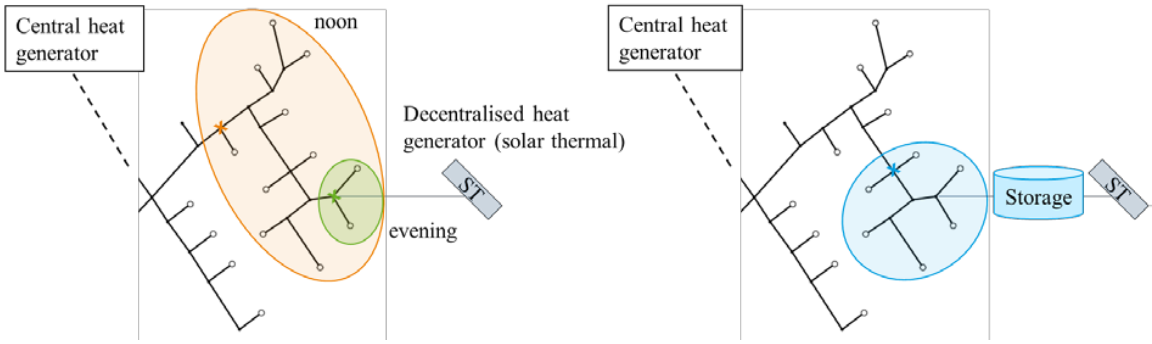

Fig. 6: Decentralised feed-in with moving supply frontiers (left) and local heat retention (right)

In the following, the measure is demonstrated based on decentralised solar thermal feed-in. However, other sources of feed-in, such as waste heat or heat pumps, are also suitable. Cell 1 (see Fig. 1) is equipped with a solar thermal plant of different sizes and is compared with and without large-scale heat storage directly at the solar thermal plant.

In Table 1 the connected load of the consumers in cell 1, as well as the annual consumption is compared to the solar thermal feed-in peak load and the annual heat generation by solar yields.

Table 1: Comparison of connected load/consumption of consumer in cell 1 with solar thermal peak load/yields for different plant sizes

variant	connected load [kW]	consumption [MWh/a]	peak load feed-in [kW]	solar yields [MWh/a]
consumer	1.130	1.757	-	-
ST 500 m²	-	-	315	264
ST 1.000 m²	-	-	630	533
ST 1.500 m²	-	-	945	805
ST 2.000 m²	-	-	1.260	1.076

As seen, the peak load of the feed-in can exceed the connected load of all consumers in cell 1. In the summertime, the daily amount of heat by feed-in of solar thermal power can be the multiple of the required consumer heat. Especially if large open spaces are available for solar thermal plants or industry with waste heat, it can happen that there is a significant surplus of heat available locally. This means that the excess heat must be distributed to the main network without shutting off, which should be avoided for efficiency reasons. For this purpose, it can be suitable to store the heat locally and only/mainly distribute it in a certain area, the cell. Having a look at the impact of variant with 1.000 m² solar thermal plant in cell 1, for hydraulic reasons a useful parameter is the mass flow at the entrance of cell 1. See Fig. 7, one can see the comparison of the nominal mass flow with solar feed-in without storage (orange) and with an additional decentral storage in the cell (dark-red). During the time of higher solar yields, a significantly increased mass flow into the main network can be seen in the variant without storage, due to an excess of heat in cell 1 (negative mass flow according to nominal flow direction). With the integration of a heat storage, the exchange with the main heating network can be reduced to a minimum and the heat is distributed in the cell with a time delay.

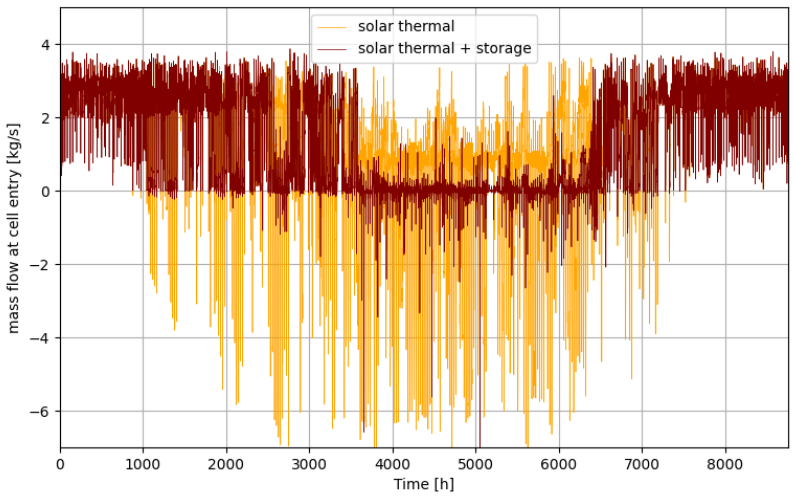

Fig 7: Comparison of mass flow at the entry of cell 1 and solar thermal feed-in with and without storag; positive mass flow means nominal flow (demand in the cell)

The local heat retention can significantly reduce the heat distribution to the main network, which can lead to a reduced effort for feed-in pumps. In addition, a reduction in heat losses is conceivable, since with the help of the feed-in and storage of the heat, the cell is independent of the main network with regard to the flow temperature.

5. Local and temporal adaption of flow temperature

5.1 Temporal adaption of flow temperature

Usually, the central supply temperature (from the central heat generator) in heating networks is controlled by means of a fixed, outdoor temperature-dependent operation mode. The aim is usually to ensure that a minimum supply temperature specified in the Technical Connection Condition (TCC) is maintained at each consumer (on the network side). However, usually the supply temperature actually achieved there is *not* evaluated/measured and accordingly no short-term adjustment of the centrally fed supply temperature takes place. Only longer-term adjustments are relatively common, for example if complaints from customers suggest that the supply temperature achieved at the customer's system is not sufficient. This procedure may lead to higher supply temperatures being operated in heating networks than would actually be necessary to comply with the TCC. If, in the future, real-time data of the network-side temperatures at the consumers become increasingly available due to advancing digitalisation, new types of possibilities for controlling the central supply temperature could arise.

Therefore, a supply temperature operation mode was developed that uses the lowest supply temperature measured at the consumer substation to control the DH network temperature at the central heat generator. The point with the lowest supply temperature is called Temperature Index Circuit (TIC), comparable with the pressure index circuit usually used to control the main pump in the network.

In Fig. 8 the TIC operation mode is illustrated. The temperatures at the TIC are usually above the minimum temperatures according to the TCC (see Fig. 8, left). The difference between the TIC und the required minimum temperature according to the TCC shows the potential for reduction of the network supply temperature. In Fig. 8 (right) the supply temperature at the heat generator is temporally adapted considering the minimum required temperature of the consumers.

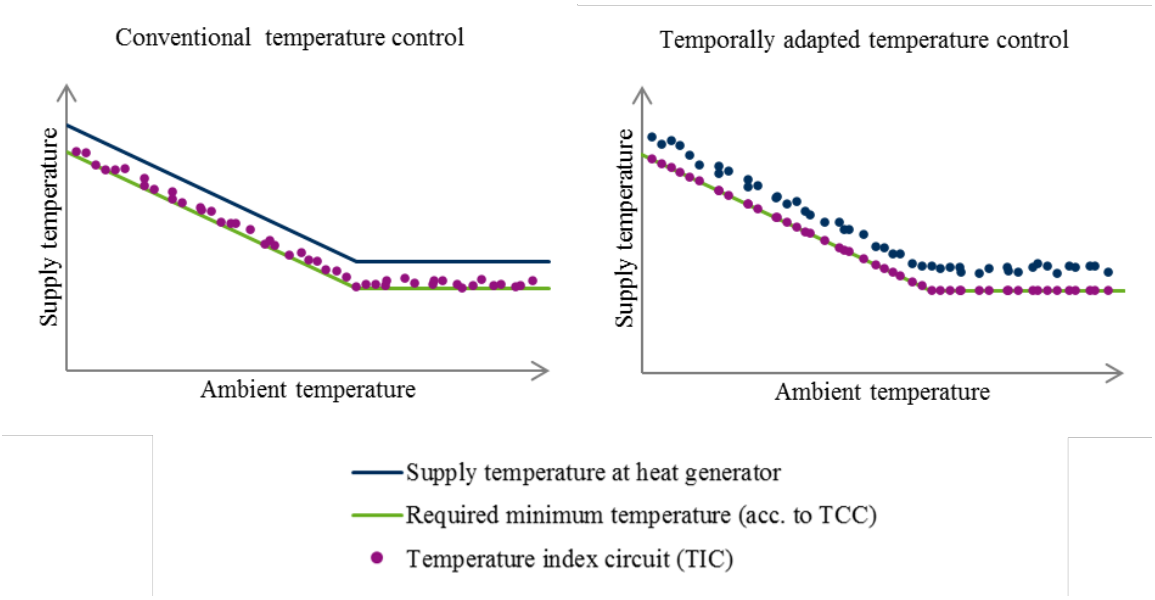

Fig. 8: Schematic diagram of conventional network temperature control (left) and temporally adapted temperature control with respect to the Temperature Index Circuit (right)

The current work deals with criteria and minimum requirements for TIC operation:

- How many metering points are required in the network?
- What type of consumers (e.g. commercial, residential) or consumer size is preferable from a measurement point of view?
- What is the minimum flow rate that the consumer must have after a shut-off period?

Evaluations on this will be published with the completion of the project in 2023.

5.2 Local adaption of flow temperature

Another aspect of flow temperature adjustment is the local decreasing or increasing of the supply temperature. The local increase can be useful if there are network sections that have a higher supply temperature requirement than the main network. Up to now, the supply temperature for the entire network has often been raised centrally in order to guarantee supply. However, this leads to significantly higher network losses and inefficient operation. It would be conceivable to raise the supply temperature in sections, e.g. using a heat pump, waste heat or similar.

More often, however, individual network sections have a significantly lower flow temperature requirement than the main network, e.g. because the network has been extended with more modern buildings. In this case, a local flow temperature reduction is a comparatively simple option. This can be done by mixing the return flow into the supply flow with a pump to overcome the pressure difference. In the case of the example network, cell 2 (see Fig. 2) is lowered in stages. The reduction of heat losses in the network can be seen in Fig. 9. The consumption of the mixing pump can be neglected in comparison to the heat losses.

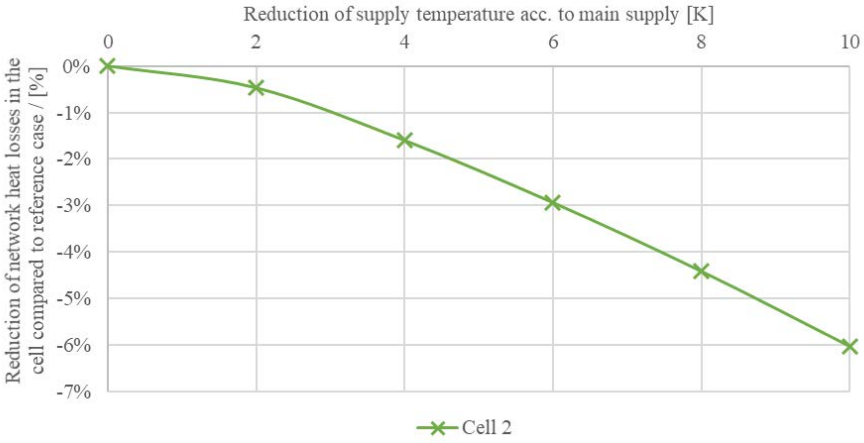

Fig. 9: Reduction of network heat losses by decreasing the supply temperature via a bypass at cell 2

6. Requirements and challenges

The cell boundaries presented in Fig. 1 have been selected manually on the basis of various criteria for the example network and tested and evaluated with the measures presented. However, the aim of the project is to develop generally applicable criteria for defining cell boundaries. As known from the electricity sector, these cells do not necessarily have to be fixed, but can move based on changing boundary conditions.

An important condition for this is the spatially and temporally resolved knowledge of the heat demand and possible heat input. The required flow temperature of the consumers is also relevant. In this regard, studies have already been conducted to evaluate the use of automated clustering methods (Mann, 2020).

Furthermore, the usually installed volume flow limitation in the consumer substations can restrict flexibility measures such as pulsation operation or a reduction of the flow temperature, although the energy-saving effect is obvious.

The necessary measurement data from the networks are often not currently available. Knowledge about the condition of the entire network can often only be estimated on the basis of a few measuring points. For this reason, large-scale digitalisation of the heating networks is an important criterion for efficient, decentralised and flexible operation.

7. Conclusion and Outlook

A decentralised heat supply in the future, especially in existing urban heating networks, poses a major challenge for many energy providers. Network operation must become more flexible, considering the requirements of the consumers. This article has shown the first approaches to flexibilisation, which will be investigated and expanded

in more detail. It has been shown that the conventional operation with an overall network view can be replaced by a cellular operation if detailed information about the consumer behaviour is known.

Within the research project, the approaches presented here will be further deepened and necessary requirements will be developed. With the advancing digitalisation of the heating networks, flexibility measures can be put into practice and evaluated in the future.

8. Acknowledgements

This project was founded by the Federal Ministry for Economic Affairs and Climate Action (FKZ: 03EN3001)

9. References

Boß, V. et. al., 2022, Flexibilität der Wärmeversorgung – Untersuchungen zum pulsierenden Netzbetrieb, EuroHeat&Power 4-5/2022. Technische Universität Dresden, Professur für Gebäudeenergietechnik und Wärmeversorgung.

Euring, M., 2020, Wärmenetzplanung 4.0: Quartier ist nicht gleich (Neubau-) Quartier, Netz ist nicht gleich Netz, EuroHeat&Power 7-8/2020. Enerpipe GmbH.

Euring, M., 2017, Smarte Wärmeverteilung in Neubaugebieten reduziert Wärmeverluste auf ein Minimum, EuroHeat&Power 5/2017. Enerpipe GmbH

Mann, L., 2020, Vorlauftemperaturvariable Zellbildungsverfahren für Wärmenetze, Studienarbeit. Technische Universität Dresden, Professur für Gebäudeenergietechnik und Wärmeversorgung.

Rapp, H., Digitalisierung von energieeffizienten Quartierslösungen in der Stadtentwicklung mit intelligenten Fernwärme-Hausanschlussstationen – iHAST (Ohasen 1-2), AGFW, Frankfurt a. M.

Viessmann, 2021, Datenblatt Vitocell 100-E und 100-W, Steinhaus bei Wels und Allendorf, Viessmann GmbH & Co. KG

Optimized Adsorption Heat Pump for Efficiency Increase of District Heating Networks

Emanuele Piccoli[1], Romain Civioc[1], Sandra Galmarini[1], Xavier Jobard[2], Alexis Duret[2], Xavier Daguenet[3] and Paul Gantenbein[3]

[1] Empa, Dübendorf (Switzerland)

[2] HEIG-VD, Yverdon-les-Baines (Switzerland)

[3] OST, Rapperswil (Switzerland)

Abstract

Adsorption heat pumps can provide cooling based on renewable district heat or waste heat, thus expanding the scope of district heating networks (DHN) and making better use of existing renewable heat sources. On the other hand, they can also provide heat while significantly reducing the return flow of the district heating network, thus increasing the efficiency of district heating supply. However, commercially available sorption machines are not designed for DHN. Therefore, new and sustainable adsorbent materials ideally suited for the temperatures and applications of district heating networks are developed and incorporated in a heat & mass exchanger designed for reversible adsorption heat pumps. The new sorption heat and mass exchanger is subjected to performance measurements. The results are used to carry out simulations to demonstrate the advantages of adsorption heat pumps for the supply of cooling and heating in district heating networks.

Keywords: Renewable heating and cooling, Adsorption heat pumps, Activated carbon adsorbent, Prototype testing, Energy system efficiency

1. Introduction

Due to climate change and the ensuing rise of the outdoor temperatures, the cooling demand in buildings will increase in the future (Birol, 2018). Nevertheless, the heating demand in Europe will remain high in wintertime (Settembrini et al., 2017). In order to achieve the energy turnaround for Europe and to reduce drastically greenhouse gas emissions, innovative, integrated and eco-friendly heating and cooling solutions are required to supply the building stock as well as processes with heating and cooling. On the one hand, the CO2 footprint of the energy mix during peak load in winter is high. On the other hand, during summer, large amounts of heat remain unused from waste incineration plants and other industrial processes because of the low heat demand during this season. In Switzerland, a large majority of Municipal Waste Incineration Plant (MWI) are connected to large DHN. This source of heat represents close to a third of the heat distributed in DHN in 2020[1]. The MWI typical efficiency combining heat and electricity production in 2020 is in average around 70%[2]. So 30% of the heat could still be valorized. The thermal losses are mainly occurring in summer time where the heat demand is low. The extra heat unused in summer time can be estimated to around 800Wh. This heat can be used in summer to power adsorption heat pumps (adHP) and supply eco-friendly and cost-effective cooling energy to various cooling consumers (e.g. buildings and industries) (Hassan et al., 2020).

District heating networks (DHN) are a well-known solution to lower the carbon footprint for heating in winter and recover otherwise unused waste heat (Puschnigg et al., 2021). However, DHN suffers from two important drawbacks, which limits their energy efficiency and operability: 1) Low efficiency caused by high operating temperatures, especially high return temperatures. 2) Low utilization of the DHN in summer time, which leads to inefficient operating conditions. The impacts of those two drawbacks are reduced heat distribution capacity for a given pipe diameter (due to limited temperature differences), high heat distribution costs (pumping energy and heat losses)

[1] https://www.fernwaerme-schweiz.ch/fernwaerme-franz/Verband/Jahresbericht.php
[2] https://vbsa.ch/donnees/energie-charts/?lang=fr

© 2022. The Authors. Published by International Solar Energy Society
Selection and/or peer review under responsibility of Scientific Committee
doi:10.18086/eurosun.2022.04.10 Available at http://proceedings.ises.org

and lower energy efficiency in the heating station (more energy to produce one unit of useful heat).

This work investigate the integration of reversible adsorption heat pumps into DHN to use untapped waste heat and increase the energy efficiency of district heating networks. Two particularly promising integrations of adHP in DHN have been identified. The DHN return temperature reduction operating mode (Figure 1 (a)) integrate an adHP at substations (SST) providing heat at the building level. The adHP uses the SST return flow as a heat source for the evaporator and thus reduces the temperature of the DHN return flow. This mode of operation increases the temperature difference between the forward and return of the DHN resulting saving on the pumping energy or in heat delivery capacity increase of a given thermal grid. Additionally, it also reduces heat losses since the return temperatures are lowered. The same adHP and the DHN heat supply can also supply comfort cooling (Figure 1(b)) to the buildings in summer time. This enables the DHN operators to offer a new energy service to their customers, while increasing the sale of heat in summer and thus the profitability of the DHN (40.8% and 31.8% of the heat distributed respectively)[3]. Since a major part of heat is either renewable or waste heat in Swiss DHN, this cold supply will also be renewable. The major challenge for this mode of operation is to dissipate and/or recover condensation and adsorption heat at intermediate temperature without extra cost, for with pre-heating of domestic hot water.

These innovative conceptual modes of operation have been evaluated separately with numerical models reflecting the current state of the art of the sorption technology and with experimental work carried out on commercial units by (Jobard et al., 2020). It results that the commercial units currently available are not adapted for integration in DHN and do not meet the requirements of DHN operators, especially in terms of temperature drop at the desorber in cooling mode. They suffer also from low power density and low thermal efficiency. Therefore, new adsorption materials are needed as well as new concept for reversible DHN SSTs for heating and cooling of buildings.

In this work, we move towards the design of such systems. In a first section, we analyze the requirements of the DHN applications based on surveys. Afterwards, we propose a novel sustainable adsorbent material suitable for the application and we analyze its performance by models and simulations. At last, we present the characterization methods to measure the performance of adHP prototypes.

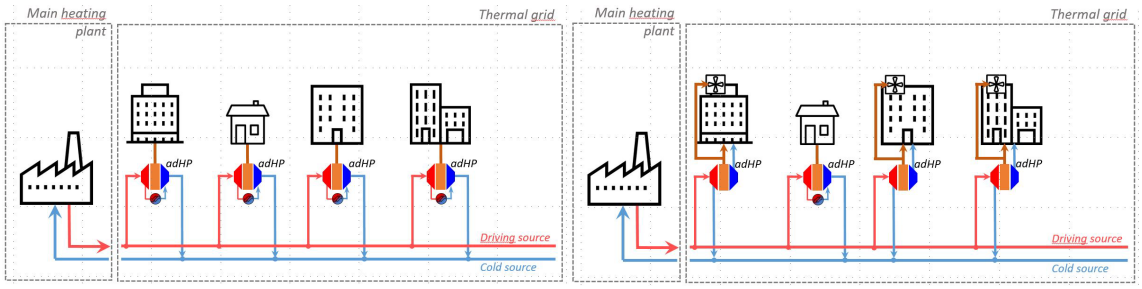

Figure 1 - Schematic view of the two applications of adHP in DHN targeted: a) return temperature reduction and b) cooling. The adHP are used in the substations to serve the DHN users.

2. DHN implementation requirements

This section presents the requirements necessary to drive the development and optimization of the adsorption materials for DHN applications. These requirements are the expected operating conditions for both heating and cooling modes. These conditions are defined with the T_{hot}, T_{con} and T_{eva}. T_{hot} is directly set from the supply of the DHN, T_{con} depends on the space heating and domestic hot water distribution system; T_{eva} depends on the space heating return temperature and on the cooling distribution system (radiant ceiling or air conditioning unit), respectively in heating mode and cooling mode. Their ranges were derived from field surveys as well as from discussion with DHN operators and are gathered in Table 1.

In the heating mode, the purpose of the substation is to satisfy the building needs in space heating and domestic hot water. The adHP is implemented in this configuration to reduce the return temperature to the grid. Therefore, the DHN efficiency and capacity are improved. The Figure 2 present the simplified hydraulic of the substation. In this mode, the DHN drives the adHP at a given temperature T_{hot} and supplies heat to the space heating loop via the

[3] https://www.fernwaerme-schweiz.ch/fernwaerme-franz/Verband/Jahresbericht.php

heat produced at the adsorber and condenser of the adHP. A heat exchanger is present to cool down the heat carrier from the desorber below the condensing temperature. This is possible with low space heating return temperature. For this to function the adsorption temperature T_{ads} must be higher than T_{con}.

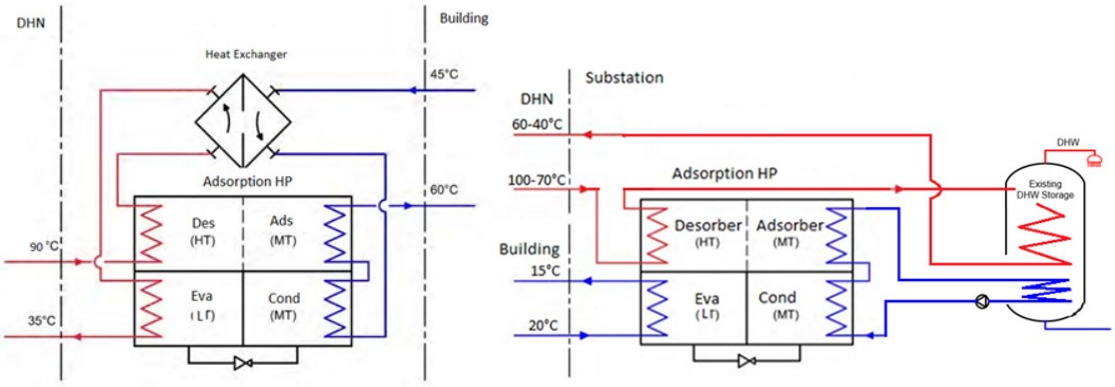

Figure 2 - Simplified hydraulic diagrams with example of possible temperature levels of each loop for the heating mode (left) and the cooling mode (right)

For implementation in existing DHN, the substation has to follow prescription given by the operators of the network that ensure a coherent integration and the supply temperature is fixed. Since DHN must supply temperature high enough for Domestic Hot Water (DHW) preparation at 60°C, as reported by (Quiquerez, 2017) supplied temperature are usually above 70°C and smaller than 110°C. Higher temperatures might in general be needed improve the COP of the machine and cooling power at the evaporator, especially considering that the desorption temperature must be below the hot source temperature to guarantee effective heat transfer. However, selecting the right adsorbent material can guarantee successful desorption. The temperature for the space heating loop is given by the characteristics of the building i.e., its energy standard and heat emission system. High temperature radiators with temperature need above 60°C are excluded because the needed temperature is to close from the supply temperature. Supply temperature of the space heating loop can be as low as 30°C for floor heating system in well insulated buildings. The evaporating temperature depends on the space heating return temperature and the pinch of the heat exchanger assumed at 5K. These are estimated with the temperature drop possible in the space heating loop. For radiators with supplied temperature of 65°C, a temperature drop of 10K and a pinch 5K induces a temperature at the evaporator inlet of 50°C. For floor heating, the temperature drop can only be of 5K, resulting in 20°C.

In the cooling mode, the adsorption pump in the substation is used to cool down buildings. In order to be able to operate in cooling mode without dry cooler to get rid heat rejection, different strategies have to be evaluated in order to valorize the rejection heat locally. One of the most promising local application for heat rejection valorization is DHW preheating. Alternatively, the heat rejected could be used as cold source for a heat pump for DHW preparation. The challenge with this local heat valorization is that the DHW need consumption affects the amount of cooling which can be produced by the AdHP. In order to operate successfully AdHP using heat supplied by a DHN, it is necessary to enlarge the temperature difference on the primary side and simultaneously to use heat at the lowest possible temperature. This represents a challenge as most of the adsorption chiller commercially available today are operated with a maximum 5°C difference and needs heat at minimum 60-65°C. This application could be interesting for DHN operators. It will intensify the heat demand in summer time when the DHN infrastructure are underused. Moreover, as most of DHNs today use a large fraction of renewable heat in their energy mix, this new application will make available renewable heat in dense urban area.

Figure 2 shows a possible hydraulic integration of an AdHP in cooling mode in a substation where the heat rejected is valorized to preheat DHW. This configuration is interesting as it eliminates the need of a dry cooler. On the other hand, it has to be operated with an important constraint: there must simultaneously cooling and DWH. Consequently, it will not be possible to produce cooling when there is no DHW demand. A compression HP could be integrated between the heat rejected by the AdHP and the DHW tank to give a bit more operating flexibility.

The Table 1 shows the operating conditions of the AdHP in cooling mode. Those conditions are derived from exchange with various DHN operators. The cooling is produced between 6 and 15°C. The forward temperature

must be at least 60°C in order to reduce too much the cooling COP. In addition, as mentioned above, it is important to insure a large temperature difference between the DHN forward and return stream for not deteriorating the DHN distribution losses and pumping energy consumption.

Table 1 - DHN temperature requirements in heating and cooling modes.

Scenario	Heating Mode			Cooling Mode		
	T_{hot}	T_{con}	T_{eva}	T_{hot}	T_{con}	T_{eva}
min-max	343-383 K	303-338 K	293-323 K	333-363 K	303-338 K	279-288 K

3. Adsorbent Material Development

Current state-of-the-art activated carbons (AC) are synthesized mostly by a bottom-up approach using toxic chemicals such as resorcinol and formaldehyde to form porous networks (Alshrah et al., 2017) which are then pyrolyzed and activated (Huber et al., 2016). The corresponding activated carbons can display a variety of microstructures and properties, making them interesting for different applications – including water sorption (Civioc et al., 2020; Huber et al., 2019). In the existing literature, green alternatives to petroleum-derived phenolic networks have been thoroughly studied to great avail (Nowicki et al., 2010; Prauchner and Rodríguez-Reinoso, 2012). However, none of them displays the array of properties required in our current work (e.g. able to adsorb and desorb in both heating and cooling mode).

Therefore, we herein study an alternative starting material: an activated carbon derived from spent coffee grounds (SCG). The properties and microstructure of the corresponding pyrolyzed material, arising from a more sustainable feedstock (thus greatly improving the carbon footprint of the adsorption heat pump) are studied. Its water adsorption characteristic is comparable with the one from more traditional resorcinol-based activated carbons; retaining an optimal performance is crucial for the efficiency of the project overall.

However, one of the main advantages of traditional resorcinol-based ACs is their monolithicity; they can be tailored thanks to the bottom-up synthesis approach by pouring the sol into a box of the desired shape. In this regard, SCG are more restrictive because of their granulated nature. Therefore, in this work we opted for a minimal usage of resorcinol and formaldehyde as a binder, effectively forming a matrix around SCG. It allows the materials to reach a monolithic state while being mostly sustainable. Importantly, this does not compromise the water adsorption performance of the materials.

Our synthesis protocol involves the collection of spent coffee grounds, which are then mixed with a minimal amount of resorcinol and formaldehyde. Typically, 30g of dry SCG and 25 mL of ethanol are mixed with 6g of resorcinol and 12 mL of commercial formaldehyde aqueous solution. A catalytic amount of ammonia in the form of an aqueous solution, around 1 mmol, is then added to the mixture. It is then poured into polypropylene boxes of the desired shape. The materials are left to cure and dry in a convection oven before being pyrolyzed and physically activated in a one-step heat treatment within a tube furnace – at 800 °C for 4 hours under a CO2 atmosphere. The result is a monolithic activated carbon, depicted in Figure 3, which can be characterized as necessary and is ready for water sorption applications.

As a finer particle size of the AC could be beneficial from the mechanical standpoint, it was decided to test the AC obtained from the fraction of the green body with the smaller diameter. Before synthesis, SCGs were sieved and only the fraction whose diameter did not exceed 200 micrometers was used – resulting in a drastic improvement of the adsorption characteristic (60% more water capacity) , as visible in Figure 4. This result, which surpasses the state-of-the-art carbons, opens very promising applications and should be further investigated, especially given the low desorption temperatures required. However, the material evaluation was performed on the basis of the more complete information available for the AC obtained from the not sieved SCG.

The ACs are currently sporting a slab shape. Therefore, envelope density ρ_{env} was calculated using a caliper to measure the dimensions of the materials. Subsequently, skeletal density ρ_{skel} was measured by means of helium pycnometry (Accupyc, Micromeritics). This calculations allows for the determination of the entirety of the pore volume within the materials, including their microporosity mesoporosity, and macroporosity (d > 50 nm) without further quantitative information.

The porosity of those materials was further characterized using nitrogen physisorption and carbon dioxide physisorption. For nitrogen sorption, an NLDFT kernel based on (Tarazona, 1985) was chosen. For CO2 sorption, an NLDFT kernel based on (Olivier, 1995) was used. The as-obtained isotherms are subsequently merged using the 3Flex software from Micromeritics. Thus, the microporosity v_μ (diameter < 2nm) and mesoporosity v_m (2 nm < diameter < 50 nm) of the materials was characterized both qualitatively and quantitatively, assuming respectively a slit and a cylindrical geometry. The amount of macroporosity was then determined by subtracting those two values from the total pore volume calculated as in Eq. 1. The volumetric pore fraction of the material ε can be then calculated as in Eq. 2.

$$v_t = \frac{1}{\rho_{env}} - \frac{1}{\rho_{skel}} \quad \text{Eq. 1,} \qquad \varepsilon = v_t \cdot \rho_{env} \quad \text{Eq. 2}$$

The wet thermal conductivity k_{50} of the ACs was determined using a custom-made guarded hot plate device (Stahl et al., 2012) at 30 °C and 50% relative humidity. Finally, dynamic water sorption isotherms were recorded on an isothermal gravimetric device (VTI-SA+ Water Vapor Sorption Analyzer, Porotec) between 5% and 80% relative humidity. For the ACs under analysis, the water adsorption characteristic be described following the Dubinin-Astakhov model (Dubinin and Astakhov, 1971):

$$w = W \cdot \exp\left(-\left(\frac{F}{C}\right)^N\right) \quad \text{Eq. 3,} \qquad F = -\frac{R}{M} \cdot T \cdot \ln\left(\frac{p}{p_{sat}}\right) \quad \text{Eq. 4}$$

The results are gather in Table 2. For the sieved SCG+RF AC, the water adsorption parameters were found to be $W = 0.48$, $C = 186$, $N = 2.4$, which means that the total capacity was enhanced without changing the type of adsorption sites.

The thermophysical properties of the AC strongly influence the performance of the adHP. To estimate the achievable performance of the SCG-based adsorbent monoliths, a dynamic model was used to calculate the energy efficiency and the power that the materials can deliver under the working conditions defined in Section 2. The model was developed in OpenModelica, following the lumped-parameter approach described in (Piccoli et al., 2021). Using such an approach assumes that the global adsorption dynamic can be sufficiently well described as if happening a single effective thermodynamic state (temperature, pressure, loading), instead of simulating all the local thermodynamic states developing within the adsorbent. Such a model includes only the heat and mass transfer within the material itself, therefore can be used as a term of comparison for different materials, boundary conditions and geometries, and not as a reference for whole adHPs.

The model is composed by a temperature boundary condition (representing the HEx fin temperature), a heat transfer resistance (representing the conduction within the AC), a heat and mass balance (representing the adsorption reaction in the pores), a mass transfer resistance (representing the vapour diffusion in the pores), one pressure boundary conditions (representing the evaporator/condenser). All these elements are connected in this order, such that the adsorption dynamics calculated in the heat and mass balance depend on the materials properties and on the boundary conditions.



Figure 3 – SCG+RF monoliths before (left) and after (right) pyrolysis

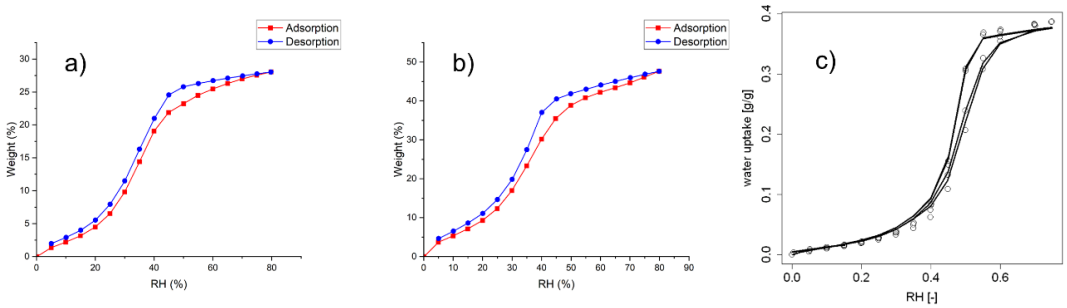

Figure 4 – Water adsorption isotherms at 30°C of not sieved (a) and sieved (b) SCG+RF AC and of RMF AC (c).

Table 2 – Thermophysical properties of the SCG+RF AC monoliths

Property	ρ_{env}	ρ_{skel}	v_M	v_m	v_μ	ε	k_{50}	W	C	N
Value	0.56 [g/cm³]	1.6 [g/cm³]	0.83 [cm³/g]	0.03 [cm³/g]	0.30 [cm³/g]	66 [%]	0.092 [W/m/K]	0.29 [g/g]	185 [J/g]	2.6 [ ]

The temperature and pressure boundary conditions are modelled as square waves oscillating between the adsorption and the desorption heat transfer fluid temperatures and evaporator and condenser pressure, respectively. Moreover, a control mechanism forbids flow reversal for the pressure boundary condition.

The heat transfer resistance R_{heat} within the monolith is modelled as transient 1-D conduction:

$$R_{heat} = \frac{(2 \cdot s)^2}{\pi^2 \cdot \alpha \cdot V_t \cdot c \cdot \rho_{env}} \cdot \left(1 - 0.3 \cdot \exp\left(-\frac{\tau}{8.9e-4}\right) - 0.7 \cdot \exp\left(-\frac{\tau}{1.3e-2}\right)\right) \quad \text{Eq. 5}$$

The adimensional time τ, determining the transient term, is the equivalent of the Fourier Number in absence of adsorption. However, the adimensional time is stretched due to the additional adsorption energy terms in the heat balance and by its entanglement with the mass transfer. To compensate for this, it is implicitly extracted from the state of the material:

$$\frac{T - T_i}{T_f - T_i} = 1 - 0.82 \cdot \exp\left(-\frac{\tau}{1.0e-1}\right) - 0.18 \cdot \exp\left(-\frac{\tau}{4.6e-3}\right) \quad \text{Eq. 6}$$

Similarly, the mass transfer resistance within the monolith is modelled as microscopic surface diffusion and a transient 1-D macroscopic diffusion:

$$R_{mass} = \frac{r_\mu}{3 \cdot D_\mu \cdot \rho_{env} \cdot s \cdot a_{surf} \cdot A_s} + \frac{s}{D_{M*} A_s} \cdot \left(0.3 \cdot \exp\left(-\frac{\tau}{8.9e-4}\right) - 0.7 \cdot \exp\left(-\frac{\tau}{1.3e-2}\right)\right) \quad \text{Eq. 7}$$

Eq. 3 implies that the size of the bigger porosity is not limiting the gas mean free path and therefore no major difference among more or less porous materials should be expected. Furthermore, given the characteristic lengths at play in the microscale and in the macroscale ($r_\mu \sim 1\ \mu m$ and $s \sim 1\ mm$) the macroscopic diffusion is by far the limiting mechanism, especially at low values of τ. This is similar to the trends observed for coatings (Ammann et al., 2019).

In Eq.1, Eq. 2 and Eq.3 the exponential equations are numerically derived from the analytical solutions (Carslaw and Jaeger, 1959) of the average thermal resistance and of the average temperature of infinite slabs, respectively. It can be noticed how the transient term of the heat and mass transfer resistances are complementary. The reason is that the effective state of the material represents also the position in the monolith in which the adsorption is occurring. At the beginning of each step, the adsorption is temperature driven, so it happens at a minimum distance from the fin surface and at a maximum distance from the vapour interface (R_{heat} is small and R_{mass} is big), while at the end of the step, the opposite will happen.

The essence of the heat and mass balance consists in two equations, entangled by the water loading w:

$$\frac{T_f - T}{R_{heat}} + \dot{m}_v \cdot (h_{ext} - h_{int}) = (m_s \cdot c_s + m_a \cdot c_a) \cdot \frac{\partial T}{\partial t} - H \cdot m_s \cdot \frac{\partial w}{\partial t} + m_v \cdot \frac{\partial h_{int}}{\partial t} + h_{int} \cdot \frac{\partial m_v}{\partial t} \quad \text{Eq. 8}$$

$$\frac{\gamma_{ext}-\gamma_{int}}{R_{mass}} = \gamma_{int} \cdot \frac{\partial V_v}{\partial t} + V_v \cdot \frac{\partial \gamma_{int}}{\partial t} + V_t \cdot \rho_{env} \cdot \frac{\partial w}{\partial t} \quad \text{Eq. 9}$$

The state of the AC is determined by its properties, namely thermal diffusivity α, specific heat capacity c, envelope density ρ, thickness s and water adsorption characteristic $w = w(p,T)$. As stated above, one of the advantages of using ACs as adsorbent material is the possibility of tailoring their properties to a given application. In particular, for SCG this can be controlled by changing the pyrolysis process to have more or less microporosity and macroporosity. This will influence the adsorption characteristic, the density and the thermal diffusivity. In order to understand how the different pyrolysis conditions (CO_2 flowrate, max temperature and time above the critical temperature of the coffee) affect these properties, a Design of Experiment based on a central composite design was performed on the SCG. Regarding the adsorption characteristic and the density, we established that the flow of CO_2 does not have a significant influence within the range studied, while the maximum temperature and the pyrolysis time have a great influence. The thermal diffusivity, instead, strongly depends on the process of creation of the monolith from the AC powder. As this would add more parameters to the analysis, it was not included and the reference thermal conductivity of 0.067 W/m/K (obtained for a highly macroporous RMF AC monolith) was used instead. This means that the thermal resistance might be overestimated for the denser samples. Moreover, the specific heat capacity was assumed to be similar to the one measured for the RMF AC (Piccoli et al., 2021).

In general, each material property P can be described as a function of the maximum pyrolysis temperature $T \in [632{,}968\ °C]$ and the duration of the pyrolysis above 300°C $D \in [244{,}429\ min]$:

$$P = a \cdot T + b \cdot D + c \cdot T \cdot D + d \quad \text{Eq.10}$$

Table 3 summarizes the results obtained for the SCG AC powder.

Table 3 – Description of SCG AC properties as a function of the pyrolysis parameters

Material Property	Symbol [Units]	Temperature coeff. a	Time coeff. b	Temp./Time coeff. c	Constant coeff. d
Saturation Water Capacity	$W\ \left[\frac{g_w}{g_s}\right]$	0	-1.3e-3	2.4e-6	0
Char. Energy of Adsorption	$C\ \left[\frac{J}{g}\right]$	0.43	1.2	-2.0e-3	0
Ads. Curve Shape Factor	$N\ [-]$	0	0	0	2.0
Skeletal Density	$\rho_{skel}\ \left[\frac{g}{cm^3}\right]$	0	-2.1e-3	2.9e-6	1.7
Envelope Density	$\rho_{env}\ \left[\frac{g}{cm^3}\right]$	5.6e-4	1.4	2.4e-6	0

Given the requirements of DHN for heating and cooling purposes, the performance of the SCG ACs should be tailored accordingly. Therefore, we used the dynamic adsorption model to simulate the Key Performance Indicator (KPI) of the material in a range of process, material and application parameters. The KPI was selected to be a tradeoff between energy efficiency and specific cooling power reached by an adsorption/desorption cycle in steady state (i.e. after 50 cycles):

$$KPI_{heating} = \frac{(E_{con}+E_{ads})^2}{E_{hot} \cdot t_{cycle}} \quad \text{Eq. 11,} \qquad KPI_{cooling} = \frac{(E_{eva})^2}{E_{hot} \cdot t_{cycle}} \quad \text{Eq.12}$$

In order to ensure a feasible heat exchange to with the heat transfer fluid, the desorption temperature is assumed to be 5 K below T_{hot} and the adsorption temperature is assumed to be 5 K above T_{con}. To minimize the number of simulation required, the working temperatures $T_{eva}, T_{con}, T_{hot}$ were fixed to 293, 308, 368 K for the heating mode and to 288, 303, 363 for the cooling mode respectively. Firstly, the best pyrolysis conditions for the (improvable) not sieved SCG+RF AC were defined by calculating the KPI for long cycles (reaching full equilibrium). The best material was selected for 3 scenarios, for which the total KPI was calculated as $KPI_t = \left(\frac{\varphi_h}{KPI_{heating}} + \frac{\varphi_c}{KPI_{cooling}}\right)^{-1}$:

- Current Demand (CD), serving only heating, with $\varphi_h = 1, \varphi_c = 0$
- Moderate Cooling (MC), where the cooling demand is less important than the heating demand, with $\varphi_h = 0.67, \varphi_c = 0.33$
- High Cooling (HC), where cooling demand is as important as the heating demand, with $\varphi_h = 0.5, \varphi_c = 0.5$

The pyrolysis conditions delivering the ideal materials for the three scenarios are listed in Table 4. The material design is clearly limited by space in which they were investigated: higher temperature and lower duration of pyrolysis would be beneficial. Moreover, the cooling mode is by far the most constraining and it dominates the choice for MC and HC scenarios.

Table 4 – Optimal pyrolysis parameter for the different application scenarios

Parameter	Current Demand	Moderate Cooling	High Cooling
T	968 °C	968 °C	968 °C
D	275 min	244 min	244 min

For the investigation of the optimal material thickness and cycle time, the material for MC and HC was used. When simulating different monolith thicknesses, thinner materials were able to produce much higher power, and therefore preferred. For example, a thickness of 1 mm (one order of magnitude higher than conventional coatings), delivered maximum KPI with a full cycle time of about 25 s, that is at the limit of the capacity of conventional heat exchangers, which have important thermal inertia. This means that for thin coatings, work should be done towards fast heat exchangers design. For 2 mm monoliths, however, the ideal cycle time increase to 100 s, as shown in Figure 5. The achieved thermal coefficient of performance reached 0.79 and the $KPI_{cooling}$ 1.4 kW/kg. This means that the monolithicity of the adsorbent offers a great advantage in the design of the heat exchanger.

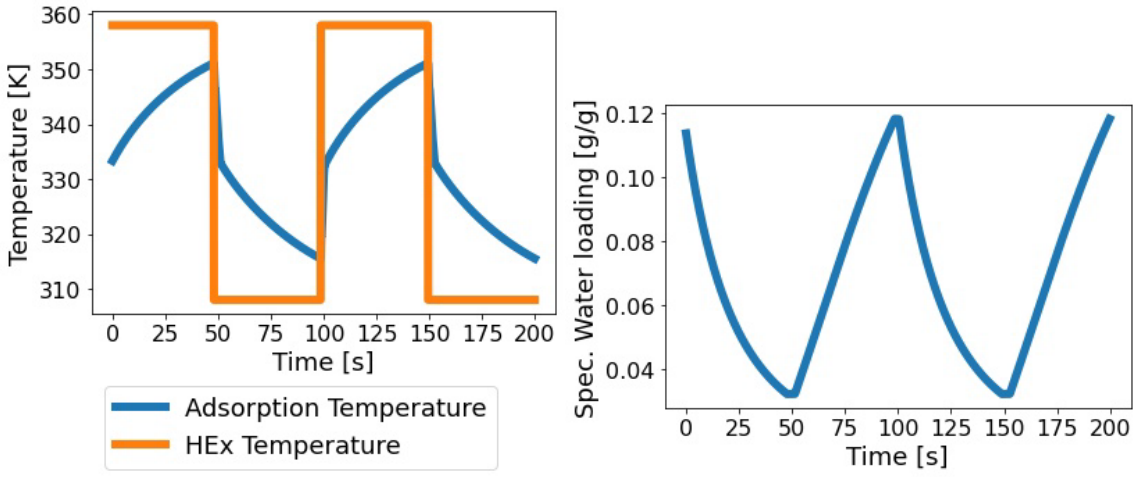

Figure 5 - Steady state cooling cycle for a 2 mm monolith. The adsorption temperature (left) increases fast due to the locality of the heat transfer. The adsorption on the materials (right) happens at a fast rate throughout the cycle.

4. Adsorption Heat and Mass Exchanger Characterization

For an adHP design in the power range of several kW, small-scale adsorber-desorber heat exchanger (A-D HEx) cyclic experiments around 1 kW open the possibility to investigate and optimize the HEX design. The design and manufacturing of the AC-based A-D HEx unit is one of the key tasks in the development of an adHP (Mohammadzadeh Kowsari et al., 2018). To characterize the A-D HEx efficiency, the sorbate mass is measured dynamically in-situ for both half cycles (adsorption and desorption). By knowing the dry mass and the adsorption potential (pressure/temperature conditions) in function of the sorbate loading on the adsorbent material, the adsorbed sorbate acts as a reference for the power (i.e. the external heat transfer loop efficiency).

In the adsorber - desorber characterization the mass uptake w(t) in the adsorption and mass loss in the desorption cycling is measured. The amount of w(t) multiplied by the heat of evaporation L of the sorbate is used as a benchmark for the efficiency of the heat and mass exchanger. L is a function of temperature T and in case of water L (20

°C) = 2537.5 kJ/kg (VDI-Wärmeatlas, Springer-Verlag Berlin Heidelberg 2013).

Therefore, the measurement setup of the SNF THRIVE project (Gantenbein et al., 2017) was modified. This comprised the modification of the external heat transfer fluid loops and additional sensors – like a new balance beam (HBK Plattformwägezelle 1-SP4MC6MR/7KG-1) of a higher resolution (mass m +/- Δm of 0.5 g).

Figure 6 shows the graphical user interface (GUI) of the NI LabVIEW data acquisition system. The principle of the setup with heat sources and heat sinks can be seen. Therefore, 3 thermostatic baths are used to perform adsorption and desorption (with the A/D HEX) as well as evaporation (evaporator) and condensation (condenser) of sorbate in the cycles. With a 4th thermostat the double jacked is thermostated to avoid heat transfer from and to the environment (the inner vacuum envelope surface) from and to the A/D HEX. In Figure 8 part of the open single chamber with the installed A/D HEX I (suspended at the beam balance) is shown and the right of this figure shows a section of the activated carbon sorbent disks stack.

Prior to cyclic adsorption and desorption measurements with sorbate, a calibration procedure without sorbate has to be performed for each cycle time t_{cycle}. These calibrations account for all "virtual" mass changes induced by thermal expansion of the A/D HEX, pressure oscillations in the heat transfer fluid and any heat input from the surrounding. Figure 7 shows weight measurement data for both adsorption and desorption. At the onset of adsorption (resp. desorption) the behaviour with a high mass uptake (resp. decrease) per time can be seen. In the curve fitting the coefficients a_l, d_k and the indices l, k have to be determined for each temperature quadruple and cycle time. After this procedure the functions can be used to parameterise a sorption heat pump model.

After the measurements with the sorbent-sorbate combination, an appropriate data procedure follows to determine the efficiency parameters. The power of the A/D HEX I was determined by the sorbate mass uptake w(t) and mass loss through the adsorption desorption cycles. Although the sorbent shows a high kinetic behavior (steep increase of the mass uptake at the onset of adsorption) a low power in the range of 100 W was reached (SCP: 300 W/kg) due to a long cycle time t_{cycle}. A close look to the mass curve w(t) indicates to shorten the t_{cycle} down to approx. one half – and therefore nearly a double of the SCP would be reached. An even higher SCP is expected with unaged sorbent material and an unaged A/D HEX (no peeling/dissolution of sorbent from the heat conduction Copper fins). In fact, the sorbent aging depends of the interaction with the sorbate and should not occur in normal operating conditions.

Based on the defined temperatures of the scenarios the sorbate vapor pressure p_s is in the range of 17.1 mbar (15 °C) and 42.5 (30 °C) sub-atmospheric pressures. The understanding of the sorption kinetics in the 1 kW power range allows for the scaling of results to a several kW (heating and cooling) power adsorption heat pump (Dague-net-Frick et al., 2017).

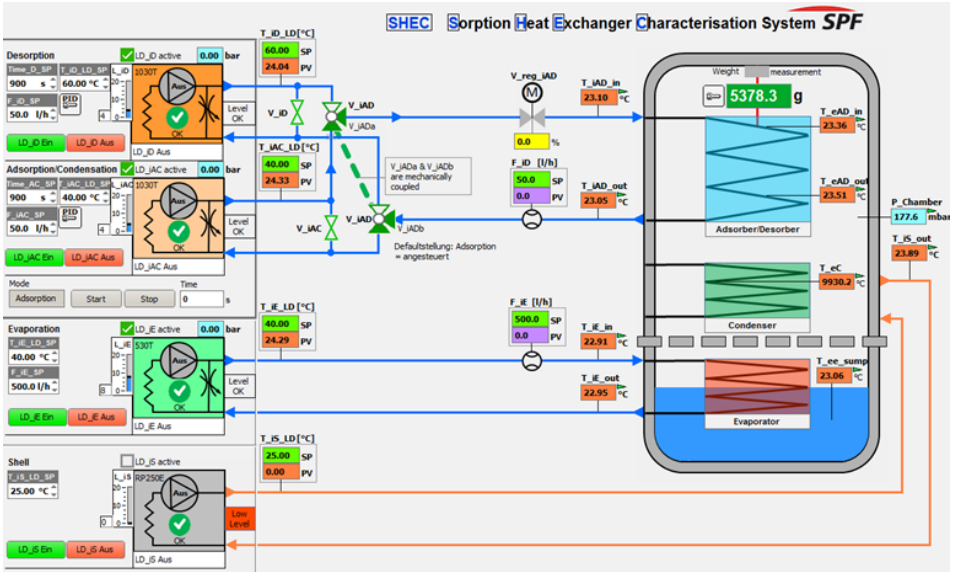

Figure 6 - graphical user interface (GUI) of the NI LabVIEW data acquisition system: 4 thermostatic baths as heat sources and heat sinks (left), single chamber setup with double jacket envelope and installed evaporator and adsorber/desorber (right), tubing and sensors. The original condenser is not installed – but the evaporator has a double function for evaporation and condensation.

Therefore, the evaporator is partly immersed in the liquid sorbate (blue color and temperature sensor T_ee_sump). While the lower part acts as an evaporator, the upper part acts as a condenser.

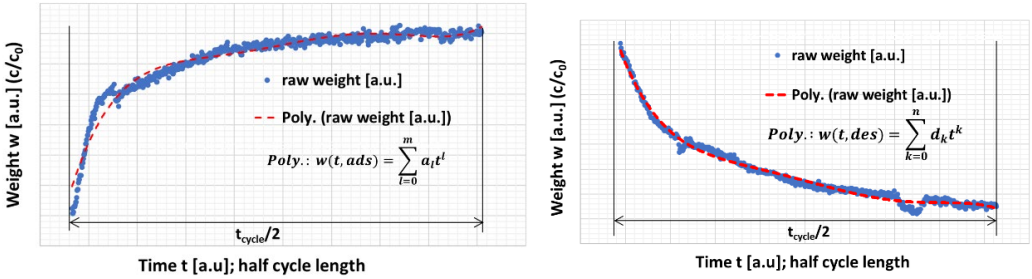

Figure 7 - Measurement data: adsorption (left) resp. desorption (right) curve over the half cycle time (a. u. = arbitrary units) and concept of data curve analysis with peace wise fit functions.

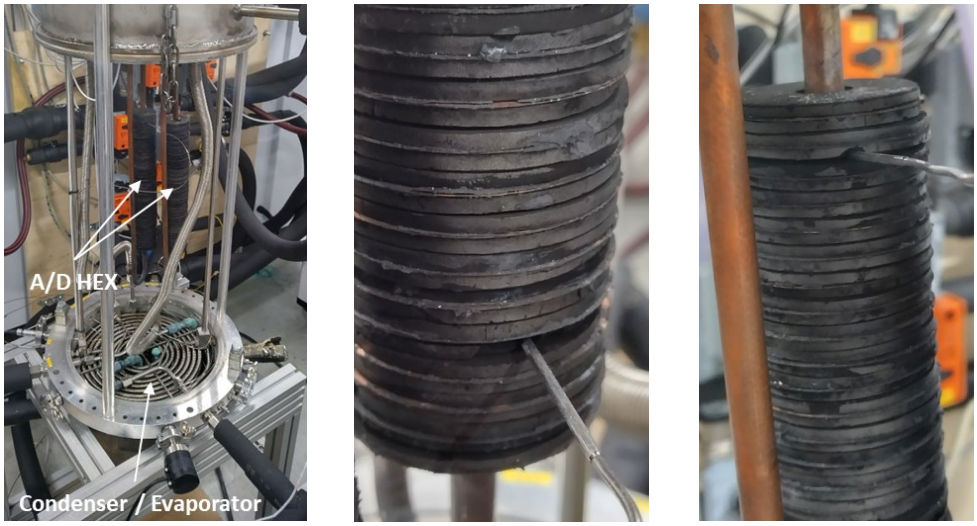

Figure 8 - SHEC and installed activated carbon sorbent disks stack: photo of the open single chamber measurement setup (left) and a section of the A/D HEX I with clamped Pt 100 temperature sensors (right). The sorbent disks sandwich the heat conducting Copper fins.

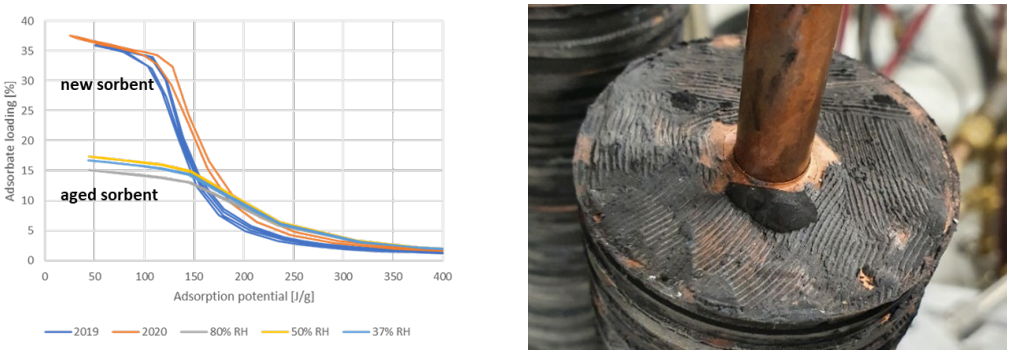

Figure 9 - sorbent ageing and peeling of the Copper fins: the sorbent shows an intrinsic ageing behavior after a 3 years exposure to sorbate vapor (left graph with the adsorbate loading in function of the age of the sorbent) and the sorbent disk peeled of the copper fin due to ageing of the glue (right picture).

5. Conclusions

In this work, we presented relevant progress obtained towards the design of adsorption heat pumps capable of improving district heating network efficiency in both heating and cooling mode. Firstly, the needs of DHN operators are examined and the most useful applications were selected. Specifically, in the heating mode the adHP can reduce the return temperature of the network, while in cooling mode the waste heat usage is increased.

The adsorbent material developed, an activated carbon (AC) obtained from spent coffee grounds, is a much more sustainable material than state-of-the-art ACs. The obtained adsorbent delivers satisfactory performance for the application studied. In particular, the pyrolysis process gives a good control over the adsorption characteristic curve, and should be further explored for sieved green body and towards higher temperatures and lower durations. Moreover, the models and the simulations of the AC gave useful insight on further development. Thin monoliths (<1mm) can be more performant than thicker ones, but they will be limited by the HEx design. Thicker monoliths are compatible with conventional HEx and are therefore very promising, as they provide a unique solution for effective HEx are usage.

Lastly, we built and tested a 1kW-prototype characterization setup with increased capacity and accuracy, which will be fundamental for further development of the adHP. In this setup, we could evaluate the effects of bad material handling and ageing.

6. Acknowledgments

We acknowledge the support of the Swiss Federal Office of Energy, as well as the contributions received from Juan Antonio Pérez López, Sahana Tavaragondi and Riccardo Torreggiani during their stay at Empa.

7. Nomenclature

Quantities					
Quantity	**Symbol**	**Unit**	**Quantity**	**Symbol**	**Unit**
Specific heat	c	J/kg/K	Area	A	m^2
Thermal conductivity	k	W/m/K	Specific area	a	m^2/g
Diffusion coefficient	D	m^2/s	Enthalpy	h	J/kg
Sat. water capacity	W	g/g	Mass	m	kg
Char. ads. energy	C	J/ g	Heat	E	J
Thermal diffusivity	α	m^2/s	Mass flow rate	$\dot{m}$	kg/s
Ads. char. shape factor	N		Heat transf. resistance	R_{heat}	K/W
Porosity	ε		Heat flow rate	Q	W
Specific pore volume	v	cm^3/g	Mass transf. resistance	R_{mass}	s/m^3
Density	ρ	kg/m^3	Temperature	T	K
Time	t	s	Pressure	p	Pa
Adimensional time	τ		Gas concentration	γ	kg/m^3
Radius	r	m	Volume	V	m^3
Specific ads. loading	w	g/g	Thickness	s	m
Adsorption energy	H	J/kg	Adsorption energy	F	J/g
Evaporation enthalpy	L	J/kg			

Subscripts			
Quantity	**Symbol**	**Quantity**	**Symbol**
Fin	f	Skeletal	$skel$
Saturation	sat	Adsorbate	a
Evaporator	eva	Adsorbent	s
Condenser	con	Vapour	v
Adsorption	ads	Macroscopic	M
Hot source	hot	Microscopic	μ
Internal	int	Mesoscopic	m
External	ext	Initial	i
Envelope	env		

8. References

Alshrah, M., Tran, M.-P., Gong, P., Naguib, H.E., Park, C.B., 2017. Development of high-porosity resorcinol formaldehyde aerogels with enhanced mechanical properties through improved particle necking under CO 2 supercritical conditions. Journal of Colloid and Interface Science 485, 65–74. https://doi.org/10.1016/j.jcis.2016.09.030

Ammann, J., Michel, B., Ruch, P.W., 2019. Characterization of transport limitations in SAPO-34 adsorbent coatings for adsorption heat pumps. International Journal of Heat and Mass Transfer 129, 18–27. https://doi.org/10.1016/j.ijheatmasstransfer.2018.09.053

Birol, D.F., 2018. The Future of Cooling 92.

Carslaw, H.S., Jaeger, J.C., 1959. Conduction of Heat in Solids, 2nd ed. Oxford University Press, Great Britain.

Civioc, R., Lattuada, M., Koebel, M.M., Galmarini, S., 2020. Monolithic resorcinol–formaldehyde alcogels and their corresponding nitrogen-doped activated carbons. J Sol-Gel Sci Technol 95, 719–732. https://doi.org/10.1007/s10971-020-05288-x

Daguenet-Frick, X., Moullet, Y., Gantenbein, P., Persdorf, P., Notter, D., 2017. Adsorption Heat Pump Upscaling from 1 KW to 10 KW of Cooling Power: Experimental Based Modelling, in: International Sorption Heat Pump Conference 2017. Presented at the International Sorption Heat Pump Conference 2017, Tokyo.

Dubinin, M.M., Astakhov, V.A., 1971. Development of the concepts of volume filling of micropores in the adsorption of gases and vapors by microporous adsorbents 5.

Gantenbein, P., Daguenet-Frick, X., Bont, F., Persdorf, P., Notter, D., 2017. Cooling power determination by measuring the adsorbed vapor mass variations: comparison of mass adsorption cooling power correlation and external fluid loop power measurement, in: International Sorption Heat Pump Conference 2017. Presented at the International Sorption Heat Pump Conference 2017, Tokyo.

Hassan, A.A., Elwardany, A.E., Ookawara, S., Ahmed, M., El-Sharkawy, I.I., 2020. Integrated adsorption-based multigeneration systems: A critical review and future trends. International Journal of Refrigeration 116, 129–145. https://doi.org/10.1016/j.ijrefrig.2020.04.001

Huber, L., Hauser, S.B., Brendlé, E., Ruch, P., Ammann, J., Hauert, R., Widmer, R.N., Ubert, C.J., Matam, S.K., Yoon, S., Zhang, Y., Koebel, M.M., 2019. The effect of activation time on water sorption behavior of nitrogen-doped, physically activated, monolithic carbon for adsorption cooling. Microporous and Mesoporous Materials 276, 239–250. https://doi.org/10.1016/j.micromeso.2018.09.025

Huber, L., Ruch, P., Hauert, R., Matam, S.K., Saucke, G., Yoon, S., Zhang, Y., Koebel, M.M., 2016. Water sorption behavior of physically and chemically activated monolithic nitrogen doped carbon for adsorption cooling. RSC Adv. 6, 80729–80738. https://doi.org/10.1039/C6RA18660B

Jobard, X., Padey, P., Guillaume, M., Duret, A., Pahud, D., 2020. Development and Testing of Novel Applications for Adsorption Heat Pumps and Chillers. Energies 13, 615. https://doi.org/10.3390/en13030615

Mohammadzadeh Kowsari, M., Niazmand, H., Tokarev, M.M., 2018. Bed configuration effects on the finned flat-tube adsorption heat exchanger performance: Numerical modeling and experimental validation. Applied Energy 213, 540–554. https://doi.org/10.1016/j.apenergy.2017.11.019

Nowicki, P., Pietrzak, R., Wachowska, H., 2010. Sorption properties of active carbons obtained from walnut shells by chemical and physical activation. Catalysis Today 150, 107–114. https://doi.org/10.1016/j.cattod.2009.11.009

Olivier, J.P., 1995. Modeling physical adsorption on porous and nonporous solids using density functional theory. J. Porous Mater. 2, 9–17.

Piccoli, E., Frazzica, A., Galmarini, S., 2021. D4.3: Model capable of estimating the performance of a given adsorption chiller set-up and a given adsorber material for a given application scenario, Hycool project public deliverables.

Prauchner, M.J., Rodríguez-Reinoso, F., 2012. Chemical versus physical activation of coconut shell: A comparative study. Microporous and Mesoporous Materials 152, 163–171. https://doi.org/10.1016/j.micromeso.2011.11.040

Puschnigg, S., Jauschnik, G., Moser, S., Volkova, A., Linhart, M., 2021. A review of low-temperature sub-networks in existing district heating networks: examples, conditions, replicability. Energy Reports 7, 18–26. https://doi.org/10.1016/j.egyr.2021.09.044

Quiquerez, L., 2017. Décarboner le système énergétique à l'aide des réseaux de chaleur: état des lieux et scénarios prospectifs pour le canton de Genève. https://doi.org/10.13097/ARCHIVE-OUVERTE/UNIGE:93380

Settembrini, G., Domingo-Irigoyen, S., Heim, T., Jurt, D., Zakovorotnyi, A., Seerig, A., Zweifel, G., Menti, U.P., 2017. ClimaBau - Planen angesichts des Klimawandels. Lucerne University of Applied Sciences and Arts.

Stahl, Th., Brunner, S., Zimmermann, M., Ghazi Wakili, K., 2012. Thermo-hygric properties of a newly developed aerogel based insulation rendering for both exterior and interior applications. Energy and Buildings 44, 114–117. https://doi.org/10.1016/j.enbuild.2011.09.041

Tarazona, P., 1985. Free-energy density functional for hard spheres. Physical Review A 31, 2672.

EuroSun 2022

Direct Excess Heat Utilization from a High Performance Computer in an Existing Unrenovated Building: A Case Study

Dr. David Sauerwein[1], Frederik Feike[2]

[1]Institute for Sustainable Building Design, Technische Universität Darmstadt

[2]Institute for Technical Thermodynamics, Technische Universität Darmstadt

Summary

This study quantifies the savings potential of fossil district heat for the case study of the architecture building of the Technische Universität Darmstadt by directly using excess heat of a high performance computer (HPC). It is based on the already implemented demonstrators of a hot-water-cooling system for the new HPC and on the integration of low temperature ceiling heating systems in the otherwise unrenovated architecture building. As a result, with an excess heat utilization rate of 52 %, more than 60 % of the fossil building's district heating demand can be saved.

Keywords: excess heat utilization, low temperature heating, high performance computer, building renovation

1. Introduction

For the decarbonization of the building sector, there is no alternative to reducing the demand for fossil fuels. Currently, about 75 % of the German building stock is heated with natural gas or oil (dena, 2021). The current energy crisis has further increased the urgency of substituting fossil fuels. Accelerated and comprehensive implementation of alternative heat supply concepts through increased use of renewable energies and excess heat in buildings is a key to this. Whereas new buildings have very good energetic properties, existing buildings often have high specific heat demands and make up the majority of the current building stock. Additionally, old buildings also require high supply temperatures, thus it is difficult to supply them with renewable heat that can mainly only be used efficiently at lower temperatures.

The advancing digitalization leads to an increasing growth of data center capacities, resulting in an increasing demand for electric energy (Hintemann, 2020). The resulting excess heat is mainly dissipated to the environment. This increasing potential can be used as a valuable resource to cover the heat demand of adjacent buildings. To balance the differences between demand and supply and to increase the potential of excess heat utilization, low-temperature district heating networks are well suited. In existing district heating networks, the connected buildings have to be addressed first to reduce the temperature levels (Averfalk et al., 2021).

2. HPC excess heat utilization

Data center excess heat temperatures depend strongly on the implemented cooling technologies, which can be divided into four different approaches. The most common is server cooling via the data center room air, using computer room air handlers or computer room air conditioners. The second method cools the air locally at the server through rear door air-water heat exchangers. The third method is a combination of direct water-cooling of the hottest server components and air-cooling for the remaining parts. The last approach is to fully emerge the server in a dielectric fluid. While the most widespread

© 2022. The Authors. Published by International Solar Energy Society
Selection and/or peer review under responsibility of Scientific Committee
doi:10.18086/eurosun.2022.04.11 Available at http://proceedings.ises.org

heat transfer medium is air, water-cooling offers many advantages. It reduces the additional energy required for cooling, enables higher power densities, and allows higher excess heat temperatures (Davies et al, 2016).

According to Ebrahimi et al. there are several possibilities to utilize data center excess heat: space heating and hot water preparation, district heating, power plant co-location to preheat boiler water, absorption refrigeration, Organic Rankine Cycles, piezoelectrics, thermoelectrics, biomass co-location and desalination. When using the excess heat to supply buildings, heat pumps are often used to raise the temperature level to meet the building's requirements. In newer buildings, direct excess heat utilization without heat pumps is usually possible (Ebrahimi et al., 2014).

In this work, only excess heat utilization for the provision of space heating is investigated, since the HPC is located in close vicinity to larger university buildings. In addition, direct excess heat utilization without the use of heat pumps is particularly energy efficient.

3. Temperature reduction in buildings

Decarbonization of the heat demand in existing buildings can be achieved by saving heat through measures to improve the energetic quality of the building envelope. This has been sufficiently researched and is state of the art. However, if an increased substitution of heat demand with renewable heat is aspired, the level of system temperatures is the key target. Renewable excess heat potentials, which are often at a low temperature level, can only be used efficiently by reducing the temperature in the building heating system.

In order for renewable heat to be efficiently integrated into building energy systems, it is important that the return temperature is as low as possible in addition to the level of the supply temperature. Various structural and operational measures can be used to reduce system temperatures in building heating systems to different degrees. A low-investment measure is the installation of string-balanced valves and pre-set radiator valves including a hydronic balancing of the heating system (Schmidt et al., 2017). Based on this, the heating curve can be lowered step by step. By replacing critical or undersized radiators, the supply and return temperature for the entire building can be reduced (Østergaard et al., 2016). A great temperature reduction can be achieved once by refurbishing the building envelope and thus reducing the heating load. Another strategy is to increase the heating surfaces by installing surface heating systems, which allows the same heating load to be delivered at a lower temperature (Lund et al., 2014; Sauerwein et al., 2023). The implementation of surface heating systems in new buildings is state of the art. Particularly for the use of ceiling heating systems in the unrenovated non-residential building stock, there are often concerns regarding negative effects on thermal comfort.

4. Implementations at Technische Universität Darmstadt

As part of the "EnEff:Stadt Campus Lichtwiese" research project, a concept for the excess heat utilization of the HPC located on the campus “Lichtwiese” of Technische Universität Darmstadt was developed (Oltmanns et al., 2020) and subsequently implemented. To ensure high excess heat temperatures, the HPC is cooled via hot-water-cooling (Fig. 1 left). The excess heat is further upgraded via a heat pump and eventually fed into the return line of the university’s district heating network. This setup needs additional electric energy to use the excess heat, but because of the high excess heat temperatures, the operation of the heat pump is very efficient. Since the excess heat utilization went into operation in the beginning of 2021, an average COP higher than 5 could be achieved (Feike et al., 2021).

To analyze and optimize this concept, an additional monitoring system was implemented. Among other parameters, the available excess heat of the HPC as well as the corresponding temperatures are measured, which fluctuate depending on the computational load of the HPC (Fig. 2 left). The excess heat varies quite strongly between 160 kW and 410 kW with an average output of 351 kW. The

fluctuation of the excess heat temperature is relatively small in a range between 45 °C and 52 °C with an average value of 47.2 °C.

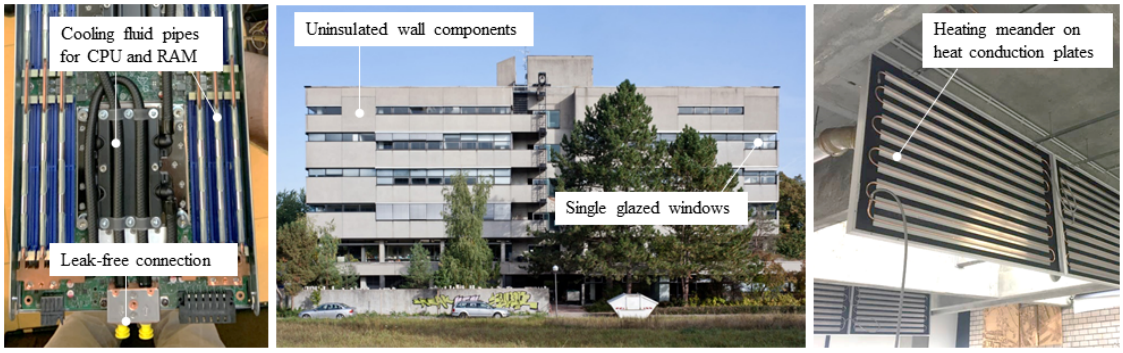

Fig. 1: Hot-water-cooling on a server blade (left), listed architecture building (source: Jakob Philipp Weise) (middle), integration of ceiling heating panels (right)

In another part of the research project, the potential for temperature reduction in unrenovated existing buildings by installing a low-temperature heating system inside the listed architecture faculty building (Fig. 1 middle) is investigated. Space heating is covered by ceiling heating panels (Fig. 1 right) together with the existing radiators at the same temperature level. This makes it possible to achieve a high level of thermal comfort even for workplaces close to the facade: In addition to a reduced cold air drop in the window area, the radiation temperature asymmetry between the cold facade and the warm ceiling is effectively limited. In operation, it was possible to reduce the supply temperature by more than 30 K to 45 °C at very low outside temperatures (Fig. 2 right), while complying with normative thermal comfort requirements (ISO 7730).

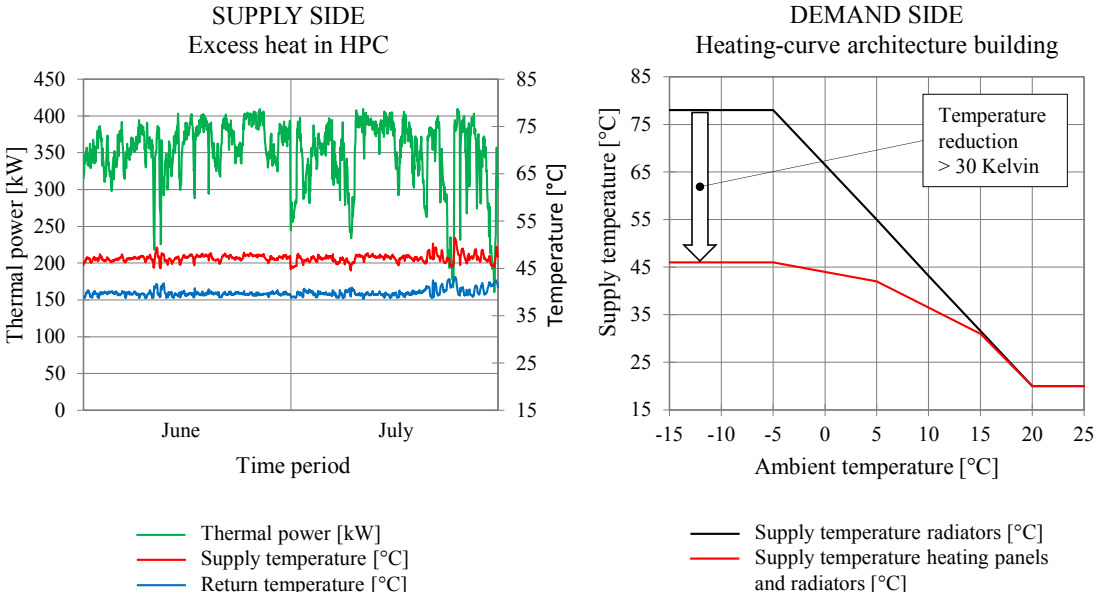

Fig. 2: Supply side: Excess heat HPC (left), Demand side: Heating-curve architectural building (right)

5. Direct utilization of excess heat

Based on measured data during the operating phase regarding the excess heat potential of the HPC and the low-temperature compatibility of the architecture building, the interconnection of supply and demand by a direct excess heat utilization shall now be investigated (Fig. 3).

For this purpose, the share S_u of usable excess heat Q_u in the available excess heat Q_a and the share S_d of usable excess heat Q_u in the total heat demand of the building Q_d is quantified in the following according to (eq. 1) and (eq. 2).

$$S_u = \frac{Q_u}{Q_a} \qquad \text{(eq. 1)}$$

$$S_d = \frac{Q_u}{Q_d} \qquad \text{(eq. 2)}$$

On the supply side, a temperature loss of 2 K per heat exchanger and distribution losses in the pipes of 5 % are assumed. This reduces the average heat output on the building side to 334 kW at 43 °C. For the demand side, an annual load curve, mass flows and system temperatures are thermally simulated in hourly resolution using a validated building model in the software IDA-ICE 4.8. The heating loads are primarily covered by excess heat. If the temperature level of 43 °C is not sufficient, or the heating load exceeds the available excess heat capacity, the remaining heat demand is covered by district heating (Fig. 3). The calculations were first carried out with the average values of the excess heat power and temperature and in the next step with the dynamic, fluctuating measured values. For this purpose, an annual profile was extrapolated from the measured data for June and July 2022, because the HPC was operated as intended during this time period.

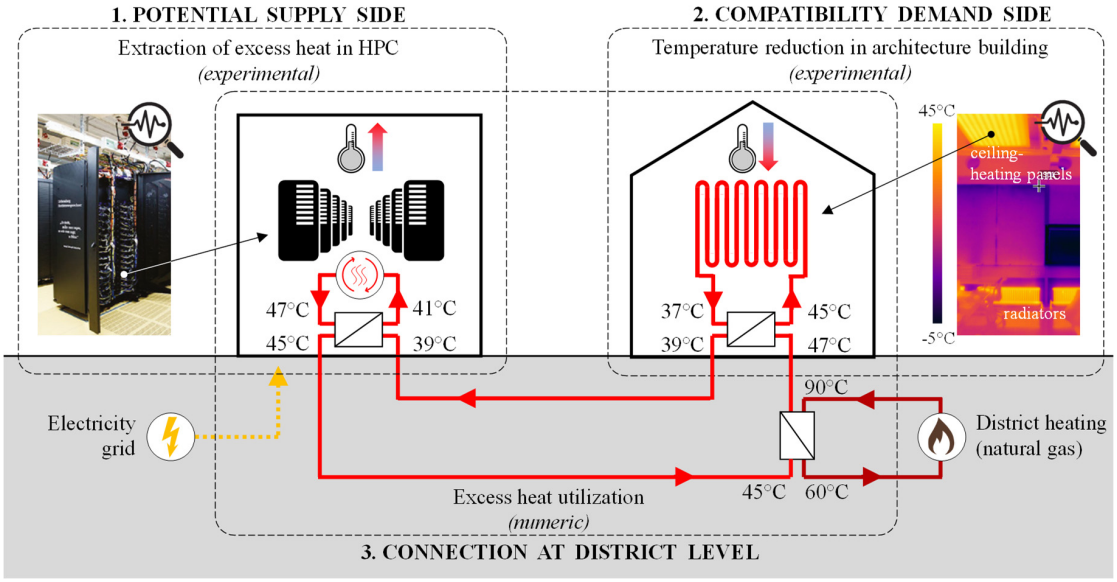

Fig. 3: Energy concept and research design of direct excess heat utilization in the architecture building

6. Evaluation and conclusion

The results show that approximately 63 % (S_d) of the total annual heat demand can be substituted directly by usable excess heat of 1,527 MWh/a. The remaining demand of 910 MWh/a (37 %) must be covered by fossil district heating. Due to the seasonal discontinuity of the heat demand approximately 52 % (S_u) of the available excess heat of the HPC can be used (Fig. 4 left). In winter, S_u reaches 98 %, but in summer S_u drops to 0 % because of non-existent heat demand. In this case, the available excess heat has to be dissipated to the environment via free cooling. In the comparison between the calculation approach with average or fluctuating values for the excess heat power and temperature, only marginal differences of less than 0.5 % are found.

Considering the unrenovated building envelope and the unchanged high heating loads, the result of this study is encouraging: By integrating low-temperature ceiling heating systems, excess heat can be efficiently integrated into the heat supply at a low temperature level and more than half (63 %) of the demand for fossil district heating can be replaced.

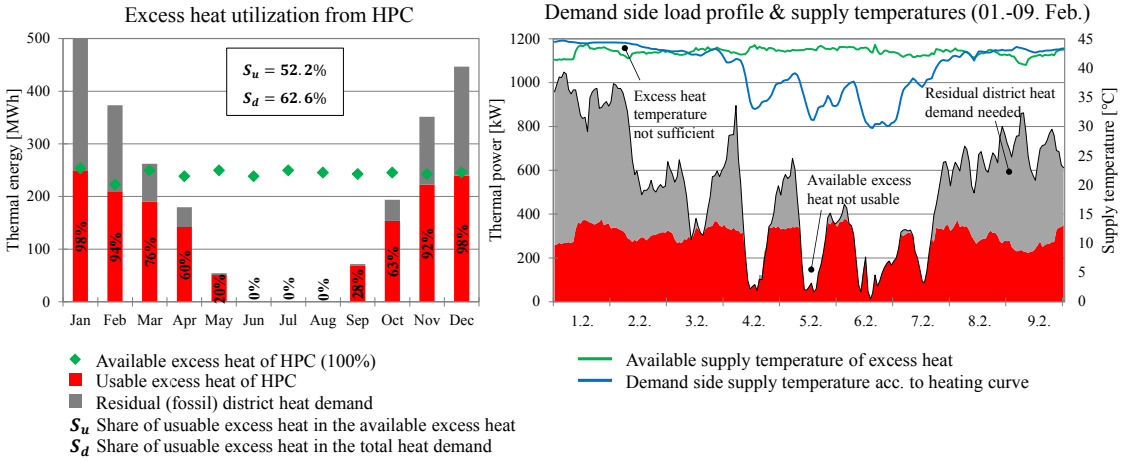

Fig. 4: Excess heat utilization from HPC (left), demand side load profile & supply temperatures (right)

The results also show, that for the decarbonization of heating networks through increased integration of renewable (excess) heat, the temperature reduction potential on the building side should also be considered. A holistic planning of district energy systems should integrate actors from the energy supplier side as well as from the building side into the planning process at an early stage.

In this case, a static calculation based on mean values is legitimate for quantifying the share of excess heat utilization and the share of heat demand covered by excess heat. The calculation considering a dynamic profile has less impact on the characteristic values than initially expected. In times of high heat demand, which have a particularly dominant effect on the characteristic values, the complete excess heat can be used regardless of whether it has a constant or fluctuating character.

Compared to solar thermal potentials, the results show a comparatively high excess heat utilization potential, since the supply profile does not show any seasonal characteristics.

7. Outlook

The knowledge gained from this study will be used to implement direct excess heat utilization of the HPC in the nearby test halls in the next phase of the research project and to determine the actually usable excess heat potential. Furthermore, it is of interest to what extent the district heating demand can be additionally reduced by increasing the degree of excess heat utilization through load shifting measures during the transitional seasons.

In the context of the rapid expansion of data center capacities, their excess heat should also be increasingly used to heat buildings. The implementation of hot-water-cooling significantly improves the possibility to do so.

More surface heating systems should be installed, especially in existing buildings, in order to be able to integrate more local renewable (excess) heat. This should also be done if a facade renovation is not (yet) possible. In the sense of a strategy of "small steps" this can be a cost-effective option on the way to complete renovation.

As an alternative to the concept described here, buildings that still require very high supply temperatures can be supplied by decentralized heat pumps that use excess heat as a heat source. This could lead to a complete substitution of fossil fuels.

Considering the excess heat availability outside the heating season, the use of a seasonal low-temperature heat storage could also increase the coverage rate of the heat demand.

8. Acknowledgements

Technische Universität Darmstadt is funded for this research by the Federal Ministry of Economic Affairs and Climate Action (BMWK) in the project “EnEff:Stadt Campus Lichtwiese” (03ET1638).

9. References

Averfalk, H. et al., 2021. Low-Temperature District Heating Implementation Guidebook. IEA DHC Report

Davies, G., Maidment, G., Tozer, G., 2015. Using data centres for combined heating and cooling: An investigation for London. Applied Thermal Engineering. 94 (2016), 296-304. doi: 10.1016/j.applthermaleng.2015.09.111

Deutsche Energie-Agentur GmbH (dena), 2021. Dena-Gebäudereport 2021-Fokusthemen zum Klimaschutz im Gebäudebereich, Berlin.

Ebrahimi, K., Jones, G.F., Fleischer, A.S., 2014. A review of data center cooling technology, operating conditions and the corresponding low-grade excess heat recovery opportunities. Renewable and Sustainable Energy Reviews 31. 622-638. doi: 10.1016/j.rser.2013.12.007

Feike, F., Oltmanns, J., Dammel, F., Stephan, P., 2021. Evaluation of the excess heat utilization from a hot-water-cooled high performance computer via a heat pump. Energy Reports 7, 70-78. doi: 10.1016/j.egyr.2021.09.038

Hintemann, R., 2020. Rechenzentren 2018. Effizienzgewinne reichen nicht aus: Energiebedarf der Rechenzentren steigt weiter deutlich an. Online. https://www.borderstep.de/wp-content/uploads/2020/03/Borderstep-Rechenzentren-2018-20200511.pdf

Lund, H., Werner, S., Wiltshire, R., Svendsen, S., Thorsen, J., Hvelplund, F., Mathiesen, B., 2014. 4th Generation District Heating (4GDH): Integrating smart thermal grids into future sustainable energy systems. Energy. 68, 1–11. doi: 10.1016/j.energy.2014.02.089.

Oltmanns, J., Sauerwein, D., Dammel, F., Stephan, P., Kuhn, C., 2020. Potential for waste heat utilization of hot-water-cooled data centers: A case study. Energy Science & Engineering. 2020 8, 1793-1810. doi: 10.1002/ese3.633

Østergaard, D. S., Svendsen, S., 2016. Replacing critical radiators to increase the potential to use low-temperature district heating – A case study of 4 Danish single-family houses from the 1930s. Energy. 110, 75–84. doi: 10.1016/j.energy.2016.03.140.

Sauerwein D., Fitzgerald N., Kuhn C., 2023. Experimental and Numerical Analysis of Temperature Reduction Potentials in the Heating Supply of an Unrenovated University Building. Energies. 16(3), 1263. doi:10.3390/en16031263

Schmidt, D., Kallert, A., Blesl, M., Svendsen, S., Li, H., Nord, N., Sipiläf, K., 2017. Low Temperature District Heating for Future Energy Systems. Energy Procedia. 116, 26–38. doi: 10.1016/j.egypro.2017.05.052.

Low Temperature District Heating as a Key Technology for a Successful Integration of Renewable Heat Sources in our Energy Systems

Dietrich Schmidt[1] and Kristina Lygnerud[2]

[1] Fraunhofer Institute for Energy Economics and Energy System Technology IEE, Kassel (Germany)

[2] IVL Swedish Environmental Research Institute, Gothenburg (Sweden)

Abstract

Low temperature district heating is a heat supply technology for efficient, environmental friendly and cost effective community supply. Moreover, it is recognized as a key technology for transforming and decarbonating heat energy systems by efficient integration of renewable energy sources as solar thermal, geothermal and other waste heat sources.

The results from the international cooperation activity IEA DHC Annex TS2 on "Implementation of Low-Temperature District Heating Systems" provide advice and recipes for obtaining lower network temperatures as well as information on other features to include in existing and new district heating systems (Averfalk et al. 2021). Accomplished by summarizing the economic benefits of low-temperature district heating and gained experiences from early adopters in various urban areas throughout Europe. Lessons learned can be applied in new and expanding district heating systems and are presented in this paper. We discuss economic benefits, temperature levels in buildings, temperature levels in district heating systems, an applied case, competitiveness of low temperature district heating and transition strategies for cities with existing district heating systems.

Keywords: Low temperature district heating, 4th generation DH, energy transition, integration of renewable heat sources

1. Introduction

In many urban areas, district heating systems are used to move heat through pipes from available heat sources to buildings and processes that require heat. Major heat sources include recycled heat from processes that have considerable amounts of residual heat (e.g. thermal power plants and industrial processes generating an excess of heat) but some heat is obtained from renewable energy sources (e.g. solar thermal systems or geothermal wells). Fossil fuels have continued to be used as a primary energy source for combustion. Future district heating systems will have market conditions that differ from those of current systems where the omission of fossil fuels is one.

It is expected that energy efficiency measures will reduce the heat demand and on the supply side, renewables and heat recycling will replace current energy generation systems that rely on processes having fossil fuels as primary energy sources. Hence, future systems will have to use upgraded district heating technology to accomplish decarbonization. An integration of renewable heat sources into the systems is an important step. To ensure efficient, renewable systems, lowering heat distribution temperatures is key.

During the last decade, the collective label 'fourth-generation district heating' (4GDH) has been used to describe these enhanced district heating systems. The overarching goal with these systems is to obtain fully decarbonized district heating systems (Frederiksen & Werner 2013). According to the 4th generation definition (Lund et al. 2014), such systems should have the following abilities:

- To supply low-temperature district heating for space heating and hot water preparation
- To distribute heat with low grid losses
- To recycle heat from low-temperature sources

© 2022. The Authors. Published by International Solar Energy Society
Selection and/or peer review under responsibility of Scientific Committee
doi:10.18086/eurosun.2022.04.12 Available at http://proceedings.ises.org

- To integrate thermal grids into a smart energy system
- To ensure suitable planning, cost and motivation

The transition from traditional district heating systems to completely decarbonized systems will support international, national, and local ambitions for decarbonization by obtaining lower CO_2 emissions. The conclusion from the EU carbon dioxide emissions reduction path is that the rate of change up to 2030 should increase more than five times compared to the previous goal for 2020 (illustrated below). Hence, the increased usage of low temperature district heating networks is important and desirable.

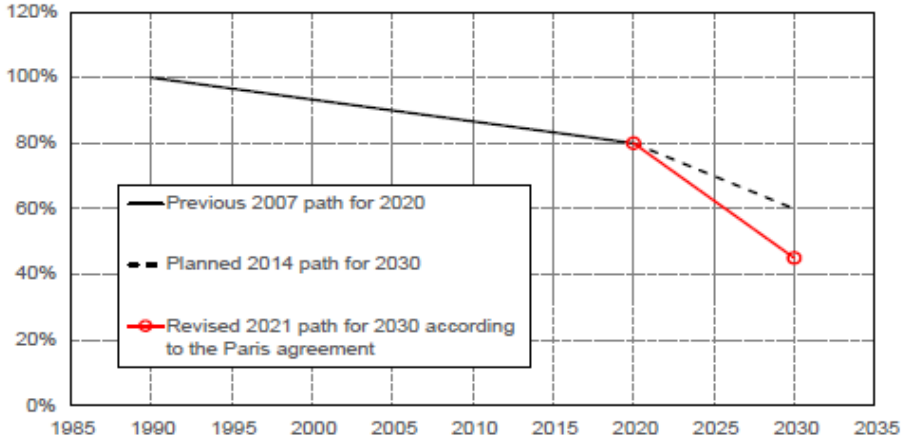

Fig. 1: Three paths for reduction of the EU carbon dioxide emissions until 2020 and 2030.

The IEA-DHC Annex TS2 definition of low temperature district heating applies to all new technological features and concepts using low temperatures, which are considered best available from 2020 onward. As experienced in previous technology generations, a wide diversity of technology choices is expected. Hence, cold district heating systems are also included in our definition of low temperature. The corresponding technology comprises all heat distribution technologies that will utilize supply temperatures below 70 °C as the annual average. 4GDH technology is a family of many different network configurations for heat distribution. Notably, cold and warm networks are siblings in this family of configurations.

2. Gains from low temperature

Heat distribution with supply temperatures below 70 °C will increase the profitability of implementing geothermal heat, heat pumps, industrial excess heat, solar collectors, flue gas condensers, and heat storage options into district heating systems.

At lower distribution temperatures, the economic benefits of renewables and recycled heat are based on the following nine efficiency gains:

1. More heat extracted from geothermal wells since lower temperatures of the geothermal fluid can be returned to the ground.
2. Less electricity used in heat pumps when extracting heat from heat sources with temperatures below the heat distribution temperatures since lower pressures can be applied in the heat pump condensers.
3. More excess heat extracted since lower temperatures of the excess heat carrier will be emitted to the environment.
4. More heat obtained from solar collectors since their heat losses are lower, thereby providing higher conversion efficiencies.
5. More heat recovered from flue gas condensation since the proportion of vaporized water (steam) in the emitted flue gases can be reduced.
6. More electricity generated per unit of heat recycled from steam combined heat and power (CHP) plants since higher power-to-heat ratios are obtained with lower steam pressures in the turbine condensers.
7. Higher heat storage capacities since lower return temperatures can be used in conjunction with high-

temperature outputs from high-temperature heat sources.
8. Lower heat distribution losses with lower average temperature differences between the fluids in heat distribution pipes and the environment.
9. Ability to use plastic pipes instead of steel pipes to save cost.

Additional benefits include a reduced risk of low-cycle fatigue for steel pipes (due to less variation in supply temperatures); smaller temperature drop in the flow direction, allowing for lower supply temperatures from heat supply plants (since less heat will be lost), and a lower risk of scalding during pipe maintenance (lethal accidents have occurred in high-temperature systems).

To quantify the cost reductions related to lower temperatures for various heat supply technologies, a key performance indicator called 'cost reduction gradient' (CRG) is used (Averfalk & Werner, 2020). Examples of CRG for different heat supply technologies are presented in Table 1.

Tab. 1: Overview of assessed economic effects, indicated with the cost reduction gradient (CRG) in euro/(MWh·°C), of reduced system temperatures

Assed heat supply technology (either by itself or dominating in a system)	Cost reduction gradient (CRG) in €/(MWh·K)	
	Investment cases when investment costs are reduced	Existing cases when operating costs are reduced
Low-temperature geothermal heat	0.45-0.74	0.67-0.68
Heat pump	0.41	0.63-0.67
Low-temperature waste heat	0.65	0.51
Solar thermal – flat plate collector	0.35-0.75	Not available
Solar thermal – evacuated tube collector	0.26	Not available
Biomass-boiler with flue gas condensation	Not available	0.10-0.13
Biomass-CHP with back-pressure turbine	Not available	0.10-0.16
Biomass-CHP with extraction turbine	Not available	0.09
Waste-CHP with flue gas condensation	Not available	0.07
Daily storage as tank thermal storage	0.01	0.07
Seasonal storage as pit thermal storage	0.07	0.07
Heat distribution losses	Not available	0-0.13

Table 1 reveals that traditional combustion processes in CHP plants without flue gas condensation have CRGs between 0.10 and 0.13 euro/(MWh·°C). In addition, corresponding CRGs for low-temperature heat sources, such as geothermal, heat pumps and waste heat, are between 0.5 and 0.7 euro/(MWh·°C). Hence, these new low-temperature heat sources have CRGs that are approximately five times higher than those for traditional heat supply.

Therefore, the cost savings for European low-temperature district heating systems is forecasted to be roughly 0.5 euro/(MWh·°C), which results in a total cost reduction potential of 14 billion euro per year, assuming the future annual EU district heat sales of 950 TWh and a temperature reduction of 30 °C. This cost reduction represents a net present value of more than 200 billion euro.

To arrive at low temperatures in the district heating systems both building and network configurations need updating. Lower temperatures in buildings is addressed first (3) then temperatures in networks (4).

3. Lower temperatures inside buildings

In most cases, district heating temperatures are higher than needed to comply with national temperature requirements to control the Legionella risk and typical comfort requirements for space heating. The main obstacles to lower district heating temperatures are the occurrences of simple malfunctions and faults in the district heating substations, and which, therefore, need to be eliminated. Additionally, proper maintenance and automatic fault detection in building substations should be applied in district heating systems (see also Averfalk et al 2021).

Legionella treatment is an area of focus when discussing low-temperature operation (Euroheat & Power, 2008;

HOFOR, 2019). The main risk of Legionella growth is often due to the poor design or operation of internal building installations. Alternatives to thermal treatment of Legionella are available, but in most existing buildings, district heating companies must rely on frequent wireless readings of energy meters to ensure the district heating supply temperature on entry to each customer is high enough to meet national requirements for the thermal treatment of Legionella in domestic hot water installations.

For the long term, energy renovations will enable lower district heating temperatures by reducing the heat demands in existing buildings and, therefore, reducing the space heating temperatures needed in commonly over-sized existing heating systems. The clever design of new heating installations (in existing and new buildings) using robust components will allow for lower temperatures in the future (Østergaard & Svendsen 2016, Østergaard & Svendsen 2017).

Longer thermal lengths in heat exchangers (Averfalk & Werner, 2017). Legionella-safe supply of domestic hot water and the automatic balancing of space heating systems are crucial for low temperature heating. Current, best-available technologies in this regard include externally accessible flat stations for domestic hot water supply and smart return temperature thermostats with automatic balancing functionalities.

For the design of new space heating systems and domestic hot water installations, new standards are needed to address the use of low-temperature heating based on renewable heat sources in the future. Research is needed to develop more solutions to provide Legionella-safe and comfortable domestic hot water without the current high heat requirement (Schmidt et al. 2017).

4. Lower temperatures in heat distribution networks

Five major takeaways have been identified in regards to lower temperatures in heat distribution networks (Averfalk & Werner 2018, Averfalk et al. 2021).

(1) Before investing in any improvement measure, it is necessary to compare customer supply temperatures requirements with the primary supply side temperatures. In some cases, the critical supply temperatures needed by customers and those provided by the district heating network do not match. This happens because the district heating operator does not know the exact supply temperature required by customers and, thus, ensures that the temperature supplied is never below that needed to guarantee comfort.

(2) When replacing existing substations or when designing new ones, heat exchangers with longer thermal lengths should be preferred as these will enable to obtain low supply and return temperatures.

(3) Many systems have already started their transformation to lower temperatures, demonstrating the wide range of possibilities and proven solutions that exist. However, it is important to maintain focus to avoid undermining improvement efforts.

(4) All temperature reduction experiences should be utilised; this means taking advantage of the lessons learned by forerunners and the knowledge transfer that occurs within the district heating community.

(5) Low-temperature systems contribute to the reduction of greenhouse gas emissions. Targeted policy instruments and effective subsidies enable accelerated transformation. It is particularly important to raise awareness and sensitize political decision-makers to the necessity of low-temperature systems, especially given current energy policy frameworks hardly address their importance.

5. Darmstadt applied study

An applied study of temperature reduction in the district heating network at TU Darmstadt's Campus Lichtwiese served as a showcase of an existing district heating system and is equally applicable to many other district heating systems. The study shows that operational errors within the building heating infrastructure lead to considerable increases in the network temperatures and that problems in a few buildings can have a significant impact on the entire network. In addition, addressing the most critical issues helps to reduce network temperatures considerably, especially on the return side (Oltmanns et al. 2018).

The study also reveals a major barrier: as long as the heat generation in a district heating system is realized via

CHP plants and boilers, reduced network temperatures will not immediately improve cost because many benefits presented in Section 2 do not apply to a fossil- based energy system. Additionally, renewable heat sources, such as geothermal, solar thermal or local waste heat, are low-temperature heat sources, which are neither economically nor energetically feasible in high temperature district heating systems. In a high-temperature district heating network, low-temperature renewable heat can only be integrated using a heat pump at low efficiencies, resulting in high electric energy demands. For an effective transition from fossil-based to renewable district heating, a transition from high-temperature district heating to low-temperature district heating is first necessary (Oltmanns et al. 2020).

6. Competitiveness of low-temperature district heating

Increased operational efficiency from lower system temperatures and optimized technical configurations for low-temperature heat distribution are frequently discussed. Less discussed are the competitive advantages of low-temperature solutions. Therefore, this paper addresses how a stand-alone low-temperature district heating solution, or a combination of conventional district heating and low-temperature solutions can increase the overall competitiveness of the district heating business case. First, an overall business model perspective and a national viewpoint are presented. The discussion is concluded with a more detailed analysis of the heat distribution cost in the low-temperature district heating context.

From an overall perspective, traits in low-temperature district heating business models can be complementary to the conventional district heating model. The selling point of a combination for an existing district heating system or of a stand-alone solution in greenfield investments is that local resources are used, minimizing the carbon footprint. In an era of increased digitalization, engaging in dialogue and establishing long-term relationships are valuable, an upside for the low temperature district heating prosumer relationship (Lygnerud, 2019).

The market maturity of low-temperature district heating is low, and as such, an emphasis is placed on ensuring functional, technical solutions rather than a simultaneous development of the business case. For future installations, tandem development is recommended.

Retaining heat distribution costs in district heating systems at feasible levels is vital to maintain competitiveness. The most significant component of the heat distribution cost is the specific capital cost that is higher in low heat density areas. Second is the cost of the heat distribution loss. But only the latter cost can be considerably reduced by low-temperature heat distribution, since only the ability to use plastic pipes can reduce the capital cost for LTDH.

Furthermore, LTDH should be able to be supplied (input at heating plants) with heat from low-temperature heat sources, which are expected to yield a lower heat generation cost. In low heat density areas, lower heat generation costs and lower heat distribution losses obtained by LTDH cannot completely compensate higher specific capital costs. Hence, it is impossible to increase the total competitiveness of district heating with LTDH in low heat density areas.

7. Practical implementation of low-temperature district heating

The introduction and application of new concepts and technologies, such as low-temperature district heating, often face concerns of feasibility and reliability. The earlier sections discuss measures to be taken on a building and system level and show the various technical and economic benefits of low-temperature district heating. This sections highlights that many innovative low-temperature district heating systems have already been built and operate successfully.

The demonstrators considered in this paper include various system configurations and different boundary conditions such as already realized low temperature community energy system concepts as well as planned or designed systems. Furthermore, projects showing an innovative use or operation of buildings, advanced technologies and the interaction between components within a system are included.

In total six classes of demonstrators have been identified. As they are:

- realized demonstration project on existing or conversion areas with an existing heating network
- realized demonstration project on existing or conversion areas with a new heating network
- realized demonstration projects on new constructed areas with a new heating network
- simulation and design studies on areas
- realized demonstration projects on the single building scale
- demonstrators on a laboratory scale

15 selected demonstration activities out of 40 within Europe were analyzed in detail. Cases from other countries are included in the guidebook (Averflak et al. 2021). Figure 1 shows all collected demonstration cases within Europe. Additionally to that, a gross list with approx. 150 realized low temperature district heating systems all over the world were collected (see Averfalk et al. 2021). This impressively proves the feasibility and applicability of LTDH technology.



★ Cases analysed in detail and presented (see table 2)
● Cases analysed in detail in this project (see Averfalk et al 2021)
○ Cases described in the gross list of low-temperature initiatives (see Averfalk et al 2021)

Fig. 1: Locations of the regarded demonstrator cases. © Fraunhofer IEE, own representation. Map taken from Eurostat: https://ec.europa.eu/eurostat

Tab. 2: Selected and described demonstrators for the implementation of low temperature district heating systems.

City and Area	*Country*	*Class*	*Temp. level*[1]	*Heat Supply*	*System size*[2]
Gleisdorf Transition strategy	Austria		Warm (80/50°C)	biomass & gas boilers, solar collectors	Medium (6,374 m)
Wüstenrot Weihenbronn	Germany		Warm (70/40°C)	Biomass boiler, solar collectors	Micro (371 m)
Darmstadt Lichtwiese	Germany		Warm (88/58°C)	District heating-cooling with absorption chiller	Medium (4,200 m)
Heerlen Parkstad Limburg	The Netherlands		Cold (28/16°C)	Mine water	Big (40 km)
Zürich FGZ	Switzerland		Cold (<25°C)	Data centre	Small (2,125 m)
Salzburg Lehen	Austria		Warm (65/40°C)	Solar collectors, heat pump, district heating	Small (680 m)
Graz Reininghaus	Austria		Warm (69/43°C)	Industrial excess heat, heat pump	Medium (6,000 m)
Braunschweig Rautheim	Germany		Warm (70/40°C)	Data centre	Small (2,750 m)
Lund Brunnshög	Sweden		Warm (65/35°C)	Excess heat from research facilities	Medium (6.5 km)
Kassel Feldlager	Germany		Cold (40/30°C)	ATES, GSHP and solar collectors	Medium (5.7 km)
Bamberg Lagarde	Germany		Cold & Warm (1- -2/80-50)	GSHP, sewage, CHP, district heating	Small (1,200 m)
Bjerringbo Tyttebærvej	Denmark		Warm (50/30°C)	Industrial excess heat, ATES, heat pump	n.a.
Viborg Multifamily home	Denmark		Warm (68/40°C)	District heating	Big (344.8 km)
Frederiksberg Multifamily home	Denmark		Warm (80/48°C)	District heating	Big (181.5 km)
Kassel District LAB	Germany		Cold & warm (5-130/varying°C)	Heat pump, boiler	Micro (390 m)

Core objective for the description of case studies was to identify and collect innovative demonstration concepts as examples of success stories for communities interested in developing LTDH systems. There was a total of 40 case studies from Austria, Denmark, Germany, Ireland, Norway, Switzerland, Sweden, The Netherlands and United Kingdom (see Averfalk et al. 2021). The district heating systems were of very different sizes, from miniature to city wide systems. Network lengths were from approx. 370 m to more than 340 km. The connected buildings were detached, terraced and block houses, and many low energy or passive houses. Sources of heat were solar collectors, heat pumps, CHP plants, excess heat from industry or the systems were connected to a larger network close by with heat exchangers. The temperature levels recorded were typical for cold and low-temperature systems, varying from -2 to 88 °C in supply and 16 to 58 °C in return. Savings and increased efficiencies were observed in every case studied.

Particularly from the displayed case studies, the following main conclusions can be drawn:

- From a technical point of view, the large variety of system configurations shows the flexibility in the implementation and realization of low-temperature district heating systems. For the operation, a sufficient monitoring and management system secures the success of the project. For the integration of multiple heat sources and more complicated systems, a wider digitalization of the processes is needed.
- The regulatory boundary conditions are not always beneficial. So, for example, the integration of geothermal heat requires a long (or too long) approval process, which can potentially derail the implementation. Furthermore, real cross-sectoral energy systems are not foreseen with today's rules, which makes a realization complicated.

[1] Typical/mean supply and return temperature
[2] Trench length

- The cases clearly show that a high connection rate and support from the customer could be gained when the system is owned by the municipality or a cooperative.
- From a business point of view with the above-mentioned ownership issue, interest rates might be lower, and long payback times are manageable. Some cases show that a transition to low-temperature district heating systems is economically feasible; some cases indicate the price level for the heat supply could be up to 10% lower compared to a conventional solution, even without accounting for future damage cost from global warming.

These conclusions prove that low-temperature district heating is a market-ready heat supply technology that can operate under various boundary conditions. Furthermore, case experiences show the need for digitalization measures to secure a successful operation under the new boundary conditions, such as the integration of fluctuating renewable or waste heat sources or changed network (bidirectional) operation.

8. Transition strategies

The essence of conversion, transformation and transition is that all humans are capable of profound change. Required changes in our communities can be initiated, communicated, and implemented by three steps – (1) visions, (2) strategies and (3) planning measures. Changes to our energy system should also be identified at all levels in our global community. Although changes are necessary and inevitable in all areas, they are often accompanied by concerns. The eighth chapter shows how local transition strategies have addressed these apprehensions in some urban areas.

Adopted visions, strategies, and planning measures from five urban areas are presented when the heat distribution temperature issue is properly identified within the decarbonization context (Stadt Gleisdorf, 2012, AEE INTEC, 2020, Abildgaard, 2017, Regieringsrat des Kantons Basel-Stadt, 2017, Küng, 2019, Secretariat du Grand Conseil, 2013, Quiquerez et al. 2017, Durandeux, 2019, Henke et al. 2015, Frey & Miller, 2017, Stadtwerke München, 2017, Theis, 2019). The three steps are vital to implementing district heating and cooling systems based on renewable or recycled heat or cold in every urban area. Additional university examples are briefly provided since some universities are forerunners in low-temperature district heating.

The major conclusions concerning visions, strategies, and planning measures within the local transition strategies are the following:

- Lower distribution temperatures are necessary in transition strategies for the decarbonization of district heating systems.
- Cooperation with research organizations should be considered when new technologies are implemented in local district heating systems.
- University campuses are often forerunners with new technologies for heat distribution.

9. Conclusions

Conclusions about technological development, nontechnical aspects, and policy implications, along with recommendations, are summarized here.

Tangible proper technologies and methods are available for the implementation of low-temperature district heating. Early adopters have tested and implemented lower temperatures in existing and new heat distribution networks. Building owners can and should adopt the technology now for the utilization of lower temperatures in the future. Reductions of specific heat demands will also facilitate lower temperatures. However, current technologies and methods can be further elaborated and refined by research and development.

The primary non-technical barrier to undertaking a low-temperature district heating investment is the resistance to change. One major factor that can explain the limited interest in future-proof low-temperature district heating technology is that the risk of limited heat supply in 2050, since current fossil fuels will not be available, has not yet become apparent for most end users and heat providers.

The economic benefit of low-temperature district heating can reduce the levelized cost of heat from future district heating systems, but the savings in current systems is limited. Hence, this advantage is not now strong enough

alone to encourage a transition towards more decarbonized district heating systems. Carbon pricing or other efficient policy drivers must be used as strong parallel economic drivers for incentivizing decarbonization. In addition, old institutional rules require proper revision for better alignment with low-temperature district heating.

Low-temperature district heating is easier to implement than many people fear, but adequate organization is required. In the transition work, long term visions express the future direction for the decarbonization, short and long term strategies identify what to do, and short and long term planning measures outline the steps to take.

The three main conclusions from the published guidebook from IEA DHC Annex TS2 (Averfalk et al 2021) are the following:

- Low-temperature district heating together with expected national carbon pricing schemes are major economic drivers for the decarbonization of the European district heating systems.
- The implementations of low-temperature district heating are possible since several early adopters have provided clear evidence for its suitability.
- However, the hurdles to start the transition are old habits and lock-in effects from application of current technology together with a lack of understanding of how to efficiently link stakeholders to each other.

10. Acknowledgments

The here presented results of the work within the IEA DHC Annex TS2 has been a collaborated effort from all participants. The authors and all participants would like to thank the various involved national funding agencies and industry partners for funding this research.

11. References

Abildgaard, M. (2017). Data Centers and 4GDH in practice - the case of Viborg. Paper presented at the 3rd International Conference on Smart Energy Systems and 4th Generation District Heating, 12-13 September, Copenhagen. https://www.4dh.eu/ images/VF_-_Data_Centers_and_4DH_in_practice.pdf

AEE INTEC. (2020). THERMAFLEX - Thermal demand and supply as flexible elements of future sustainable energy systems. Retrieved from https://www.aee-intec.at/thermaflex-thermal-demand-and-supply-as-flexible-elements-of-future-sustainable-energy-systems-p238

Averfalk, H., & Werner, S. (2017). Essential improvements in future district heating systems. Energy Procedia, 116, 217–225. https://doi.org/10.1016/j.egypro.2017.05.069

Averfalk, H., & Werner, S. (2018). Novel low temperature heat distribution technology. In Energy 145 (2018) (S. 526-539). ELSEVIER.

Averfalk, H., & Werner, S. (2020). Economic benefits of fourth generation district heating. Energy, 193, 116727. doi:https://doi. org/10.1016/j.energy.2019.116727

Averfalk, H., Benakopoulus, T., Best, I., Dammel, F., Engel, C., Geyer, R., Gudmundsson, O., Lygnerud, K., Oltmanns, J., Nord, N., Ponweiser, K., Schmidt, D., Schrammel, H., Østergaard, D. S., Svendsen, S., Tunzi, M., & Werner, S. (2021). Implementation of Low-Temperature District Heating Systems. A Guidebook from the IEA Technology Collaboration Programme on District Heating and Cooling including Combined Heat and Power, Final report of IEA DHC|CHP Annex TS2, Fraunhofer Publisher, Stuttgart, Germany

Durandeux, S. (2019). Abaissement des pics de demande dans les reseaux thermiques. SVGW Fachtagung Fernwärme October 31. https://www.aquaetgas.ch/aktuell/branchen-news/201912- 11-fernw%C3% A4rmetagung-bern-2019/

Euroheat & Power. (2008). Guidelines for District Heating Substations

Frederiksen, S., & Werner, S. (2013). District Heating and Cooling. Sweden: Studentlitteratur, page 408.

Frey, J., & Miller, A. (2017). The Munich renewable energy strategy. https://www.ca-eed.eu/content/download/3956/file/Dis-trictHeatingVision2040-StadtwerkeMuenchenSWM.pdf/ attachment

Henke, S., Kröper, T., Spannig, J. (2015). EnEff:Wärme | LowEx-Systeme: Breitenanwendung von Niedertemperatur-Systemen für eine nachhaltige Wärmeversorgung. Retrieved from https://www.agfw-shop.de/agfw-fachliteratur/lowex-systeme-breitenanwendung-von-niedertemperatur-systemen.html

HOFOR. (2019). Typiske fejl i varmekælderen [Common malfunctions in the district heating substation].

Küng, M. (2019). Eröffnungsreferat - Basel Fernwärme. SVGW Fachtagung Fernwärme October 31. https://www.aquaetgas.ch/ aktuell/branchen-news/201912-11-fernw%C3%A4rmetagung-bern-2019/

Lund, H., Werner, S., Wiltshire, R., Svendsen, S., Thorsen, J.E., Hvelplund, F. & Mathiesen, B.V. (2014). “4th Generation District Heating (4GDH) Integrating smart thermal grids into future sustainable energy systems”. Energy 68 (2014): 1-11

Lygnerud, K. (2019). Business Model Changes in District Heating: The Impact of the Technology Shift from the Third to the Fourth Generation. Energies, 12(9), 1778.

Oltmanns, J., Freystein, M., Dammel, F. & Stephan, P. (2018). Improving the operation of a district heating and a district cooling network. In: Energy Procedia 149, pp. 539-548, 2018.

Oltmanns, J., Sauerwein, D., Dammel, F., Stephan, P., Kuhn, C. (2020). Potential for waste heat utilization of hot-water-cooled data centers: A case study. Energy Science & Engineering, 8(5), 1793–1810. DOI: https://doi.org/10.1002/ese3.633.

Østergaard, D. S. & Svendsen, S. (2017). Space heating with ultralow-temperature district heating - a case study of four single-family houses from the 1980s. In: Energy Procedia, Vol. 116, 2017, p. 226-235.

Østergaard, D. S., & Svendsen, S. (2016). Theoretical overview of heating power and necessary heating supply temperatures in typical Danish single-family houses from the 1900s. Energy and Buildings, 126, p. 375–383. https://doi.org/10.1016/j.enbuild.2016.05.034

Quiquerez, L. (2017). Transformation Roadmap from High to Low Temperature District Heating Systems. IEA-DHC TC annex 11. Retrieved from https://www.iea-dhc.org/fi¬leadmin/documents/Annex_XI/IEA-DHC-Annex_XI_Transfor-mation_Roadmap_Final_Report_April_30-2017.pdf

Regierungsrat des Kantons Basel-Stadt. (2017). Energieverordnung 772.110, Verordnung zum Energiegesetz vom 29. August. Retrieved from https://www.gesetzessammlung.bs.ch/ frontend/versions /pdf_file_with_annex/4540

Schmidt, D. & Kallert, A. (ed.) (2017). Future Low Temperature District Heating Design Guidebook Final Report of DHC Annex TS1. ISBN 3-899999-070-6, AGFW Project Company, Frankfurt am Main, Germany

Secrétariat du Grand Conseil. (2013). Rapport du Conseil d’Etat au Grand Conseil sur la conception générale de l’énergie 2005- 2009 et projet de conception générale de l’énergie 2013. RD986 Retrieved from http://ge.ch/grandconseil/data/texte/ RD00986.pdf

Stadt Gleisdorf, 2012, Aktionsplan für nachhaltige Energie (Action plan for sustainable energy). Retrieved from https://mycovenant.eumayors.eu/docs/seap/3264_1386074394.pdf

Stadtwerke München. (2017). Shaping the heating turnaround: District heating - 100 percent renewable. Retrieved from htt-ps://www.swm.de/dam/swm/dokumente/english/district-heating-shaping-turnaround.pdf

Theis, A. (2019). Renewable District Heating for Munich. Paper presented at the Konferenz zum Thema Städte als Akteure der Energiewende. Paris 13. März. https://energie-fr-de.eu/de/veranstaltungen/leser/konferenz-zum-thema-staedte-als-akteure-der-energiewende.html

Integration of Different Solar Collectors into District Heating Networks and Floor Space Allocation

Maximilian Stahlhut[1], Cornelius Ackermann[1] and Thorsten Urbaneck[1]

[1] Chemnitz University of Technology, Department of Mechanical Engineering, Professorship Applied Thermodynamics, 09107 Chemnitz (Germany)

Abstract

For the direct integration of solar thermal systems into district heating networks many collectors with different design and thermal behavior are possible. This paper investigates four suitable collectors under different operating temperatures ($T_{DH,sup}$ = 95…140 °C) representing different generations of district heating networks. A flat-plate collector, a compound parabolic concentrator (CPC) collector and two parabolic trough collectors (PTC) were modeled in TRNSYS and simulated over a period of one year in three different scenarios and with different collector row distances. To determine a favorable collector, the heat production cost was calculated for the four collectors. The results show that in the investigated temperature range the CPC collector is the most suitable one. Depending on the defined scenario the CPC collector provides a specific annual yield (based on gross area) of 460…565 kWh m^{-2} a^{-1} with heat production cost of 33.41…40.85 € MWh^{-1}. This indicates that for most district heating applications the CPC collector is favorable.

Keywords: solar thermal, collector, field, shading, district heating, simulation, cost, floor space utilization

1. Introduction

Integration of collector fields into district heating (DH) networks is possible in various ways. A common variant is to build a solar secondary network. This integration is particularly recommended when planning new urban areas or developing neighborhood concepts, since the heating technology of the new buildings can be adapted to the lower temperatures of the solar local heating network. The low supply temperatures (e.g. $T_{DH,sup}$ = 75 °C in the solar local heating network in Chemnitz (Urbaneck et al., 2020) enable efficient use of flat-plate collectors (FPC). However, the construction of a suitable local heating network is not always feasible. In many cases, the solar heat must be fed into the existing network with supply temperatures varying from $T_{DH,sup}$ = 95…140 °C. Since heat supply with FPCs becomes increasingly inefficient at high temperature levels, these non-concentrating collectors are hardly used in district heating systems above 95 °C. For low and medium temperature ranges (100…150 °C) the stationary compound parabolic concentrator (CPC) collector and the parabolic trough collector (PTC) with single-axis tracking are suitable (Giovannetti and Horta, 2016). Both collectors have already been integrated in DH networks (Tian et al., 2018; Perers et al., 2013; Meißner and Moschke, 2016). Nonetheless, a comparison of the different solar collectors in terms of suitability for DH applications is not yet available. In this work a FPC, a CPC collector and two PTCs are modeled in the simulation software TRNSYS (Klein et al., 2017). Three scenarios are introduced which represent different operating conditions of the DH network. For comparing the collectors, they are simulated over the period of one year in three scenarios and with different floor space utilizations f_{col}. To determine a favorable collector and an optimal floor space utilization, the method of minimal heat production cost was applied.

2. Modeling in TRNSYS

2.1 Solar collectors

In this study, four commercially available collectors were modeled. The selection is intended to represent different collector setups which are suitable for low and medium operating temperatures. The modeling of the solar collectors includes one FPC *collector A)*, one CPC *collector B)* and two PTCs *collector C)* and *collector D)*. The two PTCs collector C) and collector D) differ by their concentration ratio *C*. *C* is the ratio of the aperture to the absorber surface. In principle, an increasing concentration ratio allows higher collector temperatures. Collector D) has a higher concentration ratio (*C* = 15) than collector C) (*C* = 8.5). The efficiency parameters of the collectors are summarized in Table 1. The quasi-dynamic collector model according to the European Standard EN 12975-2 (CEN, 2006) was

© 2022. The Authors. Published by International Solar Energy Society
Selection and/or peer review under responsibility of Scientific Committee
doi:10.18086/eurosun.2022.04.13 Available at http://proceedings.ises.org

used (Equation 1). The incidence angle modifier (IAM) for the beam radiation is summarized in the Appendix. The parameters a_3, a_4, a_5 and a_6 are not considered in the calculations (wind influence on heat losses, irradiance dependence on heat losses and thermal capacitance).

Tab. 1: TRNSYS Types for solar collectors and collector efficiency parameters based on gross area (K_d for collector B) is calculated in Type 71),

Collector	TRNSYS	η_0	a_1 [W m^{-2} K^{-1}]	a_2 [W m^{-2} K^{-2}]	K_d
A) FPC	Type 1289	0.763	1.971	0.015	0.873
B) CPC	Type 71	0.627	0.531	0.003	Type 71
C) PTC with C = 8.5	Type 1288	0.697	0.730	0.000	0.120
D) PTC with C = 15	Type 1288	0.717	0.107	0.001	0.000

$$\dot{q}_{\mathrm{col}} = \eta_0\left(K_{\mathrm{b}}G_{\mathrm{b,tilt}} + K_{\mathrm{d}}G_{\mathrm{d,tilt}}\right) - a_1(T_{\mathrm{m}} - T_{\mathrm{a}}) - a_2(T_{\mathrm{m}} - T_{\mathrm{a}})^2 \qquad \text{(eq. 1)}$$

The stationary collectors collector A) and collector B) are positioned with an azimuth of γ_{col} = 180° and a surface tilt of β = 35°. The two PTCs collector C) and collector D) are operated with a continuous single-axis tracking to reduce the incident angle Θ,i on the collector surface. In principle, a distinction can be made between two tracking variants for single-axis tracking:

- alignment of the collector axis in north-south direction (N-S) with a continuous tracking from east to west,
- alignment of the collector axis in east-west direction (E-W) with a continuous change of the surface tilt.

By changing the tracking angle β with the position of the sun, the angle of incidence in the transverse plane to the absorber tube is continuously zero degrees. An angular deviation is only perceivable in the longitudinal plane.

A deviation from the optimal angle of incidence Θ,i = 0° leads to a lower usable radiation fraction and thus to so-called cosine losses. The cosine losses result from a non-optimal angle of incidence of the beam radiation on the collector surface, whereby the relationship according to Equation 2 applies.

$$G_{\mathrm{b,tilt}} = G_{\mathrm{b},\Theta,\mathrm{i}=0°} \cdot cos\Theta,\mathrm{i} \qquad \text{(eq. 2)}$$

Figure 1 shows the beam irradiation for the collectors with a fixed surface tilt of β = 35° and for the PTCs with a continuous single-axis tracking in N-S and E-W alignment. Figure 1 further provides the direct normal irradiation (DNI). DNI is the amount of solar radiation received if the collector plane is always held perpendicular to the solar beam rays (no cosine losses). It can be seen that the tracking increases the amount of usable beam irradiation. The N-S orientation has advantages in the summer period, while the E-W orientation can use more beam irradiation in winter. For Chemnitz (Germany) the N-S orientation is preferable due to lower cosine losses. Therefore, this orientation is favored in the further study.

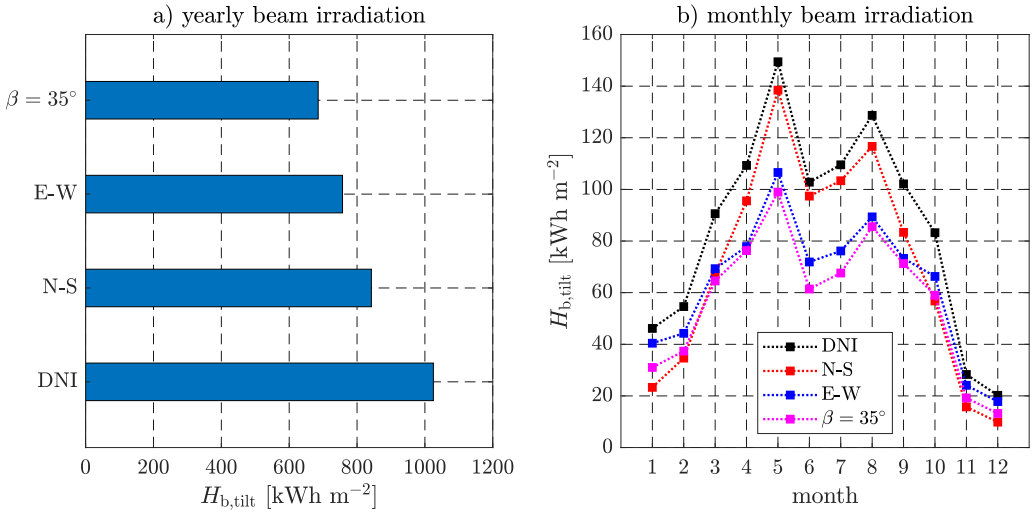

Fig. 1: Yearly and monthly beam irradiation for a fixed surface tilt of β = 35° and γ_{col} = 180°, continuous tracking with E-W alignment, continuous tracking with N-S alignment and DNI

2.2 Collector array shading

An essential aspect in the planning of a collector field is the consideration of collector array shading. These shading losses vary with the altitude and the azimuth of the sun and are significantly influenced by the collector tilt and the floor space utilization f_{col}. The floor space utilization is defined by the ratio between the distance of two collector rows and the collector length. It indicates how much of the field area is used by the solar collectors. As f_{col} increases, the distance between the collector rows decreases and the losses due to shading rise.

Figure 2 shows the losses due to row shading (exemplary for October 21) for different floor space utilizations for non-tracking ($\beta = 35°$) and single-axis tracking collectors with N-S alignment. The calculations were performed using TRNSYS and the Type 30 (TRNSYS model) for the non-tracking collectors A) and B), and using the Type 1262 for the tracking collectors C) and D) with N-S alignment. It can be seen that the shading curves differ significantly.

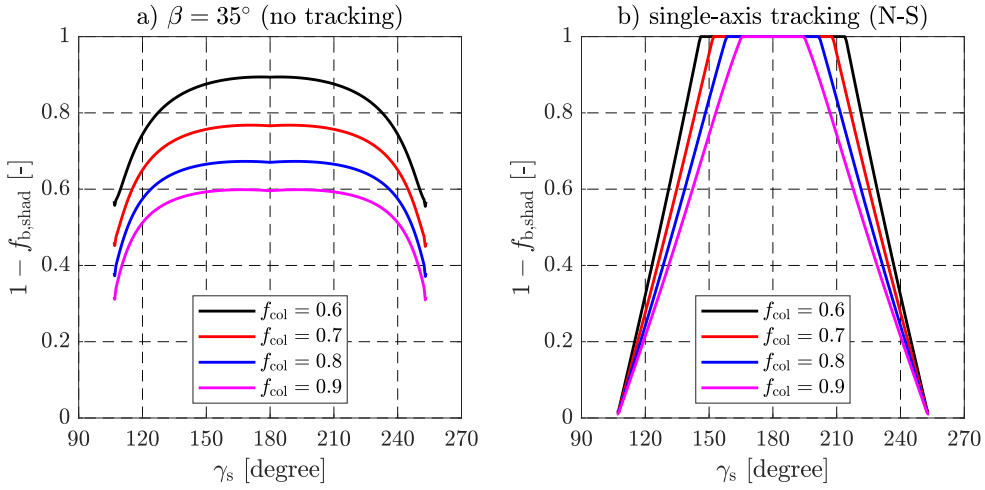

Fig. 2: Influence of collector array shading on October 21 for a) non-tracking collectors with $\beta = 35°$ and $\gamma_{col} = 180°$ and b) single-axis tracking with N-S alignment

In the morning and evening hours, the relative shading losses $f_{b,shad}$ dominate for the tracking collectors C) and D). At maximum solar elevation, no shading losses occur for the tracking collectors regardless of the floor space utilization. At this time of the day the tracking collectors are in a horizontal position. In the case of the collectors A) and B) with a fixed slope, shading losses can also occur at midday, depending on the elevation of the sun and the distance between the collector rows.

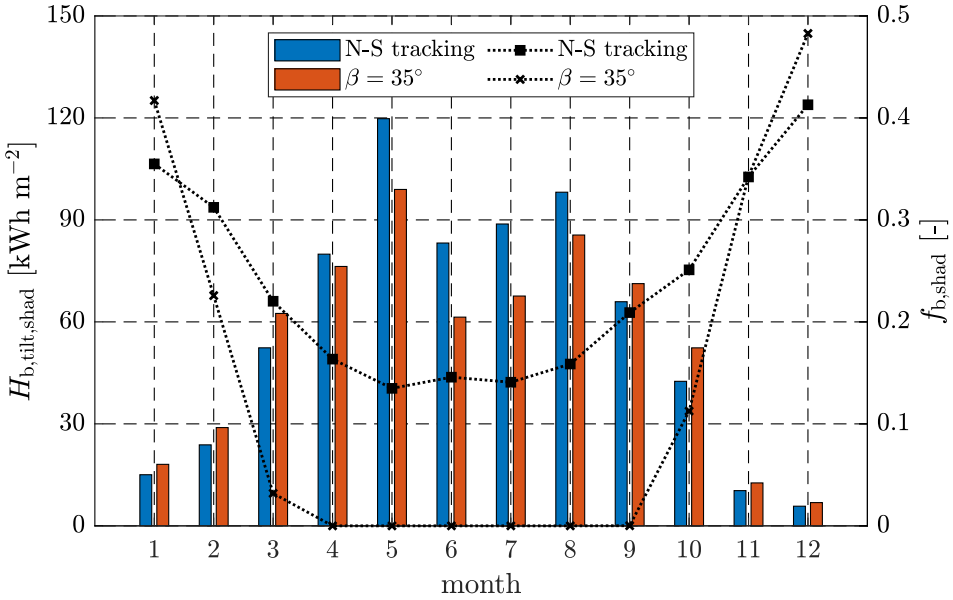

Fig. 3: Beam irradiation subtracted by shading losses for non-tracking ($\beta = 35°$ and $\gamma_{col} = 180°$) and tracking collectors (N-S) for $f_{col} = 0.6$

Figure 3 shows the beam irradiation subtracted by the shading losses for the non-tracking and tracking collectors for $f_{col} = 0.6$. In the summer months the collectors C) and D) cannot use 10…20 % of the beam irradiation due to shading losses. For the collectors A) and B) only a small amount of shading occurs in the months March to September. In total, 6% of the annual beam irradiation is shaded for collectors A) and B) and 18% for collectors C) and D). Figure 4 illustrates the reason for the higher shading losses. Despite the greater shading losses for the two PTCs, the usable beam irradiation is greater than for the non-tracking collectors due to fewer cosine losses.

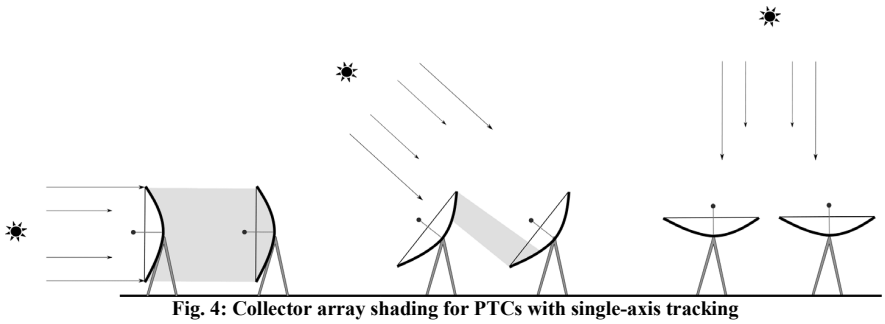

Fig. 4: Collector array shading for PTCs with single-axis tracking

2.3 District heating network

The four collectors were modeled in the simulation program TRNSYS in a system according to Figure 5. The heat transfer medium is taken from the return line of the DH network and heated by the solar system and then fed into the supply line of the DH network. The outlet temperature of the collector is set, so that the supply temperature of the DH network is reached. If the outlet temperature is too small, the three-way valve TWV1 is in position 2 and the collector fluid is preheated.

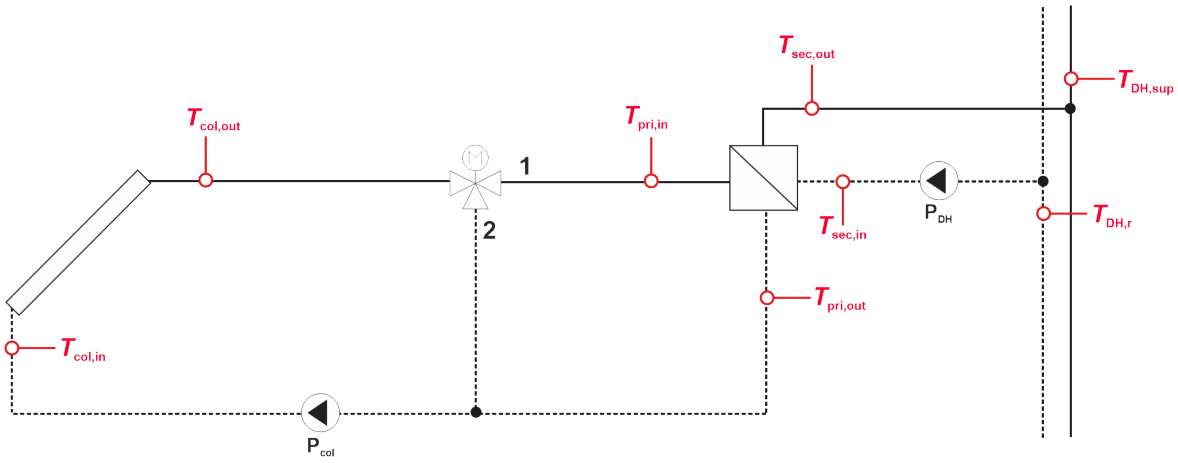

Fig. 5: Hydraulic scheme for solar collectors with direct integration in the DH network

The system in Figure 5 was simulated over a period of one year. Two weather data sets (test reference year, TRY) for Chemnitz (Germany) are used within the scope of this study: current TRY (2015) and a forecast TRY (2045). Both data sets were obtained by the online databank of the DWD (2021). The ambient temperature as well as the irradiation in the weather dataset for the year 2045 is slightly increased compared to the current weather data set. Furthermore, the proportion of the yearly beam irradiation is higher in TRY 2045. This weather dataset intends to map the impact of climate change.

For considering different operating temperatures of the DH system three scenarios are introduced:

Scenario 1 assumes an operation with a continuous adjustment of the supply temperature according to the outdoor temperature:

- $T_{DH,sup} = 110$ °C if $T_a < -10$ °C and $T_{DH,sup} = 95$ °C if $T_a \geq 15$ °C, in between linear interpolation
- $T_{DH,r} = 55$°C = constant

This is a possible future scenario, which is why the weather data set for the year 2045 was used for the simulation. In this scenario, the supply and return temperatures of the DH networks are the lowest compared to the other scenarios.

In *Scenario 2*, there is a monthly adjustment of the supply and return temperature:

- January to March and October to December $T_{DH,sup}$ = 120 °C and $T_{DH,r}$ = 62 °C
- April to December $T_{DH,sup}$ = 100 °C and $T_{DH,r}$ = 70 °C

This scenario reflects a typical contemporary grid operation with relatively low temperatures. The current weather data set is used.

Scenario 3 also uses a monthly adjustment of the supply and return temperatures:

- January to March and October to December $T_{DH,sup}$ = 140 °C and $T_{DH,r}$ = 65 °C
- April to December $T_{DH,sup}$ = 120 °C and $T_{DH,r}$ = 70 °C

However, higher grid temperatures are assumed. Since this is a representation of the current situation, the simulation also uses the current weather data set.

2.4 Heat production cost

For the selection of an optimal floor space utilization, a simplified economic evaluation is carried out on the basis of minimum heat production costs with the annuity method according to VDI 2067 (VDI, 2012). A technical utilization period of the entire plant of 25 years and an interest rate of 1 percent per year are assumed. The demand-related costs refer to the electricity consumption of the pumps and take into account an electricity price of k_{el} = 0.30 € kWh^{-1}. The operation-related costs can arise, among other things, from maintenance and servicing of the system. The operation-related costs are given in VDI 6002 (VDI, 2014) as approximately 1 percent of the investment costs. For the two parabolic trough collectors, the annual operating costs are estimated at about 3 percent of the investment costs. Due to the tracking as well as a possible cleaning of the reflectors, the operating costs assumed higher for this collector design.

The investment costs (excluding the costs for collectors) are supposed to be equal for all collector technologies with K_{Inv} = 10,685,000 €. The collector-specific costs are based on the following values:

$$k_{\mathrm{col}} = \begin{cases} 211\,\frac{€}{m^2} \cdot A_{\text{collector A)}} \\ 223\,\frac{€}{m^2} \cdot A_{\text{collector B)}} \\ 350\,\frac{€}{m^2} \cdot A_{\text{collector C)}} \\ 350\,\frac{€}{m^2} \cdot A_{\text{collector D)}} \end{cases} \qquad \text{(eq. 3)}$$

3. Results

An increase in the floor space utilization f_{col} increases the collector's annual yield. At the same time, the shading losses increase with decreasing row spacing, so that the annual yield does not increase linearly with f_{col}. Figure 6 illustrates the annual yield for the four collectors at f_{col} = 0.4…0.9 and the defined scenarios for a field area of approximately 98,525 m^2 (Mücke et al., 2021). It can be seen that collector B) provides the most annual yield in all three scenarios independent of the floor space utilization. Looking at the curve shapes of all four collectors, it is noticeable that the two PTCs, collector C) and collector D) have a flatter curve than collector B). This can be attributed to a greater increase in shading losses for the collectors with single-axis tracking. Collector A) (flat-plate collector) has a similar curve as collector B) in scenario 1. Up to a floor space utilization of f_{col} = 0.7, the curve is almost linear and then it starts to flatten. In scenario 2 and scenario 3 (at a higher temperature level) the flattening of the curve begins earlier for collector A). Collector B) has the steepest curve in comparison to the other collectors. Rising f_{col} increases the annual yield the most for this collector. The yield differences of the two PTCs collector C) and collector D) are marginal.

Figure 7 shows the heat production cost for the four collectors for different degrees of floor space utilization f_{col} as well as the defined scenarios. It can be seen that collector B) has the lowest cost in all three scenarios independent of f_{col}. The heat production costs of the CPC collector are almost half less than for the two PTCs, collector C) and collector D). In Scenario 1 collector A) has lower heat production cost in comparison to the collectors C) and D) at f_{col} = 0.4 and f_{col} = 0.5. In scenario 2 and scenario 3, collector A) has the highest heat production cost at all floor space utilizations. The lower investment cost cannot compensate for the low annual yield.

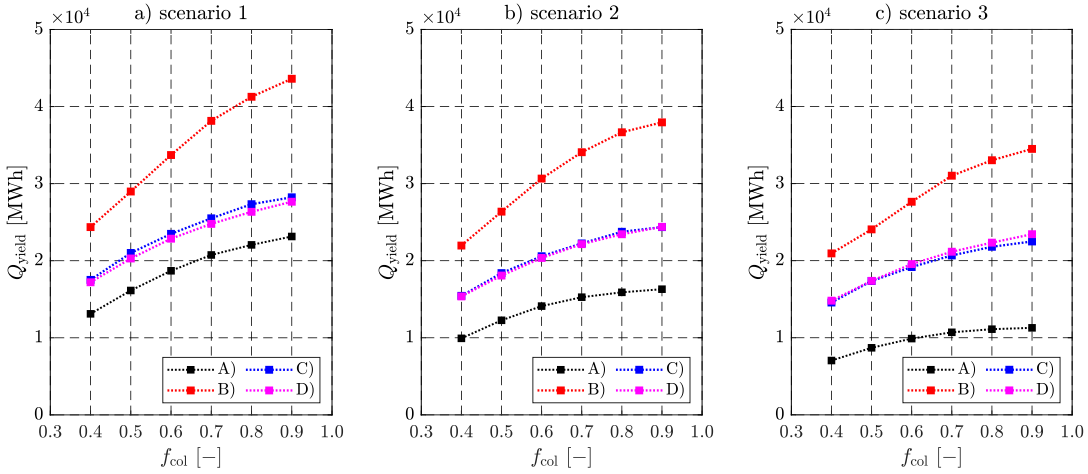

Fig. 6: Annual yield for the collectors A), B), C) and D) for different f_{col} and scenarios for a field area of 98,525 m²

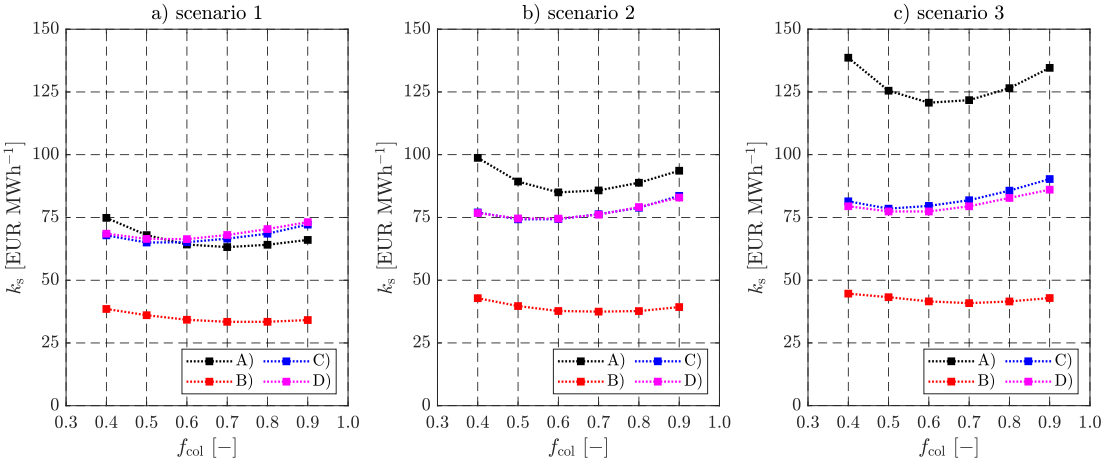

Fig. 7: Heat production cost k_s for the collectors A), B), C) and D) for different f_{col} and scenarios

Tab. 2: Floor space utilization f_{col} and specific annual yield q_{yield} (based on gross collector area) at minimum heat production cost for the collectors A), B), C), D) and for the different scenarios

scenario	f_{col}	k_s [€ MWh^{-1}]	q_{yield} [kWh m^{-2}a^{-1}]
collector A) – flat-plate collector			
scenario 1	0.7	63.14	310
scenario 2	0.6	84.92	246
scenario 3	0.6	120.62	172
collector B) – CPC collector			
scenario 1	0.7	33.41	565
scenario 2	0.7	37.47	505
scenario 3	0.7	40.85	460
collector C) – PTC C = 8,5			
scenario 1	0.5	65.01	430
scenario 2	0.5	74.24	377
scenario 3	0.5	78.48	356
collector D) – PTC C = 15			
scenario 1	0.6	66.36	399
scenario 2	0.6	74.52	355
scenario 3	0.6	77.37	341

Figure 7 also displays that the optimal floor space utilization f_{col} differs between the collectors. The PTC tends to have a minimum of k_s at a smaller floor space utilization than the CPC. This can be explained with higher shading losses for the PTC due to the tracking mechanism. At an optimum floor space utilization of f_{col} = 0.7 the collector B) has k_s of 33.41 € MWh^{-1} for scenario 1, 37.45 € MWh^{-1} for scenario 2 and 40.85 € MWh^{-1} for scenario 3. The specific annual yield (based on gross area) for collector B) in scenario 1 is 565 kWh m^{-2} a^{-1}, in scenario 2 505 kWh m^{-2} a^{-1} and in scenario 3 460 kWh m^{-2} a^{-1}. Increasing the floor space utilization to f_{col} = 0.9 increases the annual yield Q_{yield} about 11.2% - 14.3% while decreasing k_s about 2.1% - 5.0%.

4. Discussion

The results of the investigation show that collector B) (CPC collector) provides the most yield in the three defined scenarios and thus in the temperature range of $T_{DH,sup}$ = 95...140 °C at the floor space utilizations f_{col} = 0.4...0.9. Moreover, the heat production cost of collector B) is the lowest at all floor space utilizations. The minimum heat production costs result at f_{col} = 0.7 with k_s = 33.41...40.85 € MWh^{-1}. When comparing collector B) with the two PTCs, collector C) and collector D), it becomes clear that due to greater shading losses, the optimal floor space utilization for the PTCs is lower than that of the CPC collector. Thus, the single-axis tracking collectors use the total collector field area less efficient.

Although single-axis tracking increases the usable fraction of beam radiation by reducing cosine losses, collector C) and collector D) provide less annual yield than the non-tracking collector B). This can be mainly attributed to the fact that at the investigation area (Chemnitz, Germany) about 52% of the annual global irradiation is diffuse. Due to the relatively large concentration ratio of the parabolic trough collectors, only a small part of the diffuse radiation arriving from a wide angular range can be utilized for heat generation.

The results of the study confirm that the direct integration of solar systems into district heating networks is efficiently possible without the construction of a secondary network. For an efficient use of the solar heat it should be integrated in the district heating network in such a way that largest possible coverage of the district heating load is achieved by the solar system in the summer period.

5. Acknowledgments

The authors would like to thank *inetz* for providing and allowing the use of information. Special thanks also go to the Chemnitz city administration for commissioning and cooperating in the project "*Erstellung eines Klimaschutzteilkonzeptes für die Stadt Chemnitz zur Erschließung der Potenziale regenerativer Energien im Hinblick auf die CO_2-Reduktionsziele 2050*."

6. References

CEN European committee for standardization, 2006. EN 12975-2:2006 Thermal solar systems and components – Collectors – Part 2: Test methods.

Deutscher Wetterdienst, 2021. Testreferenzjahr Standort Chemnitz, https://www.dwd.de (last accessed on 10.03.22).

Giovannetti, F., Horta, P., 2016. Comparison of process heat collectors with respect to technical and economical conditions. International Energy Agency, Solar Heating & Cooling Programme, Task 49.

Klein, S. A. et al., 2017. TRNSYS 18: A Transient System Simulation Program. Solar Energy Laboratory, University of Wisconsin, Madison, USA, http://sel.me.wisc.edu/trnsys.

Meißner, R., Moschke, D., 2016. Senftenberg – Ergebnisse des ersten Betriebsjahres. https://www.ritter-xl-solar.de/senftenberg-ergebnisse-des-ersten-betriebsjahres/ (last accessed on 10.03.22).

Mücke, J. M., Böhme, H., Urbaneck, T., 2021. Klimaschutzteilkonzept Stadt Chemnitz - Erschließung der Potenziale regenerativer Energien im Hinblick auf die CO_2-Reduzierungsziele 2050. Abschlussbericht, www.chemnitz.de 17.03.2021. – ISBN 987-3-9812586-6-0

Perers, B., Furbo, S., Dragsted, J., 2013. Thermal performance of concentrating tracking solar collectors. Technical University of Denmark, Department of Civil Engineering. DTU Civil Engineering Reports No. R-292

Tian, Z., Perers, B., Furbo, S., Fan, J., 2018. Thermo-economic optimization of a hybrid solar district heating plant

with flat plate collectors and parabolic trough collectors in series. Energy Conversion and Management. 92-101. – ISSN 0196-8904 https://doi.org/10.1016/j.enconman.2018.03.034.

Urbaneck, T.; Shrestha, N. Lal; Oppelt, T.; Frotscher, O.; Göschel, T.; Uhlig, U.; Frey, H., 2020. Solare Fernwärme für das Quartier Brühl in Chemnitz – Begleitforschung (SolFW). Technische Universität Chemnitz, Fakultät für Maschinenbau, Professur Technische Thermodynamik (Ed.), inetz GmbH (Ed.) - ISBN: 987-3-9812586-5-3, Open Access: https://nbn-resolving.org/urn:nbn:de:bsz:ch1-qucosa2-390452

VDI Verein deutscher Ingenieure, 2012. VDI 2067 Part 1 Economic efficiency of building installations – Fundamentals and economic calculation.

VDI Verein deutscher Ingenieure, 2014. VDI 6002 Part 1 Solar heating in portable water – Basic principles – System technology and application in residential buildings.

Abbreviations

Quantity	Symbol
Compound parabolic concentrator	CPC
Deutscher Wetterdienst	DWD
Direct normal irradiation	DNI
District heating	DH
East-West alignment	E-W
Flat-plate collector	FPC
Incidence angle modifier	IAM
North-South alignment	N-S
Parabolic trough collector	PTC
Pump	P
Test reference year	TRY
Three way valve	TWV

Symbols

Quantities

Quantity	Symbol	Unit
Area	A	m^{-2}
Heat loss coefficient at $(T_m\text{-}T_a) = 0$	a_1	W m^{-2} K^{-1}
Temperature dependence of the heat loss coefficient	a_2	W m^{-2} K^{-2}
Concentration ratio	C	
Factor	f	
Floor space utilization	f_{col}	
Beam irradiance	G_b	W m^{-2}
Diffuse irradiance	G_d	W m^{-2}
Beam irradiation	H_b	kWh m^{-2}
Diffuse irradiation	H_d	kWh m^{-2}
Incidence angle modifier	K	
Electric cost	k_{el}	€ kWh^{-1}
Investment cost	K_{Inv}	€
Heat production cost	k_s	€ MWh^{-1}
Heat quantity	Q	MWh
Specific heat quantity	q	kWh m^{-2}
specific Heat	$\dot{q}$	W m^{-2}
Temperature	T	°C
Surface tilt	β	0 to ± 90°; toward the equator is +ive
Azimuth (of surface)	γ	0 to 360°; clockwise from North is +ive
Incidence (on surface)	Θ,i	0 to + 90°
Longitudinal incidence angle	Θ,L	0 to + 90°
Transversal incidence angle	Θ,T	0 to + 90°
Zero loss efficiency	η_0	

Subscripts

Quantity	Symbol
Ambient	a
Beam	b
Collector	col
Diffuse	d
District heating	DH
Electric	el
Incidence	i
Investment	Inv
Mean	m
Primary	pri
Return	r
Solar	s
Secondary	sec
Shading	shad
Supply	sup
Tilted surface	tilt

Appendix: INCIDENCE ANGLE MODIFIER FOR BEAM RADIATION

Tab. 1: IAM beam radiation for collector A)

Θ_i	0°	10°	20°	30°	40°	50°	60°	70°	80°	90°
K_b	1.00	1.00	0.99	0.98	0.96	0.91	0.82	0.53	0.27	0.00

Tab. 2: IAM beam radiation for collector B)

Θ_L , Θ_T	0°	10°	20°	30°	40°	50°	60°	70°	80°	90°
$K_b(\Theta_L)$	1.00	1.00	0.99	0.96	0.93	0.9	0.87	0.86	0.43	0.00
$K_b(\Theta_T)$	1.00	1.02	1.03	1.03	1.03	0.96	1.07	1.19	0.60	0.00

Tab. 3: IAM beam radiation for collector C)

Θ_L , Θ_T	0°	10°	20°	30°	40°	50°	60°	70°	80°	90°
$K_b(\Theta_L)$	1.00	0.99	0.99	0.98	0.96	0.91	0.77	0.53	0.18	0.00
$K_b(\Theta_T)$	1.00	1.00	1.00	1.00	1.00	1.00	1.00	1.00	1.00	0.00

Tab. 4: IAM beam radiation for collector D)

Θ_L , Θ_T	0°	10°	20°	30°	40°	50°	60°	70°	80°	90°
$K_b(\Theta_L)$	1.00	0.95	0.92	0.88	0.82	0.71	0.55	0.31	0.00	0.00
$K_b(\Theta_T)$	1.00	1.00	1.00	1.00	1.00	1.00	1.00	1.00	1.00	0.00

Development of a combined model predictive and adaptive Control Strategy for the Operation of a cold District Heating Network

Jens Ullmann[1], Harald Drück[1], Bernd Hafner[2]

[1] Institute for Building Energetics, Thermotechnology and Energy Storage, Stuttgart (Germany)

[2] Viessmann Climate Solutions SE, Allendorf (Germany)

Abstract

Cold district heating networks, also called 5th generation district heat and cold or 5GDHC, reduce thermal losses induced by high operating temperatures using relatively low temperatures for energy distribution and storage. In order to optimize the operation of such a network a model predictive control (MPC) including an adaptive control strategy is developed and investigated for controlling both, the heating and cooling supply. An ice store with a large thermal capacity of 75 MWh represents the main thermal energy store and acts as a heat source for decentralized heat pumps being part of the investigated network. Since the ice store is discharged during winter for heat supply and is charged during summer for cooling purposes it functions as a seasonal thermal energy store. Using model predictive controls over such a long period of time is not feasible due to computational restrictions. Hence an adaptive control part is proposed and implemented into an MPC for an optimum operation of the ice store throughout the year. First system simulation results for the optimum seasonal operation of the ice store are presented using a non-predictive control as well as a model-predictive control.

Keywords: model predictive control (MPC), adaptive control, 5th generation district heat and cold (5GDHC), anergy network, ice store, heat pump

1. Introduction

District heating networks represent a cost effective alternative for the heat supply with large fractions of renewable energies compared to decentralized heating systems installed in each single house. As standard district heating networks using high supply temperatures face the disadvantage of high heat losses, especially when comprising long distance piping, so-called 5th generation district heat and cold or 5GDHC reduces this disadvantage using low supply temperatures. In this contribution a 5GDHC network is being investigated using a large ice store with a water volume of 770 m³ as the main central and seasonal thermal energy store. As the main source for environmental and solar thermal energy a large so-called thermal sun-air-collector (Lott, S. 2022) field is connected to the network. The network includes decentralized heat pumps supplying small buffer heat (hot water) stores of the heating systems of the buildings with temperatures in the range of 25 to 45 °C. When required the heat pump also supports the cooling which is primarily performed using the ice store while regenerating it for the heating period. As the standard, non-predictive control for the CDHN a so-called state machine is being used selecting corresponding modes of operation depending on the ambient conditions and the system conditions. The heating system within the buildings is controlled using a simple stand-alone controller. In order to further optimize the control of the CDHN a model predictive control (MPC) strategy is developed in order to better utilize thermal capacities within the buildings and heat stores and hence reduce unnecessary thermal overheating or losses.

The temperatures within buildings are strongly depending on “disturbance factors” such as the solar irradiance, the ambient air temperature and internal heat sources such as e. g. the number of persons in a building. Regular heating controls take into account only current measurement data for controlling, such as the current ambient air temperature. Model predictive controls predict the future behavior of systems taking into account the predicted disturbance factors such as the forecasted weather conditions or predicted internal loads. Model predictive controls use these predictions in order to compute an optimal control input over a finite time period (prediction horizon) using system simulations. Control inputs are varied within system simulations and an optimum is being determined for a defined target function, such as e. g. a minimum of a cost function, while satisfaction of given system constraints is being ensured. That means the predicted disturbance factors are taken into account during the current control step. This can prevent

© 2022. The Authors. Published by International Solar Energy Society
Selection and/or peer review under responsibility of Scientific Committee
doi:10.18086/eurosun.2022.04.14 Available at http://proceedings.ises.org

heating systems from heating up rooms to a set point temperature, which are then finally overheated by in- or external disturbance factors such as solar irradiance shortly after. So, taking predictions into account during the current control step potentially reduces thermal loads and can also optimize the overall thermal energy supply. E. g. the thermal losses of heat stores can be reduced by only heating up the stores when heat supply is required using an MPC.

2. 5th generation district heat and cold (5GDHC)

A simplified scheme of the investigated 5GDHC network is shown in Fig. 1. Heat loss reduction is being achieved using relatively low network (orange hydraulics in Fig. 1) temperatures for heat distribution. These low temperatures are being realized using both, a centralized ice store and a centralized so-called thermal sun-air-collector field as the main thermal energy sources of the heating and cooling system. Thermal energy for heating is shifted from low temperature level supplied by the sources via the network to higher temperatures using decentralized heat pumps combined with buffer stores in each building (red hydraulics in Fig. 1). The thermal sun-air-collector field can either regenerate, or charge, the ice store (green hydraulics in Fig. 1) or directly supply the heat pumps as well (not shown in Fig. 1). Using the "mixed discharge mode" for heating (see table 1) the heat pumps are supplied by both, thermal energy from the thermal sun-air-collectors and the ice store at the same time using a temperature controlled mixer for keeping the heat pump evaporator supply temperature above a specific minimum temperature.

In addition to supplying heat the ice store can also be used for cooling the buildings during summer. This operation mode is called "natural cooling" (blue hydraulics in Fig. 1). If the cooling power provided by the ice store is not sufficient, cooling can be performed by the heat pump, this is called "active cooling" (not shown in Fig. 1). The excess heat produced during active cooling is emitted to the ambient via the thermal sun-air-collectors (required hydraulics not shown in Fig. 1). If the temperature of the ice store rises above a set point value, it can also be pre-conditioned. During pre-conditioning the ice store is actively discharged analog to the active cooling mode.

The design capacity of the ice store is related to the heating and cooling demand of the connected buildings. It is operated as a seasonal thermal energy store being cooled, or discharged, during the winter when energy for heating the buildings is extracted by the heat pumps and being regenerated, or charged, during the summer by cooling the buildings. The domestic hot water is generated exclusively by means of electric instantaneous water heaters (Lott, S. 2022).

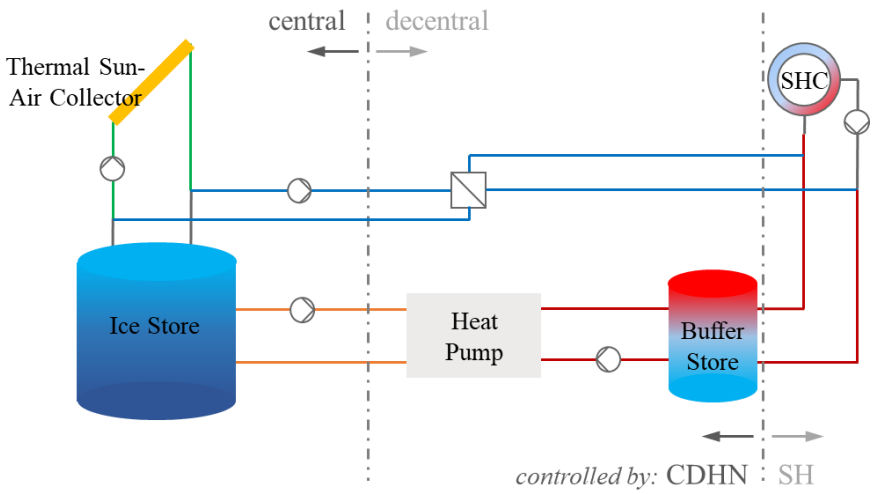

Fig. 1: Simplified hydraulic scheme of the investigated 5th generation district heat and cold (5GDHC) network for space heating and cooling (SHC), orange: low temperature heat supply, red: heating mode, blue: cooling mode, green: regeneration of ice store

The standard control of the investigated CDHN is implemented as a so-called state machine which selects one of 15 different so-called "modes of operation" depending on the actual system and boundary conditions. The state machine controls only the central part of the system as well as the heat pumps and buffer stores. The control of the underfloor space heating (SH) is controlled by a separate two-point controller. There are several operation modes for heating as the "mixed discharge mode" described above, cooling the building or conditioning the ice store. Each operation mode represents a specific set of actor settings controlling e. g. pumps or valves. The state machine is implemented in MATLAB® Simulink. In order to perform annual system simulations using the simulation software TRNSYS the Simulink model of the state machine is integrated as a co-simulation. At the beginning of each TRNSYS time step

the state machine model is called returning the operation mode for the TRNSYS simulation to use as well as the setting for each network component or actor. The most important modes of operation are shown in table 1. As an example for the actor settings, the setting of the heat pumps is shown. Other actor settings besides on and off are possible e. g. related to the switching of valves. Considering the decentralized buildings, the TRNSYS building model Type 56 is used for system simulations and is controlled by a simple two-point controller.

Tab. 1: Modes of operation utilized by the state machine used as the standard controller for the CDHN; SoC: state of charge of ice store (see chapter 3.2 for definition)

Mode of operation	No.	Purpose	Heat pump operation
Discharge mode	2	Heating mode using the ice store as main heat source	On
Mixed discharge mode	3	Heating mode using both, ice store and absorber as heat sources	On
Absorber direct mode	4	Heating mode using the absorber as main heat source	On
Regeneration	5	Charge ice store using absorber as heat source	Off
Pre-conditioning (active)	-	Reduce SoC of ice store for natural cooling	On
Natural cooling	-	Coolin of building and charging ice store using building as heat source	Off
Active cooling	-	Cooling of building and use of heat pump and absorber to re-cool excess heat	On

3. Model predictive and adaptive control

As an alternative to the standard control based on actual system data a model predictive control (MPC) was implemented in order to take future system conditions into account when making actual control decisions. The time horizon considered by a model predictive control is usually between one to several days. The thermal capacity of the ice store is very large in comparison to the thermal capacity of the buildings. Hence an MPC is not suitable to optimize the control strategy for the operation of the ice store as a seasonal thermal energy store because the MPC would require very long computation times. Additionally, the MPC would require a full year weather forecast. For an optimum utilization the ice store has to be fully charged (heated up) at the beginning of winter and fully discharged or cooled down resulting in a maximum ice fraction at the beginning of the summer. This aim however can be contradictive to the aim of an MPC which is to minimize energy consumption and maximize energy gains from renewable sources such as the thermal sun-air-collectors. Hence in order to achieve an optimum seasonal performance of the entire heating and cooling system including the ice store an adaptive control strategy needs to be implemented separately and be connected to the MPC. This can be achieved using the so-called state of charge (SoC) of the ice store as the measurable key figure for its control (see Fig. 3). The state of charge by definition reaches its minimum value when the ice store is fully solid with a temperature of 0 °C. The maximum value is reached when the ice store is fully melted and its maximum operation temperature is reached (see definition in chapter 3.2). The permissible or optimum range of the state of charge for a given control step is calculated using the adaptive control strategy (described in chapter 3.2) and is then passed to the MPC as restrictive constraints as shown in Fig. 2. Restrictive constraints represent boundary values of system components that should not be exceeded. As an example of a restrictive constraint the room air temperatures should not drop below 20 °C during the heating season.

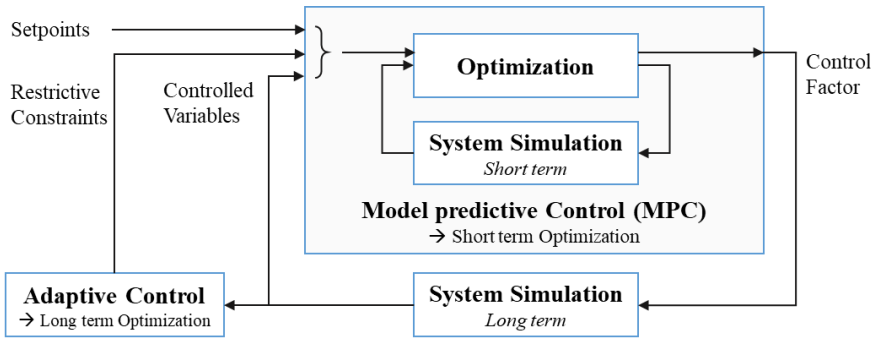

Fig. 2: Simplified procedure of system simulations using model predictive control (MPC) including an adaptive control for the optimum seasonal control of a 5GDHC network for heating and cooling with an integrated ice store.

System simulations using the MPC as system control are performed using TRNSYS including the building model Type 56. The MPC is implemented in MATLAB® using its genetic algorithm for optimization. As well as the

standard control the MPC is integrated into the TRNSYS system simulation using the TRNSYS Type 155 (TRNSYS-MATLAB interface). The adaptive part of the control is implemented within MATLAB as an artificial neuronal network (ANN) returning the restrictive constraints in terms of the permissible state of charge of the ice store depending on the actual system and boundary conditions.

3.1. Model predictive control (MPC)

The MPC is used in order to calculate a course over time for the modes of operation which reduces the demand of electrical energy for the heat pumps and increases the amount of gained environmental thermal and solar energy. Therefore, optimization simulations are being performed using the system simulation model which is used for the overall or main (annual) system simulations as well. The optimization simulations are performed varying the course for the operation mode over the prediction horizon (approx. 1 to 3 days) and analyzing the simulation results in terms of the energy demand or gain while keeping the set point room air temperature within the buildings. The simulation results are evaluated using the so-called target function. The target function contains all energy flows or values to be taken into account for the control. Its result is a scalar calculated as shown exemplary in equation 1:

$$\min \begin{pmatrix} Z * \sum_{k=0}^{N_p} \left(\left(R * Q_{el,k} \right) \right) - Y * \sum_{k=0}^{N_p} \left(Q_{renewable,k} \right) \\ + X * \sum_{k=0}^{N_p} \left(Q_{\Delta T,k}^2 \right) + W * \sum_{k=0}^{N_p} \left(Q_{HSloss,k} \right) + V * \sum_{k=0}^{N_p} \left(Q_{\Delta SoC,k} \right) \end{pmatrix} \quad \text{(eq. 1)}$$

$Q_{el,k}$ electric energy consumption of heat pump [kWh]

$Q_{renewable,k}$ in- and output of renewable energy [kWh]

$Q_{\Delta T,k}$ difference between actual value and set point value of energy within room air zones [kWh]

$Q_{\Delta HSloss,k}$ heat losses of the decentralized heat stores [kWh]

$Q_{\Delta SoC,k}$ difference between actual value and set point value of energy within ice storage [kWh]

R, Z, Y, X, W, V weighting factors

N_p number of time steps within prediction horizon

k timestep within prediction horizon

For computational reasons the target function is defined as a continuous function. Therefore, the restrictive restraints to the control such as the deviation from room air temperature or the deviation from the permissible state of charge of the ice store are considered within the target function like the other energy flows or values. Since the weighting factors determine the behavior of the MPC the energies considered for the restrictive constraints are potentiated in order to behave as de-facto restrictive constraints returning very high target function results when differing from set point values. The target function value is then minimized by the MATLAB genetic algorithm (GA). This is performed by repeating the optimization simulation with varying courses of operation modes until the result value of the target function reaches a minimum. The variation of the course of the operation mode is perform by the GA.

3.2. Adaptive control

As the ice store is used as a seasonal thermal energy store for heating and cooling the adaptive control has to ensure it is fully charged at the beginning of the heating season and fully discharged at the beginning of the cooling season. In order to control the seasonal course of the energy state of the ice store, the adaptive control uses the so-called “state of charge” (SoC) as the measurable key figure of the ice store. The state of charge is defined using two reference states: solid ice with a temperature of 0 °C is represented by a value of 0 or 0 % and liquid water with a temperature of 0 °C is represented by a value of 1 or 100 % (see Fig. 3, left). The maximum state of charge of the ice store within the investigated system reaches 125 % at its maximum temperature of 20 °C.

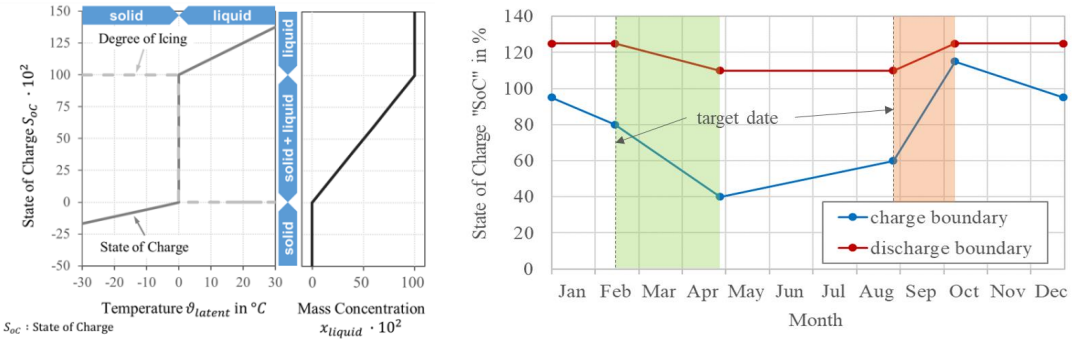

Fig. 3: Definition of the State of Charge or SoC (left) and seasonal course of the State of Charge with boundaries for charging (blue) and discharging (red) of the ice store throughout one year used in order to condition ice store for cooling (green area) and heating (red area) period.

To ensure for example that the ice store is sufficiently discharged at the beginning of the cooling period the adaptive control starts to discharge (or condition) the ice store towards the end of the heating season by using the discharge mode rather than the mixed discharge mode. The mixed discharge mode uses also the sun-air-collector and can result in higher supply temperatures and thus increase the heat pump performance. But accepting a lower heat pump performance in favor of a further discharged ice store can benefit the overall seasonal performance of the system. This is due to higher thermal ice store capacity available as a heat sink for natural cooling. This can very well reduce the amount of active cooling required during the cooling season.

The conditioning of the ice store is activated by the control using the so-called charge (blue line in Fig.3, right) and discharge (red line in Fig.3, right) boundaries as trigger-signals. During preparation for the cooling period (green area in Fig. 3, right) the control keeps the SoC of the ice store below the charge boundary. The charge boundary defines the start or target date and duration of the ice store conditioning. The duration required in order to discharge or charge the ice store is depending on the ratio of the total heat capacity of the ice store to the total heating (or cooling) demand. If the ice store has a high capacity in relation to the heating or cooling demand of the entire system, the target date needs to be shifted to an earlier date because the required duration will extend.

In order to determine the best target date and appropriate duration for the ice store conditioning an artificial neuronal network (ANN) will be trained with data resulting from a parametric simulation study. The parametric simulation study will be performed using TRNSYS system simulations using the standard state machine control varying the ratio of heating demand to ice store capacity as well as the time and duration for charging / discharging (or conditioning) of the ice store. The in- and output data for training the ANN is shown in Fig. 4. As a result, the ANN is trained to return the target date and duration for charging and discharging. The MPC can than retrieve target date and duration from the ANN using the input data at an actual control step.

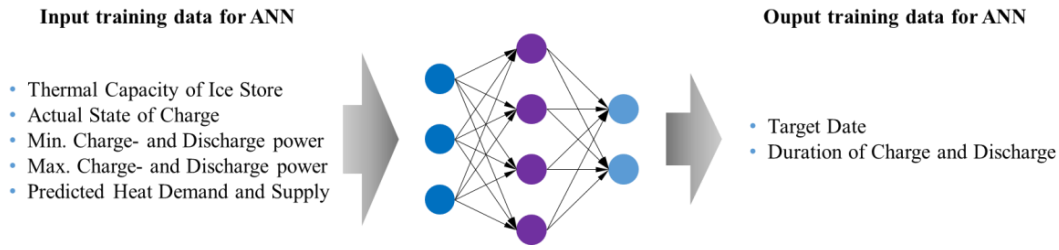

Fig. 4: Training data for artificial neuronal network (ANN) in order to return permissible charge and discharge boundaries for the model predictive control (MPC)

4. Results

First results of the system simulations using the standard state machine control are presented in chapter 4.1. The results comprise exemplary energy quantities required or delivered from the system components as well as exemplary seasonal courses of the state of charge depending on different ratios between heating demand and ice store capacity. The results also show the effect of shifting the charge boundary for the ice store to an earlier target date.

First results concerning the MPC are shown in chapter 4.2. The influence of the building initialization for the optimization simulation is described as well as the general functionality of the MPC and its capability to shift loads

and e.g. preheat the buffer store already before the heat demand increases (see Fig. 9). It is also shown that further adaption of the target function weighting factors needs to be performed for the MPC to reduce the electrical energy consumption of the heat pumps though.

The domestic hot water is generated exclusively by means of electric instantaneous water heaters and is therefore not taken into account in the system simulation.

4.1. 5th generation district heat and cold (5GDHC)

First annual system simulations were performed using the standard state machine control. The overall heat demand of the modeled building is 253 MWh/a and the overall cooling demand is 58 MWh/a. The effective usable thermal capacity of the ice store is 75 MWh resulting in a ratio of heat demand to ice store capacity of 3.4. Thermal losses of the distribution network are not considered within this simulation. Because the network temperatures are between -10 °C and 20 °C, the network is estimated to loose very little thermal energy or even gain thermal energy from the surrounding soil. First exemplary results of the annual system simulation are shown in Fig. 5. The narrow columns represent a thermal energy gain into the overall system when being positive and a thermal energy loss from the overall system when being negative (thermal energy loss from thermal sun-air-collector to ambient for cooling purposes during July and August). Concerning the broad columns positive values represent losses or demands such as space heating demand. Negative values represent thermal gains to the system. The ice store's change in internal thermal energy is represented by a broad column as well. A negative value represents a discharging of the ice store and a positive one represents a charging of the ice store.

The seasonal performance factor of the heat pump within this exemplary result is 4.6 regarding heating supply and 3.6 regarding cooling supply. The seasonal performance factor for heating is defined as the ration of heating energy delivered to the building divided by the demand of electrical heat pump energy during the heating season. The seasonal performance factor for cooling is defined as the ratio of delivered cooling energy to the building divided by the electric energy demand of the heat pump during active cooling mode or ice store conditioning.

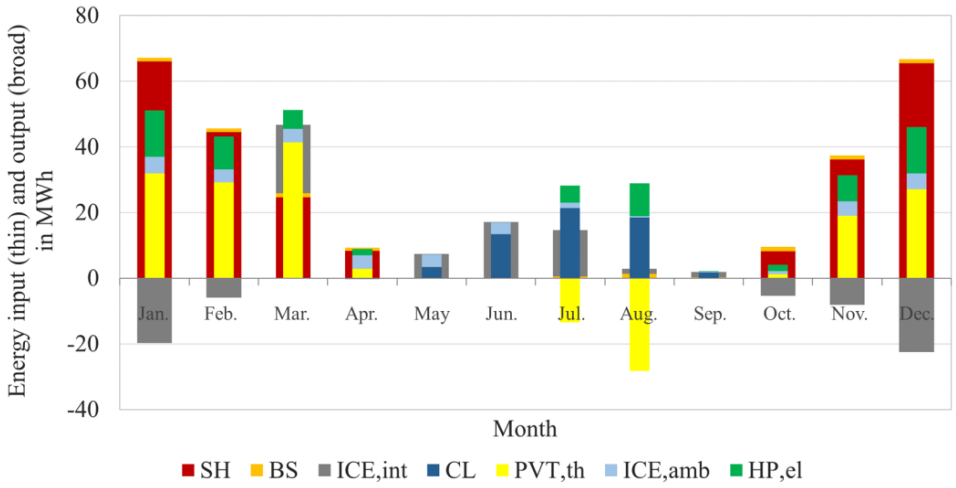

Fig. 5: Energy input (positive inner thin column) and output (positive outer broad column); SH: space heating, BS: buffer stores, ICE: ice store (int: internal energy change, amb: thermal environmental gains), CL: cooling PVT,th: thermal gain from sun-air-collectors, HP,el.: external electrical energy of heat pumps.

The influence of the ratio between heat demand and ice store capacity as well as the target date for the ice store conditioning on the seasonal course of the state of charge is shown in Fig. 6.

The seasonal course of the SoC resulting from the simulation results shown in Fig. 5 for a ratio of heat demand to ice store capacity of 3.4, is represented by the solid blue line in Fig. 6. In comparison the solid red line shows the seasonal course of the SoC for a ratio of heat demand to ice store capacity of 1.7. The lower related heating and cooling demand results in a much slower and lower amplitude of discharging and charging of the ice store.

Fig. 6 also shows the seasonal course of the SoC for two different charging boundaries; solid: CB1 and dotted: CB2 green line, for a heat demand to ice store capacity ratio of 3.4. Compared to CB1, the ice store is discharged earlier using CB2. Since the ice store is only discharged using heating modes during the heating season the ice store can be discharged further using CB2 because the buildings heating demand is higher during this earlier time of the year. This can potentially reduce the overall electrical energy demand for the heat pumps as the effect on the seasonal performance factor for heating is very low, but the ratio of cooling demand and electrical energy for cooling rises

from 3.8 to 5.6 when using CB2.

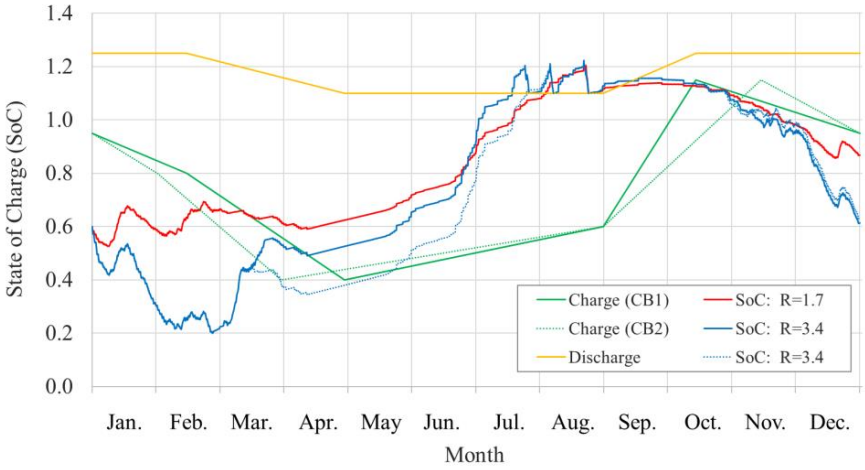

Fig. 6: Seasonal course of the state of charge (SoC) for two different ratios (R) of heat demand to ice store capacity and two different charge boundaries (CB1 and CB2) for R = 3.4.

4.2. Model predictive control (MPC)

Using the software TRNSYS it is not possible to pause a running system simulation and start a new simulation using the actual state of the paused simulation as the initialization state of the new simulation. So in order to perform optimization simulations by the MPC new system simulations have to be performed. These new system simulations have to be initialized according to the actual state of the main system simulation at the beginning of the present prediction horizon. This is possible for most used component models or TRNSYS types respectively. Concerning the initialization of TRNSYS Type 56 (building model) the room air temperatures can be initialized, but the temperatures of the wall structure cannot. This results in high deviations between room air temperatures during optimization simulation and room air temperatures during the main simulation. This deviation is represented in Fig 7 by the difference between the room temperature of the main simulation and the room temperature of the optimization simulation without “settling time”.

As no alternative building model is available, a so-called transient or settling time was used as an alternative for quasi-initialization. Thus, the optimization simulation starts at the beginning of the control horizon minus the settling time. During the settling time, the previously determined operation mode course of the main simulation is used. As a compromise, the use of a 48 hour settling time is considered to be a reasonable compromise between simulation effort and the quality of the initialization of the optimization simulation.

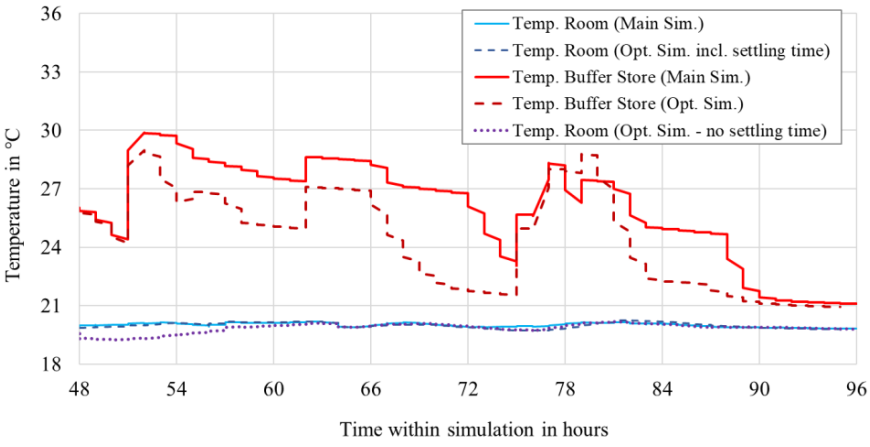

Fig. 7: Comparison between room air temperature and buffer store temperature during main simulation and optimization simulation using “settling time” as well as no settling time for room air temperature.

First exemplary results of annual system simulations using a MPC are shown in Fig 8 in terms of the room air temperatures as well as the ambient and heat store temperatures for the heating season. Additionally, the course of the operation mode being relevant for heating is shown on the right axis. These first results only show a basic functionality as the room air temperatures 1 to 3 demonstrate that the MPC is capable of keeping the set point

temperature of 20 °C for most of the heating season. Temperature drops of rooms 2 and 3 at the end of the heating season are probably caused by a high temperature rise within the room 1. The difference between actual and set air temperature of all 3 rooms is first added up and later evaluated by the target function using weighting factors within this simulation. It is estimated that treating all rooms separately by the target function will solve this unwanted behavior.

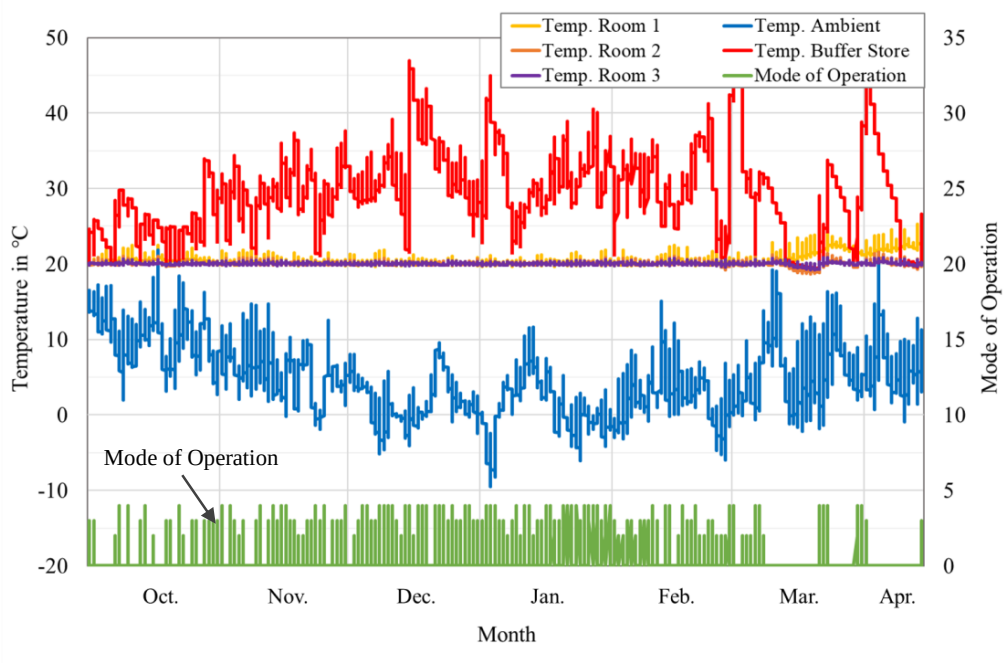

Fig. 8: Exemplarily results for room, ambient and heat store temperatures determined using system simulations applying model-predictive control (MPC) as well as the mode of operation (see table 1) during heating season (October to April).

The electrical energy demand of the heat pumps is not reduced by the MPC while keeping the same comfort level as using the standard state machine control so far. It is estimated that further adaption of the target function parameters will show a distinct increase in the performance of the MPC compared to the actual results.

The results show that the buffer store temperature mainly ranges between 25°C and 35°C during winter months and only occasionally reaches 50°C. The buffer store temperature shows that the buffer store is only heated up when increased demand is predicted. In Fig. 9 this behavior can be well observed on day 5 when the buffer store is heated up to above 40 °C during the first half of the day but the ambient temperature drops not before the second half. The model-predictive control therefore generally exploits the flexibility of the system to shift loads.

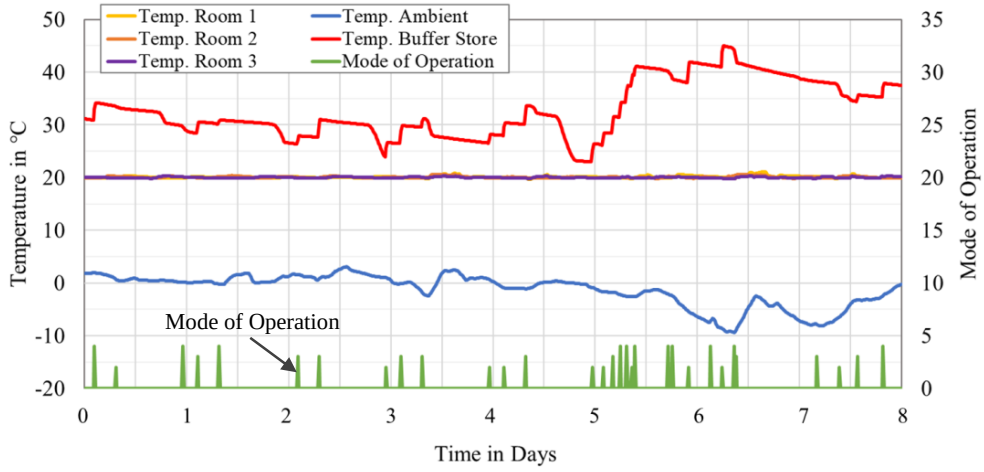

Fig. 9: Load shifting effect of the model-predictive control (MPC) in terms of room, ambient and buffer store temperatures determined using system simulations applying MPC as well as the mode of operation during one week of heating season (see table 1).

Further system simulations have shown that using the same weighting factors of the target function for cooling that

are used for heating does not result in good control results for cooling in terms of room air temperature not being kept under set point temperature. Thus different weighting factors will be determined for heating and cooling.

At present the disturbance factors are predicted exactly for optimization, meaning the same disturbance factors (e.g. weather or thermal gains) are used for main simulation and for optimization simulations. Furthermore, the MPC has to be expanded by rules handing large deviations between actual and predicted disturbance factors.

The use of the system model as a functional mockup unit (FMU) using the functional mockup interface (FMI) was no option since TRNSYS version 18 was used and only one tool was available performing FMU model conversion for TRNSYS version 17. Co-Simulation using FMI in general could be an option but would does not solve the problem of initializing building model walls of TRNSYS Type 56.

5. Conclusion and outlook

The introduced 5GDHC network for heating and cooling was modeled using the simulation software TRNSYS for system modeling and MATLB® SIMULINK for modeling the standard state machine as well as the model predictive control. First results of the system simulation using the standard control show high seasonal performance factors (SPF) of the heat pumps of well above 4 during heating season. The seasonal course of the state of charge (SoC) of the ice store depends on the ratio of heating and cooling demand to the thermal capacity of the ice store. The variation of the target date of the ice store conditioning strongly influences the seasonal course of the SoC and hence the heating or cooling capacity of the ice store at the beginning of the heating or cooling period and the SPF of the heat pumps accordingly. In order to determine the control parameters for an optimum seasonal course of the SoC a parameter study will be performed. The parameter study results will be used to train an artificial neuronal network (ANN). The trained ANN can then supply the MPC with optimized control parameters for the SoC boundaries being permissible at the current control step.

In order to further optimize the CDHN control a concept has been proposed to combine a model predictive control and an adaptive control strategy in order to further optimize the operation of the CDHN. The aims of both, the MPC used for short term optimization can be contradictive to the long term adaptive control part used for conditioning of the ice store for the heating or cooling period. Thus the adaptive control strategy overrules the MPC delivering permissible boundary conditions for the state of charge of the ice store at any given time during the year. The permissible boundary conditions are delivered by the ANN that has been trained with the result of the parameter study and returning the control parameters resulting in the optimum seasonal course of the SoC as described above. First results of system simulations presented in this paper show that the MPC is generally functional during the heating season. Room air temperatures are kept above set point values and load shifting can be observed. The weighting factors of the MPC's target function require further adaption in order to achieve an overall reduction in electrical energy demand of the heat pumps. It is estimated that further work on the parametric values of the target function will result in a reduction of electrical energy demand.

6. Acknowledgments

The activities of IGTE and Viessmann described in this paper are being supported by the German Federal Ministry for Economic Affairs and Climate Action (BMWK) based on a decision of the German Bundestag by Projektträger Jülich (PtJ) within the project 'Development of integrated solar supply concepts for climate-neutral buildings for the "city of the future" (Sol4City)' under grant numbers 03ETW019 A\B. The authors gratefully acknowledge this support and carry the full responsibility for the content of this publication.

7. References

Dittmar, R., Pfeiffer, B.-M., 2004. Modellbasierte Prädiktive Regelung. De Gruyter, ISBN-13: 978- 3486275230.

JUNGWIRTH, J. Lastmanagement in Gebäuden. München, Technische Universität München, Diss., 2015. München, 2015, urn:nbn:de:bvb:91-diss-20150128-1221398-0-6.

Prívara, S., Široký, J., Ferkl, L., Cigler J., 2011. Model predictive control of a building heating system: the first experience: Elsevier; Energy and Buildings 43 (2–3) (2011), pp. 564–572.

Zakulaa, T., Armstrong, P.R., Norford, L., 2014. Modeling environment for model predictive control of buildings. Elsevier, Energy and Buildings 85 (2014), pp. 549–559.

WIMMER, R.W. Regelung einer Wärmepumpenanlage mit Model Predictive Control, 2004, IMRT Press c/o Institut für Mess- und Regeltechnik, ETH Zentrum, https://doi.org/10.3929/ethz-a-004904606.

SOLAR ENERGY LABORATORY, UNIVERSITY OF WISCONSIN-MADISON. TRNSYS 16 Nutzerhandbuch. Getting started. Wisconsin.

MathWorks®, 2022. Global Optimization Toolbox Documentation (r2022a). Retrieved May 03, 2022 from https://de.mathworks.com/help/gads/.

Lott, S., Fischer, S., Drück, H., Hafner, B., 2022. Quasi-Dynamic Testing of Thermal Sun-Air-Collectors and Numerical Simulations of a Cold District Heating Network, EuroSun 2022 Conference Proceedings (to be published).

Techno-Economical Assessment of a Solar Regenerated Borehole Heat Exchanger Field with PVT Collectors for District Heating

Finn Weiland, Niklas Kracht, Bharat Chhugani and Peter Pärisch

Institute for Solar Energy Research in Hamelin (ISFH), Emmerthal (Germany)

Abstract

Cold district heating networks distribute heat with few losses or even gains from the heat source to decentralized heat pumps in residential districts. These so called fifth-generation district heating systems have the possibility of being operated entirely by renewable energies and often use a borehole heat exchanger field as the primary heat source. The paper presents a case study and discusses the sustainable dimensioning of borehole heat exchanger fields for district heating by means of system simulations with TRNSYS, focusing on the solar regeneration of the ground with photovoltaic thermal collectors. The simulation results show that the combination with solar regeneration allows the reduction of the ground source by 53 %, increases the efficiency by approx. 5 %, minimizes the levelized cost of heat and improves sustainability in terms of long-term operation.

Keywords: solar regeneration; ground source heat pump; borehole heat exchanger; PVT; 5th gen. district heating

1. Introduction

Several field studies in Germany have shown that the average seasonal performance factor (SPF) of ground source heat pump systems is significantly higher than that of air source heat pump systems (Auer and Schote, 2009; Miara et al., 2011; Günther et al., 2020). The difference between the efficiency levels is most significant in winter, when the ambient temperatures are lowest and the heat demand is at its peak. Therefore, ground source heat pumps with borehole heat exchangers (BHE) should substantially contribute to the future heat supply based on renewable resources. With rising market penetration, the interaction of individual BHEs in large borehole heat exchanger fields or in a cluster of individual BHE systems is at the focus of scientific discussions (Witte, 2018; Fascì et al., 2021). The sustainable operation of BHE fields and clusters requires regeneration with solar, environmental or waste heat. Persdorf et al. (2015) and Sauter et al. (2021) show that the regeneration with solar energy prevents undercooling of the ground in densely populated areas with BHE clusters. However, BHEs for single buildings are expensive and especially cold district heating networks with connected heat prosumers can reduce the specific costs of the shared BHE field. A number of research projects, like +Eins, SmartQuart, EASyQuart, EnVisaGePlus and KNW-Opt, use field tests and simulations to analyze the behavior of cold district heating networks.

This paper discusses the effect of solar regeneration of a BHE field in a residential district heating system using a simulation study with the transient system simulation program TRNSYS. A schematic of the district heating concept is shown in figure 1.

The district comprises 37 multi-family houses (MFH), designed almost according to the Passive House standard, with 450 apartments for 800 inhabitants. The heat for space heating (411 MWh), domestic hot water (DHW, 315 MWh) as well as distribution losses inside the buildings (266 MWh) is provided by heat pumps, which use the cold district heating network as the heat source. A BHE field and a photovoltaic thermal (PVT) collector field that also allows regeneration of the ground provide the required heat to the network. The BHEs are 150 m deep and the cold district heating network has a total length of about 1 km. This type of cold district heating is a so called fifth-generation heating network, which means that the transmission temperatures are commonly in the range of approx. 5 °C to 25 °C and therefore have relatively low heat losses or even gains. The PVT collectors correspond in their design to uncovered thermal collectors, also known as wind and/or infrared sensitive collectors (WISC), and thus efficiently supply heat at or below the ambient temperature (0 °C to 30 °C) as well as electrical energy (not considered in this paper).

© 2022. The Authors. Published by International Solar Energy Society
Selection and/or peer review under responsibility of Scientific Committee
doi:10.18086/eurosun.2022.04.15 Available at http://proceedings.ises.org

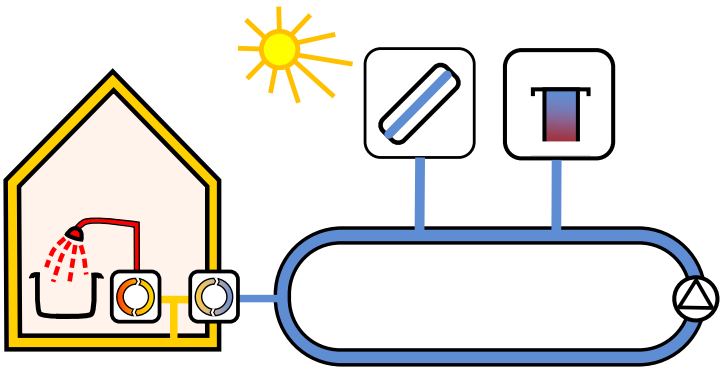

Figure 1: The cold district heating network supplies the heat pumps in the MFHs using the ground (BHE field) as a primary heat source. The PVT collectors assist and regenerate the BHE field.

2. Simulation model and boundary conditions

The heat demand of the district for space heating is simulated with a time step of 15 min in TRNSYS TRNBuild, using the properties of the building materials, the shading, the geometry and the ventilation of the buildings. This results in an average specific space heating demand of 19.2 kWh/(m²·a) and a total of 411 MWh for all MFH. The demand of the domestic hot water is calculated using the district heating load profiles of the software DHWcalc, Version 2.02b (Braas et al., 2020). A demand of 20 l/d per person, based on a hot water temperature of 60 °C and a cold water temperature of 10 °C, results in a specific demand of 14.7 kWh/(m²·a) and a total of 315 MWh for the district. Within the building, the heat is distributed by a 2-pipe-system to heat interface units, which can provide space heating as well as domestic hot water and simultaneously reduce the required flow temperature to approximately 50 °C according to German temperature standards (DVGW, 2004; DIN, 2012). Losses for storage and building internal pipe network increase the demand by 266 MWh. Thus, the heat pumps have to deliver 955 MWh of heat to the buffer storages. To account for simultaneity effects the load profile is aggregated to 1 h-data. Figure 2 (left) shows the yearly heat load profile for the district before storage.

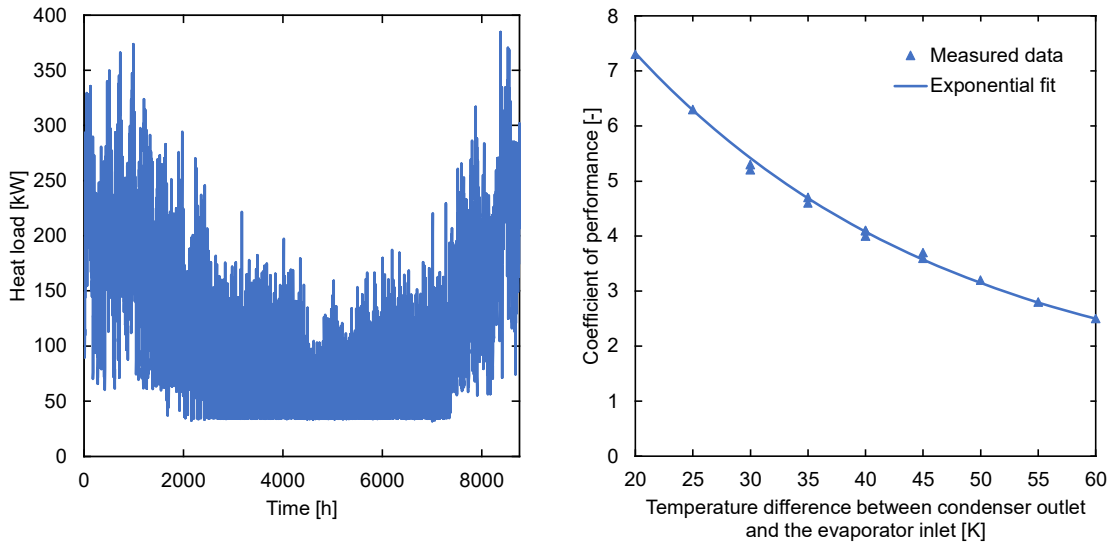

Figure 2: Heat load profile for the district before storage (left) and simplified exponential fit of the coefficient of performance of the heat pump model based on measured data (right)

The load profile for the total heat demand on the load side of the heat pumps (condenser) is read as an input in the following simulation model. The heat pump is modeled with an approximation of the coefficient of performance (COP), assuming no dependency of compressor speed. The simplified fit is based on heat pump test results of the Heat Pump Test Center in Buchs of the Eastern Switzerland University of Applied Sciences (Wärmepumpen-Testzentrum WPZ, 2021). The COP is dependent on the condenser outlet temperature $T_{out,cond}$ and the evaporator

inlet temperature $T_{in,evap}$ (see figure 2, right) according to the following equation:

$$COP_{HP} = 13e^{-0.036\cdot(T_{out,cond}-T_{in,evap})} + 1 \quad \text{(eq. 1)}$$

The condenser outlet temperature is constant and set to 51.8 °C, which is a simulated average value needed to ensure a flow temperature of 50 °C at the heat interface unit. Using the COP and the current heating load of the heat pump condenser, the heat flow rate of the evaporator is calculated as follows:

$$\dot{Q}_{HP,evap} = \dot{Q}_{HP,cond} \cdot \left(1 - \frac{1}{COP_{HP}}\right) \quad \text{(eq. 2)}$$

The mass flow through the evaporator is controlled by a constant temperature difference of the heat pump evaporator of 3 K. To simplify the simulations of the cold district heating network and the heat pumps, all heat pumps in the district are combined into a single heat pump. This combined heat pump is located at a common connection point with a shared evaporator inlet temperature. To illustrate the method used to model the network and the setup of the system simulations, figure 3 shows a map of the district on the left side and a system diagram on the right side.

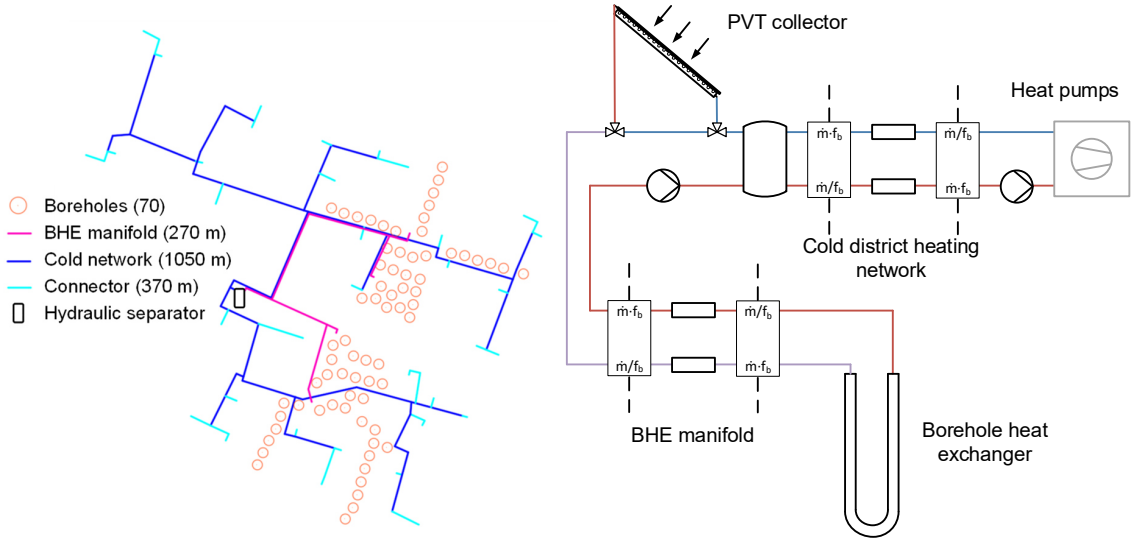

Figure 3: Map of the district with the route of the network and BHE manifold as well as projected positions of BHEs (left) and schematic of the source side model of the heat supply system (right). The PVT collector field is integrated in the return flow and will regenerate the borehole heat exchanger field. The cold district network and the BHE are hydraulically decoupled.

The complex structure of the network, consisting of connecting pipes to each building, the cold thermal network from the hydraulic separator, the BHE manifolds and the BHE distribution pipes (not shown in figure 3), is simplified with the help of a branching factor. To reduce simulation time, the branches of the network are aggregated and combined into a single flow pipe and a single return pipe. Similarly, the connectors to the buildings and the manifolds and the distributors of the BHE field are aggregated into single pipes for flow and return. To account for the branches of the network and to calculate a mass flow through the simulated pipes, we calculate a branching factor f_b of each subsection of the network. This branching factor is defined by the ratio of the total length of the corresponding network l_{tot} and the average length to the connection points l_{avg}:

$$f_b = \frac{l_{tot}}{l_{avg}} \quad \text{(eq. 3)}$$

For example, the length of the simulated pipe of the cold network is the average length between the central hydraulic separator and all connectors of the MFH. Table 1 contains the average lengths of the simulated pipes and the total lengths of the subsections of the network as well as the branching factors. The values for the BHE distributors vary depending on the number of boreholes. The values in the table are given for the case of 70 boreholes.

Table 1: Branching factors of the subsections of the cold district heating network.

Subsection	Pipe diameter	Average pipe length	Total pipe length	Branching factor
Cold network	170 mm	185 m	1054 m	5.7
Connectors	26 mm	10.4 m	364 m	36.0
BHE Manifolds	170 mm	116 m	267 m	2.3
BHE Distributors (70 boreholes)	40.8 mm	35.5 m	617 m	17.4

For calculating the heat transfer of each subsection of the network, the total mass flow is divided by the branching factor of the simulated pipe and the resulting heat transfer of the single simulated pipe is subsequently multiplied by the branching factor. To calculate the heat transfer between the cold district heating network and the surrounding ground the Buried Noded Twin Pipe model (Type 951) developed by TESS is used.

Inside the cold network are two circulation pumps. Their power consumptions $P_{el,i}$ are modeled depending on the mass flow and their respective maximum power consumption:

$$P_{el} = P_{el,max} \cdot \left(0.2 + 0.8 \cdot \frac{\dot{m}}{\dot{m}_{max}}\right) \quad \text{(eq. 4)}$$

The maximum power consumption $P_{el,max}$ is calculated from the maximum volume flow, the corresponding pressure drop of that part of the network Δp and an efficiency of 0.75:

$$P_{el,max} = \frac{\dot{V}_{max} \cdot \Delta p}{0.75} \quad \text{(eq. 5)}$$

To estimate the pressure drop, the pipe diameters and average pipe lengths were used. For the cold grid and the connectors this results in a cumulated pressure drop of 39 kPa. The sum of the pressure drops over the BHE manifolds and distributors depends on the number of boreholes. It varies between 59.3 kPa and 66.2 kPa in the case of 30 and 70 boreholes respectively.

The BHE loop is hydraulically decoupled from the evaporator loop by a hydraulic separator. A circulation pump ensures a turbulent flow through the BHE field all year long. The turbulent flow, a borehole diameter of 152 mm and a shank spacing of the double U-tube heat exchanger of 60 mm result in an internal borehole resistance (R_a) of 0.29 (m·K)/W, an external borehole resistance (R_b) of 0.09 (m·K)/W, and an effective borehole resistance (R_b^*) of 0.0978 (m·K)/W. These values are calculated with the software Earth Energy Designer (EED). The ground properties are provided by a thermal response test. The test results for the depth of 150 m show an average undisturbed ground temperature of 12 °C. The thermal conductivity of the ground is specified as 2.1 W/(m·K), the volumetric heat capacity amounts to 2200 kJ/(m³·K), and the density is estimated at 1650 kg/m³. The measured effective borehole resistance is at 0.08 (m·K)/W and thus corresponds very well with the calculated values.

The initial design of the BHE field includes 70 boreholes of 150 m depth each. This is the maximum number of boreholes, that can be built on this site. The location of the individual boreholes is determined by the positioning of buildings, property lines, and other open space planning of the district. The initial configuration design with 70 boreholes is shown on the left side of figure 4. In a parameter study, the number of boreholes is varied between 30 (4500 m total length) and 70 (10500 m total length) in steps of five boreholes each, resulting in nine variants. For the variants, the outer most boreholes are successively removed from the field. The resulting configuration of 30 boreholes is exemplified on the right side of figure 4.

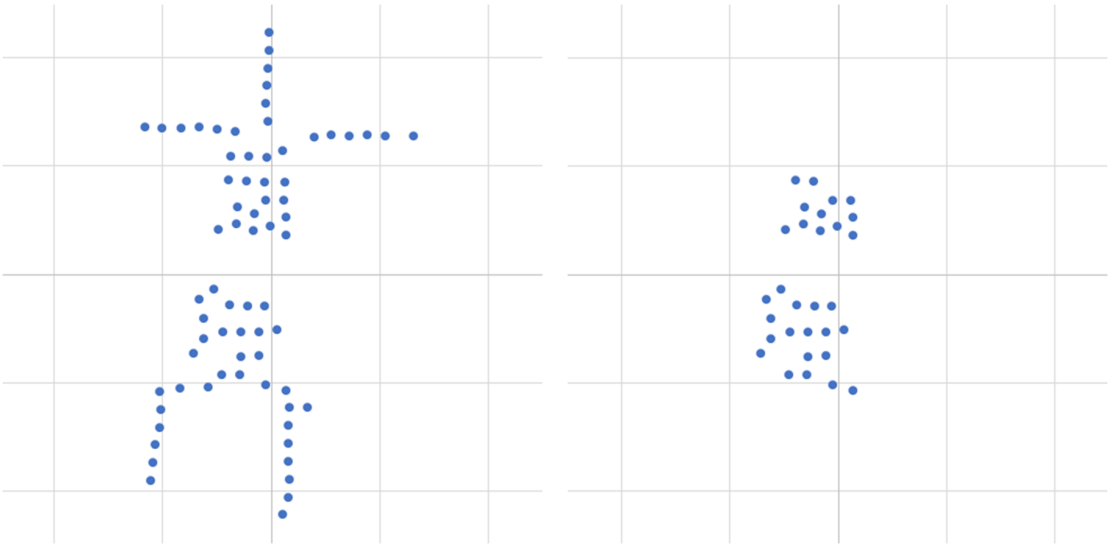

Figure 4: Exemplary BHE field configurations for the parameter study: 70 boreholes on the left side and 30 boreholes on the right side. Each quadrant has a length of 50 m.

The regeneration of the ground is implemented by using PVT collectors, which are incorporated on the return line to the borehole heat exchanger field. The thermal efficiency parameters of the PVT modules are specified by Chhugani et al. (2020) and are shown in table 2:

Table 2: Thermal efficiency parameters of the PVT collector for the open circuit state.

Parameter	Value	Unit	Definition
η_0	0.632	-	zero-loss efficiency of PVT, 0.53 (@MPP)
b_1	19.08	W/(m²·K)	Heat loss coefficient of PVT / c_1
b_2	3.69	J/(m³·K)	Wind dependency of heat loss coefficient / c_3
b_u	0.126	m/s	wind correlation of optical efficiency of PVT collector

The collector field has a slope of 30° and is facing directly south. For the parameter study, the collector area is increased in steps of 100 m² from 0 m² (without regeneration) to 900 m². These ten variants combined with the variations of the BHE field result in a parametric array of 9x10, a total of 90 simulations.

The energetic evaluation criteria of the simulations are the sustainable use of the ground and the efficiency of the heat pumps. In order to ensure a sustainable operation of the geothermal source, the requirements for the use of the ground and the operational restrictions of borehole heat exchangers have to be fulfilled. In Lower Saxony, Germany, the minimum BHE inlet temperature is limited to -3 °C at its peak and to 0 °C for a monthly average (base) to avoid frost conditions in the filling material of the boreholes (Jensen et al., 2022). In contrast, we chose the lowest temperature in the system (evaporator outlet) to incorporate a safety margin. In addition, any long-term increase in groundwater temperature should be avoided. When regenerating the BHE field, this can be achieved if less heat is injected into the ground than extracted. The PVT collectors deliver heat if the temperature hysteresis is 5 K (on) and 2 K (off).

The simulation period as well as the evaluation period is set to 50 years to ensure a long-term operation of the ground source.

The efficiency is evaluated based on the average SPF of the simulation period. The selected evaluation boundaries are decisive for this criterion. In the frame of the IEA SHC TASK 44, Malenkovic et al. (2013) give an overview of the different evaluation boundaries and their suitability for the comparison of different heat supply systems with heat pumps. Gehlin et al. (2022) specify the system boundaries explicitly for ground coupled heat pump systems as part of the IEA HPT Annex 52. Two system boundaries were chosen to assess the efficiency of the system configurations. The first boundary *H1* includes only the heat pump without auxiliary energy (SPF_{H1}). In

addition to the heat pump, the second selected system boundary $H2+$ includes electrical energy for the circulation pumps and fans on the source-side as well as solar regeneration (SPF_{H2+}).

3. Simulation results

To evaluate whether the individual parameter variation complies with the minimum temperature requirements, the lowest monthly average fluid temperature at the outlet of the evaporator (figure 5, left side) and the lowest hourly evaporator outlet temperature (figure 5, right side) are considered. The heat pump systems are designed to operate in monovalent mode. Therefore, configurations that do not meet the minimum temperature requirements are prohibited and marked grey.

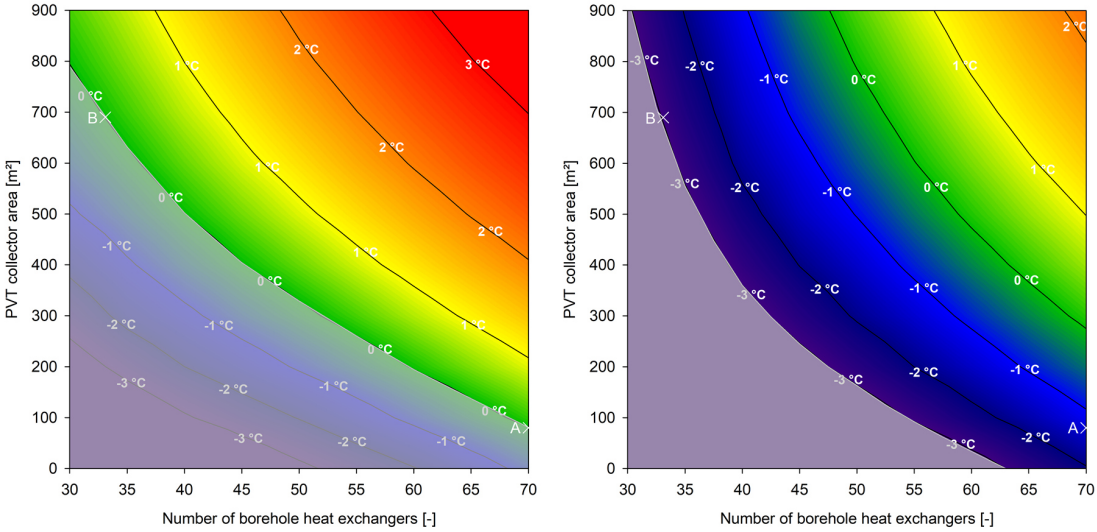

Figure 5: Minimal monthly average evaporator outlet temperature (left) and minimal hourly evaporator outlet temperature (right), A: 70 borehole heat exchangers and 80 m² PVT collectors, B: 33 borehole heat exchangers and 690 m² PVT collectors.

When combining the two minimum temperature requirements the base load is almost exclusively the significant criterion. Only for the smallest BHE field configuration with 30 boreholes, the peak load is the decisive criterion (see figure 6). This can be explained by the fact that a smaller number of boreholes results in a lower usable heat capacity of the surrounding ground to support the heat extraction peaks. Thus, the entire parametric array can be divided into an approvable and a non-approvable (grey) section. Notably, a BHE field with 70 boreholes is not sufficient to be operated without regeneration. The interpolated minimal PVT collector area needed to operate this BHE field is 80 m². This is the base scenario for our further evaluation.

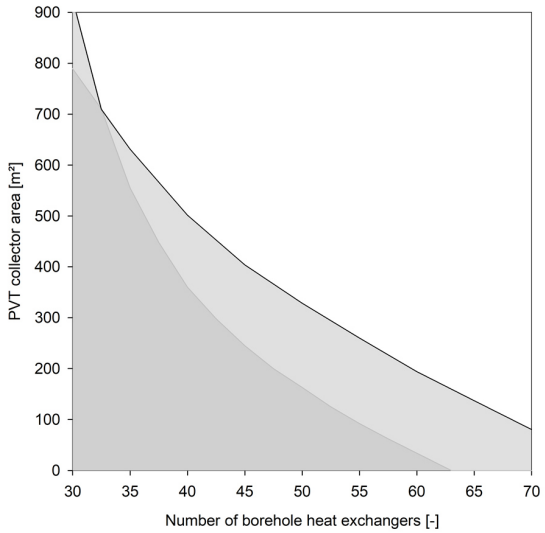

Figure 6: Combined minimum temperature requirement for both base and peak load

The resulting efficiencies of the parameter array are shown in figure 7. The left side features the SPF for the heat pump SPF_{H1}, and the right side features the efficiency of the heat pump including the source-side SPF_{H2+}.

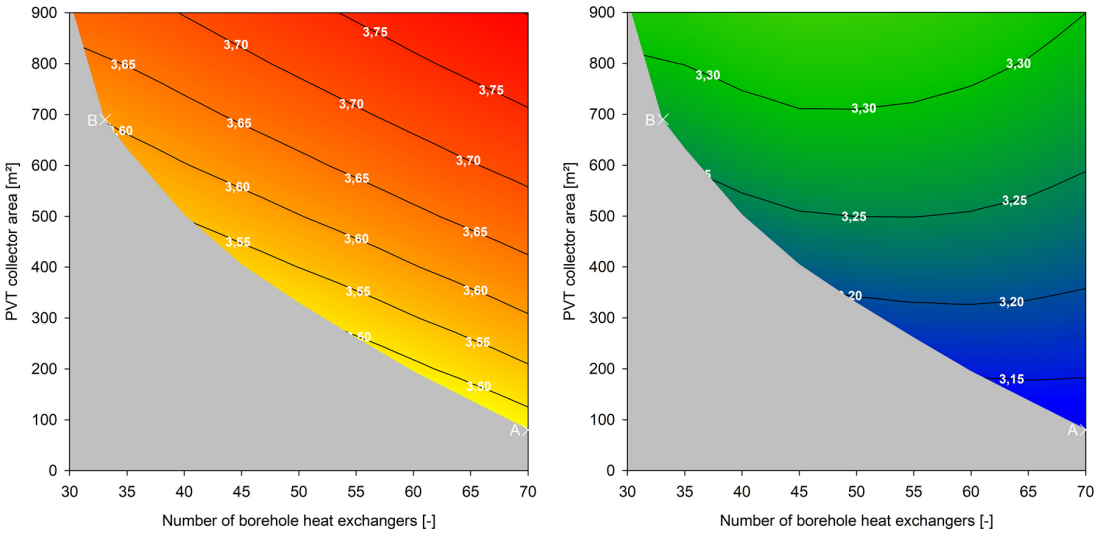

Figure 7: SPF of the heat pumps SPF_{H1} (left) and including the source-side SPF_{H2+} (right) for different no. of BHEs and PVT collector areas. The configurations in the grey area do not meet the sustainability criteria for minimum temperatures, A: 70 borehole heat exchangers and 80 m² PVT collectors, B: 33 borehole heat exchangers and 690 m² PVT collectors.

The results in figure 7 left show that the performance of the heat pump SPF_{H1} improves both with increasing number of boreholes and with increasing PVT collector area. Increasing the number of boreholes by 5 (≙750 m) results in an increase of the efficiency by roughly 0.02. Solar regeneration improves the efficiency of the system approximately by 0.05 per 100 m². In the base scenario of 70 boreholes and 80 m² of PVT collectors an SPF_{H1} of 3.47 is achieved. By using additional 610 m² of PVT panels, the length of the BHE can be reduced by 53 % from 70 to 33 boreholes, or 10500 m to 4950 m, and simultaneously raise the heat pump efficiency to 3.61.

When considering the electrical energy consumption of the circulation pumps on the source side SPF_{H2+} (figure 7 right), the lines with constant efficiency show an optimum. For a given PVT area the efficiency shows a flat minimum, which lies in the range between 45 to 60 boreholes. Due to the higher consumption of the BHE loop circulation pump at higher borehole count, a further increase of the geothermal plant while maintaining the same PVT area, does not improve the SPF_{H2+}.

To further evaluate the results towards a sustainable operation, the net heat extraction from the ground is investigated. The net heat extraction Q_{net} corresponds to the total heat extraction from the ground $Q_{BHE,out}$ minus the amount of heat that is injected into the ground via the borehole heat exchangers $Q_{BHE,in}$ during the same period:

$$Q_{net} = Q_{BHE,out} - Q_{BHE,in} \quad \text{(eq. 6)}$$

In relation to the total source-side heat at the evaporator of the heat pump $Q_{HP,evap}$, the net heat extraction results in the degree of regeneration f_{reg}:

$$f_{reg} = \frac{Q_{HP,evap} - Q_{net}}{Q_{HP,evap}} \quad \text{(eq. 7)}$$

On the left side of figure 8, the achieved degrees of regeneration for the last year of the simulation period are plotted. Additionally, the temperature drops over the last five years of the simulation period is shown in figure 8, on the right side. These temperature differences refer to the end-of-year temperatures of the 45th and the 50th year at the evaporator outlet of the heat pump. A small temperature difference corresponds to a more sustainable operation.

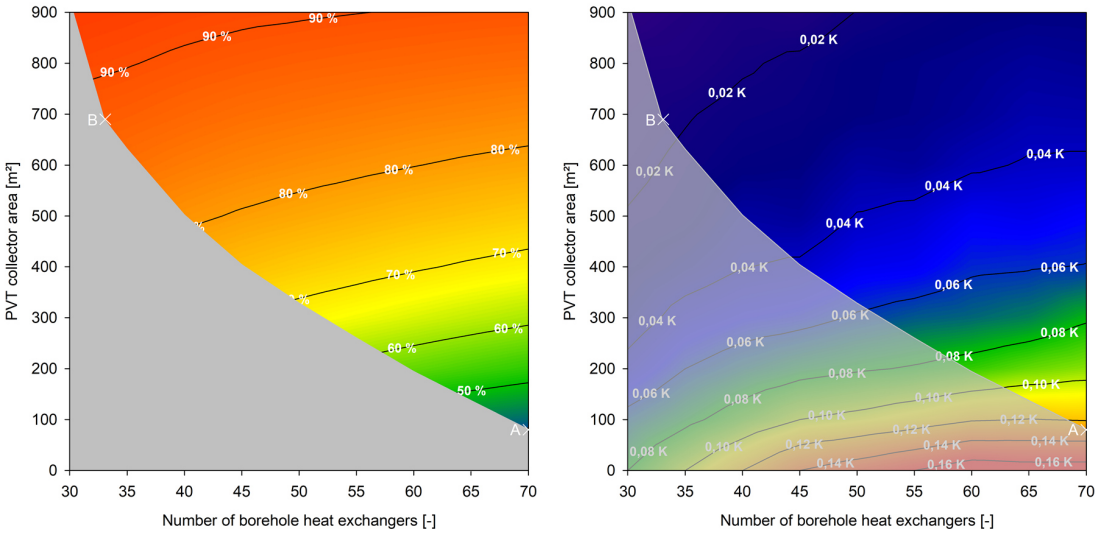

Figure 8: Degree of regeneration (left) and drop of the heat pump evaporator temperature over the last 5 years (right), A: 70 borehole heat exchangers and 80 m² PVT collectors, B: 33 borehole heat exchangers and 690 m² PVT collectors.

The highest degree of regeneration is achieved with the smallest number of BHE and the largest PVT collector area, but stays below 100 %. Smaller fields have higher regeneration degrees than larger fields, since the system is more sensitive to heat loads and the temperatures drops are stronger and thus higher regeneration performances are achieved. However, a complete regeneration or even a net heat injection into the ground is not desirable, since urbanization has already increased groundwater temperatures. A net extraction from the ground can counteract this development to a certain degree.

A higher degree of regeneration leads to a lower long-term reduction of the system temperatures. Thus, a lower temperature difference represents a more sustainable operation. From this point of view, an option with as few boreholes as possible and as much PVT collector area as possible is the most sustainable. The impact of (un)regenerated systems on the ground can also be seen in the horizontal temperature cuts of the two following exemplary variants of 70 BHEs with 100 m² of PVT regeneration and 35 BHEs with 700 m² of PVT regeneration after 50 years of operation (see figure 9).

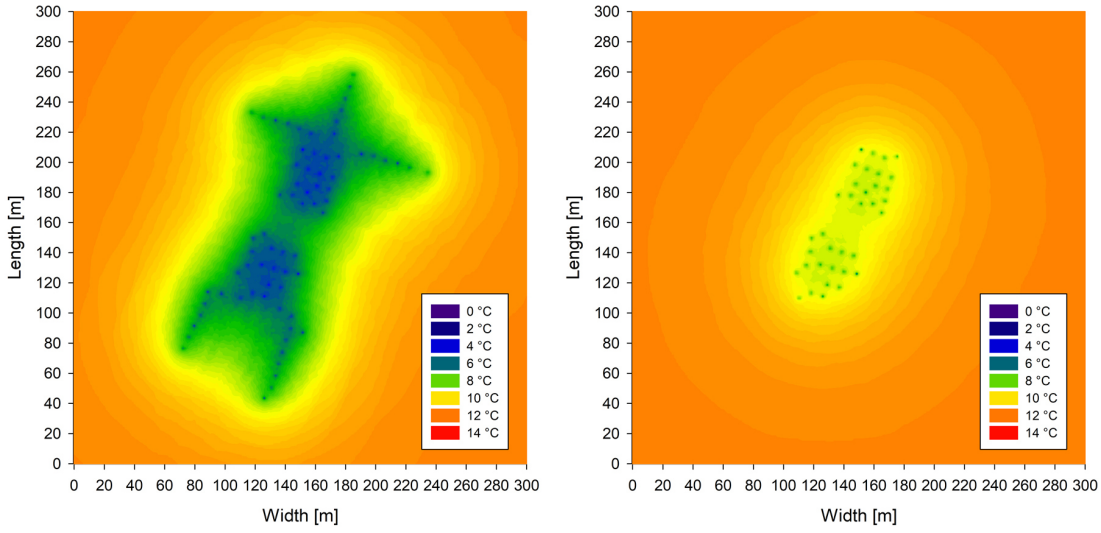

Figure 9: Horizontal temperature cuts at a depth of 75 m after 50 years of operation for a system with low regeneration (left, 70 BHEs and 100 m²PVT) and a system with high regeneration (right, 35 BHEs and 700 m²PVT)

4. Cost analysis

The economic evaluation of the system is based on the static approach of the levelized cost of heat (LCOH)

methodology, as defined by Zenhäusern et al. (2020):

$$LCOH = \frac{K_{INV} - S + \sum_{t=1}^{T} OM_t \cdot (1+r)^{-t}}{\sum_{t=1}^{T} Q_{HP,const,t} \cdot (1+r)^{-t}} \quad \text{(eq. 8)}$$

It includes initial investment costs for the drilling of the borehole heat exchangers, the regeneration with PVT collectors and the cold thermal network K_{INV} as well as a subsidy share S of 49 % of the investment costs and a further construction cost subsidy.

The price assumptions are based on information of an associated planning bureau from 2021. Current developments of inflation and high price increase are not reflected. The specific investment costs for the boreholes k_{BHE} were assumed to be 86 € per meter drilled. For the PVT collectors, only the additional costs compared to simple PV modules are considered, since the areas that are not used for PVT collectors will be used for PV modules any way. These additional specific costs k_{PVT} are assumed to be 370 €/m². The 1912 k€ is the investment costs for the overall cold thermal network including the pipes, sensors, control units and planning. The investment costs are calculated as follows:

$$K_{INV} = 1912\ k€ + k_{BHE} \cdot 150\ m \cdot n_{BHE} + k_{PVT} \cdot A_{PVT} \quad \text{(eq. 9)}$$

The remaining investment costs after deduction of the subsidy and the construction cost subsidy are financed by a loan with a term of T=50 years and at an interest rate r of 5 %. The annual operating and maintenance costs OM_t are dependent on the investment costs:

$$OM = 19\ k€ + (1070\ k€ + k_{BHE} \cdot l_{BHE} + k_{PVT} \cdot A_{PVT}) \cdot 0.0209 \quad \text{(eq. 10)}$$

Earnings due to selling the PV-electricity are not considered and the operating and maintenance costs are kept constant. The electricity price k_{el} used in the calculations is assumed to be 30 ct/kWh. From these generalized assumptions, the Levelized Cost of Heat using the net present value method with the present value $pv = 18{,}3$ is calculated accordingly.

$$LCOH = \frac{(K_{INV} \cdot 0.51 - 1027\ k€ + OM \cdot pv + W_{el} \cdot k_{el} \cdot pv)}{(Q_{HP,cond} \cdot pv)} \quad \text{(eq. 11)}$$

The resulting heat production costs are shown in figure 10.

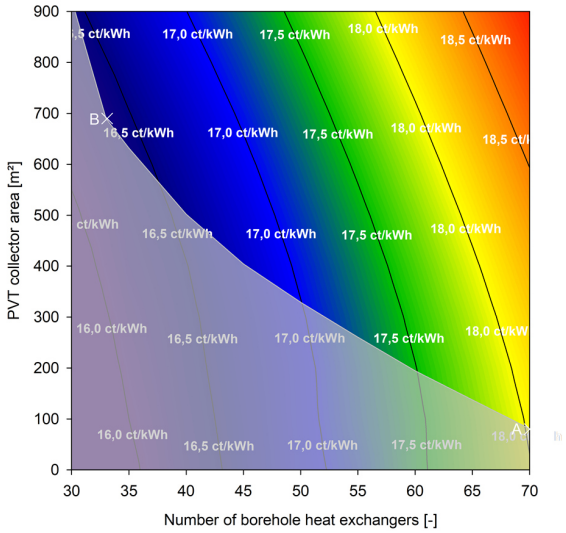

Figure 10: Levelized cost of heat, A: 70 borehole heat exchangers and 80 m² PVT collectors, B: 33 borehole heat exchangers and 690 m² PVT collectors.

The graph shows that solely increasing the PVT collector area is not a profitable option. Thus, for the most favorable number of boreholes, the minimum required collector is always the economically best option. The results show furthermore that variations with a small array of boreholes and a large PVT area are most cost efficient. However, it appears that at about 33 (interpolated) borehole heat exchangers, some sort of tipping point may be reached, beyond which further reduction will drive up the minimum required PVT area such that the Levelized Cost of Heat will be higher. The economically optimal variant is the one with 33 borehole heat

exchangers and 690 m² PVT collectors at below 16.4 ct/kWh. At the current state of the planning process, it seems possible to install the optimal 690 m^2 of PVT collectors. If there appears an installation limit for PVT collectors below 690 m^2 in later stages of the planning or construction process it may be necessary to drill more boreholes.

5. Summary

This paper presents a case study for the sustainable, efficient and cost-effective dimensioning of a cold thermal network with borehole heat exchangers and PVT collectors as the source of a heat pump-based district heating concept with 37 multi-family houses. The results of the TRNSYS simulations can be summarized in the following three statements:

- Firstly, small BHE fields with high degrees of regeneration are more efficient than large fields with little regeneration. For the operation of the largest possible BHE field with 70 boreholes at least 80 m^2 of PVT collectors is needed. By using additional 610 m² of PVT panels, the number of boreholes can be reduced by 53 % from 70 to 33, and the 50-year average SPF_{H2+} is simultaneously rising from 3.1 to 3.27.
- Secondly, small numbers of BHE with large areas of PVT result in the lowest long-term cooling of the ground, and thus are the most sustainable option for using the ground as a heat source for district heating systems.
- Lastly, small BHE fields with minimal required regeneration represent the most cost-effective option. The lowest heat production cost of 16.4 ct/kWh is achieved for the variant with 33 boreholes and 690 m² of PVT collectors. Further addition of PVT collectors to increase system efficiency is not cost effective.

This concludes that saving boreholes by using regeneration should always be considered in the planning phase of large renewable heat supply solutions with heat pumps.

6. Acknowledgement

The joint project "Sustainable operation of large geothermal heat pump systems by regeneration with solar, environmental and waste heat" (Geo-Resume) is funded by the state of Lower Saxony and the German Federal Ministry for Economic Affairs and Climate Action under the reference number 03EE4021A on the basis of a resolution of the German Bundestag. The authors thank for the support as well as for the fruitful cooperation with the project partners of University of Göttingen, LBEG and iNeG. The responsibility for the content of this publication lies exclusively with the authors.

7. References

Auer, F. and Schote, H., 2009. *Zweijähriger Feldtest Elektro-Wärmepumpen am Oberrhein: Nicht jede Wärmepumpe trägt zum Klimaschutz bei*, Final Report, Lahr, Agenda 21 - Gruppe Energie in Lahr.

Braas, H., Jordan, U., Best, I., Orozaliev, J. and Vajen, K., 2020. *District heating load profiles for domestic hot water preparation with realistic simultaneity using DHWcalc and TRNSYS*, *Energy*, vol. 201, 117552. DOI: 10.1016/j.energy.2020.117552.

Chhugani, B., Pärisch, P., Kirchner, M., Littwin, M., Lampe, C. and Giovannetti, F., 2020. *Model Validation and Performance Assessment of Unglazed Photovoltaic-Thermal Collectors with Heat Pump Systems*, *Proceedings of the ISES EuroSun 2020 Conference – 13th International Conference on Solar Energy for Buildings and Industry*, Online, International Solar Energy Society. DOI: 10.18086/eurosun.2020.05.13.

DIN, 2012. *DIN 1988-200:2012-05 Codes of practice for drinking water installations - Part 200: Installation Type A (closed system) - Planning, components, apparatus, materials; DVGW code of practice*, Berlin, Deutsches Institut für Normung. DOI: 10.31030/1887421.

DVGW, 2004. *DVGW W 551:2004-04 Drinking water heating and drinking water piping systems - Technical measures to reduce Legionella growth - Design, construction, operation and rehabilitation of drinking water installations*, Bonn, Deutscher Verein des Gas- und Wasserfaches.

Fascì, M. L., Lazzarotto, A., Acuña, J. and Claesson, J., 2021. *Simulation of thermal influence between independent geothermal boreholes in densely populated areas*, *Applied Thermal Engineering*, vol. 196, 117241. DOI: 10.1016/j.applthermaleng.2021.117241.

Gehlin, S., Spitler, J. D., Witte, H., Andersson, O., Berglöf, K., Davis, M., Javed, S., Bockelmann, F., Turner, J. and Clauss, J., 2022. *Guide for analysis and reporting of GSHP system performance - system boundaries and key performance indicators (KPI)*, IEA HPT Annex 52 - Long-term performance monitoring of GSHP systems for commercial, institutional, and multi-family buildings. DOI: 10.23697/XA7Z-VD92.

Günther, D., Wapler, J., Langner, R., Helmling, S., Miara, M., Fischer, D., Zimmermann, D., Wolf, T. and Wille-Hausmann, B., 2020. *WPsmart im Bestand - Felduntersuchung optimal abgestimmter Wärmepumpenheizungssysteme in Bestandsgebäuden beim Betrieb im konventionellen sowie im intelligenten Stromnetz (Smart Grid)*, Final Report, Version 2.1., Freiburg. DOI: 10.2314/KXP:1747246166.

Jensen, H., Pester, S., Schöner, R., Dube, C., Lipkow, U., Hause, A., Duddek, M. and Fischer, K., 2022. *Leitfaden Erdwärmenutzung in Niedersachsen: Rechtliche und technische Grundlagen für erdgekoppelte Wärmepumpenanlagen*, Landesamt für Bergbau, Energie und Geologie. DOI: 10.48476/GEOBER_24_2022.

Malenkovic, I., Pärisch, P., Eicher, S., Bony, J. and Hartl, M., 2013. *Definition of Main System Boundaries and Performance Figures for Reporting on SHP Systems*, IEA SHC Task 44 / HPP Annex 38. DOI: 10.18777/ieashc-task44-2013-0009.

Miara, M., Günther, D., Kramer, T., Oltersdorf, T. and Wapler, J., 2011. *Wärmepumpen Effizienz: messtechnische Untersuchung von Wärmepumpenanlagen zur Analyse und Bewertung der Effizienz im realen Betrieb*, Final Report, Freiburg, Fraunhofer ISE. DOI: 10.2314/GBV:665477864.

Persdorf, P., Ruesch, F. and Haller, M., 2015. *RegenOpt - Optionen zur Vermeidung nachbarschaftlicher Beeinflussung von Erdwärmesonden: energetische und ökonomische Analysen*, Final Report, Zurich, Switzerland, City of Zurich.

Sauter, D., Hunziker, M., Poppei, J., Cochand, F., Hubbuch, M. and Rohrer, J., 2021. *Solar Thermal Regeneration of Borehole Heat Exchangers in Urban and Suburban Districts*, *Journal of Physics: Conference Series*, Lausanne, Switzerland, vol. 2042, 012094. DOI: 10.1088/1742-6596/2042/1/012094.

Heat Pump Test Center WPZ, 2021. *Test results brine / water & water / water heat pump*, Eastern Switzerland University of Applied Sciences [Online]. URL: https://www.ost.ch/en/research-and-consulting-services/technology/system-technology/ies-institute-for-energy-systems/heat-pump-test-center-wpz/test-results-of-heat-pump Accessed 12 September 2022.

Witte, H. J. L., 2018. *A Novel Tool for Assessing Negative Temperature Interactions between Neighbouring Borehole Heat Exchanger Systems*, Adana, Türkiye.

Zenhäusern, D., Gagliano, A., Jonas, D., Tina, G. M., Hadorn, J.-C., Lämmle, M. and Herrando, M., 2020. *Key Performance Indicators for PVT Systems*, IEA SHC Task 60. DOI: 10.18777/ieashc-task60-2020-0007.

F. Innovative Industrial Process Heat

Non-Tracking Asymmetric Shadeless (NASH) Solar Collectors for Decarbonizing Industrial Process Heat

Yogesh Bhusal[1], Bennett Widyolar[1], Jordyn Brinkley[1], Mahmoud Abido[2], Roland Winston[1]
[1]Winston Cone Optics, Merced-CA (USA)
[2]University of California Merced-CA (USA)

Abstract

This work reports the development and year-long performance of an innovative non-tracking asymmetric shadeless (NASH) solar collector designed using nonimaging optics. The NASH collector can efficiently convert solar irradiance into thermal energy that is suitable for industrial process applications that need temperatures up to 200 °C. NASH design eliminates the need for row-to-row spacing as in conventional tilt-installed collectors and can be installed on ground and flat or slant roof without wasting any space. The collector has a nonimaging reflector that concentrates sunlight (from acceptance angle -75° to 5° from vertical) on the evacuated receiver tube with a geometric concentration ratio of 1.72X. Five early prototype modules are fabricated and tested for performance measurement. The collectors have demonstrated an optical efficiency of 58-60%, a peak efficiency of 50% while operating at 120 °C and full-year-average daily solar to thermal conversion efficiency of 42% for the year of 2022, while operating around 120 °C. The collectors were also tested at operating temperature of 150 °C and achieved solar-to-thermal conversion efficiency of >40%. The thermal energy generation of the collector at or near 120 °C ranged from 1 to 3.5 kWh/m^2/day over the year with lowest in winter months and highest in summer months.

Keywords: nonimaging optics, XCPC, NASH, solar thermal collector, solar thermal energy

1. Introduction

In 2021 out of 97.3 quadrillion BTUs (28516 TWh) total primary energy consumption in US, the industrial end use sector accounted for its 35% and was responsible for 30% of the total energy related CO_2 emissions in US. The majority (40%) of the energy consumption in the industrial sector is provided by natural gas and second to that (34%) by petroleum. Moreover, thermal energy consumption in industrial, residential and commercial sectors account for 23%, 7% and 4% respectively, of the total primary energy consumption in US (B. Widyolar et al. 2021). About 33% of this thermal energy consumed in industrial sector is utilized in process applications below 100 °C, about 44% between 100-500 °C, 13% between 500-1000 °C and 9% above 1000 °C (McMillan et al. 2021). Solar thermal energy technology is a promising renewable energy option to decarbonize these industrial thermal processes applications. In solar thermal energy technology, the more common flat plate collectors and evacuated tube collectors are mostly used for residential purposes and are not efficient at the temperatures above 80 °C and high-concentration solar thermal systems like PTC and Heliostat towers are economical only in large scale installations. Our team led by professor Roland Winston has developed and demonstrated the external compound parabolic concentrator (XCPC) technology since 2009 at the University of California Merced for applications like food processing (drying), wastewater evaporation and solar cooling with double effect LiBr absorption chiller.(B. Widyolar et al. 2021; Ferry et al. 2020; B. Widyolar et al. 2014; Milczarek et al. 2017; B. K. Widyolar et al. 2019). XCPC collectors are designed using nonimaging optics, can collect solar radiation throughout the day and year-round from a stationary position (non-tracking) and have no moving parts except for the pump for heat transfer fluid. During module level testing, at peak solar irradiance normally incident upon them, XCPCs have efficiently generated thermal energy at 100 °C and 200 °C at 60% and 50% solar to thermal conversion efficiency respectively(B. Widyolar et al. 2018).

In this work we report the development of an innovative variation of XCPC, called non-tracking asymmetric shadeless (NASH) collector which has an aperture parallel to the horizontal and can be installed flat on any surface without requiring row to row spacing. We have built and tested five prototype modules of the NASH collector each with an aperture area of 2.85 m^2 at UC Merced research facility in Atwater, CA. Among these five prototype modules, two modules are tested for a yearlong performance measurement while operating at ~120 °C, two modules are tested using vacuum intact (good vacuum) receiver tubes on one module and vacuum-lost (bad vacuum) receiver tubes on

© 2022. The Authors. Published by International Solar Energy Society
Selection and/or peer review under responsibility of Scientific Committee
doi:10.18086/eurosun.2022.05.01 Available at http://proceedings.ises.org

the other module, for performance comparison while operating above 100 ºC and the fifth module is tested for stagnation with both good and bad vacuum receiver tubes. The NASH collector design including optical parametric optical simulations, FEA thermal fluid modeling and the experimental results of all three tests are discussed in this paper.

2. Collector Design

In this work we have redesigned the optics of external compound parabolic concentrator (XCPC) to develop an innovative stationary, non-tracking asymmetric shadeless (NASH) collector that is capable of efficiently converting solar irradiance into thermal energy up to 200 ºC. The original nonimaging XCPC collectors were installed in a conventional tilt design generally at latitude angle tilt, requiring the spacing between the rows to prevent the self-shading. The proposed new design NASH collector can be installed with horizontal aperture parallel to the ground/flat roof/slant roof (with some modification) and eliminates the need for spacing between the rows, thus allowing the land area that would otherwise be wasted to prevent row-to-row shading, to be utilized for active solar collection. This distinction between tilt collectors and proposed NASH collector is illustrated in **Figure 1 left**. No row-to-row spacing enables the equivalent-sized NASH solar collector array to be installed on a much smaller land footprint than the tilt design XCPC collectors. Moreover, this reduces the balance of system (BOS) costs by reducing the pipe lengths, insulation length, fluid volume thus reducing system warming up heat and heat losses from the longer pipes otherwise. The compact and low-profile flat installation causes low wind load on the collector and reduces structural design requirements against high winds. The NASH collectors can be installed on flat roof, slant roof, on ground and on façade without need for tilted frames. The collector modules are of robust construction made of Aluminum square tube framing and can be stacked on top of each other or be laid on their sides for transportation from one site to another. Also, the components can be easily disassembled and transported separately from one site to another site of installation.

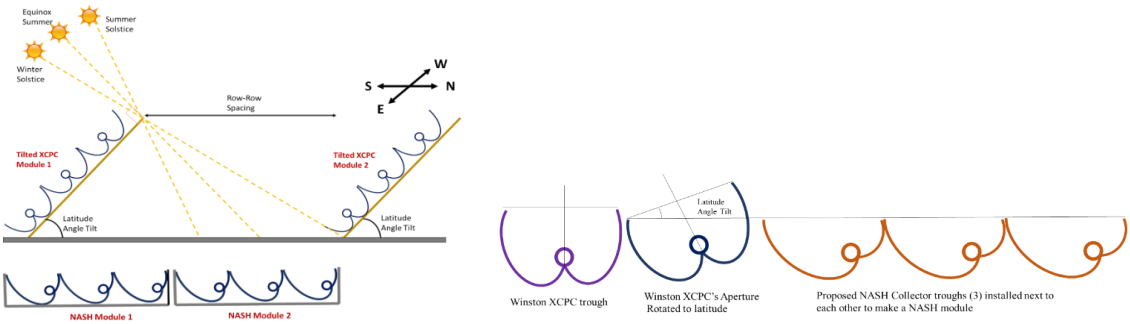

Figure 1.(left) Comparison of tilt installed XCPC collectors with row-to-row spacing and proposed shadeless NASH collector (right) Design steps of NASH collector.

The NASH design involves first generating the original XCPC trough for two inputs, a desired absorber diameter and acceptance angle, as described in the previous work (B. Widyolar et al. 2018; Winston, Jiang, and Ricketts 2018). Then the XCPC is rotated in an anticlockwise direction, usually at an angle equal to the latitude of the location to be installed on. Then the right-side reflector curve of XCPC is cut to the height of the left-side reflector curve to create horizontal aperture. Then the second similar trough can be placed next to the first one, in contact, without causing shading from the first trough, as illustrated in **Figure 1 right**. The shape of NASH collector shown in the paper does not represent the exact design curvature and is sketched only for illustration because of a patent in process.

A NASH collector module with a 2.85 m^2 aperture area has a gross land footprint of 3.64 m^2, giving the land fill-factor of 78%. Design specifications of a NASH module are listed in **Table 1**. **Figure 2** shows a CAD model and fabricated prototype of a three-tube NASH collector module. A NASH module has five major components- Frame, Reflector (3 troughs), Evacuated receivers (3 tubes) and Manifold. The reflector troughs and receivers are oriented in east-west directions just like the original XCPC collectors. Each trough's aperture can accept the sunlight between the acceptance angle of -75º to +5º due south from the vertical, enabling the collection of sunlight between the summer and winter solstice without any mechanical tracking. This angle is selected for NASH collector designed for latitude range (32-42º) of California USA but can be custom designed for any other latitude locations.

In each trough the nonimaging reflector of aperture 498 mm provides the geometric concentration of 1.72X at the 90 mm diameter absorber in metal-glass sealed vacuum receiver. The selectively coated Aluminum absorber fin (solar absorptance 95% and <8% infrared emittance) in the receiver tube absorbs 95% of the concentrated sunlight and limits the infrared re-radiation to less than 8% and the vacuum insulation in the receiver prevents the convection heat losses to the environment, thus ensuring efficient operation of the collector regardless of the ambient temperatures. The 80 inches long vacuum receiver is a borosilicate glass tube that houses a selectively coated low-cost Aluminum absorber fin in a decagon cross-section and a copper U-tube fluid channel that is ultrasonically welded to the inner surface of the absorber fin to ensure optimal conduction heat transfer from Aluminum absorber fin to the U-tube copper fluid channels. The reflectors are low-cost Aluminum sheet metal laminated by Mylar film and shaped to a nonimaging concentrator shape. These reflectors are paired with patented metal-glass vacuum receiver tubes and assembled on a robust Aluminum ribs and framing.

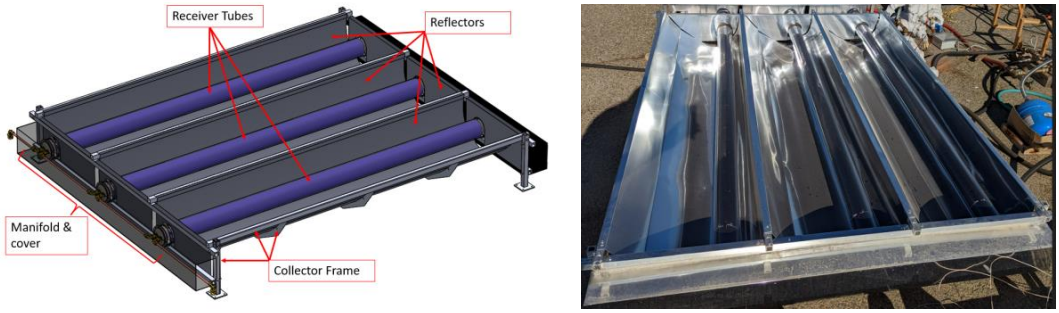

Figure 2. (left) Solid model of the NASH collector module and (right) prototype module.

Table 1. Design specifications of NASH collector module

Aperture area	2.85 m^2
Concentration ratio	1.72 X
Acceptance angle	±40° from 35° Latitude tilt or -75° to +5° from vertical
Troughs/tube length orientation	East-West
Land footprint/ Fill factor	3.64 m^2 / 78%
Collector height / weight	1 ft / 88 lbs
Working temperature	up to 200 °C

3. Performance Modeling

Firstly, a curvature of NASH reflector was generated using edge ray principle and string method of nonimaging optics by using the absorber size and acceptance angle and steps discussed in Design section. Then the corresponding optical model was created in a ray tracing simulation software, Light tools. **Figure 3** shows the optical model of the NASH collector trough of three design considerations: rotated and cut CPC (proposed design), full ACPC (alternative design) and half ACPC (alternative design). A parametric analysis was conducted to compute the shape efficiency or the intercept factor by considering ideal optical properties of reflector, glass tube and absorber, as a function of solar incidence angle from -90 to +90 degrees that represents the seasonal variation of the Sun's position in sky. An ideal solar collector will have shape efficiency/intercept factor of 1 for all angles within the acceptance angle. All three designs of NASH collector are developed to accept/collect the solar radiation incident from the range of -75° (rays coming from the left side of the vertical, representing solar incidence during equinox, winter solstice and most of the summer) to +5° (right side of the vertical, representing solar incidence during peak summer).

Again, the optical efficiency was also computed by assuming the incident light had a ±0.25° beam angle to approximate the solar disk angle, a reflector with 88% reflectance (Mylar film), a Borosilicate Glass tube envelope with Fresnel losses (4% loss on both glass surface) and the absorptance of the selectively coated absorber as 95%. The shape efficiency or intercept factor and optical efficiency of different designs of NASH collector are shown in plots in **Figure 4 and Figure 5.** The optical efficiency is the average of these shape efficiency/intercept factor at

different solar incidence angles within the acceptance angle range. The average optical efficiency of the NASH collector was computed to be 70%.

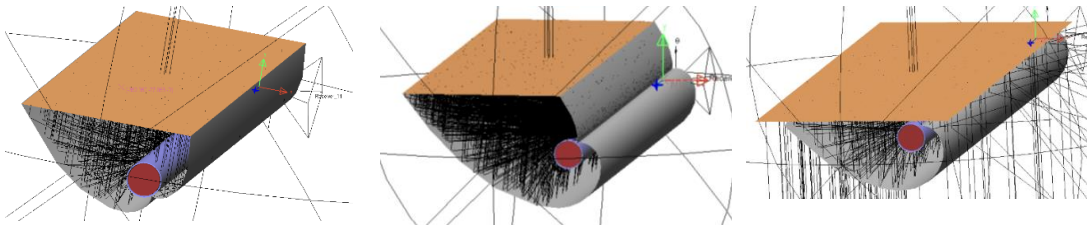

Figure 3. Ray-tracing simulations of different NASH collector designs: (left) Rotated and cut CPC, (middle) Full ACPC and (right) half ACPC

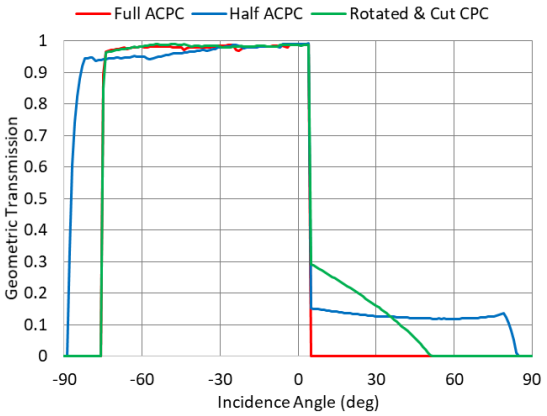

Figure 4. Intercept factor of different designs of NASH collector as a function of solar incidence angle

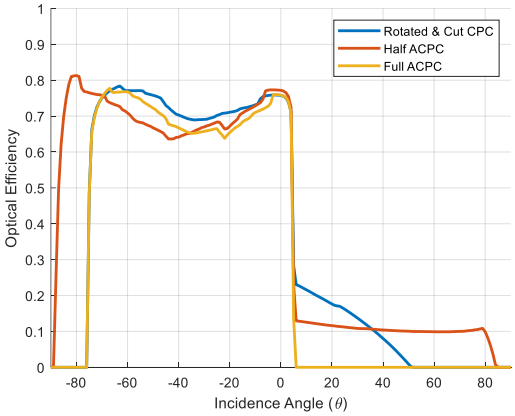

Figure 5. The optical efficiency of different designs of NASH collector as a function of solar incidence angles.

Using the average optical efficiency and the energy balance of incident solar power on to the absorber, thermal losses from the absorber at elevated temperature the theoretical thermal model of the NASH collector was developed and is shown in **Figure 6.** The plot shows the average optical efficiency from optical model (~70%) and the estimated solar to thermal energy conversion efficiency using the 25 g/s flow rate of 50/50 water/propylene glycol heat transfer fluid (HTF) under 1000 W/m^2 solar irradiance, at different working temperatures. The efficiency of the collector keeps decreasing as the working temperature increases and the collector stagnates (zero efficiency) at 370 ^{o}C. **Figure 7** shows the solar-to-thermal conversion efficiency plot of the proposed NASH collector at standard solar irradiance of 1000 W/m^2 and the lower levels of solar irradiances. The same collector will perform with lower thermal efficiency at the same temperature and will also stagnate at lower temperature. **Figure 8** shows the solar-to-thermal performance of NASH collector at solar irradiance of 1000 W/m^2 for varying flow rates of 50/50 water and propylene glycol. The curves show that the turbulence of HTF in the fluid channels is very important for efficient heat transfer from fluid channel walls to the HTF.

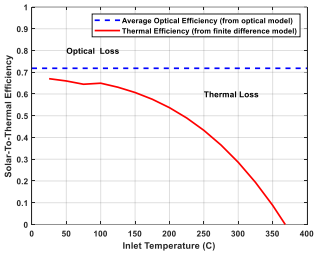

Figure 6. Modeled instantaneous solar-to-thermal efficiency of NASH collector with 25 g/s flow rate of 50/50 water/propylene glycol HTF under 1000 W/m^2 solar irradiance.

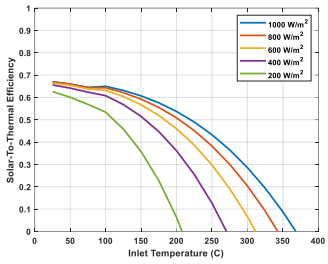

Figure 7. Solar-to-thermal performance of the NASH collector with a 25 g/s flow rate of 50/50 water/propylene glycol HTF under varying solar irradiance.

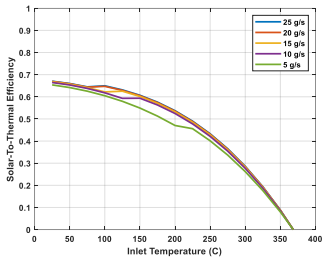

Figure 8. Solar-to-thermal performance of the NASH collector with 50/50 water/propylene glycol HTF under 1000 W/m^2 solar irradiance at varying flowrates.

Then, using the hourly solar resource data from TMY3 database for Merced, CA, an annual model was created which shows the daily solar energy available (solar insolation KWh/m^2/day), the solar energy absorbed by the collector at its optical efficiency also in (kWh/m^2/day) and the thermal energy generation (kWh/m^2/day) by the NASH collector while operating at 150 ^{o}C and are plotted in **Figure 9(left).** Moreover, the solar thermal power available, solar thermal power absorbed at optical efficiency and solar thermal power generated (at 150 ^{o}C) throughout the day in March 20, 21 and 22 of a typical year are shown in **Figure 9(right).** This thermal generation is obtained by subtracting the radiation losses from the collector at the operating temperature (here 150 ^{o}C) from the solar power absorbed by collector at its optical efficiency. The model does not consider the thermal losses from plumbing, storage tanks and other parasitic losses that depend on installations and thermal load types.

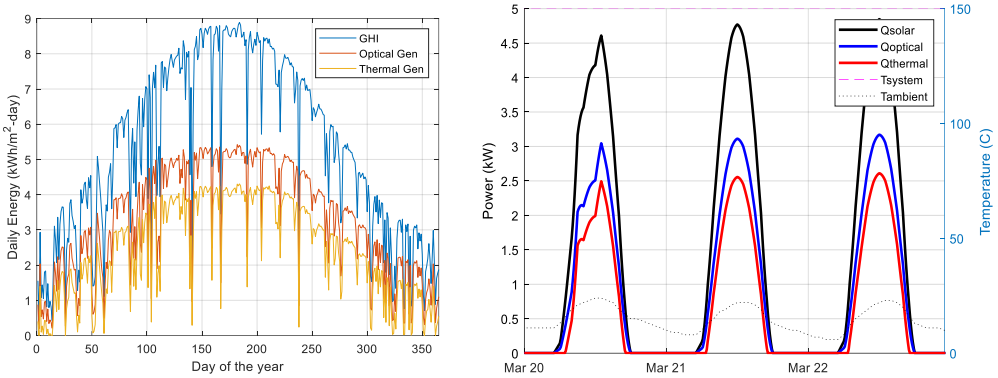

Figure 9. (left) Modeled daily available solar energy using TMY3 Global Horizontal Irradiance data, optical generation (energy absorbed by collector) and useful thermal energy carried by HTF while operating at 150 ^{o}C, all in KWh/m^2/day, from NASH collector in Merced, CA. (right) The solar incident power, absorber power and thermal generation (at 150 ^{o}C system operation) by two NASH modules (6 troughs, 6 tubes)

Moreover, FEA simulations were performed in COMSOL Multiphysics to determine the absorber fin material and the fin thickness. The thermal energy is generated at the absorber fin by the impingement of concentrated sunlight. This heat then transfers from the fin surface to the fluid channels (via conduction) through the 5 mm wide ultrasonic weld (contact surface of fluid channel and fin). Then the heat transfers from the inner surface of fluid channel to fluid by internal forced convection. The concentrated heat flux input was assigned to the specific boundary of the decagon absorber fin. The radiation boundary condition was applied to the full surface of the decagon absorber, the convection boundary condition (h) was applied to the inside surface of the fluid channels and the conduction was considered in all solids. The model was then meshed and computed for temperature distribution. The simulated stagnation temperature at the decagon shape absorber fin and U tubes are illustrated in **Figure 10** where it is seen that the highest temperature at absorber fin is 370 ^{o}C which is at the region of absorber fin where the sunlight is concentrated (at right surface of decagon fin) at vertical solar incidence and at the fluid channel is ~330 ^{o}C. **Figure 11** shows the temperature distribution at absorber fin and fluid channel when a 50 ^{o}C water flows through the fluid channel (copper tube) at 100 g/s. **Figure 12** shows the temperature distribution at absorber fin and fluid channel when a 200 ^{o}C duratherm oil is flowing through the collector at 100 g/s. There is approximately 40 ^{o}C temperature gradient

between the hottest spot in the absorber fin (a section of decagon absorber fin where concentrated sunlight impinges) and the U tube fluid channel. Eventually after conducting the FEA simulations and considering the much lower cost of Aluminum and yet its decent conductivity, an Aluminum absorber fin of 0.4 mm thickness and Copper U tube fluid channel of 6.5mm ID, 8 mm OD were selected for manufacture.

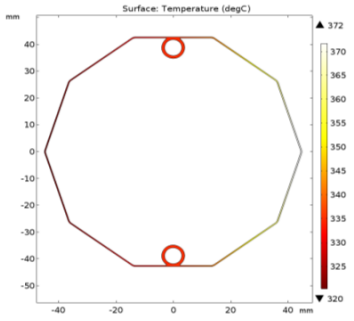

Figure 10. Stagnation temperature of aluminum fin and copper tube fluid channel

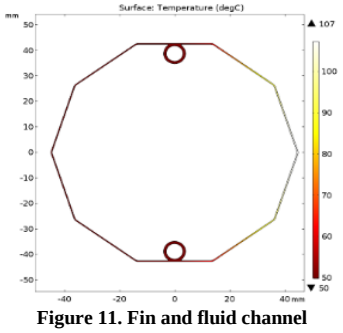

Figure 11. Fin and fluid channel temperatures as 50 ºC water flows through the tubes at 100 g/s

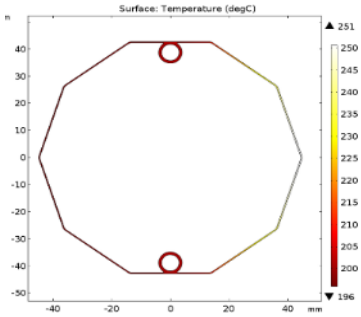

Figure 12. Fin and tube temperatures as 200 ºC duratherm oil flows through the tubes at 100 g/s

4. Experimental Results

4.1. Stagnation Temperature

To measure the highest collection temperature of the collector, a NASH module with one good vacuum receiver tube and two vacuum-lost receiver tubes, referred to as bad vacuum tube, was tested to stagnate on Sun with no heat transfer fluid moving through the collector, shown in **Figure 13**. In this case, the only heat lost by the absorber is the infrared thermal radiation emitted by the selective coated absorber in the vacuum tube. The top tube is non-evacuated and provides the maximum temperature achieved by a receiver tube that has lost its vacuum. The middle tube is evacuated, providing the maximum temperature achieved by the receiver tubes. Temperatures are measured using thermocouples directly inserted into the heat transfer fluid channels, so they are roughly in the middle of the tube, along the length. The evacuated tube has two thermocouples, one inserted in the receiver tube channel facing the short reflector length and one inserted into the opposite receiver tube channel facing the long reflector length (higher concentration ratio of light focused onto this side). The stagnation temperatures of these good and bad vacuum tubes were measured from June 8th to July 20th, 2022. The module under stagnation and the stagnation temperature data are shown in Figure 14. The evacuated receiver tube on a cleaned collector reached a maximum stagnation temperature of up to 330 ºC and remained >300 °C even on partly cloudy days and with dusty reflectors. The bad vacuum or non-evacuated tube reached a temperature of about 230 °C.

We performed a more than a month-long stagnation test of the collector as destructive testing to understand the worst-case operating condition of the collector. In real world installation, the solar thermal array and the heat transfer fluid loop should be engineered to avoid stagnation. Stagnation of solar thermal array can occur if the HTF pump stops either due to power outage or pump failure. This causes the stagnant overheating of heat transfer fluid and extreme pressures build up inside the collectors' fluid channels and fluid handling system. This could cause undesirable thermal loop expansion, a plumbing system failure, equipment failure and personal injury. The stagnation control strategy such as installation of mechanical pressure relief valve (PRV) at the outlet is important to prevent system failure due to pump-failure stagnation. Whereas sometimes the high temperatures can build up when heat transfer fluid cannot dump heat to the load. In this case, a temperature control heat dump (radiator and fan) should be installed to control the temperature rise in the solar array.

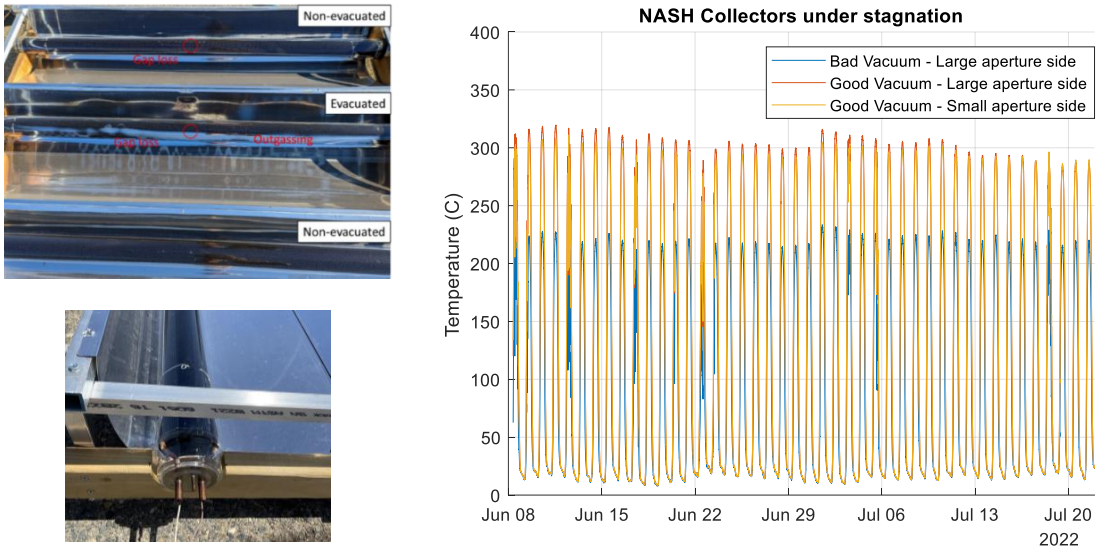

Figure 13. (left) A NASH module with two bad vacuum receiver tubes and one good vacuum receiver tube under stagnation test, and closeup of thermocouple wires inserted into a receiver tube and (right) the stagnation temperature plot.

4.2. First Two Prototype Modules (Full Year Testing)

The first two prototype modules (Aperture area 2 x 2.85m^2=5.7 m^2) of NASH collectors were connected in series and set for long-term performance measurement while operating above 100 ^{o}C. **Figure 14** shows the first and second prototypes of NASH collectors undergoing long-term testing. A solar circulating pump station (SRS-145-5.1) is used to circulate the heat transfer fluid(water) through the collectors and internal copper heat exchanger coils in the 53-gallon solar hot water tank (DUDA Solar). The pump control system turns the pump on every morning when the solar sensor measures the irradiance of 150 W/m^2 or if the solar loop fluid goes below 0 ^{o}C (for freeze protection) and keeps the pump turned off otherwise. During sunny hours, the water in the tank is indirectly heated by the HTF in heat exchanger coils. The water in the tank is free to evaporate out of the tank-top opening to the atmosphere as it is heated to 100 ^{o}C by the circulating HTF. The mass flow rate in the loop is measured by using a Coriolis flowmeter with frequency output. A PSP solar sensor (voltage output) placed on the same horizontal plane as the collector aperture measures the incoming Global Horizontal Irradiance (GHI). Temperatures at the collector inlet/outlet and tank inlet/outlet are measured by thermocouples directly inserted into the flow path. The data is logged every 5 seconds using the DI 808 web-based data logger from DATAQ instruments. Loop pressure was measured using an absolute pressure transmitter with a 0-5 V signal output.



Figure 14. Prototype 1 and 2 undergoing long-term testing at temperatures >100 ^{o}C

Every 5 seconds, the GHI, collector inlet/outlet temperatures and flowrate are recorded. The thermal power absorbed by the HTF is calculated by the product of mass flow rate, specific heat capacity and temperature rise in the collector inlet/outlet. The thermal power absorbed is divided by the incident solar power (product of GHI and collector aperture) to give the instantaneous solar to thermal conversion efficiency.

$$\eta = \frac{mc_p(T_o - T_{in})}{\text{GHI} * \text{Collector Aperture Area}} \qquad \text{(eq. 1)}$$

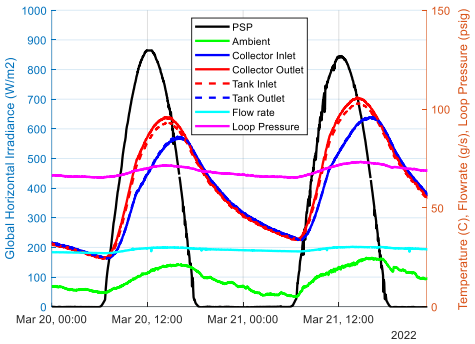

Figure 15. Instantaneous plot of GHI, collector and tank inlet/outlet temperatures, mass flowrate and loop pressure

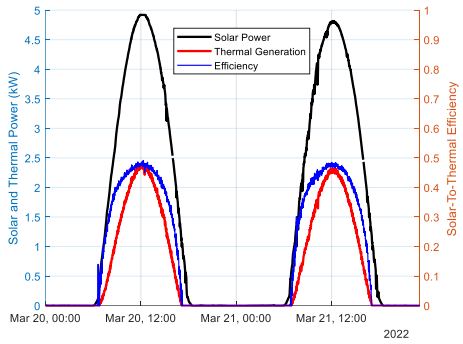

Figure 16. Instantaneous plot of incident solar power, thermal power generated and the instantaneous efficiency.

Figure 15 and **Figure 16** show the instantaneous plots of operating temperatures and instantaneous incident solar power, thermal power generated by the collector and the instantaneous efficiency of the collector. Then for each full day, the area under the thermal generation curve (power x timestep = kWh) is divided by the area under incident solar power (also in kWh) to obtain the solar to thermal conversion efficiency of that day, called daily efficiency. For each month these daily efficiencies and other measurements were consolidated and plotted for the full month starting in Figure 18. The left plot on each figure shows the daily data such as maximum ambient temperature, maximum temperature on solar HTF, maximum tank temperature, maximum and minimum loop pressure, and maximum wind speed. The right plot shows the solar insolation (KWh/m^2) measured every day.

Figure 17 shows the performance data measured during the month of January. Due to the ambient temperature below 0 ºC during January, the loop did not go above 100 ºC except during one temporary stagnation that recorded higher temperature. Average daily efficiency for the month of January was 49%.

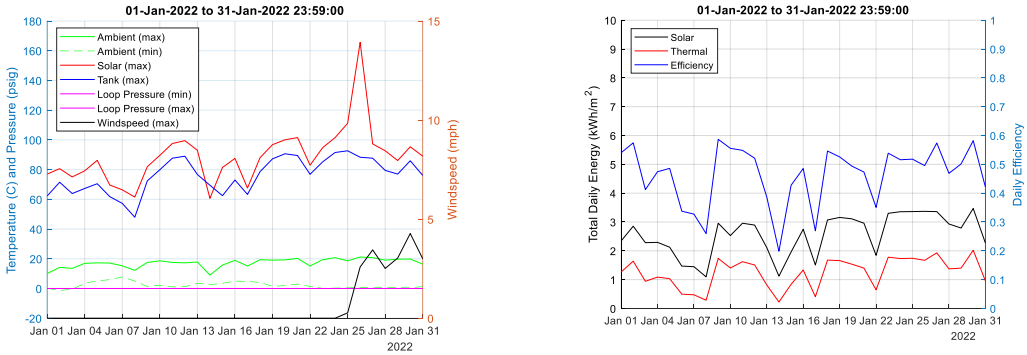

Figure 17. January performance measurement

Figure 18 shows the performance in June, which was also as expected, and the average daily efficiency in June was 42%.

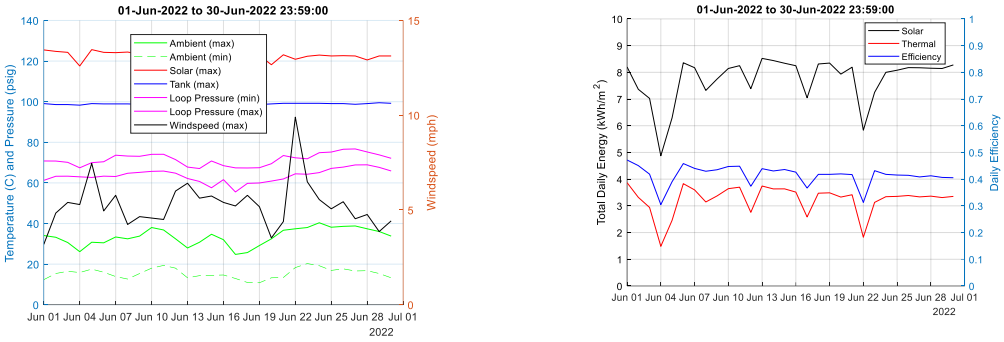

Figure 18. June performance measurement

Figure 19. shows the performance in July, which was also as expected, and the average daily efficiency in July was 45%.

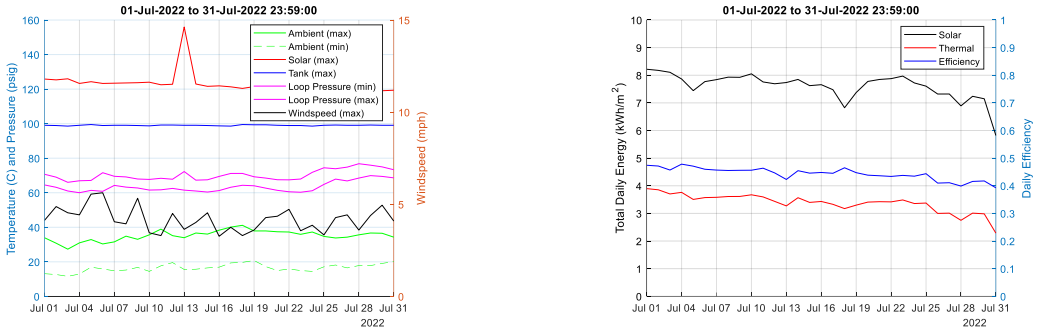

Figure 19. July performance measurement

These measurements were recorded for each day in the year 2022 starting January 01 to Dec 31. The collectors were cleaned on the first day of each month. The monthly averages of modelled solar, measured solar, modelled thermal generation, measured thermal generation are also calculated and plotted in **Figure 20**. It seems that thermal energy generation by NASH collectors (purple line) ranges between **1 kWh/m^2/day** in the winter months to upto **3.5 kWh/m^2/day** in summer months. The measured thermal generation seems to be approximately equal to 42% of total measured solar insolation (GHI), which is shown as new model curve. Due to the horizontal aperture NASH collector collects maximum solar insolation during the summer months when the cosine effects are minimum. The daily thermal energy generation by the NASH collector averaged over 365 days was 2.16 kWh/m^2/day, which means 1 square meter aperture of NASH collector will generate **~800 kWh** of thermal energy at or near 120 ºC, over a full year. The daily solar insolation in test location in Atwater, California averaged over all 365 days was 5.16 kWh/m^2/day.

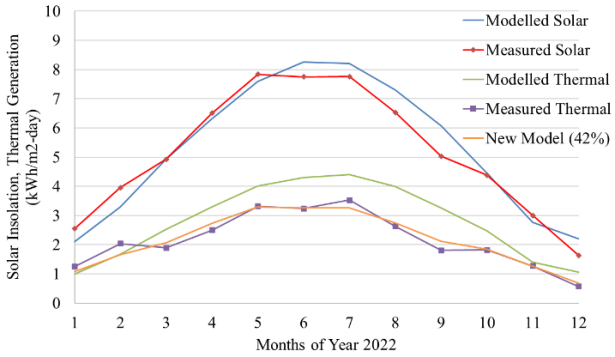

Figure 20. A yearlong performance of 2 modules of NASH collectors

The NASH collector module performance turned out to be 77% of the originally modelled performance. The 23% difference can be attributed to the optical transmission losses due to fabrication and assembly errors, soiling in reflectors and glass tube, heat losses from manifold and lower than modelled solar irradiance. In January and February, it is seen that the collector is producing more than expected because in these winter months, the collector was operating under 100 ºC and was producing more energy than modeled for operating at 120 ºC.

4.3. Third & Fourth Prototype- Good Vacuum and Bad Vacuum Test

A separate test loop was set up for performance measurement of the third and fourth prototype modules. The experiment aimed to understand the difference in the performance of module #1 good vacuum collector and module #2 bad vacuum collector at temperatures as high as 150 ºC. The test loop setup is shown in **Figure 21,** and the test started in June 2022. Module #1 on the right has three evacuated receiver tubes and module #2 in the left has three non-evacuated receiver tubes. A preheater calorimeter is installed before the collector modules such that the calorimeter, module #1 and module #2 are plumbed in series. The heat transfer fluid (Water) first goes through Calorimeter, then to the good vacuum tube collector, then to the bad vacuum tube collector, and recirculates, thus has a same flow rate for all three systems. The thermocouples were placed at inlet/outlet of calorimeter, outlet of module #1 and outlet of module #2. The thermocouple at outlet of the calorimeter would serve as the inlet temperature of the fluid entering the good-vacuum module. The outlet of the good-vacuum module would be an inlet of the bad-vacuum module. Finally, the outlet temperature of the bad vacuum modules was measured. Also, the Global Horizontal Irradiance was measured by the PSP placed at the horizontal plane. The calorimeter served as the flow rate measurement device. By measuring the current (I_c) and voltage (V_c) at the calorimeter terminals, using their product as input thermal power, and using specific heat capacity of water and using the inlet and outlet temperatures at calorimeter, we could calculate the flow rate in the loop. The calorimeter was insulated and assumed that the electrical power in the calorimeter was fully converted to heat.

To account for any heat loss from the calorimeter or the thermal energy not transferred to the fluid going through calorimeter, we measured the temperature gained by fluid across the calorimeter inlet/outlet while Calorimeter is on and measured the temperature drop of fluid across the calorimeter inlet/outlet while Calorimeter is intentionally turned off and added these and equated with the Calorimeter input electrical power. This will give us the accurate mass flowrate across the loop. The temperature drop across the calorimeter while it is turned off during high-temperature operation is essentially the heat loss from the calorimeter at that temperature, which is not actually being utilized even while it is turned on and hence should be deducted from the calorimeter power (IV) to accurately calculate flow rate.

$$I_c V_c = \left(mc_p(Tc_o - Tc_i)\right)_{\text{Cal on}} + \left(mc_p(Tc_i - Tc_o)\right)_{\text{cal off}} \qquad \text{(eq. 2)}$$

By calculating the flow rate from the above equation, the instantaneous solar thermal efficiency of both good vacuum and bad vacuum collectors were calculated using the temperature rise across these modules.

$$\eta = mc_p(T_o - T_{in})\ /\text{GHI} * \text{Collector Aperture Area} \qquad \text{(eq. 3)}$$

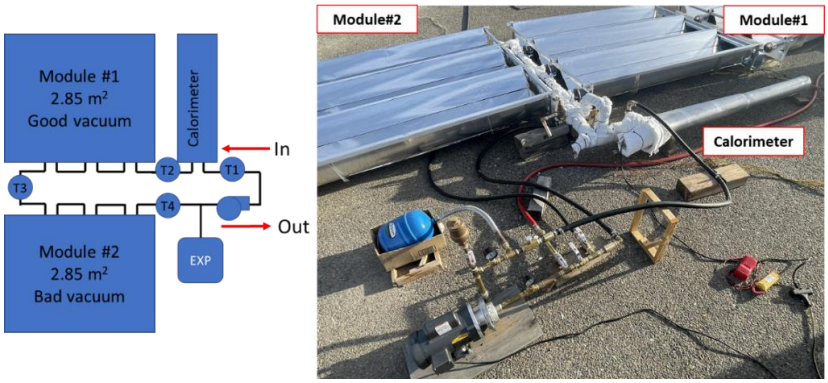

Figure 21. East-west oriented third and fourth prototype NASH collector modules during on-Sun test with Calorimeter.

The efficiency is plotted against mean temperature of the collector (the average of the collector inlet and outlet) and against the reduced temperature (T*) as shown in **Figure 22 (left) and (right)** respectively. Reduced temperature $T^* = \frac{T_m - Ta}{GHI}$ where T_m is a collector mean temperature (average of inlet and outlet temperatures) is a normalized temperature parameter that incorporates the combined effects of operating temperature, ambient temperature, and variable solar radiation to the instantaneous efficiency. The instantaneous efficiency of solar thermal collectors is generally plotted against this parameter. The collector demonstrated an efficiency >40% at temperatures above 100 ^oC and up to 150 ^oC. We can also see that the vacuum integrity of the receiver tubes is very important for efficient operation of the collectors. The distinction in the performance of good and bad vacuum collectors can be seen even at the operating mean temperature of 50 ^oC. The efficiency of a bad vacuum module is significantly lower than that of a good vacuum module beyond operating temperatures of 100 ^oC.

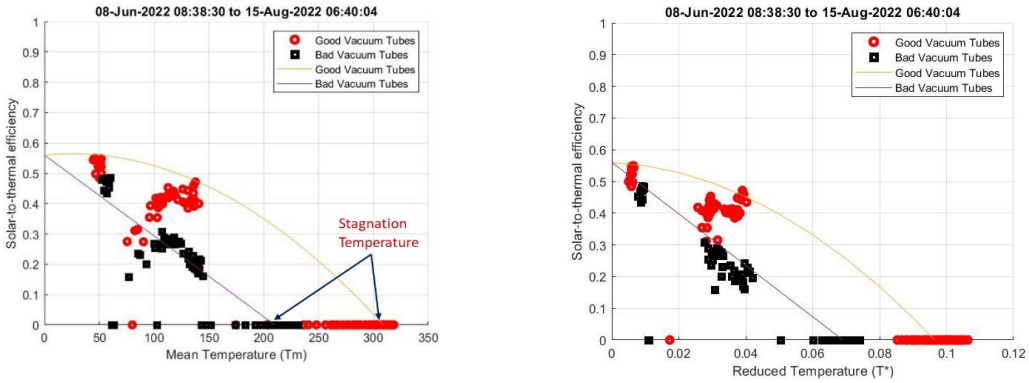

Figure 22. (left) Thermal efficiency at different mean fluid temperature, for good vacuum and bad vacuum collectors and (right) thermal efficiency as a function of reduced temperature parameter.

To summarize, in all five prototype modules we notice that the measured efficiency is lower than the modeled efficiency. This is mainly because of the imperfections in the reflector fabrication, meaning the exactness of reflector curvature. Imperfect reflector curvature reflects the incoming solar radiation away from the absorber thereby reducing the optical efficiency. The modeled optical efficiency was about 70%. However, the measured optical efficiency is around 56-58%. As the operating temperatures go higher, the solar-to-thermal energy conversion efficiency reduces due to thermal radiation loss from the collector. In **Figure 23** we can see the blue color of the sky on the reflectors instead of the dark blue color of the absorber. This means that the light incident on those sky-blue parts of the collector from your viewing angle or camera angle will not be directed to the absorber and will be reflected to the sky. Furthermore, soiling is a very important factor that reduces the efficiency of the collector, especially when the collectors are installed around dusty environments like farmland and construction regions. In addition to the working temperature, the efficiency can be impacted by ambient temperature, wind conditions, incident solar irradiance and dust level on the collector; hence, the efficiency is not consistent even for the same operating temperatures on different days.



Figure 23. Gap losses and other optical losses due to reflector imperfections in NASH prototype modules.

5. Conclusion

We presented optical design and modeling and thermal performance modeling of the NASH collector at elevated temperatures. The NASH collector could readily achieve the optical efficiency of ~65-70% if they are developed using standard manufacturing methods where the optical imperfections due to fabrication errors and gap losses are avoided. Moreover, we presented the results of experimental testing of prototypes 1 & 2, 3 & 4, and 5. We reported that the NASH collector with 1.72X concentration ratio achieved a stagnation temperature of up to 330 ^{o}C, optical efficiency of 56-58% (on early prototypes), an instantaneous peak efficiency of 50% while operating at 120 ^{o}C and average daily efficiency of 42% in the Year 2022, while operating around 120 ^{o}C. In the good vacuum versus bad vacuum module testing the NASH collectors operated between 100 ^{o}C and 150 ^{o}C and achieved solar-to-thermal conversion efficiency of >40%. We understood from the good vacuum and bad vacuum modules experiment that the vacuum integrity is crucial at high temperatures for efficient operation, however, bad vacuum tubes collector still can provide positive heat generation at temperatures up to 230 ^{o}C. These prototype modules had optical imperfectness due to early-stage fabrication methods that can be improved in the future. We have not observed any problems with the collectors in the instances of weather conditions like snowing in Winter, high winds on test site recorded up to 55 mph and stagnation with HTF measuring up to 260 ^{o}C and high pressure (100 psi relief valve). The team is working towards employing low-cost materials and manufacturing methods to reduce the Levelized cost of heat (LCOH) of these collector systems.

6. Acknowledgment

This work has been funded by California Energy Commission (CEC), USA under the grant number PIR-20-004. The authors are thankful to Robyn Lukens for her contribution to this research project.

7. References

Ferry, Jonathan, Bennett Widyolar, Lun Jiang, and Roland Winston. 2020. “Solar Thermal Wastewater Evaporation for Brine Management and Low Pressure Steam Using the XCPC.” *Applied Energy* 265 (December 2019): 114746. https://doi.org/10.1016/j.apenergy.2020.114746.

McMillan, Colin, Carrie Schoeneberger, Jingyi Zhang, Parthiv Kurup, Eric Masanet, Robert Margolis, Steven Meyers, Mike Bannister, Evan Rosenlieb, and William Xi. 2021. “Opportunities for Solar Industrial Process Heat in the United States. (Under Review).,” no. January: NREL/TP-6A20-77760.

Milczarek, Rebecca R., Jonathan J. Ferry, Fatima S. Alleyne, Carl W. Olsen, Donald A. Olson, and Roland Winston. 2017. “Solar Thermal Drum Drying Performance of Prune and Tomato Pomaces.” *Food and Bioproducts Processing* 106 (November): 53–64. https://doi.org/10.1016/J.FBP.2017.08.009.

Widyolar, B.K., L. Jiang, J. Ferry, J. Brinkley, Y. Bhusal, and R. Winston. 2019. “Nonimaging Solar Collectors toward Net-Zero GHG Emission.” In *Proceedings of SPIE - The International Society for Optical Engineering*. Vol. 11120. https://doi.org/10.1117/12.2534513.

Widyolar, Bennett, Lun Jiang, Yogesh Bhusal, Jordyn Brinkley, and Roland Winston. 2021. “Solar Thermal Process Heating with the External Compound Parabolic Concentrator (XCPC) – 45 m 2 Experimental Array Performance , Annual Generation (KWh / m 2 -Year), and Economics.” *Solar Energy* 230 (July): 131–50. https://doi.org/10.1016/j.solener.2021.10.027.

Widyolar, Bennett, Lun Jiang, Jonathan Ferry, and Roland Winston. 2018. “Non-Tracking East-West XCPC Solar Thermal Collector for 200 Celsius Applications.” *Applied Energy* 216 (January): 521–33. https://doi.org/10.1016/j.apenergy.2018.02.031.

Widyolar, Bennett, Roland Winston, Lun Jiang, and Heather Poiry. 2014. “Performance of the Merced Demonstration XCPC Collector and Double Effect Chiller.” *Journal of Solar Energy Engineering, Transactions of the ASME* 136 (4): 1–13. https://doi.org/10.1115/1.4027726.

Winston, Roland, Lun Jiang, and Melissa Ricketts. 2018. “Nonimaging Optics: A Tutorial.” *Advances in Optics and Photonics* 10 (2): 484. https://doi.org/10.1364/AOP.10.000484.

Techno-environmental comparison of steam generation systems with industrial heat pumps

Abdulrahman Dahash, Johannes Riedl, Sabrina Dusek, Bernd Windholz and Franz Helminger

[1] Sustainable thermal energy systems, Center for Energy, AIT Austrian Institute of Technology GmbH, Vienna (Austria)

Abstract

Steam generation significantly contributes to the energy demand in industry since steam is widely used as energy carrier. To cope with energy efficiency measures, it becomes crucial to recover the waste heat as it is an inevitable product. Thus, the incorporation of a heat pumps might assist in this recovery for steam generation applications. In this work, the industrial steam generation with the aid of a heat pump is investigated. The integration of the heat pump into the process is realized for three main approaches: 1) direct steam generation, 2) steam generation with a flash tank and forced circulation and 3) steam generation with a drum for natural circulation. In the second approach, a circulation pump is needed. The last approach relies on natural circulation. This work conducts a simulation-based analysis to examine the performance of 4 configurations. The findings reveal a promising applicability of such systems with notable performance, which allows in promoting the energy efficiency measures in industry with great savings in CO_2 emissions compared to a conventional steam generation system (e.g. gas-fired steam generator).

Keywords: Heat pump, steam generation, natural circulation, flash tank, plate heat exchanger, plate and shell heat exchanger.

1. Introduction

Nowadays, the decarbonization of the industrial sector is broadly discussed and profoundly stressed out due to the increasing awareness against climate change, pollution and depletion of fossil fuels. Thus, several states began to introduce a set of policy measures in order to pave the way for a smooth transition to a low-carbon, sustainable and affordable energy future (Singh Gaur et al., 2021). If properly defined, such measures should ultimately lead to the decarbonization of the several energy sectors. Amongst others, industry sector arises as one of the most energy-intensive sectors that plays a significant role in emissions when fossil fuels are used (Kim, 2022). Thus, the industrial sector inevitably is no exception in any decarbonization plan. Subsequently, many states worldwide started embarking ambitious goals for expanding the share of renewable energy resources (RES) in their future energy system scheme. In this context, it is noteworthy to highlight that the share of RES is increasing in the electricity mix and, therefore, electrification might be a viable option for the aimed sustainable energy future (Kim et al., 2022).

Amongst others, industrial steam generation accounts for a significant share in the industrial applications due to its emergence as an interesting energy carrier for applications in which process heat is demanded and, subsequently, is extensively consumable in the industry (Liu et al., 2022). Often, steam (elevated temperature, superheated) is highly desirable in several industrial applications such as drying, refining and food processing. Steam can be offered for industrial applications by means of several methods: 1) offsite generation and transferred to demand side, 2) conventional boilers and 3) combined heat and power (CHP) systems (Kang et al., 2019). In the first method, steam might lose its quality when transported due to heat losses. As for conventional boilers, they exploit the combustion of natural gas and, subsequently, they contribute to greenhouse gas emissions (GHG). Likewise, CHP units might tend to use natural gas as fuel for large portion of its installations.

Noticeable is that the foregoing methods significantly rely on the combustion of fossil fuels (e.g. natural gas) to achieve high-temperature steam. This will lead to an increase in emissions with other drawbacks, e.g. violation to security of supply due to increase in gas prices as seen after Ukraine crisis. Inevitably, one of the key measures to achieve industrial decarbonization and independency from conventional fuels is the increase in energy efficiency measures for steam generation given its tremendous potential. In this context, waste heat recovery (WHR) arises as a promising measure for efficient steam generation due to its capability to utilize medium to elevated temperature heat sources for steam generation (Broberg Viklund and Johansson, 2014).

© 2022. The Authors. Published by International Solar Energy Society
Selection and/or peer review under responsibility of Scientific Committee
doi:10.18086/eurosun.2022.05.02 Available at http://proceedings.ises.org

Subsequently, heat pumps are commonly attractive solutions for enhancing process energy efficiency via waste heat recovery, lowering pollutant emissions, and improving the utilization of primary energy resources (Arpagaus et al., 2016). Thus, several policy makers have paid notable attention to such technology due to its key role in the achievement of sustainable energy future. In this regard, heat pump technology is powered by electricity to lift the heat captured from industrial waste heat at low temperature level to medium or elevated temperature level. Owing to its low environmental impact and desired energy efficiency, this work examines the potential of heat pumps assisted steam generation and quantifies four configurations for heat pump integration to achieve high steam quality.

2. Literature review

Despite the low expansion level for heat pumps in industry, adoption of such a technology is drastically increasing besides the soaring in the gas prices, which might later lead to undesired impacts (e.g. increase in product unit prices due to increase in OPEX). The significant importance of heat pump technology is owed to its potential to reduce emissions by reuse of industrial waste heat and use of electricity (or surplus electricity from RES) to lift the waste heat to higher temperatures and use it for industrial applications. As a result, it is anticipated that heat pump installation will witness a drastic deployment in the coming years.

In this context, steam generation with the aid of heat pumps has been widely discussed in several research studies. For instance, (Liu et al., 2022) recently suggested a new concept for high-temperature heat pumps for efficient and economic steam generation applications. The work revealed the capability of the proposed heat pump to produce steam with temperatures up to 154°C and this generation can be realized with a cascade energy inputs. Aiming at a novel high-temperature heat pump, (Mateu-Royo et al., 2019) proposed a layout with a modified scroll compressor and an internal heat exchanger. The work conducted a steam generation analysis with the refrigerant “HFC-245fa” and, accordingly, the heat pump was capable to produce steam with a temperature of 140°C.

On their part, (Meroni et al., 2018) paid considerable attention to the design of heat pump compressors in order to reduce the energy input with higher operation performance. The work presented a mean-line model for centrifugal compressors design, optimization and analysis. The model was later validated against a set of design and off-design conditions. The work revealed the potential of multi-stage compressor with steam as working medium for achieving the highest performance compared to other counterparts. For steam generation with the aid of heat pumps including a flash tank, (Chen et al., 2021) proposed such a system for deep recovery of waste heat and conducted a techno-economic analysis to show the potential and generation capacity of the suggested system. The outcomes highlighted the prominence of the proposed system for efficient and feasible recovery of the waste heat.

Owing to their importance, heat exchangers (i.e. condenser and evaporator) design is a crucial aspect in industrial heat pumps. This is attributed to the resulting heat transfer coefficient and the heat transfer area. In this regard, plate heat exchanger (PHE) found its place favorably in several industrial applications such as chemical processes and food processing due to its low cost and high heat transfer performance resulting from high heat transfer area to volume ratio for such heat exchangers and,, thus, PHEs are characterized with design compactness (Abu-Khader, 2012). Yet, PHEs are often limited in the operation range (temperature and pressure) and, thus, they are not suitable for high-temperature industrial applications (> 150°C). Besides, they are prone to fouling issues that might lead to impact on thermo-hydraulic behavior in heat exchangers. As a results, plate-and-shell heat exchangers (PSHE) are envisioned as alternative candidates to PHE to overcome the above-mentioned drawback. In this context, (Jo et al., 2020) experimentally compared both types in order to evaluate the evaporative heat transfer characteristics and address their applicability for industrial heat pumps employing R-1234ze(E) as a refrigerant. Compared to its PHE counterpart, the work concluded that PSHE showed better performance in terms of heat transfer.

To reduce the refrigerant temperature at the inlet of the throttling valve, an internal heat exchanger (IHX) is implemented in the heat pump system. The main goal of IHX is to transfer heat from the liquid refrigerant side to the vapor refrigerant side in order to boost the system performance and increase the temperature (or quality) of the steam (Cao et al., 2019). Accordingly, industrial heat pumps are equipped with an internal heat exchanger (IHX) to boost their performance. The work concluded a significant increase in the heating coefficient of performance when an IHX present in the heat pump cycle.

On the sink side, the lukewarm water can be circulated with the aid of either forced circulation or natural circulation. In the first method, a circulation pump is dedicated to accomplishing this task by steering the feedwater through the heat pump condenser to absorb the heat and eventually boils. Such a method has no segregation in the process and can be called “direct steam generation”. Natural circulation, on the other hand, is characterized with the presence of drums that captures the resulted mixture after the condenser and releases only saturated steam. The forced circulation

can operate at higher pressures and temperatures, whereas the natural circulation has lower pressure drop. Yet, it is noteworthy to mention that the absence of drums and its equipment (i.e. downcomers and risers) make options with forced circulation more attractive due to lighter weight. Yet, the desire to decrease the operational expenditure drives the efforts to integrate drums in order to generate a pressure difference sufficient to naturally circulate the feed water.

In this context, (Keshavar et al., 2019) numerically studied the dynamics of natural circulation for heat recovery steam generation. The work investigated the role of the drum design parameters heat rate input and feed water flowrate on the steam quality. The work concluded that increasing the feed water flow rate results to a decrease in the steam quality when heat rate input kept constant. Whilst the increase in heat rate input with a constant feed water flow rate led to an increase in the steam quality. Yet, the foregoing study with existing literature (such as (Naim Hossain et al., 2022), (Bilde et al., 2019)) are all limited to the application of natural circulation for boilers.

Although the aforementioned studies identified significant results and contributed to the knowledge of heat pumps, the authors highlighted and discussed the shortcomings associated. In this study, the authors aim to investigate the steam generation with the aid of heat pumps in order to take advantage of the waste heat and recover it for further use. Thus, this work will conduct a simulation-based analysis to examine the performance of each of the proposed configurations for industrial steam generation (section 3.1).

3. Methodology

3.1. Configurations for industrial steam generation

This work examines the heat pump-assisted steam generation enabling the recovery of industrial waste heat. Thus, several configurations for the heat pump integration can be noticed to realize steam generation. These configurations are as below:

- Configuration a: A circulation pump (forced circulation) with a flash tank as shown in Figure 1,
- Configuration b: Direct steam generation whereby the condenser is a plate heat exchanger (PHE) with no flash tank as illustrated in Figure 2,
- Configuration c: Direct steam generation whereby the condenser is a plate-and-shell heat exchanger (PSHE) with no flash tank as presented in Figure 2, and
- Configuration d: Herein, the circulation pump is eliminated due to the natural circulation that is carried out with the aid of the drum, downcomers and risers. This configuration is displayed in Figure 3.

In this context, it is noteworthy to highlight that both configurations (b and c) are similar with main exception in the condenser type. To gain further insights, Figure 4 shows exemplary sketches to illustrate the difference between a plate heat exchanger and a plate-and-shell heat exchanger. Another remark is that configuration (d) is also similar to the sketch of configuration (a). Yet, the circulation pump and the flash valve are eliminated. The flash tank is substituted with a drum to realize the natural circulation. Figure 5 shows a typical industrial heat pump with all components used. Such a heat pump will be used for the configurations investigated in this work.

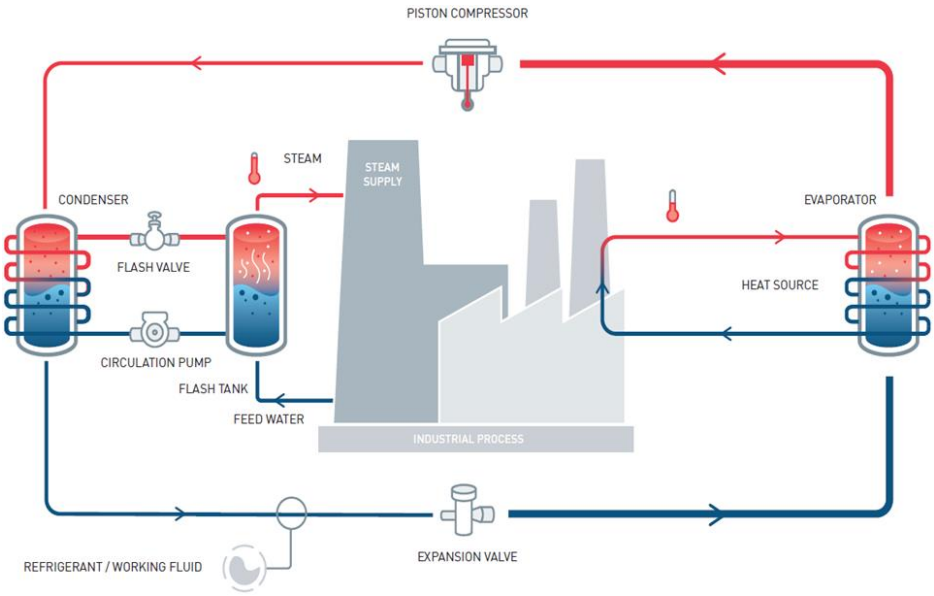

Figure 1: Steam generation with forced circulation and flash tank, configuration a.

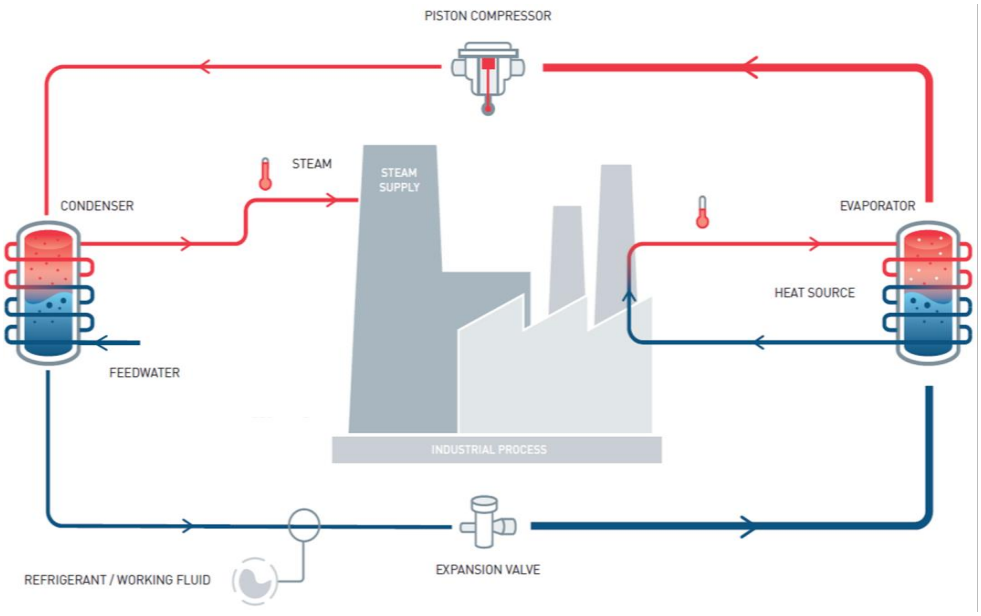

Figure 2: Direct steam generation without flash tank, configurations b and c.

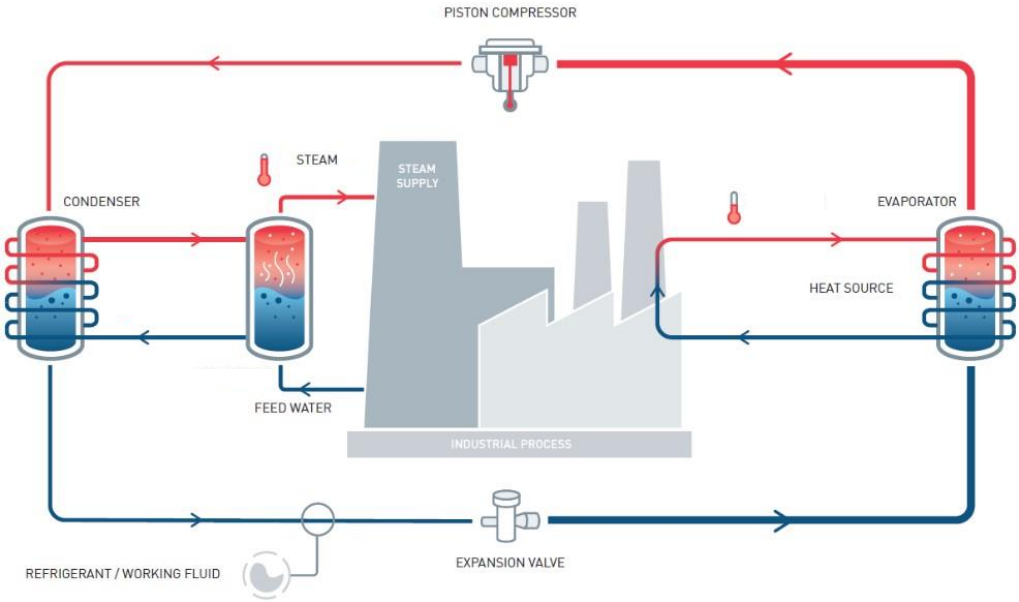

Figure 3: Steam generation with drum and natural circulation, configuration d.

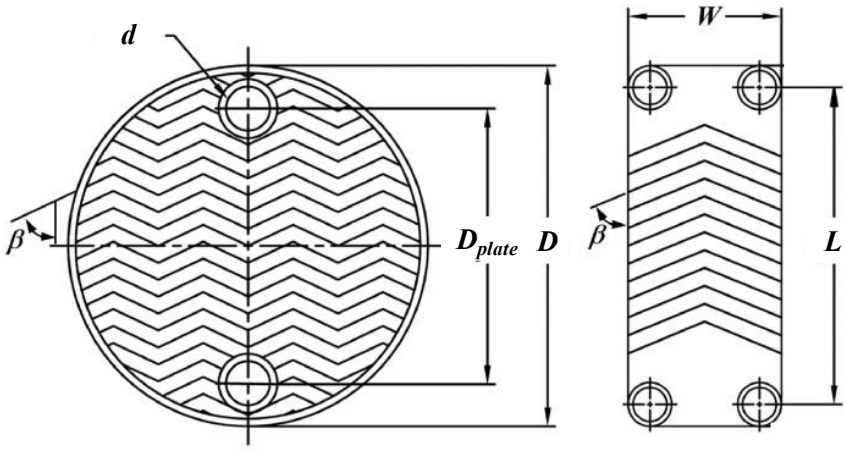

Figure 4: An exemplary sketch for the plate-and-shell heat exchanger (PSHE) and plate heat exchanger (PHE) (reproduced from (Jo et al., 2020)).

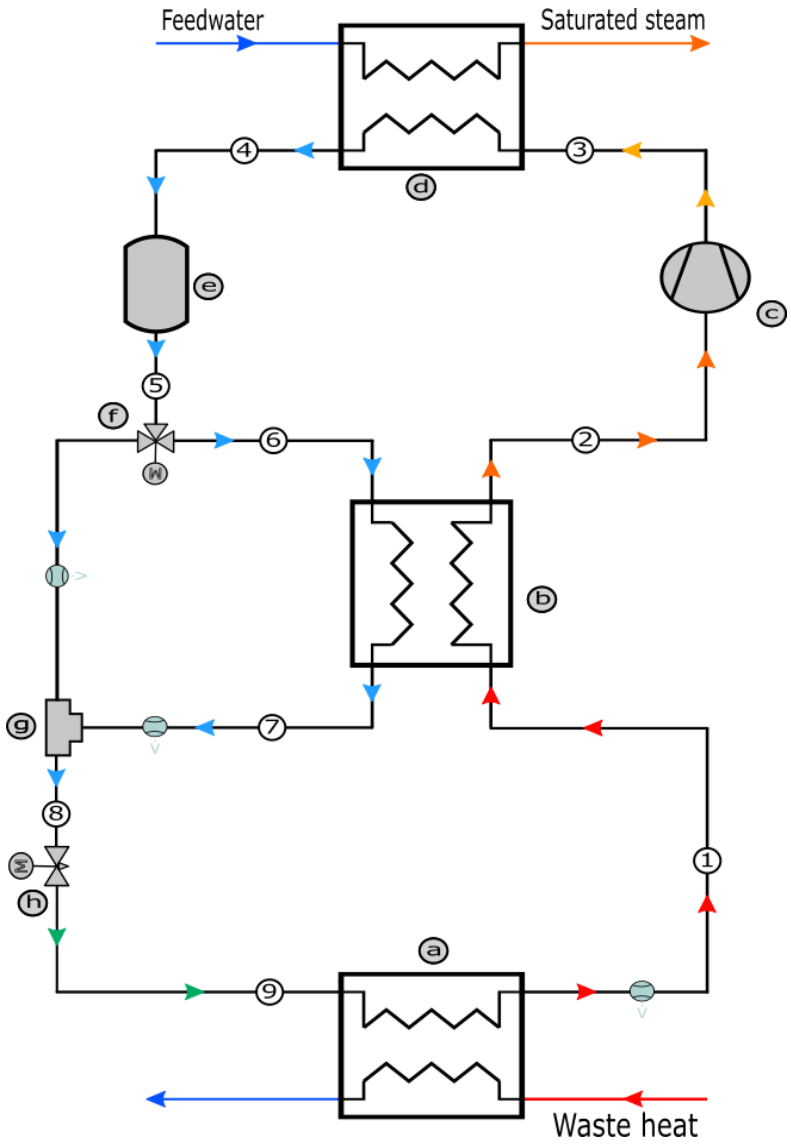

Figure 5: A typical industrial heat pump installation for the investigated configurations in this work. Heat pump components: (a) evaporator, (b) internal heat exchanger, (c) compressor, (d) condenser, (e) liquid/gas separator, (f) 3-way valve, (g) junction and (h) expansion valve.

3.2. Dynamic system simulations

For all configurations, the heat pump system together with the required components (e.g. drum, flash tank) are all modeled with the aid of the object-oriented, equation-based, open-source modeling language Modelica. To run the simulations, Dymola 2022x is used as simulation environment. For the system simulations, basic components (heat exchangers, expansion valve, separator) are used from the commercial library TIL 3.10.0 developed by TLK Thermo GmbH (Gräber et al., 2010) (TLK Thermo GmbH). This library is supported by a TILMedia to emulate the thermophysical properties for all working media (e.g. refrigerants, water/steam). With the aid of this library, other models (e.g. drum, compressor, flash tank, plate-and-shell heat exchanger) are developed in house. The developed models shall obey the energy conservation and mass balance.

Moreover, the drum model is developed with the two volumes since two distinct phases (i.e. liquid and vapor) are present in the component. Besides, it is presumed that there might be a non-ideal phase interaction between both phases and, thus, a thermal non-equilibrium state. Accordingly, the liquid phase might have a different temperature from that of the vapor one. Yet, both volumes can exchange heat and mass between each other. Besides, the model can consider the pressure difference due to friction inside the drum and the geostatic effects (i.e. impact of ports location). Furthermore, the developed drum model also includes a simplified form for momentum balance including the forces of static pressure, friction and gravity. In summary, the following assumptions are considered for the models development:

1. The system configurations shall operate under steady-state conditions,
2. The thermal losses in the evaporator, compressor, condenser, internal heat exchanger, drum and flash tank are neglected, and
3. Expansion is an isenthalpic process.

The reader is directed to (Gräber et al., 2010) in case further information is needed for modelling of the components. Plate and shell heat exchanger is thoroughly described in (Dusek et al., 2020).

3.3 System boundary conditions

This work investigates the foregoing configurations for a saturated steam generation ($\kappa = 1$) with a pressure of 2 bar_a and saturation temperature of 120.2°C. The heat pump configurations all operate with R1233zd(E) as refrigerant owing to its low global warming potential (GWP) and high heat transfer coefficient resulting in lower heat transfer areas as demonstrated in (Dawo et al., 2022).

The industrial waste heat is available as hot water with a temperature of 70°C and allows for a decrease of 5 K over the source side (evaporator) and, subsequently, the flowrate is regulated. The evaporator is a PHE type with 140 plates made of stainless steel. Table 1 reports other geometrical characteristics for the chosen heat exchangers in the analyzed configurations. The water side has a heat transfer coefficient of 2500 W/(m^2.K), whereas the refrigerant evaporation heat transfer coefficient is set to 10,000 W/(m^2.K). Furthermore, this work presumes a zero pressure drop over the evaporator length for both sides. Moreover, the heat pump compressor is capable to achieve a maximum flowrate of 216 m^3/hour and a maximum outlet temperature of 140°C. The heat pump condenser type is subject to examination and, accordingly, its design is determined by the configuration.

Table 1: Geometrical characteristics of the heat exchangers used in the configurations of heat pump.

Parameter	**Evaporator**	**IHX**	**Condenser**		
			Confs. (a, c)	**Conf. (b)**	**Conf. (d)**
Type	PHE	PHE	PHE	PSHE	PHE
Plate width, *W*	304 mm	364 mm	304 mm	364 mm	364 mm
Plate length (port to port), *L*port	601 mm	284.5 mm	597 mm	284.5 mm	284.5 mm
Angle of the corrugation, β	35°	35°	35°	89°	35°
Corrugation pitch	12.6 mm	12.6 mm	12.6 mm	1.2 mm	12.6 mm
Number of plates	140	40	120	114	150
Plate diameter, D_{plate}	-	-	-	440 mm	-
Shell diameter, *D*	-	-	-	732 mm	-

The investigated exemplary system demands a predefined superheating temperature of 15 K for the refrigerant at the inlet of the condenser. Thus, there is an IHX used in order to respect this this constraint (15 K). Consequently, it is crucial to implement a bypass that allows the refrigerant to proceed flowing to the throttling valve without passing through IHX if the constraint violated (> 15 K). This means that the condenser inlet temperature has a higher priority than that of the throttling valve. Moreover, the heat pump system comprises a separator post to the condenser to ensure a liquid refrigerant flow prior to the evaporator.

The configuration (d) with natural circulation encompasses a vertical drum component with a total length of 2.4 m. The downcomer port is located at 0.1 m, whereas the riser port is situated at a height of 2.1. The feed water inlet port is located at 0 m and the steam outlet port is at 2.4 m.

3.4 Performance indicators

In order to evaluate the technical capability of the configurations, the work analyzes the heat pump configurations by two performance indicators; one is the coefficient of performance (COP) for the heat pump integrated and the other is steam generation rate. All solutions that violate the constraint of compressor outlet temperature will be disregarded.

For heating applications, the coefficient of performance is the quotient of the useful heat delivered at the condenser (Q_{cond}) to the electricity input to the compressor (W_{comp}). Accordingly:

$$COP_{\mathrm{h}} = \frac{Q_{\mathrm{useful}}}{W_{\mathrm{in}}} = \frac{Q_{\mathrm{cond}}}{W_{\mathrm{comp}}} \quad (1)$$

4. Results and discussion

This study addresses a simulation-based analysis of heat pump configurations for steam generation. The simulations are conducted in Dymola 2022x environment with DASSL solver and a tolerance of 10^{-4}. In order to ensure a steady-state operation condition, the simulation time is set to a single day (24 hours). The goal of this analysis is to achieve a saturated steam at a temperature of 120,2°C and a pressure of 2 bar_a.

4.1 Heat pump cycle

Figure 6 reveals the log(*p*)-*h* diagram of the refrigerant R1233zd(Z) circulating in the heat pump. Noticeable is that all configurations had comparable refrigerant cycles with similar characteristics (e.g. temperature, pressure) despite the slight differences (< 1%). For instance, it can be observed that the pressure ratio for the used refrigerant remained at a value of appx. 3.78 for the configurations (a) and (c) whereby the evaporator and condenser pressures were 4.4 bar_a and 16.7 bar_a, respectively. This pressure ratio dropped down to 3.73 and 3.7 for the configurations (b) and (d), respectively. However, it was possible for all configurations to comply with the compressor outlet temperature constraint (< 140°C). For example, configuration (a) achieved a compressor outlet temperature of 138°C, whereas configuration (d) attained a value of 137°C. Despite this slight difference, all configurations led to a condenser outlet temperature of 123°C corresponding to a fully liquid refrigerant.

Furthermore, Figure 6 illustrates that the refrigerant further cooled down to (294.7 kJ/kg and 75.85°C) over the internal heat exchanger releasing a portion of heat (Δh_{IHX} = 66.5 kJ/kg) to the vapor refrigerant side. Yet, the outcomes highlighted that only a small portion of the refrigerant mass (13%) was directed in the IHX path, whilst the remainder (87%) flowed further to the junction component and remixed with the rest (13%) (compare Figure 5). Subsequently, such a behavior was obvious in the heat pump cycle as both flows mixed resulting in an enthalpy with a value of 352 kJ/kg. Post to the junction, the refrigerant expanded in the throttling valve leading to a refrigerant in a vapor phase with a quality of 43% for the configurations investigated.

By virtue of the waste heat (5 K, 21 kJ/kg and 4.14 kg/s), the refrigerant with 43% vapor quality absorbed this heat over the evaporator and, thus, it was slightly superheated. Later, the refrigerant received more heat through IHX and superheated further. In summary, the heat pump cycle could achieve a heating COP of 3.1 for all configurations investigated. Moreover, the cycle analysis pinpointed the role of IHX in the heat pump cycle and showed its minor impact in the entire operation and, thus, further work should consider and estimate the cost-to-benefit for such a component in steam generation heat pumps. Furthermore, the analysis showed that the changes in the heat pump configuration (e.g. PHE or PSHE) did not lead to significant changes on the refrigerant side under the considered boundary conditions (i.e. operational and geometrical).

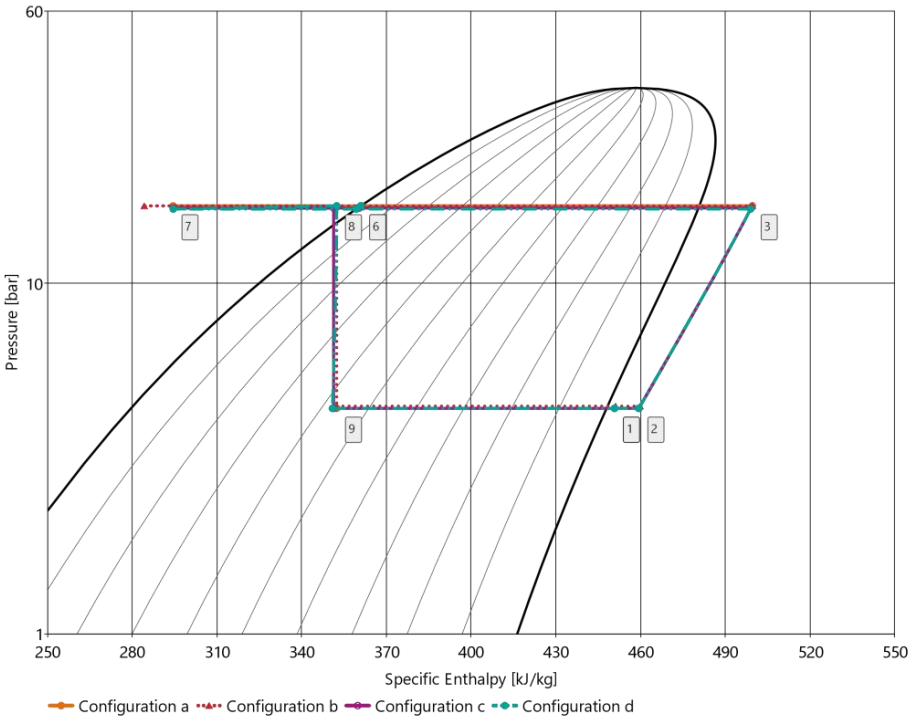

Figure 6: The log(p)-h diagram of the R1233zd(E) for the proposed steam generation heat pump configurations.

4.2 Steam generation analysis

Bearing in mind that the configurations showed no meaningful change in the heat pump cycle, it becomes crucial to evaluate the steam generation rate and its quality for the configurations investigated. For steam generation, the configurations were all supplied with feed water at a pressure of 2 bar_a and a temperature of 20°C (84.4 kJ/kg). Besides, it is worthwhile to inspect the geometrical parameters of the heat pump condenser to gain further insight into the heat pump suitability for steam generation.

Table 2: Summary of heat pumps configurations considered in this work for steam generation.

	Configuration (a)	**Configuration (b)**	**Configuration (c)**	**Configuration (d)**
Heating COP	3.1	3.1	3.1	3.1
Steam generation rate [kg/hr]	169	166	169	167
Condenser heat transfer area [m^2]	22.7	22.7	18.5	22.7
Circulation	Yes (Forced)	No	No	Yes (Natural)

The outcomes indicated the application of the steam generation configurations and they resulted in a similar generation rate with slight deviation (< 1%). In this context, both configurations (a) and (c) produced highest steam rate, but main difference was the condenser design. For configuration (a), a PHE with a heat transfer area of 22.7 m^2 was used, whereas configuration (c) included a PHSE condenser with a heat transfer area of 18.5 m^2. Besides, configuration (a) incorporated a flash tank and a circulation pump, whilst (c) did not. Despite the notable layout differences, both configurations led to comparable results (COP and steam). Moreover, it must be mentioned that the material volume used for heat exchangers manufacturing is surely of high importance as less volume demanded means lower investment costs.

The work also investigated a heat pump system with natural circulation (configuration (d)). Compared to its counterparts, such a configuration led to a generation of saturated steam with 167 kg/hour and a comparable COP. In such a configuration, a PHE with 120 plates and total heat transfer area of 22.7 m^2 was used at the sink side (i.e. condenser). Thus, it was possible to control the quality of the steam generated and ensured a statured steam. Herein, it must be mentioned that a drum was an essential component in this configuration in order to realize the natural circulation and eliminate the circulation pump.

4.3 Impact of evaporator temperature on steam generation

To understand the impact of the evaporator temperature difference on the steam generation rate, it is important to investigate a configuration that shows complexity. Therefore, this work considers configuration (a) for further analysis. Herein, the configuration composes of a heat pump system coupled to a flash tank with a forced circulation through the condenser. The foregoing analysis presumed a temperature difference of 5 K for the waste heat over the evaporator. Thus, this examination is extended to consider two other temperature differences of 10 K and 15 K over the evaporator, whereas the flowrate of water (i.e. waste heat carrier) is reduced to maintain a constant heat rate over the evaporator. Such a variation in temperature might be observable depending on the application. Moreover, other boundary conditions will be maintained.

In this context, Figure 7 shows the heat pump cycle for the configuration (a) under the analyzed boundary conditions for the variants of 5 K, 10 K and 15 K. Obviously, the decrease in temperature downstream the condenser leads to a notable change in the evaporator pressure as depicted in Figure 7. This is attributed to the control of the heat pump as it is required to maintain a superheating temperature of 3 K post to the evaporator on the refrigerant side. Thus, it is crucial to operate the heat pump at lower pressures to comply with this constraint.

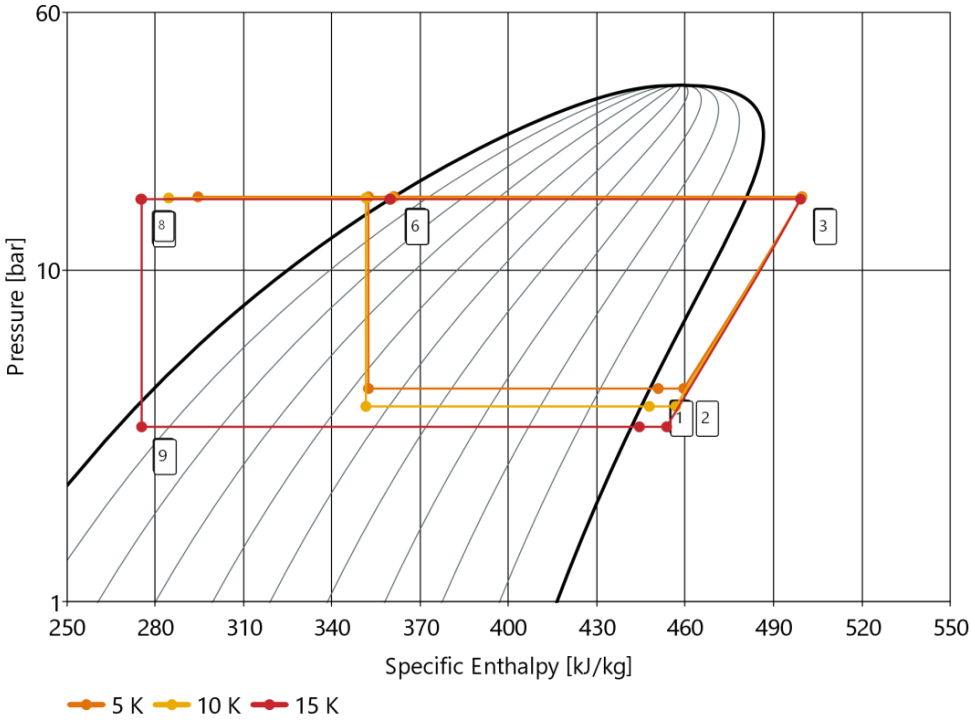

Figure 7: Impact of evaporator temperature difference on the heat pump cycle of configuration (a).

The increase of useful temperature difference from 5 K up to 15 K leads to a remarkable decrease in the refrigerant velocity as shown in Figure 8. This inevitably means that the refrigerant at the evaporator upstream is denser as the temperature difference increases. For instance, when considering the 15 K variation, the refrigerant has higher density and accordingly lower steam quality to that of the 5 K variation. This is evidently revealed in Figure 7. Inevitably, this decrease in refrigerant velocity will eventually lead to an increase in the compressor pressure ratio to fulfill the requirements of 15 K as superheating temperature with a maximum temperature of 140°C for the condenser upstream. Thus, compressor power input will increase and, consequently, this increases the operational expenditure.

Moreover, the outcomes revealed a decrease in heating COP from 3.1 for the 5 K variation down to 2.8 for the variation of 15 K. The heating COP is 2.9 for the 10 K variation. In this context, noticeable is the reduction that occurs in the steam generation rate as it drops from 169 kg/hr for 5 K variation down to 119 kg/hr for variation of 15 K, whereas a rate of 144 kg/hr is obtained for 10 K variation. The quality and temperature of the produced steam remain for all variations as required (i.e. saturated steam at 2 bar_a and 120.2°C).

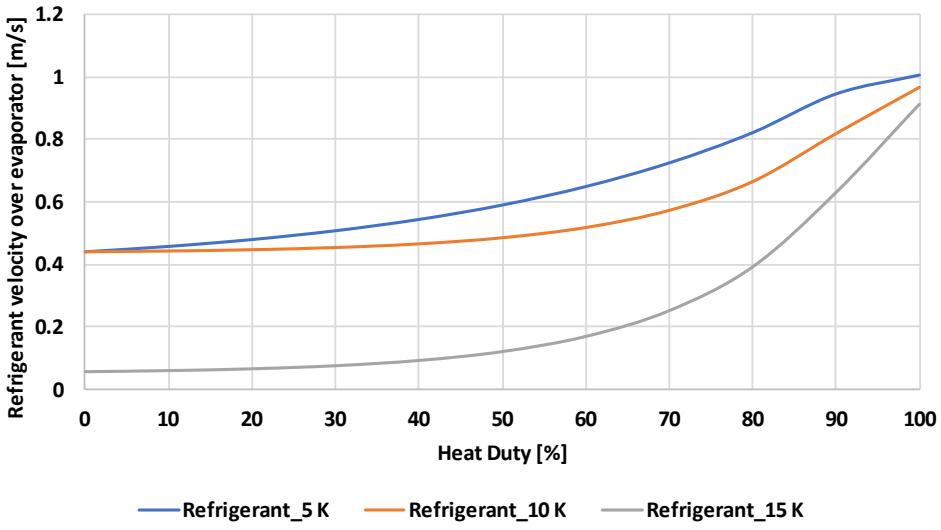

Figure 8: Refrigerant velocity over the length of a single plate in the evaporator.

4.4 Environmental analysis

In order to understand the environmental impact of steam generation with the aid of industrial heat pumps, it is essential to compare the emissions produced against a conventional system. In this manner, the foregoing findings underline that the heat pump condenser has a heating rate of 125 kW to produce steam with a rate of 166 kg/hr – 170 kg/hr. Thus, a gas-fired steam generation with a heating power of 125 kW and efficiency of 90 % arises as a conventional candidate that is used as a benchmark.

For the environmental analysis, the carbon dioxide emissions can be determined:

$$M_{\mathrm{CO}_2} = f_{\mathrm{CO}_2} \cdot E \quad (2)$$

Herein, f_{CO_2} represents the annual averaged emission factor in [kgCO2/kWh] following the Austrian guidelines for each energy form, whereas E stands for the annual energy consumption required in [kWh/a] for steam production. Heat pumps consume electricity from the power grid and, thus, the emission factor is 219 kg_{CO2}/kWh_{el} (Umweltbundesamt GmbH, 2021). The conventional system, on the other hand, consumes natural gas with an emission factor of 268 kg_{CO2}/kWh_{gas} (Umweltbundesamt GmbH, 2021). To determine the annual energy consumption, it is assumed that an industrial plant runs for 7320 hours/a, and the rest is for maintenance. Accordingly, **Table *3*** reports the savings in carbon dioxide emissions for heat pumps steam generation systems compared to the conventional system. Therein, it is obviously seen that a total of 208 tCO_2 can be saved on annual basis when heat pumps selected for steam generation.

Table 3: Summary of environmental analysis between steam generation with aid of heat pumps and a gas-fired steam generation.

System	Steam generation rate [kg/hr]	Heating power [kW]	Annual electricity [MWh_{el}/a]	Annual Gas consumption [MWh_{gas}/a]	Annual CO_2 emissions [tCO_2/a]
Heat pump steam generation	166 – 170	125	295	-	64.5
Gas-fired steam generation	170	125	-	1016.5	272.5

5. Conclusions

Process heating plays a significant role in the industrial energy demand whereby 20% of this process heating is required at temperatures between 100°C and 200°C. For such a temperature range, steam arises as an interesting energy carrier for industrial applications. Besides, the importance of steam emerges from its application as heat transfer medium and reaction medium as well. However, steam generation might be costly and unfriendly for environment when conventional fuels are used. In order to increase the energy efficiency measures and reduce the CO2 emissions, the use of waste heat is required.

In this work, 4 configurations for steam generation with the aid of heat pumps were investigated with the aid of numerical simulation in Modelica/Dymola. The configurations were: (a) direct steam generation with a HP equipped with a plate-type condenser, (b) direct steam generation with a HP equipped with plate and shell-type condenser, (c) steam generation with a HP coupled to a flash tank and a circulation pump and (d) steam generation with a HP coupled to a drum to realize natural circulation allowing the elimination of the circulation pump. For the analysis, the aim is to supply industry with saturated steam at 2 bar_a and 120°C.

The refrigeration cycle analysis revealed same heating coefficient of performance ($COP_{heating}$) for the heat pumps in the investigated configurations. The findings revealed that those configurations slightly differed from each other with the amount of steam generated. Compared to its counterparts with plate-type condenser, configuration (b) showed smaller heat transfer area with a reduction of 19 % for the heat pump condenser due to the implementation of a plate-and-shell heat exchanger. Thus, this reduced the land availability, which is an important aspect considered by industry of installation.

Moreover, the work conducted a comparison against a conventional steam generation system (i.e. gas-fired steam generator with 90% efficiency) to examine the environmental impact of steam generation with heat pumps. The outcomes showed significant CO_2 savings of around 80% when heat pumps used for steam generation compared to gas-fired steam generator under same boundary conditions.

6. Acknowledgments

The project has received funding from the European Union's Horizon 2020 programme for energy efficiency and innovation action under grant agreement No. 820771.

7. References

Abu-Khader, M. M. (2012). Plate heat exchangers: Recent advances. *Renewable and Sustainable Energy Reviews, 16*(4), 1883-1891. doi:10.1016/j.rser.2012.01.009.

Arpagaus et al. (2016). Multi-temperature heat pumps: A literature review. *International Journal of Refrigeration, 69*, 437-465. doi:10.1016/j.ijrefrig.2016.05.014.

Bilde et al. (2019). Mathematical model of natural circulation biomass boilers during start-up. *International Journal of Heat and Mass Transfer, 143*. doi:10.1016/j.ijheatmasstransfer.2019.118477.

Broberg Viklund, S. and Johansson, M. T. . (2014). Technologies for utilization of industrial excess heat: Potentials for energy recovery and CO2 emission reduction. *Energy Conversion and Management, 77*, 369-379. doi:10.1016/j.enconman.2013.09.052.

Cao et al. (2019). Theoretical analysis of internal heat exchanger in transcritical CO2 heat pump systems and its experimental verification. *International Journal of Refrigeration, 106*, 506-516. doi:10.1016/j.ijrefrig.2019.05.022.

Chen et al. (2021). Proposal and comprehensive analysis of an innovative steam generation system by deep recovery of low-grade waste heat. *Journal of Cleaner Production, 310*. doi:10.1016/j.jclepro.2021.127509.

Dawo et al. (2022). R1224yd(Z), R1233zd(E) and R1336mzz(Z) as replacements for R245fa: Experimental performance, interaction with lubricants and environmental impact. *Applied Energy, 288*. doi:10.1016/j.apenergy.2021.116661.

Dusek et al. (2020). Analysis of a steam generating high temperature heat pump for industrial waste heat recovery. *Proceedings of 13th IEA Heat Pump Conference 2020*, (pp. 559-568). Jeju, Korea. Retrieved August 17th, 2022, from https://heatpumpingtechnologies.org/publications/paper-no-097-analysis-of-a-steam-generating-high-temperature-heat-pump-for-industrial-waste-heat-recovery-13th-iea-heat-pump-conference-jeju-korea/

Gräber et al. (2010). Modelling of heat pumps with an object-oriented model library for thermodynamic systems. *Mathematical and Computer Modelling of Dynamical Systems, 16*(3), 195-209. doi:10.1080/13873954.2010.506799

Helminger et al. (2016). Hochtemperatur warmepumpen messergebnisse einer laboranlage mit HFO-1336MZZ-Z bis 160 °C kondensationstemperatur. *Proceedings of the 14. Symposium Energieinnovation* (pp. 1-20). Graz, Austria: TU Graz. Retrieved August 03, 2022, from https://www.tugraz.at/fileadmin/user_upload/Events/Eninnov2016/files/lf/Session_F2/LF_Helminger.pdf

Jo et al. (2020). Comparative evaluation of the evaporation heat transfer characteristics of a low-GWP refrigerant R-1234ze(E) between shell-and-plate and plate heat exchangers. *International Journal of Heat and Mass Transfer, 153*. doi:10.1016/j.ijheatmasstransfer.2020.119598.

Kang et al. (2019). Experimental study on the performance of a steam generation heat pump with the internal heat exchanging effect. *International Journal of Refrigeration, 108*, 154-162. doi:10.1016/j.ijrefrig.2019.09.003.

Keshavar et al. (2019). Dynamic simulation of a heat recovery steam generator dedicated to a brine concentration plant. *Journal of Thermal Analysis and Calorimetry, 135*, 1763–1773. doi:10.1007/s10973-018-7448-8

Kim et al. (2022). Heat integration of power-to-heat technologies: Case studies on heat recovery systems subject to electrified heating. *Journal of Cleaner Production, 331*. doi:10.1016/j.jclepro.2021.130002.

Kim, J.-K. (2022). Studies on the conceptual design of energy recovery and utility systems for electrified chemical processes. *Renewable and Sustainable Energy Reviews, 167*. doi:10.1016/j.rser.2022.112718.

Liu et al. (2022). Experimental investigation of a high-temperature heat pump for industrial steam production. *Applied Energy, 312*. doi:10.1016/j.apenergy.2022.118719.

Mateu-Royo et al. (2019). Experimental exergy and energy analysis of a novel high-temperature heat pump with scroll compressor for waste heat recovery. *Applied Energy, 253*. doi:10.1016/j.apenergy.2019.113504.

Meroni et al. (2018). Design of centrifugal compressors for heat pump systems. *Applied Energy, 232*, 139-156. doi:10.1016/j.apenergy.2018.09.210.

Naim Hossain et al. (2022). Integrated thermal modeling, analysis, and sequential design of heat exchanger surfaces of a natural circulation RDF boiler including evaporator tubes. *Applied Thermal Engineering, 211*. doi:10.1016/j.applthermaleng.2022.118455.

Singh Gaur et al. (2021). Heat pumps and our low-carbon future: A comprehensive review. *Energy Research & Social Science, 71*. doi:10.1016/j.erss.2020.101764.

TLK Thermo GmbH. (n.d.). TIL – Model library for thermal components and systems. Retrieved August 25, 2022, from https://www.tlk-thermo.com/index.php/en/til-suite

Umweltbundesamt GmbH. (2021). Retrieved September 19, 2022, from Berechnung von Treibhausgas (THG)-Emissionen verschiedener Energieträger: https://secure.umweltbundesamt.at/co2mon/co2mon.html.

Modeling of a Solar Heat for Industrial Processes (SHIP) System using Fresnel Collectors

Marco A. David-Hernández, Antonio Cazorla-Marín, José Gonzálvez-Maciá, Jorge Payá

Instituto Universitario de Investigación en Ingenieria Energética

Universitat Politècnica de València

Camino de Vera s/n, 46022, Valencia, Spain

Abstract

A quasi-dynamic model has been developed to simulate the dynamics and energy performance of a Solar Heat for Industrial Process (SHIP) system with Fresnel collectors under different control schemes and with variable heat demand. The model validation has been carried out with measurements obtained from the SOLPINVAP experimental facility in Almassora (Spain) during the summer of 2021 and 2022. This facility comprises a modular Fresnel collector solar field and a kettle reboiler. The results show that the predicted energy generation is in the same order of magnitude as in the measurements, and the overall system dynamics are reproduced accurately.

Keywords: Solar Heat for Industrial Process, Modelling, Fresnel collector, Quasi-dynamic model

1. Introduction

Solar Heat for Industrial Process (SHIP) is the implementation of current and proven solar technologies to supply the heat demand needed in different manufacturing processes of the industry sector. The industrial sector represents one-third of the global energy demand, and SHIP systems have become a growing option for the decarbonization of this sector. SHIP systems have been pushed forward as an alternative to fossil fuel-based boilers. In these kinds of systems, predicting the components' behavior, dynamics, and performance under different demand, control conditions, and integration with the heat demand is of great interest.

In the field of SHIP, there are two main common technologies: non-concentrating, such as flat plate and evacuated tube collectors, and concentrating collectors for example parabolic trough and linear Fresnel. The industrial processes can be divided depending on the temperature level required by the process: low, medium and high temperature heat (Kumar, Hasanuzzaman and Rahim, 2019). Linear Fresnel collectors are commonly used to generate medium temperature heat ($150\ ℃ - 400\ ℃$). As reported in the Solar Heat World Wide report (Weiss and Spörk-Dür, 2022), by the end of March 2022 SHIP plants by collector type in operation there are 20 linear Fresnel collectors SHIP systems.

SHIP systems are used to harness the incident irradiance from the sun and deliver it in the form of heat to an industrial process. The useful heat is transmitted by means of a heat transfer fluid, which usually is thermal oil, water, or steam. In this field, experimental on-site documentation of SHIP systems using linear Fresnel collectors is rather limited, being the case of a pharmaceutical plant in Jordan (Berger *et al.*, 2016) the one with more documentation.

In the present work, a quasi-dynamic model that simulates the dynamics and performance of a SHIP system, with a modular Fresnel collector solar field and a modified kettle reboiler, has been developed within the frame of the SOLPINVAP project (INDERTEC, 2020). Experimental measurements have been carried out during the summer of 2021 and 2022 at the experimental facility SOLPINVAP, located in Almassora, Spain. Two measured days have been selected based on the measured irradiance. Simulations with the characteristics and control parameters of the SOLPINVAP solar field have been carried out with the developed model. The validation of the developed model with the simulation results and the measurements of the selected days is shown in the following sections.

© 2022. The Authors. Published by International Solar Energy Society
Selection and/or peer review under responsibility of Scientific Committee
doi:10.18086/eurosun.2022.05.03 Available at http://proceedings.ises.org

2. Methodology

2.1. System Model

A mathematical quasi-dynamic model has been developed and built inside the object-oriented programming environment of MatLab. The latter was selected as modeling software due to its built-in libraries capable of solving differential algebraic equations systems (DAE). Each physical component has been programmed as an individual object with a set of equations, inputs, and outputs. The reason for using objects is to give the model the flexibility to assemble a system with any number of components and connections scheme.

The present work analyzed a system that comprises a shell and tube heat exchanger named kettle reboiler, a modular Fresnel collector solar field, a circulation pump, a filling pump, a steam extraction valve, and pipelines. In Fig. 1, the system components are represented with their thermodynamic interface (dots) between objects.

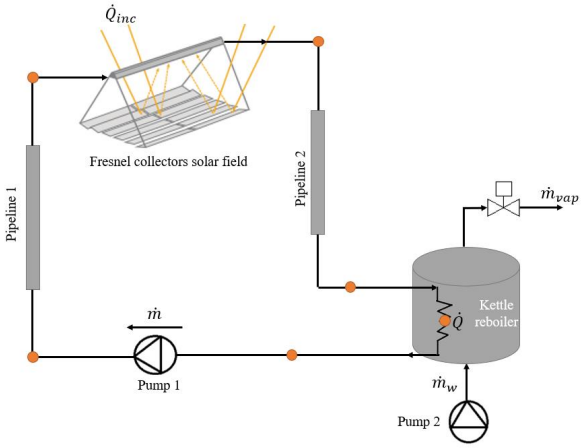

Fig. 1: System diagram with the model components on Indirect Steam Generation mode

Pressurized water has been used as heat transfer fluid throughout the solar field. The REFPROP library (NIST, 2013) has been included in MatLab to calculate the thermodynamic properties of the fluid. The main components shown in Fig. 1 are explained in the following sections.

2.2. Kettle Reboiler Model

The kettle reboiler installed at the experimental platform has been modified to work in two modes: Indirect Steam Generation (ISG) and Direct Steam Generation (DSG). It has two main functions: to separate the liquid water from steam and to accumulate energy.

Complex models for a tank with a 2-phase working fluid can be found in the literature. Such models consider the 2-phase fluid as two separate fluids. Thus, the thermodynamic state of each phase is known at any given time step (Stevanovic, Maslovaric and Prica, 2012). These models are helpful when the steam and liquid water have different temperatures. However, in SHIP systems, that is rarely the case. In this work, a simplified tank model has been developed, where the 2-phase fluid inside the kettle reboiler is considered in thermodynamic equilibrium at each time step. Thus, the thermodynamic state of the 2-phase fluid can be known by calculating two independent properties. The properties selected for the calculation are its density ρ and specific internal energy u, as shown in equations (eq. 1) to (eq. 3). Furthermore, the kettle reboiler has been assumed as a cylinder for simplification purposes.

$$\frac{d\rho}{dt} = \frac{\sum \dot{m}_{in} - \sum \dot{m}_{out}}{V_T} \quad \text{(eq. 1)}$$

$$\frac{dU}{dt} = \dot{Q}_{in/out} + \sum(\dot{m}_{in} \cdot h_{in}) - \sum(\dot{m}_{out} \cdot h_{out}) \quad \text{(eq. 2)}$$

$$U = \rho \cdot V_T \cdot u + M_M \cdot C_{p,M} \cdot T_M \quad \text{(eq. 3)}$$

The kettle reboiler is modeled with a differential-algebraic equations system. Where (eq. 3) represents the total internal energy of the tank: the sum of the energy of the 2-phase fluid and the tank's mass. V_T is the total internal volume of the kettle reboiler, M_M and $C_{p,M}$ are the tank material's mass and specific heat, respectively. In (eq. 1), $\dot{m}_{in}$ and $\dot{m}_{out}$ are the inlet and outlet mass flow rates, respectively. On the right-hand side of (eq. 2), $\dot{Q}_{in/out}$ represents any heat flow rate going into/out the kettle reboiler, for example, input heat from the shell and tube heat exchanger or heat loss to the ambient. It has been assumed that, when the fluid is in saturation state, the temperature

of the tank material, T_M, is the same as the temperature of the fluid inside the tank. Then, this temperature can be calculated as a function of the density and the specific internal energy of the 2-phase fluid: $T_M = T_{fl} = f(\rho, u)$.

2.3. Fresnel Collector Model

The Fresnel module collector model has been created as a black box, where the inputs were reduced to weather data and inlet mass flow, enthalpy, and pressure of the flowing water.

A pyranometer for the measurement of global horizontal irradiance has been installed at the experimental plant. However, there is no other instrument to measure or calculate the direct normal irradiance (DNI). Thus, on the lack of this information, a clear-sky model has been implemented to estimate the DNI. In the present work, the selected model is the clear-sky model presented in the ASHRAE handbook (ASHRAE, 2013). The disadvantage of this methodology is that it works on the assumption of a clear atmosphere.

A simple Incident Angle Modifier (IAM) based model has been implemented to calculate the incident heat on the collector absorber. The longitudinal and transversal IAM (IAM_l and IAM_t respectively) were calculated with the Monte Carlo Ray Tracing software tool Tonatiuh (CENER, 2017). Thus, the incident heat on the absorber tube can be calculated as shown in (eq. 4) (Morin *et al.*, 2012). Where A is the total reflective effective aperture area on the horizontal plane of a Fresnel module, N_{mod} is the number of modules, and Cl is a factor related to the cleanliness of the reflective surface.

$$\dot{Q}_{inc} = \eta_0 \cdot IAM_l \cdot IAM_t \cdot Cl \cdot A \cdot N_{mod} \cdot DNI \quad \text{(eq. 4)}$$

No thermal inertia is considered in the Fresnel collector model, as the developed quasi-dynamic model assumes that the thermal inertia is concentrated in the kettle reboiler.

2.4. Heat Loss Model

A simple thermal loss model has been used for the pipelines and the kettle reboiler. Both components have been assumed to be cylinders. The heat loss depends on the temperature difference ΔT between the temperature of the fluid and the ambient temperature, as shown in equation (eq. 5), where R_t is the thermal resistance. The model is used to simulate the thermal loss of each component throughout the simulation. The heat loss through the walls on both bases of the cylinder is also considered in the kettle reboiler.

$$\dot{Q}_{loss} = \frac{\Delta T}{R_t} \quad \text{(eq. 5)}$$

3. Experimental Facility

The experimental solar platform, SOLPINVAP, is located in Almassora, Spain (39.958, -0.074). The facility is comprised of a single row of 6 collector modules in series. There is a total of 9 absorber tubes for a total length of $35.12\ m$. The Fresnel solar collector modules have been manufactured by Solatom (Solatom CSP, 2018). Each module has a reflective aperture area of $26.4\ m^2$. The optical efficiency of the Fresnel modules, calculated with Tonatiuh, is $\eta_0 = 66.7\%$. The kettle reboiler is located inside a skid structure on the southern side of the solar field. The solar field is north-south oriented with a deviation of $32°$ northeast (being north $0°$ and south $180°$). In Fig. 2 a) and b), the Fresnel solar field and the kettle reboiler are shown.



a) b)

Fig. 2: Photos taken at the SOLPINVAP experimental plant, where in a) the Fresnel module collector field and in b) the kettle reboiler inside the skid

3.1. Control Parameters of the Solar Field

The circulation pump of the primary circuit of the solar field is turned on when the global irradiance, measured by the pyranometer, is greater than $150\ W/m^2$. It is turned off when there is not enough irradiance or when the measured liquid water level inside the tank is lower than a critical level of $-80\ mm$ (where $0\ mm$ is at the center of the kettle reboiler). The level inside the tank is kept between a maximum and minimum value by filling the tank with treated water.

The steam extraction is carried out by controlling the aperture of two pneumatic valves. The first valve keeps the pressure inside the tank, and the second keeps the pressure inside an expansion tube. The latter has the function of imitating the demand side (with a constant process pressure). In the skid installation, a flow meter has been added to measure the steam mass flow rate, as shown in Fig. 3.



Fig. 3: Steam mass flow meter installed at the extraction side of the skid

4. Results and Discussions

As mentioned in section 2.2, the solar field SOLPINVAP was designed to work on ISG and DSG modes. Two measurement campaigns on the ISG mode have been carried out at the experimental solar plant SOLPINVAP to validate the developed model. In ISG mode, the kettle reboiler receives the heat absorbed from the solar field through the tube heat exchanger.

The first measurements were done during the summer of 2021, and the following measurements were acquired during the summer of 2022. Two separate days are analyzed in the present work, one from each campaign. The first is June 24, 2021, and the second on June 12, 2022.

4.1. Weather Data

In Fig. 4 the global, direct normal, and diffuse irradiance for both June 24, 2021, and June 12, 2022, are shown as

reported in the measurements from the Valencia airport in Manises. Although the SOLPINVAP facility is 63 km away from Valencia Airport, it has been assumed that the weather does not significantly change around the same region.

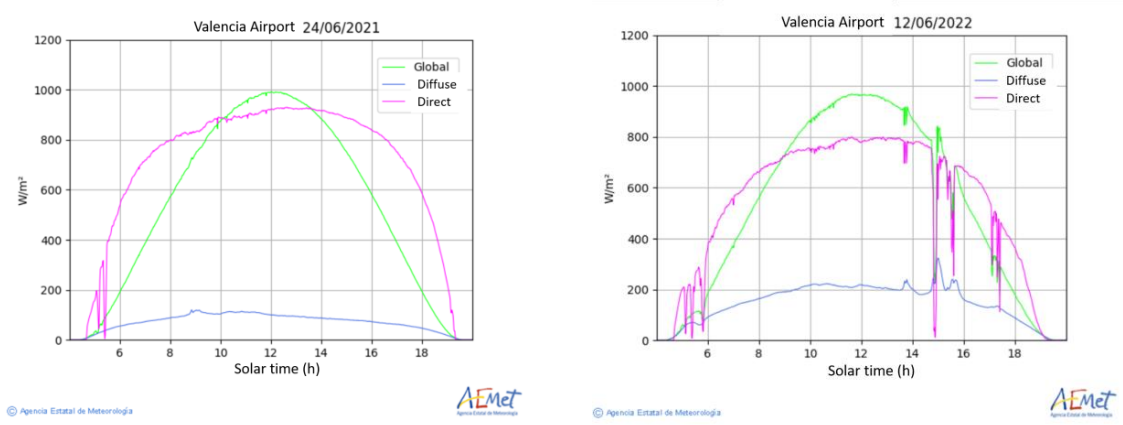

a) b)

Fig. 4: Global (green), direct normal (magenta) and diffuse (blue) irradiance measured at Valencia airport for a) June 24, 2021 and b) June 12, 2022 (taken from the Agencia Estatal de Meteorología – AEMET, Gobierno de España)

As shown in Fig. 4, both days presented a global irradiance with similar behavior to clear-sky conditions. Thus, the conditions are met for the use of a clear-sky model. As mentioned in section 2.3, the ASHRAE clear-sky model has been used for the calculations. The model uses optical depth indexes for the direct τ_b and diffuse τ_d irradiance, which depend on the location. These two indexes embody clear-sky conditions like precipitable water, aerosols, ozone, Etc. (ASHRAE, 2013). The optical depth indexes for both days have been estimated using the ASHRAE model, and the measurements are shown in Fig. 4. In Tab. 1 are listed the estimated optical depth indexes for each day, respectively.

Tab. 1: Optical depth indexes calculated with the clear-sky model and the irradiance measured at Valencia Airport

Optical Depth Index	June 24, 2021	June 12, 2022
τ_b(-)	0.4978	0.6969
τ_d(-)	2.4953	1.7500

In Fig. 5, the globlal irradiance measured by the pyranometer at the SOLPINVAP facility and the simulated irradiance, with the implemented clear-sky model using the optical depth indexes of Tab. 1, are shown. The root mean square error between the measured and simulated with the clear-sky model global irradiance on June 24, 2021 (Fig. 5 a)) is 16.05 W/m^2, whereas, on June 12, 2022 (Fig. 5 b)), the root mean square error is 69.9 W/m^2.

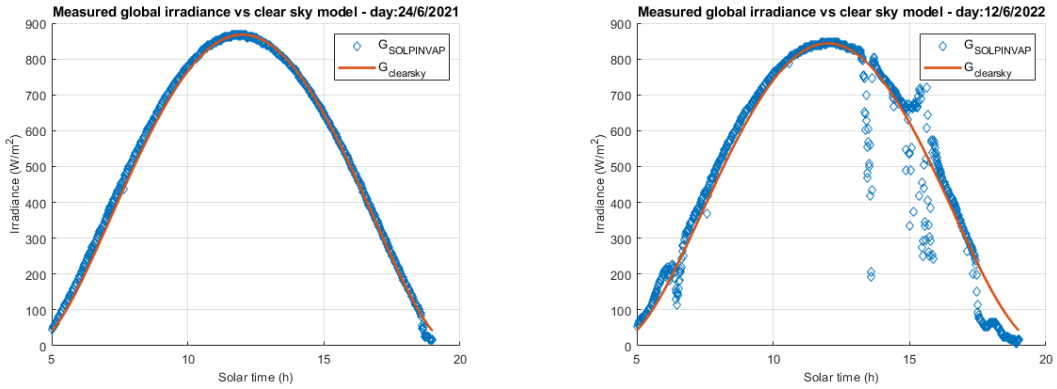

a) b)

Fig. 5: Global irradiance measured by the pyranometer at SOLPINVAP facility and the simulated with the clear-sky model and the respective optical depth indexes

4.2. Experimental Measurements

As mentioned above, two days are going to be analyzed in the present work. The measurements carried out during the two experimental campaigns at the SOLPINVAP plant are shown in Fig. 6. In both cases, the steam extraction was done through a steam valve controlled by a PID control scheme. Fig. 6 a) shows the temperatures at the inlet of the solar field $T1$ and the outlet $T2$, the temperature inside the kettle reboiler T_{tank}, the water level, and the measured steam mass flow rate at the extraction. The pressure inside the kettle reboiler is shown in Fig. 6 b). On June 24, 2021, solar energy was absorbed in the solar field, and there was steam extraction. The filling pump has turned on for 5 minutes during the measurements, as observed in Fig. 6 a). On June 24, 2021, the system was in function until the water level of the kettle reboiler reached a critical minimum. In Fig. 6 c) and d), the corresponding variables are shown on June 12, 2022. On June 12, 2022, solar energy was absorbed in the solar field, steam was extracted, and the water level control was active, as shown in Fig. 6 c).

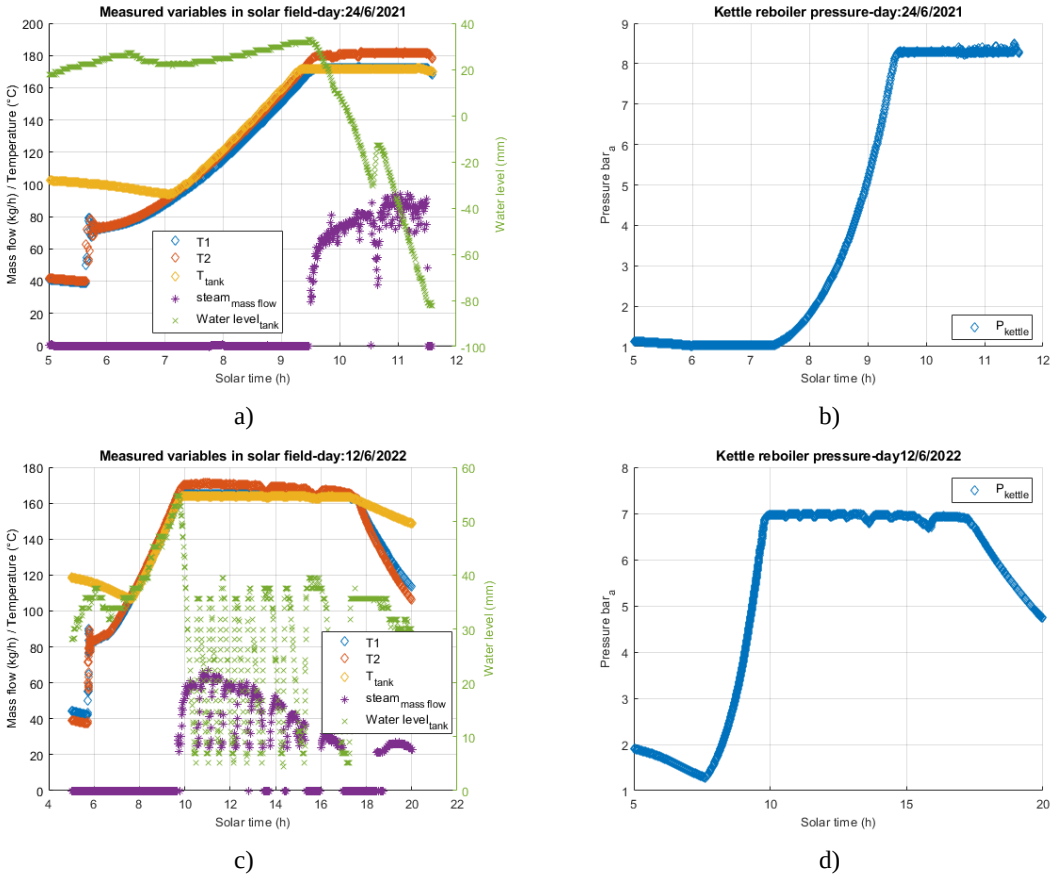

Fig. 6: Experimental measurements at SOLPINVAP. In a) and b) are the results on June 24, 2021, and in c) and d) the corresponding for June 12, 2022

The developed model is intended to simulate the system under normal working conditions with different control schemes and heat demands. In the following sections, the validation of the model with the experimental measurements of two days is presented, first on steady state and then on transitory and steady state. The DNI has been calculated during every time step with the optical depth indexes for the corresponding day and the clear-sky model.

4.3. Steady State

First, the Fresnel module collector model has been validated with the experimental measurements in the steady state period, i.e., a period where the temperature measurements in the solar field do not vary significantly. The inputs given to the model were the temperature at the inlet of the solar field, the water mass flow, and the clear-sky DNI. This validation was also used to estimate a clean factor for both measured days. Fig. 7 a) and b) present the validation results for June 24, 2021, and June 12, 2022, respectively, where $T2_{sim}$ and $T2_{exp}$ are the simulated and experimental temperatures, respectively, at solar field outlet. $T1_{exp}$ is the measured temperature at the inlet of the solar field, and $Mass\ flow_{solar\ field}$ is the mass flow rate of the pressurized water. On June 24, 2021 (Fig. 7 a)), the clean factor was estimated to be 70%, and the root mean square error between the simulated and measured solar field outlet

temperature was 0.3 K. It can also be observed that the model correctly follows the temperature tendency when there is a sudden change in water mass flow.

In the same way, the experimental measurements on June 12, 2022 (Fig. 7 b)) have been used to validate the Fresnel collector model. The estimated clean factor is 64%, and the root mean square error between the simulated and measured solar field outlet temperature is 0.19 K. In Fig. 7 b), decrements in the solar field inlet temperature and, consequently, at the outlet temperature can be observed. These decrements are due to the introduction of cold water when the filling pump is activated to increment the water level inside the kettle reboiler. Fig. 7 a) and b) also show no significant thermal inertia in the collector tubes.

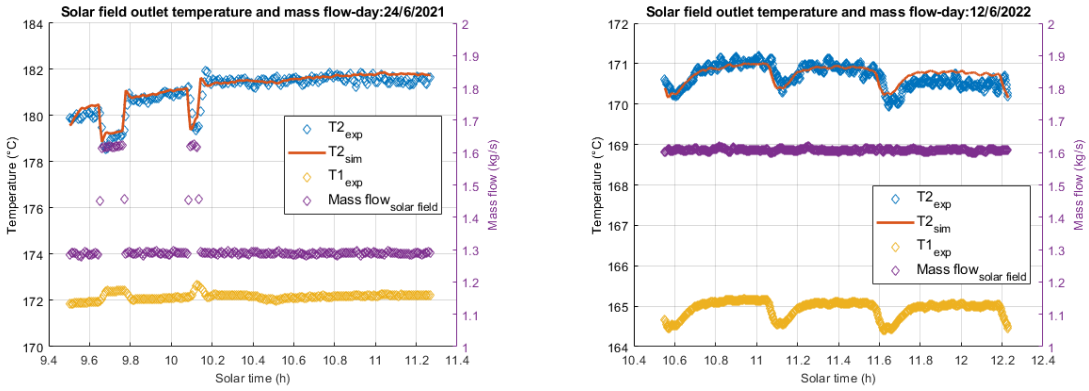

a) b)

Fig. 7: Predicted solar field outlet temperature, both simulated and measured, the solar field inlet temperature and water mass flow for: a) June 24, 2021 and b) June 12, 2022

The general model is then validated with the estimated clean factors in the same steady state time period. The general model is referenced as the complete system with all the components (see Fig. 1). The inputs to the general model are the weather data, the measured water mass flow rate, and control factors for steam extraction. A simple proportional control has been implemented to simulate the aperture of the steam extraction valve. Below, in Tab. 2, are listed the initial model parameters used for the simulation of the general model. As mentioned in section 3.1, the water level is referenced to the center of the kettle reboiler. Thus, a positive level value is above the center of the tank, and a negative value is below that point.

Tab. 2: Initial parameters for the simulation with the general model on steady state

Parameter	24/06/2021	12/06/2022	Unit
τ_b	0.4978	0.6969	-
τ_d	2.4953	1.7500	-
Clean Factor	70	64	%
Kettle Metal Mass	3079	3079	kg
Initial Kettle Pressure	8.1	6.9	bar_a
Initial Water Level	+25	+36	mm
Max Pressure	8.7	8.4	bar_a
Min Pressure	8	6	bar_a
Max Water Level	+10	+35	mm
Min Water Level	-81	+5	mm
Fill Water Temperature	50	50	℃

The comparison between the measured (subscript “exp”) and simulated (subscript “sim”) parameters of the solar

field in steady state are shown in Fig. 8. Where in Fig. 8 a) are the inlet and outlet solar field temperatures and water mass flow, Fig. 8 b) the kettle reboiler pressure and water level, and in Fig. 8 c) the extracted steam mass flow of June 24, 2021. In Fig. 8 d), e) and f), the respective comparison of the parameters mentioned before, on June 12, 2022, is graphed. In Tab. 3 are listed the corresponding root mean square error for each relevant variable for June 24, 2021 and June 12, 2022. Moreover, the relative difference between the experimental measured and simulated extracted energy is presented in Tab. 4. The generated energy is referred to as the integrated steam mass flow during the analyzed period.

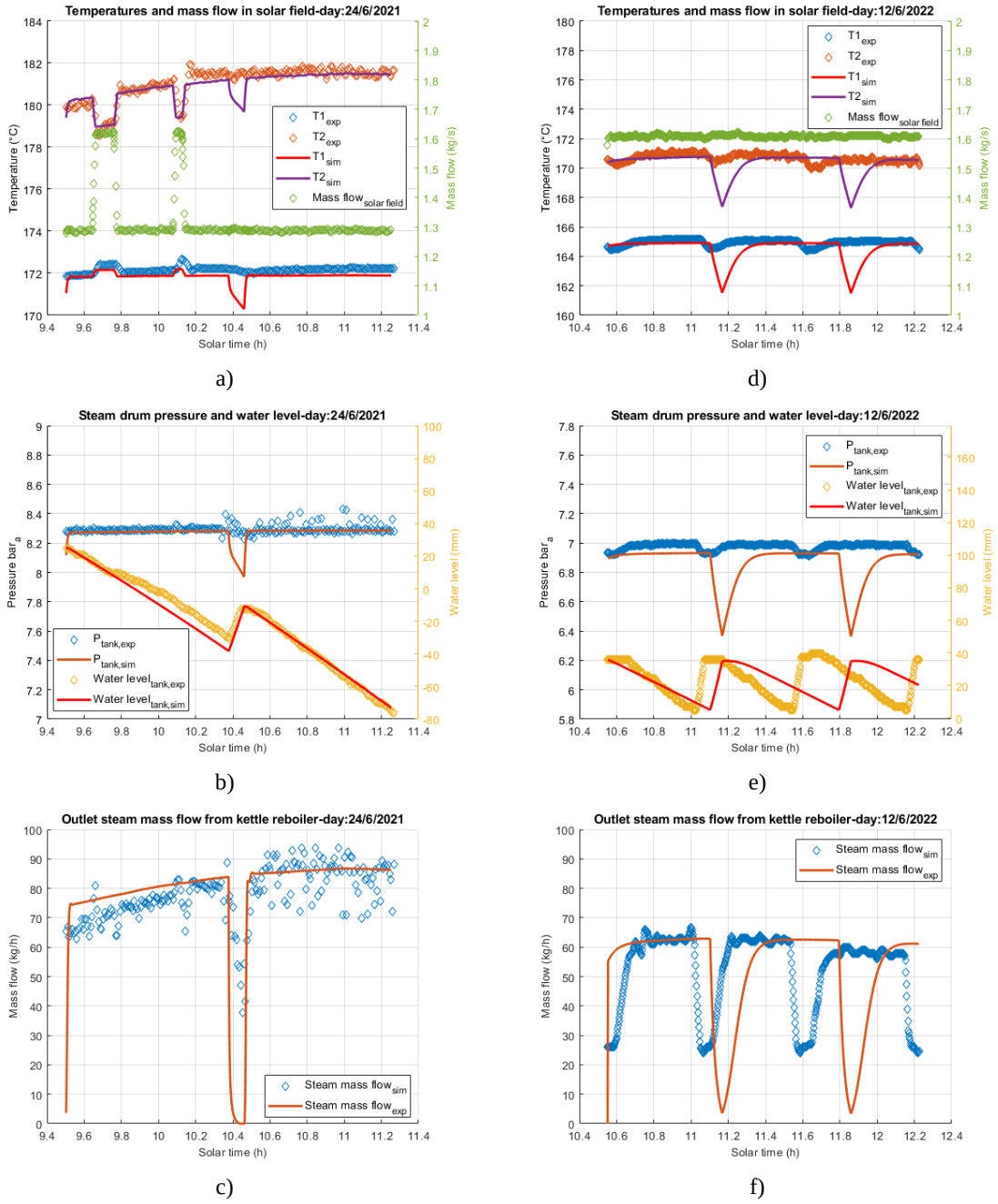

Fig. 8: Validation of the model on steady state time period. In a), b) and c) the results of June 24, 2021, and in d), e) and f) the simulation results of June 12, 2022 are shown.

Tab. 3: Root mean square error of the relevant parameters of two days in the analyzed time period

	Root Mean Square Error		
Parameter	**24/06/2021**	**12/06/2022**	**Unit**
$T1$	0.53	0.95	K
$T2$	1.02	0.91	K
P_{tank}	0.08	0.18	bar_a

Tab. 4: Comparison between measured and simulated generated energy in the analyzed time period

Parameter	**24/06/2021**	**12/06/2022**	**Unit**
Experimental Energy Extracted	380.52	241.2	MJ
Simulated Energy Extracted	378.43	242.32	MJ
Relative Difference	0.05	0.5	%

On both days, the filling pump introduced cold water into the kettle during the analyzed period. It can be observed how the model predicts a decrease in pressure greater than the measured by the pressure sensor, $0.31\ bar_a$ in the case of June 24, 2021 (Fig. 8 b)) and $0.56\ bar_a$ on June 12, 2022 (Fig. 8 e)). This is because the model considers a homogeneous 2-phase fluid inside the kettle reboiler; this means the 2-phase fluid is in thermodynamic equilibrium at every time step. However, this is not true in reality because there exists a stratification when cold water enters the tank. Nevertheless, the decrease in pressure predicted by the model does not significantly affect the energy generated by the system, as presented in Tab. 4.

4.4. Transient and Steady State

In this section, the model is validated with the experimental measurements, including the initial transient state of the system. The latter means when the day starts, and the pressurized water is heated up, and the kettle reboiler is pressurized up to the desired pressure level. The simulations in this section were carried out from the point where the inlet solar field temperature has reached $100\ ℃$, ensuring that the fluid inside the kettle reboiler is in saturation state.

In Tab. 5 are listed the initial parameters for the transient and steady state simulation. As mentioned before, on June 24, 2021, the main circulation pump and the system were turned off when the kettle reboiler water level reached a critical minimum. Thus, the simulation was carried out until that moment of the day. In the case of June 12, 2022, the simulation was done until there is presence of clouds, as observed in Fig. 5 b) and Fig. 6 c). The sky model does not simulate cloud presence. Therefore, the model validation was carried out just during the clear-sky section of the day.

Tab. 5: Initial parameters for the simulation with the general model on transient and steady state

Parameter	24/06/2021	12/06/2022	Unit
τ_b	0.4978	0.6969	-
τ_d	2.4953	1.7500	-
Clean Factor	70	64	%
Kettle Metal Mass	3079	3079	kg
Initial Kettle Pressure	1	1.28	bar_a
Initial Water Level	+23.6	+35.7	mm
Max Pressure	8.7	8.4	bar_a
Min Pressure	8	6	bar_a
Max Water Level	+10	+35	mm
Min Water Level	-81	+5	mm
Fill Water Temperature	50	50	℃

In Fig. 9, the validation of the general model, including the transient and steady state, with the measurements carried out on June 24, 2021, and June 12, 2022, is presented. Where the subscript "sim" stands for simulation and the subscript "exp" is for the experimental measurement. Fig. 9 a) and d) show the inlet and outlet solar field temperature and water mass flow. In Fig. 9 b) and e), the evolution of the pressure and water level throughout the day can be observed. Furthermore, the extracted steam mass flow on June 24, 2021, and June 12, 2022, is graphed in Fig. 9 c) and f) respectively, on each mentioned figure. The comparison between the measured and simulated extracted energy and the relative difference for both June 24, 2021, and June 12, 2022, is presented in Tab. 6.

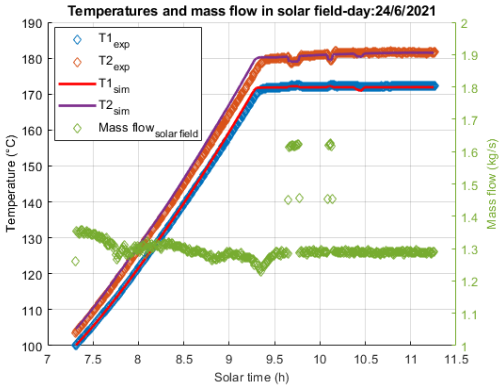

a)

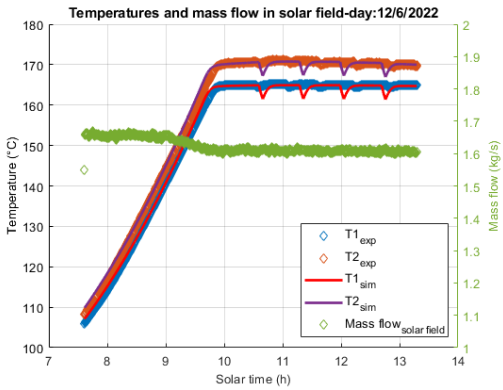

d)

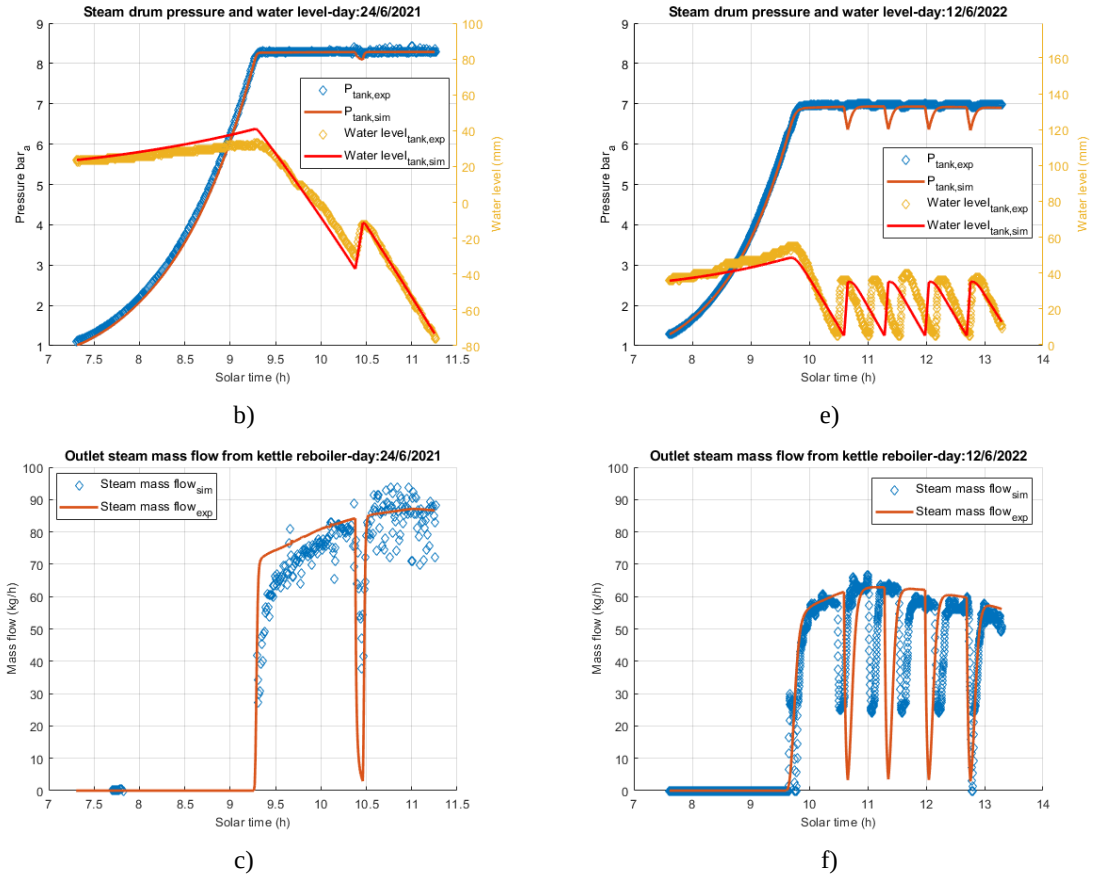

Fig. 9: Validation of the model on transient and steady state. In a), b) and c) the results of June 24, 2021, and in d), e) and f) the simulation results of June 12, 2022 are shown.

Tab. 6: Comparison between measured and simulated generated energy in the analyzed time period

Parameter	24/06/2021	12/06/2022	Unit
Experimental Energy Extracted	406.8	493.2	MJ
Simulated Energy Extracted	424.8	500.4	MJ
Relative Difference	4.4	1.5	%

Fig. 9 a), b), d), and e) show that, on both days and with their respective initial parameters, the model follows the tendency of the inlet and outlet solar field temperatures and the kettle reboiler pressure along the transient part of the day. During the steady state part of the simulation, the model predicts a decrease in pressure due to the introduction of cold filling water, as observed in Fig. 9 b) and e). The pronounced decrease of the simulated pressure occurs because the model does not account for stratification in the liquid phase when cold water is introduced. In Fig. 9 c) and f) shows that the simulated steam mass flow also decreases more than in reality when cold water fills the kettle reboiler. Nevertheless, as presented in Tab. 6, the latter does not significantly affect the final predicted energy generated by the system.

5. Conclusions

A quasi-dynamic model has been developed in MatLab that is able to simulate the dynamics, behavior, and performance of a SHIP system with a modular Fresnel collector solar field. The developed model simulates any collector module arrangement thanks to its object-oriented structure. It has been structured only to change few initial parameters considering weather data, the clean factor, and control variables. Thus, the rest of the parameters depend on the inputs mentioned before.

In order to estimate the DNI, measurements from the Valencia airport were used to estimate optical depth indexes

required for the implemented clear-sky model. The SHIP model has been validated with experimental measurements from the SOLPINVAP experimental platform during the summer of 2021 and 2022. The validation results show that the model correctly reproduces the temperatures and pressure tendencies in the transient and steady state. On steady state, the model simulates the solar field temperatures and pressure inside the kettle reboiler with small error. The model predicts a sudden pressure drop when cold water is introduced to the kettle reboiler, thus decreasing the predicted steam mass flow. The pressure drop may be smaller in reality because there is a stratification in the liquid phase when cold water enters the tank, and the same occurs with the extracted steam mass flow. However, it has been shown that the decrease in pressure does not significantly influence the simulated final energy generated compared with the experimentally measured energy generated.

Thus, the developed quasi-dynamic model is able to simulated accurately the behavior, dynamics, and performance and accurately predict the energy generated by a SHIP system that comprises a Fresnel collector solar field.

6. Acknowledgements

The authors gratefully acknowledge the company SolatomCSP, for all the information and operational data from the SHIP facility used in the present work, and for all the technical support. This work was partially supported by the Research and Development Aid Program (PAID-01-20) of the Universitat Politècnica de València for receiving the Research Fellowship FPI-UPV-2020. This publication has been carried out in the framework of the project "DECARBONIZACIÓN DE EDIFICIOS E INDUSTRIAS CON SISTEMAS HÍBRIDOS DE BOMBA DE CALOR", funded by the Spanish "Ministerio de Ciencia e Innovación (MCIIN)" with code number PID2020-115665RB-I00.

7. References

ASHRAE (2013) 'Handbook Fundamentals, Chapter 14. Climatic Design Information', *Atlanta*, 1952, pp. 1–56.

Berger, M. *et al.* (2016) 'First Year of Operational Experience with a Solar Process Steam system for a Pharmaceutical Company in Jordan', *Energy Procedia*, 91, pp. 591–600. Available at: https://doi.org/10.1016/j.egypro.2016.06.209.

CENER (2017) *Tonatiuh, Monte Carlo Ray Tracer Software*. Available at: https://iat-cener.github.io/tonatiuh/ (Accessed: 21 February 2022).

INDERTEC (2020) *Indertec desarrolla SOLPINVAP: Energía SOLar de Media Temperatura para procesos INdustriales con demanda de VAPor*. Available at: https://indertec.com/2020/01/19/indertec-desarrolla-solpinvap-energia-solar-de-media-temperatura-para-procesos-industriales-con-demanda-de-vapor/ (Accessed: 8 June 2020).

Kumar, L., Hasanuzzaman, M. and Rahim, N.A. (2019) 'Global advancement of solar thermal energy technologies for industrial process heat and its future prospects: A review', *Energy Conversion and Management*, 195(February), pp. 885–908. Available at: https://doi.org/10.1016/j.enconman.2019.05.081.

Morin, G. *et al.* (2012) 'Comparison of Linear Fresnel and Parabolic Trough Collector power plants', *Solar Energy*, 86(1), pp. 1–12. Available at: https://doi.org/10.1016/j.solener.2011.06.020.

NIST (2013) *REFPROP*. Available at: https://www.nist.gov/srd/refprop (Accessed: 23 September 2021).

Solatom CSP (2018) *SolatomCSP*. Available at: http://www.solatom.com/ (Accessed: 8 June 2020).

Stevanovic, V.D., Maslovaric, B. and Prica, S. (2012) 'Dynamics of steam accumulation', *Applied Thermal Engineering*, 37, pp. 73–79. Available at: https://doi.org/10.1016/j.applthermaleng.2012.01.007.

Weiss, W. and Spörk-Dür, M. (2022) 'Solar Heat World 2022. Global Market Development and Trends 2021. Detailed Market Figures 2020', p. 87. Available at: https://www.iea-shc.org/Data/Sites/1/publications/Solar-Heat-Worldwide-2021.pdf.

A novel method for assessing the techno-economical compatibility of solar thermal integrations

Andrea Gambardella[1] and Puneet Saini[2,3]

[1] Absolicon Solar Collectors AB, Fiskaregatan 11, Härnösand 87133, Sweden

[2]Absolicon Solar Collectors AB, Fiskaregatan 11, Härnösand 87133, Sweden

[3]Department of Energy and Construction Engineering, Dalarna University, Falun S-79188, Sweden

Abstract

In this work we present a method to evaluate the compatibility of a solar thermal integration in an industrial process. We introduce two indicators to quantify in a comprehensive way all the financial and technical boundaries influence on the design choices and on the costs of a solar thermal integration.

Both the indicators are measures of the divergence of an integration from a fictive (yet technically possible) ideal case and from a "do-nothing" case. In this way, the incompatibilities of the integration are associated to the consequences that the non-ideal factors have on both costs and performances. Moreover, the value of the indicators is normalized between a minimum and a maximum being the "do-nothing" and the ideal cases respectively.

We then used these indicators on a real case scenario to compare the pros and cons of two different solar thermal integration approaches (hot water vs steam) to a beer brewery in southern Europe.

The results show that retrofitting part of the existing appliance to be fed with hot water rather than steam enhances the compatibility of solar thermal with the brewery. Nevertheless, we measured no relevant improvement to the compatibility of solar thermal when designing a brewery from scratch with the same characteristics but were the solar thermal system could have been integrated "ad-hoc" rather than retrofitted.

Keywords: solar thermal integration, compatibility, low pressure industries, brewery

Introduction

The challenges of integrating a solar thermal system into an industrial process can be overcome at a cost which will surely affect the design of the optimal solution.

These challenges can be of different nature, from purely thermodynamical to logistical, to geographical, etc. and they can also influence each other so that mitigating a problem could worsen, ease and/or create other problems. Thus, normally the optimal solution consists of those precise temperature setpoints, that specific heat-exchanger, and all those other design choices corresponding to the right trade-off between being technically ideal (best performances) and economically ideal (best price). This procedure is not different from other common designing processes, after all, it is nothing more than a quality-price evaluation, but what makes the case of solar thermal different is that the quality of an integration does not depend exclusively on deterministic factors, it also depends on the compatibility between the solar energy nature and the industrial process it will serve. The lack of understanding of this compatibility can lead to an imbalance between expectations and reality.

In this work, we show a techno-economic analysis of solar thermal integration designs that with few terms reflects the influence that the compatibility has on the optimal solution.

© 2022. The Authors. Published by International Solar Energy Society
Selection and/or peer review under responsibility of Scientific Committee
doi:10.18086/eurosun.2022.05.04 Available at http://proceedings.ises.org

Background

When comparing different potential solar thermal integrations in an industrial process we often found ourselves ranking the solutions by several parameters of different nature and magnitude such as the Levelized Cost of Energy (LCoE), the pay-back period, the energy delivered/wasted, the investment costs etc. Since different integration solutions have different pros and cons, in most of the cases, each ranking is different depending on which parameter is it based on, and even within each ranking the scoring system might not be always univocal. Unless the priorities of the integration are clearly defined, it is hard to set an unambiguous score that is comprehensive of all the other parameters and with which it is possible to draw an overall ranking of the different potential solar thermal integrations. We decided to refer to this score as "compatibility".

The key for understanding the compatibility of the integration of a solar energy technology with a specific process is to define other reference cases first, specifically we need to define a best-case scenario (ideal case) and a worst case scenario (no-integration or "do-nothing" case). These cases would score respectively top and bottom of our overall ranking. Once that those cases are defined both in technical and economic terms, we identify the compatibility of the integration in the relative divergence between the optimal solution and the ideal one.

It is important to distinguish between the ideal and the optimal cases.

By ideal case we refer to a fictive (yet possible) scenario where we assume that all the process specific needs can be fulfilled by solar energy without the need for complementary components and without any unnecessary energy loss and/or extra costs.

That implies, for example, that in the ideal case the solar energy production always matches exactly the energy needs, therefore the temporal component causing any mismatch between the energy production and utilization can be disregarded.

Moreover, the heat is always transferred at process level and at the lowest allowable temperature difference according to pinch analysis (to minimize thermal losses).

Finally, in the ideal case, no logistic constraint applies, and the space availability is virtually unlimited while the cost of the solar collectors is equal to their production cost (no profit margins or expenses due to transport etc.).

By optimal case instead, we refer to the real scenario proposed for the integration as a result of the techno-economical designing process.

Beside these two cases, we refer to the no-integration case (or worst case) as the current state of the system: without any solar thermal integration.

At this point we need to assess the divergence between the optimal solution and the ideal one.

In order to explain and give a measure to this divergence, a little bit of terminology is necessary, and the following graph helps visualizing better the up-coming concepts

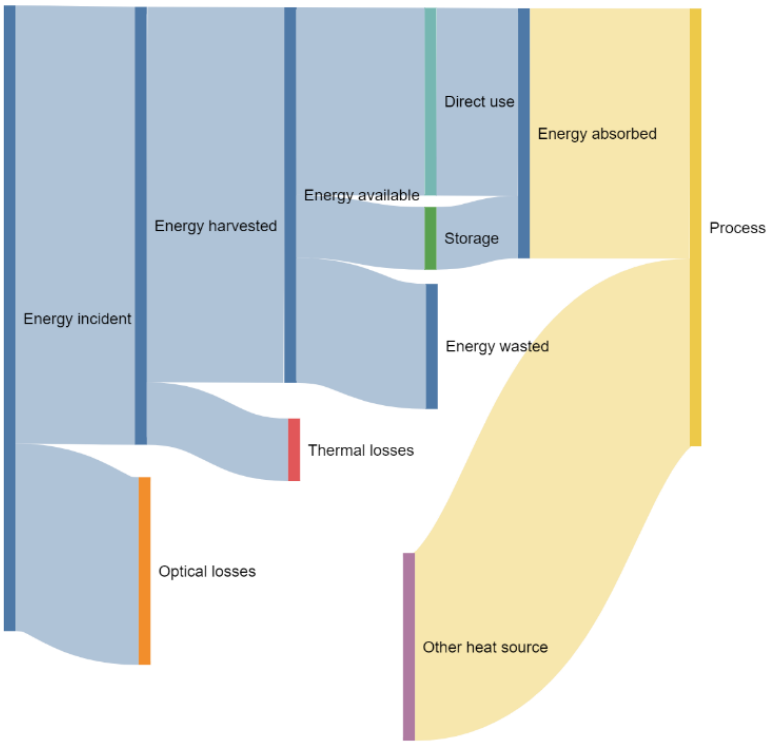

Fig.1: Solar thermal integration energy Sankey diagram

Fig. 1 shows the solar energy flows [in MWh/year] of a generic solar field to the target user. We define as:

- Energy incident, the amount of solar radiation reaching the solar thermal collectors
- Optical losses, the amount of energy incident not transferred to the heat carrier of the solar system. These losses are inevitable, so they compare also in the ideal case. Nevertheless, external factors (such as shading from surrounding structures or ground tilt) influence these losses. In the ideal case, the environment does not affect these losses.
- Energy harvested, the difference between energy incident and optical losses
- Thermal losses, the amount of energy harvested lost to the environment by heat transfer. These losses are also inevitable, but they can be mitigated to a certain extent. In the ideal case these losses are reduced to their physical possible minimum.
- Energy available (Q_A), the difference between energy harvested and thermal losses
- Energy absorbed (Q_S), the amount of energy available that is used by the process either directly or via a thermal storage. In the ideal case the energy absorbed equals the energy available and it only consists of direct use (no storage).
- Energy wasted (Q_D), the amount of energy available that was never used by the process because of a mismatch between heat production and demand.
- Heat load (Q_0), the total energy needed by the process.

Furthermore, we define the following adimensional parameters:

- Solar fraction (S_F), the ratio between the energy absorbed and the heat load. Obviously, this parameter ranges between 0 and 1 and in the ideal case is 1 while is 0 for the no-integration case.
- Capacity reserve (C_R), the ratio between energy wasted and energy available. This parameter also ranges between 0 and 1, but it is 0 for both the ideal and the no-integration case.

Finally, we define the following financial parameters:

- Levelized cost of energy ($LCoE$) measured in €/MWh, by the following formula [2]:

$$\mathrm{LCoE} = \frac{sum\ of\ costs\ over\ project\ lifetime}{sum\ of\ energy\ load\ over\ project\ lifetime} = \frac{\sum_{t=1}^{n}\frac{I_t+O_t}{(1+\alpha)^t}}{\sum_{t=1}^{n}\frac{Q_t}{(1+\alpha)^t}} \quad \text{(eq.1)}$$

where:

- I_t are investment expenditures in the year t
- O_t are operational costs (fuel and maintenance) in the year t
- Q_t is the heat load in the year t
- n is the lifetime of the project in years
- α is the discount rate

n and α must be equal in the ideal, optimal and no-integration cases for the comparison to make sense. Moreover, the LCoE must consider the effects associated with the energy production and demand mismatch and thus, in the formula, we must use the value of the solar energy absorbed, rather than the energy available. That also implies that in the investment expenditures we must include the cost of thermal storages and any other non-exclusively-solar related costs (such as piping, foundations etc.)

- The fuel price (F) measured in €/MWh
- The cost of the investment in the ideal case (I_{ideal}) and in the optimal case (I_{opt}) measured in €

For simplicity, we will assume as investment expenditures the total cost of the solar thermal integration and as operational costs no other costs but the fuel costs

The LCoE alone does not reflect all the solar thermal integration gains, indeed basing the design on the LCoE alone could results in the tendency of preferring cost-reducing installations over other factors such as energy efficiency or sustainability [4]. On the other hand, it is comprehensive of both the technical and the financial aspects of the case. In other words, the LCoE is a quite good "overall" scoring system, not for nothing it is widely acknowledged as a convenient summary measure of the competitiveness of an energy technology [4], but it should not be the only indicator to consider, and it also lacks some form of reference values in order to contextualize and give some significance to its bare figure.

Obviously, for the solar thermal integration to even make sense economically, the relation between the LCoE for the reference cases must be as follows:

$$LCoE_0 > LCoE_{opt} > LCoE_{ideal} \quad \text{(eq.2)}$$

We have in this way indirectly ranked the integration cases (no-integration as the worst, ideal as the best). This allows to measure the divergence between the optimal and the ideal cases and to normalize that value having both the best and worst cases as reference

$$\Phi = \frac{LCoE_0 - LCoE_{opt}}{LCoE_0 - LCoE_{ideal}} \quad \text{(eq.3)}$$

We introduce the financial compatibility (Φ) defined above as one of the indicators of the solar thermal technology integration compatibility with the process.

If we take the conservative assumption that the current cost of energy will not adjust for the discount rate, we can expand the terms of the financial compatibility and we can rewrite the eq.3 as:

$$\Phi = \frac{S_F - {rI_{opt}}/{Q_0 F}}{1 - {rI_{ideal}}/{Q_0 F}} \quad \text{(eq.4)}$$

where

$$r = \frac{1}{\sum_{t=1}^{n}\frac{1}{(1+\alpha)^t}} \quad \text{(eq.5)}$$

and where ${rI}/{Q_0 F}$ is another adimensional number representing the costs of the solar thermal investment as a portion of the current value of the energy costs each year of the no-integration case. We will refer to it as the relative weight of the investment with the symbol χ so that

$$\Phi = \frac{S_F - \chi_{opt}}{1 - \chi_{ideal}} \quad \text{(eq.6)}$$

Summing up, we can now observe that:

- The financial compatibility's value is bounded between 0 and 1.
- We can express it as function of two adimensional parameters being the solar fraction and the relative weight of the investment.
- It is comprehensive of both technical and financial aspects.
- It is contextualized with the current price of energy and with the best possible price achievable with solar thermal

Just like the LCoE, when comparing two possible integration solutions, Φ is very powerful to understand if it is more convenient to opt for more solar energy or for cheaper solar energy. In addition, since its value is bounded, it gives a measure of the limitations that the costs and the technical boundaries pose on the optimal solution.

At first glance, it might seem that the financial compatibility is not affected by the capacity reserve. That is because from a purely economic point of view, the capacity reserve has only significance as a theoretical limit on the economic benefits acquirable through a thermal storage.

On the other hand, in a purely energetical compatibility perspective, the capacity reserve plays a much more important role. That can be shown following the same conceptual procedure of measuring the divergence between the optimal and the ideal cases, but according to energetical aspects only.

In order to do that, we define a two-dimensional geometrical space consisting of the energy absorbed and the energy wasted (we will represent them as the x and the y respectively of a Cartesian coordinate system).

The three cases can now be represented as points in this space:

- No-integration correspond to the space origin (0;0) having neither energy wasted nor absorbed
- Ideal case is on the x-axis (Q_0; 0)
- Optimal case is the generic point (Q_S; Q_D)

We can now introduce the energy compatibility (Ψ) as the divergence between optimal and ideal cases normalized by the divergence between ideal and no-integration cases where we measured divergences as distance between points.

$$\Psi = \frac{Q_0 - \sqrt{(Q_0 - Q_S)^2 + (Q_D)^2}}{Q_0} \quad \text{(eq.7)}$$

we can rewrite this expression as

$$\Psi = 1 - \sqrt{(1 - S_F)^2 + \left(\frac{S_F C_R}{1 - C_R}\right)^2} \quad \text{(eq.8)}$$

We can observe that:

- The energy compatibility's value is < 1 but theoretically it is not inferiorly limited like the financial compatibility. This is because we have not yet imposed that that the divergence between optimal and ideal cases had to be smaller than the divergence between ideal and no-integration cases (which for the financial compatibility must happen for the integration to be economically meaningful and it is expressed by eq.2).
- Like we did for the financial compatibility, but in an energy-wise dimension only, if we had to impose a constraint to the energy compatibility's lower limit and justifying it as the minimum condition for the case to be meaningful, that would eventually translate into a relation between the solar fraction and the capacity reserve resulting in the domain of the meaningful solutions shown in Fig.2:

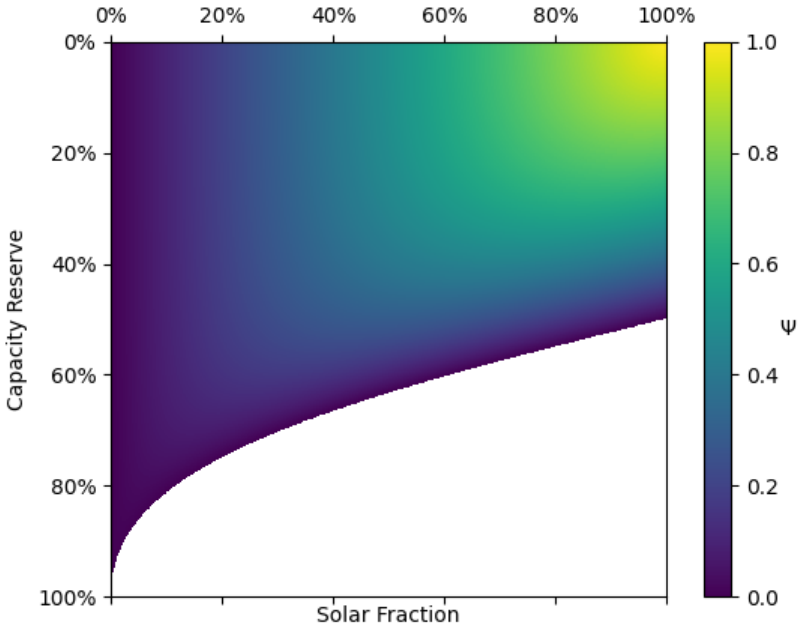

Fig.2: Values of the energy compatibility in the domain of the energy meaningful solution

- We can express it as function of two adimensional parameters being the solar fraction and the capacity reserve
- It's expressed by only energy related variables, thus it does not reflect the economics of the integration although they influence the choice of the optimal case.

Ψ becomes very useful when comparing two possible integration solutions to understand, from an energy point of view, whether is it worth to waste more to deliver more.

Methodology

We will now use the energy and financial compatibility to characterize different possible integration cases in a real scenario of a beer brewery in southern Europe. The main difference between the integration cases is the heat carrier media on the brewery side. More specifically, we want to assess through the compatibility KPIs if it is beneficial to convert the brewery, or part of its processes to use hot water instead of steam as heat carrier.

To evaluate each case, a simulation software has been developed. The software calculates all the energy flows of a solar integration corresponding to the weather condition, the heat demand, the solar thermal system layout, the current plant layout and the process physical boundaries (such as operational temperatures and pressures). Adding information about investments and current energy prices for each configuration, the software also finds the solar thermal system layout that score best in terms of financial compatibility for that specific configuration. We have chosen those layouts as the optimal cases for each scenarios and then we compared them.

The first step is to define some boundary conditions and general data inputs. Two indispensable inputs are the typical meteorological year profile and the brewery heat load profile. Without them it is impossible to assess the mismatch between production and demand of solar energy. Our source of typical meteorological year profile for this case is Meteonorm [5], while for the brewery heat load profile we used the steam consumption data from the brewery's SCADA system.

The solar collectors used for the simulation are "Absolicon T160" solar parabolic trough concentrators [6]. The bare minimum price of the collectors for the ideal case is 200 €/$m^2_{aperture}$ while we will consider an actual price for the chosen location of 350 €/ $m^2_{aperture}$. Regarding the thermal energy storages, we will consider 2000 €/m^3 for pressurized storages and 400 €/m^3 for atmospheric pressure storages.

The plant currently uses heavy fuel oil (HFO) to fire the boilers. They have a taxation on their carbon emissions and their boiler efficiency is circa 85%. All in all, the cost for MWh turns to be approximately 110 €/MWh.

Considering that the total yearly load amounts to 36700 MWh/year the current annual energy cost (which is nonetheless than the no-integration case reference) is 4.037 M€/year.

We will consider a discount rate of 7% and project's lifetime of 20 years.

The boilers at the facility are fed with de-aerated water at 103°C and they produce saturated steam at 160°C (slightly above 6 bar), but all the processes occur at temperatures under 103°C. By definition, in the ideal case the heat is always transferred at process level and at the lowest allowable temperature difference according to pinch analysis. Given the heat loads and temperatures of each process in the brewery and assuming a pinch temperature difference of 5°C the pinch analysis shows that the input and output temperatures of the solar field heat carrier for the ideal case will be respectively 50°C and 110°C.

Technically, all the heat loads could be fed at process level, however mashing and wort boiling are very sensitive processes that the brewery did not want to retrofit for the fear of altering the beer taste. Therefore, although in the ideal case we include all the processes, for the hot water case we will then only consider the load fraction of the targetable processes.

Even though some of the processes are operated in batch mode, for the pinch analysis we considered them to be simultaneous with a time averaging approach by calculating each process energy consumption and dividing it by its operation time [1][3].

To integrate solar thermal energy at boiler level, the collectors field operates parallelly to the boilers: it receives a part (or all) of the boilers' feedwater in input and it outputs steam to be sent back to the plant steam distribution system (via the manifold right after the boilers). The steam produced by the solar field has properties similar to the boilers steam: it has just slightly higher pressure (to have flow priority into the system), but almost identical in temperature (since the solar steam is at saturation conditions while the boiler steam is slightly overheated to reduce condensation along the steam distribution system).

During the designing phase, the process engineers have decided to produce solar steam with a parallel flow heat exchanger. That is for enhancing a thermos-syphon effect replacing a circulation pump on the cold side of the heat exchanger. The drawback of this decision is that the pinch point temperature is now higher than the steam saturation temperature forcing the solar collectors to also operate at higher temperatures and causing higher heat losses.

Furthermore, the process engineers have also estimated that the appropriate temperature difference between input and output of the solar field should be of 20°C. The trade-off is that higher input-output temperature difference increases the heat losses but reduces the flow and therefore the cost of piping and other equipment (such as the circulation pump).

Concerning the hot water case, the pinch analysis suggest that the optimal case should have as inlet and outlet temperatures on the collector side respectively 30°C and 120°C. That results in an average mean temperature (and thus thermal losses) of the collector even lower than the ideal case, but this advantage is only a small side-effect of a major drawback for this case which is the impossibility of targeting the entire brewery heat load since the processes of mashing and worth boiling had to be excluded. That implies that the solar fraction of this case cannot exceed the value of 52%.

To avoid this problem, a third hybrid case (steam + hot water) was also investigated. This case is similar to the hot water one, but in addition, it can provide steam to the brewery. The steam is generated only with excess solar energy that would otherwise be wasted. The steam cannot be generated with energy coming from the thermal storage and cannot be stored in turn (energy to make steam can only be absorbed as direct use energy).

The hot water case requires a bigger initial investment than the steam case since it requires additional retrofitting measures, and the hybrid case requires an even bigger initial investment for the same reason.

All in all, Tab 1. summarizes the characteristics of each case.

Tab. 1: Summary of simulation results and economical choices of each considered integration case

Case	*No-Integration*	*Ideal*	*Steam*	*Hot Water*	*Hybrid*
Integration type	None	Process level	Boilers level	Process level	Process and Boilers level
Targeting load	Total load	Total load	Total load	Partial load	Total load for direct heat. Partial load for storage
Type of storage	No storage	No storage	Pressurized	Non-pressurized	Non-pressurized
Collectors' inlet temperature [°C]	-	50	165	30	30 or 165
Collectors' outlet temperature [°C]	-	110	185	120	120 or 185
Price of field [€/m2]	0	200	350	350	350
Price of storage [€/m3]	0	0	2000	400	400
Optimal field area [m2]	0	37437	12069	15325	18390
Optimal storage volume [m3]	0	0	190	1456	1571
Extra integration costs [M€]	0	0	0.1	1.0	1.5
Solar thermal investment [M€]	0	7.487	4.703	6.946	8.565
Energy produced [MWh/year]	0	36700	9093	15193	17684
Energy absorbed [MWh/year]	0	36700	7733	14050	15904
Energy wasted [MWh/year]	0	0	1361	1143	1780
Heat rate [kWh/m2/year]	0	0.980	0.641	0.917	0.865
LCoE [€/MWh]	110	18.00	98.13	84.59	82.92
Payback period [years]	-	2	11	7	9
Solar fraction	0%	100%	21%	38%	43%
Capacity reserve	0%	0%	15%	8%	10%

In addition, we also investigated a case of a hybrid steam-water greenfield scenario. For this case the investment cost must also account for the cost of the boilers. The boiler size is dimensioned after the solar field performances to be complementary to it. The boiler size of each case is obtained as the maximum value of the power not delivered by solar energy. The boiler prices are estimated from a linear regression of commercially available boilers prices vs their nominal powers [7]. The relation obtained is shown in eq.9

$$B = 0.2782P_w + 29.849 \quad \text{(eq.9)}$$

Where B is the boiler price is thousands € and P_w is the boiler's nominal power in kW.

Obviously, the non-integration case must be updated with the cost of a full-sized boiler that we will add to the extra integration costs and that will impact on the LCoEs calculation.

Despite our expectations, the boiler size of the optimal case was not reduced a lot showing that the peak power demand hours did not match well the solar thermal production. This mismatch is a true form of incompatibility and thus will be reflected both in the financial and in the energy compatibility as we have defined.

Tab 2. summarizes the updates to the reference case and the results of the simulation for the greenfield scenario.

Tab. 2: Summary of simulation results and economical choices the greenfield integration case

Case	*No-Integration*	*Ideal*	*Greenfield (Hybrid)*
Optimal field area [m2]	0	37437	18333
Optimal storage volume [m3]	0	0	1613
Extra integration costs [M€]	3.038	0	2.924
Total investment [M€]	3.038	7.487	9.986
Energy produced [MWh/year]	0	36700	17670
Energy absorbed [MWh/year]	0	36700	15903
Energy wasted [MWh/year]	0	0	1767
Heat rate [kWh/m2/year]	0	0.980	0.867
LCoE [€/MWh]	117	18.00	86.33
Solar fraction	0%	100%	43%
Capacity reserve	0%	0%	10%

Results and conclusions

Before revealing the values of financial and energy compatibility of each case, we can make some judgments over their simulation results and economical choices.

From both an energy and an economical perspective, the water integration case is surely more compatible with solar thermal than the steam integration since it can deliver more and waste less energy by also costing less at the same time. The energy and the economical compatibility definition were still useful to measure and quantify objectively how much more compatible is the water integration respect to the steam one. Indeed, without using the energy compatibility as we defined, the answer would be subjective to the personal interpretation of the trade-off between higher solar fractions and lower capacity reserves. Similarly, it is hard to understand the scale of the economical improvements without contextualizing the LCoEs of the two cases with the current price of the energy, the increase of energy delivered and the different investment costs.

The difficulties of comparing unequivocally the compatibility of the integrations are even more evident when comparing the hot water integration case with the hybrid (steam and hot water) integration case. Indeed, the multitude of pros and cons of the two cases do not allow for an obvious interpretation and even less for a quantifiable measure of the compatibility.

The hybrid case costs more than the hot water case, it wastes more energy (thus it has a lower heat rate) and has a longer payback period. On the other hand, the hybrid case also delivers more energy and has a slightly lower LCoE than the hot water case.

Furthermore, the optimal sizes of field and storage of the hybrid case as retrofitting and as greenfield scenarios are almost identical. The boiler costs for the no-integration and the greenfield optimal case are also very similar. This suggest that the only advantage that the solar thermal integration would have as a greenfield project rather than as a retrofitting project for this specific case are due to the increased relative cost of the no-integration case.

In the next figures are shown the simulation outputs for Φ and Ψ for the considered solar field aperture and storage volume ranges. The red star represents the optimal case for each scenario.

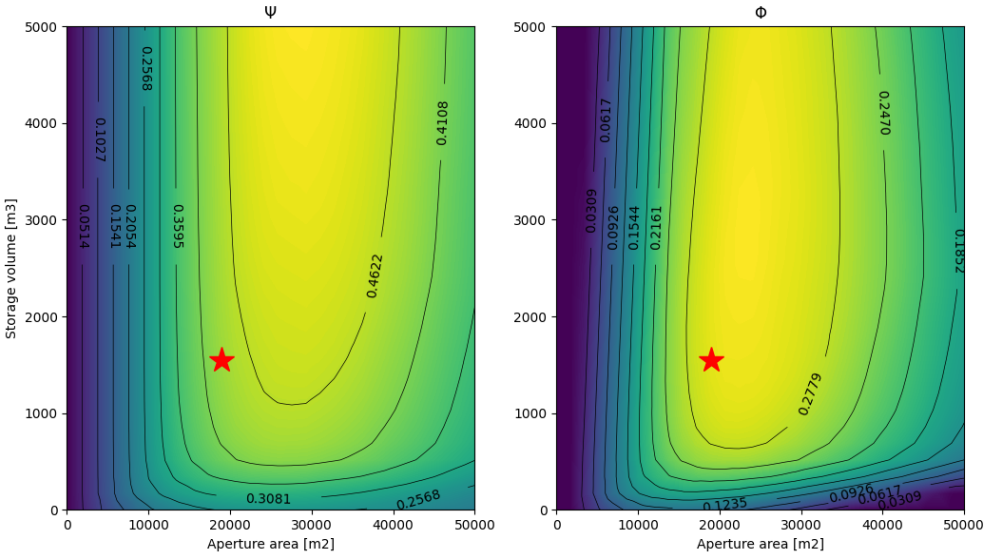

Fig.3: Parametric analysis results for energy and economic compatibility (hybrid case)

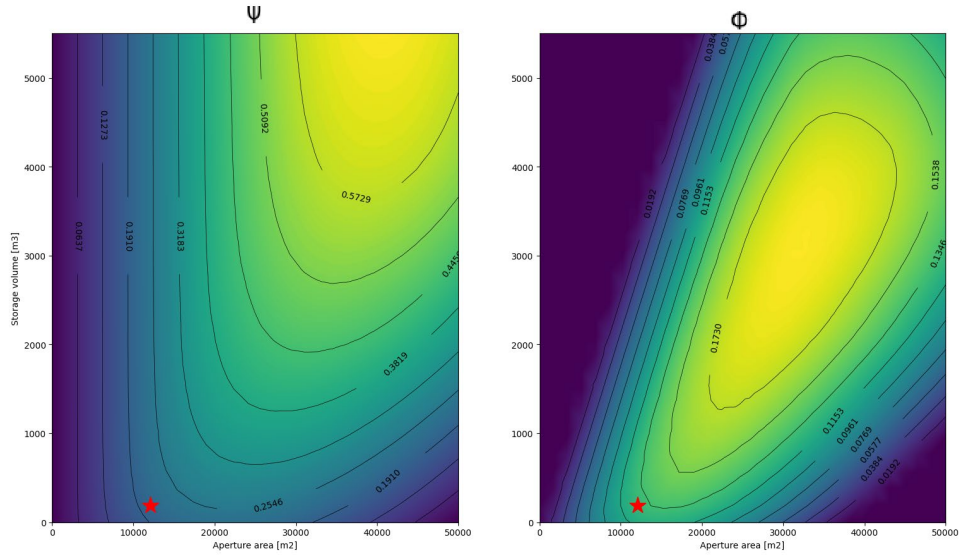

Fig.4: Parametric analysis results for energy and economic compatibility (steam case)

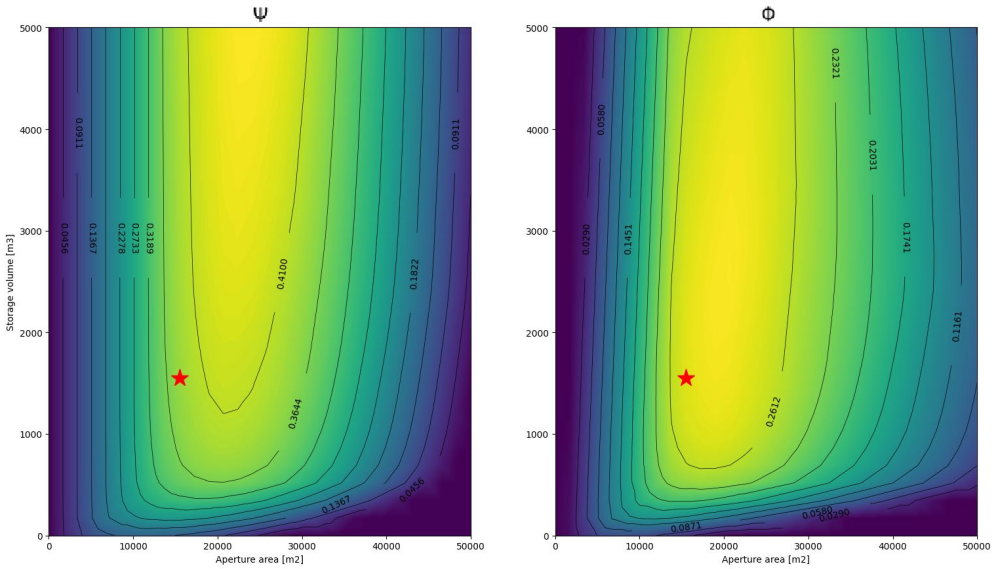

Fig.5: Parametric analysis results for energy and economic compatibility (hot water case)

Note how the trends of the contour lines for Φ and Ψ have similar shapes but different values across both the different scenarios and the two indicators themselves.

Finally, Tab. 3 shows the results for the financial and energy compatibility of all the considered optimal cases.

Tab. 3: financial and energy compatibility of each integration optimal case

Case	*Steam*	*Water*	*Hybrid*	*Greenfield (Hybrid)*
Ψ	21%	38%	43%	43%
Φ	13%	28%	29%	31%

As expected, the steam integration ranks the lowest for both financial and energy compatibility, nevertheless we had expected the energy compatibility gap between the two scenarios to be much larger since the actual gap is comparable to the solar fractions gap and we thought that the capacity reserve would have contributed to enlarge it even further. The reason of that is because the capacity reserve negative impact on the energy compatibility increases with the solar fraction too (the absolute amount of wasted energy of the two cases is quite similar).

The financial compatibility, on the other hand, is more than double as high for the water compared to the steam integration case, but almost identical to the financial compatibility of the hybrid case suggesting that the economical advantages achievable through technical improvements in the hybrid case are proportional to their costs.

As we expected, both the energy and the financial compatibility of the hybrid case does not increase much in a greenfield scenario either, since the power peaks mismatch makes impossible to reduce the boiler size.

In all the cases, the energy compatibility results higher than the financial one which means that the ideal conditions for this integration are easier to achieve from an energy point of view rather than from an economical point of view regardless the layouts.

In conclusion, according to the indicators presented in this work, there is a substantial improvement from both economic and financial perspective in choosing hot water rather than steam as heat carrier for the considered

solar thermal integration. There is an additional yet less remarkable improvement in choosing a hybrid system of hot water and steam.

In the case of a greenfield project, where the solar thermal integration and the plant can be designed to meet each other needs much better than in a retrofitting project, we assessed the scale of the advantages to be relatively small.

References

[1] Tibasiima, N. and Okullo, A. (2017) Energy Targeting for a Brewing Process Using Pinch Analysis. Energy and Power Engineering, 9, 11-21. doi: 10.4236/epe.2017.91002.

[2] Lai, Chun Sing; Jia, Youwei; Xu, Zhao; Lai, Loi Lei; Li, Xuecong; Cao, Jun; McCulloch, Malcolm D. (December 2017). "Levelized cost of electricity for photovoltaic/biogas power plant hybrid system with electrical energy storage degradation costs". Energy Conversion and Management. 153: 34–47. doi:10.1016/j.enconman.2017.09.076.

[3] Dumbliauskaite, M., Becker, H. and Maréchal, F. (2010) Utility Optimization in a Brewery Process Based on Energy Integration Methodology. Proceedings of ECOS, 91-98.

Web references

[4] Walter Short; Daniel J. Packey; Thomas Holt (March 1995). "A Manual for the Economic Evaluation of Energy Efficiency and Renewable Energy Technologies" (PDF). www.nrel.gov. National Renewable Energy Laboratory. pp. 47–50. Retrieved 17 July 2022.

[5] Meteonorm 8 release notes. https://meteonorm.com/assets/publications/5BV.3.8_pvsec_2020_mn8.pdf Retrieved 17 July 2022.

[6] Solarkeymark database. Search for “Absolicon” in the database for the model T160 measured results https://solarkeymark.eu/database/ Retrieved 17 July 2022.

[7] State of Michigan, prices of appliances by different nominal powers https://www.michigan.gov//media/Project/Websites/treasury/VOL/Vol236UIP12MiscellaneousIndustrialCosts.pdf?rev=b2a14a143c11493e8d0a30587afaa282 Retrieved 17 July 2022.

Using heat maps to assess the energy efficiency of industrial companies

Stephen Holway[1], Felix Pag[1], and Klaus Vajen[1]

[1] University of Kassel, Institute of Thermal Engineering, Kassel (Germany)

Abstract

New solutions are required to reduce the CO_2 emissions of industrial companies, as currently most of the heat is generated by burning fossil fuels. Here, not only more efficient technologies, but technologies which incorporate renewable heat sources are required. Industrial heat consumption makes up a large portion of the overall heat consumption. Before individual decarbonisation roadmaps can be developed it is imperative to assess the current heat consumption of an industrial plant. This presents a major problem, as industrial complexes can be large and consist of many individual buildings. Thus, it is often unclear where to begin. The heat map in this work is used to visualise key figures of each individual building in an industrial site allowing the comparison between the buildings with respect to different aspects. It displays the heat consumption of each individual building in an industrial complex visually. For example, this makes it possible to compare the specific heat consumption, and to identify which buildings possibly represent the largest potential for energy efficiency measures. The specific heat consumption on building level also makes it possible to compare the buildings with those of other plants, with similar usage. The heat map can also be used to analyse the local distribution of waste heat and heat sinks.

Keywords: heat map, specific heat consumption, heat consumption, process heat

1. Introduction

Considering the current climate crisis, countries all over the globe are aiming to reduce their CO_2 emissions. Although heat represents the largest share of energy end usage with almost 50 %, a lot of the focus has been placed on renewable electricity generation in the past, which makes up a share of 20 %, transport makes up the remaining 30 % of energy end usage. Of this heat consumption industrial processes make up about 51 % and 46 % are consumed for space and hot water heating in buildings. Currently, this heat is mainly generated by burning fossil fuels (IEA, 2021). To reduce greenhouse gas emissions, energy efficiency measures must be taken to reduce the heat consumption, while at the same time increasing the share of renewable heat. However, before respective roadmaps for the transition of industrial companies can be developed, the current heat consumption needs to be determined based on available data. Here, large urban industrial complexes present a challenge, as these mostly consist of a great number of individual buildings. The question arises which buildings should be analysed first and how this can be illustrated clearly. The heat map presented in this paper provides various building specific data, which makes it possible to compare the buildings to one another using key figures of the buildings. In this paper, two key figures are defined regarding the specific heat consumption, the heat consumption divided by the floor space and heat consumption divided by the building volume. Moreover, the resolution of the heat consumption on building level makes it possible to include the usage of the buildings and the types of heat consumers inside. Based on the comparison of building parameters, energy efficiency potentials can be identified, and the different buildings can be prioritised. The resolution of the heat consumption on building level also makes it possible to not only assess the energy efficiency of the respective buildings but also identify the reasons for this higher specific heat consumption. Furthermore, best practise examples can be identified and adapted to other buildings. Another way of reducing the overall heat consumption of an industrial plant is the identification and utilisation of waste heat potentials. Again, large industrial plants present the problem of consisting of many different buildings. Here, the heat map can be used to show the location of the waste heat sources and the heat consumption on the map. The heat map is then used to identify suitable heat sinks for nearby waste heat sources. This is invaluable as the economic viability for the utilisation of waste heat decreases with greater distances between sinks and sources, as additional piping and systems are needed. In this study, the heat map will show the heat consumption of an automotive manufacturing plant.

© 2022. The Authors. Published by International Solar Energy Society
Selection and/or peer review under responsibility of Scientific Committee
doi:10.18086/eurosun.2022.05.05 Available at http://proceedings.ises.org

2. Methodology - Developing the heat map

For the creation of a heat map sufficient data on the objects, which are to be mapped, is required. In this case study the data is supplied by various sources. The operator of the automotive manufacturing plant supplied heat flow meter data for some individual buildings, building complexes, and supply lines. Furthermore, data on the installed heat consumers, such as the installed heating capacity, and their location in the plant is given. To supplement this data, heat flow measurements are performed with ultrasonic flow meters. As the heat consumption of most of the buildings is not measured individually, it is necessary to estimate the heat consumption of these buildings based on the knowledge of the heat consumers, the available flow meters, and own measurements. It is then possible to estimate the individual heat consumption of the buildings. This standardised annual heat consumption is shown in Figure 1. At this point, the specific values are calculated, but not shown here, as they include third party data. Thus, the heat consumption of the buildings is normalised, to show the buildings heat consumption in relation to each other. The map itself is created with the OpenStreetMap data bank (OpenStreetMap contributors, 2022). Even though the absolute value of the heat consumption of individual buildings in industrial companies is needed for the design of the required heat generation units or the local district heating grid, it is of little use when comparing the buildings within the industrial site or even with similar buildings in other sites. Because the various buildings differ greatly in size (Figure 1). For this comparison and further evaluation of the heat consumption, specific values are required. For this purpose, the building parameters, such as inside air volume and floor space are needed. This data is supplied by the operator of the automotive manufacturing plant. For some buildings this data is not available, so it is calculated based on the blueprints provided by the plant operator.

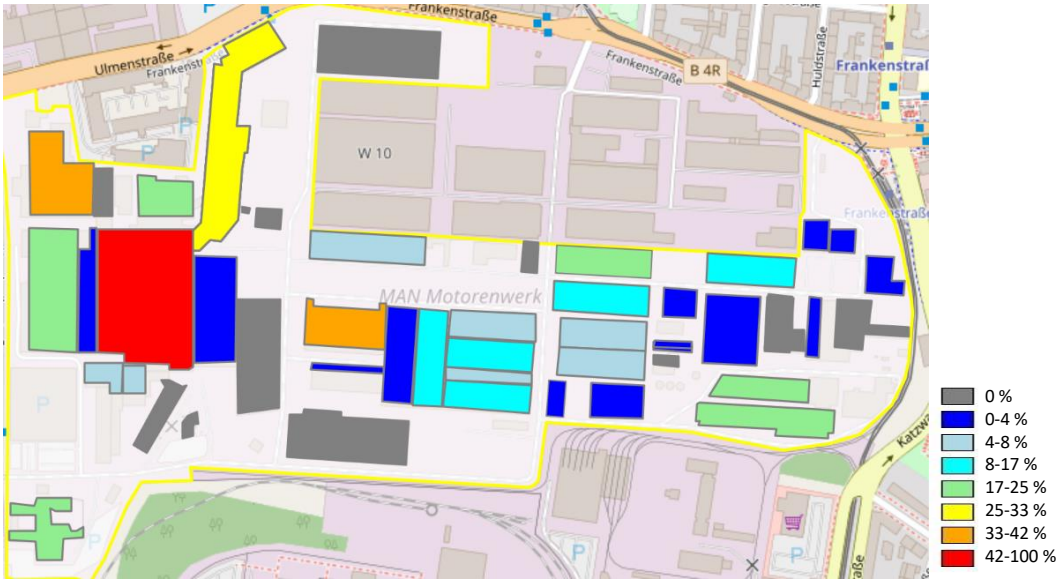

Figure 1: Standardised annual heat consumption of the different buildings in an automotive manufacturing plant

3. Results - Utilising the heat map

In this example, the heat consumption of the production site is dominated by space heating through ventilation and recirculation systems which are used to ensure fresh air and space heating in the big manufacturing halls. Typical process heat systems such as washing machines, heated baths, or drying processes play a minor role in the heat consumption of the manufacturing plant, as they amount to about 18 % of the heat consumption. Thus, the specific heat consumption can be used to pre-evaluate the thermal efficiency of the buildings. Nevertheless, it must be kept in mind, that some buildings have a significant process heat consumption and thus show a higher specific heat consumption, even if they have a higher thermal efficiency. One example of a building with a high process heat demand is the yellow building in Figure 1 which houses the paint shop with various drying processes. The two key figures for the annual specific heat consumption are shown in Figure 2 with the heat consumption divided by the floor space and in Figure 3 with the heat consumption divided by the gross building volume. Figure 2 shows two buildings in orange with a high area-specific heat consumption and identifies these as buildings with a potential for increasing the energy efficiency. Thus, these buildings are analysed more closely to find the reasons for this high specific heat consumption. Contradictory to this, Figure 3 shows that, the right of the two orange buildings has a low volume-specific heat consumption. Consequently, in this case the specific heat consumption, regarding the buildings

floor space is not sufficient to compare the energy efficiency of the buildings, as the volume of the buildings also has a great influence on the heat consumption. Therefore, the specific heat consumption regarding the buildings inside air volume represents a better key figure than the specific heat consumption based on the floor space, as the heat consumption for space heating increases with the buildings volume: The air flow is mostly dependent on the buildings inside air volume because the ventilation units are designed to provide certain air exchange ratios. As the inlets of the ventilation units are mostly situated directly under the roof the whole building volume is exchanged. However, additional factors influence the buildings heat consumption, these include the control of the ventilation and recirculation systems as well as the utilisation of heat recovery systems.

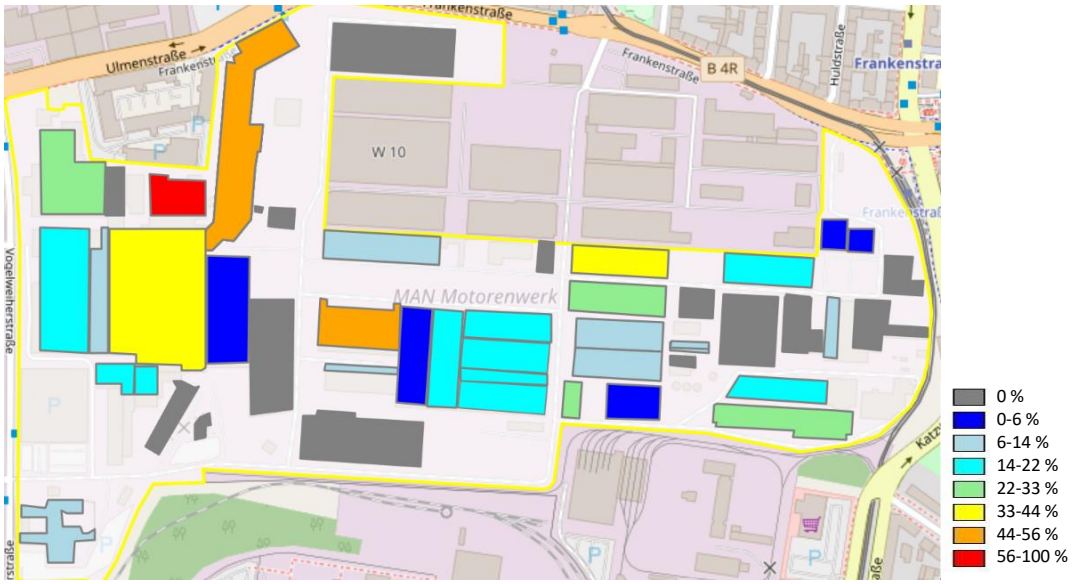

Figure 2: Standardised specific annual heat consumption of the different buildings in an automotive manufacturing plant (floor space)

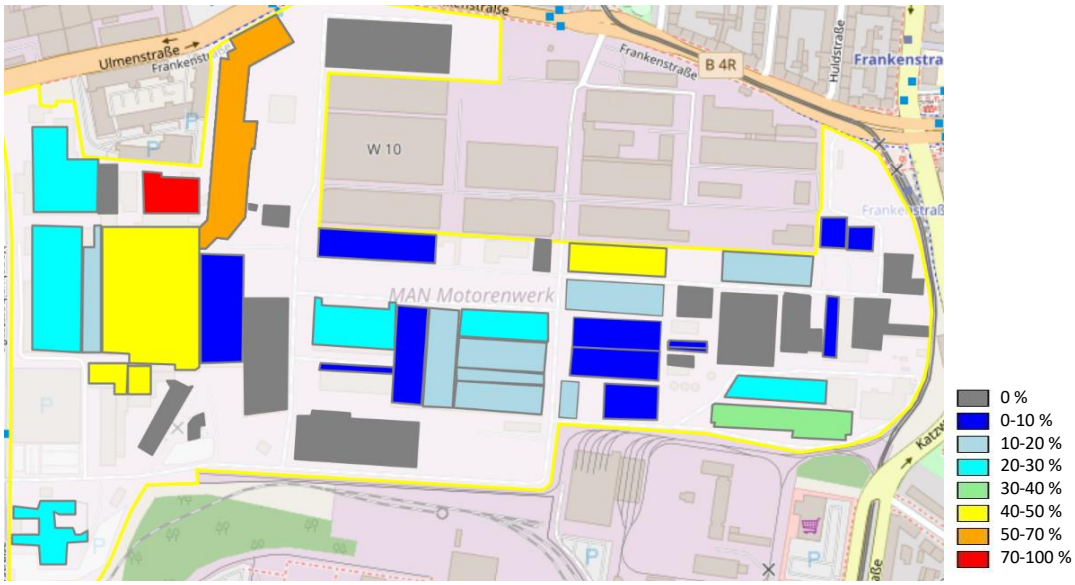

Figure 3: Standardised specific annual heat consumption of the different buildings in an automotive manufacturing plant (gross building volume)

In residential buildings the heat losses are dominated by transmission, as the walls, buildings and windows are badly insulated, and these buildings commonly are not fitted with air ventilation units. After energetic renovations the transmission heat losses and the air permeability are reduced, and air ventilation units are required. Here, the buildings volume becomes more important, as the ventilation units then provide certain air ventilation ratios. However, as the ceiling height of most buildings is similar the volume correlates with the floor space. In this automotive manufacturing plant, the heat losses are dominated by ventilation heat losses, as the installed ventilation

units provide high air exchange ratios. Consequently, in this case the gross building volume is of interest, as a higher building volume results in higher volume flows.

A multitude of production processes take part in an industrial manufacturing plant e.g., washing, drying, tempering, and the generation of compressed air. With some exceptions, such as washing machines radiating waste heat directly into the halls, the waste heat generated in these processes, is rejected to the environment with cooling units or compression chillers. The utilisation of this waste heat presents a large potential to reduce the heat consumption within an industrial site. At this point, not only the amount of waste heat but also the location of the waste heat sources in the industrial site, in relation to the location of heat consumers, is of interest. The standardised waste heat potential of the automotive manufacturing plant is presented in Figure 4. The waste heat potential was standardised to the same value as the heat consumption in Figure 1, to be able to compare them to each other. These potentials include waste heat from compression chillers, various production processes, server cooling, and engine tests. The manufacturing plant includes test stands for the serial tests of engines (yellow building) and test stands for research and development (red building), in Figure 4. The waste heat potentials of the air compression units (green and light blue building) are estimated based on the electricity demand, provided by the plant operator. For the engine tests, the energy content of the consumed diesel was used to estimate the waste heat potential, from which the electricity generation is subtracted. Further data is obtained by own heat flow measurements with ultrasonic flow meters. The overlay of the two maps in Figure 1 and 4 makes it possible to assess if the waste heat can be used locally in the same building, buildings close by, or if the heat must be transported to other buildings of the plant. The Figures 1 and 4 show, that in the west of the plant the waste heat potential could be utilised to also meet the high heat consumption in the west of the plant. The building on the bottom left of Figures 1 and 4 also shows a sufficient heat sink for its own waste heat. On the other hand, the red building (Figure 4) on the bottom right shows a higher waste heat potential than heat consumption. Thus, this waste heat must be distributed to other nearby buildings. In this case, the heat map can supply a first indication to the relation and position of waste heat potentials and heat consumption within the plant. This makes it possible to prioritise the utilisation of waste heat sources, depending on absolute amount of waste heat and the availability of nearby heat sinks. This information also allows to identify which heat sinks and waste heat sources need to be examined more closely, regarding the simultaneity of heat consumption and waste heat potential.



Figure 4: Standardised annual waste heat potential of the different buildings in an automotive manufacturing plant

4. Conclusion and outlook

When developing different energy efficiency and decentralised renewable heat generation roadmaps for a large industrial site, it is imperative to first estimate the current heat consumption. The developed heat map allows a graphical comparison of key figures of different buildings within a plant and gives the opportunity to compare them to similar buildings of other plants. This enables the users to quickly identify buildings with a higher specific heat consumption. Based on this, an assessment can be made which buildings already consume less heat and which buildings should be the focus of potential energy efficiency measures. Moreover, estimating the heat consumption

on building level makes it possible to examine the different buildings individually and account for their usage and the different heat consumers within. This is necessary as they directly impact the heat consumption of the building. Furthermore, the heat map offers the opportunity to show the location of waste heat sources and heat sinks, making it possible to prioritise the utilisation of waste heat potentials in the vicinity of heat sinks and identify which heat sinks should be supplied by which waste heat source.

This heat map shows the heat consumption and waste heat potential as annual values and therefore cannot be used to assess the simultaneity of the heat consumption and the waste heat potential. In consequence, the individual heat sources and sinks need to be examined more closely, than done in this study. This also means, that it cannot be used to calculate the maximum heat load of the system. The creation of a heat map requires a lot of data on the buildings, which are to be mapped. The bigger the industrial complex and the more numerous the data the more a heat map can help to get a better overview of the specific buildings in a plant. This heat map is used to identify buildings with a lower energetic efficiency, within the automotive manufacturing plant. From this base, the different buildings were prioritised for the implementation of energy efficiency measures. The heat map is then also used to identify possible heat sinks for waste heat sources. In the next step the heat map shall show how the heat consumption of the buildings changes when implementing different energy efficiency measures and the integration of waste heat. This will make it possible to quantify the remaining heat consumption, which is to be decarbonised.

5. Acknowledgments

The authors thank the Federal Ministry for Economic Affairs and Climate Action for the funding of the project (03EN3023A) as well as the project partners for the good cooperation and the supply of data.

6. References

IEA (2021) ‘Renewables 2021: Analysis and forecast to 2026’. Available at: https://www.iea.org/reports/renewables-2021.

OpenStreetMap contributors (2022), 14 September. Available at: www.openstreetmap.org.; Available from: https://www.iea.org/reports/renewables-2021

Effect of HTF flow direction on thermal performance in upward facing cavity receiver

Shivam Kumar[1], Shridhar Laxman Bapat[2] and Shireesh Balwant Kedare[1]

1 Indian Institute of Technology Bombay, Mumbai, India

2 Indian Institute of Technology Dharwad, Dharwad, India

Abstract

An analysis is carried out to examine the influence of heat transfer fluid (HTF) flow direction on thermal performance in an upward-facing cone-cylindrical receiver. The receiver is modeled as a cone-cylindrical helical coil receiver which is subjected to concentrated solar flux from a 60 sq.m. Scheffler parabolic dish. The receiver is inclined at an angle equal to 25˚. Therminol-55 is taken as the HTF flowing through the coil receiver. A numerical approach is adopted to evaluate the convective and radiative heat loss parameters from the coil receiver. These parameters are used to evaluate the thermal efficiency of the coil receiver for two-fluid flow configurations: a) Up-flow (bottom-to-mouth), and b) down-flow (mouth-to-bottom). It is observed that for the down-flow configuration, the mean coil temperature is lower than the upward flow configuration, resulting in reduced thermal losses and higher thermal efficiency up to 5-10% under different operating conditions. The results will help in designing optimal helical coil solar cavity receivers for medium and high-temperature decentralized power generation applications, and, industrial process heat

Keywords: Solar, Cavity, Receiver, Helical Coil, Scheffler dish, Thermal performance, Industrial process heat

1. Introduction

Solar dish concentrator systems have been seen as a promising technology for decentralized power generation, and industrial process heat for a long time. These systems are point focus systems and use a cavity receiver, placed at the focus, to absorb the reflected solar radiation. The most used dish concentrator systems are parabolic dish concentrators, where, a downward-facing receiver is attached to the dish where the incoming high-density solar flux is absorbed (Hafez et al., 2016). A HTF circulates across the walls of the receiver and absorbs heat from the receiver wall. The temperature range achieved in a parabolic dish system is ideal for applications like generating hot compressed air for air Brayton cycles and supercritical carbon dioxide (s-CO2) for closed Brayton cycles. However, it is difficult to connect high-pressure pipelines to a moving receiver mounted on a dish, as shown in Fig 1. One solution to overcoming this issue is to use another category of the parabolic dish which provides a static focus at the ground level, called the Scheffler Dish (Munir et al., 2010). This aids in the installation of high-pressure lines and can also be used in the form of multiple clusters for scaled-up CSP applications (India-One, 2010). To overcome these issues, Scheffler dish technology could be used as it has a static focus, as shown in Fig 2 (Munir et al., 2010). The Scheffler dish rotates about the polar axis to perform daily tracking while keeping the receiver fixed, as shown in Fig 3. The receiver has an upward-facing orientation and is kept inclined at an angle equal to the local latitude.

Various parameters for an upward-facing cavity receiver like cavity shape, aperture ratio, wind effect, etc. are previously analyzed (Leibfried and Ortjohann, 1995). However, one parameter that is still not looked at is the effect of the flow direction in the cavity receiver with thermic oil as the HTF. In this paper, a cone-cylindrical-shaped helical coil cavity receiver is subjected to concentrated solar flux from 60 m^2. Scheffler dish, and is analyzed to evaluate the thermal efficiency of the coil receiver for two-fluid flow configurations: a) Up-flow (bottom-to-mouth), and b) down-flow (mouth-to-bottom). During this analysis, the thermal performance for two flow configurations for a range of mass flow rates will be analyzed. This study will be very useful in designing helical coil solar cavity receiver for medium and high-temperature decentralized power generation applications, that uses an upward-facing dish concentrator technology.

© 2022. The Authors. Published by International Solar Energy Society
Selection and/or peer review under responsibility of Scientific Committee
doi:10.18086/eurosun.2022.05.06 Available at http://proceedings.ises.org

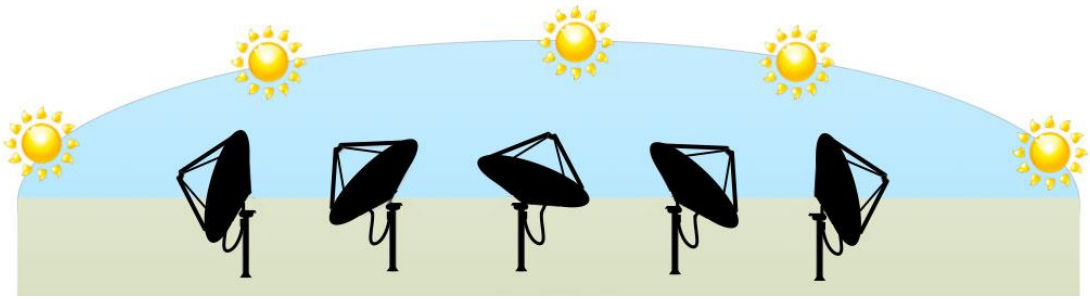

Figure 1: Movement of the receiver with dish during day tracking



Figure 2: Scheffler Dish with static focus receiver

2. System Description

An upward-facing cavity receiver is assumed under concentrated solar flux after reflection from a 60 m^2 Scheffler paraboloid reflector. The dimension of the Scheffler reflector in the current analysis is based on the dish used at the India One Solar Thermal Power Plant, Abu Road, India, as shown in Fig 4, and its dimensional details are shown in Table 1. Assuming no optical errors in the dish, ray tracing is performed for flux analysis of the cavity receiver, for which the reflector surface is discretized into 10^4 points, and each point impinges with a solar ray. The position of the sun for this analysis is assumed to be at solar noon on equinox with a DNI value of 800 W/m^2. Each solar ray follows the trajectory wherein it first falls onto the dish surface, gets reflected and it then passes through the focus of the dish and finally hits the receiver, as shown in Fig 3.

The cavity receiver in the current analysis is assumed to have a cone-cylindrical shape, which is the most optimal shape in terms of thermal efficiency among the six shapes analyzed by Kumar et al (Kumar et al, 2018). The receiver is made of a helical coil, as shown in Fig 5, and its coil and tube dimensional details are shown in Table 2. The receiver is assumed to have an inclination of 25˚ (local latitude of Abu Road, India), which makes the normal vector from the receiver aperture parallel to the polar axis of the earth (the axis about which the Scheffler dish performs its day tracking operation). The receiver is positioned 375 mm behind the focus of the dish to ensure that all the solar flux is intercepted with no spillage. The schematic of the Scheffler Dish-cavity receiver system, shown in Fig 3, shows the effective aperture area of the Scheffler dish. The mathematical value of effective aperture area on equinox for a 60 m^2 Scheffler dish is evaluated using eq 1 and is found to be 43.72 m^2. For equinox, the declination angle is equal to zero and the shape of the aperture area is a circle.

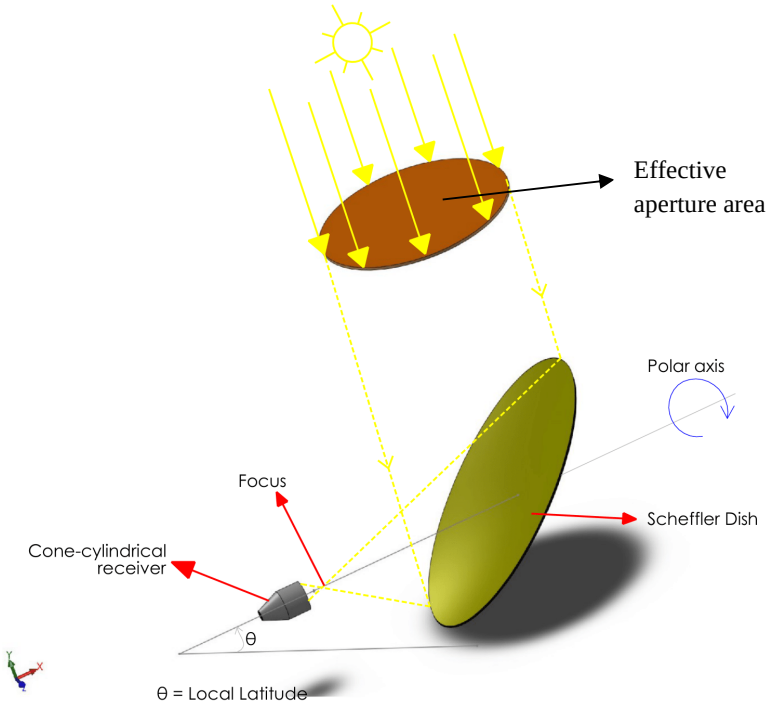

Figure 3: Schematic of Scheffler dish-cavity receiver system

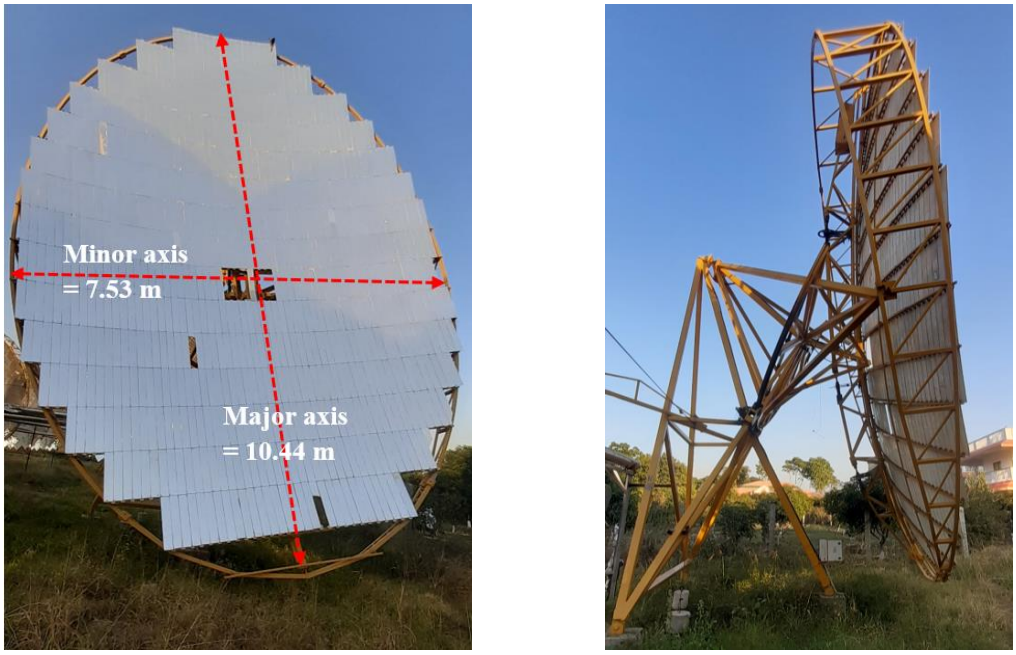

(a) Front View of Scheffler Dish **(b) Lateral View of Scheffler Dish**

Figure 4: Details of 60 m2 Scheffler Dish System

Table 1: Dimensional details of Scheffler Paraboloid Reflector at India-One

Focal Length	3.79 m
Number of rectangular mirrors	770
Dimension of a rectangular mirror	650 x 120 mm
Major axis of the elliptical outline of the dish	10.44 m
Minor axis of the elliptical outline of the dish	7.53 m

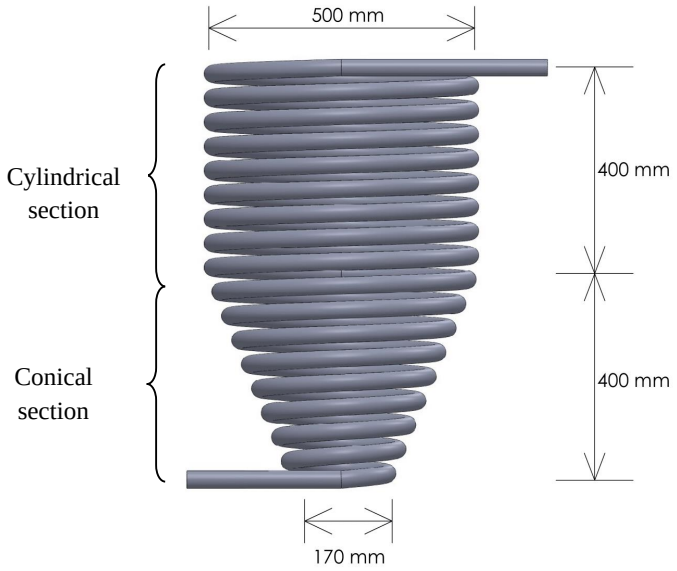

Figure 5: Helical coil Cone-Cylindrical Receiver

Table 2: Dimensional detail of Cone-cylindrical receiver

Tube Outer Diameter	33.4 mm
Tube Inner Diameter	26.4 mm
Number of turns in coils	17
Pitch of coil	47 mm
Ratio of Cone to Cylindrical section	1:1
Coil Diameter at bottom	170 mm
Coil Diameter at Top	500 mm
Coil Material	ASTM A 53-68 Welded & Seamless Steel Pipes

$$Aperture\ Area = Reflector\ Area \cdot \{\cos\left(43.23^\circ - \frac{\delta}{2}\right)\} \quad \text{eq. (1)}$$

Where δ is the solar declination angle

In the current analysis, the aim is to analyze the effect of HTF flow direction on the thermal performance of the receiver. The two flow configurations are a) Up-flow, and b) Down-flow. In the Up-flow configuration, the cold HTF flows from the bottom of the receiver and exits the mouth of the receiver as hot HTF, whereas in the Down-flow configuration, the cold HTF flows from the mouth of the receiver, and exits as hot HTF from the bottom of the receiver. Both flow configurations are shown in Fig 6. The HTF chosen under analysis is Therminol-55, a synthetic fluid that is an efficient and reliable HTF for medium temperature-range operations up to 593 K.

3. Methodology

The thermal performance of the cone-cylindrical receiver under different flow configurations is compared by evaluating their respective thermal efficiencies, which is the ratio of net energy absorbed to the net incident flux. The value of total incident heat flux at the receiver aperture can be calculated by the eq (2):

$$Incident\ Solar\ Flux = (DNI) \cdot (Dish\ Apperture\ area) \quad \text{eq (2)}$$

However, for estimating the incident heat flux on each coil can be estimated by using ray tracing. To perform ray tracing, the entire cone-cylindrical receiver is divided equally into 10 sections along the axis 1-1', as shown in Fig 7, and the flux map is plotted for each section using discretized ray tracing operation. The resulting flux map is shown in Fig 8. The numerical values of flux map intensities are mentioned in Table 3 for each coil section.

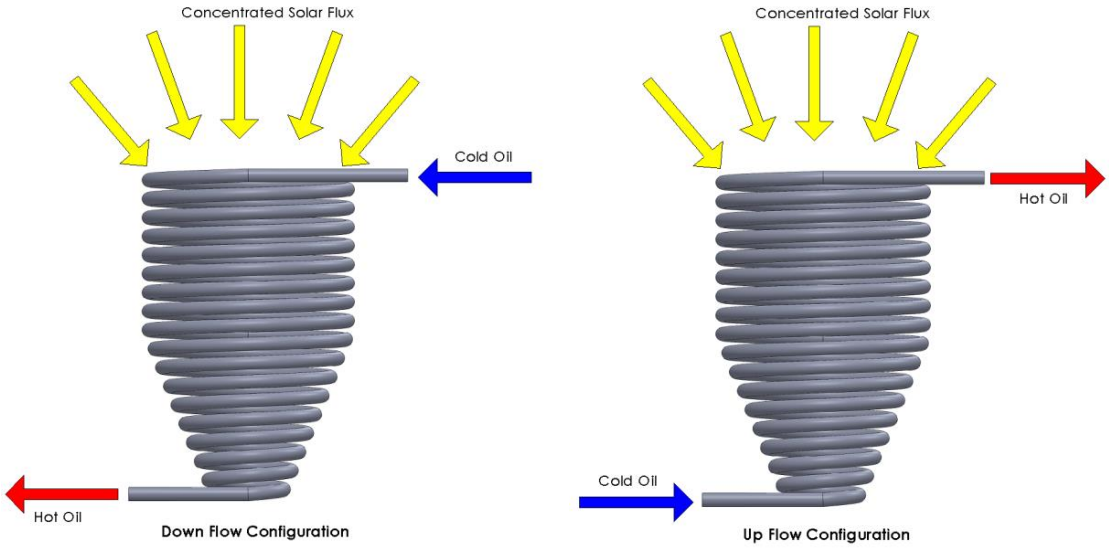

Figure 6: Flow configuration for Heat Transfer Fluid

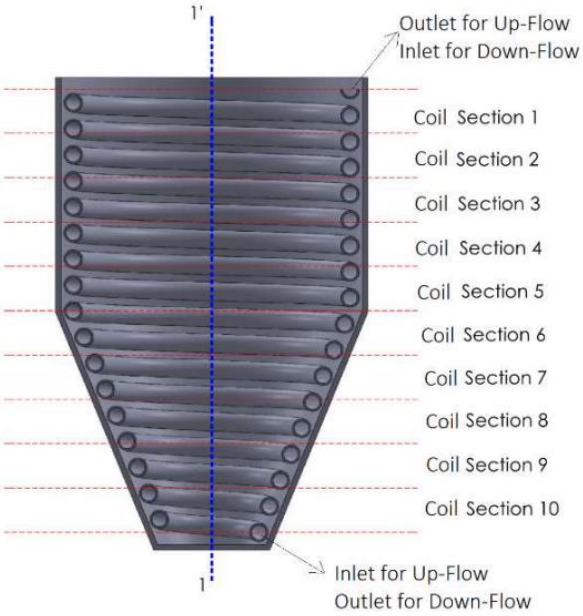

Figure 7: Cone-cylindrical coil receiver divided equally along the axis into 10 sections

The incident flux intensities value at each coil section can be used in the steady state energy balance equation, which equates it to the summation of their respective useful heat gains and thermal heat loss, as shown in eq (3):

$$Incident\ heat\ flux = Energy\ Absorbed\ by\ Coils + Thermal\ losses \quad \text{eq (3)}$$

$$Thermal\ heat\ loss = Q_{cond} + Q_{conv} + Q_{rad} \quad \text{eq (4)}$$

$$Heat\ gain\ by\ HTF = \dot{m} \cdot C_p \cdot \Delta T \quad \text{eq (5)}$$

As both terms on the right-hand side of eq (3), i.e., energy absorbed and thermal losses are unknown, an iterative method is proposed to evaluate these values. The flowchart for the iterative method is shown in Fig 9.

Table 3: Section-wise flux distribution details on Cone-cylindrical receiver

Coil Section No.	Coil Length (m)	Flux intensity (W/m^2)
10	1.087	6496
9	1.439	7920
8	1.791	9776
7	2.143	12320
6	2.495	15816
5	2.671	8304
4	2.671	11144
3	2.671	15552
2	2.671	22672
1	2.671	35392

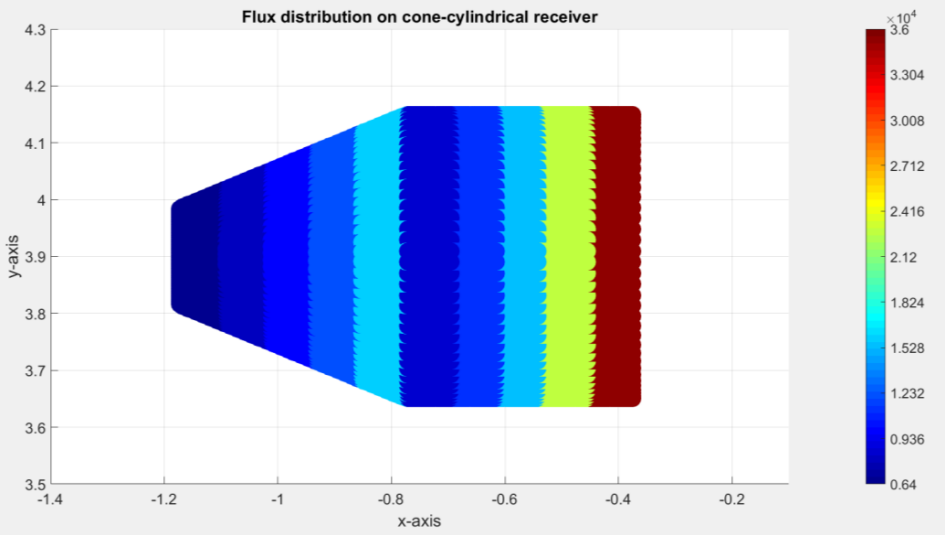

Figure 8: Flux map distribution section-wise on the cone-cylindrical receiver

3.1 An iterative method for estimating heat absorbed and heat losses at the coil section

Step 1: Choose the flow configuration between Up-flow & Down-flow with a mass flow rate, $\dot{m}$, and assume the inlet temperature $T_{_f_IN_1}$ at the 1st coil section.

Steps 2 & 3: The entire coil length is divided into 10 equal sections of axial length about axis 1-1', as explained earlier. Using discretized ray tracing, average flux intensities are estimated at each coil section, with their respective values mentioned in Table 3, and these values are assigned as $Q_{incident}$.

Step 4: A fraction of $Q_{incident_1}$ at coil section 1 is assumed to be Q_{abs_1}, and it is equal to the useful heat gain for the HTF flowing through this coil section. For this assumed value of Q_{abs_1}, and $T_{_f_IN_1}$ from Step 1, calculate the outlet temperature $T_{_f_OUT_1}$, using eq (6). Using the temperatures at the inlet and outlet, the surface temperature of the coil section is evaluated.

$$Q_{abs_1} = \dot{m} \cdot C_p \cdot (T_{_f_OUT_1} - T_{_f_IN_1}) \qquad \text{eq (6)}$$

Step 5: The calculated value of outlet temperature at coil 1 is assigned as the inlet temperature at coil 2, i.e., $T_{_f_OUT_1} = T_{_f_IN_2}$

Step 6: The process of Steps 4 & 5 are repeated for all the coil sections, and the surface temperature at all coil sections is estimated.

Step 7: For the respective coil surface temperatures, the Q_{conv} and Q_{rad} are evaluated using eq (7) and eq (8) respectively. The h.t.c. value in eq (7) and view factor value in eq (8) are estimated using ANSYS Fluent.

Step 8: After estimating the Q_{conv} and Q_{rad} from the previous step, the energy balance equation is checked. If the energy conservation holds good, then the initial guess of $T_{_f_IN_1}$ and Q_{abs} are correct. If not, then the process is repeated with a new guess of $T_{_f_IN_1}$.

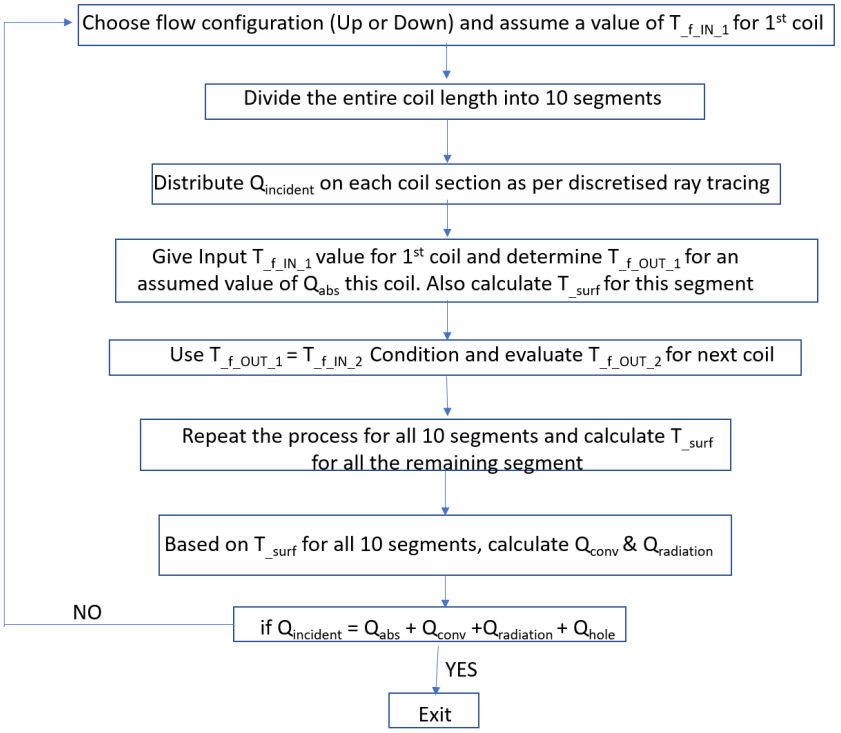

Figure 9: Iterative method to estimate useful heat gain and thermal losses

3.2 Heat transfer coefficient and View factor value for cone-cylindrical coil receiver to estimate Q_{conv} & Q_{rad}

For estimating the convection and radiation heat losses, eq (7) and eq (8) respectively can be used:

$$Q_{conv_i} = h \cdot A_i \cdot (T_{surf_i} - T_{amb}) \qquad \text{eq (7)}$$

$$Q_{rad_i} = \sigma \cdot \epsilon \cdot F_{i_aper} \cdot A_i \cdot \left({T_{surf_i}}^4 - {T_{amb}}^4\right) + \sigma \cdot \epsilon \cdot F_{i_insulation} \cdot A_i \cdot ({T_{surf_i}}^4 - {T_{insulation}}^4) \qquad \text{eq (8)}$$

However, the values of h.t.c. in eq (7) and view factor (F_{ij}) in eq (8) are very complex to determine and there is no straightforward empirical relation in the literature for determining these values. Therefore, these values for each coil section are estimated using ANSYS Fluent.

For h.t.c. estimation, CFD analysis is conducted by building the geometry and simulating it inside a large enough air enclosure, as shown in Fig 10. The enclosure is filled with air at ambient conditions (300 K and 1 atm) uniform throughout. Next, the model is meshed suing fine meshing near the coil section, and the mesh coarsens as the mesh goes far away from the coil area. The number of elements in the mesh is counted to be 7402418. For boundary conditions, an isothermal temperature condition is put at the coil surface, and this temperature for each coil section is estimated by the iterative methodology of section 3.1. The resulting h.t.c. values from CFD analysis are shown in Table 4.

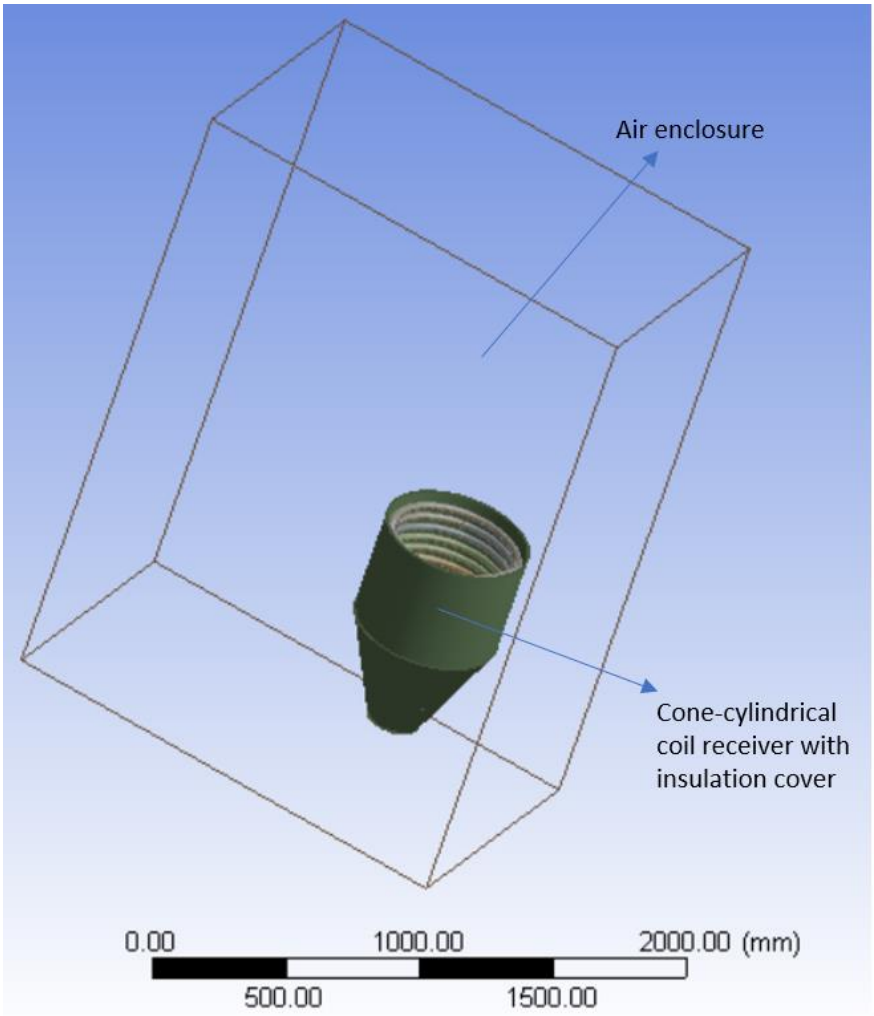

Figure 10: Coil receiver in air enclosure

Table 4: h.t.c and view factor values for Up-flow configuration with inlet temp of 573 K and mass flow rate of 0.312 kg/s

Coil No.	Surface Temp (K)	h.t.c. (W/m^2-K)	View factor from coil to aperture, F_{i_aper}	View Factor from coil to insulation: $F_{i_insulation}$
1	577	8.64	0.02	0.45
2	579	8.24	0.03	0.42
3	581	7.77	0.04	0.45
4	583	7.38	0.05	0.41
5	587	7.56	0.06	0.45
6	585	8.39	0.05	0.44
7	588	6.57	0.07	0.42
8	592	6.93	0.09	0.41
9	599	7.9	0.12	0.4
10	609	7.87	0.25	0.38

The radiation heat loss will comprise two radiative heat loss terms: radiation from the coil to receiver opening, and radiation from the coil to insulation cover. The view factors for both cases are shown in Table 4 and were calculated using ANSYS Fluent by applying a surface-to-surface radiation module. The temperature of the insulation cover is assumed to be 300 K in the present analysis.

4. Results & Discussion

The system is analyzed for Up-flow and Down-flow configurations using the iterative methodology explained in section 3.1. The corresponding temperature profiles are shown in Fig 11 and Fig 12. The corresponding mass flow rate, average Reynolds number, and thermal efficiencies are also mentioned in the plots of the temperature profile.

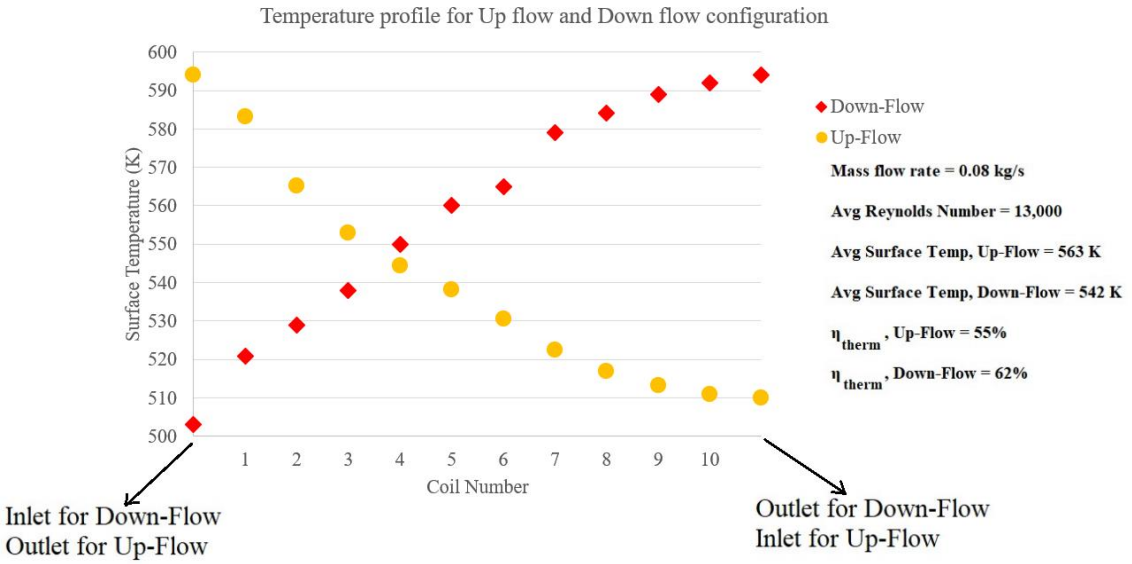

Figure 11: Temperature profile for Up-flow and Down-flow configuration at 0.08 kg/s mass flow rate

From the temperature profiles in Fig 11 and Fig 12, it is observed that the average surface temperature is lower when the flow configuration is Down-flow. This can be attributed to the fact that cold HTF enters from the top of the receiver and absorbs the most concentrated solar flux. As the temperature is low in the Down-flow configuration at the top, the heat losses are substantially less, resulting in higher thermal efficiency. However, it is also observed that as the Reynolds number is increased from 13000 to 50000, the difference in thermal efficiency between up-flow and down-flow reduces. This is because as the Reynolds number increases, the flow rate increases which results in a smaller temperature difference between coil surface temperature and HTF mean temperature.

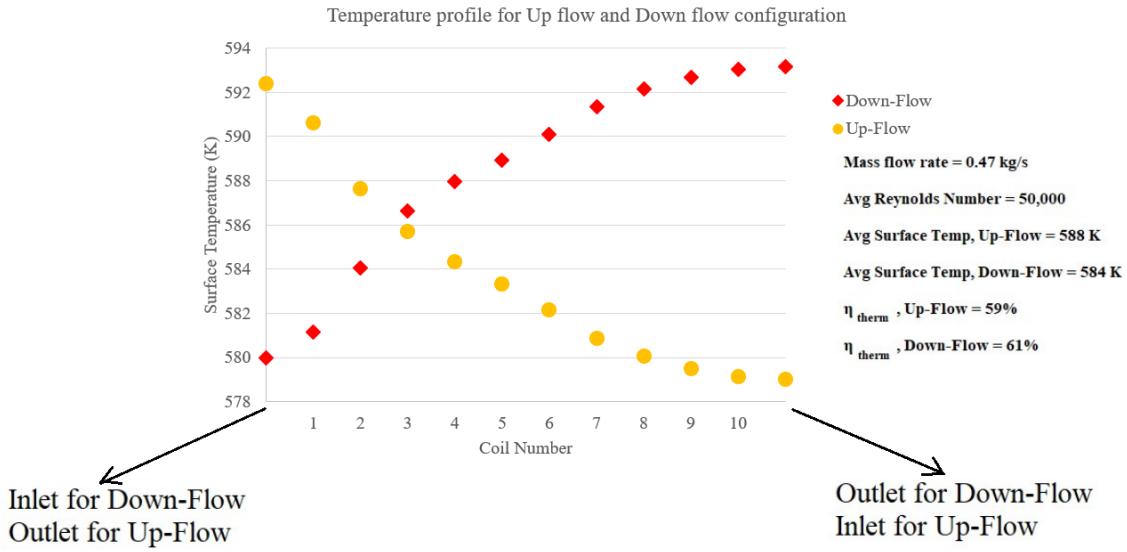

Figure 12: Temperature profile for Up-flow and Down-flow configuration at 0.47 kg/s mass flow rate

5. Conclusion

A cone-cylindrical cavity receiver was analyzed for two flow configurations: Up-flow & Down-flow. The cone-cylindrical receiver is assumed to be under concentrated solar flux incoming from a 60 m^2 Scheffler dish reflector. The HTF assumed for the analysis is Therminol-55, a synthetic fluid for moderate temperature operation. The analysis was conducted for two flow rates of 0.08 kg/s and 0.47 kg/s. It was observed that irrespective of the flow rates, the down-flow configuration had better thermal efficiency. This was attributed to the fact that in the down-flow configuration, the average surface temperature was lower than in the up-flow configuration, leading to lower thermal losses. However, as the flow rates increased, the temperature difference between fluid flow and coil surface reduced, which reduced the gap between thermal efficiencies of up-flow and down-flow.

Acknowledgment

The authors acknowledge the support provided by the ONGC Energy Center, New Delhi for carrying out this work.

References

Hafez, A.Z., Soliman, A., El-Metwally, K.A., Ismail, I.M., 2016, Solar parabolic dish Stirling engine system design, simulation, and thermal analysis, Energy Conversion and Management. 126, 60-75

“India One” Solar Thermal Power Plant,” World Renewal Spiritual Trust, [Online]. Available: https://india-one.net/. [Accessed 9 September 2022].

Munir, A., Hensel, O., Scheffler, W., 2010, Design principle and calculations of a Scheffler fixed focus concentrator for medium temperature applications, Solar Energy. 84(8), 1490-1502

Leibfried, U., Ortjohann, J., 1995, Convective Heat Loss from Upward and Downward-Facing Cavity Solar Receivers: Measurements and Calculations, Journal of Solar Energy Engineering. 117, 75-84

Kumar, S.; Shendage, D. J.; Doke, P.; Kedare, S. B., Bapat, S. L.; Numerical Investigation of Convective Heat Loss from Upward Facing Cavity Receivers of Different Shapes at Different Inclinations and Temperatures, International Journal of Environment and Sustainable Development. 8, 7-11. DOI: 10.47469/JEES.2019.v08.100082

Scenario Based Heating and Cooling Load Profiles in Piglet Production Systems

Konstantin König[1], Felix Pag[1], and Klaus Vajen[1]

[1] University of Kassel, Institute of Thermal Engineering, Kassel (Germany)

Abstract

Highly industrialized factory farming of pigs is energy-intensive, because efficient pig production is only possible under optimal climatic housing conditions, as the highly bred breeds are temperature-sensitive. To keep production costs as low as possible, the heating and cooling supply must be operated as efficiently as possible. However, as regulatory requirements are constantly adjusted and market demand changes, pig farmers need to adapt and improve their pig production, which affects the efficiency of the heat and cooling supply concept. A case study in a large piglet farm is used to develop a tool for predicting annual heating and cooling requirements that can be used in other farms with similar boundary conditions. The tool allows a quick classification of changes in the production system in terms of their impact on heating and cooling demand. The forecast of the scenario-based heating and cooling load profiles provides an important starting point for increased efficiency and further development of a renewable heating and cooling supply concept.

Keywords: Heating demand, Cooling demand, Pig farming, Pig housing, Piglet production systems

1. Introduction

Today's world requires constant adaptation and further development of the operating conditions of piglet production systems because the demands of the market are changing, and legal requirements are constantly being increased. The pig farmers must react to the volatile conditions to be able to hold their market share. This can include structural changes to the pig housing, with an impact on the number of animal places and thus an increase in heat demand. But also optimising the housing climate through cooling during the summer months to increase the efficiency of production and wellbeing of the animals can be a measure. Each measure has an impact on the heating and cooling demand and can thus affect the efficient operation of existing heating and cooling systems. Solar cooling as cooling system could be an interesting solution, as the stables are equipped with enough roof area and thus offer good conditions for solar thermal energy. Based on measurement data collected at a piglet production system, a tool is developed as a decision-making basis for the improvement and further development of the heating and cooling supply concept. This tool aims at helping piglet farmers to consider and compare different scenarios for the heating and cooling demand in order to have a decision-making basis for the expansion, conversion, or new construction of the heating and cooling supply systems. For this purpose, the tool determines future heating and cooling load profiles based on current heat demand and housing climate data. The focus is exclusively on intensive pig production systems with an emphasis on piglet production.

2. Pig production system and requirements of indoor environment in pig housing systems

The process of pig production can be divided into piglet production/rearing and fattening of pigs. The gestation period of the sow is between 112 and 115 days. The weaned piglets remain with the sow for 21 to 28 days and are suckled by her. After weaning, the piglets are taken to the piglet housing for about 5 weeks. At a live weight of 30 kg, they are transferred from the piglet housing to the fattening housing. Piglet production/rearing extends overall over about 170 days and is thus a main driver of heat demand in the value chain of pig production (Giner Santonja et al., 2017). In all process steps of pig production, heat demand has the largest share with respect to the total energy demand (Seifert et al., 2009): Within the piglet production system, heat demand accounts for 87% of

© 2022. The Authors. Published by International Solar Energy Society
Selection and/or peer review under responsibility of Scientific Committee
doi:10.18086/eurosun.2022.05.07 Available at http://proceedings.ises.org

the total energy demand. In sow housing, heat demand has a share of 66% (Seifert et al., 2009). In consequence, heat supply has a significant impact on the energy efficiency of pig production systems.
Depending on the process stage and the age of the piglets, different house climates are optimal for the performance of the animals (Blaha et al., 2010). Tab. 1 shows the performance-oriented optimal temperatures. Those optimal air temperatures are the main reason for the heating and cooling demand in the housing.

Tab. 1: Optimal air temperature in pig housing (DIN 18910, 2017)

Pig Housing	Optimal air temperature of the stable air [°C]
Mating and gestating sows	20 to 16
Farrowing sows	20 to 16
Weaners	32 to 20
Piglets	30 to 20

3. Head demand scenario

The case study is about a German pig farm which includes 5,000 sows and 160,000 piglets per year with an annual heat demand of 5 GWh and an annual electricity demand of 2.6 GWh. Like most farmers with highly industrialised factory farming, the case study only had data about the annual electricity consumption but no information on the heat consumption. In this case study, measuring the heat demand is only possible by retrofitting appropriate heat meters, which involves a great deal of effort and costs. Due to sector-typical restrictions, mobile heat flow meters cannot be used within the stables ensuring that the animals do not get in contact with human germs. This means that mobile heat flow meters can only be installed outside the stable, for example at the heating distributer, which does not allow measurement of the individual compartments. The electricity consumption or the electricity load profile can be obtained from the energy supplier and with this, it is easily accessible. Thus, the first step is to use the electricity load profile and come to first conclusions. Focus here is the ventilation system because it impacts the housing climate and depends on the stable temperature and the outside temperature. This allows initial conclusions to be drawn about the daily/weekly/seasonal heat demand based on the electricity load profile.

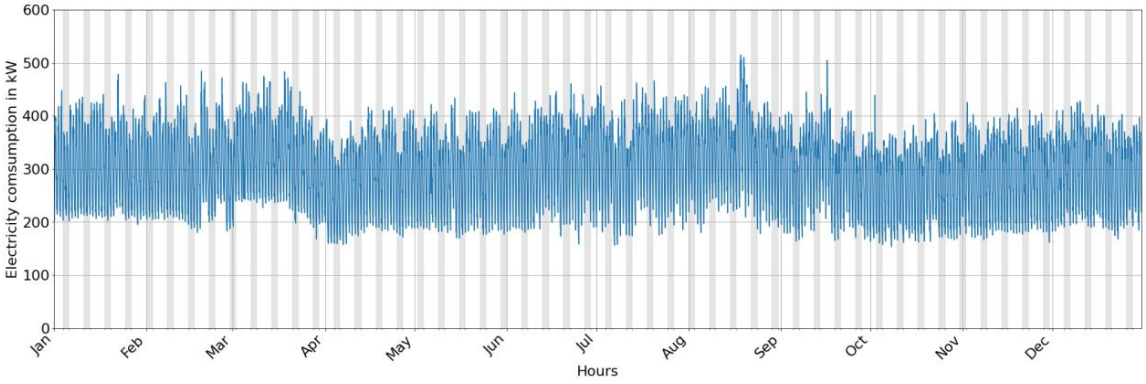

Fig. 1: Annual electricity load profile of the investigated piglet frame in hourly resolution for the year 2020

Fig. 1 shows the electricity load profile for the year 2020, which is representative in comparison to the years before. The comparison also shows that there are no significant differences between the years, which also indicates constant production and a regular cycle at farrowing, which is also assumed for the determination of the heat demand. The analysis of the profile does not indicate a strong seasonality of the electricity profile.

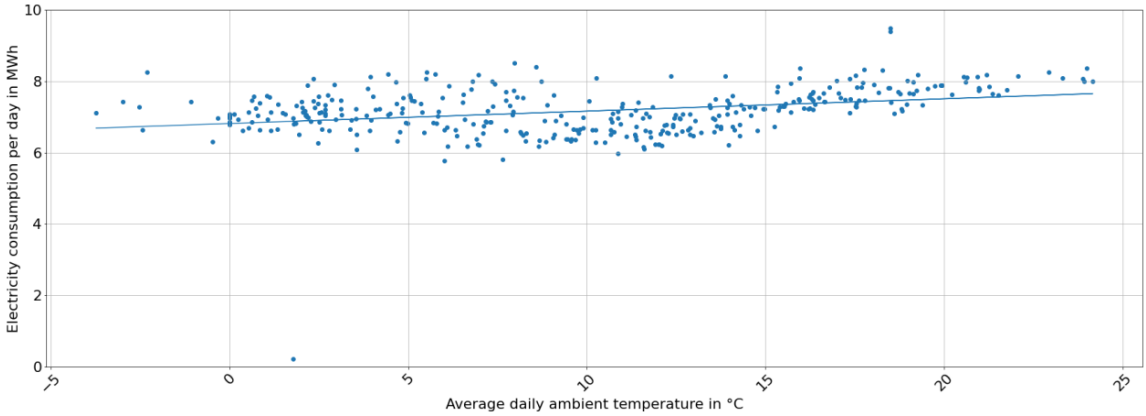

Fig. 2: Dependence of the electricity consumption on the average ambient temperature of the investigated piglet frame

In contrast to Fig. 1, Fig. 2 shows that the electricity consumption is slightly dependent on the ambient temperature. This dependency is due to the rising ambient temperatures, which leads to increased stable temperatures. To ensure the well-being of the pigs and to maintain the optimal air temperatures, the air exchange rate of the ventilation systems is increased. This dependency is also supported by the fact that in winter the air exchange rate is deliberately reduced by the farmers to reduce heat losses. Thus, the electricity load is subject to the climatic regulations of the stable and is therefore related to the heat demand. This means that the heat demand is also subject to an ambient temperature dependency as shown in Fig. 3.

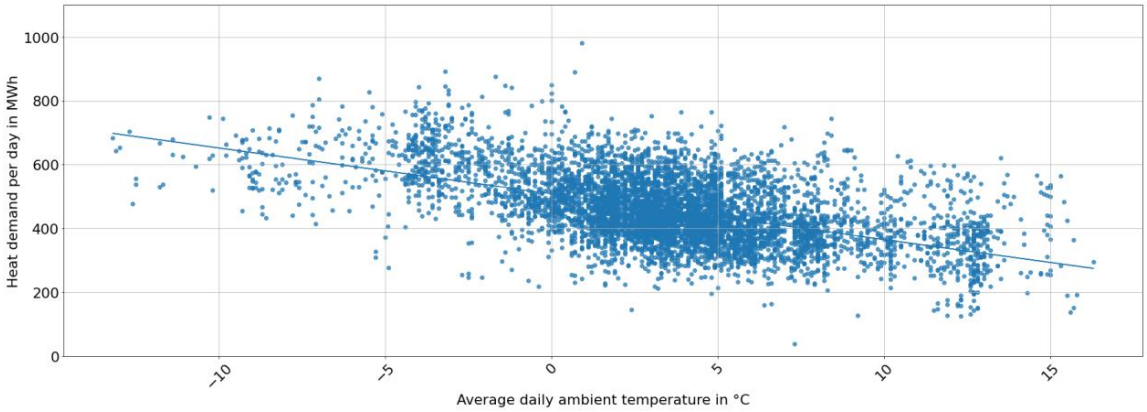

Fig. 3: Dependence of the heat demand on the average ambient temperature of the investigated piglet frame, hourly resolution

The annual load profile for the heat demand is created based on a heat flow measurement over a shorter period. The results show that there is an ambient temperature dependency of the heat load profile as found by Jesper et al., (2021). So, the heat load profile of the investigated piglet farm is calculated for the entire year as shown in Fig. 4.

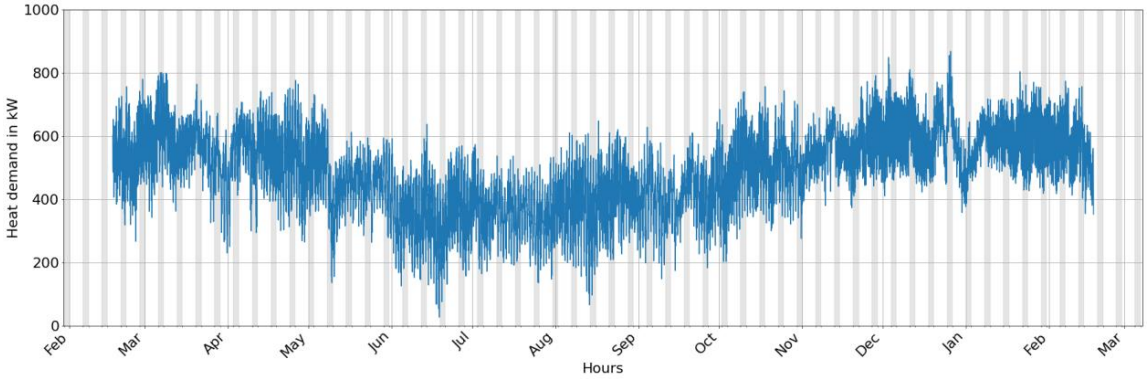

Fig. 4: Annual heat load profile of the investigated piglet frame in hourly resolution for the year 2021/22

4. Cooling demand scenario

Fig. 5 exemplifies the farrowing stable temperature of the investigated piglet frame. It shows a year-round deviation between set and stable temperature. This is probably due to faulty control, but nevertheless the deviation increases in the summer months despite the increased air exchange rate. This temperature overshoot is the main reason why some farmers have already installed cooling systems and why the cooling demand must be considered when designing an efficient energy concept.

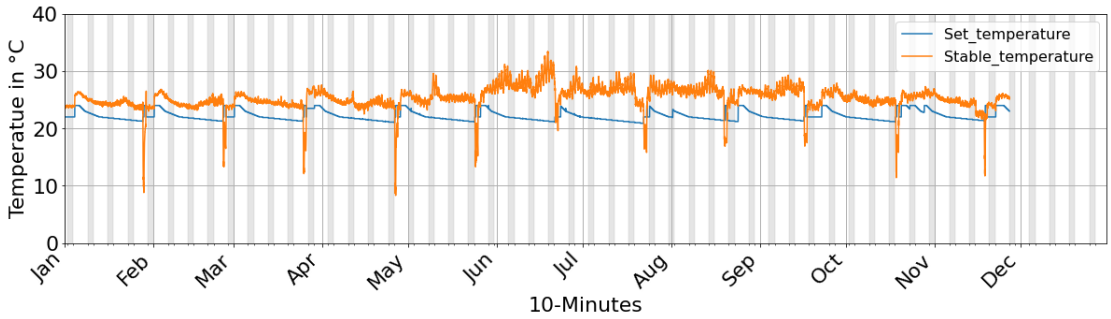

Fig. 5: Example of set temperature and stable temperature for one farrowing stable of the investigated piglet frame in 10 minutes resolution

In addition to the ambient temperature, the sensitive heat production of the animals must be taken into account when calculation the cooling demand of a stable. The decisive factors for the sensitive heat production are the number of animals per compartment, their weight, and their daily weight gain. Considering those factors, the sensitive heat production can be determined with eq. 1 according to (DIN 18910, 2017). For the case study the farrowing pen and the gilts pen are most interesting for cooling, in order to avoid overheating of the farrowing sows and to optimise production and growth of the gilts.

Sensitive heat production:

$$q_{sen} = 0.62 * q_{tot,cor} - \frac{q_{tot}}{1000} * (1.15 * 10^{-7} * T_i^6) \quad \text{(eq. 1)}$$

Corrected Heat production on ambient temperature

$$q_{tot,cor} = q_{tot} * \left(1 + G * (20 - T_i)\right) \quad \text{(eq. 2)}$$

Farrowing pen (DIN 18910, 2017):

$$q_{tot} = 4.85 * m^{0.75} + 28 * Y_1 \quad \text{(eq. 3)}$$

Gilts (DIN 18910, 2017):

$$q_{tot} = 4.85 * m^{0.75} + 8 * 10^{-5} * p^3 + 78 * Y_2 \quad \text{(eq. 4)}$$

$G = species\ specific\ gradient$
$T_i = Stable\ Temperature\ in\ °C$
$m = Weight\ animal\ in\ kg$
$Y_1 = Milk\ outpu\ in\ l/d$
$p = Pregnat\ phase$
$Y_2 = daily\ weight\ gain\ in\ kg/d$

The cooling demand for the investigated piglet farm is shown in Fig. 6, with a reasonable peak during the summer period, what makes solar cooling a suitable option to meet the demand. But must intensive pig production systems,

as well as this case study have a biogas plant with an CHP unit. For the case study the cooling demand overlaps with the excess heat of the CHP unit, for most of the time as shown in Fig. 6. This makes it possible to use the excess heat for cooling the air supply by absorption cooling and adjust the stable temperatures to the optimal temperatures. This solution has the advantage of better housing climate without or only few additional energy input, as the excess heat is currently dissipated during the summer period. In the current situation, with the current incentives, solar cooling is not an attractive solution for the farms, because the excess heat from the CHP is available during the summer period.

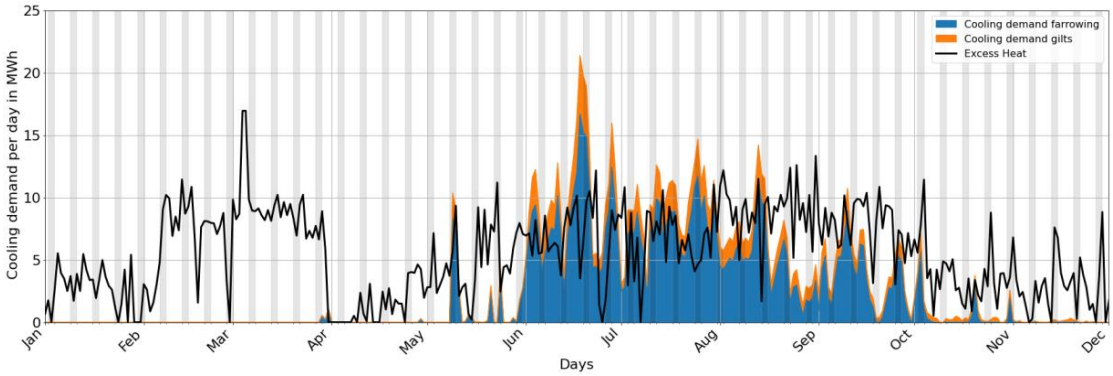

Fig. 6: Cooling demand of the stables and excess heat of the CHP of the investigated piglet farm

5. Conclusion

The consideration of different heating and cooling demand scenarios in the design of a heating and cooling supply concept offers the advantage that future changes can already be considered. Likewise, the forecast of the heating and cooling load profiles can serve as a basis for decision-making for planned measures. For detailed planning, the specific conditions of the operation site must be considered. The full paper presents the methodology how the heating and cooling load profile for a piglet farm can be calculated based on different boundary conditions such as size of the housings, number of pigs, and location as well as the installed facilities for heat recovery, cooling, etc. This methodology is exemplified by the case study but can be transferred to other intensive pig production systems, as the circumstances such as the layout of the stables and the presence of a biogas plant are very similar. The results show that the profile of the excess heat of the existing CHP, which is currently dissipated during summertime, goes along with the calculated cooling demand for the stables. In consequence, an absorption cooling process with the excess heat of the CHP is a more attractive solution to increase breading efficiency and animal welfare at the same without additional energy input, as solar cooling.

6. References

Blaha, Hoy, Schulte-Wülwe, Stalljohann, Brede, Sieverding, 2010. Animal Health Pig [Tiergesundheit Schwein].

DIN 18910, 2017. Thermal insulation of closed barns - Thermal insulation and ventilation - Planning and calculation principles for closed forced-ventilated barns [Wärmeschutz geschlossener Ställe - Wärmedämmung und Lüftung - Planungs- und Berechnungsgrundlagen für geschlossene zwangsbelüftete Ställe]. Accessed 6 April 2022. doi:10.31030/2680106

Giner Santonja, G., Georgitzikis, K., Maria Scalet, B., Montobbio, P., Roudier, S., Sancho, L.D., 2017. Best Available Techniques (BAT) Reference Document for the Intensive Rearing of Poultry or Pigs. Publications Office of the European Union. doi:10.2760/020485

Seifert, C., Wietzke, D., Fritzsche, S., 2009. Energy for heating and ventilation in practical pig farming [Energie für Heizung und Lüftung in der praktischen Schweinehaltung]. Landtechnik. doi:10.15150/LT.2009.709

Design of a Small-Scale Solar Maize Dryer

Peace Muusha, Blessed Sarema and Samson Mhlanga

National University of Science and Technology, Bulawayo (Zimbabwe)

Abstract

Maize is the most widely grown cereal crop in Zimbabwe. At harvest, the content of moisture in maize is usually above 25 % which is undesirable for safe storage throughout the year. The acceptable moisture content for prolonged storage of maize is about 12.5 %. Most farmers in Zimbabwe use the traditional way of drying maize by exposing it to the sun for a prolonged period. The drying period can span up to three months using these traditional methods. This delays the delivery of the grain to the market as well as the quality of the product resulting in post-harvest losses. This paper is a documentation of the project that was supported and sponsored by the Southern African Solar Thermal Demonstration Initiative (SOLTRAIN) to design a small-scale solar grain dryer for maize in Zimbabwe. Drying experiments were conducted in the laboratory to determine the drying parameters that were used in the design. An optimum drying temperature of 60 °C was determined against a drying time of 6 hours to reach the acceptable moisture levels using a drying vessel of a capacity of 1.5 tonnes and a collector area of 48 m^2 using flat plate air collectors. The control system of the dryer was also developed

Keywords: Solar drying, grain drying, flat plate air collectors, drying chamber

1. Introduction

The main goal of this project was to improve the quality of the maize whilst reducing waste associated with the drying process by making use of renewable solar thermal energy. This undertaking drives towards the achievement of Sustainable Development Goal 7 which calls for the provision of clean and affordable energy. The present common maize drying techniques in Zimbabwe are monotonous, time-consuming as far as productivity is concerned (Lambert et al., 2018). The developments that have occurred over the years use non-renewable energy sources (Meyer and Greyvenstein, 1992). These are not readily accessible in Zimbabwe, and they also compromise the natural environment. There is need to spare time, reduce labour, enhance the quality of dried maize with a better clean drying technique. Many farmers suffer post-harvest losses as well as delayed marketing of grain due to the current natural drying techniques (Herald,2016). Hence the need to develop a simple grain dryer that is usable at a small-scale level.

2. Experimental Setup

Experiments were conducted to analyse the effect of temperature on drying rate and moisture content in order to determine and optimise the drying parameters for drying grain. A Thermotec 40 litre laboratory oven was used for the experiment which has a temperature range of 0-150℃ and constant airflow rate of 1.5m/s. Three temperature levels were selected according to the Taguchi Design of Experiments that are 40 °C, 50 °C and 60 °C. The mass of the grain was recorded at 5 min intervals until the moisture content of grain reaches the desired 12.5%. A stopwatch was used to measure the drying time for the various experiments. The results of the experiments are as shown in Fig 1 and Fig 2.

© 2022. The Authors. Published by International Solar Energy Society
Selection and/or peer review under responsibility of Scientific Committee
doi:10.18086/eurosun.2022.05.08 Available at http://proceedings.ises.org

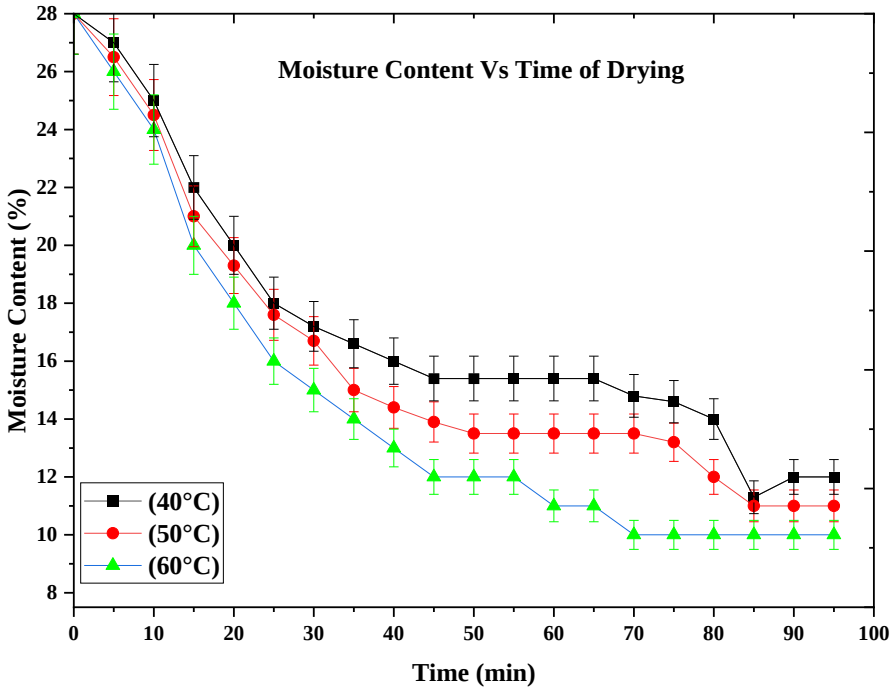

Fig.1. Moisture Content Vs Time of Drying Maize at Varying Temperatures

Fig 1 shows the variation of moisture content and drying time for the three temperature levels, while Fig 2 shows the drying rate against the drying time.

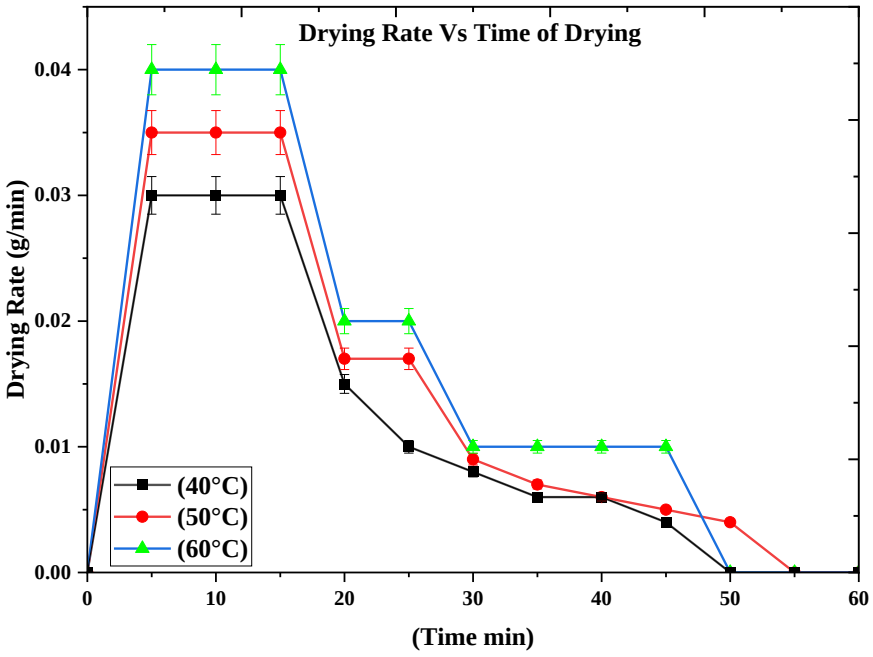

Fig.2. Drying Rate Against the Drying Time

By applying the large is better, the optimum values can be deduced from the graphs. It was concluded that dryer is sensitive to temperature more than the other parameters. Initial mass and drying period needed not be too large and too small for effective drying to take place.

3. System Design

A maize dryer was designed with a capacity of drying 1500 kg of maize from 25 % to 12.5 % moisture content in 8 hours, using a collector efficiency of 33.2 %, and a 30 % pickup efficiency as well as 30 % system efficiency. The system efficiency is within the range of efficiency for forced convection dryers, that is, 20-30 % (Fuller, 2012). The design was made up of two different systems. The first system is the heating system process that uses the flat plate solar collectors (Bala and Janjai, 2012). A dehumidifier to control the humidity and temperature of air was also included. The second system consists of the grain handling circuit for efficient drying of grain. All the electrical components were designed to be powered by an external solar photovoltaic system. Fig 3 shows the schematic of the heat collection, heat storage and drying chamber layout design. The major design considerations for the maize dryer system include the solar collector unit sizing, design of ductwork, drying chamber sizing, dehumidifier sizing, photovoltaic system sizing and the control system sizing. The solar collector design followed guidelines from Duffie and Beckman (2006) as well as Tan and Charters (1970).

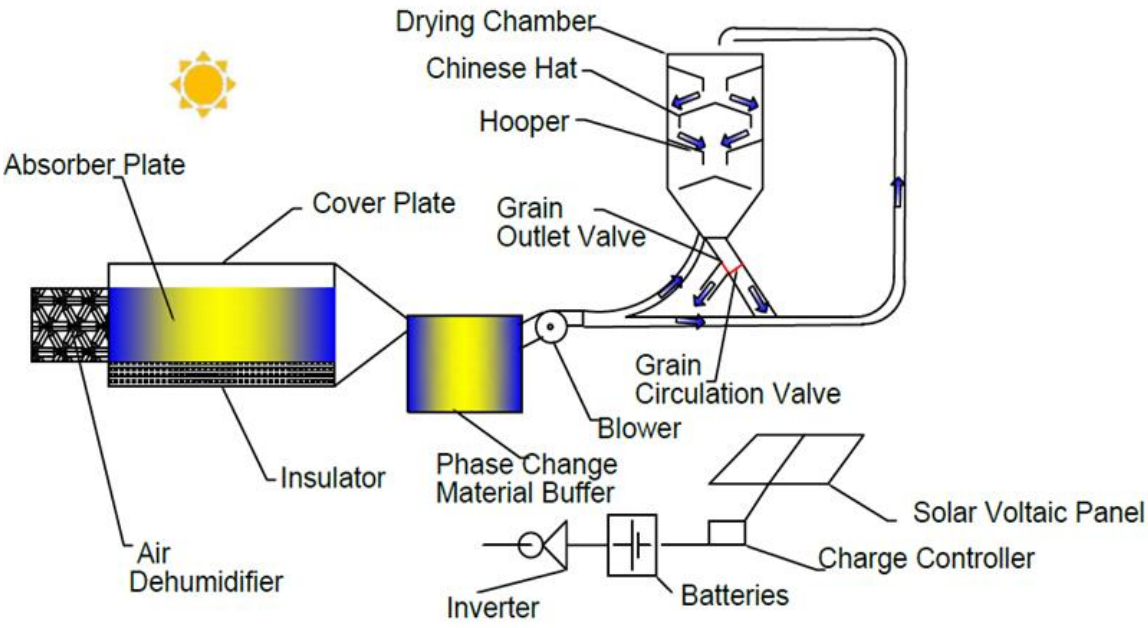

Fig.3. Maize Dryer System Layout

3.1 Design of a Solar Collector Unit

The drying heat load, Q_{load} determines the area of a solar heat collector. The heat load is determined by the amount of grain to be dried, its initial and final moisture contents, and the time required to complete the drying operation. 1500 kg of maize at 25 % moisture content needs to be dried to 12.5 % in 8 hours. The initial amount of moisture in the grain, w_i , is:

$$m_i = 25\% * 1500kg = 375\ kg \quad (1)$$

and the dry matter weight, m_{dm}, is:

$$m_{dm} = 1500\ kg - 375\ kg = 1125kg \quad (2)$$

The final amount of moisture in the grain, m_f, at 12.5 percent moisture content, is found from the relationship:

$$12.5\ \% = \frac{m_f}{m_f + m_{dm}} kg$$

Hence,

$$m_f = \frac{12.5\ \% * 1125\ kg}{0.875} = 160.71kg \quad (3)$$

The amount of moisture to be removed, m_w, is therefore:

$$m_w = 375\ kg - 160.71\ kg = 214.29kg \quad (4)$$

The total heat energy required to evaporate the water and dry maize to the required moisture content for the total drying process is calculated using Equation 5.

$$Q_{load} = m_p C_f (T_f - T_i) + m_w h_{fg} \quad (5)$$

Where:

- m_p = mass of a maize, kg
- C_f = average specific heat capacity of the maize, 1.552 kJ/kgK
- T_f (65 °C) and T_i (28 °C) is the final and initial temperatures of air respectively, ℃
- m_w = is the mass of the water to be removed during drying, kg
- h_{fg} = latent heat of vaporisation, kJ/kg. (2304 kJ/kg from steam tables)

$$Q_{load} = 1500\ kg \times 1.552\ kJ/kgK \times (65 - 28)℃ + 214.29\ kg \times 2304\ kJ/kg \quad (6)$$

$$Q_{load} = 332.792\ MJ$$

If a conservative collector efficiency of 30% is considered, and an average irradiation of 800.48 W/m^2 for Mashonaland Central in Zimbabwe is used, the useful heat gain in the collector, q_u, is:

$$q_u = 30\% * 800.48\ {}^{W}/_{m^2} = 240.14\ {}^{W}/_{m^2} \quad (7)$$

Assuming that radiation is available 8 hours a day, hence, using 8 hours of operation, the total collector heat gain, q_{ut}, is:

$$= 240\ {}^{W}/_{m^2} * 8\ h = 1920\ {}^{Wh}/_{m^2}\ or\ 6.916\ kJ/m^2$$

Therefore, the total area of a bare plate solar heat collector,A_c, is given by Equation 8.

$$A_c = \frac{Q_{load}}{q_{ut}} \quad (8)$$

$$A_c = \frac{Q_{load}}{q_{ut}} = \frac{332.79}{6.916} = 48m^2$$

The average drying rate for the drying system is calculated using Equation 9:

$$\dot{m}_{dr} = \frac{m_w}{t_d} \quad (9)$$

Where:

- t_d = total time to reach the equilibrium moisture, sec

$$\dot{m}_{dr} = \frac{214.29\ {}^{W}/_{m^2}}{8\ h \times 60\ min \times 60\ s}$$

$$\dot{m}_{dr} = 7.44\ \times\ 10^{-3} kg/s$$

The mass flow rate of air required for the drying process is evaluated using the Equation 10:

$$\dot{m}_a = \frac{\dot{m}_{dr}}{(W_f - W_i)} \quad (10)$$

Where:

- $\dot{m}_{dr}$, is the average drying rate, kg/hr;
- W_f; W_i are final and initial humidity ratio, ${}^{kgH_2O}/_{kg\ (dry\ air)}$ (Determined from Psychrometric Charts)

$$\dot{m}_a = \frac{7.44\ \times\ 10^{-3}\ kg/s}{(0.20579 - 0.024226)\ {}^{kgH_2O}/_{kg\ (dry\ air)}}$$

$$\dot{m}_a = 0.041\ kg/s$$

Power required for the drying process is calculated using Equation 11:

$$Power, P = \frac{Q_{load}}{t_d} \quad (11)$$

$$P = \frac{332.792 \times 10^6 J}{8\ h \times 60\ min \times 60\ s}$$

$$P = 1.156 \times 10^4 W$$

3.2. Design of Ductwork

The air return system requires sizing of ducting for efficient circulation of steam. To design ducting system, a proper fan needs to be selected, evaluation of volumetric flow rate, fan horse power and the determination of the duct area. The equations to design the maize dryer ductwork include:

The volumetric flow rate required for the drying rate is evaluated as follows in Equation 12.

$$V_a = \frac{\dot{m}_a}{\rho_a} \tag{12}$$

Where:

- $\dot{m}_a =$ is the mass flow rate of air, kg/s
- $\rho_a =$ density of air at 65℃ = 1.0447 kg/m^3

$$V_a = \frac{0.041\ kg/s}{1.0447\ kg/m\text{^}3}$$

$$V_a = 0.0392\ m^3/s = 79.68\ cfm$$

Fan horsepower is then evaluated using Equation 13.

$$Fan\ HP = \frac{Air\ Flow \times Static\ Pressure}{6320 \times Fan\ Efficiency} \tag{13}$$

$$Fan\ HP = \frac{79.68\ cfm \times 469.74}{6320 \times 0.85}$$

$$Fan\ HP = 6.70511 HP \approx 5\ kW$$

Most fans have efficiency ranges between 70% and 85%. Having a working temperature of 65℃ = 149℉ and approximating 469.74 inches from the static pressure.

The average velocity of heated air is 200fpm (1.016 m/s) (Ashrae, 2010). The duct area for the pipe system that transport heated air from thermal energy storage tank to drying chamber is determined as shown in Equation 14.

Therefore, the duct area is calculated as;

$$Duct\ Area\ = \frac{Air\ Flow(cfm)}{velocity(fpm)} \tag{14}$$

$$Duct\ Area\ = \frac{79.68\ cfm}{200\ fpm}$$

$$= 0.394 ft^2$$

3.3 Drying chamber sizing

To size the drying chamber, knowledge of amount on maize to be dried per batch as well as the volume of maize is vital. Also, the volume of the screw conveyor in the chamber is considered by addition of 30% volume of the volume of maize. The total volume is 1500kg of maize which occupies an approximate f 1.93m^3 space. With a 1.5m height, the radius of cylinder is calculated using the relationship in Equation 15.

$$Radius, r = \sqrt{\frac{V}{\pi h}} \tag{15}$$

Where,

- V = Volume of drying chamber, m^3
- h = height of drying chamber, m

$$Radius, r = \sqrt{\frac{1.3 \times 1.93\ \text{m}^3}{\pi \times 1.5\ m}}$$

$$= 0.72\ m$$

3.4 Dehumidifier Sizing

Assuming that the initial humidity of moist air is 80% relative humidity, the desired relative humidity is 50%, the atmospheric room temperature and pressure is 28 °C and 760mmHg respectively. The size of the dehumidifier is obtained by use of Equation 16.

$$Dehumidification\ capacity\ per\ hour, kg/hr\ = (H_{a1} - H_{a2})V_r \quad (16)$$

Where:

- H_{a1} = is present absolute humidity of air, mmHg
- H_{a2} = is desired absolute humidity of air, mmHg
- V_r = Volume of room to be dehumidified, i.e., solar collector volume ($9\text{m} \times 9\text{m} \times 0.5\text{m} = 40.5\text{m}^2$)

The present absolute humidity of air (H_{a1}) in mmHg is given by Equation 17 as:

$$H_{a1} = \frac{P_i \times M_w}{(P - P_i)M_{wdry}}\ mmHg \quad (17)$$

Where:

- P_i = Partial pressure of water at given relative humidity, mmHg
- P = Atmospheric pressure of water at given relative humidity, mmHg
- M_w = Molecular weight of water, g/mol
- M_{wdry} = Molecular weight of dry air, g/mol

From Equation 17 H_{a1} and H_{a2} were determined as follows:

$$H_{a1} = \frac{P_i \times M_w}{(P - P_i)M_{wdry}} = \frac{22.61\ mmHg \times 18\ g/mol}{(760 - 22.61)mmHg \times 29 g/mol} = 0.019 mmHg$$

$$H_{a2} = \frac{P_i \times M_w}{(P - P_i)M_{wdry}} = \frac{14.13\ mmHg \times 18 g/mol}{(760 - 14.13)\ mmHg \times 29 g/mol} = 0.0118 mmHg$$

This implies that using Equation 16, the dehumidification capacity would be:

$$(0.019 - 0.0118) mmHg \times 40.5\ \text{m}^2 = 0.293\text{kg/hr}$$

3.5 Photovoltaic System Design

The sizing of the photovoltaic system was done in 5 steps. The steps included estimating the electrical load, battery sizing, solar array sizing, inverter sizing, and charge controller sizing.

(i) Estimating the Electric Load

The biggest load in the design is the blower fan of 5 kW, followed by dehumidifier load estimated to be 0.28 kW. Other loads include LED lights of 30 W and microcontroller of 20 W. The blower is run intermittently during the drying process as the dryer also takes advantage of the natural convection process. It is estimated that the blower runs for an hour cumulatively during the day. The other components will operate for about 8 hours a day. A combined daily energy demand of 10 kWH was used in the design to also cater for system efficiencies.

(ii) Battery Sizing

The battery capacity is determined by the daily energy demand, the system voltage and the depth of discharge. A 12 V system, for a 10-kWH daily energy demand and depth of discharge of 50 % yields a battery capacity of about 1 700 AH. This capacity is based on one day operation. The battery capacity could be increased to give more days of autonomy, but since the solar dryer is not expected to work without radiation, therefore it is prudent to use one day of autonomy to minimise costs.

(iii) Array Sizing

The solar PV array is sized by considering the daily load demand, the peak sun hours and the system efficiency.

The location for which the dryer should be utilised has about 6.5 hours of sunshine. Considering system efficiency of 95 % between the charge controller and the array, the size of the array should be 1619 W. The selection of the panels will depend on the available solar panels on the market.

(iv) Inverter Sizing

The inverter is sized to take both linear and non-linear loads. The capacity of the inverter is should be oversized to allow for a higher power draw at equipment start-up. In this design the inverter should be able to cater for the 5 kW motor and 330 W additional components for lights, controller and dehumidifier.

(v) Charge Controller Sizing

The charge controller should be sized according to the maximum current flowing in the circuit. The maximum power from the solar generator is 1619 W and with a system voltage of 12 V the maximum amperage is around 135 Amps. The current can be reduced by increasing the system voltage to 24, 36 or 48 Volts.

3.6 Control System Design

Process control is the active changing of the drying parameters based on the results of process monitoring. The monitoring sensors measures actual values of parameters and displays them on an HML. The drying chamber will have two humidity sensors (at top and bottom) which works to measure the humidity in the dryer.

When the difference in humidity is measured and is found to be more or less the same, the buzzer system rings to alert the operator to close circulation valve. The operator will then open the offloading valve to take a sample of maize only and check if the moisture content has reached desired level. If the humidity difference between the two sensors is not within threshold, the maize offloading valve is closed whilst the circulation valve is open to allow grain circulation.

The temperature sensors measure current temperature and they shut down the blower when the temperatures in the drier are not within threshold. In the design of the control system, an Arduino controller is used to control the system automatically.

4. System Flow

The system flow can be explained by two different systems. The first system is the heating system process that uses the flat plate solar collectors, dehumidifier to heat air to required temperatures. The second system consist of the grain handling circuit for efficient drying of grain.

4.1 The Heating Circuit

The heating circuit is made up of the flat plate solar collector, dehumidifier, PID controller. The heat energy is collected by the flat plate solar collector and stored in the heat storage tank. From the heat storage tank, there is a valve to regulate the amount of heat energy passing through. As heat passes through the valve, it is then blown to grain at required temperatures for drying.

The drying chamber has temperature sensors to check the current temperatures of the heat transferred to maize. The valve opening levels are controlled by use of PID controller. The PID controller sends a voltage pulse depending with the calculated error. Therefore, the valve is either partially opened or closed as it allows heat to pass through to compensate for the disturbances.

4.2 Grain Handling Circuit

The grain handling system is made up of the drying chamber with hoppers and Chinese hats, valves and two blowers. Grain is loaded into drying chamber by blowing it to the top after which the blower is switched of. As grain falls through the opening of the hopper, it receives heat energy from the heated air and in doing so it starts to dry gradually.

After passing through the top hopper, grain is channeled (by means of Chinese hats) to the constructed gaps between the inner surfaces of the drying chamber and Chinese hats and in doing so increases the holding time of

grain in the chamber. From the Chinese hats, grain continue falling down to the conical shaped bottom of the drying chamber by means of gravity.

The tip opening of the conical shaped bottom of the drying chamber has a pipe which collects grain that falls on it. This pipe is Y shaped with single valves for each. One pipe is for grain discharge after drying and the other is for circulation of grain to be blown back to the top chamber hopper such that the process repeats itself until grain reaches the required moisture content.

5. Results

The designed dryer has a capacity of drying 1 500 kg of maize from 25% to 12.5% moisture content in 8 hours. The solar dryer has a collector efficiency of 43.2%, and a 30% pickup efficiency as well as 30% system efficiency. The system efficiency is within the range of efficiency for forced convection dryers, that is, 20-30 %. The collector efficiency is within the range of 30-40 % for the given collector area. This implies that the project is economically feasible and a desirable option.

A working prototype which is shown in Figure 4 was fabricated. The prototype was made up of a flat plate solar collector, heat storage tank, a blower, a drying chamber, as well as the control unit. A flat plate solar collector was made up of a glass cover plate, anodic aluminum absorber plate and a wooden insulator plate. The drying chamber, as well as the heat storage tank, were made of a galvanized metal sheet. Control system was made up of Arduino Mega microcontroller connected to two DHT temperature and humidity sensors and a DSB 108 temperature sensor. A buzzer and an LED light with two colors green and red showing comprised the control system.



Fig.4.Fabricated Prototype

6. Conclusion

The project consists of the design of a solar thermal dryer for use by A1 communal farmers in Zimbabwe. It gives an understanding of harnessing solar energy for the benefit of the farmers thereby increasing the efficiency of drying grain during harvest period. The design can dry 1.5 tons per day on a normal sunny day. This will go a

long way in reducing post-harvest losses and farmers can deliver their grain to the market at a faster rate thereby improving their cash flows compared to natural drying.

7. Acknowledgements

The authors extend thanks to Austrian Development Agency, OFID and SOLTRAIN - Southern African Solar Thermal Training and Demonstration Initiative for funding this project. The funding allowed for further experimental work, fabrication of a prototype to conduct experiments that supported the research and funded other activities to gather data from affected farmers and Grain Marketing Board. Special thanks are also given to the NUST Department of Industrial and Manufacturing for supporting this project.

8. References

Ashrae. 2010. Handbook of Fundamentals. New York: American Society of Heating, Refrigerating and Air-Conditioning Engineers.

Bala, B. K., & Janjai, S., 2012. Solar drying technology: potentials and developments. In Energy, Environment and Sustainable Development (pp. 69-98). Springer, Vienna.

Duffie, J. A., & Beckman, W. A., 2006. Solare energy thermal processes. New York: John Willey and Sons.

Fuller. J. R., 2012. Solar Drying - A technology for Sustainable Agriculture and Food Production. Solar Energy Conversion and Photoenergy Systems, III.

Herald., 2016. Emerging_Farmer. from How to grow maize in Zimbabwe: http://www.emergingfarmer.com/2016/10/how-to-grow-maize-in-zimbabwe.html [Online] Accessed March 15, 2019.

Lambert, J., Angus, D., & Reid, D., 2018. FAO. Retrieved January 6, 2019, from Agriculture Engineering in Process: http://www.fao.org/docrep/t0522e/t0522e08.htm

Meyer, J. P., & Greyvenstein, G. P., 1992. The drying of grain with heat pumps in South Africa: A technoeconomic analysis. International Journal of Energy Research, 16(1), 13-20.

Tan, H. M., & Charters, W. W. S., 1970. An experimental investigation of forced-convective heat transfer for fully developed turbulent flow in a rectangular duct with asymmetric heating. Solar Energy, 13(1), 121-125.

How to Combine a Solar Heating Plant and a CHP Most Efficiently for Industrial Applications?

Felix Pag[1], Alan Pino[2] and Klaus Vajen[1]

[1] University of Kassel, Institute of Thermal Engineering, Kassel (Germany)

[2] University of Seville, Department of Energy Engineering, Sevilla (Spain)

Abstract

To successfully decarbonize the industrial heat demand efficient solutions to reduce the CO_2-emissions of the industrial heat supply are required. Since solar heating plants usually cannot supply a company's low temperature heat demand, they must be combined with other low carbon technologies. Combined heat and power plants represent one of the most efficient technologies for generating heat and electricity from fossil fuels. In the future, CHP plants fueled by H_2 or biogas can be an important component of sector coupling. Nevertheless, the operation of CHP plants with fossil fuels causes CO_2 emissions, and renewable fuels are scarce. Therefore, a combination with e.g. solar thermal is recommended in order to reduce the operating hours. This study analyzes the combination of solar heating plants and CHPs based on TRNSYS simulations. Variations of the hydraulics, system design and operation, as well as control, result in an optimized system design considering the diverse industrial boundary conditions. The assessment is performed considering a technical evaluation. This work is conducted within the framework of IEA SHC Task 64/IV Subtask A.

Keywords: Solar heating plant, SHIP, CHP, TNRSYS, Task 64/IV

1. Introduction

The decarbonization of industrial heat demand is a huge challenge world-wide. In contrast to the higher temperature level above 200 °C, the low- and medium-temperature heat demand is suitable to be provided with solar collectors also in regions with lower direct normal irradiation. However, recent studies of the authors highlight two aspects that underline the importance of efficient hybrid heat concepts. Firstly, industrial heat demand is not constant throughout the year, but ambient temperature dependent heat plays a significant but often underestimated role in industry (Jesper et al., 2021). Consequently, the potential solar fractions are also in industrial application often limited by the seasonality of the heat load profile as it is usual in residential applications. Secondly, the availability of roof area is a strongly limiting factor in various industries, especially in the sectors with a high summer heat demand and a correspondingly high solar collector area potential (Pag et al., 2022). The VDI guideline 3988 (Association of German Engineers, 2020) is an established pre-design methodology for solar process heat plants in European countries. Here, the solar thermal system is designed with respect to the summer heat demand as key design parameter following the idea, to fully cover this heat demand on a sunny summer day. Consequently, only little solar excess heat is generated, but only comparably small solar fractions are possible if the summer heat demand is significantly smaller than winter heat demand. With respect to the climate change mitigation goals and in order to massively reduce the CO_2-emissions, solar heating plants have to be combined with other renewable or least most efficient technologies. Currently, there is not enough renewable electricity to cover world-wide heat demand with heat pumps. In addition, there is not always a suitable heat source for heat pumps and ambient heat is only available at a low temperature level with respect to the temperature requirements in industry. CHP are one of the most efficient solutions to use fossil fuels. Fueled with H_2 or biogas, CHP can play an important role for sector coupling or in regions with a very heat demand density (e.g. industrial companies). Therefore, also efficient combined heat and power (CHP) modules in combination with solar heating plants can be a solution to reduce CO_2-emissions if there are integrated efficiently. However, design guidelines and detailed information on how to combine both technologies are rare. In this study, an efficient system design and operation of solar heating plants and CHPs is defined with respect to different boundary

© 2022. The Authors. Published by International Solar Energy Society
Selection and/or peer review under responsibility of Scientific Committee
doi:10.18086/eurosun.2022.05.09 Available at http://proceedings.ises.org

conditions. Different hydraulics, design-strategies, and operation modes are compared employing TRNSYS (Klein, 2017) simulations, whose results are evaluated technically.

2. TRNSYS Simulation Models

In order to analyze how to combine solar heating plants and CHPs most efficiently, two different hydraulics are implemented in TRNSYS (Fig. 1). The first system follows the idea of "keeping it simple". Both technologies charge one shared buffer storage which supplies the heat for the process. In the second system, each of the technologies charges an independent storage. The storages are discharged alternating: if there is enough solar heat available, the solar buffer storage is discharged with priority; otherwise, if at the top the solar storage the process set temperature is not reached, the heat is supplied from the CHP storage. In both cases, the solar heating plants is operated with a set temperature control with variable flows in the primary and secondary circuit to always provide the set temperature if enough irradiation is available. The CHP efficiency is modelled with characteristic curves, calculating the thermal and electrical efficiency based on the net power and the part load ratio. The CHP is controlled with respect to the temperatures of the respective storage. Different switch-off criteria for the CHP are analyzed in the one-storage system allowing the CHP less (only top 10 %) or more (up to 60 %) usage of the storage by varying the position of the respective temperature sensor. In the two-storage system, the CHP starts operation if the top temperature of "its" storage falls below the set temperature and stops operation if the storage is fully loaded. Furthermore, the CHP has a minimum runtime of one hour and a standby time of 0.5 hours reducing interval operation.

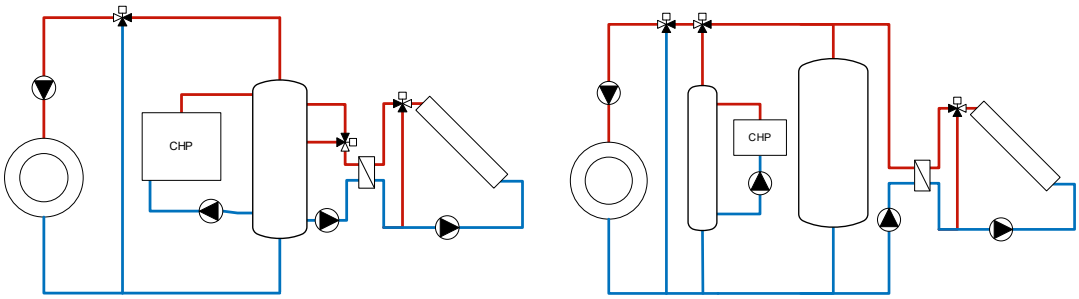

Fig. 1 Scheme of the two simulated hydraulics, left: one-storage system, charged by both solar collectors and CHP, right: solar collectors and CHP charge the corresponding storages independently.

3. Pre-design of simulation cases

To evaluate the system design and performance with different boundary conditions, the reference profiles from Jesper et al. (2021) are used. The respective regression profiles are shown in Fig. 2, (a) representing the profiles for working days and (b) for weekend days as well as holidays. Each of the profiles represents a different ambient temperature dependency (cluster) and the profiles for weekdays and weekend days can be combined as needed. In the further work, the combination of these cluster profiles is represented by the following nomenclature (working day cluster, weekend day cluster). According to the most often cluster combinations given by Jesper et al. (2021) the following cluster combinations are selected: (0,0), (0,1), (1,2), (2,3), (3,4). Potsdam, Germany, is chosen as location and the respective temperature profile is used to calculate the actual heat load profile. The annual heat demand is varied between 1, 3, and 5 GWh/a which is relevant for scaling effects on the one hand and for the thermal and electrical efficiency curves of the CHP modules. The process temperatures are set to 80 °C for the flow stream and 60 °C for return, which is typical for low temperature process heat (Lauterbach et al. 2012; Brunner et al. 2012).

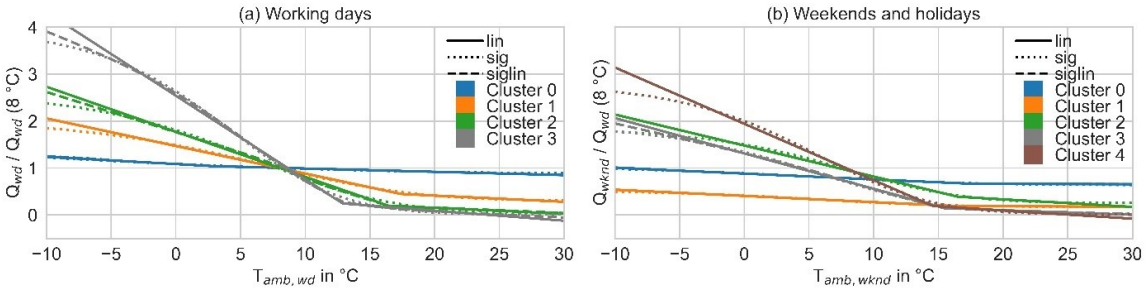

Fig. 2: Heat load profile regressions as a function of the ambient temperature from (Jesper et al., 2021)

The solar heating plant is designed according to the VDI guideline 3988. The collector area is sized to fully cover the summer heat demand of a standard production day on a good summer day in combination with a buffer storage. Consequently, solar excess heat is avoided to improve economics. Consequently, only low solar fractions can be reached (Pag et al., 2022), especially by companies with a significant ambient temperature dependency of the heat load and by companies with a limited roof area. For each of the four heat load profiles, the CHP is designed with various net capacities considering different full load hours (3000 to 7000 full load hours) in a year. Typically, this is done based on a sorted load curve. Therefore, the annual solar yield is estimated based on the load profile and the VDI guideline. Then, the solar yield is distributed in an hourly resolution employing the efficiency curve of the collector. Based on this, the residual heat load is calculated, and the CHP size is determined according to a given full load hour value. For the given cases, the CHP net electrical power varies between 50 and 300 kW_{el}. For the one-storage system, the storage size is determined with respect to the collector area based on the VDI recommendations. The same is done for the solar storage in the two-storage system; however, the CHP storage is sized to buffer one hour of full capacity operation of the CHP without heat demand.

4. Comparison of system performance of one- and two-storage system

To compare the technical performance of a one-storage system with a two-storage system, the system design shown in Tab. 1 is used.

Tab. 1: Parameters of the system design to compare one- and two-storage system

Parameter	Value
Solar collector size	1,660 m^2_{gr}
Solar storage	166 m^3 (100 l/m^2_{gr})
CHP capacity	422 kW_{th}, 324 kW_{el}
CHP storage size	18 m^3
Working day cluster	1
Weekend day cluster	2
Annual Heat Demand	3 GWh

Fig. 3 shows the difference between the one- and the two-storage system for several parameters. Consequently, the storage losses (*Q_loss,st*) are higher in the two-storage system as a second storage is installed which is only fed by the CHP unit. In contrast, the solar yield (*Q_sol,st*), calculated as the solar heat which is fed into the storage, is higher in the one-storage system compared to the two-storage system. This can be explained by the fact the storage is discharged continuously, so the mean bottom storage temperature throughout the year is lower compared to the two-storage system. Here, the solar storage is discharged discontinuously (only if the top of the storage reaches the set temperature) and only when discharged "cold" return water is fed into the storage at the bottom. Due to higher storage losses and less solar yield, more heat has to be provided by the CHP (*Q_CHP*, +1 %) in the

two-storage system. Nonetheless, also slightly less heat is provided by solar heating plant and CHP compared to the one-storage system (*Q_load,covered* -1 %).

To sum up, with respect to an efficient system design, the one-storage system offers a more efficient system performance and should be preferred if a system is built from scratch. Apparently, the efficiency of the solar thermal system is not affected by the CHP unit which feeds into the same storage.

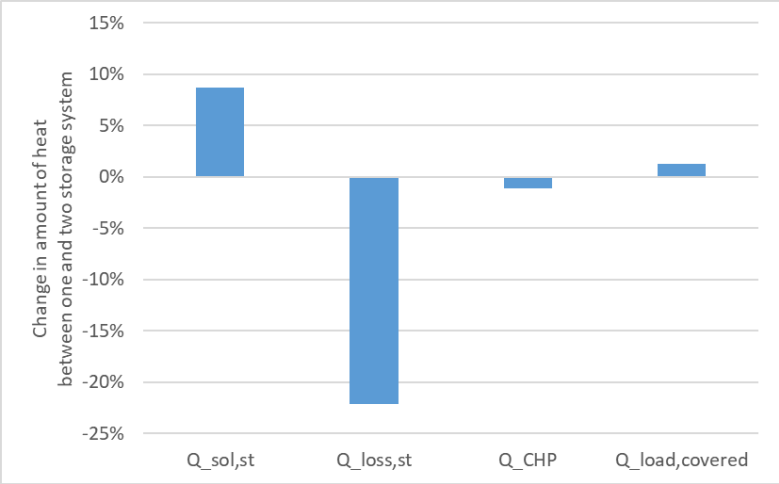

Fig. 3: Comparison of the one- and two-storage system for the selected system design

5. Technical performance of different system designs with the one-storage system

The results presented in section 4 highlight that a combined storage of solar heating plant and CHP is beneficial for the overall system performance. The efficiency of the solar heating plant is not significantly affected by the CHP. This can be explained by the fact that the CHP is only allowed to charge the top 10 % of the storage whereas the rest of the storage is only charged by the solar heating plant. With respect to the CHP this might lead to undesirable side effects, such as continuous switch-on and switch-off operation. As indicated in section 2, further simulations are done, analyzing the system performance if the CHP is allowed to heat up a higher share of the storage (top 30 % and top 60 %). Furthermore, the system performance is analyzed for the different load profiles. Fig. 4 shows the results for the different system simulations as a function of the full load hours of the CHP (inversely proportional to CHP capacity) exemplarily with an annual heat demand of 1 GWh/a – (a) showing the respective solar yield and (b) the starts of the CHP per year. Apparently, the heat load profile has a slight influence on the solar yield which is mainly due to a lower heat demand on week-end compared to production days (cluster (0,1), (2,3), and (3,4)). Furthermore, the capacity of the CHP does not show a clear influence on the solar yield, but only for cluster (0,1). Here, with higher CHP full load hours which is correlated with a lower CHP capacity, the solar yield is increasing. This might be an effect of the minimum run time of the CHP which is set to one hour. The higher the capacity of the CHP the more the storage is heated up which reduces the solar yield by higher storage temperatures. This is most significant for cluster (0,1) as the week-end heat load is especially low in comparison to the production day heat load here. The results show that the more the CHP is allowed to heat the storage, the more the solar yield decreases. Whereas the difference between the placement of the CHP control node, which stops the CHP operation if the set temperature is reached here, at 10 (blue) or 30 % (orange) of the storage height does not significantly affect the solar yield. allowing the CHP to heat up to 60 % of the storage decreases the solar yield by up to 10 %. This effect is stronger, if the heat load is more seasonal (cluster (2,3) and (3,4)) or if the CHP capacity is high. Fig. 4 (b) analyzes the number of CHP starts with the same variations. The influence of the position of the CHP control node is even stronger here. By allowing the CHP up to 60 % of the storage, the number of starts can be significantly reduced, partially up to 80 %. The influence of the CHP capacity and the seasonality of the load profile only shows a minor importance. The effect on economics can be hardly numbered, but it is common sense, that a smoother operation of CHPs with less starts has a positive effect on maintenance costs and lifetime.

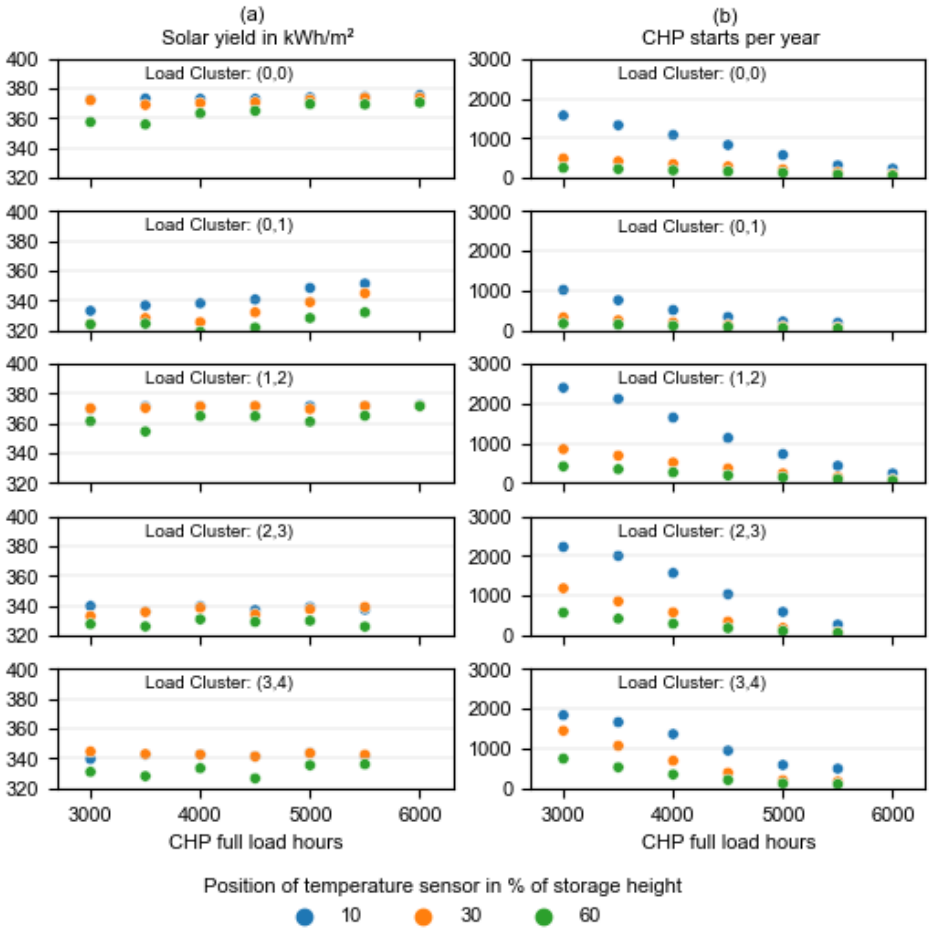

Fig. 4: TRNSYS simulation results: specific solar yield and CHP starts per year as a function of the CHP capacity for the different clusters and different heights of the CHP control node, annual heat demand 1 GWh/a

6. Conclusion and Outlook

The combination of solar heating plant and CHP is analyzed under various boundary conditions with TRNSYS simulations to evaluate how to combine both technologies most efficiently. The comparison of a one- and two-storage system shows that the technical performance of the one-storage system is beneficial. But as the system performance does not differ that significantly, both hydraulics can be realized efficiently, but are going to have different applications. If a CHP is already existing, the two-storage system can be the best option, as a smaller CHP storage is already existing, and the solar thermal system can simply be installed in parallel. If a new system is going to be implemented, the one-storage system should be installed as it is easier to control and only one storage is needed which reduces the investment. Furthermore, it is shown that the CHP operation can benefit of a large solar storage by reducing the starts and stops throughout the year which reduces the maintenance costs and extends the lifetime. The analysis of the CHP control highlights that the CHP should not be allowed to heat up the entire solar storage as this reduces the solar yield significantly from a certain point. These results can also be transferred to the combination of solar heating plants with other technologies such as biomass or heat pumps which must and can be operated more flexible compared to solar heating plants.

7. Acknowledgments

The authors gratefully acknowledge the financial support provided by the German Federal Ministry for Economics and Climate Action for the projects AnanaS (03ETW014A).

8. References

Association of German Engineers, 2020. Solar thermal process heat. Beuth Verlag GmbH, Berlin 27.160.

Jesper, M., Pag, F., Vajen, K., Jordan, U., 2021. Annual Industrial and Commercial Heat Load Profiles. Modeling Based on k-Means Clustering and Regression Analysis. Energy Conversion and Management: X 10 (3), 100085. https://doi.org/10.1016/j.ecmx.2021.100085

Klein, S.e.a., 2017. TRNSYS 18: A Transient System Simulation Program. Solar Energy Laboratory, University of Wisconsin, Madison, USA.

Pag, F., Jesper, M., Kusyy, O., Vajen, K., Jordan, U., 2022. Solar fractions of SHIP plants considering the availability of roof area based on OpenStreetMap data. Solar Energy Advances (2). https://doi.org/10.1016/j.seja.2022.100017

Techno-economic comparative analysis of solar thermal collectors and high-temperature heat pumps for industrial steam generation

Puneet Saini [a,b,c], Mohammed Ghasemi[b], Cordin Arpagaus[d], Frédéric Bless[d], Stefan Bertsch[d], Xingxing Zhang[b].

[a] Absolicon solar collectors AB, Fiskaregatan 11, Härnösand, Sweden. 87133.
[b] Department of Energy and community buildings, Dalarna University, Sweden.
[c] Department of Engineering Sciences, Civil Engineering and Built environment, Uppsala University, Sweden.
[d] Eastern Switzerland University of Applied Sciences, Institute for Energy Systems, Werdenbergstrasse 4, 9471 Buchs, Switzerland
*Corresponding author. Email address: puneet@absolicon.com, pks@du.se. Phone: +46(0)700264251.

Abstract

Industrial heat production is responsible for around 20% of total greenhouse gas emissions in Europe. To achieve the climate change goals defined in the Paris Climate Agreement, the EU commission has shifted its focus on sustainable means to generate heating. Moreover, global dependencies are leading to a re-organization of natural gas supplies. Therefore, there is a need for less vulnerable and less price volatile solutions for heating. This paper focuses on two decarbonization technologies for industrial process heat supply: (a) electricity-driven steam-generating high-temperature heat pumps (HTHP), a technology that is more efficient than fossil fuel boilers in generating steam, and (b) solar parabolic trough collector (PTC), which can produce heat economically and at a minimal carbon footprint compared to other technologies. The main aim of this paper is to evaluate the levelized cost of heat (LCOH) of these technologies to fulfill a comparative techno-economic analysis. A maximum PTC collector's solar fraction limit is defined to indicate when the LCOH for these two technologies is equal. This limit allows distinguishing between the economic stronghold of each technology. The evaluation is carried out through the annual energy simulations using TRNSYS and Excel spreadsheets for HTHPs, while TRNSED and OCTAVE are used for the solar thermal part. Boundary conditions for European geographical constraints have been applied to establish use cases for the analysis. The result shows that the design of a PTC system with optimal SF can reach cost parity with HTHP for most of the analyzed locations. The developed methodology serves as a valuable guide to quickly determine a preferred lower carbon heat solution, thus easing the decision-making for industries.

Keywords: High-Temperature Heat Pump; Parabolic Trough Collector; Solar Fraction; Techno-economic analysis

1. Introduction

"Heat is half" of the global primary energy consumption, while the other half is due to energy use in transport and electricity sector [1]. The generation of heat from various fuel sources results in nearly 40% of the global CO2 emissions. Therefore, the decarbonization of the heating supply is the "elephant in the room" and needs significant attention from policymakers to promote the right technological solution to facilitate the rapid replacement of gas, coal, and other fossil fuels. Heat is consumed in buildings for space heating, domestic hot water, and industries to generate steam or hot water. The major focus regarding technical solutions for clean heating is often on electrification using electrical heaters or heat pumps (HPs). Residential heating demand can be decarbonized using commercial HPs, and their significance is further emphasized in Repower EU, which aims to deploy 60 million HPs by 2030, a projected 4 fold increase from current numbers [2].

It is important to note that industrial process heating demand constitutes 66% of the EU's overall heating demand [3]. In addition, the concepts of positive energy district (PED) and climate-neutral city are promising nowadays, but they have not yet included industrial heating demand within their boundaries. With the ongoing challenges in gas supply, natural gas prices have increased exponentially in the past few years, thus creating an energy-tense situation in the EU [4]. This implies that a less price volatile and reliable supply of fuels for industrial process

© 2022. The Authors. Published by International Solar Energy Society
Selection and/or peer review under responsibility of Scientific Committee
doi:10.18086/eurosun.2022.05.10 Available at http://proceedings.ises.org

heat should be prioritized. The process heat required in most industries is in the medium temperature range (i.e., 80 to 250 °C). Several technologies in the market can achieve this temperature with low carbon emissions, such as solar thermal (ST) collectors, high-temperature heat pumps (HTHP), and boilers utilizing green fuels such as waste biomass or biogas, or renewable electricity.

Industries typically use fossil fuel boilers to generate steam, which is used as a heat transfer fluid to carry out several processes. Retrofitting any new technology in an existing boiler system requires a detailed understanding of system boundary conditions. Therefore, economic feasibility is a crucial decisive criterion for industries to evaluate any technology. From market experience, it is realized that large multinationals can facilitate the capital expenditure (CAPEX) for an efficiency improvement process (such as the implementation of ST, HTHP) only if the payback is attractive (typical expectation is less than 5 years).

An indicative pre-feasibility assessment using economic key performance indicators (KPIs) can facilitate industries toward quick decision-making for a go/no-go decision concerning a detailed evaluation of any technology. Therefore, this paper is themed around doing a comparative techno-economic analysis for heat generation using typical boundary conditions encountered in industries. The focus is on two specific technologies to generate steam, i.e., (a) electricity-driven steam-generating HTHPs and (b) solar-powered parabolic trough collectors (PTC), which is a type of concentrating ST collector.

2. Objectives

The central objective of this paper is a comparative analysis of both HTHP and PTC systems for steam applications using industrial boundary conditions. Previous studies have performed a general feasibility analysis for solar thermal technologies or HPs. However, only a few have investigated comparing these technologies on a large spatial scale with techno-economic boundaries. Moreover, there is a lack of studies comparing HTHP for the steam generation with PTC-based collectors.

Perez et. al compared the techno-economic performance of 3 types of ST collectors, and photovoltaic powered heat pumps [5]. The methodology used to compare ST and PV systems is based on the calculation of the levelized cost of energy and greenhouse gas emissions. However, only a residential heat pump with maximum temperature upto 60 ºC is considered without dynamic modelling, and the ramping up of temperature upto set point is done by resistance heater. Neyer et. al compared the techno-economic assessment by comparing an air/water heat pump with photovoltaic and solar thermal, to support for a small multifamily house located in Madrid [6]. However, the results are restricted to residential temperature range, and does not apply for industrial sectors. A similar study concluded that a hybrid system of solar thermal collector with Natural gas boiler is competitive to air source HP system, with boundary conditions applied to residential buildings in Europe [7]. There is a lack of studies dealing for decarbonising heating technologies for industries, specifically comparing HTHP for the steam generation with PTC-based collectors. The most relevant work to the current paper is by [8], where the authors have developed a techno-economic comparison methodology using maximum turn-key solar investment as an indicator. This methodology can be used as a criterion to quickly compare and select between solar thermal and heat pumps based on boundary conditions. However, even the study did not consider the effect of SF on LCOH. This variation is critical to consider while comparing technologies, especially with high-temperature solar thermal, due to the lack of steam storage technologies. The LCOH of the ST system increases exponentially after a threshold SF due to the diminishing added value of heat storage. Therefore, when comparing other technologies with ST, the SF is a critical criterion to define and is not considered in previous studies. The current paper has overcome the limitations by using comprehensive variables as a comparison basis for both HTHP and ST. The paper also considers updated analysis from a techno-economic perspective capturing the recent development in PTC and HTHP while considering the effects of improved efficiency and cost reductions. The next sections provide an overview of research methodology

3. Research methodology

This study aims to assess the energy and economic performances of industrial PTC and HTHP in the context of the European climates. Figure 1 shows the flow chart of the methodology used for analysis. First, the evaluation

is carried out through annual energy simulations performed with dynamic simulation software. After this, a systematic approach is followed to provide the reader with the information needed to understand the results. . The analysis is carried out for 3 different load profiles with constant peak demand to capture a broad range of industrial load conditions. The geographical focus for simulations is limited to Europe. However, the results obtained are parametrized to direct normal irradiation (DNI) and can be used to assess the performance for any given location.

In Step 1, simulations for HTHP are conducted using TRNSYS for given load profiles to calculate the COP and thermal output. The outputs are based on a performance map obtained from an HTHP supplier (ref) for a broad range of operating conditions.
In Step 2, dynamic simulations for PTC collectors are done. The product chosen for this study is restricted to a PTC manufactured by a Swedish company named Absolicon solar collector AB [9]. The product is designed for industrial applications and fits this study well.
Simulation of the PTC system is done in two sub-steps. The component performance is analysed using TRNSED, and the system performance is simulated using the developed model in OCTAVE. Storage sizing optimization obtains each location's SF vs. LCOH curve. The LCOH calculations for ST and HTHP are done using a developed model in Excel.
Finally, in Step 3, based on the results obtained, the LCOH of both technologies is compared to provide boundary conditions to identify the strong economic hold of each technology. An indicator SF_{limit} is introduced to distinguish the economic advantage and to generalize the results.



Figure 1 Flow chart for the methodology used for this study

4. Boundary conditions

4.1 Load profiles and heating demand

The heat demand in the industries depends on the process characteristics and varies, which is difficult to capture by one study. However, the selection of load profiles to represent a significant share of industries is the focus of this paper. Three different load demand profiles are considered for the analysis. The peak heat demand is fixed at 500 kW_{th} (steam flow of 0.8 tonnes per hour), typical of many process industries. As ST and HTHP are subjected to the same load constraints, the comparative results are not affected by the selection of peak load value. The steam demand is assumed at a constant temperature of 140 °C (saturation pressure 3.7 bar_a). The steam temperature range is commonly used in many food processing industries and fits well with temperature constraints for both medium-scale PTC and HTHP products.

The 3 chosen load profiles are explained as follows:

- **Continuous demand**: Uniform demand throughout the year with 8760 annual operational hours, which results in annual heat demand of 4380 MWh/year. Such load profiles are prevalent in many large production factories, such as the pharmaceutical sector.
- **Weekday demand**: Uniform demand throughout the weekdays of the year (no operation during the weekend). The annual heat demand for this case is 3132 GWh/year, corresponding to real cases in industrial load. An example of this load variation can be found in the food and beverage sector.
- **Daytime demand**: Uniform demand only during the day (10 hours per day starting 8:00 to 18:00 for whole week), resulting in an annual heat load of 1825 GWh/year. This load profile is typical for a small/medium production facility.

A summary of the considered load profile cases for simulations is shown in Table 1.

Table 1 Summary of the load profiles considered for simulations

Load profile	Nos of operational days per year	Operational days per week	Operational hours per day	Peak Power [kW]	Annual heating load [GWh]	Time
1	365	7	24	500	4.38	24*7*365
2	261	5	24	500	3.13	24*5
3	365	7	10	500	1.82	8:00 to 18:00 each day

Weekly variation for considered load profiles is shown in 2 . The presented week pattern is repeated for a whole year to obtain the annual heat demand.

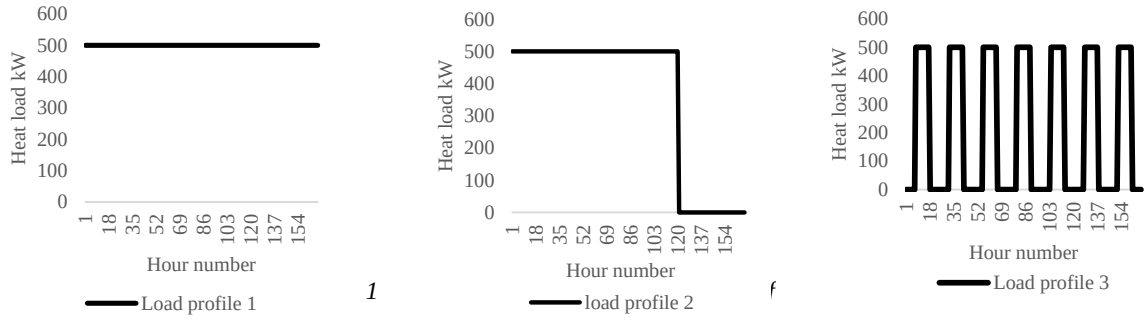

Figure 2 Weekly variation of different load profiles considered for the analysis.

4.2 HTHP boundaries

The HTHP is designed for peak heating capacity in this study. Therefore, it is considered the sole heat source for the energy system without any backup boiler. On the source side, the available wastewater stream is considered

at the inlet, which transfers heat to the HP refrigerant and exits at a lower temperature depending on the temperature glide. On the sink side, the feed water stream enters the inlet and receives heat from HP to convert to steam, which is fed to the process line. A commercial HTHP (Kobelco model 165) capable of generating steam at a maximum temperature of 165 °C is used to meet the steam requirement [10]. The HP used for this study can produce steam up to maximum temperature and pressure of 165 °C and 0.8 MPa-gauge, respectively. The applied refrigerant in this HP is a mixture of R134a and R245fa. The HP utilizes a semi-hermetic inverter twin screw compressor. The rated COP of the modelled HTHP is 2.5, specified at source and sink temperatures of 70 °C and 165 °C, respectively. A performance map based on data from the commercial HTHP is used to calculate the electricity consumption. The performance map consists of the COP of the HTHP for various temperature lifts, as shown in the Figure 3. The temperature lift represents the difference between the fluid temperature at the heat source inlet and the heat sink outlet. The HP has a variable speed capacity to operate at the part load conditions. The electrical consumption derived from the annual simulations is then used to calculate the LCOH.

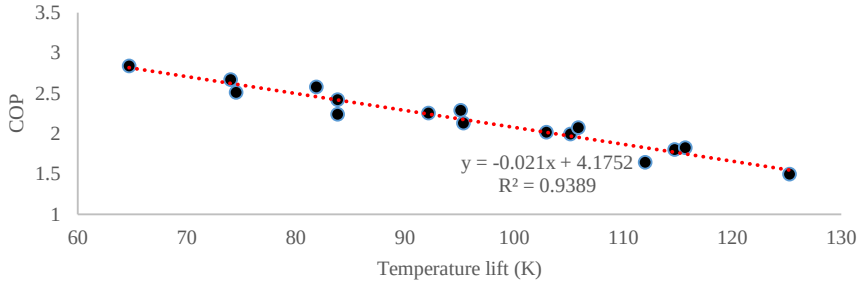

Figure 3 Variation of HP COP with temperature lift

The source for the HP evaporator is considered a wastewater stream with a fixed temperature of 40 °C, available throughout the year. A temperature glide of 6 °C is considered on the evaporator. The resulting temperature lift of the HTHP is 100 °C , corresponding to steam temperature of 140 °C. The feedwater temperature entering the HTHP arrives at 110 °C, resulting in a 30 °C temperature difference on the heat sink side. The flow rate in the source and sink are varied to obtain the designed temperature glide and thermal capacity, respectively. The HP is designed for peak heating demand of 500 kW; the specifications are shown in Table 2.

Table 2 *Specifications of HP considered in this study* [34].

Parameter	*Value*
Compressor	Semi-Hermetic Inverter Twin Screw
Refrigerant	Mixture of HFC134a & HFC245fa
Dimensions [mm]	W4400 H3180 L2810
Weight [kg]	7090
Heating capacity[t/h] @0.6MPaG, source 70°C	0.839 @20°C supply
Power [kW] @0.6MPaG, source 70°C	253.9
Heating COP@0.6MPaG, source 70°C	2.5

Economic inputs for HTHP

For the HP LCOH, it is necessary to include various costs. The analysis is done for 3 different capital expenditures (CAPEX) of 500, 1000, 1500 Euro/kW_{th} values derived from data based on implemented HTHP case studies [11]. The operational costs for HTHP consider the electricity to run the HP compressor and fluid pumps. The operation and maintenance (O&M) costs for HTHP are usually higher than those for boilers and are set to 5% of CAPEX value. The relevant parameters for HTHP thermo-economic modelling are shown in the Table 3. The LCOH of both HTHP and PTC systems are compared for time horizon of 15 years. The period is chosen to reflect the suitable timeline considered by various multinational companies for energy related investments. Three different electricity prices are chosen for analysis considering the range of industrial electricity tariffs in EU.

Table 3 Assumptions regarded in HTHP simulations

Parameter	*Abbreviation*	*Value*	*Units*
System degradation rate	SD	0.5	%

Capital expenditure	CAPEX	500/1000/1500	Euro/kW_{th}	
O&M cost	$EX_{o\&M}$	5	%	of CAPEX
HP lifetime		15	Years	
LCOH analysis period		15	Years	

For sensitivity analysis of LCOH, a total of 27 cases are analyzed, accounting for 3 different values of three variables (i.e., CAPEX, electricity price, and load profiles). The values of these variables are shown in Table 4.

Table 4 Different scenarios for the variables used in HTHP LCOH calculations.

Description	*Abbreviation*	*Case 1*	*Case 2*	*Case 3*
HP CAPEX [Euro/kW_{th}]	CAP	500	1000	1500
Electricity Price [Euro/MWh]	ELP	70	100	150
Load Profile [h/year]	LPR	8760	6264	3650

4.3 Solar thermal collector simulations

3.3.1 PTC product description

The ST product considered for analysis is a PTC collector manufactured by the Swedish company Absolicon solar AB. The product T160 is a concentrating parabolic trough collector that focuses direct solar irradiance onto an absorber tube that runs along the focal line of the concentrator and contains a working fluid that gets heated when solar radiation is concentrated on it. The collector works on single axis tracking using the astronomical watch which tracks the solar collectors so they always face the sun. The product can generate steam and hot water from 60 °C to 160 °C, and is therefore suitable for many industrial sectors (e.g dairy, brewery, chemical etc). The collector can be categorized as a small PTC type and is certified by solar Keymark. The optical efficiency of the collector is 76.6 % based on aperture area. The key technical specifications of the collector are shown in Table 5. The main components of a collector consist of:

- Reflector, which reflects the incoming radiation onto the receiver.
- The receiver tube absorbs reflected radiation and converts it into heat; this heat is then dissipated by the agent fluid that is pumped through the receiver tube
- The protective glass avoids heat losses and protects the collector from dust, snow etc.

Table 5 Key technical specifications of T160 PTC collector

Item	*Description*
Collector type	Glass-covered PTC with one-axis tracking
Recommended heat transfer fluid	Water. Propylene Glycol (max 40%)
volume of heat transfer fluid in receiver tube[Liter]	2.2
Operational temperature [°C]	60 to 160
Stagnation temperature [°C]	460
Maximum operating pressure[bar]	16
Receiver	Stainless steel, optically selective coating
Glass	4mm hardened glass, anti reflective coating
Reflector	Polymer embedded silver on steel sheet
Weight [kg]	148

3.3.2 Collector integration in the system

The overall system is divided into 2 circuits. The pressurized water stays in a closed loop called the solar loop, or primary loop. Pressurized water is warmed up by circulating in the solar collectors and is later cooled down through the heat exchanger, which has its secondary side connected with a steam separator. The steam separator is a vessel which contains a mixture of steam and hot water. When the required pressure is reached in the vessel, the steam will be sent to the customer's main steam line.

The generated steam is separated from the remaining saturated liquid in the steam separator, and it has priority over the boilers-generated steam due to small overpressure. Its primary use is maintained high by the small

overheating. The saturated liquid separated from the steam in the steam separator is mixed with the incoming water from the deaerator and recirculated to the steam heat exchanger. The separation of steam and water (that occurs by gravity) creates inside the steam separator two regions (one of steam and one of liquid at nearly the same temperature), the volumes of which can fluctuate and absorb small power surges or reductions
The system arrangement considers PTC collector fields with a storage system to generate steam at 140 °C with feedwater temperature at 110 °C, same as considered for HTHP. Whenever solar production exceeds the demand, heat is diverted to thermal storage. The storage system is considered a pressurized tank using water as a storage media. When the storge is fully charged, the water Is heated to a maximum temperature of 160 °C. After discharging, the tank is cooled down, corresponding to the bottom temperature in the steam separator (approximately 140 °C). This results in an effective temperature difference of 20 °C In the thermal storage between charging and discharging.

3.3.3 Modelling of PTC system

A dynamic simulation of the collector performance was carried out for a statistically normal year based on climate data from Meteonorm using time step of 15 minutes. Simulations are based on the Solar Keymark ISO 9806 collector parameters of the Absolicon T160.
The simulation approach for PTC is based on 2 steps. In the first step, the collector is modelled without interacting with the heating load. This can be considered as if the collector operates under infinite load, and thus all the heat generated by the collector is fully utilized. The simulations are done using TRNSED, which is an add-on to TRNSYS. The collector performance parameters based on the aperture area used in the TRNSED are shown in Table 6.

Table 6 Input Performance characteristics of T160 collector used for model [29]

Parameter	Value
Optical efficiency	76.6 %
a_1 [W/m^{2}K]	0.368
a_2 [W/m^{2}K^2]	0.00322
K_d [-]	0.120
β, tilt [°]	Single-axis tracking E-W
γ, azimuth [°]*	0

3.3.5 Economic boundaries & geographical inputs

The data for PTC economic analysis includes the capital and O&M cost. The economic input values are based on data collected from the PTC manufacturer as shown in Table 7.

Table 7 Assumptions regarded in PTC T160 simulations

Item	*Symbol*	*Value*	*Unit*	*Remarks*
Capital expenditure	CAPEX	350	Euro/m^2	Represents the installed cost
O&M cost	$EX_{O\&M}$	0.1	%	% of CAPEX
Solar collector lifetime		25	Years	
LCOH evaluation period		15	Years	
System degradation rate	SD	0.1	%	

The simulation for PTC is done for various locations in Europe, as shown in 4. If the country's direct normal irradiance (DNI) is spatially uniform, then one city from each country is used for simulations. However, some of European countries (for e.g France, Italy and Germany), have a significant variation of DNI. Therefore, multiple cities within the same country are selected for better representation. The LCOH results of PTC for each country would be compared with the LCOH of HTHP to determine the solar fraction threshold below which ST is more economically attractive than HTHP.



Figure 4 Map representing the various locations used for PTC simulations

4. Results

4.1 HTHP simulation results

Table 8 shows the results for LCOH calculations for HTHP for 27 simulated scenarios representing variation in the load profiles, investment cost, and electricity price. For any specific load profile, the CAP1-ELP1 represents the LCOH of HTHP assuming capex 1 (500 €/kWth), and Electricity prices 1 (70 €/MWhe), as shown previously in Table 4. The results show that the LCOH of HTHP varies from 45-130 €/MWh for the simulated scenarios. The minimum LCOH (45 €/MWh) is obtained for the lowest CAPEX and ELP values in LPR1, when the HTHP is utilised throughout the year. For the same CAP and ELP combination, LCOH increases while moving from LPR1 to LPR3 due to decreasing operational hours. Furthermore, for the same CAP value and any load profile, the LCOH increase with a higher electricity process (when moving from ELP 1 to ELP 3).

Case	HP CAPEX EUR/kW	Electricity price EUR/MWh	*LCOH of HTHP (Euros/MWh)*		
			Load profile 1 LPR.1 8'760 h/a	Load profile 2 LPR.2 6'264 h/a	Load profile 3 LPR.3 3'650 h/a
CAP.1-ELP.1	500	70	45	49	58
CAP.1-ELP.2	500	70	59	63	73
CAP.1-ELP.3	500	70	84	88	98
CAP.2-ELP.1	1'000	100	51	58	75
CAP.2-ELP.2	1'000	100	66	73	89
CAP.2-ELP.3	1'000	100	91	98	114
CAP.3-ELP.1	1'500	150	58	67	91
CAP.3-ELP.2	1'500	150	73	82	106
CAP.3-ELP.3	1'500	150	98	107	130

4.2 PTC simulation results

The results from PTC simulations suggest that LCOH has higher variation than HTHP. The reason can be attributed to a wide range of solar irradiation variations across simulated European locations. Furthermore, the LCOH also varies with solar fraction for any specific location. The range of LCOH obtained from PTC varies from 28 to 160 €/MWh. The lowest LCOH is obtained for high DNI regions (for example, cities in Spain, Portugal and Southern Italy), and at a lower solar fraction. Figure 5 shows the variation of LCOH for PTC collectors at 3

different solar fractions (5%, 25%, and 50%) and for LPR1 (8'760 h/a) using all simulated locations. There is decreasing trend of LCOH with increasing DNI due to high collector output. Furthermore, for the same DNI, the LCOH increases with increase in solar fraction due to lower utilisation of heat.

It is also important to consider that LCOH not only depends on the absolute annual DNI value, but also on the temporal variation. The high temporal variation makes it difficult to achieve large SF due to large tank volume needed, thus increasing the LCOH. This can be seen by comparing the 2 data points in 5 at 50 % SF (compared data points are marked black border). These 2 locations have nearly the same annual DNI value of around 1500 kWh/m^2. However, the LCOH for one location is much higher (147 €/MWh) compared to the other location (75 €/MWh).

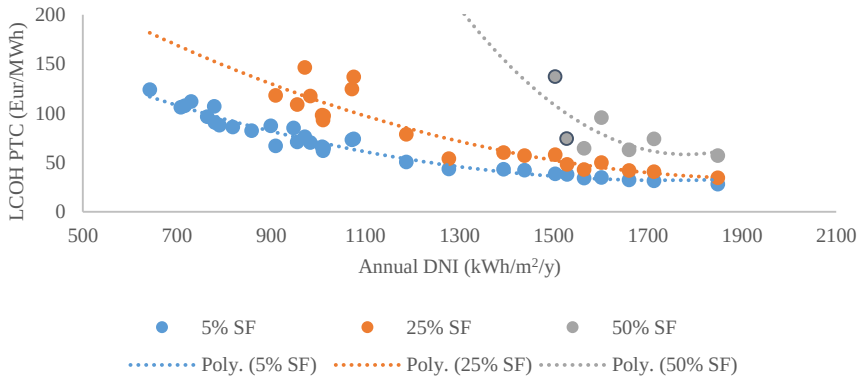

Figure 5 Variation of LCOH with SF for all locations at 3 different solar fractions and load profile 1 (8760 h/a)

The range of PTC LCOH for all 3 load profiles is shown in Figure 6. Results indicate that load profile 3 has the lowest LCOH at high solar fraction (50 %), due to high coincidence in solar irradiation and load demand. LPR2 has the highest LCOH at any SF. This is due to the lack of heating load during the weekend in LPR2, which results in high storage volume or heat spillage from the collectors.

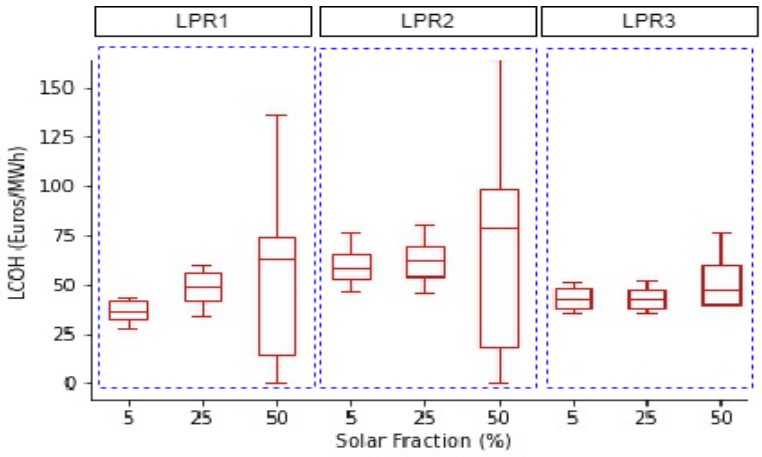

Figure 6 Range of PTC LCOH for 3 load profiles and 3 different solar fractions for all simulated locations

Based on the analysis in section above sections , the values of SF_{limit} for all simulated cases is quantified, and normalised to DNI as shown in Figure 7.

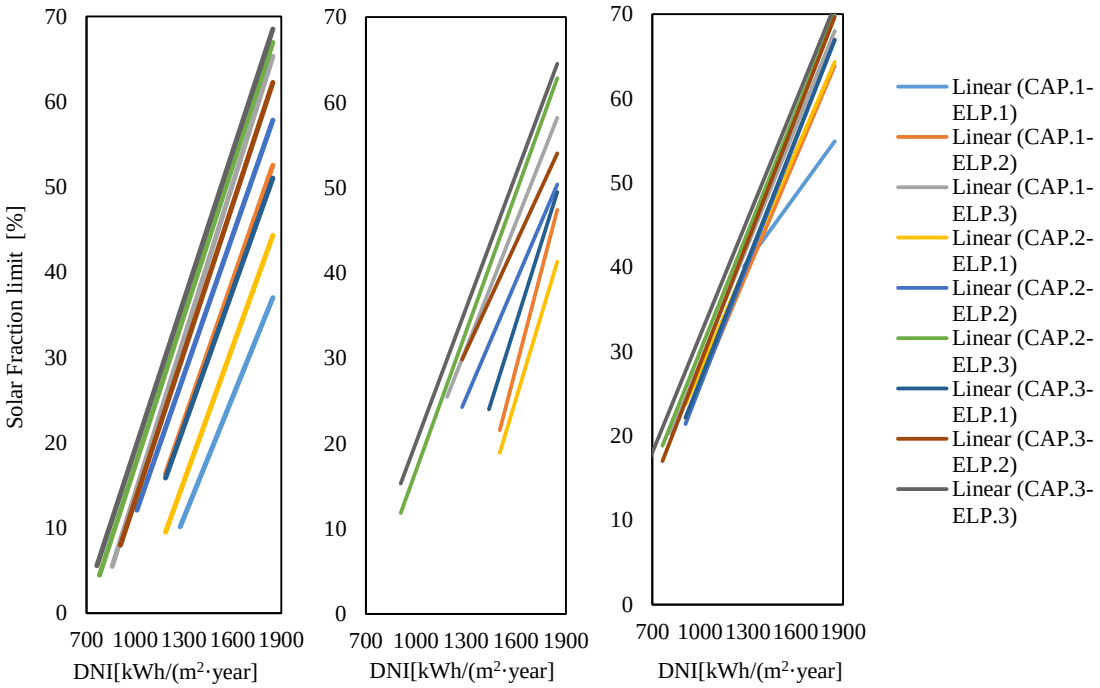

Figure 7 Variation of SF_{limit} with DNI for LPR.1 (left), LPR.2 (middle), and LPR.3 (right)

In high DNI regions (1'500 to 2'000 kWh/m^2), the average SF_{limit} varies from 25 % to 55 %, indicating that ST technologies are a cheaper way of reducing the emission by at least 1/4th. In such regions, the demand up to 55% can be met by solar thermal collectors at economical LCOH if the load profiles are favourable (LPR3). In medium DNI regions (1'001 to 1'499 kWh/m^2), SF_{limit} varies from 15 % to 30 %, lower than the high DNI regions. If the boundaries favor HTHP (low CAPEX, low electricity price, and high operational hours), the DNI at any location must be higher than 1200 kWh/m^2 for PTC to compete. In low DNI regions (500 to 999 kWh/m^2), the maximum SF_{limit} obtained is 10 %. In such regions, HTHP is cheaper than PTC for low and medium CAPEX/el price value. However, if the electricity and CAPEX are high, PTC can compete with HTHP at a minimum DNI of 764 kWh/m^2.

Comparing the results for different load profiles, there is an increasing trend of SF_{limit} with increasing DNI when moving from LPR.1 to LPR.3, indicating better economic results for PTC. When the consumption and production have high coincidence for example in LPR.3, there is a small need for storage, which would result in lower LCOH for PTC collector, and therefore higher value of SF limit can be seen. For all load profiles, Higher SF_{limit} can be obtained for high DNI locations, due to high thermal output of the collectors. In LPR 3, a SF_{limit} can be obtained even for low DNI (764 kWh/m^2) due to favourable match in DNI and load. Such figures can be used to do a quick cost feasibility analysis for both ST and HTHP, and can be very useful tool for designers.

5. Conclusions

This paper compares the techno-economic aspects of HTHPs and PTC collectors for various industrial boundary conditions for 3 load profiles. The focus is on steam generation at 140 °C (3.6 bar_a), commonly used in many process heating industries. The characteristics of commercial HTHP and PTC products are used as input in the simulation model to obtain energetic results. For LCOH calculation, an excel model is used. Finally, results are generalized using SF_{limit} as an indicator to distinguish the economic advantage of each technology.

The major conclusions of the study are as follows:

- The LCOH of HTHP for the analyzed boundary conditions ranges from 45 to 130 €MWh. There is a clear trend of increasing LCOH with higher electricity prices and specific CAPEX costs. As the HTHP was sized for a peak load capacity of 500 kW, the total CAPEX is the same for all 3 load profiles. However, the LCOH can be lowered by operating the HTHP for more hours. Therefore, the LCOH in scenario LPR1 is always lower than in LPR2 and LPR3 for the same cost of electricity prices.

- The least obtained LCOH comes from the PTC collector for high DNI regions and low solar fractions. If the meteorological conditions are suitable, PTC is a cheaper alternative to generate steam compared to HTHP. The LCOH range obtained from PTC simulations is 28 to 160 €/MWh up to 50% SF. Lower values of LCOH can be observed for high DNI regions and vice versa. High DNI regions are, for example, Spain, Portugal, and Southern Italy. Furthermore, LCOH has an increasing variation with SF. The SF-LCOH curve is not dependent on the absolute DNI but on the distribution of the DNI on a temporal basis, which decides the storage volume needed to increase the SF.

- As the LCOH increases with SF, an SF_{limit} exists when producing heat from ST gets expensive compared to HTHP. This limit is higher for high DNI regions and lower for low DNI regions. The limit increases with higher ELP and CAP for the HP. In low CAPEX and electricity cost situations for an HTHP, a threshold DNI of 764 kWh/m^2 is needed for PTC to produce heat at a cheaper rate. In the high CAPEX scenario, this threshold DNI changes to 1'200 kWh/m^2, and the average SF limit varies from 25% to 55%. In high DNI locations (1’500 to 2’000 kWh/m^2), 15% to 30% for medium DNI (1’001 to 1’499 kWh/m^2), and 0% to 10% for low DNI locations (0 to 999 kWh/m^2).

- Industry segment has high synergies if it is considered in PED concept, while both HTHP and PTC can be the key technologies for a fully decarbonised urban energy system.

References

[1] "Heating – Analysis - IEA." [Online]. Available: https://www.iea.org/reports/heating. [Accessed: 14-Aug-2022].

[2] "Article - EHPA." [Online]. Available: https://www.ehpa.org/about/news/article/repowereu-heat-pump-strategy-required-to-help-sector-deliver/. [Accessed: 14-Aug-2022].

[3] "Heating and cooling." [Online]. Available: https://energy.ec.europa.eu/topics/energy-efficiency/heating-and-cooling_en. [Accessed: 14-Aug-2022].

[4] L. Cebotari, "EU-Russia energy relations: problems and perspectives," *Proc. Int. Conf. Bus. Excell.*, vol. 16, no. 1, pp. 1001–1014, Aug. 2022.

[5] E. Pérez-Aparicio, I. Lillo-Bravo, S. Moreno-Tejera, and M. Silva-Pérez, “Economical and environmental analysis of thermal and photovoltaic solar energy as source of heat for industrial processes,” AIP Conf. Proc., vol. 1850, no. 1, p. 180005, Jun. 2017.

[6] D. Neyer, M. Ostheimer, C. Dipasquale, and R. Köll, “Technical and economic assessment of solar heating and cooling – Methodology and examples of IEA SHC Task 53,” Sol. Energy, vol. 172, pp. 90– 101, Sep. 2018.

[7] S. Alberici et al., “Subsidies and costs of EU energy Final report,” 2014.

[8] “IEA SHC || Task 64 || Solar Process Heat.” [Online]. Available: https://task64.iea-shc.org/. [Accessed: 14-Aug-2022].

[9] "Absolicon - Production Line for T160 concentrating solar collector." [Online]. Available: https://www.absolicon.com/. [Accessed: 14-Aug-2022].

[10] "Standard Compressors/ KOBELCO COMPRESSORS CORPORATION | KOBELCO Kobe Steel,. Ltd." [Online]. Available: https://www.kobelco.co.jp/english/products/standard_compressors/. [Accessed: 14-Aug-2022].

[11] "HTHP Symposium 2022." [Online]. Available: https://hthp-symposium.org/hthp-symposium-2022/. [Accessed: 14-Aug-2022].

Upgradation of Khoa Production method in Manchar, India using Solar Powered System

Swanand Tadlimbekar[1], Dr. Herena Torio[2]

[1] Masters Student, University of Oldenburg, Oldenburg (Germany)

[2] University of Oldenburg, Oldenburg (Germany)

Abstract

India is one of the largest milk producers and converts 50-55% of the produce into milk products and sweets. One of the base milk products in Indian sweets in *Khoa*, which is traditionally produced locally in an open pan heated by burning firewood. This manuscript aims to replicate the *khoa* production facility of Mahesh Khawa Kendra (MKK) to simulate and cater the heat requirement of temperatures using solar thermal energy and replace the existing wood-fired boiler setup. The storage based evacuated tube solar collector model is simulated using MATLAB Simulink CARNOT Toolbox supported by designing procedure and critical assumptions. The simulation results performed are analyzed on monthly and annual basis and monitored through performance parameters like solar fraction, fractional energy savings, collector field efficiency, collector yield as well as utilizibility. The simulated results are promising to run the replicated system purely on solar energy with solar fraction of 1.06 of the annual operation and deliver average of 68% fractional energy savings.

Keywords: India, milk, khoa, solar, collector, fractional energy savings, solar fraction, utilizibility, CARNOT

1. Introduction

The world milk production is projected to increase by 175 million tons (23%) by 2024 when compared to the base years (2012-14), the majority of which (75%) is anticipated to come from developing countries, especially from Asia ('Dairy', 2015). Besides higher profitability, traditional dairy products have acquired an interest in large-scale production to meet consumer demands (Velpula, 2018). India ranks first among the world's milk producing nations since 1998 and has the largest bovine population in the world (*Solar Heat for Industry India*, 2020). About 50-55% of milk produced in India is converted into a variety of milk products through processes such as heat desiccation, heat acid coagulation and fermentation times (Velpula, 2018) .The thermal energy accounts for approximately 70% of the total energy needs in dairy value chains for processes like powering chilling and storage units, sterilization processes, spray drying, evaporation, pasteurization, and other processes (Greening the Indian Dairy Value Chain, 2019). Solar thermal systems can contribute enormously to driving various thermal processes in the dairy industry, which demand water temperatures at <120°C (*Solar Heat for Industry India*, 2020). Among all the milk-based products, this project focusses on Khoa. Khoa, one of the most important heat-desiccated products, is used as the base material for a large variety of sweet delicacies (Rasane, Beenu and Dey, 2015). About 600,000 metric tons of khoa is produced annually in Indian sub-continent, utilizing 7% of total milk production just in India (Rasane, Beenu and Dey, 2015).

1.1 Motivation

The first author of this manuscript likes to consume sweets on regular basis which led to curiosity in local sweetshop varieties and therefore, the local khoa manufacturing setups were explored near-by the city of Pune, Maharashtra India. In Manchar, three different khoa manufacturers were personally visited where firewood was the fuel to supply heat either to the khoa making pan directly or burning firewood to heat water, which in turn heats the milk using a steam/water jacket. The level of sophistication varied across manufacturers based on the investment made. Mahesh Khawa Kendra (MKK), located in Machar, Nashik Road, district Pune, is sophistically well equipped with wood-fired boiler and vertical open drum Scrap Surface Heat Exchanger (SSHE) machines for khoa manufacturing. The manufacturer openly discussed the ongoing problems regarding his woodfired boiler and related issues, and his willingness to shift to solar thermal technology as per feasibility. As a renewable energy

© 2022. The Authors. Published by International Solar Energy Society
Selection and/or peer review under responsibility of Scientific Committee
doi:10.18086/eurosun.2022.05.11 Available at http://proceedings.ises.org

enthusiast, personally, this was one of the big opportunities to work on an actual live project and potentially assess the transition of wood-fired boiler application to a partially or totally renewable energy-powered application. The core of this work is thus devoted to check the performance of a typical system and simulate the system components and based on the final performance, the design is finalized for khoa production process.



Fig. 1: Wood-fired boiler and firewood at Mahesh Khawa Kendra, Manchar, India (Source: Self-clicked) and Khoa making in-process in one of the khoa manufacturing machines (Source: Self-clicked)

2. Literature review

For finding relevant literature on the internet, renowned search engines, as well as scientific publishing literature platforms, were used, for example, Web of Science (*Web of Science*, no date), Scopus (*Scopus*, no date) and Google Scholar (*Google Scholar*, no date)along with the search portal provided by the University of Oldenburg, Orbis Plus (*ORBIS Plus Suchportal*, no date)

To segregate the results based on the target product to be produced, keywords like 'Khoa', 'Khoya', 'Khawa', 'Khava', 'Khowa', 'Khova', 'Mawa' were used to aim for literature for khoa production. To comply with the words used on the international level, additional keywords in the context of milk, like 'desiccated', 'dehydrated', 'dehydration', 'condensation', and 'condensed' were used as needed in sub-search options as needed. Not only these, the process of prolonged boiling milk to form khoa and the heat transfer processes involved were also included (for example, words like 'heat', 'transfer', 'convective').

2.1 Khoa

As per the Bureau of Indian Standards, IS:4883 (1980) states the definition of Khoa as followed: "KHOA (KHAVA, MAWA, and PALGHOA) refers to the milk product prepared by partial dehydration of milk by heating under controlled conditions" (BIS, 1980). It also states, "Buffalo's milk is usually preferred over cow's milk for KHOA production since the former gives greater yield and a more desirable body and texture". As per M. Hickey (2009), "Condensed milk (plain) – is defined as obtained by partial removal of water from milk to which sugar may have been added" (Hickey, 2009). Concentrated semi-dried milk Khoa is produced by prolonged boiling of milk in shallow pans and drying it to a total solid amount of about 70 percent through a process of rapid evaporation of its water content (Nandi, 2009).

2.2 Khoa Production temperatures

Mahesh Kumar (Kumar *et al.*, 2011; Kumar, Prakash and Kasana, 2012), did extensive research through his studies for Khoa production including pool boiling of milk to assess khoa production temperatures. For his study, Kumar et al. considered the temperature range 90-95°C for nucleate boiling. Another team (More, no date) also developed a steam jacketed semi-mechanized Khoa-making equipment that maintained the temperature in the range of 60-120°C which varied across the drum length to control the quality and texture of khoa produced. Working in association with the local sweetmeat production units, it was ascertained that the operating temperature required for the preparation of Khoa is in the range of 95°C to 101°C (Nandi, 2009). To support the above-mentioned arguments, the Fig. 2 from the Solar Heat for Industry India (2020) report determines different solar collector technologies, temperature ranges as well as the applications for which the technologies are selected. Pasteurization and subsequent khoa production are considered in applications under 150°C. For temperatures specifically in the range 100-150°C evacuated collectors are considered.

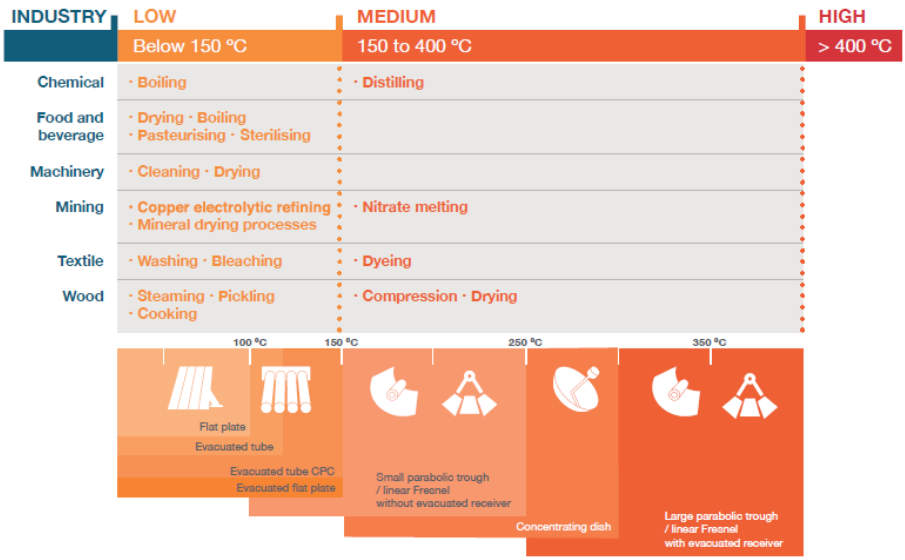

Fig. 2: Selection of different solar collector technologies as per temperature range and application requirement (*Solar Heat for Industry India*, 2020)

2.3 Khoa production using Solar Thermal Energy

With relevance to solar thermal energy, Chaudhary and Yadav, (2020) conducted a study using an evacuated tube solar collector to power a simultaneous two-staged cooking system for cooking rice and khoa production. They observed temperatures in the range of 76 to 132°C with an average solar intensity of 857.96 W/m^2. The khoa was produced successfully with moisture removal of up to 73%. Nandi (2009) demonstrated khoa production using a parabolic concentrator system with 50% efficiency which would achieve temperatures for khoa production as well as other sweetmeats. Rao and team (Rao *et al.*, 2020) did a study on the economic analysis of khoa production in an open pan (kadhai) which used 60 kg of firewood to produce 11.5 kg of khoa using 40 liters of milk. Other papers were also available that dealt with economic analysis, but the specific fuel consumption was not mentioned. The paper from Rao et. al. can be referred to as one of the processes using firewood as fuel to produce khoa.

3. Methodology

The existing setup comprises a wood-fired boiler with helical water heating coil, flue gas-based water preheater, electric motor, two khoa manufacturing open drum-type SSHEs, pumps, and motors. The reason behind using specific firewood, *Acacia nilotica*, locally also known as *Babool/Babul treewood*, has the highest calorific value of 6130 kcal/kg (Chakradhari and Patel, 2016) or 25.6 MJ/kg. At MKK, mainly three products are manufactured namely Khoa, Basundi, and Pedha. Khoa being the most temperature intensive, high demand and with a long duration of cycle time (on full heat supply), it is being targeted for this application. Benchmarking was performed for the existing setup according to working hours, cycle times, operational pressures and assuming temperatures from the literature for khoa production, i.e., 105°C. These are crucial for feeding the data as per setup to the model.

To model the system, MATLAB Simulink was used with the help of the CARNOT toolbox as an add-on. The toolbox comes with existing models and blocks modelled with the help of S-functions and experimentally validated operational parameters presented in validation files which are available on the CARNOT database as well as in the help section (*Verification of Models - CARNOT Toolbox manual*, no date). However, all the data points mentioned by default in the existing models are not in-line with the khoa production system to be modelled. Meaningful connections, operational parameters as well as user-defined inputs (author's) were made to obtain fruitful results.

An important assumption here for load calculations is the milk is being treated as a fluid (liquid) throughout the khoa production process. It is necessary because CARNOT treats all the fluids in the connections as liquids. If at any certain point in the connection the gaseous phase (or water + steam) phase exists, the simulation would terminate. To understand the limitations of the tool to be used for simulations as well as to adhere to the heating temperatures as per the literature, the load calculations are performed by treating milk as an emulsion fluid. The

khoa (milk fats) would be obtained simply by evaporation of water out of the emulsified mixture of milk. This is the reason the load calculations are not performed precisely based on energy demand as per products. Instead, the load calculations as per the load profile introduced will be calculated by CARNOT itself to eliminate any human ambiguity in the energy calculations.

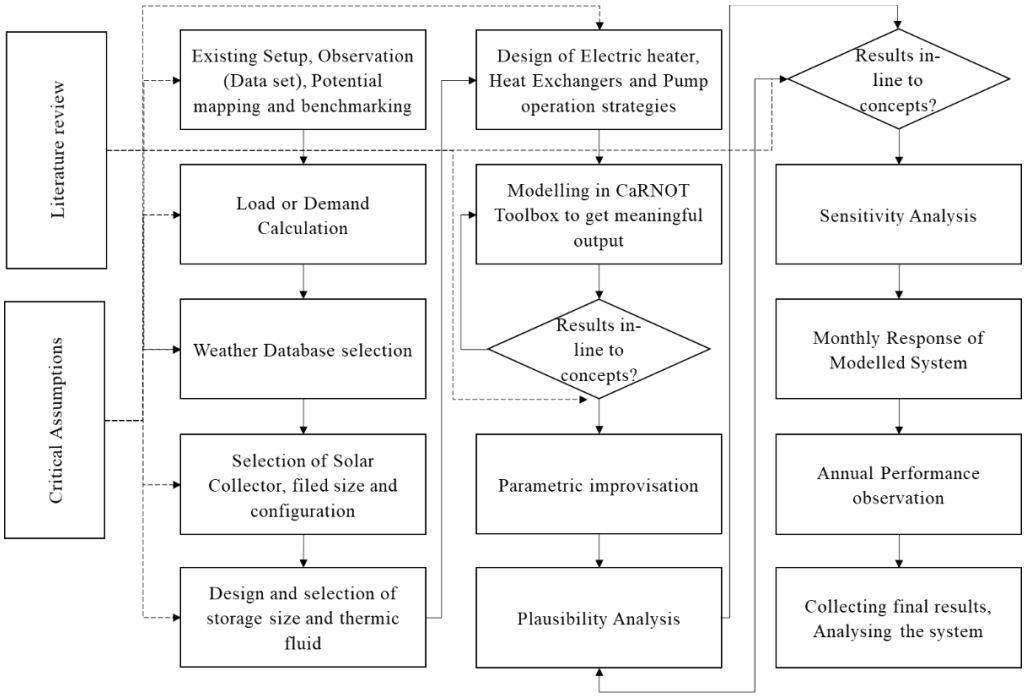

Fig. 3: Methodology flowchart of the steps for design procedure for the model supported by literature and critical assumptions (Source: Self derived)

Tab. 1: Load profile depicting the actual products used and the quantities

Parameter	Unit	Pasteurization	Khoa	Basundi	Pedha
Batches/vessel	40 liter Cans	9 (total)	5	2	2

The Weather Data Bus (WDB) in CARNOT processes the data in S-function and creates an input reference .mat file. Among all the datasets explored, the NREL NSRDB IDOC PSM v3 data (*NREL India Data*, no date) proved to be the most promising dataset available and averaged for 14 years from 2000 to 2014 and in line to the data demanded by the WDB. To avoid multiple changes in the tilt angle per year, JRC-PVGIS (*JRC PVGIS*, no date) suggests an optimum tilt angle that fits the best for seasonal variation. For the proposed system, although the location latitude is 18˚, the tilt angle suggested is 26˚. This has been fed to the WDB as well as in the model for solar collectors. The WDB averaged data also takes care of the seasonal variation in India with Summer, monsoons and winter roughly spanning across four months period each annually. To summarize, the WDB was fed for referring to the location coordinates of the khoa manufacturing facility (18.9828 N, 73.9446 W) with the optimized tilt angle of 26° facing to the south as provided from the JRC-PVGIS. The steps are summarized and represented in block diagram in Fig. 4.

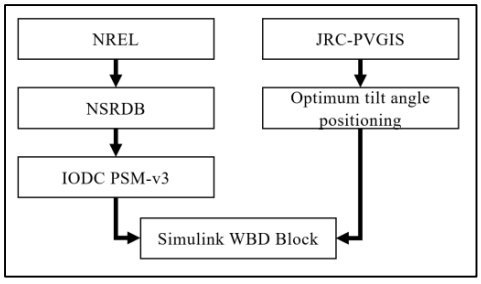

Fig. 4: Weather database source selection (Source: Self-derived)

For selection and adhering to the scientific details available for the collectors, evacuated tube solar collectors from Solflex (*Solflex Catalogue*, no date) make were used in this project. Before the solar collector field is sized, it is important to know how much solar radiation or solar energy is received at the location of MKK. This data was procured through an online portal developed by Solar GIS (*Solar Radiation Atlas*, no date), which could give a resolution of 10 km × 10 km. As per this source, MKK in Manchar receives GHI 1813.5 kWh/m^2/year. The sizing of the collector field is explained in Table 2.

Tab. 2: Calculations for collector field area and storage sizing

Parameter	Unit	Value	Storage size selection multiplying factor	Volume (m^3)
Annual demand	MWh/year	454.504		
Annual demand	kWh/year	454504.5		Selected as per Remmer (Torio, 2019)
Energy received at location (GHI)	kWh/year/m^2	1813.5		
Collector field area	m^2	250.62	As per Size (*150 lit)	37.59
Number of collectors	-	188.43		

As no guidelines are available for a storage-based khoa production system, the available literature for Domestic How Water (DHW) system was referred to and applied to the system design to simplify and justify the storage size selected. From guidelines provided by Remmer and Eicker (Torio, 2019) the storage size is parametrically obtained in liters as 150 times the collector field area calculated. The storage is assumed to lose heat/self-discharge only due to radiative losses from the side walls. This is supported by the assumption that the bottom of the standing cylindrical storage tank is in contact with the ground and zero radiative losses are expected from the base. And for the top of the cylindrical tank, it is assumed to have some air level at the top (not filling the tank completely). The dimensions of the tank are selected with a height to diameter ratio (H/D ratio) of a minimum of 2 to ensure enough stratification of hot and cold fluid inside the storage (Torio, 2019).

For effective heat transfer to take place on the primary and secondary sides, a heat transfer capacity of 505 W/K for each SSHE with 1.6 kg/s on the primary side and 0.069 kg/s on the secondary side resulted in effectiveness of 0.999 which is perfect for heat transfer. Accessorial components like load profiles for milk flow, water + glycol thermic fluid mixture, storage flow control in collector and khoa production loop were crucial for optimizing the flow to reduce unnecessary flow in components to reduce energy consumption, especially during non-sunny hours and night times. To get overview of all the steps followed in the methodology, please refer to the flowchart in Fig.3.

4. Results and discussions

For the system modelled, it is important for the components to align with the theoretical concepts to understand and meet the actual goals of the project. The plausibility analysis was performed, and the components behavior subjected to changing input conditions for a time scale of few days to two weeks depending on the component, temperatures achieved and on/off behavior as per load profiles. The simplified model is shown in Fig. 5.

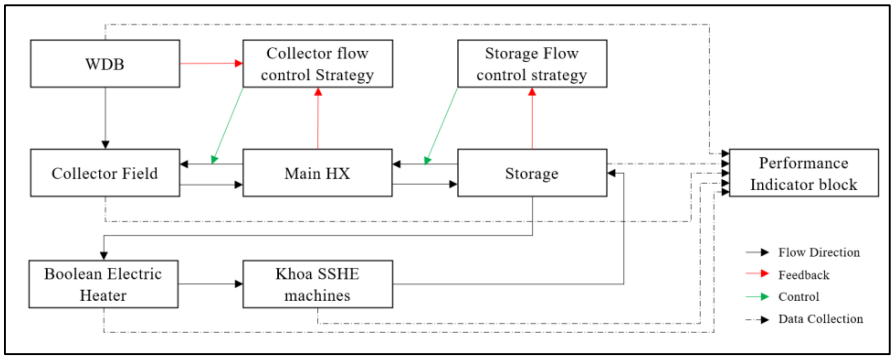

Fig. 5: Overview of the Simulink Model with components interacting among each other (Source: Self-derived)

The simulations performed were using sensitivity analysis as a tool to understand how the system is responding to the changes in system sizes as well as changes in input conditions. The response of the system is studied for a period of 60 days in such a way that on cold starting of the system, the storage can ramp up and achieve required

delivery temperatures for khoa production systems at the end of the simulations. This is necessary to ensure that the errors would not be accumulating over different components and stacking up to a diverging trend for the entire system output.

Tab. 3: Components analyzed based on parameters changed and subsequent parameters for observing the component behavior

Component	Parameter changed	Analyzed using:
Collector field	• Field area (size) • Tilt angle • Mass flow rate	○ Cumulative Collector field energy
Storage	• Size	○ Cumulative Storage Energy ○ Instantaneous internal energy
Boolean Electric heater	• Storage size	○ Cumulative Electrical energy ○ Fractional energy savings
Khoa making process	• Milk input mass flow rate • Milk input temperature	○ Cumulative khoa energy ○ Khoa production temperature

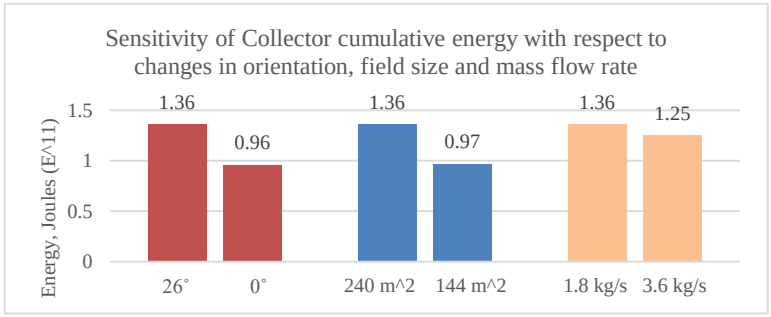

Fig. 6: Response in collector cumulative energy on different operating sizes and conditions represented sensitivity aspects

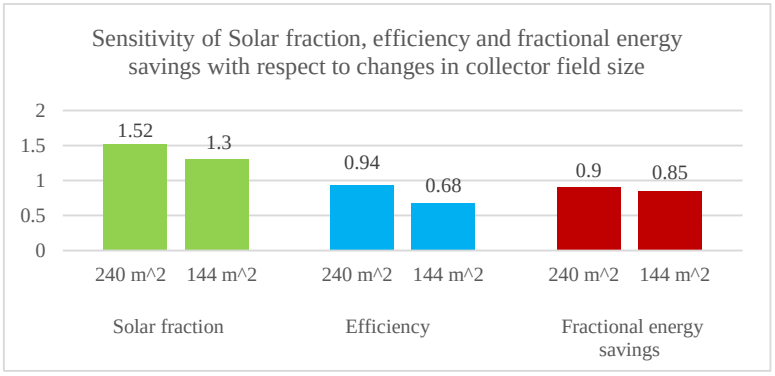

Fig. 7: Response of collector field to the performance parameters to change in field size

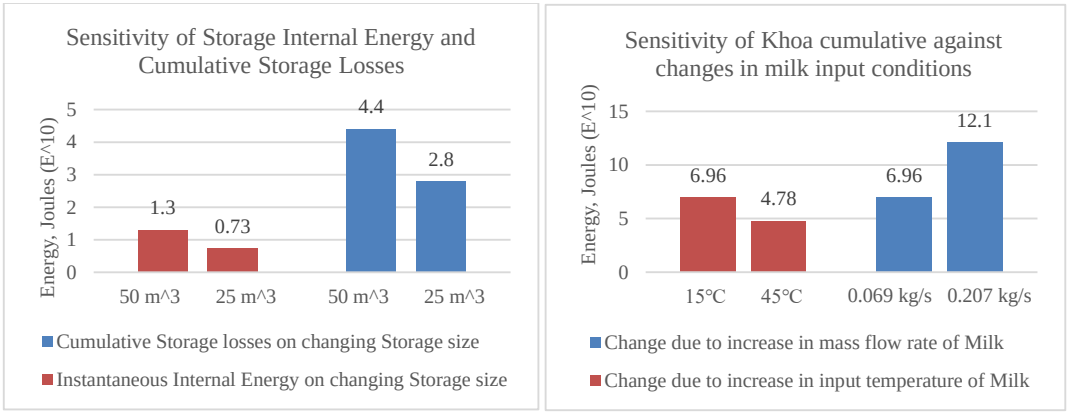

Fig. 8: Response of storage parameters on changing size and changes in khoa production energy on varying milk input conditions

Although the system sizing has been calculated using DHW as a starting point, the system size had to be optimized for the khoa production in such a way that the response of the system in terms of monthly and seasonal variation is better that the sized one as well as reconsidering the size of the system for economic investment if the real-time implementation is implements in future. The size reduction is a concern mainly for the size of storage as well as collector field. For the components used, different aspects had to be considered for performing the sensitivity analysis of the performance, which are specified in Table 3 and the changes in system sizes with respect to performance parameters are graphically depicted in Fig, 6, Fig. 7 and Fig. 8. The collector size was found 144 m^2 (reduced by 60% of design size) during the sensitivity analysis and simultaneously, as the storage size being dependent on collector field size, the optimized size is 22 m^3. Based on this, further performance analysis is proposed for the system using performance parameters.

4.1 Energy balance of the system

It is important to note that the energy balance is considered only using cumulative energy generated/consumed by the system across one operational year only. Ideally, it is expected to see the operation and balance for the long run (i.e., 3-4 years) but due to limitations of the tool to simulate and visualize properly for one operational year, the limit is up to one year only. Simulink was unable to compile the results for WDB for consecutive two years leading to the crashing of the entire MATLAB. Although thermally the heat transactions are expected to be the same at the start and end of the year, it is translated to the mathematical sum which should be ideally zero at the start and end of the year. The energies recorded by Simulink blocks on a cumulative basis are noted at the end of every year's simulation results to check the difference in the correct range. As it can be seen in Fig. 9, the heat sources are mentioned on the left-hand side and energies are flowing from the left to right direction. The energies considered here are irrespective of the signs (absorption or rejection) but are purely limited to consider only their magnitude. In an ideal case, the length of the bars on the left-hand side determined by the type of heat source must be equal to the final product expected on the right-hand side.

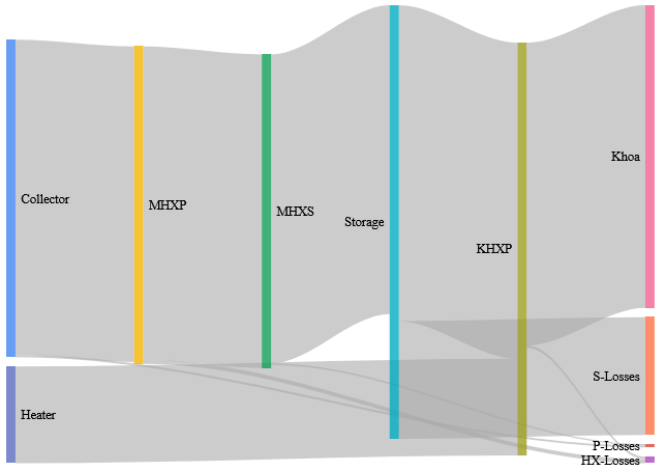

Fig. 9: Sankey diagram representing energy transfer among components for final system design (Source: Self Customized using JS Fiddle code)

4.2 Evaluating the system performance using performance parameters

The performance parameters considered mainly are solar fraction, fractional energy savings, system efficiency, utilizability and collector yield. The solar fraction was mainly used for optimization for collector field and storage resizing and ultimately helping other performance parameters close by to justify the trade-off for a better, smaller system size with close performance. The fractional energy savings are considered against an identical system model with same input parameters, difference being a boiler with efficiency of 90%, electric heater with efficiency of 95% and a small storage of 10 m^3. Please refer to the graphs below in Fig. 11. Please take a note, the time series represented is in seconds, but separated for the seasonal variations as per color coding. Respective months of the seasons are discussed as per performance of the system for clarify for the reader.

- The solar fraction at the end of the year: 1.05
- Solar collector field efficiency at end of the year: 34.1%
- System Utilizability: 820.5 $kWh/m^2/yr$

- Solar collector yield: 868.8 kWh/m^2/yr
- Fractional energy savings at the end of the year: 0.68
- Fractional energy savings average (with instantaneous behavior): 0.76
- Solar fraction Annual average (with instantaneous behavior): 1.18

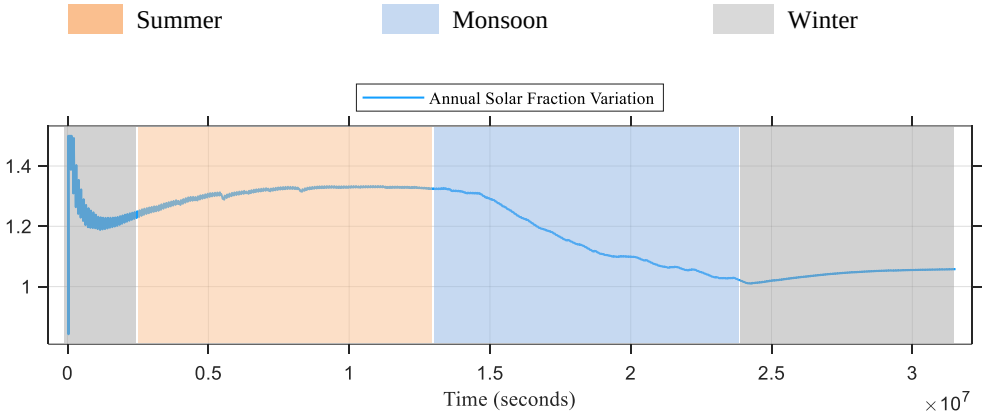

(A)

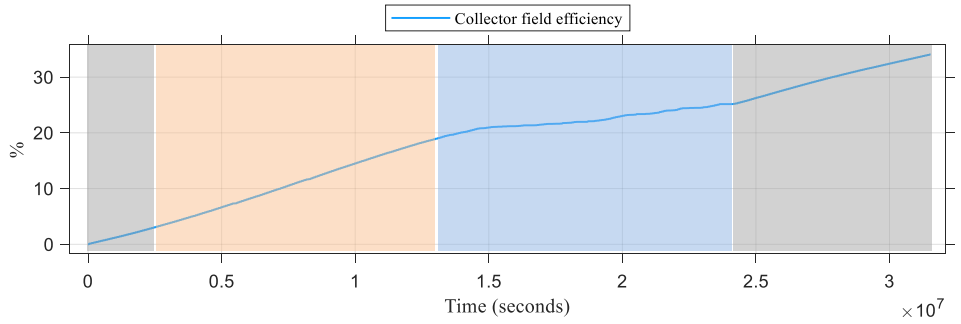

(B)

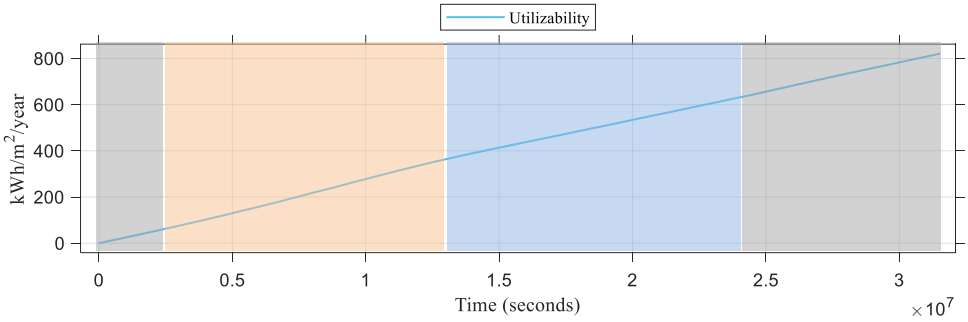

(C)

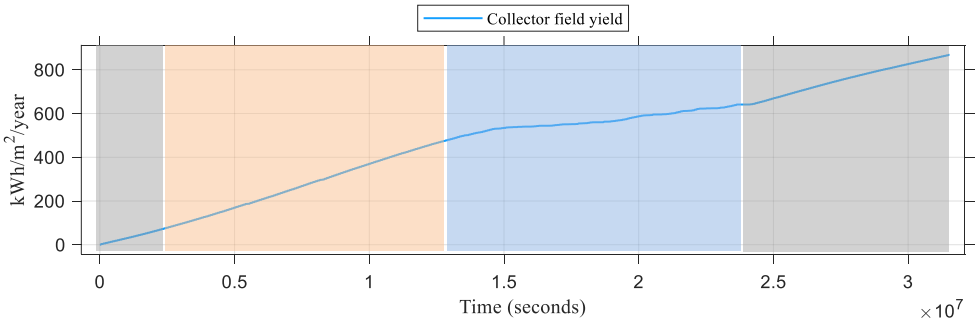

(D)

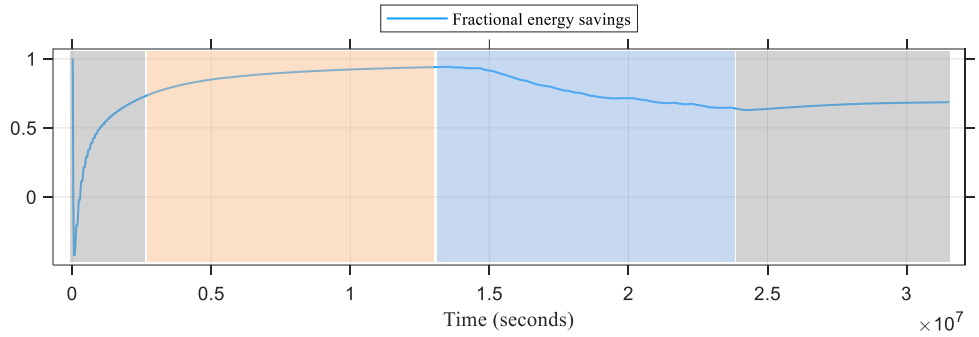

(E)

Fig. 11. Seasonal representation for explaining the share of solar energy in the khoa production system (A) Annual variation in solar fraction with values more than unity throughout the year (B) Collector field efficiency on cumulative basis(C) Utilizability and its trend with cumulative energies for calculation (D) Collector field yield with gradual decrease in slope for the monsoon season (E) Fractional energy savings against system's energy utilization from the heat source of solar collector field and Boolean electric heater

The seasons are represented as per time (seconds) namely March-May for summer, June-September for monsoons, and October to February for Winter. The graphs are to be seen one below the other and observe different parameters simultaneously as per season. As the system starts on the 1st of January, it is almost the peak of the Winter season and the energy requirements to ramp up the system are high. Although solar radiation is available, solar fraction drops down along with the fractional energy savings to charge the storage and gain energy. Gradually, as visible in Fig. 11 (E) the fractional energy savings are positive (after about 15 days) stating the system is now ramped up with the required temperature and actual benefits from the solar energy can be reaped. The participation of Boolean electrical heater (cumulative energy) stabilizes after this stage which reflects into fractional energy savings as well.

In the summer season, the system tries to run purely on solar energy which translates into minimum dependency on an electric heater and maximum savings (value approaching close to 1) as shown in Fig. 11 (E). For solar fraction, the system is approximately 130% efficient (as per system results, an error) and no dependence on external heat is observed. Logically and theoretically, it cannot be more than 100%, but can be supported with the statement of purely running on solar energy, without dependant on electric heater.

For the months of monsoon, the dependence on solar energy decreases as due to low available radiations, and simultaneously the cumulative Boolean electric heater energy increases due to low solar radiations and discharging storage energy, which reflects in Fig. 11 (A). The solar fraction decreases simultaneously reflecting into the increasing boolean electric energy, which in turn dips the fractional energy savings in Fig. 11(E). As the monsoon is over and the onset of winter, the solar radiations are back, but not with the same intensity as cumulative solar energy picks up and reflects onto the increasing trend of the solar fraction. This momentum is expected to continue and increase savings for the incoming summer season in the upcoming month and next year.

From the above discussions and inferences, it is clear that solar energy can play a majority role in powering the system thermally and reinforce the decision of running the khoa production system purely on solar energy. A boolean electric heater is an indispensable part of the system, but the maximum benefits are reaped using the designed collector field, storage as well as temperatures achieved and maintained in the system. This is in line with the expectations from the system in comparison to the traditional wood-fired boiler-powered system. The carbon savings achieved from solar energy as discussed in the upcoming chapter.

4.3 Emission savings using the proposed system

From the previous chapter, it is evident from the results and inferences drawn that the solar thermal system designed for khoa production can run on an average of 68% purely using solar energy. The remaining energy demands are catered to using electrical energy. The system, originally and currently running on wood fired boiler, can be run using solar energy and it can reinforce the objective of taking on this project initiative. As inferred in from the methodology chapter, the MKK uses Babul firewood. As per the literature survey conducted, there were no carbon sequestration reports available for babul firewood stating the exact emissions per kilogram of wood burnt or per kilo-Watt-hour energy produced. Instead, the IPCC guidelines (Freund *et al.*, no date) to choose

carbon emissions in terms of CO_2 equivalent are used to calculate the annual CO_2 emissions from the MKK using babul firewood. If the solar thermal powered system is implemented assuming wood fired boiler as an auxiliary source of heat, the system would ideally save 68% of firewood consumed and replace it through purely solar energy. This is equivalent to 307.7 tonnes of CO_2 emitted every year saved.

But, as per the proposed system, the electrical energy is used to cater to the requirements of the khoa production system. Although the boolean electric heater is purely based on the temperature deficit-based operation system, for the calculation of carbon emissions, the electrical heater can be assumed to be operated using a fossil fuel-powered electrical grid. The carbon intensity of India's power sector is 725 grams of CO_2 per kilowatt hour (g CO_2/kWh), compared with a global average of 510 g CO_2/kWh ('India Energy Outlook', 2021).

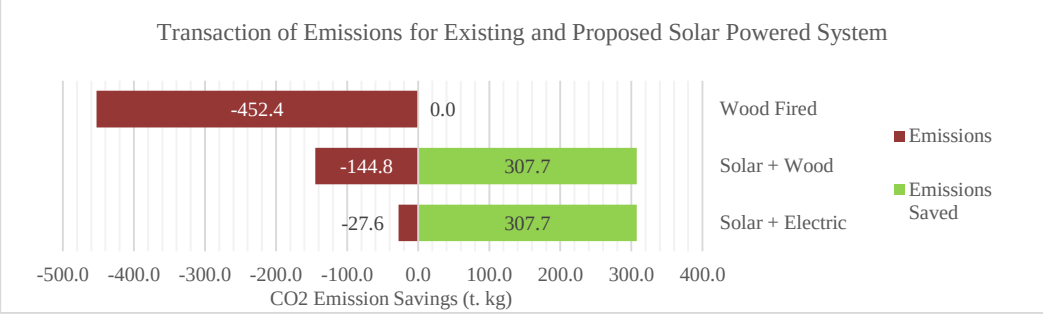

Fig. 12. Transaction for carbon emissions of existing and proposed solar powered system

It is quite evident that running the system with grid powered electrically heater-assisted solar thermal system is better than a wood-fired system and concretizes operationality as well as carbon savings of proposed system. It will be interesting to observe the system behaviour in the long run in-terms of solar fraction and fractional energy savings. The energy packages interacting in storage can be explored deeply along with minimizing dependency on electric heater. After all, the initiative to take up this project was to realize it on long-sustainable terms, the challenge is much bigger to learn during the process of implementation and pitch the product as 'green' khoa, with no/minimum emissions are involved in its production.

5. Conclusion

A genuine attempt was made to simulate an existing wood-fired khoa production system to work purely using solar thermal energy at Mahesh Khawa Kendra in Manchar, India. The system design is crucial in terms of the complexity of the processes involved and this being an attempt for a sophisticated yet novel system, the thumb rules for DHW systems proved to be helpful as a starting point. Although the system is slightly overdesigned in terms of the solar fraction of 1.06 for a simulation period limited up to one year period, the fractional energy savings achieved are satisfactory (68%) as compared to the existing wood-fired system in terms of emissions saved as well as partial dependence on the electrical heater. The overdesigning of the system is a result of diversion from the thumb rules considered and redefined for a khoa production system as per the demand assumed and results obtained for khoa production. The system highlights the dynamic behavior as per seasonal variation through numerous performance parameters, thanks to the reliable weather database file fed to the simulations. Plausibility analysis and sensitivity analysis proved to be important tools to explore component-by-component response and the performance of the system as a whole to exploit the performance as well optimize to a better sizing of the final system. After all, in comparison to the objectives of the project to simulate this system, the system performance is positive and promising to reduce the emissions significantly based on the firewood consumption and fractional energy savings on annual basis. The system is not perfect in terms of the expectations of shifting to 100% renewable energy, but the results are in a positive direction and capable to bring further insights with a better tool and a better approach. The technology simulated is promising and personally appealing to be extended further for implementation and gaining the confidence of the solar system manufacturers and dairy industry operators to head towards sustainable, green, emission-free dairy product manufacturing.

6. Acknowledgments

I would like to express my sincere gratitude to owners of Mahesh Khawa Kendra who gave the freedom to observe and improvise the existing setup, Dr. Herena Torio for guiding me regarding this project and my friends, family and critics who kept me pushing towards continuous improvement.

7. References

BIS. (1980). *Specification for Khoa*. Available at: https://archive.org/details/gov.in.is.4883.1980

Chakradhari, S. and Patel, K.S. (2016) 'Combustion Characteristics of Tree Woods', *Journal of Sustainable Bioenergy Systems*, 06(02), pp. 31–43. Available at: https://doi.org/10.4236/jsbs.2016.62004

Chaudhary, R. and Yadav, A. (2020) 'Twin vessel solar cook stove for the simultaneous cooking of two different cooking articles', *Solar Energy*, 208, pp. 688–696. Available at: https://doi.org/10.1016/j.solener.2020.08.032

'Dairy' (2015) in OECD and Food and Agriculture Organization of the United Nations, *OECD-FAO Agricultural Outlook 2015*. OECD (OECD-FAO Agricultural Outlook). Available at: https://doi.org/10.1787/agr_outlook-2015-11-en

Freund, P. *et al.* (no date) 'Properties of CO2 and carbon-based fuels', p. 18. Available at: https://www.ipcc.ch/site/assets/uploads/2018/03/srccs_annex1-1.pdf

Google Scholar (no date). Available at: https://scholar.google.com/ (Accessed: 10 September 2022).

Hickey, M. (ed.) (2009) 'Current Legislation on Concentrated and Dried Milk Products', in *Dairy powders and concentrated products*. Chichester, U.K: Wiley-Blackwell (Society of Dairy Technology series), p. 28-98

'India Energy Outlook' (2021), p. 251, Available at: https://iea.blob.core.windows.net/assets/1de6d91e-e23f-4e02-b1fb-51fdd6283b22/India_Energy_Outlook_2021.pdf

JRC PVGIS (no date). Available at: https://re.jrc.ec.europa.eu/pvg_tools/en/tools.html (Accessed: 22 August 2022).

Kumar, M. *et al.* (2011) 'Experimental study on heat and mass transfer for heating milk', *Journal of Energy in Southern Africa*, 22(3), pp. 45–53. Available at: https://doi.org/10.17159/2413-3051/2011/v22i3a3221.

Kumar, M., Prakash, O. and Kasana, K.S. (2012) 'EXPERIMENTAL INVESTIGATION ON NATURAL CONVECTIVE HEATING OF MILK: STUDY ON NATURAL CONVECTIVE HEATING OF MILK', *Journal of Food Process Engineering*, 35(5), pp. 715–726. Available at: https://doi.org/10.1111/j.1745-4530.2010.00620.x

More, G.R. (no date) 'Development_of_Khoa_Making_Equipment', *National Dairy Research Institute*.

Nandi, P. (2009) 'Solar Thermal Energy Utilization in Food Processing Industry in India.', . *Number*, 10(1), p. 9. Available at: http://www.akamaiuniversity.us/PJST10_1_123.pdf

NREL India Data (no date). Available at: https://www.nrel.gov/analysis/india-renewable-integration-study.html (Accessed: 22 August 2022)

ORBIS Plus Suchportal (no date). Available at: https://plus.orbis-oldenburg.de/primo-explore/search?vid=ORB_V2

Rao, C.S. *et al.* (2020) 'Economic analysis in mechanized production of Khoa', 22(2), p. 5. Available at: https://cigrjournal.org/index.php/Ejounral/article/view/4248/3327

Rasane, R., Beenu, T. and Dey, A. (2015) 'Khoa: A Heat Desiccated Indigenous Indian Dairy Product', *Research Journal of Pharmaceutical Biological and Chemical Sciences* [Preprint]. Available at: https://www.researchgate.net/profile/Prasad-Rasane/publication/281677356_Khoa_A_Heat_Desiccated_Indigenous_Indian_Dairy_Product/links/55f3ebd608ae7a10cf88e330/Khoa-A-Heat-Desiccated-Indigenous-Indian-Dairy-Product.pdf

Scopus (no date). Available at: https://www.scopus.com/search/form.uri?display=basic

Solar Heat for Industry India (2020). BSW - Bundesverband Solarwirtschaft e.V., pp. 29–46. Available at: https://www.solar-payback.com/wp-content/uploads/2020/06/SHIP-india-26-06-20.pdf

Solar Radiation Atlas (no date). Available at: https://mapserver.niwe.res.in/gisportal/home/webmap/viewer.html?webmap=16d20b45e4234603ae4a219f26792e95 (Accessed: 22 August 2022).

Solflex Catalogue (no date). Available at: http://www.solfex.co.uk/uploads/downloads/Solar_Thermal_Brochure_small.pdf (Accessed: 22 August 2022).

Torio, Dr.H. (2019) 'Thermal Storage - PPRE Solar Thermal Energy'. Winter Semester, University of Oldenburg

Velpula, S. (2018) 'Commercial Production Scenario of Traditional Indian Dairy Products: A Review', 7, p. 5. Available at: http://www.bepls.com/beplsfeb2018/17.pdf

Verification of Models - CARNOT Toolbox manual (no date). Available at: https://www.fh-aachen.de/fileadmin/ins/ins_sij/Carnot_Downloads/Manual.html

Web of Science (no date). Available at: https://www.webofscience.com/wos/woscc/basic-search (Accessed: 23 August 2022).

Energy Savings for Gas Preheating in the Gas Transport Sector with Air Dehumidification and Expansion Turbines

Lisa Völker[1], Yoann Louvet[1], Daniel Fleig[1], Felix Pag[1], Ulrike Jordan[1], Klaus Vajen[1]

[1] University of Kassel, Institute of Thermal Engineering, Kassel (Germany)

Abstract

In gas pressure regulating and metering stations (GPRMS) natural gas is reduced from high pressure to almost atmospheric pressure for the end consumer. To avoid, among others, freezing of pipelines and other components which the natural gas passes through, the gas is preheated before the throttling process. This work presents two different technologies with the objective to reduce the primary energy demand for the preheating of the natural gas: the dehumidification of the air of the gas expansion room and the combination of an expansion turbine with electrical heat pumps. The energy savings regarding the air dehumidification of a GPRMS could be evaluated based on measured data. A long-term field test with a novel liquid desiccant air conditioning system was carried out and based on the measured data the primary energy demand of the studied GPRMS could be reduced about 12 % for the year 2021 compared to a reference case without dehumidification. First theoretical investigations reveal that by designing the expansion turbine and heat pump unit to cover the total typical heat demand of the studied GPRMS in summer, 90 % primary energy savings can be achieved on typical summer days, 39 % in autumn / spring and 19 % in winter, considering the total energy consumption of the GPRMS (electric power and heat demand).

Keywords: gas pressure regulating and metering station, energy efficiency, liquid desiccant, dehumidification, expansion turbine

1. Introduction

Gas pressure regulating and metering stations (GPRMS) are important facilities in natural gas distribution networks, in which the gas pressure is reduced from the high pressure required to transport it over long distances to almost atmospheric pressure for the end consumers. GPRMS are an equivalent to transformer stations in the electric grid. In GPRMS the natural gas is usually throttled, leading to a temperature decrease of the gas of between 0.4 and 0.7 K/bar, depending on its composition and the operating conditions (Mischner et al., 2015). In Germany, in order to avoid freezing in the GPRMS and downstream pipelines after the throttling process, it is state of the art to preheat the natural gas with gas boilers. The energy requirement for preheating depends on the natural gas mass flow through the station, which is driven by demand and on the physical properties of the gas. In total, all German GPRMS consume about 2 TWh/a primary energy for natural gas preheating (Mischner et al., 2019).

An analysis of existing heating systems in GPRMS shows that several efficiency measures can usually be taken to reduce the energy consumption for preheating. Optimised control strategies and adapted hydraulic concepts can, for example, reduce the heat demand and further lower the flow temperature level required for preheating, usually to between 40 and 80 °C. This favours the integration of energy efficient heat supply technologies in a second step. In previous studies by Wimmer et al. (2019) and Louvet et al. (2021) several strategies are presented that include the combination of innovative technologies, which have been applied at several GPRMS in Germany to reduce their primary energy consumption. Two additional innovative technologies, not investigated so far and aiming at further reducing the primary energy consumption of GPRMS, are presented in this work. These are the dehumidification of the room where the gas expansion takes place (gas expansion room) and the combination of expansion turbine and heat pumps. Regarding the energy saving potential due to dehumidification a long-term field test was carried out at an existing commercial GPRMS and measurement data are analysed whereas for the latter presented investigations and results are based on theoretical calculations in this paper.

2. Studied GPRMS

Both GPRMS which are the focus of the present study are installed in Central Germany and are already equipped with solar heat for industrial processes (SHIP) plants and with gas absorption heat pumps (GAHPs) in addition to

© 2022. The Authors. Published by International Solar Energy Society
Selection and/or peer review under responsibility of Scientific Committee
doi:10.18086/eurosun.2022.05.12 Available at http://proceedings.ises.org

conventional gas boilers for the preheating of the natural gas.



Fig. 1: Pictures of the GPRMS Ostheim with a 295 kW_{th} SHIP plant and 123 kW_{th} GAHP (left) and the GPRMS Neu-Eichenberg with a 95 kW_{th} SHIP plant and 123 kW_{th} GAHP (right).

The GPRMS Ostheim (Fig. 1, left) has a useful heat demand more than twice as large as the GPRMS Neu-Eichenberg (Fig. 1, right). The shares of the total useful heat demand covered by the different technologies are summarised in Tab. 1. Primary energy savings of 36 % (GPRMS Ostheim) and 33 % (GPRMS Neu-Eichenberg) are achieved with the existing innovative technologies in comparison to a calculated reference scenario, in which the energy for preheating is supplied only with gas boilers. In addition, the downstream gas temperature is assumed to be constant throughout the year at 10 °C in the reference scenario, whereas both stations are equipped with a dew point control of the downstream gas temperature, also contributing to the total primary energy savings indicated.

Tab. 1: Useful heat demand and share covered by the different heating technologies for the studied GPRMS

GPRMS	Useful heat demand in MWh/a	Share gas boiler in %/a	Share GAHPs in %/a	Share SHIP plant in %/a
Ostheim	1,450	57	29	14
Neu-Eichenberg	690	43	50	7

The approximation method for calculating the heat capacity for preheating the natural gas $\dot{Q}_{phys,PH}$ to compensate the gas temperature reduction is specified by the DVGW regulations G 499 (DVGW, 2015) according to equation 1.

$$\dot{Q}_{phys,PH} = \dot{V}_n \cdot \rho_n \cdot c_{p,m} \cdot \left(\mu_{JT,m} \cdot (p_u - p_\mathrm{d}) + T_\mathrm{d} - T_u\right) \qquad (1)$$

In addition to the natural gas volume flow $\dot{V}_n$ in the standard state (T_n = 273,15 K und p_n = 1013,25 mbar), the heating capacity depends on the composition of the natural gas as well as the pressure and temperature before heating (p_u, T_u) and after expansion (p_d, T_d). The natural gas inlet temperature T_u approaches the ground temperature. The gas outlet temperature T_d (GOT) is the decisive variable to be controlled to reduce the heat demand for gas preheating. Since the actual heat consumption in a GPRMS is higher due to system and heat losses, the one calculated according to equation (1) is also referred to as the physical heat demand and represents a theoretical value.

3. Dehumidification of GPRMS with liquid desiccant air conditioning (LDAC) system

To avoid condensation on the pipe surfaces after expansion of the natural gas a dew point controller can be implemented. This ensures that the natural gas outlet temperature (GOT) is always a defined temperature difference higher than the dew point temperature of the gas expansion room. The energy demand for preheating the natural gas can be further reduced by dehumidification of the room air. Assuming a minimal allowable GOT of 4 °C and a temperature difference of 3 K for the dew point control the dew point temperature of the gas expansion room should be at least 1°C which corresponds to a humidity ratio of air of 4.5 g/kg. Conventional dehumidifier working with dew point cooling cannot be operated economically at this level of humidity anymore, because icing of the cooling coil leads to energy consuming defrosting. Another way of dehumidification uses sorption processes, either adsorption (with desiccant wheels) or absorption processes. The latter are realized in liquid desiccant air conditioning (LDAC) systems, considered in the present research.

3.1. Operating principle of LDAC system and integration to GPRMS

Fig. 2 (a) shows the operating principle of such a system which consists mainly of two heat and mass exchangers –

the absorber (conditioner) and the regenerator –, a solution-to-solution heat exchanger and a solution tank. The hygroscopic solution (LiCl-H_2O) gets into direct contact with the outdoor air (OA) in the dehumidifier. Because of the difference in water vapor partial pressure between the ambient air and above the solution surface, water molecules of the air are absorbed by the solution and the air is dehumidified. During the absorption process heat is released. In the LDAC system investigated in this project, the absorber can be cooled internally by a pipe coil through which water flows. Compared to systems without internal cooling, this offers the advantage that the heat released during absorption can be removed by the cooling water which improves the dehumidification efficiency. However, operation without cooling water (adiabatic mode) is also possible for the used LDAC system. After the absorption process the diluted solution is concentrated again in the regenerator. For that process heat is required on a temperature level of 50 to 80 °C depending on the needed dehumidification. The cooling water is provided by a wet-cooling tower and the heat for the regeneration process is provided by a solar thermal plant and gas absorption heat pumps as mentioned before. LDAC systems like the described one have so far only been used in a few pilot systems in Europe.

An LDAC system was implemented at GPRMS Neu-Eichenberg in 2020 (see Fig. 2 (b)) and has been monitored since then in a long-term test. For GPRMs state of the art is that the fresh air supply for the gas expansion room is realized by natural ventilation with louvre in the wall. For the field test mechanical ventilation was implemented to supply the dehumidified fresh air to the gas expansion room.

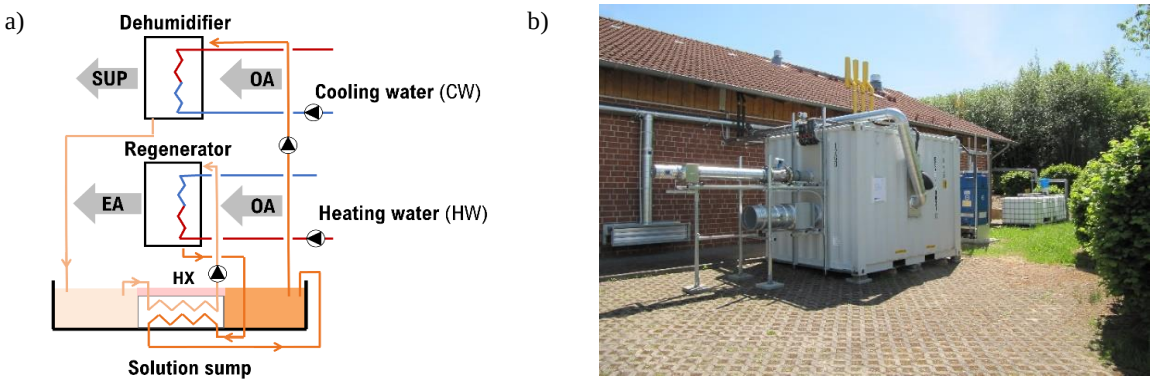

Fig. 2: (a) Operating principle of LDAC system and (b) LDAC system in a maritime container in front of GPRMS Neu-Eichenberg

3.2. Method

In order to determine the reached yearly energy savings through dehumidification, the physical heat demand is first determined according to equation 1 using the measurement data from the gas network operator ($Q_{phys,meas}$) for the year 2021. For the reference case, the physical heat demand must also be determined in the event that no air dehumidification takes place ($Q_{phys,ref}$). For this reference case, it is assumed that the humidity ratio in the gas expansion room corresponds to that of the outside air (natural ventilation). Thus, the dew point temperature in the room and also the GAT can be determined for the reference case. In 2021, the offset from the measured dew point temperature in the gas expansion room to the GOT was 5 K until July and 3 K from August. The same offset is also assumed for the reference case. Since heat (Q_{reg}) is required for the regeneration process, this must be taken into account when determining the savings, so that the heat saved (Q_{save}) based on the calculation of the physical heat demand, can be calculated according to equation 2.

$$Q_{save} = Q_{phys,PH,ref} - Q_{phys,PH,meas} + Q_{reg} \quad (2)$$

Based on measurement data for the to be depressurized natural gas and the heating gas consumption for the year 2017-2019 the average ratio of energy supplied by fossil fuel (heating gas) to calculated physical heat demand is 1.15. Assuming that value also for the reference case without dehumidification the heating gas consumption (for the boiler and GAHPs) can be estimated. Thus, besides the savings based on the theoretical physical heat demand also the primary energy savings can be determined. Therefore also the electrical power consumption of the LDAC system is considered with primary energy factor for electricity of 1.8.

It turned out, that the deviation of the measurement data for the relative humidity of the air at the absorber inlet is outside the measurement uncertainties of the sensors. The relative humidity (RH) is used to calculate the dew point

temperature for the reference case without dehumidification. In order to be able to estimate the savings in preheating despite the measurement deviation, a correction curve was determined by calibrating the sensors, which was applied to the measurement data for 2021. For areas that the correction curve cannot depict (RH > 90%), data from a nearby weather station are used. In addition, the measurement data for the pressure of the natural gas before expansion and the measurement data for the gas outlet temperature (in minute time steps) are missing for August 2021. Since the gas pressures remained almost constant over the entire considered period, the inlet pressure for August is assumed to be 50 bar and hourly measured values were used for the GOT.

3.3. Measurement data and results

The measured volume flow rate at standard conditions for the to be depressurized natural gas is shown in Fig. 3 for the year 2021. The total gas volume for the year 2021 was 80.7 10^6 Nm³. The mean daily upstream pressure in 2021 was 51 bar and the mean daily downstream pressure was 14.4 bar in summer and 8 bar in winter. Fig. 4 shows the measured humidity ratio of the air at the absorber inlet $\omega_{abs,in}$ and absorber outlet $\omega_{abs,out}$ as well as the necessary humidity ratio to reach the minimal GOT of 4 °C (ω_{goal}) for the year 2021. Also in the winter months there is a need for dehumidification on some days, since the humidity ratio of the air is above ω_{goal}. In July 2021 the temperature difference (between the GOT and the dew point temperature of the air) of the dew point control was reduced from 5 K to 3 K which results in an increase of ω_{goal}.

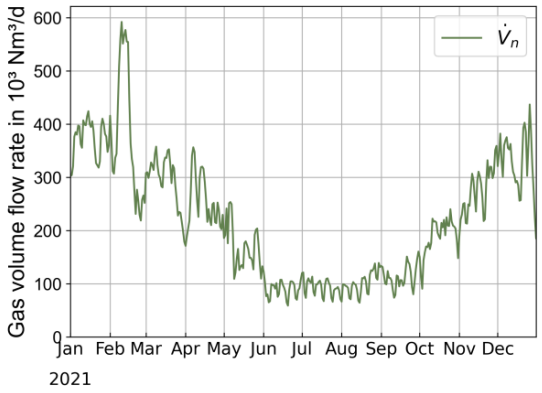

Fig. 3: Measured volume flow rate at standard conditions of the to be depressurized natural gas for the year 2021

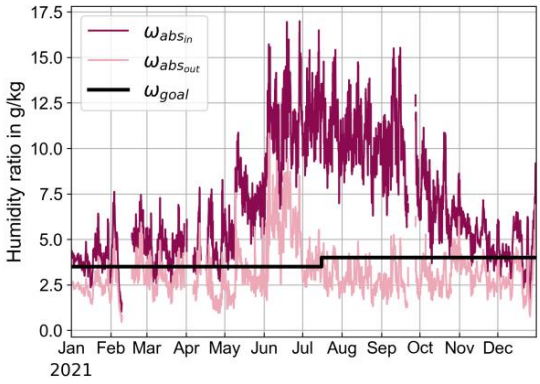

Fig. 4: Measured humidity ratio at absorber inlet $\omega_{abs,in}$ and outlet $\omega_{abs,out}$

The wet cooling tower to provide the cooling water for the absorber was put into operation in April 2021. During the year 2020 the LDAC system was operated adiabatic (without cooling of the absorber). The evaluation of the measurement data show that the dehumidification is more effective with internal cooling as shown in Fig. 5. The mean hourly humidity ratio difference $\Delta\omega$ of inlet and outlet humidity ratio depending on the inlet humidity ratio at the absorber is plotted for the operation of the LDAC system with and without internal cooling (adiabatic) for the years 2020 and 2021. Especially in summer for higher outdoor air humidity ratios the humidity ratio difference $\Delta\omega$ can be more nearly doubled if the absorber of the LDAC system is cooled by the wet cooling tower and heat supply to the regenerator is sufficient. Taking as example an inlet air humidity ratio of 13 g/kg an average humidity ratio difference of 5 g/kg and 9.4 g/kg is reached in adiabatic operation and with internal cooling respectively.

The results of the dehumidification regarding the GOT for the year 2021 are shown in Fig. 6. The measured GOT with dehumidification ($T_{d,meas}$) and a calculated GOT without dehumidification ($T_{d,ref}$) assuming that the dew point temperature of the gas expansion room is equal to that of the ambient air (due to natural ventilation) are plotted. Due to the dehumidification, the minimum GOT of 4 °C is reached in about 80% of the operating hours. In total, the GOT of 4 °C was exceeded for 1,800 hours, of which approx. 750 hours can be traced back to June and September, when the LDAC system ran faulty or was completely out of order. In June the major problem was the heat supply for the regeneration so that the mean hot water inlet temperature at the regenerator was only 38 °C whereas it was 58 °C for the remaining summer month. Due to the lower hot water temperatures in June the dehumidification is clearly restrained. As mentioned before the hot water for the regeneration is supplied by the GAHPs and the solar thermal plant and for that reason is somehow districted. By the dehumidification the GOT could be reduced by an average of 12 K in summer and 2 K in winter month.

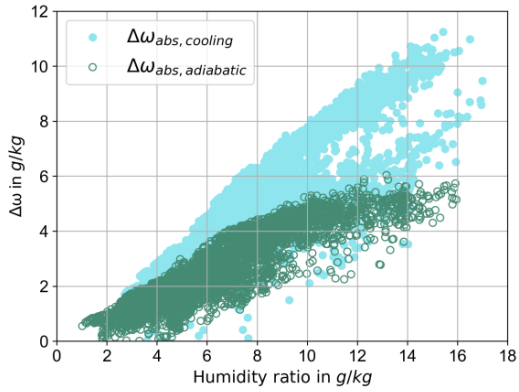

Fig. 5: Mean hourly humidity ratio difference $\Delta\omega$ of inlet and outlet humidity ratio depending on the inlet humidity ratio at the absorber for the operation of the LDAC system with and without internal cooling (adiabatic) for the years 2020 and 2021

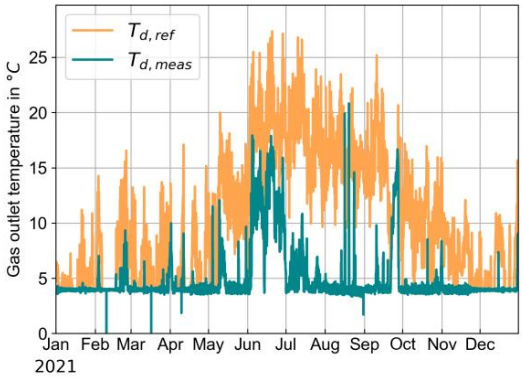

Fig. 6: Measured GOT with dehumidification (T_{meas}) and theoretical GOT without dehumidification (T_{ref}) for the year 2021

Based on the given GOT the physical heat demand for the measured data $Q_{phys,meas}$ and the reference case $Q_{phys,ref}$ is calculated and shown in Fig. 7. Besides the physical head demand also the measured heat for the regeneration Q_{reg} is considered. The physical heat demand $Q_{phys,meas}$ amounts to a total of 608 MWh and the heat consumption for the regeneration Q_{reg} to 40.5 MWh for 2021. If a GOT of 4 °C had been realized the whole year the physical heat demand would have been 589 MWh which corresponds to the maximal energy saving potential. This means the maximal potential regarding only the physical heat demand was missed by 3.2 %.

The physical heat demand $Q_{phys,ref}$ for the reference case without dehumidification is 747 MWh. As expected, the savings regarding the physical heat demand are highest in the summer months when outdoor air humidity ratio is high as shown in Fig. 8. The faulty operation of the LDAC system due to problems with hot water supply are clearly noticeable for the month June. Further although the natural gas volume flow rate is the lowest during summer month, highest savings can be determined during that time. However, this also requires the highest heat consumption for the regeneration (see Fig. 7). In 2021, the heat demand was reduced by a total of 99 MWh taking into account the regeneration heat, compared to the reference case thanks to the dehumidification of the gas expansion room air. This corresponds to a reduction of 13.2 %. Without the failure of the heat supply in June and the shutdown of the LDAC system in September, the reduction would have been even higher. In addition to the required regeneration heat, however, the power consumption for the LDAC system must also be taken into account. In 2021, this amounts to 3 MWh for the LDAC system.

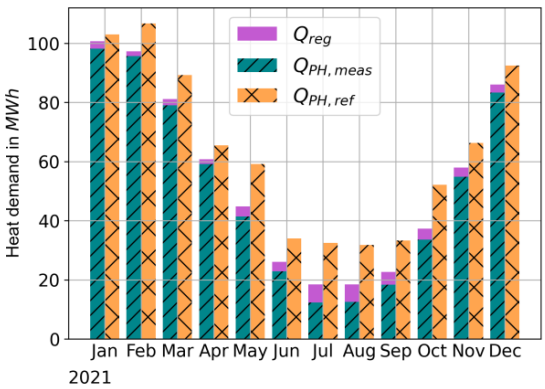

Fig. 7: Monthly physical preheating demand for the measured data $Q_{phys,PH,meas}$ and the reference case without dehumidification $Q_{pys,PH,ref}$ as well as the measured heat demand for the regeneration Q_{reg} for the year 2021

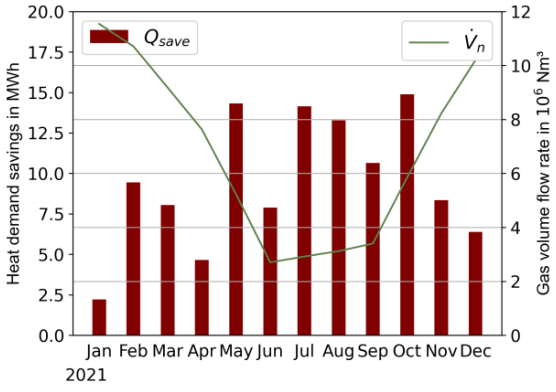

Fig. 8: Calculated monthly savings Q_{save} in physical heat demand based on measured data compared to reference case without dehumidification and natural gas volume flow rate at standard conditions for the year 2021

The heating gas consumption for the GAHPs and the gas boiler was 74,160.3 Nm³ in 2021 which corresponds to a total heat input by fossil fuels of 754 MWh. It should be considered that from the middle of November until the end of the year 2021 the regenerative heat supply (GAHPs and ST) was not in operation. During that time only the gas boilers covered the preheat demand which led to higher heating gas consumption during that month compared to other years. The primary energy input including the electricity consumption for the LDAC system is 834.8 MWh. Assuming a ratio of 1.15 of physical heat demand to heat input by fossil fuels the primary energy input for the reference case is 945 MWh. Based on this assumption the primary energy could be reduced by 11.6 % for the year 2021.

4. Combination of expansion turbine and heat pumps

During the throttling process, the potential energy contained in the gas at high pressure is not used. Alternatively, the gas can be expanded in an expansion turbine to generate electricity. It is reported that in Germany expansion turbines with a total capacity of 70 MW_{el} are already installed at GPRMS (Mischner et al., 2015). However, the installed turbines are in the range of several 100 kW_{el}, which limits their scope of application to the largest GPRMS with a high gas throughput. A research project was initiated aiming at developing a smaller turbine in the range of a few tens of kilowatts and at demonstrating its application in combination with electric heat pumps, with the aim of supplying the energy demand for gas preheating of the GPRMS.

The pressures indicated in this chapter are absolute pressures. The calculations are performed with the programming language Python, notably using the library NeqSim (Solbraa, 2022) for the determination of the physical properties of the gases considered.

4.1. The natural gas expansion process

The gas expansion process in an expansion turbine is presented in Fig. 9. The gas states before and after the expansion turbine (Fig. 9, left) are represented in a (h-s) diagram in Fig. 9 (right). The ideal expansion, between the points *u,ex* and *ds,ex* is isentropic. The corresponding change in enthalpy Δh_s expresses the theoretical work that can be transferred outside of the system. The work actually transferred from the gas stream to the turbine wheel is characterised by the isentropic efficiency η_s of the expansion turbine. For the considered application isentropic efficiencies between 0.6 and 0.7 can be expected.

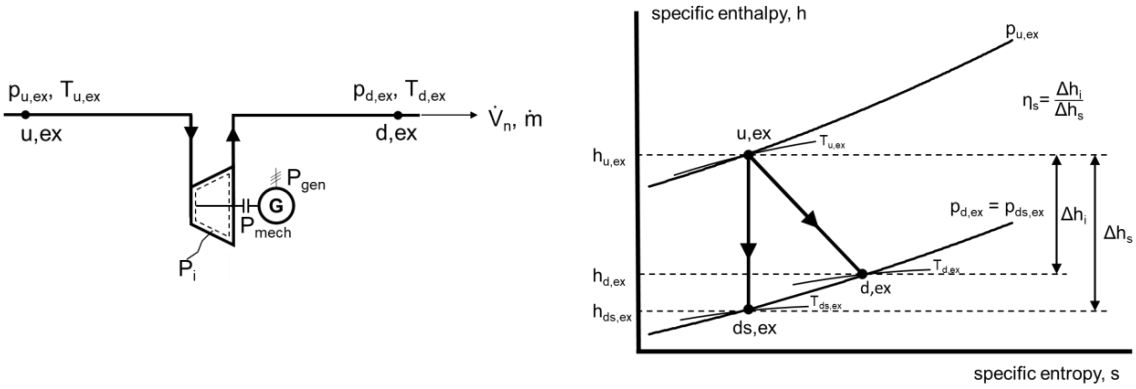

Fig. 9: Hydraulic scheme of an expansion turbine in a gas pipeline (left) and representation of the expansion process in a (h-s) diagram (right) adapted from Mischner et al. (2015)

An impulse turbine is the chosen technology to achieve the gas expansion. With this type of expansion turbine the gas pressure reduction (from $p_{u,ex}$ to $p_{d,ex}$) takes place exclusively in the nozzle situated before the turbine wheel and results in an increase of the gas kinetic energy, which is maximal at the nozzle outlet. For converging nozzles, the gas velocity at the nozzle outlet is limited by the sound velocity. This implies that for a given nozzle exit (throat) area the maximum possible gas flow rate is achieved when the gas reaches sonic velocity. This state corresponds to the so-called critical condition for operating the nozzle. In a nozzle, pressures and velocity are linked. The critical velocity therefore corresponds to a given pressure ratio between the downstream and upstream pressures of the nozzle, which depends on the gas composition and the operating conditions (gas pressures and temperatures). For methane for instance, in the temperature and pressure ranges relevant for GPRMS, the pressure ratio varies between 0.50 and 0.55. As an example for $p_{u,ex}$ = 40 bar, critical velocity is reached for $p_{d,ex}$ = 21 bar. In this condition the pressure reached downstream is called the critical pressure and is usually referred to as p^*. It is possible to further

reduce the pressure at the nozzle (i.e. expansion turbine) outlet below p^* and operate the expansion turbine in supercritical conditions. In this case the gas experiences a post-expansion at the nozzle outlet from p^* to the expansion turbine downstream pressure (lower than p^*). Another solution consists in using a converging-diverging nozzle, also called de Laval nozzle. In this configuration supersonic gas velocities can be achieved at the outlet of the nozzle.

The flow in the nozzle is almost isentropic, which means that the gas temperature at the outlet of the nozzle is close to $T_{ds,ex}$. Considering methane, for an upstream pressure of 40 bar, a pressure ratio of 0.5, η_s = 0.6 and $T_{d,ex}$ = 5 °C the calculated $T_{ds,ex}$ amounts to -10.3 °C. It remains to be clarified if this local, between nozzle outlet and turbine wheel, low gas temperature could be a problem for the operation of the turbine. One option to avoid low temperatures at the nozzle outlet is to increase the downstream gas temperature $T_{d,ex}$, which would result in an almost equivalent increase in $T_{ds,ex}$. However, this is not optimal from an energetic point of view, as it also corresponds to an almost equivalent increase in $T_{u,ex}$.

4.2. Integration of the expansion turbine combined with a heat pump in an existing GPRMS

Keeping the required upstream gas temperature of the turbine $T_{u,ex}$ to the lowest level possible is indeed crucial, as the main idea of the project consists in using heat pumps in combination with the expansion turbine to provide the requested energy to preheat the gas. The heat pump should use the ambient air as heat source and should be driven by the expansion turbine. A hydraulic scheme of the integration of an expansion turbine combined to an electric heat pump in an existing GPRMS is presented in Fig. 10. The existing installation in grey consists of two redundant parallel gas lines. More information about the function of the different components can be found in Wimmer et al. (2019) and Louvet et al. (2021) for instance. The expansion turbine is connected in parallel to the existing pressure reduction lines and aims at reducing the pressure of part of the gas flow circulating through the station. The pressure of the remaining gas flow being reduced with a gas pressure regulator in the existing gas lines. The components required to integrate the expansion turbine are indicated in green in the block marked T-U (expansion turbine unit). It consists in different valves and safety devices as well as an additional gas preheater, as the required upstream gas temperature of the expansion turbine is higher than the one required before the gas pressure regulator. Also, an additional gas pressure regulator might be required in the expansion turbine unit (not represented) if the design pressure ratio of the expansion turbine is higher than the ratio between downstream and upstream GPRMS pressures. The combination of the expansion turbine, the heat pump and the related components is marked T-HP-U (expansion turbine and heat pump unit).

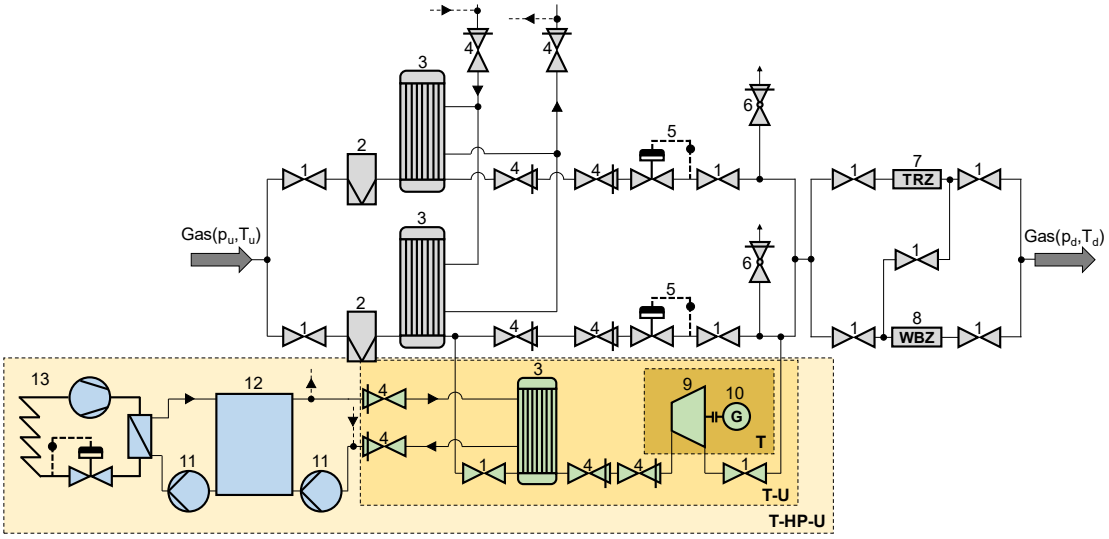

1 Shut-off valve
2 Filter
3 Gas preheater
4 Safety shut-off valve
5 Gas pressure regulator
6 Safety relief valve
7 Turbine wheel flow meter
8 Vortex flow meter
9 Turbine
10 Generator
11 Pump
12 Heat storage
13 Air-source heat pump

Fig. 10: Hydraulic scheme of the integration of an expansion turbine combined to a heat pump in an existing GPRMS

Dimensioning the expansion turbine is a complex task, depending on several technical, economic and regulatory parameters. To illustrate part of the challenges, measurement data from the GPRMS Ostheim are shown for the year 2020 in Fig. 11 with a daily resolution. The gas volume flow rate (Fig. 11, left) varies greatly along the year due to the seasonality of the gas demand. There is a factor eight between the mean daily gas volume flow rate in the summer

months and the peak volume flow rate at the end of January. There is thus a first compromise to make between reaching a high number of full load hours (FLH) for the expansion turbine and heat pump unit corresponding to an economic optimum and minimising the CO_2 emissions of the GPRMS. The higher the nominal gas flow rate the expansion turbine and heat pump unit is designed for, the less remaining heat demand for gas preheating the auxiliary gas boiler needs to cover, but the lower the number of FLH of the unit. The pressure levels at the GPRMS (Fig. 11, right) also play an important role in the design of the expansion turbine as mentioned in section 4.1. The mean daily upstream pressure experiences important variations along the year of 26.6 bar between its minimum and its maximum. On the opposite the mean daily downstream pressure is set to a constant value. Two different operating levels of 15.5 bar in the winter and 10.8 bar in the summer (between mid-April and beginning of October) can be identified.

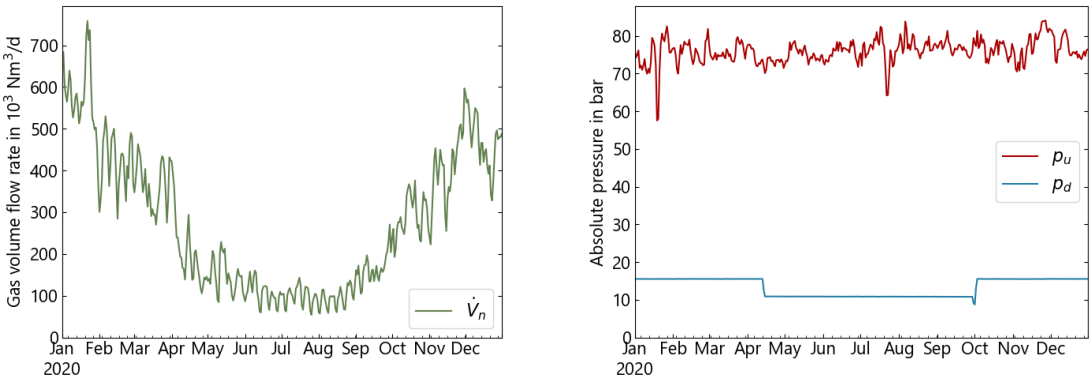

Fig. 11: Measured daily gas flow rate (left) and mean daily pressure levels (right) at the GPRMS Ostheim for the year 2020

Varying pressure conditions are a challenge as the expansion turbine (nozzle, turbine wheel) is designed for given pressure levels. Deviating from the nominal parameters, not only pressures but also flow rate, results in a decrease of the efficiency of the expansion turbine, and thus a lower power output at the generator. The varying upstream pressure is not a relevant issue for the considered GPRMS, as the total pressure reduction is anyway too important to be achieved solely by the expansion turbine. This is illustrated in Fig. 12, representing the calculated required gas temperature upstream of the expansion turbine (red dots) depending on the upstream pressure for a set downstream pressure of 12 bar as well as set downstream temperatures of 5 °C (Fig. 12, left) and 15 °C (Fig. 12, right) for methane. The isentropic efficiency of the expansion turbine is set to 0.65. The evolution of the upstream gas temperature required for the expansion process with the turbine follows a logarithmic pattern. With the considered assumptions, reducing the gas pressure from 58 to 12 bar with the expansion turbine requires an upstream gas temperature of 83 °C. Assuming a logarithmic mean temperature difference (LMTD) of 10 K at the gas preheater and considering distribution losses, this would require the heat pump to supply a flow temperature of at least 95 °C, outside the range of what air-source heat pumps can deliver. For the GPRMS Ostheim it is therefore necessary to reduce the upstream gas pressure before the expansion turbine to an acceptable level. The observed variations of the gas upstream pressure are thus not a problem for the design of the expansion turbine as far as the nominal upstream pressure is not higher than the minimum supply upstream pressure of the GPRMS. This minimum upstream pressure is usually contractually defined between the operator of the GPRMS and the upstream gas network operator.

For comparison purposes the required upstream gas temperature for the same pressure reductions but achieved with a gas pressure regulator (throttling) is also represented (blue dots) in Fig. 12. The upstream gas temperature required for the throttling increases almost linearly with the upstream pressure at a rate of 0.4 to 0.5 K/bar in the ranges considered. Compared to the expansion process, the required upstream gas temperature and therefore the required energy for preheating is significantly lower for the throttling.

The comparison of both downstream gas temperature levels (Fig. 12 left and right) also shows that an increased downstream gas set temperature, for instance in summer to avoid water vapour condensation on the outer surface of downstream pipes, correspond to an equivalent increase in the required upstream gas temperature. With an upstream gas pressure of 58 bar, the increase of 10 K of the downstream gas set temperature requires an increase of 10.9 K of the upstream gas temperature.

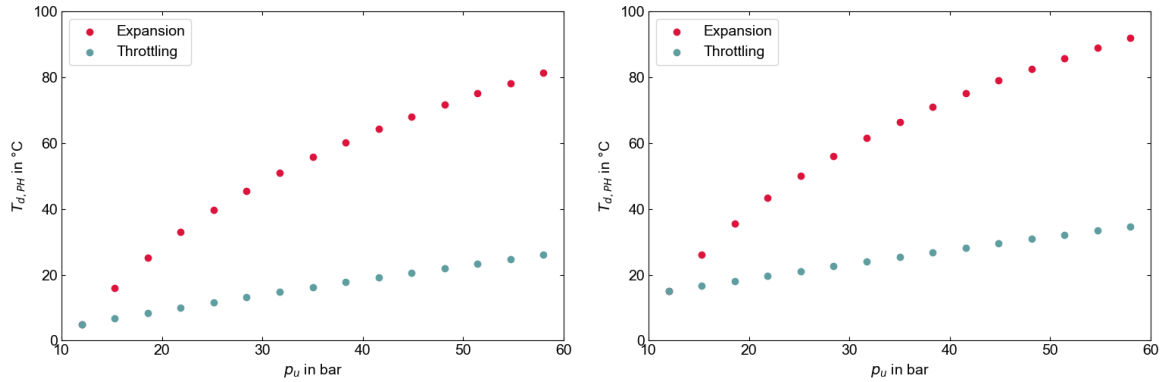

Fig. 12: Calculated upstream gas temperatures for different upstream gas pressures for an expansion process and a throttling process. Calculated for methane with a fixed downstream pressure p_d = 12 bar and a fixed downstream temperature T_d = 5 °C (left) and T_d = 15 °C (right). For the expansion process the isentropic efficiency is fixed, η_s = 0.65.

The variations of the gas downstream pressure (Fig. 11, right) are more problematic for the design of the expansion turbine. Several options can be considered. One consists in designing the expansion turbine for a downstream pressure situated in-between the pressure levels in summer and in winter, so that the expansion turbine never operates in nominal conditions, but the operating point is never "too far" from the design point. The installation of an additional gas pressure regulator downstream of the expansion turbine is another option, linked to increased investment costs and more space requirements. At network level, keeping a constant downstream pressure throughout the year could be also considered, if the operation of downstream GPRMS allows it.

The rated capacity of the power line connecting the GPRMS to the grid is also an important parameter to consider for the design of the expansion turbine. GPRMS are usually situated outside inhabited areas, thus far from main power lines, so that an extension of the rated capacity of the connecting line is often not an option due to the high related costs. The capacity of the line might then be a limiting factor when the expansion turbine additionally to covering the needs of the heat pump is designed to cover the power needs of the GPRMS and export surpluses to the grid. Even if attractive on paper, connecting the expansion turbine to the grid also comes with complications. Indeed, only small network operators as defined by the regulator (BMJV, 2021) are allowed to supply power to the grid due to EU rules on unbundling in the energy sector. According to the current legislation, larger network operators would have to delegate the operation of the expansion turbine to a contractor if they aim at supplying power surpluses to the grid.

4.3. Energetic comparison between throttling process and expansion process

A comparison of the energy flows between the conventional throttling process and the process including an expansion turbine combined to a heat pump is presented in Fig. 13 for identic upstream and downstream conditions.

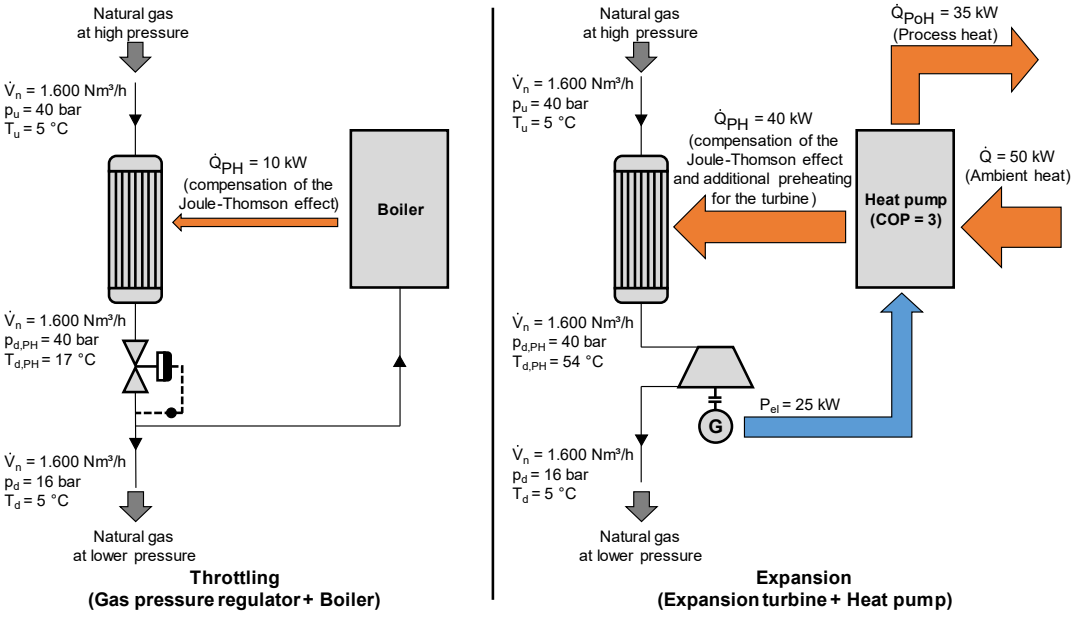

Fig. 13: Schematic comparison of the energy flows in the throttling process (left) and in the process including the expansion turbine (right)

As mentioned in section 4.2 the required gas temperature $T_{d,PH}$ at the outlet of the gas preheater is significantly higher before the expansion turbine than before the gas pressure regulator. In the presented case the heating power needed to preheat the gas is four times higher when using the expansion turbine. Also, the expansion turbine is designed to supply the heat pump exclusively. With an assumed coefficient of performance (COP) of 3, 53 % of the heat output of the heat pump is used to preheat the gas before the expansion turbine, while the remaining 47 % ($\dot{Q}_{PoH}$) can be used to preheat the rest of the natural gas flowing through the GPRMS, for which the pressure is reduced with a conventional throttling process instead of using an expansion turbine.

To theoretically compare the conventional throttling process with the expansion process from an energetic point of view, the GPRMS Ostheim in 2020 is taken as case study (see Fig. 11). For the integration of the expansion turbine unit, the hydraulic configuration presented in Fig. 14 is considered. All the gas flowing through the station is preheated in a first gas preheater, to a temperature allowing to reach the set GOT (T_d) after throttling. Part of the total gas stream flowing through the station flows through the expansion turbine unit while the rest of the gas stream passes through the existing line with the conventional gas pressure regulator. The gas stream flowing through the expansion turbine unit requires a pre-throttling and an additional preheating before passing through the expansion turbine for the reasons explained in section 4.2.

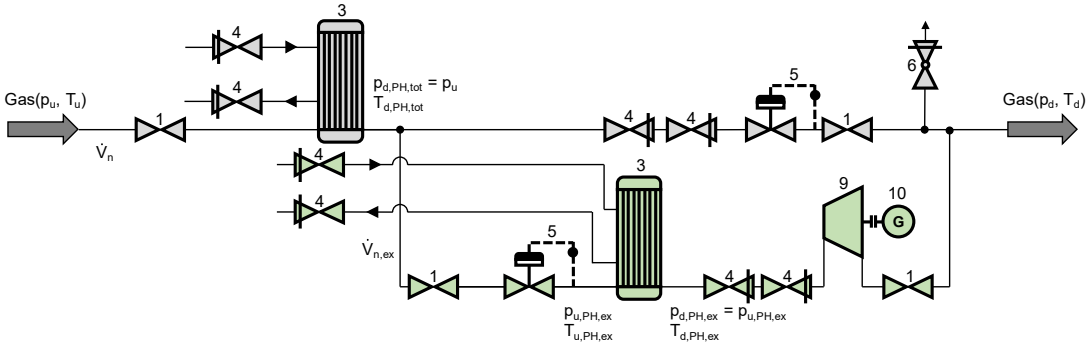

Fig. 14: hydraulic scheme of the considered integration of the expansion turbine unit at the GPRMS Ostheim. The description of the components is given in Fig. 10.

Three operating conditions are compared, corresponding to average operating conditions at the GPRMS Ostheim in summer (mean from June to August), winter (mean from December to February) and autumn / spring (mean from September to November and March to Mai). The temperatures and gas flow rate are averaged over these periods. The measured upstream gas temperature follows the ground temperature at a depth of 1.5 m and the set GOT varies along the year and follows the dew point of the ambient air to avoid condensation on the outside of downstream pipes and components. For simplification purposes the upstream and downstream pressures are considered constant over the year at 76 bar, respectively 14.5 bar corresponding to the flow rate-weighted averages.

The expansion turbine and heat pump unit are designed to cover the entire heat demand of the station for gas preheating on average summer operating conditions. The upstream pressure of the expansion turbine $p_{d,PH,ex}$ is set to 27 bar, so that the converging nozzle operates just below critical conditions. The calculations are performed with methane. The COP of the heat pump is calculated with equation 4-6.2 from Jesper et al. (2021) for standard heat pumps with hydrofluorocarbons or hydrofluoroolefins as refrigerant. The temperature of the source (ambient air) is reduced of 5 K to take into account a higher LMTD at the evaporator as the heat pumps considered in Jesper et al. are water-water heat pumps and not air-water heat pumps. The flow temperature of the heat pump is set to $T_{d,PH,ex}$ + 12 K, assuming a LMTD of 10 K at the gas preheater and heat losses in the distribution loop. In summer a second scenario is considered, where the expansion turbine additionally covers the power demand of the GPRMS amounting to 5 kW_{el}. For the calculation of the electric power of the generator of the expansion turbine, the isentropic efficiency, mechanical efficiency, and generator efficiency are fixed to 0.65, 0.97, and 0.975 respectively. To calculate the primary energy savings, a gas boiler utilisation ratio of 0.85 (based on net calorific value) is considered as well as primary energy factors of 1.1 for natural gas and 1.8 for electricity. The savings are calculated for the total energy demand of the GPRMS (power and heat for gas preheating) compared to a case where the pressure reduction takes place with a conventional throttling.

Tab. 2: Calculated temperatures and performance of the expansion turbine and heat pump unit for different representative operating conditions of the year. The expansion turbine unit is designed to meet the total heat demand of the station in a typical summer day. Values marked with an asterisk (*) are measured.

Parameter	Unit	Summer (mean Jun-Aug)	Summer (mean Jun-Aug) incl. GPRMS power	Winter (mean Dec-Feb)	Autumn / spring (mean Sep-Nov & Mar-Mai)
$\dot{V}_n$ (*)	m³/h	4,170	4,170	20,418	10,926
T_u (*)	°C	13.8	13.8	7.9	10.7
T_d (GOT) (*)	°C	15.7	15.7	4.8	8.1
$T_{d,PH,tot}$	°C	40.6	40.6	31.5	34.3
$T_{u,PH,ex}$	°C	21.6	21.6	11.5	14.2
$T_{d,PH,ex}$	°C	46.3	46.3	34.9	38.5
T_{amb} (*)	°C	18.3	18.3	4.0	10.0
COP	-	3.6	3.6	3.3	3.5
$\dot{V}_{n,ex}$	m³/h	2,214	2,842	2,214	2,214
$P_{el,ex}$	kW	25.0	32.1	24.0	24.4
$\dot{Q}_{HP}$	kW	89.0	96.5	80.0	85.5
$\dot{Q}_{aux}$	kW	0.0	0.0	220.0	86.0
$\dot{Q}_{PE,save}$ (GPRMS)	%	90.0	100.0	19.4	39.1

The results are presented in Tab. 2. At the design point in summer, 53 % of the total gas flowing through the station flows through the expansion turbine unit. The expansion turbine has an electric power of 25 kW respectively 32 kW (+28 %) if the power demand of the GPRMS is also covered. It results in primary energy savings of 90 % respectively 100 % in summer. With this dimensioning of the expansion turbine, primary energy savings of 39 % can be achieved in autumn / spring and 19 % in winter. The savings would be increased by 4, respectively 3 %-point if the power consumption of the station was additionally covered by the expansion turbine (not presented in Tab. 2). As indication, 42 % of the total annual energy demand for gas preheating took place in 2020 over the three winter months, 47 % during the six autumn / spring months and the remaining 11 % during the three summer months. The slight decrease of the expansion turbine electrical power observed in autumn / spring and winter compared to summer is caused by different gas properties due to lower gas temperatures. Interestingly the COP of the heat pump does not significantly vary along the year as the lower ambient air temperatures are compensated by lower GOT in winter and autumn / spring than in summer, due to lower water vapor dew point temperatures.

5. Conclusions and outlook

Novel concepts for the decarbonisation of gas preheating in the gas transport sector are presented in this work. Air dehumidification by a novel liquid desiccant air conditioning system could already be realized in a long-term field test and showed additional primary energy savings of 11.6 % for a year compared to a reference case without dehumidification. The solution combining an expansion turbine with heat pumps is still in the design phase, but preliminary investigations also showed a good potential for further savings. By designing the expansion turbine and heat pump unit to cover the total typical heat demand of the studied GPRMS in summer, 90 % primary energy savings can be achieved on typical summer days, 39 % in autumn / spring and 19 % in winter, considering the total energy consumption of the GPRMS (electric power and heat demand). Increasing the nominal power of the 25 kW_{el} expansion turbine by 28 % enables covering the power demand of the GPRMS, and thus allows further primary energy savings. Further investigations, including economic considerations are foreseen to compare the different configurations in more details. Whether these systems will be adopted in the future remains to be seen, depending on possible regulatory barriers and their economic viability.

6. Acknowledgments

The authors are thankful to the Federal Ministry for Economic Affairs and Climate Action (BMWK) for funding the research project ASTEREX (grant number: 03EE5101A) and to State of Hesse for funding the project LDAC-Anlage (grant number: 20005248) through the European Regional Development Fund.

7. References

BMJV, 2021. Energiewirtschaftsgesetz vom 7. Juli 2005 (BGBl. I S. 1970, 3621), das zuletzt durch Artikel 84 des Gesetzes vom 10. August 2021 (BGBl. I S. 3436) geändert worden ist, EnWG.

DVGW, 2015. Technische Regel – Arbeitsblatt – DVGW G 499 (A) – Erdgas-Vorwärmung in Gasanlagen. DVGW, Bonn.

Jesper, M., Schlosser, F., Pag, F., Schmitt, B., Walmsey, T.G., Vajen, K., 2021. Large-scale heat pumps: Uptake and performance modelling of market-available devices, Renewable and Sustainable Energy Reviews, Volume 137, https://doi.org/10.1016/j.rser.2020.110646

Louvet, Y., Ritter, D., Pag, F., Heinzen, R., Grebe, D., Vajen, K., 2021. Innovative erneuerbare Wärmeversorgungskonzepte für die Dekarbonisierung des Gastransportsektors, in: Proceedings 31. Symposium Solarthermie und innovative Wärmesysteme. Bad Staffelstein, Germany.

Mischner, J., Fasold, H.-G., Heymer, J., Förster, F., Altfeld, K., Deutsch, M., 2015. Gas2energy.net: systemplanerische Grundlagen der Gasversorgung, 2., überarbeitete und erweiterte Auflage. ed, Edition gwf Gas, Erdgas. DIV, Deutscher Industrieverlag, München.

Mischner, J., Köstner, R., Krause, K., 2019. Schaltungen zur Energierückgewinnung für die Gasvorwärmung in Gasdruckminderungsanlagen, Fachberichte Neue Technologien. gwf Gas + Energie.

Solbraa, E., 2022. NeqSim - an open source process simulation software [WWW Document]. NeqSim. URL https://equinor.github.io/neqsimhome/ (accessed 7.22.22).

Wimmer, L., Ritter, D., Louvet, Y., Heinzen, R., Grebe, D., Vajen, K., Jordan, U., 2019. Monitoring of renewable process heat plants within the gas sector, in: Proceedings of the ISES Solar World Congress 2019. Santiago, Chile, doi:10.18086/swc.2019.12.14

List of symbols

$c_{p,m}$	mean isobaric specific heat capacity in J/kg/K
h	specific enthalpy in J/kg
p	absolute pressure in bar
p^*	critical pressure in bar
P_{el}	electric power in W
$\dot{Q}$	heating capacity in W
Q	heating energy in J
s	specific entropy in J/kg/K
T	temperature in °C
$\dot{V}_n$	gas volume flow rate at standard temperature and pressure (STP) in m³/s
Δh_i	specific enthalpy difference (real) in J/kg
Δh_s	specific enthalpy difference (ideal) in J/kg
$\Delta\omega$	humidity ratio difference in kg/kg
η_s	isentropic efficiency
$\mu_{JT,m}$	Joule-Thomson coefficient in K/bar
ρ_n	gas density at STP in kg/m³
ω	humidity ratio in kg/kg

Subscripts

abs,in	absorber inlet
abs,out	absorber outlet
amb	ambient
aux	auxiliary heater
d	downstream
ds	downstream, ideal isentropic expansion
ex	expansion turbine
goal	ideal set point
HP	heat pump
meas	measurement
PE	primary energy
PH	preheating
phys	physical
PoH	process heat
ref	reference
reg	regenerator
save	saved
tot	total
u	upstream

G. Solar Air Conditioning and Refrigeration

Experiments On a Solar Vapour Absorption Refrigeration Cold Storage System

Mani A[1] and Vijayakumar S[1]

[1]Department of Mechanical Engineering

Indian Institute of Technology, Chennai, India.

Abstract

Combining two rapidly growing technologies, such as solar energy and vapour absorption refrigeration cold storage, will result in an innovative solution to address the increasing demand for cold storage for food preservation systems. The effects of several operational parameters such as condenser temperature, evaporator temperature, and generator temperature on the performance of a solar vapour absorption refrigeration cold storage system were studied in this work. Using solar energy, vapour absorption refrigeration system, a cold room cabin temperature of 8°C was achieved with a cooling load of 3.5 kW capacity and a hot water inlet temperature of 103.1°C, and a cooling water inlet temperature of 32.6°C during experimentation.

.

Keywords: Solar energy, Vapour Absorption Refrigeration, Cold storage, R134a-DMF

1. Introduction

Absorption refrigeration is being investigated as an alternative to vapour compression refrigeration due to its potential use of solar energy, waste heat utilisation, etc. In India's, the world's energy and environmental scenarios are rapidly changing. As a result of this, renewable energy was considered as one of the options to the Second Law standpoint of energy conversion. According to the World Economic Forum, India has one of the highest rates of food losses as waste in the world, with yearly harvest and post- harvest losses in fruits, vegetables, and grains reaching to Rs 440 billion. One of the primary causes of food waste and loss is a lack of cold chain infrastructure, which includes refrigerated transport, pack houses, collection centers, and cold storage. As a result, in order to reduce wastage of the above, the development of a solar cold storage technique will solve the above, as well as energy and environmental challenges in the natural and international scenarios. Remote places/villages, farmers with enormous output capacity, and others will benefit from a solar-powered cold storage system. Combining two growing technologies like solar energy and vapour absorption cold storage will result in an innovative solution that is environmentally friendly. Solar cold storage systems also have negligible operational costs.

2. Literature Review

Numerous researchers have experimented with different solar-based heating and cooling system applications. Using solar energy, Sozen et al. (2002) conducted experimental research on a prototype aqua-ammonia absorption heat pump system. A parabolic-shaped collector was incorporated into the system's design to provide the generator with the high-temperature water it needs, and a thermodynamic analysis demonstrates that the absorption system's performance depends on both losses and irreversibility. According to research, the system's evaporator and absorber parts of the system have more exergy loss than the other parts. In (2002), Sumathy et al. developed a 100 kW LiBr-H_2O absorption chiller. By utilising a two-stage chiller, the proposed method can achieve nearly the same total COP as the conventional system at a cost reduction of about 50%. It can be used when the generator temperature is between 60 °C and 75 °C. Shaarawi et al. developed solar-powered LiBr-water absorption air conditioning for a typical family home's continual cooling demand of 5 kW. The results show that the most efficient design for consistently delivering the cooling effect throughout the day is the hybrid cold and refrigerant storage system.

The performance of VARS is influenced by the heat of vaporization of the refrigerant, solubility of the refrigerant in solvent and pressure range of the refrigerant over the operating cycle. The choice of the system's working fluids

© 2022. The Authors. Published by International Solar Energy Society
Selection and/or peer review under responsibility of Scientific Committee
doi:10.18086/eurosun.2022.06.01 Available at http://proceedings.ises.org

should take into account the system's economic, environmental, and thermodynamic characteristics. The commercial working fluids for absorption refrigeration systems are the refrigerant-absorbant combination like Ammonia - Water and Water - LiBr. However, there are significant drawbacks associated with the above two pairs, such as toxicity and corrosion for ammonia systems and vacuum pressure, crystallizationsation effect for LiBr systems. Due to these limitations, alternative refrigerants have been explored by with R134a-DMF emerging as one of the option due to its good thermodynamic, chemical, and transport properties and ODP of 0.001.

Yokozeki (2005) estimated the performance of VARS by combining various absorbents with various refrigerants. R134a-DMF pair has a greater COP than other R134a combinations and requires a lower circulation ratio than other combinations. The performance of the intended solar collector will have the most impact on the choice of an absorption cooling device. The most popular kind of solar collector is flat-plate collectors, including a metallic absorber and an insulated housing on top of which are placed glass plates. In high temperatures, evacuated collectors function better and lose less heat. In order to endure the pressure differential between the atmosphere and the vacuum, evacuated collectors are commonly constructed with a metallic absorber placed within an evacuated glass tube. The experimental investigation of a LiBr-water absorption system run by evacuated tubes and flat plate solar collectors was provided by Darkwa et al. (2012). There are four hot water storage tanks connected to the system. According to the experiment results, water heated to 96.3 °C and supplied by solar collectors can achieve a coefficient of performance (COP) of 0.69.

Numerous experts have reported on the impact of different designs and parameters that are operational on the COP of solar refrigeration systems. The generator that is optimal was determined to be greater than the constant temperature process under constant pressure, according to a study on phase-change materials, the system's COP can increase by up to 2.4 times compared to a single stage as the latent heat of the refrigerant increases. The efficiency of the absorption that is solar is increased when a heat pump is added to the refrigeration system, making it easier to achieve cooling under various climatic conditions.

3. Fabrication of solar cold storage system

The three main categories in which the fabrication work for the solar cold storage system is done are Vapour absorption refrigeration cold storage systems, solar photovoltaic systems and solar thermal collection systems. The schematic diagram for the solar cold storage system shown in Fig.1 is created by combining these three subsystems.

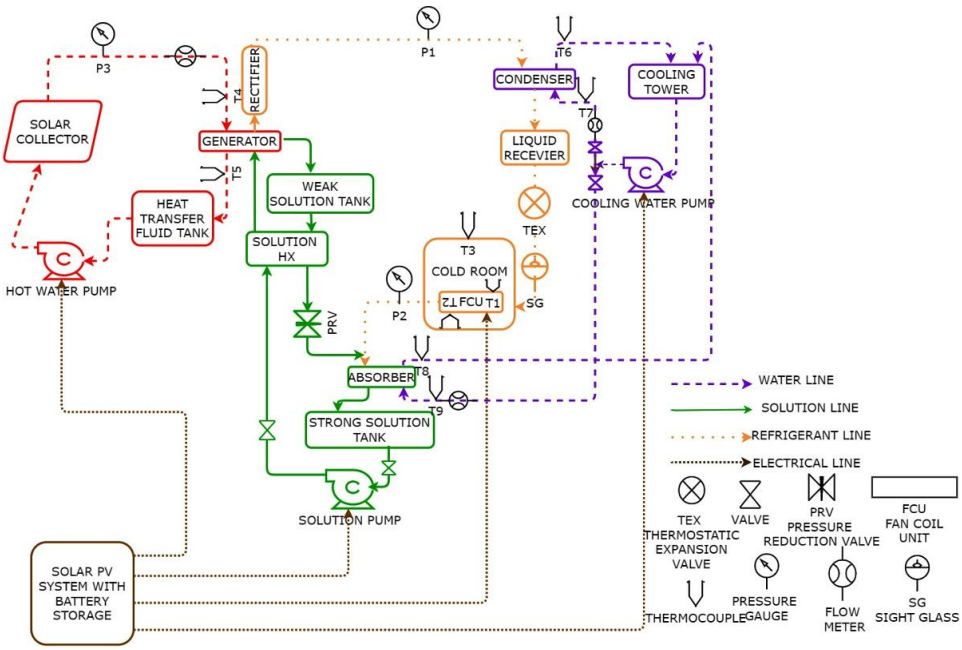

Fig. 1: Schematic diagram of solar cold storage experimental setup.

3.1 Solar PV system

Solar Photovoltaic system is designed to supply the electrical power required to run Pumps, Fans of the system. In general, the Solar PV system mainly consists of solar panels, Inverter, battery, electrical control system with necessary electrical wiring connections. Solar panels are used to convert incident solar energy into electrical energy. Crystalline silicon is the predominant material used in most of the solar panels. Inverter is used to convert the DC power produced by solar panels into AC power. Battery is used to store the DC power for back up time duration likely considering cloudy phenomena. Electrical control system mainly consists of Variable frequency drive along with electrical switches, relays and PLC's.

A 36 panels of 11.5 kW (34 × 325W, 2 × 340W) capacity is installed for running cooling water pump, hot water pump, solution pump, cooling tower motor, evaporator unit fan and lighting arrangements of the cold room. First of all, the supporting structure made up of aluminium frames for placing the panels are installed. Over the supporting structure, the panels are mounted in series array arrangement. The supporting structures are further strengthened by providing concrete civil work to withstand natural disasters like cyclone. Figure.2 shows the assembled view of Solar PV Panels.

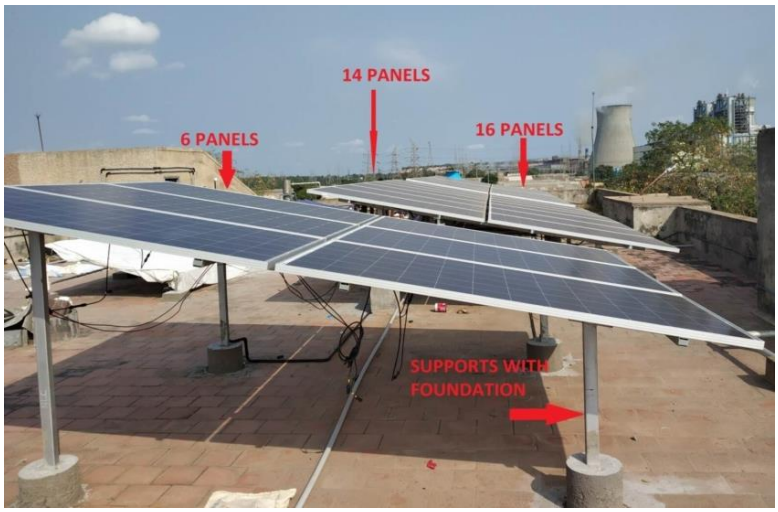

Fig. 2: Photograph of solar photovoltaic panels

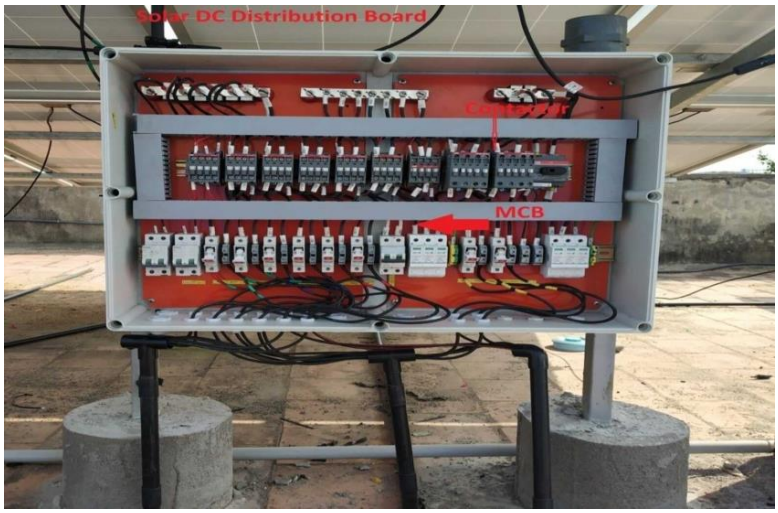

Fig. 3: Photograph of solar DC distribution board

The electrical connections from the panels are connected to Inverter through DC distribution board. DC distribution board mainly consist of contactors, Multiple Circuit Breaker and fuse arrangements as shown in Figure 3. The DC distribution is connected in such way that 2 series of 18 panels each for the rated supply to cater all pumps and fans. However, in starting time of system operation, a delay of two minutes is required to start the motor of solution pump. The energy produced from solar in that two minutes are used to charge the battery backup. A 10 kVA capacity Inverter is used to convert the solar produced DC power to AC power to run the pumps, fans and lighting arrangements. The inverter, battery bank and control board are shown in Figure 4. The electrical control board consist of two VFD's , PLC with Relay arrangement, MCB and control switches to motors of each pump separately. One VFD is used to control the cooling water pump, hot water pump, cooling tower motor and another is used to control the solution pump.

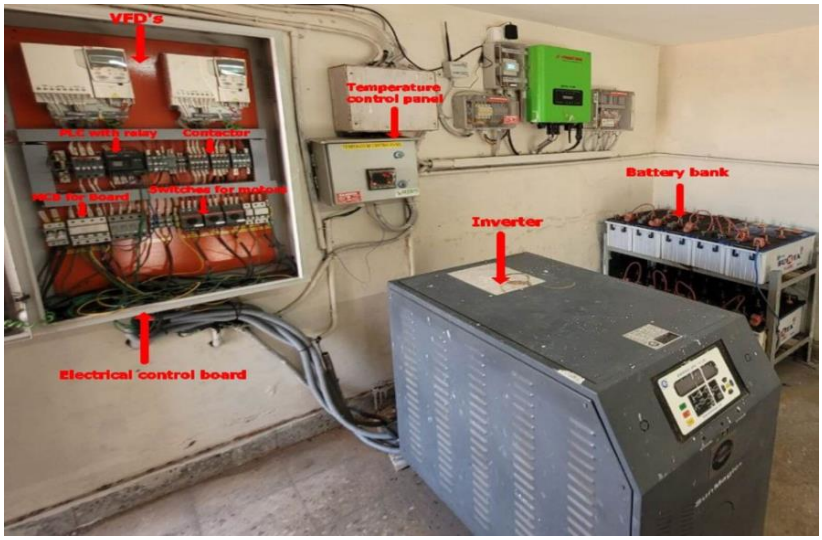

Fig. 4: Photograph of electrical control panel containing inverter, VFD, battery bank etc.,

3.2 Solar thermal collection system



Fig. 5: Solar thermal evacuated tube collector system

Solar collectors are special kind of heat exchangers that transform solar radiation into heat. The collector is a device which absorbs the incoming solar radiation, converts it into heat, and transfers this heat to water flowing through the collector. Evacuated tube collectors (ETC) are used in this project because of their excellent performance at high temperatures. ETC mainly made up of evacuated tube, heat pipe with heat transfer fluid, heat transfer fins. Solar thermal system consists of ETC, solar thermal energy storage tank, hot water pump with required pipe connections. In the system De-Mineralized water is used as heat transfer fluid to transfer the heat from collector system to vapour absorption refrigeration system. Solar ETC collector system is shown in Figure.5



Fig. 6: Sensible thermal storage tank with hot water pump



Fig.7: Cooling tower with cooling water pump

The piping connections involved in the solar collector system are well insulated in such a way that there will be minimal heat loss during the transfer of DM water from one component to another. A 70 mm thickness of glass wool is used as an insulating material. Figure.6 shows the sensible thermal storage tank and hot water pump. Figure.7 shows the cooling tower with cooling water pump which is used to chill the heated water coming from the condenser and absorber by rejecting heat to ambient air.

3.3 Vapour absorption refrigeration and cold storage system

Liquid refrigerant evaporates in the evaporator by absorbing heat from the product's cold room thereby producing refrigeration. Refrigerant vapour from the evaporator is absorbed in the absorber by a stream of weak refrigerant solution. The heat of mixing is removed by the cooling water. Strong refrigerant solution formed after absorption is pumped to the generator by solution pump. Solar energy in the form of hot water is supplied to the generator to boil off the refrigerant vapour from the strong solution. This vapour also contains some absorbent vapour due to affinity between refrigerant and absorbant and low boiling point difference between absorbant and refrigerant. The refrigerant vapour is rectified in the heat exchanger to get refrigerant vapour. This vapour is condensed in condenser by supplying cooling water, and liquid refrigerant is stored in the condensate tank. This tank supplies liquid refrigerant to the evaporator through thermostatic expansion valve and capillary tube. Weak refrigerant solution leaving the generator is sent to absorber for absorption through pressure reduction valve. A solution heat exchanger is provided to cool the weak hot solution before entering the absorber and preheat the strong solution before entering the generator. Thus VARS undergoes cyclic operation to produce continuous refrigeration effect. Cooling water is supplied by cooling tower through cooling water pump to both absorber, condenser by parallel connection. Figure.8 shows cold room with Vapour Absorption Machine.



Fig.8: Vapour absorption refrigeration and cold storage system

4. Experimental setup and Procedure

To experiment with the system, first, ensure that all of the panels are correctly connected according to the design. Then, turn on all of the MCBs in the solar DC distribution panel and ensure that the DC power produced by the solar panels is sent to the inverter. Then, turn on the inverter input, output, battery, and solar MCB in the inverter board, and press the START button in the inverter panel. After that, turn on the MCBs in the control panel in the following order: solar supply, input to control board, PCU switch, pressure switch, output to DC distribution board, and all motors and then, test the solar collector system's functioning. Check that all valves in the vapour absorption refrigeration system are open for operation. Open the bypass valve in the pump line at first, and gradually close it as the pressure rises. Take temperature and pressure readings at all pre- determined locations and combine them. To find the water flow rate at the absorber, generator, and condenser, measure the pressure drop across the respective orifice plates. Measure the airflow rate and temperature differential across the evaporator coil for evaporator side cooling. To examine the performance of the system using time-to-time operation, repeat the observations for each predetermined time interval of 30 minutes.

For evaluating the performance of vapour absorption refrigeration system (VARS), the following procedures are followed.

Evaporator load, Qe :

$Q_e = m_a \times Cp_a \times \Delta T_e - (Q_{losses,wall})$

Where,

ma = mass flow rate of air across evaporator

T_3= Average air side temperature around the evaporator fan coil unit

T_{10}=Ambient Temperature

ma = ρa × Acoil × Vair

A_{coil} = Area of FCU coil

Condenser heat rejection rate, Qc :

$Q_c = m_{cw,c} \times C_{pw} \times \Delta T_{cw.c}$

Where,

$m_{cw,c}$ = mass flow rate of cooling water across condenser = ρw × Qcw,c

$V_{cw,c}$ = 6.943984 × 10-6 × √(ΔP2)

$\Delta_{Tcw,c}$ = cooling water temperature difference across condenser

Absorber heat rejection rate, Qa :

$Q_a = m_{cw,a} \times C_{pw} \times \Delta T_{cw,a}$

Where,

$m_{cw,a}$ = mass flow rate of cooling water across absorber = $\rho_w \times Q_{cw,a}$

$V_{cw,a}$ = 6.943984 × 10-6 × √(ΔP3)

$\Delta_{Tcw,a}$ = cooling water temperature difference across absorber

Generator heat load, Qg :

$Q_g = m_{hw,g} \times C_{pw} \times \Delta T_{hw,g}$

Where,

$m_{hw,g}$ = mass flow rate of hot water across generator = $\rho_w \times Q_{hw,g}$

$V_{hw,g}$ = 5.980159 × 10-6 × √(ΔP1)

$\Delta_{Thw,g}$ = hot water temperature difference across generator

Coefficient of Performance for VARS, COP = Q_e / Q_g

Where,

Qe = evaporator load

Qg = generator heat load

5. Results and Discussion

From the experimental studies, the overall performance of the vapour absorption refrigeration system is presented based on the various operational parameters like hot water and cooling water inlet and outlet temperatures.

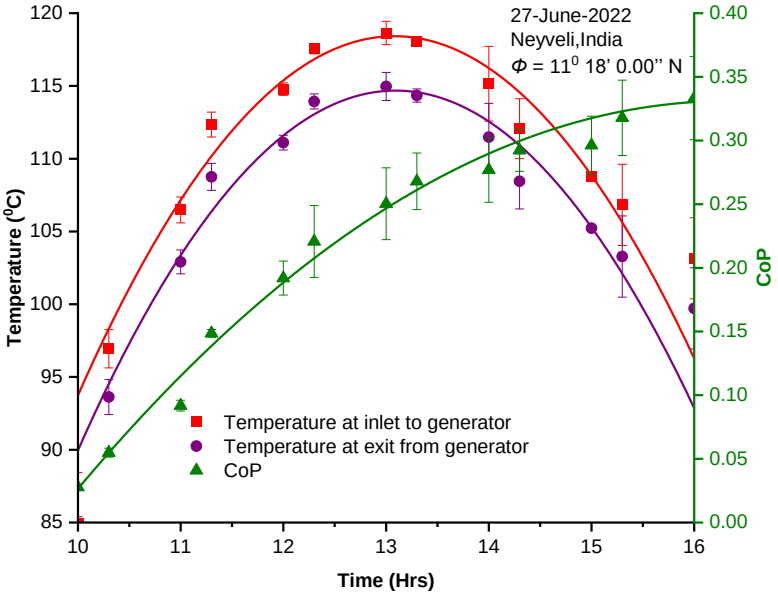

Fig. 9: Effect of variation of generator temperature and CoP with time

The performance of the VAR system along with generator inlet and outlet temperature with respect to time is shown in Fig.9. The hot water give heat to generator, as the outlet temperature is always less than that of inlet conditions. As the hot water inlet temperature increases with time, the generation of refrigerant vapour increases. So the evaporator temperature in cold room cabin decreases as the result of increased CoP.

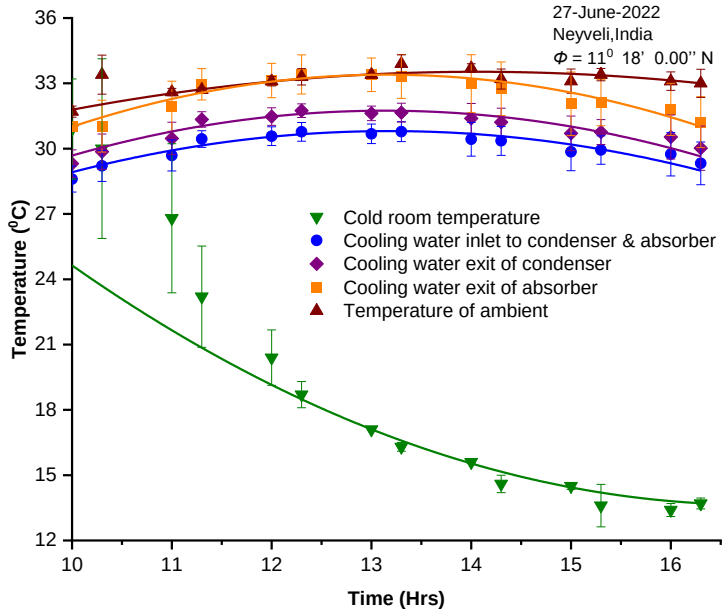

Fig. 10: Variation of cold room temperature, Ambient temperature, Cooling water inlet temperature for condenser and absorber and Cooling water outlet temperature for condenser and absorber with time

Variations of cold room cabin temperature, ambient temperature, cooling water inlet temperature for condenser and absorber and outlet temperature of condenser and outlet temperature of absorber variation with time is shown in Fig.10. The cooling water inlet to both absorber and condenser is made in parallel connection to increase the performance of the system, so that inlet condition of cooling water to both absorber and condenser is same. As the cooling water in absorber and condenser upon removing the heat from the respective components, the outlet conditions is higher than that of inlet conditions.

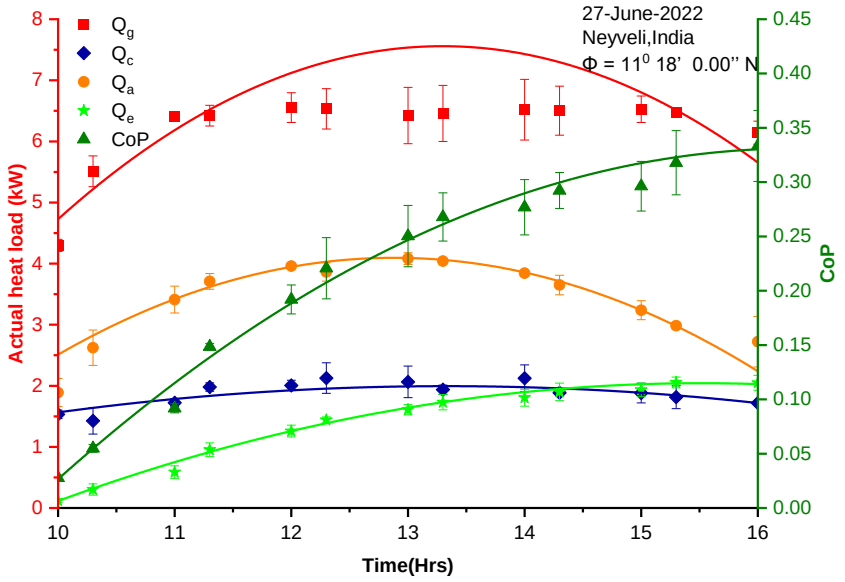

Fig. 11: Effect of variation of actual heat load and CoP with time

From Figure 11. The generator and evaporator heat load increases with time and then decreases. CoP of the system increases with time as the increases in Q_e is higher than Q_g.

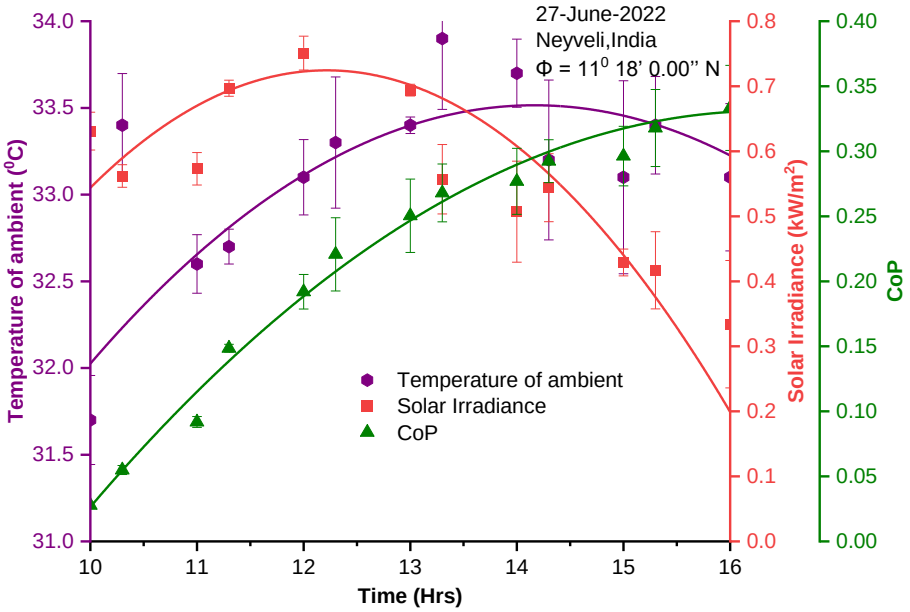

Fig. 12: Effect of variation of solar irradiance, ambient temperature and CoP with time

Figure.12 shows the variation of the ambient temperature, solar irradiance, and COP with time. The Solar Irradiance increases with time and then decreases and ambient temperature keeps in phase with time. CoP of the system increases with time due to increase in Q_e.

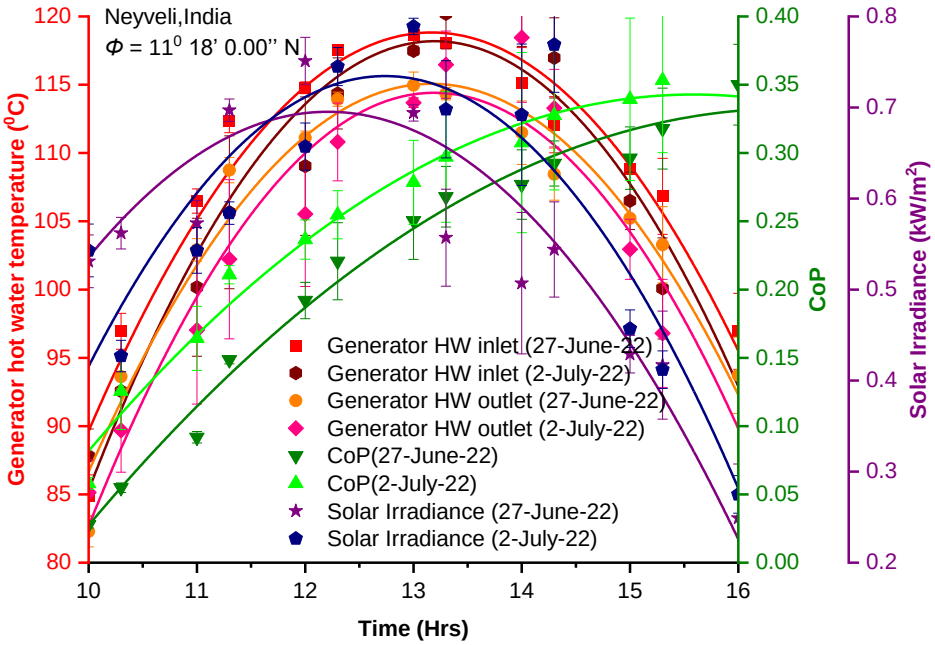

Fig. 13: Variations of operational parameters in the solar vapour absorption refrigeration system.

Temperature at the generator's hot water inlet and outlet vary in phase with solar irradiance on two distinct days. Thus, whenever solar irradiance increases, the Coefficient of performance of the system increases as shown in figure 13.

6. Conclusions

The influence of different operational parameters such as condenser temperature, evaporator temperature, and generator temperature on the performance of the solar Vapour absorption refrigeration cold storage system has been carried out. From the system's performance, the following conclusions have been drawn.

i. As the generator temperature rises, the evaporator temperature decreases, increasing the condenser heat rejection rate. As the generator's heat load decreases, the system's overall performance improves.

ii. The generator hot water inlet temperature, generator hot water exit temperature and CoP increase with increasing solar Irradiance.

Acknowledgments

Thankfully acknowledge the financial and administrative support of Centre for Applied Research and Development, Neyveli Lignite Corporation India Limited, Neyveli.

References

Adnan Seozen and Duran Altıparmak (2002) Development and testing of a prototype of absorption heat pump system operated by solar energy, Applied Thermal Engineering, 22,1847–1859

Balamurugan. P and Mani. A (2012) Experimental studies on heat and mass transfer in tubular generator for R134a-DMF absorption refrigeration system, International Journal of Thermal Sciences, 61, 118-128

Darkwa , S. Fraser and D.H.C. Chow (2012) Theoretical and practical analysis of an integrated solar hot water-powered absorption cooling system Energy, 39 ,395-402

Gosney, W.B. Principles of Refrigeration. Cambridge University Press, London, 1982.

Muthu, V., R. Saravananand S. Renganarayanan (2008) Experimental studies on R134a-DMAC hot water-based vapour absorption refrigeration systems. International Journal of Thermal Sciences, 47, 175-181

Radwan A. Almasri and Nidal H. Abu-Hamdeh (2022) Thermal solar sorption cooling systems - A review of principle, technology, and applications, Alexandria Engineering Journal 61, 367–402

Sumathy and Huang (2002) Solar absorption cooling with loaw grade heat source-A strategy of development in south china, Solar Energy 72,155–165

Saravanan, R., and Maiya, M.P., (1998) Thermodynamic comparison of water-based working fluid combinations for a vapour absorption refrigeration systems. Applied Thermal Engineering, 18, 553–568

Venkatesh A and Mani. A (1989) Comparison of performance of single stage and two-stage intermittent ammonia water solar refrigeration system, International Journal of Solar and Wind Technology, 6 (1), 75-78

Yokozeki, A. (2005) Theoretical performances of various refrigerant-absorbent pairs in a vapour absorption refrigeration cycle by the use of the equation of state, Applied Energy, 80, 383-39

Xingjian Zhang, Hui Li and Chunxin Yang (2015) A novel solar absorption refrigeration system using the multi-stage heat storage method, Energy and Buildings 102, 157–162

https://www.iea.org/reports/renewables-integration-in-india

http://www.fnbnews.com/Top-News/cold-storage-infrastructure-and-wastage-of-perishables-64154

Appendix: Units and Symbols

Table 1: symbols for miscellaneous quantities

Quantity	Symbol	Unit
Area	A	m^2
Volume flow rate	V	$m^3\ s^{-1}$
Mass flow rate of air	m_a	$kg\ s^{-1}$
Mass flow rate	$\dot{m}$	$kg\ s^{-1}$
Evaporator load	Q_e	kW
Condenser heat rejection rate	Q_c	kW
Absorber heat rejection rate	Q_a	kW
Generator heat load	Q_g	kW
Temperature	T	^0C
Overall heat transfer coefficient	U	$W\ m^{-2}\ K^{-1}$
Efficiency	η	
Density	ρ	$kg\ m^{-3}$
Time	t	s

Abbreviations

VARS- Vapour Absorption Refrigeration system

ODP- Ozone depletion potential

DMF-Dimethylformamide

CoP-Coefficient of Performance

PV-Photovoltaic

VFD-Variable Frequency Drive

PLC-Programmable logic controller

DC-Direct current

AC-Alternating current

MCB-Multiple circuit breaker

ETC-Evacuated tube collector

DM-Demineralized

VAM-Vapour Absorption Machine

Adapted components and showcases on solar cooling systems in sunbelt region countries

Marco Beccali[1], Salvatore Vasta[2], Wolfgang Weiss[3], Ben Alex Baby[1] and Marina Bonomolo[1]

[1] Università degli Studi di Palermo, Dipartimento di Ingegneria, Palermo (Italy)

[2] Consiglio Nazionale delle Ricerche, ITAE, Messina (Italy)

[2] Ergosol, Fairfield (United States)

Abstract

As global temperatures are hitting new heights, demand for air-conditioning is increasing. In this light, the improvement of solar cooling systems and their actual performance need to be investigated. IEA – SHC Task 65 Solar Cooling for Sunbelt regions focuses on innovations for affordable, safe, and reliable Solar Cooling systems. The project focuses on solar energy, either solar thermal or solar photovoltaic, in the Sunbelt region, taking into account the different boundaries worldwide (sunny and hot, and humid climates, between the 20th and 40th degrees of latitude in the northern and southern hemisphere). The task consists of four main subtasks to investigate different aspects of the study: adaptation, demonstration, assessment & tools, and dissemination. This paper presents the results of a survey conducted within the activities of two subtasks: adapted components (A2) and showcases on system and component level (B1).

Keywords: solar cooling, adapted component, case study, Sunbelt region

1. Introduction

The population is growing, the incomes are rising, the rise in global temperature, and the increase in comfort standards are causing the increase in air-conditioning demand. Nowadays, air conditioners and electric fans account for about a fifth of the total electricity in buildings around the world – or 10% of all global electricity consumption (IEA, 2018). If measures are not taken to counteract this increase, the space cooling demand will almost triple by 2050; it can reach 6,200 TWh or 30% of the total electricity use in buildings. Such estimations are generally based on the most recently available conventional technologies for air-conditioning and refrigeration.

While the OECD (Organisation for Economic Co-operation and Development) countries in Europe, the US, Australia etc., are taking the lead in solar cooling technology both in thermal and photovoltaic (PV), most of the countries in the Sunbelt regions need more momentum in terms of technology and funding to propel this further. Countries that fall between 20 and 40 degrees of latitude face an increase in cooling demand on one side and higher solar irradiation on the other, thus making it a one-stop solution to utilize the potential of solar cooling and try to invert the current trend. The Green Cooling Initiative (Gloel et al., 2015) estimates a steep rise in the use of conventional air conditioning units from 918 million to 3.5 billion by 2050.

In this light, IEA Solar H&C PROGRAM task 65 focuses on innovations for affordable, safe, and reliable solar cooling systems. The project focuses on solar energy, either solar thermal or solar photovoltaic, in the Sunbelt region, taking into account the different boundaries worldwide (sunny and hot, and humid climates, between the 20th and 40th degrees of latitude in the northern and southern hemisphere).

Solar cooling systems have gained significant attention as an environmentally friendly and sustainable solution for meeting the cooling demands in Sunbelt region countries. These systems incorporate adapted components and are tailored to these countries' unique requirements and climatic conditions. By harnessing abundant solar energy and optimizing cooling technologies, solar cooling systems in Sunbelt region countries offer immense potential for reducing energy consumption, enhancing comfort, and mitigating climate change impacts.

The above-mentioned task consists of four main subtasks to investigate different aspects: adaptation, demonstration,

© 2022. The Authors. Published by International Solar Energy Society
Selection and/or peer review under responsibility of Scientific Committee
doi:10.18086/eurosun.2022.06.02 Available at http://proceedings.ises.org

assessment & tools and dissemination. This paper presents the results of a survey conducted within the activities of two subtasks: Adapted components (A2) and showcases on system and component level (B1). The expected goal of the project is to deepen the understanding of how varying climatic conditions and operating parameters affect the choice of components and identify the factors that enable or pose challenges to widespread application in the region. Indeed, solar cooling systems designed for sunbelt region countries incorporate components specifically adapted to the local climate and environmental conditions. These components are selected to optimize the system's performance and ensure its reliability in high-temperature regions. Some of the key adapted components include Solar Collectors: Solar collectors used in sunbelt region countries are designed to capture and convert a maximum amount of solar radiation into thermal energy. Furthermore, they are optimized to operate efficiently even in high ambient temperatures, ensuring optimal energy generation throughout the year.
Sorption Chillers: sorption chillers are commonly employed in solar cooling systems. These chillers use the heat generated by solar collectors to drive the cooling process. Adapted chillers have improved heat transfer capabilities, enhanced efficiency, and increased tolerance to higher inlet temperatures, making them suitable for sunbelt region countries.
Heat Rejection Systems: Heat rejection systems, such as cooling towers or dry coolers, are essential for dissipating excess heat generated during the cooling process. Adapted heat rejection systems are designed to operate effectively in hot climates, providing efficient heat transfer and reducing water consumption where applicable.
Thermal Energy Storage: To overcome the intermittent nature of solar energy availability, solar cooling systems in Sunbelt region countries often incorporate thermal energy storage solutions. These storage systems are optimized for higher ambient temperatures and offer effective energy storage and retrieval capabilities, ensuring uninterrupted cooling during periods of low solar radiation. To investigate how a solar cooling system must be adapted in such a severe climate area, scientists developed specific tools and conducted focused experimental campaigns. For example, (Ssembatya et al. 2014) evaluated the performance of solar cooling systems in the UAE climatic conditions by TRNSYS simulation. The system used for simulations was developed to assess the potential of solar cooling systems in this region. The tool developed showed that the system can operate with a thermal COP of 0.60 – 0.80. The experiments then validated such results on a typical day, thus proving that an adapted system can meet its cooling requirement for almost 2/3rd of the year without backup heating and/or cooling.

Litardo (Litardo et al., 2022) recently reviewed all the cooling strategies for warm and humid climates. The authors examined and identified possible solutions for space cooling in hot-humid climates (air system with heat recovery, radiant ceilings coupled with AHU, etc.), including an assessment of the application of these solutions on a case-study building in Mogadishu, Somalia, from the point of view of the cooling demand to the energy consumption of the selected cooling systems. The findings of this work provide helpful information about the performance of the cold delivery systems in harch climatic areas, thus allowing the extrapolation of data for solar-assisted systems. Also (Bentayeb et al.) provided valuable data about such a class of systems. In their study, the authors presented a model that considers the actual functioning of an adsorptive solar fridge that employs activated carbon-methanol pairs regarding weather conditions such as ambient temperature and insolation. The model simulates the cooling performance in two distinct Moroccan climates: Rabat (humid and temperate) and Marrakech (hot and arid). The numerical simulation reveals that the solar refrigerator operates differently in each climate. In Rabat, which has a Mediterranean climate, the cold room temperature can be sustained below 5°C; conversely, in Marrakech, which has a pre-Saharan climate, the system can overheat during the summer and the cold room temperature can reach 17°C. The simulation also indicates that the studied unit poses a problem in both climates as the cold room temperature can drop below 0°C, with a minimum of -15°C during winter.

2. Methodology

The survey was shared and sent to solar cooling experts, researchers and manufacturers. Moreover, to have a more extensive database of information, the survey was upgraded with other data from literature review studies. The survey was divided into two main parts. Each part included information related to one of the two subtasks. In particular, the first part was associated with a first exploratory survey of demonstration cases: it included information such as title, typology of the case (if implemented, detailed project, concept, etc.), the name of the implementer and the owner, the location, the related climate condition, the application sector (process industry, distribution of goods, fish industry, buildings, mining, etc.), technology information of the Thermal Driven Chiller (STD), Solar Thermal collectors (ST), of the PV panels, of the storage, of the heat and cold back up, and the Heat Rejection System (HRS), the description of the demo case, the profile of the energy needs, availability of space for the installation of renewable/energy-efficient technologies, the potential of replication, and availability of data/monitoring system. The

second part included information regarding the actual performance of the components such as thermally driven chiller, electric chiller unit/backup, ST collectors, PV panels, storage, heat and cold backup, heat rejection system, and the description of possible precautions adopted for operation in climatic conditions of the Sunbelt area.

3. Solar Cooling System Types: an overview

This section provides a basic description of solar cooling technologies and focuses on identifying components suitable for different solar cooling systems based on weather profiles. The primary solar cooling systems are illustrated in Figure 1.

One prominent solar cooling system is the PV-assisted system, which primarily utilizes solar energy to generate electricity. This electrical energy is then used to power a conventional vapour compression system. In addition, hybrid Photovoltaic-Thermal (PVT) collectors are employed in cases where the thermal energy from solar radiation is extracted. This integration of PVT collectors has been shown to enhance the efficiency of PV panels.

The following subsections further elaborate on the specific details and workings of PV-assisted systems and PVT collectors.

Another significant solar cooling technology is Solar Thermal (ST) cooling, which encompasses various types and applications. ST energy is harnessed to drive chillers of multiple typologies. The section comprehensively describes ST cooling, including detailed discussions on system components such as solar collectors, thermal energy storage, chillers, and heat rejection methods. Each component is described, highlighting its functionalities and significance within the ST cooling system.

By categorizing the components suitable for different solar cooling systems and considering weather profiles, the section offers valuable insights into the design and implementation of solar cooling technologies. Furthermore, it emphasizes the utilization of solar energy in both PV-assisted systems and ST cooling, showcasing the potential of these systems to provide sustainable and efficient cooling solutions in various applications.

Overall, the section provides a foundational understanding of solar cooling technologies, offering a basis for further exploration and research in the field. In addition, it sets the stage for subsequent discussions on system optimization, performance analysis, and advancements in solar cooling systems for diverse climate conditions.

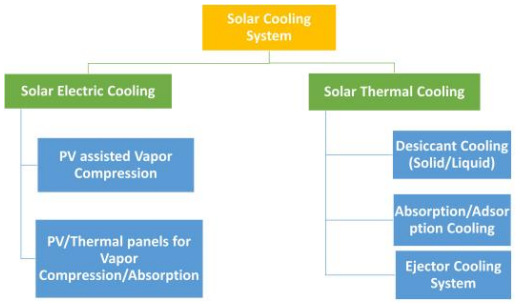

Fig. 1: Solar Cooling System Classification

3.1 PV-assisted Solar Cooling

Solar electric cooling utilizing the electric energy from a PV panel combined with vapour compression systems is an effective form of solar cooling technology in many scenarios because PV panels integrated into existing buildings do not need any additional allied parts to support the cooling process. Furthermore, with the current PV panel efficiencies at 15% to 20% and the use of Maximum Power Point Tracking (MPPT) to optimize solar energy utilization, PV-assisted vapour compression cooling is more economically and technologically viable.

Optimizing the effective utilization of solar fraction incident on the PV panel to meet the energy demand of a building, the ratio of peak-rated power of panels to the chiller-rated power is a critical design consideration (Li, Y., 2018). Also, different energy storage options, such as cold storage using phase change materials (PCM) and batteries, are considered to increase the overall system effectiveness (Wang and Dennis, 2015), Albatayneh et al. (2021a) made an experimental evaluation between PV air conditioner and ST cooling system. While ST cooling had a LCOE value of $2.35/kWh, the value for the air conditioning system coupled with PV is under $0.05/kWh for an Eastern Mediterranean region characterised by a hot, dry climate. When considering different techno-economic parameters,

the choice of appropriate solar collector technology and efficient solar cooling device are critical determining factors (Mokhtar *et al.*, 2010).

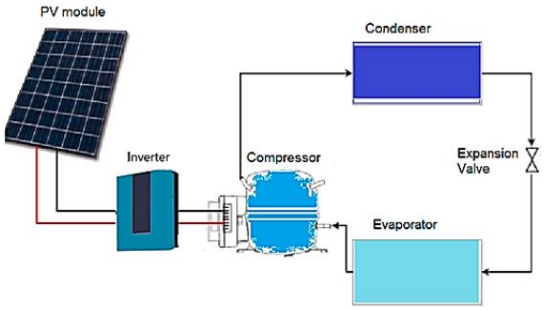

Fig. 2: PV-assisted solar cooling (Albatayneh *et al.*, 2021)

3.2 Vapor absorption Cooling

A vapour absorption cooling system consists of an absorber, generator and pump (the thermal compressor), a condenser, an expansion valve and an evaporator. The system can be divided into three circuits: a) Hot water flow; which supplies the heat to the absorber, b) Cold water flow; which is responsible for drawing heat from the space to be cooled and c) Cooling water flow; here the heat generated by both the above flows are removed by a cooling tower and released to the environment.

Various researchers developed and studied different systems configurations, demonstrating that systems could be enhanced at various stages to increase their overall performance. Alghool et al., (2020) studied to store the ST energy, a storage tank and/or an auxiliary heater are used to keep the hot water supply consistent and to compensate for any intermittency in solar insolation and prolonged usage over a day. They found that solar collectors covered 46% of the chiller's heat demand. Lòpez et al. (2020) employed a biomass boiler to account for hot water in the solar energy and a ClimateWell-CW10 absorption chiller. It has two different subsystems that can alternatively charge and discharge independently in the same project. The machine achieves good COP values that match the literature references, but results predict that extra use of auxiliary heating systems may be needed for applications with low insolation levels. Yu et al. (Yu *et al.*, 2019) showed that in high-rise building applications using a hybrid refrigeration system combining absorption and compression cycle, COP is improved by up to 22.2% and 19.8% on sunny days and cloudy days, respectively.

Another good action can be the integration in this kind of system of chilled water. This tank is usually a cold backup to ensure space cooling at all times of the day. E.g. for residential and multi-family building applications, domestic hot water (DHW) can be extracted from the cooling tower water circuit and heat extraction from the water to be cooled reduces the size of the cooling tower (Bilardo *et al.*, 2020).

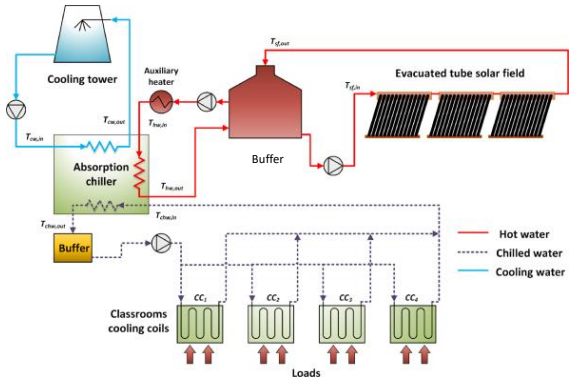

Fig. 3: Schematic diagram of an absorption cooling system (Aguilar-Jiménez et al., 2020)

3.3 Vapor Adsorption Cooling

Solar adsorption air conditioning system (SADCS) uses low-grade heat to power their adsorption/desorption cycle to bring about a cooling effect. SADCS can be broadly categorized as open and closed system adsorption cooling. In an open cycle adsorption cooling, the latent heat of cooling is reduced by adsorbing moisture to the adsorbant surface, and working air is in direct contact with the adsorbant. On the other hand, a closed system produces chilled water

that brings about the cooling effect (Mat Wajid et al., 2021). An open cycle solar adsorption cooling comprises two main components a dehumidifier and cold storage. The working principle is detailed in the figure below. It entails an open adsorption heat pump with intermittent operation. Furthermore, an air solar-driven absorption system is designed with the additional use of an auxiliary heater and cold storage (Nielsen et al., 2022).

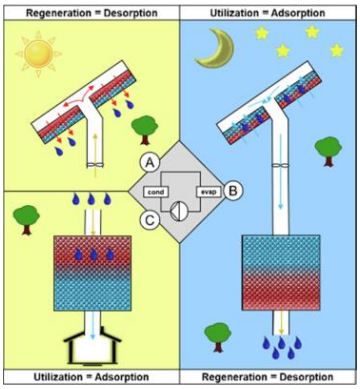

Fig. 4: Working principle of solar adsorption cooling (Nielsen et al., 2022)

In a closed system adsorption cooling, there are three independent water streams i) connected to the solar heating system to heat the adsorber beds ii) cools down the condenser and the bed iii) chilled water loop cooling the indoor space(Almohammadi and Harby, 2020). To enhance the adsorption cycle for more demanding applications, there are additional components with two adsorption chambers so that they can function alternately and get a continuous useful effect (see figure 5). When ads 1 is in cooling mode (adsorber) ads 2 will be in heating mode (desorber). Cooling towers like in the absorption cycle take away the heat from the condenser and are part of the heat rejection cycle of the refrigeration cycle.

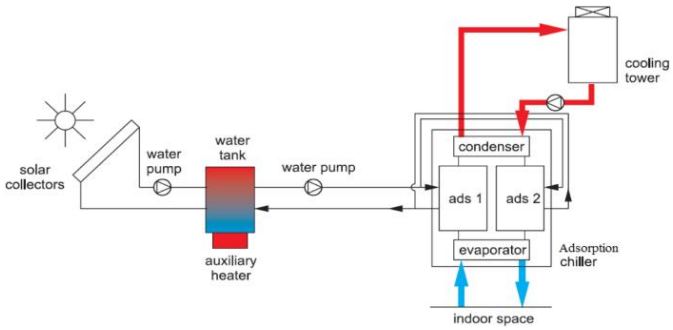

Fig. 5: Schematic of solar adsorption cooling (Dorota Chwieduk et al., 2014)

3.4 PV/T Solar Cooling

A PV/T solar cooling system is a hybrid system that combines photovoltaic and thermal technologies to provide both electricity generation and cooling capabilities. It integrates photovoltaic (PV) modules with solar thermal collectors, commonly known as Photovoltaic-Thermal (PV/T) collectors, to maximize solar energy utilisation and improve overall system efficiency.

In a PV/T solar cooling system, the PV modules convert sunlight directly into electricity, which can be used to power the cooling system components. Simultaneously, the PV/T collectors absorb solar radiation and extract thermal energy. This thermal energy is then used in the cooling process, typically through an absorption or adsorption chiller.

The PV/T collectors in a solar cooling system are designed with a dual-purpose structure. First, photovoltaic cells are embedded within the collector, allowing for simultaneous electricity generation and thermal energy collection. The advantage of this configuration is that it maximizes the system's overall energy output while utilizing the available solar energy resource more efficiently.

The thermal energy collected by the PV/T collectors can be used in several ways for cooling purposes. One common approach is to drive an absorption chiller, where thermal energy is utilized to generate a cooling effect through the absorption process. Another option is to employ an adsorption chiller, where the thermal energy is used to desorb adsorbent materials, creating a cooling effect through evaporation and condensation cycles.

The integration of PV/T technology into solar cooling systems offers several advantages. Firstly, it allows for the simultaneous generation of electricity and thermal energy, increasing the system's overall energy efficiency.

Secondly, it reduces the space requirements compared to separate PV and solar thermal installations, making it more suitable for constrained areas. Additionally, PV/T solar cooling systems contribute to reducing greenhouse gas emissions by utilizing renewable energy sources and reducing reliance on conventional cooling methods.

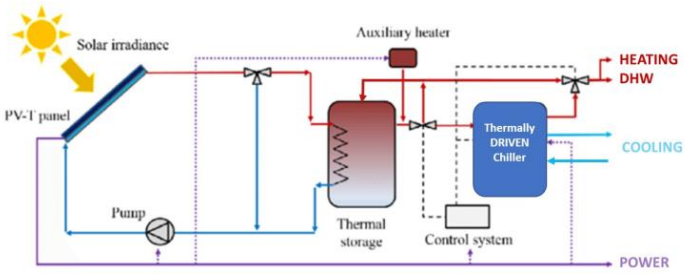

Fig. 6: Schematic of a PV/T solar sorption cooling system.

3.4 Solar Assisted Ejector Cooling

The overall system consists of a solar collector loop, a generator loop, and an ejector loop. The ejector cooling cycle (ECC) replaces the compressor in a vapour compression cycle by thermodynamic mixing of two working fluids in a convergent-divergent nozzle, as shown in Fig 6. Ejector cooling system has a more straightforward design and low equipment cost than absorption/adsorption cooling, although thermal efficiency is low (Saito et al., 2014). Alternate working fluids that can be used in this system make it an attractive option (Varga, S.. 2017). As shown in Fig. 7, solar ECC has two main streams, the solar conduit and ejector cooling cycle. A heat transfer fluid is generally used in the system to transfer heat from the solar collector to the working cooling refrigerant in the generator (Braimakis, 2021).

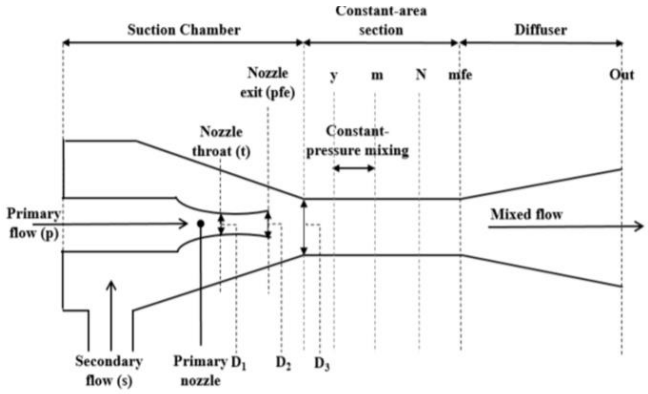

Fig. 7: Schematic of an ejector (Eveloy and Alkendi, 2021)

Eveloy and Alkendi, (2021) studied the use of a three-stage ejector cooling system powered by an evacuated tube collector for a small-scale building. The proposed system is shown to have reduced 42% of the annual energy consumption for a building in the United Arab Emirates, a country in the Sunbelt region.

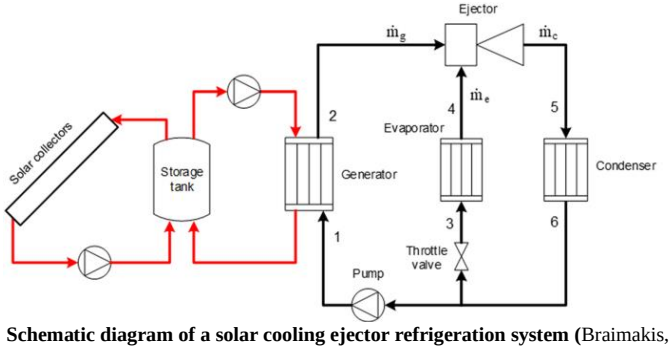

Fig. 8: Schematic diagram of a solar cooling ejector refrigeration system (Braimakis, 2021)

Owing to its low COP, ejector cooling devices are coupled with other effective cooling technologies such as solar ejector-vapour compression and ejector-absorption cycles, which are promising in achieving COP improvements

(Buyadgie, D,2012). Zarei et al., (2020) demonstrated the use of a novel combined solar cooling system using PVT panels and an ejector compression cooling system. The heater, compressor, and pumps were electrically powered by the PV panel and the output thermal energy from the PVT system was used to cool the condenser and the sub-cooler. The study shows that the PV panel efficiency and COP of the system can be improved by up to 11.1%

4. Results of the survey

Solar cooling has the potential to be an effective and efficient solution for decarbonization in countries across the Sunbelt region. With an expected increase in the cooling demands in these countries, it could be an excellent opportunity to identify the correct component choice and analyze existing projects to further catapult its reach and impact. The study summarizes 32 works from across 18 countries in the Sunbelt region. The distribution of projects is depicted below.

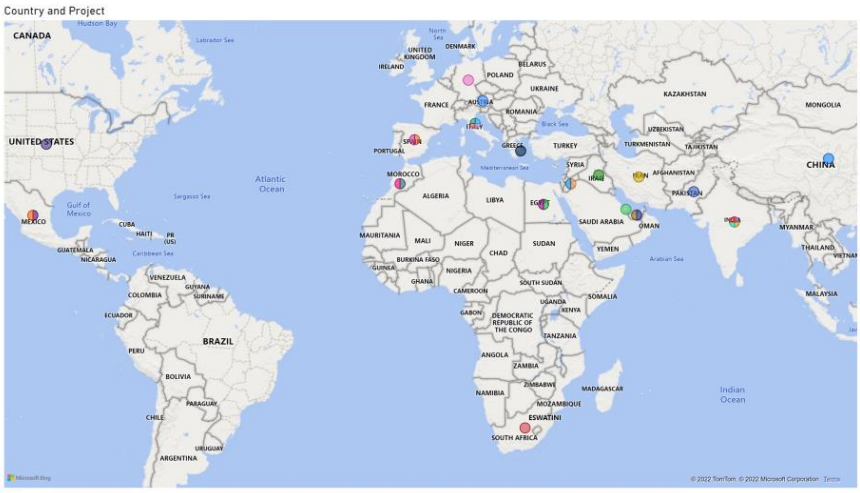

Fig. 9: Representation of projects from across different countries

4.1 Koppen-Geiger climate classification

Koppen-Geiger climate classification divides climate across the globe into five main categories, the equatorial zone(A), the arid zone (B), the warm temperate zone (C), the snow zone D, and the polar(E) and 31 sub-types adding in additional ranges for precipitation and air temperature. It is classified based on monthly air temperature precipitation and maximum and minimum values. Knowing each country's climate zone can be a critical criterion for choosing the right type of cooling system and solar energy collectors. Figure 10 shows the distribution of our projects studied across various climate classification zones.

Table1: ***Koppen-Geiger climate classification***

Main climates	Precipitation	Temperature
A: equatorial	W: desert	a: hot summer $T_{max} \geq +22$ ˚C
B: arid	S: steppe	b: warm summer not (a) and at least 4 $T_{mon} \geq +10$ ˚C
C: warm temperate	f: fully humid	c: cool summer not (b) and $T_{min} > -38$ ˚C
D: snow	s: summer dry	d: extremely continental like (c) but $T_{min} \leq -38$ ˚C
E: polar	w: winter dry	h: hot arid $T_{ann} \geq +18$ ˚C
	m: monsoonal	k: cold arid $T_{ann} < +18$ ˚C
		F: polar frost
		T: polar tundra

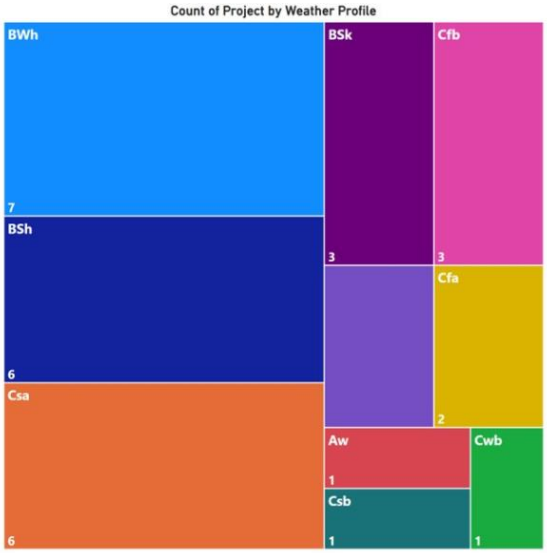

Fig. 10: Representation of projects studied and their climate classification

The temperature criterium estimates the intensity of solar insolation, the number of sunny days, and maximum and minimum temperatures in a zone. Countries in the Sunbelt region fall in the range between Group A (tropical climates), Group B (dry climates) and Group C (temperate climates). The solar cooling projects included in this study are located (actually or simulated) in 60% of the Sunbelt region throughout 9 sub-types. Most of the projects reported are from BWh (Hot desert) (23%), and BSh (Hot semi-arid) & Csa (Hot summer-Mediterranean) (both 20%) climate regions.

4.2 Projects Typologies

The studies were from a wide range of types as shown in Figure 11. 50% of the projects are in the implementation phase at various stages while 18% of the works are operational projects with established results. A quarter of these works are project concepts studied for implementation in nature.
Others have been simulated by using tools such as TRNSYS, Python, Matlab, and other mathematical modelling tools that can effectively estimate a system's performance before its implementation. Some published works of laboratory experiments and simulations validated by real-time building energy use have also been used in our survey for a broad range of analyses. Projects of different categories are studied to enhance the understanding of their performance and generate design rules that apply to different climate zone. The design rules encompass various components in a specific weather zone.
As shown in the following figure, almost 70% of the projects studied are either implemented or detailed projects, 25 % are concepts, and 6% are experimentations and validated using real-time buildings.

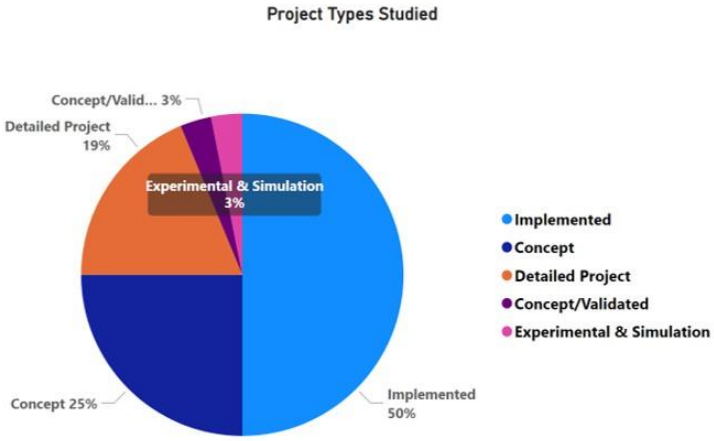

Fig. 11: Project typology distribution

4.3 Solar Collector types

Solar Cooling uses a range of solar energy harnessing devices. Evacuated tube collectors constitute 30% of the projects studied, and flat plate collectors and Fresnel collectors are equally next in usage. The studies also noted that Fresnel and flat plate collectors are the most popular options in implemented projects, with evacuated tubes the highest in simulation projects.
The distribution of different solar collectors over various temperature profiles gives a fair understanding of which is most suitable in different scenarios. As shown below (Figure 12.) Evacuated tube collectors have widespread application over three climate regions, BSk, BWh, and Csa and similarly with Flat plate collectors in Bsh, Cfb, Bwh, and Csa.

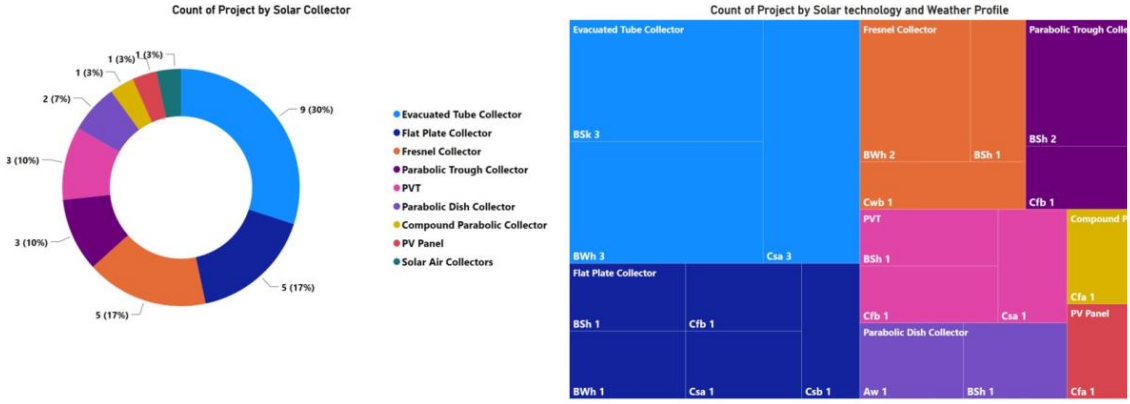

Fig. 12: Solar Collector types (left) and Representation of Solar collector type by weather profile (right)

ST cooling is the most applied solar cooling technology over solar electric cooling. Out of which, 30% of cases studied use evacuated tube collectors, Flat plate collectors (17%), Fresnel collectors (17%), Parabolic trough collectors (10%) and PV panels (10%). These are some of the most preferred options.

4.4 Solar cooling applications

In most cases studied, solar cooling systems are installed in public buildings such as offices, schools, and university buildings, making it suitable to use the sun during the daytime directly for utilization. Domestic buildings appear to be the next most studied because of their widespread need in the Sunbelt region for enhancing indoor comfort. They also have good potential for sectors like food preservation, process industries, etc.

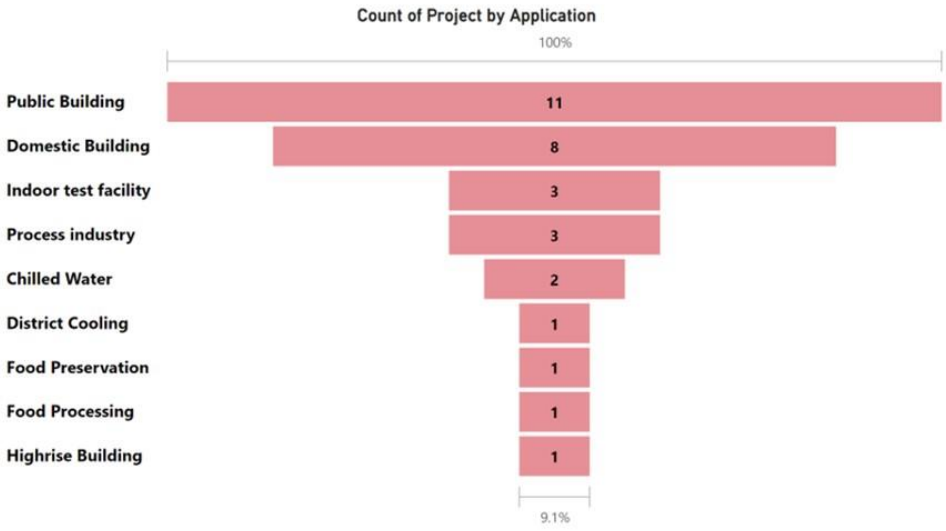

Fig. 13: Solar cooling applications

4.5 Adapted components

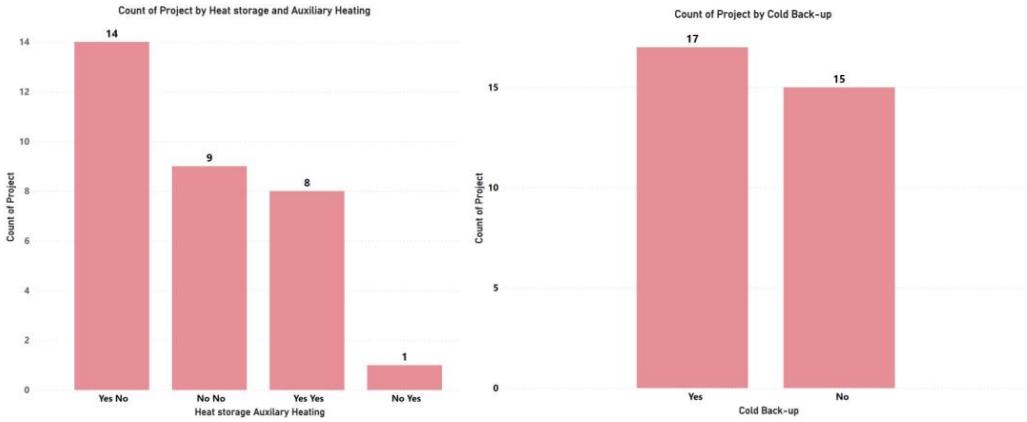

Fig. 14: Heat storage auxiliary heating in projects (left) and cold backup in projects (right)

As mentioned in section 3, heat storage tank and auxiliary heating are used to meet the cooling load when there is low or zero (es. during nighttime) solar radiation. In public buildings such as office spaces and educational institutions, the cooling load is mainly concentrated during the daytime, reducing the need and capacity of these components. However, cooling demand could be needed throughout the day for domestic applications such as villa houses, multi-family buildings, and process industries. Cold backup components include devices that can prolong the cooling effect even when the solar cooling device does not function such as a vapor compression system. In particular, cold backup was comparatively less in use with 53% when compared to heat-back up. To account for the intermittency of solar radiation, heat storage or auxiliary heating is observed to be the common practice. Indeed, hot water storage or heat backup by auxiliary heating was used in 72% of the projects with heat storage being more popular over heat backup.

4.6 Three-way Sankey diagram

The chart below depicts the interrelation between the climate classification each project has been based on, to the solar collector used, and the adopted solar cooling system. This gives an insight into commonalities in the appropriate component and system use about the climatic zone a project falls into. For example, when the maximum number of projects are from BWh (hot desert climate), Fresnel and evacuated tube collectors are mostly preferred over flat plate collectors and others to harness solar energy. Similarly, most studies show evacuated tube collectors are chosen in Csa (Hot summer Mediterranean) and BSk (Tropical and subtropical steppe climate). Of the available ST cooling techniques, 71% use solar absorption, whereas 19% use solar adsorption cooling and other technologies such as Ejector cooling, PV assisted cooling (3% each).

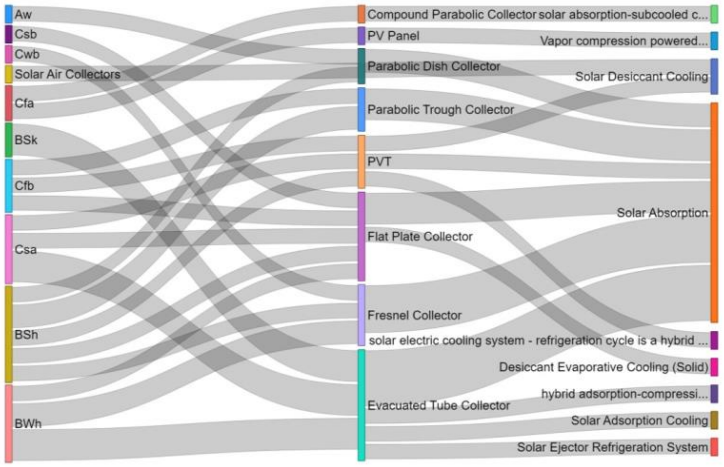

Fig. 15: Representation of weather profile with solar collector and solar cooling technology used

The survey results demonstrated a favourable environment to prove the maturity of solar cooling technology. Insights

drawn from this study could benefit a range of stakeholders: private users, public entities, 'hard to abate industrial sectors', policymakers, etc. Moreover, the outcome of this study, and in general the expected results of Task 65, will facilitate tracing the pathway to decarbonization goals and contribute towards energy transition in the region. With the certainty of different case studies presented, energy professionals can take a more informed decision in choosing components and system adaptions suitable for varying climatic conditions. The first presented results are drawn from 32 projects across 18 countries representing a range of 10 weather profiles such as the tropical wet and dry (Aw), hot desert (BWh), hot semi-arid (BSh), hot summer-Mediterranean (Csa), Warm-summer Mediterranean (Csb), Humid subtropic (Cfa), Monsoon-influenced humid subtropical (Cwa), Hot summer humid continental climate zones.

5. Conclusion

This paper aimed to present the first survey results conducted within the activities of two IEA Task 65 subtasks: Adapted components (A2) and showcases on system and component level (B1). The first presented results are drawn from 32 projects across 18 countries representing a range of 10 weather profiles. The 32 projects studied are over 17.06 MW of thermal cooling projects, which are summarized as follows:

- Most of the projects reported are from BWh (Hot desert) (23%), and BSh (Hot semi-arid) & Csa (Hot summer-Mediterranean) (both 20%) climate regions.
- Almost 70% of the projects studied are implemented or detailed, with 25 % being concepts. In addition, 6% of the project is experimentation and validated using real-time buildings.
- ST cooling is by far the most applied solar cooling technology over solar electric cooling. Out of which 30% of cases studied use evacuated tube collectors, Flat plate collectors (17%), Fresnel collectors (17%), Parabolic trough collectors (10%) and PV panels (10%). These are some of the most preferred options.
- Of the available ST cooling techniques, 71% of them use solar absorption, whereas 19% use solar adsorption cooling and other technologies such as Ejector cooling, PV assisted cooling (3% each)
- Hot water storage or heat backup by auxiliary heating was used in 72% of the projects with heat storage being more popular over heat backup.
- Cold backup was comparatively less in use with 53% when compared to heat-back up. To account for the intermittency of solar radiation, heat storage or auxiliary heating is observed to be the common practice.

The primary application was on the public buildings (34%) with an average working span of 8hr/day. In comparison, some others were utilized in the domestic building (25%), process industry (9%), and food processing sector.

6. References

- Aguilar-Jiménez, J.A., Velázquez-Limón, N., López-Zavala, R., González-Uribe, L.A., Islas, S., González, E., Ramírez, L., *et al.* (2020), "Optimum operational strategies for a solar absorption cooling system in an isolated school of Mexico", *International Journal of Refrigeration*, Elsevier Ltd, Vol. 112, pp. 1–13, doi: 10.1016/j.ijrefrig.2019.12.010.
- Albatayneh, A., Jaradat, M., Al-Omary, M. and Zaquot, M. (2021), "Evaluation of coupling pv and air conditioning vs Solar cooling systems—case study from Jordan", *Applied Sciences (Switzerland)*, MDPI AG, Vol. 11 No. 2, pp. 1–15, doi: 10.3390/app11020511.
- Alghool, D.M., Elmekkawy, T.Y., Haouari, M. and Elomri, A. (2020), "Optimization of design and operation of solar assisted district cooling systems", *Energy Conversion and Management: X*, Elsevier Ltd, Vol. 6, doi: 10.1016/j.ecmx.2019.100028.
- Almohammadi, K.M. and Harby, K. (2020), "Operational conditions optimization of a proposed solar-powered adsorption cooling system: Experimental, modelling, and optimization algorithm techniques", *Energy*, Elsevier Ltd, Vol. 206, doi: 10.1016/j.energy.2020.118007.
- Bentayeb, F., Lemmini, F., & Guilleminot, J. J. (1995). Adaptation of an adsorptive solar refrigerator to Moroccan climates. Renewable Energy, 6(7), 867-882. ISSN 0960-1481. https://doi.org/10.1016/0960-1481(94)E0020-6.
- Bilardo, M., Ferrara, M. and Fabrizio, E. (2020), "Performance assessment and optimization of a solar cooling system to satisfy renewable energy ratio (RER) requirements in multi-family buildings", *Renewable Energy*, Elsevier Ltd, Vol. 155, pp. 990–1008, doi: 10.1016/j.renene.2020.03.044.
- Braimakis, K. (2021), "Solar ejector cooling systems: A review", *Renewable Energy*, Elsevier Ltd, 1 February, doi: 10.1016/j.renene.2020.09.079.
- Buyadgie, D., Buyadgie, O., Drakhnia, O., Artemenko, S. and Chamchine, A., 2012. Solar cooling technologies using ejector refrigeration system. Energy Procedia, 30, pp.912-920.
- Dorota Chwieduk, Andrzej Grzebielec and Artur Rusowicz. (2014), "Solar cooling in buildings", doi: https://doi.org/10.4467/2353737XCT.14.222.3310.

- Eveloy, V. and Alkendi, Y. (2021), "Thermodynamic performance investigation of a small-scale solar compression-assisted multi-ejector indoor air conditioning system for hot climate conditions", *Energies*, MDPI AG, Vol. 14 No. 14, doi: 10.3390/en14144325.
- Gloel, J., Oppelt, D., Becker, C. and Heubes, J. (2015), *Green Cooling Technologies Market Trends in Selected Refrigeration and Air Conditioning Subsectors*, Eschborn.
- IEA. (2018), *The Future of Cooling Opportunities for Energy-Efficient Air Conditioning Together Secure Sustainable*, Paris.
- Li, Y., Zhao, B.Y., Zhao, Z.G., Taylor, R.A. and Wang, R.Z. (2018), "Performance study of a grid-connected photovoltaic powered central air conditioner in the South China climate", *Renewable Energy*, Elsevier Ltd, Vol. 126, pp. 1113–1125, doi: 10.1016/j.renene.2017.05.064.
- Litardo, J., Del Pero, C., Molinaroli, L., Leonforte, F., & Aste, N. (2022). Sustainable active cooling strategies in hot and humid climates – A review and a practical application in Somalia. Building and Environment, 221, 109338. ISSN 0360-1323. https://doi.org/10.1016/j.buildenv.2022.109338.
- López, M.J.S., Prieto, J.I., Blanco, E. and García, D. (2020), "Tests of an Absorption Cooling Machine at the Gijón Solar Cooling Laboratory", *Energies*, MDPI AG, Vol. 13 No. 15, doi: 10.3390/en13153962.
- Mat Wajid, N., Zainal Abidin, A.M., Hakemzadeh, M., Jarimi, H., Fazlizan, A., Fauzan, M.F., Ibrahim, A., *et al.* (2021), "Solar adsorption air conditioning system – Recent advances and its potential for cooling an office building in tropical climate", *Case Studies in Thermal Engineering*, Elsevier Ltd, Vol. 27, doi: 10.1016/j.csite.2021.101275.
- Mokhtar, M., Ali, M.T., Bräuniger, S., Afshari, A., Sgouridis, S., Armstrong, P. and Chiesa, M. (2010), "Systematic comprehensive techno-economic assessment of solar cooling technologies using location-specific climate data", *Applied Energy*, Elsevier Ltd, Vol. 87 No. 12, pp. 3766–3778, doi: 10.1016/j.apenergy.2010.06.026.
- Nielsen, E., Becker-Hardt, S., Englmair, G., Kong, W. and Furbo, S. (2022), "Investigation on an air solar-driven open sorption system for comfort cooling", *Solar Energy*, Elsevier Ltd, Vol. 231, pp. 57–71, doi: 10.1016/j.solener.2021.11.018.
- Saito, Y., Ito, T., Matsuo, A. and Sato, H., 2014. Ejector configuration for designing a simple and high performance solar cooling system. Energy Procedia, 57, pp.2564-2571.
- Ssembatya, M., Pokhrel, M. K., & Reddy, R. (2014). Simulation Studies on Performance of Solar Cooling System in UAE Conditions. Energy Procedia, 48, 1007-1016. ISSN 1876-6102. https://doi.org/10.1016/j.egypro.2014.02.115.
- Varga, S., Oliveira, A.C., Palmero-Marrero, A. and Vrba, J., 2017. Preliminary experimental results with a solar driven ejector air conditioner in Portugal. Renewable energy, 109, pp.83-92.
- Wang, X. and Dennis, M. (2015), "Influencing factors on the energy saving performance of battery storage and phase change cold storage in a PV cooling system", *Energy and Buildings*, Vol. 107, pp. 84–92, doi: https://doi.org/10.1016/j.enbuild.2015.08.008.
- Yu, J., Li, Z., Chen, E., Xu, Y., Chen, H. and Wang, L. (2019), "Experimental assessment of solar absorption-subcooled compression hybrid cooling system", *Solar Energy*, Elsevier Ltd, Vol. 185, pp. 245–254, doi: 10.1016/j.solener.2019.04.055.
- Zarei, A., Liravi, M., Babaie Rabiee, M. and Ghodrat, M. (2020), "A Novel, eco-friendly combined solar cooling and heating system, powered by hybrid Photovoltaic thermal (PVT) collector for domestic application", *Energy Conversion and Management*, Elsevier Ltd, Vol. 222, doi: 10.1016/j.enconman.2020.113198

The application of concentrating solar thermal systems in hospital buildings

Vavalos P.[1], Drosou V.[2], Christodoulaki R.[2], Zoras S.[1] and Dimoudi A.[1]

[1] Department of Environmental Engineering, Democritus University of Thrace, Xanthi, Greece,

[2] Solar Thermal Department, Centre for Renewable Energy Sources and Saving, Pikermi, Greece

Abstract

One of the basic objectives of EU is to decarbonize the building sector by the year 2050. To achieve this goal, energy renovation of the building stock across Europe will be initiated in order to improve the energy performance of buildings and reduce greenhouse gas emissions. Hospital buildings are often large scale buildings that accommodate energy intensive uses, such as space heating and cooling with specific thermal comfort settings, high hot water requirements, equipment, lighting. This results to very high energy consumption in hospital buildings and consequently, high energy bills.

The aim of this paper is to investigate the application of concentrating solar thermal for space conditioning needs in hospitals buildings in Greece and enhance their application in the building sector. The paper will present the techno-economic and environmental assessment for a hospital building targeting to reduction of the carbon footprint of these buildings.

Keywords: Net Zero Buildings, Hospitals, Thermal Energy, Concentrating solar thermal systems.

1. Introduction

One of the basic objectives of EU is to decarbonize the building sector by the year 2050. To achieve this goal energy renovation of the building stock across Europe will be initiated in order to improve energy performance of buildings and reduce greenhouse gas emissions.

Hospital buildings are big buildings that accommodate energy intensive uses like space heating and cooling with special comfort settings, high hot water requirements, equipment, lighting. This results to very high energy consumption in hospital buildings and consequently high energy bills (Dimoudi et al. 2022).

Final energy use intensities of health care buildings in EU countries varies from 656,5kWh/m^2 in Bulgaria, 147,8kWh/m^2 in Estonia, 228,2kWh/m^2 in France, 1.124,3kWh/m^2 in Spain and 516,2kWh/m^2 in the United Kingdom (Balaras et al, 2017). In other studies, differences on hospital's energy recordings were found. Energy intensity of 20 hospitals in Spain was recorded at 270kWh/m^2 and of 48 hospitals in UK at 289kWh/m2 (Bawaneh et al, 2019) while at 195kWh/^{m2} in France (Nourdine, Saad, 2020).

The energy intensity per bed or per employee also varies between countries, ranging from an average consumption at 29.000kWh/bed for heating and 6.000kWh/bed for electricity in a survey of 2.100 hospitals in Germany and in Spain electricity recordings fluctuate between 8.888kWh/bed and 10.004kWh/bed for small (under 300 beds) and big hospitals (González et al, 2018), while in France 26.000kWh/bed (Nourdine, Saad, 2020).

A survey on energy consumed in fourteen hospitals in North-West Greece, reported that the average thermal annual consumption was 179kWh/m^2, the average electricity energy consumption was 118kWh/m^2 and the average electricity consumption per bed was at 10.483kWh and per employee at 4.461kWh (Kostadimas et al. 2022).

The aim of this paper is to investigate the application of concentrating solar thermal for space conditioning needs in hospitals buildings in Greece and enhance their application in the building sector. The paper will present the

© 2022. The Authors. Published by International Solar Energy Society
Selection and/or peer review under responsibility of Scientific Committee
doi:10.18086/eurosun.2022.06.03 Available at http://proceedings.ises.org

techno-economic and environmental assessment for a hospital building targeting to reduction of the carbon footprint of these buildings.

2. Analysis of the energy consumption of the hospital building - simulation

The energy profile of a General Hospital located at the A Climatic zone is used in the study. The simulation for its energy performance were carried out with two collaborating energy simulation tools: the EnergyPlus and the DesignBuilder software.

The General Hospital was built in a site area of 40.000 m^2 which is located in the center of a small city. The total premises of the hospital nowadays consist of 2 buildings which were constructed in different time periods. The construction permission for the main hospital building was issued in 1983 and it was completed almost 5 years later in 1987/8, according to the regulations of the permit year. A new wing which is connected to the main facilities, was added to the building compound later at 2010.

The total area of the General Hospital after the addition of the new building, amounts almost 13.000 m^2, distributed in 5 floors in the main hospital (Basement Floor B', Basement Floor A', Ground Floor, First Floor and Second Floor), and 3 floors in the new building (Basement Floor, Ground Floor and First Floor). Almost 9.000 m2 is conditioned while the other 4.000 m^2 (Basement B' with mechanical equipment, mechanical rooms in both buildings, storage rooms, etc.) is unconditioned.

Due to its complex structural design and its energy consumption diversities between its internal spaces, the General Hospital was separated into four distinct conditioned thermal zones which demonstrate the same use and activity schedules, have the same HVAC systems and operate at the same temperatures set-points. Those four thermal zones, were divided into smaller thermal zones according to their floor or orientation but still following the same attributes as their parent zone. The unconditioned zones which include the floor with the mechanical service room, equipment, storage rooms and auxiliary spaces were designed as well into the software.

The hospital's envelope is insulated and its windows are divided between doubled glazed with old or new aluminum frame.

The facilities are able to hospitalize more than 4.000 patients per year, while there are 120 available beds able to satisfy the needs of the hospital, so occupancy profiles, internal gains for occupants, clothing and activity rate were taken into account for the energy performance simulation. The operation hours of the building differ greatly due to the different activities between the zones. The operating hours of the hospital per day may vary in its different zones between 8 to 24 hours. Therefore, each zone was created with its unique operation schedules and temperature set-points. The lighting and mechanical equipment follow the operation schedules of their zone.

The HVAC systems of the General Hospital consist of equipment that was installed in the old building during its construction, along with the equipment that was provided at later stages which are diesel boilers, air cooled chillers and air handling units (AHUs).

The General Hospital has two separate Heating, Cooling and Ventilation systems, in its two buildings (old building and new wing). The hospital consists of two separate heating systems with diesel boilers and two separate cooling systems with air cooled chillers which are used for the two buildings. The mechanical ventilation equipment of the hospital consists of air handling units conditioning all 4 thermal zones. The AHUs are operating following the working profile of the occupants of the thermal zones and are separated into two different categories according to their characteristics. The needs for domestic hot water are satisfied by the diesel boilers in both buildings throughout the year.

The main heating system of the old building that operates separately from the new building, consists of two diesel boilers of 1.046,00 kW power (900.000 kcal/h), operating simultaneously, according to the needs of the hospital (Fig. 1). The hot water loop consists of a two-pipe system of supply and return, distributed from the heating collector to the thermal heating units (convectors) located in all areas of the building areas, and also to the heating

coils located to the air handling units and the reheat coils in their terminal units inside the zones. So, the air handling units can be used for heating purposes as well.

Two diesel boilers of 407,00 kW power (350.000 kcal/h) located in the mechanical room of the new wing basement, operate alternately and not at the same time, covering the needs of the new wing of the hospital (Fig 2).

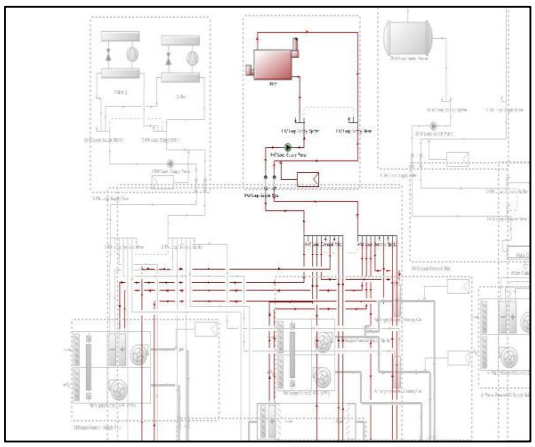

Fig. 1: Schematic of the heating system of the General Hospital (new wing)

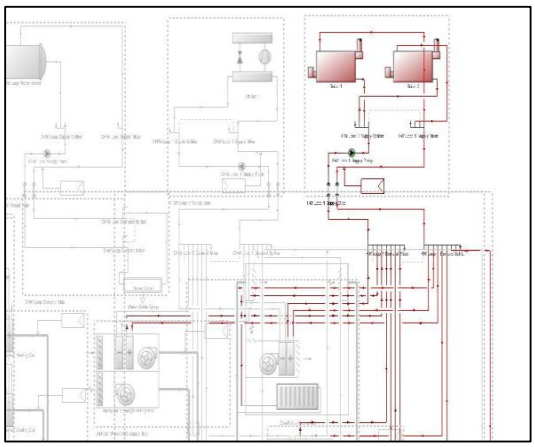

Fig. 2: Schematic of the heating system of the General Hospital (old building)

Three air cooled chillers are installed in the hospital to cover the needs for the cooling loads. Two of them, of 440 kW with refrigerant R134a, are located in the roof of the new building (Fig. 3) while the older one is found in the old building (Fig. 4). Those air cooled chillers are connected to the chilled water loop of their wing respectively. The chilled water loop includes a two pipe system of supply and return which provides chilled water to cooling coils located in the air handling units.

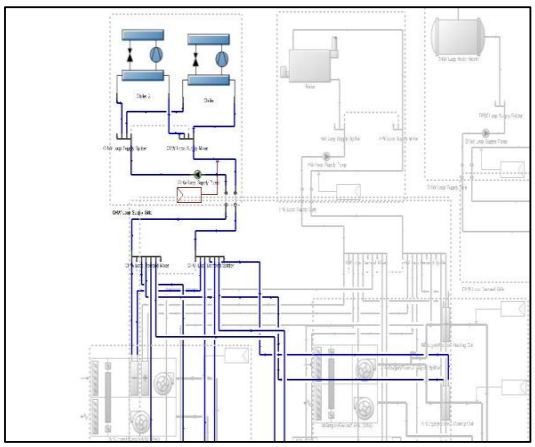

Fig. 3: Schematic of cooling system of the General Hospital (new wing)

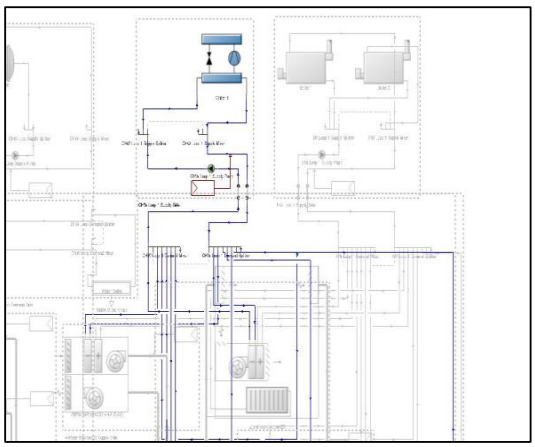

Fig. 4: Schematic of cooling system of the General Hospital (old building)

There are totally 10 AHUs installed in the hospital, located in different sections, meeting the required conditions of each specific space, with total 410,13 kW cooling capacity and 347,82 kW heating capacity. All of them are variable speed units with preheat and reheat in order to reduce energy consumption but they are separated in two types: a) AHUs with a two-pipe system of supply and return (Fig. 5), b) AHUs with a dual duct air loop consisting of a four-pipe system, where the heating and cooling is mixed (Fig. 6).

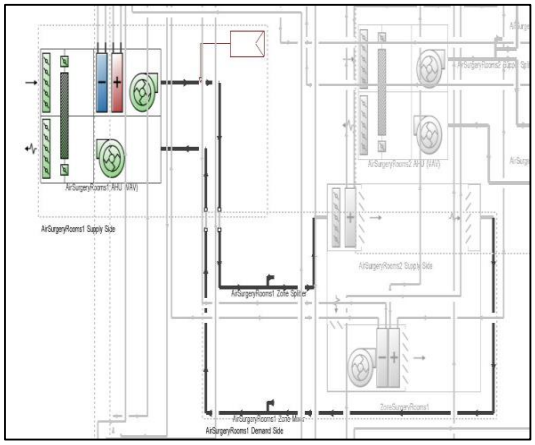

Fig. 5: Schematic of AHUs with a two-pipe system of supply and return

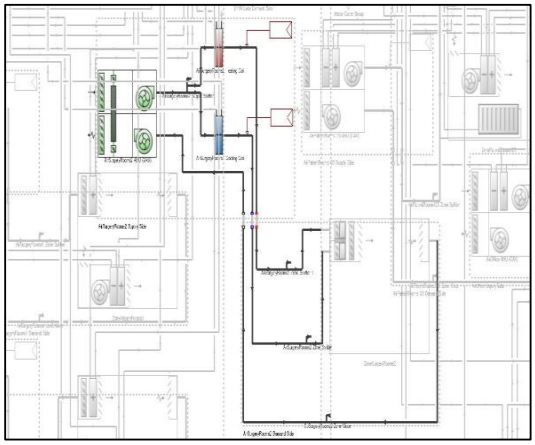

Fig. 6: Schematic of AHUs with a dual duct air loop consisting of a four-pipe system

The simulation was performed with four time steps per hour, evaluating the energy consumption of the building.

After the simulation of the energy performance of the existing base building, results about the electricity and heat consumption were extracted. The total net energy consumption of the hospital is 1.866,6 MWh, out of which 1.320,2 MWh is the electricity consumption (cooling, lighting, equipment and other appliances) and 546,4 MWh is the diesel consumption (heating and DHW). The total source (primary) energy is 4.429,5 MWh, out of which 3.828,5 MWh is the source electricity consumption and the 601,0 MWh is the source diesel consumption (ZenH Balkan, 2021).

Figures 7 and 8 present the percentage distribution (%) of each consumption per use and per category. The source diesel consumption has 14% of the total source consumption, while source electricity consumption covers the 86%, and out of the electricity total, the interior lighting has 22%, the interior equipment has 7%, the cooling has 44%, the other appliances have 13%.

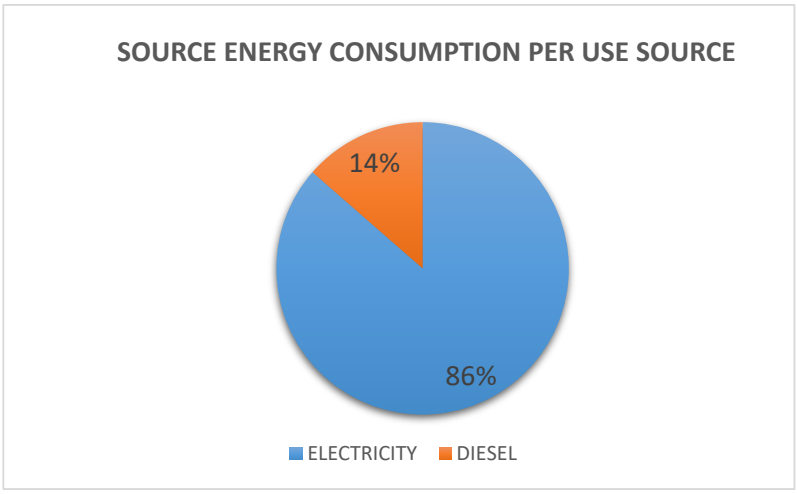

Fig 7: Distribution of source energy consumption per use, in percentage (%)

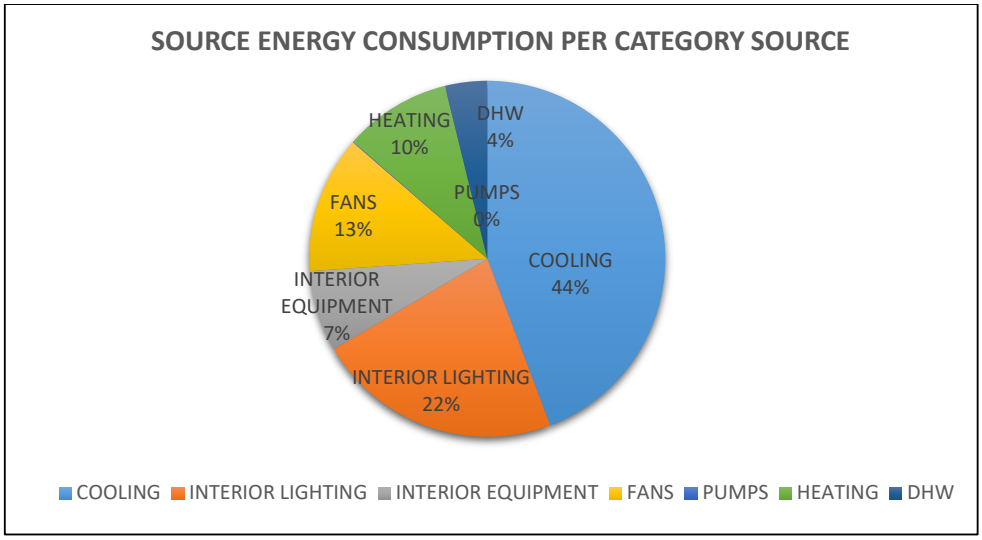

Fig 8: Distribution of source energy consumption per category, in percentage (%)

After the energy evaluation of the case study building and simulation of its energy performance, 9 different energy efficiency scenarios were examined in order to reduce the energy needs of the building. Those scenarios were categorized according to the source they targeted and they included insulation of the external walls and roof of the building with mineral wool insulation, replacement of its windows with new PVC framed ones, double glazed with low-e coating, replacement of old lights with led lights, installation of a Building Energy Management System (BEMS) to control the lighting system according to occupancy profiles and illuminance level (lux set-points), addition of shading devices at the windows and control of them according to solar radiation, natural ventilation control according to occupancy schedules for temperature reduction during summer period, and implementation of cool roof material.

After the simulation of all examined scenarios, the source (primary) electricity energy consumption is reduced by 33.3%, corresponding to 1.273,6 MWh and the diesel consumption is reduced by 25,5% (Tab. 1). The total reduction of primary energy consumption, considering all scenarios from 1 to 9 is 1.426,6 MWh, corresponding to 32,2%. The specific total primary energy consumption is reduced by 162 kWh/m^2, corresponding to specific total primary energy consumption of 341,4 kWh/m^2 (Tab. 2, Fig. 9).

Tab. 1: Source energy consumption (in MWh) and energy savings (in %) from scenarios 1 to 9

	Case building consumption	**Scenarios 1-9 consumption**	**Energy savings**	
	Source energy, MWh	Source energy, MWh	MWh	%
Electricity	3.828,5	2.554,9	1.273,6	33,3%
Diesel	601,0	448,1	153,0	25,5%
Total	4.429,5	3.002,9	1.426,6	32,2%

Tab. 2: Specific source energy consumption (in kWh/m2) and energy savings (in %) from scenarios 1 to 9

	Case building consumption	**Scenarios 1-9 consumption**	**Energy savings**	
	Source energy kWh/m^2	Source energy kWh/m^2	kWh/m^2	%
Electricity	435,2	290,4	144,8	33,3%
Diesel	68,3	50,9	17,4	25,5%

Total	503,5	341,4	162,2	32,2%

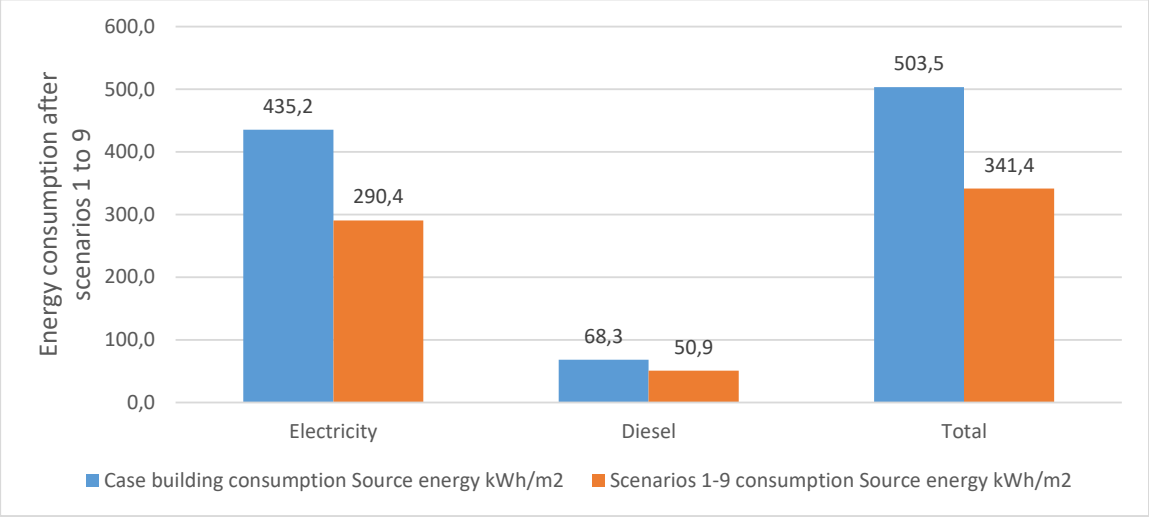

Fig. 9: Specific source energy consumption (in kWh/m^2) per energy source from scenario 1 to 9

Table 3 presents the distribution of the source (primary) energy consumption (in MWh) and the energy savings for each separate category use (in MWh and %) for all scenarios. The diesel energy consumption is decreased by 153,0 MWh (35,5%) while the electricity consumption for cooling is decreased by 381,3 MWh (19,4%).

With the aim of achieving a nearly zero energy building, after the implementation of the 9 energy efficient scenarios and reduction of the energy needs of the building, exploitation of RES systems was investigated. The current study focus on investigating exploitation of solar energy for space cooling with concentrated solar thermal collectors.

Tab. 3: Source energy consumption (in MWh) and energy savings (in %) per category from scenario 1 to 9

	Case building Energy consumption	**Scenario 1-9 Energy consumption**	**Energy Savings [Scenario 1-9]**	
	Source energy, MWh	Source energy, MWh	MWh	%
Cooling	1.960,8	1.579,5	381,3	19,4%
Interior Lighting	986,0	218,9	767,1	77,8%
Interior Equipment	326,3	326,3	0,0	0,0%
Fans	552,2	427,7	124,5	22,5%
Pumps	3,3	2,5	0,8	23,7%
Heating	431,4	278,4	153,0	35,5%
DHW	169,7	169,7	0,0	0,0%
Total	4.429,5	3.002,9	1426,6	32,2%

3. Performance Analysis of the solar cooling system

In this section, the energy performance of a concentrating solar thermal system for covering part of the cooling loads of the aforementioned hospital building is described. The energy performance assessment is elaborated in Greenius - The Green Energy System Analysis Tool, developed by German Aerospace Center DLR - Institute of Solar Research, Solar High Temperature Technologies. Meteorological data for Kefalonia, Greece in the form of typical meteorological year record (TMY) are extracted from Meteonorm and inserted into the Greenius tool, as it

can be seen in Fig. 10. The cooling loads of the hospital, as presented in the previous section “case building energy consumption”, are inserted into the Greenius tool.

Load Curve and OS : Hospital load

The annual sum of the load is 525,65 MWh and the average load 60,01 kW,
whereas the annual load minimum is 0,00 kW and the maximum 470,00 kW.
January 1st of the typical refence year is a Monday.
Operating strategy is: Hospital load

Meteo : Kefalonia_Hospital

It is located at 38,17°N 20,50°E, 177 m (timezone 2,0 h).
Temperature min. is 2,1 °C, max. 36,2 °C, mean 18,3 °C.
The annual sum of global irradiation GHI is 1754 kWh/m² and the sum of direct normal irradiation DNI is 1908 kWh/m²
The annual sum of diffuse irradiation Diff is: 603 kWh/m²
Max wind speed is 15,5 m/s, mean is 3,0 m/s.

Fig. 10: Input data for the project site; cooling load and meteorological data

The solar thermal system is comprised of concentrating parabolic collectors, thermal chiller, hot water storage tank and the auxiliary hydraulic equipment. The technical characteristics of the selected solar collectors are seen in Fig. 11. The solar collectors’ field consists of 3 rows with 15 solar collectors each, resulting in 594m^2 total collectors’ area (Fig. 12). The selected fluid in the field is Dowtherm A and the temperature exiting the field depends on the chiller operational temperature and it is set at 180ºC. Thermal storage of 2.000kWh is also foreseen, that results in 3 hours of full load storage, on an average summer day. The selected thermal chiller is double effect, utilizes absorption technology and the cooling capacity is 583kW. Detailed technical characteristics of the chiller are shown in Fig. 13.

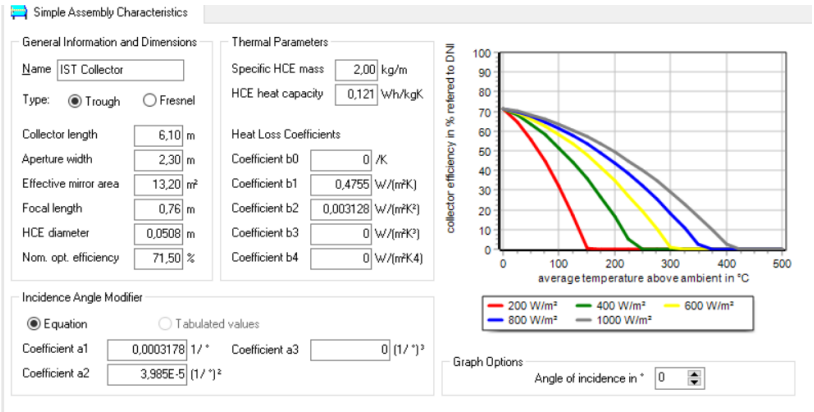

Fig. 11: Input data for the solar collectors

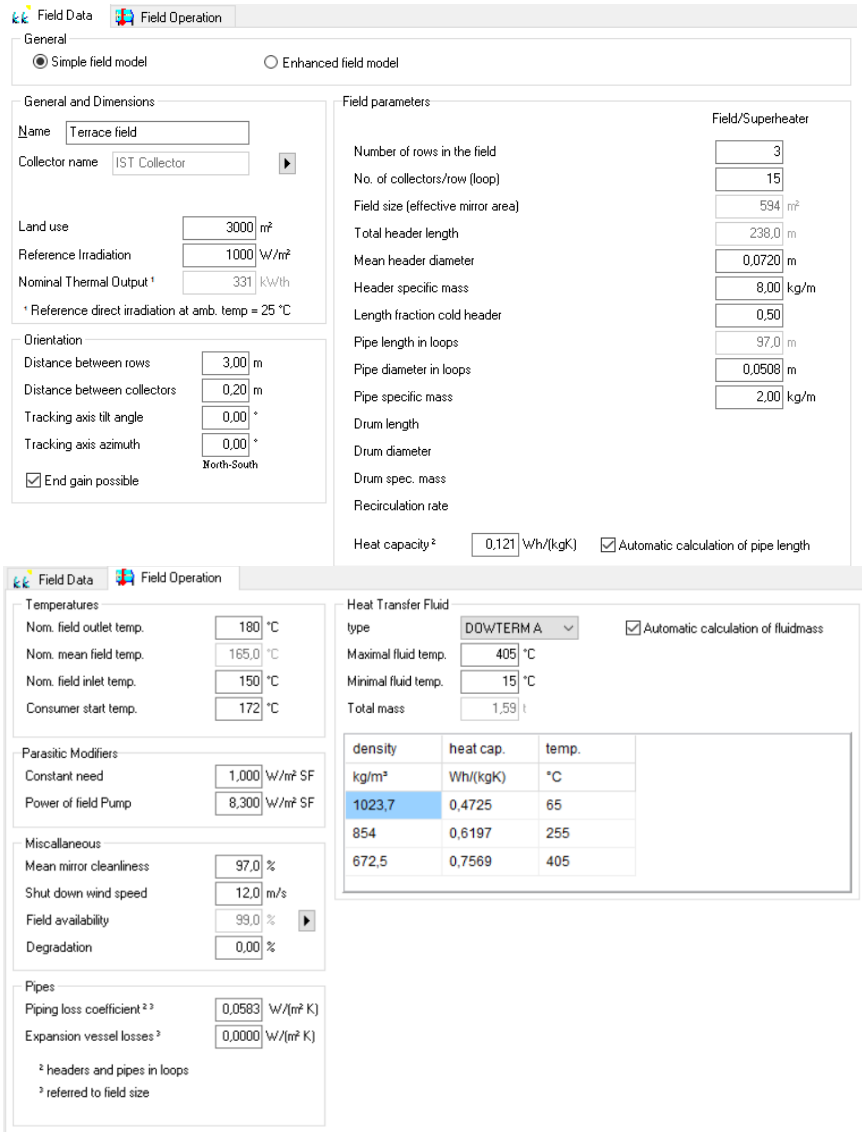

Fig. 12: Input parameters for the solar collectors' field

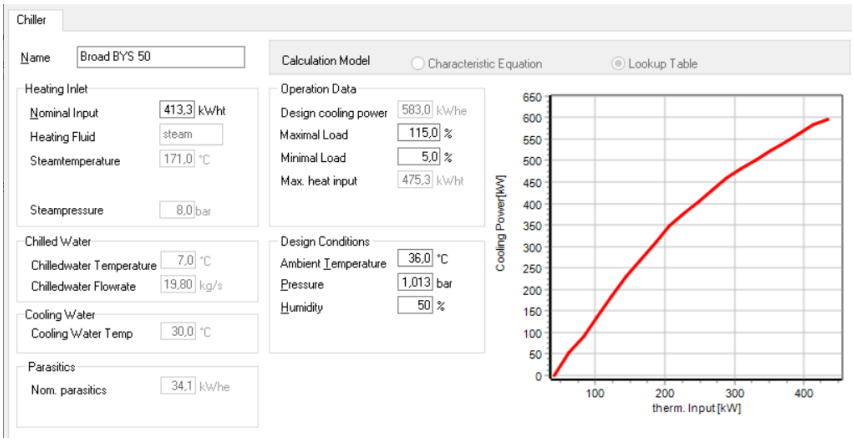

Fig. 13: Input data for the absorption chiller

Following the data input of all operational parameters regarding the site, the building load and the cooling system, the simulation procedure follows. The results of the simulation for each month are shown in Table 4. The annual sum of the Direct Normal Irradiation onto the collectors' area is 1.133MWh. Taking into consideration the thermal and optical losses, the thermal energy produced by the collectors is 334MWh, whereas that of the solar field is 272MWh. The double effect solar thermal chiller produces 240MWh of cooling energy and an amount of 172MWh of thermal energy is stored. The annual average solar fraction of this solar thermal system is 39%, which means that the designed solar cooling system can provide the 39% of the cooling load of the building. The average annual field efficiency is 19% and the average annual collectors' efficiency is 26%.

Tab. 4: Simulation results in tabular form

	DNI	**DN_c**	**H_{dn}**	**T_{amb}**	**Q_{load}**	**Q_{cool}**	**Q_{field}**	**Q_{col}**	**$Q_{Storage}$**	**Solar Cooling Fraction**
	W/m²	W/m²	MWh	°C	MWh	MWh	MWh	MWh	MWh	%
Average				**18**						**39%**
Sum	1.908.109	1.695.066	1.133		526	240	272	334	172	
January	105	68	46	11	0	0	2	6	3	
February	125	91	50	11	0	0	3	7	4	
March	177	154	78	13	0	0	14	19	22	
April	254	239	109	16	0	0	29	35	46	
May	290	283	128	20	59	10	39	46	42	0.17
June	311	305	133	24	117	66	45	51	5	0.56
July	353	345	156	27	141	84	55	61	4	0.60
August	328	313	145	27	146	71	45	52	1	0.49
September	237	212	101	23	63	10	24	30	20	0.16
October	179	142	79	20	0	0	11	17	18	
November	137	92	59	16	0	0	3	7	4	
December	111	69	49	13	0	0	1	5	2	

Graph 14 shows the annual distribution of the building's cooling load (red line) in comparison to the Direct Normal Irradiation on the collectors' area. This graph visualizes the advantage of the solar cooling concept; that is the time coincidence of the cooling loads with the availability of solar irradiation.

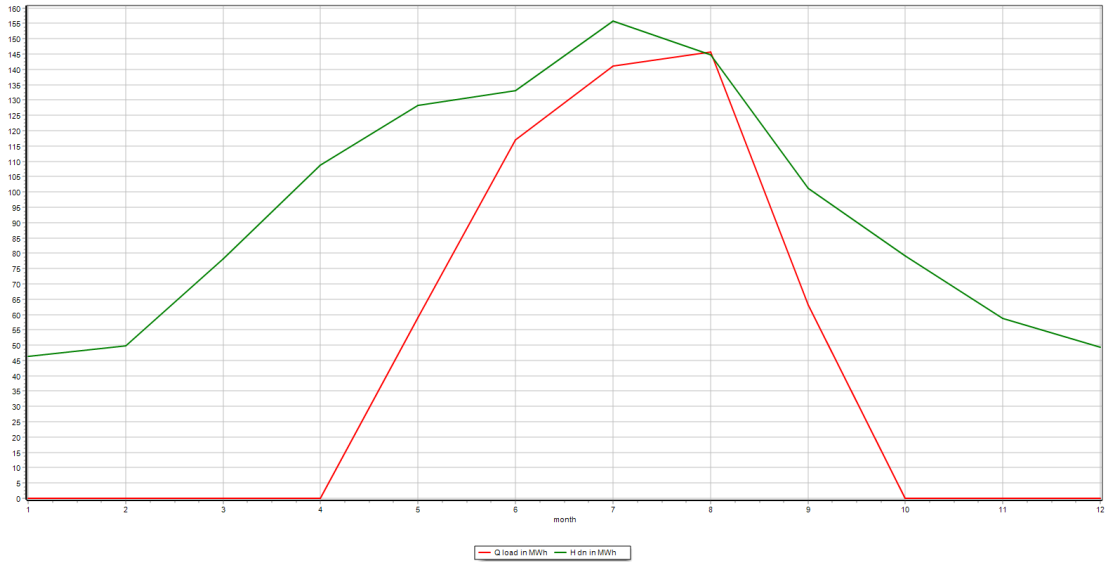

Fig. 14: Direct Normal Irradiation on the collectors' area (green line) and annual distribution of the hospital's cooling load (red line), in MWh

Fig. 15 shows the annual distribution of the cooling load (red line), in comparison to the cooling energy produced from the chiller (green line). The areas that occupy these two lines show that the selected capacity of the chiller and the parameters of the solar system are sufficient to cover approximately half of the cooling energy demands. Moreover, this graph illustrates the stored thermal energy happening during the spring and autumn periods, whereas in summer, the stored energy is minimized, due to its direct use in the thermal chiller. The blue line shows the heat produced by the solar field.

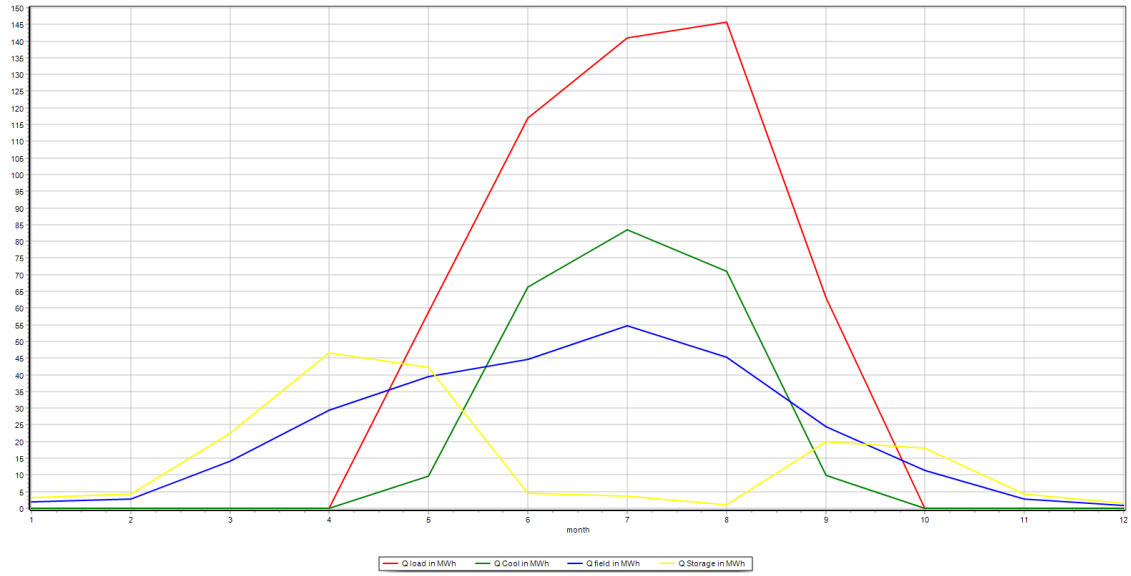

Fig. 15: Annual distribution of the hospital's cooling load (red line), cooling output from the chiller (green line), heating output from the solar collectors' field and stored heat (yellow line), in MWh

The economic evaluation of the system has been based on a previous work of the authors (Drosou et al, 2016) and the most important considerations are shown below. As such, Table 5 provides the initial, operation and maintenance costs of the solar cooling system.

Tab 5: Solar Cooling System Costs

Initial Costs		
Component	**Price**	**Unit**
Solar field	350	€/m^2
Chiller	200	€/kW
Cooling tower, hydraulics, other components	135	€/kW
Installation & Commissioning	15% of components cost	
Total system cost	**463,686**	**€**
Total system specific cost	**781**	**€/m^2**
Annual Operation & Maintenance Costs		
Solar field	4	€/m^2
Chiller	2.8	€/MWh
Cooling tower, hydraulics	0.2% of total system cost	
Total O&M cost	**3,813**	**€/a**
Total O&M specific cost	**6**	**€/m^{2}a**

A preliminary economic analysis based on the aforementioned data shows that the total investment cost sums up to 463,686 €, thus, resulting in a specific cost of 781 € per m2 of net solar collector area. Assuming the current electricity price of large consumers at 0.14€/kWh and considering the total investment cost, the annual energy savings of this system are 9,567 €/a, the IRR is negative and the Levelised Cost of Energy is 0.2672. These figures are far from attractive and indicate that this investment could be acceptable under specific circumstances. For example, the use of incentives could make the system costs more appealing. Additionally, new tighter legislation towards net zero emissions that applies penalties for CO_2 emitters could also fix the economics of this system.

4. Discussion and Conclusion

This work described the energy performance of a concentrating solar thermal system for covering part of the cooling load of a hospital building in Greece. Following a thorough analysis of the building's cooling loads, these were estimated at approximately 525MWh/a. The solar system comprised of 594m^2 concentrated parabolic collectors and a 2.000kWh thermal storage and 413kW double effect thermal absorption chiller. The energy performance assessment of the cooling system was elaborated in the Greenius tool and the results showed that the designed system provided 39% of the cooling loads of the building. The average annual field efficiency was calculated at 19% and the average annual collectors' efficiency was 26%. The annual sum of the Direct Normal Irradiation onto the collectors' area is 1.133MWh. Taking into consideration the thermal and optical losses, the thermal energy produced by the solar field is 272MWh. The double effect solar thermal chiller produces 240MWh of cooling energy and an amount of 172MWh of thermal energy is stored. The economic figures of the system, that is the Levelised Cost of Energy 0.2672 and the negative IRR imply that this system could be economically viable under specific circumstances.

In the direction of the future decarbonization of buildings, the use of RES heating and cooling systems is getting necessary. Peak space cooling needs also coincide with peak solar energy availability and solar thermal systems can contribute to space cooling and avoidance of interior overheating. The results of this analysis can be also useful for engineers and developers during the design and dimensioning process of solar concentrating thermal systems for heat production.

5. Acknowledgements

The simulation work was performed in the frame of the "ZenH Balkan" project, co-funded by the Interreg Balkan-Mediterranean Programme and National Funds.

6. References

Balaras, C. A., Dascalaki, E. G., Droutsa, K. G., Micha, M., Kontoyiannidis, S., & Argiriou, A. A. (2017). Energy use intensities for non-residential buildings. Zbornik Međunarodnog kongresa o KGH, 48(1), 369-389.

Bawaneh, K., Ghazi Nezami, F., Rasheduzzaman, M., & Deken, B. (2019). Energy consumption analysis and characterization of healthcare facilities in the United States. Energies, 12(19), 3775.

Dimoudi A. Kantzioura A., Toumpoulides P., Zoras St., Dimitriou St., Thravalou St, Metaj M., Mara E., Dorri A., Serghides D. 2022. The Energy Performance of Hospital Buildings in the South Balkan Region: The Prospects for Zero-Energy Hospitals. In: Sayigh A. (eds) Sustainable Energy Development and Innovation. Innovative Renewable Energy. Springer, Cham. https://doi.org/10.1007/978-3-030-76221-6_83.

Drosou V., Kyiaki E., Dimoudi A., Papadopoulos A. 2016. Concentrating solar thermal collectors for cooling of buildings: An assessment for Greece. 47th International Congress and Exhibition on Heating, Refrigeration and Air-Conditioning, 30 Nov-2 Dec, Belgrade (Serbia).

González G., A., García-Sanz-Calcedo, J., & Rodríguez Salgado, D. (2018). Evaluation of energy consumption in German hospitals: Benchmarking in the public sector. Energies, 11(9), 2279.

Greenius - The Green Energy System Analysis Tool, DLR - Institute of Solar Research.

International Energy Agency IEA. 2011. Solar Heating and Cooling Program - Task 38 Solar Air-Conditioning and Refrigeration - Monitoring Procedure for Solar Cooling Systems, A joint technical report of subtask A and B.

Kostadimas C., Dimoudi A., Zoras S. 2022. First Actions to Decarbonization of Buildings in the Health Sector: Investigation of their Energy Profile in the Area of Central and Western Macedonia in Greece. Intern 2020 Decarbonization Confer. ASHRAE, 5-7 Oct.

Nourdine, B., & Saad, A. (2020, March). Energy consumption in hospitals. In 2020 International Conference on Electrical and Information Technologies (ICEIT) (pp. 1-6). IEEE.

ZenH Balkan - Retrofit Assessment of the General Hospital of Kefalonia. 2021. Final Report, ZenH Balkan Project, INTERREG Balkan- Med Programme.

Annual Energy Performance of a Solar/Biomass HVAC System: Experimental Characterization through Concise Cycle Tests

Matteo Dongellini[1], Robert Haberl[2], Lukas Omlin[2], Szabolcs Varga[3], Claudia Naldi[1] and Gian Luca Morini[1]

[1] Department of Industrial Engineering, University of Bologna, Bologna (Italy)

[2] Institute for Solar Technology, Eastern Switzerland University of Applied Sciences, Rapperswil-Jona (Switzerland)

[3] Institute of Science and Innovation in Mechanical and Industrial Engineering, Porto (Portugal)

Abstract

This paper presents main results of Concise Cycle Tests (CCTs) carried out on the HVAC system developed under the Hybrid-BioVGE H2020 project. This system is driven by renewable energy sources (i.e., solar energy and biomass) and provides for space heating and cooling for small-scale residential and commercial buildings. The most innovative element of the HVAC system is a thermally-activated variable geometry elector (VGE) chiller, which provides for the building cooling load. Seasonal performance of the Hybrid-BioVGE system were assessed experimentally for both heating and cooling operating mode, according to the Whole System Testing (WST) methodology implemented by Institute SPF. Some components of the system were physically installed in the test bench, while other elements were simulated in TRNSYS and their performance was emulated and given to the test rig actuators according to the Hardware-in-the-Loop approach. Results point out that a significant part of the system energy demand can be satisfied by solar energy during the heating season: solar fraction is higher than 83% and, consequently, only 17% of the space heating energy need is provided by the back-up biomass boiler. On the contrary, the system energy performance for cooling operating mode is much lower than expected from numerical simulations. No sufficient cooling energy is supplied to the building due to the lack of cooling power from the VGE. Test results point out that a different control function to manage VGE operation must be defined necessarily.

Keywords: Whole system testing, Hardware-in-the-Loop, Variable-geometry ejector, Concise cycle test

1. Introduction

Nowadays, building sector is responsible for a large share of energy consumptions and greenhouse gas emissions, up to 40% worldwide (Alazazmeh and Asif, 2021). Furthermore, according to Braulio-Gonzalo et al. (2021), about 26% of final energy consumption in the European Union is associated to the use of energy in residential buildings (e.g., for space heating and cooling, domestic hot water production and appliances). Moreover, it is well known how the overall thermal energy demand of buildings depends on several drivers, such as climate, user behavior, envelope thermal properties and the availability of HVAC technologies. It is evident that, due to climate change, energy consumptions linked to space cooling are expected to grow significantly in the next future (Mutschler et al., 2021). In fact, a warmer climate results in a considerable increase of cooling energy demand in regions characterized by mild ambient temperatures during the hot season, thus resulting in a growing share of population installing an air conditioning device.

Currently, cooling energy need is mainly met by electric-driven vapor-compression units. Consequently, the forecasted growth of cooling demand will strongly impact power systems, for example affecting the electricity peak demand, especially during the hot season, and increasing the electricity off-take from the grid. Nowadays, decarbonization of energy systems is still ongoing and, for this reason, carbon emission factor for electricity from the distribution network maintains a high value (Ramsebner et al., 2021), since the highest share of electric energy is produced by fossil fuels in large and decentralized power plants.

© 2022. The Authors. Published by International Solar Energy Society
Selection and/or peer review under responsibility of Scientific Committee
doi:10.18086/eurosun.2022.06.04 Available at http://proceedings.ises.org

In this alarming framework, to limit the environmental impact and mitigate the climate change, a wider diffusion of sustainable HVAC systems, combined with on-site renewable energy systems, must be achieved in new and existing buildings. As pointed out by the open literature, solar-driven ejector cooling has high emission saving potential for space cooling applications. In fact, it is a simple, low-cost technology and an intrinsic correlation between solar irradiation and cooling demand can be found in common applications (Allouche et al., 2017).

Nevertheless, ejector-based cooling systems are typically characterized by low energy efficiency: the ejector Coefficient of Performance (*COP*) is lower than 0.3 in stationary operating mode and, furthermore, its performance is strongly influenced by current operating conditions (i.e., generator, condenser and evaporator temperature) and the adopted working fluid (Braimakis, 2021). Moreover, the best ejector energy performance can be achieved only for a narrow range of operating conditions. In fact, traditional fixed-geometry ejectors are sized for design working conditions and, under floating operating mode, the ejector fluid dynamics is strongly penalized, resulting in a significant reduction of *COP* (Varga et al., 2017). For above-mentioned reasons, the adoption of variable-geometry ejectors can improve sharply both the flexibility and the seasonal energy performance of this kind of systems (Van Nguyen et al., 2020).

Within this framework, the H2020 Hybrid–BioVGE project (Hybrid-BioVGE project, 2019) aims to design and demonstrate the energy saving potential of an innovative hybrid HVAC system, by means of which the energy needs for both space heating and cooling of residential and small-scale commercial buildings can be satisfied. The system developed along the project is driven by heat during the whole year, exploiting two renewable energy sources: solar energy and biomass. Its major components are solar thermal collectors, a biomass boiler, used as auxiliary heating device, two thermal energy storages and a thermally-driven variable geometry ejector (VGE) chiller, the most innovative element of the system.

Previous numerical works have pointed out the clear potential of the proposed VGE-based HVAC system in the current energy transition towards renewables. Dongellini et al. (2021) demonstrated that during the cooling season, almost 75% of the ejector's generator heat demand can be provided by solar energy, while about 90% of the system energy input is covered by renewable energy. Nonetheless, experimental tests are fundamental to assess the effective performance of Hybrid-BioVGE system and confirm its strong energy saving potential.

In this context, a reliable experimental evaluation of the Hybrid-BioVGE system performance is a difficult task, due to complexity of the system, dynamic operating conditions, interaction between components and master control logic. For this reason, Whole System Test (WST) approach is the only reliable test procedure to evaluate the effective performance of this system (Haller et al., 2013). In fact, when a complex HVAC system is used in a real building, transient phenomena which cannot be easily quantified by single component tests may arise, such as on-off cycling and stand-by losses. WST methods are based on the "Hardware-in-the-Loop" (HiL) concept and allow to test complete systems with realistic boundary conditions and for almost main operating modes, supporting the extrapolation of annual performance data of the tested system (Papillon et al., 2011). In recent years, dynamic WST methods have been developed and implemented in several European institutes to perform reliable tests on complex HVAC systems (Menegon et al., 2020).

In this context, the aim of the present paper is to evaluate the effective energy performance of the Hybrid-BioVGE system according to the WST methodology. Main components of the developed system are installed in an indoor test rig located at the institute OST-SPF, in Switzerland. The test rig is composed by four hydronic loops, by means of which heating and cooling loads of a building, as well as solar collector field or boiler outputs can be emulated in real time and given as boundary conditions to tested components. Simulation models of emulated subsystems are implemented within the dynamic software TRNSYS 18.

In order to extrapolate directly the seasonal performance of the Hybrid-BioVGE system from WST results, two Concise Cycle Tests (CCTs) have been defined, one for the heating operating mode and one for the cooling operating mode. Each CCT involves a series of days, representative of the whole season. In detail, seven and six typical days have been selected from the Meteonorm (Meteonorm, 2022) weather database with 1 hour time resolution to define test sequences for heating and cooling seasons, respectively. Weather data from both test sequences are emulated in the test rig as well.

In this work, the results of CCTs carried out on the Hybrid-BioVGE system for both heating and cooling operating mode are reported. The energy performance of the system has been assessed experimentally, obtaining the seasonal solar fraction (i.e., the share of building energy demand covered by solar energy), the seasonal coefficient

of performance of the VGE and the overall primary energy consumption of the system.

2. Methodology

CCTs performed at the institute OST-SPF aimed to evaluate the energy performance of the Hybrid-BioVGE system installed in one of the demonstrator of the project, located in Porto (Portugal).

2.1. Description of the Hybrid-BioVGE system

The HVAC system proposed by Hybrid-BioVGE consortium and studied in this work is coupled to a single-family detached home built during 2020 in Porto. The building presents an unheated basement, where the HVAC system technical room is present, and three heated floors (i.e. ground, first and second floor). The total net floor area of conditioned zones is equal to 186.3 m^2, while the heated volume of the building is 426.6 m^3. The building is characterized by a highly-performant envelope. For sake of brevity, thermal properties of envelope components can be found in Moser and Schranzhofer (2020).

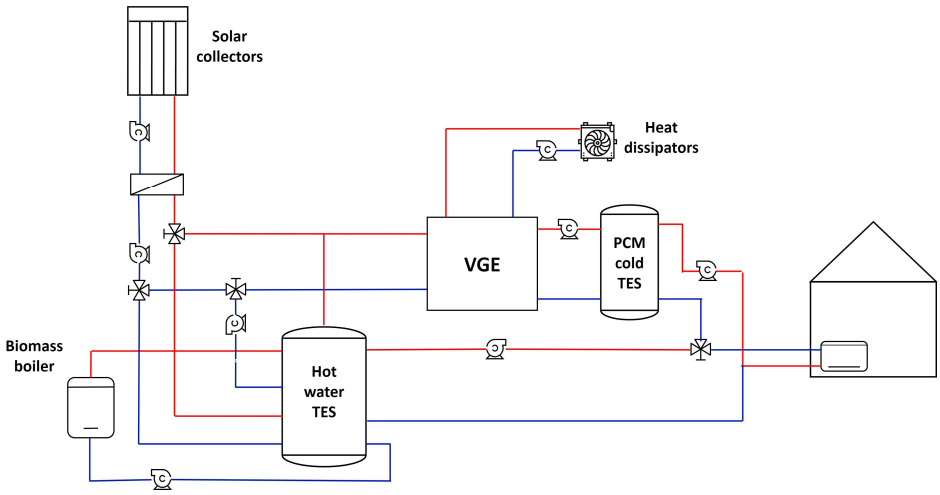

Fig. 1: Layout of the Hybrid-BioVGE HVAC system installed in the demonstrator in Porto

As pointed out in the previous section, the HVAC system developed by Hybrid-BioVGE consortium is composed by several components. In Figure 1, the simplified layout of the system is represented. Additional details on the complete design of the whole system are reported in Kalkgruber (2021).

Heat is mainly provided during both the seasons by nine flat plate collectors, installed on the building roof. Solar thermal collectors have a surface tilt (β) equal to 35°, while the azimuth (γ) is equal to 0° (i.e., collectors facing South). Optical efficiency η_0, 1st and 2nd order heat loss coefficients are equal to 0.706, 3.503 W/m^2K and 0.011 W/m^2K^2, respectively. These data, provided by the manufacturer, are related to the gross area of each collector, equal to 2.78 m^2. As pointed out in Figure 1, a plate heat exchanger decouples the solar collector field from the remaining part of the system.

During the heating season, solar collectors charge a 1000 liters hot water Thermal Energy Storage (TES). Heat is stored in the hot TES and then is provided to the building by means of radiant floor surfaces. A biomass boiler, fueled by pellet chips and characterized by a nominal heating capacity of 12 kW, is used as back-up heat generator during cloudy days with low values of solar irradiation.

The VGE chiller is most innovative element of the Hybrid-BioVGE project and is connected to several components of the HVAC system. The cooling device operates with R152a as refrigerant fluid and has been designed for a nominal cooling capacity of about 5 kW. As pointed out before, the ejector has the capability to adjust its geometry to maximize both the secondary mass flow rate (i.e., to obtain the highest cooling power) and the *COP*, depending on current operating conditions. In particular, the device has two degrees of freedom: i. the nozzle throat area can be varied by means of a movable spindle; ii. the relative position of the primary nozzle exit section with respect to the entrance section of the ejector throat can be adjusted by changing the nozzle position. Two linear stepper motors are coupled to the ejector to vary its geometry. In Figure 2, a picture of the whole VGE cooling device is reported.



Fig. 2: Variable geometry ejector cooling system

The VGE cooling system presents three plate heat exchangers to exchange heat between refrigerant and water. The generator of the ejector-based unit is mainly driven by solar energy. As pointed out by the hydraulic scheme shown in Figure 1, the VGE chiller is directly fed by solar collectors when high levels of solar irradiation are present. On the contrary, generator receives heat from the hot TES during days characterized by low irradiation (e.g., cloudy or rainy days). In this way, thermal energy collected by the solar field in previous days with better climatic conditions can be exploited, increasing the overall solar fraction of the system. Finally, the biomass boiler is operated as back-up system when no solar irradiation is present and, simultaneously, the hot TES is discharged. VGE evaporator is coupled to the HVAC system distribution network by means of a 500 liters sensible-latent thermal storage, which stores refrigerated water and encapsulated PCM modules. About 30% of the cold TES volume is occupied by disk-shaped modules, filled with ATS15, a salt-hydrate PCM having a melting temperature of 15°C (Axiotherm, 2022). In this way, the storage capacity of the system can be improved at the same volume, allowing a better operation of the VGE, since the TES temperature remains higher after the phase change, during the charging process. Finally, heat from the condenser is rejected to the ambient air by means of two commercial dissipator units, connected in parallel and installed on the building roof, having a rated heating capacity of 25 kW.

Control logic of the VGE and master control strategy of the whole system have been defined by the consortium. The complete description of control rules adopted for the Hybrid-BioVGE system supervision (i.e., list of variables, possible operating modes, setting of parameters) can be found in Morini et al. (2021).

2.2. Description of the experimental test rig for Concise Cycle Tests

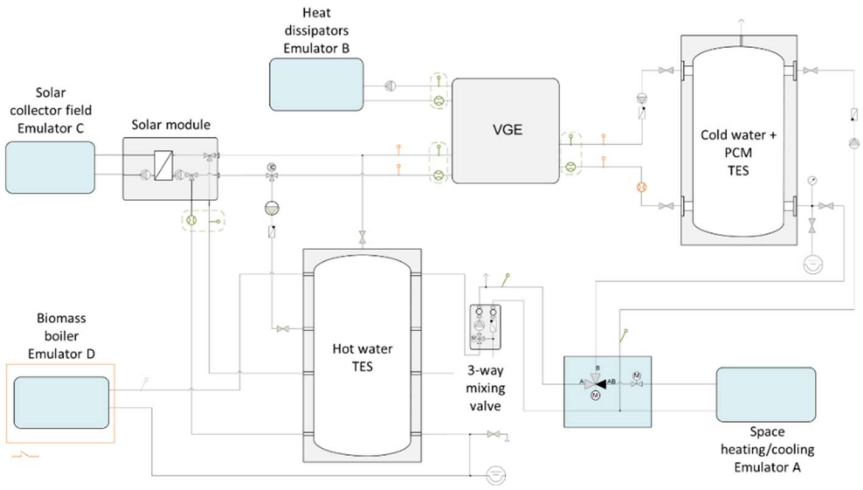

Fig. 3: Simplified hydraulic scheme of the experimental test rig installed at OST-SPF, with emulated and real installed components of the Hybrid-BioVGE system

The experimental test rig used to carry out CCTs on the Hybrid-BioVGE system is made of several components. Some of them are elements of the real HVAC system, others emulate pieces of equipment not installed within the

test rig or the building thermal load. The overall layout of the experimental setup is reported in Figure 3.

As pointed out by that figure, both the hot water TES and the cold latent-sensible TES are installed at OST-SPF institute. They are hydraulically connected to the VGE cooling systems with pipes. Other elements of the real HVAC system, such as the solar module and the 3-way mixing valve module, are connected to the experimental test rig. In Figure 4, pictures of the main elements of the Hybrid.BioVGE system installed in the laboratory are reported.

On the other hand, the performance of solar collectors, biomass boiler and heat dissipator units is reproduced by emulators B, C and D, respectively, since these elements are not physically installed within the test rig. The building thermal load for space heating/cooling, evaluated by dynamic simulations, is emulated as well by means of emulator A. Additional data needed to run a CCT, such as weather data (i.e., ambient temperature, solar irradiation incident on solar collectors) and room temperatures, are reproduced by electronic devices and given to emulators and installed devices as inputs.

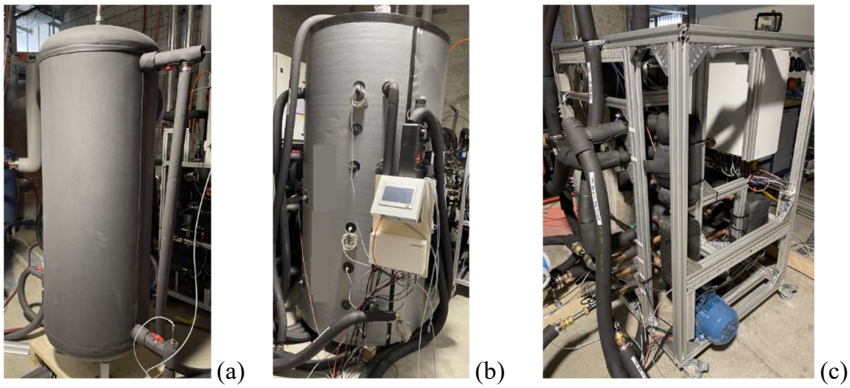
(a) (b) (c)

Fig. 4: Components of the Hybrid-BioVGE system installed in the test rig: cold sensible-latent TES (a), hot TES (b) and VGE chiller (c)

Simulation models of emulated components are implemented in the dynamic software TRNSYS 18 (Klein et al., 2017). Building heating and cooling loads are evaluated by means of Type 56 (Multi-zone building model). Solar collector model is “Flat plate collector with capacitance – Type 539”. Biomass boiler model is “Simple boiler with efficiency from data file – Type 751”, coupled to a series of equations needed to model the boiler control strategy (e.g., deashing procedure, hot and cold start-up). Both Type 539 and Type 751 can be found within TESS libraries. Heat dissipator units coupled to the VGE are modelled through the “Multi-dimensional data interpolation – Type 751” model, by means of which performance data of dissipators (i.e., thermal power and fan power input), given by the manufacturer, are interpolated as functions of fan speed, ambient air temperature and inlet water temperature.

2.3. Selection of heating and cooling test sequences

The heating and cooling demand of the building, as well as the yield of solar collector field, is of course dependent on the selected weather data. Therefore, two different test cycles were extracted from the annual weather data set for the Porto site, which was used for previous simulations. The first test sequence has been defined for the heating operating mode and the second test cycle has been designed for the cooling period. The reason for splitting into two sequences is the large inertia of the thermal masses involved in the system (i.e., building, hot and cold TES).

The test sequence from the heating period is composed by 7 days and consists of the week ranging from January 22nd to January 28th. On the other hand, the sequence from the cooling period consists of six selected days between May 28th and September 2nd. The selected days during the year can be seen in Figure 5, while the 7-day heating cycle and the 6-day cooling cycle are reported in Figure 6 and Figure 7, respectively. It is evident from these figures that selected sequences represents different climatic conditions occurring in Porto during the whole season. For example, the 6-day cooling cycle includes days with high values of both ambient temperature and solar irradiation (e.g., Day 1 and 3), as well as periods characterized by low solar irradiation and low or high ambient temperatures (e.g., Day 2 and Day 5, respectively).

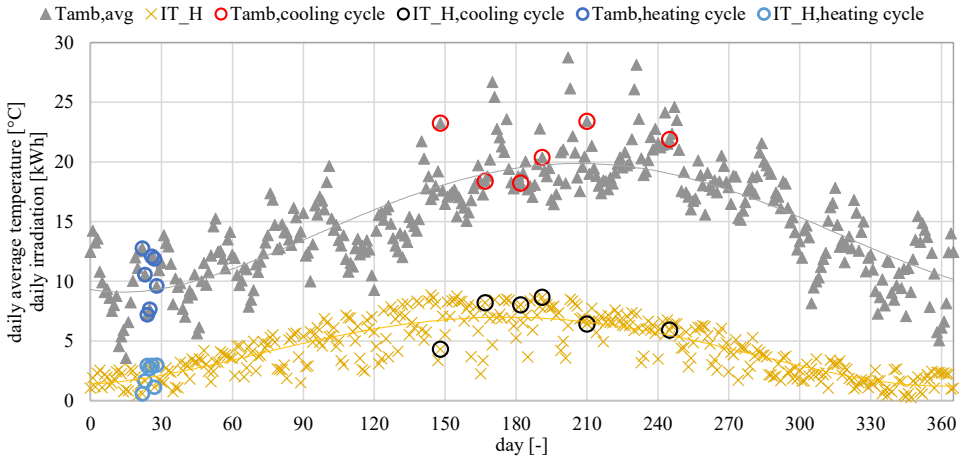

Fig. 5: Annual weather data with markings of the days selected for heating and cooling test cycles ($T_{amb,avg}$ = daily average ambient temperature, IT_H = daily global horizontal irradiation)

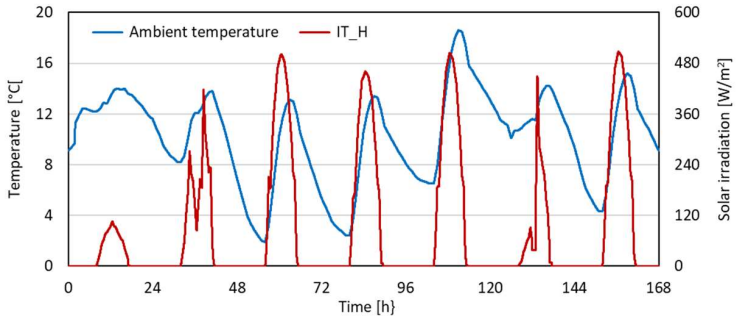

Fig. 6: Weather data of the 7-day heating cycle

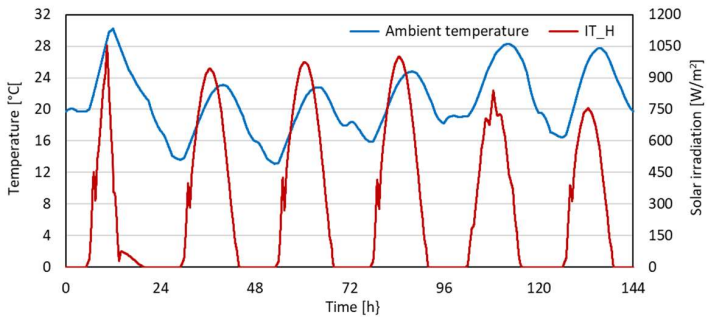

Fig. 7: Weather data of the 6-day cooling cycle

3. Results and discussion

3.1. Heating operation

Results of CCT carried out for heating operating mode are reported in Figure 8 and Table 1. As pointed out by outcomes of experimental tests, the Hybrid-BioVGE system is characterized by excellent energy performance. Globally, a total of 189.4 kWh of heat was supplied to the building for space heating. Solar collectors provided about 224.1 kWh, while the biomass boiler energy output was equal to 31.9 kWh. Consequently, the system solar fraction for heating mode (SF_h), defined as the share of building's thermal energy demand for heating provided by solar energy, is very high and equal to 1 for 6 days of the sequence (i.e., space heating energy need totally satisfied by solar collectors' yield and no energy supplied by the biomass boiler). The back-up boiler delivers heat to the hot TES and, consequently, provides for the space heating, only during the third day of the sequence, characterized by very low values of ambient temperature during the night (see Figure 6 and Table 1 for reference). The overall solar fraction of the Hybrid-BioVGE system throughout the heating cycle is 0.83. Therefore, test

results perfectly agree with previous numerical simulations. Moreover, the electric energy demand of controllers and pumps was limited to 6.7 kWh, corresponding to about 3.5% of the building energy demand.

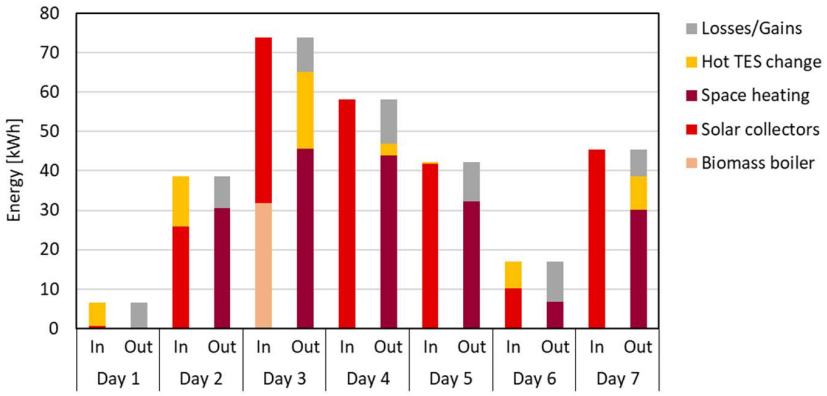

Fig. 8: Results of the 7-day heating cycle with inputs/outputs on a daily basis

Tab. 1: Results of the 7-day heating cycle

Day	$T_{amb,avg}$ (°C)	$I_{tot,hor}$ (kWh/m^2)	Q_{sh} (kWh)	Q_{col} (kWh)	Q_{bmb} (kWh)	Q_{hTES} (kWh)	SF_h
1	12.5	0.574	-0.2	0.6	0.0	6.1	1.00
2	10.6	1.662	-30.5	25.8	0.0	12.8	1.00
3	7.2	2.950	-45.7	41.9	31.9	-19.5	0.30
4	7.7	2.699	-44.0	58.2	0.0	-2.8	1.00
5	12.1	2.945	-32.2	41.8	0.0	0.5	1.00
6	11.9	1.120	-6.7	10.3	0.0	6.7	1.00
7	9.6	2.979	-30.1	45.5	0.0	-8.4	1.00
Total	10.2	14.929	-189.4	224.1	31.9	-4.6	0.83

$I_{tot,hor}$ = total solar irradiation on horizontal; Q_{sh} = space heating energy; Q_{col} = collector field energy input; Q_{bmb} = energy supplied by biomass boiler; Q_{hTES} = change of hot TES stored energy (positive values: discharge of TES, negative values: charge of TES)

From the results it can be seen that a significant amount of heat is collected by the solar field during the heating cycle and, consequently, during the whole heating season. It is evident how the largest quantity of solar energy is collected during days 3, 4, 5 and 7, having high values of solar irradiation and a significant thermal load from the building. In these days, in fact, the energy demand for space heating is significant during night and early morning hours and, for this reason, the hot TES is discharged before daytime. Consequently, water temperature within the storage decreases and a huge amount of heat can be potentially collected by the solar field, charging the hot tank and avoiding stagnation phenomenon. In this way, thermal energy stored in the hot TES can be exploited during the following days, if needed. Results confirm that, typically, the energy content of the storage is sufficient until the time when solar energy is available. As an example, during the second day of the heating cycle, space heating energy is higher than solar energy collected by the solar field and hot TES is partially discharged to provide for building's thermal energy demand. On the contrary, a low amount of solar energy is collected during days characterized by higher values of ambient temperature and, consequently, lower heating load from the building. In this case, which is very frequent in locations as Porto characterized by a mild winter, the hot thermal storage is charged rapidly during the morning and stagnation of solar collectors cannot be prevented.

One of the most significant findings of CCT performed for heating operating mode of the Hybrid-BioVGE system is the significant influence of thermal losses on the system energy performance. As pointed out by Figure 8, daily average thermal losses are equal to 8.8 kWh, with a maximum value of 11.3 kWh obtained on the sixth day of the

sequence. Along the overall heating cycle, almost 28% of heat collected by the solar field is dissipated from the hydraulic circuit. Since thermal losses from emulators and piping can be neglected, heat is mainly dissipated from the hot TES. In fact, experimental data point out that the temperature of water stored within this tank is very high. The average hot TES temperature throughout the heating cycle is equal to 70°C and rises to 74.8°C and 74.3°C during day 5 and day 6, respectively. It is worth to mention that for the sixth day of the sequence, thermal losses are almost equal to collector field energy input. This outcome is a strong indication that particular effort has to be paid to the minimization of heat losses from the storage system. For example, the hot TES should be located in environments having a warm temperature throughout the heating season, such as the building basement, and additional layers of thermal insulation should be included in the blanket.

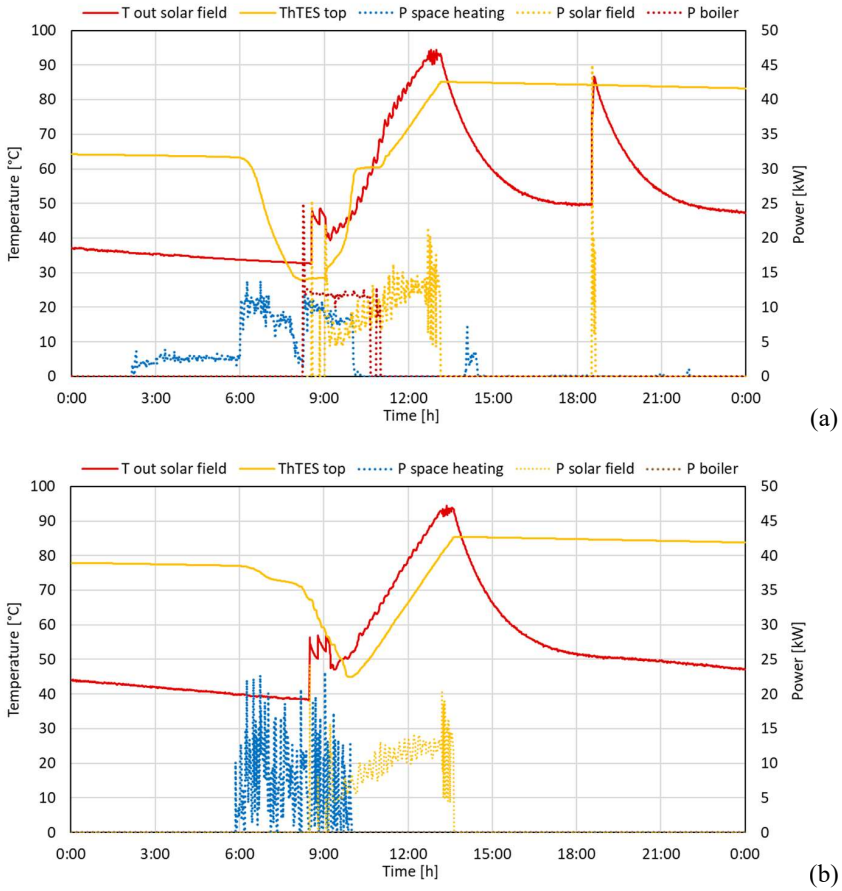

Fig. 9: Excerpt from the heating cycle CCT, showing the effective behavior of the system: day 3 (most severe day) (a) and day 7 (typical winter day with high solar irradiation and low ambient temperature) (b)

In order to highlight the potential of this kind of test, in Figure 9 an excerpt from heating cycle test data is shown. More in detail, test results from day 3 and day 7 of the heating cycle are reported in Figure 9a and 9b, respectively.

As pointed out by Figure 6, day 3 is the most severe day of the selected heating test sequence. Minimum and average ambient temperature are equal to 2°C and 7.2°C, respectively. During the night, the energy content of the hot TES is not particularly high, due to the low solar irradiation of the previous day, but the storage is able to provide for the building thermal load. Since the building space heating is linked to a time program, every morning at 6:00 rooms' internal set-point increases and required thermal power sharply rises to 10 kW. The thermal storage is discharged very fast and the biomass boiler is activated before solar energy is available. Then, as soon as solar irradiation increases and rooms are heated up, the boiler is switched off and solar collectors charge the storage until the maximum allowed temperature (85°C) is reached.

On the other hand, day 7 of the heating cycle represents a typical winter day for the Porto site. It is characterized by high solar irradiation and low ambient temperature ($I_{tot,hor}$ and $T_{amb,avg}$ equal to 2.979 kWh/m^2 and 9.6°C, respectively). Graph reported in Figure 9b shows that the storage tank has stored a significant amount of energy throughout the previous day, with a temperature in the upper part of the hot TES close to 80°C. Thereby, the

building space heating energy is supplied with no activation of the biomass boiler and the tank is discharged. Then, solar collectors charge the thermal storage in about 3-4 hours and sufficient heat is stored for the next day.

In conclusion, measurements show that, in case of the heating season, the capacity of the hot TES is sufficiently large to store energy throughout the day and provide for the space heating demand when it is needed in the next morning. In combination with the time program of the building emission sub-system, a very high solar fraction can be achieved. Nevertheless, the storage tank is charged to its maximum energy content on a significant part of the heating cycle (i.e., four out of seven days). Consequently, the solar field is in stagnation while the supply of energy to the building is inactive. To further decrease the biomass consumption, the building could be heated to higher temperatures and store thermal energy in the envelope.

3.2. Cooling operation

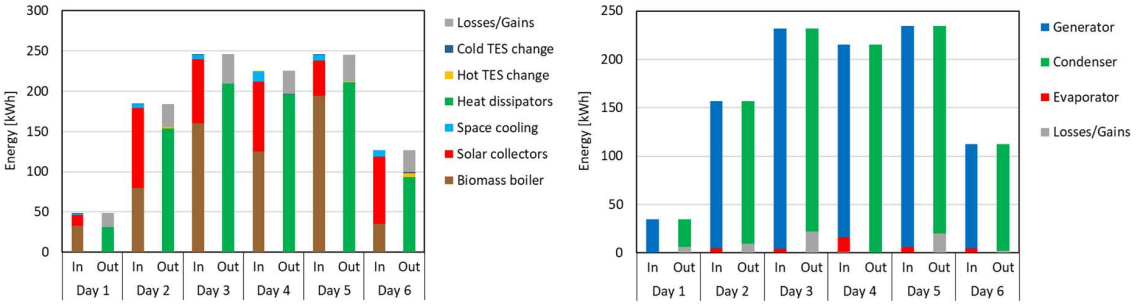

(a) (b)

Fig. 10: Results of the 6-day cooling cycle with inputs/outputs on a daily basis for Hybrid-BioVGE system (a) and VGE chiller (b)

Tab. 2: Results of the 6-day cooling cycle

Day	1	2	3	4	5	6	Total
$T_{amb,avg}$ **(°C)**	23.1	18.5	18.2	20.4	23.3	22.0	20.9
$I_{tot,hor}$ **(kWh/m²)**	4.311	8.204	8.559	8.675	6.420	5.904	42.072
Q_{sc} **(kWh)**	1.2	4.4	5.8	13.0	6.8	7.7	38.9
Q_{col} **(kWh)**	13.8	99.8	79.3	86.7	44.1	84.1	407.8
Q_{bmb} **(kWh)**	32.8	79.8	160.4	125.0	194.1	34.9	627.0
Q_{hTES} **(kWh)**	0.5	-1.7	0.0	0.4	-0.6	-4.1	-5.5
Q_{cTES} **(kWh)**	0.5	0.2	0.3	-0.7	0.5	-1.9	-1.1
Q_{gen} **(kWh)**	34.9	152.1	227.6	199.1	228.5	107.5	949.7
Q_{cond} **(kWh)**	-28.7	-147.3	-209.8	-215.2	-214.3	-110.7	-926
Q_{eva} **(kWh)**	0.0	4.5	4.4	15.0	6.1	5.1	35.1
Q_{dis} **(kWh)**	-31.5	-153.6	-209.4	-196.2	-211.3	-93.7	-895.7
SF_c	0.06	0.48	0.30	0.37	0.15	0.68	0.34

Q_{sc} = space cooling energy; Q_{cTES} = change of cold TES stored energy (positive values: discharge of TES, negative values: charge of TES); Q_{gen} = energy provided to VGE generator; Q_{cond} = energy rejected by VGE generator; Q_{eva} = energy absorbed by VGE evaporator; Q_{dis} = energy rejected by heat dissipators

Results from the cooling cycle CCT are reported in Figure 10, Figure 11 and Table 2. Along the cooling cycle, a total of 38.9 kWh of cooling energy is supplied to the building. Solar collectors' yield and biomass boiler energy output are equal to 407.8 kWh and 627 kWh, respectively. The room temperatures obtained from the virtual building highlight that there is no sufficient cooling energy supplied to the building thermal zones. In particular,

rooms at the first floor reach a maximum temperature of 28.5°C, significantly far from the desired value (25°C). The main KPI of the system is the solar fraction for cooling mode (SF_c), defined as the share of thermal energy demand of the VGE generator provided by solar energy. SF_c ranges from 0.06 to 0.68 on a daily basis and its average value throughout the cooling cycle is equal to 0.34, almost the half of the expected value.

As will be pointed out later, the cooling system operates permanently and, for this reason, the electric energy demand for auxiliaries (e.g., controllers, pumps, actuators) is very high. The total electric energy consumption is 68.9 kWh, almost the double of supplied cooling energy, a significant part of which (33.7 kWh) is needed for the VGE chiller only. It is evident that the Hybrid-BioVGE system expected performance is not achieved and a dramatic difference between test results and numerical simulations is obtained.

Experimental results point out that during the first day of the cooling cycle, characterized by: low solar irradiation and very high ambient temperature, the VGE cannot operate due to excessively high condensing temperature. For this reason, the VGE operation should be shifted to periods with lower ambient temperatures to store cooling energy in the cold PCM thermal storage.

Furthermore, a critical behavior of the Hybrid-BioVGE system can be observed also for other days of the cycle. Due to safety limits, the hot TES can be heated up to 85°C by solar collectors and the biomass boiler (for scarce availability of solar energy) and the capability to store heat from the solar field is limited. Moreover, as soon as the VGE is activated and thermal power is required to drive the ejector, the water temperature within the tank drops fast to 75-80°C . Consequently, the temperature available for the generator is too low and no cooling power can be obtained, even for low condensing temperatures. In addition, test results reveal that even with an inlet temperature to the generator higher than 100°C, in correspondence of high solar irradiation and direct feeding of the VGE through solar collectors, only a small cooling effect can be realized at the evaporator. Therefore, the maximum cooling power achieved by the VGE is equal to 1 kW, which is not sufficient to charge completely the cold TES. In fact, the lowest tank temperature obtained during the cooling cycle is 13°C, above the supercooling temperature of PCM modules. Thus, the room temperature cannot be maintained within the desired range.

Moreover, it is important to highlight how the relevance of thermal losses strongly increases for cooling operating mode. Test results point out that heat losses from hot TES and piping range between 17.3 kWh and 36.4 kWh per day, having an average value along the cooling cycle of 28.6 kWh/day. Thereby, a significant share of the system thermal energy input (i.e., solar field yield and biomass boiler output) is dissipated with no useful effect.

In Figure 11 an excerpt from cooling cycle test data is shown. In this figure, measurements for Hybrid-BioVGE system and VGE chiller from day 4 of the cooling cycle are reported. (Figure 11a and Figure 11b, respectively).

As mentioned before, an extremely high deviation between test results and numerical simulations of the VGE performance is achieved. A series of findings from experimental tests will be implemented in the next prototype, which will be installed in two demonstrators (the residential building in Porto and a small office building in Austria). For example, measurements not reported in this paper for sake of brevity point out that very large pressure drops, up to 6 bar, occur between internal pump outlet and generator inlet on the refrigerant side of the VGE. The cause of such dramatic pressure loss is a valve, installed between above-mentioned components, which will be eliminated in the next release of the VGE chiller since its presence is redundant.

As pointed out before, the building room temperature cannot be lowered due to the lack of significant cooling output of the VGE. Thereby, a permanent cooling demand on the system is present and the operating time of the VGE is correspondingly high, up to 24 hours per day. In order to prevent a not efficient operation of the VGE, an additional setting has been implemented in the system controller. The ejector-based chiller can be activated only when the difference between the temperature available to drive the generator and the ambient temperature is higher than 60°C.

Moreover, measurements in the cooling operating mode shows that the hot TES is discharged in less than 2 hours by the operation of the VGE chiller. It is evident from Figure 11 that when the VGE is operated, water temperature within the storage tank drops sharply and this leads to the activation of the biomass boiler to provide heat. Therefore, the capacity of the hot TES is not sufficient to extent the VGE operation with solar energy during periods characterized by colder climatic conditions and, consequently, better coefficient of performance.

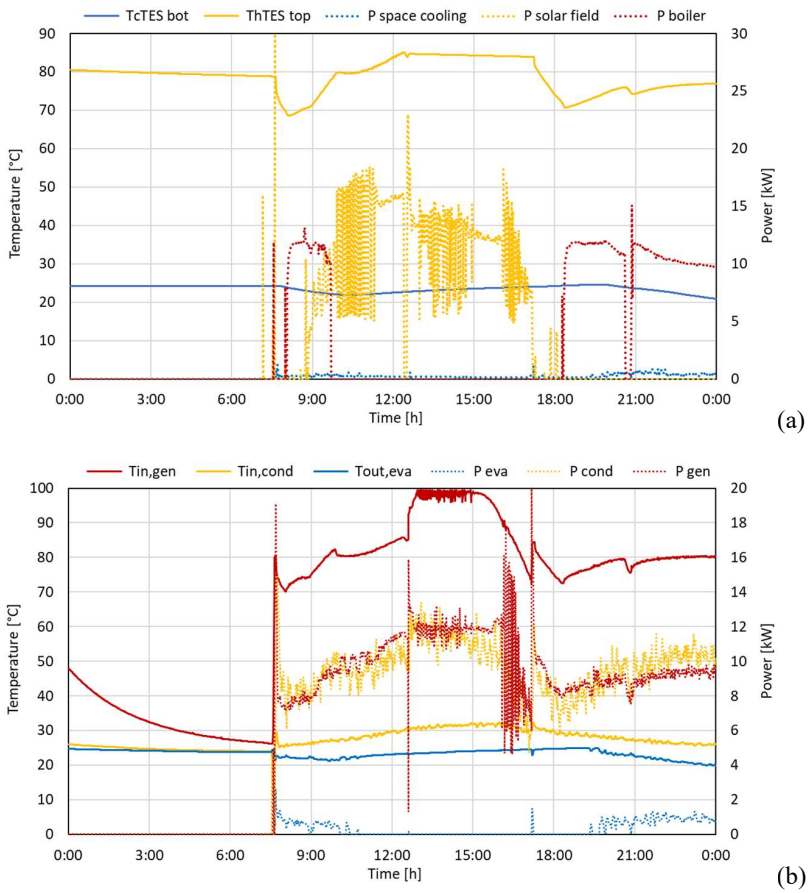

Fig. 11: Excerpt from day 4 of the cooling cycle: effective behavior of the Hybrid-BioVGE system (a) and VGE chiller (b)

To conclude, test results point out that a strong improvement concerning both the piping and control strategy of the VGE has to be performed in the development of the next chiller prototype. In particular, measurements show that a different function, based on the actual generated cooling power is necessary to control the VGE operation.

4. Conclusions

In this paper, findings of experimental tests carried out on the HVAC system proposed by the Hybrid-BioVGE project, according to the Whole System Testing methodology, are reported. Some components of the system, such as variable-geometry ejector (VGE) chiller, hot and cold thermal storages, were physically installed in the test bench, while other elements, such as solar collectors, biomass boiler, heat dissipators, building load and climatic data are emulated. A seven-day and a six-day test sequence were defined to assess the effective performance of the system for heating and cooling operating mode, respectively.

Results point out that the Hybrid-BioVGE system has an excellent potential during the heating season. A very high share of the building space energy demand, up to 83%, can be provided by solar collectors and the biomass boiler consumption is limited. Moreover, arrangement and capacity of the hot thermal storage is coherent and the daily demand of heat can be satisfied even for severe climatic conditions by thermal energy stored from the previous day.

On the contrary, measurements show that the tested prototype of VGE cooling system cannot deliver the planned cooling capacity. Main reasons for this unexpected behavior are the presence of very high pressure drops on the refrigerant side of the VGE, caused by a valve placed among the internal pump and the generator, and a not optimal control strategy. Adjustments on the dimensioning of VGE piping and heat exchangers are necessarily for the development of further prototypes, as well as the implementation of a different control function, which has to include the actual generated cooling power in its algorithm.

5. Acknowledgments

This paper is supported by European Union's Horizon 2020 research and innovation programme under grant agreement N° 818012, project Hybrid-BioVGE (Hybrid Variable Geometry Ejector Cooling and Heating System for Buildings Driven by Solar and Biomass Heat).

6. References

Alazazmeh, A. Asif, M., 2021. Commercial building retrofitting: Assessment of improvements in energy performance and indoor air quality. Case Studies in Thermal Engineering. 26, 100946.

Allouche, Y., Varga, S., Bouden, C., Oliveira, A.C., 2017. Dynamic simulation of an integrated solar-driven ejector based air conditioning system with PCM cold storage. Applied Energy. 190, 600–611.

Axiotherm (Accessed on July 27 2022). Axiotherm product HeatStixx and HeatSel. https://heatstixx.de/en/produkte-heatstixx/.

Braimakis, K., 2021. Solar ejector cooling systems: A review. Renewable Energy. 164, 566-602.

Braulio-Gonzal, M., Bovea, M.D., Jorge-Ortiz, A., Juan, P., 2021. Contribution of households' occupant profile in predictions of energy consumption in residential buildings: A statistical approach from Mediterranean survey data. Energy and Buildings. 241, 110939.

Dongellini, M., Naldi, C., Moser, C., Varga, S., Morini, G.L., 2021. Primary energy saving potential of a solar-driven ejector cooling system: a case study for a Portuguese residential building. Journal of Physics: Conference Series. 2116 (18), 012117.

Haller, M., Haberl, R., Persson, T., Bales, C., Kovacs, P., Cheze, D., Papillon, P., 2013. Dynamic whole system testing of combined renewable heating systems – The current state of the art. Energy and Buildings. 66, 667-677.

Hybrid-BioVGE project, 2019. EC H2020 Grant Agreement No. 818012. https://hybrid-biovge.inegi.up.pt/.

Kalkgruber, J., 2021. H2020 Hybrid-BioVGE Project. Deliverable 4.1 – Final designs of the 3 prototypes.

Klein, S.A. et al. 2017. TRNSYS 18: A Transient System Simulation Program, Solar Energy Laboratory, University of Wisconsin, Madison, USA, http://sel.me.wisc.edu/trnsys.

Menegon, D., Persson, T., Haberl, R., Bales, C., Haller, M., 2020. Direct characterisation of the annual performance of solar thermal and heat pump systems using a six-day whole system test. Renewable Energy. 146, 1337-1353.

Meteonorm, (accessed on July 25, 2022). https://meteonorm.com/en/.

Morini, G.L., Naldi, C., Biserni, C., Fabbri, G., Valdiserri, P., 2021. H2020 Hybrid-BioVGE Project. Deliverable 5.1 – Control strategy/algorithms.

Moser, C., Schranzhofer, H., 2020. H2020 Hybrid-BioVGE Project. Deliverable 2.1 - Report on thermal simulation of selected buildings.

Mutschler, R., Rüdisüli, M., Heer, P., Eggimann, S., 2021. Benchmarking cooling and heating energy demands considering climate change, population growth and cooling device uptake. Applied Energy. 288, 16636.

Papillon, P., Albaric, M., Haller, M., Haberl, R., Persson, T., Pettersson, U., Frank, E., Bales, C., 2011. Whole System Testing: The Efficient Way to Test and Improve Solar Combisystems Performance and Quality. *ESTEC – 5th European Solar Thermal Energy Conference*, Marseille 20–21 October.

Ramsebner, J., Haas, R., Auer, H., Ajanovic, A., Gawlik, W., Maier, C., Nemec-Begluk, S., Nacht, T., Puchegger, M., 2021. From single to multi-energy and hybrid grids: Historic growth and future vision. Renewable and Sustainable Energy Reviews. 151, 111520.

Van Nguyen, V., Varga, S., Soares, J., Dvorak, V., Oliveira, A.C., 2020. Applying a variable geometry ejector in a solar ejector refrigeration system. International Journal of Refrigeration. 113, 187–195.

Varga, S., Oliveira, A.C., Palmero-Marrero, A., Vrba, J., 2017. Preliminary experimental results with a solar driven ejector air conditioner in Portugal. Renewable Energy. 109, 83–92.

Analysis of Constructive Modifications for Enhancing the Performance of Solar Collector/Regenerators for Liquid Desiccant Systems

Fernando Manuel Gómez Castro[1], Ursula Eicker[2], Ulrike Jordan[1]

[1] Institute for Thermal Engineering, Kassel University, Kassel (Germany)

[2] Next-Generation Cities Institute, Concordia University Montreal, Montreal (Canada)

Abstract

This paper presents an investigation of a solar collector/regenerator (C/R) that is designed as a direct solar thermally-driven liquid desiccant system, in which the diluted desiccant solution is regenerated by simultaneously exposing it to solar radiation and air streaming along the liquid surface. Numerical finite element models of the device are developed to improve the heat and mass transfer processes within the collector/regenerator. Constructive modifications of the analysed design are based on adding an upper air-preheating channel, an artificially roughened absorber plate and a flat bottom reflector. The results demonstrate that the air-preheating channel has a moderate impact on the regeneration efficiency, whereas the turbulators and the solar concentrator exhibit high potential to boost the performance of the collector/regenerator.

Keywords: Thermally-driven liquid sorption system, collector/regenerator, numerical finite element models, upper air-preheating channel, turbulators, flat bottom reflector

1. Introduction

Solar-driven liquid desiccant systems are regarded as a sustainable and environmentally friendly technology to provide suitable thermal comfort conditions in buildings and to sanitise indoor air. The systems rely on the capacity of hygroscopic solutions to directly remove the moisture from the air by the absorption process and on the solar heat to regenerate the liquid sorbent within a temperature range of 40 to 80 °C (Katejanekarn and Kumar, 2008).

In a collector/regenerator (C/R), the heat collecting fluid is a hygroscopic liquid film flowing down the absorber plate. The liquid desiccant is reconcentrated by exposing it to air circulating in the regenerating channel. However, this device is not yet commercially available due to its large dimensions to satisfy the regeneration requirements of liquid desiccants. Large dimensions limit not only the wettability of the absorber plate but also its modularity and scalability, thus making it quite difficult to install it on the building envelope.

Some performance enhancement methods such as the double-glazed arrangement have been analysed in the literature for shortening the solar C/R length without damaging its operation. By using the counter-flow pattern between the liquid and gas phases, a performance improvement of about 3% was obtained for the device with upper air-preheating channel (Yang and Wang, 1998) under the hot and humid climatic conditions of Kaohsiung, Taiwan.

Zheng and Worek (1996) experimentally investigated a mechanical method for enhancing the heat and mass transfer during the evaporation of water from a liquid film in a channel consisting of adding cylindrical rods to a plate transversely to the direction of fluid motion. The average Nusselt and Sherwood numbers first increased to peak values at an optimal spacing of the rods and then decreased with further augmentation in rod pitch since the eventual diminution in surface roughness reduced both the flow separation/reattachment processes in the gas-phase and the mixing in the liquid-phase.

Flat reflectors are a well-established, cost-effective way to boost the operation of solar devices. Chen and Kao (1990) experimentally compared the performances of a closed C/R, a natural-flow C/R and a natural-flow C/R augmented with an external flat reflector using LiCl solution with mass fractions between 30% and 35%. The results demonstrated that adding a reflective mirror enhanced the evaporation rate by 20%.

© 2022. The Authors. Published by International Solar Energy Society
Selection and/or peer review under responsibility of Scientific Committee
doi:10.18086/eurosun.2022.06.05 Available at http://proceedings.ises.org

This paper presents a numerical investigation of constructive modifications for promoting the heat and mass transfer phenomena in the regenerating panel. The modifications include the attachment of an upper air-preheating channel. In a second step, an artificially roughened absorber plate is used. Furthermore, a ray tracing algorithm is developed in Mathematica to evaluate the contribution of a flat bottom mirror to the optical performance of a south-facing C/R under the typical meteorological conditions of Stuttgart, Germany.

2. Heat and mass transfer in solar collector/regenerators

Fig. 1 shows the investigated C/R constructions. The upper air-heating channel shown in Fig. 1(a) is constructed with an additional glass cover on top of the existing one with a change in flow direction of the air at the end of the device. The roughened absorber plate shown in Fig. 1(b) is modelled as multiple V dimpled patterns from computational models implemented in Wolfram Mathematica. To evaluate the impact shading between the C/R and the flat bottom mirror a construction as shown in Fig. 1(c) is considered.

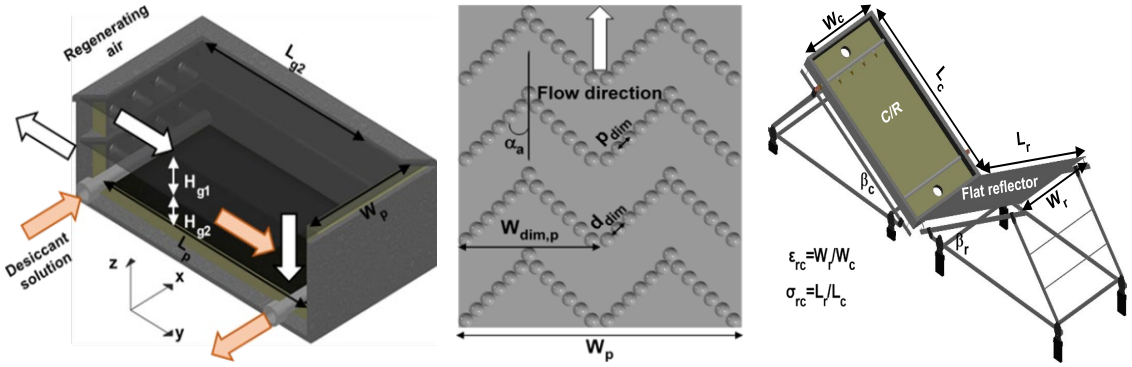

(a) Upper air-preheating channel (double-pass double-glazed C/R)

(b) Artificially roughened absorber plate (dimples)

(c) Flat bottom reflector

Fig. 1: Analysed constructive modifications of the solar collector/regenerator.

2.1. Single-pass single-glazed collector/regenerator

Six nodes normal to the flow directions of the fluids are used to analyse the coupled heat and mass fluxes in the finite element of the single-pass single-glazed C/R (SG-C/R) as shown in Fig. 2. These are: (I) the glass cover, (II) regenerating air, (III) desiccant solution, (IV) porous fabric, (V) absorber plate and (VI) collector housing.

To model the heat and mass transfer, a basic set of equations was developed based on the mass and energy balances for each node.

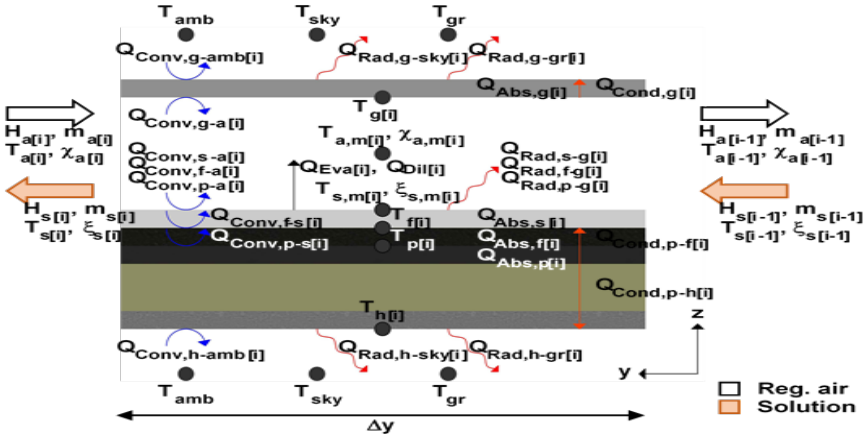

Fig. 2: Finite element of the single-pass single-glazed C/R in counter-flow.

2.2. Double-pass double-glazed collector/regenerator

The finite element of the double-pass double-glazed C/R (DG-C/R) illustrated in Fig. 3 comprises eight nodes normal to the flow directions of the fluids. These are: (I) the outer glass cover, (II) regenerating air in upper channel, (III) inner glass cover, (IV) regenerating air in lower channel, (V) desiccant solution, (VI) porous fabric,

(VII) absorber plate and (VIII) collector housing.

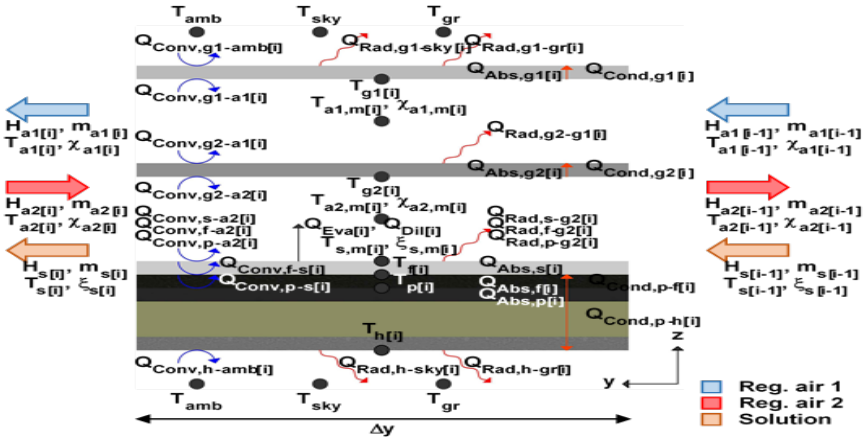

Fig. 3: Finite element of the double-pass double-glazed C/R in counter-flow.

The DG-C/R model is an extension of the SG-C/R model with an additional upper channel with transparent walls for preheating the air stream prior to the solution regeneration process. Therefore, the set of governing equations from the SG-C/R is extended by three additional ones describing the energy balance of the outer glass cover, of the regenerating air in the upper channel, and the inner glass cover.

The combined effects of the thermal and solutal buoyancy forces on the mixed convective heat and mass transfer during water evaporation from the liquid desiccant film in a smooth channel are considered by applying the law of cosines to the correlations proposed by Azevedo and Sparrow (1985) (natural convection) and by Gnielinski (2010) (forced convection) for laminar air flow and to those given by Fedorov and Viskanta (1997) (natural convection) and by Taler (2017) (forced convection) for turbulent air flow. In the case of an artificially roughened channel, the calculations for the forced flow are done based on the unified formulation developed by Brkic and Praks (2018), in which the correlations of Kumar et al. (2017) for multiple V-dimpled patterns are used in the fully developed rough turbulent regime.

2.3. Solar concentration with a flat bottom reflector

The optical path of a sunlight ray through the concentrating system can be fully described from the vector analysis based on transformation matrices among the coordinate systems of the horizontal (X, Y, Z), reflector (X', Y', Z') and collector (X'', Y'', Z'') planes. Fig. 4 shows the shading of the flat reflector by the collector, which can occur if the sun is situated behind the receiver. This situation leads not only to the self-shading of the collector but also to the total/partial obstruction of the sunlight falling on the opposite bottom mirror.

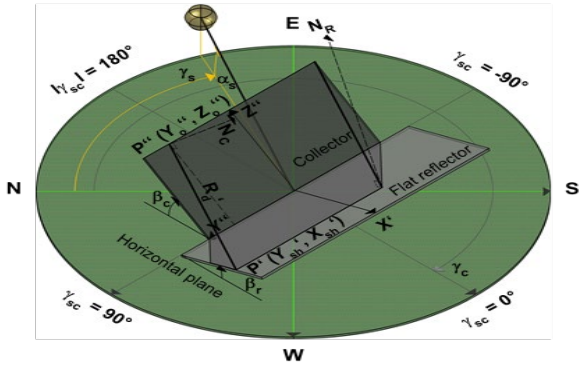

Fig. 4: Intersection point (Ysh', Xsh') of a sunlight ray transmitted from the collector to the reflector.

Fig. 5(a) shows the self-shading of the reflective surface, which simultaneously casts a total or partial shadow on the opposite collector. The optical path of the sunlight rays incident on and reflected by the flat booster mirror towards the collector plane is depicted in Fig. 5(b). Some of these rays are accepted on the receiver aperture area, while others are lost.

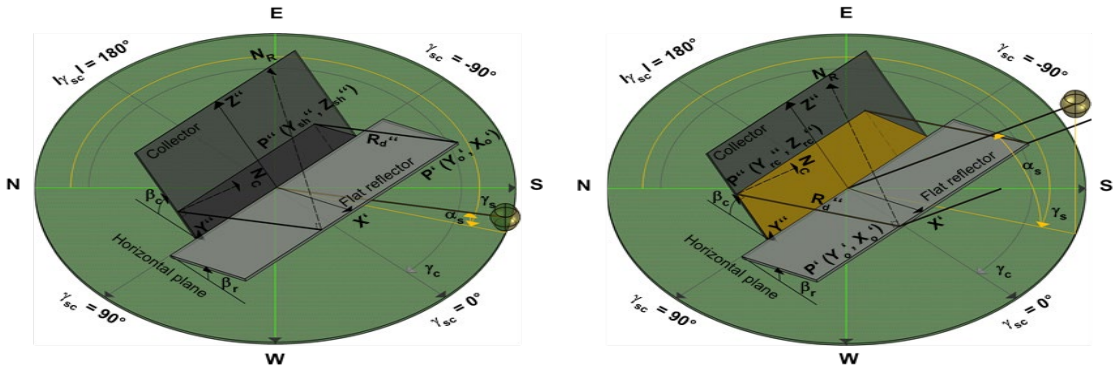

(a) (b)

Fig. 5: Intersection points of a sunlight ray (a) transmitted from the reflector to the collector and (b) reflected from the reflector to the collector.

Convex 2D polygons that describe the shading onto the collector and reflector planes as well as the sunlight concentrated by the mirror onto the collector plane are clipped in turn against each boundary of these surfaces according to the algorithm of Sutherland-Hodgman (1974) to estimate the available global irradiance on the tilted receiver from the method of Baccoli et al. (2018).

3. Performance indicators

In order to characterise the mass transfer mechanism of the studied devices, the regeneration efficiency (η_{Des}) is introduced as the ratio of the latent heat required by the desorption of the water from the diluted desiccant solution trickling down the absorber plate (ΔH_{Des}) to the global irradiance on the aperture area of the tilted collector ($Q_{\beta c}$) (Peng and Zhang, 2015):

$$\eta_{Des}=\frac{\Delta H_{Des}}{\dot{Q}_{\beta c}}\times 100=\frac{\dot{m}_{Des}\cdot\left(h_{fg}+h_{Dil}\right)}{G_{\beta c}\cdot A_c}\times 100 \qquad \text{(eq. 1)}$$

With $\dot{m}_{Des}$ as the water desorption rate; h_{fg} as the enthalpy of evaporation; h_{Dil} as the specific enthalpy of dilution; $G_{\beta c}$ as the global solar irradiance collected on the tilted surface; A_c as the aperture area of the collector.

For the purpose of considering the power required to blow air through an artificially roughened channel, the thermohydraulic performance factor ($PF_{th,SGr}$) is assessed (Lewis, 1975):

$$PF_{th,SGr}=\frac{Nu_{Dh,SGr}/Nu_{Dh,SG}}{\left(f_{d,SGr}/f_{d,SG}\right)^{1/3}} \qquad \text{(eq. 2)}$$

Where $Nu_{Dh,SGr}$ and $f_{d,SGr}$ are the Nusselt number and Darcy friction factor for the structured duct, whereas $Nu_{Dh,SG}$ and $f_{d,SG}$ are the Nusselt number and Darcy friction factor for the smooth channel.

Additionally, the optical performance factor (PF_{opt}) denotes the potential benefit/drawback of coupling a flat bottom reflector to the collector/regenerator. It is defined as the ratio of the global tilted solar radiation harvested by the boosted regeneration unit ($I_{\beta rc}$) to the global tilted solar radiation collected by the conventional one without reflecting surface ($I_{\beta c}$) during a given time period (Rehman and Uzair, 2021):

$$PF_{opt}=\frac{I_{\beta rc}}{I_{\beta c}}=\frac{\int G_{\beta rc}\cdot dt}{\int G_{\beta c}\cdot dt} \qquad \text{(eq. 3)}$$

With $G_{\beta rc}$ and $G_{\beta c}$ as the global solar irradiance on the tilted receiver with and without the booster mirror.

4. Results and discussion

4.1. Double-pass double-glazed collector/regenerator

The single-pass single-glazed (SG-C/R) and double-pass double-glazed collector/regenerators (DG-C/R) with smooth absorber plates are compared for the same operating conditions with aqueous LiCl as desiccant solution. The parameters taken into account along with their values are listed in Tab 1.

Tab. 1: Ranges and reference values of the control parameters for SG- and DG-C/Rs.

Type	Variable	Symbol	Unit	Range	Reference value
Meteorological parameters	Global solar irradiance on the tilted surface	$G_{\beta c}$	W/m^2	400, 700, 1000	700
	Barometric pressure	p_b	Pa	-	97657
	Wind speed	V_w	m/s	-	2
Parameters of the air	Inlet temperature	$T_{a,in}$	°C	-	30
	Inlet humidity ratio	$\chi_{a,in}$	g/kg	-	12
	Volumetric flow rate per cross-sectional area	$\dot{V}_a$	m^3/(m^2·h)	200-3600	-
Parameters of the desiccant solution	Inlet temperature	$T_{s,in}$	°C	-	40
	Inlet mass fraction	$\xi_{s,in}$	%	-	30
	Volumetric flow rate per cross-sectional area	$\dot{V}_s$	l/(m^2·h)	-	500
Geometric parameters	Width × length	$W_c \times L_c$	m × m	-	1 × 2
	Gap height(s)	H_{gi}	cm	-	5
	Tilt angle	β_c	°	-	35°

The ratio of the regeneration efficiency of the double-pass double-glazed C/R to that of the single-pass single-glazed one is plotted for Reynolds numbers of the air (with the channel hydraulic diameter D_h as characteristic length) of $Re_{a,Dh} \in [314, 6033]$ and a Reynolds number of the liquid desiccant of $Re_s^*=12.8$, see Fig. 6(a). The three lines depict the efficiency ratios for an irradiance on the tilted collector surface of 400 W/m², 700 W/m² and 1000 W/m².

According to the left y-axis in Fig. 6(a), the efficiency ratio sharply decreases by increasing the air Reynolds number, which indicates that the second glass cover is only advantageous for low air Reynolds numbers. This happens since the temperature rise of the air passing the upper channel is also high for low air Reynolds numbers as shown in Fig. 6(b). The air-preheating is promoted at high irradiance levels, as the warmer liquid film transfers more heat to the inner glazing.

For irradiance levels of 400 W/m² and 1000 W/m², the DG-C/R outperforms the SG-C/R ($\eta_{Des,DG}/\eta_{Des,SG}>1$) in the laminar air flow regime with air Reynolds numbers below about 2100 and 1400, respectively (see left y-axis in Fig. 6(a)). That means, the higher the solar irradiance, the lower the maximum air Reynolds number with a positive effect of the air-preheating upper channel. This occurs because the greater solar heating of the desiccant solution at high irradiance levels requires greater air-preheating to reduce the thermal dissipation from the liquid film, which in turn enhances the mass transfer driving potential at the liquid-air interface.

From the right y-axis in Fig. 6(a), an upward trend in the regeneration efficiency is observed with augmenting air Reynolds number. In transitional and turbulent flow regimes, the additional glazing and air passage of the DG-C/R negatively affect the system performance. For a Reynolds number of the air of about 6000, corresponding to a mean air velocity in the channel of about 1 m/s and a solar irradiance on the tilted collector plane of 700 W/m², the regeneration efficiency of the DG-C/R drops by approximately 5.1% with respect to the SG-C/R, from $\eta_{Des,SG}$=37.9% to $\eta_{Des,DG}$=36%. This occurs because the weak air-preheating prevailing in such conditions (see Fig. 6(b)) cannot sufficiently diminish the heat fluxes from the liquid desiccant to compensate for the low optical efficiency of the device. Thus, the highest performance benefit of the DG-C/R is obtained at low air flow rates under reduced sunlight conditions.

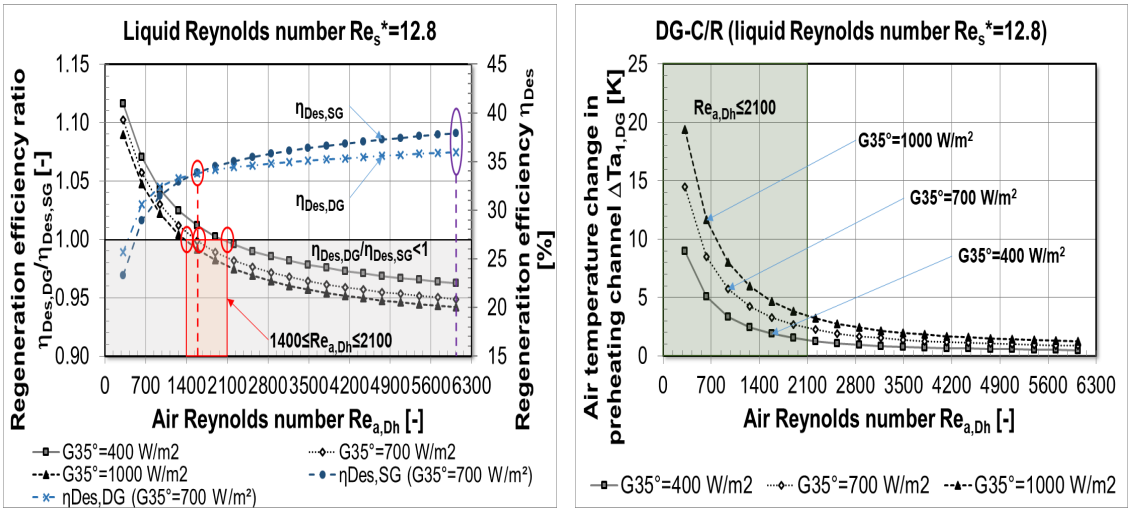

(a) Efficiency ratio

(b) Air-preheating effect

Fig. 6: Ratio of the regeneration efficiency of the DG-C/R with respect to the SG-C/R (a) and air-preheating effect (b) over the Reynolds number of the air at different global tilted solar irradiance levels.

4.2. Artificially roughened single-pass single-glazed collector/regenerator

The single-pass single-glazed collector/regenerators with smooth (SG-C/R) and artificially roughened (SGr-C/R) channels are benchmarked at the operating conditions and geometric parameters specified in Tab. 1 using aqueous LiCl as hygroscopic liquid. The absorber plate of the SGr-C/R is texturized by multiple V-dimples arranged according to the optimal configuration reported by Kumar et al. (2017) (see Fig. 1(b)) with a relative roughness depth of κ_r=0.037 (ratio of the dimple depth to the hydraulic diameter of the channel), relative roughness width of ω_r=5 (ratio of the plate width to the width of the dimpled pattern), δ_r=1 (ratio of the dimple depth to dimple diameter), relative roughness pitch of π_r=9 (ratio of the distance between two consecutive dimples to the dimple depth) and angle of attack of α_a=55° (angle between the dimple line and the air flow direction).

The left y-axis in Fig. 7(a) represents the ratio of the regeneration efficiency of the artificially roughened single-pass single-glazed C/R to that of the smooth single-pass single-glazed one for air Reynolds numbers ranging from 314 to 6033 and a liquid Reynolds number equal to 12.8. The efficiency ratio curves are obtained for solar irradiances on the tilted collector surface of 400 W/m², 700 W/m² and 1000 W/m². It is found that the SGr-C/R strongly outperforms the SG-C/R ($\eta_{Des,SGr}/\eta_{Des,SG}>1$) within the considered range of $Re_{a,Dh}$. This behaviour is even more noticeable at low solar irradiance thanks to the minor thermal dissipation of the liquid film with its surroundings.

According to the left y-axis in Fig. 7(a), the efficiency ratio first increases until it reaches its maximum value, after which it decreases smoothly with rising air Reynolds number. This fact reveals that there is a limit at which the remarkable intensifications in the convective heat and mass transfer coefficients caused by the successive flow separation/reattachment in the gas-phase and mixing in the liquid-phase can no longer compensate for the lessenings in the temperature and vapour pressure gradients at the liquid-air interface as the air flow rate augments. For irradiance levels of 400 W/m² and 1000 W/m², the optimal air Reynolds numbers lie in the early stage of the turbulent flow and in the transitional flow with $Re_{a,Dh}\approx4400$ and $Re_{a,Dh}\approx3800$, respectively. Thereby, the higher the solar irradiance, the lower the optimal air Reynolds number with the maximised operational benefit of the structured absorber plate. This can be explained by the fact that a lower convective heat transfer coefficient inhibits the thermal losses from the hotter liquid film at high solar irradiance collected on the tilted surface, which improves the mass transfer driving force.

The right y-axis in Fig. 7(a) shows an ascending tendency in the regeneration efficiency by increasing air Reynolds number. For $Re_{a,Dh}\approx6000$, corresponding to a mean air velocity in the channel of approximately 1 m/s, and a solar irradiance on the tilted collector surface of 700 W/m², the regeneration efficiency of the SGr-C/R rises by about 9.9% with respect to the SG-C/R, from $\eta_{Des,SG}$=37.9% to $\eta_{Des,SGr}$=41.7%, due to the combined effects of enhancing the convective heat and mass transfer coefficients by adding multiple V-dimples.

The thermohydraulic performance factor of the artificially roughened single-pass single-glazed C/R to that of the

smooth single-pass single-glazed one is plotted for air Reynolds numbers of $Re_{a,Dh} \in [314, 6033]$, a liquid Reynolds number of $Re_s^*=12.8$ and solar irradiances of 400 W/m², 700 W/m² and 1000 W/m² falling on the tilted absorbing surface, see Fig. 7(b). Values of $PF_{th,SGr}$ greater than unity denote the overall advantage of roughening the absorber plate of the SGr-C/R, since the most efficient device maximises the Nusselt number while minimising the friction factor and, consequently, the fan power consumption. The use of the SGr-C/R over the SG-C/R is recommended only for air Reynolds numbers beyond about 2500 with the thermohydraulic performance factor rising monotonically up to about 1.6.

The optimal operating points found for the SGr-C/R at $Re_{a,Dh}\approx4400$ and $Re_{a,Dh}\approx3800$ under solar irradiances of 400 W/m² and 1000 W/m² have thermohydraulic performance factors of $PF_{th,SGr}\approx1.3$ and $PF_{th,SGr}\approx1.1$, respectively, while the operating point $Re_{a,Dh}\approx6000$ at a solar irradiance of 700 W/m² reaches a value of $PF_{th,SGr}\approx1.5$. This demonstrates that the procedure for optimising the geometry and operating conditions of the SGr-C/R must be based on the combined analysis of the curves of efficiency ratio (see the left y-axis in Fig. 7(a)) and thermohydraulic performance factor (see Fig. 7(b)). By contrast, below $Re_{a,Dh}\approx2500$, modest increases in heat transfer are obtained within the structured channel in comparison to the high air flow pressure drops, so that the high energy requirements of the fan are not justified.

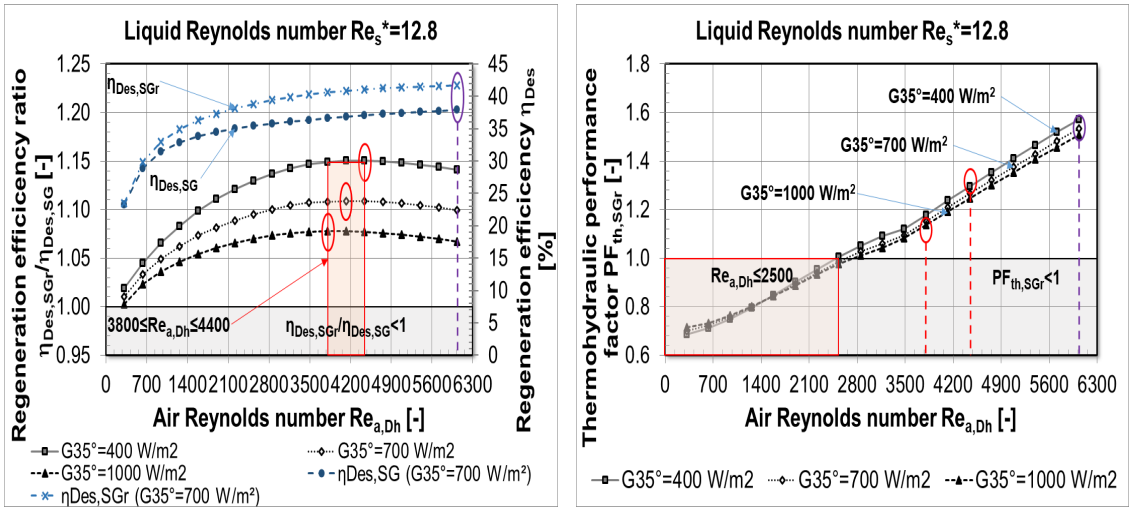

(a) Efficiency ratio

(b) Thermohydraulic performance factor

Fig. 7: Ratio of the regeneration efficiency (a) and thermohydraulic performance factor (b) over the Reynolds number of the air at different global tilted solar irradiance levels.

4.3. Solar collector/regenerator with booster mirror

Fig. 8. shows the contour plots of the total annual global radiation on the tilted surface ($I_{\beta rc}$) and the annual optical performance factor (PF_{opt}) for Stuttgart, Germany (48.8° N 9.2° E) obtained from the weather data of the typical meteorological year (TMY) generated by Meteonorm. The analysed low concentrating system comprises a C/R of 1 m width × 2 m length coupled to a flat bottom mirror with the same dimensions ($L_r/L_c=1$ and $W_r/W_c=1$) and a reflectivity of 0.9. The performance indicators $I_{\beta rc}$ and PF_{opt} are calculated for representative average days for each month throughout the year (Klein, 1977) with 5° steps for the inclinations of the collector ($0°\leq\beta_c\leq90°$) and reflector ($0°\leq\beta_r\leq90°$) by only discarding the case of $\beta_c=\beta_r=90°$. The total annual global solar radiation available on the C/R reaches a maximum value of about 1400 kWh/(m²Y) at collector inclinations of $30°\leq\beta_c\leq60°$ and reflector tilt angles of $10°\leq\beta_r\leq35°$ with annual optical performance factors of $1.05\leq PF_{opt}\leq1.12$. Finally, optical performance factors less than unity occur in the regions limited by $0°\leq\beta_c\leq90°$ and $40°\leq\beta_r\leq90°$, which indicates the shading of the collector either by itself (see Fig. 4) or by the planar mirror (see Fig. 5(a)).

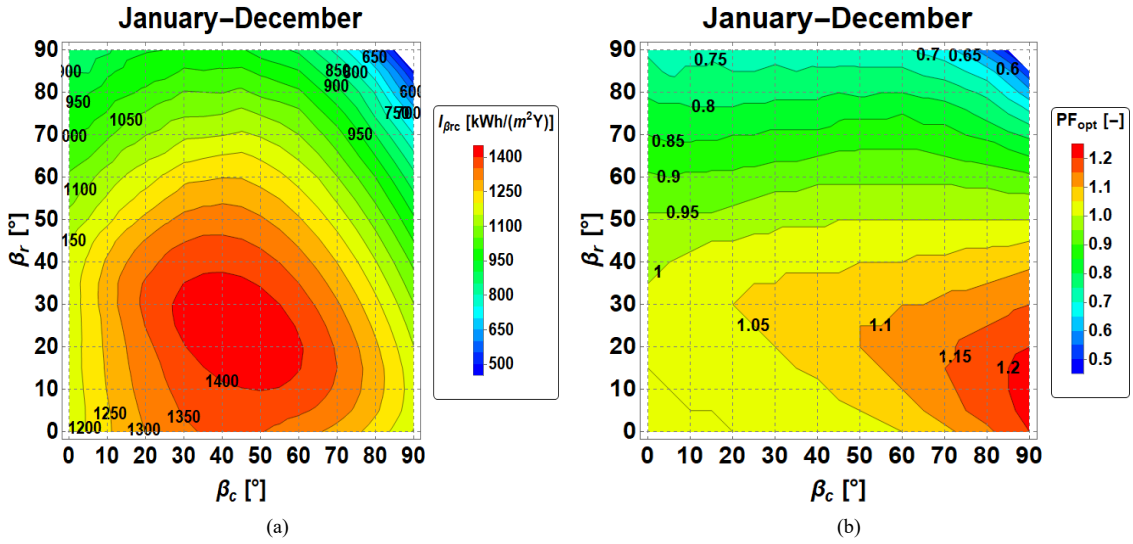

(a) (b)

Fig. 8: Variation of (a) the total annual global solar radiation on the tilted surface and (b) the annual optical performance factor for the C/R with booster reflector (L_r/L_c=1 and W_r/W_c=1) in Stuttgart, Germany.

5. Conclusions

This paper presents an investigation of the impact of three measures on the performance of a solar collector/regenerator: Adding an upper air-preheating channel, using a structured absorber plate and coupling a flat bottom mirror to the direct solar regeneration unit.

For the operating conditions and geometry considered here, it was found that the double-pass double-glazed configuration (DG-C/R) improves the regeneration efficiency relative to the single-pass single-glazed one (SG-C/R) for small Reynolds numbers. The reason for this lies in the fact that the air preheated in the double-pass construction contributes to decrease the thermal dissipation from the desiccant solution, which leads to an increase in the liquid-air interfacial vapour pressure gradient. However, this air preheating effect weakens as the air flow approaches the transitional and turbulent regimes and may even negatively impact the solution regeneration process. For example, for an air Reynolds number of approximately 6000, corresponding to a mean air velocity in the channel of about 1 m/s and a solar irradiance collected on the tilted plane of 700 W/m², the regeneration efficiency of the DG-C/R falls by about 5.1% with respect to the SG-C/R, from $\eta_{Des,SG}$=37.9% to $\eta_{Des,DG}$=36%.

In contrast, the structured single-pass single-glazed device (SGr-C/R) enhances the regeneration efficiency relative to the smooth single-pass single-glazed one (SG-C/R) by intensifying the convective heat and mass transfer coefficients via the continuous flow separation/reattachment in the gas-phase and mixing in the liquid-phase. The optimal values of air Reynolds numbers that maximise the efficiency ratios obtained for the analysed operating conditions and geometric configuration reveal the counterproductive effects of this measure on the temperature and vapour pressure gradients at the liquid-air interface (and consequently, on the effective mass flux of water vapour) if the device operates beyond them. For a Reynolds number of about 6000 and a solar irradiance available on the tilted collector of 700 W/m², the structured surface results in an increase of the regeneration efficiency by approximately 9.9%, from $\eta_{Des,SG}$=37.9% to $\eta_{Des,SGr}$=41.7%, and a thermohydraulic performance factor of 1.5.

Finally, a ray-tracing model was developed to evaluate the effect of an additional mirror on the collector efficiency. For a low concentrating system installed in Stuttgart, Germany, the maximum total annual global solar radiation yields to about 1400 kWh/(m²Y), which can be attained at collector tilt angles between 30° and 60° and reflector inclinations between 10° and 35°. This corresponds with an increase of the annual optical performance of 5 to 12%.

In order to realistically evaluate the suitability of the measures discussed here, annual simulations of the systems are necessary. Besides the heat and mass transfer exchanges occurring in the direct solar regenerators and the optical performance of the flat booster mirror described in the proposed models, other factors must be considered in the analyses such as the additional power consumption of the fan due to the upper channel and the 180° air

deflection in the DG-C/R and the structured absorber plate in the SGr-C/R as well as their construction and operating costs. This paper provides a good basis for this future research.

Acknowledgments

The funding provided by the Federal Ministry of Education and Research in framework of the program "Research at Universities of Applied Sciences-Funding Scheme Young Engineers" (contract number 03FH0041X4) during the initial stages of this research (2015-2018) is gratefully acknowledged.



References

Azevedo, L. F. A., Sparrow, E. M., 1985. Natural convection in open-ended inclined channels. Journal of Heat Transfer, 107(4), 893-901, DOI: 10.1115/1.3247518.

Baccoli, R., Frattolillo, A., Mastino, C., Curreli, S., Ghiani, E., 2018. A comprehensive optimization model for flat solar collector coupled with a flat booster bottom reflector based on an exact finite length simulation model. Energy Conversion and Management, 164, 482-507, DOI: 10.1016/j.enconman.2018.02.091.

Brkic, D., Praks, P., 2018. Unified friction formulation from laminar to fully rough turbulent flow. Applied Sciences, 8(11), 2036, DOI: 10.3390/app8112036.

Chen, L. C., Kao, F. K., 1990. The experimental study of three types of regenerator/collector for solar liquid desiccant cooling. Clean and Safe Energy Forever. International Solar Energy Society Proceedings Series, 1, 840-844, DOI: 10.1016/B978-0-08-037193-1.50171-3.

Fedorov, A. G., Viskanta, R., 1997. Turbulent natural convection heat transfer in an asymmetrically heated, vertical parallel-plate channel. International Journal of Heat and Mass Transfer, 40(16), 3849-3860, DOI: 10.1016/S0017-9310(97)00043-4.

Gnielinski, V., 2010. G2 Heat transfer in concentric annular and parallel plate ducts, in VDI Heat Atlas (2nd). Springer, Berlin, Heidelberg, pp. 701-708, DOI: 10.1007/978-3-540-77877-6_35.

Katejanekarn, T., Kumar, S., 2008. Performance of a solar-regenerated liquid desiccant ventilation pre-conditioning system. Energy and Buildings, 40(7), 1252-1267, DOI: 10.1016/j.enbuild.2007.11.005.

Klein, S. A., 1977. Calculation of monthly average insolation on tilted surfaces. Solar Energy, 19(4), 325-329, DOI: 10.1016/0038-092X(77)90001-9.

Kumar, A., Kumar, R., Maithani, R., Chauhan, R., Sethi, M., Kumari, A., Kumar, S., Kumar, S., 2017. Correlation development for Nusselt number and friction factor of a multiple type V-pattern dimpled obstacles solar air passage. Renewable Energy, 109, 461-479, DOI: 10.1016/j.renene.2017.03.030.

Lewis, M. J., 1975. Optimising the thermohydraulic performance of rough surfaces. International Journal of Heat and Mass Transfer, 18(11), 1243-1248, DOI: 10.1016/0017-9310(75)90232-X.

Peng, D., Zhang, X., 2015. A modified model of solar collector/regenerator considering effect of the glazing temperature. International Journal of Refrigeration, 49, 151-159, DOI: https://doi.org/10.1016/j.ijrefrig.2014.10.004.

Rehman, N. U., Uzair, M., 2021. Hybrid ray tracing model and particle swarm optimization for the performance of an internally reflecting solar still with a booster reflector. Arabian Journal for Science and Engineering, 46, 2021-2032, DOI: 10.1007/s13369-020-04963-z.

Sutherland, I. E., Hodgman, G. W., 1974. Reentrant polygon clipping. Communications of the ACM, 17(1), 32-42, DOI: 10.1145/360767.360802.

Taler, D., Taler, J., 2017. Simple heat transfer correlations for turbulent tube flow. E3S Web of Conferences, 13(4), DOI: 10.1051/e3sconf/20171302008.

Yang, R., Wang, P. L., 1998. Experimental study for a double-glazed forced-flow solar collector/regenerator. Journal of Solar Energy Engineering, 120(4), 253-259, DOI: 10.1115/1.2888128.

Zheng, G. S., Worek, W. M., 1996. Method of heat and mass transfer enhancement in film evaporation. International Journal of Heat and Mass Transfer, 39(1), 97-108, DOI: 10.1016/S0017-9310(96)85009-5.

A New Method for Determining the Nusselt and Sherwood Numbers in Simultaneous Heat and Mass Transfer in Solar Collector/Regenerators

Fernando Manuel Gómez Castro[1], Ursula Eicker[2], Ulrike Jordan[1]

[1] Institute for Thermal Engineering, Kassel University, Kassel (Germany)

[2] Next-Generation Cities Institute, Concordia University Montreal, Montreal (Canada)

Abstract

This paper presents a new method to evaluate Nusselt and Sherwood numbers for solar collector/regenerators. The method is based on dimensionless groups of the thermophysical properties, temperature and mass concentration gradients, heat and mass transfer coefficients and system geometry. The resulting relations for the Nusselt and Sherwood numbers are reliable to obtain good results of the coupled heat and mass exchange within forced-flow direct collector/regenerators. Unlike conventional relations, these are general expressions valid for different liquid desiccants. In this study the relations are validated with own measurements and with relations from literature.

Keywords: Nusselt number, Sherwood number, collector/regenerators, coupled heat and mass exchanges, liquid desiccants

1. Introduction

The overall performance of a direct solar regenerated liquid desiccant system strongly depends on the solar collector/regenerator (C/R), which adjusts the mass fraction of the hygroscopic solution used for dehumidifying air. A detailed understanding of the coupled heat and mass fluxes at the liquid-gas interface in the C/R is required to derive new correlations for the Nusselt and Sherwood numbers for refining the accuracy of computations.

Yang and Wang (1994) derived empirical correlations for the Nusselt and Sherwood numbers in a 2 m width × 9 m length single-glazed counter-current C/R in the humid climate of Kaohsiung, Taiwan, and analysed the impact of operating conditions on the water desorption rate of both forced- and natural-flow C/Rs with a parameter study. Their results indicate that the forced convection C/R outperforms the natural convection one at low mass fractions of lithium chloride (LiCl).

Li and Yang (2010) conducted laboratory-scale tests with a 1 m width × 2 m length single-glazed parallel-flow C/R for assessing the effects of parameters on the regeneration of an aqueous lithium bromide (LiBr) solution. Although high air mass flow rates improved the C/R performance at high solar irradiances, it was better to keep low air flow rates at cloudy conditions. Besides, empirical correlations for the heat and mass transfer coefficients were proposed as functions of the solar irradiance, the temperature, humidity ratio and mass flow rate of the air plus the temperature and mass fraction of the solution.

Finally, Peng and Zhang (2016) studied experimentally the regeneration process in a 1 m width × 2 m length single-glazed counter-flow solar C/R in terms of the inlet conditions of the air and aqueous LiCl solution and weather conditions in Southern China. They observed an optimal air flow rate that maximised the regeneration efficiency, whose value decreased by rising the flow rate of the solution at near ambient temperature, whereas the inverse trend was obtained at moderate solution temperature. They also proposed correlations for the Nusselt and Sherwood numbers with the Reynolds number, Prandtl and Schmidt numbers, inlet solution mass fraction, solution-to-air mass flow rate ratio and air-to-solution temperature ratio as arguments.

The correlations resulting from the above-mentioned researches are, nevertheless, only suitable for a specific liquid sorbent under transitional and turbulent air flow in the C/R channel. This paper presents general equations for the coupled dimensionless heat and mass transfer coefficients valid for aqueous solutions of $CaCl_2$, LiCl and LiBr obtained from both, own measurements and experimental data of Alizadeh and Saman (2002), Li and Yang

© 2022. The Authors. Published by International Solar Energy Society
Selection and/or peer review under responsibility of Scientific Committee
doi:10.18086/eurosun.2022.06.06 Available at http://proceedings.ises.org

(2010), and Peng and Zhang (2015; 2016).

2. Description of the test rig

The tests were performed in the lab-scale arrangement comprising a forced-flow regenerating panel operating in counter-current mode with respect to aqueous calcium chloride ($CaCl_2$) trickling on its heat collecting surface, fans, solution tanks, pumps, flow regulator/indicator, PID controller and data acquisition devices. The single-pass single-glazed C/R consists of a transparent cover and a housing made of Plexiglas and is thermally insulated from its surroundings via 25 mm thick polystyrene sheets. Its tilt angle from the horizontal plane can be variably set from 15° to 30°. This device has a total area of 2.4 m² (1 m width × 2.4 m length), a sprinkling area of 2 m² (1 m width × 2 m length) and a gap height of 10 cm (see Fig. 1(a)). A black cotton fabric is used for ensuring both high absorption of solar irradiance and uniform wetting. The distribution of the hygroscopic liquid is carried out from top of the C/R via a drip system. The regenerating air enters the device through a circular inlet located in the centre of a lower distribution box. For a preferably even air streaming profile in the channel, 12 flow openings are distributed over the entire width of the inlet and outlet ports as shown in Fig. 1(b).



(a) C/R prototype (b) Air distribution chamber

Fig. 1: Free-standing collector/regenerator.

3. Instrumentation and experimental setup

Fig. 2 depicts the test rig of the direct solar regeneration unit with the installed measurement and system technology, which comprises subsystems for supplying forced air and for circulating and storing desiccant solution. The regenerating air is provided by an axial fan with continuous flow control in the range of 50 to 250 m³/h, whereas the weak $CaCl_2$ solution is delivered to a PVC liquid distributor header (located at the top of the C/R) with symmetrically arranged openings with an inner diameter of 0.7 mm and a separation distance of 1 cm by a plastic solution pump at volumetric flow rates between 5 and 30 l/h. The temperature of the incoming solution to the C/R is controlled by the combination of an ARCTIC cold bath/circulation thermostat HAAKE AC 150-A10 and a plate heat exchanger B3-12A-30-2.0. The strong hygroscopic liquid is then collected in a gutter and pumped back to a PVC solution tank. The volumetric flow rates and temperatures of the fluids, air relative humidity and solution density are measured at the inlet and outlet of the C/R once the fluids conditions approach steady-state.

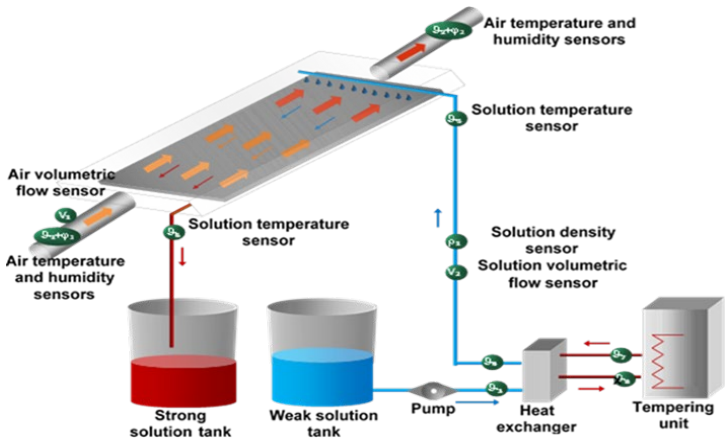

Fig. 2: System sketch of the C/R prototype.

4. Calculation of Nusselt and Sherwood numbers from experimental data

The convective heat and mass transfer coefficients in the gas-phase streaming within the C/Rs have been determined from data both, measured in the test rig and published by Alizadeh and Saman (2002), Li and Yang (2010) and Peng and Zhang (2015; 2016) with the logarithmic mean difference method:

$$h_{Conv,s\text{-}a} = \dot{m}_{da} \cdot c_{p,a} \cdot \left(T_{a,out} - T_{a,in}\right) / \left(A_s \cdot \Delta T_{LM,s\text{-}a}\right) \quad \text{(eq. 1)}$$

$$h_{Conv,mD,s\text{-}a} = \dot{m}_{da} \cdot \left(\chi_{a,out} - \chi_{a,in}\right) / \left(A_s \cdot \Delta \rho_{LM,s\text{-}a}\right) \quad \text{(eq. 2)}$$

With $\dot{m}_{da}$ as the mass flow rate of the dry air and $c_{p,a}$ as the isobaric specific heat capacity of the moist air; ($T_{a,out}$, $\chi_{a,out}$) and ($T_{a,in}$, $\chi_{a,in}$) as the pairs of the temperatures and humidity ratios of the air at the top and bottom of the counter-flow C/R; A_s as the area of the liquid sorbent; $\Delta T_{LM,s\text{-}a}$ and $\Delta \rho_{LM,s\text{-}a}$ as the logarithmic mean temperature and mass concentration differences at the liquid-air interface, which are given by:

$$\Delta T_{LM,s\text{-}a} = \left(T_{a,out} - T_{a,in}\right) / \left(Ln\left(T_s - T_{a,in}\right) - Ln\left(T_s - T_{a,out}\right)\right) \quad \text{(eq. 3)}$$

$$\Delta \rho_{LM,s\text{-}a} = \left(\rho_{a,out} - \rho_{a,in}\right) / \left(Ln\left(\rho_s - \rho_{a,in}\right) - Ln\left(\rho_s - \rho_{a,out}\right)\right) \quad \text{(eq. 4)}$$

Where are T_s and ρ_s are the temperature and mass concentration of water vapour of the desiccant solution.

The dimensionless heat transfer coefficient, the Nusselt number ($Nu_{s\text{-}a,Dh}$), is then defined as:

$$Nu_{s\text{-}a,Dh} = h_{Conv,s\text{-}a} \cdot D_h / k_a \quad \text{(eq. 5)}$$

With D_h as the hydraulic diameter of the air channel and k_a as the thermal conductivity of the moist air.

The dimensionless mass transfer coefficient, the Sherwood number ($Sh_{s\text{-}a,Dh}$), is given by:

$$Sh_{s\text{-}a,Dh} = h_{Conv,mD,s\text{-}a} \cdot D_h / D_{12} \quad \text{(eq. 6)}$$

Where D_{12} is the diffusivity of water vapour in the air.

5. Proposed approach

The comprehensive database of Nusselt and Sherwood numbers evaluated from both the measurements in previously described test rig and the experimental results extracted from Alizadeh and Saman (2002), Li and Yang (2010) and Peng and Zhang (2015; 2016) has been used to derive new empirical correlations for assessing the heat and mass exchanges within the C/R. In simultaneous heat and mass transfer, the Nusselt and Sherwood numbers are influenced by several major parameters including the thermophysical properties of the liquid and gas phases, latent heat of evaporation and specific enthalpy of dilution during phase change, temperature and mass concentration gradients due to the phase change, single-phase convective heat and mass transfer coefficients, gravitational acceleration and system geometry:

$$Nu_{s\text{-}a,D_h}=f\left(\rho_a,\mu_a,\beta_a,c_{p,a},k_a,\beta_{c,a},D_{12},h_a,u_a,\rho_s,\mu_s,\sigma_s,u_s,h_{fg}+h_{Dil},\Delta T_{s\text{-}a},\Delta\rho_{s\text{-}a},h_{Conv,s\text{-}a,0},g\cdot Sin(I_c),D_h,L_p,\delta_s\right) \quad \text{(eq. 7)}$$

$$Sh_{s\text{-}a,D_h}=f\left(\rho_a,\mu_a,\beta_a,c_{p,a},k_a,\beta_{c,a},D_{12},h_a,u_a,\rho_s,\mu_s,\sigma_s,u_s,h_{fg}+h_{Dil},\Delta T_{s\text{-}a},\Delta\rho_{s\text{-}a},h_{Conv,mD,s\text{-}a,0},g\cdot Sin(I_c),D_h,L_p,\delta_s\right) \quad \text{(eq. 8)}$$

Consequently, eqs. 7 and 8 comprise 21 variables with 4 primary dimensions (i.e. kg [M], m [L], s [t], K [T]). Based on the dimensional analysis, 17 dimensionless parameters should be required in both the Nusselt and Sherwood number correlations, which can be reduced to the following pre-defined dimensionless numbers:

Dimensionless parameters for the Nusselt number correlation:

$$Re_{a,Dh}=\frac{u_a\cdot D_h}{\nu_a} \qquad Gr_{a,ch,Dh}=\left|\frac{g\cdot\beta_a\cdot\Delta T_{s\text{-}a}\cdot {D_h}^3}{{\nu_a}^2}\right|\cdot\left(\frac{D_h}{L_p}\right)\cdot Sin(I_c)$$

$$Le_{a,ev}=Le_a\cdot\left(\frac{h_{fg}+h_{Dil}}{h_a}\right) \qquad Ka_s=\left(\frac{\rho_s\cdot{\sigma_s}^3}{g\cdot Sin(I_c)\cdot{\mu_s}^4}\right)^{1/3}$$

$$Re_s^*=\frac{4\cdot u_s\cdot\delta_s}{\nu_s}$$

$$Nu_{s\text{-}a,Dh,0}=\frac{h_{Conv,s\text{-}a,0}\cdot D_h}{k_a} \qquad Gr_{a,m,ch,Dh}=\left|\frac{g\cdot\beta_{m,a}\cdot\Delta\rho_{s\text{-}a}\cdot {D_h}^3}{{\nu_a}^2}\right|\cdot\left(\frac{D_h}{L_p}\right)\cdot Sin(I_c) \quad \text{(eq. 9)}$$

Where $Re_{a,Dh}$ is the gas-phase Reynolds number (ratio of the inertial forces to viscous ones in the gas-phase); $Gr_{a,ch,Dh}$ is the channel thermal Grashof number (ratio of thermal buoyant forces to viscous ones acting on the gas-phase); $Le_{a,ev}$ is the Lewis number of evaporation for the gas-phase (product of the Lewis number and the enthalpy ratio), firstly introduced by Enayatollahi et al. (2017); Ka_s is the liquid-phase Kapitza number (ratio of surface tension forces to inertial ones in the liquid-phase); Re_s* is the liquid-phase Reynolds number (ratio of the inertial forces to viscous ones in the liquid-phase); $Gr_{a,m,ch,Dh}$ is the channel solutal Grashof number (ratio of solutal buoyant forces to viscous ones acting on the gas-phase) and $Nu_{s\text{-}a,Dh,0}$ is the single-phase Nusselt number.

Dimensionless parameters for the Sherwood number correlation:

The dimensionless parameter $Nu_{s\text{-}a,Dh,0}$ is substituted with the single-phase Sherwood number $Sh_{s\text{-}a,Dh,0}$.

The formulations are developed by logarithmically normalising the dimensionless groups with respect to their corresponding limits as suggested by Larachi and Levesque (2008). The Nusselt number for coupled heat and mass exchanges ($Nu_{s\text{-}a,Dh}$) at the liquid-air interface is given as the sum of the components for sensible ($Nu_{s\text{-}a,Dh,s}$) and latent ($Nu_{s\text{-}a,Dh,l}$) heat transfer (Cherif et al., 2011):

$$Nu_{s\text{-}a,Dh}=Nu_{s\text{-}a,Dh,s}+Nu_{s\text{-}a,Dh,l} \quad \text{(eq. 10)}$$

Here, $Nu_{s\text{-}a,Dh,s}$ is assessed from conventional expressions for the single-phase Nusselt number in a channel ($Nu_{s\text{-}a,Dh,0}$), e.g. Gnielinski (2010) for laminar flow and Taler (2017) for turbulent one, whereas $Nu_{s\text{-}a,Dh,l}$ is defined as:

$$Nu_{s\text{-}a,Dh,l}=(-0.905+11.467\cdot S)\cdot Nu_{s\text{-}a,Dh,0} \quad \text{(eq. 11)}$$

The normalised output function S is obtained from the following expression:

$$S=LR1+\sum_{i=1}^{7}LR2_i+\sum_{i=1}^{7}LR3_i \quad \text{(eq. 12)}$$

The auxiliary functions for the multiple linear regressions without interaction terms (LR1), with two-way interaction terms ($LR2_i$) and with three-way interaction terms ($LR3_i$) are defined as:

$$LR1=a_0+\sum_{i=1}^{7}a_i\cdot U_i \quad \text{(eq. 13)}$$

$$LR2_i=U_i\cdot\sum_{j=1}^{8-i}b_{i,j}\cdot U_{j+(i-1)} \quad 1\le i\le 7 \quad \text{(eq. 14)}$$

$$LR3_i=U_i^2\cdot\sum_{j=1}^{7}c_{i,j}\cdot U_j \quad 1\le i\le 7 \quad \text{(eq. 15)}$$

With their normalised inputs (U_i) and their ranges of validity given below:

$$U_1=\frac{Log\left(\frac{Re_{a,Dh}}{142.252}\right)}{4.675} \qquad U_2=\frac{Log\left(\frac{Gr_{a,ch,Dh}}{112.33}\right)}{8.839} \qquad U_3=\frac{Log\left(\frac{Le_{a,ev}}{19.529}\right)}{1.552}$$

$$U_4=\frac{Log\left(\frac{Ka_s}{288.24}\right)}{3.15} \qquad U_5=\frac{Log\left(\frac{Re_s^*}{0.773}\right)}{4.691} \qquad U_6=\frac{Log\left(\frac{Gr_{a,m,ch,Dh}}{458.766}\right)}{6.26}$$

$$U_7=\frac{Log\left(\frac{Nu_{s\text{-}a,Dh,0}}{23.957}\right)}{1.313} \quad \text{(eq. 16)}$$

Domain of applicability:

$142.252 \leq Re_{a,Dh} \leq 1.525 \cdot 10^4$ $112.33 \leq Gr_{a,ch,Dh} \leq 7.75 \cdot 10^5$
$19.529 \leq Le_{a,ev} \leq 92.204$ $288.24 \leq Ka_s \leq 6723.739$
$0.773 \leq Re_s^* \leq 84.273$
$23.957 \leq Nu_{s\text{-}a,Dh,0} \leq 89.011$ $458.766 \leq Gr_{a,m,ch,Dh} \leq 2.4 \cdot 10^5$

The numerical values of coefficients a_i, $b_{i,j}$ and $c_{i,j}$ in eqs. 13-15 for the transitional and turbulent air flow regimes are presented in Tab. 1.

Tab. 1: Coefficients a_i, $b_{i,j}$ and $c_{i,j}$ of the normalised output function for computing the Nusselt number in solar C/Rs according to the coupled calculation approach ($Re_{a,Dh} \geq 2300$).

a_i	0	1	2	3	4	5	6	7
	-5.871	52.179	17.256	18.346	-28.291	10.54	-41.606	-49.969
$b_{i,j}$	**0**	**1**	**2**	**3**	**4**	**5**	**6**	**7**
1		-29.103	-140.65	12.651	-0.006	-39.327	93.66	59.98
2		29.778	13.005	42.779	1.367	11.231	30.584	
3		-42.305	-13.642	-3.914	-18.839	25.694		
4		18.459	-15.537	-4.337	45.935			
5		14.552	4.884	-8.342				
6		23.421	-40.896					
7		10.908						
$c_{i,j}$	**0**	**1**	**2**	**3**	**4**	**5**	**6**	**7**
1		-8.931	85.955	-36.57	4.941	32.539	-37.092	-29.949
2		2.438	-7.356	-31.329	-49.056	19.557	5.869	2.438
3		41.616	16.256	-0.277	7.261	3.181	14.112	-23.01
4		5.371	24.736	2.741	-10.783	0.917	-18.798	-42.38
5		-5.621	-27.108	1.309	11.087	-4.773	9.019	21.173
6		-41.785	-10.22	14.051	26.282	-13.327	-9.081	33.897
7		14.405	-35.095	-3.449	-13.391	-20.337	11.934	4.918

The procedure outlined in eqs. 10-15 is called the coupled evaluation method, since it includes dimensionless parameters corresponding to both the temperature and concentration gradients, i.e. U_2 and U_6 (see eq. 16), as expected in simultaneous heat and mass transfer processes. Similarly, the Sherwood number for simultaneous heat and mass transfer processes ($Sh_{s\text{-}a,Dh}$) at the liquid-air interface is assessed in terms of the component obtained by applying the heat/mass transfer analogy to the single-phase Nusselt number ($Sh_{s\text{-}a,Dh,0}$) and the convection contribution due to phase change ($Sh_{s\text{-}a,Dh,l}$) as follows:

$$Sh_{s\text{-}a,Dh} = Sh_{s\text{-}a,Dh,0} + Sh_{s\text{-}a,Dh,l} \quad \text{(eq. 17)}$$

Where the component $Sh_{s\text{-}a,Dh,l}$ is given by:

$$Sh_{s\text{-}a,Dh} = (-0.733 + 11.161 \cdot S) \cdot Sh_{s\text{-}a,Dh,0} \quad \text{(eq. 18)}$$

With the normalised output function S and auxiliary functions LR1, $LR2_i$ and $LR3_i$ already defined by eqs. 12-15. Only the normalised input U_7 changes:

$$U_7 = \frac{Log\left(\frac{Sh_{s-a,Dh,0}}{23.127}\right)}{1.28} \quad \text{(eq. 19)}$$

Domain of applicability:

$23.127 \leq Sh_{s\text{-}a,Dh,0} \leq 83.189$

In this case, the coefficients a_i, $b_{i,j}$ and $c_{i,j}$ in eqs. 13-15 for the transitional and turbulent air flow regimes are summarised in Tab. 2.

Tab. 2: Coefficients a_i, $b_{i,j}$ and $c_{i,j}$ of the normalised output function for calculating the Sherwood number in solar C/Rs according to the coupled evaluation method ($Re_{a,Dh}$≥2300).

a_i	0	1	2	3	4	5	6	7
	29.79	-23.657	-88.397	-6.121	-1.497	-12.306	-23.806	35.304
$b_{i,j}$	**0**	**1**	**2**	**3**	**4**	**5**	**6**	**7**
1		45.896	17.759	31.526	-88.239	1.292	55.27	-10.944
2		50.09	9.419	91.958	3.028	79.645	-29.584	
3		-9.558	-6.018	2.72	-15.502	8.253		
4		5.111	12.751	-21.025	-63.391			
5		7.078	-2.297	14.395				
6		-11.28	-14.142					
7		-49.812						
$c_{i,j}$	**0**	**1**	**2**	**3**	**4**	**5**	**6**	**7**
1		-55.795	56.915	-31.063	79.57	-8.884	-38.248	11.133
2		-77.33	31.253	-10.724	-11.79	4.499	-83.69	19.426
3		9.86	-1.488	2.853	-0.029	0.522	7.715	-10.426
4		8.003	-56.905	8.312	0.116	-0.346	16.286	29.694
5		9.816	-3.125	-4.984	-8.874	-2.101	3.194	-7.826
6		-23.58	26.376	10.252	12.13	-6.798	-3.402	19.069
7		68.029	3.338	7.905	2.815	-2.742	17.64	-32.332

6. Performance indicators

The performance of the C/R is characterised on the basis of the water desorption rate ($\dot{m}_{Des}$), which is the change in the amount of water evaporated from the weak solution, and therefore transferred to the air stream per unit time:

$$\dot{m}_{Des}=\dot{m}_{da}\cdot(\chi_{a,out}-\chi_{a,in}) \quad \text{(eq. 20)}$$

Where $\dot{m}_{da}$ is the mass flow rate of the dry air; $\chi_{a,out}$ and $\chi_{a,in}$ are the humidity ratios of the air at the top and bottom of the counter-flow sorption unit.

Finally, the average relative deviation (ARD) is selected as statistical indicator for comparing the results obtained from experiments ($P_{Exp[i]}$) and calculations ($P_{Mod[i]}$) (Qi et al., 2013):

$$ARD=(1/n)\cdot\sum_{i=1}^{n}\left|(P_{Exp[i]}-P_{Mod[i]})/P_{Exp[i]}\right|\cdot 100 \quad \text{(eq. 21)}$$

With n as the number of data set.

7. Results and discussion

The parity plot comparisons for the Nusselt and Sherwood numbers obtained from own experimental data and the literature data (Alizadeh and Saman, 2002; Li and Yang, 2010; Peng and Zhang, 2015, 2016) and the corresponding estimated from the coupled computational method are depicted in Fig. 3. The predicted Nusselt numbers exhibit a good fit to the experimental values, with an average relative deviation of ARD=12.7% and almost 90% of the data within the error bands of ±30% (R^2=0.98). On the other hand, approximately 94% of the Sherwood numbers estimated with the proposed correlation lie within the limits with ARD=10.5% (R^2=0.98). These results confirm the appropriate choice of the dimensionless groups used in the correlations to represent in a generalised and compact way the thermophysical properties of the fluids, temperature and mass concentration gradients between the liquid and gas phases, heat and mass transfer coefficients for the gas-phase, system geometry and other parameters that strongly influence the combined heat and mass exchanges in the regeneration of diluted desiccant solution within solar collector/regenerators.

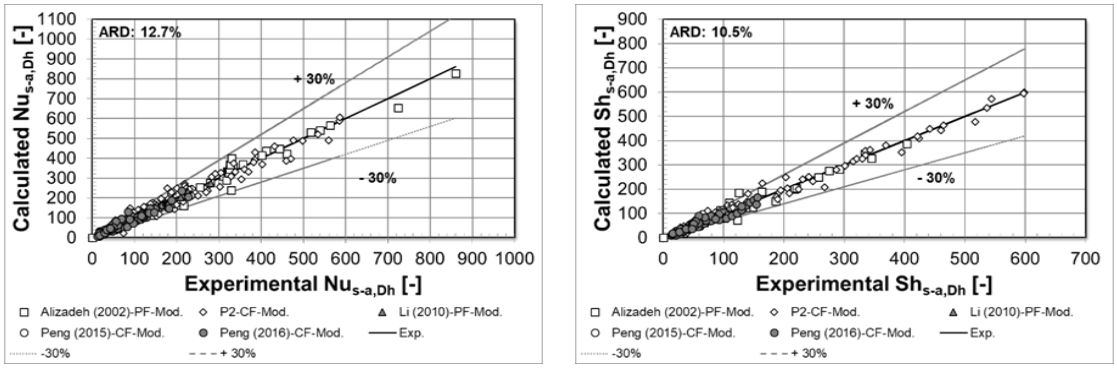

(a) Nusselt number (b) Sherwood number

Fig. 3: Comparison between calculated and experimental Nusselt and Sherwood numbers for simultaneous heat and mass fluxes in solar C/R.

Fig. 4 shows the parity plots between the water desorption rates determined from measurements in the test rig with aqueous $CaCl_2$ solution and those predicted from the new approach under the following boundary conditions: Global solar irradiance on the tilted collector varying between 925 and 1165 W/m²; air volumetric flow rate changing from 47 to 252 m³/h; inlet air temperature of about 32 °C; inlet air humidity ratio of approximately 12 g/kg; solution volumetric flow rate ranging between 4.8 and 30.1 l/h; inlet solution temperature of about 35 °C and inlet solution mass fraction of approximately 41%. The good matches achieved not only in the temperature changes of the liquid desiccant (ARD=8.3%) and air (ARD=11.8%) but also in the variations of the solution mass fraction (ARD=12.6%) and air humidity ratio (ARD=11.7%) at the inlet and outlet openings of the collector/regenerator contribute to enhance the accuracy of simulation by keeping the average relative deviation between the experimental and numerical values of the water desorption rate as low as 11.6% with almost 95% of the computations within uncertainty bands of ±30%.

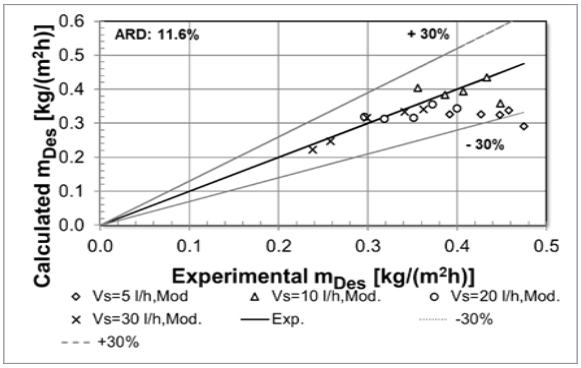

Fig. 4: Comparison between the calculated and experimental values of the water desorption rate obtained with the C/R prototype.

A group of experimental data reported by Peng and Zhang (2016) for a counter-flow solar C/R of 1 m width × 2 m length using aqueous LiCl solution has been selected for comparison with the numerical results obtained with the formulae derived by Peng and Zhang (2016) and by the authors of this work under following conditions: Global solar irradiance collected on the tilted plane varying between 419 and 786 W/m²; air volumetric flow rate changing from 69.8 to 350 m³/h; inlet air temperature fluctuating between 28.6 and 36.6 °C; inlet air humidity ratio ranging from 9.1 to 20 g/kg; solution volumetric flow rate varying between 12.1 and 18.1 l/h; inlet solution temperature changing from 24.8 to 31.6 °C and inlet solution mass fraction fluctuating between 23.7 and 25.7%. The model based on the expressions of Peng and Zhang (2016) gives a deviation of ARD=22.3% and keeps low dispersion against experimental data since all of its results are within error bands of ±30% (see Fig. 5(a)). However, the best outcomes are reached with the new correlations with a deviation of ARD=18.3% (see Fig. 5(b)). This can be explained by the inclusion of the coupled thermal and solutal buoyancy effects on the solution regeneration process in the collector channel through the heat and mass transfer Grashof numbers as well as the physical properties of the liquid sorbent through the Kapitza number in the new correlations, which improves the accuracy of the computed changes in the temperature and mass fraction of the desiccant solution.

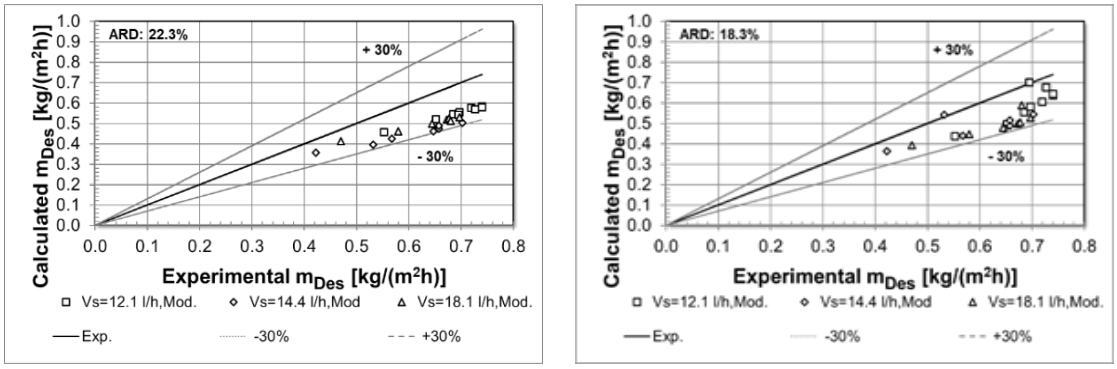

(a) Correlations of Peng and Zhang (2016) (b) Proposed correlations

Fig. 5: Comparison of the experimental water desorption rates reported by Peng and Zhang (2016) with the values predicted from the analysed formulations.

8. Conclusions

This paper presents new correlations for computing the Nusselt and Sherwood numbers in combined heat and mass transfer processes occurring in the regeneration of a liquid desiccant film flowing down the absorber plate of a solar collector/regenerator (C/R). These expressions were developed from measurements in the test rig using an aqueous solution of $CaCl_2$ with air flow in the turbulent regime and experimental data published in the literature using aqueous solutions of $CaCl_2$, LiBr and LiCl with air flow in the transitional and turbulent regimes.

The results show good agreements between the experimental and calculated values of the Nusselt and Sherwood numbers with average relative deviations of 12.7% and 10.5%, which demonstrates the suitability of the selected dimensionless groups for describing the simultaneous heat and mass fluxes occurring during the regeneration of weak solution within the device.

The coupled evaluation method of dimensionless convective heat and mass transfer coefficients is applied along with the energy and mass balances of the collector prototype in order to determine the water desorption rate of a diluted aqueous solution of $CaCl_2$ flowing in counter-current direction with air circulating through its channel. An average relative deviation of 11.6% is obtained for the water desorption rate under the analysed operating conditions due to the improved accuracy of the computations of the changes in the temperatures, mass fraction and humidity ratio of the fluids entering and leaving the C/R.

Further benchmarking is done to ascertain whether the new correlations developed in this work are more accurate than those proposed by Peng and Zhang (2016). For this purpose, experimental data published by Peng and Zhang (2016) for a counter-flow regenerating panel operating with aqueous LiCl solution are compared with the simulation results achieved from the above-mentioned formulations. Although the numerical results generated under the considered boundary conditions with both methodologies show low dispersion with respect to the experimental data, the computational model based on the new correlations provides the lowest average relative deviation with a value of 18.3%. In contrast, the mathematical model relying on the formulae of Peng and Zhang (2016) yields an average relative deviation equal to 22.3%. This is because the proposed methodology includes dimensionless groups that consider the combined effects of the thermal and solutal buoyancy forces and the physical properties of the liquid desiccant on the solution regeneration process.

The comparative analyses presented in this study have demonstrated the reliability and versatility of the new coupled evaluation method to simulate the simultaneous heat and mass exchanges taking place in the solar collector/regenerator when a liquid desiccant film is regenerated. Although this formulation is only valid for aqueous solutions of $CaCl_2$, LiBr and LiCl and air flow in the transitional and turbulent regions, it can be extended to other types of liquid sorbents and other air flow regimes by fitting it to newly available experimental data.

The new correlations developed in this work can be easily integrated into design or simulation programs to predict the thermodynamic performance of the solar collector/regenerator with high accuracy. This provides a good basis for future research aimed at analysing the technical and economic feasibility of direct solar regenerated liquid desiccant systems and evaluating measures for improving the heat and mass exchanges in a regenerating panel.

Acknowledgments

The funding provided by the Federal Ministry of Education and Research in framework of the program “Research at Universities of Applied Sciences-Funding Scheme Young Engineers” (contract number 03FH0041X4) during the initial stages of this research (2015-2018) is gratefully acknowledged.



References

Alizadeh, S., Saman, W. Y., 2002. An experimental study of a forced flow solar collector/regenerator using liquid desiccant. Solar Energy, 73(5), 345-362, DOI: 10.1016/S0038-092X(02)00116-0.

Cherif, A. S., Kassim, M. A., Benhamou, B., Harmand, S., Corriou, J. P., Jabrallah, S. B., 2011. Experimental and numerical study of mixed convection heat and mass transfer in a vertical channel with film evaporation. International Journal of Thermal Sciences, 50(6), 942-953, DOI: 10.1016/j.ijthermalsci.2011.01.002.

Enayatollahi, R., Nates, R. J., Anderson, T., 2017. The analogy between heat and mass transfer in low temperature crossflow evaporation, International Communications in Heat and Mass Transfer, 86, 126-130, DOI: 10.1016/j.icheatmasstransfer.2017.06.002.

Gnielinski, V., 2010. G2 Heat transfer in concentric annular and parallel plate ducts, in VDI Heat Atlas (2nd). Springer, Berlin, Heidelberg, pp. 701-708, DOI: 10.1007/978-3-540-77877-6_35.

Larachi, F., Levesque, S., 2008. Seamless mass transfer correlations for packed beds bridging random and structured packings. Industrial and Engineering Chemistry Research, 47(9), 3274-3284, DOI: 10.1021/ie070718o.

Li, Y., Yang, H., 2010. Experimental study of an open-cycle solar collector/regenerator using liquid desiccant for air conditioning. International Journal of Green Energy, 7(3), 273-288, DOI: 10.1080/15435071003796038.

Peng, D., Zhang, X., 2015. A modified model of solar collector/regenerator considering effect of the glazing temperature. International Journal of Refrigeration, 49, 151-159, DOI: 10.1016/j.ijrefrig.2014.10.004.

Peng, D., Zhang, X., 2016. Experimental investigation on regeneration performance, heat and mass transfer characteristics in a forced solar collector/regenerator. Energy, 101, 296-308, DOI: 10.1016/j.energy.2016.02.028.

Qi, R., Lu, L., Yang, H., Qin, F., 2013. Investigation on wetted area and film thickness for falling film liquid desiccant regeneration system. Applied Energy, 112, 93-101, DOI: 10.1016/j.apenergy.2013.05.083.

Taler, D., Taler, J., 2017. Simple heat transfer correlations for turbulent tube flow. E3S Web of Conferences, 13(4), DOI: 10.1051/e3sconf/20171302008.

Yang, R., Wang, P. L., 1994. Experimental study of a forced convection solar collector/regenerator for open-cycle absorption cooling. Journal of Solar Energy Engineering, 116(4), 194-199, DOI: 10.1115/1.2930081.

Parabolic Trough Collector(PTC) system for combined cooling and heating supply for a factory building in Turkey

Dr.- Ing. Ahmet Lokurlu[1], Ing. Akshay Ramesh[2]

[1] SOLITERM Group GmbH, Aachen (Germany)

[2] SOLITERM Group GmbH, Aachen (Germany)

Abstract

In 2021, the construction of the solar thermal plant for the combined cooling and heating supply of a factory building in Turkey started. The use of an absorption chiller enables the support of the air conditioning of the factory building during the summer months. In the winter months, the generated heat is used to heat the hall. This combination allows the solar gains to be optimally utilized. The collector field is the largest in Europe built for the use of solar thermal cooling. The plant was commissioned at the end of 2021 and formally inaugurated in June 2022.

In a Mediterranean country like Turkey or any other sunny country, almost all hotels, hospitals, and other public facilities must be air-conditioned during the summer months. This requires a very high amount of energy, as most modern air conditioning systems are driven by refrigerant through electrically powered compression chillers. Since solar radiation occurs simultaneously with the air conditioning demand, it can be assumed that cooling systems with double-acting absorption chillers in combination with parabolic trough collectors can be operated more suitably and intelligently than conventional systems.

Keywords: sustainable energy, parabolic trough collector, solar cooling, high temperature solar thermal systems, solar air conditioning

---

1. Introduction

Nowadays, our society faces many energy problems because of fossil fuel depletion, the increasing rate of CO2 emissions, the increasing rate of electricity price, and the new lifestyle trend which are fully connected with high energy consumption. These problems can be easily faced by using renewable and sustainable energy sources. Solar energy utilization is the most widespread method for covering a part of the thermal or electrical needs of buildings. An application that can use Solar energy to reduce electricity consumption is solar cooling technology, a combination of solar thermal energy and absorption cooling chillers.

The sun is the ultimate source of energy. Its energy exceeds the world's primary energy demand by a factor of ten thousand. SOLITERM's ultimate goal is to optimize the use of this enormous energy potential, as it will account for the largest share of the future energy mix.

The SOLITERM Group as an innovative company develops and sets up an absorption chiller-based solar thermal cooling system operated with its own developed and patented parabolic trough collectors (SOLITERM PTC), which not only reduces the high electricity demand and costs for air conditioning, cooling, and warm water generation but also supply a CO2 emission-free energy for the buildings.

Using an Absorption chiller in combination with concentrated collectors is an interesting idea that is investigated over the last few years. Especially for countries with high irradiation levels, the use of solar technologies can be an attractive investment that is also environmentally friendly.

The SOLITERM Group under the direction of Dr. Ahmet Lokurlu planned and installed Europe's largest industrial solar thermal cooling plant at the Mayr-Melnhof Graphia Group in Turkey in 2021. Since then, the cooling system has been operating successfully. At present we are installing some other systems in different

© 2022. The Authors. Published by International Solar Energy Society
Selection and/or peer review under responsibility of Scientific Committee
doi:10.18086/eurosun.2022.06.07 Available at http://proceedings.ises.org

countries intending to supply air conditioning and steam for summer applications, as well as warm water for winter applications in hotels, hospitals, and industrial facilities.

The presented paper will show and describe the example application of the installed SOLITERM Systems at the Meyr-Melnhof Graphia in Turkey.

2. Selection of technology

An interesting application is to use solar thermal in combination with absorption chiller technology to provide cooling thereby reducing the conventional energy required for cooling. Absorption chillers consist of four main parts: Generators, condensers, evaporators, and absorbers.

A double-effect absorption chiller has the same basic components as a single-effect but also includes an additional generator, heat exchanger, and pump. In this cooling system heat input from the collector is used at the generator to separate the refrigerant vapor from the solution. Li-Br and H2O solutions are used as refrigerant solutions in the absorption system.

The quality of energy transformation from heat to chilling energy for an absorption chiller is given by the coefficient of performance, COP=Chilling capacity/heating capacity.

Mostly single effect absorption chillers are available with a limited operating temperature of the heat (< 100 °C) along with low COP values (annualized) (< 0,6). Double effect absorption chillers offer higher COPs by converting the solar heat more efficiently into chilling energy. Therefore, high-temperature heat should be used in double effect absorption chillers which require a temperature of approximately 140 °C. The elevated temperatures lead to higher thermal losses in the collector – the conversion efficiency overcompensates this effect by far though [1][2]. As is seen in Table 1, double effect absorption chillers are mostly steam-powered.

Table 1: Properties of single effect and double effect absorption chillers

	Single effect	Double effect
Heating Temperature	max 110°	Min 140°
Fluid	water	Steam
COP (annual Value)	0,4...0,7	1,2...1,5

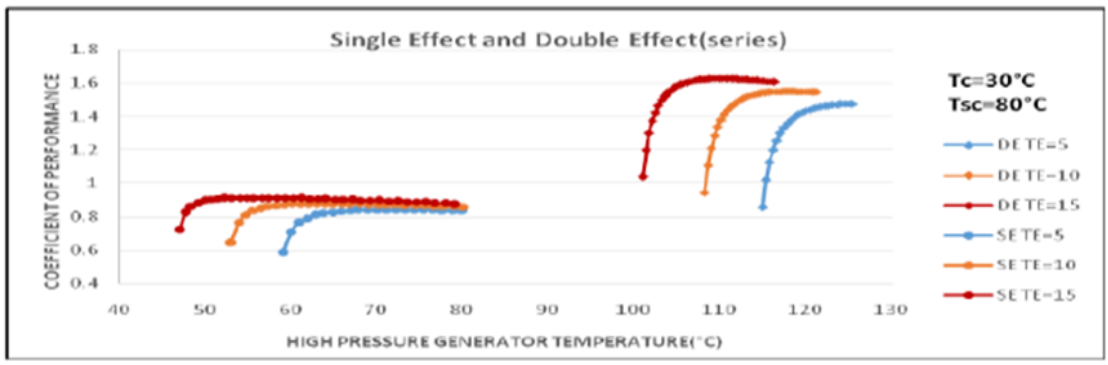

Fig. 1: Variations in COP of single effect and double effect flow cycles with generator temperature at different values of temperatures in the evaporator and the condensers at various pressure levels [3]

The use of solar cooling technologies can be an attractive investment, which is environmentally friendly, especially for countries with high irradiation levels. The combination of double effect absorption chillers and solar thermal technologies has proven its efficiency. Solar thermal is categorized into two groups: concentrating and non-concentrating.

Flat plate and evacuated tube collectors belong to the non-concentrating category. The biggest problem of flat plate and evacuated tube collectors is their low outlet temperature and their low efficiency at high temperatures which prevents them from being efficiently used for air conditioning due to a COP (Coefficient of Performance) of approx. (0.4 to 0.6) for small-sized applications. To satisfy a certain demand, a larger collector area is needed. But at many locations, like hotels, especially on roofs of buildings, space is limited. As a result, the application range of conventional solar systems is limited.

Comparison between PV and PTC:

To compare the two technologies the following calculations, refer to the specifications of a cooling demand of 500kW and a DNI (Direct Normal Irradiance) of 2000 kWh/m² annum. According to the calculations stated above, we would need an available surface of around 1400 m², because the process efficiency of the PV technology is less than 15%. In the case of a PTC Application, 66 PTC modules and therefore only a surface of 540 m² and a process efficiency is around 70% is needed in this case. Considering these drawbacks of PV technology, solar thermal concentrating technology combined with a double effect absorption chiller is much more effective and efficient for cooling applications.

3. PTC system by SOLITERM

The application potential of the solar thermal PTC system by SOLITERM is nearly endless, as it can be installed in any location worldwide. Energy consumers with various energy demands and various boundary conditions can benefit from this technology worldwide, but also in regions with low radiation this represents a highly feasible solution, as the system can be integrated into any infrastructure and reduce the usage of conventional energy supply and the use of fossil fuels. There is no particular target group or industry since the PTC system can be custom-tailored to meet any temperature level (6 °C – 350 °C), pressure level (0-25bar) and provide any form of energy (steam, cooling, heating, warm water, process cooling, sea-water desalination, and electricity). The PTC system by the SOLITERM Group can be combined with any conventional or renewable energy source, making it a highly compatible, flexible, and outstanding solution for any kind of industrial, Commercial, or individual application.

The PTC model used is specially manufactured by SOLITERM in a robot-controlled, automated production line and has an optical efficiency of 99 %. If there is enough space the PTC system can even cover up to 100 % of the energy demand of the end consumer whoever that might be, such as the food and beverage industry, the textile and chemical industry, hotels, shopping malls, airports, public buildings, private buildings, data centers, and many other potential clients.

The use of SOLITERM solar energy systems in combination with highly efficient 2-stage absorption chillers allows the use of solar energy in areas where – during the summer months – cooling requires such a great amount of electricity that tariffs are sky-high and power grids are used to their utmost capacity or even beyond. The connection to steam generators and to the hot water cycle allows supplying even more kinds of energy consumers with solar-powered clean energy. So, the SOLITERM systems are applicable all over the world in a wide range of possible applications, both industrial and commercial. The system at hand represents a universal and at the same time highly customized, as well as a flexible solution towards lowering emissions, becoming independent from fossil fuels, saving money, re-investing in more important aspects, and ultimately building a socially responsible, environmentally friendly, and sustainable economy and world.

To widen the application range for solar energy, SOLITERM developed different-sized Parabolic Trough Collectors (PTC): The SOLITEM PTC 1800 for large applications as well as the small-sized PTC 1100 for residential buildings. Both collectors can supply temperatures about 300 °C to 350 °C and are suitable for roof mounting. As well as the PTC 3000, 4000 and 5000 which are used for solar thermal power plants.

4. Parabolic Trough Collectors

To deliver high temperatures with good efficiency a high-performance solar collector is required. PTCs can effectively produce heat at temperatures between 50°C and 400°C. Parabolic trough collectors are made by bending a sheet of reflective material into a parabolic shape. A black metal tube, covered with a glass tube to reduce heat losses, is placed along the focal line of the receiver. When the parabola is pointed toward the sun, parallel rays incident on the reflector are reflected onto the receiver tube. The concentrated radiation reaching the receiver tube heats the fluid that circulates through it, thus transforming the solar radiation into useful heat. The collector can be oriented in an east-west direction, tracking the sun from north to south, or in a north-south direction, tracking the sun from east to west.

For applications up to 180 °C, the use of pressurized water is established. Higher temperatures can be achieved by using thermal oils. To achieve the required temperature, individual collectors are combined in groups that have their circuits for the heat transfer fluid.

The surface of the receiver is typically plated with a selective coating that has a high absorptance for solar radiation but a low emittance for thermal radiation loss.

A tracking mechanism must be reliable and able to follow the sun with a certain degree of accuracy, return the collector to its original position at the end of the day or during the night, and track during periods of intermittent cloud cover. Additionally, tracking mechanisms are used for the protection of collectors, i.e., they turn the collector out of focus to protect it from hazardous environmental and working conditions, such as wind gusts, overheating, and failure of the thermal fluid flow mechanism.

The sun tracking system with a precision of 0.1° in every row ensures maximizing the energy yield, making it more efficient compared to other solar thermal technologies, such as a flat plate or other collectors.

5. A Model Application for an Integrated Energy Supply System for combined cooling and heating supply of a factory building in Turkey

The production site MM Graphia in, which belongs to Mayr-Melnhof Karton AG, was confronted with increasing energy consumption, which led to high energy costs and greenhouse gas emissions. Therefore, the management decided to find a solution, to improve the environmental and economic situation of the production facilities in Turkey, and potentially all the company's other facilities worldwide. The company turned to SOLITERM Group GmbH, which, based on technical data on-site implemented a solar thermal system to substitute fossil fuels, reduce electricity fossil fuels, reduce electricity consumption, and cover the energy demand as economically and economically, and environmentally friendly.

5.1 Weather Analysis

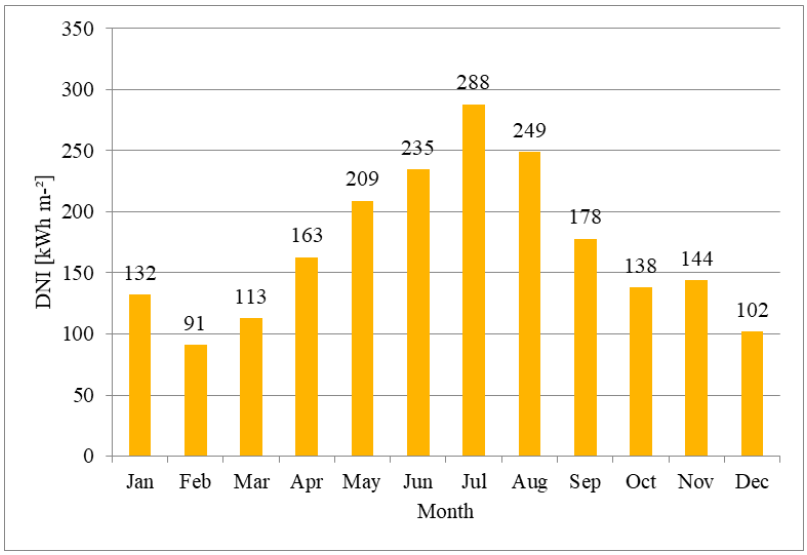

Fig 2: Monthly Direct Normal Irradiance (DNI) data for the project location in Turkey

The conditions for the construction of a solar thermal plant are above average here. Solar data, determined with the database of Meteonorm, show a value of 2049 kWh m^{-2} per year for the direct normal irradiation (DNI). The annual distribution is illustrated by the monthly values, which are shown in Figure 2.

As expected, solar irradiation is higher in summer than in winter. This is due to the long sunshine duration caused by the inclination of the globe in summer. This graph shows essential direct radiation for the parabolic trough. In contrast to many non-concentrating systems, the diffuse part of the global radiation cannot be used. A difference of 197 kW m^{-2} can be observed between the worst month (February) and the month with the highest solar radiation (July). This significant difference represents a major challenge for the design of the system to the process of operation. To use the high gains from the summer on the one hand and to have used for the solar energy in the winter, on the other hand, a combined cooling and heating system was developed.

5.2 Process demands

For the design of the plant, the various process requirements of the plant operator were taken into account. The project aimed to intercept the region's power outages and ensure 24-hour operation. Four halls are available for production, which have different requirements for temperature, air exchange, and humidity. These can be classified as follows:

- The production process for paper requires a steady room temperature of 30 °C.
- For the printing area, a steady temperature of 28 °C is required. In addition, an air exchange of 2 air changes per hour and an air discharge of 1.5 air changes per hour is required.
- For the paper cutting room, a steady humidity of 35% and a temperature range of 28°C - 30°C are required.
- For the board cutting and packaging area, a temperature range of 26°C - 32°C is sufficient to provide suitable working conditions.

As the temperatures at the site show very high seasonal fluctuations, the integration of a combined cooling and heating system was necessary to cool the hall in summer and heat it in winter. Before the integration of solar thermal energy, electric compression chillers with a total capacity of 2050 kW (1150 kW, 550 kW, 350 kW) were used for cooling. For heating, a gas burner with a capacity of 1 MW was used.

5.3 Solar Plant

The solar field consists of a 5.000 m² collector surface area and extends over the roof surfaces of the factory building. Due to the local conditions, it was necessary to realize the field in two stages.

The collectors have an aperture area of 9 m² (5m x 1.8m) and are combined in modules. A module is composed of 6 collectors, which have a common drive and solar tracking systems. The tracking Motor has a precision of 0.1° in every row which ensures maximizing the energy yield, making it more efficient compared to other solar thermal technologies, such as a flat plate or other collectors. The nominal thermal output of a collector is 4.97 kW at an irradiance of 850 W m^{-2} (Direct Normal Irradiance). This results in a specific output of 552 W m^{-2}.

5.4 System Operations

We use our solar field to provide air conditioning for the factory buildings. These factory buildings have different demands in summer and winter.

Summer mode:

The solar field is operated from April to October in summer mode reaching a maximum temperature of 180°C in the absorber tube and providing chilled water for cooling. Fan coils (15kN) and air Handling Units are used to condition and distribute the air in the building to a temperature of 8°C.

Winter mode:

In winter the system generates hot water using fewer collectors compare with cooling for heating. Since the required temperatures are lower in winter, lower temperatures can also be used in the solar field.

The total thermal capacity of the collector array is approximately 2.5 MW. This results in a cooling capacity of a two-stage absorption chiller of 3.5 MW. The absorption chillers used are each matched to the size of the associated collector field so 2 chillers with 1.4 MW and 2.1 MW were used. The double effect absorption

chiller has a coefficient of performance value that can achieve up to 1,40. The system was integrated into the heating and cooling supply lines of the facilities, using the existing conventional components as backup systems for safety and emergency cases. The entire plant has an integrated SCADA system that is fed with meteorological data and controls the collectors accordingly, ensuring fully automatic energy optimization, and supply and thus a reduction in unnecessary energy consumption in production and offices.



Fig. 3: SOLITEM PTC 1800 Parabolic Trough Collectors in the project location in Turkey

The implementation of the system described led to numerous benefits, not only for the business but also for the people in and around the company. Firstly, it led to energy savings in form of fuel savings of 1.780 MWh annually and electricity savings of 3.500 MWh annually, while more than 90 % of the annual process cooling, air conditioning, and warm water supply will be provided by the PTC plant. A reduction of 2.000 tons of CO2 emissions is achieved every year, as conventional sources are being used much less.

6. Conclusion

SOLITERM Parabolic Trough Collectors can deliver high-temperature heat. These systems offer a wide range of opportunities to reduce the costs of energy supply. Combined with double effect steam or hot water powered absorption chillers, Parabolic Trough Collectors make highly efficient solar thermal cooling possible.

SOLITERM supplied, installed, and commissioned Europe's largest industrial solar thermal cooling system at Mayr-Melnhof Graphia Group in Turkey. The project paves the way for an economical, renewable energy supply and enables potential and flexibility to adapt to different energy demands as well as the decarbonization of industry.

Besides the ecological and economic aspects, the social impact of the project was great. New jobs for technical management, monitoring, and maintenance have been created, giving young and ambitious people the chance to be part of a revolutionary, innovative, and highly sustainable project. The existing employees were educated and trained with regards to the PTC system and also regarding innovative, as well as renewable technologies. This in turn created awareness among people in and around the client company, leading to an awareness of renewable energy, sustainability, and more careful use of energy in general. Further details of the concept will be presented at the conference.

7. References

(1) Lokurlu, A., Y.Akin (2007) 'Intelligent and Advanced Solar Cooling System based on the Novel Technological Development "SOLITEM Parabolic Trough Collector PTC 1800". *SOLITEM estec2007 conference Proceedings.*

(2) Krüger, D., Pitz-Paal, R., Lokurlu, A. and Richarts, F. (2002) 'Solar cooling and heating with parabolic trough collectors for a hotel in the Mediterranean'. *Proceedings of the Solar Paces 11th International Symposium*, Zürich, 4–6 September. ISBN: 3-9521409-3-7. https://elib.dlr.de/2593/

(3) Khan, (2016) 'COMPARATIVE ANALYSIS OF SINGLE AND DOUBLE EFFECT LiBr-WATER ABSORPTION SYSTEM'. *4th International Conference on recent Innovations in Science Engineering and Management*, India, 20 March. (PDF) COMPARATIVE ANALYSIS OF SINGLE AND DOUBLE EFFECT LiBr-WATER ABSORPTION SYSTEM (researchgate.net)

Energy Analysis of a Solar-Driven Hybrid Air Conditioning System with an Absorption Heat Pump and a Desiccant Evaporative Cooling System.

Juan Prieto[1], Ruslán Kotegov[1], Francisco Comino[2], José Ignacio Ajona[3], Manuel Ruiz de Adana[2], Alberto Coronas[1]

[1] Universitat Rovira i Virgili, Mechanical Engineering Department, CREVER, Avda. Països Catalans 26, 43007, Tarragona (Spain)

[2] Dto. De Química-Física y Termodinámica Aplicada, Escuela Politécnica Superior, Universidad de Córdoba, Campus de Rabanales, Antigua Carretera Nacional IV, km 396, 14071, Córdoba (Spain)

[3] Seenso Renoval S.L, C. Aravaca 30, 28040, Madrid (Spain)

Abstract

In this paper it is presented a HVAC system with a solar driven single-effect absorption heat pump with condensation heat recovery and an air-handling unit with a desiccant wheel and an evaporative cooler. The integration of both cooling technologies allows to achieve a good overall performance as the desiccant system handles the latent loads and the absorption chiller the sensible loads. Moreover, the desiccant system is activated with the heating provided by the condensation heat from the absorption heat pump, which minimizes the amount of heating that must be provided by a solar concentrator coupling flat sun-tracking mirrors to a fixed tilt evacuated tubular collectors.

The size and the operational conditions of the integrated system are selected in order to optimize the overall performance of the system under different ambient conditions (solar radiation, ambient temperature and ambient humidity ratio). An overall thermal COP of 1.21 is reached in the hybrid system.

Keywords: Type your keywords here, separated by commas, in italic

1. Introduction

In this work, it is presented a solar cooling system with an absorption heat pump (AHP) with condensation heat recovery and an air-handling unit (AHU) with a desiccant wheel (DW), and an indirect evaporative cooler (IEC). The integration of both cooling technologies allows achieving a good overall performance as the desiccant system handles the latent loads and the AHP the sensible loads. Moreover, the desiccant system is activated with the heating provided by the condensation heat from the AHP, which minimizes the amount of heating that must be provided by the solar panels.

Therefore, the main objective is the energy analysis of an integrated solar cooling system comprised of the mentioned technologies when it is implemented in Tarragona, Spain. The expected results are referred to the number of solar panels, the AHP cooling and heating capacity, the AHU cooling capacity at nominal conditions, and the operating conditions that maximizes the overall performance of the system.

2. System description

A hybrid solar cooling system comprised of an AHP with condensation heat recovery and AHU with a desiccant wheel (DW) and an indirect evaporative cooler (IEC) is evaluated. The activation heat required by the AHP is provided by evacuated tube solar collectors (ETC) with low concentrator (<2) in both sides of them. In addition, the released heat in the AHP condenser is used to regenerate the DW. The description of each component of the system and the integration of all of them is presented below.

2.1. Absorption heat pump

The AHP is based on a single-effect absorption H_2O/LiBr chiller with its cycle modified to recover the heat of condensation at a useful temperature level (Juan Prieto et al. 2022). Thereby, the performance of the AHP is improved and enables the delivery of two useful outputs simultaneously. Besides, part of the condensation heat is also used internally for the LiBr solution preheating to reduce the generator heat input. Figure 1 shows a schematic

© 2022. The Authors. Published by International Solar Energy Society
Selection and/or peer review under responsibility of Scientific Committee
doi:10.18086/eurosun.2022.06.08 Available at http://proceedings.ises.org

layout of the AHP. As it can be seen in this Figure, two new components are incorporated: a preheater (PH) and a water-solution heat exchanger (WSHE). The weak, in LiBr, solution is preheated before entering to the solution heat exchanger (SHE) by using the heat released during condensation of part of the vapor leaving the generator (stream 7). The PH is implemented in parallel with the condenser (C). The water-solution heat exchanger cools the strong, in LiBr, solution leaving the SHE while producing hot water. Moreover, the heat released by the condenser is at useful temperature level so that it can be also used for heating applications. Thus, the hot water leaving the WSHE and the C is supplied to regenerate the DW of the AHU.

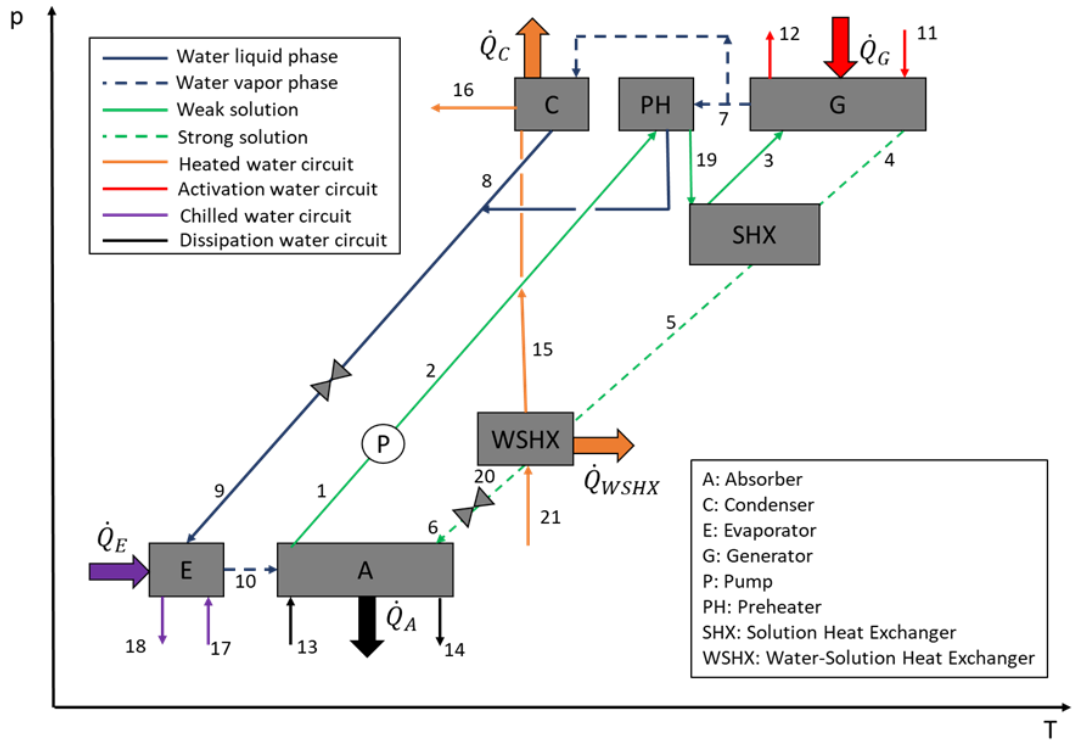

Fig. 1: Single-effect absorption heat pump for simultaneous heating and cooling production (Juan Prieto et al. 2022).

Along with the components of the cycle, the working conditions have also been changed in this system. The Dühring plot for the improved absorption HP with CHR is represented in Figure 2. Red lines illustrate the conditions of the proposed single-effect H_2O/LiBr AHP. Conditions in Figure 2 correspond to the thermodynamic states of the system in Figure 1. As it can be noted, this system also operates at two different pressure levels. The absorber and evaporator operate at a low-pressure level, which is around 1 kPa. The condenser, generator, preheater, solution heat exchanger, and water-solution heat exchanger operate at a high-pressure level of around 15 kPa. In opposition to the conventional cycle, the high pressure is doubled up. The temperature of condensation depends upon the actual pressure, the greater the pressure the greater the condensing temperature. Thus, the elevated pressure permits to make use of condensation heat for a variety of heating applications and for preheating the weak solution as well. Furthermore, due to changes in the operating conditions, a few alterations should be made to enhance the overall efficiency of the absorption cycle.

In this regard, the cycle operates at four temperature levels in place of three (J. Prieto et al., 2022):

- The evaporator produces cooling, and the temperature ranges from 5 to 15 °C;
- The absorber dissipates heat to the ambient because the heat is useless for most applications at these temperature levels. The temperature ranges from 25 to 40 °C;
- The condenser heating (condensation heat) can be used, as the temperature ranges from 50 to 60 °C;
- The generator requires a heat supply, and the temperature ranges from 85 to 120 °C.

As it can be observed, Figure 2 clearly shows that crystallization risk under these conditions is minimal because Point 6 is far from the crystallization line. Consequently, the new cycle operates under more favorable conditions compared to the conventional cycle. In this sense, the generator operating temperatures can be greater

than in the conventional cycle. Besides, the lack of crystallization allows the use of a SHE with higher effectiveness, and, as a result, the total cycle COP is higher. Furthermore, the preheated condition at State 19 before the SHE leads to a higher temperature at State 5. This fact allows the incorporation of the WSHE into the system after the SHE to extract additional heat from the cycle.

Eventually, the differential between the strong and poor solution mass fraction is lower contrasted with the conventional cycle. Consequently, to obtain the equivalent amount of heating and cooling it is imperative to increase the solution mass flow rate, and it implies that a more powerful solution pump must be installed.

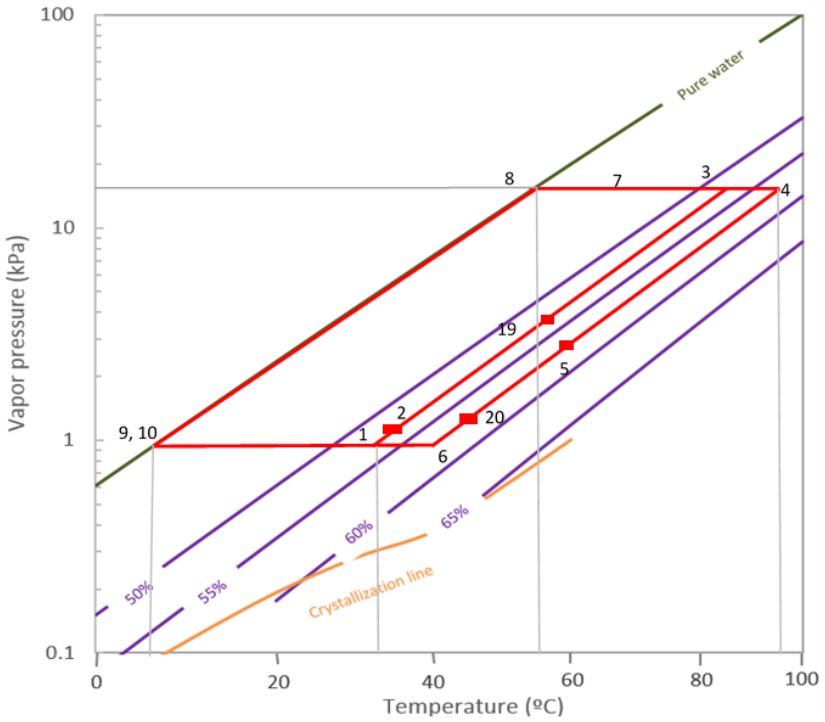

Fig. 2: Dühring plot for the proposed single-effect H_2O/LiBr absorption heat pump for combined heating and cooling production. (J. Prieto et al., 2022)

2.2. Air handling unit

The AHU is comprised by a DW, an IEC, a heating coil (HC) and a cooling coil (CC). The AHU can independently control the air temperature (by means of the IEC and the CC), and the air humidity (by means of the DW and HC), thereby optimizing indoor air conditions (Comino et al. 2019). A schematic of the AHU is shown in Figure 3. The DW is activated by means of a heating coil, HC. This HC is fed by a water flow, which is heated by the hot water coming from the AHP condenser and water-solution heat exchanger. The CC is fed by chilled water coming from the AHP evaporator. The process and the regeneration air streams come from the outdoor air (100% outdoor air), as shown in Figure 3.

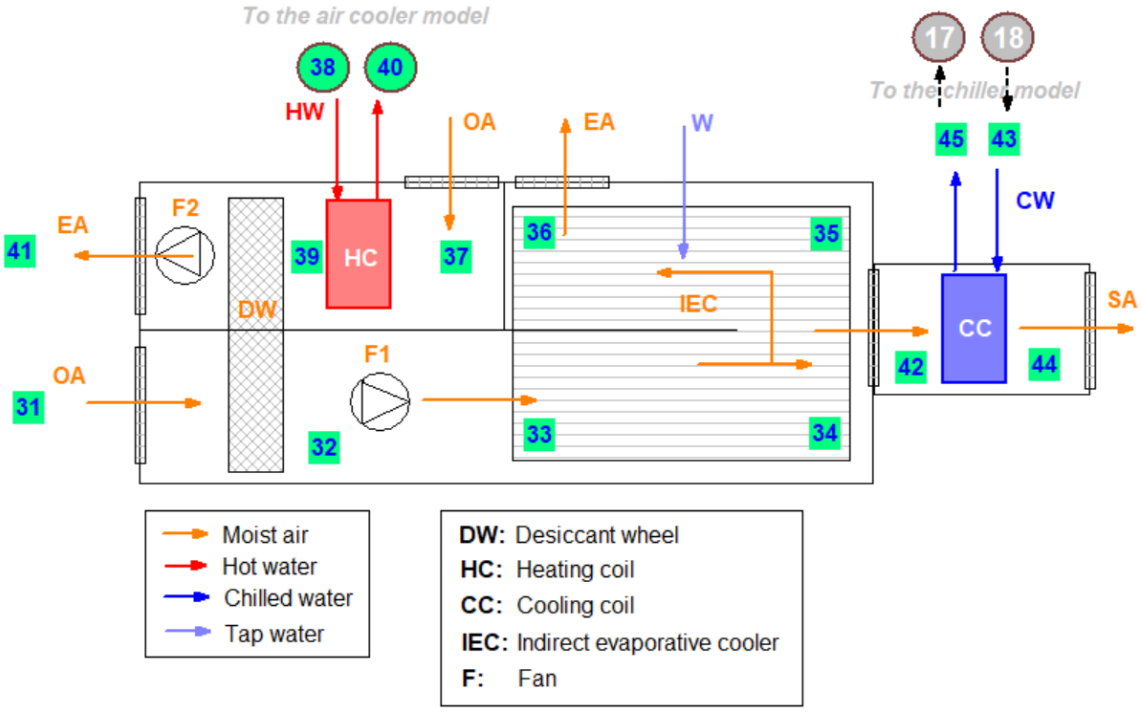

Fig. 3: Air handling unit with desiccant wheel, indirect evaporative cooler, heating coil and cooling coil.

2.3. Solar concentrator thermal collectors

The WeSSun solar concentrator couples flat sun-tracking mirrors to a fixed tilt solar collector (flat plate or evacuated tubular collectors - ETC). It is a low-concentration Design (<2) that, producing a quasi-homogeneous distribution of solar radiation over the solar absorber, increases solar productivity per m^2 of aperture. Moreover, it offers an automatic and simple protection against wind overloads and/or excessive temperatures, by closing the mirrors over the collector, and can be used with existing solar thermal products (see Figure 4 for an example coupling WeSSun with an ETC) (José Ignacio Ajona 2021).



Fig. 4: WeSSun solar concentrator coupling flat sun-tracking mirrors to a fixed tilt evacuated tubular collectors

2.4. Integrated system

The integrated system is a hybrid air conditioning system with the described AHP and the AHU. Figure 5 illustrates how the system is integrated. The AHP is providing chilled water to the cooling coil and hot water to activate the desiccant evaporative cooling system. In this case, chilled water temperature can be increased as the latent heat is handled by the desiccant system. This allows to operate the AHP at higher evaporator temperature.

Therefore, heating rate in the condenser and the water-solution heat exchange is used to activate the desiccant wheel. In this case, hot water passes first through the water-solution heat exchanger and then through the condenser. However, absorber heating rate cannot be used for this application as temperature requirements for the desiccant system are higher than the provided by it. Therefore, absorber heating rate must be dissipated through a cooling tower.

Finally, hot water temperature required for the activation heat is provided by the described solar thermal collectors.

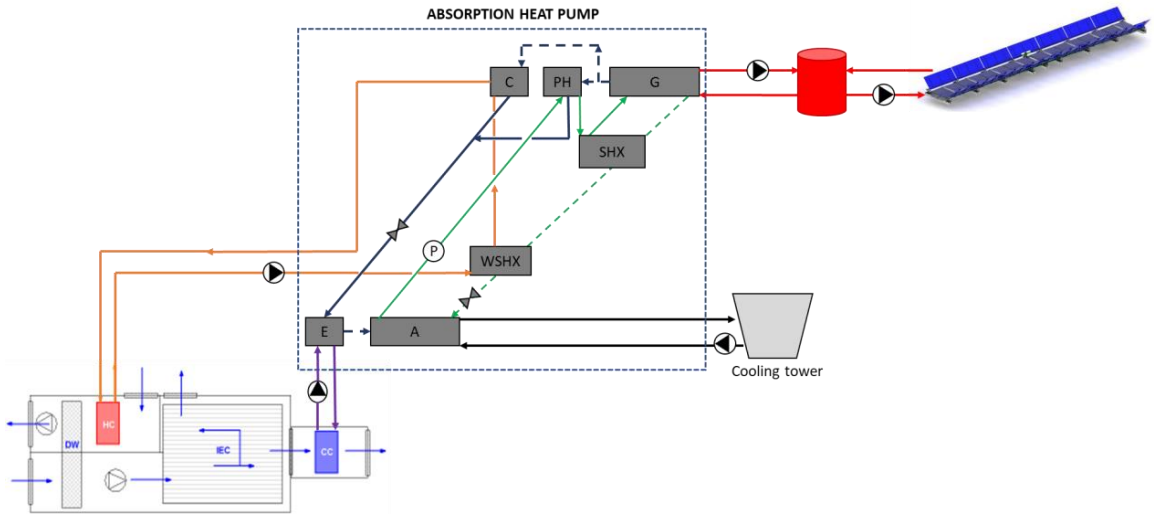

Fig. 5: Overall scheme of the integrated system.

3. Methodology

Models of the single technologies are first developed with Engineering Equation Solver (EES) using the Engineering Equation Solver software package (EES). For the case of the AHP and the AHU, these models are based on energy and mass balances, and heat transfer equations are applied on the thermal components of the system. For the case of the solar thermal collectors, the model is based on the efficiency curve and the incidence angle modifier. Once the models are developed, a performance analysis of the single technologies is firstly done to obtain the optimal working temperatures and flow rates for each one. Then, the technologies are coupled in an integrated model that is used to obtain the component size and nominal conditions that maximizes the system performance in terms of cooling capacity, and overall COP.

3.1. Absorption heat pump model

To model the system properly, typical assumptions for a Water/LiBr absorption cycle are used. The assumptions of the H_2O/LiBr absorption cycle are:

- The absorption cycle operates under equilibrium conditions.
- Losses of heat and pressure decays are neglected.
- Kinetic and potential energies are negligible.
- The water/LiBr solution leaving the absorber is saturated at low pressure.
- The water/LiBr solution leaving the desorber is saturated at high pressure.
- The pure water vapor (refrigerant) leaving the evaporator is saturated at the low pressure.
- Counter-flow desorber is considered, the refrigerant vapor leaving the desorber is in equilibrium with the entering water/LiBr solution.
- Water (refrigerant) at the exit of the condenser is saturated at the high pressure.
- Water (refrigerant) at the exit of the preheater is saturated at the high pressure.
- Preheater and condenser are arranged in parallel, in other words, in both components inlet and outlet conditions are the same.
- The solution pump is isentropic, and the expansion valves are isenthalpic.

Water conditions of the external circuits are calculated with the UA value of each component. Table 1 shows the UA values for all the components of the AHP.

Table 1. UA values for each component of the AHP.

Component	Characteristics	Value	Unit
Evaporator	UA	14.33	kW/C
Condenser	UA	4.734	kW/C
Absorber	UA	27.07	kW/C
Desorber	UA	58.17	kW/C
Preheater	UA	3.00	kW/C
Solution heat exchanger	UA	8.074	kW/C
Water-solution heat exchanger	UA	2.964	kW/C

3.2. Air-handling unit model

To model the system properly, typical assumptions for desiccant systems are used. The assumptions for the AHU are:

- The air-handling unit operates under steady-state conditions.
- Processes occurring in the desiccant wheel are adiabatic.
- There is no mass transfer in the HC, the air humidity ratio ω at the inlet and outlet is constant.
- Cooling process in the IEC occurs at a constant humidity ratio.

The air-handling unit components are modelled by assuming UA value for the heating coil, the thermal effectiveness for the indirect evaporative cooler, the mass effectiveness for the desiccant wheel and the bypass factor for the cooling coil. Table 2 contains the assumed values for each component of the air-handling unit.

Table 2. Specifications of the AHU.

Component	Characteristics	Value	Unit
Heating coil	UA	0.6468	kW/C
Indirect evaporative cooler	ε_t	0.727	-
Desiccant wheel	ε_m	0.52	-
Cooling coil	F	0.2875	-

3.3. Solar thermal collectors

Solar thermal collectors are modelled with the efficiency method, considering that the incidence angle modifier changes with longitudinal and transversal angles. In this sense, the thermal efficiency of the solar collectors is calculated with the following equation:

$$\eta_{SC} = \frac{\dot{Q}_{SC}}{G_0} = a_0 \cdot K(\theta) - a_1 \cdot \frac{(T_{av} - T_{amb})}{G_0} - a_2 \cdot \frac{(T_{av} - T_{amb})^2}{G_0}$$

where $\dot{Q}_{SC}$ is the fluid heating rate in the solar collectors, G_0 is the total solar irradiance, T_{av} is the average temperature of the solar collectors, T_{amb} is the ambient temperature, θ is the incidence angle, a_0, a_1, a_2 are the efficiency parameters, and $K(\theta)$ is the incident angle modifier, which are empirical values provided by the manufacturer. The incident angle modifier is calculated as the product of a transversal (K_T) and a longitudinal (K_L) function:

$$K(\theta) = K_T(\theta_L = 0; \theta_T) \cdot K_L(\theta_L; \theta_T = 0)$$

Figure 6 shows the transversal and the longitudinal incidence angle modifiers as function of the incidence angle.

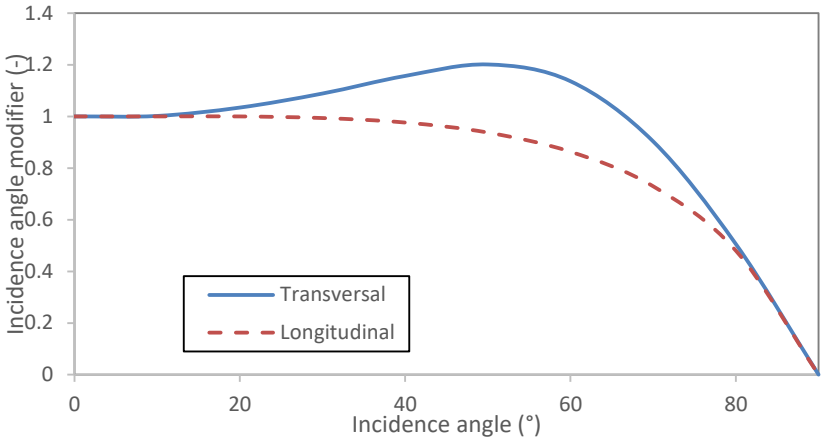

Fig. 6: Solar thermal collector longitudinal and transversal incidence modifiers.

The technical characteristics of the solar thermal collectors are included in Table .

Table 3. Technical characteristics of the solar thermal collectors.

Parameter	Value	Description
Dimensions (mm)	1420, 2050, 100	Length, width, height
Aperture area (m^2)	4.46	-
Number of vaacuum tubes (-)	21	-
Concentration ratio (-)	1.704	-
a_0 (-)	0.642	Based on aperture area
$a_1 \left(\frac{W}{m^2 \cdot K}\right)$	0.89	Based on aperture area
$a_2 \left(\frac{W}{m^2 \cdot K^2}\right)$	0.001	Based on aperture area
Volume Flow rate (l/h)	10-500	-
Max. operating pressure (bar)	10	-
Stagnation temperature (ºC)	272	-
Mirror solar reflectivity	> 94 %	-
Mirror dimensions (mm)	1495, 1605, 4	Length, width, heigth

The total number of solar thermal collectors is 20 and the water tank volume is 9.0 m^3.

4. Results

Results section is divided into two subsections. The first subsection is focus on the performance evaluation of the AHP. The second subsections is focus on the performance evaluation of the integrated system.

4.1. Performance evaluation of the AHP

Figure 7 shows the AHP Cooling coefficient of performance (COP_C) and heating coefficient of performance (COP_H) as function of the outlet condenser temperature, the chilled water temperature, the ambient temperature and the activation temperature. In terms of COP_C, values follow the typical trend of the single-effect absorption chillers, but with higher values (from 0.82 to 0.93) due to the lower heat input required in the generator. The COP_H is especially influenced by the driving hot water inlet temperature, with stable values (0.87–0.93).

The summary of the trends for the COP_C and the COP_H is included in Table 4. In general, the higher the condenser and the chilled water temperatures, the higher the COP_C and COP_H. On the other hand, the higher the ambient temperature, the lower the COP_C and COP_H. The activation temperature has an opposite effect on the COP_C and the COP_H. In this sense, the higher the activation temperature, the higher the COP_C and the lower the COP_H.

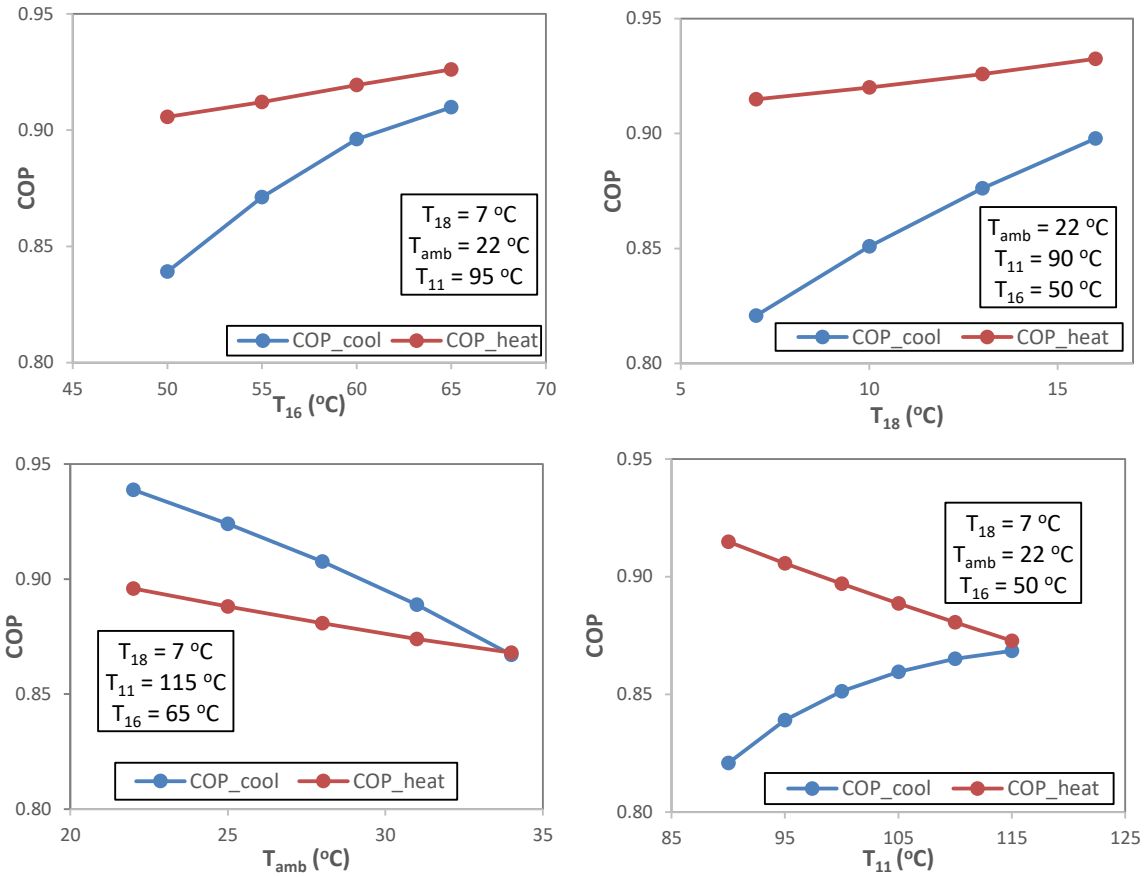

Fig. 7: AHP Cooling COP and heating COP as function of the outlet condenser temperature (top-left), the chilled water temperature (top-right), the ambient temperature (bottom-left) and the activation temperature (bottom-right).

Table 2. Results of the mathematical modelling of the AHP.

Indicator	Trend	COP_{cool} Trend	COP_{heat} Trend
T_{16}	increase ↑	increase ↑	increase ↑
T_{18}	increase ↑	increase ↑	increase ↑
T_{amb}	increase ↑	decrease ↓	decrease ↓
T_{11}	increase ↑	increase ↑	decrease ↓

4.2. Performance evaluation of the integrated system

Once the performance of the AHP is evaluated, the performance of the integrated system is carried out. Table 5 shows the input parameters considered for the simulation of the integrated system. Ambient temperature ranges from 22 °C to 34 °C. Ambient relative humidity ranges from 0.4 to 0.8. Chilled water temperature ranges from 7 °C to 10 °C, outlet condenser temperature ranges from 60 °C to 65 °C and activation temperature ranges from 100 °C to 105 °C. In total, 120 operational conditions are evaluated from the integrated system.

The performance of the integrated system is evaluated in terms of total cooling ($Q_{cool,tot}$), which is calculated as the total cooling production of the system (the provided by the IEC and the CC); total COP (COP_{tot}), which is calculated as the $Q_{cool,tot}$ over the activation heat required in the AHP.

Table 5. The updated list of input parameters for the simulation of the integrated system.

RH_{amb}	T_{amb} ºC	T_{18} ºC	T_{16} ºC	T_{11} ºC
0.4	22	7	60	100
0.6	25	10	65	105
0.8	28			
	31			
	34			

The main results of the simulations are included in Table 6. This Table shows the highest COP_{tot} and $Q_{cool,tot}$ achieved by the integrated system under different ambient conditions, and the operational conditions that allow to achieving this performance. Generally, the highest COP_{tot} is achieved at T_{16}=65 ºC and T_{11}=100 ºC. On the other hand, the highest $Q_{cool,tot}$ is achieved at T_{18}=10 ºC, T_{16}=60 ºC, and T_{11}=105 ºC.

Table 6. Operating conditions at RH_{amb} = 0.6 and different ambient temperatures T_{amb} = 22 - 34 ºC.

T_{11} = 105 ºC		COP_{tot}	$Q_{cool,tot}$	T_{18} ºC	T_{16} ºC	T_{11} ºC
T_{amb}=22 ºC	Highest COP_{tot}	1.113		7	65	100
RH_{amb}=0.6	Highest $Q_{cool,tot}$		84.35	10	60	105
T_{amb}=25 ºC	Highest COP_{tot}	1.143		7	65	100
RH_{amb}=0.6	Highest $Q_{cool,tot}$		76.60	10	60	105
T_{amb}=28 ºC	Highest COP_{tot}	1.16		7	65	100
RH_{amb}=0.6	Highest $Q_{cool,tot}$		68.93	10	60	105
T_{amb}=31 ºC	Highest COP_{tot}	1.209		10	65	100
RH_{amb}=0.6	Highest $Q_{cool,tot}$		61.33	10	60	105
T_{amb}=34 ºC	Highest COP_{tot}	1.192		10	65	100
RH_{amb}=0.6	Highest $Q_{cool,tot}$		53.79	10	60	105

5. Conclusions

This study presents an energy analysis and performance evaluation of an integrated solar-driven air conditioning system using an AHP with condensation heat recovery and an AHU with a DW and IEC. The AHP is activated with ETC with mirrors with low concentration design (<2). The single components of the system and the integrated system have been numerically evaluated.

First, the performance of the AHP is separately evaluated. The results for the AHP simulations are presented in Figure 7 and Table 4. In general, the higher the condenser and the chilled water temperatures, the higher the COP_C and COP_H. On the other hand, the higher the ambient temperature, the lower the COP_C and COP_H. The activation temperature has an opposite effect on the COP_C and the COP_H. In this sense, the higher the activation temperature, the higher the COP_C and the lower the COP_H.

The, the integrated system is studied. In this case, the highest COP_{tot} achieved by the system is 1.21, which is reached with an ambient temperature of 31 ºC, a chilled water temperature of 10 ºC, an outlet condenser temperature of 65 ºC and an activation temperature of 100 ºC. The highest cooling capacity achieved by the system is 84.35 kW, which is reached with an ambient temperature of 22 ºC, a chilled water temperature of 10 ºC, an outlet condenser temperature of 60 ºC and an activation temperature of 105 ºC.

6. Acknowledgments

This work has been supported by the European WEDISTRICT project (grant agreement N°857801) co-founded by the EC under the call H2020-LC-SC3-2018-2019-2020.

7. References

Ajona, J.I, 2021. Advanced Tracking Concentrator for Fixed Tilt solar thermal Collectors. European Federation of Agencies and Regions for Energy and Environment (FEDARENE)

Prieto, J., Ayou, D.S., Coronas, A. 2022. Energy and Exergy Analysis of H_2O/LiBr Absorption Heat Pumps for Combined Heating and Cooling Applications. CYTEF 2022 − XI Congreso Ibérico | IX Congreso Iberoamericano de Ciencias y Técnicas del Frío, Cartagena, Spain, 17-19 April, 2022.

Comino, F., Castillo, J., Navas, F.J., Ruiz de Adana, M.. Experimental assessment of a hybrid solar HVAC system based on desiccant wheel and an indirect evaporative cooling. Preliminary experimental results. Conference: II International Engineering Thermodynamics Congress, Albacete, Spain, June, 2019

Hybrid Solar Thermal Field (FPC-PTC) Applied for Solar Heating and Cooling Process in the Agroindustry Sector

Josue F. Rosales-Pérez[1], Andrés Villarruel-Jaramillo[1], Juan Diego Gil[2], Manuel Pérez-García[2], José M. Cardemil[1] and Rodrigo Escobar[1,3]

[1] Pontificia Universidad Católica de Chile, Santiago(Chile)

[2] CIESOL Research Center on Solar Energy, Joint Center UAL-CIEMAT, University of Almería, Almería (España)

[3] Centro del Desierto de Atacama, Pontificia Universidad Católica de Chile, Santiago (Chile)

Abstract

In the Agroindustry, as in the rests of productive sectors, the current need to reduce CO_2 emissions and reaching sustainable growth justifies the necessity to integrate renewable energy sources. Greenhouses facilitate the improvement of the agricultural production process, but they also need an adequate energy supply to ensure the ideal ambient conditions for crop growth. The use of solar energy is a convenient solution due to its easy access in rural locations in many world areas. However, sizing the solar field for greenhouses, both in terms of area and technology, has the challenge of supplying the seasonal demand of thermal loads. The objective of this work is to evaluate the advantages of using a hybrid solar field with FPC-PTC in series integrated with an absorption chiller to provide the heating and cooling demand of a greenhouse of tomatoes in Almería, Spain. It was considered solar fields between 80 m^2 to 540 m^2. The results show that a hybrid configuration with 50% of PTC increases the energy contribution of the solar systems in the summer months and allows a solar fraction over 0.96 with a solar field area smaller than half of the greenhouse area. In comparison with the solar field with FPC, the hybrid configuration increased the solar fraction in summer months up to 32 percent.

Keywords: absorption chiller, hybrid solar field, greenhouse

1. Introduction

Industry requires a decrease in fossil energy consumption and CO_2 emissions, especially the food sector, which is highly related to population growth to reach the goal of decarbonized energy. In this sense, temperature control is a key factor in industrial production for cooling and heating processes (Villarruel-Jaramillo et al., 2021). Furthermore, high-efficiency agricultural production is one of the essential tools to satisfy the growing demand for food. Modern agrarian production facilities are designed for the optimal use of land, water, and energy, making agricultural exploitation a semi-industrial production process (Cabrera et al., 2017). Greenhouses are ideal for the optimal use of the resources required for agricultural production because they allow controlling primordial variables for crop growth like ambient temperature, and the correct irrigation of water and fertilizers (Cabrera et al., 2017). Depending on the location's weather characteristics and temperature requirements of the crop, temperature control inside greenhouses produce heating and cooling demands that need to be supplied with sustainable energy resources. The agricultural sector is mainly located far from residential areas and tends to burn liquefied petroleum gas (LPG) for heat processes. One of the solutions for sustainable agroindustry is the incorporation of solar energy into the production process (Prieto et al., 2021). However, the demands for heating and cooling can generate a sizing challenge when considering the variables given by the quantity of product, weather conditions, and characteristics of the space to be heated (Gil et al., 2021).

Solar systems have been shown to be able to satisfy the energy requirements of greenhouse facilities (Lazaar et al., 2015; Mahmood and Al-Ansari, 2021; Prieto et al., 2021; Sajid and Bicer, 2021). However, using solar energy to meet thermal demand in summer for cooling could be a challenge due to the high energy consumption of the absorption chiller, and the flat plate collectors (FPC) tend to generate low heating rates in the first hours of the day. Consequently, it is necessary to use an auxiliary boiler to supply heat that increases fossil fuel consumption in hours with solar radiation availability. For this reason, implementing schemes that improve the solar system's energy performance under the seasonal energy demand of greenhouse applications could encourage the application of solar technologies in the agro-industrial sector. Tian et al. (2018) evaluated the behavior of a hybrid solar field (HF) with parabolic trough collectors (PTC) connected in series with FPC for district heating. The HF showed the ability to

© 2022. The Authors. Published by International Solar Energy Society
Selection and/or peer review under responsibility of Scientific Committee
doi:10.18086/eurosun.2022.06.09 Available at http://proceedings.ises.org

improve the energy output on summer days of the solar system compared to an individual field with FPC. However, the system's behavior has not been explored considering high demands in cooling processes during summer with thermal machines, a seasonal period in which the HF mostly benefited. In this sense, HF could have the potential to outperform the seasonal performance of FPC solar systems in thermal cooling applications, where demand increases simultaneously when HF performance grows. This works aims to evaluate the energy performance of FTC-PTC hybrid systems under the seasonal energy requirements for cooling and heating a greenhouse.

2. Methodology

2.1 Case Study

The evaluations were carried out considering the meteorological data of a location in the Andalusia Province in Spain (Lat: 36.85°, Long: -2.38°) and the thermal demand of a tomato production greenhouse with an area of 680 m2. The cooling and heating loads were calculated using the methodology presented by (Cabrera et al., 2017), considering set-point temperatures of 12 ºC and 27 ºC for the night and day periods, respectively, and relative humidity inside the greenhouse of 80%. The monthly cooling and heating demand are shown in fig. 1c. The system is configured with a hot thermal storage tank (HTES), a solar field, an absorption chiller with a nominal capacity of 70 kW for cooling, and a gas auxiliary boiler to supply the required heat when the solar systems cannot supply all the chiller or heating demand. Two configurations of solar fields are evaluated: 1) individual solar field with FPC (FPC-IF), and 2) hybrid solar field with FPC and PTC with east-west tracking integrated in series with an area proportion of 50 % of FPC. The scheme of the system with the hybrid solar field is shown in fig. 1b. A seasonal operation strategy with two control modes is implemented. In control mode 1, solar energy is stored to supply the night heating demand, and only excess energy is used to supply the chiller's energy requirements. In control mode 2, solar energy is used to supply the chiller's demand, and the stored energy is used for the night heating load. In fig. 1c is shown the periods of the year when control modes 1 and 2 are activated.

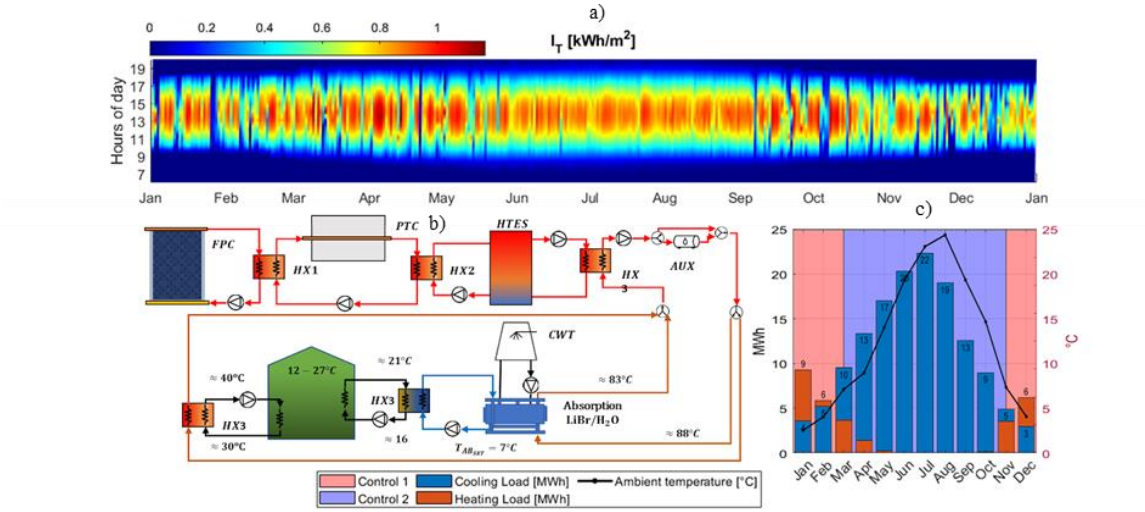

Figure 1: a) Total irradiance on tilted surface; b) FPC-PTC+ABS hybrid solar field diagram for greenhouse air conditioning and c) Monthly thermal demand for cooling and heating, and intervals of control strategy

2.2 Numerical model and system sizing

The software to simulate the proposed scheme is TRNSYS, which uses the norm EN12975-2 Dynamic Efficiency Approach with the types 1289 and 1288 for resolving the numerical model of the FPC and PTC, respectively (TRNSYS, 2017). On the other hand, thermal storage (HTES) is modeled with Type 158, simulating a constant volume stratified storage tank with a vertical configuration. Type 91 simulates heat exchangers with constant effectiveness (ε) of 0.7. Finally, the chiller is modeled using Type 107, which requires a data file that contains the instant capacity and the capacity fraction for each inlet temperature of the generator (T_{gen}), cooling water tower (T_{cwt}), and the setpoint temperature for the chilled water (T_{chi}) obtained from the nominal data and operation curves of the catalog (TRNSYS, 2019). Table 1 shows the types and parameters used in the numerical simulation.

Tab. 1: Model parameters for TRNSYS simulation (Janotte et al., 2009; SP Technical Research Institute of Sweden, 2016)

Component	TRNSYS Type	Parameters	Value	Unit
Flat plate collector (HTHEATboost 35/10)	1289	$\eta_{0,b}$	0.779	-
		C_1	2.41	W/(m^{2}K)
		C_2	0.015	W/(m^{2}K^2)
		C_5	6.798	kJ/(Km^2)
		K_d	0.98	-
Parabolic trough collector (Solitem PTC1800)	1288	$\eta_{0,b}$	0.683	-
		C_1	0	W/(m^{2}K)
		C_2	0.015	W/(m^{2}K^2)
		C_5	6.798	kJ/(Km^2)
		K_d	0.012	-
Storage tank	158	Loss Coefficient	0.923	W/(m^{2}K)
Heat exchangers	91	ε	0.7	-
Absorption chiller (Yazaki SC-20)	107	$Cap_{nominal}$	70.33	kW
		Q_{Gen}	100.5	kW
		COP	0.7	-
		T_{gen}	70-95	°C
		T_{cwt}	26-33	°C
		m_{chi}	10992.6	kg/hr
		m_{gen}	17283.8	kg/hr
		m_{cwt}	36725.3	kg/hr

The solar field pre-sizing is based on the F-Chart method, which estimates the solar field's monthly heat production in function of the monthly irradiation on the inclined plane (IT), temperature ambient (Tamb), and the thermal demand of the process. In that sense, the solar field is designed to reach different solar fractions between low to high solar coverage of the energy required for heating (Q_{LH}) and the energy needed for the generator (Q_{Gen}) of the absorption chiller to meet the cooling demand. For the case of the hybrid solar field, a criterion parameter is introduced for the area sizing called fraction area (FA), as shown in the flow chart in Fig. 2. FA estimates the area of FPC based on a fraction of the total area of the solar field, for this work FA=0.5.

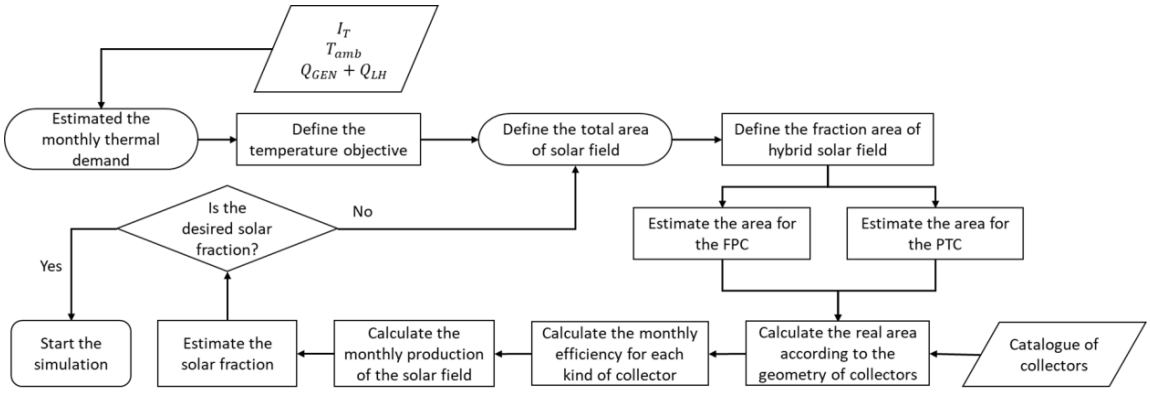

Figure 2. Flow chart for the pre-sizing of the hybrid solar field.

2.3 System energy efficiency

The system energy efficiency is calculated like the ratio between the useful energy delivered by the system to the greenhouse and the input energy from the solar radiation and gas consumed by the auxiliary boiler (Dias et al., 2019). The system energy efficiency for the FPC-IF and the HF are calculated from Eq. 1 and Eq. 2 respectively.

$$\eta_{sys_{FPC-IC}} = \frac{Q_{heating}+Q_{cooling}}{Q_{FPC-IC}+Q_{backup}} \quad \text{(eq. 1)}$$

$$\eta_{sys_{HF}} = \frac{Q_{heating}+Q_{cooling}}{Q_{FPC-HF}+Q_{PTC-HF}+Q_{backup}} \quad \text{(eq. 2)}$$

Where $Q_{heating}$ and $Q_{cooling}$ are the energy delivered for the system to the heating and colling demand respectively, Q_{FPC-IC} is the solar energy received by the FPC solar field with individual configuration, Q_{FPC-HF} and Q_{PTC-HF} are the energy received by the FPC and PTC solar fields of the HF and Q_{backup} is the energy consumed by the auxiliary boiler.

3. Results

Fig. 3 shows the monthly solar fields' energy losses ($QL_{SolarField}$), the solar fields' useful energy ($QU_{SolarField}$), the backup energy (Q_{BackUp}) and the solar fraction (SF) for the smallest evaluated area and the area with the best relation between solar fraction and efficiency (204 m^2 and 208 m^2 for the FPC and HF, respectively). Results indicate that the HF allows having a more constant SF throughout the year while FPC presents higher differences between the summer and winter months. Fig. 3(a2) and Fig. 3(b2) show that for similar solar field areas, the HF reaches higher SF from April to September, where the highest demand requirements for the greenhouse are concentrated. In these months, the HF allows SF improvements with 32 % and 25 % values over the FPC in June and July, respectively.

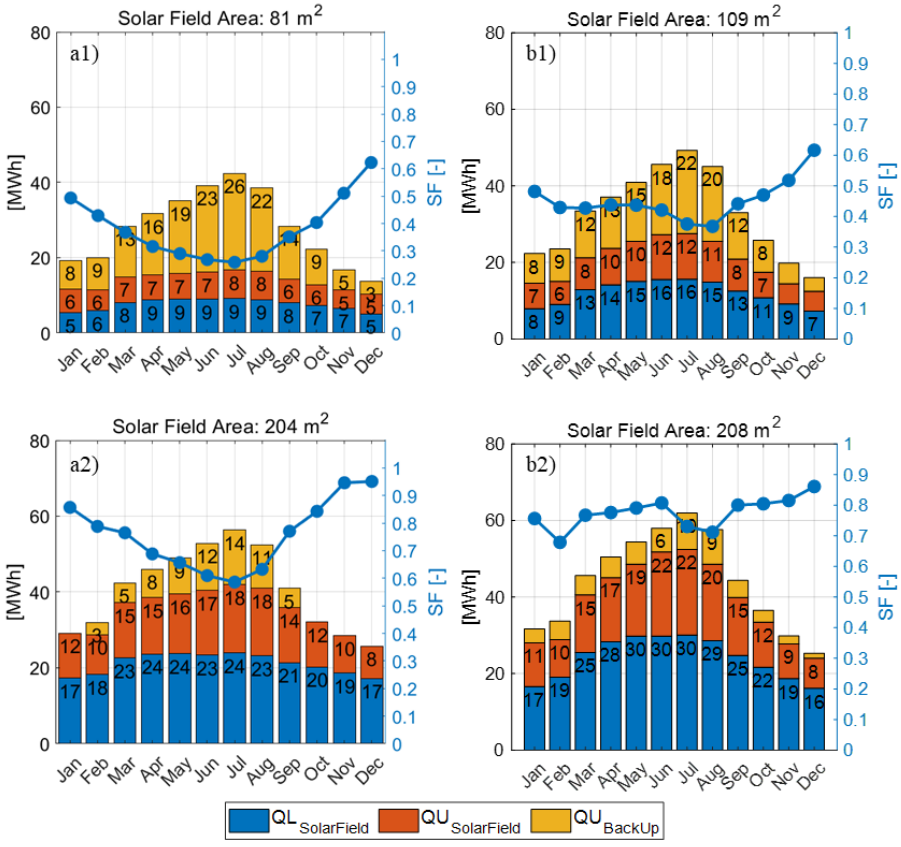

Figure 3: Monthly energy for the two solar field configurations (a. FPC solar field and b. FPC-PTC solar field)

In Fig. 4 are presented the heat flow rate maps of heating and chiller's heat demand (Fig. 4a), the heat flow rate produced by the FPC-IF with a total area of 204 m^2 (Fig. 4b), and the heat flow rate produced by the HF with a total solar field area of 208 m^2. Fig. 4a shows that heating requirements occur at night and in the early morning and late afternoon. Fig. 4b, while Fig. 4c indicates that the HF supplies more heat than the FPC-IF in the morning and noon hours of days in summer, allowing it to reach higher values of SF in the months with the biggest heat requirements of the greenhouse, which is consistent with the behavior observed in Fig. 3. In Fig. 4 we can also observe that the seasonal operation strategy allows that in winter months the FPC-IF and the HF have similar and high coverage of the heating demand, but the FPC-IF has slightly better coverage of the small cooling energy requirements in this period.

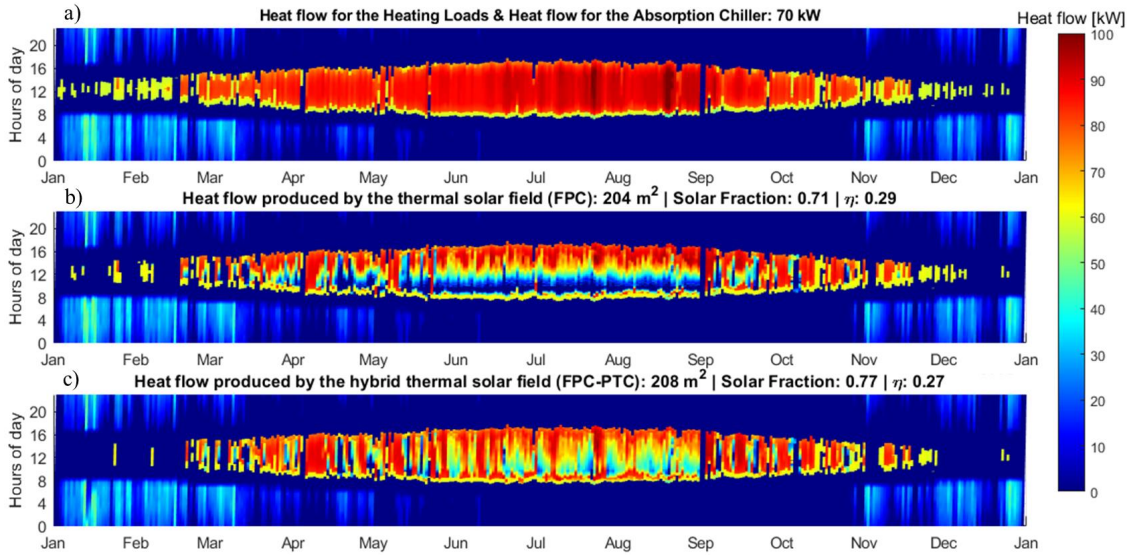

Figure 4: Heat flow rate maps of a) heating and chiller's heat demand; b) heat flow rate produced by the FPC-IF with a total area of 204 m^2 and c) heat flow rate produced by the HF with a total solar field area of 208 m^2

In Fig. 6 is shown the comparison of the solar fraction and efficiency of the FPC-IF and HF for different values of the total solar field area. Results indicate that for the smallest areas evaluated, both configurations have similar values of SF. Nevertheless, for larger areas, the HF has higher values of SF than the individual configuration, presenting a difference of 7% for areas of 300 m^2, allowing the HF to reach values of SF over 0.96 with areas smaller than half of the greenhouse area.

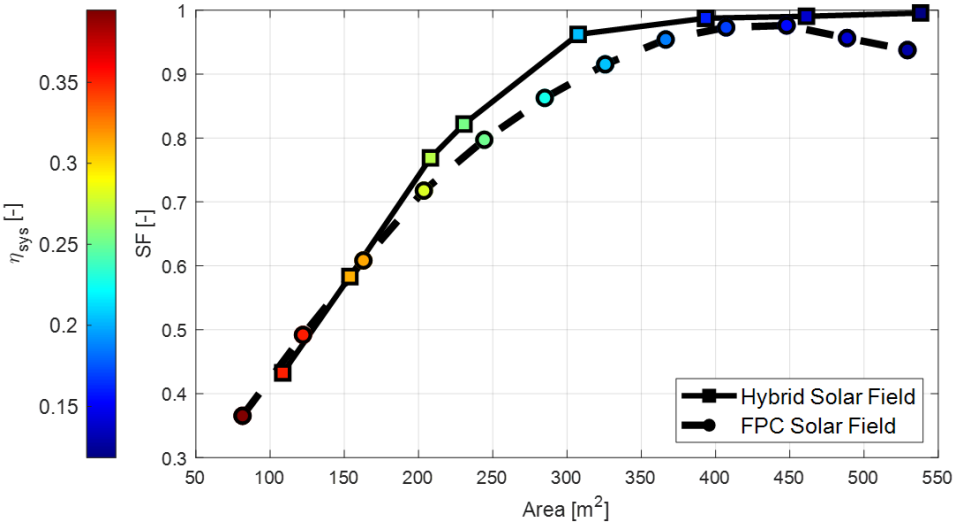

Figure 6: Comparison of solar fraction and efficiency of the system between FPC and hybrid solar field (FPC-PTC) schemes.

According (Sadi and Arabkoohsar, 2020), the solar cooling systems with PTC presented low performance with respect to the use of FPC due to the highest temperature of PTC reducing the coefficient of performance (COP) of the absorption chiller. In contrast, the results observed in this study show that the hybridization of FPC-PTC allows higher solar coverture with a smaller area, representing a clear advantage with respect to the FPC due to the backup

energy savings during summer.

Results of this work indicate that the HF allows a more constant SF throughout the year, attenuating the decrease in energy production observed in the FPC in the summer months. The HF has been shown to produce a better energy coverage than the FPC in most hours of summer days, a period of time when the heat requirement of the greenhouse is bigger. This is due to two main factors: 1) the improvement in the PTCs performance with the higher levels of direct radiation in summer; 2) the higher reduction of the FPC efficiency with the increment of the solar field operation temperature due to the requirements of the chiller generator. The improvement of the solar energy coverage with the HF in the summer months agrees with the findings of (Tian et al., 2018), and shows the potential of this type of configuration to supply solar energy to facilities with seasonal energy demands of cooling and heating.

4. Conclusion

This work evaluated the energy performance of hybrid solar systems with FPC-PTC to satisfy the energy requirements for heating and cooling of a greenhouse for tomato production in the south of Spain. The energy performance of the hybrid solar field was compared with an FPC solar field with individual configuration. The comparison was made in terms of heat flow rate, total monthly energy and annual solar fraction, and the systems were simulated using TRNSYS software.

Results show that a HF can mitigate the reduction of the energy coverage observed in the FPC in the months with higher greenhouse energy consumption. The HF allows improvements in the solar fraction up to 32 % and 25% in June and July, respectively, and significant enhancements in the other months between April and September. The findings of this work indicate the capacity of the FPC-PTC hybrid configuration to improve the energy performance of solar systems under seasonal energy demand for heating and cooling. Also, the HF system shows the potential to provide energy to other productive processes with seasonal energy demand and higher temperature requirements. In future works, the economic feasibility of this system and its performance under other solar resources and process temperature requirements will be evaluated.

5. Acknowledgments

J. Rosales-Pérez would like to acknowledge the funding from National Agency for Research and Development ANID BECAS/DOCTORADO NACIONAL 21200844, and A. Villarruel-Jaramillo acknowledge the funding from National Agency for Research and Development ANID BECAS/DOCTORADO NACIONAL 2120082.The authors gratefully acknowledge the MICROPROD-SOLAR project of the Spanish State Research Agency (ref. PCI2019-103378), which supports the CYTED program call for Strategic Projects on distributed generation, renewable energies and microgrids in Strategic Enclaves of Latin America.

6. References

Cabrera, F., Sánchez-Molina, J., Zaragoza, G., Pérez-García, M., Rodríguez-Díaz, F., 2017. Renewable energy technologies for greenhouses in semi-arid climates, in: Geothermal, Wind and Solar Energy Applications in Agriculture and Aquaculture. pp. 153–193.

Dias, F., Brondani, M., Vasquez, M.C., Hoffmann, R., Silva, E.E., 2019. Revisiting energy efficiency, renewability, and sustainability indicators in biofuels life cycle: Analysis and standardization proposal. https://doi.org/10.1016/j.jclepro.2019.119850

Gil, J.D., Ramos-Teodoro, J., Romero-Ramos, J.A., Escobar, R., Cardemil, J.M., Giagnocavo, C., Pérez, M., 2021. Demand-side optimal sizing of a solar energy–biomass hybrid system for isolated greenhouse environments: Methodology and application example. Energies (Basel) 14. https://doi.org/10.3390/EN14133724

Janotte, N., Meiser, S., Krüger, D., Lüpfert, E., Pitz-Paal, R., Fischer, S., Müller-Steinhagen, H., 2009. QUASI-DYNAMIC ANALYSIS OF THERMAL PERFORMANCE OF PARABOLIC TROUGH COLLECTORS. J Sol Energy Eng 132.

Lazaar, M., Bouadila, S., Kooli, S., Farhat, A., 2015. Comparative study of conventional and solar heating systems under tunnel Tunisian greenhouses: Thermal performance and economic analysis. Solar Energy 120, 620–635. https://doi.org/10.1016/J.SOLENER.2015.08.014

Mahmood, F., Al-Ansari, T.A., 2021. Design and thermodynamic analysis of a solar powered greenhouse for arid

climates. Desalination 497. https://doi.org/10.1016/J.DESAL.2020.114769

Prieto, J., Ajnannadhif, R., Fernández-del Olmo, P., Coronas, A., 2021. Integration of a system with solar thermal energy and biomass for the heating and cooling control of a greenhouse in Mediterranean climates.

Sadi, M., Arabkoohsar, A., 2020. Techno-economic analysis of off-grid solar-driven cold storage systems for preventing the waste of agricultural products in hot and humid climates. J Clean Prod 275. https://doi.org/10.1016/J.JCLEPRO.2020.124143

Sajid, M.U., Bicer, Y., 2021. Performance Assessment of Spectrum Selective Nanofluid-Based Cooling for a Self-Sustaining Greenhouse. Energy Technology 9, 2000875. https://doi.org/10.1002/ENTE.202000875

SP Technical Research Institute of Sweden, 2016. Solar Keymark Certificate No. SP SC0841-14. Borås.

Tian, Z., Perers, B., Furbo, S., Fan, J., 2018. Thermo-economic optimization of a hybrid solar district heating plant with flat plate collectors and parabolic trough collectors in series. Energy Convers Manag 165, 92–101. https://doi.org/10.1016/j.enconman.2018.03.034

TRNSYS, 2019. TRNSYS 18 - Mathematical Reference.

TRNSYS, 2017. TESS COMPONENT LIBRARIES General Descriptions [WWW Document]. TRNSYS Documentation. URL http://www.trnsys.com/tess-libraries/TESSLibs17_General_Descriptions.pdf (accessed 9.6.22).

Villarruel-Jaramillo, A., Pérez-García, M., Cardemil, J.M., Escobar, R.A., 2021. Review of Polygeneration Schemes with Solar Cooling Technologies and Potential Industrial Applications. Energies 2021, Vol. 14, Page 6450 14, 6450. https://doi.org/10.3390/EN14206450

Covering energy demands of Africa with radiative cooling and solar collection using a single device

Roger Vilà[1], Jesús Monterrubio[1], Cristian Solé[1], Albert Castell[1] and Marc Medrano[1]*

[1] Sustainable Energy, Machinery and Buildings (SEMB) Research Group, INSPIRES Research Centre, Universitat de Lleida, Pere de Cabrera s/n, 25001 Lleida, Spain

* Corresponding author: marc.medrano@udl.cat

Abstract

The Radiative Collector and Emitter (RCE) is a renewable technology which enables heating and cooling in a single device. It is an innovative concept which reduces the dependency on fossil fuels, and therefore diminishes the carbon footprint. Africa as a whole, presents a high demand of cooling, and covering these needs with renewable energy is possible thanks to Radiative Cooling (RC). Three simulations were performed in Africa (Agadez, Calvinia and Libreville) to determine the relation between cooling and Domestic Hot Water (DHW) demands compared with the renewable energy produced with the RCE. Results show an annual coverage of the cooling demand of 26.80% at Agadez and 8.72% at Libreville, while at Calvinia there are surpluses almost all the year. DHW is fully covered with solar collection The simulations also show that temperatures below the ambient may be achieved in cold storage tanks. Actually, these temperature differences are 5.56ºC, 3.36ºC and 4.50ºC at Agadez, Calvinia and Libreville, respectively.

Keywords: Radiative cooling, solar thermal collection, renewable energy, energy demand, Africa

1. Introduction

Residential and commercial buildings are responsible for the consumption of 40% of the energy of the world (Atmaca and Atmaca, 2022). Part of this energy is used to refrigerate by means of non-renewable energy sources and, thus greenhouse gases are emitted. If nothing is done, the situation may become cyclic, as shown in Fig. 1.

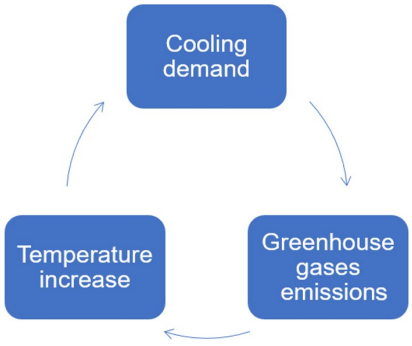

Fig. 1: Hypothetical situation derived from covering cooling demands with contaminant energy sources

An alternative presented is known as Radiative Collector and Emitter (RCE): the combination of radiative cooling and solar heating in a single device, producing heat during daytime and cold during nighttime. It is an innovative concept which helps to reduce the dependency on fossil fuels, and therefore reduces the carbon footprint.

The Radiative cooling (RC) is being studied as a passive cooling strategy which cools without any electricity input, having an important impact on global energy consumption (Raman et al., 2014). The aim is to radiate heat to outer space through the infrared atmospheric window between 8 and 13 μm wavelengths (Li et al., 2019), obtaining temperatures below the ambient.

© 2022. The Authors. Published by International Solar Energy Society
Selection and/or peer review under responsibility of Scientific Committee
doi:10.18086/eurosun.2022.06.10 Available at http://proceedings.ises.org

According to Vall et al. (2018) and Castell et al. (2020), the RCE (Fig. 2 and 3) has a similar shape to a flat plate solar thermal collector with two working modes: solar collection and radiative cooling. The water flowing through the device is heated during the day and chilled during the night. Different material characteristics are needed to operate under these different modes, and for this reason, it incorporates a movable cover. The collector is placed horizontally to maximize radiation to the sky. The solar collection cover lets solar radiation get to the collecting surface while mid and far infrared radiations are blocked. On the other hand, the radiative cooling cover lets emit thermal radiation into the atmosphere.



Fig. 2: RCE prototype with a movable cover. Extracted from Castell et al. (2020)

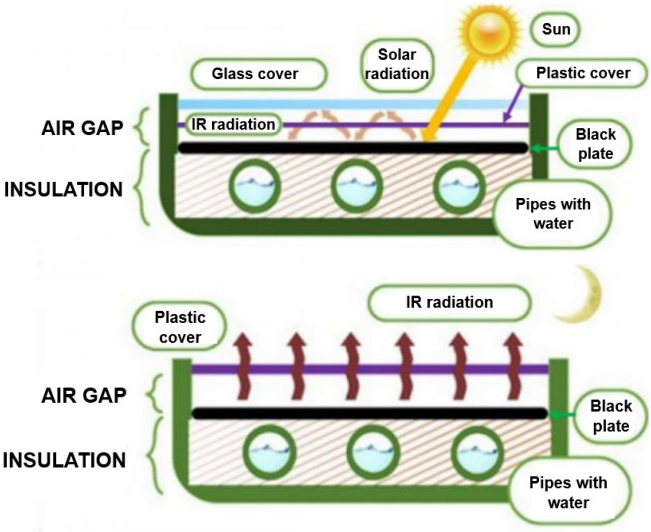

Fig. 3: RCE components for the heating mode (top) and cooling mode (bottom)



Fig. 4: Selected locations to obtain the energy demand and production

Regarding the maps created by Aili et al. (2021), high values of annual mean net cooling power are found in most parts of Africa. Considering the RC potential, three African regions can be distinguished: the Sahara Desert with the highest RC power potential, the tropical area remarkable for low values and the south of Africa with values in between.

This study presents an analysis related to the demands of cooling and domestic hot water (DHW) of three identical office buildings in Africa compared with the RCE's energy production. As it can be seen in Fig. 4, the offices are specifically located in Agadez (high RC power potential), Libreville (low RC power potential) and Calvinia (cooling potential in between).

2. Data acquisition and methodologies

Meteorological information was obtained from the Meteonorm database (Remund et al., 2019), corresponding to the radiation period from 1991 to 2010 and the temperature period from 2000 to 2009. DHW and cooling demands were obtained from the EnergyPlus simulation software, in which office buildings were taken from the USA Department of Energy, DOE ("Commercial prototype Building Models," n.d.) (Fig. 5). The same modifications were made as those implemented by Vall et al. (2018), that is to say, set point temperature schedules at 25/27ºC and natural ventilation through occupants controlled windows (7-22 h). The same building (Tab. 1) was used in the three locations in order to get comparable results, as the offices usually have the same comfort indoor conditions in all locations.

Tab. 1: Geometric parameters of the offices simulated

Wall area [m^2]	Window area [m^2]	Net conditioned area [m^2]	Roof area [m^2]
1,978.00	652.60	4,982.20	1,660.50

The Trnsys software was used to simulate the facility shown in Fig. 6 and to determine the production of energy. During the day, water from the hot tank was heated in the RCE, while during the night, water from the cold tank was refrigerated.

The results obtained (energy demand and production) were then analyzed using RStudio.

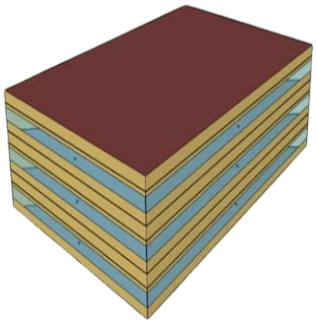

Fig. 5: Office building simulated in EnergyPlus

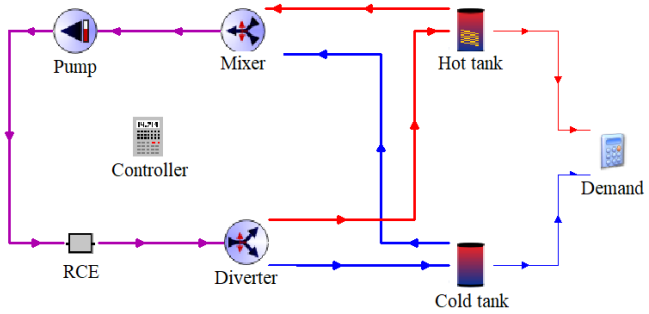

Fig. 6: Scheme of the facility simulated in Trnsys

The RCE device was presented as a Trnsys type, simulating the model developed and experimentally validated by Vall et al. (2020), in which parameters like the difference between the fluid temperature at the inlet and outlet of the RCE were calculated using energy balances between the device, the ambient air and the sky. The working mode (daytime solar collection or nighttime radiative cooling) was also considered.

Hot and cold tanks were used to store water obtained from heating and cooling modes, respectively, and to cover demands when needed. The demand was simulated in the following way: water from the hot and cold tanks was replaced by grid water at 20ºC during the night and during the day, respectively.

The controller type determined whether the RCE worked as a solar collector or as a radiative cooler, and modified both the pump flow rate (changing its speed) and the cover properties of the RCE (allowing the correct operation in each mode). The daily sunrise and sunset time were used to determine whether it was nighttime or daytime, and thus select the radiative cooling or solar collection mode, respectively.

The total roof surface in the analyzed building was 1,660.5 m^2. In this study, 1,330.0 m^2 (A_{RCE}), 80% of the total roof surface, was filled with RCEs in order to cover as much cooling demand as possible. A reasonable 20% of the roof was left for other uses. As the RCE's surface is 2 m^2, a total amount of 665 plates were required. The main technical characteristics of each RCE are presented in Tab. 2.

Tab. 2: Technical data of the RCE

Pipe diameter	**Pipe thickness**	**Insulation thickness**
8.00 mm	0.60 mm	30.00 mm
Cover solar absorptivity (heating mode)	**Cover solar transmissivity (heating mode)**	**Cover solar reflectivity (heating mode)**
0.05	0.90	0.05
Cover > 4 µm absorptivity (heating mode)	**Cover > 4 µm transmissivity (heating mode)**	**Cover > 4 µm reflectivity (heating mode)**
0.80	0.10	0.10
Cover solar absorptivity (cooling mode)	**Cover solar transmissivity (cooling mode)**	**Cover solar reflectivity (cooling mode)**
0.10	0.80	0.10
Cover > 4 µm absorptivity (cooling mode)	**Cover > 4 µm transmissivity (cooling mode)**	**Cover > 4 µm reflectivity (cooling mode)**
0.10	0.80	0.10
Radiator solar absorptivity	**Radiator solar transmissivity**	**Radiator solar reflectivity**
0.95	0.00	0.05
Radiator > 4 µm absorptivity	**Radiator > 4 µm transmissivity**	**Radiator > 4 µm reflectivity**
0.95	0.00	0.05

The tanks were dimensioned to store the heated and cooled water obtained during the daytime or nighttime hours, respectively, allowing their future use when required. The volume of the cold tank ($V_{cold\ tank}$) was determined using eq. 1 and the water flow rate for the cooling mode ($\dot{m}_{RC}$) was obtained using eq. 2.

$$V_{cold\ tank} = \frac{q_c \cdot A_{RCE} \cdot t_{RC}}{C_p \cdot \Delta T_{tank} \cdot \rho_w} \quad [m^3] \quad \text{(eq. 1)}$$

$$\dot{m}_{RC} = \frac{q_c \cdot A_{RCE}}{C_p \cdot \Delta T_{RCE}} \quad [kg/s] \quad \text{(eq. 2)}$$

where q_c is the expected RC power ($50\ Wm^{-2}$), t_{RC} is the time in which RC can be applied ($8\ h/day = 28{,}800\ s/day$), C_p is the water specific heat ($4{,}192\ J/(kg \cdot K)$), ΔT_{tank} is the temperature decrease of the water in the tank ($10\ K/day$), ρ_w is the water density ($1{,}000\ kg/m^3$) and ΔT_{RCE} is the temperature difference between the inlet and outlet of the RCE ($2\ K$). It should be noted that the mentioned values of q_c, ΔT_{tank} and ΔT_{RCE} are possible and reasonable according to the results from Castell et al. (2020).

On the other hand, the daytime facility was sized accomplishing the recommendations given by the Spanish public organization called IDAE (Institute for the Diversification and Saving of Energy) depending on the collecting surface (A_{RCE}): minimum volume of the hot tank of $75\ L/m^2$ and water flow rate of $40 - 60\ L/(h \cdot m^2)$.

To sum up, the dimensioning of the installation is shown in Tab. 3.

Tab. 3: Facility parameters in each working mode

Working mode	Water flow rate [kg/s]	Tank volume [m^3]
Solar collection (day)	22.17	99,750
Refrigeration (night)	7.93	45,687

As the water pump is a variable speed one, its flow rate is governed by the eq. 3.

$$\dot{m}_{RCE} = \gamma \cdot \dot{m}_{max} \quad [kg/s] \quad \text{(eq. 3)}$$

where $\dot{m}_{RCE}$ is the mass flow rate flowing through the RCE, $\dot{m}_{max}$ is the pump maximum speed (22.17 kg/s – solar heating mode) and γ is the coefficient in charge of modifying the pump speed ($\gamma = 0.36$ for the cooling mode).

In addition, the monthly energy values produced were calculated using eq. 4 and 5.

$$E_{RC,month} = \sum_{month}(P_{RC} \cdot \Delta t) \quad [kWh/(m^2 \cdot month)] \quad \text{(eq. 4)}$$

$$E_{SH,month} = \sum_{month}(P_{SH} \cdot \Delta t) \quad [kWh/(m^2 \cdot month)] \quad \text{(eq. 5)}$$

where P_{RC} is the radiative cooling power obtained in the RCE $[kW/m^2]$, P_{SH} is the solar heating power obtained in the RCE $[kW/m^2]$ and Δt is the period of time $[h]$ in which P_{RC} and P_{SH} are obtained.

3. Results and discussion

A comparison between the energy produced during daytime (solar heating mode) and nighttime (RC mode), for a year, is presented in Fig. 7, 8 and 9. It can be observed that solar collection increases during summer months, when solar radiation is higher. On the other hand, during the summer months, RC is lower in Niger and Calvinia, which is known as seasonal anomaly (Aili et al., 2021).

The three locations are far away from each other. In fact, Agadez is in the northern hemisphere and Calvinia is in the southern hemisphere, which means that seasons are reversed. As Libreville is near the equator, the climate is quite stable all over the year and the results prove that.

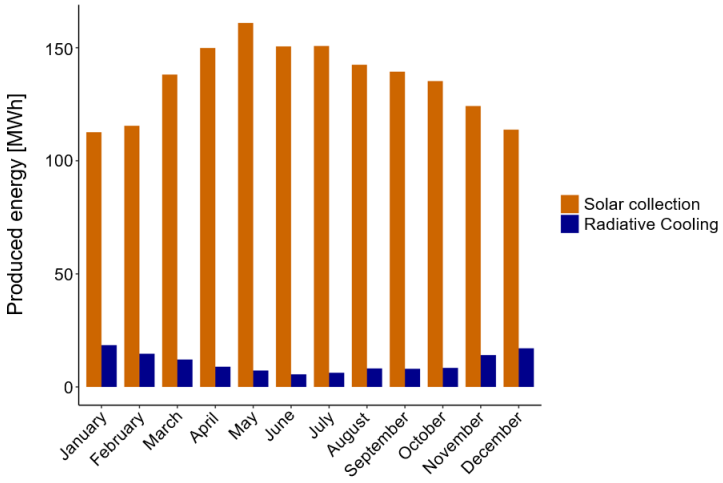

Fig. 7: Monthly energy production in an office building at Agadez (Niger)

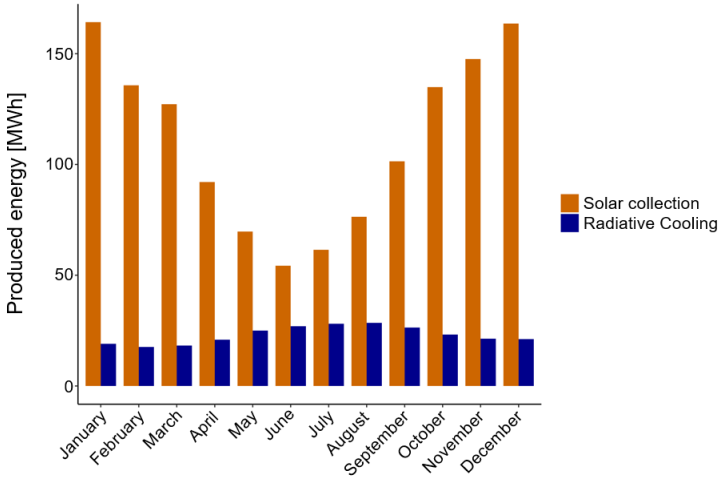

Fig. 8: Monthly energy production in an office building at Calvinia (South Africa)

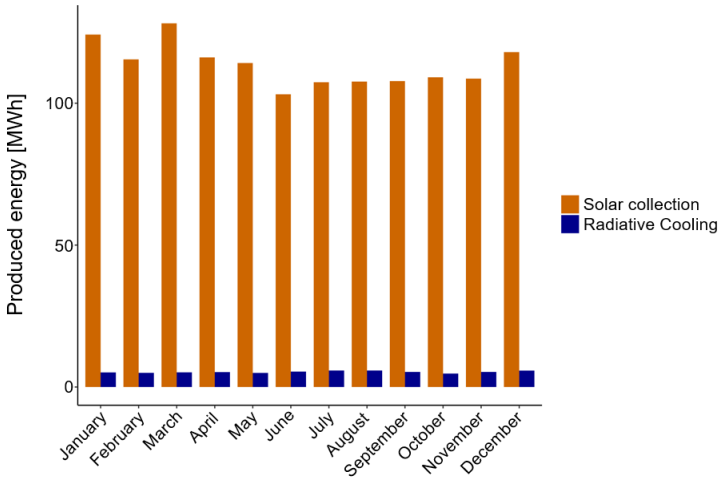

Fig. 9: Monthly energy production in an office building at Libreville (Gabon)

Fig. 10, 11 and 12 compare the cooling demand with the refrigeration energy production using radiative cooling, while Tab. 4 and 5 present the energy demand per square meter. The cooling demand at Agadez and Libreville is partially covered, while at Calvinia there are energy surpluses almost all the year (except January, February and March). Actually, Tab. 6 indicates that the mean annual cooling demand covered at Agadez and Libreville are 26.80% and 8.72%, respectively. In addition, the energy production at the capital of Gabon is quite stable, so the refrigeration covered is almost constant all the year (between 7.19% and 10.86%).

Tab. 4: Monthly DHW energy demand per square meter at each location [Wh/m²]

	January	February	March	April	May	June
Agadez	196.84	177.66	205.51	184.99	194.62	190.93
Calvinia	187.28	170.69	201.28	186.59	201.94	202.28
Libreville	196.07	177.45	205.52	185.06	194.76	190.78

	July	August	September	October	November	December
Agadez	182.32	198.57	182.85	191.16	189.87	191.68
Calvinia	194.80	210.20	189.84	192.87	186.50	184.22
Libreville	182.47	198.57	183.02	191.34	189.99	191.34

Tab. 5: Monthly cooling energy demand per square meter at each location [Wh/m²]

	January	February	March	April	May	June
Agadez	4,765.18	6,305.88	10,018.44	11,956.56	13,943.80	14,200.91
Calvinia	5,239.93	5,192.33	4,352.99	2,034.34	357.98	122.97
Libreville	12,716.65	12,355.99	14,268.66	13,124.59	13,903.82	12,120.44

	July	August	September	October	November	December
Agadez	14,592.36	14,962.17	12,875.00	11,720.39	8,453.95	5,820.12
Calvinia	176.26	102.77	406.39	1,813.79	2,647.50	4,172.68
Libreville	10,751,45	11,640.36	11,022.00	11,754.51	12,008.53	12,752.14

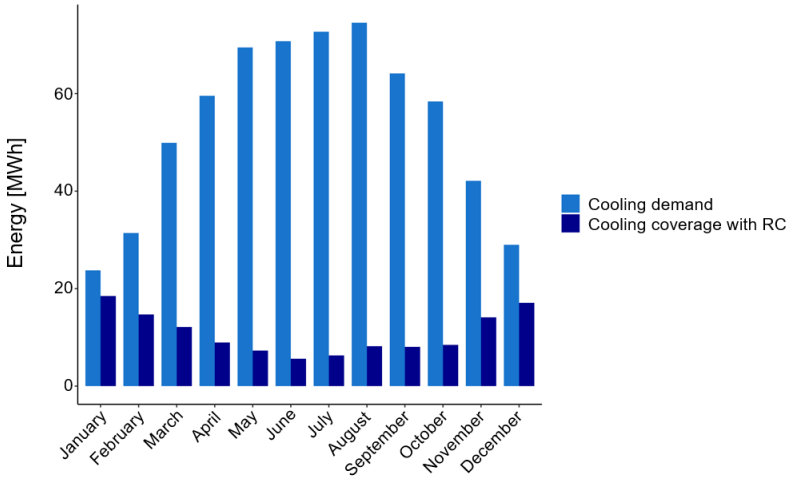

Fig. 10: Monthly refrigeration coverage in an office building at Agadez (Niger)

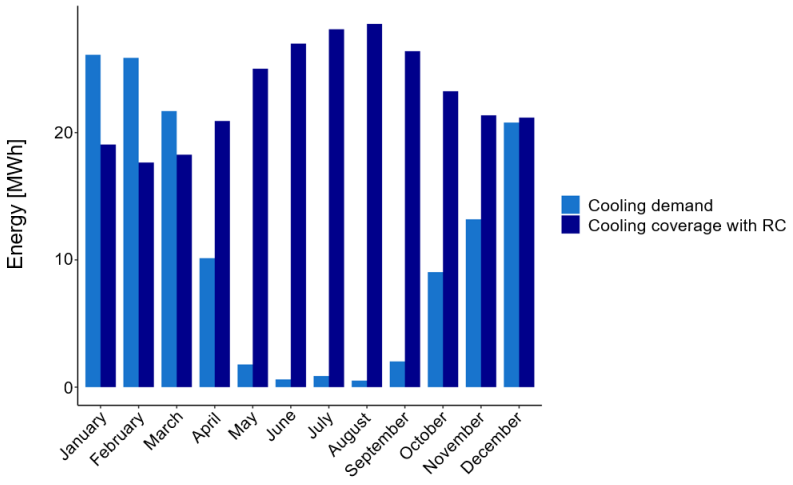

Fig. 11: Monthly refrigeration coverage in an office building at Calvinia (South Africa)

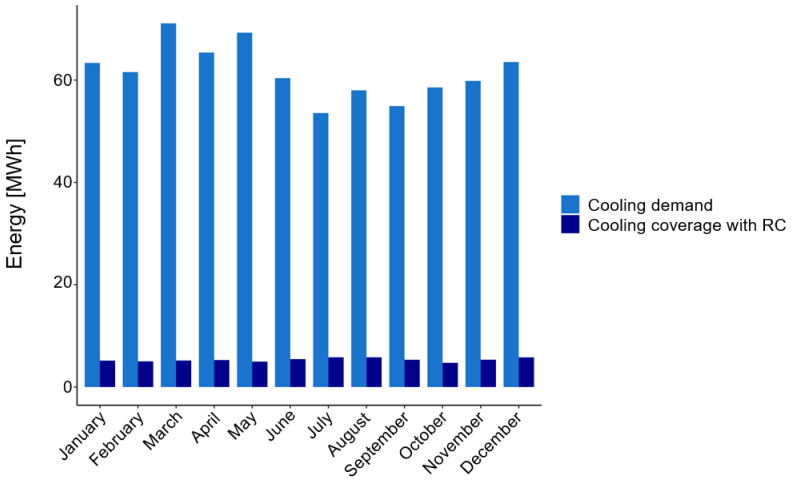

Fig. 12: Monthly refrigeration coverage in an office building at Libreville (Gabon)

Tab. 6: Percentages of cooling energy coverage ("surp." indicates that there are surpluses that specific month)

	January	February	March	April	May	June
Agadez	77.91	46.79	24.32	15.03	10.50	7.94
Calvinia	73.00	68.21	84.22	surp.	surp.	surp.
Libreville	8.16	8.16	7.28	8.09	7.19	9.03

	July	August	September	October	November	December
Agadez	8.66	10.99	12.56	14.50	33.50	58.95
Calvinia	surp.	surp.	surp.	surp.	surp.	surp.
Libreville	10.86	10.03	9.69	8.09	8.93	9.11

On the other hand, Fig. 13, 14 and 15 compare the DHW demand with the heating energy production using solar collection. A clear difference in the order of magnitude is observed between the heating and cooling energy production. It is important to highlight that office building demands count with lower DHW demands per square meter than other buildings typologies, such as hotels or residential buildings (Vall et al., 2018). As the facility was dimensioned to achieve the maximum cooling energy in an office building, there are many DHW surpluses in all the locations (additional energy accumulated after having covered all the DHW demand). Possible uses of these DHW surpluses include district heating in cold regions in Africa, industrial cleaning or water preheating in industries.

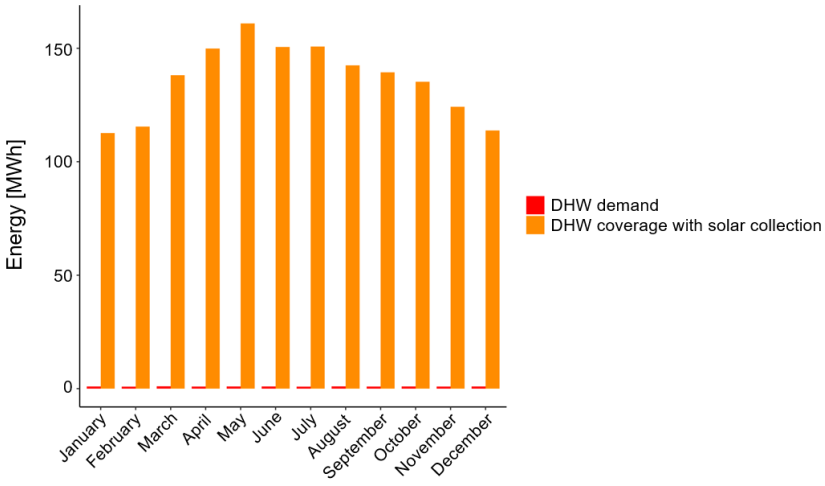

Fig. 13: Monthly DHW coverage in an office building at Agadez (Niger)

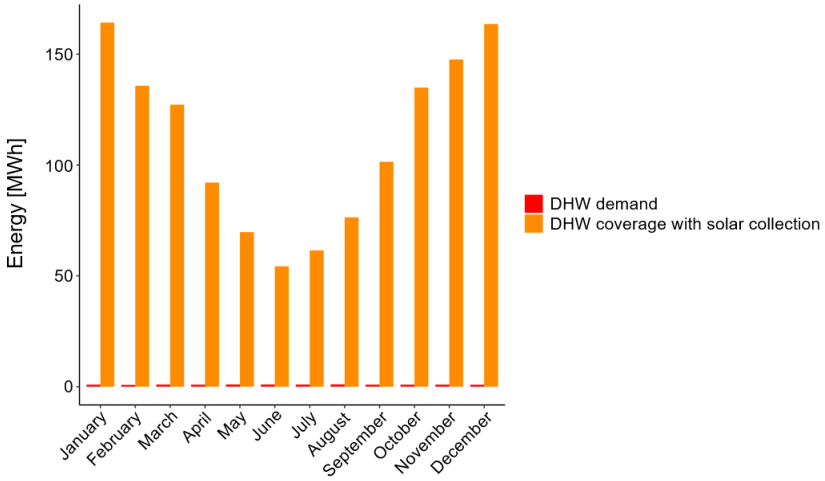

Fig. 14: Monthly DHW coverage in an office building at Calvinia (South Africa)

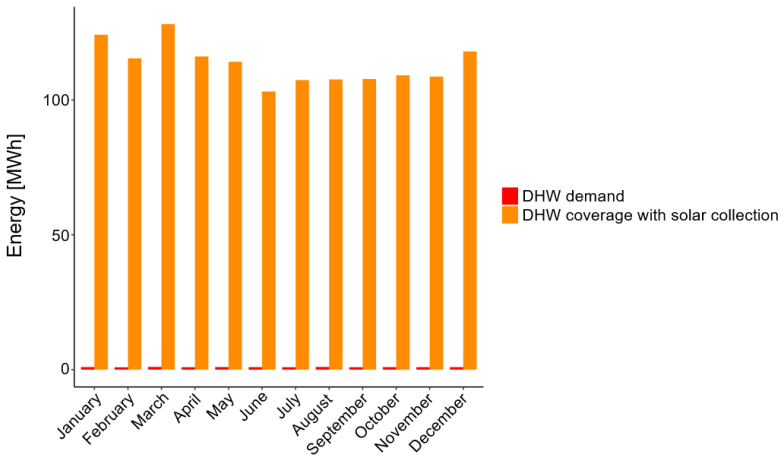

Fig. 15: Monthly DHW coverage in an office building at Libreville (Gabon)

Furthermore, Tab. 7 shows differences between the temperatures just before and after the Radiative Collector and Emitter. Higher changes of temperature are observed during daytime working mode (solar collection). Although the best performance is observed at Agadez when considering daytime mode, the best results are achieved at Calvinia for nighttime hours.

Tab. 7: Mean temperature changes between the inlet and outlet of the RCE

	Mean temperature reduction (nighttime)	Mean temperature increase (daytime)
Agadez	0.89 ºC	3.95 ºC
Calvinia	1.68 ºC	3.65 ºC
Libreville	0.41 ºC	2.90 ºC

Moreover, results extracted using RStudio show that sub-ambient temperatures may be achieved thanks to radiative cooling. As an average, the simulations indicate that during the night, temperatures of the cold tanks at Agadez, Calvinia and Libreville are 5.56ºC, 3.36ºC and 4.50ºC below the ambient, respectively.

Fig. 16 through 21 show the inlet and outlet temperatures of an RCE, the temporal profile of solar radiation, and the net power obtained per square meter of RCE (heating or cooling power). Negative values are used to represent cooling. For each location, data from the 10th to the 17th of January and July are presented. This allows the analysis of the RCE's performance under different weather conditions in each city.

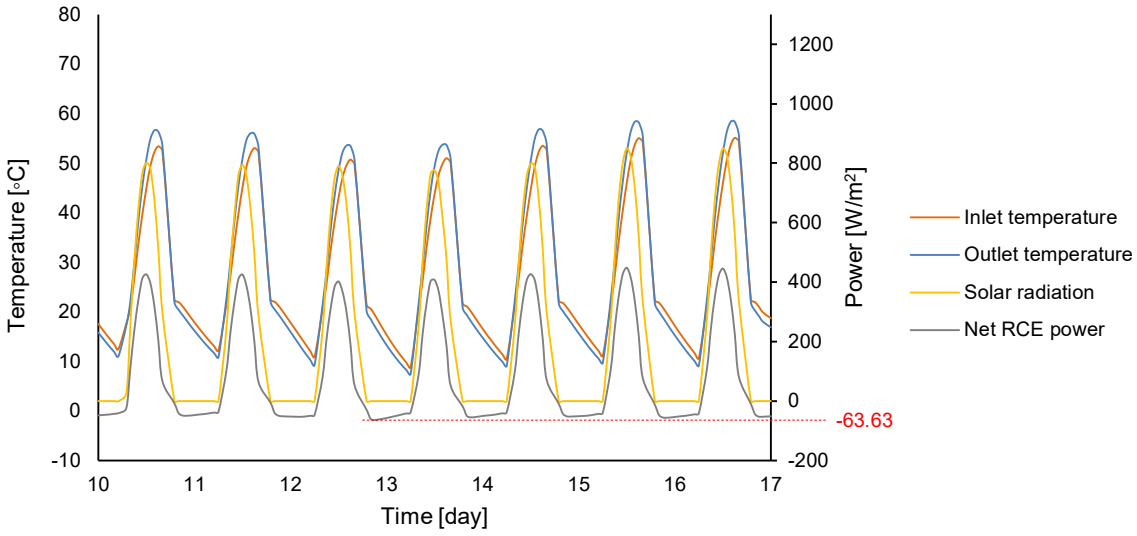

Fig. 16: Weekly RCE data from the 10th to the 17th of January at Agadez

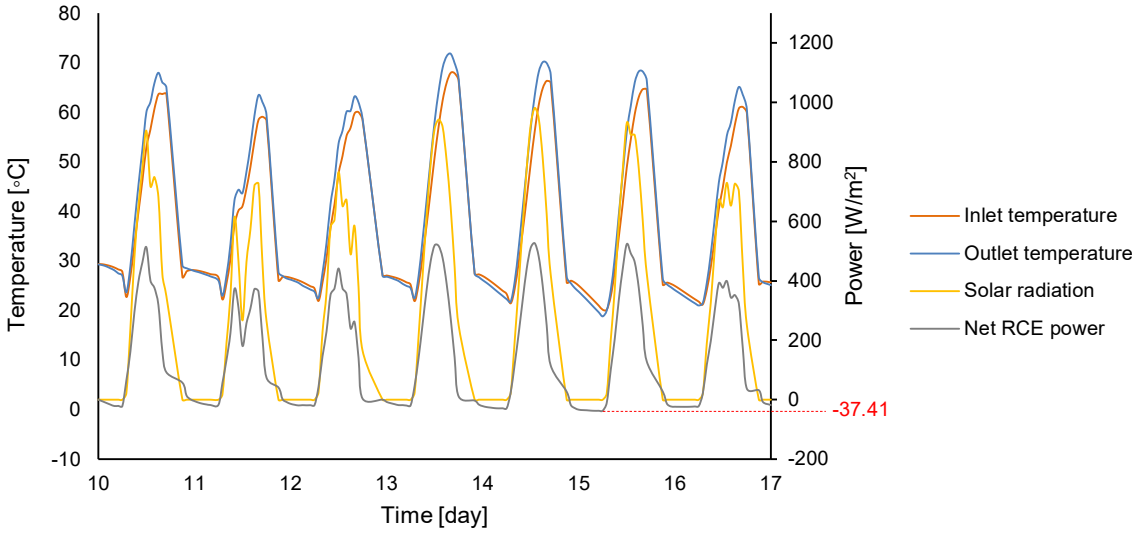

Fig. 17: Weekly RCE data from the 10th to the 17th of July at Agadez

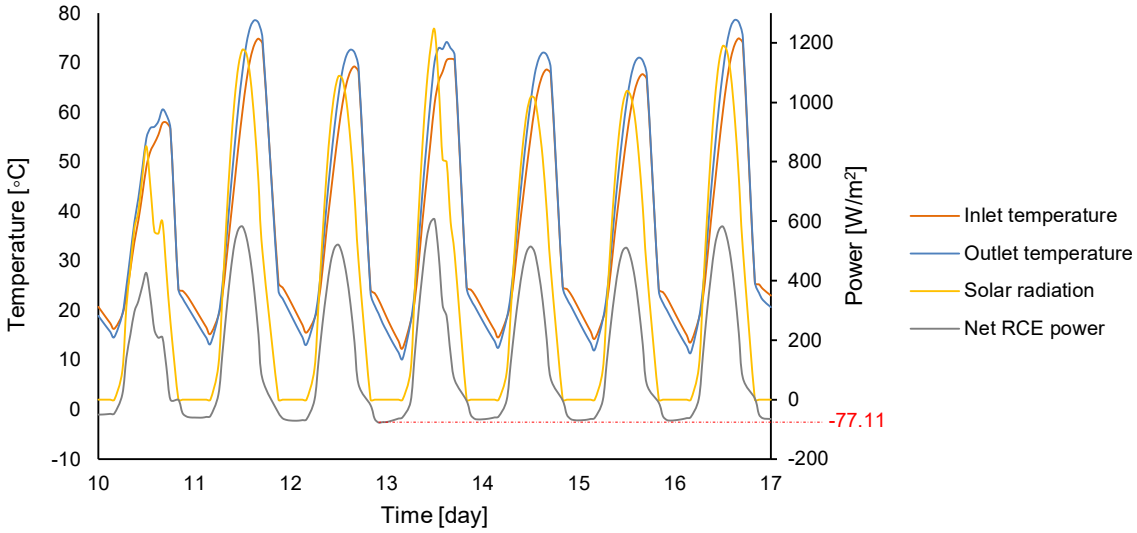

Fig. 18: Weekly RCE data from the 10th to the 17th of January at Calvinia

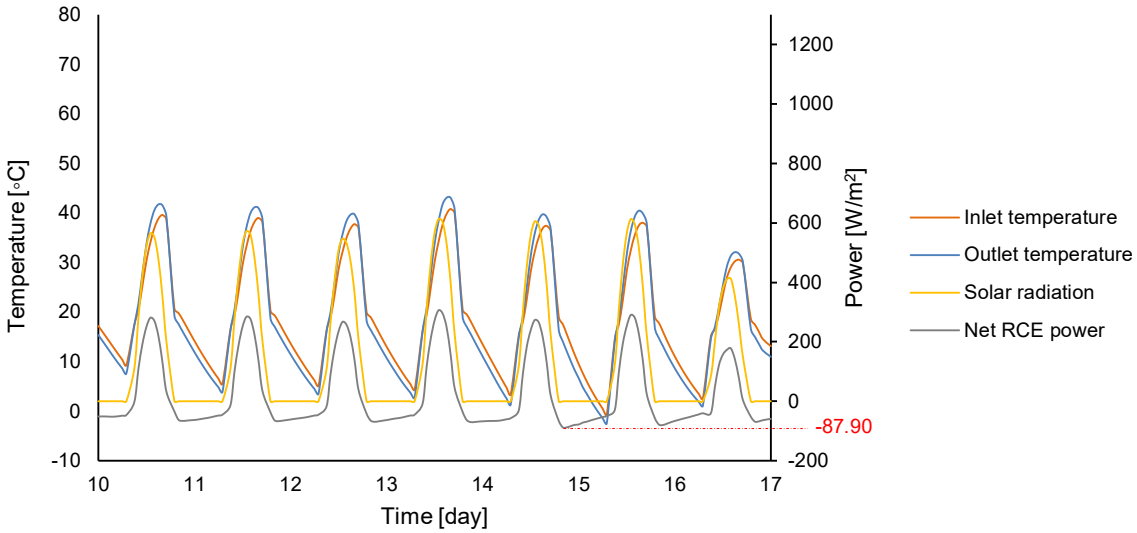

Fig. 19: Weekly RCE data from the 10th to the 17th of July at Calvinia

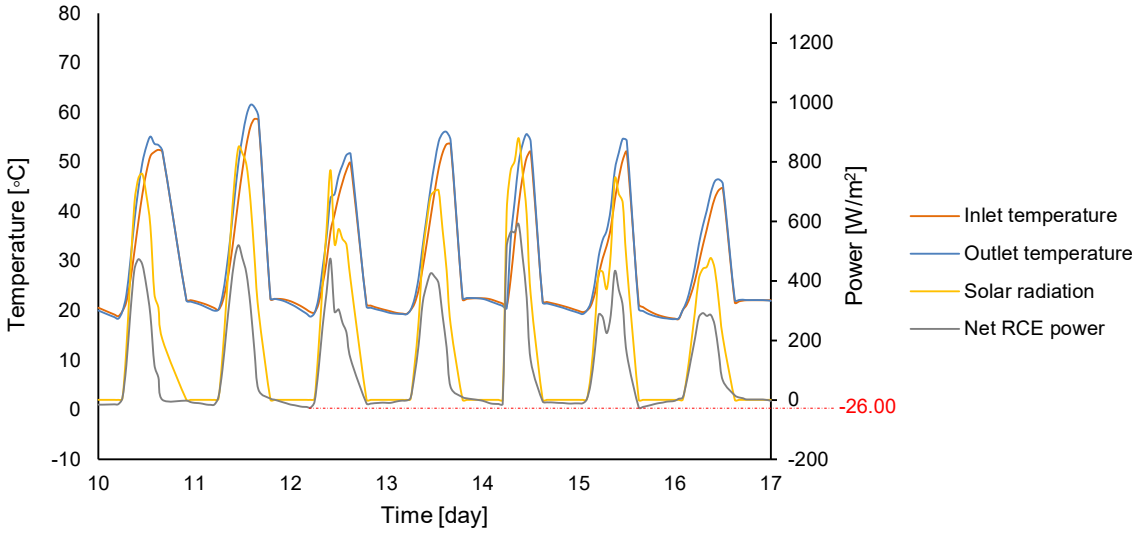

Fig. 20: Weekly RCE data from the 10th to the 17th of January at Libreville

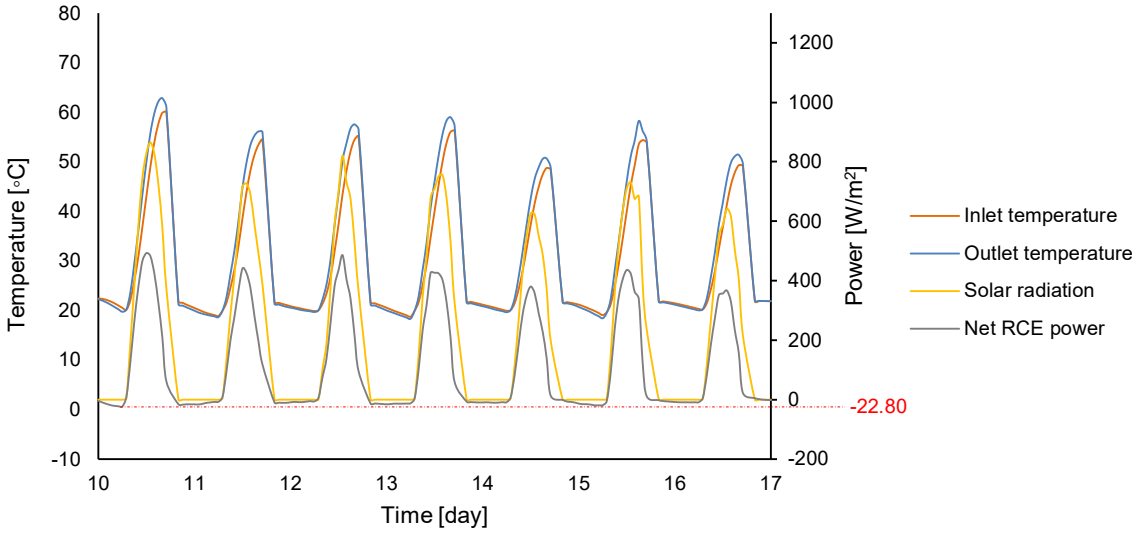

Fig. 20: Weekly RCE data from the 10th to the 17th of July at Libreville

It can be observed that when solar radiation is at its maximum, the net power is also at its highest. In the opposite case, when radiation is low or null, cooling power is maximized thanks to the RC. It can also be appreciated that the cooling power is of a different order of magnitude than the solar collection power, as mentioned before. The solar collection mode allows higher temperature changes compared to the Radiative Cooling mode, but the temperature reduction is enough to extract heat from the offices using close to ambient refrigeration systems, such as radiant floors or ceilings. The highest cooling potential results for these weeks are found in Calvinia.

4. Conclusions

As it was expected, the solar heating energy produced is higher than the energy obtained with RC. Mean annual values of heating energy production at Agadez, Calvinia and Libreville are 136.14 MWh/month, 110.73 MWh/month and 113.33 MWh/month, respectively; while the results of cooling energy production are 10.78 MWh/month, 23.06 MWh/month and 5.33 MWh/month, respectively.

While the cooling demand at Agadez and Libreville is partially covered (26.80% and 8.72%, respectively), at Calvinia there are surpluses almost all year. On the other hand, there are many Domestic Hot Water surpluses in all the locations. This extra energy could be used in nearby buildings or industries for other heating purposes such as building heating, commercial laundry or industrial pre-heating processes.

The seasonal anomaly described by Aili et al. (2021) has also been observed, especially in Agadez and Calvinia, where less RC power is obtained during the summer months.

The results also show that temperatures below the ambient may be achieved thanks to radiative cooling. In fact, mean annual temperature differences between the cold tanks and the ambient of 5.56ºC, 3.36ºC and 4.50ºC are observed at Agadez, Calvinia and Libreville, respectively.

5. Acknowledgments

The authors would like to thank Generalitat de Catalunya for the project grant given to their research group (2017 SGR 659). The work was partially funded by the Spanish government under grant agreement RTI2018-097669-A-I00 (Ministerio de Ciencia, Innovación y Universidades). Jesús Monterrubio would like to thank Ministerio de Educación y Formación Profesional of the Spanish government for his fellowship of collaboration in University Departments.

6. References

Aili, A., Yin, X., Yang, R., 2021. Global Radiative Sky Cooling Potential Adjusted for Population Density and Cooling Demand. Atmosphere 12, 1379. https://doi.org/10.3390/atmos12111379

Atmaca, A., Atmaca, N., 2022. Carbon footprint assessment of residential buildings, a review and a case study in Turkey. Journal of Cleaner Production 340, 130691. https://doi.org/10.1016/j.jclepro.2022.130691

Castell, A., Medrano, M., Martorell, I., Solé, C., Rincón, L., 2020. Desarrollo y evaluación de un equipo para producción combinada de frío y calor mediante refrigeración radiante y captación solar.

Li, M., Peterson, H., Coimbra, C., 2019. Radiative cooling resource maps for the contiguous United States. Journal of Renewable and Sustainable Energy 11, 036501. https://doi.org/10.1063/1.5094510

Raman, A.P., Anoma, M.A., Zhu, L., Rephaeli, E., Fan, S., 2014. Passive radiative cooling below ambient air temperature under direct sunlight. Nature 515, 540–544. https://doi.org/10.1038/nature13883

Remund, J., Müller, S., Kunz, S., Huguenin-Landl, B., Studer, C., Cattin, R., 2019. Meteonorm. Meteotest, Switzerland.

U.S. Department of Energy. Commercial prototype Building Models, n.d. https://www.energycodes.gov/prototype-building-models#Commercial (accessed August 31, 2022).

Vall, S., Castell, A., Medrano, M., 2018. Energy Savings Potential of a Novel Radiative Cooling and Solar Thermal Collection Concept in Buildings for Various World Climates. Energy Technology 6, 2200–2209. https://doi.org/10.1002/ente.201800164

Vall, S., Johannes, K., David, D., Castell, A., 2020. A new flat-plate radiative cooling and solar collector numerical model: Evaluation and metamodeling. Energy 202, 117750. https://doi.org/10.1016/j.energy.2020.117750

Optimal operation and conceptual design of a novel façade-integrated adsorption cooling system

Simon O. Weber[1], Olaf Böckmann[2], Andreas Greiner[3], Sumee Park[4], Micha Schäfer[2], Martin Ostermann[3] and Philip Leistner[1]

[1] Institute for Acoustics and Building Physics, University of Stuttgart (Germany)

[2] Institute for Building Energetics, Thermotechnology and Energy Storage, University of Stuttgart (Germany)

[3] Institute for Building Construction, University of Stuttgart (Germany)

[4] Fraunhofer Institute for Building Physics, Valley (Germany)

Abstract

About 5% of the world's energy consumption is used for indoor air conditioning Construction (UN 2021 Status Report). This study expects it to increase by up to 157% by 2050 under stated policies scenario. This could be accompanied by an increasing risk of power outages. To meet the enormous summer cooling demand of buildings, a component is therefore needed that provides cooling energy off-grid and emission-free. The façade-integrated adsorption cooling concept presented in this paper provides cooling energy in a decentralized and nearly emission-free way. By using this concept, large pipe routes can be dispensed with, the use of environmentally harmful coolants can be avoided, and power generation peaks can be reduced. For this purpose, an optimization-based operation strategy for a novel adsorption cooling system is presented in this paper. In addition, to support an optimal conceptual design, the critical building parameters are identified, their number is reduced and varied with respect to energy efficiency.

By applying a novel operation strategy, the system can be controlled more efficiently and in a more comprehensive adsorber orientation range compared to the previous operation strategy. In this context, the reduction of power consumption on the hottest day of the year shows a strong dependence on the adsorber orientation and the area ratio of the adsorption cooling components. In the optimal parameter configuration and using the new operating strategy, the power consumption can be reduced by 70%.

Keywords: optimal operation, conceptual design, façade integration, adsorption cooling

1. Introduction

According to the UN's recently published 2021 Global Status Report for Buildings and Construction (UN 2021 Status Report), the building sector contributes 37% of global carbon dioxide emissions and 36% of global energy consumption. Building cooling accounts for 5% of energy consumption annually. In addition, global energy demand for building cooling will increase between 29% to 157% by 2050, depending on the stated policies scenario. This could be accompanied by an increase in the risk of power outages. On the one hand, due to the simultaneous supply of the increasing cooling demand and, on the other hand, due to the drought-induced shutdown of power plants.

Within this background, the Collaborative Research Centre 1244 (CRC 1244) at the University of Stuttgart interdisciplinary investigates adaptive building skins and structures to reduce resource consumption in building construction as well as energy consumption in building operation. Based on the results of the first research phase, the world's first adaptive high-rise experimental building (D1244) was inaugurated this year (Blandini et al., 2022). They showed that lightweight adaptive buildings can reduce the greenhouse gas emissions over the entire life cycle (material + operation) by 40%. Unlike conventional massive buildings, lightweight buildings have low inherent thermal capacity and thus are prone to thermal oscillations.

© 2022. The Authors. Published by International Solar Energy Society
Selection and/or peer review under responsibility of Scientific Committee
doi:10.18086/eurosun.2022.06.11 Available at http://proceedings.ises.org

The novel façade-integrated adsorption cooling system used in this work relies on the previous work of Boeckmann et al. (2021) and Heidingsfeldt et al. (2022). It addresses several challenges at a time by offering the possibility to provide energy for building cooling in a nearly climate-neutral and decentralized way and by refraining from the use of environmentally harmful coolants. Thus, it contributes to the reduction of emissions in construction and operation as well as to grid resilience.

Prieto et al. (2017) and Almasri et al. (2022) supply a broad overview on current work on façade-integrated cooling and solar sorption cooling systems, respectively. Accordingly, solar energy is either converted into electricity in PV modules or into heat in solar collectors. From that cooling energy is mainly generated by using compression or sorption chillers, respectively. In the group of solar thermal cooling systems, which are studied widely, the most installations are either absorption or adsorption systems (Settino et al., 2016). The systems presented in the quoted technology overview have separated solar thermal collectors and sorption units, which are usually placed on the building's roof or in the basement. In contrast to these systems, the adsorption system in this work combines the adsorber and the solar collector into one component, which allows it to be façade integrate able. This is favourable due to the high potential of solar energy harvesting in this area. Furthermore, the integration into the façade reduces the competition for space on the roof surface between HVAC systems, photovoltaics, terrace use or greenspace applications.

The integration into the facade also leads to certain challenges. For example, the adsorber orientation must be adapted to the location. The mutual dependence of the adsorber orientation, the switching times of the operating phases and the cooling demand in the room must be coordinated. This requires a control concept that can consider the influencing factors presented. The current control concept, in the following called rule-based strategy, switches the phases based on predefined heuristics. External signals such as the solar energy input and internal states such as the pressures of the individual components are considered. This results in the main tasks of this work. In addition to the development of an optimization-based operating strategy of the facade-integrated adsorption cooling system, an efficiency analysis of selected system parameters is carried out. The discussion of the simulation results focusses on the following hypotheses:

- The optimisation-based operation strategy enables lower power consumption than the rule-based strategy
- The performance of the system strongly depends on the building orientation as well as the area ratio of the components

The paper is organized as follows: In Section 2, the models of the adsorption cooling, the additional compression cooling, the air conditioning system, and the building are described. Furthermore, the control strategies of the total system and the adsorption cooling are explained and the parameters for the parametric study are introduced. The simulation results are presented and discussed in detail in Section 3. Finally, the study is concluded in Section 4.

2. Methods

The system consists of the building and the HVAC equipment. This includes the heat pump (HP), ventilation (AHU), compression cooling (COCH) system and the novel facade-integrated adsorption cooling (ADCH) system. All models and controls were created in Dymola with the modelling language Modelica.

2.1. Building

For the building model, the zonal model from the IBPSA library was used. This library forms the core of the validated Modelica building models Aixlib, Buildings, BuildingSystems and IDEAS. The building model was created for one squared building storey of the D1244 high-rise, with an internal ground area of 5.11m x 5.11m and 2.85m height. The variable volume of the evaporator is then subtracted from the room volume V_Z. Weather data were generated for the location of D1244 on the university campus (N 48.749°, E 9.112°) using Meteonorm software. For all results, July 8 was selected as the hottest day of the test reference year.

The building zone is surrounded by four types of facades, whose dimensions are the subject of parameter variation, the floor and roof. The facade types include a lightweight wall, a window wall, the adsorber and condenser components. The lightweight wall is constructed in five layers, their thicknesses and material properties are shown in Table 1. The window-to-frame ratio f_{WF}, the secondary heat gain coefficient q_i and other properties of the window wall are shown in Table 2. The window data were generated for a triple low-e argon glazing and vinyl

frame within the WINDOW 7.8 software. The properties of the adsorber and condenser facade are presented in the subsection 1.c. The floor and ceiling were modelled as a 13cm thick steel-concrete layer ($c_p = 1000\frac{J}{kgK}, \lambda = 2.5\frac{W}{mK}, \rho = 2500\frac{kg}{m^3}$). This corresponds approximately to the dimensions of adaptive ceiling systems, which are investigated within other subprojects of the CRC 1244. The internal and external combined convective-radiative heat transfer coefficients were taken from the EN ISO 6946 standard ($h_{ind} = 7.7\frac{W}{m^2K}, h_{ext} = 25\frac{W}{m^2K}$). The outermost short wave radiation absorption coefficient was set to 0.3.

Table 1: Properties of the lightweight wall

Layer	Material	$s\ [cm]$	$c_p[\frac{J}{kgK}]$	$\lambda[\frac{W}{mK}]$	$\rho[\frac{kg}{m^3}]$
1 / outermost	Plaster lime mortar	2	1000	0.869	1800
2	Medium-density fibreboard	2	1700	0.130	650
3	Mineral wool	10	840	0.032	30
4	Medium-density fibreboard	2	1700	0.130	650
5 / innermost	Plaster gypsum	1.5	1000	0.333	1200

Table 2: Properties of the window wall

$g[-]$	$q_i[-]$	$U[\frac{W}{m^2K}]$	$f_{WF}[-]$
0.279	0.09	0.942	0.1

The building model is influenced by heat flows due to the interaction with the ambient temperature, the solar gains, internal gains, and those heat flows of the HVAC systems. The internal gains are active only in the range of working hours from 7-18h, where 2 people emit the total heat output $\dot{Q}_{IG} = 440W$. This results from the radiative and convective heat flows of each person and the convective heat flow of two PC (DIN V 18599-10 Table A.2).

2.2. Heat pump, ventilation, compression chiller

A simple COP model is used for the heat pump and the compression chiller, cf. equations 1 and 2. The ventilation exchanges the room volume at the given air exchange rate acr with ambient air without heat recovery, cf. equation 3. The EPM Pabst 6312 TDH fan, cf. equation 4, is assumed for the energy consumption of the ventilation. The total energy consumption is then calculated as the integral of all power components over the specified day, cf. equation 5.

$$\dot{Q}_{HP} = COP_{HP}\, P_{HP} \qquad COP_{HP} = 4 \qquad \text{(eq. 1)}$$

$$\dot{Q}_{COCH} = -COP_{COCH}\, P_{COCH} \qquad COP_{COCH} = 3 \qquad \text{(eq. 2)}$$

$$\dot{Q}_{AHU} = \frac{c_{p,air}\,\rho_{air}\,V_Z}{3600}(T_a - T_Z)acr \qquad \text{(eq. 3)}$$

$$acr = 13.55\frac{m^3}{Wh}\frac{1}{V_Z}P_{AHU} \qquad \text{(eq. 4)}$$

$$E_{tot} = \int_0^{24} P_{HP} + P_{COCH} + P_{AHU}\,dt \qquad \text{(eq. 5)}$$

2.3. Façade-integrated adsorption chiller

In contrast to the technical systems mentioned in subchapter 2.b, the novel facade-integrated adsorption system provides cooling without emissions during operation. The cooling system consists of the components adsorber, condenser and evaporator which are vacuum-tight and separably connected by valves. Figure 1 shows the schematic structures of each component. The adsorber contains zeolite as the adsorbent and water as the adsorptive. Zeolite is used because of its well-documented properties. Material optimization is the subject of future

work. To introduce the heat and maintain the vacuum medium, the adsorbate is encased and permeated with aluminium fins. It is decoupled from the interior of the room by a 4cm layer of vacuum insulation panel ($c_p = 1000\frac{J}{kgK}, \lambda = 0.003\frac{W}{mK}, \rho = 150\frac{kg}{m^3}$). An air gap and glazing separate the adsorber from the environment. Switchable dampers are placed at the outlets and inlets of the air gap. The condenser is also encased and permeated with fins. It condenses water vapor and releases the heat to the environment. It is also insulated by a 4cm thick layer of vacuum insulation panel to the room. The evaporator is installed under the ceiling of the room. It is also

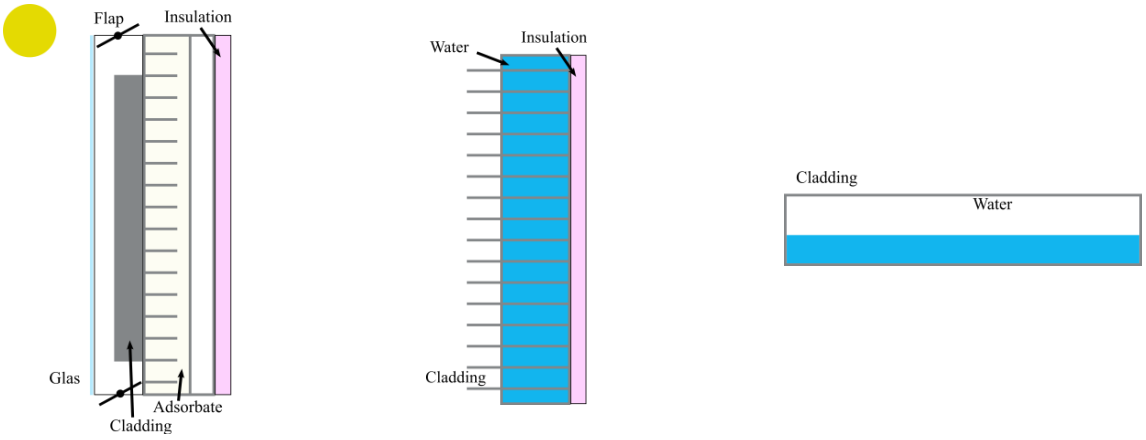

Figure 1: Schematic construction of adsorber (left, side view), condenser (center, top view) and evaporator (right)

encased and extracts the heat necessary for evaporation from the room.

The components are connected to each other by valves depending on the operating phase, cmp. Figure 2. In phase 1, the intermediate heating, all valves are closed and the adsorber is heated up by the absorbed solar radiation. In the subsequent desorption phase, phase 2, the valve from the adsorber to the condenser is opened. Water vapour desorbs out of the zeolite and is liquefied in the condenser. Then follows phase 3, the intercooling phase. During this phase, all valves are closed and the adsorber is cooled down to a lower temperature level. This cooling process is accelerated by opening the dampers. These dampers enable free convective cooling of the air gap in the adsorber. In the actual cooling phase, phase 4, opening the valve between the evaporator and the adsorber starts the adsorption process of water vapour from the evaporator to the zeolite. The dampers are opened to dissipate the heat generated in the process. The evaporation of the water cools it down, whereby heat is extracted from the room via the finned evaporator shell. The implemented model equations for the adsorption system are presented in the paper by Heidingsfeld et al. (2022).

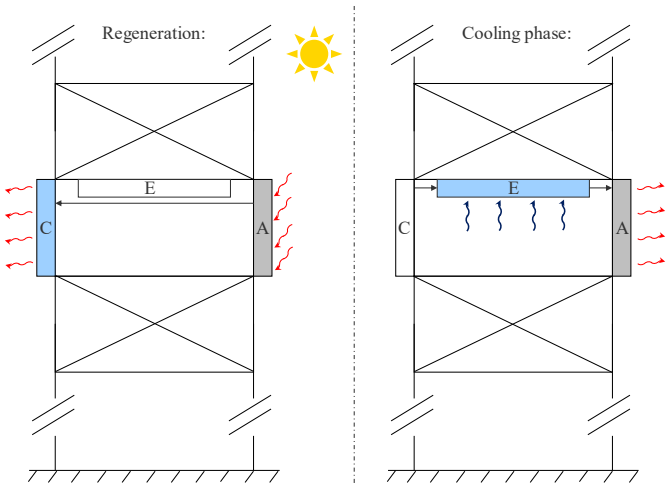

Figure 2: Operation principle of the façade-integrated adsorption cooling system

2.4. Control concept

A control concept was created for the building model, which specifies the control variables of the system and efficiently operates the system. The following manipulated variable and state constraints must be fulfilled. Within working hours, the room temperature must be between $21°C$ and $24°C$ (DIN 18599-10 Table A.2). Outside working hours, the limits are extended by $5K$. In addition, an air exchange rate acr between 2 h^{-1} and 3 h^{-1} must be achieved during working hours. This range was also expanded outside working hours to 0 h^{-1} and 6 h^{-1}. The control concept is shown in Figure 3. In the first link of the control chain, the set point of the total cooling capacity $\dot{Q}^*_{tot}$ is determined from a set point/ actual value comparison of the room temperature. If the room needs to be warmed up, the heating output is transferred to the heat pump. However, this is not necessary for the selected day and is therefore not depicted. In the split unit, the individual systems are added one after the other. First, an attempt is made to achieve the total cooling capacity through the ventilation $\dot{Q}^*_{AHU}$. If this cooling capacity is not sufficient, the adsorption cooling system is given the remaining cooling capacity $\dot{Q}^*_{ADCH}$. Finally, the remaining differential power is set to the compression cooling system $\dot{Q}^*_{COCH}$.

A blind is added to each window. To represent a realistic solar energy input with minimal computational effort, the mitigation factor F_c value was set constant ($F_c = 0.1$) for all blinds. The control variables of the ventilation and compression cooling are the air change rate acr and electric power P_{COCH}, respectively. They are set within their own PID control loops such that the specified setpoint is maintained. The manipulated variables of the adsorption cooling system are the valve positions between the evaporator and adsorber and between the adsorber and condenser, the damper positions dmp in the adsorber air channel and the signal of the pump pmp between the condenser and evaporator. In order not to open the two valves simultaneously, their valve signal is combined. Negative values of the combined signal enable desorption, only the valve to the condenser is opened. In contrast, only the valve from the evaporator to the adsorber is open for positive values vlv. At zero, both valves are closed. The combined valve signal vlv is at zero in phases 1 and 3, at a constant -1 in phase 2 and at 1 in phase 4 if the applied setpoint cooling capacity $\dot{Q}^*_{ADCH}$ is greater than the actual cooling capacity $\dot{Q}_{ADCH}$ from the evaporator. The dampers in the adsorber gap are opened as described above to support adsorber cooling in phases 3 and 4 and are closed in phases 1 and 2. Irrespective of the operating phase, the pump pumps water into the evaporator in the morning hours until a predefined water mass is reached.

Decisive for the control of the valve and the air dampers is the selection of the phases in the SEL_{Phase} block, cmp. Figure 3. Two approaches are compared in this work. The so-called rbd-approach (rule-based) switches the phase starting from phase 1 using fixed switching heuristics. The switching conditions are first published by Heidingsfeldt et al. (2022). With rbd-strategy, the phase is switched from 1 to 2 as soon as the adsorber pressure exceeds the condenser pressure ($p_{ads} > p_{con}$). Intercooling starts as soon as the irradiation drops ($\dot{G}_s < 0$), the irradiation on its surface is below a threshold ($G_s < 200$) and the adsorber loses more heat than it receives ($\Delta\dot{Q}_{ads} < 0$). The cooling phase 4 starts if the evaporator pressure exceeds the adsorber pressure ($p_{eva} > p_{ads}$) and steps to intermediate heating with the sunrise at the next morning ($\dot{G}_s > 0$ & $G_s > 0$).

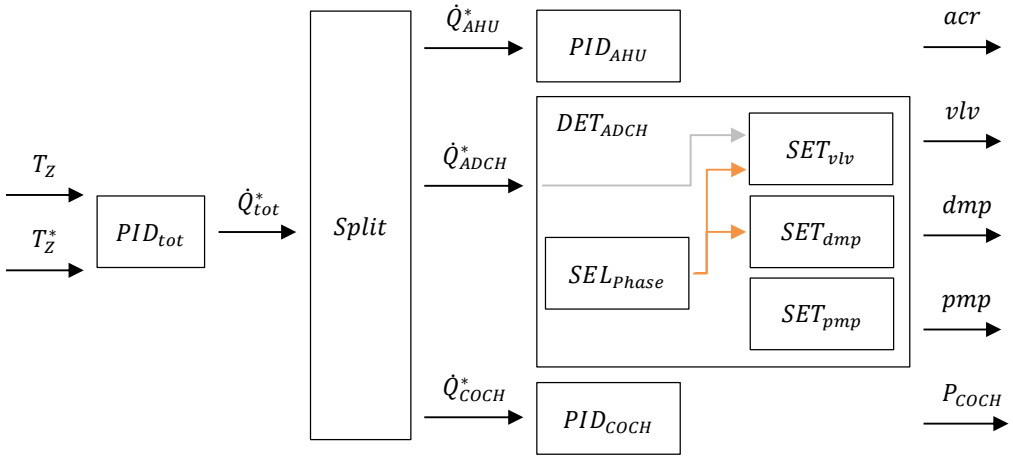

Figure 3: Schematic illustration of the control concept, set points with *

The second obd-approach (optimisation-based) switches the phase number based on predefined points in time. The phase also starts at phase 1 and changes from 1 to 2 at time t_{12}. For the subsequent switching times, the variables t_{23} and t_{34} were also introduced. The optimal times were determined for each set of configuration parameters such that the total energy consumption is minimal. To obtain the total energy consumption for a parameter set, the entire model was exported as an fmu-model and simulated in Python with fmpy. The optimal energy consumption under variation of the time variables was achieved by coupling the fmu-model with the solver scipy-optimize-minimize, using the Powell method.

2.5. Parameter variation

To verify the third central hypothesis of this work, the parameters that decisively influence the cooling performance of the façade-integrated adsorption cooling are varied and optimised in addition to the operating strategy. From the set of system parameters, 6 parameters were identified and reduced to 2 parameters. The parameters include the position of the adsorber or_{ads} and condenser or_{con}, the facade area ratios of adsorber f_{ads} and condenser f_{con}, the floor area ratio of the evaporator f_{eva} and the azimuthal building orientation γ_{build}.

The façade area ratios f_{ads}, f_{con} are limited by the defined areas of the windows and the total area. Each orientation has one window with the area ratio $f_{win} = 0.25$. The sum condition must hold for each orientation: $f_{ads} + f_{con} + f_{win} + f_{wal} = 1$. The façade area of the lightweight wall type f_{wal} is adjusted so that the condition is fulfilled. The façade area ratios are proportional to the mass of zeolite and the heat exchange area of all three components. In this work the area ratios are set equal, $f_{ads} = f_{con} = f_{eva} = f$. This scales the cooling capacities and exchange areas together. However, this reduction in complexity prevents the identification of dominant cooling capacity limitations.

To consider a maximum angular range of the adsorber orientation γ_{ads}, the adsorber is always placed in the position $or_{ads} = 1$. The positions $or_j = \{1,2,3,4\}$ correspond to a south, west, north or east orientation, respectively, as long as the building is oriented towards the south $\gamma_{build} = 180°$. By varying the building orientation γ_{build}, the adsorber orientation γ_{ads} changes to the same extent. The condenser is always placed in position 3 since the modelling of the condenser does not yet include any interaction with solar irradiance and the north orientation is dominated by shadow.

In summary, this paper considers the system efficiency analysis with respect to the façade area ratio f and the adsorber orientation γ_{ads}.

To obtain comparable energy consumptions, the initial temperatures of the room, adsorber, condenser and evaporator were set to a fixed value ($T_Z = T_E = 24.3°C, T_A = 47.2°C, T_C = 25.7°C$). The initial value of the loading was chosen to satisfy the periodicity condition ($|x_{ads}(t = 0) - x_{ads}(t = 24h)| < 10^{-4}$). This condition was achieved by iteratively setting the final value of the loading to the initial value until it was satisfied. This periodicity condition was applied to both operating strategies individually.

3. Results & Discussion

3.1. Comparison of the operating strategy

To visualize the influence of the different operating strategies, the time trends in Figure 4 are used first. These show the operating phases, the adsorber loading and the current cooling capacity for both operating strategies. In this context, all area ratios are set to the value $f = 0.5$ and the building is oriented in south-southeast direction $\gamma_{ads} = 160°$ like the D1244.

The phase curve depicted in Figure 4 shows that by using the obd-strategy, desorption starts later, intercooling and the cooling phase start earlier. Along with the delayed start of desorption, there is no premature increase in loading as with the rbd-operating strategy. This increase in the desorption phase leads to opposite mass flows from the condenser to the adsorber and, as a result of its temperature increase, to lower cooling capacity. Flap

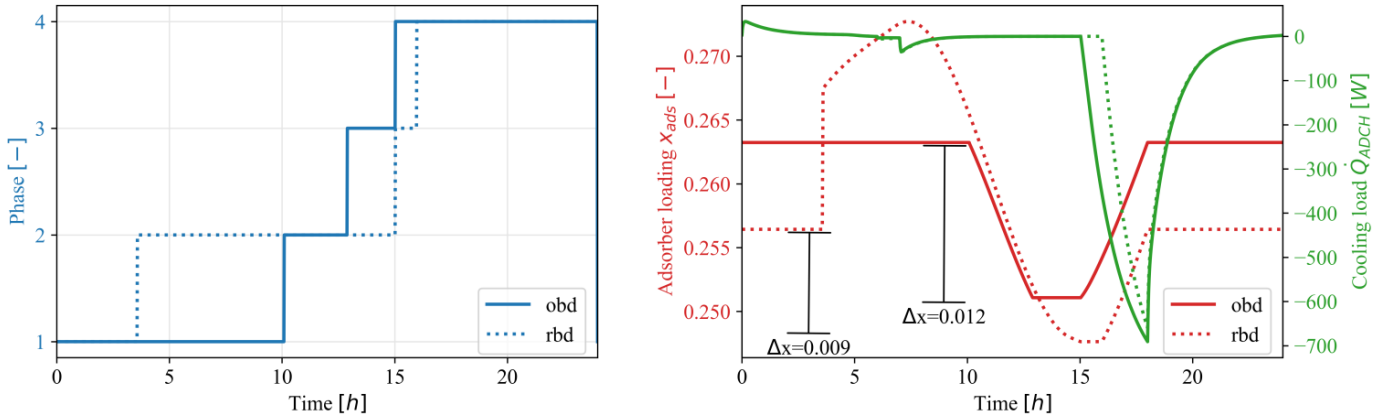

Figure 4: Time behaviour of the operating phases (left) and the adsorber loading x_{ads} and cooling capacity $\dot{Q}_{ADCH}$ (right) in comparison to both operating strategies

valves could be used to stop the backflow. The loading difference for the obd operating strategy is slightly larger, although the initial loading is larger. The cooling capacity drops earlier according to the earlier switching time t_{34} and reaches a higher cooling load as with the rbd-strategy. The slightly increased loading difference in combination with the avoidance of backflows and the earlier start of the cooling phase finally leads to a higher cooling energy and 5.6% lower total electricity consumption E_{tot}.

Next, the dependence of the total energy consumption E_{tot} on the building orientation and the operating strategy was investigated, cmp. Figure 5. As before, the area ratios were set to f=0.5.

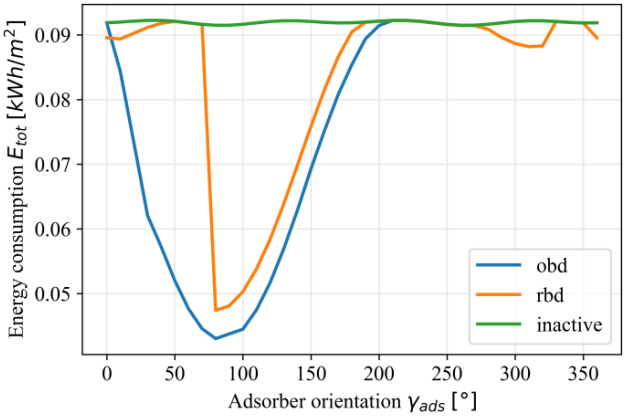

Figure 5: Total daily energy consumption E_{tot} versus adsorber orientation γ_{ads} with varying operating strategy.

The green curve results from an overall model with an inactive adsorption cooling system. In this case, the phase is kept constant at 1. This curve shows that the solar energy gains uniformly occur across all building orientations. This depends solely on the distribution of the windows across the building orientations. In comparison, the energy consumptions with active adsorption cooling system are consistently lower. The total energy consumption with rbd-operating strategy drops very sharply from a threshold orientation in the range of $\gamma_{ads} \in \{70°, 80°\}$. Prior to this threshold orientation, the switching condition from phase 4 to 1 holds at noon instead of in the morning on the following day due to a short and small increase in solar irradiation. As a result, the cooling phase, and the associated cooling power $\dot{Q}_{ADCH}$ are lower in this range, and the total power consumption is significantly higher. Compared to the rbd-operating strategy, the obd-operating strategy enables lower energy consumption in the predominant range. Most importantly, it enables efficient operation in the range below the threshold orientation. In the range of west orientation $\gamma_{ads} > 180°$, the rbd-operation strategy is slightly more suitable. Its curve shows a second smaller minimum. Due to an early switchover to phase 1 or 2 at noon, the loading is desorbed in the evening. As a result, the load unexpectedly increases in the morning and decreases in the evening, the loading lift is reversed. The obd-operating strategy is not able to perform a reverse loading lift due to the fixed switchovers and fixed initial phase. A slight adjustment by coupling the initial phase and phase development to the building

orientation could offer significant advantages for both operation strategy for western adsorber orientations.

3.2. Comparison of the system parameter

To eliminate the small fluctuation of the energy consumption when the adsorption cooling is inactive with the adsorber orientation, cmp. Figure 5 green line, the relative difference to the consumption with an active adsorption cooling system is considered. These relative energy consumption reductions are shown in Figure 6 for both operating strategies and for a variable facade area ratio f. The facade area ratio is varied up to a maximum value of $f_{max} = 0.75$.

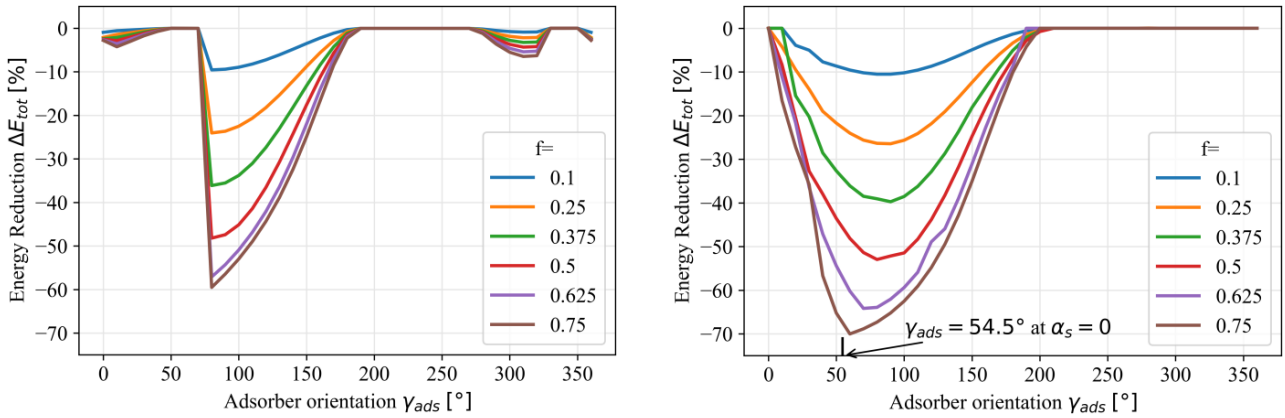

Figure 6: Energy savings by using facade-integrated adsorption cooling and by using the rbd-operating strategy (left) or obd-operating strategy compared to the azimuthal orientation of the adsorber γ_{ads} with variable facade area ratio f

The energy reduction curve is similar to that of the absolute total electricity consumption in Figure 5, since the reference value with inactive adsorption cooling systems is nearly constant. Accordingly, the energy savings applying the rbd-operating strategy reveals the same drop as in the previously discussed results. Now it is shown that this threshold orientation is the same for all area ratios. This is because the switching criterion depends only on the solar radiation. As Figure 7 (left) clarifies for obd-strategy, the reduction in consumption decreases proportionally with the facade area ratio up to a ratio of $f = 0.6$. With the increasing area ratios, the adsorbate quantity and the heat exchange areas increase, providing more cooling capacity. From an area ratio $f = 0.6$ the reduction decreases less and the optimum shifts to the solar azimuth at sunrise $\gamma_{ads} = 54.5°$. As Figure 8 reveals, the adsorption cooling system now takes over the complete cooling task. The compression cooling is reduced. A further saving is thus only possible if the desorption and thus the adsorption starts earlier. This angle change is also illustrated in Figure 7 (left). Figure 7 (right) shows the switching times for obd-strategy versus building orientation for all possible facade area ratios. In the range from the solar azimuth at sunrise to the south orientation $54.5° < \gamma_{ads} < 180°$ all curves cluster into three nearly distinct lines. These describe from bottom to top the

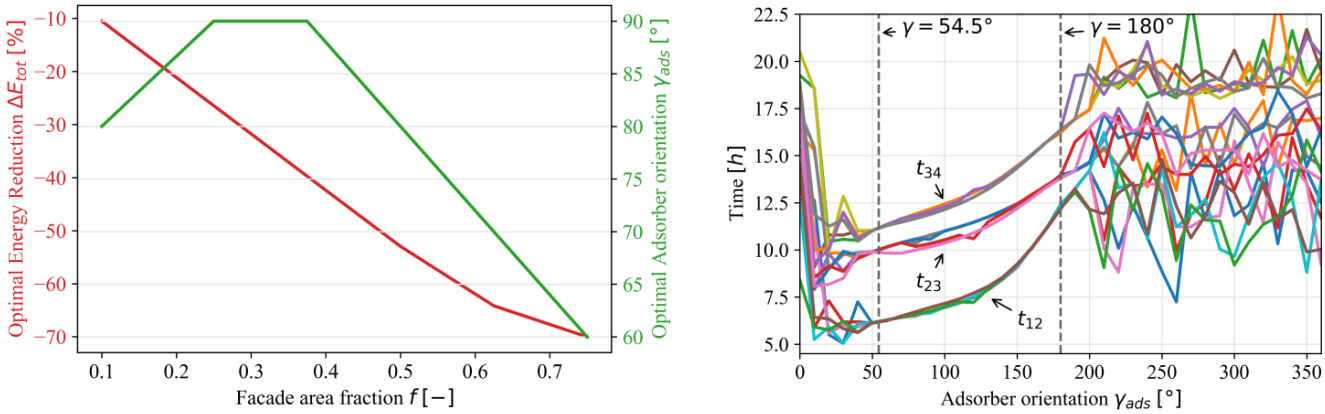

Figure 7: Left: Optimal energy reduction ΔE_{tot} and adsorber orientation γ_{ads} versus facade area ratio f, Right: Switching times between phases versus adsorber orientation γ_{ads} at all facade area ratios, both subfigures for obd-strategy

switching times t_{12}, t_{23}, t_{34} versus the adsorber orientation. In this range, the switching times are nearly independent of the facade area ratio. In the range $54.5° > \gamma_{ads} > 180°$ there is no unique clustering. In this range, the obd-operating strategy does not provide unique switching times. However, these uncertainties do not affect the curves of the energy reduction in Figure 6. It remains open whether this is the result of purely numerical or also physical reasons.

Figure 8 shows the time curves of the loading, the total cooling power $\dot{Q}_{tot}$, the cooling power by the compression cooling $\dot{Q}_{COCH}$ as well as that of the adsorption cooling $\dot{Q}_{ADCH}$, each for initial (init, $f = 0.5, \gamma_{ads} = 160°$) and the optimal parameter set (opti, $f = 0.75, \gamma_{ads} = 60°$).

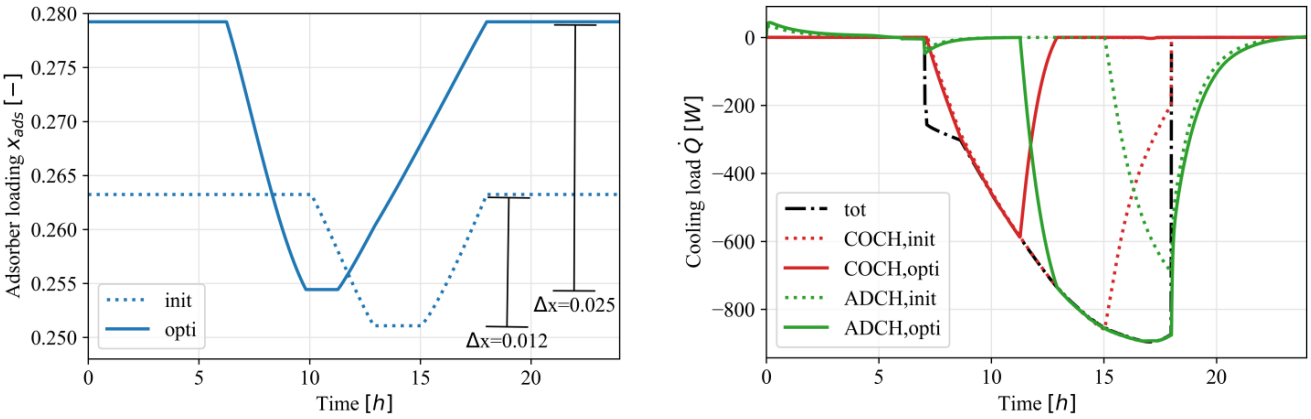

Figure 8: Time curves of the operating phases (left) and of the adsorber loading x_{ads} and cooling capacities $\dot{Q}$ (right) with obd-operating strategy in comparison between the initial and optimal parameter set.

The loading stroke with an optimum parameter set is more than twice as large as in the comparison case. The cooling demand at the beginning of the working time is covered by the ventilation if the outside temperature is lower than the upper room temperature limit at $24°C$. Thereafter, the adsorption and compression cooling system are added. In the optimum case, the cooling load is taken over by the adsorption cooling system at about 1 p.m., about 5 hours earlier. The course of the cooling capacity by the compression cooling system is shifted to the morning hours. Accordingly, a second, perhaps small adsorption cooling system in a western orientation would be suitable to cool the system completely emission-free.

4. Conclusion

In this paper, a new optimization-based operation strategy and an efficiency analysis on a novel façade-integrated adsorption cooling system were presented. The main contributions of this work are as follows:

By applying the obd-operation strategy, energetically more optimal switching times can be found compared to the rbd-operation strategy. By applying optimal system parameters and the obd-strategy, power consumption can be reduced by additional 10% compared to the rbd-strategy. This confirms the first hypothesis of this work. Applying the obd-strategy shows a distinct minimum of total electricity consumption with building orientation and area ratios. This confirms the second central hypothesis. In comparison, the rbd-operating strategy can only be applied up to a certain threshold orientation, which was attributed to a switching condition. In contrast, it allows for a small second minimum of energy reduction in the western orientation region. This reveals that the coupling of the switching criteria to the adsorber orientation is indispensable. The time behaviour of the solar energy gains is defined by the area ratios of the windows and the dimensions of the building. Accordingly, the location of the optimal parameter configuration (building orientation, component area ratio) is coupled to it. However, under the assumptions of this work, which among other things provides for a uniform distribution of the windows and certain facade dimensions, the optimal orientation of the adsorber is $\gamma_{ads} = 60°$, and the optimal facade area ratio is $f = 0.75$. In this case, the total electricity consumption can be reduced by 70% through the novel facade-integrated adsorption cooling.

Future work should further develop the obd-operation strategy so that the phase selection is coupled to the adsorber orientation and thus it can optimally operate the system in both orientations. Accordingly, it must be

investigated to what extent the additional compression cooling machine can be dispensed with by using a second adsorber-condenser system in the opposite orientation. In this case, the coordination between the components becomes much more challenging as the interconnection possibilities between the components increase. This can make the application of model-predictive control concepts necessary. Here, it must be investigated to what extent the loading is suitable as a unique and continuous manipulated variable for each adsorber system. In this work all area ratios were kept equal. To overcome this condition should be part of future work. Thereby, threshold values for heat transfer barriers could be investigated and considered in the design.

5. Acknowledgements

This work was carried out within the Collaborative Research Centre CRC1244 ‘Adaptive skins and structures for the built environment of tomorrow’ subproject C06, which are funded by the German Research Foundation under the Project-ID 279064222.

6. References

Almasri, R.A., Abu-Hamdeh, N.H., Esmaeil, K.K., Suyambazhahan, S., 2022. Thermal solar sorption cooling systems - A review of principle, technology, and applications. Alexandria Engineering Journal 61, 367–402. https://doi.org/10.1016/j.aej.2021.06.005

Blandini, L., Haase, W., Weidner, S., Böhm, M., Burghardt, T., Roth, D., Sawodny, O., Sobek, W., 2022. D1244: Design and Construction of the First Adaptive High-Rise Experimental Building. Frontiers in Built Environment 8.

Boeckmann, O., Schaefer, M., 2021. Modellierung und Simulation eines fassadenintegrierten Adsorptionssystems zur solaren Gebäudekühlung. DECHEMA Thermodynamik Kolloquium, Chemnitz

Curcija, C., Vidanovic, S., Hart, R., Jonsson, J., Powles, R., 2018. WINDOW Technical Documentation 220.

DIN V 18599-10:2018-09, Energetische Bewertung von Gebäuden_- Berechnung des Nutz-, End- und Primärenergiebedarfs für Heizung, Kühlung, Lüftung, Trinkwarmwasser und Beleuchtung-Teil 10: Nutzungsrandbedingungen, Klimadaten, n.d.. Beuth Verlag GmbH. https://doi.org/10.31030/2874436

Heidingsfeld, J.L., Boeckmann, O., Schaefer, M., Böhm, M., Sawodny, O., 2022. Low Order Hybrid Model for Control Design. CCTA Conference, Trieste

Jorissen, F., Reynders, G., Baetens, R., Picard, D., Saelens, D., Helsen, L., 2018. Implementation and verification of the IDEAS building energy simulation library. Journal of Building Performance Simulation 11, 669–688. https://doi.org/10.1080/19401493.2018.1428361

Müller, D., Lauster, M., Constantin, A., Fuchs, M., Remmen, P., n.d. AIXLIB – AN OPEN-SOURCE MODELICA LIBRARY WITHIN THE IEA-EBC ANNEX 60 FRAMEWORK 8.

Nytsch-Geusen, C., Huber, J., Ljubijankic, M., Rädler, J., 2013. Modelica BuildingSystems − eine Modellbibliothek zur Simulation komplexer energietechnischer Gebäudesysteme. Bauphysik 35, 21–29. https://doi.org/10.1002/bapi.201310045

Prieto, A., Knaack, U., Auer, T., Klein, T., 2017. Solar coolfacades: Framework for the integration of solar cooling technologies in the building envelope. Energy 137, 353–368. https://doi.org/10.1016/j.energy.2017.04.141

Settino, J., Sant, T., Micallef, C., Farrugia, M., Spiteri Staines, C., Licari, J., Micallef, A., 2018. Overview of solar technologies for electricity, heating and cooling production. Renewable and Sustainable Energy Reviews 90, 892–909. https://doi.org/10.1016/j.rser.2018.03.112

UN 2021 Status Report, United Nations Environment Programme (2021) 2021 Global Status Report for Buildings and Construction: Towards a Zero-emissions, Efficient and Resilient Buildings and Construction Sector – Full report. Available at: https://www.unep.org/resources/report/2021-global-status-report-buildings-and-construction (Accessed: 8 September 2022)

Wetter, M., Zuo, W., Nouidui, T.S., Pang, X., 2014. Modelica Buildings library. Journal of Building Performance Simulation 7, 253–270. https://doi.org/10.1080/19401493.2013.765506

H. PV and PVT Systems for Buildings and Industry

Decarbonizing Heating Supply Systems in Existing Single-family Houses Through PVT - Heat Pump Systems

Bharat Chhugani[1], Peter Pärisch[1], Federico Giovannetti[1]

[1] Institute for Solar Energy Research Hamelin (ISFH), Emmerthal (Germany)

Abstract

Photovoltaic - Thermal (PVT) collectors are a silent, invisible and almost everywhere available heat source for heat pumps to decarbonize the existing building stock. The ongoing research project investigates PVT - assisted heat pump systems in the building sector, aiming to increase market awareness of this technology. The paper presents the simulative comparison of different heat supply systems for an existing state single-family house. The results show that the PVT - heat pump achieves higher efficiency than an air-source heat pump. With 30 m² PVT provided with an optimized (air) heat exchanger, the heat pump achieves ≈14 % higher efficiency than the air source heat pump (seasonal performance factor 3.59 PVT - heat pump to 3.10 air source heat pump). PVT (30 m²) as a sole heat source for the heat pump system reduces the CO_2 emissions up to 49 % compared to a condensing gas boiler and 25 % compared to air-source heat pumps. Combining PVT with borehole heat exchanger (BHE) with brine-water heat pump systems reduces 54 % CO_2 emissions compared to the gas boiler while simultaneously enabling smaller dimensioning of BHE with summer regeneration with PVT heat. Hence the results confirm the good performance of the PVT as a single or additional heat source for heat pumps. The paper also shows that PVT's design and performance are more important if it works as a sole heat source than if it assists a borehole heat exchanger.

Keywords: Photovoltaic-Thermal (PVT) collector, TRNSYS Simulation, Monitoring, heat pump system

1. Introduction

The heat supply to buildings constitutes about 40 % of the total energy demand in Germany. Around half the energy for heat generation in Germany is currently provided by natural gas (BDH 2021). According to BDH (Federation of German Heating Industry), around half of all heating systems in Germany are outdated (BDH 2021). Not only with a view to the climate goals and the necessary reduction of CO_2 emissions but the current political situation between Ukraine and Russia and a shortage of gas supplies to Europe strongly encourage us to accelerate more into renewable energy, especially in the heating sector. Heat pump (HP) systems offer a promising opportunity to replace conventional fossil fuel-based heating systems for space heating and domestic hot water (oil and gas boilers). Besides renovating the buildings to achieve low supply temperatures, searching for a suitable heat source is challenging. Photovoltaic-thermal (PVT) collectors can be used as a direct or additional heat source for brine-water heat pumps. PVT collectors combine a solar thermal collector and a photovoltaic module in a single component, simultaneously generating power and heat from the same area. They are silent, invisible, and feasible almost everywhere. Therefore, PVT can be a crucial technology for future energy supply systems by maximizing the fraction of local renewable energy source utilization and making a decisive contribution to the realization of the climate-neutral building stock.

The ongoing project “integraTE” investigates PVT collectors with heat pumps and tries to increase market awareness of this technically attractive energy supply system for the building sector. PVT collectors can be used as a single heat source for the heat pump or as an additional heat source with ground heat exchangers, like borehole heat exchangers (BHE). In the project, ten demonstration systems are part of ongoing monitoring, as presented in detail in Helmling et al. (2022). Among all the systems, five systems use PVT collectors as a single heat source for the heat pump, and the remaining five systems combine the PVT with at least one additional heat source, such as a borehole heat exchanger (BHE). Apart from the monitoring, the project aims to carry out detailed simulative investigations of different energy supply systems. The first simulation study

© 2022. The Authors. Published by International Solar Energy Society
Selection and/or peer review under responsibility of Scientific Committee
doi:10.18086/eurosun.2022.07.01 Available at http://proceedings.ises.org

compares various energy supply systems for a new single-family with a PVT - heat pump, and the detailed results are presented in Chhugani et al. (2023).

This paper investigates different energy supply concepts for an existing single-family house for the German climate and mainly focuses on PVT-assisted heat pump systems. The simulation study compares two PVT systems and six reference systems. As for the PVT- heat pump systems, PVT collectors are used as a single and additional heat source for heat pumps. All simulated systems are listed below and shown in Fig. 1.

- PVT - heat pump systems
    1. PVT - heat pump
    2. PVT - borehole heat exchanger (BHE) - heat pump
- Reference heat pump systems
    3. Air source heat pump
    4. PV - air source heat pump
    5. Borehole heat exchanger - heat pump
    6. PV - borehole heat exchanger - heat pump
- Gas heating systems
    7. Gas condensing boiler
    8. Solar thermal collectors - gas condensing boiler

The contribution also includes a description of different boundary conditions, system components, and control strategies of the simulations. The simulations are performed using the software TRNSYS v17.01.0028. Two different PVTs collectors (uncovered or WISC: Wind and Infrared Sensitive Collector) are analyzed regarding system performance with heat pumps for sensitivity analysis. The system evaluation is carried out based on two assessment criteria: CO_2 emissions and seasonal performance factors.

PVT systems

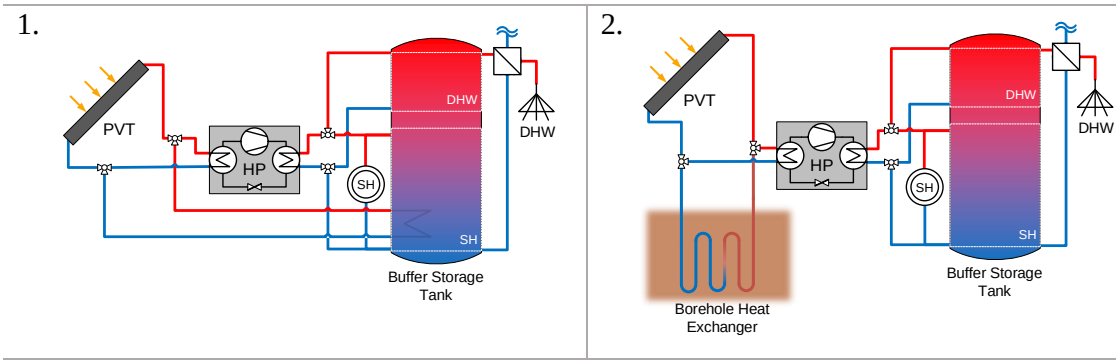

Reference systems

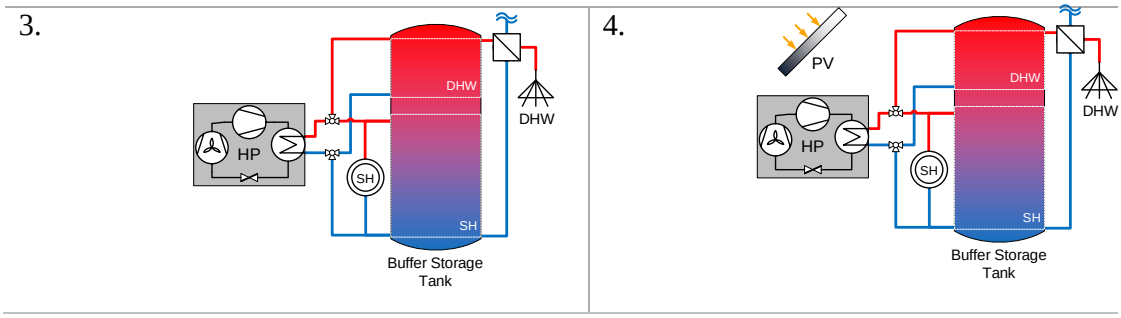

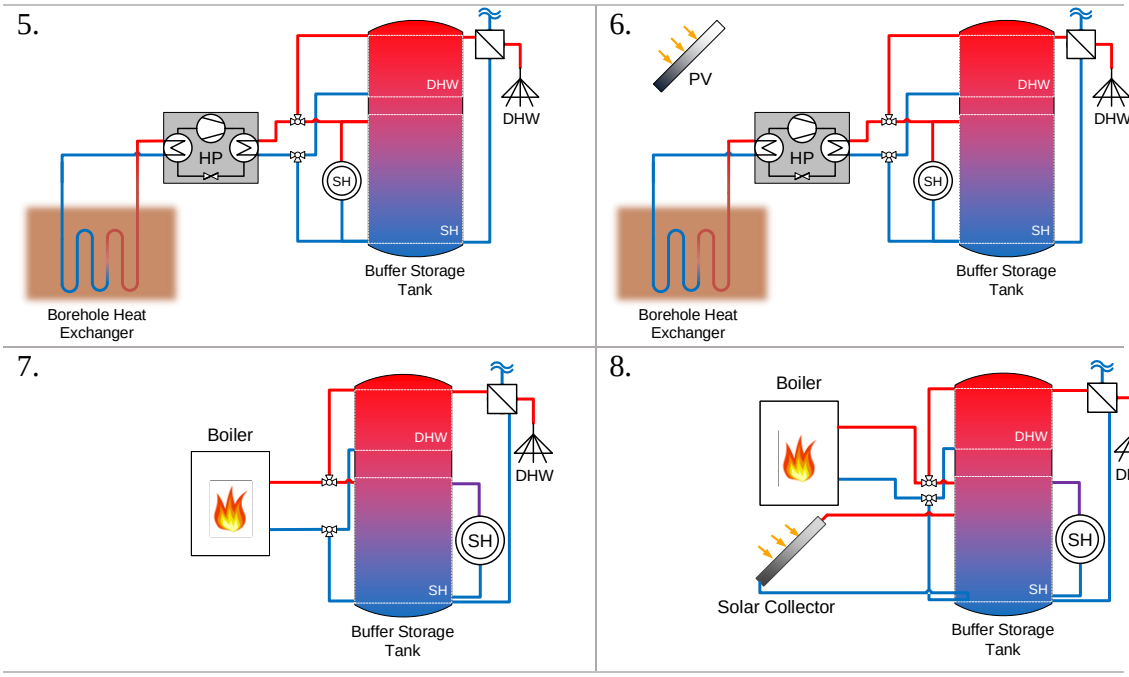

Fig. 1: Simulated PVT- heat pump and reference systems

2. Simulation boundary conditions and methodology

2.1 Building

The reference IEA SHC Task 44 single-family house (SFH100) has been chosen for the simulation, which corresponds to an existing building (built or renovated 25 years ago) for European Climate. In Task 44, the building heating demand was investigated for the reference climate Strasbourg, with a heating demand of 100.2 kWh/(m²·a) and all boundary conditions of the building described in Dott et al. (2013). In the project "integraTE", the heating demand of this building is investigated for the German location Wuerzburg with the Meteonorm one-minute weather data. It is approx. 108 kWh/m²a, which is supplied with radiators, and the heating characteristic curve has a maximum supply temperature of 55 °C

2.2 Household electricity

The photovoltaic-thermal collectors provide electricity and heat; therefore, the household electricity profile has been defined and presented. For this purpose, the (VDI-Richtlinie 4655:2021) electrical profile for an existing single-family house is used, with annual electricity consumption of ≈ 4039 kWh. The yearly electrical profile is shown in Fig 2.

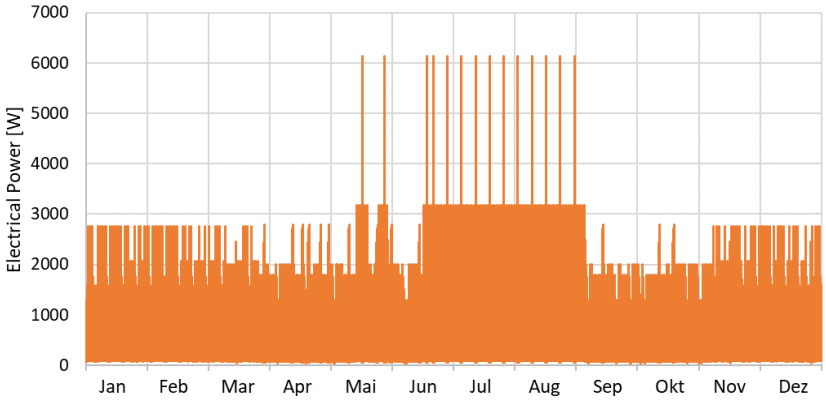

Fig 2: Household electricity demand of the existing SFH according to VDI 4655

2.3 Domestic hot water

The tap profile for domestic hot water (DHW) demand of the single-family house is derived from IEA SHC Task 44 (Haller et al. 2013). The energy demand of the DHW is approx. 5.8 kWh/d (15 kWh/m²a), with a total daily hot water demand of 145 l/d and the hot water tap at 45 °C without hot water circulation. The DHW profile is shown in Fig. 3. An instantaneous water heater efficiently delivers DHW to the building, which has a UA value according to (eq. 1).

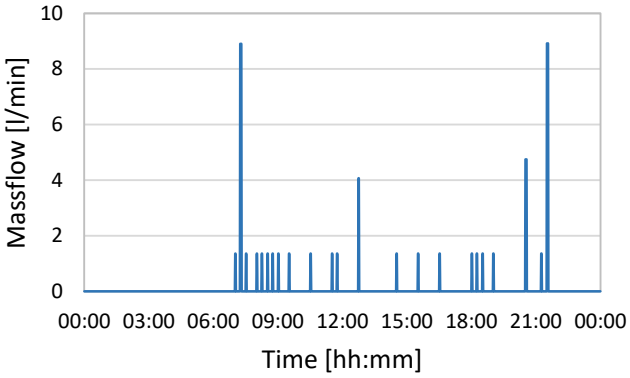

Fig. 3: Domestic hot water demand (DHW) of the building at 45°C

$$UA = -1{,}8\frac{W/K}{(kg/min)^2} \cdot \dot{m}_{sec}{}^2 + 240\frac{W/K}{kg/min} \cdot \dot{m}_{sec} + 600\frac{W}{K} \qquad \text{(eq. 1)}$$

2.4 Photovoltaic - Thermal (PVT) collectors

As mentioned before, two different market-available PVT collectors are used for the sensitivity analysis in the study. The first collector is an uncovered/WISC PVT collector with a finned air heat exchanger on the back side, developed explicitly for heat pump applications. The thermal parameters of the collector are determined using outdoor tests (Giovannetti et al. 2019) and compared to TRNSYS simulations, especially under frost conditions (Chhugani et al. 2020). The second PVT collector is a standard uncovered/WISC PVT collector without fins, whose parameters are taken from the Solar Keymark test certificate. Both collector parameters are shown in Tables 1 and 2.

For the simulation of the PVT collector in TRNSYS, type 203 has been used, which was explicitly developed for uncovered PVT collector simulations (Stegmann et al. 2011). This model combines two performance models, the thermal part of the model is based on (EN 12975-2:2006), and the empirical effective solar cell model defines the electrical side of the collector (PV module) by Wagner (2010). For the dynamic PVT simulations, collector parameters are required from performance tests and manufacture standard data sheets. Both characteristic models are interconnected for the calculation of correct PV cell temperature. The detailed PVT model is described in (Stegmann et al. 2011).

For the configuration of PVT to heat pump (in Fig. 1(1)), the PVT collector is used as the only heat source for the heat pump, and in summers if the PVT temperature is higher than the buffer storage tank, then PVT heat is used directly to storage tank. Both PVTs in simulations are regularly defrosted to account for model uncertainties below 0 °C as explained in (Chhugani et al. 2020). In the PVT with borehole heat exchanger (BHE) to heat pumps (in Fig. 1(2)) configuration, PVT is only used if the collector temperature is 5K higher than BHE, and on sunny days BHE is regenerated with PVT heat when the heat pump is not running, and PVT temperature remains higher than BHE.

Tab 1: Thermal PVT parameter sets (MPP-related)

	η_0 [-]	c_1 [W/(m²·K)]	c_3 [J/(m³·K)]	c_4 [-]	c_5 [kJ/(m²·K)]	c_6 [s/m]
PVT (WISC) with fins	0.532	19.08	3.69	0.434	26.05	0.067
Standard PVT (WISC)	0.570	11.02	4.80	0.620	42.20	0.011

Tab 2: Electrical PV parameter at Standard Test Conditions (STC)

	P_{mpp} [Wp]	A [m²]	η_{el} [-]	V_{mpp} [V]	I_{mpp} [A]	V_{oc} [V]	I_{sc} [A]	TC [%/K]
PVT (WISC) with fins	340	30	17.5	37.6	9.05	48.0	9.45	-0.39
Standard PVT (WISC)	300	30	18.3	32.6	9.19	39.9	9.77	-0.39

2.5 Brine water heat pump

For the PVT to heat pump (HP) simulation, a modulating brine-to-water heat pump with a thermal capacity of 12.46 kW and a COP of 4.13 at B0/W35 has been used. This HP is suitable for integration with PVT collectors as the only heat source and can operate down to a minimum inlet temperature of -15 °C on the evaporator side. Fig. 4 shows the characteristic curve of the heat pump. If the temperature falls below the minimum source inlet temperature, the integrated auxiliary heater (12 kW) in the heat pump takes over the charging of the storage tank as a bivalent-alternative operation. For compressor protection, as in actual heat pump operation, the heat pump has a minimal pause time of 20 min.

The TRNSYS type 401 is used for heat pump simulations developed by (Afjei and Wetter M. 1997). This type can simulate different heat pumps, such as air-source and brine-water. The heat pump model is based on biquadratic polynomials for condenser power and compressor power calculated from the heat pump characteristic data obtained from experiments, as shown in Fig. 4(b) for the heat pump used in this simulation. The modulation is modeled with three instances of type 401 in parallel and linear interpolation, as proposed by (Hüsing und Pärisch 2020).

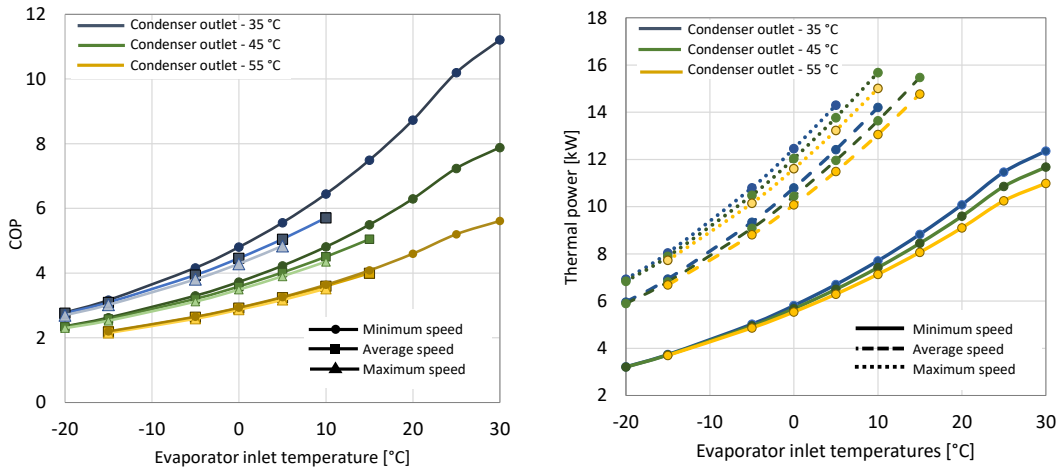

Fig. 4: Characteristics data of the heat pump, (a) coefficient of performance (b) thermal power, at different evaporator inlet temperatures (x-axis) and condenser outlet temperatures (blue 35 °C, green 45 °C, yellow 55 °C) for three different compressor speeds

2.6 Borehole heat exchanger (BHE)

Besides, BHE as a single heat source for heat pumps, a combination of BHE and PVT with heat pumps is also simulated and investigated. They are connected in parallel, and the higher temperature source is preferred when the HP is running. The reason for these simulations is the high efficiency and the opportunity to shorten the required length of BHE by regeneration of the ground in the summer through PVT. For the simulation, a 120 m deep BHE was simulated with 30 m² of PVT and 180 m BHE as the only heat source. TRNSYS Type 451 was validated through the experimental system at ISFH for TRNSYS simulation (Pärisch et al. 2015). The simulation with a borehole heat exchanger runs for two years, and the second year's simulated result is evaluated and presented here in the paper.

2.7 Air source heat pump

The air-source heat pump of the reference system has a thermal heating capacity of 11.2 kW and a COP of 3.5 at A2/W35, including defrosting losses. TRNSYS type 401 (Afjei und Wetter M. 1997) is also used for the air source heat pump simulations with the built-in COP-reduction for defrosting. However, the air-source heat

pump modeling considers other electrical stand-by losses and thermal losses due to the frosting processes of the air heat exchanger outdoor unit. These losses are simplified in type 401 by a modified Gauss function representing the percentage reduction in COP as a function of the outdoor temperature, and the method is explained in Afjei and Wetter M. (1997). The COP reduction function of the simulated heat pump in this paper is derived according to experimental investigations from ISFH. This COP reduction function at different relative humidity levels is presented in Chhugani et al. (2023). Moreover, as in a real system, de-icing can occur every 30 to 60 minutes on colder winter days; at that time, the heat pump can no longer supply energy to the building, and then the electric rod often starts; this effect cannot be simulated with type 401.

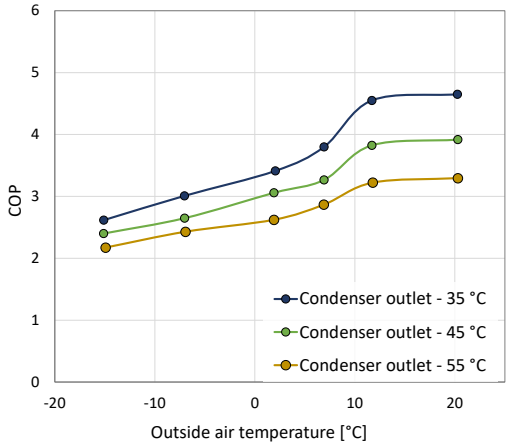

Fig. 5: Air source heat pump coefficient of performance for different air temperatures (x-axis) and condenser outlet temperatures (35 °C, 45 °C, 55 °C) with defrosting losses

2.8 Buffer storage tank

The building is simulated with a buffer tank of 560 liters on the sink side of the heat pump. Three immersion temperature sensors are used for the controller. The upper temperature (relative height 0.9) sensor records the temperature of the standby section for domestic hot water demand; the middle-temperature sensor (relative height 0.5) for the space heating. Furthermore, there is a solar part for direct solar gains in the summer and defrosting in the winter (rel. height 0.2). For the dynamic simulation of the thermal buffer storage tank, stratified fluid storage tank TRNSYS Type 340 has been used (Drück 2006).

The simulation is carried out with a “PV-based control strategy”, where the storage tank is charged with two different temperature setpoints in this strategy. If the total irradiance on the collector plane is higher than 500 W/m², the heat pump heats the domestic hot water zone to a maximum temperature of 60 °C with a hysteresis of -3 K. Afterwards, if irradiance is still higher than 500 W/m², the bottom part of the storage tank for the space heating is charged. This bottom layer is heated up 10 K higher than the heating characteristic for the SFH100, according to (Dott et al., 2013) with -3 K hysteresis. And when the irradiance drops below 500 W/m², the heat pump heats the domestic hot water zone at a maximum of 55 °C with a -5 K hysteresis. The space heating zone is charged based on the outside temperature according to the heating characteristic curve for the SFH100 with -3 K hysteresis with a maximum temperature of 55 °C at -14 °C.

2.9 Condensing gas boiler

The gas boiler is a classic condensing modulating boiler with a nominal heating power of 25 kW and water content of 7.3 liters. The boiler's efficiency at nominal load is 96.59 % based on a higher heating value. The boiler is simulated with the Type 204 developed at ISFH and extensively presented in (Glembin and Rockendorf 2010).

2.10 Solar collectors

The next reference system is a solar combi system equipped with the same gas condensing boiler as explained above and an additional 15 m² solar thermal system. The system combines a 1050 l buffer storage tank to use high solar potential. The parameters of the solar flat plate collector are shown in Table 3.

Tab 3: Efficiency parameters of the solar flat plate collector used for the reference system (Solar Keymark Test)

	η_0 [-]	a1 [W/(m²K)]	a2 [W/(m²K²)]
Flat plate solar collector	0.81	3.757	0.014

The secondary pump (between the heat exchanger and storage tank) switches on when the heat exchanger input temperature on the primary side exceeds the lower storage tank temperature by 7 K. The operating mode of the pumps is low-flow with 20 kg/(m²·h). The secondary pump is switched off when the difference falls below 5 K.

2.11 Key performance indicators (KPIs)

The heat supply systems presented in the paper are evaluated and analyzed based on different key performance indicators (KPIs). Two categories characterize these KPIs; 1) Environmental indicators and 2) Energy-related indicators.

- Environmental indicator

The CO_2 emissions of all the systems are calculated as the sum of the energy consumption values (gas or electricity) by the respective energy supply system, each multiplied by the corresponding emission factors according to the German Building Energy Act (GEG). The CO_2 emission factors for the two energy sources, natural gas and electricity according to GEG, are given below and used in the calculation with equation 2.

$$CO_{2,Emissions} = Final\ energy\ consumption\ (Gas/Electricity) \cdot x_{CO_2} \quad \text{(eq. 2)}$$

x_{CO_2}: CO_2- Emission factors (x_{CO_2}) in kg CO_2-Equiv. /kWh
Natural gas: 0.24 kg/kWh,
Electricity: 0.56 kg/kWh (electricity taken from Grid)
Electricity: 0.0 kg/kWh (generated by PV/PVT panels and consumed by the system)

- Energy-related indicators

In order to analyze the performance of the systems, two different seasonal performance factors SPF_{bSt} and $SPF_{bSt}^{(Grid)}$ are used and explained in equations 3 to 6 for different systems. The performance factors have been adjusted according to the individual system, but reference is taken from Task 60 and Task 44, as explained in (Malenković et al. 2012; Zenhäusern et al. 2020). Although the system boundary "before storage" SPF_{bSt} gives the better results and doesn't consider the overall system losses (Pärisch et al. 2013); it is also taken for our simulations because it allows comparison to the field tests performed by Fraunhofer ISE, similarly explained in (Helmling et al. 2022). The different heat pump systems are presented with their respective square views (Fig. 6 and Fig. 7) for simplification.

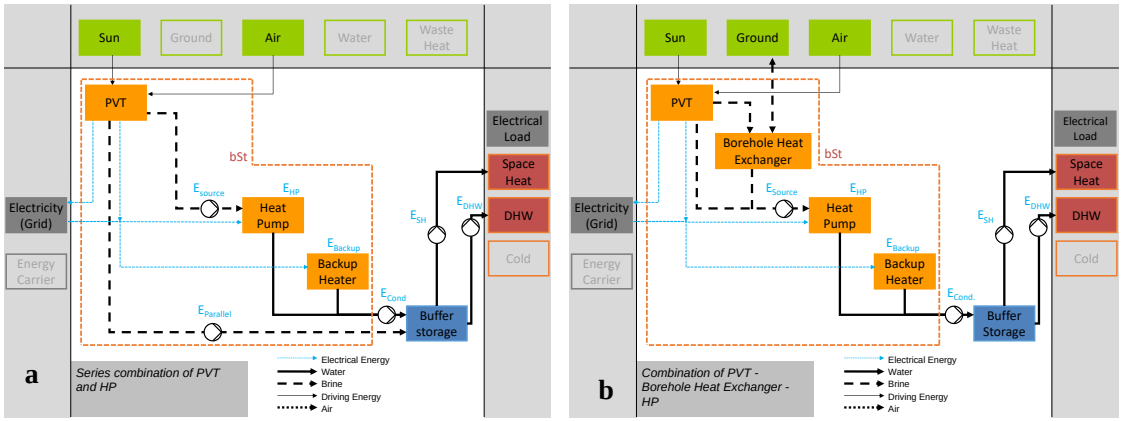

Fig. 6: Square-views of different heat pump systems (a) PVT - heat pump (b) PVT - BHE - heat pump for boundary bSt (before storage in dashed line)

$$SPF_{bSt} = \frac{\int(\dot{Q}_{HP} + \dot{Q}_{Backup} + \dot{Q}_{PVT,parallel})\,dt}{\int(\dot{E}_{HP} + \dot{E}_{Backup} + \dot{E}_{Pumps})\,dt} \quad \text{(eq. 3)}$$

$$SPF_{bSt}^{(Grid)} = \frac{\int(\dot{Q}_{HP} + \dot{Q}_{Backup} + \dot{Q}_{PVT,parallel})\,dt}{\int_{>0}(\dot{E}_{HP} + \dot{E}_{Backup} + \dot{E}_{Pumps} - \dot{E}_{PVT_el_Self})\,dt} \quad \text{(eq. 4)}$$

For the PVT - heat pump system in Fig. 6(a), SPF_{bSt} is the ratio of the heat quantities supplied to the buffer storage by the heat pump ($\dot{Q}_{HP}$), the auxiliary heating ($\dot{Q}_{Backup}$) and the PVT direct charging as well as defrosting ($\dot{Q}_{PVT,parallel}$) divided by the electrical energy consumed within this system boundary, and explained in eq. 3. $\dot{E}_{HP}$ is the electrical energy of the heat pump, $\dot{E}_{Pumps}$ is the pump energy of source pumps, and for PVT direct charging/defrosting pump. Besides, $\dot{E}_{Backup}$ is the electrical energy of the auxiliary heater.

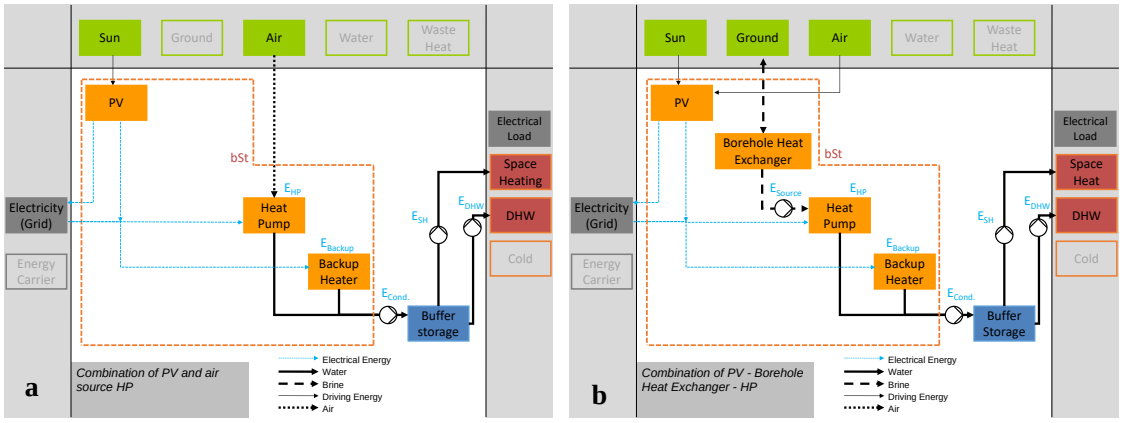

Fig. 7: Square-views of different heat pump systems (a) PV - Air source heat pump (b) PV - BHE - heat pump for boundary bSt (before storage in dashed line)

SPF_{bSt} for rest of the heat pump systems for Fig. 6 (b) and Fig. 7(a,b) is calculated using eq. 5, which considers energy supplied by the heat pump ($\dot{Q}_{HP}$) and the auxiliary heating ($\dot{Q}_{Backup}$) to the buffer storage and devided by the electrical energy consumed within its system boundary.

On the other hand, $SPF_{bSt}^{(\mathrm{Grid})}$, which considers self-consumed PVT/PV electricity in the bSt boundary, is calculated using eq. 4 (for PVT - heat pump system in Fig. 6 (b)) and eq. 6 (for all the remaining heat pump systems). This means that the generated electrical power of PVT/PV is used simultaneously for the electrical consumption of the heating system (simulation time step = 1 min) without battery storage.

$$SPF_{bSt} = \frac{\int(\dot{Q}_{HP} + \dot{Q}_{Backup})\,dt}{\int(\dot{E}_{HP} + \dot{E}_{Backup} + \dot{E}_{Pumps})\,dt} \quad \text{(eq. 5)}$$

$$SPF_{bSt}^{(Grid)} = \frac{\int(\dot{Q}_{HP} + \dot{Q}_{Backup})\,dt}{\int_{>0}(\dot{E}_{HP} + \dot{E}_{Backup} + \dot{E}_{Pumps} - \dot{E}_{PVT/PV_el_Self})\,dt} \quad \text{(eq. 6)}$$

For the heat pump systems according to configurations 3 and 5 from Fig. 1, where there is no PV/PVT available then the $SPF_{bSt}^{(\mathrm{Grid})}$ is not calculated.

Additionally, in the $SPF_{bSt}^{(Grid)}$ factor, produced PVT/PV electricity is used for the heat pump system with the first priority, which increases self-consumption of PVT/PV electricity for the heat pump system hence the $SPF_{bSt}^{(Grid)}$ upsurges. However, in reality, household electricity should be given first priority because household electricity is more expensive than heat pump tariff. Many heat pump suppliers use this approach to make their

products attractive. In order to make things more transparent, two different electricity distribution priorities have been simulated and compared in this simulation study. In priority-A, the heat pump system benefits more from PVT/PV electricity regardless of household demand, and with priority-B, the benefit enormously depends on the household energy demand.

Priority-A:
1. Heat pump system
2. Household electricity
3. Grid feed-in

Priority-B:
1. Household electricity
2. Heat pump system
3. Grid feed-in

3. Results

Fig. 8 shows the seasonal performance factors (SPF) of the different simulated heat pump systems. The simulation result with Priority-A is shown in Fig. 8 (a), and that with Priority-B is illustrated in Fig. 8 (b).

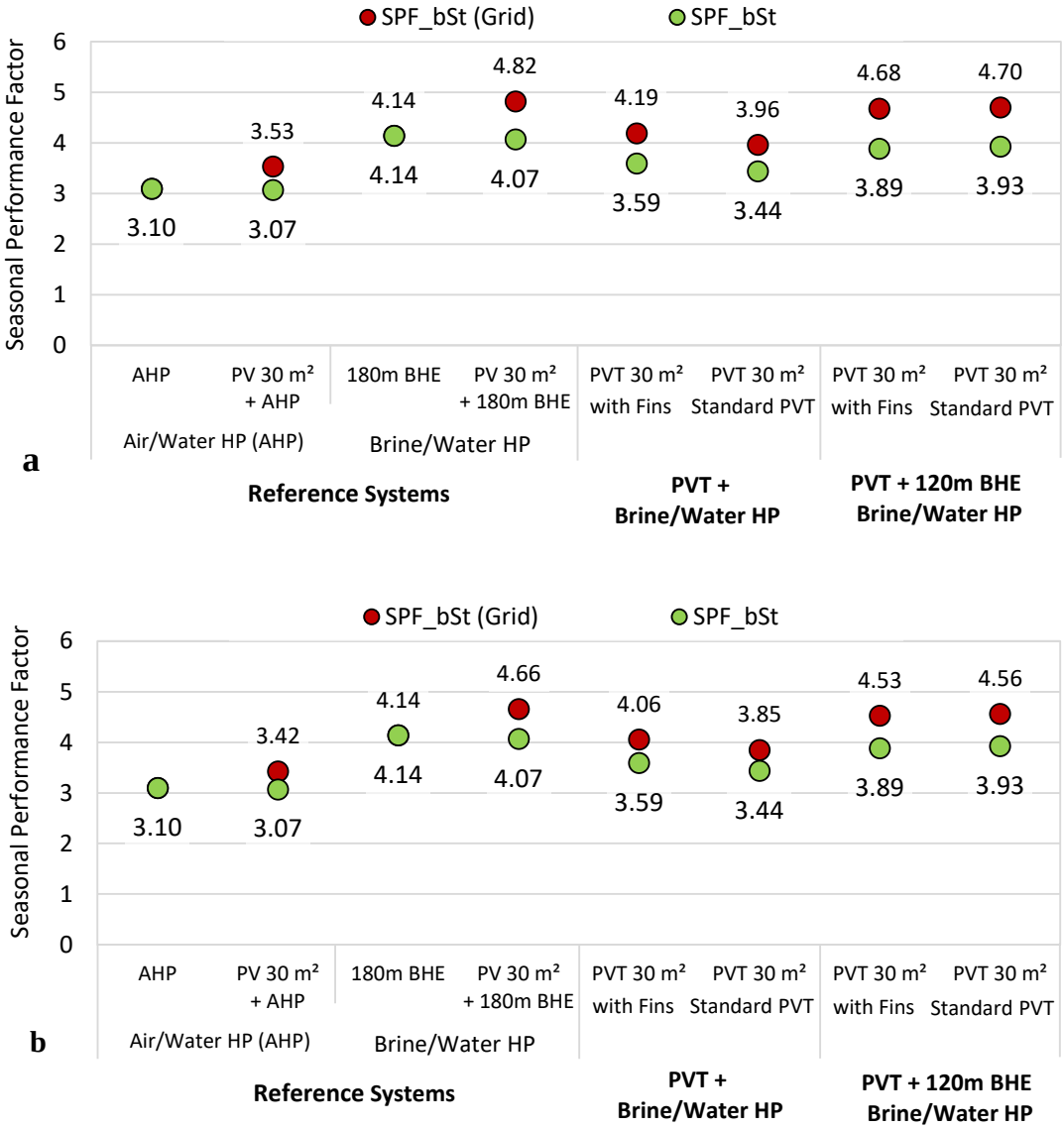

Fig. 8: SPF (Seasonal Performance Factor) of different systems (a) with Priority-A (heat pump as a first priority) (b) with Priority-B (household electricity as a first priority)

The difference between these two electricity priorities is visible in the $SPF_{bSt}^{(Grid)}$ factor. However, the discrepancy between these two priorities is very low, approx. 3% for any heat pump systems where PV/PVT electricity is available and directly used for the heating system. This indicates that produced PVT/PV can be used with any priorities. However, there is no battery storage here; if the battery storage is considered, the

results might be different because the stored electricity will be first used for household electricity, and the rest will only be used for heat pumps.

With priority-A, the direct comparison of the air-source HP with PVT to HP proves that systems PVT systems are more efficient. The PVT with fins (PVT 30 m²) achieves SPF_{bSt} of 3.59 against SPF_{bSt} of 3.10 for the air-source heat pump. The same 30 m² PVT - heat pump system reaches $SPF_{bSt}^{(Grid)}$ of 4.19 compared to $SPF_{bSt}^{(Grid)}$ of 3.53 with 30 m² of PV - air source heat pump. A heat pump with 180 m deep BHE achieves SPF_{bSt} of 4.14, and combining 30 m² of PV with the geothermal heat pump system boosts the $SPF_{bSt}^{(Grid)}$ to 4.8.

On the other hand, 30 m² PVT with 120 m deep BHE achieves $SPF_{bSt} \approx 3.9$ and $SPF_{bSt}^{(Grid)} \approx 4.7$ regardless of PVT collector. Hence, it is crucial to understand that the PVT combination with BHE opens the possibility of reducing BHE length (here reduced by ≈ 33 %, from 180 m to 120 m) without significantly affecting system efficiency. This aspect becomes economically more relevant for larger systems with two or more boreholes. On the other hand, ground source regeneration via PVT heat generally ensures a sustainable system operation, and it can compensate for planning uncertainty even for small BHE installations.

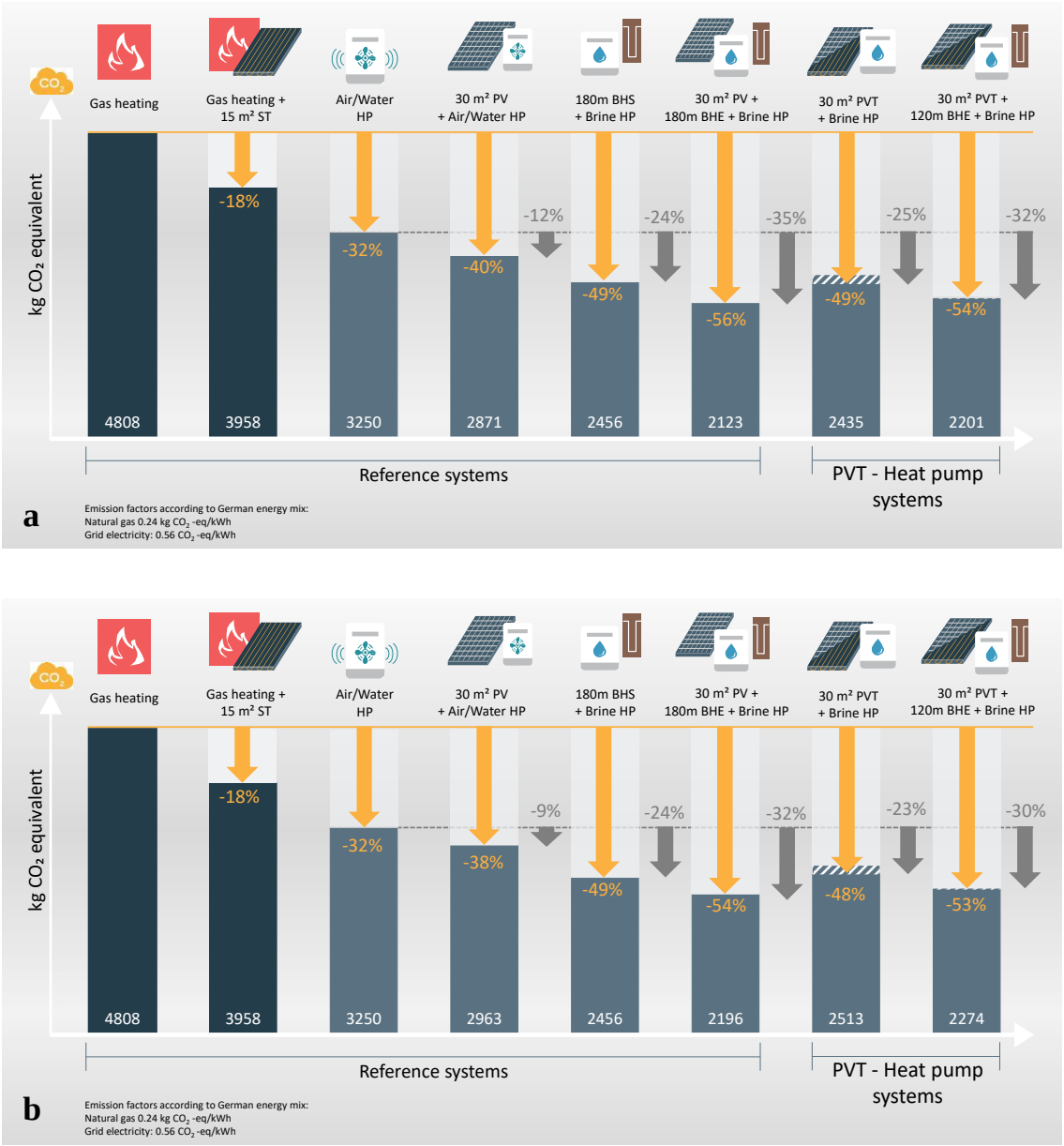

Fig. 9: CO_2 emissions of different simulated heat supply systems (a) with Priority-A (heat pump as a first priority) (b) with Priority-B (household electricity as a first priority)

Fig. 9 shows the CO_2 emissions with different energy supply systems with different electricity distribution priorities and calculated according to equations 2. The calculations of CO_2 emissions for the heat pump systems are carried out with a PV-based control strategy and based on electricity taken from the grid only for the heating system. As shown in Fig. 9, the highest amount of CO_2 emissions is produced with a condensing gas boiler with 4808 kg CO_2 equivalent, as expected. The solar thermal combi system (15 m²) reduces CO_2 emissions by 18 %. The heat pump systems show significant potential for CO_2 reduction compared to the gas boiler. An air-source HP reduces CO_2 emissions by 32 %, whereas PV with an air-source heat pump reduces emissions by 40 % with Priority-A and 38% with Priority-B. There is also substantial potential for CO_2 reduction by replacing the heating system with PVT - heat pump systems. PVT with fins (30 m²) with heat pump reaches CO_2 savings of 49 % (B: 48 %), same as 180 m BHE - heat pumps. In general, the PVT collector coupled with the HP system offers high CO_2 saving potential and represents an attractive alternative to the PV-air source or the geothermal heat pump.

On the other hand, 30 m² PVT with BHE (120m) with heat pumps are proven to be similarly efficient as 30 m² PV with BHE and heat pump. PVT with BHE combination reduces CO_2 emissions by 54 %, whereas PV wot BHE decreases CO_2 emissions by 56% (With Priority A). The hatched area shows the variation between the two PVT designs. Unlike the system used as an only heat source, the PVT design is not essential for the investigated combination of PVT and BHE.

4. Conclusion

The ongoing research project “integraTE” aims to comprehensively assess PVT- heat pump systems and increase market awareness of this new technology for the building energy supply sector. Detailed simulative investigation in the project generates information and allows understanding of the performance of this PVT - heat pump systems for existing German buildings.

The following points summarize the essential findings of the simulations:

- The seasonal performance factors (SPF_{bSt}) of PVT with fins as a single heat pump source is 14 % higher than that of PV to air source heat pump (both PVT and PV area 30 m² with priority-A)
- Considering PV electrical generation significantly enhances the system performance factor: with PV based control strategy without battery storage, the system reaches $SPF_{bSt}^{(Grid)}$ to 4.19 for 30 m² of PVT with fins for heat pump source with priority-A, whereas 30 m² PV - air source heat pump reaches only 3.53.
- PVT (30 m²) to heat pump system reduces the CO_2 emissions up to 49 %, dependent on the PVT design, compared to condensing gas boiler and 25 % CO_2 emissions reduction compared to air-source heat pumps.
- Combining PVT with borehole heat exchanger (BHE) in brine-water heat pump systems saves up to 54 % CO_2 emissions and reduces the required length of BHE from 180 to 120 meters, independently of the PVT design.

Summing up, direct coupling of PVT collectors with heat pumps as a single source (thermal side) achieves good system efficiency and represents a promising alternative to air source and geothermal heat pumps. PVT with boreholes (approx.≈33 % smaller) shows very good system efficiency, similar to PV with borehole systems. In the PVT-BHE configuration, PVT can favorably supply the heat to the heat pump directly or regenerate the ground source. Solar regeneration enables a sustainable operation of the BHE field by avoiding long-term cooling effects. It plays an important role, especially with larger installations, where smaller dimensioning of BHE is possible or required.

5. Acknowledgments

The presented work and results are part of the research project “integraTE - 03EGB0023” funded by the German Federal Ministry for Economic Affairs and Climate Action (BMWK) and supported by the Lower Saxony Ministry of Science and Culture. Furthermore. We thank our partners Fraunhofer ISE, IGTE of University Stuttgart and Solrico for the collaboration. Further, thanks go to blue energy systems (nD-Systeme), PA-ID Process, Architektur- und TGA-Planungsbüro Carsten Grobe, SunMaxx, Splus2, TripleSolar, and Consolar - Solare Energiesysteme for their financial support. The authors are grateful for the support and are responsible for the content of the publication.

6. References

Afjei, T.; Wetter M. (Hg.), 1997. Type 401, TRNSYS Compressor heat pump including frost and cycle losses, version 1.1. Available online at https://trnsys.de/download/en/ts_type_401_en.pdf.

BDH, 2021. BDH Federation of German Heating Industry, Efficient systems and renewable energies Technology and Energy Panel 2021.

Chhugani, B., Pärisch, P., Helmling, S., Giovannetti, F., 2023. Comparison of PVT - heat pump systems with reference systems for the energy supply of a single-family house. In: Solar Energy Advances 3, 100031. DOI: 10.1016/j.seja.2022.100031.

Chhugani, B., Pärisch, P., Kirchner, M., Littwin, M., Giovannetti, F., Lampe, C., 2020. Model Validation and Performance Assessment of Unglazed Photovoltaic-Thermal Collectors with Heat Pump Systems. EuroSun 2020: 13th International Conference on Solar Energy for Buildings and Industry. DOI: 10.18086/eurosun.2020.05.13.

EN 12975-2, 2006. DIN Deutsches Institut für Normung e.V., 2006. Thermische Solaranlagen und ihre Bauteile, Kollektoren, Teil 2: Prüfverfahren, Deutsche Fassung EN 12975-2:2006, Beuth Verlag, Berlin. Available online at https://www.beuth.de/de/norm/din-en-12975-2/83764314.

GEG. Gesetzes zur Vereinheitlichung des Energieeinsparrechts für Gebäude und Änderung weiterer Gesetze, Artikel 1, Gesetz zur Einsparung von Energie und zur Nutzung erneuerbarer Energien zur Wärme- und Kälteerzeugung in Gebäuden (Gebäudeenergiegesetz - GEG) Bundesgesetzblatt Jahrgang 2020 Teil I Nr. 37, ausgegeben am 13. August.2020.

Giovannetti, F., Lampe, C., Kirchner, M., Littwin, M., Asenbeck, S., Fischer, S., 2019. Experimental Investigations on Photovoltaic-Thermal Arrays Designed for the Use as Heat Pump SourceSantiago, Chile. DOI: 10.18086/swc.2019.05.03.

Glembin, J., Rockendorf, G., 2010. Abschlussbericht für das Teilprojekt des ISFH: Integration von Heizkesseln in Wärmeverbundsysteme mit großen Solaranlagen, Teil 2: Kesselmodell und Parametrierung, Förderkennzeichen: 0325958A.

Haller, M. Y., Dott, R., Ruschenburg, J., Ochs, F., Bony, J., 2013. The Reference Framework for System Simulations of the IEA SHC Task 44 / HPP Annex 38. Part B: Buildings and Space Heat Load, A technical report of subtask C Report C1 Part A.

Helmling, S., Langner, R., Geimer, K., 2022. Betriebsanalyse von 5 PVT-Wärmepumpensystemen auf Basis von Feldmessdaten über 12 Monate im Rahmen des Projektes integraTE. 32. Symposium Solarthermie Und Innovative Wärmesysteme, In Kloster Banz, Bad Staffelstein.

Hüsing, F., Pärisch, P., 2020. Modelling of Inverter Heat Pumps in TRNSYS. EuroSun2020: 13th International Conference on Solar Energy for Buildings and Industry. DOI: 10.18086/eurosun.2020.04.08.

Malenković, I., Pärisch, P., Eicher, S., Bony, J., Hartl, M., 2012. Definition of Main System Boundaries and Performance Figures for Reporting on SHP Systems, Deliverable B1, IEA SHC Task 44/ HPP Annex 38.

Pärisch, P., Mercker, O., Oberdorfer, P., Bertram, E., Tepe, R., Rockendorf, G., 2015. Short-term experiments with borehole heat exchangers and model validation in TRNSYS. In: Renewable Energy 74, 471-477. DOI: 10.1016/j.renene.2014.07.052.

Stegmann, M., Bertram, E., Rockendorf, G., Janßen, S., 2011. Model of an unglazed photovoltaic thermal collector based on standard test procedures. ISES Solar World Congress 2011, Solar Heating and Cooling, International Solar Energy Society, Kassel, Germany.

VDI-Richtlinie 4655, 2021. VDI-Richtlinie, Reference load profiles of residential buildings for power, heat, and domestic hot water as well as reference generation profiles for photovoltaic plants.

Wagner, A., 2010. Photovoltaik Engineering. Handbuch für Planung, Entwicklung und Anwendung. 3., erw. Aufl. Heidelberg: Springer (VDI-Buch).

Zenhäusern, D., Gagliano, A., Jonas, D., Marco Tina, G., Hadorn, J.-C., Lämmle, M., Herrando, M., 2020. Key Performance Indicators for PVT Systems. SHC Task 60/Report D1. DOI: 10.18777/ieashc-task60-2020-0007.

Simplified thermal performance model for the design of a PVT heat exchanger dedicated to solar-assisted heat pump

Valentin Delachaux[(1)(2)], Laetitia Brottier[(1)] and Rachid Bennacer[(2)]

(1) DualSun, Marseille (France)

(2) Université Paris-Saclay, ENS Paris-Saclay, CNRS, LMPS, Gif-sur-Yvette (France)

Abstract

With the aim of designing the most efficient photovoltaic-thermal hybrid solar panel (PVT) dedicated to solar-assisted heat pump, it has been built a simplified steady-state 1D-2D numerical model to compare different solutions from their heat gain factor with the ambient air. It allowed apprehending thermal couplings between the different constituent elements from conductive and/or convective heat transfers, and the different contributions linked with geometry variability. While keeping a global vision of the problem, it has been possible to focus on key choices (number of risers, absorber plate thickness, fin height, number of fins) and find optimum solutions. This work would later benefit from being confronted to experimental results and being completed by dynamic modelling and complete CFD simulations for validation and finer understanding purposes.

Keywords: hybrid solar collectors (PVT), sheet-and-tube, unglazed, heat pump (HP), solar-assisted heat pump, thermal performance, free convection, fin-and-tube, numerical model

1. Introduction and objective

The potential of systems based on the coupling of a water/water heat pump and photovoltaic-thermal hybrid solar panels (PVT) as its low temperature source has been highlighted by research projects at European scale such as Sunhorizon and Integrate, studies (Harrison, 2017), , and market trends with the rise of manufacturers of patented dedicated solutions such OptiSolar (FR3040473B1, 2017), Li-Mithra (EP3270084A1, 2018) and Consolar (WO2018033409A1, 2018),

Indeed, this kind of solution makes better use of the strengths of the PVT (low temperature, electric back-up), is more universal (vs. direct DHW preheating limited to systems regularly supplied with cold water) and allows a much higher coverage rate over the year.

First, the main determinant of the performance of such a coupling is the ambient air heat gain factor of the PVT panel to provide thermal power when the solar radiation is low or even zero. Second, a satisfactory level of heat transfer with the PV panel should be maintained, both to collect heat from the sun and cool down the photovoltaic cells. Thus, as part of our own approach to designing a dedicated hybrid panel with any set of constraints (among which the dimensions of the panel), it is at stake to predict thermal performance indicators for any suggested design.

The main idea is to increase the heat transfer surface between the calorific fluid and the air by adding surface extensions (e.g., fins). Any surface extension corresponds to additional heat transfer which depends on geometry, contact surface, base temperature, and convection air flow. To our knowledge, there is only few literatures which considers such new features on PVT heat exchangers with strong coupling between the conduction and convection regimes. The objective is to understand these coupled thermal behaviours and to find optimums for different heat exchanger geometries.

© 2022. The Authors. Published by International Solar Energy Society
Selection and/or peer review under responsibility of Scientific Committee
doi:10.18086/eurosun.2022.07.02 Available at http://proceedings.ises.org

2. Numerical model description

2.1 State-of-the-art

The first step was to write a steady-state 1D-2D numerical model in Python[1] for a basic sheet-and-tube unglazed PVT, either a harp or a meander. It is based on the component called *Type 560* which was developed as part of the Electrical Library by Thermal Energy System Specialist (TESS, 2022). As it is mentioned in (Annis, 2015), this algorithm comes from the Hottel-Whillier models for flat-plate solar heat collectors presented in (Duffie and Beckman, 1991) and adapted in (Florschuetz, 1979). Then in (Lovvik and Bergene, 1995) it was developed a very similar but more detailed steady-state model to predict the performance of water-type PVT.

Our model roughly corresponds to the steady-state 2D model of (Zondag et al., 2002). It developed and validated a 3D dynamical model and three steady state (3D, 2D and 1D) models of a double-glazed PVT collector. As in the following, the electric modelling was based on the power coefficient approach to correct the power production at different temperatures. Numerical data agreed with experimental ones within 5%. For the calculation of the daily yield, the simple 1D model performed almost as good as 3D dynamic model.

Another work (Chow, 2003) presented an explicit dynamic thermal model (for a single-glazed flat plat PVT) suitable for system simulation with the control-volume finite difference approach (the PVT panel is assimilated to a network of characteristic volumes) to generate results for hourly performance analysis and provide information on the transient performance. This model was later updated and validated by (Bhattarai et al., 2012) through a comparison with experimental data. It was found that the maximum differences between the measured and predicted values was 1.17 K for water temperature at collector outlet, 2% for collector thermal efficiency and 0.2% for collector electrical efficiency.

A dynamic model was developed on Matlab in (Guarracino et al., 2016) for unglazed, single glazed and double-glazed sheet-and-tube PVT collector. The model assumed constant temperature along the layer thickness (1D along the z direction) but variable temperature along the layer plane (2D finite element method on the x-y plane). In our paper, such 2D aspect is considered only for the absorber sheet through a fin heat conduction analytical solution; for the other layers, the average temperature on the plane is computed. The Matlab model was validated both in steady-state and in dynamic conditions against third party available data. An agreement within ± 8% for fluid temperature difference and thermal efficiency in steady-state conditions was found, whereas in dynamic condition the model was able to compute the time constant of the PVT collector tested by (Amrizal et al., 2013) very closely. Later, this dynamic model was used and integrated in (Sredenšek et al., 2021) for describing the entire photovoltaic/thermal system with a specific thermal energy storage tank; then validated against measurements data on a dedicated experimental system.

In (Simonetti et al., 2018), it went a step further: (i) considered all the layers (the maximum ever: 11) and materials that are used to build the PVT collector, (ii) used the five parameters electric equivalent approach to account for PV power production introducing a more physical way to deal with PV cell connection in series, and (iii) modelled the heat transfer between the tube and the coolant fluid with a fin behavior. Moreover, differently from previously published papers, the validation of the model was carried out considering both "slow variation" and "steep variation" of working conditions and under clear sky and cloudy sky days. This allowed to stress the model and put in evidence its limitations.

2.2 Dedicated steady-state 1D-2D numerical model

In the following, the model is chosen to be suitable for implementation of different types of surface extension and geometries. The objective is to compare their average thermal performance so that the steady-state simulation is adequate. The PV panel is segmented in the direction parallel to the tubes. Each "slice" i corresponding to one tube is considered separately which is legitimized by symmetry assumptions. If the heat exchanger is a meander, these slices are in series, if it is a harp, they are in parallel. It has been kept as an option to slice the panel perpendicular to the tubes depending on the location of the fins.

[1] https://github.com/valentindelachaux/PVT-thermal-performance-model

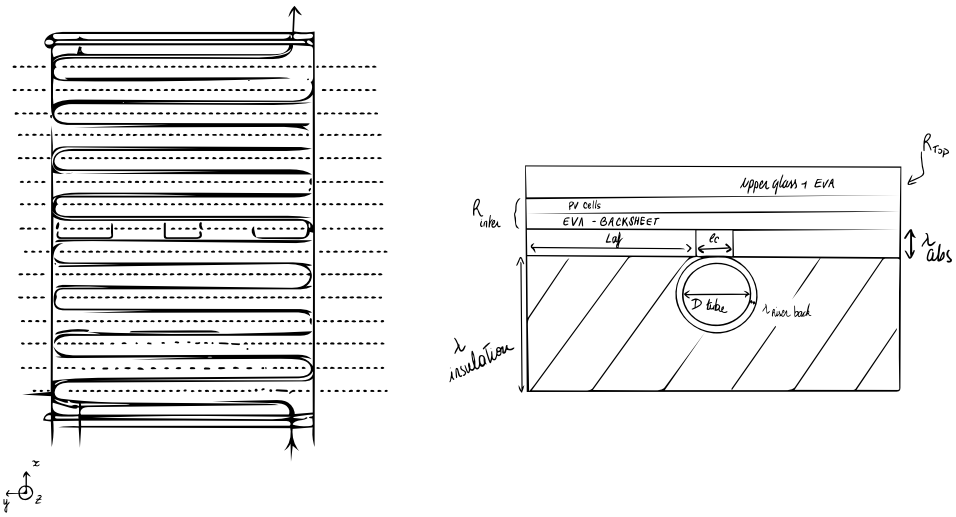

Fig. 1: basic sheet-and-tube PVT panel, the heat exchanger is a meander with horizontal manifolds

These main assumptions – common in the literature mentioned above – are listed below:

- the layers are thin enough to consider temperature constant along each layer thickness: the model is 1D in z direction,
- for any layer except the absorber sheet, the temperature considered is the mean temperature across the x-y plane,
- temperature gradients in the direction of flow and between the tubes can be treated independently: for the absorber sheet, the x-dependency of the temperature is considered while it is averaged along y-direction. Moreover, even if in the case of a meander, the temperature profile between two adjacent pipes is symmetrical and the temperature has a maximum on the symmetrical axis,
- the side effects are not considered,
- the optical properties of all relevant materials are constant,
- all material properties are presumed to be independent of temperature and equal on both sides,
- water flow rate is evenly distributed between the pipes and the thermal losses and mixing effects at the inlet and outlet manifolds are negligible,
- the flow is fully developed in tubes,
- the headers cover a small area of the collector and its effect on the temperature distribution on the absorber can be neglected,
- the incident irradiance G, the wind speed and the ambient temperature are uniform boundary conditions at the surface of the PVT collector,
- it is assumed that there is no dust or partial shading on the collector,
- the reflection, absorption and transmission factors are calculated only for the incident solar irradiance.

Our model uses the notations of the *Type 560* component. Here is the main nomenclature:

Tab. 1: Nomenclature

β	slope of the collector surface	Eff_T	coefficient for the PV cell efficiency as a function of the cell temperature
ε	emissivity	Eff_G	coefficient for the PV cell efficiency as a function of the incident radiation
θ_L	longitudinal angle of incidence	IAM	incidence angle modifier
θ_T	transversal angle of incidence	k	thermal conductivity

λ	thickness of a layer	$R_{abs,back}$	resistance to heat transfer from the absorber to the ambient air at the back of the collector (insulation + convection)
$\tau\alpha$	transmittance-absorptance product for the solar collector	$R_{tube,back}$	resistance to heat transfer from the tube to the ambient air at the back of the collector (insulation + convection)
χ	resistance to heat transfer from the tube to the internal fluid	R_{ins}	resistance provided by the insulation
A_G	gross collector area	R_{inter}	resistance to heat transfer from the PV cells to the absorber plate
C_p	specific heat of the fluid flowing through the PV/T collector	R_{top}	resistance to heat transfer from the upper glass + EVA to the PV cells
C_B	the conductance between the absorber plate and the bonded tube	R_{tube}	resistance provided by the thickness of the tube

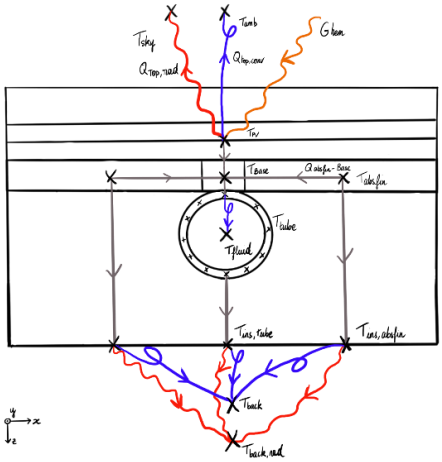

Fig. 2: vertical cross-section of a slice of the PVT panel and diagram of temperature nodes and heat transfers

Let us recall the equations obtained from four energy balances in order to understand how the model is modified to consider the addition of fins.

Energy balance on the PV cells layer

Neglecting conduction along the surface, the energy balance at any point along the surface gives:

$$S = \frac{T_{PV}-T_{amb}}{R_{top}} + h_{rad}\left(T_{PV} - T_{sky}\right) + \frac{T_{PV}-T_{abs}}{R_{inter}} \qquad \text{(eq. 1)}$$

where $T_{PV} = \overline{T_{PV}}^{x,y}$ and $T_{abs} = \overline{T_{abs}}^{x,y} = \frac{l_c \overline{T_B}^{y} + L_{af}\overline{T_{absfin}}^{y}}{W}$

S is the net absorbed solar radiation i.e., the total absorbed solar radiation minus the PV power production:

$$S = (\tau\alpha)_{\theta_L,\theta_T} G_{hem}(1-\eta_{PV}) \qquad \text{(eq. 2)}$$

$(\tau\alpha)_{\theta_L,\theta_T} = IAM(\tau\alpha)_n$ is the transmittance-absorptance product at an angle of incidence (θ_L, θ_T) and should be estimated with the appropriate optical model.

The conversion efficiency η_{nom} of the incident sunlight into electricity is assumed to decrease linearly with increasing cell operating temperature T_{PV}. The electrical model used is the most common one, the power coefficient approach:

$$\eta_{PV} = \eta_{nom}\left(1 + \mathrm{Eff}_T\left(T_{PV} - T_{ref}\right)\right)\left(1 + \mathrm{Eff}_G\left(G_T - G_{ref}\right)\right) \quad \text{(eq. 3)}$$

The PV cells layer transfers heat with the ambient air through the layers above it (glass, EVA) and by convection. The latter is represented by a heat transfer coefficient h_{top} which is calculated for mixed-regime as in (Guarracino et al., 2016) or (Simonetti et al., 2018):

$$h_{top} = \left(h_{free}^3 + h_{forced}^3\right)^{1/3} \quad \text{(eq. 4)}$$

For the upper side of the panel, h_{free} follow these correlations (replacing g by $g\cos(\beta)$ in the Ra number):

Tab. 2: Correlations for the free convection heat transfer coefficient between the upper side of a hot or a cold plate and the ambient air

Name	Case	Validity conditions	Formula
(Churchill and Chu, 1975)	Hot plate	$\beta \geq 45°$ and laminar flow $(10^4 \leq Ra_L \leq 10^9)$	$Nu_L = 0.68 + 0.67Ra_L^{1/4}\left[1 + \left(\frac{0.492}{Pr}\right)^{\frac{9}{16}}\right]^{-\frac{4}{9}}$ (eq. 5)
(Churchill and Chu, 1975)	Hot plate	$\beta \geq 45°$ and turbulent flow $(Ra_L \geq 10^9)$	$Nu_L = 0.10Ra_L^{1/3}$ (eq. 6)
Raithby and Hollands in (Rohsenow et al., 1998)	Hot plate	$\beta < 45°$, $0.024 \leq Pr \leq 2000$, and $Ra_L \geq 10^7$	$Nu_L = 0.14Ra_L^{1/3}\frac{1+0.0107Pr}{1+0.01Pr}$ (eq. 7)
(Fujii and Imura, 1972)	Cold plate	$\beta \geq 2°$ and $(10^5 \leq Ra_L \leq 10^{11})$	$Nu_L = 0.68 + 0.67Ra_L^{1/4}\left[1 + \left(\frac{0.492}{Pr}\right)^{\frac{9}{16}}\right]^{-\frac{4}{9}}$ (eq. 8)

The same correlations are used for the free convection heat transfer coefficient between the lower side of such a plate and the ambient air, by reversing the "hot" and "cold" cases. So they are used for h_{back} computation as well. See the Github repository documentation for the modelling of forced convection at the front.

The radiative heat transfer coefficient is designed to respect the Stefan-Boltzman law:

$$h_{rad} = \varepsilon_{PV\ cells}\sigma\left(T_{PV} + T_{sky}\right)\left(T_{PV}^2 + T_{sky}^2\right) \quad \text{(eq. 9)}$$

(Guarracino et al., 2016) stated that the common model for T_{sky} from (Duffie and Beckman, 1991) (usually valid for clear sky conditions) would lead to less than 1% of error for the value of the collector thermal and electrical output.

$$T_{sky} = 0.0552T_{amb}^{1.5} \quad \text{(eq. 10)}$$

In an ISO/DIS 9806 steady-state indoor test, there is an artificial cold sky so that $T_{sky} = T_{amb}$

Energy balance equation on the "absorber-fin"

The absorber above the tube is considered as two symmetrical fins of length L_{af} with conduction along x-direction. On each side of the absorber-base, the following differential equation for the temperature profile at a given y is found:

$$k_{abs}\lambda_{abs}\frac{d^2T_{abs}}{dx^2} = \frac{T_{abs} - T_{amb}}{R_{abs,back}} - \frac{T_{PV} - T_{abs}}{R_{inter}} \quad \text{(eq. 11)}$$

With these boundary conditions:

$$\begin{cases} T_{abs}\left(x = L_{af}\right) = T_B \\ \frac{dT_{abs}}{dx}(x = 0) = 0 \text{ (symmetry)} \end{cases} \quad \text{(eq. 12)}$$

This equation is solved below:

$$T_{abs}(x, y) = \frac{b}{j} + a_{abs}(y) \times \cosh(mx)$$

with $a_{abs}(y) = \frac{1}{\cosh(mL_{af})}\left(T_B(y) - \frac{b}{j}\right)$ and $m = \sqrt{\frac{F\prime j}{k\lambda}}$ (eq. 13)

At a given y in the fluid direction, $T_{abs}(x) = \overline{T_{abs}}^{y}(x) = \frac{b}{j} + \overline{a_{abs}(y)}^{y} \times \cosh(mx)$ (eq. 14)

With the following parameters:

$F' = \frac{1}{h_{rad}R_{inter} + \frac{R_{inter}}{R_{top}} + 1}$; $b = S + h_{rad}T_{sky} + \frac{T_{amb}}{R_{top}} + \frac{T_{back}}{R_{abs,back}F\prime}$; $j = \frac{1}{R_{inter}F\prime} + \frac{1}{R_{abs,back}F\prime} - \frac{1}{R_{inter}}$ (eq. 15)

Energy balance on the absorber-base

$l_B = l_c + \iota$ is the width of the base of the fin. l_c is the width of the weld. An energy balance on the base (non-fin) area of the absorber plate shows:

$$q'_{Base-tube} = l_c \frac{T_{PV} - T_B}{R_T} - \iota \frac{T_B - T_{back}}{R_{abs,back}} + 2q'_{absfin} \quad \text{(eq. 16)}$$

Assuming $T_B = b_1 q'_{tube-fluid} + b_2 T_{fluid} + b_3 T_{back}$, we get:

$$q'_{Base-tube} = -\theta_{Bt} q'_{tube-fluid} + \kappa_{Bt} T_{fluid} + \epsilon_{Bt} \quad \text{(eq. 17)}$$

Energy balance on the tube

$$q'_{tube-fluid} = q'_{Base-tube} - q'_{tube-back} = C_B(T_B - T_{tube}) - \gamma_{back}(T_{tube} - T_{back}) \quad \text{(eq. 18)}$$

With $C_B = \frac{l_c k_{riser}}{\lambda_{riser}}$ and $\gamma_{back} = \frac{p_{ext,tube}}{R_{tube} + R_{tube,back}} + h_{back,rad} p_{ext,tube,rad}$

The Millman's theorem gives c_1, c_2, and c_3 in $T_{tube} = c_1 T_B + c_2 T_{fluid} + c_3 T_{back}$ and then find b_1, b_2, and b_3. In this calculation, we need $\chi = \frac{1}{h_{fluid} p_{int,tube}}$ and so the internal heat transfer coefficient h_{fluid}. We chose the correlation from (Taler and Taler, 2017) which is valid for $Pr \in [0.6,160]$, $Re \geq 10^4$ and $L/d_w \geq 60$:

$$h_{fluid} = \frac{k_{fluid} Nu}{D_{tube}} \; with \; Nu = 0.023 Re^{0.8} Pr^n, n = 0.7 \quad \text{(eq. 19)}$$

Substituting $q'_{Base-tube}$ from (eq. 17) into (eq.18), we find the heat transfer to fluid (per unit of length in the fluid direction in W/m) as a function of T_{fluid} with three key parameters:

$$q'_{tube-fluid}(y) = \frac{\kappa_{tf}}{\theta_{tf}} T_{fluid}(y) + \frac{\epsilon_{tf}}{\theta_{tf}} \quad \text{(eq. 20)}$$

See the GitHub repository documentation for the expression of κ_{Bt}, θ_{Bt}, ϵ_{Bt}, (b_i), (c_i), κ_{tf}, θ_{tf}, and ϵ_{tf}.

Energy balance on a differential section of fluid moving through the tube

$$\frac{\dot{m} C_p}{N_{harp}} \frac{dT_{fluid}}{dy} = q'_{tube-fluid}$$
(eq. 21)

$$\frac{dT_{fluid}}{dy} = a_f T_{fluid} + b_f \text{ where } \begin{cases} a_f = \frac{N_{harp}}{\dot{m} C_p} \frac{\kappa_{tf}}{\theta_{tf}} \\ b_f = \frac{N_{harp}}{\dot{m} C_p} \frac{\epsilon_{tf}}{\theta_{tf}} \end{cases} \quad \text{(eq. 22)}$$

Finally, we get the temperature field of the fluid in the tube:

$$T_{fluid}(y) = \left(T_{fluid,in} + \frac{b_f}{a_f}\right) \exp(a_f y) - \frac{b_f}{a_f} \quad \text{(eq. 23)}$$

Likewise, see the GitHub repository documentation to find the expression of the average temperature of the fluid along the tube $\overline{T_{fluid}}$, the heat transfer q'_{fluid}, the average temperature of the base of the absorber along the tube $\overline{T_B}$, the average temperature of the absorber-fin on either side of the tube $\overline{T_{absfin}}$, the average temperature of the absorber $\overline{T_{abs}}$ and the average temperature of the PV cells layer $\overline{T_{PV}}$.

The solution of this set of equations requires an iterative approach until convergence.

2.3 Implementation of fins

The second step consisted in the implementation of surface extensions in these equations. They are either against tubes (e.g., a fin-and-tubes heat exchanger usually found as a heat pump evaporator, a finned-tubes heat exchanger) or against the absorber plate. In the latter, fins are in series with the "absorber-fin".

Fins welded on the tubes (f0) and (f1)

The fins (f0) are welded vertical against the tubes, and perpendicular to the fluid direction y, so that they are parallel to the free convection air flow. Each fin is characterized by the number of Biot $Bi = \left(1 + \frac{\lambda_{fin}}{\delta_{fin}}\right)\frac{\lambda_{fin} h_{back}}{k_{fin}}$.

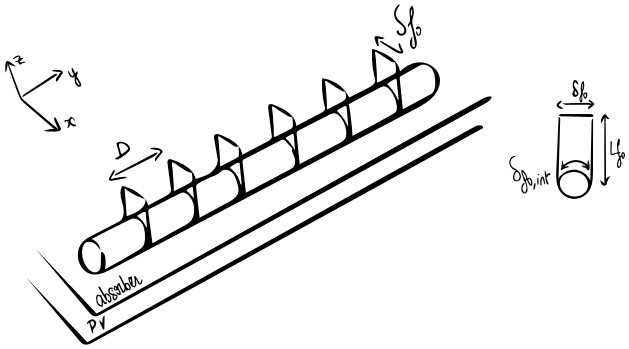

Fig. 3: vertical fins welded perpendicular to the tubes (f0)

Here is the heat equation:

$$\frac{d^2 T_{fin}}{dx^2} - \frac{2Bi}{\lambda_{fin}^2}\left(T_{fin}(x) - T_{ext}\right) = 0 \qquad \text{(eq. 24)}$$

Boundary conditions if symmetry or zero-flux end:

$$\begin{cases} T_{fin}(x = 0) = T_{tube}(y) \\ \frac{d}{dt} T_{fin}\left(x = L_{fin}\right) = 0 \end{cases} \qquad \text{(eq. 25)}$$

Boundary conditions if free-flux end:

$$\begin{cases} T_{fin}(x = 0) = T_{tube}(y) \\ k\frac{dT_{fin}}{dz}\left(z = L_{fin}\right) = -h_{back}\left(T_{fin}\left(z = L_{fin}\right) - T_{back}\right) \end{cases} \qquad \text{(eq. 26)}$$

Solving this equation requires the computation of γ, fin and flow characteristic number:

$$\gamma = \frac{\frac{\alpha}{\lambda_{fin}}\sinh\left(\frac{\alpha}{\lambda_{fin}}L_{fin}\right) + \frac{\beta\alpha}{\lambda_{fin}}\cosh\left(\frac{\alpha}{\lambda_{fin}}L_{fin}\right)}{\cosh\left(\frac{\alpha}{\lambda_{fin}}L_{fin}\right) + \beta\sinh\left(\frac{\alpha}{\lambda_{fin}}L_{fin}\right)} \text{ with } \alpha = \sqrt{2Bi} \text{ and } \beta = \frac{\sqrt{Bi/2}}{\left(1 + \frac{\lambda_{fin}}{\delta_{fin}}\right)}$$

(eq. 27)

Without detailing it here, horizontal fins (f1) welded from one tube to the other have been modelled as well. For a slice *i* of the panel, at a given *y*, the average heat transfer through the fins on back and on either side is:

$$q_{f0}{}' = \gamma_0^{int}(T_{tube}(y) - T_{back}) \text{ with } \gamma_0^{int} = k_{f0}\gamma_0 \frac{\lambda_{f0} N_{f0} \delta_{f0}^{int}}{L_{tube}} \qquad \text{(eq. 28)}$$

$$q_{f1}{}' = \gamma_1^{int}(T_{tube}(y) - T_{back}) \qquad \text{with } \gamma_1^{int} = 2k_{f1}\frac{\lambda_{f1} N_{f1} \delta_{f1}^{int}}{L_{tube}} \frac{\sqrt{2Bi_{f1}}}{\lambda_{f1}} \tanh\left(\sqrt{2Bi_{f1}}\frac{L_{f1}}{\lambda_{f1}}\right) \qquad \text{(eq. 29)}$$

Then, we adapt the model with these additional heat transfers:

$$\gamma_{back} \leftarrow \gamma_{back} + \gamma_0^{int} + \gamma_1^{int} \qquad \text{(eq. 30)}$$

Fins welded on the absorber plate (f2)

These are also vertical and perpendicular to the fluid direction y.

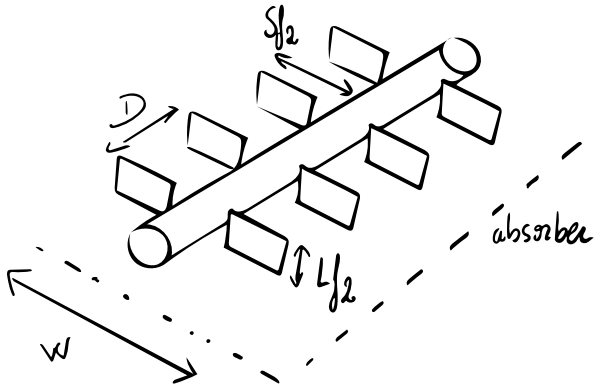

Fig. 4: vertical fins welded on the absorber plate, perpendicular to the tubes (f2)

For half of the fin on one side of the tube, the heat transfer in $W/(m^2 of contact)$ is:

$$q_{f2} = \gamma_2^{int}\left(\overline{T_{abs}}^{y}(x) - T_{back}\right) \text{ with } \gamma_2^{int} = k\gamma_2 \frac{\lambda_{f2} N_{f2} \delta_{f2}}{L_{tube}\delta_{f2}} \quad \text{(eq. 31)}$$

The b and j coefficients from $T_{abs}(x) = \overline{T_{abs}}^{y}(x) = \frac{b}{j} + \left(T_B(y) - \frac{b}{j}\right)\frac{\cosh(mx)}{\cosh(mL_{af})}$ become:

$$b \leftarrow b + \frac{\gamma_2^{int} T_{back}}{F'} \qquad j \leftarrow j + \frac{\gamma_2^{int}}{F'} \quad \text{(eq. 32)}$$

3. Methodology

We developed a numerical model which predicts the steady-state thermal power output of one PVT panel under a set of meteorological (irradiance, ambient temperature, wind) and system parameters (inlet fluid temperature, flow rate). By running this simulation into a sample of test data, so it is possible to get the a_i coefficients which characterize the panel according to (eq. 42) from ("ISO/DIS 9806:2017 Solar energy — Solar thermal — Test methods," 2017).

$$\dot{Q} = A_G\left(\eta_{0,hem}K_{hem}G - a_1(T_m - T_a) - a_2(T_m - T_a)^2 - a_3u'(T_m - T_a) + a_4G' - a_6u'G - a_7u'G' - a_8(T_m - T_a)^4\right) \quad \text{(eq. 33)}$$

Since the latest version of this standard, the coefficients a_2 and a_8 are often set to zero for PVT panels because the thermal power is considered linearly dependent on the temperature difference. Besides, the heat exchanger being in a narrow space between the panel and the roof, it has been assumed that the wind does not modify the convective heat transfers on the rear side. Therefore, the information of geometry impact on free convection air flow is contained only in the a_1 coefficient. The information of forced convection impact is theoretically contained only in a_3.

In the following, the optical efficiency $A0 = a_0 - a_6u'$ and the heat loss coefficient $A1 = a_1 + a_3u'$ are retained as the two main thermal performance representative values. An average wind speed of u = 1.3 m/s is assumed so that u' = -1.7 m/s.

This model includes modelling temperature fields in and over the constituent elements of the exchanger and fluid flow geometry (having an impact on internal heat transfer coefficient and temperature field along its path). It allows analysing the different contributions by heat transfer type (conduction, convection, radiation) and by source (sun irradiance, ambient air) linked with geometry variability and finding optimum solutions.

In the following, we analyse a basic PVT prototype. We do not consider the manifolds. We use our numerical model directly without calibration following the experimental tests

4. Results

4.1. Number of risers

A specific PVT panel prototype has been studied. The heat exchanger is a meander made up with 16 risers bonded against an aluminum absorber sheet. The latter is plated against the backsheet of the PV panel.

Tab. 3: PVT panel prototype characteristics

Parameter	Symbol	Value
Nominal efficiency	η	20%
Power decrease coefficient	Eff_T	-0.0034 /K
Tilt	β	45°
Number of risers	N	16
Gross area	A_G	1.93 m^2
Absorber length	L_{abs}	1,550 mm
Absorber width	w_{abs}	1,080 mm
Tube diameter	D_{tube}	8 mm
Weld width	l_c	4 mm
Absorber conductivity	k_{abs}	226 W/mK
Absorber thickness	λ_{abs}	0.4 mm

A greater number of risers makes it possible to collect heat transfer from the absorber more efficiently. Above a certain number, the absorber surface associated with each tube is sufficiently small for a major part of these transfers to be collected. Note that we are in the case of a meander exchanger, the flow rate is therefore constant, as is the internal heat transfer coefficient of the fluid.

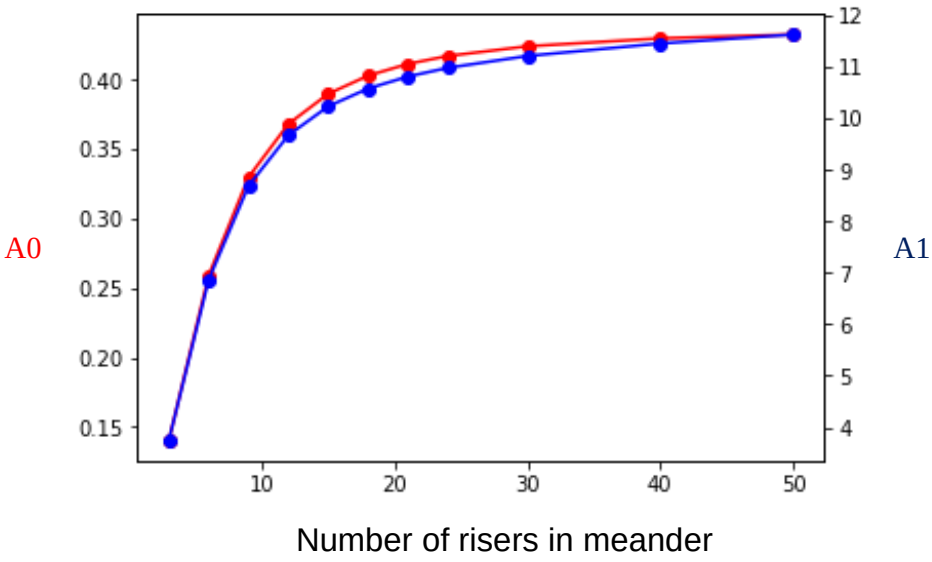

Fig. 5: A0 and A1 (for u = 1,3 m/s) dependency on the number of risers for our meander PVT panel

4.2 Absorber thickness

The absorber, on either side of each tube, acts as a fin:

- One face being in direct contact with the backsheet, transmits the heat from sunlight, radiative transfer, and convection on the upper side
- The other side transmits the heat from convection on the lower side

This function makes it possible to exploit the entire surface of the collector. To improve A0 and A1 coefficients, the fin must therefore play its role as well as possible.

With the same panel, here is a parametric study about the absorber plate thickness. Indeed, it behaves like a fin on each side of each tube, so its conductance (product of thermal conductivity and thickness) is highly influent on thermal performance.

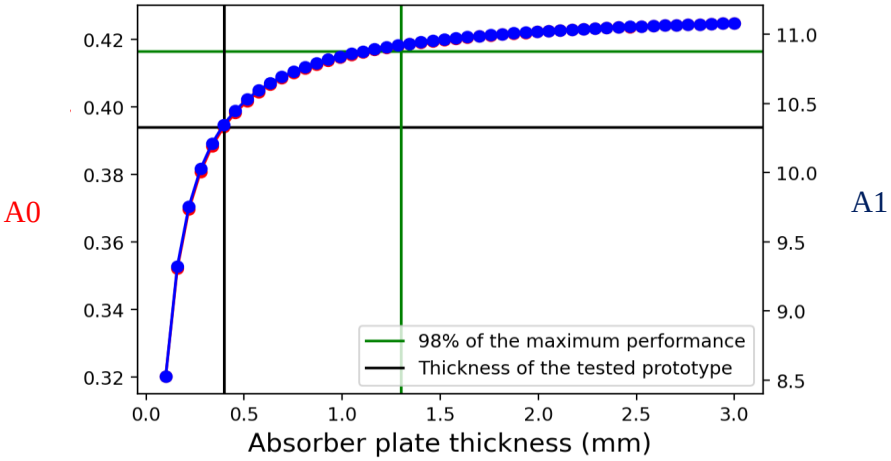

Fig. 6: A0 and A1 (for u = 1,3 m/s) dependency on absorber plate thickness for our meander PVT panel

It is found that the aluminum absorber plate should have a thickness of at least 1.3 mm to get a minimum of 98% of the maximum value reached for about 27 mm of thickness. If the absorber plate of the prototype is replaced by a 1.3 mm-thick one, the A0 would increase by about 3 points which corresponds to about 7% more energy produced every year.

4.3. Fins height L

Tab. 4: PVT panel prototype characteristics

Number of fins	N_{f2}	120
Fin spacing	D	9 mm
Fins conductivity	k_{f2}	226 W/mK
Fins thickness	λ_{f2}	1.5 mm

As shown above, the behavior of rectangular vertical fins plated on the absorber is known with an analytical solution giving the incoming heat flux at the base of each fin according to their geometry. Specifically, the influence of their height L is well known. It significantly increases the heat flux until some point. Beyond the threshold value of $L < \frac{\sqrt{ka}}{h}$, the rest of the fin is “useless”. Here the calculated threshold value with an average rear side heat transfer coefficient of h = 3,6 W/m^{2}K is about 31 cm. The simulation for this PVT panel, with fins perpendicular to the tubes and plated against the absorber plate, reflects this phenomenon, and gives approximate expected values for the performance indicators A0 and A1.

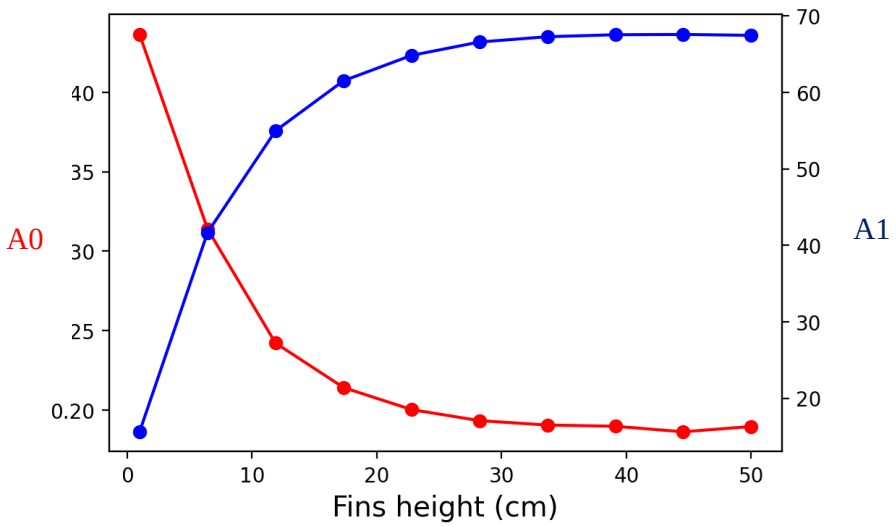

Fig. 7: A0 and A1 (for u = 1,3 m/s) dependency on fins height for the PVT panel with fins perpendicular to the tubes and plated against the absorber plate (120 aluminum fins, 1.5 mm thick, fin spacing of 9 mm,)

4.4. Fins number

Tab. 4: PVT panel prototype characteristics

Fins length	L_{f0}	20 mm
Fins width	δ_{f0}	10 mm
Contact width between fins and tube	δ_{f0}^{int}	$(\pi D_{tube})/2$ = 13 mm

As another example, the PVT heat exchanger has fins perpendicular to the tubes and welded against them. A key choice, in such a design, is the number of fins (i.e., the fin spacing) because it negatively influences the heat transfer coefficient on the back of the panel h_{back} as (Tari and Mehrtash, 2013) shows. It dealt with free convection heat transfer from plate-fin heat sinks and gave a complete set of Nusselt number correlations covering all inclination angles. As Fig. 8 shows, it allows finding the optimum fin spacing to maximize the global heat loss coefficient A1 or optimizing the number of fins against weight and/or cost constraints.

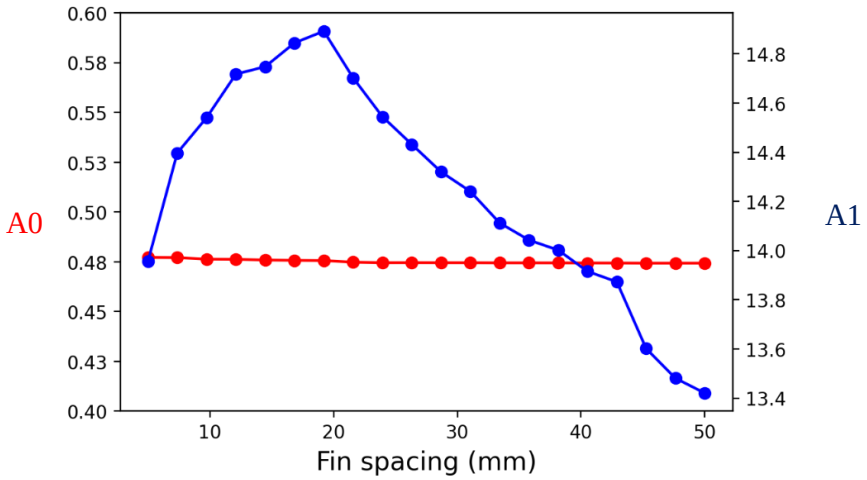

Fig. 8: A0 and A1 (for u = 1,3 m/s) dependency on fin spacing for the PVT panel with fins perpendicular to the tubes and welded against them (52 mm long fins, 1.5 mm thick)

5. Conclusion

This model allowed us to study thermal performance of a variety of heat exchanger pre-designs and understand the determinants of different contributions. While keeping a global vision of the problem, it has been possible to focus on key choices and find optimum solutions for the number of tubes, the absorber thickness, the fins height or spacing. In our approach, the model has been assumed to be relevant to compare geometries with each other. First, it would benefit from being confronted with experimental results. Indeed, quantification of uncertainties is at stake as (Huang and Shah, 1992) showed. Second, a dynamic modelling of thermal performance would complete the analysis, e.g. by adapting the model of (Guarracino et al., 2016). Third, CFD simulations could contribute to the validation of optimizations and to the understanding of thermal couplings with the consideration of temperature inhomogeneities, as shown in (Singh et al., 2015), (Taler et al., 2019) and (Marcinkowski et al., 2021). It has been shown that the impact of the heat exchanger geometry, the frame of the panel, and the incidence angle on the free convection air flow should be studied to optimize such a PVT panel dedicated to a solar-assisted heat pump.

6. References

Amrizal, N., Chemisana, D., Rosell, J.I., 2013. Hybrid photovoltaic–thermal solar collectors dynamic modeling. Appl. Energy 101, 797–807. https://doi.org/10.1016/j.apenergy.2012.08.020

Annis, N.C., 2015. Performance analysis and modelling of hybrid photovoltaic-thermal solar panels.

Bhattarai, S., Oh, J.-H., Euh, S.-H., Krishna Kafle, G., Hyun Kim, D., 2012. Simulation and model validation of sheet and tube type photovoltaic thermal solar system and conventional solar collecting system in transient states. Sol. Energy Mater. Sol. Cells 103, 184–193. https://doi.org/10.1016/j.solmat.2012.04.017

Chow, T.T., 2003. Performance analysis of photovoltaic-thermal collector by explicit dynamic model. Sol. Energy 75, 143–152. https://doi.org/10.1016/j.solener.2003.07.001

Churchill, S.W., Chu, H.H.S., 1975. Correlating equations for laminar and turbulent free convection from a vertical plate. Int. J. Heat Mass Transf. 18, 1323–1329. https://doi.org/10.1016/0017-9310(75)90243-4

Duffie, J.A., Beckman, W.A., 1991. Solar Engineering of Thermal Processes 928.

Florschuetz, L.W., 1979. Extension of the Hottel-Whillier model to the analysis of combined photovoltaic/thermal flat plate collectors. Sol. Energy 22, 361–366. https://doi.org/10.1016/0038-092X(79)90190-7

Fujii, T., Imura, H., 1972. Natural-convection heat transfer from a plate with arbitrary inclination. Int. J. Heat Mass Transf. 15, 755–767. https://doi.org/10.1016/0017-9310(72)90118-4

Guarracino, I., Mellor, A., Ekins-Daukes, N.J., Markides, C.N., 2016. Dynamic coupled thermal-and-electrical modelling of sheet-and-tube hybrid photovoltaic/thermal (PVT) collectors. Appl. Therm. Eng. 101, 778–795. https://doi.org/10.1016/j.applthermaleng.2016.02.056

Harrison, S., 2017. The Potential and Challenges of Solar Boosted Heat Pumps for Domestic Hot Water Heating. Presented at the 12th IEA Heat Pump Conference, Rotterdam.

ISO/DIS 9806:2017 Solar energy — Solar thermal — Test methods, 2017.

Lovvik, O.M., Bergene, T., 1995. Model calculations on a flat-plate solar heat collector with integrated solar cells 10.

Marcinkowski, M., Taler, D., Taler, J., Węglarz, K., 2021. Thermal Calculations of Four-Row Plate-Fin and Tube Heat Exchanger Taking into Account Different Air-Side Correlations on Individual Rows of Tubes for Low Reynold Numbers. Energies 14, 6978. https://doi.org/10.3390/en14216978

Rohsenow, W.M., Hartnett, J.P., Cho, Y.I. (Eds.), 1998. Handbook of heat transfer, 3rd ed. ed, McGraw-Hill handbooks. McGraw-Hill, New York.

Simonetti, R., Molinaroli, L., Manzolini, G., 2018. Development and validation of a comprehensive dynamic mathematical model for hybrid PV/T solar collectors. Appl. Therm. Eng. 133, 543–554. https://doi.org/10.1016/j.applthermaleng.2018.01.093

Singh, S., Sørensen, K., Condra, T., 2015. Multiphysics Numerical Modeling of a Fin and Tube Heat Exchanger. Presented at the The 56th Conference on Simulation and Modelling (SIMS 56), October, 7-9, 2015, Linköping University, Sweden, pp. 383–390. https://doi.org/10.3384/ecp15119383

Sredenšek, K., Seme, S., Štumberger, B., Hadžiselimović, M., Chowdhury, A., Praunseis, Z., 2021. Experimental Validation of a Dynamic Photovoltaic/Thermal Collector Model in Combination with a Thermal Energy Storage Tank. Energies 14, 8162. https://doi.org/10.3390/en14238162

Taler, D., Taler, J., 2017. Simple heat transfer correlations for turbulent tube flow. E3S Web Conf. 13, 02008. https://doi.org/10.1051/e3sconf/20171302008

Taler, D., Taler, J., Wrona, K., 2019. Transient behavior of a plate-fin-and-tube heat exchanger taking into account different heat transfer coefficients on the individual tube rows. E3S Web Conf. 137, 01036. https://doi.org/10.1051/e3sconf/201913701036

Tari, I., Mehrtash, M., 2013. Natural convection heat transfer from horizontal and slightly inclined plate-fin heat sinks. Appl. Therm. Eng. 61, 728–736. https://doi.org/10.1016/j.applthermaleng.2013.09.003

TESS, 2022. TESS Component Libraries v18.

Zondag, H.A., de Vries, D.W., van Helden, W.G.J., van Zolingen, R.J.C., van Steenhoven, A.A., 2002. The thermal and electrical yield of a PV-thermal collector. Sol. Energy 72, 113–128. https://doi.org/10.1016/S0038-092X(01)00094-9

Investigation of Creep-Fatigue Lifetime in Solar Photovoltaic Module Interconnections

Alireza Eslami Majd[1], Nduka Nnamdi Ekere[2], Armin Rahmati Darvazi[3], Ali Amini Sedehi[4] and Fideline Tchuenbou-Magaia[1]

[1]Faculty of Science and Engineering, University of Wolverhampton, Wolverhampton (UK)
[2]Faculty of Engineering and Technology, Liverpool John Moores University, Liverpool (UK)
[3]Faculty of Technology and Engineering, University of Guilan, Rasht (Iran)
[4]Faculty of Mechanical Engineering, University of Kashan, Kashan (Iran)

Abstract

The growing demand for utilization of solar photovoltaic (PV) module puts increased pressure on manufacturers to improve the reliability of PV modules for meeting their lifetime warranty. The PV module interconnection which is one of the key components of the module is reported to account for about 40% of the failure of the module. In this study, Finite Element Analysis using ABAQUS software was used to investigate the creep-fatigue behavior of the solder joints for convectional PV module interconnection with different dimensions. The exponent factor of the Coffin–Manson–Arrhenius approach for estimating the creep-fatigue life of the PV module interconnections was determined to be -1.8 and was used to predict the solder joint's creep-fatigue life under thermal cycling operating conditions. Our results also suggest that optimal dimensions for higher creep-fatigue life and PV interconnection reliability are 20µm solder thickness, 40µm-50µm silver-pad thickness, 150µm copper thickness and 1mm ribbon width.

Keyword: PV Module Interconnection, Reliability, Creep-Fatigue, Life Time.

1. Introduction

As the PV Solar module technology is being developed to play a more significant role in the replacement of fossil fuel sources with renewable energy sources, the challenge to improve the reliability of the PV modules is getting more attention. According to a recent IRENA (International Renewable Energy Agency) report (IRENA 2019), solar PV will become the second-largest power generation source by 2050 (just behind wind power) and will be the catalyst for the transformation of the global electricity sector, generating some 25% of total electricity needs globally. In order to grow the global share of electricity generation of Solar PV from the current 3% (IEA, 2020) to the projected 25% by 2050, there is an urgent need for improving the reliability of PV modules, which have been reported to fail due to adverse operating conditions such as thermal cycling, damp heat and UV exposure. For example, thermal cycling can cause PV module interconnection solder joint failures and cracks in solar cells (Ogbomo, et al., 2018).

Solar PV module manufacturers are also keen to achieve higher reliability products in order to match their offer of power output warranties of 25 years (with early and premature failures covered by the warranty and the free replacement of the solar PV module). Study of the potential failure modes of PV module have shown that one of the major PV module's reliability challenges is the failure of the solder joint materials used for connecting the ribbon to the cell. This is because the daily power-up and shut-down and the associated heating and cooling down of the PV module results in thermal cycling and ageing of the PV module. Consequently, the solder joints used for the PV module interconnection can experience very high stress and strain levels due to the coefficient of the thermal expansion (CTE) mismatch between the adjacent materials (Itoh, et al., 2014). The induced stress and strain in the solder joints result in high levels of energy accumulation that can significantly reduce the creep-fatigue life of the interconnection and the long-term reliability of the PV module (Ogbomo, et al., 2018). Also, during the high temperature manufacturing processes of the PV module (e.g. EVA lamination), the CTE mismatch between the materials can cause the micro-cracks in the solder joints, which can then result in a premature interconnection failure (Majd, Ekere, 2020a).

© 2022. The Authors. Published by International Solar Energy Society
Selection and/or peer review under responsibility of Scientific Committee
doi:10.18086/eurosun.2022.07.03 Available at http://proceedings.ises.org

The models for estimation of the fatigue life of solder joints can be sub-divided into three categories, namely: stress-based, strain-based and energy-based approaches. According to the stress-based approach, fatigue failure occurs when the accumulated stress reaches a trigger threshold (Li, et al., 2017; Han, Han, 2014). The strain-based approach is the most widely reported method in the literature for the computational study of creep-fatigue behavior of the solder joints. For strain-based fatigue models, the strain is composed of the elastic strain, plastic strain, creep strain components, which are not easily distinguishable (Knetch, Fox, 1990). The Coffin-Manson model and the Total Strain model are two of the most popular strain-based models used for the prediction of the thermal fatigue life of materials (Li, et al., 2017; Lee, et al., 2000). The Coffin-Manson model uses the plastic strain amplitude over a cycle to estimate the number of cycles to failure. Several modifications of the Coffin-Manson model have been used for the prediction of the fatigue life of materials in specific conditions (Chen, et al., 2017). For example, Yunxia Chen et al. used the modified Coffin-Manson equation to introduce a coupling damage model considered low-cycle fatigue and creep (Chen, et al., 2021). It was also found that for strain levels less than 1%, the Coffin-Manson model cannot accurately estimate the creep-fatigue life, and hence is not recommended, as the strain is mostly composed of creep and elastic strains rather than plastic strain (Hund, Burchett, 1991). The total strain model was introduced as a modified form of the Coffin–Manson model to incorporate both the elastic and plastic strain terms (Lee, et al., 2000; Yao, et al. 2017).

In terms of the energy-based models used for predicting the creep-fatigue life of materials, the Morrow Energy Density model (Andersson et al., 2006; Zhu et al., 2014), is one of the most widely used methods. In this approach, the plastic strain energy density is used instead of the plastic strain values. The advantage of this method is that it incorporates the effects of both plastic strain and plastic stress on the cumulative energy. In the Morrow Energy Density model, the number of cycles to failure (N_f) is a function of the plastic strain energy density, which is obtained from the hysteresis stress-strain loops for each cycle. In another study, Akay et al. developed the model for predicting the creep-fatigue life based on the total strain energy, rather than the plastic strain energy density (Akay, et al., 2003). The stress–strain hysteresis energy is also important for predicting the fatigue failure life (Steinhorst, et al., 2013)). For example, Darveaux proposed a fatigue model with consideration of the accumulated stress–strain hysteresis energy in the material to derive the equation for the crack initiation cycle number and crack propagation rate (Darveaux, 2002).

The strain and the energy terms used in the models discussed above for the estimation of the fatigue life of materials can be found by using the analytical constitutive models of creep behavior. Examples of the constitutive models used for the prediction of the creep fatigue life of materials include the following: (a). Garofalo or Hyperbolic Sine (Syed, 2004; Depiver, et al., 2021), (b). Anand (Baber, Guven, 2017; Cho, et al., 2018), (c). Johnson-Cook (Halounai, et al., 2020) and (d). Power Law (Zhang, et al., 2008; Ma, 2009).

In this study, the Hyperbolic-Sine creep model in ABAQUS software was used to study the creep behavior of the solder joints for PV module interconnection with different dimensions. The total dissipated energy extracted from FEM simulation was used to find the number of cycles to failure for the solder joints using reliability formulation. For this reliability, a Coffin–Manson–Arrhenius exponent factor was found by comparing different thermal cycling conditions. Then this factor was used to determine the creep-fatigue life of the solder joints in PV module interconnection under arbitrary thermal cycling conditions.

2. Methodology

2.1. Creep Investigation Model

Previous studies on the failure of solder materials showed that they exhibit elastic, bilinear kinematic hardening plastic behavior after yielding (Che, Pang, 2004). The Hyperbolic-Sine creep model is perhaps, one of the most widely reported in the literature for investigating the effect of temperature and strain rate on the elastic plastic creep behavior of materials. Amalu, et al. (2016) compared different set of creep parameter values of the lead-free solder joints to select a suitable constitutive model based on the Hyperbolic-Sine creep model to predict the accurate creep parameters (Amalu, Ekere, 2016). Equation 1 shows the formula for the Hyperbolic-Sine creep model.

$$\dot{\varepsilon}_{cr} = A\left(\sin \mathrm{h}(\beta\sigma)\right)^{n} exp\left(-\frac{Q}{RT}\right) \qquad \text{(eq. 1)}$$

where $\dot{\varepsilon}_{cr}$ is the scalar creep strain rate, A is Boltzmann's constant, β and n are constants, σ is the von-mises effective stress, Q is activation energy, R is gas constant and T is the absolute temperature. The values of the parameters in the hyperbolic sine creep equation for popular SAC (Tin, Silver, Copper) solder alloys (e.g. Sn3.8Ag0.7Cu, Sn3.5Ag0.75Cu and Sn3.5Ag0.5Cu) have been found to be as follows: β is 0.02447 1/MPa, n is 6.41, R is 8.314 J·Mol−1·K−1 and $\frac{Q}{R}$ is 6500 (Schubert, et al., 2003).

2.2. FEM Simulation

In this study, the FEM simulation for different dimensions of the conventional PV module interconnection ribbon was performed in ABAQUS 2019 and the Hyperbolic-Sine creep model was applied to the solder joint material. Tab. 1 presents the mechanical properties of the material used for the FEM simulation. As the plastic behavior of the solder joint material is considered temperature dependent, the values for the coefficient of thermal expansion of the materials, the Young's Modulus and the plastic stress for the solder joint material used for investigating the effect of temperature on the elastic plastic creep behavior of materials are given in Tab. 2.

Tab. 1: Mechanical Properties of material used in the FEM simulation of PV module interconnection (Majd, Ekere, 2020a).

	IMC-Copper (Cu5Sn6)	IMC-Silver (Ag3Sn)	Solder (SAC)	Silver	Al	Copper	EVA	Silicon	Tedlar	Glass
Elastic Modulus (GPa)	110	79	See Tab. 2	69	68.3	121	11	130	2.138	73.0
Poisson's Ratio	0.3	0.3	0.35	0.365	0.34	0.34	0.499	0.28	0.4	0.235
Yield Stress (MPa)	-	-	-	43	85	121	12	170	41	-
Thermal Expansion Coefficient (ppm/K)	See Tab. 2	See Tab. 2	See Tab. 2	See Tab. 2	See Tab. 2	See Tab. 2	270	See Tab. 2	78	8.0
Plastic Stress (MPa) @ Strain	-	-	See Tab. 2	43@0.001 120@0.04	85@0.001 100@0.12	121@0.001 217@0.01 234@0.02 248@0.04	-	-	41@0.00 55@0.9	-

Tab. 2: Temperature dependency of the material properties used in the FEM simulation (Majd, Ekere, 2020a).

Temp. (°C)	Interpolated data for the Coefficient of Thermal Expansion (ppm/K)							Young's Modulus (GPa)	Yield Stress (MPa)	Plastic Stress (MPa) at 0.065 Strain
	Copper	Silver	Al	Silicon	IMC-Copper (Cu5Sn6)	IMC-Silver (Ag3Sn)	Solder	Solder (SAC)		
0	16.22	18.67	22.50	2.35	17.7	19	21.3	49	71	145
30	16.60	18.98	23.29	2.63	18	19.4	21.81	46.9	52	131
60	16.91	19.20	23.85	2.87	18.3	19.8	22.32	44.8	16	110
90	17.22	19.42	24.41	3.04	18.6	20.3	22.83	42.7	-	-
120	17.53	19.65	24.97	3.20	19	20.7	23.34	40.6	-	-
150	17.76	19.91	25.40	3.36	19.8	21.1	23.85	38.5	-	-

To increase the computational solution speed, the 2D plane-strain elements were used since the geometry of the models have a high ratio of the interconnection length to the other dimensions of model. The symmetry boundary condition was applied to the mid-point of the interconnection section and bottom-end of the Tedlar material was closed. Fig. 1 is a schematic view of the cross section of the conventional PV module interconnection showing the applied boundary conditions and the solder joint mesh design used for the FEM simulation in ABAQUS. The models were subjected to a homogenous thermal cycling load, with time history in accordance with the IEC 61215-2:2016 standard (the temperature of cycle uniformly changes between the

minimum temperature (-40°C) and maximum temperature (85°C) with the rate 100°C/hr during 15 minutes and with 10 minutes dwell time) (International Electrotechnical Commission, 2016). In this study, the thickness of the materials used for the models (namely, aluminum, silicon cell, EVA, glass and Tedlar layers), were assumed to be 25µm, 200µm, 460µm, 3mm and 190µm, respectively. Also, the thickness of the IMC (intermetallic compound) layer in the boundaries of the solder joint with the copper and silver-pad materials is considered to be 4 µm. The interconnection width and the thickness of other component parts including silver-pad, copper, and the solder joints are then varied to investigate the effect of interconnection design on the creep-fatigue response.

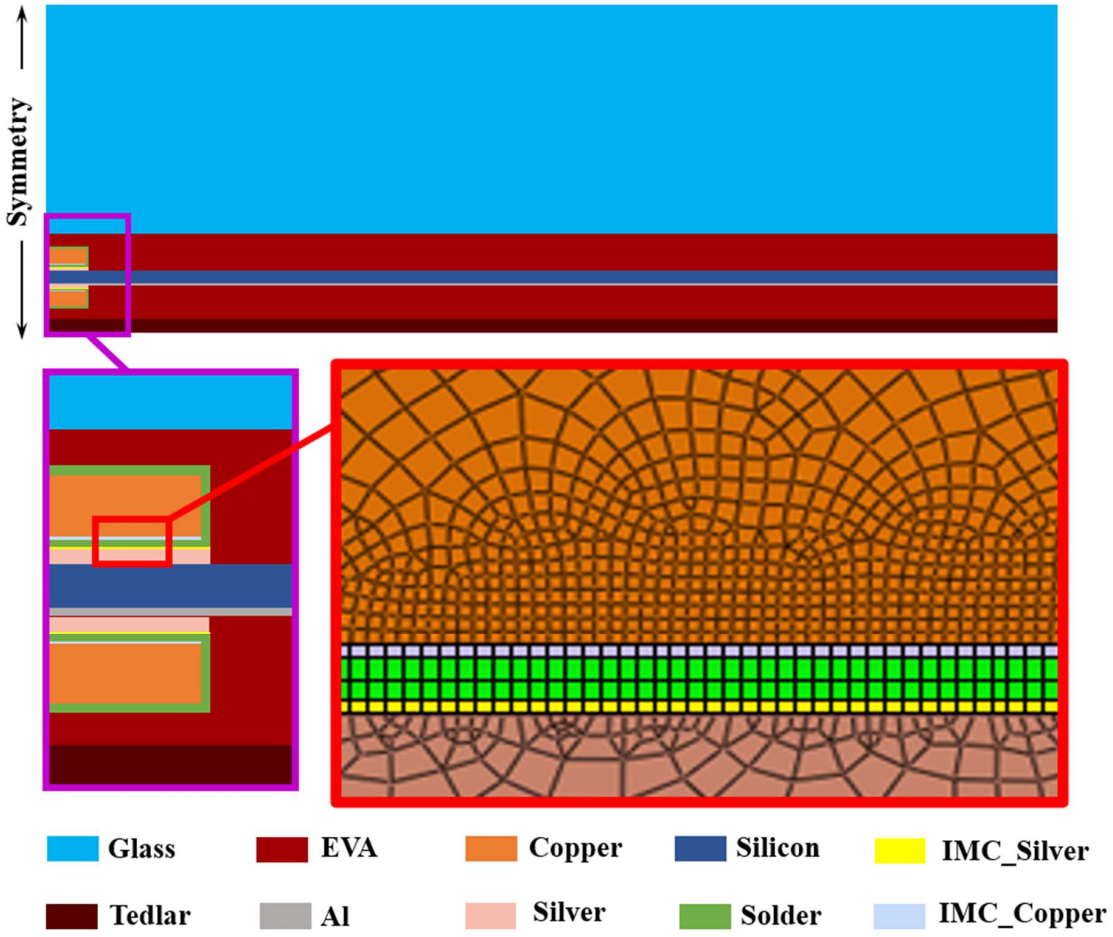

Fig. 1: Schematic view of the simulated conventional PV module interconnection showing the boundary conditions, arrangement of materials and solder joint meshing style.

2.3. Validation of the Methodology

To validate the methodology used for creep-fatigue investigation in this work (including element type, mesh size, and the formulation to estimate the creep-fatigue lifetime), the results of a simulation of SAC solder joint in Wafer Level Chip Scale Packages (WLCSP) were compared with the literature.

Tab. 3 compares the number of cycles to failure (N_f) estimated using the present methodology with the N_f reported in the literatures. There were good agreements between the estimated N_f using the present methodology in this study and the N_f reported from the experiment (9.8% error) as highlighted in Tab.3. Hence, the present practiced methodology to predict the creep-fatigue lifetime of the solder joints can be reasonably used for the lifetime estimation of the creep-fatigue failure in the PV module interconnection solder joints.

Tab. 3: Lifetime model parameters and estimated N_f for the solder joint used in WLCSP.

Lifetime Model Parameters $N_f = C(w_{acc})^{\eta}$	**FEM Simulation** (Lee, Chiang, 2019)	**FEM Simulation** (Tsou, et al., 2017)	**Present FEM Simulation**
w_{acc} (from FEM)	0.35	0.39	0.44
C	145	175	526
η	-2	-1.9	-1
N_f	1152	1058	1112
N_f from experiment (Hsieh, Tzeng, 2014)			
Error for the N_f	13.7%	4.4%	9.8%

3. Results and Discussion

3.1. Creep Behavior of the PV Module Interconnection Solder Joint

The FEM results of the creep stress/strain for each PV module interconnection configuration investigated in this study for 5 thermal cycles are discussed in this section. Fig. 2 shows the equivalent creep strain (CEEQ) distribution in the solder joint of the conventional PV module interconnection with 20µm, 40µm, 200µm and 1000µm in solder, silver, copper thickness and ribbon width, respectively, after 5 thermal cycles (ranging from -40°C to 85°C). The results showed that the maximum CEEQ in the solder joint is located at the side of solder joint, and that the middle of the solder joint experiences minimum CEEQ. The location for the maximum CEEQ found in the solder joint was near to the location of the crack initiation in PV module interconnection solder joint subjected to the high temperature of lamination process found in previous studies (Majd, et al., 2019, 2020a, 2020b, 2022).

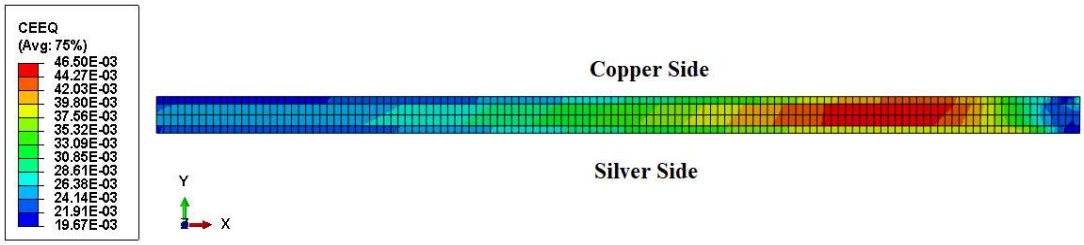

Fig. 2: Equivalent creep strain distribution (CEEQ) in the PV module interconnection solder joint after 5 thermal cycles.

Fig. 3 shows the plot of the hysteresis stress-strain (creep) in shear direction at the element with maximum CEEQ for the solder joint shown in Fig. 2. Fig. 3 suggests that the area enclosed by the stress-strain curve increases marginally with increase in the number of cycles; and this means that the accumulated creep energy in the solder joint increases with thermal cycling which may cause thermal fatigue failure of the solder joint. This increase in the accumulated creep energy is more apparent when using the hysteresis plot of the maximum principle stress via CEEQ for the first 5 thermal cycles, (in Fig. 4) in which the area enclosed by the curve is almost linearly increases by number of cycles.

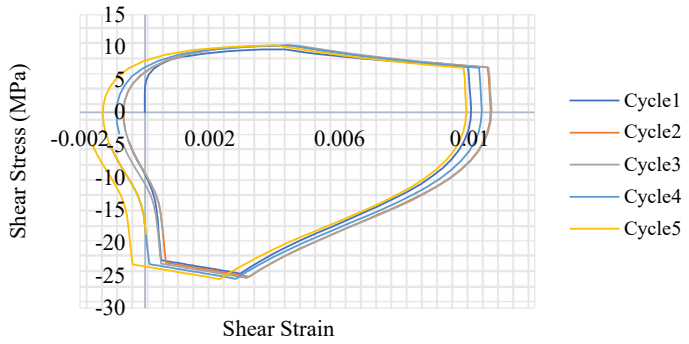

Fig. 3: Plot of the hysteresis shear stress-strain at the element with maximum CEEQ (for 5 thermal cycles).

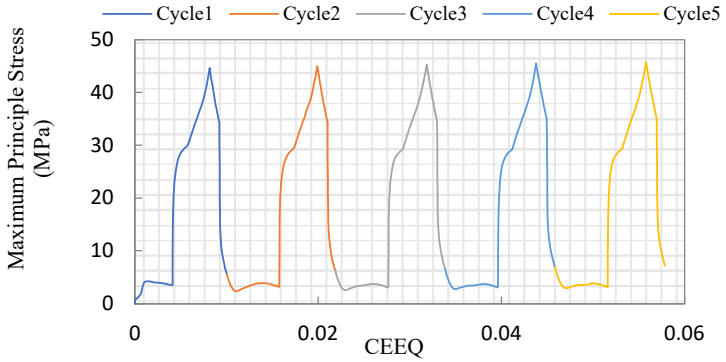

Fig. 4: Plot of the hysteresis maximum principle stress-CEEQ (at the element with maximum CEEQ).

Fig. 5 shows the distribution of the creep-dissipated energy per unit volume for the solder joint shown in Fig. 4, for 5 thermal cycles (ranging from -40°C to 85°C). It can be seen that the distribution of the creep dissipated energy is very similar with the that of the CEEQ (shown in Fig. 2). This indicates that where the CEEQ is maximum, the creep-dissipated energy exhibits the maximum value and vice-versa. Also, the changes in the creep dissipated energy (ECDDEN) at the element with the maximum CEEQ during the first 5 thermal cycles is shown in Fig. 6. As it can be seen in Fig. 5, the side of solder joint exhibits a maximum creep energy and it increases with an increase of the cycle number. This trend is clearly shown in Fig. 6, where by increasing the time (cycle number), the magnitude of the maximum creep dissipated energy increases.

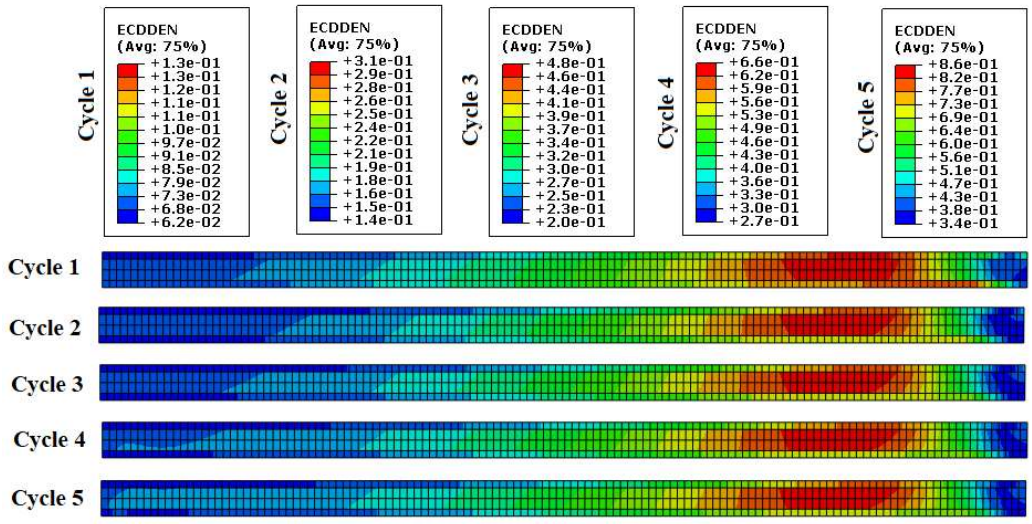

Fig. 5: Distribution of the creep dissipated energy (mJ/mm3) in the solder joints.

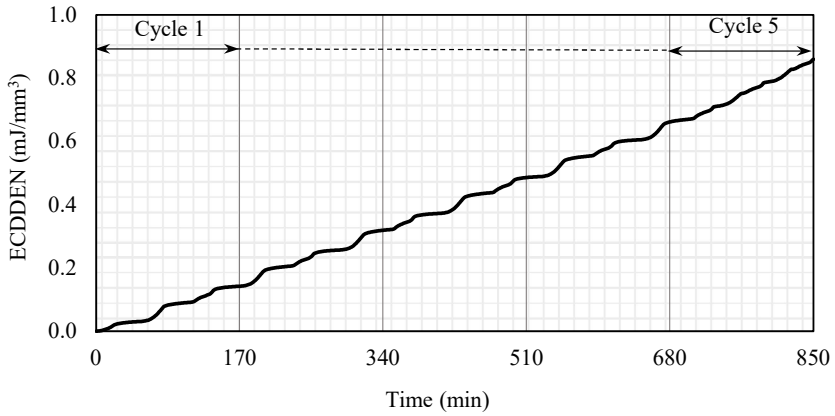

Fig. 6: Creep dissipated energy at the element with maximum CEEQ.

3.2. Fast Cycling Test for Creep-Fatigue Failure Estimation

The empirical models for estimating the creep-fatigue life of SAC (Tin, Silver, Copper) solder alloys joints have been developed by Syed (Syed, 2004). In this approach, he correlated the creep fatigue damage data obtained from laboratory experimental studies with the results of the FEM simulation (i.e. accumulated creep strain and energy density per cycle) to predict thermal creep fatigue life of SAC. His results show that the number of cycles to failure (N_f) for the solder joints under thermal cycling loads are given by the following equation:

$$N_f = (W' w_{acc})^{-1} \qquad \text{(eq. 2)}$$

where W' is the energy density constant for failure (0.0019 for that SAC solder joints) and w_{acc} is the average accumulated creep energy density (per cycle). The average accumulated creep energy density for the solder joints is then given by the following equation:

$$w_{acc} = \frac{\sum W_i V_i}{\sum V_i} \qquad \text{(eq. 3)}$$

where V_i and W_i are the element volume and the accumulated creep energy for each element, respectively.

The Modified Coffin–Manson–Arrhenius lifetime model is one of the most widely used approach for studying the behavior of materials under thermal cycling fatigue; and has been used for predicting the creep life of the solder joints. The solder joint fatigue failure is the mechanical degradation of the solder material due to deformation under cyclic loading and this is known to occur at stress levels below the normal yield stress of solder due to either repeated temperature fluctuations, or mechanical vibrations, or mechanical loads (or combined temperature fluctuations, vibrations and loading). However, in the Coffin-Manson method, the cycling temperature is considered as the main parameter that affects the creep fatigue life. Previous studies have reported on the use of the Modified Coffin-Manson-Arrhenius model for estimating the number of cycles to failure of solder joints for different cycling temperature ranges (Samavatian, et al., 2020; Guyenot, et al., 2011). Held, et al. reported on the creep behavior of the solder joints under fast thermal cycling test and they proposed a descriptive model based on the modified Arrhenius lifetime model for predicting the number of cycles to failure (Nf) for solder joints. The analytical formula that describes the relation between the number of cycles to failure, Nf and cycling temperatures (see equation 4) has been reported by Held, et al. (1997) (Held, et al., 1997).

$$N_f = A * \Delta T^{\alpha} * \exp\left(\frac{Q}{RT_m}\right) \quad \text{(eq.4)}$$

where, Nf *is* the number of cycles to failure, ΔT is the cycling temperature (in Kelvin, R and Q are the gas constant and internal energy, respectively, Tm is the mean cycle temperature (in Kelvin), α is the exponent factor (dependent to the design) and A is a constant for the material.

The exponent factor (α), can be found by rearranging equation 4 for the Field Conditions ($N_{f_{field}}$) and the test conditions ($N_{f_{test}}$), as follows:

$$\frac{N_{f_{field}}}{N_{f_{test}}} = \left(\frac{\Delta T_{field}}{\Delta T_{test}}\right)^{\alpha} * \exp\left(\frac{Q}{R}\left(\frac{1}{T_{m_{field}}} - \frac{1}{T_{m_{test}}}\right)\right) \quad \text{(eq.5)}$$

$$\alpha = \frac{1}{\ln\frac{\Delta T_{field}}{\Delta T_{test}}} \ln\left(\frac{N}{N_{f_{test}} * \exp\left(\frac{Q}{R}\left(\frac{1}{T_{m_{field}}} - \frac{1}{T_{m_{test}}}\right)\right)}\right) \quad \text{(eq.6)}$$

In this study, the exponent factor (α) for the conventional PV module interconnection under any field condition, was found by comparing the correlated FEM results for different temperature intervals (ΔT) with the test condition. Tab. 4 shows the calculated values of accumulated creep energy density per cycle ($wacc$) for different cycling conditions. The values of $wacc$ were calculated (by using equation 3) for the first 5 cycles of each load cycling scenario, and the average is used to estimate the number of cycles to failure (N_f) (see equation

2). Then, using equation 6 gives the value of α based on the comparison of the each field thermal cycling condition with the test thermal cycling condition (temperature ranging from -40°C to 85°C). The results of the study presented in Tab. 4, shows good convergence in the values of $wacc$ for each of the five cycles used for investigating the thermal cycling scenarios; and this provides confirmation that the FEM simulation of the PV module interconnection has been implemented accurately.

To find the generic value of α_m for a given field thermal cycling condition and design, we use the mean value of the calculated α values (see Tab. 4), which was found to be α_m -1.8. This α_m (generic value) found for the conventional PV module interconnection operating under any field thermal cycling condition, can be substituted into equation 4 to determine the number of cycles to failure (N_f) and the associated the creep-fatigue life. This generic value for the exponential factor found in this study can be used for evaluating potential design changes and to facilitate design for reliability validation of different configurations to improve the long-term PV module system reliability.

Tab. 4: Averaged accumulated creep energy density and α for different thermal cycling condition.

T_{min} (°c)	T_{max} (°c)	T_m (k)	ΔT (k)	accumulated creep energy density per cycle (w_{acc})					N_f	α
				w_{acc_1}	w_{acc_2}	w_{acc_3}	w_{acc_4}	$w_{acc_{ave}}$		
-40	**85**	**296**	**125**	**0.157**	**0.158**	**0.158**	**0.158**	**0.158**	**3333**	-
-20	70	298	90	0.088	0.088	0.088	0.088	0.088	5983	-1.93
-10	70	303	80	0.071	0.072	0.072	0.072	0.072	7351	-2.11
-10	60	298	70	0.055	0.055	0.055	0.053	0.055	9530	-1.90
-10	50	293	60	0.042	0.042	0.042	0.040	0.042	12592	-1.74
-10	40	288	50	0.030	0.030	0.030	0.030	0.030	17311	-1.63
-20	60	293	80	0.070	0.070	0.070	0.068	0.070	7271	-1.70
-20	50	288	70	0.055	0.055	0.055	0.055	0.055	9510	-1.54

3.3. Creep-Fatigue Lifetime Estimation

The number of cycles per day used for calculating the creep-fatigue life for PV module operating under thermal cycling has generally been assumed to be l.5 cycles per day (Guyenot, et al., 2011); and this rate 1.5 cycles per day was then used with the calculated number of cycles to failure to determine the numbers of years to failure (Creep-Fatigue lifetime). The effect of different parameters (namely: solder thickness, silver-pad thickness, copper thickness and ribbon width), on the creep-fatigue lifetime of the conventional PV module interconnection (operating under 3 different thermal cycling loads, namely: from temperature ranges of 10°C to 50°C, 0°C to 50°C and 0°C to 60°C) are presented in Fig. 7 to 10. The results showed that for all PV module interconnection dimensions studied, the creep-fatigue lifetime calculated for the thermal cycling loads (namely: the 10°C to 50°C and the 0°C to 50°C) were identical. The results indicate that for all cases studied, the maximum temperature of the cycling load massively impacts the creep-fatigue lifetime; as by increasing the maximum temperature from 50°C to 60°C, the creep-fatigue lifetimes experience 50% decrease. Equally, the results showed that the minimum temperature of the cycling load has much less effect on the creep-fatigue lifetime.

Fig. 7 shows that for solder joints thicker than 20µm, there is no or little change in the creep-fatigue lifetime with increase in the solder joints thickness. The calculated creep-fatigue lifetime of the solder joint of interconnection under thermal cycling in range of 0°C to 50°C (ΔT=50°C) was 26.5 years which is in very good agreement with the reported life (25 years) for similar configuration studied by Guyenot, et al. (2011) (Guyenot, et al., 2011). This provides further validation for the methodology used for this study, as reported in our previous study (Majd, Ekere, 2020a). Fig. 8 shows that the creep-fatigue lifetime increases linearly with increasing silver-pad thickness. For example, increasing the silver-pad thickness from 20µm to 50µm resulted in an increase of about 50% in the creep-fatigue lifetime.

Changing the copper thickness and ribbon width had very marginal effect on the creep-fatigue lifetime (less than 10%) as highlighted by Fig. 9 and Fig. 10. However, for reducing the electrical resistance in the ribbon, the ribbon should be designed to provide enough cross section of ribbon (at least 0.15mm^2). Hence, the

minimum acceptable copper thickness is considered as 150µm when the ribbon width is no less than 1mm. Alternatively, for the ribbons width with less than 1mm (e.g. 900µm), the copper with thickness higher than 150µm should be used. Our results shows that the ribbon with ribbon width of 900µm and copper thickness of 175µm has about 1% less creep-fatigue life compared to the ribbon with 1mm width, and 150µm copper thickness.

In summary, the methodology developed for this study to investigate the effect of the four geometrical parameters on the creep-fatigue lifetime of conventional PV module interconnection provided the results for determining the optimal design for long-term reliability. Our results recommend the 20µm solder thickness, 40µm-50µm silver-pad thickness, 150µm copper thickness and 1mm ribbon width geometry.

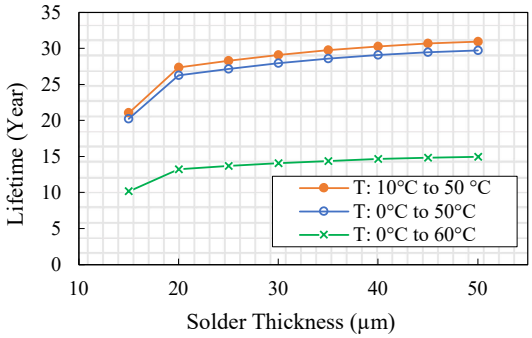

Fig. 7: Effect of solder thickness on the creep-fatigue lifetime of the conventional PV module interconnection operating under 3 different thermal cycling conditions.

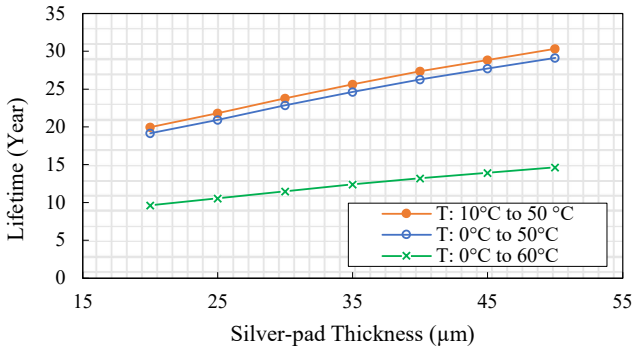

Fig. 8: Effect of silver-pad thickness on the creep-fatigue lifetime of the conventional PV module interconnection.

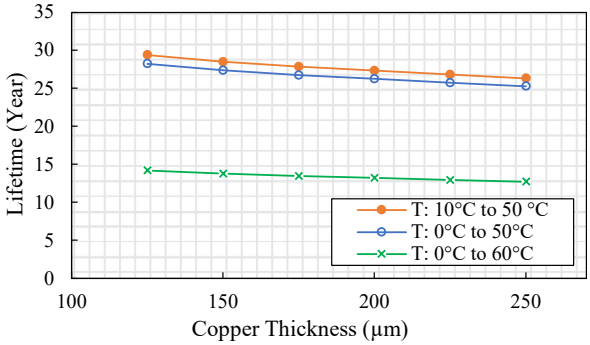

Fig. 9: Effect of copper thickness on the creep-fatigue lifetime of the conventional PV module interconnection.

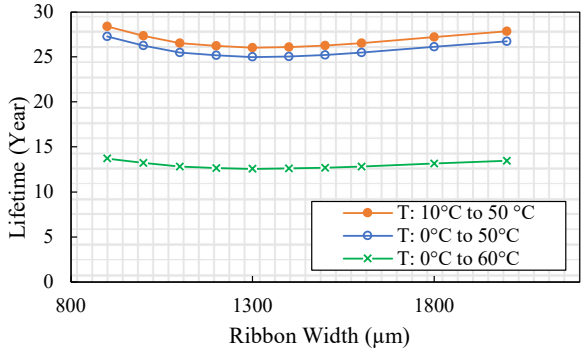

Fig. 10: Effect of ribbon width on the creep-fatigue lifetime of the conventional PV module interconnection.

4. Conclusion

The strain and stress induced by the field thermal cycling loads leads to the creep-fatigue failure mode of the solder joint which adversely affect the reliability of the PV module. An attempt has been made to investigate the creep behavior of the solder joints for the conventional PV module interconnection with different dimensions using the FEM simulation in ABAQUS software. Our results showed that the maximum shear creep strain in the solder joint was located at the corner of the connection area in copper side; and that this location exhibited the highest propensity for creep fatigue failure during the operation. In the study, the total dissipated energy was used to find the number of cycles to failure for each of the PV module interconnections operating under the test and field thermal cycling load. The exponent factor of Coffin–Manson–Arrhenius approach for determining the Creep-Fatigue life of the PV module interconnections was determined to be -1.8; and this generic exponent factor value was then used to determine the solder joint's creep-fatigue life under thermal cycling operating conditions. It was found that, for all cases studied, the maximum temperature of the cycling load massively impacts the creep-fatigue lifetime with a 50% decrease in creep-fatigue lifetimes when the maximum temperature was increased from 50°C to 60°C. On the other hand, the minimum temperature of the cycling load showed much less effect on the creep-fatigue lifetime. There was little or no change in the creep-fatigue lifetime with increase in the solder joints thickness for solder joints thicker than 20µm. similarly, changing the copper thickness and ribbon width had very marginal effect on the creep-fatigue lifetime (≤ 10%) whereas the creep-fatigue lifetime increases linearly with increasing silver-pad thickness. Our results recommend the 20µm solder thickness, 40µm-50µm silver-pad thickness, 150µm copper thickness and 1mm ribbon width geometry. The presented results of the PV module interconnections study can be used to evaluate potential design changes and facilitate the design for reliability validation of different configurations for improving the long-term PV module system reliability.

5. Acknowledgment

The authors would like to acknowledge the support of the Faculty of Science and Engineering, University of Wolverhampton for providing the sponsorship to Dr. Alireza Eslami Majd's Ph.D. study. This work was also partially supported by the INNOVATE UK project No: 833831.

6. References

Akay, H.U., Liu, Y., Rassaian, M., 2003. Simplification of finite element models for thermal fatigue life prediction of PBGA packages. Journal of Electronic Packaging, Transactions of the ASME. 125 (3), 347–353. DOI:10.1115/1.1569956

Amalu, E.H., Ekere, N.N., 2016. Modelling evaluation of Garofalo-Arrhenius creep relation for lead-free solder joints in surface mount electronic component assemblies. Journal of Manufacturing Systems. 39, 9–23. doi.org/10.1016/j.jmsy.2016.01.002

Andersson, C., Sun, P., Liu, J., 2006. Low cycle fatigue of Sn-based lead-free solder joints and the analysis of fatigue life prediction uncertainty. Proceedings of the eight IEEE CPMT International Symposium on High Density Packaging and Component Failure Anlaysis (HDP´06), Shanghai, 09 October. 272–279. DOI: 10.1109/HDP.2006.1707606

Baber, F., and Guven, I., 2017. Solder joint fatigue life prediction using peridynamic approach.

Microelectronics Reliability. 79, 20–31. doi.org/10.1016/j.microrel.2017.10.004

Che, F.X., and Pang, J.H.L., 2004. Thermal fatigue reliability analysis for PBGA with Sn-3.8 Ag-0.7 Cu solder joints. Proceedings of 6th Electronics Packaging Technology Conference (EPTC 2004). (IEEE Cat. No. 04EX971), Singapore, 08-10 December. 787–792. DOI: 10.1109/EPTC.2004.1396715.

Chen, Y., Jin, Y., and Kang, R., 2017. Coupling damage and reliability modeling for creep and fatigue of solder joint. Microelectronics Reliability. 75, 233–238. doi.org/10.1016/j.microrel.2017.03.016

Chen, Z., Zhang, Z., Dong, F., Liu, S., and Liu, L., 2021. A Hybrid Finite Element Modeling: Artificial Neural Network Approach for Predicting Solder Joint Fatigue Life in Wafer-Level Chip Scale Packages. Journal of Electronic Packaging.143 (1). doi.org/10.1115/1.4047227

Cho, Y., Jang, J., and Jang, G., 2018. Sensitivity analysis on the fatigue life of solid state drive solder joints by the finite element method and Monte Carlo simulation. Microsystem Technologies. 24 (11), 4669–4676. doi.org/10.1007/s00542-018-3819-0

Darveaux, R., 2002. Effect of simulation methodology on solder joint crack growth correlation and fatigue life prediction. Proceedings of 50th Electronic Components and Technology Conference (Cat. No.00CH37070), Las Vegas, 21-24 May. 124 (3), 147–154. DOI: 10.1109/ECTC.2000.853299

Depiver, J. a, Mallik, S., and Harmanto, D., 2021. Solder joint failures under thermo-mechanical loading conditions–A review. Advances in Materials and Processing Technologies. 7 (1), 1–26. doi.org/10.1080/2374068X.2020.1751514

Majd, A., and Ekere, N.N., 2019. Numerical analysis on thermal crack initiation due to non-homogeneous solder coating on the round strip interconnection of photo-voltaic modules. Solar Energy. 194, 649-655. doi.org/10.1016/j.solener.2019.10.092

Majd, A., Ekere, N.N., 2020. Study of High Temperature Crack Initiation and Growth in Light Capturing Ribbon (LCR) PV Module Interconnection. Advanced Materials Science and Technology. 2(2). doi.org/10.37155/2717-526X-0202-3

Majd, A., Ekere, N.N., 2020. Crack initiation and growth in PV module interconnection. Solar Energy. 206, 499-507. doi.org/10.1016/j.solener.2020.06.036

Majd, A., Ekere, N.N., Darvazi, A.R., Sedehi, A.A., 2022. Creep- Fatigue Lifetime Estimation of Efficient Photovoltaic Module Ribbon Interconnection. Microelectronics Reliability. 139, 114831. doi.org/10.1016/j.microrel.2022.114831

Guyenot, M., Peter, E., Zerrer, P., Kraemer, F., and Wiese, S., 2011. Enhancing the lifetime prediction methodology for photovoltaic modules based on electronic packaging experience. 12th Intl. Conf. on Thermal, Mechanical & Multi-Physics Simulation and Experiments in Microelectronics and Microsystems, Linz, 18-20 April. 1–4. DOI: 10.1109/ESIME.2011.5765781

Halouani, A., Cherouat, A., Miladi Chaabane, M., Haddar, M., 2020. Modeling and experimental investigation of damage initiation and propagation of LQFP package under thermal cycle. Microsystem Technologies. 26, 3011–3021. doi.org/10.1007/s00542-020-04884-9

Han, C., Han, B., 2014. Board level reliability analysis of chip resistor assemblies under thermal cycling: A comparison study between SnPb and SnAgCu. Journal of Mechanical Science and Technology. 28 (3), 879–886. doi.org/10.1007/s12206-013-1154-z8

Held, M., Jacob, P., Nicoletti, G., Scacco, P., Poech, M.-H., 1997. Fast power cycling test of IGBT modules in traction application. Proceedings of second international conference on power electronics and drive systems, Singapore, 26-29 May. 1, 425–430. DOI: 10.1109/PEDS.1997.618742

Hsieh, M., Tzeng, S., 2014. Solder joint fatigue life prediction in large size and low cost wafer-level chip scale packages. 15th International Conference on Electronic Packaging Technology, Chengdu, 12-15 August. 496–501. DOI: 10.1109/ICEPT.2014.6922704

Hund, T.D., Burchett, S.N., 1991. Solder fatigue reduction in point focus photovoltaic concentrator modules. Proceedings of The Conference Record of the Twenty-Second IEEE Photovoltaic Specialists Conference, Las Vegas, 07-11 October. DOI: 10.1109/PVSC.1991.169310

IEA, 2020. Solar PV - Analysis - IEA.

International Electrotechnical Commission, 2016. IEC 61215-2: Terrestrial Photovoltaic (PV) Modules – Design Qualification and Type Approval -Part 2: Test procedures.

IRENA, 2019. Future of solar photovoltaic: Deployment, investment, technology, grid integration and socio-economic aspects (A Global Energy Transformation: paper).

Itoh, U., Yoshida, M., Tokuhisa, H., Takeuchi, K., Takemura, Y., 2014. Solder joint failure modes in the conventional crystalline Si module. Energy Procedia, 55, 464–468. doi.org/10.1016/j.egypro.2014.08.010

Knecht, S., Fox, L.R., 1990. Constitutive relation and creep-fatigue life model for eutectic tin-lead solder. IEEE Transactions on Components, Hybrids, and Manufacturing Technology. 13 (2), 424–433. DOI: 10.1109/33.56179

Lee, W.W., Nguyen, L.T., Selvaduray, G.S., 2000. Solder joint fatigue models: review and applicability to chip scale packages. Microelectronics reliability. 40 (2), 231–244. doi.org/10.1016/S0026-2714(99)00061-X

Lee, Y.C., Chiang, K.N., 2019. Reliability Assessment of WLCSP using Energy Based Model with Inelastic Strain Energy Density. Proceedings of International Conference on Electronics Packaging (ICEP), Niigata, 17-20 April. 329–332. DOI: 10.23919/ICEP.2019.8733436

Li, X., Sun, R., Wang, Y., 2017. A review of typical thermal fatigue failure models for solder joints of electronic components. Proceedings of IOP Conference Series: Materials Science and Engineering, 3rd International Conference on Applied Materials and Manufacturing Technology (ICAMMT 2017), Changsha, 23–25 June. 242 (1). DOI:10.1088/1757-899X/242/1/012103

Ma, H., 2009. Constitutive models of creep for lead-free solders. Journal of Materials Science. 44 (14), 3841–3851. doi.org/10.1007/s10853-009-3521-9

Ogbomo, O.O., Amalu, E.H., Ekere, N.N., Olagbegi, P.O., 2018. Effect of operating temperature on degradation of solder joints in crystalline silicon photovoltaic modules for improved reliability in hot climates. Solar Energy. 170, 682–693. doi.org/10.1016/j.solener.2018.06.007

Samavatian, V., Iman-Eini, H., Avenas, Y., Samavatian, M., 2020. Effects of creep failure mechanisms on thermomechanical reliability of solder joints in power semiconductors. IEEE Transactions on Power Electronics. 35 (9), 8956–8964. DOI: 10.1109/TPEL.2020.2973312

Schubert, A., Dudek, R., Auerswald, E., Gollhardt, A., Michel, B., Reichl, H., 2003. Fatigue life models for SnAgCu and SnPb solder joints evaluated by experiments and simulation. Proceedings of 53rd Electronic components and technology conference. New Orleans, 27-30 May. 603–610. DOI: 10.1109/ECTC.2003.1216343

Steinhorst, P., Poller, T., Lutz, J., 2013. Approach of a physically based lifetime model for solder layers in power modules. Microelectronics Reliability. 53 (9–11), 1199–1202. doi.org/10.1016/j.microrel.2013.07.094

Syed, A., 2004. Accumulated creep strain and energy density based thermal fatigue life prediction models for SnAgCu solder joints. Proceedings of 54th electronic components and technology conference. (IEEE Cat. No. 04CH37546), Las Vegas, 04-04 June. 1, 737–746. DOI: 10.1109/ECTC.2004.1319419

Tsou, C.Y., Chang, T.N., Wu, K.C., Wu, P.L., Chiang, K.N., 2017. Reliability assessment using modified energy based model for WLCSP solder joints. Proceedings of International Conference on Electronics Packaging (ICEP), Yamagata, 19-22 April. 7–15. DOI: 10.23919/ICEP.2017.7939312

Yao, Y., Long, X., Keer, L.M., 2017. A review of recent research on the mechanical behavior of lead-free solders. Applied Mechanics Reviews. 69 (4). doi.org/10.1115/1.4037462

Zhang, X.P., Yin, L.M., Yu, C.B., 2008. Thermal creep and fracture behaviors of the lead-free Sn–Ag–Cu–Bi solder interconnections under different stress levels. Journal of materials science: materials in electronics. 19 (4), 393–398. doi.org/10.1007/s10854-007-9351-0

Zhu, Y., Li, X., Gao, R., Wang, C., 2014. Low-cycle fatigue failure behavior and life evaluation of lead-free solder joint under high temperature. Microelectronics Reliability. 54 (12), 2922–2928. doi.org/10.1016/j.microrel.2014.08.016

Energy Performance Investigation of PVT assisted Heat Pump System for a Net Zero Office Building

Min-Hwi Kim[1], Jongkyu Kim[1], Gwangwoo Han[1], Youngsun An[1], and Hongjin Joo[1*]

[1] Renewable Heat Integration Laboratory/Korea Institute of Energy Research, Daejeon (South Korea)

Abstract

This paper investigated the energy saving potential of the photovoltaic and solar thermal panel (PVT) assisted multi-source heat pump system for net zero office buildings. We proposed the schematic of the PVT assisted multi-source heat pump system to serve heating and domestic hot water load. The energy saving potential of the proposed system was also analyzed by simulation research compared with the conventional system. The conventional system composed of the air-source heat pump integrated with PV system. It was found that the proposed system can save 33% of operating energy consumption compared with conventional system. The renewable energy penetration rate of the proposed system showed 14.8% higher than the conventional system.

Keywords: PVT assisted heat pump system, multisource heat pump, BIPVT

1. Introduction

Over the last decades, the interests in terms of the renewable energy system has been raised to improve the renewable energy penetration rate and energy efficiency of the building service system. Recently, photovoltaic and solar thermal panel (PVT) system has been interested caused by the energy generation density per unit area is much higher than the conventional photovoltaic (PV) and solar thermal collector. The temperature raises of PV panel surface is critical causes of the degradation of power generation. PVT is one of the solutions to cool the PV panel and also produce thermal energy sources for heat pump system to serve heating and domestic hot water. Also, recently researches have been conducted to reduce the installation cost of PVT, the PVT panel is integrated with the building surfaces and wall, so it calls building integrated PVT (BIPVT). Thermal demand of heating season is much higher than the cooling season. The south-facing vertical wall is good place to install the solar thermal panel. It caused that the solar radiation of the south-facing wall in cooling season is much lower than that in heating season. The stagnation problem of solar collector can be solved by installing the PVT into the south-facing wall. This paper presents the energy saving potential of the PVT assisted multi-source heat pump compared with the conventional air-source heat pump system.

2. PVT assisted multi-source heat pump system

Figure 1 shows the schematic of PVT assisted multi-source heat pump system and conventional heat pump system. In this proposed system, the PVT system simultaneously produced electric and thermal energy. When the solar irradiation reached panel, about 20% of electricity and 25% of thermal energy were produced. The electricity is directly used building or operation of heat pumps, the thermal energy is stored into the buffer thermal energy storage (TES). The temperature above 50 °C can supply directly to the heating demand or hot water demand, but the high temperature leads the degradation of power generation in PV panel. In this research, the target temperature of PVT outlet water is set at 35 °C. Then, the stored thermal energy is used as a heat source of heat pump. The heat pump produces over 50 °C hot water and stored into another TES. The size of this TES should be covered by the daily thermal load. During the heating season, the daytime stored thermal energy is used as a heat source of heat pump during the daytime. Caused by the weather condition, the PVT cannot produce thermal energy, the air-source heat pump is operated. In cooling season, the thermal energy produced by the PVT is stored into the buffer TES during the daytime, and cooling water is produced by the heat pump with air-source. Then, during the nighttime, the hot water is produced by the heat pump with buffer TES heat source.

© 2022. The Authors. Published by International Solar Energy Society
Selection and/or peer review under responsibility of Scientific Committee
doi:10.18086/eurosun.2022.07.04 Available at http://proceedings.ises.org

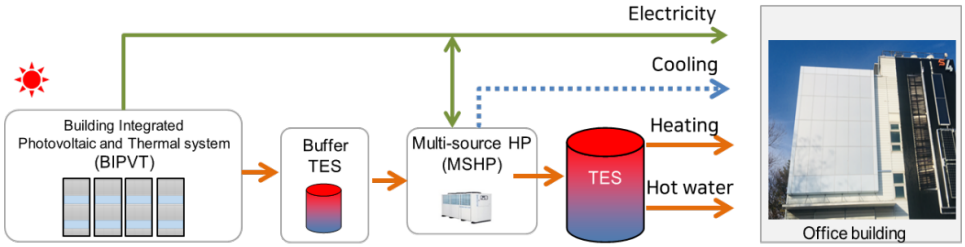

(a) PVT assisted heat pump system

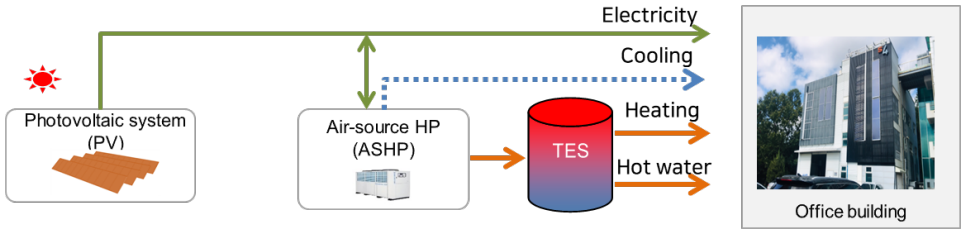

(b) Conventional system

Fig. 1: Overview of system schematics

3. Simulation study

The energy saving potential of the proposed system was analyzed by the simulation work. In order to simulate the PVT panel, the manufactured data was used in Polysun software. The power generation and thermal energy output was simulated using Polysun software (Fig.2). The selected office building is four-story and total floor are of 400 m^2, it is assumed that the PVT panel is installed into the south-facing wall. The electric load and thermal load (i.e., heating, hot water and cooling demand) have been monitored, and we used measured data. We found that the annual heating and hot water load of the building in each floor is 10,291 kWh_{th}. For the heat pump simulation, experimental data for multi-source heat pump was used. This multi-source heat pump is installed in the greenhouse, and 30 RT capacity of heating and cooling. This heat pump uses air source and water source, and the heat source can be selected manually or automatically. The heat pump operation schematic is that the water source is primary used as a heat source, but when the temperature of heat source is lower or higher than the target temperature, the heat pump is automatically changed by the air-source operation mode. The heat pump simulation model is generated by the measured data, and it serves the coefficient of performance (COP) depends on the inlet source side water temperature, flow rate, outlet load side water temperature, and flow rate. In order to serve heating and domestic hot water, about 1000 Liter of storage tank was used for the PVT source heat pump system. The air-source heat pump system used 300 Liter and 600 Liter of water storage tank for serving domestic hot water and heating, respectively.

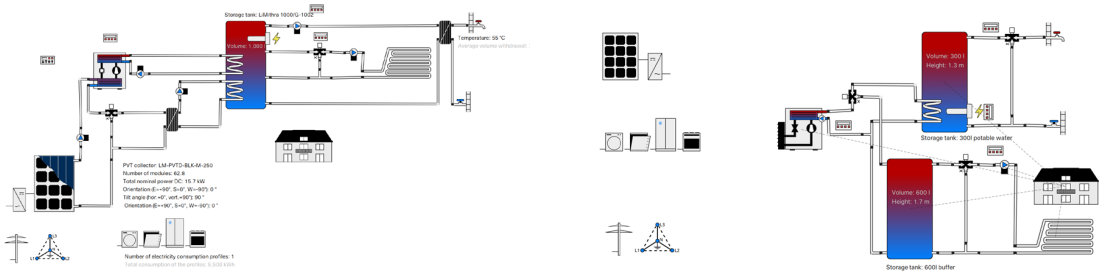

(a) PVT source heat pump system configuration (b) PV and air-source heat pump system configuration

Fig. 2: Overview of system schematics

4. Results

In Table 1 below, hourly simulation based annual energy performance on the proposed system was investigated compared with the conventional system. The installation capacity of PVT is 15.4 kWp and 88 m^2 in each floor. The total annual power generation of PV is 6.1 MWh. The heat pump operating energy consumption of the proposed

system can save 33% for serving heating and hot water demand via conventional system. It mainly caused that the proposed heat pump enhanced over 30% of COP compared with air-source heat pump. It was found that the renewable energy penetration rate is predicted to be 82.0% and 96.8 % of conventional system and proposed system, respectively. The proposed system can improve 14.8% point of renewable penetration rate.

Tab. 1: Impact of system configurations

	PV-ASHP	PVT-MSHP
Heating and hot water demand	10,291 kWh_{th}/a	10,291 kWh_{th}/a
Cooling demand	12,134 kWh_{th}/a	12,134 kWh_{th}/a
Heat pump power consumption	7,475 kWh_{el}/a	6,332 kWh_{el}/a
PV generation	6,132 kWh_{el}/a	6,132 kWh_{el}/a
Net-zero	82.0%	96.8%

5. Conclusions

In this paper, the energy saving potential of the PVT assisted multi-source heat pump has been investigated via compared with the conventional air-source heat pump system. It was found that heat pump operating energy consumption of the proposed system can save 33% for serving heating and hot water demand via conventional system. It was also found that the renewable energy penetration rate of the proposed system can improve 14.8% point of compared with that of the conventional system.

6. Acknowledgments

This work was conducted under framework of the research and development program of the Korea Institute of Energy Research (C2-2474).

7. References

Miglioli, A., Aste, N., Del Pero, C., Leonforte, F., 2021. Photovoltaic-thermal solar-assisted heat pump systems for building applications: Integration and design methods. Energy and Built Environment.

Simonetti, R., Molinaroli, L., Manzolini, G., 2019. Experimental and analytical study of an innovative integrated dual-source evaporator for solar-assisted heat pumps. Solar Energy. 194, 939-951.

Qu, M., Chen, J., Nie, L., Li, F., Yu, Q., Wang, T., 2016. Experimental study on the operating characteristics of a novel photovoltaic/thermal integrated dual-source heat pump water heating system. Applied Thermal Engineering. 94, 819-826.

Wang, G., Quan, Z., Zhao, Y., Sun, C., Deng, Y., Tong, J., 2015. Experimental study on a novel PV/T air dual-heat-source composite heat pump hot water system. Energy and Buildings, 108, 175-184.

Fire protection requirements and solutions for the implementation of BIPV on a high-rise residential building in Frankfurt/Germany

Michael Krause[1], Peter Funtan[1], Christof Erban[2], Roland Müller[3]

[1] Fraunhofer Institute for Energy Economics and Energy System Technology IEE, Kassel (Germany)

[2] SUNOVATION Produktion GmbH, Elsenfeld (Germany)

[3] bauart Konstruktions GmbH & Co. KG, Darmstadt (Germany)

Abstract

Especially for high-rise buildings with their limited roof areas, the activation of the façade with photovoltaics is an important opportunity to improve the energy efficiency of these buildings. With respect to a residential high rise building in Frankfurt, Germany, the research project PV-HoWoSan has been investigating the most important issues for installing photovoltaics in the façade from the point of view of the building owner: statics, fire protection, secure distribution of the generated electricity, Life-cycle assessment and economic efficiency. A major task in order to install the system at the building has been to go through the approval process. PV modules are classified according to an adapted US standard being different to the European standardization system. However, since PV modules usually contain polymer, a classification as non-flammable is not possible within EN 13501. Thus, the investigations within PV-HoWoSan focused especially on the aspect of fire protection. Therefore, a new façade system based on stainless steel material and several fire protection features has been designed. In order to get the required authority approvals, a system burning test was carried out at an official test facility. The paper deals with the experience of the design and approval process.

Keywords: PV façade system, High-rise buildings, system burning tests, PV fire classification

1. Introduction

According to Diefenbach et al., the majority of high-rise residential buildings in Germany and Europe has been built in the period 1985-1978 and are now in a state to be retrofitted. In the context of upcoming renovation measures, the activation of the building envelope with photovoltaics (PV) in combination with thermal insulation offers the opportunity to generate electricity locally in such buildings and to give them a modern and future-oriented design. Often, supposedly high investment costs and uncertainties in the planning process (fire protection, building law, building physics, statics) prevent the use of PV façades.

To overcome these obstacles, the research project "PV-HoWoSan: Development and demonstration of a cost-reduced, industrially produced PV façade system for the renovation of multi-storey residential high-rises buildings", funded by the German Federal Ministry for Economic Affairs and Energy BMWi started November 2017. The research project set itself the goal of using an actual high-rise residential building to investigate the most important issues from the point of view of the housing association - statics, fire protection, secure distribution of the generated electricity, LCA and economic efficiency - to go through the approval process and to install the system on the building. In order to develop an economical and permit-capable BIPV façade system, additional experts have been integrated into the research project.

2. The Demo Building

Fig. 1 shows the demonstration building before renovation. The high-rise residential building of ABG Holding Frankfurt, the biggest local housing company in Frankfurt, built in 1976, has 102 residential units on 16 floors, a height of approx. 47 m and a total floor space of approx. 7,500 m². The existing façade consists of concrete sandwich elements that have a polystyrene core as internal insulation. For the renovation of the façade, the use of a composite thermal insulation system was planned, in which 2 PV strips with a total area of 120 m² were intended

© 2022. The Authors. Published by International Solar Energy Society
Selection and/or peer review under responsibility of Scientific Committee
doi:10.18086/eurosun.2022.07.05 Available at http://proceedings.ises.org

to be additionally installed on the southern building side. As a high-rise building, the building is classified for approval purposes according to the German “Musterbauordnung” as a special building in building class 5 (GK 5). With respect to this, the Hessian Building Code (HBO), the Administrative Regulation on Technical Building Regulations (H-VV TB) and the Hessian High-Rise Building Guideline (H-HHR-2012) had to be considered. The central fire protection requirement of GK5 is that exterior walls must consist only of non-combustible building materials. In accordance with the high-rise building directive, this requirement also applies to the exterior wall cladding (insulation and facades) of high-rise buildings. The planned use of the PV elements from the project partner SUNOVATION, which are classified as "flame-retardant" (B1), and the necessary electrical cabling represented a deviation from the building regulations (in this case, the special building regulation H-HHR) due to the lack of a generally valid building classification approval for use on a high-rise building.



Fig. 1: Left: View of the façade of the demonstration building in Frankfurt foreseen for the installation of two strips PV. Right: CAD-Model visualizing the planned PV-strips (ABG)

3. Fire protection requirements and design approach

Immediately at the kick-off meeting of the PV-HoWoSan project, it became clear that the fire at the Grenfell Tower in London in June 2017 would also have an impact on the PV-HoWoSan project. Initial discussions with the Frankfurt building inspectorate and the responsible fire protection expert led to the expectation that the design requirements for ensuring fire protection would be higher than assumed at the time of the project application.

Right from the start, the Frankfurt building inspectorate considered the aluminum substructure material commonly used for PV systems to be inadequate in terms of fire protection, so that it was necessary to switch to (stainless) steel. Furthermore, additional design measures were required to prevent the spread of fire. These referred, for example, to integrate cables in special fire protection ducts, the floor-by-floor partitioning of fire compartments by means of specially developed fire bars or to measures for the thermal separation of the PV façade from the concrete sandwich elements (in particular to the combustible insulation of the sandwich elements) of the existing façade.

In a further coordination meeting with the building inspectorate and the Frankfurt Fire Department, the performance of a fire test at a accredited testing and certification center for fire protection was required as a prerequisite for the issuance of an individual approval (ZIE). At the same time, planning for the refurbishment of the Mainfeld 7 high-rise building resulted in a short time slot for the installation of a PV façade by the client,

ABG, which effectively reversed the planned course of the project. According to the project plan, the knowledge gained from the design, assembly and installation of the test façade to be built at Fraunhofer IEE was intended to be incorporated into the demo project. As a consequence, it was decided to contact various testing institutes as soon as possible. With MFPA-Leipzig, a test institute could be identified at which it was possible to carry out a fire test in May 2018. With this date, it seemed possible to align the necessary building applications and installation work of the PV façade with the construction schedule of ABG for the renovation of the Mainfeld 7 high-rise building. Therefore, it was decided to start with the development of the novel PV façade system designed by the Richard-Grün-Institut (RGI) for the demo façade and not to wait for the developments on the test façade at Fraunhofer IEE. Due to the short lead time until the fire test, the essential requirements of the building inspectorate and fire department were adopted 1-to-1 in the creation of the fire test model.

The facade system chosen was the suspended pilaster strip approach of the Richard Grün Institute, which promised prefabrication of the facade and rapid on-site assembly. Fig. 2 illustrates the structural design, which consists of horizontal transoms and vertical pilaster strips. The pilaster strips hold the PV modules statically via a suspension system and accommodate the vertical cabling by being designed as a closed channel. Due to the uncertainty about the load-bearing capacity of the existing curtain wall, it was decided to implement the load transfer using the roof. By doing this, the entire structure suspends from the parapet of the high-rise building via the pilaster strips. The horizontal transoms have been designed as closed fire ledgers which are responsible for the residual load-bearing capacity as well as the absorption of the wind loads through the integrated facade anchors.

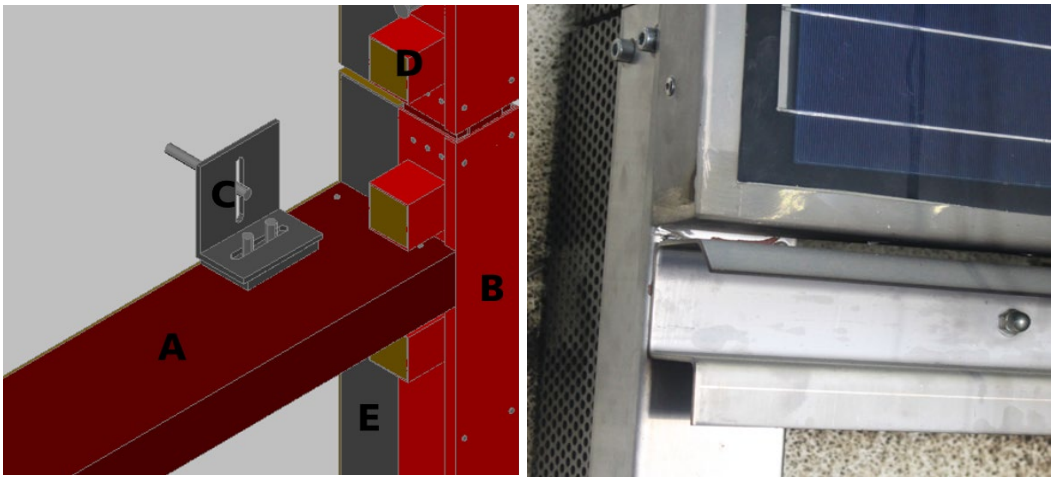

Fig. 2: Left: Structural design of the façade system (A: horizontal fire bar filled with mineral wool, B: vertical pilaster strip, C: façade anchors with slotted holes, D: cable outlets, E: perforated plate reinforcement for horizontal rear ventilation) (RGI). Right: Suspended PV module above the fire bar that extends into the plane of the PV modules.

Fig. 3 illustrates how the fire test was carried out at MFPA Leipzig GmbH. Due to the unavailability of a hall for large-scale fire tests, a full-scale fire test simulating a room fire was carried out in coordination with the Frankfurt Building Inspectorate and in accordance with DIN 4102:20:2017-10 (Fire behavior of building materials and components - Part 20: Supplementary verification for the assessment of the fire behavior of exterior wall claddings). Due to the compromise regarding the test facility, the actual test and thus assessment duration was extended from the required 20 minutes to 30 minutes. The evaluation factors for the fire test were:

- *No enlargement of the primary fire (gas burner) due to the PV design*
- *Effectiveness of fire bars to prevent fire spreading across floors*
- *No independent further burning of the PV construction after the primary fire was distinguished*
- *No dripping of burning components of the construction. Only individual drops of cable insulation can be tolerated*
- *No falling down of construction parts, except for shattered glass*
- *Assessment of smoke development*
- *Assessment of the overall structure under fire exposure*
- *Evaluation of the temperature development behind the External Thermal Insulation Composite System on the surface of the raw test stand (surface of masonry) in order to predict the expected temperature*

development of the facing layer / polystyrene insulation.

- *Proof of the effectiveness of the fire protection bricks installed in the pilaster strips.*



Fig. 3: Carrying out a fire test at MFPA Leipzig. Left: Before the start. Middle: During the test. Right: After distinguishing the primary burning flame

The fire test showed that the essential requirements for fire behavior have been fulfilled by the developed design. Apart from a slight burning of the flamed PV module, the associated low smoke development and the bursting of only small glass surfaces in the area of the primary flame, the PV module stops to burn shortly after the primary flame was extinguished. Thus, it could be shown that the developed construction behaves approximately like a non-combustible system despite consisting of combustible components. Following this, the use in the planned high-rise building renovation appeared to be approvable.

Due to the increased fire protection requirements, which specifically demanded the use of stainless steel instead of aluminum, as well as detailed design adjustments to the RGI basic concept, a significant cost increase for the demo façade was to be expected compared to the original assumption at the time of the project application. Therefore, it was decided that only one PV strip would be realized due to the limited funding volume.

4. First construction phase: insulation measure and facade anchors

On the basis of the fire successful test carried out in May 2018, the application for constructional permit for the statically relevant fastening points for setting the anchors, as well as the roof retaining points was then submitted in October 2018. The planned fixing points of the PV façade construction, based on the fire test, especially the façade anchors with thermal separation via two non-combustible calcium silicate plates (Fig. 4, left), were described in the application. By notification in December 2018, this building application for the installation of the attachment points for a PV strip was approved, so that the planning and implementation of the necessary work could be pursued. This included, for example, the development of a possibility for strain relief of the cabling within the pilaster strip (comp. Fig. 4, right)

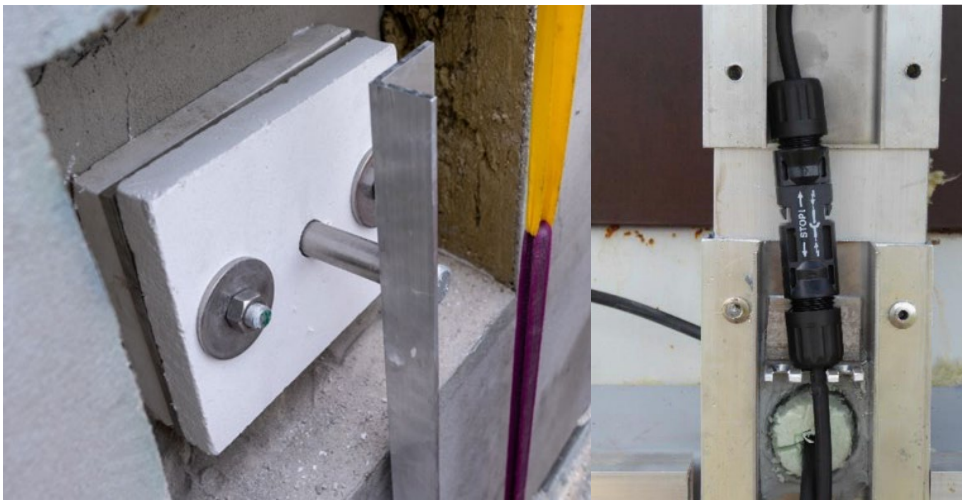

Fig. 4: Left: Facade anchors with thermal separation via calcium-silicate plates (Stark Ingenieure). Right: Strain relief within the pilaster strips

An additional core drilling in the area of the anchors and the replacement of the EPS in the area of the core drilling by mineral wool within the facing shell were to be dispensed when installing the PV facade anchors due to costs and structural reasons. Since this represented a deviation from the fire test carried out at the MFPA in Leipzig, an additional thermal simulation of the anchor situation was carried out. Based on these simulations, the building application was adapted and the execution was approved by the building supervisory authority in November 2019. With the installation of the facade anchors to accommodate the PV facade, the energy refurbishment of the building "Im Mainfeld 7" was completed in May 2019, as shown in Fig. 5. By using these fixed points, almost any facade design could be implemented later on, taking into account the static boundary conditions.

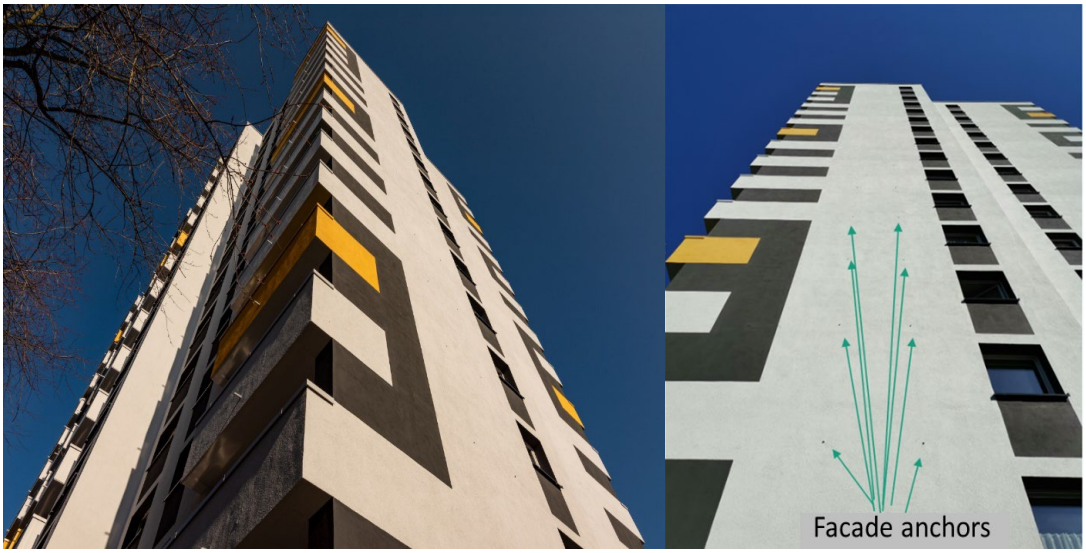

Fig. 5: Demo facade with facade anchors after renovation (ABG).

For the implementation of the second construction phase - the installation of the PV façade structure a decision about responsibilities had to be taken. Due to warranty aspects that could not be fulfilled by the research consortium, an external contractor was planned to be assigned for the installation of the façade. For this purpose, intensive discussions took place with external companies regarding interfaces and responsibilities. However, a bid submitted by a large façade company in March 2020, together with the costs incurred anyway for e.g. PV modules, inverters, implementation planning, fire protection and structural analysis reports, building applications, ZIE, significantly exceeded the originally estimated costs despite the reduction to only one PV-strip. The reasons for the high costs include:

- *High fire protection requirements--> Stainless steel as material, fire bar, bulkheading*

- *Newly developed type of construction, which includes specific elements especially for fire protection reasons → No use of standard profiles*
- *No experience with newly developed system and lack of implementation planning → Risk surcharge*
- *The installation concept, for which the scaffold was no longer available, via access cages and/or industrial climbers*
- *Cross-trade construction → Coordination effort between electrical and facade construction with regard to planning and execution*
- *Existing building → Prefabrication difficult, tolerance*
- *Warranty coverage → High replacement costs in case of damage*
- *Relatively small PV area leads to high kW_{peak} costs*
- *Uncertainties about load transfer of floor slabs → Suspension system*
- *High-rise building → Static requirements, wind loads (static, especially in case of fire), working at height, time required for installation*

5. Further developments at the Fraunhofer IEE test stand

To overcome some of these aspects, the development of a test façade was pursued in parallel. The test façade was to be set up at the Fraunhofer IEE test stand and was planned to be investigated by measurement. Specific approaches were the development of prefabrication potentials, the assembly options, and the optimization of rear ventilation to increase the PV performance, especially in the case of full-surface occupancy of the facade with PV modules.

For this purpose and to support the construction of the façade, a 3-D model of the planned PV installation was developed. The implementation of the test façade is based on the construction principle of the frames and façade construction parts developed for the demonstration building in Frankfurt, whereby the façade approach was selected so that different module sizes can be integrated. As with the demonstration building in Frankfurt, the façade system was suspended from the roof, with additional anchoring in the floor slabs. Furthermore, the central fire protection requirements from Frankfurt were adopted. Significant extensions of the original approach are:

- *Due to the elemented construction method, arbitrarily designed facades with windows, doors, porches, etc. can be served*
- *All perimeter building endings were developed and integrated (floor, roof and side finishes, as well as building corners).*
- *Two energy processing concepts were implemented in the facade: string inverter and module inverter*
- *Line installations can be made in vertical and horizontal way*
- *The assembly and installation work clearly demonstrated the optimization potential of the system.*

Fig. 6 illustrates the assembly process (left), in which a wire rope hoist attached to the roof was used to mount the modules as well as the finished structure (right) facing south-east on the right-hand side and south-west on the left-hand side. The development of the test façade and the test setup have shown that the pilaster strip suspension system further developed in the project can be used to realize a PV façade as a curtain-type rear-ventilated façade with all the required fire protection elements. At the same time, however, it was also shown that a lack of experience with a new system approach as well as manufacturing tolerances can greatly complicate and thus delay the construction and assembly process.



Fig. 6: Left: Test facade during assembly (left) and after finalization (right).

On the basis of the experience gained at the test stand, discussions were held with other façade manufacturers, with whom, however, it was still not possible to achieve a significant cost reduction. In some cases, a bid was not submitted due to technical issues (again, the warranty aspects). Since the building owner cannot assume the additional costs arising in the current situation and the costs are not yet in a justifiable ratio to the electricity yield, the implementation of the developed PV façade cannot be pursued at the demonstration building at the present time, despite the façade anchors already installed.

6. Conclusions

The research project PV-HoWoSan on which this experience report is based, has shown that the implementation of BIPV on high-rise buildings faces great challenges. However, the possibility of developing suitable solutions and of obtaining approval for the construction of a photovoltaic façade designed was demonstrated using an intensive dialog with the responsible approval authorities. The central boundary conditions and possibilities with regard to the approval process are:

- *The use of photovoltaics on a high-rise building always represents a deviation from the respective building code.*
- *In the building class for special constructions, no time limits for the finalization of the approval process are specified by the authorities, which may have a significant impact on the construction process and may represent a risk difficult to be considered.*
- *In close coordination with the building inspectorate and, if necessary, the fire department, ways can be identified so that a building component consisting in part of flame-retardant materials behaves like a non-combustible building component/system*
- *For the design of such systems, the exact analysis of the present building situation is necessary. Important aspects here are:*
    - *Building height*
    - *Access for the fire department*
    - *Hazard situation of the facade where PV is to be installed:*
        - *Arrangement of windows, distance to windows and openings*
        - *If applicable, accessible spaces below the facade*

  - *Fire alarm system and/or extinguishing system available*
  - *Structure of the existing facade: combustible materials installed*
  - *Type of PV modules: Glass-glass or glass-foil modules*
- *Fire tests, both Single Burning Item (SBI) and large-scale fire tests can show important information regarding the fire behavior of products or new system approaches*
- *Existing buildings often have uncertainties regarding the load-bearing capacity of e.g. facing shells or also regarding the exact position of floor slabs. Alternative fastening options such as the roof suspension developed in the project offer promising possibilities to ensure stability even for high-rise buildings*

However, the project has further shown that standardized systems are not available for the implementation of PV on buildings with high fire safety requirements, such as those from building class 5. Significant deviations from standardized designs, however, can result in significant additional costs and are often difficult to implement economically without additional funding. This affects all phases of the implementation of such projects, from preliminary and detailed design, through installation and commissioning, to the warranty period. Here, it is important to have a coordinated and experienced interdisciplinary team in which the interfaces and responsibilities are clearly defined, e.g. by a general contractor. In addition, a close connection to the approval authorities need to be ensured. The PV-HoWoSan project has shown that legally reliable and generalizable statements on new technology approaches can only be obtained to a limited extent from both the approval authorities and the specialist planners.

Furthermore, façade-integrated photovoltaics generally have lower yields compared to roof systems due to their less favourable orientation, which is why economic viability cannot be achieved through electricity feed-in alone. However, the electrical yield of façade-integrated systems is better suited to the use of electricity in the building compared to roof integrated systems. Thus, since contract models for direct use of electricity by tenants are becoming increasingly popular in multi-storey residential buildings, a high rate of owner-use significantly improves economic viability. This is additionally supported if a high-quality façade, e.g. a ventilated façade or a curtain wall, is to be realized with a high-quality appearance even without photovoltaics. In this case, costly substructures do not have to be financed by the electricity yield alone.

The same applies to the question of whether Building Integrated PV (BIPV) is to be attached to new or to existing buildings. With regard to statics and a high degree of prefabrication, integration in existing buildings can lead to great uncertainties, which are usually not be faced in new buildings. The same applies to the issue of fire protection. In buildings classified as special-purpose buildings, high fire protection requirements must be met in new buildings anyway. Hereby, fire alarm systems and extinguishing systems, which can be for example extended to extinguish fire in the facade, are usually available as well as access options for the fire department and sufficiently dimensioned escape routes. All this can facilitate the argumentation of deviations from the building code in the fire protection concept.

In summary, the PV-HoWoSan research project has shown important boundary conditions and obstacles for the implementation of BIPV on special buildings like high-rise buildings. In particular, even if the actual implementation on the demo building was not realized due to cost reasons, a path for planning, approval and implementation could be shown. Such a path could be followed in case of significantly more favourable boundary conditions at alternative buildings.

7. Acknowledgments

The research project PV-HoWoSan has been funded by the Federal Ministry for Economic Affairs and Climate Actions (BMWK) based on a decision of the German Bundestag.

8. References

Diefenbach et al.: Grundlagen für die Entwicklung von Klimaschutzmaßnahmen im Gebäudebestand – Untersuchung über die bautechnische Struktur und den Ist-Zustand des Gebäudebestandes in Deutschland, Juli 2007, Editor: BMVBS /BBR BBR-Online-Publication 22/07

HBO: Hessische Bauordnung HBO (2018): Hessische Gesetze und Verwaltungsvorschriften, July 2018. Hessisches Ministerium für Wirtschaft, Energie, Verkehr und Wohnen, Referat VII 3 (Baurecht)

H-VV TB: Hessische Verwaltungsvorschrift Technische Baubestimmungen (H-VV TB), Hessisches Ministerium

für Wirtschaft, Energie, Verkehr und Wohnen

H-HHR: Hessische Richtlinie über den Bau und Betrieb von Hochhäusern (Hessische-Hochhaus-Richtlinie - H-HHR) Hessische Gesetze und Verwaltungsvorschriften, 2012, Appendix HE 12 to lfd. Nr. A 2.2.2.7 of the Hessischen Verwaltungsvorschrift Technische Baubestimmungen (H-VV TB)

DIN 4102:20:2017-10 Brandverhalten von Baustoffen und Bauteile – Teil 20: Ergänzender Nachweis für die Beurteilung des Brandverhaltens von Außenwandbekleidungen, 2017

Performance of Heat Pump Systems with PVT Collectors with optimized Finned Heat Exchangers integrated as single Heat Source

Manuel Lämmle[1,2] and Gunther Munz[1]

[1] Fraunhofer Institute for Solar Energy Systems ISE, 79110 Freiburg (Germany)

[2] INATECH - Albert-Ludwigs Universität Freiburg, 79108 Freiburg (Germany)

Abstract

Novel photovoltaic-thermal PVT collectors with an optimized finned heat exchanger were designed, built and tested. The test results indicate an excellent convective heat transfer coefficient for the air-to-water heat exchange. The system performance is evaluated by simulation of a heat pump system, where PVT collectors are integrated as the only heat source to the evaporator. Due to the operating temperatures below ambient, the PVT collector harvests both ambient and solar heat and therefore can be considered as a solar air-to-water heat exchanger. The PVT heat pump system achieves a good overall system performance, depending on the PVT area and type of heat exchanger construction. The novel double-finned multichannel heat exchanger achieves a seasonal performance factor of SPF of 3.6 with a relatively small PVT collector area of 3 m^2/kW_{th} and thus consumes 9 % less electricity than a PV-coupled air source heat pump system.

Keywords: Photovoltaic-thermal collectors; heat pump systems; renewable heating; solar heating

1. Introduction

In recent years, photovoltaic-thermal PVT collectors received increasing interests, as these hybrid systems combine the solar generation of heat and electricity in a single component. Different design and types of PVT collectors emerged, which can be classified according to their suitable temperature range (Lämmle et al. 2020).

A promising system design concerns the combination of heat pumps, where PVT collectors comprise the only heat source. The operating conditions of solar thermal collectors integrated as heat source in heat pump systems differ substantially from the conventional operating conditions of solar collectors for hot water preparation. Fluid temperatures near and below ambient air temperatures occur frequently, particularly during the heating season in winter. As a consequence, collector and system must be ideally designed in such a way, that sufficient low temperature heat is supplied to the heat source also during cold winter days without sunlight.

2. Design of optimized PVT collectors with finned heat exchanger

Two innovative PVT collectors were designed, built, and tested, which are optimized towards an enhanced air-to-water heat exchangers on the backside of the PV module (Figure 1). To increase the surface area usable for heat exchange, finned aluminum heat exchangers are used:

- Collector 1 uses a microchannel absorber with a double finned heat exchanger which is glued to a PV module with a gross area of 1.98 m² and a rated electrical efficiency of η_{STC} = 17 %. The fins on both sides of the microchannel absorber utilize solar heat from the PV module as well as heat from the environment.
- Collector 2 uses a finned sheet-and-tube absorber design. A perforated aluminum sheet is glued to the backside of a commercial glass-glass PV module with a gross area of 1.61 m² and a rated electrical efficiency of η_{STC} = 17 % ((Munz et al. 2022).

Both collector design differ in their specific construction, but both aim at making use of solar energy via a good conversion factor $\eta_{th,hem}$ and aim at increasing convective heat transfer of via an increased UA-value (a_1 and a_3). The latter comprises a considerable difference to conventional, insulated solar thermal collectors, which aim at reducing their convective heat loss coefficients.

© 2022. The Authors. Published by International Solar Energy Society
Selection and/or peer review under responsibility of Scientific Committee
doi:10.18086/eurosun.2022.07.06 Available at http://proceedings.ises.org

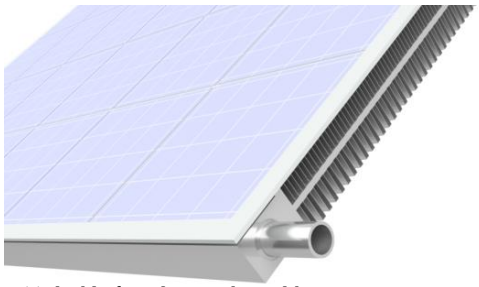

(a) double finned microchannel heat exchanger



(b) finned sheet and tube heat exchanger (SOLAB GmbH)

Figure 1: Design of the optimized PVT collectors

3. Performance of optimized PVT collectors with finned heat exchangers

The collectors underwent standardized performance characterization tests, carried out at the TestLab Solar Thermal Systems at Fraunhofer ISE (Figure 2).





Figure 2: Collectors during outdoor (microchannel heat exchanger) and indoor (finned sheet-and-tube heat exchanger) performance testing

Table 1 reports the test results of characterizing the thermal performance of the PVT collector following the collector equation of WISC collectors according to ISO 9806:2017:

$$\dot{Q} = A_G \left[\begin{array}{l} \eta_{0,\mathrm{hem}} G_{\mathrm{hem}} - a_1 \left(\vartheta_m - \vartheta_a\right) - a_2 \left(\vartheta_m - \vartheta_a\right)^2 - a_3 u' \left(\vartheta_m - \vartheta_a\right) + \\ a_4 \left(E_L - \sigma T_a^4\right) - a_6 u' G_{\mathrm{hem}} - a_7 u' \left(E_L - \sigma T_a^4\right) - a_8 \left(\vartheta_m - \vartheta_a\right)^4 \end{array} \right] \quad \text{(Eq. 1)}$$

Mind that the new standard ISO 9806:2017 reports the coefficients a_3 and a_6 as a function of the reduced wind speed u' = u-3m/s. Comparing performance parameters with measurements according to older standards therefore requires a conversion of the parameters from u to u'.

Performance tests of the PVT collector with double-finned microchannel HX were carried out under quasi-dynamic outdoor testing conditions in hybrid PVT mode of simultaneous thermal and electrical power conversion. The heat output strongly depends on convective heat transfer and wind speed u' as can be seen at the high value of a_3. In general, a very high value of a_1=71.1 W/m²K is achieved, which indicates the high heat transfer capacity UA of the finned heat exchanger.

Performance tests of the PVT collector with finned sheet-and-tube HX were carried out under steady-state indoor testing conditions, also in hybrid PVT mode of simultaneous thermal and electrical power conversion. The solar conversion is improved considerably, compared to the double-finned microchannel HX due to a better thermal coupling of PV cells and fluid. Yet, the convective heat transfer, as indicated by a_1 and a_3 is smaller than in the double-finned microchannel HX.

The different test procedures were selected due to the different season during which the tests were carried out. Both test procedures can be applied interchangeably and achieve similar results. However, the steady-state indoor method does not provide performance values for the thermal capacity a_5 and the optical incidence angle modifiers.

	$\eta_{0,hem}$	a_1	a_2	a_3	a_4	a_5	a_6	b_0	K_d	A_G
	[-]	[W/m²K]	[W/m²K²]	[Ws/(m³K)]	[Ws/(m³K)]	[J/(m²K)]	[s/m]	[-]	[-]	[m²]
Double-finned microchannel HX	0.3747	71.1	0	16.7	0	41668	0.05	0.18	1.014	1.98
Finned sheet-and-tube HX	0.528	25.7	0	3.372	0.528	-	0.031	-	-	1.61
PVT products according to their Solar Keymark Data sheets										
Finned sheet-and-tube HX	0.137	84.35	0	22.03	0.44	41580	0.111	0	1	1.98
Non-insulated PVT collector	0.425	19.65	0	1.85	0	20800	0.018	0.2	0.88	1.88
Insulated PVT collector	0.543	8.95	0	0.783	0.45	47777	0.039	0.05	0.84	1.88

Table 1: Performance data of the optimized PVT collectors with finned heat exchangers compared to commercial PVT products according to their Solar Keymark Data sheets (CEN 2022).

The performance data of commercial PVT products, all unglazed WISC PVT collectors, are included for reference purposes. The commercial finned sheet-and-tube PVT collector (Leibfried et al. 2019) achieves excellent values of a_1 and a_3. The effect of fins to increase the overall UA-value can be assessed qualitatively by comparing the a_1 and a_3 values with the non-insulated and insulated PVT collectors without fins. Hereby, it is important to keep in mind that all performance coefficients a_1 – a_6 are obtained from multi-linear regression. Therefore, there is a high likelihood that these parameters are cross-corelated, which is why they should not be interpreted singularly.

4. Performance of single-source PVT heat pump systems

To assess the performance of PVT collectors integrated as single low temperature heat source to the heat pump's evaporator, we modelled a thermo-hydraulic system in Dymola/Modelica, including PVT collector, heat pump, electrical back-up heater, hot water storage and corresponding system control. Figure 2 shows a simplified hydraulic sketch of the PVT heat pump system. The considered building with its demand profiles and supply temperatures represents an existing multi-family building with a retrofitted PVT heat pump system. The heat pump and building model are described in Lämmle et al. 2022, yet nominal supply and return temperatures for space heating of 40/35°C, corresponding to a radiant floor heating system are used.

The thermal output of the PVT collectors are calculated based on the standardized, dynamic performance model in (ISO 9806 2017). Field tests of collector 2 showed, however, that the performance model is only partially applicable for sub-ambient temperatures (Munz et al. 2022). Chhugani et al. 2020 found a similar deviation between solar keymark test parameters and parameters identified from field tests. Therefore, the performance model is mostly valid for the solar operation mode with fluid temperatures above ambient, and the simulation results should be primarily used for comparing the different PVT technologies.

To ensure a resilient operation of the PVT system throughout the year, an electrical resistance heater is integrated in the primary heat pump loop. It supports the PVT collector when brine temperature drops below the minimum evaporator temperature of -10°C.

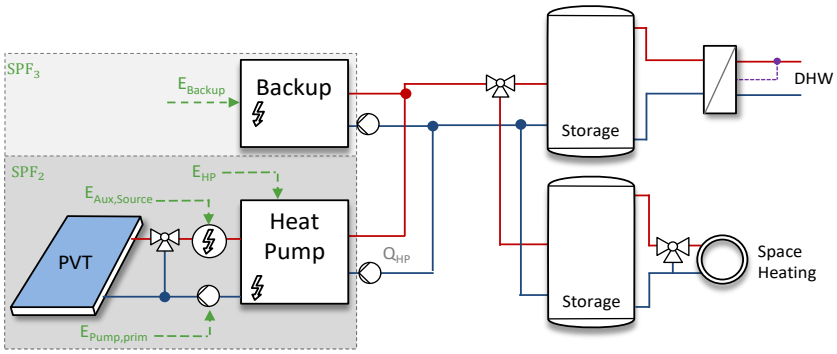

Figure 3: Hydraulic layout of thermo-hydraulic heat pump system model

The seasonal performance factor of the heat pump system SPF_2 is evaluated as the key performance indicator to

consistently compare different types of heat pump systems (PVT-source, air-source and ground-sources). The following definition for SPF_2 based on Zottl et al. 2012 considers the system boundaries as shown in Figure 3 and includes the electricity consumption of the heat pump E_{HP}, auxiliary heater in the brine loop $E_{Aux,Source}$ and primary pump $E_{Pump,prim}$:

$$SPF_2 = \frac{Q_{HP}}{E_{HP} + E_{AuxSource} + E_{Pump,prim}} \quad \text{(Eq. 2)}$$

The seasonal performance factor of the heat pump system SPF_3 additionally considers the electricity and heat supplied by the backup heater. In our case, the backup heat is supplied by an electrical resistance heater with an assumed ideal efficiency of 100%.

$$SPF_3 = \frac{Q_{HP} + Q_{Backup}}{E_{HP} + E_{AuxSource} + E_{Pump,prim} + E_{Backup}} \quad \text{(Eq. 2)}$$

The total heat gain and the system performance depends significantly on the size of the PVT collector array: the larger the area of the PVT collectors, the higher are the evaporator temperatures and the higher is the efficiency. Therefore, the size of the PVT collector array is varied, with relative values of 1 – 5 m² of collector area per kW_{th} of the nominal heat output of the heat pump.

Figure 3 also includes the evaluated SPF of a reference air-source (SPF_2 = *3.3*) and a ground-source heat pump system (SPF_2 = *4.2*). The PVT heat pump system with double-finned microchannel HX achieves the SPF of an air-source heat pump at a relative area below 2 m² per kW_{th} of nominal heat pump power. With a larger area of the PVT collector, the SPF increases further with a maximum SPF_2 = *3.7*. At a relative area of 3m²/kW_{th} the PVT heat pump system achieves an SPF_2 = *3.6* and thus consumes 9 % less electricity than the air-source heat pump system.

The heat pump system with finned sheet-and-tube PVT heat exchangers achieves a lower heat output and therefore a lower SPF_2 = *3.1* at a relative area of 3 m²/kW_{th}. Consequently, this system consumes 5 % more electricity than the air-source heat pump system.

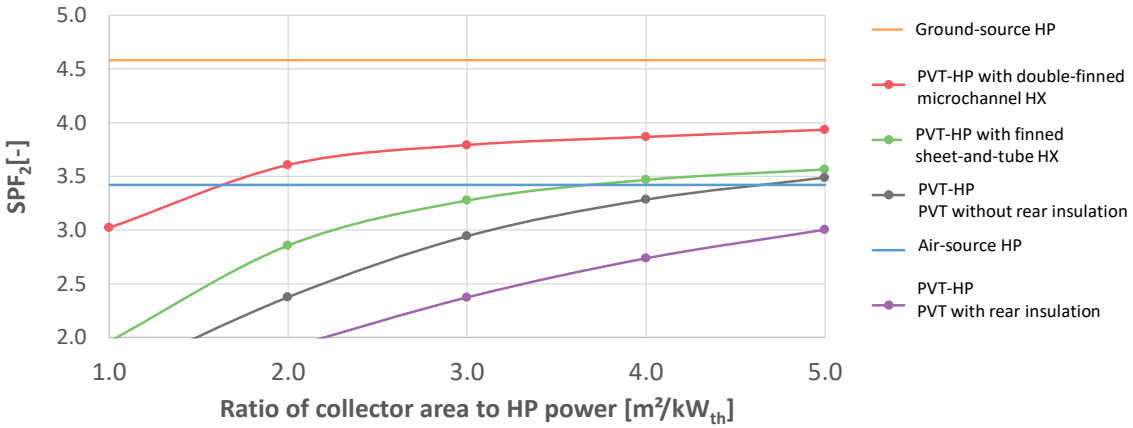

Figure 4: Seasonal performance factor SPF_2 of a PVT heat pump compared to reference air and ground source heat pumps.

The following figure plots the curves of the seasonal performance factor SPF_3 of the heat pump system, including the contribution from the backup unit. Due to the additional electricity requirement, the SPF_3 of all systems drop slightly by 0.1 – 0.2 points.

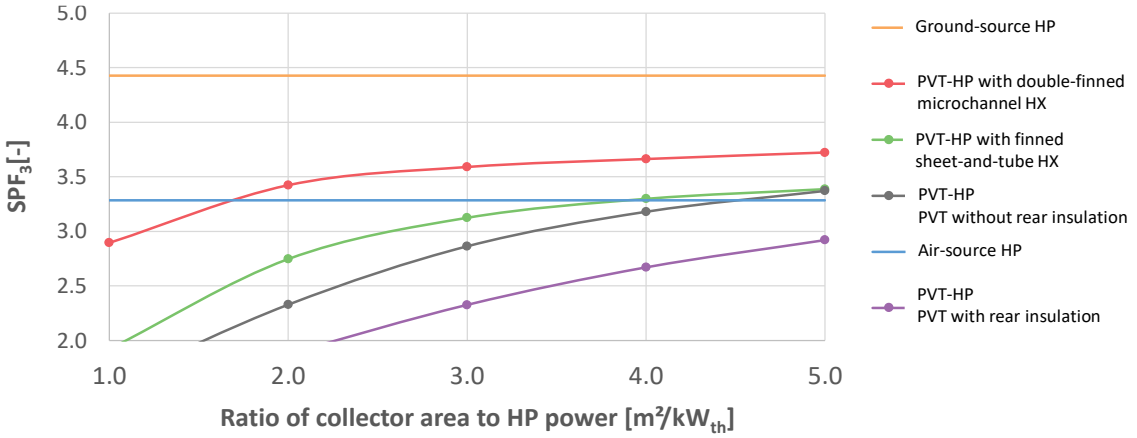

Figure 5: Seasonal performance factor SPF_3 of a PVT heat pump system compared to reference air and ground source systems.

5. Summary and conclusion

Due to the nature of integrating PVT collectors into heat pump systems, these collectors operate most frequently below ambient temperatures at $\Delta T = T_m - T_{amb} < 0$. As these collectors harvest both solar and ambient heat, this type of PVT collector should be considered as a solar air-to-water heat exchanger instead of a pure solar thermal collector. These considerations result in a new design options: the optimization of convective heat gains is of particular importance during nighttime operation or in winter when irradiation levels are low. Solar gains play a secondary role in integration as the single heat source.

Two novel types of PVT collectors were designed, built and tested. The first design features a double-finned multi-channel heat exchanger. The second design integrates a smaller fin construction added to an aluminum sheet-and-tube PVT absorber. Performance measurements indicate increased U-values for enhanced convective heat gains for both collectors.

System simulations of both PVT collectors integrated as the single source to a heat pump system demonstrate the capability of this system type. The finned heat exchanger achieves a seasonal performance factor in the order of magnitude between air and brine heat pumps. Next to the collector design, the area of the PVT collector array plays a central role. With a relative collector area of 3 m² per kW_{th} of heat pump power, the double-finned microchannel PVT collector achieves an SPF_2 of 3.6 and thus consumes 9 % less electricity than an air-source heat pump system. The finned sheet-and-tube PVT collector achieves slightly lower efficiency and requires 4 m^2/kW_{th} to achieve the same performance as an air-source heat pump system.

Condensation and frosting are not considered in the simulations yet. On the one hand, the condensation and frosting enthalpy is utilized thermally. On the other hand, icing of the surface of the PV module can reduce electrical power output of the PVT collector. Secondly, icing of the rear side heat exchanger may reduce the heat transfer capability temporarily, which may require defrosting of the PVT array. Both effects should be subject to further research.

6. Acknowledgements

We gratefully acknowledge financial support of the German Federal Ministry for Economic Affairs and Climate Action (BMWK) due to an enactment of the German Bundestag under grant number 03ETW011A. We would like to thank all project partners Solab GmbH and Solvis GmbH for the fruitful cooperation.

7. References

CEN (2022): Solar Keymark Database. The Solar Keymark CEN Keymark Scheme. https://solarkeymark.eu/database/. Brussels.

Chhugani, Bharat; Pärisch, Peter; Kirchner, M.; Littwin, Matthias; Lampe, Carsten; Giovannetti, F. (2020): Model Validation and Performance Assessment of Unglazed Photovoltaic-Thermal Collectors with Heat Pump Systems. In *EuroSun 2020: 13th International Conference on Solar Energy for Buildings and Industry - Proceedings*, pp. 1–12. DOI: 10.18086/eurosun.2020.05.13.

ISO 9806 (2017): ISO 9806:2017 Solar energy - Solar thermal collectors - Test methods, checked on 2017-09.

Lämmle, Manuel; Bongs, Constanze; Wapler, Jeannette; Günther, Danny; Hess, Stefan; Kropp, Michael; Herkel, Sebastian (2022): Performance of air and ground source heat pumps retrofitted to radiator heating systems and measures to reduce space heating temperatures in existing buildings. In *Energy* (242), Article 122952. DOI: 10.1016/j.energy.2021.122952.

Lämmle, Manuel; Herrando, María; Ryan, Glen (2020): Basic concepts of PVT collector technologies, applications and markets -. SHC Task 60/Report D5. IEA SHC Task 60. DOI: 10.18777/ieashc-task60-2020-0002

Leibfried, Ulrich; Fischer, Stephan; Asenbeck, Sebastian (2019): PVT-Wärmepumpensystem SOLINK - Systemvalidierung und zwei Jahre Praxiserfahrung. In *Symposium Thermische Solarenergie Bad Staffelstein*.

Munz, Gunther; Hesse, Gunther; Wartusch, Volker; Lämmle, Manuel; Helmling, Sebastian; Mehnert, Stefan (2022): PVT-Kollektoren als Luftwärmeübertrager - Leistungscharakterisierung und Performance in einem Wärmepumpensystem. In *Tagungsband 32. Symposium Solarthermie und innovative Wärmesysteme*.

Zottl, Andreas; Nordmann, Roger; Coevoet, Michel; Riviere, Philippe; Miara, Marek; Benou, Anastasia; Riederer, Peter (2012): Sepemo Report D4.2. /D 2.4. - Concept for evaluation of SPF Version 2.2. A defined methodology for calculation of the seasonal performance factor and a definition which devices of the system have to be included in this calculation. Heat pumps with hydronic heating systems.

Failure Risk Analysis of Photovoltaic Systems Based on Literature Review

Alexandre MATHIEU[1,2,3], Gilles FRAISSE[2], Martin THEBAULT[2], Simon THEBAULT[3], Simon BODDAERT[4], Leon Gaillard[1]

[1] Heliocity, Grenoble FRANCE

[2] LOCIE, Université Savoie Mont Blanc, CNRS UMR5271, F- 73376 Le Bourget du Lac, FRANCE

[3] CSTB, Saint Martin D'Hères FRANCE

[4] CSTB, Sophia Antipolis FRANCE

Abstract

In the context of the quick expansion of photovoltaic (PV) capacity, monitoring and correcting system failures are crucial to maximize performance. To reduce these sources of underperformance, a well-rounded knowledge of failures becomes essential. This paper highlights the most critical photovoltaic failure modes using the Failure Mode Effect and Criticality Analysis (FMECA) methodology. A review of the current knowledge of failures in PV systems, their detection methods, and their relationships is first performed. Then, this study ranks the failures based on their Risk Priority Number (RPN) deducted from their severity, occurrence, and detection score. The novelty of the approach relies on the adaptation and combination of assigned scores from different literature sources. The failure risk analysis especially outlines that critical failure modes occur in any component of the PV installation and every single part of the system needs special attention to manage underperformances.

Keywords: PV system, Failure risk analysis, FMECA

1. Introduction

Acknowledging the devastating consequences of climate change such as the dramatic increase in temperature, the rising water levels, and the intensification of extreme meteorological events (Pachauri, 2014) strong incentives at the European level have led to a massive deployment of renewable energies to mitigate energy-related environmental impact. The International Renewable Energy Agency forecasts a striking expansion of the photovoltaic capacity to 14 TW in 2050 in the 1.5°C scenario (International Renewable Energy Agency, 2021) which would correspond to 15 times more than in 2020 (Masson and Kaizuka, 2021). At the dawn of an energy paradigm shift, developing a PV performance guarantee becomes crucial to meet the objectives of climate plans and European directives such as the Energy Performance of Building Directive, EPBD (European Union, 2018).

In recent decades, the photovoltaic (PV) market has grown rapidly but the operation of PV installations continues to face significant challenges. With a 23% increase in capacity in 2020 (Masson and Kaizuka, 2021), the global photovoltaic market is experiencing unprecedented growth. On the other hand, substantial production losses subsist and around 5% of the total theoretical production could be recoverable (Leloux et al., 2011; Raycatch, 2021) if adequate operation and maintenance are ensured. Therefore, the investigation and alleviation of underperformance sources become essential to optimize the production of solar installations.

Mitigating failures reduce the Levelized Cost of Energy (LCOE) by increasing the operating lifetime of PV systems (Aghaei et al., 2022) and making power plants financially more viable. As mentioned by Catelani (Catelani et al., 2013), failures and their maintenance are rarely taken into account in the initial phases of PV projects. However, reducing underperformance effects would significantly improve the overall business cases of PV plants.

This study aims to map PV failures and rank them based on risk. Inspired by (Catelani et al., 2013; Colli, 2015; Collins et al., 2009; Milic et al., 2018; Rajput et al., 2019; Rongbin et al., 2015; Villarini et al., 2017), the failures Risk Priority Numbers (RPN) are computed from its performance reduction, occurrence, and detection ability as in a Failure Modes, Effects and Criticality Analysis (FMECA) process. A sampling method taking scores according to several data sources is then established to alleviate knowledge bias and take full benefit of the available information. Finally, the most critical failures are short-listed and described extensively.

© 2022. The Authors. Published by International Solar Energy Society
Selection and/or peer review under responsibility of Scientific Committee
doi:10.18086/eurosun.2022.07.07 Available at http://proceedings.ises.org

2. State of the art on photovoltaic failure modes and detection methods

In this section, the failure scope is defined to further list failure modes. Then, failure losses are dissociated from normal photovoltaic losses, and detection methods are collected to identify and avoid significant power losses. Finally, the inhomogeneous relationship between failures and detection methods is highlighted.

1. Failure Scope

This study focuses on failure modes that directly impact system performance on the following components: PV array, cables, and inverter. Even though PV systems are defined by their integration, even sometimes on buildings, failure modes specific to these features are accounted for as changes to PV array performance. This choice keeps the failure list generic and exploitable to any photovoltaic installation. Similarly, auxiliary systems are excluded from consideration as in most cases they do not affect the production generation itself (Bun, 2011; Villarini et al., 2017), and the failure of protection systems may be assumed negligible (Miquel et al., 2018) except for fuse faults that can be included in the "Combiner box failure" and "Inverter defect" category.

Each of those system sub-components is subject to failures along its life and might impact the system performance at different levels.

2. Power photovoltaic underperformances: expected losses vs failure

All photovoltaic systems are affected by underperformance which results from expected losses. Those can be estimated at the design phase and should not be considered as failures. These can be divided into six categories (Bun, 2011):

- **Module temperature losses**: the efficiency of PV cells varies with temperature, and temperature coefficients are commonly specified on manufacturer datasheets.
- **Non-optimal irradiance collection:** effects including spectral response (Lindsay et al., 2020) and shading.
- **Non-optimal array production extraction:** Mismatches between PV modules and strings due to the slight differences in electrical characteristics cause some inevitable losses.
- **Natural system aging:** materials and components naturally degrade over time and induce a degradation rate in the order of percentages per year. Regarding the PV modules themselves, the manufacturer warranty usually conforms with a 20 % reduction in 25 years.
- **Joule losses in the cables:** The intrinsic resistive nature of the cables leads to power being cleared up into joule losses.
- **Inverter losses:** The conversion from DC to AC in the inverter unavoidably involves some power losses.

All losses that come in addition to the previous ones are then considered as failure losses. For instance, unexpected shading or module under-ventilation leads to additional losses compared to the estimation and falls in the failure category.

Several projects (Aghaei et al., 2022; Bansal et al., 2021; Bun, 2011; Colli, 2015; Köntges et al., 2017, 2014; Miquel et al., 2018; Rongbin et al., 2015) aim at listing and describing failures. For the Agence Qualité Construction (AQC), which lists 37 faults (Miquel et al., 2018), a failure is characterized by its phase of appearance (design, installation, operation) and its target component (module/field, inverter, system, connectors, protection system, sensor). The frequency (low/high) and the risk (electric shock, fire) must also be considered when it comes to prioritizing failures. The causes of failures are very diverse and complex to anticipate from environmental stress, poor quality in commissioning, unexpected events to accelerated aging.

A total of 26 failure modes was identified and Table 1 collects the failures per system component. The failure modes have been initially collected from the AQC report (Miquel et al., 2018) and, then, rearranged to find intersections with the failure lists from IEA (Herz et al., 2022) and Long Bun (Bun, 2011) in order to complete

information and counter-check the relevance of the given occurrence and performance scores.

Table 1: PV failure modes

Failure mode	Component	Failure mode	Component
Insulation failure and ground connection defect	**System**	Corrosion	**Module/Array**
Inverter defect	**Inverter**	Delamination	**Module/Array**
Inverter overheating	**Inverter**	Encapsulant degradation	**Module/Array**
Unexpected inverter voltage input	**Inverter**	Frame/Mounting structure defect	**Module/Array**
Combiner box defect	**Wiring**	Glass breakage	**Module/Array**
Connector defect	**Wiring**	Hot spot	**Module/Array**
DC cable defect	**Wiring**	Junction box defect	**Module/Array**
Anti-reflective coating degradation	**Module/Array**	Light Induced Degradation (LID) and Light and elevated Temperature Induced Degradation (LETID)	**Module/Array**
Backsheet degradation	**Module/Array**	Module under-ventilation	**Module/Array**
Burn marks	**Module/Array**	Not conform power rating	**Module/Array**
Bypass diode defect	**Module/Array**	Potential Induced Degradation (PID)	**Module/Array**
Cell cracks	**Module/Array**	Shading	**Module/Array**
Cell interconnection defect	**Module/Array**	Soiling	**Module/Array**

Most of the failures are related to “Module/Array” because of its sophisticated photoelectric phenomenon. Then, the wiring category is comprised of three failure modes accounting for each of its elements. Inverters are at the crossroads of important PV array segments which might induce significant performance losses in case of failures. Finally, “Insulation failure and ground connection defect” can appear in any location of the installation.

Active research is undertaken to avoid the apparition of failures and the first step towards risk mitigations is the implementation of detection methods.

3. Detection methods

A detection method is defined as follows according to the AQC report (Miquel et al., 2019): “Method that is manual or automated, enabling the detection of one or more dysfunctions of a system, and alerting the user”. In Table 2, the detection method list has been inspired by the AQC report.

Table 2: PV detection method characteristics

Category	Detection method	Maturity	Cost	Accessibility
Electrical test	Insulation test	Mature	€€	On-site
Electrical test	Isc measurement	Mature	€€	On-site
Electrical test	IV tracer	First prototypes/Mature	€€	On-site
Electrical test	Signal transmission method	Mature	€/€€	On-site
Electrical test	Voc measurement	Mature	€€	On-site
Imaging method	Electroluminescence	Mature	€€/€€€	On-site
Imaging method	Infrared thermography	Mature	€€	On-site
Imaging method	UV fluorescence imaging	First prototypes/Mature	€€	On-site
Monitoring	Inverter monitoring	Mature	€	Remote
Monitoring	IV monitoring	First prototypes	€€	Remote

Monitoring	Monthly net-metering	Mature	€	Remote
Monitoring	Platform monitoring	Mature	€€	Remote
Visual inspection	Visual inspection	Mature	€/€€	On-site

The “Visual inspection” category depicts the simple observation, ideally, of a specialist on the installation sub-components. The “Imaging method” covers all methods processing images of PV modules under stressed or normal operating conditions. The “Electrical tests” are all measurements that can be performed during a maintenance visit where measured values are compared to theoretical ones. Finally, “Monitoring” methods track the performance of the system from a remote location. Each method detects a specific spectrum of failures according to its methodology and its area of operation (Aghaei et al., 2022; Herz et al., 2022; Köntges et al., 2014).

4. Failure mode - detection method correspondence

A detection method can notice underperformances from several failures and a failure can usually be noticed from several detection methods. More specifically, Figure 1 displays the relationships between all failures and detection methods of the datasets previously developed.

A disparity in the associations between the 26 failure modes (red squares) and 13 detection methods (blue dots) is brought to light. There are failures such as “Shading” or “Cell interconnection defect” that can be detected with up to 9 detection methods but “Anti-reflective coating degradation” can only be discovered with “Visual inspection”. On the other hand, some detection methods like “Visual inspection” have a wide spectrum of detection with 21 detectable failures while some others such as “Isc measurement” detect only 4 failures.

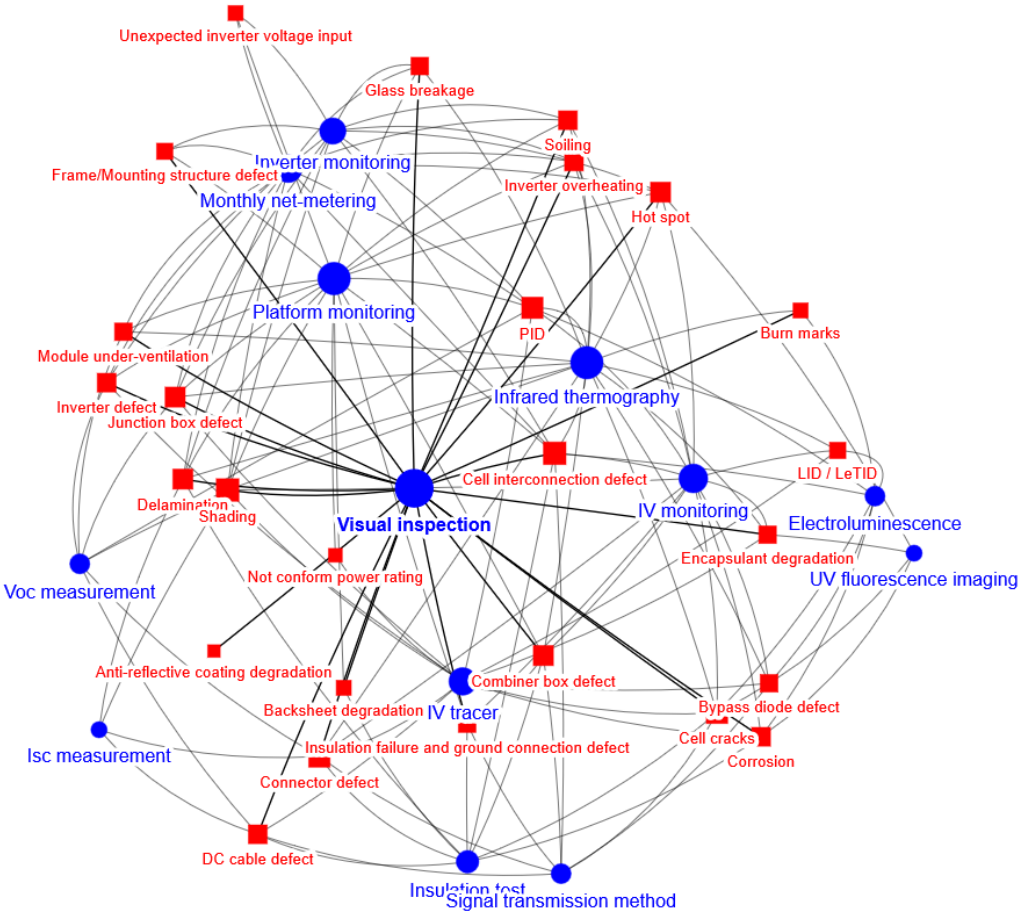

Figure 1: Network maps of failure and detection method

Figure 1 shows the relationship between "detection methods" and failure modes only with the "detection" signification that actually differs from "identification". A "detection method" notices underperformances without being able to associate them with a specific failure. It is usually the case with monitoring methods where a drop in performance can be easily observed, accounting for a failure although identifying the exact cause of the failure might require some more developed techniques. On the other hand, an "identification method" can locate exactly the failure and characterize it fully in detail for further correction purposes. In the rest of the paper, the "identification" signification is retained since those methods are mandatory to identify the exact root of the failure and suggest a correction. Each failure will be associated with at least one "identification" method.

3. Methodology to rank failures via FMECA based on different data sources

This paper introduces a new way to adapt score scales from different literature data sources. Compared to other PV FMECAs (Catelani et al., 2013; Colli, 2015; Collins et al., 2009; Milic et al., 2018; Rajput et al., 2019; Rongbin et al., 2015; Villarini et al., 2017), the detection score also takes into account the maturity of the associated identification method. Then, a new methodology to combine different literature sources through a random score generation is investigated.

In this section, the Failure Modes, Effects, and Criticality Analysis (FMECA) is first introduced and the score-sampling methodology for each failure is then explained.

1. Failure Modes, Effects, and Criticality Analysis

Failure Modes and Effects Analysis (FMEA) is based on expert opinions and would coincide during the early phase of strategy implementation (Herz et al., 2022) such as failure mitigation. FMEA is particularly suited since operational data is limited due to the relatively recent uprise of the photovoltaic sector, the lack of systematic failure reporting (Moser et al., 2017), and the large diversity of technologies and climates.

Failure modes may be prioritized according to their importance and this process is referred to as Failure Modes, Effects, and Criticality Analysis (FMECA). As defined by Milic (Milic et al., 2018) in Figure 2, the FMECA starts with defining the scope of the PV system, identifying the failures modes, characterizing its causes as well as effects, and assigning severity/occurrence/detection scores to calculate the Risk Priority Number (RPN) in order to diagnose corrective measures.

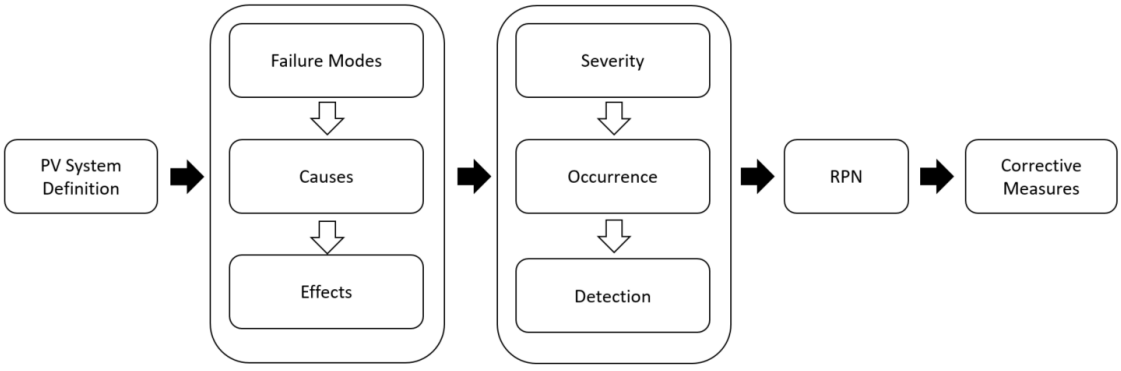

Figure 2: FMECA flow chart (Milic et al., 2018)

The Risk Priority Number (RPN) in Equation 1 reveals the criticality of each failure and is calculated with the product of three decision criteria: severity, occurrence, and detection. The severity (S) is an estimate of how strongly the failure will affect the system (Milic et al., 2018). The effect on the performance raised by that failure mode is specific to each site. The occurrence (O) represents the likelihood that the failure mode might occur and

lead to the indicated severity of the consequence. It may be defined according to the computed frequency of each failure mode. Detection (D) approximates the ability to identify and prevent the failure before the system is impacted.

$$RPN = S * O * D \quad \text{(eq. 1)}$$

Table 3: Severity, Occurrence, and Detection scoring systems partially from (Milic et al., 2018)

Score	Severity (S)	Occurrence (O)	Detection (D)
1	**Insignificant**, no effect on the performance	**Remote**, unlikely	**Undemanding**, mature identification method with low costs
2	**Low**, slight impact on the system performance	**Low**, rare apparition	**Straightforward,** detection with low requirements
3	**Moderate**, noticeable degradation of parts of the system performance	**Moderate**, occasional downtime	**Intermediate**, identification method with moderate cost and maturity
4	**High**, high degradation, non-functionality/loss of performance	**High**, frequent apparition	**Complex detection** with high requirements
5	**Hazardous**, system interruption or severe loss of performance	**Very High**, almost certain apparition	**Highly complex**, not mature, and high costs

The performance and occurrence scores from the AQC (Miquel et al., 2018), IEA (Herz et al., 2022), and (Bun, 2011) have been adapted to fit the presented scoring system in Table 3. The AQC performance scoring includes five possible categories comparable to the chosen ones and then, the scores have been moved up by 1 additional point from the AQC's 0-4 scale to fits the 1-5 given performance scoring range. Regarding the AQC's occurrence scores, they have been updated from "+"," ++"," +++" to 1,3,5 respectively to fill the whole score range. Similarly, L. Bun's occurrence and severity scores got revised from 1,2,3 to 1,3,5.

In the aim of following the same systematic method, the qualitative costs and maturity levels given from another AQC report (Miquel et al., 2019) are used to compute scores for all identification methods. The qualitative costs given by the AQC are translated from (€, €€, €€€) to (1,2,3). Then some points are added depending on the maturity level: 2 points are added if the maturity is at "First prototypes", 1 point is added if the identification method is in between "First prototypes" and no point is added if the method is "Mature". The detection score D of each failure is then set by the lowest score of its associated "identification" methods.

$$D = M + C \quad \text{(eq. 2)}$$

Where:

- **D**: detection score of the identification method, between 1 and 5
- **M:** Market maturity of the method, between 0 and 2
- **C:** Identification method intervention cost, between 1 and 3

Regarding the adopted identification method for each failure, the correspondence with failure has been inspired and completed thanks to the AQC (Miquel et al., 2019) and IEA report (Herz et al., 2022).

In some cases, multiple severity and occurrence scores can be assigned to a failure from Table 1. The IEA report generally lists several score "options" out of five for the same failure mode. Also, several sub-"associated" failure modes from a data source can sometimes match only one failure from Table 1 and would correspond to variants or alternatives. All those failures were retained to randomly generate scores in the sampling methodology presented later.

All severity, occurrence, and detection scores are collected and a sample of five failures is shown in Table 4. If there are several sub-"associated" failures from a data source to a failure "k" from Table 1, the scores are listed with a comma separator. In the case a data source gives a range of different score "options" for the same sub-"associated" failure, those are all informed with a semicolon separator. When the data source does not contain any info about severity or occurrence, no score is shown.

Table 4: Five PV failures with performance, occurrence, and detection scores

Failure mode	Severity (S)			Occurrence (O)		Associated identification methods	Detection score (D)
	AQC (Miquel et al., 2018)	IEA (Herz et al., 2022)	(Bun, 2011)	AQC (Miquel et al., 2018)	(Bun, 2011)		
Inverter defect	5	1;2;3;4;5	[5, 5, 5, 5, 5, 3, 1, 1, 1, 1]	3	3	Visual inspection	1.5
Inverter overheating	5	[3;4;5, 1;2;3;4;5]	[5, 5]	3	3	Platform monitoring	2.0
Unexpected inverter voltage input	2		[5, 5, 5, 3, 3, 3]	3	5	Platform monitoring	2.0
Anti-reflective coating degradation	1		3	1	1	Visual inspection	1.5
Backsheet degradation	4	[1;2;3;4;5, 1]		1	1	Visual inspection	1.5

2. Random FMECA score-sampling

To fully take advantage of the available information from the diverse data sources, a methodology has been developed to randomly generate scenarios. Each scenario especially represents a point of view on the failure risk at three different levels: data source, sub-"associated" failures, and score options. Since there is not any valuable argument to trust more any data source, any sub-"associated" failure, or score options, an even distribution is applied to pick each of the levels starting from the data source, through the sub-"associated" failures to the score options.

For each scenario of each failure, the severity and occurrence scores are randomly picked separately with the following steps:

i. The data source is randomly picked with uniform weights.

ii. Since, sometimes, several sub-"associated" failures from a data source are associated with only one failure from the list from Table 1. An "associated" failure is uniformly randomly picked.

iii. If the IEA source has been picked, the final score is randomly picked among the failure score options from IEA.

The example below illustrates the random pick of the severity score for the delamination case.

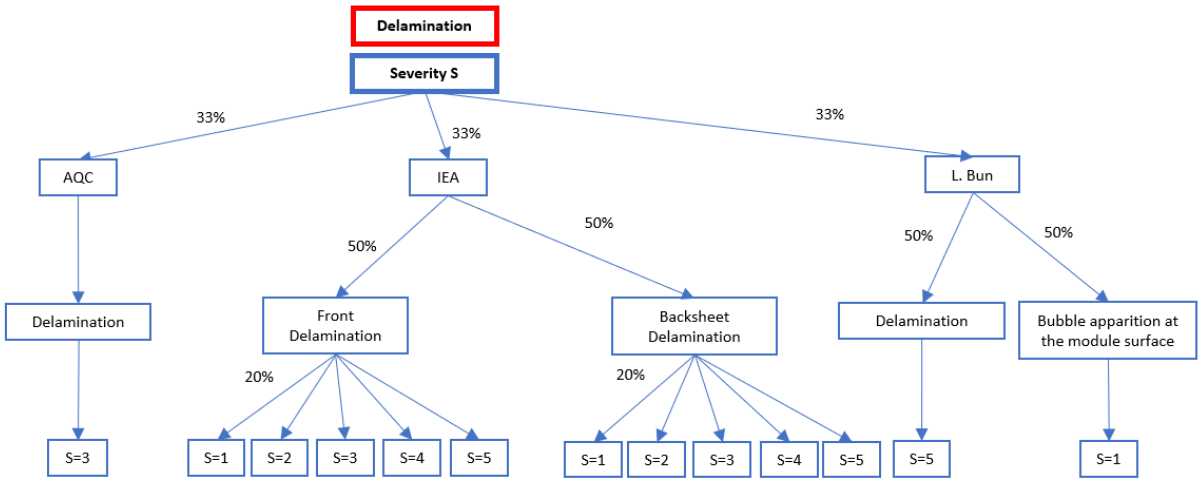

Figure 3: Severity random sampling, "delamination" case

A total of N_s = 5000 scenarios are further generated with the severity and occurrence score picked distinctly for each scenario. The severity, occurrence, and detection scores are then combined to get the RPN score for each scenario "n" as in Equation 3 which enables to create a RPN distribution for each failure "k".

$$RPN_{k,n} = S_{k,n} * O_{k,n} * D_k \quad \text{(eq. 3)}$$

In order to compare failures to each other from their RPN distribution, a final score indicator $RPN_{RMS,k}$ for each failure k, is defined in Equation 4. The Root Mean Square (RMS) method penalizes more significantly the failures containing $RPN_{k,n}$ with higher scores in their distributions.

$$RPN_{RMS,k} = \sqrt{\frac{1}{N_s}\sum_{n=1}^{N_s} RPN_{k,n}{}^2} \quad \text{(eq. 4)}$$

RMS has the advantage to grasp a whole distribution through one indicator. It assigns more weight to the highest scores and, ineluctably, is sensitive to any outlier. The regular mean of the distribution could have been instead applied but its uniform weights would not promote critical failures with distribution with a fat tail risk. The RMS indicator is thereafter applied to rank and shortlist the most critical failures.

4. Results of the FMECA applied to photovoltaic failures

Sample generation has been performed according to the presented methodology and the first noteworthy observations come from the Severity (S) and Occurrence (O) scores. In Figure 4, the S and O means have been collected for all failures.

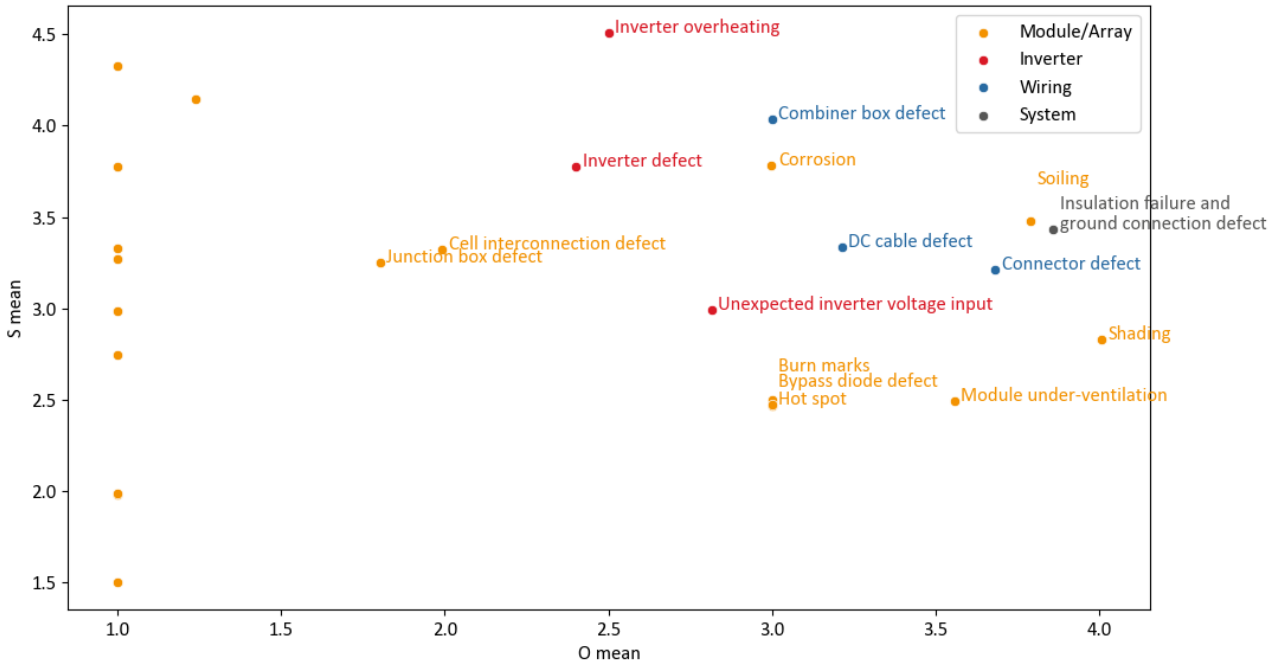

Figure 4: Severity (S) and Occurrence (O) mean scores from the sample generation

The focal position of the inverter conveys the consequences of any failure mode on a large section of the PV array and includes the most dangerous financial repercussions according to Tjengradwira (Tjengdrawira et al., 2017). Legitimately getting severity scores over 3 and coupled with steady occurrence scores, the "Inverter" component needs to actively be supervised to mitigate risks.

Similarly crucial to the architecture, the "Wiring" category bundles high severity and occurrence results. "Insulation failures and ground connection defect" has also the potential to lead to serious consequences. The wiring and insulation failures have the highest safety-risk scores in (Miquel et al., 2018) and, from a safety and

performance perspectives, are definitely to prioritize

The number of failures related to “Module/array”, 19, does not necessarily reflect more severe consequences compared to other components but highlights rather the complexity of the PV technology. 12 out of 19 of the failures obtain a mean occurrence score lower than 2 and are rather negligible in terms of technical risks. On the other hand, still some failures such as “Corrosion”, “Soiling” and “Shading” remain with very high scores and need special care during maintenance visits.

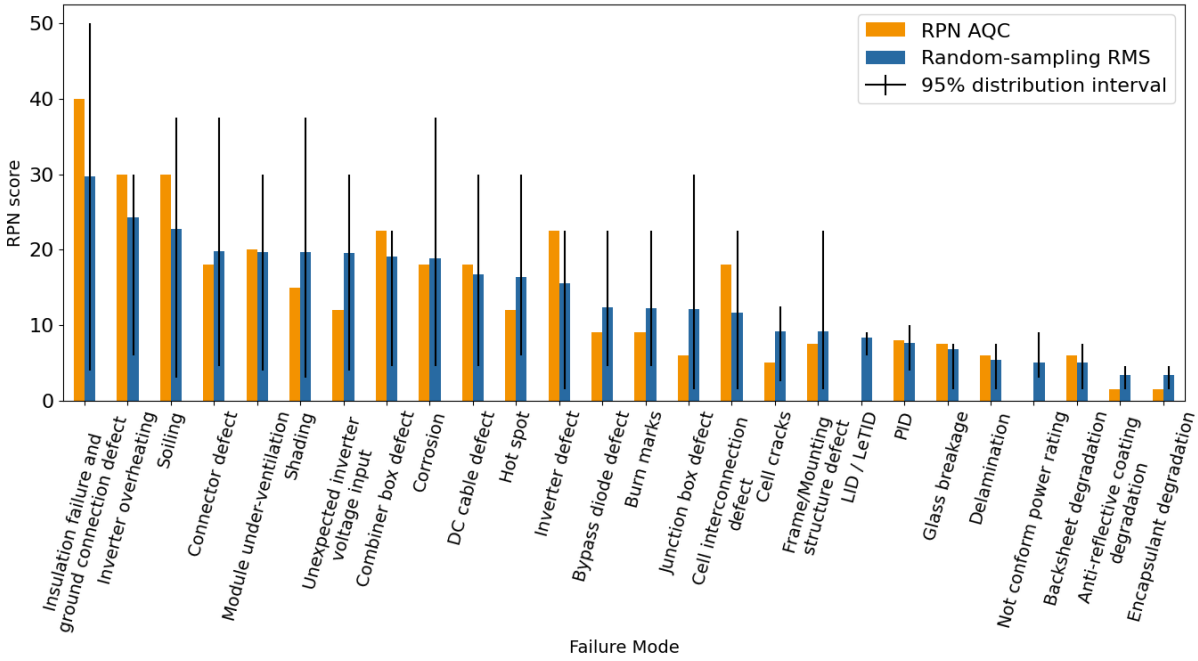

Figure 5: RPN scores from AQC and sampling RMS with 95% confidence interval

Appending the detection score in the random sampling, RPN scores have been calculated in Figure 5. The AQC dataset in orange is introduced as a benchmark. The RPN_{RMS} calculated for each failure with Equation 4 from the sampling distribution associated with the 95% confidence interval is displayed in blue and the failures are ordered according to their RPN_{RMS} score.

The variations in AQC and RMS scores globally follow each other although the latter has less amplitude since it gets flattened with the inclusion of different score sources. The RPN score distribution for each failure stays wide because the IEA report usually suggests large score intervals. Indeed, failure modes can impact the performance at different degrees such as soiling of which impact is a function of its homogeneity (Maghami et al., 2016).

Some of the failures with a low RPN score need special consideration. The “LID / LeTID” and “Not conform power rating” failure modes that were not considered in the AQC dataset stay at the low end of the ranking. For LID, this low score is particularly valid for all technologies except for amorphous silicon where the module power degradation can reach 10 – 30 % according to Gostein (Gostein and Dun, 2011). “PID” is also a well-identified failure mode with significant impact (Dhimish and Tyrrell, 2022; Luo et al., 2017) reaching sometimes 40 % of losses on real installations (Libby, 2014) but its low occurrence keeps the failure away from the top 15.

Regarding the changes from AQC to the RMS method, Table 5 highlights the respective scores and rankings.

Table 5: PV failure ranking

Failure mode	Score RPN_AQC	Ranking AQC	Score RPN_RMS	Ranking RMS
Insulation failure and ground connection defect	**40**	**1**	**29,8**	**1**
Inverter overheating	**30**	**2**	**24,6**	**2**
Soiling	**30**	**2**	**22,6**	**3**

Unexpected inverter voltage input	**12**	**12**	**19,9**	**4**
Module under-ventilation	**20**	**6**	**19,8**	**5**
Connector defect	**18**	**7**	**19,7**	**6**
Shading	**15**	**11**	**19,4**	**7**
Combiner box defect	**22,5**	**4**	**19,1**	**8**
Corrosion	**18**	**7**	**18,9**	**9**
DC cable defect	**18**	**7**	**16,9**	**10**
Hot spot	**12**	**12**	**16,4**	**11**
Inverter defect	**22,5**	**4**	**15,8**	**12**
Bypass diode defect	**9**	**14**	**12,3**	**13**
Cell interconnection defect	**18**	**7**	**11,6**	**16**

The retained failure modes to further establish risk mitigation strategies are the RMS top 12. Those are nearly the same as the AQC top 12 and capture the agreement between all data sources on the failure batch to mitigate. The RMS score also steps down by 3,5 significant points between the 12th and the 13th place which separates the top 12 from the rest of the failures.

The failures contained in the Top 12 almost do not change between the AQC and RMS methods but the internal ranking gets modified. The "Cell Interconnection defect" is ejected from the top 12 to the 16th place in the RMS ranking due to the IEA report and L. Bun assigning more moderate severity and occurrence scores. In addition, the IEA report and L. Bun consider realistically more different failure alternatives for "Inverter defect" compared to AQC which has high scores, and the RMS makes it drop from the 4th to the 12th place in the final ranking. Finally, L. Bun has more severe scores for "Unexpected inverter voltage input" and significantly increases its ranking to 4th place.

The failures excluded from the top 12 are all categorized in the Module/Array category. It particularly underlines that any failure mode appearing in the inverter, wiring, or system component is considered critical. On the other hand, it also stresses that all components need attention when it comes to monitoring underperformances since they all contained at least one failure in the top 12.

5. Discussion

The outcome of the FMECA is confirmed by the literature. "Insulation failure and ground defect" is generally in the very top priorities (Catelani et al., 2013; Colli, 2015; Milic et al., 2018; Villarini et al., 2017). "Inverter defect" and "inverter overheating" are well advised, usually in the top 5 (Milic et al., 2018; Villarini et al., 2017). The "abnormal values of the voltage" (Villarini et al., 2017) and "improper function" (Milic et al., 2018) could reflect the "Unexpected inverter voltage input" and has a more versatile ranking but generally in the first half of the ranking. "Shading" and "Soiling", often combined, are frequently in the most critical failures (Basu, 2015; Catelani et al., 2013; Milic et al., 2018) and "Hot spot" in the top 10 (Catelani et al., 2013; Milic et al., 2018). "DC cable defect", "Connector defect" and "Corrosion" defect are never in the top priorities but maintain consistent scores (Basu, 2015; Milic et al., 2018; Villarini et al., 2017). "Module under-ventilation" has not been identified in the literature except by Basu (Basu, 2015) considering rooftop PV applications where its score is relatively low. However, when considering building-mounted installations, it might be relevant to account for it due to the complex integration. "Combiner box defect" has also not been found cited as such in the literature and represents one of the specificities of the analysis.

The presented study showcases the advantages of looking into a whole system with well-defined and counter-checked scores from different literature sources. Some studies have already looked into the FMECA but at the PV module level only (Catelani et al., 2013; Rajput et al., 2019; Rongbin et al., 2015). Some other studies analyze the whole system (Colli, 2015; Collins et al., 2009; Milic et al., 2018; Villarini et al., 2017) without analyzing the sensitivity of the RPN coefficients. Also, a thorough methodology is developed in this study to calculate detection scores as of the qualitative cost/maturity detection scores from the literature (Miquel et al., 2019). Finally, as mentioned by Villarini (Villarini et al., 2017) different climate conditions might affect the FMECA analysis,

datasets, and using datasets from different sources would showcase a generic analysis covering most of the cases.

Moreover, some additional features might improve the presented methodology. As mentioned by (Villarini et al., 2017) the FMECA could eventually be updated with live data provided by reliability maintenance systems, and/or the occurrence score could be fed according to Mean Time Between Failure (MTBF) figures as examined in (Colli, 2015; Collins et al., 2009). A complete data-driven FMECA from (Filz et al., 2021) with a detection score based on forecasting model accuracies could eventually be extended to the severity and occurrence scores.

Additionally, FMECA scores could be improved to consider a higher level of detail. For instance, shading might lead to additional failures such as hot spot and bypass diode defects. Also, the concomitance of "Soiling" and "Potential Induced Degradation (PID)" could lead to more serious power reduction than when each phenomenon is considered separately (Luo et al., 2017). Modeling capabilities with empirical studies would additionally improve the understanding of performance impact such as the impact of PID (Annigoni et al., 2016) and LID as mentioned by (Woodhouse et al., 2020).

Having identified the most critical failures, the next steps would logically be to optimize the inspection methodology along the life of any PV installation in terms of frequency and content. Modeling more precisely the failure performance impact with their evolution in time and the interactions between them would give indications on how and when to perform diagnostics with which identification methods. From those simulations, a failure-correction decision support tool could also be envisioned to optimize the energetic, environmental, and financial value of the PV plant. All those suggestions together could come to fruition with a PV performance guarantee.

6. Conclusion

In this article, all photovoltaic failure modes are listed and associated with identification methods. The Failure Modes, Effects, and Criticality Analysis (FMECA) methodology assigns criticality scores to each failure based on its severity, occurrence, and detection ability. Based on the information from different data sources, score samples are randomly generated to take into account the different failure variants, eliminate knowledge bias, and obtain a generic overview. Those failures are finally ranked according to the Root Mean Square (RMS) of their respective score distribution.

Results demonstrate that all PV components from "Module/Array", "Wiring", "Inverter" to "System" contain critical failures in the top 12, and not any of those can be set aside to develop a strategy to decrease underperformances. In the first place, the "Insulation failure and ground defect" can occur in any part of the installation and has among the highest severity and occurrence scores because of its major safety and performance consequences. All failure modes collected in the inverter and wiring components are in the top 12 because of their central position in the PV architecture. Due to its technology complexity, "Module/Array" collects 19 failure modes while only 5 are in the top 12: "Hot spot", "Corrosion", "Shading", "Soiling" and "Module under-ventilation".

7. Acknowledgement

The authors of the article would like to thank the ANRT funding as well as the co-financing between Heliocity and CSTB for the project "Methodology development to guarantee building photovoltaic systems' performance including failure modeling". This work has been supported by the French National Research Agency, through the Investments for Future Program (ref. ANR-18-EURE-0016 – Solar Academy).

8. References

Aghaei, M., Fairbrother, A., Gok, A., Ahmad, S., Kazim, S., Lobato, K., Oreski, G., Reinders, A., Schmitz, J., Theelen, M., Yilmaz, P., Kettle, J., 2022. Review of degradation and failure phenomena in photovoltaic modules. Renew. Sustain. Energy Rev. 159, 112160. https://doi.org/10.1016/j.rser.2022.112160

Annigoni, E., Jankovec, M., Galliano, F., Li, H.-Y., Perret-Aebi, L.-E., Topic, M., Sculati-Meillaud, F., Virtuani, A., Ballif, C., 2016. Modeling Potential-Induced Degradation (PID) in crystalline silicon solar cells: from accelerated-aging laboratory testing to outdoor prediction. Presented at the 32nd European Photovoltaic Solar Energy Conference and Exhibition, Munich, Germany, pp. 1558–1563. https://doi.org/10.4229/EUPVSEC20162016-5BO.11.2

Bansal, N., Jaiswal, S.P., Singh, G., 2021. Comparative investigation of performance evaluation, degradation causes, impact and corrective measures for ground mount and rooftop solar PV plants – A review. Sustain. Energy Technol. Assess. 47, 101526. https://doi.org/10.1016/j.seta.2021.101526

Basu, J.B., 2015. Failure Modes and Effects Analysis (FMEA) of a Rooftop PV System. Int. J. Sci. Eng. Res. 3, 51–55.

Bun, L., 2011. Détection et localisation de défauts dans un système photovoltaïque (Theses). Université de Grenoble.

Catelani, M., Ciani, L., Cristaldi, L., Faifer, M., Lazzaroni, M., 2013. Electrical performances optimization of Photovoltaic Modules with FMECA approach. Measurement 46, 3898–3909. https://doi.org/10.1016/j.measurement.2013.08.003

Colli, A., 2015. Failure mode and effect analysis for photovoltaic systems. Renew. Sustain. Energy Rev. 50, 804–809. https://doi.org/10.1016/j.rser.2015.05.056

Collins, E., Dvorack, M., Mahn, J., Mundt, M., Quintana, M., 2009. Reliability and availability analysis of a fielded photovoltaic system, in: IEEE Photovoltaic Specialists Conference (PVSC). pp. 002316–002321. https://doi.org/10.1109/PVSC.2009.5411343

Dhimish, M., Tyrrell, A.M., 2022. Power loss and hotspot analysis for photovoltaic modules affected by potential induced degradation. Npj Mater. Degrad. 6, 11. https://doi.org/10.1038/s41529-022-00221-9

European Union, 2018. DIRECTIVE (EU) 2018/844 OF THE EUROPEAN PARLIAMENT AND OF THE COUNCIL of 30 May 2018 amending Directive 2010/31/EU on the energy performance of buildings and Directive 2012/27/EU on energy efficiency.

Filz, M.-A., Langner, J.E.B., Herrmann, C., Thiede, S., 2021. Data-driven failure mode and effect analysis (FMEA) to enhance maintenance planning. Comput. Ind. 129, 103451. https://doi.org/10.1016/j.compind.2021.103451

Gostein, M., Dun, L., 2011. Light Soaking Effects on PV Modules: Overview and Literature Review. Presented at the IEEE Photovoltaic Specialists Conference, Seattle, WA, USA. https://doi.org/10.1109/PVSC.2011.6186605

Herz, M., Friesen, G., Jahn, U., Köntges, M., Lindig, S., Moser, D., 2022. Quantification of Technical Risks in PV power Systems (No. IEA-PVPS T13-23:2021). IEA PVPS.

International Renewable Energy Agency, 2021. World Energy Transition Outlook: 1.5 °C Pathway. IRENA.

Köntges, M., Kurtz, S., Packard, C., Jahn, U., Berger, K.A., Kato, K., Friesen, T., Liu, H., Van Iseghem, M., 2014. Review of Failures of Photovoltaic Modules (No. IEA-PVPS T13-01:2014). IEA PVPS T13.

Köntges, M., Oreski, G., Jahn, U., Herz, M., Hacke, P., Weiss, K.-A., 2017. Assessment of photovoltaic module failures in the field (No. IEA-PVPS T13-09:2017). IEA PVPS.

Leloux, J., Narvarte, L., Trebosc, D., 2011. Performance analysis of 10,000 residential PV systems in France and Belgium. Presented at the 26th European Photovoltaic Solar Energy Conference and Exhibition, Hamburg, Germany.

Libby, C., 2014. Literature Study and Risk Analysis for Potential Induced Degradation (No. 3002003737).

Lindsay, N., Libois, Q., Badosa, J., Migan-Dubois, A., Bourdin, V., 2020. Errors in PV power modelling due to the lack of spectral and angular details of solar irradiance inputs. Sol. Energy 197, 266–278. https://doi.org/10.1016/J.SOLENER.2019.12.042

Luo, W., Khoo, Y.S., Hacke, P., Naumann, V., Lausch, D., Harvey, S.P., Singh, J.P., Chai, J., Wang, Y., Aberle, A.G., Ramakrishna, S., 2017. Potential-induced degradation in photovoltaic modules: a critical review. Energy Env. Sci 10, 43–68. https://doi.org/10.1039/C6EE02271E

Maghami, M.R., Hizam, H., Gomes, C., Radzi, M.A., Rezadad, M.I., Hajighorbani, S., 2016. Power loss due to soiling on solar panel: A review. Renew. Sustain. Energy Rev. 59, 1307–1316. https://doi.org/10.1016/J.RSER.2016.01.044

Masson, G., Kaizuka, I., 2021. Trends in Photovoltaic Applications (No. IEA-PVPS T1-41:2021). IEA PVPS.

Milic, S., Katic, V., Cickaric, L., 2018. Failure Modes and Effects Analysis of Urban Rooftop PV Systems – Case Study, in: International Symposium on Industrial Electronics (INDEL). Banja Luka, Bosnia and Herzegovina. https://doi.org/10.1109/INDEL.2018.8637640

Miquel, C., Stravrou, C., Lebert, N., Sarantou, J., 2019. Méthodes de détection des dysfonctionnements électriques des installations photovoltaïques. (No. ETUC2P1901). AQC - HESPUL.

Miquel, C., Stravrou, C., Lebert, N., Sarantou, J., 2018. Dysfonctionnement électriques des installations photovoltaïques: points de vigilance. (No. PTVIGI1801). AQC - HESPUL.

Moser, D., Del Buono, M., Jahn, U., Herz, M., Richter, M., Brabandere, K., 2017. Identification of technical risks in the photovoltaic value chain and quantification of the economic impact: Economic impact of technical risks in photovoltaic plants. Prog. Photovolt. Res. Appl. 25. https://doi.org/10.1002/pip.2857

Pachauri, R.K., 2014. Climate change 2014: synthesis report. Contribution of working groups I, II and III to the fifth assessment report of the Intergovernmental Panel on Climate Change., IPCC.

Rajput, P., Malvoni, M., Kumar, N.M., Sastry, O.S., Tiwari, G.N., 2019. Risk priority number for understanding the severity of photovoltaic failure modes and their impacts on performance degradation. Case Stud. Therm. Eng. 16, 100563. https://doi.org/10.1016/J.CSITE.2019.100563

Raycatch, 2021. Solar Asset Optimization, Industry Benchmark Study. Tel Aviv, Israel.

Rongbin, Y., Guixiong, L., Xiaoli, 2015. Failure Risk Analysis of the Photovoltaic Modules Based on the Improved FMECA Method. Presented at the International Conference on Instrumentation and Measurement, Computer, Communication and Control (IMCCC), Qinhuangdao, China, pp. 1166–1170. https://doi.org/10.1109/IMCCC.2015.250

Tjengdrawira, C., Moser, D., Ulrike Jahn, Armansperg, M. v., Theologitis, I.-T., Heisz, M., 2017. PV Investment Technical Risk Management (No. 649997). Solar Bankability.

Villarini, M., Cesarotti, V., Alfonsi, L., Introna, V., 2017. Optimization of photovoltaic maintenance plan by means of a FMEA approach based on real data. Energy Convers. Manag. 152, 1–12. https://doi.org/10.1016/j.enconman.2017.08.090

Woodhouse, M., Repins, I., Miller, D., 2020. LID and LeTID Impacts to PV Module Performance and System Economics DRAFT Analysis.

Comparative Analysis of the Performance of Four Different Photovoltaic-Thermal Modules

Maxime Mussard[1]*, Pierre Maret[2], Junjie Zhu[1], Sean Erik Foss[1], Zhengping Li[3], Wenzhong Shen[3], Yao Zhao[4], Yanjun Dai[4]

[1] Institute for Energy Technology, Kjeller (Norway)

[2] Diplôme Énergétique et Environnement, ENSI Poitiers, Université de Poitiers, Poitiers (France)

[3] Institute of Solar Energy, Shanghai Jiao Tong University, Shanghai (China)

[4] Institute of Refrigeration and Cryogenics, Shanghai Jiao Tong University, Shanghai (China)

*Corresponding author: maxime.mussard@ife.no

Abstract

An experimental comparison between four different PVT modules is made, the modules being identical apart from their PV technology. Two experiments are run simultaneously comparing two sets of PVT and PV modules with the same solar cell technology. The passivated emitter and rear cell (PERC) technology with white back sheet is used as reference module, all the others are compared to it during one day of experimentation for each technology. For the thermal output of the PVT, the results show an improvement for the modules using PERC with black back sheet by more than 10 %, while there is no significant evidence of change for the silicon hetero-junction (SHJ) or tunnel oxide passivated contact (TOPCon) technologies. For the electrical output, none of the technologies outperforms the others in terms of performance ratio; but the PERC with black back sheet PVT-module sees a significant improvement of 2.5 % of its performance ratio compared to its PV counterpart.

Keywords: Photovoltaic-thermal, Comparative analysis, Performance Ratio, PERC, SHJ, TOPCon

1. Introduction

A photovoltaic-thermal (PVT) module gives the possibility to both extract thermal energy from photovoltaic cells, and cool them down, thus improving their electrical performance.

Several comparative analyses among PVT-modules or between PVT-modules and PV-modules have been performed. Han et al. (2021) show that a set of PVT modules combined with another set of solar thermal modules are outperforming PV and solar thermal combined when the ambient temperature tends to be high, the irradiance strong and/or the inlet temperature of the coolant lower. Carmona et al. (2021) compare a PVT-module with integrated phase change material (PCM) to a PV-module: an increase of AC output by 7.43 % is observed thanks to the cooling system. Good et al. (2015) compare PV+solar thermal, uncovered PVT, covered PVT+PV, and only PV for housing in Norway: the "only PV" configuration seems to get the closest to net zero energy balance when using energy for a building, but the result could be different by changing slightly the criteria of the comparison.

While these research works compare either PVT with PV or different PV technologies, there is little research about the comparative behavior of PVT equipped with different solar cell technologies. This article is a first attempt to fill the gap. In this article different PVT-modules equipped with the exact same cooling loop but with different solar cell technologies are compared: Si passivated emitter and rear cell with white back sheet (PERC white), Si passivated emitter and rear cell with black back sheet (PERC black), Si heterojunction with intrinsic thin layer (SHJ) and Si tunnel oxide passivated contact (TOPCon). All modules are having the same size and the same number of cells, the PV technologies differ by their electrical efficiencies and temperature coefficients.

© 2022. The Authors. Published by International Solar Energy Society
Selection and/or peer review under responsibility of Scientific Committee
doi:10.18086/eurosun.2022.07.08 Available at http://proceedings.ises.org

2. Experimental setup

2.1. Overview of the test platform

The test platform is situated at Kjeller, Norway at the following coordinates: N 59.9732, E 11.0537. It is made of four modules: one PV and one PVT module with PERC white (as PVT reference), one PVT and one PV module of another type (from left to right on Figure 1). The PVT module consists of a PV module mounted with a cooling system and a layer of insulation on its backside (cf. 2.3.). The setup allows direct comparisons between:

- Modules of identical PV technology with (PVT) and without (PV) cooling element
- Modules of different PV technology with cooling element
- Modules of different PV technology without cooling element

The irradiance I_{rr} (W/m^2) is measured via a calibrated thermopile pyranometer placed on the same test platform. The four panels tested at a given time are connected to an inverter. The electrical output of each module is recorded via the inverter (model QS1 from AP Systems) and a communication device about every 5 minutes.



Fig. 1: Experimental setup with PERC white (PV and PVT) and PERC black (PVT and PV) modules

2.2. Characteristics of the modules

All eight modules tested are initially characterized for their nominal power at STC P_{nom} under standard test conditions (STC) in a lab: irradiance G_{STC} = 1000 W/m^2 and corrected temperature T_{STC} = 25°C. The characteristics of the modules are indicated in Table 1, the temperature coefficient being taken from the manufactuer. All of them have the same geometry of cells: half-cells of M6 format wafers, 166 mm of side-length. All the modules have the same size: 1.04 m by 1.76 m. Each panel thus consists of 120 half-cells.

Tab. 1: Module characteristics

Cell technology and application	Color of backsheet	Temperature coeff. (%/°C)	Power at STC, P_{nom} (W)	P_{nom} difference compared to PVT reference (%)
PERC PV	White	-0.38	347.3	-1.59
PERC PVT	White	-0.38	352.9	0
PERC PV	Black	-0.38	358.0	+1.45
PERC PVT	Black	-0.38	358.7	+1.64
SHJ PV	White	-0.26	362.4	+2.69
SHJ PVT	White	-0.26	354.5	+0.45
TOPCon PV	White	-0.31	364.4	+3.26
TOPCon PVT	White	-0.31	363.4	+2.98

2.3. Design of the cooling elements of the PVT modules

The cooling system is made of eight copper tubes, 1 cm external diameter, connected at the bottom and the top to two larger horizontal pipes. The system is insulated with a foam about 2 cm thick. The pipes are welded to an aluminum backplate itself in contact with the module. Figure 2 shows two views of the cooling configuration on the backside of the panel.



Fig. 2: Cooling loop design on the backside of the PVT module, and PVT module with insulation installed on the rack

2.4. Hydraulic loop

Each of the two PVT modules is connected to a hydraulic cooling loop (Figure 3). A pipe connects the PVT outlet to the top of a 200 l water tank; another pipe leaves the water tank close to its bottom to the PVT inlet, via a pump and a flow meter. The cooling loop is filled with water. Temperatures are recorded at the inlet and outlet of the PVT module. The pump is set constantly at its minimum power, equal to 50 % of its maximal power. The power consumption of the pump is about 21.5 W all along the experiments.

The recommendations of the norm for solar thermal collectors testing (ISO 9806:2017) are followed as closely as possible:

- The temperature probes are insulated and situated less than 200 mm from the inlet and outlet of each PVT-module
- The flow rate is maintained below 0.028 kg/(s·m^2), as close as possible to the norm: constant flow rate of 0.02 kg/(s·m^2)

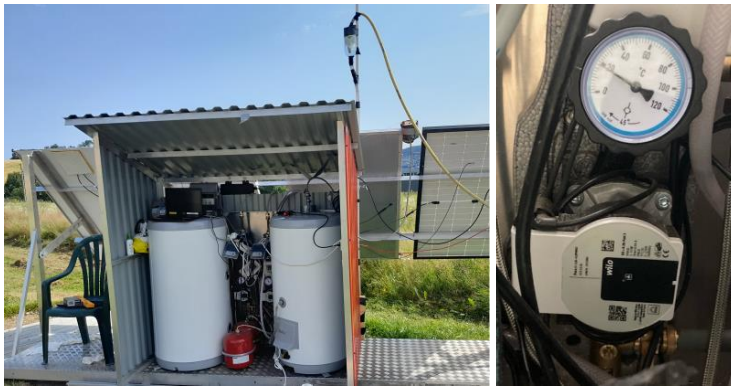

Fig. 3: Water tanks and hydraulic pump

2.5. Experiments

Four modules are tested simultaneously: the PERC white PV and PVT, and a set of PVT and PV modules of one of the other three technologies: PERC black, TOPCon and SHJ. Thermal and electrical outputs are measured.

Data is recorded every 10 seconds, except the electrical output of the modules recorded about every 5 minutes. The displayed data are computed using a moving average of 10 minutes.

The experiments are run during the days shown in Table 2 where the meteorological conditions are indicated together with the tested technologies. All technologies are tested with the PERC white as reference for both PVT

and PV. On the 22nd of August, the reference PV module (PERC white) could not be connected and a comparison was made with the PERC black PV another day.

Tab. 2: Information on experiments

Date	Technology tested with reference	Weather
Aug. 22nd, 2022	PERC black	Sunny, up to 21°C
Aug. 23nd, 2022	SHJ	Sunny with sparse clouds, up to 22°C
Aug. 24nd, 2022	TOPCon	Mixed sunny-cloudy, up to 23°C

3. Energy analysis

3.1. Flow rate measurement and assumptions

Each loop is equipped with a flow meter. By controlling the flow manually on a regular basis, it is noted that only one flow meter is reliable. As the loops and pumps are nominally identical, the two flow rates are necessarily very similar and stable over time; however minor changes in the loop may slightly impact the flow rate at equal pumping power.

The flow rate through the reference PVT module (PERC white) is therefore measured manually at the end of each day and the flow rate values during the day extrapolated from the flow meter values of the other PVT module. The flow difference between the two setups is between 0 and 3 % depending on the days. This method gives an additional uncertainty of ± 2 % for the flow rate of the reference PVT.

3.2. Calculation of efficiencies

The thermal and electrical energy outputs are correlated with the insolation reaching the module and displayed. The thermal efficiency is found using the following formula:

$$\eta_{th} = \frac{Q.\Delta t}{G.\Delta t} \qquad \text{(eq. 1)}$$

where:
Q is the thermal power output of the module (W, cf. 3.3.);
G is the irradiance on the module (W) ;
Δt is the timestep (s);

while electrical efficiency is given by the following formula:

$$\eta_{el} = \frac{P_{AC}.\Delta t}{G.\Delta t} \qquad \text{(eq. 2)}$$

where P_{AC} is the electrical power output (W).

3.3. Thermal analysis and assumptions

To calculate the thermal output the equation used is the following:

$$Q = \dot{m} \cdot C_p \cdot \Delta T \quad \text{(eq. 3)}$$

where:
$\dot{m}$ is the mass flow rate (kg/s);
C_p is the heat capacity of water, considered constant: 4180 J/(kg·°C);
ΔT is the temperature difference between the outlet and inlet of the PVT module (°C).

To effectively compare the modules, it is important to keep the inlet temperatures of water as close as possible to each other. This is not always possible, due to different starting temperatures, and different stratification behaviour of the two water tanks (despite being near identical).

To compensate for differences of temperature at the inlet, the following assumptions are made:

- The temperature difference between the two modules is equal to the one of the two water inlets
- The additional losses due to the temperature difference of the inlets are proportional to it
- The losses occur only on the front side of the PVT module
- The radiative emissivity of the modules is set at $\varepsilon = 0.7$ and the sky temperature at $T_{sky} = 0°C$, both used in radiative losses calculation
- The convective heat transfer coefficient is set to: $h = 6$ W/(m²·°C) , used in convective losses calculation (typical for low wind velocity)

By calculating the difference of energy emitted by radiation (Stefan-Boltzmann equation) and lost by convection (Newton's law of cooling) between the two modules, we obtain the results shown in Table 3.

Tab. 3: Evolution of heat losses difference between two PVT modules for 1°C of difference at the inlet for cold, warm and hot inlet temperatures

Temperature at the inlets (°C)	**Difference in thermal losses (W/°C)**
15 and 16	17.5
25 and 26	18.3
35 and 36	19.1

From Table 3, it is possible to see that the difference of losses per °C of temperature difference at the inlet is rather constant. A value of $q_{dif} = 18$ W/°C is chosen for the rest of the study to account for additional thermal losses.

The additional thermal losses to compensate to get a proper comparison are equal to: $q_{dif}\Delta T_{in}$ (in W).

The rate of thermal energy conversion after electrical energy conversion (thermal energy converted divided by thermal energy available) is: $\frac{\eta_{th}}{1-\eta_{el}}$. Indeed, the rate must be calculated considering that a part of the solar energy has been converted to electricty before the thermal exchanges occur.

By multiplying the virtual additional heat available to the rate of thermal energy conversion A thermal output Q_{add} is thus added to Q for every timestep following this formula:

$$Q_{add} = \frac{q_{dif} \cdot \eta_{th}}{1-\eta_{el}} . \Delta T_{in} \qquad \text{(eq. 4)}$$

where:
ΔT_{in} is the temperature difference between the two inlets (°C).

A similar adjustment is made for the electrical output: the difference of temperature between modules is considered equal to the difference of temperature at the inlet of the hydraulic loop, and a term $P_{AC\text{-}add}$ is added to the electrical output P_{AC} when the temperature of a module is higher:

$$P_{AC-add} = P_{AC} \cdot TC \cdot \Delta T_{in} \quad \text{(eq. 5)}$$

where TC is the temperature coefficient (cf Table 1).

Note that Q_{add} and $P_{AC\text{-}add}$ are introduced when normalizing the efficiencies to compare the energy outputs in part 4 (Figures 5, 7 and 9) and calculating the performance ratios in part 5.

4. Experimental results

4.1. PERC black PVT test

The evolution during the test of the electrical and thermal efficiencies for the PERC black and PERC white PVT modules are displayed in Figure 4. Due to the relatively stable irradiance, the efficiencies are also rather stable during the day. Comparing the electrical and thermal efficiencies of both modules will give a first insight on their relative performances. Figure 5 shows the evolution of the inlet temperatures, and the ratios of thermal and electrical outputs (output PERC black/output PERC white), both before and after the normalization described in 3.3: the large difference in inlet temperatures have a certain impact on the two ratios.

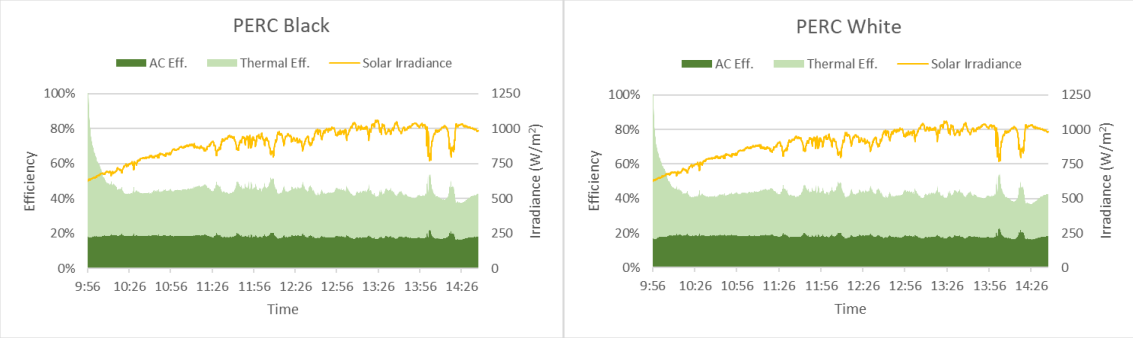

Fig. 4: Energy efficiencies for PERC black and PERC white – 22nd/08

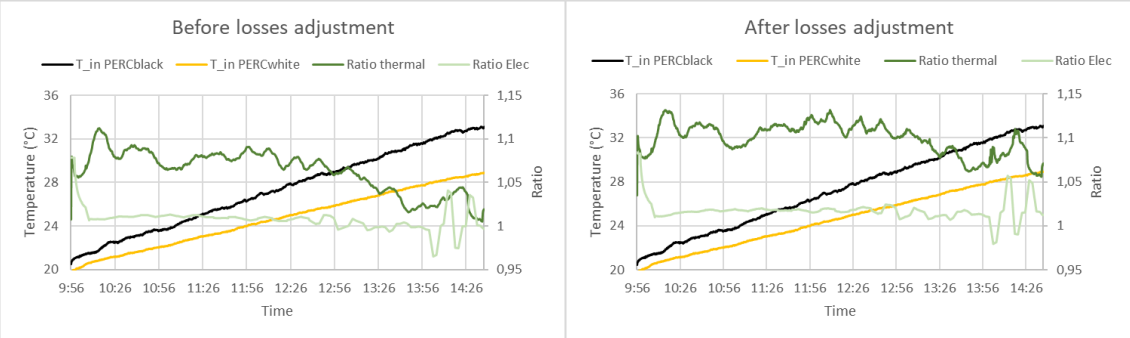

Fig. 5: Evolution of inlet temperatures and ratios of efficiencies before and after normalization – Aug. 22nd, 2022

4.2. SHJ PVT test

The evolution of the electrical and thermal efficiencies for the SHJ and PERC white PVT modules are displayed in Figure 6.

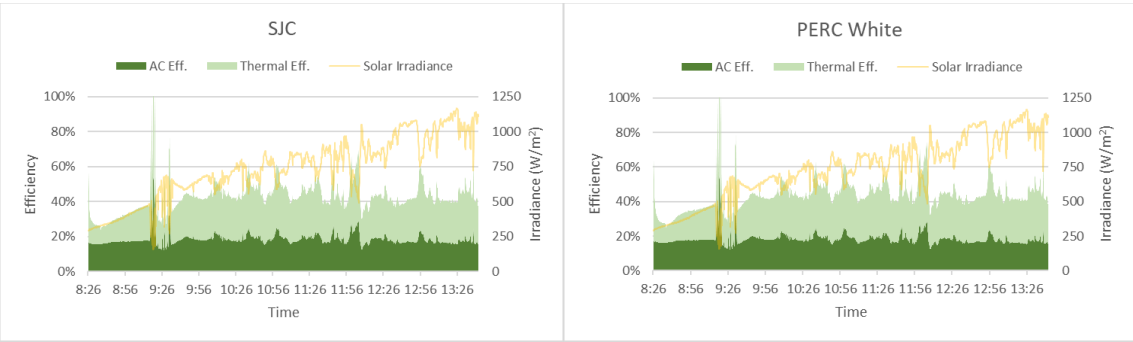

Fig. 6: Energy efficiencies for SHJ and PERC white – Aug. 23rd, 2022

The results are less regular due to the alternating bright and partially covered sun. The peaks in efficiency are due to the inertia of the thermal system and electrical recording. Figure 7 shows as Figure 5 the impact of the thermal loss correction on the ratios (output SHJ/output PERC white): the impact is much more modest here.

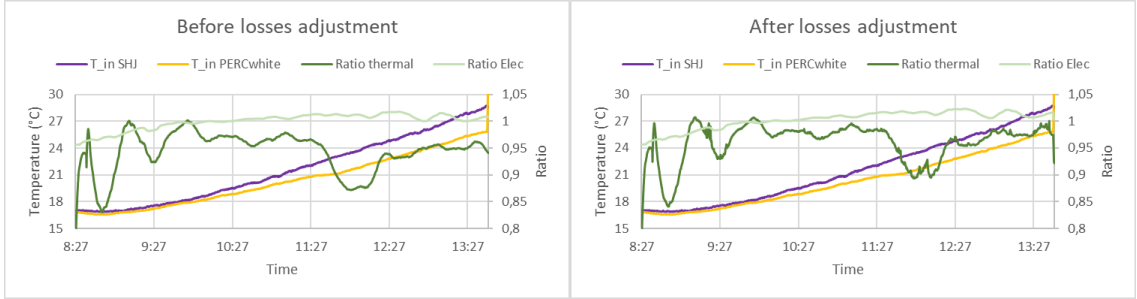

Fig. 7: Evolution of inlet temperatures and ratios of efficiencies before and after normalization – 23rd/08

4.3. TOPCon PVT test

The evolution of the electrical and thermal efficiencies for the TOPCon and PERC white PVT modules are displayed in Figure 8. This time, the results are very irregular due to the rapid alternation between sunny and cloudy weather. Figure 9 shows the influence of the correction to account for thermal losses on the ratios (output TOPCon/output PERC white), which is small here due to the reduced temperature difference between the two inlets.

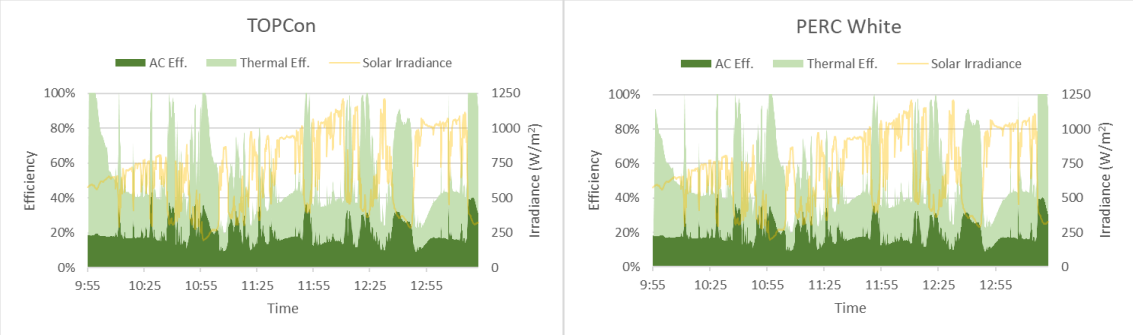

Fig. 8: Energy efficiencies for TOPCon and PERC white – 24th/08

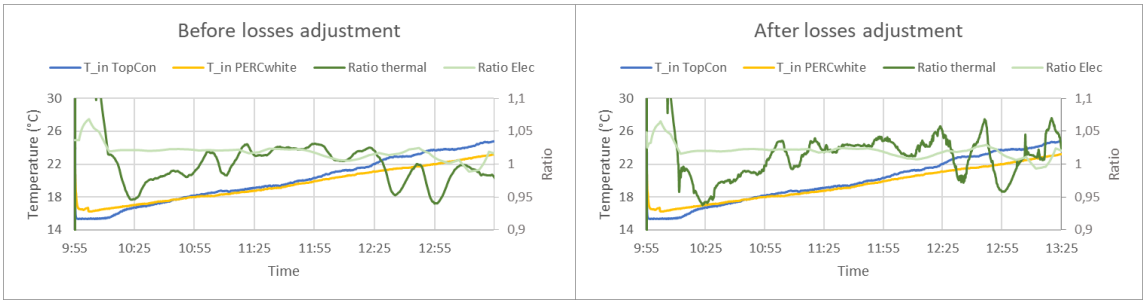

Fig. 9: Evolution of inlet temperatures and ratios of efficiencies before and after normalization – 24th/08

4.4. Infrared imaging

Infrared (IR) pictures have been taken during all experiments to identify any malfunction of the cooling loop, with color scales indicated on the side.

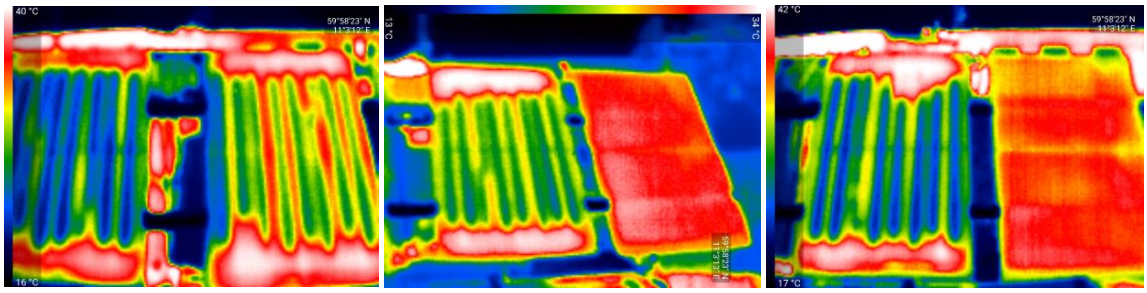

A **B** **C**

Fig. 10: IR imaging of PVT modules - A: PERC white (left) and black (right) PVT - B: SHJ PVT (left) and PV (right) - C: TOPCon PVT (left) and PV (right)

Figure 10 shows slight imperfections on the panels. Both modules on picture A (PERC white and black) seem to behave as expected, the black one being hotter. Picture B shows the SHJ PVT and PV modules: there is apparently a non-optimal heat exchange on the PVT for one of the channels. Likewise, picture C shows the TOPCon PVT and PV, and the contact of one of the channels on the PVT seems questionable. These pictures may help to give a different perspective on the interpretation of the data. Furthermore, the color scale helps to estimate the temperature difference between the PV and the coldest point of the PVT: potentially more than 10°C.

5. Comparative analysis and interpretation

5.1. Energy outputs compared to the reference PVT

Each PVT module performance is compared to the reference PVT module during the same day. The electrical and thermal performance of the reference is set at 100 % for each day and the performance of the other technologies are calculate relative to this. Figure 11 shows that the difference in electricity production is small, from 0 to 2 % increase compared to PERC white depending on the technology. Concerning the thermal output, the PERC black produces about 7 % more, the SHJ 8 % less and the TOPCon 4 % less than the reference. It is now important to adjust the data to ensure that the trends are not biased due to inlet temperature differences.

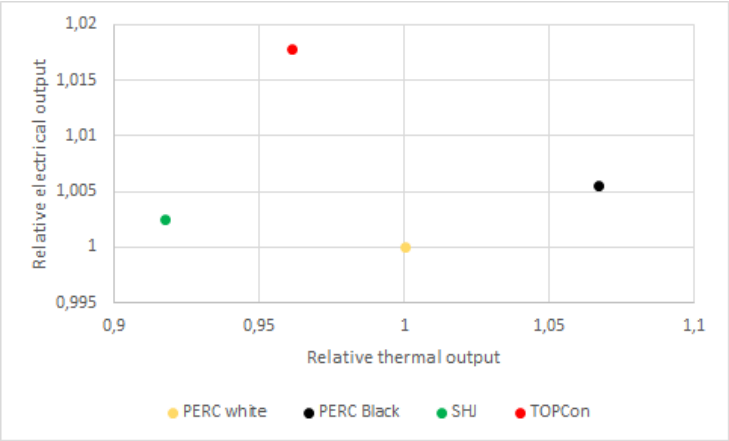

Fig. 11: AC and thermal output compared to PERC white

5.2. Normalized energy outputs compared to the reference

The difference in inlet temperatures biases the results in favour of the PVT module with the coldest inlet temperature (generally the PERC white, reference module), both for thermal and electrical outputs. The adjustments described in 3.3 are applied to get a normalized comparison to the reference if the conditions at the inlet were the same (Figure 12). Note that the normalization adjusts for differences due to temperature, but not due to differences in P_{nom}, this adjustment will be considered when performing the performance ratio analysis.

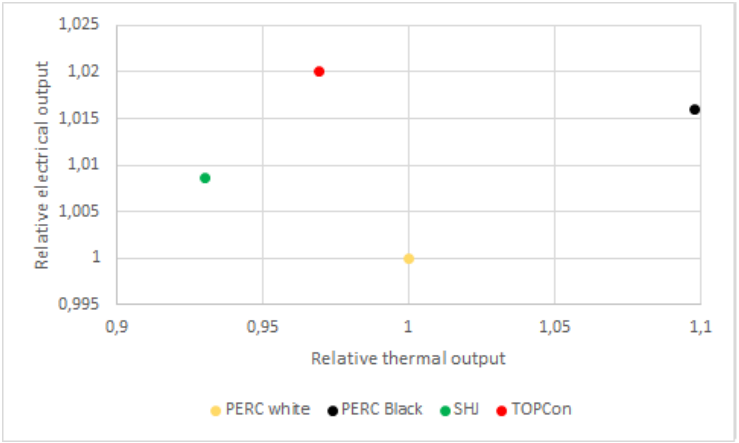

Fig. 12: Corrected AC and thermal output compared to PERC white

After the adjustments, the trend of the thermal outputs are confirmed. The black module produces over 10 % more thermal power: it can be explained by the black back sheet absorbing more radiation with its higher absorptivity. The SHJ underperforms thermally by about 6 % and the TOPCon by 3 % compared to the reference. The imperfections from Figure 10 may explain the lower thermal output for SHJ and TOPCon; also their higher electrical output may impact negatively but marginally the thermal output. There is thus no major evidence of differences of behavior for SHJ, TOPCon and PERC white for the thermal energy extracted.

In terms of electrical output, the PERC black and TOPCon modules produce less than 2 %, and SHJ less than 1 %, more compared to PERC white. Note that the nominal power of all the other panels are significantly higher than PERC white, it is thus relevant to perform an analysis of the performance ratios.

5.3. Performance ratio analysis

The performance ratio formula is the following (IEA-PVPS report, 2021), based on the AC power instead of DC:

$$PR = \frac{E.G_{STC}}{P_{nom}.H_{POA}} \qquad \text{(eq. 6)}$$

where:

E is the AC energy produced over a given time (J)
H_{POA} is the plane-of-array irradiation over the same given time (J/m^2)

Ratios of PR are calculated. A PR analysis can bring help in comparing the electrical performance of different systems. First, the PR of each setup for each experimental day is estimated from experimental data, including the normalization described in 3.3 when applicable (Table 4). Then, the ratio of the PR of the PVT module tested a given day to the PR of the reference module (PERC white) the same day is calculated and displayed in Table 5.

Tab. 4: PV performance ratios of all the modules PVT and PV tested

Performance Ratios of the modules					
22.08.2022		**23.08.2022**		**24.08.2022**	
PERC White		**PERC White**		**PERC White**	
PV	PVT	PV	PVT	PV	PVT
No Data	0.942	0.991	0.981	0.967	0.951
PERC Black		**SHJ**		**TOPCon**	
PV	PVT	PV	PVT	PV	PVT
0.919	0.932	1.006	0.978	0.938	0.930

Tab. 5: Ratios of PR of PVT modules by PR of the reference

Technology	**$PR_{PVT}/PR_{PVT\text{-}PERCwhite}$**
PERC Black	0.999
SHJ	1.004
TOPCon	0.991

The results show that the PRs remain very close to each other. It is important to remember that these values are calculated including the thermal losses normalization, and this model may have its limits and margin of errors. Only the TOPCon gives a slightly lower ratio, but it is also the one having the smallest correction due to thermal losses. Therefore there is no evidence of major improvement or deterioration of PR of the PV element when changing the technology.

Tab. 6: Ratios of PR of PVT modules by PR of PV modules of the same technology

Technology	**PR_{PVT}/PR_{PV}**
PERC White 23rd/08	0.989
PERC White 24th/08	0.983
PERC Black	1.025
SHJ	0.979
TOPCon	1.004

Finally, Table 6 compares the PR of the PVT to the PR of the same PV under the same conditions. Note that only two measurements are displayed for the reference module, as explained in 2.5. The PR of PERC White and SHJ are slightly larger in their PV version, while the TOPCon gets identical PR for PVT and PV, and the PERC black gets a larger PR when used on PVT configuration. It is important to interpret these results with care due to the use of the thermal loss correction; however the PERC black improvement (2.5 %) is larger than the improvement due

to this correction (which is about 1 %). Also, a better design of the cooling on the backside may have a positive impact on the PR_{PVT}.

The quality of the thermal contact for the SHJ and TOPCon PVT modules being under question, it could have an influence on the ratios in Table 5 and 6 for these two technologies, which may be higher with a standard contact.

6. Conclusion

Three experiments comparing couples of PV and PVT modules of a given solar cell technology are run.

Concerning the thermal output:

- The PERC black outperforms the other three technologies by 10 %, the black color giving a certain advantage for solar radiation collection.
- Among PERC white, TOPCon and SHJ, there is no evidence of superiority of one of these technologies over the other: the margin of errors and imperfections of the backside can explain the differences observed and more advanced experiments are needed before concluding.

Concerning the electrical output:

- There is no evidence of major differences on the other, the performance ratios remain very similar for all PVT modules. The questions about quality of thermal contact keep the discussion open.
- The PERC black PVT gets a slightly better performance ratio than its PV counterpart; while PERC white and SHJ PVT do not match the performance ratio of the corresponding PV.

From these experiments, the PERC black seems to be the most competitive configuration, by having both the best increase in thermal output and in PV performance ratio.

The differences between setups are small: the uncertainties concerning flow measurements, different weather conditions for different experiments (cells can be more effective under certain conditions), difference of quality among cooling setups and limitation of the thermal loss model must be underlined. It is likely that their cumulated impact remains small, but it may limit the breadth of the conclusions.

A deeper analysis on the influence of temperatures on all the PV and PVT modules must be done on the current set of data to sharpen the understanding and will be likely discussed in future research works.

The following recommendations are listed for future experiments:

- Extended testing in parallel during a larger period of time
- Improved cooling structure, both in design, quality, and consistency between modules
- More advanced equipment: control on the inlet temperature, accuracy of flow rate measurement

7. Acknowledgments

This publication has been jointly written within the cooperative project “Key technologies and demonstration of combined cooling, heating and power generation for low-carbon neighborhoods/buildings with clean energy – ChiNoZEN”. The authors gratefully acknowledge the funding support from the Research Council of Norway (NRC project number 304191 - ENERGIX) and from the Ministry of Science and Technology of China (MOST project number 2019YFE0104900). In addition, the authors would like to acknowledge Jan Thomas Haraldsen for building the platform, Nathan Roosloot for running the characterization of the modules; and Sigurd Brattheim, Joar Amundsen and Bent Thomassen for their availability and help on a regular basis. This work could not have been performed without all these participants.

8. References

Carmona, M., Palacio Bastos, A., Doria Garcia, J., 2021. Experimental evaluation of a hybrid photovoltaic and thermal solar energy collector with integrated phase change material (PVT-PCM) in comparison with a traditional photovoltaic (PV) module. Renewable Energy 172, 680-696.

Gao, B., Shao, Y., Liu, W., Xiang, H., Yu, Y., Liu, Z., 2022. Out-door reliability and degradation of HIT, CIGS, n-type multi-busbar, PERC, and CdTe modules in Shanghai, China. Solar Energy Materials and Solar Cells 236, 111490.

Good, C., Andresen, I., Hestnes, A. G., 2015. Solar energy for net zero energy buildings – A comparison between solar thermal, PV and photovoltaic–thermal (PV/T) systems. Solar Energy 122, 986-996.

Han, Z., Liu, K., Li, G., Zhao, X., Shittu, S., 2021. Electrical and thermal performance comparison between PVT-ST and PV-ST systems. Energy 237, 121589.

IEA-PVPS T13-22:2021 report. *Assessment of Performance Loss Rate of PV Power Systems*.

International Organization for Standardization. (2017). *Solar energy – Solar thermal collectors – Test methods* (ISO Standard No. 9806:2017)

A PVT Driven Direct Expansion Heat Pump Field Operation Results

Asier Sanz[1], Antonio J. Martín[2], Ainhoa Pereda[1], Eduardo Roman[1], Pedro Ibañez[1] and Raquel Fuente[2]

[1] TECNALIA, Basque Research and Technology Alliance (BRTA), Derio (Spain)

[2] Energy Panel, Lucena (Spain)

[3] University of the Basque Country UPV/EHU, Bilbao (Spain)

Abstract

The high energy-consuming building sector needs to meet both electricity and heat demands. In a nearly zero energy building scenario, most of the consumed energy would be generated locally by means of renewable solutions that nowadays seem not to provide an attractive performance or cost-competitiveness. Solar-based technologies tend to be the most promising ones, but for high densely populated areas, the usual photovoltaic or thermal single approaches may not be efficient enough. The current work is focused on several day intraday performance analysis for the dual use of the solar resource by means of hybrid PVT collectors and their smart combination with direct expansion heat pumps through predictive control strategies. To that end, the solution was developed, two systems were installed in real-use single-family houses at Mediterranean and continental climates as a domestic hot water application, operated and monitored. The presented analysis is based on several key performance indicators calculated for the tested-period one representative day (considering meteorological boundaries and system operation) for both locations. The results (Mediterranean/continental) show 91/98% renewable energy share, 72/147% self-sufficiency ratio, 53/81% heat pump self-consumption and 26/99% of the solar fraction.

Keywords: PVT, heat pump, hybrid system, control, field results.

1. Introduction

Solar energy is available all over the face of the earth. Thus, buildings should try to take higher value from every beam of light reaching their envelopes. Today, photovoltaics (PV), and in the past, solar thermal (ST) applications, are becoming widely used for built environment on-site generation. Nevertheless, for high densely populated and shadow restricted areas, these kind of single approaches are not enough to satisfy building energy needs. Detailed analysis of solar resources in built environments shows that not only roofs but also façades should be considered with higher efficiency solar conversion devices such as PVT.

Harnessing solar energy should be a must for new and refurbished buildings, but when the sun is not shining and energy stores are empty, solar base solutions always require back-up systems, which reduces their competitiveness. The electrical grid makes things easier, but thermal needs are still highly fossil fuel-dependent in a great part of Europe. However, heat pumps (HP) seem a promising technology for a reduction in building thermal comfort-related CO_2 emissions and enable the use of the electrical infrastructure to use them as a back-up (Gaur, 2021). Therefore, if solar and HP are individually suitable for electricity and heat generation, merging them in a unique hybrid system will enable to obtain higher benefits (Hadorn, 2015). Anyway, it is usually hard to compare technologies and quantify those real benefits to simply conclude which one shows overall greater performance. Thus, an experimental approach is proposed to shed some light on the real field performance of such systems.

The proposed solution is a solar hybrid PVT dually coupled HP. It is a fully integrated system comprising an unglazed hybrid solar collector, a direct expansion solar assisted HP (DX-saHP) and an overall system control (Fig. 1). The base of the technology has been widely studied before by different research groups for comparative analysis (Sanz, 2018) and experimental studies (Pei, 2008). The union of PV and solar thermodynamic technologies in one collector enables simultaneous electricity and heat generation and in a kind of symbiosis both technologies work optimally without mismatching the other's performance (Ji, 2009), as occurs in conventional PVT where a trade-off between

© 2022. The Authors. Published by International Solar Energy Society
Selection and/or peer review under responsibility of Scientific Committee
doi:10.18086/eurosun.2022.07.09 Available at http://proceedings.ises.org

the thermal and electric performance is needed. Thus, the dually assisted HP significantly increases the total annual use of the solar resource while primary energy consumption is reduced.

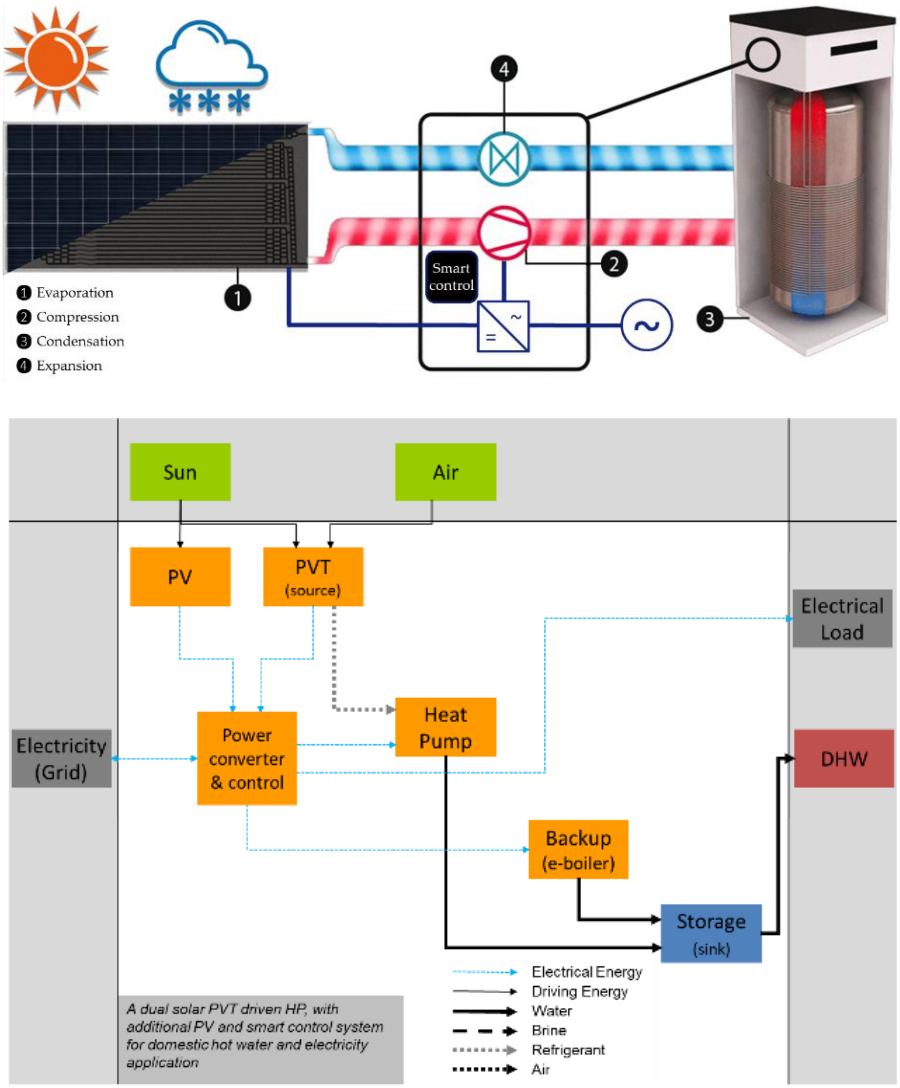

Fig. 1: A representation of the PVT dually coupled HP technology. Physical scheme of main system elements (up) and proposed representation of IEA square view (down).

2. Materials and Methods

In order to prove the previously exposed potential benefits, a couple of prototypes (Fig. 2) of the proposed solution were developed, installed and operated for one entire year in a real-use ap-plication. The objective of the test is double. First, to experimentally determine the technical performance of the whole solution by means of accurate monitoring. Second, to validate the robustness of the system under extreme working conditions.

2.1. Real-Use DHW Application

The demonstrator baseline is a single-family house. One of them is located at Jablonec nad Nisou (Czech Republic) and the other at San Martino di Lupari (Italy). The new solution has been installed to fully supply hot tap water for a 3 and 4 members family, respectively, replacing the previously existing gas boiler energy supply.



Fig. 2: The single-family house considered for the test previous (up) and post intervention (down), located at Jablonec nad Nisou (50.7N, 15.1W coordinates, left) and San Martino di Lupari (45°38'N, 11°51'W coordinates, right).

2.2. Components Sizing

The DHW application that has been chosen for validation purposes determines the strategy to be used for system sizing. Thus, according to the expected DHW day demand and its consumption profile, the thermodynamic bloc comprising the HP and the thermal energy store (TES) is selected. Traditionally, for DX-saHP, the key parameter to explore at this point is the time interval needed to ensure the entire tank water is heated at the set point. Usually, a maximum time is established. Then the HP and TES are selected to guarantee that in the worst-case scenario the elapsed time needed to reach the setpoint is below the defined one. For the current case study, at the coldest, lower solar resource and higher DHW demand months of January and December, with a 2.5 kW of heat output HP and a 200 l (Czech Republic) and 175 l (Italy) TES the elapsed period is below 2 h.

However, the new solution to be tested pretends to run mainly on solar resources. For this reason, an inverter HP has been selected. Even at its maximum regime, an output of 2.5 kW of heat would be reached, it will regularly work at lower operation points. Thus, a slightly higher TES volume has been selected. The final volume is increasing around 50% the TES capacity (till 300 l) and enabling us to heat it up during solar resource availability periods. Thus, the risk of reaching premature HP stops due to the maximum TES temperature being reduced.

Finally, for the selected thermodynamic block, the collection field is sized according to the required cold power for the HP in the previously commented winter period worst-case scenario. For the current case study, with a conventional DX-saHP system, a total of 2.72 m^2 (2 units of 1.36 m^2) of black painted roll bond solar thermodynamic collectors would be enough. However, the new solution is based on PVT collectors and the front layer might have a lower heat transfer capacity. Thus, the selected collection area is increased. For the Italian prototype the collection area has been increased by 17.6% up to 3.2 m^2 (2 units of 1.6 m^2). In the Czech Republic prototype up to 4.8 m^2 (3 units of 1.6 m^2). Even though 2 units might be enough to thermally run the HP, the additional collector is supposed to add a plus for the critical winter season. To avoid undesired excessive summer HP suction temperatures, independent blocking valves are added to each one of the collectors in both locations. An additional PV module is also added in order to enable a comparison of electrical yields for the Czech case study.

2.3 Instrumentation and Data Acquisition

The experimental activity requires accurate monitoring of energy fluxes and further relevant boundary variables to determine the technical performance of both system components and the complete solution. Thus, different kinds of sensors are displayed along the prototype. The most significant variables to measure meteorological conditions, energy collection (solar field), conversion (power electronics for PV and) HP and store (hot water tank) have been considered. A summary of them is listed below (Tab. 1).

Tab. 1: A selection of the most significant monitored variables, including the instrumentation features.

Instrument	Units	Description	Symbol	Range and Units	Accuracy
MET calibrated cell (Atersa)	2	Global plane of array irradiance	G_{PoA}	0 … 1400 W/m^2	±2.2%
	1	Ambient temperature	T_{amb}	−20 … 100 °C	±0.8 °C
	1	Wind speed	*ws*	2 … 140 km/h	±3% *[1]
	1	Crystalline silicon PV module reference temperature	T_{PVref}	−20 … 100 °C	±0.8 °C
RTF-100-S4B 5.0-C8 PT100 (Labfacility)	1 per collectors or module	Middle absorber/backsheet temperature	$T_{PVT,2}$ $T_{PVT,3}$ T_{PV}	−50 … 150 °C	±1%
VMU-E DC energy meter (Carlo Gavazzi)	4 one per collector	Voltage	$V_{PVT/PVm,X}$	0 … 400 V	±0.5% *[2]
		Current	$I_{PVT/PVm,X}$	0 … 20 A	±0.5% *[3]
		Power	$P_{PVT/PVm,X}$ *[5]	0 … 8 kW	±1%
		Energy	$E_{PVT/PVm,X}$ *[5]	*na* kWh	±1%
EM110 AC energy meter (Garlo Gavazzi)	3 Grid balance PV generation HP consumption	Energy	E_{Grid} E_{PVm} E_{HP}	*na* kWh	±1% *[4]
µPC HP controller (Carel)	1	Compressor voltage	V_{Comp}	*na* V	±1%
		Compressor current	I_{Comp}	*na* A	±1%
		Evaporation temperature	T_{Eva}	−50 … 100 °C	±1 °C
		Suction temperature	T_{Suc}	−50 … 100 °C	±1 °C
		Discharge temperature	T_{Dis}	−50 … 100 °C	±1 °C
		Condensation temperature	T_{Con}	−50 … 100 °C	±1 °C
		TES load temperature	$T_{TES,load}$	−50 … 100 °C	±1 °C
		TES middle temperature	$T_{TES,mid}$	−50 … 100 °C	±1 °C
		Condenser outlet temperature	T_{COut}	−50 … 100 °C	±1 °C

*[1] The accuracy for wind speed is valid for 15 … 140 km/h range, but always greater than ± 1 km/h. *[2] The accuracy for DC voltage is valid for 10 … 400 V range. *[3] The accuracy for DC current is valid for 0.05 … 20 A range. *[4] The accuracy for AC energy is 1.5% for a range of 0.25 … 0.5 A, according to EN50470-3. *[5] The term E_{PV} is left for the total solar field electrical output.

2.3. Data Analysis, Cleaning, Processing and Key Performance Indicators

The gathered system performance is first analyzed in detail. The day-based files have an automatic checking algorithm. The procedure only enables us to filter entire day performance days with all dataset variables in range. Furthermore, all days are carefully manually analyzed using specific timeseries templates to filter any additional errors. Thus, days with partial operation, monitored variable outlyers or additional reported phenomena are removed at this stage. Any kind of gap filling is not considered. The analysis continues only with the valid-day dataset. For this selection, several intraday parameters and day-aggregated energy values are calculated. Additionally, day representative key performance indicators (KPI) are obtained. The determination of these KPIs is performed according to the common agreed procedure established within the International Energy Agency Solar Heating and Cooling programme (Zenhäusern, 2020).

3. Results and Discussion

The described systems have been operated for more than one entire year. Some of the obtained results are discussed below. The current work is focused on the intraday performance of the system. Thus, one hole year representative day is presented for each one of the locations,

3.1. Mediterranean prototype

The selected day for the analysis is the 25 May (Fig. 3). It is a fully sunny day without any cloud and a total of 2.9 kWh/m^2 of plane irradiation, 27.8 °C mean ambient temperature and no wind (0.13 m/s). The system presents a day operation starting previously than the smart controller expected (8h27), due to a sudden DHW consumption provoking a critical morning low TES average temperature (24.8 °C). Thus, the HP begins operation at a high booster mode to continue working at lowest speed due to the still poor morning PV production. The process is repeated at 10h15 with a new DHW consumption that moves the operation to a low booster operation mode for approximately half an hour. After this morning period the machine starts to run in regulation mode, following the PV production setpoint. For 1.55 h of operation the HP moves again to low regime. Finally, after 2.5 h of operation, the TES is completely heated, and in consequence the HP is stopped. During the evening, a first low DHW consumption event could be noticed around 19h30, but the second one at 20h00 significantly reduces the TES available heat. However, the TES average temperature does not go below 30 °C so the controller does not force the non-solar operation.

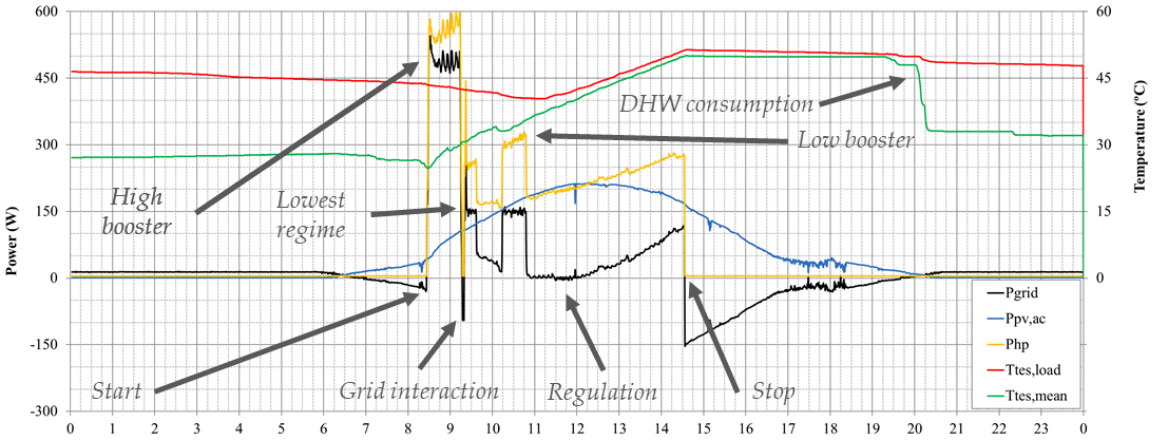

Fig. 3: Main system electric power and TES state of charge profiles for the 25 May.

The system-level KPIs show 91.4% value for renewable energy share (RES). The performance in term of self-sufficiency ratio (SSR) reaches 72.1%, below expected. This figure is aligned with the self-consumption ratio (SCR), an 80.7%. The main reason underling these KPIs is the still potentially optimizable control performance in other to avoid early morning booster activation and evening no HP operation. The narrow HP operation periods, due to high solar potential and lower thermal loads should limit the solar fraction (SF). Although SF is widely used for thermal systems, for DX-saHP solutions might not have sense, as the ambient air contribution is much greater than the solar gain. However, the day performance show also that operation during high ambient temperatures (>36 °C at 14h25) is possible, validating the system concept also for hot locations.

3.2. Continental climate

The considered day for the analysis is the 21 April (Fig. 4). This spring day has a 6.8 kWh/m^2 plane irradiation, a 17.0 °C mean ambient temperature and almost no wind (0.09 m/s). The smart controller of the solution starts up the operation at 8h41, with a relatively high TES average temperature of 37.9 °C. The HP starts operation in regulation mode, copying the PV production till 9h25, when it reaches the maximum regime. After this event the HP continues running at its maximum for more than 4 h, showing a non-constant consumption due to the dynamic PVT collector field contribution and TES status. At 13h45 the 50 °C setpoint is reached and the HP operation is stopped. In the operation period, the TES mean temperature is reduced to 35.7 °C at 10h35 due to a medium DHW consumption, although the load temperature does not go below 47.4 °C. During the almost 5-h operation the HP works almost at its full regime with almost no regulation. The evening period seems not to be needed for high irradiation and warm days, as the system is capable to heat up the entire TES without impacting the grid consumption or affecting user comfort.

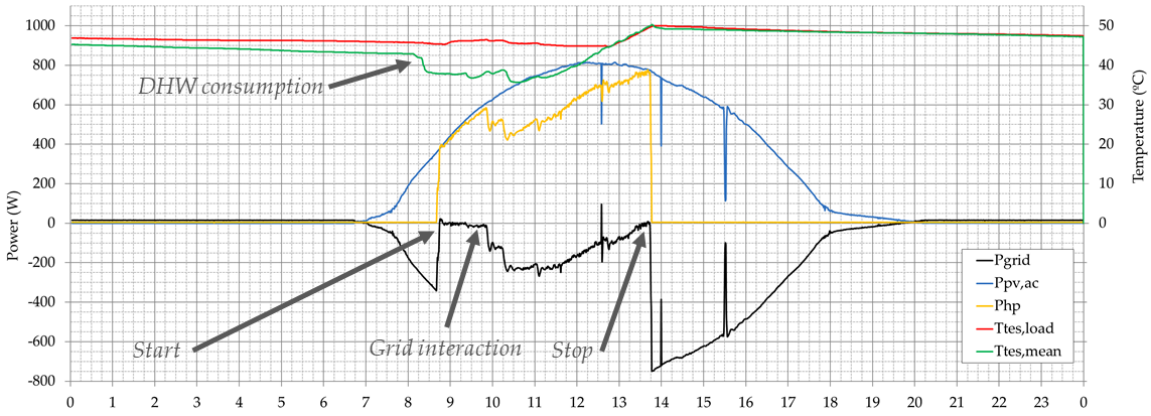

Fig. 4: Main system electric power and TES state of charge profiles for the 21 April.

The system-level KPIs evidence great figures for RES (97.8%) and SSR (147.2%), mainly driven by good solar resources. The non-evening operation reduces the SCR to 52.6%, but still shows a high capability to self-consume almost all the energy of the operating. The non-HP operation period and the low regime during operation are responsible for not gathering higher SF (25.9%). A half of SF is scored by electricity production, which shows that for such a day there is still much more potential heat to be produced.

4. Conclusions

The current work is focused on the analysis of the performance of the dual use of the solar resource by means of hybrid PVT collectors and their smart combination with direct expansion HPs through predictive control strategies. For that purpose, a solution with several innovations in the collector and in the overall control strategy was developed. A couple of real-use single-family houses have been selected for hosting the tests, at the Mediterranean climate location of San Martino di Lupari (Italy) and the continental climate representative location of Jablonec nad Nisou (Check Republic), both for a DHW application over one-year of operation. The sizing of the system has been carried out. The system comprising several PVT collectors and one PV module (only for Czech prototype), dually connected to an inverter DX-saHP with an oversized TES and a predictive control has been properly installed, commissioned and fully accurately monitored. The recorded dataset has been postprocessed according to specific internationally recognized procedures for PVT plus HP systems. The presented study is based on the intraday analysis of one representative day of the tested period for both location.

The experimental campaign feeds the calculation of the proposed system-level KPIs for two different days (one for each location). The presented figures show 91.4% for RES, 72.1% for SSR, 80.7% for SCR with an incoherent SF value for the Mediterranean prototype, while for continental climate the figures are 97.8% for RES, 147.2% for SSR, 52.6% for SCR and 25.9% for SF. The high RES is essentially based on HP performance and enhanced by solar field contribution. The obtained SCR shows good underlying control performance, although there is still big potential to better predict the optimum operation period and avoid early morning grid energy consumption (for booster or low regime HP operation) and the undesired unused evening solar resource. The obtained SSR and SF results are huge, but somehow artificially boosted due to the high solar resource and DX-saHP ambient heat collection. The short operation days caused by common high energy resource and limited TES buffering are an additional features to look at during system sizing. Further simulation and sensitivity analysis might be helpful in order to determine the required trade-off between objectives to achieve.

5. Acknowledgments

The work carried out is comprised under the HANDLE innovation project between Tecnalia Research & Innovation, Energy Panel S.L, Termoidraulica Brotto, Termosol and InnoEnergy, with the collaboration of the University of the Basque Country.

6. References

Gaur A.S., Fitiwi, D.Z., Curtis, J., 2021. Heat pumps and our low-carbon future. Energy Res. Soc. Sci. 2021, 71,

101764.

Hadorn, J.C., 2015. Solar and Heat Pump Systems for Residential Buildings, 1st ed.; Wiley: en, NJ, USA.

Ji, J., He, H., Chow, T.T., Pei, P., He, W., Liu, K., 2009. Distributed dynamic modeling and experimental study of PV evaporator in a PV/T solar-assisted heat pump. Int. J. Heat Mass Transf., 52, 1365–1373.

Pei, G., Ji, J., Chow, T.T., He, H., Liu, K., Yi, H., 2008. Performance of the photovoltaic solar-assisted heat pump system with and without glass cover in winter. Proc. Inst. Mech. Eng. Part A J. Power Energy, 179–187.

Sanz, A., Fuente, R., Martin, A.J., 2018. Solar hybrid PVT coupled heat pump systems towards cost-competitive NZEB. In Proceedings of the EuroSun 2018, Rapperswil, Switzerland.

Zenhäusern, D., et. al., 2020. IEA SHC Task 60, Key Performance Indicators for PVT Systems; A Technical Report of Subtask D; IEA SHC: Cedar, MI, USA

Energy Performance of Four Prototypes of PVT Collectors. A Comparative Study

Raquel Simón-Allué, Adriana Coca-Ortegón, Yolanda Lara and Isabel Guedea

[1] ENDEF Solar Solutions, Zaragoza (Spain)

Abstract

This work focuses on the energy evaluation of different liquid-based PVT collectors, with the view to obtain a PVT collector able to operate at high temperatures (above 50ºC) with acceptable thermal efficiency. To that end, the use of semi-transparent PV laminates is explored. Four prototypes were developed, tested and evaluated in controlled environment: two models with conventional silicon photovoltaic laminate and two models using a semitransparent photovoltaic laminate. Results show that the glazed PVT with frontal cover models offer better overall energy performance for STC conditions and maintain acceptable thermal efficiencies (30% and 45% depending on the PV laminate) when working at temperatures above 50ºC. Prototypes without frontal cover show good thermal efficiency at STC but present a strong dependency with the operational temperature and wind velocity. Semi-transparent PV laminate remains as an interesting possibility when the PVT collector must operate at high temperature but the electricity production is reduced, still needs to improve the ratio between electricity and thermal energy.

Keywords: PVT; glazed, unglazed, transparent laminate, experimental performance.

1. Introduction

Photovoltaic-thermal (PVT) collectors combine in a single panel, electricity and thermal energy production. PVT collectors usually have a frontal photovoltaic laminate with a rear absorber or heat exchanger (HX), through which thermal energy is extracted at low temperatures. Main classifications are performed based on the heat transfer fluid used (mainly liquid-based, air-based and refrigerant-based); type of solar input (concentrated, flat plate, parabolic, etc.); type of PV technology (mono-Si, poly-Si, other PV tech) and thermal absorber designs (copper sheet and tube, aluminum roll bond, polymeric box) (Herez et al., 2020; Joshi and Dhoble, 2018; Sultan and Ervina Efzan, 2018; Wu et al., 2017). In general, compared to the PV technology, PVT collectors get better overall energy efficiency (electrical and thermal) by unit area, therefore this technology is gaining interest for the development and implementation of net zero and positive energy buildings.

The most extended PVT type used is the liquid-based PVT collector, which represents 59% of the total area installed in the existing PVT system (Baggenstos et al., 2020). Solar technologies, PVT included, have grown in the global market significantly during the past 5 years, as shown in recent reports by the International Energy Agency (IEA). Specifically, PVT technology is growing in the European and Asian markets, dedicated mostly to domestic hot water production (IEA-SHC, 2022). Their potential was also highlighted by the IEA through the Task 60 (IEA-SHC, 2018), dedicated exclusively to the PVT systems and applications.

This technology may be used for diverse applications, such as pool heating, domestic hot water production, heating space, solar drying, and heat production for processes at low temperatures. However, the temperature requirements of the final application also determine the most suitable PVT collector type for each case. The higher temperature production, the lower thermal efficiency is finally obtained from the PVT collectors. Also, depending on climatic conditions the production temperature is limited according to the thermal behavior.

Thermal insulation level is a key factor that directly affects the energy performance of the PVT collector in both the thermal and electrical contribution. Depending on the insulation level there are two main types of liquid-based PVT collectors: *Unglazed PVTs*, with rear insulation layer but the PV module directly in contact to the environment; and *Glazed PVTs,* with an additional glass cover on the frontal face to limit thermal losses and to improve the thermal production of the PVT collector.

The purpose of this work is to study the performance of different PVT prototypes capable of working with good thermal efficiency even at high temperatures. The objective is to obtain a PVT collector suitable for applications

© 2022. The Authors. Published by International Solar Energy Society
Selection and/or peer review under responsibility of Scientific Committee
doi:10.18086/eurosun.2022.07.10 Available at http://proceedings.ises.org

where electricity and hot water above 50-55ºC are required. To that end, we explored the possibility of increasing the incident solar radiation on the thermal absorber by using a semi-transparent PV laminate. Thus, four different prototypes were defined, developed, and tested in the frame of the European H2020 MiniStor project. The testing procedure was performed under steady state conditions, following the requirements of the UNE-EN-ISO 9806 (ISO 9806, 2017). Thermal and electrical performance were compared between prototypes at different operating temperatures.

2. PVT Prototypes Description and Methodology

2.1 MiniStor Project background

The research presented in this paper was developed in the context of H2020 European Project, MiniStor (Minimal Size Thermal and Electrical Energy Storage System for In-Situ Residential Installation), which focuses on the design of a novel compact integrated thermal storage system for achieving sustainable heating, cooling and electricity storage that can be adapted to existing systems in residential buildings. This system is based on a Thermochemical (TCM) reactor combined with hot and cold phase-change materials (PCM), and in parallel with an electrical storage system based on Li-ion batteries. The MiniStor system can be activated by different Renewable Energy Sources (RES), such as hybrid Photovoltaic-Thermal (PVT) collectors, Flat-Plate solar thermal Collectors (FPC), biomass and other local RES.

The TCM storage system requires temperatures above 50°C to start the corresponding reactions and storage of the heat produced by the RES. One of the goals of MiniStor project was the design a solar system using PVT subsystem to produce heat for the activation of the TCM with suitable overall energy efficiency (electrical and thermal); in this line, several PVT prototypes were developed, tested and included in several simulations of the overall system. This paper presents the main results obtained for four PVT prototypes developed and tested during the MiniStor project. Most promising prototypes were considered for its integration with the TCM storage system. More information about this integration (between solar subsystem and general system) and the whole storage system under development in MiniStor project can be found in Zisopoulos et al., 2021.

2.2 PVT prototypes description

Four PVT models were designed, developed and tested in a controlled environment. Prototypes 1 and 2 are based on conventional silicon PV laminates, while prototypes 3 and 4 use a semi-transparent PV laminate, so the incident solar radiation can pass directly onto the thermal absorber. At the same time, thanks to the PV laminate cells, it is also possible the simultaneous production of electricity. Figure 1 shows the corresponding layer configuration used in each one, while Tab. 1 gathers the main technical characteristics.

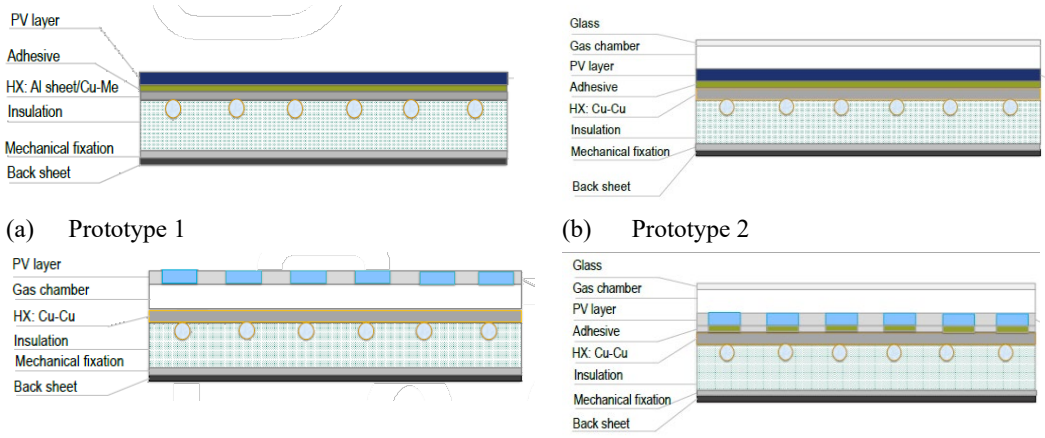

Figure 1: Sectional view of the different PVT tested prototypes.

Tab. 1:Technical characteristics of PVT prototypes.

	Prot. 1	**Prot. 2**	**Prot. 3**	**Prot. 4**
External configuration	Unglazed	Glazed	Unglazed	Glazed
Gross area [m^2]	1.7	1.63	1.62	1.62
Aperture area [m^2]	1.64	1.58	0.89	0.89
Absorber area [m^2]	1.31	1.53	1.53	1.53
PV technology	Mono - Si	Poly - Si	Semitransparent Poly - Si	Semitransparent Poly - Si
Peak power [W]	320	270	160	160
Nominal efficiency [%]	18.8	16.6	9.91	9.91
V_{mpp} [V] - I_{mpp} [A]*	33.4 / 9.58	31.19 / 8.67	19.05 / 8.43	19.05 / 8.43
Temperature coefficient of voltage / current [%/K]	- 0.29 / 0.05	-0.30 / 0.038	-0.345 / 0.046	-0.345 / 0.046
Absorber material	Copper + aluminium	Copper	Copper	Copper
Absorber geometry	Sheet & tubes (meander)	Sheet & tube (harp)	Sheet & tube (harp)	Sheet & tube (harp)
Tested flow [l/h]	85	125	125	125

* Measured at Standard Testing Conditions (STC): 1000W/m2; cell temperature at 25ºC; AM1.5.

Prototype 1 is an unglazed PVT collector. It has a PV laminate with a gross area of 1.7 m^2, made of monocrystalline silicon cells (peak power of 320 W). The thermal absorber design is Sheet & Tube type absorber made of an aluminum sheet with copper tubes in a meander arrangement (Figure 1.a). The integration between the PV layer and the thermal absorber was performed by using mechanical methods and an adhesive acrylic type. Finally, the rear enclosure was added with a 30 mm thick rock-wool insulation layer.

Prototype 2 is a glazed PVT collector, with a PV laminate with a gross area of 1.63 m^2 made of polycrystalline silicon cells (peak power of 270 Wp). The thermal absorber design is Sheet & Tube made with a copper sheet and copper tubes arranged in harp (Figure 1.b). The integration between the PV layer and the thermal absorber was performed also using mechanical methods combined with an adhesive acrylic type. This prototype has a frontal transparent insulation cover, composed of a 3.2mm glass and a gas chamber, as well as a rock wool rear insulation layer.

Prototype 3 is an unglazed PVT collector that uses a semi-transparent PV laminate with a gross area of 1.62 m^2. The silicon cells cover only 54% of their gross surface transparent, so the nominal electrical power is lower, with a value of 160 Wp. This prototype uses the same type of thermal absorber as prototype 2, but the PV laminate is not in direct contact with the copper sheet since there is an internal air camera between both components. As a result, the solar incident radiation arrives at the thermal absorber (Figure 1.c).

Prototype 4 is a glazed PVT collector that has the same components of Prototype 3 (semi-transparent PV laminate and copper absorber) but the air camera is located on the frontal face of the collector. Thus, the frontal cover implies frontal insulation as introduced in Prototype 2, as well as a rock wool rear insulation layer (Figure 1.d).

In all cases, PV layer includes also several sub-layers in all prototypes: the first is a protective photovoltaic glass, followed by the silicon cells, encapsulated in EVA, and finally a back sheet.

2.3 Testing methodology

The testing procedure were carried out according to EN-ISO 9806 standard (ISO 9806, 2017), following the static testing methodology. For each prototype, the tests were carried out for several days, to ensure different levels of wind severity. Experimental tests were performed under natural irradiance in Zaragoza (Spain). PVT prototypes were placed in an in-house testing rig with an inclination of 45º and were manually oriented to the sun to guarantee a constant solar irradiation during several hours each day (between 900-1000W/m2). During the testing period, panels were forced to operate in a close hydraulic loop at different inlet temperatures with the PV laminate performing at MPPT (maximum production point).

Thermal performance was obtained by using temperature sensors (PT-100), flow meter (Pulse Teko TC1) and pressure gauge (Unik 5000), while the electrical performance was evaluated by measuring the current and voltage generated in CC in the panel. Environmental data (global irradiance, ambient temperature and wind speed) were measured through a weather station composed of a pyranometer (LP Pyra 03) and a wind gauge (Thies 4.3303.22). All sensors reported data with a frequency of 1 min, which was registered in a PLC Modicon 241 for the subsequent analysis. A scheme of the testing rig and main components is shown in Figure 2, with the hydraulic (in blue), electrical (in red, CC in continuous and CA in dash line) and monitoring (in purple dash line) connections.

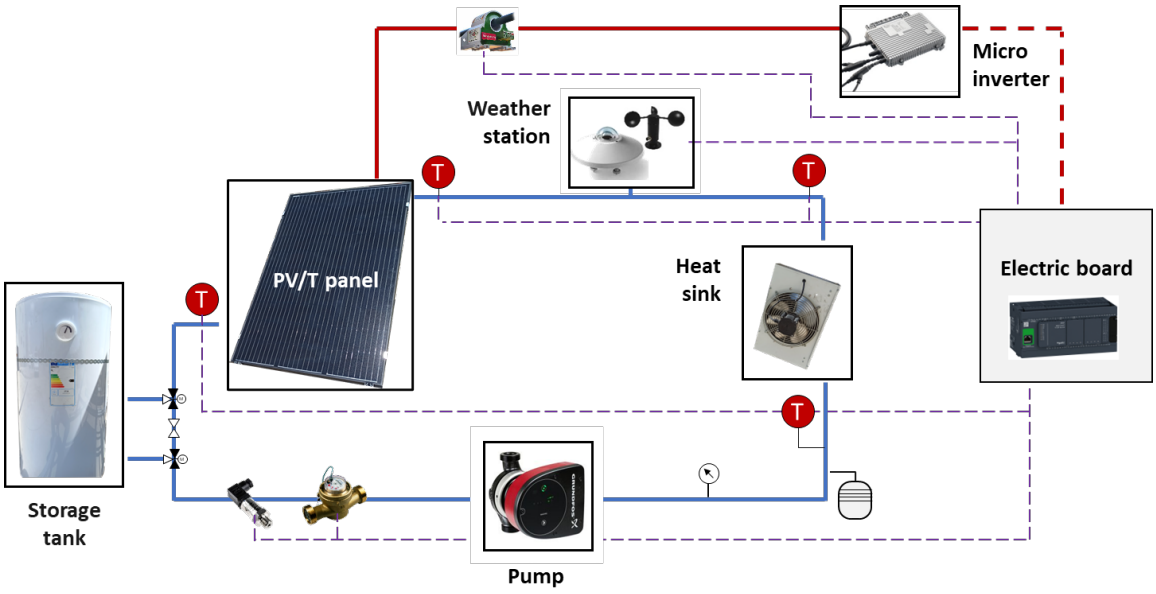

Figure 2: Flow diagram of the PVT testing rig.

2.4 Mathematical considerations

The instantaneous thermal effective power generated by each prototype is calculated after the testing procedure through the equation (eq. 1). This equation is based on the thermal gap of the fluid measured between the outlet and the inlet of the panel (ΔT), the flow rate inside the circuit ($\dot{m}$) and the specific heat of the water (c_f). Then, the instantaneous thermal efficiency was calculated through (eq. 2, considering the solar irradiance (G) and the gross area of the PVT panel (A_G).

$$\dot{Q} = \dot{m} \cdot c_f \cdot \Delta T \qquad \text{(eq. 1)}$$

$$\eta_{th} = {\dot{Q}}/{(A_G \cdot G)} \qquad \text{(eq. 2)}$$

The electrical power of each prototype was also registered during the testing, measuring the electrical current circulating through the panel (I_p) and calculated through the (eq. 3) . The voltage was estimated from the V_{mppt} value of the PV panel, considering the penalization of temperature, following the relation:

$$W_p = I_p \cdot V_p \quad \text{(eq. 3)}$$

$$V_p = V_{mppt}\,(1 - \alpha_{PV}\,(T_c - T_{STC})) \quad \text{(eq. 4)}$$

Where α_{PV} is the voltage temperature coefficient of each PV laminate (indicated in Tab. 1), T_c the cell temperature and T_{STC} the cell temperature at standard test conditions (T_{STC}=25°C). The cell temperature has been estimated based on the environmental conditions (solar radiation and temperature) and the nominal operating temperature of the cell, T_{NOC}, set by the manufacture as 45ºC.

Then, the instantaneous electrical efficiency was calculated by means of (eq. 5).

$$\eta_{PV} = {W_p}/{(A_{PV} \cdot G)} = {(I_p \cdot V_p)}/{(A_{PV} \cdot G)} \quad \text{(eq. 5)}$$

2.4.1 Thermal characterization

The parameter identification of the PVT panels has been performed according to the international standard ISO 9806, corresponding to each type of collector here tested. The most updated standard, ISO 9806, 2017, indicates the obtaining of eight parameters to define the thermal performance of a collector, as well as the considerations of reduced wind speed ($u' = u - 3\ m/s$) instead of direct wind measurement and net irradiance on the collector plane. In this article, the procedure indicated in the ISO 9806, 2013 is preferred through, as has been used by other authors (Bianchini et al., 2017; Brötje et al., 2018; Jonas et al., 2019; Simón-Allué et al., 2022), since it is considered that favors the comparison between different collectors.

For steady-state collector efficiency tests, the ISO 9806, 2013 differentiates the thermal model characterization as a function of the collector type, discretizing the performance of uncovered or WISC collectors (wind and/or infrared sensitive) with a linear mathematical model and the glazed collectors with a quadratic model.

According to this standard, the thermal performance of a covered collector is characterized through the quadratic relation depicted in (eq. 6, where η_0, a_1, a_2 are the thermal performance coefficients of the collector. η_0 is the optical efficiency and represents the collector efficiency at $T_m = T_a$, while $a_1$and a_2 are the linear and quadratic heat loss coefficient respectively. T_m is calculated as the average between the inlet and outlet collector temperature, calculated as stated in the standard. This formula is function of the collector operating parameter ($T_m - T_a$), mean fluid temperature and ambient temperature and G, solar irradiance.

$$\eta_{th} = \eta_0 - a_1\left(\frac{T_m - T_a}{G}\right) - a_2 G\left(\frac{T_m - T_a}{G}\right)^2 \quad \text{(eq. 6)}$$

The thermal performance of the uncovered or WISC model is characterized through the linear relation of (eq. 7, where η_0, b_u, b_1, b_2 are the thermal performance coefficients of the collector. In this case, η_0 is the optical efficiency, b_u is the wind dependence of collector efficiency coefficient, $b_1$the linear heat loss coefficient and b_2 the wind dependence of the heat loss. The WISC model includes the dependency with u, wind speed, and G'', the net irradiance. This magnitude can be calculated following the (eq. 8, according to the ISO 9806, 2013, where α is the solar absorptance, ε is the hemispheric emittance and E_L the longwave irradiance.

$$\eta_{th} = \eta_0\,(1 - b_u u) - (b_1 + b_2 u)\frac{T_m - T_a}{G''} \quad \text{(eq. 7)}$$

$$G'' = G + \frac{\varepsilon}{\alpha}\,(E_L - T_a^4) \quad \text{(eq. 8)}$$

Operational parameters T_m, T_a, G and u are directly measured during the testing procedure. Thermal performance coefficients are calculated by least-squares approximation, through curve fitting of the experimental data. Quadratic model was used for the characterization of Prot. 2, 3 and 4 and linear model was used for the characterization of Prot. 1, based on the experimental measurements.

2.4.2 Statistical analysis

An additional statistical analysis has been applied to the parameter characterization in order to assess the suitability of the model assumptions presented here and the goodness of the final fit. The strength of the relationship between thermal performance and the abscissa operational parameter $\left(\frac{T_m - T_a}{G}\right)$ has been evaluated through the calculus of the Pearson's correlation (r_{xy}) coefficient for the Prot. 1 (expected linear relation). It indicates the level of linear dependency between both variables: perfect fitting (r=1), no relation (r=0), positive dependency (r>1) or inverted dependency (r<0).

For Prots. 2 – 4, Spearman coefficient has been used instead, to determine if thermal efficiency and the abscissa operational parameter $\left(\frac{T_m - T_a}{G}\right)$ are monotonically related, even if their relationship is not linear, as it expected. The analysis of this coefficients is the same of the Pearson's one.

Besides, the goodness of the regression is assessed through the coefficient of determination R^2, calculated as indicated in (eq. 9) between the experimental measurement y_i and the numerical approach $\bar{y}$.

$$R^2 = \frac{\sum(\hat{y}_i - \bar{y})^2}{\sum(y_i - \bar{y})^2} \qquad \text{(eq. 9)}$$

3. Results & discussion

3.1 Energy efficiency

A summary of the electrical and thermal efficiencies obtained for the four different PVT collectors is provided in Figure 2, with energy efficiency values placed in the y-axis and the operating parameter $\left(\frac{T_m - T_a}{G}\right)$ in the x-axis. Experimental data were obtained slightly displaced on the X-axis depending on the season where they were tested. Thermal efficiency is shown in blue and electrical value in red. An overall performance has been calculated considering electrical and thermal efficiency as the direct sum of both quantities, as performed in previous works (Fayaz et al., 2019; Ozgoren et al., 2013). Although the addition of two different types of energy should be taken with caution, having a single factor to compare the overall efficiency of collectors is useful.

Efficiency results indicate that Prototypes 2 and 4 (both with frontal cover) exhibited the highest values for overall performance (63.4% and 64% respectively in STC) while maintaining an acceptable thermal performance for high operation temperature (thermal efficiency around 30% and 45% respectively when working 25ºC above environment). Prototypes 1 and 3, on the contrary, showed lower thermal and overall efficiency for the whole testing range (overall efficiency: 56.5% - 46.1% respectively under STC, and 26.2% - 20.1% when working 25ºC above environment).

Regarding the electrical performance, better results were found for the unglazed model as expected, not only for the higher nominal efficiency of the PV laminate, but also for the lower operational temperature due to the absence of frontal cover.

The incorporation of semi-transparent PV laminates severely decreases the electrical production of the panel, as the PV panel has half nominal power of the PV laminated used in Prot. 1. This should provoke direct benefits on the thermal performance since more amount of solar radiation is able to reach the thermal absorber. However, according to the experimental results, this benefit is obtained when the PV laminate is direct contact to the absorber (Prot. 4) and not when an air camera separates both components (Prot. 3). No significant improvement in electrical production is found in this case when the semi-transparent PV laminate is in direct contact to the surrounding ambient (Prot. 3) versus the same configuration with the frontal cover (Prot.4), probably because refrigeration effect of the thermal absorber contributes in this last case to decrease the operational cell temperature.

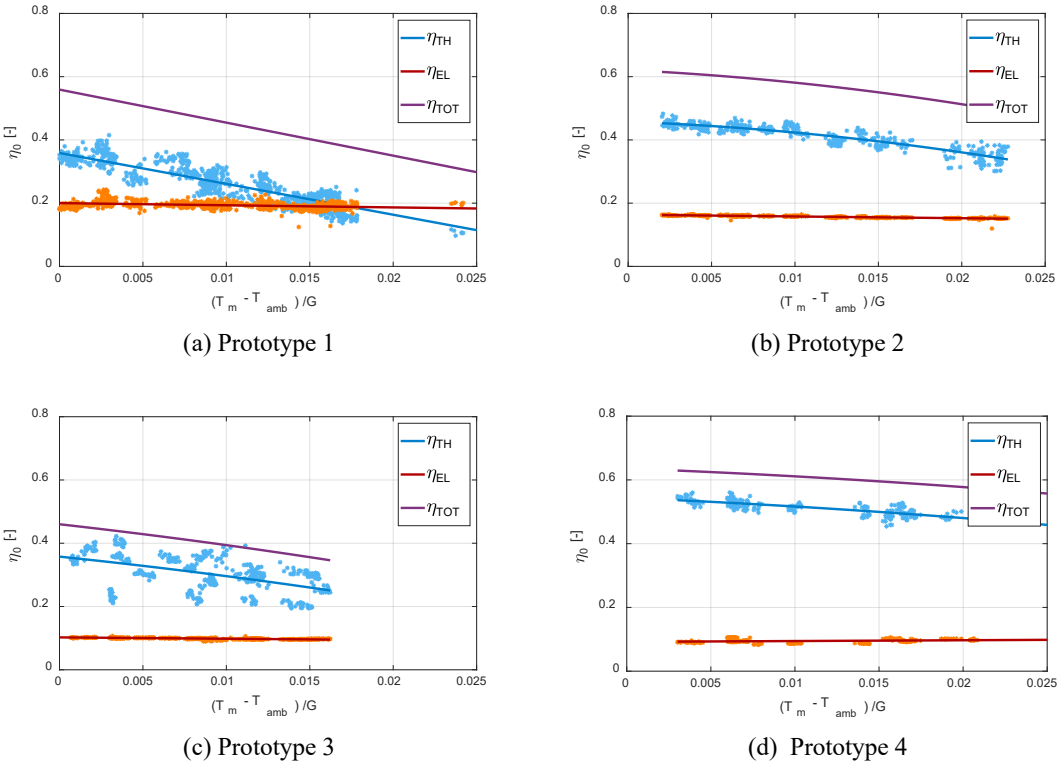

(a) Prototype 1 (b) Prototype 2

(c) Prototype 3 (d) Prototype 4

Figure 3: PVT efficiencies.

3.2 Thermal parameter characterization

The values of the thermal performance coefficients, defined as stated in the ISO 9806, 2013, are calculated for all prototypes based on the eq. 6 and eq. 7. The values obtained for each case are gathered in Tab. 2, together with technical values to assess the goodness of the adjustment.

Prototypes with frontal glazing present higher values of optical efficiency (η_0) followed by the uncovered panel (Prot. 1) and the one with rear camera (Prot. 3). For the Prot. 1, higher values of η_0 were expected due to the absence of frontal cover at low operational temperatures. An optical efficiency value below the other prototypes can be explained due to the material composition of the thermal absorber (sheet of aluminum instead of copper), the geometry (meander instead of harp configuration), lower operational flow rate or an enhanced electrical generation.

Prot. 1 also presents the higher linear heat loss coefficient (b_1) which implies that the thermal efficiency is strongly decrease when the operational temperature is increased, as it is the main purpose in this project. Glazed prototypes, on the contrary, show the lower values of heat loss coefficients, indicating that they are able to maintain acceptable efficiency levels even when the collector increases temperature. Between these two cases, it is highlighted the Prot. 4, which also presents a lower value of $\boldsymbol{a_2}$(quadratic term). This implies a better efficiency than Prot. 2 when the PVT panels performs at high temperature.

Tab. 2:Thermal performance coefficients and main adjustment characteristics. *Electrical efficiency value is given for Tm = Ta.

	η_0	b_u	b_1 / a_1	b_2 / a_2	η_{EL}*	N	SE	r (Pearson)	ρ (Spearman)	R^2
Prot. 1	0.380	0.0312	9.77	-0.122	0.20	911	0.0258	-0.9228	-0.9199	0.8717
Prot. 2	0.457	-	2	0.148	0.163	427	0.0160	-0.9057	-0.8803	0.8363
Prot. 3	0.358	-	5.49	0.0712	0.102	537	0.0466	-0.5989	-0.6044	0.3597
Prot. 4	0.544	-	2.25	0.00576	0.093	247	0.0145	-0.9026	-0.8398	0.8268

Tab. 2 also includes some information about the quality of the numerical adjustment obtained with the thermal coefficients. Particularly, this table shows for each prototype case: N, as the number of individual measurements, SE as the Standard Error of the regression, *r* as the Pearson coefficient, ρ as the Spearman coefficient and R^2 as the determinant coefficient, all of them defined in Section 2.4.2.

The value of Pearson's (***r***) and Spearman (***ρ***) coefficients reflects a negative relation, which means that the thermal efficiency decreases as the variable $\left(\frac{T_m - T_a}{G}\right)$ increases. Pearson's coefficient show a strong linear relation between variables ($-0.9 > \boldsymbol{r} > -1$) for all prototypes except the Prot. 3, where a poor relation is found ($\boldsymbol{r} > -0.6$). Spearman's coefficient supported this finding, demonstrating that the behaviour of Prot. 3 is not only not linear, but seems to depend on some additional variable besides the temperature gap and the solar irradiation.

3.3 Uncertainty analysis

All PVT prototypes exhibit some level of dispersion in the experimental data, as expected in measurements taken with real environmental data. However, both prototypes without frontal cover (Prot. 1 and 3) present much higher dispersion level than the prototypes with (Prot. 2 and 4), although the nature for this dispersion seems to come from different sources. To better evaluate this effect, we include in Figure 4 the histogram of errors, a graphical analysis of the error committed in the thermal efficiency when is calculated through the numerical characterization of Section 2.4.1 (η_{cal}) or experimental measurements (η_{exp}). For each case, determination coefficient R^2 is included in each subfigure, also added in Tab. 2.

For uncovered prototype case (Prot. 1, Figure 4 (a)), the range of error between theoretical and experimental thermal efficiency is wider than in other cases, however, the coefficient of determination R^2 is closer to 1, which should indicate better adjustment. This can be explained because the number of measurements taken during the testing of Prot. 1 (N=911) is much greater than those used in Prot. 2 and 4 (N=427 and N=247 respectively). As the number of items are much higher, the possibility to obtain bigger errors increases, although the general adjustment considering the whole period testing is better.

Moreover, it should be remarked that this model depends not only on the $\left(\frac{T_m - T_a}{G}\right)$ parameter, but also on the wind speed (see (eq. 6)). The theoretical model incorporates this variable, but the graphical representation of Figure 3 (a) is shown for the average wind speed measured during the testing. The dispersion found in this figure around the linear performance is then a consequence of the different wind levels registered during the testing, and not an inaccuracy of the thermal model.

The prototype with the rear camera (Prot. 3) is different. In this case the graphical dispersion shown in Figure 3 (c) is higher than any other case, as is the error range between theoretical and experimental results shown in Figure 4 (c). Moreover, the gaussian curve generated in the histogram of Prot.3 has a much flatter profile than the other three cases, which presents a sharper profile with higher frequencies located close to zero. This poor adjustment is clearly represented by the R^2 value of 0.3597 calculated for this case. This fact indicates that the thermal model considered for this prototype may not be suitable, since this theoretical model is not able to reproduce the experimental performance with enough accuracy.

Two approaches are proposed to address the adjustment to this model. First one is to include some dependency of the wind speed, since it has been noticed during the testing that this variable has some influence on the final thermal performance. As the relation with the temperature parameter $\left(\frac{T_m - T_a}{G}\right)$ has proved to be clearly quadratic, the question remains whether the relationship with wind is quadratic or linear. Second one exposes the possibility of developing a new theoretical model to characterize this particular solar panel, since none of the models presented in ISO 9806, 2013 seems to be able to predict the thermal performance due to the presence of air camera between the PV and absorber.

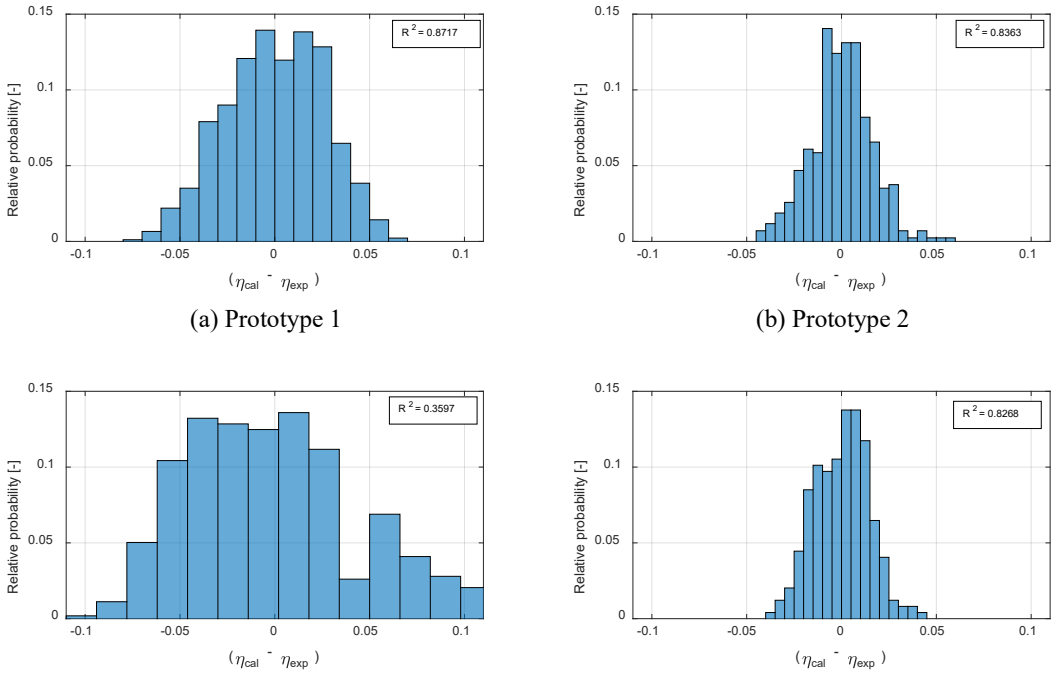

(a) Prototype 1 (b) Prototype 2

(c) Prototype 3 (d) Prototype 4

Figure 4: Histogram of error committed between theorical data (η_{cal}, calculated from linear or quadratic models) and experimental data (η_{exp}), and coefficient of determination R^2 for each adjustment.

3.4 Power production

As explained in 2.1, the objective of the project was to find a PVT panel able to work at 50ºC with still useful thermal efficiency. In order to assess the appropriateness of prototypes at the operating conditions required in end use, we have calculated the power production (thermal and electrical) of each prototype when working at mean operational temperature of 50ºC. For this comparison, STC conditions (1000W/m^2, Ta=25ºC, wind=1m/s) are considered. Graphical results are shown in Figure 5 while particular values for operational temperature of $\boldsymbol{T_m}$= 50ºC are gathered in Tab. 3.

In these figures, the relation of each prototype with regard to the thermal losses is graphically shown. At STC conditions, Prot. 1 (Figure 5 (a)) presents full linear behavior with a strong negative slope, as stated by the linear coefficient (b_1=9.77). Lower thermal efficiencies are expected for higher values of wind speed. Thanks to the electrical potential of this PV laminate, the total power generated by this prototype at 50ºC is 286.5 W/m^2, where only 104.7 W/m^2 provided for thermal process.

Prot. 3 (Figure 5 (c)) presents better thermal generation but lower electrical production than Prot. 1, in a slightly smaller gross area. As a consequence, the total power production is a bit lower (270.3 W/m^2), but more thermal contribution can be provided to the end user. This estimation however should be analyzed with more detail since the evaluation of the adjustment and the thermal model used cannot be considered as satisfactory.

Finally, both glazed models (Prot. 2 and 4, Figure 5 (b) and (d)) present reasonable total energy productions at 50ºC, which reached to 473.9 W/m^2 for the Prot. 2 and 571.5 W/m^2 for Prot. 4. The main difference lay in the thermal-electrical ratio obtained in each model, which was 66-34% for Prot. 2 and 84-16% for Prot. 4. Based on this data, it is concluded that both collectors are recommended for their use in the final application.

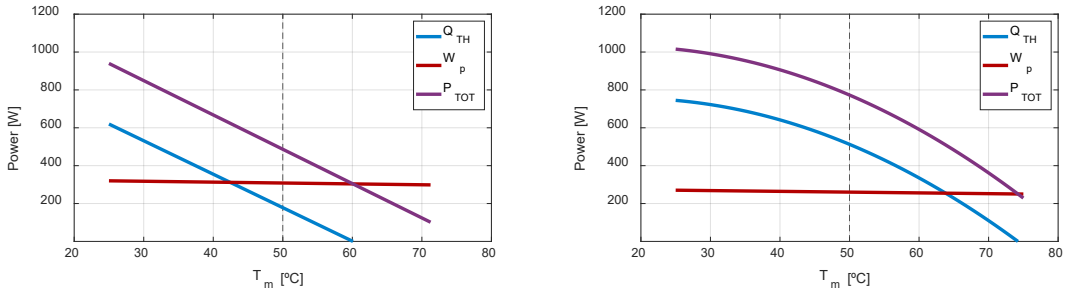

(a) Prototype 1

(b) Prototype 2

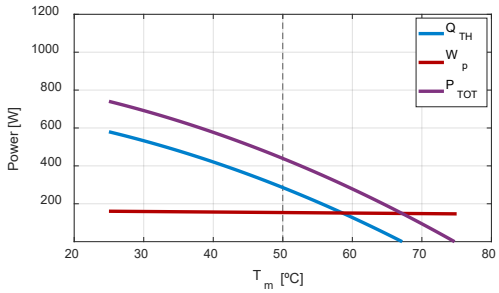

(c) Prototype 3

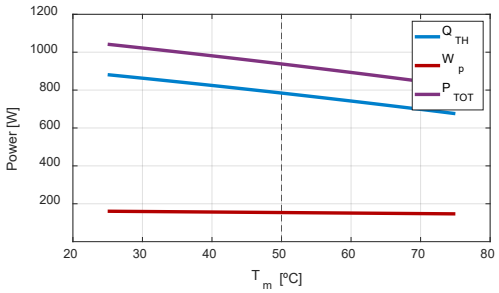

(d) Prototype 4

Figure 5: PVT power production at STC (1000W/m², Ta=25ºC, wind=1m/s).

Tab. 3: Estimated power production of PVT prototypes at 50ºC and STC.

	Prot. 1	**Prot. 2**	**Prot. 3**	**Prot. 4**
Thermal power [W]	178	512	285	784
Thermal power [W/m²]	104.7	314.1	175.9	481
Electrical power [W]	309	260.5	153.5	153.8
Electrical power [W/m²]	181.8	159.8	94.4	90.5
Total power [W/m²]	286.5	473.9	270.3	571.5

This study is not exempt form limitations. Although the analysis fulfilled its objective of selecting suitable and most promising PVT prototypes for their ulterior integration with TES system, the characterization of Prot. 3 should be improved. One possibility would be to develop a mathematical model for this particular PVT design. A second and more recommended way would be to obtain the thermal characterization through the 8-parameter equation indicated in the updated version of the standard, ISO 9806, 2017. The main future line of this study is to develop a procedure to be able to characterize the four prototypes here proposed under the last version of the standard, and compare numerical approaches.

4. Conclusions

This work presents the results of testing four liquid-based PVT prototypes considered for their future use as thermal and electricity collectors, in the frame of an electrical storage system developed under a H2020 European project. Prototypes were designed, manufactured and tested according to EN-ISO 9806 standard (CEN, CENELEC 2017).

Experimental testing and subsequent numerical analysis allowed to characterize the thermal behavior of prototypes based on the models given in the ISO 9806, 2013. Statistical analysis indicated a good quality of the thermal adjustment, with the exception of Prot. 3 with rear air camera, which exhibited uncertain adequacy of the

numerical model applied. Further study is recommended for this case. For the rest of cases, optical efficiency and heat loss coefficients were calculated with good statistical indicators, which enables the estimation of the thermal and electrical power productions at certain external conditions (solar irradiance, ambient temperature and wind speed). This approach has been then used to determine their potential at the required operational temperature (above 50ºC).

From the prototypes proposed, two PVT models without frontal cover (unglazed collector with high performance PV laminate and collector with intermediate camera with semi-transparent PV laminate) showed low thermal efficiency for the required operational temperature. Particularly, unglazed case presented the highest electrical performance (around 19%) but really low thermal generation (105 W/m^2) at high temperatures, which dismisses its use for this application but remain for others where lower temperatures or more electrical efficiency are sought. On the other hand, the other two prototypes exhibited acceptable thermal productions at 50ºC. Both prototypes include a frontal cover that minimizes the heat losses on the collector. As a consequence, they reach to produce up to 314 W/m^2 (Prot. 2 with full PV laminate) and 481 W/m^2 (Prot. 4 with semi-transparent PV laminate). The difference between them remains also in the electrical production, with greater values for the case of full laminate rather than semi-transparent PV laminate, up to 70% higher.

Results indicate that the incorporation of semi-transparent PV laminate may help to improve the thermal performance of the glazed PVT collectors, especially when working at high temperatures (around 25ºC above environment, as required for this project). However, it reduces the electrical production, so their use should be reserved for applications where thermal contribution is crucial.

5. Acknowledgments

This work has been carried out in the framework of the European Union's Horizon 2020 research and innovation programme under grant agreement No 869821 (Minimal Size Thermal and Electrical Energy Storage System for In-Situ Residential Installation - MiniStor). This project was funded by the European Commission within the Eighth Framework Programme H2020, throughout the. LC-EEB-05-2019-20 call.

6. References

Baggenstos, A., Mellor, A., Gagliano, A., Corino, C., Zenhäusern, D., Cabral, D., Ryan, G., Guedea, I., Brottier, L., Ruoff, U., Schubert, M., Lämmle, M., Pellegrini, M., Dannemand, M., Cañada, M., Radish, N., Pokorny, N., Ramshack, T., 2020. Existing PVT systems and solutions. IEA SHC Task60, PVT Systems, Report A1, 1st ed. https://doi.org/10.18777/ieashc-task60-2020-0001

Bianchini, A., Guzzini, A., Pellegrini, M., Saccani, C., 2017. Photovoltaic/thermal (PV/T) solar system: Experimental measurements, performance analysis and economic assessment. Renew. Energy 111, 543–555. https://doi.org/10.1016/j.renene.2017.04.051

Brötje, S., Kirchner, M., Giovannetti, F., 2018. Performance and heat transfer analysis of uncovered photovoltaic-thermal collectors with detachable compound. Sol. Energy 170, 406–418. https://doi.org/10.1016/j.solener.2018.05.030

Fayaz, H., Rahim, N.A., Hasanuzzaman, M., Rivai, A., Nasrin, R., 2019. Numerical and outdoor real time experimental investigation of performance of PCM based PVT system. Sol. Energy 179, 135–150. https://doi.org/10.1016/j.solener.2018.12.057

Herez, A., El Hage, H., Lemenand, T., Ramadan, M., Khaled, M., 2020. Review on photovoltaic/thermal hybrid solar collectors: Classifications, applications and new systems. Sol. Energy 207, 1321–1347. https://doi.org/10.1016/j.solener.2020.07.062

IEA-SHC, 2022. Solar Thermal Market Records Year of Growth, Solar update. The Newsletter of the IEA Solar-Heating and Cooling Programme. USA.

IEA-SHC, 2018. Task 60 - PVT Systems: Application of PVT Collectors [WWW Document]. URL https://task60.iea-shc.org/

ISO 9806, 2017. Solar energy - Solar thermal collectors - Test methods. Second Edition.

ISO 9806, 2013. ISO 9806:2013 Solar energy - Solar thermal collectors - Test methods.

Jonas, D., Lämmle, M., Theis, D., Schneider, S., Frey, G., 2019. Performance modeling of PVT collectors: Implementation, validation and parameter identification approach using TRNSYS. Sol. Energy 193, 51–64. https://doi.org/10.1016/j.solener.2019.09.047

Joshi, S.S., Dhoble, A.S., 2018. Photovoltaic -Thermal systems (PVT): Technology review and future trends. Renew. Sustain. Energy Rev. 92, 848–882. https://doi.org/10.1016/j.rser.2018.04.067

Ozgoren, M., Aksoy, M.H., Bakir, C., Dogan, S., 2013. Experimental performance investigation of photovoltaic/thermal (PV-T) system, in: European Physical Journal Conferences. https://doi.org/10.1051/epjconf/20134501106

Simón-Allué, R., Guedea, I., Coca-Ortegón, A., Villén, R., Brun, G., 2022. Performance evaluation of PVT panel with phase change material: Experimental study in lab testing and field measurement. Sol. Energy 241, 738–751. https://doi.org/10.1016/j.solener.2022.05.035

Sultan, S.M., Ervina Efzan, M.N., 2018. Review on recent Photovoltaic/Thermal (PV/T) technology advances and applications. Sol. Energy 173, 939–954. https://doi.org/10.1016/j.solener.2018.08.032

Wu, J., Zhang, X., Shen, J., Wu, Y., Connelly, K., Yang, T., Tang, L., Xiao, M., Wei, Y., Jiang, K., Chen, C., Xu, P., Wang, H., 2017. A review of thermal absorbers and their integration methods for the combined solar photovoltaic/thermal (PV/T) modules. Renew. Sustain. Energy Rev. 75, 839–854. https://doi.org/10.1016/j.rser.2016.11.063

Zisopoulos, G., Nesiadis, A., Atsonios, K., Nikolopoulos, N., Stitou, D., Coca-Ortegón, A., 2021. Conceptual design and dynamic simulation of an integrated solar driven thermal system with thermochemical energy storage for heating and cooling. J. Energy Storage 41. https://doi.org/10.1016/j.est.2021.102870

Prefabricated Renewable Energy Façades For Cost-Effective Buildings (Prefab)

Corry de Keizer[1], Maarten Dörenkämper[1] and Simona Villa[1]

[1] TNO Energy Transition, Eindhoven (the Netherlands)

Abstract

The integration of solar energy in prefabricated façade elements is a promising technology. The energy transition requires a large amount of space, and especially for high-rise buildings the roof area is not sufficient to comply with modern building codes regarding energy performance. Prefabricated or 'industrial' building is getting more popular, as it leads to lower costs for installation and allows for better quality control. Within this project, a consortium developed prefab façade elements with integrated photovoltaic (PV) modules. A demonstrator was designed and constructed, which includes PV modules with several innovative technologies with regards to size, form, colour and transparency. Different colour techniques were used. The performance of the demonstrator is extensively analysed based on measurements and detailed modelling.

Keywords: BIPV, façade, industrial building, coloured PV, prefab

1. Introduction

The energy transition requires a lot of space for implementing renewable energy technologies. Solar energy systems are especially suited to be integrated in e.g. roofs, facades or infrastructure. Especially for high rise buildings, the roof surface alone is insufficient to meet the energy demand and therefore integration of photovoltaics in the façade offers an interesting opportunity. In the Netherlands, there is a potential of about 660 km^2 for solar energy integration in the façade (Van Hooff, et al., 2021). Solar façades could potentially produce 32 TWh per year which is nearly 30% of the electricity demand of the Netherlands (CBS, 2021).

There are many examples of photovoltaics integrated or added to facades (Corti et al., 2020). Demonstration projects with different technologies, colours and ways of integration have been implemented since the 1990's. There are several ways to integrate PV in the building skin that depend on the construction of the façade. Rainscreens, also known as cold or ventilated façades consist of a load-bearing substructure, an air gap and a cladding. Usually, PV modules are integrated in a similar way to non-PV claddings. Curtain wall façades are external and not ventilated, these can be totally or partially glazed and are supported by a substructure. It is designed to resist air and water infiltration. PV elements can replace the non-PV glass. A double skin façade consists of two glazed skins, photovoltaics is integrated in the outer skin that should be able to withstand wind loads. The cavity functions as insulation and can be actively ventilated. Accessory façade are for example balconies with bifacial PV. Lastly prefabricated or multifunctional facades are preassembled and have multiple functions like thermal and acoustic insulation, weather protection, energy production, etc. (ICARES, 2019).

The aim of the PREFAB project is to develop integration of PV into prefabricated façade elements that are aesthetically pleasing and affordable. The potential advantage of integrating PV into prefabricated façade elements is an improved process efficiency, lower installation cost and avoided costs for cladding materials, improved quality and safety management. It can also result in a reduced installation time on often busy building locations and less transport movements and therefore lower CO_2 emissions. Further advantages may include a better freedom of design. It is expected that integrating PV in facades of high-rise and low-rise office buildings or dwellings will become important in the next decade, especially in densely populated countries like the Netherlands.

In the PREFAB project, we have been working on developing technologies that allow aesthetic solar panels to be integrated into prefabricated façades of buildings. Several innovative technologies with regards to the size, 3D shape, colour and transparency of the PV modules are researched and implemented in a demonstrator. The

© 2022. The Authors. Published by International Solar Energy Society
Selection and/or peer review under responsibility of Scientific Committee
doi:10.18086/eurosun.2022.07.11 Available at http://proceedings.ises.org

demonstrator includes modules with several PV technologies, different PV colouring technologies, module packaging and mounting method. The PREFAB demonstrator was installed on an outdoor research location and extensively measured for a year. Furthermore, the PV performance model BIGEYE (Janssen, 2018; Burgers, 2018) is validated for PV panels in the façade by using measured data from the PREFAB demonstrator.

The PREFAB project has been running from 2019 to 2022 and was carried out by a broad consortium that includes prefab building companies (TGM, Emergo), a BIPV façade supplier (Studio Solarix), engineering and installing companies (Sanko Solar, SCX Solar), a company on composites who integrate PV (Flexipol), software developers (Novasole) and a research institute (TNO). The ambition of the commercial project partners is to develop products that can be introduced to the market after the end of the project.

In this paper, we will focus on the design and different technologies of the demonstrator and installed measurement equipment (Chapter 2). The field test (chapter 3) is described with a focus on the analysis of weather and performance of the individual modules. Furthermore, electrical PV simulations on the PREFAB system are performed in order to investigate further the electricity generation potential of such a BIPV system, as well as to improve the understanding on specific aspects, such as shading and albedo effect (Chapter 4).

2. PREFAB demonstrator

2.1 The PREFAB demonstrator

The demonstrator is shown in Figure 1, while the installation of a prefab element is shown in Figure 2. The demonstrator consists of two prototypes. The left prototype (1.80 m wide, approx. 4 m high) has an aluminium frame as is typically used for high-rise office or residential buildings. This façade element was assembled in the factory and mounted directly from a crane. The right side prototype has a wooden frame typically used in low-rise dwellings. The PV modules are mounted on site.

Several different (PV) technologies are implemented in the demonstrator:

- PV cell types: Crystalline silicon and CIGS
- Colouring technology: coloured foil and ceramic printed ink on glass
- Module packaging: frontsheet – backsheet (solar foil), glass-backsheet and glass-glass modules
- Form and size: CIGS PV foil is integrated in a 3D composite module, the cells are in two surfaces facing different directions.
- Prefabrication and mounting: one façade element is fully assembled in the factory and mounted from a crane, the other one is partially prefabricated (including window) and PV modules are mounted on site.



Fig. 1: PREFAB demonstrator, consisting of two façade elements, on the outdoor research facility



Fig. 2: Installation of a PREFAB element

The specifications of the installed modules and the colouring technology are described in Table 1. Solarix supplied the coloured foils for the different modules and the coloured etched glass of module J1. They supplied modules A, C2, E and D. Module J1 was produced by TNO. The CIGS module (foil) for panels G, H and I were produced by TNO part of Solliance. The CIGS foil was laminated within a composite 3D shaped module by Flexipol. A printed foil is used to colour the modules. The STC rated power was measured by TNO and is shown in the last column per m^2 cell area. This column shows quite some differences due to the reference technologies and the method for the colour technology. A print with ceramic ink results in lower losses due to colour. The printed foil was a first innovative solution and will be further improved with regards to losses due to colour. Due to the different dimensions, all modules have a different part of the area of the module that is filled with cells,.

The demonstrator is installed on SolarBEAT, the outdoor research location of TNO on the TU Eindhoven campus. The façade of the demonstrator is oriented towards the south. A full year performance was measured from August 2021 to July 2022.

Tab 1: Specification of the modules in the demonstrator



Panel	Cell-type	Colour technology	P_{mpp} (W)	Module area (m^2)	Cell area (m^2)	Area Fill (%)	Rated W/m^2_{cell}
J1	c-Si (MWT*)	Ceramic ink on glass	165.0	1.55	1.22	79	135
E	c-Si	Printed foil	48.5	0.85	0.54	63	90
D	c-Si	Printed foil	107.9	1.47	1.17	80	92
A	c-Si	Ceramic ink on glass	143.5	1.41	1.10	78	130
C2	c-Si	Ceramic ink on glass	114.4	1.11	0.81	73	141
G	CIGS	Printed foil	27.3	0.48	0.29	61	93
H	CIGS	Printed foil	33.7	0.53	0.33	63	101
I	CIGS	Printed foil	21.7	0.48	0.29	61	74

* Metal Wrap Through (MWT) back contact technology

2.2 Installation and measurement equipment

The PV modules are kept in maximum power point and are connected to the grid by making use of DC-DC power optimizers and a inverter (SolarEdge). For every module (except module E), the DC current, voltage and power are measured with a AcuDC 243 power analyser that is installed between the power optimizer and the PV module. Since module E had a too low V_{OC} for the power optimizer, this module is measured using an IV tracer. T-type thermocouples are mounted on the rear side of the PV panels. In the case of the composite panels (G, H, I), the thermocouples are laminated within the composite structure. Irradiance in the plane of the façade is measured using two EKO MS80 pyranometers, which are mounted at two different heights on the west-side of the demonstrator (see Figure 1). The different irradiance levels at different heights are further measured by 8 different photodiodes (EKO ML-01) installed on a so-called irradiance beam located in the middle of the setup.

On SolarBEAT a solar measurement station is installed that measures Global Horizontal Irradiance (GHI) using an EKO MS-802 pyranometer. Diffuse Horizontal Irradiance (DHI) is measured with a similar pyranometer combined with a EKO MB-12 shading ball, which is mounted on a EKO Str-22G sun-tracker. On the same sun-tracker, Direct Normal Irradiance (DNI) is measured with a pyrheliometer of the type EKO MS-86. Furthermore, several meteorological parameters (ambient temperature, wind speed, wind direction, air pressure, precipitation) are measured using a Lufft WS 600 weather-station.

Every day all measured data with a time resolution of 1 minute is uploaded to an SQL-database.

3. Performance analysis

3.1 Irradiation and wind speed

The irradiation profile over a year is very different for a façade in comparison to the irradiation for a horizontal or optimally inclined plane. Figure 3 shows the monthly measured in-plane or plane of array irradiation (POA) in the façade and the monthly measured global horizontal irradiation (GHI). The highest monthly irradiation for the façade is not found in the summer months, but during spring and autumn as the elevation angle of the sun is more advantageous for planes with a tilt angle of 90°. During summer, the sun is high in the sky and often beyond the vertical façade, which sees a smaller sky portion than, for instance, an horizontal or slightly tilted PV module. Also direct irradiation from northeast or northwest is not received by a south facing façade. The annual irradiation on the south façade from August 2021 to July 2022 was 917 kWh/m^2, this is approximately 18% lower than the global horizontal irradiation and 27% lower than irradiance on a 35° tilted roof. It was a very sunny year.

The wind compass in Figure 4 shows the frequency of wind speed and direction. The building on the north influences the wind profile.

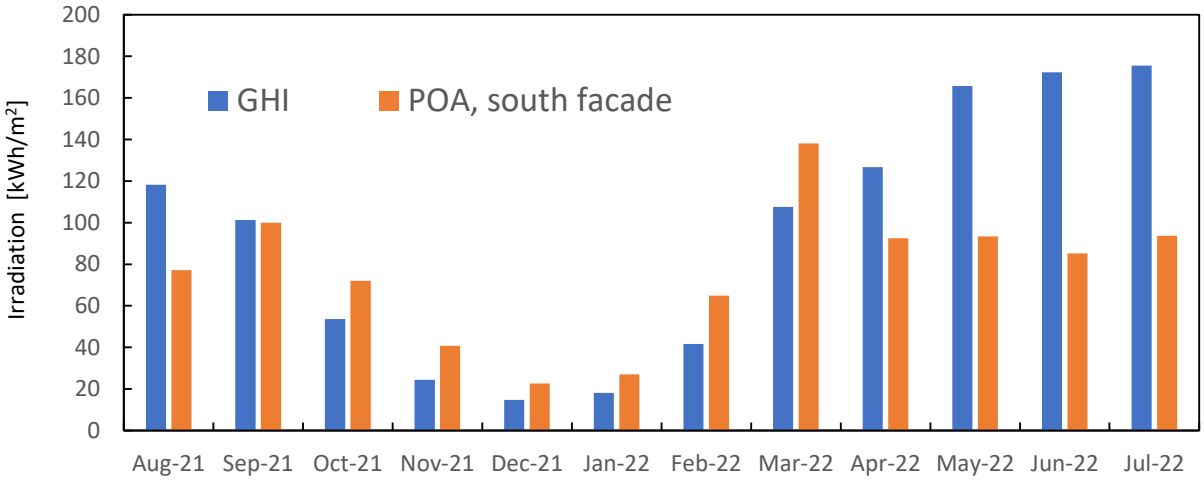

Fig. 3: Measured monthly in-plane irradiation (POA) in the south façade and the monthly global horizontal irradiation (GHI)

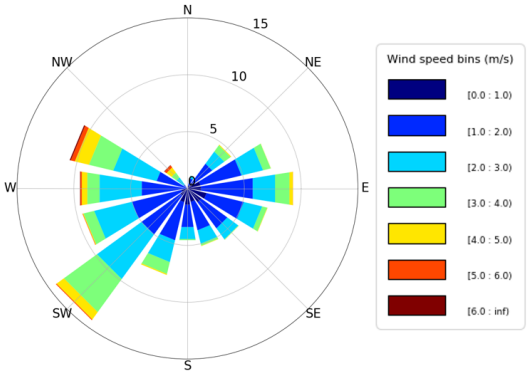

Fig. 4: Wind compass

3.2 Energy performance of the coloured modules

In this section, we evaluate the DC performance of the different PV modules. The PREFAB elements and the individual PV panels were affected by external factors, like shade (see Figure 5), and factors that are system specific. To allow for a fair comparison between the different PV modules, data during times when at least one of the PV panels is affected has been filtered out. The following filters have been applied to the data set:

- Shading: The azimuth angle should be between 130° and 242° (with 180° as south) and an elevation angle higher than 14°
- Voltage blocking effect due to the many different module sizing and specifications in combination with the DC-bus of the Solar Edge system: the output voltage of the power optimizer should be lower than 78V.
- All modules should be functioning, times when some power optimizers start up late, due to the rated power of the modules, are excluded

This results in a smaller dataset, where about one-third of the annual irradiance is still included. The effect of shading (see also Figure 5) will be evaluated by simulations in Chapter 4.



Figure 5: Left: Shade patterns in the morning of the 17th of April of 2022 caused by the neighbouring PV setup (ZigZag) Right: Shade on panel D, caused by the protruding part of panel C2 in the afternoon of the 17th of April 2022.

Figure 6 shows the monthly DC performance ratio (PR_{DC}) for three of the modules.

$$PR_{DC} = \frac{E_{DC} \cdot G_{STC}}{P_{STC} \cdot I_{POA}}$$

Where E_{DC} is the DC energy yield, G_{STC} the irradiance at standard test conditions (1000 W/m^2, 25°C), P_{STC} is the installed DC power and I_{POA} is the solar irradiation.

The trend throughout the year shows slightly higher performance ratios in winter and slightly lower performance ratios in summer, probably due to temperature effects. The slightly lower PR of the foil coloured modules could be due to inaccuracies in STC power ratings. The lower PR of the CIGS modules is possible caused by a mismatch due to irradiance on two planes. Figure 7 shows the 30-minute instantaneous PR_{DC} of module G. It clearly shows a dependence on the azimuth of the direct sunlight that is caused by the cells in two different planes. Figure 8 shows the DC performance ratio and the annual expected DC yield for an unshaded situation in kWh/m^2 cell area. The modules with a ceramic ink colouring show a higher calculated annual yield due to a higher peak power, as well as a higher performance ratio. The expected DC yield for the unshaded situation is calculated by multiplying the module specific rated peak power (W/m^2) with the performance ratio and the annual irradiation.

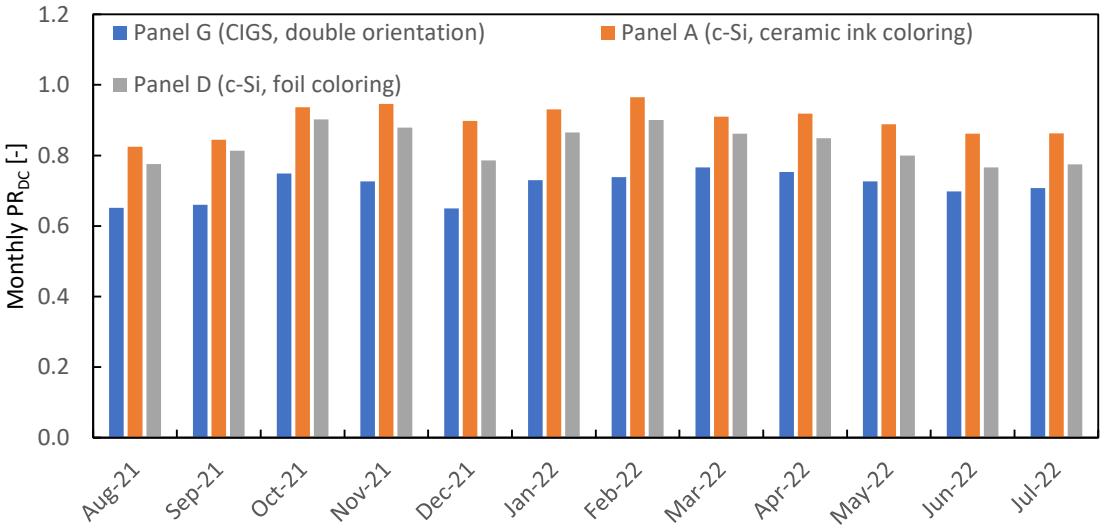

Figure 6: Monthly DC performance ratio for selected modules

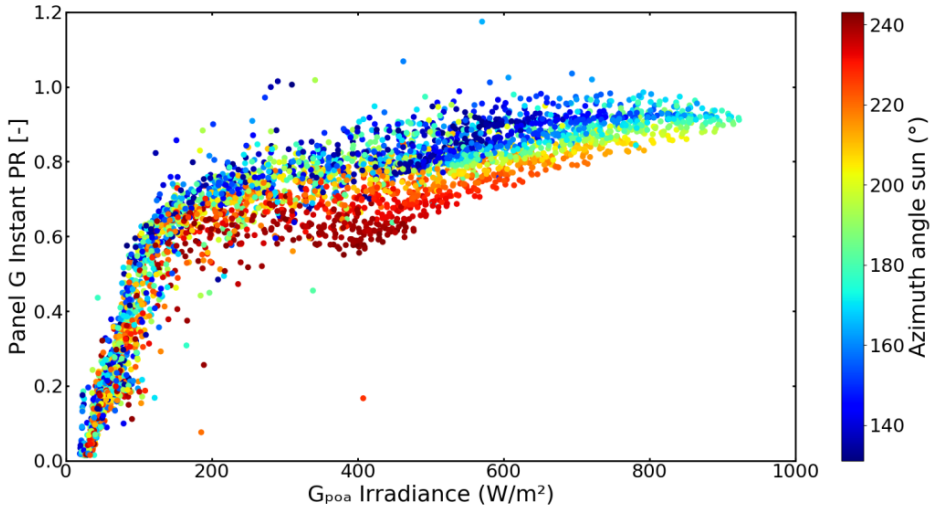

Figure 7 Temperature corrected instantaneous PR_{DC} of panel G as a function of the G_{POA} irradiance. The colour code represents the azimuthal position of the sun. One datapoint represents 30minutes.

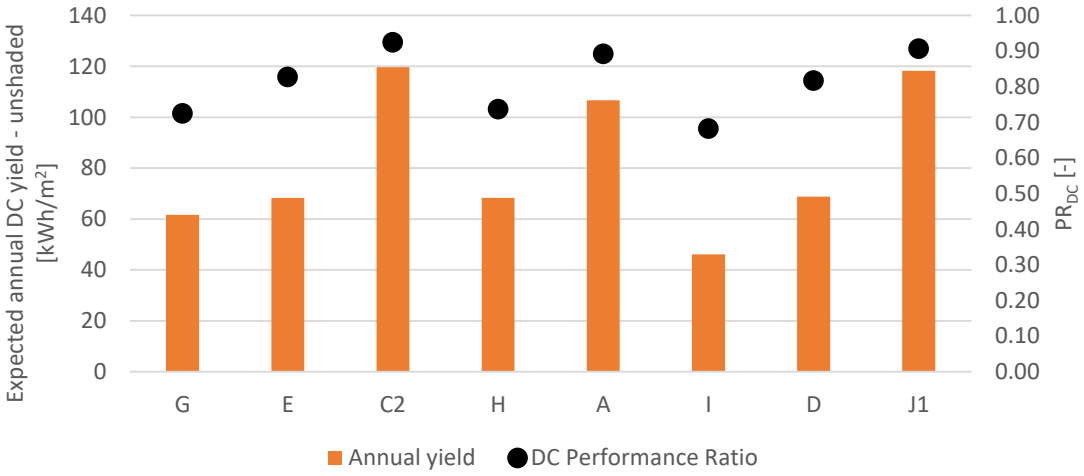

Figure 8 Annual DC performance ratio for unshaded situation as measured (on the right axis) and expected DC annual yield (on the left axis) for an unshaded situation. The DC annual yield is calculated by multiplying PR_{DC} with irradiation and rated specific module power.

4. Simulation of annual energy yield

4.1. BIGEYE Model

The energy yield is modelled with BIGEYE, an in-house developed software for PV system modelling (Janssen et. al., 2018, Burgers et.al.,2018). The effect of self-shading (from the construction itself) will be evaluated. At first, we model the PREFAB modules as closely as possible to the real demonstrator built at SolarBEAT, considering the real geometry of the system with all its sources of shade. In such a way, we can validate the model using the real outdoor measured data. Then, typical meteorological year data are used to estimate the annual generation potential of the PREFAB façade mockup in its current configuration.

With BIGEYE, PV systems at any location and of any configuration (e.g. bifacial) can be modelled. Using weather and environmental data, the electricity produced can be calculated on a minutely, hourly, daily, monthly or yearly basis. With the software it is possible to accurately reproduce the geometry of the studied system, and account for external shading objects, which will act in the model as dummy elements. BIGEYE user interface requires two input files: a geometry file and a meteorological file.

In the PREFAB modelling work, the most challenging part resulted to be the realization of the geometry file, due to the high customization of the façade and variety of modules' shapes, dimensions and orientations. In order to take into account the mutual shading, it was crucial to accurately reproduce not only the PV modules, but also all the dummy non-PV active panels which are part of the facade, with their exact dimension and relative spacing. In fact, most of the modules within the PREFAB system are subjected to multiple sources of shading, such as construction-shading from their own support or shading from external objects (e.g. the other cabins at SolarBEAT). Figure 9 shows the schematic of the modelled geometry of the system in BIGEYE, including both the PV-active elements (A, C2, D, E and J1) and the dummy elements responsible for casting shades. Modules G, H and I are not modelled.

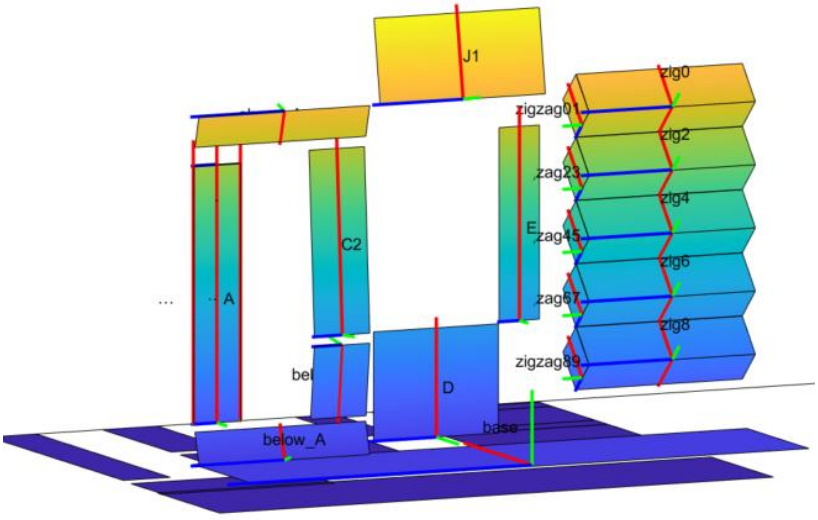

Figure 9. BIGEYE modelled geometry of the PREFAB system, including both PV active elements (A, C2, J1, D, E) and dummies.

The losses due to the colour coatings (ink printed dots on glass or coloured foil) on the actual PREFAB modules are almost purely optical, meaning that they mainly translate in a current decrease.

4.2. Validation of the model

The module was validated by comparing measured and simulated power for several sunny and cloudy days in different seasons. An example for module J1 on the April 17, 2022 is shown in Figure 10. From the results of the validation we can state that BIGEYE is successful in accurately modelling the current, voltage and power output of the different modules. With a good degree of accuracy (typically $R^2 > 0{,}996$), we could validate the model with the measured data.

The simulations also helped in understanding specific issues that were encountered in the real life demonstrator, such as specific shading patterns and power electronics issue. For example, on the selected sunny day, we can see

the effect of the power optimizer issue (i.e. voltage blocking) on module J1 (Figure 10). It can be observed that, before 9:30 am and after 17:30 the measured Impp slightly decreases (limited by the reached max PO voltage) while the Vmpp slightly increases, when compared to the simulated curves which present instead smooth profiles.

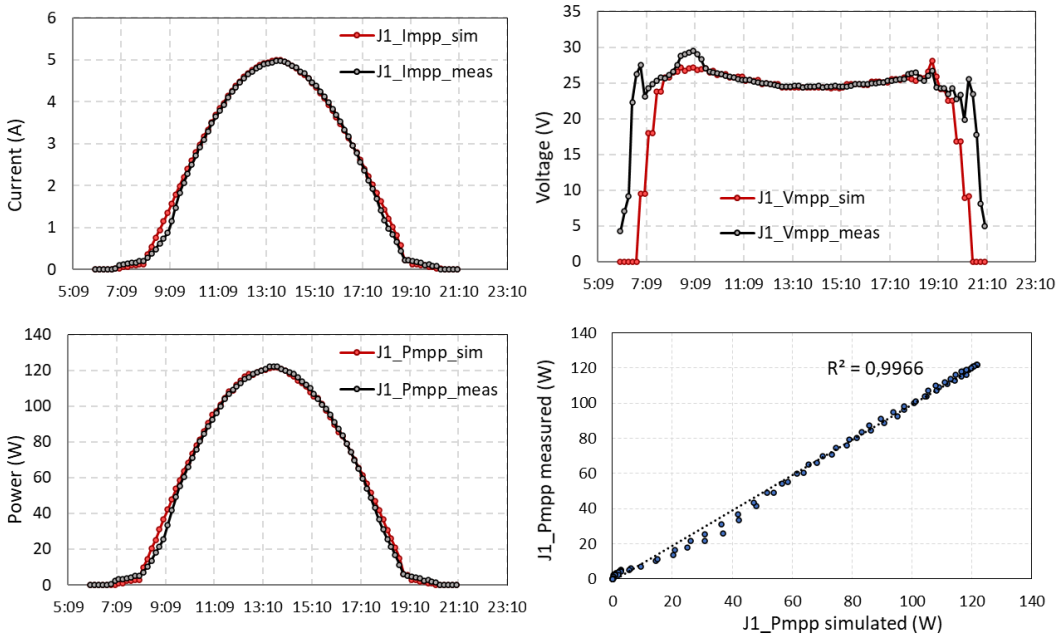

Figure 10. Model validation module J1 (sunny day 17/04/2022): comparison measured data vs simulation.

4.3. Shading losses

For each simulation, BIGEYE also allows to compare the electrical power output both including and excluding the presence of shading elements. In such a way it is immediately possible to see to what extent shading affected and limited the power production. For the same reference sunny day as before, this is shown in Figure 11. For each module we compare the simulated power generation including all sources of shade (as in real life – red curves) versus the hypothetical power production if no shading sources would be present (blue curves). It can be seen that for this sunny day, modules D and E are the most affected by the shade, reporting a loss of more than 9%. In that case the shade is coming mainly from the zigzag structure next to the PREFAB one, as visible from the webcam photo in Figure 5. Module A shows a 7% loss (over this day) which is attributed to its own support structure and the titled dummy panel above it. On the other hand, modules C2 and J1, which are not vertical but slightly tilted towards the sky (3° and 5° respectively), are not affected by any shade, thus reporting no loss.

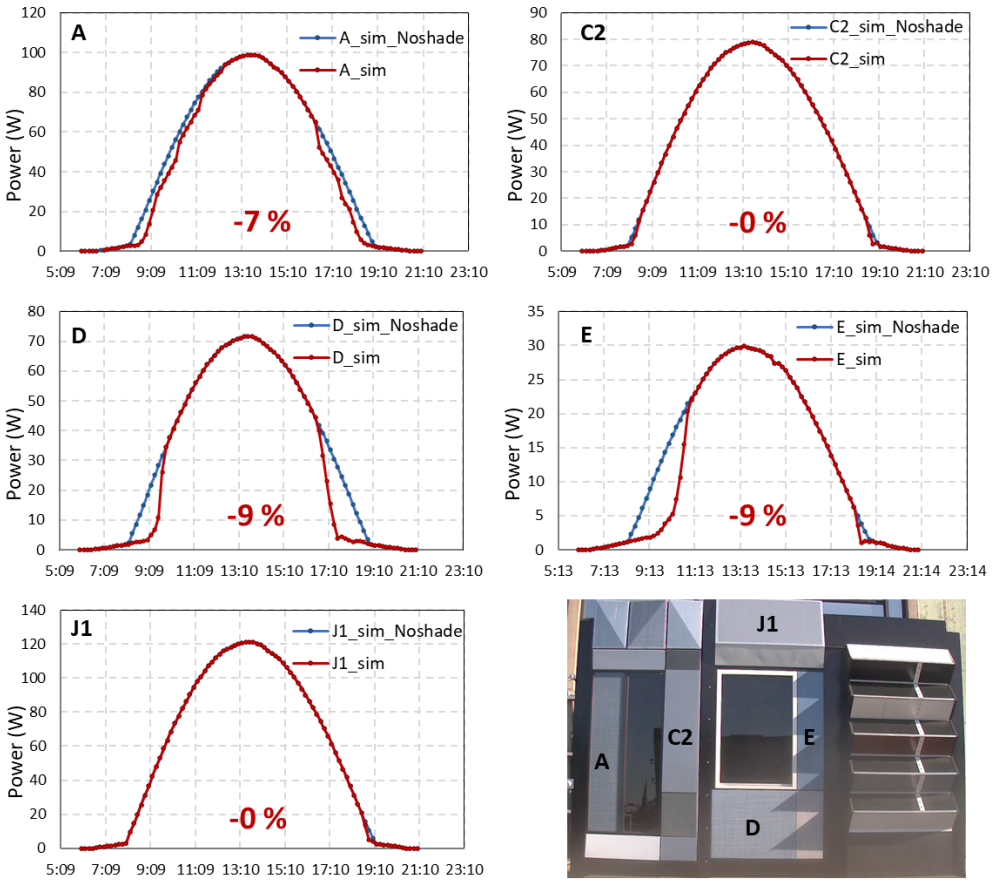

Figure 11. Simulations showing power loss due to shading for each module during sunny day 17/04/2022. The power production including all sources of shade (in red) is compared to the hypothetical power production in case of no shading elements (in blue). The percentage indicates the total daily power loss.

4.3. Simulation for a typical meteorological year

A full year simulation was performed for one representative module of the PREFAB system, i.e. module D. The simulation is run using weather data for a typical meteorological year (TMY) from Meteonorm software, with a 1-h timestamp. Please note that the irradiation of the TMY is significantly lower than the measured weather data during the PREFAB field test. Figure 12 shows the results of the simulation as a monthly energy yield bar plot, where we also compare the energy generation in case of presence and absence of shading. The presence of shading elements as we have them at SolarBEAT is actually representative of a real case scenario, where such a module would be installed in the façade (south-facing, in this case) of a building in a city environment, which is plenty of possible sources of shade (other buildings, trees, etc.). In the simulated case, we found that most shading losses are in spring/autumn and summer, and for the full year they account for around 4 to 5%. The simulation also shows that the energy yield is the highest in the spring and autumn season, and slightly decreased in summer. All in all, the energy production of a vertical façade system is more evenly distributed over the year than a standard tiled-roof top installation. This aspect, in particular, is relevant now that we are facing problems like energy grid congestion issues and grid overload. Avoiding excess energy production when there is less demand (i.e. sunny summer day) while producing more when there is more need (e.g. winter) is a beneficial aspect of vertical PV façade installations.

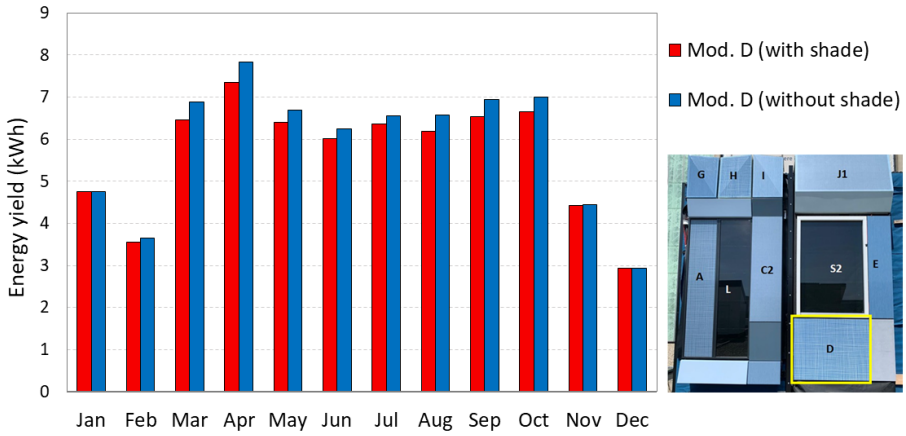

Figure 12. Modelled monthly energy production of one of the PREFAB modules (module D), both including (in red) and excluding (in blue) the presence of shading elements. The simulation is run with a TMY meteo file.

5. Conclusion

Within the PREFAB project, a consortium developed prefab façade elements with integrated photovoltaic (PV) modules. A demonstrator was designed and installed, which includes PV modules with several innovative technologies with regards to size, form, colour and transparency. One of the elements was mounted directly from a crane. Different module colour techniques were used.

The performance of the demonstrator was extensively analysed based on measurements and modelling. The DC yield and PR of the very versatile panels, in terms of colour, shape and PV-technology, has been presented. Mismatch losses can occur when a single PV panel has multiple orientations. The dependence of the azimuthal angle of the sun on the performance of the 3D shaped panel used in the PREFAB demonstrator has been visualized.

The advanced simulation tool BIGEYE resulted to be suitable for modelling opaque aesthetical BIPV façades. Despite the complexity and diversification of the PREFAB system, we could successfully validate the model with the measured data. The model could be further improved by fine tuning the geometrical input file according to an even more precise representation of all dimensions and spacing between the modules and dummy elements casting a shade on them. The current model however gives already very good correlations.

Additionally, the model also allowed to quantify the losses due to shading to the total power generation. The (TMY) year simulation provided an estimation of the total energy yield that could be generated by one of the coloured PREFAB modules when placed in a south-facing vertical façade, both in a shaded and shade-free scenario.

6. Acknowledgments

This work is supported by the Netherlands Enterprise Agency (RVO) and the Dutch Topteam Energy via the project: ‘PREFAB’, TKI Hernieuwbare Energie with grant number TEHE118026.

7. References

Burgers, A.R., Janssen, G.J.M., van Aken, B.B., 2018. BIGEYE: Accurate energy yield prediction of bifacial PV systems. In: BifiPV Workshop, Denver, USA, September 10-11

CBS, 2021. https://www.cbs.nl/nl-nl/nieuws/2021/09/elektriciteitsproductie-stijgt-in-2020-naar-recordhoogte, accessed 9 September 2022.

Corti, P., Bonomo, P., Frontini, F., Macé, P., Bosch, E., 2020. Building Integrated Photovoltaics: A practical handbook for solar buildings' stakeholder; Status Report, SUPSI, Becquerel Institute.

Hooff, W. van, Kuijers, T., Quax, R., Witte, J., 2021. Ruimtelijk potentieel van zonnestroom in Nederland,

Generation.Energy / TKI Urban Energy, Netherlands
https://www.topsectorenergie.nl/sites/default/files/uploads/Urban energy/publicaties/Ruimtelijk potentieel van zonnestroom in Nederland.pdf (topsectorenergie.nl)

ICARES (Becquerel Institute), 2019. BIPV market and stakeholder analysis, BIPV Boost. https://bipvboost.eu/public-reports/download/update-on-bipv-market-and-stakeholder-analysis, accessed 9 September 2022.

Janssen, G.J.M., Burgers, A.R., Binani, A. Carr, A.J., Van Aken, B.B., Romijn, I.G., Klenk, M., Nussbaumer, H. and Baumann, T., 2018. How to Maximize the kWh/kWp Ratio: Simulations of Single-Axis Tracking in Bifacial Systems. In: Proceedings of the 35th European Photovoltaic Solar Energy Conference and Exhibition, 1573-1577. https://doi.org/10.4229/35thEUPVSEC20182018-6BO.7.5.

I. Solar Energy and Heat Pumps

Modular Refurbishment of multi-family Houses with PVT-PCM Heat Pump Systems and self-learning Energy Management

Thomas Bernard[1], Steffen Wallner[1], Ulrich Leibfried[2] Simon Stürtz[3] and Florian Schlosser[4]

[1] Fraunhofer IOSB, Karlsruhe (Germany)

[2] Consolar Solare Energiesysteme GmbH, Lörrach (Germany)

[3] COMGY GmbH, Berlin (Germany)

[4] Universität Paderborn, Paderborn (Germany)

Abstract

This paper presents a retrofit concept, especially for multi-family houses, where the two retrofit measures are decoupled in time. The heating system is based on a hybrid system with a PVT-driven heat pump and an energy management system that ensures the dynamically optimized use of the different energy sources in terms of minimized CO_2 emissions and costs. The renovation concept consists of supplementing an existing gas boiler with a heat pump with SOLINK PVT collectors in the first step. If necessary, the gas boiler can also be replaced with a small investment. In a typical dimensioning, the heat pump capacity is 50 % of the maximum heating capacity, but supplies - partly in parallel operation - about 80 % of the heating energy over the year. If the building envelope is renovated in a second step, the share of the gas boiler can be reduced to zero. However, no energy management solutions are yet available on the market with which optimized and monitored operation with minimized grid power consumption can be realized in a simple manner, especially in multi-family houses and quarters. Hence a predictive and self-learning energy manager has been developed and implemented as cloud-based service. The functionality of the energy manager is investigated and proven on the basis of three properties. In a simulation study, a typical renovation process of a multi-family house is shown in two steps.

Keywords: modular refurbishement, PVT, heat pump, predictive energy management

1. Introduction

According to the Paris Climate Agreement, climate neutrality is required for Germany by 2035 (Rahmstorf, 2019). In Germany, buildings and quarters account for around 35 % of energy consumption, of which over 90 % is used to provide heat (BMWK, 2022). In particular, the three million medium-sized multi-family houses (3 - 12 housing units) are responsible for about 37 % of about 105 million t CO2 emissions of the German residential building stock (Mauch, Greif, 2021). Overall, only 13.6% of all German buildings are fully renovated or new buildings (Metzger et al., 2019). In order to achieve the climate target in this sector, a significantly greater and more consistent renovation rate is required above all. This involves, on the one hand, the replacement of fossil-fuel heat generators and, on the other hand, the insulation of the building envelope. However, the switch to an efficient low-temperature heating system with a high proportion of renewable energies often fails because the building would first have to be renovated to reduce the heat demand and the temperature level of the heating circuit. Coupled with the lack of suitable energy management, this leads to high coverage shares of fossil or purely electrical redundancy systems.

The paper is structured as follows: In section 2 the two-stage refurbishment concept with PVT is presented. The impact on energy savings and CO2 emissions is discussed by means of simulation results. Some first impressions from real world application of the concept are shown. Section 3 focuses on the predictive, self-learning energy manager. Results from the cloud based implementation in properties are discussed.

© 2022. The Authors. Published by International Solar Energy Society
Selection and/or peer review under responsibility of Scientific Committee
doi:10.18086/eurosun.2022.08.01 Available at http://proceedings.ises.org

2. Two-stage refurbishment concept with PVT

2.1 General concept

Besides the problem of missing low-temperature heating systems, the use of heat pumps often fails, especially in densely built-up urban areas, because ground probes or ground heat exchangers are not possible or desired, while air-source heat pumps are not target-oriented due to noise emissions and/or high-power consumption. Special PVT heat pump collectors (SOLINK) with heat transfer surface on the back side can be used as a sole, efficient, and silent heat source for heat pumps due to their high heat transfer capacity to ambient air (Leibfried et al., 2019). At the same time, they produce electrical power - due to the cooling on the back side with higher yield than pure PV modules.

The renovation concept consists of supplementing an existing gas boiler with a heat pump with SOLINK collectors and the substitution of the sensible thermal energy storage (TES) by a TES using phase change materials (PCM) in the first step. If necessary, the gas boiler can also be replaced with a low investment volume. In a typical dimensioning, the heat pump capacity is 50 % of the maximum heating capacity, but supplies - partly in parallel operation - about 80 % of the heating energy over the year. If the building envelope is renovated in a second step, the share of the gas boiler can be reduced to zero. The renovation concept is sketched in Fig. 1.

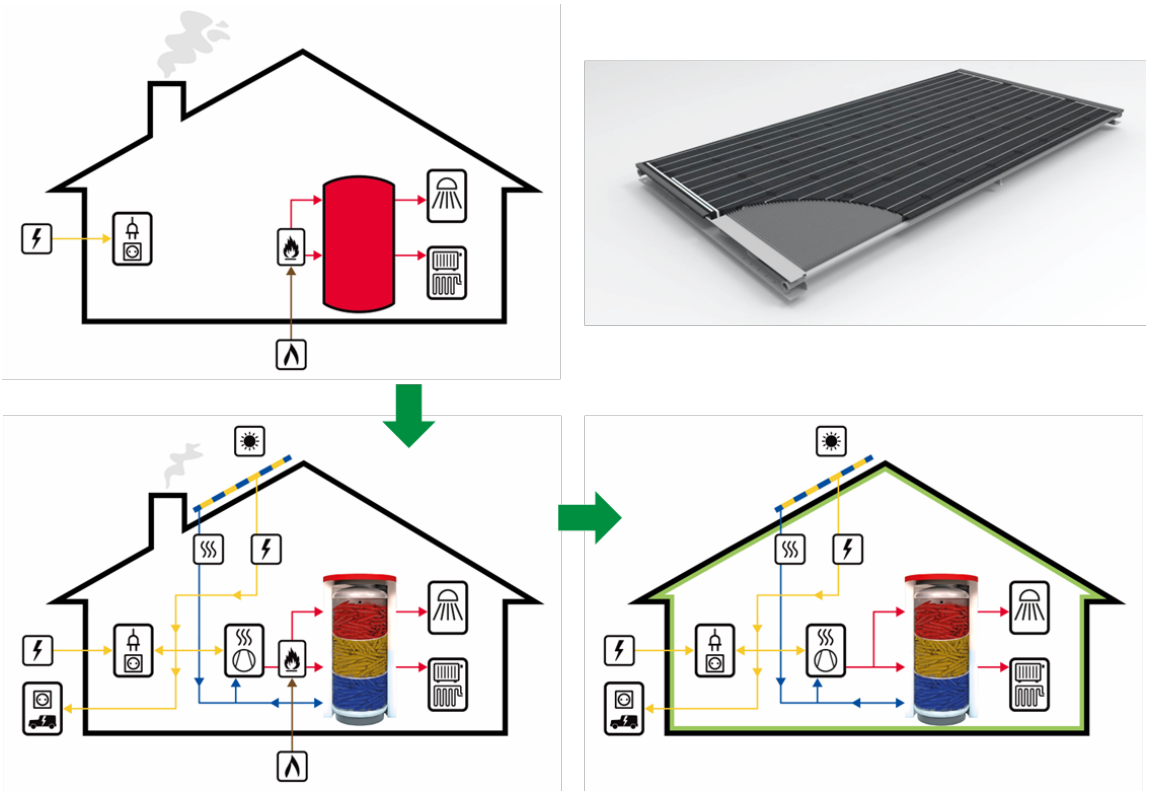

Fig. 1: Two-stage refurbishment:
left: uninsulated building envelope, SOLINK heat pump combined with peak-load gas boiler;
right: insulated building, full supply with SOLINK.

SOLINK heat pumps represent a third class of heat pump systems, now proven in over 1000 installations, alongside ground-source/groundwater-coupled heat pumps and air-source heat pumps. SOLINK systems ensure that the decarbonization of heating technology is accompanied by the necessary increase in renewable electricity production.

The use of PCM-TES instead of sensible TES has the following advantages: (1) A high specific storage capacity allows the installation of storage units even in small installation spaces. In this way, energy management can be used to selectively shift heat pump operation to favorable times and to temporarily store the heat that is not needed. (2) In contrast to conventional water-based buffer TES, the temperature of PCM storage tanks does not rise significantly, so that the efficiency of the heat pump remains consistently high. A narrow temperature window is particularly relevant because in existing buildings even higher flow temperatures are required in the heating

system. (3) Different temperature levels can be realised in one storage tank, for example for radiator or surface heating on the one hand and for domestic hot water supply on the other.

As part of the SOLINK project funded by the DBU, it was shown that SOLINK heat pumps in single-family and multi-family homes achieve comparable, and in some cases better, economic efficiency than air-source or ground-source heat pumps combined with a PV system. The PVT collectors, when typically sized, produce in a year the electrical energy that the system consumes. Although most of the electricity is produced when there is no demand for heating but hot water, with appropriate load management with heat and battery storage, 50% or more of the electricity demand can still be met directly. In the previous studies and in the following ones, the use of self-generated electricity for households/tenants in multi-family houses has not yet been taken into account, as the current bureaucratic requirements for this are a deterrent for many landlords. The economic efficiency can therefore be improved even further if households/tenants also use their own electricity.

2.2 Simulation of a step-by-step redevelopment

In a simulation study, a typical renovation process of a multi-family house was mapped in two steps. Tab. 1 shows the boundary conditions on which the simulation study was based.

Tab. 1: Ambient conditions, building and heat generator for simulation study

Redevelopment stage	Unit	unrenovated	hybrid system	Renovated building without gas
Location		Würzburg	Würzburg	Würzburg
heated living space	m²	800	800	800
Heating demand	kWh/a kWh/(m² a)	77400 97	77400 97	43000 54
Warm water withdrawal Warm water heating demand	l/d kWh/a	1450 22080	1450 22080	1450 22080
Orientation / inclination collector field		-	South / 40°	South / 40°
General electricity (uses PV yield) [1]	kWh/a	6000	6000	6000
Hot water preparation		Central WW heating, 60°C circulation	Four-wire network, decentralized Fresh Water, 50 °C circulation	Four-wire network, decentralized Fresh Water, 50 °C circulation
Heating circuit temperatures FT/RT	°C	60/50	60/50	40/35
Gas boiler power	kW	40	40	-
Heat pump capacity (two-stage) for B0/W35 / B-15/W35	kW	-	34 / 23	34 / 23
Area of SOLINK PVT collectors	m²	-	79	79

[1] General electricity excludes the household electricity in the appartments

In the fully refurbished Stage 3, a reduction in the heating requirement of 45 % is assumed. The existing heating surface then only has to transmit significantly less power, so that the flow and return temperatures can also be reduced. The simulations were performed with Polysun. Fig. 2 and Fig. 3 show the hydraulics modeled in each case. In all three cases, a 1000 l buffer tank is provided for the heating circuit and another for the hot water preparation.

Annual simulations were used to calculate the reductions in consumption costs and CO_2 emissions caused by the heating system. The following assumptions were made:

- Energy price heat generator (gas): 6 cents/kWh
- Energy price heat generator (electricity): 22 cents/kWh
- Energy price auxiliary energy (electricity): 29,2 Cent/kWh
- Feed-in tariff: 9,03 Cent/kWh
- CO_2 factor electricity: 537 g CO_2eq/kWh
- CO_2 factor gas: 202 g CO_2eq/kWh

When calculating the costs, the feed-in tariff was deducted from the consumption costs. For CO2 emissions, on the other hand, the CO2 credit from PV feed-in was not taken into account.

Fig. 4 shows the annual CO_2 emissions and operating costs of the three stages. The first renovation stage reduces CO_2 emissions by 37%, the second by 65% compared to the baseline. This does not take into account CO_2 avoidance by feeding PV electricity into the grid. The cost savings - here considering the feed-in tariff - are similar: 39% in the first stage, 67% in the second. This corresponds to CO_2 emissions of 11.2 kg CO_2 per m2 of living space and thus achieves the target value of ≤ 12 kg CO_2/m2 for residential buildings in the existing stock which corresponds to the target of maximum global warming of 1.5 °C.

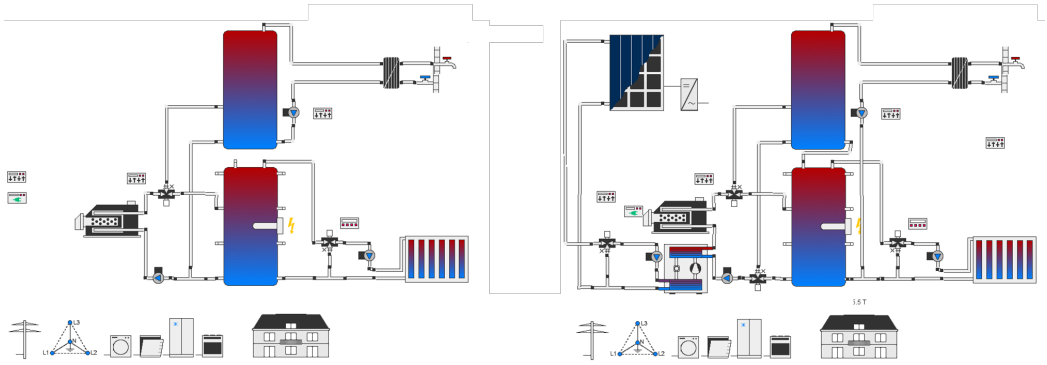

Fig. 2: Hydraulic schemes shown in simulation: left unrefurbished with gas boiler, right with hybrid system: heat pump with SOLINK PVT collectors and gas boiler connected in series.

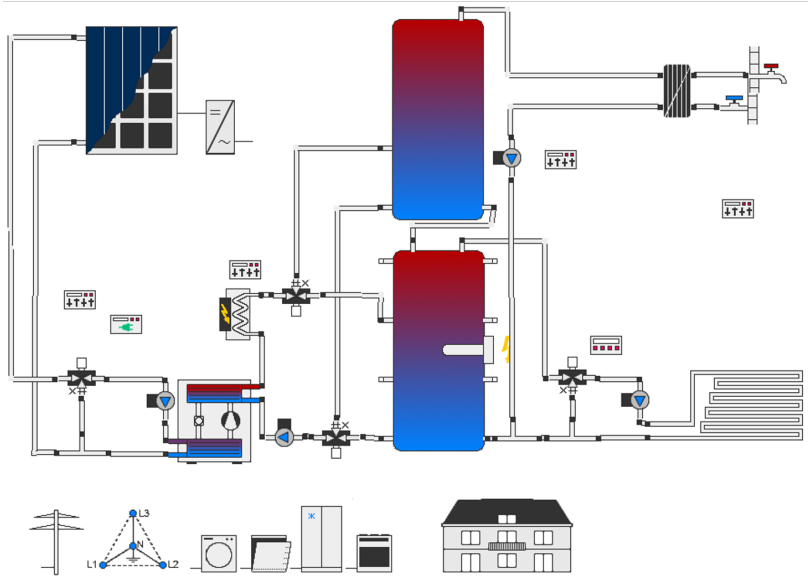

Fig. 3: Hydraulics of the second renovation stage for monoenergetic heat pump operation. The return of the circulation line for hot water preparation is connected to the heating buffer tank at the bottom. Due to this optimized connection, the heating buffer tank can also be used for energy management, i. e. storage heating in case of PV surplus, in summertime hot water operation only.

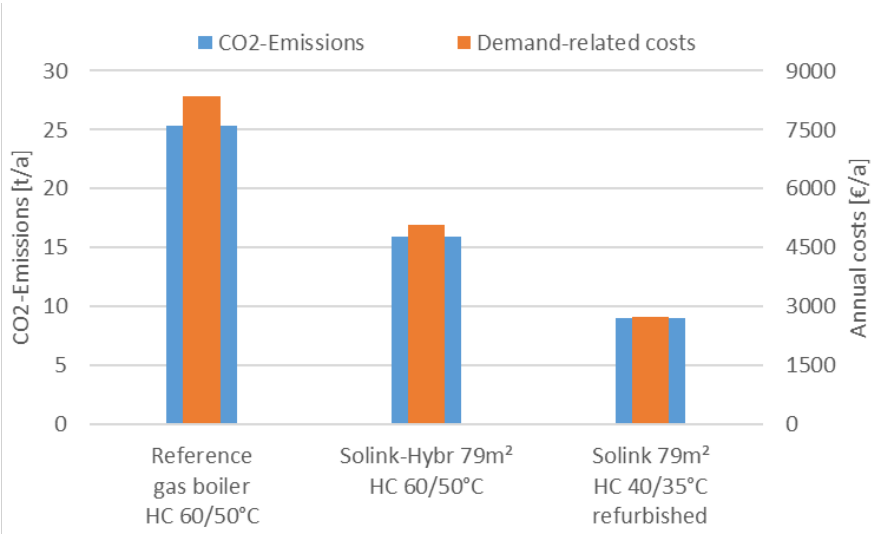

Fig. 4: Costs and CO_2 emissions of the baseline condition and the two refurbishment stages.

In the first refurbishment stage, the gas boiler supplies only 22 % of the annual heat demand, 78 % comes from the SOLINK heat pump. The reason that the costs and emissions in the fully refurbished stage do not decrease further compared to the first stage is that the total heat demand is not halved, but still accounts for 65 % of the consumption in the first refurbishment stage. Heating consumption drops to 55%, but hot water consumption remains the same. Also, the better thermal insulation leads to a reduction of the heating operation in the transition period - i.e. the times that could also be supplied very efficiently with heat pump and PVT.

Fig. 5 shows the energy consumption of the three variants in detail as well as important key figures. The self-consumption shares of stage 2 and 3 is about 40 % in each case, i.e. almost half of the electrical energy produced by the SOLINK collectors is used directly for the heating system or for general electricity. If the PV yield were also used directly for households, this share and thus also the economic efficiency could be increased even further. The prerequisite for this to be implemented in practice is that the German government fulfills its obligation to adapt the EEG in this respect in conformity with European law, so that electricity produced in a building can be used directly without bureaucratic hurdles and levies. The German government is currently (early 2023) in the process of changing the rules so that all electricity consumed by all households can initially be covered by that produced locally, without triggering a huge amount of bureaucracy.

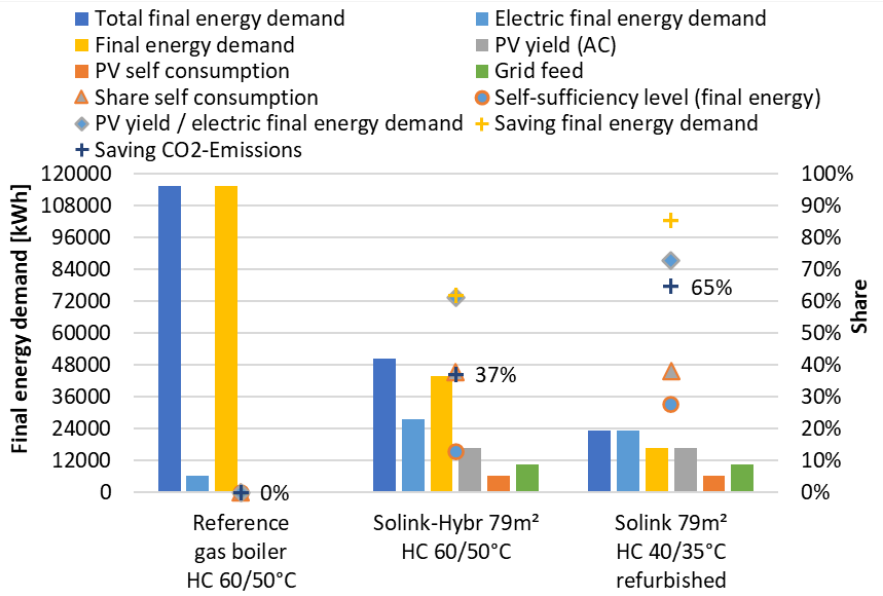

Fig. 5: Energy consumption and key figures of the three variants (see also Table 1)

Total final energy demand	Total consumed energy (electricity and gas)
Final energy demand	= Total final energy demand - PV Self consumption
PV Self consumption	Part of the energy produced by PV which has been directly consumed
Share self consumption	Relation PV Self consumption to total PV yield
Self-sufficiency level (final energy)	The share of the annual final energy consumption that is directly (simultaneously) covered by PV output
Saving final energy demand	Savings in relation to the reference, the gas boiler (electricity and gas added).

Table 1: Definition of the key figures shown in Fig. 5

The result of bivalent systems, here the partially renovated "Solink Hybrid" variant, depends strongly on the control concept in terms of cost and CO_2 savings. Here, a bivalence point dependent on the outdoor temperature with parallel operation was applied: the boiler is only enabled in addition to the heat pump below 0 °C ambient temperature. Furthermore, a simple non-predictive energy management is implemented: If the PV grid feed-in exceeds a threshold, the set temperature of the heat pump, with which it heats the buffer tank, is raised.

2.3 Real application

The heat supply of an apartment building of the Volkswohnung Karlsruhe, which was built in 1963 and renovated in the 80s and 90s, was renovated in 2020 with a SOLINK heat pump and a peak load gas boiler. The brine heat pump has an output of 43 kW_{th} (B0/W35), the peak load gas boiler has an output of 60 kW_{th}, and the SOLINK collector array has an area of 200 m2. Fig. 6 provides an impression of the SOLINK PVT collectors.

The system is metrologically supported by Fraunhofer ISE as part of the *Smart Quartier Karlsruhe-Durlach (SQ-Durlach)* project.



Fig. 6: Transport of SOLINK collectors to the roof of the apartment building (left). SOLINK collectors installed on the roof (one half of the roof and one half of the field) (right)

2.4 Summary and conclusion

SOLINK PVT heat pump systems enable the use of efficient heat pumps even in densely built-up urban areas. The decisive advantages over an air-to-water heat pump with PV system are the higher system efficiency and the absence of noise pollution. Compared to ground-source heat pumps, there are no restrictions due to space requirements or geological prerequisites for drilling. In connection with a temporally decoupled renovation of heating technology and building envelope, they open new possibilities for the energetic renovation of existing buildings.

3. Predictive, self-learning energy manager

Previous control concepts for heating systems are not designed to operate various components in a network or in a quarter in a holistically energy-optimised manner. In order to ensure energy-efficient operation and the highest possible degree of energy autarky even with changing utilisation concepts or energy demands - for example, after

thermal insulation - a self-learning energy management system is presented in this work. For this purpose, the energy manager developed in the project dynOpt-En (dynOpt-En, 2022) is to be used locally in the individual properties.

3.1 Concept of the energy manager

The basic concept of the optimizer is illustrated in Fig. 7. The energy manager uses a prediction algorithm to optimise heat generation in buildings and quarters. For this purpose, the optimisation continuously calculates consumption forecasts from the meter data available for energy billing in combination with weather forecasts and other sensor data. These are used to optimally match different heat generators to each other, in addition to heat pumps and gas boilers, also CHP units, each combined with PV or solar heating systems.

The optimisation algorithm requires no complex and individual programming and only a small number of sensors. The basic algorithmic principle of the optimizer is nonlinear model predictive control. The single components of the energy system (PV(T), heat pump, CHP, heat/electricity storage) are modeled by simple static equations resp. 1st order storage models.

The optimizer has an internal prediction horizon of e.g. 36 hours. The internal time sample time of the predictor is 1 hour. The optimization calculation typically takes less than a minute and is updated e.g. every 10-15 minutes.

It is important to note that the optimizer does not replace the basic control of the aggregates. The result of the optimizer are "activation commands" for the individual aggregates (heat pump for heating or cooling, CHP, battery charging). For modulating heat pumps, the activation level is also optimized. The activation commands are also transmitted to the metering service provider via Internet interface. The latter implements the activation commands via its connection to the actuator system in the property. This is done, for example, via relays or, in the case of heat pumps, via a Smart Grid Ready interface (SG Ready interface for short)

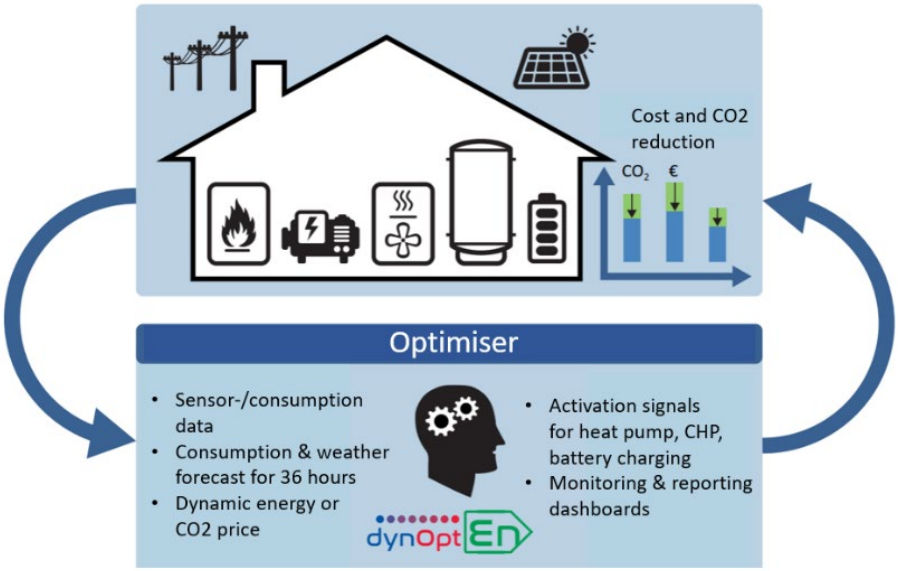

Fig. 7: Basic concept of the predictive energy manager

3.2 Cloud-based implementation of the energy manager

The consistent design of the energy manager as an online cloud service means that hardly any on-site installations are necessary. All data are available via data interface (e.g. REST API). Via a gateway, the data from the meters already available for consumption billing are transferred in 15-minute resolution to the energy manager, which runs on an external server. Via the gateway and interfaces provided for this purpose, such as the SG-Ready interface of a heat pump, the operating request for the heat generators is also set. For this purpose, either gateways can be used as a plug-and-play solution or already installed data collectors and controls can be integrated. Energy management can thus be offered as a service of the metering service. As a further service, the monitoring of energy consumption and costs can take place with a comparison of the real values with those expected for the respective weather conditions.

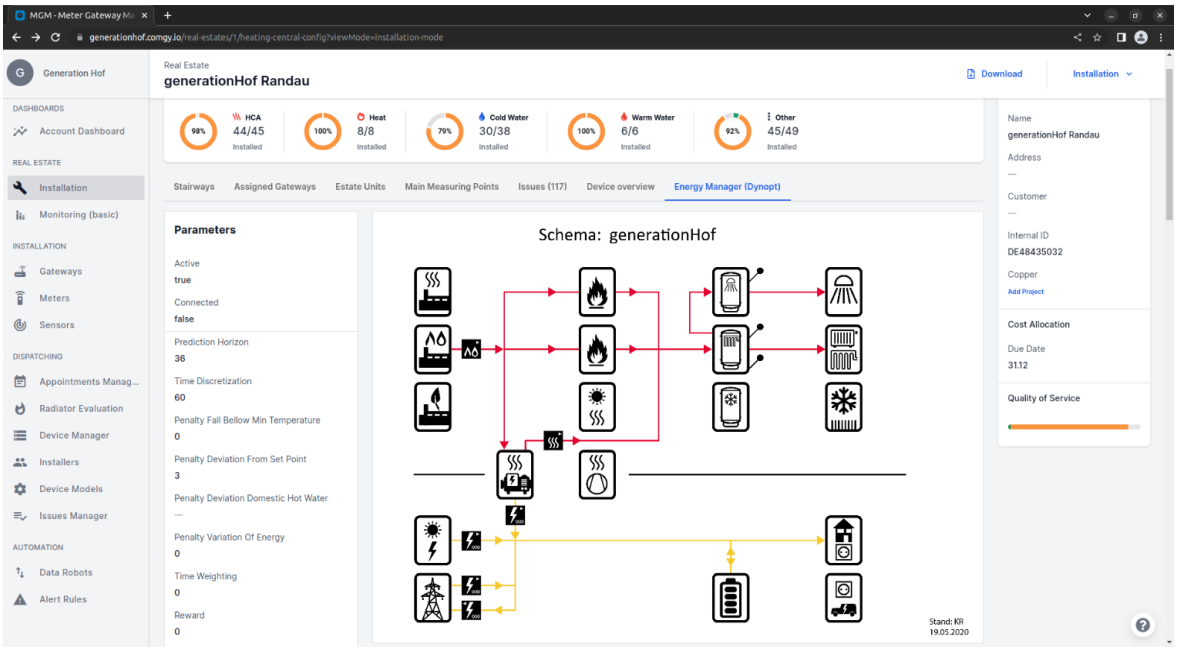

Fig. 8: Cloud-based portal for plant configuration and parameterization of the optimizer

The plant structure of the properties can be stored with graphic symbols via a web-based portal (Fig. 8). Here, the physical and control linkage of the energy generators with the energy storage systems and the main consumers is mapped - thermal and electrical in each case. Via the graphical user interface, meters and sensors are linked to the optimizer. Furthermore, it is possible to adjust parameters of the plant (e.g. volume of the thermal storage) and the optimizer directly at runtime. The suitable communication with the optimizer takes place via a REST-based interface. For this, the configuration model and the external functions of the optimizer have been defined in the form of the Energy Manager API and described in the open standard OpenAPI (OpenAPI, 2022).

Communication with the optimizer is encrypted, since the optimizer API is only accessible via HTTPS. To control access to the assets created in the optimizer, clients - such as the configuration portal - must authenticate themselves with predefined bearer tokens (IETF, 2022). At this point it is important to emphasize that the optimizer only returns "recommended actions" (e.g. setpoints; activation of the heat pump etc.) via the API. The client installed in the property implements these. The optimizer therefore never intervenes directly in the system control.

3.3. Results of the application of the predictive energy manager

The energy manager dynOpt-En is primarily intended for commercial properties such as multi-family houses and quarters in which several components such as heat pumps, PV systems, solar heating systems, gas boilers or CHP units are operated in conjunction with each other. Furthermore, dynOpt-En monitors energy consumption and costs and compares the real values with those expected for the respective weather conditions. In this way, malfunctions can be detected promptly and signaled via a clear visualization. In the project, the functionality of the energy manager was tested on the basis of 3 properties with different system configurations (including PV, heat pump, CHP, thermal and electrical storage; heating and cooling operation was investigated).

In annual simulations it could be proven for an exemplary property with PV and heat pump that by using the predictive energy manager compared to a non-predictive energy manager, the operating costs and also CO2 emissions are reduced by approx. 15% per year. The self-consumption fraction (i.e., the ratio of PV energy used to operate the heat pump to the electrical heat pump energy required) was increased by about 20%.

Thus, the use of the predictive energy manager makes economic sense for larger properties. An essential prerequisite for the performant use of the energy manager is a sufficiently large thermal storage. Especially for the operation with heat pumps, a clean separation between a zone with higher temperatures for water heating and a zone with lower temperatures for heating is necessary. As part of the dynOpt-En project, Consolar Solare Energiesysteme developed a new type of two-zone heat pump storage tank for this purpose (Leibfried et al., 2022).

Fig. 9 shows data from a real property in Lörrach/Germany (period 17 - 24.5.2021). In this property the operation of heat pump has been optimized. A web-based dashboard has been implemented, which visualizes all relevant data (outdoor climate, sensor data, optimizer calculations, activation of heat pump), see Fig. 9.

Furthermore, a live visualization of the "internal optimizer view" was realized. From the monitoring dashboard, the prediction of the optimizer at this point in time can be displayed in a simple way (right mouse click on any point in time). This is shown as an example in Fig. 10. From the selected point in time, the visualization shows the prediction over the next 36 hours. In Fig. 10 it can be seen that the activation of the heat pump is done in an optimized way, so that no activation of the heat pump is necessary during the next day.

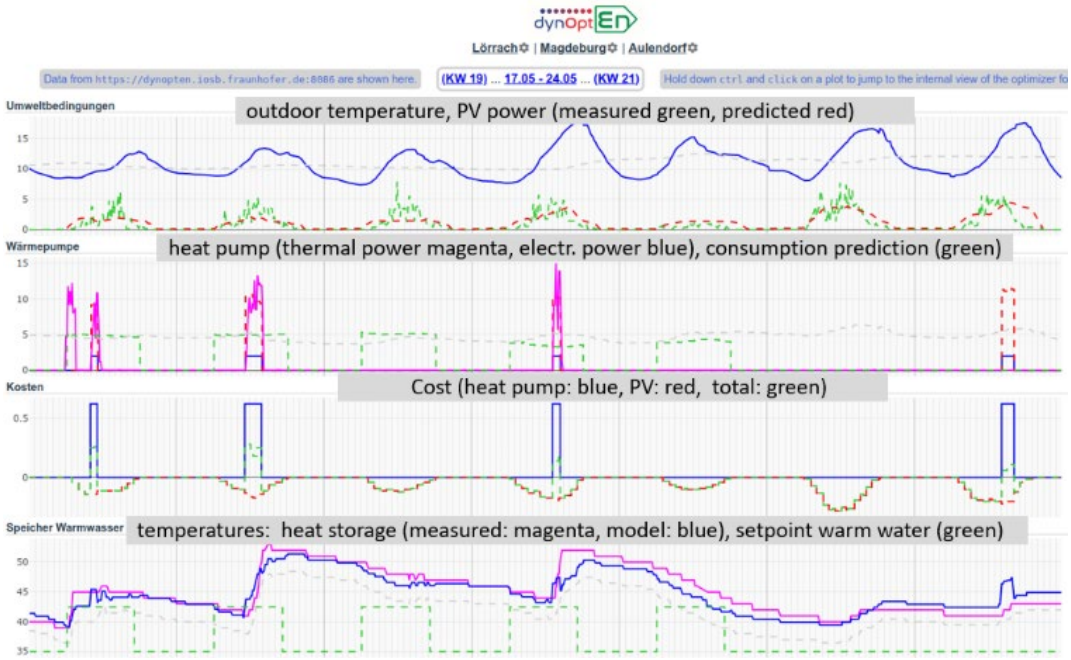

Fig. 9: Data from a real property in Lörrach/Germany with optimized operation of a heat pump (period 17 - 24.5.2021)

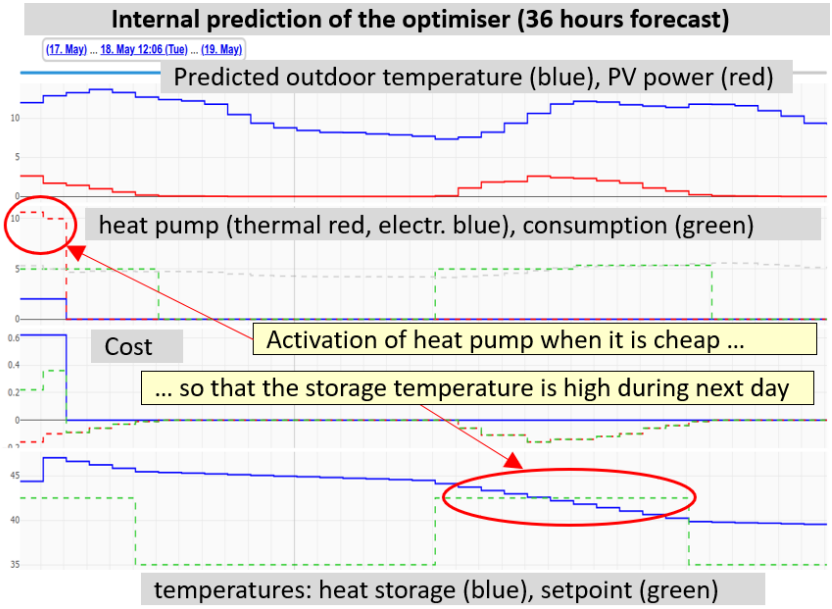

Fig. 10: Internal prediction of the optimiser (data from a property in Lörrach/Germany, period 17 - 18.5.2021)

3.2 Monitoring of key performance and efficiency indicators

For monitoring, a distinction is made between evaluations and presentations for the operator (e.g. housing association) and the end customers. Algorithms for the provision of performance and efficiency indicators have been developed and implemented in clearly arranged dashboards. The key figures (e.g. costs, CO2 emissions, thermal/electrical energy consumption or energy provision) are output in daily, weekly or monthly aggregation. Fig. 11 shows a dashboard for visualizing monthly averages of costs per thermal kilowatt hour, CO2 emissions per thermal kilowatt hour, CO2 emissions of the heat pump and outdoor temperature of a property. From Fig. 11, it can be seen that only in the months of December, January, and February of the study period 2020/2021 does non-renewable energy need to be purchased. During the rest of the period, the predictive energy manager ensures that the thermal energy is provided regeneratively and thus free of charge.

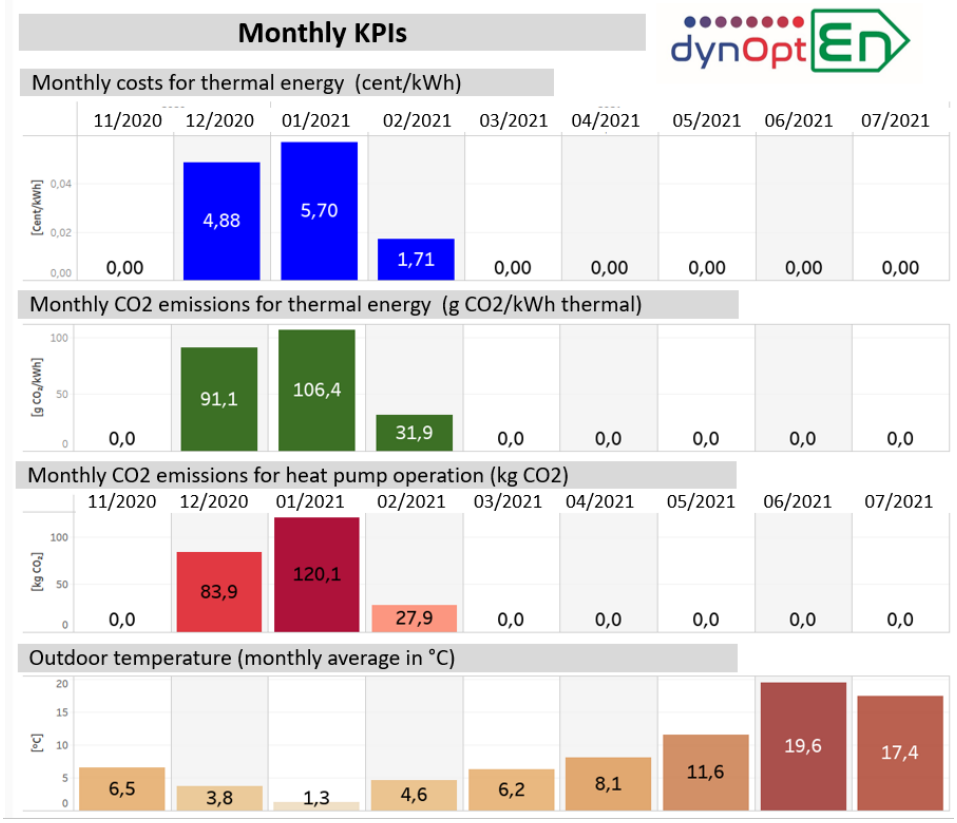

Fig. 11: Dashboard visualizing monthly average values of a property in Lörrach/Germany in the period November 2020 - July 2021

4. Summary and Outlook

4.1 Summary

In this paper we have presented a two-stage refurbishment concept with PVT. In a simulation study, a typical refurbishment process of a multi-family house is shown in two steps: status quo - hybrid operation - full refurbishment. First real results of a multi-family house refurbished with PVT heat pump and gas peak load boiler are presented. Furthermore, a predictive and self-learning energy manager has been developed and implemented as cloud-based service. The energy manager has been deployed in 3 larger properties with different system configurations (including PV, heat pump, CHP, thermal and electrical storage). It has been shown that with the cloud-based service, maintenance-friendly and robust operation is possible. According simulation and experimental results the energy savings of typical properties are approximately 15 %. The energy self-consumption of PV power has been increased by approx. 20%.

4.2 Outlook

To reduce expansion of grids and costs, the autarky of quarters must be increased. This requires a superordinate instance having knowledge about the storage levels, renewable electricity generation potential of the individual properties and about energy prices. In addition, further research is required in the selection and development of PCM suitable for the required temperature range, in optimised heat transfer and in the monitoring of the storage charge level for optimised operation. Therefore, the aim of a planned project is to develop a central energy manager that minimises the energy consumption of the individual properties with regard to electricity grid purchases. For this purpose, the central energy manager of one quarter communicates with the local energy managers of the multi-family-houses and gives incentive signals based on forecasts for generation, demand and electricity price. The central energy manager shall detect changes in user behaviour and energy demand in the quarters (e.g., through refurbishment) and shall adapt the parameterization of the model in a self-learning manner without any extensive adjustments in the central control system. Moreover, the central energy manager shall work on the principle of predictive control with a powerful optimiser. Weather forecasts and predicted consumption (electricity and heat) of the properties are considered. Methods for automated consolidation of measurement data need to be developed to ensure optimal use for the data-driven models. Two-level energy management will then be practically investigated in a multi-family house and virtually tested in a quarter via software-in-the-loop simulation with realistic load cases and scenarios. In addition, the new project aims to reduce the transaction costs of modular refurbishment by digitally supporting the inventory, pre-design, parameterisation of predication models and commissioning.

5. Acknowledgement

The authors would like to thank the german ministry BMWK for funding the project dynOpt-En (grant number 03ETS001). Thanks to Sebastian Asenbeck (IGTE der Universität Stuttgart) for performing the simulations. This contribution was supported by the Fraunhofer Cluster of Excellence Cognitive Internet Technologies (CCIT), Machine Learning Research Center.

6. References

BMWK (German Federal Ministry for Economic Affairs and Climate Action), 2022: http://www.energieforschung.de/energieforschungspolitik/energieforschungsprogramm/foerderschwerpunkte/#guq (Access: 08.04.2022)

dynOpt-En: Project ‚Dynamisches Optimierungsmodul zur angebots- und bedarfsgerechten Zuschaltung von Energieträgern kombiniert mit wärmepumpentauglichem Wärmespeicher‘, project website www.dynopt.de, accessed 08.09.2022

IETF - Internet Engineering Task Force, 2022, https://datatracker.ietf.org/doc/html/rfc6749, accessed 08.09.2022

Leibfried, U., Fischer, S., Asenbeck, S., 2019. PVT-Wärmepumpensystem SOLINK – Systemvalidierung und zwei Jahre Praxiserfahrung, Symposium Thermische Solarenergie 2019.

Leibfried, U., Bernard, B., Stürtz, S., 2021. Energetische Sanierung von Mehrfamilienhäusern mit PVT-Hybridsystem und Messdienst-basierten Energiemanagement, Symposium Thermische Solarenergie 2021

Leibfried, U., Asenbeck, S: Wärmepumpenspeicher: Kombispeicher, getrennte Speicher – geht beides?, Proceedings 32. Symposium Solarthermie und innovative Wärmesysteme, 03. - 05. Mai 2022, Kloster Banz, Bad Staffelstein

Mauch, W.; Greif, S.,2021. Grundlagenstudie Wärmepumpen-Fahrplan. https://www.waermepumpe.de/fileadmin/user_upload/waermepumpe/07_Publikationen/Sonstige/Vortrag_Berliner-Energietage_Folien_FfE.pdf (Access: 12.04.2022)

Metzger, S., Jahnke, K., Walikewitz, N., Otto, M., Grondey, A., Fritzm, S., (2019). Wohnen und Sanieren. Empirische Wohngebäudedaten seit 2002. Hg. v. Umweltbundesamt.

OpenAPI Initiative, 2022, https://www.openapis.org/, accessed 08.09.2022

Rahmstorf, S, 2019. Potsdam Institut, https://scilogs.spektrum.de/klimalounge/wie-viel-co2-kann-deutschland-

noch-ausstossen/emissionen-deutschland-3/ (Access: 08.04.2022)

Solar-Thermal Activation of Rear-Ventilated Façades as a Source for Heat Pump Based Heat Supply Systems

Christoph Büttner[1], Edward Frick[1], Federico Giovannetti[1]

[1] Institute for Solar Energy Research in Hamelin (ISFH), Emmerthal (Germany)

Abstract

The envelope of multi-storey residential buildings offers an untapped potential for the integration of regenerative energy supply systems. Due to their specific assembly, rear-ventilated façades exhibit particularly suitable features: high design flexibility, modularity, easy installation and maintenance, and the possibility to hide the systems engineering in the ventilation gap. We analyzed solar thermally activated façade claddings made of concrete focusing on their thermal performance. Based on these results, the potential of the concrete façade as an additional source in a ground source heat pump system is assessed by building simulations with the software TRNSYS. A comparison of different heating systems shows that for a multi-storey building of about 1400 m² living space with an opaque wall area of nearly 1010 m², a 75 m² light grey concrete façade can reduce the borehole heat exchanger (BHE) by 25% to 600 m without a reduction of performance thanks to active regeneration. In addition, the façade can be used to further heat the BHE outlet. Significantly higher efficiency is expected for larger areas and better performing façade claddings in combination with different operation modes.

Keywords: rear-ventilated façades, solar thermal collectors, TRNSYS, multi-storey residential buildings, heat pump, building envelope, building integration

1. Introduction

To reduce both energy demand and CO_2 emissions, it is necessary to significantly increase the use of renewable energies and implement more severe energy efficiency measures. For this purpose, EU directives and national laws are tightening the requirements for existing and new buildings, focusing on higher renovation rates and a more effective substitution of fossil fuels. The combination of solar-thermal energy and heat pump can make a decisive contribution towards a climate neutral heat supply. Whereas both technologies are already well established in the sector of single-family houses, there is a lack of economical and architecturally appealing solutions in the field of multi-family buildings. The most critical points for heat pumps are noise emissions in the case of air-water systems and a lack of space for suitable heat sources in the case of ground source systems. For solar-thermal energy usual factors include a limited space for solar collectors, costs, and the technically complex implementation.

2. Solar-thermal activation of a building envelope

Façade-integrated solar-thermal collectors offer untapped potential for the implementation of new, aesthetically appealing solutions for multi-family buildings. Rear-ventilated façades are particularly suitable for solar-thermal activation due to their advantages in terms of building physics, modularity, and the large number of cladding materials that can be used. Furthermore, the ventilation gap between the façade cladding and the mineral insulation of the building provides enough space for the invisible installation of the components of the system. In the scope of a current research project, different concepts for thermally active rear-ventilated façades are being developed and the energy potential of the façades as alternative or additional heat sources in heat pump-based heat supply systems is being evaluated experimentally and theoretically (Frick, Büttner, et al., 2021). The basic approach consists in activating the façade using components that are already available on the market without modifying their original appearance so that the active modules cannot be distinguished from the common ones. As façade

© 2022. The Authors. Published by International Solar Energy Society
Selection and/or peer review under responsibility of Scientific Committee
doi:10.18086/eurosun.2022.08.02 Available at http://proceedings.ises.org

claddings, concrete, metal, and glass (single- and double-glazed) are investigated. For each material, specific activation approaches were chosen (Frick, Kirchner, et al., 2021). To evaluate the behavior of the investigated façade types as part of the heat supply system of a multi-family building, system simulations using TRNSYS (Klein, 2010), a simulation program used in the fields of renewable energy engineering and building simulation with a focus on active and passive solar use, were carried out. The experimental investigations and numerical modeling of the different facade panels were used to determine the collector parameters. According to the collector equation *(eq. 1)* used in TRNSYS Type 832 by Haller et al. (2014), the relevant collector parameters were determined and are shown in Tab. 1 (see appendix for an explanation of the used quantities). As a reference, a typical flat plate collector (Solar Keymark Database, 2019) both for rooftop and façade installation is included. For the façade collector, the heat loss coefficient a_1 is reduced, to account for the lower convective heat transfer in a vertical air gap (Bartelsen et al., 1999).

Tab. 1: collector parameters, based on gross area

		façade cladding				collector	
Parameter	**Unit**	**Concrete**	**Metal**	**Glass unglazed**	**Glass double-glazed**	**Flat Plate Tilt 45°**	**Flat Plate Tilt 90°**
η_0, $F'(\tau\alpha)$	-	0.40	0.59	0.774	0.58	0.78	0.78
b_0	-	0.055	0.055	0.055	0.081	0.13	0.13
K_{diff}	-	1	0.98	1	0.86	0.88	0.88
a_1	W m^{-2} K^{-1}	11.30	11.33	9.33	4.982	3.35	3.05
a_2	W m^{-2} K^{-2}	0	0	0	0.0212	0.013	0.013
a_3, $c_{w,hl}$	J m^{-3} K^{-1}	4.04	1.22	3.74	0	0	0
a_4, c_{IR}	-	0.761	0.212	0.691	0	0	0
a_5, C_{eff}	J m^{-2} K^{-1}	282000	22755	11000	23060	6220	6220
a_6, $c_{wF'}$	s m^{-1}	0.056	0.0144	0.0224	0	0	0

$$\dot{q}_{out} = F'(\tau\alpha) \cdot K_b \cdot I_b + F'(\tau\alpha) \cdot K_d \cdot I_d - c_{w,F'} \cdot u_w \cdot (I_b + I_d) + c_{IR} \cdot (I_{IR} - \sigma \cdot T_{amb}^4) - a_1 \cdot \Delta T_{amb} - a_2 \cdot |\Delta T_{amb}| \cdot \Delta T_{amb} - c_{w,hl} \cdot u_w \cdot (\Delta T_{amb}) + \dot{q}_{lat} - C_{eff} \cdot \frac{d\vartheta_m}{dt} \quad \text{(eq. 1)}$$

with

$$\Delta T_{amb} = \vartheta_m - \vartheta_{amb};\ u_w = wf \cdot u_{w,0};\ I_{IR} = rf \cdot I_{IR,0} + (1 - rf) \cdot \sigma \cdot T_{amb}^4$$

The potential of the thermally activated façade can be estimated by a heat yield investigation. For a constant inlet temperature, the yield is determined depending on weather data and orientation and is plotted in Fig. 1. A demonstration building with a solar active concrete façade is planned in Pforzheim, Southern Germany, therefore weather data for the corresponding location are used. The data were taken from Meteonorm, using the Hofmann model hourly values are converted into minute values (Meteotest, 2022; Hofmann et al., 2014). Compared with a common flat plate collector mounted on the roof, the façade cladding acts as an uncovered collector (or WISC, Wind and Infrared Sensitive Collector) and allow the use of environmental heat at low temperatures.

The operation temperature of the façade must be taken into account. Operation at low temperatures promises high yields because a lot of environmental heat can be gained. However, dew formation or even icing may occur which can be undesirable due to algae formation and optical changes of the concrete surface. Other materials (e.g., metal) might be better suited to withstand lower temperatures and exhibit a higher potential for this application. To use the façade as a source for the heat pump, the operating limits of the evaporator side must be taken into account. Other use cases for the façade are the regeneration of the borehole heat exchanger and, at suitably high temperatures, the direct loading of the buffer storage tank. However, high temperatures must be reached, façade claddings like glass, especially the double-glazed design, or metal are suitable for this.

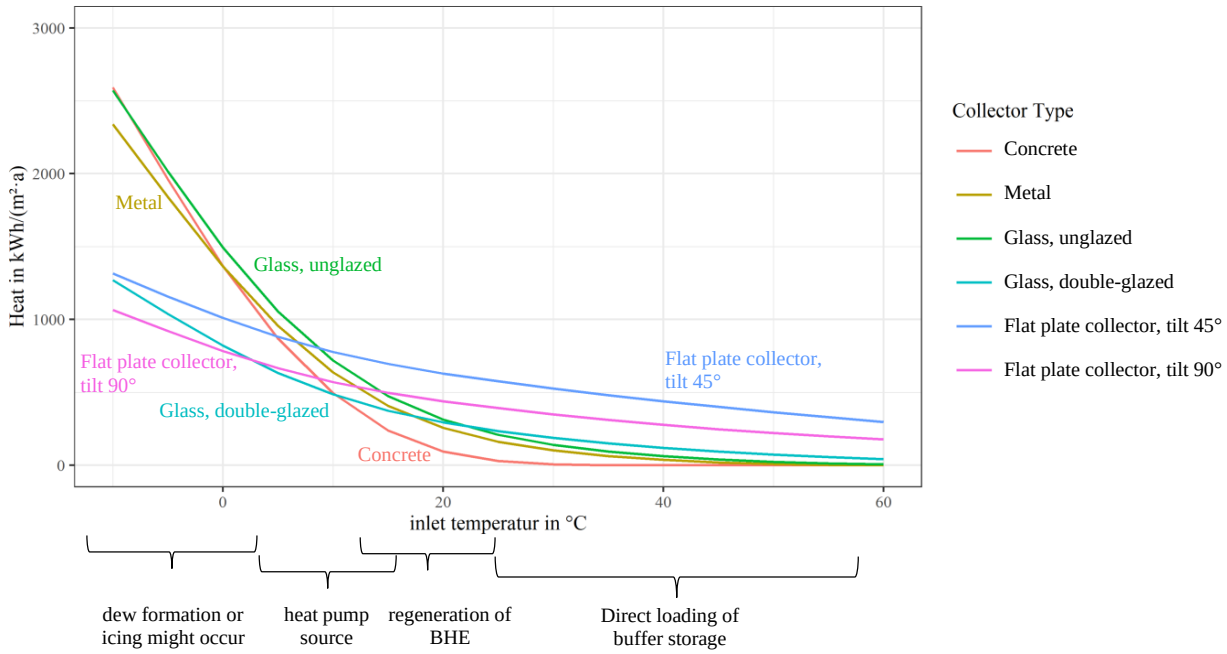

Fig. 1: yearly gross heat yield of different façade claddings (concrete, metal, glass, insulated glass) and rooftop collector facing West for constant inlet temperatures and possible application fields

The temperature range between 5 and 25 °C is well suited as a supplementary heat pump source. At higher temperatures (e.g., 15 to 28 °C) regeneration of the ground source (e.g., borehole heat exchanger) of the heat pump becomes possible. Due to the arrangement (façade, vertical alignment) and thermal characteristics, the yield is low at even higher temperatures. Thus, both the lower and upper limits might be fixed, depending on the heating supply concept and operation mode. With higher operating temperatures the yield decreases and thus the contribution of the facade to the overall system.

The distribution of the heat output in the annual and daily course for differently oriented concrete façades for 5 and 20 °C inlet temperatures is shown in Fig. 2.

At low temperatures, the façade can supply useful heat throughout the year, but its operation at higher temperatures is only possible in transition and summer periods. Because the façade also acts as an environmental heat exchanger, in summer useful gains with over 200 W/m² are possible even at nighttime. Depending on the orientation of the facade, the maximum values are reached in the morning hours (facing east), at midday (facing south), or in the afternoon hours (facing west).

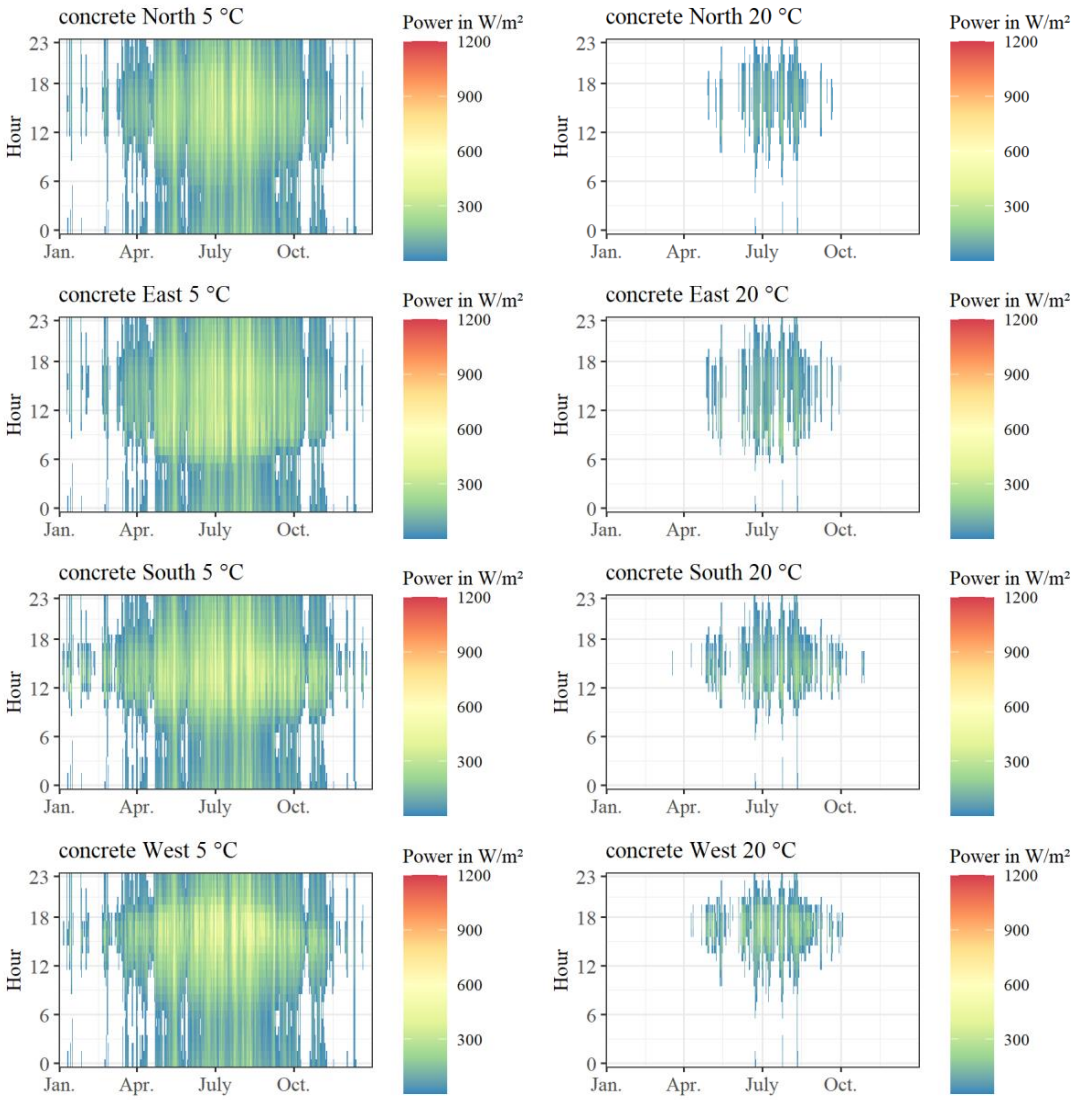

Fig. 2: annual and daily distribution of heat flux for the concrete façade facing different directions at a constant inlet temperature of 5 and 20 °C

3. System Concept

The heat for the investigated multi-storey residential building is primarily generated by a brine-to-water heat pump and stored by using the thermal mass of the building as well as a common buffer storage. The façade serves as a solar collector and environmental heat exchanger. The gained energy can be used in different ways, depending on the system configuration: it allows the regeneration of the borehole heat exchanger, heats the ground source outlet, or can be directly used for the heat pump as an additional source. The investigation aims to assess the potential of the façade as a heat pump source, depending on its characteristic performance values and the specific function. Fig. 3 shows the general scheme of the investigated system.

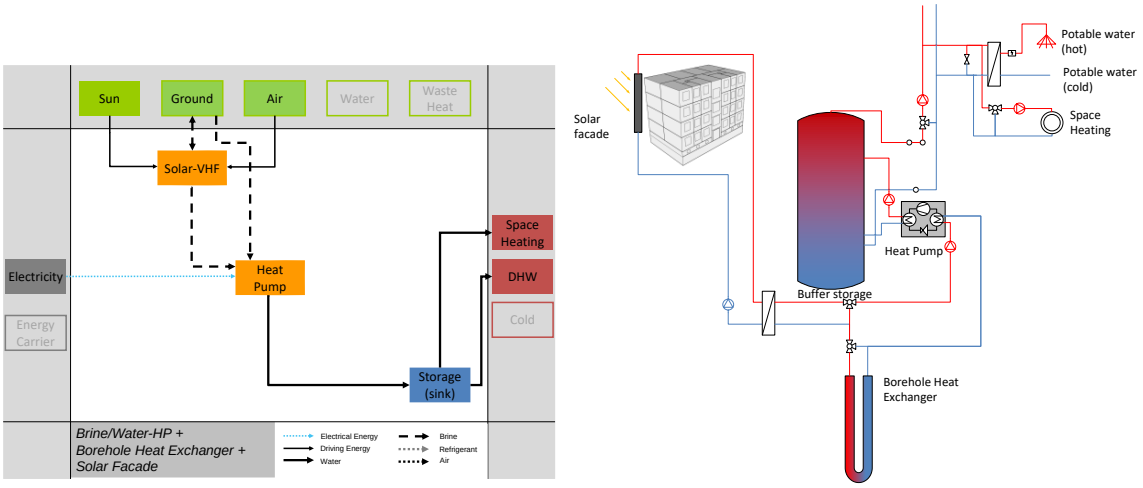

Fig. 3: Left: Schematic of energy flows in the investigated heat supply system (green: environmental energy, orange: energy conversion, blue: thermal energy storage, red: useful energy). Right: Schematic diagram of the heat supply system under investigation

Using TRNSYS, a multi-family building, consisting of 19 apartments each with 84 m² net space was modeled using Type 56. The heat demand of the building is 52.5 MWh/a, with an additional hot water demand of 19.5 MWh/a (Jordan et al., 2019). The building heat supply system consists of a modulating brine-water heat pump (Type 401), the solar-thermal active façade with heat exchanger (Type 832 by Haller et al., 2014), a borehole heat exchanger (Type 346), a centralized 2000 l buffer storage (Type 340) and decentral instantaneous water heaters in each apartment. The brine-water heat pump uses mainly the borehole heat exchanger as a heat source and loads the buffer storage so that a supply temperature of 35 °C is available at the instantaneous water heaters. The decentralized stations use this supply temperature directly for the floor space heating. Via a heat exchanger and an additional electric rod, the potable hot water (45 °C) is produced directly according to demand and in a hygienic manner. The façade is used as an additional source as long as the outlet temperature is above 5 °C (to reduce dew formation and prevent icing) and below 25 °C (max. inlet temperature of heat pump source side). For façade outlet temperatures above 11 °C, the borehole heat exchanger as a source is deactivated. Additionally, the façade enables the regeneration of the borehole heat exchanger, ensuring their sustainable operation and offering the possibility to significantly reduce their size. For a visualization and explanation of the different energy flows see Fig. 4.

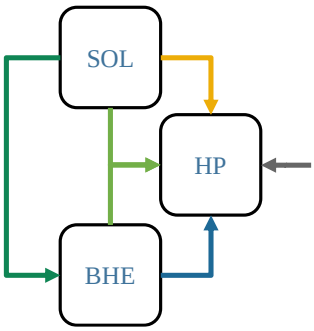

SOL -> BHE:	Solar façade (SOL) for active regeneration of Borehole Heat Exchanger (BHE)
BHE + SOL -> HP:	Outlet of BHE additionally heated by SOL as a source of a heat pump (HP)
SOL -> HP:	SOL as a source of HP
BHE -> HP:	BHE as a source of HP
-> HP:	Power consumption of HP compressor

Fig. 4: Color-coded energy flows with description

4. Results

The system with the thermally activated concrete façade is compared with a common system consisting of a gas boiler or brine-water heat pump. According to the requirements of the German building energy act (GEG, 2020), a heating system with fossil energy sources needs a share of renewable energy sources, therefore the system with a gas boiler includes a suitably dimensioned solar thermal collector (COL) for direct loading of the storage (ST). The systems are described in the following and the results are shown in Fig. 5. The area of the active façade is based on the plan for the demonstration building.

1. HE + COL: Gas condensing boiler with solar support (35 m² flat plate collectors with south orientation and 45° inclination).
2. HP + BHE: brine-water heat pump with ground source (8 x 100m borehole)
3. HP + SOL + BHE (red.): like 2, but additionally with solar thermal activated façade (75 m² east and 25 m² west) and a reduction of the number of boreholes by 25% (6 x 100 m)

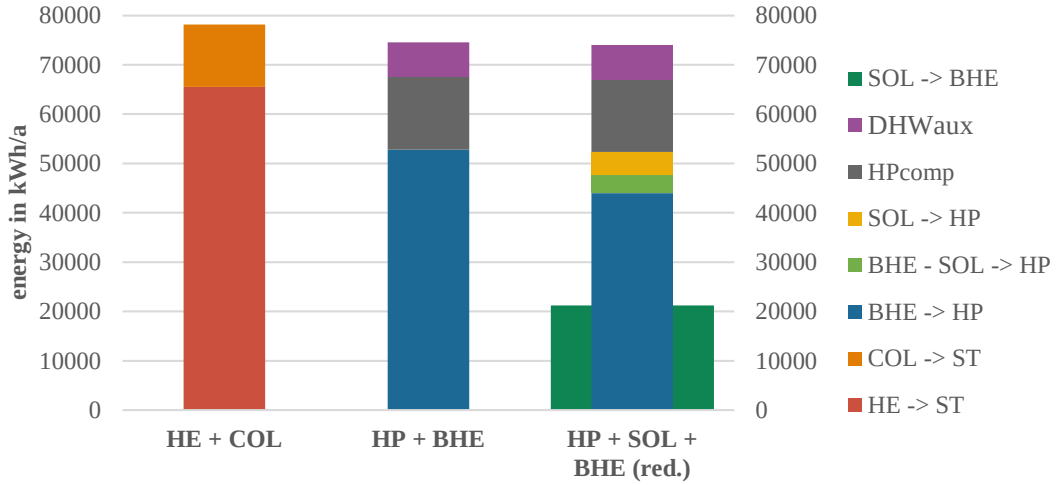

Fig. 5: Representation of the energy flows for 3 heat supply concepts

In addition to the energy flow and its color coding, already described in Fig. 4, the figure also shows the power consumption of the heat pump compressor (HPcomp) and the electric heating of domestic hot water in the instantaneous water heater (DHWaux). The sum of the heat quantity of the different sources, as well as the electricity consumption less the system losses (storage and distribution losses) results in the useful heat quantity of approx. 72 MWh/a.

The gas boiler supplies the buffer storage with approx. 65 MWh/a and the roof-mounted flat plate collector supplies 13 MWh/a heat to cover the useful heat demand. No additional electrical heating through the instantaneous water heater is needed (HE + COL).

The heating systems with a heat pump are using a lower set temperature in the buffer storage, which improves the efficiency of the heat pump and reduces the system losses. But additional electrical heating (approx. 7 MWh/a) is required for the domestic hot water preparation. The heat input to the storage tank is reduced to approx. 68 MWh/a of which approx. 53 MWh/a are drawn from the borehole heat exchanger (HP + BHE).

The use of the thermally activated building envelope in combination with a 25% smaller ground source can reduce the heat extraction from the ground to 44 MWh/a. More than 8 MWh/a from the facades are used as a heat pump source. In addition, more than 21 MWh/a are used to regenerate the borehole heat exchanger, which reduces the drop in ground temperature during the operating time and also ensures high annual performance factors after decades of operation (HP + SOL + BHE (red.)).

Tab. 2: Annual performance factor for different heat supply concepts, calculated as the ratio of condenser output to work of the compressor

	HEATING CONCEPTS	SPF
2:	HP + BHE (8x 100 m)	4.58
3:	HP + BHE + SOL (6x 100 m)	4.60

As a result, the borehole heat exchanger field can be reduced by 25% with the support of a relatively small solar-activated façade without a reduction of the heat pump's performance (see Tab. 2). Using Earth Energy Designer

(Hellström and Sanner, 2000), the influence of the regeneration on the ground temperatures over several years can be calculated. Using the results of the system simulation, the unloading and loading of the borehole heat exchanger were used for the simulation of the BHE and ground temperature for a period of 35 years.

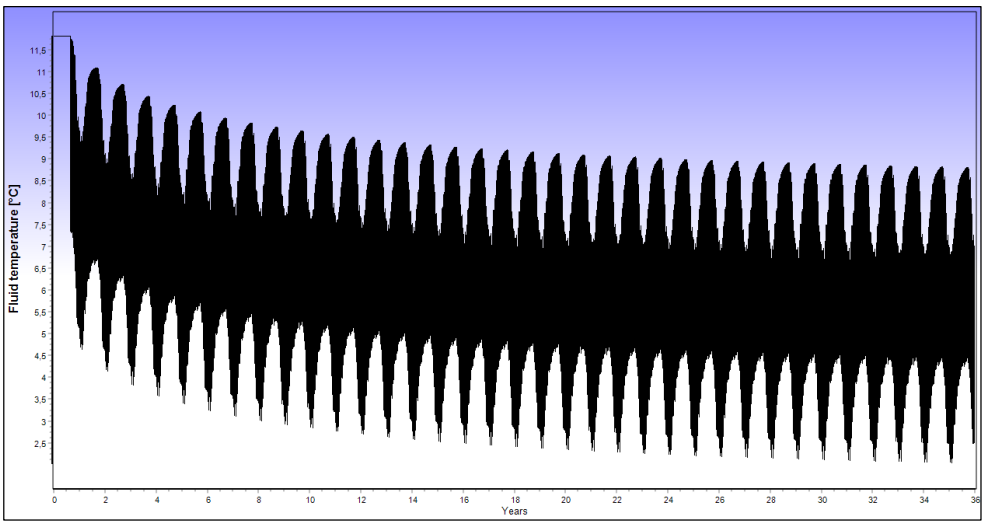

Fig. 6: mean fluid temperature of the borehole heat exchanger (8x 100m) during 35 years for the concept HP + BHE

In the system without active regeneration, the ground temperature and thus also the fluid temperature of the borehole heat exchanger decreases in the first years of operation. The temperature drop amounts to approx. 2.0 K after 10 years, and 2.5 K after 35 years (see Fig. 6).

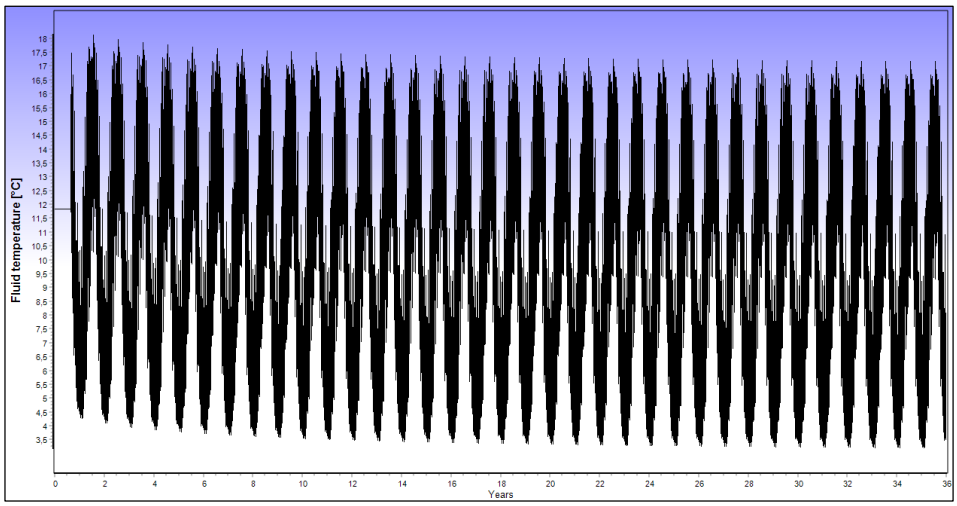

Fig. 7: mean fluid temperature of borehole heat exchanger (6x 100m) during 35 years for concept HP + BHE + SOL

Due to the active regeneration of the BHE (see Fig. 7), the cooling effect of the fluid during the operating time is lower, and the temperature does not decrease further after the first years. The temperature drop amounts to approx. 1.0 K after 10 years, and 1.2 K after 35 years. In addition, high temperatures of up to 17 °C are available after active regeneration, thus even with a reduced ground source, a higher heat pump performance is still reached.

4.1 Façade orientation

Fig. 8 shows the influence of the different orientations of the solar façade. In each case, 75 m² of the solar thermally activated concrete façade are considered for either the north, east, west, or south façade.

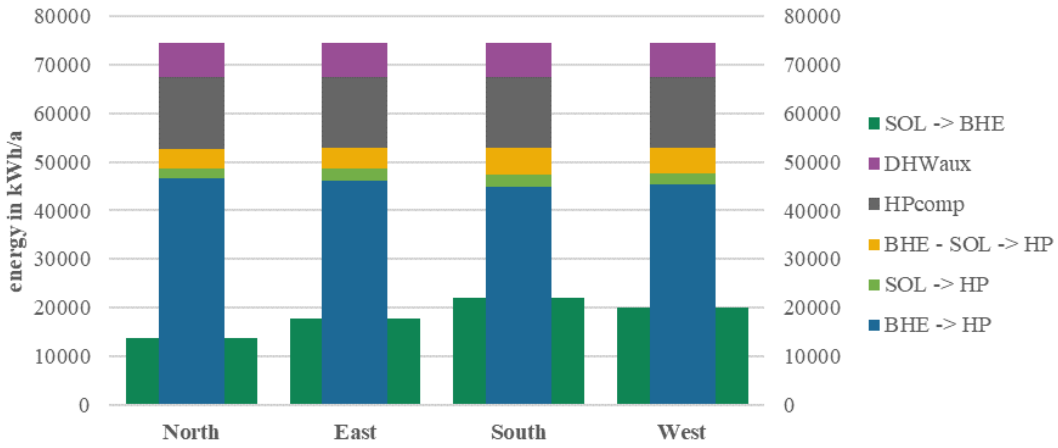

Fig. 8: Distribution of the heat yields of a 75 m² concrete facade for different orientations

The orientation has a significant influence on the yields of the façade, especially for the active regeneration of the borehole heat exchanger field. For this operation mode, the solar thermal activated facades serve both as environmental heat exchangers and solar collectors.

Tab. 3: yield of the concrete façade for different operation modes

				without regeneration (without SOL->BHE)		**with regeneration (with SOL -> BHE)**	
orientation	**SOL -> BHE**	**SOL -> HP**	**BHE + SOL -> HP**	**in kWh/a**	**in kWh/ (m²a)**	**in kWh/a**	**in kWh/ (m²a)**
North	13659	4017	2148	6165	82	19824	264
East	17766	4321	2391	6712	89	24478	326
South	21972	5363	2657	8020	107	29992	400
West	19973	5233	2225	7458	99	27431	366

To meet the increased demand for heat and daylight in living and recreational rooms, these are often orientated to the south. Although this orientation is also advantageous for the solar facade (see Tab. 3), solar thermal activation of a larger contiguous opaque area is often not possible due to the interruption by windows. For this purpose, especially in freestanding buildings, the facade areas with west and east orientation are better suitable. A solar facade with a west orientation has higher yields compared to an east facade. The east facade can gain energy from solar radiation in the morning hours but is at a lower temperature level overall due to its thermal capacity and the low outdoor temperatures at night. The west façade heats up over the course of the day and reaches its highest temperatures during the afternoon and evening hours. In addition, the heat demand might be higher in the afternoon and evening hours, as the buffer tank needs to be recharged more frequently. Thus, the west façade is more likely to meet the simultaneous supply and demand requirement and thus achieve higher yields. The north facade acts as an environmental heat exchanger and has still significantly yields by approximately 80% of the east facade, 72% of the west facade, and 66% of the south facade, respectively.

4.2 Façade area

Fig. 9 shows the energy flows of the sources for different facade areas and orientations (east and west).

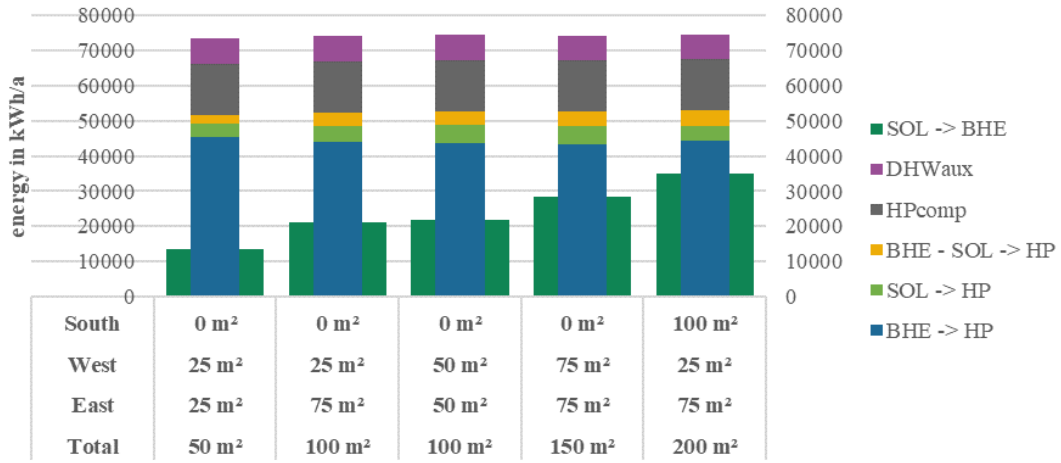

Fig. 9: Effect of different areas of the concrete facade for 6x100m borehole heat exchanger

For the same total area, the variant with a higher proportion of activated west façade shows higher yields. The larger the area of the solar facade, the more environmental heat can be used for the regeneration of the ground. At 100 m², about half of the heat extracted from the ground can be reloaded. By using a south facade, the proportion of the solar facade as a source for the heat pump is only minimally increased (compare 100 m² and 200 m²), but significantly more yield can be used for active regeneration of the ground. Since the source side of the heat pump has a limitation of the temperature range (-10 °C to 25 °C), other concepts are necessary for the use of the facade yields at higher temperature levels, e.g., due to orientation (south facade) or efficiency (darker concrete facade or facade materials made of glass or metal).

4.3 Façade color

Fig. 10 shows the effect of different efficiencies of the facade (zero-loss efficiency η_0) on the system performance. These can be achieved, for example, by different coatings or concrete colors that have different optical properties. For this purpose, specific spectrometric investigations were carried out in the project on small-format concrete samples.

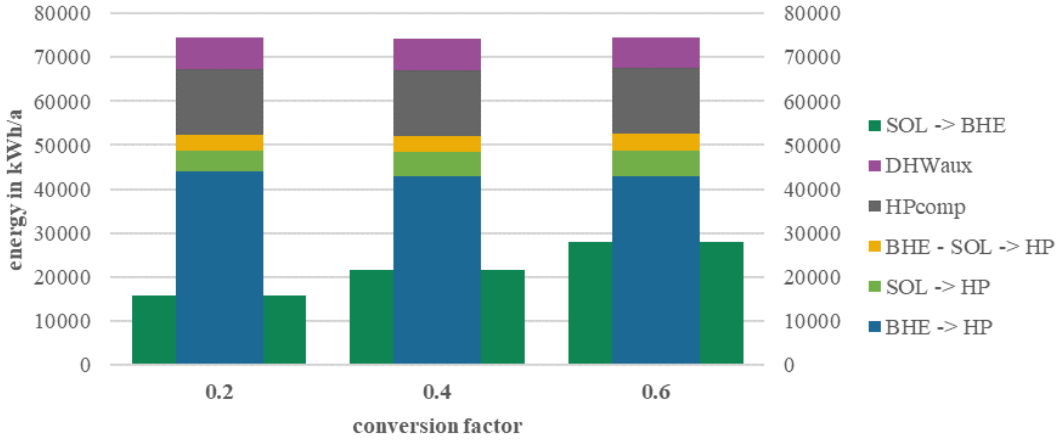

Fig. 10: Variation of the visual characteristics of the concrete facade, 6x100m borehole heat exchanger, 75 m² east and 30 m² west facade

A very light-colored facade exhibits a low (0.2), light-grey concrete, as planned in the demo object, exhibits a medium efficiency (0.4). In the implemented concept, the facade color has a significant influence on the amount of heat introduced into the ground for active regeneration but doesn't play an important role in the use as a source of the heat pump.

5. Conclusion and Outlook

The simulation results based on measured data of a concrete solar façade show the following effects on the considered heat pump system and operation mode:

- The amount of heat extracted from the ground can be significantly reduced.
- The remaining environmental heat is provided by the solar-thermal façade, whether as a sole source or in combination with the borehole heat exchanger.
- Most of the heat gained by the facade is used for the regeneration of the ground source.

By lowering the amount of extracted heat and by regenerating the ground source through a small thermally active façade, a reduction of the ground source of about 25% (either length or number of boreholes) can be achieved, compared to a system with a conventional rear-ventilated façade without impairing the heat pump performance. Higher efficiency can be achieved with larger activated areas or darker colors of the concrete claddings.

Such a system is currently implemented as a demonstration multi-family building in Southern Germany. Heating concepts for active facades with different claddings (e.g. metal and glass), operating over a larger temperature range, and considering direct loading of the buffer storage are currently being investigated. These concepts increase the complexity of the system, but can further reduce or even eliminate the ground source of the heat pump.

6. Acknowledgments

The project “Solar thermal activation of rear-ventilated facades for multi-storey residential buildings: Development, integration into the energy supply system and demonstration” underlying this publication was funded by the State of Lower Saxony and by the German Federal Ministry for Economic Affairs and Climate Action (reference number 03ETW013) based on a decision of the German Parliament. The authors are grateful for this support. The responsibility for the content of this publication lies with the authors.

7. References

Bartelsen, B., Kiermasch, M. and Rockendorf, G., 1999. *Inclination dependency of flat plate collector heat losses, ISES 1999 Solar World Congress, Jerusalem, Israel, July 4-9, 1999: conference proceedings*, Jerusalem, Israel, Elsevier Science Ltd, 72–75.

Frick, E., Büttner, C., Kirchner, M. and Giovannetti, F., 2021. *Solar thermal, rear-ventilated façades as heat pump sources in multi-storey buildings*, *ISES SWC 2021: Solar World Congress, Virtual Conference, 25-29 October 2021: Conference Proceedings*, 1158–1168.

Frick, E., Kirchner, M., Palm, J. and Giovannetti, F., 2021. *Solarthermische Aktivierung vorgehängter, hinterlüfteter Fassaden: Konzepte, numerische Modellierung und experimentelle Untersuchungen von Fassadenpaneelen*, *Tagungsband des 31. Symposiums Solarthermie und innovative Wärmesysteme*, Symposium Solarthermie und innovative Wärmesysteme, Bad Staffelstein, OTTI e.V., Regensburg, vol. 31.

GEG, 2020. *Gesetz zur Einsparung von Energie und zur Nutzung erneuerbarer Energien zur Wärme- und Kälteerzeugung in Gebäuden (Gebäudeenergiegesetz–GEG)*, [Online]. Available at www.gesetze-im-internet.de/geg/ Accessed 18 February 2021.

Haller, M., Perers, B., Bales, C., Paavilainen, J., Dalibard, A., Fischer, S. and Bertram, E., 2014. *TRNSYS Type 832 v5.10 „Dynamic Collector Model by Bengt Perers“: Updated Input-Output Reference*, Report.

Hellström, G. and Sanner, B., 2000. *Earth Energy Designer - User Manual 2.0*, [Online]. Available at http://www.buildingphysics.com/manuals/eed.pdf.

Hofmann, M., Riechelmann, S., Crisosto, C., Mubarak, R. and Seckmeyer, G., 2014. *Improved Synthesis of Global Irradiance with One-Minute Resolution for PV System Simulations*, *International Journal of Photoenergy*,

Hindawi, vol. 2014, e808509 [Online]. DOI: 10.1155/2014/808509.

Jordan, U., Braas, H., Best, I., Orozaliev, J., Vajen, K. and Kassel, U., 2019. *DHWcalc Update 2.02: Programm zur Generierung von Trinkwasser-Zapfprofilen auf statistischer Basis*, Kloster Banz, Bad Staffelstein, Conexio GmbH, 14.

Klein, S. A., 2010. *TRNSYS 17: A Transient System Simulation Program*, Solar Energy Laboratory, University of Wisconsin, Madison, USA [Online]. Available at http://sel.me.wisc.edu/trnsys.

Meteotest, 2022. *Meteonorm 8*, 3012 Bern, Schweiz, Meteotest AG [Online]. Available at meteonorm.com Accessed 1 September 2022.

Solar Keymark Database (2019) *Annex to Solar Keymark Certificate: SolvisCala 254-AR* [Online]. Available at www.duurzaamloket.nl.

Appendix

Tab. 4: collector parameters for basic equation according to Type 832 Haller et al., 2014

Quantity	Symbol	Unit
heat output of the collector per area	$\dot{q}_{out}$	W m^{-2}
latent (condensation + sublimation) heat gains	$\dot{q}_{lat}$	W m^{-2}
zero loss efficiency of the collector, sometimes referred to as η_0	$F'(\tau\alpha)$	-
incidence angle modifier for beam radiation	K_b	-
beam radiation incident on collector plane	I_b	W m^{-2}
incidence angle modifier for beam radiation	K_d	-
diffuse radiation incident on collector plane	I_d	W m^{-2}
factor for a wind dependency correction of F' (and thus the zero-loss coefficient $F'(\tau\alpha)$), used for unglazed collectors	$c_{w,F'}$	s m^{-1}
wind speed parallel to the collector plane	u_w	m s^{-1}
first order heat loss coefficient	a_1	W K^{-1} m^{-2}
second order heat loss coefficient	a_2	W K^{-2} m^{-2}
arithmetic mean of the collector temperature	ϑ_m	°C
ambient temperature at location of collector field	ϑ_{amb}	°C
absolute ambient temperature at location of collector field	T_{amb}	K
wind speed dependency of heat losses	$c_{w,hl}$	J m^{-3} K^{-1}
long wave irradiation dependency of heat losses (or gains)	c_{IR}	-
long wave irradiation on collector plane	I_{IR}	W m^{-2}
Stefan Boltzmann constant	σ	W m^{-2} K
time	t	s
effective thermal capacitance of the collector (including fluid)	C_{eff}	J m^{-2} K^{-1}
wind speed from wind data	$u_{w,0}$	m s^{-1}
wind speed factor	wf	-
sky radiation factor	rf	-
long wavelength radiation downwards from sky	$I_{IR,0}$	W m^{-2}

The Potential of Combined PV and Air Source Heat Pump Systems in German Residential Buildings

Kristina Dabrock,[1] Kevin Knosala,[1] Noah Pflugradt,[1] Henning Beuth,[1] Leander Kotzur,[1] and Detlef Stolten[1,2]

[1] Institute of Energy and Climate Research (IEK-3), Techno-Economic Systems Analysis, Forschungszentrum Jülich GmbH, Wilhelm-Johnen-Str., D-52428, Germany

[2] Chair for Fuel Cells, RWTH Aachen University, c/o Institute of Energy and Climate Research (IEK-3), Techno-Economic Systems Analysis, Forschungszentrum Jülich GmbH, Wilhelm-Johnen-Str., D-52428, Germany

Abstract

Heat pumps are considered a cornerstone of the process of decarbonizing building stock. Especially in combination with electricity provided by rooftop photovoltaic (PV) systems, a large-scale roll-out of heat pumps will constitute a valuable element in the EU's endeavor to increase both energy efficiency and the share of renewable power utilized in buildings. However, the installation of both PV systems and heat pumps is subject to various constraints, e.g., roof shapes for the former and available space for the latter. Therefore, we are investigating the feasibility of extensively implementing air source heat pumps combined with PV. This paper introduces a detailed spatial analysis of the available space around buildings that could be available for heat pumps, and couples it with an overview of the rooftop PV potential of these buildings. The analysis is carried out for two example regions in North Rhine-Westphalia, Germany. The results for the city of Cologne show that the combination of an outdoor air source heat pump with rooftop PV is feasible for 47% of residential buildings. In rural Winterberg, the share of suitable buildings is 74%. This illustrates both the potential for a large-scale roll-out of heat pumps in combination with PV in some regions, as well as the relevance of limiting factors such as available space in others. Furthermore, the results underline the importance of detailed spatial analyses for assessing the potential of the large-scale roll-out of heat pump–PV systems in Germany.

Keywords: Heat pumps, air source heat pumps, feasibility analysis, outdoor space, spatial analysis, Germany, decarbonization, residential, PV

1. Introduction

Buildings account for 40% of the total energy consumption in the EU and 36% of greenhouse gas emissions. Therefore, they will play a central role in the EU's goal of reaching climate neutrality by 2050, as defined in the European Green Deal (European Commission, 2020a). The electrification of the heat supply and increasing the share of renewable energy used are two measures that can contribute to the decarbonization of the building sector (European Commission, 2020b; Thomas et al., 2022). Heat pumps are one of the main technical solutions available for this, carrying many potential economic and environmental advantages (Wang et al., 2020). Operating heat pumps in residential buildings using electricity from rooftop photovoltaic (PV) installations will lead to an efficient and decentralized zero-emission heat supply, which is necessary for achieving the emissions reduction goals.

However, even the installation of the most popular and easiest-to-install type of heat pumps, namely the air-sourced model, is subject to a range of constraints. These include indoor and outdoor space availability, acceptable noise levels, roof load, and heat supply temperatures. The feasibility of rooftop PV, on the other hand, depends largely on roof shape. Whether an existing building is suitable for the installation of an air source heat pump combined with PV therefore depends on its individual characteristics.

On the one hand, the political agenda and conceptual decarbonization pathways clearly aim to increase the number of heat pumps and PV systems in buildings (Bundesministerium für Wirtschaft und Klimaschutz and Bundesministerium für Wohnen, Stadtentwicklung und Bauwesen, 2022; Bundesverband Wärmepumpe (BWP) e. V, 2021; Prognos et al., 2020; Stolten et al., 2022). On the other, studies analyzing the feasibility of

© 2022. The Authors. Published by International Solar Energy Society
Selection and/or peer review under responsibility of Scientific Committee
doi:10.18086/eurosun.2022.08.03 Available at http://proceedings.ises.org

combined heat pump and PV installations primarily focus on individual buildings or building types. Rieck et al. (2020), Bee et al. (2019), and Pena-Bello (2021), though with slightly differing emphases and approaches, all investigate the feasibility of PV-powered heat pump systems for individual buildings using house and grid simulations. Solar generation potential for Germany has been evaluated using spatial analyses and simulations by, e.g., Risch et al. (2022). Spatial analyses addressing heat pumps, such as Volkova et al. (2021), focus on using them for district heating and not for individual buildings or assessing the potential of ground source heat pumps (Konetschny et al., 2018). The link between the two levels, i.e., the techno-economic modeling of individual building heating systems on the one side and the political goal of the large-scale decarbonization of the heating sector via air source heat pumps and renewable energy on the other is, to our knowledge, not clearly understood.

In order to contribute to quantifying the potential of combined PV and air source heat pump systems, this study conducts a detailed, building-level spatial analysis using the example of two regions in the federal state of North Rhine–Westphalia in Germany. In order to account for characteristic regional differences, we analyze one region each from the two ends of the spectrum defined by the RegioStaR classification (Bundesministerium für Digitales und Verkehr, 2018), with Winterberg serving as a representative example of a rural/village area and Cologne being representative of a metropolis. The goal is to determine the percentage of residential buildings with sufficient outdoor space for setting up an easy-to-install air source heat pump, as well as sufficient rooftop PV potential.

2. Methodology

In our study, we employ a two-step approach. First, we analyze the space availability of buildings (sub-sections 2.1.–2.2.). Then, we calculate and evaluate the ratio between yearly solar generation potential and yearly heat demand for those buildings (subsections 2.3.–2.5.). Based on the results of these two analyses, we can draw conclusions regarding the share of buildings in our example areas that fulfill both the space requirement and meet the targeted ratio threshold (subsection 2.6.).

2.1. Outdoor space requirements of air source heat pumps

As a first step, a thorough analysis of the outdoor space requirements for air source heat pumps of different capacities and by various producers is carried out. This is performed by drawing on the information provided in the product sheets published on producers' websites.

2.2. Spatial analysis of outdoor space availability

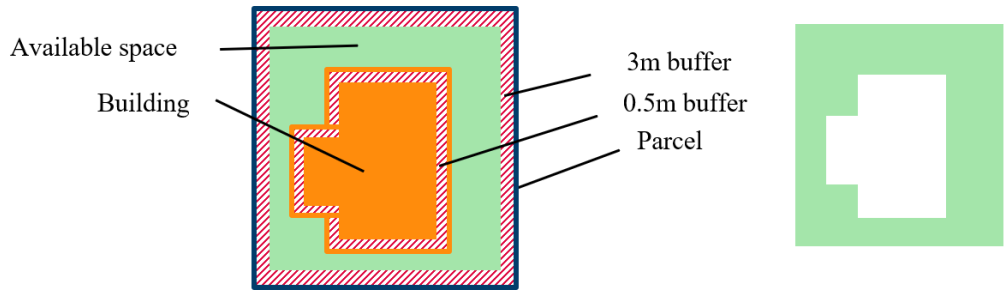

Fig. 1: Illustration of available space around a building. On the left: parcel with a 3m buffer inside the polygon and buildings with a buffer of 0.5m on the outside; on the right: the remaining available space after removing the buffer and building areas.

The basis for a detailed spatial analysis is data on individual building footprints and associated plot areas for the building stock. For North Rhine–Westphalia, open governmental 3D data of buildings in level of detail 2 (LoD2) is available (Bundesamt für Kartographie und Geodäsie, 2021). All ground surface areas present in the data are extracted and considered as building footprints in the subsequent analysis.

Buildings are then divided into residential, non-residential, and irrelevant instances. All buildings below a footprint area threshold of 30 m² are considered irrelevant, thus excluding structures such as garages and garden sheds from the analysis. Residential and non-residential buildings are then differentiated by spatially joining the European settlement map "ESM 2015 – R2019" (Corbane and Sabo, 2019). This raster dataset labels every 10m x 10m grid cell in Europe as residential or non-residential. Buildings are classified by

calculating the zonal statistics of their footprint polygon with the rasterstats package (Perry, 2022). Each building is thereby assigned the most frequently-occurring raster cell value from the European Settlement Map that its footprint polygon touches.

Based on the assumption that the available outdoor space of a building is best estimated by the size of the parcel on which it is located, cadastral parcels are the second dataset required for the space availability analysis. For North Rhine–Westphalia, this data is openly available (Geobasis NRW, 2022). Parcels are assigned to buildings by spatially-joining both datasets. All buildings, the centroid of which intersect a parcel polygon, are assigned such a parcel. For the space availability analysis, the total parcel area is reduced (1) by a buffer of 3m within the parcel polygon based on the German standard border margin for buildings as defined by federal building regulations; and (2) by the area of all buildings located on the parcel plus a buffer outside of them of 0.5m. The remaining space is then deemed potentially available for a heat pump (see Figure 1).

Finally, we analyze whether a heat pump of size 1m x 1.5m as derived from the product research described in 2.1 fits into the available space. For this, we first rasterize the remaining parcel area in 0.1m x 0.1m raster cells, resulting in a matrix in which free and occupied space are represented by zeroes and ones. Then, we rasterize the heat pump at the same resolution, i.e., a heat pump with the aforementioned dimensions is described by a matrix with the dimensions 10 x 15 filled with ones. This heat pump matrix is rotated by 45°, 90°, and 320° to account for different possible orientations of the heat pump on the parcel, and for each of these we test whether the heat pump matrix can be found in the matrix describing the parcel. As a result, it can be determined whether each residential building has sufficient outdoor space for an air source heat pump or if space could be a critical factor.

2.3. Heat demand assignment

The basis for an estimation of the buildings' yearly heat demand is the EU project Hotmaps (Hotmaps Consortium, 2022), which calculated residential heating demand for each hectare based on statistical values. For our analysis, each residential building's yearly heat demand was determined by spatially-joining the building centroids with the Hotmaps raster data for residential buildings (*Hotmaps Project, D2.3 WP2 Report – Open Data Set for the EU28*, 2018). A raster grid cell value as given by Hotmaps was divided amongst the residential buildings that lie within that raster cell proportionally to the buildings' footprint areas.

2.4. Rooftop PV potential analysis

Another input dataset for our analysis was rooftop PV potential. Specifically, we employed the data generated by Risch et al. (2022). The underlying data were: (1) LoD2 building models for Germany (Bundesamt für Kartographie und Geodäsie, 2021), providing information about roof area, tilt, and orientation; and (2) the surface solar radiation dataset by EUMETSAT (EUMETSAT, 2019). Based on this data, the potential for every roof surface was simulated using RESKit (Ryberg et al., 2022).

The time series generated during the simulation were aggregated into a single yearly generation value per roof. We then assigned these values to the buildings based on roof positions. All roof centroids that lie within the building footprint polygons were then summed up and assigned to the respective building.

2.5. Ratio threshold approximation

We define a target of 50% of heat demand supplied from PV. This means that the local PV generation can account for 50% of the electricity supply that is needed by the heat pump over the course of the year. Because of the inverse yearly profiles of heating demand and solar generation, the temporal fluctuation over the course of a year must be considered, which is why we calculate a monthly profile from the aggregated yearly value for both heat demand and PV generation potential. The yearly heat demand was distributed to all months of a year proportionally to the heating degree method with data provided by the Institut Wohnen und Umwelt (IWU) (2022), whereas the yearly solar generation was distributed to all months based on the monthly horizontal irradiation with data from the same source. To give an indication of the variability of data based on the geographical location under consideration, especially with the aim of extending our analysis to a larger geographical scope, we carried out the calculation for four locations in Germany. The analyzed locations were in the North (Glücksburg-Meierwik), South (Freiburg), West (Nideggen-Schmidt) and East (Dresden-Hosterwitz) of the country. We first extracted the degree-day numbers from the IWU for each month of the year 2021 for the respective location. Then, we calculated the share of each month by dividing the monthly

degree-day numbers by the sum of all values of the year. With this as a factor, we distributed yearly energy demands for heating to all months to obtain an estimation of the monthly heat demand. Similarly, we extracted monthly horizontal global irradiation values from the IWU for the year 2021 for all four locations, calculated the monthly share and used this to distribute yearly PV generation to the corresponding months. With these monthly profiles and assuming a very conservative coefficient of performance (COP) of 3 for a heat pump, we calculated for each month how much of the energy required for heating could be provided through the PV system. Summing up the amount of thermal energy covered in each month and dividing it by the total heating demand leads to an approximation of how much of the heating demand can be supplied by PV over the course of the year, depending on the ratio between the yearly electrical energy provided through PV to the yearly thermal energy required for heating. Using monthly values also has the advantage of leveling out daily fluctuations, which provides a first approximation of the existence of heat storage and building thermal mass and reduces the calculation times for this first calculation to manageable amounts. We evaluate this relation for a range of yearly heat demands of between 5 and 35 MWh and yearly solar generation potentials of between 1 and 25 MWh. Finally, we can estimate a ratio of yearly PV generation to yearly heat demand that corresponds to a 50% electricity supply to the heat pump by PV over the course of a year.

2.6. Consolidation of the results

In a final step, the results from the outdoor space availability analysis, heat demand assignment, and rooftop PV potential analysis were consolidated. All buildings with sufficient outdoor space available were preselected. For those buildings, the ratio of yearly solar generation potential to yearly heat demand was calculated. Above the previously defined ratio threshold, buildings were deemed suitable for the installation of a combined heat pump–PV system. Based on this, we calculated the share of buildings that are suitable for the installation of a combined heat pump–PV system in both regions.

3. Results

3.1. Required space

The space requirements of the outside unit of 82 air source heat pumps from eight different producers is shown in Figure 2, in which the unit's depth is plotted against its width. The cluster at the bottom left comprises heat pumps of dimensions of up to 1m x 1.5m and the cluster to the top right comprises heat pumps of dimensions greater than this. The space requirements of the outside unit of split constructions are lower than those of monoblocs and these heat pumps all fall within the first cluster. However, as split constructions are more complex in their installation and our focus lies on quantifying the potential for easy-to-install systems, monobloc sizes are more relevant for our analysis. We therefore set the heat pump size for which we analyze the space availability to 1m x 1.5m, which is larger than that for split constructions but lies within a medium range for monoblocs.

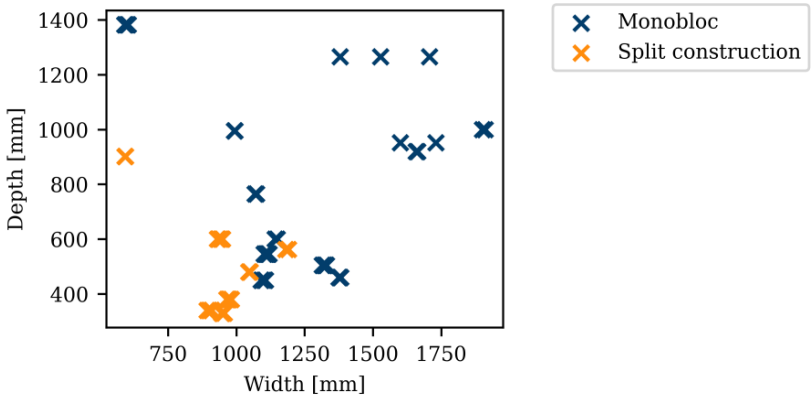

Fig. 2: Dimensions of an outdoor unit of 82 air source heat pumps for both monoblocs and split constructions. A small scatter of a maximum 10mm has been added to the x-component of every point for better visibility of duplicates.

3.2. Available space

The analysis of available space shows that after ignoring buildings to which no parcel could be assigned, only 3% of buildings have insufficient space for a heat pump with 1m x 1.5m dimensions in provincial/rural Winterberg (category 225 of RegioStaR17), whereas 18% of buildings in metropolitan Cologne (category 111 of RegioStaR17) have insufficient space (see Figure 3). We analyzed the space availability of 223,178 residential buildings in Cologne and 8,940 residential buildings in Winterberg.

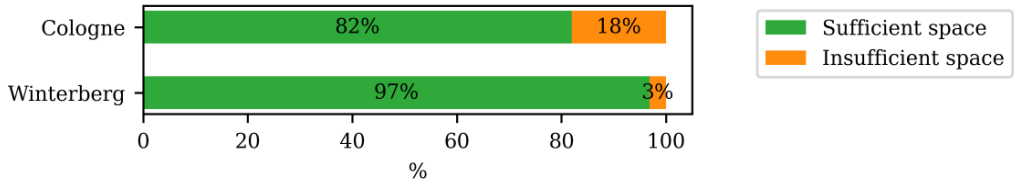

Fig. 3: Percentage of buildings with and without sufficient outdoor space for installing a heat pump with dimensions of 1m x 1.5m in Cologne and Winterberg. The total numbers of classified buildings are 223,178 and 8,940 for Cologne and Winterberg, respectively.

Figure 4 shows small extracts of the analyzed areas as an example of the spatial distribution of building footprints colored according to space availability, with buildings with insufficient space depicted in red and those with sufficient space in green. On the left is shown a densely built-up area in central Cologne, whereas the right depicts a more sparsely built-up area in Winterberg.



Fig. 4: Buildings classified according to their space availability in small extracts from the analyzed areas. Red symbolizes insufficient space, whereas green represents sufficient space. The map on the left shows an area in central Cologne, and that to the right is in Winterberg.

3.3. Ratio threshold estimation

Figure 5 illustrates the relationship between yearly solar electricity generation potential to the yearly heat demand ratio and the share of heat demand that can be covered by a PV-powered heat pump of COP 3, taking the yearly profiles into consideration. Results are shown for four locations in Germany. Approximately 50% of heat demand is met with a PV-powered heat pump over the course of a year, corresponding to a ratio of around 40% yearly solar generation potential to yearly heat demand. The values lie in similar ranges for all four locations, especially for lower yearly ratio values. The higher the yearly ratio, the more the values diverge. For a ratio of yearly electricity generation by PV to a yearly heat demand of 40%, the maximum and minimum still lie within a range of 7 percentage points.

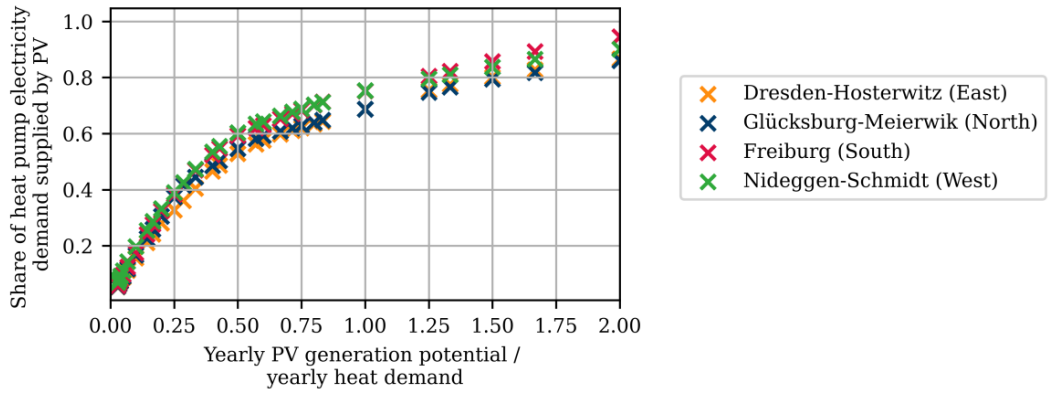

Fig. 5: Relationship between the yearly solar generation potential to yearly heat demand ratio (x-axis) and the share of heat demand that can be covered by a PV powered heat pump of COP 3, taking the yearly profiles into consideration (y-axis) for four locations in Germany.

3.4. Heat demand and solar potential ratio

Based on the yearly heat demand values and yearly solar generation potential values assigned to residential buildings, a ratio between the yearly potential for electrical energy generated via PV and yearly thermal energy demand for heating can be calculated. A histogram combined with a cumulative curve of these ratios for all buildings that have previously been found to have enough space and to which we could assign both a yearly solar generation potential and level of heat demand is shown in Figure 6. For most buildings, the ratio lies below a value of 1, meaning that the electrical energy provided via PV is lower than the thermal energy required for heating. The histogram of Winterberg has a peak at approximately 0.5, whereas that of Cologne is slightly shifted to the left and peaks at ca. 0.4. The dashed line represents the yearly value ratio threshold of 40% calculated in the previous step.

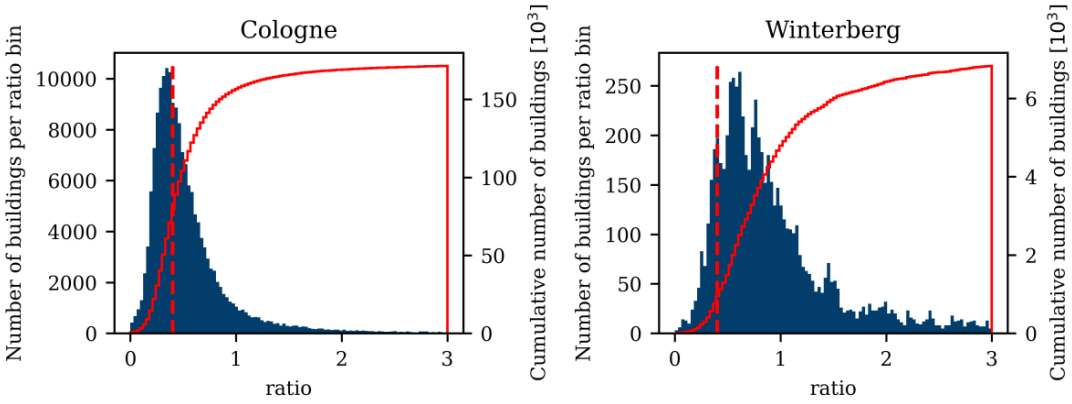

Fig. 6: Histogram of ratios of electrical energy generation potential through rooftop PV to thermal energy demand for heating for each building (excluding missing values) in Cologne (left) and Winterberg (right). The dashed red line represents the 40% ratio threshold.

As is shown in Figure 6, approximately 89% of buildings in Winterberg and 59% of buildings in Cologne lie above the 40% ratio threshold. However, the buildings depicted in Figure 6 are only those to which both PV generation and a heat demand profile could be assigned, and so we were able to calculate a ratio. We also calculated the share of buildings with a ratio above 50% when including the buildings without any ratio. This yields a share for Winterberg of 78%, and of 57% for Cologne.

3.5. Building stock suitability for a combined system

Figure 7 displays a summary of all results for both regions. It depicts the share of buildings with insufficient or undefined space availability and for buildings with sufficient space, it shows the share of buildings above and below our defined ratio, as well as the undefined share. The total share of buildings in Cologne with both enough space and a ratio above the threshold is 47%. The same category of buildings has a share of 74% in

the building stock of Winterberg. A higher share of undefined values for both space availability and ratio can be observed in those in Winterberg.

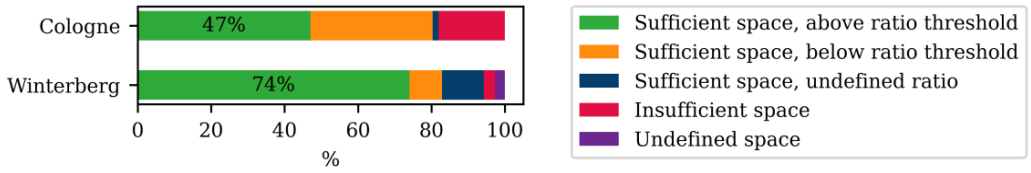

Fig. 7: Share of buildings classified according to their space availability for a heat pump of dimensions 1m x1.5m, as well as the ratio between solar generation potential and heat demand in Cologne and Winterberg.

4. Discussion

The results of the space availability analysis show that how large the share of buildings with sufficient outdoor space for an air source heat pump depends heavily on the region. Although space availability is generally not a major issue in the sparsely built-up rural area of Winterberg, it can become a challenge in densely populated urban areas such as Cologne. This difference is to be expected and can be understood intuitively by envisioning a typical city center with small, if any, garden patches and neighboring houses standing wall-to-wall and comparing this with a suburban or village setting in which many houses are single-family dwellings surrounded by larger gardens and standing several meters apart from neighboring houses. It can be concluded that space availability is a limiting factor for the large-scale rollout of heat pumps in Cologne, and likely in other urban areas of similar characteristics, which should be addressed to increase the number of buildings that qualify for the installation of air source heat pumps. One possible solution could be the use of split systems instead of monoblocs because of their smaller outside units. However, this has the drawback of entailing greater installation efforts. Roof installations are another option to consider, although they carry own challenges, e.g., permissible roof loads or competition for space with PV systems.

The ratio between PV generation potential and heat demand further reduces the number of houses that qualify for combined heat pump–PV systems according to our self-set energy threshold. Not only the space availability but also the ratio varies by region. The ratios of buildings in Cologne tend to be lower than those in Winterberg, which means that a smaller amount of the electric energy required by a heat pump could be provided by a PV installation. This is due to there being a significantly higher average heat demand per building in Cologne, combined with only slightly higher PV generation potential compared to Winterberg. One possible explanation for this could be the lower ratio of roof areas to living space in multi-level buildings in densely populated urban areas. To increase the share of buildings with a higher ratio, the energy demand of buildings would have to be reduced, e.g., through targeted energy retrofitting activities. It is also important to keep in mind that setting the amount of electricity that should be supplied by the PV system to 50% is arbitrary. Lower numbers, although resulting in a reduced level of self-sufficiency, could also be acceptable or even preferable. Furthermore, we calculated the ratio threshold based on degree-day numbers and irradiation values for one year only. Yearly weather variability, with cold and overcast years on the one hand and warm and sunny years on the other, could have a significant effect on the determined ratio. And, although we do not consider this in our analysis, it should not be forgotten that electricity generated by PV is not only useful for powering a heat pump but also for household appliances and, especially in a future transport system, battery electric vehicles.

Combining the results from both the space availability analysis and PV potential/heat demand ratio analysis, it can be stated that in rural Winterberg, there is not only more space available but also a large proportion of buildings (74%) exceed our defined ratio for being able to provide enough electricity for heating. In Cologne, many buildings are already excluded due to lack of available space. Of the share remaining, only approximately half (47%) of the buildings have the potential to provide sufficient electricity for heating with PV. The difference in results for Winterberg and Cologne underlines the importance of taking regional disparities into account when analyzing the practical feasibility of the large-scale roll-out of heat pumps. It also emphasizes the relevance of spatial analyses at the building level compared to statistical analyses at an aggregated one. Even within regions, characteristics vary. And although we did not quantify them, a qualitative visual analysis showed that space availability is less of an issue in the suburbs of Cologne than in the city center. Although

the potential for combined air-sourced heat pump–PV systems is high in rural areas, it is limited in urban ones by both space availability and the ratio between solar potential and heat demand. At the same time, the absolute number of buildings in urban areas is significantly higher than in rural ones. Therefore, when aiming for a large-scale roll-out of combined systems, the absolute number of buildings in cities where the installation of a combined system is feasible will still be considerable. It is also important to note that the amount of PV-generated electricity we base our calculations on constitutes the maximum electricity produced that is available for the heat pump, as in reality the heat pump will compete with other electricity-consuming household appliances.

Our study provides a first approximation regarding the potential for combined air-sourced heat pump–PV systems. By choosing two regions at the ends of the RegioStaR classification spectrum with very different characteristics, we can give an indication of the range of values we can expect for the entirety of Germany. However, the numbers we provide must be seen as preliminary, as this study is subject to several simplifications that require further research. First, all ground surface areas from the building data were taken as independent units. This results in an overestimation of the total number of buildings, which makes an analysis of the absolute numbers unreliable. This could be remedied by defining building complexes in which multiple smaller constructions are considered as one and the roof areas of buildings currently defined as irrelevant could be included as part of larger structures, leading to an increase in PV generation potential for some buildings. Furthermore, the ratio threshold we define is an approximation, as we only consider monthly values and do not take building-specific or regional characteristics into account. Additionally, solutions for inconsistencies between our building footprints and the Hotmaps raster data that leads to missing data for the heat demand of buildings must be found. A study addressing these issues and extending the analysis to all of Germany will follow in the form of a journal publication.

5. Conclusion and outlook

This study demonstrates the feasibility of the chosen approach. While we identified some areas that need further improvement, the preliminary results are very promising. It was possible to show that in metropolitan areas such as Cologne for about 47% of residential buildings a combined air source heat pump–rooftop PV system is feasible and can cover over 50% of the yearly heating demand. For rural areas such as Winterberg the share of buildings that can be supplied in the same way exceeds 70%. The results emphasize the importance of detailed spatial analyses for assessing the potential of decarbonization measures, such as the large-scale roll-out of heat pump–PV systems.

This research has far-reaching implications for the next few years. With rising gas prices, the option of switching to a hybrid system by installing a combined heat pump–PV system on top of an existing gas heating, which is feasible especially in rural areas, becomes increasingly attractive. If gas prices stay high, it is very economical in such a hybrid system to only draw gas from the grid during periods of extreme cold and low solar radiation, leading to significantly reduced full-load-hours of the gas grid. This means that the price per unit must be increased to cover the high fixed costs of the gas grid, which effectively leads to an additional rise in consumer prices. Given sufficiently high production and installation capacities for rooftop PV and heat pumps, this might even lead to a death spiral of the entire rural gas grid, in which rising gas prices and the switch to hybrid heating systems accelerate each other. This will be analyzed in detail in further studies.

6. References

Bee, E., Prada, A., Baggio, P., Psimopoulos, E., 2019. Air-source heat pump and photovoltaic systems for residential heating and cooling: Potential of self-consumption in different European climates. Build. Simul. 12, 453–463. https://doi.org/10.1007/s12273-018-0501-5

Bundesamt für Kartographie und Geodäsie, 2021. 3D-Gebäudemodelle LoD2 Deutschland [WWW Document]. URL https://gdz.bkg.bund.de/index.php/default/3d-gebaudemodelle-lod2-deutschland-lod2-de.html (accessed 4.6.22).

Bundesministerium für Digitales und Verkehr, 2018. Regionalstatistische Raumtypologie (RegioStaR) des BMVI für die Mobilitäts- und Verkehrsforschung.

Bundesministerium für Wirtschaft und Klimaschutz, Bundesministerium für Wohnen, Stadtentwicklung und Bauwesen, 2022. Breites Bündnis will mindestens 500.000 neue Wärmepumpen pro Jahr [WWW Document]. URL https://www.bmwk.de/Redaktion/DE/Pressemitteilungen/2022/06/20220629-breites-buendnis-will-mindestens-500000-neue-waermepumpen-pro-jahr.html (accessed 8.26.22).

Bundesverband Wärmepumpe (BWP) e. V, 2021. Roadmap Wärmepumpe - Der Weg zur Dekarbonisierung des Gebäudesektors.

Corbane, C., Sabo, F., 2019. European Settlement Map from Copernicus Very High Resolution data for reference year 2015, Public Release 2019. https://doi.org/10.2905/8BD2B792-CC33-4C11-AFD1-B8DD60B44F3B

EUMETSAT, 2019. Surface Solar Radiation Data Set - Heliosat (SARAH) - Edition 2.1 [WWW Document]. URL https://navigator.eumetsat.int/product/EO:EUM:DAT:0022 (accessed 4.6.22).

European Commission, 2020a. Powering a climate-neutral economy: An EU Strategy for Energy System Integration.

European Commission, 2020b. In focus: Energy efficiency in buildings [WWW Document]. European Commission - European Commission. URL https://ec.europa.eu/info/news/focus-energy-efficiency-buildings-2020-lut-17_en (accessed 4.4.22).

Geobasis NRW, 2022. Grundrissdaten [WWW Document]. URL https://www.opengeodata.nrw.de/produkte/geobasis/lk/akt/gru_xml/ (accessed 8.26.22).

Hotmaps Consortium, 2022. Hotmaps Project - The open source mapping and planning tool for heating and cooling [WWW Document]. Hotmaps Project. URL https://www.hotmaps-project.eu/ (accessed 8.26.22).

Hotmaps Project, D2.3 WP2 Report – Open Data Set for the EU28, 2018.

Institut Wohnen und Umwelt (IWU), 2022. Gradtagszahlen Deutschland.

Konetschny, C., Schmid, T., Greif, S., 2018. Potenzialanalyse zur Nutzung von Erdwärmepumpen im Gebäudebestand - Oberflächennahe Geothermie im außerstädtischen Wohngebäudebestand. FfE München, BWK – Das Energie-Fachmagazin.

Pena-Bello, A., Schuetz, P., Berger, M., Worlitschek, J., Patel, M.K., Parra, D., 2021. Decarbonizing heat with PV-coupled heat pumps supported by electricity and heat storage: Impacts and trade-offs for prosumers and the grid. Energy Conversion and Management 240, 114220. https://doi.org/10.1016/j.enconman.2021.114220

Perry, M., 2022. rasterstats: Summarize geospatial raster datasets based on vector geometries.

Prognos, Öko-Institut, Wuppertal-Institut, 2020. Klimaneutrales Deutschland. Studie im Auftrag von Agora Energiewende, Agora Verkehrswende und Stiftung Klimaneutralität.

Rieck, J., Taube, L., Behrendt, F., 2020. Feasibility analysis of a heat pump powered by wind turbines and PV-Applications for detached houses in Germany. Renewable Energy 162, 1104–1112. https://doi.org/10.1016/j.renene.2020.07.011

Risch, S., Maier, R., Du, J., Pflugradt, N., Stenzel, P., Kotzur, L., Stolten, D., 2022. Potentials of Renewable Energy Sources in Germany and the Influence of Land Use Datasets. Energies 15, 5536. https://doi.org/10.3390/en15155536

Ryberg, D.S., Heinrichs, H., Robinius, M., Stolten, D., 2022. RESKit - Renewable Energy Simulation toolkit for Python. FZJ-IEK3.

Stolten, D., Markewitz, P., Schöb, T., Kullmann, F., Risch, S., Groß, T., Hoffmann, M., Franzmann, D., Triesch, T., Kraus, S., Maier, R., Gillessen, B., Heinrichs, H., Pflugradt, N., Grube, T., Linnsen, J., Kotzur, L., 2022. Neue Ziele auf alten Wegen? Strategien für eine treibhausgasneutrale Energieversorgung bis zum Jahr 2045. Schriften des Forschungszentrums Jülich, Energie & Umwelt / Energy & Environment 577, 99.

Thomas, S., Schüwer, D., Vondung, F., Wagner, O., 2022. Heizen ohne Öl und Gas bis 2035 – ein Sofortprogramm für erneuerbare Wärme und effiziente Gebäude. Im Auftrag von Greenpeace e.V. Greenpeace.

Volkova, A., Pieper, H., Koduvere, H., Lepiksaar, K., Siirde, A., 2021. Heat Pump Potential in the Baltic States.

Wang, X., Xia, L., Bales, C., Zhang, X., Copertaro, B., Pan, S., Wu, J., 2020. A systematic review of recent air source heat pump (ASHP) systems assisted by solar thermal, photovoltaic and photovoltaic/thermal sources. Renewable Energy 146, 2472–2487. https://doi.org/10.1016/j.renene.2019.08.096

Comparison of a Centralized with Decentralized Heat Pump Systems in a Multi-Family Building

Robert Haberl[1], Kanchan Bohara[1], Dr. Michele Zehnder[2] and Michel Y. Haller[1]

[1] SPF Institute for Solar Technology, Eastern Switzerland University of Applied Sciences (OST), Rapperswil (Switzerland)

[2] CTA AG, Münsingen (Switzerland)

Abstract

The goal of the project "HpCosy", from which the work presented here originates, is the development of decentralized heat pump systems, which are to be combined into a swarm for the optimal use of PV electricity. In order to be able to quantify the effects of this swarm control at a later stage, the first step was to compare one centralized with six decentralized heat pump systems in a multi-family home.

In a first step, the thermal load of the building was defined with the help of simulations using the program TRNSYS with its Type 56 building model. The internal load due to occupancy and user behavior as well as the domestic hot water profile is based on individual profiles generated with the program loadprofilegenerator. In the next step the heating system was calculated. These calculations were performed using a multidimensional performance model provided by the heat pump manufacturer. The calculation of the heat pump takes into account both the necessary compressor speed to cover the load and the required flow temperature depending on the outside temperature respectively the status of the storage tanks.

The calculations reveal an electric energy saving potential of more than 30% through the use of decentralized units for domestic hot water and space heating instead of central systems. The focus here is on domestic hot water circulation: The circulation required in multi-family home necessitates high setpoint temperatures in the storage tank. In addition, the ability to individually adjust setpoint temperatures for space heating also has a positive effect, as a single user cannot dictate inefficient operation for the entire building through high temperature demands.

Keywords: Heat pump, domestic hot water recirculation, space heating, energy savings.

1. Introduction

Heat pumps are a key technology for supplying buildings with domestic hot water (DHW) and space heating (SH). They will play a key role in an energy transition in which the geographical distribution of energy sources will increasingly be based on electrical energy. Hot water and the provision of cooling will become increasingly important due to better insulation of buildings, increased comfort requirements and, last but not least, advancing climate change. The obvious solution is to supply space heating, hot water and cooling with one device and, as much as possible, with locally produced PV electricity. In view of this development, the challenges facing system suppliers today no longer lie solely in the design and construction of a heat pump unit, but increasingly in system integration and control. What is needed are compact system solutions that are able to provide heating while at the same time reacting flexibly to the supply of photovoltaic electricity or to tariff incentives for load shifting (demand side management). In this paper, a comparison is made between flexible decentralized heat pump heating systems and a centralized solution for a multi-family home, in order to be able to compare the advantages and disadvantages without the influence of special control strategies.

© 2022. The Authors. Published by International Solar Energy Society
Selection and/or peer review under responsibility of Scientific Committee
doi:10.18086/eurosun.2022.08.04 Available at http://proceedings.ises.org

2. Procedure

2.1 Boundary conditions

A combination of building simulations using TRNSYS software and heat pump system calculations using spreadsheets was used to compare a centralized vs. decentralized heat pump systems in a multi-family home (MFH).

The modeling of the building was done with "Type 56" in the software TRNSYS(Klein et al, 2017; SPF-OST, 2021). It is a three-story renovated building consisting of six apartments: three on the east side and another three on the west side (Mojic et al., 2019). In the simulation model, the building is divided into eight thermal zones: six apartments, the basement, and the stairwell that connects to each apartment. Both, the internal loads of the apartments and the DHW demand are determined individually, with different occupant profiles. Details of the building and the load profiles are shown in Tab. 1. The occupant profiles are based on profiles from the tool loadprofilegenerator (Pflugradt, 2010). The naming of the profiles used is given in brackets.

The city of Zurich was used as the location of the building. The total heat demand of each apartment as the sum of SH at ideal heating with set temperature 21 °C and DHW can be seen in Fig. 1. In total, the heat demand adds up to 50 MWh for SH and 17 MWh for DHW.

Tab. 1: Details of the building and the residents.

	West	East
3. Floor	148.9 m^2 / 2 Persons (CHR55)[B]	167.8 m^2 / 4 Persons (CHR18)
2. Floor	148.9 m^2 / 4 Persons (CHR27)	167.8 m^2 / 2 Persons (CHS04)
1. Floor	148.9 m^2 / 2 Persons (CHR33)	167.8 m^2 / 4 Persons (CHR44)
Energy reference area	1'302 m^2	
Net floor area	1'103 m^2	
Specific heat demand	45 kWh/(m^2.a)	
Shape factor[A]	1.3	

[A] Shape factor = thermal envelope divided by energy reference area

[B] In brackets: Name of the household from the tool loadprofilegenerator.

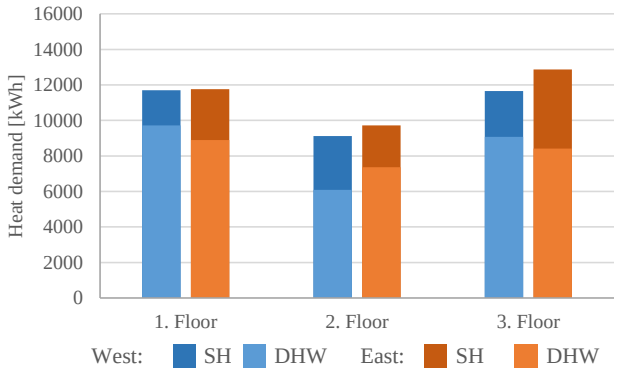

Fig. 1: Heat demand for SH and DHW per apartment.

2.2 Modelling and dimensioning of the heating systems

Centralized heating system

The main components of the centralized heating system are, in addition to the inverter-controlled 26 kW heat pump itself, two DHW tanks, each with a volume of 600 l, and a SH buffer tank with a capacity of 850 l. Fig. 2 shows the hydraulic scheme of the system. A central pump supplies the space heat distributor from which the individual apartment units are supplied. Each apartment is equipped with a room-temperature controlled thermostatic valve. An overflow valve is integrated into the heating circuit system to keep the pressure constant and prevent the pump from working against closed valves. The domestic hot water distribution is kept warm by hot-water (circulation).

It is worth mentioning that, in agreement with the Swiss standard SIA 385/1:2020 ("SIA 385/1: Anlagen für Trinkwarmwasser in Gebäuden - Grundlagen und Anforderungen," 2020), the hot water recirculation is calculated with 60/55 °C in flow and return, with the corresponding effects on the set temperature in the DHW storage tank. Because of temperature limitations of the heat pump, part of the heat must be supplied directly electrically by an electric heating element in order to reach the required 60 °C. The flow and return setpoint temperatures for space heating at reference conditions are 35/30 °C. The actual flow temperature set point for each hour of the heating season is calculated based on a heating curve that takes into account the ambient outside air temperature. Additionally, 2 K have been added to the central supply flow temperature setpoint in order to compensate for losses.

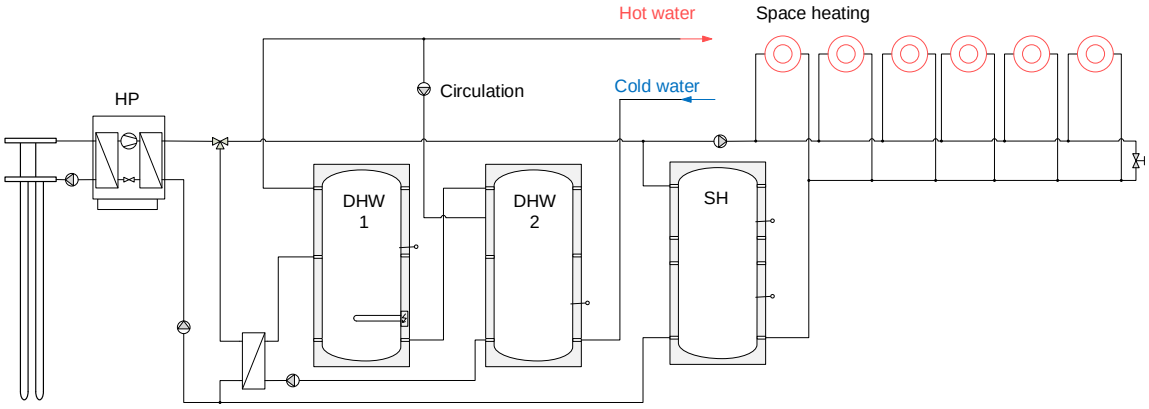

Fig. 2: Hydraulic scheme of the centralized heating system.

The dimensioning of the heat pump for the central heating system was based on the heat demand of the building described above. The aim of the design was a model that can cover the heat demand with 2500 full load hours. The total space heating demand (including losses) in the building is about 58 MWh. Considering the full load hours of 2500 for the heat pump operation, the heat pump capacity is 23.1 kW. The Optiheat Inverta 17e model from CTA AG with an output of 25.6 kW at a compressor speed of 70 rps was selected as the basis for the calculations. The COP of this HP as a function of the condenser outlet temperature and the compressor speed is shown in Fig. 4 on the left.

Decentralized systems

The decentralized systems were modeled as compact units with integrated DHW storage tanks (220 l) and direct connection to space heating without a SH buffer tank. The set temperature in the DHW tank is 55°C (SIA 385/1:2020 for systems without DHW recirculation), which can be achieved by the heat pump without the use of an electric heating element; the space heating curve can be set individually in each unit according to the preferences of the occupants and the heat loss rate of the apartment, which is higher for apartments just under the roof or in contact with the basement.

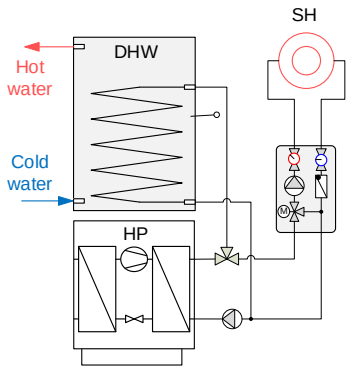

Fig. 3: Hydraulic scheme of a single decentralized unit.

The parameterization of the heat pumps, that determines the heating capacity and electric power consumption, was done according to the Optiheat Inverta 4esr TWW model of the company CTA AG: The COP of this HP as a function of the condenser outlet temperature and the compressor speed is shown in Fig. 4 on the right.

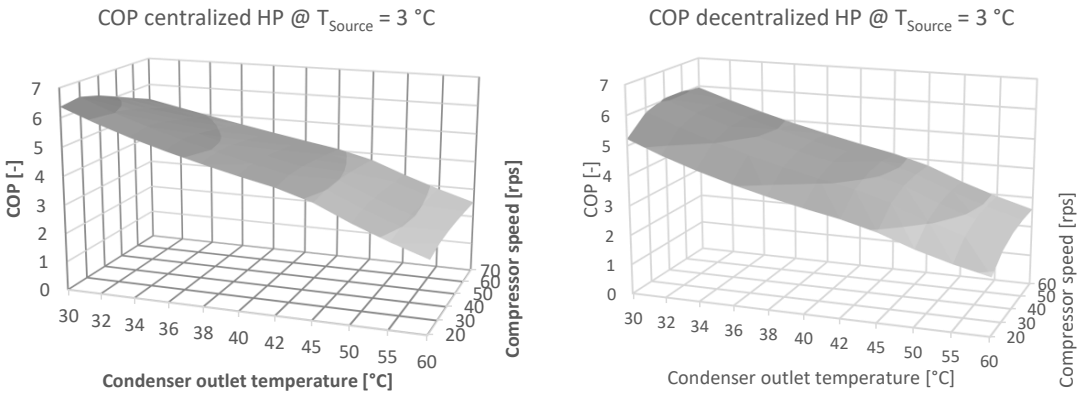

Fig. 4: COP of the central HP (left) and the decentralized HPs on the right as a function of condenser outlet temperature and compressor speed.

2.3 Variation of room set temperatures

A significant advantage of the decentralized systems is that different comfort requirements of the residents can also be served precisely. For example, a higher room temperature setpoint for one of the apartments on the upper floor does not lead to a general increase in the heating circuit flow temperature, since the other apartments can be served independently. Accordingly, it can be expected that the advantage of the decentralized systems will come into effect primarily when the demands on the room setpoint temperatures in the individual apartments differ significantly.

To investigate the influence of the room setpoint temperatures on the results, Monte Carlo simulations were performed in which different setpoint temperatures for the individual apartments were randomly assumed in the range 21 - 25 °C (in one-degree increments).

As described, the heating curve in the decentralized units was adjusted to the respective demand or the desired temperature, whereas the flow temperature supplied by the central system is determined by the apartment with the highest room setpoint temperature.

3. Results

3.1 Comparison with Identical Room Temperature Setpoints

Heat balance

The heat balance of the different versions is shown in Fig. 5. The total heat demand for SH and DHW is identical. The variants differ only in the heat losses via the storage tanks and the distribution and/or circulation:

Considering the DHW storage losses, two factors in particular have an influence. The six storage tanks together have a larger surface area than the two central storage tanks at a very similar storage volume. This fact leads to an increase of the DHW storage losses of the decentralized units. The temperature difference between the storage tanks and the environment speaks in favor of the smaller decentralized storage tanks: first, the temperature set point of the decentralized storage tanks is lower than in the central storage tanks, and second, they are located in a warmer environment. In the apartments the room temperature is 21°C, in the installation site of the central system a temperature of 15°C was assumed. In total, the heat losses of the six small DHW tanks are slightly higher than those of the two DHW tanks from the centralized system.

In addition to the storage losses, there are thermal losses in the decentralized system due to the pipes for distribution and circulation that are kept warm. With 4650 kWh, these losses are approx. 70 % higher than the storage losses.

The difference in the SH part is comparatively low. The storage tank losses of the buffer tank, that are small due to the small temperature difference to the ambient, and the losses for distribution of heat to the apartments amounts to approximately 3% of the heat demand. The decentralized systems have no losses at all, since they do not have a space heat storage and heat transfer from the pipes to the surrounding contributes to the heat the apartment and is therefore not lost.

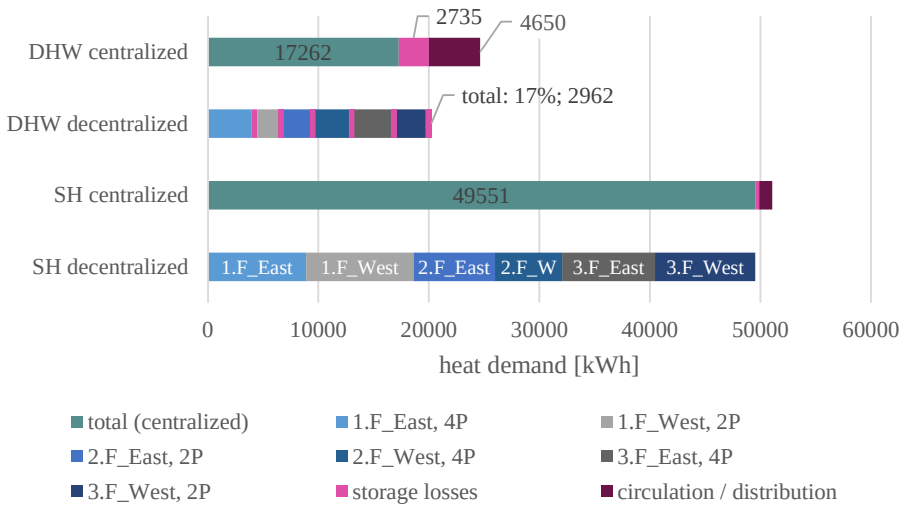

Fig. 5: Heat balance of the centralized / decentralized variants.

Electricity demand

Fig. 6 shows the total electric energy demand and the extra electric energy use that is needed for covering losses and inefficiencies (e.g. reduced COP of the heat pump or the use of electric heating elements instead of the heat pump at higher temperatures) for the centralized as well as for the decentralized system.

With a target room temperature of 21 °C in each apartment, the decentralized systems could save 12 % of the electrical energy used for space heating. Looking at DHW preparation only, the total electricity savings of the decentralized systems compared to the centralized is 53 %, which is a result of lower temperature setpoint requirement for storage tanks of decentralized systems without recirculation (55 °C vs. 60 °C), and spared losses of the recirculation itself.

The total saving of electric energy in the presented case is 28 %.



Fig. 6: Electricity demand to cover SH and DHW and the respective extra-electricity for covering losses and inefficiencies, for a centralized heating system compared to 6 decentralized systems.

Performance factors

The seasonal performance factors were calculated for different subsectors: for DHW, SH and for the total heat demand. In the case of the central system, Fig. 7 also lists the PF to cover the various losses. This illustrates above all the influence of the high temperature requirements of the circulation, which must be covered for the most part by heat provided directly electrically (supply 60 °C, return 55 °C).

The resulting SPF of the decentralized system is finally 4.0, while the decentralized systems each achieve an SPF of approximately 5.

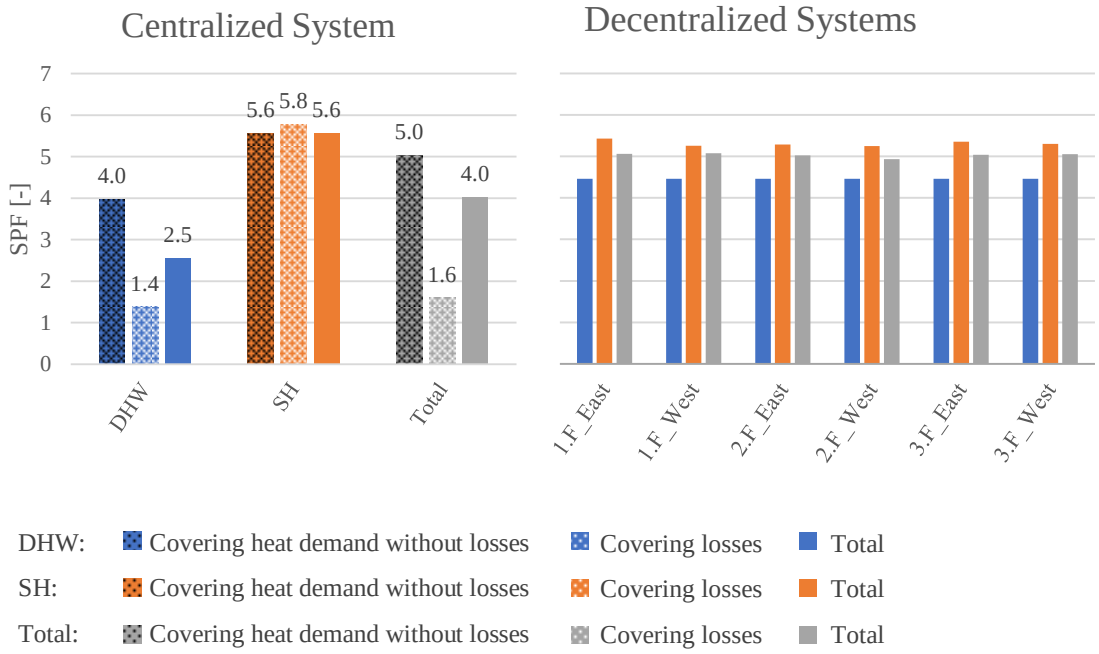

Fig. 7: Overall SPFs of the centralized and decentralized systems

3.2 Comparison with Individual Room Temperatures

As described above, a variation of randomly selected room set temperatures was calculated to investigate the influence on the overall systems. Fig. 8 gives an overview on the room temperature setpoints (in the graphic on top) and the achieved savings in electric energy in total (middle) as well as the difference in subsectors (bottom).

- The total savings differ between 25% and 31%.
- The lowest savings compared to the central system are achieved in the case where the majority of apartments request a high set point temperature in the apartment units (Tset2).
- The highest savings in percentage can be seen in the case, where the maximum set temperature in a single apartment is 23 °C.
- The highest savings in total (kWh) can be seen in the case with the largest difference between the maximum and the median set temperature (Tset1).

The difference in electricity consumption for DHW preparation is naturally very small, since the variation has no effect on the load to be covered. Nevertheless, there is a small difference to be seen. That is due to the influence of thermal losses: the higher the room set temperature, the lower the thermal losses of the distributed storage tanks. Since the storage losses were considered as passive gains in the apartment, this also changes the heat demand to be covered for space heating. Of course, the different room setpoint temperatures and also the interaction between the zones play a disproportionately larger role.

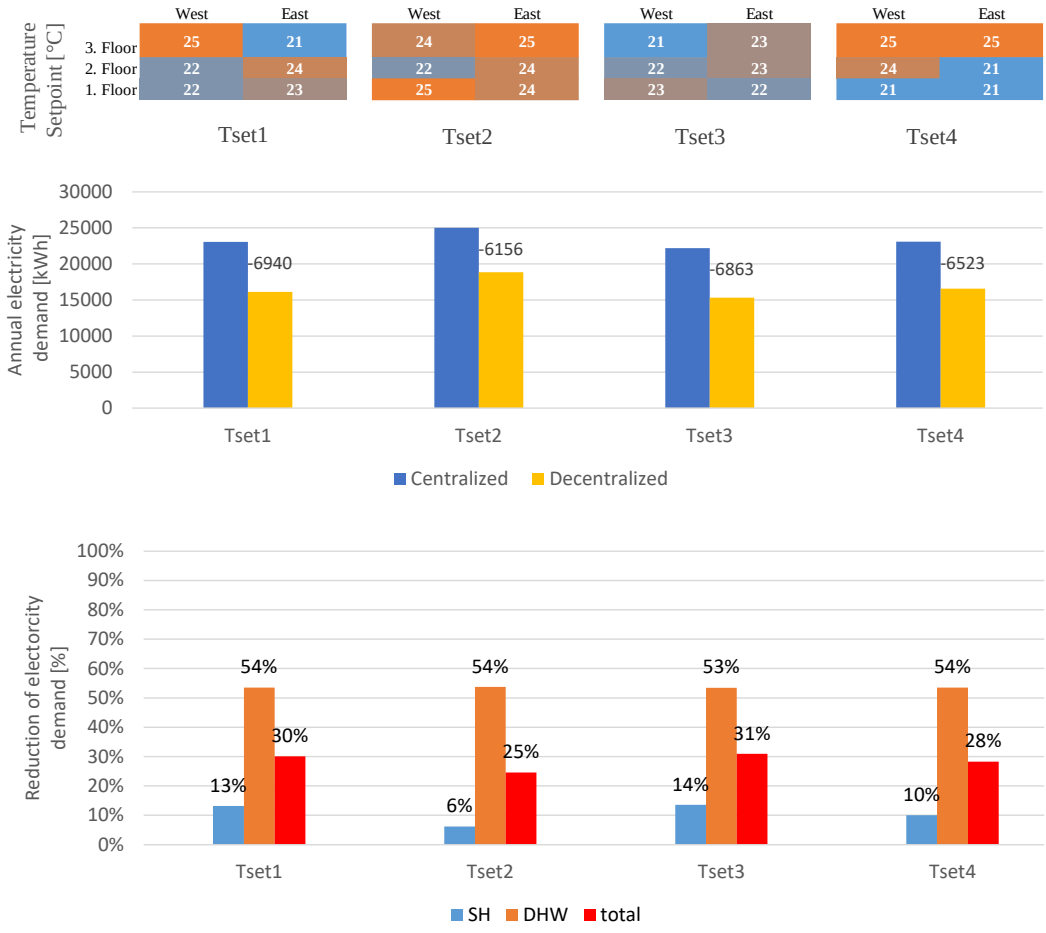

Fig. 8: Set temperatures in the apartments and the achieved savings in electric energy.

4. Summary

The comparison between a centralized and several decentralized heat pump systems clearly shows great advantages of the decentralized solutions, even in a purely demand controlled operation without taking PV electricity or swarm control into account.

The savings in the base case with a room set temperature of 21 °C are 28 % in electric energy. The variation of room set temperatures revealed that the savings could increase up to 31 % when only one of the apartments demands a high room temperature. However, the largest share of the energy saved is due to the elimination of DHW circulation.

5. Outlook

In a next step, the possibilities of a swarm control of the decentralized units will be investigated with the aim of using PV electricity as efficiently as possible. Here, too, various advantages of the decentralized solution are expected:

- The individual, power-controlled systems allow precise and finely graduated adjustment to the current PV yield.
- The individual hot water tanks are not subject to the restrictions of circulation with its high flow temperature, which must be guaranteed at all times. This means the timing of recharging can be coordinated with the availability of PV electricity.
- The individual systems allow individual decisions regarding the comfort criteria for room temperatures. In this way, it may be possible to better exploit the potential for storing heat in the thermal capacitance of the hydronic floor heating systems.

6. Acknowledgement

The authors would like to thank the Swiss Federal Office of Energy for supporting the project "HpCosy - Heat Pump Comfort System" under contract number SI/502088-01, the partners of the institute INEB at the University of Applied Sciences and Arts Northwestern Switzerland and the industry partner from the company CTA AG.

7. References

Klein et al, S.A., 2017. TRNSYS 18: A Transient System Simulation Program, Solar Energy Laboratory, University of Wisconsin, Madison, USA [WWW Document]. URL http://sel.me.wisc.edu/trnsys/

Mojic, I., Crameri, S., Caflisch, M., Carbonell, D., Haller, M., 2019. Reference Framework for Building and System Simulations: Multifamily Reference Building.

Pflugradt, N., 2010. Load Profile Generator Version 1.3.5. Prof. Technische Thermodynamik, Germany, Chemnitz.

SIA 385/1: Anlagen für Trinkwarmwasser in Gebäuden - Grundlagen und Anforderungen, 2020.

SPF-OST, S.I. for S., 2021. SPF-OST/pytrnsys_gui.

Increasing PV self-consumption with heat pumps – sense or non-sense of additional electric heaters

Michel Y. Haller[1], Andreas Heinz[2]

[1] SPF Institute for Solar Technology, Eastern Switzerland University of Applied Sciences (OST), 8640 Rapperswil (Switzerland)

[2] Institute of Thermal Engineering (IWT), Graz University of Technology, 8010 Graz (Austria)

Abstract

Hot water and space heating are increasingly being provided by photovoltaics in combination with heat pumps. In most cases, end user purchase tariffs for electric energy are significantly higher than feed-in tariffs for photovoltaic electricity. Therefore, increasing self-consumption of locally produced photovoltaic electricity makes economically sense, if a corresponding reduction of electric energy consumed from the grid can be achieved. At the same time, the self-consumption measures must not lead to a too high increase in system energy consumption, which also causes a strong reduction of PV feed-in. In this contribution it is shown that the optimization of thermal storage management by the heat pump is advantageous, while the use of electric heaters in order to heat the storage further when the heat pump has reached its maximum supply temperature generally leads not only to energetic inefficiency, but also to a financial loss for the end user or owner of the system.

Keywords: Heat pump, domestic hot water, space heating, PV self-consumption, control, thermal storage

1. Introduction

With a change from cost-covering feed-in tariffs for photovoltaics (PV) to one-time subsidies and feed-in tariffs that are lower than the tariffs for electricity that is consumed from the grid, the optimization of self-consumption of PV electricity has become economically interesting. Domestic hot water (DHW) and space heating are increasingly being provided by photovoltaics in combination with heat pumps (HP). In combination with thermal storage for DHW only or for storage of DHW and space heat in so called stratified combi-tanks, optimal control for charging of these storages in order to achieve higher PV self-consumption and thereby less cost for electric energy that is purchased from the grid is an attractive and low-cost solution for the optimization of self-consumption.

PV-coupled residential HP systems and measures for increasing PV self-consumption have been analyzed by several authors during recent years. Battaglia et al. (2017) analyzed the potential for increasing the self-sufficiency by overheating a thermal energy storage (TES) with a PV-coupled air-source HP system in a simulation study for a single family house, reporting savings in grid electricity consumption of 11 % using a water TES. PV-coupled air-source HP systems in renovated single family buildings coupled with a radiator heating system were analyzed by Heinz and Rieberer (2021), using different rule-based control strategies for increasing the self-sufficiency. Thür et al. (2018) studied a PV-coupled ground-source HP and used thermally activated building systems and water TES together with a rule-based control. Toradmal et al. (2018) also used the thermal mass of the building and a water TES both for PV-coupled air- and ground-source HPs. The results of these two studies showed that the building itself can offer significant thermal storage capacity, avoiding an additional large TES. An additional possibility for significantly increasing self-consumption in PV-HP systems is to use a battery. This was also demonstrated in the above mentioned publications by Toradmal et al. (2018) and Battaglia et al. (2017). However, both studies state that a water TES is economically beneficial compared to batteries, which are significantly more expensive.

It is important to note that energy storage comes along with energetic losses, and for the case of thermal storage with HPs, increasing the temperature of the thermal storage decreases the efficiency of the HP that is charging the storage. Thus, because of losses and inefficiencies of storage, the reduction of electric energy consumption from the grid is often quite lower than the increase of PV self-consumption and corresponding reduction of feed-in

© 2022. The Authors. Published by International Solar Energy Society
Selection and/or peer review under responsibility of Scientific Committee
doi:10.18086/eurosun.2022.08.05 Available at http://proceedings.ises.org

suggests.

Assuming self-consumption optimization that can be achieved by control only, for which no additional investment cost has to be accounted for, increasing self-consumption is only financially of interest if the net-cost of energy exchanged with the grid (NC, €/a) can be reduced:

$$NC = GC \cdot GT - PVF \cdot FT \qquad \text{(Eq. 1)}$$

where GC (kWh/a) is the annual consumption of electricity from the grid, GT (€/kWh) is the tariff for electricity consumed from the grid, PVF (kWh/a) is the locally produced electricity fed into the grid, and FT (€/kWh) is the corresponding feed-in tariff. (Eq. 2) shows the condition that must be met in order to reduce NC and to benefit financially from an increase of PV self-consumption. From this equation, it can be deduced that if the ratio of grid-tariff to feed-in-tariff is 2:1 (e.g. GT = 0.2 €/kWh, FT = 0.1 €/kWh), an increase of self-consumption is only economically interesting if the ratio of decrease of grid feed-in (ΔPVF, equals increase of self-consumption) to the decrease of consumption from the grid is lower than 2:1:

$$\frac{\Delta PVF}{\Delta GC} < \frac{GT}{FT} \qquad \text{(Eq. 2)}$$

2. Procedure

This study was carried out for two types of systems, both based on an air-to-water HP. On the one hand, a DHW-only system was considered and, on the other hand, a combi-system for DHW preparation and space heating. The most important assumptions concerning the two systems and the used boundary conditions are described in the following sections.

2.1 Domestic hot water system

System layout and simulation tool

Domestic hot water systems with PV, HP and electric heater were simulated with an own developed code written in python. Figure 1 shows the relevant components and the hydraulic layout of the considered system, that contains a DHW storage tank that is charged via a heat exchanger and discharged directly, an air source HP, a PV field, household electricity consumption and a connection to the electricity grid. The developed python code calculates energy transfers and temperatures of the relevant system components based on quarter hourly timesteps for one year based on simplified efficiency assumptions that allow for fast calculation of a whole year within a few seconds. Different sizes have been assumed for the PV system that is always oriented south with an inclination of 45°. PV yield (AC) was calculated based on the total irradiance on the collector plane and an average efficiency of 17% for the PV modules, losses for cables, soiling etc. of 7% and inverter efficiency of 94%.

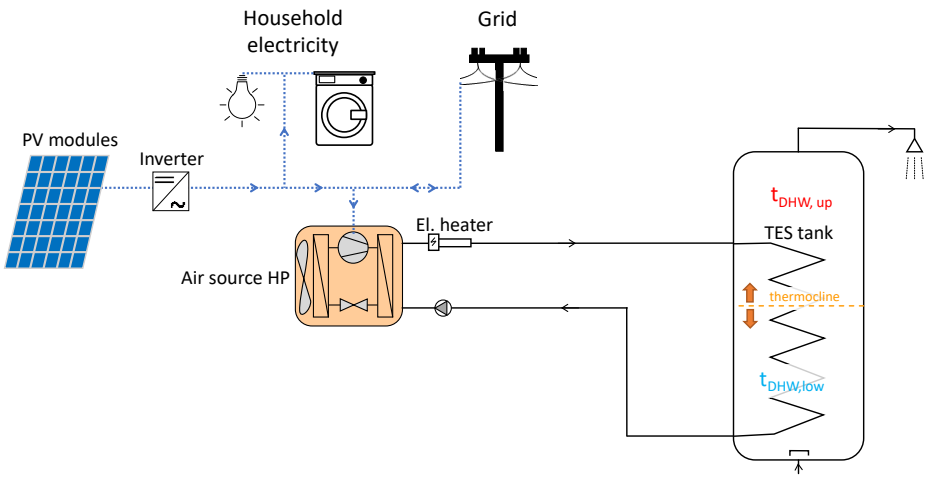

Figure 1: Hydraulic layout of the considered DHW system setup.

Heat pump model

The COP of the HP is calculated as a fraction ($\eta_{hp} = 0.45$) of the carnot efficiency (maximum possible efficiency) of a cycle, using the assumed evaporation (t_{evap}) and condensation (t_{cond}) temperatures of the working fluid:

$$COP_{hp} = \eta_{hp} \cdot \frac{t_{cond} + 273\ K}{\max(t_{cond} - t_{evap},\ \Delta t_{min})} \qquad \text{(Eq. 3)}$$

In order to avoid unrealistically low differences between the evaporation and the condensation temperature ($t_{cond} - t_{evap}$) a minimum temperature difference of $\Delta t_{min} = 5K$ was introduced. Evaporation and condensation temperatures differ from the temperatures of the heat source and the heat sink by the temperature difference needed for heat transfer through the heat exchanger, which was represented by ($\Delta t_{hp,hx} = 5K$). Due to reasons of simplicity, the same value was used here for the evaporator and for the condenser:

$$t_{cond} = t_{c,wat,in} + \Delta t_{hp,hx} \qquad \text{(Eq. 4)}$$

$$t_{evap} = t_{e,air,in} - \Delta t_{hp,hx} \qquad \text{(Eq. 5)}$$

In the case of the condenser, the inlet temperature $t_{c,wat,in}$ is again higher than the temperature in the DHW storage while charging because of the heat exchanger that transfers heat from the condenser water loop to the DHW of the storage tank ($\Delta t_{TES,hx}$ = 5 K):

$$t_{c,wat,in} = t_{TES,charge} + \Delta t_{TES,hx} \qquad \text{(Eq. 6)}$$

The temperature $t_{TES,charge}$ is taken as the average of the corresponding TES zone(s) over the timestep of charging. Nominal capacity of the HP ($Q_{hp,nom}$) was assumed to be 10 kW and not varied (no power modulation and no dependency on temperatures).

TES model

The thermal storage tank is simulated as a two-zone model with sharp thermocline. Hence there is only two volume elements and corresponding temperatures in the tank. During HP charging, it is assumed that first the lower volume ($t_{DHW,low}$) is heated until it reaches the upper volume's temperature ($t_{DHW,up}$), and then both volumes are heated uniformly to the required set temperature. Discharging is carried out by volume displacement, i.e. the upper volume of the TES decreases and the lower increases by an amount that leads to the discharged energy that corresponds to the DHW tapping profile. This kind of discharge simulation corresponds to a perfectly stratifying discharge process. Consequently, inefficiencies due to fluid mixing in the tank are not simulated directly, but included in the term $\Delta t_{TES,hx}$ that is used to express the increase in HP delivery temperatures caused by heat exchange AND ineffiencies due to unperfect temperature stratification as a lumped factor.

Electric heater

The electric heater is assumed to have a maximum power of $P_{elrod,max} = 5\ kW$ and is power modulating, i.e. it will never consume more electricity than would be fed to the grid if the heater was not switched on:

$$P_{elrod} = \min(\max(P_{el,PV,ac} - P_{el,hh}, 0), P_{elrod,max}) \qquad \text{(Eq. 7)}$$

Additionally, the electric heater operation was limited to times after 2 p.m., i.e. after the time-window for TES charging by the HP.

Boundary conditions

The climate used for the simulation was based on weather data from Zurich, a test reference year developed by SPF (CCT climatic data described in Haller et al. 2013), with an annual average of the outdoor temperature of 9.1 °C and solar radiation of 1111 kWh/(m²a) on the horizontal.

The tap profile for DHW as well as the household electricity demand was based on the reference multifamily building profiles described by Mojic et al. (2019), that are based on the software LoadProfileGenerator V.8 (Pflugrath 2016, https://www.loadprofilegenerator.de). For a single household, the total DHW consumption and household electricity of the multifamily building with six apartments was divided by six, leading to an annual consumption of 2'935 kWh/a for DHW (heat) and of 3'288 kWh/a for household electricity.

Control

The HP was set to charge the storage after midday from noon to 2 p.m. to 55 °C. Additionally, if the TES volume above the thermocline was lower than a threshold needed for supplying a quarter hour peak demand (maximum quarter hourly demand of the year), then the HP was allowed to recharge the TES also outside the given time window up to a level that allows for serving the quarter hourly demand at all times. The electric heater was run exclusively with PV electricity and only after 14:00 (i.e. after the time window of HP charging) and up to a temperature of 60 °C. Other maximum temperatures for electric heater charging were tested but did not lead to significantly different results (i.e. only to results that are worse than the one shown from an economic point of view). For this reason, results with other end-temperatures for the electric heater are not shown for the DHW system.

2.2 Combi-system for space heating and DHW

System layout and simulation tool

For the analysis of the combi-system, a detailed TRNSYS system model was used. The model was established in previous work and described in more detail in (Heinz et al., 2020) and (Heinz and Rieberer, 2021).

The considered system consists of an air-to-water HP with speed-controlled compressor, a thermal energy storage (TES), a so-called combi-tank, a PV-system and an electric heater in the flow line of the HP, as shown Figure 2. The HP is connected to the TES, which was considered with two different volumes of 0.5 and 1 m³. The heat losses of the TES were assumed with efficiency class B according to (EC, 2013). Using three-way-valves, the HP can charge either the DHW zone of the TES via the two connections on the top or the space heating zone via the lower connections. The TES is connected to the HP in parallel to the space heating system. This means, when the store is being charged for space heating by the HP, some of the flow will go via the space heating distribution loop and the rest will go through the store. The proportions depend on the current operating conditions (current flow) of the space heating loop. DHW preparation is done via a freshwater station (external plate heat exchanger) to a temperature of 45 °C. The PV system is considered in three different sizes (4, 7 and 10 kWp), oriented to the south and with an inclination of 45°.

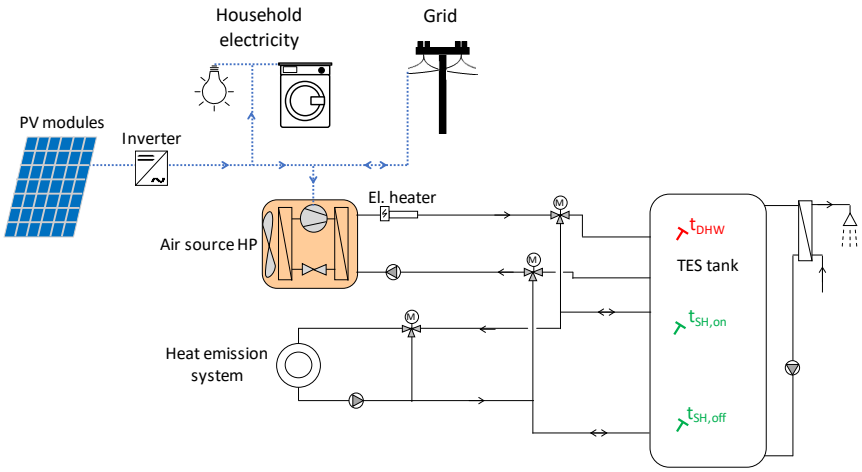

Figure 2: Hydraulic layout of the considered combi-system for space heating and DHW.

Boundary conditions

The system was implemented in a single family residential building with a gross floor area of 185 m², based on the statistical average living space per person in Austria of 45.3 m² per person (Statista, 2020) and a four-person-household. The wall structures were chosen on the basis of Austrian building typologies that were defined in the European project TABULA (2014). The basis was a “usual renovation“ scenario of a building with the according wall structures, as defined in TABULA for the age class 1961-1980. Using this data, a detailed building model with one thermal zone was developed in TRNSYS Type 56. The resulting space heating demand is 10’700 kWh/a in the climate of Zurich, with an annual average of the outdoor temperature of 9.1 °C, heating degree days of

3'553 Kd/a and solar radiation of 1'111 kWh/(m²a) on the horizontal. The heat emission system was considered in two variants, on the one hand radiators with design flow/return temperatures of 56/48 °C, and on the other hand a floor heating system (design flow/return 35/30 °C).

The tap profile for DHW was taken from the FP7 project MacSheep, with details described in (Bales et al., 2015). A realistic DHW profile was chosen with a two-minute time step with many variations in flow rates. The profile was derived for a family of four people with the software DHWcalc (Jordan and Vajen, 2012), which is based on the theory described in (Weiss, 2003). It uses statistical probabilities of different types of discharge and their flow rates and duration. The total heat demand for DHW of the used profile is 3'038 kWh/a.

For the household electricity a detailed annual profile with a time resolution of one minute was created for a four-person-household (both parents employed, two school-aged children) with the software LoadProfileGenerator (Pflugrath 2016, https://www.loadprofilegenerator.de). This profile has a total electricity consumption of 3'058 kWh/a.

Control

Normal charging with the HP: If there is no (or not enough) PV excess yield (as described in the next paragraph), the HP begins to charge the DHW zone of the TES if $t_{DHW} < 45$ °C (sensor position in Figure 2) and stops, when $t_{DHW} > 55$ °C. The DHW zone is charged only in a time window from 12:00 to 14:00, in order to shift HP charging into times of available PV electricity. In order to ensure comfort, an "emergency charging" is started if t_{DHW} drops below 40 °C outside of the foreseen time window. The space heating zone is charged, if $t_{SH,on} < t_{fl}$ and stopped when $t_{SH,off} > t_{fl} + 2$ K, where t_{fl} is the set space heating flow temperature depending on the ambient temperature. During DHW charging, the compressor is operated constantly with 75 % of the maximum speed. In space heating operation, the compressor speed is adapted via a PI-controller in order to reach the set flow temperature t_{fl} at the outlet of the condenser.

Overcharging with the HP: Whenever the available PV excess yield is higher than 0.7 kW, the system is switched to "overcharging mode". This means that the DHW zone and the space heating zone (only within the heating season) of the TES are both heated to higher set temperatures. Due to the operational limits of the used compressor, overheating is done dependent on the ambient temperature to max. 60 °C when $t_{amb} > 5$ °C and to 56 °C at $t_{amb} \leq 5$ °C. Overcharging is stopped when either the TES temperature reaches this temperature limit or PV excess drops below a threshold of 0.6 kW. During overcharging, the speed of the compressor is adapted in order to match the electricity consumption of the HP to the available PV excess electricity (considering the speed limitations of the used compressor). The aim is to make maximum use of the PV yield and to draw as little energy as possible from the grid.

Overcharging with the electric heater: In case of enough available PV excess yield (as described in the last paragraph) the maximum temperature that can be achieved by overcharging with the HP is limited. In this case, the electric heater can be used for additional overheating to higher temperatures. It is assumed to be operated only if the TES has already been heated to the max. possible temperature by the HP. The lower part of the storage (space heating zone) is only overcharged with the electric heater during the heating season. In order to study the effect on the results, additional overcharging was done to different max. temperature levels of 65, 75 and 85 °C. In addition, to limit the overheating by the electric heater to a reasonable temperature level based on the demand, a simple predictive control was implemented in the simulation. The aim here was to overheat only in order to be able to bridge the next night without having to activate the HP. For this purpose, an (ideal) forecast of the outdoor temperature for the period from 18:00 to 6:00 of the next night was used. This variant is referred to as demand oriented overheating "t_{opt}" in section 3.2.

2.3 Key performance indicators

Self-consumption ratio ($E_{PV,self}/E_{PV}$, -) and degree of self-sufficiency ($SS = E_{PV,self}/E_{total}$, -) are often used as key performance indicators for PV self-consumption strategies. However, SC and SS are not suitable for system optimization since they tend to optimize towards inefficient systems. For this reason, neither SC nor SS will be used in this contribution, but the share of grid consumption (SGC) will be used instead:

$$SGC = (E_{total} - E_{PV,self})/E_{total,ref} \quad \text{(Eq. 8)}$$

In this equation, $E_{total,ref}$ refers to the total electric consumption of the system without additional self-consumption measures, and E_{total} refers to the total electric consumption for the system under investigation, i.e. with the corresponding self-consumption measures.

In order to generalize the result and make them applicable to a wide range of systems, for the DHW system the size of the PV system is given as PV production ratio (PV_{ratio}):

$$PV_{ratio} = E_{PV}/E_{total} \quad \text{(Eq. 9)}$$

where E_{PV} (kWh) is the electric energy (AC) produced by the PV system.

3. Results

3.1 Domestic hot water systems

Figure 3 shows the reduction of the share of grid consumption (SGC) for a typical household with a standard DHW demand, depending on the size of the installed PV system. The red curve is valid for "systems without DHW HP" as well as for systems with a DHW HP that is allowed to charge randomly at any time of the day. It is to be noted that "systems without DHW HP" refers to systems where E_{total} as well as $E_{total,ref}$ includes only household electricity consumption, i.e. it excludes energy used for DHW or for space heating, whereas systems with DHW HP refers to systems where E_{total} as well as $E_{total,ref}$ includes electricity used for DHW preparation by a HP. Consequently, a particular point of the red curve, e.g. where PV_{ratio} = 1.0, corresponds to quite different values for E_{total} and as $E_{total,ref}$, depending on the question whether DHW preparation is included or not, and hence also the size of the PV system that corresponds to this PV_{ratio} is different for the two systems. Furthermore, the same set of curves can be used for a single home or for a multifamily building, since the size of the required PV system to reach a certain PV production ratio just scales with the size of the electricity demand of the object.

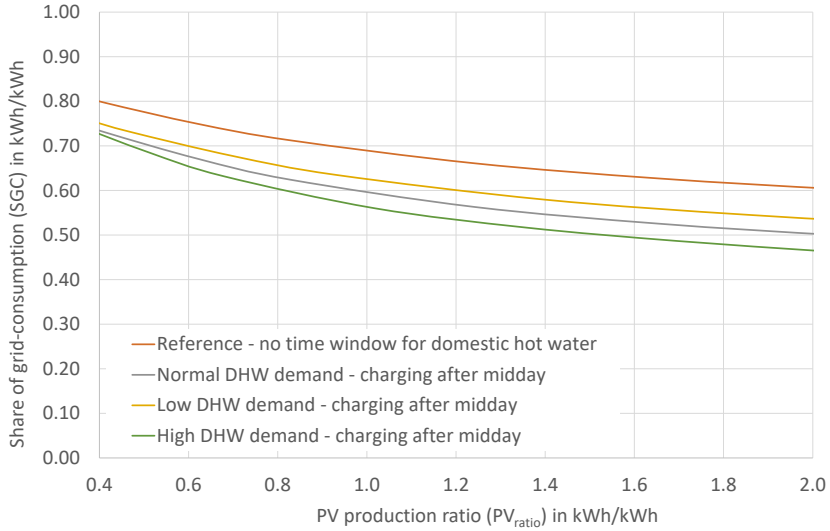

Figure 3: Share of total electric energy consumption covered by the grid as a function of the PV size (PV production ratio) for systems with different DHW demand and charging strategies.

The other curves are valid for normal (grey), low (yellow) or high (green) DHW demand in combination with a HP that is only allowed to charge the storage after midday, i.e. from 12:00 to 14:00. Low DHW demand was assumed to be 50% of the normal, high demand 200% of the normal DHW demand of 2'935 kWh/a for a single apartment or living unit. Also here, the same curves can be applied for single as well as for multi-family buildings, following the same rules as described above. If results are generalized in this way, then normal, low and high DHW demand correspond to a ratio of DHW demand ($Q_{DHW,dem}$) to household electricity consumption ($P_{el,hh}$) as shown in Table 1.

Table 1: General ratio of DHW demand and household electricity represented by the curves in Figure 3.

	DHW demand		
curve color	label	general ratio $Q_{DHW,dem}/P_{el,hh}$	$Q_{DHW,dem}$ for given example
grey	normal	0.89	2'935 kWh/a
yellow	low	0.45	1'468 kWh/a
green	high	1.78	5'870 kWh/a

Results so far have not included the use of an electric heater in order to charge more energy into the DHW storage, and thereby increase PV self-consumption, after the HP has charged the storage (i.e. after 14:00 when the time window for HP charging ends) for cases where there is still a surplus of locally produced PV electricity available. Figure 4 shows the increase of PV self-consumption that is achieved for the investigated system by using an electric heater after 14:00 (i.e. after the time-window where the HP charges) in order to increase the storage tank temperature from 55 °C to 60 °C, for cases where the storage volume at 55 °C is able to cover 100% of the average daily heat demand. Obviously, this kind of control leads to a significant increase of PV self-consumption, i.e. also to an equal amount of reduction of PV electricity that is fed to the grid and reimbursed according to the feed-in tariff. With other words, there is a loss of income for the owner from the reduction of PV feed-in. The thinking behind this kind of control is that while the self-consumption increases, the amount of energy purchased from the grid decreases and thus there is a reduction of cost for energy purchased from the grid that compensates for the loss of income from feeding in.

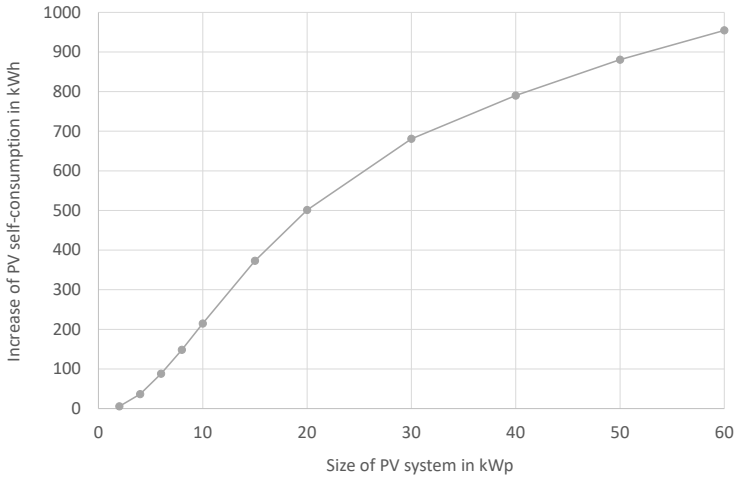

Figure 4: Increase of PV self-consumption achieved by heating the storage from 55 °C to 60 °C with an electric heater after HP charging (i.e. after 14:00), whenever sufficient PV electricity is available, for storage sizes that covers 100% of the average daily DHW demand when heated at 55 °C.

Figure 5 shows for different sizes of storage volumes (different colors) and different sizes of PV systems (size of PV system increases from left to right for each set of values) the reduction of electricity that is purchased from the grid (y-axis) together with the reduction PV energy fed into the grid (equals increase of self-consumption). Strikingly, for all data points the achieved reduction of grid purchase differs substantially from the increase in self consumption or decrease of feed-in, with reduction of feed-in generally being 3.5 to 5 times higher than the corresponding reduction of grid purchase. This means that only if the ratio between the purchase tariff and the feed-in tariff is 3.5 to 5 or higher, an economic benefit can be achieved for this consumer or owner of the system.

A typical current situation in Switzerland is a ratio of tariffs of approximately 2:1 (e.g. 0.2 €/kWh for purchase and 0.1 €/kWh for feed-in). For this case, heating with an electric heater from 55 °C to 60 °C with PV electricity, after the HP has reached the required hygienic temperature of 55 °C, leads to financial losses. For a DHW storage that is sized to cover only 50% of the average daily DHW demand, i.e. the storage must be charged several times a day, the minimum ratio of tariffs above which the electric heater does not lead to a financial loss is between 3:1 and 4:1. If the DHW storage is sized to cover the average daily DHW demand (100%), the ratio must be higher than 5:1. With other words: if the purchase tariff is 0.2 €/kWh, feed-in tariff must be lower than 0.04 €/kWh before an economic advantage can possibly result from the electric heater.

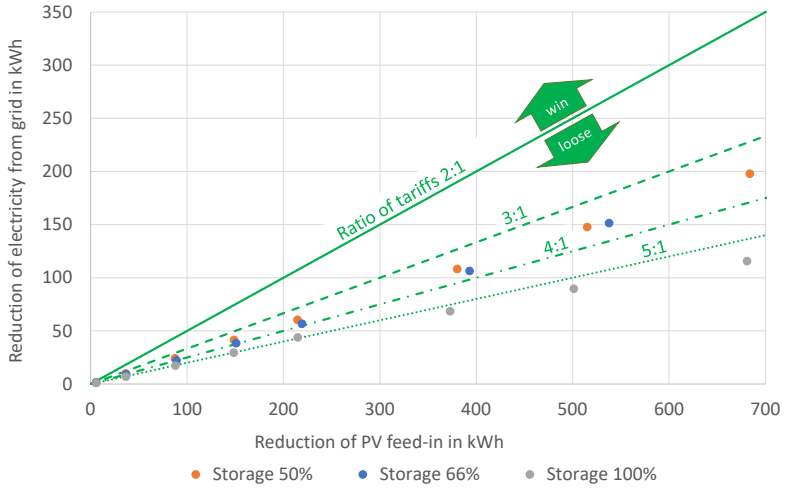

Figure 5: Reduction of electricity from the grid, depending on reduction of PV feed-in, achieved by heating the storage from 55 °C to 60 °C with an electric heater after HP charging (i.e. after 14:00), whenever sufficient PV electricity is available, for storage sizes that cover 50%, 66% or 100% of the average daily DHW demand.

3.2 Combi-system

For the combi-system, the results for the share of grid consumption (SGC) are shown for all simulated variants in Figure 6. As expected, SGC is decreasing with increasing PV size and increasing storage volume. Compared to the reference system (Ref), where overheating of the TES is only done with the HP, SGC can be improved (=decreased) by additional overcharging with the electric heater. The extent of the improvement depends on the available storage volume and the max. temperature to which the el. heater is allowed to overheat the TES. Higher temperatures allow a stronger decrease in grid consumption and, therefore, SGC. However, the reduction in SGC is only a few percent at most. For the system with a radiator heating system (Figure 6, right) the reduction is higher than for the floor heating system. This is due to the lower storage capacity available for overheating with the HP with higher space heating temperatures, which leads to higher savings in grid consumption if additional storage capacity is activated with the electric heater. Moreover, the difference in COP between heat provision by the HP and the electric heater (COP ~ 1) is lower for the radiator system due to higher heat sink temperatures.

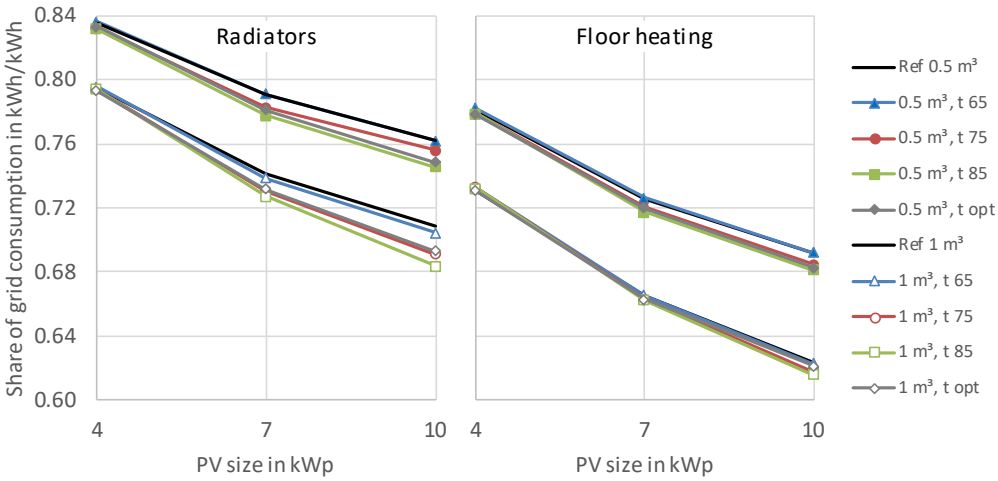

Figure 6: Share of grid consumption (SGC) as a function of the PV size for heating the TES from 60 °C to different max. temperatures (e.g. "t 75" means max. electrical overheating to 75 °C) with an electric heater after HP charging; storage sizes 0.5 and 1 m³, PV sizes 4, 7 and 10 kWp; "Ref" is the reference system without additional electric overheating.

Monthly and annual electric energy balances of three system variants with 7 kWp of PV, a TES volume of 1 m³ and the radiator heating system are shown in Figure 7. The top-most figure shows the reference system with overheating of the TES by the HP only. Here, there is also a very small amount of electric heating in the winter months, which is only due to the HP not being able to operate at very low ambient temperatures. If the electric

heater is used with max. overheating to 75 °C (Figure 7, centre), heat provision from the electric heater increases to 1'931 kWh. This increases the total el. consumption of the system from 5'697 kWh to 7'064 kWh. While the consumption from the grid decreases by only 59 kWh compared to the reference system, the feed-in of PV electricity decreases strongly by 1'426 kWh. It is quite obvious from the results in Figure 7 (centre) that with this strategy a lot of overheating occurs during the warmer transitional period. Here, a lot of PV yield is available, but on the other hand there is only a small heat demand.

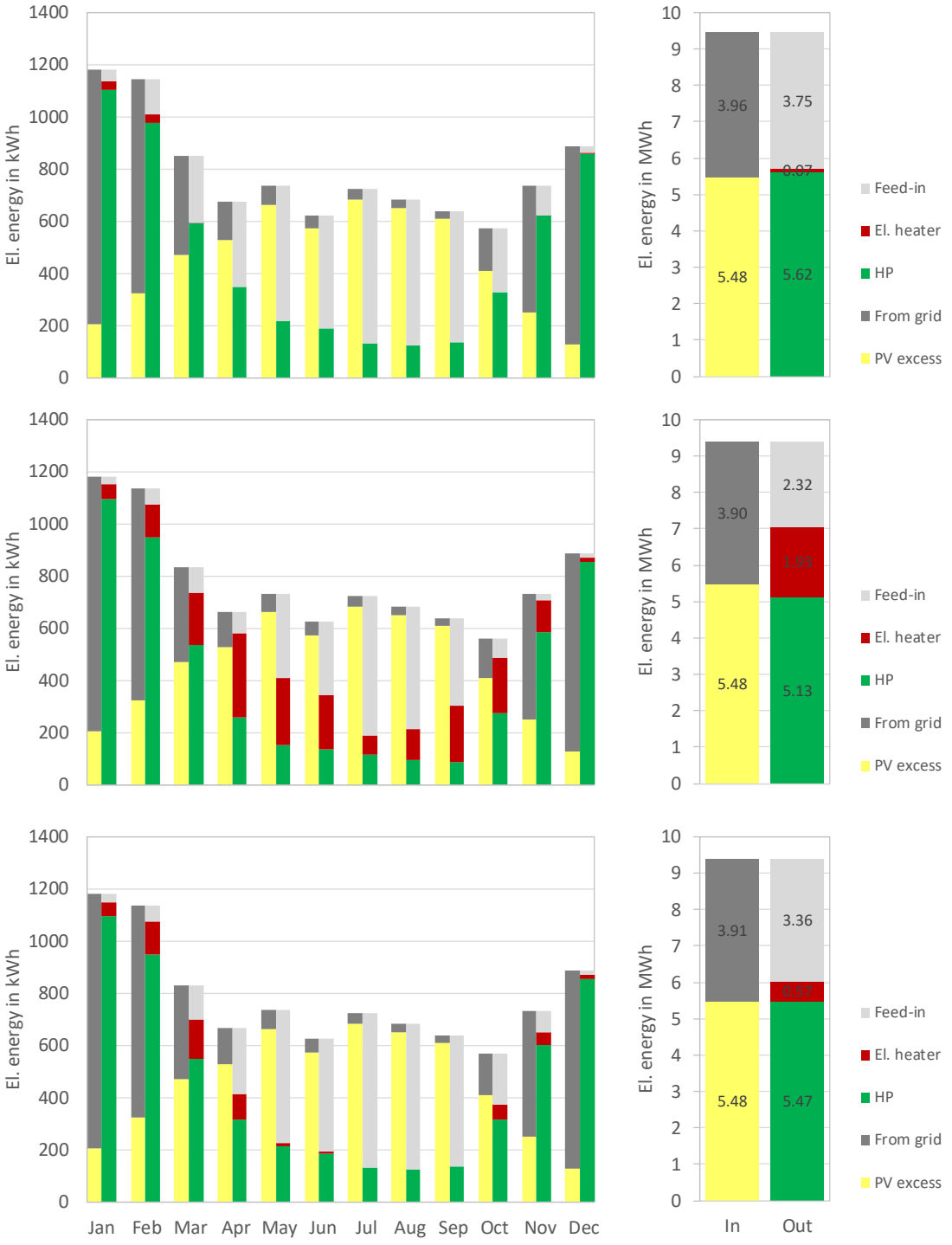

Figure 7: Monthly (left) and annual (right) energy balance of the combi-system with radiator heating system, 7 kWp of PV and a TES volume of 1 m³; Top: no additional overheating with electric heater (Ref); Centre: overheating to max. 75 °C; Bottom: demand oriented overheating ("t_{opt}")

Therefore, the demand oriented overheating strategy ("t_{opt}") was implemented (see section 2.2), with the results shown on the bottom of Figure 7. Using this strategy, heat provision by the electric heater is reduced mostly during the transitional period, where the heat demand is low. The consumption of the electric heater decreases to 573 kWh and the overall system consumption to 6'039 kWh. Compared to the reference system, overall grid consumption is reduced by 52 kWh and PV feed-in by 394 kWh. These results are more promising than with max. overheating to 75 °C. However, with a significantly higher reduction of the feed-in compared to the grid consumption, the question remains, if there can be an economic benefit compared to the reference system.

This is addressed in Figure 8, in the same way as before for the DHW-only system in section 3.1 (Figure 5). The results show, that, due to the strong increase in system electricity consumption and a very high reduction of feed-in, for most considered configurations the ratio of tariffs has to be higher than 20:1 in order to achieve a financial benefit compared to overcharging with the HP only. Some of the simulated configurations even show a slight increase in grid consumption of a few kWh. With a radiator heating system, the results are better than with a floor heating system (Figure 8, left vs. right) for the same reasons as discussed for Figure 7. The different max. temperatures used for the electric heater show a massive reduction of PV feed-in with increasing temperatures due to increased PV self-consumption and system electricity consumption. However, increasing the temperature can nevertheless lead to a better (but still bad) financial result (e.g. "t 65" vs. "t 75" in Figure 8 left). The best results of all variants with additional electric overheating are achieved with the demand-oriented optimized control ("t_{opt}"). However, e.g. with radiator heating, a TES volume of 1 m³ and 7 kWp of PV, still a tariff ratio of 7.5:1 or higher is necessary to achieve a financial benefit. Thus, considering current tariffs, no configuration could be found in which the additional use of electric heating could economically compete with using only the HP to optimize PV self-consumption.

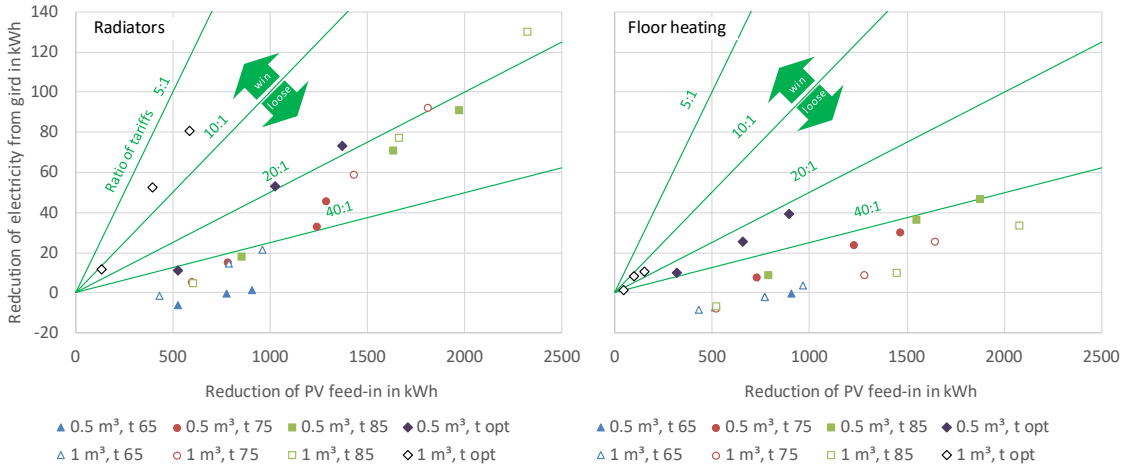

Figure 8: Reduction of electricity from the grid, depending on reduction of PV feed-in, achieved by heating the storage from 60 °C to different max. temperatures (e.g. "t 75" means max. electrical overheating to 75 °C) with an electric-heater after HP charging; storage sizes 0.5 and 1 m³, PV sizes 4, 7 and 10 kWp (PV size increases from left to right).

4. Summary and Outlook

Hot water and space heating are increasingly being provided by photovoltaics in combination with heat pumps. Due to PV feed-in tariffs being quite lower than the grid purchase tariffs of electricity in many countries or regions, an increase of PV self-consumption and decrease of grid purchase can be achieved by letting the heat pump operate more than usual and use PV electricity instead of feeding it to the grid. Since in this case the momentary heat generation is higher than the demand, heat is stored either in a technical thermal storage or in the thermal mass of the building itself. Thus, thermal storages reduce the need of electrochemical batteries that could be used with the same goal. When thermal storages are charged with a heat pump, the efficiency of the heat pump is generally decreasing with increasing state of charge, since condenser temperatures increase in parallel to the temperatures of the heat storage. However, despite this loss of efficiency, the use of thermal storage in combination with heat pumps to optimize self-consumption, when properly done, is of economic benefit and interest for the end-user. This has been shown e.g. by Battaglia et al. (2017), Thür et al. (2018), and Heinz and Rieberer (2021), and is also

confirmed by the work presented in this publication.

The simulations of the two systems that are presented in this article were carried out with two different simulation tools and different experts carrying out the simulations independently from each other. It has to be mentioned that the assumptions concerning the maximum temperature to which the heat pump is able to heat the storage (55 °C in the study for the DHW-only system and 60 °C in case of the combi-system) were different. This may have some influence on the results, but an adjustment of the assumptions would probably not change the basic statement and conclusions of this work. While some might criticize the approach of merging results from two different studies that were carried out independently, it may also be seen as an advantage, since it leads to more robust conclusions where they match between the two studies. Results are less prone to be influenced by specifics of a tool or a team or expert's influence on the settings and parameterizations used.

While the optimization of thermal storage management by the HP has been shown clearly to be advantageous already before, this work also presents results on the additional use of an electric heaters for increasing the PV self-consumption. The electric heater is used to heat DHW-only storages or combi-storages for DHW and space heating further, after the heat pump has charged the storage to the maximum temperature it is capable of, and locally produced PV electricity is still available in abundance. This mode of operation is tempting, since self-consumption of PV electricity can be increased substantially, which was confirmed by our results. However, results also show that while self-consumption increases, grid-purchase does not decrease nearly in the same way. For DHW systems the decrease of grid purchased energy stayed 3.5 to more than 5 times lower than the increase of PV self-consumption. For the combined DHW and space heating systems the ratio between increase of PV self-consumption and decrease of grid-consumption was more than 7.5 for systems with radiators for space heating, and more than 20 for most systems with low temperature floor heating. One of the reasons for this is the fact that the electric heater is, depending on the temperatures needed, 3-6 times less efficient than the heat pump. Thus, it is hardly imaginable that the ratios between the increase of PV self-consumed and the decrease of grid purchased energy is lower than 3, even if the electric heater consumes only PV electricity and the heat pump would have had to provide this heat exclusively using electricity from the grid. However, in many cases also the heat pump could have provided this heat – at a later time when storage temperatures have dropped again - using PV electricity. This is e.g. the case for a DHW storage tank that has been charged by the heat pump at mid-day and is then able to cover the demand of 24 hours if the next day is again a sunny day. In this case, the use of an electric heater after heat pump charging on day one does not lead to any reduction of grid purchased energy, but only to an increase of PV self-consumption. An increase of PV self-consumption is at the same time a decrease of PV feed-in by the same amount. If there would have been a financial reimbursement for the PV feed-in, the use of the electric heater is a financial loss for the owner, even if the heater and its control were for free. If additional CAPEX cost must be accounted for the electric heater and its control, the result will be even worse from an economic point of view.

Finally, it can be stated that for the current situation in Austria and Switzerland, where PV feed-in tariffs are in most cases about 2 to 3 times lower than the tariffs for grid purchase of electricity, the operation of an electric heater after heat pump operation that reaches the hygienic temperature, cannot be recommended due to its inefficiency and the resulting financial loss for the owner. Only when feed-in tariffs are 3.5 – 5 times lower (DHW system) or 7.5 – 20 times lower (combi-system) than the grid purchase tariffs, our results show a potential financial benefit for the owner. However, even in the unlikely cases where the owner could profit financially, the question must be raised whether this kind of inefficient use of PV electricity is beneficial from a socio-economic point of view, since there is likely more efficient and more meaningful use for this renewable energy in the neighborhood or in the country's energy system.

5. Acknowledgments

The work on DHW systems was carried out with financial support of the Swiss Federal Office of Energy (SFOE) contract SH8100380-01-01-18. The work concerning the combi-system was done within the project "HybridHeat4San", which was funded by the Austrian Climate and Energy Fund and carried out as part of the Energy Research Program 2016.

6. References

Bales, Chris, Stefano Poppi, Tomas Matuska, Jan Sedlar, Borivoj Sourek, Jiri Petrak, Andreas Heinz, and Franz Hengel. 2015. 'Deliverable 7.3 - Optimized Solar and Heat Pump Systems, Components and Dimensioning, FP7 Project MacSheep (Grant Agreement 282825)'. https://www.spf.ch/fileadmin/user_upload/macsheep/dokumente/MacSheep_D7-3_Simulations_M36_v150618_Final_revised.pdf.

Battaglia, Mattia, Robert Haberl, Evelyn Bamberger, and Michel Haller. 2017. 'Increased Self-Consumption and Grid Flexibility of PV and Heat Pump Systems with Thermal and Electrical Storage'. Energy Procedia 135 (October): 358–66. https://doi.org/10.1016/j.egypro.2017.09.527.

EC. 2013. 'Commission Delegated Regulation (EU) No 812/2013 of 18 February 2013 supplementing Directive 2010/30/EU of the European parliament and of the Council with regard to the energy labelling of water heaters, hot water storage tanks and packages of water heater and solar device'. 06-Sep-2013; https://eur-lex.europa.eu/legal-content/DE/TXT/PDF/?uri=OJ:L:2013:239:FULL&from=DE.

Haller, M.Y., Robert Haberl, Thomas Persson, Chris Bales, Peter Kovacs, David Chèze, and Philippe Papillon. 2013. "Dynamic Whole System Testing of Combined Renewable Heating Systems – The Current State of the Art." *Energy and Buildings* 66 (November): 667–77. https://doi.org/10.1016/j.enbuild.2013.07.052.

Heinz, Andreas, Christian Gaber, Robert Haberl, Michel Y. Haller, Joachim Kalkgruber, and Rüdiger Schober. 2020. 'Photovoltaic Heat Pump System for Renovated Buildings – Measures for Increased Efficiency'. In Proceedings of EuroSun 2020, 1–10. Athens, Greece, Virtual Conference: International Solar Energy Society. http://proceedings.ises.org/paper/eurosun2020/eurosun2020-0036-Heinz.pdf.

Heinz, Andreas, and René Rieberer. 2021. 'Energetic and Economic Analysis of a PV-Assisted Air-to-Water Heat Pump System for Renovated Residential Buildings with High-Temperature Heat Emission System'. Applied Energy 293 (July): 116953. https://doi.org/10.1016/j.apenergy.2021.116953.

Jordan, Ulrike, and Klaus Vajen. 2012. 'DHWcalc - Tool for the Generation of Domestic Hot Water (DHW) Profiles on a Statistical Basis'. Universität Kassel, Institut für Thermische Energietechnik.

Mojic, Igor, Sascha Crameri, Marco Caflisch, Dani Sanchez Carbonell, Michel Haller. 2019. 'Reference Framework for Building and System Simulations: Multifamily Reference Building', Version: 1.1, https://www.spf.ch/fileadmin/user_upload/spf/SPF/Produkte/Referenz-MFH/Referenz-MFH_2019-12-05_Multifamily_Reference_Building_SPF_V1.1.pdf.

Pflugradt, Noah Daniel. 2016. "Modellierung von Wasser- und Energieverbräuchen in Haushalten." Ph.D. Thesis, Technische Universität Chemnitz. https://monarch.qucosa.de/api/qucosa%3A20540/attachment/ATT-0/.

Statista. 2020. 'Österreich - Wohnfläche pro Person in Hauptwohnsitzwohnungen 2019'. Statista. 2020. https://de.statista.com/statistik/daten/studie/512938/umfrage/wohnflaeche-pro-person-in-hauptwohnsitzwohnungen-in-oesterreich/.

Tabula. 2017. 'TABULA WebTool'. 2017. http://webtool.building-typology.eu/?c=all#bm.

Thür, Alexander, Toni Calabrese, and Wolfgang Streicher. 2018. 'Smart Grid and PV Driven Ground Heat Pump as Thermal Battery in Small Buildings for Optimized Electricity Consumption'. Solar Energy 174 (November): 273–85. https://doi.org/10.1016/j.solener.2018.08.087.

Toradmal, Ajit, Thomas Kemmler, and Bernd Thomas. 2018. 'Boosting the Share of Onsite PV-Electricity Utilization by Optimized Scheduling of a Heat Pump Using Buildings Thermal Inertia'. Applied Thermal Engineering 137 (June): 248–58. https://doi.org/10.1016/j.applthermaleng.2018.03.052.

Weiss, Werner. 2003. Solar Heating Systems for Houses: A Design Handbook for Solar Combisystems. 1. Edition. London: Taylor & Francis Ltd., ISBN 978-1-902916-46-0

Numerical study of the effect of hybrid solar collectors on the performances of the system combining PVT with heat pumps

Mohamad Ali Jaafar[1], Bharat Chhugani[2] and Laetitia Brottier[1]

[1] DualSun, Marseille (France)

[2] Institute for Solar Energy Research Hamelin (ISFH), Emmerthal (Germany)

Abstract

Photovoltaic Thermal solar panels (PVT) are an interesting technology that converts solar energy into both electricity and heat in only one unit. This technology improves the conversion process efficiency of solar energy and optimizes the occupied area on the roof. PVT can be used as a heat source for heat pumps (H.P.), and the system can provide both space heating and domestic hot water efficiently and environmentally. Additionally, the electricity produced from PVT can be consumed directly by the heat pump system. The given paper presents a numerical study based on the characteristics of PVT and its effect on the system's performance. Transient simulations are performed with TRNSYS using a variable speed heat pump. Results show that, for the same number of installed PVT, the most influencing parameter is the first order heat losses coefficient (b_1) compared to the optical efficiency (η_0) of PVT, and system performance is improved when b_1 increases. For instance, with 20 PVT, the SPF is increased from 1,96 to 3,67 when the b_1 is increased from 5 to 35 (while the η_0 constant and equal to 50%). The numerical study presented herein is beneficial to design an efficient PVT dedicated to being coupled with heat pumps based on ratios combining costs and system performances.

Keywords: hybrid solar collectors (PVT), heat pump (H.P.), numerical simulations

1. Introduction

Hybrid solar panels, also known as Photovoltaic-Thermal collectors (PVT), supply heat and electricity simultaneously when exposed to sunlight. This technology improves solar energy conversion efficiency while optimizing the occupied area on the roof. Indeed, with similar dimensions to a photovoltaic panel, PVT can produce more than 2 times the total energy over the year. A real opportunity to use the produced energy of PVT efficiently all over the year is to combine them with brine/water heat pumps, as illustrated in figure 1. This attractive combination significantly improves the system performance by feeding the evaporator with the produced heat and covering part of the electrical consumption with the produced electricity. It allows using solar heat to provide space heating and domestic hot water for any residential building; however, buildings with higher heating demand require a more extensive PVT area.

Studying PVT-HP systems has attracted much attention during the last decade. Bai et al. (2012) have analyzed the performance of a PVT-HP system for sports center hot water production using TRNSYS. They showed that the achieved coefficient of performance is 4.11 in Hong Kong, with 66 % of the fraction of energy savings. In other cities in France, the obtained COP is more than 4.3, and the fraction of energy savings is more than 67%. Abu-Rumman et al. (2020) have established a PVT-Ground source heat pump (GSHP) system model using TRNSYS software to study the system performance enhancement. They showed that the average coefficient of performance of the HPs increased from 4.6 to 6.2 with a decrement of electricity consumption by more than 25%. In addition, they showed that such a system could reduce the photovoltaic panels' temperature by more than 20 °C, and improve the efficiency of electricity production by 9.5%. Chhugani et al. (2020) have investigated a system coupling unglazed liquid-based PVT collectors and heat pumps by means of yearly dynamic simulations in TRNSYS for space heating and domestic hot water. They showed that when PVT is used as a single heat source for heat pumps, the system efficiency is significantly increased and can be used as an alternative to an air source heat pump. Also achieved seasonal performance factors (SPF) are 3.18 and 3.49 (considering the electrical self-consumption of the HP) for the location of Zurich (Switzerland) with cold winters and warm summers. Del Amo et al. (2019) have analyzed the performance of a solar-assisted heat pump fed by PVT collectors using a validated TRNSYS model in Zaragoza (Spain). The obtained results show that the annual COP is 4.62 and that 67.6% of the PV yearly total production is directly consumed by the HP (37.8% of total electrical consumption of the HP).

© 2022. The Authors. Published by International Solar Energy Society
Selection and/or peer review under responsibility of Scientific Committee
doi:10.18086/eurosun.2022.08.06 Available at http://proceedings.ises.org

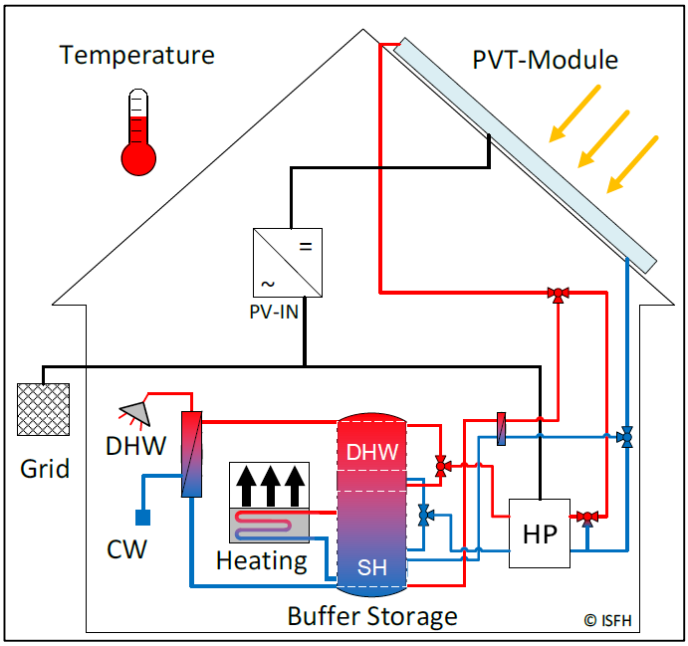

Fig. 1: System combining PVT modules with brine/water heat pumps

In order to reach the climate targets set by the European Commission for 2050, among other projects, the SunHorizon project, funded by the European Union's Horizon 2020 Research and Innovation Programme, has initiated in 2018. It aims to demonstrate the benefits in terms of GHG emissions and primary energy savings of the combination of PVT and HP for heating and cooling applications through eight European pilot sites (Chèze, 2021; Scotton et al., 2019). The main results show that more than 40% of GHG emissions and primary energy are saved compared to conventional systems. In a similar way, the « IntegraTE » European project, initiated in December 2019, aims to bring the PVT-HP system closer to the general public through five lighthouse projects. Main results show that PVT offers additional potential in addition to their capacity as an electricity source: they can provide HP with heat all year at a temperature level that improves system performances (Helmling et al., 2021).

However, many questions are still not answered about this system's design and sizing of PVT. This is the main reason behind the present study aiming to provide numerical results on the effect of the number and the characteristics of the used PVT on the performance of the PVT-HP system used for heating and domestic hot water needs. A variable speed HP is considered, and PVT are used alone to feed the evaporator directly with no intermediate tank. Simulations are carried out using the dynamic simulation software TRNSYS. In the following sections, the methodology used and the main assumptions are defined, and the obtained main results are discussed.

2. Methodology

The numerical simulations are performed using software TRNSYS v17.01.0028, where several models, so-called TRNSYS types were assembled to form and simulate the complete system. The PVT model for simulation (Type 203) was developed by the Institute of Solar Energy Research in Hamelin and validated for standard unglazed PVT collectors (Stegmann et al., 2011). The corresponding hydraulic diagram is shown in Fig. 2. PVT are used as a single heat source of the HP feeding directly the evaporator with no intermediate water tank. They are also connected to the bottom of the tank via an external exchanger. This loop is used for the PVT defrosting process; direct solar heating of the tank is not simulated here.

Simulations are performed for a single-family house SFH 45 located in Strasbourg (France) where the average outdoor temperature is 11 °C. The floor area of the building is 140 m^2 with a floor heating demand of approx. 42.5 kWh/(m^2a), with a one-minute weather data file from Meteonorm 8. Detailed building boundary conditions of this building are explained in (Dott et al., 2013). On the sink side, a hot water tank of 560 L is used for domestic hot water preparation and space heating.

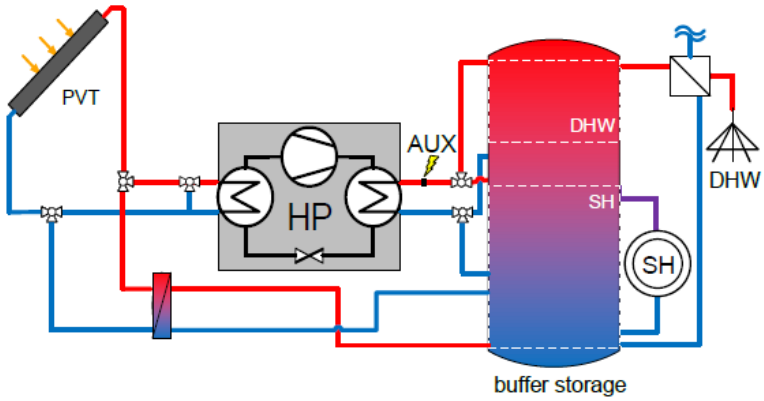

Fig. 2: Hydraulic diagram of the system with direct coupling system of PVT-HP

Fig. 2 shows the simulated PVT to heat pump configuration; the PVT collector works as the only heat source for the heat pump until the PVT outlet temperature falls below -12 °C. In the summer, if the PVT temperature is higher than the buffer storage tank, the heat pump is off then PVT heat is used directly to the storage tank. A brine-water inverter heat pump has been used with thermal power of 9.1 kW and a COP of 4.13 at B0/W35. **Erreur ! Source du renvoi introuvable.** shows the characteristic curve of the simulated variable speed heat pump.

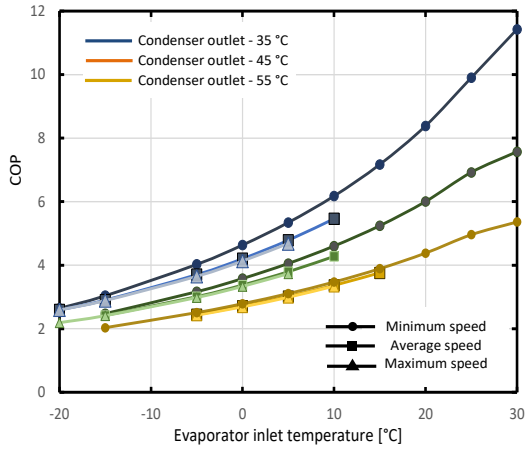

Fig. 3: Coefficient of performance (y-axis) for different evaporator inlet temperatures (x-axis) and condenser outlet temperatures (blue 35 °C, green 45 °C, yellow 55 °C) for three different compressor speeds

An electrical backup heater of 6 kW is used and located in the flow pipe of the heat pump. This heater takes over the charging of the storage tank when the temperature at the evaporator inlet at the heat pump drops below -12 °C. For the heat pump modelling, TRNSYS type 401 was used. A mixing valve is used at the evaporator inlet of the heat pump to protect from high temperatures coming from solar fields, and the maximum allowable temperature is 25 °C.

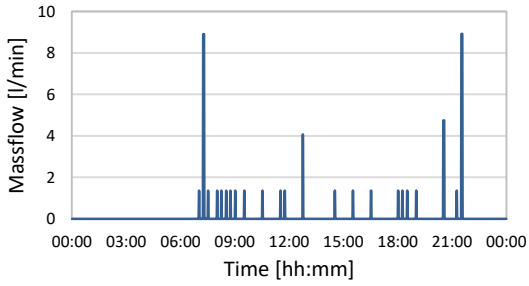

Fig. 4: Domestic hot water demand (DHW) of the building

The domestic hot water consumption is 145 L/d at 45 °C (2141 kWh/year), and water is tapped at 45 °C according to the daily DHW tap profile shown in Fig. 4.

In order to investigate and quantify the impact of PVT on system performance, different PVT collectors have been simulated and compared. The simulated collector parameters are presented below in Table 1. The unglazed PVT collector is liquid-based, with each module having 400 Wp of nominal power and 1.875 m^2 of area. In the PVT-heat pump systems, if the PVT collector temperature on cold days falls below the dew point of the air, then condensation (dew point > 0 °C) or frosting (dew point < 0 °C) occurs. The formation of frost reveals latent heat but inhibits the convection and irradiation gains. The required amount of heat for melting the frost depends furthermore on the PVT design. Now, there is no model to describe and simulate these effects accurately; however, defrosting is simulated as suggested in Chhugani et al. (2020) to reduce the uncertainty of TRNSYS type 203 for extreme conditions. Defrosting takes place when the following conditions meet, if the ambient air and dew point temperatures are below 0 °C, the heat pump is not running for at least 20 minutes, and still PVT collector temperature remains below -3 °C (frost point), then defrosting of PVT takes place and it stops once the temperature of the collector reaches 2 °C again.

Tab. 1: PVT characteristics

η_0 [-]: optical efficiency	0.35	0.35	0.5	0.5	0.5	0.65	0.65
b_1 [W/m^2.K]: first order heat losses coefficient	5	20	5	20	35	20	35
b2 [J/m^3.K]: efficiency coefficient	0						
bu [s/m]: efficiency coefficient (in terms of wind)	0						
Number of PVT [-]	12 ; 20 ; 28						

3. Results

3.1. Simulations without defrosting

For each number of PVT (*N_PVT*), seven simulations are performed with different η_0 (optical efficiency) and b_1 (first order heat losses coefficient), whereas the efficiency coefficient b_2 and the efficiency coefficient (in terms of wind) *bu* are considered zero. Table 2 provides the obtained results for the case without defrosting. *Q_eva*, *Q_cond* and *Q_backup* stand for the annual thermal energy absorbed by the evaporator of the HP (which is produced by solar collectors), the thermal energy produced by the HP condenser (transferred to the water tank and then used for the house space heating and domestic hot water) and the produced thermal energy by the electrical heater, respectively. *E_HP* and *E_pump* stand for the annual electrical consumption of the heat pump (including the compressor and the evaporator pump) and the annual electrical consumption of the condenser pump, respectively.

Tab. 2: PVT-HP system results without defrosting

N_PVT [-]	η_0 [-]	b_1 [W/m².K]	Q_eva [kWh]	Q_cond [kWh]	E_HP [kWh]	E_pump [kWh]	Q_backup [kWh]	SPF [-]
12	0.35	5	3683	4922	1285	55.5	3652	1.61
12	0.35	20	5848	7832	2060	50.4	751	2.80
12	0.5	5	3598	4789	1236	56.2	3783	1.58
12	0.5	20	5786	7746	2033	50.4	833	2.75
12	0.5	35	6364	8461	2180	49.2	124	3.41
12	0.65	20	5770	7715	2019	50.4	862	2.74
12	0.65	35	6366	8461	2178	49.3	124	3.41
20	0.35	5	4622	6132	1567	53.0	2434	1.98
20	0.35	20	6386	8449	2145	49.3	142	3.43
20	0.5	5	4575	6049	1531	53.5	2511	1.96
20	0.5	20	6355	8406	2132	49.3	180	3.40
20	0.5	35	6538	8590	2136	49.0	0	3.67
20	0.65	20	6328	8360	2113	49.4	230	3.35
20	0.65	35	6537	8589	2136	49.0	0	3.67
28	0.35	5	5270	6966	1761	51.3	1587	2.36
28	0.35	20	6509	8554	2129	49.0	31	3.63
28	0.5	5	5114	6734	1683	51.8	1818	2.26
28	0.5	20	6505	8555	2132	49.0	31	3.62
28	0.5	35	6574	8590	2101	48.9	0	3.73
28	0.65	20	6507	8546	2121	49.1	46	3.62
28	0.65	35	6575	8593	2102	49.0	0	3.73

For the evaluation of the system performance, the SPF_{SHP} is considered according to IEA Task - 44 SHP boundary conditions and explained in Malenković et al. (2012), which is the ratio between the annual heat delivered by the system (for space heating and domestic hot water) and the electrical energy consumed by the system (the compressor, evaporator and condenser pumps, the electrical heater and the defrosting pump). The formula is given by the following equation:

$$SPF = \frac{\int(\dot{Q}_{SH}+\dot{Q}_{DHW})dt}{\int(\dot{E}_{HP}+\dot{E}_{pump}+\dot{E}_{backup}+\dot{E}_{defrosting})} \quad \text{(eq. 1)}$$

It is worth noting here that the consumed PVT electricity directly by the heating system is not subtracted from the electrical consumption of the system. Only the thermal performance is calculated here, even if it is well known that this self-consumption of PVT electricity could enhance the system's performance.

Figures 5 to 7 illustrate the results obtained by variation of PVT panels 12, 20 and 28. *E_system* stands for the electrical energy consumed by the whole system. For all simulations, the system covers both space heating and domestic hot water demands; when the HP reaches its operation limits, the electrical heater takes over the charging of the storage tank.

When figures 5 to 7 are compared, the results show that no matter the PVT characteristics; η_0 (optical efficiency) and b_1 (first order heat losses coefficient), the system performance is enhanced when the number of PVT panels increases: the total heat absorbed by the evaporator increases and the total electrical energy consumed by the system decreases. This is normal and expected; however, this has a significant impact on solar installation. It

requires a higher initial cost for the additional PVTs, and more roof area for these PVTs to be installed. Moreover, the effect of the increased number of PVT is more significant for the least efficient PVT. This effect is less noticeable for the PVT with higher characteristics. This can also be explained by the limited heat consumption of the house.

When the obtained results of each figure (the same number of PVT) are compared, one common thing that can be presumed is that the system performance is highly influenced by $b_{1,}$ and the $\eta 0$ has almost no effect on the solar produced heat and the consumed electricity of the whole system. This means that PVT is not required to be efficient in converting solar radiations into heat (high optical efficiency η0), but it should work as an environmental heat exchanger with a higher heat loss coefficient (b_1). There are several reasons behind this; firstly, the PVT operation temperature is often less than the ambient temperature during colder winter days or at night; hence, high heat exchange to the ambient air is very beneficial. The calculated average temperature during the running time in PVT for all performed simulations is about -0,61 °C. Secondly, the heat demand is higher during cold winters so that during periods in which the solar radiations are very low or null, an optically performant PVT would behave in the same manner as a non-performant one. The third specific reason is the hydraulic system configuration: the direct heating of the water tank by PVT is not considered, and no buffer storage tank between the PVT and the evaporator of the HP is integrated.

Moreover, it is noticed that the system performance enhancement is more significant between the smallest and the moderated heat loss coefficients (from b1: 5 to b1: 20 W/m²K) than between the moderated and the largest ones (from b1: 20 to b1: 35 W/m²K). This means that a moderated heat loss coefficient (here b1: 20 W/m²K) is sufficient for a PVT – heat pump operation. The moderated heat loss coefficient can be obtained by choosing a very conductive material and by improving the design of the heat exchanger on the back side PVT by adding fins, for instance. These could lead to significantly higher costs for one PVT. We believe these results are more beneficial when converted into ratios considering the manufacturing cost of one PVT.

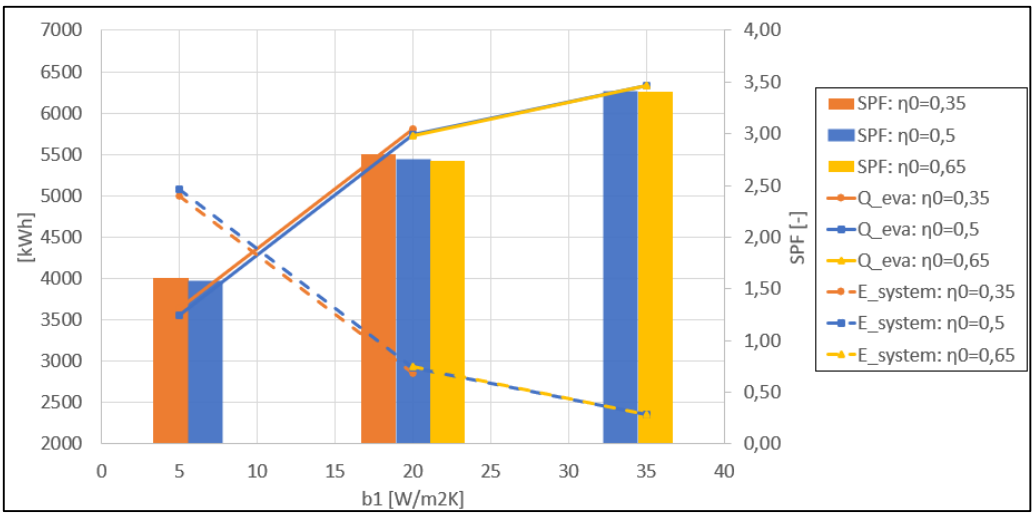

Fig. 5: Simulation results with 12 PVT

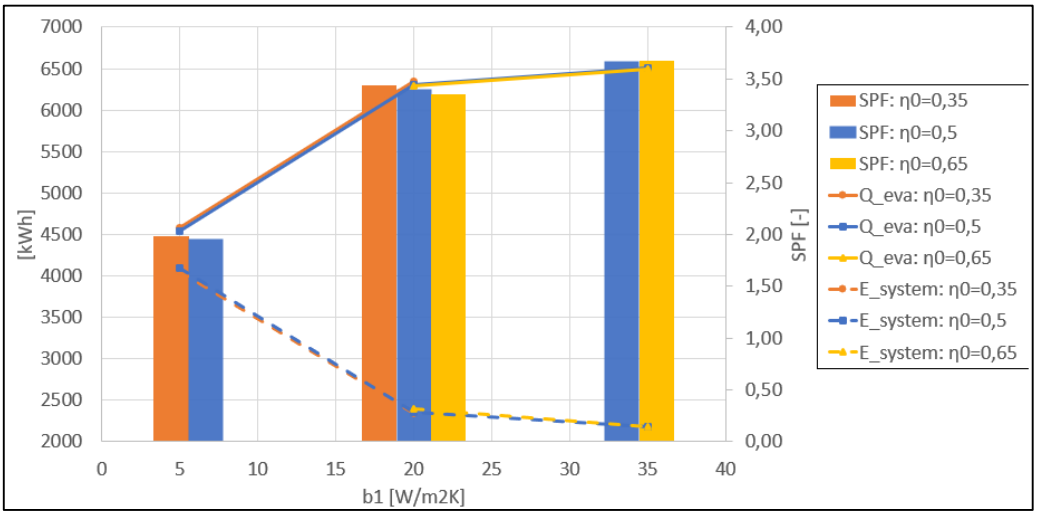

Fig. 6: Simulation results with 20 PVT

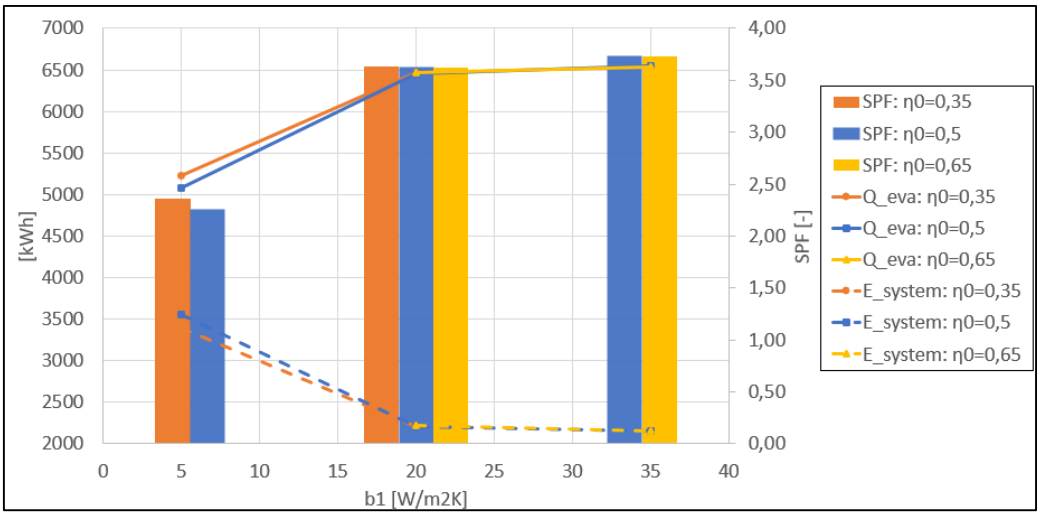

***Fig. 7:* Simulation results with 28 PVT**

3.2. Simulations with defrosting

This sub-section provides the numerical results with defrosting process considered (table 3). When compared to the results of table 2 (without defrosting), it is commonly seen that for the same case (same number and characteristics of PVT), the seasonal performance factor of the system with defrosting is slightly lower than the system without defrosting. In some cases (the first one in the tables, for instance), in which the energy consumed by the electrical heater is lower with defrosting, the results show that the energy needed to defrost the PVT is higher than the difference between the needed energy consumed by the backup to take over the heating of the water tank. For other cases (the cases with 20 PVT and optical efficiency of 0.5, for instance), it is seen that even if the PVT is defrosted, the electric heater can consume more energy than the cases without defrosting deteriorating the system seasonal performance (the difference is noticeable more with lower b_1 (5 W/m²K) than the moderate/higher b_1). It proves that for the same η_0 (here is 0.5), higher heat loss coefficients play an essential role in efficient PVT – HP operation and can make a very robust system.

Tab. 3: PVT-HP system results with defrosting

N_PVT [-]	η_0 [-]	b_1 [W/m².K]	Q_eva [kWh]	Q_cond [kWh]	E_HP [kWh]	E_pump [kWh]	Q_backup [kWh]	Q_defrost [kWh]	SPF [-]
12	0.35	5	3900	5213	1361	58.4	3783	-420.19	1.54
12	0.35	20	5960	7981	2098	51.6	806	-208.47	2.71
12	0.5	5	3779	5018	1286	58.5	3971	-417.12	1.51
12	0.5	20	5902	7894	2068	51.7	902	-215.37	2.65
12	0.5	35	6442	8565	2207	50.1	159	-139.51	3.31
12	0.65	20	5924	7923	2074	51.9	886	-229.98	2.66
12	0.65	35	6432	8552	2203	50.1	168	-134.18	3.31
20	0.35	5	4871	6458	1648	55.8	2572	-463.30	1.87
20	0.35	20	6472	8563	2173	50.3	200	-174.43	3.30
20	0.5	5	4740	6254	1573	56.4	2800	-485.55	1.81
20	0.5	20	6469	8556	2169	50.5	232	-198.30	3.27
20	0.5	35	6647	8737	2176	49.9	0	-145.73	3.60
20	0.65	20	6456	8536	2162	50.7	262	-211.07	3.23
20	0.65	35	6647	8738	2177	49.9	0	-149.37	3.59
28	0.35	5	5375	7081	1773	54.4	1935	-452.73	2.12
28	0.35	20	6644	8739	2180	50.1	29	-178.38	3.54
28	0.5	5	5209	6832	1688	55.0	2197	-466.12	2.03
28	0.5	20	6653	8753	2183	50.2	31	-193.79	3.53
28	0.5	35	6689	8747	2145	49.9	0	-156.17	3.64
28	0.65	20	6663	8755	2176	50.4	56	-220.11	3.50
28	0.65	35	6688	8751	2149	49.9	0	-161.95	3.64

As mentioned before, the reason for implementing defrosting in simulations is that frost is a very common phenomenon with PVT-heat pump operation, as explained in Chhugani et al. (2020). The ice formation on the collector field hinders the heat transport from the ambient to the collector, and this occurs when PVT operates under extreme conditions (heat pump running continuously, no direct sunshine for many days), which can be reduced by higher heat loss coefficient. It is also worth mentioning that the defrosting phenomenon requires the installation of an extra hydraulic circuit with a heat exchanger and a pump. In addition, the water tank needs to be upgraded with one extra heat exchanger. All of these have an extra cost to be added to the system.

4. Conclusion

The present paper focuses on the energy system combining hybrid solar panels (PVT) and heat pumps (HP) to provide both space heating and domestic hot water needs. It presents a numerical study investigating the effect of PVT characteristics and numbers on the system's performance. Transient simulations are performed using TRNSYS for a single-family house located in Strasbourg (France).

The obtained results showed that the PVT characteristics and number are crucial on the system annual performances which vary between 1.5 and 3.7. They also showed that no matter the PVT characteristics; η_0 (optical efficiency) and b_1 (first order heat losses coefficient), the system performance is enhanced when the number of PVT panels increases. however, this has a significant impact on solar installation cost. When the same number of PVT is considered, the system performance is shown to be highly influenced by b_1, and the $\eta 0$ has almost no effect on the solar produced heat and the consumed electricity of the whole system. Therefore the involved PVT is not

required to be efficient in converting solar radiations into heat (high η_0), but it should work as an environmental heat exchanger with a higher heat loss coefficient (b_1).

Simulations with PVT defrosting process considered showed that the system performance is detorierated compared with simulations without defrosting. This is explained by the extra consumed thermal energy by the system to defrost PVT. However, these results are more realistic since the implemented model, like others, is not able to correctly simulate the variation of the convective heat transfer coefficient of the PVT with the air when frost is produced which is still a very complex topic. The energy needed to defrost PVT compensates losses in the convective heat coefficient of the PVT.

5. References

Abu-Rumman, M., Hamdan, M., & Ayadi, O. (2020). Performance enhancement of a photovoltaic thermal (PVT) and ground-source heat pump system. *Geothermics*, *85*(January), 101809. https://doi.org/10.1016/j.geothermics.2020.101809

Bai, Y., Chow, T. T., Ménézo, C., & Dupeyrat, P. (2012). Analysis of a hybrid PV/thermal solar-assisted heat pump system for sports center water heating application. *International Journal of Photoenergy*, *2012*. https://doi.org/10.1155/2012/265838

Chèze, D. (2021). *Four Innovative Solar Coupled Heat Pump Solutions for Building Heating and Cooling*. 1–12. https://doi.org/10.18086/eurosun.2020.04.07

Chhugani, B. (2020). *Model Validation and Performance Assessment of Unglazed Photovoltaic-Thermal Collectors with Heat Pump Systems*. 1–12. https://doi.org/10.18086/eurosun.2020.05.13

Del Amo, A., Martínez-Gracia, A., Bayod-Rújula, A. A., & Cañada, M. (2019). Performance analysis and experimental validation of a solar-assisted heat pump fed by photovoltaic-thermal collectors. *Energy*, *169*, 1214–1223. https://doi.org/10.1016/j.energy.2018.12.117

Dott, R., Ruschenburg, J., Ochs, F., Bony, J., & Haller, M. (2013). The Reference Framework for System Simulation of the IEA SHC Task 44 / HPP Annex 38 - Part B: Buildings and Space Heat Load. *Technical Report of Subtask C of the IEA SHC Task 44*.

Malenković, I., Pärisch, P., Sara Eicher, J. B., & Hartl, M. (2012). Definition of Main System Boundaries and Performance Figures for Reporting on SHP Systems. *IEA SHC Task 44 - Subtask B*, *Aralık*, 1–26. http://www.iea-shc.org/task44%0ANomenclature

Scotton, S., Decorme, R., Calderoni, M., Costa, S. V., Cuneo, A., Frazzica, A., Barberis, S., Fuligni, F., Martinelli, F., & Magrassi, F. (2019). *Sun and Thermal Energy: Europe's Precious Energy Sources for Efficient Industries and Buildings*. 3. https://doi.org/10.3390/proceedings2019020003

Stegmann, M., Bertram, E., Rockendorf, G., & Janßen, S. (2011). Model of an unglazed photovoltaic thermal collector based on standard test procedures. *30th ISES Biennial Solar World Congress 2011, SWC 2011*, *4*, 2639–2647. https://doi.org/10.18086/swc.2011.19.30

Testing a Flexible Configuration of a Solar-Assisted Heat Pump with PVT Collectors for Domestic Hot Water Production

George Meramveliotakis[1,2], George Kosmadakis[1], Marika Pilou[1] and Sotirios Karellas[2]

[1] Thermal Hydraulics and Multiphase Flow Laboratory, National Centre for Scientific Research "Demokritos", Agia Paraskevi (Greece)

[2] Laboratory of Steam Boilers and Thermal Plants, Zografou, School of Mechanical Engineering, National Technical University of Athens, 9 Heroon Polytechniou St., Zografou Campus, 15780 Athens, (Greece)

Abstract

A solar energy based pilot system located in Athens, Greece, is examined experimentally for covering hot water demand. The system consists of a heat pump with vapor injection coupled with low concentrating stationary PVT collectors in a flexible configuration. The produced heat of the collectors is delivered to the hot water tank directly covering the demand with the heat pump operating as an air-source unit and supporting the charging when its temperature gets below 45 ^{o}C. This work examines the performance and the capacity of the system with two different draw-off profiles (medium and large) based on EU standard EN16147:2017 simulated by an electronic valve with a constant water mass flow rate and a pre-defined time schedule during the day. Tests have been conducted for both profiles during summer days with the aim to evaluate the system performance in terms of heat balances and net electricity consumption once considering the power production of the PVT collectors as well.

Keywords: Heat pump, PVT collector, residential building, domestic hot water, tapping profile

1. Introduction

The total required energy for space heating (SH) and domestic hot water (DHW) is estimated to more than 20% of the entire energy demand in EU28 buildings (Bertoldi et al., 2018). According to Pezzuto et al. (Pezzutto et al., 2019), over 85% of the total energy (about 3315 TWh/y) is provided for space heating while about 600 TWh/y is used for DHW needs. Also, 84% of the total energy demand for space heating and DHW production is covered by fossil fuels (e.g. gas boilers) while only 16% from renewable energy sources (Galindo Marina et al., 2016). At the same time, the European council has set 4 key milestones within the 2030 framework for climate and energy including a 40% cut in greenhouse gas (GHG) emissions compared to 1990 levels, such as at least a 32% share of renewables (Bertoldi et al., 2018). As a result, the adoption of renewable energy solutions in the building sector is getting more than crucial in order these targets to be achieved.

Several regulations and policies that have been into force have led to the decrease of space heating demand through actions such as building insulation and energy management advancements. On the other hand, the domestic hot water demand remains about the same (Guo and Goumba, 2018). Additionally, the DHW preparation is something strongly behavioral related to the occupants that requires consideration of both the energy system and the draw-off profile, which affects the energy consumption and consequently the performance and efficiency of the systems (Zhou et al., 2022). Thus, the relevant objective is formed to introduce higher efficiency systems combining also renewable energy sources and to consider the effect of draw-off profile variation to the system operation.

The use of solar energy is one of the most promising renewable energy sources to meet the needs for heating and DHW with wide use. The benefits are mainly related to the significant reduction of operational costs especially during mid-seasons and summer due to the adequate amounts of solar irradiation which eliminates the operation of typical boilers during those periods (Tian et al., 2019). On the other hand, solar collectors can only provide hot water when irradiation is sufficient emerging the need of integrating thermal storage and auxiliary systems in order to ensure that heat is delivered when needed. A promising auxiliary heating system is a heat pump whose use is increasing because it combines high efficiency, flexibility in integration with renewables, and reduced final energy consumption, especially when it is supplied with low temperature heat instead of ambient air (Pilou et al., 2021). Additionally, many efforts are on-going to decrease the carbon footprint of heat pump systems especially by employing new low global warming potential (GWP) refrigerants such as natural refrigerants like carbon dioxide

© 2022. The Authors. Published by International Solar Energy Society
Selection and/or peer review under responsibility of Scientific Committee
doi:10.18086/eurosun.2022.08.07 Available at http://proceedings.ises.org

(R744), propane (R290), and new generation hydrofluoroolefins (HFOs) (Meramveliotakis et al., 2022, 2021).

Air-source heat pumps for DHW production have a large potential and much research has been done to explore it. The main interest focuses on methods to enhance the system performance (expressed through the coefficient of performance – COP) and capacity, with vapor injection technique (Li et al., 2022) introducing significant improvements, especially in cold climates. At the same time, decreasing the GWP of the heat pump system is a crucial objective and for that natural refrigerants such as CO_2 or CO_2/Ammonia (Ju et al., 2018) blends are examined.

A more efficient alternative is the solar-assisted heat pump (SAHP) which combines solar thermal collectors and a heat pump in a single configuration to meet DHW demand (Sun et al., 2015). The operation and performance of SAHP systems have been studied both numerically (Sterling and Collins, 2012) and experimentally (Panaras et al., 2014) resulting to significant energy savings compared to fired heaters (Panaras et al., 2013). Another study (Long et al., 2021) investigated a hybrid solar hot water and air source heat pump flexible system allowing in series, parallel and preheating type connection of solar water for hot water heating. The results showed that the external conditions (ambient temperature and solar irradiation) play an important role in the overall performance and the combined heating system showed 8.4%, 7.1% and 15.8% better seasonal performance compared to the parallel, in series and preheating systems as single units.

By further advancing the SAHP configuration, the solar collectors can be replaced by hybrid photovoltaic thermal (PVT) collectors that produce both heat and electricity (Lämmle et al., 2017). This concept increases the solar energy utilization compared to separate PV and solar thermal systems (Vaishak and Bhale, 2019). Pilou et al. (Pilou et al., 2022) investigated numerically the integration of PVT collectors, multi-source heat pump and ground heat exchanger in office buildings for cold (Copenhagen) and hot (Athens) climates pointing out a high COP of the heat pump (about 4.2 for winter in Athens and 3.8 for winter in Copenhagen) with also high share of renewables reaching values over 75% for Athens and 50% for Copenhagen.

Based on the above, a coupling of a dual-source heat pump (air or water) with PVT collectors as part of a pilot system located in Athens, Greece, is examined. The system design allows exploiting all the produced PVT heat by either directly charging the DHW tank or charging a separate tank at a low temperature which acts as the heat source to the heat pump, for increasing its COP (Buker and Riffat, 2016). In this study, the performance of the air-source only system is investigated experimentally with the high temperature heat production of the PVT charging a tank to cover hot water demand whereas the heat pump is the auxiliary system to support the heat production. The system is tested under two taping water profiles according to the EN16147:2017 standard for water-heaters, corresponding to the "M" (Medium) and "L" (Large) profile of the standard.

2. System description

2.1. Experimental Setup

The experimental setup consists of a solar assisted heat pump with a heating capacity of 15 kW initially designed for heating, cooling and DHW production. The main system components are highlighted in Fig. 1 including the PVT collectors for producing heat and electricity and the heat pump providing either cooling or heating via reversing its thermodynamic cycle with the use of 4-way valves.

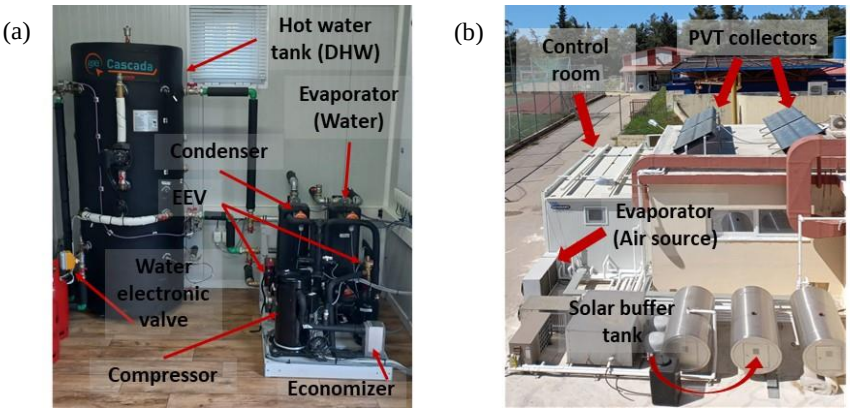

Fig. 1: The main components of the experimental setup. (a) Heat pump and DHW tank inside the control room, (b) Outdoor installation highlighting the PVT collectors, air source evaporator and auxiliary units

The schematic diagram of the complete experimental setup is shown in Fig. 2, with the main interest focused on

DHW production, while the system components which are not in operation are illustrated with gray transparent color (mainly the solar buffer tank that is charged by the collectors and enables the solar-assisted heat pump operation). The heat pump is working only with ambient air as heat source (evaporator side) while the hot side (condenser) is delivering the produced heat to the DHW tank through a closed loop water circuit. Additionally, the same tank is connected with 4 PVT collectors installed in series by two, achieving a parallel integration between solar circuit and heat pump.

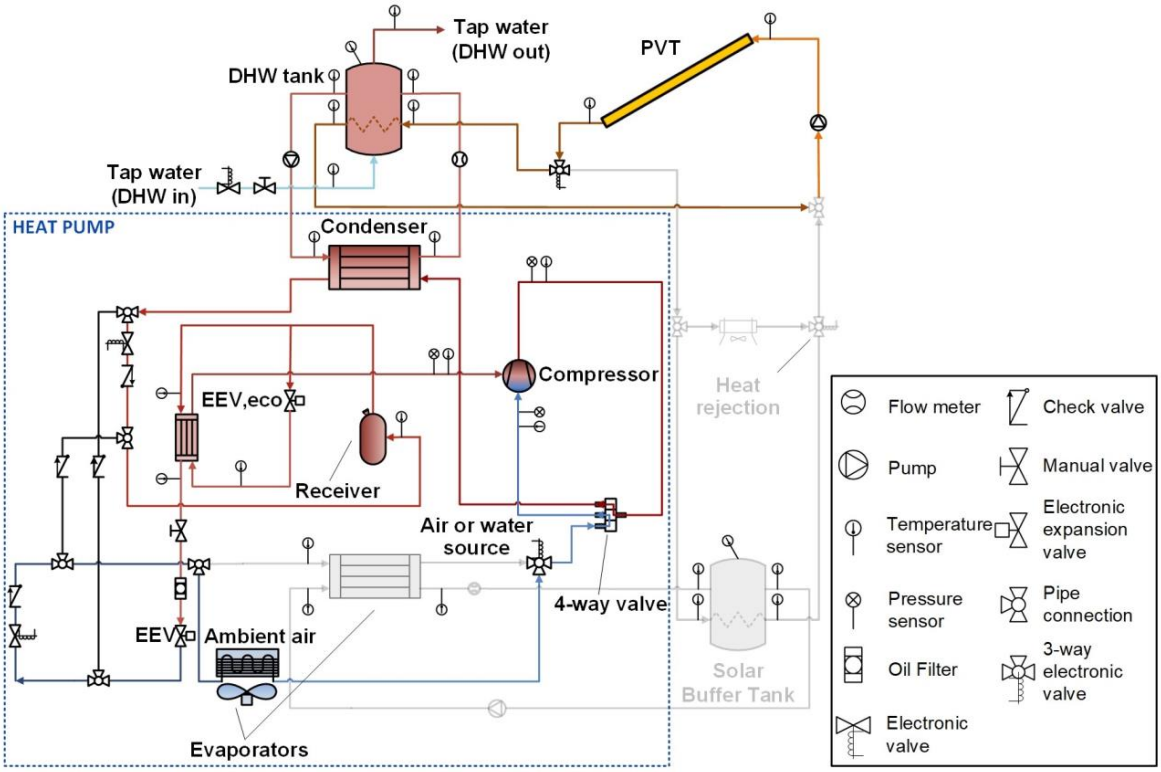

Fig. 2: Schematic diagram of the solar assisted heat pump integrated with the DHW water tank

2.2. Heat pump

The heat pump is equipped with a Copeland ZH13KVE scroll compressor initially provided for R407C with 11.7 m^3/h displacement at 50 Hz. The compressor is intended for heating applications equipped with an economizer port to allow vapor injection operation. The refrigerant is the HFO blend R454C with a low GWP of 148, zero ozone depletion potential (ODP) and was selected due to its similar properties to R407C and its performance was initially assessed with the use of a validated heat pump model in EES software (Kosmadakis et al., 2020). The total charge is 5 kg of refrigerant and a receiver with a volume of 1.5 lt has been placed after the condenser to account for changes in the operating conditions. All three plate heat exchangers (HEX) (Fig. 2) are manufactured by SWEP with some over-surfacing to ensure the performance of the heat exchanger is kept at desirable levels even during dynamic operation. Also, a custom-made fin and tube air heat exchanger is included, with 55.47 m^2 total exchange surface and capacity of 21.77 kW. The selection of either air or water source evaporator is attained by adjusting the flow direction of an electronic 3-way valve installed at the refrigerant circuit, and thus generating two different options for the working fluid accordingly. In this work, this valve always directs the refrigerant flow through the air source evaporator.

In the heat pump configuration, a vapor injection circuit (VI) is also implemented to enhance its performance and increase the system's capacity (Kwon et al., 2017; Tello-Oquendo et al., 2019). The injection mass flow rate is adjusted by an electronic expansion valve placed at the economizer line, with a fixed superheat of 7 K. A part of the main flow is expanded to an intermediate pressure and then directed to the economizer to be evaporated by the liquid flow. The vapour then enters the compressor and is mixed with the compressed vapour, resulting to a lower superheat of the mixture. The main liquid flow of the refrigerant passes through the main electronic expansion valve also with a fixed superheat of 7 K and then enters the air source evaporator and finally to the compressor suction, closing the cycle. Tab. 1 shows the main components of the heat pump.

Tab. 1: Main components of the heat pump

Component	Type	Description
Copeland ZH13KVE	Scroll compressor with VI port	11.70 m^3/h displacement at 50 Hz
SWEP B80Hx30/1P	Plate heat exchanger	30 plates with 1.68 m^2 of total heat transfer area for both evaporator and condenser
SWEP B5THx34/1P	Plate heat exchanger	34 plates with 0.384 m^2 of total heat transfer area for the economizer
Danfoss T2/TE2 134	Electronic expansion valve	Expansion valve for vapor injection circuit with 7 K adjusted superheat
Parker Sporlan ODF ST SEI-1-10-S	Electronic expansion valve	Main expansion valve with 7 K adjusted superheat
Custom made air fan coil	Fin and tube heat exchanger	4 circuits, with 3 rows (16 tubes/row) with a total surface of 55.47 m^2
OCS, type RV1CC130X250	Refrigerant receiver	Volume of 3.0 lt, design pressure 32 bar
RANCO, V10-314120200	4-way valve	Nominal capacity of 35 kW, for switching heating and cooling mode
Castel 6690M/7A6	3-way valve	For switching water and air source evaporator

2.3. PVT collectors

The PVT collector of the pilot system includes a low-concentration (concentration factor 1.5) stationary parabolic reflector with an improved design for increasing the incidence angle modifiers (IAMs) over a large range of incident angles. The solar irradiation is concentrated onto an aluminium absorber that carries on both upper and bottom side PV cells laminated with a highly transparent and electrically insulating silicone. The upper side operates exactly as a standard PV module, while the bottom side receives the concentrated solar radiation from the reflector. Also, a glazed protection is installed and the supporting housing of the collector is made of plastic and metal compounds. The cooling medium in the PVT solar circuit is a water/glycol (Tyfocor L) mixture with 40% by volume concentration of glycol, including also anticorrosive additives to protect the aluminium receiver. The produced heat is delivered through stainless steel piping to the DHW tank with an immersed heat exchanger with a total surface of 1.7 m^2. The total area of each PVT collector is 2.31 x 0.955 m (2.15 m^2) and its thermal and electrical capacity is 1250 and 250 W respectively at standard conditions. The experimental setup consists of 4 collectors placed with 31º tilt and south orientation (zero azimuth angle), connected in series by two (due to the expected pressure drop in each collector) creating two parallel loops. The flow rate of each loop is calculated with the use of a typical specific flow rate of 0.02 lt/m^2s, resulting to about 155 lt/h per loop and 310 lt/h in total. Furthermore, as depicted in Fig. 1, the solar circuit is equipped with a Wilo circulating pump, type Para 25-130/7-50, and a heat rejection dry cooler system with a capacity of 5 kW to protect the collectors from over-heating.

2.4. Domestic hot water tank

The experimental setup includes a 300 liters capacity water tank for domestic hot water preparation. The tap water is heated and then discharged (open type). A controllable valve is placed at the water inlet with an on-off functionality based on a tapping profile. Temperature sensors are installed at the inlet and outlet of the tank to measure the cold and hot water temperatures as well as a flow rate meter. In addition, temperature sensors are placed in available slots at different heights of the tank. The PVT collectors charge the bottom part, while the heat pump the upper one. This results to a strong stratification and therefore this tank is placed vertically as it is shown in Fig. 2. The DHW tank includes two immersed heat exchangers (spiral coils) made of stainless steel 316L, one for the solar circuit and another for the tap water. Furthermore, the design of the tank includes also a Grundfos water pump to recirculate the tap water and achieve the defined supply temperature for domestic hot water, which is defined at 45 ºC at all times.

2.5. Measuring instruments and their accuracy

Various sensors are installed for measuring temperatures, pressures and flow rates at different positions of the pilot system. All the measurements are collected every one minute by a PLC unit which acts both as control device of the

heat pump and as a data logger by implementing additional analog to digital communication cards with analog inputs from various sensors. The selected PLC is the Mitsubishi FX5U-32MR-ES with 16 digital inputs and 16 digital outputs and two integrated channels with analog input and 1 analog output. Concerning the heat pump configuration, there are 3 pressure and 12 temperature sensors (8 for the refrigerant and 4 for the water lines). The power consumption of the heat pump (three-phase) and the power production of the collectors (single-phase, AC side) is recorded by two power meters. Additionally, two pyranometers are used to measure total and diffuse solar irradiation in order to provide a direct evaluation of the PVT collectors performance. With the use of the above sensors it is possible to process the measured data and calculate the thermal flows of all components, the electricity consumption and production as well as performance and efficiency indicators. The list of sensors is given in Tab. 2, providing their type, accuracy and measured property.

Tab. 2: List of sensors in the pilot system with their accuracy

Property	Sensor type	Accuracy	Quantity	Description
Temperature	Pt100 3-wire, with transducer (4-20 mA)	<0.1 K	18	Temperature of water, brine and refrigerant calibrated in the range of 0-100 ºC for water and -20 – +80 ºC for refrigerant
Temperature	NTC, 2-wire	0.1 K	2	Temperatures of the refrigerant at the outlet of evaporator and economizer for superheat control
Outdoor temperature	Pt100, 4-wire with radiation shield	<0.4 K	1	Outdoor temperature for evaluating PVT collector performance and air-source operation of the heat pump
Pressure	Pressure transmitter ESCP-MIT1	0.25% of FS	3	0-10 bar for the evaporator and economizer lines, 0-30 bar for the condenser line
Flow rate	Electromagnetic flow rate meter with ModBus	<0.5% of measured value	4	Flow rate of DHW profile, solar brine and water flow in the evaporator and condenser
Electricity	Power meter with current transformers and ModBus	<0.2% of measured value	2	Electricity consumption of the heat pump and all auxiliaries. Electricity production of the PVT collectors (total).
Total solar irradiation	Pyranometer with ModBus	<5 W/m^2	1	Total solar radiation on the collector's surface (mounted on one collector with the same tilt and azimuth)
Diffuse solar irradiation	Pyranometer with shadow ring with analog signal 0-20 mV	<10 Wm^2	1	Diffuse radiation with shadow ring blocking the direct irradiation to the sensor

3. Experimental Design and performance calculations

3.1. Experimental procedure and DHW profiles

The experimental procedure is structured in a way to examine the performance of the pilot system in terms of DHW production. For that reason, the sub-system that includes the heat pump (air-source operation) – PVT collectors – DHW tank was evaluated under two test series performed using two different taping profiles (different daily loads) in two consecutive summer days (30 and 31 of July 2022) at the facilities of the National Center of Scientific Research "Demokritos" in Athens, Greece. Each experiment lasted for 24 hours in order to obtain the daily behavior of the system. Also, prior to the experimental procedure, the system has been operated for at least 2 days in order to minimize temperature fluctuations aiming to initialize the measuring conditions exactly as a typical operational day and to avoid taking into account fewer or more thermal loads. The DHW profile is pre-defined according to the

EN16147:2017 standard for water heaters, hot water storage appliances, and water heating systems ("Directive 2009/125/EC"). This standard defines a 24-h tapping cycle with a draw temperature and variable flow rate leading to the calculation of a total thermal energy demand per day. Taking into consideration the monthly average tap water temperature, the average daily thermal energy demand has a seasonal variation during the months with higher values in the winter (lower tap water temperature) and lower values in the spring and summer. According to this standard, the "M" (Medium profile – Day 1) and "L" (Large profile – Day 2) profiles have been selected and the average daily demand has been calculated as 4.68 kWh for "M" and 9.34 kWh for "L" profile during July. In order to integrate the two DHW profiles into the system operation, the hourly based DHW demand in kWh needs to be converted into an integral number which represents the opening time in minutes of an on-off electronic valve (constant water flow rate) placed at the inlet piping of DHW flow (Fig. 1). As a result, the two tapping profiles have been converted into valve opening time profiles with a flow rate of 0.355 m^3/h estimated with a best-fit procedure in order to achieve very close agreement with the standard's defined profiles. Both the tapping profiles of the standard and the time-dependent profiles of the electronic valve are depicted in Fig. 3.

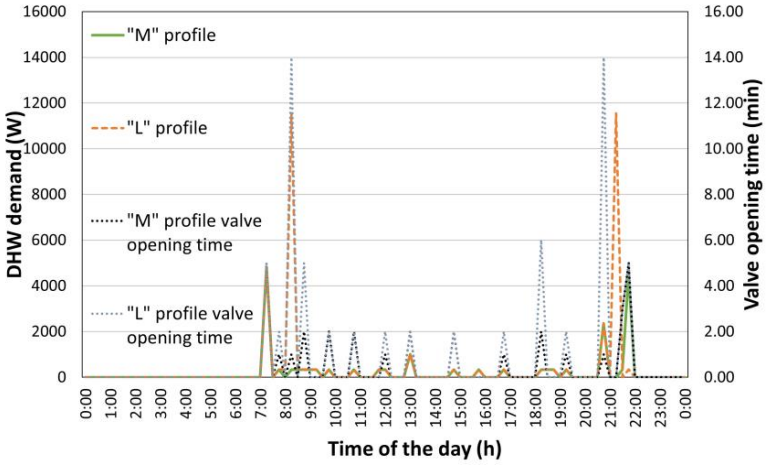

Fig. 3: DHW demand with "M" and "L" profiles of the EN16147:2017 standard and converted electronic valve opening profiles

3.2. Performance calculations

In this section, the basic performance indicators are presented. Concerning the heat pump evaluation, its capacity $\dot{Q}_{cond}$ is identified from the measured data (Eq. 1) while the system's COP is calculated with Eq. 2.

$$\dot{Q}_{cond}=\dot{m}_{w,cond}\cdot c_{p_{w,cond}}\cdot\left(T_{w,cond,out}-T_{w,cond,in}\right) \quad \text{(eq. 1)}$$

$$COP=\frac{\dot{Q}_{cond}}{P_{elec,tot}} \quad \text{(eq. 2)}$$

$\dot{m}_{w,cond}$ (kg/s) is the water mass flow at the condenser calculated from water flow measurements, c_p (kJ/kg·K) is the heat capacity at constant pressure and T (K) the temperature at specific conditions.

Regarding the PVT collectors, the heat production is identified via Eq. 3 while the produced electricity (P_{PVT}) is directly measured by the power meter. The collector's thermal and electrical efficiency is determined by Eqs. 4 and 5 while the total heat and electrical production is estimated by integrating the 1 – minute values over the whole day operation.

$$\dot{Q}_{th,PVT}=\dot{m}_{br,PVT}\cdot c_{p_{br,PVT}}\cdot\left(T_{br,PVT,out}-T_{br,PVT,in}\right) \quad \text{(eq. 3)}$$

$$n_{th,PVT}=\frac{\dot{Q}_{th,PVT}}{I_{t,total}*A_{col,tot}} \quad \text{(eq. 4)}$$

$$n_{el,PVT}=\frac{P_{PVT}}{I_{t,total}*A_{col,tot}} \quad \text{(eq. 5)}$$

where $I_{t,total}$ (kW/m^2) is the total solar irradiation on the titled collector surface and $A_{col,tot}$ the total surface of the 4 PVT collectors.

For DHW tank calculations, the heating load $\dot{Q}_{w,DHW}$ is determined by Eq. 6, while the total daily need for domestic hot water $Q_{w,DHW}$ in kWh is calculated by the integral of Eq. 7.

$$\dot{Q}_{w,DHW}=\dot{m}_{w,DHW}\cdot c_{p_{w,DHW}}\cdot\left(T_{w,DHW,out}-T_{w,DHW,in}\right) \quad \text{(eq. 6)}$$

$$Q_{w,DHW}=\frac{\int \dot{Q}_{w,DHW}\cdot dt}{60} \quad \text{(eq. 7)}$$

where the differential dt refers to the 1 – minute intervals while the value 60 is used for converting minutes to hours.

3.3. Uncertainty analysis

The propagation of sensors accuracies through the calculated properties is identified according to (Meramveliotakis et al., 2022) with the systematic error ε of a given calculated value y estimated by Eq. 8.

$$\varepsilon_y=\sqrt{\sum_i \left(\frac{\partial y}{\partial x_i}\right)^2 \varepsilon_{x_i}^2} \quad \text{(eq. 8)}$$

where $\varepsilon_{\chi i}$ is the uncertainty of the independent variables and $\frac{\partial y}{\partial x_i}$ the partial derivative of the y function with respect to every independent variable x_i.

4. Results and Discussion

4.1. Ambient conditions on reference days

According to the previous analysis, the experiments took place at 30-31 of July 2022 in Athens. The Day 1 refers to the "M" DHW profile while the Day 2 to the "L" one. The ambient conditions of these days are depicted in Fig 4 with an average ambient temperature of 29.24 during Day 2.

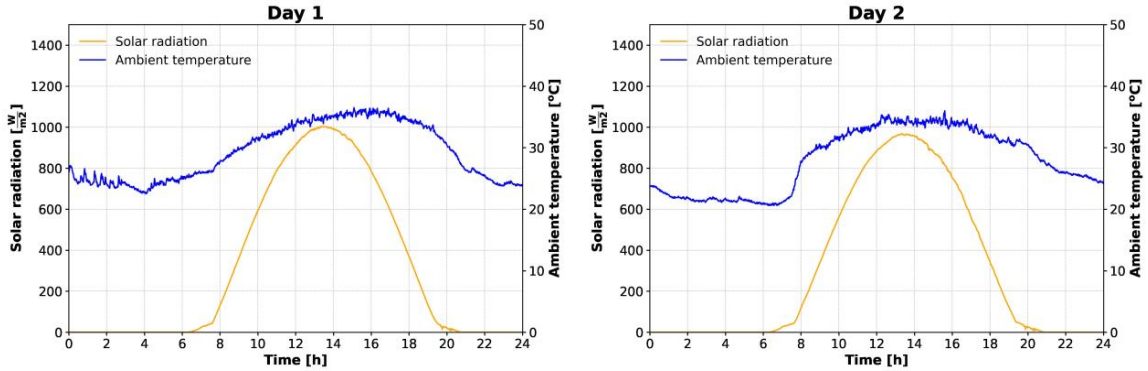

Fig. 4: Ambient temperature and solar radiation during the two days

The average daylight was about 14 hours and 9 minutes of clear sky for both days. As a result, the incident radiation on the surface of the collectors has very similar values for both days with a peak of about 1000 W/m^2 at 13:20 local time which coincides with the solar noon hour. It is obvious that due to the high ambient temperature and the plenty of solar irradiation the heat pump is expected to operate for a very short period of time during the day and especially when DHW is needed and there is no availability of solar irradiation (for example early in the morning or at night).

4.2. System performance

4.2.1. PVT performance

The performance of the PVT collectors is examined next. The heat and electricity production in accordance to the inlet and outlet brine temperatures of the collectors is shown in Fig. 5, as well as the thermal and electrical efficiency.

The control of the pump in the solar circuit was set to operate when the inlet temperature of PVT collectors is above 20 ^{o}C and the temperature difference between inlet and outlet brine is greater than 1 K. For that reason, at about 09:00 am, some fluctuations of heat production are observed, due to the fact that a period of time is needed in order to balance the transient phenomena and to obtain constant positive temperature difference between inlet and outlet flows at the collectors. The duration of heat production from PVTs during the day was about 7.5 hours for both days starting at about 9:20 and until 16:50. Also, heat production and thermal efficiency curves have the same peaks at almost identical times in both days, when the DHW tank is discharged due to taping, reducing the tank temperature, which is beneficial for the PVT efficiency. The maximum thermal performance of the PVTs occurs at noon between 12:00 and 14:00 with an average maximum production of 1.43±0.09 kW.

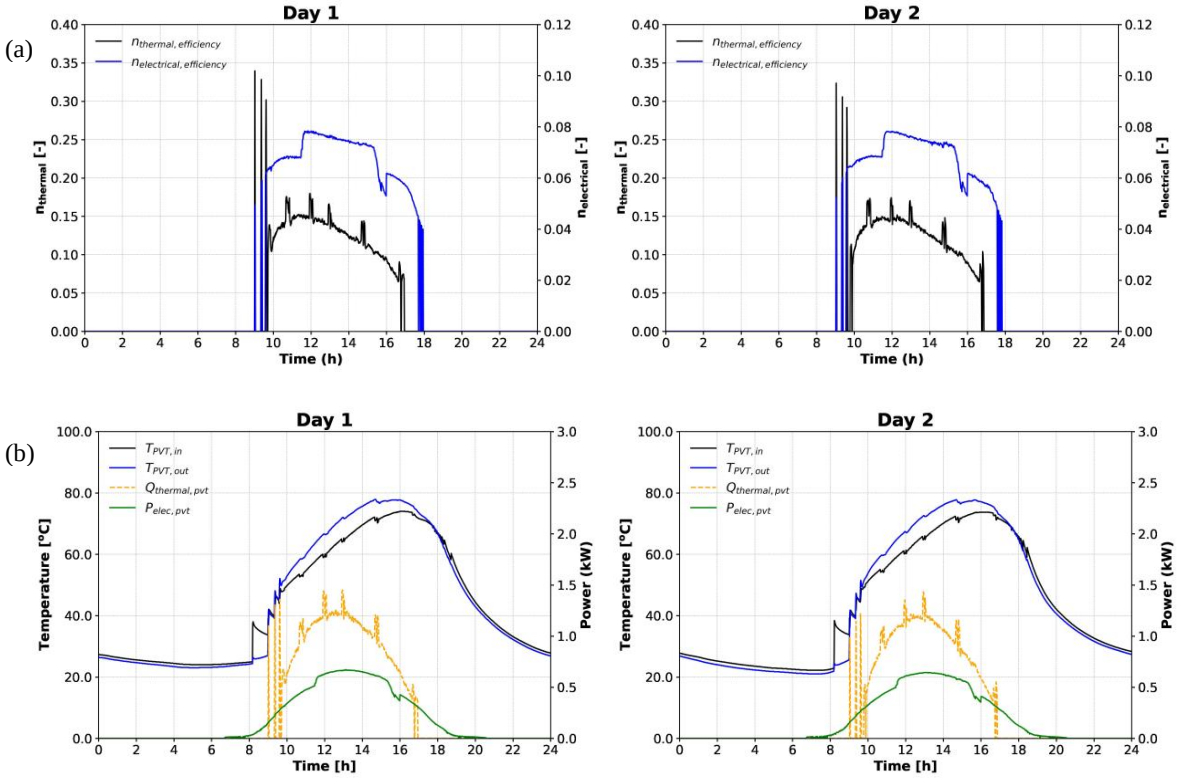

Fig. 5: PVT collectors performance indicators. (a) Thermal end electrical efficiency; (b) inlet and outlet temperature, heat and electricity production

Focusing on the electrical part of PVT collectors, the PV cells produce electricity for about 11 hours and 18 minutes from 7:54 to 19:12 on both days. The electricity generation follows an almost smooth curve with some fluctuations depending on the sun availability and brine temperature. From Fig. 5 is shown that the peak production occurs from 12:00 to 14:00 showing a maximum performance of 0.66±0.03 kW on average, due to the higher IAM values depending on the incidence angle of solar radiation on the tilted collectors. This effect is caused by movement of the shade created by the aluminum frame on both the reflector trough and the reflector underside as the sun moves from horizon to zenith affecting the energy generation of the PV cells on the lower side (Gomes et al., 2014).

The main performance indicators of PVT collectors are shown in Tab. 3 indicating an average daily efficiency for the electricity production of 6.97±0.04% and for heat of 12.69±0.03%. Concerning the production over the whole day, the heat production was about 6.77±0.09 kWh and the electrical production 4.31±0.14 kWh.

Tab. 3: Performance indicators of the PVT collectors

Performance indicator	Units	Day 1	Day 2
Peak heat production	kW	1.44	1.43
Daily thermal energy	kWh	7.00	6.54
Peak thermal efficiency	%	33.95	32.35
Average thermal efficiency	%	12.76	12.63
Peak electrical production	kW	0.67	0.644
Daily electric energy	kWh	4.40	4.23
Peak electrical efficiency	%	7.83	7.82
Average electrical efficiency	%	6.96	6.99

4.2.2. DHW production

The daily variation of the properties relevant to the DHW tank is shown in Fig. 6. The average inlet temperature of the tapping water is about 30 ºC (significantly high due to the summer days) with some fluctuations at the time when the DHW valve opens and the standing water inside the piping starts to circulate. The average DHW outlet temperature is about 50 ºC and the water tank is 60 ºC in both days. From Fig. 6 it is observed that the outlet water temperature reaches almost the tank temperature with a small margin of 2-3 ºC especially from 14:00 to 18:00 when the tank temperature is high due to the charging from the collectors.

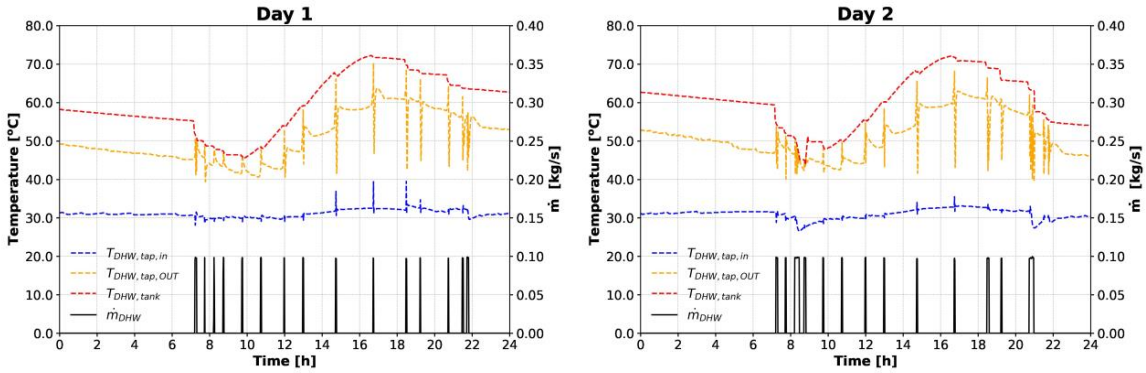

Fig. 6: Water temperatures and mass flow rate of the DHW tank during both days

The water temperatures and DHW production are shown in Tab. 4 for both days, with the measured DHW consumption being 5.73±0.38 kWh (22% higher in Day 1 with "M" profile) and 9.62±0.38 kWh (3% higher in Day 2 with "L" profile) compared to the reference values of the standard. This discrepancy depends mostly on the variation of the water inlet temperature along with the time period which is required for the electronic valve to fully open (about 0.5 min) and to fully close (about 1 min) during the operation.

Tab. 4: Main indicators of domestic hot water production in both days

DHW production	Units	Day 1	Day 2
Daily DHW production	kWh	5.73	9.62
DHW thermal energy (reference)	kWh	4.68	9.34
Total time of DHW valve opening	min	31.00	62.00
Average DHW inlet temperature	ºC	31.14	31.01
Average DHW outlet temperature	ºC	50.79	51.26
Average DHW tank temperature	ºC	59.68	60.30

4.2.3. Heat pump operation

The DHW tank temperature is kept above the threshold of 45 ºC during most of testing period, due to the high ambient temperatures, the high temperature of tapping water (about 30 ºC) and the plenty of solar irradiation. This leads to no or very little operation of the heat pump. According to Fig. 7, when the "M" profile is considered, the heat pump does not operate during the day as the DHW tank temperature is always above the setpoint. Otherwise, during the second day the energy demand is higher and the heat pump needs to operate to increase the tank temperature to 50 ºC which is the upper margin of the on-off control (Fig. 6). As a result, the heat pump operates for 10 minutes during the whole day and specifically from 08:47 until 08:57 to provide the required thermal energy to the system.

The average electrical consumption of the compressor is about 3.80±0.19 kW (0.511±0.07 kWh during the day) operating at 50 Hz when the tank temperature is much lower than the set-point (electrical consumption about 4.5±0.22 kW) with the inverter adjusting its speed and gradually reduce it to 35 Hz (electrical consumption about 3.4±0.17 kW) when the tank temperature reaches the setpoint with 1 K margin. Additionally, the capacity of the heat pump reaches high values resulting to an average of 17.43±0.69 kW, due to the high outdoor temperature of about 30 ºC, charging the tank with 2.17±0.11 kWh during this period. The system and compressor COP have an average value

of 3.42±0.21 and 3.85±0.21 respectively (main difference is the power of the air fans, about 0.43 kW) while the PVT daily electrical production is 6 times higher than the electricity demand. Tab. 5 shows the performance indicators of the heat pump only during the second day with the "L" profile.

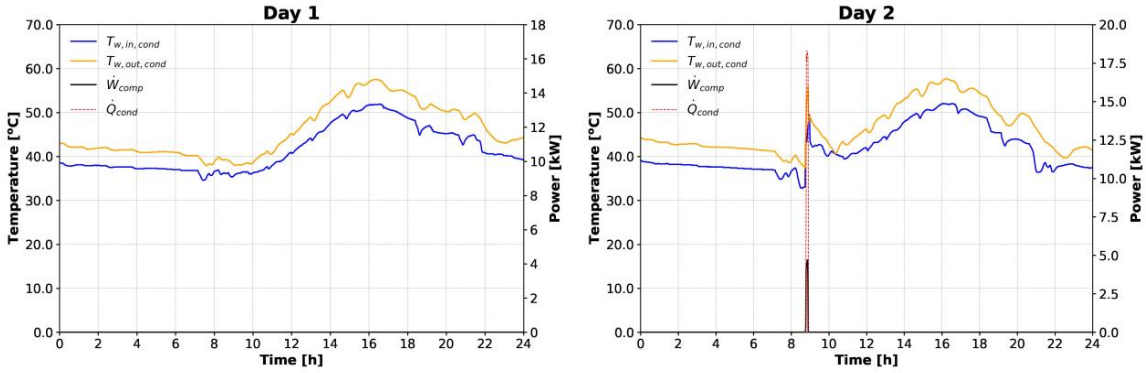

Fig 7: Heat pump operation during the days of the measurements

Tab. 5: Performance indicators of the heat pump during the second day

Heat pump performance	Units	Day 2
Average compressor COP	-	3.85
Average system COP	-	3.42
Average heating capacity	kW	17.43
Daily heat production	kWh	2.17
Daily electricity consumption	kWh	0.58
Daily compressor electricity consumption	kWh	0.51

5. Conclusions

A renewable energy system combining a dual source heat pump and four PVT concentrating stationary collectors is examined experimentally for domestic hot water production. The tests took place in two consecutive summer days in Athens, Greece, with two different tapping water profiles (one for each day) with a calculated thermal energy draw-off profile of 4.68 kWh for the first day ("M" profile) and 9.34 kWh for the second one ("L" profile) according to the EU standard.

The experimental procedure revealed that the PVT collectors provided an average thermal and electrical capacity of 6.8 kWh and 4.3 kWh respectively being similar for both days, resulting to 12.7% thermal and 7% electrical efficiency. Both thermal and electrical production have their peak during noon from 12:00 to 14:00 due to higher IAM values and the increased solar irradiation availability. Owing to the summer ambient conditions and the high temperature of the tapping water (about 30 ^{o}C) the PVT heat production is capable to keep the temperature of the DHW tank above 45 ^{o}C for the whole day with the "M" profile, while with the "L" profile requires a very little use of the heat pump in order to maintain the water temperature in the tank within the desired levels. Concerning the performance of the heat pump, it is operated only on air source heating mode for about 10 minutes during the second day. The average system and compressor COP was 3.42 and 3.85 respectively providing 2.17 kWh of thermal energy to the DHW tank. Because of the limited (day with "L" profile) or no (day with "M" profile) use of the heat pump over the day, the daily produced electricity of the PVT collectors is about 6 times higher than the electricity consumption of the heat pump, indicating that the system can provide domestic hot water and electricity exclusively derived from renewables during the summer days. However, this is expected to greatly decrease during intermediate seasons and especially winter.

In the next steps, the system will be examined experimentally for the whole year introducing not only different

tapping profiles but also different configurations of the heat pump and PVT collectors, also under SAHP operation, taking advantage of the flexibility of the pilot system. After that, a complete evaluation of the system can be accomplished, examining the performance of every component with special attention to the heat pump operation under both water and air source operation. In parallel, optimization control algorithms will be integrated to combiner the different functionalities of the system and thus minimize the net electricity consumption by increasing at the same time as much as possible the exploitation of renewable energy sources.

6. Acknowledgments

This work has been performed within the RES4BUILD project (Renewables for clean energy buildings in a future power system) – Horizon 2020 program, Grant Agreement no. 814865.

7. References

Bertoldi, P., Diluiso, F., Castellazzi, L., Labanca, N., Serrenho, T., 2018. Energy consumption and energy efficiency trends in the EU-28 2000-2015. JRC Report, European Commission.

Buker, M.S., Riffat, S.B., 2016. Solar assisted heat pump systems for low temperature water heating applications: A systematic review. Renewable and Sustainable Energy Reviews 55, 399–413. https://doi.org/10.1016/J.RSER.2015.10.157

Directive 2009/125/EC of the European Parliament and of the Council with regard to ecodesign requirements for water heaters and hot water storage tanks, EU Regul. No 814/2013 2 August 2013 – Available at: https://eur-lex.europa.eu/eli/reg/2013/814/2017-01-09 (Accessed at: 25 August 2022)

Galindo Marina, Roger-Lacan Cyril, Gährs Uwe, Aumaitre Vincent, 2016. Efficient district heating and cooling markets in the EU: Case studies analysis, replicable key success factors and potential policy implications. Publications Office of the European Union, Luxembourg (Luxembourg). https://doi.org/10.2760/371045

Gomes, J., Diwan, L., Bernardo, R., Karlsson, B., 2014. Minimizing the Impact of Shading at Oblique Solar Angles in a Fully Enclosed Asymmetric Concentrating PVT Collector. Energy Procedia 57, 2176–2185. https://doi.org/10.1016/J.EGYPRO.2014.10.184

Guo, X., Goumba, A.P., 2018. Air source heat pump for domestic hot water supply: Performance comparison between individual and building scale installations. Energy 164, 794–802. https://doi.org/10.1016/J.ENERGY.2018.09.065

Ju, F., Fan, X., Chen, Y., Ouyang, H., Kuang, A., Ma, S., Wang, F., 2018. Experiment and simulation study on performances of heat pump water heater using blend of R744/R290. Energy Build 169, 148–156. https://doi.org/10.1016/J.ENBUILD.2018.03.063

Kosmadakis, G., Arpagaus, C., Neofytou, P., Bertsch, S., 2020. Techno-economic analysis of high-temperature heat pumps with low-global warming potential refrigerants for upgrading waste heat up to 150° C. Energy Convers Manag 226, 113488. https://doi.org/10.1016/j.enconman.2020.113488

Kwon, C., Kim, Mo Se, Choi, Y., Kim, Min Soo, 2017. Performance evaluation of a vapor injection heat pump system for electric vehicles. International Journal of Refrigeration 74, 138–150. https://doi.org/10.1016/J.IJREFRIG.2016.10.004

Lämmle, M., Oliva, A., Hermann, M., Kramer, K., Kramer, W., 2017. PVT collector technologies in solar thermal systems: A systematic assessment of electrical and thermal yields with the novel characteristic temperature approach. Solar Energy 155, 867–879. https://doi.org/10.1016/J.SOLENER.2017.07.015

Li, J., Fan, Y., Zhao, X., Bai, X., Zhou, J., Badiei, A., Myers, S., Ma, X., 2022. Design and analysis of a novel dual source vapor injection heat pump using exhaust and ambient air. Energy and Built Environment 3, 95–104. https://doi.org/10.1016/J.ENBENV.2020.11.004

Long, J., Xia, K., Zhong, H., Lu, H., A, Y., 2021. Study on energy-saving operation of a combined heating system of solar hot water and air source heat pump. Energy Convers Manag 229, 113624.

https://doi.org/10.1016/J.ENCONMAN.2020.113624

Meramveliotakis, G., Kosmadakis, G., Karellas, S., 2022. Identifying the performance and losses of a scroll compressor with vapour injection and R1234ze(E). Open Research Europe 2, 49. https://doi.org/10.12688/openreseurope.14658.2

Meramveliotakis, G., Kosmadakis, G., Karellas, S., 2022. Methods based on a semi-empirical model for simulating scroll compressors with HFC and HFO refrigerants. Open Research Europe 1, 148. https://doi.org/10.12688/openreseurope.14313.3

Nuntaphan, A., Chansena, C., Kiatsiriroat, T., 2009. Performance analysis of solar water heater combined with heat pump using refrigerant mixture. Appl Energy 86, 748–756. https://doi.org/10.1016/J.APENERGY.2008.05.014

Panaras, G., Mathioulakis, E., Belessiotis, V., 2014. A method for the dynamic testing and evaluation of the performance of combined solar thermal heat pump hot water systems. Appl Energy 114, 124–134. https://doi.org/10.1016/J.APENERGY.2013.09.039

Panaras, G., Mathioulakis, E., Belessiotis, V., 2013. Investigation of the performance of a combined solar thermal heat pump hot water system. Solar Energy 93, 169–182. https://doi.org/10.1016/J.SOLENER.2013.03.027

Pezzutto, S., Croce, S., Zambotti, S., Kranzl, L., Novelli, A., Zambelli, P., 2019. Assessment of the Space Heating and Domestic Hot Water Market in Europe—Open Data and Results. Energies (Basel) 12, 1760. https://doi.org/10.3390/en12091760

Pilou, M., Kosmadakis, G., Meramveliotakis, G., Krikas, A., 2022. Towards a 100% renewable energy share for heating and cooling in office buildings with solar and geothermal energy. Solar Energy Advances 100020. https://doi.org/10.1016/J.SEJA.2022.100020

Pilou, M., Kosmadakis, G., Meramveliotakis, G., Krikas, A., 2021. Renewable Energy Based Systems with Heat Pumps for Supplying Heating and Cooling in Residential Buildings. https://doi.org/10.5281/ZENODO.5291855

Sterling, S.J., Collins, M.R., 2012. Feasibility analysis of an indirect heat pump assisted solar domestic hot water system. Appl Energy 93, 11–17. https://doi.org/10.1016/J.APENERGY.2011.05.050

Sun, X., Dai, Y., Novakovic, V., Wu, J., Wang, R., 2015. Performance Comparison of Direct Expansion Solar-assisted Heat Pump and Conventional Air Source Heat Pump for Domestic Hot Water. Energy Procedia 70, 394–401. https://doi.org/10.1016/J.EGYPRO.2015.02.140

Tello-Oquendo, F.M., Navarro-Peris, E., Barceló-Ruescas, F., Gonzálvez-Maciá, J., 2019. Semi-empirical model of scroll compressors and its extension to describe vapor-injection compressors. Model description and experimental validation. International Journal of Refrigeration 106, 308–326. https://doi.org/10.1016/j.ijrefrig.2019.06.031

Tian, Z., Zhang, S., Deng, J., Fan, J., Huang, J., Kong, W., Perers, B., Furbo, S., 2019. Large-scale solar district heating plants in Danish smart thermal grid: Developments and recent trends. Energy Convers Manag 189, 67–80. https://doi.org/https://doi.org/10.1016/j.enconman.2019.03.071

Vaishak, S., Bhale, P. v., 2019. Photovoltaic/thermal-solar assisted heat pump system: Current status and future prospects. Solar Energy 189, 268–284. https://doi.org/10.1016/J.SOLENER.2019.07.051

Wang, W., Li, Y., 2019. Intermediate pressure optimization for two-stage air-source heat pump with flash tank cycle vapor injection via extremum seeking. Appl Energy 238, 612–626. https://doi.org/10.1016/J.APENERGY.2019.01.083

Zhou, X., Tian, S., An, J., Yan, D., Zhang, L., Yang, J., 2022. Modeling occupant behavior's influence on the energy efficiency of solar domestic hot water systems. Appl Energy 309, 118503. https://doi.org/10.1016/J.APENERGY.2021.118503

Emission-Free Heat Supply of Residential Districts with Solar Thermal Energy and a Heat Pump Storage System

Dimitri Nefodov, Shengqing Xiao, Markus Richter, Thorsten Urbaneck

Chemnitz University of Technology, Professorship Applied Thermodynamics, Chemnitz (Germany)

Abstract

The European Union is aiming at a massive reduction of annual greenhouse gas emissions. Moreover, due to the ongoing and ever worsening energy crisis, costs for consumers are continously rising. Under these conditions, new concepts for heat supply are once again gaining in importance. One approach to avoiding emissions involves the use of highly efficient collector fields in combination with a heat pump-storage system. Here, supply security and economic efficiency are crucial aspects. This paper deals with the conception and possible implementation variants of a corresponding heat supply centre in a residential area (quarter). TRNSYS (TRNSYS, 2019) was used to simulate the system. Parameter studies show the influence of different variables such as collector area, storage volume, etc. The hydraulic circuit as well as the refrigerant of heat pumps exert high influence on the energy efficiency, the heat production costs and the technical safety of the heat supply centre. A variation of heat pump circuits is presented and discussed. The steady-state simulations were performed with the software EBSILON®Professional (Steag, 2019).

Keywords: heat supply, small-scale district heating, store, heat pump, quarter, dimensioning, solar thermal energy, heat production costs

1. Introduction

The European Union aims at reducing annual greenhouse gas emissions by 55% by 2030. It is envisaged that by 2050 Europe should be climate neutral (BPA, 2020). For several months now, the prices of fossil fuels have been rising very sharply leading to a comprehensive increase of costs in all areas of life, i.e., it is a significant macroeconomic phenomenon. In order to counteract these developments and trends in the long term, it is necessary to implement concepts which are largely independent of economic and political developments. Solar thermal energy, photo voltaics (PV) and wind energy are suitable as basic renewable energy sources, which is known for many years. The implementation plans so far, especially in heat supply, have never been failed due to the technical, economic or ecological potentials. Singular considerations (e.g., comparison of the heat production costs without consideration of subsequent costs) often prevents the necessary entry and expansion of solar technologies.

Within the scope of the project „Demonstration of German Energy Transition in Zwickau“ (Leonhardt et al., 2018; Projektträger Jülich, 2019), concepts (such as decentralised and centralised heat supply centres, using digital technologies to minimise the heating load, mobility solutions, etc.) of a comprehensive transformation for the Marienthal residential district (quarter) in Zwickau into a zero-emissions district (living lab) were developed from 2017 to 2022. This paper deals only with the central heat supply. To avoid emissions, the heat supply system must use very high shares of renewable energy (e.g., wind power, PV, solar thermal energy). Other objectives of this subproject are the security of supply and low-heat production costs. The last point particularly takes into account the social aspect of an affordable heat supply. Relatively low and stable prices are especially important considering acceptance by residents. In order to fulfil the above-mentioned objectives, an optimal design is necessary. Against this background, the EBSILON®Professional (Steag, 2019) and TRNSYS 18 (TRNSYS, 2019) software packages were used for optimisation purposes. The presented investigations are divided into two parts. In the first part TRNSYS was used for modelling and simulation of the heat supply system. This simulation also allowed parameter variations (see section 4). The key performance indicators are then used to assess the fulfilment of the objectives. The system under study uses compression heat pumps with fixed coefficient of performance $\varepsilon_{\mathrm{HP}}$. When using solar thermal energy as a heat source, several challenges may arise for the heat pumps. For example, a large temperature range between the heat source and the heat sink as well as variable source temperatures from the solar thermal system are determinants of the

© 2022. The Authors. Published by International Solar Energy Society
Selection and/or peer review under responsibility of Scientific Committee
doi:10.18086/eurosun.2022.08.08 Available at http://proceedings.ises.org

system operation and the coefficient of performance. In the second part based on modelling and simulations using EBSILON, the influence of the design of the heat pump circuit and the used refrigerant were investigated.

In comparison to the preliminary works (Hornberger, 1994; Raab, 2006; Marx, 2015) (solar local heating systems with heat pumps: The combination of solar thermal systems together with heat pumps has been applied for a long time. A detailed description is provided by (Nefodov, 2019).), the system under study has a solar fraction of 100%. In addition, the boundary conditions in the district (e.g., available areas) and unfavourable operating conditions (e.g., stagnation in the collectors) must be considered to ensure the security of supply.

2. Reference district and heat supply system

The reference district of the current considerations is the Marienthal residential district, which is located in the west of the city of Zwickau in Germany. The buildings in this district are three- or four-storey GDR (*German Democratic Republic*) -type buildings, which were built between 1957 and 1964 (Leonhardt et al., 2018). They were renovated after 1990 and insulated according to the regulations at that time. Natural gas fired boilers cover the space heating (supply and return temperatures of 70 and 55 °C), and domestic hot water heating is partly provided by electric instantaneous water heaters. For both, change was sought. Further modernisation of the existing buildings was not planned. Marienthal district offers excellent conditions for a local heating supply and already has a local heating network which needs to be modernised.

In Fig. 1, the electrical-thermal interconnection system is shown including the balance limits (several technical solutions were investigated in the project, which are not presented here). The main point of the present work relates to the local heating system (central heat supply). The balance limit of interest here is described using the term “heat supply” in Fig. 1. I.e., the supply of electrical energy and the purchase of renewable electricity are initially hidden. The technical approach provides the following essential points:

- use of highly efficient collectors to form a large-scale and cost-effective field,
- use of compression heat pumps,
- use of water stores (5…95 °C) with low losses and very good stratification behaviour (Urbaneck, 2018a, 2018b),
- optional securing of the local power supply with an electrochemical storage system. As part of another subproject, the heat recovery was planned here.

The operating mode for the local heating system is described below. In the case of high irradiation in summer, both storage tanks TES1 and TES2 can be loaded directly via the collectors. Storage tanks operate as seasonal thermal energy storages at a high-temperature level to exploit the solar irradiation potential during the summer. Discharge in summer and autumn takes place directly, which makes the heat pumps unnecessary. In the winter period, the heat pumps use heat water store TES1 as a heat source and charge heat water store TES2 at high temperatures. During the winter and transition periods, the collector field operates at low temperatures, whereby the specific yield increases significantly. At low temperatures in the water store TES1, two-stage operation with HP1 and HP2 is planned for technical and energy reasons. The operation of heat pumps depends on the supply of electricity from renewable energy sources in order to keep CO_2 emissions as low as possible. Thereby the water store TES2 decouples heat load from heat pump operation. The heat pumps and auxiliary units are powered by renewable electricity, which can be obtained from the electrical grid or local PV fields. Further information can be found in Leonhardt et al. (2018) and Nefodov et al. (2019).

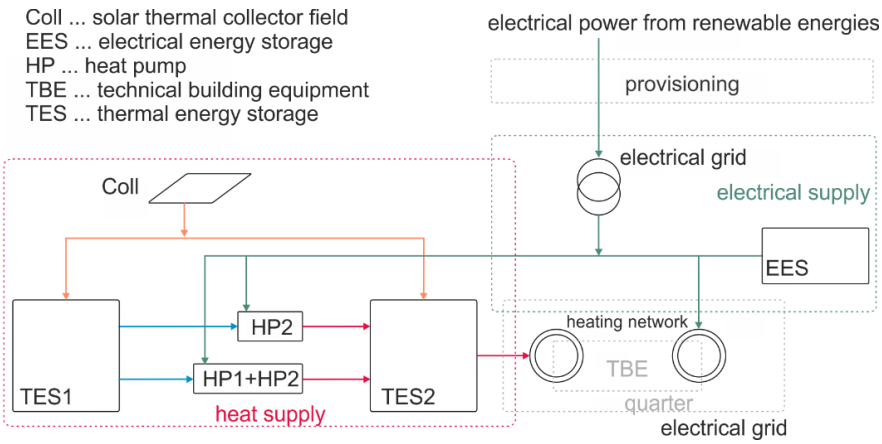

Fig. 1: Electrical-thermal interconnection system with central organisation, scheme of the technical concept and energy flows as well as balance limits (Urbaneck, 2017a)

3. System modelling with TRNSYS

The local heating system (Fig. 2) was modelled and simulated using the simulation software TRNSYS. Meeting the project objectives requires an optimal design and an optimal system operation. For this reason, after modelling, many simulations were carried out with parameter variations (e.g., size of the collector field and storage tank). Subsequent parametric studies show the influence of important parameters (e.g., size of the collector field, heat production costs, etc.), which allows a targeted system design.

In this paper, the heat supply for 133 residential units (7,776.5 m² usable area A_Q. This variant only supplies a relatively small part of the district. Here, from a practical point of view, only solar radiation is available as a heat source) is investigated. The annual heat demand Q_{Net} is approx. 908 MWh a^{-1}, and the test reference year TRY2011 (Zone 9) (DWD, 2018) was chosen as the data basis for the climatic boundary conditions. Technical specifications of a large-area collector were used as parameters for the collector area (TRNSYS type 1: solar collector). The following parameters of the collector efficiency equation were assumed: visual efficiency 85.7 %, linear heat loss coefficient 3.083 W m^{-2} K^{-1}, quadratic heat loss coefficient 0.013 W m^{-2} K^{-2}. The field has a slope of 45 ° and is ideally oriented towards the south. Furthermore, both Thermal Energy Storages (TES1 and TES2, Fig. 1) have been combined into a single heat storage tank (TRNSYS type 340: stratified fluid storage tank) with the height-to-diameter ratio of one. In this case, the heat storage tank has two temperature zones (high-temperature (ht) and low-temperature zone (lt) as illustrated in Fig. 2). The compact storage tank therefore has relatively low heat losses.

In the TRNSYS simulation, no specific heat pump (the selection of suitable refrigerants for heat pumps is described in Xiao et al. (2022)) was modelled. Initially, a simple heat pump model with a constant coefficient of performance of 3.3 was used. This is a simplification, which is necessary in the first step to understand the system behaviour and to make a first dimensioning. This constant value corresponds to the annual performance factor of a typical heat pump (the value was calculated by means of EBSILON simulations, product research confirms this value). The heat pump model consisted of a cooler (TRNSYS type 238, custom-programmed) and a heater (TRNSYS type 138: auxiliary fluid heater), where the cooler represented the evaporator side, and the heater represented the condenser side. This approach made it possible to calculate the heat flows, simplifying the heat pump operation mode. The heat pump model was configured in a way which can cover the maximum network heating load. Moreover, the system had a virtual electric back-up heater to compensate for a lack of heating capacity (e.g., undersizing of the collector array, discharged TES1 storage tank, insufficient heating capacity of the heat pump).

Regarding the loads (heating network in Fig. 2), there were no measured values available for the network or the buildings. As the building density in the area is relatively high, the network losses can be assumed to be low. Experience shows that in a network of this type, the annual heat losses are around 7% of the amount of heat consumption (Urbaneck, 2017a; Shrestha, 2019). To calculate the network load (without considering the network heat losses), the building heating loads were created using the software solar computer (module W38: cooling load and room temperature VDI 2078/6007 for Germany) and the domestic hot water heating loads

(domestic hot water profiles according to VDI 6002, part 1 (VDI, 2014)) were used. The influence of the user remains largely unconsidered in the solar computer simulations. The room temperatures according to EN 12831 supplement 1.

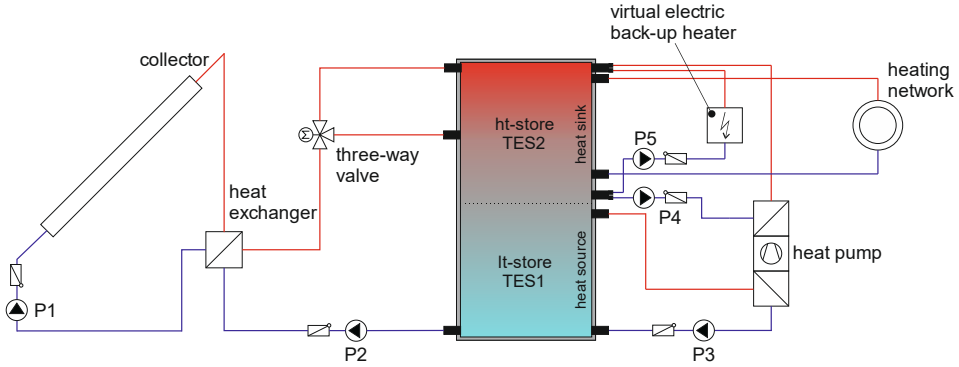

Fig. 2: Scheme of the local heating system and principle structure of the simulation with one heat pump, technical solution for the balance limit heat supply in Fig. 1 (according to Nefodov et al. (2020))

The ordered and normalised values for the network heating load are shown in Fig. 3 a). For a better assessment of the plausibility, three curves are shown in Fig. 3 a):

- the simulated network heating loads (TRY2011 as the basis for the space heating load) without network losses,
- the simulated network heating loads (TRY2011 as the basis for the space heating load) including network losses,
- measured values of the Brühl solar district heating system in Chemnitz (2018) (Urbaneck, 2017a). The heat supply system Brühl is significantly larger than the solution investigated here. However, the network temperatures and the houses (renovated apartment buildings with commercial units) with the corresponding use are partially similar. The climatic conditions also coincide. Therefore the measured values are used for comparison.

In all cases, there is a pronounced peak load range (values from 0.7 to 1.0). In the medium load range (values from 0.2 to 0.7) and in the base load range (values less than 0.2), the simulated values (blue curves) are lower than the measured values of the comparison system. The higher measured values in the medium load range can be explained by the type of use (partly commercial use at the Brühl), the user behavior (e.g., elderly people with high presence time in the apartment) or the occupancy. Load curves calculated for the Marienthal district show that the network losses (as expected) have the highest influence on the base load range.

Monthly heat amount to the network are shown in Fig. 3 b). The conversion of the annual heat demand to the areas in the district provides then the following key figures. The specific annual heat demand (using the simulated values without network losses) is 117 kWh m^{-2} a^{-1} which is related to the net effective area of the building. When converted to the useful building area according to §19 EnEV (BMJ, 2019), the value is then 97 kWh m^{-2} a^{-1}. These values are higher than the data in energy certificates of buildings in the Marienthal district (average of approx. 70 kWh m^{-2} a^{-1} in 2017, useful building area according to §19 EnEV (BMJ, 2019)). Therefore, the uncertainties mentioned above must be considered as well.

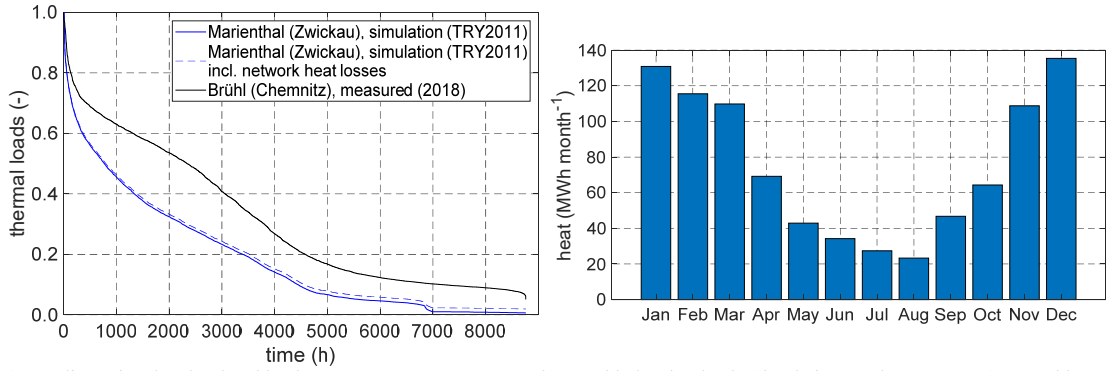

a) non-dimensional and ordered load curves

b) monthly heating loads (simulation results, TRY2011), annual heat quantities of 908.48 MWh a^{-1}

Fig. 3: Standardized network heating loads as well as monthly heat quantities into the heating network (according to Nefodov et al. (2020))

4. TRNSYS parameter study

The two most important parameters of the system are the collector area A_{coll} and the storage volume V_{TES} or storage capacity. In this parameter study these parameters were varied. Thereby, an automatic dimensioning of the system took place (e.g., volume flow in the collector circuit). Otherwise, typical values were used (e.g., thermal insulation of the storage tank). The system's main heating load remained identical in all simulations (Fig. 3:).

The use of non-renewable primary energy is to be minimised. The solar fraction f_{sol} (eq. 1) was used here as the evaluation parameter. In the simulation, the use of virtual back-up heater (Fig. 2) indicated an under-coverage by the collector array or heat pump. I.e., only at this point was non-renewable primary energy used. In case of a total avoidance of non-renewable primary energy, the solar fraction assumes 100%. The losses, which occur in particular with seasonal storage was also considered by eq. 1. Furthermore, the electricity provided for the heat pump must come from renewable energy sources (e.g., photovoltaic system, wind power). If the parameter f_{sol} takes a value of 100%, it means that the heat supply is emission-free. Otherwise, it is fraught with emissions.

$$f_{\mathrm{sol}} = \left(1 - \frac{Q_{\mathrm{VH}}}{Q_{\mathrm{Net}} + Q_{\mathrm{TES,loss}}}\right) \cdot 100 \qquad \text{(eq. 1)}$$

The dependence of the solar fraction on the collector area and the storage volume is shown in Fig. 4. Relatively large collector areas and storage volumes are necessary to completely cover the given heat load. The shown area of the solar fraction has a relatively even course. Theoretically, several system variants achieve a solar fraction f_{sol} of 100% (equivalent for an emission-free heat supply). Further analyses are to find an optimal design.

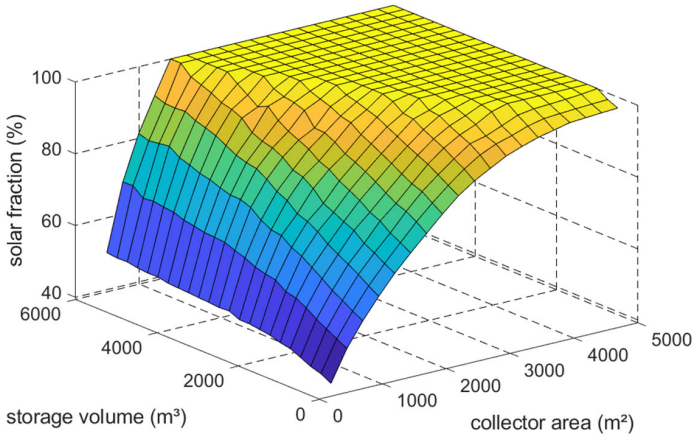

Fig. 4: Influence of the collector area and storage volume on the solar fraction, TRNSYS simulations (according to Nefodov et al. (2020))

Low heat production costs are the next evaluation parameter in this investigation. After the automatic dimensioning of the components, the investment costs were calculated on the basis of specific costs (values, functions, the reference year for the economic calculations is 2019). These investment costs were then included in the calculation of the heat production costs based on the VDI 2067. The annuity factor in the present case was 6.51% (5% interest, 30 years technical service life for all components). The heat pump operation requires a very high amount of electricity, so this cost group has a major influence. The electricity costs here were 0.16 € kWh^{-1}. Furthermore, planning, land, development and investment costs for virtual back-up heater as well as value added tax and a financial subsidy were not considered.

The heat production costs k_{h} are shown in Fig. 5 a). For better orientation, the following diagrams show the isolines (black dash lines) for the solar fraction f_{sol} of 50%, 80% and 100%. It should also be noted that in systems with high solar fractions or with an increasing ratio of collector area to storage volume, stagnation cases occur more frequently. These stagnation cases lead to a failure of the collector circuit for at least one day, to an increased thermal load on the system and possibly to consequential damage as well as to additional operation-related costs (e.g., personnel deployment for control and recommissioning). For the present evaluation, it was determined that the additional costs are 2,000 € per day with stagnation (according to assumptions, no specific measures are foreseen to avoid stagnation). The usual hourly consideration of the stagnation time does not provide information on how many days per year the system is out of operation. For this reason, it is useful to specify the number of days when stagnation occurs. In the following diagrams (Fig. 5, Fig. 6), two borderlines (red dotted lines) have been drawn for the number of stagnation days (1 and 30 days). These two borderlines divide each diagram into three sections. No stagnation occurs in the left section. I.e., the system operation proves to be safe. In the transition zone, between both limits for the stagnation time of 1 and 30 days, stagnation cases occur with increasing frequency. In the last section, the frequency of failures increases to such an extent that it is generally not advisable to design in this area for safety reasons.

In order to achieve the objective, a solar fraction of 100% is appropriate. Under consideration of the above mentioned aspects and additional costs, the optimal heat production costs in Fig. 5 a) (points L_{C1}, L_{C2}, cf. with Tab. 1) on the boundary curve for f_{sol} of 100% lie in the left-hand diagram area. I.e., optimal conditions are at low ratios of collector area to storage volume.

Fig. 5 b) additionally shows the specific investment costs $k_{\mathrm{I,spec}}$ for the systems. The investment costs here are set in relation to the annual network heat load. Increasing values indicate specifically high investments. Fig. 5 b) shows that for the f_{sol} limit curve of 100% the values are in a certain cost range. When the above-mentioned aspects are disregarded, design points in the right-hand diagram area would also be possible.

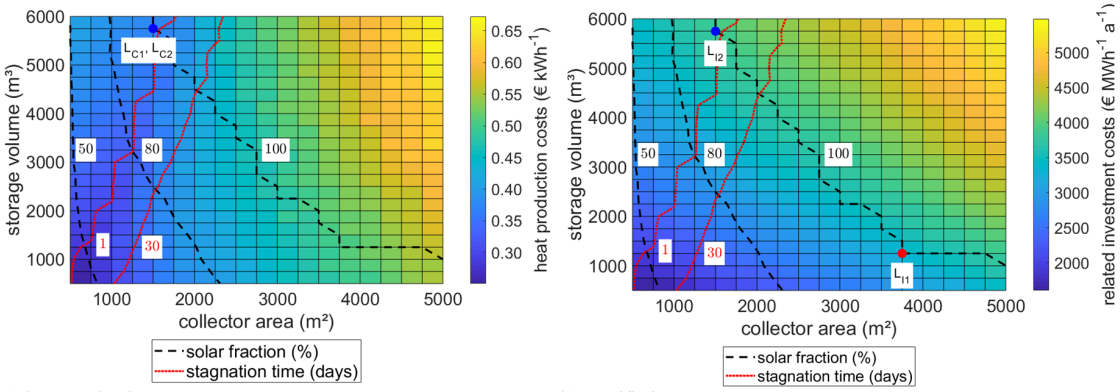

a) heat production costs b) specific investment costs

Fig. 5: Costs for different system dimensions (according to Nefodov et al. (2020))

The system requires floor area, in particular for the collector field, the storage tank and for a building (technical centre). The simplified view neglects, e.g., pipeline routes. Here it is assumed that the collector field is realised as a free-standing installation (a theoretically closed surface). This means that a minimal amount of land is used for the field. Other field constructions (e.g., roof integration on the respective buildings) and system concepts (e.g., three- and four-pipe systems) remain unconsidered. In this consideration, the urban development aspect of the consumption of floor area A_{F} for the system according to Fig. 2 should also be taken into account. The district is relatively densely built up. Distances between the existing buildings and new buildings

(e.g. supply centre) should be maintained. Existing green spaces (e.g., with laundry place or playgrounds) must be preserved at all costs. On the periphery of the district, many areas (e.g., gardens, garages) are not available for the installation of technical equipment. This is why variants with minimal land use are interesting here and in other cases as well.

Fig. 6 provides an estimate of the minimum required floor areas A_F for the system. The point $L_{a,min}$ marks the point with a minimum ground area (1,686 m²). At the same time, the secondary conditions apply that the solar fraction is 100% and no stagnation occurs. The optimum design is again in the left diagram area with low collector area-storage volume ratios.

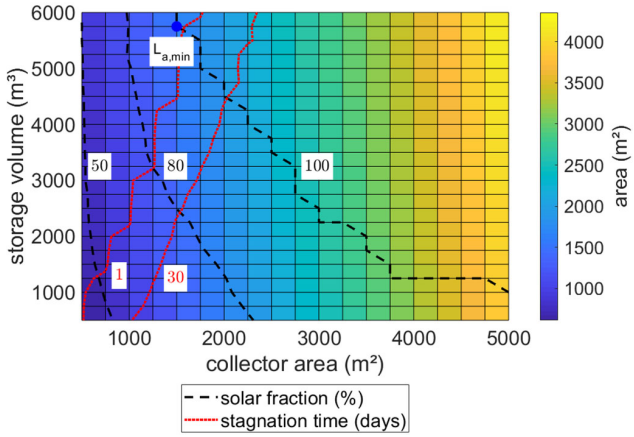

Fig. 6: Estimation of the minimum area required for the system, idealised assumptions (according to Nefodov et al. (2020))

Tab. 1 provides an overview of the discussed points L. Index 1 shows the minimum costs in each case. With index 2, the previous variants are additionally evaluated according to the minimum floor area requirement. Tab. 1 also shows key figures that are suitable for a system comparison.

Tab. 1: Overview of the points with an design according to the given criteria and key figures (according to Nefodov et al. (2020))

Location	A_{coll}	V_{TES}	A_F	k_h	$k_{I,spec}$	$\frac{A_{coll}}{V_{TES}}$	$\frac{A_{coll}}{Q_{Net}}$	$\frac{A_{coll}}{A_Q}$
	(m²)	(m³)	(m²)	(€ kWh^{-1})	(€ MWh^{-1} a^{-1})	(m² m^{-3})	(m² MWh^{-1} a^{-1})	(m² m^{-2})
L_{c1})	1,500	5,750	195.0	0.37		0.261	1.65	0.193
L_{c2})	1,500	5,750	195.0	0.37		0.261	1.65	0.193
L_{I1})	3,750	1,250	310.5		3,447.06	3.000	4.13	0.482
L_{I2})	1,500	5,750	195.0		3,924.44	0.261	1.65	0.193

By considering the stagnation cases in the cost calculations (Fig. 5 a)), there is an overlap of the points L_{c1} and L_{c2}. Thus, the minimum heat production costs are the same in both cases. The minimum specific investment costs (Fig. 5 b), point L_{I1}) are in an unfavourable range with a very high number of stagnation cases. By additionally considering the floor area requirement (Fig. 6), it turned out that the costs for L_{I2} also become minimal in the L_{c2} point. The key figures in Tab. 1 show relatively small collector areas. This seems plausible because seasonal storage is required. These ratios are approximately consistent with the literature sources or similar works (Hornberger, 1994), (Marx, 2015), (Raab, 2006).

The point L_{c2}) therefore provides the values for an optimal design of the system. With a more exact modeling of the system(e.g. heat pump operation, purchase of renewable electricity) or the boundary conditions are changed, a shift in the points shown is possible or probable.

5. Further investigations of heat pump circuits

Xiao et al. (2020) presented detailed research of the six heat pump circuits for use in the ZED project. Initially, the refrigerant R134a was used. This refrigerant damages the ozone layer and should be avoided in future applications. For this reason, further investigations were carried out. The refrigerant R134a was changed to R1234ze(E) (GWP < 1) (Regulation, 2017; Honeywell, 2017) as substitute refrigerant. To make it easier to compare the variants later, an ending was added to the variant number. Refrigerant R134a is used with the

suffix "a" and refrigerant R1234ze(E) with the suffix "ze". Tab. 2 provides an overview of the circuits considered and the attainable coefficients of performance for refrigerant R134a from Xiao et al. (2020). This section compares selected heat pump circuits (variants 1, 5 and 6 according to Xiao et al. (2020)) for both refrigerants, with the aim of identifying the advantages and disadvantages.

Tab. 2: Overview of the investigated heat pump circuits (according to Xiao et al. (2020))

variant	name	ε_{HP} (-)
1a	single-stage compression	2.62
2a	two-stage compression with subcooler economiser	3.02
3a	two-stage compression with an open-flash-economizer	3.13
4a	refrigerant circuit cascade	3.03
5a	series connection a) with common connections to the storage tank	3.21
6a	series connection b) with separate connections to the storage tank	4.16

In the following discussion, the relevant circuits (without consideration of the refrigerants) are presented first. The circuit for the heat pump system with single-stage compression (variant 1, Fig. 7) has a simple structure. Here, the essential components are: an evaporator, a condenser, an expansion valve and a compressor. With this variant, the refrigerant will be compressed directly from the evaporating pressure up to the condensing pressure. The single-stage compression heat pump process behaves less favourably with increasing pressure ratio p_c/p_0 due to the increasing compressor losses and the decreasing volumetric efficiency.

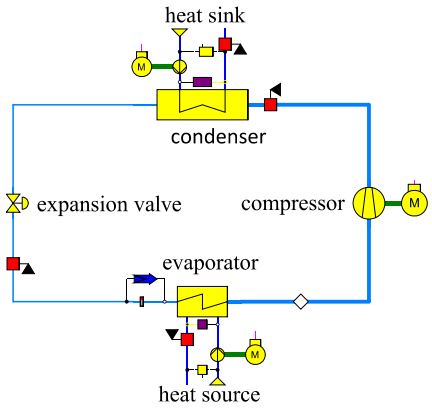

Fig. 7: Heat pump system with single-stage compression (EBSILON model), variant 1 (according to Xiao et al. (2020))

Compared to other variants, variants 5 and 6 proved to be advantageous during the investigations (Xiao et al., 2020). Here, a series connection of two single-stage heat pumps was modelled. In this case, two separate refrigerant circuits exist at different temperature levels.

At variant 5 (Fig. 8), the two refrigerant circuits are coupled with the storage tank through common connections. On the heat sink side, the water from the storage tank flows through two condensers connected in series (inlet temperature 55 °C). On the heat source side, the water is then passed analogue through two evaporators and cooled down (inlet temperature 20 °C). With variant 5, a relatively high temperature spread from 20 K can be achieved on the load side (connection of the heating network). However, with this series connection, the inlet temperature of the storage water on the heat source side (lt-store, Fig. 2) must be above the evaporation temperature in the ht-cycle (Fig. 8). Furthermore, it must be noted that if the temperature on the heat source side (lt-store, Fig. 2) is too low, operation of the ht-cycle (Fig. 8) is not possible. This reduces the available storage capacity on the heat source side.

At variant 6 (Fig. 9), both heat pump circuits have their own connections (heat sink and heat source) to the storage tank and are decoupled. For this reason, the problem mentioned in variant 5 is avoided. Since several charging and discharging devices are required here, a higher technical effort is required for storage design and operation. In this case the lt-cycle raise on the heat sink side the temperature by 40 to 45 °C and the ht-cycle by 65 to 75 °C.

Following Xiao et al. (2020), the coefficient of performance ε_{HP} is used for the energetic evaluation of heat pump circuits. Boundary conditions of the modelling and simulation are summarised in Tab. 3 and Tab. 4.

Pressure ratios may vary according to system requirements. The refrigerant mass flow of the lt-cycle of variant 6 is controlled in such a way that the heat output of the lt-cycle covers the heat extraction of the ht-cycle.

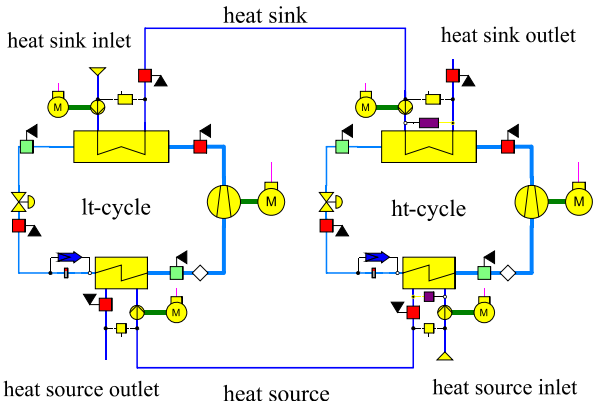

Fig. 8: Heat pump system with series connection a) (EBSILON modell), variant 5 (according to Xiao et al. (2020))

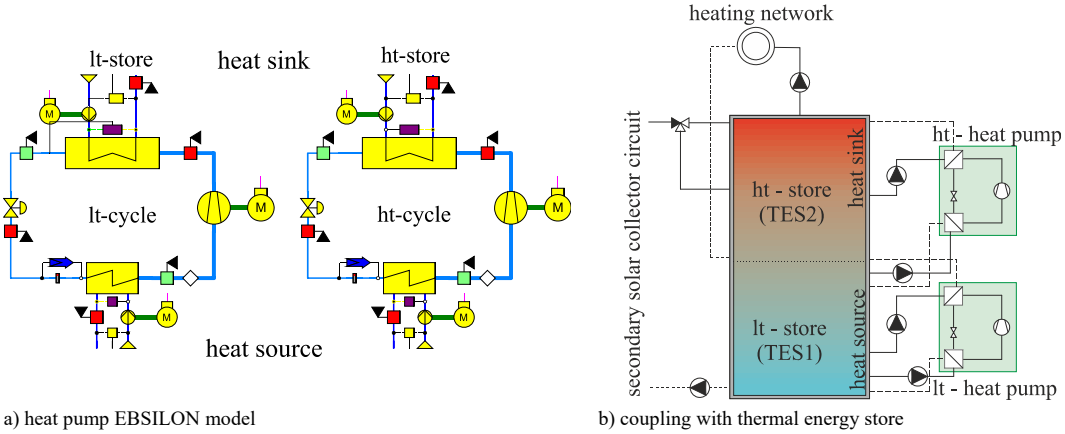

Fig. 9: Heat pump system with series connection b), variant 6 (modified according to Xiao et al. (2020))

Both variants 5 and 6 have two circuits. This allows the coefficients of performance of the lt-cycle and ht-cycle to be considered separately. The system coefficients of performance $\varepsilon_{HP,total}$ of both variants are shown in Tab. 5 and Fig. 10. Here, the coefficient of performance $\varepsilon_{HP,total}$ represents ratio of provided heat after each cycle (lt-, ht-cycle) to the electrical effort of the compressors.

The simulation results clearly show the influence of the selected refrigerants. With variant 1ze, the coefficient of performance ε_{WP} increases by 9.54% compared to variant 1a. At the same time, the heat pump heating capacity decreases by 16.2%. In variant 5, the coefficients of performance $\varepsilon_{WP,total}$ for both refrigerants remain almost identical. There is a slight improvement of 1.55% with the new refrigerant. On the other hand, the heat pump heating capacity drops by 14.08% (lt-cycle) and 14.72% (ht-cycle) compared to the circuit with refrigerant R134a. The highest coefficient of performance is achieved by the variant 6ze. The coefficient of performance increases by 36.30% compared to the circuit with the refrigerant R134a. For the lt-cycle, the heating capacity is identical in both cases. The electricity consumption with the refrigerant R1234ze(E) is reduced by 34.50% compared to the reference. At the ht-cycle, the heating capacity drops by 9.0% compared to reference refrigerant R134a. At the same time, the electricity demand decreases, so that a very high coefficient of performance is achieved overall. In total, the circuits with refrigerant R1234ze(E) show better coefficients of performance, but less heating capacity, than circuits with R134a.

Tab. 3: Basic assumptions for all EBSILON models (modified according to Xiao et al. (2020))

refrigerant	R134a	R1234ze(E)
refrigerant mass flow in the main circuit (kg s^{-1})	1.0	
subcooling of the refrigerant in the condenser (K)	0.0	
inlet temperature. heat sink (condenser) (°C)	65	
outlet temperature. heat sink (condenser) (°C)	75	

refrigerant	R134a	R1234ze(E)
overheating of the refrigerant in the evaporator (K)	10	5
inlet temperature. heat source (evaporator) (°C)	15	
outlet temperature. heat source (evaporator) (°C)	10	
pressure drop in heat exchanger (bar)	0…0.05	
minimum value for the pinch point in the heat exchangers (K)	3.0	
isentropic efficiency of the compressors (-)	0.85	
mechanical efficiency of the compressors (-)	0.99	
mechanical loss of the compressors (kW)	0.0	

Tab. 4: Further boundary conditions for the evaluation of the EBSILON circuit models (modified according to Xiao et al. (2020))

	variant 5	variant 6
supply temperature, heat source, lt-cycle (°C)	15	
supply temperature, heat source, ht-cycle (°C)	20	45
supply temperature, heat sink, lt-cycle (°C)	55	40
supply temperature, heat sink, ht-cycle (°C)	65	
refrigerant mass flow, lt-, ht-cycle (kg s^{-1})	1	

Tab. 5: Summary of the simulation results for the circuit models considered (modified according to Xiao et al. (2020))

Variant	Refrigerant	$\dot{Q}_c$ (kW)	$\dot{Q}_0$ (kW)	P_{el} (kW)	ε_{HP} (-)
1a	R134a	145.68	90.09	55.51	2.62
1ze	R1234ze(E)	122.07	79.44	42.51	2.87

Variant	Refrigerant	lt-cycle				ht-cycle				$\varepsilon_{HP,total}$ (-)
		$\dot{Q}_{c,lt}$ (kW)	$\dot{Q}_{0,lt}$ (kW)	$P_{el,lt}$ (kW)	$\varepsilon_{HP,lt}$ (-)	$\dot{Q}_{c,ht}$ (kW)	$\dot{Q}_{0,ht}$ (kW)	$P_{el,ht}$ (kW)	$\varepsilon_{HP,ht}$ (-)	
5a	R134a	155.84	110.03	45.99	3.39	142.82	96.01	46.93	3.04	3.21
5ze	R1234ze(E)	133.89	94.52	39.53	3.39	121.79	83.00	38.86	3.13	3.26
6a	R134a	104.69	75.92	28.29	3.70	133.33	103.92	28.98	4.60	4.16
6ze	R1234ze(E)	104.69	85.53	18.53	5.65	121.34	99.50	21.37	5.68	5.67

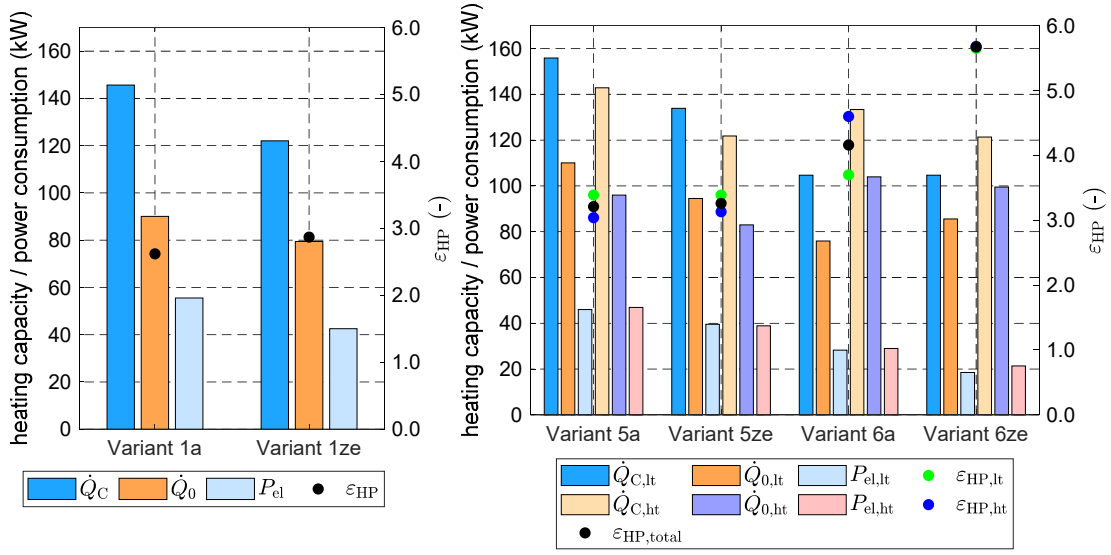

Fig. 10: Summary of the simulation results for circuit models (modified according to Xiao et al. (2020))

6. Summary and outlook

In the present paper, the feasibility and a concept for a solar local heating supply with the use of heat pumps were investigated. A heat supply in the Marienthal district (Zwickau, Germany) is possible with 100% renewable energy. The parameter study has shown that the large number of possibilities are severely limited by technical and economic criteria as well as the amount of floor space required in the district. The investigation provides preliminary parameters and key figures for an optimal system design.

The heat production costs for emission-free supply provide a moderate value of 0.37 € kWh^{-1} (for comparison: Solar local heating systems without heat pumps could achieve solar fractions of f_{sol} = 40…50 % in Germany (no emission-free). The solar heat production costs in the period from 1998 to 2004 were in the range of 0.23 € kWh^{-1}. With an increase in the solar fraction, a very strong rise in solar heating costs was observed. Further optimisation of the presented system allows for significant cost reductions, according to experience). It should be noted that the system with seasonal storage is relatively small (heat supply of 133 residential units). With increasing system size, a cost degression is to be expected. Furthermore, the system supplies a residential district with existing buildings, which are largely equipped with conventional heating technology.

Further investigations on the selected heat pump circuits using EBSILON software showed that R1234ze(E) refrigerant is well suited for heat pump operation. Compared to refrigerant R134a, higher coefficients of performance are achieved, but with lower heating capacity. For the assumed conditions, the series connection of two heat pumps with the separate connections to the storage tank is excellently suited for heat supply (variant 6). According to present investigations, a coefficient of performance of 5.67 can be achieved here.

The presented system offers even more possibilities for optimisation. Increasing the number of residential units or increasing the size of the system can further reduce specific investment costs. The inclusion of other heat sources (e.g., sewage water, geothermal energy, etc.) allows to reduce the collector size and increase the coefficients of performance in winter months. The optimisation of the heat pumps and the storage tank as well as the improvement of the system operation and control strategies will be the focus of further investigations.

Acknowledgments

The realization of the project and the scientific work is supported by the Federal Ministry for Economic Affairs and Climate Action (BMWK) on the basis of a decision by the German Bundestag (funding code 03SBE114C). The authors gratefully acknowledge this support and carry the full responsibility for the content of this paper.

References

Bundesministerium der Justiz und für Verbraucherschutz. *Verordnung über energiesparenden Wärmeschutz und energiesparende Anlagentechnik bei Gebäuden*. [Online] Available from: https://www.gesetze-im-internet.de/enev_2007/__19.html [accessed: 20.07.2019].

Der Deutsche Wetterdienst. *Wetter und Klima - Deutscher Wetterdienst - Der DWD*. [Online] Available from: https://www.dwd.de/DE/derdwd/derdwd_node.html [accessed: 08.01.2018].

Honeywell Belgium N.V., 2017. Solstice® ze Refrigerant (HFO-1234ze).

Hornberger, M., 1994. Solar unterstützte Heizung und Kühlung von Gebäuden. Bd. 47, Diss., Deutscher Kälte- und Klimatechnischer Verein, Stuttgart, Universität.

Leonhardt, S., Höhne, E., Neumann, T., Teich, T., Bodach, M., Hoffmann, M., Kretz, D., Hempel, T., Schwind, M., Franke, S., Urbaneck, T., Gill, B., Schneider, M., 2018. Demonstration einer energieeffizienten und sozialgerechten Quartiersentwicklung auf Basis elektrisch-thermischer Verbundsysteme in Zwickau Marienthal – Projekt ZED: Zwickauer Energiewende demonstrieren, in: Pöschk, J. (Eds.), Energieeffizienz in Gebäuden – Jahrbuch 2018. VME – Verlag und Medienservice Energie, Berlin, pp. 147-154.

Marx, R., 2015. Integration von Wärmepumpen in solare Nahwärmeanlagen mit saisonaler Wärmespeicherung. Diss., Shaker, Stuttgart, Universität, Aachen.

Nefodov, D., Xiao, S., Urbaneck, T., 2019. Emissionsfreie Wärmeversorgung – Stand der Technik und ein neuer Ansatz. Lüftung/Klima, Heizung/Sanitär, Gebäudetechnik (HLH), VDI Fachmedien 70, Nr. 9, pp. 90-97.

Nefodov, D., Xiao, S., Urbaneck, T., 2020. Solarthermie als Schlüssel für eine emissionsfreie Wärmeversorgung auf Quartiersebene. Lüftung/Klima Heizung/Sanitär Gebäudetechnik (HLH), VDI Fachmedien 71, Nr. 9, pp. 38-44.

Oppelt, T., Urbaneck, T., Otto, S., Heinrich, I., Schmidt, A., Göschel, T., Uhlig, U., Frey, H., 2018. Development of a software system for optimal operation of heating networks with central solar plant. *ISES EuroSun 2018 Conference – 12th International Conference on Solar Energy for Buildings and Industry.* Rapperswil, Switzerland.

Projektträger Jülich (PtJ) (2019) Solares Bauen/Energieeffiziente Stadt. [Online] Available from: https://www.ptj.de/solares-bauen-energieeffiziente-stadt [accessed: 10.02.2019].

Raab, S., 2006. Simulation, Wirtschaftlichkeit und Auslegung solar unterstützter Nahwärmesysteme mit Heißwasser-Wärmespeicher, Diss., Cuvillier Verlag, Stuttgart, Universität.

Regulation (EU) No 517/2014 of the European parliament and of the Council of 16 April 2014 on fluorinated greenhouse gases and repealing Regulation (EC) No 842/2006. Official Journal of the European Union. 20.5.2014.

Shrestha, N. L., 2019. Internal information. Technische Universität Chemnitz, Chemnitz.

STEAG Energy Services GmbH, 2019. EBSILON®Professional.

The Press and Information Office of the Federal Government (BPA) (2020) *The EU should be climate-neutral by 2050*. [Online] Available from: https://www.bundesregierung.de/breg-en/issues/climate-action/more-climate-protection-in-eu-1797114 [accessed: 21.07.2022].

TRNSYS: A TRaNsient SYstems Simulation Program - Version 18, 2019. Solar Energy Laboratory, Univercity of Wisconsin-Madison und Transsolar Energietechnik GmbH, Stuttgart.

Urbaneck, T., 2017a. Internal information. Technische Universität Chemnitz, Chemnitz.

Urbaneck, T., Findeisen, F., Mücke, J. M., Lang S., Gensbaur, M., Bestenlehner, D., Drück, H., Beyer, R., Pieper, K., 2014 - 2018. Oberirdische Speicher in Segmentbauweise für Wärmeversorgungssysteme – OBSERW; Abschlussbericht zum Verbundvorhaben. 2018a. Förderkennzeichen: 03ET1230A/B/C. [Online] Available from: http://nbn-resolving.de/urn:nbn:de:bsz:ch1-qucosa2-210713 [accessed: 12.02.2019]

Urbaneck, T., Oppelt, T., Sehwöster, I., Bank, E. F., 2018b. Große Druckbehälter als thermische Energiespeicher, Teil 1: Vor- und Nachteile sowie Einsatzgrenzen. EuroHeat&Power, VWEW Energieverlag 47, issue 11-12, pp. 18-23.

Urbaneck, T., Oppelt, T., Shrestha, N. Lal, Platzer, B., Göschel T., Uhlig, U., Frey, H., 2017b. Technische Umsetzung der solaren Fernwärme Brühl. EuroHeat&Power, VWEW Energieverlag 46, issue 11, pp. 20-23.

VDI 6002 Blatt 1, März 2014. Solare Trinkwassererwärmung Allgemeine Grundlagen, Systemtechnik und Anwendung im Wohnungsbau. Beuth Verlag GmbH, Berlin.

Xiao, S., Nefodov, D., McLinden, Mark O., Richter, M., Urbaneck, T., 2022. Working fluid selection for heat pumps in solar district heating systems. Solar Energy, Elsevier 236, pp. 499-511. https://doi.org/10.1016/j.solener.2022.02.036

Xiao, S., Nefodov, D., Urbaneck, T., 2020. Untersuchungen von Wärmepumpenschaltungen – Simulationen von Kompressionswärmepumpen mit großem Temperaturhub und variablen Quelltemperaturen, in: Deutscher Kälte- und Klimatechnischer Verein e. V. DKV (Eds.), Deutsche Kälte- und Klimatagung 2019 Ulm.

Nomenclature

Symbol	Description	Unit
Latin letters		
A	area	m²
f_{sol}	solar fraction	%
k_{h}	heat production costs	€ kWh^{-1}
$k_{\mathrm{I,spec}}$	specific costs	€ MWh^{-1} a^{-1}
P_{el}	electric power	W
p_0	evaporator pressure	Pa
p_{c}	condenser pressure	Pa
Q	heat quantity	MWh a^{-1}
$\dot{Q}_0$	thermal capacity, evaporator	W
$\dot{Q}_{\mathrm{c}}$	thermal capacity, condenser	W
V	volume	m³
Greek letters		
$\varepsilon_{\mathrm{HP}}$	coefficient of performance	-

Indices and abbreviations	
a	area
BMBF	Bundesministerium für Bildung und Forschung (engl.: Federal Ministry of Education and Research)
BMWK	Bundesministerium für Wirtschaft und Klimaschutz (engl.: Federal Ministry for Economic Affairs and Climate Action)
c	heat production costs
coll	Collector
DWD	German Meteorological Service
F	floor
HP	heat pump
ht	high temperature
I	investment costs related to the annual heat load
L	location
lt	low temperature
Net	local heating network
P	pump
Q	living space
TES	thermal energy storage
VH	virtual back-up heater
ZED	Demonstration of German Energy Transition in Zwickau

ANALYSIS OF THE ELECTRICAL CONSUMPTION OF AN AIR-COOLED SINGLE EFFECT AMMONIA/WATER CHILLER

María Esther Palacios-Lorenzo[1], José Daniel Marcos[1]

[1]Dept. of Energy Engineering, Universidad Nacional de Educación a Distancia, UNED, Madrid, (Spain)

Abstract

In this work it is analyzed the effect of the air-coolant flow rate on the absorption chiller performances. With this purpose, a discrete mathematical model has been developed and implemented in Engineering Equation Solver Software, on the bases of mass, species and energy conservation balances. The model has been validated with experimental data of the commercial chiller ROBUR model ACF60-00 LB. Results show that a moderate decrease of the air-coolant velocity may have a positive effect on the chiller performances due to leads to reduce the thermal load of the solution heat exchanger and, simultaneously, the high-level pressure. On the other hand, the electric COP increases due to the marginal decrease in theair-coolant mass flow rate per absorber surface. The drawback is the increase of the absorber size.

Keywords: *air-coolant chiller; ammonia-water; absorption chiller; ASTEP Project; solar cooling*

1. Introduction

Heat supply systems based on absorption heat pump have great potentials on energy saving and emission reduction being able to be powered by waste thermal energy and solar energy, reducing notable electricity consumption. The most common working fluid in absorption refrigeration cycles able to achieve subzero cooling temperatures is the ammonia/water pair. The European ASTEP project is being developed within this framework, and one of its main objectives is to demonstrate the feasibility of the application of solar thermal energy to partially cover the cooling demands at an industrial site, the MANDREKAS dairy company, with a cooling demand at 5ºC. Within that project, the present work aims to study the feasibility and main constrains to use a commercial air-cooled ammonia/water absorption chiller driven by a patented solar concentrator (sun dial) to satisfy the MANDREKAS's cooling demand at different outdoor conditions.

A key feature of the air-cooled absorption chillers is its electrical consumption mainly the amount of air-coolant flow, which should be minimized in order that to be competitive to the vapor compressors of similar cooling capacity (Izquierdo et al., 2012). To evaluate the electrical consumption of the air-cooled chilled when operating in different conditions, the main components of the chiller, namely, distillation column, air-cooled absorber, evaporator and condenser, have been modelled by implementing a discrete model, and subsequently integrated to the whole chiller.

This study analyses the electrical consumption required to cool down the air-cooled absorber and condenser. In particular, the commercial chiller ROBUR model ACF60-00 LB, indirectly fired by pressurized hot water, has been considered.

2. Methods

To study the performance of the single effect air-cooled ammonia/water absorption chiller, a mathematical model has been implemented in Engineering Equation Solver Software, on the bases of mass, species and energy conservation balances (Herold et al. 2016). The material thermal properties have been evaluated from Ibrahim et al (1993). Figure 1 shows a schematic diagram of the chiller. The geometry of the different devices of which the chiller consists, are detailed in Table 1. The distillation column includes a rectifying section and a stripping section, located respectively, above and below of the column feed entry point. A rectifier completes the purification system to achieve vapor refrigerant with a high grade of purity. The lack of appreciable benefits that the rectifying section entails, beside the decrease of COP associated with the use of coupled fluid-cooled rectifier (Fernández-Seara et al., 2002, 2003). and the schematic diagram of the ROBUR (Pereira et al., 2017) justifies considering the purifying system to consist of a distillation column

© 2022. The Authors. Published by International Solar Energy Society
Selection and/or peer review under responsibility of Scientific Committee
doi:10.18086/eurosun.2022.08.09 Available at http://proceedings.ises.org

fed from above (only with striping section) helped by a concentrated solution-cooled rectifier to obtain refrigerant vapor of the required purity. On the other side, the refrigerant absorption process in the concentrated solution-cooled absorber has been neglected, being then replaced by the solution heat exchanger.

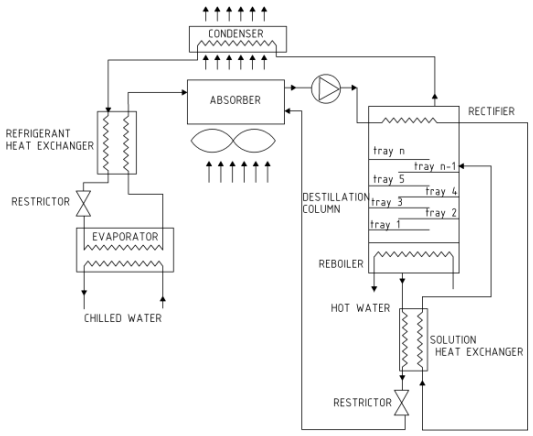

Fig. 1: Schematic diagram of the air-cooled ammonia-water absorption machine

Condenser, absorber, and evaporator tubes are described by its inner diameter, D_i, and thickness, e. The number of tubes is fixed for condenser, absorber, and evaporator, while the tubes length for these devices are obtained in the design process. Conversely, the evaporator tubes length, L, is fixed, while the number of baffles for the chilled water passage is obtained in the design process. The geometry of the finned surface for condenser and absorber, determined by the fin thickness, t_m, hydraulic diameter, D_h, minimum free flow area per frontal area, σ, and heat transfer area to total volume, α, are shown in the table. The reboiler is assumed to be a cylinder equipped externally with annular fins, with the hot water in cross flow over the cylinder, through the resulting fined annuli passage. Geometry of the reboiler annuli finned surface is defined by the length, h_f, thickness, t_m, and pitch, s, of the fins. The distillation column geometry is defined by its inner diameter D_i, hole diameter, d_h=0,00381 m, tray thickness, e_{tray}, tray spacing, S_t, weir length, l_w, hole pitch, s_h=3 d_h, weir height, h_w. and two relationships, f_1 and f_2 (Coker, 2010), being A_t=π/4 D_i^2, A_d, and A_a=A_t-2A_d, the column area, the downcomer area and the active area, respectively.

Table 1. Chiller geometry

Condenser/Absorber		**Distillation column**		**Evaporator**		**Reboiler**	
D_e [m]	0,1638	D_i [m]	0,075	D_i [m]	0.015	h_f [m]	0,01
t_m [m]	0,0004	A_d [m^2]	0,12 A_t	e [mm]	0.002	t_m [m]	0,0004
s [m]	0,00327	S_t [m]	0,15	s [m]	1,15(D_i+e)	s [m]	0,003
D_h [m]	0.0068	h_w [m]	0,1 S_t	N_{tube}	35		
σ	0.499	e_{tray} [m]	0,003	$D_{i,shell}$ [m]	(N_{tube} +1) s		
α [m^2/m^3]	269	A_d/A_t	$f_1(l_w/D_i)$	L [m]	1,1		
N_{tube}	2	A_h/A_a	$f_2(d_h/s_h)$				

Table 2 includes the effectiveness for reboiler, evaporator, condenser and air-cooled absorber, at the design point, required to determine the tubes length of absorber, and condenser, the number of baffles of the evaporator and the height of the reboiler. The effectiveness for these devices is evaluated when the chiller operates at any off-design condition. Conversely, for simplicity, the effectiveness of both internal heat exchangers (solution and refrigerant heat exchangers) is assumed to be constant in every operating condition. In addition, both the ammonia refrigerant mass fraction and the refrigerant quality at the exit of

evaporator are fixed values to limit the refrigerant temperature glide. e_w refers to the weight of the liquid entrainment per unit weight of vapor flowing in the distillation column

Table 2. Chiller parameters

Performance constrictions			**Design point**			
$x_{m,ref}$	0,99		**Coupling fluids temp. change**		**Miscellaneous**	
$Q_{out\ evap}$	0,92		$\Delta T_{cf\ abs}$[C]	1,5	$\dot{Q}_{evap}$[kW]	7,5
e_w	0,05		$\Delta T_{cf\ cond}$ [C]	5	T_{amb} [C]	35
Internal heat exchanger effectiveness	ε_{shx}	0,5	$\Delta T_{cf\ evap}$ [C]	5	$T_{cf\ evap\ out}$ [C]	-5
	ε_{rhx}	0,85	$\Delta T_{cf\ desb}$ [C]	5		

A lumped steady state model has been developed based on the application of global mass, species and energy balance and heat transfer equations and heat exchange effectiveness. The effectiveness of the evaporator, ϵ_e, is defined as (Kim et al. 2008).

$$\epsilon_e = \frac{t_{ei} - t_{eo}}{t_{ei} - T_e} \qquad \text{(eq. 1)}$$

where T and t refer to the temperature of the working fluid and the secondary fluid, respectively. The subscripts i and o refers respectively to the inlet and outlet of the condenser. Therefore, the temperature at the evaporator outlet is calculated as

$$T_e = t_{eo} + \Delta T_{cf\ evap}\left(1 - \frac{1}{\varepsilon_e}\right) \qquad \text{(eq. 2)}$$

being $\Delta T_{cf\ evap}$ the temperature increase suffered by the chilled water as it flows past the evaporator. Similarly, the temperature at the condenser outlet, T_c, may be calculated as

$$T_c = t_{ci} + \frac{\Delta T_{cf\ cond}}{\varepsilon_c} \qquad \text{(eq. 3)}$$

where the effectiveness of the condenser, ϵ_c, is defined as

$$\epsilon_c = \frac{t_{co} - t_{ci}}{T_c - t_{ci}} \qquad \text{(eq. 4)}$$

being $\Delta T_{cf\ evap}$ the temperature increase suffered by the air coolant as it flows past the condenser. In Eqs. (1) and (2), the refrigerant stream is the lowest heat capacity since it undergoes phase change. Note that

$$t_{ci} = T_{amb} + \Delta T_{cf\ abs} \qquad \text{(eq. 5)}$$

where $\Delta T_{cf\ abs}$ refers to the increase of the air coolant temperature as it flows past the absorber. The ammonia mass fraction of both the concentrated, $x_{m\ CS}$, and the diluted solution, $x_{m\ DS}$, is obtained from the reboiler and absorber effectiveness, ϵ_g, ϵ_a, expressed respectively as,

$$\epsilon_g = \frac{T_{go} - T_{gi}}{t_{gi} - T_{gi}} \qquad \text{(eq. 6)}$$

$$\epsilon_a = \frac{T_{ai} - T_{ao}}{T_{ai} - t_{ai}} \qquad \text{(eq. 7)}$$

where the lowest heat capacity is the working stream due to its lower mass flow rate. The temperature of the working fluid at the outlet and inlet of each device is obtained assumed saturated state.

Diluted and concentrated solution flow rates are obtained from the Eqs. (8)-(9) based on mass and species balance in the absorber

$$\dot{m}_s(x_{CS} - x_{DS}) = \dot{m}_r\, x_{CS} \qquad \text{(eq. 8)}$$

$$\dot{m}_{DS} + \dot{m}_r = \dot{m}_{CS} \qquad \text{(eq. 9)}$$

where the refrigerant flow rate, $\dot{m}_r$,is evaluated as

$$\dot{m}_r \approx \frac{\dot{Q}_e}{h_c^{fg}} \qquad \text{(eq. 10)}$$

In addition, the heat transfer rate for absorber or condenser, $\dot{Q}$, is determined with the energy balance, Eq. (11), at the component

$$\dot{Q} + \sum_k \dot{m}_k \cdot h_k = 0 \qquad \text{(eq. 11)}$$

where the solution mass flow rate is denoted by $\dot{m}_k$. The subscript *k* refers to each one of the flows involved in the device. Finally, the mass flow rate of the coupling fluids for evaporator, (chilled water), absorber and condenser (air coolant) are determined.

To determine the reboiler heat transfer rate, the set consist of the reboiler, the purification system and the solution heat exchanger have been modelled. The commercial chiller includes an adiabatic tray type distillation column. Negligible benefit is expected from the rectification section due to its low efficiency (Fernández-Seara et al., 2003). Accordingly, the rectifying section of the distillation column is avoided in the model. Vapor generated in a lower tray experiences liquid-vapor contact with colder solution from the upper tray. The coupled heat and mass transfer process leads to a temperature reduction and purification of the vapor. The liquid flow leaving the tray is assumed to be at thermodynamic equilibrium. Conversely, the ammonia molar fraction of the vapor leaving the i-tray, $\bar{x}_{v,i}$, is obtained calculating the Murphree vapor plate efficiency, e_M. In that way,

$$\bar{x}_{v,i} = \bar{x}_{v,i-1}(1 - e_M) + e_M \bar{x}_{v\,e,i} \qquad \text{(eq. 12)}$$

where $\bar{x}_{v\,e,i}$, refer to the molar fraction of the vapor leaving the i-tray at thermodynamic equilibrium. The Murphree vapor plate efficiency is obtained as

$$e_M = 6.8 \left(N_{R_e} N_{S_c}\right)^{0.1} \left(N_{D_g} N_{S_c}\right)^{0.115} \qquad \text{(eq. 13)}$$

where N_{R_e}, N_{S_c}, N_{D_g} are dimensionless groups depending on some thermodynamic properties of the liquid (σ_L, μ_L, ρ_L, diffusivity of the liquid light key component, evaluated with the Wilke-Chang expression (Coker, 2010), vapor velocity and geometrical characteristics of the column (fractional free area, A_h/A_t, and weir height, h_w). The effect of the liquid entrainment in the Murphree vapor plate efficiency has also been considered by using the Fair method (Coker, 2010). The reboiler Murphree efficiency is assumed to be 1. The vapor purification process is eventually completed by partial condensation in the liquid-cooled rectifier.

Conservation equations for mass, species and energy in every tray are added to the equation set (14)-(25), being reboiler and rectifier considered as additional trays.

Tray without feed:

$$\dot{m}_{L,i+1} + \dot{m}_{V,i-1} = \dot{m}_{L,i-1} + \dot{m}_{V,i+1} \qquad \text{(eq. 14)}$$

$$x_{L,i+1}\dot{m}_{L,i+1} + x_{V,i-1}\dot{m}_{V,i-1} = x_{L,i-1}\dot{m}_{L,i-1} + x_{V,i+1}\dot{m}_{V,i+1} \qquad \text{(eq. 15)}$$

$$h_{L,i+1}\dot{m}_{L,i+1} + h_{V,i-1}\dot{m}_{V,i-1} = h_{L,i-1}\dot{m}_{L,i-1} + h_{V,i+1}\dot{m}_{V,i+1} \qquad \text{(eq. 16)}$$

Reboiler:

$$\dot{m}_{L,1} = \dot{m}_{DS} + \dot{m}_{V,1} \qquad \text{(eq. 17)}$$

$$x_{L,1}\dot{m}_{L,1} = x_{L,i-1}\dot{m}_{DS} + x_{V,1}\dot{m}_{V,1} \qquad \text{(eq. 18)}$$

$$h_{L,1}\dot{m}_{L,1} + \dot{Q}_{reboiler} = h_{PS}\dot{m}_{DS} + h_{V,1}\dot{m}_{V,1} \qquad \text{(eq. 19)}$$

Feed tray:

$$\dot{m}_{L,F} + \dot{m}_{L,i+1} + \dot{m}_{V,i-1} = \dot{m}_{L,i-1} + \dot{m}_{V,i+1} \qquad \text{(eq. 20)}$$

$$x_{L,F}\dot{m}_{L,F} + x_{V,i-1}\dot{m}_{V,i-1} = x_{L,i-1}\dot{m}_{L,i-1} + x_{V,i+1}\dot{m}_{V,i+1} \qquad \text{(eq. 21)}$$

$$h_{L,F}\dot{m}_{L,F} + h_{V,i-1}\dot{m}_{V,i-1} = h_{L,i-1}\dot{m}_{L,i-1} + h_{V,i+1}\dot{m}_{V,i+1} \qquad \text{(eq. 22)}$$

Rectifier:

$$\dot{m}_{V,i-1} = \dot{m}_R + \dot{m}_C \qquad \text{(eq. 23)}$$

$$x_{V,i-1}\dot{m}_{V,i-1} = x_R\dot{m}_R + x_{ref}\dot{m}_{ref} \qquad \text{(eq. 24)}$$

$$\dot{Q}_{rect} + h_{V,i-1}\dot{m}_{V,i-1} = h_R\dot{m}_R + h_C\dot{m}_{ref} \qquad \text{(eq. 25)}$$

where *R*, *C* and *ref* subscripts refer to reflux and vapor refrigerant coming into the condenser, respectively. Subscript *DS* refers to the diluted solution coming out to the reboiler.

2.1. Solution method

The previous formulation may be used in two different ways, namely in the design process of the chiller and as a tool to analyses its off-design performance. In the design process, the value of $\Delta T_{cf\ abs,}$ $\Delta T_{cf\ cond\ ,}$ $\Delta T_{cf\ desb}$ and $\Delta T_{cf\ \ evap}$ are fixed, what lets to determine the length of the condenser and absorber tubes, L_{cond}, $L_{abs,}$ the reboiler heigh, h_{reboil}, and the number of baffles of the evaporator, $N_{baffles}$. In that way, the whole geometry of the chiller may be determined. Chiller performance at off-design conditions may be analysed then, but now $\Delta T_{cf\ abs,}$ $\Delta T_{cf\ cond\ ,}$ $\Delta T_{cf\ desb}$ and $\Delta T_{cf\ \ evap}$ are unknown magnitudes. The solution method for both design chiller and analysis of off-design performances requires an iterative process to match assumed and calculated values for effectiveness of the external heat exchangers and for the temperature change suffered by the corresponding coupling fluid.

Therefore, additional modelling for the external heat exchangers has been developed and implemented. All these models provide the temperature change suffered by the coupling fluid associated with each external heat exchanger. Then, mathematical models for the absorber, condenser, evaporator and reboiler, based on mass, and energy balance, and heat and mass transfer equations, have been developed and implemented. These models are of discrete type for the absorber, condenser and evaporator, and of lumped type for the reboiler. Specifically, the energy balance at the tube solid wall stablishes that

$$\dot{Q}_{l,out} = \dot{Q}_c \qquad \text{(eq. 26)}$$

In Eq. (26), $\dot{Q}_{l,out}$ is the heat flow from the bulk refrigerant to the wall,

$$\dot{Q}_{l,out} = U_{out} \cdot (T_{bL} - T_w) \cdot dA_c \qquad \text{(eq. 27)}$$

where the overall heat transfer coefficient, U_{out}, is given by Eq. (28)

$$U_{out} = \frac{1}{\frac{D_{wo}}{2 \cdot k_w} \ln\frac{D_{wo}}{D_{wi}} + \frac{D_{wo}}{h_{lw} \cdot D_{wi}}} \qquad \text{(eq. 28)}$$

being D_{wi} and D_{wo} the inner and outer tube diameter, respectively. dA_c is the inner heat transfer area from the tube wall to the coolant. h_{lw} refers to the heat transfer coefficient between the liquid phase and the inner tube wall. In addition, $\dot{Q}_c$ is the heat flow transferred from the wall to the air coolant, which is calculated from Eq. (29)

$$\dot{Q}_c = h_{t,c} \cdot \Delta T_{lm} \cdot dA_c \qquad \text{(eq. 29)}$$

being $h_{t,c}$ is the heat transfer coefficient between the wall and the air coolant and ΔT_{lm} the logarithmic mean temperature difference, which is defined as

$$\Delta T_{lm} = \frac{(T_w - T_{ci}) - (T_w - T_{co})}{\ln\frac{T_w - T_{ci}}{T_w - T_{co}}} \qquad \text{(eq. 30)}$$

where the subscripts *ci* and *co* refer to coolant inlet and coolant outlet of the differential control volume, respectively. Eq. (26) lets, known the bulk temperature of the liquid phase, T_{bL}, to obtain T_{co}, and eventually, ΔT_{cf} for each external heat exchanger.

2.1.1 Air-cooled absorber

Bulk temperature of the liquid phase, T_{bL}, is obtained by means of mass, species and energy balance at the vapor and liquid interface. Namely, mass balance at interface, which states than the mass transfer between the vapor and the liquid phases must be equal, can be expressed as Eq. (31), where a film model is used. Eq. (32) is obtained stating a balance energy at the liquid vapor interface (Fernández-Seara et al., 2002, 2003; Sieres et al., 2007)

$$f_1(T_i, z) = 0 \qquad \text{(eq. 31)}$$

$$f_2(T_i, z) = 0 \qquad \text{(eq. 32)}$$

In these equations, *z* refers to the ratio of ammonia to total molar flux through the interface and T_i is the temperature interface. An iterative process leaves to calculate total and partial mass fluxes transferred

through the interface, $\dot{m}$, $\dot{m}_{NH3}$ and $\dot{m}_{H2O}$. New vapor condition is calculated from mass and energy balance in the bulk vapor phase based on the differential control volume, which stablish that

$$d\dot{m}_v = -\dot{m} \quad \text{(eq. 33)}$$

$$d(x_{vb}\dot{m}_v) = -\dot{m}_{NH3} \quad \text{(eq. 34)}$$

$$d(h_{vb}\dot{m}_v) = -\left(\dot{m}_{NH3} \cdot h_{v,NH3} + \dot{m}_{H2O} \cdot h_{v,H2O} + \dot{q}_v\right) \quad \text{(eq. 35)}$$

Similarly, flow rate, temperature and composition of the liquid phase at the exit of the control volume may be obtained with mass balance in the bulk liquid, which states that

$$d\dot{m}_l = \dot{m} \quad \text{(eq. 36)}$$

$$d(x_{lb}\dot{m}_l) = \dot{m}_{NH3} \quad \text{(eq. 37)}$$

$$d(h_{lb}\dot{m}_v) = -\left(\dot{m}_{NH3} \cdot h_{l,NH3} + \dot{m}_{H2O} \cdot h_{l,H2O} + \dot{q}_v\right) \quad \text{(eq. 38)}$$

2.1.2 Condenser and evaporator

Bulk temperature of the liquid phase, T_{bL}, is obtained by means of mass and energy balance at the solution biphasic side.

2.2. Heat and mass transfer coefficients

In the reboiler, the heat transport coefficient between the finned tube wall and the coolant is obtained from (Kay, 1984) and the heat transfer coefficient in the solution side is calculated from Táboas et al., (2007), to consider the mass transfer resistance though the liquid-vapor interface at solution side. The correlation proposed by Klimenko (Mills, 1999) is used between the biphasic refrigerant and the tube surface. In the evaporator, the heat transport coefficient between the tube wall and the coolant is obtained following the procedure described in VDI Heat Atlas (Wärmeatlas, 2010) for the shell-side heat transfer in baffled shell-and-tube heat exchangers. In the condenser and in the absorber, the heat transfer coefficient between the liquid and the tube surface is calculated from the film wise condensation theory in a horizontal tube. In laminar regime, the heat transfer coefficient is obtained from the Nusselt equation for a smooth film (Wärmeatlas, 2010), ignoring the vapor shear stress effect. The increase in heat transfer due to the waviness of the film flow is considered with the Kutateladze and Gogonin equation (Wärmeatlas, 2010). In turbulent regime, the Yüksel and Müller equation (Wärmeatlas, 2010) has been used to calculate the heat transfer coefficient. Corrections proposed by Numrich equations (Wärmeatlas, 2010) have been applied to consider the effect of the shear stress at the condensate film surface, both in laminar and turbulent regime. The heat transport coefficient between the solid surface and the coolant for absorber and condenser has been evaluated by the EES software (7.75-5/8T type) (Kay, 1984). In the absorber, the heat transfer coefficient between the liquid and the liquid vapor interface is assumed to be equal to the heat transfer coefficient between the liquid and the tube wall. The heat transfer coefficient in the refrigerant vapor phase is obtained from Gnielinski (Wärmeatlas, 2010). The mass transfer coefficient is calculated by means of the Chilton and Colburn analogy (Wärmeatlas, 2010) from the heat transfer coefficient.

2.3 Mathematical model validation

The implemented mathematical model has been validated considering the COP and cooling capacity data provided by the manufacture. Note certain discrepancy between experimental data and predicted for chilled water temperature at -5 ^{o}C figure 2 (left) when the outdoor temperature is at 40 ^{o}C. This is attributable to the implemented model is no longer being adequate when the distillation column operates at weep mode, as it may happens when the chiller cooling capacity is very low.

3. Results

The air-coolant absorption chiller, powered by hot water flow, rejects thermal energy from the absorber-condenser assembly to the ambient and so, it can capture energy from the flow water to be chilled in the evaporator. Therefore, the state of the coupling fluids, namely inlet temperature and mass flow rate of the feed water, coolant air and chilled water, determines the performance of the air-cooled absorption chiller. In this work, the inlet temperature of chilled water instead of the outlet temperature is adopted as chiller parameter due to its practical interest. Particularly, the velocity of the air-coolant flow exerts a major influence not only in the size of the absorber-condenser assembly but in the electrical consumption of the chiller.

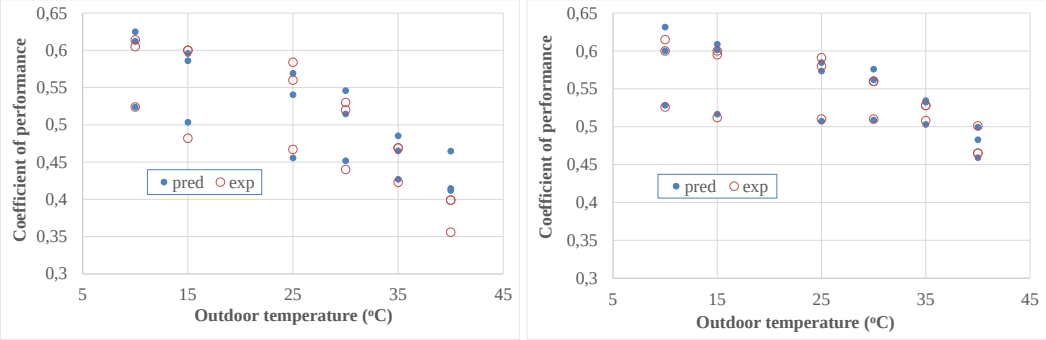

Fig.2: Predicted and manufacture COP data versus outdoor temperature. Hot water mass flow rate: 3500 l/h. Chilled water mass flow rate: 2600 l/h. Hot water temperature: 160, 185 and 240 ºC. Chilled water temperature: -5 ºC (left), 0 ºC (right).

Several cases have been analysed, which characteristics are described in table 1. Firstly, case A is studied. Then, the role of the velocity air-coolant flow is analysed by comparing case B

For each case studied, cooling capacity and COP has been provided by the manufacture, the value of all other significant parameters has been predicted with the implemented model.

Table 3.- Description of the studied cases

	Feed water flowrate (l/h)	**Chilled water flowrate (l/h)**	**Air-coolant velocity (m/s)**	**Chilled water outlet temp. (ºC)**	**Outdoor temp. range (ºC)**	**Feed water temp. range (ºC)**
Case A	3500	2600	2	-5	10-40	160-210
Case B	3500	2600	1	-5	10-40	160-210

3.1. Analysis of the absorber size

The refrigerant absorption in the absorber involves heat and mass transfer processes which rate are partly governed by the absorber thermal resistance, closely related to the air-coolant velocity The refrigerant absorption rate for a variety of working condition has been evaluated. Figure 3 presents the average refrigerant mass flowrate per absorber surface, $\dot{m}_{ref,Aabs}$, when the size of the absorber is the minimum to assure the complete absorption of the refrigerant flow as it passes through the absorber. Similar values were found in water-cooled ammonia-water absorbers (Fernández-Seara et al., 2005). The figure shows that $\dot{m}_{ref,Aabs}$ behaves asymptotically as the air-coolant velocity increases. Therefore, results reveal the existence of a practical maximum for the air-coolant velocity beyond which no further reduction in the absorber size is expected. In this study, the maximum air-coolant flow velocity is set at 2 m/s for the finned surface used to model the absorber.

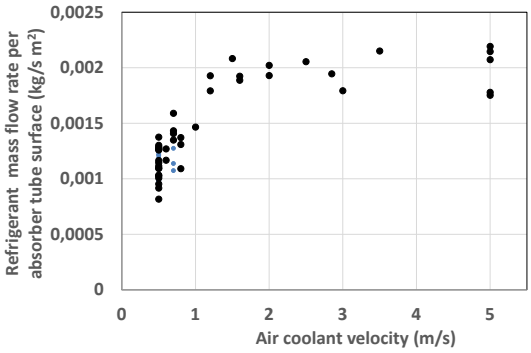

Fig 3: Average refrigerant mass flowrate per solid absorber wall surface versus air coolant velocity.

3.2 Case A

Figure 4 left shows the evolution of the high-pressure level in case A. Note that this magnitude mainly increases as the outdoor temperature does, as expected. Interestingly, it is also increases as the feed water

temperature does. This is attributed to the rise in the cooling capacity, and so, in the thermal load of the absorber. The absorber load influences the condenser performance because they are configured in parallel.

Figure 4 right shows the reflux ratio behaves as the high-pressure level does. This is due to when the high-pressure level increases, the ammonia separation in the reboiler deteriorates as the solution vapor pressure rises.

Figure 5 left presents the effective surface for the condenser, that is, the surface of the where mass transfer processes take place, normalized to its total surface. The condenser effective surface is expected to decrease as the air-coolant mass flow rate increases, due to the heat and mass transfer rate enhancement. In addition, the condenser effective surface increases as the thermal load of the absorber-condenser assembly does, that is, as the cooling capacity increases (or/and the COP decreases). Note the condenser effective surface reaches its higher values when the cooling capacity does.

As regard the electric COP, figure 5 right reveals that it is roughly governed by the outdoor temperature.

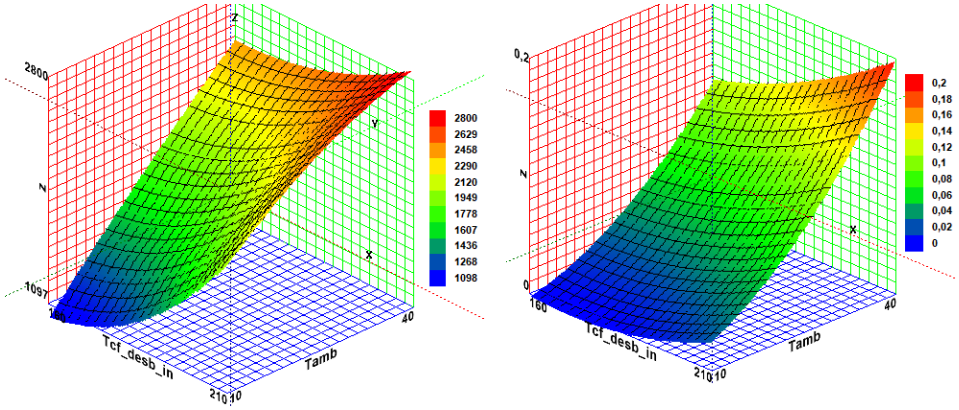

Fig. 4: High-pressure level, in kPa (left). Reflux ratio (right). Case A

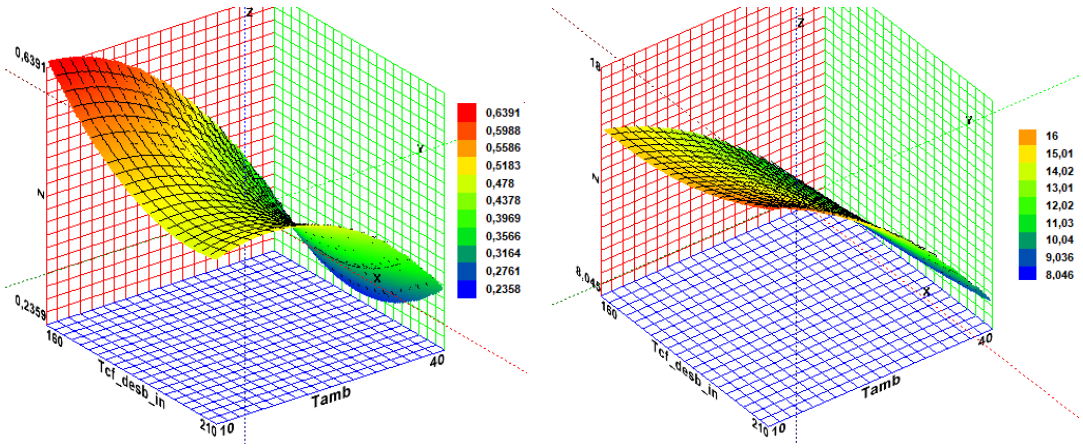

Fig. 5: Condenser effective surface (left). Electric COP (right). Case A

3.3 Case B

Case B characterizes by the fact that the air-coolant velocity is one-half of that one in case A. The distinctive features between case A and B are the followings. Firstly, the high-pressure level has decreased as compared to case A, particularly when the thermal load of the absorber-condenser assembly is maximum. (Figure 6 left). This is a consequence of the decrease in the mass and heat transfer rate. In addition, the thermal load of the solution heat exchanger decreases (Figure 6 right), because of the high-pressure level decrease.

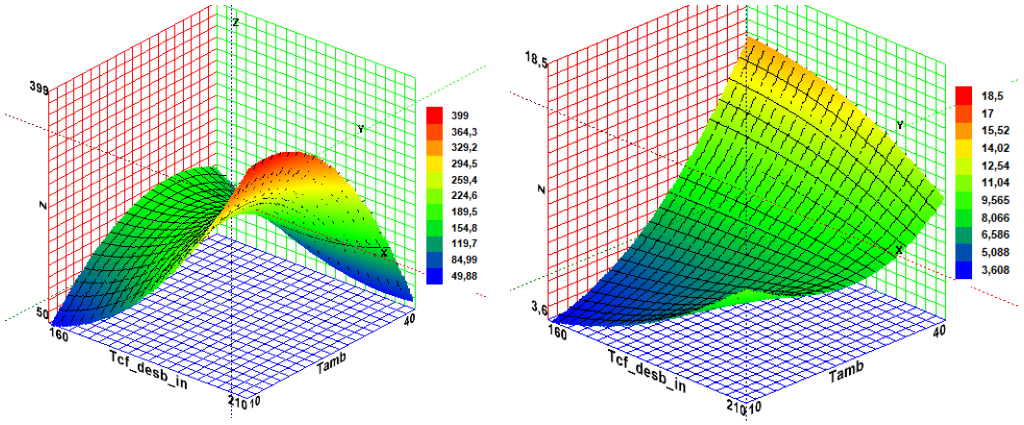

Figure 6: Decrease in the high-pressure level (left), and in the solution heat exchanger thermal load (right), when case B is compared to case A

It is highlighted that the effective surface of the absorber-condenser assembly increases as the air-coolant velocity decreases due to the decay in the mass and heat transfer process (Figure 3). However, the air-coolant mass flowrate increase due to the larger surface of the absorber-condenser assembly is surpassed by the decreases in the air-coolant velocity. Then, figure 7 left shows how the marginal air-coolant mass flow rate per absorber surface decreases in all working conditions. Finally, figure 7 left shows the increases experienced by the electric COP, particularly when the outdoor temperature is low.

4. Conclusion

In this work it is analyzed the effect of the air-coolant flow rate on the absorption chiller performances. With this purpose, a discrete mathematical model has been developed and implemented in Engineering Equation Solver Software, on the bases of mass, species and energy conservation balances. Results show that a moderate decrease of the air-coolant velocity may have a positive effect on the chiller performances due to leads to reduce the thermal load of the solution heat exchanger and, simultaneously, the high-level pressure. On the other hand, the electric COP increases due to the marginal decrease in theair-coolant mass flow rate per absorber surface. The drawback is the increase of the absorber size.

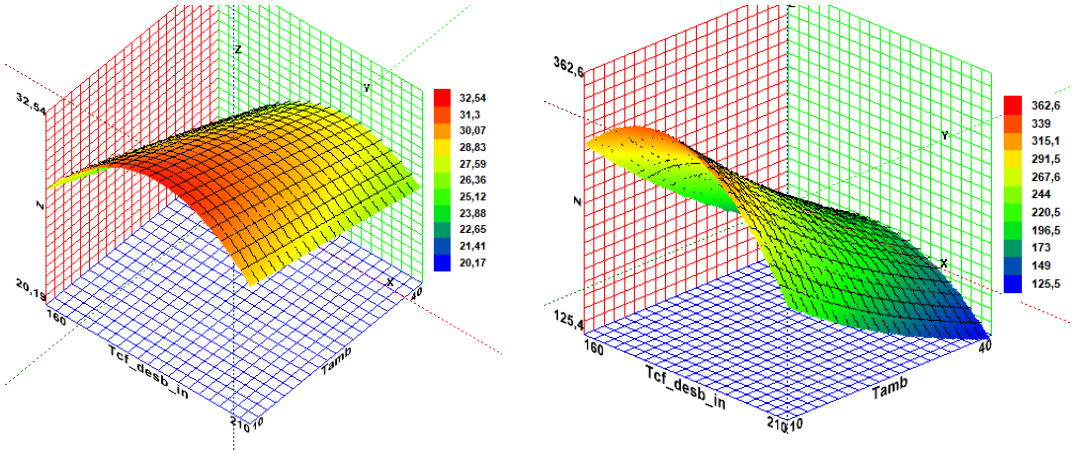

Figure 7: Marginal decrease in the air-coolant mass flow rate per absorber surface, in percentage, (left) and electric COP increases (right) when case B is compared to case A

5 Acknowledgements

This work has been developed in the frame of the ASTEP project, funded by the European Union's Horizon 2020 research and innovation program under grant agreement No 884411 and the ACES2030-CM project, funded by the Regional Research and Development in Technology Program 2018 (ref. P2018/EMT-4319)

6 References

Coker, A. K., 2010. Ludwing's Applied process design for chemical and petrochemical plants. Elsevier, 4th edition

Fernández-Seara, J., J. Sieres, M. Vázquez, 2002. Simultaneous heat and mass transfer of packed distillation for ammonia-water absorption refrigeration systems. Int J. Thermal Sciences, 41, 927-935

Fernández-Seara, J., J. Sieres, M. Vázquez, 2003. Distillation column configurations in ammonia-water absorption chiller refrigeration systems. Int. J. Refrigeration, 26, 28-34

Fernández-Seara, J., J. Sieres, C. Rodríguez, M. Vázquez, 2005. Ammonia–water absorption in vertical tubular absorbers. Int J. Thermal Sciences, 44, 277-288

Herold, K.E., R. Radermacher, S.A. Klein, 2016. Absorption chillers and heat pumps, CRC Press, 2nd edition

Ibrahim, O.M., S.A. Klein, 1993. Thermodynamic properties of ammonia-water mixtures. ASHRAE Trans: Symposia, 21, 2, 1495

Izquierdo M., Marcos J.D., Palacios M.E., González-Gil A., 2012. Experimental evaluation of a low-power direct air-cooled double-effect LiBr-H2O absorption prototype. Energy, 37, 737-748

Kay, W.M., A.L. London, 1984. Compact heat exchangers, McGrawHill, 3rd edition

Kim DS., Infante Ferreira CA., 2008. Analytic modelling of steady state single-effect absorption cycles, Int J. Refrigeration 31, 1012-1020

Mills, A.F., 1999. Transferencia de Calor, McGrawHill, 1st edition

Pereira, J.J., C.A. Cabral, C. Almir, J. Batista, A.A. Ochoa, J.C Charamba, 2017. Energetic analysis of a commercial absorption refrigeration unit using an ammonia-water mixture. Acta Scientiarum, Technology, 39, 439-448

Sieres, J., J. Fernández-Seara, 2007. Modelling of simultaneous heat and mass transfer processes in ammonia-water absorption systems from general correlations. Heat Mass Transfer, 44, 113-123

Táboas, F., M. Vallès, M. Bourouis, A. Coronas, 2007. Pool boiling of ammonia/water and its pure components: comparison of experimental data in the literature with the predictions of standard correlations. Int. J. Refrigeration, 30, 778-788

VDI Wärmeatlas, 2010. VDI Heat Atlas, Springer, 2nd edition

Zamora M., Bourouis M. Coronas A., Vallès M., 2014. Pre-industrial development and experimental characterization of new air-cooled and water-cooled ammonia/lithium bitrate absorption chillers, Int J. Refrigeration 45, 189-197

Experimental Investigation on Solar-Driven GAX-based Absorption Heat pump for Domestic Hot Water production

Hai Trieu Phan, Fabio Aste and Hélène Demasles

Université Grenoble Alpes, CEA, Liten, Campus INES, 73375 Le Bourget du Lac, France

Abstract

This paper presents a new development of NH_3-H_2O absorption heat pump designed with plate heat exchangers and market ready components in order to offer a compact machine easy-to-manufacture. An innovative architecture based on GAX (Generator Absorber Heat Exchange) cycle has been proposed for an optimal use of the internal heat of the cycle for absorption and desorption processes. A model has been built for design of a prototype with the production target of 25 kW of hot water (> 60°C) from a lower-temperature heat source of around 30°C. The prototype has been tested under various conditions. The thermal Coefficient Of Performance (COP) and the electrical coefficient of performance (ECOP) obtained at nominal conditions are respectively 1.52 and 130. Furthermore, the machine shows its capacity to operate over a wide conditions range, especially in term of the inlet temperature of the heat source from 110°C to 170°C.

Keywords: Absorption heat pump, Ammonia/water, GAX, prototype

Nomenclature

			Subscripts	
C_P	Specific heat	[J/kg.K]	A	Absorber
DX	Concentration difference between rich and poor solution	[-]	abs	absorption
DT	Temperature glide	[K]	C	Condenser
E_K	Kinetic energy	[J]	des	desorption
E_Z	Potential energy	[J]	el	electric
h	Enthalpy	[J/kg]	E	Evaporator
$\dot{m}$	Mass flow	[kg/s]	G	Generator
P	Pressure	[bar]	in	input
Q	Heat exchange rate	[W]	m	motor
T	Temperature	[K]	out	output
x	Ammonia concentration	[-]	sat	saturation
W	Work	[W]	sp	poor solution
			sr	rich solution
Acronyms			v	vapour
COP	Coefficient Of Performance	[-]	w	water
ECOP	Electrical coefficient of performance	[-]		

1. Introduction

In France, the residential and industrial sectors account for 23Mtoe of electric consumption, while the natural gas consumption attests on 24Mtoe (IEA database). In general, these two sectors are responsible of the 43.2% of the French total final consumption, and a great part of this share is converted into heat. In the residential sector, the 78% of the consumption is dedicated to space heating and cooling through systems that are fed for 58% with fossil fuels (https://www.ceren.fr/). Industry is as well dependent on fossil fuels (61% of the total consumption) for heat generation, with even a small share of the electricity consumption (18%, i.e. 21 TWh in 2013) used for thermal production. During the processes, about the 25-60% of the heat is lost to the environment, for a total amount of 8.56 Mtoe of waste heat (https://www.ademe.fr/). However, this rejected heat is available at different temperature levels: almost a third is available at >100°C and can be re-used on site

© 2022. The Authors. Published by International Solar Energy Society
Selection and/or peer review under responsibility of Scientific Committee
doi:10.18086/eurosun.2022.08.10 Available at http://proceedings.ises.org

or for feeding heating networks; the second third, between 40°C and 100°C, can be enhanced in temperature by heat pumps; the remaining third is rejected at a temperature < 40°C and is hardly exploitable. The challenge is saving the medium-and-low-temperature heat from being wasted, increasing the overall process performance and reducing the Greenhouse Gas (GHG) emissions. In this context, one of the most adapted solutions is represented by the absorption heat pumps, which use natural fluids and allow upgrading low-temperature sources to a higher temperature level using heat as fuelling. In addition, such systems can also be configured in reverse mode to produce cooling, addressing both industrial and residential needs.

To operate, absorption machines need a heat source that can be indifferently gas, renewable heat (solar, geothermal, biomass) or waste heat, with an increased economical end environmental interest in the two last cases. Concerning heating, absorption heat pumps can effectively contribute to lower the global energy consumption for both residential and industrial sectors, thus reducing the GHG emissions in accordance with the European Energy-Climate Framework 2030 and the international goals for limiting the global warming.

As absorption cycles require two fluids for operating, refrigerant and solvent, many possibilities of coupling exist in the literature according to Sun J. et al. (2012). The most diffused are ammonia-water and water-lithium bromide due to their interesting thermophysical properties. This last couple has historically been chosen for air conditioning, and in the last decades, it found application even in some heat pumps [Aprile M. et al. (2016), Dai E. et al. (2018) and Wang J. et al. (2019)]. Despite its good efficiency, especially in multi-stage systems, H_2O/LiBr has two important drawbacks: a limited operating field, by both crystallization risk and water freezing temperature, and an important cost. Ammonia-water couple avoids these problems, being suitable to operate in large temperature fields and having a lower cost, as ammonia is a common product. For the pursuit of the work, NH_3/H_2O will be the chosen fluid couple.

Amongst the different ammonia-water absorption cycles, the Generator-Absorber heat eXchanger (GAX) cycle is the most interesting due to its flexibility and increased performance compared to the single stage cycle. This cycle can effectively operated as a chiller, down to -40°C, or as a heat pump, even above 70°C with high efficiency. Despite that, few GAX heat pumps exist on the market and most of them base on expensive and bulky heat exchangers in the form of distillation columns.

According to the literature, Aprile M. et al. (2016) tested an industrial gas-driven, GAX heat pump that produces 20 kW of hot water at 60°C or 45°C (evaporator temperature $T_{E,in}$=10°C) with Coefficient of Performances (COP) of 1.6 and 1.73 respectively. Dai E. et al. (2018) tested an industrial 55 kW absorption heat pump that can produce 55°C hot water with an optimal COP of 1.63 at $T_{E,in}$=20°C and generator temperature $T_{G,in}$=200°C. The other heat pump present in the literature is a prototype made by Wang J. et al. (2019), where the main heat exchangers consist in tailored-made shells-and-tubes exchangers, thus not compact. The best performance obtained is COP = 1.51 with $T_{E,in}$=15°C and $T_{G,in}$=193°C. According to these works, the development of GAX heat pumps is particularly interesting for high-temperature waste heat recovery and, due to the COPs above 1.5, even the case of fuelling with fossil sources (gas, biomass, etc.) becomes environmentally and economically attractive.

In this paper, a novel GAX architecture is presented, together with the related numerical model. The prototype is designed, fabricated and tested according to this architecture using only commercially available components, such as plate-type heat exchangers in order to improve the compactness, the amount of charge (ammonia) as well as the minimize the constraint related to high pressure. During the experimental investigations in the laboratory test rig, a particular attention has been given to the operating conditions, which have been varied to test the response of the system in different situations. The experimental results are then discussed to analyse the impact of the main parameters, such as the generator temperature, the evaporator temperature and the solution flow rate.

2. Cycle description

As introduced before, NH3/H2O is chosen for the study due to its favourable properties. In addition, this fluid couple is particularly interesting from an industrial point of view, being ammonia a well-known element used in plenty of domains, thus largely available and cheap. In this sense, the components of the GAX heat pump

that is further proposed are chosen amongst commercial parts, as plate heat exchangers and pressurized tanks, to demonstrate the viability of such absorption systems.

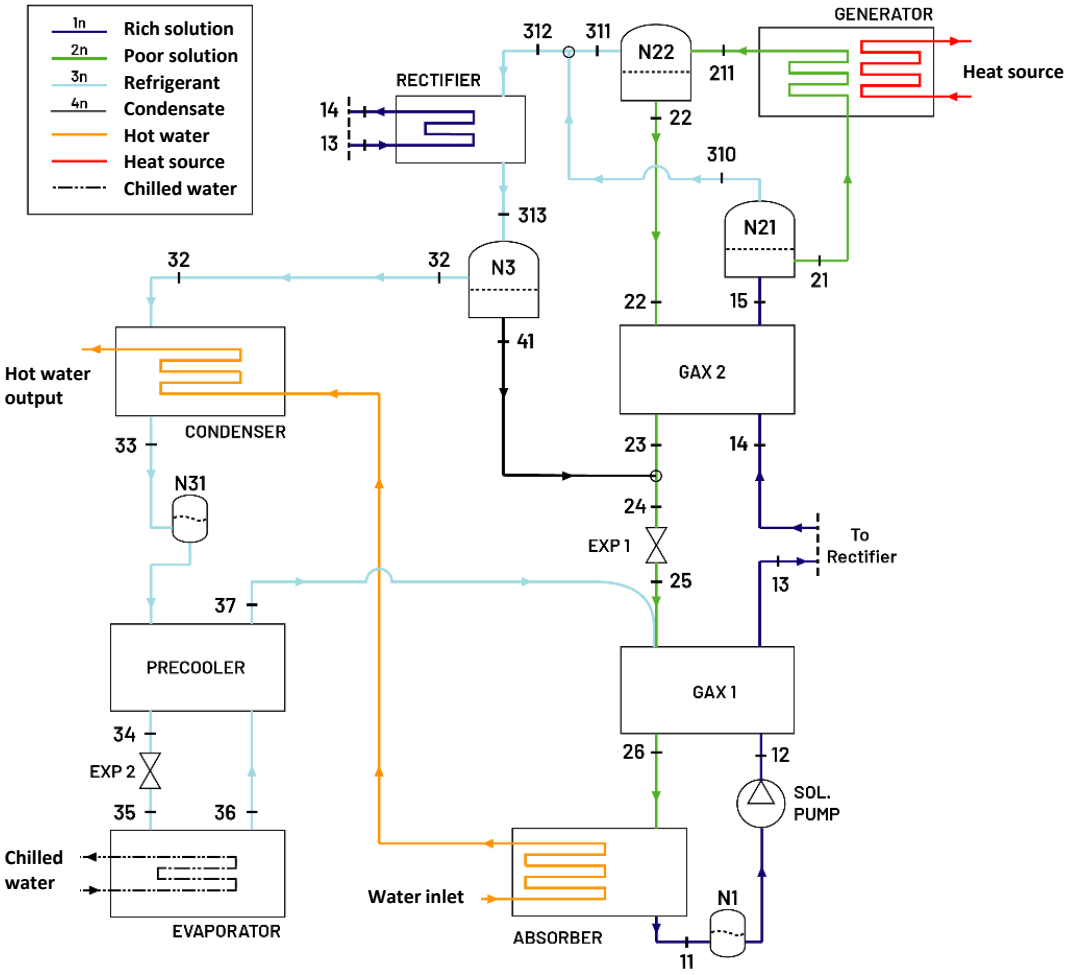

Figure 1: Scheme of GAX prototype architecture

Detailing the architecture, the GAX heat pump cycle shown in Figure 1 features a novel architecture where the vapour generation process is discretized via different components, three heat exchangers (GAX2, generator and rectifier) and three pressurized tanks (N21, N22 and N3). This approach is quite the opposite of the standard one, which involves a single element for both heat and mass transfers. A similar case can be made about the absorber too.

2.1 Working principle

As this study concerns a heat pump, the absorber and the condenser are cooled in series to maximise the cooling fluid output temperature. After preliminary simulations, the cycle is found to perform better if the absorber is entered first. In heat pump mode, the useful effect consists in the heat delivered to the cooling fluid, while the high-temperature heat entering the generator acts as the driving power. The heat flux entering the evaporator is seen as a free input.

For a convenient description, the heat pump cycle is roughly divided into three subcycles according to the different fluids: refrigerant, rich solution and poor solution.

- Refrigerant subcycle

Rich solution diphase flows coming from GAX2 and generator enter the two separation tanks N21 and N22 respectively: there, the vapour separates by gravity from the liquid solution. Due to the difference in the saturation pressures, the liquid is richer in water and the vapour is richer in ammonia, but it is generally not pure. Therefore, the vapour is sent to the rectifier to be enriched in ammonia. The purification occurs through

the refrigerant cooling, which causes a partial condensation of the fluid: the water-rich condensate is recirculated to the poor solution line. In parallel, the purified refrigerant is firstly condensed, then subcooled in the precooler before throttling, and finally vaporized in evaporator. After that, the vaporous refrigerant flows through the low-pressure side of the precooler and reaches the GAX1, where the absorption reaction with the poor solution begins.

- Rich solution subcycle

The rich solution is obtained as the product of the absorption reaction, which begins in the GAX1 and ends in the absorber. There, the ammonia-water mixture presents the highest richness in ammonia and its thermodynamic state is subcooled liquid, which allows protecting the pump. This last component increases the pressure of the rich solution that is subsequently delivered to the GAX1 (12) to be warmed. In this first heating phase, desorption might already occur. The desorption process continues in the rectifier and in the GAX2, as the rich solution recovers the available internal heat of the other fluid lines. Being diphasic after the GAX2, a first phase separation is performed in the N21 tank to avoid sending some vapour in generator inlet. Here, the remaining rich solution is heated to the highest temperature to continue desorption process. The two-phase fluid undergoes a second and final phase separation in the N22 tank, resulting in the poor solution and some additional refrigerant vapour at the outlets.

- Poor solution subcycle

After phase separation in the N22 tank, the poor solution features the lowest richness in ammonia in the cycle and the highest temperature too. A first heat recovery occurs towards the rich solution in the GAX2. Then, the poor solution is mixed with the condensate, increasing ammonia richness and decreasing the temperature. The resulting solution is throttled before entering the GAX 1 (25). There, the ammonia vapour coming from the refrigerant subcycle (37) is absorbed by the poor solution and, as the absorption reaction is exothermic, heat generation occurs. The internal recovery is realized by the rich solution (13). The complete absorption in GAX1 is limited by the temperature level of the rich solution used for the cooling. Thus, the reaction is continued in the absorber where further absorption is done by cooling with a colder external source.

- GAX effect

The GAX cycle is particularly interesting when a large temperature overlap between the generator and absorber occurs: in this case, absorption excess heat is partially available at a temperature that allows the rich solution desorption in GAX1. In GAX2 and rectifier, the desorption continues thanks to the internal heat recovery from the poor solution. Taking advantage of this temperature overlap decreases the input heat in the absorber and the generator, improving the global performance and reducing the absorber and generator components size.

2.2 Comparison with literature architectures

Only little experimental work has been done on GAX systems configured as heat pumps. Aprile M. et al. (2016) tested an absorption heat pump manufactured by the Robur Company in Germany, Dai E. et al. (2018) tested one manufactured by the Vicot Company in China, and only Wang J. et al. (2019) tested a self-made prototype.

The main difference between the proposed architecture and the existing ones consists in the vapour generation system and the absorption system. An immediate finding can be made about the rich solution circuit, which shows a different path: instead flowing first through the rectifier and then through the GAX, in the proposed version it encounters first the GAX1, then the rectifier, and finally the GAX2. This variation results from the pinch analysis of the system fluid lines and optimizes the internal heat recovery.

A more technical aspect concerns the heat exchangers technology. In the literature, the technologies used for the components where absorption takes place (GAX1 and absorber) vary according to the authors : two separated falling film heat exchangers tubes in tubes type [Aprile M. et al. (2016) and Wang J. et al. (2019)] or shell-and-tubes exchangers, which allows piling the two units to form a single component [Dai E. et al. (2018)]. However, all authors choose the same technology for the desorption block : Generator, GAX2 and rectifier are shell-and-tubes exchangers, which allows piling the three units where the ammonia vapour flows in counter-current respect to the solution, being cooled and rectified all along as in a distillation tower. Therefore, the refrigerant vapour is already purified when exiting the generation column and the condensate resulting from rectification is directly recirculated in the underlying sections. Since the vapour generation and

separation occur simultaneously, the generation block is sized taking into account the two process. The novel architecture proposed in this work avoids dealing with this point: as the heat and mass transfers and the phase separation occur separately, each component is optimally sized to its function.

Another aspect to be considered is the system manufacturing. Generally, these distillation-column-like elements consist in a cylindrical vessel where the different sections are heated or cooled by coil exchangers. Such assembly requires a complex manufacturing and, due to the low heat transfer coefficient of coil exchangers, it presents a considerable volume that cannot be split without losing all the advantages of a coupled vapour generation and separation. Differently, the proposed architecture involves many smaller units that can be distributed in the space, thus allowing a more rational positioning inside the system and an easy maintenance.

3. Modelling approach

To determine the most efficient solution for the novel GAX ammonia-water cycle, many architectures have been modelled and then implemented in the software EES (Engineer Equation Solver, http://www.fchart.com/) to be numerically studied. EES internally provides NH_3/H_2O mixture thermodynamic properties, which are calculated through the correlations proposed by Ibrahim O.M. and Klein S.A. (1993). By specifying the heat and mass efficiencies of the components and integrating the hypothesis listed in Table 1, the model returns the thermodynamic conditions of the state points of the cycle and the global performances.

Table 1: Hypothesis of the model for the prototype design

The system is at steady state;	Adiabatic components and pipes;
ΔE_K and ΔE_Z are negligible	Ideal heat sources and sinks;
Pressure drops are negligible;	Pump has $\eta_{el} = 0.9$ and $\eta_m = 0.8$;
Saturated fluid at separation tanks outlet;	The heat transfer efficiency is 0.8;
The approach temperature in heat exchangers is 5°C;	Absorption efficiency is 0.8 and desorption efficiency is 1 according to Boudehenn F. et al. (2014);
Evaporator temperature glide is 5°C;	

The model is established considering each component as a control volume, thus is 0D: the internal dynamics are excluded from the study, as the behaviour of the component is considered as a whole and included in the relative efficiency. Even if simple, this approach is reliable for the scope, as it has been largely demonstrated in previous works [Herold K. E. et al. 1996].

For each control volume, mass and energy conservation equations have been defined:

$$Total\ mass\ conservation \rightarrow \sum \dot{m}_{in} - \sum \dot{m}_{out} = 0 \quad \text{Eq. 1}$$

$$Refrigerant\ mass\ conservation \rightarrow \sum \dot{m}_{in}\, x_{in} - \sum \dot{m}_{out}\, x_{out} = 0 \quad \text{Eq. 2}$$

$$Energy\ conservation \rightarrow \sum \dot{m}_{in}\, h_{in} - \sum \dot{m}_{out}\, h_{out} + \sum \dot{Q} - \sum \dot{W} = 0 \quad \text{Eq. 3}$$

In the last equation, Q and W are the heat and work fluxes exiting the system boundary. Signs respect the traditional convention.

The evaporator temperature glide is defined as $T_{36} - T_{35}$.

Finally, the Coefficient Of Performance (COP) of a generic heat pump is defined as the ratio between the heat rejected to the external cooling fluid at the condenser and the energy input in the compressor. In the case of absorption cycles, a heat rejection occurs also in the absorber, as the absorption reaction is exothermic. This heat being recuperated by the external cooling fluid, it becomes a part of the useful effect. The energy input

changes too: in fact, besides the electric energy consumption, an additional and more consistent high-temperature heat consumption is necessary to power the system. Generally, it is good practice to distinguish the type of COP between electrical (ECOP) and thermal (COP) for the continuation, as heat consumption largely prevails on the electric). In particular, doing techno-economic analysis one of the two parameters is often negligible while the other drives the decision.

$$Electrical\ Coefficient\ Of\ Performance \rightarrow ECOP = \frac{\text{useful energy}}{\text{electric cost}} = \frac{\mathrm{Q_A} + Q_C}{\mathrm{W_{el,pump}}} \quad \text{Eq. 4}$$

$$Thermal\ Coefficient\ Of\ Performance \rightarrow COP = \frac{\text{useful energy}}{\text{heat cost}} = \frac{\mathrm{Q_A} + Q_C}{Q_G} \quad \text{Eq. 5}$$

According to simulations, the best performance considering both COP and ECOP is obtained for the architecture given in Figure 1. This model has also been used to size all the components of the prototype.

4. Experimental system

4.1 Prototype

The sizing conditions are reported in Table 2. The generator inlet temperature is set at 170°C, corresponding to the optimal numerical COP. The target of the machine is to produce 25 kW of hot water (> 60°C) from a lower-temperature heat source (~ 30°C).

Table 2: Prototype sizing point

Parameters	Value	Measure Unit
Generator inlet temperature	170	°C
Absorber inlet temperature	30	°C
Evaporator inlet temperature	35	°C
Target hot fluid outlet temperature	> 60	°C
Target heating capacity	25	kW

Using these values as model inputs, the characteristic parameters of the components have been defined. Then, each element has been identified on the market, purchased and assembled. To respect the technological readiness asset, only industrial brazed/welded plates heat exchangers are implemented, as those last components are standardized and produced in series. Instead, the piping and separation tanks, even if they are well known industrial elements, must be designed and singularly manufactured to fit the operating conditions. In addition, as the ammonia/water mixture is very corrosive, a special care is taken by selecting only resistant components, mostly made in stainless steel. Considering the material costs of the assembly without instrumentation, the pressurized tanks (36%) and the piping (25%) represent a great share, while the plate heat exchangers affect for a littler amount (13%). A picture of the prototype is shown in Figure 2.

Three stainless steel tanks are used to separate refrigerant vapour and liquid solution at the outputs of generator, GAX2 and rectifier. Two other tanks are provided as fluid storages: one to store the poor solution before pumping, in order to avoid pump cavitation during the start-up phase; the other one to store the refrigerant after the condenser. These two last tanks allow the heat pump to be operated over a wide temperature range. However, the system is filled with relatively low quantities of water and ammonia, 1.4 kg of water and 2.4 kg of ammonia. Finally, the GAX1 heat exchanger features an original, double distributor system for the poor solution and refrigerant inlet, allowing liquid and gas flows to be uniformly distributed into each channel.

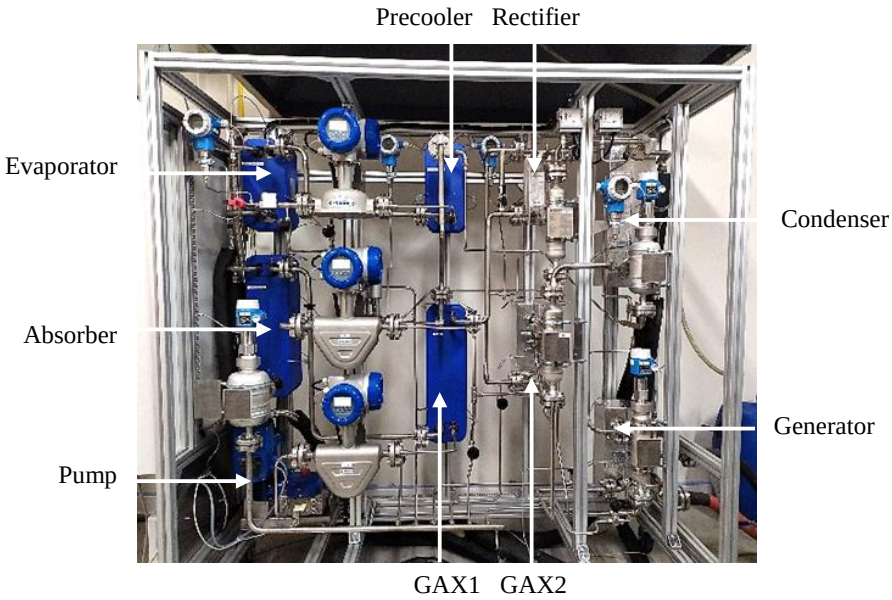

Figure 2: Front view of the GAX prototype

4.2 Characterization

Experimental tests were performed at the INES (French National Institute for Solar Energy) facility in a test rig that allowed providing adjustable temperatures and powers for the external fluids. The fluid chosen for all external circuits is pressurized water. The heat pump operating field during the tests is reported in Table 3.

Table 3: GAX heat pump operating range during experimental test. Data refers to external-side fluid for Evaporator, Absorber, Condenser and Generator and to the internal-side fluid (rich solution) for the Pump. In the case of the Pump, both upstream and downstream pressures are indicated.

		Evaporator	Absorber	Condenser	Generator	Pump
Inlet temperature [°C]	Nominal	34.6	29.5		170	41
	Minimal	25	29.5		110	35
	Maximal	50	29.5		170	47
Pressure [bar]	Nominal	9	10.5	23.4	23.6	10.5/23.6
	Minimal	7.5	7.5	19	19	7.5/19
	Maximal	13	13	24	24	13/24
Power [kW]	Maximal	13.4	16	14.6	18.9	0.2
Mass flow rate [kg/h]	Minimal	1700	320	320	950	
	Maximal		865	865		

4.3 Measurement apparatus

The prototype is instrumented with high-precision sensors in order to measure the parameters needed for a thorough comprehension of its functioning. Temperature sensors are positioned on the heat exchangers inlet/outlet. Pressure sensors are positioned on the high- and low-pressure solution and refrigerant circuits. Coriolis flowmeters are employed to measure mass flow, density and temperature of the internal fluids. Liquid level sensors are placed inside the pressurized tanks to measure the amount of the stocked liquid, thus describing the fluid distribution in the prototype. In addition, the level sensor in the storage tank upstream the pump has a protection function, as it shuts off the pump when the stocked liquid level is too low.

Type and uncertainty of the instrumentation are described in Table 4.

Table 4: Instrumentation characteristics

Parameters	Sensors type	Quantity	Uncertainty (+/-)

Heat transfer fluid temperature	Pt100	8	0.1 K
Refrigerant/Solution temperatures	Thermocouples	25	0.3 K
Refrigerant/Solution pressure	0-10 bar and 0-40 bar	4	0.2% full scale
Refrigerant/Solution flow	Mass flowmeter	3	0.20%
External fluid flow	Mass flowmeter	4	0.30%
Density	Mass flowmeter	3	2 kg/m^3
Liquid level	Capacitance level sensor	3	0.50%

4.4 Data processing

Despite the number of sensors deployed across the system, many parameters cannot be directly measured and need to be calculated afterwards. In particular, it is the case of the flow rates in the poor solution and condensate lines, and the heat fluxes in the heat exchangers. The firsts are determined through total mass and refrigerant mass balances; the lasts require energy balances in addition. The heat flux can be properly calculated only on absorber, generator, condenser and evaporator where the measures are accurately done on external fluid. As an example, the absorber heat flux is defined:

$$Q_A = \dot{m}_A c_{P,w}\left(T_{A,out} - T_{A,in}\right) \quad \text{Eq. 6}$$

Where $C_{P,w}$ is the specific heat of water and $\dot{M}$ is the heat carrier fluid flow. However, on internal heat exchangers where there are absorption or desorption reactions, the heat flux cannot be calculated as it is impossible to know the enthalpy of the fluid precisely.

4.5 NH_3 concentration

Determining the ammonia concentration of the solution is an essential point to qualify the functioning of the system. Therefore, ammonia fractions are calculated from measured density, temperature and pressure through reverse correlations based on Ibrahim O.M. and Klein S.A. (1993). The maximum error is ±2.5%.

5. Experimental results

5.1 Performance comparison to state-of-the-art systems

To facilitate the comparison of absorption chillers performances, the COP is generally showed in relation to the Carnot COP, a conventional parameter that characterizes the operating conditions of the system. The definition of the Carnot COP can be found in the literature [Boudehenn F. et al. (2014)]. This same logic can be applied to heat pumps, although a modification of the formulation is required.

On the presented prototype, the useful effect occurs throughout the absorber and the condenser as the absorption and condensation heat is released to the external fluid, which heats up to the $T_{AC,out}$ temperature. Considering the heat fluxes, the First Law of Thermodynamics gives:

$$Q_G + Q_E + Q_{(A+C)} = W \quad \text{Eq. 7}$$

With the mechanical work provided by the pump being negligible compared to the energy fluxes. Then, under the hypothesis of cycle reversibility, the Second Law Thermodynamics can be written as:

$$\frac{Q_G}{T_{G,in}} + \frac{Q_E}{T_{E,in}} + \frac{Q_{(A+C)}}{T_{AC,out}} = 0 \quad \text{Eq. 8}$$

Where $T_{AC,out}$ represents the temperature of the useful heat production, $T_{G,in}$ represents the high-temperature heat source that feeds the generator and $T_{E,in}$ represents the low-temperature heat source that interfaces with the evaporator. From Eq. 16 and Eq. 17, the Carnot COP for heat pumps can be derived as:

$$COP_{Carnot} = \frac{T_{G,in} - T_{E,in}}{T_{G,in}} \cdot \frac{T_{AC,out}}{T_{AC,out} - T_{E,in}} \quad \text{Eq. 9}$$

In Figure 3, the experimental COPs of the presented prototype and other different GAX heat pumps are reported for comparison, giving an overview of the ammonia-water heat pumps global panorama. The current work prototype shows the same performance of Wang J. et al. (2019)'s prototype. Better performances are obtained by Aprile M. et al. (2016) and Dai E. et al. (2018), which have both chosen commercial systems for their studies.

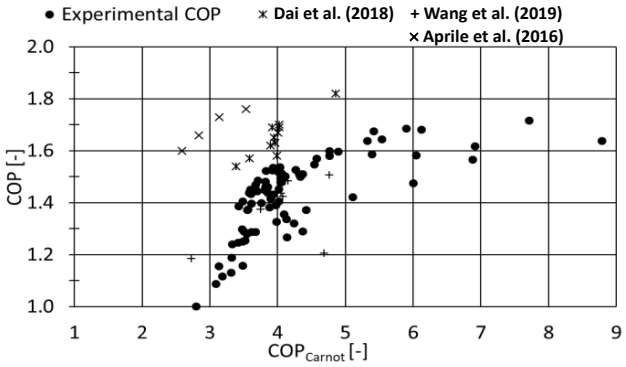

Figure 3: Comparison of thermal COP as function of the Carnot efficiency

Some general considerations can be done about the working fields of the presented systems. Dai E. et al. (2018) concentrate in a narrow area corresponding to a precise Carnot COP, varying their performance mainly depending on the absorber inlet temperature. Instead, Wang J. et al. (2019) and Aprile M. et al. (2016) systems cover a wider area, with COP trends that seem reaching a plateau after a certain Carnot COP. The current work shows a significantly large Carnot COP field, with average performances higher than Wang's et al. prototype and maximum COP in line with Dai E. et al. (2019)'s results.

Finally, observing the point distribution, a denser area is visible at Carnot COP next to 4.0. Many tests have been performed around this condition as it coincides with the sizing point of the system. The rest of the measured points are relatively scattered, which is due to working in a wide field of solution flow rates and temperatures. A summary of the operating conditions and the performances at the nominal point and at the maximum-power point is reported in Table 5.

Table 5 : Operation conditions and performances at the nominal and maximum-power points

	$T_{E,in}$	$T_{A,in}$	$T_{G,in}$	$T_{C,out}$	M_{12}	Q_G	Q_{A+C}	COP	COP_{Carnot}
Nominal	35	30	170	60	100	16	25	1.52	4.0
Max Q_{C+A}	49.4	29.3	150	60	113	18.6	32	1.72	7.7

5.2 Comparison at nominal conditions

A focus on the performance at sizing conditions is reported in Figure 4. The generator, evaporator and absorber inlet temperatures are respectively 170°C, 35°C and 29.5°C, while the outlet target temperature is 60°C. To attend this value, the absorber and condenser external fluid flowrates are varied between 570 kg/h and 700 kg/h. Instead, the external flow rates in generator and evaporator are kept constant at respectively 950 kg/h and 1700 kg/h to guarantee a proper temperature pinch. The rich solution flowrate is approximately 100 kg/h. As the average useful heat power produced in the absorber/condenser is 23.7 kW (13.6/10.1 kW), and as the average heat input in the generator is 15.6 kW, then the resulting COP is 1.52.

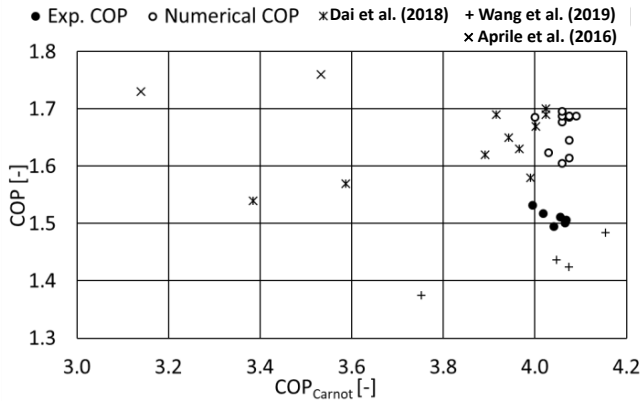

Figure 4: Numerical and experimental COP as function of the Carnot efficiency with focus on the prototype nominal conditions

Figure 4 allows comparing the numerical COP obtained from the numerical model with the experimental observations. In general, the measured performances are 10% lower than the simulated values. This might be due to different reasons: an improper configuration of the absorber, constraints in the prototype operation due to a limited thermo-mechanical resistance of the components and a reduced control of the rectification in some operating conditions. Nevertheless, if the numerical performances are in line to those of Dai E. et al. (2018), they remain lower than those of Aprile M. et al. (2016). A possible explication can be found in the technology chosen for the vapour generation. Both literature authors utilise tubes-and-shell exchangers, because this solution allows different sections to be stacked together creating a single exchange volume where refrigerant vapour and liquid solution are in counter-current, which favours heat and mass transfers. Instead, the adoption of plate heat exchanger technology allows having a more compact and easy-to-manufacture system, but with a lower mass transfer efficiency. Aste F. and Phan H.T. (2022) numerically compared these two technologies and observed that there is an impact of up to 20% in the COP for GAX systems. An interesting compromise has been introduced by Wirtz M. et al. (2021), who proposed a plate heat exchanger where the generation and rectification sections are stacked. This concept takes advantage of the refrigerant vapour and liquid solution counter-current flow, yet remaining compact.

5.3 Effects of operating conditions

As the experimental campaign was carried through the conditions reported in Table 3, the impact of different parameters on the system performance has been evaluated. In particular, the study concerns the influences of the solution flowrate, the generator temperature and the evaporator temperature.

Some preliminary observations can be presented with reference to Figure 5. The target temperature for the hot water production ($T_{C,out}$=60°C) is reached for most points, despite the wide field of working conditions. Moreover, the hot water outlet temperature seems being stable at different system heat duty (from -50% to +30% nominal power), meaning that off-design operation is feasible.

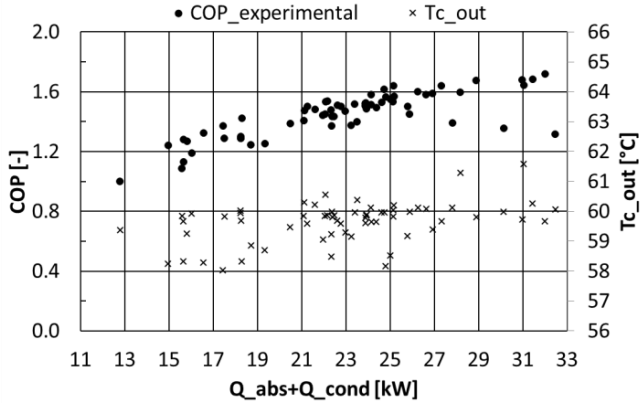

Figure 5 : COP and the outlet hot water temperature as functions of the heating capacity

Nevertheless, the COP strongly depends on the operating conditions, which reflect onto the absorber and condenser heat duties, with a sharp decrease below the nominal value (25 kW). Besides, in Figure 6 the ECOP has an almost linear tendency with reference to the increase of the useful heat production Q_A+Q_C. The highest heating power, 33kW, the best COP of 1.72 and the best ECOP of 170, are reached at 150°C, 30°C and 49.4°C respectively as generator, absorber and evaporator inlet temperatures.

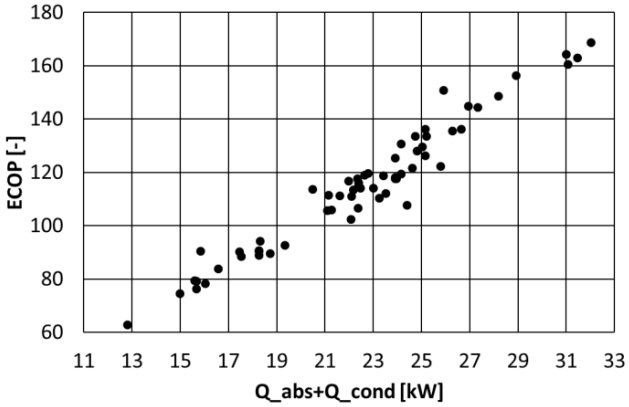

Figure 6 : Electrical COP (ECOP) as a function of the heating capacity

- Rich solution flow variation

The impact of rich solution flow rate ($\dot{m}_{12}$) is studied at the nominal temperatures of $T_{a,in}$=29.4°C, $T_{g,in}$=169.8°C and $T_{e,in}$= 34.5°C. Figure 7(a) shows that an increase in the rich solution flow rate leads to an increase in powers output of all heat exchangers, except for the evaporator. Despite the augmentation in the refrigerant vapour flow $\dot{m}_{32,}$ its exchanged heat does not follow the same trend. The evaporator appears to be limited by its size, since a decrease of the temperature glide is observed, as shown in Figure 7(b), even when a control target is set at 5K. In addition, we observed that the increase of the exchanged power in the absorber is smoother than in the generator (Figure 7(a)). A possible explanation is that the mass transfer by absorption process in GAX1 and in the absorber deteriorates with an increase of liquid fraction at the outlet of the evaporator due to lower temperature glide. Indeed, a numerical calculation shows that at measured ammonia concentration of 96%, 80% of the refrigerant exits as vapour with a 5K glide at the evaporator outlet, while only 45% exits with a 1K glide.

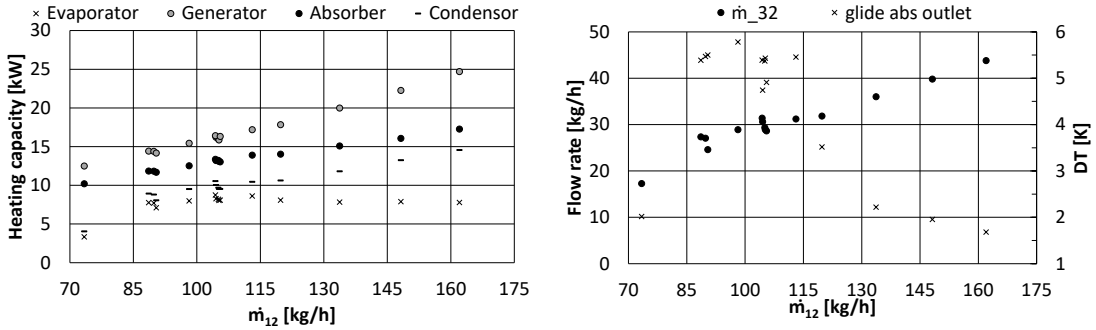

(a) Heating capacity

(b) Mass flow of the refrigerant flow and the temperature glide

Figure 7: Rich solution flow variation impact on different parameters with $T_{g,in}$=169.8°C, $T_{a,in}$=29.4°C, $T_{e,in}$= 34.5°C

- Generator temperature variation

The inlet temperature of the hot fluid at the generator is a relevant parameter because a flexibility in this sense would allow an easier management of the energy source and an increased working period. For a given solution flowrate, absorber temperature and evaporator temperature, Figure 8(a) shows a COP increase with the generator temperature. This is in line with the observations about ammonia concentration in the solution. Indeed, increasing the temperature lead to increases in the capacities of absorption and desorption represented

by $DX_{abs}=X_{12}-X_{24}$ and $DX_{des}=X_{12}-X_{22}$. In the order of magnitude, the heat production in the absorber and condenser is linked to DX_{abs} while the heat consumption in the generator is linked to DX_{des}. Therefore, the ratio between DX_{abs} and DX_{des} would represent the performance. As shown in Figure 8(b), its tendency with the generator temperature is in agreement with that of the COP.

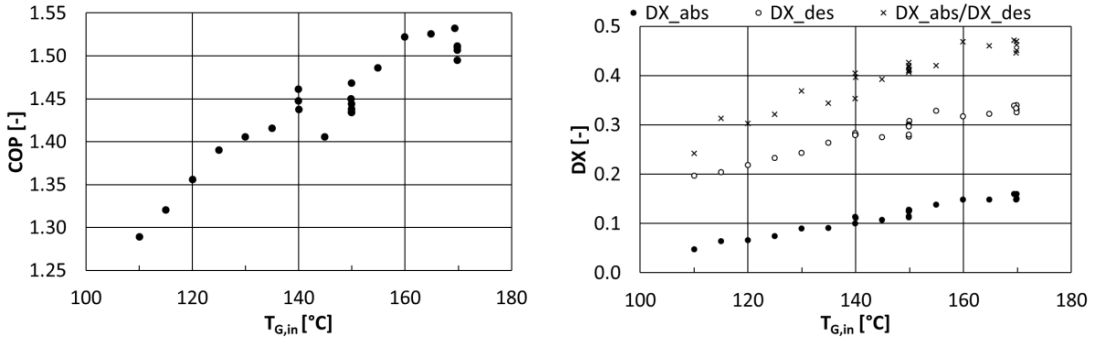

(a) COP (b) DX

Figure 8: Generator temperature variation impact on different parameters with Ta,in=29.4°C, Te,in=34.6°C, MSR=106 kg/h

The inlet evaporator temperature is representative of the low-temperature source that feeds the cycle. However, it is not necessary the ambient that would provide the input heat: for example, low-temperature waste heat could be used for this task, with positive effects on the cycle performances.

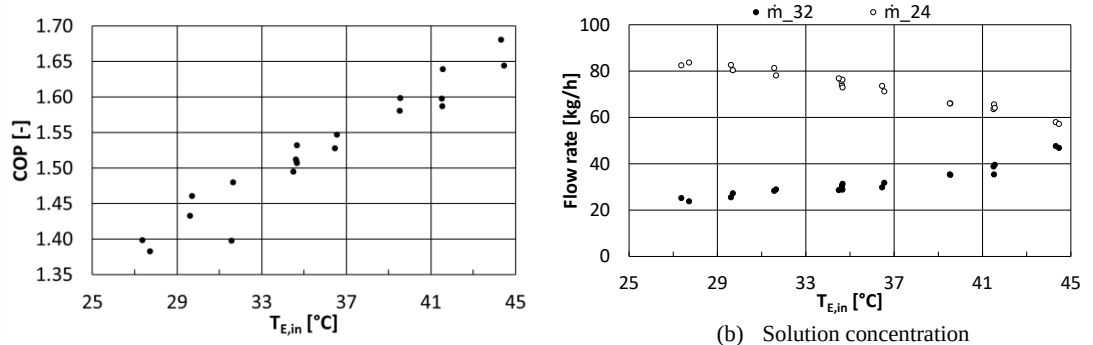

(a) COP (b) Solution concentration

Figure 9: Evaporator temperature variation impact on different parameters with $T_{a,in}$=29.4°C, $T_{g,in}$=169.8°C, M_{SR}=106kg/h

According to the expectations, increasing $T_{e,in}$ leads to a better COP, as illustrated in Figure 9(a). In particular, if the refrigerant evaporation can occur at higher temperatures, then higher pressures are allowed in the low-pressure side of the system. Operating at higher pressure is advantageous for the absorption reaction, as the equilibrium ammonia fraction of the rich solution increases with the pressure. As a result, the vapour generation flow rate ($\dot{m}_{32}$) increases with the evaporator temperature (while the poor solution mass flow rate $\dot{m}_{24}$ decreases due to a fixed pump flow rate), as shown in Figure 9(b), leading to higher COP.

6. Conclusions

This paper presents a new architecture GAX NH_3-H_2O absorption heat pump designed with plate heat exchangers in order to offer a compact machine easy-to-manufacture. An innovative architecture has been proposed with the particularity of using an internal heat exchanger (GAX1) at two level of pressure: in one side, absorption occurs at low pressure and the heat produced is transferred to other side where the desorption at high pressure can be initiated. The desorption process is internally carried out by heat recovery in the rectifier and the solution heat exchanger (GAX2). A model has been developed for design and performance simulations. Based on the numerical results, a prototype has been built with a production target of 25 kW of hot water (> 60°C) from a lower-temperature heat source of around 30°C. At nominal conditions ($T_{e,in}/T_{a,in}/T_{g,in}$)=(35/30/170)°C, the machine produces has a thermal coefficient of performance (COP) of 1.52

and an electrical coefficient of performance (ECOP) of 130. In favourable conditions, the maximum COP and power output are 1.72 and 32 kW, respectively. The tests show the capacity of the machine to operate in a wide range, especially in term of the inlet temperature of the heat source from 110°C to 170°C, with average performances in line with level of the literature. However, the experimental COPs are 10% lower than the simulated values. This might be due to different reasons: such as an improper configuration of the absorber and a limited control of the rectification in some operating conditions. These observations will be taken into account for further improvement of the prototype.

7. Declaration of Competing Interest

The authors declare that they have no known competing financial interests or personal relationships that could have appeared to influence the work reported in this paper.

8. Acknowledgements

The authors would like to express their gratitude to the French Alternative Energies and Atomic Energy Commission and the Auvergne-Rhône-Alpes region for the financial support.

9. References

Aprile M., Scoccia R., Toppi T., Guerra M. & Motta M. Modelling and experimental analysis of a GAX NH3-H2O gas-driven absorption heat pump. International journal of refrigeration, Vol. 66, pp. 155-155, 2016.

Aste F., Phan H.T., Numerical Study on Multi-effect and Multi-stage NH3/H2O Absorption Chillers for Negative Cooling in SHIP Systems, SolarPACES 2021 Conference Proceedings, 2022.

Boudehenn F., Bonnot S., Demasles H.& Lazrak A., Comparison of different modeling methods for a single effect water-lithium bromide absorption chiller. EuroSun 2014 Conference Proceedings, 2014.

Dai E., Lin M., Xia J. & Dai Y. Experimental investigation on a GAX based absorption heat pump driven by hybrid liquefied petroleum gas and solar energy. Solar Energy, Vol. 169, pp. 167-178, 2018.

Herold K. E., Radermacher R. & Klein S. A. Absorption Chillers and Heat Pumps. CRC Press, 1996.

Ibrahim O.M. and Klein S.A. Thermodynamic Properties of Ammonia-Water Mixtures. ASHRAE Trans.: Symposia, Vol. 21 (2), pp. 1495-1502, 1993.

Sun J., Fu L. & Zhang S. A review of working fluis of absorption cycles. Renewable and sustainable energy review, Vol. 16, pp. 1899-1906, 2012.

Wang J., Wu W., Shi W., Li X. & Wang B. Experimental investigation on NH3-H2O generator-absorber heat exchange (GAX) absorption heat pump. Energy, Vol. 185, pp. 337-349, 2019.

Wirtz M., Stutz B., Phan H.T. & Boudehenn F., Numerical modeling of falling-film plate generator and rectifier designed for NH3-H2O absorption machines. Heat and Mass Transfer, Vol. 58, pp. 431-446, 2021.

Experimental Investigation of a Novel Hybrid Heat Pump

Tobias Reum, Thorsten Summ, Mathias Ehrenwirth and Tobias Schrag

Institute for new Energy Systems (InES), Technische Hochschule Ingolstadt, Germany

Abstract

Heat pumps can employ renewable electrical energy to generate domestic heat without the use of fossil fuels. Hybrid heat pumps aim at utilizing different low-temperature heat sources. In this study, a hybrid heat pump is developed which can draw ambient energy from either a ground source heat exchanger or an air source heat exchanger depending on their corresponding temperature levels. To fully exploit the energetic potential, additional operation modes are enabled. These include efficient parallel operation of both ambient heat sources, novel defrosting interconnections as well as active regeneration of the soil. A novel two-compressor refrigerant cycle is developed. The hybrid heat pump is tested in a laboratory under realistic conditions and the refrigerant cycle behavior is analyzed. The single-source operation results promise comparable efficiencies with conventional ground source heat pumps. Switching between the single source operation mode requires a procedure to not loose refrigerant mass in the unused part-cycle. The PID controller of the air refrigerant part-cycle expansion valve is not optimized and leads to minor fluctuations on evaporation pressure, superheating temperature and heating power. Parallel operation shows high efficiency at low ambient temperatures while requiring low heating power from the heat sources. The evaporation pressures are properly separated and stable. Further operation modes like defrosting and active regeneration of the ground heat source still need to be tested.

Keywords: hybrid heat pump, novel refrigeration cycle, parallel operation, experimental investigation

1. Introduction

Heat pumps are heat generators for both space heating (SH) and domestic hot water (DHW). Most heat pumps operate with electrical energy and can therefore be operated renewably by employing renewable electrical energy sources like wind turbines and photovoltaics. Differently from direct electric heaters, heat pumps can deliver a larger amount of heat energy than electrical energy consumed. This is due to the utilization of low-grade thermal energy from ambient heat sources like air, ground water or the soil. A so-called refrigerant cycle is needed to utilize these low-temperature sources. An ideal refrigerant cycle is a reverse Carnot cycle. Its efficiency is dependent on the boundary conditions, namely the temperature levels of the heat source T_{so} and the heat sink T_{si}. The maximum theoretically possible efficiency is described by the reverse Carnot efficiency η_{carnot}:

$$\eta_{\mathrm{carnot}} = \frac{T_{\mathrm{si}}}{T_{\mathrm{si}} - T_{\mathrm{so}}} \qquad \text{(eq. 1)}$$

In practice, a heat pump's efficiency is calculated as the ratio between the heating power $\dot{Q}_{\mathrm{heat}}$ and the electrical power P_{el} and is called the coefficient of performance (COP):

$$\mathrm{COP} = \frac{\dot{Q}_{\mathrm{heat}}}{P_{\mathrm{el}}} \qquad \text{(eq. 2)}$$

Commonly, COPs vary between 2 and 6 depending on the temperature levels of the heat source and heat sink (SH or DHW) (John Cantor Heat Pumps, n.d.; Naldi, et al., 2014; Natural Resources Canada, 2022). The heating power $\dot{Q}_{\mathrm{heat}}$ is calculated via the mass flow $\dot{m}$, the specific heat capacitance c_p, and the temperatures of inlet and outlet flow, T_{in} and T_{out} respectively:

$$\dot{Q}_{\mathrm{heat}} = \dot{m} * c_p * (T_{\mathrm{out}} - T_{\mathrm{in}}) \qquad \text{(eq. 3)}$$

Air source heat pumps (ASHP) are heat pumps with an air source heat exchanger (ASHX) as the heat source, ground source heat pumps (GSHP) are connected to ground source heat exchangers (GSHX), usually via a brine cycle. While ASHPs usually have lower investment costs, the annual efficiency is generally lower than that of a GSHP, since the soil is a large heat storage and is usually on a higher temperature level during winter. An increased source temperature leads to an increased efficiency according to equation 1.

© 2022. The Authors. Published by International Solar Energy Society
Selection and/or peer review under responsibility of Scientific Committee
doi:10.18086/eurosun.2022.08.11 Available at http://proceedings.ises.org

Superheating temperature T_{sup} is a major criterium for a properly operating refrigerant cycle. Superheating of the refrigerant is necessary at the inlet of the compressor. Superheating temperature is an increase of the refrigerant temperature at compressor inlet $T_{\mathrm{comp,in}}$ above the evaporation temperature T_{evap}. Fluid parts would damage the compressor and reduce the service life significantly. Therefore, the expansion valves control the mass flow through the evaporator to allow superheating of the refrigerant. Superheating temperature is then defined as:

$$T_{\mathrm{sup}} = T_{\mathrm{comp,in}} - T_{\mathrm{evap}} \qquad \text{(eq. 4)}$$

The fluids within refrigerant cycles are called refrigerants. They change their phase between liquid and gaseous, absorbing or dissipating heat accordingly. They need to evaporate and condensate at usable temperature ranges and require high specific vaporization capacities for compact component design. There is a strong need for new refrigerants due to formerly employed fluids being either damaging to the ozone layer and current ones having high global warming potentials when released. A Europe-wide phase down of harmful refrigerants is pursued (EU, 2014). While natural refrigerants like propane (R290) are promising regarding the environmental impact as well as thermodynamically, their flammability still prevents broad usage. A large number of mixtures is currently on the market, weighing up environmental impact and safety of use.

Research is going on to combine several heat sources within one single heat pump. These are commonly referred to as hybrid heat pumps (HHP). One research group employed two separate GSHXs together with an air-based regenerator as the heat source for a HHP. The system was optimized for an office building and the cooling load was dominant. The heat pump purely operated with the GSHXs, while the air-based regenerator supported in keeping these at low-enough temperature levels for passive cooling. The two GSHXs were operated serially for heating, cooling or being allowed to regenerate (passively or actively via the ASHX). Still, they found a decrease of 47 % in borehole sizing when compared to a single ground-source heat pump system. (Allaerts, et al., 2014)

Another project analyzed a HHP with an air and a ground heat source. The heat pump could switch between either heat source and deliver heating power to an office building. They found comparable efficiencies to a GSHP while having half the area for a horizontal GSHX. The interconnection did not allow parallel operation of both heat sources or novel defrosting methods. Only passive regeneration of the GSHX was possible. (Corberan, et al., 2018)

Within the research project Hybrid Heat Pump+, funded by the Federal Ministry for Economics and Climate Action, Germany, parallel operation of two heat sources was identified as a major innovation. The basic scheme can be seen in Figure 1.

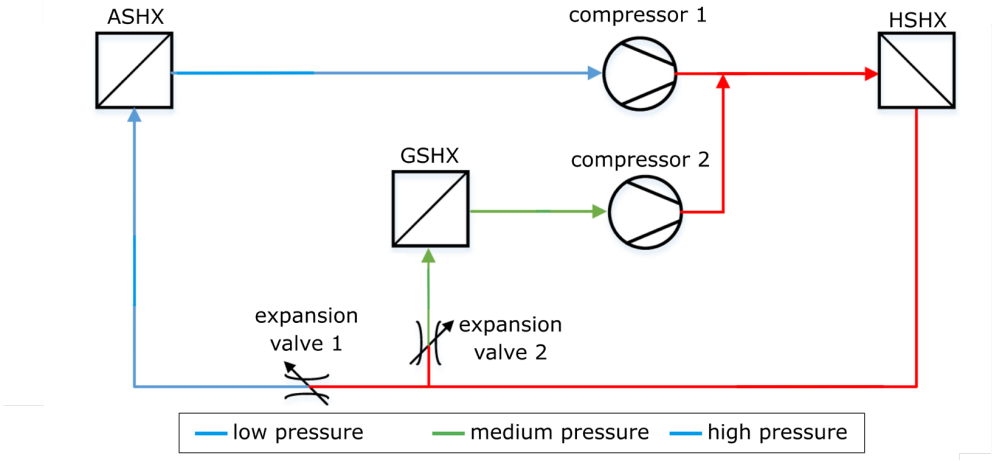

Figure 1: Scheme of the initial idea of a refrigerant cycle with two heat sources, two compressors and two expansion valves. This allows separated evaporation pressures (blue and green) to supply one condensation pressure (red).

An ASHX as well as a GSHX was chosen. Both heat sources can be designed at lower power, since peak loads can be supplied by both heat sources in parallel. Also, flexible variation of the load on the sources helps managing the energy content of the GHSX while preventing freezing. To allow efficient parallel operation, an interconnection using two compressors needs to be developed. Further operation modes were to be realized: First, defrosting of the ASHX using the GSHX is more efficient, since reverse cycle defrosting always draws energy from the heating system heat exchanger (HSHX). Second, active regeneration of the GSHX during times of comparatively high ambient air temperatures can reduce the necessary area of the GSHX even further compared to previous research results. These required additional valves and control algorithms.

For an evaluation of these operation modes, a prototype needs to be built and experimentally investigated. The novel refrigerant cycle operation is analyzed. Of special interest are superheating temperatures of the refrigerant within the heat sources, stability of the expansion valve controls and refrigerant amount within the operating part-cycle. Based on the efficiency findings during single-source operation, a comparison of the COPs with a conventional heat pump line is drawn. This allows evaluation of the impact of the increased complexity of the refrigerant cycle on single source operation. Parallel operation can be analyzed first regarding the refrigerant cycle stability concerning superheating, refrigerant amount and overall stability of the operation. Also, the parallel operation COP as well as the power needed from the GSHX can be compared to the single source operation.

2. Methodology

An interconnection was designed based on a refrigerant cycle with two heat sources and two compressors connected to a single HSHX. The implications on the refrigeration cycle had not been analyzed before and were a major evaluation point for the experimental investigation. Additional valves and components can influence the single-source operation. In parallel operation, it was unknown how the superheating of the refrigerant after the evaporators and the expansion valves will behave. Also, the refrigerant mass needed to be supervised closely to avoid a lack during certain operation modes or when switching from one operation mode to another.

Apart from the single source and parallel operation of both sources, the interconnection was required to allow several further operation modes:

- Defrosting using reverse cycle mode, where the ASHX is defrosted using the HSHX as the heat source.
- Defrosting of the ASHX using the GSHX as the heat source.
- Active cooling using either the ASHX or the GSHX as the heat sink for the HSHX.
- Active regeneration of the GSHX, both serially to heating as well as parallel to ASHP operation.

The HHP was manufactured by the industry partner ratiotherm GmbH & Co. KG and implemented into a thermal test bench, where the boundary conditions could be set. Testing for the single source operation modes was done based on the standard DIN EN 14511 (DIN e.V., 2019). This is the commonly used standard for heat pump efficiency testing in Europe and allows for comparable results. Market-available heat pumps from the same manufacturer were used for a comparison of the single-source operation. This allows a determination of the impact of the additional components within the refrigerant cycle on the efficiency.

The parallel operation mode of both heat sources was tested at low ambient temperatures. Since this operation mode is supposed to cover primarily peak loads, both compressors are supposed to run at full speed at design ambient temperatures according to (DIN e.V., 2020). For the location of the test bench, Ingolstadt yields a design ambient temperature of $T_{\mathrm{a,design}} = -13.3\ °C$. At highest possible load, the total efficiency was measured and compared to the extrapolated single source operation efficiencies of the HHP. Internal sensors of the HHP allowed a supervision of the superheating and the control of the expansion valves. For this control, a temperature sensor was located at the inlet of the compressor. The evaporation temperature is commonly determined by the evaporation pressure along with a lookup table of the specific refrigerant.

For all experiments, the refrigerant amount was supervised. A large refrigerant collector was included in the interconnection to buffer the necessary refrigerant amount. However, if refrigerant is locked out of the operated part-cycle into a non-operated part-cycle by valves, a lack of refrigerant mass can impact the efficiency significantly. Two methods were used to detect this behavior:

- A flow sight glass within the refrigerant cycle, commonly placed in front of the expansion valve, allowed a determination of the refrigerant's state at this point. Usually, the refrigerant is supposed to be fully liquid at this point. Gas bubbles are an indicator for too low refrigerant amount within the currently operated part-cycle of the HHP.
- The evaporation pressure got reduced when the amount of refrigerant was lowered. This could help when comparing different experiments with each other for example after an operation mode switch (e.g., from ASHP operation to GSHP operation and back). If the evaporation pressure is reduced, this is an indicator for a loss of refrigerant mass to the non-operated part-cycle.

3. Thermal Test bench

A thermal test bench was used to emulate the ambient conditions during the testing of the HHP. It consists of a hydraulic test bench, sensors and actuators as well as a control program written in LabVIEW on a connected PC. The hydraulic part has a heat source and a heat sink. The heat source is supplied by electric heaters and can deliver the heat via a brine cycle to the heat pump. This allows source temperatures below water freezing point. The heat sink is a water-based cycle connected to a cooling machine.

Both hydraulic cycles can control the volume flow and the temperature return flow. The volume flow is controlled by a flow valve. The current volume flow is measured continuously and a PID controller withing the LabVIEW control program changes the opening of the flow control valve accordingly. The temperature return flow to the heat pump is controlled by a mixing valve, comparing the currently measured return temperature to the setpoint. Similar to the volume flow control, a PID controller is implemented in the LabVIEW control system. Pipe lengths between the controlled components and the measuring sensors lead to delays especially when operating with low volume flows.

Insulated tubes connect the test bench to the HHP. They lead to an additional delay when changes to the setpoints occur. To avoid major impacts of these delays, static tests are conducted.

To allow ASHP tests, there is also a climate chamber where the ASHX was placed. The climate chamber is supplied by an air conditioning system and an exhaust in flow-through connection. Sensors allow control of the temperature and the relative humidity in the climate chamber. Since the ASHX extracted additional heat from the climate chamber, the setpoints of the air conditioning system needed to be adjusted. Again, static tests are beneficial to avoid complex control challenges.

The LabVIEW program as well as the monitoring system of the HHP store the measurement data continuously. This allows evaluation of the experiments using MATLAB.

4. Results and Discussion

This chapter is divided into three parts: First, the designed interconnection is shown and explained. Second, the experimental results for single source operation are discussed. Third, parallel operation is analyzed.

4.1. Designed interconnection of the HHP

The HHP was designed as a split heat pump, which means the ASHX is within a different casing than the compressors and connected via refrigerant-filled pipes. This allowed usage of existing parts from the industry partner as well as simple connection to the test bench's climate chamber. To tackle the challenge of the refrigerant phase-down, a novel blend was used. R-454B has a significantly lower GWP than common refrigerants for heat pumps, but has an ASHRAE classification of A2L (Chemours, 2021). This means it is flammable. Refrigerant sensors had to be added to the test bench facilities to reduce risks.

To allow the additional operation modes, several components had to be added. These included magnetic valves, one-way valves as well as several manual ball valves as two-directional flow valves. For a full automation of the heat pump, the manual valves need to be substituted. A large refrigerant gatherer was included to buffer the refrigerant amount needed for different operation modes. Additional heat exchangers were added: a high-temperature heat exchanger for a second heating system on an increased temperature level was included into the GSHP branch. An economizer was added into the ASHP branch, which is increasing the efficiency by transferring heat from the condensated high pressure refrigerant flow into the superheated refrigerant flow before the compressor (Jin, et al., 2016). These heat exchangers were constructive adjustments from the industry partner to be able to use existing parts. Further operation modes are possible, but within this paper, the focus lies on these aforementioned ones. The full interconnection is shown in Figure 2.

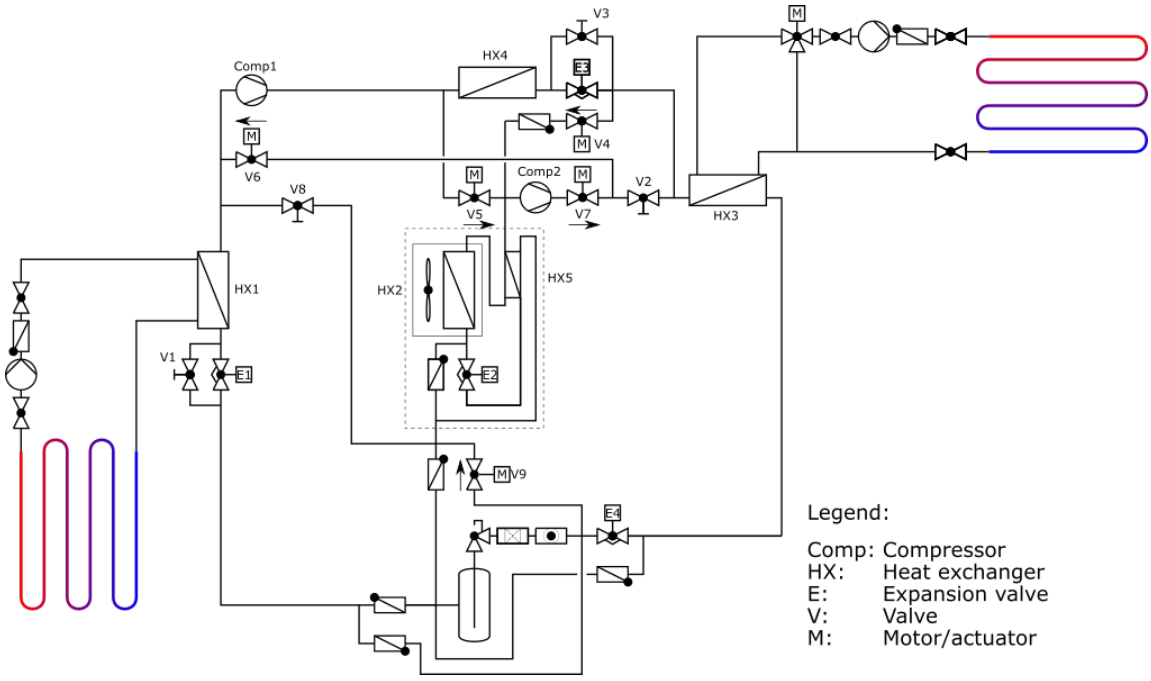

Figure 2: Interconnection of the novel HHP including all components. Sensors are not shown. Both ground source as well as heating system are shown schematically.

During GSHP operation, HX1 is the GSHX and the refrigerant is compressed by Comp1. HX4 is the high temperature heat exchanger and currently not used. Through the ball valve V3, the refrigerant reaches the HSHX HX3 and condenses. Through one-way valves and the refrigerant gatherer along with filters and the sight glass, the liquid refrigerant reaches the expansion valve E1. After the pressure reduction, the refrigerant is fed into HX1, closing the cycle.

ASHP operation uses Comp2, HX2 and E2 respectively. Different valves need to be opened to allow the refrigerant cycle, namely the manual ball valve V2 and the magnetic valves V7 and V9. The economizer HX5 is used here.

Parallel operation is the combination of both previous operation modes, ASHP and GSHP. Both compressors are run as well as both expansion valves and the aforementioned valves have to be opened accordingly.

Defrosting can be done using a reverse cycle principle. By operating Comp1 and opening the ball valve V2 and the magnetic valves V5 and V6, heat can be taken from HX3 on a low pressure and the refrigerant condenses within the ASHX HX2. In this case, E4 acts as the controlling expansion valve.

The second defrosting mode is using the GSHX HX1 as the heat source and Comp1 as the compressor. Opening the magnetic valve V5 and controlling with the expansion valve E1 closes the cycle.

Active regeneration of the GSHX HX1 can be done by using the Comp2 to compress the evaporated refrigerant from the ASHX HX2. Through the magnetic valves V6 and V7, the refrigerant reaches HX1. The ball valve V1 leads the refrigerant to the refrigerant gatherer and the magnetic valve V9. E2 acts as the expansion valve.

4.2. Single source operation

The single source operations were measured according to (DIN e.V., 2019). The standard defines source and sink temperatures, tolerances and test durations. The test bench cannot fulfill all the requirements (e.g., temperature sensors and electricity meter exceeded tolerances). But the measurement points regarding source and sink temperatures were followed, so the measurements for both the air source as well as the ground source operation were based on this standard.

For the evaluation, the COP was calculated using equation 2. Over the duration defined in the aforementioned standard, the heating power using equation 3 as well as the electrical power of the compressor were measured. The division lead to the COP.

Figure 3 shows the results for the single source operations and compares these with a market-available heat pump of the industry partner ratiotherm. As expected, lower sink temperatures T_{si} lead to higher efficiencies COP. With increasing source temperatures (ambient air temperature and brine temperature respectively), the COP increases as

well. The comparison is done with heat pumps from the Max-line of ratiotherm (ratiotherm GmbH & Co. KG, n.d.). They contain several similar components like the heat exchangers, but different compressors and most notably a different refrigerant. Another factor is, that the HHP COPs do not include peripheral power for pumps, ventilators and electrical components. While these generally play a minor role compared to the compressor, this lowers the total electrical consumption and therefore increases the COP. These are the major reasons for the improved COP of the HHP compared to the market-available Max-line heat pumps. It can, however, be said, that the HHP does not suffer from the additional complexity of the hydraulic refrigerant cycle to a large extent.

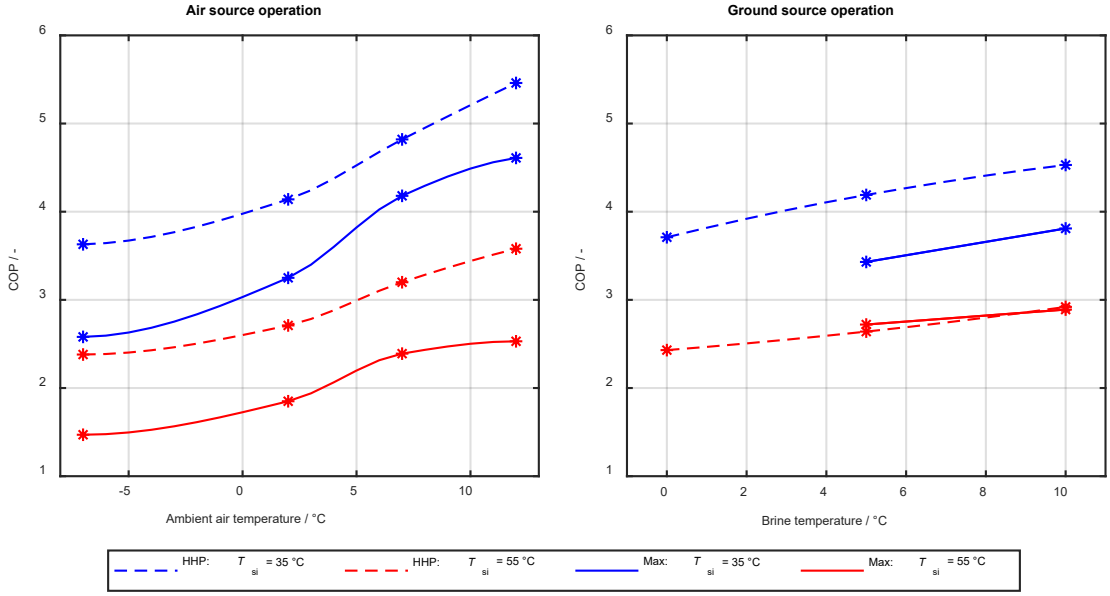

Figure 3: Experimentally derived COPs of the HHP. Different heating temperatures T_{si} are shown in red and blue. Dashed lines show the HHP measurement results, the full line the comparison with heat pumps from ratiotherm's Max production line. The measurement points are interpolated using monotone piecewise cubic interpolation (Fritsch and Carlson, 1980).

During the measurements of the air source operation, a significant fluctuation of the COP was detected. This was a result of significant fluctuations of the evaporation pressure. This in turn is a result of fluctuating superheating temperature T_{sup}, which is again a result of fluctuating expansion valve opening. This behavior is shown in figure 4. The expansion valve was not controlled appropriately, fluctuating between 21 and 37 % PWM opening degree. The most likely reason is improper PID parameters within the HHP software. This needs to be considered when analyzing further operation modes.

A shift of the refrigerant mass was detected as well. When switching between the single source operations, a significant lack of refrigerant occurred. This could be seen in both the sight glass before the expansion valve as well as in decreasing evaporation pressures compared to previous experiments in the same operation mode. To avoid this, all valves had to be opened when switching between the operation modes, allowing the refrigerant to spread in the whole refrigerant cycle instead of gathering in the evaporators. Since this procedure took time and even had to be repeated occasionally, a more careful analysis and a proper procedure still needs to be developed to tackle this difficulty.

4.3. Parallel operation

As discussed, parallel operation was tested in low ambient air temperature conditions to be able to cover peak loads. Due to a mechanical issue with the air source compressor (Comp2 in figure 2), full loads were not possible anymore without overloading the inverter and an error stopping the operation. Therefore, the test was conducted at lower inverter frequency $f = 50$ % and increased ambient air temperature $T_a = -10$ °C instead of at full load at the design ambient temperature $T_{a,design} = -13.3$ °C. Theoretically, parallel operation therefore could deliver more heating power, but the general behavior regarding refrigerant amount and superheating temperature should remain the same. If possible, this should be examined in future tests.

Figure 5 shows the heating and electrical power as well as the COP during parallel operation. Over the shown duration, the average COP was 3.43. To compare this with the single source operation, the air source operation needed to be extrapolated and resulted in a COP of 2.69. The brine source operation yielded a COP of 3.71 at similar

boundary conditions. While the latter is better than the parallel operation, parallel operation is more efficient than the air source operation. The main benefit is the omission of any other peak load heat generators: In practice, electrical heating rods are often used to cover peak loads, adding an electrical efficiency of 1. The parallel operation of the HHP is significantly more efficient in these low temperature ambient air conditions. The second benefit is a significantly lower load on the GSHX. While the HHP extracted about 3.7 kW from the brine cycle, the single source operation would need 5.8 kW to cover the same heating power of about 8 kW, which the HHP delivers during this experiment. This is a reduction to about 64 %.



Figure 4: Graph of the air source operation focusing on evaporation temperature and superheating. The fluctuations derive from an improper PID controller for the expansion valve.

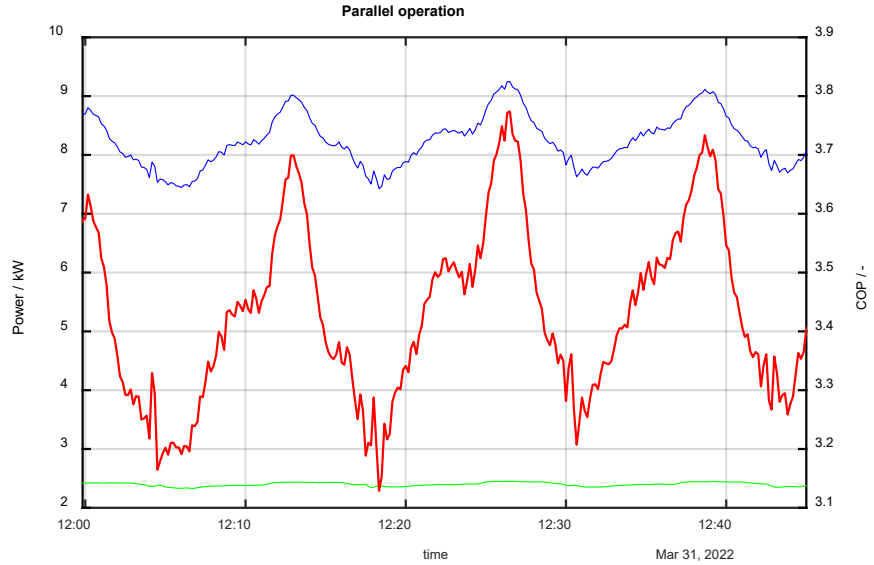

Figure 5: Overview of the parallel operation at ambient temperature $T_a = -10$ °C, brine temperature $T_{brine} = 0$ °C and sink temperature $T_{si} = 35$ °C.

The fluctuations of the COP and the heating power during parallel operation were significant. As seen in the single source operation, the issue lies within the control of the expansion valve within the ASHX part-cycle. Figure 6 shows the behavior of evaporation temperature and superheating of both part-cycles. While the operation was stable for the GSHX part-cycle, the values fluctuated for the ASHX part-cycle. This is a fundamental issue with the expansion valve control and not of the parallel operation.

The refrigerant amount was found to be no issue, since both part-cycles are actively taking part in the operation. No lack of refrigerant was detected, even during switching to and from parallel operation.

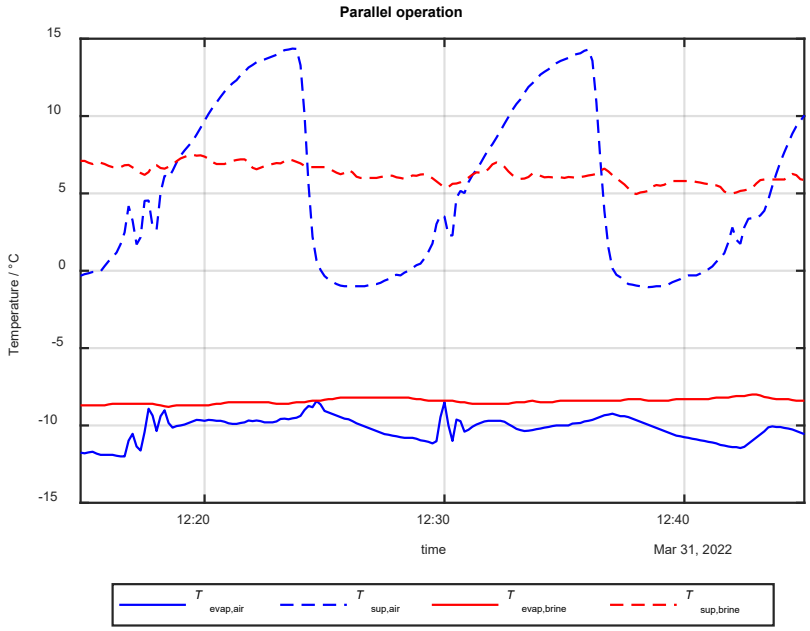

Figure 6: Graph of the parallel operation focusing on evaporation temperatures and superheating. The fluctuations of the air source part-cycle are based on an improper PID controller of the expansion valve.

5. Conclusions and Outlook

The developed interconnection for the HHP is significantly more complex than traditional heat pumps. Not only two compressors and expansion valves need to be controlled, the number of valves is a challenge not only economically but also for the control strategy. Whether the full list of operation modes is necessary and ecologically as well as economically feasible needs to be determined further.

First tests with the HHP in single source operation showed promising results. Even though the complexity of the refrigerant cycle is increased and additional components are placed in the refrigerant flow, the efficiency was comparable with market-available heat pumps. Detailed analysis including the electric power consumption of the periphery as well as optimization of the PID control of the air source operation expansion valve need to follow. One more challenge was detected: The refrigerant amount was not easily available to the other single source operation when changing the heat source. Further investigation of this behavior and development of a proper control strategy might further increase the complexity of the HHP control.

Parallel operation of both heat sources proved to be possible. The evaporation pressures were separated during operation and the expansion valves controlled independently. The efficiency was promising: It was an improvement compared to air source operation, while – expectedly – not reaching efficiencies of brine source operation. However, the heating power was significantly increased over the single source operations. Also, the power extracted from the GSHX could be reduced to almost 64 % by parallel operation at this specific measurement point. The issue with the air source part-cycle expansion valve fluctuating could be seen in this operation mode as well, leading to an overall fluctuating heating power and COP. No issue with the shifting refrigerant amount was observed.

The remaining operation modes need to be analyzed in detail. The refrigerant amount issue needs to be evaluated and possible control strategies to be developed. For an energetic evaluation, an annual simulation using models derived from the experimental data and an optimal control strategy needs to be conducted. These are further steps to tackle the challenges of the novel HHP.

6. Acknowledgments

The authors would like to thank the Federal Ministry for Economics and Climate Action (BMWK) for the financial support within the funding programme Central Innovation Programme for small and medium-sized enterprises (ZIM).

7. Reference

Allaerts, K., Coomans, M. & Salenbien, R., 2014. Hybrid ground-source heat pump system with active air source regeneration. *ELSEVIER Energy Conversion and Management*, 04 November, pp. 230-237. https://doi.org/10.1016/j.scs.2014.02.005.

Chemours, 2021. *Opteon™ XL41; Refrigerant (R-454B): Product Information.* [Online] Available at: https://www.opteon.com/en/-/media/files/opteon/opteon-xl41-product-information.pdf [Accessed 21.04.2023].

Corberan, J., Cazarlo-Marín, A., Marchante-Avellaneda, J. & Montagud, C., 2018. Dual source heat pump, a high efficiency and cost-effective alternative for heating, cooling and DHW production. *International Journal of Low-Carbon Technologies, 13*, pp. 161-176. https://doi.org/10.1093/ijlct/cty008.

DIN e.V., 2019. *DIN EN 14511:2019-07, Air conditioners, liquid chilling packages and heat pumps for space heating and cooling and process chillers, with electrically driven compressors.* Berlin: Beuth Verlag GmbH.

DIN e.V., 2020. *DIN/TS 12831-1:2020-04, Method for calculation of the room heat load - Part 1: National addition to DIN EN 12831-1.* Berlin: Beuth Verlag GmbH.

EU, 2014. Regulation (EU) No 517/2014 of the European Parliament and of the Council of 16 April 2014 on fluorinated greenhouse gases and repealing Regulation (EC) No 842/2006 Text with EEA relevance. *OJ L 150*, 20 05, pp. 195-230.

Jin, L. et al., 2016. Performance Comparison of Air-source Heat Pumps Using Economizer Vapor Injection and Internal Heat Exchanger in Cold Regions. *International Refrigeration and Air Conditioning Conference*, West Lafayette.

John Cantor Heat Pumps, n.d.. *https://heatpumps.co.uk.* [Online] Available at: https://heatpumps.co.uk/heat-pump-information-without-the-hype/what-is-the-cop/ [Accessed 01.09.2022].

Naldi, C., Zanchini, E. & Morini, G. L., 2014. A method for the choice of the optimal balance-point temperature of air-to-water heat pumps for heating. *Sustainable Cities and Society*, 07. https://doi.org/10.1016/j.scs.2014.02.005.

Natural Resources Canada, 2022. *Heating and Cooling With a Heat Pump.* [Online] Available at: https://www.nrcan.gc.ca/energy-efficiency/energy-star-canada/about/energy-star-announcements/publications/heating-and-cooling-heat-pump/6817 [Accessed 01.09.2022].

ratiotherm GmbH & Co. KG, n.d.. *Wärmepumpen WP Max und WP Grid vom Hersteller.* [Online] Available at: https://ratiotherm.de/waermepumpen/ [Accessed 01.09.2022].

PV driven Air Heat Pump using Overheating Effects as Thermal Battery in Single Family Houses

Alexander Thür, Bernhard Schett, Fabian Leu

Unit of Energy Efficient Building / University of Innsbruck, Innsbruck (Austria)

Abstract

Theoretical investigations based on TRNSYS simulations are carried out for an electric driven air heat pump in combination with different concepts of thermal activation of the building mass and a water storage in small single-family buildings. Building mass and water storage are acting as thermal battery for local produced photovoltaic electricity. Several different heat pump characteristics and control strategies in combination with a low energy house (new built or after renovation) and different heat capacities (concrete or screed and different water storage volumes) are investigated. Using PV with 7,362 kWh electricity gain per year the household grid electricity consumption of 3,058 kWh/a can be reduced by 35% resulting in 1,987 kWh/a. Additionally the air heat pump grid electricity consumption of 3,169 kWh/a as reference case can be reduced by only 15% (without any thermal activation) resulting in 2,676 kWh/a grid consumption. When using building mass and water storage as thermal battery for the photovoltaic - heat pump system, up to 60% less grid electricity consumption resulting in 1,251 kWh/a grid electricity consumption can be achieved. Photovoltaic self consumption for household and heat pump electricity on the other side can be increased from 22% in the reference case up to 46% in the best case, thus more than doubling. In fact the heat storage effect in the screed of the floor heating system or the concrete ceiling is in the range of about 30 kWh per day which is in the same magnitude of the potential of a 800 liter water storage. Operating cost can be reduced by ca. 30% using existing thermal mass just by simple advanced control strategies.

Keywords: heat pump, photovoltaic, thermal battery, single-family house, building mass activation

1. Introduction

Electrical driven air heat pumps in combination with thermally activated building systems (TABS) and conventional hot water tanks as thermal energy storage (TES) can be used as thermal batteries for electricity produced by a photovoltaic (PV) system with the goal to realize a maximum of PV self-consumption and minimized electricity grid consumption respectively.

Within the national research project “Energieschwamm”, it was investigated how an air heat pump system in combination with different building types with different designed TABS (thermal activation of the building mass) can act as a thermal battery when supplying space heating and domestic hot water to the building with different control strategies (Heinz et al., 2022). The project was based on a set of theoretical simulations in combination with some field measurements in real buildings and the experience of the recent research project TheBat (Thür et al., 2018).

An air heat pump can be operated in different ways like: a) power controlled depending on availability of photovoltaic electricity, b) with or without using a desuperheater for domestic hot water (DHW) preparation, c) charging a TES up to different temperature levels or up to different volumes or d) heating the building to room temperatures with more or less hysteresis of the set room temperature. Within this study it is investigated, which operation modes, parameter settings and design parameter are best to achieve high PV self consumption and low electricity operating cost in combination with no additional investment cost beside some adaption of the controller setup. Household electricity as a realistic load profile created with the Load Profile Generator (Pflugradt, 2016, 2018) is taken into account, but no strategies like load shifting or use of an electric battery for improvement of PV self consumption is used (see Fig. 1, left). In general, always the PV electricity first is used to serve the household electricity, only the remaining excess PV electricity is further used for heat pump operation. Also the

© 2022. The Authors. Published by International Solar Energy Society
Selection and/or peer review under responsibility of Scientific Committee
doi:10.18086/eurosun.2022.08.12 Available at http://proceedings.ises.org

DHW tap-profile (see Fig. 1, right) created with DHWcalc (Jordan, 2005) in all simulations is the same, e.g. no optimization of tappings in point of time is done.

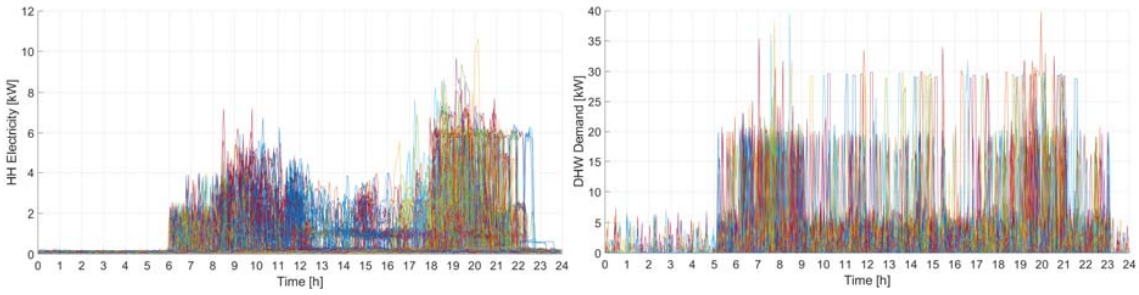

Fig. 1 Load profile as 24h-lines for 365 days for household electricity (left) and DHW tapping (right) in 3 minute time steps.

2. System description

Simulations are done for a single family house (based on the IEA SHC Task44 reference building) with low energy standard (RES45: 45 kWh/m^{2}a nominal space heating demand) at central European climate in Innsbruck, Austria. Different thermal active mass variations of floor heating (FH) or concrete ceiling activation (CCA) with different heat capacities and different configurations of the TES were investigated.

In Fig. 2 the potential heat capacities of the different components used in this study as "thermal battery" are shown. Air itself to store heat is useless as well known. The screed of the floor heating system with 0.08 m thickness in a 140 m^2 single-family house has about the same potential (31.12 kWh) as the 0.8 m^3 water tank (37.22 kWh), where the concrete ceiling with 0.2 m thickness as a potential has a threefold capacity (93.38 kWh) compared to 0.08 m screed and 0.8 m^3 water tank. The "dynamic" heat capacity during operation, which finally really can be activated, is strongly depending on several boundary conditions, as the most important are: a) stratification and temperature level in the water tank, b) u-value and temperature difference between heating water and screed/concrete, c) available power of PV and heat pump, d) length of period how long excess PV electricity is available, e) actual DHW demand and heating load of the building, etc.

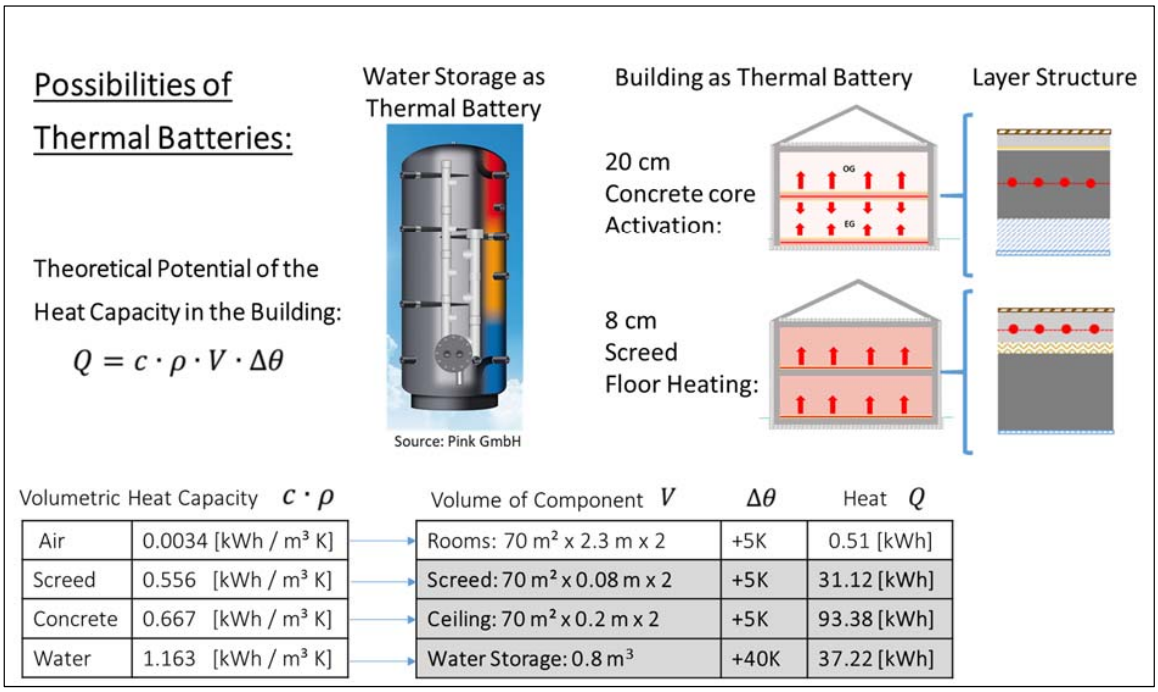

Volumetric Heat Capacity $c \cdot \rho$		Volume of Component V	$\Delta\theta$	Heat Q
Air	0.0034 [kWh / m³ K]	Rooms: 70 m² x 2.3 m x 2	+5K	0.51 [kWh]
Screed	0.556 [kWh / m³ K]	Screed: 70 m² x 0.08 m x 2	+5K	31.12 [kWh]
Concrete	0.667 [kWh / m³ K]	Ceiling: 70 m² x 0.2 m x 2	+5K	93.38 [kWh]
Water	1.163 [kWh / m³ K]	Water Storage: 0.8 m³	+40K	37.22 [kWh]

Fig. 2 Characteristic figures of the different materials used as thermal mass in the RES45 building.

In Tab. 1 the main characteristic figures of the reference building and the PV - heat pump system are shown.

In Fig. 3 the hydraulic scheme of the PV - heat pump system and the main control settings are shown. The heat pump is operated in a) standard mode or b) PV-overheating mode. PV-overheating mode is possible when excess PV electricity is available with sufficient power to run the heat pump in space heating mode or in DHW mode. Based on technical data of the heat pump at any time a theoretical "dummy heat pump" is calculated in parallel based on the actual boundary conditions (air temperature, set space heating flow temperature, bottom tank temperature) for minimal possible compressor speed. If the resulting electricity consumption is less than the available PV excess electricity, the heat pump starts operation in PV-overheating mode, first priority in DHW mode or second priority in space heating mode.

Tab. 1 Characteristic key figures of the reference building RES45 and the heat pump system.

Name	Value	Unit
Space heating consumption	6,726	kWh/a
Treated floor area	140	m^2
Room set temperature @standard control	21	°C
Room max. temperature @PV-overheating control	24	°C
Domestic hot water consumption @Tap-Temp.: 45°C	2,980	kWh/a
Household electricity consumption	3,058	kWh/a
PV system	40	m^2
PV gain	7,231	kWh/a
PV tilt angle	45	deg
PV azimuth	South	-
Heating season	Oct 1st – March 31st	-
Air - water heat pump A2/W35	5.92	kW_{th}
Water storage tank	0.8	m^3

The air heat pump has a condenser and a desuperheater. During space heating mode the water mass flow is split by a controlled 3-way valve after the condenser in order to have a controlled mass flow passing the desuperheater to reach a set outlet temperature of 53°C in standard mode or 62°C in PV-overheating mode, which is fed into the TES at the top for DHW preparation. Condenser outlet temperature is controlled by the compressor speed to reach the set temperature according to the heating curve depending on the ambient temperature. The total water mass flow passing the condenser is directly coupled to the compressor speed. The heat pump starts, when the TES outlet temperature (out 4) falls below the actual set space heating flow temperature for more than 15 minutes. The heat pump stops when the bottom sensor of the water tank exceeds the set space heating flow temperature by the hysteresis of 4K in standard mode or when the bottom sensor of the water tank exceeds 54°C in PV-overheating mode.

For heating the TES for DHW the total water mass flow passes condenser and desuperheater in series and is controlled to reach the set outlet temperature of 53°C in standard mode while the compressor runs at a fixed speed.

In PV-overheating mode the compressor speed is controlled to consume the excess PV-power (within minimum and maximum limits) and the water mass flow is controlled to reach the set outlet temperature of 62°C. The heat pump starts, when the upper temperature sensor (below "in 1") falls below 46°C at any time. During defined time windows (in this study: 5-7 and 17-19 or 11-16) the heat pump starts when the lower temperature sensor (above "in 3") falls below 46°C. The heat pump stops in all cases when the lower temperature sensor (above "in 3") of the water tank exceeds the set temperature of 52°C in standard mode or 61°C in PV-overheating mode.

DHW is prepared via an external heat exchanger unit (fresh water unit) by a speed controlled pump to reach the set tap temperature of 45°C in all cases of DHW flow rates.

Space heating loop is fed from the water tank via a mixing valve with controlled flow temperature according to an ambient temperature depending heating curve (see Fig. 4). The flow temperature is controlled in three different modes: a) standard mode, b) PV-overheating with flow temperature reinforced by +3K or c) PV "Boost" overheating with flow temperature reinforced by +10K. Space heating mass flow is individual controlled for each of the 10 thermal zones. The flow rate is constant according to the design value for each zone and just switched on or off based on a special control concept of the space heating controller to reach the set room temperature of 21°C in standard mode. In PV-overheating mode the control valve of each zone is open as long as the PV-overheating set room temperature of 24°C is reached. Additionally as a basic setting for each zone it can be defined if PV-overheating in general shall take place or not, e.g. no PV-overheating of the parents sleeping room.

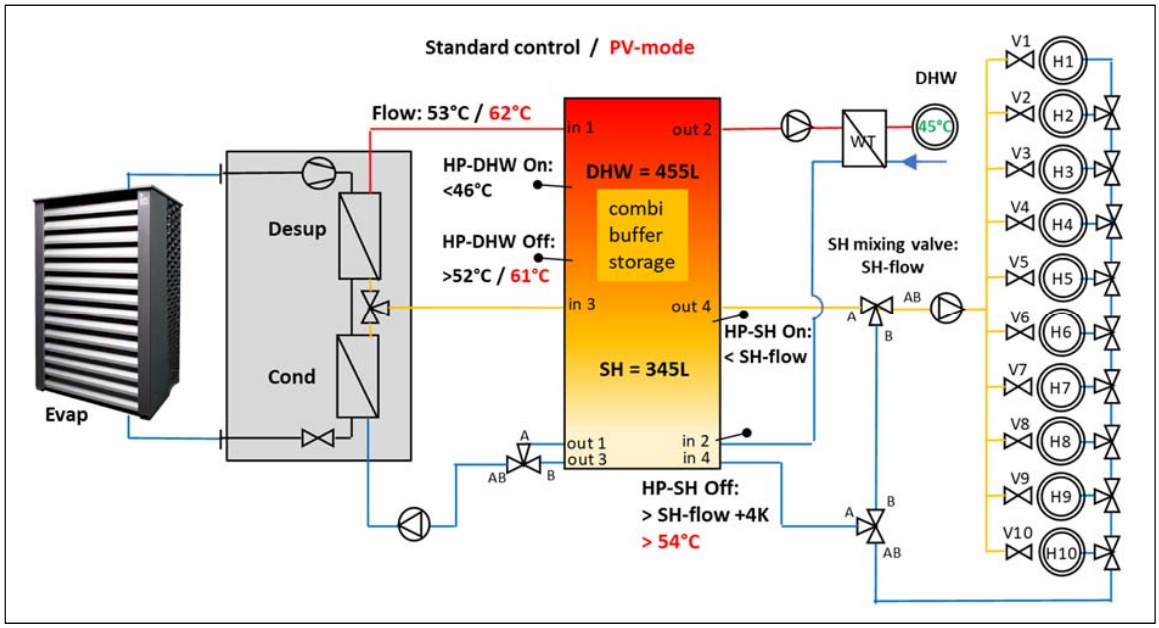

Fig. 3 Hydraulic scheme of the PV – heat pump system with a combi buffer storage as TES and a fresh water unit for DHW preparation @45°C and 10 space heating loops for 10 individual thermal zones in the RES45 single-family house.

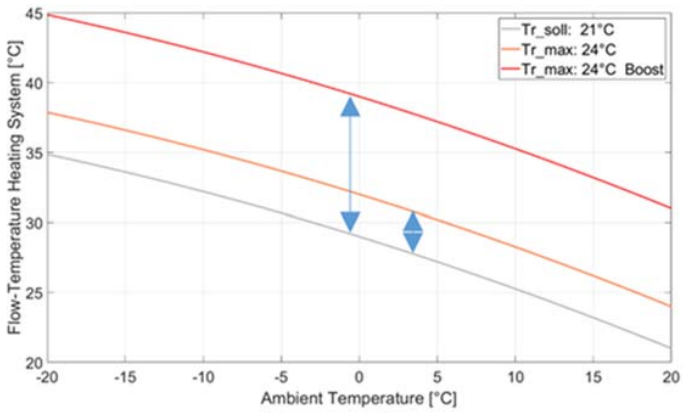

Fig. 4 Heating curve for space heating depending on ambient temperature for a) standard mode, b) PV-overheating with +3K flow temperature, c) PV "Boost" overheating with +10K flow temperature.

3. Results - Virtual 24h-day for one year

Simulation results first are presented in a qualitative way to show principle effects of different system behavior. In Fig. 5, Fig. 6 and Fig. 7 electric energies of the whole year are summed up for each hour resulting in one virtual "day" of the air heat pump system with a 40 m^2 PV system. Grid electricity consumption for household (HH) and heat pump (HP) is negative on the y-axis and the use of PV electricity for household (HH) and heat pump (HP) and remaining PV feed in (PV feed in) is positive on the y-axis.

In Fig. 5 the left graph shows the reference system without PV and with standard control system. For DHW preparation two time-slots are defined from 5 h to 7 h and 17 h to 19 h, which is a typical standard setting with the goal to be sure to have sufficient DHW during the typical peak tapping periods in the morning and in the evening. Therefor at 5 h and at 17 h a clear peak of electricity consumption from grid of the heat pump can be observed.

In Fig. 5 the right graph shows the result when the 40 m^2 PV system is added, but without any changes of the control strategy of the system. First, the PV is used to serve for household electricity (HH from PV) as much as possible, but still around two third of household electricity consumption is covered by the grid and a huge amount of PV electricity (about 85%) is available. From 7 h to 13 h a small additional fraction of PV production (7%) can be used for the heat pump, mainly for space heating, therefor still 78% of PV production must be fed into the grid. The two time slots for DHW preparation hardly can use PV electricity because of luck of sunshine at that time.

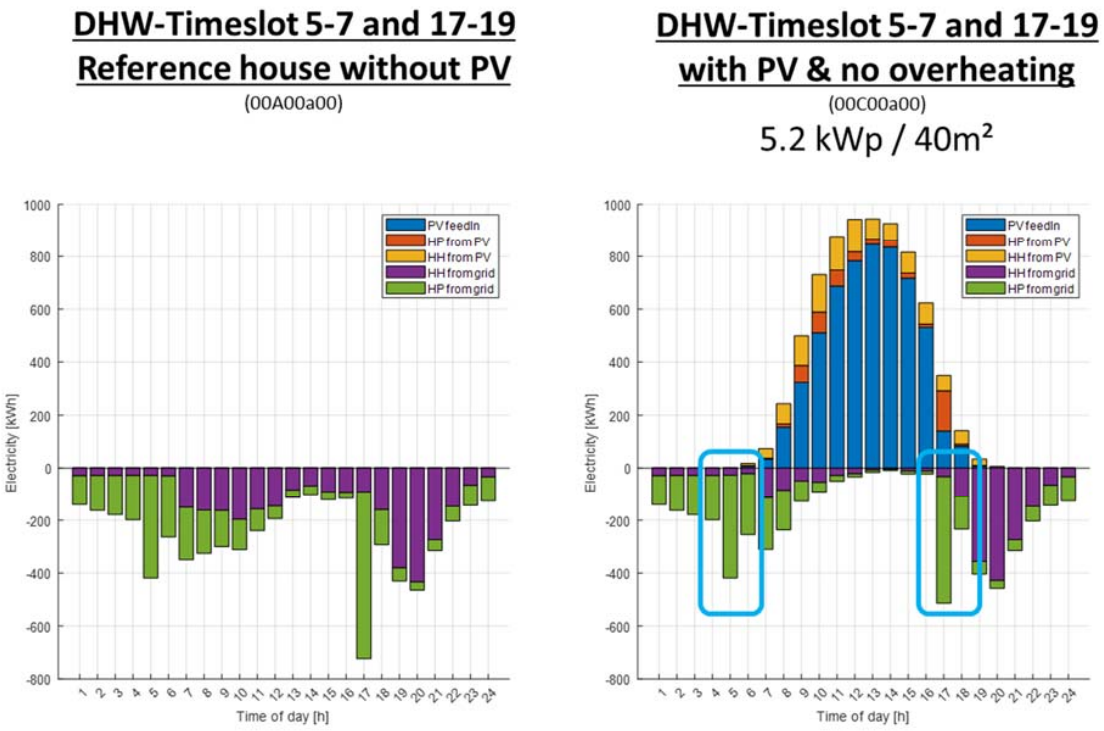

Fig. 5 Virtual 24-hour day of the whole year for the reference case without PV system (left) and with PV system (right) but without any changes of the control strategy.

In Fig. 6 the left graph shows already a significant change when just the time slots for DHW preparation is shifted to only one time slot from 11 h to 16 h. At 17 h the grid consumption of the heat pump for DHW preparation has completely disappeared and only very little space heating operation remains. At 5 h the grid consumption for DHW preparation also disappears almost completely. At 11 h the major part of DHW preparation takes place and at that time around two third can be covered by PV. Since 455 liter of the 800 liter tank are reserved for DHW, the daily consumption easily can be covered by only one defined time slot for DHW preparation. There is no need to define two time slots at very disadvantageous points in the early morning and late afternoon.

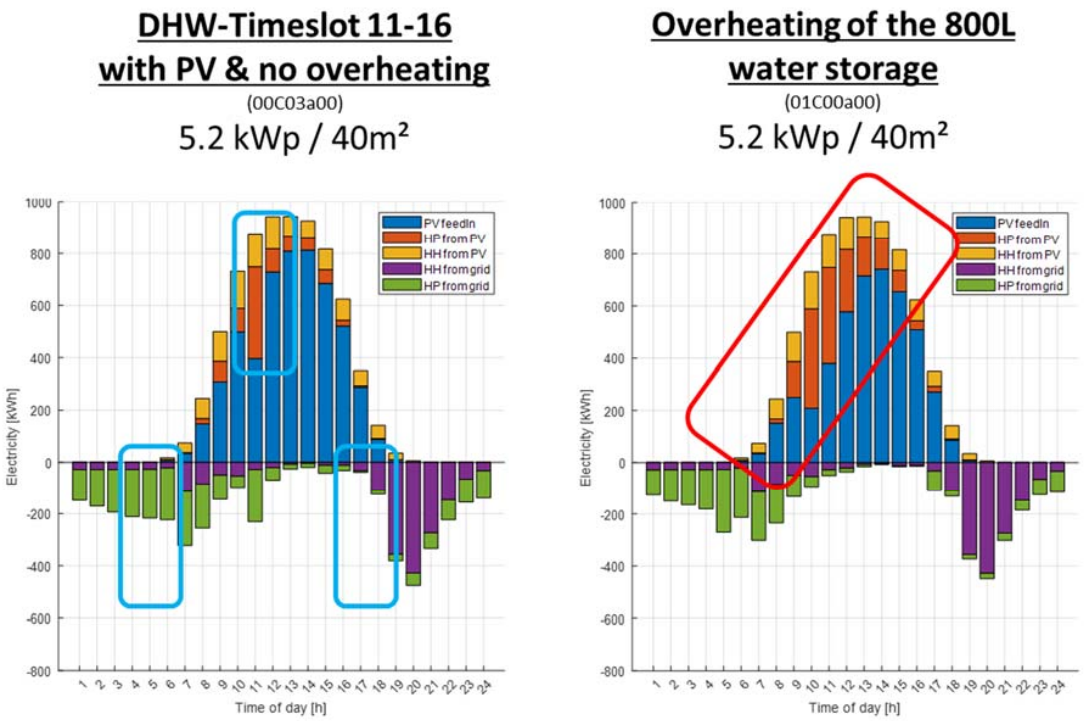

Fig. 6 Virtual 24-hour day of the whole year for the system with PV system but DHW time slot changed to only one from 11 h to 16 h (left) and the system with overheating the 800 liter water storage (but no overheating of the building) in DHW mode or space heating mode at any time whenever excess PV is available at high enough power.

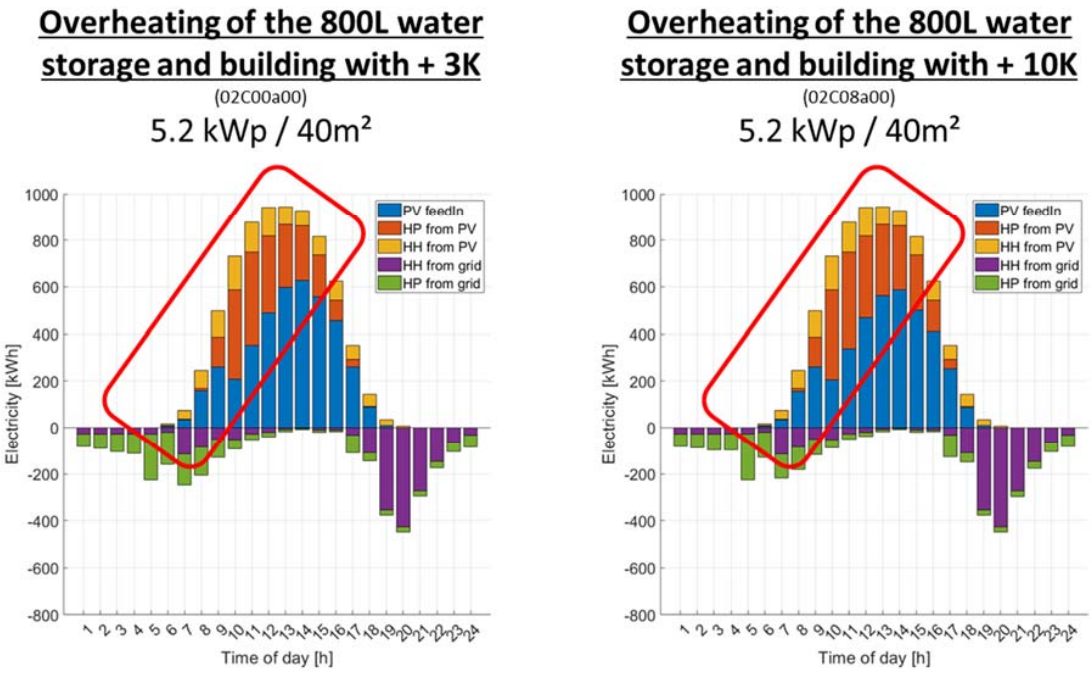

Fig. 7 Virtual 24-hour day of the whole year for the system with PV system with overheating the 800 liter water storage and overheating of the building with an extra lift of +3K of the flow space heating temperature (left) and an extra lift of +10K of the flow space heating temperature at any time whenever excess PV is available at high enough power.

In Fig. 6 the right graph shows a further significant improvement, when the control concept allows the heat pump to overheat the 800 liter water storage in DHW mode or space heating mode at any time (but no overheating of the building), whenever excess PV is available at high enough power. Even though the DHW time slots are defined again from 5 h to 7 h and 17 h to 19 h, what can be observed at 5 h with slightly higher HP grid consumption

compared to the left graph.In Fig. 7 the left graph shows the next step of significant improvement, when the control concept allows the heat pump to overheat beside the 800 liter water storage also the building at any time, whenever excess PV is available at high enough power. Overheating the building takes place with an extra lift of +3K of the flow space heating temperature and is allowed until the room temperature reaches 24°C as a maximum, but only if excess PV electricity is available.

In Fig. 7 the right graph shows almost no further improvement anymore, when overheating of the building takes place with an extra lift of +10K of the flow space heating temperature and again until the room temperature reaches 24°C as a maximum.

In general, when comparing the four graphs above (Fig. 6 and Fig. 7), it can be observed, besides less operation of the heat pump with grid electricity, a significant shift of the air heat pump operation more and more to day time instead of operation during night time. This leads not only to much more air heat pump operation powered by the PV electricity, but also to operation during daytime periods with significant higher ambient air temperature with higher COP, even though the flow temperatures during PV-overheating modes are higher compared to standard DHW or space heating modes (see also Fig. 9).

4. Overall Efficiency

In Fig. 8 as the results of the effects discussed before the electricity balance for several variants of floor heating systems and screed thickness (above the line) and concrete ceiling (below the line) with different space heating flow temperatures for overheating is shown.

In each bar from the left to the right the following electricity energies are shown: grid consumption for household electricity (HH grid), PV self consumption for household electricity (HH PV), grid consumption for heat pump operation (HP grid), grid electricity savings for the heat pump in comparison to the reference system shown in the first bar (Grid savings), PV self consumption for heat pump operation (HP PV) and finally the remaining excess PV electricity which is fed into the grid (PV FeedIn).

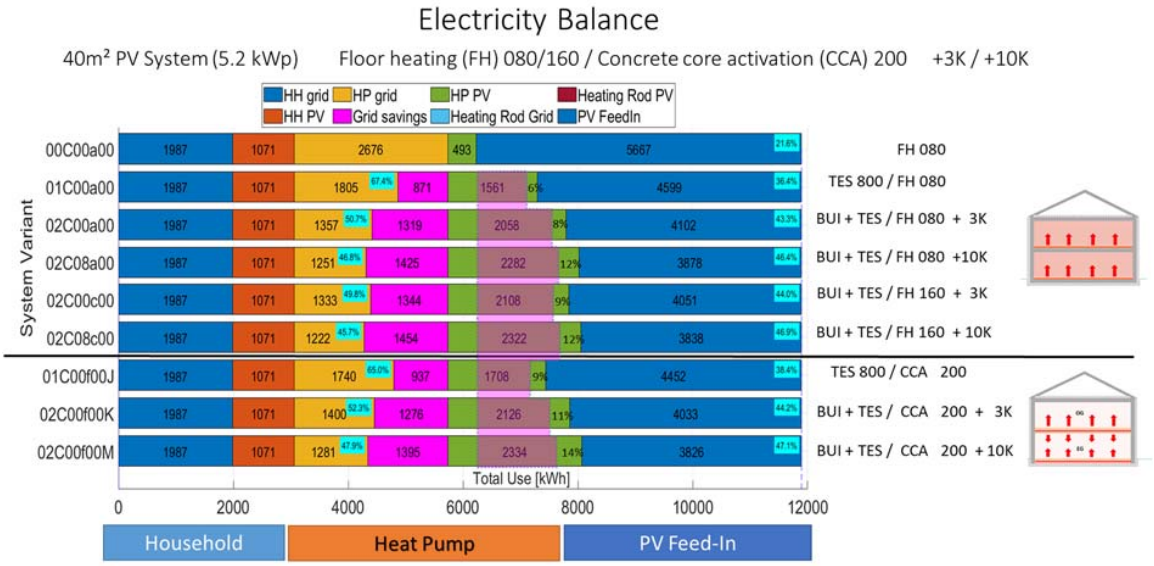

Fig. 8 Electricity Balance for several variants of floor heating systems and screed thickness (above the line) and concrete ceiling (below the line) with different space heating flow temperatures for overheating.

Within the green bar (HP PV) the Grid savings are mirrored to show at the right the remaining part of (HP PV), which in fact is the amount of additional electricity consumption of the heat pump, which is needed to cover the additional heat losses due to the overheating of the water storage and the building respectively. Therefore, just overheating the 800 liter water storage causes 6% [=(1805+1561)/(2676+493)] additional electricity consumption for the heat pump to cover the additional heat losses just of the water storage (see second bar: TES 800 / FH 080). When additionally the building is overheated with "+3 K" in the case of floor heating, the additional annual electricity consumption is 246 kWh (= 2058+1357-2676-493) or 8%, just 2%-points higher (see third bar:

BUI+TES / FH 080 +3K). However, the grid savings can be increased from 871 kWh to 1319 kWh by 51%. In other words, the grid consumption (HP grid) of the heat pump can be reduced to 50.7% in comparison to the reference case: from 2676 kWh to 1357 kWh.

If the overheating takes place with "+10K" instead of "+3K" the grid saving can further be increased from 1319 kWh to 1425 kWh or by 8%. But the additional electricity consumption significantly increases from 8% to 12%, which is +50% relatively. In terms of operating cost Fig. 14 further down will show that the economic advantage is only very little.

Also doubling the screed thickness from 0.08 m (FH080) to 0.16 m (FH160) does not improve the result significantly. Surprising is the fact, that concrete core activation with 0.2 m thickness (CCA 200) with threefold theoretical thermal capacity as potential compared to 0.08 m screed (see Fig. 2) has even worse results of grid savings: 1276 kWh for (BUI+TES / CCA 200 + 3K) compared to 1319 kWh for (BUI+TES / FH 080 + 3K). With Fig. 12 an explanation will be given for this effect.

As mentioned already in the chapter before, due to the PV-overheating the operating conditions for the heat pump can change significantly in both directions: beneficially or disadvantageous. As shown in Fig. 9, based on different definitions of seasonal performance factors (SPF) the system behavior and the heat pump itself can be analyzed. For electricity consumption in general the overall consumption of the heat pump including fan of evaporator but excluding the water pump is used. There is just to differentiate between $P_{el.sys}$ and $P_{el.grid}$. Where $P_{el.sys}$ counts all electricity consumption of the heat pump but $P_{el.grid}$ counts only the electricity delivered from grid.

SPF_{use} is a clear indicator of the overall system performance because as useful heat beside the constant DHW demand always the reference space heating demand is used. Therefore, due to the additional overheating losses of all other variants the reference system (FH 080) shows the highest SPF_{use}.

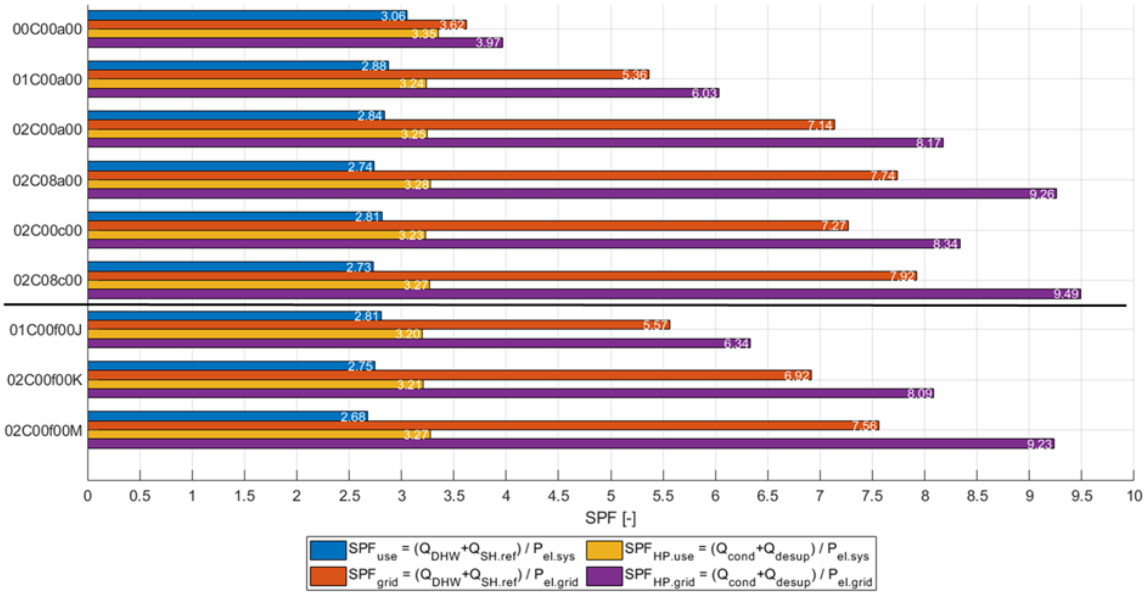

Fig. 9 Differently defined seasonal perfomance factors for several variants of floor heating systems and screed thickness (above the line) and concrete ceiling (below the line) with different space heating flow temperatures for overheating (according to Fig. 8).

For the heat pump itself the $SPF_{HP.use}$ shows already interesting effects in overheating cases ($SPF_{HP.use}$ anyway is highest in the reference case "FH080": 3.35). As more as the floor heating is used for overheating $SPF_{HP.use}$ is increasing slightly. Just using the TES leads to $SPF_{HP.use}$ of 3.24 (TES 800 / FH080) where overheating with "+3K" leads to $SPF_{HP.use}$ of 3.25 and "+10K" leads to $SPF_{HP.use}$ of 3.28. PV-overheating of the water storage stops at 54 °C, where the space heating flow temperature including overheating of "+3K" or even more "10K" leads to about 32°C and 38°C respectively at ambient temperature of 0°C. Therefore overheating the floor heating in average leads to lower condenser outlet temperatures than overheating the water storage. In the case "+10K" more heat can be stored in the screed what additionally leads to the effect that the heat pump has less operating hours during cold night with significant lower evaporator temperature. Nevertheless due to the overheating losses SPF_{use} is lowest in case "+10K".

SPF definitions using only the grid electricity consumption ($P_{el.grid}$) gives an indication how big is the PV contribution in comparison including all heat losses (SPF_{grid}) or just for the heat production of the heat pump itself ($SPF_{HP.grid}$). For example the system PV-overheating the water storage plus the floor heating screed with "+3K" (BUI+TES / FH 080 + 3K) in comparison to the reference system with PV but without any adaption of the control strategy (FH 080) shows SPF_{grid} of 3.62 and 7.14 respectively, which is a difference of factor 2. This fits to the result in Fig. 8 showing a heat pump grid electricity consumption (HPgrid) of 50.7% of the PV-overheating system compared to the reference system.

Due to PV-overheating additional heat losses of the building and the water storage take place which causes a negative effect. In Fig. 10 is shown how big this effect in comparison to other possibilities of energy storage technologies is. The blue circles "Strategies" show how big is the effect of "Effective Use" (which is equal to the reduction of grid electricity consumption) in comparison to the "PV electricity use" which is directly used to operate the air heat pump. In average around 80% of "PV electricity use" in the end leads to "Effective Use" in terms of grid electricity savings.

As an alternative, the excess PV electricity could be fed into the grid and "stored" in a pumped storage hydro power station und consumed by the air heat pump later for standard operation. Assuming 75% efficiency of the pumped storage hydro power station and 5% electricity grid losses in total an efficiency of around 70% can be expected, which is shown by the red circles "GridStorage".

Another option is the installation of a chemical battery in the house. A battery with 1 kWh capacity typically can store around 250 kWh per year in terms of full-cycles. Therefore, a battery with 5 kWh capacity would lead to annual "Effective Use" of 1250 kWh per year, which is in the same range as the two other options called "Strategies"and "GridStorage". BUT: for the battery a severe investment is needed and the lifetime is quite limited and for storing in the pumped storage hydro power station quite a significant fee has to be paid per kWh. The building mass and the water storage as a "thermal battery" are available anyway and therefore do not cause any additional investment cost nor operation cost and also maintenance cost are negligible.

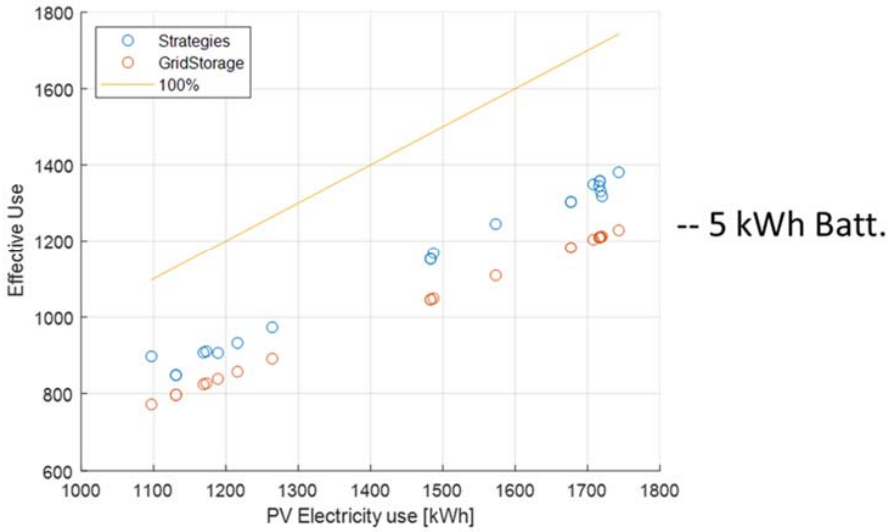

Fig. 10 Comparison of PV self consumption efficiency "Strategies" with pumped storage hydro power station "GridStorage" and chemical battery "5 kWh Batt."

5. System behaviour in detail

Overall evaluations have shown significant effects and grid electricity savings on an annual basis. Details how the effect of PV-overheating works can be observed in Fig. 11 and Fig. 12 where the simulation results of five days (Jan 4th – 9th) are shown in detail.

First clear to see is the replacement of space heating power of the water flow into the floor heating screed from night and early morning hours (90h to 102h, red lines) mainly to the sunny afternoon the day before (86h to 90h, blue lines) in Fig. 11. This is the result of storing heat in the screed with an amount of approx. 23 kWh as indicated

in Fig. 12. Similar behavior can be observed two days later but with slightly less PV power resulting in just 12 kWh storing heat in the floor heating screed. In comparison the day between with almost no PV production (96h to 120h) causes almost the same behavior of the heating system from late afternoon until late morning (112h to 128h).

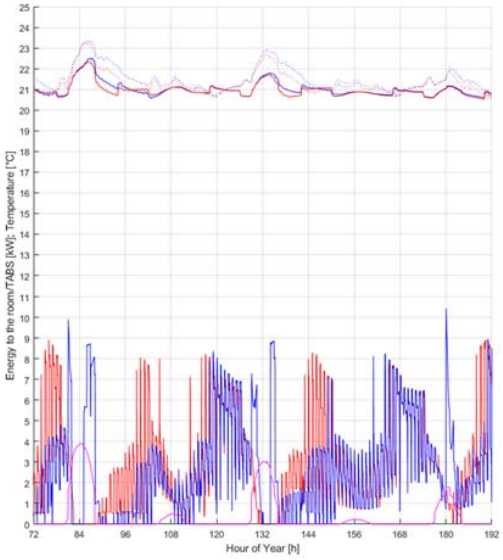

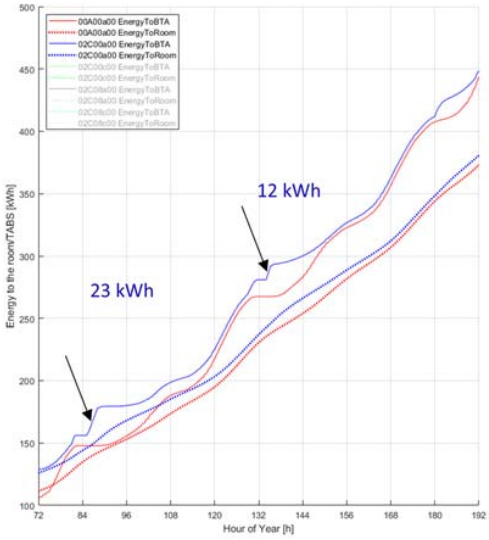

Fig. 11 left: Evolution over time of PV production power (rosa solid line) in combination with space heating power of the water flow (lower curves) and room air temperatures (upper curves: living room dotted line, parents sleeping room solid line) for the reference system (red) and the system with PV-overheating (blue);

Fig. 12 right: The cumulative curve of space heating energy from floor to room air (EnergyToRoom, dotted line) and of space heating energy of the water flow (EnergyToBTA, solid line) showing the storage effect of overheating for the reference system (red) and the system with PV-overheating (blue).

Second also clear to see is, that the room temperature evolution shows minimal higher peak room temperatures during sunny days due to overheating but significant higher room temperatures lasting until after midnight. However, "significant higher room temperatures" has to be interpreted carefully, since the difference is just around 0.5 K!

Therefore, solar radiation into the room and internal loads due to electricity household consumption and persons being in the rooms have much more significant influence than the PV-overheating control concept.

Based on Fig. 11 and Fig. 12 it can also be explained, why the increase of screed thickness or concrete ceiling activation does not result in significant additional savings of grid electricity consumption and increase of PV self consumption. Even during a very sunny day the potential to store heat in the building mass is limited due to the following facts: a) around noon a significant part of excess PV electricity is used to overheat the water storage for DHW, b) the time window with sufficient excess PV power to run the heat pump beside overheating the water storage is limited, especially in the winter period and c) the heating power of the heat pump is limited according to the standard design rules and it is not economic to install a more powerful heat pump just to be able to use some kWh PV excess electricity more.

An overview of the resulting room air temperatures only during the winter season (Oct 1st – March 31st) is shown in Fig. 13 with box-plots showing the median (red line) and 50% of the data in the blue box. The "+3K" PV-overheating strategy also here shows just marginal increase of the room air temperature: just 0.3K increase of the median and the maximum does not reach 24°C (beside some whiskers). The "+10K" PV-overheating strategy shows significant increase of the room air temperature in all cases of creed thickness or concrete ceiling, but still within potentially acceptable limits. However, the energetic benefit of the "+10K" PV-overheating strategy is as limited as the economic, what will be shown in the next chapter.

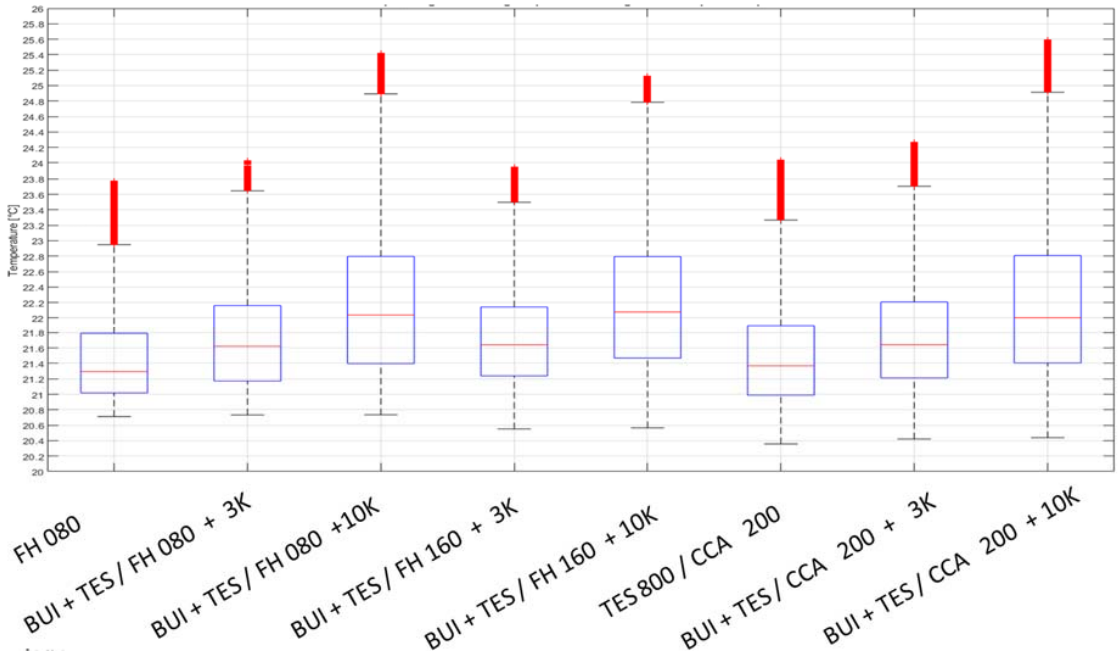

Fig. 13 Room air temperature for several variants of floor heating systems (FH) and different screed thickness and concrete ceiling (CCA) with different space heating flow temperatures for overheating.

6. Operating Cost

Final discussion is done based on Fig. 14, for the economic point of "operating cost" only, since there are no (or just marginal) differences in investment cost of the different simulation variants related to the goal of increasing the system performance based on simple control strategies.

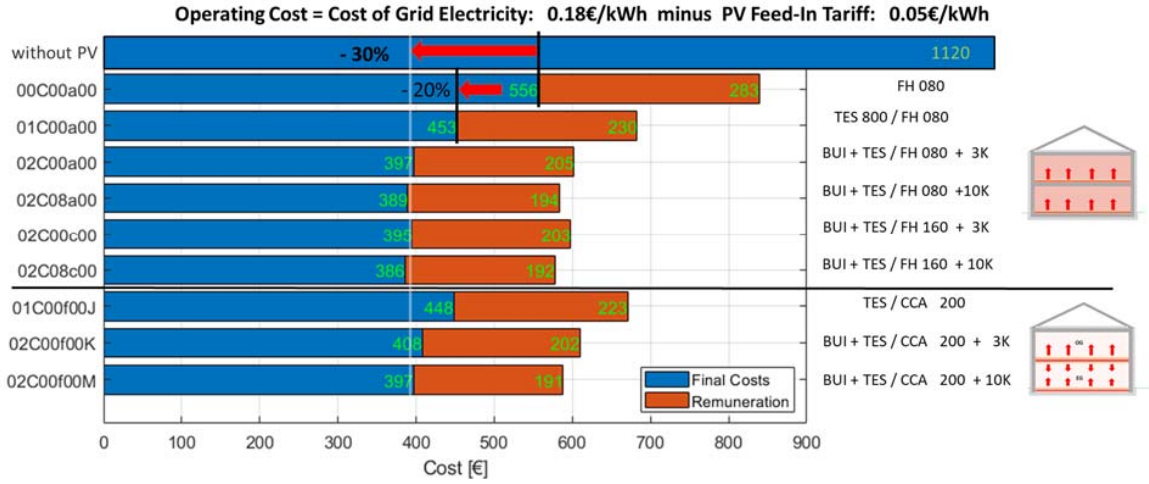

Fig. 14 Final operating cost of electricity (cost of grid minus PV feed in remuneration) including household electricity for several variants of floor heating systems and screed thickness (above the line) and concrete ceiling (below the line) with different space heating flow temperatures for overheating.

Operating cost are defined as cost of grid electricity (0.18 EUR/kWh) for the heat pump and the household electricity consumption minus the remuneration (0.05 EUR/kWh) for the excess PV fed into the grid and sold to the utility. This financial assumption was taken in 2018 based on the actual situation at that time.

The reference system without PV has overall cost of 1,120 EUR per year, as Fig. 14 shows. After installation of the 40 m^2 PV system, cost savings due to PV self-consumption result in 839 EUR per year (75%) minus 283 EUR remuneration leading to 564 EUR per year for refinancing the PV system. Using the "+3K" PV-overheating strategy (BUI+TES / FH 080 + 3K) the remaining operating cost are 397 EUR per year and the saved amount for

refinancing increases to 723 EUR per year, which is significantly 28% more. As it can be observed, all variants of screed thickness or concrete ceiling from an economic point of view are in the same range. Just using the 0.8 m3 water storage (TES800/FH080 and TES/CCA200) already has a significant effect, of course mainly due to the fact that only with the water storage the DHW demand can be covered and especially in the summer period almost 100% of the DHW demand can be covered by the PV heat pump system.

7. Conclusions

For a PV air heat pump system in a single-family house designed as a low energy building the grid electricity consumption can be halved compared to a PV – air heat pump system without overheating control concept. Several boundary conditions and parameters were studied concluding that the standard screed thickness (0.08 m) of a floor heating system with about +3K increased space heating flow temperature during PV-overheating already results in around 30% additional operating cost savings compared to a standard control concept.

PV self consumption just for heat pump operation can be quadruplicated. Including household electricity consumption for the entire system still the PV self consumption can be doubled. This is roughly the same effect as a chemical battery typically can achieve (with typical design of: 5 kWh capacity for a 5 kW_p PV system), but much more cheaper since no investment cost occur for the "thermal battery", which is anyway in the house.

Even though the room air set temperature during PV-overheating is increased from 21°C to 24°C, the finally resulting room air temperature as mean value in the winter period just increases by 0.3K. The peak temperatures during day shows almost no increase but the period from late afternoon to after midnight stays at about 0.5K to max 1K higher after a sunny day.

8. Acknowledgments

The project "Energieschwamm" was elaborated in the frame of the research program "City of the Future" in co-operation with the research partners Technische Universität Graz - Institut für Wärmetechnik, Grazer ENERGIEAgentur GmbH and the companies iDM Energiesysteme GmbH and Pink GmbH Energie- und Speichertechnik.

City of the Future is a research and technology program of the Federal Ministry of Transport, Innovation and Technology. It is managed on behalf of the BMVIT by the Austrian Research Promotion Agency together with Austria Wirtschaftsservice Gesellschaft mbH and the Austrian Society for Environment and Technology ÖGUT.

9. References

Bales, C.; Betak, J.; Broum, M.; Chèze, D.; Cuvillier, G.; Haberl, R. et al. (2015): Optimized solar and heat pump systems, components and dimensioning. MacSheep - New Materials and Control for a next generation of compact combined Solar and heat pump systems with boosted energetic and exergetic performance. Deliverable 7.3.

Heinz, A., Gritzer, F., Thür, A., 2022. The effect of using a desuperheater in an air-to-water heat pump system supplying a multi-family building, Journal of Building Engineering, vol. 49, p. 104002. https://doi.org/10.1016/j.jobe.2022.104002

Jordan, U., Vajen, K., 2005. DHWcalc: PROGRAM TO GENERATE DOMESTIC HOT WATER PROFILES WITH STATISTICAL MEANS FOR USER DEFINED CONDITIONS, Proc. ISES Solar World Congress, Orlando (US), 8. - 12.8.2005

Pflugradt, N. D., 2018. Load Profile Generator, Available online at https://www.loadprofilegenerator.de/ , checked on 20/9/2022.

Pflugradt, N. D., 2016. Modellierung von Wasser und Energieverbräuchen in Haushalten. Technische Universität Chemnitz, Chemnitz. Available online on 20/9/2022 at https://nbn-resolving.org/urn:nbn:de:bsz:ch1-qucosa-209036.

Thür, A., Calabrese, T., Streicher, W., 2018. Smart grid and PV driven ground heat pump as thermal battery in small buildings for optimized electricity consumption. Solar Energy. 2018, vol. 174, p. 273-285. https://doi.org/10.1016/j.solener.2018.08.087

J. Water Purification through Renewable Energy

Experimental studies on Solar Multi - Effect Desalination system

Thilagan Kannappan[1] and Mani Annamalai[1]

[1]Department of Mechanical Engineering

Indian Institute of Technology Madras, Chennai, Tamil Nadu, 600036 (India)

Abstract

A Multi – Effect Desalination system with a capacity of 10 m^3 has been designed, erected and tested to convert seawater into potable water using solar energy. This solar desalination will produce drinking water for a small community. The steam is flashed initially from a flash chamber of the desalination plant, using hot water from a solar flat plate collector field and fed to the first stage of the multi-stage evaporator. The average hot water outlet temperature from the collector field is in the range of 60ºC - 65ºC. In a multi-stage evaporator, seawater is sprayed parallelly to produce water vapor. This water vapour loses heat and forms condensate by losing the latent and sensible heat through the tube surface. The brine and condensate is carried to the last stage of the multi-effect desalination (MED) system. It is observed that during peak production of potable water, maximum temperature difference between inlet and outlet of cooling water is 10ºC in the condenser. Experimental studies on the solar MED system are made to understand the performance of the system using solar energy alone. The solar MED system with a maximum production rate of 1.008 $m^3\ h^{-1}$ is observed during peak sunshine hours. The distillate TDS is tested and is in the range of 1 ppm - 5 ppm.

Keywords: Multi - Effect Desalination, Solar energy, Sea water, Ejector

1. Introduction

Water naturally occurs and is a basic need for all forms of life. Among the total water availability in the world, 2.5% of water is potable for drinking. The scarcity of potable water is increasing day by day due to the increase in population and increase in industrial activities. The conversion of sea or brackish water into potable water will meet the demand through desalination techniques. Converting sea or brackish water into potable water is an energy-intensive process and can be made viable using accessible renewable energy sources like solar energy, geothermal, ocean thermal gradient, etc.

Among the available forms of renewable energy, solar energy is abundantly, distributed form and freely available throughout the year. There are different techniques of desalination using solar energy. Solar still is one of the oldest and most famous techniques in desalination. The detailed experimental studies are carried out on single sloped solar still (Mani, 1982a, 1982b). The researchers have developed a vacuum-based desalination system to commercialize desalination technology. In 1991, Low and Tay developed and tested the vacuum based desalination process using sea water (Low and Tay, 1991). Later, this experiment is extended using waste heat from a steam turbine for desalination (Tay et al., 1996).

In the desalination system, vacuum pump plays a significant role in maintaining the system's vacuum pressure. The vacuum pump will consume high-grade energy. The researchers later started working for alternate solutions and found an ejector to maintain the desalination system's vacuum pressure. Lot of simulations and experimental trials have been conducted for different configurations of ejector to replace vacuum and reduce the electrical power cost (Arun et al., 2017; Parveen Banu and Mani, 2019). Simulation studies for desalination systems have been validated with experimental results for a lab-scale desalination test rig (Kudish et al., 2003).

In this paper, experimental studies have been carried out at Vivekananda Kendra, Kanyakumari, India [Latitude : 8.08ºN and Longitude : 77.53ºE], by designing, fabricating, erecting and testing a solar multi - effect desalination plant with a capacity of 10 m^3 per day. This paper presents the design details and experimental performance of the

© 2022. The Authors. Published by International Solar Energy Society
Selection and/or peer review under responsibility of Scientific Committee
doi:10.18086/eurosun.2022.09.01 Available at http://proceedings.ises.org

plant.

2. Principle of operation

Figure 1 shows the schematic view of the Solar Multi - Effect Desalination (MED) system. The system consists of solar flat plate collector (FPC) field, flash chamber, multi - effect evaporator (MEE), condenser, solar photovoltaic power plant, ejector, hot water recirculation pump, brine pump, distillate pump, MED pump and seawater intake pump. The ejector is used for the creation of a vacuum in MED to maintain the system at the saturation state. The pressurized hot water from solar FPC field enters the flash chamber. Hot water is flashed to steam at saturation pressure of the flash chamber, and the remaining water is recirculated back to the solar FPC field. The generated steam is sent to the first stage of MEE by pressure difference.

The sea water is sprayed and flashed in MEE over the tubes of MEE, where it gets vaporized by taking heat of condensation. Also, due to flashing at the corresponding evaporator pressure, steam flows to the next stage of the evaporator in MEE. The condensed steam and the remaining brackish sea water are collected at the distillate box and brine box, respectively and are sent to the next stage of MED by manometric effect. This process continues till the distillate reaches the condenser. At the condenser, incoming sea water is used to condense the steam and reduce the temperature of distillate from the last stage of MEE. The condensed water is sent to the distillate storage tank by pump and the brackish seawater collected at the last stage of MEE is pumped back to sea. The entire Solar MED plant is powered by a solar photovoltaic power plant with a battery backup of half an hour. The MED plant is operated solely using solar energy.

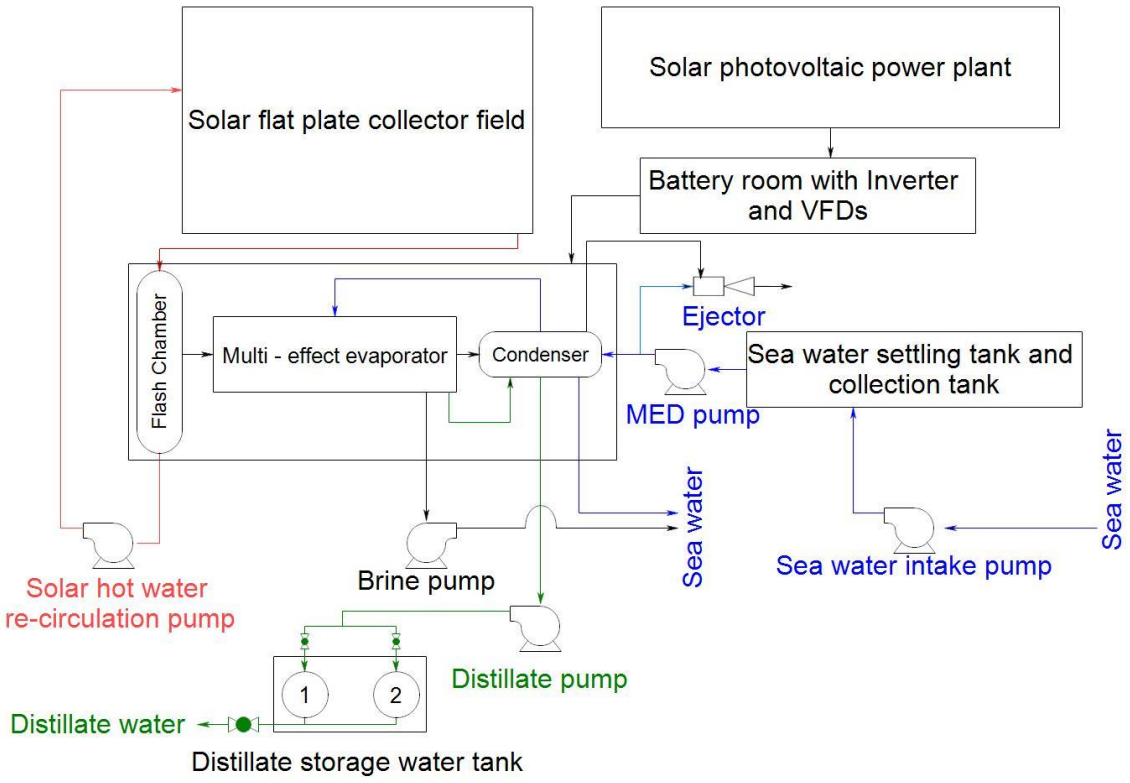

Fig. 1: Schematic diagram of Solar Multi - Effect Desalination (MED) system

3. Design of the system

Solar MED plant layout diagram is shown in Fig. 2. The plant component details are narrated below.

3.1. Solar flat plate collector field

Solar flat plate collectors are used to raise the water temperature from 60ºC to 70ºC at a varying flow rate ranging from 26,800 kg hr^{-1} to 29,800 kg hr^{-1}. A large area of solar collector field is required to raise the water temperature.

Based on Eq. 1, the total number of solar flat plate collectors required to raise the temperature of water from 60°C to 70°C is 315 (Duffie and Beckman, 2013). The area required for the solar flat plate collector field is 630 m^2. The specification of a single flat plate collector is given in Table 1.

$$\dot{m}\, C_p\, \Delta T = I\eta N \qquad \text{(eq. 1)}$$

where, $\dot{m}$ = Mass flow rate of solar FPC (kg hr^{-1}) ; C_p = Specific heat of water (J kg^{-1} K^{-1}) ; ΔT = Temperature difference between inlet and outlet of solar FPC (°C) ; I = Incident Solar Radiation (W m^{-2}) ; η = Efficiency of solar FPC (%) ; N = number of collectors.

The collector field is installed in such a way that every seven collectors are connected in series to form an array. The array arrangements will enhance heat transfer. There are 45 arrays in parallel, and they are arranged in seven rows in parallel. A ball valve operates each row to ensure a uniform flow rate in all the rows. The entire field is oriented to face south with an inclination angle of 8° to maximize solar energy falling on the collectors.

Tab. 1: Details of solar flat plate collector

Area	2 m^2 ± 0.1 m^2
Absorber Material	Copper
Fin Material	Aluminium
Reflector	Aluminium foil
Max. pressure	6 bar
Collector box	Extruded aluminium L : 2050 mm x B : 1040 mm x H : 100 mm ± 0.2 mm
Back insulation	Rockwool

3.2. Flash chamber

The hot water from solar FPCs is fed into the flash chamber. The hot water is made to flash using upward spray flashing mode (Goto et al., 2008). At saturation pressure of the flash chamber, hot water is flashed to steam. The remaining water is sent back to the solar field for recirculation using a solar hot water pump. The steam is sent to the first stage of the MED system by a difference in vacuum pressure.

Based on Eq. 2, the efficiency of the flash chamber is computed

$$FC = \frac{H^L_{IN} - H^L_{OUT}}{H^V_{OUT} - H^L_{OUT}} \qquad \text{(eq. 2)}$$

where, FC = Flash chamber efficiency (%) ; H^L_{IN} = Flash chamber inlet liquid enthalpy at temperature and pressure (J kg^{-1}) ; H^V_{OUT} = Flash chamber outlet flashed vapour enthalpy at pressure and corresponding saturation temperature (J kg^{-1}) ; H^L_{OUT} = Flash chamber outlet unflashed liquid enthalpy at pressure and corresponding saturation temperature (J kg^{-1}).

3.3. Multi-Effect Evaporator (MEE)

In the first stage of MEE, seawater is sprayed over the tubes of each evaporator using spray nozzle parallelly. The water from the spray nozzle gets atomized and absorbs the heat of condensation from the tube wall. At saturation pressure of each effect of MEE, water gets flashed, and the remaining concentrated brine solution is sent to the next effect of MEE by manometric effect. The condensed steam is collected and carried to the next effect by manometric effect. This process is continued until the distillate reaches the condenser and the brine solution is ejected from the system using the brine solution pump.

3.4. Condenser

The distillate and flashed steam from the last stage of MEE is condensed in the condenser by using incoming seawater at the flow rate of 20.6 $m^3\,h^{-1}$. The condensed distillate is pumped to the distillate tank using a distillate pump. During the process of flashing in the flash chamber, water level reduces and part of the distillate is

redirected to the flash chamber outlet (or) suction of solar recirculation pump as makeup water to the solar heating system. During the condensation process, most of the seawater is sent back to sea, which acts as a sink and the remaining seawater is sent to the spray nozzles of MEE in parallel mode at the rate of 1.2 $m^3 h^{-1}$.

3.5. Ejector

The ejector system is used to maintain vacuum pressure of the MED system during operation. In ejector, primary stream is admitted with a given flow rate of seawater. The non-condensable gases from the condenser of the MED system is entrained through the secondary stream of the ejector. The ejector is powered by seawater at the primary stream.

Based on Eq. 3, the entrainment ratio of the ejector is computed (Arun et al., 2019)

$$Entrainment\ ratio = \frac{\dot{m}_s}{\dot{m}_p} \qquad \text{(eq. 2)}$$

where, $\dot{m}_s$ = Mass flow rate of secondary stream (kg h^{-1}) ; $\dot{m}_p$ = Mass flow rate of primary stream (kg h^{-1}).

3.6. Pumps

In the solar MED system, six pumps as shown in Table 2 are used to run the plant.

Tab. 2: Details of pumps

Sl.No.	Pump	Make	Details
1.	Solar recirculation pump	Grundfos	Power – 10 hp / 7.5 kW 3 Phase ; 380-415 V ; 50 Hz Max. discharge – 30 $m^3 h^{-1}$
2.	Brine pump	Grundfos	Power – 1.5 hp / 1.10 kW 3 Phase ; 380-415 V; 50 Hz Max. discharge – 5.8 $m^3 h^{-1}$
3.	Distillate pump	Grundfos	Power – 0.37 kW / 0.5 hp 3 Phase ; 380-415 V; 50 Hz Max. discharge – 1.8 $m^3 h^{-1}$
4.	Ejector pump	PSG	Power – 3.7 kW / 5 hp 3 Phase ; 380 V ; 50 Hz Max. discharge – 24 $m^3 h^{-1}$
5.	MED pump	Kirloskar Brothers Ltd	Power – 5.5 kW / 7.5 hp 3 Phase ; 415 V ; 50 Hz Max. discharge – 25.6 $m^3 h^{-1}$
6.	Seawater intake	Johnson Pump	Power – 2.2 kW / 3 hp 3 Phase ; 415 V ; 50 Hz Max. discharge – 40 $m^3 h^{-1}$

3.7. Solar Photovoltaic panels

The pumps of solar MED plant require 20 kW of power to run the plant. The installed solar photovoltaic power plant is 20 kW with a battery backup of half an hour. Batteries are used to start and run the motors at lower solar radiation in the morning and evening hours. Inverters are used to convert DC to AC current. The specification details of solar photovoltaic panels, batteries and inverters are shown in Table 3.

Tab. 3: Details of solar PV panels and subsystems

Sl.No.	Materials	Numbers	Details
1.	Solar Photovoltaic Panels	100	PV panel capacity – 200 W Type of PV cell – monocrystalline silicon cell
2.	Batteries	14	Type of battery – Tubular battery Voltage – 12 V A.H. capacity – 75 Ah
3.	Inverters	3	Capacity – 10 kWh [Two Nos.] Capacity – 3 kWh

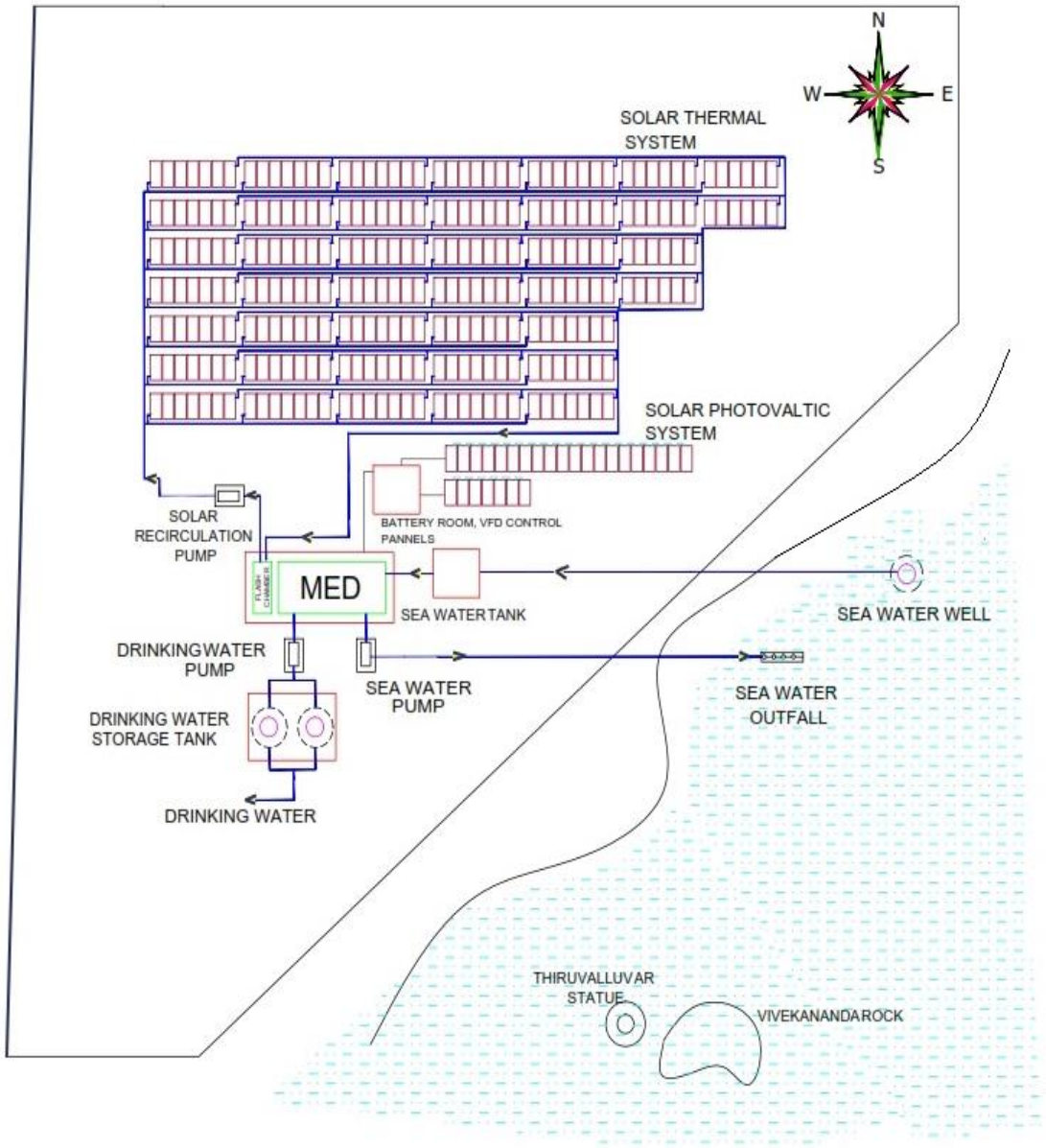

Fig. 2: Schematic diagram of Solar Multi - Effect Desalination (MED) system

4. Experimentation

Solar MED plant components are successfully designed, fabricated, erected and integrated at the project site at Vivekananda Kendra, Kanyakumari, India. The solar thermal FPC field is tested for pressure up to 4 bar in order to check leakage. Entire MED plant is tested under vacuum pressure up to 30 mbar to check vacuum leakage.

Calibrated bourdon type pressure gauges are installed at the inlet of solar FPC field, sea water inlet and primary stream of ejector. Calibrated bourdon type vacuum gauges are used at flash chamber, each effect of MEE and condenser of MED plant. Temperatures of solar MED plant are measured at different locations using calibrated T - type thermocouples. Calibrated orifice plates are used at solar FPC field inlet, brine discharge, distillate discharge and seawater inlet and are used to measure differential pressure across the orifice plates using digital differential manometer. Using the measured differential pressure readings, flow rates are calculated. Level indicators are installed at flash chamber, distillate line and bine line in order to maintain the level during operation of the plant. Solar radiation and wind speed are measured using calibrated pyranometer and anemometer respectively. The details of measuring instruments used for experimentation are shown in Table 4.

Tab. 4: Accuracy and range of measuring instruments

Sl.No.	Instrument	Accuracy	Range
1.	T type thermocouple	± 0.1 ºC	-60 ºC to 120 ºC
2.	Pressure gauge	± 1% FS	0 to 10 bar
3.	Vacuum pressure gauge	± 1% FS	0 to -1 bar
4.	Differential pressure manometer (digital)	± 0.5% FS	0 to 200 psi
5.	Pyranometer	± 10 W m^{-2}	0 to 1999 W m^{-2}
6.	Anemometer	± 3%	0 to 30 m s^{-1}

Seawater is drawn from the sea, 20 m away from the desalination plant. Sand and other particles are made to settle in the settling tank and collected in collection seawater tank. The collected seawater is sent to the plant by MED pump. Before entering the condenser, fine meshes are kept to avoid chocking of fine particles at the spray nozzles of MEE. During experimental days, sea water flow rate is maintained at 20.6 $m^3 h^{-1}$ with the pressure of 0.8 bar.

The entire MED plant is kept below 150 mbar using an ejector. In solar FPC, water is circulated until it reaches the required temperature. The average temperature of water is maintained between 65ºC - 70ºC. The water is flashed and sent to the first stage of MEE by pressure difference. The remaining water in flash chamber is recirculated to the solar FPC field using solar recirculation pump. Seawater is sent to each stage of MEE from the spray nozzles. The sprayed seawater forms steam by taking the heat of condensation and flashing, and carries to the next stage of MEE by differential pressure. The condensed steam and brine water are carried to the next effect by using manometric effect and continues till it reaches the last effect of MEE. The brine water from the last effect of MEE is pumped back to the sea using brine pump. The steam and distillate water from the last effect of MEE are condensed in the condenser and pumped to distillate tank using a distillate pump. During condensation, the ejector rejects the non-condensable gases (NCGs). The level of distillate, brine and flash chambers are monitored continuously for effective operation.

5. Results and discussion

Solar MED plant is tested for different operating conditions on different days. This paper discusses a typical operation condition for a given single day. The plant is operated between 8:00 h to 17:00 h of IST.

5.1. Experimental investigation of collector performance

Solar flat plate collector (FPC) field performance curves are shown in Fig. 3. It is observed that the temperatures of inlet and outlet increase initially and later decrease. This is due to the incident solar radiation falling on solar FPC. The maximum hot water outlet temperature is realized in the range of 74ºC - 76ºC with solar radiation

variation in the range of 1050 W m^{-2} - 1100 W m^{-2}. The average differential temperature between inlet and outlet of the collector field is maintained above 10°C with solar radiation variation in the range of 900 W m^{-2} - 1100 W m^{-2}. At least solar radiation, the collector filed is able to maintain the temperature difference in the range of 6°C - 8°C.

The solar flat plate collector field's efficiency is calculated and shown in Fig. 3. The collector field's efficiency is low during the initial period due to the cold start of solar FPC with water. As solar radiation increases, efficiency of the solar FPC field increases and later decreases when solar radiation decreases.

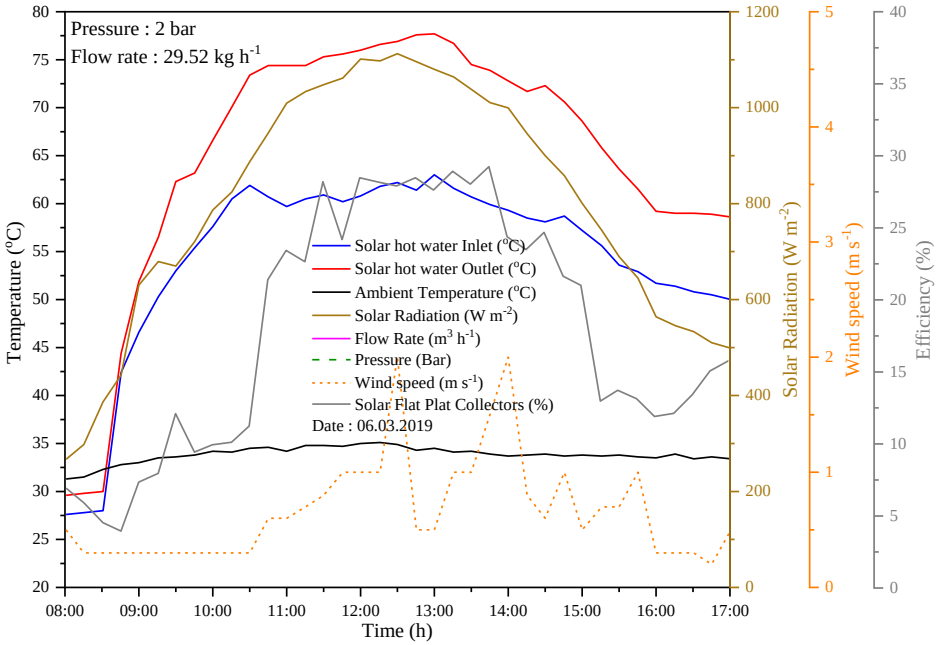

Fig. 3: Performance of solar flat plate collectors

5.2. Experimental investigation of Flash chamber performance

Figure 4 shows the performance of flash chamber. It is observed that the temperatures of flashed steam, hot water inlet and outlet of flash chamber increase and later decrease. This is due to varying hot water inlet temperature from solar field. The hot water from solar FPC is flashed to steam at saturation pressure of flash chamber. The maximum steam temperature is realized in the range of 60°C - 65°C at the corresponding flash chamber pressure of 0.13 bar - 0.18 bar.

The efficiency of flash chamber is calculated and is shown in Fig. 4. Initially the temperature of hot water is lower and does not match with the saturation pressure of flash chamber. So, the efficiency of flash chamber is lower and increases as time progresses. After reaching the flashing point of hot water, the flash chamber efficiency is in the range of 65% - 75%. The decreasing trend in the efficiency of flashing is due to lower hot water temperature of the flash chamber.

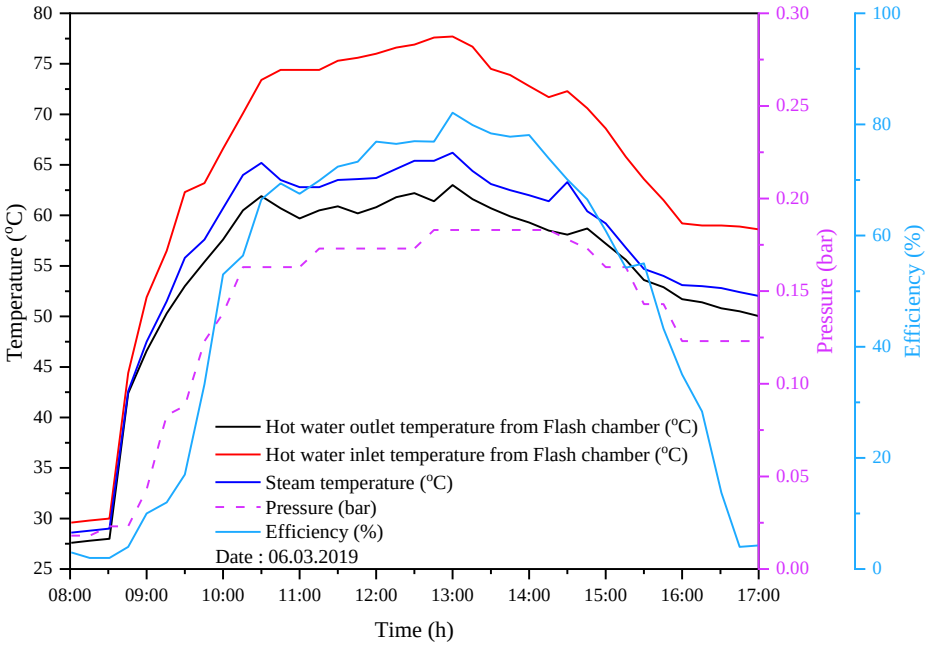

Fig. 4: Performance of Flash Chamber

5.3. Experimental investigation of Multi-stage evaporator performance

Multi Effect Evaporator performances are studied based on the temperatures of flashed steam, brine water, distillate water and non - condensable gases (NCGs) in each effect.

Steam temperatures of the first and the last effects of MED at the corresponding pressure are shown in Fig. 5. It is observed that the steam temperatures of all the effects are initially at lower temperatures. This is due to cold start of the system. As time progresses, the steam temperatures are in the increasing trend till reach peak production rate and later decrease due to decrease in chamber pressure of MEE.

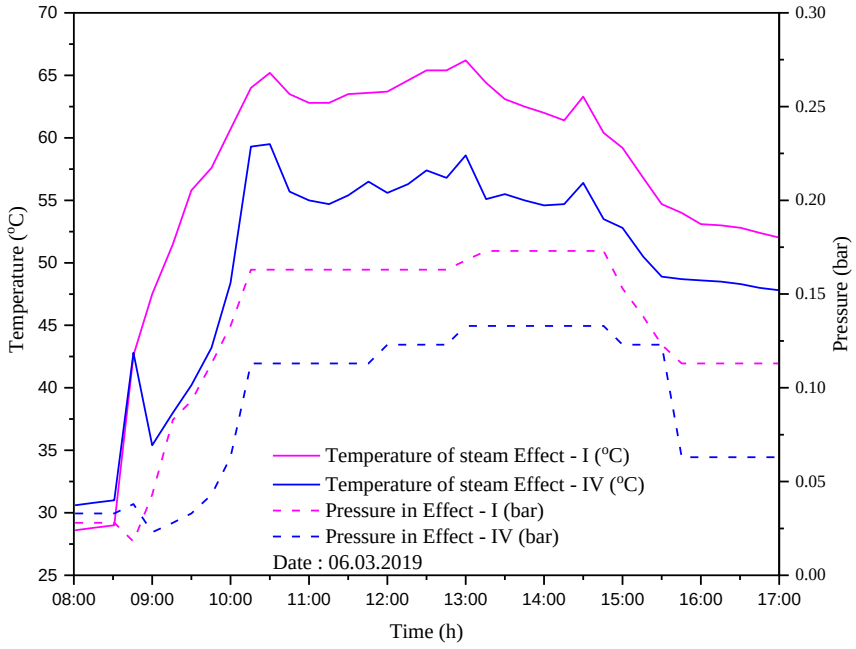

Fig. 5: Variation of steam parameters in MED

Brine water temperatures of all the effects in MED are shown in Fig. 6. The temperature profiles of brine water increase initially and later decrease. It is also observed that the brine water temperature in the first effect is higher when compared to the other effects. This is due to sea water's temperature after the steam generation at saturation

pressure of the chamber. The average brine water temperature from the last effect of MEE is in the range of 45ºC - 47ºC, with chamber pressure in the range of 0.09 bar - 0.13 bar.

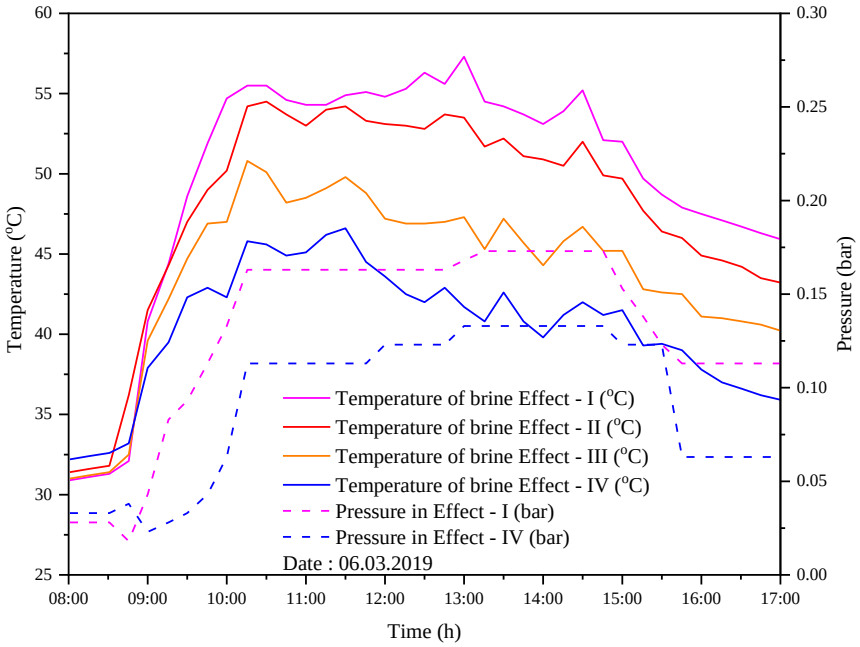

Fig. 6: Variation of brine parameters in MED

Distillate water temperatures of all the effects in MED are shown in Fig. 7. The temperature profiles of distillate water increase initially and later decrease. It is also observed that the distillate water temperature in the first effect is higher when compared to the other effects. The average distillate water temperature from the condenser is in the range of 40ºC - 45ºC.

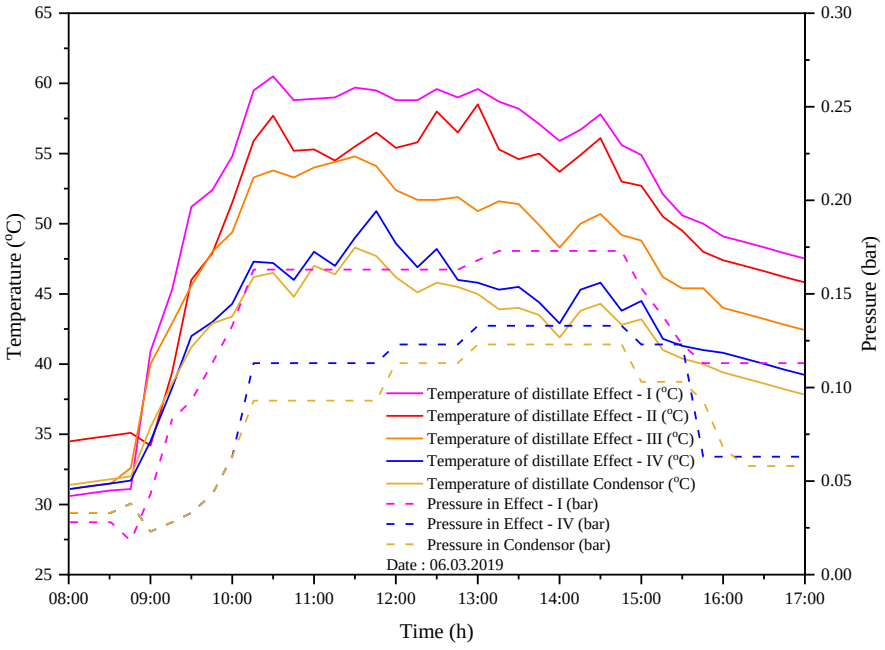

Fig. 7: Variation of distillate parameters in MED

Non – Condensable Gases (NCGs) temperatures of all the effects in MED are shown in Fig. 8. The temperatures of NCGs increase initially and later decrease.

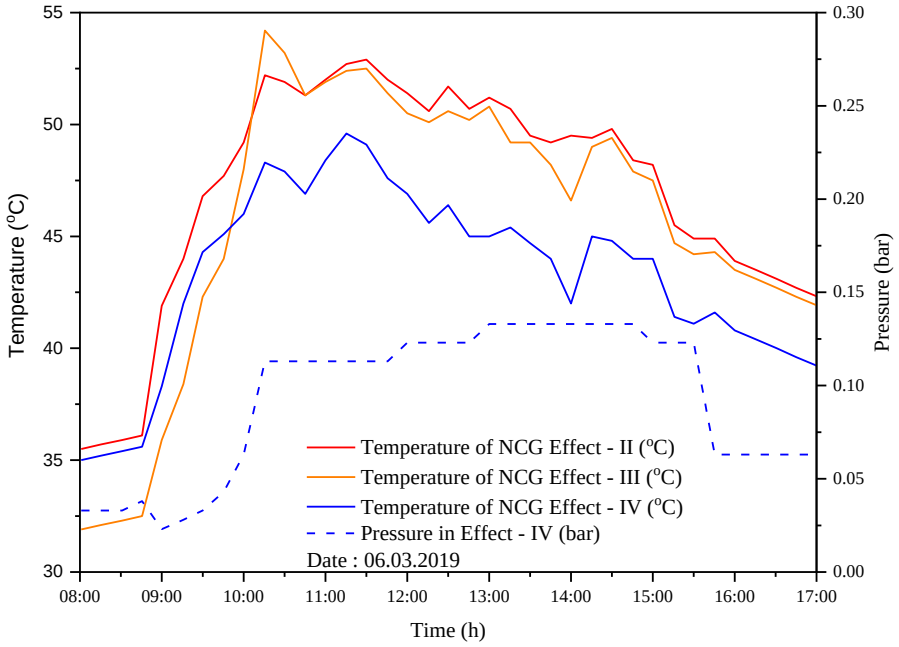

Fig. 8: Variation of NCGs parameters in MED

5.4. Experimental investigation of condenser performance

Figure 9 shows the performance of the condenser. In the condenser, sea water inlet flow rate is maintained at 20.6 $m^3 h^{-1}$ with a pressure of 0.8 bar. The average sea water inlet temperature is 30°C. It is observed that the average outlet temperature of sea water is in the range of 40°C - 43°C. During this period, the maximum outlet flow rate of distillate is observed, when the average condenser differential temperature is in the range of 10°C - 13°C. The average distillate water flow rate during the production period is l.04 $m^3 h^{-1}$.

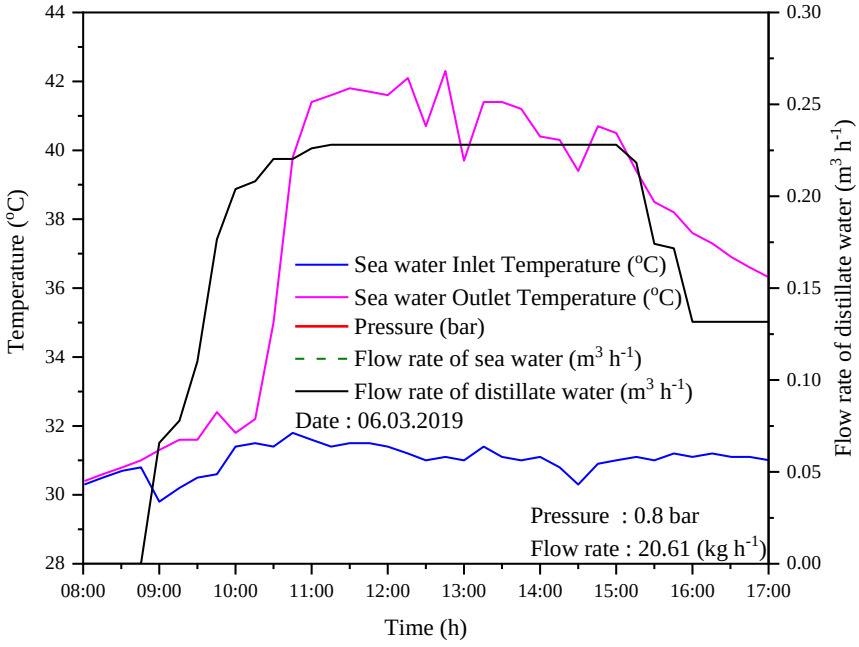

Fig. 9: Variation of parameters in condenser

5.5. Experimental investigation of ejector performance

The entrainment ratio of the ejector is studied for the performance of ejector of the solar MED plant as shown in Fig. 10. It is observed that the entrainment ratio of the ejector increases initially. Due to the initial starting condition, NCGs are accumulated at the condenser. As time progresses, distillate water production increases along

with NCGs in the condenser. The entrainment ratio is maintained as constant at peak production rate of distillate. Later, the entrainment ratio decreases due to less distillate production rate.

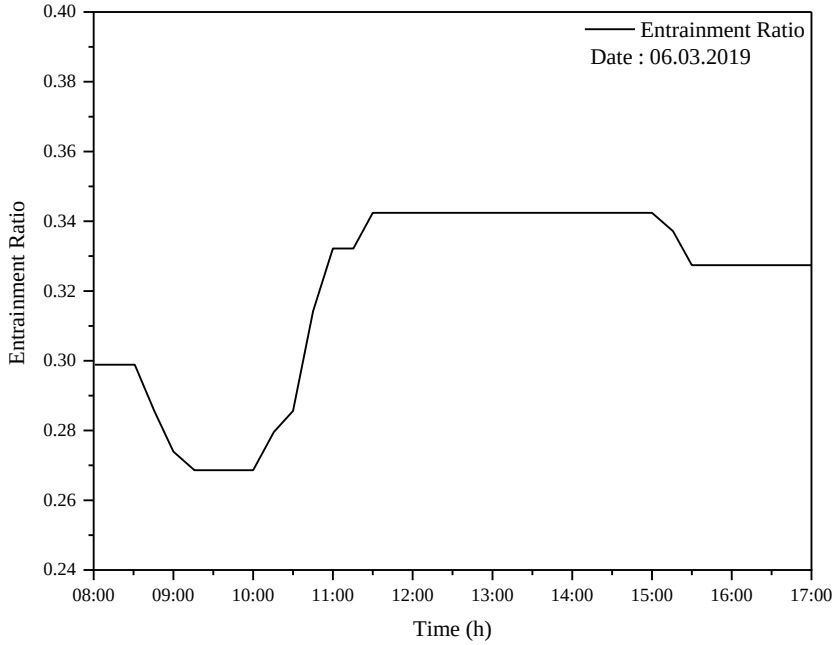

Fig. 10: Variation entrainment ratio

5.6. Quality analysis of water

The quality of distillate water is tested in terms of Total Dissolved Salts (TDS) and the unit of TDS is ppm. The distillate TDS from the plant is tested every 15 minutes of time interval on all the experimental days. Figure 11 shows the variation of distillate TDS from the plant. It is observed that the distillate TDS is 20 ppm initially and as time progresses, the average quality of distillate TDS is realized in the range of 1 ppm - 5 ppm.

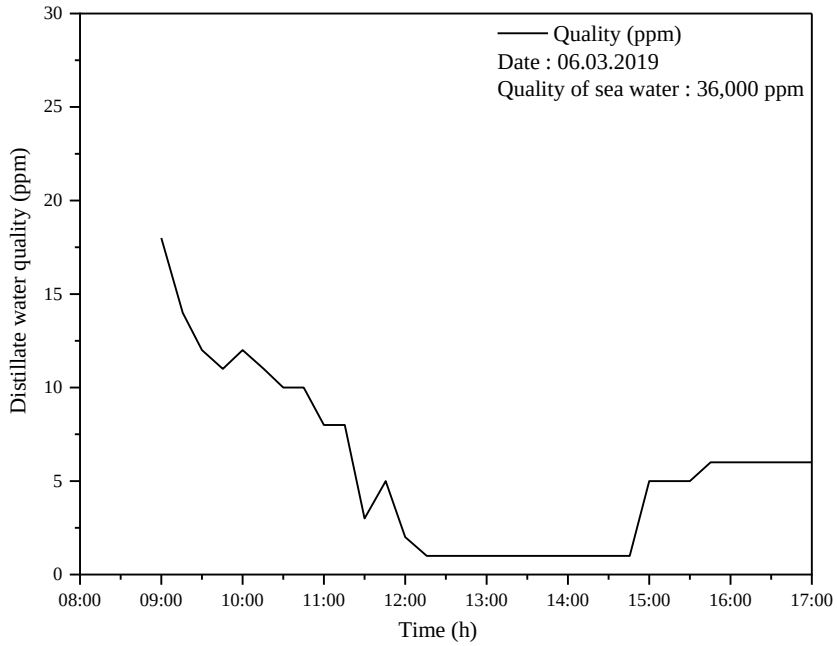

Fig. 11: Variation of distillate TDS in the desalination system

6. Conclusions

Solar Multi-Effect Desalination plant components are integrated and tested using sea water at Vivekananda Kendra, Kanyakumari, India. Solar MED plant performance is studied by varying the flow rate of solar flat plate collector field and keeping plant inlet sea water flow rate and vacuum pressure at condenser as constant on all the experimental days. The solar flat plate collector performance is studied and observed that the maximum efficiency of solar FPC is in the range of 30% - 35%. The maximum hot water outlet temperature from solar FPC is realized in the range of 70ºC - 76ºC. During the operation of the plant, vacuum pressure is maintained by using an ejector. The average entrainment ratio is in the range of 0.3 - 0.35 during peak operational hours. The desalination plant produces 6,400 liters per day using solar energy. The maximum production rate of 1.008 $m^3 h^{-1}$ is observed during peak sunshine hours. The distillate TDS is tested and is in the range of 1 ppm - 5 ppm.

7. Acknowledgments

The authors would like to thank the Ministry of Earth Sciences, Government of India, New Delhi, for providing financial assistance and National Institute of Ocean Technology (NIOT), India, for helping in erecting sea well and assisted systems at the project site. Vivekananda Kendra, Kanyakumari, India for providing land for the erection and commissioning of solar multi-effect desalination plant for the project.

8. References

Arun, K.M., Tiwari, S., Mani, A., 2019. Experimental studies on a rectangular ejector with air. Int. J. Therm. Sci. 140, 43–49. https://doi.org/10.1016/j.ijthermalsci.2019.02.014

Arun, K.M., Tiwari, S., Mani, A., 2017. Three-dimensional numerical investigations on rectangular cross-section ejector. Int. J. Therm. Sci. 122, 257–265. https://doi.org/10.1016/j.ijthermalsci.2017.08.024

Duffie, J.A., Beckman, W.A., 2013. Solar Engineering of Thermal Processes, Wiley. https://doi.org/10.1002/9781118671603.fmatter

Goto, S., Yamamoto, Y., Sugi, T., Yasunaga, T., Ikegami, Y., Nakamura, M., 2008. A Simulation Model of Spray Flash Desalination System. IFAC Proc. Vol. 41, 15909–15914. https://doi.org/10.3182/20080706-5-kr-1001.02689

Kudish, A.I., Evseev, E.G., Walter, G., Priebe, T., 2003. Simulation study on a solar desalination system utilizing an evaporator/condenser chamber. Energy Convers. Manag. 44, 1653–1670. https://doi.org/10.1016/S0196-8904(02)00180-2

Low, S.C., Tay, P.J.H., 1991. Vacuum desalination using waste heat from a steam turbine. Desalination 81, 321–331. https://doi.org/10.1016/0011-9164(91)85066-4

Mani, A., 1982a. Experimental studies on single sloped solar still. Indian Institute of Technology Madras.

Mani, A., 1982b. Studies on single sloped solar still, in: National Solar Energy Convention, IIT, New Delhi. pp. 14–17.

Parveen Banu, J., Mani, A., 2019. Numerical studies on ejector with swirl generator. Int. J. Therm. Sci. 137, 589–600. https://doi.org/10.1016/j.ijthermalsci.2018.11.033

Tay, J.H., Low, S.C., Jeyaseelan, S., 1996. Vacuum desalination for water purification using waste heat. Desalination 106, 131–135. https://doi.org/10.1016/S0011-9164(96)00104-X

Falling Film Measurements using High Speed Camera and High Speed Infra-Red Camera

Thilagan Kannappan[1] and Mani Annamalai[1]

[1]Department of Mechanical Engineering

Indian Institute of Technology Madras, Chennai, Tamil Nadu, 600036 (India)

Abstract

In this paper, a non-intrusive technique was developed to measure falling film thickness and temperature simultaneously based on the image processing techniques. This non-intrusive technique is used to study the heat and mass transfer characteristics. The enhanced heat and mass transfer of falling film over the tube will be used in the desalination system for distillate water production. The A high speed camera and a high speed infra-red camera are used to record falling film formation and temperature respectively over a horizontal plain tube at the rate of 10,000 fps by simultaneous triggering. The recorded images are processed using image processing software packages to determine film thickness and temperature profile at different circumferential angles ranging from 0° to 180° with tube impingement height of 5 mm. Film thickness over the horizontal plain tube is taken at different flow rates in the range of 0.6 lpm to 2 lpm. Measured film temperatures and film thicknesses are compared with the literature data. It is observed that the error band for falling film thickness is in the range of ±3.20% to ±8.29% for different falling film Reynolds numbers. Also, the error band for falling film temperature is in the range of ±0.08% to ±1.57%, when compared with calibrated thermocouples.

Keywords: Film thickness, Film temperature, Horizontal plain tube, Image processing

1. Introduction

A falling film is a common and effective mode of heat transfer application in many industries, such as desalination for potable drinking water, refrigeration for cooling and cold storage, Ocean thermal energy conversion (OTEC) for power generation, dairy farms and so on. The most common and widely used type of heat transfer is in multi-effect desalination (MED) application for producing fresh water on a large commercial scale (Al-Shammiri and Safar, 1999; Khawaji et al., 2008; Nair and Kumar, 2013; Ophir and Lokiec, 2005). In order to enhance the effective heat transfer using the falling film method, a proper and accurate measuring technique needs to be developed to measure thin film thickness over the horizontal tubes in the evaporation of the MED system (Chen et al., 2015; Xu et al., 2004).

Researchers have developed numerical models to determine film thickness at different circumferential angles. In 1916, Nusselt numerically modelled film thickness measurement by considering thermophysical properties, fluid flow rate and acceleration due to gravity (Nusselt, 1916). Later, researchers found that there was a lacuna in Nusselt's numerical model to determine film thickness. In 2012, Hou et al. found that the diameter of the pipe and impingement height between pipes will play a major role in determining the film thickness. So, authors modified the Nusselt's equation by giving the ratio of impingement height between pipes and diameter of the pipe with constant values based on their experimental trials (Hou et al., 2012; Nusselt, 1916).

Many researchers have attempted to measure film thickness by intrusive and non–intrusive methods. In intrusive methods, Hou et al. 2012, measured the film thickness using displacement micrometer measurement with the tube impingement height ranging from 10 mm to 40 mm with Reynolds numbers ranging from 150 to 800. The working fluids used for their experiment were pure water and seawater. They observed that Nusselt's numerical model gave a relatively reasonable prediction of the film thickness around the upper perimeter of the tube; but a poor prediction around the lower perimeter (Hou et al., 2012). Zhang et al. 2020, measured falling film thickness over a horizontal corrugated tube using a displacement micrometer. They used pure water, maintained at 20°C, as working fluid with Reynolds numbers ranging from 150 to 1000 and observed that the film thickness of the corrugated tube

© 2022. The Authors. Published by International Solar Energy Society
Selection and/or peer review under responsibility of Scientific Committee
doi:10.18086/eurosun.2022.09.02 Available at http://proceedings.ises.org

increases with the increase of the film Reynolds number, which is the thinnest for circumferential angle ranging from 90° to 120°. The film thickness decreases by increasing the tube spacing, increasing the tube diameter and corrugation radius (Zhang et al., 2020).

Researchers have started developing non-intrusive methods to evaluate the characters of the liquid film. In 2019, Jayakumar et al. have measured the falling film thickness using an air-coupled ultrasonic transducer for plain horizontal tube. They used drinking water, maintained at 25°C, as the working fluid for different Reynolds numbers ranging from 130 to 350. They measured the film thickness for the circumferential angle ranging from 40° to 130°. They observed fluctuation in film thickness with increase in flow rate and this technique can also process film thickness data with better accuracy in minimal time (Jayakumar et al., 2019). Later in 2021, Maliackal et al. measured the falling film thickness using a laser interferometric technique. They used drinking water, which was maintained in the range from 70°C to 90°C, as the working fluid for different Reynolds numbers ranging from 350 to 900. They used an optical shadow graph technique to evaluate the falling film thickness around the circumference of a horizontal tube. Mach Zehnder Interferometer (MZI) was utilized to visualize the isotherm formation. The film thickness was measured at the circumferential angles ranging from 10° to 170° and observed that the film thickness variation around the tube circumference shows an increasing trend with increase in Reynolds number, but a change in trend with varying feed inlet temperatures (Maliackal et al., 2021). In 2022, Maliackal et al. were able to measure the film interface temperature (Maliackal et al., 2022a, 2022b). The characteristics of falling film of a horizontal tube is purely depend on liquid film temperature and thickness. Based on the work carried out by the researchers using non-intrusive techniques, a simultaneous measurement is developed for the different film characteristics.

This work presents a novel image processing technique for simultaneous measurements of falling film thickness and temperature of a horizontal plain tube of a falling film evaporator of a Multi-Effect Evaporator of desalination system.

2. Principle of operation

Experimental setup consists of a uniform water distributor tank, measuring tube and dummy tubes in a horizontal arrangement, constant temperature water bath, ultrasonic type flow meter and recirculation pump. The uniform water distributor tank is of dimension 60 mm x 50 mm x 150 mm (height x width x length). A baffle is provided at the height of 40 mm from the bottom of the uniform water distributor tank. A slot opening of 1 mm at the top of the uniform water distributor tank is provided for uniform sheet flow to simulate the flow conditions of the evaporator in the desalination plant.

The working fluid for the experiment is taken as drinking water. The water temperature is maintained using a constant temperature water bath. Water is pumped to the uniform water distributor tank from the constant temperature bath. Water flows through the distributor tank's slot and flows over the first three consecutive dummy tubes, measurement tube (fourth tube) and dummy tube (fifth tube) as shown in Fig. 1. The first three dummy tubes are used for flow stabilization and for uniform film formation over the measurement tube. The fifth dummy tube is used to avoid splashing of water before it collects in the water collection tank. The tube dimension, spacing and other characteristics are given in Table 1. At the bottom, water gets collected in the collection tank and flows back to the constant temperature water bath tank. The operating conditions for the experimental study are given in Table 2. The flow rate and working fluid temperatures before and after the measurement tube are continuously monitored using a calibrated ultrasonic flow meter and T - type thermocouples respectively. T - type thermocouples are inserted through the body of the experimental setup and touches the water without disturbing the film formation. Figure 2 shows the photographic view of falling film experimental setup.

Tab. 1: Tube characteristic.

Tube material	Copper
Tube Diameter (ID)	25.4 mm
Tube thickness	0.2 mm
Effective tube length	150 mm
Number of dummy tubes	4
Number of dummy catch tube	1

Ambient Temperature	28ºC

Tab. 2: Experimental operating conditions.

Working fluid	Drinking water
Operating working fluid flow rate	0.6 – 2 lpm
Operating working fluid temperature	60 ºC

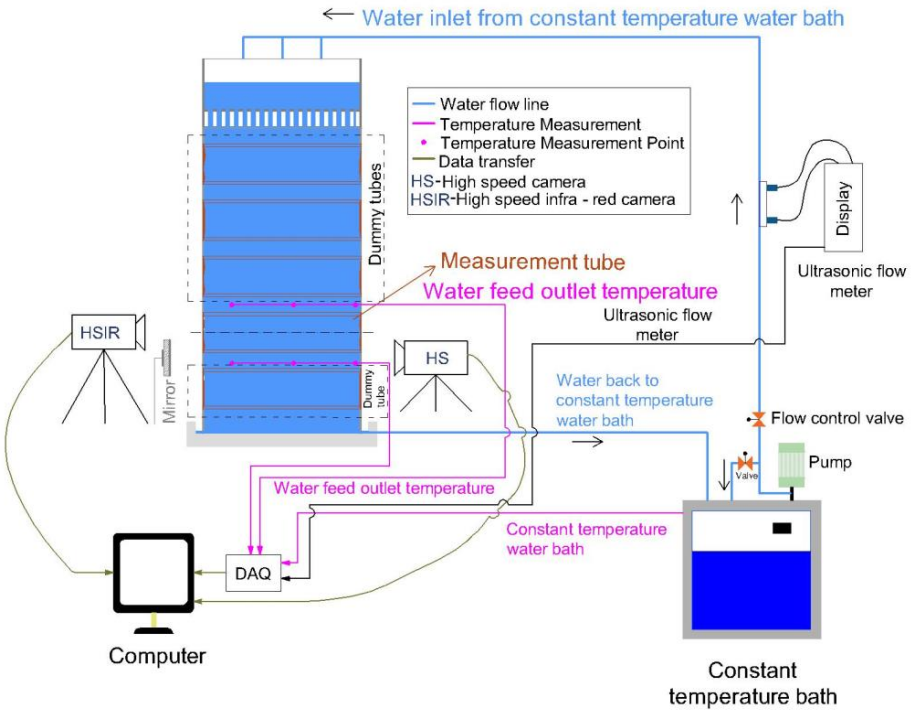

Fig. 1: Schematic diagram of falling film experimental setup.

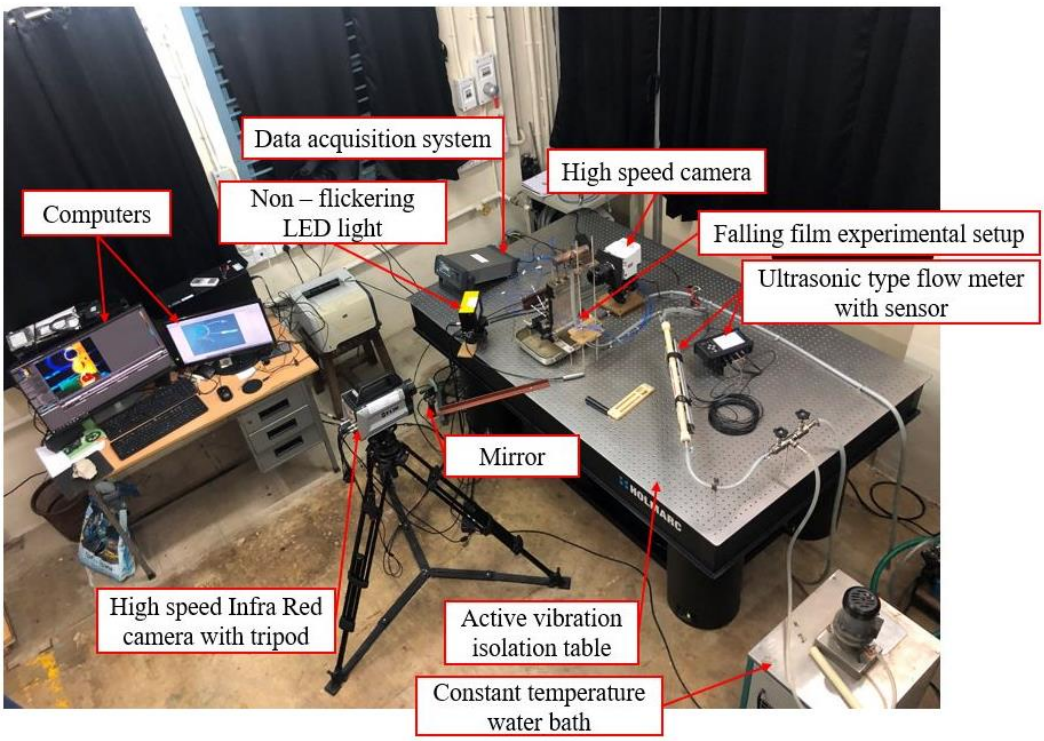

Fig. 2: Photograph of falling film experimental setup.

3. Falling film thickness and temperature measurement

Figure 3 shows the flow process for the mean film thickness and temperature measurements at each 10° circumferential angle of plain horizontal tube. After stabilization of film formation over the measuring horizontal tube, non – flickering light is positioned. The position of non-flickering light is kept in such a way that reflection of light from mirror, falling film and other surfaces should be minimal. Phantom VEO 1310L high-speed camera is made to focus the film formation from the mirror with surface finish of λ/10 and FLIR X6901sc high-speed infra-red camera is made to focus the film falling over the horizontal tube. After aligning non-flickering light, high-speed camera and high-speed infra-red camera, trial shots are recorded to check the focus and aligning. On completion of this process, high-speed camera and high-speed infra-red camera are triggered simultaneously to capture the film formation and temperature of falling film over the horizontal tube respectively.

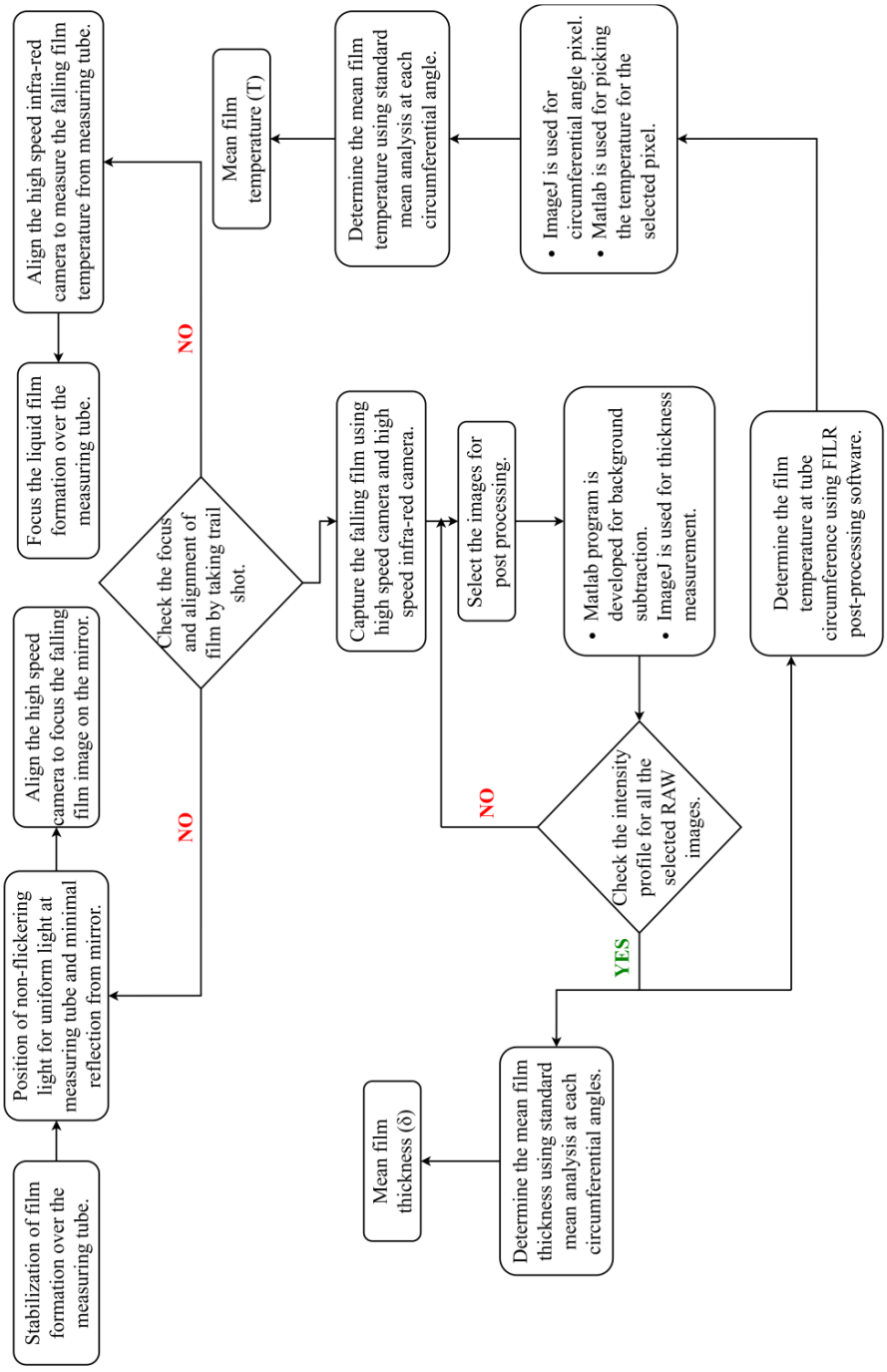

Fig. 3: Process flow chart for film thickness and temperature measurements.

After simultaneous capturing, random images of high speed camera are selected for post processing. An in house MATLAB program is developed to remove unwanted noises like reflection of light and to identify liquid film flow. Figures 4a and 4b show the raw images of high speed camera without flow and with flow respectively before post processing. Figures 5a and 5b show the images of high speed camera without flow and with flow respectively after post processing for the flow rate of 1 lpm corresponding to Reynolds number of 1008.94.

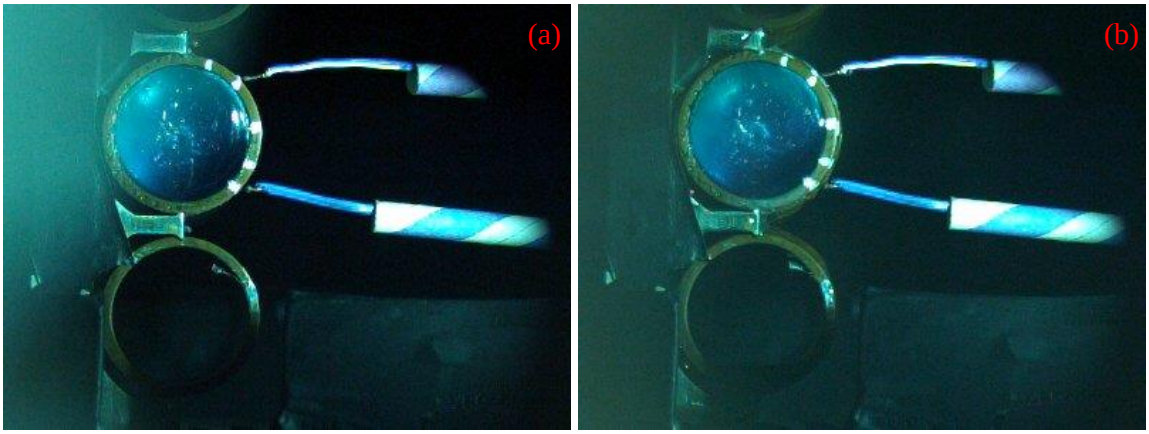

Fig. 4: Raw image of high speed camera (a) without flow and (b) with flow.

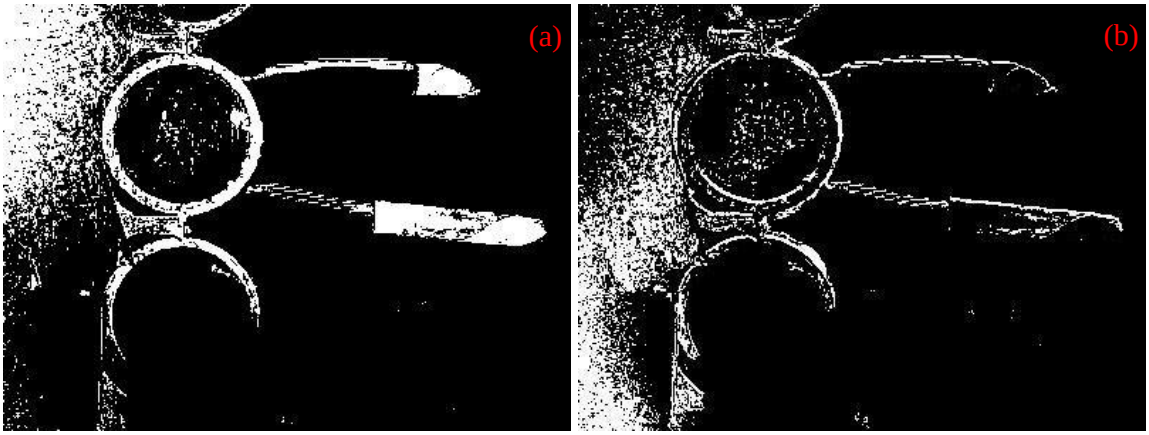

Fig. 5: Processed image of high speed camera (a) without flow and (b) with flow.

An in house ImageJ macro program is developed to identify the circumferential angle and generate radial intensity profile for without flow and with flow processed images. Figures 6a and 6b show the radial intensity profile for without flow and with flow processed images respectively. The macro program is developed for each circumferential angle of the plain tube ranging from $10^{o} \leq \theta \leq 170^{o}$ to obtain film thickness data.

After acquiring film thickness, the selected frames of high speed camera and the corresponding frames in high speed infra-red camera are used for the post processing using FLIR software. ImageJ macro program and MATLAB program are developed to identify the circumferential angle and to obtain film temperature. Figure 7 shows the temperature gradient around plain tube using FLIR software.

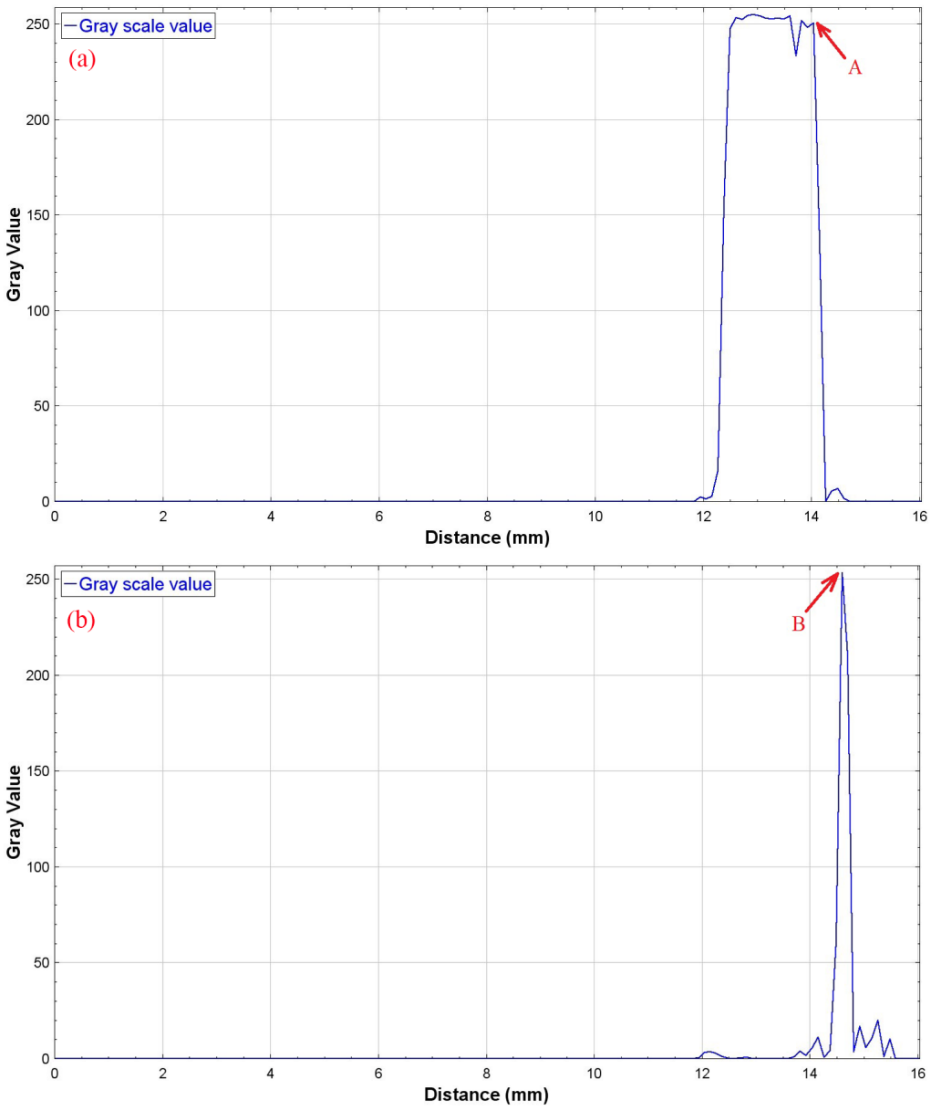

Fig. 6: Radial intensity profile for (a) without flow and (b) with flow of processed images at 80º circumferential angel.

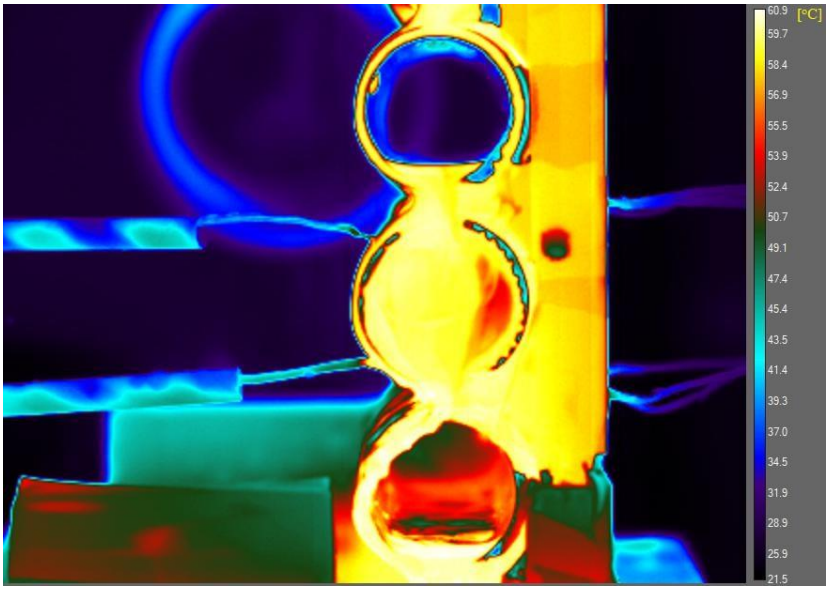

Fig. 7: Temperature gradient around plain tube using FILR software.

4. Empirical relations and Error analysis

4.1. Empirical relations

The falling film thickness (δ) over horizontal tube empirical Eq. 1 is given by Nusselt (Nusselt, 1916).

$$\delta = \left(\frac{3\mu_l \Gamma}{\rho_l(\rho_l - \rho_g) g \sin\theta}\right)^{1/3} \quad \text{(eq. 1)}$$

Where, μ_l – Liquid Dynamic viscosity [kg.m^{-1}.s^{-1}] ; Γ – Film flow rate per unit length on one side of the tube [kg.m^{-1}.s^{-1}] ; ρ_l – Liquid Density [kg.m^3] ; ρ_g – Vapor Density [kg.m^3] ; g – Acceleration due to gravity [m.s^{-2}] ; θ - Circumferential angle

In Nusselt's Eq. 1, falling film momentum effect was not taken into account. Therefore, Hou et al. has modified the Eq. 1 by considering diameter of the tube and impingement height, and the modified equation is given in Eq. 2.

$$\delta = C\left(\frac{3\mu_l \Gamma}{\rho_l(\rho_l - \rho_g) g \sin\theta}\right)^{1/3} \left(\frac{S}{D}\right)^n \quad \text{(eq. 2)}$$

Where, S – Impingement height [m] ; D – Tube diameter [m] ; n – Refractive index

$$C = \begin{cases} 0.97540, & 0^o < \theta \leq 90^o \\ 0.84978, & 90^o < \theta \leq 180^o \end{cases} \quad ; \quad n = \begin{cases} -0.16670, & 0^o < \theta \leq 90^o \\ -0.16479, & 90^o < \theta \leq 180^o \end{cases}$$

Reynolds number (Re) for falling film around the horizontal tube is given in Eq. 3.

$$Re = \frac{4\Gamma}{\mu_l} \quad \text{(eq. 3)}$$

4.2. Error analysis

A standard error mean analysis is carried out for all data sets for each circumferential angle (θ). Mean film thickness (δ_{mean}) and mean film temperature (T_{mean}) are computed by Eq. 4 and Eq. 5 respectively.

$$\delta_{mean} = \frac{\sum_{i=1}^{N} \delta_{i=1}}{N} \quad \text{(eq. 4)}$$

$$T_{mean} = \frac{\sum_{i=1}^{N} T_{i=1}}{N} \quad \text{(eq. 5)}$$

The standard deviation (SD) for the data sets is computed by Eq. 6.

$$SD = \sqrt{\frac{\sum_{i=1}^{N} (\delta_{mean} - \delta_i)^2}{N-1}} \quad \text{(eq. 6)}$$

The standard error mean (SEM) analysis is computed by Eq. 7.

$$SEM = \delta_{mean} \pm \frac{SD}{\sqrt{N}} \quad \text{(eq. 7)}$$

5. Results and discussion

Experimentation is carried out to determine the falling film thickness and temperature. The circumferential angle of falling film thickness and temperature are measured simultaneously, in the range $10^o \leq \theta \leq 170^o$ and $10^o \leq \theta \leq 180^o$, respectively, with an increment of 10°.

5.1. Comparison with numerical correlation

Figure 8 shows the variation of falling film thickness around the circumference of the plain tube for the flow rate of 2 lpm, which corresponds to the Reynolds number of 1981.82. The momentum effect of liquid film from 80° of plain tube circumferential angle is accounted as in Eq. 2. The surface tension force of liquid film plays an important role in the shift in minima from 90° to 110° circumferential angle of the plain tube. The film thickness at circumferential angels in the range of 0° to 20° and 160° to 180° of plain tube are higher and so, the liquid film has to slide over the vertical wall, reducing the momentum transfer. These regions are known as impingement zones and have the maximum error in the range of ±10.57% to ±12.27% for the film thickness. The average error

is in the range of ±1.77% to ±6.00% for the circumferential angles ranging from 30º to 150º. The present study for the circumferential angle at 80º with variation of Reynolds numbers for plain tube is compared with the experimental results carried out by Jayakumar and Mani, 2022 for plain tube with varying Reynolds numbers as shown in Fig. 9. The temperature of working fluid is maintained at 25ºC for Reynolds number ranging from 356 to 715, which corresponds to the flow rate of 0.72 lpm to 1.43 lpm. It is observed that the maximum error for the present study is in the range of ±3.2% to ±8.29%. The local heat transfer coefficient (h) with unit $W.m^{-2}.ºC^{-1}$ for different circumferential angles of plain tube is computed from Eq. 8 and plotted as shown in Fig. 10.

$$h = \frac{k_{eff}}{\delta_{mean}} \qquad \text{(eq. 8)}$$

Where, k_{eff} – effective thermal conductivity [m] ; δ_{mean} – Mean film thickness [m]

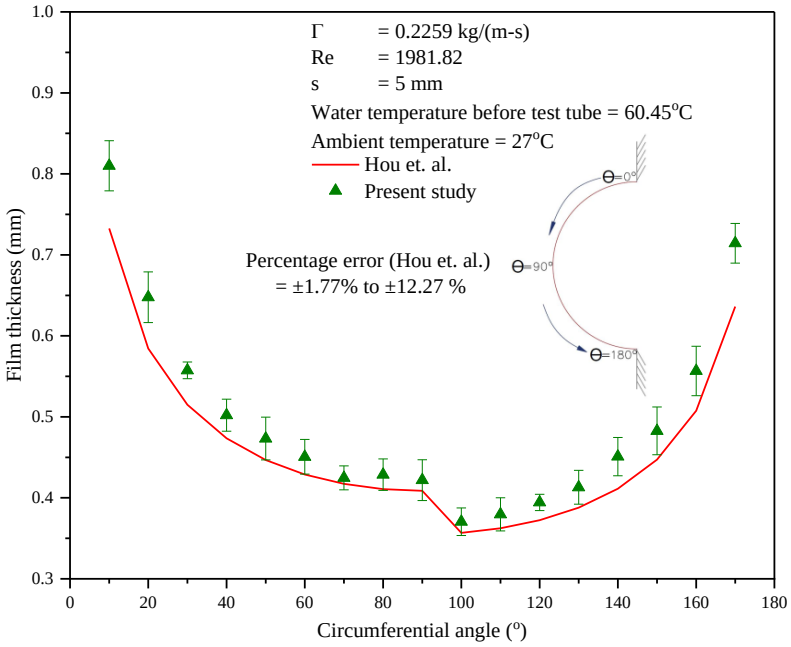

Fig. 8: Comparison of film thickness along circumferential angle with literature data.

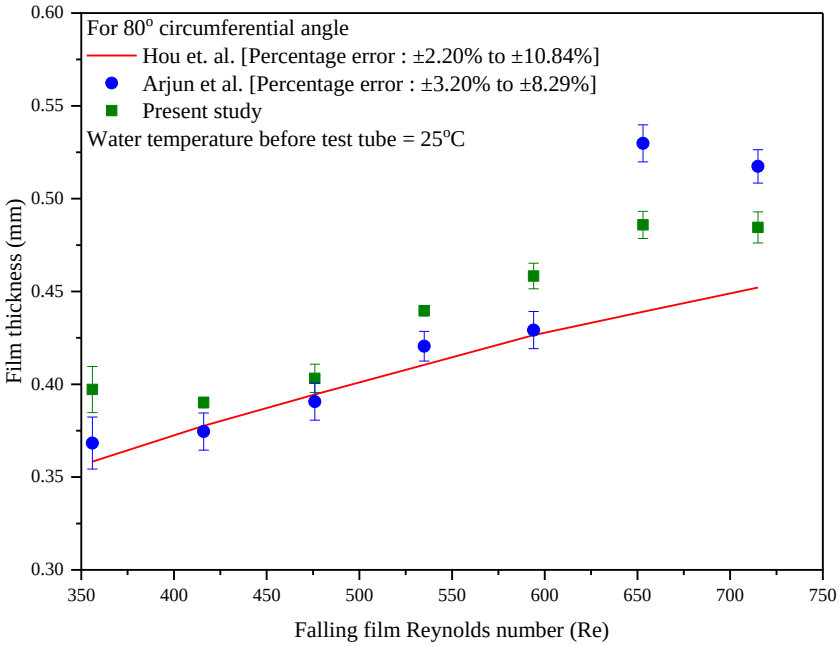

Fig. 9: Comparison of falling film thickness with different Reynolds numbers with literature data.

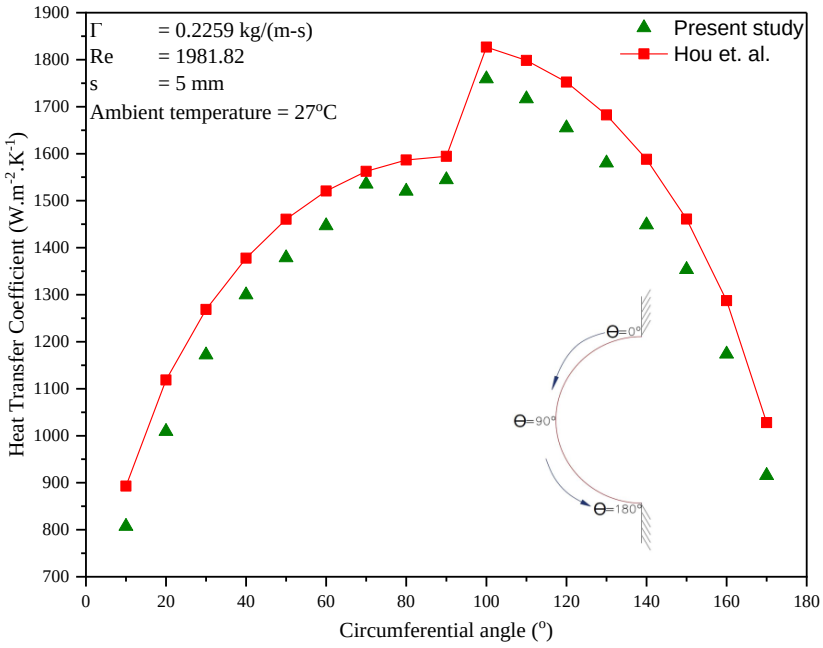

Fig. 10: Comparison of heat transfer coefficient along circumferential angle with literature data.

5.2. Effect of Reynolds number

Figure 11 shows the variation of falling film thickness around the circumference of the plain tube as a function of feed Reynolds number. The range of feed Reynolds number for typical MED operation is $448.213 \leq Re \leq 1981.82$. All the film thickness measurements are taken for complete wetting and taken as the effective length of plain tube and steady flow rate. It is observed that the falling film thickness variation around the circumferential angle of plain tube shows a strong correlation with Reynolds number variation.

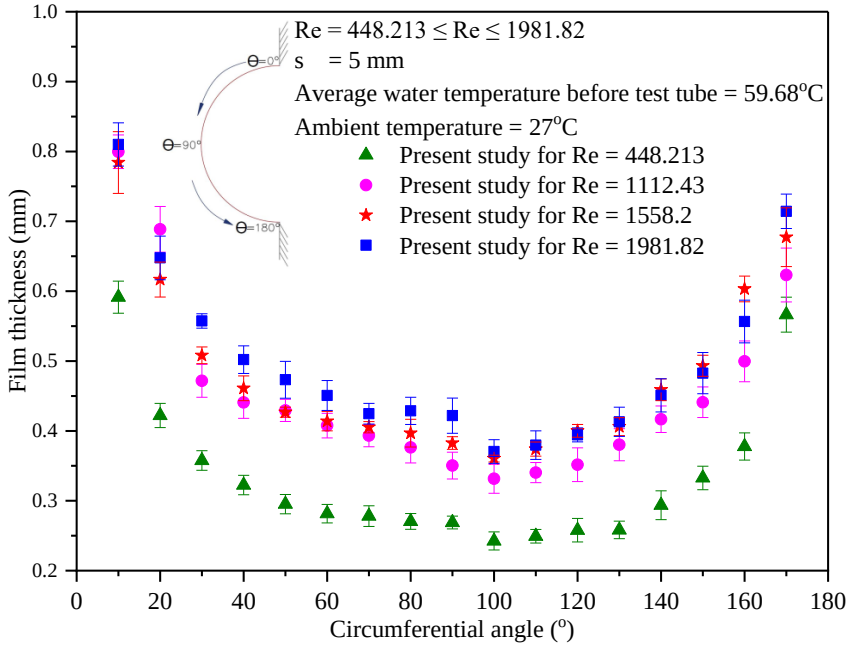

Fig. 11: Variation of falling film thickness with circumferential angle for different Reynolds numbers.

5.3. Effect of feed inlet temperature

Figure 12 shows the variation of falling film temperature around the circumference of the plain tube for the Reynolds number of 1981.82 which corresponds to 2 lpm. The average feed inlet temperature of test tube is 60°C.

All the temperature measurements are taken for complete wetting of the effective length of plain tube. The temperature data at 0º, 45º, 135º and 180º circumferential angles are measured using calibrated thermocouples. The error band of High Speed Infra-Red (HSIR) data is in the range of ±0.08% to ±1.57% when compared with calibrated T - type thermocouple. Figure 13 shows the variation of falling film temperature around the circumference of the plain tube as a function of feed Reynolds number.

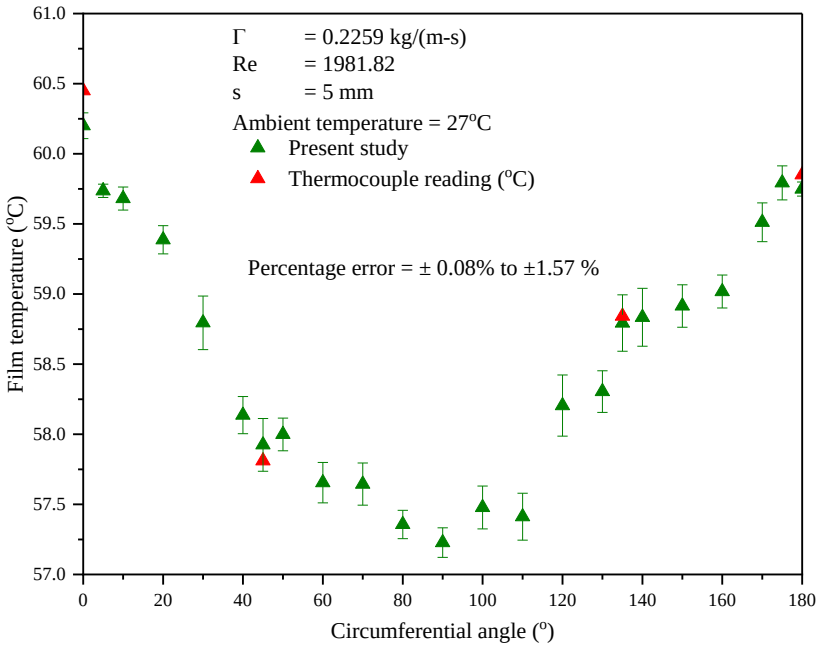

Fig. 12: Variation of falling film temperature with circumferential angle.

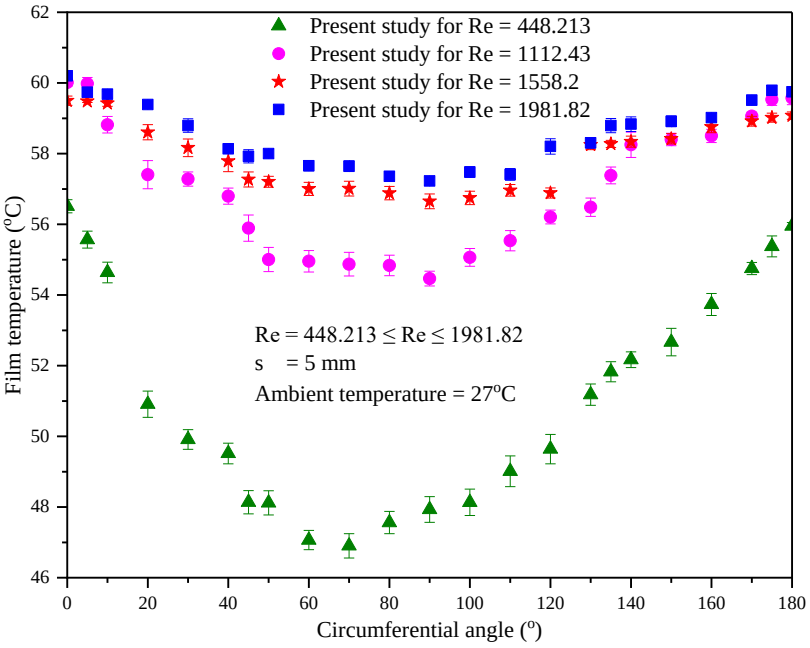

Fig. 13: Variation of falling film temperature with circumferential angle for different Reynolds numbers.

6. Conclusions

In this paper, an image processing technique (non - intrusive method) is used to evaluate the falling thin film thickness and film temperature around the circumference of a plain horizontal tube. This study is carried out for the circumferential angles ranging from 10º to 170º for film thickness and 0º to 180º for film temperature. The

film thickness follows the Hou et al., 2012 empirical model with the error band of ±1.77% to ±6.00% at non - impingement zones. Also, the present study of film thickness is compared with Jayakumar and Mani and has error band of ±3.20% to ±8.29% for different Reynolds numbers. The error band for falling film temperature is in the range of ±0.08% to ±1.57%, when compared with calibrated thermocouples.

7. References

Al-Shammiri, M., Safar, M., 1999. Multi-effect distillation plants: State of the art. Desalination 126, 45–59. https://doi.org/10.1016/S0011-9164(99)00154-X

Chen, X., Shen, S., Wang, Y., Chen, J., Zhang, J., 2015. Measurement on falling film thickness distribution around horizontal tube with laser-induced fluorescence technology. Int. J. Heat Mass Transf. 89, 707–713. https://doi.org/10.1016/j.ijheatmasstransfer.2015.05.016

Hou, H., Bi, Q., Ma, H., Wu, G., 2012. Distribution characteristics of falling film thickness around a horizontal tube. Desalination 285, 393–398. https://doi.org/10.1016/j.desal.2011.10.020

Jayakumar, A., Balachandran, A., Mani, A., Balasubramaniam, K., 2019. Falling film thickness measurement using air-coupled ultrasonic transducer. Exp. Therm. Fluid Sci. 109, 109906. https://doi.org/10.1016/j.expthermflusci.2019.109906

Jayakumar, A., Mani, A., 2022. Experimental and Numerical Study of Hydrodynamic and Heat Transfer Characteristics of Falling Film over Metal Foam Layered Horizontal Tube. J. Heat Transfer 144, 1–11. https://doi.org/10.1115/1.4053203

Khawaji, A.D., Kutubkhanah, I.K., Wie, J.M., 2008. Advances in seawater desalination technologies. Desalination 221, 47–69. https://doi.org/10.1016/j.desal.2007.01.067

Maliackal, A.K., Ganesan, A.R., Mani, A., 2022a. Heat transfer enhanced surfaces for horizontal tube falling film evaporator characterized using laser interferometry. Appl. Therm. Eng. 210, 118303. https://doi.org/10.1016/j.applthermaleng.2022.118303

Maliackal, A.K., Ganesan, A.R., Mani, A., 2022b. A novel interferometric method for simultaneous measurement of film thickness and film interface temperature for a horizontal tube falling film evaporator for MED systems. Int. J. Heat Mass Transf. 183, 122231. https://doi.org/10.1016/j.ijheatmasstransfer.2021.122231

Maliackal, A.K., Ganesan, A.R., Mani, A., 2021. Interferometric analysis of flow around a horizontal tube falling film evaporator for MED systems. Int. J. Therm. Sci. 161, 106745. https://doi.org/10.1016/j.ijthermalsci.2020.106745

Nair, M., Kumar, D., 2013. Water desalination and challenges: The Middle East perspective: A review. Desalin. Water Treat. 51, 2030–2040. https://doi.org/10.1080/19443994.2013.734483

Nusselt, W., 1916. Die oberflachenkondensation des wasserdamphes. VDI-Zs 30, 541.

Ophir, A., Lokiec, F., 2005. Advanced MED process for most economical sea water desalination. Desalination 182, 187–198. https://doi.org/10.1016/j.desal.2005.02.026

Xu, L., Ge, M., Wang, S., Wang, Y., 2004. Heat-transfer film coefficients of falling film horizontal tube evaporators. Desalination 166, 223–230. https://doi.org/10.1016/j.desal.2004.06.077

Zhang, Y., Wang, D., Liu, Y., Tang, M., Zhang, S., 2020. Distribution characteristics of falling film thickness around a horizontal corrugated tube. Int. J. Heat Mass Transf. 154. https://doi.org/10.1016/j.ijheatmasstransfer.2020.119773

Nexus Energy & Water: Integration concepts for solar energy in industrial water and waste water treatment

Sarah Meitz[1], Christoph Brunner[1], Bettina Muster-Slawitsch[1]

[1] AEE - Institute for Sustainable Technologies, Gleisdorf (Austria)

Abstract

The main objective of IEA SHC Task 62 is to increase the use of solar thermal energy in industry, to develop new collector technologies and to open up industrial and municipal water treatment as a new area of application with high market potential for solar thermal energy. The nexus between solar thermal energy and water treatment enables the development of new and innovative technology combinations and the change to a sustainable, resource- and energy-efficient industry. For the best possible integration of solar energy in waste water treatment integration concepts incorporated into a decision-making tool provide a basis information platform for decision-making and system integration.

Keywords: Solar waste water treatment; industry; energy efficiency; resource recovery

1. Introduction

Based on data available, the industrial sector in EU member states accounts for ~21 % of the waste water demand, with only 36% of this amount being treated (5,293 million m^3 of industrial waste water generated vs. 1,927 million m^3 of industrial waste water being treated) (Alabaster et al., 2021). The collection and treatment of waste water plays an essential role within the transition towards circular value chains in industry, thus efforts need to be taken to increase treatment capacities. Within this transition, wastewater purification and recovery technologies take an essential role in augmenting water and valuables from wastewater streams without placing an excessive strain on limited energy supplies. The efficient supply of energy, the best possible integration of renewable energy sources and the recovery of resources in the sense of circular economy need to go hand in hand. Within this background the use of solar process heat represents a large, but so far largely untapped potential in industry. Innovative and concrete solutions are required for the long-term and successful introduction of solar thermal energy. The integration of solar process heat to supply technologies for water treatment and purification represents a new field of application with great technical and economic potential for solar energy. The efficient interaction, the nexus between solar energy and water, opens up new and innovative approaches to solutions, which are dealt with within the framework of the International Energy Agency's Solar Heating and Cooling Task 62 (IEA SHC Task 62).

2. IEA SHC Task 62: Targets

IEA SHC Task 62 takes up selected focus areas and results from IEA SHC Task 49/IV (https://task49.iea-shc.org/) and research projects to address the opportunities, challenges and benefits of integrating solar energy into wastewater treatment in an industrial context. The main objectives are (1) to increase the use of solar thermal in industry, to (2) develop new collector technologies, and to (3) open up industrial as well as municipal water treatment as a new application area with high market potential for solar thermal. The nexus between solar thermal and water treatment enables the development of new and innovative technology combinations and the shift towards a sustainable, resource and energy efficient industry. By combining water treatment technologies with solar thermal collectors, an innovative and economically attractive overall solution can be created for the industry.

2.1. Thermally driven water separation technologies and recovery of valuable resources

One research focus of IEA SHC Task 62 is the combination of solar thermal collectors with technologies for the treatment of waste water to an innovative and economically attractive overall solution for industry. The use of thermally operated separation technologies such as membrane distillation in combination with solar process heat represents an energetically and economically promising alternative to conventional electrically operated separation technologies. Within the scope of the work, a technical and economic potential assessment for the use of solar-powered water treatment with a focus on membrane distillation will be carried out. The aim is to initiate

© 2022. The Authors. Published by International Solar Energy Society
Selection and/or peer review under responsibility of Scientific Committee
doi:10.18086/eurosun.2022.09.03 Available at http://proceedings.ises.org

new implementations and define further research and development issues.

2.2. Solar water decontamination and disinfection systems

In addition to thermal technologies, IEA SHC Task 62 focuses on processing technologies that use direct UV radiation. New industrial application areas for these solar water decontamination and disinfection systems will be identified, and by identifying technical, economic and political barriers to new decontamination and disinfection systems in industrial water and wastewater management, ongoing work can be better tailored to the needs of industry, integration facilitated and the number of implementations increased. The simultaneous utilization of heat and UV light in one technology represents new areas of application for solar energy (UV, photocatalytic applications, etc.) in industry.

2.3. System integration and decision support for end user needs

The developed concepts for the integration of solar energy in waste water and process water treatment will be available in a decision support tool to stakeholders (industrial companies, plant planners, technology providers, etc.) as a tool to support decision making and detailed planning of overall systems (further combination with waste heat, other renewables, etc.). This can overcome barriers to implementation due to a lack of user know-how and facilitate the market penetration of solar-based separation technologies.

3. Methodology

To deliver system integration and decision support for end user needs within the Nexus of Energy & Water, the methodological approach is structured as follows: (1) Identification of suitable industrial sectors and processes as well as other application areas (e.g., municipal waste water treatment) for the use of solar-driven separation technologies and definition of their requirements (e.g., components, concentrations [mg/L], amounts [m^3/day]). (2) Elaborating integration concepts, combining separation and purification technologies with energy supply from solar thermal technologies, other renewable energies and excess heat from industrial processes. (3) Setting up a decision-making tool based on Excel to identify most reasonable options for solar waste water treatment in industry from a technical and an economical point of view.

4. Results

4.1. Integration concepts

The elaborated integration concepts describe, how solar thermal energy can be integrated in combination with thermal separation technologies like Membrane Distillation (MD), to provide the thermal energy demand in a renewable way. The integration concepts are modular. Each concept has at least one base module for the renewable process heat supply, like solar thermal (illustrated in Figure 1) or heat pump. Also, the possibility for waste heat integration is available.

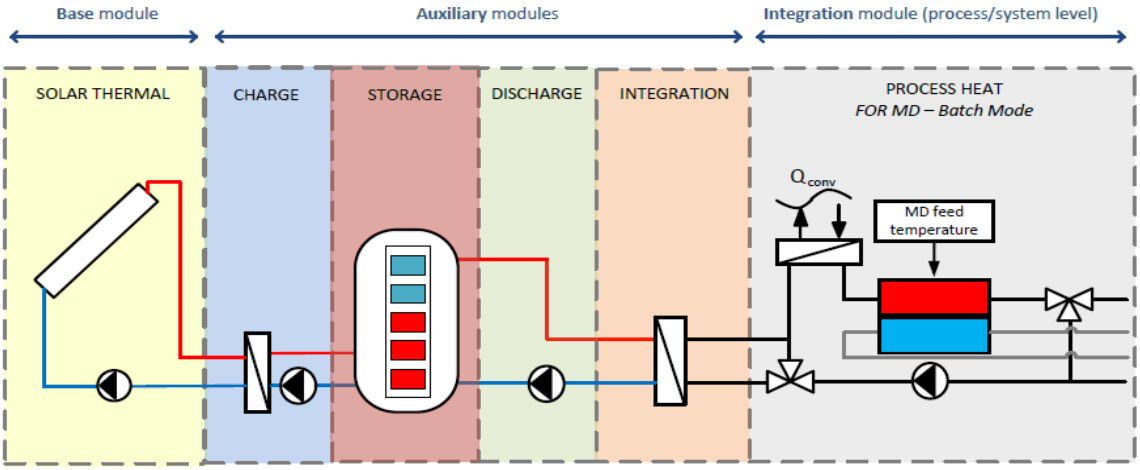

Fig. 1: Example for an integration concept combining solar thermal for the process heat supply of Membrane Distillation

In addition to the base modules, there is a large number of auxiliary modules (e.g., charge, storage, discharge,

integration). Auxiliary modules enable the integration of renewable process heat modules to supply heat on process or system level and allow adaption of the concept depending on the specific requirements given. In Figure 2 exemplary the heat supply for MD on process level is illustrated. The MD process module changes based on requirements like batch or continuous operation as well as internal heat recovery (HR) realized.

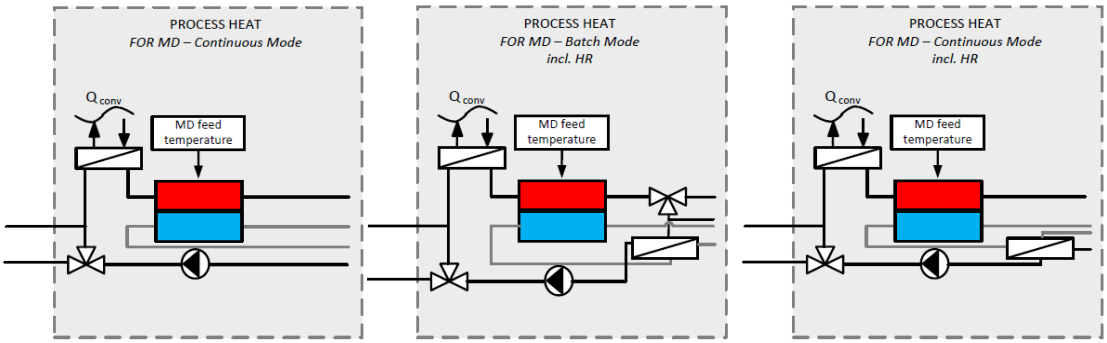

Fig. 2: Integration for MD supply on process level (batch mode with/without heat recovery, continuous mode with/without heat recovery)

4.2. Decision-Making process

4.2.1 Decision-making tool

To support the decision-making process, the integration concepts are part of the decision-making tool. The tool shows industrial companies (e.g., food and beverage industry, galvanic industry) and (municipal) waste water treatment plant operators which options/integration concepts are available to them for solar water treatment under certain framework conditions (location, land availability, waste water requirements, etc.) and which represents the most technically viable variant. The tool is available as an Excel tool to give a wide application possibility. Depending on the input (data basis) of the water treatment task (waste water characteristics, waste heat characteristics, location of industry, etc.) and selecting the treatment target (e.g., concentration or separation of specific compounds) as well as selecting the technology, the tool performs calculations (mass and energy balances) to present rough performance values (energy demand, solar yield, collector area etc.) and give recommendations for the integration. The waste water calculations are based on integrating membrane distillation as treatment technology. In terms of the energy supply solar thermal or waste heat in stand-alone mode or in a combined energy system can be selected. The basis set-up of the tool is presented in Figure 3.

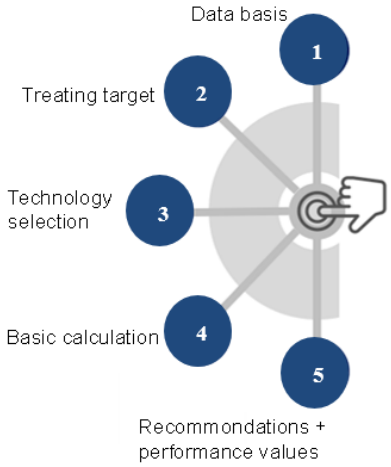

Fig. 3: Structure of the decision-making tool

4.2.1 Nomograms

Based on the calculated results from the tool, nomograms for the solar thermal and/or waste heat driven waste water treatment have been created to assist in evaluating the dependencies of a renewable supplied energy system for MD. Following parameters are included to the nomograms:

- Country: As local conditions influence the renewable energy potential (f.i. irradiation), nomograms are available for different countries. In a first step European countries Austria (Vienna) and Spain (Madrid) have been evaluated.
- Solar fraction [%]: The solar fraction is defined by the amount of energy provided by the solar thermal plant, referred to the total energy demand needed.
- GOR efficiency [-]: The Gained output ration (GOR) is defined as the ration of the latent heat of evaporation of the produced water to the total heat supplied to the system.
- Energy demand ext. [MWh/a]: The external energy demand given in MWh per year gives the remaining demand of energy needed for the MD process, depending on the solar fraction.

Exemplary nomograms are shown in Figure 4 and 5. Calculations are based on location Vienna (Austria) and a system of MD supplied by solar thermal and used for concentrating (concentration factor of 2) waste water via separating water from a waste water stream at 80°C operating temperature.

The total energy demand (calculated by the sum of the energy demand provided by solar thermal and energy demand external) to supply MD increases with an increased volume [L/h] to be treated. The energy demand of MD can be reduced, applying optimization like optimum operation conditions, module design and configurations etc. By reducing the energy demand an increase in GOR is possible. To show the influence of GOR on the whole systems energy demand, Fig. 4 illustrates that by keeping the solar fraction constant at 50% and increasing the efficiency of the waste water treatment system from GOR 0,5 to 2,5 an enormous reduction of the external energy demand is possible.

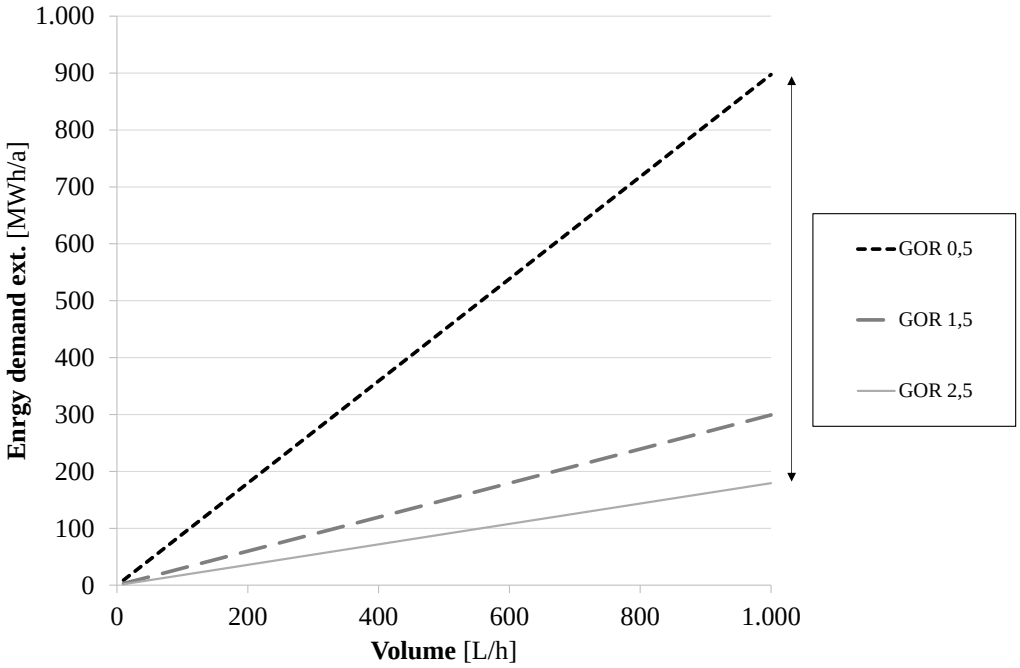

Fig. 4: Structure of the decision-making tool

Fig. 4. shows the correlation between the volume of waste water to be treated and external energy demand to be provided, depending on the given solar fraction at a constant GOR of 0,5. The external energy demand decreases by increasing the solar fraction – so the bigger the solar thermal plant the higher the coverage range of energy demand for MD.

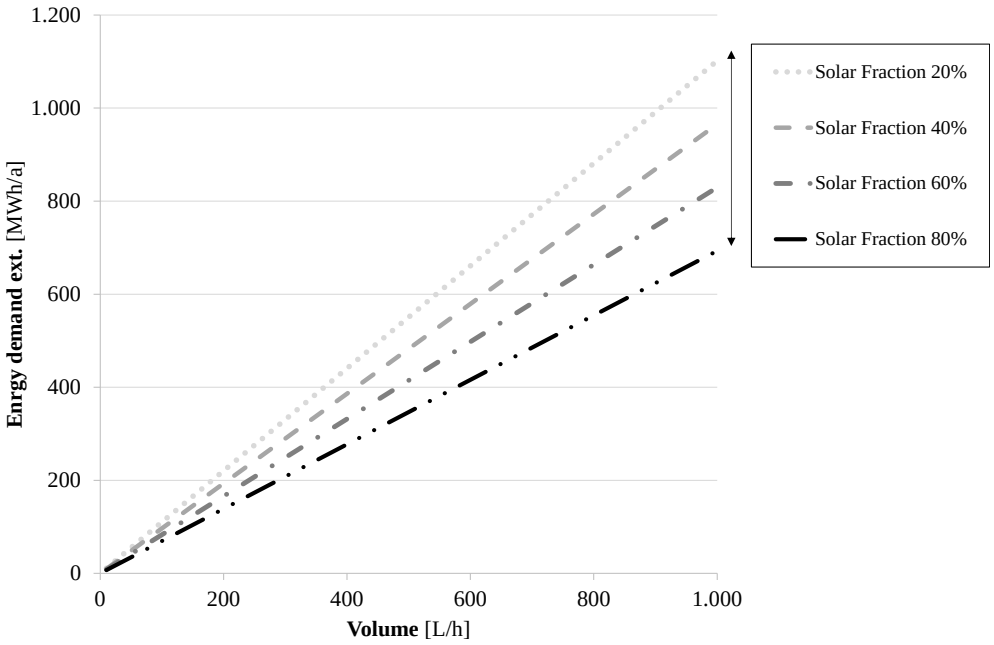

Fig. 4: Structure of the decision-making tool

5. Outlook

The use of solar wastewater treatment by solar thermal energy supply represents a large, but so far largely untapped potential in industry. Integration concepts offer a good possibility to show planners, technology providers and end-users the different options for integrating solar thermal driven water treatment technologies.
To further promote solar wastewater treatment, upcoming activities of the IEA SHC Task 62 include the completion of the decision-making tool, which is currently under validation, to show industrial companies which options/integration concepts are available for solar water treatment under certain conditions (energy demand, location, space availability, etc.) and which are the technically feasible variants.

6. Acknowledgement

The IEA SHC Task 62 project is funded by the Austrian Federal Ministry of Climate Protection, Environment, Energy, Mobility, Innovation and Technology within the IEA Call for Proposals 2018 (project number: 870651).

7. References

Alabaster, G., Jonston, R., Thevenon, F., Shantz, A., 2021. Progress on Wastewater Treatment - Global status and acceleration needs for SDG indicator 6.3.1. UN Habitat and WHO, 202

K. Carbon Neutral University Campus

EuroSun 2022

Measures for energy optimization for resource-saving consumption development on a university campus

Markus Arendt[1], André Kremonke[1] and Clemens Felsmann[1]

[1] Institute of Power Engineering, Chair of Building Energy Systems and Heat Supply, TU Dresden, Dresden (Germany)

Abstract

The CAMPER-MOVE research project addresses the challenges arisen in connection with the transformation processes that a university campus is currently undergoing. Further to the recognition of undesirable developments and the development of effective counteracting strategies, the main objective of research project is the scientific monitoring, evaluation and optimization of the practical implementation of measures of a constructional-technical nature as well as supporting an economical user behavior. The experience to be gained in this process will be incorporated in further conceptual considerations to reduce energy consumption.

Keywords: Sector Coupling, Waste Heat Utilization, Autonomous Power Supply, Energy Management, User Behavior

1. Introduction

Founded in 1828 as a technical educational institution, the Technische Universität Dresden (TUD) is today one of the largest and oldest universities in Germany. Due to its former orientation as a technical university, scientific and engineering disciplines still dominate the university today. This is reflected by a significant number of buildings with a high to very high proportion of laboratory/experimental space. The TUD is a classic campus university with a historic core campus, the main campus, south of the city center. In addition, the university also includes several sites away from the main campus, such as the Botanical Garden, the Forest Botanical Garden and the Faculty of Medicine. However, the majority of university buildings are located on the main campus.

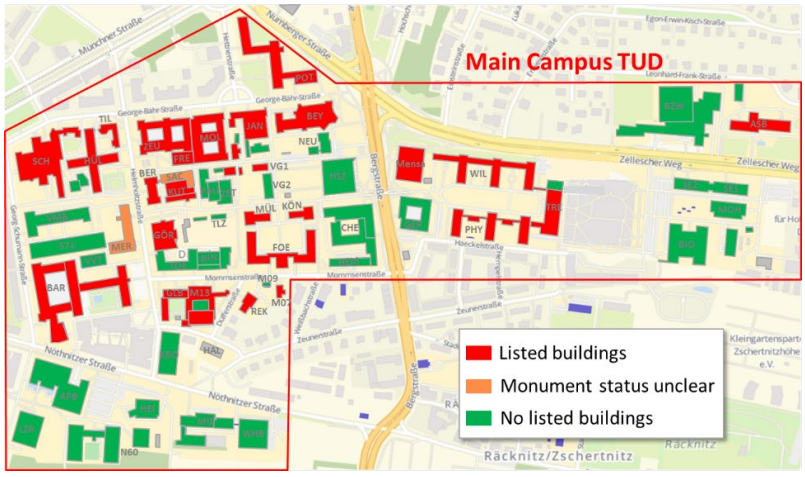

Fig. 1: Monument status of the buildings of the main campus of the TU Dresden

More than 50% of the buildings need renovation, whereas a majority of the buildings are historic monuments, which poses particular challenges for the energy retrofitting and integrating renewables (Fig. 1).

© 2022. The Authors. Published by International Solar Energy Society
Selection and/or peer review under responsibility of Scientific Committee
doi:10.18086/eurosun.2022.10.01 Available at http://proceedings.ises.org

In total, the main campus comprises 50 larger building complexes with a net floor space of approx. 390 000 m². In addition, a low-temperature local heating network of smaller size exists at the south end of the campus, which is used to transport waste heat from the university's largest data center to surrounding buildings (Fig. 2).

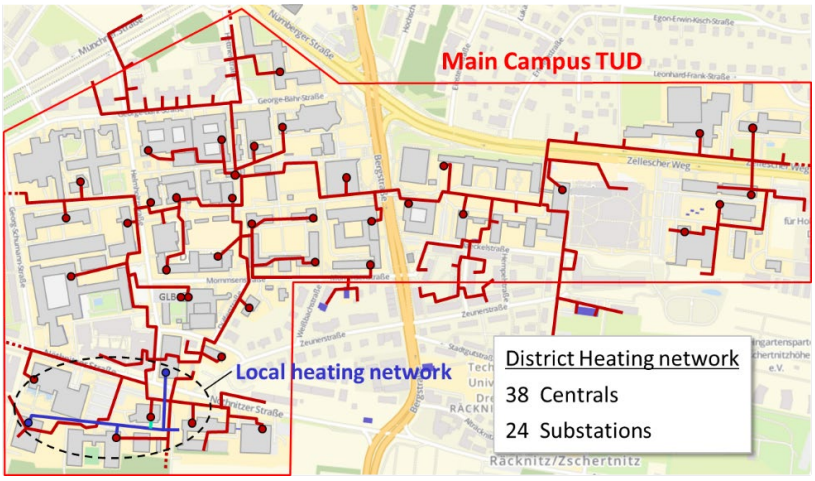

Fig. 2: District heating network in the area of the main campus of the TU Dresden

The cooling supply for the campus is provided by seven smaller local cooling networks as well as a number of decentralized small cooling generators. In total, cooling generators with a nominal capacity of approx. 25 MW are installed on the main campus, thus reaching the level of the heat supply. The cooling is mainly required for technological processes in laboratories and workshops, for cooling computer technology and for lecture hall air conditioning.

The electrical power supply of the main campus is connected to the public power grid at two central transfer stations. From there, seven internal medium-voltage rings supply all buildings. This also enables the flexible redistribution of electricity generated on the campus, which is produced regeneratively with the help of PV systems (currently approx. 350 MWh/a).

2. Analysis of energy consumption since 1998

If one examines the development of land consumption over the past 20 years, one initially sees a fairly moderate increase in the main usable area of the university of about 36 % (Fig. 3). It must be taken into account here that in the wake of the political turnaround in 1990, various restructuring of academic departments and partial realignments took place. A more detailed analysis reveals a disproportionately strong increase in highly technical areas (laboratory, server room and technical areas) by approx. 70 %. In the recent past in particular, there has been a flurry of new construction activity. In particular, buildings were constructed for institutes of the natural sciences with a high level of technical equipment and numerous laboratories. In return, rented buildings were handed over and older buildings were partially demolished.

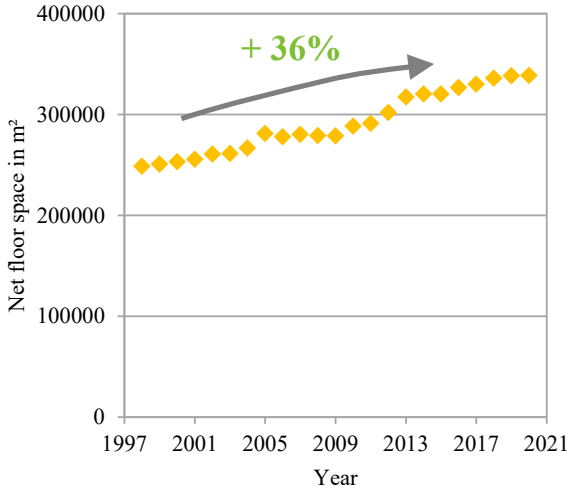

Fig. 3: Net floor space in m² without medical school (CAMPER, 2015 and CAMPER-MOVE, 2019)

The university is aware of its pioneering role and ecological responsibility and regularly initiates energy efficiency measures in its existing buildings. Newly constructed buildings have a high level of structural thermal insulation. Despite the increase in space, the heat consumption of the university campus has thus been kept at an almost constant level over the years. A slight increase has only been recorded since 2016 (Fig. 4). Due to the fact that the campus buildings are predominantly supplied with district heating from Sachsen Energie, with a high CHP share from a highly efficient combined cycle power plant (CCPP), the heat consumption also has a lower impact on the greenhouse gas (GHG) balance. Nevertheless, heat demand is highly relevant, as it generates significant energy costs and causes significantly higher emissions in other neighborhoods (with less efficient heat supply).

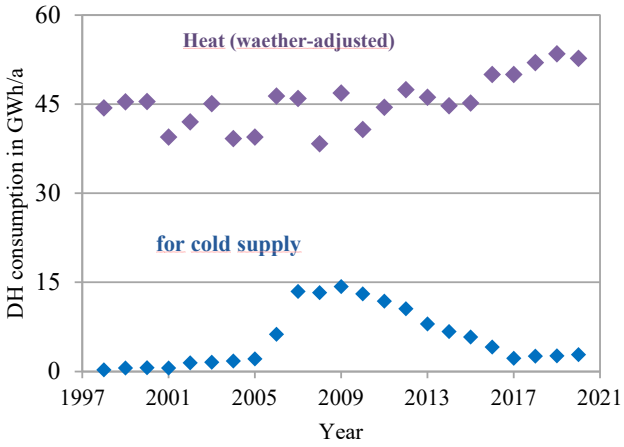

Fig. 4: DH consumption in GWh/a without medical school and weather-adjusted (CAMPER, 2015 and CAMPER-MOVE, 2019)

If we look at district heating consumption differentiated by building, we see large individual differences. The bandwidth of the area-specific heat consumption ranges from approx. 30 to 400 kWh/(m²a), in individual cases even up to 700 kWh/(m²a). Taking into account the varying use and equipment of the buildings (depending on the assigned departments and shares of use/technology areas according to DIN 277-1 (2016)). Buildings with large laboratory and test areas, as well as the sports halls and the botanical garden (many greenhouses) have the highest area-specific heat consumption. In the case of completely or partially renovated buildings, the consumption of district heating decreases on average by 30 to 40%, which is partly due to the relocation or decommissioning of large-scale consumers (such as the refectory, test stands). On average, reductions and increases in building consumption offset each other. The area-specific DH consumption of the entire campus has been consistently in the range of approx. 100...120 kWh/(m²a) over the last 20 years, which corresponds to energy efficiency class C to D according to EnEV (2015). In view of the age and condition of the campus buildings, this represents a rather low consumption value.

With the development of the local cooling supply, the district heating consumption increased temporarily due to the use of absorption chillers from 2006 to 2015 (Fig. 5). In the meantime, however, most of the systems have been converted to electrically driven compression chillers, so that the growing demand for cooling has since been reflected primarily in electrical energy consumption. In the past, there was an almost linear increase in electrical energy consumption (Fig. 6), which has more than doubled in the last 20 years. This development is driven by the growth in computing capacities (the first high-performance data center went into operation in 2006) and laboratory facilities, new buildings with a high proportion of glass (solar loads), and increased occupational health and safety regulations, which result in higher requirements for cooling and ventilation of these usable areas and thus additional electrical energy requirements. The reduction in the consumption of electric power due to the onset of the COVID pandemic can be seen (highlighted in red).

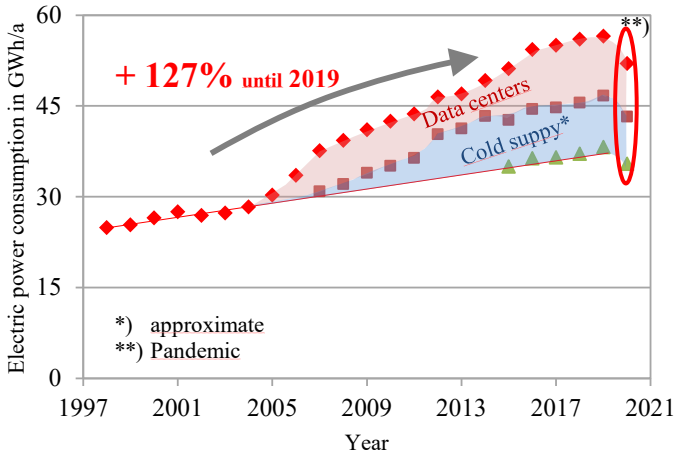

Fig. 5: Electric power consumption in GWh/a without medical school (CAMPER, 2015 and CAMPER-MOVE, 2019)

In light of these findings, consumers of, in particular, electrical energy were examined in more detail (Fig. 6). In this regard, laboratories, cooling generators and data centers are the main consumers. The increase in the distribution of technical equipment in university buildings (with laboratory and computer technology), in conjunction with stricter safety and comfort requirements in the faculties of natural sciences and engineering, creates a growing demand for cooling and ventilation.

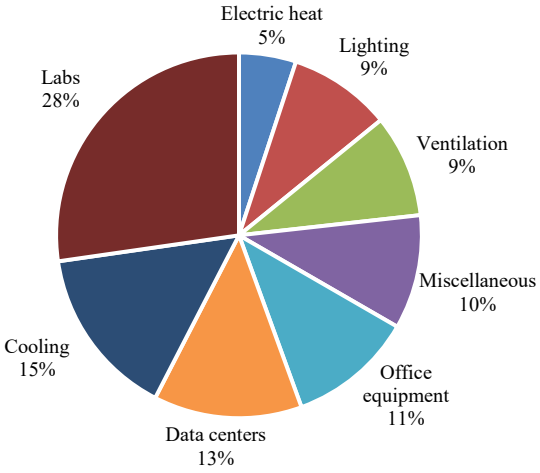

Fig. 6: Electricity consumption by use (CAMPER-MOVE, 2019)

3.1. Current data from 2019 and 2020

Figure 7 shows the currently verified final energies. On the left side the values from 2019 and on the right side those from 2020 are plotted. Furthermore, the gasoline equivalent of the mobility is also plotted to have a comparison. The first influences of the COVID pandemic can be seen. Due to the use of mobile working, the consumption of electrical energy has slightly increased, while the heat consumption has remained almost constant. The share of self-generated electric energy in the years was about 0.57% which corresponds to an energy of about 360 MWh per year.

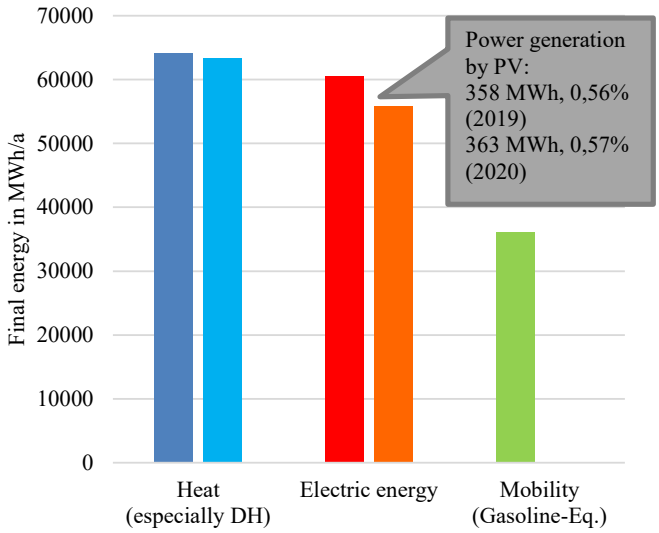

Fig. 7: Final energy in GWh/a without medical school (left: 2019; right: 2020) (CAMPER-MOVE, 2019 and Richter, *et al.*, 2017)

For comparison with Fig. 7, the GHG emissions are plotted in Fig. 8. A clear difference can be seen here. While the final energies were at a similar level, the GHG emissions are different. Electricity consumption causes significantly more emissions than heat consumption and attempts by far the highest emissions. Heating energy (mainly from district heating) is ecologically less harmful. Mobility causes many times more emissions than heating. The differences between the two years are due to changes in the respective GHG factors.

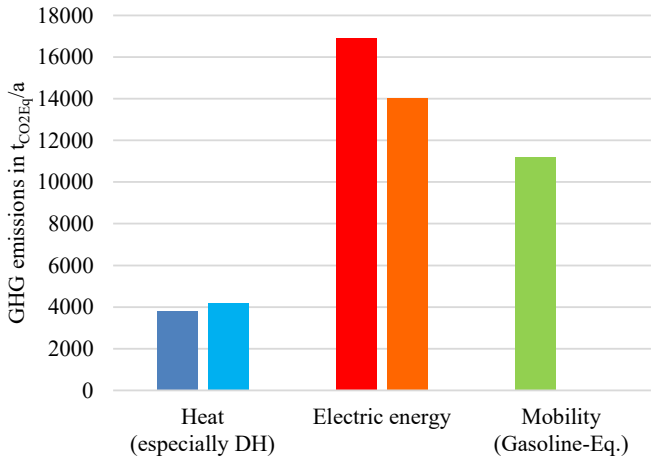

Fig. 8: GHG emissions in t_{CO2Eq}/a without medical school (left: 2019; right: 2020) (CAMPER-MOVE, 2019 and Richter, *et al.*, 2017)

Fig. 9 shows the energy costs for heat and electricity. The cost of electrical energy in 2020 was 13.8 million euros and the total annual cost of energy was 18.5 million euros.

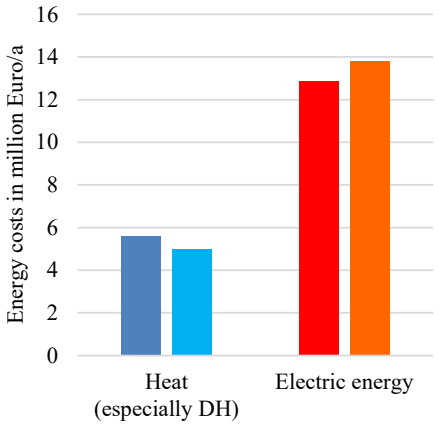

Fig. 9: Energy costs in million Euro/a without medical school (left: 2019; right: 2020) (CAMPER-MOVE, 2019)

3. GHG emissions and mobility

Figure 10 documents the percentages of the different energy sources in the final energy consumption and GHG emissions. The respective percentages in regard to the supply of heat (with district heating or natural gas/oil) and of electricity were similar, i.e. just below 40% of the total. Approximately 22% of the final energy consumption can be attributed to the mobility (gasoline equivalent) of employees and students (commuting, business trips, vehicle fleet). Looking at the GHG balance, a different picture emerges: With 63%, electrical energy consumption accounts for by far the largest share of GHG emissions. Mobility accounts for 26% of the emissions, and only about 11% is linked to the supply of heat. In total, emissions of approx. 44 000 t CO_2 equivalents were reached.

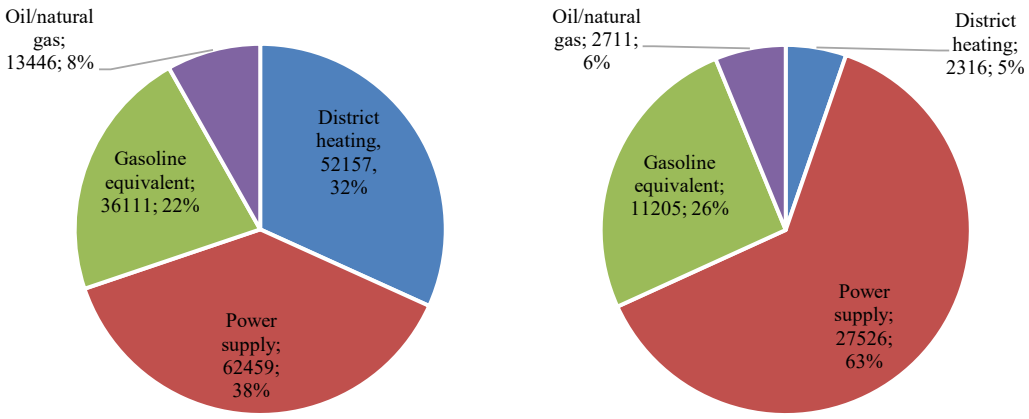

Fig. 10: Final energy consumption in MWh/a (left) and GHG emissions in t_{CO_2Eq}/a (right) (CAMPER-MOVE, 2019 and Richter, *et al.*, 2017)

In the case of mobility, the high personal final energy consumption results primarily from employees' private motorized transport including business trips by air (Fig. 11). In absolute terms, students' final energy consumption for their commute to and from work is at a similarly high level. Yet, with approx. 36 000 students compared to approx. 8 000 employees and approx. 4 300 air travelers, this relates to a larger group of persons. Overall, the mobility behavior of students may be assessed quite positively already at this point. Thanks to the mandatory semester ticket, which is valid throughout the state, students rarely resort to private motor vehicles. However, also as a result of the semester ticket, proportionately fewer students than employees use bicycles or walk for their commute - despite short distances for these ways. In combination with the high number of students, this leads to a considerable final energy consumption for public transport. The fuel consumption of buses and cars is particularly problematic in terms of the local air pollution caused. Air traffic, on the other hand, has a strong impact on the global greenhouse effect.

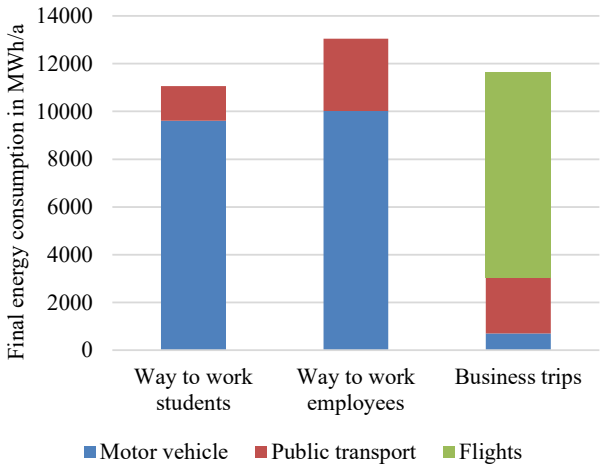

Fig. 11: Final energy consumption via mobility in MWh/a (Richter, *et al.*, 2017)]

4. Energy supply strategies

A significant number of remedying measures were identified for the university campus. If implemented in a consistent manner, these measures could lead to a significant long-term reduction in final energy consumption and greenhouse gas (GHG) emissions without impairing teaching and research. The analysis of the campus revealed serious differences in the development of consumption and the resulting environmental impact of the various energy sources (heat, electricity, mobility). Therefore, the research project will focus on the practical implementation of measures to effectively contribute to reducing the final energy consumptions and GHG emissions. The following main topics are considered:

1. reducing the energy consumption of cooling supply
2. increasing autonomous power supply through solar energy and sector coupling (power-to-cool, power-to-mobility)
3. enhancing the utilization of local, district and waste heat supplies at low-temperature levels (LowEx)
5. furthering the development of the university energy management
4. supporting an efficient user behavior (incl. mobility)
6. monitoring and updating of development planning

5. Summery

With consistent implementation of a wide range of individual measures to reduce the useful energy demand in conjunction with an optimized, increasingly regenerative energy supply (centralized and decentralized), significant energy and GHG savings can be achieved for the TU Dresden campus. However, this requires significantly stronger efforts than before. In particular, a trend reversal must be brought about in electrical energy consumption. This can be achieved by the use of energy-saving computer technology and laboratory equipment as well as a demand-oriented operation of the equipment, the reduction of the cooling energy demand (e.g. through improved summer heat protection) as well as an efficient cooling generation, an increased solar power supply of the campus and an extended energy controlling / energy management. The reduction of the absolute heating energy demand can be achieved in spite of planned campus expansions, if existing and, if necessary, expanded campus-internal heating networks are put to extended use and process-related heat sources are consistently included. The mobility-related energy consumption and emissions caused by employees' commutes and business trips should not be neglected. New mobility concepts with appropriate incentives for ecologically advantageous user behavior are needed here.

6. Outlook

The next steps in the project processing are to analyze the data of all business trips of the TU Dresden from 2017 until now. Here, the influence of the pandemic is particularly interesting and whether the behavior of business travel is gradually changing from less business travel by plane to more by train and the replacement of travel by using web meetings.

Additionally, a further investigation will be started with the approach to check whether the introduction of modern radiator controllers can make a significant and minimal-investment contribution to the reduction of heating energy at the TU Dresden.

7. Acknowledgments

The results were produced as part of the CAMPER-*MOVE* research project with the support of the Directorate 4 - Facility Management of the TU Dresden and the Chair of Transport Ecology. We would like to thank both partners for the good cooperation in the research project, the stimulating technical discussions and the provision of building data, operating and consumption information. The sponsor of the research initiative is the Federal Ministry for Economic Affairs and Climate Action (BMWK).

8. References

CAMPER, 2015. Forschungsprojekt CAMPER – CampusEnergieverbrauchsReduktion: Auf dem Weg zum Energieeffizienz-Campus der TU Dresden. Im Rahmen des 6. Energieforschungsprogramms der Bundesregierung, Förderschwerpunkt EnEff:Stadt des Bundesministeriums für Wirtschaft und Energie (BMWi) - FKZ 03ET1319A.

CAMPER-MOVE, 2019. Forschungsprojekt EnEff:Stadt - CAMPER-*MOVE:* CampusEnergieverbrauchsReduktion – Maßnahmen zur energetischen Optimierung für eine ressourcenschonende VerbrauchsEntwicklung. Auf dem Weg zum Energieeffizienz-Campus der TU Dresden. Im Rahmen des 7. Energieforschungsprogramms der Bundesregierung, Förderschwerpunkt EnEff:Stadt des BMWi - FKZ 03ET1656.

Richter, F., et al., 2017. Mobilität: Bilanzierung und Maßnahmen. Hoch-N – Nachhaltigkeit an Hochschulen, TU Dresden, Lehrstuhl für Verkehrsökologie.

DIN 277-1, 2016. Grundflächen und Rauminhalte im Bauwesen – Teil 1: Hochbau. Beuth Verlag Berlin.

EnEV, 2015. Verordnung über energiesparenden Wärmeschutz und energiesparende Anlagentechnik bei Gebäuden (Energieeinsparverordnung - EnEV). Zuletzt geändert durch Art. 3 V v. 24.10.2015 I 1789.

Identification of waste heat potentials and their integration into a district heating subgrid

Weena Bergstraesser[1], Aeliskumar Vachhani[1], Janybek Orozaliev[1], Klaus Vajen[1]

[1] University of Kassel, Institute of Thermal Engineering, Department Solar and Systems Engineering, Kassel (Germany)

Abstract

The University Campus of Kassel is supplied by a district heating subgrid using district heating (DH) and a gas combined heat and power (CHP) unit. To make the transition to a climate neutral heat supply possible, the network temperatures need to be lowered and local renewable energy sources need to be integrated into the DH network. Waste heat potentials can play an important role here. Therefore, waste heat potentials from a data center, chillers and compressor units were investigated. The data center and chillers show high potential for an integration into the DH network. Two of the chiller's waste heat potentials can be used when their temperature level is risen by heat pumps. These could supply about 15 % of the heat needed in the subgrid. Even though the waste heat is economically competitive to district heating, the revenues from electricity sales of the CHP unit are high enough to make the heat demand scenario more expensive than with just CHP unit and DH. This stands in contrast with the transformation to a renewable energy system. With changing energy prices this dilemma might resolve itself, if the relation between gas and electricity price changes.

Keywords: district heating, waste heat, heat pumps, chillers, University Campus

1. Introduction

On the University campus "Holländischer Platz" in Kassel a district heating subgrid supplies 20 buildings (19 substations) with district heating from the local city network and a gas CHP unit. The buildings on campus include laboratories, lecture halls, office space and a library, as well as some student accommodation. The DH subgrid of Kassel University was built in the 1980s and therefore requires renovation. This offers the possibility for structured planning to achieve efficiency gains and lower greenhouse gas emissions. Currently, measures for temperature reduction in network and building temperatures are being developed.

One approach to lower greenhouse gas emissions is the integration of waste heat sources into the energy supply of the DH network. The local district heating supplier plans to decarbonize the district heating network (Städtische Werke Energie + Wärme GmbH) additionally the city of Kassel plans to be climate neutral by 2030 (Stadt Kassel). The renewable energy sources inside the city are limited, therefore it is reasonable to identify potentials on the University campus. Essentially these are solar energy and waste heat potentials. The existing sources for waste heat at the University Campus are a data center, compressor units and chillers. In this paper it will be evaluated which sources can be used and weather this is profitable. If the integration of renewable sources should prove not profitable in present conditions, the focus should lie on the transformation to profitable conditions.

2. Methodology

2.1 Current heat supply

As discussed before, the current heat supply of the subgrid at the University campus "Holländischer Platz" in Kassel consists of gas-powered CHP unit and district heating from the local city network. A current typical share of district heating is about 80 %, while the CHP unit makes out about 20 % (data from 2019). The share of the CHP unit is lower than possible since there were some breaks in operation. The network temperatures in the subgrid are rather high, 115 to 75 °C supply temperature and 65 C return temperature, as shown by the straight lines in Figure 1. The current and future return temperature (RT) and supply temperature (ST) are shown in dependence of the outdoor temperature. The supply temperature is dependent on the city network since currently no hydraulic separation between the subgrid and the city network exists. In future, the modification of the substation to achieve

© 2022. The Authors. Published by International Solar Energy Society
Selection and/or peer review under responsibility of Scientific Committee
doi:10.18086/eurosun.2022.10.02 Available at http://proceedings.ises.org

hydraulic separation will be realized, additionally measures to reduce the supply and the return temperature are planned. The resulting estimated operating curves are shown by dashed lines. These two temperature levels are an important parameter that influences the efficiency of renewable energy sources and are used as a basis for further calculations.

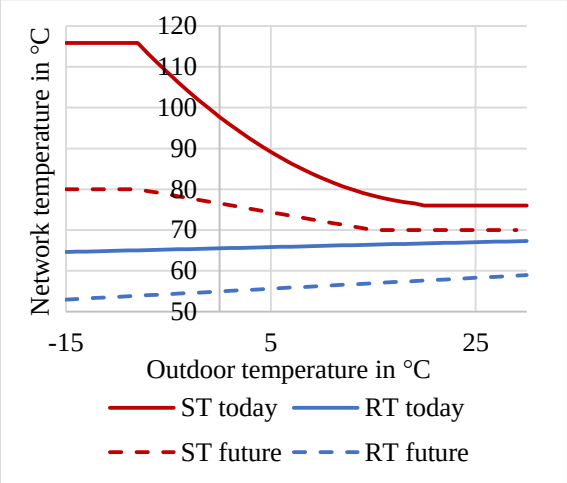

Figure 1:Operating curve of network temperatures

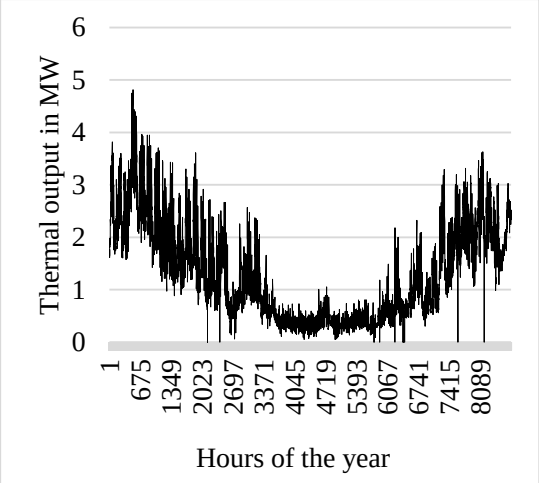

Figure 2: Heat use profile subgrid

Figure 2 shows the heat load profile from the year 2019 that had typical weather conditions and operation of the CHP unit. The heat load profile shows a well-defined seasonality with a peak demand of 4.8 MW and a heat demand in summer of around 0.4 MW.

2.2 Selection of suitable waste heat sources

As described before the waste heat potentials at the University campus “Holländischer Platz” consist of a data center, compressor units and chillers. The compressor units supply laboratories with compressed air, however the waste heat from these units proved to be unusable since the waste heat temperatures fluctuate strongly, due to start-stop operation of the compressor units. The data center is the biggest available waste heat source, but only part of the potential waste heat can be utilized since the data center is currently air cooled. Additionally, the data center is still undergoing reconstruction and has not yet reached its peak demand. Therefore, the current analysis is focused on the chillers as a waste heat source. The chillers supply laboratories with cooling water and air conditioning systems. To determine the best integration of the waste heat potentials from the chillers, the following steps were taken:

- measurements at condenser cooling circuits (several weeks in summer 2021)
- rough calculation of energy efficiency ratios (EER) of chillers depending on cooling demand (whole year)
- assessment of temperature level: possibility of direct use of waste heat?
  → heat pump (HP) to raise temperature necessary?
- estimation of seasonal coefficient of performance (SCOP) of a heat pump to decide on hydraulic integration
- calculation of actual possible waste heat that can be used to substitute district heating and gas CHP
  → possible share of waste heat

To determine waste heat potentials and temperature levels, measurements were conducted for several weeks in summer at the condenser cooling water circuits of three different chillers. The temperature level in these circuits is around 35 to 40 °C, so a direct utilization is not possible, thus the temperature level needs to be raised by a heat pump. As described in (Rühling, K. et al. 2019) the integration of renewable energy sources, in this case heat pumps, into DH networks can be achieved by different configurations. They can reach from direct use in the building on the secondary side of the substation to direct feed-in into the district heating grid. Direct use of the waste heat can be limited when the potential is higher than the building demand, while the feed-in into the district heating network ensures maximum use of waste heat potential. The three chillers that were investigated all showed

significant waste heat potential, but for one of them the integration into the district heating network proved too difficult due to the local conditions. Therefore, two of the chillers remain as potential waste heat sources. Table 1 shows some defining parameters as well as the chosen hydraulic configuration.

Table 1: Heat pump integration and parameters

	Heat pump 1	**Heat pump 2**
Chosen hydraulic configuration	feed-in into DH network	direct use in building behind substation
Source temperature	35 °C	40 °C
Yearly waste heat potential (source)	372 MWh	1303 MWh
Sink temperature	supply temperature (95-76 °C)	80 °C
SCOP	4.24	3.98
Yearly waste heat potential (sink)	486 MWh	1195 MWh

To calculate the SCOP, the following Equation 2-1 was used, it was deduced from operational data of standard heat pumps and high temperature heat pumps with hydrofluorocarbons and hydrofluoroolefin refrigerants (Jesper, M. et al. 2021). In the case of a changing sink temperature, the mean value of the various COPs is the SCOP.

$$COP = a \cdot \left(\Delta T_{lift} + 2 \cdot b\right)^{c} \cdot \left(T_{h,out} + b\right)^{d}$$ (eq. 1) (Jesper, M. et al. 2021)

COP	Coefficient of performance	a	$1.4480 \cdot 10^{12}$
ΔT_{lift}	Temperature lift between source and sink	b	88.730
$T_{h,out}$	output temperature sink	b	-4,9460
		d	0

Once the decision for the integration of waste heat from two chillers was made, a profile for the hourly waste heat usage of the heat pumps was calculated based on an assumed future operating curve for the grid temperatures, see Figure 1 (dashed lines). To calculate the SCOP of the heat pumps, see Table 1, eq. 1 was used on an hourly basis and the average value represents the SCOP.

2.3 Heat supply scenarios and additional renewable potentials

In order to evaluate the integration of the waste heat sources, their combination with other heat sources, existing as well as additionally built, has to be assessed. Especially the CHP operation is an important factor, since it produces the highest amount of greenhouse gas emissions. District heating will provide the heat that can't be generated by other sources. The main focus lies on the integration of the waste heat sources and other renewable energy sources. In addition to waste heat sources solar thermal potentials were investigated. They are the only other usable renewable heat source. However, most roof areas are already used for PV-plants or unsuitable due to constructive reasons. One large roof area could be identified, it has an area of about 1400 m² and could contain 700 m² of flat plate collector area.

To determine the best heat supply scenario, input data was fed into an energyPRO-model, where an hourly heat generation profile for each scenario is determined. The investigated scenarios relating to heat sources are:

- DH + CHP (reference)
- DH + CHP +HPs
- DH + CHP + HPs + ST
- DH + HPs + ST

To determine which heat source is used when, the priority of heat sources needs to be defined. A high priority

means that the heat source will be used first and at maximum possible level. Only then the next source can generate heat as well. The use of this approach is that some heat sources have production costs e. g. for gas or electricity. If the heat sources exist in the scenario, their priority from high priority to low priority is as follows: Solar thermal energy, waste heat pumps, CHP and district heating. In addition to the variations in heat sources the temperature operation curve was varied between the current network temperatures and the future network temperatures.

3. Results

3.1 Contribution of heat sources to the heat supply over the course of a year

To give some insight into the simulation results the scenario DH + CHP + HPs + ST with future network temperatures will be discussed in detail as an example. Figure 3 shows the share of energy sources when solar thermal and the waste heat pumps are integrated into the subgrid. The mayor part is still supplied by district heating (49 %) while the CHP plant reaches about a third (34,5 %) of the total supplied energy. The amount of solar thermal is limited by the available collector area and therefore supplies only a small portion (2.0 %) while the two waste heat pumps can supply 14,5 % of the required heat.

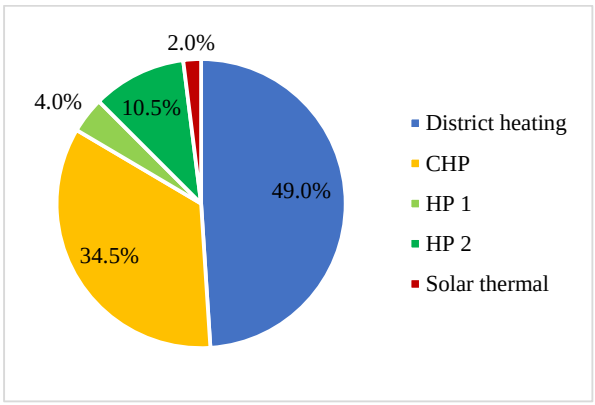

Figure 3:Share of energy sources to supply the subgrid's heat demand (future network temperatures)

The contribution of the heat sources to the heat demand over the course of a year is shown in Figure 4. Additionally, a sorted annual load curve is displayed in Figure 5. Both diagrams show that the heat demand in summer can be supplied largely by the renewable energy sources that therefore operate at base load. During summer the CHP unit is only active for short intervals to fill the storage, this can be seen very clearly in Figure 5 by yellow peaks above the total heat use line and empty spaces below. During the rest of the year the CHP unit operates continuously, whenever possible at nominal load and DH supplies the peak load for the subgrid.

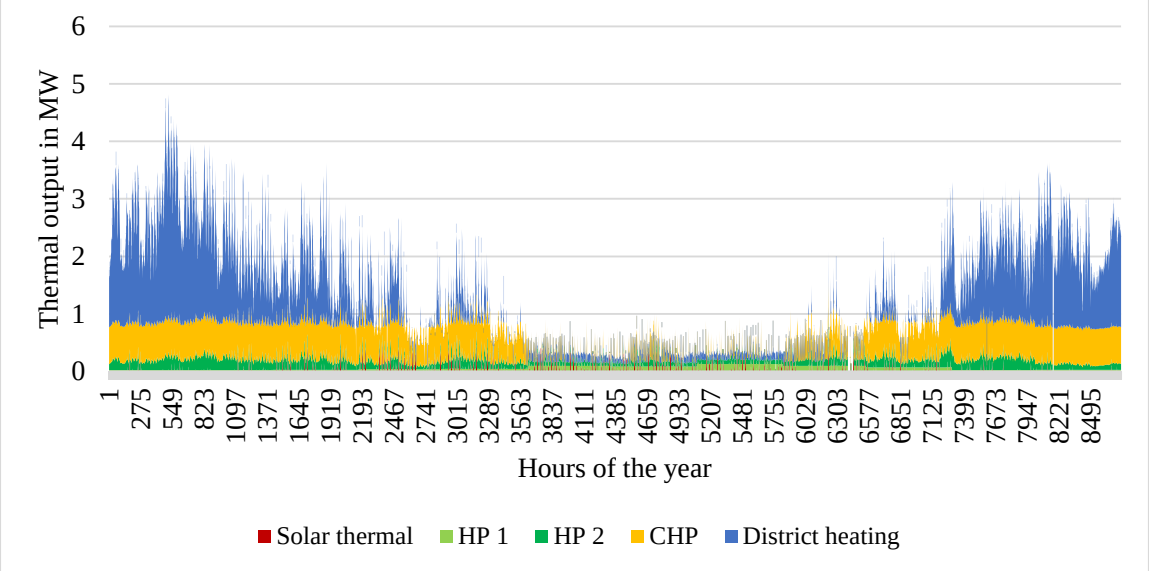

Figure 4: Thermal output of energy sources over the year with waste heat integration (future network temperatures)

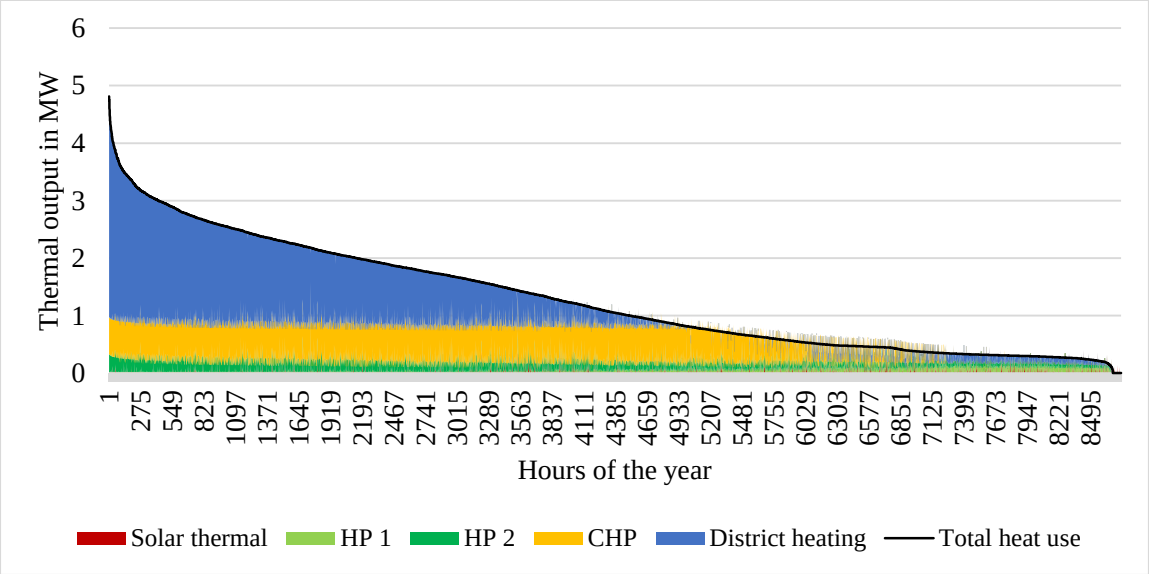

Figure 5: Thermal output of energy sources sorted by total heat use (future network temperatures)

3.2 Comparison of heat supply scenarios

Figure 6 shows how the contribution of heat sources changes from scenario to scenario, in this example it is shown for future network temperatures. When waste heat sources are integrated into the network, the amount of heat generated by the CHP plant is reduced. If solar thermal energy is integrated additionally, it further replaces the CHP plant and to a lesser degree the waste heat provided by heat pumps. Without the CHP plant its former share is replaced by district heating.

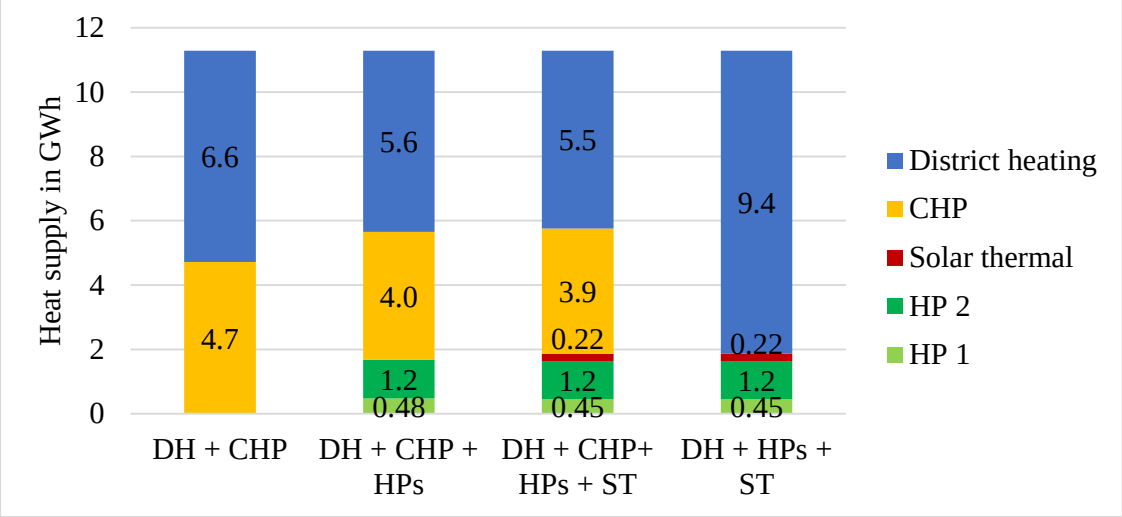

Figure 6: Thermal output of heat supply scenarios (future network temperatures)

3.3 Economic analysis

The levelized cost of heat (LCOH) is composed of investment costs for the integration of heat sources and operation costs, such as energy or fuel costs and maintenance in relation to the generated heat. The approaches to estimate cost components are summarized in Table 2. To merge investment costs with operational costs annuities for the investment costs have been calculated with a weighted average capital cost (WACC) of 8 % and a period under review of 15 years. In the case of the CHP plant proceeds from the electricity have been deducted from the costs. The investment for the solar thermal system and the waste heat pump was reduced by 40 % due to subsidies from the "Bundesförderung für effiziente Wärmenetze" (BEW) (Bundesministerium für Wirtschaft und Klimaschutz 2022).

Table 2: Approaches for cost components for LCOH calculation

Cost category	Cost approach (standardized to 2021)	Source
Investment CHP retrofitting	200000 €	(Building department University of Kassel 2022)
Investment Solar thermal high temperature flat collector (rooftop)	649.06 €/m^2	(Heymann, M. et al. 2019)
Investment HP (main component and integration)	$1649.1 \cdot x^{-0.363}$ x = thermal power output	(Wolf, S. 2017)
Maintenance CHP	6.33 €/operating hour	(Building department University of Kassel 2022)
Maintenance solar thermal	2.5 €/MWh	own assumption
Maintenance heat pump	2 €/MWh$_{th}$	(Große, R. et al. 2017)
Price electricity (2021)	0.22 €/kWh	(Building department University of Kassel 2022)
Price district heating (2021)	0.085 €/kWh	(Building department University of Kassel 2022)
Price gas (2021)	0.05 €/kWh	(Building department University of Kassel 2022)

Table 3 shows the calculated LCOH for each heat generation technology. The LCOH for the CHP plant is negative and its use therefore very profitable. The LCOHs for waste heat and solar thermal heat need to be evaluated in relation to the district heating price. The solar thermal LCOH of 11.5-14.4 €ct/kWh_{th} is higher than the district heating price and solar thermal therefore not profitable with current energy prices. The waste heat pumps reach a LCOH of 6.4-8.2 €ct/ kWh_{th} below the DH price and are therefore profitable in comparison.

Table 3: LCOH by energy source

LCOH energy sources in €/kWh_{th}	**DH + CHP**		**DH + CHP + HPs + ST**		**DH + CHP + HPs**		**DH + HPs + ST**	
	Operation curve present	**Operation curve future**	**Operation curve present**	**Operation curve future**	**Operation curve present**	**Operation curve future**	**Operation curve present**	**Operation curve future**
ST (after subsidies 40 % of investment)	-	-	0.144	0.115	-	-	0.144	0.115
CHP fuel	0.093	0.093	0.098	0.098	0.098	0.098	-	-
CHP balance (costs minus profits)	-0.061	-0.061	-0.056	-0.055	-0.055	-0.056	-	-
Waste heat HP 1 (after subsidies 40 % of investment)	-	-	0.082	0.064	0.081	0.061	0.082	0.064
Waste heat HP 2 (after subsidies 40 % of investment)	-	-	0.065	0.065	0.065	0.065	0.065	0.065
Waste heat total (after subsidies 40 % of investment)	-	-	0.069	0.065	0.069	0.063	0.069	0.065
DH price	0.085	0.085	0.085	0.085	0.085	0.085	0.085	0.085

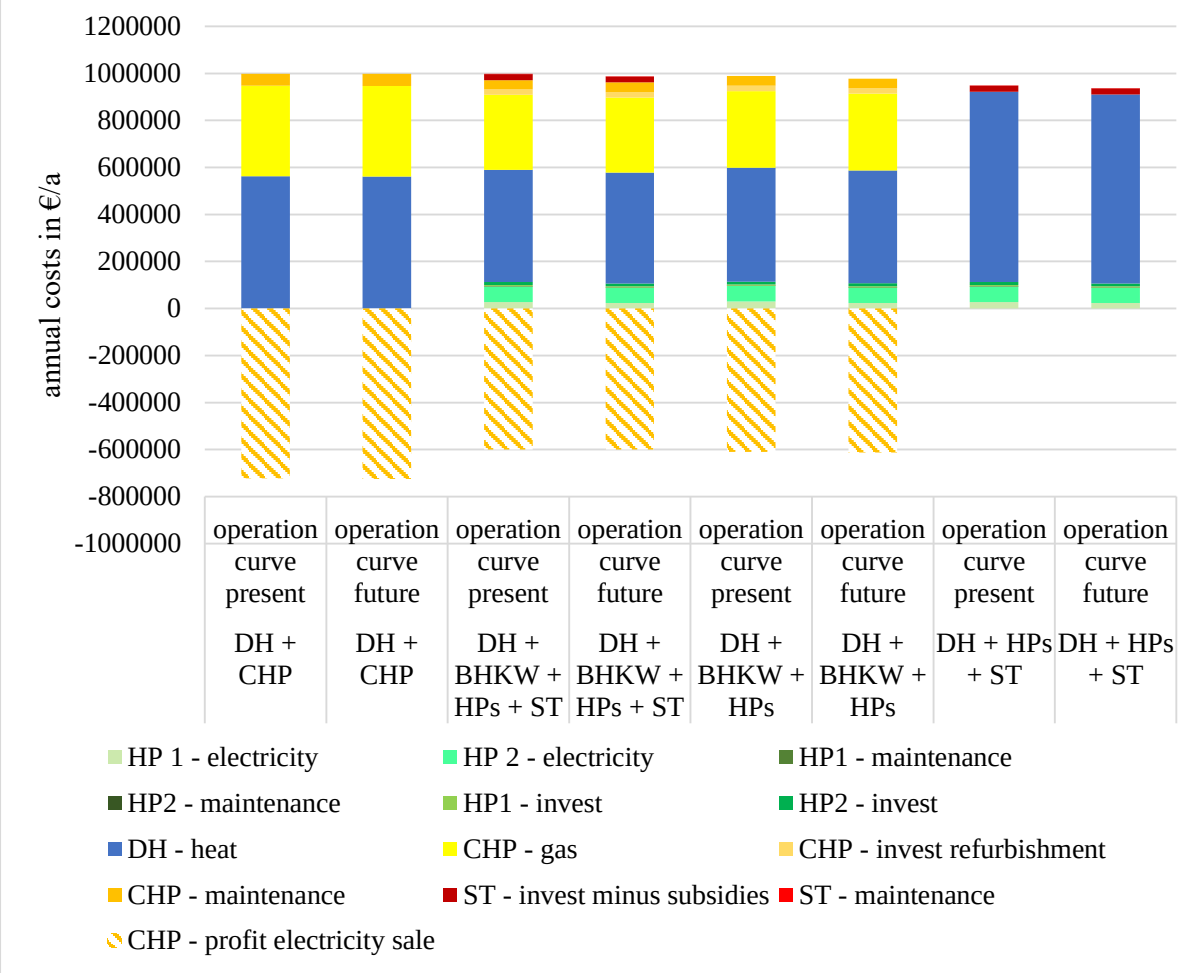

Figure 7: Annual costs and profits different scenarios

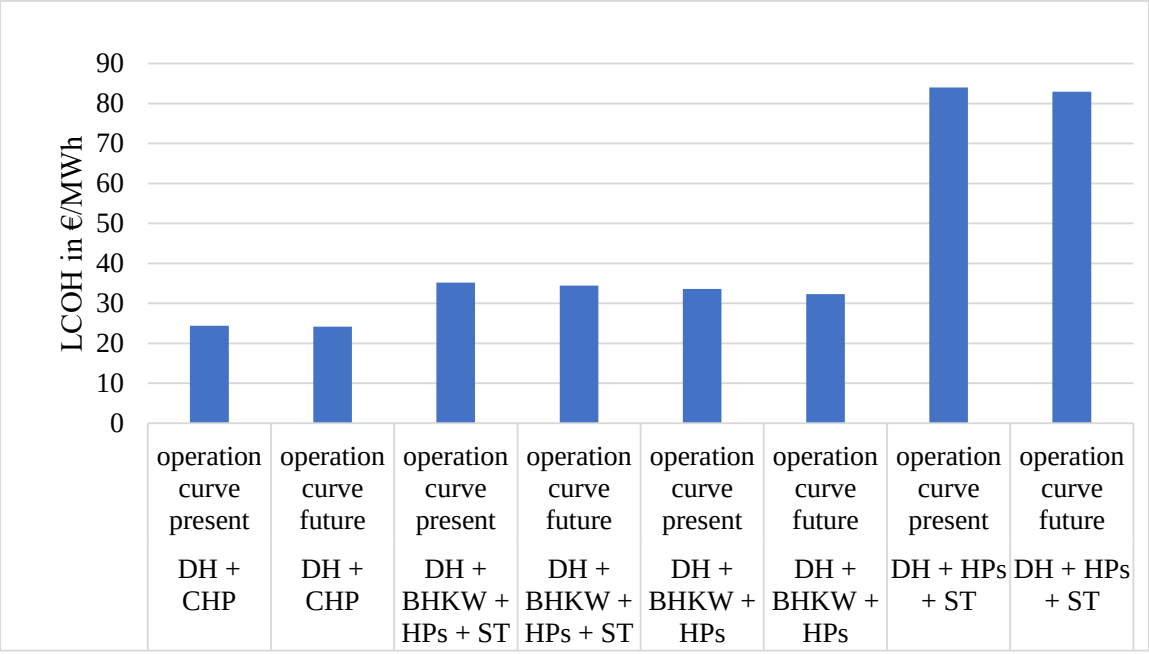

Figure 8: LCOHs of different scenarios

In addition to the economic evaluation of the heat generation scenarios the environmental impact can be assessed by comparing greenhouse gas emissions. In this case the scope for greenhouse gas emissions focusses on the emissions generated by the energy sources used. The greenhouse gas emissions of the energy sources use a CO_2-equivalent of 202 g/kWh for gas, 0 g/kWh for green electricity (HPs) and 133 g/kWh for the local district heating network (Building department University of Kassel 2022). Figure 9 shows the LCOH and CO_2-equivalents for the heat generation scenarios with future network temperatures. Both parameters are contrary to each other, a low LCOH corresponds to a high CO_2-equivalent and the other way around. This means that the current economic framework for renewable heat sources in this context does not reflect the environmental impact. Particularly the relation between gas and electricity prices has a big influence.

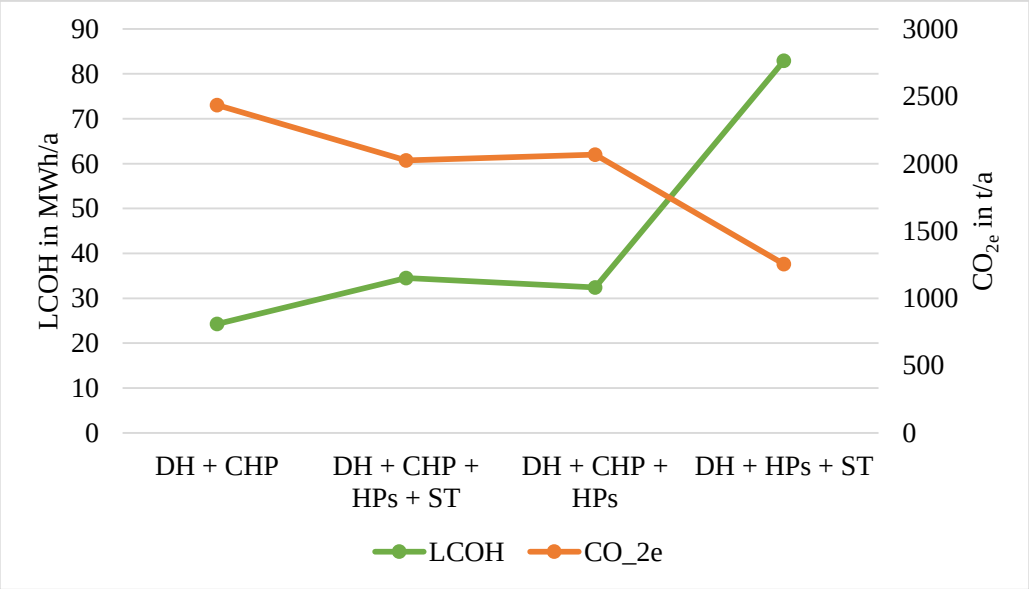

Figure 9: LCoH and CO_{2e} (future network temperatures)

4. Conclusions and outlook

Significant waste heat potentials from the chillers could be identified. Two of the waste heat sources can be used by raising their temperature level with heat pumps. Heat pump 1 can use the waste heat potential directly inside the building behind the substation while heat pump 2 would feed the waste heat directly into the district heating subgrid. The also investigated solar thermal potentials are not profitable under current conditions. The waste heat pumps are economically competitive to district heating and could supply about 15 % of the heat needed in the district heating subgrid. However, heat supply scenarios that use the waste heat pumps are less profitable than scenarios that use more heat from the CHP unit, this is due to the high revenues from the electricity sale. This stands in contrast to the greenhouse gas emissions where the gas-powered CHP unit is responsible for most. This dilemma can only be overcome if the relation between gas and electricity price changes. In further research, it could be interesting to calculate the LCOH under different pricing conditions, especially since gas prices have risen dramatically since the war in Ukraine started this year.

5. Acknowledgements

The project “EnEff:Stadt/Campus: Campus Kassel 2030 – Konzepte und Maßnahmen für die beschleunigte Umsetzung der Energiewende im Hochschulbereich” this paper is based on is supported with funds of the Federal Ministry of Economy Affairs and Climate Action (funding code 03EN3013A).

6. References

Building department University of Kassel 2022.

Bundesministerium für Wirtschaft und Klimaschutz. Richtlinie für die Bundesförderung für effiziente Wärmenetze „BEW“. 2022. https://www.bundesanzeiger.de/pub/de/amtliche-veroeffentlichung?1. Accessed 23

Sep 2022.

Große R., Christopher B., Stefan W., Geyer R., Robbi S. Long term (2050) projections of techno-economic performance of large-scale heating and cooling in the EU: External study performed by ILF Consulting Engineers Austria GmbH, and AIT Austrian Institute of Technology GmbH for the Joint Research Centre; 2017.

Heymann M., Rosemann T., Rühling K., Hoppe S., Wudenka E., Hafner B. Kostenreduktionspotential beim Ausbau der Solarisierung von Fernwärmenetzen durch Standardisierung: Koordinierter Schlussbericht - SOLSTAND (FKZ: 0325553A+B). Dresden, Allendorf; 2019.

Jesper M., Schlosser F., Pag F., Walmsley T. G., Schmitt B., Vajen K. Large-scale heat pumps: Uptake and performance modelling of market-available devices. Renewable and Sustainable Energy Reviews. 2021;137:110646. doi:10.1016/j.rser.2020.110646.

Rühling K., Gnüchtel S., Felsmann C., Heymann M., Rosemann T. Kostenreduktionspotential beim Ausbau der Solarisierung von Fernwärmenetzen durch Standardisierung: Koordinierter Schlussbericht – SOLSTAND; 2019.

Stadt Kassel. Die Klimaschutzziele. https://www.kassel.de/buerger/umwelt_und_klima/umwelt_und_klimaschutz/klimaschutz/inhalt-klimaschutzziele.php. Accessed 6 Aug 2022.

Städtische Werke Energie + Wärme GmbH. Wir über uns. https://www.ew-kassel.de/10/.

Wolf S. Integration von Wärmepumpen in industrielle Produktionssysteme: Potentiale und Instrumente zur Potentialerschließung [Dissertation]. Stuttgart: Universität Stuttgart; 2017.

Comparison of the Simulated and Measured Performance of the PV Plant of Austria's Largest (Plus-)Plus-Energy Office Building

Alexander David[1], Sabine Sint[1] and Thomas Bednar[1]

[1] Research Unit of Building Physics, TU Wien, Vienna (Austria)

Abstract

The (Plus-)Plus-Energy Office High-Rise Building near the centre of Vienna is a highly energy-efficient office tower block that is designed according to a net-zero energy concept. The main component of the net-zero energy concept is the building's PV plant. An extensive energy monitoring system is integrated into the building. As it also logs the electricity production of the plant's 19 PV inverters, it allows for a more detailed analysis of the PV electricity production. In this research the monitoring data of the PV plant that was obtained during 2018 is analysed. The design performance of different parts of the plant is contrasted with the monitored performance. Moreover, the building's PV self-consumption is analysed. Even though there were several inverter faults during the years, the PV plant generally achieved its design performance. Due to the fact that the building's consumption exceeds the design consumption, the building's PV self-consumption is significantly increased.

Keywords: university campus, office building, building integrated photovoltaic, performance monitoring, coverage of self-consumption

1. Introduction

Net-zero energy building concepts are one of the key elements necessary to reduce the energy consumption in the building sector and to achieve the EU's climate goals (European Parliament, 2018). The design concept of TU Wien's (Plus-)Plus-Energy Office High-Rise Building at the University Campus "Getreidemarkt" proves that it is theoretically possible to develop even high-rise buildings as net-zero energy buildings (Schöberl et al., 2014). One important component for achieving the net-zero energy concept is the building's PV plant.

In order to enable the assessment of the real building performance, the (Plus-)Plus-Energy Office High-Rise Building is equipped with an extensive energy monitoring system. Further, this system is used to aid in commissioning and optimising the building. Previously published results of the building's energy monitoring showed the difference between the building's theoretical design performance and its real performance (David et al., 2017, David and Bednar, 2020). Even though several of the planned energy reduction potentials could be realised, some could not be realised and due to various reasons, such more IT equipment in the offices than planned, the real energy consumption exceeds the design value. However, the electricity production of the building's PV plant generally achieved its design performance, although there were several inverter faults during the years (David et al., 2017; David and Bednar, 2020).

There are several papers presenting different surveys on the monitoring data of building integrated PV (BIPV) systems (Klugmann-Radziemska and Rudnicka, 2020; Imenes 2016). Some studies do also discuss the comparison of the measured and the simulated performances of BIPV systems (Bellazzi et al., 2018; Maturi et al., 2010). All these papers have in common that they only focus on the electricity yield of the entire PV system. As in case of the (Plus-)Plus-Energy Office High-Rise Building there is monitoring data available for each of the inverters, we analyse in our research the specific annual electricity yield of different parts of the PV plant.

Since one of the main aspects of the building's energy concepts is that in the yearly energy balance the PV electricity production should cover the building's energy consumption, this paper also addresses the building's self-consumption. As the two main options to increase the self-consumption are (battery) energy storages and demand side management (Luthander et al., 2015), the maximum electricity surplus that can be expected to occur during the course of a year is calculated. Further, we investigate the absolute minimum battery size that would be

© 2022. The Authors. Published by International Solar Energy Society
Selection and/or peer review under responsibility of Scientific Committee
doi:10.18086/eurosun.2022.10.03 Available at http://proceedings.ises.org

necessary for the building to be self-sufficient in terms of electricity consumption, and the impact of different battery sizes on the self-consumption.

For these purposes, we used the data from 2018 for the analyses conducted in this paper. The data forms a good basis since 2018 was the first year after building's optimisation and there are no gaps in the monitoring data. More recent data could currently not be used since it is not processed yet. The main reasons for that are that the official monitoring and optimisation project ended after 2018 and that the data processing involves several labour-intensive tasks, e.g., filling gaps in the data with manually extracted data from the building operation system.

Since the (Plus-)Plus-Energy Office High-Rise Building itself is only a part of a larger building complex, its system boundaries also had to be considered during all analyses (David et al., 2017). For instance, only energy consumption that occurred inside the boundaries was part of the building's energy balance. The same principle had to be applied to the electricity production by the building's PV plant – i.e., the electricity supplied by PV modules that are outside the system boundary had to be excluded from the energy balance. As eight of the high-rise's ten floors equipped with building integrated PV (BIPV), the electricity production of the entire PV was multiplied by the factor 0.8 to calculate the production that can be considered to be "inside the system boundary". In Section 4 all results that are marked with "boundary zone PV" refer to this electricity production "inside the system boundary". Results without mark or that are marked with "entire PV plant" refer to the electricity production of the entire PV plant – i.e., without any scaling.

2. Specifications of the PV plant

In this section, we give an overview of the specifications of the PV plant of the TU Wien's (Plus-)Plus-Energy Office High-Rise Building.

Fig. 1 gives a general view over the four parts of the building's PV plant: (i) southwest roof, (ii) southwest façade, (iii) southeast PV insulating glass, and (iv) southeast façade.

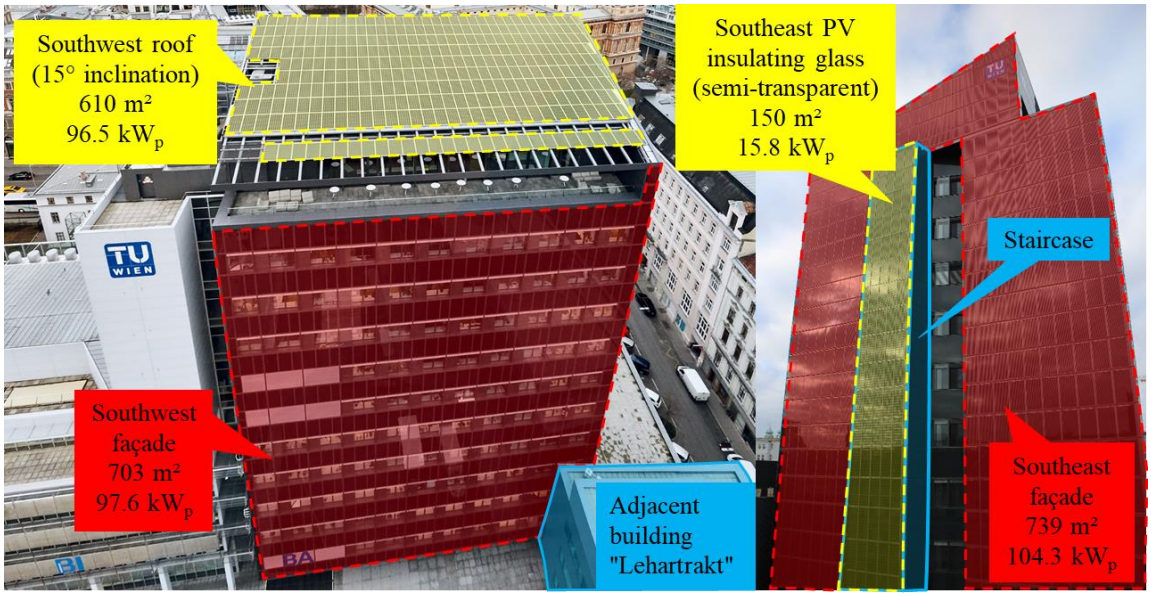

Fig. 1: Overview of the parts of the (Plus)-Plus-Energy Office High-Rise Building's PV plant

The building is the only high-rise building in the vicinity, i.e., there is almost no shading from the surrounding buildings. Just the adjacent TU Wien building "Lehartrakt" sometimes casts a shadow on the lower parts of the PV modules integrated into the southwest façade. Another reason for partial shading is the building's staircase which is protruding from the rest of the southeast façade. This leads to shading of parts of the southeast façade's left side in the morning. The part of the PV plant that is totally free of shading is the PV system on the roof.

Fig. 2 illustrates the schematic overview of this PV system on the building's roof. The areas marked with A_i in Fig. 2 highlight the different sub-surfaces of the PV system. All modules of the same sub-surface are connected to the same inverter I_i. The different colouring indicates different PV module types.

As it can be seen in Fig. 2, there are two gaps in the layout: (i) one on the left side of the PV system and (ii) one between the last and the second last row at the bottom side. The reason for (i) is that this is the location of the outlet of the ventilation shaft of the building's night ventilation system. The reason for (ii) is that this gap is needed in case of snowfall. If snow accumulates on the PV system on the roof, it must be ensured that this snow does not slide into the inner courtyard. Due to the height of the building, this snowfall might inflict serious damage to passers-by, items or infrastructure. Thus, the PV system on the roof was designed accordingly.

The PV plant on the roof has a 15° inclination towards southwest. Below the modules there is a hollow space between the real, flat roof of the building and the surface that is formed by the PV modules. All modules are standard monocrystalline modules with glass on the frontside and a plastic layer on the backside.

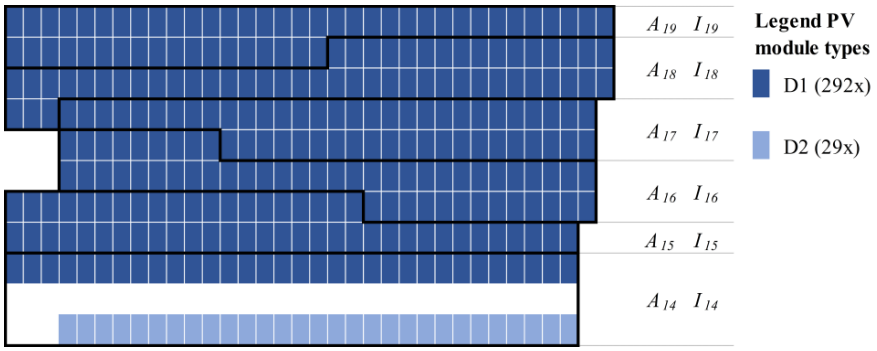

Fig. 2: Schematic representation of the PV system on the roof

Fig. 3 shows the schematic overview of the PV system integrated into the building's southwest façade in the same manner as Fig. 2. In the southwest façade the PV modules are installed in the parapet area of each floor – the only exceptions being single modules on the left and right edges of the façade. The gaps between the PV modules indicate the location of the building's windows. The gap in the right bottom corner is caused due to the connection to the adjacent building "Lehartrakt". All of the southwest façade's PV modules are monocrystalline double glass modules.

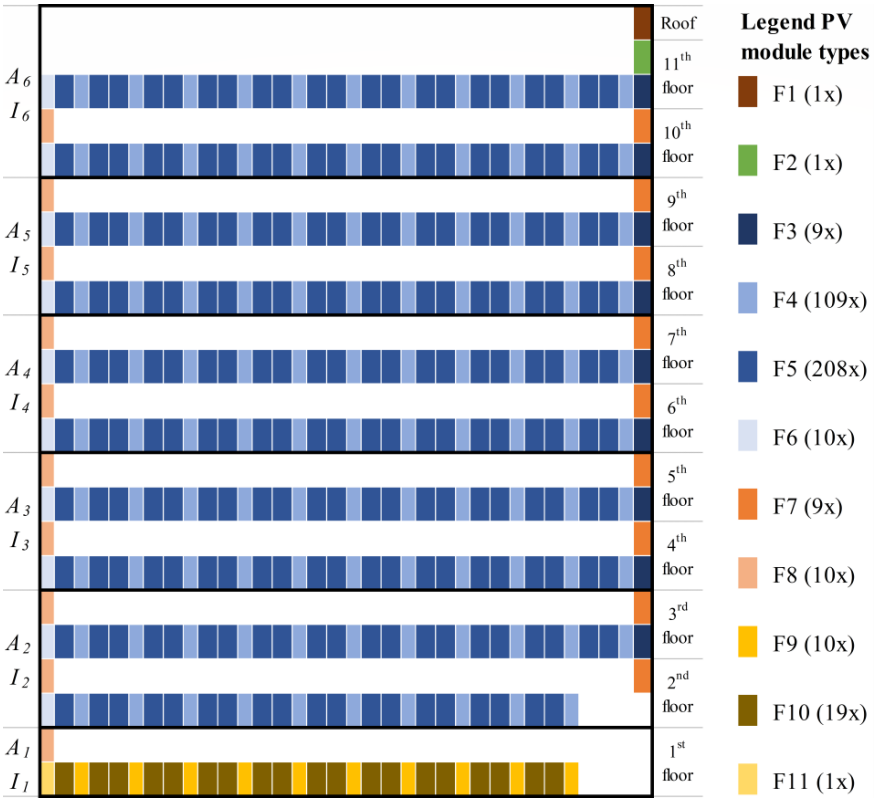

Fig. 3: Schematic representation of the PV system integrated into the southwest façade

The schematic overview of the PV system integrated into the southeast façade is displayed in Fig. 4 in the same manner as the schematics in Fig. 2 and Fig. 3. It shows that almost the entire southeast façade is equipped with PV modules.

Modules with the prefix “F” are monocrystalline double glass modules and modules with the prefix “S” are monocrystalline PV insulating glass modules. As can be seen in Fig. 4, only the staircase (sub-surface A_{13}) is equipped with insulating glass modules – the rest of the façade is equipped with double glass modules, such as the southwest façade.

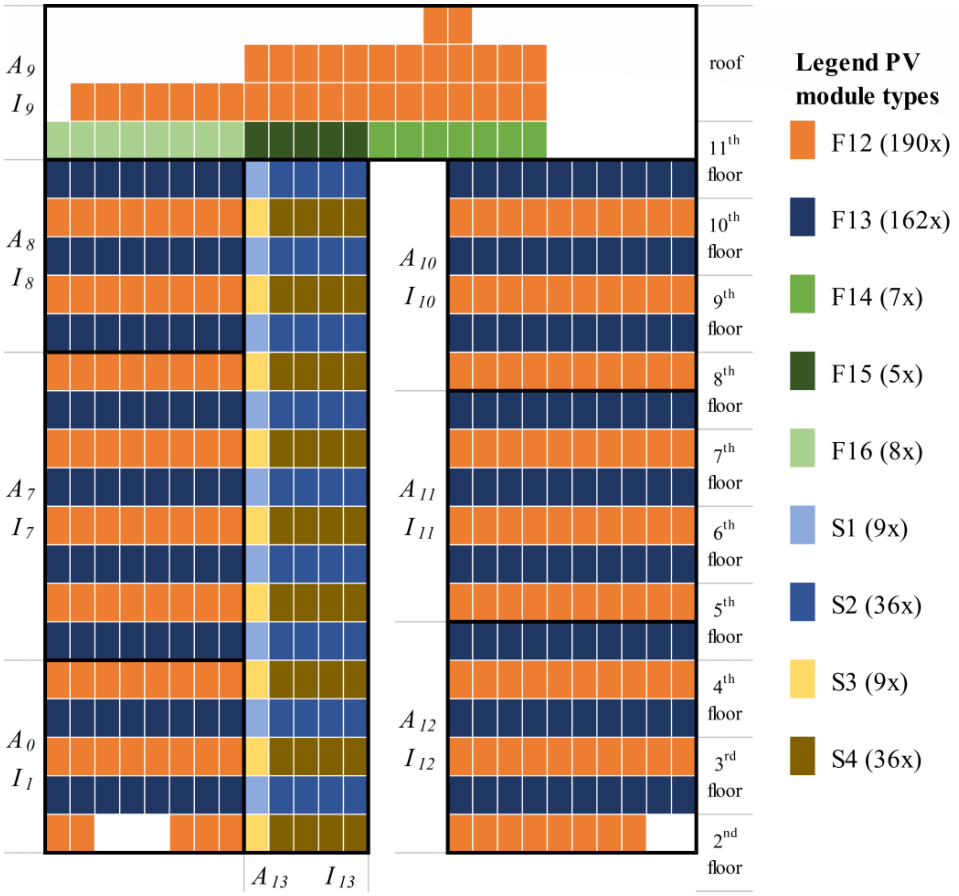

Fig. 4: Schematic representation of the PV system integrated into the southeast façade

Tab. 1 gives an overview of the installed PV modules. Their designation matches the module type designations in Fig. 2, Fig. 3 and Fig. 4. The table shows that all modules have monocrystalline wavers. The majority of the modules has a nominal power of approximately 300 W, a length of 2 m and a breadth of 1 m. Generally, the PV insulating glass installed in the southeast staircase façade is slightly smaller in size but disproportionally smaller in terms of nominal power. The reason for the disproportionally lower power is that the modules are semi-transparent, i.e., the gap between the PV modules silicone wavers is significantly larger than usual.

All of the installed modules are fairly common modules that were available on the market. Their only real special feature is that each module had to be equipped with a power optimiser. This additional component optimises the energy yield per module and prevents a single shaded PV module from reducing the output of all other modules that are connected in the string. The use of such a power optimiser is particularly useful for PV systems that are often partially shaded during the day. Since the (Plus-)Plus-Energy Office High-Rise Building is the only high-rise in the area, its PV systems are hardly shaded. The reason why power optimisers were installed is that they have a special safety feature that allows the DC voltage to be reduced to touch-safe values at the module level. This safety function was a requirement from the firefighters. It ensures that the PV modules do not pose any danger to them.

Tab. 1: Overview of the installed PV modules

Module	Type	Number	Part of	Length in mm	Breadth in mm	Power in W
F1	Double glass module (monocrystalline)	1	Southwest façade	1,580	1,021	225
F2		1		1,585	1,021	225
F3		9		2,000	1,021	300
F4		109		2,000	736	200
F5		208		2,000	1,051	300
F6		10		2,000	531	100
F7		9		1,845	1,021	275
F8		10		1,845	531	92
F9		10		1,660	736	150
F10		19		1,660	1,051	225
F11		1		1,660	531	75
F12		190	Southeast façade	1,845	1,056	275
F13		162		2,000	1,056	300
F14		7		1,080	1,056	150
F15		5		1,010	1,056	125
F16		8		1,585	1,056	225
S1	PV insulating glass (monocrystalline, semi-transparent)	9	Southeast staircase façade	2,046	846	185
S2		36		2,046	841	185
S3		9		1,901	846	165
S4		36		1,901	841	165
D1	Standard module (monocrystalline)	292	Roof	1,949	989	305
D2		29		1,629	989	255

Tab. 2: Overview of the sub-surfaces of the PV plant

Sub-surface	Inverter	Part of	Area (total aperture area) in m²	Power (total nominal power) in W
A_0	I_1	Southeast façade	74.7	10,575
A_1		Southwest façade	47.2	5,942
A_2	I_2		124.9	17,434
A_3	I_3		132.6	18,534
A_4	I_4		132.6	18,534
A_5	I_5		132.6	18,534
A_6	I_6		133.0	18,617
A_7	I_7	Southeast façade	129.9	18,400
A_8	I_8		81.9	11,600
A_9	I_9		91.0	12,550
A_{10}	I_{10}		121.8	17,250
A_{11}	I_{11}		121.8	17,250
A_{12}	I_{12}		117.9	16,700
A_{13}	I_{13}	Southeast staircase façade	149.6	15,750
A_{14}	I_{14}	Roof	108.4	17,155
A_{15}	I_{15}		100.2	15,860
A_{16}	I_{16}		100.2	15,860
A_{17}	I_{17}		98.3	15,555
A_{18}	I_{18}		102.2	16,165
A_{19}	I_{19}		100.2	15,860
Southwest façade sum			702.9	97,595
Southeast façade sum			739.0	104,325
Southeast staircase façade sum			149.6	15,750
Roof sum			609.6	96,455

Tab. 2 gives an overview of the sub-surfaces of the PV plant. It presents the total aperture area and the total nominal power of each surface. Further, the table shows how the sub-surfaces are connected to the plant's inverters. As it can be seen in the table, each sub-surface is generally connected to only one inverter – with one exception: Sub-surface A_0 of the southeast façade and A_1 of the southwest façade share inverter I_1. The designations of the surfaces and the inverters in Tab. 2 match the designations in Fig. 2, Fig. 3 and Fig. 4.

3. Method

In this section, we explain how the PV electricity generation of the inverters of the different sub-surfaces is measured by the building's energy monitoring, and how the measurements were prepared before comparing them with the electricity yield that the PV should have according to the simulations. Further, we describe the calculations that were made in order to investigate the building's self-consumption in dependence of battery size.

There are two energy monitoring systems: (i) the main building energy monitoring system that is heavily

interconnected with the building operation system and (ii) the energy monitoring system of the manufacturer of the inverters and power optimisers. While (ii) has the advantage that it is accessible via a web interface, the data that can be extracted from this interface is limited. Basically, only data from the energy yield of the entire PV plant can be exported. To get a more detailed look on the performance of the PV plant, its inverters were connected to (i) and thus data from their internal electricity meters became accessible. Therefore, in the main building energy monitoring system there is data from 20 electricity meters related to the PV plant: The 19 electricity meters of the 19 inverters and the PV main meter in the low-voltage main distribution.

Besides these 20 electricity meters, the main building energy monitoring system also logs data from other energy meters (electricity and thermal energy for heating and cooling), operational data (sensor data, setpoints and control signals) and weather data (external air temperature, global radiation, wind speed, …).

As the monitoring data from 2018 has practically without gaps, it was chosen as basis for this work. Even though the monitoring system worked almost flawlessly, some of the inverters of the PV plant did not. There was an issue with inverter I_{14}, which lasted until 2nd May of 2018, and another issue with inverter I_3, which started on 15th September 2018. During the stated timespans, both inverters did not transform and supply any of the energy provided by the PV modules connected to them. To estimate the yield that those inverters would have had if there were no issues, the monitoring data from the inverters of the neighbouring sub-surfaces were used for extrapolations.

During the planning of the PV plant, simulations were conducted with PV*SOL Expert 6.0 (R8) to calculate the electricity yield that can be expected by the plant. As the provided report of the calculation results only shows the monthly yield of each of the four main surfaces (roof, southwest façade, southeast façade and southeast staircase façade), the comparison between the simulated yield and the measured yield had to be conducted on that level of detail.

As the (Plus-)Plus-Energy Office High-Rise Building was designed to be a net-zero energy building instead of a fully self-sufficient building, it is dependent on the connections to the Viennese energy grids (electricity grid and district heating). Electricity that is not provided by the local energy sources is drawn from the grid and a surplus of electricity is fed back into the grid. As the buildings of the university campus at the "Getreidemarkt" are connected, the surplus electricity is not really fed back, but practically always consumed by other university buildings. For easier readability of this work the phrase "electricity fed back into the grid" also refers to the electricity surplus that is consumed by the other buildings at the campus.

During the planning of the building there was the premise that only measures that are economically feasible (when considering life cycle costs over 50 years) shall be implemented. Designing the building as self-sufficient building appeared to be so unfeasible that it was never even considered an option. With the data from the building's planning and the monitoring data from 2018 this option was now explored and the results are presented in this work.

It was assumed that the building was equipped with a battery storage. If there was a surplus from the PV plant this surplus electricity would be fed into the battery until it was full. Only then further surplus electricity would be fed into the electric grid. In the case that there is not enough electricity from the PV to cover the building's consumption, the missing electricity would be drawn from the battery until it was empty. Only when the battery was empty further electricity would be obtained from the electric grid. For the sake of simplicity, the processes of feeding electricity in the battery and drawing electricity from the battery, were considered lossless.

The battery capacity of this fictional setup was varied and the respective load cover factor (LCF) and supply cover factor (SCF) were calculated as shown in eq. 1 and eq. 2 by using the following inputs:

- P_{SC} ..... the electric power of the PV plant that is self-consumed by the building
- $P_{B,out}$ ..... the electric power drawn from the battery
- $P_{B,in}$ ..... the electric power fed into the battery
- P_C ..... the total electric power consumed by the building
- P_{PV} ..... the total electric power provided by the PV plant

$$LCF = \frac{\int P_{SC} + P_{B,out}\, dt}{\int P_C\, dt} \qquad \text{(eq. 1)}$$

$$SCF = \frac{\int P_{SC} + P_{B,in}\, dt}{\int P_{PV}\, dt} \qquad \text{(eq. 2)}$$

The equations were not solved analytically, but instead approximated by an hourly time discretisation. While the LCF expresses how much of the load can be covered by the local PV supply (incl. battery), the SCF expresses how much of the entire local PV supply can be consumed on site. An LCF of exactly one would indicate that the building is self-sufficient and a SCF of exactly one would indicate that all of the PV supply is consumed on site.

Considering that the building's heating demand is covered by heat from the Viennese municipal heating grid and partially by the building's server waste heat recovery, the fictional setup is not complete – the calculated LCF and SCF only represent the electricity supply and consumption. To setup the (Plus-)Plus-Energy Office High-Rise Building as true fully self-sufficient building, the heat would have to come from a local resource (e.g. a heat pump) and the electricity needed to draw heat from this resource would have to be considered when calculating the LCF and SCF.

4. Results

Based on the setup and specifications presented in the previous sections, we now show the results for the comparison simulated and measured performance of the PV plant of the (Plus-)Plus-Energy Office High-Rise Building for the data of 2018.

Fig. 4 illustrates the specific annual yield of electric energy of each of the sub-surfaces of the PV plant – calculated out of the energy monitoring data from 2018. The surfaces are coloured according to the value of the specific annual yield – ranging from blue (the lowest value) over grey up to orange (the highest value).

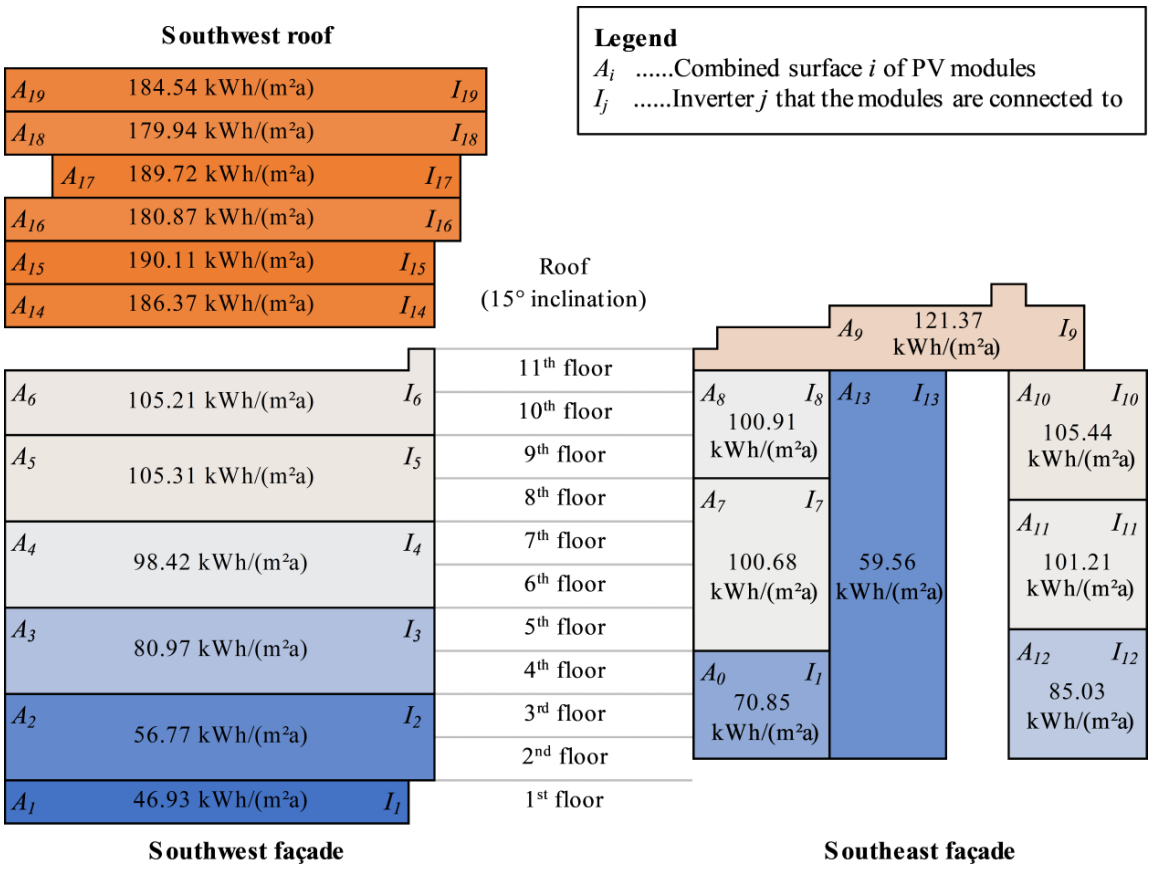

Fig. 4: Overview of the specific annual yield of electric energy of each sub-surface of the PV plant (the shown values are the extrapolation without inverter faults)

In Fig. 4 the values of inverter I_3 and I_{14} are the extrapolated values that the inverters were expected to have had if they were functioning properly without faults.

The distribution of the specific annual yield looks as expected: A sub-surface on the southwest oriented roof can provide much more electricity than each of the sub-surfaces of the façades. The higher up a façade sub-surface is, the higher its yield. Even though the building is the only high-rise in the vicinity, its lower façade sub-surfaces are still affected by the shading of the surrounding buildings. The results from the southwest façade indicate that only sub-surfaces above the 6th/7th floor appear to be unaffected by the shading of the surrounding buildings.

The sub-surface A_9 on the top of the southeast façade has a significantly higher yield than the sub-surfaces directly below it (A_8 and A_{10}). It appears that the reason is the partial shading by the protruding staircase (A_{13}).

Fig. 5 shows the absolute monthly yield of electric energy that each of the four main surfaces (roof, southwest façade, southeast façade and southeast staircase façade) had during 2018 and contrasts it with the simulation results from the planning. As there was no correction for different weather conditions in the simulation and the monitoring, the graph can only indicate general tendencies.

The displayed values from 2018 are the real measurements – the total monthly yields that were expected if there were no inverter faults are displayed separately as short black lines. As inverter I_{14} did not work properly until 2nd May and as it is one of the inverters of the PV system on the roof, the missing electricity yield is relatively significant. This becomes especially obvious when analysing the yield of April – the faulty inverter reduces the yield by 8%. Even though inverter I_3 (which failed after 15th September) is only an inverter of a lower façade sub-surface, the impact of its failure is significant as well – its failure reduces the yield of October by 5%.

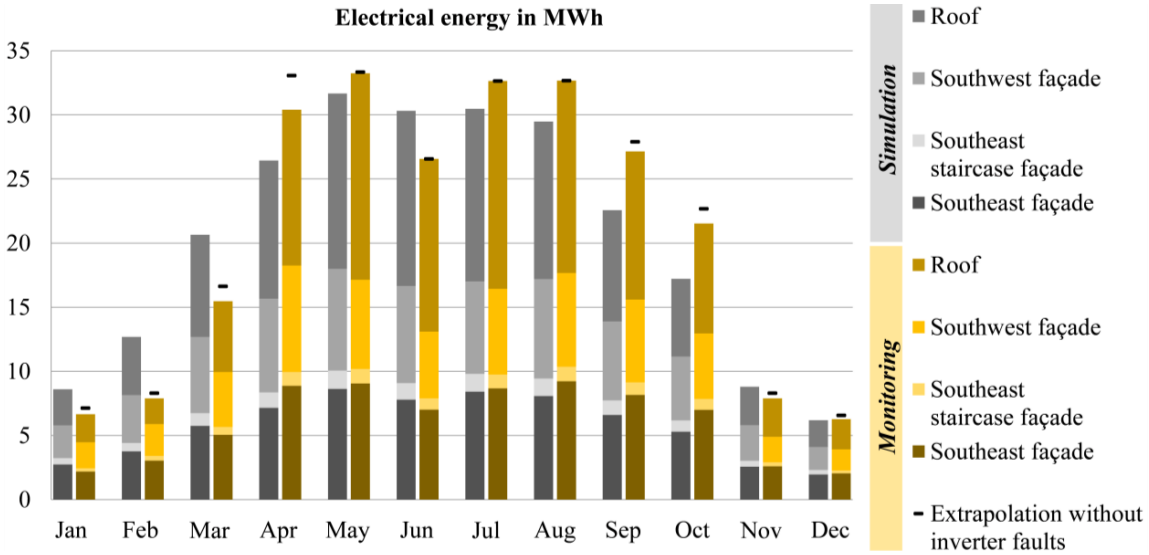

Fig. 5: Comparison of the PV plant's design performance and the performance measured in the year 2018 (Basis: AC-side of the inverters)

The general magnitude of the simulated and the measured yield in Fig. 5 is identical – the simulation seems to be a valid way to predict the real performance of the PV plant. When analysing the proportions of the yield of each of the main surfaces, there are slight indications that: (i) the PV system on the roof performs better than in the simulation, (ii) the system of the southeast façade (without staircase) performs as expected and (iii) the systems of the southeast staircase façade and the southwest façade perform worse than in the simulation.

For a more detailed comparison, the simulation would have to be repeated with the weather data measured during 2018.

As the main aspect of the (Plus-)Plus-Energy Office High-Rise Building is not only its PV plant but also the goal of producing more electricity on site than the building consumes during the year, the following analyses focus on the interplay between production and consumption. By calculating the difference between the PV electricity production and the building's consumption for every hour during the year and ordering the values in a descending order, the load duration curve – see Fig. 6 – can be calculated. It is a characteristic curve that illustrates the levels

of electric power that the building feeds into the electric grid (positive values) or draws from the electric grid (negative values) during the course of a year.

Fig. 6 shows the load duration curve for four cases, where the PV production is varied between the measured values of 2018 and estimated values if there would not have been inverter faults, and where the building consumption is varied between the measured values of 2018 and the design consumption. It can be seen that the maximum electricity surplus that can be expected to occur in the building is approximately 150 kW. In the case of design consumption and the extrapolated PV production, this value increases to 160 kW. With the ability to shift or store electrical power up to values of 100 kW, almost all of the building's surplus energy could be utilised.

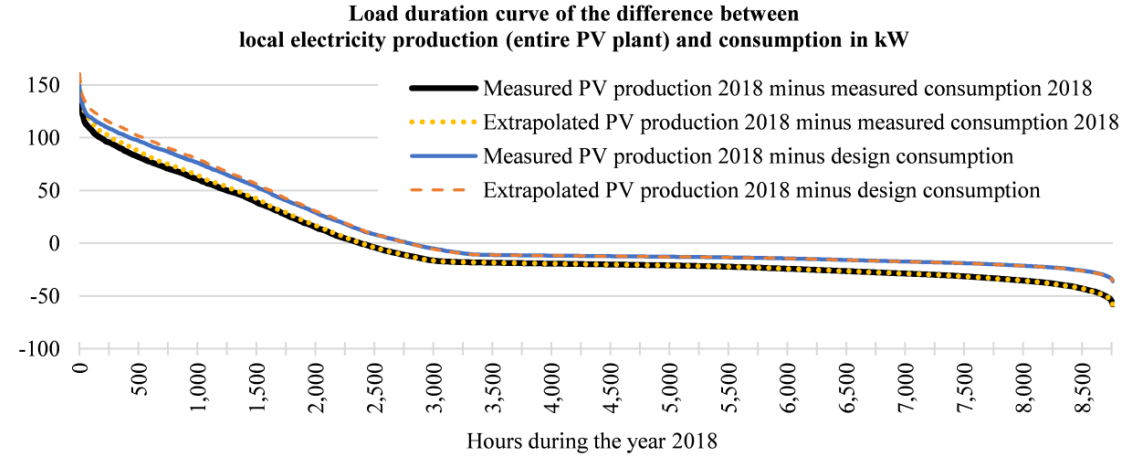

Fig. 6: Load duration curves calculated for four different cases (Basis: PV main meter; entire PV plant)

Further, it can be seen that in the cases with the measured consumption of 2018 during almost half of the year the electrical power drawn from the grid is between a band of 15 kW and 30 kW. For the case of the design consumption the power drawn from the grid lies between a band of 10 kW and 20 kW for a duration of slightly more than half a year.

As the entire PV plant also covers some building parts outside of the system boundary zone of the (Plus-)Plus-Energy Office High-Rise Building, Fig. 7 shows the same graph as in Fig. 6 for the case where only the PV inside the boundary zone is considered in the calculations. The right side of both graphs is identical – the course of the curve on the left side between hours 0 and 3,000 is flatter. Resulting in a maximum surplus of approximately 118 kW (extrapolated PV production and measured consumption) or 126 kW (extrapolated PV production and design consumption). With the ability to shift or store electrical power up to values of 80 kW, almost all of the building's surplus energy could be utilised.

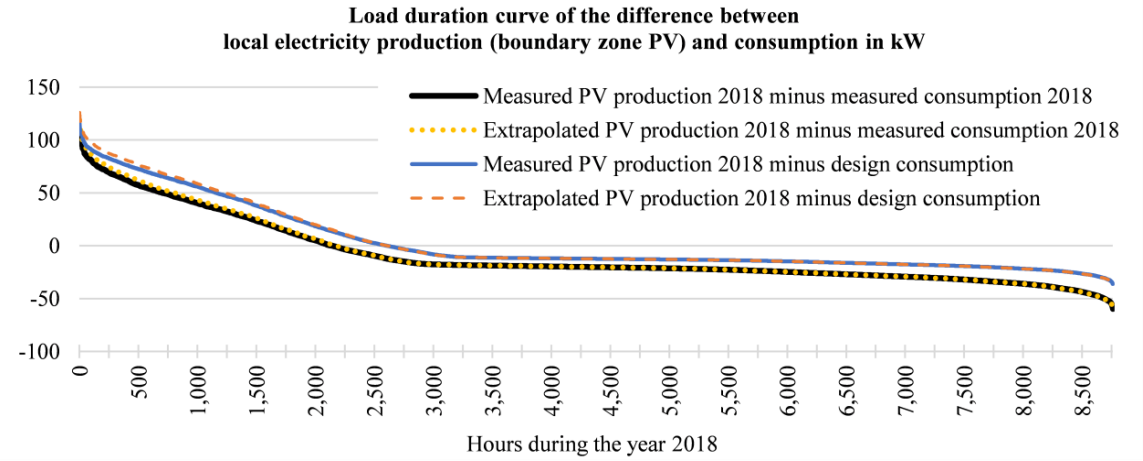

Fig. 7: Load duration curves calculated for four different cases (Basis: PV main meter; only the part of the PV plant that is assigned to the plus-energy boundary zone)

A more detailed view of the electricity surplus that can be expected by the (Plus-)Plus-Energy Office High-Rise Building's PV plant is illustrated in Fig. 8. This figure shows two of the days of 2018 which had the highest PV electricity surplus – one day of the work-week and one day of the weekend. If the building would have the design consumption and there would not have been inverter faults during 2018, the surplus of these days is estimated as 0.76 MWh (entire PV plant 1.04 MWh) and 0.87 MWh (entire PV plant 1.12 MWh). A surplus of 0.87 MWh is enough to cover the electricity consumption of more than one day (average daily consumption as measured during 2018: 0.743 MWh) respectively almost two days (average daily consumption as designed: 0.464 MWh).

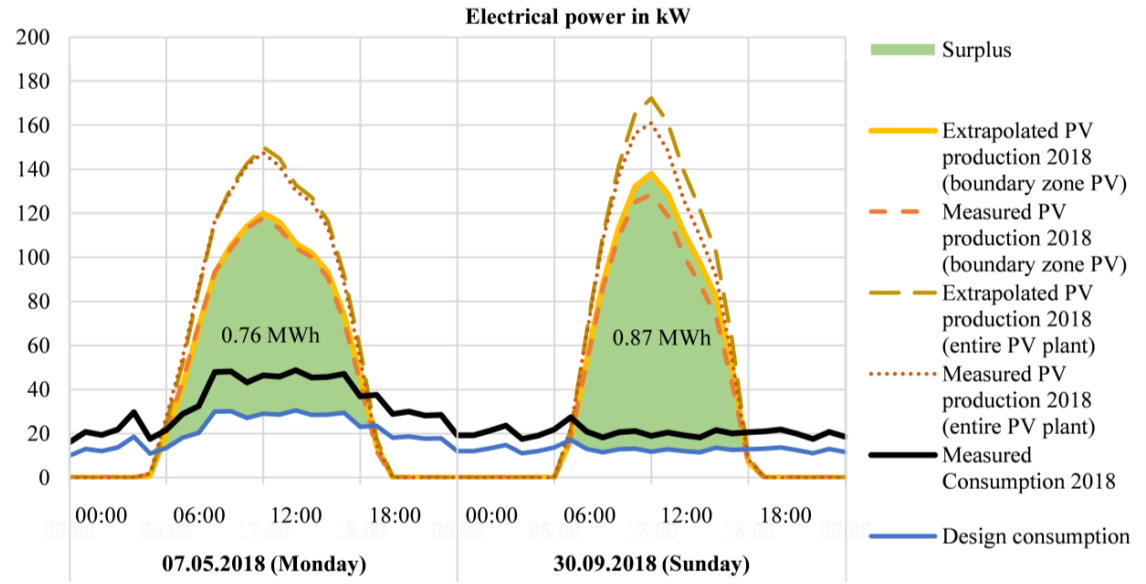

Fig. 8: Electricity supply and consumption load profiles of the two days of 2018 which had the highest PV surplus (Basis: PV main meter)

For the case that the building would achieve the design consumption, 37.8% of the PV production (boundary zone PV; extrapolated PV production) would be self-consumed and 44.3% of the load would be covered by it. According to the unaltered monitoring (boundary zone PV; measured PV production) the self-consumption was 54.6% and 40.0% of the load was covered during 2018. All these values can also be found in Fig. 9 at a battery capacity of 0 kWh.

Fig. 9 illustrates the results of a fictional setup where the building is assumed to be equipped with a battery storage. This is basically the first step of a simplified feasibility study. In this setup the battery capacity was varied and the corresponding load cover factors (LCF) and supply cover factors (SCF) were calculated as described in Section 3. The maximum value for the battery capacity was chosen so that the LCF reached a value of exactly one for the case of the design consumption. This capacity is the absolute minimal capacity that the battery of the building would have to have in order that its electricity system is fully self-sustaining.

Given the situation that the building would achieve its design consumption and the PV production would be like the one of 2018 without inverter faults (extrapolated PV production), this minimal capacity would be 32 MWh. If the PV production would be like the one of 2018 with inverter faults (measured PV production), the minimal capacity would increase to 34 MWh. Considering that in reality there are losses when loading and unloading the battery, and that a true self-sustaining system should have some reserves to compensate for further failures, unexpected weather conditions and the degradation of the PV modules, the real capacity would have to be much higher. As even the lowest minimal capacity of 32 MWh equals the energy of 69 days with average daily consumption (0.464 MWh as designed), the goal of setting up the building as a self-sustaining building appears unreasonable. Especially when considering the fact that the consumption measured during 2018 exceeded the design consumption and the fact that the fictional setup only addressed the electricity demand and not the heating demand, it becomes obvious that fully self-sustaining office high-rise buildings are a technological and economical challenge.

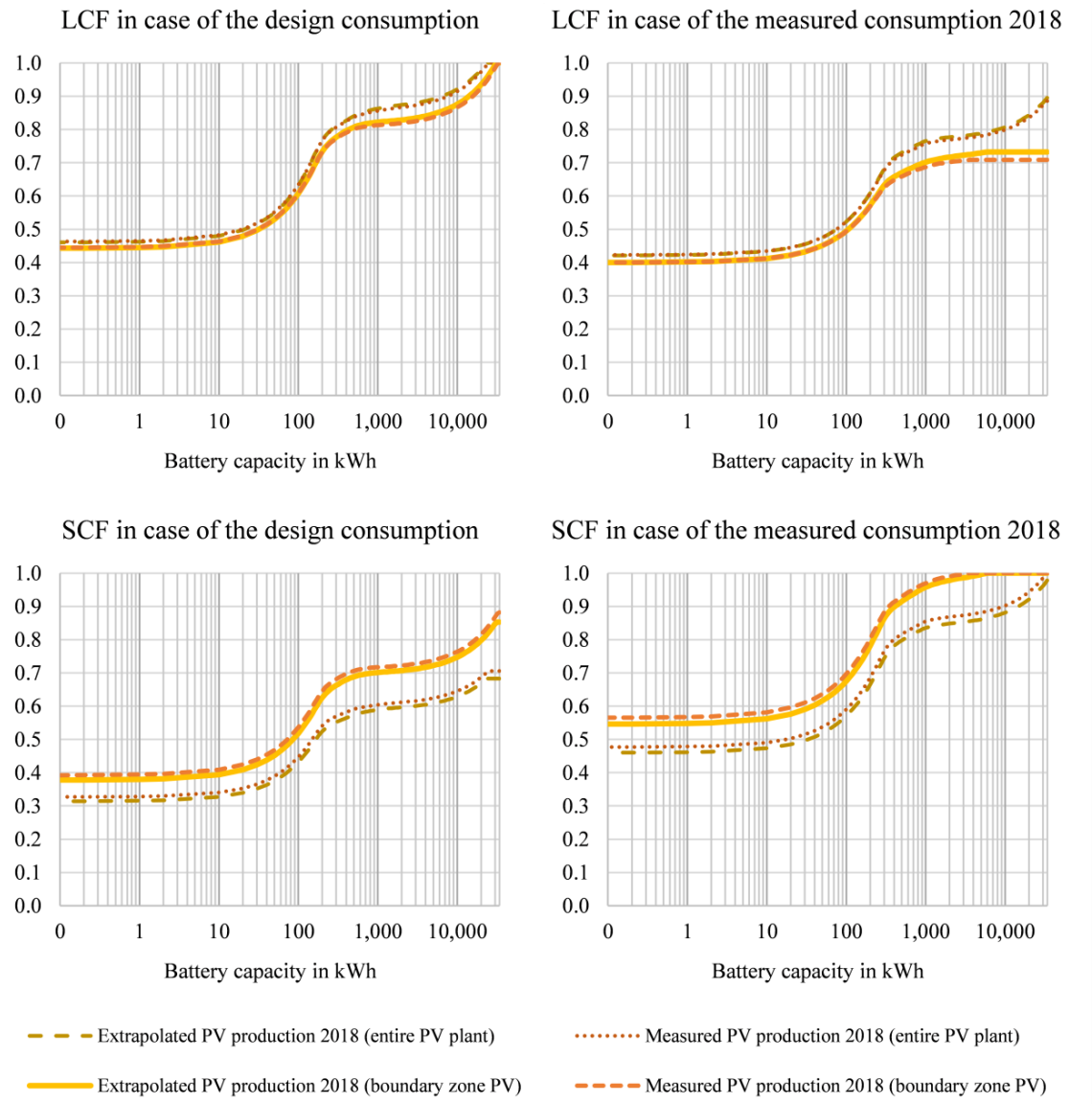

Fig. 9: Overview of the load cover factors (LCF) and supply cover factors (SCF) that could be theoretically achieved if the (Plus)-Plus-Energy Office High-Rise Building would be equipped with batteries of different sizes (losses are neglected)

5. Conclusion

Even though there were some inverter failures, the monitoring data of the PV plant of TU Wien's (Plus-)Plus-Energy Office High-Rise Building seems to fit the simulation results. The net-zero energy concept of the building works well within the setting of the whole university campus – there are enough other buildings that consume the electrical surplus of the PV plant. If the high-rise building would not be connected to the other university buildings or if they would have comparable energy concepts, there should be possibilities to shift more than 0.87 MWh (entire PV plant 1.12 MWh) electrical energy with an electrical power of 80 kW (entire PV plant 100 kW) from one day to another.

Depending on the real consumption of the high-rise building, the self-consumption of a comparable building without capabilities to shift or store electricity, can be expected to be between 37.8% and 54.6%. Further, it can be expected that between 44.3% and 40.0% of the building's electricity load will be covered by the PV supply. Even if a comparable building would achieve the design performance of the (Plus-)Plus-Energy Office High-Rise Building, it is not reasonable to set this building up as self-sustaining building – it would need battery capacities large enough to store more than three months' worth of electricity consumption.

6. Acknowledgement

The authors acknowledge the BMVIT (Federal Ministry of Transport, Innovation and Technology), Kommunalkredit Public Consulting GmbH and MA20 (Vienna's municipal department for "Energy Planning") for funding this project. The authors also acknowledge all projects partners, the TU Wien, the consortium of the Architects Hiesmayr-Gallister-Kratochwil as well as the Bundesimmobiliengesellschaft as the building owner and operator.

7. References

Bellazzi, A., Belussi, L., Meroni, I. (2018). Estimation of the performance of a BIPV façade in working conditions through real monitoring and simulation. Energy Procedia 148, 479-486. https://doi.org/10.1016/j.egypro.2018.08.123

David, A., Leeb, M., Bednar, T., 2017. Comparison of the planned and the real energy consumption of the world´s first (Plus-)Plus-Energy Office High-Rise Building. Energy Procedia 132, 543-548. https://doi.org/10.1016/j.egypro.2017.09.726

David A., Bednar, T., 2020. Transition towards an energy-efficient scientific Office Setup in Austria's largest (Plus-)Plus-Energy Office Building - An Analysis. E3S Web Conference. http://dx.doi.org/10.1051/e3sconf/202017222008

European Parliament, 2018. Directive 2018/844/EU. http://data.europa.eu/eli/dir/2018/844/oj

Imenes, A. G., 2016. Performance of BIPV and BAPV installations in Norway. *2016 IEEE 43rd Photovoltaic Specialists Conference (PVSC)*, 3147-3152, 5-10 June. https://doi.org/10.1109/PVSC.2016.7750246

Klugmann-Radziemska, E., Rudnicka, M., 2020. Energy yield generated by a small building integrated photovoltaic installation. Ecological Chemistry and Engineering 27 (3), 335-346. https://doi.org/10.2478/eces-2020-0021

Luthander, R., Widén, J., Nilsson, D., Palm, J., 2015. Photovoltaic self-consumption in buildings: A review. Applied Energy 142, 80-94. https://doi.org/10.1016/j.apenergy.2014.12.028

Maturi, L., Sparber, W., Kofler, B., Bresciani, W., 2010. Analysis and monitoring results of a BIPV system in northern Italy. *Proceedings of the 25th European Photovoltaic Solar Energy Conference and Exhibition and the 5th World Conference on Photovoltaic Energy Conversion*, Valencia 6-10 September.

Schöberl, H., Hofer, R., Leeb, M., Bednar, T., 2014. Berichte aus Energie- und Umweltforschung, Schriftenreihe 47/2014: Österreichs größtes Plus-Energie-Bürogebäude am Standort Getreidemarkt der TU Wien. Vienna: Bundesministerium für Verkehr, Innovation und Technologie.

Identification of Temperature Reduction Potentials in Heating Circuits based on Measurements

Stina Fox[1], Maike Schüler[1] and Prof. Dr.-Ing. Jens Knissel[1]

[1]University of Kassel, Department of Building Services, Kassel (Germany)

Abstract

This paper aims to find the potential for decreasing system temperatures of the district heating network at the University of Kassel. The district heating network as well as many of the supplied buildings was constructed in the 1980s. Embedded in the development of an overall concept to decarbonize the heat supply on the university's campus the Department of Building Services is evolving a methodology to estimate the contribution of supply temperature reduction. This research involves the systematically investigation of the highest possible supply temperature decrease without impairing the buildings' heat supply. The methodology includes three steps: 1. Identification of the critical buildings; 2. Identification of the critical heating circuits in the critical buildings; 3. Identification of the critical rooms in the critical heating circuits.

Keywords: heat supply, district heating, non-residential building, supply temperature reduction, heating circuits, heating control, heating-up trial, temperature measurement

1. Introduction

The research project "EnEff:Stadt/Campus: Campus Kassel 2030 - Concepts and Measures for the Accelerated Implementation of the Energy Transition in Higher Education" aims the development of an overall concept for the reduction of greenhouse gas emissions (GHG) regarding the heat supply at Kassel University. A district heating network built in the 1980s supplies 17 non-residential and 3 residential buildings at Campus "Holländischer Platz Süd" with heat. The district heating network is connected to the city network. It was designed to operate on a temperature level of 130 °C (supply temperature) and 75 °C (return temperature). The evaluation of measurement data shows that the effective operating temperature level is 105 °C/65 °C. Due to the high system temperatures, a potential to decrease the resulting distribution losses and greenhouse gas emissions by lowering the supply temperature exists. There is no reliable information of how far the heating network temperature can be reduced without impairing the heat supply of the buildings. The paper aims to give an insight into the approach to quantify the possible reduction of the supply temperatures in non-residential buildings based on measurements.

In the determination of reduced supply temperatures in heating systems studies are mainly related to residential buildings. Benakopoulos et al. (2022) present "a strategy for low-temperature operating of a radiator system by calculating the minimum supply temperature required in the system […] by using data from electronic heat cost allocators" for the study of a multi-family apartment building. However, they do not focus on specific heating circuits in different buildings. In the course of optimizing radiator heating systems in residential buildings, Jagnow et al. (2006) deal with the question of how a new temperature level can be identified and realized. For more complex non-residential buildings, Oltmanns (2021) developed a detailed dynamic simulation model of the energy system of "Campus Lichtwiese" at TU Darmstadt to determine the reduction potential of the district heating network among other aspects. The approach presented in this paper focuses on the use of measurement data.

1.1. System description

To examine the temperature reduction potentials, those buildings and those heating circuits are to be identified that are expected to be critical to decreased supply temperatures. "Critical" refers to the ensuring of heat supply for the connected buildings. Thus, the heat load of the buildings and heating circuits have to be quantified. The design outdoor temperature (T_A^*) is an important criterion for this examination. In Kassel, the design outdoor temperature is -12 °C. The analysis takes place in three steps as shown in Fig. 1.

© 2022. The Authors. Published by International Solar Energy Society
Selection and/or peer review under responsibility of Scientific Committee
doi:10.18086/eurosun.2022.10.04 Available at http://proceedings.ises.org

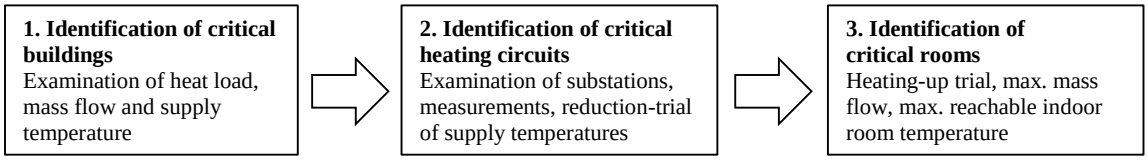

Fig. 1: systematic structure of the overall approach

The building-level (step 1) analyzes buildings on the primary (network) side. It focusses on the heat exchangers and tries to detect buildings, which might be critical in relation to a system temperature reduction and should be prioritized for further examination. It is described in more detail in a separate conference paper entitled: "Transformation of a University Campus: Comparison of Ranking Methods for Temperature Reduction from Network and Building Perspective" (Bergsträßer, Neusüß et al., 2022).

The presented paper gives an insight into the work of heating circuit level (step 2) and room level (step 3). The work focuses on the secondary side of the heating network. On heating circuit level, measurement data from different heating circuits are analyzed concerning the potential of temperature reduction. A decrease of the supply temperature during a reduction trial in several heating circuits should identify errors or insufficient heating regulation and critical rooms. Furthermore, a promising approach is the analysis of measured temperatures in rooms from heating circuits during a heating-up trial on the room level. Step 2 and 3 are still in progress.

1.2. Approach

The non-residential buildings on the university's campus supplied by the heating network are equipped with diverse fluid heating circuits of different types. Those types include static circuits, using radiators as transfer systems, dynamic circuits to heat the supply air of ventilation systems and warm water circuits, and panel heating systems using floor heating or radiant ceiling panels as transfer systems. The circuits require different supply temperatures (Sangi et al., 2015). Most of the existing heating systems at the university are in its original state from the 1980s and run on high temperatures, exposed from interviews with technical staff, from documents archived by the building department and from little measurement data of the substations. There are sparse information in relation to the designed system temperatures for the secondary side. Fig. 2 displays a simplified hydraulic diagram of a typical substation at Kassel University describing the primary and secondary side.

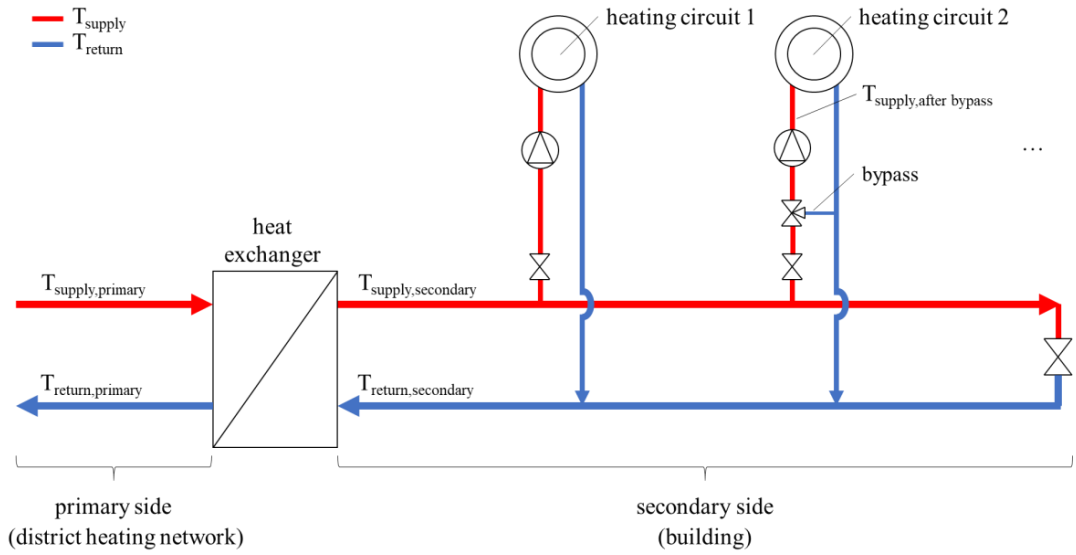

Fig. 2: Simplified hydraulic diagram of a typical substation at Kassel University

The design temperatures for the heating circuits of only seven buildings, built in 1985 to 1988, are available. In these cases, the supply/return temperature for T_A^* are 90/70 °C. It is not clear, which system temperatures are currently required in the buildings because mostly there exist no measurement points on the secondary side of the substations. It is necessary to analyze the needed supply temperatures and heat loads of heating circuits for the design outdoor temperature of -12 °C. Therefore, measurements must be taken. They are described in the following chapter.

2. Heating Circuits

As mentioned before, the buildings at Kassel University have different heating systems like static, dynamic and panel heating. Within the framework of CampusKassel2030, five buildings with different main usages were examined. Tab. 1 provides an overview of these buildings that includes the main use, the installed heating circuits and photos taken by the authors. The numbers show the amount of the measured heating circuits. The numbers in parentheses display the total amount of the existing heating circuits in the building.

Tab. 1: Overview of the measured buildings

Picture of the building (pictures taken by the authors)	**Building function/ description**	**Number of static heating circuits**	**Number of dynamic heating circuits**	**Number of panel heating circuits**
	Office and institute building with a cafeteria	2 (2)	2 (2)	1 (1)
	Lecture hall	1(1)	1 (1)	2 (2)
	Library	2 (5)	0 (2)	-
	Technical institute with laboratories and offices	3 (3)	1 (1)	-
	Residential building with student apartments	2 (6)	0 (2)	-

The measurements took place during the heating season from October 2021 to April 2022. In this period, seventeen heating circuits were evaluated in total. According to Jacob (2010), short-term measurements should exceed at least 14 continuous days to get reliable data. The measurements of the heating circuits were taken in a minimum of 14 days.

In the following sections, exemplary measurement data from different heating circuits are shown and a comparison is made. To eliminate outliers and measurement errors the 0.05 quantile and 0.95 quantile were determined. All measurements include supply and return temperatures and the mass flow of every heating circuit. Outdoor

temperatures and sporadic room temperatures were measured as well. Additionally, supply and return temperatures on the primary and on the secondary side of the heat exchangers were evaluated. To identify the heat load of a specific heating circuit out of this measurement data, the following equation (eq. 1) can be applied. The required heat load is a key value to quantify a temperature reduction potential.

Assumption: c_p = *constant*

$$\dot{Q}_{demand} = \dot{m}_{hc} \cdot c_p \cdot (T_{supply} - T_{return}) \quad \text{(eq. 1)}$$

$\dot{Q}_{demand}$	heat load demand [kW]
$\dot{m}_{hc}$	mass flow [kg h^{-1}]
c_p	specific heat capacity of water [kWh kg^{-1} K^{-1}]
T_{supply}	supply temperature [°C]
T_{return}	return temperature [°C]

2.1. Static heating circuits

In static heating circuits radiators function as heat transfer system for space heating. There exist different types of radiators, e.g. steel column, cast-iron column and panel radiators (Sangi et al., 2015). The heat is distributed by hot water. The water circulates on the secondary side of the heat exchanger at the substation and supplies the heating circuits and by this the rooms. A circulation pump regulates the mass flow. The supply temperature usually is dependent on the outdoor temperature. In many EU countries the design supply temperature is 90 °C whereas the operating supply temperature mostly is under 90 °C (Sarbu, Sebarchievici, 2015). The majority of the heating circuits in the examined buildings are designed with supply and return temperatures of 90/70 °C as well.

In some cases, bypasses are used to regulate the supply temperature in the heating circuits (see simplified heating diagram, Fig. 2). A bypass pipe with a valve connects the return pipe to the supply pipe. Depending on the set point supply temperature the valve opens gradually and cooler water from the return pipe is mixed into the supply to cool it down (Sangi et al., 2015). At Kassel University, bypasses are integrated in the static heating circuits.

As shown in Tab. 1, ten static heating circuits were measured during the heating season 2021/2022. Exemplary measurement data for a static heating circuit in the office and institute building are shown in Fig. 3

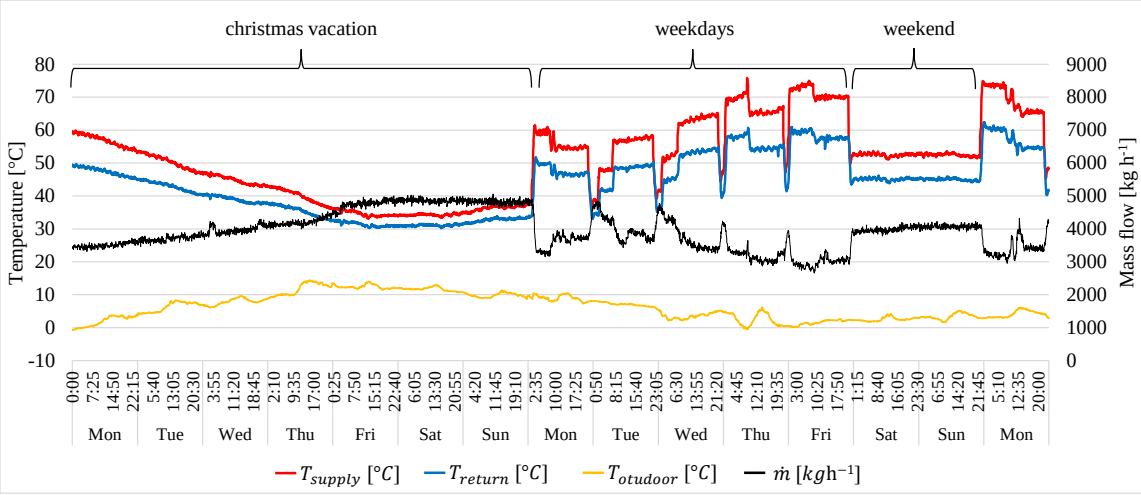

Fig. 3: Measurement data of a static heating circuit in the office and institute building with system temperatures (left axis) and mass flow (right axis), 12/27/2021-01/10/2022

Fig. 3 displays a short section of the measurement from Dec. 27th 2021 to Jan. 10th 2022. A bypass is installed between the supply and return pipe. The supply temperature, measured behind the bypass, is shown in red, the return temperature in blue, the outdoor temperature in yellow (left axis) and the mass flow in black (right axis).

The measurement section shows different periods of use. For regular usage time during the semester, the figure indicates typical weekdays and weekends. A night and weekend temperature reduction is clearly visible. In contrast to the system temperatures, where the supply is lowered by almost 20 K, there is no mass flow reduction during the night and weekend. It actually increases to 5,000 kg h^{-1}. Due to the reduced supply temperature, the thermostatic valves in the rooms open and the mass flow enhances. The room temperature does not drop significantly. The measure values from Monday to Sunday on the left half of Fig. 3 point out the control behavior of the heating circuit during the Christmas vacations. Analogous to the previous observations, the mass flow is not lowered either. This leads to unnecessary heat loss and pump power consumption, which indicates optimization potential in the heating control. The supply temperature decreases continuously to a minimum of 35 °C as the outdoor temperature rises. At the end of vacation the supply temperature increases up to 75 °C, whereas the mass flow decreases. The heat flow is just under 45 kW. Analyses of the whole measurement period resulted in a maximum heat flow of 70 kW appearing at -12 °C outdoor temperature. Despite the closing days and, in some rooms, reduced indoor temperatures of 14 °C, the maximum was not required during the heating phase. An inspection directly after the vacations showed that not all rooms were used and heated up again by turning up the thermostatic valves.

An analysis of the bypass and the bypass valve in the heating circuit over the entire measurement period shows that the actual supply temperature is lowered by the bypass function by around 20 K on average. The supply temperature on the secondary side of the substation has its maximum at 90 °C. The supply temperature measured behind the bypass in the static heating circuit in average is 70 °C. In heating up phases, the supply temperature increases up to 73 °C and the mass flow is 6,500 kg h^{-1}. A heating-up trial, described in chapter 3.1, demonstrated that the maximum mass flow for this heating circuit is 8,000 kg h^{-1}. Compared to the values shown in Fig. 3 this indicates an existing reduction potential even greater than 15 K. Measurements of other static heating circuits revealed the same heating control errors, bypass functions and similar temperature levels.

2.2. Dynamic heating circuits

Dynamic heating circuits heat the supply air of ventilation systems as shown exemplary in Fig. 4. Heat recovery is integrated in the ventilation systems of the examined buildings at the campus. The heating circuit distributes hot water to a heat exchanger, the so-called heater that is connected to the incoming air duct. This heats the supply air temperature to a predetermined set point. The heater does not operate if the outdoor temperature is sufficiently high or if the air temperature provided by the existing heat recovery system is sufficient. In this case, the heating circuit merely circulates without supplying heat to the ventilation system. Generally, the dynamic heating circuit runs as a circulation line like drinking water systems, which leads to circulation losses (Beckmann, 2020).

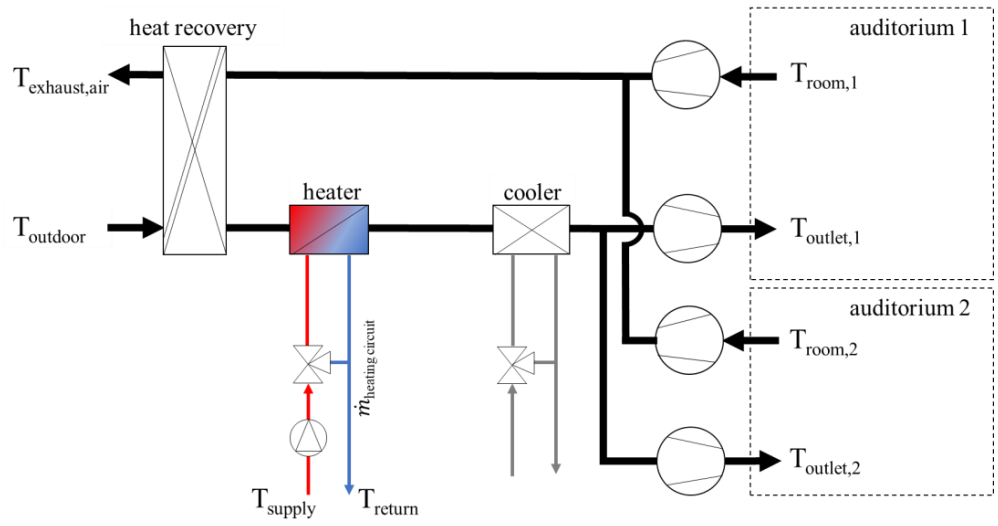

Fig. 4: Simplified diagram of an air ventilation system in a lecture hall at Kassel University

Mass flow, supply and return temperature were measured for four dynamic heating circuits. The heating circuits are connected to air ventilation systems. All of them are equipped with heat recovery as described before. Measurement data indicate that the heating circuits run on high temperature levels, similar to the static heating circuits.

In the lecture hall measures were taken from Feb. 1st to Feb. 16th 2022. Fig. 5 exemplary shows the measured values from Feb. 2nd to 8th. The supply temperature is plotted in red, the return temperature in blue, the outdoor temperature in yellow (left axis) and the mass flow in black (right axis). The heating circuit supplies two auditoriums of approximately the same size. The grey line shows the room temperature for one auditorium. Regarding the room temperature of both rooms, the average is 20.2 °C and 20.5 °C. During the night or at the weekend, the room temperatures do not fall below 18.6 °C respectively 17.2 °C.

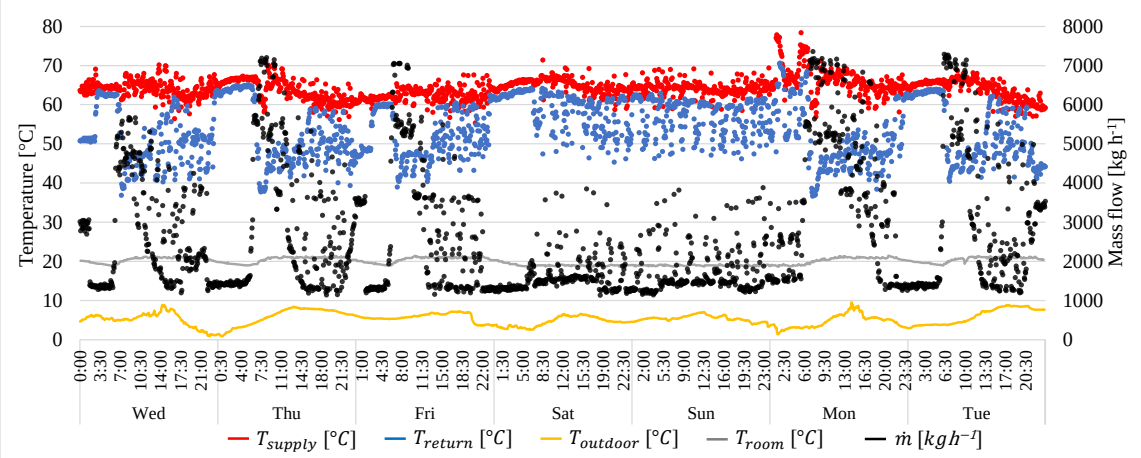

Fig. 5: Measurement data of a dynamic heating circuit in the lecture hall with system temperatures (left axis) and mass flow (right axis), 02/02/2022 – 02/08/2022

Fig. 5 pictures different relations and results of the dynamic heating circuit described above. The mass flow increases when the room temperature falls below 19 °C (set point). In this case, heat is transferred to the ventilation system and the return temperature drops at 40 °C. When there is no heat transfer, the return temperature is similar to the supply temperature, which ranges from 60 °C to 70 °C. The heating circuit runs like a circulation line. This is a common regulation for dynamic heating circuits (Oltmanns, 2021).

Further measurements, not shown in Fig. 5, were analyzed. They point out that the maximum outlet air temperature of the ventilation system, measured behind the heater (see Fig. 4), is nearly 47 °C at T_A^*. It is assumed that this temperature is required to ensure a room temperature of 19 °C. By increasing the mass flow, the supply temperature for the dynamic heating circuit could be reduced. A more detailed analysis is needed at this point.

2.3. Floor heating

In Panel heating systems, large heating surfaces take over the heat exchange. They use the (under-)floor, wall or ceiling as heat transfer systems. Due to the large surfaces panel heating systems can operate at lower temperatures. Floor heating for example runs on a low supply temperature level between 40 °C and 60 °C (Wu et al., 2015). Ceiling radiation panels in high rooms operate at higher temperatures. (Hainbach, 2020). This section takes a closer look at the floor heating system.

Fig. 6 shows exemplary results for a floor heating circuit in a cafeteria from Jan. 5th to 10th 2022. The supply temperature is plotted in red, the return temperature in blue (left axis) and the mass flow in black (right axis). Additionally, the room temperature and the outdoor temperature are pictured in grey and yellow.

The mass flow is almost constant at 1,500 kg h^{-1}. The difference between the supply (on average 38 °C) and return (on average 31.5 °C) temperature is almost constant at 6.5 K. The room temperature averages 21.5 °C and does not fall below 20 °C. There is no reduction in temperatures or mass flow outside cafeteria operating hours. Since floor heating is an inertial system it is not necessary to reduce temperatures for short operating periods (Pech, Klaus, 2015). Furthermore, this system covers the base load depending on the outdoor temperature.

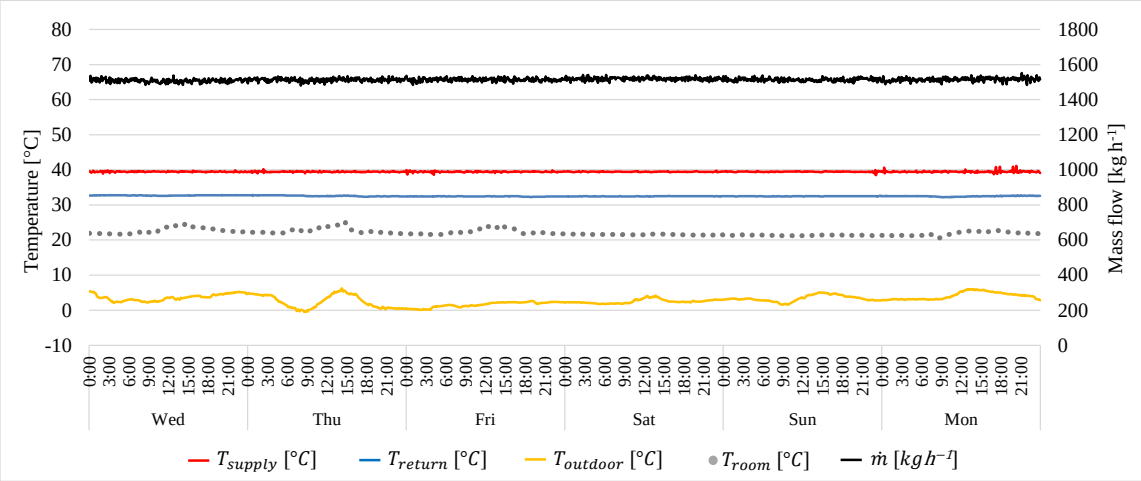

Fig. 6: Measurement data of a floor heating system in the cafeteria of the office and institute building with system temperatures (left axis) and mass flow (right axis), 05/01/2022 – 01/10/2022

Further measurements from February 2022 examined ceiling radiation panels in a lecture hall. Some differences compared to the floor heating system investigated above became apparent. One important point is the higher supply temperature (varies between 50 and 70 °C). In addition, the mass flow fluctuates in a high range. Whereas the return temperature was nearly constant. Thus, that the heating circuit is controlled by the return temperature. At this point, the examination of the ceiling panels is not discussed in detail.

3. Further Approaches

Additionally to measurements addressed in 2. Heating Circuits a heating-up trial and an experimentally reduction-trial of supply temperatures in several buildings and heating circuits were implemented to analyze the impact on the heating system and the room temperatures.

After identifying a critical heating circuit, the critical room(s) regarding possible reduced supply temperatures have to be analyzed. The desired room temperature is considered the criterion and threshold for critical rooms. In Germany, technical workplace regulations preset among other aspects a minimum room temperature depending on the work activity (ASR A3.5). The desired indoor temperature for typical workspaces like offices is 20 °C. This value is defined as set point for the identification of critical rooms.

The reachable room temperature depends on various factors. These include for example the thermal transmission coefficient (U-value) and the thermal mass storage, the geometry, the ratio between external wall area and spatial volume, the placement in the building, the usage, internal and external heat gains (irradiation) and the heat transfer system itself (Bredemeyer et al., 2022). Before installing measurement instruments, those aspects were checked by an on-site inspection. Using a floor plan that marks rooms connected to a specific heating circuit and a prediction which rooms are critical to a reduction of the supply temperature was made after the inspection.

Prediction:

- Rooms on the top floor that are at the end of the heating circuit.
- Rooms that are located in the northern corner of the building.
- Rooms with obvious deficiencies in respect of the heating transfer system.
- Rooms with a large ratio between the external wall surface and the heated volume.

3.1. Heating-up trial

In conjunction with the as critical predicted rooms, measurement instruments were installed and a heating-up trial was implemented in the office and institute building (Tab. 1). The considered static heating circuit supplies 55 rooms, including offices, seminar and conference rooms. The indoor temperature was measured in 20 rooms in which column radiators with thermostatic valves are installed. Furthermore, the supply and return temperatures of radiators were measured in the rooms predicted as critical. In arrangement with the facility management, the

thermostatic valves were adjusted to the maximum on Friday, 17th of December 2021. On Monday, 20th of December, the thermostatic valves were adjusted to the baseline again.

As already described before in 2.1. Static heating circuits, the supply temperatures in static heating circuits are usually reduced at weekends. In addition to the reduced temperature (around 40 °C), the thermostatic valves are turned up to the maximum. As illustrated in Fig. 7 the mass flow rate (black) increases probably to its maximum of 8,400 kg h^{-1}. Compared to other measured values, this maximum does not occur during the typical time of use. This mass flow increase leads to a return temperature of around 35 °C (blue). In addition, the supply temperature is shown in red and the outdoor temperature in yellow. In the right third of Fig. 7, the outdoor temperature drops to a range between -10 and 0 °C. Due to the heating circuit control, the supply temperature level increases by about 20 Kelvin to a maximum of 82 °C.

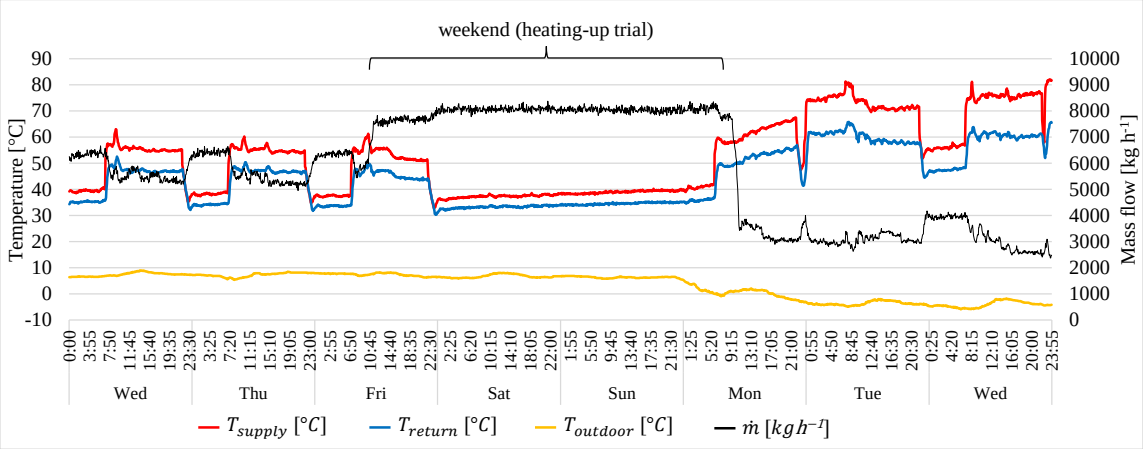

Fig. 7: Measurement data of the heating-up trial in the office and institute building, 12/15./2021 – 12/22/2021

The measured room temperatures during the heating-up trial are shown in Fig. 8. The outdoor temperature drops at a minimum of -1.0 °C on Monday. The average is 5.8 °C. Most of the rooms reach a maximum temperature of around 22 °C. Three outliers reach a maximum of 24 °C to 26 °C (IDs 1103, 1219, 3217). Two offices and one seminar room (IDs 1217, 3104 and 3105) stand out because the temperature does not hit the set point of 20 °C.

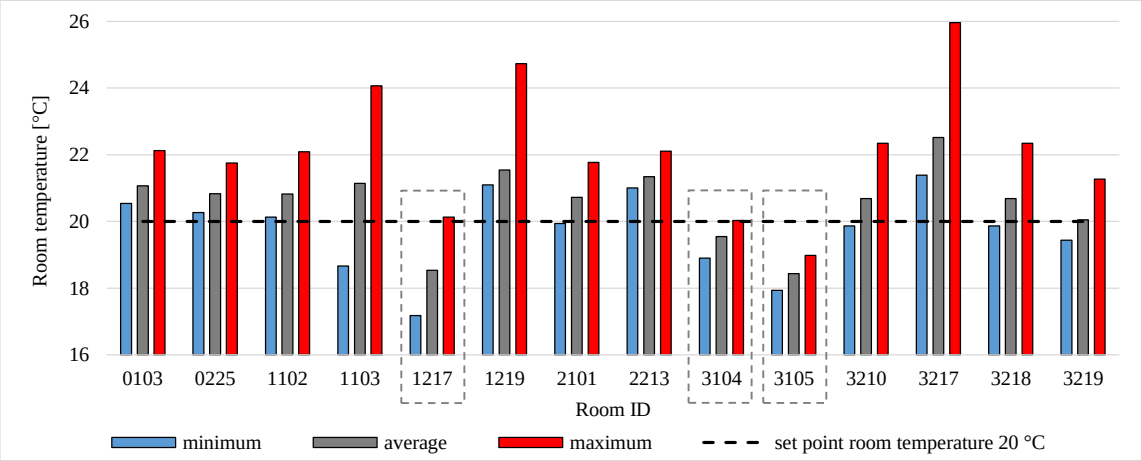

Fig. 8: Measured room temperatures during heating-up trial

In consideration to the predictions, the two offices are located at the end of the heating circuit on the highest floor. The seminar room is located in the corner on the northern side of the building. Besides the location, the seminar room is twice the size of the offices and has two radiators. One radiator is incorrectly connected to the hydraulic system. This needs to be improved. Alternatively, radiators with larger dimensions can replace the existing radiators. This measure leads to a higher radiator capacity and, as a result, a higher room temperature.

The fact that room temperatures of 26 °C are reached in conveniently located rooms indicates the oversizing of radiators. Hasan et al. (2008) state that this is a common practice. For example, the size of radiators often is

selected aligning the width of the window "in order to overcome cold draught problems" (Hasan et al., 2008). The oversized radiators are an advantage in regard to possible supply temperature reduction because they "may not necessarily need to be enlarged when operating with a low temperature system" (Hasan et al., 2008).

To examine if the radiator is sufficiently dimensioned with regard to a supply temperature reduction, the general radiator equation (eq. 2) can be used. The installed radiator capacity $\dot{Q}_{90/70}$ for the design otudoor temperature can be detemined by the radiator type and standard boundary conditions (DIN EN 442-2). In this case, the logarithmic mean temperature difference (LMTD, eq. 4) has to be calculated with the design system temperatures. For the office and institute building the design supply and return temperatures are 90/70 °C. The heat load $\dot{Q}_{\mathrm{demand}}$ that is acutally required can be analyzed by measurement data. If there is no valid data, the heat load can be estimated using the "Method for calculation of the design heat load - Part 1: Space heating load" described in DIN EN 12831-1. Eq. 3 delivers the required LMTD. With this information, possible temperature pairs (supply and return temperature) can be formed (Jagnow et al., 2003). This approach is currently being tested with further measurement data and will be implemented as an evaluation tool (4.2 Further Works).

$$\frac{\dot{Q}_{demand}}{\dot{Q}_{90/70}} = \left(\frac{\Delta T_{ln,demand}}{\Delta T_{ln,90/70}}\right)^{n} \quad \text{(eq. 2)}$$

$$\Delta T_{ln,demand} = \Delta T_{ln,90/70} \left(\frac{\dot{Q}_{demand}}{\dot{Q}_{90/70}}\right)^{\frac{1}{n}} \quad \text{(eq. 3)}$$

$$\Delta T_{ln} = \frac{T_{supply} - T_{return}}{\ln\left(\frac{T_{supply} - T_{room}}{T_{return} - T_{room}}\right)} \quad \text{(eq. 4)}$$

$\dot{Q}_{demand}$	heat load demand [kW]
$\dot{Q}_{90/70}$	installed radiator capacity at 90/70 °C [kW]
ΔT_{ln}	logarithmic mean temperature difference [K]
n	radiator exponent [-]

Moreover, a hydraulic balancing is an option to improve the heating circuit (Cho et al., 2020). For example, by reducing the maximum mass flow in rooms with the significantly higher maximum room temperature they would no longer be such outliers. In addition, the reduced mass flow in these rooms could then help to supply the undersupplied rooms.

The heating-up trial additionally indicates the maximum mass flow of the examined static heating circuit. Fig. 7 shows a maximum of 8,000 kg h^{-1}. With the known maximum mass flow and the required heat load, the return temperature can be determined at different supply temperatures (Benakopoulos, 2022).

3.2. supply temperatures reduction-trial

The reduction of supply temperatures in several heating circuits pursued the aim to investigate the development of room temperatures in the buildings. Furthermore, the complaint management was monitored. In preparation, the users were not informed about the trial to avoid foredooming complaints about the temperatures and comfort.

The supply temperatures for the static heating circuits in the library and in the institute building with laboratories were decreased by changing the supply temperature control curve with parallel shift. The university's technical operating department reduced the supply temperature in two 5 K steps. In one heating circuit from 90 °C to 80 °C and in another one from 80 °C to 70 °C for the T_A^* of -12 °C.

The arrow in Fig. 9 marks the date of the 10 K reduction for a heating circuit in the library. In this case, the heating threshold outdoor temperature of 16 °C is already reached and the supply temperature is on a low level (40 °C). In the next days the outdoor temperature decreases constantly to 0 °C. The supply temperature increases to a maximum of around 60 °C and a temperature difference of around 10 K. The considered set point room temperature of 20 °C was reached during the entire test phase. Moreover, there were no complaints from the users regarding the indoor temperatures or comfort. Despite the short period of time and the partly rather high outside temperatures, the trial was successful. The comparison of the four heating circuits involved in the test shows no significant differences in terms of the reduced supply temperature levels.

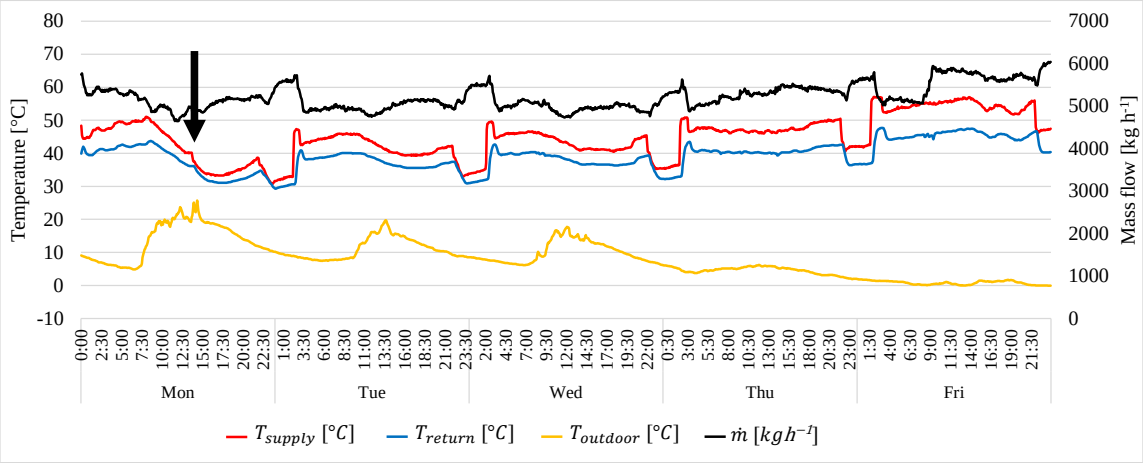

Fig. 9: Supply temperature reduction of 10 K in a static heating circuit in the library

Based on the experiences further trials with reduced supply temperatures are planned for the upcoming heating season (2022/2023). The reduction should be carried out at significantly lower outdoor temperatures and should be increased up to 15 K to 20 K in order to achieve more significant results.

4. Conclusion and Outlook

The research of the Department of Building Services at Kassel University within the project "CampusKassel 2030" is still in progress. The approaches and measurements described above show the further research potential of this project. In this chapter, the optimization potential identified for the different heating circuits and the related heating technology, such as heat exchangers or heating circuit pumps, so far will be highlighted. Furthermore, a transferable methodology for the identification of temperature reduction and optimization potentials will be developed. The current status of this methodology and the further procedure are described below as well.

4.1. Identified optimization potential

The measurements of different heating circuits showed that there exist several optimization factors regarding the temperature reduction potential. Those factors mainly relate to the heating control and components. The on-site inspections showed that water circuit pumps and heat exchangers are partly up to 40 years old with a high energy demand. The connection between heating pipes and renewed pumps are not insulated. Especially the insulation of flanges often is a weak point. As a result, distribution losses of the heating systems increase unnecessarily. Those vulnerabilities easily can be avoided. In many heating circuits bypasses are integrated that lower the supply temperature of the water on the secondary side of the heat exchanger (substation) before entering the heating circuit. This indicates the potential for reduced system temperatures. Furthermore, efficient plate heat exchangers have better transformation values compared to the existing heat exchangers and can therefore be decisive for a network temperature reduction. At Kassel University, the building service department is gradually renewing the heating circuit distribution stations. The presented results support this renewing process.

In the static heating circuit described above (chapter 2.1.) it is highly recommended to implement a night and weekend shut-off to the water circulation pump. Attention must be paid to higher heating loads during heating phases in the morning or after weekends. It should be verified that the energy savings are commensurate with the additional expense. This is transferable to other static and partly dynamic heating circuits. Efficient circuit pumps with an efficient control should be integrated in a first step. This step leads to reduced power consumption for the pumps and through a suitable regulation to fewer distribution losses outside operating hours. By increasing the mass flow, the supply temperature can be decreased. For example, the supply temperature of examined office and institute building can be reduced by at least 15 K in relation to the design outdoor temperature as explained in chapter 2.1. This reduction is currently being implemented as part of the renewal of the substation.

Regarding the dynamic heating circuits (chapter 2.2), a large reduction in supply temperatures is possible by setting user-oriented target values. In one case, the examination revealed that the supplied rooms need to be cooled instead of being heated. Still, the dynamic heating circuit runs on high supply temperatures with no efficient circuit pump regulation. An outdoor temperature range must be defined above which pump shutdown can occur.

The evaluation of the measured values shows that the floor heating system has the lowest system temperatures, as expected. There exist no reduction potential for the considered heating circuit in chapter 2.3. Panel heating circuits like ceiling radiation panels operate at a higher temperature level. In a further step it has to be worked out how large the reduction potentials are in this systems.

Examination on the room level lead to the identification of critical rooms in a specific static heating circuit (chapter 3.1) regarding the temperature reduction potential. In a next step the heat load of those rooms and the dimension of the radiators are to be calculated. With this information, radiators with correct dimension can replace the undersized radiators in the critical rooms.

It is difficult to give an overall advice for a quantification of temperature reduction potential. The non-residential buildings at Kassel University are very different in addition to their use, year of construction, types of heating circuits and especially their heat demand. An increased mass flow enables reduced supply temperatures with the required heat flow (see eq. 1). At the same time an enhanced mass flow results in a higher electricity demand. An optimum is to be determined. Thereby, it is important to integrate a gradual temperature reduction as described in 3.2. Reduction of supply temperatures. Low outdoor temperatures should be a condition for safe and satisfactory implementation.

4.2. Further Works

To make use of the results described above a universal methodology to identify temperature reduction and optimization potential for the investigated non-residential buildings based on measurement data, a “minimum temperature analysis” will be developed. The aim of this analysis method is to make a qualified statement about the minimum supply temperature for space heating in non-residential buildings based on district heating with little data. The method is implemented as an evaluation tool in Microsoft Excel. It displays a substation, heating circuits including bypasses and water pumps and rooms of a building. The heat load of the building and the heating circuits will be modeled with measurement data. Based on these information, a parametric study with various supply temperatures, mass flows and heating control can be made. This methodology is to be verified by measurements in the next heating period and by further experimentally supply temperature reductions. In general, the methodology will be developed with the aim of evaluating different campus buildings and making the approach transferable to other areas and universities.

In addition, cooperation with the building service department should be maintain. The identification of critical buildings and critical heating circuits can lead to a changed sequence for the renewal of the heating substations. Furthermore, hydraulic balancing of the heating circuits should be implemented. Subsequently, identified weak points on the room level can be eliminated by activities such as window replacement or heating surface extension.

In the future, the minimum temperature analysis could be used to map large building pools such as the University of Kassel to determine system temperature reduction potentials with little measurement effort. After the implementation and the commissioning of relevant measures, reduced supply temperatures of specific heating circuits can be optimized and adjusted step by step.

5. Acknowledgments

The project “EnEff:Stadt/Campus: Campus Kassel 2030 – Konzepte und Maßnahmen für die beschleunigte Umsetzung der Energiewende im Hochschulbereich” this paper is based on is supported with funds of the Federal Ministry of Economy Affairs and Climate Action (funding code 03EN3013A).

6. References

ASR A3.5 (2010). Room temperature. Technical rules for workplaces. In accordance with the Workplace Ordinance of August 12th, 2004 (BGBl. I p. 2179), last amended by Article 4 of the Act of December 22, 2020 (BGBl. I p. 3334).

Beckmann, N., 2020. Heizungssysteme, in: Beckmann, N., Energieeffizientes Bauen und wie es sich lohnt, Kaltenkirchen, pp. 235-236. https://doi.org/10.1007/978-3-658-28543-2

Benakopoulos, T., Tunzi, M., Salenbien, R., Hansen, K., Svendsen, S., 2022. Implementation of a strategy for

low-temperature operation of radiator systems using data from existing digital heat cost allocators. Journal Energy, Volume 251. https://doi.org/10.1016/j.energy.2022.123844

Bredemeyer, J., Fischer, J., Walsdorf-Maul, M., Schaudienst, F., 2022. 1. Wärmeschutz, in: Vogdt, F. (Ed.), Bauphysik. Grundwissen für Architekten. Springer Vieweg Verlag, Wiesbaden, pp. 27-161

Cho, H.-I., Cabrera, D., Patel, M., 2020. Estimation of energy savings potential through hydraulic balancing of heating systems in buildings. Journal of Building Engineering, Volume 28. https://doi.org/10.1016/j.jobe.2019.101030

DIN EN 12831-1:2017-09, Energy performance of buildings – Method for calculation of the design heat load – Part 1: Space heating load, Module M3-3.

DIN EN 442-2:2014, DIN EN 442 – Part 2: Test methods and rating; German version EN 442-2:2014

Hainbach, C., 2020. Systeme und Bauteile der Heizungstechnik, in: Grote, KH., Bender, B., Göhlich, D. (Eds.), Dubbel Taschenbuch für den Maschinenbau 3: Maschinen und Systeme. Springer Vieweg Verlag, Berlin, Heidelberg, pp. 827-841. https://doi.org/10.1007/978-3-662-59715-6

Hasan, A., Kurnitski, J., Jokiranta, K., 2008. A combinde low temperature water heating system consisting of radiators and floor heating. Journal of Energy and Buildings. 41, pp. 470-479. https://doi.org/10.1016/j.enbuild.2008.11.016

Jacob, D., 2012. Teilenergiekennwerte bei Nichtwohngebäuden - Leitfaden zur Hochrechnung von Kurzzeitmessungen - Entwurf, Fraunhofer Institut für Solare Energiesysteme (ISE) Freiburg.

Jagnow, K., Halper, C., Timm, T., Sobirey, M., 2003. Optimierung von Heizungsanlagen im Bestand.

Oltmanns, J., 2021. Analysis and Improvement of an Existing University District Energy System. Dissertation. TU Darmstadt. https://doi.org/10.26083/tuprints-00017367

Pech, A., Klaus, J., 2005. Heizung und Kühlung. SpringerWienNewYork. Wien, pp. 99-100.

Sangi, R., Baranski, M., Oltmanns, J., Streblow, R., Müller, D, 2015. Modeling and simulation of the heating circuit of a multi-functional building. Journal of Energy and Buildings. 110, pp. 13-22. https://doi.org/10.1016/j.enbuild.2015.10.027

Sarbu, I., Sebarchievici, C., 2015. A study of the performance of low-temperature heating systems. Journal of Energy Efficiency 8 (3), pp. 609-627. http://dx.doi.org/10.1007/s12053-014-9312-4

Wu, X., Zhao, J., Oelsen, B. W., Fang, L., Wang, F., 2015. A new simplified model to calculate surface temperature and heat transfer of radiant floor heating and cooling systems. Journal of Energy and Buildings. 105, pp. 285-293. https://doi.org/10.1016/j.enbuild.2015.07.056

Nomenclature:

ΔT_{ln}	logarithmic mean temperature difference [K]	T_{A^*}	design outdoor (ambient) temperature [°C]
c_p	specific heat capacity of water [kWh kg^{-1} K^{-1}]	$T_{exhaust,air}$	air temperature released to the outside [°C]
hc	heating circuit [-]	T_{outlet}	air temperature conducted into a room [°C]
$\dot{m}$	mass flow [kg h^{-1}]	T_{return}	return temperature [°C]
n	radiator exponent [-]	T_{room}	indoor temperature [°C]
$\dot{Q}$	heat load [kW]	T_{supply}	supply temperature [°C]

Towards a more sustainable campus, proposal of improvement through renewable energies implementation

Diego Granados-López[1], Ignacio García[1,2], David González-Peña[1], Manuel García-Fuente[1], Elena Garrachón-Gómez[1], Sol García-Rodríguez[1], Ana García-Rodríguez[1]

[1] Solar and Wind Feasibility Technologies (SWIFT), Burgos (Spain).

[2] Institute of Smart Cities (ISC), Pamplona (Spain).

Abstract

The implementation of photovoltaic (PV) panels on building surfaces allows taking advantage of the building's energy potential through the distributed generation of electricity at the consumption point. Thus, electricity generation would be possible in remote areas, while avoiding transportation costs and electrical losses. This study analyzes the feasibility of installing PV panels in eleven buildings of the Universidad de Burgos. To achieve a correct implementation, possible shadows produced by nearby obstacles were avoided. Skelion, a plug-in incorporated in the image rendering software Sketchup, has been used. According to the results obtained, only two buildings do not offer good adequation to justify the photovoltaic installation.

Keywords: Solar Energy, Photovoltaic panels, Renewable energy, Energy performance, Simulation

1. Introduction

The relevance of renewable energies in the current energy scenario has notably increased compared to fossil fuels. At the present-day, the international entities are proposing new strategies to promote the development and implementation of technologies to promote the use of energies and ensure environmental conservation, such as the European Green Deal (European Commission, 2019). In the local context, the Spanish government is promoting multiple measures to reinforce energy savings. Regarding the regulatory framework, through the Integrated National Energy and Climate Plan 2021-2030, Spain commits to tackling climate change to get the condition of a carbon-neutral country in 2050, when the 42% of end-use energy should be came from renewable sources (INECP, 2021).

Of particular concern is the energy consumption of buildings, which are also responsible for approximately 36 % of all CO2 emissions of the European countries, a situation that is especially aggravated by the Union energy dependence (Directive (EU), 2018). In particular, public facilities are bound to have excessive or inefficient energy use, usually because of their size and age of construction (Granados-López et al, 2020).

Facing this challenge, it is of good interest to make the campus of the Universidad de Burgos (Spain) more sustainable by the renewable energy implementation. Nowadays, the market of the renewable energies is leaded by the photovoltaic technologies, that have improved to the point to reach profitable energy production (Suárez-García et al., 2017).

This work analyzes the viability of the implementation of photovoltaic (PV) panels on non-used surfaces of a set of buildings of the campus (buildings description in Fig. 1). This would make it possible to produce electricity near the consumption points and to avoid transportation cost and electrical losses. Besides, it describes the estimation process of photovoltaic production by 3-D modeling to ensure a correct implementation of the PV panels avoiding the shadows produced by the close obstacles.

© 2022. The Authors. Published by International Solar Energy Society
Selection and/or peer review under responsibility of Scientific Committee
doi:10.18086/eurosun.2022.10.05 Available at http://proceedings.ises.org

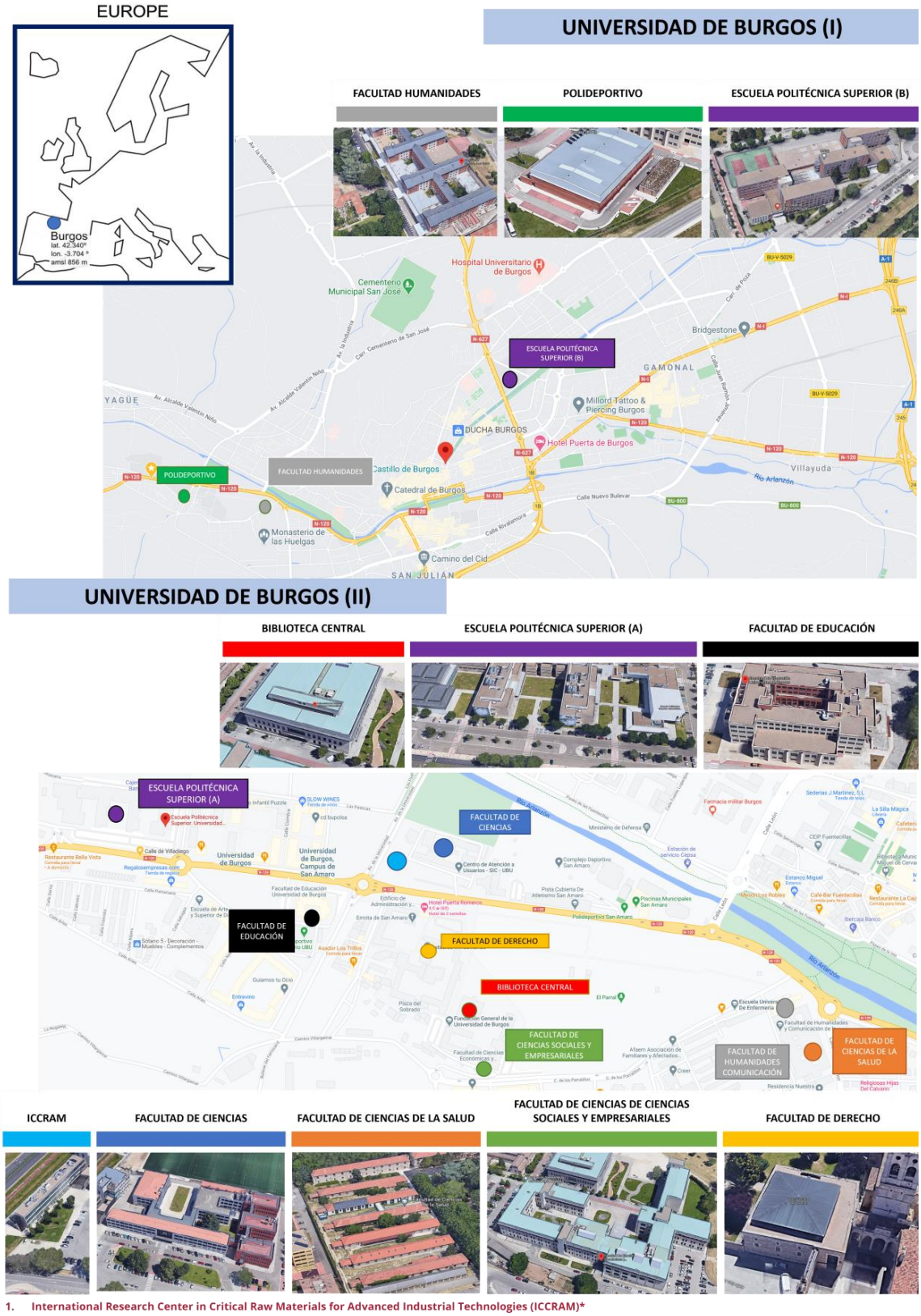

Fig. 1: Description of the Campus (II) of the Universidad de Burgos (Spain)

2. Methodology description: Campus description and PV-Simulation

The feasibility of implementing photovoltaic installations in a total of 11 buildings of the University of Burgos, was studied. As some of them are quite old, in some cases the orientation of the building may not be the adequate or are conditioned by several limiting factors. Therefore, the buildings have been divided into three groups according to the possibilities of improvement, see Tab 1: I) Installation of panels on flat roofs at 45 degrees, facing south. II) Installation of panels supported on simple auxiliary structures, on the slope of the roof, and facing the direction of the building facade (which may not be south), III) buildings that do not allow improvement, either by the obstacles of the environment, the characteristics of the building, or by legislation.

Tab. 1: Building stock description.

Group	Buildings belonging to each group
I	Facultad de Ciencias Sociales y Empresariales, Escuela Politécnica Superior (A), Escuela Politécnica Superior (B), Facultad de Educación, Biblioteca Central, and Polideportivo. **Limiting factors** -
II	Facultad de Ciencias de la Salud, Facultad de Humanidades, and Facultad de Ciencias **Limiting factors** • Facultad de Ciencias de la Salud is oriented to South - West • Facultad de Humanidades is oriented to South - West • Facultad de Ciencias is South - East.
III	ICCRAM, and Facultad de Derecho. **Limiting factors** • ICCRAM- It has all the cooling systems on the roof, and the vertical facades are glazed. • Facultad de Derecho - Placed in a historic setting, with high trees surrounding it.

This work uses the rendering technique to consider the shape of the building and its surrounding area. Therefore, all the possible obstacles are considered, and the solar irradiance that reaches the surfaces of interest can be calculated. As this first step is not limited to specific modeling programs, the Sketchup software was selected, a freeware license that has a large variety of plugins and pre-built designs (Sketchup, 2022). In the particular context of PV simulation, the Skelion plug-in (Skelion, 2022) is used due its versatility and its virtual interface. Thus, the sequence to estimate the PV production of a building is the following: First, the studied building and the surroundings are modeled by the software Sketchup. Then, the weather database Photovoltaic Geographical Information System (PVGIS) is selected (PVGIS, 2022). Finally, by the implementation of Skelion the PV production is obtained (see Fig. 2).



Fig. 2: Workflow for PV-Simulation

2.1. Building modeling - Sketchup

In urban environments, the shape and orientation of buildings can present very diverse and complex combinations, it mainly hinders the planification of energy retrofit process to fulfill the desired energy savings in each location. Currently, throughout the simulation it is possible to model the nuances with good detail level anywhere. Nonetheless, it is limited by the software and the researcher knowledge. In this work, Sketchup has served to 3D model several facilities of The Universidad de Burgos, which is a university that is located inland North of Spain (42°21′04″N; 3°41′20″O; 856 m above mean sea level), in Fig.1.

2.2. Photovoltaic simulation – Skelion

The objective of the proposed energy rehabilitation is to harvest solar radiation at the roofs. So, Skelion plug-in has been used to simulate and test the performance of the photovoltaic installation. The proposed PV-designs are shown below, Fig. 3 and 4. Panel specifications are 160 Power (W), 1.5 Length (m), 0.7 Width (m).

First, the proposal of photovoltaic installation for the Group I buildings are shown, see Tab. 1. In all of them, the roof is flat, consequently, it has been provided with panels, inclined at 45 degrees, approximately the latitude of Burgos, perfectively oriented to the South, Fig. 3.

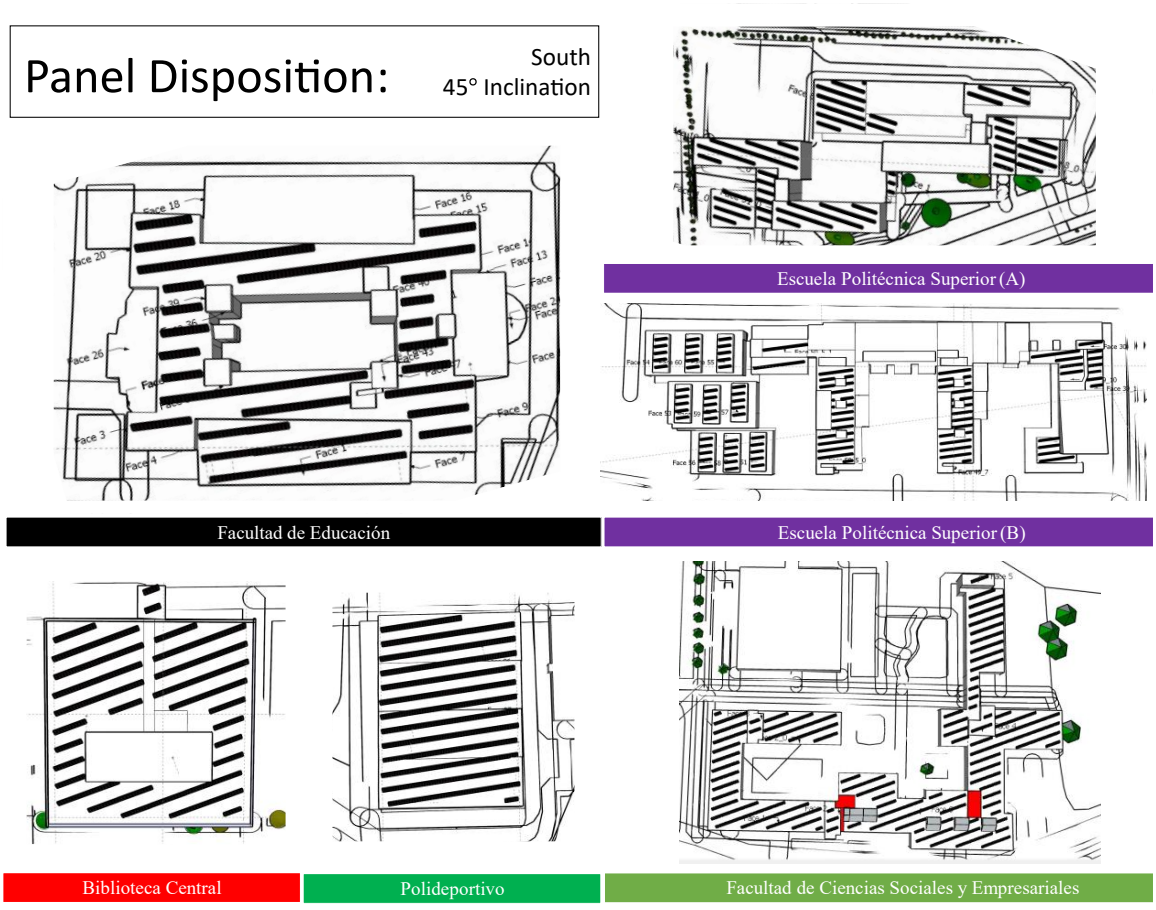

Fig. 3: PV installation on the Universidad de Burgos, Group I.

Moreover, note that in the facilities of Group II: “Facultad de Ciencias de la Salud”, “Facultad de Humanidades” and “Facultad de Ciencias”, the moderate slope of the roofs is characteristic of the building, for it, in these situations, the panels have been arranged directly on the roof, respecting the natural slope and orientation, Fig 4.

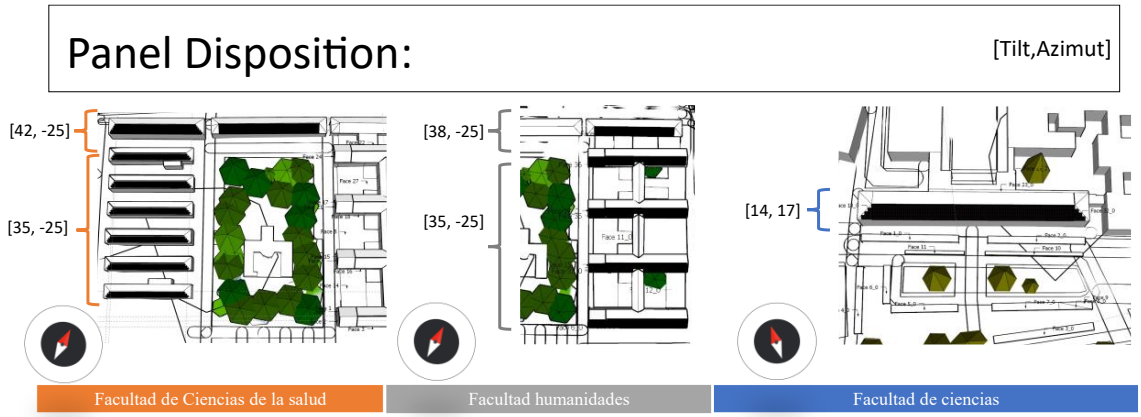

Fig. 4: PV installation on the Universidad de Burgos, Group II.

Tab.2 summarizes the basic characteristics of the proposed PV installations. In the case study, only two of eleven facilities of the Campus do not have adequate conditions to host photovoltaic installations: “Facultad de Derecho”, and “ICCRAM”.

Tab. 2: Panel distribution.

Facility	[Azimuth, Tilt]	Number of panels	Physical PV implementation
Facultad de Ciencias Sociales y Empresariales	[0,45]	1453	Yes
Escuela Politécnica Superior (A)	[0,45]	669	Yes
Escuela Politécnica Superior (B)	[0,45]	1294	Yes
Facultad de Ciencias	[17,14]	508	Yes
Facultad de Educación	[0,45]	519	Yes
Facultad de Humanidades	[-25,35] and [-25,42]	2582	Yes
Facultad de Ciencias de la Salud	[-25,31] and [-25,38]	1308	Yes
Facultad de Derecho	-	-	No
Biblioteca Central	[0,45]	474	Yes
ICCRAM	-	-	No
Polideportivo	[0,45]	655	Yes

2.3. Weather Database

Skelion Plugin provides an estimation of PV-production by using the previously 3D-model, its geographic location and shadows cast by near buildings and terrain (obstacles). Moreover, it uses the insolation dataset, that is ideally recorded near the location, in this case it has been obtained from the Photovoltaic Geographic Information System (PVGIS) database, a software tool of the European Union for the promotion of renewable energies implementation (PVGIS, 2022).

3. Results

The installed power and the annual energy production is calculated. Table 3 demonstrates that the viability of the self-sufficiency using photovoltaic energy for singular facilities depends on the building shape as well as the surroundings. In particular, the dimensions of the “Facultad de Humanidades” allows to host an installed power 5.4 times bigger than the “Biblioteca Central”, which is also transposed as larger total annual energy production, 612 versus 111 MWh.

Tab. 3: Study of viability for the facilities of the Universidad de Burgos

Facility	Power (kWp)	Energy (MWh) (yearly)
Facultad de Ciencias Sociales y Empresariales	232	340
Escuela Politécnica Superior (A)	107	144
Escuela Politécnica Superior (B)	207	305
Facultad de Ciencias	81	116
Facultad de Educación	83	121
Facultad de Humanidades	413	**612**
Facultad de Ciencias de la Salud	209	311
Facultad de Derecho	-	-
Biblioteca Central	76	**111**
ICCRAM	-	-
Polideportivo	105	154

The facilities analyzed have very different available useful areas and, consequently, host a useful power of different orders of magnitude. To facilitate the comparison of the facilities, the annual energy produced has been divided by the number of panels. Also, by using the meteorological data, Skelion estimates the percentage of solar energy that is missed due to near shadings. The analysis of the annual installed energy production per panel as well as the shading loses shows that the facility with the worst performance is "Escuela Politécnica Superior (A)", with 215 kWh/panel), Tab 4.

Tab. 4: Study of viability for the facilities of the Universidad de Burgos,

Facility	Power (kWp)	Energy (kWh/panel) (yearly)	Shading loses (%)
Facultad de Ciencias Sociales y Empresariales	232	234	2.11
Escuela Politécnica Superior (A)	107	**215**	**9.63**
Escuela Politécnica Superior (B)	207	236	1.31
Facultad de Ciencias	81	228	0.11
Facultad de Educación	83	233	2.61
Facultad de Humanidades	413	**237**	**0.7**
Facultad de Ciencias de la Salud	209	238	0.41
Facultad de Derecho	-	-	-
Biblioteca Central	76	234	1.91
ICCRAM	-	-	-
Polideportivo	105	235	1.47

Moreover, Monthly Energy production of the highlighted facilities ("Facultad de Humanidades" (larger production), "Biblioteca Central" (lower production), "Escuela Politécnica Superior (A)" (bigger shading loses)) is shown in Fig. 4. All of them presents a maximum in the central months of the year and a minimum production in the wintertime. But The production of the "Facultad de Humanidades" is not symmetrical along the year as it is facing South-west. It should be emphasized that even if the orientation and tilt is the same in "Escuela Politécnica Superior (A)" and "Biblioteca Central", the production of "Biblioteca Central" is always better as it has much less shading loses.

On the other hand, in the "Facultad de Humanidades", where the panels have been placed directly on the roof

respecting its inclination, several benefits have been found a) first, the production of this facility is similar to the others studied, b) since it requires a simple auxiliary structure, it is more economical, c) it allows placing the panels without separation (they will not generate shadows between them).

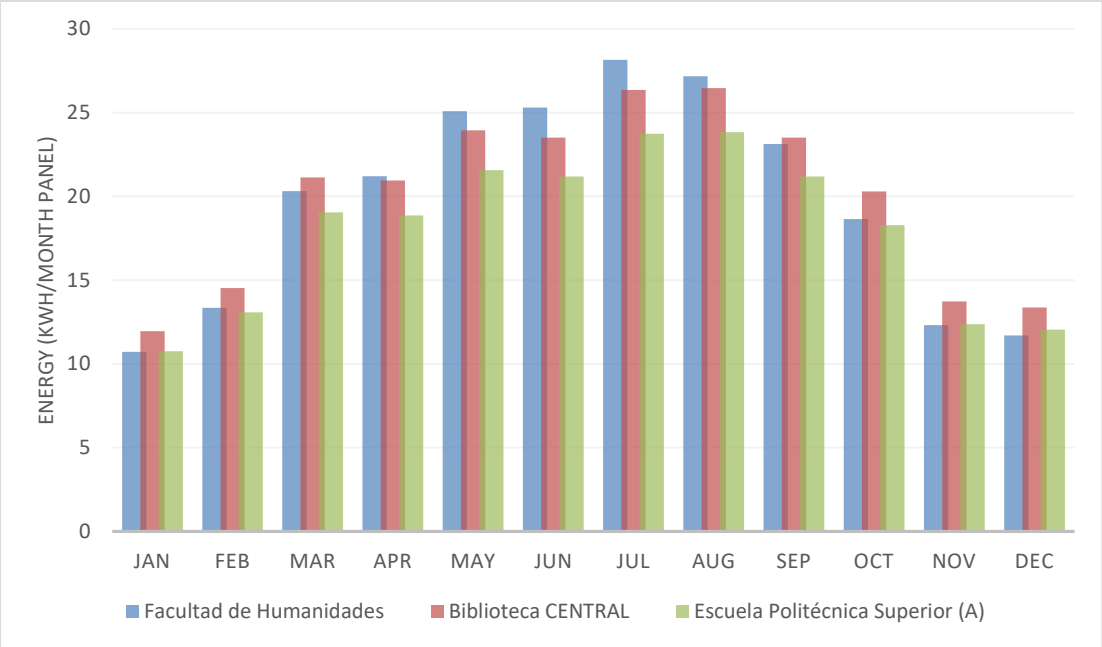

Fig. 4: Monthly Energy production

4. Conclusions

This study looks forward achieving a more sustainable campus, by proposing PV installation as renewable energies alternative to increase the sustainability and energy performance. Indeed, the implementation of photovoltaic (PV) panels on building surfaces allows taking advantage of the building's energy potential through the distributed generation of electricity at the consumption point. The following conclusions are derived:

1. Only two buildings cannot host the photovoltaic installation: “Facultad de Derecho”, and “ICCRAM”.
2. The PV installation designed of “Facultad de Humanidades” has the largest production, 612 MWh, using 2584 PV Si-monocrystalline panels wrapping the building's useful surface.
3. It can be very profitable to have the panels on sloping roofs, especially when the slope is very close to latitude, in addition to the economic benefit, it allows to host a high concentration of panels, Tab. 2.
4. Energy production per panel is very similar in all facilities, this has been achieved by avoiding nearby obstacles as well as the panels shading each other.
5. The energy saving is around 27%, this saving will be "approximately" the same in the months of January, February, March, November, and December. In the months of April, May, June, July, August, September, and October the savings can be increased (possibly to double 30-35%).

5. Acknowledgments

This research was funded by Spanish Ministry of Science and Innovation, grant number RTI2018-098900-B-I00 and Junta de Castilla y León, grant number INVESTUN/19/BU/0004 and INVESTUN/22/BU/0001. Diego Granados-López thanks grant PIRTU Program, ORDEN EDU/556/2019, for financial support. And Ignacio García thanks to the Spanish Ministry of Universities and the European Union-Next Generation EU for their financial support (Program for the requalification of the Spanish university system 2021-2023, Resolution 1402/2021).

6. References

Granados-López D. et al , 2020. Towards net-zero public buildings through BIPV: a case study in Castilla-León (Spain). *37th PVSEC, European Photovoltaic Solar Energy Conference and Exhibition. Online, 7-11 September*.

Directive(EU), 2018. Directive (EU) 2018/844 of the European Parliament and of the Council of 30 May 2018 amending Directive 2010/31/EU on the energy performance of buildings and Directive 2012/27/EU on energy efficiency. Off. J. Eur. Union, L 156/75 75–91. Available in:https://eur-lex.europa.eu/eli/dir/2018/844/oj.

European Commission, 2019. The European Green Deal. Eur. Comm. COM(2019) 640 Final Commun.

PVGIS, 2022. Photovoltaic Geographical Information System. Oficial webpage. https://joint-research-centre.ec.europa.eu/pvgis-p. Available in:https://joint-research-centre.ec.europa.eu/pvgis-photovoltaic-geographical-information-system_en, Last accessed 11/09/2022.

Skelion, 2022. Skelion. Oficial webpage http://www.skelion.com/, Last accessed 11/09/2022.

Sketchup, 2022. Sketchup. Oficial webpage. https://www.sketchup.com/es, Last accessed 11/09/2022.

Suárez-García, A. et al., 2017. Estimation of photovoltaic potential for electricity self-sufficiency: A study case of military facilities in northwest Spain. J. Renew. Sustain. Energy 9(5). https://doi.org/10.1063/1.4995687.

SmartPrio^{GIS}

A concept for recording, holding and evaluating data as a contribution to CO_2 reduction for the Kassel University campus

Swen Klauß, Anton Maas, Rolf Gross, Lukas Lohse

University of Kassel, Kassel (Germany)

Summary

The basic idea of the new SmartPrio^{GIS} concept is to collect building-related data from different formats and from different sources in a structured system. At the beginning of the process, it is important to get a broad overview of the properties and not to collect the best possible level of detail for all potential applications right from the start. By collecting the information with a geo-data referenced application such as ArcGIS from Esri, a quick overview of relevant data is made possible. Due to the successive detailing of the data collection with progressive concretization of measures, significantly fewer human resources are required at the beginning of the process to collect building data. The closer the implementation of energy retrofit measures gets, the more extensive and detailed the available information becomes, making the digital image of the campus increasingly accurate. During the overall process, prioritization options emerge by identifying potential CO_2 savings.

Keywords: concept, energy retrofit, data collection, data management, data evaluation, prioritization, successive detailing, building, university campus, implementation orientation

1. Introduction

As part of the "CampusKassel2030" research project funded by the German Federal Ministry of Economics and Climate Protection, the new SmartPrio^{GIS} methodology for data collection, storage and evaluation is being developed and tested using the University of Kassel campus as an example. With regard to energy refurbishment and efficiency improvement to accelerate the energy transition, the concept is designed to be implementation-oriented and to provide concrete support for the responsible decision-makers in dealing with the properties. Transferability to similar building areas is an important aspect.

The basic idea behind the innovative approach is to reduce the use of resources when collecting data. Neighborhood concepts usually begin with a complete data collection at the start of the project in order to be able to record the variables and boundary conditions for determining the energy balance as comprehensively as possible. This requires a great deal of time and personnel, although the relevance of the results for a longer-term transformation process is comparatively low. Particularly in the case of a university campus, those responsible are familiar with the properties managed and the fundamental aspects of the buildings.

With the SmartPrio^{GIS} concept, an implementation-oriented approach is developed that collects only a basic set of few, but relevant data for all buildings at the beginning of the process. The scope and detail of the database is successively updated as measures are concretized in the course of the process. This means that data collection is largely supported by planning steps that are necessary anyway and does not tie up any additional resources.

This makes the concept fundamentally different from other approaches and projects for collecting and using energy-related data to save energy or increase efficiency. Other projects also use geoinformation systems to collect, manage and apply the data. Examples to be mentioned in this context are:

- Wärmeatlas 2.0 - GIS model of the useful energy demand for space heating and hot water in the German building stock [1]

© 2022. The Authors. Published by International Solar Energy Society
Selection and/or peer review under responsibility of Scientific Committee
doi:10.18086/eurosun.2022.10.06 Available at http://proceedings.ises.org

- ENA - Energy master planning for grid-connected waste heat utilization; sub-project: GIS-based energy master planning system, stakeholder-specific requirements of municipalities and development of guidelines [2]
- GIS building energy - national database for energy deliveries to buildings [3]

However, the methodology of data collection of the examples mentioned does not follow the new approach described here of collecting a relevant but small amount of data at the beginning of the project by prioritization with as little effort as possible and successively expanding it during the course of the project.

The first task is to collect the data available in various places and in different formats and to structure them in such a way that central access is possible. For this purpose, data sets available as Excel sheets or CVS files, for example, are loaded into a database and further processed by means of SQL commands in order to be able to use and visualize them in ArcGIS. The data originate almost exclusively from the construction department of the University of Kassel or are coordinated with it. Thus, the data quality in terms of goal achievement can be rated as very high. Figure 1 schematically illustrates the described procedure using a concrete example. In the future, consumption data from the building management system (BMS) could be sent directly to an Oracle database to be configured accordingly, which would simplify the process and enable prompt visualizations of measured values and results.

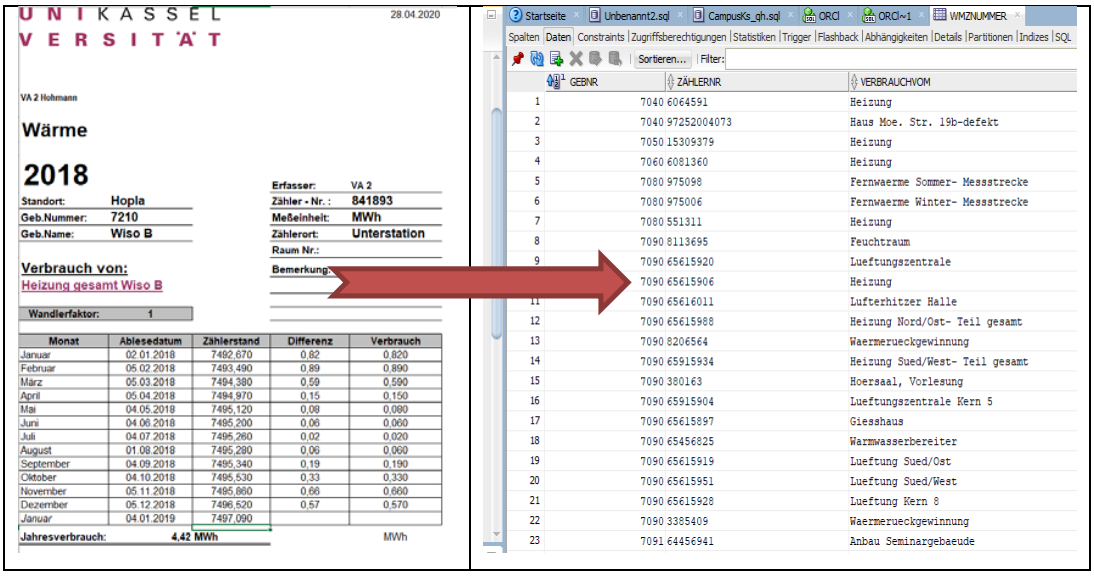

Figure 1: Transfer of consumption data from Excel sheets to a database

In addition to the advantages of the methodical approach, the approach of managing the collected data with a geo-data referenced application from the beginning in order to be able to evaluate them within a system for strategic planning, if required, is to be regarded as innovative. Through GIS-based data management, various types of information from different data sources can be summarized, localized and visualized on a building-by-building basis. With the appropriate structuring and processing of the data, it becomes possible to make information available at "one glance" that was previously stored in various places and whose existence was sometimes only known to a small group of people. In addition to the strategic component, the transparency of information and the usability of data within departments and also across divisions are significantly improved.

2. Methodological approach and data collection

The SmartPrio^{GIS} concept is based on a three-level approach, with each level differing in its level of detail, and with more and more concrete information being obtained as the levels are processed.

In line with the research approach, the concept initially refers to a purely energetic view of the refurbishment options and the increase in efficiency. Cost-effectiveness considerations are not included. However, this does

not rule out the possibility of further development at a later date. The evaluation criterion is CO_2 emissions, which can be calculated from the consumption for heating the properties and generating hot water as well as the electricity consumption multiplied by the respective emission factor.

The methodological principle is based on the fact that data is successively collected based on a mandatory data set depending on the available information. Ultimately, there should be a high density of information on the buildings at the end of the transformation process. However, the achievement of this optimal data situation for the campus is not bound to a tight time schedule. The information will primarily be obtained in connection with measures that are due to be implemented anyway.

The conceptual approach and the basic technical structure are shown in Figure 2. The continuous georeferenced data management is implemented in the project with the software ArcGIS of the company Esri.

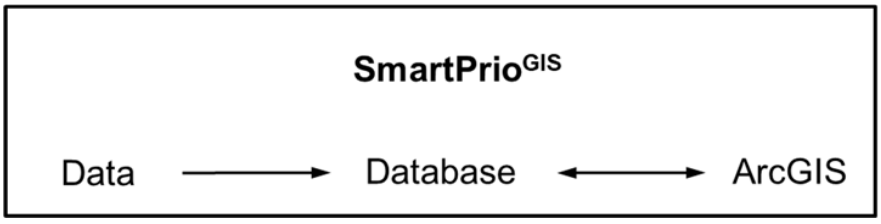

Figure 2: Illustration of the SmartPrio^{GIS} concept and the basic technical structure

The innovative character consists in the gradual acquisition of data and the successive increase in the level of detail and the scope of data in the course of the processing. At the beginning of the project, only a few data on the individual buildings are available, the so-called basic data. With the help of this basic data, an overview of the building stock should be made possible and thus an energy assessment should be carried out.

It is particularly worth mentioning that the scope of the basic data as well as the type and scope of the data to be collected later were coordinated with the university's building department from the very beginning of the project. This promotes the practicality and applicability of the concept and consistently develops the methodology in an implementation-oriented manner.

Figure 3 shows an example of the evaluation of the final energy consumption of the buildings in comparison. The larger a circle, the greater the final energy consumption for heat generation or power supply. The diagram on the right side of Figure 3 shows the final energy consumption of heat generation for eleven buildings. The buildings are sorted in descending order according to their final energy consumption for heat.

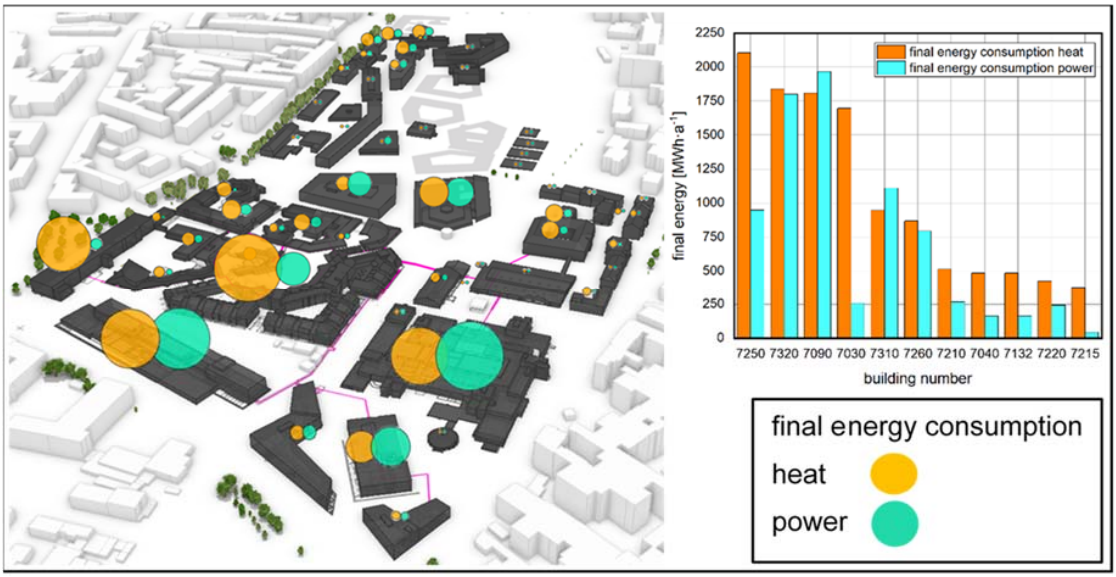

Figure 3: left extract campus overview, right final energy consumption per building – both from ArcGIS

The described methodology and the three-level model of building-related data collection can be extended beyond the energy aspects discussed here to other areas. By considering the idea of transferability, the use of the SmartPrio^{GIS} approach is explicitly connectable beyond the area of the university campus under consideration and offers corresponding development potential.

The concept is presented and described in more detail below. The illustrations refer to the consideration of greenhouse gas emissions via CO_2 equivalents. Of course, other variables such as final energy demand or consumption can also be considered and presented. A distinction is made between expenditures for the provision of heat and electricity, as there are differentiated options for influencing these.

Figure 4 shows the overview and a kind of flowchart for the application of the SmartPrio^{GIS} concept on the three levels.

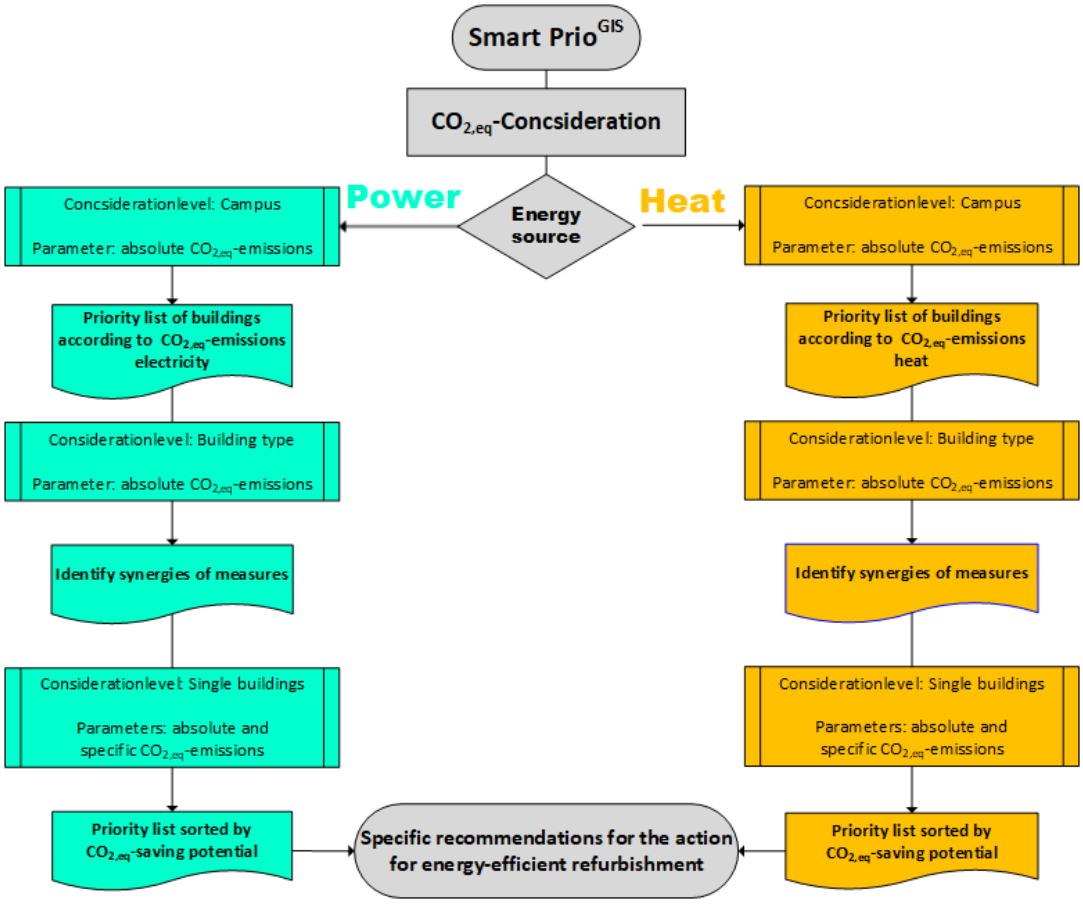

Figure 4: Overview and paths of the SmartPrio^{GIS} concept for the aspects electricity and heat

Consideration level - Campus

The top level of consideration is the campus or area under consideration. Nine baseline data were identified in coordination with the building department and collected for each building within the area of consideration. Specifically, these are

- Building name and number,
- Year of manufacture,
- Construction type,
- Usage,
- Location,

- Area (net floor area),
- Energy consumption in the last three years and
- the main energy sources.

This information as well as the calculated CO_2 emissions can be displayed in the interactive map by clicking on a building.

As a result, at the "building" level of analysis, a table is created differentiating between electricity and heat, in which the buildings are sorted according to the level of equivalent CO_2 emissions. This allows an initial assessment and classification of the buildings and an estimate of their energy quality. The evaluation of CO_2 emissions is analogous to the evaluation of final energy consumption in Figure 3.

In the course of the project, the practical advantages of successive data acquisition and synergy effects from the comprehensive view of the campus became apparent. CAD plans were extracted from the ArcGIS data to support the planning of the university's heating network. On this basis, the heat network was georeferenced as part of an external planning service, and this information was imported into ArcGIS and thus made usable for the project as well as the digital campus image. This generated only a small direct effort, since it was a planning service that was pending anyway. The level of detail of the data and the informative value of the digital campus image could be significantly increased as a result.

Cross evaluations are possible by linking the basic data. The geo-referenced visualization of the buildings and data allows a clear illustration that shows energy facts about the campus at a glance.

Consideration level - building type

The previously collected data is used directly at this observation level or evaluated to identify building types. This allows building clusters of the same age and construction to be formed. As a result, detailed information of individual buildings is derived and transferred under certain conditions and assumptions.

For this purpose, additional data on the building envelope and the systems engineering are recorded and evaluated. Analogous to the building level, the building types are sorted and displayed according to CO_2 emissions. This offers the advantage that critical or energetically unfavorable building types can be quickly identified.

As can be seen in Figure 5, the formation of building clusters also has the advantage that possible synergy effects of renovation or efficiency measures can be derived. In combination with the geo-referenced representation, not only the same building characteristics become visible, but also a possibly given spatial proximity can be recognized directly. From this, in turn, packages of measures can be planned that go beyond dealing with individual buildings.



Figure 5: Excerpt of the paths for the "building type" consideration level

Here, too, as at the "campus" level, the advantage of successive data collection becomes apparent. Thanks to the existing overall view and the exchange with the building department and external service providers, upcoming blower door measurements could be used to couple them with thermographic images on the one hand and to use the data directly on the other. Through clustering, it is also known which buildings have the same construction and thus potentially similar weak points. Coordinated improvement measures can thus be planned and synergy effects exploited.

Consideration level - building

This level has the highest level of detail. The data obtained at the other levels and in the course of the project are supplemented by building-specific information. The focus is initially on the buildings that can be assigned to the critical building types as a result of the clustering. At this point, it is important to emphasize once again that this information is not obtained specifically to improve the data situation. Following the approach of successively obtaining data that are collected anyway, this information can be obtained for different reasons. One reason would be that concrete energy refurbishment measures are pending for a building and for this reason detailed data collection is necessary. The more intensive examination of individual buildings can also take place in connection with student work. For example, bachelor's and master's theses are carried out in the course of the project, the relevant results of which are then added to the digital campus image in ArcGIS.

At the "building" level, findings from more detailed investigations of the building envelope and systems engineering are recorded. In this context, the overall energy balance of the buildings according to DIN V 18599 is a calculation method that produces detailed results. However, determining the energy requirements according to this method for the university buildings, some of which are in mixed use, involves the corresponding effort. Here, in particular, it becomes apparent that it makes sense to not only want to collect this data in order to have a comprehensive data base. The collection of such detailed data can only be efficient and resource-saving if these tasks are pending anyway or if they are processed in the course of parallel projects.

Like the overall energy balance according to DIN V 18599, the creation and evaluation of thermographic images involves considerable effort. This would not be justified just for the sake of the breadth of the data base. However, to collect this information in connection with student work can be understood as a “necessary anyway measure”, which provides the students with very practical and concrete references in addition to the increase in knowledge. For the successive data collection of the digital campus image, the benefits can be seen in Figure 6. In this view, each point on the left side of the image shows a location for which thermography evaluations are available. These can be viewed directly by selecting a point. The right side of Figure 6 shows the pictorial representation and key data, and other relevant information can also be displayed.

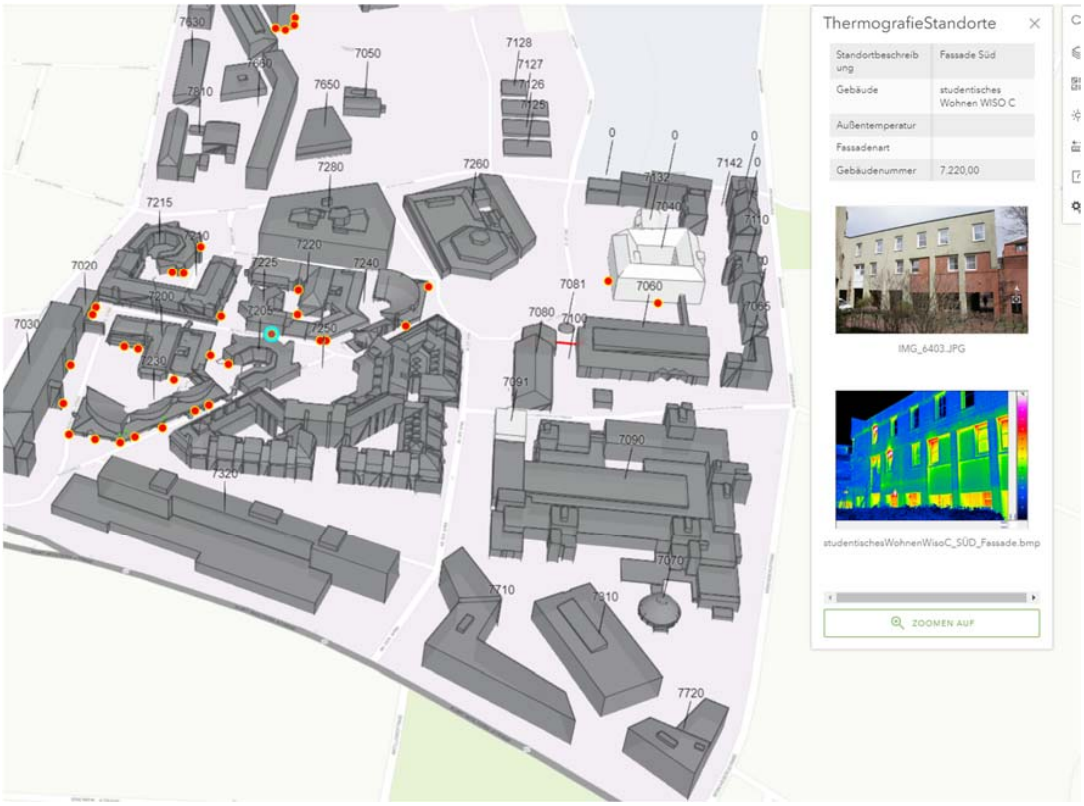

Figure 6: Exemplary representation of thermographic images from student work.

The compiled data and calculation results can be used, for example, to develop renovation measures and quantify savings potential. This can be done for individual buildings as well as for clusters of buildings by means of possible cross-analyses. Of course, the ultimately comprehensive and detailed data at the end of a data collection process also allow statements to be made about the campus balance sheet and savings associated with renovation measures.

3. Procedure using the example

An efficient approach to data collection is to use the smartphone app "Field Maps" from ArcGIS. The browser-based map, which depicts the campus, is used on a mobile basis with the smartphone. This makes it possible to directly record information identified during property inspections and to assign it to a specific location. This means that any data, such as system components (HVAC elements, transfer stations, etc.), thermographs, endoscopies and photos can be georeferenced and assigned to the buildings on the digital map using field maps.

With the help of the online map, in which the own position is displayed, relevant points can be found quickly. Figure 7 shows an example of the procedure for detecting a thermal bridge by means of a thermographic image. A situation (e.g. representation of a thermal bridge, defects, technical faults, etc.) can be evaluated on site and immediately stored digitally in the map as information. Every user of the map thus has direct access to current information.

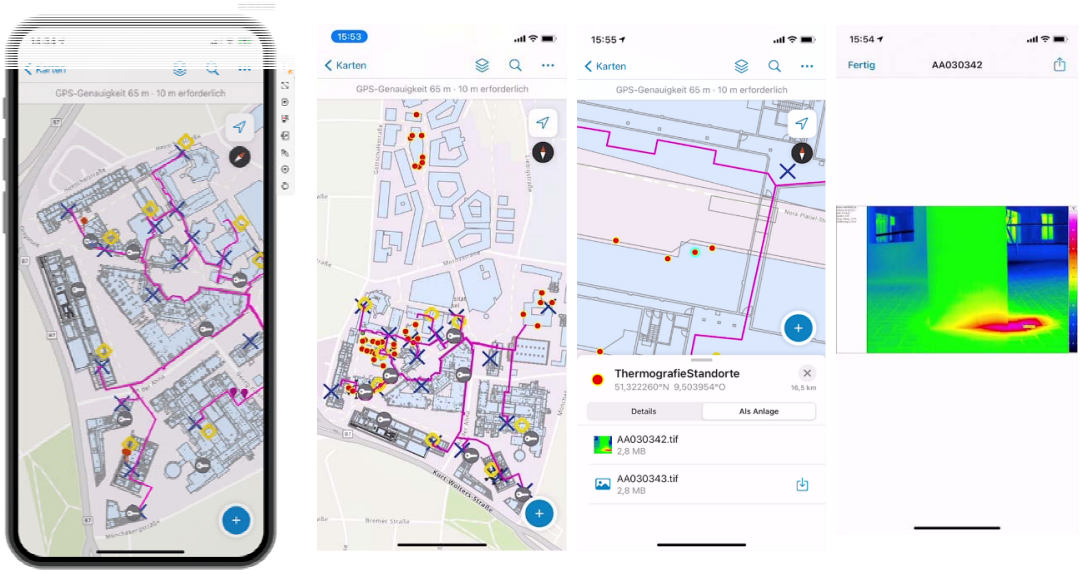

Figure 7: Illustration of the application of the smartphone app "Field Maps" using the example of a thermal bridge

In the future, the information collected in this way need not be limited to energy-related aspects. It is conceivable that the procedure could also be used in other contexts, e.g. for damage reports, for complaint management or for room bookings. For this, it would be necessary to use further functions of the ArcGIS software and to adapt them as required. However, this is easily possible for experienced users, which allows a very individual use of the data and functionalities on the basis of the campus image created.

4. Summary and outlook

The SmartPrio^{GIS} concept developed and available at provides a working basis that can be used and expanded in a variety of ways. In addition to the basic conceptual idea of not having to collect all possible data for a campus at the beginning of a process, but rather to compile this data successively during the course of the process, a resource-saving approach is demonstrated. In conjunction with georeferenced data collection and storage, a digital campus image is created that can be expanded and also used for other subject areas. In this case, only the aspects of energy refurbishment and efficiency improvement are considered. The commercial

product ArcGIS from Esri is used as the software for georeferenced data acquisition and storage, since the University of Kassel has a campus license and therefore uses it extensively. The concept can of course also be used in conjunction with other tools.

In the specific case of the application of the SmartPrio^{GIS} concept combined with ArcGIS for the campus of the University of Kassel, it can be stated that the findings to date are very promising. A large amount of data and information is naturally available in the building department, but access is not always possible centrally and across topics. The structured compilation of the data and the central availability of the information on a platform alone, in combination with visualization, offer enormous advantages in terms of meaningfulness and applicability. This could be further optimized so that, ideally, the existing data and their storage location could be found via a central access point (ArcGIS).

At the moment, only a small part of the software's functionalities is used. Above all, there is potential in the area of data evaluation and automated data transfer. In this context, the implementation of a dedicated geodata server could open up further areas of application.

Using functionalities such as "stories" or "dashboards" it is conceivable that the stored data could also be used to inform, sensitize, and activate people for energy-related issues. This could address employees of the University of Kassel as well as students. The use of ArchGIS in various departments would also allow the information already collected about the campus to be used and supplemented in research and teaching.

5. References

[1] ifeu Heidelberg gGmbH; GEF Ingenieur AG; geomer GmbH. Wärmeatlas 2.0 - GIS-Modell des Nutzenergiebedarfs für Raumwärme und Warmwasser im deutschen Gebäudebestand. 2019. URL: https://www.ifeu.de/fileadmin/uploads/Modellbeschreibung_W%C3%A4rmeatlas_2.0.pdf

[2] EnEff:Wärme: ENA – Energieleitplanung zur netzgebundenen Abwärmenutzung; Teilvorhaben: GIS-basiertes Energieleitplanungssystem, akteursspezifische Anforderungen Kommunen und Erstellung Leitfäden. ifeu –Institut für Energie- und Umweltforschung Heidelberg gGmbH. Laufzeit: 04.2020 bis 12.2023. Aktenzeichen 03EN3011A. URL: https://ewb.innoecos.com/Group/03EN3011A/Informationen/Start/Blog

[3] SIA - Schweizerischer Ingenieur- und Architektenverein; OPAN concept SA. GIS-Gebäudeenergie - Nationale Datenbank für Energielieferungen in Gebäude. 2015. URL: https://www.sia.ch/fileadmin/content/bilder/Themen/Energie/150316_GIS-Geb%C3%A4udeenergie_D.pdf

DERIVATION OF HEATING LOAD PROFILES ON THE BASIS OF DEMAND-CONSUMPTION ANALYSES

Michael Krause[1], Til Stricker[2], Leon Schellhase[3], Swen Klauß[2] and Anton Maas[2]

[1] Fraunhofer Institute for Energy Economics and Energy System Technology IEE, Kassel (Germany)

[2] Department of Building Physics, Kassel University (Germany)

[3] Department of Integrated Energy Systems, Kassel University (Germany)

Abstract

Without having extensive measurement equipment installed, only annual or monthly values of the energy consumption of existing buildings are usually available. The same applies to demand analyses, for which usually monthly and annual values for net, final and primary energy requirements are calculated. However, a higher temporal resolution of the consumption/demand data can be an important decision-making assistance both in the design of new buildings and in the planning of renovation and reconstruction measures. However, the determination of the time-resolved energetic behavior of buildings with the help of dynamic simulation models is very complex. As an alternative, a method was developed that allows hourly heating load and final energy profiles to be derived on the basis of comparatively simple approaches. The method was tested using an existing building in the local heating network of Kassel University, on a new building of the university campus being in the planning phase as well on the new institute building of Fraunhofer IEE being recently completed.

Keywords: space heating load, building heating load, energy balancing, thermal-dynamic simulation, demand-consumption balancing, DIN V 18599, DIN/TS 12831-1, method development

1. Introduction

Without extensive monitoring equipment, usually only annual or monthly values of the electrical and thermal energy consumption of buildings exist. In the case that demand analyses have been carried out, e.g. on the basis of DIN V 18599, only monthly and annual values for net, final and primary energy demands were evaluated. The procedure for calculating the space heating load according to DIN/TS 12831-1 also does not consider thermal dynamics of the buildings.

Both in the design of new buildings and in the planning of renovation and conversion measures, a higher temporal resolution of consumption/demand data can be important in various contexts. This applies, for example, to the planning of thermal and electrical storage systems, to possibilities for optimizing local heating networks in the provision and transfer of heating and cooling, or to the integration of load shifting strategies and measures for sector coupling.

For the investigation of the thermal dynamics of buildings and supply systems, the use of simulation environments such as TRNSYS, Modelica or IDA ICE is a good choice. The creation of dynamic simulation models quickly becomes very time-consuming, both for complex buildings or if a larger number of buildings is to be considered. With the complexity, the error sensibility of the numerical modelling increases at the same time, so that a validation on alternative data, e.g. from a consumption measurement or a normative demand calculation, is essential. In addition, the necessary building and plant engineering data is in many cases not fully available in order to parameterize detailed simulation models in a suitable way. For existing buildings, construction plans are often insufficiently available or inaccurate, if, for example, conversion measures have taken place or supply systems have been adapted. Parameterization in the above-mentioned simulation environments is therefore extremely difficult or does not adequately represent the existing situation. In case of new building projects, especially in the early planning stage, only limited information is available or for many aspects, no specification has been be made

© 2022. The Authors. Published by International Solar Energy Society
Selection and/or peer review under responsibility of Scientific Committee
doi:10.18086/eurosun.2022.10.07 Available at http://proceedings.ises.org

yet. If not even the cubature or orientation of the building has been determined during preliminary investigations, the application of detailed simulation tools would be of limited use. Nevertheless, for many conceptual investigations it is necessary to consider results with a higher temporal resolution, for which simplified mapping methods could represent good compromises.

2. Methodical Approach

Based on these basic considerations, a mapping method for buildings was developed in the CampusKassel2030 research project funded by the BMWK. With this method, which is further described in (Stricker 2022), the modeling and calculation effort for the required hourly profiles, e.g. for heating load or final energy demand, can be kept as low as possible. The method is based on the calculation rules of DIN V 18599 and is supported by the procedure for calculating the space heating load according to DIN/TS 12831-1 as well as by a demand-consumption comparison. The variables to be calculated within the method, using for the climate consideration test reference year data of the DWD, are:

$$\Phi_{HL,zone} = \Phi_{T,zone} + \Phi_{V,zone} - \Phi_{I,zone} - \Phi_{S,zone} + \Phi_{SpAufh,zone} - \Phi_{SpAus,zone}$$

With being:

$\Phi_{HL,zone}$	W	Heat Load of the respective zone
$\Phi_{T,zone}$	W	Transmission heat loss of the zone
$\Phi_{V,zone}$	W	Ventilation heat loss of the zone
$\Phi_{I,zone}$	W	Internal heat gains of the zone
$\Phi_{S,zone}$	W	Solar heat gains of the zone
$\Phi_{SpAufh,zone}$	W	Power for preheating the zone and its thermal mass
$\Phi_{SpAus,zone}$	W	Power taken from the thermal mass to the zone

In principle, the methodology can also be applied to weather-adjusted consumption data. For this, the availability of monthly consumption data would be desirable. However, annual consumption data are also sufficient.

The transmission heat sinks are evaluated by determining the heat transfer coefficient H_T via an indirect determination from the calculation methodology according to DIN V 18599-2. With regard to the determination of the ventilation heat sinks, infiltration and ventilation air exchanges have to consider times of building use and non-use and as well as the heat recovery efficiency. Internal heat sources are taken into account according to the specifications of DIN V 18599-10 and are integrated in the calculation methodology. The evaluation of solar heat sources requires a conversion of the hourly values of direct and diffuse horizontal radiation of the test reference year data into radiation intensities on planes of other orientations. The solar heat inputs are then calculated by multiplication with the transmission coefficients of the transparent building components and the reduction factors and shading ratios, e.g. by a manual shading control, according to DIN V 18599-2.

Especially for questions of load smoothing or load shifting as well as for the evaluation of the impact of temperature reduction during nights and heating times, the correct mapping of the building inertia is essential. Without the possibility of transient consideration of the thermal storage behavior of a room or the whole building, an hourly steady-state storage model is used within the developed method. For this purpose, the thermal mass of the building is assumed like a kind of battery storage. For this purpose, the definition of the heat storage capacity C_{wirk} within DIN V 18599-2 is used. Furthermore, a maximum transfer capacity between storage tank and room has been defined. For this purpose, the basic heating value from DIN/TS 12831-1 was used as an approximation of the maximum heat flow. Following this, the necessary storage limits are defined and the effective charging and discharging capacities can be calculated. For evaluating final and primary energy demand of buildings, the consideration of building systems is necessary. For thermal storages like e.g. ice storage systems, the charging and discharging processes are again integrated in the calculation method according to battery storages with maximum and minimum charging capacities.

In addition to thermal aspects of buildings, the determination of the electrical power demand is an important target

value, particularly for questions of sector coupling, especially if the building has its own power generation systems. In contrast to DIN V 18599, it is not sufficient to limit the calculation to the electricity demand of the building systems so that an estimation of the user consumption is necessary for the calculation procedure. In this context, it is important to distinguish between periods of use and periods of non-use. To avoid overly regular profiles, the stochastic smoothing of utilization profiles and thus of internal gains and electrical consumption is integrated in the developed method. The degree of stochastic variations is a parameterization variable and can be selected individually in the procedure.

3. Use Cases

The developed method has been applied to three different use cases. In a first step, the method was tested for the determination of possible temperature reductions within the heating network of Kassel University. For this, the existing building of the headquarter of Kassel University was investigated in detail. In addition, the new building for the natural sciences at Kassel University currently being in the design phase was modeled with the developed method in order to give conceptual support to the planning team. Finally, the new institute building of Fraunhofer IEE being recently completed has been investigated for evaluating and optimizing the energy supply system based on an ice-storage heat pump system.

3.1. Headquarter of Kassel University

Fig. 1 shows the investigated headquarter of Kassel University. The building has been analyzed by means of two approaches. On the one hand, the overall energy balance is calculated using the static calculation method of DIN V 18599, and on the other hand, thermal-dynamic simulations are carried out for the building using the IDA ICE application from EQUA. The calibration of both the time series calculation and the IDA ICE simulation is carried out in the present case with consumption data of the building.



Fig. 1: Digital twin of the headquarter of Kassel University (https://kassel.virtualcitymap.de)

As can be seen in Fig. 2, the static calculation method according to DIN V 18599, in this case performed with the software ZUB Helena from ZUB Systems, overestimates the measured final energy consumption (district heat) by roughly a factor of two. When adjusting the monthly balancing method to the real user behavior, the deviation reduces. However, a significant deviation remains both to the measured consumption as well as to the simulated demand. A further reduction seems only possible with more in deep adjustments of the building parameters and the user behavior.

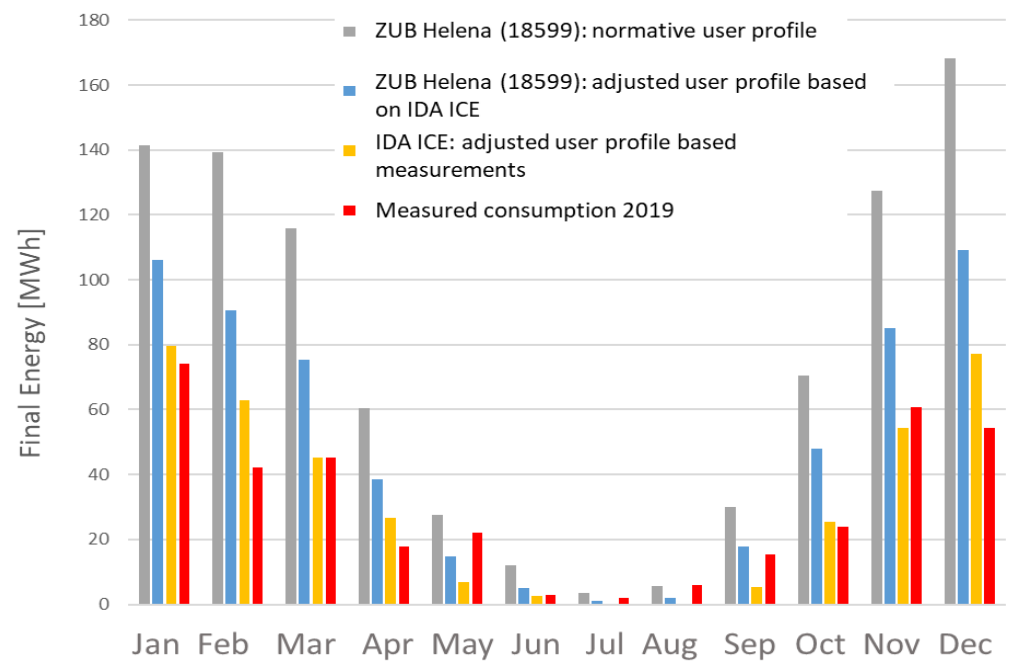

Fig. 2: Comparison of the calculation methods ZUB Helena and IDA-ICE with the measured values of district heat supply.

Fig. 3 shows the determined heat load profiles of the head quarter of Kassel University determined with the static method developed in the research project CampusKassel2030 using the approaches of DIN/TS 12831-1. As can be seen, the static calculation method using energy balances according to the method of DIN V 18599 follows the simulated load profiles with a good tendency, however, the method overestimates the simulated values by approximately 30 %. Hereby, the deviations are in the same range as shown in Fig. 2. Nevertheless, considering the systematic deviations, the load profile generation represents a smart method for determining time serials, especially in cases when a static model according to DIN V 18599 is available. Taking into account the systematic deviations, the method still serves as a good basis for optimizing the local heating network of the Campus Holländischer Platz of Kassel University.

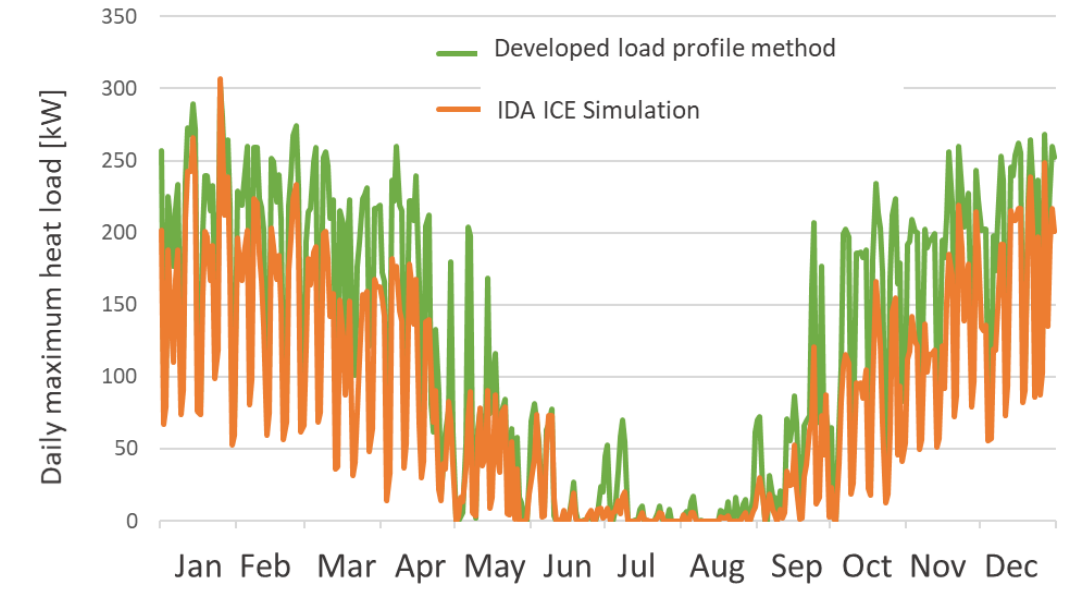

Fig. 3: Determination of hourly heat load profiles and comparison to IDA ICE Simulation

3.2. Building for natural sciences at Kassel University

The new building complex for natural science to be developed at the Campus Holländischer Platz at Kassel University is currently within the design phase cf. Fig. 4. In order to support the design process, the method of heat load derivation of existing buildings was extended to the evaluation of new buildings. For this, a zone-based exemplary geometry of the main building of the natural science complex was developed considering the space requirement of the different faculties as well as the planning specifications of the laboratory planner. The building was modelled according to the parameterization within DIN V 18599.

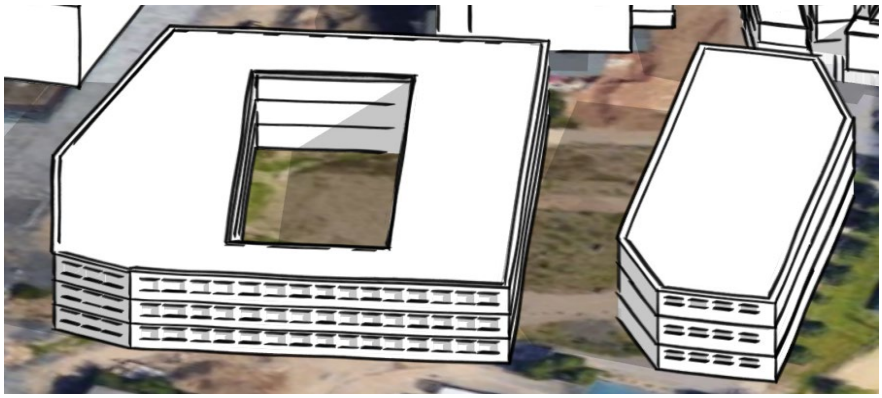

Fig. 4: Selected architectural design for the new Natural Sciences Building complex consisting of a main building (left) and a cleanroom building (right).

With the help of the developed static procedure, conceptual investigations of the heating and cooling supply were then carried out. Hereby, the investigations especially focussed on was heating and cooling concepts based on heat pump technology supported by photovoltaic systems as well as thermal storage systems. In order to estimate the resulting final energy demand profile of the building, the time serial method has been extended among the electricity consumption caused by light, technical systems as well as the electricity consumption of building users (e.g. computers, laboratories, etc.). For this, measured consumption data from (Biechele 2015) have been used for parametrization. In addition, a randomize function has been integrated to consider simultaneity. As shown in Fig. 5, the method serves as a good indication for electricity consumption and generation and helps to dimension heat pumps and PV-systems.

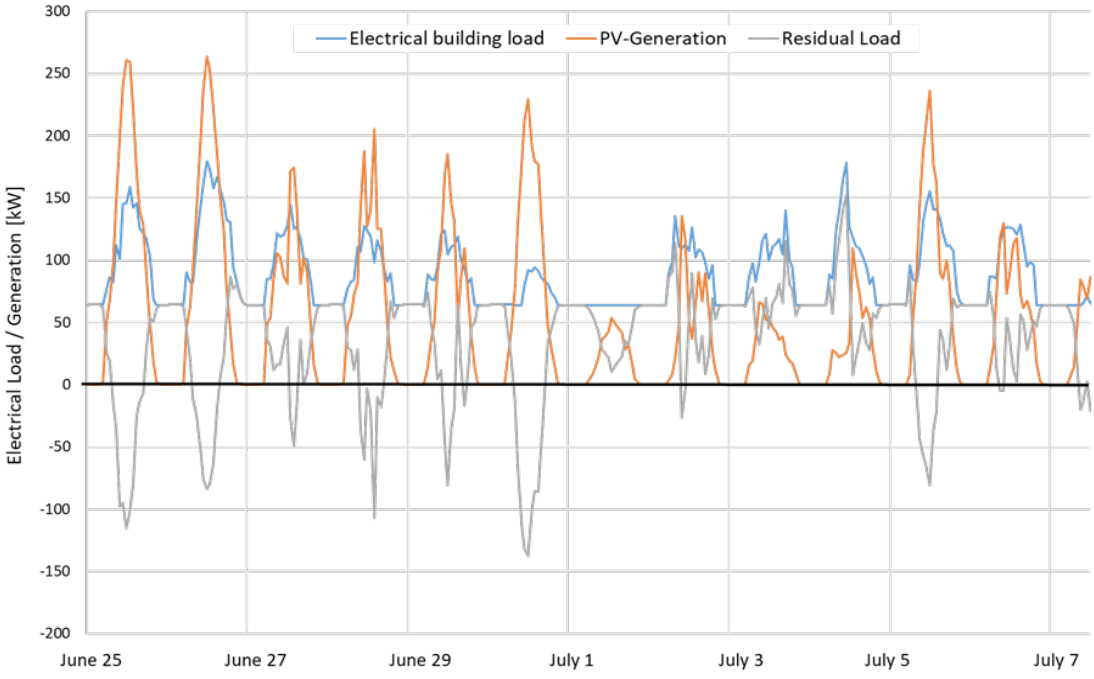

Fig. 5: Resulting electricity balance for a summer period within the new Natural Science Building at Kassel University

3.2. New Institute Building of Fraunhofer IEE

The new institute building of Fraunhofer IEE as shown in Fig. 6 started its operation in 2022 having first staff moving in in May 2022. The building can host approximately 350 people and has a very ambitious energy supply concept based on an ice-storage heat pump system. The heat system uses waste heat from the data center of the office building. Only in peak load times, the heating generation is supported by a cascade of gas burners. Regarding room comfort and indoor air quality, decentral ventilation units with high heat recovery are supplying fresh air to the respective rooms of the building.



Fig. 6: New institute building of the Fraunhofer IEE in Kassel

For the evaluation of the building performance, the developed tool for time serials investigation has been applied to the building and its heating and cooling concept. For this, a storage model for the ice storage has been integrated in the time serial model, considering sensible and latent storage capacities. Since the energy efficiency of the building concept depends on the available of the waste heat from the data center, the energy performance has been evaluated with different electrical load assumptions as well as different scenarios for regenerating the ice storage. In order to remain the availability to cool the office rooms of the building during the summer period, both waste heat and heat from solar thermal collectors were not used for the regeneration of the ice-storage in early/mid-summer within the parametrization of the model. As can be seen in Fig. 7, with low waste heat being available from the data center, the proportion of heat pump supplying heat to the building is very limited. With an average server activity of about 150 kW, the heat pump system can serve the majority of the heat demand of the building reaching the planned value of final energy demand estimated within the building energy certificate.

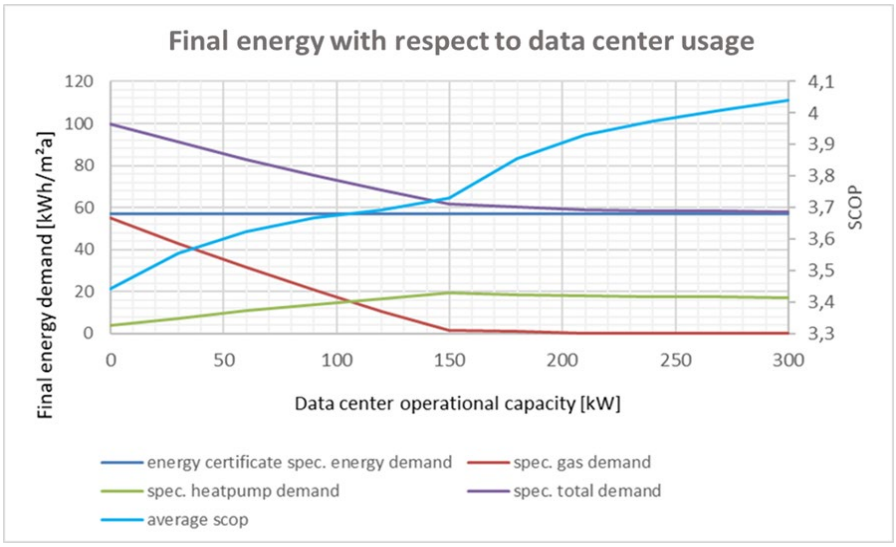

Fig. 7: Final energy performance of the heating supply concept of the new building of Fraunhofer IEE depending on the electrical consumption of the data center.

4. Conclusion

With the developed simplified method of determining time serials for heat load as well as final energy demands based on the method of DIN V 18599, useful investigations to evaluate and optimize buildings and their energy supply systems can be carried out. Typical use cases are for example the determination of load profiles, the evaluation of load shifting options especially regarding electricity generation and consumption scenarios as well scenarios including thermal and electrical storages. However, the investigation showed that the simplified method cannot easily reach the accuracy of dynamic thermal simulations like TRNSYS or IDA ICE. However, the effort of developing a validated numerical simulation model of a building, it´s technical system and their corresponding control systems is significantly higher than for the presented static time serial approach. In addition, simulation models are often not very flexible in terms of changing specific system designs or operation modes. Following this, the method can be recommended for first guess investigations of specific aspects like the examples given in this paper. Further investigations to improve the method should focus on an improved consideration of the building inertia, especially to predict cooling load profiles as well as the passive use of solar irradiance with higher accuracy.

5. Acknowledgments

The research project *CampusKassel2030* is funded by the Federal Ministry for Economic Affairs and Climate Actions (BMWK) based on a decision of the German Bundestag. The research project *IEE-Neubau* is funded by Hessian Ministry of Economics, Energy, Transport and Housing in combination with EFRE finances of the European Commission.

6. References

DIN 2017: DEUTSCHES INSTITUT FÜR NORMUNG E.V: DIN EN 12831-1:2017-09. Energetische Bewertung von Gebäuden – Verfahren zur Berechnung der Norm-Heizlast – Teil 1: Raumheizlast. Berlin. Beuth Verlag GmbH, 2017.

DIN 2018: DEUTSCHES INSTITUT FÜR NORMUNG E.V: DIN V 18599-2:2018-09. Energetische Bewertung von Gebäuden – Berechnung des Nutz-, End- und Primärenergiebedarfs für Heizung, Kühlung, Lüftung, Trinkwarm-wasser und Beleuchtung – Teil 2: Nutzenergiebedarf für Heizen und Kühlen von Gebäudezonen. Berlin. Beuth Verlag GmbH, 2018

HELENA 2021: ZUB SYSTEMS GMBH: *ZUB Helena.* 2021. URL: https://www.zub-systems.de/de/produkte/helena

IDA 2013: EQUA SIMULATION AB: *Handbuch. IDA ICE. Version 4.5.* 2013.

Stricker, T. 2022:Gesamtenergetische Bilanzierung eines Verwaltungsgebäudes der Universität Kassel auf Basis der DIN V 18599 und vergleichende Berechnungen mit dem Simulationswerkzeug IDA ICE im Rahmen des Forschungsprojekts „Campus-Kassel2030“, Master thesis Kassel University, 2022

Biechele, B., 2015: Energieeffizienz von Hochschulgebäuden. Analyse, Bewertung und Verbesserungsansätze, Kassel University Press, 2015

TRANSFORMATION OF A UNIVERSITY CAMPUS: COMPARISON OF RANKING METHODS FOR TEMPERATURE REDUCTION FROM NETWORK AND BUILDING PERSPECTIVE

Henrik Neusüß[1] | Weena Bergsträßer[2] | Dr.-Ing. Janybek Orozaliev[2]

Prof. Dr.-Ing. Jens Knissel[1] | Prof. Dr. Klaus Vajen[2]

[1] University of Kassel, Department of Building Services, Kassel (Germany)

[2] University of Kassel, Department of Solar and Systems Engineering, Kassel (Germany)

Abstract

This paper aims to find an approach to reduce temperature levels in a district heating subgrid and the supplied buildings at the University Campus in Kassel. The Campus consists mostly of non-residential buildings with high building supply temperatures. The district heating network was built in the 1980s. Consequently, there is a need for structured renovation to achieve higher energy efficiency, better integration of renewable energy sources and therefore lower greenhouse gas emissions. Methodically, two different methods for identifying temperature reduction potentials are used to determine which buildings should be focused on when transforming to low temperature supply. The two ranking methods, the Kappa method and the excess flow method, are introduced and discussed. Since the excess flow method is more established and has already proven its uses, it has been used to validate the new Kappa method. It was shown that the ranking from the Kappa method is comparable with the excess flow ranking, while still offering a distinct viewpoint from a different technical field. The weaknesses discovered in the Kappa method will be further developed and adapted in the future using various implementable factors. Furthermore, an extrapolation approach will be used to make statements about the approximate design state of the buildings.

Keywords: district heating, temperature reduction, University Campus, non-residential building, excess flow, faulty substations, Kappa method, heating circuit, technical building equipment

Transition to 4GDH

Nomenclature:

$\dot{Q}_{Pri}$	heat demand per hour primary side [kW/h]		
$\dot{Q}_{Geb,m}$	heat demand per hour calculated with heat loss H_{ges} [kW/h]		
$\dot{Q}_{GLT,h}$	heat demand per hour calculated with heat loss $H_{eq,h}$ [kW/h]		
$\dot{Q}_{WD}$	weather-independent demand [kW/h]]		
$\dot{Q}_{demand}$	heat demand per year [MWh/a]	$H_{eq,h}$	dynamic heat loss of the building [kW/K]
κ	Kappa factor	H_{ges}	stationary heat loss of the building [kW/K]
$T_{s,h}$	hourly supply temperature [°C]	$\dot{m}$	mass flow [kg/h]
$T_{r,h}$	hourly return temperature [°C]	$\dot{m}_{max}$	maximum mass flow [kg/h]
$T_{interior}$	interior space temperature steady 20 °C	$\dot{V}_a$	annual volume flow [m³/a]
T_a	related ambient temperature [°C]	$\dot{V}_{excess}$	excess flow [m³/a]
$T_{r,a}$	annual return temperature [°C]	$\dot{V}_{target}$	target volume flow [m³/a]
$T_{r,target}$	annual target return temperature [°C]	c_p	specific isobaric heat capacity [kWh/(kg·K)]
$T_{s,a}$	supply temperature annual [°C]	ρ	density [kg/m³]

© 2022. The Authors. Published by International Solar Energy Society
Selection and/or peer review under responsibility of Scientific Committee
doi:10.18086/eurosun.2022.10.08 Available at http://proceedings.ises.org

1. Introduction

Network temperature reduction is a prerequisite to realize smart energy systems and smart thermal grids as well as 4th Generation district heating (4GDH) systems . The goal of all these concepts is a 100 % renewable energy system without greenhouse gas emissions. Fault detection and rectification plays an important role to achieve temperature reduction, especially in existing networks. Therefore measurement data is used to achieve this (Månsson et al. 2018; Xue et al. 2017; Zinko et al. 2005). Faults and other limitations to temperature reduction can be found both on the primary (district heating network) and the secondary side (building level) of the substations. Typical faults are described e. g. in (Månsson et al. 2019; Bergstraesser et al. 2021).

One field where the application of new methods to achieve temperature reduction can be tested are the universities where the research is conducted, therefore multiple projects to reduce greenhouse gas emissions are and have been realized there. For example, the Bremen University of Applied Sciences, Düsseldorf University of Applied Sciences or the University of Bremen have developed climate protection concepts (Wilk et al. 2020). Many German universities are currently working on projects to improve energy efficiency, especially in the field of district heating. The TU Dresden has taken a holistic approach to energy efficiency as part of the Leuphana University of Lüneburg Climate Neutral Campus project (Opel et al. 2018). For this purpose, the fields of energy, campus development and transport were analyzed with an integral approach. Also at the TU Dresden, research has been conducted on the decentralized feed-in of solar energy and its contribution to the decarbonization and flexibilization of modern district heating networks (Rosemann et al. 2017). The Institute for Energy and Environmental Research Heidelberg (ifeu) shows transformation strategies from fossil central district heating supply to grids with higher shares of renewable energies (Paar et al. 2013).

The research project "EnEff:Stadt/Campus: Campus Kassel 2030 - Concepts and Measures for the Accelerated Implementation of the Energy Transition in Higher Education" (CK2030) integrates into these research topics. CK 2030 deals with the climate neutrality of the University campus in Kassel. The main goal of the project is to reduce greenhouse gases emitted by the building's heating supply. The university's own local heating network supplies 20 mostly non-residential buildings with local heat and is fed from the municipal district heating network. The network of the University of Kassel was built in the 1980s and requires renovation due to its age. Since the entire network is to be rebuilt, this offers the opportunity for coordinated planning with the aim of achieving the energy efficiency targets for reducing greenhouse gases. A key goal of the project is to reduce the temperatures at which the buildings are supplied, and thus reduce the network temperature. The supply and return temperatures are currently very high (130 °C / 75 °C). With lower temperatures, renewable energies could be better fed into the heating network, and the efficiency of the grid and the buildings could be increased, because lower temperature losses occur. The research project attempts to gain a complete overview of the existing situation on the campus and to depict the current state as well as to identify potential for reduction. Here, both the viewpoints from the network perspective as well as the viewpoint from the building level, up to the heating circuit or room level, are examined. This paper deals with two methods that aim to analyze larger pools of buildings and identify buildings that are critical for lowering the grid temperatures. The newly developed Kappa method attempts to identify the dimensioning condition of mass flow and temperature levels using measurement and consumption data to produce a building ranking. The Excess flow analysis sorts buildings based on their excess volumetric flow and defines a high return temperature as critical. After the presentation of both methods, they are to be compared with each other trying to evaluate Kappa as a newly introduced method, to determine differences and to identify temperature reduction potentials.

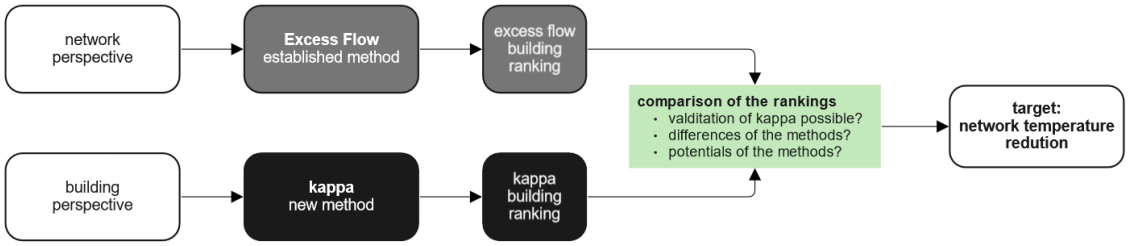

Fig. 1: Systematic structure of the overall approach

2. Kappa method

The Kappa method is currently still under development. The aim of the method is to examine a large pool of buildings for critical ones using as little measurement data as possible. For the method, only measurement data from the primary side of the buildings is used, i.e. only data from the substations heat flow meters. Heat demand, temperature, and mass flow data in hourly aggregation are evaluated at outside temperatures warmer than the design temperature for Kassel of -12 °C (acc. to DIN-TS 12831-1). Based on this data, the buildings that would be critical for a reduction of the network temperature can be identified. Once identified, the critical buildings are to be investigated in a prioritized manner at the heating circuit and room level in order to determine specific reduction potentials. These more in-depth detailed investigations are also being developed as part of the CK 2030 research project and described in the EuroSun 2022 conference paper 'Identification of Temperature Reduction Potentials in Heating Circuits based on Measurements' (Fox, Schüler, Knissel).

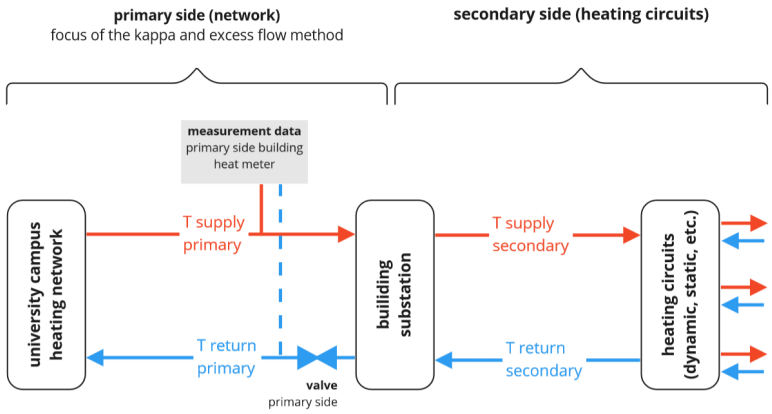

Fig. 2: Schematic diagram of a substation

Kappa combines temperature studies and mass flow studies relative to outside temperature. With the help of the Kappa factors a building ranking is to be provided, which serves for the decision of further investigations of the buildings on the heating circuit level or the room level. Kappa always aims at the design conditions of the buildings, i.e., for Kassel the required heating capacity of the buildings at -12 °C outside temperature. Since it cannot be assumed that measurements during the design state are possible, another goal of the Kappa method is to extrapolate to the design state with measurements outside the dimensioning conditions. The retrieved data from the operating technology database are in the core heating months, i.e., November through March.

Kappa factors can be used to make statements about the spread and mass flow characteristics of buildings. Buildings with a low Kappa factor have a low primary side spread and high mass flow at dimensioning conditions and buildings with a high Kappa factor have a large spread with low mass flow. To calculate Kappa with the help of capacities and to analyze further extrapolation methods, the heating loads of the buildings were calculated with different methods as a basis, the consumption analysis according to DIN-TS-12831 and the EAV analyses (energy analyses from consumption) (Wolff et al. 2019). The EAV method evaluates the efficiency of buildings and energy supply as well as user behavior based on consumption measured at monthly or weekly intervals. The calculated performances of the DIN-TS 12831 analysis were used for the further investigations.

2.1 Calculation of the Kappa factor

In the following, the calculation of the Kappa factor and its derivation is explained. The initial equation of the Kappa approach equates two heat flows (e.q. 1). $\dot{Q}_{Pri}$ describes a heat demand per hour on the primary side of the building and is calculated using the hourly values of the mass flow and the supply and return temperatures. $\dot{Q}_{Geb,m}$ calculates the heat demand via the heat loss of the building and the temperature difference between the outside and interior temperature:

$$\dot{Q}_{Pri} = \dot{Q}_{Geb,m} \text{ with } \dot{Q}_{Pri} = \dot{m}\, c_p \left(T_{s,h} - T_{r,h}\right) \text{ and } \dot{Q}_{Geb,m} = H_{ges}(T_{interior} - T_a) \quad \text{(eq. 1)}$$

H_{ges} describes the heat loss of a building and is usually based on the temperature difference of the outside temperature (often in 1 Kelvin steps). Since the determination of H_{ges} from monthly values is a steady state, an additional hourly dynamic heat loss coefficient $H_{eq,h}$ is formed to check the approach. H_{ges} corresponds to the slope of the parallel-shifted straight line from the approximate determination of the building heating load according to DIN/TS 12831-1. The analysis according to DIN 12831-1 was carried out parallel to the Kappa method using consumption data on a monthly basis of the buildings over the last three to four years. $H_{eq,h}$ as a dynamic coefficient is formed from the measured data in hourly aggregation (e.q.2).

$$H_{eq,h} = \frac{\dot{m}\ cp\ (T_{s,h} - T_{r,h})}{(T_{interior} - T_a)} \quad \text{(eq. 2)}$$

For the approach, the capacity of the different calculable heat flows are compared, so that an evaluation of the differences between dynamic and steady-state consideration is possible (eq. 3). The following heat flows are used. $T_{interior}$ is assumed as static interior temperature with 20°C acc. to (ASR A3.5 2010).

$$\dot{Q}_{GLT,h} = H_{eq,h}(T_{interior} - T_a) \text{ and } \dot{Q}_{Geb,m} = H_{ges}(T_{interior} - T_a) \quad \text{(eq. 3)}$$

If the building under consideration is a substation that simultaneously represents weather-independent demands, e.g. hot water, both the heat flow and the Kappa factor must be added by the weather independent demands (eq. 4). $\dot{Q}_{Geb,m}$ is then calculated as follows:

$$\dot{Q}_{Geb,m} = \dot{Q}_{WD} + H_{ges}(T_{interior} - T_a) \quad \text{(eq. 4)}$$

During the investigation it was found that the steady-state and dynamic heat flow are comparable. Equating the heat flows is possible because the dynamically calculated capacity $\dot{Q}_{GLT,h}$ with $H_{eq,h}$ is identical to the calculated capacity from $\dot{Q}_{Pri}$. By the equation of the two heat fluxes the following transformation for dimensionless Kappa can be derived (eq. 5).

$\dot{Q}_{Pri} = \dot{Q}_{GLT,h}$ equals $\dot{m}\ cp\ (T_{s,h} - T_{r,h}) = H_{eq,h}\ (T_{interior} - T_a)$

$$\boldsymbol{\kappa = \frac{(T_{s,h} - T_{r,h})}{(T_{interior} - T_a)} = \frac{H_{eq,h}}{c_p\ \dot{m}}} \quad \text{(eq. 5)}$$

When considering including weather-independent demands, such as water heating, the calculation must be completed with the weather-independent capacity (eq. 6).

$$\kappa = \frac{(T_{s,h} - T_{r,h})}{(T_{interior} - T_a)} = \frac{H_{eq,h}}{cp \cdot \dot{m}} + \frac{Q_{WD}}{\dot{m} \cdot c_p \cdot (T_{interior} - T_a)} \quad \text{(eq. 6)}$$

The idea of the approach is that Kappa at conditioning temperature can also be determined from the steady-state observation with H_{ges} (eq. 7). For this, however, the maximum mass flow of the system must be known. The derivation of the maximum mass flow approach and the possibility of extrapolation are explained in more detail in section 1.6.

$$\kappa = \frac{H_{ges}}{c_p \cdot \dot{m}_{max}} \quad \text{(eq. 7)}$$

$\dot{Q}_{Pri}$	heat demand per hour primary side [kW/h]		
$\dot{Q}_{Geb,m}$	heat demand per hour calculated with heat loss H_{ges} [kW/h]		
$\dot{Q}_{GLT,h}$	heat demand per hour calculated with heat loss $H_{eq,h}$ [kW/h]		
$\dot{Q}_{WD}$	weather-independent demand [kW/h]]		
$H_{eq,h}$	dynamic heat loss of the building [kW/K]	H_{ges}	stationary heat loss of the building [kW/K]
$T_{s,h}$	hourly supply temperature [°C]	$\dot{m}$	mass flow [kg/h]
$T_{r,h}$	hourly return temperature [°C]	$\dot{m}_{max}$	maximum mass flow [kg/h]
$T_{interior}$	interior space temperature steady 20 °C	c_p	specific isobaric heat capacity [kWh/(kg·K)]
T_a	related ambient temperature [°C]	κ	Kappa factor

2.2 Estimation of the Kappa factor

Using the Kappa calculation based on the temperature differences (e.q. 5), Kappa factors can be calculated for different outside temperatures and spreads. The Kappa factors are generally valid for those different temperature spreads in relation to the outside temperature and can be estimated as shown in Tab. 1. The generally valid Kappa values (y-axis) can be plotted graphically against the outside temperature (x-axis) (Fig. 3) and give an indication about the behavior of the Kappa factors in relation to the outside temperature.

Estimation of substation dimensioning	**$\Delta T_{supply-return}$ at -12 °C T_a**	**Kappa factor**
Large	10 K	0,31
Exactly	40 K	1,25
Small	60 K	1,88

Tab. 1: Estimation of Kappa factors

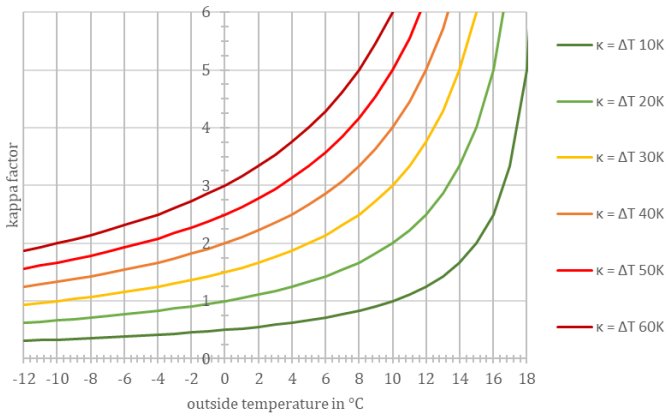

Fig. 3: General Kappa factors for different temperature spreads applied over the outside temperature

2.3 Kappa analysis for an example building

The Kappa factors that can be calculated for each building from the measurement data of the building control system can be entered in the basic diagram for better graphical classification (Fig. 4). The hourly calculated Kappa factors (y-axis) and their characteristics along the base Kappa factors can then be visualized in reference to the outside temperature (x-axis). The relationships between Kappa factor, dimensioning condition, spread, and mass flow are then easier to read in relation to the general Kappa values. Also, the behavior of the building in relation to the outside temperature is clearly readable.

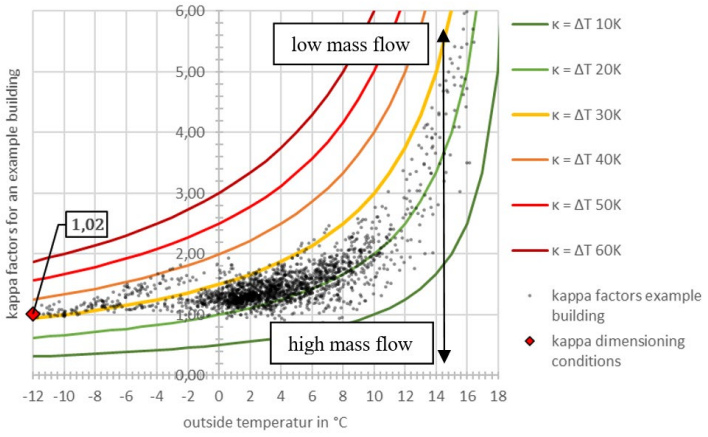

Fig. 4: Kappa factors for an example building with Kappa factor at dimensioning condition -12 °C

2.4 Results campus analysis with Kappa

The building stock of the south campus was analyzed with Kappa. Because measurement data were available that lie within the dimensioning condition – 12 °C (measurement period January 2021 to March 2021, temperatures down to approximately -17 °C), an extrapolation to dimensioning condition wasn`t necessary. The extrapolation approach is explained in more detail in section 1.6. The Kappa factors were compared in a ranking (Fig. 5). Therefore, they were graphically plotted for each building at dimensioning conditions (y-axis left) and the corresponding spreads were placed on the second y-axis for a better graphical overview. These factors are not a specific Kappa value at -12 °C but the average of the Kappa values between -11 °C and -13 °C.

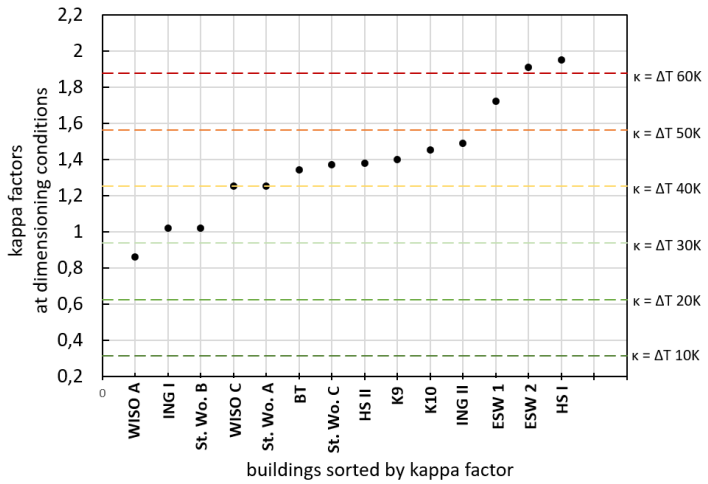

Fig. 5: Building ranking by Kappa factor – less critical with low Kappa factor, more critical with high Kappa factor for the university campus

Depending on other known building factors, such as year of construction, renovation status, etc., the result is unexpected, as new buildings are identified as critical for network temperature reduction. A low temperature spread on the primary side has a beneficial effect on the regulation of the heating circuit level. If the spread is increased on the primary side, this does not necessarily have a direct effect on the secondary side and thus does not result in an adjustment of the temperature spread on the heating circuit level. The oversizing of the substation can be used to generate the required heating output. The limiting factor of the system is then the maximum deliverable mass flow.

For each building, a Kappa diagram similar to Fig. 4 was generated. Upon closer examination of the respective Kappa data sets and examination of the resulting Kappa diagrams for each building, different types of buildings were identified.

2.5 Learnings different building types

It was discovered that the originally assumed unregulated approach (that a maximum mass flow is present in all buildings) does not apply. By comparison of all buildings graphics three building types could be identified:

- Type M: In these buildings, the maximum mass flow is applied on the primary side (Fig. 6)
- Type dT: The temperature level, spread and mass flow of the building is regulated according to the outside temperature and along a predetermined spread (Fig. 7)
- Type flex: Is unclearly regulated. By eliminating operating hours and weekend setbacks, type flex buildings can be assigned to type dT buildings.

Compared to a conventional control of substations, the type M is more unusual and not preferable. Modern substations are usually regulated in the same way as the dT building types.

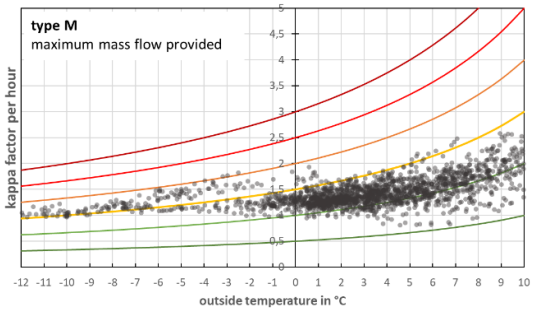

Fig. 6: Kappa analysis type M building

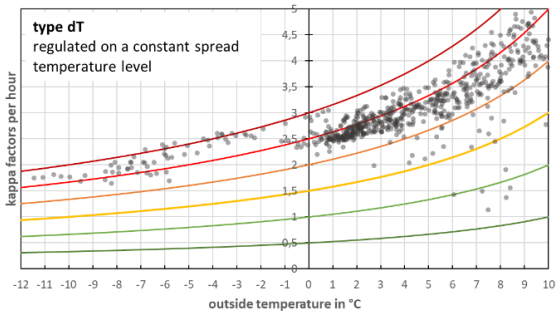

Fig. 7: Kappa analysis type dT building

2.6 Extrapolation approach dimensioning conditions

In order to test the original goal of the Kappa approach, the use of measurement data outside the dimensioning temperature and the extrapolation to dimensioning conditions, the existing measurement data was examined in different time periods. For this purpose, the original data set from January 2021 to March 2022 was divided into three monthly periods of four weeks. To check the plausibility of the individual data records and the possibility of extrapolation, the maximum mass flow calculation (eq. 7) was used for the example building. The data of the maximum mass flow was preselected and only the average of the upper 5% percentile was used. For buildings of type M, the Kappa of the dimensioning condition could be calculated approximately from these maximum mass flow Kappa values of the respective monthly periods. In comparison, the Kappa factors of the individual months are as follows: January $\kappa = 1{,}02$ (green), February $\kappa = 0{,}97$ (purple) and March $\kappa = 0{,}95$ (blue). The average Kappa factor for the example building at dimensioning condition according to Fig. 4 is $\kappa = 1{,}02$. The calculation is approximately accurate by +/- 5 K spread at design level or else deviates by 0.07 among the Kappa factors (Fig. 8). The Kappa factors were plotted against the average outdoor temperature for the measurement period. Thus, for buildings of type M a rough extrapolation to dimensioning conditions via the calculation of the steady-state heat loss coefficient and the maximum mass flow (eq. 7) is possible. For buildings of type dT and flex this does not apply. The reason for this is that the maximum mass flow cannot be derived from the Kappa factors which are controlled by a predetermined spread according to the outside temperature. Thus, it is unknown whether the Kappa factor at design condition corresponds to the maximum mass flow of the system or not. In addition, calculations were carried out for the dT types and produced unplausible results for the Kappa extrapolation.

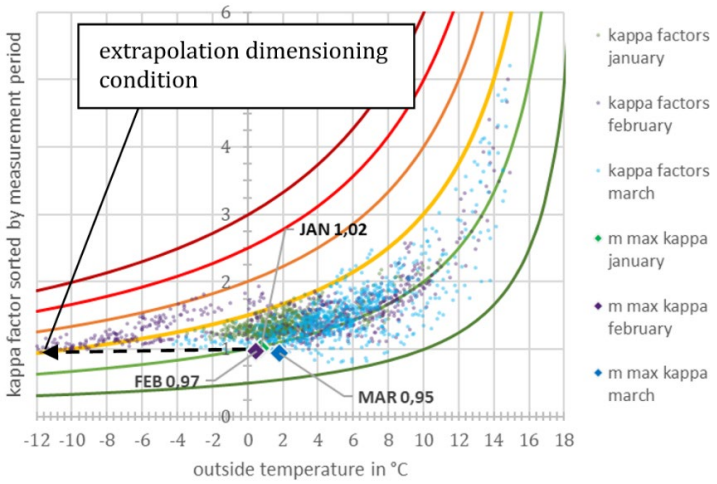

Fig. 8: Extrapolation for a Type M building to dimensioning conditions with Kappa factors and measurements beyond dimensioning condition

2.7 Outlook Kappa

The Kappa method yields a ranking prioritizing the regulation potential of a building. Buildings with a low Kappa factor should be more easily adjustable to a lower network temperatures and buildings with a high Kappa factor could be more critical. The reason for this is the assumption that buildings with a high temperature spread and high mass flow on the primary (network) side are already maxed out during dimensioning conditions and have less regulation potential on the secondary (heat circuit) side. At the moment, Kappa doesn't define a potential of temperature reduction yet and is focusing on the "as build" or better "in use" status of the buildings and heat exchangers. Fig. 5 has shown the Kappa factors for the period from 01.01.2021 to 31.03.21 and their level of temperature spread in dimensioning conditions. The Kappa factor was able to presort critical buildings out of the stock but for further analysis the ranking needs to be adjusted. In further steps Kappa needs to be corrected by other factors. To finalize the ranking aspects like the building's year of construction, the year of installation of the heat exchangers (state of renovation), the temperature spread on the heat circuit level and the kind of heat circuits (static, dynamic, hot water, etc.) could be considered and weighted. A type assignment of the different Kappa building types via the building use is currently not possible. Current evaluations show that the age of a substation could be a hint for a type M or type dT buildings.

Since Kappa can only be extrapolated for type M buildings and the mass flows for the types dT are not known, the different types and Kappa factors cannot be clearly compared. So, the goal of the extrapolation approach (Fig. 8) only works for buildings that have type M in and thus provide comparability. The goal of the upcoming research steps is also to correct the Kappa factors of the type dT buildings. Based on the available valve position data, which is accessible via the building control system, Kappa for dT buildings could be corrected. The maximum mass flow could then be calculated with this valve data and thereby provide comparability among the buildings Kappa factors. If this correction for Kappa is possible, Kappa factors could be determined for large building stocks of type M and dT with little effort. Only the information for H_{ges} from a DIN/TS 12831-1 demand analysis and the maximum mass flow (eq. 7) plus the correction factor for the valves would be needed.

3. Excess flow method

Many substations in existing district heating (DH) grids do not achieve an optimal efficiency which often corresponds to high return temperatures. In order to achieve lower return temperatures, the excess flow method was developed in the IEA DHC Annex VII "Improvement of Operational Temperature Differences in District Heating Systems" (Zinko et al. 2005). It allows to identify those customers that contribute the most to a high return temperature. Higher than required volume flow rates through a substation are the cause of unwanted high return temperatures. That is why, for each substation an excess flow is calculated, that is equal to the difference of the actual volume flow from a target volume flow, see (eq. 8).

$$\dot{V}_{excess} = \dot{V}_a - \dot{V}_{target} = \frac{\dot{Q}_{demand}}{\rho \cdot c_p} \cdot \left(\frac{1}{T_s - T_{r,a}} - \frac{1}{T_s - T_{r,target}} \right)$$

(eq. 8) (Heimo Zinko et al. 2005)

$\dot{Q}_{demand}$	heat demand per year [MWh/a]		
$T_{r,a}$	annual return temperature [°C]	$\dot{V}_a$	annual volume flow [m³/a]
$T_{r,target}$	annual target return temperature [°C]	$\dot{V}_{excess}$	excess flow [m³/a]
$T_{s,a}$	supply temperature annual [°C]	$\dot{V}_{target}$	target volume flow [m³/a]
ρ	density [kg/m³]	c_p	specific isobaric heat capacity [kWh/(kg·K)]

To define the target volume flow, a target temperature difference is needed, it is composed of the yearly mean supply temperature and a yearly mean target return temperature. All temperatures should be weighted by the volume flow to get an accurate measure of the influence on a raised return temperature. The application of the excess flow method and its validation for fault detection is described in more detail in (Bergstraesser et al. 2021).

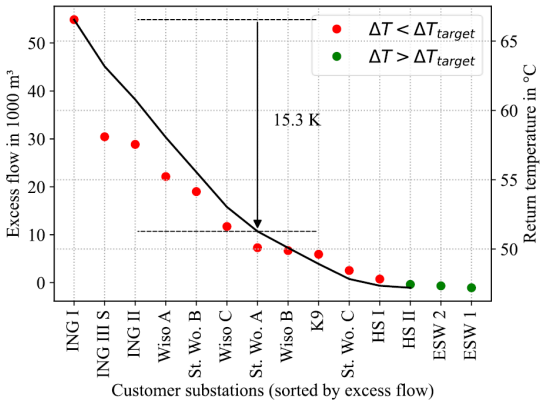

Fig. 9: Excess flow ranking with return temperature reduction

Fig. 9 shows the calculated excess flow for the year 2021 from 22.01.2021 to 26.01.2022 and includes all substations that were accessible. The substations (x-axis) are sorted by excess flow and represented by points colored in accordance with whether or not they reach the target temperature difference. A positive excess flow i.e., a higher than target return temperature is colored red, while a negative excess flow i.e. a lower than target return temperature is colored in green. Additionally, the return temperature reduction is shown when measures in substations are taken depending on the ranking by excess flow. E.g. measures in six substations, that achieve the target temperature difference, will result in a return temperature reduction of about 15 K for the whole network.

4. Comparison of the methods

Since the excess flow method has already been validated for multiple substation types, it can be used to compare the results from the Kappa method. Fundamentally, the methods show two different points of view. The excess flow method shows the view of the local heating network and ranks substations according to return temperature. The Kappa method analyses the buildings in the first step independently of the local heating network and tries to identify the regulation potential of the buildings. The secondary side (heating circuits) of the buildings is thereby not yet observed. Since one method identifies regulation potential and the other looks for errors in the regulation, the building rankings are, as expected, not identical. If the two rankings are plotted against each other, it is noticeable that they are almost opposite. This is shown in Fig. 10, which confirms the differences since a high value of Kappa, or a high excess flow is considered indicative for a critical building in both rankings.

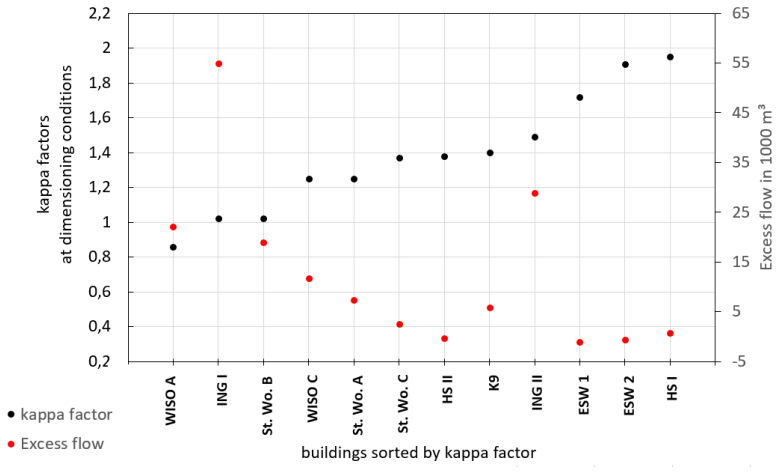

Fig. 10: Kappa ranking sorted by building and displaying the respective excess flow

By generating the reciprocal of Kappa, the readability between the two rankings was further improved (Fig. 11). It can be observed that the rankings are almost identical, with a few exceptions. Differences between the two methods can be attributed to various factors. Kappa only considers measurement data from a winter period and at dimensioning condition of -12 °C. In addition, Kappa is based on an aggregation on an hourly basis. Furthermore, different factors are included in the Kappa factor ranking, such as the measured spread, the mass flow, the heat loss coefficient, and the dimensioning temperature of the interior spaces. Excess flow is calculated on the basis of the target network temperature, the heat demand of the building and the current return temperature. These are annual average values. The excess flow ranking is also weighted by the amount of total heat demand per building/ substation. Fig. 9 shows this deviation very clearly, as the buildings ING I, K9 and ING II are buildings with a high heating requirement, building volume and floor space. These buildings differ greatly in their ranking between the excess flow and the Kappa method.

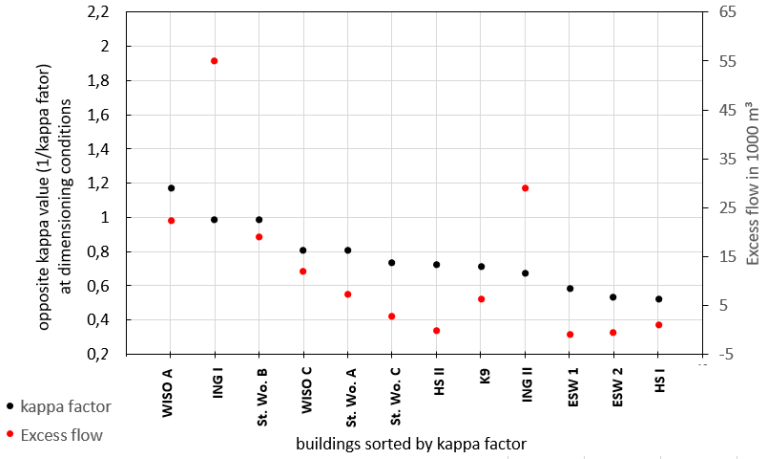

Fig. 11: Kappa ranking sorted by building and displaying the respective excess flow with opposite Kappa value (1/Kappa factor)

5. Discussion

It was shown that Kappa can be a useful approach for ranking a large building pool. However, as a newly developed method, dimensionless Kappa still requires further development and consideration. Above all, the comparability of building types M and dT is a major task for the next research steps. There are different approaches to this: Either the already described correction of the type dT buildings via the valve position in the return temperature line of the substation station, or an artificial generation of a type M building. For this purpose, the valves of the return temperature line (Fig 2) could be fully opened during the measuring phase and thus the maximum mass flow of the system artificially generated. This would result in additional losses in the heating system, but these would only be limited to the measurement period. The maximum mass flow could then be used to determine the design conditions using the simplified approach for Kappa with the heat loss coefficient (eq. 7).

The current research approach has shown in Fig. 11 that the ranking is nearly similar but does not completely match due to the size of buildings and transfer stations. The excess flow analysis approach of including the substation size could also be applicable to Kappa and could also be taken into consideration with the help of the oversizing factors of the DIN-TS-12831 analysis. As part of the research project, further building rankings were also created using the DIN/TS 12831-1 consumption analysis. There the buildings were sorted based on their oversizing factor in terms of heat demand at dimensioning condition (total heat exchanger capacity in relation to the required capacity according to DIN-TS 12831 consumption analysis). This ranking is also still in development and will be weighted, for example, by the known temperatures of the heating circuits. The Kappa method will also be compared with this ranking method in the next research step.

The dimensionless Kappa factors could be weighted by the maximum size of the substation or the actual heat demand of the buildings. This could lead to a further approximation to the excess flow method. The advantage of

a validated Kappa method would be a statement about the mass flow and spreading behavior of a building at design temperature. These statements could then be determined with a small amount of measurement data or simple measurement methods and provide a very differentiated picture of a building.

In the next step, the possibility to determine a reduction potential for the building using the Kappa factors should be developed. The idea is to be able to draw conclusions on this with the help of the investigated dimensioning condition. Therefore, a connection between the primary side (substation) and the secondary side (heating circuits) must be made. Once Kappa has been finally compared and validated with the other methods, an examination of the differences and potentials of the methods could be carried out.

6. Conclusion and Outlook

Kappa is a newly introduced calculation approach for the design state of buildings in terms of their temperature spread level and mass flow based on measured data during winter. Kappa can be calculated in two different ways, via the heat loss coefficient and mass flow or via the temperature differences (eq. 5). The calculated Kappa factors can be used as a basis to rank large building pools according to existing control potentials of the substation (primary side) from the buildings point of view. The extrapolation approach, using short measurement periods warmer than the dimensioning condition to conclude the design condition, and the simplified approach for Kappa via H_{ges} and $\dot{m}_{max}$ (eq. 7) currently only works for buildings of type M (the maximum possible mass flow is provided on the primary side).

The ranking of the Kappa method and the excess flow method can be roughly compared as shown in Fig. 11. The deviations can be explained by the differences in the period of consideration of each methodical approach and the weighted heat demand in the excess flow analysis. Kappa was validated with the help of the excess flow analysis and seems reasonable for sorting the buildings. However, further in-depth investigations are required for an exact comparison and validation of the Kappa method, especially for the different building types and the extrapolation approach.

As shown in the discussion, there are two basic approaches to correcting Kappa in the future. First, the approach of correcting kappa using the available valve position data and the artificial maximum mass flow will be tested. At the same time, kappa will be compared with the ranking from the DIN-TS-12831 analysis for further validation.

7. Acknowledgements

The project “EnEff:Stadt/Campus: Campus Kassel 2030 – Konzepte und Maßnahmen für die beschleunigte Umsetzung der Energiewende im Hochschulbereich” this paper is based on is supported with funds of the Federal Ministry of Economy Affairs and Climate Action (funding code 03EN3013A).

8. References

ASR A3.5 (2010): Room temperature. Technical rules for workplaces. In accordance with the Workplace Ordinance of August 12, 2004 (BGBl. I p. 2179), last amended by Article 4 of the Act of December 22, 2020 (BGBl. I p. 3334), 2010.

Bergstraesser, Weena; Hinz, Andreas; Braas, Hagen; Orozaliev, Janybek; Vajen, Klaus (2021): Lessons learned from excess flow analyses for various district heating systems. In: *Smart Energy* 1, S. 100005. DOI: 10.1016/j.segy.2021.100005.

Connolly, David; Lund, Henrik; Mathiesen, Brian Vad; Østergaard, Poul Alberg; Möller, Bernd; Nielsen, Steffen et al. (2013): Smart Energy Systems. Holistic and Integrated Energy Systems for the era of 100% Renewable Energy. Amsterdam, Boston. Online verfügbar unter https://vbn.aau.dk/ws/portalfiles/portal/78422810/Smart_Energy_Systems_Aalborg_University.pdf, zuletzt geprüft am 05.12.2020.

Lund, Henrik; Østergaard, Poul Alberg; Chang, Miguel; Werner, Sven; Svendsen, Svend; Sorknæs, Peter et al. (2018): The status of 4th generation district heating: Research and results. In: *Energy* 164, S. 147–159. DOI: 10.1016/j.energy.2018.08.206.

Lund, Henrik; Werner, Sven; Wiltshire, Robin; Svendsen, Svend; Thorsen, Jan Eric; Hvelplund, Frede; Mathiesen, Brian Vad (2014): 4th Generation District Heating (4GDH). In: *Energy* 68, S. 1–11. DOI: 10.1016/j.energy.2014.02.089.

Månsson, Sara; Johansson Kallioniemi, Per-Olof; Thern, Marcus; van Oevelen, Tijs; Sernhed, Kerstin (2019): Faults in district heating customer installations and ways to approach them: Experiences from Swedish utilities. In: *Energy* 180, S. 163–174. DOI: 10.1016/j.energy.2019.04.220.

Månsson, Sara; Kallioniemi, Per-Olof Johansson; Sernhed, Kerstin; Thern, Marcus (2018): A machine learning approach to fault detection in district heating substations. In: *Energy Procedia* 149, S. 226–235. DOI: 10.1016/j.egypro.2018.08.187.

Mathiesen, B. V.; Lund, H.; Connolly, D.; Wenzel, H.; Østergaard, P. A.; Möller, B. et al. (2015): Smart Energy Systems for coherent 100% renewable energy and transport solutions. In: *Applied Energy* 145, S. 139–154. DOI: 10.1016/j.apenergy.2015.01.075.

Opel, O.; Werner, K.; Gefken, J.; Tribel, A.; Strodel, N.; Brüggen, I.; Ruck, W. (2018): Klimaneutraler Campus Leuphana Universität Lüneburg. Schlussbericht Teil I + II.

Paar, A.; Herber, F.; Pehnt, M.; Ochse, S.; Richter, S.; Maier, S. et al. (2013): Transformationsstrategien von fossiler zentraler Fernwärmeversorgung zu Netzen mit höheren Anteilen erneuerbarer Energien, 2013.

Rosemann, T.; Heymann, M.; Rühling K; Hafner, B. (2017): DH Networks - Concept, Construction and Measurement Results of a Decentralized Feed-In Substation.

Wilk, A.; Pantiou, M.; Göttlicher, S.; Küster, S. (2020): Kurzstudie zu Klimaschutzkonzepten an Hochschulen, 2020.

Wolff, D.; Unverzagt, A.; Schünemann, A.; Rasche, S. (2019): DBU-Projekt Abschlussbericht „Entwicklung und Erprobung der Grundlagen für das Partnerschaftsmodell „Alliance Contracting“ in der Wohnungswirtschaft“.

Xue, Puning; Zhou, Zhigang; Fang, Xiumu; Chen, Xin; Liu, Lin; Liu, Yaowen; Liu, Jing (2017): Fault detection and operation optimization in district heating substations based on data mining techniques. In: *Applied Energy* 205, S. 926–940. DOI: 10.1016/j.apenergy.2017.08.035.

Zinko, Heimo; Hoon, Lee; Kim, Bong-Kyun; Kim, Youn-Hong; Lindkvis, Håkan; Loewen, Achim et al. (2005): Improvement of Operational Temperature Differences in District Heating Systems. Annex VII. Hg. v. IEA District Heating and Cooling.

A Holistic Energetic Transformation Concept for the Heating and Cooling Supply of a University Campus

Diana-Iulia Stanica[1], Nikolai Kononenko[2], Max Bachmann[1], **Felix Schumann**[3], **Maximilian Friebe**[1]**and Martin Kriegel[1]**

[1] Hermann-Rietschel-Institut, Technische Universität Berlin (Germany)

[2] Institut für Energietechnik, Technische Universität Berlin (Germany)

[3] Institut für Angewandte Geowissenschaften, Technische Universität Berlin (Germany)

Abstract

In order to achieve the highest CO_2 savings at a district level, a holistic planning of the renovation process is necessary in which the synergies between building retrofitting and the modernization of the energy supply are taken into account. In this study, an integrative energy retrofitting approach is applied to a small area of a university campus. It is shown that building renovations create valuable opportunities for the transformation and decarbonization of the heating and cooling supply. By considering specific boundary conditions during renovation, previously untapped waste heat potential from data centers and process cooling can be locally used for building heating, leading to CO_2-savings of 850 t/a. A modernization of the district heating network and the usage of a seasonal geothermal storage further increase the CO_2-savings up to 1100 t/a. Furthermore, the presented concept is economically attractive, with a payback period of 5-10 years and a levelized cost of energy of up to 7.5 €cents/kWh.

Keywords: building renovation, district heating and cooling, energetic district retrofitting, waste heat, geothermal storage

1. Introduction

The heating and cooling sector accounts for 50% of Europe's final energy demand and is mainly based on fossil fuels. A rapid and efficient decarbonization of this sector requires not only the acceleration of building refurbishments but also increasing the share of renewable energies and promoting the integration of waste heat into the built environment (European Comission, 2016). Because of the different stakeholder structure of the supply side and of the demand side, improvements in the energy efficiency of buildings and district energy systems (DES) are rarely considered in tandem. However, combining building retrofitting, district heating and cooling improvements and renewable energy generation into an integrative approach allows for a more cost-effective and faster decarbonization of the building stock (BPIE, 2018). This has been recognized by the European Commission in its "Renovation Wave for Europe" strategy (Europeam Commission, 2020) which explicitly addressees the importance of an integrated, neighborhood-based approach in which the co-benefits of building renovation are used to decarbonize the heating and cooling sector.

Limited studies have investigated a holistic approach to renovation at district scale and the interactions between demand and supply side energy efficiency measures. For example, (Pozzi et al, 2021) has assessed the synergies between building retrofit and district heating networks (DHN) for the city of Milano and showed that for some areas of the city, the combination of building retrofit and 4th generation district heating (4GDH) can achieve a reduction in emissions of up to 65%, larger than for other scenarios. In (Delmastro et al, 2017), a methodology for analyzing the impact on building renovation projects on the investment strategies for DHN is proposed. Furthermore, (Lündstrom and Wallin, 2015) and (Le Truong et al, 2014) have proved the necessity for considering the interaction between end-use energy saving measures and supply systems for district-heated buildings. However, the majority of these studies consider a combination of building retrofit and the construction of new low temperature 4GDH or the effects of building retrofitting on existing district heating networks.Moreover, the cooling supply and local energy resources such as waste heat potentials or renewable energies are not assessed.

In this context, this study aims to present a holistic renovation concept that showcases the synergies between

© 2022. The Authors. Published by International Solar Energy Society
Selection and/or peer review under responsibility of Scientific Committee
doi:10.18086/eurosun.2022.10.09 Available at http://proceedings.ises.org

building renovations and the transformation of the heating and cooling supply for a small campus area. A transformation strategy for the DHN to support low-temperature waste heat integration while still being able to supply unrefurbished buildings with high temperature heat is also described.

2. Description of the case study

In the framework of the "Energy Efficient Campus Berlin-Charlottenburg (EnEff:HCBC) project, refurbishment scenarios and energy efficiency solutions for heating and cooling have been assessed at the scale of a university campus district. In the first phase of the project, a decision-support methodology for the integrated energy retrofitting of the university campus was developed (Stanica et al, 2021a). This consisted of a combination of energy conservation and renewable energy generation measures. The second phase of the project focuses on detailed feasibility analyzes for holistic energetic modernization concepts that examine both the demand side and the supply of heating and cooling.

For this study, a small area of a university campus consisting of 7 buildings with an annual heat demand of ca. 10.3 GWh/a and a cooling demand of 4.7 GWh/a has been chosen (buildings B1 to B7 in Figure 1:). The building complex presents with a high waste heat (WH) potential (5.9 GWh), from data centers and process cooling that currently can't be used efficiently due to the high temperature requirements of the buildings. However, most of the buildings will be successively renovated in the next decade, creating an opportunity for the energetic transformation of the heating supply structure and for the efficient utilization of the waste heat potential. Since the building complex is supplied with heat by a branch of the 3-level municipal DHN (represented in violet in Figure 1:), a hydraulic separation of the branch from the main network is possible. This would allow a lowering of supply temperatures and the feed-in of decentralized waste heat sources into the network branch.

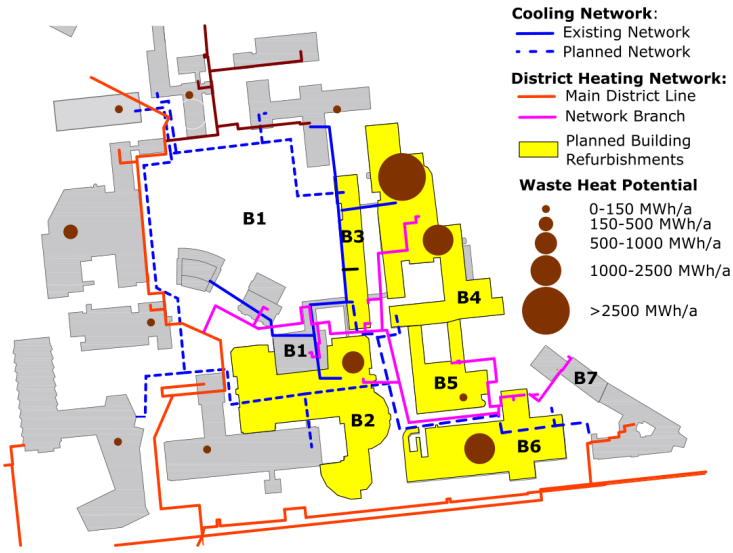

Figure 1: Campus and network layouts

To derive a holistic heating and cooling supply concept that considers the existing network infrastructure and the synergies with building renovations, a series of steps were necessary. Firstly, the existing waste heat potential was assessed and a concept for its efficient utilization was developed. Taking into account the technical requirements of the waste heat recovery and of the building heating systems, a concept for the transformation of the DHN branch was developed and its technical feasibility was assessed. Finally, the synergies and requirements for the building renovation were derived and the economic and ecologic feasibility of the proposed solutions were assessed for different scenarios.

3. Cooling supply and waste heat recovery

A concept for the modernization of the heating and cooling supply on the campus has been developed in which chillers also serve as heat pumps during the heating period (see Figure 2:). To achieve this, the temperature of the

heat sink is raised in accordance with the temperature level of the building's heating system or that of the heating network in which the waste heat will be fed in.

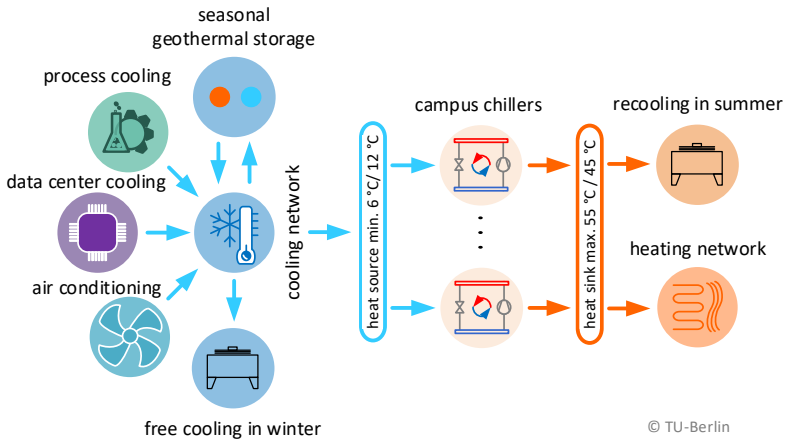

Figure 2: Waste heat recovery concept

For the concept design and the economic evaluations, a hydraulic diagram for the holistic heating and cooling generation was created (see Figure 3:.

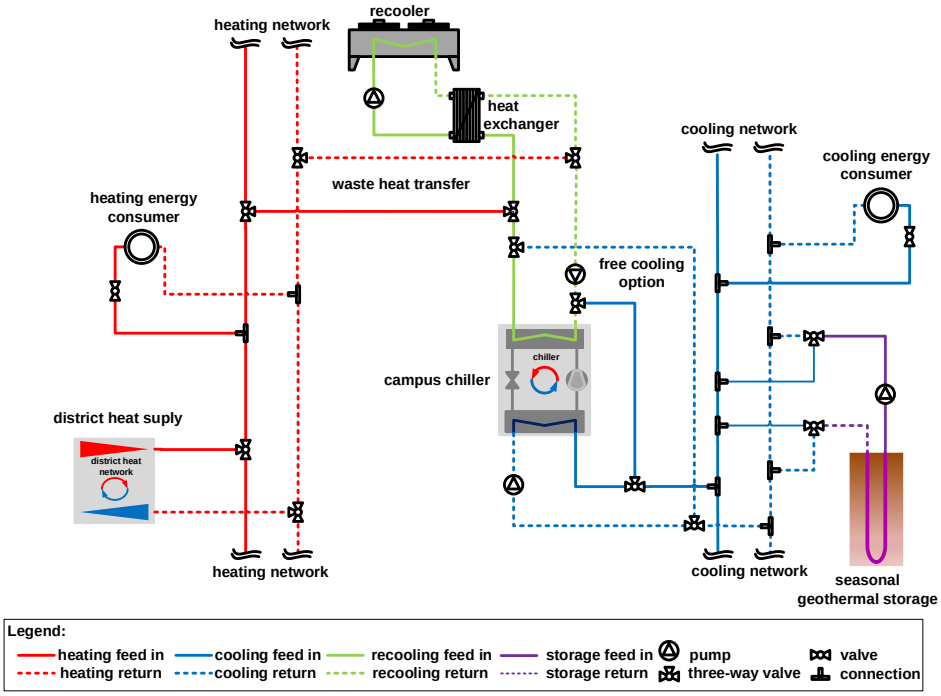

Figure 3: The hydraulic connection concept of the heating and cooling supply on campus

3.1 Cooling supply

The cooling demand of the buildings is covered by a cooling network that connects not only the buildings included in this study, but also additional buildings in their proximity. The existence of a cooling network enhances the flexibility of the concept since the cooling load can be shifted to the chillers with more favorable operating characteristics and a suitable waste heat feed-in location. By employing high-level control algorithms (Kononenko et all, 2021), the security of supply can be guaranteed and significant energy savings can be achieved.

Since the supply and return temperatures of the cooling network (6°C and 12°C respectively) are in the range of near-surface geothermal energy, a borehole geothermal system can be directly connected to the cooling network and act as a cooling storage. In winter, the geothermal borehole storage acts as an additional energy source for the heat pumps, enabling the generation of additional renewable heat. Through this process, the underground

storage is cooled and can then be used for passive cooling of the buildings in summer, thus leading to electricity savings.

Another cooling efficiency measure is the use of free cooling for low outdoor temperatures. This requires a hydraulic separation between the recooling circuit and the cooling network. The manufacturer of the chillers recommended the use of a heat exchanger between the recooler and the chiller or the cooling network. Considering the temperature difference between the two sides of the heat exchanger means that free cooling can occur for outside temperatures above 0°C.

3.2 Heat recovery and feed-in

The waste heat recovery from the chillers can be achieved by using the chillers as a heat pump and setting the condensation temperature accordingly to that of the heat demand. For the existing chillers, this requires the exchange of the air-cooled condensers with new, water-cooled ones. However, the maximum heat temperature that can be achieved is 55°C. Additionally, a temperature difference of at least 10 K between the supply and the return of the condenser needs to be guaranteed. The generated heat will then be fed in into the district heating network (see Chapter 4 and distributed to the heat consumers.

This allows the utilization of approx. 3.3 GWh/a waste heat from cooling process to be used for the heating of the buildings. The additional electrical effort for heat generation depends on the desired temperature level. For example, in the case of medium temperature radiators (see Chapter 5 amounts to only 0.5 GWh/a, resulting in an average COP(Coefficient of performance) of 6. Furthermore, by using a geothermal borehole storage for passive cooling in summer and as a heat source for the heat pumps in winter, a further 0.5 GWh/a of the heat demand can be covered by renewable energies. In this case, the additional electrical effort and the average COP are of 0.48 GWh/and 8 respectively. The lower additional electrical effort is due to the fact that, through passive cooling with the geothermal storage in summer, the power consumption for cooling in summer can be reduced by about 0.18 GWh/a, thus offsetting a part of the additional electricity consumption for the waste heat recovery in winter. For both cases, the values are well above the usual performance for conventional heat pump applications (Miara et al. 2013).

The average COP is defined as annual energy ratio between the used heat ($Q_{hr,tot}$) and the additional electrical consumption for heat recovery (see also eq. 1). The last term will be defined as the difference between the total electrical energy consumption of the chillers with heat recovery ($P_{el.,\,hr,\,tot}$) and the electrical energy consumption of the chillers in cooling mode only as a reference case ($P_{el.,cool,tot}$).

$$COP = \frac{Q_{hr,tot}}{P_{el.,hr,tot} - P_{el.,cool,tot}} \qquad \text{(eq. 1)}$$

For the scenario with geothermal storage, the term $P_{el.,hr,tot}$ also includes the electrical energy consumption of the storage pump. However, through the usage of the storage in the summertime for the passive cooling, the electrical energy consumption for cooling will be reduced and thus result in a higher COP.

4. Transformation of the district heating network (DHN)

Since the waste heat potential of some buildings exceeds their heat demand, an integration of the surplus heat into the DHN for transport to buildings without waste heat would increase its utilization rate and the CO_2-savings. Currently, the municipal district heating network is composed by two high temperature (80-110°C) supply pipes and a mixed return pipe.

In order to efficiently utilize the waste heat potential, multiple boundary conditions need to be considered. Firstly, waste heat is only available for temperatures above 0°C since below this temperature it is energetically more efficient to use free cooling. Furthermore, maximum supply and return temperatures of 55°C and 45°C respectively and a minimum temperature difference of 10K must be guaranteed on the condenser side. This means that, as a prerequisite for the waste heat integration following the renovation of the buildings, the temperature requirements for HVAC systems must be lowered (see Chapter 5). This will allow the transformation of the existing high-temperature (HT) network into a network with two temperature levels and decentralized producers as illustrated in Figure 4. In this concept, the remaining high temperature consumers (e.g. unrefurbished buildings)

will continue to be supplied with municipal district heat by a high temperature level, whereas the renovated buildings will be supplied by a low temperature network level in which waste heat is fed in.

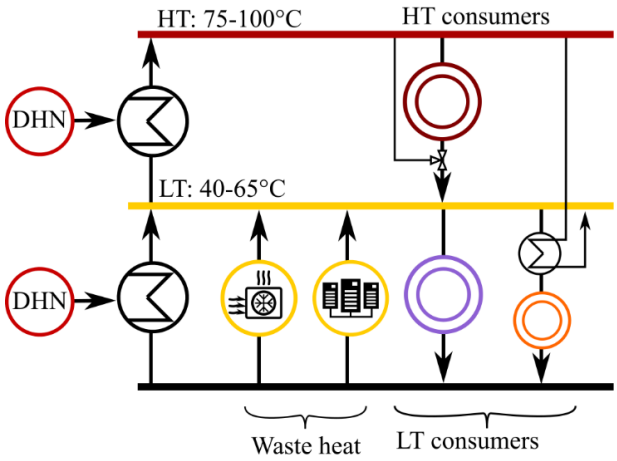

Figure 4: Concept for a DHN with two temperature levels and efficient integration of waste heat

In order to reduce the supply temperature and the pressure level in the network branch that supplies the building complex, the branch will be hydraulically separated from the primary DHN. The primary network will therefore act as a central producer to the secondary network whereas the waste heat sources will act as decentralized producers. It was shown in (Stanica et al, 2021b) that this cascading network configuration is ideal for districts with a heterogeneous building structure and for the transformation of existing high temperature networks. Because it allows an efficient integration of renewable energy resources in the heat supply of new and retrofitted buildings while also continuing to supply high temperature consumers with conventional sources, it is particularly convenient as an intermediary solution during long district renovation processes.

However, in order to transform an existing DHN branch into a cascading network with decentralized feed-in of waste heat, multiple technical constraints need to be considered.

4.1 Technical requirements for the feed-in

For the waste heat recovery to be efficient, a minimum temperature difference between the low temperature supply line and the return line of 10K needs to be guaranteed. Furthermore, after taking into account thermal losses, the maximum waste-heat feed-in temperature is of 50°C. This means that for outdoor temperatures of 0°C or higher, the temperature of the middle network line and, consequently, the supply temperature of the retrofitted HVAC systems, should be maximum 50°C. As explained below in Section 5, this can be achieved for heating systems with design temperatures of 60°C/45°C or lower.

4.2 Temperature constraints

The high temperature supply line will continue to supply the unrefurbished heating circuits of HVAC systems and the DHW systems. Due to safety regulations regarding the prevention of legionella, the DHW supply temperature needs to always exceed 70°C. Furthermore, to assure a reliable supply of the low temperature consumers, the return temperature of the high temperature consumers must not be lower than the setpoint value of the LT line. This can be achieved with the help of a controlled 3-way-valve that mixes warmer supply water into the return line when needed.

In case the temperature requirements of one or multiple consumers slightly exceed the supply temperature of the LT line, a temperature booster in the form of an electric heater or a heat exchanger supplying high temperature heat from the HT level can be installed (see Figure 4).

After considering these constraints, the supply temperature curves for the high temperature and low temperature levels of the network have been established (see Figure 5). For the low-temperature level, two scenarios have been considered: a mid-temperature level corresponding to radiators with design temperatures of 60/45°C and a low-temperature level corresponding to floor heating devices with design temperatures of 40°C/30°C.

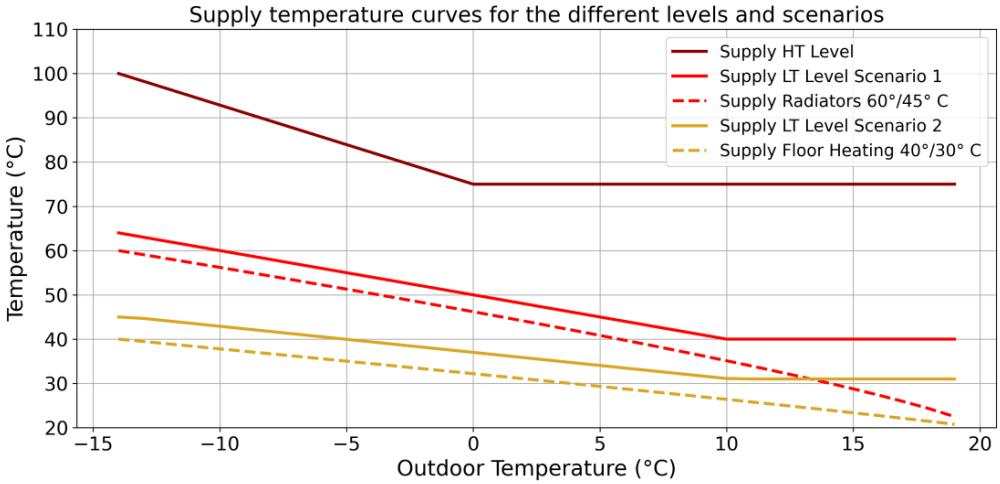

Figure 5: Temperature curves for the two supply levels and the two different scenarios

4.3 Dimensioning constraints

Due to the reduction of the supply temperature of the middle network level and to the connection of additional consumers to this level (refurbished HVAC systems that were previously connected to the HT level), an increase of the volume flow to be transported through the pipes is expected. It is therefore necessary to verify that the existing pipe diameters are sufficient and if not, to replace sections or the entirety of the LT level piping. A static analysis was carried out based on the design temperatures and expected nominal heat loads of the refurbished buildings. It could be shown that for the final state where all the planned renovations have been completed, the existing pipe dimensions are adequate. This is explained by the substantial reduction in heating load following the building renovations. This analysis can also give insights into the order of which the buildings should be retrofitted and the point at which the network transformation should be undertaken. For example, it could also be shown that the implementation of the network transformation is not possible before the renovation of the buildings B4 and B6 (see Figure 1), as in this case the existing pipes would be too small to transport the necessary heat load.

5. Building refurbishment case study

As part of the planned campus renovation and to meet current energy regulations, the building's envelopes will be refurbished and heat recovery systems for the air handling units will be installed. With the help of building simulations, the potential energy savings for the different retrofitting measures have been calculated (see Figure 6). It could be shown that the heat demand, and consequently the CO_2-emissions, of the building complex could be reduced by ca. 52% following the refurbishment. Such a significant reduction of the heat demand creates an opportunity for the lowering of the heating temperatures which in turn would allow waste heat to be used for heating.

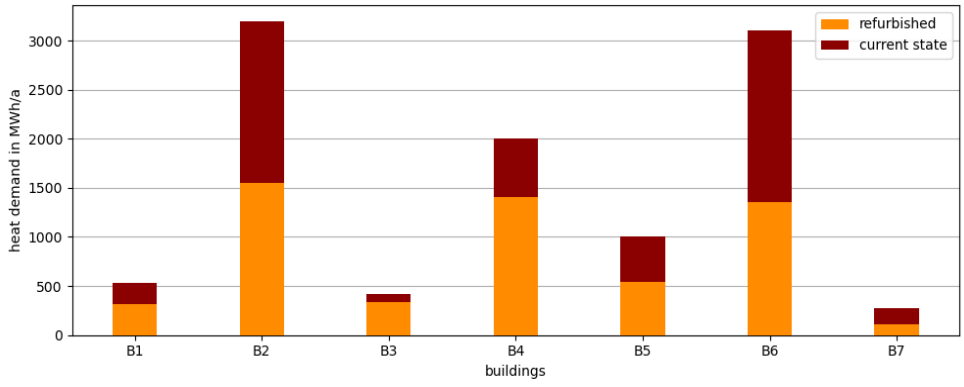

Figure 6: Heat demand of the buildings in current and refurbished state

For this, the boundary conditions of the waste heat recovery and of the heating network must be taken into account. Most buildings currently have radiators with system temperatures of 90/70 °C. As a minimum requirement, these temperatures must be lowered to 60°C/45°C as part of the renovation process (see Section 4.1). This ensures, that the buildings can use the waste heat of the chillers. However, given that the efficiency of the heat recovery depends on the temperature of the waste heat, the use of even lower temperature heating systems such as floor heating devices is recommended. Therefore, a comparative study of two systems: radiators with design temperatures of 60°C/45°C and floor heating devices with design temperatures of 40°C/30°C has been carried out.

In Figure 7: Comparison of the annuity of investment costs for radiators and floor heatingthe annual investment costs for the transformation of the heating systems in the buildings that will be refurbished is compared. An interest rate of 4% and component lifetimes from the VDI 2067-1 where assumed. It could be shown that the annuity of investment costs for installing floor heating is 57% higher than radiators.

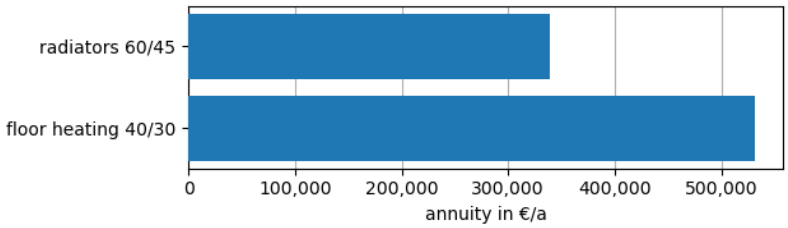

Figure 7: Comparison of the annuity of investment costs for radiators and floor heating

Furthermore, by retrofitting the air handling units with heat recovery systems, the heating demand for the air conditioning is significantly reduced, which in turn presents a good opportunity for the lowering of the supply air conditioning temperatures. If necessary, the heat exchanger of the air handling units (AHU) can be replaced in order to achieve even lower heat supply temperatures of the AHUs.

Following the implementation of the waste heat recovery measures and the transformation of the heating network, the low temperature consumers that were previously supplied by the high temperature network level (e.g the AHUs) need to be connected to the low temperature supply line of the network.

6. Seasonal geothermal storage

The heating and cooling network on the campus is to be supported by a seasonal geothermal energy storage system based on borehole heat exchangers (BHE). This will serve as a heat sink for the waste heat in summer and as a heat source for the heat pumps in winter. A central open area of 12,900 m² on the campus provides space for 120 to 150 BHEs in a hexagonal arrangement at a spacing of about five meters. Due to the good hydrogeological conditions, such as no groundwater flow and good thermal conductivity and capacity, seasonal geothermal storage is feasible and low storage losses can be expected. For the system of heating and cooling by means of chillers, the borehole thermal energy storage (BTES) should have a size of appr. 0.5 GWh (see Chapter 3). For the dimensioning of the BTES, a hydrogeological model was first created via the modeling Software FeFlow using the FEM method to determine the number of BHE and the temperature development in the underground. It should be noted that the outlet temperature of the BTES must be between the operating temperature of the chillers of 6 to 12 degrees. Initial estimates have shown that a total of approx. 80 BHE are sufficient for the needed storage size.

7. Results and conclusion

7.1 Heat recovery potential and efficiency

To assess the performance of the proposed energy retrofitting concept, an economic and ecological analysis of different scenarios has been carried out. A scenario without geothermal storage and a scenario with geothermal storage were assessed for the 2 different design system temperatures of the renovated buildings: 60°C/45°C, and 40°C/30°C, corresponding to radiators and floor heating devices (FHD) respectively. To calculate the waste heat potential and the associated electrical energy consumption, yearly simulations of the waste heat recovery from the

chillers were carried out. Depending on the scenario, the condensation temperature was set in accordance with one of the two supply temperature curves illustrated in Figure 5:. The results are summarized in Table 1. The annual average COP was calculated according to the method described in Chapter 3. It could be shown, that while all the COP values are above those of conventional heat pumps, the usage of floor heating devices in the refurbished buildings significantly increases the efficiency of the waste heat recovery. Similarly, a geothermal storage not only increases the amount of waste heat usage in the buildings through load shifting but also decreases the amount of electricity consumption of the chillers.

Table 1: Heat recovery (HR) efficiency for different scenarios

Scenario	Heating system design temperature	Waste heat recovered	Electrical consumption	annual COP	CO_2-Savings
direct HR	60°C / 45°C	3.285 MWh/a	512 MWh/a	6	704 t/a
	40°C / 30°C		205 MWh/a	16	834 t/a
with Storage	60°C / 45°C	3.858 MWh/a	483 MWh/a	8	877 t/a
	40°C / 30°C		20 MWh/a	197	1071 t/a

To understand the very high efficiency of the scenario with storage and floor heating devices, a monthly comparison of the electrical consumption for the different scenarios is illustrated in Figure 8. It can be seen that for the scenario with the lowest supply temperatures, the additional electricity consumption for the heat recovery in winter is very low and almost entirely offset by the electricity savings in summer due to the passive cooling with the geothermal storage. This is due to the fact that for this scenario, the condenser outlet temperatures are only slightly higher than currently (e.g without waste heat recovery).

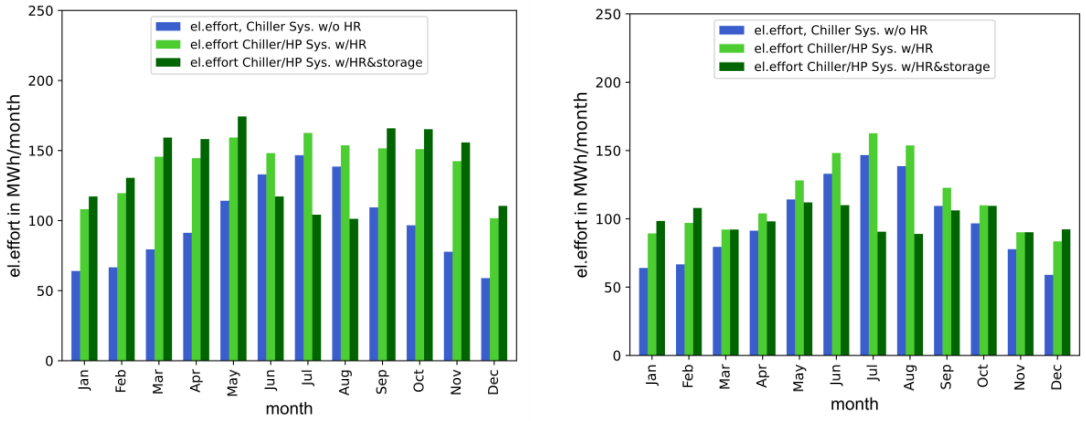

a. **supply conditions 60 °C/45 °C** b. **supply conditions 40 °C/30 °C**

Figure 8: Monthly results to electrical energy consumption of supply system for the reference (w/o HR) case and two system conceptions: direct Heat Recovery and Heat Recovery with using geothermal storage

As a consequence of the waste heat recovery and feed-in into the transformed DHN branch, the heat demand from the municipal district heating network is reduced, leading to CO_2-savings of up to 1071 t/a[1].

Figure 9illustrates the heat demand from the municipal DHN for the reference scenario without heat recovery and for the two scenarios with waste heat feed-in into the network. It shows that the combination of building refurbishment, waste heat usage and seasonal storage has the potential to reduce the dependency on fossil fuel heating sources for this building complex by 90%, with municipal DHN heat only being required for the high temperature consumers and during the periods where free cooling is prioritized above waste heat recovery.

[1] For the calculation of the CO_2-savings, the CO_2-emissions of the German electricity mix of 420 g/kWh were used (Umweltbundesamt, 2022). For the municipal DHN a CO_2-emissions factor of 280g/kWh according to (BAFA,2021) was used. It is important to note that these emission factors are specific to Germany and that for a different location, the results may differ.

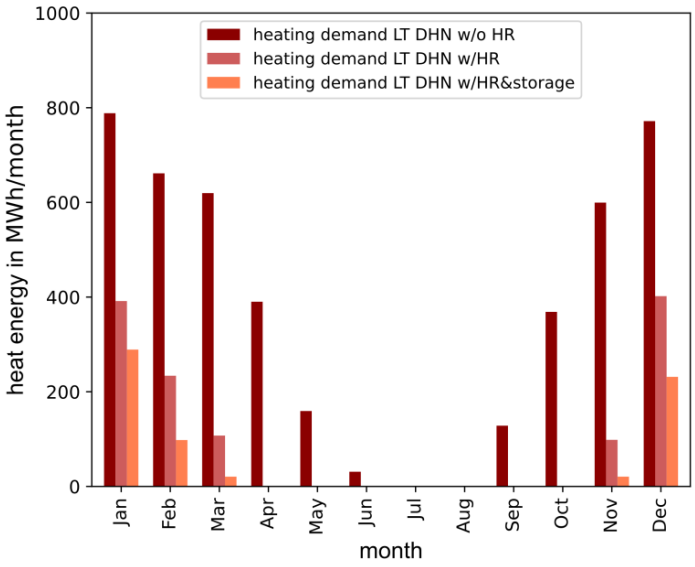

Figure 9: Monthly results of District Heat demand for the reference case (LT refurbished state w/o HR) and two system conceptions: direct Heat Recovery and Heat Recovery with using geothermal storage

7.2 Economical analysis

While it was proven that the presented concept is environmentally beneficial and leads to significant reductions in CO_2- Emissions, an economic analysis is necessary to determine its feasibility. For this, the investment costs were calculated according to manufacturer surveys and research data. The biggest investments are for the retrofitting of the chillers with heat recovery systems and for the purchase of the district network branch from the utility company (ca.0.4-0.5 million € each) closely followed by the borehole geothermal field (ca. 0.3 million €). The operation and maintenance costs were defined as a yearly percentage of the investment costs of each system. Furthermore, the cost of the additional electricity consumption for the heat recovery was added to the operation costs. The investments associated with the building retrofitting were not considered in this analysis, since these measures will be implemented regardless of the transformation of the heating and cooling supply. Therefore, the analysis only regards the economic feasibility of the heating and cooling network transformation.

A dynamic economic analysis was performed in which a service life of 20 years and an interest rate of 4% were assumed. The levelized cost of energy (LCOE) for the waste heat integration and the payback period were calculated for the 4 scenarios. It could be shown that all scenarios are profitable, with a LCOE of up to 7.5 €cents/kWh and a payback period of up to 10 years. As expected, the scenario with geothermal storage and lower temperatures largely outperforms the other scenarios, with an LCOE of 4 €cent/kWh and a payback period of 6 years. However, it is important to note that the installation of floor heating devices is more expensive than that of radiators. If the additional costs for FHD is considered, the LCOE of the low temperature scenario increases to 9 €/kWh and the amortization period to 23 years. Given that most components of the proposed system have a lifetime of over 25 years, this scenario is economically feasible. Moreover, it is important to note that for this economic analysis, the increase in energy prices has not been taken into account. Therefore, given the drastic expected increase in heating prices over the next years as well as the necessity to prioritize CO_2 savings before economic gain, the installation of FHD in the buildings is strongly recommended.

Regarding the geothermal storage, it was demonstrated that its usage increases the waste heat utilization by approx. 0,57 GWh/year and decreases the electricity demand for cooling in summer by 180 MWh/a. This results in additional CO_2-savings of ca. 200 t/a, 27% higher than the scenario without storage. Assuming a service life of 25 years, an interest rate of 4% and yearly operation and maintenance costs of 2% of the investment, a levelized cost of storage of 5.7 €cent/kWh was calculated, which is lower than the current cost of DHN heat.

7.3 Conclusion

In conclusion, this study has shown the benefits of a holistic renovation concept of a city district. It could be shown that considering the boundary conditions of the supply structure in the building renovation process creates

favorable conditions for the decarbonization of the heating and cooling supply. In total, the proposed transformation of the heating and cooling supply results in a reduction of CO_2 emissions of up to ca. 1100 t/a. Its economic feasibility is underlined by the short payback period of up to 10 years and a LCOE of max 7.5 €cent/kWh, which is much lower than the current price of municipal district heating (8.5 €cent/kWh). It was also demonstrated that while the installation of floor heating devices in refurbished buildings is significantly more expensive than that of medium-temperature radiators, it increases the efficiency of the waste heat recovery and utilization process and consequently, the CO_2-savings. This results in lower operation costs that partially offset the increased investment, especially when considering the future increase in energy prices. This example underlines the necessity to take into account the synergies between energy conservation measures at building level and the supply of energy at district level.

8. Acknowledgements

The Technische Universität Berlin is funded for this research by the German Federal Ministry of Economic Affairs and Energy (BMWi) in the project „ EnEff:HCBC" (Funding code: 03ET1632). We would also like to thank our project partner, Vattenfall Wärme Berlin AG for their technical and financial contribution to this project.

9. References

Bean, F., Volt, J., de Groote, M., Paardekooper, S., Riahi, L., 2018, Aligning district energ and building energy efficiency, Report, http://bpie.eu/wp-content/uploads/2018/11/EE-DES-BELGRADE-REPORT_WEB.pdf

Bundesamt für Wirtschaft und Ausfuhrkontrolle, 2021, Informationsblatt CO2-Faktoren, Report.

Delmastro, C., Martinsson, F., Dulac, J., Corgnati, S.P., 2017. Sustainable urban heat strategies: Perspectives from integrated district energy choices and energy conservation in buildings. Case studies in Torino and Stockholm. Energy. 138, 1209-1220, https://doi.org/10.1016/j.energy.2017.08.019

European Comission, 2016, Towards a smart, efficient and sustainable heating and cooling sector. Memo. https://ec.europa.eu/commission/presscorner/detail/en/MEMO_16_311

European Comission, 2020, A Renovation Wave for Europe - greening our buildings, creating jobs, improving lives, Brussels

Kononenko, N., Reimann, A., Ziegler. F.,2021, Modellierung des Kälteverbunds und Evaluation der übergeordneten Regelungsalgorithmen zur Effizienzsteigerung der Kälteversorgung eines Hochschulcampus , Tagungsband Deutsche Klima-Kälte-Tagung (DKV), Paper AA II.1 01, Dresden , https://www.dkv.org/index.php?id=93

Lundström, L., Wallin, F., 2016. Heat demand profiles of energy conservation measures in buildings and their impact on a district heating system. Applied Energy. 161, 290-299. https://doi.org/10.1016/j.apenergy.2015.10.024

Le Truong, N., Dodoo, A., Gustavsson, L., 2014. Effects of heat and electricity saving measures in district-heated multistory residential buildings. Applied Energy. 118, 57-67. https://doi.org/10.1016/j.apenergy.2013.12.009

Miara, M., Bongs, C., Günther, D., Helmiling, S., Krammer, Th., Oltersdorf, Th., Wapler, J., 2013, Wärmepumpen(Heat Pumps), Bine-Fachbuch, FIZ Karlsruhe

Pozzi, M., Spirito G., Fattori, F., Dénarié, A., Famigletti, J., Motta, M., 2021.Synergies between building retrofit and district heating. The role of DH in a decarbonized scenario for the city of Milano. *17th International Symposium on District Heating and Cooling*, Nottingham, UK, 6-9 September.

Stanica, D.I, Karasu, A., Brandt, D., Kriegel, M., Brandt, S., Steffan, C., 2021a. A methodology to support the decision-making process for energy retrofitting at district scale. Energy & Buildings. 238, https://doi.org/10.1016/j.enbuild.2021.110842

Stanica, D.I, Bachmann, M, Kriegel, M.,2021b. Design and performance of a multi-level cascading district heating network with multiple prosumers and energy storage. Energy Reports. 7, 128-139. https://doi.org/10.1016/j.egyr.2021.08.163

Umweltbundesamt, 2022, Entwicklung der spezifischen Treibhausgas-Emissionen des deutschen Strommix in den Jahren 1990 – 2021, https://www.umweltbundesamt.de/sites/default/files/medien/1410/publikationen/2022-04-13_cc_15-2022_strommix_2022_fin_bf.pdf

L. Urban Planning, Solar and Efficient Districts

`

Estimating Rooftops' Suitability for PVs Using Pleiades-1B Satellite Image for Charging Electric Vehicles in New Cairo, Egypt.

Shaimaa Ahmed, Mohamed Amr Serag-Eldin, and Mohamed El-Morsi
American University in Cairo, New Cairo (Egypt)

Abstract

Studying the potential of solar energy PV rooftops requires assessing solar energy and rooftop areas. First, solar radiation data on a horizontal surface were obtained from a weather station in New Cairo City (Egypt). Second, the Hay & Davies, Klucher, and Reindl (HDKR) model was used to calculate the available solar radiation on tilted surfaces. Finally, rooftops were identified and extracted from a Very High-Resolution (VHR) satellite image using Remote Sensing and Geographic Information Sciences techniques. The flat rooftops' extraction accuracy ranged between 74.6% and 96.875%. The area required for generating enough energy for one Electric Vehicle (EV) was estimated for both summer and winter. Avoiding shades from parapet walls and following the country's building codes, the water tanks and rooftop rooms were considered for PV installation. The results showed that PV rooftops could provide electricity for charging EVs in neighborhoods with different urban designs. The variables affecting the solar energy potential for EV charging are suitable rooftop areas and available solar radiation.

Keywords: PVs, rooftops, urban, neighborhoods, HDKR model, Remote Sensing, Geographic Information Sciences, very high-resolution satellite images, electric vehicles

1. Introduction

Rooftops are essential for producing solar energy using PVs in urban areas. Desert cities such as the new administrative capital (*New Administrative Capital's Map In Detail And Its Scheme*, 2019), Six of October City (*October 6*, 2022), and New Cairo City (*New Cairo*, 2022) in Egypt can benefit a lot from the abundance of solar energy (*Solar Resource Maps of Egypt*, 2019), (*Global Solar Atlas*, 2019), especially since their topography is almost horizontal. The height of buildings is almost equal in many neighborhoods and districts due to the planning laws for new cities in Egypt. However, generating solar energy from PVs installed on the rooftops of buildings is not well implemented in Egypt, and there is a lack of information about the rooftops. Therefore, mapping rooftops using VHR satellite images is important because the information is up to date, and it has more accurate measurements of the roofs.

Geographic Information Sciences (GIS) and Remote Sensing (RS) are used to detect and calculate suitable rooftop areas for generating electricity using PVs. Gassar & Cha (2021) reviewed and demonstrated 265 studies from all over the world and included one study only about solar PVs generated from rooftops in Egypt (Aboushal, 2018). In his paper, Aboushal (2018) introduced a method to identify possible rooftop areas for PVs and how to select the optimum PVs. The suggested method combined the probabilistic approach and spatial analysis to compute PV's Power Capacity Factor (PCF). The highest PCF score was selected for use in the defined urban Area in Alexandria Governorate, Egypt. Their method was based on three steps: digitizing the urban Area from Google Earth using ArcGIS, comparing PVs based on their PCF, and linking maps and PCF data.

© 2022. The Authors. Published by International Solar Energy Society
Selection and/or peer review under responsibility of Scientific Committee
doi:10.18086/eurosun.2022.11.01 Available at http://proceedings.ises.org

`

Based on the literature survey, very few detailed research studies map suitable rooftop areas for PV installation in urban areas in Egypt. For example, Taha et al. (2021) automatically identified tourist chalets from one Pleiades satellite image for Marina Resort in Egypt. They classified the satellite image using several machine learning algorisms, namely Random Forest (RF), Maximum Likelihood (ML), Support Vector Machines (SVM), and Backpropagation Neural Networks (BNN). After running these algorisms for obtaining urban and non-urban classes, they applied different morphological operations and Sobel Edge Detection techniques and conducted the quality analysis. It was concluded that RF has the highest overall accuracy and scored 97%. ML scored 95%, SVM scored 93%, and BNN scored 92%. Muhammed et al. (2021) used gamma correction, vegetation and shadow masking, k-means, and connected features, and SVM classification was applied to a satellite image to detect rooftops on an image from google earth pro. They removed the shades by creating a shades index and trained the model using digitized buildings. The accuracy assessment of SVM was 95%, and the annual PV potential was projected to be between 9.3 and 8.7 MWh/year.

Many studies investigated how solar energy could be invested in creative ways such as charging Electric Vehicles (EVs) or storing generated energy in batteries of EVs (Aljohani et al., 2020; Chandra Mouli et al., 2020; Ghotge et al., 2020; Kawamura & Muta, 2012; Mohammad et al., 2020; Vermeer et al., 2020). However, little research was conducted in the Middle East, North Africa (Alsomali et al., 2017), or Egypt (Hassan & Abdellatif, 2021; *Improving Electric Vehicle Performance Using Photovoltaic Cells*, 2018). Moreover, Egypt is developing new creative solutions to cope with the increased energy demand (*Egypt*, 2021; *Energy Consumption in Egypt*, 2020; *Energy Consumption in Egypt*, 2020; *Renewable Energy Outlook*, 2018; El-Kholy & Faried, 2011). Egypt developed a new policy towards EVs which will increase EVs usage, importing EVs (EGYPT's EVOLVING POLICY FRAMEWORK FOR ELECTRIC VEHICLES, 2020; Energy Efficiency and Renewable Energy Strategies and Policies, 2019; POLICY BRIEF: Mainstreaming Electric Mobility in Egypt: Seeing the Bigger Picture of Sustainable Cities, 2020), and manufacturing Egyptian EVs (FEV Group GmbH, 2022; State Information Service, 2022).

The optimal orientation and inclination of PVs could be horizontal or tilted on the rooftops. It is recommended that the tilted angle equals the location's latitude to obtain the maximum solar irradiance (How Does the Tilt Angle and/or Orientation of the PV Panel Affect System Performance? | Photovoltaic Lighting | Lighting Answers | NLPIP, 2021; National Solar Radiation Data Base Daily Statistics Files. National Renewable Energy Laboratory, 2005). Also, it is recommended that PVs face south in the northern hemisphere. The Hay, Davies, Klucher, and Reindl (HDKR) model (Duffie & Beckman, 2013) is highly recommended to be used when the only available data is the global solar radiation data on a horizontal surface.

It is strategic to investigate mapping rooftops to harvest energy generated from PVs to charge EVs in Egypt (Electric Vehicle Charging, 2021). This pilot study aims to map suitable areas using Pleiades-1b satellite images for PV rooftops to charge EVs. The study is conducted on compound scales in New Cairo city, and it uses solar irradiation data collected from a pyranometer located at the American University in latitude and longitude angles of 30° and 31.5°, respectively (Latitude, 2022).

According to Fakhraian et al. (2021), the hierarchical approach for estimating Solar potential on rooftops includes four stages. These stages include estimating physical potential (horizontal solar radiation), considering geographic potential (the built-up environment's impact), and estimating technical potential (the potential of generating electricity). In addition, the economic potential could be added, and it is the evaluation of the economic

`

attractiveness of PV rooftops under the present market situation. This paper demonstrates the findings for the physical and geographic potential only. Future research will discuss the technical PV potential and economic potential (Fig. 1).

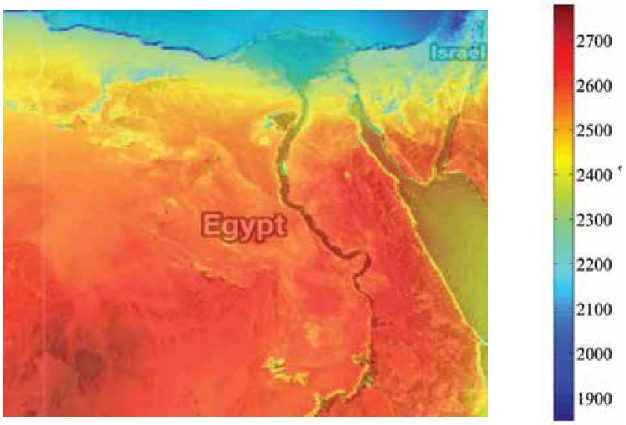

Map. 1. Egypt mean surface energy potential Adopted from (Kosmopoulos & El-Askary, 2019)

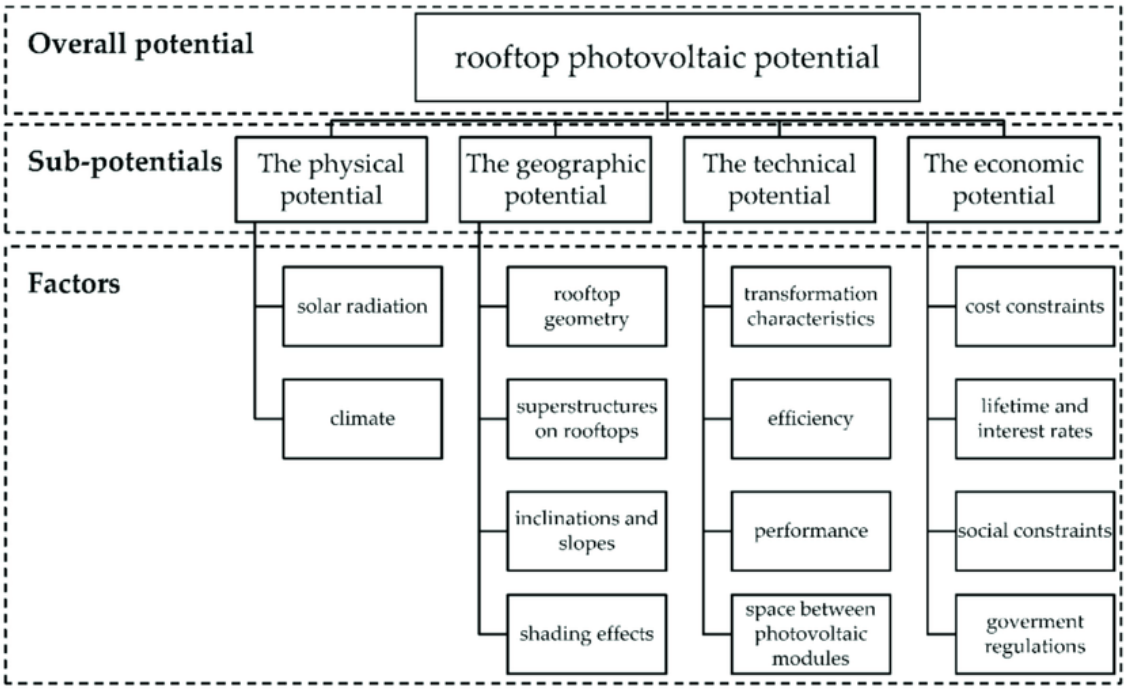

Fig. 1. Hierarchical methodology for estimating Solar potential on rooftops *(Fakhraian et al., 2021)*

`

2. Methods

1. Meteorological data

The total irradiance, G, on a horizontal surface, is measured and averaged every hour, in W/m^2, using a pyrometer, model CMP10, and manufactured by KIPP & ZONEN (*CMP10 Secondary Standard Pyranometer, CMP10 - Kipp & Zonen*, 2010). The data was collected for three years, from the end of 2018 to the beginning of 2021.

The HDKR model (Duffie & Beckman, 2013) is utilized to calculate the hourly irradiation on a tilted surface in kWh/m^2, I_T, as shown by Eq. 1, (Duffie et al., 2020). The surface is south facing and tilted at a slope $\beta = 30°$ from the horizontal.

$$I_T = (I_b + I_d A_i) R_b + I_d (1 - A_i) \frac{(1 + \cos\beta)}{2} \left[1 + f \sin^3\left(\frac{\beta}{2}\right)\right] + I \rho_g \frac{(1 - \cos\beta)}{2} \quad \text{(eq.1)}$$

I_d is the hourly diffuse irradiation in kWh/m^2, calculated using Eq. 2, Erbs' model (*Estimation of the Diffuse Radiation Fraction for Hourly, Daily and Monthly-Average Global Radiation - ScienceDirect*, 1982).

$$\frac{I_d}{I} = \begin{cases} 1 - 0.09 k_T & \text{for } k_T \leq 0.22 \\ 0.9511 - 0.1604 k_T + 4.388 k_T^2 - 16.638 k_T^3 + 12.336 k_T^4 & \text{for } 0.22 < k_T \leq 0.80 \\ 0.165 & \text{for } k_T > 0.8 \end{cases} \quad \text{(eq.2)}$$

where k_T is the hourly clearness index defined as the ratio of the hourly global (beam and diffuse) irradiation, I, received on a horizontal surface to the hourly radiation that would be received on a parallel extraterrestrial surface, I_o, as shown by Eq. 3 (Twidell & Weir, 1986)

$$k_T = \frac{I}{I_o} \quad \text{(eq.3)}$$

The global irradiation, I is calculated by integrating the total irradiance, G over an hour. The hourly values of the total irradiance, G on a horizontal surface, are available from the pyranometer measurements. While, I_o, is the integration of the solar radiation incident on a horizontal plane outside of the atmosphere, G_o, over an hour calculated according to Eq. 4 (Duffie & Beckman, 2013).

$$G_o = G_{sc} \left(1 + 0.033 \cos\frac{360n}{365}\right) \cos\theta_z \quad \text{(eq.4)}$$

Where $G_{sc} = 1.367$ kW/m^2 is the solar constant, n is the day of the year, and θ_z is the zenith angle.
In Eq. 1, the hourly beam irradiation I_b in kWh/m^2, is the difference between the hourly global irradiation, I received on a horizontal surface, and the hourly diffuse irradiation I_d

In Eq. 1, f is a modulating factor defined as $\sqrt{\frac{I_b}{I}}$, $\frac{(1+\cos\beta)}{2}$, is the view factor for the tilted surface to the sky, and $I\rho_g \frac{(1-\cos\beta)}{2}$ is the view factor for the tilted surface to the ground (Duffie & Beckman, 2013). $\rho_g = 0.2$ is the ground albedo. R_b is the ratio of beam radiation on the tilted surface $G_{b,T}$ to that on a horizontal surface G_b at any time, as defined by Eq. 5 (Duffie & Beckman, 2013)

$$R_b = \frac{G_{b,T}}{G_b} = \frac{G_{b,n} \cos\theta}{G_{b,n} \cos\theta_z} = \frac{\cos\theta}{\cos\theta_z} \quad \text{(eq.5)}$$

Where θ is the angle of incidence, and θ_z is the zenith angle.

Finally, A_i is the anisotropy index, A_i is a function of beam radiation's atmospheric transmittance. It determines the portion of horizontal diffuse to be treated as forward scattered; it is incident at the same angle as beam radiation.

`

Under clear conditions, A_i is high, and most of the diffuse are forward scattered; when the sky is totally overcast, $A_i = 0$, and diffuse is isotropic. A_i is calculated as in Eq. 6 (Duffie & Beckman, 2013)

$$A_i = \frac{I_{b,n}}{I_{o,n}} = \frac{I_b}{I_o} \quad \text{(eq.6)}$$

2. Pleiades-1B Satellite image data

The Pleiades-1B satellite image has a panchromatic band with a resolution of 50 cm (wavelength = 480-830 nm) and four multicolored bands. These bands are Blue (430-550 nm), Green (490-610 nm), Red (600-720 nm), and near-infrared (750-950 nm) bands, and their spatial resolution is 2 m (*Pleiades-1B Satellite Sensor | Satellite Imaging Corp*, 2022). The satellite image was taken on August 8, 2018. The pre-processing steps included enhancing the resolution of the satellite image and digitizing part of it. The panchromatic band increases the resolution of the multicolored bands in a process called pan-sharpen (*Earth Matters - How to Pan-Sharpen Landsat Imagery*, 2017; *Geometric Correction, Pan-Sharpening and DTM Extraction – Pleiades Satellite – CATALYST.Earth*, 2022). The resolution of the enhanced image is 0.5 m. After improving the spatial resolution, part of the image was digitized by ArcGIS software (*GIS Mapping Software, Location Intelligence & Spatial Analytics | Esri*, 2019). Next, the workflow involves extracting rooftops by applying a feature extraction module or supervised classification using RF and SVM algorism on the cloud (*Catalyst Professional – CATALYST.Earth*, 2021), comparing the two overall accuracies, and selecting the highest accuracy results or digitized maps for mapping.

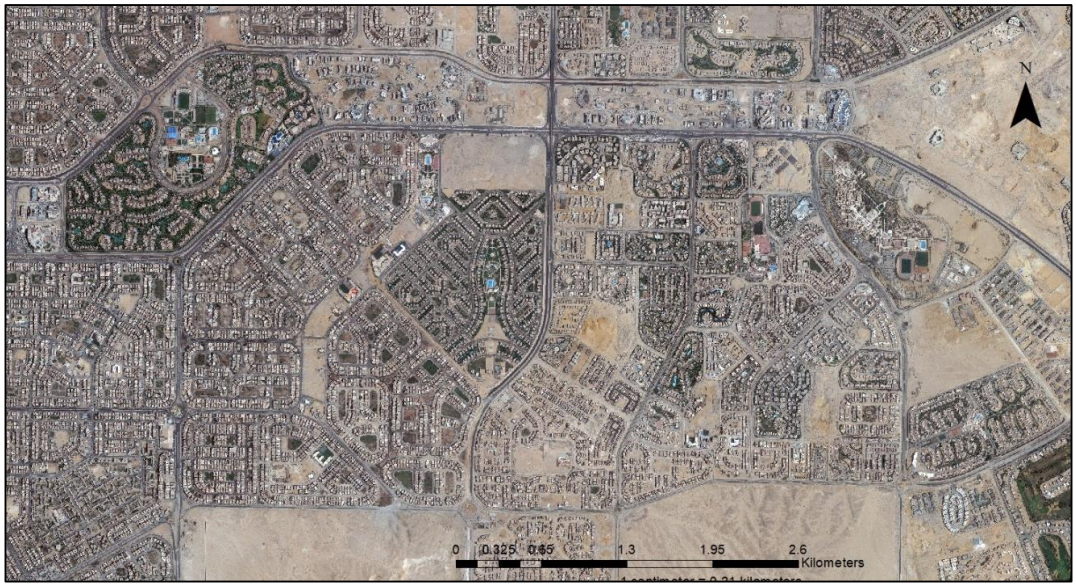

Map. 2. Pleadeas-1B satellite image for the study area after enchantment

`



Map. 3. Rooftops design in one of the samples



Map. 4. Rooftops design in one of the samples



Map. 5. Rooftops design in one of the samples



Map. 6. Rooftops design in one of the samples

3. Estimating required areas for generating electricity from rooftops

Estimating the required area to generate energy for a car is based on the average daily irradiation, the average daily electric energy required by the car for July and December.

The average measured daily irradiation, on a horizontal surface, during July is $H_{\text{July}} = 7.69 \frac{\text{kWh/m}^2}{\text{d}}$. Consequently, the average daily electric energy produced by the selected PV is $E_{PV}|_{\text{July}} = 1.3 \ \frac{\text{kWh/m}^2}{\text{d}}$.

Assuming that the average electric energy required by an electric vehicle to travel 100 km is 15 kWh. For an average daily distance of 50 km, the average electric energy required by the car is $E_{\text{car}} = 7.5\,\text{kWh/d}$.

Thus, the PV area required per vehicle during July is $A_{PV}|_{\text{July}} = \frac{E_{\text{car}}}{E_{PV}|_{\text{July}}} = \frac{7.5}{1.3} = 5.77\,\text{m}^2/\text{car}$.

For December, $H_{\text{Dec}} = 3.09 \frac{\text{kWh/m}^2}{\text{d}}$. Consequently, the average daily electric energy produced by the selected PV is $E_{PV}|_{\text{Dec}} = 0.56 \ \frac{\text{kWh/m}^2}{\text{d}}$. Thus, the PV area required per vehicle during December is $A_{PV}|_{\text{Dec}} = \frac{7.5}{0.56} = 13.39\,\text{m}^2/\text{car}$.

The PV areas required for July and December at different tilted angles are presented in Table 2

3. Results

1. Rooftops extraction

The feature extracting module, which is a part of professional catalyst software, managed to extract some of the rooftops accurately. After applying the classification function, the SVM tends to produce higher overall accuracy than the RF's algorithm, and the overall accuracy for the sample ranged between 74.6% and 96.87%. This accuracy range could be due to the overlap between the spectral signatures of different materials in urban areas. For example, the spectral reflectance of soil could be overlapped by the spectral signature of the rooftop's materials. In addition, the rooftops of buildings in desert cities could be covered by dust due to the sandy winds, and the sand's spectral signature is the same as the ground's top layer, sand. Moreover, the rooftops in one compound could be covered by different roof materials, requiring more rooftop types in the classification. Therefore, increasing the accuracy requires adding more classes and samples in the classification process.

`

To get accurate measurements for the suitable area of the rooftops', digitized maps were used. To avoid shades, the roofs of rooms or water tanks located on the rooftops were used and not the whole roof.



Map. 7. The original Satellite image of one neighborhood



Legend

Map. 8. Classified map using SMV

Table 1. 3Classification accuracy assessment for one compound

Accuracy Statistics

Overall Accuracy : 96.875% 95% Confidence Interval (91.831% 100.000%)
Overall Kappa Statistic: 0.960

Class Name	Producer's Accuracy	95% Confidence Interval	User's Accuracy	95% Confidence Interval	Kappa Statistic
shades	100.000%	(97.059% 100.000%)	94.444%	(81.085% 100.000%)	0.9243
street	84.615%	(61.156% 100.000%)	100.000%	(95.455% 100.000%)	1.0000
Green	100.000%	(93.750% 100.000%)	100.000%	(93.750% 100.000%)	1.0000
ground	100.000%	(97.222% 100.000%)	94.737%	(82.065% 100.000%)	0.9268
roof2	100.000%	(91.667% 100.000%)	100.000%	(91.667% 100.000%)	1.0000
Roof1	100.000%	(75.000% 100.000%)	100.000%	(75.000% 100.000%)	1.0000

Quantity Disagreement: 3.125% Allocation Disagreement: 0.000%

Table 1 illustrates the accuracy assessment for a neighborhood, its producer user's accuracy, kappa statistics for each class, and the overall accuracy. The overall accuracy of the SVM classification is 97.876, and urban classes are rooftops, green areas, streets, bare soil, and shades. Producer's accuracy is the number of referenced locations classified correctly / the total number of reference locations for a specific class. User's accuracy is the total number of correct classifications for a specific class/row total of the accuracy matrix. Kappa statistics evaluate how well the classification performed in compassion to randomly assigned values for this class (*Accuracy Metrics*, 2019).

2. Required rooftops area for one car

The PV area required for July & December at different tilted angles ß =10°, 20°, 30°, and 45° are presented in Table 2

`

Table 2. Estimated required area for a car for the summer and winter at different tilted angles.

Month	ß= 0°	ß= 10°	ß= 20°	ß= 30°	ß= 45°
$A_{PV}\|_{\text{July}}$ m^2/car	5.8	5.9	6	6.5	7.5
$A_{PV}\|_{\text{Dec}}$ m^2/car	13.4	11.4	10.2	9.3	8.7

In the summer, the area required for charging one electric vehicle increases when the tilted angle of the PVs increases, and the area required for charging one electric vehicle decreases when the tilted angle increases in the winter. The area difference between summer and winter could limit the number of cars charged during the year to the number of cars charged in the winter only. Moreover, the additional energy generated in the summer could 6be exported to the grid.

3. Calculating how much cars could be charged in each compound

To get the maximum energy and avoid shades, tanks or rooms on the roofs are considered, and PVs arrangement facing south (Fig. 2).



Fig. 2 Example of PVs Arrangement on Roof Tops β = 30° (tech waves, 2019)

Table 3. Available area for charging EVs and how many cars could get enough energy based on the PV's tilted angle.

Compound number	Approx. Area in m^2	Number of cars in Summer				
		At ß= 0°	At ß= 10°	At ß= 20°	At ß= 30°	At ß= 45°
1	1301	226	222	214	202	174
2	536	93	91	88	83	72
3	3441	596	586	567	533	460
4	3574	620	609	589	554	478
5	288	50	49	47	45	38
6	3325	576	566	547	515	445

`

Table 3 illustrates the compound number of the sample data, the available rooftops area in each compound, and the number of Electric Vehicles that could be charged in the summer for different tilted angles, where ß= 0°, 10°, 20°, 30° and 45°. The number of cars for each tilted angle = the total available area of rooftops of all buildings (before approximating the total available area) in a compound / the estimated required area for a car for the summer (Table 2)

Table 4. Available area for charging EVs and how many cars could get enough energy based on the PV's tilted angle

Compound number	Approx. Area in m^2	Number of cars in winter				
		At ß= 0°	At ß= 10°	At ß= 20°	At ß= 30°	At ß= 45°
1	1301	97	114	128	139	150
2	536	40	47	53	57	62
3	3441	257	301	339	369	397
4	3574	267	313	352	383	412
5	288	21	25	28	31	33
6	3325	248	291	327	356	383

Table 4 illustrates the compound number of the sample data, available rooftops area, and the number of Electric Vehicles that could be charged in the winter for different tilted angles, where at ß= 0°, 10°, 20°, 30° and 45°. The number of cars for a tilted angle = the total available area of rooftops of all buildings (before approximating the total available area) in a compound / the estimated required area for a car for the winter (Table 2)

In the summer, the number of cars that PVs could charge decreases with the increase of the inclined angle ß. The number of EVs that could be charged is the maximum when PVs are horizontal. In the winter, the number of cars that PVs could charge increases with the inclined angle ß, and the number of EVs that could be charged is maximum when PVs when ß= 45°. This suggests two scenarios for PV arrangements: arranging the PVs horizontally or at a tilted angle at ß= 45° after considering whether or not there is a plan to export the extra electricity to the grid.

4. Discussion

Using one VHR satellite image in extracting rooftop areas automatically or semi-automatically is very promising in regions with urban features with discriminating spectral reflectance. However, extracting rooftops areas is challenging in desert regions where spectral reflectance of the materials of rooftops, pedestrians, streets, and bare land are overlapped (Mohamed, 2018), (Herold et al., 2004) and (Javed et al., 2021). Therefore, it is recommended to use three images to create a third dimension which can be used as a variable or an input in automatic or semi-automatic extraction (Tian et al., 2017), (Xiang et al., 2012), (Tian et al., 2017), and (ZuWhan Kim et al., 2001). Manual extraction or digitizing rooftops produces accurate measurements but is time-consuming and costly. The design of roofs in Egypt creates an additional challenge for mapping shades. For example, the thickness of the roof's parapet is 25 cm, and its height ranges between 90 cm and 1 m. Since the parapet's width (25 cm) is less than the spatial resolution (50 cm), it was not possible to detect the parapet (0.25 pixels) or its shades (less than 2 pixels). New Cairo's topography is almost horizontal and buildings heights are almost equal because of the construction Egyptian law. However, this is not the case all over greater Cairo where buildings` height and topography of the land are changing within the same block or neighborhood. Therefore, traditional civil surveying is important to identify the height of buildings (Shaker et al., 2011) to avoid shades created by other buildings.

It is essential to avoid shades that will decrease the efficiency of the PV. Shades' avoidance is possible by grouping PVs as one block array (Fig. 2) facing south. Therefore, developing more detailed designs or architecture drawings for PV arrangements facing south with acceptable height for each building with a unique rooftop design is required. Furthermore, not all designs and shapes of rooftops were taken into consideration. Since New Cairo's

`

architectural style is designed as a mixture of the Egyptian and Western styles, many shapes and designs exist for entirely or partially tilted rooftops. Suitable rooftops design should be enforced or recommended in new desert cities to achieve the best usage of rooftops for generating energy, a.

There is a high need for accurate information about EVs, the location of charging stations, and the number of families, buildings, and cars in each compound, and the average distance a driver takes daily to get accurate areas required for charging one EV. These requirements suggest creating extensive databases and spatial databases for EVs. Since EVs market has just started, it is suggested to create this database for each new EV that enters Egypt and update it throughout the year.

5. Conclusion

Rooftops can provide enough energy for charging EVs based on two factors, the available areas of rooftops not affected by the shades and the PVs` tilted angle. VHR satellite imagery provides a wealth of information for solar planning in urban areas for desert cities in Egypt. It could be used to map urban areas such as rooftops, streets, pedestrians, and parking. VHR satellite imagery could be used for estimating suitable areas for PV installation. Accordingly, estimating energy from PVs and the area required for charging one EV is possible. Remote Sensing and GIS are recommended for use in the different stages of planning and managing cities.

The current study identified and extracted rooftops in New Cairo-Egypt from VHR satellite images using Remote Sensing and Geographic Information Sciences techniques. The area required for generating enough energy for charging one EV was estimated for both summer and winter. The results showed that rooftops could provide electricity for charging EVs in neighborhoods with different urban designs. The maximum number of EVs depends on the available area in each compound, the time of the year, and the PV tilt angle.

6. Acknowledgments

This research was supported by the American University in Cairo (SSE-ENVE-S.A-FY22-CTSG-2022-Apr-10-11-48-48 and SSE-ENVE-S.A-FY17-RSG-2019-Feb-10-01-20-3)

7. References

6th October. (2022). http://www.newcities.gov.eg/english/New_Communities/October/default.aspx

Aboushal, E. A. (2018). Applying GIS Technology for optimum selection of Photovoltaic Panels “Spatially at Defined Urban Area in Alexandria, Egypt.” *Alexandria Engineering Journal*, *57*(4), 4167–4176. https://doi.org/10.1016/j.aej.2018.11.005

Accuracy Metrics. (2019). http://gsp.humboldt.edu/olm_2019/courses/GSP_216_Online/lesson6-2/metrics.html

Aljohani, T. M., Ebrahim, A. F., & Mohammed, O. (2020). Hybrid Microgrid Energy Management and Control Based on Metaheuristic-Driven Vector-Decoupled Algorithm Considering Intermittent Renewable Sources and Electric Vehicles Charging Lot. *Energies*, *13*(13), Article 13. https://doi.org/10.3390/en13133423

Alsomali, A., Alotaibi, F., & Al-Awami, A. (2017). *Charging strategy for electric vehicles using solar energy*. 1–5. https://doi.org/10.1109/SASG.2017.8356485

Catalyst Professional – CATALYST.Earth. (2021). https://catalyst.earth/products/catalyst-pro/

Chandra Mouli, G. R., Van Duijsen, P., Grazian, F., Jamodkar, A., Bauer, P., & Isabella, O. (2020). Sustainable E-Bike Charging Station That Enables AC, DC and Wireless Charging from Solar Energy. *Energies*, *13*(14), Article 14. https://doi.org/10.3390/en13143549

CMP10 secondary standard pyranometer, CMP10—Kipp & Zonen. (2010). https://www.kippzonen.com/Product/276/CMP10-Pyranometer#.Yq_O1uxByUk

Duffie, J. A., & Beckman, W. A. (2013). *Solar Engineering of Thermal Processes*. John Wiley & Sons, Incorporated. http://ebookcentral.proquest.com/lib/aucegypt/detail.action?docID=1162079

`

Duffie, J. A., Beckman, W. A., & Blair, N. (2020). *Solar Engineering of Thermal Processes, Photovoltaics and Wind*. John Wiley & Sons.

Earth Matters—How to Pan-sharpen Landsat Imagery. (2017, June 13). [Text.Article]. NASA Earth Observatory. https://earthobservatory.nasa.gov/blogs/earthmatters/2017/06/13/how-to-pan-sharpen-landsat-imagery/

Egypt: Peak load of electricity sector 2018/2019. (2021). Statista. https://www.statista.com/statistics/1091865/egypt-amount-of-peak-load-electricity-sector/

EGYPT's EVOLVING POLICY FRAMEWORK FOR ELECTRIC VEHICLES. (2020). LYNX Business Bulletin. https://www.lynxegypt.com/assets/pdfs/EVs-Policy-Regulatory.pdf

Electric Vehicle Charging. (2021). https://www.shell.com/energy-and-innovation/mobility/electric-vehicle-charging.html

El-Kholy, H., & Faried, R. (2011). Managing the Growing Energy Demand: The Case of Egypt. *Energy & Environment*, *22*(5), 553–563. https://doi.org/10.1260/0958-305X.22.5.553

Energy consumption in Egypt. (2020). Worlddata.Info. https://www.worlddata.info/africa/egypt/energy-consumption.php

Energy efficiency and renewable energy strategies and policies. (2019). MeetMed, European Union, RCREEE. https://www.arabdevelopmentportal.com/sites/default/files/publication/meetmed_report_a1_1_final_191009.pdf

Estimation of the diffuse radiation fraction for hourly, daily and monthly-average global radiation—ScienceDirect. (1982). https://www.sciencedirect.com/science/article/pii/0038092X82903024

Fakhraian, E., Alier, M., Valls Dalmau, F., Nameni, A., & Casañ Guerrero, M. J. (2021). The Urban Rooftop Photovoltaic Potential Determination. *Sustainability*, *13*(13), Article 13. https://doi.org/10.3390/su13137447

FEV Group GmbH. (2022). *Development of the first Egyptian e-car by NASCO with FEV*. https://www.fev.com/en/media-center/press/press-releases/news-article/article/development-of-the-first-egyptian-e-car-by-nasco-with-fev.html

Gassar, A. A. A., & Cha, S. H. (2021). Review of geographic information systems-based rooftop solar photovoltaic potential estimation approaches at urban scales. *Applied Energy*, *291*, 116817. https://doi.org/10.1016/j.apenergy.2021.116817

Geometric Correction, Pan-sharpening and DTM Extraction – Pleiades Satellite – CATALYST.Earth. (2022). https://catalyst.earth/2021/07/06/geometric-correction-pan-sharpening-and-dtm-extraction-pleiades-satellite/

Ghotge, R., Snow, Y., Farahani, S., Lukszo, Z., & van Wijk, A. (2020). Optimized Scheduling of EV Charging in Solar Parking Lots for Local Peak Reduction under EV Demand Uncertainty. *Energies*, *13*(5), Article 5. https://doi.org/10.3390/en13051275

GIS Mapping Software, Location Intelligence & Spatial Analytics | Esri. (2019). https://www.esri.com/en-us/home

Global Solar Atlas. (2019). https://globalsolaratlas.info/map

Hassan, N. M., & Abdellatif, S. O. (2021). Assessing Centralized and Decentralized EV Charging Schemes using PV-Grid Connected System, Case Study in Egypt. *2021 International Conference on Microelectronics (ICM)*, 232–235. https://doi.org/10.1109/ICM52667.2021.9664915

Herold, M., Roberts, D. A., Gardner, M. E., & Dennison, P. E. (2004). Spectrometry for urban area remote sensing—Development and analysis of a spectral library from 350 to 2400 nm. *Remote Sensing of Environment*, *91*(3–4), 304–319. https://doi.org/10.1016/j.rse.2004.02.013

How does the tilt angle and/or orientation of the PV panel affect system performance? | Photovoltaic Lighting | Lighting Answers | NLPIP. (2021). https://www.lrc.rpi.edu/programs/nlpip/lightinganswers/photovoltaic/14-photovoltaic-tilt-angle.asp

Improving Electric Vehicle Performance Using Photovoltaic Cells. (2018). https://www.scirp.org/journal/paperinformation.aspx?paperid=86320

Javed, A., Cheng, Q., Peng, H., Altan, O., Li, Y., Ara, I., Huq, E., Ali, Y., & Saleem, N. (2021). Review of Spectral Indices for Urban Remote Sensing. *Photogrammetric Engineering & Remote Sensing*, *87*(7), 513–524. https://doi.org/10.14358/PERS.87.7.513

Kawamura, N., & Muta, M. (2012). *Development of solar charging system for plug-in hybrid electric vehicles and electric vehicles*. 1–5. https://doi.org/10.1109/ICRERA.2012.6477383

Kosmopoulos, P., & El-Askary, H. (2019). *The solar atlas of Egypt*. http://www.nrea.gov.eg/Content/files/SOLAR%20ATLAS%202018%20digital1.pdf

Latitude.to. (2022). *GPS coordinates of American University in Cairo, Egypt. Latitude: 30.0186 Longitude: 31.5002*. Latitude.to, Maps, Geolocated Articles, Latitude Longitude Coordinate Conversion. http://latitude.to:8080/articles-by-country/eg/egypt/10935/american-university-in-cairo

`

Mohamed, S. (2018). *Comparison of Satellite Images Classification Techniques Using Landsat-8 Data for Land Cover Extraction in Alexandria, Egypt*. International Journal of Intelligent Computing and Information Science. https://ijicis.journals.ekb.eg/article_194867_ba4b1d8f386b6b16bf0f4ee97b9b3cda.pdf

Mohammad, A., Zamora, R., & Lie, T. T. (2020). Integration of Electric Vehicles in the Distribution Network: A Review of PV Based Electric Vehicle Modelling. *Energies*, *13*(17), Article 17. https://doi.org/10.3390/en13174541

Muhammed, E., Morsy, S., & El-Shazly, A. (2021). Building Rooftops Extraction for Solar PV Potential Estimation Using Gis-Based Methods. *ISPRS - International Archives of the Photogrammetry, Remote Sensing and Spatial Information Sciences*, *44M3*, 119–125. https://doi.org/10.5194/isprs-archives-XLIV-M-3-2021-119-2021

National Solar Radiation Data Base Daily Statistics Files. National Renewable Energy Laboratory. (2005). NREL. http://rredc.nrel.gov/solar/old_data/nsrdb/dsf/

New Administrative Capital's Map In Detail And Its Scheme. (2019, September 24). Real Estate Egypt. https://realestate.eg/en/blog/new-capital-compounds/new-administrative-capital-map

New Cairo. (2022). http://www.newcities.gov.eg/english/New_Communities/Cairo/default.aspx

Pleiades-1B Satellite Sensor | Satellite Imaging Corp. (2022). https://www.satimagingcorp.com/satellite-sensors/pleiades-1b/

POLICY BRIEF: Mainstreaming Electric Mobility in Egypt: Seeing the bigger picture of sustainable cities. (2020). Friedrich-Ebert-Stiftung. https://egypt.fes.de/fileadmin/user_upload/images/FINAL_ENG_policy_brief_FES_online.pdf

Renewable Energy Outlook: Egypt. (2018). /Publications/2018/Oct/Renewable-Energy-Outlook-Egypt. https://www.irena.org/publications/2018/Oct/Renewable-Energy-Outlook-Egypt

Shaker, I., Abd-Elrahman, A., & Abdel Gawad, A. (2011). *(12) (PDF) Building Extraction from High Resolution Space Images in High-Density Residential Areas in the Great Cairo Region*. https://www.researchgate.net/publication/228735014_Building_Extraction_from_High_Resolution_Space_Images_in_High_Density_Residential_Areas_in_the_Great_Cairo_Region

Solar resource maps of Egypt. (2019). https://solargis.com/maps-and-gis-data/download/egypt

State Information Service. (2022). *The state cooperates with Egyptian scientists abroad to produce electric cars*. https://www.sis.gov.eg/Story/167112/State-cooperates-with-Egyptian-scientists-abroad-to-produce-electric-carMohamed-Ahmed-Morsi?lang=en-us

Taha, L., & Elsayed, R. (2021). Assessment of Approaches for the Extraction of Building Footprints from Pléiades Images. *Geomatics and Environmental Engineering*, *15*, 2021. https://doi.org/10.7494/geom.2021.15.4.101

techwaves. (2019, February 13). *Centralized Solar Pool Heating System* [Text]. Solar Shams. https://solarshams.com/content/centralized-solar-pool-heating-system

Tian, J., Krauß, T., & d'Angelo, P. (2017). AUTOMATIC ROOFTOP EXTRACTION IN STEREO IMAGERY USING DISTANCE AND BUILDING SHAPE REGULARIZED LEVEL SET EVOLUTION. *The International Archives of the Photogrammetry, Remote Sensing and Spatial Information Sciences*, *XLII-1/W1*, 393–397. https://doi.org/10.5194/isprs-archives-XLII-1-W1-393-2017

Twidell, J., & Weir, T. (1986). *Renewable energy resources* (second).

Vermeer, W., Chandra Mouli, G. R., & Bauer, P. (2020). Real-Time Building Smart Charging System Based on PV Forecast and Li-Ion Battery Degradation. *Energies*, *13*(13), Article 13. https://doi.org/10.3390/en13133415

Xiang, Y., Sun, Y., & Li, C. (2012). A Rooftop Extraction Method Using Color Features, Height Map Information, and Road Information. *Proceedings of SPIE - The International Society for Optical Engineering*, *8537*. https://doi.org/10.1117/12.974443

ZuWhan Kim, Huertas, A., & Nevatia, R. (2001). Automatic description of buildings with complex rooftops from multiple images. *Proceedings of the 2001 IEEE Computer Society Conference on Computer Vision and Pattern Recognition. CVPR 2001*, *2*, II-272-II–279. https://doi.org/10.1109/CVPR.2001.990971

Supply Temperature Stabilization of Decentralized Solar Thermal Collectors for Integration into District Heating and Cooling System

Raimonds Bogdanovics[1], Aleksandrs Zajacs[1]

[1] Riga Technical University, Institute of Heat, Gas and Water Technology, Riga (Latvia)

Abstract

The solar thermal collector with return/supply connection to the district heating system through a heat exchanger with a 3-way valve for temperature control was investigated. The study of supply temperature fluctuations and stabilization possibilities in northern climatic conditions was performed by an energy simulation software package and a test facility with flat plate and vacuum thermal collectors. Here we report the experimentally discovered temperature fluctuation in different working regimes (heat carrier supply temperature 80°C, 65°C, 50°C, 30°C) and different weather conditions (sunny and cloudy), as well as analyze the potential of using solar collectors for radiative cooling during the night period and present the computer model validation results.

Keywords: solar thermal collector, district heating and cooling, control accuracy

1. Introduction

The global average temperature in 2017 was about 1°C above pre-industrial levels (as a reference point for the sampling period 1850 − 1900) and continues to increase by about 0.2°C over ten years, explained by various greenhouse gas emissions based on human activity (Allen et al., 2018). Many scientists predict severe consequences for the environment as rising ocean levels, increase frequency of droughts, reduced biodiversity, reduce agricultural land and pastures, etc. As temperatures rise, so will the number of heat-related human health problems, and the spread of dangerous diseases such as malaria, tropical fever (Hoegh-Guldberg et al., 2018).

One way to slow down climate change is to pursue a carbon-neutral policy, to which 195 countries have committed themselves by 2050 under the Paris Agreement. Greenhouse gas emissions reduction can be achieved by replacing fossil fuels (coal, oil, natural gas) with renewable energy sources (solar, wind, hydro). With the development of renewable energy technologies, their efficiency is increasing but costs are falling, so households are increasingly using them to reduce the cost of heating and hot water in buildings, as well as greenhouse gas emissions.

At the end of 2019, the installed capacity of global solar collectors was 479 GWth (684 million m^2) with a total heat production of 389 TWh per year; in 2018, 12,192 m^2 flat surface solar collectors with a total capacity of 8.5 MWth and 3240 m^2 vacuum tube solar collectors with a capacity of 2.3 MWth were installed and operated in Latvia, just as in 2019 a 21,672 m^2 flat surface solar collector park with a capacity of 15 MWth was built in Salaspils (Latvia), which was connected to the existing district heating systems of the city (Weiss and Spörk-Dür, 2020). Hybrid gas boilers in combination with solar thermal panels were promoted on the market as the most efficient and environmentally friendly solutions. Nevertheless, the annual savings for a single-family house are minor and the payback time for the installation of hybrid gas/solar systems could exceed 20 years (Borodinecs et al., 2019). Despite the long payback period of solar thermal systems in Baltic countries, the market is slowly growing, mainly due to support from the EU and other funds (Valančius et al., 2020). Also, a high potential of renewable energy sources can be spotted for mobile solutions. The use of renewable energy for heat and ventilation in the mobile unit was investigated in the study (Bogdanovics et al., 2021) and solutions described in this study can be adopted for mobile use in the future.

Previous studies (Zajacs et al., 2020) confirmed that solar collectors produce the largest amount of heat energy in summer, when the solar intensity is the highest, while the heat demand during summer is the lowest because heat

© 2022. The Authors. Published by International Solar Energy Society
Selection and/or peer review under responsibility of Scientific Committee
doi:10.18086/eurosun.2022.11.02 Available at http://proceedings.ises.org

is only used to prepare hot water. During the day, hot water consumption fluctuates significantly, leading to a mismatch between heat supply and demand. This problem is partially solved by using hot water storage tanks, but if the tank volume is too small, or the household does not use hot water for a long time, solar collectors have nowhere to return heat energy, and the system temperature starts to rise and stagnation and overheating may occur. It has been found (Hillerns, 2001) that the propylene glycol-water mixture ages prematurely under the influence of high temperatures, which manifests itself as a darkening of the liquid and a decrease in the pH value, so in solar collectors, under conditions of constant stagnation, irreversible degradation of the heat carrier occurs within $2-3$ weeks. As a result of the oxidation reaction, the glycol liquid decomposes chemically, forming acidic organic compounds (lactic acid, oxalic acid, acetic acid, formic acid) as reaction products.

Almost all methods of overheating protection of solar collectors are aimed at preventing solar collectors from generating heat in the event of excess heat, thus reducing the total amount and efficiency of heat produced. If solar collectors are connected to a sufficiently large district heating network (Brange et al., 2016; Heymann et al., 2017; Lennermo et al., 2019), then the problem of stagnation could be solved without reducing the efficiency of the system, as district heating provides hot water preparation and supplies heat to factories for production processes also during the summer. Solar collectors installed in households in the summer months usually produce more heat than required, so creating a heat supply system where unused heat can be diverted to a district heating system would not only improve the overall efficiency of the system but also provide financial benefits and reduce the payback time of solar collectors.

Integrating large solar parks into a district heating system has been studied extensively (Paulick et al., 2018; Sørensen et al., 2012; Winterscheid et al., 2017). Large solar parks are mainly integrated into the district heating system, but there is very little information on small, decentralized solutions when household roof solar panels are connected to district heating networks. If energy is both consumed and produced within the household, such households are called “prosumers” or “proactive consumers”. Currently, this concept is already successfully used in the electricity market, but the concept can also be used in the field of heat energy (Brange et al., 2016).

Low heat carrier temperatures allow to significantly increase the efficiency of solar thermal collectors (Lund et al., 2021). In Strasbourg (France), the initial cost of solar collectors in the fourth-generation (annual average temperature regime 55/25°C) is reduced by 30% compared to the third-generation (80/45°C) heating system, because to achieve this the amount of heat energy per year requires a smaller solar collector area due to higher solar collector efficiency, with the percentage difference increasing in regions with the lowest solar radiation intensity (Averfalk and Werner, 2020).

Compared to the fourth-generation, the concept of the fifth-generation system includes even lower heat carrier temperatures ($20-40$°C) and the possibility to use heating networks simultaneously as a source of heat and cold for heating and cooling buildings using heat pumps. The concept of “proactive consumers” is one of the components of the fifth-generation district heating system. In total, there are at least 40 fifth-generation district heating systems in operation in Europe (mainly in Germany and Switzerland) and some of them have integrated solar systems (Buffa et al., 2019; Millar et al., 2021; Revesz et al., 2020).

In fifth-generation district heating and cooling system, radiative cooling technology – heat is radiated to outer space through a transparency window in the atmosphere between 8 and 13 μm (Bartoli et al., 1977) – can be used to produce cooling energy by solar colectors. The theoretical calculation with ZnS cover-based vacuum solar collectors shows about 75 W/m^2 cooling power at night with 5 °C difference between ambient air and absorber temperatures (Ao et al., 2021). The experimental study shows maximum net cooling power of 96 W/m^2 at night and 45 W/m^2 at noon under an average of 952 W/m^2 solar radiation (Zhao et al., 2019). As the night radiative cooling is more efficient, it is beneficial to produce heat during the day and cool during the night.

In this study, the solar thermal collector with return/supply connection to the district heating through a heat exchanger with a 3-way valve for temperature control was investigated. The study of supply temperature fluctuations and stabilization possibilities in northern climatic conditions was performed by the TRNSYS energy simulation software package and a test facility with flat plate and vacuum thermal collectors, that was placed on the university roof in Riga, Latvia. Here we report the experimentally discovered temperature fluctuation in different working regimes and different weather conditions and the computer model validation results.

2. Methods

2.1. Test facility

The test facility with flat plate and vacuum thermal collectors was created and placed on the Riga Technical University roof in Riga, Latvia, providing the location of solar collectors to the south without shading. Test facility is composed of 4 modules (see Figure 2):

- M1: parallel-connected flat plate and vacuum tube solar collectors with separate circulation pumps;
- M2: solar collector connection module for district heating system;
- M3: district heating system simulated with electric water heater;
- M4: thermal energy consumer simulated with variable speed water heating unit.

The test facility is compact and mobile (see Figure 1). Collectors slope 45°. Pipes, pumps, valves and controls are located in a water-resistant cabinet with a key. The heating unit is above the cabinet and is protected from rain. To avoid overheating, it is possible to mechanically cover collectors. Management is possible both on-site and remotely via an Internet connection. Equipment requires an electricity connection. The rig is intended to be operated at an outdoor temperature above 0°C, but for safety purposes, a water-glycol mixture (50%) is used as a heat carrier.



Fig. 1: Test facility

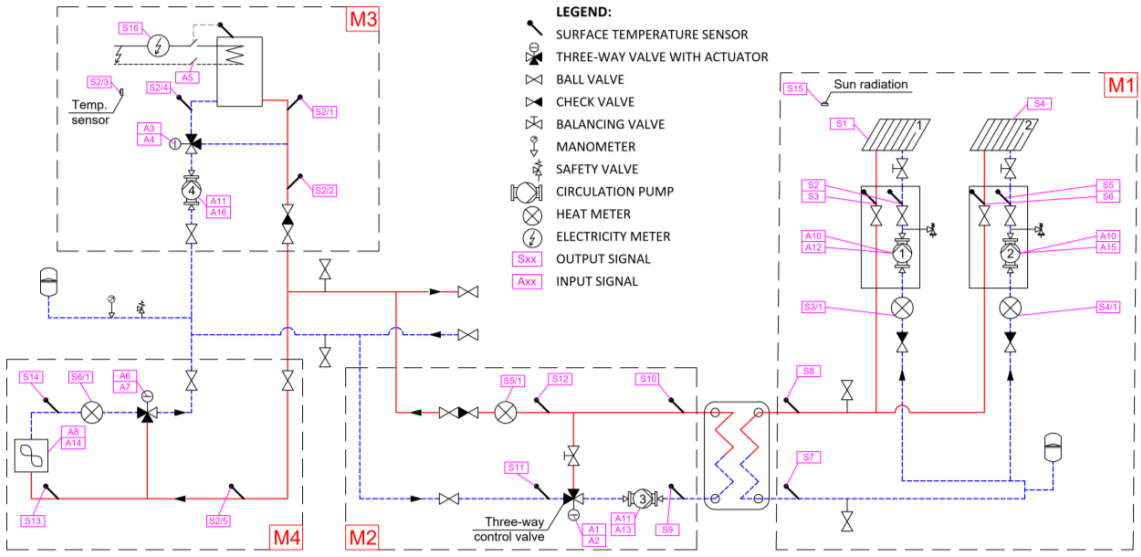

Fig. 2: Test facility schematic

The 3-way valve (see M2 in Figure 2) control speed may be changed in the range 20% − 500%, changing the time of providing a signal for opening/closing the valve (run time) and the waiting time between two consecutive opening/closing signals (see Figure 3). Three control speeds were investigated: low (20%), normal (100%), fast (500%).

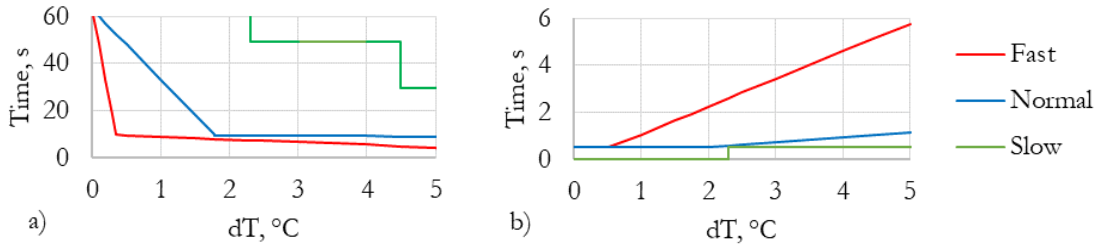

Fig. 3: Control signal (a) waiting time and (b) run time depending on the temperature difference (dT) between actual and specified heat carrier supply temperature

The experiment took place during the summer weather. Measurement step: 2.0 s. Data were filtered so only measurements then heat carrier from module M2 were injected into M4 (see Figure 2) are taken into account. Data were grouped in a way that each hour can be analyzed separately.

Hourly average solar radiation with standard deviation [W/m^2], as well as hourly average heat carrier supply temperature with standard deviation [°C], were calculated. If hourly solar radiation SD < 100 W/m^2, it is assumed that during this hour the weather was sunny, otherwise – cloudy.

During the experiment, four temperature regimes (T1/T2) for the summer period were used:

- HighT: 80/50°C, regime usually used in the big scale 3rd district heating systems;
- MediumT: 65/42°C, regime usually used in the small-scale 3rd district heating systems;
- LowT: 50/30°C, regime represent 4th generation district heating;
- UltraLowT: 30/15°C, regime represent 5th generation district heating.

Legend for cases:

- 80 / 65 / 50 / 35 - required supply temperature, °C;
- L / N / F – low / normal / fast control speed (see Figure 3);
- S / C – sunny / cloudy hour.

All temperature regimes were performed both in sunny and cloudy weather conditions and with three different 3-way valve control speeds (see Figure 3).

2.2. Computer model

The computer model (see Figure 4) was developed by TRNSYS 18 energy simulation software package. It represents the M1 and M2 modules from Figure 2. Data about M3 and M4 modules are implemented by input values based on the test facility measured values.

Input data: ambient air temperature, return heat carrier temperature and solar intensity [W/m^2] during the day based on the experiment measurement data (step 2.0 s), values between input data are linearly interpolated. Solar position from Meteonorm database for a specific day in Riga (Latvia). Pressure in the district heating system fluctuates; supply pipe 60±6 kPa, return pipe: 33±5 kPa.

Simulation time: one day from 7:00 till 19:00. Simulation step 0.1 s.

Assumptions: no specific data about wind speed, so Meteonorm database data is used; in the model heat carrier flow speed is not considered, so model response time might be faster.

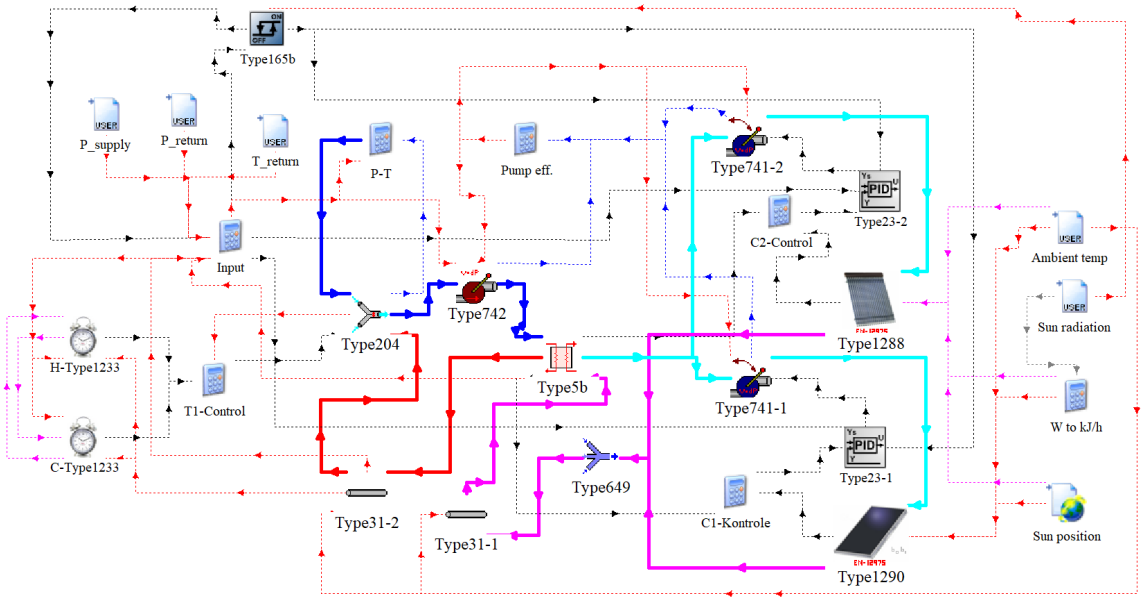

Fig. 4: Computer model created with the TRNSYS energy simulation software package

Main component parameters:

- Three-way valve with actuator (Type204). Time constant: 15 s; hysteresis: 5%; curve: linear / linear;
- Control signal (H-Type1233 and C-Type1233). The program according to Figure 3;
- Flat plate solar collector (Type1290). Area (total): 2.03 m^2; efficiency: 0.712; coefficient α_1: 3.18 W/m^2K; coefficient α_2: 0.010 W/m^2K^2; heat capacity: 6.3 kJ/m2K; slope: 45°; direction: to equator;
- Vacuum tube solar collectors (Type1288). Area (total): 1.95 m^2; efficiency: 0.362; coefficient α_1: 0.60 W/m^2K; coefficient α_2: 0.005 W/m^2K^2; heat capacity: 6.5 kJ/m^2K; slope: 45°; direction: to equator;
- Circulation pump (Type742). Pressure 42.7 kPa, efficiency 3-19% (depending on flow);
- Circulation pump (Type741). Pressure 30.0 kPa; max flow: 100 kg/h; efficiency 3-19%;
- PID controller (Type23). Gain constant: 3; integral time: 1 s; derivative time: 4 s;
- Heat exchanger (Type5b): heat transfer coefficient 425 W/K;
- Pipes with defined heat losses (Type-31). The actual loss of heat in the system is not known, therefore, for the model, heat losses are assumed to be equivalent to heat losses in DN15 (1/2'') insulated steel tube with a heat loss factor of 10 W/m^2K. The total assumed equivalent pipe length is 14 m.

3. Results

3.1. Heat carrier temperature fluctuations

For each temperature regime, average supply temperature, measurement standard deviation, kurtosis and skewness were calculated. It was found that the shape of the probability distribution plot of the heat carrier temperature deviation from desired supply temperature (see Figure 5) usually has two peaks – near 0 and some degrees Celsius behind. For instance, case 50-F-C with average temperature deviation ATD = -0.49°C, standard deviation SD = 1.11 °C, kurtosis K = 0.65 and skewness S = 0.17 or 80-L-S with ATD = -0.65 °C, SD = 2.66°C, K = 0.42, S = -0.63 has potential for control improvement. Only few cases have the ideal desired distribution characteristics like 50-N-S with ATD = 0.32°C, SD = 0.89°C, K = 21.78, S = -3.67.

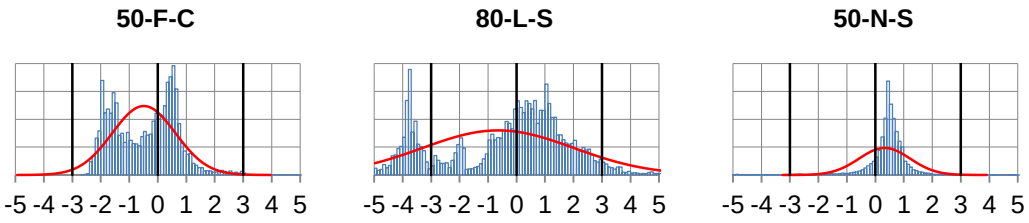

Fig. 5: Measured heat carrier supply temperature distribution; x-axis: supply temperature deviation from required temperature; y-axis: amount of measured supply temperatures; red line – normal distribution

Results show that temperature fluctuations cannot be perfectly described with normal distribution plot, but anyway, standard deviation parameter can be used to compare cases to find out the scope of temperature fluctuations (see Figure 6). The greater is the standard deviation (SD), the greater temperature fluctuates. The greatest SD = 2.85°C is found in the combination 80-L-C. The smallest SD = 0.89°C is found in the case 50-N-S. In most cases, SD in cloudy weather is greater than in sunny weather.

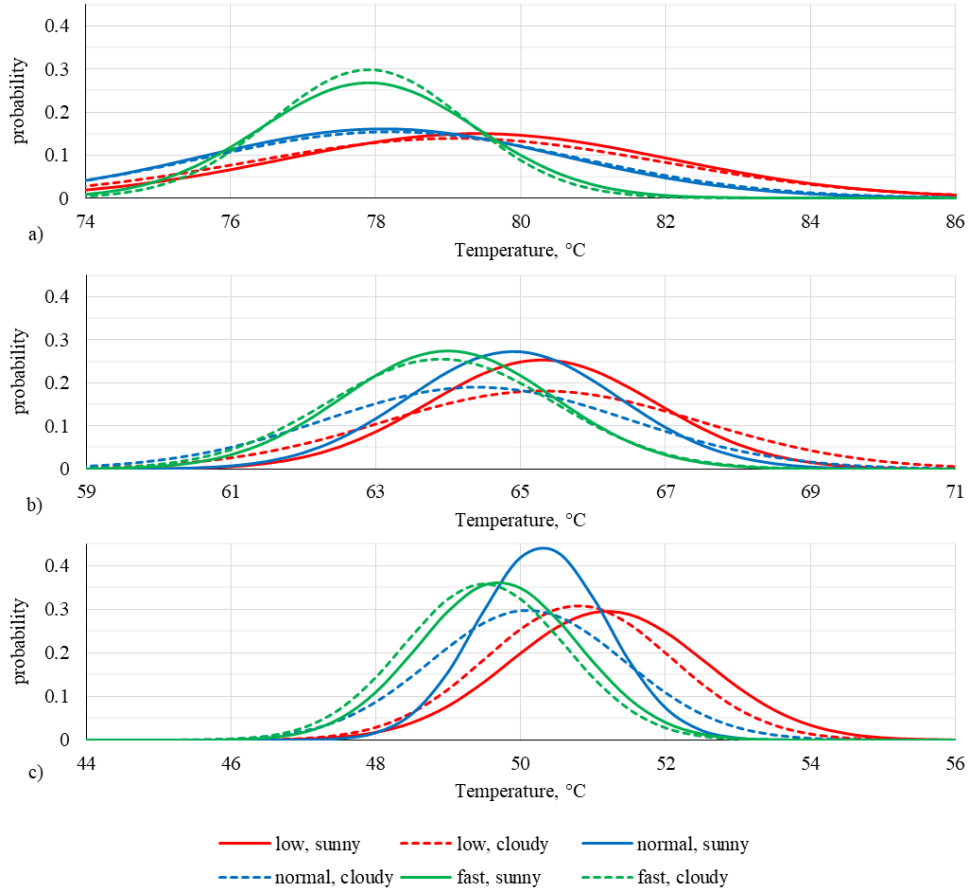

Fig. 6: Supply temperature normal distribution plots, (a) HighT: 80/50°C, (b) MediumT: 65/42°C, (c) LowT: 50/30°C

Based on the temperature regime, ranges of average temperature deviation (ATD) and standard deviation (SD):

- HighT: ATD = -2.07 – -0.65°C; SD = 1.34 – 2.85°C;
- MediumT: ATD = -1.07 – 0.34°C; SD = 1.46 – 2.19°C;
- LowT: ATD = -0.49 – 1.23°C; SD = 0.89 – 1.34°C;
- UltraLowT: ATD = -0.47 – 0.40°C; SD = 1.15 – 1.51°C.

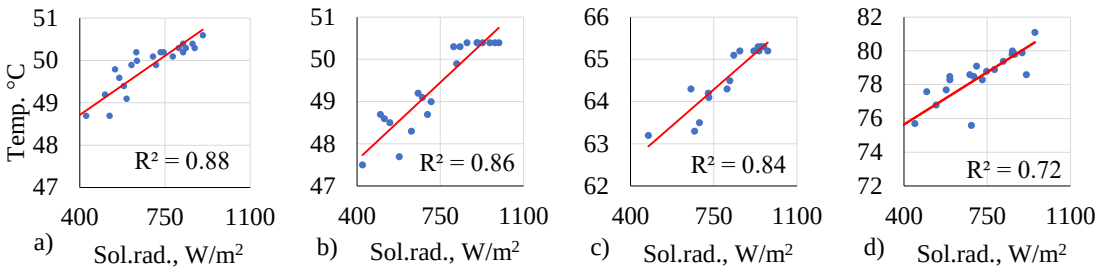

Fig. 7: Hourly average supply temperature [°C] dependence on hourly average solar radiation [W/m2], (a) 50-N-C, (b) 50-F-S, (c) 65-N-S, (d) 80-L-C

It is found (see Figure 7) that in all cases the hourly average supply temperature is lower at the lower solar radiation level and the relation between these two parameters is strong ($p < 0.05$).

3.2. Computer model validation results

Computer simulations were performed for 18 days (6 days per one temperature regime, 6 days per one control program in all possible combinations). The simulated supply temperature results were analyzed in the same way as experimentally measured data. The standard deviation of supply temperature from the experiment was compared (see Figure 8) with the standard deviation of supply temperature from the simulation based on the same weather conditions, temperature regime and control program.

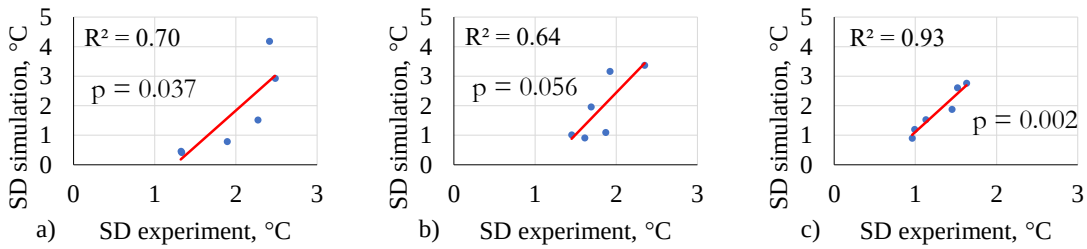

Fig. 8: Standard deviation [°C] based on experimental measurements compared to simulation results, (a) HighT: 80/50°C, (b) MediumT: 65/42°C, (c) LowT: 50/30°C

The linear regression analysis shows that there is a strong relation between experimental and simulation SD, so it is possible to use the computer model to analyze different components' impact on temperature fluctuations.

The difference between the experimental and simulation SD might be explained by assumptions and simplifications of the model that results in faster response time and higher average heat carrier temperature in the model compared to the measured temperature. The main cause might be in the simplification of the hydraulic model: no precise hydraulic resistance and geometry of facility components are used in the model as well as heat carrier flow speed is not considered. To increase the model accuracy, more measurements in different regimes should be done and more sensors, including pressure sensors, should be used.

3.3. Heating energy production

The produced energy amount from 7:00 till 19:00 was measured and simulated for 2 days – 16.08.2022 (cloudy day) and 28.08.2022 (sunny day) for MediumT (65/42°C) regime for both solar collectors. Results show that the simulated energy amount from collectors (without heat losses in pipes and system components) is 60-108% higher than measured (see Figure 9) which can be explained by high heat losses at the test facility compared to system size, so in small solar collector systems, the component proper insulation is very important.

Sunny day vacuum collector produced 2.63 kWh, flat plate collector 4.01 kWh; operation time: 10:30 – 17:30. Cloudy day vacuum collector produced 1.91 kWh, flat plate collector 2.66 kWh; operation time: 10:30 – 16:20.

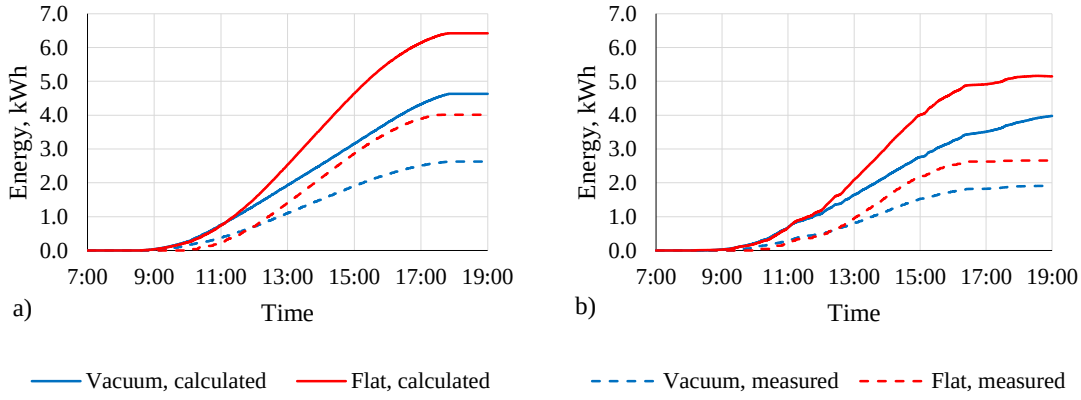

Fig. 9: Cumulative energy production, calculated and measured values, (a) sunny day, (b) cloudy day

3.4. Cooling energy production

The solar collector radiative cooling potential was investigated on 2 clear sky nights from 00:00 till 6:00.

Tab. 1: Measured values from the test facility during the night operation

Day	04.08.2022		07.08.2022	
Solar collector type	Vacuum	Flat plate	Vacuum	Flat plate
Average T to solar collector, °C	36.9	36.7	18.4	18.4
Average T from solar collector, °C	35.2	33.6	17.9	17.3
Average flow through solar collector, l/h	53.9	55.6	50.4	48.8
Average cooling power, $W/m^2_{total\ area}$	45	89	11	27
Produced cooling energy, Wh	543	1037	128	311
Average ambient air temperature, °C	19.6	19.6	14.7	14.7

Results show (see Table 1) that the cooling potential of flat plate solar collector is 2 times higher compared to vacuum tube solar collector and with higher heat carrier temperature the cooling power increase can be explained by increasing transmission heat loss. During the experiment, the heat carrier temperature was above ambient air temperature and the temperature drop in collectors was not significant.

4. Conclusion

Within this study the test facility and the TRNSYS 18 computer model were developed with the purpose to simulate and measure the performance of two types of solar collectors (vacuum tube and flat plate) in different working regimes and how they perform as a prosumer unit for thermal energy feed into the district heating network. The main desired parameter was constant supply temperature from the solar collectors' system to the district heating system. The computer model was validated within three temperature regimes and correlation coefficients for each regime were determined.

It is found that there is a difference in average supply temperature and temperature fluctuations depending on weather conditions, heat carrier temperature regime, and three-way valve control speed, achieving the best performance in sunny weather with the lower required supply temperature. With increasing the speed of the control valve, the standard deviation of heat carrier temperature fluctuations mainly decreases but the average temperature decreases too. The shape of the probability distribution plot of the heat carrier temperature deviation from desired supply temperature does not represent the normal distribution plot and usually has two peaks.

The measured produced energy demand is significantly lower than the simulated which might be explained by significant heat losses in the test facility, so additional investigations and further improvements of the test facility and computer model are going to be done in future research.

5. Acknowledgments



This work has been supported by the European Social Fund within the Project No 8.2.2.0/20/I/008 «Strengthening of PhD students and academic personnel of Riga Technical University and BA School of Business and Finance in the strategic fields of specialization» of the Specific Objective 8.2.2 «To Strengthen Academic Staff of Higher Education Institutions in Strategic Specialization Areas» of the Operational Programme «Growth and Employment». This publication was supported by Riga Technical University's Doctoral Grant programme.

6. References

Allen, M.R., Dube, O.P., Solecki, W., Aragón-Durand, F., Cramer, W., Humphreys, S., Kainuma, M., Kala, J., Mahowald, N., Mulugetta, Y., Perez, R., Wairiu, M., Zickfeld, K., 2018. Chapter 1. Framing and Context, in: Global Warming of 1.5°C. An IPCC Special Report on the Impacts of Global Warming of 1.5°C above Pre-Industrial Levels and Related Global Greenhouse Gas Emission Pathways, in the Context of Strengthening the Global Response to the Threat of Climate Change.

Ao, X., Liu, J., Hu, M., Zhao, B., Pei, G., 2021. A rigid spectral selective cover for integrated solar heating and radiative sky cooling system. Sol. Energy Mater. Sol. Cells 230, 111270. https://doi.org/10.1016/j.solmat.2021.111270

Averfalk, H., Werner, S., 2020. Economic benefits of fourth generation district heating. Energy 193, 116727. https://doi.org/10.1016/j.energy.2019.116727

Bartoli, B., Catalanotti, S., Coluzzi, B., Cuomo, V., Silvestrini, V., Troise, G., 1977. Nocturnal and diurnal performances of selective radiators. Appl. Energy 3, 267–286. https://doi.org/10.1016/0306-2619(77)90015-0

Bogdanovics, R., Borodinecs, A., Zemitis, J., Zajacs, A., 2021. Using a mobile modular energy unit with PV panels for heating. ASHRAE J. 63, 38–46.

Borodinecs, A., Bogdanovics, R., Prozuments, A., Tihana, J., Gaujena, B., 2019. Evaluation of hybrid heating systems with a combination of fossil and renewable energy sources, in: IOP Conference Series: Earth and Environmental Science. https://doi.org/10.1088/1755-1315/297/1/012050

Brange, L., Englund, J., Lauenburg, P., 2016. Prosumers in district heating networks - A Swedish case study. Appl. Energy 164. https://doi.org/10.1016/j.apenergy.2015.12.020

Buffa, S., Cozzini, M., D'Antoni, M., Baratieri, M., Fedrizzi, R., 2019. 5th generation district heating and cooling systems: A review of existing cases in Europe. Renew. Sustain. Energy Rev. 104, 504–522. https://doi.org/10.1016/j.rser.2018.12.059

Heymann, M., Rühling, K., Felsmann, C., 2017. Integration of Solar Thermal Systems into District Heating - DH System Simulation. Energy Procedia 116, 394–402. https://doi.org/10.1016/j.egypro.2017.05.086

Hillerns, F., 2001. The behaviour of heat transfer media in solar active thermal systems in view of the stagnation conditions, in: IEA-SHC Task 26 Industry Workshop. Borlänge, Sweden.

Hoegh-Guldberg, O., Jacob, D., Taylor, M., Bindi, M., Brown, S., Camilloni, I., Diedhiou, A., Djalante, R., Ebi, K.L., Engelbrecht, F., Guiot, J., Hijioka, Y., Mehrotra, S., Payne, A., Seneviratne, S.I., Thomas, A., Warren, R., Zhou, G., 2018. Chapter 3. Impacts of 1.5ºC Global Warming on Natural and Human Systems, in: Global Warming of 1.5°C. An IPCC Special Report on the Impacts of Global Warming of 1.5°C above Pre-Industrial Levels and Related Global Greenhouse Gas Emission Pathways, in the Context of Strengthening the Global Response to the Threat of Climate Change. pp. 175–311.

Lennermo, G., Lauenburg, P., Werner, S., 2019. Control of decentralised solar district heating. Sol. Energy 179, 307–315. https://doi.org/10.1016/j.solener.2018.12.080

Lund, H., Østergaard, P.A., Nielsen, T.B., Werner, S., Thorsen, J.E., Gudmundsson, O., Arabkoohsar, A., Mathiesen, B.V., 2021. Perspectives on fourth and fifth generation district heating. Energy 227, 120520.

https://doi.org/10.1016/j.energy.2021.120520

Millar, M.A., Yu, Z., Burnside, N., Jones, G., Elrick, B., 2021. Identification of key performance indicators and complimentary load profiles for 5th generation district energy networks. Appl. Energy 291, 116672. https://doi.org/10.1016/j.apenergy.2021.116672

Paulick, S., Schroth, C., Guddusch, S., Rühling, K., 2018. Resulting Effects on Decentralized Feed-In into District Heating Networks - A Simulation Study. Energy Procedia 149, 49–58. https://doi.org/10.1016/j.egypro.2018.08.168

Revesz, A., Jones, P., Dunham, C., Davies, G., Marques, C., Matabuena, R., Scott, J., Maidment, G., 2020. Developing novel 5th generation district energy networks. Energy 201, 117389. https://doi.org/10.1016/j.energy.2020.117389

Sørensen, P.A., Nielsen, J.E., Battisti, R., Schmidt, T., Trier, D., 2012. Solar district heating guidelines: Collection of fact sheets. WP3 – D3.1 & D3.2. Sol. Distric Heat. 152.

Valančius, R., Jurelionis, A., Jonynas, R., Borodinecs, A., Kalamees, T., Fokaides, P., 2020. Growth rate of solar thermal systems in Baltic States: Slow but steady wins the race? Energy Sources, Part B Econ. Planning, Policy 15, 423–435.

Weiss, W., Spörk-Dür, M., 2020. Solar Heat Worldwide. Global market development and trends in 2019.

Winterscheid, C., Dalenback, J.-O., Holler, S., 2017. Integration of solar thermal systems in existing district heating systems. Energy 137, 579–585.

Zajacs, A., Borodiņecs, A., Neviero, I., 2020. Optimal use of solar collectors in small-scale districts. IOP Conf. Ser. Mater. Sci. Eng. 869. https://doi.org/10.1088/1757-899X/869/4/042039

Zhao, D., Aili, A., Zhai, Y., Lu, J., Kidd, D., Tan, G., Yin, X., Yang, R., 2019. Subambient Cooling of Water: Toward Real-World Applications of Daytime Radiative Cooling. Joule 3, 111–123. https://doi.org/10.1016/j.joule.2018.10.006

Integration of Renewable Energies into Cityscape

Vera Boß, Karin Rühling and Clemens Felsmann

Technische Universtität Dresden, Chair of Building Energy Systems and Heat Supply, Dresden (Germany)

Abstract

A visually appealing integration of renewable energies into cityscape is important to retain acceptance. Therefore, recommendations considering aesthetic requirements have been developed for photovoltaic (PV), solar thermal (ST) and air-based heat pumps. PV and solar thermal on pitched roofs should match the roof's shape and color and do without any elevation. On flat roofs, the installations should be as invisible as possible, which can be achieved by low elevation angles and large distances to the building's edges. As visibility can often not be avoided completely, it is important to at least install the modules or collectors parallel to the roof edge. Showcase simulations have shown that an aesthetically optimized solar thermal system has a decreased energy output compared to a conventional installation, but it has almost no effect on the overall costs for heat generation in a time span of 20 years. Especially outdoor units of air-based heat pumps should be installed with some kind of noise and sight protection (e. g. enclosure).

Keywords: photovoltaic, solar thermal, heat pump, outdoor unit, cityscape, urban planning, aesthetic aspects, renewable energies, cost efficiency

1 Introduction



The acceptance of solar energy and heat pumps is high among the public in Germany (Lichtblick SE, 2020). To ensure that this remains the case, aesthetic aspects must be considered during planning. Therefore, recommendations for the integration of photovoltaic, solar thermal and heat pumps into cityscape have been developed at Technische Universität Dresden on behalf of and in interaction with Dresden's Urban Planning Office.

2 Recommendations for solar energy systems on pitched roofs

2.1 Shape and arrangement



Fig. 1: Examples for photovoltaic area matching the roof shape (left, © Felsmann) and zigzag arrangement (center, © Felsmann), further a combination of horizontal and vertical PV modules and solar thermal collectors (right, © Felsmann)

The shape of the PV or solar thermal system should be oriented towards the roof and compact areas or stripes are to be favored (see lift picture in Fig. 1). At valleys and ridges, zigzag arrangements should be avoided (see center picture in Fig. 1), meaning no fragmentation of the total area due to roof-lights or roof penetrations (see right picture in Fig. 1). Broad installations on large, continuous dormers are particularly good solutions regarding cityscape. In general, the arrangement of modules or collectors should be consistently horizontal or vertical in every area or – even better – at the whole building.

© 2022. The Authors. Published by International Solar Energy Society
Selection and/or peer review under responsibility of Scientific Committee
doi:10.18086/eurosun.2022.11.03 Available at http://proceedings.ises.org

2.2 Elevation

On pitched roofs, an elevation of solar thermal collectors or photovoltaic modules is quite common, but not acceptable from an aesthetic point of view (see left picture in Fig. 2). Considering urban planning aspects, only roof-parallel and roof-integrated systems are acceptable, as a more consistent overall appearance is achieved (see center and right picture in Fig. 2). In-roof systems are a particularly aesthetic solution but may cause a higher heat input into rooms behind. This might make stronger heat protection measures necessary or decrease thermal comfort. In case of photovoltaic, a higher module temperature decreases efficiency, whereas a solar thermal system becomes more efficient.



Fig. 2: Elevated photovoltaic modules (left, © Felsmann), roof-parallel evacuated tube collector (center, © Vaillant GmbH) and in-roof flat-plate collector (right, © Vaillant GmbH)

2.3 Color

The modules' or collectors' color plays an important role on pitched roofs. From an aesthetic point of view, their color should match the roof's color. Contrasts – as in the left picture in Fig. 3 – should be avoided. Photovoltaic in various colors is already available on the market[1]. The center picture in Fig. 3 shows red modules on a common brick-red roof. However, colored solar thermal collectors are still a subject of research. First results of a project conducted by Fraunhofer ISE are very promising (see Fig. 3 right). The developed MorphoColor™ technology for coating flat-plate collector's and PV module's glass covers allows to achieve different colors (Wessels et. al., 2021).



Fig. 3: High color contrast between roof and PV modules (left, © Felsmann), red photovoltaic on red roof (center, © BISOL Production Ltd.) and green solar thermal collector developed by Fraunhofer ISE (right, © Fraunhofer ISE (Andreas Wessels))

3 Recommendations for solar energy systems on flat roofs

3.1 Elevation

In terms of cityscape, a visibility of PV and solar thermal on flat roofs should be avoided completely, as roof edges appear erratic due to elevated modules or collectors. Besides, people tend to feel more comfortable in urban areas that are clearly delimited towards the sky. It follows that, considering urban planning requirements, the optimum elevation angle of PV and solar thermal on flat roofs is 0° and that the installation should not include any substructure. These demands are often opposed to a desired maximization of energy output. For solar thermal, elevation angles between 25° and 70° are common, for PV 30° to 45° (depending on orientation and load profile in both cases).

[1] E. g. Spectrum Series by BISOL Production Ltd., see brochure here:
https://dl.bisol.com/files/Spectrum%20Brochure/BISOL_Spectrum_Brochure_DE.pdf

Besides, minimum elevation angles usually must be abided by for static reasons. Even if an installation with almost 0° is possible, usually a substructure of 10 to 30 cm height is necessary. Hence, visibility from the surrounding urban space cannot be avoided completely.

Evacuated tube collectors that can be installed with an angle of 1° to 3° have been commercially available for more than 10 years already. The showcase collector in Fig. 4 (left picture) furthermore offers the possibility to rotate single tubes. Elevated installations are still standard though, which makes recommendations for these systems necessary (see the following paragraph 3.2).



Fig. 4: Evacuated tube collector lying flat on the roof (left, © Viessmann GmbH) and solar thermal system with orientation parallel to building's edges (right, © Ritter Energie- und Umwelttechnik GmbH & Co. KG)

3.2 Shape and arrangement

To decrease visibility from the surrounding area, the horizontal distance between module/collector and the building's edge should be as large as possible (guiding value: 1,50 m). However, this leads to decreased energy outputs as the area available for PV or solar thermal diminishes. In terms of maximum energy output, it is also possible to always choose a south exposure for the system. This cannot be favored in terms of cityscape though, as orientation should always be parallel to the roof edge (see Fig. 4 right).

4 General recommendations for solar energy systems

4.1 Roof greening

The positive effects of roof and façade greening in urban areas are well known (e.g., improvement of microclimate, sound absorption, time-delayed wastewater effect in the case of heavy precipitation, habitat for beneficial organisms in the city) and go far beyond the simple, appealing appearance that can be perceived by everyone. Despite formal competition for space, the approach of combining photovoltaic and solar thermal systems with roof greening is increasingly being adopted and available on the market (e.g., "SolarGrünDach" by Optigrün) - see Fig. 5.



Fig. 5: Showcase combination of photovoltaic and green roof (© Optigrün)

The following aspects should be taken into account in a pro and con consideration:

- Plants can bind CO_2. However, this does not lead to an actual avoidance since the CO_2 is released back into the environment at the end of the plant's lifetime. The proportion that is sequestered as carbon in the soil in the long term is relatively small: 23.6 kg_{CO2}/m^2 in 50 years (Thiele, 2015). PV or solar thermal can achieve double the amount *per year*, i.e., 100-fold values during their lifetime. In terms of maximum CO_2 avoidance, PV or solar thermal systems are therefore to be preferred over roof greening.

- Plants lead to a reduction in local and surface temperature, especially in summer. The combination with PV results in slightly increased yields, while the solar thermal energy output rather decreases.
- Greening leads to savings in heating and especially cooling demand. A general quantification and thus recommendations are difficult; individual case studies are necessary.
- In the case of construction asymmetries (chimneys, roof exits, etc.) or technically required gaps in the arrangement of PV and solar thermal fields, an architectural solution using roof greening can be extremely positive for the cityscape.

4.2 Glare effects

The cover glasses of photovoltaic modules - so-called solar glasses - reflect sunlight, so that a reflection cannot be completely prevented. Manufacturers of these solar glasses estimate the reflection percentage at approx. 8 %. The left picture in Fig. 6 shows the exemplary reflection of sunlight on PV modules.

The reflection properties of solar thermal collectors differ depending on the manufacturer/model and depend on various properties. Nowadays, the reflected portion of the incident radiation is usually well below 5 % (see right picture in Fig. 6 for an example of the reflection on vacuum tube collectors). The only exception are vacuum tube collectors with CPC reflectors - their overall reflection properties are dominated by the CPC reflector.



Fig. 6: Reflection of sunlight on photovoltaic modules (left, © SOLARWATT GmbH) and solar thermal collectors (right, © Ritter Energie- und Umwelttechnik GmbH & Co. KG)

For both photovoltaic modules and solar thermal collectors, the type of solar glass is determining for the resulting glare effect. Structured glass (microstructures on both sides, with high proportions of diffuse reflection) should be preferred over float glass (similar behavior to window glass). Moreover, flat inclination angles have a positive effect in most urban locations (e.g., no glare for traffic). Nevertheless, a glare effect cannot completely be ruled out, so that in the case of exposed locations (e.g., airport approach lane, direct view from certain city views), it may be necessary to check on a case-by-case basis.

4.3 PVT

For more than 20 years, the development of hybrid modules that provide both electrical energy and heat at low to medium temperature levels is advanced. They are referred to as PVT collectors. The basic idea addresses the drawback that the performance of current standard photovoltaic modules decreases significantly at module temperatures above 25 °C. By using a liquid or air flow, cooling of the modules is achieved, and the annual PV yield can be increased. If a designated use is found for the heat at low to medium temperature levels, the overall efficiency can be increased even further. Moreover, less area is required for installation.

4.4 Combining solar thermal or PVT collectors with heat pumps

Heat pumps are an important element when it comes to increasing the amount of renewable energy sources in the heating sector. The German federal government is aiming at installing half a million new heat pumps in Germany per year during the next few years. But tapping environmental energy as a heat source often proves problematic in urban areas, since neither the ground nor the ambient air can make significant contributions regarding the trend toward increasing building density.

A combination with solar thermal can be a very good alternative. Commercially available collectors can realize direct supply at the level needed for domestic hot water and space heating in summer and spring/fall. During the rest of the year, the solar system then serves as a heat source for the heat pump, thus contributing indirectly to the heat supply.

If PVT collectors are used, increasing the temperature level using the heat pump is required almost all year round. The situation is similar for low-cost solar thermal collectors (e.g., uncovered finned absorbers), although there is the option of using it for cooling as well if the heat pump can also realize cooling functions via additional components. In this operating mode, the collectors take over the heat dissipation to the environment.

Current research on pilot installations combining PVT collectors and heat pumps is for instance conducted by Fraunhofer ISE. Two showcase installations using PVT as the only heat source for the heat pump reached seasonal performance factors of 3.3 and 3.8 in the year 2021 (Helmling et. al., 2022), which is almost as efficient as common brine-water heat pumps with flat ground collectors as heat source.

5 Showcase simulations for solar thermal systems

5.1 Simulations of solar thermal systems with 22 collectors

The effects of aesthetical optimization measures were examined through annual yield simulations (using *Polysun*) and simple estimations of overall costs in a period of 20 years. The following boundary conditions were selected for all simulated scenarios:

- Apartment house: new building with flat roof
- Building orientation: southeast
- Floor/roof area: 28 m x 10 m
- 8 residential units with 4 persons each
- Heat demand for space heating: 30 kWh/(m²a)
- Domestic hot water demand: 50 l/d per person at 60 °C
- Solar thermal system with 22 flat plate collectors
- Collector dimension: 1.00 m x 2.00 m
- Distance to the roof edge: 1.50 m
- Buffer storage with a volume of 2,000 l
- Additional gas boiler with a capacity of 100 kW

The scenarios differ in orientation and elevation angle of the collectors (see Table 1). The reference simulation sticks to common design conventions, assuming that an elevation angle of 45° and south exposure will lead to a rather high (area-specific) heat output. In contrast, there is a scenario optimized aesthetically with a southeast orientation and an installation angle of 15° (last column in Table 1). Additionally, there are two "compromise installations" in which either only the orientation was adapted to aesthetic requirements ("parallel to roof edge") or only the installation angle ("small elevation angle").

Table 1: Overview of scenarios – 22 solar thermal collectors

Scenario	Conventional (reference)	Parallel to roof edge	Small elevation angle	Aesthetically optimized
Elevation angle	45 °	45 °	15 °	15 °
Orientation	S	SE	S	SE
	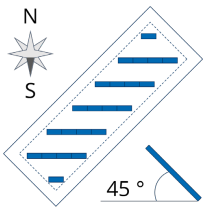	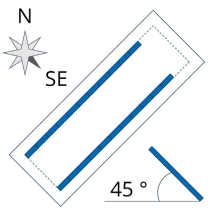	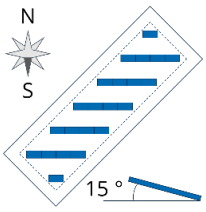	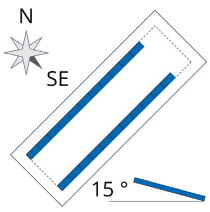

The results of the yield simulations are shown in Table 2. First, it is noticeable that the solar yields decrease at least slightly through all urban planning optimization measures (see lines 3 to 5): When placed parallel to the roof edge and continuing with a 45° installation angle, the yield decreases by 0.2 %. With an additional reduction of the installation angle to 15°, the yield even decreases by 7.0 % compared to the reference case.

When considering the natural gas consumption, however, it is noticeable: The relative increase (line 8) for the aesthetically optimized scenario is only 1.3 %. This is due to the fact that the gas boiler takes over most of the heat supply in all scenarios, which means that the reference value for this percentage is rather high in all cases.

Table 2: Results of yield simulations - 22 solar thermal collectors

0	Scenario	unit	conventional (reference)	parallel to roof edge	small elevation angle	aesthetically optimized
1	Elevation angle		45°	45°	15°	15°
2	Orientation		S	SE	S	SE
3	Solar yield	MWh/a	21.862	21.813	20.505	20.324
4	Difference compared to reference	MWh/a		-0.049	-1.357	-1.538
5	**Relative difference compared to reference**			**-0.2 %**	**-6.2 %**	**-7.0 %**
6	Natural gas consumption	MWh/a	133.502	133.576	134.998	135.186
7	Difference compared to reference	MWh/a		0.074	1.496	1.684
8	**Relative difference compared to reference**			**+0.1 %**	**+1.1 %**	**+1.3 %**
9	Consumption of electricity	kWh/a	300	300	309	305

To be able to better classify the results, a simplified profitability analysis was carried out. The assumptions made and the results are shown in Table 3. For the reference case, area-specific investment costs of 350 EUR/m² gross collector area were assumed. For the two scenarios with southeast orientation, this value was decreased by 15 % (see line 3), since two instead of seven collector rows must be installed here and thus a significantly decreased expenditure for the piping must be expected. For the two systems with a flat installation angle (15°), the area-specific costs were reduced by 10 % (see line 4), since a less complex substructure is required here.

Table 3: Estimation of overall cost – 22 solar thermal collectors

0	Scenario	unit	conventional (reference)	parallel to roof edge	small elevation angle	aesthetically optimized
1	Elevation angle		45°	45°	15°	15°
2	Orientation		S	SE	S	SE
Investment cost						
3	Factor for reduction of piping cost		1	0.85	1	0.85
4	Factor for reduction of cost for substructure		1	1	0.9	0.9
5	Area-specific cost of collector	EUR/m²	350	298	315	268
6	Overall cost of collectors	EUR	15,400	13,090	13,860	11,781
7	Cost of buffer storage	EUR	2,500	2,500	2,500	2,500
8	Cost of gas boiler	EUR	7,000	7,000	7,000	7,000
9	Assembly charges	EUR	3,000	3,000	3,000	3,000
10	Overall investment cost	EUR	27,900	25,590	26,360	24,281
Running cost						
11	Natural gas price	EUR/kWh	0.10	0.10	0.10	0.10
12	Electricity price	EUR/kWh	0.30	0.30	0.30	0.30
13	Maintenance cost in relation to investment cost		0.5 %	0.5 %	0.5 %	0.5 %
14	Yearly natural gas cost	EUR/a	13,350	13,358	13,500	13,519
15	Yearly electricity cost	EUR/a	90	90	93	92
16	Yearly maintenance cost	EUR/a	140	128	132	121
17	Overall yearly cost	EUR/a	13,580	13,576	13,724	13,732
Total cost						
18	Period under review	a	20	20	20	20
19	Total cost in 20 years	EUR	299,494	297,101	300,846	298,911
20	Additional total cost compared to reference	EUR		-2,393	+1,352	-583
21	**Relative additional cost compared to reference**			**-0.8 %**	**+0.5 %**	**-0.2 %**
22	Yearly additional cost per housing unit compared to reference	EUR/a		-15.0	+8.5	-3.64

Investment costs for buffer storage (line 7 in Table 3), gas boilers (8) and assembly (9) were assumed to be identical for all scenarios, as were natural gas and electricity prices (lines 11 and 12). A price increase in the period under consideration was neglected here for reasons of simplification. Natural gas and electric energy consumption are the result of Polysun annual simulations (see Table 2, lines 6 and 9).

A period of 20 years is considered, for which total costs of approximately 300,000 EUR result for all variants (see line 19 in Table 3). The comparison shows: The scenario "small installation angle" (15° and south orientation) has the highest total costs. Compared to the conventional reference case, this results in additional costs of about 1,350 EUR (+0.5 %).

The aesthetically optimized system is about 600 EUR (0.2 %) *less* expensive than the reference case. The most cost-effective variant is the installation parallel to the roof edge with an installation angle of 45°. Compared to the reference case, the total costs are reduced by about 2,400 EUR (0.8 %) over the observation period of 20 years. This is due to the lower investment costs resulting from the reduced effort for pipe installation, which compensate for the additional costs of the slightly higher natural gas consumption.

For a better classification, the cost differences were finally related to the number of residential units (eight) and a period of one year (see line 22 in Table 3). This results in a cost reduction of 3.64 EUR/a per housing unit for the aesthetically optimized installation compared to the conventional system.

Overall, the differences in total costs between the various scenarios are very small. The deviations of the assumptions made for e.g., costs are certainly in a similar order of magnitude. It follows that a general rejection of the urban planning optimization measures on *purely economic grounds* would not be justified.

5.2 Simulations with reduced row distance

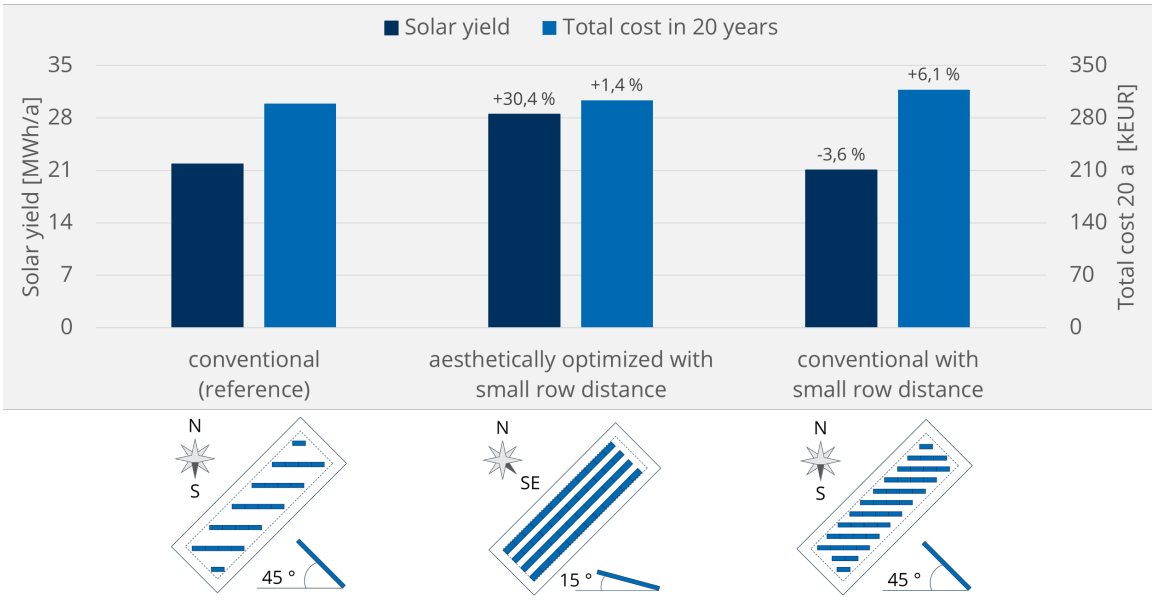

Fig. 7: Results of energetic and economic comparison of solar thermal systems with reduced row distance

It could be argued though that in terms of a *high amount of renewable energy sources* in the heating system, the reference case ("conventional") is still to be favored, as the solar thermal output is the largest. To examine this statement, another effect must be taken into account: The design of the simulated reference case was done using a common rule for determining row distances in solar energy systems. It aims at minimizing row distance, but the collectors should *not* shade each other at noon on winter solstice. The solar radiation angle is about 15.6° in Dresden at that time. This leads to a required row distance of 2.53 m and further to a total of 22 collectors fitting on the roof in the conventional scenario (45° installation angle). To simplify the comparison of the different variations, the number of 22 collectors has been assumed for *all* the simulations. However, it would also be possible to recalculate the minimal row distance for the variations with an elevation angle of 15° using the described rule. In this case, only 0.93 m would be required, leading to a total of 48 collectors fitting on the roof in case of southeast orientation ("aesthetically optimized" version).

Accordingly, another simulation with 48 collectors, 15° elevation and southeast exposure was conducted, called "aesthetically optimized with small row distance". Buffer storage size was changed to 4,000 l and its investment

costs were assumed to be 4,500 EUR. The results are displayed in Fig. 7: The thermal output of the system is about 28.5 MWh/a and thus more than 30 % higher compared to the reference case, while the overall costs are increased by only 1.4 %. So, in case the aim is to achieve a high ratio of renewable energy sources in the system, the aesthetically optimized version is to be favored over the reference case.

However, the sheer number of collectors on the roof might be the driving factor for the high heat output in this scenario. This leads to another question: Might the conventional installation – with 45° elevation and south exposure – achieve an *even higher* yield if the row distance is reduced and thus the number of collectors is increased? (This obviously means that the collectors would indeed shade each other at noon on winter solstice!) This was examined in the last solar thermal simulation: The row distance of the conventional scenario was lowered to 0.93 m (same as in 48 collector version "aesthetically optimized with small row distance"). In this case, 39 collectors fit on the roof (assumptions for buffer storage: 3,000 l and 3,500 EUR). Fig. 7 includes the results: The yield is about 3.6 % *lower* compared to the reference case (and even 26.0 % lower compared to "aesthetically optimized with small row distance"). This is due to the large amount of shading caused by the small row distance. While the system generates about 25 % more heat than the reference case during summer, the heat output in winter is drastically reduced as many of the collectors are shaded most of the time. Furthermore, it is the most expensive installation examined – the total costs are about 6.1 % higher than those of the reference case.

It can thus be concluded that in terms of total energy output *and* economic efficiency, the showcase system benefits from aesthetical optimization measures.

6 Showcase simulations for photovoltaic systems

6.1 Simulations of photovoltaic systems with 27 modules

For photovoltaic yield simulations and estimations of overalls costs, the same assumptions as for the solar thermal systems (see chapter 5) were made whenever possible. *Additional* conditions and properties include:

- Power consumption: 3,500 kWh/a per housing unit (28,000 kWh/a for the whole building)
- Module dimensions: 1.00 m x 1.72 m
- Module efficiency at STC: 17.5 %
- Number of modules: 27
- Power output: 8.09 kWp
- Investment cost: 1,500 EUR/kWp
- Feed-in tariff: 6 ct/kWh
- Maintenance charges: 1.5 % of investment cost per year

The scenarios examined are the same as in the solar thermal simulations as well: There is a conventional reference case with south exposure and 45° elevation angle, two "compromise scenarios" and the aesthetically optimized version with southeast exposure and 15° installation angle (see pictographs at the bottom of Fig. 8).

The results of the yield simulations and the overall cost estimations are shown in Fig. 8. In all scenarios, the electricity output is between 7,200 and 7,600 kWh/a and the overall cost in 20 years is between 141,000 and 145,000 EUR.

The system parallel to the roof edge with 45° installation angle generates about 2.1 % less electricity compared to the conventional (reference) case. However, the absolute self-consumption almost does not change. As feed-in remuneration is one of the driving factors regarding running cost, and investment cost are the same as in the reference scenario, both 45° scenarios result in almost the same overall cost.

In the "small elevation angle" scenario, the electrical output is almost the same as in the reference case. However, the self-consumption increases by 3.7 %. Apparently, the characteristics of the building's load and the photovoltaic output match better at 15° elevation angle in case of south exposure. Hence, less electricity from the grid is needed. This is the main reason why the "small elevation angle" scenario is the least expensive.

The aesthetically optimized installation has the lowest electricity yield (-3.4 % compared to conventional system). But as the self-consumption is still 1.1 % higher compared to the reference case, the overall costs decrease.

All in all, from a financial point of view, a 15° elevation angle is to be preferred over 45° in the given scenarios. The two main reasons for that are:

- Corresponding to the assumptions for solar thermal simulations, investment costs are reduced by 10 %, since a less complex substructure is required.
- The load curves seem to match better, resulting in a higher self-consumption and thus decreased yearly electricity costs.

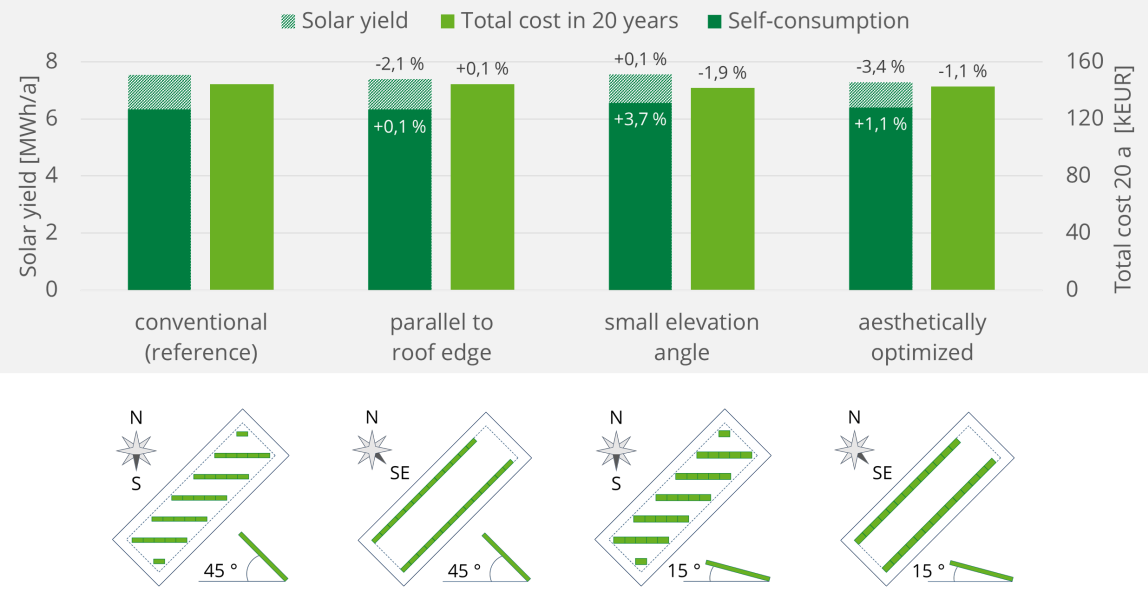

Fig. 8: Yield simulations and cost estimations including percentage of change compared to reference case for photovoltaic systems with 27 modules

6.2 Simulations with reduced row distance

According to the adaptions made for the solar thermal simulations in chapter 5.2, the row distance was decreased to 0.93 m for the aesthetically optimized as well as the conventional scenario (see pictographs on the bottom of Fig. 9). This results in 56 modules fitting onto the roof in the “aesthetically optimized with small row distance” variant and 50 for the “conventional with small row distance” case. The specific costs of the system have been lowered to 1,400 EUR/kWp in both cases (it was 1,500 EUR/kWp for the systems with 27 modules). The results of the calculations are displayed in Fig. 9.

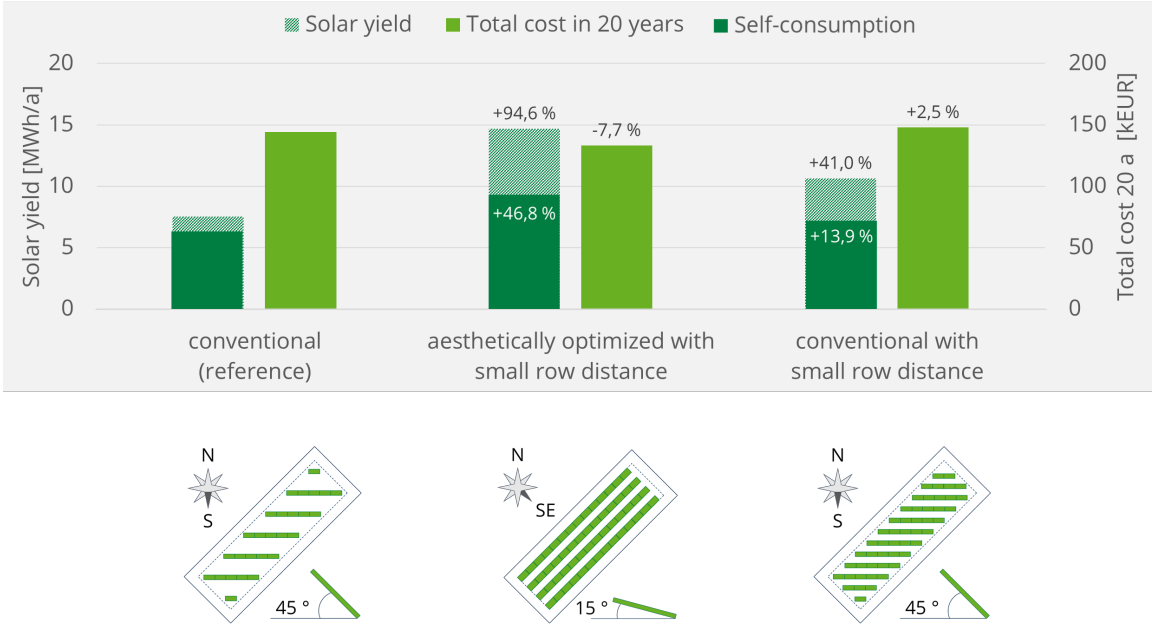

Fig. 9: Yield simulations and cost estimations for photovoltaic with reduced row distance

It is obvious that the aesthetically optimized version with small row distances generates by far the most electricity and the least cost. The conventional scenario with small row distances has a 41.0 % increased electrical output compared to the reference case, even if the number of modules is almost doubled. The self-consumption is increased by 13.9 %, but as investment cost almost doubled, the overall cost in 20 years slightly increases. This example proofs how relevant shading is for the efficiency of photovoltaic systems. It must be considered though that it is not trivial to represent shading effects in simulation software such as *Polysun*. Therefore, discrepancies between simulation and actual application cannot be excluded.

All in all, both maximizing the yield/self-consumption of the system and minimizing cost do not conflict at all with aesthetical optimization measures in the examined cases.

7 Recommendations for outdoor units of heat pumps

Besides aesthetic aspects, noise pollution is to be considered as well when planning an air-based heat pump – especially in areas with a high building density. Indoor installations generally have a smaller noise impact on the environment than split or outdoor systems. Depending on the type of installation, heat load etc., distance areas or additional noise protection measures are required.

Enclosures for heat pump's outdoor units are commercially available and provide optical improvement as well as noise prevention and access security (see left and center picture in Fig. 10). If the heat pump is not split but installed outside as a single device, sight and noise protection constructions should be considered as well. Installing the heat pump on the rooftop behind an attic or any other roof structure is a particularly good solution which also provides protection from water damage in flood-prone areas (see right picture in Fig. 10). Enclosures should not restrict the airflow to prevent performance losses in the heat pump.



Fig. 10: Enclosures for heat pump's outdoor units (left and center, © REMKO GmbH & Co. KG), rooftop installation of a heat pump with sight and noise protection (right, © iDM Wärmepumpen)

8 Summary

The most important, general design guidelines for solar thermal and photovoltaic systems are:

- For pitched roofs, the collector/module color should match the roof color, if possible. Compact surfaces or strips are preferred, and elevation should be avoided.
- On flat roofs, visibility of the collectors/modules should be avoided if possible. This means that large edge distances and flat installation angles are to be preferred. Alignment should be parallel to the roof edge.

Showcase simulations indicate that conventional design approaches for flat roofs should be reconsidered and adapted to meet requirements regarding cityscape, as this might even lead to higher yields and decreased cost. The number of collectors/modules that fit on the roof as well as the shading are essential influencing factors regarding energy output, making smaller elevation angles favorably in the examined simulations.

For heat pumps, enclosures or similar constructions ensure both an aesthetical integration into cityscape as well as noise protection without having relevant effects on the efficiency of the system as long as the airflow is not restrained.

9 References

Clemens Felsmann et. al., 2018/2020. Integration Regenerativer Energiesysteme in das Stadtbild – Ergänzendes Grundlagendokument zum Leitfaden für regenerative Energien im Stadtbild. Technische Universtität Dresden, Professur für Gebäudeenergietechnik und Wärmeversorgung, Dresden. https://tud.link/ftwu

LichtBlick SE (Volker Waltz), 2020. Repräsentative Umfrage zu erneuerbaren Energien - Mehrheit der Deutschen für Solaranlagen auf Dächern, YouGov im Auftrag der Lichtblick SE, Hamburg.

Andreas Wessels et. al., 2021. Farbige gebäudeintegrierte solarthermische Kollektoren mit hohem Wirkungsgrad. Online-Tagungsband des Solarthermie-Symposiums. Fraunhofer-Institut für Solare Energiesysteme (ISE), Freiburg.

Martin Thiele, 2015. Klimaschutzpotenzialanalyse von Dach-, Fassaden- und Straßenbaumbegrünung, Masterarbeit, Hochschule für Nachhaltige Entwicklung Eberswalde (FH).

Sebastian Helmling et. al., 2022. Betriebsanalyse von 5 PVT_Wärmepumpensystemen auf Basis von Feldmessdaten über 12 Monate im Rahmen des Projektes integraTE. Online-Tagungsband des Solarthermie-Symposiums. Fraunhofer Institut für Solare Energiesysteme (ISE), Freiburg.

Photovoltaic Panels and Planning in the UK

Luisa Brotas[1,2]

[1] Royal Borough of Kingston upon Thames, London (UK)

[2] School of Art, Architecture and Design, London Metropolitan University, London (UK)

Abstract

Photovoltaic panels rights in planning are not clearly defined in the UK. There are also no accepted criteria to assess how much is considered an acceptable reduction of solar radiation being enjoyed previously. This has even resulted in legal challenges of planning decisions. Conversely, increased global awareness to the need to reduce carbon emissions, volatile energy prices and shortage of supply, have increased the appetite for the installation of PV panels to generate renewable energy locally. This paper presents a case study of a new development in a terrace house and assesses the impact on an existing PV panel installation on a neighbouring building. Three different methods are discussed and a further detailed method of assessment that better quantifies the impact loss of the PV panels is proposed. Its rationale could lead to more informed decisions made to new developments submitted for planning.

Keywords: Photovoltaic panels, loss of performance, impact of new development

1. Introduction

The awareness of climate emergency and the need to reduce fossil fuel energy has led to an increase in use of photovoltaic panels to generate clean energy. This strategy is even more relevant in the current global energy crisis reinforcing the importance of local generation of renewable electricity. The installation of PV panels is well regulated and under certain conditions can benefit from permitted development and be exempted from planning permission. However, the impact of a new development on an existing PV is not prescribed, either expressly or by implication, in the Planning Acts or any other relevant legislation. But this type of problem can be considered a material planning consideration in the determination of applications. This paper attempts to address this problem and reviews a case study where a new extension may have an impact on a existing PV panel installation. A dwelling has Photovoltaic (PV) panels installed on its roof (referred as pv_roof) and a neighbouring dwelling (referred as new_roof) has put forward a planning application to raise its roof level. There is a concern that the extension of new_roof may potentially reduce the solar admission to the PVs and create a significant loss to the generation of renewable electricity and associated carbon emissions reductions. This paper aims to provide further insights on the case so that a more informed decision can be made on the planning application for the new_roof.

Local authorities have the duty to analyse objections raised against a planning application and decide on its merits and prevent or grant permission to the development. One aspect that has been raised in favour of protecting the solar admission to pv_roof is based on the importance of climate change and the role PV panels can have to reduce carbon emissions. Various national, governmental, local policies, programmes and incentives promoting green systems, reiterate the importance of green electricity to mitigate climate change, to reduce carbon emissions and improve associated co-benefits, e.g. local energy generation, resilience to increasing energy bills.

This was also acknowledged in a Judicial Review case McLennan v Medway Council case (McLennan, 2019) that overturned the planning permission for an extension which would have blocked a neighbour's solar panels. One basis was that the electricity generated by solar PV panels was helping to mitigate climate change.

It is also acknowledged that the 'loss of the impact of development on solar panels is a material planning consideration' and may not only affect the owner of pv_roof but may, in a small way, contribute to mitigating climate change and that the promotion of renewable energy sources is in the interest of the public as a whole.

So, it is important to have regard to the claim, even if later it may be considered not to have material consideration

© 2022. The Authors. Published by International Solar Energy Society
Selection and/or peer review under responsibility of Scientific Committee
doi:10.18086/eurosun.2022.11.04 Available at http://proceedings.ises.org

or merit. It may be relevant to weigh the impact of the loss for an informed decision to be made on the planning application.

On the other hand, local authorities are under increasing pressure to provide more social housing. It is also worth considering an increasing demand for new build in London boroughs. However, central boroughs have a limited availability of land and a relatively dense urban morphology. Increasing the buildings' height can be seen as a possible option to the housing crisis.

Each case is a case, but the decision on the new proposal for a new_roof may not deny merits to the loss of the energy generated by the neighbouring pw_roof. Equally, there is a degree of pragmatism about how constructions will have an impact on the environment. So, it is important to better assess the case study and quantify the predicted loss by the pv_roof as well as the context and opportunity of the area to expand accommodation.

2. Impact on the energy generation

Three assessments/supporting documentation in association with this case all seem to identify the potential loss on the capacity to receive solar radiation and therefore generate green energy. It is important to weigh the impact of the loss for an informed decision to be made on the planning application.

All assessments vary significantly in methodology and impact. An assessment made by the original installer for the pv_roof claims that the new proposal will reduce by 60% the electricity generated by the pv panels but does not provide a clear methodology that justifies this claim. It is an educated guess based on a review of the original installation calculations.

The promoter of the new_roof has hired a consultant, which estimates a loss of 16% during the whole year and 54% during the winter period. It also claims a reduction of around 15% (i.e. the solar panels enjoy 96% of the sunlight before the development and 81% after the development). It then concludes that the proposed development will have a low impact and sufficiently safeguards the sunlight amenity of the neighbouring building.

Another consultant commissioned by the council suggests that the PV panels simulated individually receive between 1028 and 1140kWh/m^2 solar radiation per annum. On average, this existing scenario has a 10% reduction against an ideal unobstructed scenario with panels having the same tilt and orientation (e.g. unobstructed solar irradiance of 1210 kWh/m^2). With the proposed extension new_roof the solar radiation on the PV panels is indicated that would drop to between 830 and 1012 kWh/m^2. This is considered a loss between 11 and 21% against its current value. The average of the proposed scenario would reduce to around 25% the unobstructed scenario and 16% against its current value. An assumption is made that if some incremental solar radiation reflected from surrounding surfaces is to be added, the overall reduction (existing versus proposed) is considered to average 13%.

3. Methodology

The initial three approaches differ in their methodology, and it is therefore reasonable to assess their reasoning. A new approach further attempts to come up with further insights to a more informed decision. Its rationale is also presented here.

The pv_roof installer's claim presents no calculation to how the loss is derived. However, it is worth considering that he is an accredited installer with many years of experience. So, with eventual knowhow to provide 'an educated guess'.

The consultants acting on behalf of the new_roof proposer has based their approach in estimating the Annual Probable Sunlight Hours (APSH), (Littlefair, 2001). APSH is a fairly simplified model that considers only sunlight. It is the long-term average of the total number of hours during the year in which direct sunlight reaches the unobstructed ground. A geometrical plot of 100 dots in a sky hemisphere is proportional to the probability of the sun shining from a particular area of the sky. It only assumes the sunlight contribution and its loss expressed as a percentage. No consideration is given to the angle of incidence on the PV panel nor its intensity reduction. No contribution is taken from the diffuse sky (skylight) nor any reflected contributions from nearby surfaces of influence. The variability of the diurnal daylight hours for different days of the year is also not accounted for.

For sunlight planning studies, the APSH criteria developed assumes that the loss of sunlight should be lower than

5% in winter and 25% for the whole year, or less than 0.80 times its former winter or annual value, respectively. Also that the reduction in sunlight received over the whole year is lower than 4% of annual probable sunlight hours. A recent update of the most used publication in planning for daylight and sunlight: the Building Research Establishment, BRE, Site layout planning for daylight and sunlight: A guide to good practice (Littlefair et al, 2022) suggests that where the annual probable sunlight hours received by a solar panel with the new development in place is less than 0.90 times the value before, a more detailed calculation of the loss of solar radiation should be undertaken.

It is also worth highlighting that the using the APSH criteria for solar availability on pv studies should not distinguish the winter season but consider the whole year, as PVs are expected to take advantage of most of the solar radiation available. The plots for the APSH were originally developed for vertical windows oriented south (Littlefair and Aizlewood, 1999), but can be accepted for other tilts and orientation for basic initial assessments. Lastly, it is relevant to consider that the variation of the daylight hours for different seasons (nearly 8 hours at the winter solstice versus 17 hours at the summer solstice) is not taken in consideration in this simplified assessment.

The third assessment adopts a method based on simulations using the BRE average sky. Representative sun positions at different times of the day and days of the year (1300 measures) are thoroughly assessed. Simulations also account for the diffuse sky distribution to estimate the total solar radiation reaching the two scenarios (and its loss). The sky model defined has been thoroughly validated for daylight studies, both with theoretical and real measurements collected originally in Berlin and at BRE Watford (Littlefair, 1994). This method is a significant improvement to the previous APSH method as it more accurately considers both solar geometry (i.e. position of the sun and angle of incidence) and the sky distribution (e.g. diffuse radiation) contributing towards solar irradiance. The proposed daylight modelling adopted does not consider the reflected sunlight/daylight contribution. For this case, a 3% (reduction in the loss) is put forward. The separate modelling of the eight modules in the PV array is considered important to assess the solar distribution over the various panels. But no information is given about the geometry considered nor the actual software used is presented.

The fourth proposed model attempts to estimate the annual solar radiation on the PV panels for the existing and proposed scenario based on annual simulations, with 4 time steps (i.e. every 15 min) undertaken with the weather file for Gatwick from the Energy plus software (Energyplus, 2022). This is a Test Reference Year (TRY) weather file based on statistical measurements for the location for a representative period of usually 15 years. These types of files are widely used and accepted for dynamic daylight and thermal modelling.

The model of the existing buildings with and without the proposed roof extension were modelled in Rhino. The geometry was modelled based on drawings submitted with associated planning applications. Daylight analyses were made with the widely validated RADIANCE v5.4a (Radiance, 2022) software via grasshopper, honeybee and ladybug tools v1.1.0 interface (Ladybug, 2021). IEA/SHC Task 63 (2022) has recently publish a report on existing tools for solar neighbourhood planning. The fourth method and tools indicated above align with this report and the tools adopted are widely validated. The report also highlights the lack of agreed metrics, a concerted approach on various countries or even regions in the definition of key performance indicators, KPIs, for planning with solar energy. Littlefair et al (2022) have put forward an advisory recommended minimum ratio based on the tilt of the PV (see Table 1)

Table 1 Recommended minimum ratios of solar radiation received (Littlefair et al, 2022)

Slope of solar panel in degrees to horizontal	Recommended minimum ratio of radiation received after/before
0-30	0.90
30.01-59.99	0.85
60-90	0.80

The fourth model was simplified to only include elements that may have an impact on collecting solar radiation. These include chimneys, parapets and ridges on top of the roofs. Other elements of the building at a level below the roof line, where the PV panels are located, do not contribute to the solar radiation reaching the panels, were therefore not modelled. This will significantly reduce the simulation time without reducing the accuracy of the results. The PV panels were modelled individually, and each include a grid of 96 sensors, that can highlight the spatial variances as seen in Figures 4 and 5. Other methods only considered the centre point of the panels.

However, for this initial assessment the annual cumulative results were averaged for each panel and later results averaged across the 8 panels.

All external surfaces with exception of the PV panels, were modelled as Lambertian perfect diffusers with an average reflectance of 20%. This estimation may even overestimate the real situation, as materials used on roof, walls and parapets, are dark and old and may have a lower reflectance. Nevertheless, it is relevant to assess the eventual contribution of reflected sunlight.

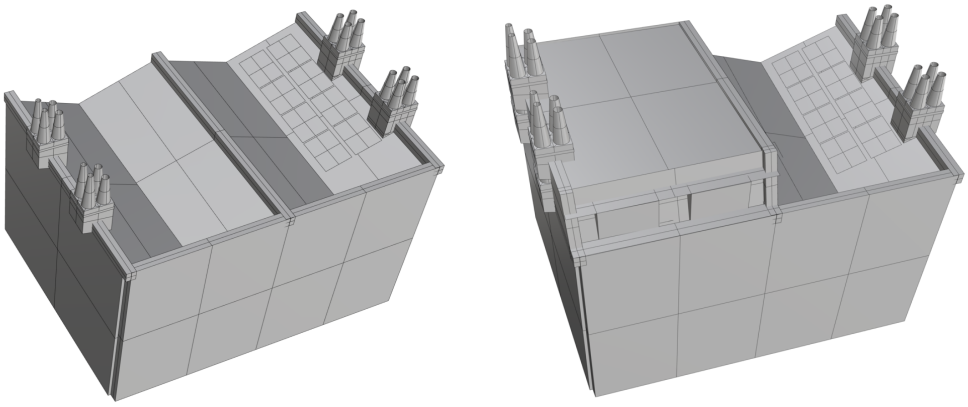

Figure 1. Volumetric scheme of buildings pv_roof without (left) and with the new_roof extension.

A desktop analysis of the urban site, based on google maps (2022), bing maps (2022) as well as views from vu-city (2022) were considered reliable to assess the volumetry and buildings surfaces that may act as reflectors or obstructions to the solar radiation reaching the panels.

Both figures 2 and 3 highlight that the neighbourhood has a low density with predominantly terrace houses. The landscape does not have significant tall volumes that may affect solar radiation reaching the PV panels. It is also relevant to highlight for planning purposes that several other terrace houses in the street and surrounding areas have already been raised by one floor. From the street view they seem acceptable.



Figure 2 : VuCITY view of the neighbourhood.



Figure 3: Street view.

4. PV panels technology

Solar photovoltaics (PVs) convert solar energy into electricity using a semiconductor material such as silicon. When solar radiation hits the semiconductor, the energy in the solar radiation is absorbed, 'exciting' the electrons in the semiconductor so that they break free from their atoms. This allows the electrons to flow through the semiconductor material producing electricity. There are different types of PV panels with different efficiencies but the ones installed at pv_roof are monocristaline and are by catalogue expected to have an efficiency of around 15%. This is an ideal 'theoretical' scenario estimated under laboratory-controlled measurements. In real life situations there are several environmental and man-made variables that may affect the overall performance of the PV panels. (Sick and Erge, 2013; Boyd and Coonick, 2015)

Maximum solar radiation is received by surfaces that are perpendicular to the solar rays. As such the orientation and tilt of the panel should therefore be adapted to the latitude of the place and position of the panel. Solar PV panels are best mounted on an inclined plane within the quadrant of the south orientation (northern hemisphere). Further orientations and tilts are still possible but with a reduced total irradiance (Littlefair et al, 2020). However, for structural aspects, to reduce problems with wind load issues as well as to promote a good visual integration, it is common to install PV panels coupled to the roof surface even if the orientation and tilt are not optimal for energy production (Holden and Robinson, 2014; Boyd 2015).

PV panels strongly rely on direct solar radiation from the sun but may also capture to a lower order of magnitude solar radiation from the sky dome. Cloud cover and shadowing can significantly reduce the amount of solar radiation and therefore the generation of electricity. Likewise, both sunlight and daylight may be reflected from obstructions and still contribute to the overall irradiance on the PV panels. The reflected contribution will strongly be affected by the reflectance of the surfaces, their specularity and roughness, the distance to the panels and the way the two surface elements 'see each other' and exchange radiation.

Sunlight availability is not that abundant in the UK (in comparison with some other locations), therefore reducing the overall performance of PVs. High capital investment needed to install PV technologies, can result in long payback periods. To promote its wide installation, there have been some government incentives in the past, namely

the 'Feed in tariff' (FIT). This incentive included a payment for generation in addition to an export fee. However, FITs had become less of an encouragement to install PV panels and more of an incitement to profit from excessive subsidies. Following a significant reduction in the cost of the PV panels, there was a reduction in both the incentive and the regular payment to generate renewable electricity.

The performance of the PV system can also be significantly affected by dust, leaves, snow or any element that covers the PV cell. Also, in a PV system, each panel has an individual maximum power point. Differences between panels introduce power losses and can lead to underperformance of the entire system over time (Pillai et al, 2022).

With traditional inverters, the weakest module reduces the performance of all modules. Newer smart systems with module-level power electronics (MLPE), e.g. microinverters and integrated power optimizer, each module produces the maximum energy, and power losses are eliminated (DOE, 2015; US DE 2015).

According to details submitted by the installer, the PV panels measure 895mm x 1320mm which results in a total area of 9.45m^2. The FIT assumed at the time of installation is 5 pence per kWh exported to the grid. No indication of the generation fee is provided. Table 1 identifies the layout of the PV panels for the results presented.

Table 1. Layout of the PV panels

A	B	C	D
E	F	G	H

5. Results and discussion

Table 2. Comparison of results from the different approaches

	INSTALLER (1nd method)	PROPOSAL CONSULTANT (2nd method)			INDEPENDENT CONSULTANCY (3nd method)			NEW APPROACH (4nd method)		
	LOSS	YEAR (WINTER) EXISTING %	YEAR (WINTER) PROPOSED %	LOSS %	EXISTING kWh/m^2	PROPOSED kWh/m^2	LOSS %	EXISTING kWh/m^2	PROPOSED kWh/m^2	LOSS %
Unobstructed	1350	100%			1210			1161		
A					1140	1012	11.2	1109	1023	7.8
B					1111	955	14.0	1089	971	10.9
C					1120	950	15.2	1086	950	12.6
D					1091	927	15.0	1072	935	12.9
E					1099	941	14.4	1059	946	10.7
F					1073	879	18.1	1031	877	14.9
G					1056	850	19.5	1015	839	17.3
H					1028	830	19.3	988	811	17.9
AVERAGE	**60**	**96 (28)**	**81 (13)**	**16 (54)**	**1090**	**918**	**15.8**	**1056**	**919**	**13.1**

Results between the different methods vary significantly. Different calculations and limitations not included in the modelling have been presented previously.

These methods also generate different amounts of global solar radiation. The installer considered a global radiation 1350 kWh/m^2 (not clear if at the panel or horizontal), which is considered above 10 and 14% the global contribution at the PV panels from the BRE average sky (adopted by the third method), and the London Gatwick

E+ sky distributions (4th method), respectively.

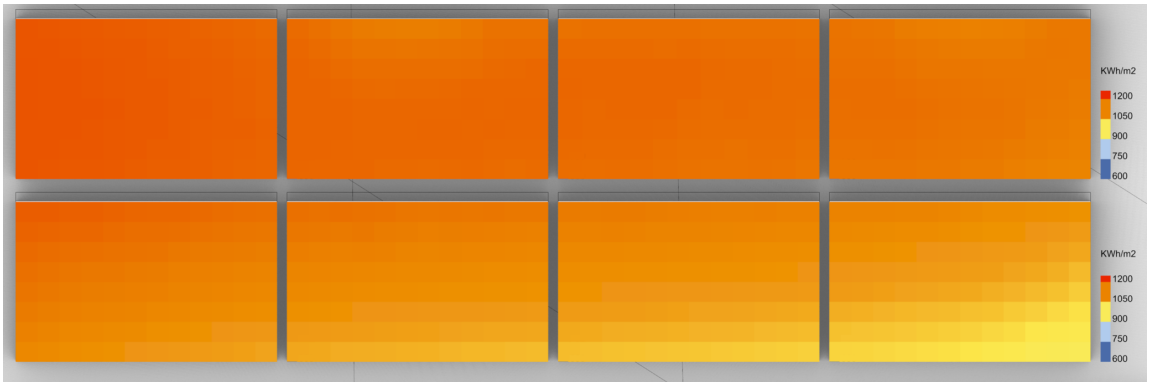

Figure 4: Total solar irradiance on PV panels at the existing scenario

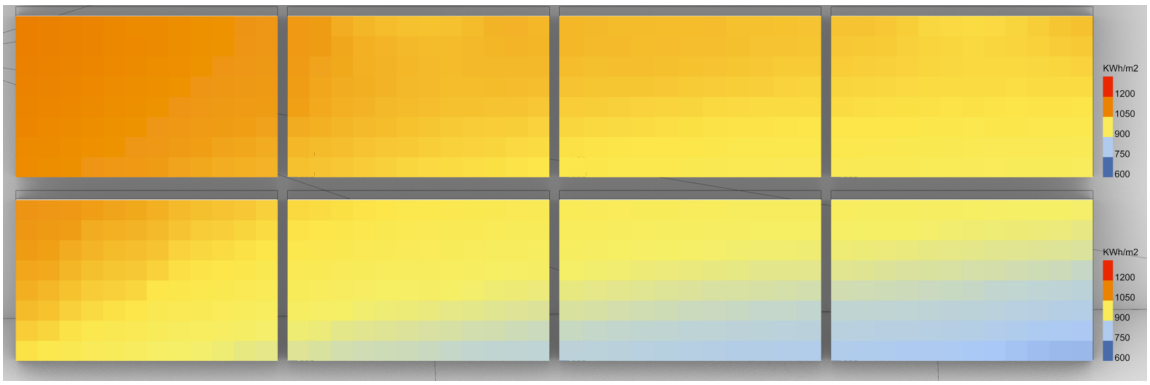

Figure 5: Total solar irradiance on PV panels at the proposed scenario

Table 3. Difference between unobstructed and average values for the different models

	3rd Method	4th method	DIFFERENCE
Unobstructed	1210	1161	4.0
Average EXISTING	1090	1056	3.1
Average PROPOSAL	918	919	-0.1

Both third and fourth results seem realistic and in a similar order of magnitude. The former third gives a higher unobstructed radiation but the loss between the existing and the proposed scenario is higher (as well as for the unobstructed) than the fourth model.

The third model did not account for the solar energy reflected by the surrounding walls, parapets and roof. It is however difficult to clearly identify further variables of influence, namely the accuracy of the modelled geometry of the proposed extension and the chimneys.

Further analyses undertaken for the fourth model with and without the contribution of reflected sunlight/skylight showed that the gain in the former model averaged less than 2%. It is worth mentioning that there are no significant obstructions on the southern side and the ground does not have an impact on the PVs. This is consistent with the educated estimation by the third consultant.

Panel H of the fourth proposed model has the lowest annual solar radiation incident, as 811 kWh/m^2. While this is an estimated reduction of 18% it is still considered an acceptable amount to produce a reasonable amount of green energy. A PV array with 1 peak power (kWp) and considering the 20% losses of the system would still generate 649 kWh of electricity per annum, above the minimum 600 kWh threshold suggested (IEA/SHC Task 63, 2022). The third worse case would for the same PV power capacity, generate slightly more electricity, estimated as 664 kWh/yr.

Figures 4 and 5 show the variation of solar radiation reaching the different panels with and without the proposed extension. The existing scenario (Figure 4) shows a more even distribution of solar radiation across all panels A-

H. It is noticeable the maximum reduction of 121 kWh/m^2 between panel A (top left) and panel H (bottom right), likely a result of the influence of the facade parapet casting a shadow on to the nearest panels. But overall all panels seem to receive a fair amount of solar radiation. For the proposed scenario the reduction between panels A and H of 212 kWh/m^2 is more significant. This would be a result of the cumulative influence of the proposed extension at the new_roof. For the lowest row E to H the reduction for the existing scenario amounts to 71 and for the proposed 135 kWh/m^2. In case of old PV panels installations it can be argued that the lowest PV panel is likely to restrict the conversion of solar radiation captured by others located in a less obstructed position.

6. Limitations

Both third and fourth models modelled the amount of solar radiation reaching the 8 individual panels. One limitation of this approach is not accounting for a loss of performance of the whole array if one PV panel is in the shadow. New developments of smart technology and improved invertors may minimize this problem. But for the panels in the study, installed in 2005, it should be assumed that if a panel in either top or lower row is obstructed and receives a reduced amount of solar radiation, then the 3 others in the row will not generate electricity above this threshold.

So, an initial estimation based on the table above should look only at the lowest solar radiation received between panels A to D and E to H or simply assume the panel that is performing worst. For the fourth model that would indicate the total solar radiation would be reduced from 988 to 811 kWh/m^2. And a loss of 18% would be reported.

This assumption should be taken with caution and the performance may be further reduced as it does not consider for the annual cumulative values estimated for each PV panel the synchronous reduction that could occur at each time step of the simulation that could affect the total output of the PVs connected in series. This study may be pursued at a later stage to estimate this loss more accurately.

7. Criteria of assessment

Rights of light are considered an easement, i.e., a right acquired by one party over another one's land. In the UK (RICS, 2016). 'Rights of Light' legally protects individuals in their access to daylighting against threats from new constructions or extensions to existing neighbouring constructions. The prescriptive right takes effect if it has been enjoyed for 20 years without interruption of a year or more, unless the right has been waived by express agreement. However, unlike rights of light that may be subject to legal remedy, access and retention of the right to solar energy does not explicitly exist in the UK law. Only recently Littlefair et al (2022) have put forward a maximum reduction considered acceptable for PV panels. However, there is no clear explanation for the criteria and how to assess how much is considered an acceptable reduction of solar radiation being enjoyed previously.

This study aimed to propose more insights to the definition of KPIs. Can we define some assessment and criteria that seem reasonable? Is an absolute value beyond which the reduction is not deemed acceptable, a valid approach? or is it a percentage of reduction versus the previous value? What could be a reasonable reduction?

Ideally a reduction of green energy generation should be minimised as much as possible. There are clear immediate benefits to generate free, clean and renewable energy. Reducing carbon emissions and mitigation of climate change, minimise the potential demand from the grid, especially at peak times, promoting resilience to the impacts of shortage of supply or be less vulnerable to the market rise of energy prices. Last but not the least, if the owner has invested in the PV infrastructure at some point in the past there is an expectation in a return of the investment. A positive return of investment may also be of more importance at later periods of life, especially when salaries/pensions may be reduced and result in an inability to pay the energy bills. PV panels providing free energy can be very important to avoid fuel poverty.

As indicated previously the price of installing a PV array has dropped significantly in the past years. But so has the payment for exporting the electricity. The Smart Export Guarantee (SEG, 2021) is the Government's successor to the FIT scheme. SEG came into force in January 2020. It applies to businesses and homes that generate solar power and other renewables on a small scale. Unlike the FIT that considered a generation and export fee there is only an agreement to pay for export electricity. The Smart Export Guarantee scheme allows companies to decide their own rates, as long as it's more than zero. Market value currently indicates between 1.5-11p/kWh (OFGEM, 2021). However, for the purpose of this estimation the price of this assessment is calculated as 5.3p/kWh of electricity exported to the grid based on the Standard Assessment Procedure, SAP10.2 (SAP 2022). Whilst the

small payment for exporting energy from the SEG is claimed to allow a return on investments at a reasonable rate, installations will remain for most an environmental rather than a financial decision. However, the recent energy crisis and the increase of energy price is changing the perception that PV panels can be a cost effective way to generate electricity against purchase form the grid.

So, responding to the question what is a recommended threshold for PVs? In a crude approach we can assume that a reduction that goes beyond a cost per kiloWatt peak (kWp) that no longer allows a reasonable positive investment is considered to have a significant negative impact. PV panels have a life time expectancy of 25 years (that excludes consideration of maintenance and replacement of other parts, namely inverters or batteries). So, a simple payback (not considering any changing value of money over time) should not go above 15 years.

Equally important is to estimate the degree of what is lost. This is important to estimate the net loss or decreased profit. It may also serve as an indication for the estimation of a possible compensation payment and a carbon offset payment to minimize the carbon emissions that would have been saved for a certain period of time.

8. Loss in FIT and reduction in carbon emissions

For this PV scheme, an area of 9.5m^2 and an efficiency estimated as 15%, results in a peak capacity of 1.425 kWp. This is considered a very small installation and therefore may be more susceptible to a higher price than an economy of scale. An estimation of a cost around £2000 for a full installation without battery is hopefully not too far from the current market. For the purpose of the following calculations a system loss that would account for cable, PCU, inverter, metering and interface losses, typically 20%, has been made.

Table 4. Simple payback analysis for the fourth model for the existing and proposed scenario

FOURTH MODEL					
		EXISTING		PROPOSED	
		Min	Average	Min	Average
Solar irradiance (kWh/m^2)		988	1056	811	919
Power rating of PV array (kWp)	1.425				
Installation cost of PV system (£)	2000				
PV generation (kWh/yr) 0.8 system losses		1126	1204	925	1048
PV export tariff (£/kWh) (SAP10.2)	0.0559				
Electricity standard tariff (£/kWh) (SAP10.2)	0.1649 (it should be noted that this cost has increased significantly in the recent months with the removal of the Energy cap and the energy crisis. But for the purpose of this assessment the price indicated at SAP is still retained)				
Annual income from PV export tariff (£)		63	67	52	59
Annual savings if all electricity is consumed (£)		186	199	153	173
Estimated PV system payback time (Years)	export	**32**	**30**	**38**	**34**
	consumed	**11**	**10**	**13**	**12**

Table 4 suggests that neither the existing nor the proposed scenario make sense from an economical point of view under the new SEG scheme to export energy generated. This is considering an export tariff of 5.59 p/kWh (no generation tariff has been included). Payback times are above 30 years. However, if we take into consideration the savings in terms of purchasing electricity at a nominal value of 35.796 p/kWh (as per indication of the unit rate of a current standard tariff from 1st Oct 2022, supplied by a mains energy company) then the PV system could have a return of investment around after 5 years. The extension of new_roof would increase the payback time by

1 years compared to the existing scenario pv_roof. No interest rates are assumed in these models.

Taking the previous scenario of the minimum and average PV solar capture, the estimated loss in FIT can be found. Estimating the carbon emissions is based on SAP 10.2 conversion factors (i.e. 0.136 kg CO_{2e} per kWh). But for ancillary purposes conversion factors from SAP 2009 and SAP10.0 (i.e. 0.591 and 0.233 kg CO_{2e} per kWh, respectively) are also presented. Much lower values are a result of the decarbonisation of the grid which has the benefit of reducing the carbon emissions associated with the consumption of electricity, but equally has the drawback of reducing the impact of green electricity generated by PV in mitigating carbon emissions. See Tables 5 and 6.

Table 5. Estimation of the total energy captured by the PV panels and the equivalent Carbon Emissions savings based on the minimum result for the fourth model

MINIMUM	TOTAL ENERGY GENERATED kWh/yr	CARBON EMISSIONS SAVINGS kg CO^2/yr [1]		
		SAP2009	SAP10.0	**SAP10.2**
EXISTING	1126	665	262	153
PROPOSED	925	547	216	126
DIFFERENCE	201	119	47	**27**
DIFFERENCE for 30 Years	**6030**	3564	1405	**820**

Table 6. Estimation of the total energy captured by the PV panels and the equivalent Carbon Emissions savings based on the average result for the fourth model

AVERAGE	TOTAL ENERGY GENERATED kWh/yr	CARBON EMISSIONS SAVINGS kg CO^2/yr [1]		
		SAP2009	SAP10.0	**SAP10.2**
EXISTING	1204	712	281	164
PROPOSED	1048	619	244	143
DIFFERENCE	156	92	36	**21**
DIFFERENCE for 30 Years	**4680**			**630**

Accounting for the minimum PV panel performance the existing scenario would generate 1126 kWh annually and 0.15 tonnes of CO_2 would be saved. The proposed scenario could reduce the energy generated annually to 925 kWh and would save 0.13 tonnes of CO_2 per annum.

The difference between the existing and the proposed scenario, of 201 kWh generated annually, is to be used for the estimation of the loss of export tariff with the proposal. For a price of 5.59 pence per kWh of electricity generated exported to the grid this amounts to £11 per year. For a price of 35.796 p/kWh of energy generated and assumed saved in energy bills this would amount to £72 per year.

Assuming a very generous life expectancy of 30 years for the PVs, the total loss of income from exporting would be £337 and a loss of £2,159 could be associated in the energy bill. These do not consider any changing value of money nor the energy price over time.

In a similar manner the loss of carbon emission savings could be estimated with a carbon offset payment, considered by the Great London Authority, currently at £95 per tonne of CO_2 accounting for a period of 30 years. This would estimate a carbon offset payment of £78.

Accounting for the average PV panel performance, in absolute values both the existing and proposed scenarios would generate higher carbon savings, but the difference between models would be lower than the difference identified accounting for the worse PV performance (i.e. minimum). A smaller difference for the average makes sense as the worst case will be more sensitive to the variation, albeit in absolute terms has, by definition a lower value, in energy generated and associated carbon emissions savings. The average quantification would reflect a lower loss of income (export £261 and £1,675 in the energy bill) and a lower equivalent carbon offset payment of £60.

[1] The carbon emission factors are 0.591 kg CO_{2e} per kWh for SAP 2009, 0.233 kg CO_{2e} per kWh for SAP10.0 and 0.136 kg CO_{2e} per kWh for SAP10.2.

9. Conclusions

As a first principle, enshrined in local, national and international policies, local boroughs should ensure that opportunities to maximise on-site generation of green electricity is pursued and maintained throughout a reasonable period.

The decarbonisation of the grid has reduced the impact PV has on carbon emission savings, but there are still several co-benefits to be considered. Reducing carbon emissions and mitigation of climate change, minimising problems with grid capacity, especially at peak times, promoting resilience to the impacts of shortage of supply or being less vulnerable to the market rise of energy prices. Last but not the least, if the owner has invested in the PV infrastructure at some point in the past there is an expectation of a return of the investment. A positive return of investment may also be of more importance at later periods of life, especially when salaries/pensions may be reduced and result in an inability to pay the energy bills. PV panels providing free energy can be very important to avoid fuel poverty.

A comparison of various methods presented from the Installer (1st method), the Consultant for the proponent of the extension new_roof (2nd method), an Expert commissioned by the borough (3rd method) or this last approach (4th method), highlight several discrepancies and a significant variation in the quantification of the loss of solar access for the PV panels of the neighbour pv_roof. However, both third and fourth methodologies seem to be more realistic and provide results in a similar order of magnitude. The other two methods are either unknown or based on simplified assessments.

Overall the loss between the existing and proposed scenario is estimated by the Installer as 60%, by the Consultant of the new_roof as 16%, and on average across all panels as 16% by the third and 13% by the fourth method.

Concerns were raised by the fact that a PV panel in shadow will affect the performance of the overall array and these potential synchronous reductions, not accounted for in the models, may further aggravate the difference between the two scenarios. New installations with module-level power electronics will mitigate this impact.

Criteria to assess the loss of energy generated by the PV panel has been put forward. However, some caution should be taken to ensure the effect is more widely tested. These highlight that the reduction in absolute terms is still considered viable to generate useful energy and possibly offset a capital investment in a reasonable payback time. This is the case for a payment of around 36 p/kWh, either saved on the energy bills, or possibly negotiated as a FIT/SEG payment, resulting in a payback of around 5 years. A reduced payment of around 6 p/kWh would not be economically viable (i.e. more than 30yrs payback time).

Further estimations of the energy generated by the fourth model for the least performance panel suggests that the loss in terms of profit is around £11 or £72 per year, depending on the price of kWh, for exporting or saving on the energy bills, is considered. Assuming a generous life expectancy of 30 years for the PVs that would result in a loss of income from the export tariff of £337 and a loss of £2,159 in the energy bill.

In a similar manner the loss of carbon emission savings could be estimated with a carbon offset payment, considered by several local authorities and the GLA, currently at £95 per tonne of CO_2 accounting for a period of 30 years. This would estimate a carbon offset payment of £78.

The estimation of the impact of the proposed development, identified as a loss of income and carbon savings reductions may be seen as low. However, significant co-benefits further associated with the local generation of green electricity should not be underestimated. Equally, lack of methods and criteria of assessment of the impact on PV panels should not give grounds for ignoring the important role that renewable energy may have, even if it is a small contribution to mitigating climate change.

An overview of the neighbouring area with similar roof extensions already permitted, may also give grounds for the acceptance of the proposed roof extension.

10. References

Bing maps (2022). https://www.bing.com/maps [Accessed Nov 2021]

Boyd, P. and Coonick, C. (2018). *BIPV in construction: the translation of product and systems into design and construction.* Technical Report. BRE National Solar Centre

BSI (2018) Daylight in buildings. BS EN 17037. London, BSI

DOE, 2015. Photovoltaic Systems with Module-Level Power Electronics, report DOE/GO-102015-4755

Energy Plus (2022). https://www.energyplus.net/weather [Accessed Aug 2022]

GoogleMaps (2022). https://www.google.com/maps [Accessed Ago 2022]

Holden, J., Robinson, P. and Building Research Establishment (2014). *Renewable energy sources: how they work and what they deliver*. Watford: Ihs BRE Press.

IEA (2020). Building Integrated Solar Envelope Systems for HVAC and Lighting, Technology Position Paper, International Energy Agency, May 2020

IEA/SHC Task 63 (2022). Identification of existing tools and workflows for solar neighborhood planning, report from SHC Task 63: Solar Neighborhood Planning and work performed in Subtask C: Solar Planning Tools Editors: Jouri Kanters, Martin Thebault, Report C1, DOI 10.18777/ieashc-task63-2022-0001, June

Ladybug Tools (2022). version 1.1.0 https://www.food4rhino.com/app/ladybug-tools [Accessed Nov 2021]

Littlefair, P. (2001). Daylight, sunlight and solar gain in the urban environment. *Solar Energy*, 70(3), pp.177–185. doi:https://doi.org/10.1016/s0038-092x(00)00099-2.

Littlefair, P.J. (1994). A comparison of sky luminance models with measured data from Garston, United Kingdom. *Solar Energy*, 53(4), pp.315–322. doi:https://doi.org/10.1016/0038-092x(94)90034-5.

Littlefair P.J. and Aizlewood M.E. (1999). *Calculating access to skylight, sunlight and solar radiation on obstructed urban sites in Europe*. BRE BR379. Watford Building Research Establishment Press

McLennan vs Midway Council (2019). Judicial case, Case No: CO/155/201 http://www.bailii.org/ew/cases/EWHC/Admin/2019/1738.html [accessed Aug 2022]

MSC (2020). The solar PV Standard, report MIS 3002 Issue 4.0

OFGEM (2022). https://www.ofgem.gov.uk/environmental-programmes/smart-export-guarantee-seg/about-smart-export-guarantee-seg [accessed Aug 2022]

Pillai, D.S., Shabunko, V. and Krishna, A. (2022). A comprehensive review on building integrated photovoltaic systems: Emphasis to technological advancements, outdoor testing, and predictive maintenance. *Renewable and Sustainable Energy Reviews*, 156, p.111946. doi:https://doi.org/10.1016/j.rser.2021.111946.

RADIANCE (2002). version 5.4a, https://www.radiance-online.org/ [Accessed Jun 2022]

Rhinoceros (2022), version 7, https://www.rhino3d.com/7/new/ [Accessed Jun 2022]

RICS (2016). Rights of light. RICS professional guidance London, RICS, 2nd edition, March.

US DE (2014). Building America Case Study: Photovoltaic Systems with Module-Level Power Electronics Photovoltaics, BRE DG 532-1, September

Vu-city (2022). https://vu.city/ [Accessed Jun 2022]

SAP (2022). The Government's Standard Assessment Procedure for Energy Rating of Dwellings Version 10.2

Sick, F. and Erge, T. (2013). *Photovoltaics in buildings: a design handbook for architects and engineers*. London: Routledge.

SEG (2020). https://solarenergyuk.org/resource/smart-export-guarantee/ [Accessed Nov 2021]

Towards Net-Zero Neighborhoods in Greece

Georgios Dermentzis, Agis M. Papadopoulos

Process Equipment Design Laboratory, Department of Mechanical Engineering, Aristotle University of Thessaloniki, GR-54124, Thessaloniki, Greece

Abstract

The paper discusses the installation of PV and solar thermal collectors on the available roof spaces, by applying heat pumps and energy efficiency standards in multi-apartment buildings, aiming to recommend measures towards net-zero neighborhoods. A real building is used varying the number of stories in the various Greek climate zones. Globally acknowledged standards such as EnerPHit are applied to investigate the potential of covering the electricity loads with PV. Besides, the choice of the heating and cooling generation system is investigated. Split units or heat pumps are used varying the COP and the design sink temperature to provide a complete overview of the energy performance. The results show that in a neighborhood with 9 buildings from 3- to 5-story buildings, the PV yield could cover 80% of the total required electricity for the year.

Keywords: Net-zero neighborhood, EnerPHit, multi-apartment buildings

1. Introduction

The need for self-production of the energy required in houses is getting more and more important in Europe. The net-zero energy goals are still not clearly defined. For example, an NZEB definition based on the type of balance (import/export, load/generation balance, or monthly net balance) is proposed (Sartori, Napolitano, and Voss 2012). Ochs, Dermentzis, and Ksiezyk (2017) highlighted the importance of considering other metrics than the mere energy balance, such as the load match factor and the PV self-consumption. In Mediterranean countries, the potential for using solar energy is very high. Besides, very good energy renovation standards such as EnerPHit (Zeno and Feist 2012) are well known to minimize building loads. De Masi, Gigante, and Vanoli (2021) proposed that a tradeoff between the thermal insulation and the installed power of renewable sources should be found. Feist (2014) suggested to use the footprint area for the specific PV electricity instead of the treated area of the building.

Papadopoulos (2016) discussed the development of regulations regarding energy standards in European countries. In a comparison between German and Greek energy regulations, the heating energy requirements were higher in Greece than in Germany since 1994 even though Berlin has almost four times higher heating degree days (HDD) than Athens. The final energy consumption in Greece increased by 7.1% from 1995 to 2011 and the residential total floor area by 16.5% (Papadopoulos 2016), meaning a reduction in the specific final energy consumption. There is a clear trend of U-value reduction over the past 40 years. Karkanias et al. (2010), in 2008 interviewed 17 persons from construction, research, and public sectors about the development of bioclimatic buildings in Greece. They concluded among others that the main barriers were the lack of adequate policy by the state, however in 2010 the a regulation on Energy Performance of Buildings (KENAK) was announced (E. G. Dascalaki et al. 2012) and revised in 2017 ("KENAK 2017. Greek Code of Energy Performance of Buildings" 2017).

Dascalaki et al. (2010) investigated a sample of 250 buildings from various areas in Greece to represent the Hellenic building stock. They found that buildings' U-values of walls, roofs, and windows, show a trend to decrease over time. In addition, the thermal energy consumption was the highest part of final energy consumption and it varied between 70 kWh/(m^2·yr) and 155 kWh/(m^2·yr) in residential buildings and 26 kWh/(m^2·yr) and 233 kWh/(m^2·yr) in non-residential buildings. The contribution of solar thermal collectors in domestic hot water production decreases the total electrical energy consumption by 27%-37% in single-family houses and 36%-57% in multi-family houses. Over 60% of the external walls do not reach the minimum U-value defined in the building codes. Space heating (SH) dominates the final energy consumption with 66% and 50.5% in residential and non-residential buildings, respectively, while the share for cooling is

© 2022. The Authors. Published by International Solar Energy Society
Selection and/or peer review under responsibility of Scientific Committee
doi:10.18086/eurosun.2022.11.05 Available at http://proceedings.ises.org

1% and 6.5%, correspondingly. However, space cooling (SC) may increase importance in Greek cities, especially in Athens due to the increase of the ambient temperature over the years and the island heat effect. Papakostas, Mavromatis, and Kyriakis (2010) calculated an increase in cooling demand in Athens by 26% between the decade 1983-1992 and 1993-2002.

This study aims to quantify the required combination of building renovation and on-site renewable sources in Greek neighborhoods towards net-zero energy. Furthermore, the impact of using split units or heat pumps is investigated aiming to provide a complete overview of possible SPF in various Greek cities.

2. Methodology

A real building that has been renovated is considered as a reference. It is modeled in PHPP (Feist 1998) such to account for varying number of floors, in different climatic conditions (10 cities), and different HVAC system and installed renewable sources. Furthermore, the obtained results are extrapolated to a typical neighborhood in Thessaloniki.

The building has been renovated according to EnerPHit standard (Zeno and Feist 2012) and it was modelled in PHPP (Feist 1998) by the Hellenic Passive House Institute. That building is chosen as a typical one having also an open space on the ground floor (often used for car parking called 'piloti'), which is very common in multi-apartment buildings in Greek cities. Split units are considered to supply both space heating and cooling. It has to be noted that split units used for cooling is a very common system in Greece. But the use of spit units for space heating is not a favorable solution from the occupant's point of view due to poor thermal comfort conditions in poor energy-performance buildings. However, this is not the case in a well-insulated building due to the high radiative indoor temperature since the internal surface of the opaque and transparent elements have high temperature due to low transmission losses of the insulated walls and good energy efficient windows. For the DHW preparation, either solar thermal collectors or electric water tank heaters are used, since both are common solutions in Greece. As an additional option, the use of air-source heat pumps to supply space heating and DHW is investigated (cooling can be also provided only if the existing radiators are changed to fan coils). The available roof space without significant shadings is fully covered with PV (in 0° inclination angle to install the maximum possible number of PV modules) and/or solar thermal.

Fig. 1 shows a typical neighborhood of a Greek city, in which the number of stories is quite different. Thus, as a next step, the number of stories as well as the location is varied in PHPP.

Besides, even though 'net-metering' is currently available in Greece, the part of PV electricity that is directly used is investigated with or without batteries. The following parameters are varied:

- The climatic conditions - 10 Greek cities
- The number of stories of the multi-apartment building - from two to eight stories
- Three HVAC systems:
    a) split units for SH and SC and solar thermal collectors (ST) for the DHW preparation (including an electric rod), the rest of the roof is covered with PV,
    b) air-source heat pump (HP) for SH, DHW and optionally SC (assuming an installation of fan coils, otherwise split units for SC), the roof is fully covered with PV and
    c) split units for SH and SC, and electric water heaters (with a tank) for the DHW preparation, the roof is fully covered with PV.
- Use of PV electricity: i) "net metering" currently available in Greece, ii) part of direct use of PV electricity without or iii) with batteries. For the share or directly used PV electricity, the "PVecon" tool is used (Ochs, Dermentzis, and Magni 2022).
- The energy performance of the split units and the heat pumps is investigated by varying: first the COP assuming a better product and second the sink temperature for supplying space heating. Four different efficiencies are considered namely 'poor', 'moderate', 'good' and 'very good', with a corresponding COP of 2.8, 3.3, 3.7, and 4.2 at 2 °C ambient temperature and 35 °C sink temperature. The sink

temperature is varied with a step of 5 K from 35 °C up to 45 °C in the case of split units and up to 60 °C in the case of HP.



Fig. 1: View of a neighborhood in Thessaloniki, Greece [from Google Earth] and a photo of the street view.

Fig. 2 presents climatic data of 10 cities from the coldest to the warmest. The maximum monthly temperature is similar in most of the cities except for the three coldest, however, the minimum monthly temperature is quite different from 2 °C in the coldest (Kastoria) to 12 °C in the warmest (Heraklion). Global radiation has a similar trend to the minimum monthly temperature with a range between 1525 to1838 kWh/(m^2 a).

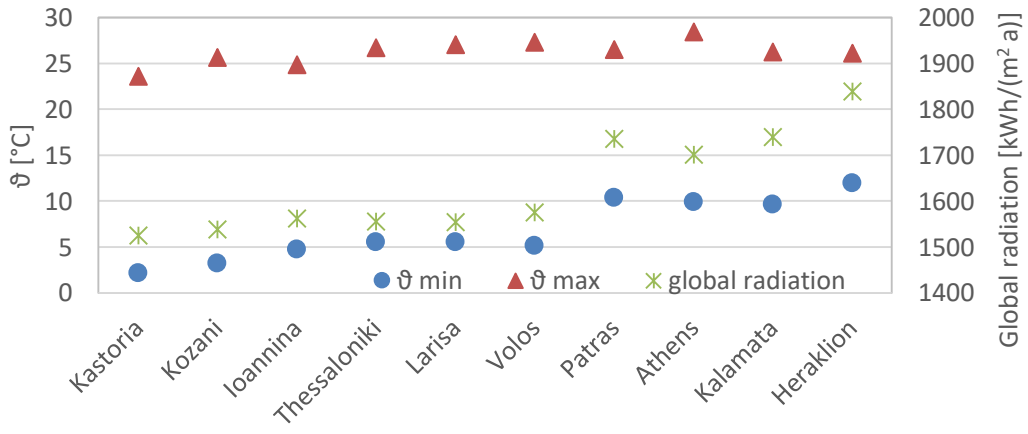

Fig. 2: Minimum and maximum monthly ambient temperature and the annual horizontal global radiation of the 10 climates (sorted from cold to warm)

In Tab. 1, the space heating and space cooling criteria to reach EnerPHit are presented as well as the calculated DHW demand and the household electricity by PHPP. The calculated number of persons in PHPP is approximately 3.6 persons per story. According to the EnerPHit standard the limit for SH is 20 kWh/(m^2 a) in the sixth colder climates and 15 kWh/(m^2 a) in the rest, while SC varies depending on each case up to a maximum of 21 kWh/(m^2 a). It is worth to be noted that the criteria to reach the Passive House standard are the same expect for the sixth colder climates in which the SH has to be 15 kWh/(m^2 a). The DHW demand varies from 11.4 to 13 kWh/(m^2 a) due to the different cold water temperatures.

Tab. 1: Space heating and cooling demands (limits according to EnerPHit standard) and DHW demand and household electricity based on PHPP.

Climate	SH demand	SC demand	DHW demand	Household electricity
	kWh/(m² a)			
Kastoria	20	15	13.0	23.9
Kozani			12.5	
Ioannina				
Thessaloniki		17	12.0	
Larisa		15		
Volos		16		
Patras	15	21	11.4	
Athens		17		
Kalamata		19		
Heraklion		20		

In order to achieve the required SH demand in each climate, the U-values vary quite significantly. Tab. 2 shows the applied values for a 3-story building located in different cities. In the coldest climate, the U-values of the insulated opaque elements are even below 0.1 W/(m^2 K) similar to the central European climate. In the rest cold climates (from Kozani to Volos), located in the North and in the middle of the country, the required U-values are between 0.12 and 0.18 W/(m^2 K). In the warmest climates, located in the southern part (such as Athens), the U-values are higher with a max of 0.47 W/(m^2 K) in Heraklion.

Tab. 2: U-values of the opaque and the transparent (as well as g-values) elements for a renovated building with 3 stories

Climate	wall	roof	slab ambient	slab ground	windows	g-value
	W/(m² K)					[-]
Kastoria	0.08	0.09	0.08	0.53	0.90	0.54
Kozani	0.12	0.12	0.12	0.53		
Ioannina	0.13	0.13	0.13	0.53		
Thessaloniki	0.17	0.18	0.17	0.53		
Larisa	0.17	0.18	0.17	0.53		
Volos	0.15	0.16	0.16	0.53		
Patras	0.28	0.31	0.31	0.54		
Athens	0.28	0.15	0.30	0.54		0.37
Kalamata	0.26	0.28	0.27	0.53		0.54
Heraklion	0.42	0.46	0.47	0.54		

3. Results and discussion

Fig 3 shows the influence of the climate on the SPF of the heat pump used for space heating and the PV yield. Presenting the climates from the colder to the warmer. It is observed that the same heat pump has better performance in south Greece from 22% (Patras) up to 32% (Heraklion) compared to the cold climate of Kastoria. The PV yield follows a similar trend but with lower values e.g., the highest increase is 20%.

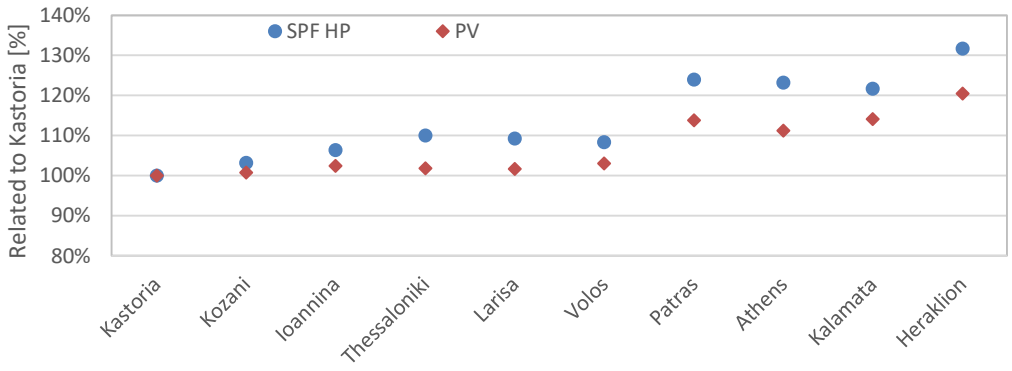

Fig. 3: Influence of the climate (10 Greek cities from cold to warm climate) on the SPF of the split units and the PV yield

A complete overview of the SPF of a heat pump used for space heating in four representative climates of Greece is presented in Fig. 4. It is observed that the choice of the heat pump has a similar impact on the SPF as the sink temperature. The latter depends on the heat emission and distribution system, the well-dimensioning/sizing of the HP, and the proper commissioning and operation (control) of the system. For example, in Thessaloniki, a poor HP that operates with a low sink temperature e.g., 45 °C leads to an SPF of 2.1, which is equal to the SPF for the case of a very good HP with a high sink temperature such as 60 °C. The choice of the HP based on its efficiency (i.e., COP) can have an impact on the electric consumption of up to 21%, e.g., in Kastoria the SPF increases from 1.6 to 2.1 (operation at 55 °C). An HP in Athens that operates at 50 °C instead of 60 °C results in 16% electricity savings and at 35 °C (by using fan coils) results in 42% or in absolute 3.1 kWh/(m^2 a) of electricity savings.

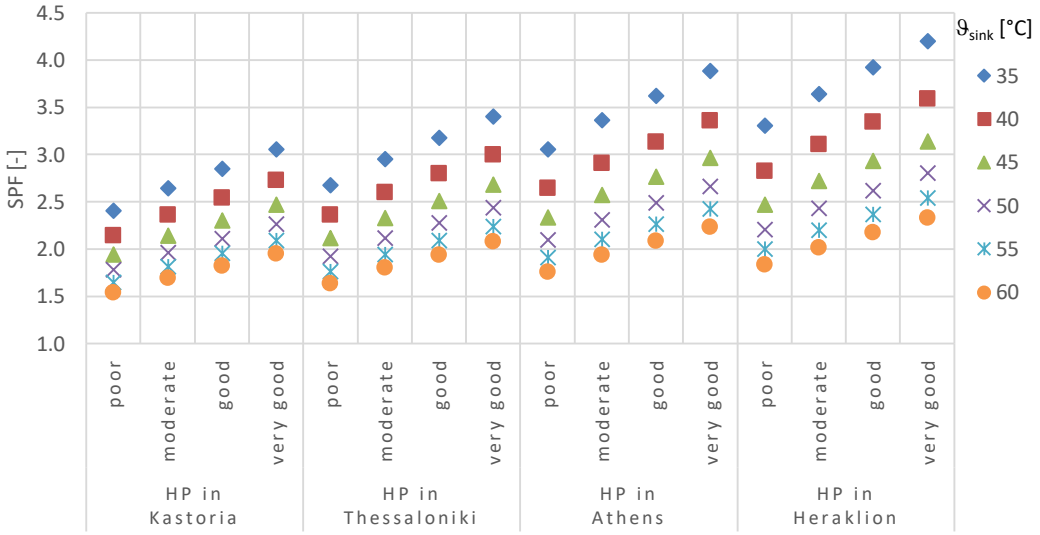

Fig. 4: Overview of the system performance factor (SPF) varying the design sink temperature, the efficiency of the heat pump, and the climate.

In Fig 5, the ratio of PV electricity and building consumption included (top) or excluding (bottom) the household electricity is presented varying the climate and the number of stories. By excluding household electricity from the balance, NZEB is possible in all climates when the building consists of a maximum of six stories. The climate influences the results; however, different measures should be applied in each climate to reach the standard (see Tab. 2). For example, the insulation thickness of the wall is 35 cm in Kastoria and six cm in Heraklion. Thus, the implementation of the building standard varies significantly, and the target of NZEB is easier to be reached in warm than cold climates due to higher SPF and PV yield that compensates for the increased cooling loads. It has to be noted that when the household electricity (23.9 kWh/(m^2 a)) is also considered in the balance, NZEB can be reached with a maximum of a 3-story building.

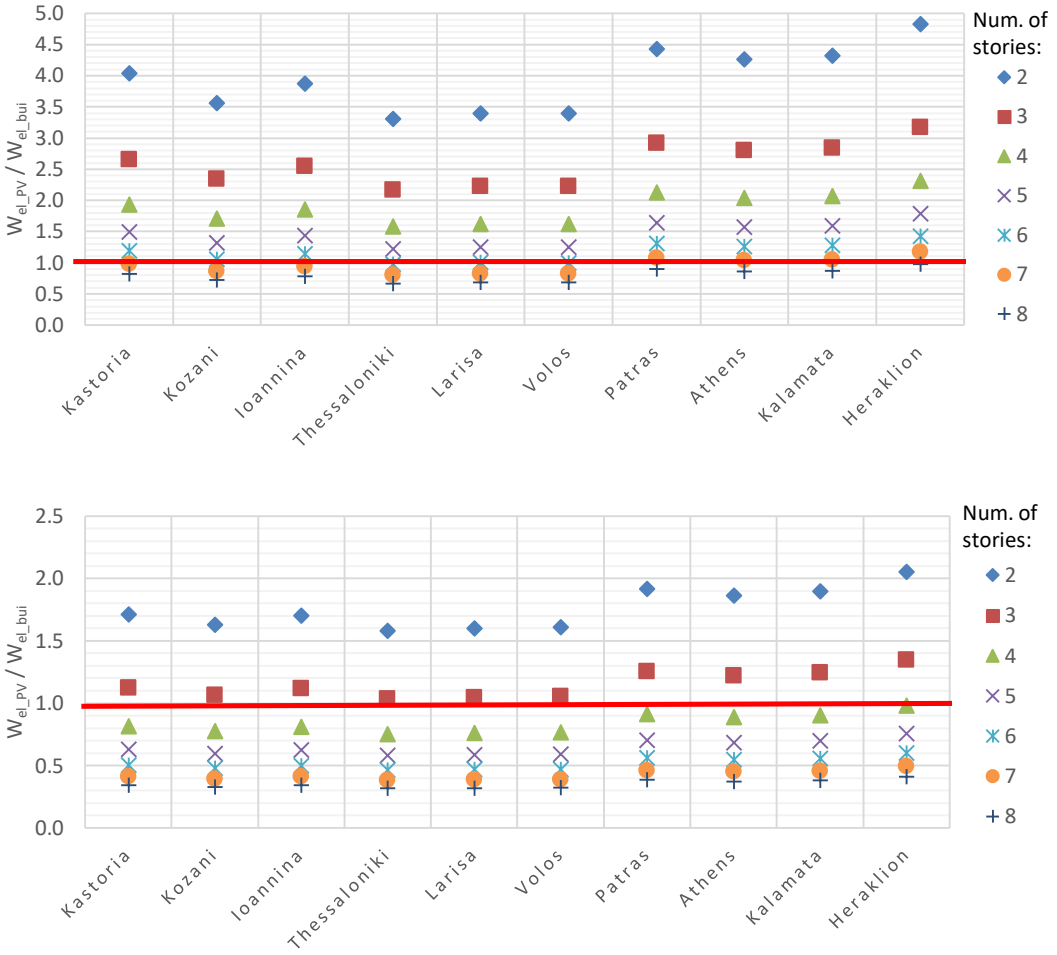

Fig. 5: Load factor considering net metering i.e., the ratio of PV electricity and building consumption over a year, depending on the climate and the number of stories including (top) or excluding (bottom) household electricity

The results are applied in a neighborhood in Thessaloniki by varying the number of stories of each building. Tab. 3 shows the influence of using solar thermal for DHW rather than electric water heaters and PV. As can be seen, even if all buildings are renovated according to very good building standards and the roof space is covered with renewable sources, the neighborhood cannot be net-zero energy since the PV production is 20% less than the electricity needed. The latter becomes 30% when the roof is fully covered with PV and electric water heaters are used for DHW (i.e., no solar thermal collectors). The results highlight that a reduction of heating demands is a priority in energy policies so that the on-site renewable sources can cover a significant part of the electricity demand towards the target of net-zero neighborhoods. PV in the façade would be also an additional option however due to very dense building areas, the shadings can be an obstacle.

Tab. 3: Ratio of PV yield and electricity demand of a neighborhood in Thessaloniki once with using solar thermal to cover the DHW demand and once without solar thermal (i.e., roof fully covered with PV)

Num. of stories	Num. of buildings	W_{el_PV} / W_{el_bui} with solar thermal	W_{el_PV} / W_{el_bui} without solar thermal
3	5	1.03	0.87
4	1	0.75	0.66
5	3	0.58	0.53
neighbourhood:	**9**	**0.80**	**0.70**

The annual remaining electricity in the neighborhood that cannot be covered by on-site renewable sources is demonstrated in Fig. 6, varying the system used for space heating and DHW, as well as the efficiency of the system and the sink temperature. In the case of split units, the sink temperature is considered to vary from 35 to 45 °C, while in the case of an HP from 35 to 60 °C, assuming using fan coils (35 up to 50 °C) or new radiators (45 up to 55 °C) or existing (or even adding some more) radiators (55 up to 60 °C). The choice of letting the electric water heaters for the DHW preparation and covering the roof with only PV (without the use of solar thermal collectors) requires almost double electricity from the grid compared to the case with ST. The use of HP for SH and DHW could lead to less required electricity from the grid, however, proper dimensioning and a choice of an HP with rather high COP are required. This is similar to the findings from an Austrian case study (Ochs, Dermentzis, and Feist 2014). Typically, often the more complex the system is, the higher the possibility for maloperation such that the HP operates at the same temperature for SH as for the DHW (Dermentzis, Ochs, and Franzoi 2021). The use of the split units for heating and cooling combined with ST for DHW are totally independent and well-established systems reducing the risk of more inefficient operation than designed.

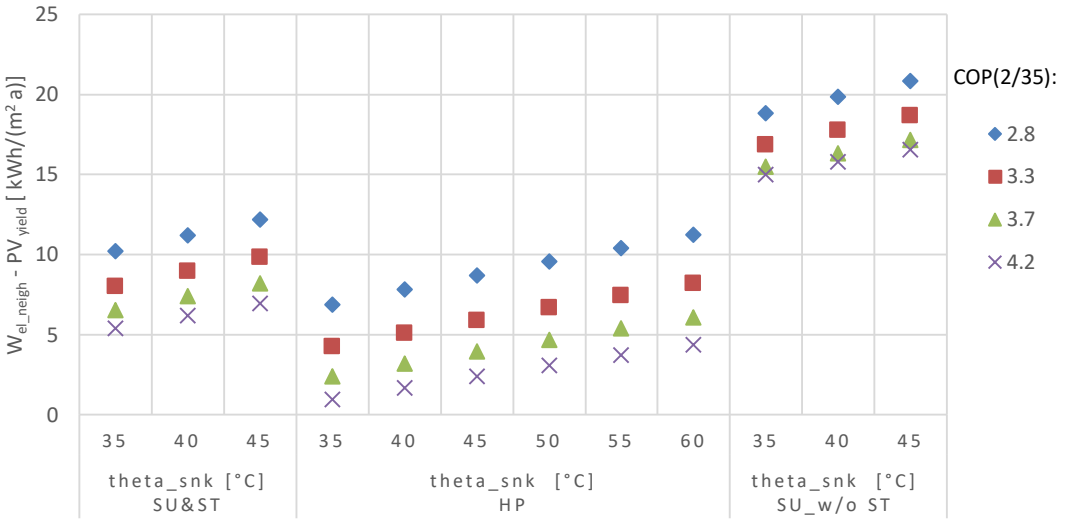

Fig. 6: Influence of the system and its performance on the final (site) energy for the neighborhood in Thessaloniki.

The annual electricity balance between PV production and electric consumption (i.e., 'net metering') that assumes the grid as ideal storage, can be misleading since the direct use of PV electricity in the building is significantly lower. Fig. 7 demonstrates the monthly electricity consumption dedicated to SH, DHW, auxiliaries, and household electricity, and the PV yield as well as the directly used electricity with or without battery installation of the 3-story building in Thessaloniki. The building is an NZEB with a ratio of 1.03 (PV yield divided by electricity consumption), however, in the winter months, the PV cannot even cover only the household electricity, resulting in high electricity demand in these months and overproduction in summer months. This need for electricity from the grid in the winter months will be significantly higher if other building standards are applied. This indicates the need for effective building energy renovations and even the need for seasonal storage. The part of the electricity consumption that is directly covered by the PV is calculated to be 0.37 in case of no batteries and 0.50 in the case with batteries. The use of batteries increases the share of direct PV electricity usage by 21%.

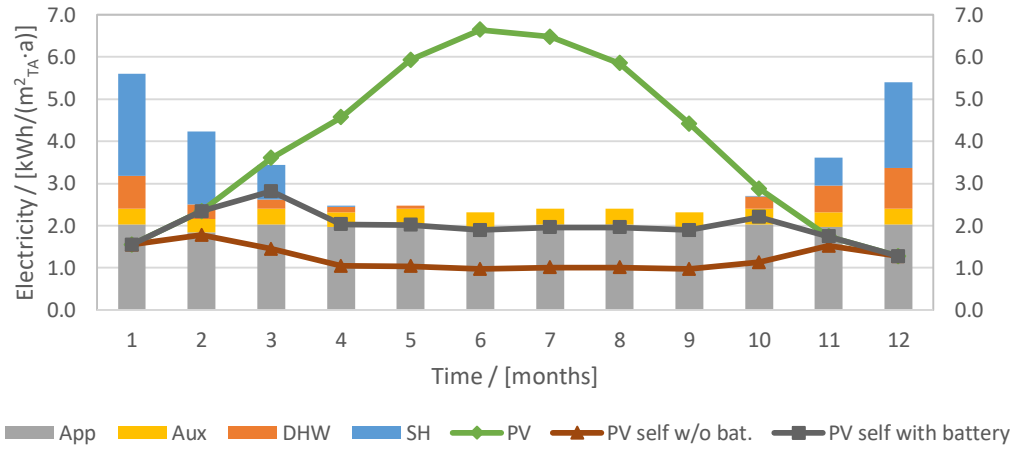

Fig. 7: Monthly electricity consumption for each application (i.e. SH, DHW, aux, and appliances) and monthly PV yield as well as the share of direct use of PV electricity with and without batteries for the 3-story building in Thessaloniki. Remark: cooling is excluded since it is not available in the current version of the PVecon tool.

New constructions consist of even more floors than the existing ones, for example, a new building in this neighborhood consists of 7 stories. This is an advantage from the space heating demand point of view due to compactness (volume/surface area). However, the remaining area for on-site renewable sources is the same, thus, other renewable sources have to be used. This increases the necessity of building new high-performance buildings and renovating the old ones with as sufficient measures as possible. Similarly, Papadopoulos et al., (2016) concluded about the real need for deep renovation of the building stock.

4. Conclusions

The study was performed to investigate the potential of applying EnerPHit standards in multi-family buildings varying the number of stories and including PV towards net-zero energy neighborhoods in Greece. The results show that PV can cover on an annual balance the electricity required for heating, cooling, DHW, and auxiliaries (excluding households) if the building is up to 6 stories in Greek climates. However, NZEB is possible up to a maximum of 3 stories when household electricity consumption is included in the balance, although the latter is not foreseen by national regulations.

The difference in climate in Greece does not have a significant influence on reaching NZEB levels, when the EnerPHit standard is applied. However, reaching the standards is much easier in the southern compared to northern climate; in the warmest climate, the required U-value of the wall is 0.42 W/(m^2 K) whilst in the coldest 0.08 W/(m^2 K); the latter figure might be challenging to achieve in practice.

The increased number of stories and also the increased compactness reduces the required measures to achieve high-performance energy standards, and at the same time, whilst the available roof space for PVs remains the same making the target of NZEB more difficult. Therefore, the implementation of a thermally well protected envelope is very important to reduce the required loads to the minimum. The choice of the heating generation system plays a major role and especially, solar thermal collectors are favorable from the energy point of view for the DHW preparation. In case of renovation, the system for DHW should be retrofitted, too and electric water heaters should be avoided even when combined with PV. Air-source HPs for supplying space heating and DHW (optional cooling, too – if fan coils are installed) combined with PVs have a potential for the highest efficiency. However, commissioning, control strategy, and sizing of the heat emission system are very important to operate the system with the lowest possible sink temperature resulting in high SPF up to 3.4 in Thessaloniki and 3.9 in Athens.

The results can be used for making policy about ways to reduce the on-site electricity consumption considering PV and solar thermal, prioritizing deep renovation concepts.

Future work should include also an economic analysis to reach the standards in several climates considering the heat and cool generation systems as well as the renewable sources.

5. Acknowledgments

This research is co-financed by Greece and the European Union (European Social Fund- ESF) through the Operational Programme «Human Resources Development, Education and Lifelong Learning» in the context of the project "Reinforcement of Postdoctoral Researchers - 2nd Cycle" (MIS-5033021), implemented by the State Scholarships Foundation (IKY). The authors would like to thank the Hellenic Passive House Institute for providing the PHPP model of the reference building in PHPP.

6. References

Dascalaki, E. G., C. A. Balaras, A. G. Gaglia, K. G. Droutsa, and S. Kontoyiannidis. 2012. "Energy Performance of Buildings-EPBD in Greece." *Energy Policy* 45 (January 2008). Elsevier: 469–477. doi:10.1016/j.enpol.2012.02.058.

Dascalaki, Elena G., Kaliopi Droutsa, Athina G. Gaglia, Simon Kontoyiannidis, and Constantinos A. Balaras. 2010. "Data Collection and Analysis of the Building Stock and Its Energy Performance - An Example for Hellenic Buildings." *Energy and Buildings* 42 (8). Elsevier B.V.: 1231–1237. doi:10.1016/j.enbuild.2010.02.014.

De Masi, Rosa Francesca, Antonio Gigante, and Giuseppe Peter Vanoli. 2021. "Are NZEB Design Solutions Environmental Sustainable? Sensitive Analysis for Building Envelope Configurations and Photovoltaic Integration in Different Climates." *Journal of Building Engineering* 39 (February). Elsevier Ltd: 102292. doi:10.1016/j.jobe.2021.102292.

Dermentzis, Georgios, Fabian Ochs, and Nicola Franzoi. 2021. "Four Years Monitoring of Heat Pump, Solar Thermal and PV System in Two Net-Zero Energy Multi-Family Buildings." *Journal of Building Engineering* 43 (March). Elsevier Ltd: 103199. doi:10.1016/j.jobe.2021.103199.

Feist, Wolfgang. 1998. "PHPP - Passive House Planning Package." Passive House Institute. http://passiv.de/en/04_phpp/04_phpp.htm.

Feist, Wolfgang. 2014. "Passive House - the next Decade." In *18th International Passive House Conference*, edited by Passive House Institute, 635–658. Aachen, Germany.

Karkanias, C., S. N. Boemi, A. M. Papadopoulos, T. D. Tsoutsos, and A. Karagiannidis. 2010. "Energy Efficiency in the Hellenic Building Sector: An Assessment of the Restrictions and Perspectives of the Market." *Energy Policy* 38 (6). Elsevier: 2776–2784. doi:10.1016/j.enpol.2010.01.009.

"KENAK 2017. Greek Code of Energy Performance of Buildings." 2017.

Ochs, Fabian, Georgios Dermentzis, and Wolfgang Feist. 2014. "Minimization of the Residual Energy Demand of Multi-Storey Passive Houses – Energetic and Economic Analysis of Solar Thermal and PV in Combination with a Heat Pump." *Energy Procedia* 48: 1124–1133. doi:10.1016/j.egypro.2014.02.127.

Ochs, Fabian, Georgios Dermentzis, and Aleksandra Ksiezyk. 2017. "Simulation and Monitoring Results of Two MFHs in PH Standard with Heat Pump, Solar Thermal and PV." In *Solar Heating Conference 2017*. Abu Dhabi, UAE.

Ochs, Fabian, Georgios Dermentzis, and Mara Magni. 2022. "PHPP vs. Dynamic Simulation – Prediction of PV-Self-Consumption with the PHPP." In *Bausim 2022*. Graz, Austria.

Papadopoulos, Agis M. 2016. "Forty Years of Regulations on the Thermal Performance of the Building Envelope in Europe: Achievements, Perspectives and Challenges." *Energy and Buildings* 127 (2016). Elsevier B.V.: 942–952. doi:10.1016/j.enbuild.2016.06.051.

Papakostas, K., T. Mavromatis, and N. Kyriakis. 2010. "Impact of the Ambient Temperature Rise on the Energy Consumption for Heating and Cooling in Residential Buildings of Greece." *Renewable Energy* 35 (7). Elsevier Ltd: 1376–1379. doi:10.1016/j.renene.2009.11.012.

Sartori, Igor, Assunta Napolitano, and Karsten Voss. 2012. "Net Zero Energy Buildings: A Consistent Definition Framework." *Energy and Buildings* 48. Elsevier B.V.: 220–232. doi:10.1016/j.enbuild.2012.01.032.

Zeno, Bastian, and Wolfgang Feist. 2012. *EnerPHit Planerhandbuch - Altbauten Mit Passivhaus Komponenten Fit Für Die Zukunft Machen*. Darmstadt, Germany. http://www.passiv.de/de/03_zertifizierung/02_zertifizierung_gebaeude/04_enerphit/04_enerphit-planer-hb.htm.

Evaluation of Angular Distribution Models to Estimate Sky Diffuse Irradiance on Tilted Planes in Urban Environments

Ignacio García[1,2], Diego Granados-López[2], David González-Peña[2], Montserrat Díez-Mediavilla[2], José Luis Torres[1] and Cristina Alonso-Tristán[2]

[1] Institute of Smart Cities (ISC), Department of Engineering, Public University of Navarre, Campus Arrosadía, 31006 Pamplona (Spain)

[2] Research Group Solar and Wind Feasibility Technologies (SWIFT), Electromechanical Engineering Department, University of Burgos, 09006 Burgos (Spain)

Abstract

The great growth of cities in the last century, together with the scarcity of developable land, has led to the growth of high-rise cities, limiting the access to solar radiation for their inhabitants. For this reason, it is crucial to have models that allow an accurate assessment of the amount of solar radiation that can be received in highly obstructed environments. In this work, it has been evaluated and compared the performance of an angular distribution model against a simpler irradiance model to estimate the diffuse irradiance received on tilted planes located in obstructed environments. To this end, a total of 320 urban scenarios were considered derived from the combination of different orientations and inclinations of the tilted plane, and different orientations and aspect ratios of the urban canyon. Models were evaluated against the diffuse irradiance values obtained by the ISO 15469:2004(E)/CIE S 011/E:2003 model and radiance measurements performed by a sky scanner at the radiometric station of the Public University of Navarre (Spain).

Keywords: Diffuse solar irradiance, Angular distribution models, Tilted planes, Urban environments

1. Introduction

For the last century there has been a growing concentration of population in cities. This tendency is expected to continue unless the necessary policy measures are taken. According to the United Nations report (United Nations, 2018), in 2018, 1.7 billion people –23 per cent of the world's population– lived in a city with at least 1 million inhabitants. In 2030, a projected 28 per cent of people worldwide will be concentrated in cities with at least 1 million inhabitants. The scarcity of available developable land has caused cities to grow in height, limiting access to solar radiation for their inhabitants. For this reason, it is crucial to have models that allow an accurate assessment of the amount of solar radiation that can be received in highly obstructed environments. Specifically, the estimation of diffuse irradiance on tilted planes –given their diffuse and anisotropic nature– requires the use of models. Depending on their complexity, such models can be classified into two main groups: (1) simple or irradiance models within which it is possible to distinguish between isotropic and pseudo-isotropic models (Liu and Jordan, 1961; Koronakis, 1986; Tian et al., 2001) and anisotropic models (Bugler, 1977; Temps and Coulson, 1977; Klucher, 1979; Steven and Unsworth, 1979; Hay and Davies, 1980; Willmott, 1982; Ma and Iqbal, 1983; Skartveit and Olseth, 1986; Saluja and Muneer, 1987; Gueymard, 1986, 1987; Muneer, 1987, 1990; Perez et al., 1987, 1990; Reindl et al., 1990); and (2) complex or angular distribution models (Matsuura and Iwata, 1990; Perez et al., 1993a; Brunger and Hooper, 1993; Igawa et al., 2004; Igawa, 2014; Lou et al., 2022).

Although numerous studies can be found in the scientific literature that evaluate the performance of these models, both simple and complex, when estimating the irradiance received on an inclined plane located in an obstacle-free environment, there are very few studies that evaluate this performance in obstructed environments. In this sense, it was carried out an evaluation of the behavior of simple or irradiance models to assess diffuse irradiance on inclined planes in urban environments in a previous work (García et al., 2021).

The current work aims to evaluate and compare the performance of an angular distribution model against a simple

© 2022. The Authors. Published by International Solar Energy Society
Selection and/or peer review under responsibility of Scientific Committee
doi:10.18086/eurosun.2022.11.06 Available at http://proceedings.ises.org

irradiance model, both widely used, in determining sky diffuse irradiance in obstructed environments. The hypothesis is that models based on the angular distribution of diffuse radiance in the sky allow for more accurate consideration of environmental obstacles than the simple models. The scope of this study is limited to sky diffuse irradiance. That is, we have not considered the reflected fluxes which, in very obstructed environments, can account for a significant part of the received energy. Therefore, this issue will be addressed with the depth it deserves in future works. The estimation of direct irradiance has also not been addressed.

This paper is organized into five sections and two appendices. The meteorological data and the quality control procedures are detailed in Section 2. Section 3 describes the general methodology and the different considered models. Section 4 presents the results obtained and the conclusions are detailed in Section 5.

2. Meteorological data

In order to compare the results obtained in this study with those obtained in the previous one (García et al., 2021), in which irradiance or simple models were evaluated, the same experimental dataset was used. Thus, the data used in this study were collected from the radiometric station of the UPNA, located on the roof of one of the buildings of the Higher Technical School of Agricultural Engineering and Biosciences (42º47'32'' N, 1º37'45'' W, 435 m a.s.l.) in Pamplona (Spain). The data series consist in 6,767 observations made between July and December 2018. Measured variables include 1-min frequency data of global irradiance on the horizontal plane, using a Kipp & Zonen CM11 pyranometer, diffuse irradiance on the horizontal plane with a Kipp & Zonen CM11 pyranometer with a shadow ball, and direct normal irradiance with a Kipp & Zonen CH1 pyrheliometer. All three instruments were mounted on a Kipp & Zonen 2AP solar tracker. In addition, the angular distribution of diffuse sky radiance was measured every 10 min using an EKO MS-321LR sky scanner. Both irradiance and angular distribution measurements corresponding to solar elevations below 5º were discarded. Irradiance measurements were further subjected to the quality control procedure proposed by the MESoR project (Hoyer-Klick et al., 2008). In the case of angular distribution of radiance, quality control was based in three criteria described in García et al. (2020).

3. Methodology

The general methodology consists of: (1) the sky classification according to the 15 types established by the ISO 15469:2004(E)/CIE S 011/E:2003 standard (2004) from radiance measurements performed by the sky scanner; (2) the estimation of the diffuse irradiance on the tilted plane from the measured angular distribution of radiance and the ISO/CIE angular distribution model, considering the obstruction provided by the urban canyon; (3) obtaining the diffuse irradiance predicted by the angular distribution model and the irradiance one, considering the effect of obstructions; and (4) the comparison of model predictions with the reference irradiance values obtained in step 2 by the ISO/CIE angular distribution model.

The computation of the diffuse irradiance received on the tilted plane of interest, indicated in steps 2 and 3 of the general methodology, was carried out by integrating the radiances corresponding to a series of visible sky elements –782,268 in this work– on such plane. In this way, those sky elements obstructed by the urban environment can be accurately discarded (see Fig. 1).

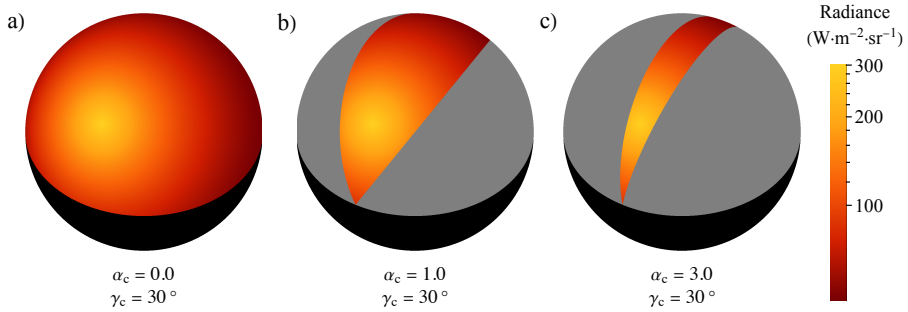

Fig. 1: Projection of the ISO/CIE sky standard 7 onto a plane with an inclination β_p = 45º and an azimuth γ_p = 30º, when the sun has a solar zenith angle of 45º and an azimuth of 30º, considering different aspect ratios (α_c) of the urban canyon. The black-shaded area is the visible part of the ground, and the gray-shaded area is the projection of the urban canyon onto the tilted plane.

The described methodology was used to compare the performance of an angular sky diffuse radiance distribution model versus an irradiance model when estimating the diffuse irradiance received on tilted planes located in urban environments with different configurations. The considered models –listed below–, as well as the reference ISO/CIE angular distribution model, are described in Subsections 3.1 to 3.3.

1. All-weather model (Perez et al., 1993a, 1993b). This is a widely used angular distribution model that uses the sky's clearness (ε) and brightness (Δ) to parameterize the angular distribution of luminance in the sky. Despite being designed to estimate the angular distribution of sky luminance, previous studies have confirmed its good performance when estimating radiance (Gracia et al., 2011).
2. Modified Perez irradiance model (Perez et al., 1987). This is a modification of the original anisotropic sky model proposed by García et al. (2021) to take into account the effect of the obstacles on the various defined sky areas (isotropic background and circumsolar region). As in the case of the All-weather model, ε and Δ are used to characterize the sky conditions.

As in the case of the data set used, a similar set of urban scenarios of the previous work was considered in order to compare the results obtained previously with simple models, and those obtained in this study from a complex one. Therefore, the general methodology was applied to a total of 320 urban scenarios resulting from the combination of 4 different orientations (γ_p) and 10 inclinations (β_p) of the tilted plane and 2 orientations (γ_c) and 4 aspect ratios (α_c) of the urban canyon, listed in Tab. 1. The aspect ratio is considered as the quotient of the height and width of the urban canyon and the azimuth origin is in the south and it increase positively towards the west and negatively towards the east.

Many urban scenarios were considered to cover as many situations as possible that can occur in a real urban environment. For all scenarios, the tilted plane of interest was considered to be in the center of the urban canyon, i.e., equidistant to the two facades that delimit the canyon.

Tab. 1: Considered configurations of the urban canyon and tilted plane.

Variable	Initial value	Final value	Increment	Cases
Urban canyon azimuth (γ_c)	0º	90º	90º	2
Urban canyon aspect ratio (α_c)	1	4	1	4
Plane tilt angle (β_p)	0º	90º	10º	10
Plane azimuth (γ_p)	-180º	90º	90º	4

The ISO/CIE angular distribution model was used to obtain the reference diffuse irradiance against which values provided by the analyzed irradiance models were compared because of two fundamental reasons. The first is the practical impossibility to install irradiance sensors in such a large number of considered scenarios. The second is to overcome data discontinuities resulting from the saturation of the sky scanner measurements of angular distribution of radiance in those patches close to the sun. The measurements of angular distribution of sky radiance were used to characterize the state of the sky according to the ISO/CIE standard. In this way, it was possible to determine the theoretical ISO/CIE radiance distribution closest to the real measured distribution. Then, the model proposed in the standard was used to obtain a continuous distribution of radiance in the sky according to the obtained ISO/CIE sky-type.

3.1. Reference luminance/radiance model: ISO/CIE angular distribution model

The standard ISO 15469:2004(E)/CIE S 011/E:2003 (2004) established a total of 15 standard sky luminance distributions. Although the ISO/CIE model is designed to describe the luminance distribution of the sky and not the radiance, García et al. (2020) found that classification in sky types from radiance and luminance measurements gives an exact match for nearly 60% of the cases and reaches 90% when, in addition to the matching classifications, the differences of 1 and 2 sky types are considered.

According to the ISO/CIE standard, the luminance relative to zenith at a given point in the sky vault, $l_{CIE}(\theta,\chi)$, is given by eq. (1).

$$l_{CIE}(\theta,\chi) = \frac{L_{CIE}(\theta,\chi)}{L_Z} = \frac{\varphi(\theta)\, f(\chi)}{\varphi(0)\, f(\theta_z)}, \qquad \text{(eq. 1)}$$

where $L_{CIE}(\theta,\chi)$ is the luminance of any sky point given its zenith angle (θ) and angular distance to the sun (χ), $f(\chi)$ is the indicatrix function, $\varphi(\theta)$ is the gradation function, θ_z is the solar zenith angle.

The gradation function, $\varphi(\theta)$, which obeys to the eq. (2), characterizes the luminance variation from the zenith ($\theta = 0°$) to the horizon ($\theta = 90°$).

$$\varphi(\theta) = 1 + a_{CIE}\,\exp(b_{CIE}/\cos\theta). \quad \text{(eq. 2)}$$

The indicatrix function, $f(\chi)$, in eq. (3) expresses the relationship between the luminance at a sky point and that at the point where $\chi = 90°$). The indicatrix function is related to the scattering of solar radiation as it passes through the atmosphere.

$$f(\chi) = 1 + c_{CIE}\,[\exp(d_{CIE}\chi) - \exp(d_{CIE}\,\pi/2)] + e_{CIE}\cos^2\chi. \quad \text{(eq. 3)}$$

Coefficients a_{CIE}, b_{CIE}, c_{CIE}, d_{CIE} and e_{CIE} included in eqs. (2) and (3) depend on the standard sky type. Consequently, in order to calculate the angular distribution of relative luminance in the sky vault at any given moment by applying eq. (1), it is necessary to know first the type of sky at that moment.

When L_Z is not a known value, it is possible to obtain the absolute luminance of the sky element, $L_{CIE}(\theta,\chi)$, from the normalization of the measured horizontal diffuse irradiance (G_d) according to eq. (4).

$$L_{CIE}(\theta,\chi) = \frac{l_{CIE}(\theta,\chi)\,G_d}{\int_{\theta=0}^{\pi/2}\int_{\gamma=0}^{2\pi}[l_{CIE}(\theta,\chi,\gamma)\cos\theta]\mathrm{d}\theta\;\mathrm{d}\gamma}. \quad \text{(eq. 4)}$$

Considering the proposed sky discretization, which consists of a large number of sky elements –782,268 in this work–, the integration of the denominator of eq. (4) can be replaced by a sum without loss of precision, as described in eq. (5).

$$L_{CIE}(\theta,\chi) = \frac{l_{CIE}(\theta,\chi)\,G_d}{\sum_{i=1}^{n} l_{CIE,i}(\theta,\chi)\omega_i\cos\theta_i}, \quad \text{(eq. 5)}$$

where n is the number of sky elements into which the sky vault is divided and ω_i is the solid angle of the sky element i.

So that, according to the ISO/CIE sky radiance distribution, the horizontal diffuse irradiance ($G_{d,CIE}$) can be obtained by integrating/summing the values of $L_{CIE}(\theta,\chi)$, according to eq. (6).

$$G_{d,CIE} = \sum_{i=1}^{n} L_{CIE,i}(\theta,\chi)\omega_i\cos\theta_i. \quad \text{(eq. 6)}$$

This last operation, as it is, may be of no interest since the value of G_d is already known. However, when calculating the diffuse irradiance received on a tilted plane ($G_{d,T,CIE}$) located in an obstructed or unobstructed environment, an analogous procedure will be applied, eq. (7).

$$G_{d,T,CIE} = \sum_{i=1}^{n} max\left[L_{CIE,i}(\theta,\chi)\omega_i\cos\theta_i', 0\right], \quad \text{(eq. 7)}$$

where θ_i' is the zenith angle relative to the normal of the tilted plane of a sky element i.

3.2. Luminance/radiance model: All-weather model

According to Perez et al. (1993a, 1993b), the relative luminance, $l_{Aw}(\theta,\chi)$, defined as the ratio between the luminance of the considered sky element, $L_{Aw}(\theta,\chi)$, and the luminance of an arbitrary sky element –generally the zenith– is given by eq. (8).

$$l_{Aw}(\theta,\chi) = [1 + a_{Aw}\exp(b_{Aw}/\cos\theta)][1 + c_{Aw}\exp(d_{Aw}\chi) + e_{Aw}\cos^2\chi]. \quad \text{(eq. 8)}$$

The coefficients a_{Aw}, b_{Aw}, c_{Aw}, d_{Aw} and e_{Aw} are adjustable coefficients that depend on two parameters used to characterize the sky conditions at a given time: sky clearness (ε) and sky brightness (Δ).

$L_{Aw}(\theta,\chi)$ may be obtained from $l_{Aw}(\theta,\chi)$, if zenith luminance (L_z) is known by eq. (9).

$$L_{Aw}(\theta,\chi) = \frac{L_{z,Aw}\,l_{Aw}(\theta,\chi)}{l_{Aw}(0,\theta_z)}. \quad \text{(eq. 9)}$$

However, the authors recommend that $L_{Aw}(\theta,\chi)$ be obtained by eq. (10) after normalization of G_d. According to the reasoning stated in Section 3.1, the integration can be replaced by a sum of very small discrete elements.

$$L_{Aw}(\theta,\chi) = \frac{l_{Aw}(\theta,\chi)\, G_d}{\int_{\theta=0}^{\pi/2}\int_{\gamma=0}^{2\pi}[l_{Aw}(\theta,\chi)\cos\theta]\mathrm{d}\theta\ \mathrm{d}\gamma} = \frac{l_{Aw}(\theta,\chi)\, G_d}{\sum_{i=1}^{n} l_{Aw,i}(\theta,\chi)\omega_i \cos\theta_i}. \quad \text{(eq. 10)}$$

Once the value of $L_{Aw}(\theta,\chi)$ is known, the calculation of the diffuse irradiance on a horizontal ($G_{d,Aw}$) or tilted plane, ($G_{d,T,Aw}$) can be carried out by eqs. (6) and (7), respectively.

3.3 Irradiance model: modified Perez model

The original model published by Perez et al. (1987) is shown in eq. (11). The three terms in this equation correspond to the diffuse irradiance from the isotropic background region, the circumsolar region, and the contribution of the horizon brightness.

$$G_{d,T,Perez} = G_d\left[(1-F_1)\left(\frac{1+\cos\beta_p}{2}\right) + F_1\frac{a}{b} + F_2\sin\beta_p\right], \quad \text{(eq. 11)}$$

where F_1 is the circumsolar brightness coefficient; F_2 is the horizon brightness coefficient; a is the solid angle subtended by the circumsolar region, weighted by its average incidence on the slope; and b is the solid angle subtended by the circumsolar region, weighted by its average incidence on the horizontal. Coefficients F_1 and F_2 depend on ε and Δ.

The proposal by García et al. (2021) modified the original model in order to take into account the effect of urban canyon on the irradiance of the isotropic background and the circumsolar region. In this regard, the first term, the contribution of the isotropic background, was modified replacing the factor $(1+\cos\beta_p)/2$ by the sky view factor (SVF). In the case of the circumsolar component, the factor a/b was replaced by the circumsolar view factor (CVF), which allows to consider the effect of the urban canyon on the circumsolar region. The term related to the horizon brightness was eliminated, in the understanding that this sky region will be obstructed, almost completely, by the urban canyon. Therefore, the modified Perez model is given by Equation (12).

$$G_{d,T,Perez} = G_d[(1-F_1)SVF + F_1 CVF]. \quad \text{(eq. 12)}$$

García et al. (2021) analyzed 5 different half-angles of opening of the circumsolar region –from point source to 45º– and demonstrated that the model that considered the 35º half-angle circumsolar region performed best when estimating the irradiance received on a tilted plane considering all studied urban scenarios. For this reason, in this work such aperture angle of the circumsolar region was selected.

4. Results and discussion

Fig. 2 shows the sky classification obtained according to the ISO/CIE standard. Clear sky types (11-15) predominate, with 56% of the records, being the sky type 13 the most frequent one. Overcast skies (types 1-5) accounted for 24.9% of the skies observed and intermediate skies (types 6-10) 19.1%.

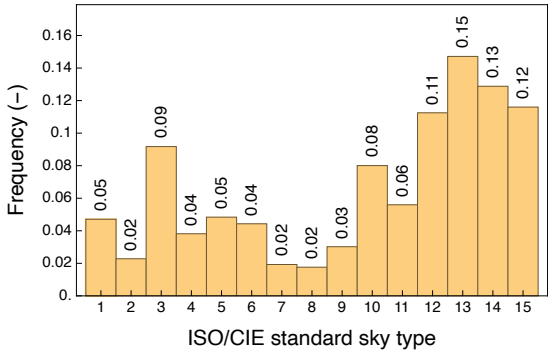

Fig. 2: Observed frequency of occurrence of each ISO/CIE Standard General Sky classification.

Once the ISO/CIE sky type was obtained, the diffuse irradiance on the inclined plane was determined for each of the 320 urban scenarios designed using the ISO/CIE angular distribution model. These irradiance values were

used as the reference against which the irradiance estimates provided by the All-weather angular distribution model, or the modified Perez irradiance model were compared. For each scenario and modified model, the performance was evaluated with the relative mean square error ($rRMSE$), according to eq. (13).

$$rRMSE(\%) = \frac{100}{\bar{G}_{d,T,CIE}} \sqrt{\frac{\sum_{i=1}^{n}\left(G_{d,T,i,CIE} - G_{d,T,i,x}\right)^2}{n}}. \quad \text{(eq. 13)}$$

where $G_{d,T,CIE}$ is the diffuse irradiance on the tilted plane calculated from the ISO/CIE angular radiance distribution model, $\bar{G}_{d,T,CIE}$ is the average of all $G_{d,T,CIE}$ values, and $G_{d,T,i,x}$ is the diffuse irradiance on the tilted plane given by the All-weather angular distribution model or the modified Perez irradiance model.

Fig. 3 shows the $rRMSE$ values obtained by the two evaluated models considering a γ_c of 0º (north-south direction) and a γ_p of -90º (east-oriented plane), Fig. 3a, and of 0º (south-oriented plane), Fig. 3b. In each of the plots we show the evolution of the errors as a function of the plane inclination and the aspect ratio of the canyon (α_c). Although 4 different orientations of the plane were considered for γ_c = 0º, only 2 have been included in Fig. 3 for space reasons. In all cases it can be observed how the error obtained by the models when estimating the diffuse irradiance on a tilted plane increases as the plane's inclination and the aspect ratio of the urban canyon rise. However, the $rRMSE$ values are significantly lower in the case of the angular distribution model compared to the irradiance model.

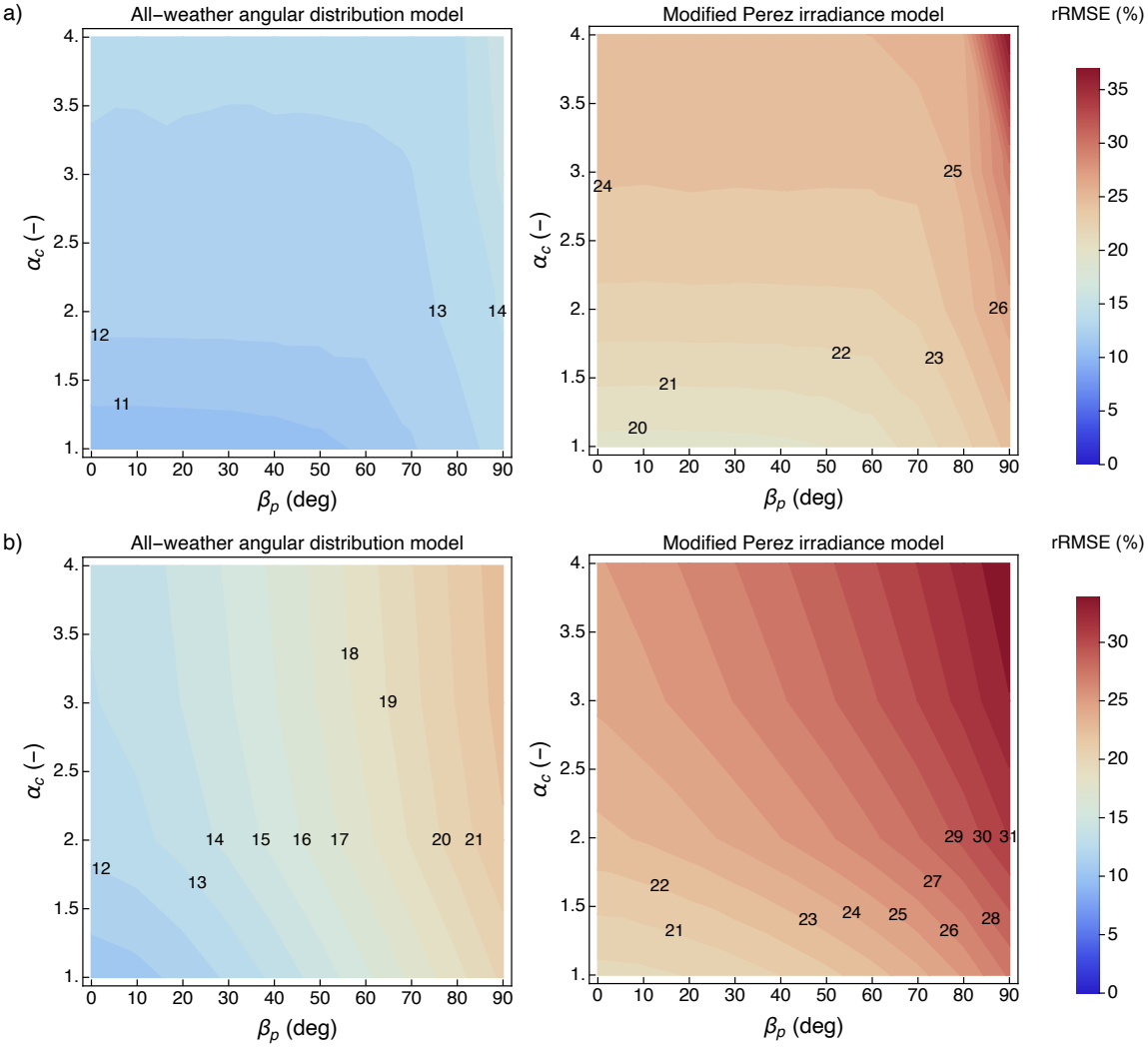

Fig. 3: $rRMSE$ (%) values of tilted diffuse irradiance obtained by each model for the different β_p and α_c combinations considering a γ_c of 0º (north-south direction) and a γ_p of (a) -90º (east facing) and (b) 0º (south facing).

Fig. 4 shows results analogous to those presented in Fig. 3, but, in this case, for a γ_c of 90º (east-west direction). Again, the trend observed in Fig. 3 can be seen. That is, the errors increase with the increase of the β_p and α_c, being significantly higher in the case of the simple model or irradiance model. For the specific case of this canyon orientation and for the reasons mentioned above, the other 2 plots corresponding to plane orientations of 90º and 180º have not been included. Thus, a total of 8 plots corresponding to the 320 scenarios considered were obtained.

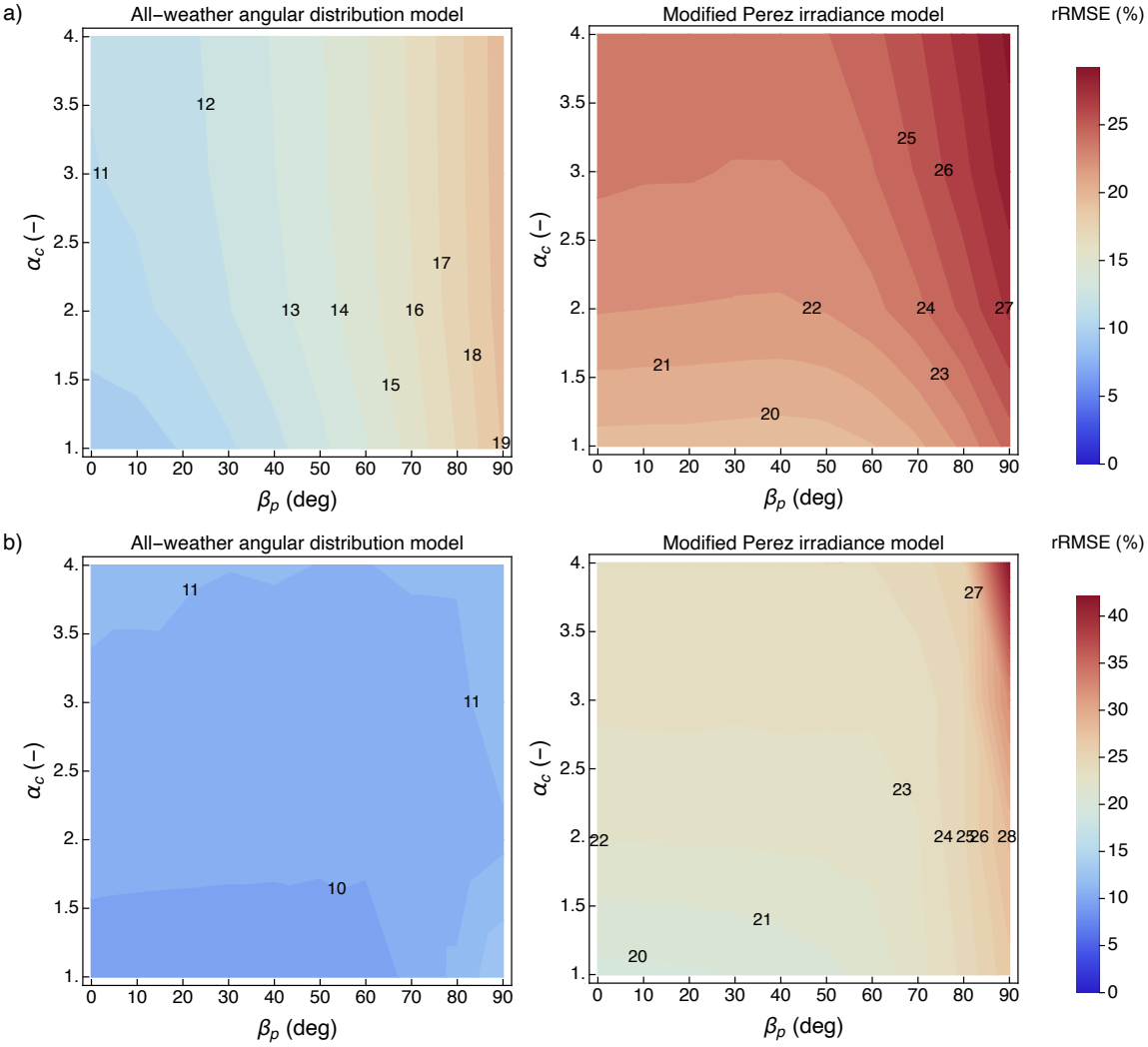

Fig. 4: $rRMSE$ (%) values of tilted diffuse irradiance obtained by each model for the different β_p and α_c combinations considering a γ_c of 90º (east-west direction) and a γ_p of (a) -90º (east facing) and (b) 0º (south facing).

Data in those 8 plots like Figs. 3 and 4 were summarized to simplify the analysis of the results. In this regard, Tabs. 2 and 3 show the $rRMSE$ values obtained for the two considered γ_c values. Each table shows the errors obtained by the two analyzed models for the different α_c. Also, for each α_c, models have been ranked according to their $rRMSE$ values and their rank order is shown in brackets.

As can be seen, in all cases the All-weather model, which considers the angular distribution of radiance in the sky vault, shows the best performance when estimating the $G_{d,T}$ values received on a plane located inside an urban canyon, with errors ranging from 11.96% in an obstacle-free environment to 15.23% when the aspect ratio of the urban canyon reaches a value of 4. In fact, the $rRMSE$ values obtained by the simple or irradiance model almost double the errors of the angular distribution model.

Tab. 2: $rRMSE$ (%) values of tilted diffuse irradiance obtained by each model for different α_c considering a γ_c of 0º (N-S). For each α_c, model rank scores are shown in parenthesis.

α_c	All-weather angular distribution model	Perez modified irradiance model
1	13.01 (1)	21.00 (2)
2	14.52 (1)	23.65 (2)
3	15.02 (1)	25.00 (2)
4	15.23 (1)	26.04 (2)

Tab. 3: $rRMSE$ (%) values of tilted diffuse irradiance obtained by each model for different α_c considering a γ_c of 90º (E-W). For each α_c, model rank scores are shown in parenthesis.

α_c	All-weather angular distribution model	Perez modified irradiance model
1	11.70 (1)	20.68 (2)
2	12.35 (1)	23.12 (2)
3	12.64 (1)	24.37 (2)
4	12.75 (1)	25.52 (2)

5. Conclusions

In this work we have evaluated the performance of an angular distribution model of diffuse sky radiance versus that of an anisotropic irradiance model, when estimating the diffuse irradiance received in a tilted plane immersed in an urban canyon. After analyzing the results considering a total of 320 urban scenarios, which arise from the combination of different orientations and aspect ratios of the canyon and different orientations and inclinations of the plane of interest, the starting hypothesis of the article has been verified. That is, the angular distribution model performs significantly better than the irradiance model. In fact, when comparing the models, it has been observed that the errors are reduced by almost half.

It should be noted that the values of sky diffuse tilted irradiance taken as a reference against which to assess the considered models have been calculated according to the ISO/CIE angular distribution model, given the practical impossibility of carrying out a measurement campaign in the 320 urban scenarios. Although this may introduce some uncertainty in the results, the use of this model, together with the sky scanner measurements, makes it possible to obtain the standard sky radiance distribution most similar to the real measured distribution.

In the future, this same study will be undertaken using HDR images of the sky calibrated in radiance, which will allow greater precision in the results. The problem of estimating reflected energy fluxes in complex environments will also be addressed.

In conclusion, the use of angular distribution models is recommended over irradiance models when estimating the diffuse sky irradiance received on planes located in urban environments.

6. Acknowledgments

The authors gratefully acknowledge the financial support provided by the Spanish Ministry of Science & Innovation under the I+D+i state program "Challenges Research Projects" (Ref. RTI2018-098900-B-I00). Ignacio García thanks to the Spanish Ministry of Universities and the European Union-Next Generation EU for their financial support (Program for the requalification of the Spanish university system 2021-2023, Resolution 1402/2021). Diego Granados-López thanks grant PIRTU Program, ORDEN EDU/556/2019, for its financial support.

7. References

Brunger, A.P., Hooper, F.C., 1993. Anisotropic sky radiance model based on narrow field of view measurements of shortwave radiance. Sol. Energy 51, 53–64. https://doi.org/10.1016/0038-092X(93)90042-M

Bugler, J.W., 1977. The determination of hourly insolation on an inclined plane using a diffuse irradiance model based on hourly measured global horizontal insolation. Sol. Energy 19, 477–491. https://doi.org/10.1016/0038-092X(77)90103-7

García, I., de Blas, M., Hernández, B., Sáenz, C., Torres, J.L., 2021. Diffuse irradiance on tilted planes in urban environments: Evaluation of models modified with sky and circumsolar view factors. Renew. Energy 180, 1194–1209. https://doi.org/10.1016/j.renene.2021.08.042

García, I., de Blas, M., Torres, J.L., 2020. The sky characterization according to the CIE Standard General Sky: Comparative analysis of three classification methods. Sol. Energy 196, 468–483. https://doi.org/10.1016/j.solener.2019.12.039

Gracia, A.M., Torres, J.L., De Blas, M., García, A., Perez, R., 2011. Comparison of four luminance and radiance angular distribution models for radiance estimation. Sol. Energy 85, 2202–2216. https://doi.org/10.1016/j.solener.2011.06.005

Gueymard, C.A., 1987. An anisotropic solar irradiance model for tilted surfaces and its comparison with selected engineering algorithms. Sol. Energy 38, 367–386. https://doi.org/10.1016/0038-092X(87)90009-0

Gueymard, C.A., 1986. Radiation on tilted planes: A physical model adaptable to any computational time-step, in: Pergamon Press (Ed.), Proceedings of INTERSOL85. Pergamon Press, Elmsford, NY, pp. 2463–2467.

Hay, J.E., Davies, J.A., 1980. Calculation of the solar radiation incident on an inclined surface, in: Proceedings of the First Canadian Solar Radiation Data Workshop. Ministry of Supply and Services, Toronto, Canada, pp. 59–72.

Hoyer-Klick, C., Beyer, H.G., Dumortier, D., Schroedter-Homscheidt, M., Wald, L., Martinoli, M., Schilings, C., Gschwind, B., Menard, L., Gaboardi, E., Ramirez-Santigosa, L., Polo, J., Cebecauer, T., Huld, T., Suri, M., de Blas, M., Lorenz, E., Pfatischer, R., Remund, J., Ineichen, P., Tsvetkov, A., Hofierka, J., 2008. Management and exploitation of solar resource knowledge, in: Proceeding of the EUROSUN 2008, 1st International Conference on Solar Heating, Cooling and Buildings. Lisbon, Portugal.

Igawa, N., 2014. Improving the All Sky Model for the luminance and radiance distributions of the sky. Sol. Energy 105, 354–372. https://doi.org/10.1016/j.solener.2014.03.020

Igawa, N., Koga, Y., Matsuzawa, T., Nakamura, H., 2004. Models of sky radiance distribution and sky luminance distribution. Sol. Energy 77, 137–157. https://doi.org/10.1016/j.solener.2004.04.016

ISO 15469:2004(E)/CIE S 011/E:2003, 2004. Spatial Distribution of Daylight – CIE Standard General Sky. Geneva: ISO, Vienna: CIE.

Klucher, T.M., 1979. Evaluation of models to predict insolation on tilted surfaces. Sol. Energy 23, 111–114. https://doi.org/10.1016/0038-092X(79)90110-5

Koronakis, P.S., 1986. On the choice of the angle of tilt for south facing solar collectors in the Athens basin area. Sol. Energy 36, 217–225. https://doi.org/10.1016/0038-092X(86)90137-4

Liu, B.Y.H., Jordan, R.C., 1961. Daily insolation on surfaces tilted towards equator. ASHRAE J. 10, 53–59.

Lou, S., Li, D.H.W., Alshaibani, K.A., Xing, H., Li, Z., Huang, Y., Xia, D., 2022. An all-sky luminance and radiance distribution model for built environment studies. Renew. Energy 190, 822–835. https://doi.org/10.1016/j.renene.2022.03.105

Ma, C.C.Y., Iqbal, M., 1983. Statistical comparison of models for estimating solar radiation on inclined surgaces. Sol. Energy 31, 313–317. https://doi.org/10.1016/0038-092X(83)90019-1

Matsuura, K., Iwata, T., 1990. A model of daylight source for the daylight illuminance calculations on the all weather conditions, in: Proceedings of 3rd International Daylighting Conference. Moscow, Russia.

Muneer, T., 1990. Solar radiation model for Europe. Build. Serv. Eng. Res. Technol. 11, 153–163. https://doi.org/10.1177/014362449001100405

Muneer, T., 1987. Solar Radiation Modelling for the United Kingdom. Council for National Academic Awards.

Perez, R., Ineichen, P., Seals, R., Michalsky, J.J., Stewart, R., 1990. Modeling daylight availability and irradiance components from direct and global irradiance. Sol. Energy 44, 271–289. https://doi.org/10.1016/0038-092X(90)90055-H

Perez, R., Seals, R., Ineichen, P., Stewart, R., Menicucci, D., 1987. A new simplified version of the perez diffuse irradiance model for tilted surfaces. Sol. Energy 39, 221–231. https://doi.org/10.1016/S0038-092X(87)80031-2

Perez, R., Seals, R., Michalsky, J.J., 1993a. All-weather model for sky luminance distribution—Preliminary configuration and validation. Sol. Energy 50, 235–245. https://doi.org/10.1016/0038-092X(93)90017-I

Perez, R., Seals, R., Michalsky, J., 1993b. To all-weather model for sky luminance distribution—preliminary configuration and validation. Sol. Energy 51, 423. https://doi.org/10.1016/0038-092X(93)90157-J

Reindl, D.T., Beckman, W.A., Duffie, J.A., 1990. Evaluation of hourly tilted surface radiation models. Sol. Energy 45, 9–17. https://doi.org/10.1016/0038-092X(90)90061-G

Saluja, G.S., Muneer, T., 1987. An Anisotropic Model for Inclined Surface Solar Irradiation. Proc. Inst. Mech. Eng. Part C J. Mech. Eng. Sci. 201, 11–20. https://doi.org/10.1243/PIME_PROC_1987_201_082_02

Skartveit, A., Olseth, J.A., 1986. Modelling slope irradiance at high latitudes. Sol. Energy 36, 333–344. https://doi.org/10.1016/0038-092X(86)90151-9

Steven, M.D., Unsworth, M.H., 1979. The diffuse solar irradiance of slopes under cloudless skies. Q. J. R. Meteorol. Soc. 105, 593–602. https://doi.org/10.1002/qj.49710544507

Temps, R.C., Coulson, K.L., 1977. Solar radiation incident upon slopes of different orientations. Sol. Energy 19, 179–184. https://doi.org/10.1016/0038-092X(77)90056-1

Tian, Y.Q., Davies-Colley, R.J., Gong, P., Thorrold, B.W., 2001. Estimating solar radiation on slopes of arbitrary aspect. Agric. For. Meteorol. 109, 67–74. https://doi.org/10.1016/S0168-1923(01)00245-3

United Nations, 2018. The World's Cities in 2018—Data Booklet (ST/ESA/ SER.A/417).

Willmott, C.J., 1982. On the climatic optimization of the tilt and azimuth of flat-plate solar collectors. Sol. Energy 28, 205–216. https://doi.org/10.1016/0038-092X(82)90159-1

COMPARISON OF SOLAR PLANNING TOOLS

Matthias Haase[1]

[1] Institute of Facility Management / ZHAW, Waedenswil (Switzerland)

Abstract

The energy master planning process for districts requires an analysis of different scenarios, which often includes the determination of the solar potential of a district. In the past, several solar planning tools were developed. These are reviewed in the first part of this paper and classified in the main part of the paper according to a list of restriction and functionality classification. Three classifications of tools were found and specified in tables. The first level comprises of stand-alone tools (e.g. PVSys, Polysun) with certain functionality restrictions. The second level comprises tools based on GIS data (e.g. PVGIS, Solroof) with restrictions by introducing reduction factor. The third level is embedded solar potential analysis in Energy Master Planning (EMP) tools (e.g. City Energy Analyst (CEA), Sympheny). By integrating comprehensive spatial and temporal analyses, along with multiple renewable energy sources, urban areas can optimize their energy utilization, minimize energy waste, and advance towards a sustainable and low-carbon future.

Keywords: Solar radiation, planning tool, simulation

1. Introduction

Climate change challenges the ambitious goals that policy makers have put in place by setting more and more ambitious energy-related building and community requirements and standards based on the Sustainable Development Goals of the United Nations (UN) [1]. The concept of Energy Master Planning (EMP) – a roadmap of planning for energy efficiency and grid optimization - can help to initiate a better planning and implementation process to fulfil these goals. Reaching for the greenhouse gas reduction goals of the Paris Agreement, stakeholders on all geographical and organisational levels from nations, regions, cities and communities are challenged. Following bottom-up approaches for energy planning on the neighbourhood level is a promising attempt to reduce energy demand, increase efficiency and lower the carbon footprint in a multi-stakeholder approach (JPI UE, 2020). Reaching for the Global Sustainability Goals, cities and communities play a prominent role as they are geographically the main cause for emissions and on the other hand play a prominent role in putting global goals into local policies and means and at the same time embedding them in the local context with site specific demands and settings

With the 2015 Paris commitment in mind it is even more important to make sure that energy generation is renewable. Since solar energy systems can replace other building materials such as cladding or shading devices, they have additional advantages compared to other heat and power production solutions (Schiefelbein 2018). Solar power as a source of low carbon energy is an essential component for the sustainability of cities and its implementation and management, through urban planning practices, can play a strategic role in improving the energy efficiency of cities. Solar urban planning is a complex process which needs to consider the interplay between multiple factors and variables, depending on urban form and solar energy inputs. In order to enhance solar considerations within the planning process, there is a great need for knowledge from different disciplines to reach the planning practice and the public (Eicker 2012, Kaiser 1996).

1.1. Urban planning process

The urban planning process is a political and technical process that balances different needs of society within a physical and spatial environment (Haase and Lohse 2019; Haase 2020). Decisions need to be taken during the process in regard to spatial, social, environmental, economical, technical and political aspirations and goals. Strategies and tools are needed to support and facilitate these decisions and to enhance solar energy considerations

© 2022. The Authors. Published by International Solar Energy Society
Selection and/or peer review under responsibility of Scientific Committee
doi:10.18086/eurosun.2022.11.07 Available at http://proceedings.ises.org

within the existing urban planning processes (Sharp et al. 2020; Schiefelbein 2018). The concept of Energy Master Planning (EMP) in Urban planning can help to initiate a better planning and implementation process to fulfil these goals through providing a roadmap for energy planning. The application of principles of a holistic approach to neighbourhood and districts, often coined community energy planning in the literature and discussed in Haase and Baer (2020). The concept of Energy Master Planning (EMP) can help to initiate a better planning and implementation process to fulfil these goals through providing a roadmap for energy efficiency in the district as a basis for energy planning that points into the future. Haase and Lohse (2019) tried to define EMP and explained the different steps involved in the process; energy efficiency (1) and comprehensive energy planning (2) (Haase and Lohse 2019). In addition, to provide the necessary methods and instruments to stakeholders involved, it is essential to identify and frame the constraints that bound the options towards an optimized energy master planning solution (Sharp et al. 2020).

1.2. Constraints and goals in Energy Master Planning

Far less common in EMP guidance and related literature is information on the identification of constraints that limit energy technology options and how stakeholders influence the decision-making process. Although the work of Sharp et al. (2020) contributes by widening the definition of constraints into EMP, it is limited in its scope while focusing on single-ownership neighbourhoods like campuses or military garrisons (Sharp et al. 2020). Not much work is available on the role constraints, stakeholders, and boundary conditions in EMP for multi-owner, multi-stakeholder neighbourhoods many cities and regions are characterized of more complex ownerships and therefore a more complex stakeholder group with more complex framing goals that can lead to further constraints in EMP. An important part is the constraints analysis as part of the assessment when energy options are developed which can be divided into the following five categories:

- Natural Locational Constraints – Resources and threats
- Distribution System & Storage Constraints
- Building and Facility Constraints
- Indoor Environment Constraints
- Building Equipment and District System Constraints

1.3 Aim of the study

As argued above there is an intrinsic need to know the natural locational constraints of a site early in the Energy Master Planning process. Especially the resources need to be evaluated to form the basis for goal setting and further steps in the EMP. The aim of this study was to collect and assess different approaches to quantify solar energy potential from photovoltaic systems in the urban context. Within this framework, the amount of energy provided by the integration of photovoltaic systems into existing buildings and their energy consumption, are two key indicators to identify the neighborhoods of the city that behave as urban units with positive, negative or balanced energy performances.

2. Methodology

We collected methods and tools from various sources. An extensive literature review was conducted, followed by a review of past and present solar neighbourhood research activities:

- *ScienceDirect and Scopus database*
- *International research activities (IEA SHC Task 51, IEA SHC Task 63, IEA EBC Annex 73, IEA EBC* Annex 83, IEA EBC Annex 75, EU projects)
- *Software databases (e.g. https://www.buildingenergysoftwaretools.com/)*
- Other research projects (e.g. national initiatives, local planning tools)

Then we adopted factors which were divided between exclusion factors and reduction factors in order to consider spatial aspects for PV arrays installation, shading effects, roof typologies and other roof uses and PV module efficiency. Other factors are related to other urban parameters and the energy demand of the buildings within the district. Table 1 provides an overview of the factors that were included in the analysis.

Tab. 1: Factors included in the analysis

Exclusion factors	Reduction factors	Urban factors
surfaces	obstructions	Morphology
technologies	Surfaces	Energy demand
Performance factors	Physical parameters	Demand profiles
Period		

It can be seen that there were factors identified that exclude certain features of solar radiation potential calculations. These refer to surfaces, technologies, performance factors and simulation periods. The second set of factors were found that reduce the amount of solar radiation, such as obstructions, surfaces and other physical parameters. Then, there are urban factors like morphology, energy demand and demand profiles of districts. Based on these functionality factors, it was possible to classify the mapped tools into three levels (level1 – 3).

3. Results

An increasing number of cities and even regions are producing online solar maps which can give building owners an indication of the solar energy potential of their roofs, and some cities are additionally including solar potential of facades. These solar maps are both urban planning and assessment tools. When reviewing the assessment tools it became clear that the tools were developed and are explored in different ways. There are three main levels of functionality. Tools which produce solar radiation on surfaces and estimate electricity production by using exclusion factors were classified as Level 1. Figure 1 shows the calculation procedure. Tools which use a digital model and combine neighboring buildings and the terrain relief were classified as Level 2. Figure 2 shows the simulation procedure. Tools which are capable of coupling solar radiation analysis with the local specificity were classified as Level 3.

3.1. Level 1

Solar maps are used to identify suitable building surfaces for the installation of solar energy systems. These maps quantify the solar potential on building roofs or facades and predict the amount of solar energy that can be generated. While most solar maps focus on displaying the existing urban landscape, some cities are exploring the possibility of incorporating these features into urban planning maps. The production of solar maps involves the use of advanced technologies such as photogrammetry and drones.

To obtain solar radiation data, various National Solar Radiation Databases (e.g., NSRDB in the US) have been established. These databases contain solar radiation and meteorological data for national and regional areas, including neighboring countries. They provide publicly available datasets that have been collected and distributed over a certain period of time. The databases typically consist of surface observations, models, satellite data, as well as measurement and modeling technologies. For example, the current NSRDB includes solar irradiance data at a 4-km horizontal resolution for every 30-minute interval from 1998 to 2016. This data is computed using the National Renewable Energy Laboratory's (NREL's) Physical Solar Model (PSM), along with products from other research labs in the US (Sengupta 2018). It is important to validate the irradiance data with surface observations, which can be done by assessing mean percentage biases for global horizontal irradiance (GHI) and direct normal irradiance (DNI).

Efforts to develop solar maps can also be observed in other countries, as indicated in Table 2. However, existing solar maps have limitations, particularly in estimating solar potential for integrated solar facade systems, as the majority of maps are designed for small-scale roofing installations (Lobaccaro et al. 2012). Furthermore, some solar energy potential assessment categories are not clearly defined (Lobaccaro et al. 2019).

Tab. 2: Solar maps

name	features	country
Aurora	AI engine, sales support, contract manager	Global
BlueSol	• BlueSol is a software for the design of photovoltaic systems in every country in the world. • It allows to perform the entire process of designing a PV system, from the preliminary assessment of producibility to the realization of the project documentation. • made with a standard Microsoft interface, easy to use and manages every detail of the PV system.	Global
Helioscope	• web-based sales and design tool for solar professionals • robust 3D design engine and bankable energy yield simulator • detailed financial calculator and drag-and-drop proposal editor	Global
Global Solar Atlas	• Regional and local geographical characteristics may represent technical and environmental prerequisites, but also constraints for solar energy development. • Ground imagery from satellite and city maps helps identify potential areas of interest. Main roads, railways, and transmission line networks help define the accessibility and feasibility of sites for the location of power plants. • Different map layers can be selected: photovoltaic electricity output (PVOUT), global horizontal irradiation (GHI), direct normal irradiation (DNI), diffuse horizontal irradiation (DIF), global tilted irradiation for fixed systems at optimum angle (GTI), optimum angle of PV modules (OPTA), temperature (TEMP), elevation (TERRAIN), satellite view (SATELLITE) and information on roads and streets (NORMAL).	Global
NREL	The maps illustrate select multiyear annual and monthly average maps and geospatial data from the National Solar Radiation Database (NSRDB) Physical Solar Model (PSM). The PSM covers most of the Americas.	US
NY Solar map	The website provides a step-by-Step approach 1. Evaluate the building's solar potential (see solar map solar potential calculator) 2. Learn about solar technologies (see solar basics) 3. Learn about available PV incentives 4. Gather energy bills and roof schematic drawings (if available), and contact solar installers using the 'solar connect' feature on the map 5. Receive remote and on-site evaluations from contractors to get at least 3 quotes 6. Evaluate if your roof needs to be reinforced or replaced 7. Contact references from solar contractors 8. Evaluate costs and financing options to decide on direct ownership or third-party ownership 9. Sign contract with selected solar installer 10. The solar contractor files applications for incentives and permits; the installation moves forward	NY, US
PV Sol Free & Premium	• PV*SOL is a software used by planners, architects, installers and skilled technicians around the world to plan and design efficient PV systems. • PV*SOL offers the most detailed configuration and shade analysis for PV systems. It calculates solar output, panel sizing and economic forecasting for a PV system.	Global
PV F-chart	PV F-CHART is a comprehensive photovoltaic system analysis and design program. The program provides monthly-average performance estimates for each hour of the day. The calculations are based upon methods developed at the University of Wisconsin which use solar radiation utilizability to account for statistical variation of radiation and the load.	Global

Polysun	Polysun software from Vela Solaris allows a multi-practice simulation of various energy system with reliable results in terms of functionality, energy efficiency and profitability – from single-family homes to districts, worldwide and for all market-standard technologies.	Global
Pylon	Web-based PV design software	US
PVsyst	• PVsyst is designed to be used by architects, engineers, and researchers. It is also a very useful educative tool. • It includes a detailed contextual Help menu that explains the procedures and models that are used, and offers a user-friendly approach with a guide to develop a project. • PVsyst is able to import meteo data, as well as personal data from many different sources.	Global
PVGIS	Free and open access to: • Electricity generation potential for different PV technologies and configurations • Solar radiation and temperature, as monthly averages or daily profiles • Full time series of hourly values of both solar radiation and PV performance • TMY data for nine climatic variables, formatted for building energy calculation tools • Application Programming Interface for fast, automated access needs • Maps of solar resource and PV potential, by country or region, in ready to print files • PVMAPS, a software suite for users to make customised maps • PVGIS uses high-quality and high-spatial and temporal resolution data of solar radiation obtained from satellite images, as well as ambient temperature and wind speed from climate reanalysis models. The PVGIS energy yield model is validated from measurements performed on commercial modules at the JRC's European Solar Test Installation (ESTI). ESTI is an ISO 17025 accredited photovoltaic calibration laboratory for all photovoltaic materials.	Europe
Solar PV map	Understand the Australian solar PV market with live generation data, historical maps and animations, and tools to explore rooftop PV potential and per-postcode market penetration.	Australia
Solar Reference map	This interactive solar reference map is intended to provide quick and intuitive access to weather data needed to install code-compliant PV systems.	Florida, US
Solcast	• Solcast takes on the many challenges of producing live and forecast solar data, • making the data as easy to access, validate and integrate as possible, which is made possible through an API Toolkit. • It provides instant access to live and forecast data products via this web interface. • These include direct estimates of global, direct and diffuse solar radiation, as well as PV power output.	Global
Solar calculator	• The residential solar calculator is a tool intended to help determine the viability of adding solar photovoltaic (PV) panels as an alternative energy source to residential buildings (single-family homes) in Calgary. • Homeowners can use this tool as a starting point to help assess their home's solar potential, and to get an idea of the estimated costs and payment options. • The residential solar calculator is intended for informational purposes only.	Calgary, Canada
SolarEdge site designer	• SolarEdge Designer is a free web-based solar design tool that helps solar professionals lower PV design costs and generate winning customer proposals. • plan, build and validate with SolarEdge residential and commercial systems from inception to installation with this powerful selling tool	Global
Solarius	Solarius PV is a professional software for technical design and economic analysis for any type of photovoltaic system connected to national electricity grids (grid-connected).	Global

	Sizing, financial analysis and single-line diagrams in a single solution, which can be used in every situation and for all kinds of needs: • for PV systems installed on new or existing buildings or even for large systems (photovoltaic farms) • in every location (geolocation with reference climate data) • in any boundary condition (near and far obstacles) • all types of Panels and Inverters (extensive library with thousands of different models)	
Solargis	• Multiple independent studies have found Solargis to be the most reliable solar database • Spatial resolution of 250 m and sub-hourly temporal resolution better represent typical and extreme weather and improve accuracy • Solutions available for all solar energy assessment needs: from prospecting to effective operation • Solargis data and services are available for any location between latitudes 60N and 50S	Global
Suncalc	SunCalc shows the movement of the sun and sunlight-phase for a certain day at a certain place. The results can be printed or given by API.	Global
Sunroof	Solar savings are calculated using roof size and shape, shaded roof areas, local weather, local electricity prices, solar costs, and estimated incentives over time. Using a sample address, the detailed estimate Project Sunroof can give output for any address.	US

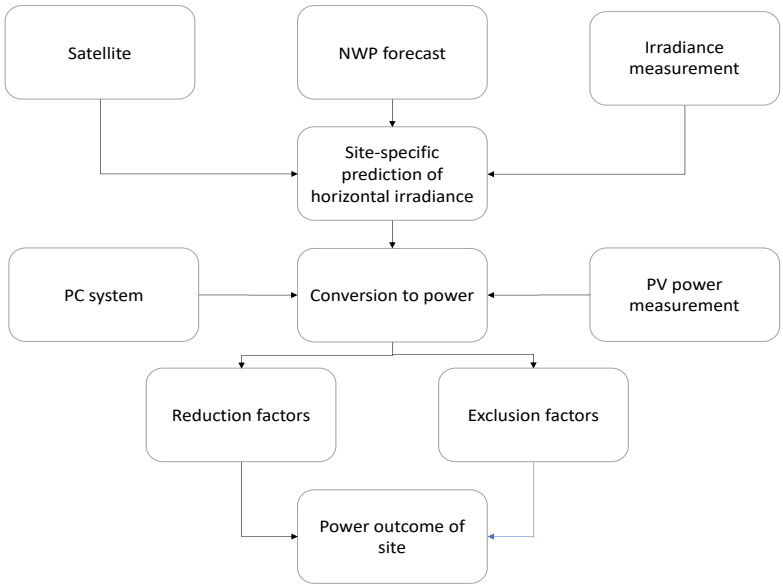

Fig. 1: Calculation illustration

3.2. Level 2

Alternatively, the solar potential of every roof and facade may be precisely calculated using a digital model which combines neighboring buildings and the terrain relief (Digital Surface Models or 3D City Models) with an adapted solar simulation software. The identified tools in this category are listed in Table 3. Such digital models are available in an increasing number of places. Solar simulation tools integrate radiation models considering urban shading effect and the possibility of reflections. Solar energy can be utilized in buildings to a much higher degree than is the case today, but the first obstacle is at the urban level. Local authorities currently lack the approaches, methods and tools to assess the potential for active solar energy. In order to perform an analysis of the solar potential of a study area, a 3D model built at a certain Level of Detail needs to be employed. According to (Biljecki, 2015), buildings are represented as footprint extrusions and with flat roofs at LOD 1 (at this level of

detail). The complexity of the built agglomerations (such as building volumes, urban or building typological factors, density, vegetation, etc.) affects the incidence of solar irradiation on the buildings' surfaces (e.g., partial shading or localized hot spots causing overheating), which may lead to power losses, non-optimal operating conditions caused by potential malfunctions, or safety and reliability reduction effects. Moreover, the determination of the solar potential of construction surfaces in a more realistic way becomes more prominent. In the analysis of constraints at the urban scale it becomes important to analyze typological factors. By introducing weighting indicators to translate the different constructive, geometric, and typological constraints that affect the solar system's integration, shading from surrounding buildings and solar inter-building reflections are becoming common solution to the deployment of solar systems on façades and roofs in such highly densified urban environments. Nonetheless, it is possible to use more detailed three-dimensional representations for analysis concerning a limited number of buildings since computation time exponentially increases with the number of modelled surfaces. Once the physical model is available, two main approaches for estimating solar irradiance values on building envelopes can be employed according to the literature review of Freitas et al. (2015): empirical based or computational based.

The empirical based models transpose the global and diffuse horizontal radiation values measured from weather stations located in open fields into the direct beam and diffuse components for any tilted surface by also considering the reflections due to the ground's albedo.

In general, there is a big consensus around the use of the Perez anisotropic sky model (Perez et al., 1987) that considers one direct beam component from the sun, three diffuse sky components e deriving from the circumsolar disc close to the sun's position, the horizon band close to the ground and the isotropic contribution from the remaining of the sky dome respectively e and the ground reflected component. However, these models fail when complex urban layouts need to be taken into account, especially when obstructions to sunlight can strongly affect solar harvesting like within dense urban environments. Consequently, the development of computational based models that mainly differ each other for the resolution (both spatial and temporal) of the analysis and the radiation components taken into account.

Tab. 3: Solar simulation

name	Description	System level
Design-Builder	DesignBuilder Software Ltd specialises in developing high-quality, easy-to-use simulation software that helps you to quickly assess the environmental performance of new and existing buildings. DesignBuilder's advanced building performance simulation tools minimise modelling time and maximise productivity. Models either imported from BIM, or built quickly within DesignBuilder, provide fully-integrated performance analysis including energy and comfort, HVAC, daylighting, cost, design optimisation, CFD, BREEAM/LEED credits, and reports complying with several national building regulations and certification standards. DesignBuilder software is distributed globally and via a network of international partners.	Building, components
District Energy Concept Adviser	This software was developed in collaboration with international partners from IEA ECBCS Annex 51 "Energy Efficient Communities" and comprises a set of individual supporting tools. The very heart of the software is a tool for the energy assessment of districts, which uses archetypes and other pre-set configurations to allow for a simple and quick data input mapping all the buildings in the district. Thus it takes the user just a few steps to identify the energy saving potential of various strategies in the areas of building construction, technical building systems, and centralized supply systems. Other included tools are a case study viewer with 19 exemplary energy efficient city quarters, information on energy efficient technologies and strategies and a benchmarking tool for measured energy use.	Building
Homer	HOMER software is built on the trusted, market-leading HOMER platform, used by more than 250,000 system designers and developers in over 190 countries. I	Building

	Whether designing hybrid microgrids or distributed generation systems, the software solution consider geographic-specific criteria and risks, such as fuel price changes, load growth, accelerated battery degradation and changing weather patterns.	
IDA ICE	IDA ICE is an innovative and trusted whole-year detailed and dynamic multi-zone simulation application for study of thermal indoor climate as well as the energy consumption of the entire building. The physical models of IDA ICE reflect the latest research and best models available, and the computed results compare well with measured data. While serving a global market, IDA ICE is adapted to local languages and requirements (climate data, standards, special systems, special reports, product and material data).	Building, components, systems
OnGrid Tool	OnGrid offers data, software, and education to solar companies — so those companies can offer effective financial presentations to their prospects. OnGrid started in 2005, in Northern California	system
Polysun	Polysun software from Vela Solaris allows a multi-practice simulation of various energy system with reliable results in terms of functionality, energy efficiency and profitability – from single-family homes to districts, worldwide and for all market-standard technologies.	Building, components, system
RETscreen	CanmetENERGY's engineering experts have developed innovative clean energy project analysis, modelling, and simulation software tools to help users: • assess various types of renewable energy and energy efficient technologies • reduce greenhouse gas emissions • optimize integrated energy efficient design in domestic and international markets • reduce operating costs & comply with code requirements • qualify for funding and incentive programs	District, systems
Sonnendach (CH), Solroof	The map shows the degree of suitability of roofs for the use of solar energy, together with the potential yield. For this purpose the course of the sun throughout the year is simulated and the level of solar radiation reaching the roof is calculated.	Building, system
Sympheny	Sympheny aims to empowers the planners and managers of buildings & local areas to drive the global energy transition. Their unique combination of digital twin technology and intelligent algorithms allows to provide for the new knowledge needs of energy planners, facility managers and site owners in the emerging energy landscape. Sympheny aims to support energy planners and energy managers in different countries and contexts around this world by providing software that is globally scalable and locally adaptable.	Building, components, systems
System Advisor Model (SAM)	The System Advisor Model (SAM) is a free techno-economic software model that can model many types of renewable energy systems. SAM simulates the performance of photovoltaic, concentrating solar power, solar water heating, wind, geothermal, and biomass power systems, and includes a basic generic model for comparisons with conventional or other types of systems. The financial models are for projects that either buy and sell electricity at retail rates (residential and commercial) or sell electricity at a price determined in a power purchase agreement (PPA). SAM's simulation tools facilitate parametric and sensitivity analyses, Monte Carlo simulation and weather variability studies. It includes a built-in scripting language called LK that automates simulations for batch processing and allows for more complex analyses and reading and writing data from files. Several macros written in LK come with SAM to help with tasks such as checking weather files, sizing photovoltaic systems, and other tasks.	Building, components, systems
TRNSYS - Solar	• TRNSYS is made up of two parts. The first is an engine (called the kernel) that reads and processes the input file, iteratively solves the system, determines convergence and plots system variables. The kernel	Building, components, systems

Thermal Energy	also provides utilities that, among other things, determine thermophysical properties, invert matrices, perform linear regressions and interpolate external data files. • The second part of TRNSYS is an extensive library of components, each of which models the performance of one part of the system. The standard library includes approximately 150 models ranging from pumps to multi-zone buildings, wind turbines to electrolyzers, weather data processors to economics routines, and basic HVAC equipment to cutting edge emerging technologies. Models are constructed in such a way that users can modify existing components or write their own, extending the capabilities of the environment.	
UrbaSun	• Meteodyn have been studying micro-meteorology since 2003. • They develop wind flow and solar radiation simulation software that is suitable for all types of terrain. • Their software and services allow the renewable energy, construction and transportation industries to accurately calculate and model wind or solar radiation.	Building

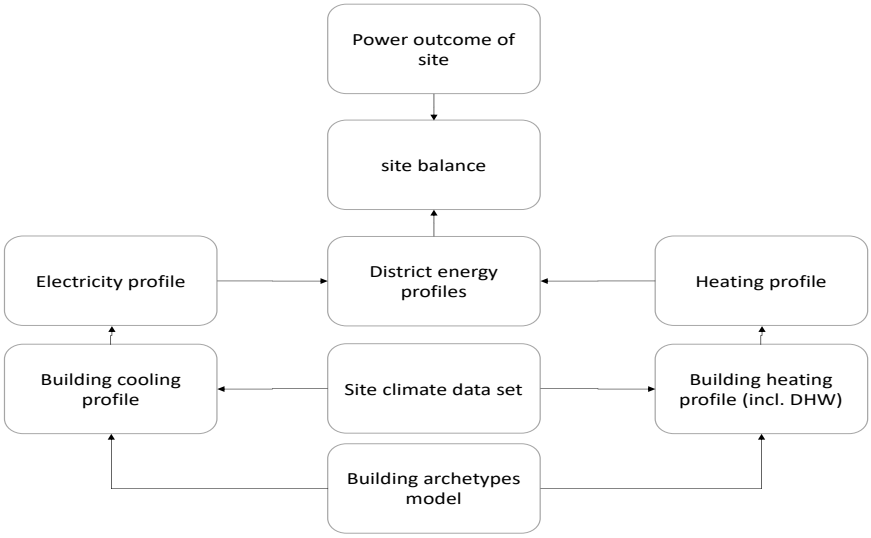

Fig. 2: Simulation illustration

3.3 Level 3

On the strategic planning level, buildings and neighborhoods can be recognized in districts. Regarding sensitivity, particularly sensitive (or non-sensitive) districts can be identified in an area that otherwise is assessed as a uniform medium-sensitive territory. In GIS zones with different heritage categories in accordance with the method of context sensitivity presented in the previous chapter can be marked in maps. As such protected zones in land use plans can be marked as highly sensitive areas, commercial and industrial zones as low sensitive areas. These considerations need to be coupled with a deep understanding of the local specificity and a constructive discussion with the local site protection authorities (Amado and Poggi 2014). Table 4 lists the tools that were identified in this category.

Tab. 4: Solar urban design tools

name	url	Urban planning level
City Energy Analyst (CEA)	https://cityenergyanalyst.com/	advanced

DIVA-For-Rhino	http://www.solemma.com	advanced
RETscreen	http://www.retscreen.net	high
Sonnendach (CH), Solroof	https://www.uvek-gis.admin.ch/BFE/sonnendach/index.html	medium
Sympheny	https://www.sympheny.com/#1	advanced

3.4 Features of Solar PV planning tools

All solar PV design software need some kind of features to match technical accuracy and urban planning criteria (e.g. gross roof area of building (m²) Calculating the shadow free area on the site, available for solar PV installation, Estimation of the annual yield for PV systems on available roof area (kWh), etc.). These are elaborated and provide useful information for further EMP.

All solar PV design software need some kind of input data, which include:

- Gross roof area of building (m²)
- Available flat roof area for PV installation considering exclusion factors (m²)
- Estimating the solar energy available at a given location – for example, rooftop of a building
- Calculating the shadow free area on the site, available for solar PV installation
- Sum of all global solar irradiation values over a year (kWh/m²)
- Mean annual global radiation on available roof area (kWh)
- Designing a solar PV installation to produce the required solar power
- Calculating the projected solar energy production
- Creating the engineering drawings and reports for the planned installation
- Available pitched roof area for PV installation considering exclusion and reduction factors (m²)
- Estimation of the annual yield for PV systems on available roof area (kWh)

The characteristics and parameters of the urban system which are required to estimate photovoltaic solar electricity have been gathered by mean of quantitative spatial analysis. According to related approaches to available roof surface area for photovoltaic energy potential evaluations, some specific criteria have to be assumed for taking into account those factors that can reduce the gross roof surface.

Table 5 shows the analysis results of the functionality levels of different solar planning tools.

Tab. 5: Analysis results of functionality levels of different solar planning tools

Planning tool	**url**	**Functionality**		
		Level 1	Level 2	Level 3
Aurora	http://www.aurorasolar.com/	X		
BlueSol	http://www.bluesolpv.com/	X		
City Energy Analyst (CEA)	https://cityenergyanalyst.com/			X
DesignBuilder	https://designbuilder.co.uk/	X	X	
District Energy Concept Adviser	https://www.district-eca.com/		X	
DIVA-For-Rhino	http://www.solemma.com			X

Helioscope	https://www.helioscope.com/	X		
Homer	https://www.homerenergy.com/		X	
IDA ICE	https://www.equa.se/de/ida-ice		X	
OnGrid Tool	http://www.ongrid.net/		X	
PV Sol Free & Premium	https://pvsol.software/en/	X		
PV F-chart	http://fchartsoftware.com/pvfchart/	X		
Polysun	https://www.velasolaris.com/	X	X	
Pylon	https://getpylon.com	X		
PVGIS tool	https://re.jrc.ec.europa.eu/pvg_tools/en/	X		
PVsyst	https://www.pvsyst.com/	X		
RETscreen	http://www.retscreen.net		X	X
SolarEdge site designer	https://www.solaredge.com/us/products/installer-tools/designer#/	X		
Solarius	https://www.accasoftware.com/en/solar-design-software	X		
Sonnendach (CH), Solroof	https://www.uvek-gis.admin.ch/BFE/sonnendach/index.html		X	X
Sympheny	https://www.sympheny.com/#1		X	X
System Advisor Model (SAM)	https://sam.nrel.gov/download		X	
TRANSYS - Solar Thermal Energy	http://www.aiguasol.coop		X	
UrbaSun	http://meteodyn.com/en/		X	

4. Conclusions

Typical-alone tools were classified as Level 1 (e.g. PVSys, Polysun). The Level 2 tools are based on GIS data (e.g. PVGIS, Solroof) and provide urban planning relevant features. Level 3 tools embedded solar potential analysis in Energy Master Planning (EMP) tools (e.g. City Energy Analyst (CEA), Sympheny).

Solar potential calculations for different buildings are incorporated into a Geographic Information System (GIS) platform, which provides a comprehensive map for clear identification of urban areas, their energy consumption, and their potential for energy production. This step allows for achieving an energy balance in urban areas and enables the identification of areas with higher energy needs. Urban parameters can then be developed to transform and adapt the energy demand and production patterns accordingly. Conversely, by analyzing areas with energy surplus, it is possible to assess buildings and make necessary adjustments or improvements to urban parameters.

However, energy balances are not the sole focus of interest. In the future, there will be a greater emphasis on spatial and temporal distributions. It will be important to consider not only diurnal variations but also seasonal differences. Solar planning tools should incorporate these developments into their analysis. Additionally, other renewable energy sources at the district scale, such as wind energy, biomass-based solutions, and geothermal energy, need to be integrated into these types of analyses. The full potential of renewable energy can only be harnessed when buildings are considered not only in terms of their surfaces (roofs and facades) but also in terms of their overall structure and fabric. Heating, cooling, and electricity demands are significant components of the equation for achieving a decarbonized future energy system.

By integrating comprehensive spatial and temporal analyses, along with multiple renewable energy sources, urban areas can optimize their energy utilization, minimize energy waste, and advance towards a sustainable and low-carbon future.

The next step will be to choose a typical district and to perform for each solar potential tool class an analysis. The

results can then be compared and used for benchmarking purposes.

5. Acknowledgments

This work has been completed within the project DECARB financed by ZHAW which is highly acknowledged.

6. References

Amado, M. and Poggi, F. Solar Urban Planning: A Parametric Approach, Energy Procedia, Volume 48, 2014, Pages 1539-1548, ISSN 1876-6102, https://doi.org/10.1016/j.egypro.2014.02.174. (https://www.sciencedirect.com/science/article/pii/S1876610214004366)

F. Biljecki, J. Stoter, H. Ledoux, S. Zlatanova, A. Çöltekin, Applications of 3D city models: State of the art review, ISPRS International Journal of Geo-Information, 4 (4) (2015), pp. 2842-2889, 10.3390/ijgi4042842

Eicker, U., Renewable Energy Sources Within Urban Areas – Results From European Case Studies, in Chicago Winter Conference 2012, Chicago, 2012.

Haase, M. and Lohse, R., Process of Energy Master Planning of Resilient Communities for comfort and energy solutions in districts, IOP Conference Series: Earth and Environmental Science, Volume 352, Number 1, IOP Publishing Ltd, https://iopscience.iop.org/article/10.1088/1755-1315/352/1/012019, access date: 09.02.2020

Haase, M. and Baer, D. (2020), Constraints, stakeholders and framing goals in energy master planning between neighbourhood and district, in Bisello, A., Vettorato, Ludlow, D., Baranzelli, C (Eds.) "Smart and Sustainable Planning for Cities and Regions - Results of SSPCR 2019 – Open Access Contributions", p. 3 – 13, SPRINGER, https://doi.org/10.1007/978-3-030-57764-3_1

IEA, (2012), "Technology Roadmap Solar Heating and Cooling", OECD/IEA, (accessed 2017-09-10 at https://www.iea.org/publications/freepublications/publication/technology-roadmapsolar-heating-and-cooling.html)

IEA, (2014), "Technology Roadmap Solar Photovoltaic Energy", OECD/IEA, (accessed 2017-09-10 at http://www.iea.org/publications/freepublications/publication/technology-roadmap-solar-photovoltaicenergy---2014-edition.html)

JPI Urban Europe / SET Plan Action 3.2 (2020). White Paper on PED Reference Framework for Positive Energy Districts and Neighbourhoods. https://jpi-urbaneurope.eu/ped/

Kaiser, N., Solar energy in architecture and urban planning, Prestel, 1996

Lobaccaro, G.; Frontini, F.; Masera, G.; Poli, T. SolarPW: A new solar design tool to exploit solar potential in existing urban areas. Energy Procedia 2012, 30, 1173–1183.

Lobaccaro, G.; Lisowska, M.M.,; Saretta, E.; Bonomo, P; Frontini, F. A Methodological Analysis Approach to Assess Solar Energy Potential at the Neighborhood Scale. Energies 2019, 12, 3554; doi:10.3390/en12183554.

Perez, R., Seals, R., Ineichen, P., Stewart, R., Menicucci, D., 1987. A new simplified version of the perez diffuse irradiance model for tilted surfaces. Sol. Energy 39, 221e231. https://doi.org/10.1016/S0038-092X(87)80031-2.

Schiefelbein et al. 2017. Implementation of energy strategies in communities – Results within the context of IEA annex 63, 30th International Conference on Efficiency, Cost, Optimization, Simulation and Environmental Impact of Energy Systems, ECOS 2017-San Diego, CA, US.

Sengupta, M., Y. Xie, A. Lopez, A. Habte, G. Maclaurin, and J. Shelby. 2018. "The National Solar Radiation Data Base (NSRDB)." *Renewable and Sustainable Energy Reviews* 89 (June): 51-60.

Sharp, T., Haase, M., Zhivov, A., Rismanchi, B., Lohse, R., Rose, J. Nord, N. (2020), Energy Master Planning: Identifying Framing Constraints That Scope Your Technology Options, ASHRAE Transactions. Atlanta: American Society of Heating, Refrigerating and Air-Conditioning Engineers, Inc

Case Study of a Positive Energy Community for Renewable Energy Sharing

Min-Hwi Kim[1], Haneol Kim[1], Dongwon Lee[1], Deukwon Kim[1], Jongkyu Kim[1] , and Youngsun An[1*]

[1] Renewable Heat Integration Laboratory/Korea Institute of Energy Research, Daejeon (South Korea)

Abstract

In this paper, we developed a positive energy community for renewable energy sharing community and investigated the positive energy performance of the proposed community compared with conventional community. The selected case study positive energy community has 56 houses and 2 non-residential buildings. This positive energy community is composed of building integrated photovoltaics (BIPV), Battery Energy Storage System (BESS), Thermal Energy Storage System (TESS). The community energy management system (CEMS) was operated to monitoring the community energy performance and energy trading of inner and outer community. This paper presents the positive energy performance and economic benefit of the proposed community. It was found that the proposed community has 229% of renewable energy penetration rate and about 30% of self-consumption rates can be improved compared with the conventional community.

Keywords: energy sharing community, electric and thermal energy sharing, self-consumption, BIPV

1. Introduction

Energy sharing community refers to the sharing of the surplus energy produced from distributed energy production systems with surrounding buildings in the community. Such energy sharing prevents the surplus energy from being supplied to the grid, thereby reducing the instability of the grid caused by renewable energy. In addition, the economic efficiency of distributed energy production systems can be secured through such energy sharing and trading even though there has been no economic benefit of surplus electricity for small-scale power generation.

2. Low-Carbon Energy Sharing Community

A low-carbon energy sharing community attempts to operate electricity and thermal energy supply chains at the same time. When prosumer buildings that produce surplus energy desire to sell surplus electricity, surrounding buildings that consume a large amount of energy purchase such surplus energy. In this instance, prosumers can sell either the surplus electricity produced from PV systems or the cold and hot energy produced using such surplus electricity. For such energy sharing/transactions, the real-time sales of energy to be produced are also possible, but energy is stored in energy storage facilities, such as energy storage systems (ESS) and thermal energy storage (TES), for sales at an appropriate time point

Figure 2 shows the conceptual diagram of the convergence energy system to obtain the optimal energy sharing effect by implementing an energy sharing platform. This convergence energy system consists of the power grid and cooling and heating networks. The electricity produced from the renewable energy systems installed in each building covers the electricity demand of each building, and the surplus electricity is supplied to the grid in the village. The surplus electricity is then shared with other surrounding buildings or stored in ESS for supply from ESS when the electricity produced from renewable energy is insufficient or the electricity cost of the grid is expensive. In addition, when ESS is fully charged with the surplus electricity, the heat pump is operated to store cold energy in summer and hot energy in winter in the heat storage tank for supply to each building.

The self-consumption rate of the convergence energy system for the community was analyzed using the load cover factor (LCF) and supply cover factor (SCF). LCF represents the proportion of the amount received from the grid (P_{imp}) to cover the power load (P_{load}), battery (P_{BESS}), and heat pump load for heat storage in the heat storage tank (P_{HP}). As it approaches 100%, it means that the proportion received from the grid is low (eq. 1). SCF represents the proportion of the amount transmitted to the grid (P_{exp}) after covering the power load (P_{load}), battery (P_{BESS}), and heat

© 2022. The Authors. Published by International Solar Energy Society
Selection and/or peer review under responsibility of Scientific Committee
doi:10.18086/eurosun.2022.11.08 Available at http://proceedings.ises.org

pump load for heat storage in the heat storage tank (P_{HP}) with the power generated from PV systems (P_{gen}). As it approaches 100%, it means that the proportion transmitted to the grid is low (eq. 2). In this instance, the power load includes all plug loads, such as lighting, in buildings. As these proportions approach 100%, the self-consumption rate becomes higher. In this study, the self-consumption rate (SLCF) was represented as the average of LCF and SCF (eq. 3).

The SCF is self-consumption, and that is defined as the fraction of the sharing the PV and BIPV generation power supplied to the load. High self-consumption and self-sufficiency means that the entire electricity load is mostly covered by the BIPV and PV. In this study, the self-consumption rate (SLCF) was represented as the average of LCF and SCF. In order to investigate the energy performance of the proposed system, the building load and BIPV was simulated by TRNSYS 18 software. This software provide hourly based dynamic simulation results.

$$LCF = 1 - \frac{\int_{t_1}^{t_2} P_{imp}(t)dt}{\int_{t_1}^{t_2}[P_{load}(t)+P_{BESS}(t)+P_{HP}(t)]dt} \quad \text{(eq. 1)}$$

$$SCF = 1 - \frac{\int_{t_1}^{t_2} P_{exp}(t)dt}{\int_{t_1}^{t_2} P_{gen}(t)dt} \quad \text{(eq. 2)}$$

$$SLCF = \frac{SCF+LCF}{2} \quad \text{(eq. 3)}$$

For the analysis of economic efficiency according to the energy cost, the following assumptions were made: Building residents purchased electricity at 100 won/kWh from the nano-grid operator and sold electricity at 50 won/kWh. In the economic efficiency analysis, the electricity cost was analyzed for energy sharing and trading with-out considering the initial cost for PV systems, ESS, and TES. In this paper, the initial cost of the systems has not been considered due to the fast change of subsidies for each systems.

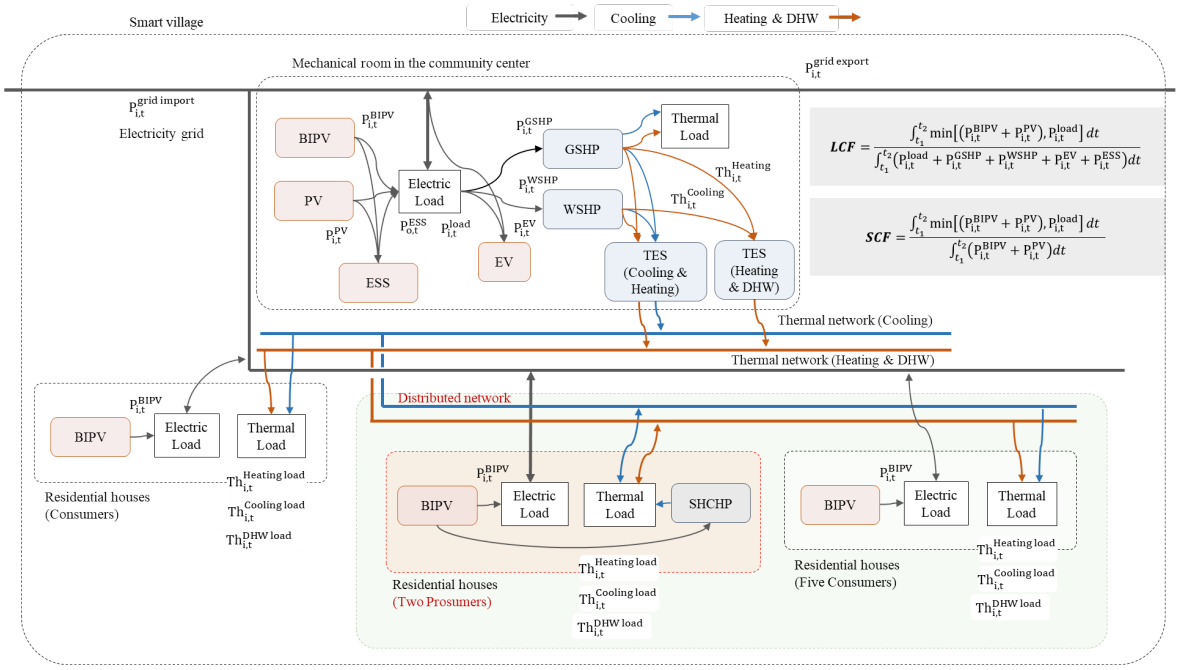

Fig. 1: Overview of conversion energy system

3. Case study: Smart Village

The smart village is located in the waterfront area of Busan Eco Delta City. It consists of 56 single-family houses and community facilities (Fig.2). It was designed with a site area of 7,202 m^2, a building area of 2,200 m^2, and a total floor area of 3,620 m^2. The single-family houses have two stories above the ground, and the community facilities have one underground story and two stories above the ground. The houses are lightweight steel structures based on the reinforced concrete structures, and the community facilities are reinforced concrete structures. The community facilities have a building area of 266 m^2 and a total floor area of 1,192 m^2. The single-family houses have a building area of 1,636 m^2 and a total floor area of 2,374 m^2 based on 19 houses. In the community buildings, locations where various renewable energy systems can be applied are roofs and walls. The building integrated photovoltaic system (BIPV) was installed on southern walls, and the installation area was 194 m^2. The building attached photovoltaic

system (BAPV) was installed on roofs, and the installation area was 108 m^2.

First, the thermal load for each house was calculated to estimate building cooling and heating loads for the 19 houses. To this end, the number of household members was randomly assumed for each house, and the schedule for the thermal load was randomly calculated. As for the reference load, the thermal load profile was applied based on the measurement data and the random range was set to 80% based on this profile to derive the load profile. The reference thermal load was based on the use of the electricity of 3,500 kWh per year, and the 19 houses were set to have a load range from 2,574 to 5,064 kWh. The average load of the 19 houses was set to 3,582 kWh.

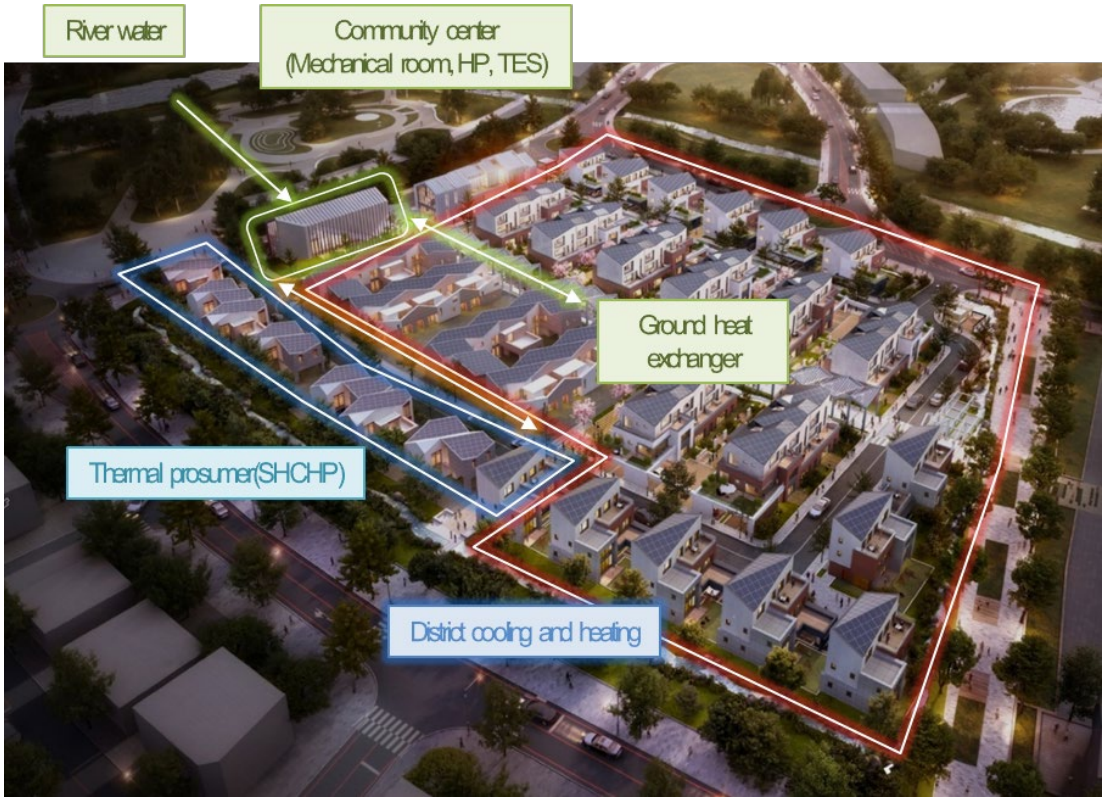

Fig. 2: Overview of smart village

4. Results

In Table 1 below, simple simulation analysis on the energy sharing improvement effect was conducted using the convergence energy system. SLCF and energy cost for the cooling period (June to August), intermediate period (March to May and September to October), and heating period (November to February) were compared between the energy transaction methods of P2G and P2P. They were also compared among the thermal energy system configurations of air-source heat pump (ASHP), central supply-type ground source heat pump (GSHP), and TES. In addition, energy performance according to the battery size was analyzed for each method.

The total capacity of the installed PV systems is 189.67 kW, and thus the total solar power generation is 220.2 MWh (Fig. 3). The total plug power consumption of buildings is 68.1 MWh. When ASHP is used, it consumes the power of 57.4 MWh. Thus, the total power consumption is 125.5 MWh, and the renewable energy penetration rate is predicted to be 180%. When GSHP is used, however, it consumes the power of 30.8 MWh and the renewable energy penetration is predicted to be 229%(Fig.4).

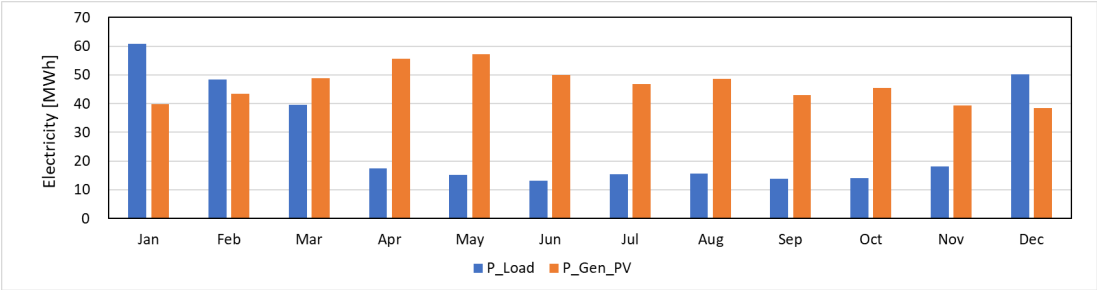

Fig. 3: Monthly power generation of BIPV and electric load

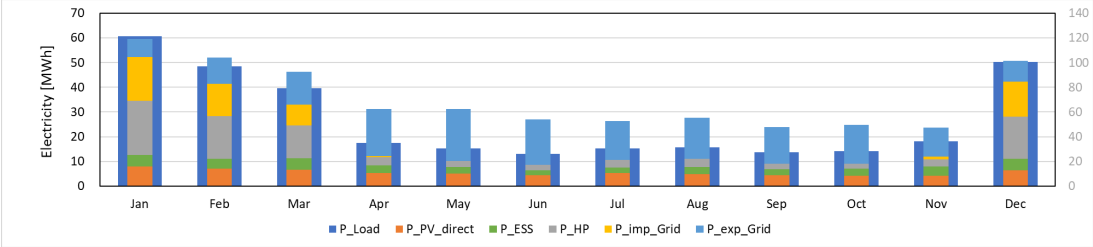

Fig. 4: Monthly power generation to ESS and heat storage

As shown in Table 1, the analysis results on seasonal and annual SLCF revealed that annual SLCF was 45.4% when energy sharing was not utilized due to P2G. When ASHP was used and energy sharing was applied, however, SLCF was 58.8% or higher. In addition, as the battery capacity increased, SLCF also increased from 58.8 to 77.5%. When central supply-type GSHP and TES were used, SLCF was more than 10% higher at the same battery capacity (100 kWh).

In terms of energy cost (Table 2), additional profits for surplus electricity could not be obtained for conventional P2G transactions. When cost benefits for surplus electricity are generated by supplying the energy produced through energy sharing to surrounding buildings and when surplus electricity is utilized using the central supply-type heat pump rather than using individual heat pumps, it was predicted that at least 2.5 million won can be obtained as a profit from the entire community. In addition, when both the battery and central supply-type heat pumps are applied, it was found that 6.5 million won per year and 340 thousand won per house can be obtained as profits for energy cost compared to the method of utilizing P2G.

Table. 1: Impact of system configurations for SLCF

Value	PV capacity [kW]	BESS [kWh]	Sum	Inter	Win	Annual
SLCF [%]	P2G, ASHP	0	48.2	45.0	43.8	45.4
	P2P, ASHP	100	63.30	59.6	54.5	58.8
		200	74.5	74.2	65.5	71.4
		300	79.5	78.4	75.0	77.5
	P2P, GSHP-TES	100	77.9	72.9	67.2	72.2
		200	79.5	77.5	83.6	80.0
		300	79.7	78.0	85.7	81.0

Table. 2: Impact of system configurations for cost

Value	PV capacity [kW]	BESS [kWh]	Sum	Inter	Win	Annual
Benefit cost [Mil.won]	P2G, ASHP	0	0	0	0	0
	P2P, ASHP	100	1.4	2.1	-0.9	2.7
		200	1.6	2.5	-0.5	3.5
		300	1.7	2.6	-0.3	4.0
	P2P, GSHP-TES	100	2.0	3.2	0.8	5.9
		200	2.0	3.2	1.0	6.3
		300	2.0	3.3	1.1	6.5

5. Conclusions

The cost benefits mentioned in this study are the simplest examples of various business models. Nano-grid operators will be able to contribute to the cost benefits of residents in the energy sharing community and create a new industry

referred to as nano-grid operators by producing various energy costs. In addition, they can minimize the instability caused by introducing renewable energy systems at very high levels, such as for net-zero, through energy sharing. Basically, energy sharing and trading can maximize the utilization of energy sharing through harmony between prosumers and consumers. To practically achieve net-zero, however, it is necessary to maximize prosumers to enable net-zero in a community. In addition, it will be possible to improve cost benefits and the self-consumption rate by supplying renewable energy to buildings where it is difficult to achieve net-zero with prosumers.

6. Acknowledgments

This work was supported by the Korea Agency for Infrastructure Technology Advancement (KAIA) granted financial resource from the Ministry of Land, Infrastructure and Transport (project number: 22PIYR-C153277-04) and framework of the research and development program of the Korea Institute of Energy Research (C2-2474).

7. References

Long, C., Wu, J., Zhou, Y., and Jenkins, N., 2018. Peer-to-peer energy sharing through a two-stage aggregated battery control in a community Microgrid. Applied energy. 226, 261-276.

Peck M.E. and Wagman D., 2017. Energy trading for fun and profit buy your neighbor's rooftop solar power or sell your own-it'll all be on a blockchain. IEEE Spectr. 54, 10, 56-61.

Wang C., Yan J., Marnay C., Djilali N., Dahlquist E., and Wu J., 2018. Distributed energy and Microgrids (DEM). Appl Energy. 210, 685–9.

Modelling and Simulation of Booster Heat Pump for DHW Preparation in a Multi-Family Building Connected to the District Heating

Mara Magni[1], Fabian Ochs[1], Georgios Dermentzis[1] and Elisa Venturi[1]

[1] University of Innsbruck, Innsbruck (Austria)

Abstract

Booster Heat Pumps (HPs) are integrated into the District Heating (DH) networks aiming at increasing the PV-self consumption. In this work, a dynamic model of a booster HP for the preparation of the Domestic Hot Water (DHW) in a typical Austrian multi-family house is developed. A series of dynamic simulations considering different controls, DHW profiles, storage quality, demand for the appliances and common areas, PV and battery sizes are performed to analyse the influence of this technology on the PV self-consumption, electricity demand and thermal energy demand from the DH network. The results show that when appliances are included in the balance, the PV yield available for the booster HP is limited. A non-optimal control logic of the booster HP could lead to an increase in electricity demand from the grid. The application of battery to increase the PV self consumption for the common areas is not beneficial as the available PV peak power per flat is limited and it would be anyway self used for appliances and HP. Batteries contribute to a slight reduction in electricity demand from the grid when the PV yield cannot be used to cover the appliances. Moreover, the operation of the booster HP influences the energy demand from the DH and makes the CO_2 emission of the building dependent on the energy mix of both DH and electricity grid.

Keywords: Booster heat pump, District heating, PV self-consumption, Domestic hot water preparation, Appliances, Battery.

1. Introduction

The buildings sector is responsible for around 37% of global CO_2 emissions (United Nations Environment Programme, 2021) and in order to achieve the 2050 neutrality targets, it will be necessary to drastically reduce current emissions and offset the rising trend in CO_2 emissions due to population growth. According to global reports (United Nations Environment Programme, 2021), it is expected that by 2050 over 85% of the buildings will be zero-carbon-ready leading to a reduction of 75% of the heating intensity of which around 50% will be covered by Heat Pumps (HP) and 10% by DH. From this framework, it is clear that in the future the HP technology will be strongly integrated with the urban DH networks (Biermayr *et al.*, 2019). In addition, HP can support the transition toward low-temperature DH since they influence the energy demand and temperature required by the buildings (Østergaard *et al.*, 2022). HP technology can be integrated in many different ways into the DH network: providing heat to the DH network, centrally for a building or a building block for heating and/or DHW preparation, or decentrally flat wise for heating and or DHW preparation. Hence, it is clear that the possibilities for integrating the HP into the DH are manifold and that this integration has consequences for the operation of the DH (see (Ochs, Magni and Dermentzis, 2022) for a comprehensive overview). Integrating HP into the DH, makes the DH dependent on the electricity network, might reduce the DH operation time (e.g. if all the buildings use a HP for the DHW preparation, the DH is not needed in summer), influences the capability of self-consume the PV yield (Ochs, Magni and Dermentzis, 2022).

Booster HPs are able to decouple the supply temperature required by the building from the DH temperature (Østergaard and Andersen, 2016) allowing to operate the DH network with a lower temperature reducing distribution losses. In addition, HPs could contribute to increase the PV self-consumption potentially offering an economic advantage from the user's point of view. This work focuses on the analysis of the flat-wise integration of a booster HP for DHW preparation, considering a newly built multifamily house building located in Innsbruck. The source of the HP is a central storage supplied by the DH network. The goal of this analysis is to assess the contribution of the booster HP to the increase of PV self-consumption by means of dynamic simulation performed with Matlab/Simulink using the CARNOT Toolbox (*CARNOT Toolbox - File Exchange - MATLAB Central*, 2020). To make this analysis more robust the simulation is performed considering different scenarios for PV and battery size, control of the booster HP, DHW tapping profile, appliances profiles, different thermal qualities of the decentral storage.

© 2022. The Authors. Published by International Solar Energy Society
Selection and/or peer review under responsibility of Scientific Committee
doi:10.18086/eurosun.2022.11.09 Available at http://proceedings.ises.org

2. Method

2.1. Building

A newly built multifamily house located in Innsbruck is used as a basis for this work. This building (see Fig. 1) is built with a Passive House standard and it is composed by 7 floors and 35 flats. The footprint area of the building is 412 m^2 and the total heated area is 2209 m^2.

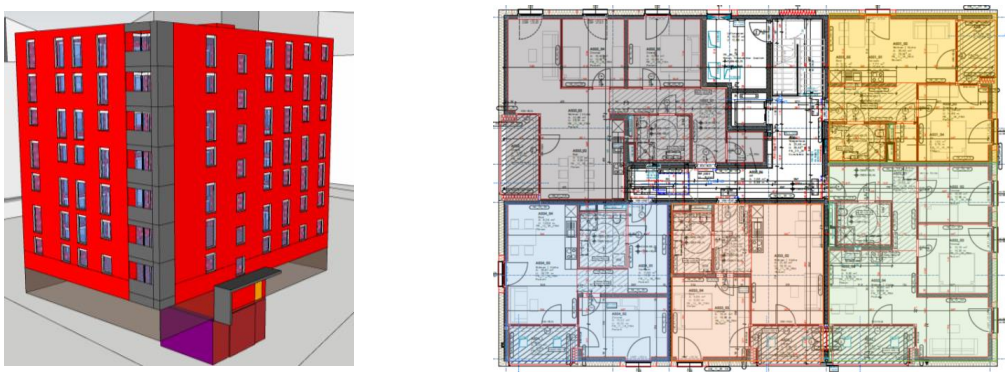

(a) (b)

Fig. 1: (a) view and (b) floor plan of the reference building (Neue Heimat Tirol - NHT)

The building is equipped with a 1000 l central storage heated by the DH network, which supplies in each flat in parallel the floor heating loop and the booster HP for the DHW preparation. The booster HP is used to charge the decentral storage of 150 l for the DHW preparation (see also Fig. 3). The PV yield is used first for the building electricity demand and the excess is delivered to the electricity grid. A battery system is used with the aim of maximizing the self-consumption of the PV for the electricity demand of the common areas.

A scheme of the developed model implemented in Matlab/Simulink is reported in Fig. 2 and each part is explained in the following sections.

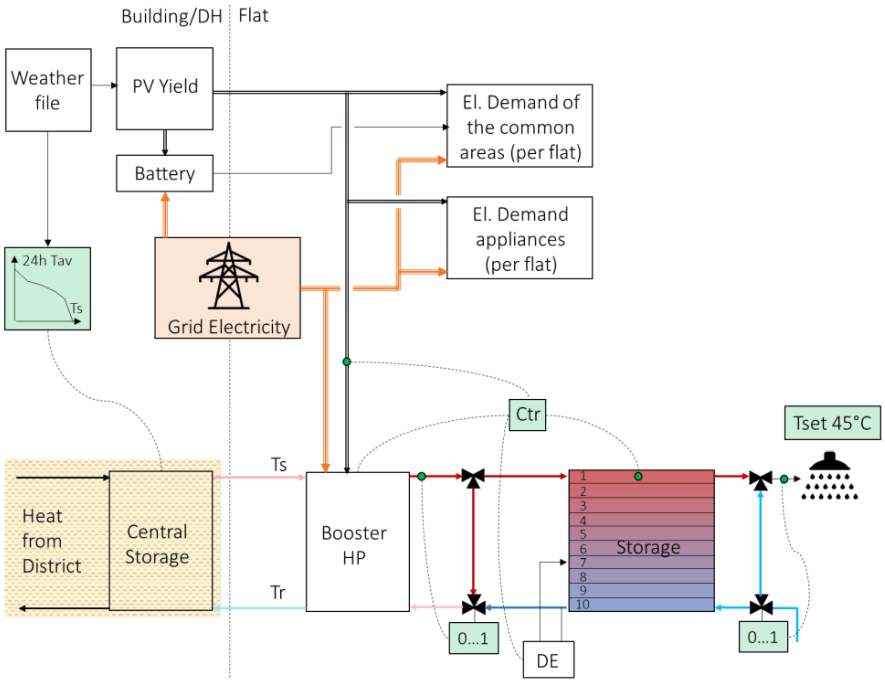

Fig. 2: Simplified scheme of the developed model of the flatwise booster HP for DHW preparation with PV and battery. The central storage (i.e. dashed area) is not modelled

2.2. Weather description

The weather file used for performing the dynamic simulations is based on the OIB 2019 (Österreichisches Institut für Bautechnik, 2019) climate for Innsbruck.

Fig. 3 shows the monthly ambient temperature (black line) and the monthly solar irradiation on a horizontal surface (red bars).

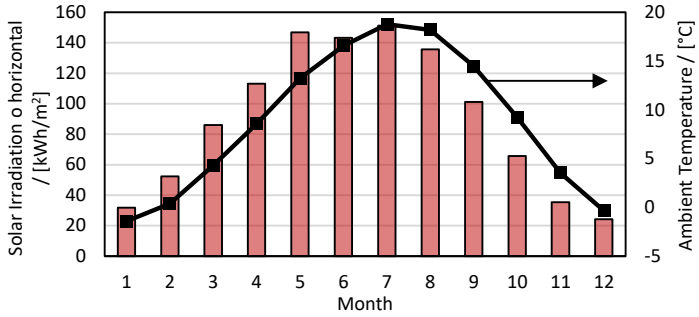

Fig. 3: Solar irradiation on a horizontal surface (left side) and monthly average ambient temperature (right side) for the climate of Innsbruck according to OIB 2019 (Österreichisches Institut für Bautechnik, 2019)

2.3. Photovoltaic Panels and Batteries

PV panels are simulated with a south orientation and 10° of inclination and they have an efficiency of 20 %. The climate of Innsbruck (OIB climate 2019 (Österreichisches Institut für Bautechnik, 2019)) is used in the calculations and simulations. An inverter efficiency of 97% is considered. Different sizes of PV are considered ranging from a peak power per flat of 0.5 kWp to 5 kWp (see Tab. 1).

A roof coverage of 60% is normally reachable while reaching a share between 60 % and 80 % is challenging and requires accurate planning. Therefore, the scenarios from PV1 to PV3 are plausible while scenarios PV4 and PV5 are only reachable for low-rise buildings, or they require to partly cover the façade of the building with PV.

Tab. 1: Analysed PV scenarios

Case	PV peak per flat [kWp/flat]	PV peak total [kWp]	Roof coverage [%]
PV1	0.5	17.5	22%
PV2	0.86	29.9	37%
PV3	2	70.0	85%
PV4	3.5	122.5	-
PV5	5	175.0	-

PV self-consumption is evaluated using the Load and Supply Cover Factors (i.e. LCF and SCF respectively) according to equations 1 and 2:

$$LCF = PVSelf / Wel,tot \quad \text{(eq. 1)}$$

$$SCF = PVSelf / PVtot \quad \text{(eq. 2)}$$

Where PVSelf is the self-consumption of the PV yield, PVtot is the total PV yield and Wel,tot is the electricity demand of the building. LCF and SCF are also calculated for the individual applications of PV energy (i.e. common area, battery, appliances, HP). In this case, PVSelf is the PV energy consumed directly for the application under study.

In addition to different PV sizes also different battery sizes, storing energy for the common areas, are analysed (see Fig. 2). The simulated scenarios regarding the batteries are reported in Tab. 2. A charging and discharging efficiency of 0.9 and a standby consumption of 10 W are considered in the simulation model.

Tab. 2: Analysed scenarios for the battery size.

Case	Battery size
BATT1	No battery
BATT2	15 kWh
BATT3	30 kWh

2.4. Booster Heat Pump

The maps of performance of the booster HP (see Fig. 4), used in the dynamic simulation model analysed (see Fig. 2), are calculated by means of a simulation of the refrigerant cycle (Monteleone *et al.*, 2022). Considering a source temperature of 35 °C and a sink temperature of 55 °C, the booster HP works with a COP of 3.06 and a compressor power of 654 Wel.

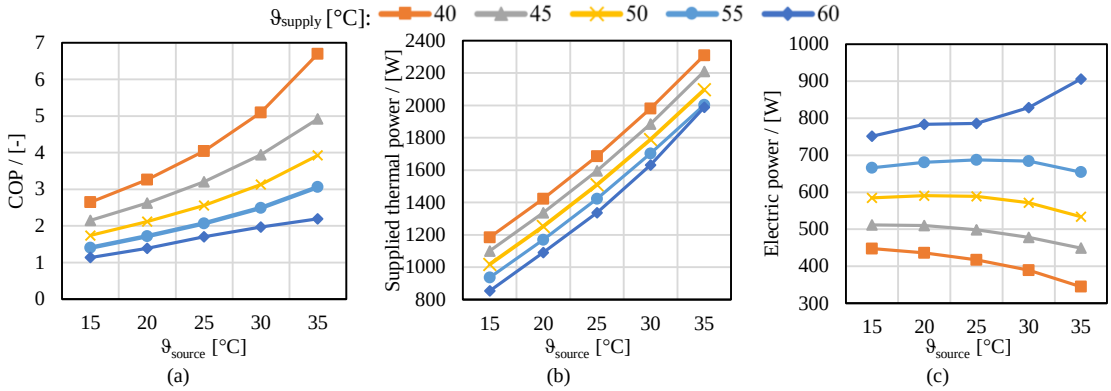

Fig. 4. Performance Maps of the booster HP: (a) COP, (b) Thermal power and (c) Electric power

The booster HP located in each flat uses as a source the energy from the DH delivered to the flats through a central storage (see Fig. 2) controlled with a set point temperature, which is a function of the ambient temperature (see Fig. 5). During the summer period (i.e. July and August) it is assumed that the HP extract heat from the floor heating loop contemporarily providing cooling energy to the building and not requiring any energy from the DH network.

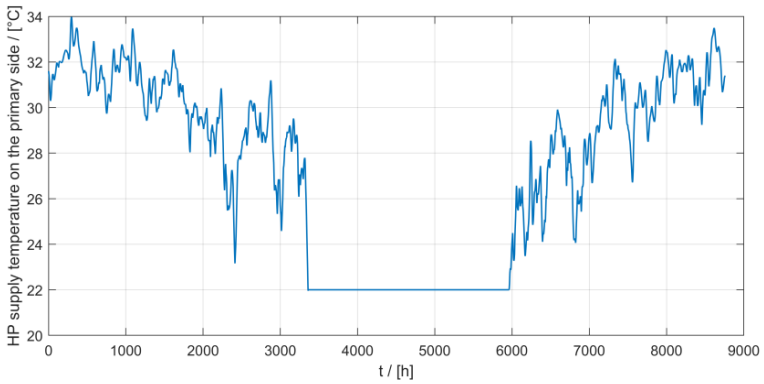

Fig. 5. Supply temperature to the booster HP throughout the year

The decentral storage, heated up by the booster HP, is a 150 l storage and it is analysed considering two different energy classes (i.e. A and B). A three-way valve between the booster and the decentral storage prevents ruining the temperature stratification of the storage (see Fig. 1). While the three-way valve after the decentral storage controls the supply temperature to the user (see Fig. 1). In addition, a minimum run time of 15 min and a minimum off time of 5 min are considered in the simulation model of the HP.

2.5. Heat Pump Control Strategies

Based on the available PV yield for the booster HP, different control logics are implemented to analyse their impact on the PV-self consumption (see Tab. 3). The standard control logic (CTR1) foresees to warm up the decentral storage to 53°C from 2 to 8 a.m. and from 3 to 9 p.m. to guarantee the comfort during the morning and evening shower, while the strategies CTR2 and CTR3 increase the set point to 60°C when power from the PV modules is available. A direct electric heater (DE) is activated in parallel to the booster only when the storage temperature drops below 47.5 °C.

Tab. 3 Control logics of the set point of the decentral storage depending on the PV yield

CTR1	CTR2	CTR3
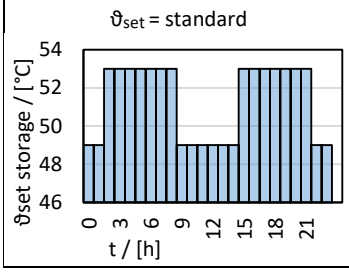	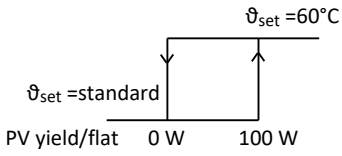	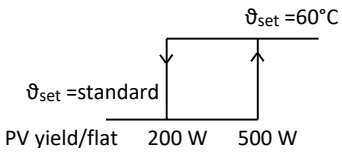

2.6. Domestic Hot Water Tapping profiles

Three different tapping profiles with the same total daily energy of 5.9 kWh/day are analysed (i.e. DHW1 considering one shower in the morning and one in the evening, DHW2 with two showers in the morning and DHW3 with two showers in the evening), see Fig. 6. The tapping mass flow is controlled with an energy-based control.

The monthly energy balances for the different cases are calculated by averaging (with equal weight) the simulation results obtained with the three different profiles as the real DHW tapping profile is not known and it affects the energy balance of the system.

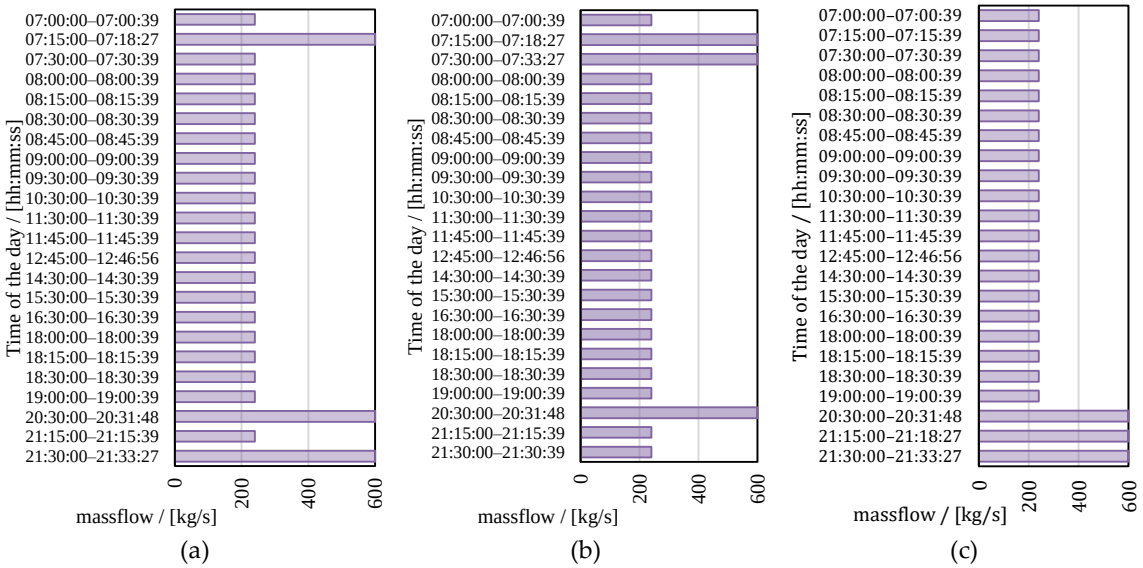

Fig. 6: Domestic hot water tapping profiles characterized by an energy of 5.9 kWh/day, but with different distribution of the showers throughout the day (a: one shower in the morning and one in the evening, b: two showers in the morning and c: two showers in the evening)

2.7. Appliances

Five different scenarios are considered regarding the electricity demand of appliances and common areas (see Tab. 4). The APP4 and APP5 scenarios consider the same electricity demand as the APP3 and APP2 scenarios, but the PV yield cannot be used directly for the household appliances.

Tab. 4: Annual electricity consumption per flat considered for the appliances and common areas for the three different variants (i.e.APP1, APP2, APP3, APP4 and APP5)

	Appliances	Possibility to use the PV yield for appliances	Common areas	Total
	[kWh/(a flat)]	Yes/No	[kWh/(a flat)]	[kWh/(a flat)]
APP1	0	Yes	0	0
APP2	1600	Yes	252	1852
APP3	2500	Yes	252	1752

APP4	2500	No	252	1752
APP5	1600	No	252	1852

A dynamic profile is used for the appliances (1600 or 2500 kWh/(a flat)), see Fig. 7, while a constant profile for the electricity demand of the common areas (252 kWh/(a flat)) is used.

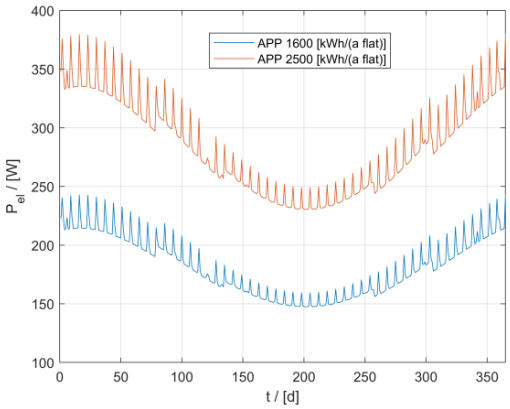

Fig. 7: Daily average appliances profiles

3. Results and Discussion

The storage quality does not significantly affect the energy balance of the flat. A class A storage compared to a class B reduces the electricity demand from the grid of maximum 3%. For this reason and for sake of simplicity only the results obtained with a class A storage are reported.

The different DHW tapping profiles (see Fig. 6) influence the temperature of the storage throughout the day and therefore the control of the HP. In Fig. 8a and Fig. 9a the temperature of the top part of the storage, as well as the set point temperature, is reported while in Fig. 8b and Fig. 9b the electric power of the HP and the PV yield are shown for different DHW tapping profiles (i.e. DHW1, DHW2 and DHW3), considering the appliances profile APP2 (see Fig. 7), the PV size PV2 (see Tab. 1) and the storage quality A. In Fig. 8 the results for the control strategy CTR1 (see Tab. 3) are reported while in Fig. 9 the results for the control strategy CTR2 are reported.

From Fig. 8 and Fig. 9 it can be noticed that the tapping profiles DHW1 (i.e. one shower in the morning and one in the evening) and DHW3 (two showers in the evening) have a similar profile of the storage temperature, the only difference is that the storage temperature is slightly lower in the evening with DHW3 and during the day with DHW1. The storage temperature during the daytime is consistently lower for the DHW2 (two showers in the morning). This allows to harvest a higher share of renewable energy during the day. With DHW1 and DHW3 the storage is quite empty in the evening leading to a night-time charge (to guarantee the comfort for the morning shower) that cannot take advantage of the PV yield. From Fig. 8b and Fig. 9b it can be seen that the charging periods are shifted during the daytime with DHW2 compared to DHW1 and DHW3. The effect of the control strategy CTR2 can be seen in Fig. 9b, in fact at around midday, when the PV yield is at its maximum, the set point of the storage is increased to 60 °C in order to enhance the PV self-consumption attempting to shift the load from the night-time to the day-time. Nevertheless, when the appliances are considered (i.e. APP2 and APP3), only a small share of PV yield is left for the HP (i.e., considering the case PV2 only 12 % with APP3 and 26 % with APP2 is available for the HP).

As explained in Section 0, the HP has a minimum run and off time. The effect of the minimum run time is visible in Fig. 8a and Fig. 9a. In fact, at around 5 a.m. when there is no DHW demand and the storage temperature falls slightly below the set point, the HP switch on and even though the set point is quickly reached, it stays on until the minimum rum time has elapsed (i.e. 15 min). The minimum run time together with the non-modulating behaviour of the HP considered in this case study, makes it difficult to match the electricity demand with the PV yield optimizing the self-consumption.

(a)

(b)

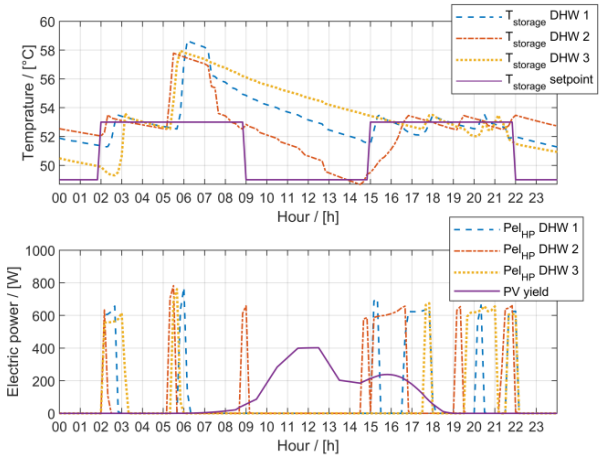

Fig. 8: (a) Storage temperature and set point and (b) electricity demand of the HP and PV yield (April 16th) for the different DHW tapping profiles considering APP2, PV2, BATT1, CTR1 and storage quality A

(a)

(b)

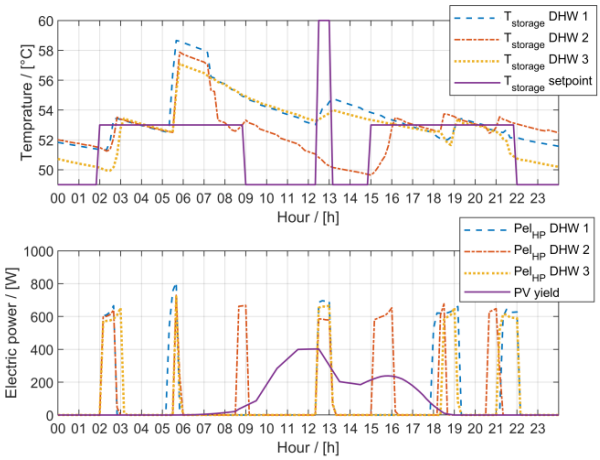

Fig. 9: (a) Storage temperature and set point and (b) electricity demand of the HP and PV yield (April 16th) for the different DHW tapping profiles considering APP2, PV2, BATT1, CTR2 and storage quality A

Fig. 10 shows the sorted plot of the (a) temperature of the top part of the storage and (b) the COP of the HP for the different control strategies and DHW tapping profiles considering APP2, PV2, BATT1 and storage quality A. From here it is visible that the control strategy CTR2 leads to a higher storage temperature, as the increase of set point to 60°C is activated more often compared to CTR3. The increased storage temperature leads to a lower COP of the HP and higher losses. In addition, when the HP is on, its power is not fully covered by the PV yield as it is not modulating, and a high share of PV is already used to cover the electricity demand in the common areas and appliances. Therefore, the control strategy that aims only at the maximization of the PV self-consumption is not always the optimal one. Disregarding the electricity demand of appliances and common areas and controlling the HP according to the total available PV yield could lead to an increase in electricity demand from the grid of up to 14% (considering the control strategy CTR2).

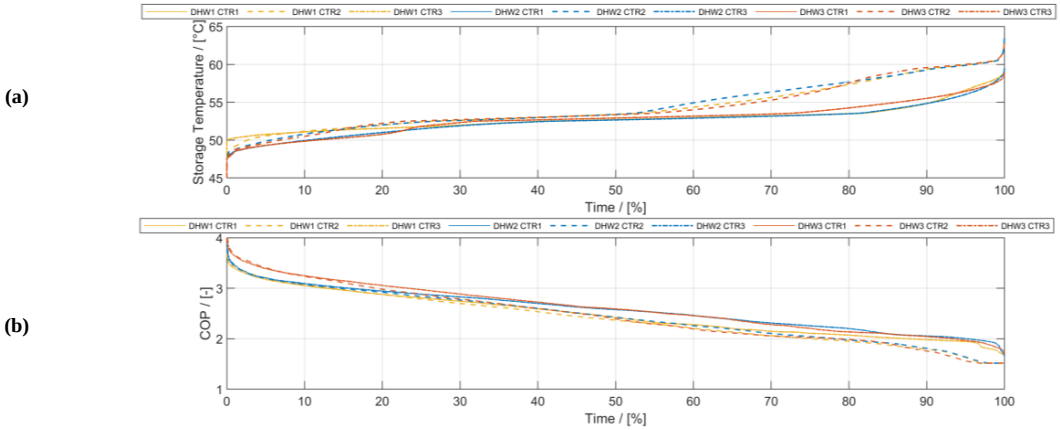

Fig. 10: (a) Sorted storage temperature, (b) sorted COP of the HP for different DHW tapping profiles (i.e. DHW1, DHW2, DHW3) and different control strategies (i.e. CTR1, CTR2, CTR3) considering APP2, PV2, BATT1 and storage quality A

Fig. 11 shows the monthly electricity balance of one flat for the case considering CTR2, DHW2, APP2, PV2, BATT1 and storage quality A. The internal green staked columns represent the electricity demand of the common area (per flat), appliances and HP, while the external staked columns represent the self-consumption of the PV yield for common areas, appliances and HP and on top (in dark brown) the electricity demand covered by the grid. The dark dashed line represents the PV yield, and the patterned part of the columns represents the PV yield fed into the grid. From Fig. 11, it is clear that the PV size of the case PV2 (see Tab. 1) barely cover the electricity demand of appliances and common areas. A small overproduction of PV is fed to the grid only during the summer months.

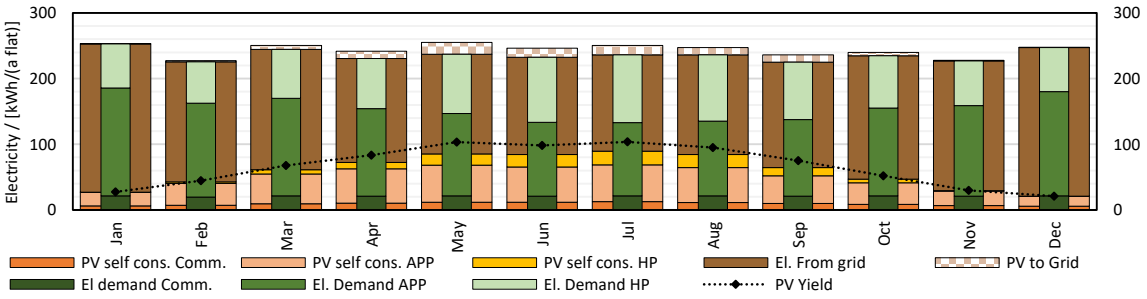

Fig. 11. Monthly electricity balance for the case considering CTR2, DHW2, APP2, PV2, BATT1 and storage quality A

In Fig. 12 the annual electricity balance of all the cases without batteries and averaging of the results for the three different DHW profiles are reported. When the appliances are included in the balance, the electricity demand of the HP is only around 25% of the total electricity demand considering APP3 and 35% considering APP2. Even in the most optimistic scenario, concerning the PV peak power (i.e. PV5), in none of the cases, a null electricity demand from the grid is achieved.

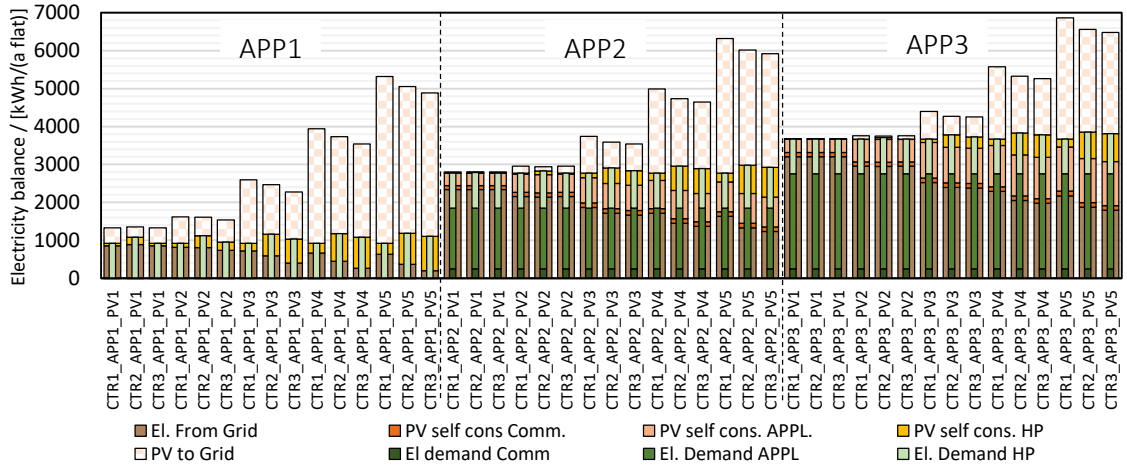

Fig. 12: Electricity balance for all the cases considering no batteries and averaged results over the three DHW profiles

Fig. 13 shows on the left y-axis the electricity demand of the HP flowing from the grid and from the PV and on the right side the share of the HP electricity demand covered by PV is reported. From here it can be noticed that the total electricity demand is always maximum applying CTR2 and that at the same time CTR2 allows to maximize the PV self-consumption for the cases PV1, PV2 and for the cases with appliances (APP2, and APP3) also for PV3. The increased set point (60°C) leads to higher storage losses and poorer COP of the HP. The Seasonal performance factor of the HP is around 2.5 when the control logic CTR1 is applied and can decrease down to 2.0 when CTR2 is used. The storage losses can increase up to 17% considering CTR2 with respect to CTR1. Thus, with the CTR2 the reduction in terms of efficiency outperforms the increased self-consumption leading to an increased electricity demand from the grid for the case APP1_PV1. In most cases, the control strategy CTR3 allows the highest reduction in terms of electricity from the grid as it activates the increased set point only when the PV yield available for the HP is higher than 500W covering most of the HP demand.

After subtracting the PV self-consumption for appliances, the PV yield available for the HP is limited especially for the cases PV1 and PV2 (a maximum of 3% of the HP electricity demand can be covered by the PV self-consumption considering APP2). When higher PV peak power per flat is available (i.e. from PV3 to PV5) it is possible to cover from 14% to 27% considering APP2 and from 8% to 19% considering APP3 of the HP electricity demand, nevertheless, these configurations are not realistic for multi-family houses.

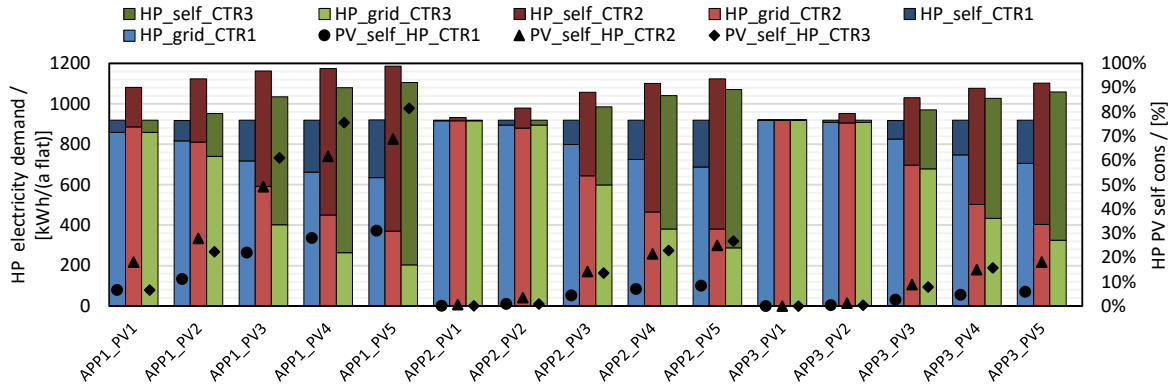

Fig. 13: Impact of the control strategy on the HP electricity demand (i.e. PV self-consumption and electricity from the grid) for all the cases considering averaged results for the three different DHW profiles

The influence of the batteries on the electricity balance is reported in Fig. 14 for the cases considering different PV and battery sizes, applying the control strategy CTR3, the appliances APP2 and APP5 and considering averaged results for the three different DHW profiles. The APP5 case considers the same electricity demand for household appliances as the APP2 case, but in APP5 the PV yield cannot be used to meet the demand of the household appliances. From Fig. 14 it can be noticed that, for the cases considering APP2, the contribution of the batteries to increase the PV self-consumption leads to a reduction of the PV self-consumption that, in the case without batteries (i.e. BATT1), would have been used for the appliances. This leads to an increase in electricity demand from the grid of 1%, 2% for the cases with small PV size (i.e. PV1 and PV2) and a maximum reduction of electricity from the grid of -6% for the case PV5. In addition, it can be seen that in the cases with APP5, the self-consumption of PV for the HP, the PV yield fed into the grid and the electricity demand from the grid are higher than in the cases with APP2, since the PV yield is not used for the appliances. Considering the APP5 cases, the batteries always lead to a reduction of energy from the grid of at least -3 % (case BATT2, PV1) to a maximum of -8 % (case BATT3, PV5).

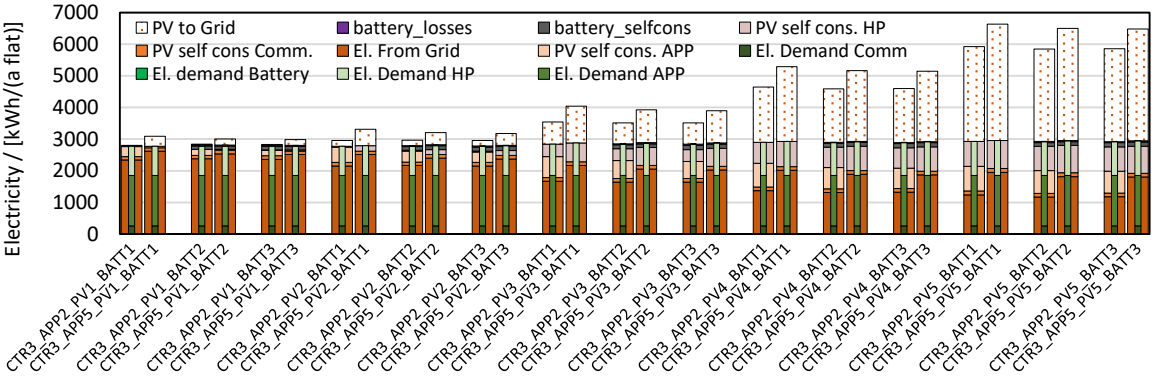

Fig. 14: Influence of the battery system on the electricity balance

Fig. 15 shows the SCF and LCF for cases with different battery and PV sizes, considering CTR3, APP2 and APP5 and averaged results for the different domestic hot water profiles. From Fig. 15 it can be seen that:

- SCF of up to 95% can be achieved for small PV systems (PV1 and PV2 cases), but for these cases only 20% to 30% of the electricity demand (i.e. LCF) can be covered by PV;
- Increasing the PVs from case PV4 to PV5 does not lead to important benefits in terms of LCF. This means that most of the additional energy generated by PVs is fed into the grid;
- Appliances make an important contribution to increasing SCF and LCF;
- If the PV output is not used for the Appliances (i.e. APP5), the batteries contribute to increase the LCF, while when the PV yield can be directly used in the flats to cover the electricity demand for appliances (i.e. APP2) the batteries lead to reduction of the LCF because they reduce the PV yield available for appliances introducing losses;
- The battery size BATT3 compared to BATT2 does not lead to a high increase in LCF for this case study.

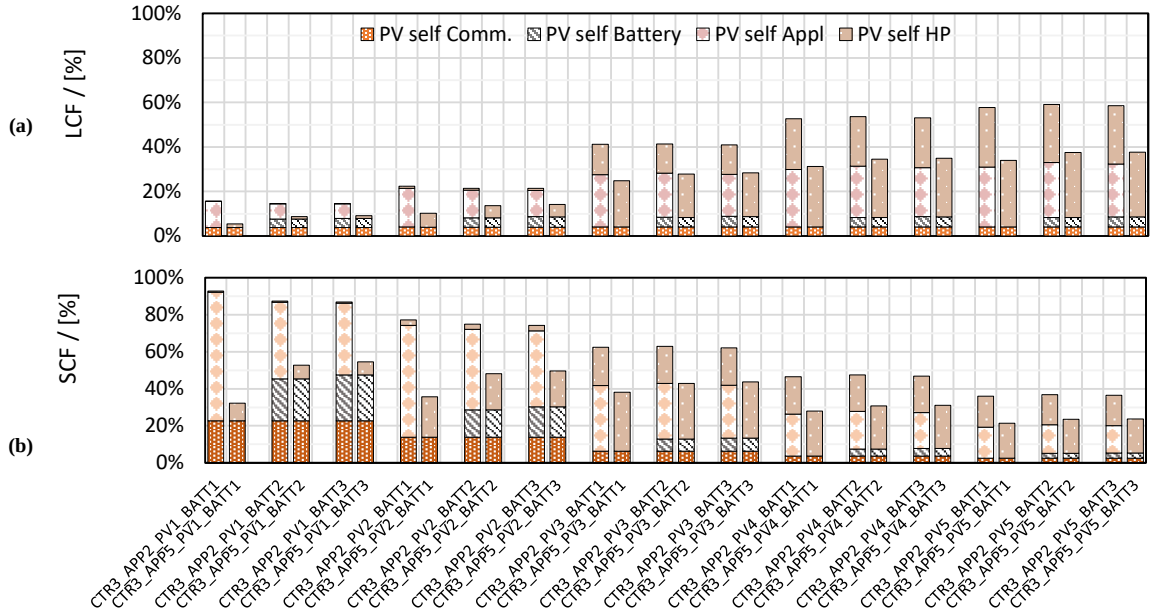

Fig. 15: Influence of the battery system on (a) SCF and (b) LCF for the cases considering CTR3 and the average results for the three different domestic hot water profiles

Fig. 16a shows the average daily state of charge (SOC) of the batteries and the electricity demand required from the grid to meet the electricity demand of the common areas when the batteries are empty, considering PV size PV2 the battery sizes BATT2 and BATT3. From Fig. 16a it can be seen that the daily mean SOC is higher on average for the case with BATT3 relative to BATT2, but in winter when solar availability is low, the grid electricity demand is similar in both cases.

Fig. 16b shows the dynamic behaviour of the batteries during the 9th day of the year for the case CTR3_DHW2_APPL2_PV2_BATT2. When the SOC is 0 (empty batteries), the power demand of the common areas and the self-discharge power of the batteries (10 W) must be covered with energy from the grid. During the day, the battery is charged with the PV electricity that is not directly used to meet the needs of the common areas. Some energy is lost during both charging and discharging (90% charging and discharging efficiency), which is shown in the graph with the green asterisks ("Losses"). When the batteries are full (SOC=1) or when the available power of the PV system is higher than the maximum charging power, the excess energy is bypassed by the battery (this is represented in the diagram by a red dashed line - "over Battery").

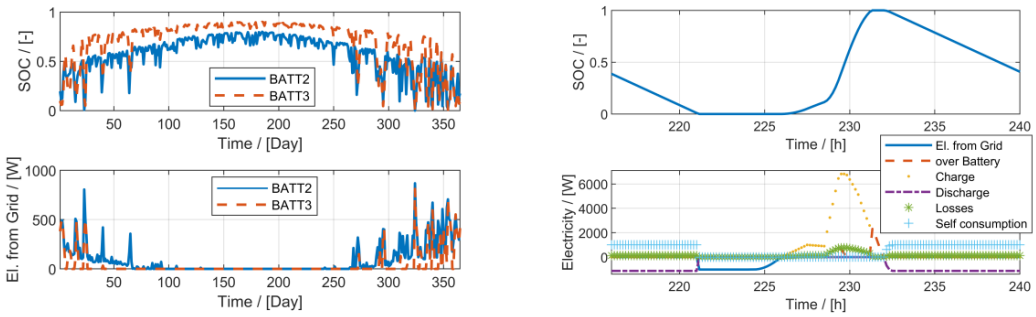

(a) (b)

Fig. 16: (a) Average daily state of charge (SOC) of the batteries and electricity demand from the grid required to meet the electricity demand of the common areas when the batteries are empty for the two cases: CTR3_DHW2_APPL2_PV2_BATT2 and CTR3 _DHW2_APPL2_PV2_BATT3; (b) dynamic behaviour of the batteries during the 9th day of the year for the case CTR3 _DHW2_APPL2_PV2_BATT2

In all the considered cases a DHW useful annual energy demand of 2133 kWh per flat is considered. Without the installation of the booster HPs in each flat, this amount of energy should be supplied by the DH network. With the booster HP a Seasonal Performance Factor of around 2.4 is achieved. This means that around 57% of the energy is still supplied by the DH network. Considering that during July and August the booster HP could be used for cooling purposes extracting energy from the floor heating loop, the energy extracted from the DH network would be around 44% of the DHW energy demand while the electricity demand is 43% of the total thermal energy demand. In all the simulated cases the energy extracted from the DH network depends on the seasonal performance factor of the HP and varies between 904 kWh/flat to 1073 kWh/flat.

The district heating network becomes, therefore, dependent on the electricity grid with regards to the price per kWh and CO_2 emission (i.e. fossil/renewables share in the district and electricity). A broad overview of the integration of HP in the district heating network is provided in (Ochs, Magni and Dermentzis, 2022).

4. Conclusions

The main motivations for the integration of booster HPs into the DH network are to increase the PV self-consumption and to decouple the supply temperature of the DH from the required temperature of the connected buildings. Within this work, the performances of a booster HP installed in a flat of a multi-family house served by the DH and equipped with PV are analysed by means of dynamic simulations. The results show that when a booster HP is solely controlled to increase the PV self-consumption, the electricity demand from the grid could actually be increased. In fact, when the solar energy is available the set point of the DHW storage is increased and the HP is switched on. In this situation the performance of the HP is reduced as the supply temperature increases, the storage losses increase, and the power of the HP is not entirely covered by the PV yield (in part because the PV yield is already used to cover the demand of the appliances and in part because the HP is not modulating). Particularly in the case of multi-family houses, the PV yield per flat is limited (as the available roof area per flat is reduced for high-rise buildings) and it could be so low that it would be almost completely used to cover the load from appliances. For this case study, the PV self-consumption is enhanced by the HP, only for a PV size bigger than 2 kWp/flat. Nevertheless, it is hardly possible to achieve this PV peak power per flat in multi-family buildings as it would require covering the building facades in addition to the roof of the building.

The domestic hot water tapping profile influences the capability of harvesting energy from the PV. A DHW tapping profile that leaves the storage empty in the morning enables to shift the load from night-time to the daytime allowing to use a higher PV share. If the tappings are concentrated during the evening, the storage will be charged overnight. For this reason, to make the analysis more robust, three different DHW tapping profiles are considered in this work.

The possibility of applying batteries to increase the self-consumption of the PV for the electricity demand of the common rooms has been also analysed. Nevertheless, for this case study, the application of batteries for a PV size below 2 kWp/flat would lead to a slight increase (i.e. around 2%) of electricity demand from the grid as the PV yield would be anyway self-consumed by the electricity demand of the appliances and the batteries only introduce additional losses. For a PV size higher than 2 kWp/flat, the batteries could lead to a maximum benefit of -6% of electricity from the grid. If the PV yield in the flats cannot be used to cover the household appliance demand, the batteries can help to reduce the electricity demand from the grid by 3% to 8% depending on the PV size. Nevertheless, the high additional cost has to be considered.

In future work, this analysis should be repeated for a modulating booster HP that would be able to cope with the PV yield increasing the self-consumption without requiring additional electricity from the grid. In addition, different profiles for the electricity demand of the common areas should be analysed.

5. Acknowledgments

The work presented in this paper was possible through the collaboration project “Rum 27” with Neue Heimat Tirol. The authors are grateful for the financial support. This work is also part of a collaboration within IEA SHC Task 66 “Solar Energy Buildings” and IEA HPT Annex 61 “Heat Pumps in Positive Energy Districts”. Financial support was provided by the Austrian Ministry for Transport, Innovation and Technology and the Austrian Research Promotion Agency (FFG) through the IEA Research Cooperation.

6. References

Biermayr, P. *et al.* (2019) *Innovative Energietechnologien in Österreich: Marktentwicklung*.

CARNOT Toolbox - File Exchange - MATLAB Central (2020). Available at: https://de.mathworks.com/matlabcentral/fileexchange/68890-carnot-toolbox (Accessed: 7 July 2022).

Monteleone, W. *et al.* (2022) ‘Development of an Air-Source Mini-Split Heat Pump for Domestic Hot Water by Means of Coupled CFD and Refrigerant Cycle Analysis’, in *ISEC Sustainable Energy Conference* . Graz, pp. 78–86.

Ochs, F., Magni, M. and Dermentzis, G. (2022) ‘Integration of Heat Pumps in Buildings and District Heating Systems - Evaluation on a Building and Energy System Level’, *Energies 2022, Vol. 15, Page 3889*. Multidisciplinary Digital Publishing Institute, 15(11), p. 3889. doi: 10.3390/EN15113889.

Østergaard, D. S. *et al.* (2022) ‘Low-temperature operation of heating systems to enable 4th generation district heating: A review’, *Energy*. Pergamon, 248, p. 123529. doi: 10.1016/J.ENERGY.2022.123529.

Østergaard, P. A. and Andersen, A. N. (2016) ‘Booster heat pumps and central heat pumps in district heating’, *Applied Energy*. Elsevier Ltd, 184, pp. 1374–1388. doi: 10.1016/J.APENERGY.2016.02.144.

Österreichisches Institut für Bautechnik (2019) *OIB-RICHTLINIE 6: OIB-RICHTLINIE 6 Energieeinsparung und Wärmeschutz*.

United Nations Environment Programme (2021) *Global Status Report for Buildings and Construction: Towards a Zero-emission, Efficient and Resilient Buildings and Construction Sector*. Nairobi.

Appendix

Abbreviations	
APP	Appliances
BATT	Battery
COP	Coefficient of Performance
CTR	Control
DH	District Heating
DHW	Domestic Hot Water
HP	Heat Pump
LCF	Load Cover Factor
PV	Photovoltaic Panels
SCF	Supply Cover Factor

Heat Pumps, Photovoltaics and Energy Storage in Buildings – Load Characteristics and Flexibility Options on District Level

Fabian Ochs[1], Alice Tosatto[1], Mara Magni[1], Elisa Venturi[1], Georgios Dermentzis[1,2]

[1] University of Innsbruck, Innsbruck (Austria)

[2] University of Thesaloniki, Thesaloniki (Greece)

Abstract

A comprehensive simulation study of (future) energy-efficient districts including building, HVAC system and energy storage is performed in order to investigate the potential and limits of storage and flexibility in buildings on the district level. Based on three existing examples of energy-efficient districts, building and district models are developed. In future decarbonized districts, the heat demand will be significantly decreased and will be provided by electric energy to a large extent: new buildings built in nZE standard, deep renovated existing buildings as well integration of heat pumps in buildings will lead to a strongly seasonal varying electricity demand. This assessment includes a detailed investigation of the PV own-consumption as well as the external (price) signal-driven energy storage in buildings. The use of the thermal mass of buildings as storage as well as the additional integration of onsite (thermal/electric) storage allows to increase the PV own consumption and further reduce the electric energy of the district, while the influence on the peak power is limited.

Keywords: Decarbonization of the Building Stock, Energy Efficient District; Energy Storage; Energy Flexibility; PV and Heat Pump; Energy Storage; Urban Planning; Energy Policy

1. Introduction

a. Energy Flexibility in Buildings

The use of heat pumps (HP) in buildings for space heating and or domestic hot water (DHW) preparation is without any doubt in most cases the best and often the only option for the decarbonization of the building stock (Wemhöner et al. 2019, Biermayr et al. 2021). The decarbonization of existing districts remains as a major future challenge (Abbasi et al. 2021). With the increasing decarbonization of the electricity mix, the use of HPs will be significantly more competitive than any other technical option. The decarbonization of the electricity system is challenging and requires the integration of renewables and also the integration of electrical and thermal energy storage in the energy system and in buildings (Kurnitski et al. 2011, Ochs et al. 2021). With the electrification of buildings (and mobility) and the integration of PV, buildings will represent an important part of the electricity system, representing both a load and a source and the impact on the electric system becomes increasingly relevant.

Energy flexibility (of buildings) has been intensively studied within the last decades. The main objective is improving the grid stability, which faces challenges with increasing share of renewables on the one hand and electrification of buildings and mobility on the other hand. Li et al. (2021) recently presented a comprehensive review of energy flexibility options in residential buildings. Demand side management is mainly used for peak power reduction, but also possible CO_2 emission savings and cost reduction potential was investigated on building and district level.

Typically, energy flexibility options are distinguished in “shift” and “shed“ (IEA HPT Annex 67). In this context “shift” means that energy consumption is increased before a peak occurs such that during usual peak times the building load can be decreased (i.e. overheating, followed by a period of reduced consumption). “Shed” instead would just cut the peak, which would lead to a reduced indoor temperature during the usual peak period. Hence, assuming violation of the thermal comfort (TC) is not acceptable, in buildings “shed” is not an option.

b. Research gap and novelty of this work.

Several studies on energy flexibility can be found and many of them are summarized within the IEA EBC Annex 67 project and follow-up projects collaborate within Annex 83. The main drawback of existing studies is that they typically lack a to analyze a complete year but concentrate on certain periods. Secondly the lack to analyze the load curve (LC) of the building stock and its future development with massive integration of PV in buildings. This

© 2022. The Authors. Published by International Solar Energy Society
Selection and/or peer review under responsibility of Scientific Committee
doi:10.18086/eurosun.2022.11.10 Available at http://proceedings.ises.org

work includes two important aspects. Firstly, a simplified building stock model (using "future" Tyrol as an example) is investigated and secondly, the entire year is analyzed showing the influence on the required grid capacity from the grid perspective and the influence on the electricity peak. For this purpose, at first, for a selection of real case studies the electric load curve resulting from space heating (SH) and domestic hot water (DHW) preparation with a HP and considering auxiliary energies as well as appliances is presented, secondly the building and building stock simulation model is presented and the introduced simplifications are justified. Then, in a sensitivity analysis, the influence on the storage efficiency, storage capacity and storage duration is analyzed. Finally, the building stock simulation results are presented and discussed, see Fig. 1.

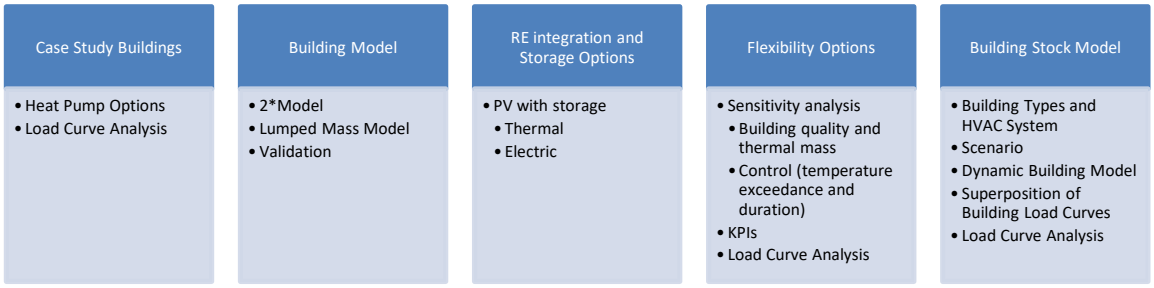

Fig. 1: Structure and method of this work

2. Case Studies

Case Studies of buildings with HP and PV are introduced (Fig. 2) in order to be able to analyse the potential of energy flexibility on building level.

Energy flexibility requires buildings with electric heating system (i.e. HP) for DHW and or SH, and. Three examples of realized buildings and districts are analyzed and used as case studies in this work:

- "Campagne Areal" (NHT and IIG, Innsbruck) around 1000 apartments in 16 buildings acc. to the Passive House (PH) Standard is supplied with DH and central ground water (GW) HPs for SH (Dermentzis et al. 2021(a)).
- In the project "Rum 27" (NHT, Innsbruck) new multi-apartment buildings are connected to District Heating (DH) and, to achieve the PH Plus Standard have a large PV system. In order to increase the PV own consumption, equipped with so-called apartment-wise booster HPs for DHW (Ochs, et al. 2022).
- The two nZE multi apartment buildings "Innsbruck Vögelebichl" (NHT, Innsbruck) represent typical new buildings and are equipped with GW-HP, solar thermal and PV (Dermentzis et al. 2021(b)).



Campagne (NHT), Passive House with District Heating for DHW and GW-HP for SH and PV

Rum 27 (NHT, renderwerk.at), Passive House Plus with district heating and booster HP for DHW and PV

Vögelebichl (NHT), Passive House Plus with GW-HP and ST and PV

Fig. 2: Example of very efficient apartment buildings (PH Standard) with different HP systems and PV

These three examples of buildings in Passive House quality can be seen as representative prototypes of buildings with very high efficiency and lowest possible grid impact. The resulting load curves of a building simulation with simplified building models representing the case study multi apartment buildings (MAB) each in PH quality (15 kWh/(m² a)) are compared in Fig. 3. The small MAB has on annual level more PV production than total electricity consumption (NZEB) and has a higher grid load peak power in summer (PV excess) than in winter. The peak power (hourly average in specific value) is similar for all three buildings and is in the range of 10 W/m² including auxiliary energy and appliances. Obviously, with increasing number of storeys, the possible PV contribution significantly reduces and NZEB is only possible up to typically 4 storeys. Passive House quality and a very efficient HP-based heating system is required to reach NZEB (see also Ochs et al. (2014)). Hence, in terms of energy, in the majority of cases buildings will represent a greater load then source. However, in terms of peak power, PV excess electricity can be more relevant for the grid. Onsite PV and energy storage in buildings influences the load characteristic and the flexibility potential of the building stock.

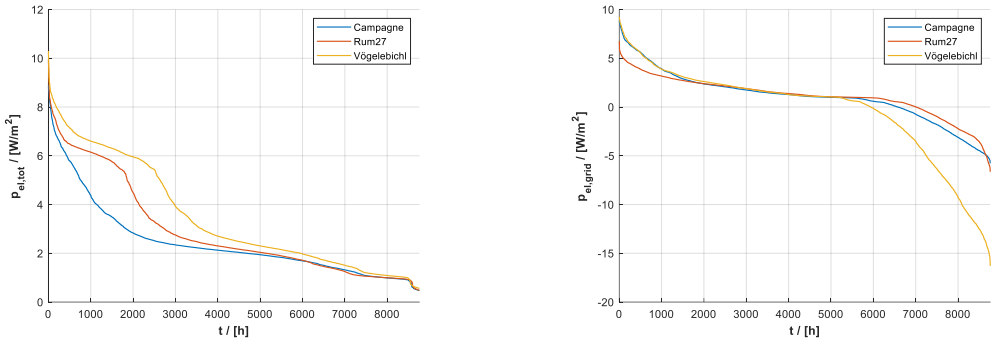

Fig. 3: Specific electric load curve (a) total electricity demand and (b) grid electricity demand of a large (10 storey) MAB with GW-HP for SH and PV, a medium (7 storey) MAB with booster-HP for DHW and PV and a small (4 storey) MAB with GW-HP for SH and DHW and PV, climate of Innsbruck.

3. PV, Energy Storage and Energy Flexibility

a. Energy Flexible Buildings

Through energy storage, energy flexibility in buildings has the potential to provide additional capacity for energy grids, and integrate RE sources in energy systems. Furthermore, there is a potential to reduce costly extensions or upgrades of energy distribution grids. The main challenge is providing thermal comfort, reducing thermal losses while ensuring an economic benefit for the building owner/operator and the utility, see (IEA EBC, Annex 67). In times of availability of abundant and cheap renewable electricity buildings can be (slightly) overheated (activation of the thermal mass) or available storage capacities (thermal/electric) can be charged such that in peak power times or when renewable energies are scarce, the load can be reduced. A flexible external signal-driven control is required for such an operation.

The thermal mass of the building and or additional thermal or electric storage can be charged prior to either expected peak load (i.e. low ambient temperature) or high energy price (i.e. low RE availability) periods. It can be expected that peak periods and high price periods frequently coincide but this is not necessarily the case. If low RE availability (in winter with low PV and hydro power and in no wind periods) coincides with low temperature and thus high demand coincide, electricity price can be expected to peak. Contrariwise, periods with high RE availability (excess electricity from wind power and PV) would lead to low electricity prices and this would be pronounced in periods with low loads e.g. high solar radiation and thus high solar gains.

b. Energy Storage Options

In buildings several options for storing energy are available. Typically, a small DHW store will be present, which covers the daily DHW demand (night/day). Optionally, a SH buffer can be present, which is typically dimensioned to prevent on/off operation of the HP. The set point temperature of the buffer storage can be increased to increase its storage capacity. In addition, the thermal mass of the building can be activated by increasing the set point from

typically 20 °C (standard assumption for calculations) or 22.5 °C (a more realistic average) to maximum 25 °C (or maybe 26 °C).

Floor heating (FH) or thermal activated building systems (TABS) will not be present in the majority of the buildings with respect to the building stock, instead radiators are the predominant heat emissions system. The flow temperature depends on the building quality and size of the radiators. Using (fan supported) convectors the flow temperature can be further reduced, which leads to lower distribution losses and to better performance of the in future predominantly used heat pumps.

Finally, batteries can be used to store surplus electricity. If present, a typical capacity is 1 kWh of battery capacity per 1 kWp of installed PV. Increasingly, as a rule of thumb batteries are dimensioned to cover the electric load of a building on an average summer day.

Table 1 gives an overview of building-integrated storage and potential storage capacities. In combination with an HP, with an average Coefficient of Performance (COP) of 3, the thermal storage capacity can be approximately converted to electric storage capacity. For DHW the daily electric storage potential is 2.3 kWh. For a typical Single Family House (SFH) the daily electricity consumption (appliances, lighting, etc.) is ranging between 6 kWh/d in summer and 8 kWh/d in winter.

Tab. 1: Example of energy storage in a SFH (150 m²), type and storage capacity (acc. to Ochs et al. 2021).

Energy	**Electric**	**Thermal**		
Type	Battery	Building Mass	SH buffer	DHW storage
Typical Size	ca. 1 kWh/kW$_p$	200 Wh/K/m²	1000 l	100 to 150 l
Storage Capacity	5 kWh$_{el}$ … 7 kWh$_{el}$	28 kWh$_{th}$/d ΔT = 1 K	23 kh$_{th}$ 50/30 °C	7 kWh$_{th}$ 50/10 °C
Converted capacity (electric)		9.3 kWh$_{el}$	7.7 kWh$_{el}$	2.3 kWh$_{el}$

c. Theoretical Savings through Energy Flexibility

Assuming a perfect prediction of the RE availability and the load curve (LC), an external signal could be used to overheat the building stock in times of low CO2-emissions and/or low energy prices and thus reduce the load in the following high energy price period.

In order to activate the thermal mass of the buildings or charging thermal storage the set point temperature can be increased, e.g. by $\Delta T_{SP} = 3.5$ K for the indoor temperature and/or by $\Delta T_{SP} = 10$ K for the DHW storage temperature.

$$T_{SP} = T_{SP} + \Delta T_{SP} \cdot (signal == 1) \quad \text{(eq. 1)}$$

Through this (additional) activation of the onsite (thermal or electric) storage capacity, peaks in the LC could be theoretically shifted to non-peak times (so-called peak shaving) or additional energy consumption can be generated in low energy demand periods thus leading to a reduced energy demand in the subsequent period. While in the first case the purpose is reducing peaks in the grid electricity, in the second case additional peaks could still occur, but shifted to later times. In any case, if under-temperature is excluded, activation of flexible storage options will increase the average building and or storage temperature and as a consequence, the total energy demand (E_{flex}) will also increase with respect to the reference case (E_{ref}) because of storage losses (E_{loss}).

$$E_{flex} = E_{ref} + E_{loss} \quad \text{(eq. 2)}$$

Thus, flexibility options will always increase the energy demand, but the additional energy demand and some of the reference energy demand ($E_{ref} \cdot a$) might be provided at lower cost or with higher share of RE and thus with lower CO_2 emissions. The losses depend on the type of storage and the storage duration. In case of the thermal mass of the building the envelope quality (EQ) and the thermal mass (TM) of the building influence the thermal losses.

4. Building and Building Stock Model

a. Dynamic Building Model

The simplified dynamic simulation model of the building includes the HVAC systems, i.e. HP or Direct Electric (DE), DHW and appliances profiles as well as storage options (thermal, electric) and PV integration. A simple dynamic 1-zone lumped capacity model developed in Matlab (ode15s solver) is used (see Ochs, et al. 2021) and compared against a 2* model with and without floor heating, see Fig. 4. Different building typologies and energy levels are implemented. The models were compared against each other and against the validated building simulation model carnotUIBK (see Magni et al. 2022).

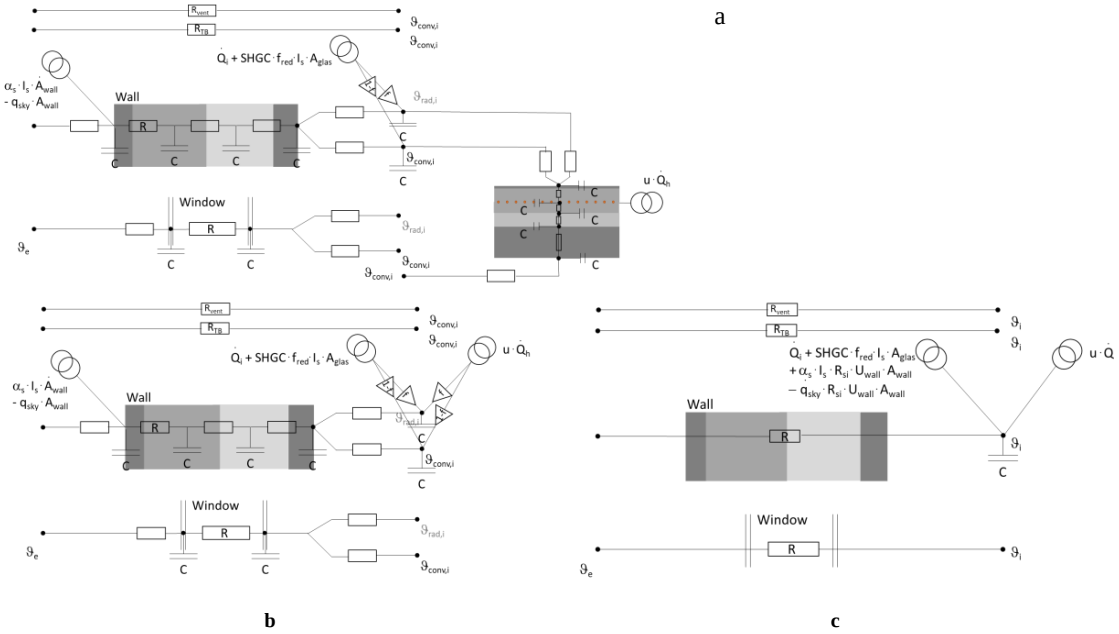

Fig. 4 (a) 2* model with 1 wall with 4 nodes, floor heating and 1 window with 2 nodes (13 ODEs), (b) 2* model without floor heating (8 ODEs) and (c) lumped capacity model (1 ODE)

b. District and Building Stock Model

The building stock electric load curve is determined by superposing the load curves of different building types. For each building type with the different HVAC configurations the load curve is simulated with the reduced order lumped capacity one zone building model with different options of PV and storage integration as well as external-signal based overheating. Each building with its representative energy demand and equipped with either an HP or a DE heating system represents a partly flexible load for the electricity grid. Buildings heated with biomass or connected to DH system represent an appliance- (and auxiliary-) based load only, which is not flexible unless electric storage is implemented (i.e. battery). The scenario under investigation assumes a total phase-out of fossil heating systems (i.e. no gas and oil boiler). The schematic representation of the building stock is shown in Fig. 5. Further details about the buildings can be found in Ochs et al. (2021).

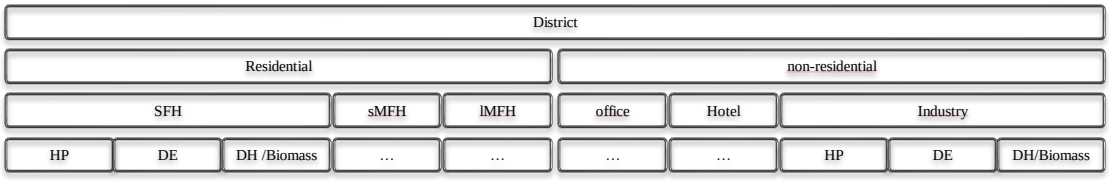

Fig. 5: Scheme of the district/building stock model with different building types (i.e. SFH: Single Family House, sMFH/lMFH: small/large Multi Family House, office, Hotel and Industry) and HVAC systems (i.e. HP: Heat Pump, DE: Direct Electric, DH: District Heating, and Biomass).

c. PV potential in building stock

Assuming PV will be installed on every roof, and given the roof area and restrictions in terms of shaded roof area

and competing roof use (chimney, window, ventilation system, etc.) the following potential PV installation is assumed (Tab. 2).

Tab. 2: PV potential and typical battery size in buildings, scenario for Tyrol 2050.

		SFH	s-MFH	l-MFH	Office	Industry	Hotel
Treated area	m²	150.8	334.4	1822.0	1153.8	1009.8	1024.6
No of storeys	-	2	4	10	5	5	5
PV	kW_p	5	9	18	25	21	22
No of Buildings	-	106579	67592	5063	10584	7461	9571

The total roof installed PV sums up approx. 18 MW_p. Remark: The actual total PV potential is significantly higher as only the heated buildings are considered and unheated buildings such as garages, stores and halls, etc. present an additional space for PV that can be integrated in the buildings energy system.

d. Climate

The climate has a significant influence on the energy flexibility. In times of low ambient temperature and low solar radiation, the overheated building will be subject to relevant thermal losses, while in times of moderated temperatures or high solar gains, the storage period is expected to be longer. For this simulation study, the climate of Innsbruck in hourly resolution is used (Meteonorm). Additionally, a synthetic climate is used to investigate the influence of the building envelope quality and thermal mass on the storage duration and storage efficiency. The ambient temperature of Innsbruck in daily resolution is shown in Fig. 6 (a), in Fig 6 (b) a period of 2.5 days in winter is shown. There are four periods of few days with very low temperature at the beginning of the year and two at the end of the year, with the lowest temperature in December and the longest cold temperature period in February. Fig. 6 (c) shows the synthetic climate used for the sensitivity analysis.

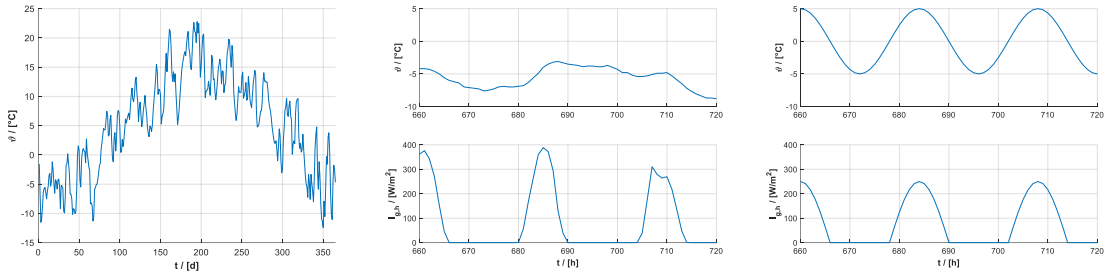

a b c

Fig. 6 (a) Daily average temperature of Innsbruck, (b) hourly temperatures and global horizontal radiation for a period of 2.5 days end of January and (c) synthetic climate in hourly resolution for a period of 2.5 days.

5. KPIs

Building time constant: If the thermal mass of the building is concentrated to one node, the building can be expressed by its time constant

$$\tau = \frac{(m \cdot c)_{eff}}{\sum UA + \rho \cdot c \cdot V \cdot n_{eff}} \quad \text{(eq. 3)}$$

Storage Duration: The storage duration is the time between the point of time when the building is heated again after the external signal driven heating (which is equal to undershoot of the SP temperature) and the point of time when the external signal is set back to zero ($signal == 0$)

$$\Delta\tau = t(heat\ on) - t(signal == 0) \quad \text{(eq. 4)}$$

Thermal Storage Capacity: The storage capacity is the difference in energy

$$Q_{out} = Q_{ref}(t(heat\ on)) - Q_{ref}(t(signal == 0)) \quad \text{(eq. 5)}$$

Thermal Storage Efficiency: The thermal storage efficiency is the ratio of heat output and input.

$$\eta_{th} = Q_{out}/Q_{in} \quad \text{(eq. 6)}$$

The heat input Q_{in} is the additional heat delivered to the building during the phase when the external signal is equal to one. It is calculated by the heat delivered to the building in that phase minus the heat delivered in that phase without overheating ($Q_{in,ref}$).

Electric Storage Efficiency: The electric storage efficiency is the ratio of electric output and electric input. The electric efficiency depends on the thermal efficiency and on the HP performance.

$$\eta_{el} = W_{out}/W_{in} \quad \text{(eq. 7)}$$

The electric efficiency can be higher or lower than the thermal efficiency. It depends on the temperature level the HP is operated during overheating and would be operated in the reference case (i.e. without overheating). A simple and clear example is an air-to-water HP for DHW preparation. When a HP is only operated during daytime with in average a couple of K higher air temperatures than during nighttime, the HP's COP would be higher leading to an increased electric storage efficiency with roughly the same thermal efficiency.

6. Results and Discussion

a. Lumped mass building model

The simplified lumped mass model used for the building stock model was compared against the more detailed 2* model with and without floor heating, see section above. The dynamic behavior with respect to the indoor (i.e. operative) temperature on hourly resolution cannot be predicted very accurately with the simplified lumped capacity model but the trend with respect to the time constant of the building is correct and the accuracy is sufficiently good with respect to the load and for the purpose of this work. This conclusion is in agreement with the results presented by Magni et al. (2021). The inertia of a floor heating system (see Fig. 7) leads to a different dynamic behavior also with respect to the heating power. However, with respect to the electric load curve, even a floor heating system in combination with a buffer storage and a HP can be predicted sufficiently well with the simplified lumped mass model.

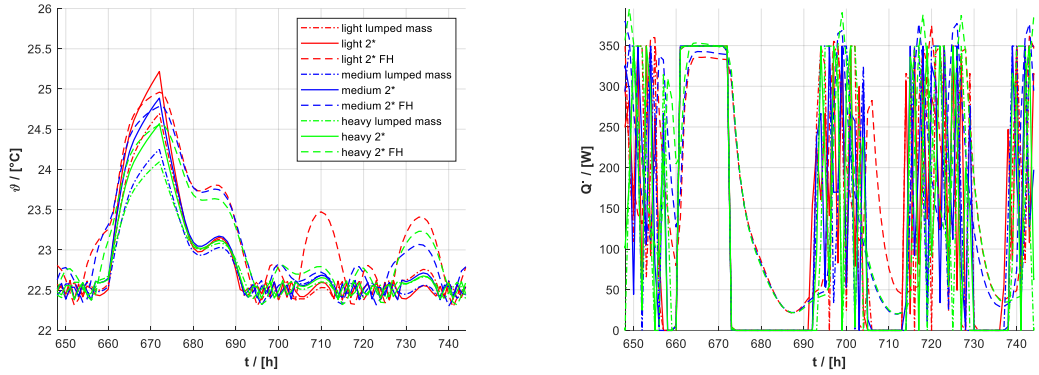

a **b**

Fig. 7 (a) temperature and (b) heating load of a signal driven overheating (synthetic climate) with different thermal mass of the building (light, medium, heavy).

b. Single Building – Influence of Building Quality and Thermal Mass

Exemplarily, Fig. 8 and 9 show the temperature development of the lumped mass building model with three different envelope qualities (EQ) and two variants of the thermal mass of the building (medium or high thermal mass (TM)) with an external signal-based overheating to 26 °C and 24 °C, respectively.

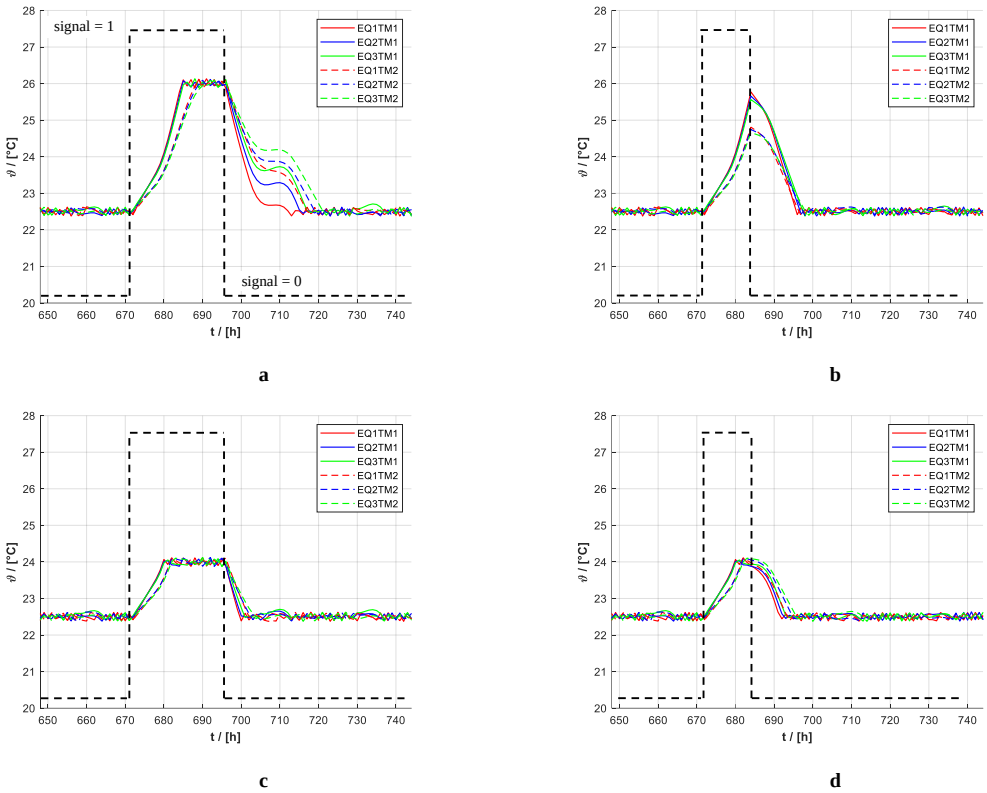

Fig. 8: (external) signal based overheating of the building starting from hour 672 ((a), (c) 24 h (b), (d) 12 h) depending on the thermal mass (i.e. TM1: medium and TM2 high thermal mass), building quality (i.e. EQ1: low, EQ2: medium and EQ3: high envelope quality) and SP ((a) and (b) + 1.5 K (c) and (d) + 3.5 K); 2*1TZ building model, with synthetic climate

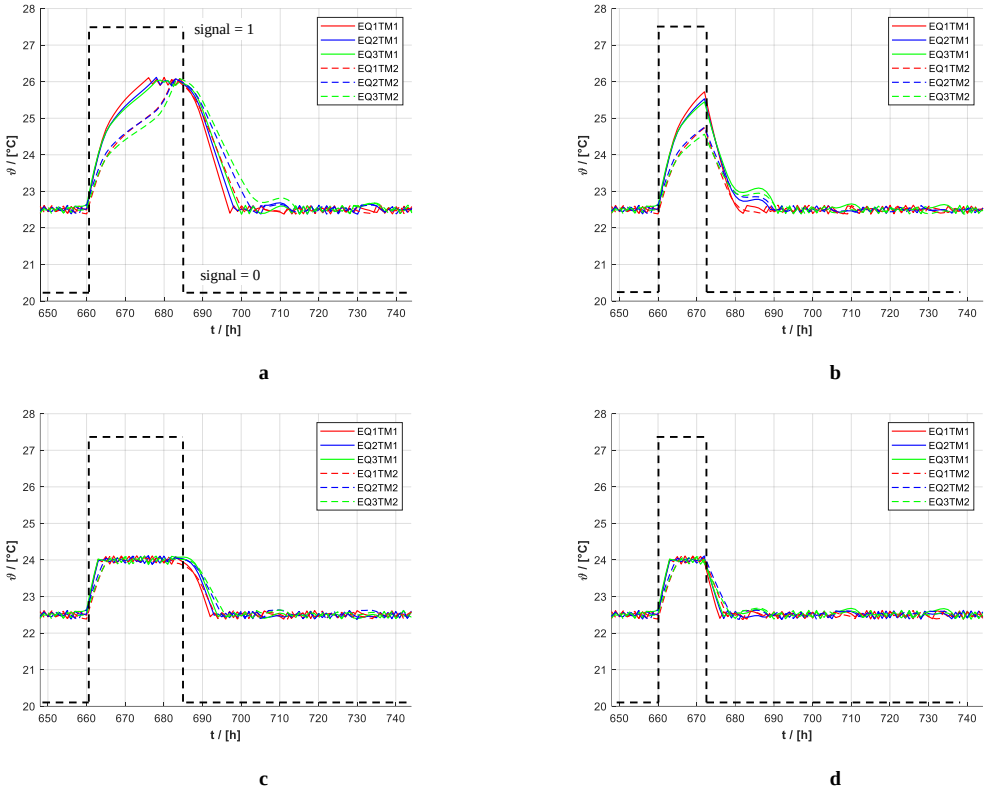

Fig. 9: (external) signal based overheating of the building starting from hour 660 ((a), (c) 24 h (b), (d) 12 h) depending on the thermal mass, building quality and SP ((a) and (b) + 1.5 K (c) and (d) + 3.5 K); 2*1TZ building model, with synthetic climate.

The maximum storage duration ($\Delta\tau$) depends on the building's envelope quality (EQ), the thermal mass (TM), i.e. its time constant τ, the SP temperature exceedance as well as on the climate (external temperature and solar radiation), i.e. on the time of the year. In cold winter times with low temperature, more energy could be theoretically stored in a building, but also the thermal losses are higher. Contrariwise, in the interim season, losses are low, but also the storage potential is low, as only little heat is required at that time at all. As shown in Fig. 8 and 9 for an external signal of 12 h and 24 h the maximum storage period for the building with high envelope quality and high thermal mass does reach 32 h at maximum. The storage duration and the storage efficiency are reported in Fig 10 (a) and (b).

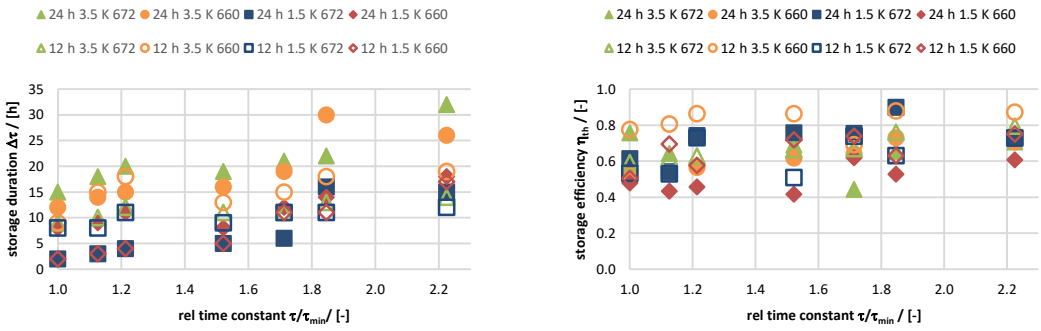

a b

Fig. 10: (a) Storage duration ($\Delta\tau$) and (b) thermal storage efficiency (η_{th}) as a function of the relative time constant of the building (τ/τ_{min}) for different overheating duration (12 h or 24 h), temperature (1.5 K and 3.5 K) and starting point (hour 660 or 672).

The efficiency is higher for short heating-up periods with higher overheating temperature. Long overheating periods with low temperature difference lead to short storage periods and poor efficiencies. The storage duration can significantly increase when the next day with increasing temperature and solar gains is reached (as in case of e.g. 24 h, 3.5 K, 660 where dt = 30 h at τ/τ_{min} = 1.85 instead of 19 h at τ/τ_{min} = 1.7 or 32 h instead of 22 h for the case 24 h, 3.5 K, 672 when the relative time constant is increased from 1.85 to 2.22).

c. Single Building – Load Duration Curve

For the example of the SFH the effect of external signal-based overheating is shown in Fig. 11 for the heating sorted heating load (a) and the load vs. ambient temperature curve (b). Peaks at low ambient temperature periods can be reduced and are shifted to times with higher ambient temperature. But this succeeds only for some peak power days and overall the peak power of the building is not reduced.

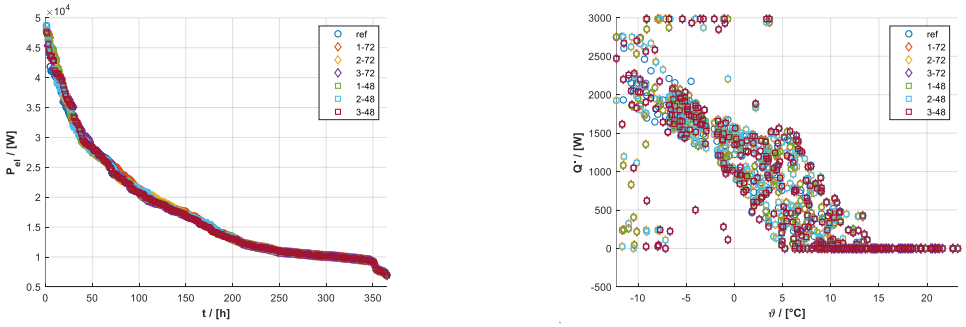

a b

Fig. 11. (a) Sorted total electric load duration curve (daily sum) with and without external signal-based overheating and (b) thermal load vs. ambient temperature in daily average for the SFH with SH of 47 kWh/(m² a); for different overheating temperature (1, 2 or 3 K and different overheating period 48 or 72 h) in comparison the the reference without overheating (ref).

In Fig. 12 for a selected period at the end of the year, the daily electric energies are shown and how (with respect to the reference without external signal-based overheating) the load is shifted by maximum 2 days. The daily maximum peak cannot be reduced when two peak periods follow with short time lag.

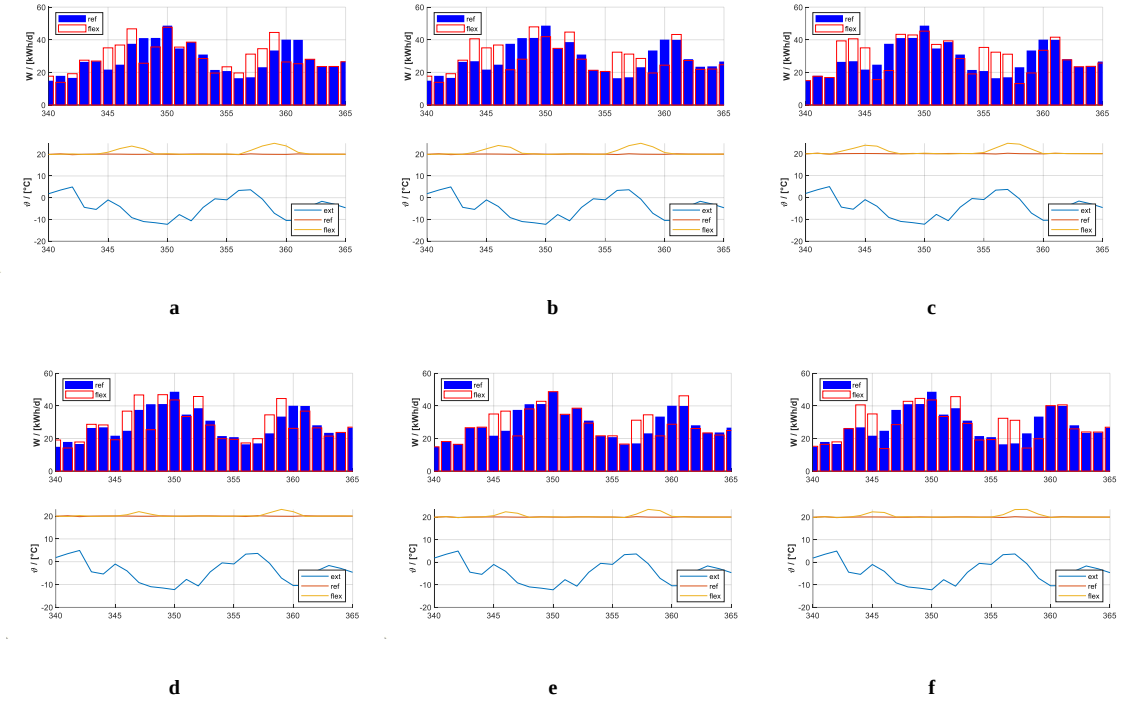

Fig. 12. Daily sum of the electric energy (from day 340 to day 365 of the year) for the SFH for overheating of (a) 1 d in advance and 72 h duration (b) 2 d in advance and 72 h duration (c) 3 d in advance and 72 h duration (d) 1 d in advance and 48 h duration (e) 2 d in advance and 48 h duration (f) 3 d in advance and 48 h duration.

d. Building Stock – Load Duration Curve

The building stock load duration curve is shown in Fig. 13. The peaks occur in times of low ambient temperatures. Based on the previous results, it can be concluded that a shift of more than 24 h cannot be achieved and cold periods are typically longer than 24 h. Peaks can occur with only a short time-lag, e.g. peak at day 352. Hence, the theoretic peak reduction potential is limited to approx. 85 % to 90 %. If in a winter period the average load curve is in the range of 80 % with respect to the peak and a peak situation is predicted in advance, the load must be increased to shave the peak. Thus, in this period the average load must increase from 80 % to e.g. 90 %. Practically, due to non-ideal prediction and non-ideal behavior, the peak power reduction might not occur at all or the peak might be only shifted by max. 24 h.

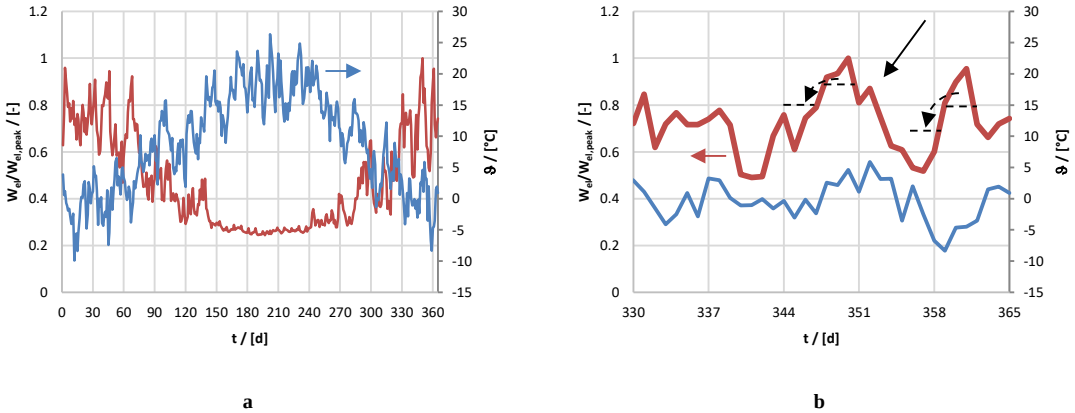

Fig. 13. Building stock electric load curve (based on scenario Tyrol 20250, Ebenbichler et al. 2020) normalized (a) hourly power and (b) daily energy with a section of few days in Winter; total electric energy demand: 1995 GWh, hourly Peak Power: 739 MW.

Fig. 14 shows the load duration curve for the building stock model (a) sorted hourly powers and (b) daily energies

with different variants: reference, with DHW preparation during daytime, with and without PV, with battery (1.35 kWh/kW$_p$). While PV has relevant influence on the load curve, in particular in summer, the integration of storage is only of low relevance for the load curve and the peak powers.

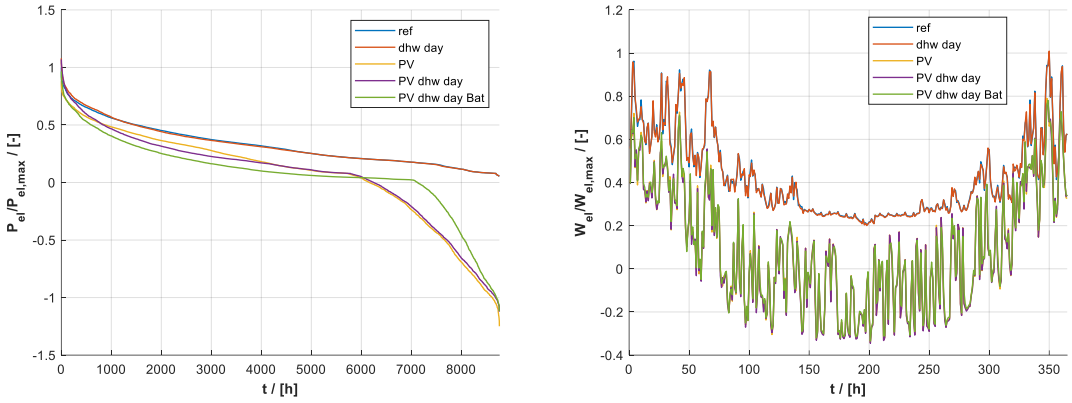

Fig. 14. Building stock load curve (based on scenario Tyrol 20250, Ebenbichler et al. 2020); (a) normalized hourly electric power (b) daily energies; total electric energy demand: 1995 GWh, hourly Peak Power: 739 MW; ref: reference without PV and storage, dhw day: ref. with day time domestic hot water storage charging, PV: with PV; PV dhw day: with PV and day time domestic hot water storage charging; PV dhw day bat with additional battery (ca. 1.35 kWh//kWp (in average).

7. Conclusions

Energy storage in buildings can be used to shift the load from peak times to few hours later, thus theoretically reducing the stress on the electric grid. On building level, thermal and electric energy storage is possible (thermal building mass, space heating (SH) buffer, DHW storage or battery, typically in combination with PV and potentially electric cars). Possibilities and limits of load shifting in buildings using the thermal mass and/or thermal or electric storage were discussed. The developed building and building stock/district models allow to evaluate the possibility to shift load through the activation of the thermal mass of the building, thermal energy storage (for SH and DHW) and batteries depending on the building energy level, the HVAC system and onsite PV.

The storage efficiency and storage duration depend on the one hand on the envelope quality of the building and its thermal mass and on the other hand on the control (overheating temperature) and the time of the year (i.e. ambient conditions). The storage duration when overheating the building thermal mass is limited to max. 48 h in the optimistic case (highly efficient building with high thermal mass and floor heating) and is significantly less as concerns the future building stock with an average space heating demand of 45 kWh/(m² a) and in the winter months with low ambient temperature. Hence, the effective storage duration is of the same order of magnitude as a typical battery charging/discharging cycle. The thermal storage efficiency varies strongly between 40 % and 90 %. On the annual perspective and from the grid point of view neither external signal-based overheating nor battery charging have a relevant influence on the peak powers. A load shift from night to day is possible and can make sense regarding renewable integration (CO_2 emission reduction, reduced energy consumption at high price periods) but the requirements on the grid capacity and the provision of peak power plants is hardly influenced.

8. Acknowledgments

The project “Energiespeicher Tirol Phase II” (Land Tirol) enabled this work. This work is also part of a collaboration within IEA SHC Task 66 “Solar Energy Buildings” and IEA HPT Annex 61 “Heat Pumps in Positive Energy Districts”. Financial support was provided by the Austrian Ministry for Transport, Innovation and Technology and the Austrian Research Promotion Agency (FFG) through the IEA Research Cooperation.

9. References

M.H. Abbasi, Abdullah B., M.W. Ahmad, A. Rostami, J. Cullen (2021). Heat transition in the European building sector: Overview of the heat decarbonisation practices through heat pump technology. Sustainable Energy Technologies and Assessments.

P. Biermayr, C. Dißauer, M. Eberl, M. Enigl, H. Fechner, B. Fürnsinn, M. Jaksch-Fliegenschnee, K. Leonhartsberger, S. Moidl, E. Prem, C. Schmidl, C. Strasser, W. Weiss, M. Wittmann, P. Wonisch, E. Wopienka, Innovative Energietechnologien in Österreich: Marktentwicklung 2020; BMK

G. Dermentzis, F. Ochs, A. Thuer, and W. Streicher (2021a). Supporting decision-making for heating and distribution systems in a new residential district - An Austrian case study, Energy, vol. 224, p. 120141

G. Dermentzis, F. Ochs, N. Franzoi (2021b). Four years monitoring of heat pump, solar thermal and PV system in two net-zero energy multi-family buildings, Journal of Building Engineering, Volume 43, November 2021.

R. Ebenbichler, A. Hertl, A. Hofmann, W. Streicher, M. Mailer, A. Tosatto, I. Anton, F. Reith, F. N. Schaaf, S. Rzehak, F. Ochs (2021): Energie-Zielszenarien Tirol 2050 und 2040 mit Zwischenzielen 2030.

J. Heier, C. Bales, V. Martin (2015). Combining thermal energy storage with buildings – a review, Renewable and Sustainable Energy Reviews, Volume 42, February 2015, Pages 1305-1325

J. Kurnitski, A. Saari, T. Kalamees, M. Vuolle, J. Niemelä, T. Tark, T. (2011). Cost optimal and nearly zero (nZEB) energy performance calculations for residential buildings with REHVA definition for nZEB national implementation. Energy and Buildings, 43(11), 3279-3288.

H. Li, Z. Zhe, T. Hong, M. A. Piette, Energy flexibility of residential buildings: A systematic review of characterization and quantification methods and applications, Advances in Applied Energy, 2021.

M. Magni, F. Ochs, W. Streicher, Comprehensive analysis of the influence of different building modelling approaches on the results and computational time using a cross-compared model as a reference, Energy and Buildings, Volume 259, 15 March 2022, 111859.

F. Ochs, M. Magni, E. Venturi, A. Tosatto, and W. Streicher (2021). Cost-optimal nZEB HVAC configurations with onsite storage, E3S Web Conf., vol. 246, p. 07001, Mar. 2021.

F. Ochs, G. Dermentzis, W. Feist, Minimization of the Residual Energy Demand of Multi-storey Passive Houses – Energetic and Economic Analysis of Solar Thermal and PV in Combination with a Heat Pump, Energy Procedia Volume 48, 2014, Pages 1124-1133

IEA EBC Annex 67, Energy Flexible Buildings; http://www.annex66.org/ (visited 2022).

C. Wemhoener, L. Rominger, S. Buesser, M. Magni, F. Ochs, C. Betzold, D. Dippel (2019). Simulation-based Methodology for Comparison of nZEB Requirements in Different Countries Including Results of Model Calibration Tests, IBPSA 2019, Rome.

Buried Twin Pipe Model Validation for System Simulations of Ice Storage Tanks in 5GDHC networks

Maike Schubert, Martin J. Neugebauer, Damian Birchler, Florian Ruesch and Daniel Carbonell

SPF Institute for Solar Technology, Eastern Switzerland University of Applied Science (OST), Rapperswil (Switzerland)

Abstract

As cooling becomes more and more important for the building sector in central Europe, low temperature 5th Generation District Heating and Cooling (5GDHC) networks are of increasing importance. Different heat sources for such networks exhibit different limitations. While waste heat is limited through its origin, the capacity of ground and lake water is limited by their temperature levels in winter, while abundant heat is available in summer times. Therefore, the integration of seasonal thermal storages can be of great benefit. One option is the implementation of ice storages as long-term load shifting elements. Moreover, peak demands during both heating and cooling periods demand for oversizing the heat/cold supply. Here ice storages can play a different role by providing additional short-term capacity for heating and cooling on the coldest and hottest days respectively. In this paper, we present 5GDHC network configurations in which ice storages can be operated in a useful manner. Furthermore, we analyze the temperature levels and differences in a 5GDHC network over a year as a basis for tuning the parameters of a buried double pipe model typically employed in such networks.

Keywords: Thermal Networks, 5GDHC, Ice Storage Tanks, Solar-Ice Systems

1. Introduction

Thermal networks running on a low temperature level are becoming more and more important all over Europe (Caputo et al., 2021). The advantage of such networks is that waste heat at low temperature levels (e.g., from sewage plants or data centers) or environmental heat from various sources (e.g., lake or ground water) can be used. Additionally, low temperature networks, also called 5GDHC (5th Generation District Heating and Cooling networks), have the potential to provide cooling in summer. About 40 % of potential sources of 5GDHC networks are, however, limited (Sres and Nussbaumer, 2014) and therefore may be short during the heating period. Storages play an important role in this context for shifting the available heat on a seasonal basis as well as on shorter timescales. Ice storages are used for heating applications as seasonal storages in solar-ice based heating systems in single and multi-family buildings (Carbonell at al., 2021). In district heating networks with anti-freeze heat transfer fluids, ice storage tanks could replace geothermal probes. While borehole fields need a temperature level of 25 °C to 30 °C for regeneration (Ruesch and Haller, 2017), ice storages can be regenerated at any temperature above 0 °C. Smaller ice storages may be used for load shifting on shorter timescales like weeks as additional heat sources for covering the coldest days. Moreover, ice storages could be used for short term cooling load shifting helping the electric grid to be more flexible, thus providing a double function for heating and cooling peak load shifting. In this paper we present results of analyzing monitoring data of a 5GDHC over year, which in turn are used to validate a network pipe model implemented in TRNSYS.

2. Network configurations compatible with ice storages

To bring the temperature level of a 5GDHC network up to a range at which the heat can be used in applications such as room heating or domestic hot water, distributed heat pumps at the user sites are employed. Besides the lower operating temperatures, the main feature distinguishing 5GDHC networks from earlier generations is the bidirectional energy flow (Caputo et al., 2021). The low temperature levels allow that different users of the same network can be in different operation modes (heating or cooling). Within such a bidirectional energy flow network,

© 2022. The Authors. Published by International Solar Energy Society
Selection and/or peer review under responsibility of Scientific Committee
doi:10.18086/eurosun.2022.11.11 Available at http://proceedings.ises.org

only certain configurations can be combined with an ice storage in a useful manner.

The three configurations we identified as useful, are shown in **Fig. *1***. In case a) the ice storage is located at the site of the central heat source. Here the ice storage can be regarded as an alternative to a borehole field. Case b) depicts a specific version of case a), in which the main heat source is represented by solar thermal collectors and/or air heat exchangers. Unlike case a), where the ice storages can be an add-on to an existing (waste) heat source, the ice storage is an integral part of the heat source in case b). Only the combination with an ice storage enables the usage of solar thermal collectors and/or air heat exchangers. Finally, in case c) one or more smaller decentralized ice storages are used at the user sites to shift loads on shorter timescales on the network end of the heat pump system. Here they can be seen as potential replacements for sensible storages.

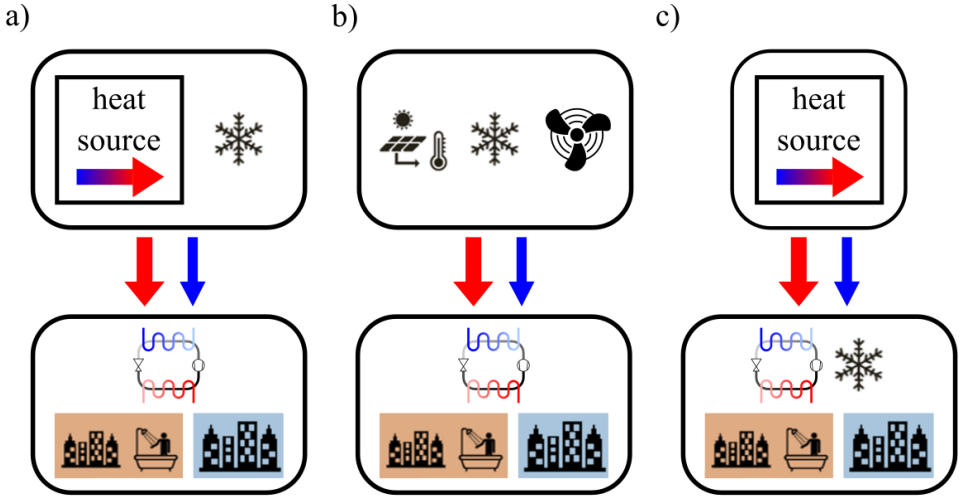

Fig. 1: Network configurations considered for implementation of ice storage tanks. a): Centralized ice storage at the location of the main (or one of the main) heat source(s). b): Combination of storage combined with air source heat exchanger and/or solar thermal collectors as the main heat source of a network. c): Decentralized ice storages (e.g., at consumer substations with cooling needs) for shorter term load shifting.

3. Analysis of existing 5GDHC network

5GDHC networks usually feature uninsulated buried double pipes. Because of the lack of insulation these pipes interact significantly with both the ground and with each other. To gain insight in the behavior of a network based on such pipes, monitoring data from a 5GDHC network in Zurich (Switzerland) were analyzed. In its final stage of extension this network is supposed to cover the heating demands of around 5500 inhabitants distributed over around 2200 dwellings in the year 2050. In 2020, which is the year analyzed in the following, the network included two data centers with a combined nominal heating demand of 80'000 MWh/a, two ground probe fields with a combined 332 probes of 250 m length and six energy substations with a total installed power of 7.3 MW. The network nominally provided 35'000 MWh heat for space heating and domestic hot water. The energy reference area serviced was 185'000 m^2. The network length is 1'500 m and the heat transfer fluid used is untreated water.

The monthly energy balance of this network for the year 2020 is presented in **Fig. *2***. Network components that add heat to the system (sources) are on the positive and components that take heat from the system (sinks) are on the negative side. All values exact for those labelled "pipes heat exchange" were extracted from monitoring sensors. The "pipes heat exchange" is simply the difference between the sinks and the sources values, ensuring that a balance is achieved. We assume that these imbalances are entirely due to thermal losses and gains that happen in the network pipes and hence named them accordingly. It can be clearly seen that the heat losses through the pipes are higher for the warmer months from April until September as compared to the remaining colder ones. Since the ground is still relatively warm in November from summer, there are slight pipe heat gains for the network during this month. The ground probe fields act as heat sinks from April to October and as heat sources for the remaining months.

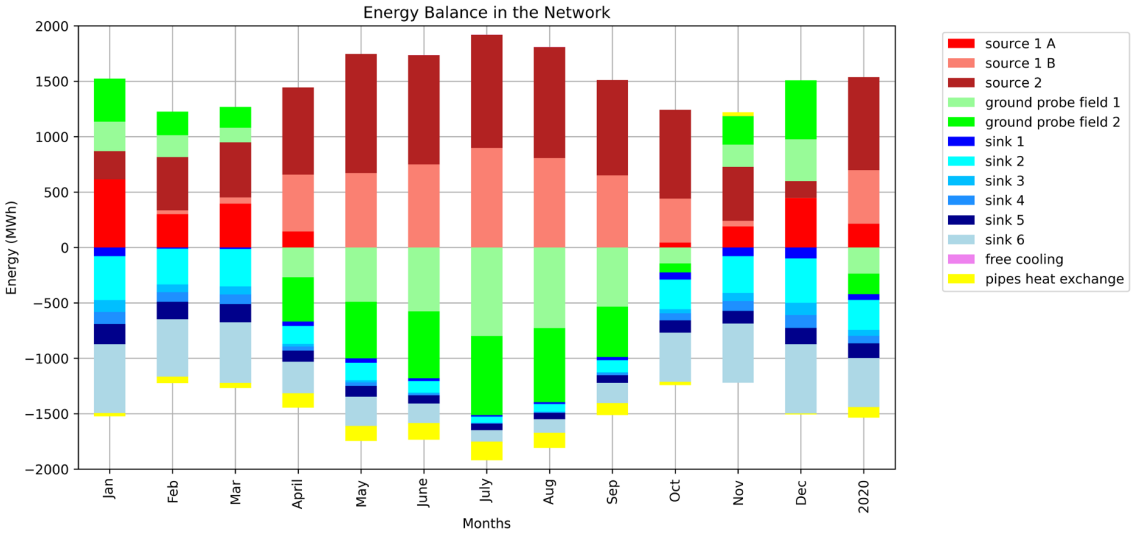

Fig. 2: Energy balance of the network for the year 2020 with all sinks and sources and the ground probe fields. Pipe heat exchange (yellow parts of the bars) on the negative side (sink-side) means overall losses, on the positive side (source-side) means overall gains of the network. The "2020" bar represents annual values which are divided by a factor of 10 for being in a similar range as the monthly bars.

There is a 580 m long section of the network between the two substations of Source1 and Groundsource2 with no further substations in between. This piece of double pipe should allow for a deeper analysis of pipe losses and gains. The respective temperatures over the year 2020 are shown in **Fig. *3***. The temperatures of the warm (solid line) and the cold (dashed line) pipes are shown at Source1 (blue) and Groundsource2 (orange) in **Fig. *3 a)***. The temperature level outside the heating period (April – October) is up to 27 °C in the warm pipe, while it stays just below 25 °C in the cold one. This is above the ground temperature even in warm summer months and explains the pipe losses. From November to March the temperature level of the network is around 15 °C in the warm and around 11 °C in the cold pipe. The drop in temperature occurring in November marks the start of the heating season.

Fig. *3 b)* shows the temperature differences for the warm (red line) and the cold (blue line) between the two substations Source1 and Groundsource2. These temperature differences directly reflect the heat losses and gains for the two pipes over the examined section. The temperature difference is taken between the downstream and the upstream point in each pipe. This means that the difference is formed in an inverse fashion between the warm and the cold pipe, since the flow directions are opposite to one another. Consequently, heat losses are reflected by positive and heat gains by negative values in the temperature difference. It should be noted that for the year 2020 there was a predominance of cooling over heating demand leading to relatively high network temperature and hence to relatively large losses. These will be reduced when more heat sinks are connected to the network, as planned.



Fig. 3: a): Absolute temperature of the network for substation Source1 and Groundsource2 (GS2). The warm/cold pipes are represented by a solid/dashed lines respectively. b): Difference of network temperature between substation Source1 and GS2 for the warm pipe in red and network temperature difference between GS2 and Source1 for the cold pipe in blue. Between substations Source1 and GS2 there is 580 m of buried, uninsulated double pipe. Note that the spike in October constitutes an outlier caused by a data logging issue.

4. Validation of double pipe model and simulation framework

The project Ice-Grid will include simulations of 5GDHC networks featuring ice storages. These will be done with the open-source simulation framework pytrnsys (SPF-OST, 2019) and TRNSYS as core engine. The pipes of the networks will be modelled through an extension of Type 951 from the TESS library (TRNSYS, 2019) representing a "buried twin pipe". Here the extension consists of adapting the model such that it supports changing flow directions in both pipes, which is not possible with the original model.

While most parameters of the pipes, like their diameter for example, are simply known from planning data, the thermal conductivities of both the pipe material and the soil are determined through fitting them to the monitoring data presented in the previous section. It should be noted that the temperature sensors from the data in **Fig. *3*** have a measurement uncertainty of 0.1 K. Therefore, the temperature loss of the cold pipe of about 0.1 K lies within the uncertainty range and even the higher temperature losses of the warm pipe of about 0.4 K are close to the uncertainty range.

In the buried double pipe model two identical pipes are symmetrically placed in a common casing with a fill material embedded by soil. The flow direction of the pipes is defined by the sign of the mass flow rate which is given as inputs to the model. Only conductive heat transfers between the pipe and the filling material and soil is considered. Thermal resistance between the pipes and between each pipe and the surrounding soil are calculated. Around the casing a finite difference model of soil conduction is employed to calculate heat accumulation and dissipation. While the volume excavated to lay the pipes and fill with filling material has a rectangular cross section in the real system, the geometry of the model is concentric around the symmetry axis of the double pipe.

Note that the radius around the symmetry axis for which interaction with soil can be considered is limited to the burying depth of the pipes. These circumstances are illustrated by **Fig. 4**.

All other geometric parameters are fixed to the physical values of the installed network. The pipes have an inner diameter of 42 cm, the distance between the centers of the pipes is around 75 cm and the pipe depth is taken to be 2 m below the surface, which is about the average of pipe depth in the relevant part of the system.

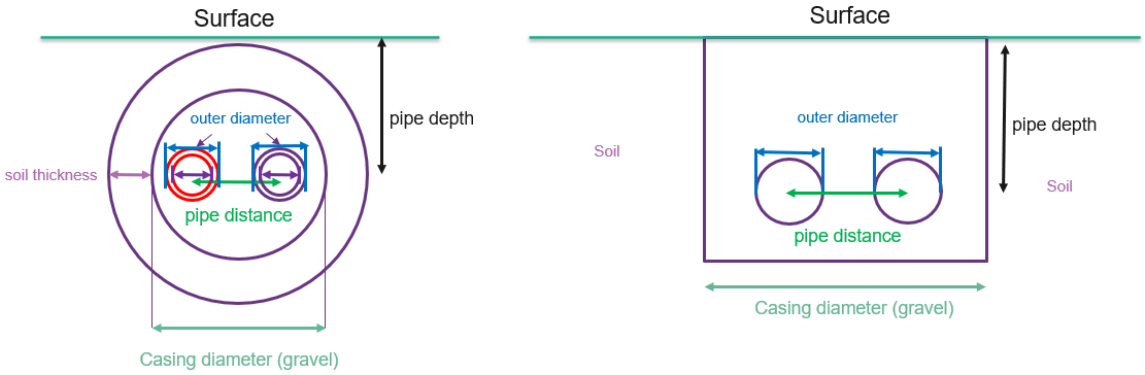

Fig. 4: Comparison of model geometry (left) and geometry in a real network (right).

In a first step the effect of the meshing resolution was analyzed by varying the number of control volumes. The accuracy did not increase when going beyond the default settings of 5 radial soil nodes and 4 circumferential soil nodes. So, the numbers of nodes were kept at these values. In a next step the effect of thermal properties (conductivity and capacity) of the fill material and surrounding soil were tested. Mainly changes in the thermal conductivity of gravel and soil have been analyzed. For the pipe itself a typical heat conductivity value for plastic pipes was selected.

Thermal conductivities of ground and filling material vary over the year depending on the water saturation of the ground. Water saturated loam or gravel have much higher thermal conductivities than their dry counterparts. A summary of thermal ground properties can be found in Santa et al. (2017). In the model used here the ground properties are assumed to be constant over time.

To calibrate the thermal conductivities of the soil around and the gravel between the pipes assumed in the model, a simple simulation was set up. This simulation includes a section of double pipe representing the 580 m long section between Source1 and Groundsource2 analyzed above. For this test simulation the inlet temperatures and mass flow rates of the two individual pipes were simply read from the measured data and the respective outlet temperatures were returned. The thermal conductivities were then varied to minimize the difference between annual losses measured in this part of the network and the annual losses determined through the simulation. Exploring different parameter variations, the best match between measurement data and model was found at a thermal conductivity of 3 W/(mK) for the filling material (gravel) and 2.35 W/(mK) for the soil. At these values the annual difference in thermal losses between the simulation and measured values is less than 5%.

The respective outlet temperatures of the pipes for two selected parts of the year are shown in **Fig. 5**. The model outputs (lines) match the measurement data (dots) well. The temporal sections in spring (April) and fall (September) were selected because they exhibit strong temperature dynamics.

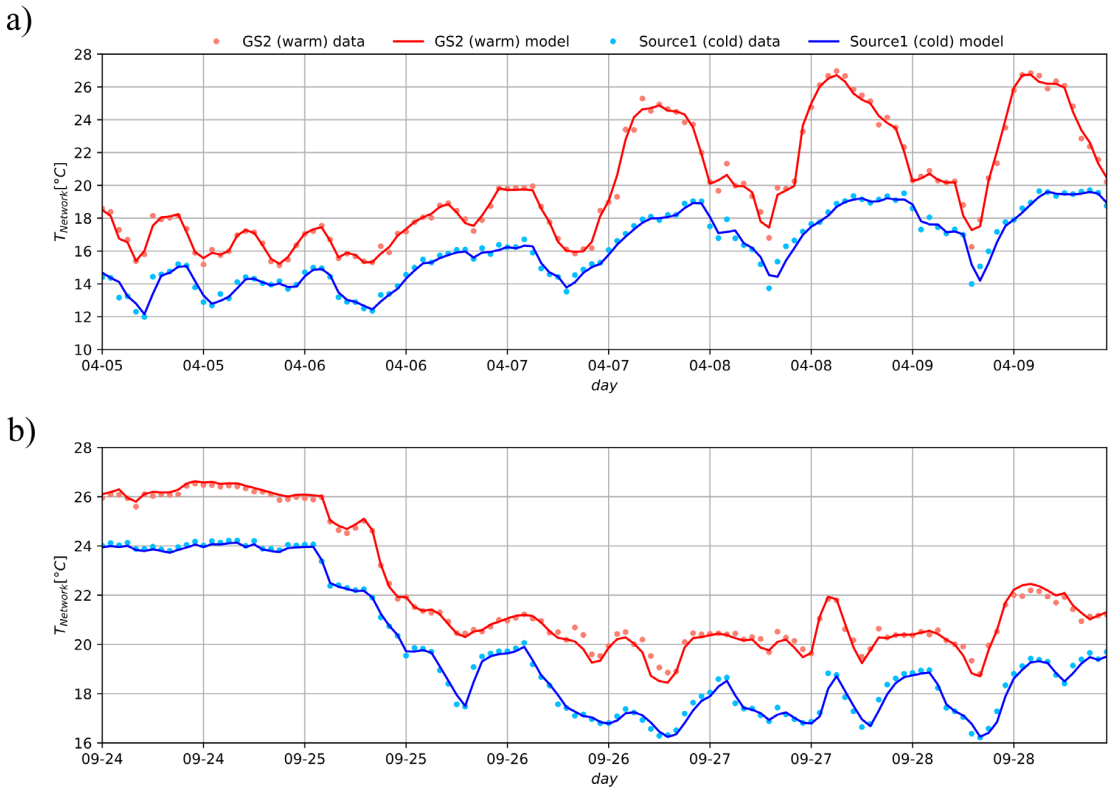

Fig. 5: Temperatures at Source1 and GS2 for warm and cold pipes. The measurement data is represented through dots and the model output by lines. Two temporal sections of the analyzed year with a pronounced dynamics were selected: April 5th to 9th in a) and September 24th to 28th in b).

The open-source TRNSYS framework pytrnsys, that will be used for the simulation in the current project also features a graphic user interface (GUI) that facilitates setting up the hydraulic systems to be simulated with TRNSYS. Pytrnsys is being currently extended from building HVAC systems to feature district heating networks within two national Swiss projects. This extension includes the possibility to connect district heating network components with double pipe connection by drag and drop, which can be automatically exported into a specific TRNSYS type handling hydraulic connections. An example of the GUI with a generic district heating network is shown in **Fig. 6**.

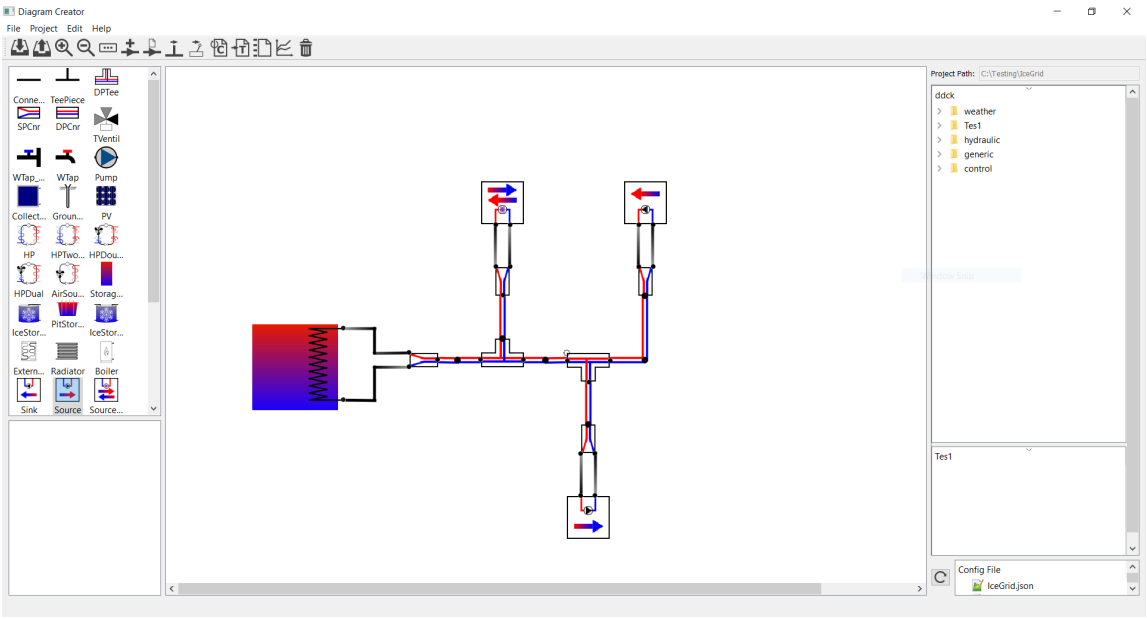

Fig. 6: Screenshot of the graphical user interface of pytrnsys while setting up a hydraulic scheme featuring a district heating network.

5. Conclusion

The qualitative behavior of the data measured on a double pipe section of a 5GDHC network is completely in line with the expectations. The beginning and end of the heating season are clearly visible as changes in the temperature level of the network. The relatively high heat losses can be attributed to a rather high temperature level overall, rooted in the abundance of heat sources as compared to sinks during the year monitored. The assumption that these losses will decrease significantly when the temperature level is decreased due to the addition of heat sinks, is well justified by the behavior of the system for the month of November. There the sudden temperature drop due to the onset of the heating season correlates even with heat gains in the network.

Employing the buried twin pipe model developed as an extension of TRNSYS TESS library type 951 during the current projects a good agreement between model output and measured data can be achieved when tuning the thermal conductivities of the filling material between the pipes and the surrounding soil while fixing the remaining model parameters to their nominal values.

Together with the identification of relevant network configurations and the extension of the TRNSYS framework pytrnsys to district network simulations, the validated buried twin pipe model forms a solid base to explore the usage of ice storages 5GDHC network through system simulations.

6. Acknowledgments

We would like to thank the Swiss Federal Office of Energy (SFOE) who supported this work within the project Ice-Grid (project nr. SI/502280-01).

7. References

Caputo, P., Ferla, G., Belliardi, M., & Cereghetti, N., 2021. District thermal systems: State of the art and promising evolutive scenarios. A focus on Italy and Switzerland. Sustainable Cities and Society, 65, 102579. https://doi.org/10.1016/j.scs.2020.102579

Carbonell, D., Schubert, M., & Neugebauer, M., 2021. BigIce—Assessment of solar-ice systems for multi-family buildings. Bundesamt für Energie BFE.

Ruesch, F., & Haller, M., 2017. Potential and limitations of using low-temperature district heating and cooling networks for direct cooling of buildings. Energy Procedia, 122(Supplement C), 1099–1104.

SPF-OST, 2021, Documentation of the pytrnsys framework, https://pytrnsys.readthedocs.io/en/latest/, © Copyright 2021, Institute for Solar Technology (SPF), OST Rapperswil (accessed 12.9.2022)

Sres, A., & Nussbaumer, B., 2014. Weissbuch Fernwärme Schweiz—VFS Strategie. Verband Fernwärme Schweiz VFS.

TRNSYS 2019, TESS Application libraries for TRNSYS 18, https://www.trnsys.com/tess-libraries/index.html (Acessed 12.09.2022)

Municipal Heat Planning to Exit from Coal, Oil and Natural Gas in a German Major City

T. Vaupel, H. Braas, I. Best, J. Orozaliev, K. Vajen, U. Jordan

University of Kassel, Institute for Thermal Engineering, Kassel (Germany)

Abstract

Following a decision by the city's municipal council in 2019, a climate protection council was formed in the German city of Kassel as an advisory body to develop possible concepts and measures with the help of specialist groups to outline how climate neutrality can be achieved in Kassel by 2030. A major challenge on the way to a climate-neutral city is the decarbonization of the heat supply. In Kassel, more than 85 % of the heat supply is based on fossil fuels. In order to investigate this transformation process as holistically as possible, using Kassel as an example, various scenarios are being developed for a heat supply without coal, oil and natural gas. These are based on a model for the development of heat demand, a building-specific heat atlas, a comprehensive determination of the local potential for renewable heat, and an hourly calculation of the heat supply variants with a subsequent profitability analysis

Keywords: district heating, transformation, district heating scenarios, roadmap, heat demand development, heat atlas, local renewable potentials

1. Introduction

An increasing number of German cities are setting themselves the goal of climate neutrality. One of these cities is Kassel, which in 2019, in connection with the "Climate Emergency Declaration", set itself the ambitious goal of becoming climate-neutral by 2030 and supplying itself with 100% renewable energies from local sources.

In some other studies, target scenarios and transformation paths to a climate-neutral heat supply are presented for large cities such as Hamburg and Berlin shown by *Egelkamp et al*. (2021) and *Kicherer et al*. (2021). However, the scenario for Hamburg only refers to the district heating supply and in the scenario for Berlin, constant assumptions were made for district heating expansion and densification. Therefore, the following study focuses on a holistic view of target scenarios and the transformation path towards decarbonization of the whole city of Kassel.

The methodology used in this study is based on procedures for municipal heat planning as described, for example, by the Climate and Energy Agency Baden-Württemberg (KEA-BW, Leitfaden kommunale Wärmeplanung by *Peters* (2020)) and already implemented, at least in part, in various research and practical projects.

Important components of municipal heat planning are, for example, an inventory analysis of heat consumption, a potential analysis for the use of renewable energies, the development of target scenarios and transformation paths from the status quo to the target scenario, an allocation of local and district heating areas and the development of concrete measures and transformation paths.

2. Heat Supply in Kassel: Status Quo

Decentralized gas heating systems cover about 2/3 of the total heat demand in Kassel. Based on data on existing oil tanks, it was estimated that about 9 % of the heat demand is generated with decentralized oil heaters. For the remaining 4 % of heat generators, the energy source is unknown; it is possible that these are also oil heating systems or other technologies, such as pellet burners and heat pumps (*Hinz* et al. 2020).

Approximately 21% of the total heat demand in Kassel is provided by a district heating network. Heat is generated

© 2022. The Authors. Published by International Solar Energy Society
Selection and/or peer review under responsibility of Scientific Committee
doi:10.18086/eurosun.2022.11.12 Available at http://proceedings.ises.org

by burning coal, waste, natural gas, processed waste wood (biomass) and sewage sludge in CHP plants, as well as fuel oil for peak load coverage. The heat supply is thus based entirely on fossil fuels and waste (see Figure 1).

The goal of the municipal energy supply company of Kassel, is to substitute coal combustion with sewage sludge and waste wood combustion by 2025. To this end, corresponding conversion measures are currently being carried out at the combined heat and power plants (Städtische Werke Kassel 2020).

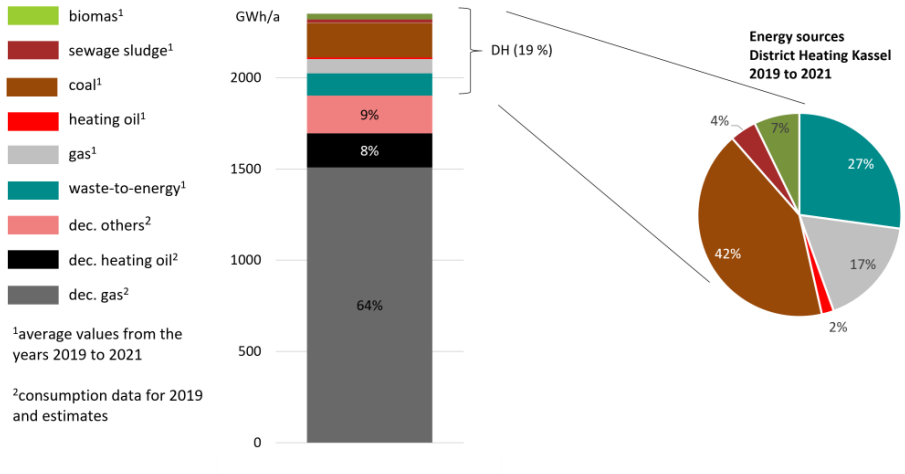

Fig. 1: Current energy sources in the heat supply of Kassel

3. Prioritization of Areas for Heat Networks and Decentralized Heat Supply

So far, about 21 % of Kassel's heat demand is provided by district heating. However, various studies on future decarbonized heat supply assume a much higher district heating share in large cities of 50 to 80 % *(Thamling and Langreder* 2020; *Gerhardt et al.* 2019; *Maaß et al.* 2021).

Figure 2 shows an example scenario for an allocation of 60 % of Kassel's heat demand. The evaluation is based on statistical blocks as the smallest administrative unit of a city, usually comprising blocks of houses separated by streets, rivers or similar (*Dieckmann and Trutzel* 1991).

Heat consumptions of individual buildings and path lengths are summed in the statistical blocks and heat occupancy densities, defined as the ratio of heat consumption to path length, are evaluated.

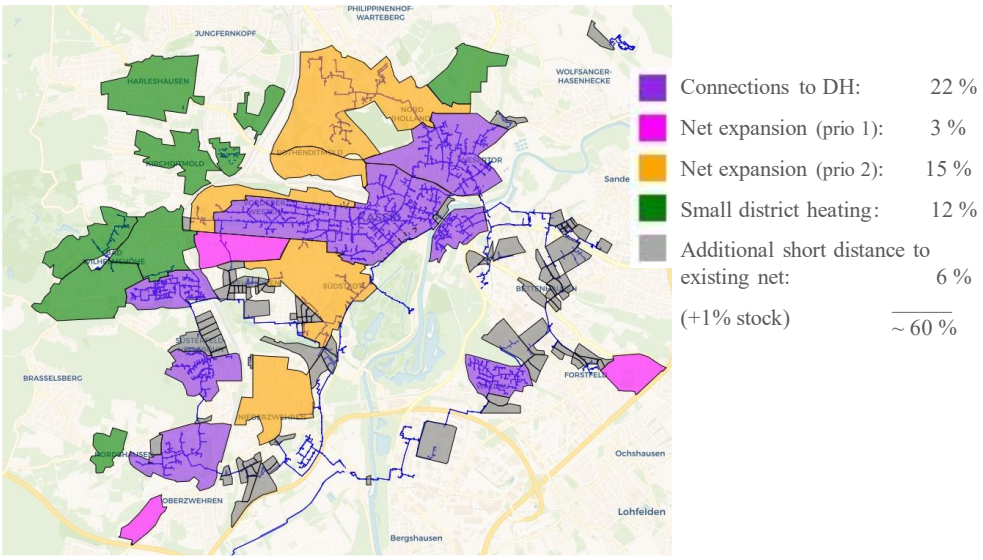

Fig. 2: Areas assigned to district heating in Kassel

4. Heat generation scenarios

4.1. Load Profile

The seasonal distribution of heat consumption is modeled by a synthetic standard load profile (SLP for short) in hourly resolution (BDEW, 2016) and it is based on an average outdoor temperature profile (Meteonorm) for the Kassel site. The load profile contains components for centralized and decentralized supply. For centralized supply, constant heat distribution losses of 15 % of the heat sales are taken into account for simplification purposes.

4.2. Calculation Tools

The heat input to the heat grid and the loading and unloading of the seasonal storage are calculated on an hourly basis using simplified Python-based balance models. The profile for solar thermal heat supply is determined by weather data (solar radiation and outdoor temperature) and the calculation of collector field efficiencies (for flat plate collectors) and then scaled over the installed area.

4.3. Future Energy Sources and Heat Pumps

The following technologies and energy sources are considered for a heat supply without coal, oil and natural gas:

- Feeding into heat grids: Waste incineration, biomass (waste wood), industrial waste heat, large-scale heat pumps, large-scale solar thermal systems, and biogas peaking boilers.
- Building-specific heat supply: Heat pumps, solar thermal and biomass boilers.

In the district heating supply, waste and sewage sludge incineration and the use of industrial waste heat serve as base loads and are assumed to be constant for simplicity. Biomass (waste wood) and biogas serve to cover peak loads. The potential of sewage sludge, waste wood and waste incineration estimated by the municipal energy supplier and the estimated waste heat potential amount to a total of approx. 700 GWh/a. This corresponds to a share of total heat consumption in Kassel of approx. 30 %. Waste and residual waste incineration already generates high surplus heat in summer, which has so far been dissipated with river water (Fulda). In order to make this surplus heat usable in winter, a seasonal storage facility is necessary.

For large heat pumps feeding into heat grids, an average system annual performance factor (SPF) of 3.1 is assumed. Possible heat sources for large-scale heat pumps are low-temperature waste heat from industry, as well as river, sewage plant and other wastewater, and shallow and deep geothermal energy.

Due to the limited availability of biomass, it is assumed that only about 5% of Kassel's total heat demand is assumed to provided by decentralized biomass. In addition, it is assumed that the summer heat demand for all biomass heating systems is covered by a solar thermal system.

Since air-source heat pumps are predominantly used in large cities and the vast majority of buildings will not have been renovated by 2030, a mean system annual performance factor (SPF) of building heat pumps of 2.7 is assumed, following the results of *Bergmann and Erhorn* (2017); *Langner et al.* (2014); *Günther et al.* (2020). In addition, it is assumed that every fourth heat pump heating system is combined with a solar thermal system.

4.4. Seasonal Storage

A pit storage tank is considered as seasonal storage. To increase the seasonal storage capacity, the storage tank is additionally charged with an internal heat pump, which cools the lower part of the store down to 20°C. The temperature in the upper part of the store is assumed to be 85°C.

Such storage facilities with volumes between approx. 60,000 m³ and 200,000 m³ have already been built in the Danish cities of Dronninglund, Marstal, Gram and Vojens, for example. Another storage facility with a volume of

700,000 m³ is currently being planned in Odense, Funen (DK).

Feasibility studies and technical investigations on the upscaling of such earth reservoirs can be found, for example, in the publications by *Tziggili et al.* (2013), *Weinhold and Rühling* (2019) and van Helden (2022), respectively. New liner materials are currently being developed that should enable a storage temperature of 95 °C in the future. The publication also shows that storage volumes of up to 2 million m³ are feasible (van Helden 2022).

4.5. Scenario with a District Heating Share of 60 %

Fig. 3 shows the seasonal distribution of the heat supply for the scenario with 60 % district heating. With the highest priority in the heat supply, combustion processes are considered from heat carriers that can only be stored to a limited extent (i.e. waste and sewage sludge) and waste heat from industry and commerce, followed by solar thermal energy. The storage is designed in such a way that no unused surpluses remain from these heat carriers. Additionally, the storage tank is fed from the internal heat pump to a certain extent.

To save as much biomass as possible for the peak load demand, the seasonal storage water is used to provide the heat demand, as soon as all heat sources other than biomass together don't cover the demand. The heat that is then still required (beyond the provision of heat from the storage and biomass), is provided by an additional peak load boiler, which can be operated with biogas, for example.

For the waste incineration plant, a maintenance interval of 2 weeks in September is taken into account, based on today's operating mode. Today, the waste incineration plant runs at reduced capacity during summer. In the scenario however, it is assumed that the waste incineration plant is also operated at full load in the summer, in order to be able to provide as much heat as possible. For peak load coverage, the discharge capacity of the storage tank is increased. The number of storage cycles per year is 1.34.

In the scenario shown in Fig. 3, the share of the overall heat demand provided by district heating is 60%, of which 12% is local heating. About 12% of the heat demand is covered by river heat pumps and 5% by the wastewater heat pump. Decentralized and large heat pumps for local heat supply cover 38% of the total heat demand of the city of Kassel. A small share of solar thermal and biomass is also planned for the local heat supply. The share of solar thermal energy from central collector fields is 2.3% of the total heat demand. This corresponds to a collector area of about 100,000 m².

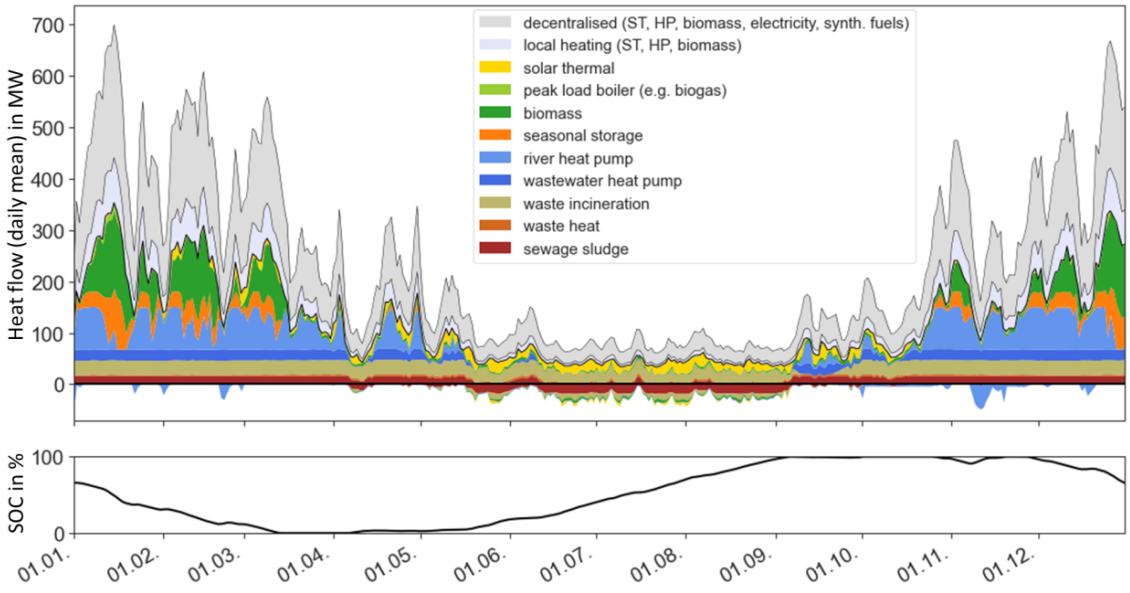

Fig. 3: Load profile of the 60% scenario with all heat generators used

5. Summary and Conclusion

A heat atlas has been developed for the city of Kassel in which heat consumption is mapped for each building. Scenarios for the development of the heat demand yield a decrease in heat demand of approx. 17 % by 2030 compared to 2019.

In order to achieve high coverage rates of renewable energies, a densification and expansion of the district heating network to approx. 60 % (includes 12% local heating) of the total heat demand of the city of Kassel is considered. Suitable district heating and local heating areas were identified using an algorithm as well as manual refinement taking into account additional constraints. The initial parameters used are the heat occupancy density and the spatial proximity of the areas to the district heating network.

For district heating, a medium-term potential for waste, sewage sludge and waste wood incineration as well as industrial waste heat of about 700 GWh/a was determined for Kassel. Biogas plants were considered to cover peak loads. Using simplified balance models, a storage volume of approx. 1 million m^3 was determined in order to use the surplus heat from the incineration processes for the existing district heating system and to successively integrate large-scale heat pumps and solar heat into the central heat supply system in the event of a district heating expansion. With district heating accounting for 60 % of total heat consumption, the storage capacity is sufficient to achieve a solar thermal share of about 2.3 % of total heat demand (4 % of district heating demand) in Kassel.

The goal of operating the heat supply system in Kassel without the energy sources coal, oil and natural gas as early as 2030 proves to be extremely ambitious. All energy-saving and supply potentials must be fully exploited without delay. This involves, for example, broad-based building refurbishment, the installation of innovative heat supply systems in buildings, and the provision of additional resources and central infrastructure, such as the expansion of heating networks, the installation of large-scale heat pumps and the development of suitable low-temperature sources, the provision of large areas of land, and the installation of solar thermal systems and storage facilities. In particular solar thermal systems and ground-source seasonal storage require system sizes that have been projected in isolated cases but have not yet been implemented on this scale. The provision of the necessary regeneratively generated electricity will also be a major challenge in the coming years.

6. Acknowledgments

The authors gratefully acknowledge the support of Städtische Werke Kassel and the Environmental and Garden Department of the City of Kassel, as well as the financial support of the research project "Wärmewende Kassel" from the State of Hessel, HMWEVW, through the European Regional Development Fund (EFRE)

7. References

Bergmann, Antje; Erhorn, Hans (2017): Energieeffizienz elektrisch angetriebener Wärmepumpen. Praxisergebnisse aus dem Monitoring

BDEW (2016): BDEW/VKU/GEODE-Leitfaden. Abwicklung von Standardlastprofilen Gas. Hg. v. BDEW Bundesverband der Energie- und Wasserwirtschaft e. V., Verband kommunaler Unternehmen e. V. (VKU) und Groupement Européen des entreprises et Organismes de Distribution d'Énergie (GEODE). Berlin.

Dieckmann, Jochen; Trutzel, Klaus (1991): Deutscher Städtetag 1991. Kommunale Gebietsgliederung.

Egelkamp, Robert; Wett, Lina; Kallert, Anna Marie Dr.-Ing. (2021): Potenzialstudie klimaneutrale Wärmeversorgung Berlin 2035. Analyse erneuerbarer Wärmepotenziale für eine klimaneutrale Wärmeversorgung in Berlin bis 2035.

Gerhardt, Norman; Ganal, Irina; Jentsch, Mareike Dr. (2019): Entwicklung der Gebäudewärme und Rückkopplung mit dem Energiesystem in -95 % THG Klimazielszenarien.

Günther, Danny; Wapler, Jeanette; Langner, Robert; Helmling, Sebastian; Miara, Marek Dr.; Fischer, David et al. (2020): Wärmepumpen in Bestandsgebäuden: Ergebnisse aus dem Forschungsprojekt "WPsmart im Bestand" (Abschlussbericht).

Hinz, Andreas; Orozaliev, Janybek Dr.; Vajen, Klaus Prof. Dr. (2020): Effizienzoptimierung und Perspektiven der Fernwärme Kassel. Kurzfassung des Abschlussberichts, Juli 2020.

Kicherer, Nina; Lorenzen, Peter; Schäfers, Hans (2021): Design of a district heating roadmap for Hamburg. In: *Smart Energy* 2, S. 100014. DOI: 10.1016/j.segy.2021.100014.

Kuhlmann, Andreas (2019): Statistiken und Analysen zur Energieeffizienz im Gebäudebestand. Dena Gebäudereport 2019.

Langner, Robert; Günther, Danny; Miara, Marek Dr.; Helmling, Sebastian; Wapler, Jeanette (2014): "WP-Monitor". Feldmessung von Wärmepumpenanlagen.

Maaß, Christian; Freiberger, Leona; Sandrock, Matthias Dr. (2021): Grüne Fernwärme für Deutschland. Potenziale, Kosten, Umsetzung, 08.03.2021.

Peters, Max Dr. (2020): Leitfaden Kommunale Wärmeplanung.

Ekaterini Tziggili, Thomas Schmidt, Dirk Mangold (2013): "Gesamtbetrachtung zu solaren saisonalen Wärmespeichern und mögliche multifunktionale Nutzungen". Forschungsbericht zum BMU-Vorhaben 0325976A.

Städtische Werke Kassel (2020): Kohleausstieg schon 2025: Neue Anlage im Fernwärmekraftwerk. Online verfügbar unter https://www.sw-kassel.de/ueber-uns/kommunikation/aktuelles/einzelansicht/kohleausstieg-schon-2025-neue-anlage-im-fernwaermekraftwerk/, zuletzt aktualisiert am 25.03.2022.

Thamling, Nils; Langreder, Nora (2020): Perspektive der Fernwärme.

van Helden, Wim (2022): Giga-scale thermal energy storage for renewable districts.

Weinhold, Katja; Rühling, Karin (2019): Grean Heat 3. Entwicklung innovativer Energieversorgungstechniken und –strukturen mit den Kernkomponenten modularer Großwärmespeicher und Maxianlage Solarthermie.

Heat Pumps in Positive Energy Districts

Carsten Wemhoener[1], Fabian Ochs[2], Franziska Bockelmann[3], Christina Betzold[4]

[1] Institute of Energy Technology, OST Eastern Switzerland Univ. of Appl. Sciences, Rapperswil (CH)

[2] Unit of Energy-efficient building, UIBK Building construction, University of Innsbruck (AT)

[3] Steinbeis Innovation Centre SIZ energieplus, Braunschweig (DE)

[4] Energy campus Nürnberg, Technische Hochschule Nürnberg Georg Simon Ohm (DE)

Abstract

The new Annex 61 in the Technology Collaboration Programme (TCP) on Heat Pumping Technologies (HPT) of the International Energy Agency IEA entitled "Heat pumps in positive energy districts" deals with in-depth investigations on heat pump (HP) application in clusters of buildings and positive energy neighbourhoods/ districts. As extension of the unique features of HP in individual buildings, the application of HP in clusters of buildings and neighbourhoods can unlock further potentials of load balancing and waste heat recovery. Based on the state of the art the Annex systematically investigates HP concepts in more detail regarding design, control and integration potentials by both system simulation and monitoring. Besides new built clusters, also renovation concepts for existing neighbourhoods are a focus to shift the balance in the direction of zero energy/emission targets. The paper gives an outline of the Annex work and more detailed insight into four exemplary case studies to be investigated within the Annex framework.

Keywords: heat pump, positive energy district, clusters of buildings, simulation, monitoring

1. Introduction

Climate protection developed as one of the largest challenges to secure the survival of mankind. The global carbon budget for keeping the 1.5 °C target established in the Paris Agreement of 2015 (UN, 2016) is reached within a time frame of less than 10 years at current CO_2-equivalent emissions (IPCC, 2021). Thus, efforts in all fields to reduce greenhouse gas emissions are urgently required and many cities have already declared climate emergency in the recent years.

The built environment is a key sector for fast emission reductions in many countries. For instance, in the EU, 36% of the emissions are due to buildings, so reaching ambitious climate targets will be strongly facilitated by transforming the building sector. For new building standards have developed to high performance requirements. Furthermore, buildings shall contribute to cover their own demand, leading to the nearly zero energy concepts (nZEB), which has been established in the EU with the recast of the Energy Performance of Buildings Directive (EPBD, EC 2010) and is the current requirement from January 1, 2021 in the EU member states. Also the USA and Canada as well as Japan and China have targets to reach Net Zero Energy Buildings (NZEB) in the time frame of 2020 to 2030. Ambitious targets, though, are harder to achieve in existing buildings. However, the latest version of the EPBD of 2018 also requires the member states to develop retrofit strategies to notably enhance the energy performance of the building stock. For new dwellings, also examples to even transcent the nZEB balance and reach a positive energy balance exist with the ability to export parts of on-site energy production to connected grids. This concept can be extended to clusters of buildings and districts deriving a positive energy district. However, former work, among others in the HPT Annex 49 on "Design and integration of HP in nZEB" confirmed, that in particular for larger residential and office buildings, reaching a positive energy balance on the individual building level can still be challenging (Wemhoener, 2020). In this sense, extension to clusters of buildings with different load structures also have potentials to enhance the heat pump (HP) performance and enable to reach ambitious energy targets.

On the other hand, in the Net Zero Roadmap of the International Energy Agency (IEA) (IEA, 2021), HP are seen as dominating heating systems with a share of 70% globally by 2050.

© 2022. The Authors. Published by International Solar Energy Society
Selection and/or peer review under responsibility of Scientific Committee
doi:10.18086/eurosun.2022.11.13 Available at http://proceedings.ises.org

While HP are already establishing as standard heating system in the new built market in many countries, application of (larger) HP for the use in cluster of buildings and neighborhoods are not yet as common. Comprehensive recommendations for the best integration of the HP from a purely decentralized use on individual building level to an entirely centralized integration are missing, and performance potentials of HP application in districts depending on load boundary conditions are not obvious. Moreover, further benefits of HP in cluster of buildings regarding storage options and unlocking of energy flexibility as well as economic implications are further investigated to entirely assess potentials and facilitate ambitious energy performance/emission reduction.

2. Outline of the HPT Annex 61

On this background, the new Annex 61 in the Technology Collaboration Programme (TCP) on Heat Pumping Technologies (HPT) of the IEA entitled "Heat Pumps in Positive Energy Districts" studies the application of HP for clusters of buildings and positive energy neighborhoods (PEN)/ -districts (PED). The focus is on smaller clusters of buildings and neighborhoods, mainly with residential and office use. While the majority of project contributions concentrate on new built clusters, quite some projects also focus on strategies to increase the energy performance of existing neighborhoods to approach a zero energy/emission balance, which is also in the scope of the Annex. Thereby renovation strategies include both the improvement of the building envelope and the integration of HP, and optimized concepts are to be evaluated.

Besides the unique performance features of HP and the ability to provide the different building services of space (SH)/domestic hot water (DHW) heating and space cooling (SC)/dehumidification (DH) even at the same time, HP are also a key technology to link the on-site electricity production and heating/cooling demands in districts, respectively. Thus, supposed benefits of the HP integration in districts are manifold.

- the high energy performance of HP enables to reach ambitious energy/emission targets
- the simultaneous operation of HP for different building services enables a waste heat recovery for other building services, e.g. by simultaneous space cooling and DHW heating within the district
- the link of electric and thermal energy allows for load balancing within the district of electric and/or thermal loads as well as on-site electricity production for enhanced self-consumption
- the load balancing can also provide energy flexibility for connected grids, so that the district can provide services for other parts of the city

In order to assess the HP potentials the Annex work follows a 4-step methodology divided into Tasks. Based on the state-of-the-art analysis of HP use in already existing clusters of buildings or PED, a concept analysis for HP in PED is carried out. For promising concepts a detailed techno-economic analysis is accomplished and backed-up by monitoring of HP operation in PED, which are evaluated in parallel to the concept analysis. Details on the individual Tasks is given in the following

- Task 1: State of the art analysis (January 2022 – December 2022)

  Starting from already existing HP systems in cluster of buildings the state of the art is characterized and boundary conditions for the follow-on tasks are gathered. As Key Performance Indicators (KPI) CO_2-eq-emissions and further ecological and economic KPI are considered. As result of Task 1 an assessment of technically realistic options for PED as well as an economic estimation of reachable ambition levels and the economic handicap could be evaluated. Therefore, standardised load profiles are generated and used for archetype district, e.g. entire residential use, mixed residential and office use etc. These archetype districts are to be characterised by the building quality reflected in the loads, the available renewable sources and the on-site energy production options.

- Task 2: Generic concepts development (July 2022 – July 2023)

  Task 1 is followed by Task 2 for the analysis of generic system concepts. Starting from decentralized concepts on individual building level as reference different categories to a central integration are defined, comprising a purely electric connections, a collective heat source, a semi-centralized integration in terms of mixed centralized and decentralized HP, e.g. a central SH HP combined with a "booster" decentralized DHW HP up to a fully centralized HP integration. Figure 1 shows the generic concepts dependent on the degree of integration of the HP in the district. For each subsystem, a short technical characterization is elaborated. As result, an overview of generic integration options of the HP in districts with pros and cons and favorable applications as well as recommendations are foreseen.

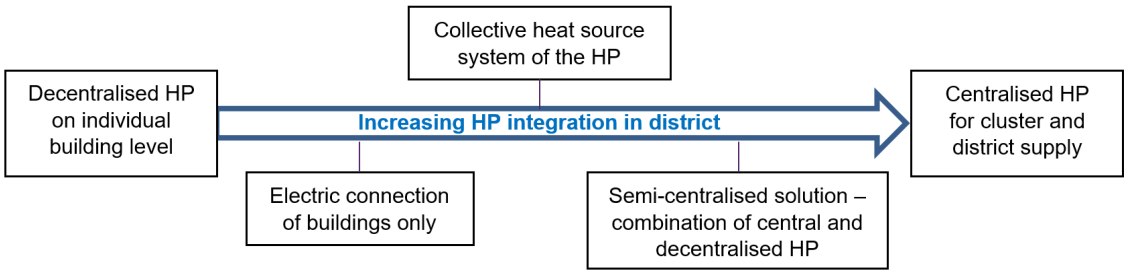

Fig. 1: Generic system concepts depending on the degree of integration of the heat pump in the district

- Task 3: Techno-economic analysis of promising concepts (January 2023 – December 2024)

Based on the favorable system concepts derived in Task 2 a more detailed techno-economic analysis is carried out, in particular regarding the design and control as well as integration with storage and other generators to optimize the HP operation regarding performance, renewable energy integration, system cost and energy flexibility. The detailed investigations are carried out by simulations where also modelling aspects of larger heat pumps are a research topic. Task 3 also serves to evaluate optimization potentials of real system in monitoring in Task 4, which in turn yield operation and performance data to validate the models.

- Task 4: Monitoring and system optimization of the real performance of HP in districts

As mentioned above Task 4 is dedicated to the evaluation of the real performance of HP in district applications and to the identification of typical optimization potentials in the real operation for the different heat pump integration options in monitoring. Moreover, a comparison and verification to simulated values is enabled by the real operational data.

- Task 5: Dissemination of interim results

All task are accompanied by dissemination activities like workshops, articles, website information and presentations, which are summarized in an overarching Task 5

Table 1 gives an overview of possible contributions of the interested and participating countries in the Annex.

Tab. 1: Possible contributions of the interested and participating countries

Country	Institution	Contributions
AT	UIBK, AIT, AEE-intec	• Concept for 7 equal multi-family houses (MFH) by simulation/monitoring • Evaluation of HP in clusters of buildings (decentral, semi-central, central)
BE	ULB, KU Leuven, Swecobelgium, Vito	• Design, simulation and monitoring of clusters of offices and neighbourhoods with sewage water heat source • Clean cluster concepts for dedicated load situations • HP in a retrofitted neighbourhood to plus energy level
CA	Concordia	• Case studies of positive energy neighbourhoods by simulation
CH	IET OST	• Simulation and monitoring of positive energy neighbourhood • Design of larger heat pumps for MFH and clusters of buildings
DE	THN, SIZ energieplus	• Model predictive control of 8 single family houses for energy flexibility • (Retrofit) concepts for MFH/neighbourhood by simulation and monitoring
IT	Univ. Firenze	• Monitoring and simulation of neighbourhood with seasonal thermal storage, HP and solar collectors/troughs
JP	Univ. Nagoya	• Evaluation of contribution of HP in positive energy district to reach climate protection targets • Case studies of simulation and monitoring of HP in districts
NL	EnergyGo	• Investigation of decentralised and centralised system concepts for HP in new built and retrofit application
SE	RISE	• HP modelling and development for the use in thermal grids • Control of HP flexibility in thermal grids and large-scale control of HP
US	NIST, ORNL, EPRI	• Simulation, testing and monitoring of high performance ground source integrated HP with different ground-source systems (horizontal/borehole)

3. Case studies in clusters and districts

In the following four examples of the contributions of Austria, Germany and Switzerland are given. The projects have a different state, since the Annex 61 is in the starting phase. The monitoring projects of Germany refer to clusters of buildings, where the monitoring is already ongoing; the projects of Switzerland and Austria refer to larger clusters of above hundred flats and are in the planning and commissioning phase. The project apply different degrees of HP integration. The ongoing monitoring in Germany refers to a cluster of eight single family plus energy houses in a semi-central configuration with central space heating and free-cooling and decentralized DHW supply. Moreover, two cluster of two and four multi-buildings, respectively, are in monitoring in Konstanz and Wolfsburg. In the Austrian project central district heating is combined with decentralized heat pumps and in the Swiss project, a centralized HP integration is investigated.

2.1 Cluster of eight terraced plus energy houses, Herzo Base, Germany

The cluster of eight terraced houses is located in Herzogenaurach, Germany in the new district Herzo Base and built in 2017. The buildings were designed as an "all electric buildings", which means that the core source of energy is electricity. A PV-system (88 kWp) on the roofs delivers an annual surplus of energy. The idea of small neighbourhoods creating an energy community and share energy systems enables higher potential to increase the PV self-consumption. Furthermore, synergies between different electrical loads lead to a more even electrical profile and reduces electrical load peaks. The terraced houses share a central heat pump system of two modulating heat pump (MHPs) of each 17 kW_{th}, with geothermal heat source as well as a battery system with a capacity of 40 kWh_{el}. The supply of domestic hot water is decentralized in each terraced house by a domestic hot water-HP (Booster), which use the heating buffer storage units as heat source. All 8 terraced houses are equipped with floor heating and decentralized ventilation devices. The objectives of the field monitoring is the evaluation of the plus energy balance and PV self-consumption. Another aspect is the field test and evaluation of advanced control strategies in order to increase PV self-consumption and reduce energy costs. Fig.2 show the building cluster and and its position in the district.



Fig. 2: Building cluster Herzo Base, Herzogenaurach, DE

In the planning phase, a plus energy balance has been envisaged and just reached. The monitoring data demonstrate a clear positive energy balance on an annual observation period. In the simulation, a standard weather data set of the German Weather Service (DWD) was used, which has lower solar radiation and outdoor temperatures compared to the monitoring. Also, in contrast to the planning phase, less electricity is consumed due to low household electricity consumption and lower number of electrical vehicles. On the other hand, the heat energy consumption is higher than expected due to higher room set point temperatures and window ventilation. Nevertheless, the supply cover factor (incl. PV and battery) is 37 % and load cover factor is 64 %.

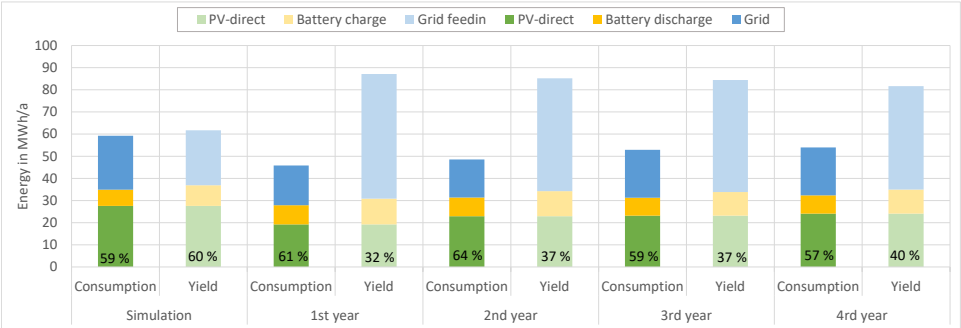

Fig. 3: Annual balance for PV yield and consumption

Fig. 3 shows the annual balance of PV yield and total electricity consumption. The total electricity consumption includes all consumers of the terraced houses: electricity for appliances, heat pumps, auxiliary energy and other consumers. By the change of control strategy of the heat pumps to a PV optimized operation in the 2nd year, the PV self-consumption could be increased by 12.5%. Regarding the efficiency of the heat pumps, the MHPs achieve a good overall system performance factor (SPF) of about 4.8. The SPF of the boosters are quite constant by 4.2, which is very good for providing high storage temperatures. The balance is based on the produced energy and the electrical power consumption of the compressor and the source circulation pump. The SPF of the system, which includes the thermal used energy (heating + DHW) and thermal losses as well as electrical energy for all heat pumps and auxiliary energy, is constant at approx. 3.3 over the years. In the winter months, the SPF of the system reaches good values of 4, but it drops to just under 2 in the summer. Due to high auxiliary energy, e.g. circulating pumps and circulation, especially in summer, the SPF of the system is only 3.3. The share of auxiliary energy is about 13% in summer and about 5% in winter. With regard to the individual heat pumps, very good SPFs are achieved. When considering the overall system, only moderate SPFs are achieved due to high auxiliary energy. Tab. 2 shows results from the monitoring over four monitoring periods.

Tab. 2: Monitoring results (average over four years (2019 – 2022)

	Building cluster Herzo Base
Heating consumption	Space heating 32.8 kWh/(m²a) (59%) Domestic hot water 22.6 kWh/(m²a) (41%)
Electricity consumption	Heat pumps 11.1 kWh/(m²a) (25%) Boosters 5.4 kWh/(m²a) (12%) Household and other technical 27.3 kWh/(m²a) (62%)
Load Cover Factor and Supply Cover Factor	LCF ~ 64% SCF ~37%
SPF HP	MHPs 4.8 Boosters 4.2 all HP together 3.3

In addition to monitoring, the operation of a model predictive control (MPC) is investigated (Betzold et al., 2022). On the one hand, a simulation study was carried out, on the other hand, the operation was implemented in real in the terraced houses. The simulation of the control strategies shows that due to the large PV production, a very high PV self-consumption is already achieved in heat-controlled operation. Advanced control strategies, like MPC, increase the load cover factor by only 2% to 3% percentage points. Energy cost savings can be achieved especially by MPC by up to 34%. In addition to operation at PV production, efficient operation with high COP at partial load is crucial for energy cost savings. The real operation of the MPC in the terraced houses shows that deviations in the prediction and modeling as well as the interpretation of the setpoint from the online simulation lead to different results in real operation. The operating costs of online simulation and measurement show deviations of -64%.

The terraced houses present the integration of renewable energies in a cluster of buildings and achieve very good values in terms of load cover factor, efficiency and operating costs. Under real weather conditions, the PV system could be scaled down to still achieve very good results.

2.2 Multi-family building clusters with EnergyPlus concept in Konstanz and Wolfsburg, Germany

The planning and implementation of a completely renewable energy supply for a block of residential buildings in an urban structure presents a challenge. This was achieved in the two projects by providing heat using a ground-coupled HP. The multi-family houses in Konstanz and Wolfsburg were completed in 2016 and supply a net floor area of 1140 and 9500 m².

Fig. 4 shows the building cluster in Konstanz (two buildings) and Wolfsburg (four buildings). The energy concepts of the residential buildings are based on heat supply via HP. The generated heat is temporarily stored in buffer tanks and delivered to the low-temperature heating systems. The DHW is heated via fresh water stations or storage tank charging systems. Decentralized exhaust air systems or central ventilation systems ensure a constant air exchange. Natural ventilation via the windows is possible in all properties.



Fig. 4: Cluster of multi-family buildings in Konstanz (left) [source: WOBAK] and Wolfsburg (right), DE

Photovoltaic systems are installed to cover the electrical energy needs of the system technology and the connected households. The system technology is optimized for so-called "PV self-consumption", which means direct use of the photovoltaic yields. Electrical energy from the PV systems that cannot be directly consumed or stored is fed into the public electricity grid. The comparison of the multi-family buildings refers to their efficiency, ecology and economy, with the overall balance and thus the total consumption of electrical energy serving as the basis for evaluation. The consumption of the buildings is made-up of the electricity consumption of HP and circulation pumps, general electricity (lift, staircase, garage, etc.) and the user electricity of the individual flats (appliances).

Tab. 3: Key data on the building and supply concept

	Konstanz	**Wolfsburg**
building	2 buildings (2016) with 12 apartments in total; 3 floors each; Net Floor Area (NFA) 1140 m² (total)	4 buildings (2016) with 68 apartments in total; 4 floors each; Net floor Area (NFA) 9500 m² (total)
PV-system	59.2 kWp on the roof; roof slope 10° to west and east	27.4 kWp on the roof of house A; Roof slope 45° to south (possible PV size ~160 kWp)
heat pump	2x brine-to-water-HP (30 + 27 kW)	2x brine-to-water-HP (90 + 50 kW) and 4x air-to-water-HP (each 14 kW)

In Fig. 5, the electricity consumption (divided into self-consumption and electricity from the grid) compared to the PV production (divided into self-consumption and grid feed-in) for the years 2018 to 2021 as well as the planning values are listed. It can be seen that the electricity requirements estimated in the planning for the buildings do not correspond to the determined electricity consumption; more electricity is consumed. This is due to higher user electricity for appliances and hot water consumption. Nevertheless, it can be shown that a solar load cover factor of up to 35% of the total energy consumption and a supply cover factor up to 40% can be realized.

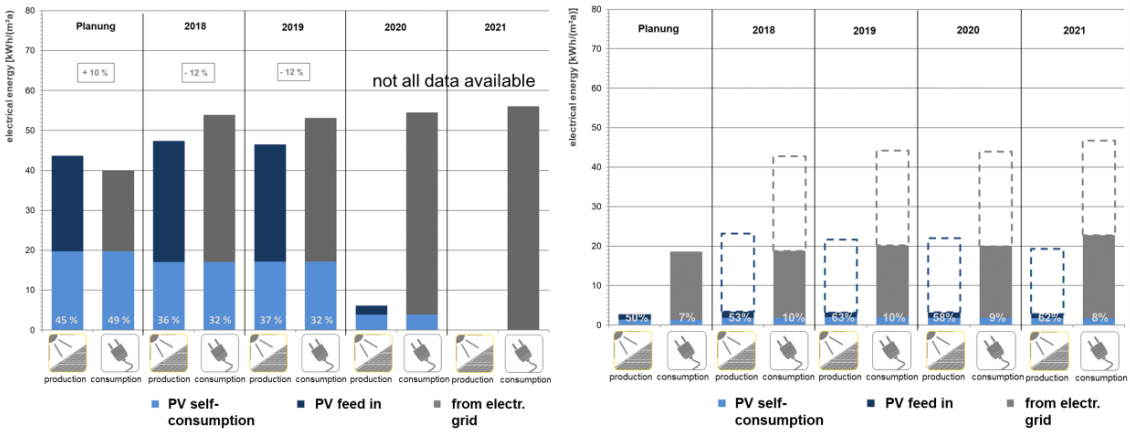

Fig. 5: Annual energy balance, multi-family buildings Konstanz (left) and multi-family buildings Wolfsburg (right) (dotted bars: possible PV yield for total PV on the roof and additional electricity for appliances), DE

The EnergyPlus balance could not achieved due to the higher electricity consumption and in the case of Wolfsburg, the possible PV area on the roofs is also too small to cover the total electricity demand (annual balance). Table 3 shows the annual averages of the four monitoring years for the multi-family houses in terms of heat and electricity consumption and coverage shares. Differences in the coverage shares between the monitoring years can be attributed to volatile PV yields and fluctuating electricity consumption.

Tab. 3: Monitoring results (average over four years (2018 – 2021)

	Konstanz	**Wolfsburg**
Heating consumption	SH 56.3 kWh/(m²a) (71%) DHW 23.0 kWh/(m²a) (29 %)	SH 41.7 kWh/(m²a) (66%) DHW 21.6 kWh/(m²a) (34 %)
Electricity consumption	HP 23.0 kWh/(m²a) (43%) appliance and other technical 31.0 kWh/(m²a) (57 %)	HP (incl. auxiliaries/general consumption) 20.0 kWh/(m²a) (46%) Appliances 24.0 kWh/(m²a) (54 %) (assumption)
Load Cover Factor/ Supply Cover Factor	LCF ~ 32% SCF ~37%	LCF ~9% * SCF ~60% *
SPF HP	3.94 (all HP together)	3.96 (all HP together)

*Includes only the technical room; without appliances

In the case of the multi-family building in Wolfsburg, it must be taken into account that only the technical room (HP and heating supply systems, auxiliaries and general electricity) is supplied with PV electricity in the evaluation and balance. The electricity for appliances is not included, as it is not measured and cannot be covered by PV electricity in the implementation. For legal reasons regarding the grid connection and supply of the four buildings, the PV system cannot be fully installed in Wolfsburg. For this reason, PV was only installed on one roof and only supplies the building technology in the technical room with electricity. Figure 4 shows the possible PV yields as dotted bars, if the cluster had been equipped with all possible PV modules and the additional electricity consumption for appliances.

A comparison for estimating the CO_2 reduction is based on the supply concepts with gas condensing boiler with solar thermal and electricity grid connection as well as district heating and electricity grid connection depicted in Fig. 6. The two example concepts are common supply concepts for multi-family houses in Germany in order to fulfil the minimum standard. No credits for feed-in of PV electricity into the grid were taken into account. It can be clearly seen that the conventional concepts emit 10 to 80 t/a or 40 – 108 % more CO_2 (depending on the concept and building) than the implemented HP concept. Both the results determined from the monitoring and the general energy conceptualization prove that, in addition to the use of HP, photovoltaic systems also represent essential building blocks for achieving the goal defined by the federal government of a nearly climate-neutral building stock by the year 2045. Both in the balancing and in future concept considerations and designs, care should be taken to ensure that the concepts are designed for an overall energy balance, i.e. heat and electricity requirements including user electricity for the entire building are taken into account.



Fig. 6: Annual CO_2 emissions compared to supply concepts with gas boiler and solar thermal or district heating (heat + electricity)

2.3 Campagne district in Innsbruck, Austria

A new low-energy residential district is being built in Innsbruck, Austria. The building owners (social housing companies) had to make decisions with respect to the energy quality of the buildings and the heating system with respect to the energy and environmental impact. The district will be composed of 16 buildings grouped in four blocks (Fig. 7). The main part of the buildings is residential and will consist of approximately 1100 new apartments for a total surface of 78027 m^2. Moreover, sport facilities, cafes, schools and kindergartens will be constructed. In the planning phase, a cooperative process was carried out, involving neighbouring residents and local associations.



Fig. 7: Building cluster of Campagne, Innsbruck, AT (source: ibkinfo.at; stadtteilzentrum-reichenau.at, Bogenfeld Architekten)

The buildings are built according to Passive House standard (space heating demand lower than 15 kWh/(m^2a)). The space heating demand is supplied by a groundwater HP and the emission system is floor heating. The domestic hot water is provided by the district heating network, which accounts for a high proportion of heat by renewable sources, industrial waste and bioenergy. The shares of renewable sources and industrial waste heat of the district heating of Innsbruck are higher than other cities in Austria and it is foreseen that these shares are going to increase in the future. Photovoltaic panels are installed on the roof on the buildings to cover the electrical demand of auxiliaries. Moreover, sustainable mobility solutions are planned to enhance the electric mobility.

A comprehensive simulation study has been carried out (Dermentzis et al., 2021) investigating different types of heat generation system (e.g. alternatives and/or combinations with HP), varying the level of centralisation of the heat generation system and the type of heat distribution system. The aim of the study was to find the best combinations with respect to energy and environmental impact. The results supported the decision-making procedure of the Campagne project. The options concerning the heating system are district heating (DH), heat pump (HP), or the combination of both (HP and DH). In the latter case, the two systems are hydraulically separated, i.e. HP covers the space heating and DH covers the DHW demand. A natural gas boiler was used as a reference heating system. The selected KPIs to compare the system concepts were the total primary energy demand (i.e. renewable and non-renewable primary energy demand) and the CO2 emissions. Besides, the KPIs were evaluated with annual or monthly conversion factors. One building was modelled and simulated in detail, and then the results were extrapolated to the whole district. The assumed characteristics of the buildings are shown in Tab. 4.

Tab. 4: Assumption of the modelled building

Space heating demand	14.5 kWh/(m^2·a).
DHW profile tapping cycle	Type M, as described in EN 16147 (2017)
Average number of persons per flat	2.1
Internal gains	3.1 kWh/day for each flat

Five concepts of pipe distribution systems including decentralized DHW systems (one per flat) were investigated:

1. a 4-pipe system with hot water circulation for DHW
2. a 4-pipe system with a fresh-water station in each flat (including a heat exchanger for the DHW)
3. a 2-pipe system with a fresh-water station in each flat (including a heat exchanger for the DHW)
4. a 2-pipe system with the so-called return-flow heat pump
5. a 2-pipe system for space heating and a simple electric boiler in each flat for the DHW preparation

The integration of HPs on building level instead of district level is significantly preferable resulting in total primary energy (PE) savings of 23%.

The most efficient distribution systems combined with an HP are a 4-pipe system with a freshwater station or a 2-pipe system with return-flow HP. A 2-pipe system with a freshwater station in combination with the highest insulation level is the optimal distribution system.

The study results show that HPs are more beneficial than DH or gas boiler for space heating and DHW preparation. Both KPIs (PE and CO_2) lead to this conclusion. This applies also to air-source HPs, which are less efficient than ground-source HPs in supplying space heating. The highest savings compared to natural gas are observed in CO_2 emissions. The use of heat pumps or district heating instead of gas boilers decreases the carbon emissions by a maximum of 75% and 52%, respectively. In this study, the design supply temperature of 35 °C for space heating is relatively low due to the combination of the low heating load of a Passive House and the use of a floor heating system. This improves considerably the performance of the HP.

Both KPIs increase for the case of HP when monthly factors are used, because of the seasonal variations of the electricity conversion factors. Moreover, the higher the share of renewables on the energy mix (e.g. for electricity or DH) is, the higher the importance of monthly conversion factors.

The results indicate that in the case of an HP, the systems with low supply temperature are preferable i.e. four pipe system with freshwater station and 2-pipes system with the so-called return-flow heat pump. Besides, the choice of one HP per building instead of one per district reduces the thermal losses by 79%. However, the maintenance effort might be lower with one central HP instead of 16 HPs. One HP per block would increase the thermal losses by 23% (compared to one HP per building). As mentioned above, the installed system consists of DH for DHW and groundwater HP for space heating. The decision of using both DH and HP instead of only HP is made mainly due to the limitation for ground water use. The installed system (4-pipe system with a fresh-water station in each flat) saves up to 44% of primary energy and 60% in CO_2 emission compared to the gas system.

A detailed monitoring system (on building and flat level) is installed in one block (consisting of 4 buildings) of the Campagne district. Several heat meters and electricity meters were installed along the production system and the distribution system to monitor both space heating and domestic hot water preparation, collecting data on building- and apartment-level. Electricity consumption for appliances and auxiliaries is also available, as well as the produced energy from the photovoltaic panels. The aim is to analyse the power consumption and the output of the heat pump, as well as the heat losses of thermal storages, heat exchangers and distribution pipes. Moreover, in one building, temperature and humidity are monitored on flat level. In the same building a CO_2 sensor is installed in each of the five central ventilation units. Design values and results of the simulation study can be confirmed by the monitoring data and potential problem can be detected. A detailed study of the distribution losses along the pipe can be carried out. Monitored data can also be used as input of further simulations to investigate alternative system using validated dynamic models.

2.3 Papieri district in Cham, Switzerland

The Papieri district in Cham, CH, is an old estate of the Paper industry, which is rebuild to a comprehensive new neighbourhood in six phases over the next years for 1000 inhabitants and 1000 additional workplaces in the final development. Fig. 8 left shows a picture of the district, the first development phase is depicted in Fig. 8 middle and the energy concept of the borehole field connected to the central HP heating and cooling is shown on the right.

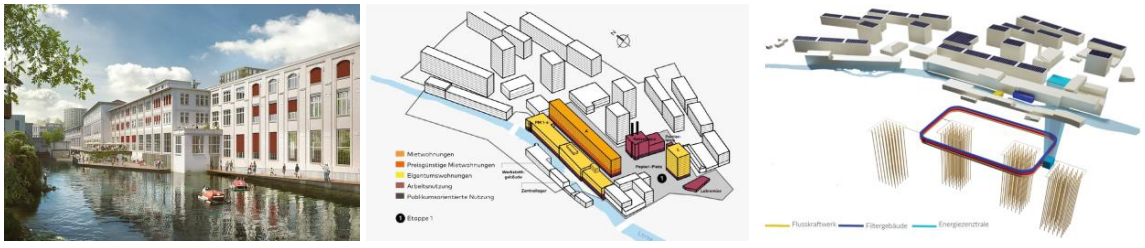

Fig. 8: Papieri neighbourhood, Cham, CH, with neighbourhood view from the river (left), buildings of the first phase (middle), and the energy concept (right) source: www.papieri-cham.ch, AWIAG, Cham group)

The neighbourhood consists of industrial heritage buildings of the paper industry which are preserved and retrofitted for a new use and are amended by new buildings, which create a mix of about 30% of existing and 70% of new buildings. In the first phase depicted in Figure 7 middle, 105 condominiums and 160 rental apartments together with 4400 m^2 floor area of commercial and office use will be commissioned by the end of 2022.

The estate development is designed in a way that all building services of heating, cooling and domestic hot water are entirely supplied by renewable energy. About 40% of the electricity use in the district is produced on-site. The electricity is produced by a 6500 m^2 PV-system of an installed peak capacity of 1.27 MWp and an estimated annual electricity production of 1.1 GWh, which is installed on the roof of the new buildings. As second electricity generator a hydro power plant with an installed capacity of 240 kW and a calculated annual production 1.25 GWh is installed in the river Lorze, which run through the district. The remaining electricity is imported as certified green electricity from the utility in order to reach a zero emission balance.

The space heating and cooling as well as the DHW production is supplied entirely renewable by four central ammonia HP of a total capacity of 4 MW, which use borehole fields of totally 192 ground probes of 320 m depth as heat source. As second heat source the river water of the Lorze is used either directly as heat source or as regeneration source for the borehole fields. The comfort cooling for the residential and office use is planned to be operated primarily by free-cooling from the boreholes. Active cooling by the HP in chiller operation is only provided for peak load cooling, whereby all the recooling (waste) heat from the active chiller operation is to be recovered for other uses like DHW production or for the regeneration of the borehole fields.

Since neither the modelling and simulation nor the monitoring has started, yet, only the above mentioned energy concept and design data are available of the neighbourhood. The HP system will be modelled, simulated and monitored in order to optimize the first operation years and retrieve on-site information for the further development of the neighbourhood in the later project phases. The evaluation includes the verification of the system performance of the centralized and the zero emission balance.

A special focus of the simulation and the monitoring is a more detailed analysis of the operation and the energy balance of the borehole fields for combined space heating, DHW and cooling operation. Moreover, the options for the interaction of the two heat sources of the borehole fields and the river water is investigated. Performance potentials are seen in the use of the source with most favorable temperature level, the regeneration of the borehole field for space heating and the simultaneous operation of the HP for heating and cooling in combination with high free-cooling shares. Thus, the objective for the system operation is the maximize the system performance of the HP by an optimized management of the borehole field as heat source and (free-)cooling heat sink and the integration of the ground and river water heat source.

4. Conclusions and outlook

Positive energy districts are an ambitious concept, which is currently promoted in order to enhance a high energy performance and on-site energy production as part of the transformation of the energy system. Extending the system boundary from the individual building to clusters of buildings and neighbourhoods offers the combination of different uses and load structures, which can unlock opportunities to increase on-site self-consumption of the produced electricity in the cluster by load balancing and to enhance the performance by waste heat recovery from one building use for another. Heat pumps can play an important role in positive energy district concepts, since they facilitate to reach ambitious energy targets by their high energy performance and can link both electric and thermal loads as well as different thermal uses like heating and cooling. As further aspect, sector coupling within the district and with connected grids can provide energy flexibility within and over the boundaries of the district.

The upcoming Annex 61 in the Heat Pumping Technologies TCP of the IEA investigate heat pump concepts for building cluster and positive energy districts. Starting with decentralized solutions on the individual building level, higher integration of the HP in the districts up to entirely centralized solutions and integration with other energy generators/supply like district heating is evaluated technically and economically. Based on generic concepts a detailed techno-economic analysis shall deliver favorable applications of HP in positive energy districts and recommendations for the integration, design and control of the HP systems.

As insight to the national contributions the paper presents four case studies with different degree of integration of the heat pump in the cluster or district. Already existing results of the case studies confirm that reaching a positive energy balance is a challenge, which requires high building performance to limit the loads, high performance generators for efficient energy supply and vast energy production with the cluster or district, in particular for larger buildings and non-residential use.

Higher integration of the heat pump can create opportunities of higher on-site energy consumption and waste heat recovery for different building services in the cluster, which may further increase the energy performance and flexibility, but may also increase the cost and losses due to necessary grid connections. Both technical and economic trade-offs with be analysed in the Annex 61.

Results of the case studies underline that HP reach high performance values in the application in clusters and can facilitate to reach ambitious objectives of zero or plus energy neighbourhoods or districts due to its unique features of even simultaneous provision of different building services with high performance. Furthermore, HP offer energy flexibility for higher PV self-consumption and reduced grid interactions. The upcoming Annex will derive favorable HP concepts for districts by simulation and monitoring in different case studies.

5. Acknowledgments

This paper presents an outline and interim results from Austria, Germany and Switzerland of the Annex 61. Acknowledgments are expressed to all present and future contributions to the Annex 61 of the Annex participants and to the Swiss Federal Office of Energy SFOE for the support and funding of the Annex 61.

This paper presents results from the projects "Herzo Base - Energy storage houses - An energy flexible building and energy concept of tomorrow" (FKZ 03ET1364A) and "Herzo Opt - Monitoring of the building envelope, thermal room comfort and energy system with operational optimization" (FKZ 03ET1641A). The project is funded by the German Federal Ministry for Economic Affairs and Energy based on a resolution of the German Bundestag.

6. References

Betzold, C., Dentel, A., 2022. Comparison and implementation of MPC and simple predictive control into a heat pump system. REHVA 14th HVAC World Congress Clima, 22nd – 25th May 2022, Rotterdam, The Netherlands.

Dermentzis G., Ochs F., Thuer A., Streicher W., 2021. Supporting decision-making for heating and distribution systems in a new residential district - An Austrian case study. Energy, 2021

EN 16147, 2017. Heat pumps with electrically driven compressors - Testing, performance rating and requirements for marking of domestic hot water units, CEN, Brussels

European Parliament, 2010. Directive 2010/31/EU of the European Parliament and Council of May 19, 2010 on the energy performance of buildings (recast), Journal of the European Union, p. L 153/13, 18. 6. 2010, Brussels

IEA, 2021. Net Zero by 2050, A Roadmap for the Global Energy Sector, revised version October 2021 (4th revision), International Energy Agency, Paris

IPCC, 2021. Summary for Policymakers. In: Climate Change 2021: The Physical Science Basis. Contribution of Working Group I to the Sixth Assessment Report of the Intergovernmental Panel on Climate Change [Masson-Delmotte, V., P. Zhai, A. Pirani, S.L.Connors, C. Péan, S. Berger, N. Caud, Y. Chen, L. Goldfarb, M.I. Gomis, M. Huang, K. Leitzell, E. Lonnoy, J.B.R. Matthews, T.K.Maycock, T. Waterfield, O. Yelekçi, R. Yu, and B. Zhou (eds.)]. Cambridge University Press, Cambridge, United Kingdom and New York, NY, USA, pp. 3−32, doi:10.1017/9781009157896.00

UN, 2016. United Nations,Treaty Series,vol. 3156, CHAPTER XXVII, ENVIRONMENT, 7. d Paris Agreement, Paris, 12 December 2015, United Nations,Treaty Series,vol. 3156, C.N.63.2016.TREATIES-XXVII.7.d of 16 February 2016 (Opening for signature) and C.N.92.2016.TREATIES-XXVII.7.d of 17 March 2016 (Issuance of Certified True Copies.

Wemhoener, C. (ed.), 2021. IEA HPT Annex 49 - Design and Integration of heat pumps for nearly Zero Energy Buildings - Executive Summary, IEA Technology Collaboration Program on Heat Pumping Technologies (HPT), Borås

M. Solar Thermal and PVT Collectors and Solar Loop Components

Spectral Beam Splitting in Compound Parabolic Collector based Photovoltaic Thermal System

Mohit Barthwal[1] and Dibakar Rakshit[1]

[1] Indian Institute of Technology Delhi, New Delhi (India)

Abstract

Spectral beam splitting (SBS) is an approach to eliminate the interdependency between photovoltaic (PV) and photothermal conversion processes in a conventional photovoltaic thermal (PVT) system. Hence, it overcomes the major shortcoming of a traditional PVT system, which is the extraction of low-temperature thermal output as it is limited by the peak operational temperature attained by the PV cells/module. The present work conceptualizes a novel compound parabolic collector (CPC)-based concentrating PVT system utilizing a nanofluid optical filter for SBS. A Monte Carlo Ray Tracing (MCRT) based optical analysis of the devised system is carried out to determine the incident heat flux. Further, the cell temperature associated with the incident flux is determined through a quasi-dynamic thermal analysis. The developed optical and thermal models are verified against the experimental and numerical findings. The devised model emphasized the effectiveness of the nanofluid optical filter by transferring the solar rays within the spectral response range to the PV array while absorbing the rest of the spectrum. The maximum array temperature is recorded to reach as high as 375 K without splitting. However, when employing the SBS approach, this equivalent temperature is retained at 328 K. Hence, the cell temperature is sustained near the standard test temperature via splitting, with no passive or active cooling. Moreover, the maximum cumulative temperature rise is observed to be 58.76 K and 71.88 K for deionized water and ZnO nanofluid, respectively.

Keywords: PVT, Spectral splitting, Compound parabolic collector, MCRT, Nanofluid

1 Introduction

The solar spectrum (250-3000 nm) includes ultraviolet (250-380 nm), visible (380-740 nm), and infrared (740-2500 nm) energy (fig. 1 (b)). However, a photovoltaic (PV) cell operates in a specific spectral response range (SRR) depending on the semiconductor material's bandgap. Most of the solar spectrum up to 1109 nm is converted into valuable electrical energy by c-Si PV cells, while the rest is dissipated as heat, which is called thermalization (Polman and Atwater, 2012). A 1°C increase in the cell temperature reduces the electrical efficiency by 0.4-0.6% (Chander et al., 2015; Kalogirou and Tripanagnostopoulos, 2006). A PVT system prevents any loss of electrical efficiency by cooling the cells while also harnessing a thermal output for various real-world applications (Sathe and Dhoble, 2017).

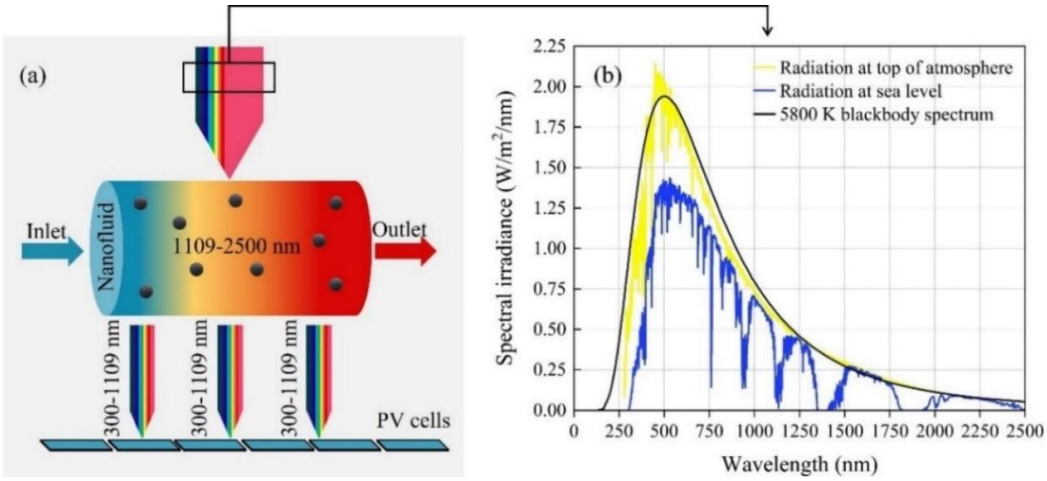

Fig. 1: (a) Concept of solar spectral beam splitting via nanofluid optical filter, and (b) AM1.5 solar spectrum.

© 2022. The Authors. Published by International Solar Energy Society
Selection and/or peer review under responsibility of Scientific Committee
doi:10.18086/eurosun.2022.12.01 Available at http://proceedings.ises.org

The highest operating temperature of the PV cells/module limits the extraction of high-temperature thermal output (Luo et al., 2020). The cooling fluid can reach 30-45°C (Barthwal and Rakshit, 2021). This low-grade heat output is appropriate only for domestic purposes. The spectral beam splitting (SBS) technique eliminates the dependencies between photovoltaic and photothermal conversions in a PVT system (Fernandes and Schaefer, 2021), allowing for a high-temperature thermal output and improving photovoltaic efficiency. SBS-based PVT divides the solar spectrum into portions based on the PV cell's bandgap cut-off wavelength. Only photons with wavelength (and energy) in the PV semiconductor material's spectral response range are used to generate electrical output to minimize undesirable thermalization.

The SBS can be realized using an optical filter for splitting the wavelengths. It is classified based on the optical filter employed. A thin nanofilm can be utilized to reflect the SRR to the PV array while transmitting the rest to a heat transfer fluid (HTF). Another way is to employ a nanofluid optical filter to absorb the non-SSR wavelengths and transmit the rest to the PV cells (fig. 1 (a)). Using a nanofilm has the drawback of high optical losses due to reflection. Moreover, synthesizing nanofilm is a complex process. On the other hand, a nanofluid optical filter is easier to synthesize and has a volumetric effect in harnessing thermal energy. Also, it is easier to regulate the heat-to-electricity ratio based on the application requirements with varying the nanoparticle concentration of the nanofluid. By employing a Fresnel lens-based CPVT system, (An et al., 2016) used Cu_9S_5 in oleylamine as a nanofluid optical filter. Compared to a typical arrangement with no optical filter, the electrical efficiency of the PV cells was increased by roughly 18% with the assistance of a nanofluid optical filter. A high temperature (100°C) thermal output was also recovered from the CPVT system. (Meraje et al., 2022) also used a nanofluid optical filter to examine the Fresnel lens-based CPVT system. A ZnO nanofluid was synthesized using water-ethylene glycol as the base fluid and visually tested for the SBS. The study suggested ZnO nanofluid for the SBS.

The literature review suggests that the SBS capabilities are investigated for a high concentration solar field-based PVT system. However, an SBS-coupled compound parabolic concentrator (CPC) has not been explored in the literature. The CPC has sparked a lot of interest in solar thermal applications. Yet, no substantial commercial development has occurred. The same is applicable for effectively implementing the SBS technique. Moreover, in order to enable applications operating at low to medium temperatures, it is crucial to investigate the development of a collector with a low concentration ratio. Furthermore, the use of CPC provides the advantage of seasonal tracking, which simplifies the PVT operation. The present work proposes a low concentration CPC-based PVT system with SBS capabilities. A c-Si PV cell with a cut-off wavelength of 1109 nm (corresponding to a 1.12 eV bandgap) is considered. PV cells have an SRR between 300 nm and the semiconductor material's cut-off wavelength (1109 nm). The proposed system's utility is evaluated using an opto-thermal analysis for the location of New Delhi, India.

2 Methodology

2.1. Physical model

Fig. 2 shows the physical model of the proposed system. The CPVT system consists of a CPC collector (fig. 2 (a)), the geometry of which is made from the profiles of two intersecting parabolas (fig. 2 (c)). A collector with a concentration ratio (CR) of 2.8 is truncated to a CR of 2.3 (tab. 1). A PV array consisting of 8 series-connected cells is placed at the absorber/detector (fig. 2 (b)). Borosilicate glass tubes containing nanofluid (as the optical filter) are placed over the PV array to absorb the infrared radiation and transmit the visible spectrum. The spectral transmissivity (τ_λ) and absorptivity (α_λ) of an ideal nanofluid optical filter is given by eq. 1 and 2, respectively. And tab. 2 describes the optical properties of all the components.

$$\tau_\lambda = \begin{cases} 1, & 380\ \text{nm} < \lambda \leq 1100\ \text{nm} \\ 0, & \lambda > 1100\ \text{nm} \end{cases} \quad \text{(eq. 1)}$$

$$\alpha_\lambda = \begin{cases} 0, & 380\ \text{nm} < \lambda \leq 1100\ \text{nm} \\ 1, & \lambda > 1100\ \text{nm} \end{cases} \quad \text{(eq. 2)}$$

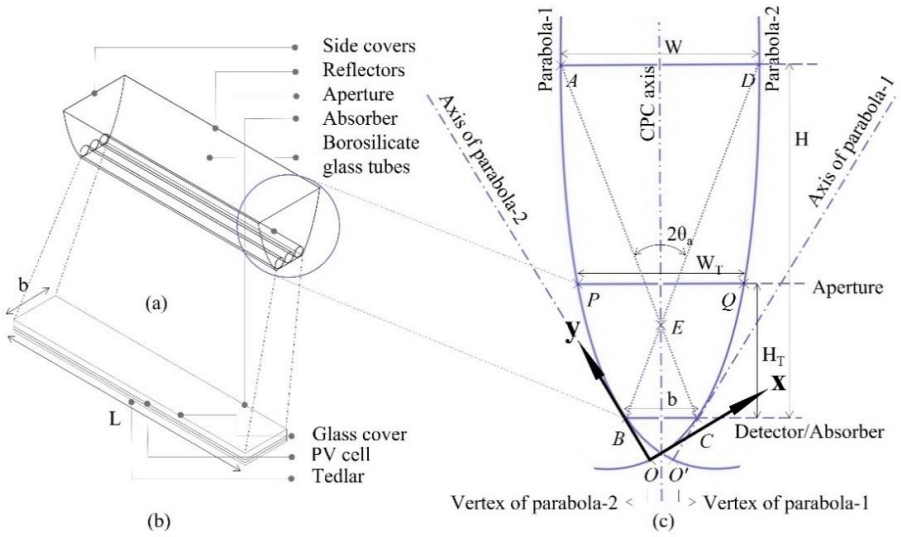

Fig. 2: Physical model of (a) devised spectral beam splitting based concentrating photovoltaic thermal collector, (b) PV array, and (c) geometrical configuration of the compound parabolic concentrator.

Tab. 1: Physical parameters of original and truncated compound parabolic collector (CPC).

Parameter	Original CPC		Truncated CPC	
Acceptance angle (°)	$2\Theta_a$	41.85	$2\Theta_a$	82.96
Concentration ratio (-)	C	2.80	C	2.34
Aperture width (mm)	W	375.20	W_T	314.50
Absorber width (mm)	b	134.00	b	134.00
Collector height (mm)	H	665.87	H_T	253.00
Collector length (mm)	L	1000.00	L	1000.00
Glass tube inner diameter (mm)	D_i	42.60	D_i	42.60
Glass tube outer diameter (mm)	D_o	44.60	D_o	44.60
Pitch (mm)	P	50.00	P	50.00

Tab. 2: Optical properties of concentrating photovoltaic thermal collector components (Parthiban et al., 2022; Zhou et al., 2015).

Component	Material	Thickness (mm)	Absorptivity (α)	Reflectivity	Transmissivity (τ)	Emissivity (ε)
Glazing	Acrylic glass	1.5	0.03	0.02	0.95	0.93
Reflector	Aluminium	1	0.05	0.92	0.03	-
Glass cover	Glass	1.5	0.03	0.02	0.95	0.93
PV cell	-	0.3	0.88	0.12	-	-

2.2. Simulation procedure

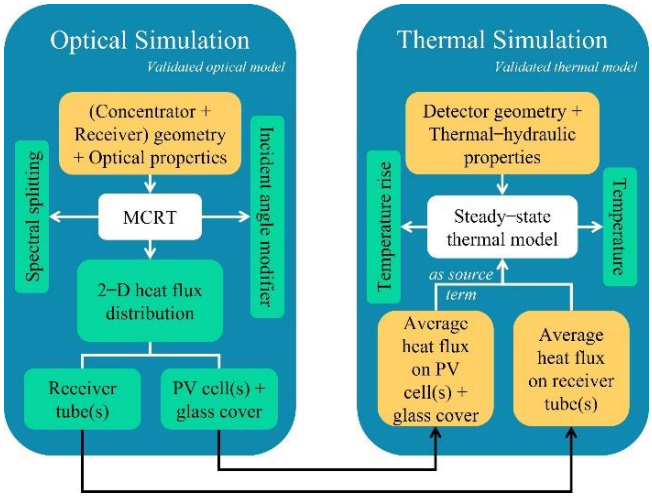

Fig. 3: Simulation methodology workflow for coupled opto-thermal analysis.

The optical simulation is carried out using the MCRT approach (Shadmehri et al., 2018). The incidence angle (Θ_i) of the rays is affected by the orientation, location, surface slope, and time of day (Barthwal and Rakshit, 2021). It is estimated for the months of January and June in New Delhi, India. The concentration and receiver geometry with optical properties are fed to the model to generate a 2-D non-uniform heat flux distribution on PV cell(s), glass cover, and nanofluid tubes. The incoming ray is traced to check if it strikes the reflector, nanofluid, and detector (PV array) or if it is overflown. If the wavelength of this incoming ray is not within the spectral response range, it is absorbed; otherwise, it is transmitted to the detector. Finally, the heat flux of the transmitted, absorbed, and overflown rays is calculated. The resultant heat flux distribution is fed to a steady-state thermal model along with detector/tube geometry and thermal−hydraulic properties to obtain the temperature distribution on the PV array. Fig. 3 shows the adopted methodology workflow.

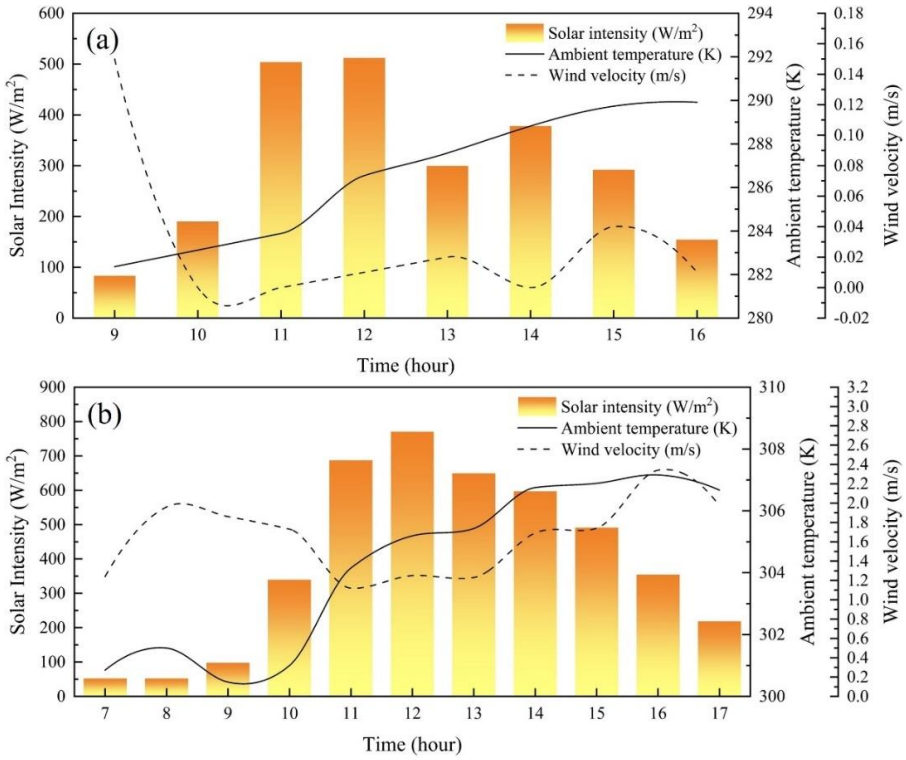

Fig. 4: Graphical representation of average climatic data for the month of (a) January, and (b) June, recorded in real-time via an in-house weather station at New Delhi (28.61°N, 77.20°E).

Because the PV array and nanofluid tube units are not considered to be thermally coupled in the current physical model, the PV array and glass tube units are analyzed separately. The developed model has been evaluated on real-time weather data (fig. 4) recorded by an in-house weather station (fig. 5) in New Delhi, India. The thermo-physical properties of the system components are listed in the tab. 3. The heat generation term ($\dot{Q}$) in eq. 3 is supplied as internal volumetric heat generation at the cell ($\dot{Q}_{cell}$) and glass cover ($\dot{Q}_g$), which are given by eqs. 4 and 5, respectively. Where G denotes the concentrated heat flux at the absorber/detector. And α_{cell}, η_{cell}, and t_{cell} denote the cell's absorptivity, reference efficiency, and thickness, respectively. Similarly, α_g, τ_g, and t_g denote the glass cover's absorptivity, transmissivity, and thickness, respectively. Fig. 6 represents the imposed boundary conditions in the simulation procedure. Cell ($\dot{Q}_{cell}$) and glass cover ($\dot{Q}_g$) heat generation is provided at the cell unit (fig. 6 (a)) along with ascribed convective and radiative heat losses determined through eqs. 6 and 8, respectively. The corresponding convective/wind (h_w) and radiative (h_r) heat transfer coefficients are quantified using eqs. 7 and 9, respectively. Where, v_w and T_{sky} denotes the wind velocity and sky temperature, respectively.

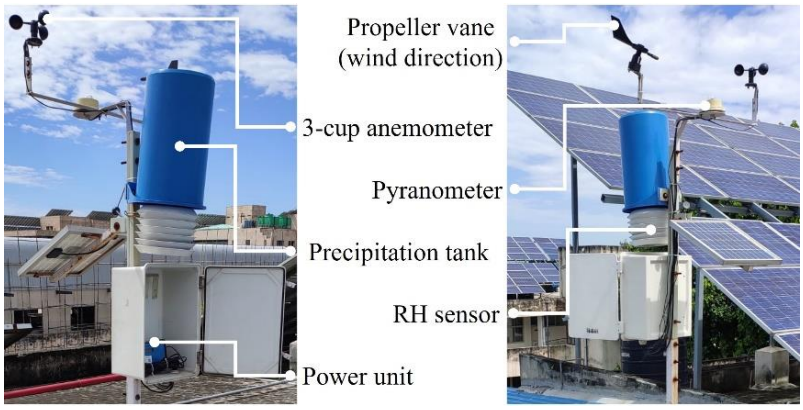

Fig. 5: Weather station for recording the climatic data.

Tab. 3: Thermo-physical properties of concentrating photovoltaic thermal collector components (Baig et al., 2018; Meraje et al., 2022).

Component	Thickness (mm)	Thermal conductivity (W m^{-1} K^{-1})	Density (kg m^{-3})	Specific heat capacity (J kg^{-1} K^{-1})	Viscosity (kg m^{-1} s^{-1})
Glass cover	1.5	1	3000	500	-
Cell	0.3	148	2330	677	-
Tedlar	0.3	0.15	1200	1250	-
DI water	-	0.606	997	4220	8.90 x 10^{-4}
ZnO nanofluid	-	0.376	1057.38	3316.08	2.0122 x 10^{-3}

$$\frac{\partial}{\partial x_j}\left(k\frac{\partial T}{\partial x_j}\right) + \dot{Q} = 0 \qquad \text{(eq. 3)}$$

$$\dot{Q}_{cell} = \frac{G\,\tau_g\,\alpha_{cell}(1-\eta_{cell})}{t_{cell}} \qquad \text{(eq. 4)}$$

$$\dot{Q}_g = \frac{G\,\alpha_g}{t_g} \quad \text{(eq. 5)}$$

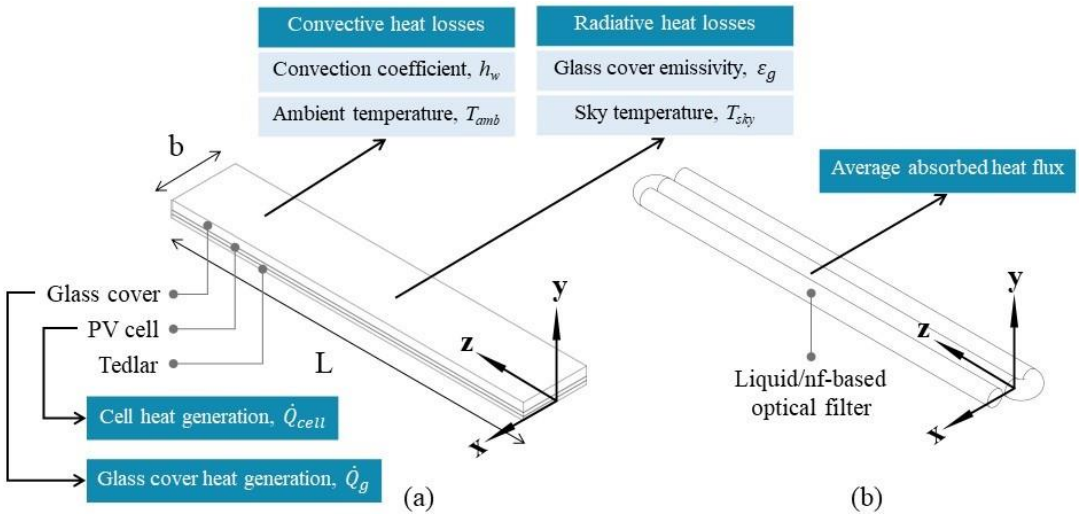

Fig. 6: Boundary conditions imposed at the (a) PV array, and (b) glass tube units.

$$Q_{c,losses} = h_w\left(T_g - T_{amb}\right) \quad \text{(eq. 6)}$$

$$h_w = 5.82 + 4.07\,v_w \quad \text{(eq. 7)}$$

$$Q_{r,losses} = h_r\left(T_g - T_{sky}\right) \quad \text{(eq. 8)}$$

$$h_r = \sigma\,\varepsilon_g\left(T_g^2 + T_{sky}^2\right)\left(T_g + T_{sky}\right) \quad \text{(eq. 9)}$$

The nanofluid in the tube is kept stationary, similar to in (An et al., 2016). For numerical modeling, a negligibly small mass flow rate (5×10^{-4} kg/s) is specified at the tube inlet, along with the hourly ambient temperature recorded by the weather station. At the nanofluid surface, the average absorbed heat flux boundary condition is employed (fig. 6 (b)). Eqs. 10, 11, and 12 give the continuity, momentum, and energy equations for the examined 3-D, steady, laminar flow in the borosilicate glass tube (Liang et al., 2019).

$$\frac{\partial}{\partial x_j}(\rho\,u_i) = 0 \quad \text{(eq. 10)}$$

$$\frac{\partial}{\partial x_j}\left(\rho\,u_i u_j\right) = -\frac{\partial p}{\partial x_j} + \frac{\partial}{\partial x_j}\left[\mu\left(\frac{\partial u_i}{\partial x_j} + \frac{\partial u_j}{\partial x_j}\right)\right] + \rho g_i \quad \text{(eq. 11)}$$

$$\frac{\partial}{\partial x_j}\left(\rho\,u_j C_p\,T\right) = \frac{\partial}{\partial x_j}\left(k\frac{\partial T}{\partial x_j}\right) \quad \text{(eq. 12)}$$

The computational mesh is generated using Ansys ICEM CFD. A grid-independence study is conducted separately for the PV array and glass tube units to make the solution free from the grid size with respect to cell (T_{cell}) and nanofluid temperature (T_{nf}), respectively (tab. 4). Eq. 13 calculates the percentage error (E_n) corresponding to the number of elements (n) based on the associated temperature value (T_i) versus the next subsequent temperature value (T_{i+1}). Finally, 21708000 and 676494 number of elements are considered for PV array and glass tube units, respectively, for further analysis. The pressure-velocity coupling is realized using the SIMPLE algorithm, and

second-order upwind discretization is employed. The convergence conditions for continuity and momentum are chosen to be < 10^{-3}, and that for energy be < 10^{-6}.

$$E_n = \left|\frac{T_i - T_{i+1}}{T_i}\right| \quad \text{(eq. 13)}$$

Tab. 4: Grid independence analysis for PV array and glass tube units for the unglazed collector.

PV array unit			Glass tube unit		
Number of elements	**T_{cell} (K)**	**E_n**	**Number of elements**	**T_{nf} (K)**	**E_n**
9648000	362.9242	0.30	44608	297.913	0.114
14472000	361.8242	0.22	83640	297.573	0.081
21708000	361.0177	0.002	210048	297.331	0.067
29547000	361.009	0.002	676494	297.131	0.037
36662400	361.001	-	1073034	297.019	0.037
-	-	-	1573200	297.910	-

3 Results and discussion

3.1. Optical analysis

The objective of the optical investigation is to determine the average heat flux received by the photovoltaic cell and the borosilicate glass tube units. The analysis has been carried out on the collector that is oriented east to west, and real-time January and June meteorological data have been utilized.

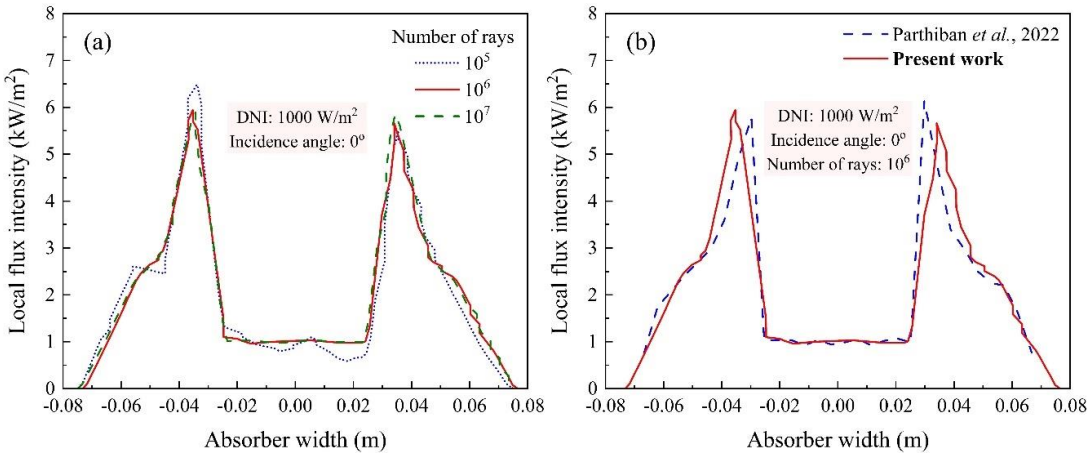

Fig. 7: (a) Ray independence study, (b) Validation of flux intensity on absorber/PV array width for present optical analysis against that by (Parthiban et al., 2022).

The optical model has been validated by the results of (Parthiban et al., 2022) (fig. 7). The reference study utilized a truncated 2.3 CR CPC as in the present work. Tracing fewer rays does not adequately represent the flux intensity at the detector. However, a greater number of rays increases the computing cost of the ray-tracing operation. A ray-independence test is performed to ensure that the local flux intensity (and hence the average flux intensity) at the absorber/detector does not fluctuate with the number of rays traced. The test is carried out with 10^5 to 10^7 rays.

Fig. 7 (a) depicts no reasonable variation in local flux intensity for 10^6 and 10^7 rays. Hence, 10^6 rays are used in further analysis. Also, fig. 7 (b) shows a reasonable agreement of local flux intensity between the present optical model and the reference study.

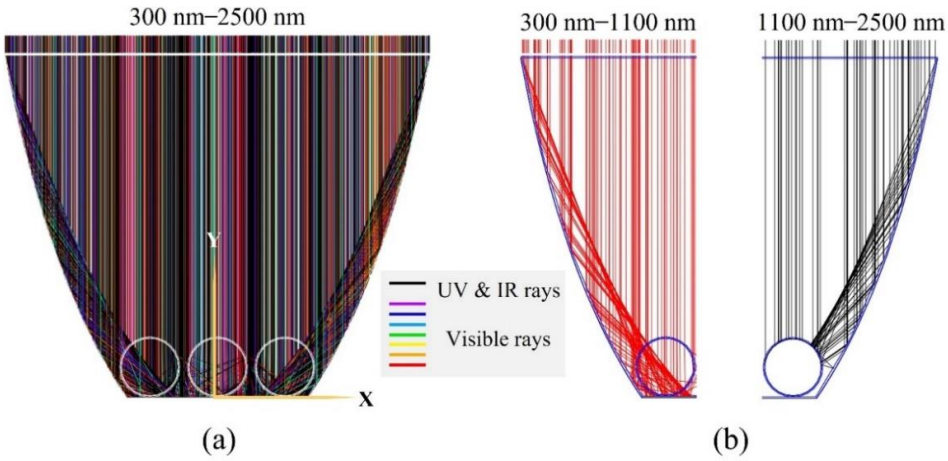

Fig. 8: (a) Traced solar spectrum, and (b) wavelength-sorted traced-rays in the devised collector (only 5% starting rays are shown for better visualization)

The rays traced on the 16th of January 2022 at solar noon (1200 hours) are depicted in fig. 8. These rays represent various wavelengths from the solar spectrum (fig. 8 (a)). In order to facilitate better viewing, only 5% of the initial rays are shown. The spectral beam splitting (SBS) process is observed in operation where rays with wavelengths within the spectrum response range (300–1100 nm) are passed through the photovoltaic array while the remaining wavelengths are absorbed by the nanofluid optical filter (fig. 8 (b)). The central part of the array has to have a uniform flux distribution since the incoming rays do not get deflected by the reflector and strike straight on the absorber/detector. On the other hand, the rays that interact with the reflector are reflected near the detector's edges. As a result, a maximum heat influx will be between the central part and the edges of the absorber/detector.

The incident angle modifier (IAM) is a significant optical analysis index. It represents the decrease in irradiance that reaches the PV cell's surface compared to normal incidence. It is obtained using a basic air-glazing model with one air-glass contact (fig. 9 inset) via eq. 14 (Sjerps-Koomen et al., 1996). The transmission-absorptance ($\tau\,\alpha$) depends on the extinction coefficient (K_e) and the thickness (t) of the glazing for incidence (Θ_i) and refraction (Θ_r) angle duos (eq. 15). Also, Snell's law (eq. 16) is used to quantify refraction angles for different ray incidents. Fig. 9 depicts the variations of IAM as a function of incidence angle. The modifier drops as the ray incidence angle rises because the first (primary) reflection becomes more significant at greater incidence angles. When sun rays enter an angle, these reflection (cosine) losses are responsible for the lower transmission of sun rays through the glass front of a solar cell/module.

$$\mathrm{IAM}(\Theta_i) = \frac{\tau\,\alpha\,(\Theta_i)}{\tau\,\alpha\,(0)} \qquad \text{(eq. 14)}$$

$$\tau\,\alpha\,(\Theta_i) = \exp\left(\frac{-K_e t}{\cos\Theta_r}\right)\left[1 - \frac{1}{2}\left\{\frac{sin^2(\Theta_r - \Theta_i)}{sin^2(\Theta_r + \Theta_i)} + \frac{tan^2(\Theta_r - \Theta_i)}{tan^2(\Theta_r + \Theta_i)}\right\}\right] \qquad \text{(eq. 15)}$$

$$\frac{\Theta_i}{\Theta_r} = \frac{n_g}{n_{air}} \qquad \text{(eq. 16)}$$

The incidence angle modifier is also interpreted in terms of the system's optical efficiency. A greater IAM value corresponds to greater optical efficiency. As the incidence angle of the entering rays rises, the cosine losses resulting from reflection become more pronounced. Consequently, similar to IAM, the optical efficiency follows a declining trend as the incidence angle increases.

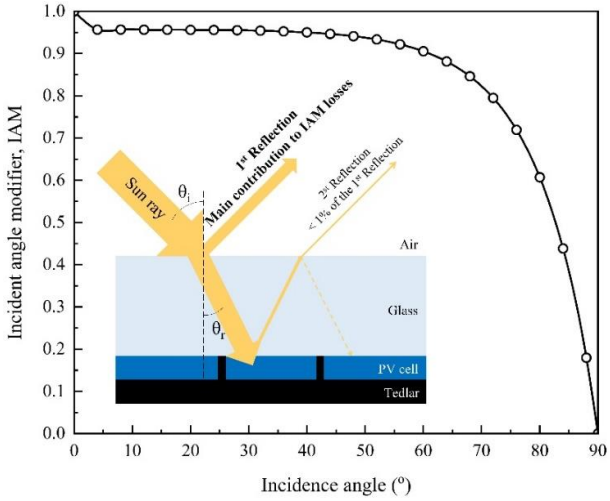

Fig. 9: Variation of incident angle modifier (IAM) with ray incidence angle. (Inset) IAM losses in one air-glass interface model.

3.2. Thermal analysis

The thermal simulation involves the individual analysis of the PV array unit and the nanofluid, as no thermal connection is assumed between the glass tube unit and the PV array. The results of the thermal analysis include validation results with the experimental findings as well as the results of spectral beam splitting in terms of cell temperature and optical filter temperature rise.

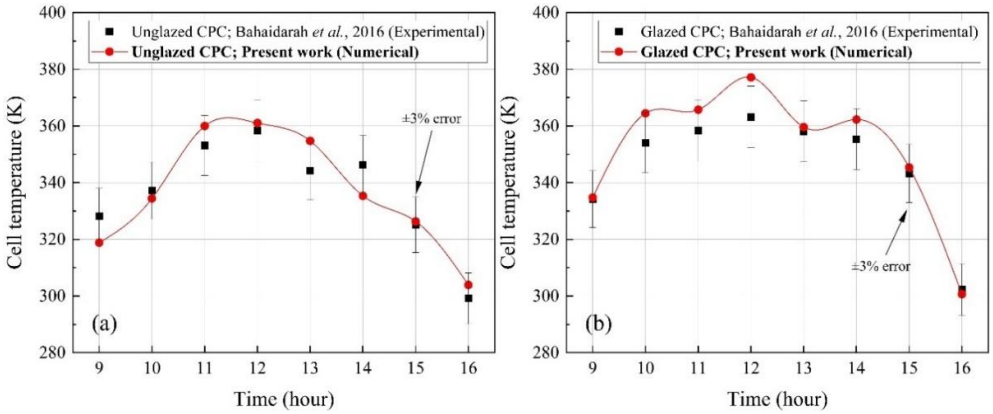

Fig. 10: Validation of temporal cell temperature for (a) unglazed, and (b) glazed collector against the experimental work of (Bahaidarah et al., 2016).

The computed cell temperature is compared to the experimental observations of (Bahaidarah et al., 2016) for both unglazed and glazed collectors to verify the current thermal model. Fig. 10 depicts the temporal variation of cell temperature. At solar noon, the highest average cell temperature is 361 K for the unglazed system and 377 K for the glazed system. When comparing the current thermal model to the experimental results, a maximum of 3% deviation in cell temperature is recorded, validating the thermal simulation approach employed. Another inference can be made in terms of the potential for cooling in concentrating PV cells. The PV cells with a concentrator ought to perform better as compared to the cells without utilizing any concentrator due to the availability of much higher incident heat flux. However, the thermalization limits the potential of the CPV system, and hence a thermal management effort is required to prevent any high temperatures. Without utilizing any passive or active cooling strategy, deionized water and ZnO nanofluids are employed as optical filters for this purpose.

Fig. 11 shows the variation of cell temperature with the time in the day for the winter (January) and summer (June) months. It is observed that the average cell temperature in a conventional CPV system can be as high as 360 K and 375 K for the months of January and June, respectively. However, the cell temperature is maintained near

standard test condition (STC) temperature (298 K) in the proposed nanofluid filter-based system.

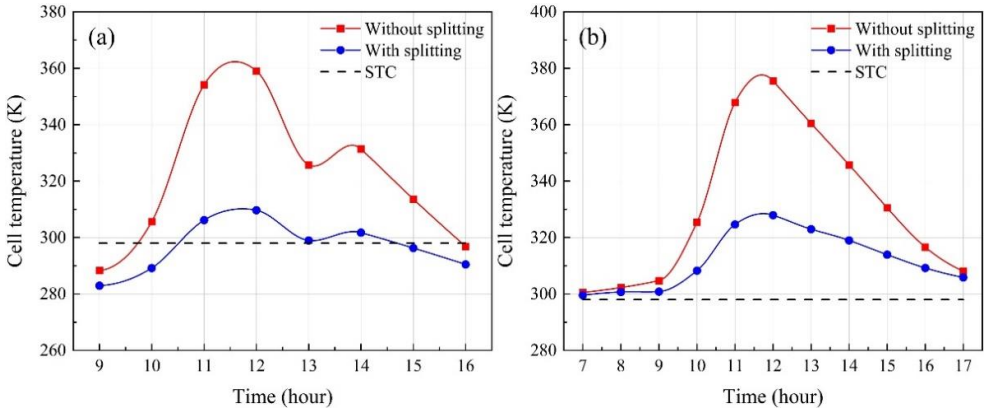

Fig. 11: Temporal variation of average cell temperature for the month of (a) January, and (b) June for the systems placed in New Delhi (28.61°N, 77.20°E).

The temperature rise of the liquid/nanofluid optical filter is also determined. The absorbed heat flux is determined using the optical simulation (fig. 3). Section 2.2 describes the simulation process. Deionized water and ZnO nanofluid (500 ppm ZnO nanoparticles in 50-50% water-ethylene glycol solution) are simulated as the optical filter. Tab. 3 lists the thermophysical characteristics of DI water and ZnO nanofluid. The cumulative temperature rise of the optical filter over time can be seen in fig. 12. The greatest cumulative temperature rise of DI water and ZnO nanofluid at 1600 hours in January is 35.62 K and 43.59 K, respectively. However, during the month of June, DI water and ZnO nanofluid had temperatures of 58.76 K and 71.88 K, respectively.

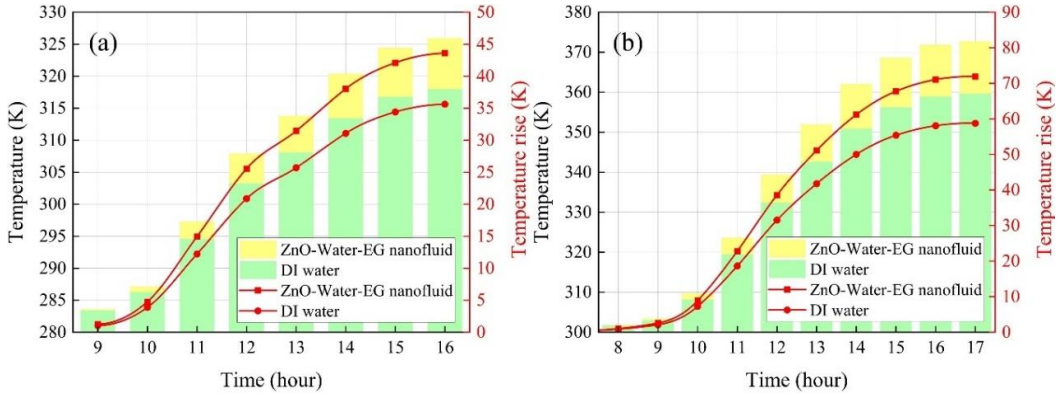

Fig. 12: Temporal variation of cumulative temperature rise of optical filters for the month of (a) January, and (b) June.

4 Conclusions

The opto-thermal analysis of a proposed novel spectral beam splitting powered compound parabolic collector-based photovoltaic thermal system is carried out. Monte Carlo ray-tracing is utilized to observe the prowess of nanofluid-based solar splitting for the cogeneration of electricity and thermal output. Moreover, a finite volume-based solver is utilized for quantifying the thermal output from the devised system. The developed opto-thermal framework is validated with respect to local flux intensity and cell temperature, justifying the methodology employed. The following main findings are summarized for the present work:

- Without resorting to active and/or passive cooling methods, the SBS approach aided in maintaining a cell temperature comparable to the STC temperature.
- The maximum array temperatures of 360 K and 375 K were observed for January and June, respectively, without the SBS employment. With the SBS technique, however, these equivalence temperatures were 310 K and 328 K, respectively.

- DI water and ZnO nanofluid observed the maximum cumulative temperature increases of 35.62 K and 43.59 K, respectively, in January. In contrast, the temperatures of DI water and ZnO nanofluid in the month of June were 58.76 K and 71.88 K, respectively.

Multiple potential intervention avenues have been identified in the current study for use in future investigations. To get a more consistent heat flux distribution, the number of quartz tubes positioned above the PV array (or the number of passes) can be adjusted. Moreover, the heat-to-electricity ratio from the designed PVT collector may be modified by varying the pitch of the tubes. In addition, thermal losses may be avoided by utilizing a concentric glass tube with a vacuum in between.

Acknowledgments

The authors thank HPC facility at IIT Delhi for computational resources. The first author would like to thank the Science and Engineering Research Board (SERB), Government of India, and IIT-Delhi for providing the necessary travel assistance-Grant numbers-ITS/2022/002055, and IITD/PGSR/2022/67221, respectively.

References

An, W., Wu, J., Zhu, T., Zhu, Q., 2016. Experimental investigation of a concentrating PV/T collector with Cu9S5 nanofluid spectral splitting filter. Appl. Energy 184, 197–206. https://doi.org/https://doi.org/10.1016/j.apenergy.2016.10.004

Bahaidarah, H.M., Gandhidasan, P., Baloch, A.A.B., Tanweer, B., Mahmood, M., 2016. A comparative study on the effect of glazing and cooling for compound parabolic concentrator PV systems – Experimental and analytical investigations. Energy Convers. Manag. 129, 227–239. https://doi.org/https://doi.org/10.1016/j.enconman.2016.10.028

Baig, H., Jani, R., Markam, B.K., Maiti, S., Mallick, T.K., 2018. Modelling and experimental analysis of a seasonally tracked V-trough PV/T system in India. Sol. Energy 170, 618–632. https://doi.org/https://doi.org/10.1016/j.solener.2018.06.018

Barthwal, M., Rakshit, D., 2021. Artificial neural network coupled building-integrated photovoltaic thermal system for indian montane climate. Energy Convers. Manag. 244, 114488. https://doi.org/https://doi.org/10.1016/j.enconman.2021.114488

Chander, S., Purohit, A., Sharma, A., Arvind, Nehra, S.P., Dhaka, M.S., 2015. A study on photovoltaic parameters of mono-crystalline silicon solar cell with cell temperature. Energy Reports 1, 104–109. https://doi.org/10.1016/j.egyr.2015.03.004

Fernandes, M.R., Schaefer, L.A., 2021. Multiparticle nanofluid optimization for spectral-splitting energy harvesting. Renew. Energy 173, 849–860. https://doi.org/https://doi.org/10.1016/j.renene.2021.02.116

Kalogirou, S.A., Tripanagnostopoulos, Y., 2006. Hybrid PV/T solar systems for domestic hot water and electricity production. Energy Convers. Manag. 47, 3368–3382. https://doi.org/https://doi.org/10.1016/j.enconman.2006.01.012

Liang, Y., Liu, P., Zheng, N., Shan, F., Liu, Z., Liu, W., 2019. Numerical investigation of heat transfer and flow characteristics of laminar flow in a tube with center-tapered wavy-tape insert. Appl. Therm. Eng. 148, 557–567. https://doi.org/https://doi.org/10.1016/j.applthermaleng.2018.11.090

Luo, K., Ji, J., Xu, L., Li, Z., 2020. Seasonal experimental study of a hybrid photovoltaic-water/air solar wall system. Appl. Therm. Eng. 169, 114853. https://doi.org/https://doi.org/10.1016/j.applthermaleng.2019.114853

Meraje, W.C., Huang, C.C., Barman, J., Huang, C.Y., Kuo, C.F.J., 2022. Design and experimental study of a Fresnel lens-based concentrated photovoltaic thermal system integrated with nanofluid spectral splitter. Energy Convers. Manag. 258, 115455. https://doi.org/https://doi.org/10.1016/j.enconman.2022.115455

Parthiban, A., Mallick, T.K., Reddy, K.S., 2022. Integrated optical-thermal-electrical modeling of compound parabolic concentrator based photovoltaic-thermal system. Energy Convers. Manag. 251, 115009. https://doi.org/https://doi.org/10.1016/j.enconman.2021.115009

Polman, A., Atwater, H.A., 2012. Photonic design principles for ultrahigh-efficiency photovoltaics. Nat. Mater. 11, 174–177. https://doi.org/https://doi.org/10.1038/nmat3263

Sathe, T.M., Dhoble, A.S., 2017. A review on recent advancements in photovoltaic thermal techniques. Renew. Sustain. Energy Rev. 76, 645–672. https://doi.org/https://doi.org/10.1016/j.rser.2017.03.075

Shadmehri, M., Narei, H., Ghasempour, R., Shafii, M.B., 2018. Numerical simulation of a concentrating photovoltaic-thermal solar system combined with thermoelectric modules by coupling Finite Volume and Monte Carlo Ray-Tracing methods. Energy Convers. Manag. 172, 343–356. https://doi.org/https://doi.org/10.1016/j.enconman.2018.07.034

Sjerps-Koomen, E.A., Alsema, E.A., Turkenburg, W.C., 1996. A simple model for PV module reflection losses under field conditions. Sol. Energy 57, 421–432. https://doi.org/https://doi.org/10.1016/S0038-092X(96)00137-5

Zhou, J., Yi, Q., Wang, Y., Ye, Z., 2015. Temperature distribution of photovoltaic module based on finite element simulation. Sol. Energy 111, 97–103. https://doi.org/https://doi.org/10.1016/j.solener.2014.10.040

Nomenclature

List of Acronyms			
CFD	Computational Fluid Dynamics	MCRT	Monte Carlo Ray-Tracing
CPC	Compound Parabolic Collector	PVT	Photovoltaic Thermal
CPVT	Concentrating Photovoltaic Thermal	SBS	Spectral Beam Splitting
CR	Concentration Ratio	SRR	Spectral Response Range
DI	Deionized	STC	Standard Test Condition
HTF	Heat Transfer Fluid	SIMPLE	Semi-Implicit Method for Pressure Linked
IAM	Incident Angle Modifier		Equations
List of Symbols			
C	Concentration ratio (-)	W	Aperture width (m)
C_p	Specific heat capacity (J/kg.K)	$\dot{Q}$	Heat generation (W/m^3)
D	Diameter (m)	b	Absorber width (m)
E	Error (-)	g	Acceleration due to gravity (m/s^2)
G	Solar radiation (W/m^2)	h	Heat transfer coefficient (W/m^2K)
H	Height (m)	n	Number of elements/Refractive index (-)
L	Length (m)	t	Thickness (m)
T	Temperature (K)	u/v	Velocity (m/s)
List of Greek Symbols			
α	Absorptivity (-)	τ	Transmissivity (-)
ε	Emissivity (-)	Θ_a	Half-acceptance angle (°)
ρ	Density (kg/m^3)	Θ_i	Incidence angle (°)
σ	Stefan-Boltzmann constant (W/m^2K^4)	Θ_r	Refraction angle (°)

Empirical Validation of Low-Temperature PVT Collector for Heat Pump Integration

Francisco Beltrán, Nelson Sommerfeldt, Hatef Madani

KTH Royal Institute of Technology, Stockholm (Sweden)

Abstract

The combination of solar photovoltaic-hybrid (PVT) and ground source heat pumps (GSHP) can be a promising pathway towards the decarbonization of heating, cooling and electricity production in buildings. However, the concept of combining both technologies is still at an early stage in commercialization. As part of an ongoing 4-year research project, numerical modelling techniques have been applied to develop a digitally optimized PVT collector prototype specifically designed for heat pump integration. The goal of this study is to validate such models with a commercially available finned PVT collector against empirical data, with experiments carried out at an outdoor laboratory in Stockholm. Thermal and electrical outputs are measured for a range of low inlet fluid temperatures with varying flow rate, ambient temperature, solar irradiance and wind speed. R^2 values of 0.99 and 0.89 for electrical and thermal output respectively, show that the numerical model can predict real world performance of the collector with a high degree of certainty. The performance results show that the studied finned PVT collector has the potential to generate 800 W/m^2 of thermal power for a temperature difference of 30 K between inlet and ambient, and a solar irradiation of 1000 W/m^2. Even at a low irradiance of 200 W/m^2, a specific thermal output of 350 W/m^2 can be achieved, for a difference between inlet and ambient temperatures of 20 K.

Keywords: *Solar PV/thermal, PVT collector, Solar Heat Pump, COMSOL, Numerical Modelling*

1. Introduction and Background

A promising pathway to the electrification and decarbonization of buildings are solar heat pumps (SHP). There are numerous methods for combining the two technologies; however, one increasingly interesting approach is the series integration of photovoltaic/thermal hybrid collectors with ground source heat pumps (Kamel et al., 2015; Sommerfeldt and Madani, 2017). The design allows for shorter borehole lengths (Bertram et al., 2012), and in larger buildings with multiple boreholes, spacing reductions can reduce land requirements by up to 87% (Sommerfeldt and Madani, 2019). PVT also has the potential to regenerate degraded boreholes in older heat pump systems without the need for additional drilling. In addition, the operating temperatures in the borehole circuit are relatively low (-10°C to +20°C), allowing for a higher PVT collector thermal and electrical efficiency, and reduces costs by removing the need for glazing or insulation on the backside. Additionally, the electrical gains from lower PV cell temperatures is enough to cover the additional pumping power, making the additional thermal gains energetically free (Sommerfeldt and Madani, 2019; Vittorini et al., 2017).

When compared to solar thermal, the PVT+GSHP concept is relatively undeveloped and thus has had little design dedicated to PVT collectors as part of a heat pump system. When the thermal gains come from the solar collector and the surrounding air, the cost-benefit balance can change meaning a comprehensive techno-economic analysis is needed to identify the improvement potential of the current design. Chhugani et al., (2021) and Schmidt et al., (2018) investigated the empirical performance of PVT collectors as a single source for a heat pump, highlighting the system performance benefits of this configuration.

A 4-year research project aims at advancing the development and commercialization of an integrated heating, cooling and electricity system solution for European buildings using solar PVT and GSHP technology. One of the work packages in this project consists of applying numerical modelling techniques to develop a digitally optimized PVT collector prototype specifically designed for heat pump integration. Several designs have been modeled and studied with particular focus on enhanced heat capture from the surrounding air. Mass and heat transfer mechanisms as well as fluid dynamics have been considered in numerical modelling tool Comsol Multiphysics. Model validation is a critical part of the prototype development, so it becomes necessary to validate the results obtained from the simulations with experimental data in outdoor laboratory conditions.

© 2022. The Authors. Published by International Solar Energy Society
Selection and/or peer review under responsibility of Scientific Committee
doi:10.18086/eurosun.2022.12.02 Available at http://proceedings.ises.org

2. Objective and Methodology

The aim of this study is twofold. Firstly, it attempts to validate the numerical model of an unglazed, uninsulated PVT collector prototype with fins, specifically designed for heat pump integration in low temperature applications. This is done by using the commercially available numerical modelling software COMSOL Multiphysics, and comparing the results with the data obtained from the experimental testing of the collector prototypes. Secondly, it aims at quantifying the performance of a finned PVT collector by presenting the thermal performance curves for different flow rates and solar irradiance levels.

The experiments are performed in an outdoor setting using various flow rates and inlet temperatures during several days in July and August 2022 in Stockholm, Sweden. This provides a suitable range of ambient temperatures and solar irradiance levels to match the range of reduced temperatures tested in the simulations. To control for dynamic conditions (e.g. wind speed), measurements are selected and discretized such that they represent a quasi-steady state for comparison to steady-state results from the numerical model. Hourly averages for 30 different empirical data points are considered for the validation of the model. Outlet fluid temperatures from the PVT collectors, as well as thermal output and electricity generation are monitored for the 14 PVT collector array. Thermal and electrical outputs are assumed to be evenly distributed between all the collectors of the array, so the measured data is divided by 14 to get the measured values for one PVT collector.

The following step is to build the numerical model, where it is necessary to manually adjust the unknown parameters, such as thermal resistance between PV and absorber or the convective heat transfer coefficient on front and rear sides of the PVT collector, so that they can fit the empirical data in the best possible way. The same boundary conditions as in the experiments are then used as input in the numerical model, where outlet temperature from the PVT and PV cell temperature are obtained. These parameters are then used to calculate the thermal power and electricity generation. Outlet fluid temperature, PV electricity production and thermal output are used as validation metrics; tested using mean absolute error (MAE), mean biased error (MBE), and coefficient of determination (R^2). The model that best fits the empirical data is then the one that minimizes the errors and gives the highest coefficient of determination. Finally, the performance curves of the PVT collector at different flow rates and solar irradiation levels is plotted against the reduced temperature difference, based results from the simulations of the numerical model.

3. Method

In order to meet the objectives, it is required to have an testing facility where the PVT collector prototypes can be evaluated, and a model in Comsol Multiphysics software. In the following sections both the testing facility and numerical model are described in detail.

3.1. Testing facility

Testing of the PVT collectors is performed at an outdoor laboratory facility, located on the roof of the Energy Technology Laboratory at KTH Royal Institute of Technology, in Stockholm, Sweden. It consists of two independent arrays of 14 PVT and 2 PVT collectors respectively, mounted on a south-facing roof with a tilt angle of 45°. For the purpose of this study, only the 14 PVT collector array is considered. The larger PVT array is made up of two subarrays connected in series, where each subarray has seven collectors connected in parallel, for a total of 14 PVT collectors. The heat transfer fluid in the PVTs is an ethylene glycol – water mixture with a volumetric ratio of 25/75. The fluid is temperature controlled using a domestic heat pump, enabling supply temperatures down to -5 °C during summer days. This is done by connecting the collector array to a 300 L cold-water storage tank, where the evaporator of a 3-12 kW variable speed ATLAS Thermia heat pump cools down the heat transfer fluid in the tank and generates the low temperatures required at the inlet of the PVT collectors. The maximum source temperature of the heat pump at the inlet of the evaporator is 20 °C, and the maximum heating capacity of 12 kW is achieved at B5/W35 and a compressor speed of 5300 rpm. The testing facility also includes a hot water storage tank and a 10 kW Alfa Laval air-water heat exchanger for heat dissipation. The PVT collector arrays and mechanical room can be seen in Fig. 1, and a flow chart of the system with its monitoring equipment can be seen in Fig. 2.

The PVT collectors have been provided by Swedish startup Solhybrid i Småland, and consist of a glass-to-glass PV module with an aluminium manifold mechanically pressed against the rear glass. Having glass on the backside of the PV panel, as opposed to conventional PV, allows for a greater contact with the heat exchanger and increases mechanical strength, at the expense of an increased thermal resistance (Sommerfeldt and Ollas, 2017). The

manifold has a trough that fits a 12 mm copper pipe, which is also mechanically fixed. Thermal grease is added between the rear glass and aluminium manifold, as well as between the pipe and the trough to improve the thermal contact between the different surfaces. The thermal absorber-exchanger consists of six aluminium manifold and copper pipe units, each 150 mm wide and 1600 mm long, and are connected in a traditional parallel/harp configuration.



Fig. 1. Testing facility with mechanical room (left) and PVT collectors (right)

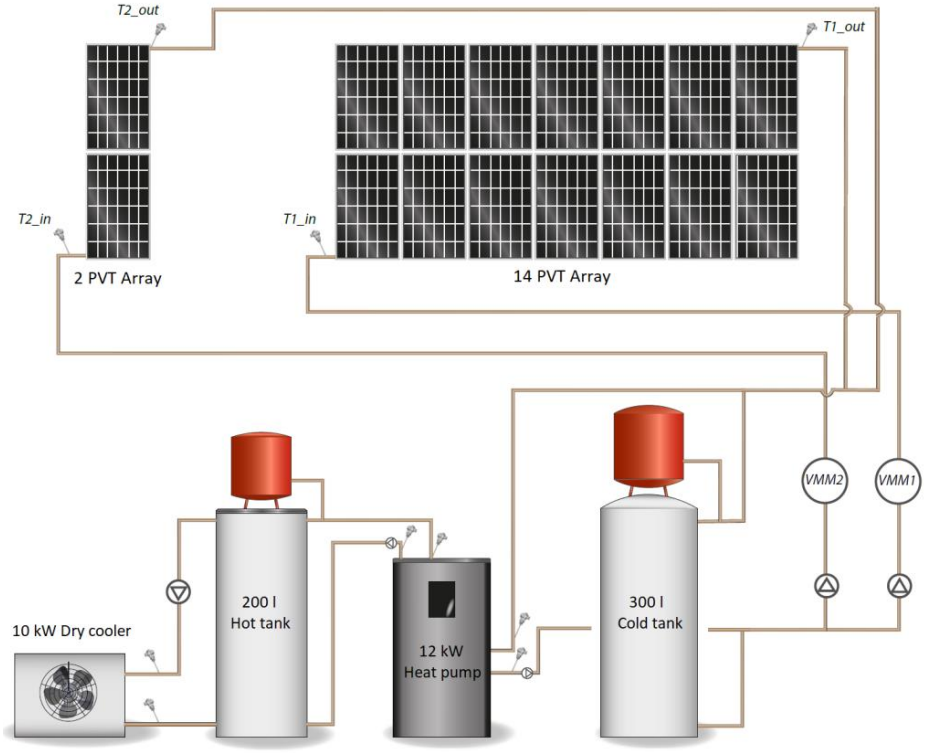

Fig. 2. System diagram with relevant measuring equipment

The PV module used for the PVT collectors is model PLM-285MA-60DG, a 60-monocrystalline-cells panel manufactured by Perlight Solar. The electrical ratings and specifications of the PV module are presented in Tab. 1. The conversion from the direct current (DC) generated by each module to alternating current (AC) is done by 14 Enphase IQ7 microinverters, one connected to each module.

Tab. 1. Electrical data of selected PV module

P_{max} (W_p)	Efficiency (η_{el})	Open-circuit voltage (V_{oc})	Short-circuit current (I_{sc})	Voltage at P_{max} (V_{mp})	Current at P_{max} (I_{mp})	Temp. coeff. P_{max} (β)
285 W	17.52 %	38.80 V	9.32 A	32.43 V	8.79 A	-0.40 %/K

A heat power meter is used to measure inlet and outlet temperatures to and from the PVT collectors, as well as flow rate and thermal power. In addition, a PT1000 temperature sensor is connected to the outlet of the PVT to

cross validate the measurements given by the heat meter. The entire system is monitored by two data loggers: one that tracks the electricity production from the microinverters, and one that tracks the heat pump performance, flow rates and the temperature levels within the system. The weather data is collected from a weather station installed directly above the PVT array, where ambient temperature, relative humidity, dew point, wind speed and direction are monitored. Solar irradiance is measured by a solar irradiance meter, located in the plane of the PVT collectors next to the array. All the measured data is obtained in 1-minute time steps, except for the electricity production that is measured every 5 minutes. A summary of the measurement equipment and the parameters that are being measured is presented in Tab. 2. Although there are other parameters that are being monitored in the system, such as compressor power or brine temperatures, only those relevant for this study are presented here.

Tab. 2. Measurement equipment and monitored parameters

Equipment	Quantity	Nomenclature
Weather Station	Ambient temperature (outdoor) [°C]	*T_amb*
	Wind speed [m/s]	*υ*
Solar irradiance meter	Incident solar irradiation [W/m^2]	*G*
Heat power meter (*VMM1* and *VMM2*)	Thermal power [W]	*Q_th*
	Volumetric flow rate [m^3/h]	*q*
	Inlet temperature to PVT [°C]	*T1_in & T2_in*
	Outlet temperature to PVT [°C]	*T1_out & T2_out*
Microinverters	Electrical power [W]	*P_el*

3.2. COMSOL model description

The PVT collector is modelled as a 1.6 x 0.9 m flat plate representing the glass-glass PV panel, and a metal thermal absorber with fins mechanically pressed to the back side. The PV panel consists of 5 layers: front glass, EVA encapsulate, silicon cells, EVA encapsulate, and rear glass, whereas the thermal absorber consists of the aluminum manifold and copper pipes that were described in the previous section. A thermal grease layer of 0.5 mm is added between the rear glass and aluminum manifold. To account for the imperfect thermal contact between the PV panel and absorber, the conductivity of the thermal grease that best fits the model is found to be 0.020 Wm^{-1}K^{-1} (thermal resistance of 0.017 m^{2}KW^{-1}) which is within the range of thermal resistance values of 0.010 – 0.040 m^{2}KW^{-1} found by Sommerfeldt and Ollas (2017) in their study of a similar collector. It is important to highlight that the thermal conductivity of the thermal grease also considers the imperfect bonding of absorber and PV, and consequent presence of air, which explains the low value. A summary of the material layers and properties is presented in Tab. 3, based on the study by Sommerfeldt and Ollas (2017).

Tab. 3. Material layers and properties

Layer	Material	Thickness [mm]	Density [kgm^{-3}]	Conductivity [Wm^{-1} K^{-1}]	Heat Capacity [Jkg^{-1}K^{-1}]
PV	Silicon	0.225	2330	148	677
EVA	EVA	0.5	960	0.7	2090
Glass	Glass	2.5	2530	1.8	500
Thermal grease	Thermal grease	0.5	2600[c]	0.02	1100[c]
Absorber plate	Aluminum	~ 1.75	2690[a]	218[a]	900[a]
Tube	Copper	1	8954	390	383
Fluid	Ethylene glycol - water	-	Vary w/temp	0.6	4186

[a] ASM International Handbook Committee, 1990

[b] Cristofari et al., 2009

[c] (Thermal Management, n.d.)

In order to reduce the required computational time and take advantage of the fact that the absorber consists of six identical and symmetrical manifold-pipe units, only one sixth of the PVT collector is modelled in COMSOL Multiphysics. An even flow distribution among all pipes and all collectors in the system is considered. A cross sectional diagram of PVT collector can be seen in Fig. 3.

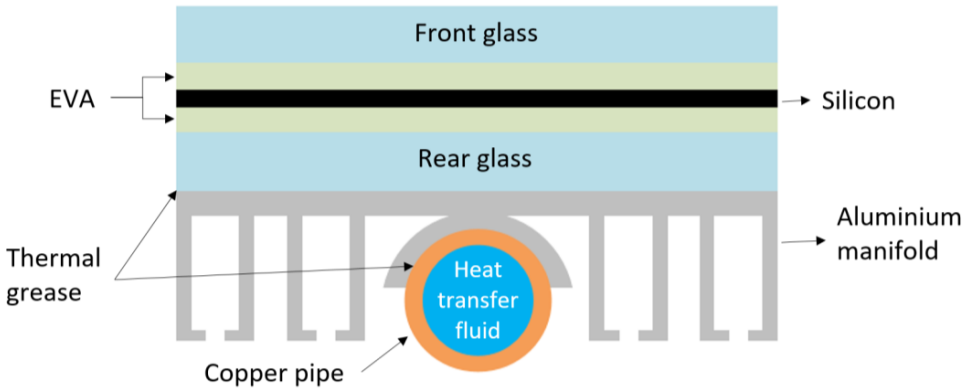

Fig. 3. Cross sectional diagram of the modeled PVT collector

Since the fluid flow falls in the laminar regime for all the measured flow rates, both laminar flow and heat transfer in solid and fluids interfaces with a non-isothermal flow multiphysics coupling are set up in COMSOL Multiphysics software. The PV part of the collector is modeled using a simple efficiency approach, where the electrical efficiency (η_{el}) is given by equation $\eta_{el} = \eta_0 \times [1 - \beta_0(T_{PV} - T_{ref})]$, being η_0 the efficiency of the PV cell at a reference temperature T_{ref}, T_{PV} the actual temperature of the PV cell, and β_0 the factor that governs the temperature dependence. The transmittance-absorptance factor is set at 0.81 (Sakellariou and Axaopoulos, 2018; Simonetti et al., 2018), whereas the sky temperature (T_{sky}) is given by expression $T_{sky} = 0.0552 \times T_{amb}^{1.5}$ (Duffie and Beckman, 1991).

The effect of wind speed on heat losses is a significant factor for unglazed PVT collectors (Sandnes and Rekstad, 2002). There are several methods to calculate the convective heat transfer coefficient in relation to wind speeds presented in the literature, but the model that best suits this case is a combination between the one presented by Cristofari et al., 2009 on the rear side of the collector, and the one presented by Watmuff et al., 1977 on the front side of the collector. According to Cristofari et al., 2009 , the convective heat transfer coefficient (h_c) with ambient air depends on whether the subject surface is on windward or leeward side and can be expressed by $h_c = 11.4 + 5.7\upsilon$ $Wm^{-2}K^{-1}$ and $h_c = 5.7$ $Wm^{-2}K^{-1}$ respectively. In this case, the rear side of the collector is considered to be on leeward, since for most of the hours in the period of study the wind is coming from the south or southwest directions. Thus, h_c is set at 5.7 $Wm^{-2}K^{-1}$. The convective heat transfer coefficient model on the front side of the collector is set at by $h_c = 2.8+3\upsilon$ $Wm^{-2}K^{-1}$ (Watmuff et al., 1977). The reason why a lower h_c might fit the model better than the higher one presented by Cristofari et al., 2009, is because of the effect of the full collector array as compared to a single collector. Frost formation, condensation gains and nighttime operation are not considered in the model.

In the testing facility there are two subarrays connected in series and each subarray has seven collectors connected in parallel. Assuming that the volumetric flow rate is evenly distributed between the PVT collectors in the array, the flow rate through each collector is calculated as 1/7 of the total volumetric flow rate into the array. Since the outlet temperature is measured at the end of the second subarray, the simulation is performed in two stages: the temperature at the outlet of the first PVT collector is obtained from the simulations, and it is used as inlet temperature for the second simulation. The results obtained from this second simulation is the one used for the calculation of the thermal output, which is then divided by two in order to calculate the value per module.

3.3. Performance evaluation

The performance of the PVT collectors is evaluated using three metrics:

- Thermal output (*Q_th)* in W for model validation
- Electrical output *(P_el)* in W for model validation
- Specific thermal output (q_th) in W/m^2 for the evaluation of the performance curves

When evaluating the thermal performance of the PVT collector for different flow rates and solar irradiation levels, the specific thermal output is plotted against the reduced temperature difference, defined as $T_{red} = (T_i - T_a)/G$ where T_i is the inlet temperature to the collector, T_a the ambient temperature, and G the solar irradiation.

To evaluate how well the numerical model fits the empirical data, three different statistical measures are used. Firstly, the Mean Absolute Error (MAE), which is calculated as the sum of the absolute errors divided by the

number of observations or data points, representing the average of the absolute errors. The expression for the calculation of MAE can be seen in (eq.1), where n is the number of observations, $\hat{y}_i$ is the simulated or predicted value and y_i the measured value.

$$MAE = \frac{1}{n}\sum_{i=1}^{n}|\hat{y}_i - y_i| \qquad \text{(eq. 1)}$$

Another statistical method used for the validation of the model is the Mean Biased Error (MBE), which is used to estimate the average bias in the prediction made by the model. A positive MBE means that the model is overestimating the dataset, whereas a negative MBE means that the model is underestimating the dataset. The expression for the calculation of MBE can be seen (eq.2).

$$MBE = \frac{1}{n}\sum_{i=1}^{n}(\hat{y}_i - y_i) \qquad \text{(eq. 2)}$$

The coefficient of determination (R^2) is the final statistical method to evaluate the accuracy of the model with regards to the measured data. It compares the variance of the dependent variable with the total variance. In other words, it helps to understand how differences in the dependent variable (simulation results), can be explained by the differences in a second variable. It shows how strong a linear relationship is between two variables, and is represented with a number between 0 (fails to explain variance) and 1 (fully explains variance). It can be calculated with (eq.3), where RSS is the sum of the squares of residuals, TSS the total sum of squares, and $\bar{y}$ the mean of the observed or measured data.

$$R^2 = 1 - \frac{RSS}{TSS} = 1 - \frac{\sum_i (y_i - \hat{y}_i)^2}{\sum_i (y_i - \bar{y})^2} \qquad \text{(eq. 3)}$$

4. Results

Of all the data gathered, 30 different hours of measurements are selected, based on the requirement that there should be 60 sequential measurements with a determined level of variance for each of the different measured parameters. If that condition is met, then it is assumed that the conditions are steady state for that hour, and it is then used as a single data point. The level of variance is determined by the Coefficient of Variation (CV), which is defined as the standard deviation divided by the mean of the sample. The acceptable CV for each of the input parameters is presented in Tab. 4.

Tab. 4. Acceptable coefficient of variation for measured parameters

Parameter	Acceptable CV
Volumetric flow rate	<10%
Inlet temperature	<10%
Ambient temperature	<10%
Solar irradiance	<30%

Although the original idea was to have a low variability of wind speed measurements, this was deemed impossible. However, the collectors have a relatively high thermal inertia, so the variance in wind speeds should have a minimal impact on the fluid temperatures (Sommerfeldt and Ollas, 2017).

Tab. 5 shows the values for the different boundary conditions. The range of measured ambient temperatures in the 30-point data set was between 13 °C and 24 °C, with an even frequency distribution along the range. Inlet temperatures varied between 1 °C and 12 °C, with 40 % of the measurements occurring between 6 °C and 8 °C. When looking at solar irradiation levels, almost half of the data points were below 400 W/m^2, however, 20 % of them were over 800 W/m^2. The variation of average wind speeds was in the range of 0 to 7 m/s, with a quite even distribution along the range. Volumetric flow rate varied was mostly around 80 lh^{-1}m^{-2}, with a few experiments performed at lower values.

The measured values of ambient temperature, inlet temperature, solar irradiance, wind speed and flow rate are used as inputs in the COMSOL model, where outlet temperature and average PV cell temperatures are obtained as outputs. Outlet fluid temperature is then used to calculate the thermal output of the PVT collector and thermal efficiency, whereas the average PV cell temperature is used to calculate the specific electrical output and the electrical efficiency.

Tab. 5. Measured values of boundary conditions

Flow rate [$lh^{-1}m^{-2}$]	Inlet Temp. [°C]	Ambient Temp. [°C]	Solar irradiance [W/m^2]	Wind speed [m/s]
81.4	6.13	24.23	73.0	4.7
81.2	5.89	22.83	23.5	4.5
81.8	6.50	21.89	300.2	4.6
79.5	5.80	19.76	142.9	6.7
82.1	6.77	19.42	712.5	6.3
27.2	5.59	19.28	0.0	3.4
44.2	5.36	16.53	46.3	2.6
30.3	5.36	18.36	0.0	1.6
30.4	4.80	16.99	0.0	2.6
81.2	5.88	20.11	274.3	5.0
81.1	5.83	20.15	191.7	5.3
34.7	5.33	17.30	83.2	2.5
39.0	6.21	16.68	42.5	1.5
82.8	7.63	16.85	450.7	6.4
82.5	7.48	18.51	53.5	6.7
84.6	8.31	18.24	256.4	4.4
27.9	5.74	18.19	0.0	1.3
82.7	8.16	13.48	221.9	0.3
74.7	7.69	15.58	174.8	0.8
43.8	7.31	14.44	66.2	0.0
85.3	9.89	18.21	1021.7	2.8
86.5	11.41	20.84	945.8	5.1
86.2	10.99	20.49	857.5	4.2
66.8	1.78	21.21	491.0	1.9
81.9	6.29	20.70	542.0	6.8
82.0	6.83	20.15	671.9	5.2
78.7	8.48	13.48	545.7	0.5
83.9	9.33	16.87	882.9	2.4
88.5	11.03	18.93	693.6	5.2
85.8	11.09	19.90	887.5	5.6

4.1. Model validation

Fig. 4 shows the measured values of outlet temperature on the x-axis, and the simulated values of the outlet temperature in the y-axis. It can be seen that the different data points are scattered close to the y=x line with a few exceptions. The model seems to be overestimating the outlet temperatures for lower values, and underestimating it for higher ones. The maximum absolute error is around 2.5 K, but the mean absolute error is considerably lower, with a value 0.70 K. A mean biased error of 0.16 K shows that the model is slightly overestimating the outlet temperature of the PVT collectors, but the value is low to consider it a problem. Finally, a coefficient of determination of 0.902 shows that more than 90 % of the variability in the simulated results of the outlet temperature can be explained by the variability in the measured data, which means that the model can represent real world performance accurately.

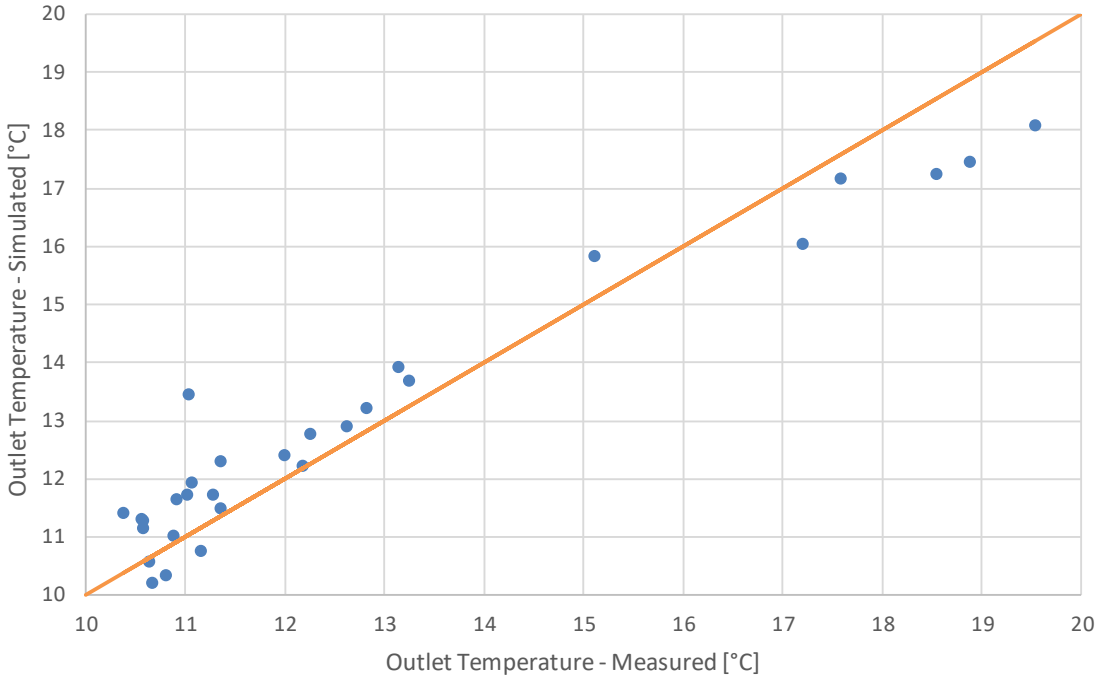

Fig. 4. Simulated outlet temperature values plotted against measured outlet temperature values

Fig. 5 shows the measured values of thermal output obtained from the heat meters on the y-axis, against the thermal output calculated with the simulation results. Once again it can be seen that the data points are scattered close to the y=x line, with the highest absolute errors occuring for the highest values of thermal output. The maximum absolute error is close to 150 W, represeting a relative difference of 25 %. However, the mean absolute error is almost four times smaller. When calculating the mean biased error, the result of 4.5 W shows that the model is overestimating the thermal power production, which is alligned with the results obtained for the outlet temperature. A coefficient of determination of 0.89, shows a good relationship between real world performance and the simulated results.

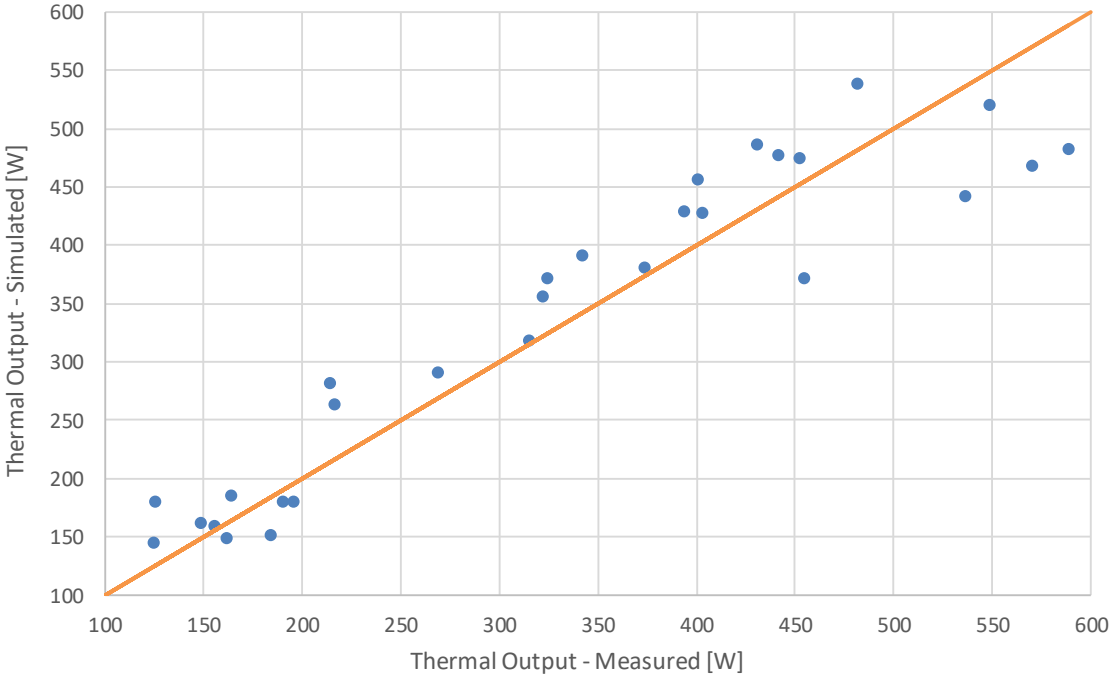

Fig. 5. Simulated thermal output values plotted against measured thermal output values

Fig. 6 shows the measured values of electrical output obtained from the microinverters on the y-axis, against the electrical output from the simulation results, using a simple efficiency approach. It can be seen that most of the

data points are close to the y=x lines, with the highest absolute errors of approximately 25 W and relative error of 10 % occurring when the electricity production is the highest. For low electricity production values, the simple efficiency approach fits the measured values precisely. A MAE of 4.20 W, a MBE of 0.48 W, and R^2 value of 0.995, shows that the simple efficiency approach can predict the electricity production from each collector in a good way.

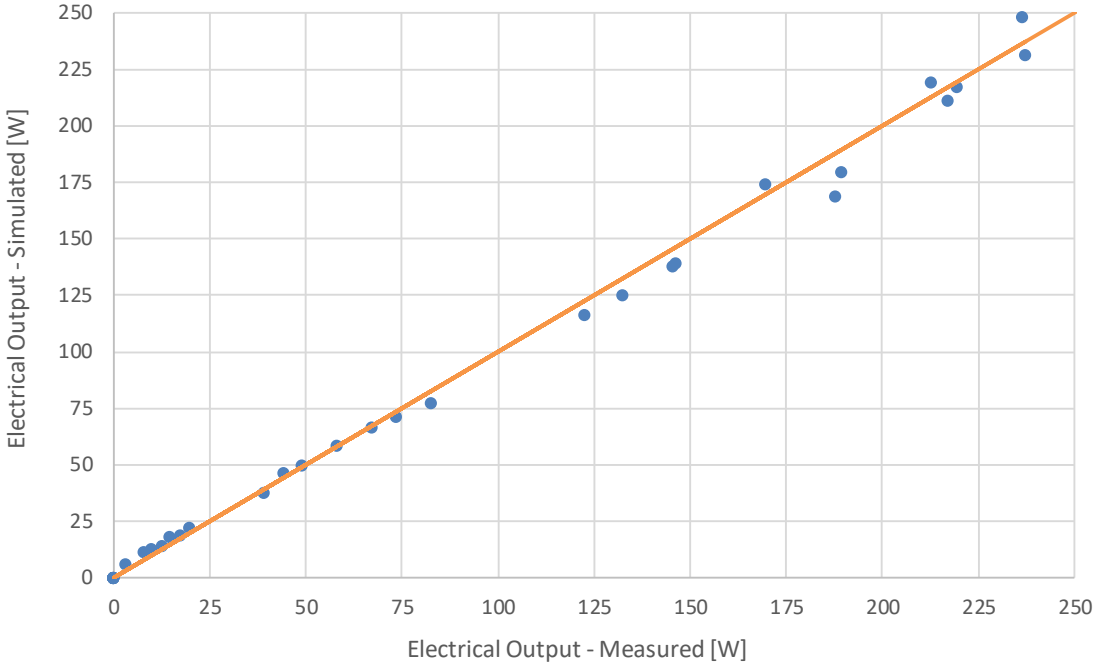

Fig. 6. Simulated electrical output values plotted against measured electrical output values

The statistical methods results for outlet temperature, thermal power and electrical power can be seen in Tab. 6.

Tab. 6. Statistical methods summary of results

	Temperature Out	Thermal Power	Electrical Power
Mean Absolute Error (MAE)	0.70 K	40.02 W	4.20 W
Mean Biased Error (MBE)	0.16 K	4.48 W	-0.48 W
Coefficient of Determination (R^2)	0.902	0.887	0.995

4.2. Performance curves

This section presents the performance curves of the studied PVT collector for different solar irradiation levels and flow rates based on the numerical modelling results. Ambient temperature is fixed at 20 °C and wind speed at 1 m/s. For the evaluation of the performance of the PVT collectors under different solar irradiation levels, a constant flow rate of 80 $lh^{-1}m^{-2}$ is considered. The results in Fig. 7 show that even when the solar irradiance is as low as 200 W/m², thermal output can be as high as 530 W/m² or 363 W/m² for reduced temperature differences of -0.15 Km^2W^{-1} and -0.10 Km^2W^{-1} respectively. As would be expected, the maximum thermal output occurs when solar irradiation is 1000 W/m² with a reduced temperature difference of -0.03 Km^2W^{-1}, which is equivalent to a temperature difference between ambient and inlet to the collector of 30 K. For this case, the specific thermal output can be as high as 800 W/m² or 1160 W/collector. The performance at a reduced temperature difference of 0 Km^2W^{-1}, varies between 26.1 W/m² for the lowest solar irradiation case, and 297.7 W/m² for the highest solar irradiation case.

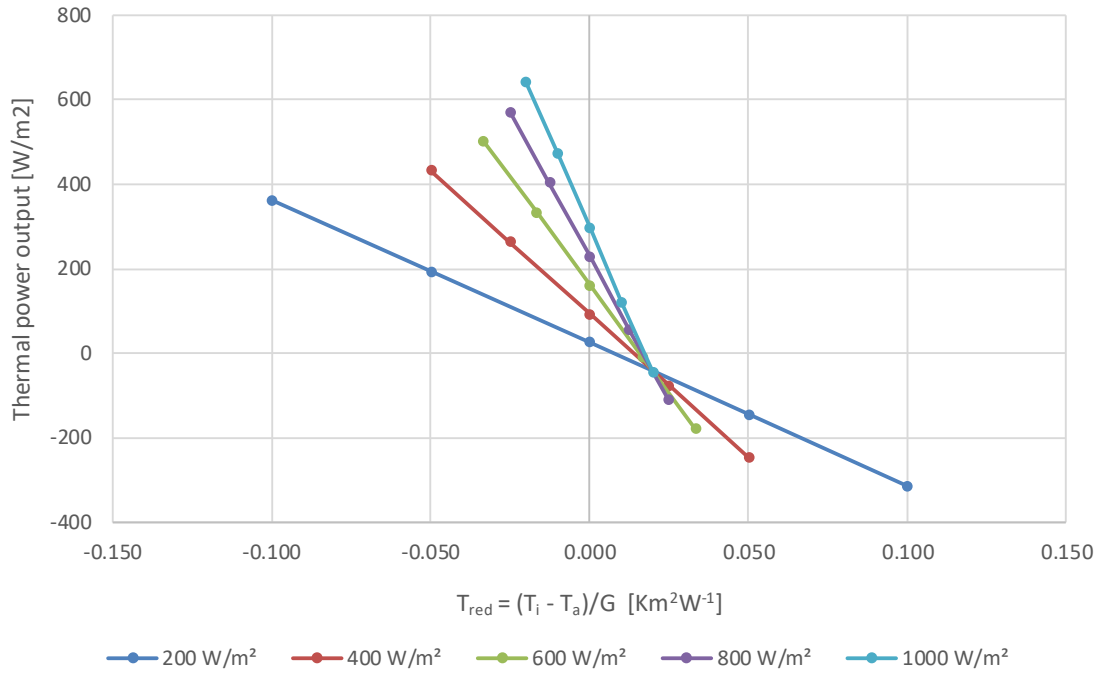

Fig. 7. Thermal performance curve of PVT collector prototype obtained from Comsol Multiphysics simulations

For the evaluation of the performance of the PVT collectors under different volumetric flow rates, a constant solar irradiation level of 1000 W/m^2 is considered. The results in Fig. 8 show that increasing the flow rate from 20 lh^{-1}m^{-2} to 100 lh^{-1}m^{-2} has diminishing returns. For a reduced temperature difference of -0.02 Km^{2}W^{-1}, increasing the flow rate from 20 lh^{-1}m^{-2} to 40 lh^{-1}m^{-2}, increases thermal output from 414.7 W/m^2 to 519.5 W/m^2, equivalent to 25.3 %. However, when flow rate is further increased to 60 lh^{-1}m^{-2}, 80 lh^{-1}m^{-2} and 100 lh^{-1}m^{-2}, the increase in specific thermal output is of 13.2 %, 9.3 % and 7.1 %. The performance at a reduced temperature difference of 0 Km^{2}W^{-1}, varies between 193 W/m^2 for a flow rate of 20 lh^{-1}m^{-2}, and 318.6 W/m^2 for 100 lh^{-1}m^{-2}, which is a lower variation than what occurs for the one occurring for the different solar irradiation levels. It is worth noting that the flow remains always in the laminar regime, with a Reynolds number of 450 at 100 lh^{-1}m^{-2}.

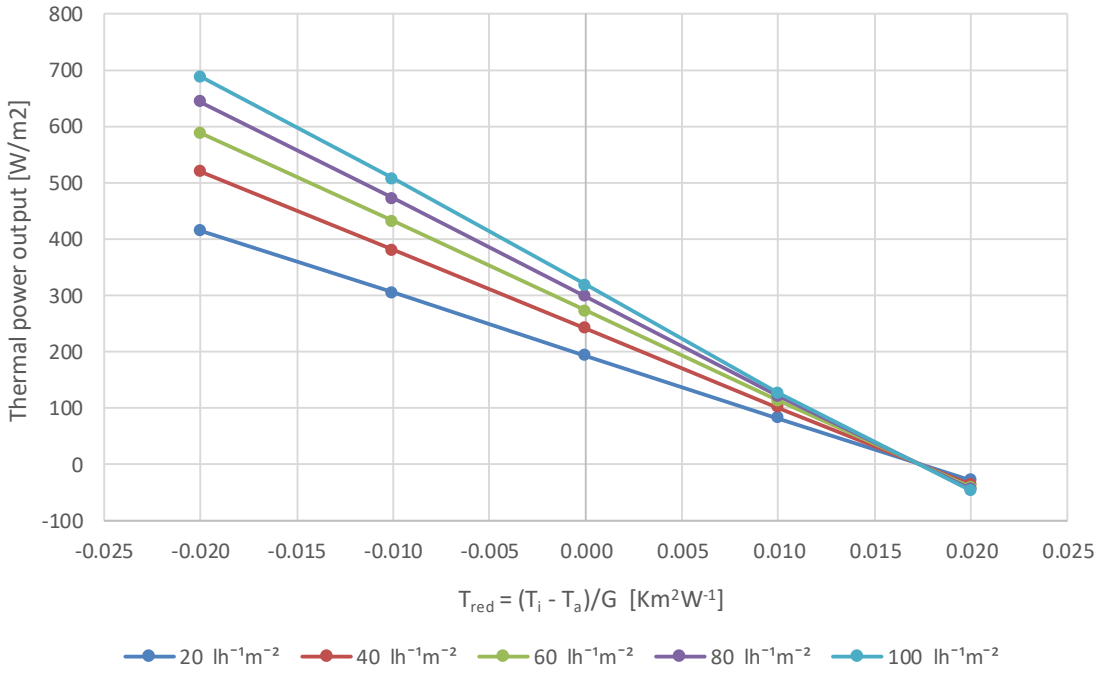

Fig. 8. Thermal performance curve of PVT collector prototype obtained from Comsol Multiphysics simulations

5. Discussion and Conclusions

The analysis presented in this paper shows that the numerical model of a sheet and tube PVT collector with fins specifically designed for heat pump integration, fits the empirical data with an R^2 value of more than 88% for the main three output parameters: outlet temperature, thermal output and electrical output. However, the MAE for outlet temperature and thermal power needs to be discussed further.

To begin, the thermal output of the full collector array was measured in the experiments and divided by 14 to calculate the value for one collector, but in the model only two collectors were considered. All collectors were assumed to generate the same amount of power, although most probably the subarray that has the lowest inlet temperature produces a higher thermal output than the following subarray, due to a higher temperature difference between inlet temperatures and ambient, enhancing the heat capture from the surrounding air. While this may be a limitation in validating a single collector, since it is expected that PVT will nearly always be installed in an array, the approach used here captures variance between individual collectors that can be missed if only using a single sample.

Condensation effects were not considered in this study, which could be an important issue when the difference between inlet temperature and dew point temperature is high. However during the experiments, no considerable amount of condensation was observed on the rear side of the PVT collectors, so it was not considered to be a critical modelling aspect for the studied data range.

It is important to highlight that even though the highest thermal output obtained from the measurements was 368 W/m^2, based on the performance curves obtained from the simulations of the validated numerical model, the thermal output of the sheet and tube PVT collector with fins could more than double that value. This can happen for example, when there is a brine temperature coming out of the borehole field below -5 °C, there is an ambient temperature of 25 °C and the solar irradiance is 1000 W/m^2. Although not a common scenario, this could be possible and helps set an upper limit for the amount of heat that can be extracted from the collector. However, even at low irradiation levels, the PVT collector can work mostly as an air-water heat exchanger achieving a specific thermal output of more than 300 W/m^2. In a study currently under peer-review, the addition of fins are shown to increase heat capture from the air by up to 60 % over unfinned designs.

The finned design is still relatively unique and a developing segment of PVT design. This work builds on the body of knowledge that defines the performance and potential of PVT heat pumps systems by describing an empirically validated numerical model. Further work in finned PVT collector development and analytical models in full systems analysis (e.g. TRNSYS) can be informed using COMSOL, reducing time and effort. Future work will quantify the full PVT+HP system performance and the benefits finned collectors provide.

6. References

ASM International Handbook Committee, 1990. ASM Handbook, Volume 02 - Properties and Selection: Nonferrous Alloys and Special-Purpose Materials. ASM International.

Bertram, E., Glembin, J., Rockendorf, G., 2012. Unglazed PVT collectors as additional heat source in heat pump systems with borehole heat exchanger. Energy Procedia 30, 414–423. https://doi.org/10.1016/j.egypro.2012.11.049

Chhugani, B., Pärisch, P., Kirchner, M., Littwin, M., Lampe, C., Giovannetti, F., 2021. Model Validation and Performance Assessment of Unglazed Photovoltaic-Thermal Collectors with Heat Pump Systems 1–12. https://doi.org/10.18086/eurosun.2020.05.13

Cristofari, C., Notton, G., Canaletti, J., 2009. Thermal behavior of a copolymer PV/Th solar system in low flow rate conditions. Sol. Energy 83, 1123–1138. https://doi.org/10.1016/j.solener.2009.01.008

Duffie, J.A., Beckman, W.A., 1991. Solar Engineering of Thermal Processes.

Kamel, R.S., Fung, A.S., Dash, P.R.H., 2015. Solar systems and their integration with heat pumps: A review. Energy Build. https://doi.org/10.1016/j.enbuild.2014.11.030

Sakellariou, E., Axaopoulos, P., 2018. An experimentally validated, transient model for sheet and tube PVT collector. Sol. Energy 174, 709–718. https://doi.org/10.1016/j.solener.2018.09.058

Schmidt, C., Schäfer, A., Kramer, K., 2018. Single source "solar thermal" heat pump for residential heat supply: Performance with an array of unglazed PVT collectors, in: 12th ISES Eurosun Conference. Rapperswil, Switzerland.

Simonetti, R., Molinaroli, L., Manzolini, G., 2018. Development and validation of a comprehensive dynamic mathematical model for hybrid PV/T solar collectors. Appl. Therm. Eng. 133, 543–554. https://doi.org/10.1016/j.applthermaleng.2018.01.093

Sommerfeldt, N., Madani, H., 2019. In-depth techno-economic analysis of PV/Thermal plus ground source heat

pump systems for multi-family houses in a heating dominated climate. Sol. Energy 190, 44–62. https://doi.org/10.1016/j.solener.2019.07.080

Sommerfeldt, N., Madani, H., 2017. Review of Solar PV/Thermal Plus Ground Source Heat Pump Systems for European Multi-Family Houses 1–12. https://doi.org/10.18086/eurosun.2016.08.15

Sommerfeldt, N., Ollas, P., 2017. Reverse engineering prototype solar pv/thermal collector properties from empirical data for use in TRNSYS Type 560. ISES Sol. World Congr. 2017 - IEA SHC Int. Conf. Sol. Heat. Cool. Build. Ind. 2017, Proc. 1121–1132. https://doi.org/10.18086/swc.2017.18.11

Thermal Management, n.d. Thermal Pastes [WWW Document]. Therm. Manag. URL https://www.thermalmgt.com/thermal-pastes/ (accessed 9.10.22).

Vittorini, D., Castellucci, N., Cipollone, R., 2017. Heat recovery potential and electrical performances in-field investigation on a hybrid PVT module. Appl. Energy 205, 44–56. https://doi.org/10.1016/j.apenergy.2017.07.117

Watmuff, J., Proctor, D., Australia, S., 1977. Solar and wind induced external coefficients-Solar collectors. COMPLES.

Experimental Testing of a Solar Thermal Collector with composite TIM of plastic Honeycomb and Silica Aerogel Polyurethane Containers

Jian Zheng[1], Rafel Febrer[1], Jesús Castro[1], and Deniz Kizildag[1]

[1] Heat and Mass Transfer Technological Center (CTTC) Universitat Politècnica de Catalunya-BarcelonaTech (UPC), Terrassa (Barcelona) (Spain)

Abstract

A new proposal of high performance flat plate solar thermal collector (FPC) based on Transparent Insulation Materials (TIM) combining silica aerogel contained in insulation containers with plastic honeycomb is evaluated and compared with similar state of the art technologies. Thus, the proposed FPC shows better performance than the basic plastic honeycomb collector at high $\Delta TT/GG > 0.074$ while potentially protecting the honeycomb layer from reaching high temperatures. This data is compared as well with a previous version of the FPC with combined TIM of plastic honeycomb with silica aerogel to demonstrate that the performance has been improvedwith a new construction strategy.

Keywords: Silica Aerogel, Flat plate solar thermal collector, Honeycomb

1. Introduction

Solar thermal collectors operated under medium temperatures have different technologies operating in the current market. Besides FPC, stationary compound parabolic collectors (CPC), evacuated tubes collectors (ETC), Fresnel lens collectors (FLC), small parabolic trough collectors (PTC) and cylindrical trough collectors (CTC) are other technological alternatives widely investigated according to Tian and Zhao 2013. Also, Sharma et al. 2013 demonstrated that a solar heated system could be employed in various applications depending on the temperature and working fluid. Many authors, e .g. Sokhansefat et al. 2018 used TRNSYS16 software for a thermoeconomic analysis of two different solar hot water systems with FPC and ETC in cold winter Iran. Their results showed that the ETC system is 41% better than the FPC systems and applying ETC in cold climates is recommended. (see Osorio el al. 2017) used TIMs in the FPCs, PTCs, and CR, then the results presented that TIM could dramatically increase the thermal efficiency at high absorber temperature. For the FPCs, when the extinction coefficient of TIM $\mu = 8m^{-1}$ and the absorber temperature $T_{abs} > 103^{\circ}C$, the FPCs with TIM have higher efficiency than the conventional ones. High performance honeycomb flat plate solar collector (FPC) using honeycomb plastic Transparent Insulation Materials (TIM) has been established as a commercial market solution (an example of that is TIGI's collector, Klier et al. 2014)) that achieve a good tradeoff between high efficiency in the high temperature range ($(T_m-T_a)/G>0.08$) with a reasonable cost compared to evacuated tube collectors. Beikircher el al. 2014 presented that optimized mounting insulation with 30mm film should yield the same results as mineral wool with 50 mm insulation thickness. Besides, the film does not store moisture, and could avoid fogging and corrosion. Zhou et al. 2019 also studied FPCs with TIM using numerical methods, and the results show that if the transmittance of TIM is below 80%, the collector with TIM shows no advantages. Bellos and Tzivanidis 2018 introduced nanofluid with solar-driven absorption chiller with nanofluid to enhance the thermal performance. Ranjith and Karim 2016 used alternate working fluid for the solar thermal system, including propylene glycol(PG). Ammar el al. 2022 used transparent insulation material parallel slats (TIM-PS) to prevent air convection in a flat plate solar air collector for industrial agriculture drying. In order to reduce the thermal loss in the collector, TIM is widely used and in works of (see Ammar el al. 2022, Kizildag et al. 2022, Kessentini et al. 2014), simulations and experiments of FPC with TIM were carried out. In order to protect TIM from the high temperature of the absorber, in Kizildag et al. 2022, an overheating protecting ventilation channel based on shape memory alloy is used in the FPC, which can ventilate the FPC and preventing the TIM from igniting. (Wu et al. 2021) introduced aerogel to the PV/T

© 2022. The Authors. Published by International Solar Energy Society
Selection and/or peer review under responsibility of Scientific Committee
doi:10.18086/eurosun.2022.12.03 Available at http://proceedings.ises.org

collector and found that the heat loss of the PV/T at 70°C could be reduced up to 75% and the thermal efficiency increased by 46%. The coefficient generally has a linear relationship with solar radiation and ambient temperature. To acquire better thermal insulation, aerogel is introduced in the solar collector due to its high transmittance and low thermal conductivity, which also has an ultra-low density. In this part, several versions of FPC are demonstrated including the manufacturing details. The experimental data is compared with each version and simulation results.

The current study intends to validate a new proposal of collector with a compound TIM cover of plastic honeycomb and a silica aerogel layer contained using insulation containers which are implemented using polyurethane. The FPC has been tested in the summer days. The design aims to reduce the thermal loss in the relatively high-temperature T_{abs}>90°C. Additionally, it is compared with state-of-the-art honeycomb and silica layer collectors from Kizildag et al. 2022.

2. Collector concept

The previous collectors developed that have been taken as a reference to evaluate the new proposal efficiency are schematically represented in Figure 1. In contrast, the collector proposed in the current study is presented in Figure 2.

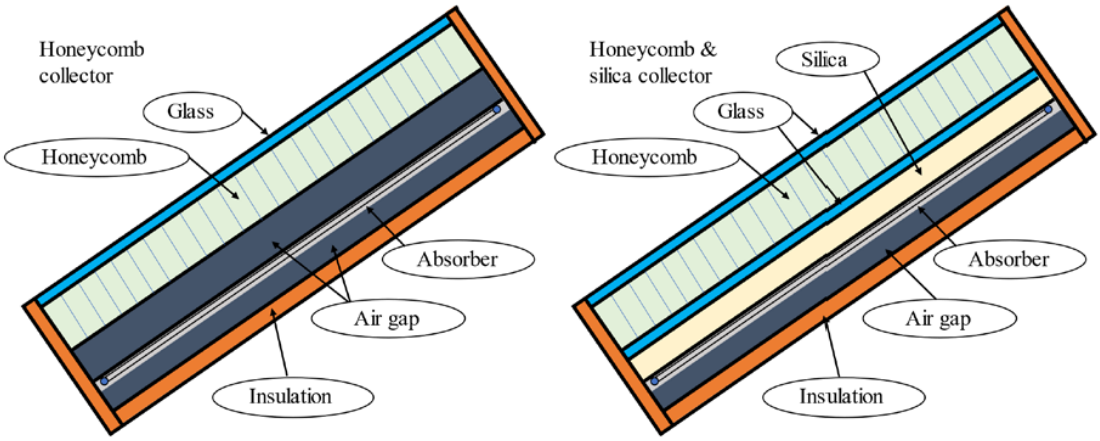

(a) Previous high performance FPC (Kizildag et al. 2022) **(b)High performance FPC in this work with TIM and aerogel**

Fig. 1: Honeycomb collector (Left), Honeycomb and silica aerogel collector (right)

Important details to assess properly the efficiency of the collectors depicted in Figure 1. Are the following:

- Both collectors have the same thickness of honeycomb (75mm)
- The glass layer of the honeycomb collector has a transmittance of 0,96 and the honeycomb and silica collector a transmittance of 0,92 for both glasses
- The silica layer of the honeycomb and silica FPC is 20mm thick
- Both collectors are equally insulated
- Both collectors have the same absorber design

Regarding the new collector, the main differences are that the silica will be distributed using polyurethane containers and vertically stacked between the honeycomb layer and the absorber. Moreover, the glass layers for this collector will be a 0.96 transmittance glass. The remaining properties will be kept the same to simplify the comparison between solar collectors.

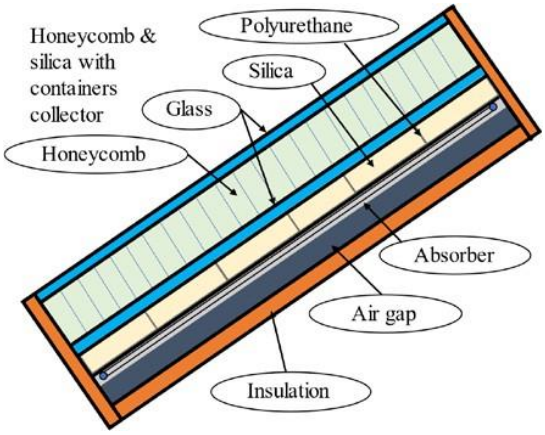

Fig. 2: Honeycomb with silica aerogel containers solar thermal collector

The test bench used to obtain the steady-state efficiency of the solar collectors compared in the current study is presented in Figure 3. The results have been recorded in accordance with ISO 9806-1:1994.

The flat plate solar collector with TIM in this work is addressed as a further development of the collector proposed at Kizildag et al. 2022, and the main difference is the insulation with aerogel. The ventilation channel is set behind the absorber since there will be barely an air gap inside the collector. The TIM used is cellulose triacetate, which has a melting point of 120-160◦C. And yellowing and embrittlement can already be observed at temperatures above 100 ◦C (see Kizildag et al. 2017). The aerogel used here has a thermal conductivity of 0.01 W·m−1K −1, a density of 0.1 g/cm3. After the absorber is fixed above the insulation, the aerogel will be tiled above the absorber with a thickness of 2 cm. Since the aerogel is in the shape of particles and the collector is inclined, an auxiliary structure should be placed to fix the aerogel layer. Seven polyurethane barriers are attached above the absorber with the same thickness as the aerogel, and another tampered glass (same as the cover) is placed on top of the aerogel and barriers, as shown in Fig 4a. And the TIM material is glued to the cover, then the cover will be fixed with the support structure. The cover should not be directly placed above the first layer of glass since the absorber may form curvature and affect the horizontal level, a small air gap (<1cm) between the first layer of glass and TIM should always be considered. Finally, the collector should be well insulated. Finally, the collector should be well insulated, as shown in Fig 4(b). The picture was taken several days after the installation of the solar collector, from which it shows clearly the aerogel above the absorber is fixed well.

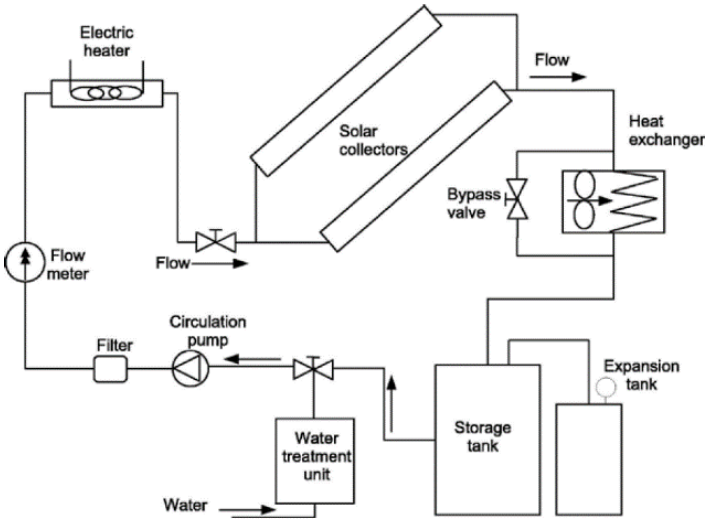

Fig. 3: Test bench used for the characterization of the solar thermal collectors



(a) **(b)**

Fig. 4: Solar collector with TIM and Silica aerogel, (a) shows the silica above the absorber with a thickness of 2cm (b) represents the collector with TIM after insulation and installation.

3. Experimental Results

The experimental results of the previous solar thermal collectors depicted in Figure 1 and the new proposal shown in Figure 2 can be seen in Figure 5. The honeycomb with silica layer without containers (previous version) has worst performance in the comparison since the reduction of the optical efficiency is not compensated with the reduction of the first and second order coefficients. In other words, the reduction in the transmittance produced by the glasses of 0.92 transmittance and the silica layer cannot be compensated with the reduction of the heat losses produced by the silica aerogel. Moreover, the silica aerogel presented important problems related to compactness that will be discussed later in section 4.

The proposed collector, represented in Figure 4, overcome the honeycomb collector when $(T_m - T_a)/G > 0.08$ area. This important finding demonstrates the applicability of the silica aerogel to obtain high efficiency collectors and that the technical difficulties could be overcome using containers to maintain silica compactness and shape.

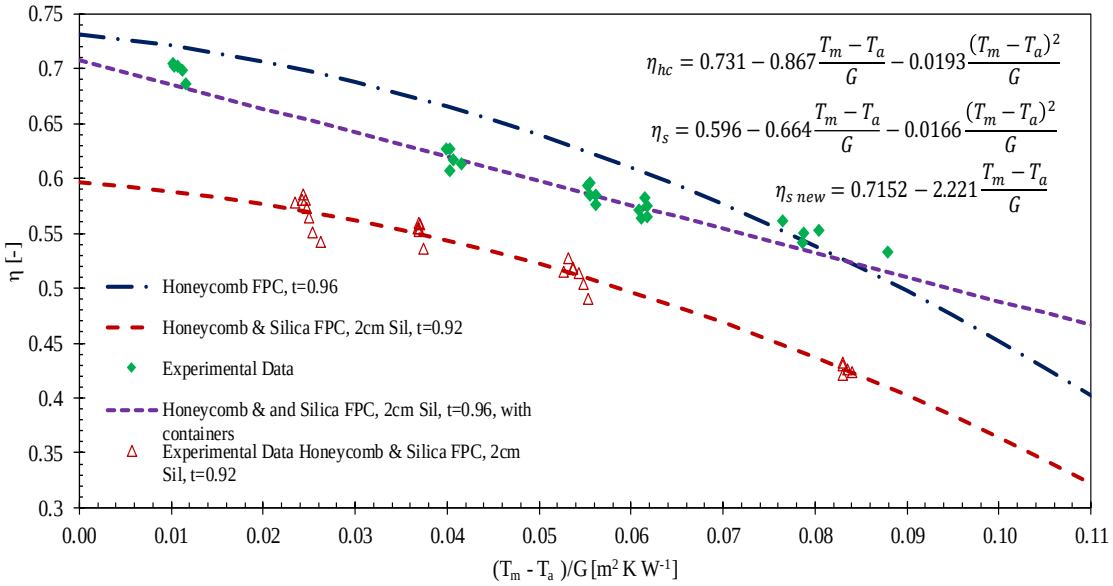

Fig. 5: Efficiency of the honeycomb FPC and the honeycomb with silica FPC collectors based on aperture area

The curve is flattened quite importantly due to the silica effect on the heat losses. Additionally, the improved compactness of the silica played a vital role in the results as will be discussed in the following section.

4. Discussion

The first version of silica aerogel with honeycomb FPC presented silica compactness related issues consequence of manufacturing the FPC without considering the movement of the silica aerogel granulates inside the collector. The implementation of containers to strategically locate silica for the second version is justified with Figure 4, since the flatness of the curve is improved. Previous design without containers struggled in containing properly the silica on the top side of the collector. Thus, the heat losses in the hottest part of the FPC were high. During the manufacturing of the new version of the collector the air-silica compactness ratio was taken importantly in consideration. The higher the stability of the silica inside the collector and the less air contained inside, the better the efficiency to be achieved.

It can be observed that although the silica-honeycomb collectors' optical efficiency is low when compared to the pure plastic honeycomb TIM collector, its efficiency becomes greater in the $\Delta T/G > 0.08$ region.

When the performance of the two versions of combined silica aerogel/plastic honeycomb TIM high performance FPC are compared. It cannot be neglected the relevant effect of using high transmittance glass in the present collector (0.96) compared to the one in the previous version (0.92).

An important aspect to be improved for the next versions of the new collector, is the optimization of the useful area, as the polyurethane bars that contain the silica aerogel occupy part of the collector area (now about 15%).

5. Conclusions

In this work, the performance of a new concept of high performance Flat Plate Collector (FPC) based on Transparent Insulation Materials (TIM) combining silica aerogel contained in insulation containers with plastic honeycomb is evaluated. The current study demonstrates that including silica aerogel without considering its compactness is not a success approach. Thus, properly compacting the silica can improve efficiency of a previously developed plastichoneycomb TIM for high temperature applications (at $\Delta T/G > 0.08$). Another important lesson learned is that a high transmittance glass cannot be avoided since the silica aerogel decreases optical performance, which is notenough compensated flattening the efficiency curve at high temperatures to have a competitive FPC.

6. Acknowledgments

Sponsored by the SUDOKET – SOE2/P1/E0677 project under the Interreg-Sudoe program.

7. References

Ammar, M., Mokni, A., Mhiri, H., Bournot, P., 2022. Parametric investigation on the performance of natural convection flat plate solar air collector with additional transparent insulation material parallel slats (TIM-PS). Solar Energy, 231(November 2021):379–401.

Beikircher, T., Berger, V., Osgyan, P., Reuß M., Streib, G., 2014. Low-e confined air chambers in solar flat- plate collectors as an economic new type of rear side insulation avoiding moisture problems. Solar Energy, 105:280–289.

Bellos, E., Tzivanidis, C., 2018. Performance analysis and optimization of an absorption chiller driven by nanofluid based solar flat plate collector. Journal of Cleaner Production, 174:256–272.

Kessentini, H., Capdevila, R., Castro, J., Oliva, A., and Bouden, C., 2014. Three dimensional heat transfer analysis of combined conduction and radiation in honeycomb transparent insulation. Solar Energy, 105:58–70.

Kessentini, H., Castro, J., Capdevila, R., Oliva, A., 2014. Development of flat plate collector with plastic transparent insulation and low-cost overheating protection system. Applied Energy, 133:206–223.

Klier, S., Klier, Z., Adel, M., Efron, R., TIGI LTD., 2014. System and method for temperature limiting in a sealed solar energy collector (US Patent Number 8857426B2) Mark M. Friedman. URL: https://patentimages.storage.googleapis.com/48/43/73/b224ddbdaebbc0/US8857426.pdf

Kizildag, D., Castro, J., Kessentini, H., Rigola, J., Oliva, A., 2017. Development, optimization and test performance of highly efficient flat plate solar collector with transparent insulation and low-cost overheating protection. In ISES Sol. World Congr. 2017-IEA SHC Int. Conf. Sol. Heat. Cool. Build. Ind. 2017, Proc, pages 2031–2042.

Kizildag, D., Castro, J., Kessentini, H., Schillaci, E., Rigola, J., 2022. First test field performance of highly efficient flat plate solar collectors with transparent insulation and low-cost overheating protection. Solar Energy, 236(December 2021):239–248.

Osorio, D., Rivera-Alvarez, A., Girurugwiro, P., Yang, S., Hovsapian, R., Ordonez, C., 2017. Integration of transparent insulation materials into solar collector devices. Solar Energy, 147:8–21.

Ranjith, V., Karim, A., 2016. A Comparative Study on the Experimental and Computational Analysis of Solar Flat Plate Collector Using an Alternate Working Fluid. Procedia Technology, 24:546–553.

Sharma, K., Sharma, C., Mullick C., Kandpal C., 2017. Solar industrial process heating: A review. Renewable and Sustainable Energy Reviews, 78(January):124–137.

Sokhansefat, T., Kasaeian, A., Rahmani, K., Heidari, A., Aghakhani, F., Mahian, O., 2018 Thermoeconomic and environmental analysis of solar flat plate and evacuated tube collectors in cold climatic conditions. Renewable Energy, 115:501–508.

Tian, Y., and Zhao CY., 2013. A review of solar collectors and thermal energy storage in solar thermal applications. Applied Energy, 104:538–553.

Wu, L., Zhao, B., Ao, X., Yang, H., Ren, X., Yu, Q., Guo, K., Hu, M., and Pei, G., 2021. Performance analysis of the aerogel-based PV/T collector: A numerical study. Solar Energy, 228(September):339–348.

Zhou, L., Wang, Y., Huang, Q., 2019. Parametric analysis on the performance of flat plate collector with transparent insulation material. Energy, 174:534–542.

Appendix: Units and Symbols

Table 1: Symbols for properties

Preferred name	Symbol	Unit
Temperature	*T*	K
Thermal conductivity	*K*	W m^{-1} K^{-1}
Thickness	*E*	m
Efficiency	*η*	
Solar irradiance on FPC	*G*	W m^{-2}

Table 2: Suffixes for properties

Suffixes	Symbol
Flat plate collector	FPC
Stationary compound parabolic collectors	CPC
Fresnel lens collectors	FLC
Small parabolic trough collectors	PTC
Cylindrical trough collectors	CTC
Sil	Silica Aerogel
Honeycomb	TIM
Absorber	abs
Ambient	a
Absorber fluid inlet	i
Outlet	o

Numerical modeling and simulation comparisons of a cost efficient novel CPVT Solar Collector

Daniel Santos[1], Jesús Castro[1], Deniz Kizildag[1], Joaquim Rigola[1] and Assensi Oliva[1]

[1]Heat and Mass Transfer Technological Center (CTTC),

Universitat Politècnica de Catalunya BARCELONA TECH (UPC),

Terrassa (Spain)

Abstract

In this work, the simulation of a Concentrated PhotoVoltaic Thermal (CPVT) solar collector system has been done by means of Finite Volume Method. The system consists of a parabolic collector, which concentrates solar irradiance onto solar cells, which are refrigerated attaching them to a pipe which contains water. At the same time, water is warmed up. Numerical results were validated with experimental data obtained within the current eranet project for the Economic Cogeneration by Efficiently Concentrated SUNlight (ECOSUN). The idea of this project is to study how to take advantage of the residual heat produced by photovoltaic elements. The CPVT model is oriented to optimize the design for solar cooling applications. Finally, a 1D model is introduced to reduce the computational cost of the simulation for obtaining key parameters.

Keywords: parabolic collector, solar energy, solar power, solar cell, FVM, CPVT.

1. Introduction

Thermal engineering and other fields of physics are combined in order to study solar cell technology. Experiments are very useful tool to understand the behaviour of any system, but on the other hand, they can be very expensive and difficult to perform. In solar cell systems, thermal and solid components are often combined with fluids in order to refrigerate them. Physics of these systems are well understood: they combine Navier-Stokes equations with energy conservation equation (and sometimes radiation equations). Despite of the fact that we know the equations, they do not have an analytical solution for the general case. One powerful tool that allows us to obtain numerical results of a solar cell system and help us in the optimizing process is Computational Fluid Dynamics (CFD) (Guadamund, et al.). Discretising properly the equations and using computational resources, we can simulate these systems and obtain information of them. Once we have our model implemented, it is important to use experimental data to assess that our model is correct, and then we can use it to simulate the system under different conditions, such as different inlet conditions, different geometrical configurations or different materials, avoiding the necessity of repeating the experiments, which is in general expensive.

ECOSun project has as main aim the cost reduction of electricity and heat co-generation via a Concentrated Photovoltaic/Thermal (CPV-T) system by applying low-cost materials and advanced industrial manufacturing methods. In the CPV-T system, the solar radiation is captured in parabolic through concentrator based on a novel support structure fabricated by injection moulding and focused on a Co-Generation Absorber Module (CAM), where special c-SiPV-cells are operated under concentration. The purpose of this project is focused on concentrated photovoltaic thermal collector (CPVT), which concentrates solar irradiance onto a row of photovoltaic solar cells (Sharaf and Orhan). At the same time, these solar cells must be refrigerated in order to work optimally. This could be done, for instance, attaching these solar cells to a pipe which contains some fluid (water in our case). One of the subtasks of the project has been to simulate properly the whole CPVT system, comparing our results against the results obtained experimentally. Different configurations of inflow water will be taken into account, using a closed system with a glass envelope and low-pressure air. The whole CPVT system can be attached to absorption machines in order to take advantage of the residual heat (Castro et al., 2021).

© 2022. The Authors. Published by International Solar Energy Society
Selection and/or peer review under responsibility of Scientific Committee
doi:10.18086/eurosun.2022.12.04 Available at http://proceedings.ises.org

2. CPVT solar cell system



Fig. 1: CPVT solar collector experimental configuration (Felsberger, et. al. 2020)

Figure 1 show the experimental configuration of the experiment carried out by Felsberger, et. al. 2020, and Figure 2 and Figure 3 show the structure of the CPVT solar cell system we want to simulate. From a numerical point of view, it consists of three parts: solid regions, fluid domains and coupling interfaces.

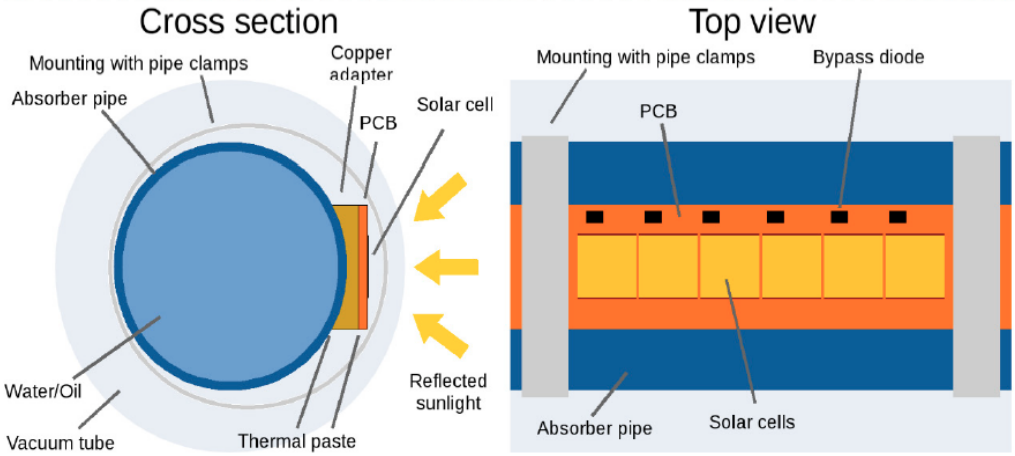

Fig. 2: Side scheme of the CPVT solar collector experimental configuration (collector not included) (Felsberger, et. al. 2020)

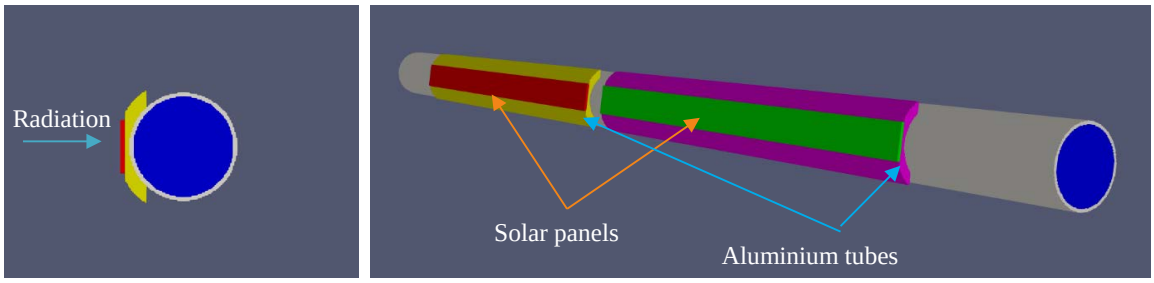

Fig. 3: CPVT cross section configuration (left); CPVT configuration front of parabolic collector (collector not included)

Figure 2 also shows the important parts of the system: i) an absorber pipe; ii) a printed circuit board (PCB) which have the solar cells attached; and iii) a piece which connects the PCB with the pipe iv) and an envelope glass to isolate the system. Finally, a parabolic solar collector is used to concentrate solar power onto the solar cells, as shown in Figure 1.

3. 3D Numerical model and validation

The equations we need to solve for each region are:

- Solid elements: energy equation conservation, (note that for this case, the velocities are equal to 0).

$$\frac{\partial T}{\partial t} + \boldsymbol{u} \cdot \nabla \mathrm{T} = \frac{k}{\rho c_p} \nabla^2 \boldsymbol{T} + \frac{J}{\rho c_p}, \qquad \text{(eq. 1)}$$

where T is the temperature, **u** is the velocity (**u**=0 for solid elements), k is the thermal conductivity, ρ is the density, c_p is the heat capacity and J is the source term.

- Fluid elements: (Eq.1) + Incompressible Navier-Stokes equations with buoyancy term (Boussinesq approximation):

$$\nabla \cdot \boldsymbol{u} = 0, \qquad \text{(eq. 2)}$$

$$\frac{\partial \boldsymbol{u}}{\partial t} + (\boldsymbol{u} \cdot \nabla)\mathbf{u} = -\frac{1}{\rho}\nabla(p - \rho \boldsymbol{g} \cdot \boldsymbol{z}) + \nu \nabla^2 \boldsymbol{u} - \boldsymbol{g}\beta(T - T_0), \qquad \text{(eq. 3)}$$

where **u** is the velocity, p is the pressure, ρ is the density, ν is the kinematic viscosity, **g** is the gravity constant, β is the thermal expansion coefficient, and T is the temperature. Buoyancy term is needed to take into account natural convection with the exterior air. Forced convection appears between the flow inside the pipe and the pipe, so this term is not really relevant there.

- Coupling interfaces (solid-solid and fluid-solid):
  - Heat flux exiting one domain enters the other: $Q_1 = -Q_2$.
  - Same temperature at the interface: $T_1 = T_2$.

Convective and radiative terms are taken into account in order to compute the heat flux. The radiation model used is the Finite Volume Discrete Ordinates Method, which solves the RTE (Radiative Transfer Equation):

$$\hat{\boldsymbol{s}} \cdot \nabla I(\boldsymbol{r}, \hat{\boldsymbol{s}}) = \kappa I_b + (\kappa + \sigma_s) I, \qquad \text{(eq. 4)}$$

applying a finite volume method (Colomer, 2006; Wang, 2020). In the previous equation, the intensity radiation field I is solved, which is defined as the energy due to radiation, propagating along a given direction $\hat{\boldsymbol{s}}$, that crosses a unit area normal to $\hat{\boldsymbol{s}}$, per unit area, unit solid angle around $\hat{\boldsymbol{s}}$, unit wavelength and time. The absorption coefficient κ and the scattering coefficient σ_s model the medium behavior.

Finally, the radiation coming from the parabolic collector is assumed as a radiative boundary condition computed as (Zarza, 2015):

$$q = \frac{W_{par}}{W_{pV}} G_b \eta_{opt}, \qquad \text{(eq. 5)}$$

where W_{par} is the aperture width of the parabola, W_{pV} is the height of the solar cells, G_b is the direct solar irradiance and η_{opt} is the optical efficiency of the parabola.

Many codes such as Ansys Fluent or OpenFOAM are able to deal with cases which need to solve the previous equations. OpenFOAM was the code chosen in our case. In particular, we selected the "chtMultiRegionFoam" solver, which can solve transient cases with conjugate heat transfer between solids and fluids. Furthermore, radiation is solved by means of fvDOM method, which is the more precise model that OpenFOAM has integrated.

This model was validated using experimental data coming from EcoSUN experimental test cases under lab tests conditions (Felsberger, et. al. 2020; Buchroithner, et al.). Besides, other experiments have been done within this configuration in order to obtain experimental data (Felsberger, et. al. 2021). Our model was capable of reproduce properly the results of these experiments. The main objective of the model was to obtain the temperature reached

by the system in the steady state. Figure 4 shows the validation of the model under lab conditions. The validation of the model is deeply examined in Santos, et.al (2021).

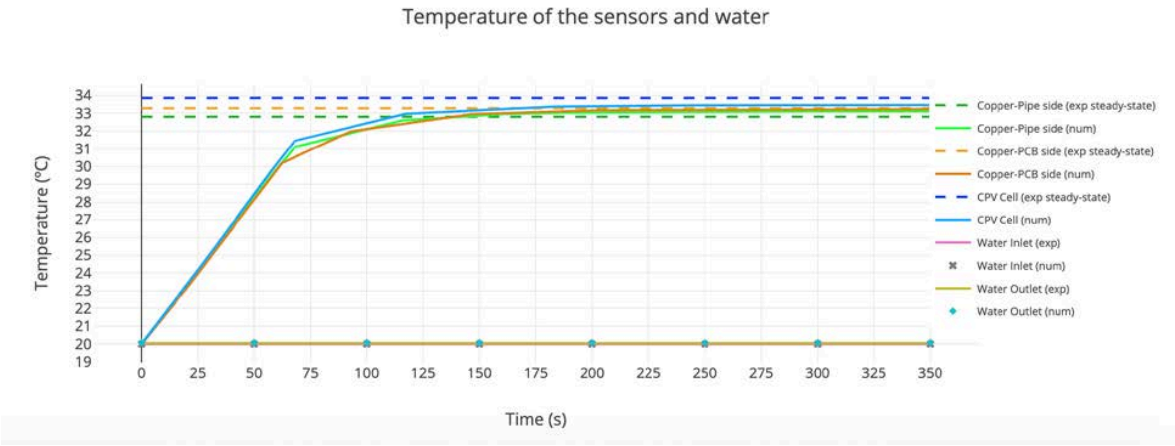

Fig. 4: Temperature obtained at temperature sensors. Water input temperature is 20.0°C. Slashed lines represent the steady state temperature found in the experiment.

Figures 5, 6 and 7 show an example of the temperature reached by the back part of the PCB in the steady state. All the results have a reliable agreement with the experimental ones (Santos, et. al. 2021).

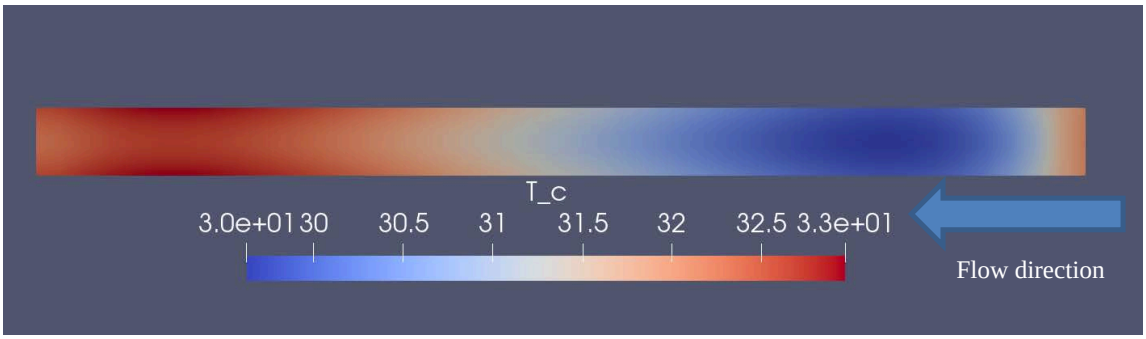

Fig. 5: HTF 17°C case. (Top) Steady state temperature profile behind the PCB. (Bottom) Temperature of the sensors over time.

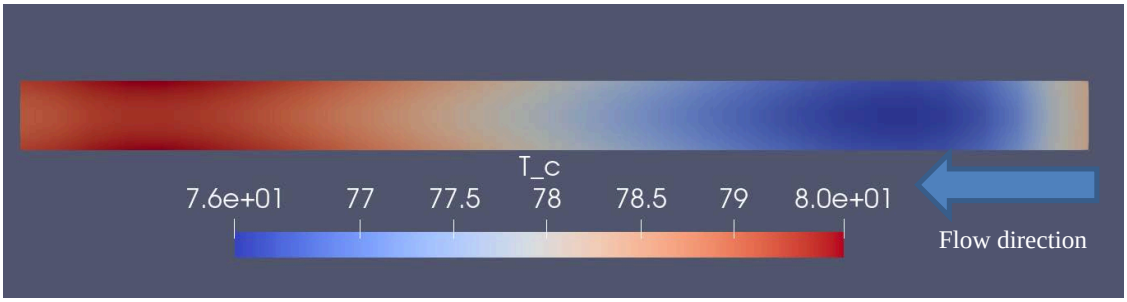

Fig. 6: HTF 65°C case. (Top) Steady state temperature profile behind the PCB. (Bottom) Temperature of the sensors over time.

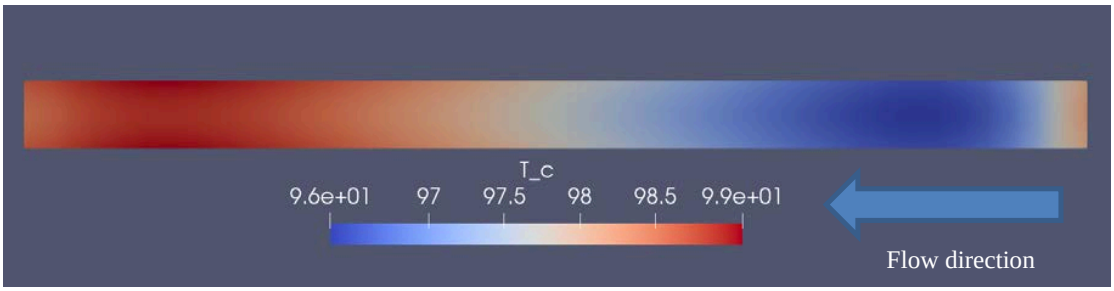

Fig. 7: HTF 90ºC case. (Top) Steady state temperature profile behind the PCB. (Bottom) Temperature of the sensors over time.

The short orange region found at the HTF entrance is caused by the heat transfer from the pipe to the PCB, and it was also observed in the experiments. Radiation also warms up the solid pipe, and part of this heat is transferred to the PCB.

4. 1D Numerical model and comparison of models

A transient 1D integration of the continuity, momentum and energy equations was done by means of finite volume method. Once we have the 1D discretization of the equations in the axial direction, they are solved by means of a step-by-step method. Some parameters such as friction factor and heat transfer coefficient are estimated using empirical correlations. In our case, the model was used to solve only the pipe, taking into account the width of the pipe and the flow. For more details of this discretization, see Morales, et. al. (2009).

Such model, due to the nature of a 1D simulation, has the advantage of needing much less computational power in comparison with a 3D simulation. On the other hand, it is only capable of providing information about some key parameters such as pressure drop, local heat transfer coefficient or outlet temperature of the HTF. For instance, it is not capable of providing information about the map temperature of the pipe or the PCB.

Another limitation of this model, which is very important in our analysis, is that it is assuming that heat flux is known as a boundary condition and it is assumed to be entering through all the pipe homogeneously. Clearly, this is not happening in our case, where the radiation enters only from the cells side and it is not arriving homogeneously to the pipe. However, as we will see now, this approximation is capable of reproducing some key aspects of the real experiments.

Tab. 1: Pressure drop, average heat transfer coefficient and outlet temperature obtained for the different test cases using both models.

	Pressure drop 3D model [Pa]	**Pressure drop 1D model [Pa]**	**Heat transfer coed 3D model [W/m2K]**	**Heat transfer coed 1D model [W/m2K]**	**Experimental outlet temperature [ºC]**	**Outlet temperature 3D model [ºC]**	**Outlet temperature 1D model [ºC]**
HTF 17ºC	9	8	703	674	17.48	17.46	17.57
HTF 65ºC	10	7	1259	1221	65.00	65.02	65.02
HTF 90ºC	25	17	2252	2221	88.68	88.67	88.69

As we can see in Table 1, the 1D model is able to obtain proper values for the pressure drop, the heat transfer coefficient and the outlet flow temperature. However, as we can see in Figures 8, 9 and 10, it is not capable of reproducing properly the fluid temperature along the pipe. This is due to the assumption that the heat flux is entering homogeneously the pipe. As the heat flux entering the system is the same in both models, the outlet temperature is very similar, but as it is entering the system homogeneously for the 1D case and in homogeneously for the 3D case, the temperature map is going to differ. From this feature, the 1D model adjusts the wall temperature to fix the flux, so the wall temperature is not going to be correct either.

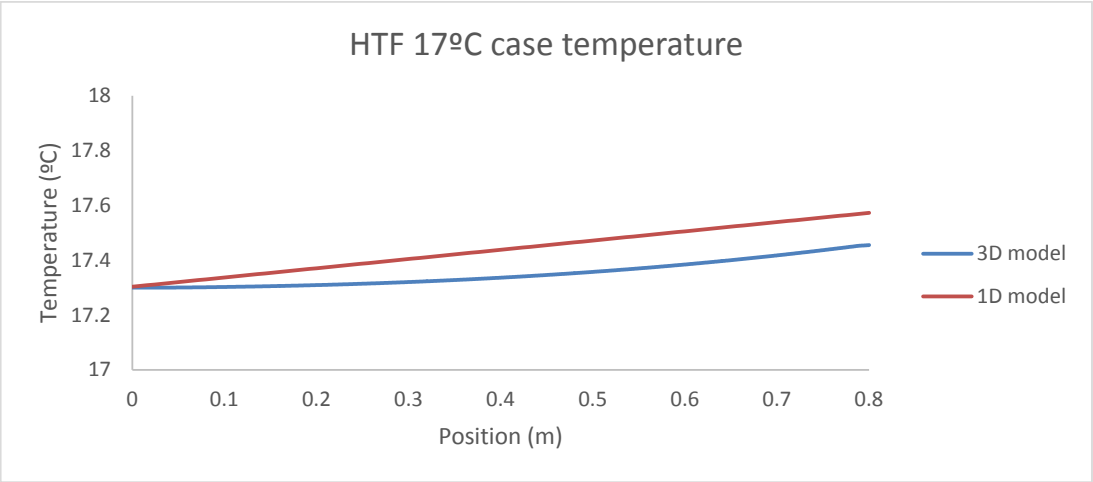

Fig. 8: Outlet temperature of the heat transfer fluid for the 17 ºC HTF case obtained using both models.

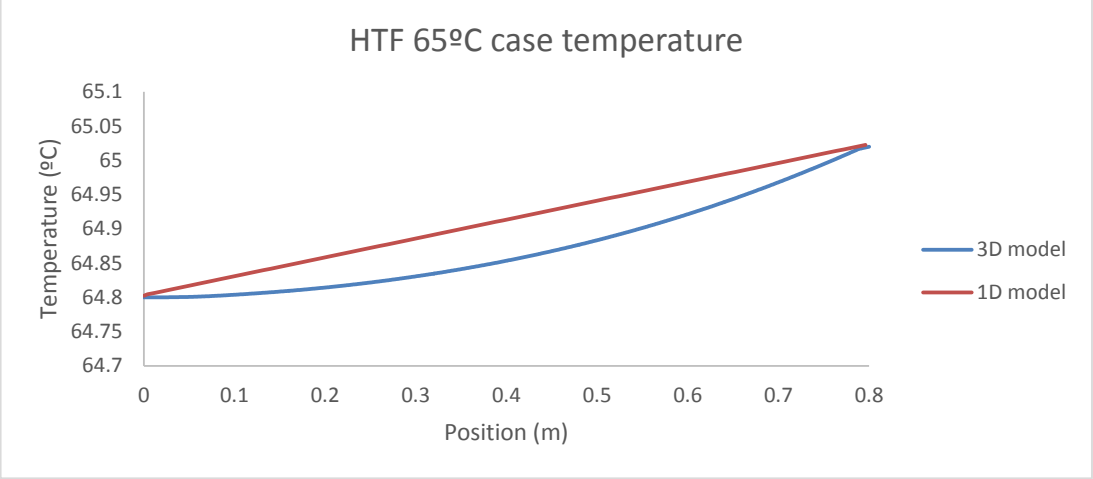

Fig. 9: Outlet temperature of the heat transfer fluid for the 65 ºC HTF case obtained using both models.

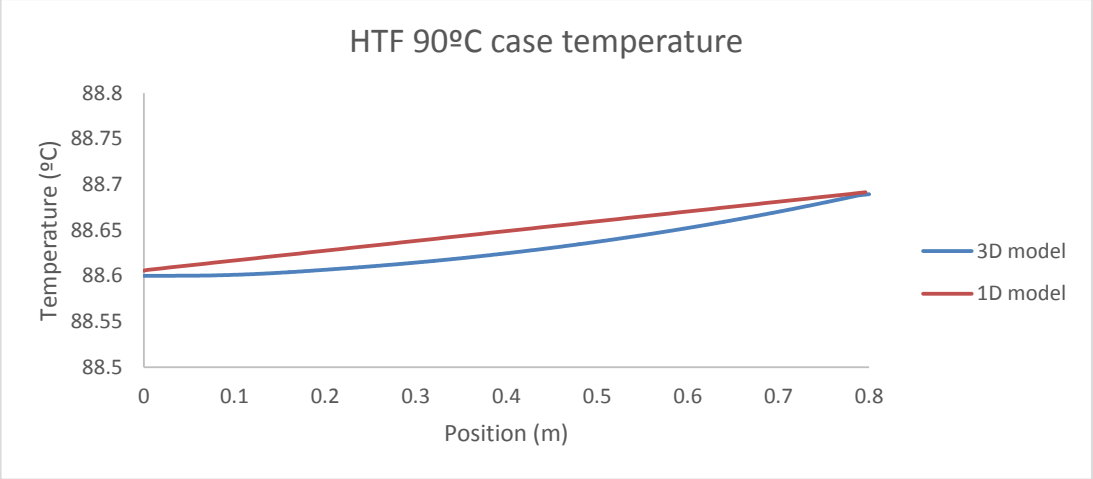

Fig. 10: Outlet temperature of the heat transfer fluid for the 90 °C HTF case obtained using both models.

5. Conclusions

A whole and detailed 3D numerical model for CPVT systems has been numerical developed, validated and experimentally tested under laboratory and real tests conditions. This model has demonstrated an excellent capability of prediction of the thermal behaviour of the system, and it can also be used as a numerical tool to study different geometries configurations for specific solar cooling application.

On the other hand, the 1D numerical model is useful for performance comparisons, but it is not bale to stablish detailed values of the system. However, it gives good results for outlet temperature, pressure drop and heat transfer coefficients.

6. Acknowledgments

This project has received funding from SOLAR-ERA.NET Cofund 2 joint call undertaking under the European Union's Horizon 2020 research and innovation programme.

7. References

Buchroithner, A., Gerl, B., Felsberger, R., Wegleiter, H., 2021. Design and operation of a versatile, low-cost, high-flux solar simulator for automated CPV cell and module testing, Solar Energy, Volume 228, Pages 387-404, ISSN 0038-092X. DOI: https://doi.org/10.1016/j.solener.2021.08.068

Castro, J., Rigola, J., Kizildag, D., Oliet, C., 2021. Preliminary assessment of a polygeneration system based on a concentrated photovoltaic thermal (CPVT) solar collector, ISHPC 2021: proceedings, Technische Universität Berlin Campus Charlottenburg, pp. 176-180. DOI: http://dx.doi.org/10.14279/depositonce-12278

Colomer, G., 2006. Numerical methods for radiative heat transfer, PhD thesis, Universitat Politècnica de Catalunya (UPC), Terrassa.

Felsberger, R., Buchroithner, A., Gerl, B., Wegleiter, H., 2020. Conversion and Testing of a Solar Thermal Parabolic Trough Collector for CPV-T Application, Energies, 13, 6142, 1-24. DOI: https://doi.org/10.3390/en13226142

Felsberger, R., Buchroithner, A., Gerl, B., Schweighofer, B., Wegleiter, H., 2021. Design and testing of concentrated photovoltaic arrays for retrofitting of solar thermal parabolic trough collectors, Applied Energy, Volume 300, 117427, ISSN 0306-2619. DOI: https://doi.org/10.1016/j.apenergy.2021.117427

Guadamund, E., Chiva, J., Colomer, G., Farnós, J., Al Mers, A., Rigola, J., Perez, C., 2017. Development of a high accurate numerical platform for the thermal and optical optimization of linear Fresnel receivers. *ISES Solar World Congress/IEA SHC Solar Heating and Cooling Conference*, pp. 2000 – 2011. DOI:10.18086/swc.2017.31.04

Morales-Ruíz, S., Rigola, J., Pérez-Segarra, C.D., García-Valladares, O., 2009. Numerical analysis of two-phase flow in condensers and evaporators with special emphasis on single-phase/two-phase transition zones, Applied Thermal Engineering, Volume 29, pp 1032-1042. DOI: https://doi.org/10.1016/j.applthermaleng.2008.05.017

Santos, D., Castro, J., Kizildag, D., Rigola, J., Oliva, A, 2021. Numerical Simulation of a Cost Efficient Novel CPVT Solar Collector. *ISES Solar World Congress*, Virtual conference, October 25-29. DOI:10.18086/swc.2021.22.08

Sharaf, O. Z., Orhan, M. F., 2015. Concentrated photovoltaic thermal (CPVT) solar collector systems: Part I – Fundamentals, design considerations and current technologies. Renewable and Sustainable Energy Reviews. Volume 50, 1500-1565. DOI: https://doi.org/10.1016/j.rser.2015.05.036

Wang, B., 2020. OpenFOAM fvDOM Model discretization notes (URL: https://boyaowang.github.io/boyaowang_OpenFOAM.github.io/2020/09/30/fvdom/). Last access: 08/10/2021.

Zarza, E., 2015. Sesión 13: Diseño de captadores y de campos de captadores cilindroparabólicos, lecture notes, Electricidad Termosolar, Escuela de Organización Industrial, delivered in 2015-2016. URL: (https://www.eoi.es/es/savia/publicaciones/25357/electricidad-termosolar-captadores-cilindroparabolicos-sesion-13-y-14). Last access: 08/10/2021.

Numerical Investigation of the Performance of a Solar Air Heater Equipped with Packed Beds

Hossein Ebadi[1], Antonio Cammi[2], Laura Savoldi[1]

[1] MAHTEP Group, Dipartimento Energia "Galileo Ferraris" (DENERG), Politecnico di Torino, Italy
[2] Department of Energy, Politecnico di Milano, Italy

Abstract

In this work, a numerical study based on pore-scale CFD analysis has been carried out on a solar air heater equipped with intermittent packed beds. Hydraulic and thermal characteristics of the air were determined by testing a range of mass flow rates and various collector configurations, including one (SAH-M1), two (SAH-M2), and three (SAH-M3) packed beds. After the validation of the numerical simulations with general correlations, results showed that as the number of packed zones increases, the total pressure drop grows. As a result, the maximum pressure drop was obtained as 115 kPa for the collector with three packed zones, operating at Re ~ 1.3×10^5. Detailed thermal analysis proved that the intermittent integration of packed beds has the potential to also increase the heat transfer exchange between each packed zone, improving the convection by 25% in the second zone to the first zone and 35% in the third zone to the second zone at Re ~ 1.3×10^5. This enhancement effect can be attributed to the increase in the turbulence conditions of the fluid regime from one bed to the other. Evaluating the effects of design parameters showed that the bed spacing could not change the thermo-hydraulic characteristics significantly, while particles' randomness may only affect the pressure drop by 13%.

Keywords: Solar air heater, Packed bed, heat transfer coefficient, porous, PCM

1. Introduction

Solar Flat Plate Collectors (FPC) are the most mature technology cases among all the other solar collectors, which have wide dissemination in both industrial and domestic applications. In general, the sample design of such collectors has a limited efficiency, which can be extended only if any other enhancement method is employed. To this achieve aim, in addition to optical augmentation, scientists have proposed various techniques to improve the nominal thermal efficiency of FPC which can be classified as passive or active solutions (Gorjian et al., 2020).

Solar Air Heaters (SAH) is one of the low-temperature solar collectors, which has wide deployment in agricultural and residential applications. According to the reports in the literature, the integration of pack beds, usually in the form of heat storage units could increase the nominal thermal efficiency further by storing the excessive heat with sensible or latent heat energy storage systems (Kumar and Kim, 2017). In general, packed bed SAHs can be formed using a metal screen, porous matrix, or packed particles to improve the heat transfer from the absorber to fluid flow. There are numerous studies that address the application of packed beds with SAH, investigating the shape, orientation, and size of the particles used in the medium. However, most of the reported works are usually experimental (Singh et al., 2013) or have a macro-scale numerical approach (Choudhury et al., 1995) due to the complexity of the simulation of packed-bed geometry. The employment of wire mesh packed beds with solar air collectors showed an 80% higher efficiency for a double pass flow. A finite difference solution algorithm was proposed using C++ language for a two-dimensional fully-developed fluid flow to predict the heat transfer coefficient for packed bed systems (Chouksey and Sharma, 2016). In an experimental study, researchers (Prasad et al., 2009) determined the heat transfer and friction characteristics of a packed bed solar air heater using wire mesh as packing material. It was found that the friction factor is a function of the system (geometrical) and operating parameters while the mass flow rate and the porosity of the bed are two important factors affecting the thermal efficiency. An analytical model was developed by scientists (Dhiman et al., 2011) to study a parallel flow solar air heater with packed material through an iterative solution procedure solving the governing energy balance equations. Results indicated that the air mass flow rate has the highest effect on the thermal efficiency of the heater where the maximum thermal efficiency increase was 20% due to the presence of the packed material. The integration of limestone and gravel as the packed-bed material with solar air heaters was also investigated both

© 2022. The Authors. Published by International Solar Energy Society
Selection and/or peer review under responsibility of Scientific Committee
doi:10.18086/eurosun.2022.12.05 Available at http://proceedings.ises.org

numerically and experimentally (Ramadan et al., 2007). Using an analytical solution of the energy-balance equations for the various elements of the system, researchers studied the effect of different operational and configurational parameters such as mass flow rate, and packed porosity on the heater performance and reported that the best performance could be achieved by materials with higher masses and lower porosities. In another attempt (Raj et al., 2019), phase change materials (PCM) were added to a solar air heater used for drying applications to extend the operating hour of the system after sunset. Therefore, several discrete metallic rectangular and cylindrical macro-encapsulate PCM units were placed inside the channel. Conducting a series of experimental tests, it was revealed that the average encapsulate efficiency can be obtained as 47.2% and 67% respectively for rectangular and cylindrical macro-encapsulates.

To open a new door in this field of research, this study aims to present a micro-scale (pore-scale) numerical analysis of a rectangular SAH duct equipped with packed bed inserts made by cylindrical particles with 3D CFD simulation using the commercial software of STAR CCM+. To reach this aim, the Discrete Element Method (DEM) was used to develop the geometry of the packed bed consisting of mm-size cylindrical particles. The credibility of this methodology for the development of porous structures with random packings has been well demonstrated in the literature (Allio et al., 2020; Savoldi et al., 2020). The beneficial effects in the augmentation of the heat transfer are specifically addressed in the analysis, with an eye on the increase of pressure drop driven by the presence of the packed bed inserts.

2. Solar collector

A typical SAH with dimensions of 726 mm × 80 mm × 30 mm was modeled, considering the solar absorber located over a rectangular duct, including running air. Since this study aims to model the inserts in the air channel and has no obligation to solve the energy equation on the collector's cover, the solution domain does not concern the heat transfers from the glass cover and the isolating materials. Therefore, the main emphasis of the current work is to study the behavior of the turbulent regime formed when the air passes through the packed medium. As known that the integration of packed beds will bring some pumping penalty due to the pressure drop within the medium, the proposed packed bed was designed as intermittent in three different zones as depicted in Figure 1 to reduce the expected pressure drop. The bed elements were cylinders with 10 mm diameter and 10 mm height to present the Phase Change Material (PCM) containers when heat storage materials are employed.

Each packed zone was simulated by a length of 42 mm consisting of 60 random cylinders as shown in Fig.1. The formation of the packed bed was achieved using DEM simulation, following the procedure introduced in the literature (Allio et al., 2020). This process was conducted in three stages, in which firstly, a container as the bulk volume of the matrix was devised and particles with the given dimensions were injected along the gravity to fill the container. The transient DEM simulation was continued until the number of particles reached the desired value of the target porosity, which for the case at hand, is 52 %. In the next step, particles were replaced with solid cylinders to form the packed matrix. Thus, the solid domain was built by combining the particles' geometries and their contact points with the channel structure, where the heat flux functions were applied to this domain as a boundary condition at the outer wall. Simulations were performed first for a smooth SAH and then the packed bed SAH with three configurations, investigating the hydraulic and thermal behaviors of the air inside the collector. The model SAH-M1 was developed with a solar heater equipped with a 42-mm-long packed bed, located as shown in Figure 1. The model SAH-M2 accounted for 2 packed beds with a 200 mm interval, and the model SAH-M3 was created with 3 packed beds, each 200 mm apart from the others. Thus, simulations were aimed to compare the effects of mass flow rate $\dot{m}$ (0.01, 0.05, 0.08 kg/s) on each of the proposed designs and understand how fluid behaves as it passes through each model. As far as the heat transfer coefficient is concerned, thermal modeling was added to the simulations investigating the convective heat transfer coefficients for a constant wall temperature of particles.

In this regard, the average heat transfer coefficient (h) between the fluid and solid rings was determined through the microscopic study and applying a constant wall temperature boundary condition to the cylinders. The intention of this investigation was to assess the air convective heat coefficient over the particles (PCM containers) representing a constant melting temperature. Therefore, a constant wall temperature of 600K was applied to the wall of the particles. The definition of the overall heat transfer coefficient is given in Eq.1.

$$h = \frac{\dot{m} C_p (T_o - T_i)}{S_S (T_s - T_m)} \quad \text{(eq.1)}$$

where T_{mo} and T_{mi} are the mean outlet and inlet bulk temperatures of fluid Computed at the inlet/outlet of the PB zones, while ΔT_{lm} indicates the log mean temperature difference, $\boldsymbol{c_p}$ is the air specific heat, evaluated at the temperature T_m, and $\boldsymbol{S_S}$ is the total particle surface.

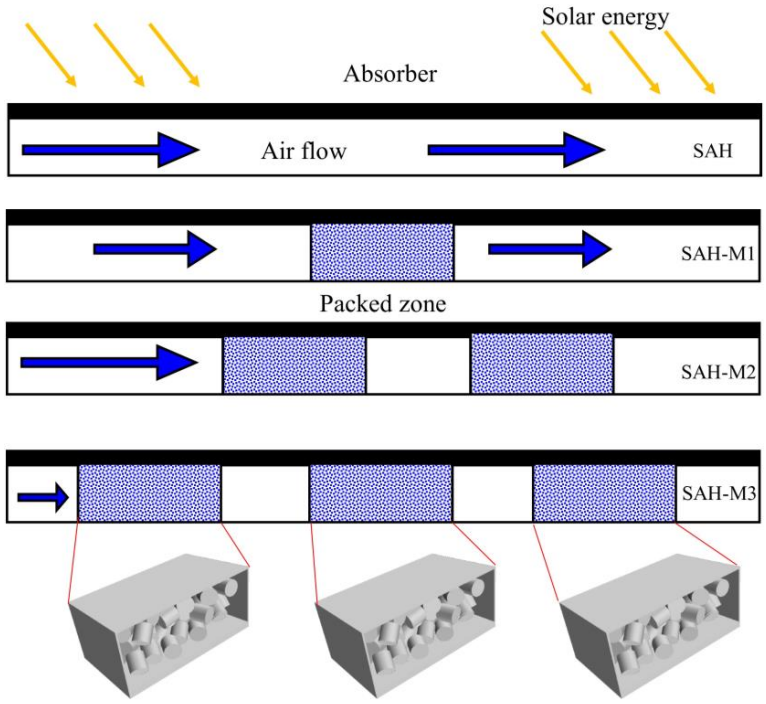

Fig. 1: Schematic of the different solar collectors equipped packed beds consisting of cylinders.

As the temperature is not uniform across the inlet and outlet cross-sectional areas, the mean inlet and out temperatures are determined using Eq.2.

$$\boldsymbol{T_m} = \frac{\int_A \boldsymbol{\rho v C_p T dA_c}}{\boldsymbol{\dot{m} C_p}} \quad \text{(eq.2)}$$

where $\boldsymbol{\rho}$ is the fluid density and v represents the fluid velocity, while the log mean temperature difference can be expressed as Eq. 3.

$$\Delta \boldsymbol{T_{lm}} \equiv \frac{(\boldsymbol{T_s - T_{mo}}) - (\boldsymbol{T_s - T_{mi}})}{\boldsymbol{ln}((\boldsymbol{T_s - T_{mo}})/(\boldsymbol{T_s - T_{mi}}))} \quad \text{(eq.3)}$$

3. Model setup

A 3D conjugate heat transfer model was selected for a steady-state condition. In order to simulate a turbulent flow inside the receiver, a two-equations Reynolds-Averaged Navier-Stokes (RANS) model, namely the two-layer realizable $k-\varepsilon$ model, was used, with a two-layer wall treatment at the wall. It is worth mentioning that $k-\varepsilon$ turbulence model is widely used in the modelling of solar tubular absorbers enhanced with inserts (Bellos et al., 2017; Bellos and Tzivanidis, 2018; Kumar and Reddy, 2020; Mwesigye et al., 2014; Yılmaz et al., 2020). The two-layer version of the $k-\varepsilon$ model adds flexibility to the wall treatment switching automatically between low-y+ and high-y+ treatments. As indicated by literature (Dixon et al., 2012), the superiority of the realizable $k-\varepsilon$ over the standard $k-\varepsilon$ model refers to the addition of an improved equation for the turbulent energy dissipation rate ε, with a variable viscosity coefficient Cμ instead of a constant value. Thus, as long as rotation boundary layers under strong adverse pressure gradients, separation, and recirculation with strong curvature are considered, similar to those found in packed tube simulation (Dong et al., 2017; Moghaddam et al., 2021), this model could result in a reasonable performance. According to the realizable $k-\varepsilon$ model, the transport equations for the turbulent kinetic energy k and for its dissipation rate ε are expressed as follows.

$$\frac{\partial}{\partial t}(\rho\kappa) + \frac{\partial}{\partial x_j}(\rho\kappa u_j) = \frac{\partial}{\partial x_j}\left[\left(\mu + \frac{\mu_t}{\sigma_\kappa}\right)\frac{\partial \kappa}{\partial x_j}\right] + G_\kappa + G_b - \rho\varepsilon - Y_M + S_\kappa \quad \text{(eq.4)}$$

$$\frac{\partial}{\partial t}(\rho\varepsilon) + \frac{\partial}{\partial x_j}(\rho\varepsilon u_j) = \frac{\partial}{\partial x_j}\left[\left(\mu + \frac{\mu_t}{\sigma_\varepsilon}\right)\frac{\partial \varepsilon}{\partial x_j}\right] + \rho C_1 S\varepsilon - \rho C_2 \frac{\varepsilon^2}{k+\sqrt{v\varepsilon}} + C_{1\varepsilon}\frac{\varepsilon}{k}C_{3\varepsilon}G_b + S_\varepsilon \quad \text{(eq.5)}$$

where G_κ and G_b refer to the kinetic energy based on mean velocity gradients and buoyancy, respectively, Y_M represents the fluctuating dilatation in compressible turbulence to the overall dissipation rate, σ_κ and σ_ε are the turbulent Prandtl numbers for the turbulent kinetic energy and its dissipation and S_κ and S_ε are source terms. Also, the eddy viscosity μ_t can be determined by Eq. 6.

$$\mu_t = \rho C_\mu \frac{\kappa^2}{\varepsilon} \quad \text{(eq.6)}$$

In the realizable $k-\varepsilon$ model, first introduced by Shih et al. (Shih et al., 1995), C_μ is a function of mean strain and rotation rates, the angular velocity of the system rotation, and the turbulence fields (k and ε) (Soe and Khaing, 2017).

The thermal analysis in this work was performed using a segregated flow temperature model and the boundary condition of a constant inlet temperature of the fluid. Since this study considers various absorber designs, a range of different boundary conditions corresponding to the flow configuration was applied in the CFD simulation as follows:

- In the case of SAH-M designs, two inlet faces were defined as mass flow inlet conditions while a pressure outlet was applied to the outlet face. In the thermal simulations, the interface between the solid and fluid domain in the packed zone was treated with a constant wall temperature to achieve the HTC in the packed zone. The collector walls were set as the adiabatic boundary conditions, while the united walls of the particles were treated with the constant wall temperature boundary conditions.
- For the validation study, a reference pressure of 1 bar was set for the simulations, while in the rest of the simulations a reference pressure of 10 bar was used to ensure the one-direction flow over the packed particles.
- To exclude the inlet effects of the running air the inlet section was elongated to a distance, which led the fluid regime to reach the necessary hydraulic characteristics related to fully developed conditions.

A polyhedral-based meshing with prismatic layers for fluid regions was employed to solve the equations. Grids were developed using a hybrid approach employing both structured and unstructured mesh. As shown in Figure 2, several custom controls were adopted to the boundary layer areas to refine the meshing with specific care, especially for the packed-bed zones where the particles are located. While in the areas, where the velocity and temperature gradients are smoother, cells become coarser and uniform along the length of the channel.

4. Validation study

An important step in the analysis of the thermal and hydraulic performance of solar air heaters is to obtain the friction factor in adiabatic conditions, which is defined through the Darcy relation (Eq. 7) for every flow. In the case of smooth SAH, a correlation is given in Eq. 8 (Azad et al., 2021).

$$f = \frac{2}{L/D_h}\frac{\Delta P}{\rho \bar{v}^2} \quad \text{(eq.7)}$$

$$f_S = 0.085 \times Re^{-0.25} \quad \text{(eq.8)}$$

where L is the length of the absorber, D_h is the hydraulic diameter of the rectangular channel, defined as $\frac{2ab}{a+b}$ in which a and b are the height and width of the channel, and v is the average inlet velocity of the air, ρ is the average density of the air, and ΔP is the pressure drop obtained through CFD simulation.

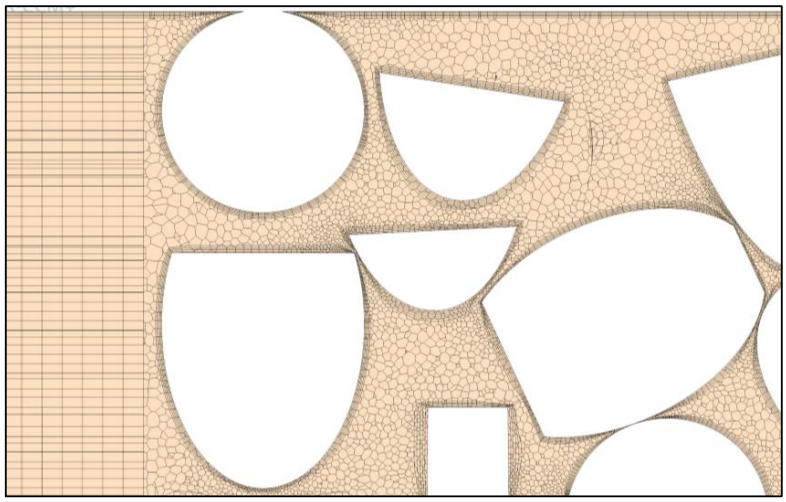

Fig. 2: Hybrid mesh used to develop the network grid for SAH-M models.

For the sake of validation in terms of Nusselt number, a smooth SAH with a constant heat load of 1000 W/m^2 was simulated and results were validated with those obtained by the Dittus-Boelter correlation as follows (Bensaci et al., 2020);

$$Nu = \frac{h \times D_h}{k} = 0.023 \times Re^{0.8} \times Pr^{0.4} \quad \text{(eq.9)}$$

$$Re = \frac{4 \times \dot{m}}{\pi D_{ri} \mu} \quad \text{(eq.10)}$$

$$Pr = \frac{\mu Cp}{k} \quad \text{(eq.11)}$$

where k is the thermal conductivity of the air computed at the average temperature T_m, and μ is the dynamic viscosity of the air. Therefore, the boundary conditions in this simulation consist of a mass flow inlet at the inlet face, and a pressure outlet at the outlet face, while a uniform heat flux was applied to the top surface of the solid plate, and an interface was defined between the fluid and solid regions.

As mentioned above, the validation process was carried out by comparing both the Nusselt number and friction factor for a range of Re numbers to check the viability of the simulation in the smooth model. According to Fig. 3a, the computation of f shows a very good agreement between the results of CFD and correlation with less than 15% error. Furthermore, as shown in Fig.3a the comparison between the values of the Nu number predicted from the correlation and those obtained with CFD simulation indicates that the discrepancy could not exceed 20%, which asserts that the current numerical procedure can capture the physics of the SAH under study.

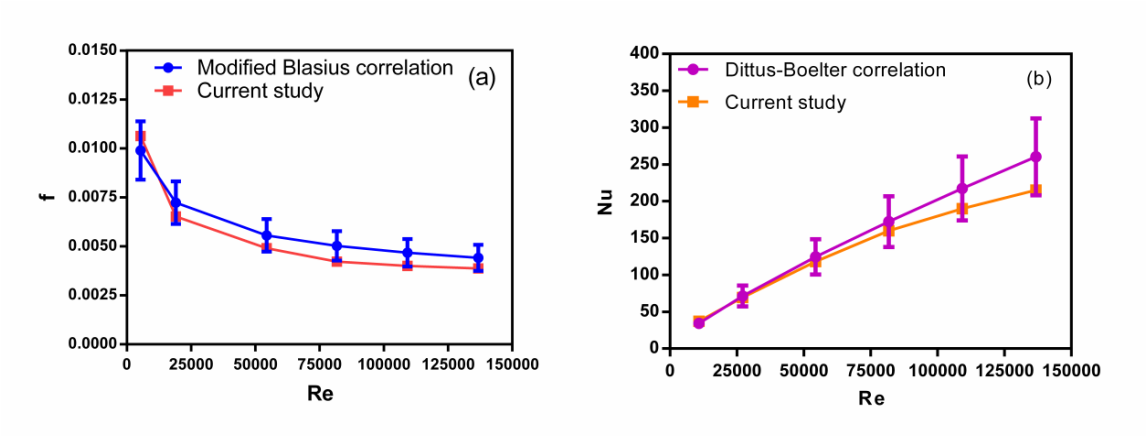

Fig. 3: Validation results: the comparison of (a) friction factor and (b) Nu number with respect to various Reynolds number.

Then to check the accuracy of the meshing grid, ensuring that results are independent of the number of cells, several cases were studied with a range of cell numbers, and the global results in terms of friction factor and Nu number were compared. The refinement of the grid has been achieved by first giving a constant base cell size and increasing the base cell size until y+ reached 1. Then, the number of prism layers was frozen, and the base cell

size was decreased until convergence was achieved in the results. Following the discussed procedure, the optimum meshes were obtained as 0.1, 17.5, 26.4, and 32.7 million cells respectively for smooth, SAH-M1, SAH-M2, and SAH-M3 models. It must be added that since y+ values were achieved as ~1 at the wall and knowing that the Prandtl number for air is close to 1, good modeling of the fluid-dynamic boundary layer (friction factor) should allow good modeling of the thermal boundary layer.

5. Results and discussion

In this section, the hydraulic performance of the proposed solar heaters is presented and flow characteristics are determined. Fig.4a shows the total pressure drops achieved through the developed models for a range of Re numbers. As shown, pressure drop increases with growth in Re number, and also increasing the number of packed beds. In more detail, when two packed beds are employed, the pressure drop increases by 100%, and when three packed beds are considered the pressure drop increases by 200% compared to the one packed bed employment. As a result, the maximum pressure drop is recorded as 115 kPa for SAH-M3 and Re ~ 1.3×10^5, and the minimum is 570 Pa in SAH-M1 and Re ~ 8×10^4. Fig.4b provides the detailed pressure drops computed over each packed bed in the model SAH-M3. As expected, in all the mass flow rates, the pressure drop increases from the first (PB1) to the second packed bed (PB2) due to the mixing induced by the presence PB1. However, this trend undergoes a very slight drop coming from PB2 to PB3.

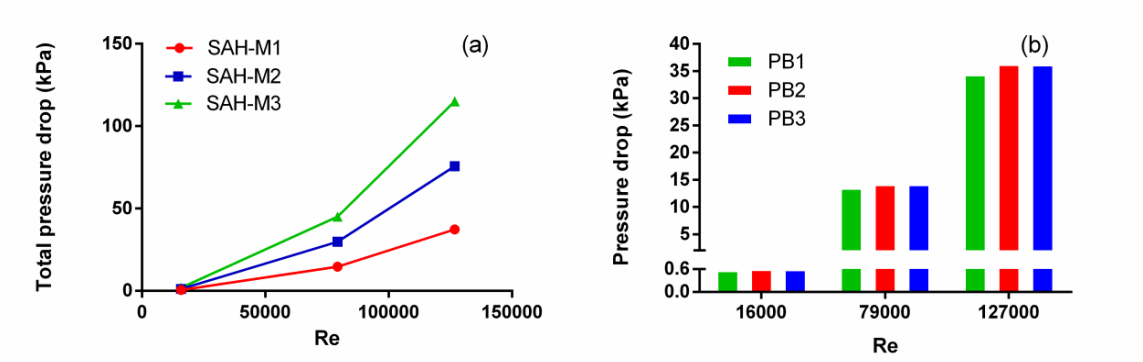

Fig. 4: (a) Total pressure drop computed for the different packed bed designs as a function of the Reynolds number; (b) pressure loss at the different porous inserts in the SAH-M3 configuration, for different values of the Reynolds number.

Fig.5 shows the air velocity counters over the first packed zones of the model SAH-M3 (Re ~ 1.6×10^4) on a cross-section along the flow axis. As shown, air attacks the first packed bed (PB1) in a fully-developed condition with no chaos in the flow. Passing through the particles, the flow boundary layers are broken, forming high-velocity contours in the narrow passages and some stagnation points where the flow passage is blocked. As a result, the air leaving the packed zone undergoes a higher turbulent condition. As observed, the particles' orientation is a factor, which affects the velocity contours formation inside the packed zone. Thus, loose packing spots can provide enough space for vortex and high-speed flow formations, while stagnation zones can be observed whiten the dense packing areas. Results follow the conclusions derived in other works (Ebadi et al., 2021).

Fig.6 represents the values of averaged air turbulent kinetic energy (TKE) obtained at the inlet of each packed bed. Results show that as the Re number increases, the value TKE grows, in view of the turbulent mixing of the flow downstream of the pebble bed, shown in Fig 5. A higher level of turbulent kinetic energy determines a higher pressure drop, as shown in Fig. 4b. Note, however, that the actual amount of the computed TKE increase is related to the distance among the PB: the smaller the distance, the higher the TKE. The distance among the PB can then become an optimization parameter to find a suitable trade-off between the increase of efficiency due to the turbulent mixing and the increase of the pressure drop.

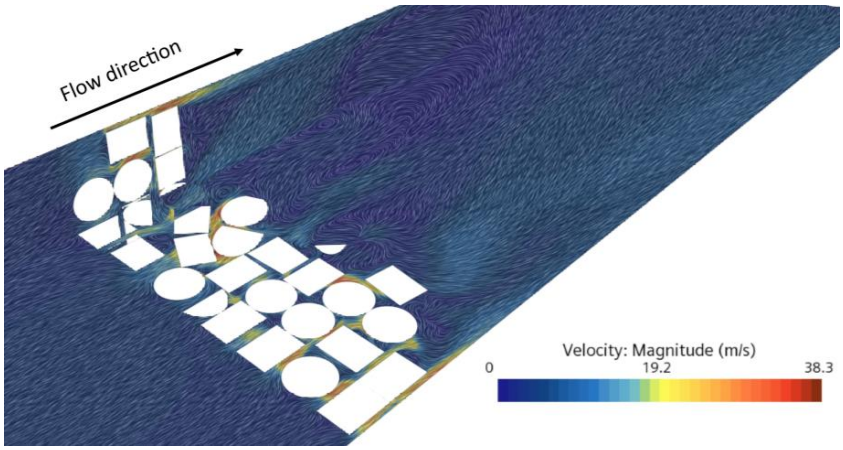

Fig. 5: Velocity field of the fluid passing through the first packed bed in the model SAH-M3 and Re ~ 16000.

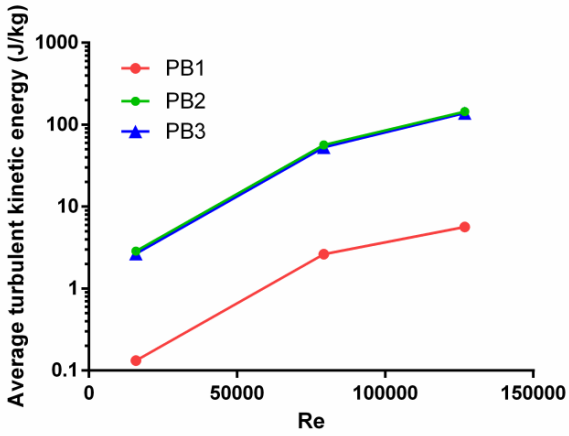

Fig. 6: The computed average turbulent kinetic energy at the inlet of each packed bed in SAH-M3 model.

Following the analysis of the flow field, an evaluation has been performed to obtain the heat transfer coefficients on various SAH designs with respect to a range of Re numbers. Figure 7 renders the air temperature profile computed along the flow direction as it passes through the first, second, and third packed zones in the model SAH-M3 and Re ~ 1.3×10^5. As shown, the random positioning of the particles plays an important role in forming the temperature contours, where those located perpendicular to the flow have a higher contribution to the air temperature increase, while others aligned with the flow direction lead to lower heat exchange.

Fig.8a illustrates the various convective heat coefficients obtained on each packed bed, respecting various Re numbers. As expected, increasing the turbulence inside the fluid regime improves the amount of heat transferred to the fluid where the maximum convective heat coefficients are obtained at Re ~ 1.3×10^5. Moreover, when the flowing air passes through the first packed bed, undergoes a sudden increase in its TKE, which improves its ability to convey the heat to the next packed bed. Furthermore, when the air reaches the third packed bed, h enhances further, hitting its maximum value under three mass flow rates. According to Fig. 8b, a comparison has been made to assess the increments in convective heat coefficients computed along each packed bed. As shown, for the low and medium mass flow rates, the increase in heat convection between the second and first packed beds is higher than that measured among the third and second packed beds. When the air mass flow rates increase to the highest value (Re ~ 1.3×10^5), the comparison results become reversed, putting the h_{PB3}/h_{PB2} ratio higher than h_{PB2}/h_{PB1}. Thus, a 25% enhancement is obtained by comparing the values of h for PB2 to those of PB1 at Re ~ 1.3×10^5. While this convection improvement continues to rise, reaching the third packed zone with a nearly 35% increase compared to PB2. As a result, the intermittent implementation of packed zones has positively affected the heat transfer improvement, increasing the turbulence conditions in the fluid regime from one bed to the other.

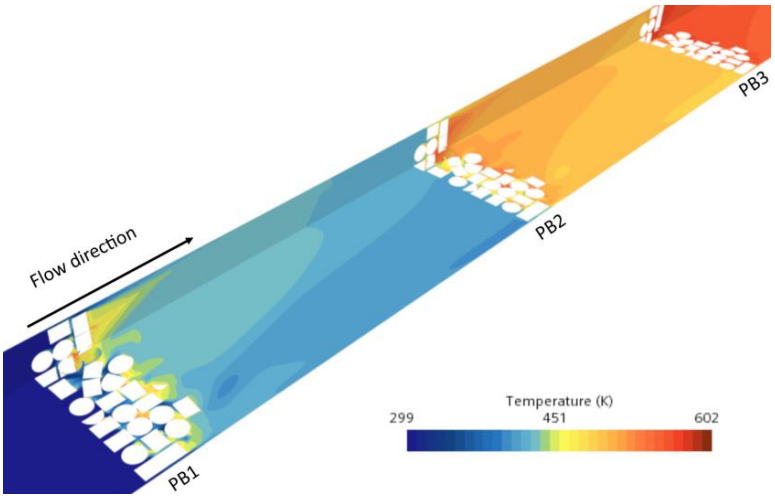

Fig. 7: Temperature map obtained for the fluid passes through each bed in the model SAH-M3 and Re ~ 127000.

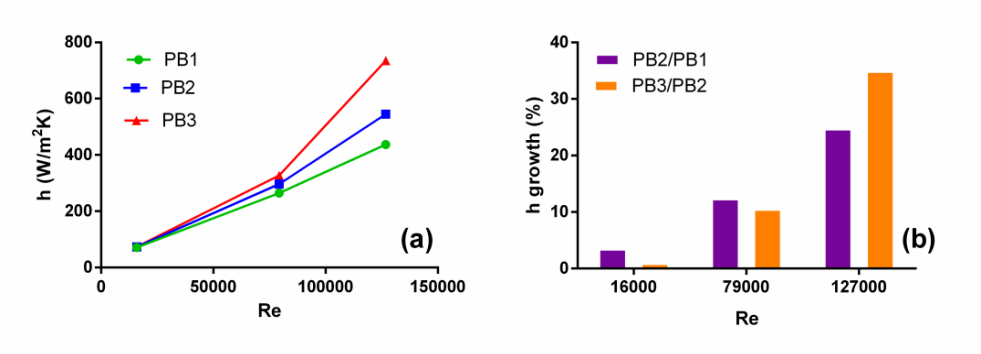

Fig. 8: (a) The convective heat transfer coefficients obtained on each packed bed in the model SAH-M3, (b) the change ratio among each packed bed.

In this section, a comparison study has been carried out to assess the effects of particle randomness and bed spacing on the hydrothermal performance of the collector with three packed beds (SAH-M3). Therefore, a number of simulations were used, where first, the flow direction is reversed compared to the default investigations to take into account the randomness parameter. Then two more configurations with different packed bed spacing, including 150 and 100 mm length were developed to find the deviations in the values of pressure drop and heat convection coefficient compared to 200 mm length. According to Fig. 9, decreasing the packed bed spacing has resulted in very small changes in the values of pressure drop, increasing it by less than 2% with Re ~ 8×10^4. When the fluid flow direction is reversed, considering a new particle packing structure, pressure drop values have changed in all the models showing that particles' orientation has a significant role in fluid hydraulic behavior. As the numerical showed, reversing the fluid flow could have a 13.5% increase in the air pressure drop determined in the model with 200 mm bed spacing, while decreasing the bed spacing to 150 mm and 100 mm eases the growth, respectively to 13 and 12%. Therefore, particle randomness is the dominant factor, affecting the pressure drop while bed spacing showed very small effects on the hydraulic behaviors of air passing through intermittent packed beds.

Figure 10 shows the heat convection coefficient calculated for various SAH-M3 configurations operating at Re ~ 8×10^4, where D indicates the direct flow and R represents reverse flow, imposed on 100, 150, and 200 mm spacing packed bed designs. One of the important points is that in all the tested models, as the air passes through the packed beds, h is increasing from the first to the second and third. Evaluating the effects of randomness, which means comparing the values in direct and reverse flows, it was revealed that the particles' orientations do not have a very large impact on the heat convection coefficient among all the packed beds, where this deviation revolves around ± 1%. Investigations for the packed-bed spacing also suggest that decreasing the length between each two consecutive packed beds could not affect the collector thermal performance significantly, where a very slight increase of 2 % might be seen when the values of PB3 are compared between the 200 and 100 mm spacing. Thus,

it can be concluded that the numerical result of this study has an acceptable accuracy to be used in further analyses regardless of the packed-bed spacing and particle randomness.

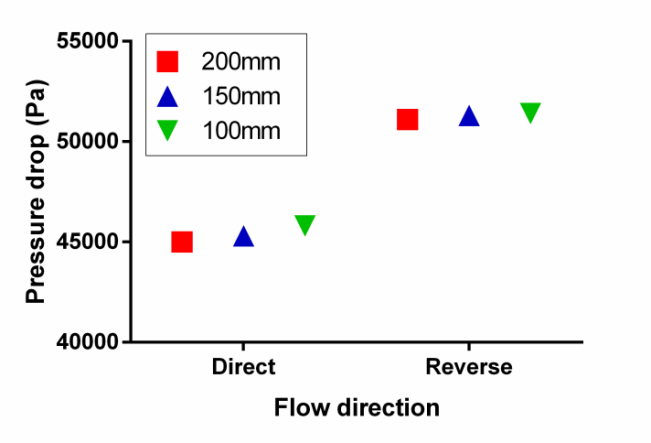

Fig. 9: Effects of flow direction (particle randomness) and bed spacing on the total pressure drop obtained along the solar collector at Re ~ 8 × 10⁴.

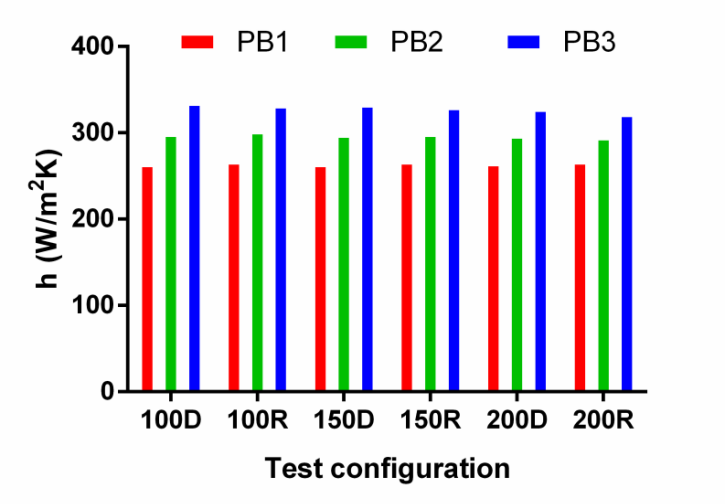

Fig. 10: The variation in heat transfer coefficient using various bed spacing and two different packing formations.

6. Conclusions

Several simulations were developed, using Star CCM+ software to study the airflow behavior inside a solar collector assisted with several intermittent packed beds at the pore scale. Reaching a good accuracy in the validation of numerical results with the general correlations, thermo-hydraulic behaviors of the collector were investigated, testing the number of packed beds and various air mass flow rates. The obtained results showed that the pressure drop could increase up to 1.15 bar when air with a mass flow rate of 0.08 kg/s passes through the three packed beds. However, the detailed analysis revealed that as the air passes through the second bed, it losses a fraction of its kinetic energy, leaving the third bed with a reduced pressure drop. The thermal results proved that the intermittent implementation of packed zones leads the heat transfer improvements at high Re, increasing the turbulent conditions in the fluid regime from one bed to the other. Thus, the values of the heat transfer coefficient rise by almost a factor of 2 for the packed bed number 1 and 3 at Re ~ 1.3×10^5. This enhancement suggested that at the highest airflow rate considered in this study, it is boosted by the thermal mixing that occurred in the porous structure of the beds. Finally, the sensitivity study showed that the thermal performance of the proposed solar collector has the least dependency on the parameters such as particles' orientation and bed spacing with only 2%, while hydraulic results may alter up to 13.5% if the packing structure differs.

7. Acknowledgments

We acknowledge the use of the computational resources provided by hpc@polito, which is a project of Academic Computing within the Department of Control and Computer Engineering at the Politecnico di Torino (http://hpc.polito.it). This work has also been supported by Italian Super Computing Resource Allocation (ISCRA-CINECA) within the Application ID: GRECIAN – HP10C6U7V4.

8. References

Allio, A., Difonzo, R., Leggieri, A., Legrand, F., Marchesin, R., Savoldi, L., 2020. Test and Modeling of the Hydraulic Performance of High-Efficiency Cooling Configurations for Gyrotron Resonance Cavities. Energies.

Azad, R., Bhuvad, S., Lanjewar, A., 2021. Study of solar air heater with discrete arc ribs geometry: Experimental and numerical approach. Int. J. Therm. Sci. 167, 107013.

Bellos, E., Tzivanidis, C., 2018. Investigation of a star flow insert in a parabolic trough solar collector. Appl. Energy 224, 86–102.

Bellos, E., Tzivanidis, C., Tsimpoukis, D., 2017. Thermal enhancement of parabolic trough collector with internally finned absorbers. Sol. Energy 157, 514–531.

Bensaci, C.-E., Moummi, A., Sanchez de la Flor, F.J., Rodriguez Jara, E.A., Rincon-Casado, A., Ruiz-Pardo, A., 2020. Numerical and experimental study of the heat transfer and hydraulic performance of solar air heaters with different baffle positions. Renew. Energy 155, 1231–1244.

Choudhury, C., Chauhan, P.M., Garg, H.P., 1995. Economic design of a rock bed storage device for storing solar thermal energy. Sol. Energy 55, 29–37.

Chouksey, V.K., Sharma, S.P., 2016. Investigations on thermal performance characteristics of wire screen packed bed solar air heater. Sol. Energy 132, 591–605.

Dhiman, P., Thakur, N.S., Kumar, A., Singh, S., 2011. An analytical model to predict the thermal performance of a novel parallel flow packed bed solar air heater. Appl. Energy 88, 2157–2167.

Dixon, A.G., Walls, G., Stanness, H., Nijemeisland, M., Stitt, E.H., 2012. Experimental validation of high Reynolds number CFD simulations of heat transfer in a pilot-scale fixed bed tube. Chem. Eng. J. 200–202, 344–356.

Dong, Y., Sosna, B., Korup, O., Rosowski, F., Horn, R., 2017. Investigation of radial heat transfer in a fixed-bed reactor: CFD simulations and profile measurements. Chem. Eng. J. 317, 204–214.

Ebadi, H., Allio, A., Cammi, A., Savoldi, L., 2021. First numerical evaluation of the thermal performance of a tubular receiver equipped with Raschig rings for CSP applications, in: Power 2021. ASME.

Gorjian, S., Ebadi, H., Calise, F., Shukla, A., Ingrao, C., 2020. A review on recent advancements in performance enhancement techniques for low-temperature solar collectors. Energy Convers. Manag. 222, 113246.

Kumar, A., Kim, M.H., 2017. Solar air-heating system with packed-bed energy-storage systems. Renew. Sustain. Energy Rev. 72, 215–227.

Kumar, B.N., Reddy, K.S., 2020. Numerical investigations on metal foam inserted solar parabolic trough DSG absorber tube for mitigating thermal gradients and enhancing heat transfer. Appl. Therm. Eng. 178, 115511.

Moghaddam, E.M., Foumeny, E.A., Stankiewicz, A.I., Padding, J.T., 2021. Heat transfer from wall to dense packing structures of spheres, cylinders and Raschig rings. Chem. Eng. J. 407, 127994.

Mwesigye, A., Bello-Ochende, T., Meyer, J.P., 2014. Heat transfer and thermodynamic performance of a parabolic trough receiver with centrally placed perforated plate inserts. Appl. Energy 136, 989–1003.

Prasad, S.B., Saini, J.S., Singh, K.M., 2009. Investigation of heat transfer and friction characteristics of packed bed solar air heater using wire mesh as packing material. Sol. Energy 83, 773–783.

Raj, A.K., Srinivas, M., Jayaraj, S., 2019. A cost-effective method to improve the performance of solar air heaters using discrete macro-encapsulated PCM capsules for drying applications. Appl. Therm. Eng. 146, 910–920.

Ramadan, M.R.I., El-Sebaii, A.A., Aboul-Enein, S., El-Bialy, E., 2007. Thermal performance of a packed bed double-pass solar air heater. Energy 32, 1524–1535.

Savoldi, L., Allio, A., Bovento, A., Cantone, M., Fernandez Reche, J., 2020. Experimental and numerical investigation of a porous receiver equipped with Raschig Rings for CSP applications. Sol. Energy.

Shih, T.-H., Liou, W.W., Shabbir, A., Yang, Z., Zhu, J., 1995. A new k-ϵ eddy viscosity model for high reynolds number turbulent flows. Comput. Fluids 24, 227–238.

Singh, H., Saini, R.P., Saini, J.S., 2013. Performance of a packed bed solar energy storage system having large sized elements with low void fraction. Sol. Energy 87, 22–34.

Soe, T.M., Khaing, S.Y., 2017. Comparison of Turbulence Models for Computational Fluid Dynamics Simulation of Wind Flow on Cluster of Buildings in MandalayNo Title. Int. J. Sci. Res. Publ. 7, 337–350.

Yılmaz, İ.H., Mwesigye, A., Göksu, T.T., 2020. Enhancing the overall thermal performance of a large aperture parabolic trough solar collector using wire coil inserts. Sustain. Energy Technol. Assessments 39, 100696.

Validation of an Alternative Methodology for Direct Steam Generation Modelling in Parabolic Collectors

Eduardo González-Mora[1] and Ma. Dolores Durán-García[1]

[1] Facultad de Ingeniería/Universidad Autónoma del Estado de México, Toluca (México)

Abstract

The analysis of the two-phase flow in linear concentrators remains a fundamental part of implementing the concept known as direct steam generation in concentrated solar thermal plants. The models developed to date require, on the one hand, an iterative analysis to estimate the coefficient h, and, on the other hand, high demand for computational fluid dynamics calculations. In the present work, with the help of Adiutori's methodology, a one dimensional thermo-hydraulic model of a parabolic trough collector in the direct steam generation is described. The difference between the present model, which stands out from the rest, is that for the analysis of convective heat transfer, a functional of the temperature is evaluated, instead of dimensionless groups to estimate the h coefficient, a similar approach is used for the pressure drop instead of the fluid friction factor. This allows to solve directly, and without the need for iterative processes, the model to predict the temperature rise and the pressure drop along the receiver, especially in the two-phase flow zone. The results obtained are similar to the experimental data published by different researchers, which validates the developed model, and will allow simulations to be carried out in a more agile way and reduce calculation errors. This ensures the usefulness of the model for further analysis.

Keywords: Thermo-hydraulic model, two-phase flow, heat transfer, boiling, parabolic collector

1. Introduction

Solar plants for conversion of thermal energy into electrical energy through power cycles (CSP) have been oriented to solar fields with parabolic trough collectors (PTC), using mainly thermal oil as heat transfer fluid (HTF), so two different circuits are operating with two different fluids, the solar field operating with thermal oil and the feed block operating with water/steam (Moya, 2021).

The next evolution in linear concentrating systems has been to implement HTFs that operate at higher temperatures, where an alternative is a process called direct steam generation (DSG), where steam is generated directly in the solar field (Giglio et al., 2017; Hakkarainen and Kannari, 2015; Zarza Moya, 2017). Establishing the behavior of CSP systems is important for this technology to begin to be introduced into the energy matrix because although there are currently approximately 120 plants of this type, the installed capacity is of the order of 6387 MW (IRENA, 2022a), which corresponds to less than 2% of the installed capacity of renewable energy sources (IRENA, 2022b).

The main issue with DSG modeling is the two-phase flow zone, due to the inherent complexity of the boiling process in a stream of water flowing inside a tube (Alobaid, 2018; Hewitt, 1998). To date, there is considerable progress in DSG analysis (Giglio et al., 2017; Islam et al., 2018; Sandá et al., 2019), however, they all resort to the concept of classical heat transfer, with the calculation of the convective coefficient h, in combination with the friction factor f, to understand the thermo-hydraulic behavior of the installation, even in CFD models (Lobón et al., 2014; Pal and K, 2021).

Adiutori (2017) has proposed a generalized methodology to eliminate the convective heat transfer coefficient h and the friction factor f to model more simply the behavior of thermo-hydraulic systems, known as "The New Engineering". This methodology requires transforming the Nusselt number relationships and the Moody diagram

© 2022. The Authors. Published by International Solar Energy Society
Selection and/or peer review under responsibility of Scientific Committee
doi:10.18086/eurosun.2022.12.06 Available at http://proceedings.ises.org

to obtain functional relationships dependent on measurable variables such as pressure and temperature. Thus, it is possible to solve a thermohydraulic model without the need of iterative processes, reducing the calculation time and the error in the solution. In previous work (González-Mora and Duran García, 2022), we proposed a methodology, summarized in Section 2. However, its validation was pending. In this current work, we aim to validate this methodology by comparing it with experimental data reported by other researchers, as described in Section 3. This validation will establish the reliability and applicability of our proposed thermo-hydraulic model for future analyses.

2. Thermo-hydraulic model

The developed model takes as reference those described by other authors (Forristall, 2003; Hachicha et al., 2018; Montes Pita, 2008; Sun et al., 2015; Vasquez Padilla, 2011). The general one dimension (1D) modeling approach consists of subdividing the receiver into smaller HCE (heat collector element), averaging the physical quantities ψ over the cross-sectional area A perpendicular to the flow direction x_1 by:

$$\int_V \psi \, \mathrm{d}V = \int_{\Delta x_1} \left[\int_A \psi \, \mathrm{d}A \right] \mathrm{d}x_1 \qquad \text{(eq. 1)}$$

where Δx_1 is the increment in length. The purpose of the 1D models is to understand the behavior of the systems using the balance equations, complemented with the constitutive equations (El Hefni and Bouskela, 2019). The difference in the model to be developed lies in the fact that we will opt for a methodology that does not require iteration to solve the heat flows and associated temperatures in the thermal model, as proposed by Adiutori (2017).

2.1. Assumptions

Temperature, heat fluxes, and thermodynamic properties are assumed to be uniform around the circumference of each HCE. The optical properties of all materials involved are considered as constant isotropic quantities and independent of temperature, except for the emittance of the receiver. Radiation fluxes in opaque (such as absorber) and semitransparent (glass cover) materials are approximated to surface phenomena (Howell et al., 2015; Özışık, 1973).

The Eurotrough parabolic collector is 12,27 m long, and the supports are placed at 4,06 m from each other. Here it will be assumed that each module has 3 supports, so the effective length of each module will be 12,12 m, however, it is initially assumed that the remaining 12 cm corresponds to protective shields and joints that allow connecting the modules to form a loop and that in this small section, there are no heat losses, nor considerable pressure drops.

2.2. Model description

As the HTF absorbs energy, the HCE increases in temperature. Due to the difference between the average fluid temperature at each cross-section and the ambient temperature, heat losses will exist. Fig. 1(a) allows for identifying the heat flows in the HCE, where the heat losses through the supports are also identified; and Fig. 1(b) shows the thermal resistance model specifying the surfaces involved.

With these schematics, it is possible to establish the balance equations applying the first law of thermodynamics, considering flows per unit length, we can define the equations for the thermal resistance model shown in Fig. 1(b).

$$\dot{q}'_{12,conv} = \dot{q}'_{23,cond} \qquad \text{(eq. 2)}$$

$$\dot{q}'_{3,SolAbs} = \dot{q}'_{34,conv} + \dot{q}'_{34,rad} + \dot{q}'_{23,cond} + \dot{q}'_{38,cond} \qquad \text{(eq. 3)}$$

$$\dot{q}'_{45,cond} = \dot{q}'_{34,conv} + \dot{q}'_{34,rad} \qquad \text{(eq. 4)}$$

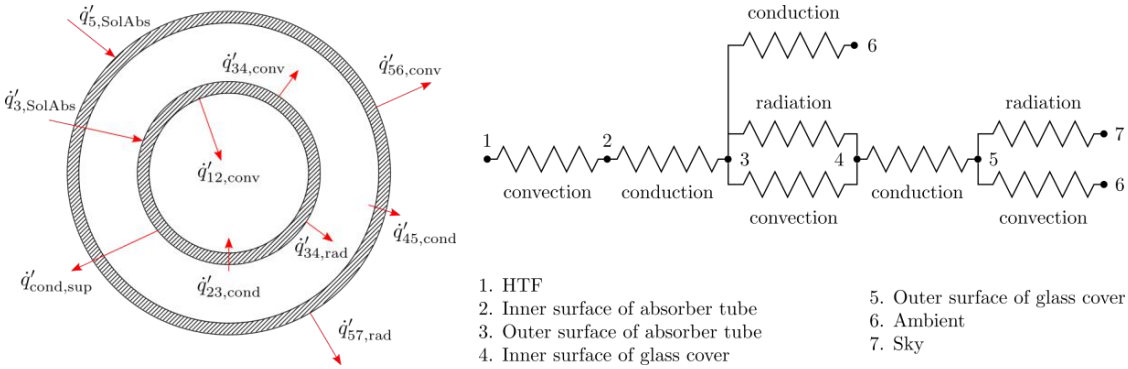

a) Heat fluxes on the HCE **b) Thermal resistance model**

Fig. 1: Thermal model

$$\dot{q}'_{45,cond} + \dot{q}'_{5,SolAbs} = \dot{q}'_{56,conv} + \dot{q}'_{57,rad} \quad \text{(eq. 5)}$$

$$\dot{q}'_{12,conv} = \dot{m}(h_{in} - h_{out}) \quad \text{(eq. 6)}$$

where each of the heat fluxes can be expressed as:

$$\dot{q}'_{i,SolAbs} = IAM\rho_{PTC}(\alpha\tau)_i W G_{bn} \quad \text{(eq. 7)}$$

$$\dot{q}'_{ij,cond} = \frac{2\pi k_{ij}(T_i - T_j)}{\ln D_j/D_i} \quad \text{(eq. 8)}$$

$$\dot{q}'_{ij,rad} = \frac{\sigma\pi D_i\left(T_i^4 - T_j^4\right)}{\frac{1}{\varepsilon_i} + \frac{(1-\varepsilon_j)D_i}{\varepsilon_j D_j}} \quad \text{(eq. 9)}$$

$$\dot{q}'_{ij,conv} = h_{ij} D_j \pi\left(T_j - T_i\right) = f(\Delta T) \quad \text{(eq. 10)}$$

where IAM is the incidence modifier angle, ρ_{PTC} is the reflectance of the mirrors, $(\alpha\tau)_i$ is the product of the absorptance and transmittance of surface i, W is the trough width, G_{bn} is the incident solar radiation in the normal direction, k is the surface conductivity, T is the temperature, D is the diameter, σ is the Stefan-Boltzmann constant, ε is the emittance and h is the convective coefficient. The subscripts i and j allow us to identify each of the surfaces, according to Fig. (1b). Note that Eq. (10) initially involves the coefficient h, which will be replaced in its entirety by a functional of the temperatures, as explained below. In the present work, it is worth mentioning that only Eq. (10) is discussed, as it presents the novelty of the thermal model, while Eqs. (2) to (9) are not ignored since they are used to solve the system of equations.

The annulus formed between the absorber tube and the glass envelope is modeled as free convection between two cylinders because the receiver is evacuated. Between the glass cover and the environment the convection can be forced or natural. In the first case the Žhukauskas equation is used, while the Churchill and Chu equation is adequate for the second case (Bergman et al., 2011). For convection between the absorber tube and the heat transfer fluid, there are two cases: the Pethukhov or Gnielisnki equation (Bergman et al., 2011) for single-phase fluid, and the Gungor and Winterton correlation for two-phase flow (Gungor and Winterton, 1986).

2.3. Transformation of heat transfer equations according to Adiutori's methodology

Traditionally, when temperatures and heat fluxes are unknown in a heat transfer problem, it is necessary to resort

to iterative processes to get to know these unknowns. The problem becomes more complex when the three transfer phenomena are coupled since the equations are highly nonlinear. Special attention is given to convection due to the nature of the Nusselt relations that allow determining the convective coefficient h, generating great interest in fluids with phase change. Adiutori (2017) has proposed a methodology that allows giving a more agile solution to heat transfer problems where temperatures and heat fluxes are unknowns, without the need for iterative processes.

In this methodology, the aim is to obtain functionals of separable variables that allow the solution of any heat transfer problem. Conventional heat transfer coefficient correlations are easily transformed in the new engineering by replacing h with $q/\Delta T$, then separating q and ΔT, which allows obtaining correlations of the type $q = f(\Delta T)$ or $\Delta T = f^{-1}(q)$. Thus, dimensionless group parameters are replaced by individual parameters, and those that are temperature-dependent are replaced by temperature functions.

In this study, we present an approach that allows for the evaluation of parameters without relying on dimensionless groups as stated by Adiutori (2017). This reveals the direct relationships between individual parameters, enabling correlations to be developed based solely on experimentally measurable quantities. This approach facilitates the computation of current phenomena under specific operating conditions.

For comparison, Fig. 2 illustrates the flowcharts used to obtain the convective heat flow in the two-phase zone. In the traditional methodology (Fig. 2(a)), one needs to consider an initial value of $\dot{q}'_{21,conv}$, determine h_{FC} and h_{NB} using the Bo number, compute $\dot{q}'_{21,conv}$ and iterate until convergence is achieved. However, Fig. 2(b) shows that by substituting $\dot{q}'_{21,conv}/\Delta T$, one can obtain a functional that can be separated and solved more easily. This transformation, according to Adiutori's methodology, proves to be more appropriate, resulting in lower solution times. Overall, our proposed approach offers a more efficient and effective way to evaluate parameters, and the results demonstrate its superiority over the traditional methodology in terms of computational efficiency.

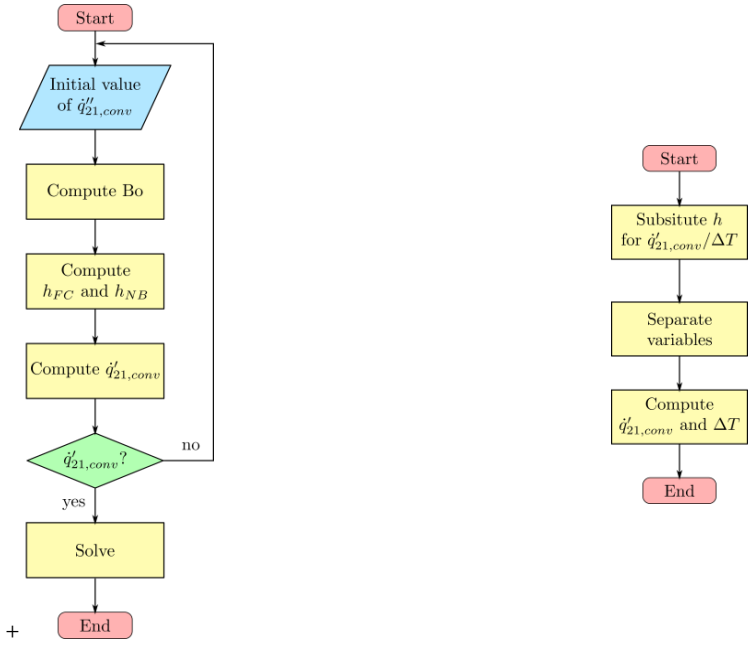

a) Calculation with traditional methodology **b) Calculation with the proposed methodology**

Fig. 2: Comparison of methodologies for heat flow calculation

2.4. Transformation of the two-phase flow equation and friction factor

The Gungor and Winterton correlation involves two convective coefficients, one for forced convection and the other for nucleated boiling; where a boiling factor (F) dependent on the Martinelli parameter (X) and the boiling number by (Bo) is involved:

$$h_{12} = h_{FC} + h_{NB} \qquad \text{(eq. 11)}$$

$$h_{FC} = 0{,}023\mathrm{Re}_l\mathrm{Pr}_l^{0,4}(k_l/D_2)F \quad \text{(eq. 12)}$$

$$h_{NB} = 55p_r^{0,12-\log\varepsilon} - \log^{-0,55} p_r\, PM^{-0,5}\left(\dot{q}'_{12,conv}\right)^{0,67} S \quad \text{(eq. 13)}$$

$$F = 1 + 2{,}4 \times 10^4 \mathrm{Bo}^{1,16} + 1{,}37X_{tt}^{-0,86} \quad \text{(eq. 14)}$$

$$X = \left(\frac{x}{1-x}\right)^{-0,9}\left(\frac{\rho_l}{\rho_g}\right)^{-0,5}\left(\frac{\mu_g}{\mu_l}\right)^{-0,1} \quad \text{(eq. 15)}$$

$$\mathrm{Bo} = \frac{\dot{q}'_{12,conv}\pi D_2^2}{4\dot{m}h_{fg}} \quad \text{(eq. 16)}$$

$$S = \left(1 + 1{,}15 \times 10^{-6}F^2\mathrm{Re}_l^{1,17}\right)^{-1} \quad \text{(eq. 17)}$$

$$\mathrm{Re}_l = \frac{4\dot{m}^2(1-x)}{\pi\mu_l D_2} \quad \text{(eq. 18)}$$

where Re is the Reynolds number, Pr is the Prandtl number, k is the conductivity, p_r is the reduced pressure, ε is the pipe roughness, PM is the molecular weight, x is the vapor quality, ρ is the density, μ is the viscosity and h_{fg} is the enthalpy of vaporization; with subscript l for the liquid phase and subscript g for the vapor phase.

Incorporating the methodology outlined in the previous section, we can rewrite Eqs. (11) to (13) to establish a relationship between the two-phase convection heat flow ($\dot{q}'_{12,conv}$) and the temperature difference (ΔT) between the fluid and the receiver surface. This relationship can be expressed in the following form:

$$\Delta T = C_1\dot{q}'_{12,conv}\left[C_2\left(C_3 + C_4{\dot{q}'_{12,conv}}^{1,16}\right)^2 + C_5 - \frac{C_6{\dot{q}'_{12,conv}}^{0,67}}{C_7\left(C_8+C_9{\dot{q}'_{12,conv}}^{1,16}\right)^2 - 1}\right]^{-1} \quad \text{(eq. 19)}$$

Each C_i in the functional parameter of temperature is clearly positive ($C_i > 0$), and can be obtained from any thermodynamic properties database. The general behavior of the function is illustrated in Fig. 3(a), revealing a continuous function with a unique correspondence between ΔT and $\dot{q}'_{12,conv}$. This implies that there is no need for iterations in the solution of the heat transfer in each HCE. In Fig. 3(b), the reported behavior of the boiling curve as a function of temperature is presented. By comparing the results with the reported boiling curves, it can be confirmed that the transformation is indeed adequate, further validating the proposed methodology.

The friction factor is obtained in an iterative manner from

$$\frac{1}{\sqrt{f}} = -2\log\left(\frac{\varepsilon/D_2}{3{,}7} + \frac{2{,}51}{\mathrm{Re}_D\sqrt{f}}\right) \quad \text{(eq. 20)}$$

because it represents the Moody diagram (Bergman et al., 2011), with the variables:

$$f = \frac{\mathrm{d}P}{\mathrm{d}x}\frac{2D}{\rho u_m^2} \cong \frac{\Delta P}{L}\frac{2D}{\rho u_m^2} \quad \text{(eq. 21)}$$

$$\mathrm{Re}_D = \frac{\rho u_m D}{\mu} \qquad \text{(eq. 22)}$$

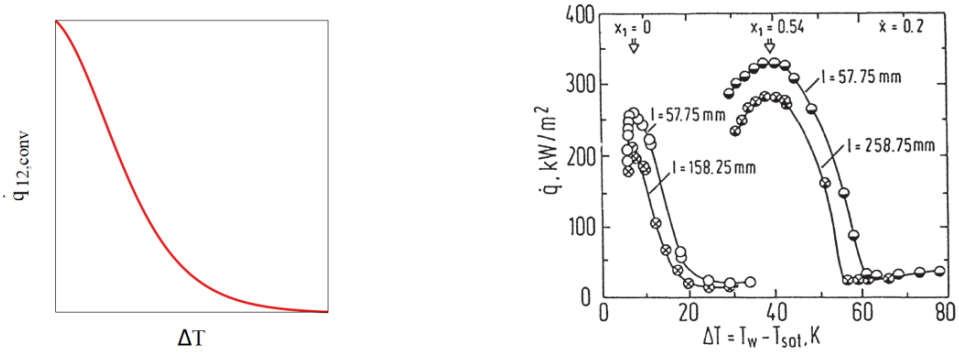

a) Boiling curve for the proposed model

b) Boiling curves for pure substances x=0 and mixtures with a concentration x=0.54 (Auracher and Marroquin, 2019)

Fig. 3: Convection of the two-phase flow inside the tube

and the ratio ε/D. Multiplying the friction factor by $0{,}5\mathrm{Re}^2$ yields a set of parameters $(D^3 g\rho/L\mu^3)\Delta P$, which is independent of $\dot{m}$. Thus, by plotting the parameter $(D/\mu)\dot{m}$ on the abscissae, and the parameter $(D^3 g\rho/L\mu^3)\Delta P$ on the ordinates, the resulting plot will have the form of pressure drop behavior concerning mass flow, i.e., it will have the form $\Delta P = \Delta P(\dot{m})$, i.e., since they are independent parameters, iterative processes will not be necessary to estimate the pressure drop. Fig. 4(a) shows the conventional Moody diagram, while Fig. 4(b) shows the modified Moody diagram.

3. Model evaluation and validation

To validate the thermo-hydraulic model, a two-part approach was employed to ensure the reliability of the results. This unique methodology eliminates both the convective heat transfer coefficients (h) and, the friction factor (f). The first part of the validation focused on verifying the two-phase flow pattern, while the second part involved analyzing the pressure drop and temperature increase along the loop. This separation was necessary as the model employs an alternative approach compared to traditional models, and it was crucial to ensure its full applicability and accuracy in both aspects of the validation process.

3.1. Two-phase flow regime

When two-phase flow circulates within a pipe, different flow patterns can occur (see Fig. 5), each with very special thermal and hydrodynamic characteristics (Tomei et al., 2015), therefore, characterizing the type of flow is of utmost importance. It has been described in the literature that an annular flow should be used in DSG plants since this minimizes the deformations of the absorber, and maximizes its useful life (Almanza et al., 1997; Cui et al., 2013; Khanna et al., 2014; Li et al., 2017), in addition, to enhance the heat transfer (Eck and Steinmann, 2005; Montes Pita, 2008; Zarza Moya, 2003).

To identify the type of flow, at least two maps have been proposed. The first of these maps was developed by Taitel and Dukler (1976), involving various dimensionless groups (such as the Froud number), or the more recently developed map of Barnea (1987) relating the velocity of stream and water. It has been decided to use the Taitel and Dukler map due to its ease of use, and its solution is quite large with well-defined flow intervals.

Fig. 6 shows a comparison of the results obtained in the DUKE loop (Feldhoff et al., 2016) plotted using a dashed line with black marker, and those obtained using the proposed model (solid orange line), for a mass flow of 1,3 kg s^{-1}, an irradiance of 900 Wm^{-2}, and a pressure of 80 bar. One can see that the black and orange lines are superimposed, thus the solution obtained is adequate. The bibliography mentions that caution must be taken in the use of this diagram, especially in the area near the beginning or end of evaporation, since some type of stratification may occur (Hirsch et al., 2014). When analyzing the results shown, it can be seen that at the beginning of the evaporation (Martinelli numbers X higher than 1.6), there is an intermittent flow. The presence

of intermittent flow in the initial stages of boiling process in a horizontal pipe carrying water-steam mixture, as explained by Feldhoff et al. (2016), may not be a cause for concern if it eventually evolves into an annular flow. The transition to annular flow results in a more stable and predictable two-phase mixture, and the pressure drop across the pipe becomes more consistent, as stated in the same reference.

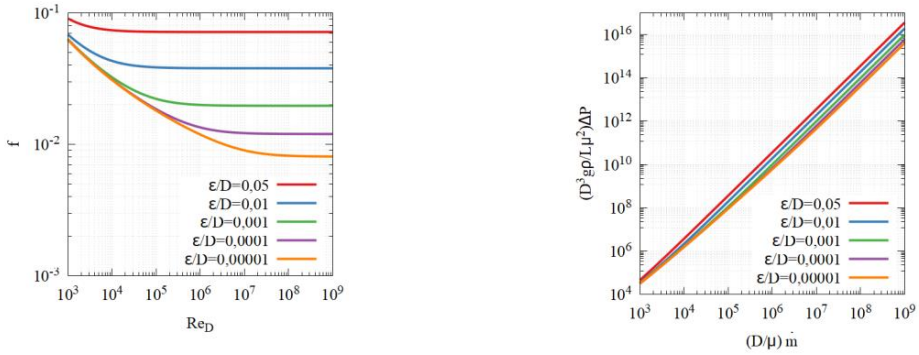

a) Moddy's diagram **b) Modified Moddy's diagram**

Fig. 4: Pressure drop model

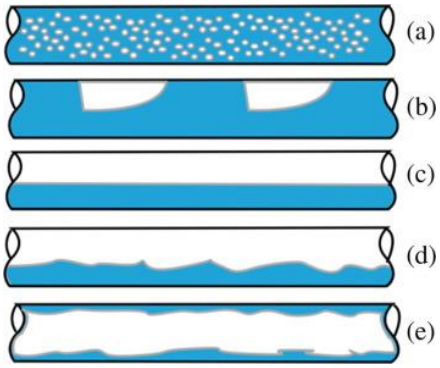

Fig. 5: Flow pattern for horizontal pipes. (a) Disperse bubble. (b) Intermittent. (c) Smooth stratified. (d) Wavy stratified. (e) Annular (López et al., 2016)

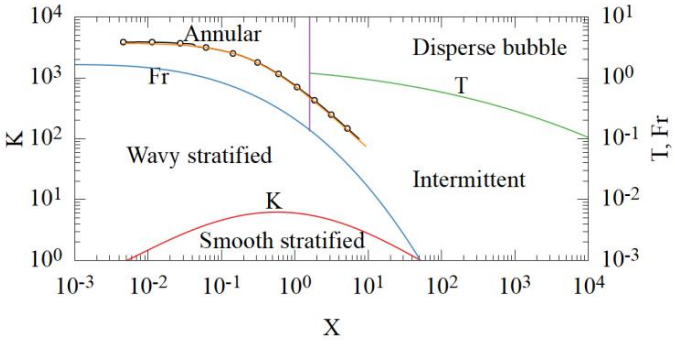

Fig. 6: Superposition of the simulation flow regime on the generalized flow regime map for two-phase flow in horizontal pipes. Adapted from (Feldhoff et al., 2016)

Once the flow pattern in the two-phase zone has been verified, it is possible to compare the pressure drop in this zone with Eck's model (2005), emphasizing that Eck's model employs a "traditional" model, in addition to being an approximation of a 2D model to 1D, by considering the wet angle inside the pipe; while the model developed is 1D. In this case, a flow of 1 kg s^{-1} has been simulated for a pipe of 50 mm inner diameter.

The results of both simulations are presented in Fig. 7, with solid lines representing the simulation results of the developed model, and dashed lines with markers representing Eck's results (2005) . It is evident that the profiles are quite similar, with only slight deviations observed in the developed model, where the values are slightly higher

by no more than 15% for Δ*P*, and less of 1% for the total pressure along the loop, for each case (30, 60 and 100 bar). . This outcome aligns with the findings of Montes (2008), which suggested that the values should be slightly higher in comparison to 2D or 3D models. However, it is worth noting that a potential limitation is the need to generate a new heat transfer function when changing the operating conditions, such as pressure.

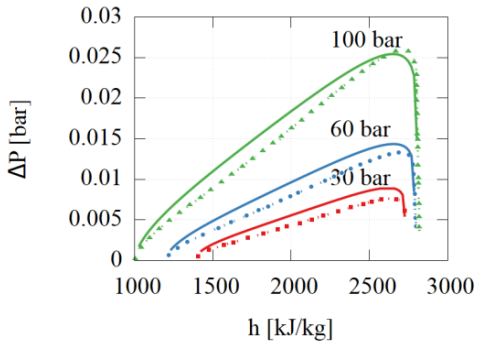

Fig. 7: Pressure drop in the two-phase flow region. Adapted from (Eck and Steinmann, 2005)

3.2. Temperature rise and pressure drop evolution through the loop

The last stage of the validation consisted of analyzing the entire loop to determine the evolution of the water temperature and pressure drop along the loop as a whole. For this, the operating parameters and the experimental results of the DISS loop were taken (Lobón et al., 2014): a mass flow of 0,59 kg s^{-1}, an irradiance of 807 W $m^{-2,}$ and a pressure of 101,9 bar at the loop inlet. Fig. 8 shows the experimental results (markers) and the continuous line shows the simulation results, where the convergence of the results of the developed model can be seen. In this case, the error between temperatures is less than 1%, so the model is validated.

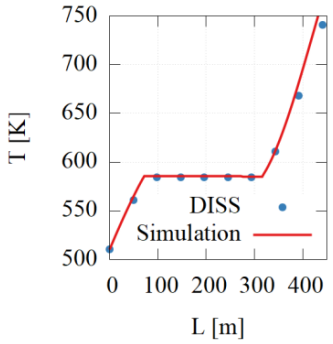

Fig. 8: Pressure drop in the two-phase flow region. Adapted from (Eck and Steinmann, 2005)

4. Conclusions

The energy model developed allows evaluating without complications the evolution of temperature and pressure drop along the parabolic trough loop. It has been identified that the flow pattern can be predicted according to the Taitel and Dukler diagram (see Fig. 6) and that when simulating the DUKE loop conditions obtained experimentally [8], a mostly annular flow pattern is verified, except for the beginning of the boiling zone, which is intermittent. The transition from intermittent to annular flow during the boiling process in a horizontal pipe carrying water-steam mixture is not a concern if it evolves to an annular flow.

The thermohydraulic model was fully validated by estimating the evolution of temperature and pressure drop along the loop. In both cases, the difference between the results obtained by the developed model and the experimental results in the DISS loop (Eck and Steinmann, 2005) is less than 1%, as shown in Fig. 8, which ensures the convergence of the analysis.

With the aforementioned, the proposed methodology can be confidently applied to various future works, such as the modeling of a conceptual DSG plant in the Northwest region of Mexico. This methodology can effectively establish the operating parameters and design conditions for concentrating solar power systems that utilize direct

steam generation. The robustness and reliability of this methodology make it a valuable tool for advancing research and development in the field of solar energy technologies.

5. Acknowledgments

Authors acknowledge CONACyT for a Ph.D. grant for EGM.

6. References

Adiutori, E., 2017. The New Engineering, 3rd ed. Ventuno Press, Naples, FL.

Almanza, R., Lentz, A., Jiménez, G., 1997. Receiver behavior in direct steam generation with parabolic troughs. Sol. Energy 61, 275–278. https://doi.org/10.1016/S0038-092X(97)88854-8

Alobaid, F., 2018. Process Simulation, in: Numerical Simulation for Next Generation Thermal Power Plants. pp. 15–86. https://doi.org/10.1007/978-3-319-76234-0_2

Auracher, H., Marroquin, A., 2019. Critical heat flux and minimum heat flux of film boiling of binary mixtures flowing upwards in a vertical tube, in: Convective Flow Boiling. CRC Press, pp. 213–218.

Barnea, D., 1987. A unified model for predicting flow-pattern transitions for the whole range of pipe inclinations. Int. J. Multiph. Flow 13, 1–12. https://doi.org/10.1016/0301-9322(87)90002-4

Bergman, T.L., Lavine, A.S., Incropera, F.P., Dewitt, D.P., 2011. Fundamentals of Heat and Mass Transfer, 7th ed. John Wiley & Sons, Inc.

Cui, W., Li, H., Li, L., Liao, Q., 2013. Thermal stress analysis of DSG solar absorber tube in stratified two-phase regime. AIP Conf. Proc. 1558, 2217–2220. https://doi.org/10.1063/1.4825979

Eck, M., Steinmann, W.-D., 2005. Modelling and Design of Direct Solar Steam Generating Collector Fields. J. Sol. Energy Eng. 127, 371–380. https://doi.org/10.1115/1.1849225

El Hefni, B., Bouskela, D., 2019. Introduction to Modeling and Simulation, in: Modeling and Simulation of Thermal Power Plants with ThermoSysPro. Springer International Publishing, Cham, pp. 1–10. https://doi.org/10.1007/978-3-030-05105-1_1

Feldhoff, J.F., Hirsch, T., Pitz-Paal, R., Valenzuela, L., 2016. Analysis and potential of once-through steam generators in line focus systems – Final results of the DUKE project. AIP Conf. Proc. 1734, 100006. https://doi.org/10.1063/1.4949194

Forristall, R., 2003. Heat Transfer Analysis and Modeling of a Parabolic Trough Solar Receiver Implemented in Engineering Equation Solver. Colorado.

Giglio, A., Lanzini, A., Leone, P., Rodríguez García, M.M., Zarza Moya, E., 2017. Direct steam generation in parabolic-trough collectors: A review about the technology and a thermo-economic analysis of a hybrid system. Renew. Sustain. Energy Rev. 74, 453–473. https://doi.org/10.1016/j.rser.2017.01.176

González-Mora, E., Duran García, M.D., 2022. Propuesta de eliminación del coeficiente convectivo h para el modelado de flujo bifásico en concentradores parabólicos, in: XVIII Congreso Ibérico y XIV Congreso Iberoamericano de Energía Solar. Mallorca.

Gungor, K.E., Winterton, R.H.S., 1986. A general correlation for flow boiling in tubes and annuli. Int. J. Heat Mass Transf. 29, 351–358. https://doi.org/10.1016/0017-9310(86)90205-X

Hachicha, A.A., Rodríguez, I., Ghenai, C., 2018. Thermo-hydraulic analysis and numerical simulation of a parabolic trough solar collector for direct steam generation. Appl. Energy 214, 152–165. https://doi.org/10.1016/J.APENERGY.2018.01.054

Hakkarainen, E., Kannari, L., 2015. Dynamic Modelling of Concentrated Solar Field for Thermal Energy Storage Integration, in: 9th International Renewable Energy Storage Conference (IRES 2015), At Düsseldorf.

Hewitt, G.F., 1998. BOILING, in: Rohsenow, W.M., Hartnett, J.P., Cho, Y.I. (Eds.), Handbook of Heat Transfer. McGraw-Hill Education, New York.

Hirsch, T., Feldhoff, J.F., Hennecke, K., Pitz-Paal, R., 2014. Advancements in the Field of Direct Steam Generation in Linear Solar Concentrators—A Review. Heat Transf. Eng. 35, 258–271. https://doi.org/10.1080/01457632.2013.825172

Howell, J.R., Menguc, M.P., Siegel, R., 2015. Thermal Radiation Heat Transfer, 6th ed. CRC Press, Boca Raton. https://doi.org/10.1115/1.3449647

IRENA, 2022a. Solar energy [WWW Document]. URL https://www.irena.org/solar (accessed 5.9.22).

IRENA, 2022b. Statistics Time Series [WWW Document]. URL https://www.irena.org/Statistics/View-Data-by-Topic/Capacity-and-Generation/Statistics-Time-Series (accessed 5.9.22).

Islam, M.T., Huda, N., Abdullah, A.B., Saidur, R., 2018. A comprehensive review of state-of-the-art concentrating solar power (CSP) technologies: Current status and research trends. Renew. Sustain. Energy Rev. 91, 987–1018. https://doi.org/10.1016/J.RSER.2018.04.097

Khanna, S., Kedare, S.B., Singh, S., 2014. Deflection and stresses in absorber tube of solar parabolic trough due to circumferential and axial flux variations on absorber tube supported at multiple points. Sol. Energy 99, 134–151. https://doi.org/10.1016/J.SOLENER.2013.11.005

Li, L., Sun, J., Li, Y., 2017. Thermal load and bending analysis of heat collection element of direct-steam-generation parabolic-trough solar power plant. Appl. Therm. Eng. 127, 1530–1542. https://doi.org/10.1016/J.APPLTHERMALENG.2017.08.129

Lobón, D.H., Baglietto, E., Valenzuela, L., Zarza, E., 2014. Modeling direct steam generation in solar collectors with multiphase CFD. Appl. Energy 113, 1338–1348. https://doi.org/10.1016/j.apenergy.2013.08.046

López, J., Pineda, H., Bello, D., Ratkovich, N., 2016. Study of liquid–gas two-phase flow in horizontal pipes using high speed filming and computational fluid dynamics. Exp. Therm. Fluid Sci. 76, 126–134. https://doi.org/10.1016/j.expthermflusci.2016.02.013

Montes Pita, M.J., 2008. Análisis Y Propuestas De Sistemas Solares De Alta Exergía Que Emplean Agua Como Fluido Calorífero. Universidad Politécnica de Madrid.

Moya, E.Z., 2021. Parabolic-trough concentrating solar power systems, in: Concentrating Solar Power Technology. Elsevier, pp. 219–266. https://doi.org/10.1016/B978-0-12-819970-1.00009-8

Özışık, M.N., 1973. Radiative Transfer and Interactions with Conduction and Convection, 1st ed. Wiley.

Pal, R.K., K, R.K., 2021. Thermo-hydrodynamic modeling of flow boiling through the horizontal tube using Eulerian two-fluid modeling approach. Int. J. Heat Mass Transf. 168, 120794. https://doi.org/10.1016/j.ijheatmasstransfer.2020.120794

Sandá, A., Moya, S.L., Valenzuela, L., 2019. Modelling and simulation tools for direct steam generation in parabolic-trough solar collectors: A review. Renew. Sustain. Energy Rev. 113, 109226. https://doi.org/10.1016/J.RSER.2019.06.033

Sun, J., Liu, Q., Hong, H., 2015. Numerical study of parabolic-trough direct steam generation loop in recirculation mode: Characteristics, performance and general operation strategy. Energy Convers. Manag. 96, 287–302. https://doi.org/10.1016/j.enconman.2015.02.080

Taitel, Y., Dukler, A.E., 1976. A model for predicting flow regime transitions in horizontal and near horizontal gas-liquid flow. AIChE J. 22, 47–55. https://doi.org/10.1002/aic.690220105

Tomei, G.L., Wilcox, B., Company, B.& W., 2015. Steam: Its Generation and Use. Babcock & Wilcox Company.

Vasquez Padilla, R., 2011. Simplified Methodology for Designing Parabolic Trough Solar Power Plants. University of South Florida.

Zarza Moya, E., 2017. 5 – Innovative working fluids for parabolic trough collectors, in: Blanco, M., Ramirez Santiagosa, L. (Eds.), Advances in Concentrating Solar Thermal Research and Technology. pp. 75–106. https://doi.org/10.1016/B978-0-08-100516-3.00005-8

Zarza Moya, E., 2003. Generación directa de vapor con colectores solares cilindro parabólicos. Proyecto DIrect Solar Steam (DISS). Universidad de Sevilla.

Effects of Atmospheric Gases on the Efficiency of Heating and Cooling Supply Components: Experimental Investigation of Plate Heat Exchangers

Martin Heymann, Franziska Koch and Karin Rühling

Chair of Building Energy Systems and Heat Supply, TU Dresden (GER)

Abstract

The paper presents measurement results for the influence of bubble flow (gas volume fraction up to 6 %) on the pressure drop und heat transfer in three plate heat exchanger test objects, which are operated with water as heat transfer fluid. The gas content effects the efficiency and auxiliary energy consumption of solar thermal systems. Therefore, the plate heat exchanger as one of their main components is investigated in detail.

Keywords: plate heat exchanger, two-phase flow, water, nitrogen, pressure drop, heat transfer

1 Introduction

As is well known, free gases in heat transfer media can cause a wide variety of problems in energy heating systems. In solar thermal systems, for example, these are flow instabilities and partial stagnation. The investigations of the joint research project ImpactGas (Funded by Federal Ministry for Economic Affairs an Climate Action on the basis of a resolution of the German Bundestag, Funding Reference Number: 03EN1001A, research partners Hochschule Zittau/Görlitz and Fraunhofer IFAM Dresden) generally focus on the effects of free gases on the heat output and the pressure loss of individual components. The project team is investigating different types of heat exchangers and is going to study solar thermal collectors. These are the components in solar thermal systems that are expected to have the greatest impact on heat output and hydraulic functioning. The results apply to other types of systems as well.

This paper presents the investigation of three plate heat exchanger test objects. The plate heat exchangers have the same design and differ only in the number of plates. In the following, the component test stand for water/water heat exchangers is presented. It enables the setting of variable gas contents in the heat transfer medium. The measurement concept for determining the flow pressure losses and the heat transfer in the test objects is presented and the influence of free gases with a volume fraction ε of 2 to 6 % is discussed.

The effects of the relevant gases nitrogen, oxygen and carbon dioxide on thermal heating systems are manifold and depend on the control concept used.

In Scenario 1, the control system will try to continue to fulfil the supply task despite a disturbance by free gases. For example, it will increase the heat capacity rate via the pump speed to such an extent, that the target temperature and thus the necessary transmission capacity are reached. For this scenario, it could be shown that the flow pressure losses of all test items increase significantly, but for load cases with at least 50% of the design volume flow only minor effects on the heat transfer are to be expected.

In Scenario 2, the control system cannot compensate for the disturbances caused by the free gases. This can be the case, for example, if the system is already working close to the maximum point or the control only takes into account environmental influences but not process variables. In this case, the total volume flow remains the same, but the heat capacity rate decreases.

© 2022. The Authors. Published by International Solar Energy Society
Selection and/or peer review under responsibility of Scientific Committee
doi:10.18086/eurosun.2022.12.07 Available at http://proceedings.ises.org

2 Concept/Methodic

2.1 Heat Exchanger Test Objects

The test objects Hex20, Hex30 and Hex40 are plate heat exchangers from a well-known manufacturer. They have the following parameters:

Tab. 1: Parameters of the plate heat exchanger test objects

Test object	Number of plates	Number of passages	Stamping Angle	Design heat transmission capacity	Design volume flow
			°	kW	m³/h
Hex20	20	1	44 resp. 78	20	0,59
Hex30	30	1	44 resp. 78	30	0,89
Hex40	40	1	44 resp. 78	40	1,19

2.2 Test Rig

Fig. 1 shows the simplified schematic of the component test rig. A well degassed Reference Circuit represents the primary side of the heat exchanger test specimen, i.e. the heating side, and supplies it with temperature-controlled heat transfer fluid.

The so-called Test Circuit supplies the secondary side of the test object with heat transfer medium, which is also temperature-controlled. It has the option to set the gas fraction for dissolved gases (Gas Admission I, not shown here), with nitrogen, technical air and, if necessary, carbon dioxide to produce a defined content of dissolved gases. The heat transfer medium conditioned in this way is stored in a pipe storage tank (not shown here). Gas Admission II can provide a defined fraction of undissolved gases (bubble flow).

All variables required for balancing around the test objects, such as volume flows (F), pressures (P) and the differential pressure (ΔP) as well as the temperatures (T) are measured. The temperatures T21/T22 are the inlet and outlet temperatures on the Test Circuit side, T31/T32 on the Reference Circuit side. For the volume flows, F31 is the sensor on the Reference Circuit side. On the Test Circuit side, there is the sensor F11 located upstream of Gas Admission II which measures the water volume flow $\dot{V}_W$, F12 measures the total volume flow $\dot{V}_W + \dot{V}_G$ accordingly. In the following evaluation, the gas volume flow $\dot{V}_G$ is calculated via the gas mass flow sensor F40, since a higher accuracy can be assumed here. The associated gas volume fraction calculates according to $\varepsilon = \dot{V}_G/(\dot{V}_W + \dot{V}_G)$ – also referred to as void fraction. This definition corresponds to the definition for the homogeneous gas volume fraction according to (VDI-Wärmeatlas, 2013).

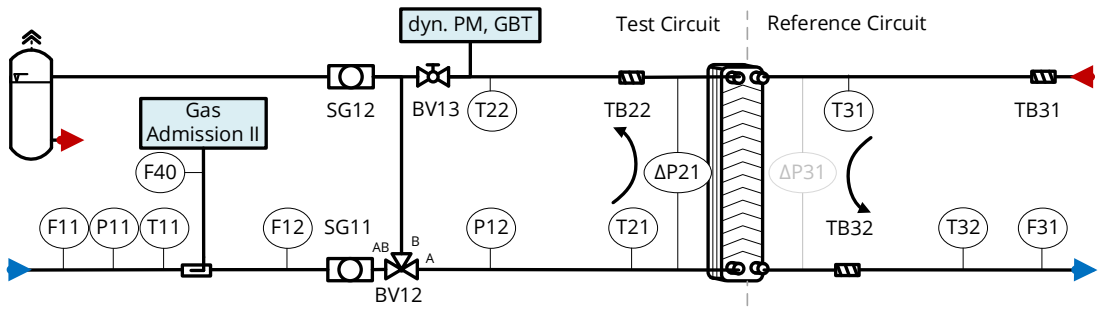

Fig. 1: Component test rig for water-to-water heat exchangers, simplified schematic, F … volume flow sensor, T … temperature sensor, P … pressure sensor dyn. PM ... dynamic pressure maintenance, GBT … "Gas Bubble Test" BV … ball valve, TB … turbulator, SG ... sight glass

The direction of flow was chosen so that the gas-laden side of the heat exchanger test object flows from the bottom to the top. This represents the thermo-hydraulically plausible installation position recommended by the manufacturer. In practice, this should definitely also be taken into account during planning. The side with the greater risk of gas desorption should be flowed through from bottom to top. This is either the circuit with a potential gas entry (e.g. geothermal probe circuit, drinking water, side with compressor pressure maintenance) or the side to be heated, since with water as the heat transfer medium the solubility limit decreases with temperature.

Whether gases have accumulated in the test object during the course of the tests can be determined with a very high degree of accuracy using the measurement method according to (Heymann, et al., 2014) or (VDI 4708-2:2022-04) the so called "Gas Bubble Test". In the heat exchanger component test stand, the inflow of gases via Gas Admission II is first stopped and the test waits until no more gas bubbles can be seen in the SG12 sight glass. Then the pipe section around the test object is shut off by means of the ball valves BV12/BV13 and the pressure is increased via the dynamic pressure maintenance. The initial pressure is restored by draining medium into a collecting vessel. The gas bubble volume can be determined via the measured variables of pressure and volume of drained heat transfer medium. Normalization to the volume of the test circuit side of the test heat exchanger results in the gas volume fraction in the test object $\varepsilon_{\mathrm{Hex}}$.

2.3 Experimental Design

All operating conditions are approached with degassed medium on both sides at first. This represents the Reference Case (RC), which serves as the reference condition for the comparative evaluation. This is followed by the Test Cases (TC) with a well degassed medium (water) at the inlet to the test object and a defined volume fraction of free gases of ε = 2, 4 and 6 %. The selected gas volume fractions correspond to potential conditions in practice. This results in the test matrix shown in Tab. 2. The tests were conceived in such a way that the Reference Case and the Test Case have the same water volume flow $\dot{V}_{\mathrm{W}}$, i.e. they reflect the conditions according to Scenario 1.

The three right-hand columns of Tab. 2 show for which evaluations the tests were used. The column $\varepsilon_{\mathrm{Hex}}$ stands for the investigations on gas accumulation in the test object, Δp and k for the investigations on pressure loss and heat transfer.

Tab. 2: Testing matrix, volume flow rate data in % of the design case

	Hex20	**Hex30**	**Hex40**				
Design volume flow	0,59 m³/h	0,89 m³/h	1,19 m³/h				
T31/T21 °C	**F31/F11** % of design volume flow			**ε** % (v/v)	**$\varepsilon_{\mathrm{Hex}}$**	**Δp**	**k**
25/25	–/000, –/025, –/050, –/075, –/100, –/125, –/150, –/175			RC: 0, TC: 2, 4, 6	●	●	
65/25	050/050, - 100/100, 125/125, 150/150	050/050, - 100/100, 125/125 -	050/050, 075/075, 100/100 - -			●	●
65/35						●	●
75/40						●	●

The selected test points correspond to the specifications made in DIN EN 1148/A1:2005-12 for the performance testing of water/water heat exchangers. For each heat exchanger, this results in approx. 30 operating conditions in the cold state and in total 36 operating conditions for the tests with heat transfer. After setting the test boundary conditions, a settling time of three minutes is waited for the cold tests and five minutes for the warm tests. These time periods were determined in preliminary tests and are intended to take into account the capacitive effects of heating up the heat exchanger and, if necessary, the accumulation of free gases in the test objects. The measurement time for an operating state set in this way is then two minutes for cold tests and five minutes for warm tests.

The tests at ambient temperature require a significantly shorter test duration, as the conditioning of the Test Circuit and the setting of the test boundary conditions are easier to realize. Therefore, significantly more measuring points were approached for this temperature level (25/25). This means that the influence of the gas loading on the pressure loss in the cold state is particularly well investigated.

A comparable study can be found in the literature (Kreissig & Müller-Steinhagen, 1992). Here, analogous to Scenario 1, the individual tests were compared based on the mass flow density in the flow cross-section. The study investigates the pressure losses of an air-water flow on two plate heat exchangers, for each of which the number of plates can be varied. The aim was to use the air-water flow to model the conditions for the usage as an evaporator. Therefore, the area of investigation with gas volume fractions of up to 100 % differs significantly from the investigation presented here. Furthermore, the flow through the plate heat exchanger was from top to bottom, which complicates the interpretation and evaluation due to the possible accumulation of gases in the test objects.

2.4 Evaluation methodology

In the following, the procedure for evaluating the measurement data will be described in more detail. First, selected calculations are made with the raw measurement data in the time ranges of the steady-state operating conditions. The temporal resolution is one second.

- Further calibration functions are applied to selected measured values in addition to the basic calibration.
- With the pressure and temperature measurement data, the fluid properties (density, specific enthalpy, dynamic viscosity) are determined at the relevant points. These are the inlet and outlet sides of both circuits as well as fluid properties at medium conditions.
- Derived state variables (gas volume fraction), process variables (heat outputs, balance errors) and key Fig.s (pressure loss coefficient, characteristic numbers) are calculated.

For all these variables, averaging takes place over the stationary time range.

- Using the averaged values, selected values (heat transfer coefficient) are calculated.
- An important point of the chosen evaluation methodology is the formation of models for the gas-free Reference Case by means of regressions. These are determined, for example, for the flow pressure losses and the heat transfer, but also for other key Fig.s. In each case, individual trial functions are used that represent the required quantity as a function of the water volume flow and the average temperatures. This procedure makes it possible to assign an exactly matching (modelled) Reference Case to each measured Test Case. In this way, unavoidable variance in the test conditions can be compensated and the validity of the evaluation can be increased.
- The quantities related to the gas-free Reference Case are formed for all Test Cases. The assignment of the Test Case to the Reference Case is carried out for Scenario 1 via the water volume flow rate $\dot{V}_{\mathrm{W}}$. For Scenario 2, the corresponding Reference Case with the same total volume flow $\dot{V}_{\mathrm{tot}} = \dot{V}_{\mathrm{W}} + \dot{V}_{\mathrm{G}}$ can be determined using the model approaches. For the related pressure loss and heat transfer coefficient, the values are calculated according to Equation (1) and (2). For the Reference Case, the model value at volume flow and mean temperature of the Test Case is used:

$$\frac{\Delta p_{\mathrm{f}}}{\Delta p_{\mathrm{f,RC}}} = \frac{\Delta p_{\mathrm{f,TC}}}{\Delta p_{\mathrm{f,RC,Model}}(\dot{V}_{\mathrm{TC}}, T_{\mathrm{m,TC}})} \quad (1)$$

$$\frac{k}{k_{\mathrm{RC}}} = \frac{k_{\mathrm{TC}}}{k_{\mathrm{RC,Model}}(\dot{V}_{\mathrm{TC}}, T_{\mathrm{m,TC}})} \quad (2)$$

The resulting factors can be interpreted analogously to the two-phase multiplier described in (VDI-Wärmeatlas, 2013).

- The determined quantities are plotted against the gas volume flow rate to show the influence of the bubble flow (compare Fig. 3c and 4c). This influence is mapped with a simple (linear) regression function.

According to the (VDI-Wärmeatlas, 2013), the pressure drop of an adiabatic gas-liquid flow in pipelines is composed of

- the acceleration component Δp_{A},
- the hydrostatic component Δp_{g} and
- the actual friction component Δp_{f}.

$$\Delta P21 = p' - p'' = \Delta p_{\mathrm{f}} + \Delta p_{\mathrm{A}} + \Delta p_{\mathrm{g}} \quad (3)$$

The acceleration component Δp_{A} results from a change in momentum of the heat transfer medium if, for example, the flow velocity changes significantly between inlet and outlet, as in an evaporator. This is taken into account in the evaluation, but is negligible for all operating points. With the homogeneous model (see (VDI-Wärmeatlas, 2013) and (Michaelides, et al., 2016)), however, there would be a relevant resulting hydrostatic fraction Δp_{g}, which arithmetically leads to higher friction pressure losses with a measured total pressure. This produces an inconsistent picture in the evaluations and is probably not valid. In the ascending two-phase flow, slip occurs which just compensates the hydrostatic component. Therefore, the evaluation does not consider the hydrostatic component.

In the investigations of (Kreissig & Müller-Steinhagen, 1992) the hydrostatic pressure loss component is considered mathematically. However, in this case, there is a downwards flow and the investigation area is much broader with gas volume fractions of up to 100%. According to the paper, the measurement results were also difficult to reproduce with existing model approaches.

For each operating condition according to Tab. 2, the test boundary conditions are set. These are the inlet temperatures into the test object in the Test and Reference Circuits T21 and T31, the water volume flows in both circuits F11 and F31 as well as the dissolved gas content (here: degassed water) and the gas volume fraction ε set via Gas Admission II. After waiting for the settling time, the outlet temperatures T22 and T32 are set in as the system reaction. The gas bubble volume that may have accumulated $\varepsilon_{\mathrm{Hex}}$ in the test object also represents a system reaction.

3 Results

3.1 Gas accumulation in heat exchanger test objects

For selected tests in the cold state (25/25), the accumulated volume of free gases was determined using the methodology described above ("Gas Bubble Test") and the gas volume fraction in the test specimen $\varepsilon_{\mathrm{Hex}}$ was calculated. Fig. 2 shows the results for all three of the test objects. From a volume flow of 0.5 m³/h upwards, gas contents of less than 2.5 % (v/v) were measured, with a few exceptions, which is close to the expected measurement accuracy. Here, no significant additional effect of an accumulated gas bubble on the heat transfer or the pressure losses is to be expected. The determined effects are then mainly due to the gas bubbles transported along in the flow.

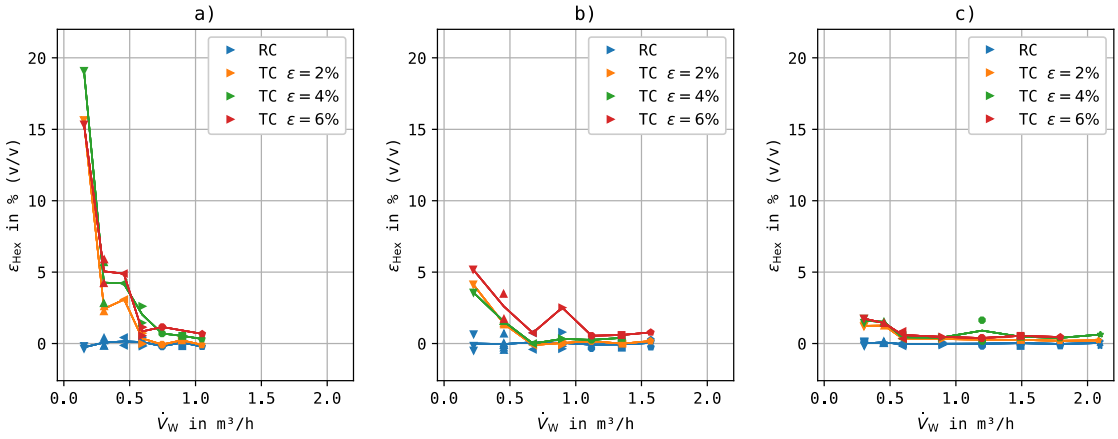

Fig. 2: Gas accumulation, gas volume fraction $\varepsilon_{\mathrm{Hex}}$ in test object, Test Circuit
a) Hex20 with 20 plates, b) Hex30 with 30 plates, c) Hex40 with 40 plates

3.2 Effects on Pressure Drop

Fig. 3 shows measurement results for the pressure loss of test object Hex40 on the Test Circuit side. The tests took place without heating by the Reference Circuit at a media temperature of approx. 25 °C. The gas-free Reference Cases are marked in blue and the Test Cases with a gas volume fraction of ε = 2, 4 and 6 % are shown in yellow, green and red respectively. The gas volume fraction ε is determined with the homogeneous model from the measured values of gas mass flow (F40) and water volume flow (F11) as well as from the corresponding fluid properties. The volume flow F11 corresponds to the volume flow of the pure water $\dot{V}_{\mathrm{W}}$ without the gas component, since the sensor is located upstream of Gas Admission II. It is varied from 0 to approx. 2.1 m³/h (175 % of design volume flow). The evaluation follows the logic of Scenario 1, in which operating states with approximately the same capacity flow rate are compared, which would fulfil very similar supply tasks in practice. An analogue evaluation is available for all three test objects and four temperature levels.

Diagram a) shows the flow pressure loss over the water volume flow rate $\dot{V}_{\mathrm{W}}$. A slight fanning out of the measured values due to an increased gas volume fraction ε can be observed, but general correlations are not yet recognizable in this representation. An empirical model is used to calculate the friction pressure loss Δp_{f} in the Reference Case by means of a trial function depending on volume flow and temperature. The results of the model are shown in the diagram as a blue dotted line.

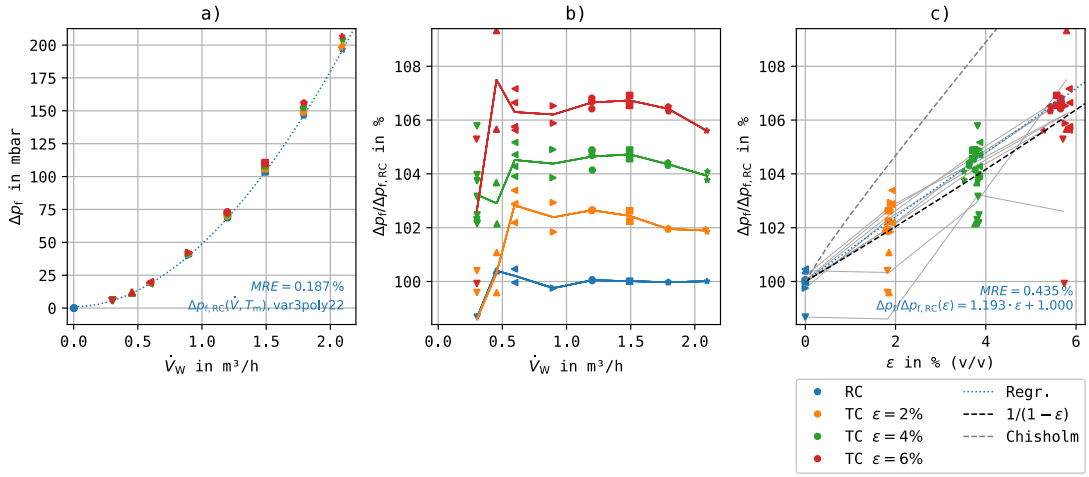

Fig. 3: Flow pressure drop Δp_f in test object Hex40 depending on the gas volume fraction, Scenario 1
a) Plotted over the water flow rate $\dot{V}_W$, reference case model function
b) Related pressure drop $\Delta p_f/\Delta p_{f,RC}$, plotted over the water flow rate $\dot{V}_W$
c) Related pressure drop $\Delta p_f/\Delta p_{f,RC}$, plotted over the gas volume fraction ε, modelling approaches

The modelling of the pressure loss is based on the definition of the pressure loss coefficient ζ in plate heat exchangers from (VDI-Wärmeatlas, 2013) and on a mixed second order polynomial with the volume flow and the mean temperature as variables. The model allows a correction of the Reference Case point in the following.

Diagram b) plots the pressure losses related to the modelled Reference Case $\Delta p_f/\Delta p_{f,RC}$ over the water volume flow $\dot{V}_W$. Significantly increased pressure losses can be seen for the gas-laden Test Cases. In some cases, operating conditions were approached several times. The colored lines in the diagram run along the mean values of these experiments. From a water volume flow $\dot{V}_W$ of 0.5 m³/h, the lines run almost parallel to the abscissa. The related pressure losses here are therefore less dependent on the water volume flow and more on the gas volume fraction ε. Below 0.5 m³/h, the related pressure losses rise sharply in some cases or drop below 100 %. On the one hand, this can be explained by the accumulation of gas cushions (slightly increased values for ε_{Hex}), on the other hand, with the very small numerical values of the measured pressure difference, measurement errors of the sensor and model deviations have a disproportionate effect.

In Diagram c) of Fig. 3 the pressure losses related to the modelled Reference Case $\Delta p_f/\Delta p_{f,RC}$ are plotted over the gas volume fraction ε. The assignment to the volume flow rate is possible via the marking symbol used.

The pressure drop increases steadily with the gas volume fraction ε in the investigated area. The result is a pressure loss that increases by approximately one percentage point per percentage point of gas volume fraction. The measuring points for all volume flows greater than 0.5 m³/h are grouped very closely around a straight line with an increase of 1.2 and with a MRE (Mean Relative Error) of 0.44 %. This is an indication of the high accuracy of the differential pressure sensor used and confirms the evaluation methodology applied. The regression lines $\Delta p_f/\Delta p_{f,RC} = f(\varepsilon)$ were formed for all test objects and temperature pairings and will be discussed later.

The pressure loss coefficient of a two-phase flow ζ is formed according to (Huhn & Wolf, 1975) with effective fluid properties and with a hydraulic diameter defined specifically for plate heat exchangers according to (VDI-Wärmeatlas, 2013). Equation (4) applies to the related pressure loss. With the assumption that the pressure loss coefficients formed in this way depend primarily on the geometry and surface properties of the duct walls (and thus $\zeta/\zeta_{RC} \approx 1$ applies), the following simple approach can be derived:

$$\frac{\Delta p_f}{\Delta p_{f,RC}} = \frac{\zeta}{\zeta_{RC}} \cdot \frac{1}{1-\varepsilon} \approx \frac{1}{1-\varepsilon} \tag{4}$$

This approach is presented in the diagram and follows the measured values of Hex40 very well. The approach described in (VDI-Wärmeatlas, 2013) for predicting the related pressure drop (called Two-Phase Multiplier) according to Chisholm also only assumes a dependence on the gas mass fraction $\dot{x}$ and thus of ε. The related pressure loss $\Delta p_f/\Delta p_{f,RC}$ is thus also seen as independent of the volume flow or the flow velocity. However, this approach leads to a significant overestimation of the gas influence.

3.3 Effect on heat transfer

Fig. 4 shows an example of the measured heat transfer coefficients for test object Hex40 and the temperature level 65/25. An analogous evaluation is available for all three test objects and four temperature levels.

Diagram a) represents the heat transfer coefficients as $k \cdot A$. Here A is the transfer area of the test object taken from the data sheet.

$$k \cdot A = \frac{\dot{Q}_1}{\Delta T_m} \tag{5}$$

The heat transfer coefficient is determined according to Equation (5). Here $\dot{Q}_1$ is the heat flow on the gas-free Reference Circuit side. The heat transfer coefficients increase with increasing water volume flow due to the higher capacity flow, as more heat can be transferred. The determined logarithmic temperature difference ΔT_m also increases. Operating states with higher water volume flow correspond to states with lower Number of Transfer Units NTU (dimensionless heating area). The dimensionless temperature change Φ (operational characteristics) also decreases (not shown here). Diagram a) does not allow any statements about the influence of the gas volume fraction.

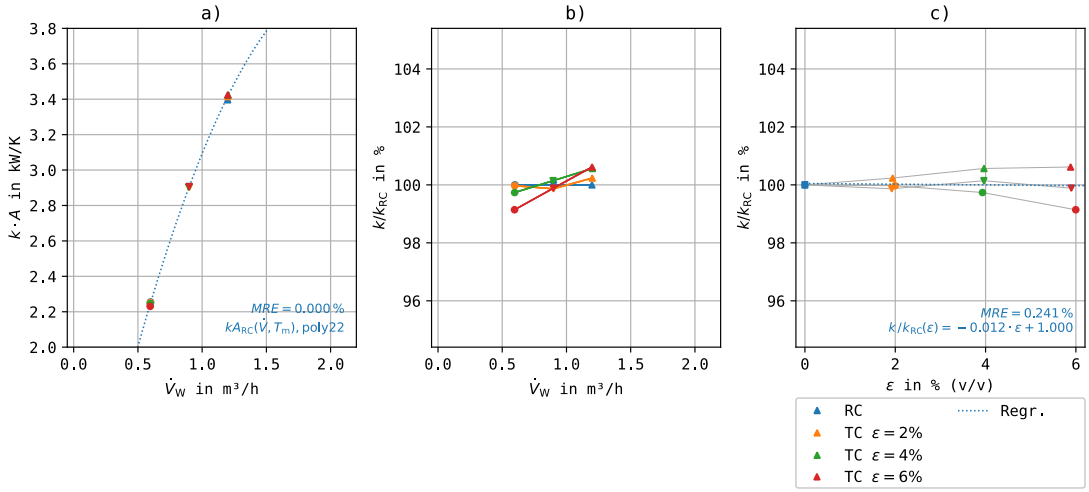

Fig. 4: Heat transfer coefficient k in test object Hex40 depending on the gas volume fraction, Scenario 1
a) Plotted over the water flow rate $\dot{V}_W$, reference case model function
b) Related heat transfer coefficient k/k_{RC}, plotted over the water flow rate $\dot{V}_W$
c) Related heat transfer coefficient k/k_{RC}, plotted over the gas volume fraction ε, modelling approach

Diagrams b) and c) from Fig. 4 show that an increase in the gas volume fraction ε of up to 6 % has only a slight effect on the heat flow coefficients k. The related heat transition coefficient k/k_{RC} varies by a maximum of ±1 %. A slight tendency can be recognized that at high gas volume fractions ε the heat transfer is slightly worse for low volume flow rates and slightly better for high volume flow rates. The deviations are within the range of measurement accuracy and just about balance each other out over all operating points. Regression lines $k/k_{RC} = f(\varepsilon)$ were formed for all test objects and temperature pairs. The gas volume fraction on average shows no influence in the other characteristic Fig.s NTU and Φ in comparison to the Reference Case.

3.4 Overview for all Test Objects and Temperature Levels (Scenario 1 and 2)

In summary, Fig. 5 shows the effects of the bubble flow for Scenario 1. Diagrams a) and b) contain the regressions of the related pressure losses and related heat transfer coefficients for all heat exchanger test objects and investigated temperature pairings. In systems that adjust the water volume flow via a control system so that the supply task is still fulfilled with free gases in the system (Scenario 1), the following statements can be made:

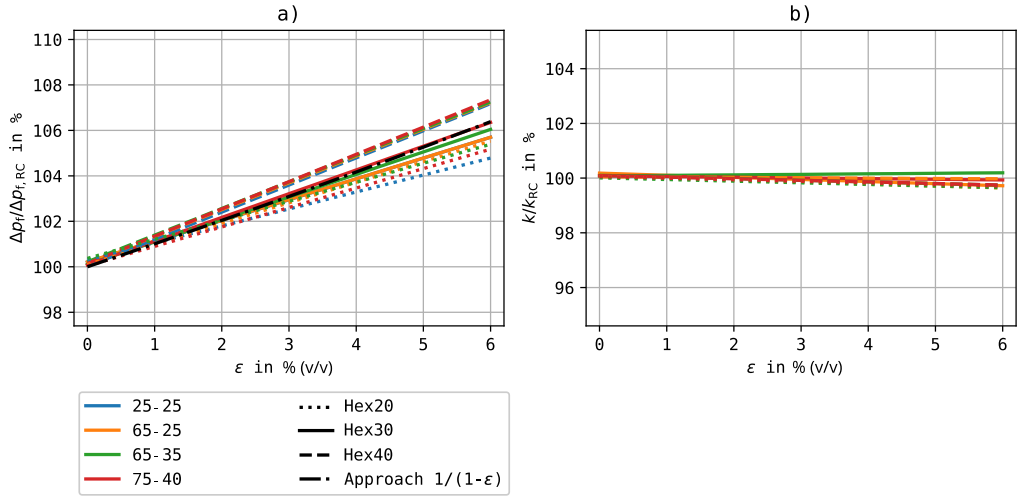

Fig. 5: Overview graph for all heat exchanger test objects and temperature pairings, Scenario 1
a) Related pressure drop $\Delta p_f/\Delta p_{f,RC}$, plotted over the gas volume fraction ε, modelling approach
b) Related heat transfer coefficient k/k_{RC}, plotted over the gas volume fraction ε

The measurements cannot prove an influence of free gases on the heat transfer. Averaged over all volume flows, all regression lines show a gradient close to zero. With a gas volume fraction of 6 %, maximum deviations in the range of ± 0.2 % are to be expected.

Analogously, Fig. 6 shows the evaluation for Scenario 2. In this consideration, the pressure losses according to Diagram a) decrease with increasing gas volume fraction. This results from the fact that the pressure losses of a bubble flow are mainly caused by the viscosity of the water phase and correspondingly lower pressure losses occur at lower water flow velocities. Analogous to the derivation of Equation (4) it can be assumed that the pressure loss coefficients ζ between the Test and Reference Case remain approximately constant for the same water volume flow. With the additional assumption that the deviations in the water volume flow of approx. 6 % according to Scenario 2 only have a minor effect on the ζ-values, the following simple relationship can be derived for Scenario 2:

$$\frac{\Delta p_f}{\Delta p_{f,RC}} \approx 1 - \varepsilon \tag{6}$$

The regressions formed for test objects Hex20 and Hex30 correspond well to this approach for all temperature levels. For Hex40, the pressure losses decrease to a lesser extent. The analysis does not show a relevant influence of the temperature level.

Diagram b) shows a uniform decrease in the heat transfer coefficients k for all test objects and temperature pairings by approx. 4 % at 6 % gas volume fraction. This results from comparing a measured Test Case with a Reference Case with increased water volume flow corresponding to the gas volume fraction. As shown in Fig. 4, the heat flow coefficient increases with increasing water volume flow, which leads to the observed behavior.

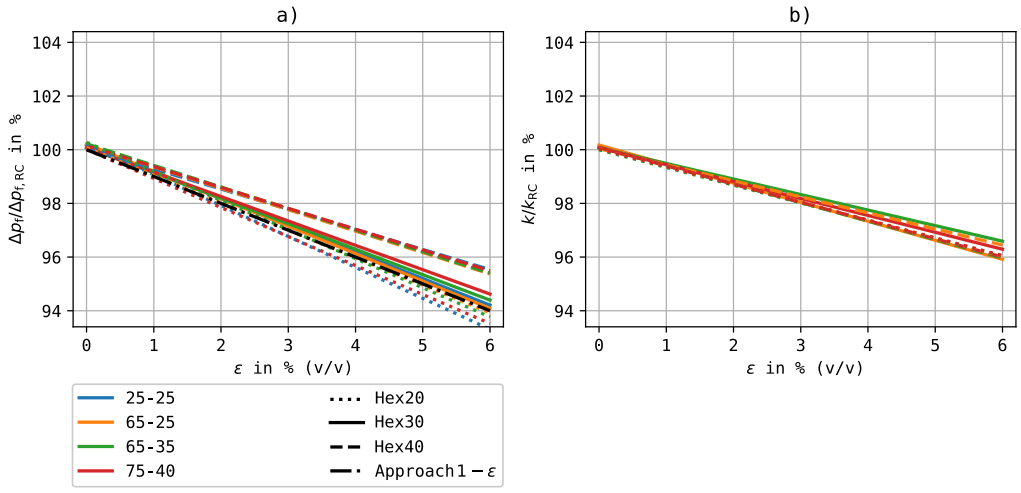

Fig. 6: Overview graph for all heat exchanger test objects and temperature pairings, Scenario 2
a) Related pressure drop $\Delta p_f/\Delta p_{f,RC}$, plotted over the gas volume fraction ε, modelling approach
b) Related heat transfer coefficient k/k_{RC}, plotted over the gas volume fraction ε

4 Conclusion/Prospect

To summarize, the experimental setup can adjust defined two-phase flows of water and free gas components of nitrogen precisely enough. The measurement technology used can represent the effect of variable gas fractions on the pressure loss and heat transfer very well. Circulating free gases in a thermal heating system – e.g. due to lack of care during commissioning or maintenance – can have a negative impact on the system operation.

In systems with a functioning control system, the disturbance caused by air bubbles can be compensated. The supply task can still be fulfilled by increasing the water volume flow via an increasing speed of the circulating pumps until the performance limit is reached (Scenario 1). In this case, however, increased pressure losses (approx. one percentage point per volume percent of gas) in the heat exchanger (and probably other system components) and thus an increased auxiliary energy demand must be expected. The effects on the heat transfer in the heat exchanger are minor in the examined area, possibly slightly depending on the operating condition.

In systems without direct control of the process variables (Scenario 2), the flow pressure losses and the heat transfer decrease accordingly due to the lower water volume flow. However, the supply task can no longer be fulfilled here.

These statements are valid for the selected, favorable mounting orientation of the heat exchanger, in which the flow through the circuit with the greater risk of gas accumulation is from the bottom to the top. It is essential to bear this in mind when designing systems. The strong accumulation of gas cushions in local high points in the system will lead to significant disturbances. At low flow rates, however, gases can accumulate in the heat exchanger even if the installation position is favorable for air removal.

This study highlights a single aspect related to atmospheric gases in the thermal system. Effects on other components such as circulation pumps, fittings, solar thermal collectors, etc. are also to be expected. Temperature and volume flow sensors relevant to control and billing may also be affected.

In any case, increased attention must be paid to the topic during design, commissioning and maintenance. Here, for example, VDI 4708-2 contains important information. It is necessary to always avoid the occurrence of free gases. Care during commissioning and vacuum or membrane degassing can achieve this. For small systems, mobile vacuum degassers that are only used during commissioning and, if necessary, at maintenance dates can be an economical solution. Free gases can be easily detected with a “Gas Bubble Test” and thus the need for action can be evaluated.

Furthermore, the research question is, whether the conclusions gained can be transferred to circuits with water-glycol mixtures.

References/Nomenclature

DIN EN 1148/A1:2005-12. Wärmeaustauscher - Wasser/Wasser-Wärmeaustauscher für Fernheizung - Prüfverfahren zur Feststellung der Leistungsdaten; German version EN 1148:1998/A1:2005. Berlin, Wien, Zürich: Beuth Verlag GmbH, DIN Deutsches Institut für Normung e. V. and DIN-Normenausschuss Kältetechnik (FNKä.). https://dx.doi.org/10.31030/9647845

Heymann, M., Panitz, F., Rühling, K. & Felsmann, C. 2014. Solubility Coefficients for Solar Liquids, a New Method to Quantify Undissolved Gases and Practical Recommendations. Energy Procedia, Band 48, pp. 721-730. https://doi.org/10.1016/j.egypro.2014.02.084

Huhn, J. & Wolf, J. 1975. Zweiphasenströmung gasförmig/flüssig. 1st. Edition. Ed. Leipzig: Fachbuchverlag. https://katalog.slub-dresden.de/id/0-1081515562

Kreissig, G. & Müller-Steinhagen, H. M. 1992. Frictional Pressure Drop for Gas/Liquid Two-Phase Flow in Plate Heat Exchangers. Heat Transfer Engineering, January, Band 13, p. 42–52. https://doi.org/10.1080/01457639208939787

Michaelides, E. E., Crowe, C. T. & Schwarzkopf, J. D. 2016. Multiphase Flow Handbook. CRC Press. https://doi.org/10.1201/9781315371924

VDI-Wärmeatlas. 2013. Verein Deutscher Ingenieure. 11th Edition. Ed. Berlin Heidelberg: Springer. https://doi.org/10.1007/978-3-642-19981-3

VDI 4708-2:2022-04. Druckhaltung, Entlüftung, Entgasung - Entlüftung und Entgasung. Berlin, Wien, Zürich: Beuth Verlag GmbH. https://katalog.slub-dresden.de/id/211-DE88829723

Appendix: Units and Symbols

Tab. 3: Symbols, Abbreviations, Indexes

Quantity	Symbol	Unit
Heat transition coefficient	k	$kW/K/m^2$
Related heat transfer coefficient	k/k_{RC}	%
Number of transfer units	NTU	-
Pressure drop	Δp	mbar
Related friction pressure drop	$\Delta p_f/\Delta p_{f,RC}$	%
Heat flow rate	$\dot{Q}$	kW
Temperature	T	°C
Log mean temperature difference	ΔT_m	K
Volume flow	$\dot{V}$	m³/h
Gas volume fraction or void fraction	ε	% (v/v)
volume fraction of accumulated gas in heat exchanger	ε_{Hex}	% (v/v)
Operational characteristics of heat exchanger	Φ	-
Pressure loss coefficient	ζ	-

Quantity	Symbol
Reference circuit	1
Test circuit	2
Friction	f
Gas	G
Heat exchanger	Hex
Mean relative error	MRE
Reference case	RC
Test Case	TC
Total	tot
Volume fraction	(v/v)
Water	W

Collector Efficiency Curves considering an Adapted Calculation Approach for Convective Heat Transfer in Insulating Gas Layers of Solar Collectors

Pascal Leibbrandt[1], Federico Giovannetti[2], Thomas Schabbach[1], Ulrike Jordan[3]

[1] Hochschule Nordhausen, Institute for Renewable Energy Technology (in.RET), Weinberghof 4, Nordhausen (Germany)

[2] Institute for Solar Energy Research Hamelin (ISFH), Am Ohrberg 1, Emmerthal (Germany)

[3] Kassel University, Institute of Thermal Engineering, Kassel (Germany)

Abstract

Recent investigations of the heat transfer in a gas layer between parallel plates heated from below indicate that there is a convective flow also below the critical Rayleigh number of 1708 in the so-called conductive flow regime. Based on experimental investigations, a correction term is proposed in this study that better characterizes the heat transfer below the critical Rayleigh number. The aspect ratio of the insulating gas layer is identified as the dependent variable of the correction function, which has a significant influence on the flow regimes and thus the heat transport phenomena that occur. This paper presents collector efficiency curves of a glass collector. Taking into account the convective flow at the critical Rayleigh number, the Nusselt number is increased by about 23 % for an aspect ratio of 48. This leads to an increase of the collector efficiency by nearly 3 % for a temperature difference of 40 K between the collector fluid and ambient temperature, and more than 6 % for a temperature difference of 60 K.

Keywords: heat transfer, convective heat transfer, conductive / postconductive regime, insulating glass, insulating gas layers, solar collector, calculation approach

1. Introduction

Aim of the presented investigation is to determine the heat transfer in inclined insulation gas layers, heated from below. The heat transfer in inclined gas layers is particularly important for standard flat-plate solar collectors as well as for novel insulating glass solar collectors.

The transition point between conductive and convective heat transfer in inclined gas layers, characterized by the critical Rayleigh number Ra_{crit}, was already studied analytically and experimentally from the 1960s and following years. All known investigations assume pure conduction below the critical Rayleigh number, whereas already Hollands et al. (1976) describe a flow with deflections at the lower and upper end of the gas layer.

However, measurements on solar flat-plate and insulating glass collectors show that heat losses are significantly higher than expected on the basis of pure heat conduction. For example, Bartelsen et al. (1993) and Föste (2013) showed deviations of up to 32 % between experimental and numerical data.

Also, previous investigations with computational fluid dynamics (CFD) simulations show that the assumption of pure heat conduction up to Ra_{crit} is only valid for very large aspect ratios. The aspect ratio $AR_{20} = L_{20}/s_{20}$, as shown in Fig. 1, describes the ratio of the length L_{20} of the gas layer and its thickness s_{20}.

This paper presents experimental investigations of insulating glazing with different geometries and aspect ratios in the subcritical Rayleigh number regime. Further details can be found in Leibbrandt et al. (2022).

© 2022. The Authors. Published by International Solar Energy Society
Selection and/or peer review under responsibility of Scientific Committee
doi:10.18086/eurosun.2022.12.08 Available at http://proceedings.ises.org

2. Heat Transfer in Enclosed Insulating Gas Layers Heated from Below

Fig. 1 shows a scheme of the investigated setup, consisting of two parallel, plane glass panes (10) and (30) with a space in between filled with argon (20). The lower glass pane (30) is heated from below to induce a uniform temperature field $T_{31}(x,y)$. The aim of the investigations presented here is to determine the convective heat transfer coefficient $h_{20,c}$ in the gas layer between surfaces (13) and (31) at temperatures $T_{13} < T_{31}$, see Fig. 1.

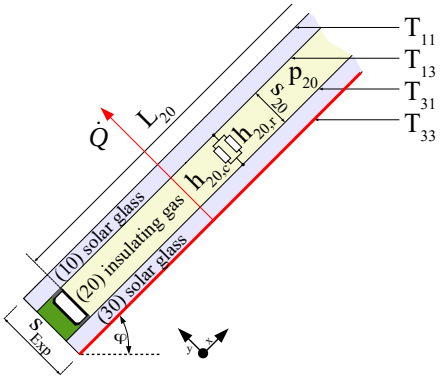

Fig. 1: Geometry and boundary conditions of the setup

The heat transfer $\dot{Q}$ between the two glass panes is determined by internal free convection and radiation. The heat transfer rate is

$$\dot{Q} = A_{20} \cdot h_{20} \cdot (T_{31} - T_{13}) \tag{1}$$

with the area $A_{20} = L_{20} \cdot B_{20}$ and the gas layer width B_{20}. The total heat transfer coefficient h_{20} is the sum of the convective heat transfer coefficient $h_{20,c}$ and the radiative heat transfer coefficient $h_{20,r}$:

$$h_{20} = h_{20,c} + h_{20,r}. \tag{2}$$

The convective heat transfer coefficient $h_{20,c}$ is calculated from the Nusselt number Nu, which is specified for free convection as a function of the Rayleigh number Ra,

$$Nu = Nu(Ra). \tag{3}$$

The Rayleigh number is the product of the Grashof number Gr, which relates the buoyancy forces to the internal viscous friction forces, and material properties, expressed by the Prandtl number Pr.

Hollands et al. (1976) developed the following Equation 4 from experimental investigations. The Equation 4 is a function of the Rayleigh number and it is divided into three parts. The operator $[...]^+ = (|[...]| + [...])/2$ elicits that only positive values of the argument are used, i.e. it eliminates the term if the argument is negative. $Ra^* = Ra \cdot \cos(\varphi)$ is also called modified Rayleigh number, where φ as the inclination angle, see Fig. 1.

$$Nu = 1 + 1.44 \cdot A \cdot [B]^+ + [C]^+ \tag{4}$$

with:

$$A = 1 - \frac{1708 \cdot (\sin(1.8 \cdot \varphi))^{\frac{1}{6}}}{Ra \cdot \cos(\varphi)} \qquad B = 1 - \frac{1708}{Ra \cdot \cos(\varphi)} \qquad C = \left(\frac{Ra \cdot \cos(\varphi)}{5830}\right)^{\frac{1}{3}} - 1$$

The heat transfer is characterized by three flow regimes:

- At lower Rayleigh numbers ($Ra^* < 1708$) the conductive behavior dominates, since the flow velocities are very small. This flow regime is called **conductive regime.**
- With increasing Rayleigh numbers ($1708 < Ra^* < 5830$) the flow velocity increases and a monocellular basic flow develops. In this range of Rayleigh numbers, the regime is called **immediate postconductive regime.**

- With an even higher Rayleigh number (Ra* > 5830) the monocellular flow decays into a multicellular flow with several convection rolls. This flow type is called **high Rayleigh number regime.**

The lowest heat transfer through the gas layer and thus the highest solar collector efficiency is reached for the distance $s_{20,opt}$, that corresponds to a modified Rayleigh number of Ra* = 1708. For Ra* = 1708 the convective heat transfer is at its minimum.

Preliminary 2D and 3D CFD simulations presented in Leibbrandt et al. (2018) found that the aspect ratio AR is an additional influencing parameter for the convective heat transfer coefficient in the gas layer for the same reference conditions as used in the experimental setup by Hollands et al. (1976).

3. Experimental Investigations on Insulating Glazing

The heat transfer through three different insulating glazings is measured in a guarded hot box according to EN 12664 (2001) specifically conceived for measurements at temperatures up to 90 °C and variable tilted angles, see Fig. 2(a). The insulating glazings, Fig. 2(b), have the basic dimensions of 500 mm x 500 mm. The length of the gas layer is L_{Exp} = 480 mm. The layer thicknesses s_{20} varied between 10, 8 and 6 mm. It can be adjusted by using different spacers. The resulting aspect ratios are AR_{Exp} = 48, 60 and 80, respectively.

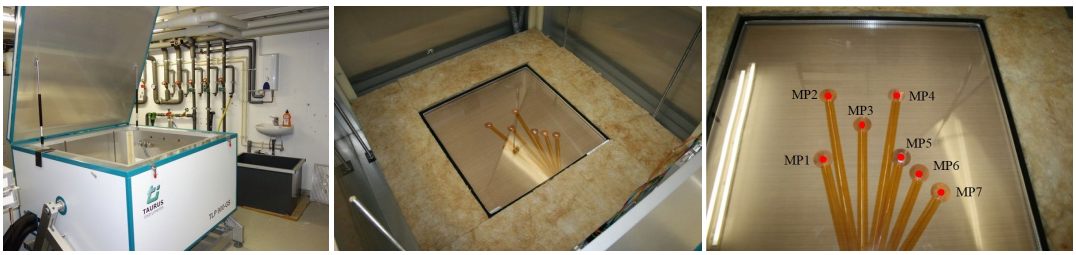

Fig. 2: 2(a) Pictoral view of the test facility, 2(b) View of the insulating glazing in the test facility, 2(c) Detailed view of the temperature sensors position on the insulating glazing

The temperature difference $\Delta T_{Exp} = T_{33} - T_{11}$ between the surfaces of the insulating glazing is measured with temperature sensors on the outer surfaces of the insulating glazing at the measuring points MP1 - MP7 on both sides of the insulating glazing, see Fig 2(c). The thermal resistance and the resulting equivalent thermal conductivity k_{Exp} (with the approach $\dot{q}_{Exp} = k_{Exp}/s_{Exp} \cdot \Delta T_{Exp}$) are determined from the measured values.

As boundary conditions for the experiment, the insulating glazing mean temperatures T_{Exp} = 20, 40, 60 and 80 °C at $\Delta T_{Exp} \approx 20$ K are set ($T_{Exp} = (T_{11} + T_{33})/2$). For each specimen of insulating glazing, the measurement is carried out for tilt angles of 0, 20, 40 and 60°.

With the measured heat flow rate $\dot{q}_{Exp}$ and the measured temperature difference ΔT_{Exp} between the surfaces of the insulating glass, the total thermal resistance of the probe R_{Exp} can be determined. The total resistance R_{Exp} is the sum of the serial resistances of the glass panes $R_{Exp,10}$ and $R_{Exp,30}$ (with k_{Gl} and s_{Gl}) and the resistance of the insulating gas $R_{Exp,20}$:

$$R_{Exp} = R_{Exp,10} + R_{Exp,20} + R_{Exp,30} \tag{5}$$

The resistance of the gas layer $R_{Exp,20}$ results from the parallel resistances for free convection $R_{Exp,20,c}$ and radiation $R_{Exp,20,r}$:

$$\frac{1}{R_{Exp,20}} = \frac{1}{R_{Exp,20,c}} + \frac{1}{R_{Exp,20,r}} \tag{6}$$

With the definition $R_i = 1/(h_i \cdot A)$ and A = const., Equation 5 in combination with Equation 6 gives the determining Equation for the convective heat transfer coefficient.

$$h_{Exp,20} = h_{Exp,20,c} + h_{Exp,20,r} \tag{7}$$

The radiative heat transfer coefficient $h_{Exp,20,r}$ in Equation 7 is calculated with an emission coefficient of ϵ_{Gl} = 83.7 % for the uncoated float glass panes. The Nusselt numbers Nu_{20} for the experimental data are determined according to the definition in Equation 8

$$Nu_{20} = h_{Exp,20,c} \cdot \frac{s_{20}}{k_{20}} \tag{8}$$

with the experimentally determined convective heat transfer coefficient $h_{Exp,20,c}$, the gas layer thickness s_{20} and the temperature-dependent gas conductivity k_{20}.

Fig 3 shows the Nu_{20} numbers determined from the measurements as a function of the modified Ra* number. For horizontal plates and Ra* just above Ra^*_{crit}, the convective heat transfer coefficient exceeds the purely conductive one by more than 30 % (Nu_{20} = 1.33); for Ra* around 2400, Nu_{20} is already very close to the value given by Equation 4, with Nu_{20}/Nu_{Holl} = 1.02.

A measurement error analysis of all influencing variables with errors occurring during the measurement and a measurement error propagation results in a maximum uncertainty with respect to the experimentally determined Nusselt number Nu_{20} of ±12.9 %. Details of the measurement error analysis and supplementary figures with error bars can also be found in Leibbrandt et al. (2022).

4. Recommended Relationship for the Nusselt Number below Ra_{crit}

The investigations show, that also below the critical Rayleigh number Ra^*_{crit} there is a convective heat transfer in the gas layer. To describe the Nusselt number Nu_{20} for Ra* < 1708, a correlation is proposed as a quadratic function of the aspect ratio for 48 ≤ AR ≤ 80. It is derived from mean values of the Nu_{20} values for each aspect ratio. The resulting correlation is given in Equation 9:

$$D = \frac{Nu_{20}}{Nu_{Holl}} = D_2 \cdot AR^2 + D_1 \cdot AR + D_0 \tag{9}$$

with:

$D_2 = 1.292 \cdot 10^{-4}$, $D_1 = -2.283 \cdot 10^{-2}$ and $D_0 = 2.035$

The correlation corrects the previous assumption of pure conduction for Ra* < 1708 in Equation 4, validated for 48 ≤ AR ≤ 80. Combining Equation 4 and 9 results in Equation 10:

$$Nu = max\begin{Bmatrix} D \\ 1 + 1.44 \cdot A \cdot [B]^+ + [C]^+ \end{Bmatrix} \tag{10}$$

The proposed correction to the Nusselt number describes convective heat transfer for small aspect ratios below the critical Rayleigh number. For an aspect ratio of 48, the relation yields a Nusselt number of about 1.23. Fig 3 indicates the impact of Equation 10 on the Nusselt number compared to the Hollands et al. (1976) approach for 48 ≤ AR ≤ 80.

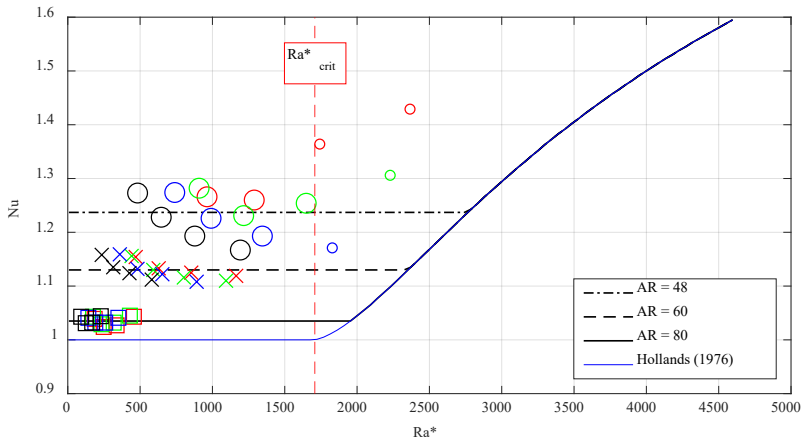

Fig. 3: Experimentally determined data (symbols) and their mean values (black lines) in comparison to the approach according to Hollands et al. (1976) (blue line). AR = 48 (O), AR = 60 (X) and AR = 80 (□), red for φ = 0°, green for φ = 20°, blue for φ = 40°, and black for φ = 60° with Ra*=Ra·cos(φ).
Measurement data above Ra* = 1708 are not accounted for the correction (small symbols).

5. Effect on collector efficiency

A collector model is used to investigate the influence of the heat transfer coefficient $h_{20,c}$ modified with the correction function on the collector efficiency of an insulating glass collector according to Leibbrandt et al. (2018).

The thermal collector model is developed as part of a research project and is described in Schabbach et al. (2018). In a thermal network with 34 temperature nodes, each node represents one isothermal subsurface of a component or an isothermal volume. A temperature difference between two nodes leads to a heat flow whose magnitude depends on the temperature difference as well as the thermal resistance between the nodes. All types of heat transfer, occurring in the solar collector, are considered in the thermal network (conduction, natural and forced convection and thermal radiation). The multidimensional thermal network is verified only in terms of the individual heat transfer resistances and the associated heat flows. It could not be validated by measurements due to problems in manufacturing the insulating glass collector. However, the method used for thermal modeling based on temperature nodes is validated on the example of standard flat-plate collectors with collector measurements. The thermal model is used here only for estimating influencing parameters on collector heat losses and collector performance.

Fig. 4 shows the influence of the heat transfer coefficient $h_{20,c}$ on the collector efficiency η. As shown in Fig. 3, the experimentally determined Nusselt number below the critical Rayleigh number is at maximum 1.3, which also increases the value of the heat transfer coefficient in the range of about 30 %, so it is $h'_{20,c} = 1.3 \cdot h_{20,c}$. The effects on the collector characteristics for an increase of the heat transfer coefficient $h_{20,c}$ by 10 % - 30 % are shown in Fig. 4.

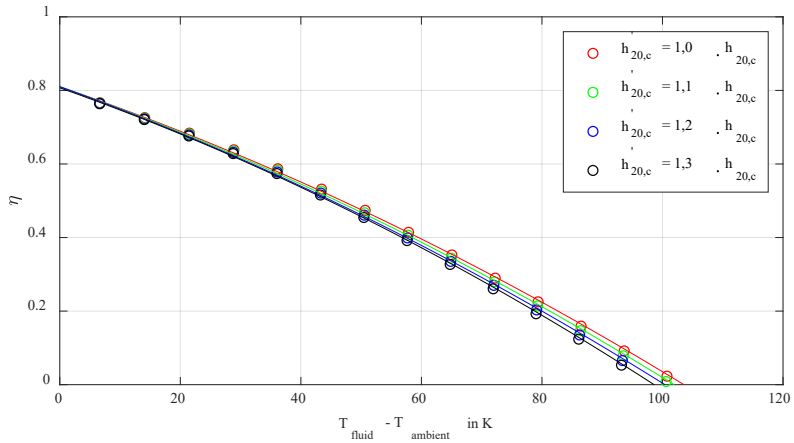

Fig. 4: Collector characteristics based on the thermal collector model with adapted heat transfer coefficients

For an increase of the heat transfer coefficient $h_{20,c}$ by 30 % and a temperature difference between the collector fluid and the ambient air of 40 K the collector efficiency η decreases by 2.7 % if the convective heat transfer in the so-called conductive flow regime is taken into account by the correction term as described in Equation 10.

If the temperature difference $T_{fluid} - T_{ambient}$ increases to 60 K, the deviation of the collector efficiency from the standard model due to the convection heat transfer, increases to about 6.4 %. Thus, the heat transfer correction is significant especially for high temperature differences.

This results in a reduction of the stagnation temperature ($\eta \rightarrow 0$) by about 5 to 6 K.

6. Conclusion

Experiments of an enclosed gas layer between two glass panes show that the heat transfer below the critical Rayleigh number Ra_{crit} is higher than the conductive heat transfer assumed so far. The investigations show that there is a convective share of the heat transfer in the gas layer also below the critical Rayleigh number.

For small aspect ratios (here 48), there is an increase of the heat transfer compared to pure conductive regime by 23 % for the examined conditions.

To describe this convective heat transfer, a novel relationship is proposed for the Nusselt number as a function of the aspect ratio, but not a dependence of the inclination angle in the subcritical regime. In particular, the transition near and above the critical Rayleigh number should be examined in detail with further experimental investigations to improve the presented results.

For a temperature difference between fluid an ambient of 60 K, the deviation of the collector efficiency from the standard model due to the convection heat transfer, increases to about 6.4 %, calculated with a thermal collector model.

References

Bartelsen, B., Jansen, S., Rockendorf, G., 1993. Heat Transfer by Natural Convection in the Air Gap of Flat Plate Collectors. Proceedings ISES Solar World Congress, pp. 267-273, Budapest, Ungarn

Föste, S., 2013. Flachkollektor mit selektiv beschichteter Zweischeibenverglasung. Dissertation, Gottfried Wilhelm Leibniz Universität Hannover

Hollands, K.G.T., Unny, T.E., Raithby, G.D., Konicek, L., 1976. Free Convective Heat Transfer Across Inclined Air Layers. J. Heat Transfer 98(2), 189-193

Leibbrandt, P., Schabbach, T., Dölz, M., Rhein, M., 2018. Untersuchungsergebnisse zur Strömung und Wärmeübertragung im Nurglaskollektor. 28. OTTI Symposium Thermische Solarenergie, Bad Staffelstein

Leibbrandt, P., Giovannetti, F., Schabbach, T., Jordan, U., 2022. Improved calculation approach of the heat transfer in inclined insulating gas layers. Solar Energy. Volume 231, January 2022, Pages 252-261

Schabbach, T., Leibbrandt, P., 2018. Abschlussbericht zum Vorhaben NUGLACOL – Nurglas-Solarflachkollektor. Entwicklung eines kostengünstigeren solaren Flachkollektorsystems auf Glas-Basis. Kurzbezeichnung: NuGlaCol. Förderkennzeichen: 0325557A. Laufzeit: 01.03.2015 - 31.05.2018. Nordhausen

Thermal performance of building materials and products - Determination of thermal resistance by means of guarded hot plate and heat flow meter methods - Dry and moist products with medium and low thermal resistance; German version EN 12664:2001

Experimental Investigation on A Novel Flat-Plate Water-Based Photovoltaic-Thermal Module

Wenjie Liu [a], Jian Yao [a], Teng Jia [a], Yao Zhao [a], Yanjun Dai [*, a]

[a] Institute of Refrigeration and Cryogenics, Shanghai Jiao Tong University, Shanghai 200240, China

Abstract

The performance of a novel flat-plate water-based PVT (photovoltaic-thermal) module was experimentally investigated under different environmental conditions in Shanghai. A novel PVT module was. An experimental bed was implemented to investigated the performance of the module on heat collection, benefit for electricity generation, and pressure drop. Additionally, the temperature unevenness of the module was discussed. The results revealed that the PVT module can contribute a 12% benefit for electricity generation compared with PV module. Additionally, the intercept efficiency factor of the module could reach over 0.8, and the heat efficiency can reach over 45%. Meanwhile, the relation between temperature unevenness and dimensionless temperature was fit.

Keywords: PVT, water-based, experimental investigation, temperature unevenness.

1. Introduction

Buildings, which offer indispensable facilities for human beings, consume about 40% of the global energy (Lin et al., 2021) and emit more than 30% of the global carbon dioxide (Costa et al., 2013). Meanwhile, the energy consumption and the carbon emission of the building section is expected to keep growing in the future (Ibn-Mohammed et al., 2013). Renewable and sustainable energy, especially solar energy, is increasingly widely applied to buildings as a more energy-saving and low-carbon approaches to face with the energy crisis and the global warming.

Solar energy technology can be roughly categorized into photovoltaic (PV) technology and solar thermal technology (Vassiliades et al., 2022). Thereinto, PV technology is widely accepted and applied in recent years due to the rapid progress in electrical efficiency (Gao et al., 2019; Zhao et al., 2008) and the reduction in the power generation costs (IRENA, 2018).

The PV modules transfer solar irradiation received into heat in addition to electricity during operation, leading to the rising modules temperature and worsening electricity efficiency due to temperature effect (Dubey et al., 2013). As some research reported, every 1 ^{o}C temperature increase will lead to 0.45-0.50% drop in relative efficiency (Siecker et al., 2017). Meanwhile, a high working temperature can also shorten the life span of PV modules. The PVT technology, which was first conceptualized by Wolf et al. (Wolf, 1976) in 1976, can serve to extract and reuse the waste heat and to lower the working temperature of PV modules by implementing a thermal absorber in the back side of the modules.

After decades of research, the PVT technology has witnessed profound progresses, including innovation on designs and working fluids. The PVT modules can be mainly categorized into the following types with respect to different working fluid: air-based (Solanki et al., 2009), water-based (Shyam et al., 2015) and refrigerant-based (Jouhana et al., 2016). Among these, the water-based PVT presents a satisfactory heat efficiency, better adaptability to large-scale system, and lower system complexity, resulting in its wide application. Aste et al. (Aste et al., 2015) reported a simulation, showing that the glazed water-cooling PVT could offer a thermal efficiency of 42% with an electrical efficiency of 13.2%.

As a heat collector, the performance of the water-based PVT module can be evaluated from the aspect of heat efficiency, which is depended on the climate conditions (ambient temperature, irradiation intensity), the operation parameters (flow rate, inlet temperature), and the design parameters. UI Abdin et al. (UI Abdin et al., 2021) conducted a simulation on a parallel-shape sheet-and-tube water-based PVT module, reporting a

© 2022. The Authors. Published by International Solar Energy Society
Selection and/or peer review under responsibility of Scientific Committee
doi:10.18086/eurosun.2022.12.09 Available at http://proceedings.ises.org

thermal efficiency varying from 32%~70% under different flow rates. Saeed et al. (Saeed et al., 2021) developed a water based PVT module, achieving a thermal efficiency varying from 38.8–43.1%.

However, the temperature unevenness of water-based PVT modules is also an important factor. Yu et al. (Yu et al., 2019) reported a temperature difference above 20 ºC for a roll-bond water-based PVT collector. Uneven temperature distribution in the solar cells (which is unavoidable because water is sensible-heat working fluid), like hot spot, will undermine the electrical performance and shorten the life span. Thus, the research on water-based PVT should consider the temperature unevenness (or uniformity) as an essential factor. The object of this paper is to experimentally investigated the temperature uniformity besides other important electrical and thermal parameters of a novel water-based PVT module.

2. System description and experimental setup

Fig. 1 briefly illustrated the structure of the water-based PVT module investigated. The working fluid inside the tube absorbs waste heat generated in the PV cells through the tube-plate heat transfer structure behind the white plate. The insulation in the backside is made of foamed polyurethane, preventing the fluid from the heat dissipation.

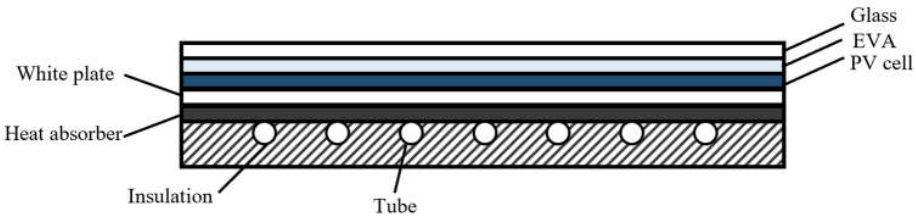

Fig. 1: The schematic diagram of the structure of the water-based PVT module.

Fig. 2(a) presented the schematic diagram of the experimental rig testing the PVT module. Two different measuring points are set at the inlet and outlet of the PVT module to measure the temperature rise and pressure drops of the module. Thermostatic tank is used to keep the inlet temperature constant. The electricity sector, including MPPT (maximum power point tracer), accumulator, and load, is used to measure and to consume the electricity power. Additionally, five temperature sensors were distributed in different position between the thermal absorber and the insulation to measure the temperature difference of the PVT module (shown in Fig. 3). The front view of the experiment rig was shown in Fig. 4.

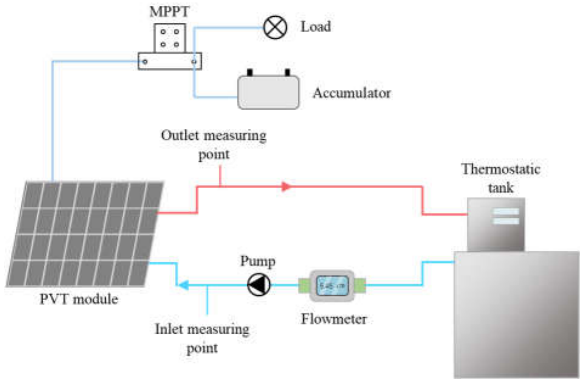

(a) The schematic diagram

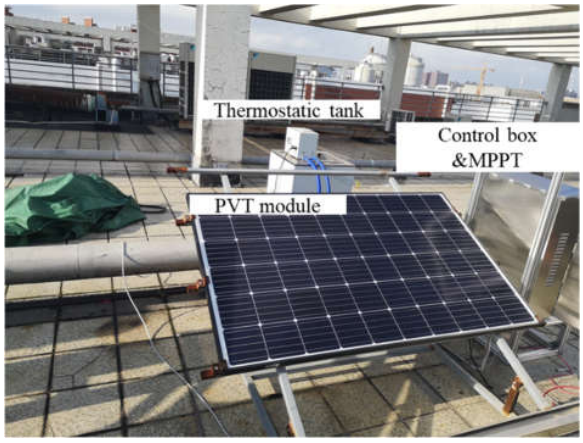

(b) The front view

Fig. 2: The experiment rig.



Fig. 3: The locations of five temperature sensors.

The field tests of the water-based PVT experiment system were conducted in a series of days from Oct. to Jan. in Shanghai. Besides the PVT module's thermal performance, its electrical performance was also experimentally investigated in comparison with a single PV module to estimate its benefit on electricity generation.

3. Results and discussion

3.1 Mathematical model

Apart from the electricity output, the PV cells convert part of the solar irradiation into heat:

$$Q_{abs} = (\tau\alpha) I_R (1 - \eta_e) \quad \text{(eq. 1)}$$

The heat dissipation from the PVT module to the ambient can be expressed by the following equation:

$$Q_L = U_L (T_p - T_a) \quad \text{(eq. 2)}$$

where T_p, T_a refer to the temperature of the PV cells and the ambient air; U_L, the heat loss coefficient, can be expressed by:

$$U_L = \frac{1}{\frac{1}{h_{cv}+h_{rd}} + \frac{L_g}{k_g}} + \frac{1}{R_{pb} + \frac{L_b}{k_b}} \quad \text{(eq. 3)}$$

where h_{cv}, h_{rd} refer to the heat transfer coefficient of the convection and radiation processes; R_{pb} is the thermal resistance between the PV cells and the heat absorber; L, k refer to the thickness and the thermal conductivity; the subscript *g, b* represent the glass cover and the back insulation, respectively.

The heat absorbed by the working fluid (water) is:

$$Q = Q_{abs} - Q_L \quad \text{(eq. 4)}$$

The thermal efficiency is defined as:

$$\eta = \frac{Q}{I_R A} \quad \text{(eq.5)}$$

Besides the thermal efficiency, two other parameters, efficiency factor and the heat removal factors were defined and calculated to evaluate the thermal performance:

Efficiency factor F' and heat removal factor F_R are defined as:

$$F' = \frac{A[(\tau\alpha)I_R(1-\eta_e)-U_L(T_f-T_a)]}{Q} \quad \text{(eq. 6)}$$

$$F_R = \frac{A[(\tau\alpha)I_R(1-\eta_e)-U_L(T_{in}-T_a)]}{Q} \quad \text{(eq. 7)}$$

where T_f is the average temperature of the working fluid, T_{in} is the inlet temperature; τ,α are the transmittance of the glass and the absorptivity of the PV cells, respectively.

An excess temperature was proposed to comprehensively consider the module temperature and the irradiation:

$$\theta = \frac{T_f-T_a}{\tau\alpha(1-\eta_e)I} \quad \text{(eq. 8)}$$

Another excess temperature, θ_f, was proposed as the ratio of the temperature rise of the fluid to the irradiation:

$$\theta_f = \frac{T_o-T_i}{\tau\alpha(1-\eta_e)I} \quad \text{(eq. 9)}$$

The temperature unevenness is defined as:

$$\Delta = T_5 - T_1 \quad \text{(eq. 10)}$$

where T_1, T_5 refer to the lowest and the highest temperature recorded by the five temperature sensors.

3.2 Comprehensive performance

The field tests were conducted under two different levels of the mass flow rate of the water (1.3 kg/min and 0.25 kg/min) in different days.

Fig. 4 presents three different experiments in Nov. 26th, Jan. 1st, and Dec. 31st, respectively.

(1) The experiment in Nov. 26th (Flow rate:1.3 L/min)

As shown in Fig. 4(a), the experiment lasted from 10:03 to 14:30, within which the average ambient temperature was 18 ℃, and the average irradiation is 477 W/m^2. During the experiment, the average temperature rise of the circulating water is 3.16 ℃, and the average electrical/thermal/overall efficiency were 14.27%/35.24%/49.51%, respectively. Besides, the average module temperature is 34.9 ℃. The maximum value of the temperature unevenness during the experiment was 19.9 ℃, while the average value of that was 16.0 ℃.

(2) The experiment in Jan. 1st (Flow rate: 0.25 L/min)

As shown in Fig. 4(b), the experiment lasted from 10:10 to 14:30, within which the average ambient temperature/solar irradiation was 10 ℃/414 W/m^2. Compared with the experiment in Nov. 26th, the average temperature rise of the circulating water improved due to the smaller flow rate (from 3.16 ℃ to 5.77 ℃). However, the convective heat transfer within the tube was undermined by the decreasing flow velocity, which leads to lower thermal efficiency. The average electrical/thermal/overall efficiency of the PVT module were 16.75%/14.29%/31.04%, respectively. Compared with the thermal efficiency of the PVT module with a flow rate of 1.3 L/min, that of the PVT module with a flow rate of 0.25 L/min decreased by 59.45%. Additionally, the maximum value of the temperature unevenness was 20.0 ℃, while the average value of that was 13.2 ℃, showed little difference from that of the PVT module with a flow rate of 1.3 L/min.

(3) The experiment in Dec. 31st (Pure PV module)

As shown in Fig. 4(c), the experiment lasted from 10:00 to 14:30, within which the average temperature is the same as that on Jan. 1st. During the experiment, the average electrical efficiency of the PV module is 14.90%, 12.4% lower than the electrical efficiency of the PVT module on Jan. 1st, proving the electricity generation benefit of the PVT module.

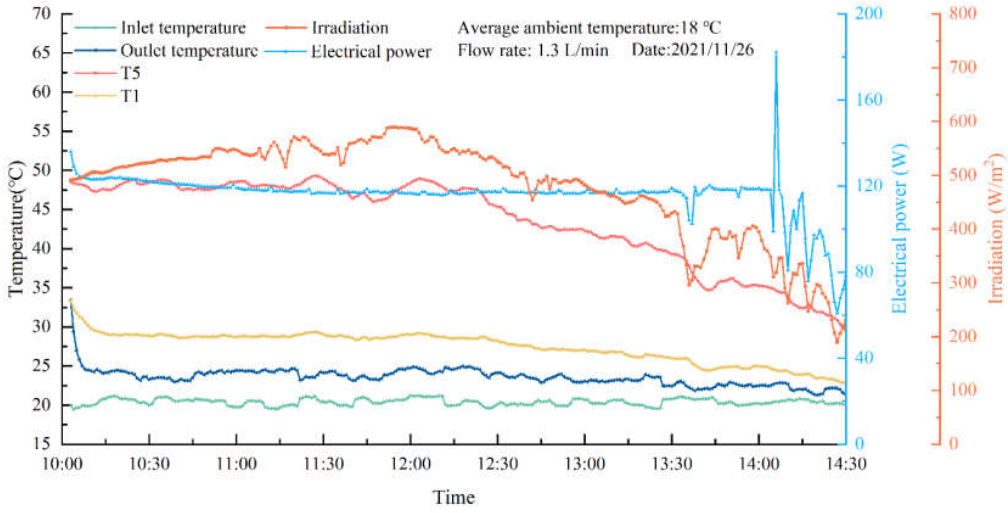

(a) Experiment in Nov. 26th

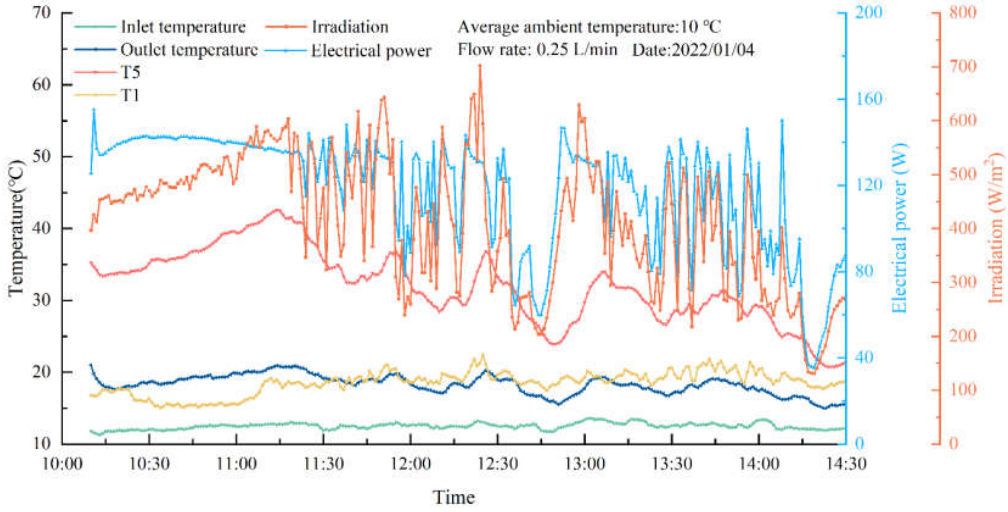

(b) Experiment in 2022/01/04

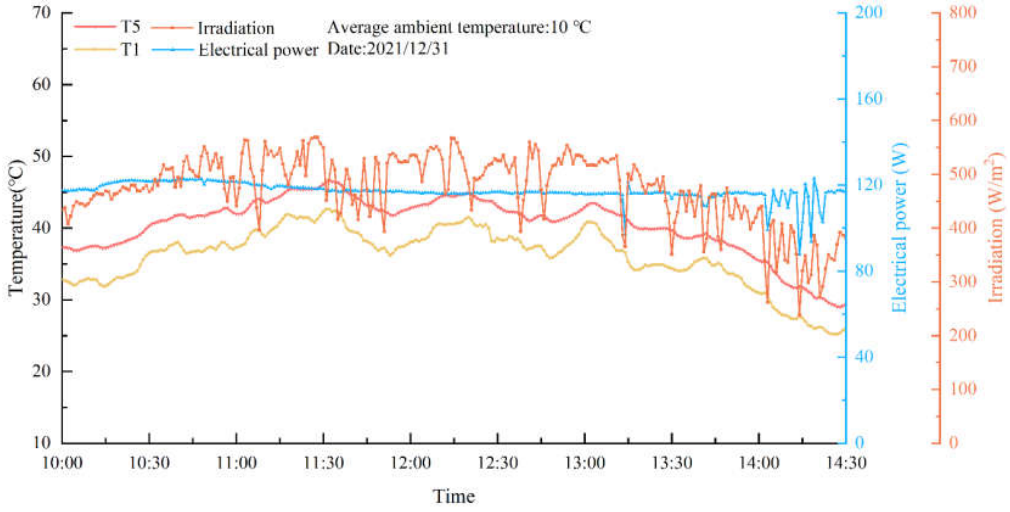

(c) Experiment in 2021/12/31

Fig. 4: The experiment results.

3.3 Thermal performance

Besides the comprehensive performance, the thermal performance of the PVT module was specifically analyzed with reference to the flat-plate collector. Some important coefficients, such as efficiency factor, heat removal factor, and thermal efficiency were investigated to reveal their relation to heat loss coefficient or excess temperature based on a series of experiment results. Meanwhile, the relation of the temperature unevenness to the excess temperature was also investigated.

Fig. 5(a) presents the relation between F' of the PVT module and U_L under different flow rate. The efficient factor decreases with the increasing heat loss coefficient to similar extend under different flow rate. The PVT module with a flow rate of 1.3 L/min has higher intercept efficiency factor (0.974) than that with a flow rate of 0.25 L/min (0.833), indicating higher flow rates leads to higher heat collection potential of the PVT modules. Fig. 5(b) presents the fitting results of F_R-U_L curves under different flow rate. These two curves present similar trend to the F'-U_L curves. The intercept heat removal factors of the PVT module were estimated to be 0.939 and 0.680 when the flow rate is 1.3 L/min and 0.25 L/min, respectively.

Fig. 5(c) illustrates the relation between thermal efficiency and the excess temperature. The experimental results showed that, the thermal efficiency varied from 20% to 45% under different climate and operating conditions with the flow rate of 1.3 kg/min, while varied from 9% to 18% with the flow rate of 0.25 kg/s. The intercept thermal efficiency were expected to be 52.57% and 21.42% for PVT modules with flow rates of 1.3 L/min and 0.25 L/min, respectively.

Fig. 5(d) shows the relation between the temperature unevenness and the excess temperature. With the increasing excess temperature, the temperature unevenness increases. In a series of experiments, the temperature unevenness varied from 12 to 21 ºC. The PVT modules with higher flow rate is estimated to have higher temperature unevenness.

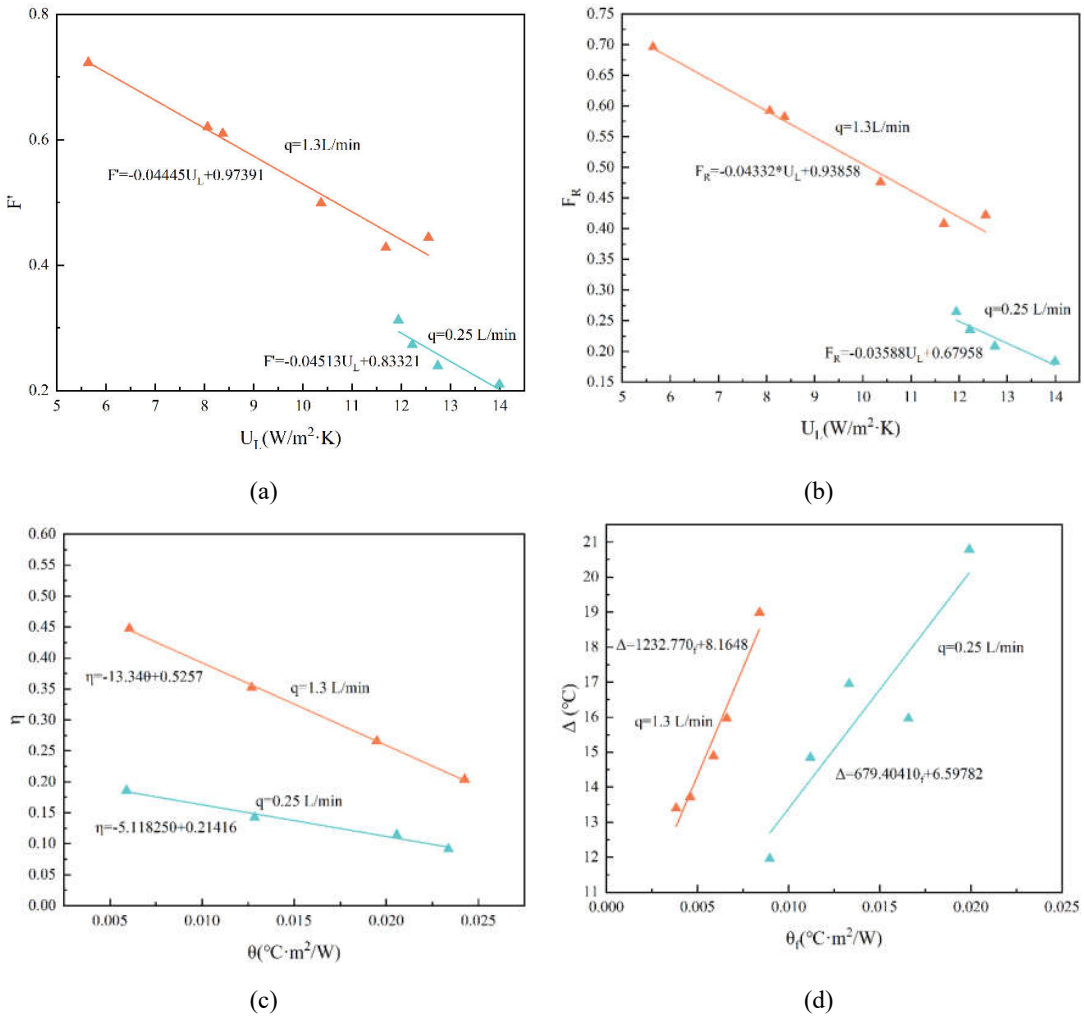

Fig. 4: The thermal performance of the PVT modules.

4. Conclusions

In this paper, a novel water-based PVT module was manufactured and experimentally investigated. The thermal and electrical of the module was evaluated. The results suggested that the PVT module has satisfactory thermal efficiency and benefit on electricity generation. The relation between efficiency/heat removal factors and heat loss coefficient was fitted to comprehensively present its thermal performance. Meanwhile, the relation between temperature unevenness and excess temperature was also discussed.

5. Reference

Costa A, Keane MM, Torrens JI, Corry E. Building operation and energy performance: Monitoring, analysis and optimisation toolkit. Applied Energy. 2013;101:310-6. DOI: 10.1016/j.apenergy.2011.10.037

Dubey S, Sarvaiya JN, Seshadri B. Temperature Dependent Photovoltaic (PV) Efficiency and Its Effect on PV Production in the World – A Review. Energy Procedia. 2013;33:311-21. DOI: 10.1016/j.egypro.2013.05.072.

Gao T, Yang Q, Guo X, Huang Y, Zhang Z, Wang Z, Liao M, Shou C, Zeng Y, Yan B, Hou G, Zhang X, Zhao Y, Ye J. An industrially viable TOPCon structure with both ultra-thin SiOx and n+-poly-Si processed by PECVD for p-type c-Si solar cells. Solar Energy Materials and Solar Cells. 2019;200. DOI: 10.1016/j.solmat.2019.109926.

Ibn-Mohammed T, Greenough R, Taylor S, Ozawa-Meida L, Acquaye A. Operational vs. embodied emissions in buildings—A review of current trends. Energy and Buildings. 2013;66:232-45. DOI: 10.1016/j.enbuild.2013.07.026

IRENA. Renewable Power Generation Cost in 2017. International Renewable Energy Agent. 2018.

Lin Y-H, Lin M-D, Tsai K-T, Deng M-J, Ishii H. Multi-objective optimization design of green building envelopes and air conditioning systems for energy conservation and CO2 emission reduction. Sustainable Cities and Society. 2021;64. DOI: 10.1016/j.scs.2020.102555

Niccolò Aste, Claudio Del Pero, Fabrizio Leonforte, Massimiliano Manfren. Performance monitoring and modeling of an uncovered photovoltaic-thermal (PVT) water collector. Solar Energy. 2016;135:551-68. DOI: 10.1016/j.solener.2016.06.029

Jouhara H, Milko J, Danielewicz J, Sayegh MA, Szulgowska-Zgrzywa M, Ramos JB, Lester SP. The performance of a novel flat heat pipe based thermal and PV/T (photovoltaic and thermal systems) solar collector that can be used as an energy-active building envelope material. Energy. 2016;108:148-54. DOI: 10.1016/j.energy.2015.07.063

J.Siecker, K.Kusakana, B.P.Numbi. A review of solar photovoltaic systems cooling technologies. Renewable and Sustainable Energy Reviews. 2017;79:192-203. DOI: 10.1016/j.rser.2017.05.053

Saeed Abdul-Ganiyu, David A. Quansah, Emmanuel W. Ramde, Razak Seidu, Muyiwa S. Adaramola. Study effect of flow rate on flat-plate water-based photovoltaic-thermal (PVT) system performance by analytical technique, Journal of Cleaner Production, 2021;321:128985. DOI: 10.1016/j.jclepro.2021.128985

Shyam, Tiwari GN, Al-Helal IM. Analytical expression of temperature dependent electrical efficiency of N-PVT water collectors connected in series. Solar Energy. 2015;114:61-76. DOI: 10.1016/j.solener.2015.01.026

Solanki SC, Dubey S, Tiwari A. Indoor simulation and testing of photovoltaic thermal (PV/T) air collectors. Applied Energy. 2009;86(11):2421-8. DOI: 10.1016/j.apenergy.2009.03.013

Ul Abdin Z, Rachid A. Bond graph modeling of a water-based photovoltaic thermal (PV/T) collector. Solar Energy. 2021;220:571-7. DOI: 10.1016/j.solener.2021.03.028

Vassiliades C, Agathokleous R, Barone G, Forzano C, Giuzio GF, Palombo A, Buonomano A, Kalogirou K. Building integration of active solar energy systems: A review of geometrical and architectural characteristics. Renewable and Sustainable Energy Reviews. 2022;164. DOI: 10.1016/j.rser.2022.112482

Wolf M. Performance analyses of combined heating and photovoltaic power systems for residences. Energy Conversion, 1976;16(1):79-90. DOI: 10.1016/0013-7480(76)90018-8

Yu Y, Yang H, Peng J, Long E. Performance comparisons of two flat-plate photovoltaic thermal collectors with different channel configurations. Energy. 2019;175:300-8. DOI: 10.1016/j.energy.2019.03.054

Zhao L, Zhou CL, Li HL, Diao HW, Wang WJ. Design optimization of bifacial HIT solar cells on p-type silicon substrates by simulation. Solar Energy Materials and Solar Cells. 2008;92(6):673-81. DOI: 10.1016/j.solmat.2008.01.018

Interception on Solar Absorbers: Ray Tracing for Comparison between a Parabolic Reflector and a Compound Parabolic Concentrator

Casiana B. Lwiwa[1] and Ole J. Nydal[1]

[1] Norwegian University of Science and Technology, Trondheim (Norway)

Abstract

A Compound Parabolic Concentrator (CPC) can direct incoming rays on an upper aperture to pass through a lower smaller aperture, giving a concentration ratio typically in the order of 4-5, depending on the acceptance angles of the CPC. The case for consideration here is for an absorber to be positioned inside the CPC, where a heat transfer fluid will circulate for heat absorption and further transport to a heat storage. Continuous solar tracking is to be avoided but tilting the concentrator 2-3 times during a day can be accepted.
A 3D CPC is compared with a normal Parabolic Reflector (PR) for similar concentration ratios. The comparison is made using ray tracing, where the sun angle is scanned over the acceptance angles and the interceptions on a cylindrical absorber are compared between the two systems. For low concentration ratios, the performances of the two reflectors are comparable, with about 10% improvements in interception ratios with the CPC over the PR. The concentration ratios for a CPC are limited. For the PR, an optimum can be considered, between increasing the concentration ratio but at the cost of decreasing the interception ratios.

Keywords: Compound Parabolic Reflector, ray tracing, optical efficiency, concentrating solar thermal, solar heat absorber

1. Introduction

Solar concentrators are lenses or reflectors which concentrates incoming solar rays on a large area (the aperture) onto a smaller area (the absorber). Solar concentration is in particular useful in solar thermal systems, where solar radiation is converted to heat. A range of direct heat collector systems are available for low temperature applications (typically flat panels or evacuated tube collectors for hot water systems). For higher temperature needs, typically, above 200 degrees C, concentrating solutions are required.

Reflectors, or lenses, which converge solar rays onto an absorber, require solar tracking with accuracies depending on the concentration ratios of the system. The geometrical concentration ratio is defined as:

$$C_r = \frac{A_{in}}{A_{abs}} \qquad \text{(eq. 1)}$$

where A_{in} is the aperture area for the incoming solar rays and A_{abs} is the area of the absorber. If the concentration ratio is high, the solar tracking must be accurate, as even small misalignments with the sun direction (often less than one degree) can shift the focal area away from the small absorber area. The range of sun angles where the incoming solar rays still terminate on the absorber can be called the acceptance angle. High concentration ratios then lead to small acceptance angles.

When designing a concentrating system for solar thermal energy collection, the temperature requirements at the absorber needs to be balanced by the precision requirements of the solar tracking system. Although solar tracking solutions are available, there are cases where the demand for robustness excludes solar tracking systems. The question then is what level of performance can be achieved with a concentration system based on minimal requirements for solar tracking (e.g., 2-3 adjustments of a concentrator during a day). A CPC can potentially meet these requirements.

© 2022. The Authors. Published by International Solar Energy Society
Selection and/or peer review under responsibility of Scientific Committee
doi:10.18086/eurosun.2022.12.10 Available at http://proceedings.ises.org

The aim is to achieve both high energy efficiency and high temperatures at a thermal absorber positioned at the focal area of a solar reflector. The temperature rise on the absorber due to the solar radiation is:

$$\rho A_{abs} \delta c \frac{dT}{dt} = P_{abs} - Q_{loss} \qquad \text{(eq. 2)}$$

An absorber shell with area $A_{abs}\,(m^2)$, thickness $\delta\,(m)$, heat capacity $c\,(J/Kkg)$ and density $\rho\,(kg/m^3)$ obtains a rate of change of temperature (dT/dt) due to the solar power onto the absorber $P_{abs}(W)$, minus the thermal losses to the ambient and/or to a heat transfer medium at the absorber $Q_{loss}(W)$. With no optical losses, the power on the absorber is equal to the incoming solar power on the aperture of the concentrator. Optical losses are due to imperfect reflectivity on the concentrator surface, to rays not hitting the absorber as a result of surface irregularities and to the geometrical design of the concentrator system. The cases for analysis here are the geometrically based losses, the design aspects which leads to interception ratios less than one. The interception ratio, η is defined as the ratio of the sun rays hitting the absorber to the incoming rays on the reflector opening. The power on the absorber then becomes:

$$P_{abs} = P_{in}\eta = I_{sun} A_{in} \eta \qquad \text{(eq. 3)}$$

$P_{in}(W)$ is the sun power into the concentrator, $I_{sun}(W/m^2)$ is the sun intensity and A_{in} is the aperture area of the concentrator.

The temperature rise on the absorber then increases both with increasing interception ratios and concentration ratios (neglecting Q_{loss} for simplicity).

$$\rho \delta c \frac{dT}{dt} = I_{sun} \frac{A_{in}}{A_{abs}} \eta = I_{sun} C_r \eta \qquad \text{(eq. 4)}$$

When designing a concentration system with relaxation on the tracking accuracy, a larger absorber gives less interception losses (higher η) and higher concentration ratios (C_r). A smaller absorber may give higher temperatures, although overall lower energy efficiencies.

The performances of two types of reflectors are presented in this study: a Parabolic Reflector (PR) and a 3D Compound Parabolic Concentrator (CPC). The comparisons are made using an in-house ray tracer named TraceIt, varying the solar angles and the concentration ratios (size of the absorber). A cylindrical shaped absorber was chosen, as this will be easier to encapsulate with a glass cover (for reduction of convective heat losses) than for a spherical shaped absorber.

2. Parabolic reflector

A parabolic reflector (PR) focus incoming parallel rays along the z axis, on a focal point f (m) from the base of the PR. The shape of the reflector is given by:

$$z = \frac{r^2}{4f} \qquad \text{(eq. 5)}$$

For a two dimensional reflector (2D trough), r = x, and for a three dimensional reflector (3D dish), $r = \sqrt{x^2 + y^2}$. The depth h of the dish is related to the diameter of the dish, d, for a given focal length f by (follows from geometrical considerations):

$$h = \frac{d^2}{16f} \qquad \text{(eq. 6)}$$

3. Compound Parabolic Reflector, CPC

A CPC is the combination of two parabolic reflectors (PRs) as shown in Fig. 1. Early descriptions of CPCs are given in (Winston and Hinterberger, 1975) and (Rabl, 1976). A review of various applications of CPCs is given in (Tian et al., 2018). A particular CPC application for concentrating Photo Voltaics is provided in the review by (Parretta et al., 2003).

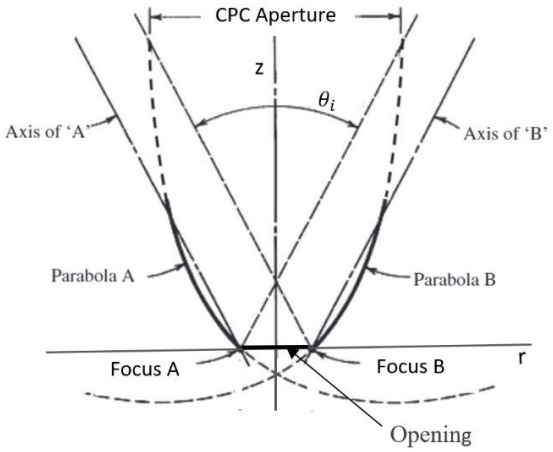

Fig. 1: The CPC (Lwiwa and jørgen Nydal, 2022)

The two parabolas are rotated and shifted opposite along the r axis, such that the focal point of one parabola is at the surface position of the other parabola. The parts of the parabola walls between the Aperture and the Opening constitutes the CPC. The magnitude of the rotation determines the half acceptance angles. Increasing the rotation gives larger acceptance angle but smaller concentration ratio (smaller A_{in}). The incoming rays with angles within the acceptance angles will go through the lower opening of the CPC for the 2D case (η = 1). For the 3D case, where the surface results from a revolution around the z-axis, the interception ratio becomes less than one when the solar angles deviates from the symmetrical vertical case.

By performing the rotation and the translation of the parabolas (Eq. 5), the following equation for the CPC results (Dai et al., 2011):

$$((r+a)c+zs)^2 = 4a(1+s)(zc-rs+a) \qquad \text{(eq. 7)}$$

where $c = cos\theta_i$, $s = sin\theta_i$, θ_i, =acceptance angle, a= radius of exit opening. The illustrations in Fig. 2(a) are for a=0.1, θ_i= 15 degrees.

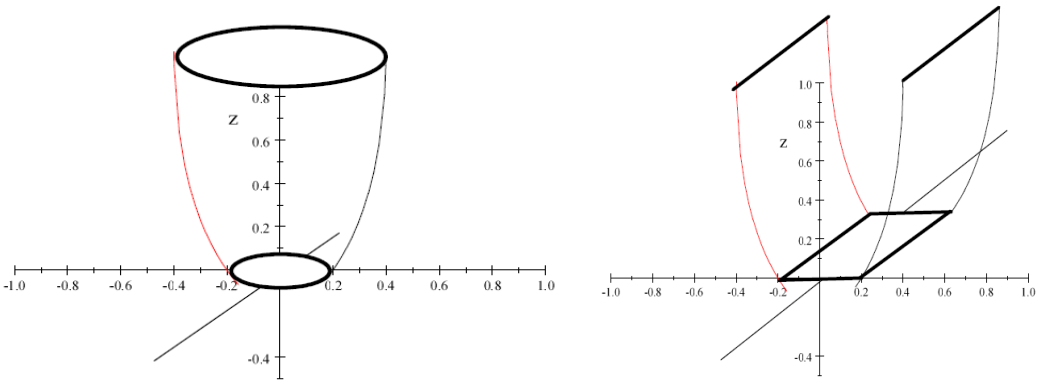

(a): 3D CPC **(b): 2D CPC**

Fig. 2: Schematic diagram of a 3D and a 2D CPC

4. Ray tracing

Ray tracing is the tracing of the individual paths of rays passing through the optical system with the purpose of finding their distribution pattern on the surfaces of interest. Each ray starts from a point of origin (the sun) and is tracked as it intersects with surfaces. A reflective surface will reflect the ray onwards and an absorbing surface will terminate the ray. The base problem is to find the interception point $\overrightarrow{P}$ with a surface f (x, y, z) = 0 for a ray with starting point $\overrightarrow{S}$ and with a direction unit vector $\vec{d}$.

$$\vec{P} = \vec{S} + u\vec{d} \qquad \text{(eq. 8)}$$

Inserting Eq. 8 on component form into Eq. 7 for the surface gives an equation for u, the distance from the origin of the ray to the interception point, (Jafrancesco et al., 2018) gives an overview of ray tracing programs.

In this work, an in-house program has been used (TraceIt is programmed in C++, Qt, OpengGL) as this gives the flexibility for direct programming of needed functionalities, see a short description in (Nydal, 2014). This tool includes the 3D model view of the data where panels can be selected for translation, rotation or deletion. Tracelt gives the user options to set up different type of geometrical shapes (eg. cylinder, flat panels, spheres, parabolas, CPCs, Scheffler, light guides, lens) which can be defined as reflectors or absorbers. The sun is user specified (sun angle, density of sun points and direction). These functionalities are missing in other commercial ray tracing tools. A screen capture of the program is shown in Fig. 3.

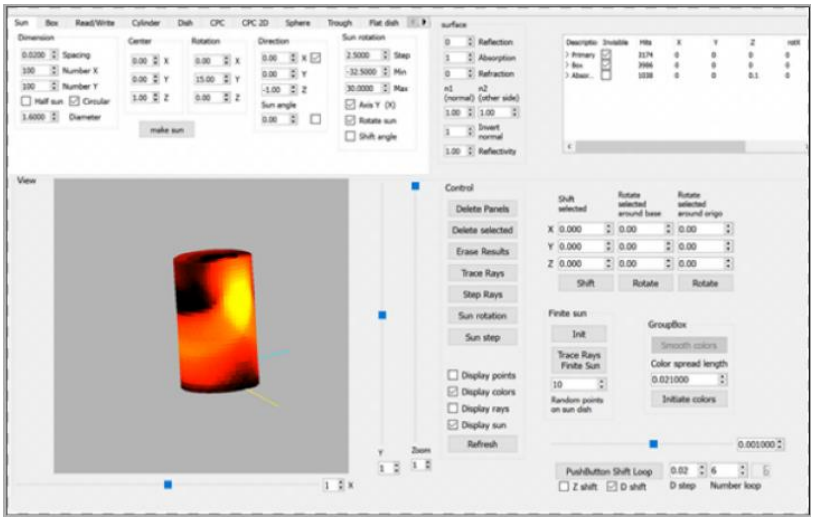

Fig. 3: A screen capture of the Tracelt program

Analytical solutions for u from Eq. 7 and Eq. 8 can be found for the classes of cylindrical, spherical, and parabolic surfaces as well as for the 2D CPC case. For the 3D CPC case, a bisect numerical solutions scheme was implemented. The results of the tracing can be exported for better graphical presentation than what is implemented in TraceIt, the result plots in this study are generated with Matlab.

5. Cases for comparisons

The cases for consideration in this study is for a cylindrical absorber to be positioned inside the CPC (Fig. 4) and the PR, varying the absorber length and the diameter.

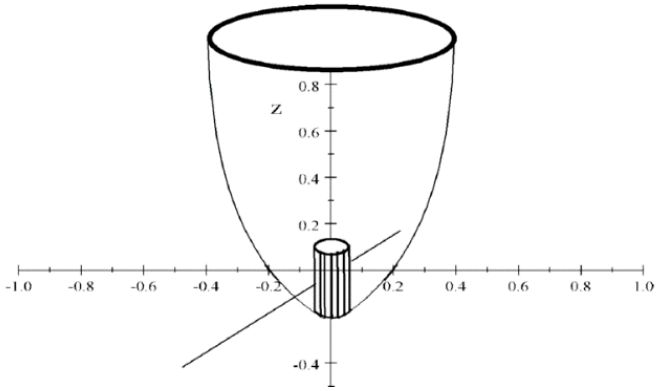

Fig. 4: Cylindrical absorber positioned inside the CPC for sensitivity analysis with changing diameter and length

A CPC is compared with a normal Parabolic Reflector (PR) for the same concentration ratios (same openings of the two reflectors and same absorber area). Loops were programmed in TraceIt for scanning of sun angles and geometrical changes (length and diameter of the absorber). The interceptions on a cylindrical absorber are compared between the two reflectors. The cases are:

- Reflectors: The CPC (acceptance angle 15 degrees) and Parabolic dish are used as reflectors. Aperture diameter=1.0 m
- Absorber length. A cylinder with length L=0.3 m and diameter D= 0.15 m is shifted downwards with step size of 0.04 m
- Absorber diameter. The diameter of a cylinder with length L=0.15 m is changed from D=0.1 m to D=0.2 m with step size of 0.02 m
- The Sun is an array of rays where each ray has a starting point and a direction. A given sun size gives better control on comparisons between cases than Monte Carlo methods. In Monte Carlo methods, rays are selected randomly and the user has to apply simulation times which are sufficiently long to give converging results. With a fixed sun, the number of sun rays are the same for both cases, and comparisons can be meaningful also with relatively few sun rays. The rays entering the reflector and the rays hitting the absorber determines the interception ratios. The applied sun dimension was a grid of 100x100 sun rays, with 0.02 m grid size of the sun ray density. This gives simulations with 10000 rays and the sun extends over a 2x2 m square region.

6. Qualitative comparisons

Fig. 5(a) illustrates the geometrical extent of the first reflected rays from a line sun (a one dimensional array of sun rays). A line sun gives the equivalent behaviour of a 2D CPC and is easier to visualize than a swarm of 3D rays. For incoming normal sun rays, the PR shows the rays passing through the focal point, whereas the CPC spreads the rays across the bottom area.

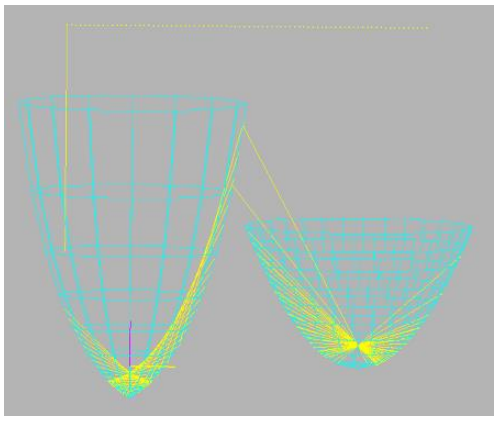

Fig. 5 (a): CPC and PR with the same concentration ratio showing the line sun and sun rays when the sun is vertical

For the maximum acceptance angle of 15 degrees, Fig. 5(b), the CPC focus the rays on the side of the reflector, which is according to the design principles of a CPC.

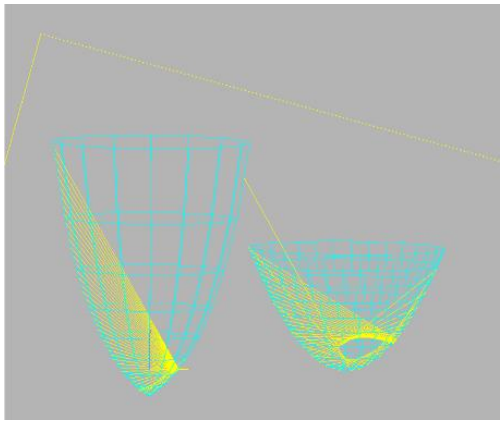

Fig. 5 (b): CPC and PR with the same concentration ratio showing the line sun and sun rays when the sun is tilted 15 degrees

With sun angles double the maximum acceptance angle, shown in Fig. 5(c), both reflectors show very large spread of the rays. The spread will be even larger with the sun rays covering the whole aperture, but the line sun serves to give an indication of how far a cylindrical absorber should extend into the reflectors.

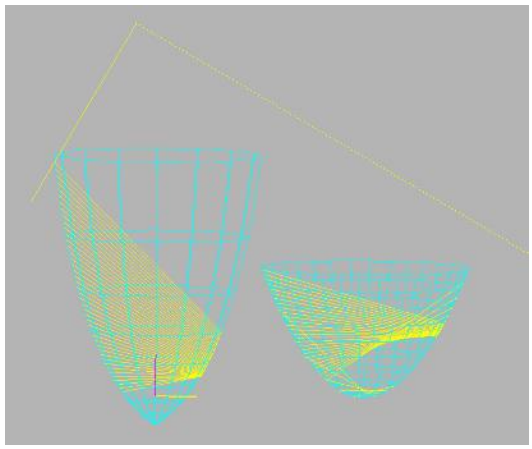

Fig. 5(c): CPC and PR with the same concentration ratio showing the line sun and sun rays when the sun is tilted 30 degrees

7. Sensitivity on absorber length

A 30 cm long cylinder with 15 cm diameter was shifted downwards and out of the reflectors in steps of 4 cm. This means the ray tracing is made with a decreasing length of the absorber. At each absorber position, the sun is scanned over a range of acceptance angles, and the accumulated averaged interception is computed for each step in sun angle. This cumulative interception at a given angle is then a measure of how much of the incoming sun rays have hit the absorber during the change in sun angle from zero to the given angle. It gives an indication of how much total energy can be collected at the absorber during the period when the sun traverses from zero to the given angle.

Fig. 6 shows the cumulative interception results for each position of the absorber. At sun angles normal to the reflectors, the interception is 1 for all absorber lengths. The upper curves are for the long absorber, and it is seen that a long absorber will accumulate more interceptions as the sun angles are increased from the zero position. As the absorber becomes shorter (as it is lowered out of the reflectors) the accumulated interception starts to decreases at earlier sun angles.

The comparisons between the CPC and the PR shows that the CPC performs better than the PR for low solar angles, although the differences are quite small for large absorbers. For higher sun angles, the PR performs somewhat better than the CPC.

We would often prefer small absorbers, in order to reach high temperatures at the absorber (high concentration ratios). At about 18 degrees sun angle, the total averaged interception for the smallest absorber is similar between the two reflectors. An optimal use of the CPC appears then to suggest reflector adjustments after 5-10 degrees change in sun angles. When the sun angle has reached 15 degrees, about 50% of the rays have been absorbed, for both the CPC and the PR.

The overall tendency is that the CPC and the PR can give similar interception values for sufficiently long absorbers (low concentration ratios). For shorter absorbers, the CPC performs better. The ray tracing also shows that the main illumination area for the CPC case is closer to the absorber base than for the PR case.

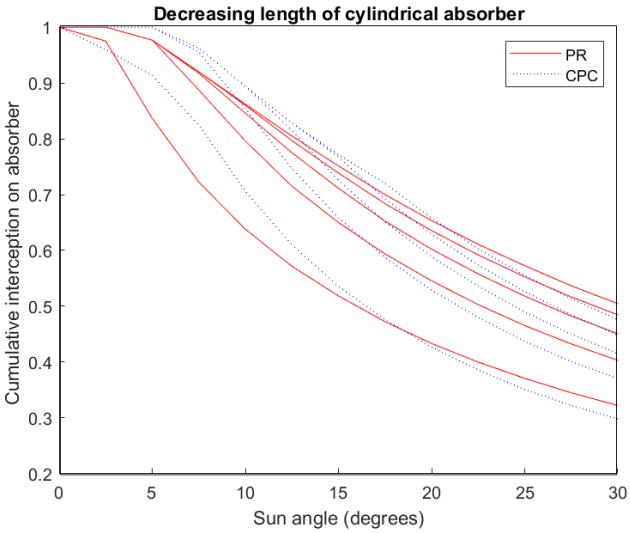

Fig. 6: Cumulative interception on sun rays on a cylindrical absorber (L=0.3 m, D=0.15 m) which is shortened in steps of 0.04 m for each curve. CPC (dashed) and PR (solid)

In order to minimize the absorber surface, an absorber length of L=0.15 m was selected for sensitivity tests on changing the absorber diameter.

8. Sensitivity on absorber diameter

A 15 cm long cylindrical absorber is positioned at the vertex of the CPC and the PR reflectors, and the diameter is changed in steps of 2 cm from an initial diameter 10 cm to the largest diameter of 20 cm. This gives a decrease in concentration ratios from about 14 to 6. Again, the solar angles are chosen to exceed the maximum acceptance angle (15 degrees) to see the effect of operating the CPC reflectors beyond the design regions as shown in Fig. 7.

If the absorber is kept in a constant vertical position, the pipe connections to the heat transfer loop can be static, as the absorber will not move. Large absorbers naturally have higher interception values, all rays are captured for a larger range of sun angles from the vertical. However, smaller absorbers are required to obtain higher temperatures (higher concentration ratios) and the interception values for smaller absorbers decay faster as the sun angles are increased.

The CPC is seen to perform better than PR at low solar angles, but somewhat worse than PR for higher solar angles, beyond the acceptance angle for the CPC.

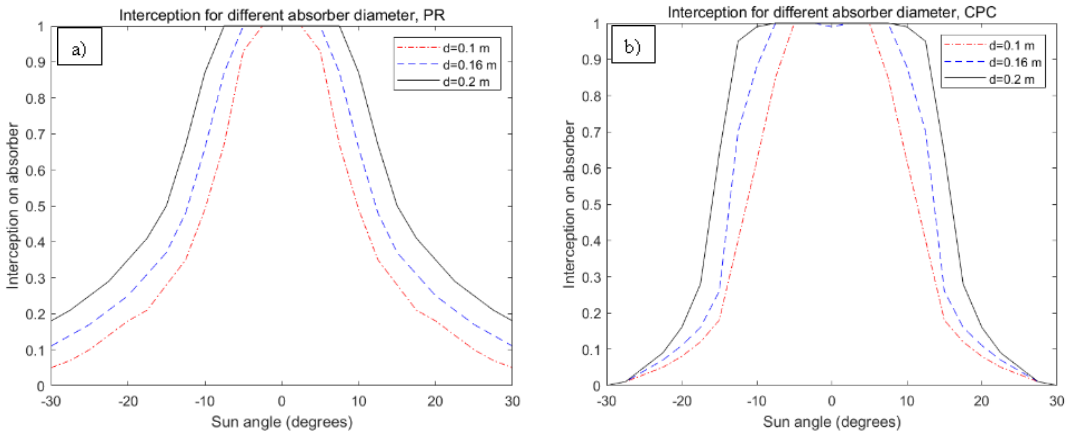

Fig. 7: Interception on cylindrical absorber with different diameters (0.1, 0.16, 0.2 m) and sun angles. a) and b) for absorber aligned with reflectors.

The accumulated interception values are shown in Fig. 8, for the symmetric cases with the absorber parallel with the sun rays at zero sun angle. The values in the figure are the averaged total interception in the intervals from zero solar angle to the actual angle on the x axis. The CPC maintains higher average interception ratios as the solar angle increases, but eventually performs weaker at very large sun angles.

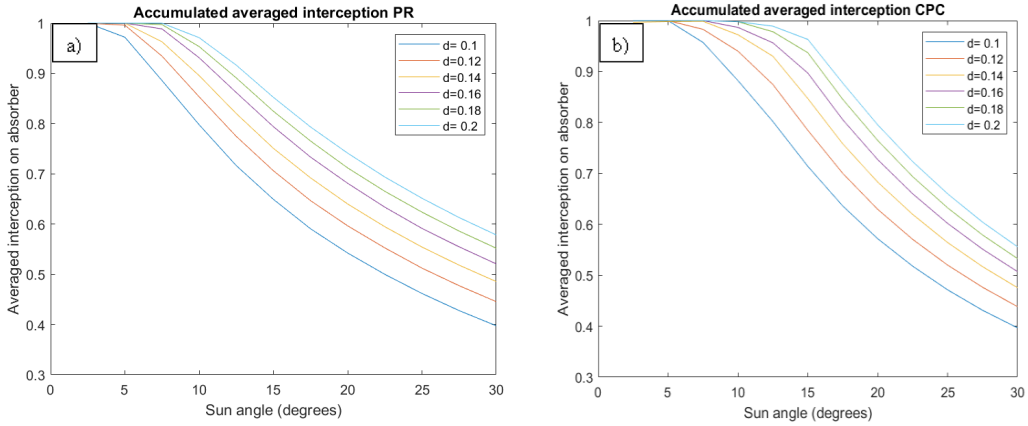

Fig. 8: Accumulated interception for sun angles deviating from the normal incident. (a) PR (b) CPC

The relative difference in accumulated interception for CPC and PR is shown in Fig. 9. The comparison is taken for selected diameters: 0.1 m, 0.16 m and 0.2 m. The differences in the interception values are quite low for lower sun angles and increases up to a maximum of about 12% for sun angle at 15 degrees (acceptance angle for the CPC).

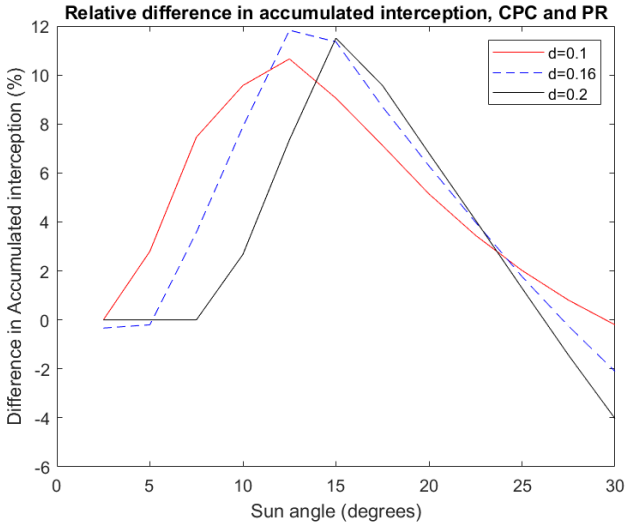

Fig. 9: Relative difference between accumulated interception of CPC and PR

9. Sensitivity on tilting the reflector

If a reflector (PR or CPC) is left to accumulate energy on a cylindrical absorber without solar tracking, the interception values with the varying sun angles have been shown above, with sensitivities on absorber length and on absorber diameter. It shows how the interception values decrease with the sun angles and will come to zero for sufficiently large sun angles. The practical use of such systems would then require some changes in the reflector angle towards the sun at some regular time interval. A solar tracking system gives continuous movement of the reflector with the sun and can then be designed to provide high concentration ratios. The benefit with a CPC is less dependency on solar alignment, but at the cost of lower concentration ratios.

As a test on the effect of tilting the reflectors on the interception ratios, the two reflectors were compared for a tilt angle of 15 degrees. This means that the absorber will be at an angle with the axes of the reflectors, and the case is no longer symmetrical as the sun angle vary.

The interception results with tilted reflectors are seen in Fig. 10, with similar diameter changes of the absorber as before. The interception values are somewhat reduced and the curves are slightly non-symmetric around the normal sun angles.

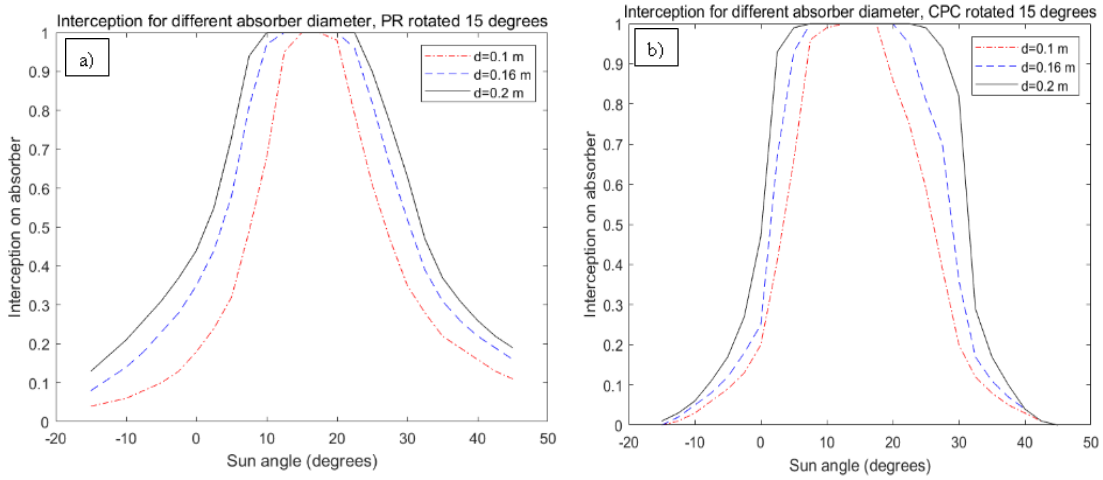

Fig. 10: Interception on cylindrical absorber with different diameters (0.1, 0.16, 0.2 m) and sun angles. a) for PR tilted 15 degrees b) for CPC tilted 15 degrees.

10. Conclusion

Ray tracing is used for comparison of a Compound Parabolic Concentrator (CPC) and a Parabolic Reflector (PR) with similar apertures (opening diameter). The cases are motivated in the application of solar cookers, where a concentrator can heat a storage in the focal area without elaborate solar tracking methods. The sensitivity of the interception ratio on the length and diameter of a cylindrical absorber positioned inside the CPC and PR is evaluated. With the quite large absorber dimensions applied in this work (concentration ratios varying from 14 to 6), the differences between the CPC and the PR are quite small, the CPC shows up to 12% better averaged performance than the PR. The CPC can tolerate shorter absorber lengths than the PR, as the intersection locations on the absorber is closer to the absorber base than for the PR. The concentration ratio for a CPC is limited (when the reflector walls become vertical) while a PR can be optimized more freely, taking into account the balance between the interception ratio and the concentration ratio.

11. Acknowledgements

The first author express her gratitude to the Norwegian University of Science and Technology, NTNU Energy strategic Area for financial support for the PhD work.

12. References

Dai, G.-L., Xia, X.-L., Sun, C. & Zhang, H.-C. 2011. Numerical investigation of the solar concentrating characteristics of 3D CPC and CPC-DC. *Solar Energy*, 85**,** 2833-2842.

Jafrancesco, D., Cardoso, J. P., Mutuberria, A., Leonardi, E., Les, I., Sansoni, P., Francini, F. & Fontani, D. 2018. Optical simulation of a central receiver system: Comparison of different software tools. *Renewable and Sustainable Energy Reviews*, 94**,** 792-803.

Lwiwa, C. B. & Jørgen Nydal, O. 2022. A Ray Tracer for optimizing solar concentrating systems: The case of discretized Compound Parabolic Concentrator. *Scandinavian Simulation Society***,** 15-18.

Nydal, O. J. 2014. Ray tracing for optimization of a double reflector system for direct illumination of a heat storage. *Energy Procedia*, 57**,** 2211-2220.

Parretta, A., Martinelli, G., Stefancich, M., Vincenzi, D. & Winston, R. Modelling of CPC-based photovoltaic concentrator. 19th Congress of the International Commission for Optics: Optics for the Quality of Life, 2003. International Society for Optics and Photonics, 1045-1047.

Rabl, A. 1976. Comparison of solar concentrators. *Solar energy,* 18**,** 93-111.

Tian, M., Su, Y., Zheng, H., Pei, G., Li, G. & Riffat, S. 2018. A review on the recent research progress in the compound parabolic concentrator (CPC) for solar energy applications. *Renewable and Sustainable Energy Reviews,* 82**,** 1272-1296.

Winston, R. & Hinterberger, H. 1975. Principles of cylindrical concentrators for solar energy. *Solar Energy,* 17**,** 255-258.

Angle-dependent properties of MorphoColor™ solar collectors: Color stability, IAM, yield

Stefan Mehnert, Thomas Kroyer, Andreas Wessels, Oliver Höhn, Benedikt Bläsi, Bruno Bueno, Helen Rose Wilson, Tilmann Kuhn

Fraunhofer Institute for Solar Energy Systems ISE, Freiburg (Germany)

Abstract

MorphoColor™ coatings were developed for application in solar thermal flat-plate collectors and their marketability was ensured in the project, "Color Collector - Concepts for Architecturally Adapted Collectors for Existing and New Buildings", which is funded by the German Federal Ministry of Economic Affairs and Climate Action (BMWK), funding code 03ETW007A. The project is coordinated by Fraunhofer ISE, which is co-operating with Interpane E&B GmbH, Siko GmbH, THIEME GmbH & Co. KG and Fuchs Design GmbH as project partners.

The influence of the color on the annual yield was minimized. The design possibilities shown in this article represent only a small portion of all possibilities. The first applications of MorphoColor™ collectors in Jenbach, Austria and Freiburg, Germany are currently being implemented and are being monitored by Fraunhofer ISE.

Keywords: Building-integrated solar thermal, high-transmittance colored coating, design, performance, simulation, monitoring

1. Introduction to MorphoColor™ technology

The German government is aiming for a climate-neutral building stock by 2045. Architecturally integrated roof and façade collectors can make a significant contribution to the transformation of the energy system. For these architecturally integrated solar thermal applications, the design of the solar collectors plays a decisive role. With the MorphoColor™ technology, we present an approach that makes aesthetically valuable solar collectors with high efficiency feasible.

The starting point for the development was a phenomenon that can be observed in the morpho butterfly. Its is distinguished by the strong blue coloration of its wings, which is produced by a 3D surface structure with lamellae on a nanometer scale. Inspired by this, glass panes with MorphoColor™ coatings were developed for use as collector covers. The color impression is created by an interference layer system on a glass substrate with a microscopically structured surface. For a description of the basic function of the MorphoColor™ layers, please refer to (Bläsi et al. 2021). The first application in solar thermal collectors is described by Wessels et al. (Wessels et al. 2021, 2021).

The glass panes coated with MorphoColor™ offer very interesting properties for solar thermal collectors:

- High solar yield (> 90% of clear glass)
- Saturated colors
- Anti-glare design
- High angular stability of the color impression
- Absorber almost completely invisible behind colored layer
- Simple integration into collectors due to thermally pre-stressable coating

© 2022. The Authors. Published by International Solar Energy Society
Selection and/or peer review under responsibility of Scientific Committee
doi:10.18086/eurosun.2022.12.11 Available at http://proceedings.ises.org

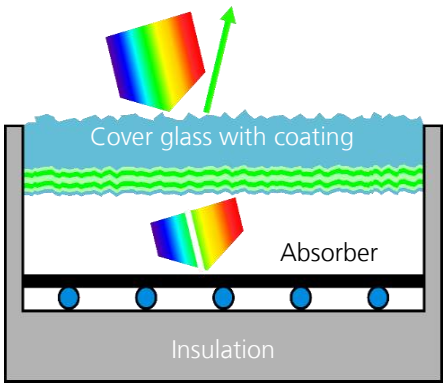

Fig. 1: Schematic illustration of a collector with a MorphoColor™ glass cover

2. Angle-dependent spectral evaluations in reflection

Angle-dependent reflectance measurements were carried out on MorphoColor™ coated, structured glasses by means of an Agilent Cary 5000 spectrometer and using the Universal Measurement Accessory (UMA). Both the angle of incidence and the angle of reflection can be varied within an azimuthal plane. Fig. 2 shows examples of reflectance spectra at different reflection angles θ_R for an angle of incidence of -30°. As can be seen in the schematic drawing in Fig. 2, all angles are defined relative to the normal to the glass sample. The spectra clearly show the narrow-band reflection peak characteristic of MorphoColor™ technology. The small spectral shift of the peak causes the colored appearance to remain very stable for different viewing angles.

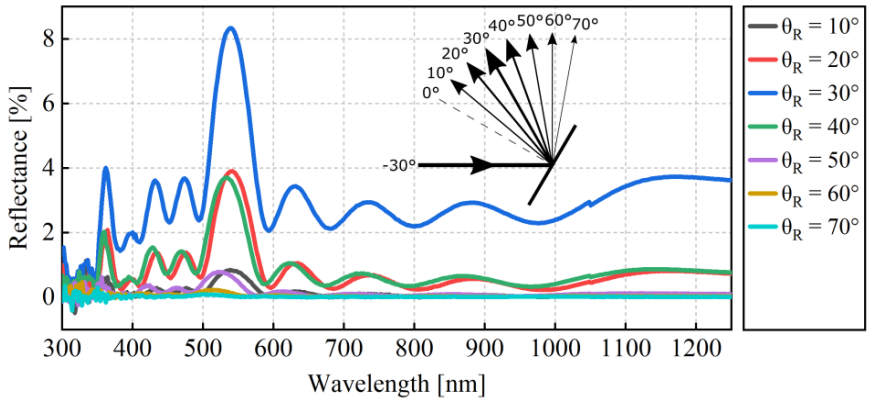

Fig. 2: Angle-dependent spectral data of a MorphoColor™ coated glass cover that is structured on one surface. The layer stack is located on the structured glass side and is designed so that the narrow reflection peak occurs at approx. 540 nm and thus looks green in reflection.

3. Color measurements with luminance camera under outdoor conditions

To visualize the appearance of MorphoColor™ solar collectors in real applications with complex environmental conditions, a demonstration collector was measured outdoors using a calibrated LMK color camera from the manufacturer, TechnoTeam. As also shown in the schematic of Fig. 1, the coated structured side of the glass cover is oriented towards the inside of the collector. The outside of the glass is not textured. Fig. 3 shows the resulting colors from different viewing angles in front of the west-facing collector. Photographs were taken both when the sky was clear (clear sky) and when it was overcast (overcast). In both cases, the sun was in the southwest. Comparing the colors under the different conditions shows clear differences. In the case of the clear sky, the direct reflection in the northwest results in significantly brighter colors than in the southwest, where the observer has the sun behind him. In the case of overcast skies, the colors appear much more homogeneous in terms of brightness due to the diffuse illumination. Looking not at the brightness but at the color tone, both sets of environmental

conditions show very good angular stability. The color remains green and it is only at very large viewing angles that a tendency to shift towards gray tones becomes visible.

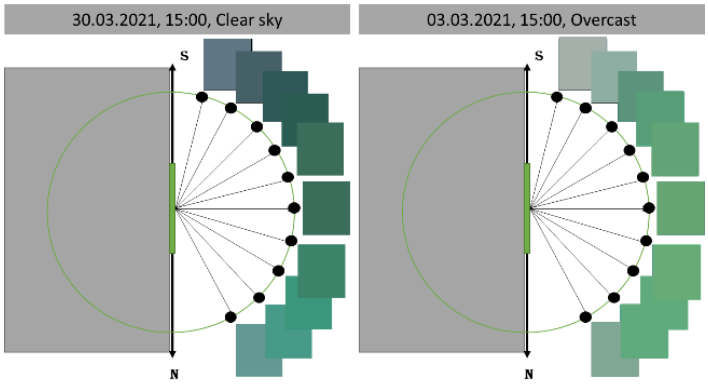

Fig. 3: Color measurements with a luminance camera under outdoor conditions. The MorphoColor™ solar collector sample was located vertically on a west-facing façade. The camera was located along the perimeter of a horizontal half-circle centered at the center of the sample.

Using a synchronized spectral weather station, both the sky and the direct irradiation of the sun were monitored in terms of their intensity and spectrum during the measurements. The combination of these data with the color data can be used in further work to calibrate and validate material models. These could be used to create a visualization tool.

4. Solar collector performance evaluation

With the aim of quantifying the performance and yield reduction of the MorphoColor™ solar collectors compared to a standard flat-plate collector (reference), the performance was characterized according to EN ISO 9806:2018, as well as the gross annual yield being simulated using ScenoCalc for different locations and collector mounting angles.

5. Efficiency curves of MorphoColor™ solar collectors

The efficiency curve of a reference collector with clear, uncoated glass was determined using the solar simulator of the TestLab Solar Thermal Systems at Fraunhofer ISE. The clear, uncoated glass cover was then replaced with MorphoColor™ coated and structured glass in the colors, blue, green, red, gold and grey and the conversion factor η_0 was determined in each case. To exclude influences on the determination of the conversion factor, the test stand configuration remained unchanged. The efficiency curves determined are shown in Fig. 4, normalized to the reference collector. The comparison of the characteristic curves shows that for the colors blue, green, and red, the reduction of the collector efficiency is in the range of 10 percentage points. This was one of the project goals and the result is consistent with the optical characterization of the MorphoColor™ glass panes.

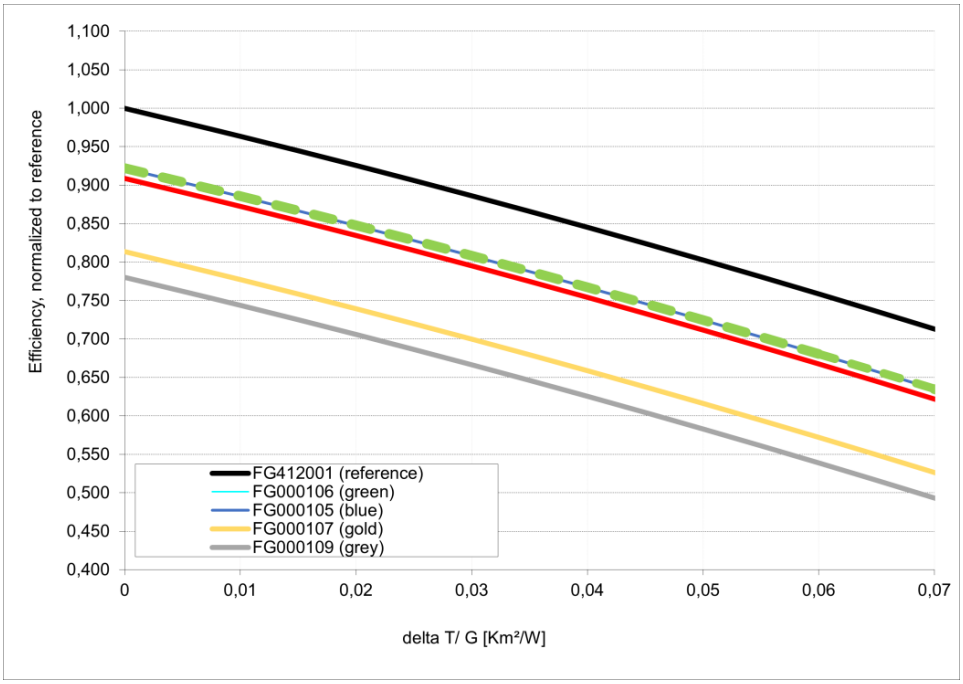

Fig. 4: Efficiency curves of the MorphoColor™ solar collectors, normalized to the reference collector.

6. Angle-dependent solar transmittance curves of MorphoColor™ glasses

The direct-hemispherical solar transmittance (Tdir-hem_sol) of MorphoColor™ glass panes in the five colors mentioned above and the glass cover of the reference collector were measured at different angles of incidence (cf. Fig. 5).

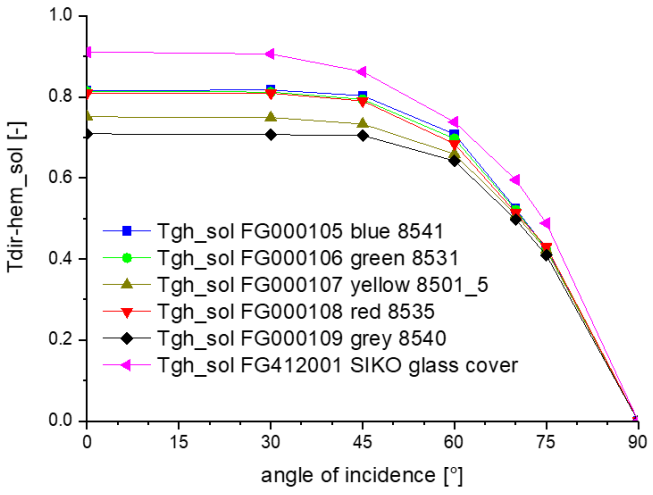

Fig. 5: Angular dependence of the direct-hemispherical solar transmittance (Tdir-hem_sol) for five MorphoColor™ glass covers in different colors and the original glass cover of a SIKO solar collector

Angle-dependent "calibration curves" for each MorphoColor™ glass pane were calculated from the ratio Tdir-hem_sol_Morpho to Tdir-hem_sol_reference. Multiplying these "calibration curves" by the IAM (Incidence Angle Modifier) curve for the reference collector leads to theoretical IAM curves for collectors covered with MorphoColor™ glass panes. The result shows no significant influence on the IAM result of collectors with MorphoColor™ glass panes for the Morpho coatings shown here. Compared to the reference, all coatings show increased IAM values. In particular, this can be observed in the range of incidence angles from 30° to 65°, which

leads to the expectation of a positive influence on the result of the annual yield simulations (cf. Fig. 6).

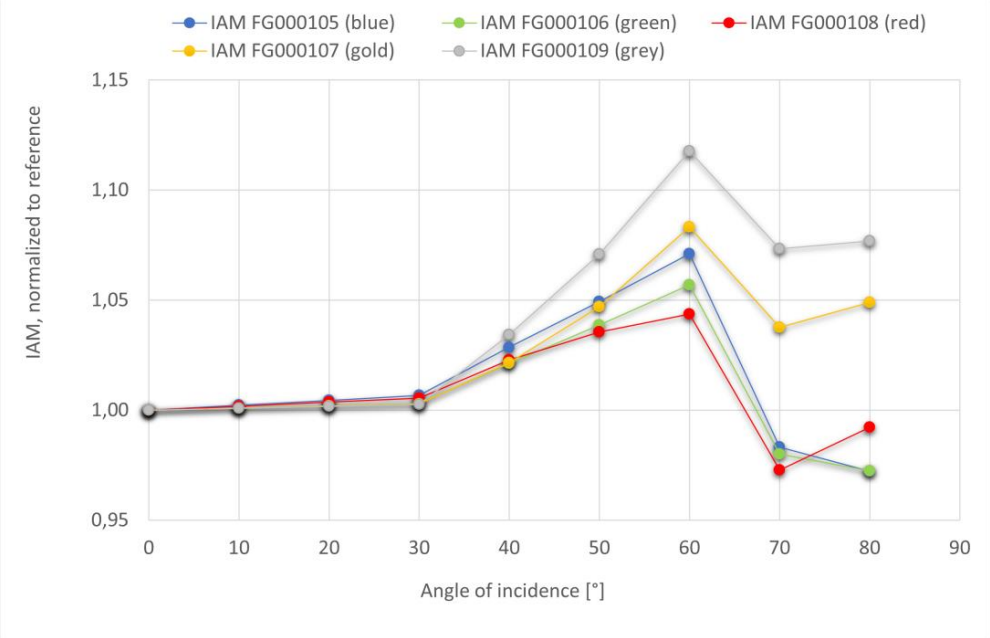

Fig. 6: Incidence Angle Modifier (IAM) of the MorphoColor™ solar collectors, normalized to the reference collector.

7. Acceptance of diffuse irradiance of MorphoColor™ solar collectors

The acceptance of diffuse irradiance K_d of the MorphoColor™ solar collectors and the reference collector were determined based on the theoretically determined IAM with the metrologically determined efficiency curves. The method used to determine the diffuse radiation acceptance is described in (EN ISO 9806:2018) and assumes an isotropic distribution of the diffuse irradiance over the sky hemisphere. The influence of the MorphoColor™ coating on the acceptance of diffuse irradiance of the MorphoColor™ solar collectors is shown in Fig. 7 normalized to the reference collector. The MorphoColor™ solar collectors show a slight increase in the acceptance of diffuse irradiance compared to the reference collector.



Fig. 7: Diffuse radiation acceptance of the MorphoColor™ solar collectors, normalized to the reference collector.

8. Gross annual yield of MorphoColor™ solar collectors

Based on the performance parameters of the indoor performance test, the theoretical IAM curves and the acceptance of diffuse irradiance, gross annual yield simulations were carried out using ScenoCalc. In addition to the tilt angles as a function of latitude, which were used in the context of collector certifications, all simulations were also carried out for vertical orientation of the collector. The simulations are based on constant collector operating temperature levels of 25°C, 50°C and 75°C. It is therefore assumed that the collector always operates

at the same temperature level throughout the year. The mass flow rate is fixed at 72 kg/m²h. Also, no energy demand profiles are considered within the ScenoCalc simulation. The total energy produced over the course of the year is accumulated in the result to give the gross annual yield. ScenoCalc does not take capacitive effects into account. The result of ScenoCalc therefore does not show the expected performance of the collector in a real solar thermal system but is particularly suitable for comparing the annual yield of different collector variants based on the performance parameters and the IAM curve.

The gross annual yield of the MorphoColor™ solar collectors is shown for the locations, Würzburg, Stockholm, Davos and Athens, both for the standard tilt angle and for vertical orientation normalized to the reference collector (Figure 8 to Figure 11). The differences between the results for the individual locations are marginal. If the tilt angle of the collector corresponds to the latitude minus 10°, yield reductions result which are between 6 to 10 %-points at the fluid temperature of 25°C and 13 to 20 %-points at the fluid temperature of 75°C for the colors blue, green and red. The colors gold and grey show somewhat higher yield reductions due to the more complex layer structure. A similar picture emerges when the collector is set up vertically. Here, the yield reduction due to the use of the respective MorphoColor™ glass at the fluid temperature of 25°C is in a range of 5 to 10 %-points and at a fluid temperature of 75°C, is between 14 and 27-%- points. The reason for the greater influence when the collector is installed vertically is the reduced duration with high irradiatiance.

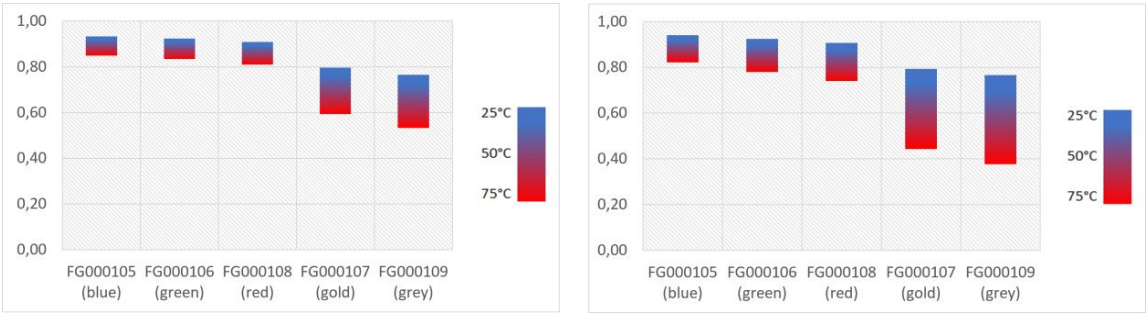

Fig. 8: Gross annual yield of MorphoColorTM solar collectors, normalized to the reference collector at the Würzburg site. Right, collector tilt angle = latitude -10°. Left, collector tilt angle = 90°.

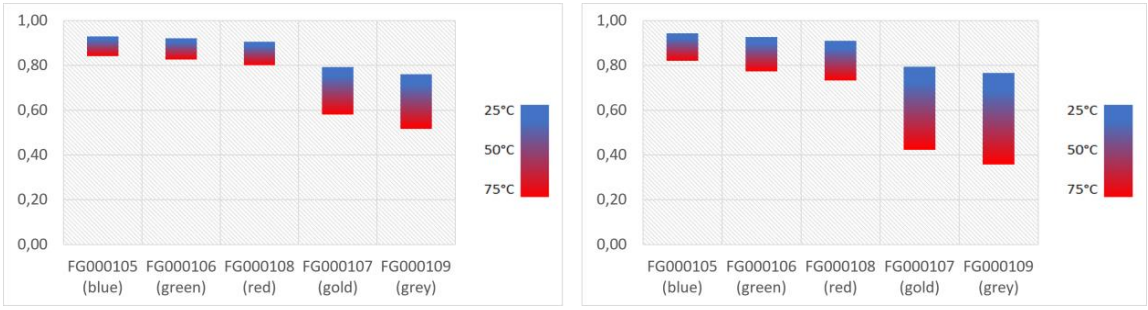

Fig. 9: Gross annual yield of MorphoColorTM solar collectors, normalized to the reference collector at the Stockholm site. Right, collector tilt angle = latitude -10°. Left, collector tilt angle = 90°.

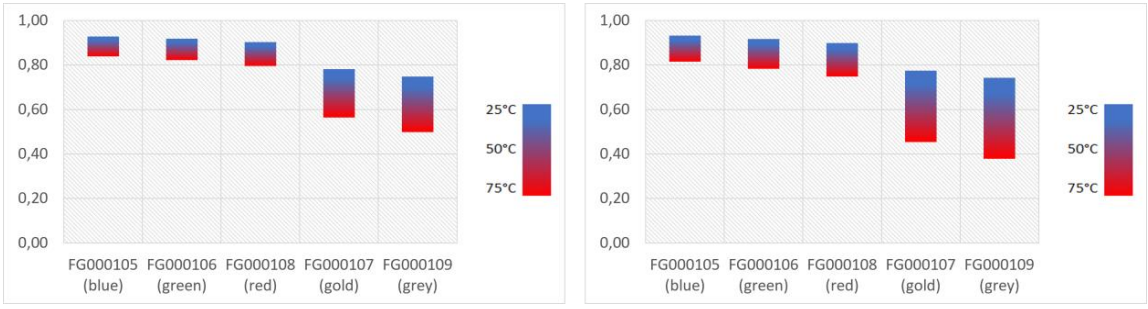

Fig. 10: Gross annual yield of the MorphoColorTM solar collectors, normalized to the reference collector at the Davos site. Right, collector tilt angle = latitude -10°. Left, collector tilt angle = 90°.

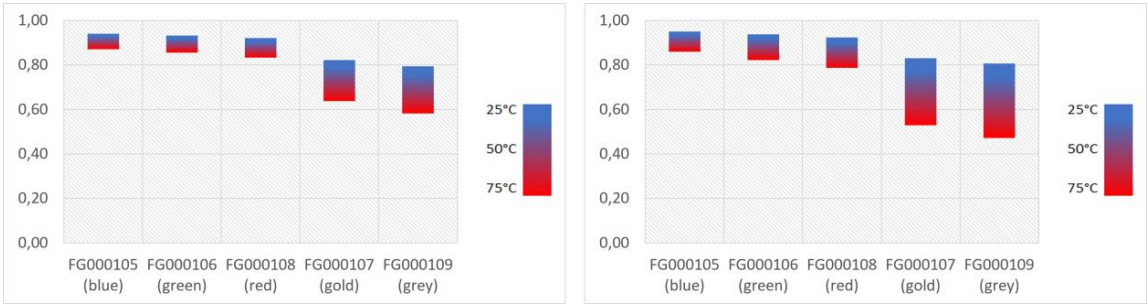

Fig. 11: Gross annual yield of the MorphoColorTM solar collectors, normalised to the reference collector at the Athens site. Right, collector tilt angle = latitude -10°. Left, collector tilt angle = 90°.

9. Marketability of MorphoColor™ solar collectors

To increase design freedom in the architectural integration of solar thermal energy as well as to ensure the marketability of MorphoColor™ glass, the goal was to achieve simple exchangeability of MorphoColor™ glass with the transparent covers of flat-plate collectors that already had a Solar KEYMARK certification.

The simplified process for the certification of collectors with MorphoColor™ glass is shown in Fig. 12. Note: The prerequisite is an existing Solar-Keymark certification of a flat-plate collector.

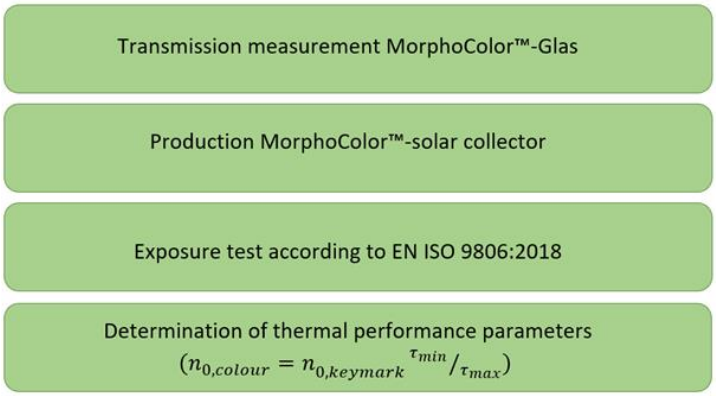

Fig. 12: Process flow for Solar Keymark certification when replacing the transparent cover of a certified flat-plate collector by MorphoColor™ glass.

10. Acknowledgments

Our thanks go to the BMWK for funding the project, to Lichtblau Architekten for their support, and to our project partners for their excellent cooperation.

Bundesministerium
für Wirtschaft
und Klimaschutz

SIKO
einfach | sauber | heizen

THIEME

AGC INTERPANE

fuchsdesign®

11. References

Bläsi, Benedikt; Kroyer, Thomas; Kuhn, Tilmann E.; Höhn, Oliver (2021): The MorphoColor Concept for Colored Photovoltaic Modules. In: *IEEE Journal of Photovoltaics* 11 (5), S. 1305–1311. DOI: 10.1109/JPHOTOV.2021.3090158.

EN ISO 9806:2018: Solar energy - Solar thermal collectors - Test methods.

Wessels, Andreas; Kroyer, Thomas; Mehnert, Stefan; Bläsi, Benedikt; Höhn, Oliver (2021): Colored building-integrated solar thermal collectors with high efficiency. 31st Symposium Solar Thermal and Innovative Heat Systems. Fraunhofer-Institut für Solare Energiesysteme ISE. Conexio GmbH, 27.04.2021.

Hardware-in-the-loop integration of PVT models using Internet of Things-enabled communication

J. Meiers[1], A. el Jeddab[2], D. Theis[2], D Jonas[1], G. Frey[1], M. Deissenroth-Uhrig[2]

[1]Saarland University, Chair of Automation and Energy Systems, Saarbrücken (Germany)

[2]htw saar, University of Applied Sciences, Saarbrücken (Germany)

Summary

This paper proposes a Hardware-in-the-Loop (HiL) simulation architecture incorporating Internet of Things (IoT)-enabled communication using Message Queueing Telemetry Transport (MQTT), a lightweight protocol, making distributed messaging possible. The communication procedure between TRNSYS, BCVTB and Matlab as the simulation part and LabVIEW as communication node to the hardware of the real system, is described. Three different HiL test approaches have been compared and the selection of representative days using k-means clustering is depicted, incorporating space heating demand and weather conditions. Results from applying the HiL framework on a parallel solar heat-pump system with emulated covered PVT collectors, show acceptable differences in the collector output temperature and the thermal power output between simulation and hardware. These are found to be caused by time delay in the communication and dynamic limits of the volume flow control in the PVT collector circuit.

Keywords: HiL, PVT, simulation, MQTT, IoT, TRNSYS, MATLAB, LabVIEW

1. Introduction

Hybrid photovoltaic-thermal (PVT) collectors represent a compact solution, converting solar energy in thermal and electrical energy, where installation area is limited but solar supported heating is desired or necessary. PVT provide an alternative heat source for heat pump (HP) systems especially in urban regions with high building density where air source heat pumps come close to their limits regarding legal requirements in relation to noise emissions. Therefore, testing PVT systems in different application scenarios (e.g. as additional energy source in fossil fuel driven heating systems or as heat source for heat pump systems) is important to figure out the potential of reducing fossil fuels consumption or electrical grid demand.

To cope with the fluctuating nature of renewable energy sources and the complexity of modern building energy systems, modeling and simulation studies offer an efficient way for scenario research, like accounting for different locations, weather conditions and building standards. Further they allow for system design and analysis of the systems dynamic behavior in different concepts, as presented in Hadorn (2015) and Frank et al. (2010) or building energy supply systems.

Hardware-in-the-Loop (HiL) approaches offer a high degree of freedom in testing. A HiL simulation combines computer simulation with a separate hardware testbed acting as an embedded system. The HiL approach is cost effective and allows to investigate the performance of a complete system or system components. It is especially useful for rapid control prototyping and validation.

In previous works, Jonas et al. (, 2019) developed a PVT model in the TRNSYS simulation tool (TRNSYS, 2020). In this contribution, the authors have developed a networked HiL framework in the solar laboratory at htw saar that emulates PVT collectors and integrate them into a complete solar heat pump (SHP) building energy system with hydraulic circuit, thermal storage tank and battery storage system. The system concept, which is under consideration in this contribution, is a *solar ground source heat pump* system with connection of the PVT collector to the thermal storage tank in *parallel* to the heat pump (SGSHP-P). Space heating (SH), domestic hot water (DHW) and domestic electric power (DEP) demand profiles have been generated from simulation data of the corresponding system using the TRNSYS model library SHP-SimLib (Jonas, 2023) for a single family household with an annual heat demand of 45 kWh/m² (SFH45) in Strasbourg.

© 2022. The Authors. Published by International Solar Energy Society
Selection and/or peer review under responsibility of Scientific Committee
doi:10.18086/eurosun.2022.12.12 Available at http://proceedings.ises.org

The HiL architecture designed in this work contains TRNSYS as simulation tool, Building Controls Virtual Test Bed (BCVTB) (Wetter et al., 2008) as middleware for real-time simulation and communication between TRNSYS and MATLAB (MATLAB, 2017) using Berkeley Socket Distribution (BSD) socket connection. MATLAB provides network communication to LabVIEW (Bitter et al., 2018), which acts as software interface to the real system testbed. In addition to acting as a software interface, BCVTB also guarantees real time synchronization of the simulation and the data acquisition and control tools in the testbed.

The paper is structured as follows: following Section 2 explains the system model incorporating the PVT collector in the simulation software TRNSYS as a use case for the HiL simulation platform. In Section 3 identification of representative days of a year for SHP system analysis is described. Section 4 discusses the Hardware-in-the-Loop framework and network communication using Internet-of-Things (IoT) messaging protocol Message Queuing Telemetry Transport (MQTT) in detail and in Section 5 key performance indicators are defined and results are discussed.

2. PVT collector system model

The simulation model has been created in TRNSYS (2020). It is part of the SHP-SimLib from Jonas (2023) and includes the developed TRNSYS Type 835 of a PVT collector (Jonas et al., 2010). The complete model can be subdivided into four sub models (cf. Fig. 1):

- PVT
- Weather
- MATLAB interface
- Output

In the PVT sub model, the collector model TRNSYS Type 832 (Haller et al., 2014) calculates the thermal collector output, where the mean fluid temperature influences the electrical power output, which is calculated in TRNSYS Type 835. Type 31 considers thermal energy losses in the inlet pipe to the collector with ambient temperature as an average of room and outside temperature. A two-point hysteresis controller controls the collector circulation pump with a constant volume flow. As input signals it needs the current temperatures in the DHW and SOLAR zone of the storage tank.

In the weather sub model, weather data for Strasbourg was generated by Meteonorm (2009). Here, long wavelength radiation downwards from sky to the collector plane will be calculated using the fictive sky temperature.

The MATLAB interface is realized by using BCVTB as middleware. Type 6666, provided by the TRNSYS vendor Transsolar, enables TRNSYS to send and receive data to and from MATLAB.

The calculated powers will be integrated over time and the resulting energies will be written to output files.

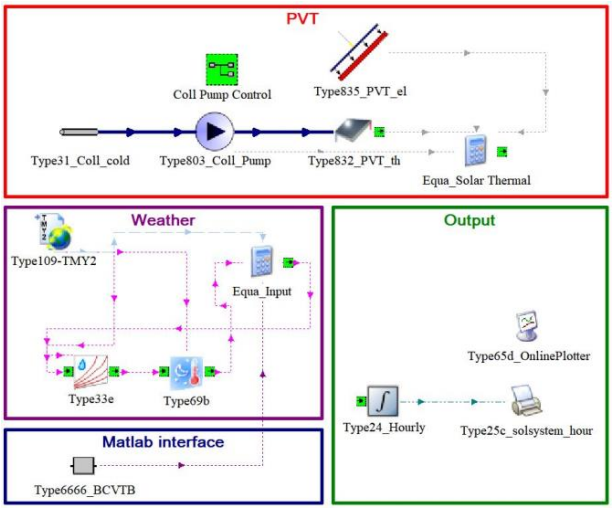

Fig. 1: TRNSYS PVT collector system simulations model

3. Choosing Representative Test Days

Within the last few years, several HiL test methods have been established for testing a SHP system, which will be described in this section. It should be noted that none of the examined methods could be completely adopted. Instead, a standalone test procedure was developed and described briefly. The common approach among the methods is the installation and testing of the system in a laboratory test bench or emulation in real time if some of the components are not installed and, mainly because of economic reasons, the choice of a set of representative days of a year. The selection of these days is still a critical step in the procedure, refer to Menegon et al. (2017). All methods describe a short test cycle and an emulation of boundary conditions. This can be a 6-day test cycle or, less often, a 12-day test cycle.
Among the existing HiL test methods, following three methods have been taken under consideration:

- *Concise Cycle Test* (CCT)
  CCT is a dynamic test method developed at the Institute of Solar Technology, Rapperswil, Switzerland (SPF) for testing systems for heat supply. The method describes a six-day test cycle in which an entire building is supplied with heat. The results should provide information about the performance data of an entire year by extrapolation (Haberl and Haller, 2018).
- *Prescribed Load Performance Extrapolation* (PLPE)
  PLPE is a test procedure that can be applied to several locations. The locations used so far are Bolzano (Italy), Zurich (Switzerland), Gdansk (Poland) and Rome (Italy). For all locations, weather data from Meteonorm have been used, while demand for SH and DHW vary depending on the locations. As with CCT, a room temperature of 20 °C is specified and a two-storey single-family house with an area of 180 m² is simulated (Menegon et al., 2017).
- *New Materials and Control for a next generation of compact combined Solar and heat pump systems with boosted energetic and exergetic performance* (MacSheep)
  As part of the EU research project MacSheep (Haberl et al., 2015), a method was developed, with the intention to harmonize the test procedure of SERC and SP (both Sweden), INES (France) and the SPF (Switzerland). In the test bench, energy storage, auxiliary heater, all devices for SH and DHW preparation, all devices related to the solar circuit, pumps and pipe connections, controllers, and temperature sensors are considered for evaluation.
  The simulation is based on EN ISO 13790-2008 considering a single family house based on the International Energy Agency (IEA) Solar Heating and Cooling Programme (SHC) Task 44 / Heat Pump Programme (HPP) Annex 38 (IEA SHC, 2013) with a heating energy requirement of 45 kWh/m²a (SFH45) for a test period of 6 and 12 days, not taking into account an electrical load profile. As reference location, Zurich has been chosen and weather data has been simulated with TRNSYS using weather dataset from Meteonorm. Tests will be done with criteria of CCT (e.g., preconditioning of the storage tank).

The test methods differ in the following points (Menegon et al., 2018):

- Choice of test sequence
- Definition of load profiles
- Emulation of the components which are not installed in the test bench
- Extrapolation of seasonal performance factors on other climates
- Application of climate data and load profiles

While MacSheep only slightly differs from the CCT method, PLPE is a completely new approach when it comes to the heat distribution and choice of weather data for the test.
Unfortunately, neither MacSheep nor PLPE describe a DEP consumption. CCT is the only available recent method, which presents a DEP load. The total DEP demand is of a high interest in a household with a SHP system, especially in the context of a Smart Grid.

CCT in the latest version (Haberl and Haller, 2018) uses an optimized ambient temperature and irradiation in the test sequence with the aim to match the annual demand after extrapolation. However, as of the latest versions of those procedures, the weather file is modeled according to the space heating demand of the simulated and emulated building, which is not the case in our approach.

In this approach the SH demand profile generated in TRNSYS and applying the k-means clustering algorithm in MATLAB, six representative days have been determined. These are selected in such a way that they are nearly

corresponding to the nominal SH demand value of 45 kWh/m²a (SFH45). From the identified clusters, days 4 and 2 are chosen in such a way that the former has a high ambient temperature at a high irradiation and the latter has a high ambient temperature at low irradiation. For the six representative days determined, this results in a total SH energy demand of 111.64 kWh, which corresponds to an annual energy demand of 6791.4 kWh after multiplication with 365/6, respectively 48.5 kWh/m²a for a SFH45 reference building with a heated living area of 140 m².

When selecting the days, the global horizontal irradiation and the ambient temperature were determined in such a way, that these days reflect the different weather conditions of the whole year.

The days of the matching sequence are 41, 101, 111, 272, 321, 331 and are listed in Table 1 with corresponding SH demand and weather conditions.

Tab. 1: Identified representative Days of the year, corresponding date and number of days in the year

No.	Number of Representative Day of the Year	Corresponding Date of the Year	Daily Space Heating Energy [kWh]	Weather Characteristic of the Day 1),2)
1	41	10.02.	39.93	GHI: high ;AT: low
2	101	11.04.	0	GHI: variable; AT: high
3	111	21.04.	2.3	GHI: low; AT: low
4	272	29.09.	0	GHI: high; AT: high
5	321	17.11.	39.15	GHI: low; AT: low
6	331	27.11.	30.26	GHI: high; AT: low
Σ			111.64	

1) GHI: Global Horizontal Irradiance (high: > 600 W/m², low: < 600 W/m²; variable: > 600 W/m²)
2) AT: Air Temperature (low: (< 15 °C, high: > 15 °C)

4. Hardware-in-the-loop framework

In this section, the development of the networked Hardware-in-the-loop framework will be described in detail. The HiL architecture incorporates TRNSYS as simulation tool, BCVTB as middleware for real-time synchronization and communication between MATLAB and LabVIEW that acts as software interface to the real system testbed. Messaging between MATLAB (simulation) and LabVIEW (real system) is established using MQTT. The developed HiL test bench allows to perform component specific test procedures on the one hand as well as dynamic tests of the complete SHP system, where different thermal and electrical sources and loads can be emulated.

Thermal and electrical demand profiles (SH, DHW, DEP) have been generated through simulation of the SGSHP-P system in TRNSYS using the defined boundary conditions of IEA SHC Task 44 / Annex 38. Here Strasbourg as location with corresponding weather conditions and a single-family household (SFH) with nominal annual space heating demand of 45 kWh/m² (SFH45) was applied. The results are converted to CSV file format and directly loaded by LabVIEW and applied to the real system.

Whole the load demand profiles are independent from the current state of the reals system, the PVT simulation model depends on the current states in the test bench, due to the input volume flow rate and input temperature from the storage tank in the real system to the PVT collector in the simulation model.

The HiL architecture uses MQTT communication protocol, which is a lightweight, open and simple messaging protocol, ideally applicable for distributed communication, transmitting data between multiple, resource-constrained devices having low bandwidth and low power requirements. Therefore, an appropriate application is transmission of sensor data in poor quality networks. MQTT runs in the application layer, over the TCP/IP layers that provide a lossless and bidirectional transmission of any type of data. It is a client-server messaging protocol that encapsulates the one-to-many message distribution of the publish-subscribe model into TCP/IP, making it suitable for use in Machine-to-Machine (M2M) communication and the Internet-of-Things (IoT) architecture, where lots of devices and sensors are connected across the Internet.

The one-to-many architecture is highly suited to control, where a single message to a single channel, called topic, could be used to control many thousands of devices at once.

The publish-subscribe model involves multiple clients with each other, without having any direct connection established between them. All clients communicate with other clients via a central server, called broker. It routes the messages to the appropriate subscribing clients.

As mentioned before, MQTT operates on a channel-wise communication, meaning that it operates on a hierarchical 'topic' structure so that systems can be logically grouped based on application requirements. For example, devices can be grouped into areas in relation to the connected infrastructure, as electrical or thermal subsystem in a residential energy system. Topic subscriptions can include wildcards so that a variety of advanced data filtering can be utilized. For example, a device can subscribe its specific control topic and publish on a specific sensor topic, while the controller subscribes all sensor topics easily through wildcard in the sensor layer in a hierarchical structure. Due to the use of TCP, MQTT connections can be made inherently secure using TLS/SSL, while additional security can easily be added to MQTT systems using authorization servers for publish or subscribe requests.

MQTT has been ratified as an OASIS (Organization for the Advancement of Structured Information Standards) standard in October 2014 (OASIS Standard, 2014) and 2016 as an ISO/IEC 20922 standard (ISO/IEC 20922:2016, 2016), which guarantees consistency across implementations. It has built-in Quality of Service (QoS) mechanisms, which can guarantee message delivery from client to broker, or vice-versa: Depending on the QoS level, communication data increases from QoS 0 to QoS 2

- QoS 0: a message is delivered at most once, without an acknowledgement.
- QoS 1: a message is delivered at least once but duplicates can occur.
- QoS 2: a message is delivered exactly once.

QoS is important because it enables to manage the network quality by controlling the protocol overhead when connection problems occur or bandwidth is low. In our contribution, where the amount of transmitted data is comparatively low, we use QoS 2 to ensure message delivery only once. Mosquitto (Light, 2017) is used as MQTT broker (server) and running on a raspberry pi embedded system.

The HiL architecture we implemented is based on a decentralized communication infrastructure and has some advantages compared to a centralized implementation:

- HiL simulation can run on different computers in the local area network (LAN). As in our work, we run the simulation with MATLAB as one client on one computer (PC1) and LabVIEW as second client and interface to the test bench on another computer (PC2). Therefore, it is also possible to run simulation via remote connection over longer distance from the test bench in a wide area network (WAN).
- In general, any simulation software or algorithm can be used that can handle received data and transmit the data in the appropriate format.
- MQTT protocol and its topics allow a hierarchical message structure depending on the system design, e.g. *\thermal system\heat pump\power consumption* or *\electrical system\PVT\power production.* This allows an efficient message handling, where devices can subscribe and publish only their specific data. For example, where MATLAB receives only data from LabVIEW of topic *\HiL_PVT\L2M* and LabVIEW from MATLAB of topic *\HiL_PVT\M2L*, it is useful, that an additional database client receives data from all topics using a wildcard *\HiL_PVT\#.*
- The extension of the system (sensors and actuators) in future works can be easily realized by installing MQTT enabled devices as provided now by leading manufacturers of instrumentation products.
- The *Last Will and Testament* feature of MQTT provides a way for clients to respond to ungraceful disconnects in an appropriate way. If a client has been disconnected in an improper way the broker sends a predefined message to all the clients. This could help to set the system in a safe state.

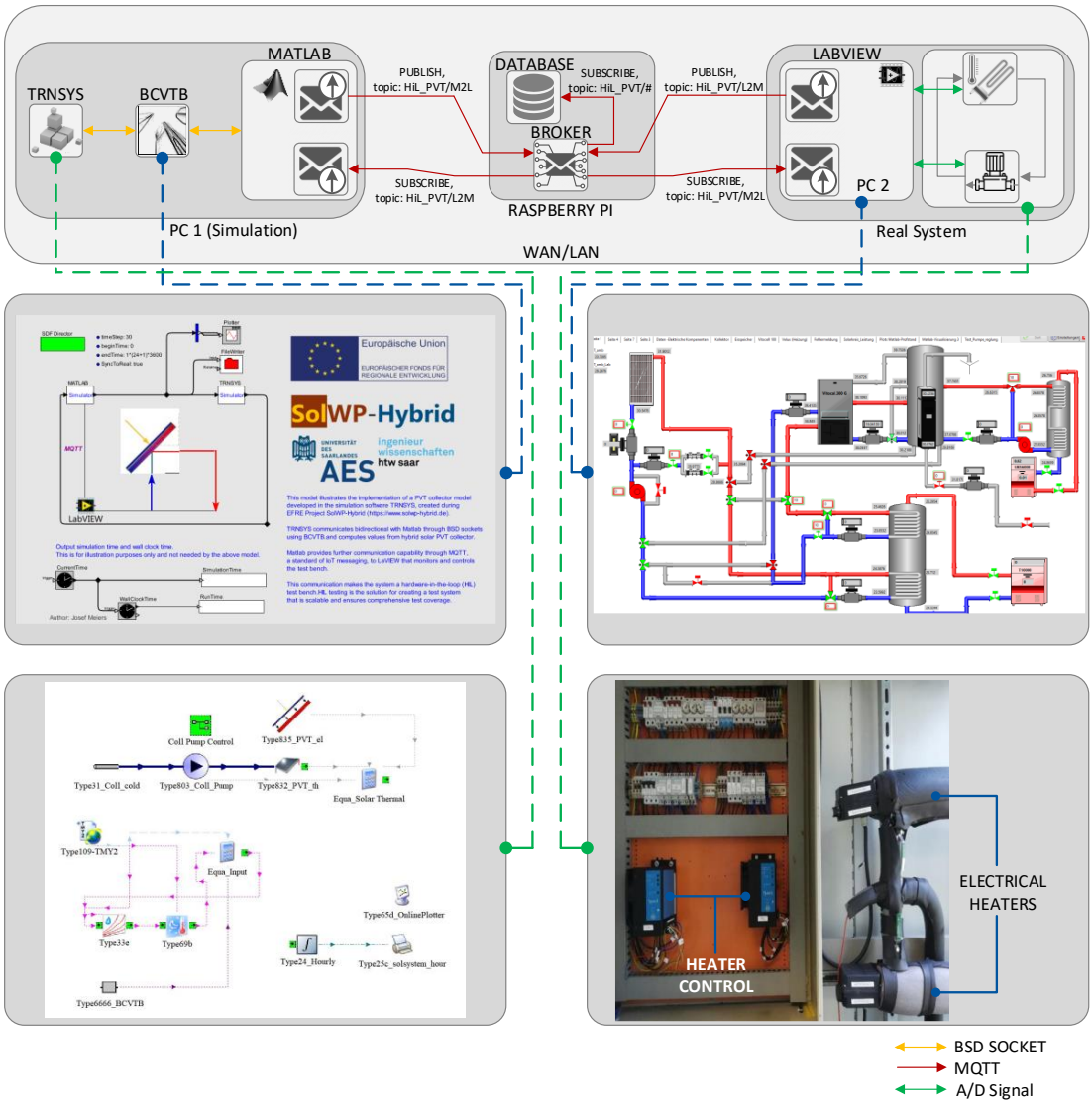

Fig. 2: Hardware-in-the-loop framework (top layer: main architecture of the software tools and communication, middle left: BCVTB model, middle right: LabVIEW visualization of the solar heat pump testbench, bottom left: TRNSYS model of PVT collector, bottom right: electrical heater for thermal power output emulation of PVT collector)

In Figure 2, the architecture of the HiL simulation is visualized, showing the software, networked interconnection with MQTT topics, BCVTB model, LabVIEW visualization of the SHP system, TRNSYS model of the PVT collector subsystem, and the heating system, which emulates the thermal power output of the simulated PVT collector.

In the HiL framework, MATLAB acts as a master to control the simulation entry point. Users start both software endpoints, MATLAB and LabVIEW. After starting MATLAB, it waits, until it receives the first message from LabVIEW, where the considered date and time is given. MATLAB then writes the TRNSYS deck-file with new start date and starts the BCVTB model via command line. BCVTB initializes the TRNSYS model and corresponding MATLAB script in a separate process.

The simulation time step in TRNSYS is 20 seconds (dt_{RT}) and the cycle time step in LabVIEW is 10 seconds (dt_{LV}), where all sensor values will be measured and send via MQTT and actuator values will be received and set. BCVTB stops execution of the simulation after each simulation time step until a real-time timer has fired. Therefore, LabVIEW will only transfer and receive at each second time step of the LabVIEW program loop messages from and to MATLAB. In case, LabVIEW will not receive any data it will do no change in the control (cf. Figure 3).

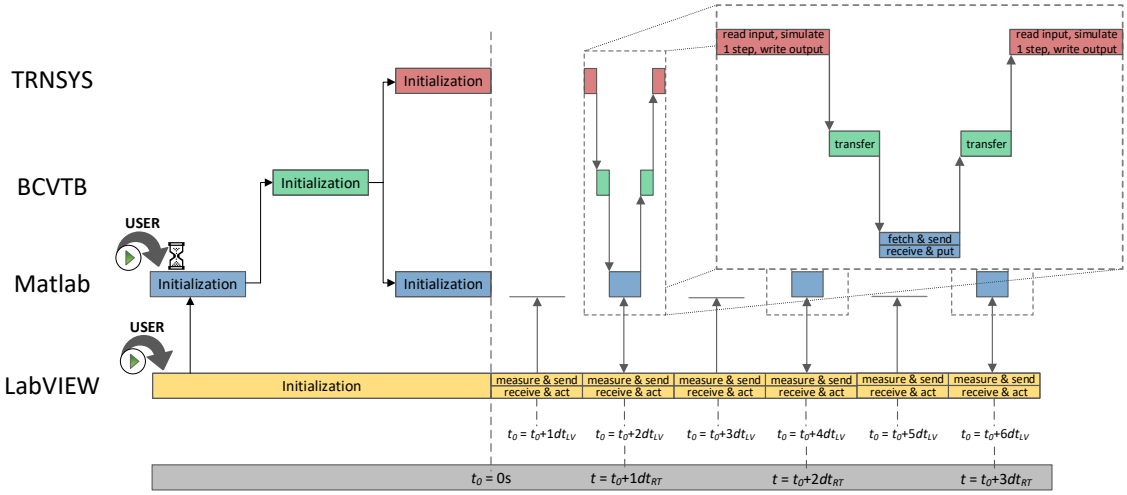

Fig. 3: Visualization of software timing schedule during Hardware-in-the-Loop simulation

In the TRNSYS model of the PVT collector system, outlet fluid temperature ($T_{PVT,out,sim}$), thermal ($\dot{Q}_{PVT,sim}$) and electrical ($W_{el,PVT,sim}$) power outputs are calculated under the given weather conditions also calculated in the simulation. Beside this, control of the PVT collector circulation pump has been implemented in the simulation model. The control signal ($s_{PVT,sim}$), whether solar circulation pump is switched on or off is also an output signal. On the other side, LabVIEW provides four measured values as input signals to the simulation. Temperature of the inlet fluid flow ($T_{PVT,in,testbench}$) and the volume flow rate ($\dot{V}_{PVT,testbench}$) have to be given to the PVT collector model, while storage tank temperature of the DHW area ($T_{ST,DHW,testbench}$) and SOLAR area ($T_{ST,SOLAR,testbench}$) need to be used for decision making of the controller of the PVT collector circulation pump. Input and Output signals are summarized in Table 2.

Tab. 2: Output and input values from and to MATLAB and LabVIEW (M2L: MATLAB to LabVIEW, L2M: LabVIEW to MATLAB)

Output (M2L)		**Input (L2M)**	
PVT collector thermal power	$\dot{Q}_{PVT,sim}$	PVT collector fluid input temperature	$T_{PVT,in,testbench}$
PVT collector electrical power	$W_{el,PVT,sim}$	PVT collector volume flow rate	$\dot{V}_{PVT,testbench}$
PVT collector fluid output temperature	$T_{PVT,out,sim}$	Storage tank DHW temperature	$T_{ST,DHW,testbench}$
PVT collector circulation pump state (ON/OFF)	$s_{PVT,sim}$	Storage tank SOLAR temperature	$T_{ST,SOLAR,testbench}$

5. Results

In this section, we will discuss the quality of the HiL simulation (cf. Section 4) and the results of simulation for the six representative days (cf. Section 3) by introducing two definitions of the seasonal performance factor (SPF) as key performance indicators depending on the system energy boundaries. The SPF quantifies the final energy efficiency of the defined system and is generally defined as the overall useful energy output to the overall driving final energy input over a period of one year.

Here, we consider the time period of the six representative days for its calculation.
SPF with focus on the heat pump (SPF_{HP}) only considers the electrical power consumption of the HP system, considering HP compressor, control system and pumps of internal circulation, heat source and heat sink side (primary and secondary circuit) from grid, PVT collector or battery storage system. Thermal energy production of the HP is measured directly at the output pipes of the HP (cf. equation 1).

Whereas SPF with focus on the solar heat pump systems (SPF_{SHP+}) additionally recognizes the electrical power demand of the SH, DHW and PVT collector circulation pumps (cf. equation 2). While in SPF_{HP} thermal output power behind the HP, at its outlet pipes, is used, in SPF_{SHP+} thermal power extraction behind the storage tank is taken into consideration.

Figure 4 visualizes the energy flows and the energy boundaries for the two SPF definitions.

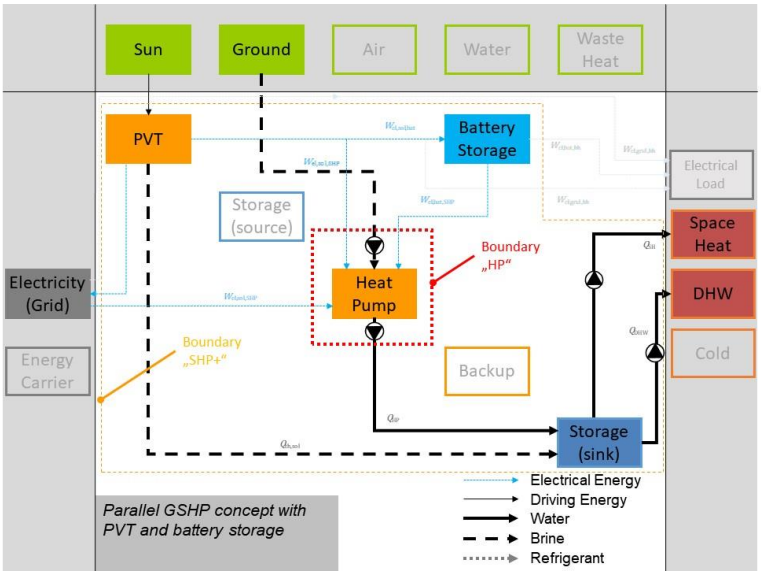

Fig. 4: Visualization of energy flows and boundaries for SPF definitions in the considered solar heat pump system

$$SPF_{HP} = \frac{Q_{HP,SH} + Q_{HP,DHW}}{W_{el,HP}} \quad \text{(eq. 1)}$$

where:

$Q_{HP,SH}$: thermal energy production of HP for SH [kWh]
$Q_{HP,DHW}$: thermal energy production of HP for DHW preparation [kWh]
$W_{el,HP}$: electrical energy demand of the HP system [kWh]

$$SPF_{SHP+} = \frac{Q_{ST,SH} + Q_{ST,DHW}}{W_{el,HP} + W_{el,DHW} + W_{el,SH} + W_{el,PVT}} \quad \text{(eq. 2)}$$

where:

$Q_{ST,SH}$: thermal energy tapping from ST for SH [kWh]
$Q_{ST,DHW}$: thermal energy tapping from ST for DHW preparation [kWh]
$W_{el,DHW}$: electrical energy demand of DHW circulation pump [kWh]
$W_{el,SH}$: electrical energy demand of SH circulation pump [kWh]
$W_{el,PVT}$: electrical energy demand of the PVT collector circulation pump [kWh]

Beside the seasonal performance factor, an equivalent definition of the daily performance is introduced with Daily Performance Factor (DPF). Equations 1 and 2 remain the same, only the time period is reduced to one day.

In Figure 5, DPF for each of the six representative days and the resulting SPF for the overall time are shown. Daily performance factors of the complete solar heat pump system (DPF_{SHP+}) range between 1.8 and 4.0, whereas values of DPF_{HP} are in the range of 1.6 to 3.7.

Except day 101, the values of DPF_{SHP+} are better than DPF_{HP}. For days 41, 272 and 331 this is reasonable to a higher usage of solar thermal energy.

Although solar thermal energy is high on day 101, DPF_{HP} is higher than DPF_{SHP+}. This can be explained due to the behavior of the HP controller. On this day, the HP is switched on in the morning to heat up the SH and DHW zone of the storage tank ($Q_{HP,SH}$, $Q_{HP,SH}$ high) although there is no space heating demand ($Q_{ST,SH}$ low). Additionally, the PVT collector will also charge the storage tank. The amount of heat produced by the heat pump on this day is higher than the heat demand, even without solar thermal energy entry.

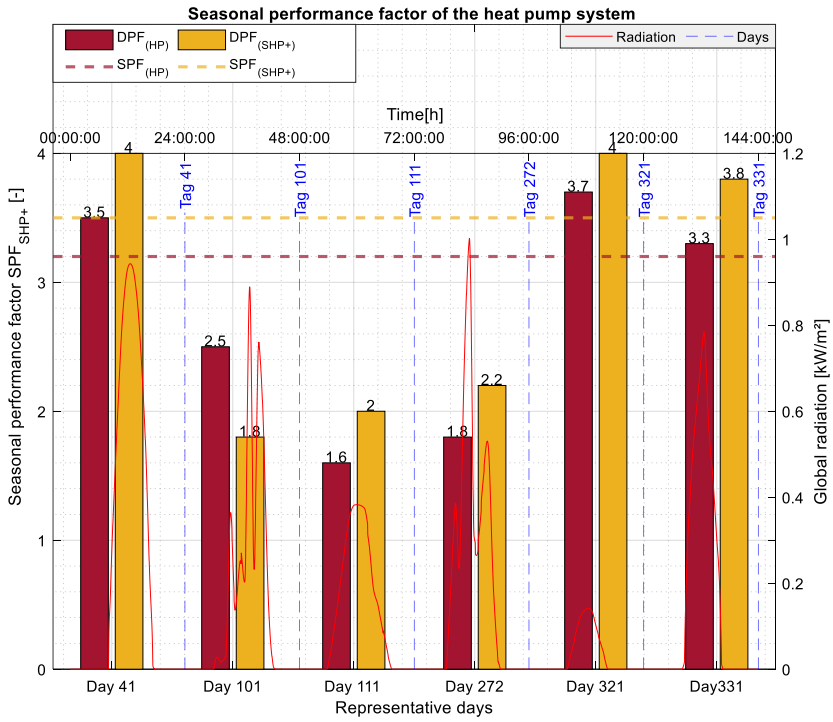

Fig. 5: Daily and seasonal performance factor for representative days and for the entire period in comparison of HP system and complete SHP system

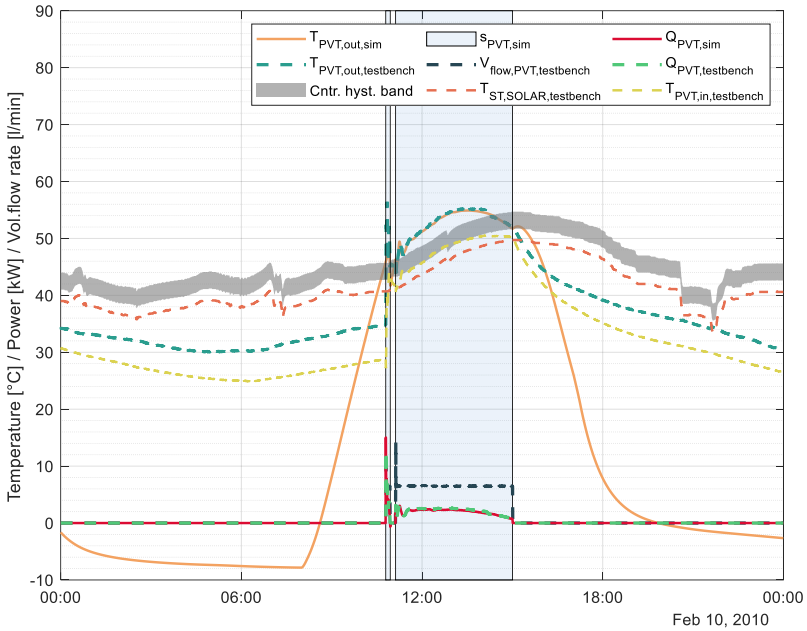

Fig 6:Comparison of simulation and measured values

From Figure 6 it can be seen that the simulated ($T_{PVT,out,sim}$) and measured values of the PVT collector output temperature ($T_{PVT,out,testbench}$) show good accordance in times where the PVT collector circulating pump is switched on ($s_{PVT,sim}$). It can also be seen clearly that there are overshoots in the PVT collector volume flow rate, when the circulating pump is switched on. This leads to oscillating behavior in the measured PVT collector output temperature. At the current state, this is an unavoidable behavior, since the installed volume flow valve is quite slow (it takes about 60 seconds for fully opening) and the implemented PID controller for the volume flow does not recognize the time delay in the simulation framework communication.

It has been observed that this time delay is three simulation time steps and leads to an oscillating behavior. This can be improved by decreasing the HiL simulation time step but is limited due to installed measuring equipment.

Since the electronic power source is very fast to emulate the simulated electric PVT collector power output, deviations can be neglected compared to the thermal system.

Table 3 shows root mean square error (RMSE) (cf. equation 3) for PVT collector output temperature and the thermal power output for each of the six representative days.

$$RMSE = \sqrt{\frac{1}{N}\sum_{n=1}^{N}\left(x - x_{ref}\right)^2} \qquad \text{(eq. 3)}$$

The error is only calculated in time steps, where the circulating pump is switched on. In day 3 and 5 there is no thermal power output, since the calculated output temperature of the PVT collector is not high enough.

Root mean square error of the PVT collector output temperature ($RMSE_T$) ranges from 1.01 to 2.12 K, error of thermal output power ($RMSE_{dQ}$) from 0.62 to 0.82 kW and thermal energy output ($RMSE_Q$) from 0.05 to 0.58 kWh (relative values from 0.8 to 7.3 %). These values derive from the continuous time delay in the communication and from the oscillating behavior of the controller.

As an additional quality criterion, comparing of energies for domestic hot water and space heating preparation and household electricity demand over the entire test sequence show relative deviations of about 1.2-2.8 % and are therefore considered to be small. Concluding from that, the HiL emulation shows satisfactory results, improvements are expected with an improved control of the volume flow rate in the PVT collector emulation loop.

Tab. 3: Root Mean Square Error of PVT collector output temperature, thermal power and thermal energy between simulation and testbench

Day No.	$RMSE_T$ [K]	$RMSE_{dQ}$ [kW]	$RMSE_Q$ [kWh]([%])
1	1.01	0.65	0.58 (7)
2	1.17	0.62	0.48 (7.3)
3	-	-	-
4	2.12	0.82	0.05 (0.8)
5	-	-	-
6	1.55	0.68	0.06 (1.5)

6. Conclusion

The proposed HiL framework is based on a decentralized communication infrastructure, which offers advantages compared to a centralized implementation such as remote simulation. The used MQTT protocol can be secured and the underlying communication protocol TCP is robust. As there is no integrated software tool that fulfills our requirements on modeling and control, we have proposed a new framework that connects the following software tools: MATLAB, TRNSYS, LabVIEW and BCVTB.

We selected six representative days, where the global horizontal irradiation and the ambient temperature were determined in such a way, that these days reflect the different weather conditions of the whole year. This method differs from described test procedures.

In conclusion the comparison of simulated and measured output temperature and thermal energy of the PVT collector in the use case shows that the error can be considered as acceptable small.

7. Acknowledgements

This work was part of the research project SolWP-Hybrid. The project was funded by the federal state of Saarland and the European Regional Development Fund (ERDF 2014-2020). The authors are grateful for this support and thank the project partners, Viessmann Heizsysteme GmbH, Sonnenkraft GmbH, DualSun and Stadtwerke Saarlouis for their support and cooperation.

8. References

Bitter, R., Mohiuddin, T., Nawrocki, M.: , 2018 *LabVIEW: Advanced programming techniques*: Crc Press.

Frank, E., Haller, M., Herkel, S., Ruschenburg, J.: , Systematic classification of combined solar thermal and heat pump systems, *EuroSun 2010, Graz (Austria), 29 September - 01 October.* http://dx.doi.org/10.18086/eurosun.2010.14.04.

Haberl, R., Haller, M.: *Concise Cycle Test - Beschreibung der Prüfmethode*. Rapperswil (CH), 2018.

Haberl, R., Haller, M. Y., Papillon, P., Chèze, D., Persson, T., Bales, C.: *Testing of combined heating systems for small houses: Improved procedures for whole system test methods: Deliverable 2.3*. MacSheep - New Materials and Control for a next generation of compact combined Solar and heat pump systems with boosted energetic and exergetic performance, 2015.

Hadorn, J.-C.: , 2015 *Solar and heat pump systems for residential buildings*: John Wiley & Sons.

Haller, M., Perers, B., Bale, C., Paavilainen, J., Dalibard, A., Fischer, S., Bertram, E.: TRNSYS Type 832 v5.10 „Dynamic Collector Model by Bengt Perers ": Updated Input-Output Reference, 2014.

IEA SHC: Task 44/HPP Annex 38: The reference framework for system simulations. *International Energy Agency Solar Heating and Cooling Programme*, 2013.

ISO/IEC 20922:2016: Information Technology — Message Queuing Telemetry Transport (MQTT) v3.1.1, 2016. URL: https://www.iso.org/obp/ui/#iso:std:iso-iec:20922:ed-1:v1:en,(2022-03-29).

Jonas, D.: *SHP-SimLib. A library of solar and heat pump subsystem simulation models in TRNSYS*, 2023. URL: https://github.com/DnJns/SHP-SimLib/,(2023-04-24). http://dx.doi.org/10.5281/zenodo.7695126.

Jonas, D., Lämmle, M., Theis, D., Schneider, S., Frey, G.: Performance modeling of PVT collectors: Implementation, validation and parameter identification approach using TRNSYS. *Solar Energy*, *193*(2), pp. 51–64, 2019. http://dx.doi.org/10.1016/j.solener.2019.09.047.

Jonas, D., Theis, D., Frey, G.: , Implementation and Experimental Validation of a Photovoltaic-Thermal (PVT) Collector Model in TRNSYS, *EuroSun 2018, Rapperswil (Switzerland),10-13 September.* http://dx.doi.org/10.18086/eurosun2018.02.16.

Light, R. A.: Mosquitto: Server and client implementation of the MQTT protocol. *The Journal of Open Source Software*, *2*(13), p.265, 2017. http://dx.doi.org/10.21105/joss.00265.

MATLAB: , 2017 *version 9.3.0 (R2017b)*. Natick, Massachusetts: The MathWorks Inc.

Menegon, D., Haberl, R., Haller, M.: , Comparison of two whole system test methods: CCT and PLPE, *EuroSun 2018, Rapperswil (Switzerland), 10-13 September.* http://dx.doi.org/10.18086/eurosun2018.12.02.

Menegon, D., Soppelsa, A., Fedrizzi, R.: Development of a new dynamic test procedure for the laboratory characterization of a whole heating and cooling system. *Applied Energy*, *205*, pp. 976–990, 2017. http://dx.doi.org/10.1016/j.apenergy.2017.08.120.

Meteonorm: *Meteonorm 6.1.0.9,: Global Meteorological Database for Engineers, Planners and Education, Software and Data on CD-ROM*. Bern, Switzerland,: Meteotest, 2009.

OASIS Standard: MQTT version 3.1. 1 Plus Errata 01: OASIS Standard Incorporating Appoved Errata 01, *1*, 2014. URL: http://docs. oasis-open. org/mqtt/mqtt/v3,(2022-03-28).

TRNSYS: *TRNSYS - A Transient System Simulation Program: University of Wisconsin, Madison, Wisconsin, United States of America.* version 18.02: Solar Energy Laboratory, 2020.

Wetter, M., Haves, P.: *A modular building controls virtual test bed for the integrations of heterogeneous systems.* Lawrence Berkeley National Laboratory, Berkeley, Calif., Oak Ridge, Tenn., 2008.

Development and Indoor Testing of a High-Performance PV/Thermal Panel with Integral Stagnation Control

Lucio Mesquita[1], Steve Harrison[2], Roy Indranil[2], and Ben Stinson[2]

[1] Natural Resources Canada, CanmetENERGY-Ottawa, Ottawa (Canada)

[2] QSBR Innovations Inc., Kingston (Canada)

Abstract

Photovoltaic-thermal (PVT) collectors, as devices that can provide both electricity and heat, have the potential to achieve lower installation costs and higher total energy production for the same roof or ground area than separate photovoltaic (PV) and solar thermal (ST) systems. High-performance PVT collectors can enhance the economics of PVT systems by producing heat that can be used directly for domestic hot water systems, space heating and industrial process applications. The increased maximum temperature in high-performance PVT collectors carries an inherent risk of absorber overheating under stagnation conditions. Many PV panels' damage mechanisms are related to higher temperatures, and some of them can lead to catastrophic failures. This work presents outdoor and indoor test results for PVT collectors equipped with an anti-stagnation mechanism, evaluating maximum absorber temperature under stagnation conditions. A glazed PVT collector prototype was built by adapting a commercially available PVT collector with an anti-stagnation device. The prototype was subsequently modified to incorporate low-emissivity glass top glazing. The testing conducted has shown the effectiveness of an air-venting channel on the back of the absorber in reducing the maximum stagnation temperature of the PVT collector, even when oriented in a relatively challenging landscape orientation. Finally, the use of a solar simulator for stagnation temperature measurement has been shown to produce results similar to those measured outdoors and offers the advantage of obtaining steady-state repeatable conditions

Keywords: *photovoltaics, solar thermal, PV/Thermal, PVT, stagnation, overheating, Canada*

1. Introduction

Increasing the use of non-emitting, renewable energy sources is an essential element of greenhouse gases (GHG) emissions reduction initiatives. In Canada, energy use in housing, buildings, and communities accounts for about a quarter of the country energy consumption (NRCan, 2019) and 17% of its GHG emissions (ECCC, 2022). Residential space heating (SH) consumed 885 PJ of energy in 2016, 47% of which was supplied by natural gas (26% by electricity) (NRCan, 2016). Domestic hot water (DHW) represented an annual load of 284 PJ of which 68% was supplied by natural gas. Photovoltaic-thermal (PVT) collectors, as devices that can provide both electricity and heat, offer interesting opportunities to support GHG emissions reductions. They have the potential to achieve lower installation costs and higher total energy production per m^2 of occupied roof space than separate photovoltaic (PV) and solar thermal (ST) systems, as shown by Lämmle et al. (2017).

As with solar thermal collectors, a PVT collector can have either a gas or a liquid as the heat transfer fluid. The collectors can also be glazed or unglazed, and non-concentrating or concentrating. Until now, most PVT collectors available in the market are liquid, unglazed and non-concentrating (De Keiser et al., 2017). This is in part because unglazed collectors have a small impact on the module's electricity production and require minimal or no changes to the standard PV panel frame. However, unglazed PVT collectors have limited potential to generate heat at temperatures that can be used directly for domestic water heating, space heating and industrial processes. Therefore, in recent years, there has been a greater effort in the development of high-temperature PVT (HT-PVT) collectors. High performance at elevated temperature levels is mostly achieved by reducing convective thermal losses, as with the vacuum insulated model developed by UK-based Naked Energy (Mellor et al, 2018) and/or by reducing the radiative thermal losses, as presented by Lämmle et al. (2016).

© 2022. The Authors. Published by International Solar Energy Society
Selection and/or peer review under responsibility of Scientific Committee
doi:10.18086/eurosun.2022.12.13 Available at http://proceedings.ises.org

2. Overheating Protection in Solar Thermal Collectors

Overheating protection has been developed for solar thermal collectors to prevent damage to the heat transfer fluid and/or to the absorber. Harrison and Cruickshank (2012) reviewed different technologies used for stagnation control in solar thermal systems. The authors divided the stagnation control approaches into system, array and collector levels. They also pointed out the main advantage of anti-stagnation technologies that are integral to the collector design: by addressing stagnation at the source, this approach maintains lower collector temperatures during stagnation, therefore eliminating negative effects of excessive temperatures, e.g., thermal stresses, over-pressures, and material and heat transfer fluid degradation.

Harrison et al. (2004a) proposed an innovative integral stagnation control. The approach uses a passive venting channel located below the absorber (Fig. 1). The bottom (or back) of the channel is insulated to reduce heat loss during normal operation. Flow through the channel is induced by buoyancy-driven natural convection, initiated by a valve assembly designed to open at a predetermined temperature. An automatic valve controls airflow through the channel, effectively reducing the maximum absorber temperature under stagnation conditions.

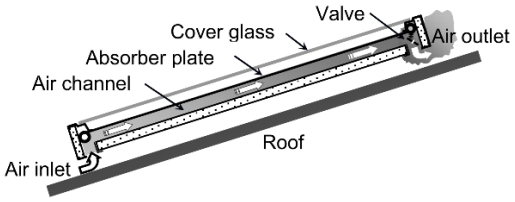

Fig. 1: Conceptual design of a solar collector with integral stagnation temperature control

The increased performance in high-temperature PVT collectors carries an inherent risk of absorber overheating. Many PV cells and their encapsulation have damage mechanisms that increase with operational temperatures, and some of them can lead to catastrophic failures, depending on the maximum temperature reached by the absorber. The collector designer has essentially two choices: to develop new PVT collectors based on new materials that can withstand the stagnation temperatures (Matuska et al., 2015) or to control stagnation maximum temperature.

3. Prototype Design

In the present work, a HT-PVT collector prototype was designed and built with the same integral stagnation control presented by Harrison et al. (2004b). The prototype was built by adapting a commercially available PVT collector, Solimpeks model Powertherm, with the anti-stagnation device. Table 1 presents the relevant specifications for the PowerTherm collector.

Tab. 1: Commercial collector specifications, from Eurofin (2011) and Solimpeks (2019).

Overall Dimensions (mm)	870 x 1640 x 105
Gross Area (m^2)	1.427
Aperture Area (m^2)	1.420* (1.268)
Absorber Area (m^2)	1.400* (1.214)
Absorber Material	copper
Absorber Thickness (mm)	0.12
Number of Risers	14
Risers OD (mm)	8
Headers OD (mm)	22
Glazing Material	low iron tempered glass
Glazing thickness (mm)	4
PV Cell Material	Si, Mono-Crystalline
Nominal PV Power (W)	180
Module Efficiency (standard conditions) (%)	12.90
Temperature coefficient of Pmax (%/°C)	-0.45

***See discussion regarding measured dimensions below.**

It is relevant to note that our measurements indicate significantly different aperture and absorber dimensions than what was reported by Eurofin (2011) and Solimpeks (2019). During this investigation, an aperture area of 1.268 m^2 and an absorber area of 1.214 m^2 was measured.

For the prototype, a 44 mm air channel and 25 mm thick polyisocyanurate (PIR) insulation board replaced the original collector's 50 mm glass wool back insulation. The 25 mm PIR insulation has approximately the same conductive thermal heat transfer coefficient as that of the 50 mm glass wool (0.93 W/m^{2}K for PIR vs 0.89 W/m^{2}K for glass wool). Temperature sensors were added to the back of the absorber and positioned as shown on Fig. 2. Both the back of the absorber and the front of the polyisocyanurate board were painted black to enhance the radiative heat transfer between the two surfaces. Air channel openings of 30 mm were installed along the full extension of the top and bottom of the collector (i.e., for the landscape orientation). Those openings were closed with foam insulation and sealed with aluminium tape during the "closed" tests, and then opened to evaluate the impact of the air channel airflow on maximum stagnation temperatures (see Fig. 3). A commercial version of such solution would have automatically operated valves/dampers as described by Harrison et al. (2004a).

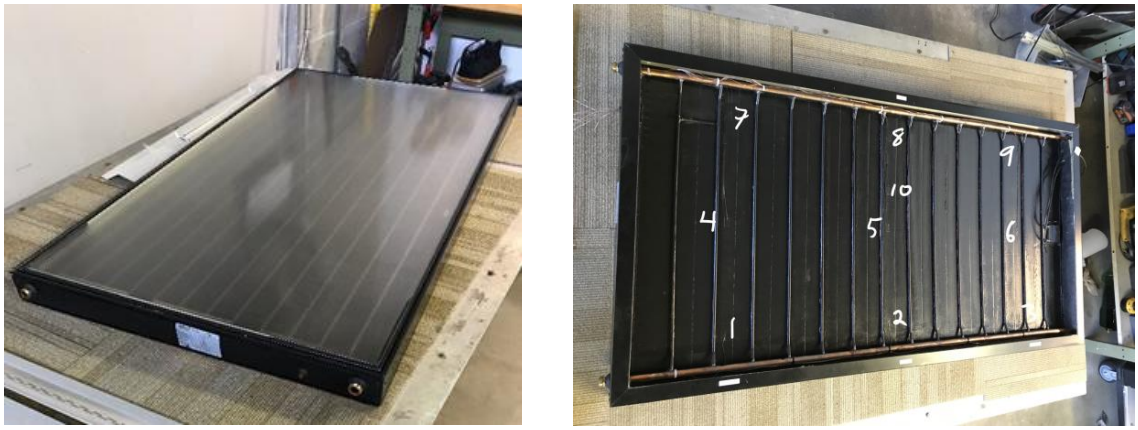

Fig. 2: Original commercial PVT collector (left) and collector being modified (right). Numbers denote the position of temperature sensors that were attached to the back of the absorber.



Fig. 3: Photo showing the 30 mm air channel openings installed along the full extension of the top and bottom of the collector (left, open channels), (right, channels sealed).

After the outdoor and initial indoor tests, the collector was modified once again. A low-iron glass with a low emissivity coating replaced the original top glazing. This glass, manufactured by Pilkington under the trade name Advantage Low-e, has, according to the manufacturer, an infrared emissivity of 0.1428.

4. Stagnation Testing

4.1 Outdoor Testing

Due to COVID-19 restrictions, the initial testing in 2020 of the prototype with the original glazing was done outdoors. The tests were conducted at NRCan's National Solar Test Facility (NSTF), in Mississauga, Ontario

(43.6°N Latitude). Although the vented air channel had been successfully used in solar thermal collectors before (Harrison et al., 2004), questions remained regarding the cooling capacity of the channel for a "landscape" configuration such as in this prototype, as there is a reduced buoyancy to drive the airflow in such configuration, as compared to a "portrait" configuration. The panel was mounted at 30° tilt, facing south. Daily irradiance, wind speed, panel and ambient temperatures were recorded with the air-vent open and closed. Figure 4 shows the prototype mounted for testing. Measured stagnation temperatures on the absorber and insulation surfaces and in the air-stream (at the center of the back of the panel) are shown on Figs. 5a and 5b for two similar days and with the vent channel closed and open. Results are summarized in Table 2. The stagnation temperature was measured by sensor 10, which is positioned at the centre of the absorber width (along the direction of the headers), and at 2/3 of the absorber height (along the direction of the risers). Under stagnation, absorber temperatures reached 124°C with the vent closed, as opposed to 95°C when the vent was open.

Tab. 2: Summary of outdoor stagnation test results for Aug 20 (channel closed) and Aug 23 (channel open).

Period 1PM to 2:30PM	Avg. Solar Rad. (W/m^2)	Avg. Amb. Temp. (°C)	Avg. Wind Speed (m/s)	Peak Absorber Temp. (°C)
Vent Closed Aug 20	1106	27	1.50	124
Vent Open Aug 23	1108	32	1.55	95



Fig. 4: Prototype undergoing outdoor stagnation testing (left), and open vent in rear of collector (right).

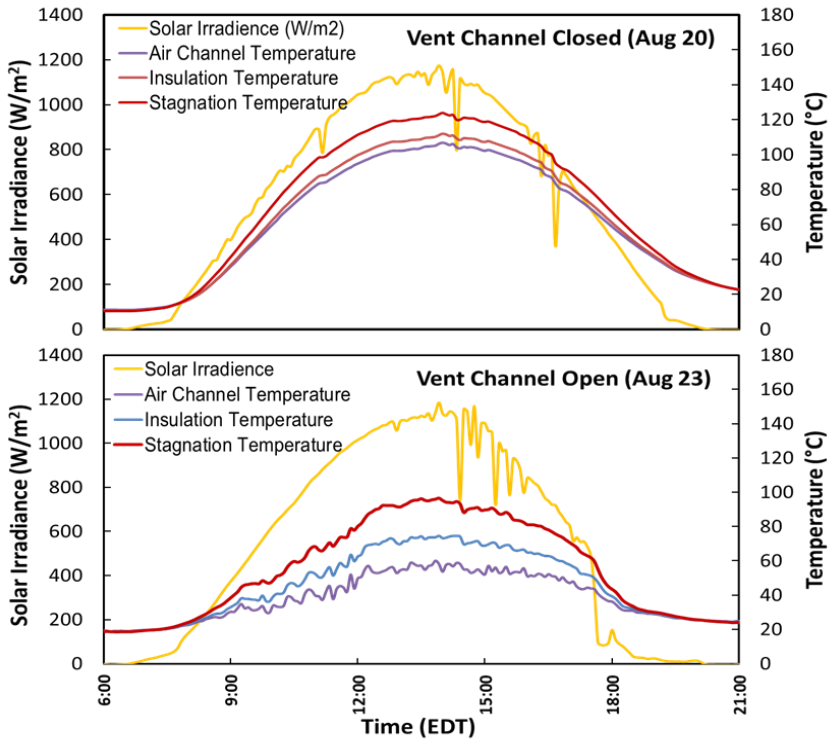

Fig. 5: Test results for prototype undergoing outdoor stagnation testing, a) top – air vent closed, b) bottom- air vent open.

4.2 Indoor Testing

Once most COVID-19 restrictions were lifted, the collector prototype was tested indoors under controlled conditions using the environmental chamber and solar simulator at the National Solar Test Facility, Fig. 6. The simulator uses a 200 kW VORTEK single-source arc-argon lamp. The prototype was mounted at 60° tilt and all tests were performed at a wind speed of 0.65 m/s. Twelve different conditions were tested, as shown in Table 3.

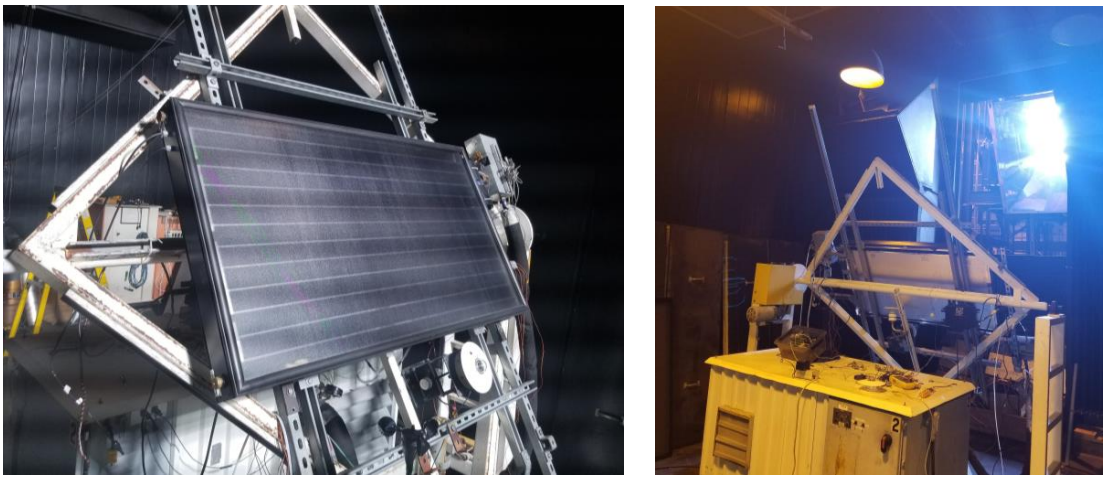

Fig. 6: Collector mounted for indoor stagnation testing using the solar simulator.

The highest stagnation temperature was achieved with the collector operating under open circuit, at irradiation level of 1000 W/m^2, closed vent and low-e glazing. In this case, the stagnation temperature reached 143.9 °C. As with the outdoor tests, opening the air vent provided significant relief regarding the stagnation temperature. For the conditions mentioned above, opening the vent reduced the stagnation temperature from 143.9 °C to 82.1°C. By reducing the heat losses, the use of low-e glazing leads to significant increases in stagnation temperatures. Under the same conditions of cases 1 and 3, the stagnation temperature for the collector with low-e glazing was 23.3°C than the collector with the original glass. However, in the case of operation with the air vent open, the collector with low-e glazing presented a stagnation temperature lower than the collector with the original glass. The explanation for this is the fact that, with the air vent open, the heat losses are dominated by convective processes and, at the same time, less irradiation reaches the absorber due to the lower solar transmittance of the low-e glass. The test results are also grouped according to their test configuration and plotted in Figs. 7 to 10 for comparison.

Tab. 3: Test cases for the indoor stagnation tests.

Case#	Nominal Irradiation (W/m2)	Vent	PV Operation	Top Glazing	T_{STAG} (°C)	Avg Irrad (W/m^2)	Avg Tamb (°C)
1	1000	Closed	OC	Low-e	143.9	1041	31.2
2	1000	Closed	MPP	Low-e	133.8	1044	31.6
3	1000	Closed	OC	Original	120.6	1059	31.4
4	1000	Closed	MPP	Original	111.2	1061	31.6
5	800	Closed	OC	Original	102.7	799	31.4
6	800	Closed	MPP	Original	94.1	799	31.3
7	600	Closed	OC	Original	88.3	603	31.1
8	1000	Open	MPP	Original	86.7	1060	31.4
9	1000	Open	OC	Low-e	82.1	1043	31.7
10	1000	Open	MPP	Original	79.7	1057	31.7
11	800	Open	OC	Original	75.4	798	31.5
12	600	Open	OC	Original	66	599	31.2
OC= open circuit, MPP= maximum power point, Tstag is the maximum temperature at sensor 10							

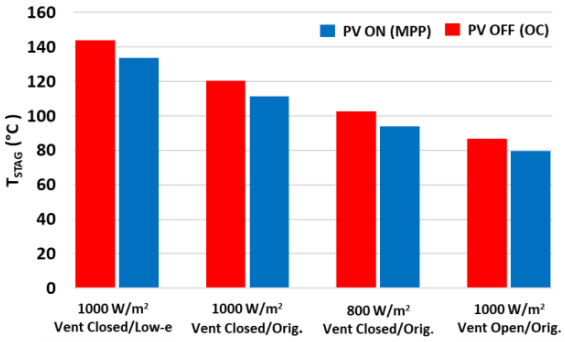

Fig. 7: Stagnation temperatures for cases with PV operating in open circuit (OC) and maximum power point (MPP).

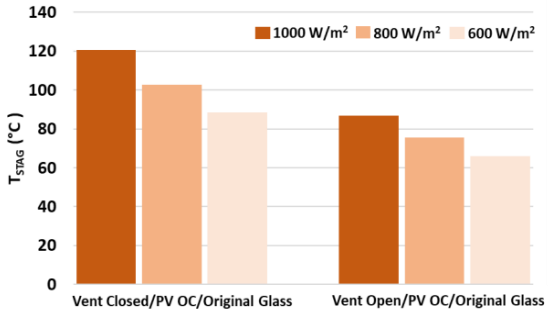

Fig. 8: Stagnation temperatures for cases with varying irradiation levels.

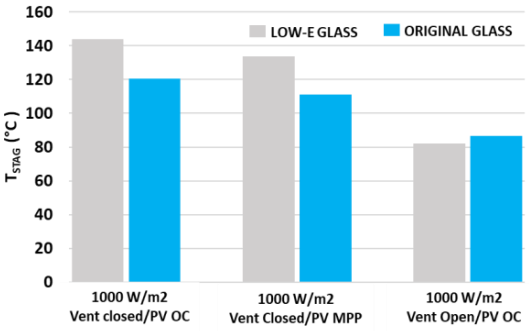

Fig. 9: Stagnation temperatures for cases with the original and low-e glazings.

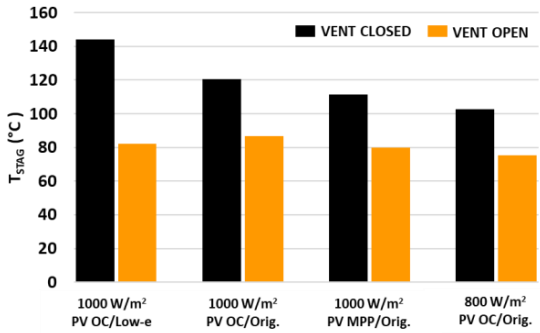

Fig. 10: Stagnation temperatures for cases with air vent channel closed and open.

5. Conclusions and Future Work

As anticipated, the results confirm that when PV output is reduced, stagnation temperatures further increased. The testing conducted has shown the effectiveness of the air channel in reducing the maximum stagnation temperature of the PVT collector, even when oriented in a relatively challenging landscape orientation.

The results also show that the addition of a Low-E coating to the interior of an exterior glazing in a PVT collector significantly increases stagnation temperature to potentially damaging levels. For the Low-E glazing used, the solar transmittance was not as high as the transmittance of the "solar" glass used in the unmodified collector. If further improvements in the solar transmittance of Low-E coated glass are made, stagnation temperatures would be significantly increased, requiring the redesign of PVT collectors, or the inclusion of active stagnation control to deal with times when the thermal and PV loads are reduced.

Finally, the use of a solar simulator for stagnation temperature measurement has been shown to produce results similar to those measured outdoors and offers the advantage of obtaining steady-state repeatable conditions. It is important to note the solar simulator facility used for this study consists of a single-source lamp equipped with water cooled mirror elements that reduce excessive thermal irradiance, while also providing a highly collimated beam that closely matches natural sunlight.

Future work will include additional testing of the prototypes to fully characterize their thermal and PV efficiency under different operational conditions.

6. Acknowledgments

The authors would like to thank Khaled Ayyad (Element Materials) for his technical support and his contribution to many discussions on the topics studied in this paper. Funding for this project was provided by NRCan's Program of Energy Research and Development (PERD).

7. References

De Keiser, C., Bottse, J. and De Jong, M., 2017, PVT Benchmark – an overview of PVT modules on the European market and the barriers and opportunities for the Dutch market, SEAC/TNO, Eindhoven, Netherlands.

ECCC, 2022. 2030 Emissions Reduction Plan: Canada's Next Steps for Clean Air and a Strong Economy. Environment and Climate Change Canada. Gatineau, Quebec.

Eurofins – Modulo Uno S.P.A, 2011, Test report M1.11.NRG.0319/43724, Torino, Italy.

Harrison, S. and Cruickshank, C., 2012, A review of strategies for the control of high temperature stagnation in solar collectors and systems. Energy Procedia, 30, pp.793-804, https://doi.org/10.1016/j.egypro.2012.11.090

Harrison, S.J., Lin, Q., Mesquita, L.C.; Valletta, D.A., 2004a, Method and apparatus for solar collector with integral stagnation temperature control - WO 2004070289 A1. Patent.

Harrison, S.J., Lin, Q., Mesquita, L.C.S., 2004b, Integral Stagnation Temperature Control for Solar Collectors. SESCI 2004 Conference, University of Waterloo, Ontario, Canada August 21st–25th, 2004.

Lämmle, M., Kroyer, T., Fortuin, S., Wiese, M. and Hermann, M., 2016, Development and modelling of highly efficient PVT collectors with low-emissivity coatings. Solar Energy, 130, pp.161-173, https://doi.org/10.1016/j.solener.2016.02.007.

Lämmle, M., Oliva, A., Hermann, M., Kramer, K. and Kramer, W., 2017, PVT collector technologies in solar thermal systems: a systematic assessment of electrical and thermal yields with the novel characteristic temperature approach, Solar Energy, 155, pp. 867-879, https://doi.org/10.1016/j.solener.2017.07.015.

Matuska, T., Sourek, B., Jirka, V., and Pokorny, N., 2015, Glazed PVT Collector with Polysiloxane Encapsulation of PV, Cells: Performance and Economic Analysis, International Journal of Photoenergy, Volume 2015, Article ID 718316., https://doi.org/10.1155/2015/718316.

Mellor, A., Alonso Alvarez, D., Guarracino, I., Ramos, A., Riverola Lacasta, A., Ferre Llin, L., Murrell, A., Paul, D., Chemisana, D., Markides, C. and Ekins-Daukes, N., 2018, Roadmap for the next-generation of hybrid photovoltaic-thermal solar energy collectors. Solar Energy, 174, pp.386-398, https://doi.org/10.1016/j.solener.2018.09.004.

NRCan, 2016, Table 7: Space Heating Secondary Energy Use and GHG Emission by Energy Source, NRCan Energy Use Statistics Residential Sector, Natural Resources Canada, Ottawa, Ontario.

NRCan, 2019, Canada's Secondary Energy Use (Final Demand) by Sector, End Use, and Subsector, National Energy Use Database, Natural Resources Canada, Ottawa, Ontario.

Solimpeks, 2019. General Catalogue - 022019/1. Available at https://solimpeks.com.tr/wp-content/uploads/dokumanlar/kataloglar/Solimpeks_EN.pdf, Accessed 07/09/2022.

Zondag, H.A., 2008, Flat-plate PV-Thermal collectors and systems: a review. Renew. Sustain. Energy Rev., 12, pp. 891-959, https://doi.org/10.1016/j.rser.2005.12.012.

A Performance Analysis of a Parabolic Trough Collector Using Numerical Computation and Real-Time Parameters

Prashant Saini[1], Pradeep Kumar[1], Atul Dhar[1], Satvasheel Powar[1]

[1] Indian Institute of Technology Mandi, Mandi, (India)

Abstract

This study models the parabolic trough collector (PTC) to assess the efficiency and heat flux distribution at the cylindrical receiver tube's outer wall. The algorithm used is Monte Carlo Ray Tracing (MCRT). A few authors have published the equations and their methods for building the MCRT-based algorithm. This work shows a simple and straightforward technique for improving the accuracy of MCRT-based algorithms while reducing processing time. For the PTC receiver tube's outside wall, the MCRT heat flux is employed as an input for numerical computation. These computations are carried out using ANSYS (Fluent 18.1). Temperature-dependent features of the heat transfer fluid and thermal radiation between the glass wrap and the absorber tube are also considered. A solar steam plant was built by Protarget, Germany, and operated by LUIT Renewables India, and the experimental results of Sandia Laboratory in the USA are within 2% of the computational results. The effect of variations in the real-time parameters, such as solar radiation, heat transfer fluid mass flow rate, wind speed, and glass envelope effect on PTC efficiency, are investigated further. According to the findings of this study, the PTC efficiency is affected by all of these parameters.

Keywords: Monte Carlo Ray Tracing, Computational Fluid Dynamics, Heat Transfer Fluid, Effective Statistic Random Method, PTC, CSC, parallel computing.

1. Introduction

Due to the growing population worldwide, energy demand for technological and industrial growth is increasing rapidly. Fossil fuels play a significant role in furnishing such energy demand, leading to conventional resource depletion and contributing to global warming (Hang et al. (2008), Fan et al. (2017), Cheng et al. (2015)). According to the U. N. Sustainable Development Goal 9 (Industry, Innovation, and Infrastructure) report, India's industrial sector consumed 32 % of energy in 2014, 74 % of which was used for heating production only. Process heat requirements in the industry vary from 50 °C to 400 °C (Chargui et al. (2021), Bellos et al. (2020)). Solar energy is a powerful resource with the potential to meet this energy/heat requirement. Solar energy is abundant in nature and technologically suitable for commercial applications (Cheng et al. (2013), Vouros et al. (2020)). According to the 2019 International Energy Agency (IEA) report, gross world energy usage in 2017 was 1.6×10^{14} kWh. The World Energy Assessment report estimated that the total energy received from the Sun to the Earth's surface is approximately 1.4×10^{14} TWh. Using 1-2 % of received power can meet world energy requirements.

Solar photovoltaic modules convert solar energy directly to electricity. But they have significantly lower efficiency as compared to solar thermal (Bartela et al. (2021)). Different solar collectors are engaged for thermal use viz flat plate collectors, evacuated tube collectors, line-focus collectors, point-focus collectors, and concentration collectors (Tzivanidis et al. (2015), Saini et al. (2018)). The option of a solar thermal collector depends on heat (outlet temperature) requirements. CSCs can achieve high temperatures ranging from 100 °C to 500 °C compared to non-concentrating solar collectors. Solar concentrators focus on the receiver using lenses or mirrors. These lenses help focus solar radiation from relatively large areas onto a (smaller area) receiver, where radiation is (usually) used to generate steam (Khandelwal et al. (2019), Wang et al. (2014)). These temperature levels can easily meet industry requirements without increasing the atmospheric carbon footprint. Many studies reported using CSCs (Concentrating Solar Collectors) and mainly focusing on solar collectors converting lower-density solar energy to mechanical energy (Cheng et al. (2014), Almanza et al. (2002), Powar et al. (2020)). When run in a temperature range of 250 °C – 565 °C, the real-world devices assert the CSCs' energy conversion efficiency between 23 % and 35 %.

Many researchers investigated the collector's optical efficiency. Burkhard et al. (1973) deduced an empirical relationship to determine solar energy flux on an absorber surface. Using this analytical relationship, Burkhard et al. (1973) assess the tube's heat flux. Evans et al. (1977) established an integral relationship governing solar energy flux distribution over parabolic trough collector (PTC) flat absorbers. The surface slope error has been investigated and reflects the effect of slope error on severity (Tyagi et al. (2007)). Jeter et al. (1986) built an

© 2022. The Authors. Published by International Solar Energy Society
Selection and/or peer review under responsibility of Scientific Committee
doi:10.18086/eurosun.2022.12.14 Available at http://proceedings.ises.org

integrated model for determining the distribution of solar energy on both types of absorber tubes, i.e., circular absorber tube and flat absorber tube. This resulting formulation helps to decide PTC's performance. Later, Jeter et al. (1986) developed a model that considered the non-uniform source and incorporated reflection, absorption, and transmission effects to determine the PTC's optical efficiency (Jeter et al. (1987)).
Since PTC efficiency is also controlled by several other factors, including solar radiation, heat transfer fluid's mass flow rate, heat transfer fluid temperature, and wind velocity, understanding the effect of these factors on PTC efficiency is required. To the best of our knowledge, no such study analyses these crucial parameters' effect on PTC conversion efficiency.
Complex mathematical equations are included in these model types (Wang et al. (2021)). Adjusting geometric and optical characteristics in these models, on the other hand, is inconvenient (Kalogirou 2012). Considering such issues, a straightforward and flexible approach is crucial for analyzing CSCs' optical performance for the various geometric conditions (Kulahli et al. (2019), Mechanics and Arbor, 1982). MCRT is one of the reliable tools to overcome these challenges (He et al. (2011)). It's a very flexible, convenient, and efficient tool for estimating and analyzing CSC's optical performance (Liang et al. (2017), Fan et al. (2018)). This article explains a simple and straightforward technique for developing an MCRT-based method to estimate solar flux distribution over the PTC receiver tube in a circumferential and axial orientation with greater accuracy. The output of the created MCRT model is coupled as one of the boundary conditions in Fluent 18.1 to predict the PTC solar flux distribution to evaluate PTC performance and heat transfer characteristics. PTC efficiency and effectiveness were investigated using numerical models for various real-time parameters (e.g., solar radiation, HTF mass flow rate, heat transfer fluid inlet temperature (HTF), and wind velocity). The effect of the glass envelope on PTC output in the absorber tube was also investigated. A new MCRT-based algorithm is developed and reported here to calculate the non-uniform heat flux on the receiver tube of PTC's outer wall, as explained in section 2. Using this algorithm, two cases (with and without a glass envelope) are simulated under different real-time parameters to determine the efficiency of PTC, as explained in section 3.

2. Model Description

This investigation has been done to determine the effect of real-time parameters that significantly impact the efficiency of PTC, including solar radiation, the mass flow rate of heat transfer fluid, the temperature of heat transfer fluid, and wind speed. An in-house MCRT code was developed to find out the heat flux on PTC. This heat flux was used as a boundary condition in Fluent for estimating the heat gain by the PTC.

2.1 Governing equations

In the presented case, the fluid flow is in a steady and turbulent state; the following governing equations have been used in the FLUENT 18.1 simulation (A. Inc. 2018, "ANSYS Fluent Theory Guide v18.1," ANSYS 18.1 Doc., vol. 15317, no. April, p. 850).
Mass conservation is represented by the continuity equation (1):

$$\frac{\partial}{\partial x_i}(\rho u_i) = 0 \qquad \text{(eq. 1)}$$

The momentum conservation integral equation is represented by equation (2):

$$\frac{\partial}{\partial x_i}\left(\rho u_i u_j\right) = -\frac{\partial p}{\partial x_i} + \frac{\partial}{\partial x_j}\left[(\mu_t + \mu)\left(\frac{\partial u_j}{\partial x_i} + \frac{\partial u_i}{\partial x_j}\right) - \frac{2}{3}(\mu_t + \mu)\frac{\partial u_l}{\partial x_l}\delta_{ij}\right] + \rho g_i \qquad \text{(eq. 2)}$$

The Reynolds analogy concept was used in turbulent momentum transfer for numerical modeling of turbulent heat transport. The modeled energy equation is represented by equation (3):

$$\frac{\partial}{\partial x_i}(\rho u_i T) = \frac{\partial}{\partial x_i}\left[\left(\frac{\mu}{Pr} + \frac{\mu}{\sigma_T}\right)\frac{\partial T}{\partial x_i}\right] + S_R + S_h \qquad \text{(eq. 3)}$$

Turbulent kinetic energy (k) is represented by equation (4), and the rate of dissipation of kinetic energy (ε) is represented by equation (5).

$$\frac{\partial}{\partial t}(\rho k) + \frac{\partial}{\partial t}(\rho k u_i) = \frac{\partial}{\partial t}\left[\left(\mu + \frac{\mu_t}{\sigma_k}\right)\frac{\partial k}{\partial x_j}\right] + G_k + G_b - \rho\varepsilon - Y_M + S_k \qquad \text{(eq. 4)}$$

ε-equation:

$$\frac{\partial}{\partial t}(\rho\varepsilon) + \frac{\partial}{\partial x_i}(\rho\varepsilon u_i) = \frac{\partial}{\partial x_j}\left[\left(\mu + \frac{\mu_t}{\sigma_\varepsilon}\right)\frac{\partial \varepsilon}{\partial x_j}\right] + C_1\frac{\varepsilon}{k}(G_k + C_{3\varepsilon}G_b) - C_{2\varepsilon}\rho\frac{\varepsilon^2}{k} + S_\varepsilon \qquad \text{(eq. 5)}$$

S_k and S_ε are user-defined source terms. k-ε model is a semi-empirical model based upon the model transport

equation to determine the turbulent kinetic energy (k) and turbulent kinetic energy dissipation rate (ε) when the flow is fully turbulent. μ_t is turbulent viscosity, and the generation of k, G_k is represented by

$$\mu_t = C_\mu \rho \frac{k^2}{\varepsilon} \text{ and } G_k = \mu_t \frac{\partial u_i}{\partial x_j}\left(\frac{\partial u_i}{\partial x_j} + \frac{\partial u_j}{\partial x_i}\right)$$

The values of the standard constants are as follows:
$C_{2\varepsilon} = 1.92$, $\sigma_\varepsilon = 1.3$, $C_\mu = 0.09$, $C_{1\varepsilon} = 1.44$, $\sigma_k = 1.0$

2.2 Integration of FLUENT and MCRT method

The distribution of circumferential solar flux on the receiver tube of PTC was estimated by MCRT (Monte Carlo Ray Tracing) in-house developed code. The estimated distribution of solar energy flux was used in FLUENT 18.1 software as the boundary condition. In the MCRT code, a data file of heat flux is generated, and the FLUENT software processes this heat flux data file as one of the boundary conditions. The governing equations used in the FLUENT are discretized by using a finite volume method. The energy equation, along with the momentum equation, is discretized by the second upwind scheme. The thermal radiation between the glass envelope and receiver tube is considered by using an additional source term method as represented by the term S_h in the energy equation (equation 3). Natural convection due to the temperature-dependent properties of heat transfer fluid (Syltherm-800) is included in the momentum equation by including the density as a function of temperature. And gravity is putting on in the Fluent.

2.3 Monte-Carlo-based Ray Tracing

The MCRT code was written in C to estimate the solar radiation distribution on the receiver tube's outer wall. The effective statistical random method was used to calculate solar flux distribution over the receiver tube, as described in the literature (Ehrlich 2002, Hoff and Janni 1989).

In the next step, the Monte Carlo method defined a virtual ray tracing plane above the PTC. The distance between this plane and the device was randomly chosen (i.e., 5m) (Fig.1), as it does not affect the solar flux calculation. Each random ray from this virtual plane is perpendicular to the absorber tube and parabolic reflector. A random generation process defines the source point on the virtual plane. The Monte Carlo method is a computational algorithm that performs repeated random sampling to obtain numerical results. The Monte Carlo method is based upon the concept of randomness to solve numerical problems.

There are five ways to define PTC geometry, and two independent geometric parameters can program the PTC.

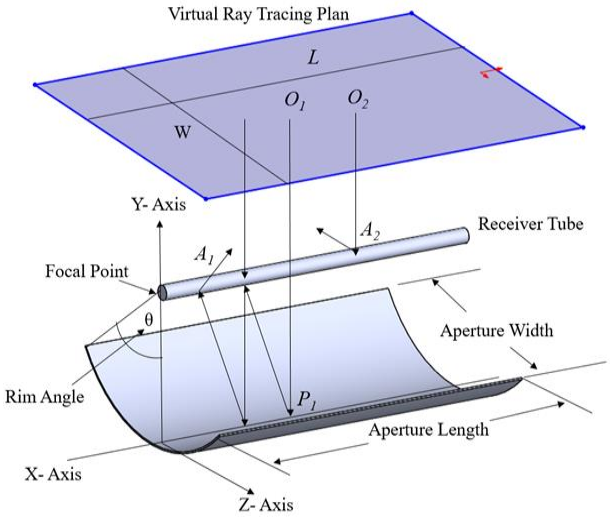

Fig. 1: Ray tracing virtual plan scheme

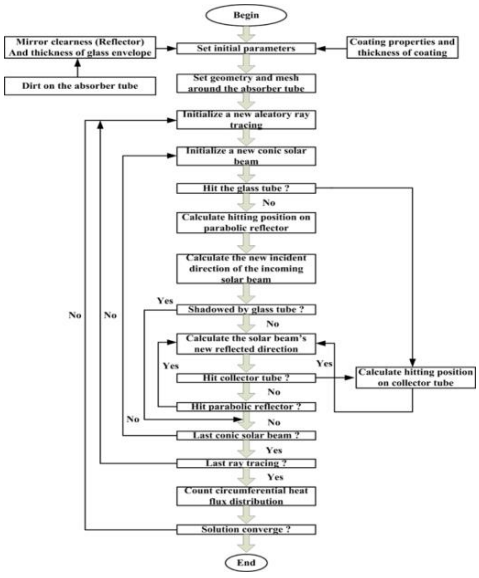

Fig. 2: Flow diagram of MCRT

The following methods can describe analytically deduced equations of PTC:

1. By specifying the focal point (f) and the parabola's aperture width (w), the rim angle (θ) is obtained. The parabola's coefficient (c) is related to focal length by equation (6).

c = 1/4f, and θ = 90° if b = 0, θ = arctan (0.5w/b) if b > 0, θ = 90° +arctan (b/0.5w) if b < 0 (eq. 6)

where b is the focal point distance.

2. By specifying the parabola's coefficient (c) and the aperture width (w), the parabola's focal point (f) is obtained by equation (7).

f = 1/4c and θ = 90° if b = 0, θ = arctan (0.5w/b) if b > 0, θ = 90° +arctan (b/0.5w) if b < 0 (eq. 7)

3. By giving the focal point *(f)* and the rim angle *(θ)*, the parabola's coefficient *(c)* is obtained from equation (6). The aperture width *(w)* is obtained by using equation (8).

$$w = \frac{-1+\sqrt{1+tan^2(\theta)}}{c*tan\,(\theta)}, if\ \theta < 90°, w = \frac{-1}{c}, if\ \theta = 90°, w = \frac{tan^2(\theta)+\sqrt{1+tan^2(\theta)}}{c}, if\ if\ \theta > 90° \quad \text{(eq. 8)}$$

4. With the specified parabola's coefficient *(c)* and the rim angle *(θ)*, the focal point *(f)* is calculated by using equation (7), and the aperture width *(w)* is obtained exactly the same as in case 3, by using equation (8).
5. With aperture width *(w)* and specified rim angle *(θ),* the focal point *(f)* is calculated by using equation (9).

$$f = \frac{w[1+\sqrt{1+tan^2(\theta)}]}{4tan\,(\theta)}, if\ \theta < 90°, f = \frac{w}{4}, if\ \theta = 90°, f = \frac{w[-tan\,(\theta)\ +\sqrt{1+tan^2(\theta)}]}{4tan\,(\theta)}, if\ if\ \theta > 90° \quad \text{(eq. 9)}$$

The total area of the absorber surface (A_a) and the estimated concentration factor are computed by using the equations (10-12).

$$A_a = 2\,\pi\,R\,L \quad \text{(eq. 10)}$$

Parabolic Reflector Surface Area (A_p) is estimated by equation (11).

$$A_p = \left[\frac{w}{2}t + \frac{1}{4c}\,ln\,ln\,(2c*w+t)\right]L \quad \text{(eq. 11)}$$

The concentrating factor (c_{fact},) relates the aperture width with the absorber's external radius, as shown by equation (12).

$$c_{fact} = \frac{w}{2\pi R} \quad \text{(eq. 12)}$$

In these equations: *R*: External radius of the absorber tube, *L*: Absorber tube length, *t* is obtained by the following equation: $t = \sqrt{(1+4w^2c^2)}$

For determining the total solar energy flux incidence on the absorber tube, an iterative process was performed. Each iterative loop generated a sequence of 1.8×10^8 rays tracing with starting points O_1, O_2, etc. (Fig. 1) located in the virtual ray tracing plane. Each ray tracing hits the system at different locations for the absorber tube (A_1) and the parabolic screen at points P_1. These hitting points are calculated by using the equations (13).

$x_i = x_i^o + t\cos(\alpha_i)$, where i = 1,2,3……, (eq. 13)

where x_i^o are the coordinates of the source points located at the virtual ray tracing plane. Cos (α_i) is the ray tracing's direction cosines (0, -1, 0), and *(t)* is a parameter related to the linear vector function.

The parameter *(t)* is computed by the analytic solution of the quadratic equation (14).

The parameter *(t)* corresponds to the minimum value between the two roots t_1 and t_2 of equation (14).

$$t = \frac{-b \pm \sqrt{b^2-4ad}}{2a}, t = \min(t_1, t_2) \quad \text{(eq. 14)}$$

The normal external vector is built at the intersection point that was previously found by equation (13).

For the parabolic screen

$$n_x = 0;\ n_y = \frac{1}{\sqrt{1+4c^2x_3^2}}, n_z = \frac{-2cx_3^2}{\sqrt{1+4c^2x_3^2}} \quad \text{(eq. 15)}$$

For the absorber tube

$n_x = 0;\ n_y = cos(\theta_c);\ n_z = sin\,(\theta_c\,)$ (eq. 16)

Equation (18) represents the direction of the solar radiation on the PTC. The mean of the intersection points determines the angle (θ_c), where θ_c is the azimuthal angle at the absorber tube.

The unit reflected vector s^r is represented by equation (17) in vector and indicial notation.

$s^r = 2|s\cdot n|n - s,\ s_t^r = 2|s_j\cdot n_j|n_j - s_j,$ (eq. 17)

For determining the portion of the surface over the receiver tube, over which the solar radiation heat flux is added, a sequential search by discrete elements was developed. Each of the discrete elements on the absorber tube is divided into triangular elements.

The intersection points ***I*** within the triangular element is computed by using the equation (18).

$$I_i = x_{si}^o + t_p\cos(\alpha_i) \quad \text{(eq. 18)}$$

For three-node elements, the parameter *(t_p)* defines the intersection ***(I)*** between the solar beam and the triangular plane. The equation (19) is used for the computation of intersection point *(I)* within the triangular elements.

$$t_p = \frac{d - a_k x_{sk}^o}{a_k \cos(\alpha_k)} \quad \text{(eq. 19)}$$

Where a_k is the plane's coefficients defined by three points, and d is an independent term in equation (19).
If the intersection point belongs to the three nodes elements, the following condition represented by equation (20-21) must be satisfied for each component:

$$I_i = \beta_k x_i{}^k \text{ and } \sum_{k=1}^{3} \beta_k = 1 \quad \text{(eq. 20)}$$

The three values of coefficients (β_k) are obtained by the solution of the expression in equation (20), which produces a set of simultaneous equations (21).

$$\begin{matrix} x_1 & x_2 & x_3 \\ y_1 & y_2 & y_3 \\ z_1 & z_2 & z_3 \end{matrix} \times \begin{matrix} \beta_1 \\ \beta_2 \\ \beta_3 \end{matrix} = \begin{matrix} I_x \\ I_y \\ I_z \end{matrix} \quad \text{(eq. 21)}$$

The solution for each coefficient in equation (21) is given by equation (22).

$$\beta_k = \frac{I_k(y_l z_m - y_m z_l) + I_y(x_m z_l - x_l z_m) + I_z(x_l y_m - x_m y_l)}{\Delta} \quad \text{(eq. 22)}$$

Where sub-indices: *k*, *l*, and *m* follow a cyclic counter-clockwise permutation: *1-2-3*, and Δ is the matrix determinant.
If equation (21) is satisfied, then the solar energy flux is computed and added to the surface discrete elements. The local radiation energy in the unit area is computed by applying the numerical equation (23) for every ray tracing impacting on a specific discrete element around the absorber tube (Ehrlich 2002).

$$\dot{q}_r^e = \rho_{cl}\gamma a_e K(\theta_i)\psi(\theta_i) I_{bn} \text{ and } \rho_{cl} = 0.935, a_e = 0.023, \psi(\theta_i) = 1 \quad \text{(eq. 23)}$$

The user specifies the solar irradiance, I_{bn}. According to Kerlin et al. (2016), a default value of *1360.8 W/m²* was set in. The value of the intercept factor *(γ = 0.84)* was obtained from equation (24) (Padilla et al. (2011)).

$$\gamma = \prod_{i=1}^{6} \gamma_i \quad \text{(eq. 24)}$$

Where γ_1 = 0.950 (black chrome), γ_2 = 0.980 (collector mirror's geometrical accuracy), γ_3 = 0.960 (mirror clearness), γ_4 = 0.980 (dirt on heat collection element, i.e., absorber tube).
The incident angle modifier function $K(\theta_i)$ is defined by equation (25) (Gorantla et al. (2017)).

$$K(\theta_i) = cos(\theta_i) + 0.000884(\theta_i) - 0.00005369(\theta_i^2) \quad \text{(eq. 25)}$$

At the end of one cycle, when the 1.8×10^8 rays hit all the elements around the absorber tube, the total solar energy flux per unit area is computed by each element according to the Monte Carlo method by equation (26).

$$\dot{q}_e^L = \left(\frac{A_a}{A_e}\right)\left[\left(\frac{1}{N_a}\right)\sum_{r=1}^{N_r^e} q_r^e\right]_L \quad \text{(eq. 26)}$$

The total solar flux per unit area collected by the absorber tube is computed at the end of one cycle with the help of equation (27).

$$\dot{q}_e^L = \sum_{r=1}^{N_r^e} q_r^e \quad \text{(eq. 27)}$$

The relative error in the cycle of 1.8×10^8 rays is computed by using the equation (28).

$$Loop_{error} = \frac{|(\dot{q}_a^L)_{new} - (\dot{q}_a^L)_{old}|}{(\dot{q}_a^L)_{new}} \quad \text{(eq. 28)}$$

If the relative error is less than 0.0001, the convergence is attained, and the computation is finished; otherwise, another cycle of 1.8×10^8 rays tracings is performed until convergence is attained. Figure 2 represents the in-house developed algorithm's flowchart to calculate the heat flux on the receiver tube's outer surface using parallel computing. SEGS LS2 parabolic trough absorber tube was used to validate with the experimental comparison of Z. D. Cheng et al. (2010), as explained in section 2.7.

2.4 Boundary conditions

At the outlet of the PTC, a fully developed flow condition was applied. At the inlet of the absorber tube of PTC, a velocity magnitude of 1 m/s and HTF temperature of 303 K was applied. Other surfaces of the absorber tube of PTC were considered as adiabatic walls. At the absorber tube's outer cylindrical surface, circumferential heat flux calculated by the in-house developed MCRT method was applied. Syltherm-800 liquid oil was used as heat transfer fluid, and its properties are specified in Table 1. To couple the velocity and pressure, a SIMPLE algorithm is used. SIMPLE is used for solving pressure equations by using a semi-implicit method for compressible and incompressible fluid flow. In the SIMPLE algorithm, a second-order upwind scheme is used. The Nusselt number and Reynold number are calculated using the relation in Incropera and DeWitt (1990). A

computation domain five times larger than the PTC geometry was used to determine the effect of air. HTF with variable temperature is used to assess the impact of wind speed on the efficiency of PTC.

Tab. 1: Thermophysical properties of Syltherm-800

Temp (°C)	Specific heat (Kj/kg K)	Density (kg/m^3)	Thermal conductivity (W/m K)	Viscosity (mPa s)	Vapour pressure (kPa)
30	1.625	934.99	0.1331	8.32	0
80	1.711	881.68	0.1237	3.86	1.46
130	1.796	837.46	0.1143	2.11	13.5
180	1.882	792.08	0.1049	1.26	59.5
230	1.967	744.3	0.0955	0.81	171.7
280	2.052	692.87	0.0861	0.54	380.2

2.5 Grid independence study

Uniform structured mesh is used across the geometry, as shown in Figure 3. A grid independence study was conducted for PTC's absorber tube to predict performance and heat transfer characteristics. The minimum number of elements with grid-independent accuracy was 0.7 million; below that level, numerical calculation accuracy and solution stability changed with grid size, as seen in Figure 4. The element size implemented in the investigated case in this study was 0.005 × 0.005 m, with 0.7 million elements. Substantial computational effort and time were observed beyond 3.9 million elements corresponding to a grid size of 0.0025 × 0.0025 m. The volume mesh used has hexahedral-shaped elements. Figure 4 shows the curves of axial temperature variation at three circumferential locations corresponding to 0.7 million, 1.1 million, and 3.9 million elements, which are almost coinciding with each other. The figure shows that all respective curves are very close to each other, and the results show that the simulation model used is independent of grid size. To verify the grid independence of the solution, the model was run at three element sizes: 0.005 × 0.005 m, 0.0040 × 0.0040 m, and 0.0025 × 0.0025 m. These element sizes resulted in 0.7 million, 1.1 million, and 3.9 million elements in the geometry. Based on the finding of this study, a 0.7 million element count was used in all the simulations.

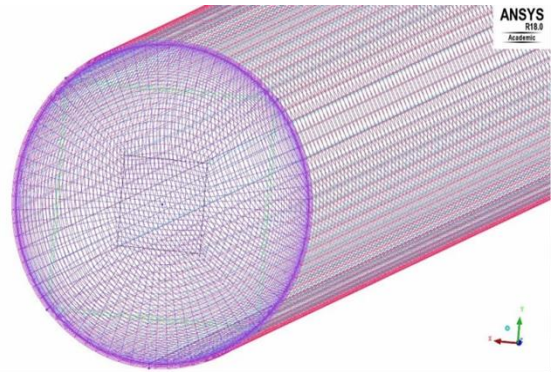

Fig. 3: Structured Mesh on the receiver tube of parabolic trough collector

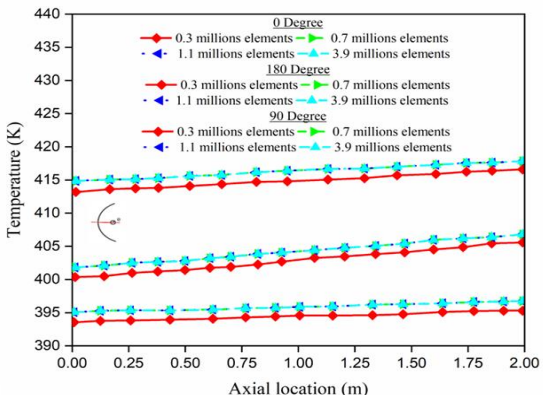

Fig. 4: Axial temperature on the receiver tube of the parabolic trough collector computed at four grid sizes (0.005 × 0.005 m, 0.0040 × 0.0040 m, 0.0025 × 0.0025 m and 0.0059 × 0.0059 m)

2.6 Experimental setup

Figure 5 (a) represents the schematic diagram of the PTC solar steam plant in Hatsun Agro Products in Salem (Tamil Nadu), India. This PTC solar steam plant has 2-rows of PTC and can be operated individually depending upon the need. This PTC solar steam plant has a minimum capacity of 900 kg of steam per day under temperature and pressure of 220 °C and 17.5 bar. The maximum capacity of this plant is 3 tonnes per day, and the average production of steam in this plant is 1.5 tonnes per day. Silicon-based heat transfer fluid is used in this system. The maximum thermal efficiency obtained in this system is 60%-65%. Figure 5 (b) depicts Hatsun Agro Products' actual PTC solar steam plant in Salem, Tamil Nadu (India).

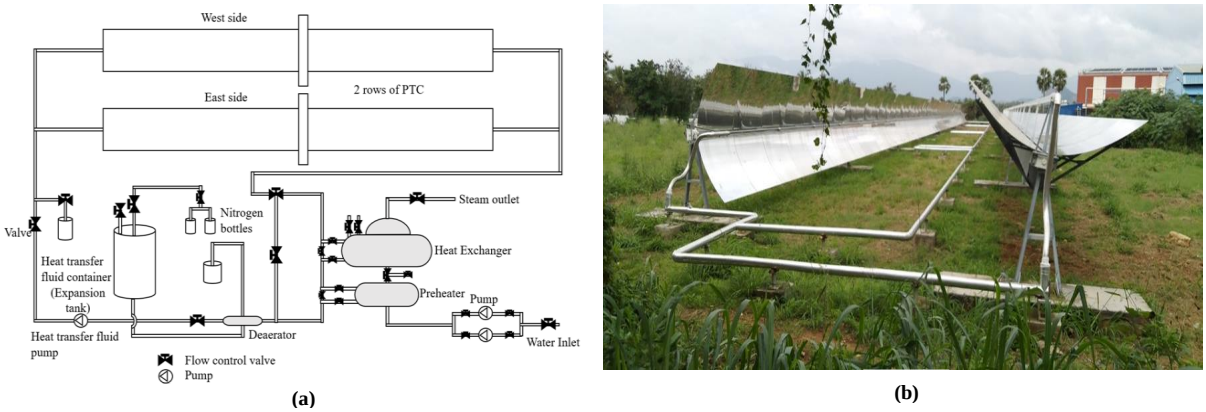

(a) (b)

Fig. 5: (a) Schematic diagram of parabolic trough collector solar steam plant in Hatsun Agro Products, Salem (Tamil Nadu), India, and (b) Parabolic trough collector solar steam plant in Hatsun Agro Products, Salem (Tamil Nadu), India

2.7 Validation

Figure 6 shows that solar flux distribution in the circumferential direction over the PTC receiver tube using the MCRT method is in good agreement with the experimental results of Z. D. Cheng et al. (2010). Table 2 displays PTC dimensions for validation analysis, similar to the SEGS LS2 parabolic trough collector module tested on AZTRAK rotating platform at SNL by Dudley et al. (1994).

Tab. 2: Dimensions of the SEGS LS2 parabolic trough collector

S. No.	Parameters	Values
1.	Length of parabolic reflector (m)	7.8
2.	Width of parabolic reflector (m)	5
3.	Focal point (m)	1.84
4.	Outer diameter of receiver tube (mm)	70
5.	Outer diameter of a glass tube (mm)	115
6.	Inner diameter of receiver tube (mm)	66

Tab. 3: Experimental data and comparison with Z.D Chang et al. (2010) results with simulation results

Cases	I_r (W/m^2)	q_m (kg/s)	T_a (°C)	T_{in} (°C)	$T_{o,exp}$ (°C)	T_o (Z. D. Cheng.) (°C)	T_o	η (Exp.) (%)	η (Z. D. Cheng) (%)	η (%)
Case1	933.7	0.6782	21.2	102.2	124.0	126.8	126.09	72.51	72.64	72.47
Case 2	937.9	0.6206	28.8	297.8	316.9	319.4	316.36	67.98	68.35	68.20
Case 3	920.9	0.5457	29.5	379.5	398.0	401.9	398.53	62.34	62.69	62.40

Tab. 4: Experimental data of parabolic trough collector solar steam plant of "Hatsun Agro Products", Salem, Tamil Nadu (India) developed by Protarget, Germany & managed by LUIT Renewables and comparison of experimental results with simulation results

Cases	I_r (W/m^2)	q_m (kg/s)	T_a (°C)	T_{in} (°C)	$T_{o,exp}$ (°C)	T_o	η (Exp.) (%)	η (%)
Case1	794.90	0.7126	34	184.2	216.9	217.8	66.74	66.57
Case 2	848.78	0.6502	37	192.1	214.1	213.60	65.25	64.80
Case 3	810.71	0.5746	36	201.5	220.5	221.5	62.41	63.40

The energy absorption efficiency of the tube was calculated by using the equation (32).

$$\eta = k[73.3 - 0.007276\Delta T_{aa}] - 0.496(\Delta T_{aa}/I) - 0.0691(\Delta T_{aa}^2/I)$$

The new model on the MCRT method is also validated by comparing the efficiency results of Z.D. Chang et al. (2010) with the current study for the three different cases. The model was further validated by experimental data obtained from the PTC solar steam plant of Hatsun Agro Products in Salem, Tamil Nadu (India),

developed by Protarget, Germany, in collaboration with LUIT Renewables. Comparisons show close agreement with experimental data in Table 3 and Table 4. The maximum difference between the computed results of this study and the experimental data is less than 2%. This confirms the reliability of the new algorithm for the analysis of PTC absorber tubes.

3. Results and discussions

The variations in real-world parameters, including solar radiation, the inlet temperature of HTF, the mass flow rate of HTF, and wind speed on the efficiency of PTC, are analyzed and presented. The geometrical details of the PTC used for the numerical simulation are displayed in Table 5. Efficiency results are presented with and without a glass envelope over PTC's absorber tube. Subsequently, adding a glass envelope increases PTC's overall performance. As it prevents surrounding convective heat losses.

3.1 Solar radiation and distribution on receiver tube

Figure 7 (a) shows the solar flux distribution circumferentially over the receiver tube for the different solar radiations. For the different solar radiations, we have different solar flux. Here, solar flux on the receiver tube is directly proportional to solar radiation. Whereas, Figure 7 (b) shows the temperature on the outer wall of the receiver tube in the axial direction for the different values of θ (i.e., θ = 0°, 90°, 180°). This rise in the temperature in the axial direction can be observed in Figure 7 (b). The temperature is highest at θ = 90° as compared to θ = 0°, 180°. This is due to the reason that θ = 90° is on the side which has higher concentrated solar radiation while θ = 0° is on that side which has the lowest solar concentration. And θ = 180° on the side, which lies in between the concentrated solar region. The trends for the temperature and the circumferential solar distribution is quite similar to that of Z. D. Cheng et al. (2010).

Tab. 5: The dimensions of the parabolic trough collector

S. No.	Parameters	Values
1.	Length of the parabolic reflector (m)	2
2.	Focal point (mm)	220
3.	Width of parabolic reflector (m)	1
4.	Outer diameter of absorber tube (mm)	32

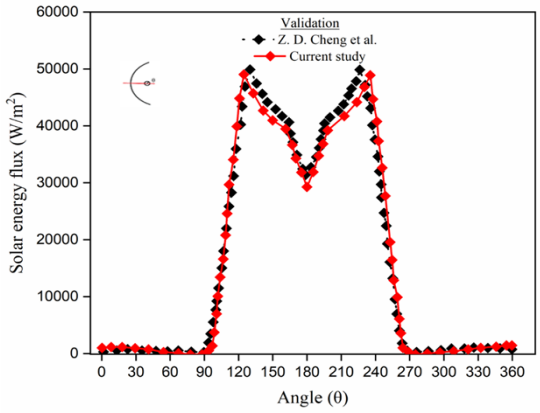

Fig. 6: Validation of solar energy flux distribution over the receiver tube circumference with 937.9 W/m² (Z. D. Cheng et al. (2010)

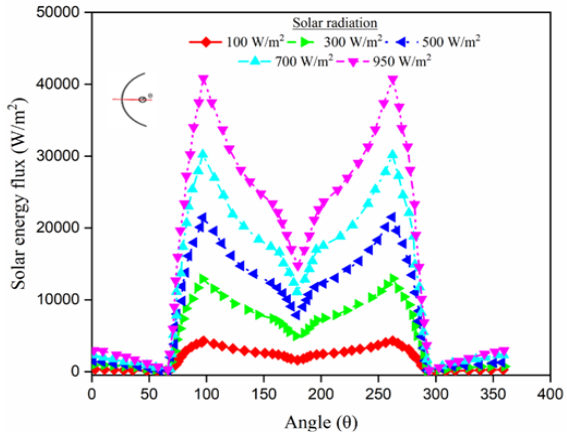

(a)

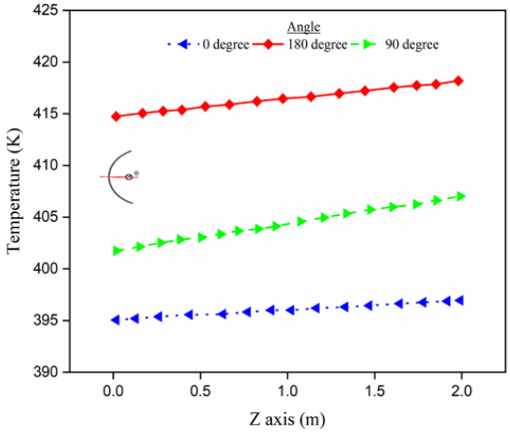

(b)

Fig. 7: Circumferential solar flux distribution on the outer wall of receiver tube of parabolic trough collector for different solar radiations, and (b) Temperature on the receiver tube of parabolic trough collector in an axial direction

3.2 Impact of solar radiation on the efficiency of PTC

Figure 8 (a) shows solar radiation's impact on PTC's efficiency. As we increase solar radiation, PTC efficiency increases by keeping HTF's mass flow rate and inlet temperature constant. (i.e.,1 m/s and 303 K) as presented in Figure 8 (a). Due to increased solar radiation, concentrated solar energy flux on the receiver tube surface also increases. Solar flux on the receiver tube surface is proportional to the solar radiation. Moreover, as the amount of solar radiation rises, the outlet temperature of HTF (Syltherm-800) also rises. The PTC's output and outlet temperature increase by inserting the glass envelope outside the receiver tube, as shown in Figure 8 (a). Efficiency increases by 0.06% by maintaining the constant flow rate and inlet temperature of HTF (i.e., 1 m/s and 303 K). The explanation is that the glass envelope reduces atmospheric convective heat losses.

Figure 8 (b) represents the relationship between the Reynolds number and Nusselt number for the varying solar radiations. Reynolds number remained unchanged as the mass flow rate and inlet flow temperature were kept constant (i.e., 1 m/s and 303 K) while studying the effect of solar radiation on the efficiency of PTC. Nusselt number varies because of the convective heat transfer coefficient change, which keeps changing with the change or increase in solar radiation. An increase in the Nusselt number increases the efficiency of the PTC, as shown in Figure 8 (a).

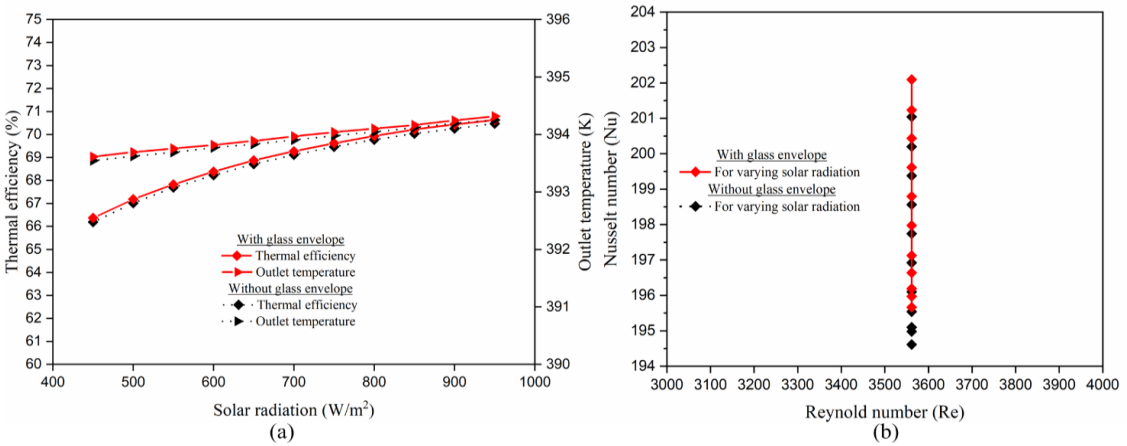

Fig. 8: (a) Efficiency of parabolic trough collector with the variation of solar radiation, and (b) Variation of Reynold number and Nusselt number with the variation of solar radiation

3.3 Impact of mass flow rate on the efficiency of PTC

Figure 9 (a) shows the impact of the mass flow rate of HTF on the PTC's efficiency. As we increase the HTF's mass flow rate, there is an increase in efficiency, but the outlet temperature of the PTC decreases. This is because of the effect of mass flow rate. A higher flow rate combined with a lower temperature difference (i.e., the temperature difference between the inlet and outlet of the absorber tube) increases PTC efficiency. And for the lower flow rate, the higher temperature difference (i.e., the temperature difference between the inlet and outlet of the absorber tube) combined with the lower flow rate reduces the overall efficiency of the PTC by keeping the solar radiation and inlet temperature of the HTF constant (i.e., 950 W/m2 and 303K). Also, for the lower mass flow rate, the higher will be the outlet temperature and the outlet temperature start reducing as we start increasing the mass flow rate of HTF because of less time for the HTF to get heated in the receiver tube of PTC. The glass envelope's addition to the absorber tube increases the efficiency and outlet temperature by 8.5% by keeping solar radiation and inlet HTF temperature constant (i.e., 950 W/m2 and 303K). This is due to less convective heat losses to the atmosphere, as depicted in Figure 9 (a). Figure 9 (b) shows the relation between the Reynolds number and the Nusselt number for varying the mass flow rate of heat transfer fluid. As the velocity of the heat transfer fluid keeps on increasing, the Reynolds number keeps on increasing. As the Reynolds number increases, the convective heat transfer coefficient also increases. This increase in the convective heat transfer coefficient increases the Nusselt number. An increase in the Nusselt number increases the efficiency of the PTC, as shown in Figure 9 (a).

3.4 Impact of HTF's temperature on the efficiency of PTC

Figure 10 (a) shows the collector's efficiency effect of HTF temperature. PTC efficiency increases rapidly for lower HTF temperature due to the higher heat transfer rate due to the higher temperature difference (i.e., the

HTF temperature difference between the inlet and outlet of the absorber tube). Whereas, if we keep raising the HTF temperature, there is no significant increase in the PTC's efficiency as we keep the mass flow rate of HTF and solar radiation constant (i.e., 950 W/m^2 and 1 m/s). The increase in HTF temperature is higher for lower inlet HTF temperature, but the heat transfer rate reduces as we raise the inlet HTF temperature. PTC's total performance and outlet temperature improved by 0.13% as we placed the glass envelope outside the receiver tube, keeping solar radiation and mass flow rate constant (i.e., 950 W/m^2 and 1 m/s). This is due to reduced atmospheric convective heat losses. Figure 10 (b) represents the relations between the Reynolds number and Nusselt number for varying inlet temperatures of heat transfer fluid. As the heat transfer fluid temperature increases, the various properties of the heat transfer fluid changes (such as density, thermal conductivity, specific heat, and viscosity). Change in the properties of the fluid increases the Reynolds number. The Nusselt number changes initially because of the high convective heat transfer coefficient, but later, the change in the convective heat transfer coefficient is not significant enough to increase the Nusselt number. Thus the efficiency of the PTC increases initially, but after that efficiency of the PTC becomes constant with an increase in the fluid inlet temperature (Figure 10 (a)).

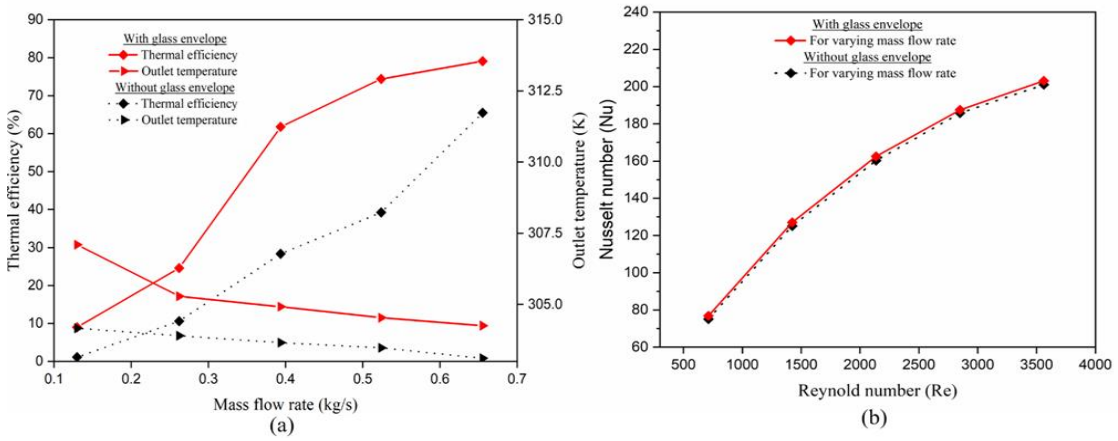

Fig. 9: (a) Efficiency of parabolic trough collector with the variation of heat transfer fluid's mass flow rate, and (b) Variation of Reynold number and Nusselt number with heat transfer fluid's mass flow rate

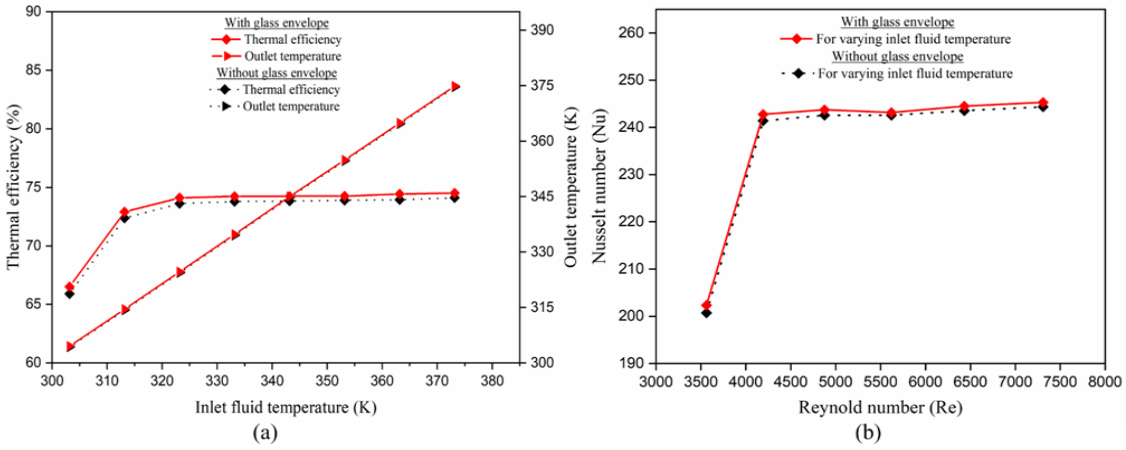

Fig. 10: (a) Efficiency of parabolic trough collector with a variation of inlet heat transfer fluid temperature, and (b) Variation of Reynold number and Nusselt number with inlet heat transfer fluid temperature

3.5 Impact of wind speed on the efficiency of PTC

Figure 12 (a) shows wind speed's effect on parabolic trough collector efficiency. PTC's performance tends to decrease with increased wind speed. It is due to increased ambient heat loss, as shown in Figure 12 (b). The convective heat loss is reduced with the glass envelope used on the absorber tube, as shown in Figure 12 (a). Figure 12 (c) represents the effect of wind speed on the Nusselt number and Reynold number. As the wind speed increases, the Nusselt number keeps on reducing because of higher convective heat loss. This reducing Nusselt number reduces the overall efficiency of the PTC. With the incorporation of glass tubes, the convective heat loss reduces, increasing the overall efficiency compared to the operation of PTC without glass tube.

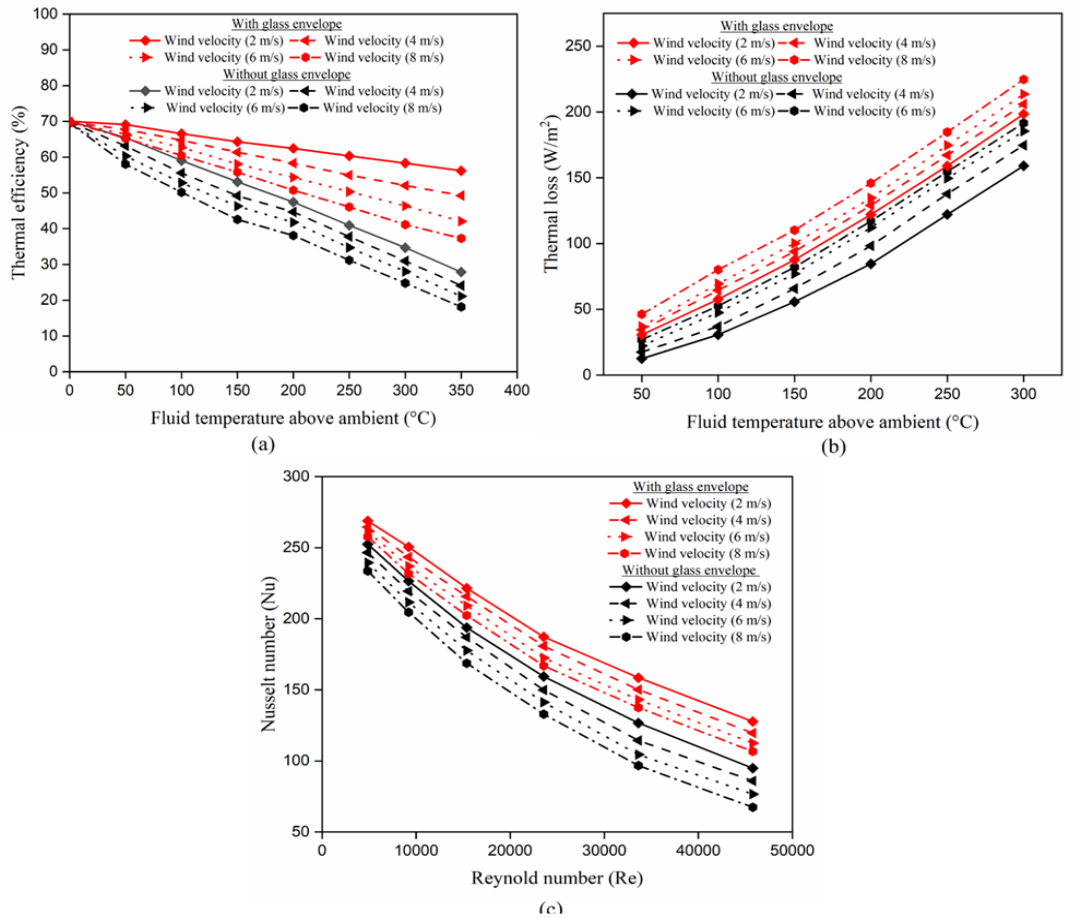

Fig. 12: (a) Effect of wind speed on the efficiency of parabolic trough collector with and without glass envelope, (b) Heat loss from the parabolic trough collector for different wind speeds, and (c) Variation of Reynold number and Nusselt number with different wind speed

4. Conclusions

This paper addressed PTC computational studies using a simple and straightforward approach based on the MCRT method. This algorithm's findings were compared with empirical and experimental research published in the literature as well as with local validation. The maximum relative difference between the new and experimental results was less than 2%. After validation with experiments, two cases were simulated using the same algorithm, i.e., with and without glass envelope, for different real-world parameters (i.e., solar radiation, HTF temperature, mass flow rate of HTF, and wind speed). The findings showed an improvement in efficiency and outlet fluid temperature with an increase in solar radiation. The efficiency and outlet temperature improved further with the addition of a glass envelope outside the receiver tube, as this envelope reduces convective losses to the atmosphere. Furthermore, the efficiency is increased by changing the mass flow rate as convective losses decrease. But the increasing mass flow rate reduces outlet temperature. There is a rapid increase in PTC efficiency for lower inlet fluid temperature, but an increase in efficiency becomes insignificant after specific inlet fluid temperature as the heat transfer rate reduces with the increasing temperature of HTF. Efficiency and outlet temperature increase by using the glass envelope. Wind speed significantly affects PTC's efficiency. PTC efficiency tends to decrease as wind velocity increases due to high convective heat loss. There, too, positioning the glass envelope on the receiver tube increases efficiency.

5. Acknowledgment

The authors gratefully acknowledge the LUIT Renewables and Himachal Pradesh State Council for Science, Technology, and Environment (SCSTE) for providing the experimental data and funding support under the aegis of "Design and development of efficient solar dryer for corrugated box drying" for conducting this research.

6. References

A. Inc., 2018. ANSYS Fluent Theory Guide v18.1," ANSYS 18.1 Doc., vol. 15317, no. April, p. 850.

Almanza, R., Jiménez, G., Lentz, A., Valdés, A., and Soria, A., 2002. DSG under two-phase and stratified flow in a steel receiver of a parabolic trough collector. J. Sol. Energy Eng. Trans. ASME, vol. 124, no. 2, pp. 140–144. https://doi.org/10.1115/1.1463734
Bellos, E., Tzivanidis, C., Said, Z., 2020. A systemetic parametric thermal analysis of nanofluid-based parabolic trough solar collectors. Sustainable Energy Technologies and Assessments, vol. 39. https://doi.org/10.1016/j.seta.2020.100714
Burkhard, D. G., Shealy, D. L., and Sexl, R. U., 1973. Specular reflection of heat radiation from an arbitrary reflector surface to an arbitrary receiver surface. Int. J. Heat Mass Transf., vol. 16, no. 2, pp. 271–280. https://doi.org/10.1016/0017-9310(73)90056-2
Chargui, R., Tashtoush, B., Awani, S., 2021. Experimental study and performance testing of a novel parabolic trough collector. International Journal of Energy Research. https://doi.org/10.1002/er.7267
Cheng, Z. D., He, Y. L., and Cui, F. Q., 2013. A new modelling method and unified code with MCRT for concentrating solar collectors and its applications. Appl. Energy, vol. 101, pp. 686–698. https://doi.org/10.1016/j.apenergy.2012.07.048
Cheng, Z. D., He, Y. L., and Qiu, Y., 2015. A detailed non-uniform thermal model of a parabolic trough solar receiver with two halves and two inactive ends. Renew. Energy, vol. 74, pp. 139–147. https://doi.org/10.1016/j.renene.2014.07.060
Cheng, Z. D., He, Y. L., Wang, K., Du, B. C., and Cui, F. Q., 2014. A detailed parameter study on the comprehensive characteristics and performance of a parabolic trough solar collector system. Appl. Therm. Eng., vol. 63, no. 1, pp. 278–289. https://doi.org/10.1016/j.applthermaleng.2013.11.011
Cheng, Z. D., He, Y. L., Xiao, J., Tao, Y. B., and Xu, R. J., 2010. Three-dimensional numerical study of heat transfer characteristics in the receiver tube of parabolic trough solar collector. Int. Commun. Heat and Mass Transf., vol. 37, no. 7, pp. 782–787. https://doi.org/10.1016/j.icheatmasstransfer.2010.05.002
Dudley, V., Kolb, G., Sloan, M., Kearney, D., 1994. SEGS LS2 solar collector — test results, Report of Sandia National Laboratories, SANDIA94-1884, USA. https://doi.org/10.2172/70756
Evans, D. L., 1977. On the performance of cylindrical parabolic solar concentrators with flat absorbers. Sol. Energy, vol. 19, no. 4, pp. 379–385. https://doi.org/10.1016/0038-092X(77)90009-3
Fan, M., Liang, H., You, S., Zhang, H., Yin, B., and Wu, X., 2017. Performance analysis of a solar heating system with the absorption heat pump and oil/water heat exchanger. Energy Procedia, vol. 142, pp. 97–104. https://doi.org/10.1016/j.egypro.2017.12.016
Hang, Q., Jun, Z., Xiao, Y., and Junkui, C., 2008. Prospect of concentrating solar power in China-the sustainable future. Renew. Sustain. Energy Rev., vol. 12, no. 9, pp. 2505–2514. https://doi.org/10.1016/j.rser.2007.06.002
He, Y. L., Xiao, J., Cheng, Z. D., and Tao, Y. B., 2011. A MCRT and FVM coupled simulation method for energy conversion process in parabolic trough solar collector. Renew. Energy, vol. 36, no. 3, pp. 976–985.
Incropera, F., DeWitt, D., 1990. Fundamentals of Heat and Mass Transfer, John Wiley and Sons, Third Edition, New York, NY.
Jeter, S. M., 1986. Calculation of the concentrated flux density distribution in parabolic trough collectors by a semi-finite formulation. Sol. Energy, vol. 37, no. 5, pp. 335–345.
Kalogirou, S. A., 2012. A detailed thermal model of a parabolic trough collector receiver. Energy, vol. 48, no. 1, pp. 298–306. https://doi.org/10.1016/j.energy.2012.06.023
Mechanics, A. and Arbor, A., 1982. An Analysis of the Technical Performance of a Parabolic for Solar Industrial and Economic Trough. Mech. Eng., vol. 25, no. 9, pp. 1427–1438.
Powar, S., Saini, P., Pandey, S., Dhar, A., 2020. System for cooking eatables. Indian Patents and Trademark Office. 202021049173.
Saini P., Patil D.V., Powar S., 2018. Review on Integration of Solar Air Heaters with Thermal Energy Storage. In: Tyagi H., Agarwal A., Chakraborty P., Powar S. (eds) Applications of Solar Energy. Energy, Environment, and Sustainability. Springer, Singapore. https://doi.org/10.1007/978-981-10-7206-2_9
Saini, P., Powar, S., Dhar A., 2020. System for drying articles. Indian Patents and Trademark Office. 201821038197.
Sokhansefat, T., Kasaeian, A. B., and Kowsary, F., 2014. Heat transfer enhancement in parabolic trough collector tube using Al2O3/synthetic oil nanofluid. Renew. Sustain. Energy Rev., vol. 33, pp. 636–644.
Tzivanidis, C., Bellos, E., Korres, D., Antonopoulos, K. A., and Mitsopoulos, G., 2015. Thermal and optical efficiency investigation of a parabolic trough collector. Case Study. Therm. Eng., vol. 6, pp. 226–237.
Vouros, A., Mathioulakis, E., Papanicolaou, E., Belessiotis, V., 2020. Modelling the overall efficiency of parabolic trough collectors. Sustainable Energy Technologies and Assessments, vol. 40.
Wang, K., Zhang, Z.D., Li, M. J., Min, C. H., 2021. A coupled optical-thermal-fluid- mechanical analysis of parabolic trough solar receivers using supercritical CO_2 as heat transfer fluid. Applied Thermal Engineering, vol. 183, 116154. https://doi.org/10.1016/j.applthermaleng.2020.116154
Zadeh, P. M., Sokhansefat, T., Kasaeian, A. B., Kowsary, F., and Akbarzadeh, A., 2015. Hybrid optimization algorithm for thermal analysis in a solar parabolic trough collector based on nanofluid. Energy, vol. 82, pp. 857–864. https://doi.org/10.1016/j.energy.2015.01.096

Modelling and Experimental Verification of an Unglazed Metal Façade Collector Model

Viacheslav Shemelin and Tomas Matuska

Czech Technical University in Prague, University Centre for Energy Efficient Buildings, 27343, Bustehrad, Czech Republic

Abstract

The paper presents a theoretical model for energy performance simulation of an unglazed metal façade collector (UMFC). Different configurations of UMFC were developed and experimentally tested with the use of an indoor solar simulator to perform a verification process. The verification of the model demonstrated that there is a good agreement between the simulated and experimentally obtained results. The sensitivity analysis has been performed to demonstrate the influence of the wind-forced convection model on the theoretically calculated efficiency. However, the results of the analysis indicated that it is extremely important to identify an appropriate wind-forced convection correlation for the estimation of the thermal performance of a UMFC. A large number of correlations for wind-forced convection presented in the literature demonstrated that there is no universally acceptable correlation. The difference was caused by different combinations of experimental and operating conditions (ambient air temperature, wind range, wind tunnel/outdoor/indoor measurement, instrumentation, surroundings, etc.). Therefore, it was highly recommended to provide a long-term verification process of the model since the climatic and operating conditions (especially wind-related conditions for instance wind speed, wind direction, wind turbulence, etc.) are different compared to an indoor verification process.

Keywords: Unglazed solar thermal collector, metal façade cladding system, building integrated solar thermal (BIST), wind-forced convection

1. Introduction

The utilization of solar energy using a building envelope becomes more and more attractive today. It offers great environmental benefits (reduction in primary energy consumption, reduction in greenhouse gas emissions, etc.) as well as economic benefits (reduction in building operating costs, sustainable operation, public subsidies, etc.). Particularly the usage of efficient, technically reliable, and time-proven solar thermal technologies has great potential. Among solar thermal technologies, unglazed solar thermal collectors have lower thermal performance compared to glazed flat-plate collectors or vacuum tube collectors. Unglazed solar thermal collectors for a long time were utilized primarily for low operation temperature heating purposes in applications such as swimming pool heating or as an evaporator in a heat pump system. The high magnitude of heat losses (mainly caused by convection) prevented their wider distribution in solar thermal applications. On the other hand, they are cheaper, lighter, and more reliable. Therefore, the combination of an unglazed solar thermal collector and a metal facade cladding system comes to mind. Such an unglazed metal façade collector (UMFC) is based on one key element (solar absorber metal sheet). Moreover, this solution brings a few advantages. Firstly, the metal cladding system is a well-established technology used by architects for new buildings, as well as for retrofit purposes. So, there is a large application potential. Secondly, a commercially available metal cladding system is available in a large palette of colours. It allows us to solve the aesthetic issues associated with the solar thermal integration processes. Thirdly, installing a UMFC system is faster than an entirely new façade solution because UMFC is based on a commercially available metal cladding system. Last but not least, the energy-active large-area building façade system can be used for direct hot water preparation and distribution, space heating in combination with a heat pump, direct space cooling (night radiative cooling), or space cooling in combination with a heat pump. It is, therefore, not surprising that metal unglazed solar thermal façade collector attracts attention from the scientific field (Probst and Roecker, 2007; Hermann et al., 2010; Giovanardi et al., 2015; Shen et al., 2016; Martinez et al., 2017; Weiland et al., 2019; Shemelin and Matuska, 2022).

© 2022. The Authors. Published by International Solar Energy Society
Selection and/or peer review under responsibility of Scientific Committee
doi:10.18086/eurosun.2022.12.15 Available at http://proceedings.ises.org

Analyzing the thermal performance of a UMFC is essential as it helps to improve the design. In fact, research and sensitivity analysis of design changes should be performed simultaneously to create an efficient device. Since the experimental study of all possible collector designs is not feasible, analytical methods such as computational modelling using a mathematical model must be employed. The benefits of computational modelling are the ability to study the thermal performance under different climatic and operating conditions which are difficult or impossible to create in laboratory conditions, to provide design changes sensitivity analysis, etc.

In the past, some studies investigated an unglazed thermal collector energy performance to create a mathematical model. For instance, Keller (1985) concluded that the significant difference in thermal performance modelling of glazed and unglazed solar thermal collectors is that the thermal performance of unglazed collectors is strongly influenced by six environmental factors (namely solar irradiance, ambient air temperature, longwave radiation, wind speed, rain, and condensation/frost.) while the thermal performance of glazed collectors primarily depends on only two environmental factors (solar irradiance and ambient air temperature). Later Morrison and Gilliaert (1992) modified the well-known Hottel-Whillier-Bliss equation (Bliss Jr., 1959; Hottel and Whillier, 1955; Hottel and Woertz, 1942; Whillier, 1967) for unglazed solar thermal collectors. It includes an allowance for longwave sky radiation and wind speed on the calculated thermal performance. Then Eisenmann et al. (2006) developed, experimentally validated, and described an additional energy gain of an unglazed metal collector, including the condensation phenomena. The condensation effect on a metal unglazed solar thermal collector heat gains was investigated and considered in several other collector models reported by (Morrison, 1994; Perers, 2010; Soltau, 1992; Stegmann et al., 2011). Later Anderson et al. (2013) investigated theoretically and experimentally the thermal performance of an unglazed thermal collector for radiant cooling. Bunea et al. (2015) developed and evaluated an unglazed solar thermal collector considering condensation/evaporation, frost/melting, and rain phenomena.

The proposed mathematical model aims best to represent the thermal behaviour under different design changes and quantify their influence on the collector's thermal performance. The presented model is a very detailed theoretical model with 17 input design parameters such as the absorber length, width, pipe thermal conductivity, bond material thermal conductivity, etc. It allows to perform a sensitivity analysis of design parameters under different climatic and operating conductions and to demonstrate their impact on the annual performance of UMFC-based solar systems. Moreover, this study outlines the influence of wind-forced heat transfer on thermal performance and indicates the importance of choosing an appropriate correlation for wind-forced convection.

2. Mathematical model

The proposed model is a detailed theoretical model of an unglazed metal façade liquid collector (see Fig. 1) that requires the geometrical (length of the metal absorber, width of the absorber, etc.), physical parameters (the metal absorber thermal conductivity, the pipe thermal conductivity, etc.), operating conditions (the collector heat transfer fluid mass flow rate, the collector heat transfer fluid inlet temperature, etc.) and climatic conditions (solar irradiance, ambient air temperature, wind velocity, etc.) to calculate the model outputs (the usable heat output, with respect to the collector area, and output heat transfer fluid temperature).

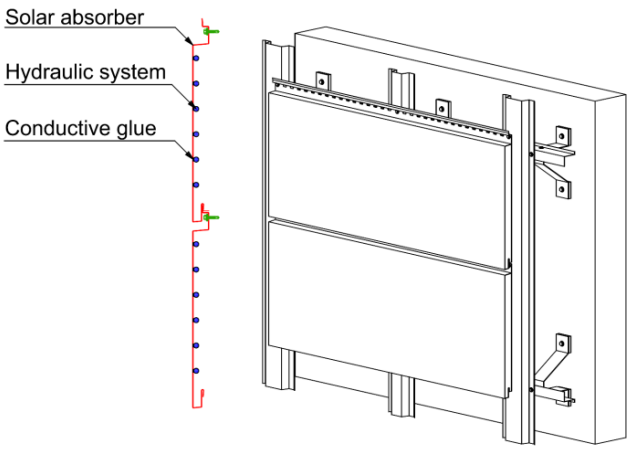

Fig. 1: The schematic layout of UMFC

The model uses the well-known one-dimensional useful energy output equation proposed by Hottel and Woertz (1942), Hottel and Whillier (1955) and Bliss Jr. (1959) so that

$$Q_{c,u} = A_{abs} F_R [\tau\alpha G - U(T_{in} - T_a)] \qquad \text{(eq. 1)}$$

where A_{abs} is the solar collector absorber area (m^2), F_R is the collector heat removal factor (-), τ is the solar transmittance of the collector cover, in the case of an unglazed solar collector it is equal to 1 (-), G is the global solar irradiance on the collector plane (W m^{-2}), U the collector overall heat loss coefficient (W m^{-2} K^{-1}), T_{in} is the heat transfer fluid inlet temperature (K), and T_a is the ambient air temperature (K).

In this equation, the fundamental difficulty is that there are two interdependent variables, the collector overall heat loss coefficient U and the collector heat removal factor F_R. The iteration cycle is introduced into the calculation process to solve this issue. In the first iteration step, the absorber T_{abs} and the heat transfer fluid T_{fluid} temperatures are estimated based on the inlet heat transfer fluid temperature T_{in}. Then, external and internal energy balances are calculated, describing the heat transfer process from the absorber surface to the surroundings and from the absorber surface to the heat transfer fluid, respectively. After that, the useful energy output is calculated according to Eq. (1). Afterwards, both estimated temperatures are recalculated. Finally, the recalculated absorber temperature T_{abs} and the heat transfer fluid temperature T_{fluid} are compared with the initial values. The calculation process continues as long as both temperatures are equal with 0.05 K difference. Typically, it takes from 3 to 5 iteration steps.

As mentioned above, the external energy balance describes the energy losses from the absorber surface to the surroundings. In the case of a UMFC, the external energy balance (see Fig. 2) consists of:

- the heat transfer processes by combined convection (forced and natural) and radiation from the front absorber surface to the ambient;
- the heat transfer processes by natural convection and radiation in the air gap between the back absorber surface and a façade wall.

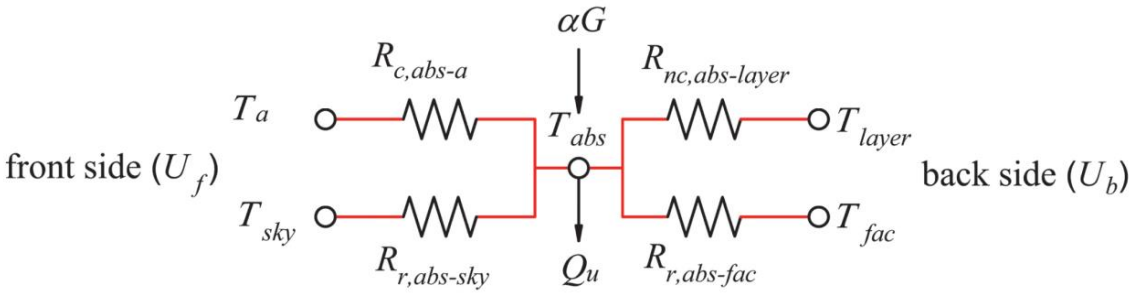

Fig. 2: Schematic layout of the external energy balance

To calculate the actual intensity of the heat transfer processes mentioned above, the absorber temperature T_{abs} should be known. On the other hand, the absorber temperature T_{abs} is dependent on the intensity of the heat transfer processes. Therefore, the absorber temperature T_{abs} in the first iteration step is estimated based on the heat transfer fluid inlet temperature T_{in}. Afterwards, the intensity of the heat transfer processes and the collector overall heat loss coefficient U are calculated based on the estimated absorber temperature T_{abs}.

The internal energy balance (see Fig. 3), contrary to the external energy balance, expresses the heat transfer processes inside a collector, from the absorber surface to the heat transfer fluid. It includes:

- the heat transfer process by fin conduction;
- the heat transfer process by bond conduction;
- the heat transfer process by pipe conduction;
- the heat transfer process by forced convection from the pipe surface to the heat transfer fluid.

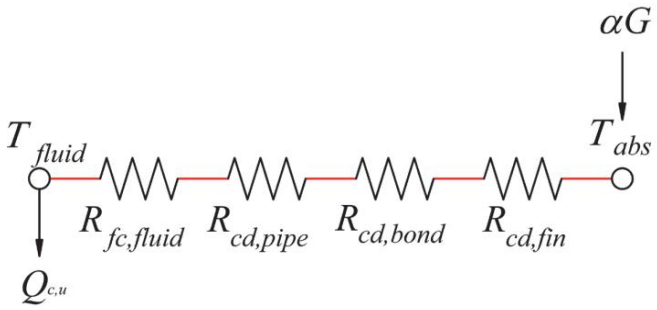

Fig. 3: Schematic layout of the internal energy balance

Here the situation here is very similar to the external energy balance. To calculate the actual intensity of the heat transfer processes, the heat transfer fluid mean temperature T_{fluid} should be known. On the other hand, the mean temperature of heat transfer fluid T_{fluid} is dependent on the intensity of the heat transfer processes. Hence, similar to external energy balance, in the first iteration step the heat transfer fluid mean temperature T_{fluid} is estimated based on the heat transfer fluid inlet temperature T_{in}. Then, the intensity of the heat transfer processes and the collector useful energy output $Q_{c,u}$ are determined based on the mean temperature of heat transfer fluid T_{fluid}.

3. Model verification

The proposed model was experimentally verified in Solar Laboratory operated under the University Centre for Energy Efficient Buildings (UCEEB) Czech Technical University in Prague. Ten UMFC prototypes different in design were produced using a commercially available metal cladding system to verify the model. Each prototype consists of a metal solar absorber with a solar absorptance α of 0.95, a longwave emittance ε of 0.95 and a hydraulic system (serpentine tube) bonded to the metal absorber sheet using conductive glue. The combinations of two pipe materials, three types of glue, three distances between pipes, and two prototype dimensions were used to demonstrate the performance sensitivity to different design parameters. A general dimensional scheme of the designed prototypes is illustrated in Fig. 4. The design parameters of the produced UMFC prototypes are presented in Tab. 1. The photos of the first experimental prototype are shown in Fig. 5.

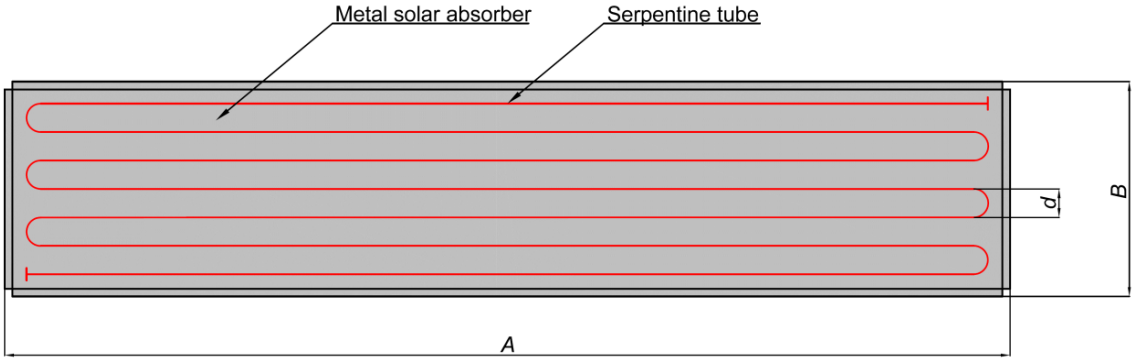

Fig. 4: The general dimensional scheme of the designed prototypes

Tab. 1: Design parameters of the produced UMFC prototypes

Prototype	Absorber material	Bond thermal conductivity (W m^{-1} K^{-1})	Distance between tubes d (mm)	Tube material	Absorber dimensions A x B (mm x mm)
1	Aluminium	2.8	90	Cu 15x1	2000 x 470
2	Aluminium	2.8	90	PEX 16x2	2000 x 470
3	Steel	1.4	90	PEX 16x2	2000 x 470
4	Steel	0.28	150	Cu 15x1	2000 x 470
5	Steel	0.28	150	PEX 16x2	2000 x 470

Tab. 1: Design parameters of the produced UMFC prototypes *(continued)*

6	Aluminium	1.4	90	PEX 16x2	3200 x 650
7	Aluminium	0.28	130	PEX 16x2	3200 x 650
8	Steel	1.4	130	Cu 15x1	3200 x 650
9	Steel	0.28	90	PEX 16x2	3200 x 650
10	Steel	0.28	130	PEX 16x2	3200 x 650



Fig. 5: Photos of the first experimental prototype

The produced prototypes were experimentally tested under stable climatic (solar irradiance, ambient air temperature, wind speed) and operating conditions (heat transfer fluid inlet temperature, heat transfer fluid flow rate) to determine the steady-state thermal output with the use of an indoor solar simulator (see Fig. 6 and Fig. 7). The sensors' type and their accuracy are given in Tab. 2.

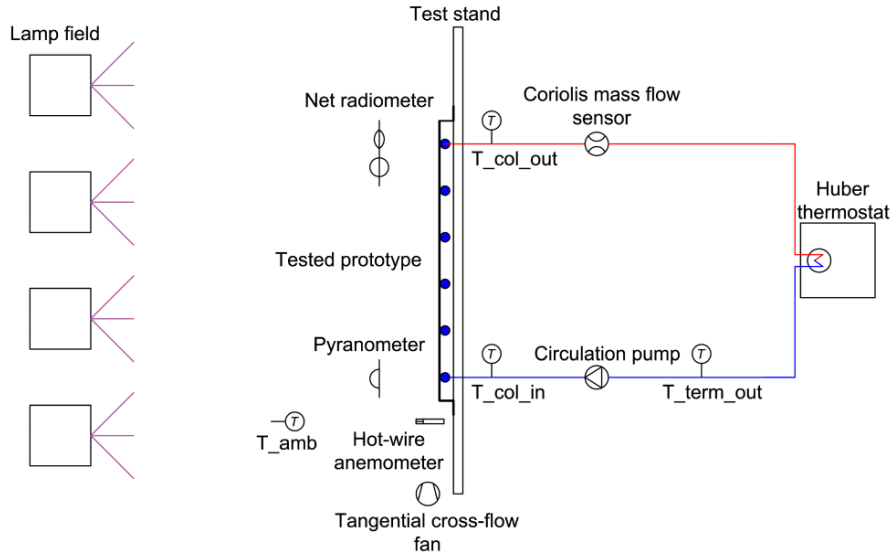

Fig. 6: An indoor solar simulator configuration



Fig. 7: UMFC prototype on the test stand

Tab. 2: The sensors' type and their accuracy

Sensor	Manufacturer	Type	Accuracy
Temperature	TMG	PT100	± 0.05 K
Flow rate	Krohne	Coriolis mass flow sensor OPTIMASS 7000 T10	± 0.002%
Solar irradiation	Kipp & Zonen	Pyranometer SMP1 1 -A	± 1.4%
Long wave irradiation	Kipp & Zonen	CNR4 Net Radiometer	± 4%
Wind velocity	Airflow Lufttechnik GmbH	Hot-wire anemometer D12-65V C	± 0.1 m/s

The prototypes were tested under three wind speeds to obtain steady-state useful thermal output $Q_{c,u}$ for at least three operation points (Fig. 6 and Fig.7). Subsequently, the instantaneous efficiency η_c was determined from Eq. (2) so that

$$\eta_c = \frac{Q_{c,u}}{A_{abs} G"} \qquad \text{(eq. 2)}$$

where $G"$ is the net irradiance at the plane of the collector (W m^{-2}). It was defined from Eq. (3) so that

$$G" = G + \frac{\varepsilon}{\alpha}(E_L - \sigma T_a^4) \qquad \text{(eq. 3)}$$

where E_L is the long wave irradiance in the collector plane (W m^{-2}).

Afterwards, the experimentally obtained useful energy output $Q_{c,u}$ and the analytically calculated instantaneous efficiency η_c were compared with the theoretically calculated characteristics provided by the model. Fig. 8 demonstrates the verification process for prototypes 1 and 3. The verification process for the other UMFC prototypes looks very similar.

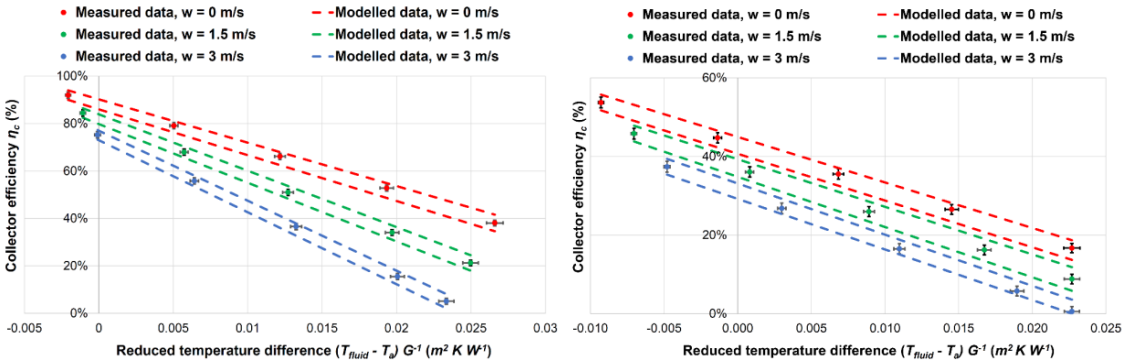

a) b)

Fig. 8: The model verification process for the prototype 1 (a) and the prototype 3 (b)

First of all, it should be noted that the experimentally obtained efficiency points are coupled with the expanded uncertainty points caused by the accuracy of the sensors (see Tab. 2) and the random variation of the measured quantities. Secondly, the theoretically modelled efficiency characteristics the model provides are influenced by the uncertainty of the input design parameters. Therefore, the theoretically calculated efficiency characteristic is presented as an efficiency area. Thirdly, it is worth noting that wind speed substantially influences the thermal performance of the tested UMFC. Finally, comparing and contrasting the experimentally obtained efficiency points and theoretically calculated efficiency area, the modelled results fit the experimentally obtained results relatively well. The flow chart of the verification process is shown in Fig. 9.

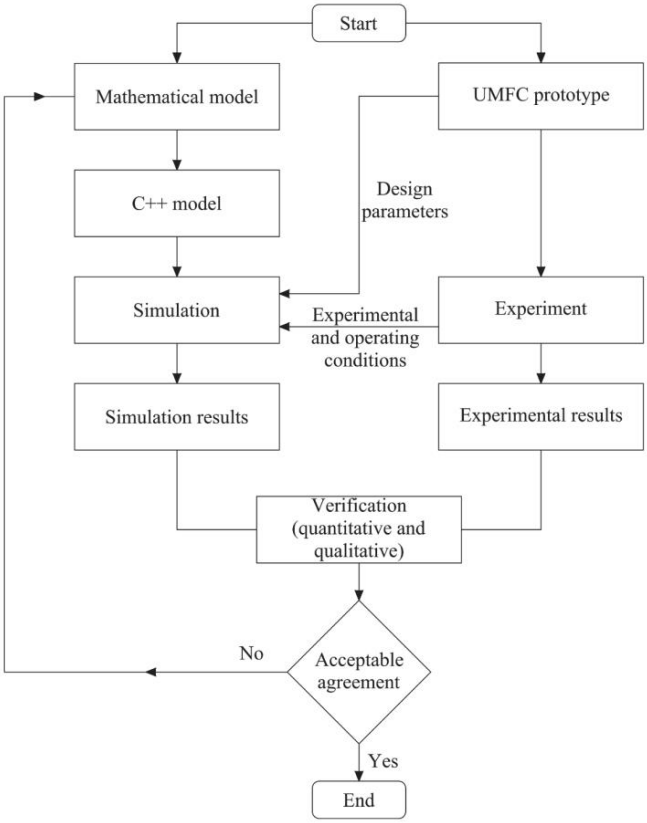

Fig. 9: Flow chart of the verification process

4. Data analysis and the model testing

The thermal performance of a UMFC is significantly affected by heat losses, especially by the front side heat losses. As mentioned above (see Fig. 2), the front side heat losses are caused by two heat transfer processes – by radiation loss from the absorber surface and by combined convection (forced and natural) loss to the ambient. It is evident that due to the relatively low operating temperatures of UMFC, the influence of the radiation heat transfer process is relatively low. On the other hand, the effect of combined convection is significant.

The combined convection heat transfer coefficient is generally calculated as a function of a forced convection heat transfer coefficient using a correlation in terms of wind speed w and natural convection heat transfer coefficient correlation represented by the temperature difference between the surface temperature T_{abs} and the ambient temperature T_a (Eq. 4).

$$h_c = f(h_w(w), h_n(\Delta T)) \qquad \text{(eq. 4)}$$

The present study analyses only the influence of the wind-forced convection model on the theoretically modelled efficiency since wind-induced convective heat transfer has a significantly greater influence than natural convective heat transfer. The issue is that up to now, there is no consensus about an appropriate procedure for the wind-forced convection heat transfer coefficient calculation (Sartori, 2006). As for today, a huge amount of work has been conducted over the last 100 years by different researchers. Palyvos (2008) has presented an exhaustive literature review on the wind-forced convection models, including more than 95 different correlations. This survey includes correlations obtained for façade surfaces and roof-mounted single-glazed solar thermal collectors. Later, Kumar and Mullick (2010) performed experiments for unglazed solar thermal collectors to estimate the wind-caused heat transfer coefficient and compared it with studies of other researchers.

Fig. 10 demonstrates the thermal efficiency area for UMFC prototype 1 with two limiting curves as a result of the proposed mathematical model calculations using 40 different wind-forced convection correlations, which are suitable for unglazed solar thermal collector modelling under the conditions of the performed experiment. First of

all, the modelling results indicate that the theoretically calculated thermal performance is highly dependent on the selection of wind-forced heat transfer correlation used in the model. Secondly, the span of the efficiency area between the limits increases with an increase in wind speed. Therefore, to calculate the thermal performance of a UMFC with a reasonable degree of accuracy, it is extremely important to identify a proper heat transfer correlation for wind-forced convection heat transfer.

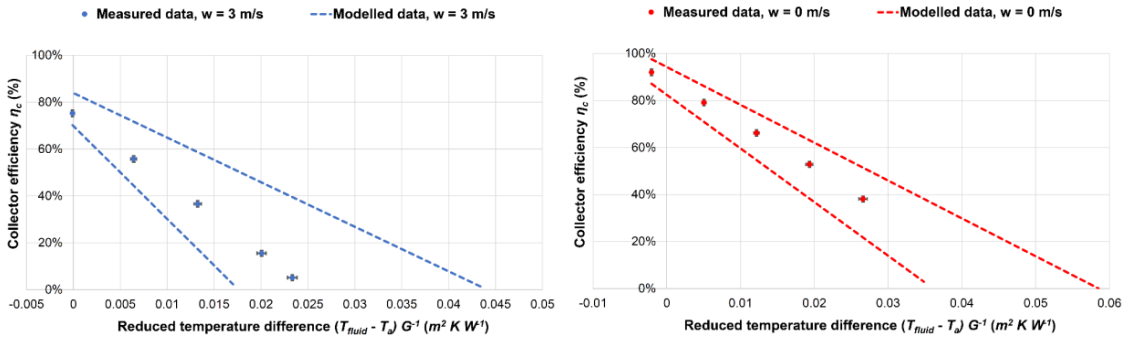

Fig. 10: The thermal efficiency area as a result of the model calculation using 40 suitable wind-forced convection correlations

Fig. 11 presents the efficiency curves as a result of the model calculation for the first UMFC prototype using 5 widely used wind-forced convection correlations (McAdams, 1954; Wattmuff et al., 1977; Test et al., 1981; Kumar et al., 1997; Sharples and Charlesworth, 1998). The simulation results are also compared with the experimental results.

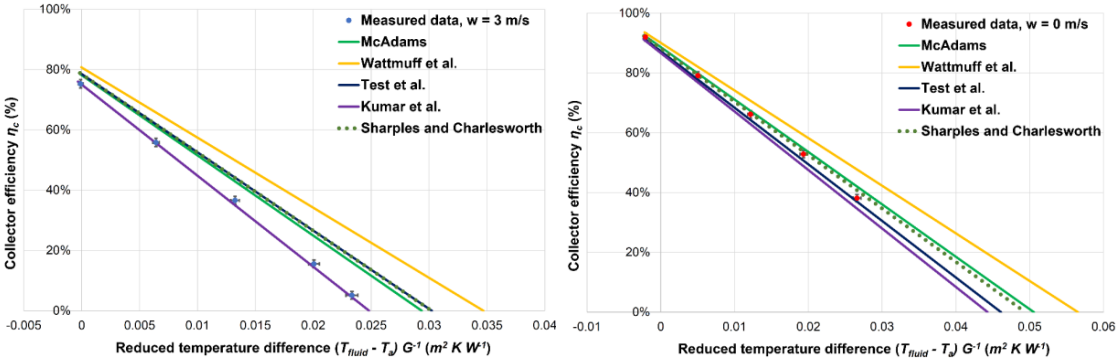

Fig. 11: The thermal efficiency characteristics as a result of the model calculation using 5 widely used wind-forced convection correlations

The simulation results indicate that the wind-forced convection correlations obtained by McAdams (1954) and Wattmuff et al. (1977) give lower values of wind-forced heat transfer coefficient and, consequently, higher efficiency values for the collector. On the other hand, the wind-forced convection correlations obtained by Test et al. (1981) and Sharples and Charlesworth (1998) give higher values of wind-transfer coefficient and, as a result, lower efficiency values. The difference in the simulation results is caused by a difference in the experimental conditions. While McAdams (1954) and Wattmuff et al. (1977) reported their correlations based on wind tunnel measurements, Test et al. (1981) and Sharples and Charlesworth (1998) performed outdoor experiments to obtain wind-forced heat transfer coefficient correlations. The point is that the amount of free stream disturbance in outdoor conditions is generally higher than in wind tunnels at the same speed. Consequently, a higher heat transfer coefficient can be expected in outdoor experiments compared to low turbulence wind tunnel measurement (Test et al., 1981). Moreover, wind flow in a wind tunnel is generally steady, while there are dynamically changing conditions for wind speed and direction during outdoor experiments.

It can also be observed that the experimental results obtained in the present study are somewhat close to the results of Kumar et al. (1997). This may be due fact that the experiment was performed in an indoor environment using an industrial fan. The constant stream disturbance (swirls and turbulence) generated by a large industrial fan can be a factor responsible for higher values of wind-forced convection heat transfer coefficient. Finally, it is evident that the experimental conditions have a crucial influence on the wind-forced heat transfer coefficient and, consequently, on the thermal performance of UMFC prototypes. Therefore, to provide solar system simulation

results with a reasonable degree of accuracy, a long-term outdoor verification process (onsite at best) is highly recommended to find an appropriate wind-forced convection correlation.

5. Conclusion

The paper presents a novel detailed mathematical model of an unglazed metal façade collector. To verify the model, ten differently designed UMFC prototypes were produced based on the conventional metal facade cladding system and experimentally tested. Comparing and contrasting the experimentally obtained efficiency points and theoretically modelled efficiency area span, it can be concluded that the model results fit the experimentally obtained efficiency points sufficiently well.

It was also shown that the thermal performance of a UMFC is greatly influenced by wind-forced convection heat transfer from the front side. Therefore, it is extremely important to identify an appropriate wind-forced convection correlation to minimize the difference between experimentally obtained and theoretically modelled results. Many correlations for wind-forced convection clearly demonstrate that there is no universally acceptable correlation. It is caused by different combinations of experimental conditions (ambient air temperature, wind range, wind tunnel/outdoor/indoor measurement, instrumentation, surroundings, etc.). It should be noted that any wind-forced heat transfer correlation obtained from experimental or analytical results is valid within specific experimental conditions. Actually, Sharples and Charlesworth (1998) and Oliphant (1980) conclusions' agree with this fact and conclude that the results from their work are strictly and only applicable to the particular experimental conditions existing at the site of the measurements. Therefore, the heat transfer model taken from its experimental conditions applied under different conditions leads to incorrect results. Hence, the verification process provided by using an indoor solar simulator in the case of an unglazed solar thermal collector is insufficient. Generally, wind flow under indoor tests is steady, whereas wind is always dynamic in the natural environment as much in wind speed as in wind direction. As a result, a long-term outdoor verification process is highly recommended to find an appropriate wind-forced convection correlation.

Future work will focus on a long-term outdoor verification process based on a large-scale UMFC demonstration under different operation conditions of potential applications (direct hot water preparation, combination with heat pump for hot water preparation and space heating, night cooling, etc.).

6. Acknowledgment

This work was developed within the project Facade system with integrated heat exchanger, CZ.01.1.02/0.0/0.0/20_321/0024470 supported by the Operational Programme Enterprise and Innovations for Competitiveness of the Ministry of Industry and Trade of the Czech Republic. The project is co-financed by the European Union.

7. References

Anderson, T.N., Duke, M., Carson, J.K., 2013. Performance of an unglazed solar collector for radiant cooling.

Bliss Jr., R.W., 1959. The derivations of several "Plate-efficiency factors" useful in the design of flat-plate solar heat collectors. Sol. Energy 3, 55–64. https://doi.org/10.1016/0038-092X(59)90006-4

Bunea, M., Perers, B., Eicher, S., Hildbrand, C., Bony, J., Citherlet, S., 2015. Mathematical modelling of unglazed solar collectors under extreme operating conditions. Sol. Energy 118, 547–561. https://doi.org/10.1016/j.solener.2015.06.012

Eisenmann, W., Mueller, O., Pujiula, F., Zienterra, G., 2006. Metal roofs as unglazed solar collectors, coupled with heat pump and ground storage. Determination of gains from condensation, system concepts; Unverglaste Metalldach-Sonnenkollektoren in Kopplung mit Waeremepumpe und Erdsonde. Bestimmung des Waermeertrag.

Giovanardi, A., Passera, A., Zottele, F., Lollini, R., 2015. Integrated solar thermal façade system for building retrofit. Sol. Energy 122, 1100–1116. https://doi.org/10.1016/j.solener.2015.10.034

Hermann, M., Lunz, K., Hillerns, F., 2010. BIONICOL. Development of a bionic solar collector with an aluminium roll-bond absorber; BIONICOL. Entwicklung eines bionischen Solarkollektors mit Aluminium-Rollbond-Absorber.

Hottel, H., Whillier, A., 1955. Evaluation of flat-plate solar collector performance. Trans. Conf. Use Sol. Energy; 3, 74–104.

Hottel, H., Woertz, B., 1942. Performance of flat-plate solar-heat collectors. Trans. ASME (Am. Soc. Mech. Eng.); (United States) 64, 91–104.

Keller, J., 1985. Characterization of the thermal performance of uncovered solar collectors by parameters including the dependence on wind velocity, humidity and infrared sky radiation as well as on solar irradiance.

Kumar, S., Mullick, S.C., 2010. Wind heat transfer coefficient in solar collectors in outdoor conditions. Sol. Energy 84, 956–963. https://doi.org/10.1016/j.solener.2010.03.003

Kumar, S., Sharma, V.B., Kandpal, T.C., Mullick, S.C., 1997. Wind induced heat losses from outer cover of solar collectors. Renew. Energy 10, 613–616. https://doi.org/10.1016/S0960-1481(96)00031-6

Martinez, R.G., Goikolea, B.A., Paya, I.G., Bonnamy, P., Raji, S., Lopez, J., 2017. Performance assessment of an unglazed solar thermal collector for envelope retrofitting. Energy Procedia 115, 361–368. https://doi.org/10.1016/j.egypro.2017.05.033

McAdams, W.H., 1954. Heat Transmission 3d Ed. McGraw-Hill, New York.

Morrison, G.L., 1994. Simulation of packaged solar heat-pump water heaters. Sol. Energy 53, 249–257. https://doi.org/10.1016/0038-092X(94)90631-9

Morrison, G.L., Gilliaert, D., 1992. Unglazed Solar Collector Performance Characteristics. J. Sol. Energy Eng. 114, 194–200. https://doi.org/10.1115/1.2930005

Oliphant, M. V, 1980. Measurement of wind speed distributions across a solar collector. Sol. Energy 24, 403–405.

Palyvos, J.A., 2008. A survey of wind convection coefficient correlations for building envelope energy systems' modeling. Appl. Therm. Eng. 28, 801–808. https://doi.org/10.1016/j.applthermaleng.2007.12.005

Perers, B., 2010. An improved dynamic solar collector model including condensation and asymmetric incidence angle modifiers, in: EuroSun. 28 September-1 October, 2010 Graz, Austria.

Probst, M.M., Roecker, C., 2007. Towards an improved architectural quality of building integrated solar thermal systems (BIST). Sol. energy 81, 1104–1116.

Sartori, E., 2006. Convection coefficient equations for forced air flow over flat surfaces. Sol. Energy 80, 1063–1071.

Sharples, S., Charlesworth, P.S., 1998. Full-scale measurements of wind-induced convective heat transfer from a roof-mounted flat plate solar collector. Sol. Energy 62, 69–77.

Shemelin, V., Matuska, T., 2022. Unglazed solar thermal collector for building facades. Energy Reports 8, 605–617. https://doi.org/10.1016/j.egyr.2022.07.075

Shen, J., Zhang, X., Yang, T., Tang, L., Wu, Y., Jin, R., Pan, S., Wu, J., Xu, P., 2016. Conceptual Development of a Compact Unglazed Solar Thermal Facade (STF) for Building Integration. Energy Procedia 96, 42–54. https://doi.org/10.1016/j.egypro.2016.09.096

Soltau, H., 1992. Testing the thermal performance of uncovered solar collectors. Sol. Energy 49, 263–272. https://doi.org/10.1016/0038-092X(92)90005-U

Stegmann, M., Bertram, E., Rockendorf, G., Janßen, S., 2011. Model of an unglazed photovoltaic thermal collector based on standard test procedures, in: Proc. of the ISES Solar World Congress. pp. 172–180.

Test, F.L., Lessmann, R.C., Johary, A., 1981. Heat Transfer During Wind Flow over Rectangular Bodies in the Natural Environment. J. Heat Transfer 103, 262–267.

Wattmuff, J.H., Charters, W.W.S., Proctor, D., 1977. Solar and wind induced external coefficients for solar collectors. Coop. Mediterr. pour l'Energie Solaire, Rev. Int. d'Heliotechnique 2, 56.

Weiland, F., Kirchner, M., Rensinghoff, V., Giovannetti, F., Kastner, O., Ridder, D., Tekinbas, Y., Hachul, H., 2019. Performance assessment of solar thermally activated steel sandwich panels with mineral wool core for industrial and commercial buildings. J. Phys. Conf. Ser. 1343, 012098. https://doi.org/10.1088/1742-6596/1343/1/012098

Whillier, A., 1967. Design factors influencing solar collector performance. Low Temp. Eng. Appl. Sol. Energy 27–40.

Agri Solar Thermal Systems: A Brief Study on the Energetic Potential of Bifacial Solar Thermal Systems

Thorsten Summ, Michael Seiler, Mathias Ehrenwirth, Christoph Trinkl and Wilfried Zörner

Institute of new Energy Systems (InES) / Technische Hochschule Ingolstadt (THI), Ingolstadt (Germany)

Abstract

The limited availability of land for large-scale solar technologies has led to the idea of combining agricultural and energetic land use. Especially bifacial Agri photovoltaics has shown to be attractive regarding low installation costs. Bifacial Agri solar thermal systems have been neither analyzed nor tested in this context, which results in a lack of research in this field. Therefore, the objective of this paper is to outline the energetic potential of a bifacial solar thermal system. An analytic modelling approach based on solar irradiance analysis was chosen to obtain the specific thermal energy yield for a whole reference year. This included considerations of incidence angle and collector efficiency along with operation temperature and model assumptions. In comparison to a conventional collector facing south and inclined at 45°, the provided annual thermal energy per m^2 collector area of the bifacial module (90° east-west oriented) was calculated to be 0.9 % less (451 kWh/m^2). The results suggest that a bifacial Agri-ST system is capable to deliver a comparable amount of thermal energy per m^2 of collector area. Furthermore, the calculations indicate an increased seasonality of the bifacial over the conventional system. By neglecting shading effects and assuming isotropic diffuse irradiance this potential was presumably overestimated in this study. System simulations should be carried out in the future to consider these effects as well as transient operation states.

Keywords: Agri solar thermal, bifacial system, incidence angle, efficiency, specific annual energy yield, solar thermal system, flat-plate collector, insulating glass flat-plate collector

1. Introduction

1.1 Background and Motivation

The use of land for the provision of renewable energies has become a topic of discussion in politics and society in recent years. While in urban areas the roof surfaces of buildings are used for renewables, rural areas offer open spaces for the use of wind energy, photovoltaics (PV), solar thermal energy (ST), and biomass. The expansion of these technologies is essential to reduce greenhouse gas emissions, but both suitable and affordable land is limited. The different utilization options are increasingly competing with each other (Epp, 2021b, 2021a; Röpcke, 2021). This problem will intensify in the upcoming years due to the required growth of renewables. Furthermore, there will be an increase in demand for solar district heating (SDH) in European countries (Epp, 2021c). However, to cover the heat demand of a community which is connected to the district heating network, several hundreds to thousands of square meters of installed collector area is required. In rural areas, this land is often used for agriculture and are therefore not available for renewable energies.

Against the background of this competition for space, two-sided irradiated (bifacial) PV modules were recently investigated for the integration of solar cells in agriculturally used areas (Gerhards et al., 2022; cf. Katsikogiannis et al., 2022). By vertical installation (90° tilt angle) and orientation to east-west, each side is exposed one half of the day to supply electrical energy. This approach promises to take up only a fraction of agricultural land by placing the modules vertically while providing renewable electricity to the nearby community. This concept is called Agri-PV and can provide combined agricultural and electricity production, making an important contribution to climate action and other Sustainable Development Goals of the UN (Huck, 2022). Agri-PV systems have become a mature technology in the last years and are considered to be state-of-the-art.

1.2 Agri-PV and Agri-ST Systems

The concept of Agri-PV has its roots in 1981 when Goetzberger and Tastrow introduced the idea of growing potatoes underneath a collector field. However, this concept did not become established until 2013 (Scharf et al., 2021). For

© 2022. The Authors. Published by International Solar Energy Society
Selection and/or peer review under responsibility of Scientific Committee
doi:10.18086/eurosun.2022.12.16 Available at http://proceedings.ises.org

this type of installation, the agricultural use is still in the foreground and may not be influenced by the electricity generation, or only insignificantly. This has also been stated in the first standard DIN SPEC 91434 (Deutsches Institut für Normung e. V., 2021). For this purpose and in order to maximize both agricultural yields and electricity production, the right system design must be selected.

The first possibility of combining agricultural use and PV on the same area is to install the PV modules above the agricultural area as a kind of roof construction (see Fig. 1). In this case, rows of stable (steel) supports are erected at a freely selectable distance. The distances between the rows are chosen in such a way that the system is integrated into the respective agricultural management and has a minimal impact on it. The system is erected with the aid of a wide variety of foundations, such as screw foundations or pile-driven foundations, which are anchored in the ground so that they provide the overall structure with sufficient stability even under varying wind loads. Concrete foundations are not used in this case, as they can disturb the ecology and workability of the soil in the long term. (Trommsdorff et al., 2020)

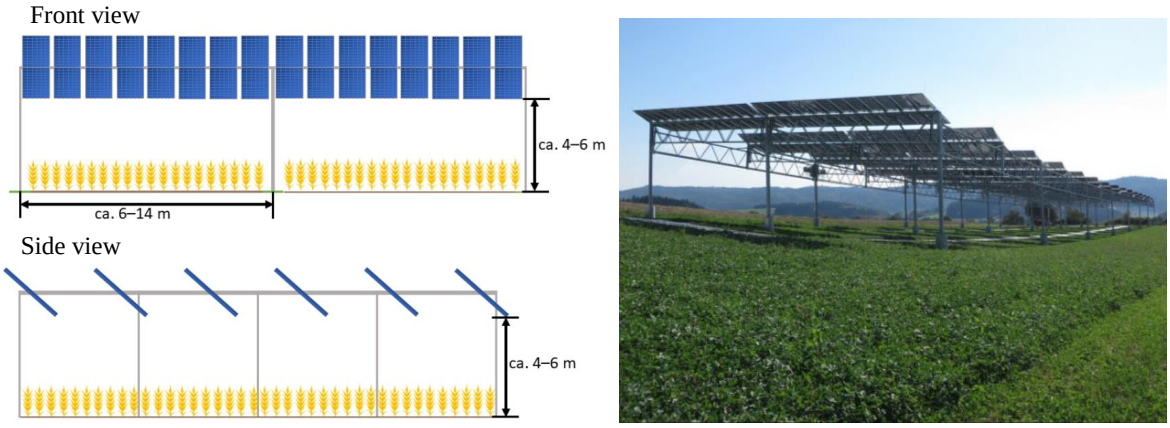

Fig. 1: Schematic illustration (left) and test plant (right) from Scharf et al. (2021) of an elevated Agri-PV system on a arable field.

This type of installation is more expensive as compared to conventional ground-mounted types (Scharf et al., 2021) which is why another type of Agri-PV has been introduced by the company Next2Sun GmbH. This so-called bifacial Agri-PV system does not require elevated mounting supports but instead the PV modules are installed vertically as seen in Fig. 2. The distance between the module rows is chosen in such a way that the agricultural machine has enough space to mow the field and thus cultivate the area. However, this vertical installation requires the collectors to be orientated toward east and west, rather than south. Therefore, the system has its peak power before and after solar noon.

So far, a solar thermal variant of this concept does not exist and thus, the problem of limited land-availability remains unsolved for solar thermal systems. Therefore, this paper focuses on Agri-ST technology. The usage of concentrators to increase the efficiency of the modules is difficult because the rear side of the module must not be covered. Generally, for a solar thermal realization, evacuated tube collectors could be considered even if compound parabolic concentrators cannot be used. However, in this study, a first potential estimation of that novel concept is done for which the investigation of flat-plate collectors (FPC) is considered to be sufficient.

Common FPCs have a non-transparent rear side which contains the solid materials to insulate the absorber and increase the efficiency. It needs to be removed in order to allow for bifacial operation. In addition, the casing of the module which is typically made of aluminum, needs to be replaced by a transparent material. The resulting design is similar to an insulating glass unit with an absorber between front and rear cover.

In the last years insulating glass flat-plate collectors have been developed and investigated thoroughly (Giovannetti et al., 2014; Giovannetti and Kirchner, 2015; Summ et al., 2020; Summ et al., 2021). The design concept is well-suited for a bifacial Agri-ST application and numerous investigations have shown that the performance is in a similar order of magnitude as compared to conventional FPCs. Additionally, Nikolić and Lukić (2015) investigated double-exposure flat-plate collectors and showed that a bifacial operation can perform significantly better with the usage of reflecting surfaces. In this study, no reflecting mirrors are considered and insulating glass FPCs are investigated in order to have a comparable bifacial setup as shown in Fig. 2.



Fig. 2: Example of an bifacial Agri-PV system. (Next2Sun GmbH, 2022). The distance between the module rows is chosen in such a way that the agricultural machine has enough space to mow the field and thus cultivate the area.

1.3 Research Gaps and Scope

A bifacial solar thermal implementation in the context of Agri-ST does not yet exist and thus, no investigations on the energetic potential of this technology have been conducted. Therefore, the objective of this paper is to outline the energetic potential and compare bifacial collectors which can be used for Agri-ST plants with a conventional collector.

2. Methodology

The objective of this paper is to provide a first estimation of the bifacial Agri-ST concept by means of specific collector yield analysis and comparison with a conventional solar thermal setup. In order to compare the south-oriented, tilted collector field with a vertical Agri-ST collector field, analyses on the solar irradiance were conducted. A conventional collector field with an inclination of 45° facing south was compared to a bifacial 90° east-west oriented collector field.

The methodological approach for the presented research work is shown in Fig. 3. The key output is the collector yield calculation and comparison which is displayed in dark green. Three sets of technical data were included consisting of collector data, weather data, and operational data. Another set of model assumptions completed the input for the modelling approach.

An analytical modelling approach was considered to be sufficient for the first specific energy yield estimation of bifacial collectors. A system simulation approach was not selected in this study, instead a linear function was used for modelling the thermal yield. In that function, the beam irradiance, diffuse irradiance, average collector efficiency, and incidence angle modifier (IAM) were considered.

Weather data from PVGIS-SARAH (European Commission, Joint Research Centre, 2022) referring to the year 2016 was used to obtain the solar irradiance on the inclined surfaces. The selected dataset refers to a location in the center of Germany near the city of Kassel. The solar angles were also extracted from the data to compute the incidence Θ between the sun rays and the collector aperture surface using the geometrical relation (Quaschning, 2013):

$$\Theta = \arccos(-\cos(\alpha)\sin(\beta)\cos(\gamma_s - \gamma_c) + \sin(\alpha)\cos(\beta)) \qquad \text{(eq. 1)}$$

α : solar elevation β : collector tilt angle γ_s : solar azimuth angle γ_c : collector azimuth angle

In that manner, the IAM can be taken into account for the computation of the thermal energy output. For both systems, the IAM values according to Tab. 1 were considered. A linear interpolation was applied to account for intermediate values of Θ. To calculate the thermal energy output q, the solar beam irradiance G_b, diffuse solar irradiance G_d, and average collector efficiency η were taken into account. q was computed and compared for both the conventional and bifacial solar thermal system. The following relation represents the modelling approach to obtain the specific thermal

energy output, where IAM is a function of Θ and η is a function of β:

$$q(t) = \int_0^t (G_b + G_d)\,\eta\,\mathrm{IAM}\,\mathrm{dt} \qquad \text{(eq. 2)}$$

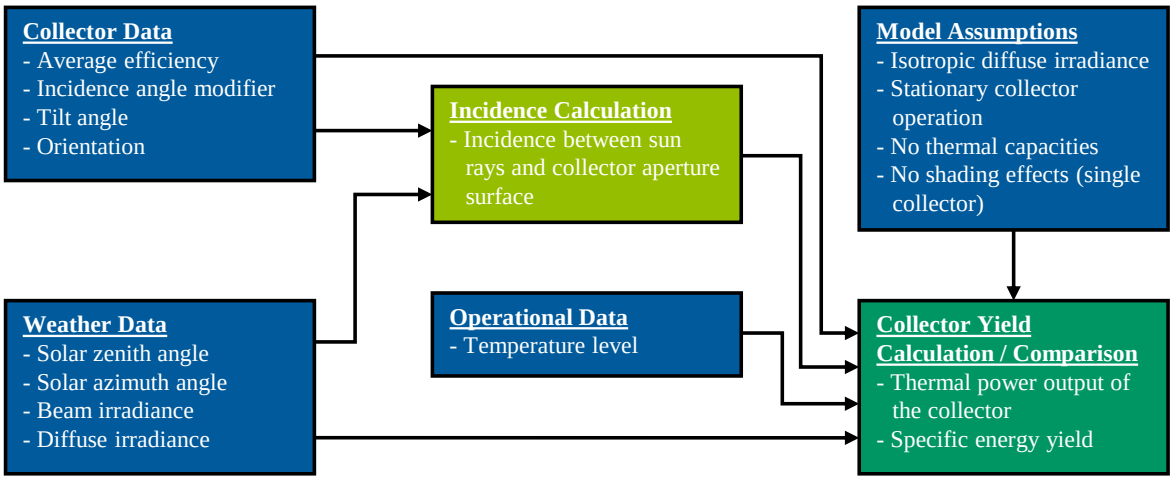

Fig. 3: Schematic illustration of the methodological approach for the presented study. Inputs are displayed in blue, intermediate computations in light green and outputs in dark green.

The thermal efficiency for the analysis was set according to the investigations of Giovannetti and Kirchner (2015) for a collector temperature level of 60 K above ambient ($\eta_{conventional} = 0.425$, $\eta_{bifacial} = 0.5$). The authors have shown, that a vertically installed collector performs better as compared to a 45° installed one. Convective losses of the module are affected by the collector tilt angle and with larger tilt, the performance will increase (Montoya-Marquez and Flores-Prieto, 2017). Hence, the vertically installed bifacial module shows a higher efficiency than the 45° tilted conventional collector. For the analysis, full-year data was used with an hourly resolution.

Tab. 1: Incidence angle modifier for both the conventional and bifacial flat-plate collectors. For intermediate values, a linear interpolation scheme was implemented.

Θ	0°	50°	70°	90°
IAM	1.00	0.98	0.80	0.00

3. Results and Discussion

The objective of this study was to provide a first estimation of the bifacial Agri-ST concept by means of specific collector yield analysis and comparison with a conventional solar thermal setup. The annual energetic comparison of the conventional and the bifacial collector is shown in Fig. 4. Both blue curves represent the cumulative specific irradiation on the aperture surface of the conventional (solid lines) and bifacial (dashed lines) collector. With a total specific irradiation of 1,185 $\mathrm{kWh/m^2}$ the south-oriented collector receives about 6.5 % more energy as compared to the bifacial system (1,108 $\mathrm{kWh/m^2}$). Between October and April, the south-oriented collector gains more energy compared to the east-west-oriented one. Yet, during the other parts of the year the bifacial collector appears to have more favorable conditions. In that time period, the slope of the dashed curve is slightly larger which suggests that more energy can be converted by the bifacial collector. Prior to the analysis, the east-west-oriented surface was expected to receive more energy during the winter period as compared to the south oriented one. The assumption was that the smaller solar elevation will be beneficial for the vertical installation and therefore the bifacial collector was expected to be preferably used during fall and winter.

However, the green curves reveal that the opposite seems to be true. Both show the cumulative specific energy yield of the collectors. The difference in total specific energy yield is smaller as for the irradiation. For the conventional collector it is 455 $\mathrm{kWh/m^2}$ and for the bifacial collector it results in 451 $\mathrm{kWh/m^2}$ which is a relative difference of only 0.9 %. This comparatively small difference is partially caused by the higher efficiency of the vertical collector (cf. section 2). As described above, the bifacial collector receives less solar energy during the wintertime but more energy during summertime. As a result, the slope of the curves deviates for these periods.

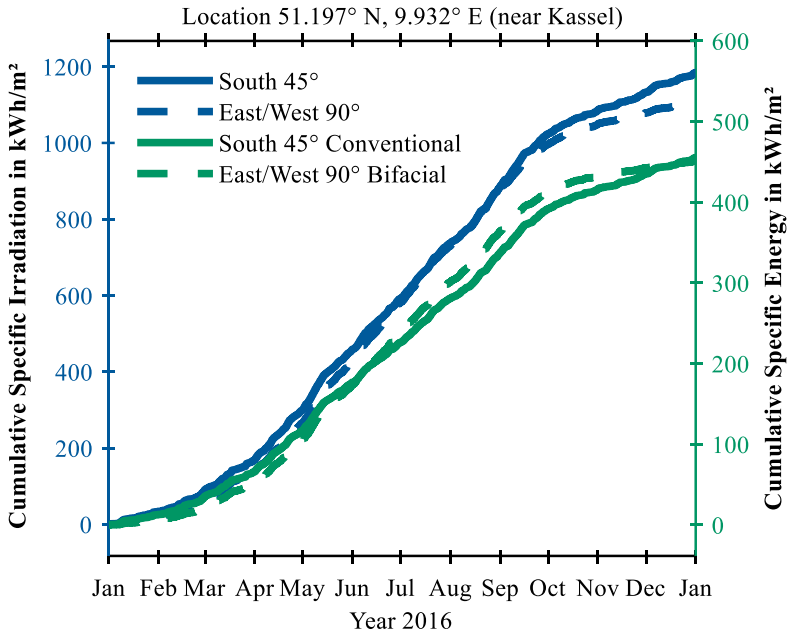

Fig. 4: Comparison of the annual cumulative specific irradiation for a 45° south-oriented (–) and a 90° east-west-oriented (- -) surface (left axis). On the right axis, the annual cumulative specific energy of a conventional (–) and a bifacial (- -) solar thermal collector is shown.

The effect of the annual solar movement on the incidence angle modifier is shown in Fig. 5. In the two plots, the IAM for the 45° south-oriented, 90° east oriented, and 90° west oriented collector aperture surface are compared. On the left, the time period during summer solstice is displayed. It can be seen that the blue area represents the east side of the bifacial collector, which is irradiated early in the morning with low incidence. Similarly, the west side is irradiated on the second half of the day, which is represented by the green area. Also as expected, the southern surface is most irradiated in the middle of the day. It is noteworthy that due to the early sunrise and late sunset, the time integral of IAM for east and west is larger than the gray area representing the conventional collector. This explains why the bifacial collector achieves a greater specific yield in summer than the conventional one. On the other hand, shading effects have been neglected in this study. Though, they could have a significant impact on the advantage which the bifacial concept offers over the conventional one. It is expected that shading in summer will partially offset the benefit of early sunrise and late sunset, and thus the bifacial system may provide less specific yield than shown here.

On the right, the same dataset is shown during winter solstice. Here, a different result emerges. The shorter days affect the bifacial collector in particular. The solar angles are less favorable in this case although the low elevations were initially assumed to be advantageous. Overall, the wintertime indicates a significantly lower energy yield compared to the conventional module.

This effect can be seen even clearer in Fig. 6, where the data from Fig. 3 is shown in the form of a bar chart for the individual months of the year. It can be seen that the months of April to August are those in which the bifacial concept delivers more thermal energy. During this period, the bifacial collector outperforms the conventional one by 15.1 %. On the other hand, the months of September to March benefits the conventional concept. Here, the collector is clearly more effective which is demonstrated by the specific energy yield which is 32.6 % higher compared to the bifacial collector in that time period.

Also noteworthy are the months of June and September, because the radiation values are significantly different from those of the other months (cf. Fig. 6). In September, the radiant energy for the bifacial collector is 12.2 % less as compared to the conventional one, whereas in June it is the other way round. The reason for the unexpected turnaround is the share of diffuse radiation, as described below.

Fig. 7 shows the time histories of the radiation values during June and September for the south-facing system. The beam radiation is shown in blue, the diffuse part of the radiation in green. It is noted that the fraction of diffuse radiation is greater in June than in September. This indicates, that the sky was cloudier in June than in September. Due to the fact that the bifacial collector can use the diffuse radiation on both sides, it can be assumed that this collector performs better on cloudy days than the conventional collector. This in turn explains why the energy values

for the conventional and bifacial collectors in Fig. 6 differ so much. However, it was assumed that the diffuse radiation is isotropic, and the collector converts the radiant energy on both sides to the same extent. In combination with the shading effects, these simplifications are likely to affect the total specific energy yield and could make the comparison work in favor of the conventional system.

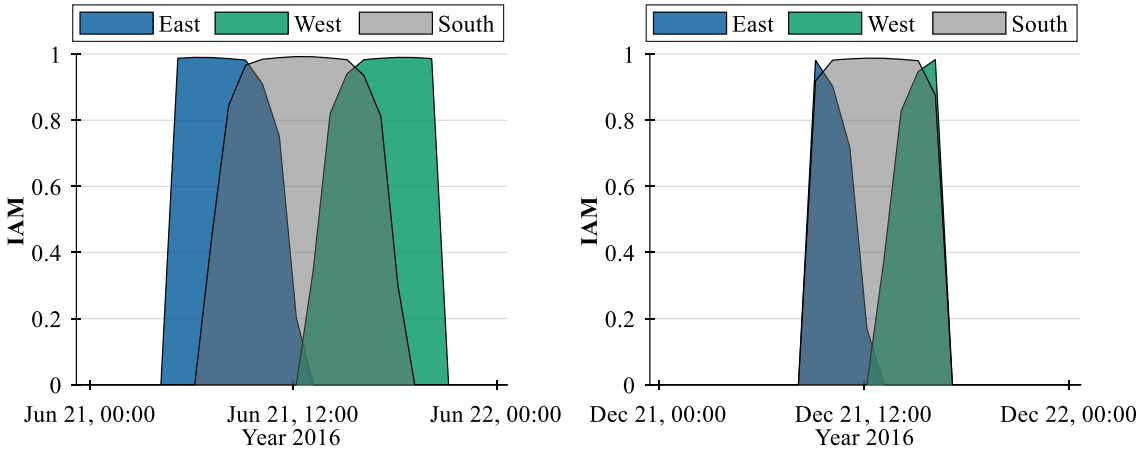

Fig. 5: Incidence angle modifier for the 45° south-oriented, 90° east-oriented, and 90° west-oriented collector aperture surfaces at the summer solstice (left) and winter solstice (right). Early sunrise and late sunset during summertime is beneficial for the bifacial system, whereas the shorter days are more favorable for the conventional installation.

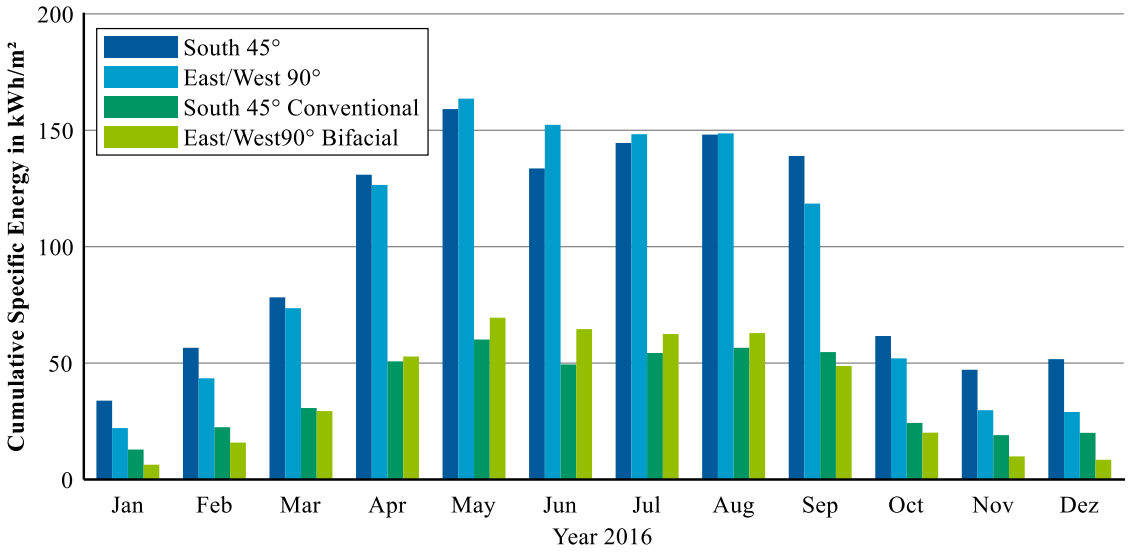

Fig. 6: Bar plot comparison of the monthly cumulative specific irradiation for a 45° south-oriented and a 90° east-west-oriented surface. The green bars represent the monthly cumulative specific thermal energy of a conventional and a bifacial solar thermal collector.

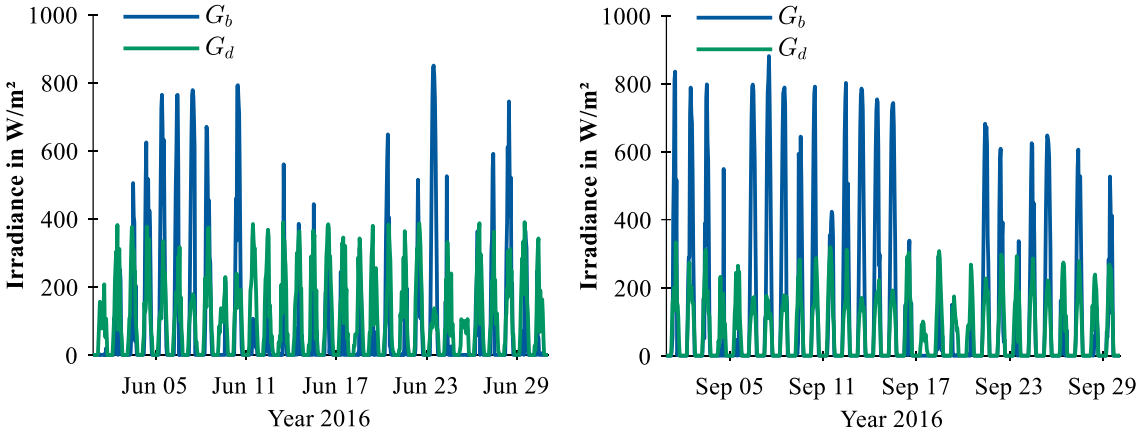

Fig. 7: Line Plot of the direct (blue) and diffuse (green) radiation fraction for the months of June (left) and September (right). It can be seen that the diffuse component is slightly larger in June than in September.

4. Conclusions

The analytical modelling approach has shown that a 45° south-oriented flat-plate collector delivers 0.9 % more thermal energy than a 90° east-west oriented bifacial flat-plate collector. Three main reasons were identified which explain this unexpected small difference. First, the efficiency of the bifacial collector is greater as compared to the conventional one because the vertical installation will positively affect the convective losses (cf. Giovannetti and Kirchner, 2015; Montoya-Marquez and Flores-Prieto, 2017). Second, the incidence and IAM during summertime are more favorable for the bifacial collector leading to a 15 % advantage regarding specific thermal energy yield. Third, the bifacial system is capable to convert the diffuse components of the radiation at the side facing away from the sun.

These results suggest that a bifacial Agri-ST system is capable of delivering a comparable amount of thermal energy per m^2 of collector area. Furthermore, an increased seasonality of an Agri-ST system can be assumed. This shift of the energy yield into the summer months can be either advantageous or disadvantageous for the thermal consumer, depending on the system design and control strategy. The energetic disadvantage of bifacial collectors appears moderate and acceptable. Additionally, under consideration that new areas for solar thermal can be opened up by using that novel system, the potential of Agri-ST is considered remarkable. However, this potential was presumably overestimated in this study by neglecting shading effects.

Shading is expected to be the most important unconsidered aspect as on the one hand it has an influence on the collector row spacing and thus the utilization rate on the fields. On the other hand, shading will reduce the solar yield and may reduce or even eliminate the advantageous summer yields for the bifacial collector. How big this influence is should be further investigated in future studies. At the same time, changing the parameters which were selected for this study, may have an impact on the results. Therefore, it is reasonable to continue these studies with an extended range of input parameters. System simulations could help to consider these aspects in future studies and also account for transient effects.

Apart from of the theoretical analysis, practical questions are still unanswered, such as the hydraulic connection of the modules or the mounting system under consideration of agricultural boundary conditions. In this respect, the results of this study are to be seen as a first assessment of the potential, which is to be verified and extended in further analyses in order to be able to demonstrate the full potential of this technology.

Acknowledgments

The work presented in this paper was funded by the Federal Ministry of Economic Affairs and Climate Action of the Federal Republic of Germany within the 7th Energy Research Program under the project “flexLAC” (Project ID 03ETW015-A). The overall aim of “flexLAC” is to design a mass-producible insulated glass flat-plate collector which is able to reduce heat generation costs for solar district heating.

References

Deutsches Institut für Normung e. V., 2021. Agri-Photovoltaik-Anlagen. Anforderungen an die landwirtschftliche Hauptnutzung. Beuth Verlag GmbH, Berlin ICS 27.160; 65.020.01. https://www.beuth.de/de/technische-regel/din-spec-91434/337886742. Accessed 5 September 2022, 26 pp.

Epp, B., 2021a. "German SDH market could be bigger, if there was enough space". https://www.solarthermalworld.org/news/german-sdh-market-could-be-bigger-if-there-was-enough-space. Accessed 8 October 2021.

Epp, B., 2021b. "Renewable heat generation should be priviledged in the Building Regulations §35". https://www.solarthermalworld.org/news/renewable-heat-generation-should-be-privileged-building-regulations-ss35. Accessed 8 October 2021.

Epp, B., 2021c. Spotlight on SDH potential in Germany, the Netherlands and Austria | Solarthermalworld. https://solarthermalworld.org/news/spotlight-sdh-potential-germany-netherlands-and-austria/. Accessed 28 February 2022.

Gerhards, C., Schubert, L., Lenz, C., Wittmann, F., Richter, D., Volz, B., 2022. Agri-PV – Kombination von Landwirtschaft und Photovoltaik. https://slub.qucosa.de/landing-page/?tx_dlf[id]=https%3A%2F%2Fslub.qucosa.de%2Fapi%2Fqucosa%253A77460%2Fmets. Accessed 11 April 2022.

Giovannetti, F., Kirchner, M., 2015. Performance and Reliability of Insulated Glass Collector Prototypes, in: Conference proceedings / EuroSun 2014, International Conference on Solar Energy and Buildings, Aix-les-Bains, France, 16 - 19 September. Proceedings of the EuroSun 2014 Conference. International Solar Energy Society, Freiburg, Germany, pp. 355–361.

Goetzberger, A., Tastrow, A., 1981. Kartoffeln unter dem Kollektor. Neuer Vorschlag der Fraunhofer-Gesellschaft. Sonnenenergie 6 (3), 19–22.
Huck, W., 2022. Resolution adopted by the General Assembly on 25 September 2015, in: Huck, W. (Ed.), Sustainable Development Goals. Article-by-Article Commentary, 1st ed. Nomos Verlagsgesellschaft, Baden-Baden, pp. 653–684.
Katsikogiannis, O.A., Ziar, H., Isabella, O., 2022. Integration of bifacial photovoltaics in agrivoltaic systems: A synergistic design approach. Applied Energy 309, 118475.
Montoya-Marquez, O., Flores-Prieto, J., 2017. The Effect of the Angle of Inclination on the Efficiency in a Medium-Temperature Flat Plate Solar Collector. Energies 10 (1), 71.
2022. Our Agro-Photovoltaic Concept. Agriculture and Livestock Farming. https://www.next2sun.de/en/our-concept/.
Röpcke, I., 2021. Solare Wärmenetze: Startschuss für SolnetPlus. https://www.solarthermie-jahrbuch.de/solare-waermenetze-startschuss-fuer-solnetplus/. Accessed 14 October 2021.
Scharf, J., Grieb, M., Fritz, M., 2021. Agri-Photovoltaik. Stand und offene Fragen. TFZ-Bericht 73. www.tfz.bayern.de. Accessed 31 August 2021.

N. Thermal Energy Storage

Investigating the use of Phase Change Materials to Reduce Space Conditioning Loads in Cold Climates

Calene Baylis[1] and Cynthia A. Cruickshank[1]

1 Carleton University, Ottawa (Canada)

Abstract

Because buildings are responsible for nearly 40% of global energy consumption, it is critical that emissions-intensive conditioning loads be minimized to achieve global climate targets. One option to decrease conditioning loads is using phase change materials (PCMs) which can be integrated into buildings to store solar gains during peak periods to decrease space cooling loads, and during the heating season, the midday stored energy can be used to decrease overnight heating loads. Reductions in cold climate heating and cooling loads with PCMs has been limited both in research and in practice, despite that the heating loads account for two thirds of energy consumption in some locations. The objective of this modelling study was to assess the ability of PCMs in full building simulations with various properties to decrease heating and cooling loads in the capital cities within Canada and Germany. It was found that in Ottawa and Berlin, space heating loads could be reduced by 4.7% and 6.5%, respectively, and cooling loads by 60.1% and 54.1%, respectively. The underlying causes of this discrepancy between space heating and cooling reductions are described within the paper. In addition, integrating PCMs with two melting temperatures was found to have limited impact compared to a single PCM with a melting temperature of 23ºC, and the greatest reductions in heating load reductions were achieved with a two-story house.

Keywords: Phase change material, latent thermal storage, EnergyPlus, full building simulation, solar gains

1. Introduction

Buildings are responsible for a substantial portion of energy consumption worldwide, and in locations such as Canada, 64% of residential energy is used to meet space heating loads (NRCan, 2018). It is critical that strategies be developed, optimized, and implemented to decrease these numbers if national and international climate targets are to be met. As such, approaches to decrease conditioning loads such as more effective utilization of solar gains are necessary. Building integrated latent thermal storage with phase change materials (PCMs) relies on a solid-liquid phase change to store solar energy during peak periods to decrease the energy that directly enters the air in a space and thus simultaneously reduces peak room temperatures and energy required for cooling. Reducing the peak cooling energy has the added benefit of limiting the utilization of peak energy throughout the summer that are often met using natural gas, which can have a significant impact on emissions. In the heating season, the energy that is stored during peak solar periods helps reduce any midday overheating that may occur. The energy can then be released in the evening or overnight to maintain room temperatures throughout the day and decrease energy required for overnight heating.

It has been found in past studies that the melting temperature was outside of the room temperature range, minimal, if any, energy reductions have been shown which is the root of the cold climate challenges with PCM (Gassar and Yun, 2017). Furthermore, improper selection of PCM melting temperatures can lead to worse performance of a building (Kheradmand et al., 2016). As such, for PCMs to be most beneficial in the reduction of space conditioning loads, their melting temperature should be near that of the room temperature setpoint. However, in locations with two distinct conditioning seasons, room temperature setpoints often vary by several degrees throughout the year, which can limit the effectiveness of the PCM for either the heating or cooling loads, depending on the PCM melting temperature selection. As such, utilization of two PCMs – one that is better suited to each conditioning load – may be a viable solution to minimize space conditioning

© 2022. The Authors. Published by International Solar Energy Society
Selection and/or peer review under responsibility of Scientific Committee
doi:10.18086/eurosun.2022.13.01 Available at http://proceedings.ises.org

loads year-round.

The objective of this study was to evaluate the ability of PCMs to decrease heating and cooling loads in Ottawa, Canada and Berlin, Germany – locations with two distinct conditioning seasons, and the capital cities of both countries assessed. This expands on past research by delving further into the factors affecting PCM implementation, including utilization of two PCMs, PCM melting and solidifying temperatures, and house layout. Without full knowledge of how each of these factors impacts building energy consumption and temperatures, and how the performance of PCMs varies between geographic locations, PCM systems will not be able to be most effectively designed and implemented. This research increases the current knowledge on PCM integration and provides insight into factors that can lead to the greatest reduction in conditioning loads and therefore emissions in Canada and Germany. This paper includes a review of related literature, description of the simulation methodology used, and results that are described and discussed.

Although PCMs have been well demonstrated to decrease cooling loads, evaluation and successful utilization of them for heating is limited. Guarino et al (2017) found that despite a 47-75% decrease in space cooling, there was a negligible difference in heating with PCM gypsum with a phase change range of 18-24°C in a building in Canada. In contrast, however, an annual heating load reduction as high as 44% was found in a review by Al-Yasiri and Szabo (2021), while Heim and Clarke (2004) found a reduction in heating loads of up to 90% at times during the winter. Various studies have been done to increase the effectiveness of PCMs, and lower thicknesses of PCM with greater surface area, which would be the case with PCM-integrated drywall, have been shown to significantly reduce conditioning energy consumption (Alam et al., 2014). This is caused by the fact that the PCM response to thermal excitations and thus ability to quickly store and release energy is limited in thicker wall assemblies (Kosny et al., 2013) or with increased insulation (Entrop et al., 2011).

PCMs have been shown to be most effective when their melting temperature is within 2ºC of the indoor temperature setpoint (Kosny et al., 2013). However, in locations with two distinct space conditioning seasons, the room temperature setpoints often vary by several degrees throughout the year, which can render a single PCM ineffective a significant portion of the time. As such, a method that has been shown to increase the effectiveness of PCMs is the utilization of two PCMs – one tailored to each the heating and cooling seasons. Memarian et al. (2018) analyzed the effects of one PCM versus two PCMs in a warm climate and found that PCMs nearly doubled the energy reduction compared to a single PCM from 8% to 15% energy load reductions. In this study, 21ºC and 29ºC melting temperature PCMs were implemented on the interior of the wallboard within a space. Other studies have shown that two PCMs increase the time during which thermal energy is stored by 57% compared to a single PCM, leading to a decrease in the peak space temperature by 2ºC (Lakhdari et al., 2020).

In an attempt to optimize PCMs for a cold Canadian climate, Beradi and Soudian (2019) studied a system with two PCM melting points in July through October. The best performance was found to be during the later months because large diurnal temperature swings occurred during the change of season from summer to fall, promoting nighttime solidification and therefore greater utilization of the latent storage capacity of the PCM. A study by Mathis et al. (2018) in Quebec, Canada also agreed that the greatest energy savings could be realized in shoulder seasons, finding 8.7%, 9%, and 41% reductions in March, April, and May, respectively. Nikoofard et al (2015) studied a single PCM system in Canada in a techno-economic analysis and concluded that a PCM with a melting temperature of 23ºC was capable of decreasing the national energy and emissions by 2.5%.

Mohseni and Tang (2020) conducted a simulation using EnergyPlus and found that regardless of the PCM location within the wall, the heating and cooling energy consumption could be decreased with a PCM melting temperature of 21ºC. Furthermore, it was concluded that the best melting temperature for cooling reductions in the summer were 25ºC and the best for heating reductions was 21ºC.

The limitations within the literature include that many studies have not been conducted on full houses – the experimental studies are limited to small test chambers and limited simulation-based research exists on full house models with two PCMs. Little to no research has been conducted on the variability of PCM performance between various housing archetypes or comparisons of PCMs in various geographic locations. In addition, limited optimization has been conducted for heating loads, and research is even more limited on

increasing the effectiveness of PCMs for both conditioning seasons.

With proper design of PCMs and thorough understanding of their performance, PCM systems can be better equipped to significantly reduce both conditioning loads. However, due to the limited research in this area and mix of results on PCM effectiveness, additional evaluation of PCM properties and integration scenarios is critical to fully understand the scenarios in which PCMs are most suitable for integration into cold climate houses. In addition, it is necessary to understand which PCM properties and house layouts within the existing building stock may contribute to differing energy savings with PCMs.

2. Methodology

Three full house models with different common layouts were developed for this analysis using EnergyPlus – an open-source building simulation tool that provides detailed predictions of building physics elements such as infiltration, heat transfer, and solar gains (US Department of Energy, 2021). The three house layouts that were considered are open concept bungalow, partitioned bungalow, and two-story. All of these were assumed to have four occupants during weekday evenings and weekends and no occupancy during the day on weekdays. The bungalows had a 164 m^2 floor area (excluding the basement) and a 30% window to wall ratio on the south façade, and the same total window area was maintained for the two-story house case. The solar heat gain coefficient (SHGC) and U-factor of the windows were 1.4 and 0.4 $W/m^2 \cdot K$, respectively. The air infiltration for the house was 2.5 ach (Placido and Pressnail, 2014), and there was a constant 600 W of electrical gains to represent lights and auxiliary electrical systems in total to the main floor and basement zones. The heating and cooling setpoints were 19ºC and 25ºC with setbacks to 16ºC overnight and during unoccupied weekdays in the winter, and 30ºC during unoccupied weekdays in the summer. The walls, floors, and roof were composed of typical residential construction components, as shown in Tab. 1, with the corresponding properties shown in Tab. 2.

Tab. 1: Building envelope construction

Exterior Wall	Interior Floor	Exterior Roof	Foundation Wall
Siding	OSB	Shingles	Concrete
Air gap	Air gap	Air gap	Insulation
OSB	OSB	OSB	Gypsum
Insulation	-	-	-
XPS	-	-	-
Gypsum	-	-	-

Tab. 2: Building material properties

	Siding	OSB	Insulation	XPS	Gypsum	Shingles	Concrete
Thickness (mm)	12.7	12.7	150	25.4	12.7	5.0	2.032
Density (kg/m^3)	2240	1000	28	55	800	800	2240
Conductivity ($W/m \cdot K$)	0.094	0.17	0.038	0.027	0.17	0.1	1.95
Specific Heat ($J/kg \cdot K$)	1170	1300	750	1210	1090	1200	900

Each house layout was simulated in Ottawa, Canada and Belin, Germany with and without PCM. The simulations were conducted using Canadian Weather for Energy Calculations (CWEC) data for Ottawa, Canada and Typical Meteorological Year (TMY) data for Berlin, Germany. PCM was implemented on the inside surface of the gypsum on all walls on the main floor, to represent PCM-integrated drywall or a simple PCM retrofit. In the case of the partitioned bungalow, the east and west walls and the partition wall in the

south zone had PCM, and for the two-story case, the east and west walls of both the main and second floors had PCM in addition to the north wall of the main floor. These PCM locations were chosen to maintain the quantity of PCM between all layouts. The PCM properties are shown in Tab. 3, which were obtained using differential scanning calorimetry (DSC) and guarded hot plate (GHP) experiments.

Tab. 3: PCM properties simulated

Property	Value
Latent Heat (kJ/kg)	160.0
Thermal Conductivity (W/m·K)	0.22
Density (kg/m^3)	900
Subcooling (ºC)	6.0
Liquid Specific Heat (kJ/kg·K)	0.98
Solid Specific Heat (kJ/kg·K)	3.96

Annual simulations were conducted while varying PCM properties such as the degree of subcooling (the temperature difference between the melting and solidifying temperatures) and PCM melting temperatures, to indicate trends and desirable properties to seek during PCM sourcing. In addition, building parameters such as layout and window locations were varied, and simulations were conducted to determine the impact of including two PCMs of different melting temperatures compared to a single PCM scenario. In terms of the PCM properties, three different degrees of subcooling were assessed: 1ºC, 3ºC, and 6ºC, which indicates the temperature difference between the melting and solidifying temperatures. For these cases, the melting temperature was held constant, and the solidifying temperature was adjusted to be the corresponding temperature below the melting temperature. Three melting temperatures were also assessed: 21ºC, 23ºC, 25ºC, which were selected to be between the heating and cooling setpoints.

In the base open concept house, three thermal zones were used – one for each the attic, main floor, and basement. The partition wall layout included four thermal zones because the main floor was split into a front and back zone, and the two-story layout included four thermal zones which included a thermal zone for the second floor. The front and back thermal zones and the second-floor zone operated identically to the single main floor zone in terms of heating and cooling setpoints and infiltration, while electrical loads and occupancy were split between the main and additional zone. The open concept house had PCM integrated into all walls on the main floor, and to maintain the same quantity of PCM, the partition wall layout did not contain PCM in the back wall. In situations where only one melting temperature PCM was used, the same total mass of PCM was used as cases with two different PCMs to further maintain similarity between the cases studied.

The limitations of the model used include utilization of the ideal heating and cooling objects for space conditioning loads. These objects do not model a central conditioning unit, but rather an independent variable air flow unit for each thermal zone that modulates the air flow rate and temperature to meet the conditioning loads. As such, there is no thermal lag that would occur with a radiant heating system, and the spaces are treated as though they have their own conditioning units. This is a limitation of the models because in a typical house, the setpoints for each space would be met using one conditioning unit that was modulated by the main zone air conditions. Independent control was chosen in this study in an attempt to maximize the usefulness of the PCM within each zone.

3. Results and Discussion

The results of the simulations conducted within this study predict the cases of PCM properties, integration methods, and house layouts that lead to reduced space conditioning loads in Ottawa, Canada and Berlin, Germany. Within a base case open concept house with no PCM, the heating and cooling loads were found to be 527.96 MJ/m^2 and 14.50 MJ/m^2, respectively in Ottawa, Canada and 329.66 MJ/m^2 and 10.23 MJ/m^2 in

Berlin, Germany. These values were compared to houses with PCM throughout the study. Tab. 4 illustrates the base conditioning loads without PCM for the three house layouts in both cities. For the partitioned wall layout, the main floor zone that was 12 m in depth in the open concept case was split into two 6 m deep zones.

Tab. 4: Base case conditioning loads without PCM

		Heating (MJ/m^2)	Cooling (MJ/m^2)
Ottawa	**Open Concept**	527.96	14.50
	Partitioned	528.18	14.47
	Two Story	533.22	30.9
Berlin	**Open Concept**	329.66	10.23
	Partitioned	328.58	10.19
	Two Story	329.01	23.58

The two-story cases had greater cooling loads due to the additional perimeter area which increased heat transfer between the outdoors and the conditioned space, as compared to the bungalow cases. Within this study, PCM properties including the difference between melting and solidifying temperatures were assessed with a single-PCM open concept house, followed by different combinations of PCM melting temperatures and different housing layouts in both cities considered.

3.1. Single PCM Open Concept House

Fig. 1 illustrates the variations that occur in annual heating and cooling loads due to single PCMs with different melting temperatures and degrees of subcooling. In these simulations, one PCM was implemented into an open concept house within Ottawa. The melting temperatures selected were 21ºC, 23ºC, and 25ºC, such that they were all within the range of space conditioning setpoints throughout the year.

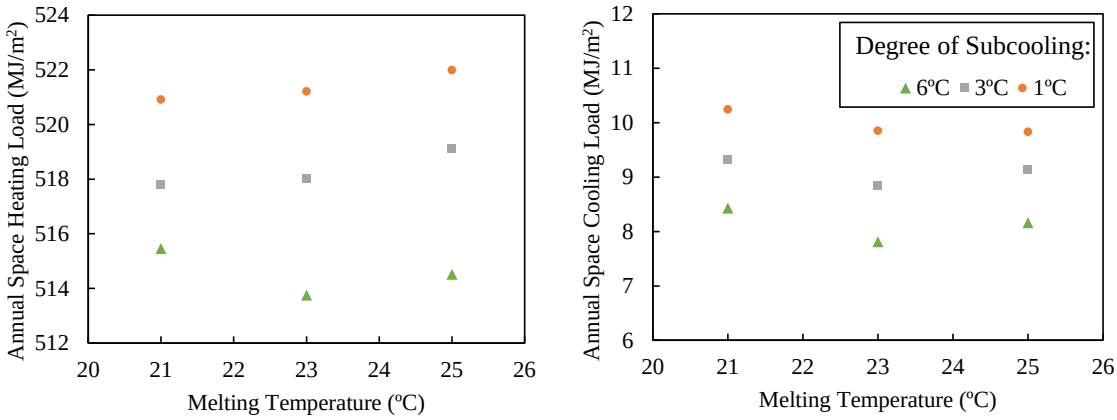

Fig. 1: Heating (left) and cooling (right) loads with a single PCM in Ottawa

It can be seen that a single PCM with a 6ºC lower solidifying temperature than the melting temperature caused the lowest annual heating and cooling loads, regardless of the melting temperatures examined. This analysis was limited to melting temperatures within the 21-25ºC range to be between the heating and cooling setpoints and thus be as effective as possible for both throughout the year. With lower subcooling, PCM melting temperatures that were closer to the space conditioning setpoint were found to minimize conditioning loads, as predicted based on past research. However, as the degree of subcooling increased to 6ºC, both the heating and cooling loads were found to be minimized with melting temperatures of 23ºC. This is caused by the PCM with this melting temperature more readily solidifying to better use the latent storage capacity, whereas with the 21ºC PCM, it would have to cool to 15ºC to fully solidify when there is a large degree of subcooling.

Based on these results, it could be recommended that PCMs be selected to have melting temperatures closer to that of the cooling setpoint with greater subcooling, particularly if the exact heating and cooling setpoints are unknown. Greater subcooling allows a PCM to be more effective over a wider range of room temperature setpoints and thus mitigates concerns of limited PCM effectiveness that have been indicated in past studies. Overall, however, the relative difference between any of the studied options is relatively low, with heating and cooling reductions from the base house without PCM varying between 1.1-2.7% and 27.5-47.7%, respectively.

3.2. Two PCM Open Concept House

Based on the results for PCM melting temperatures, the main cases studied were a single PCM with melting temperature of either 21ºC or 23ºC, two PCMs with melting temperatures of 21ºC and 23ºC, and a base case without PCMs. The space air temperature, north wall temperature, and solar gains transmitted through the window for a summer (July 2) and winter (January 24) day are shown in Fig. 2 with 21ºC and 23ºC PCM in the main zone walls of the open concept house in Ottawa.

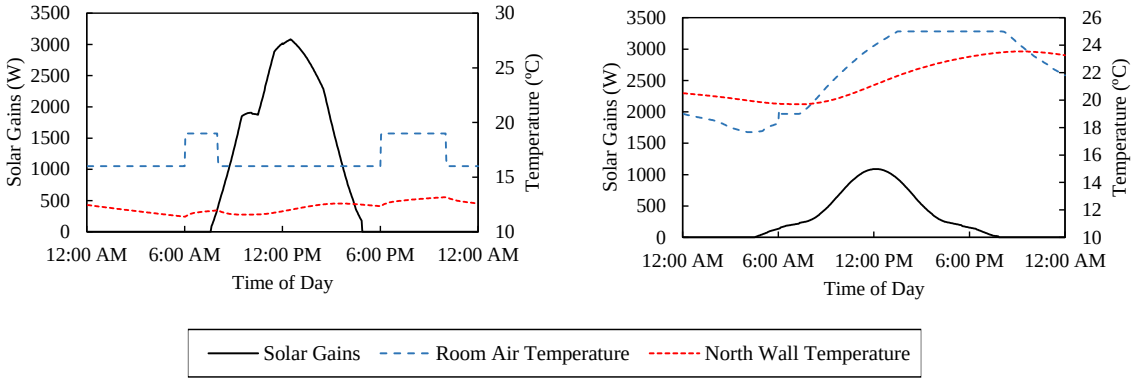

Fig. 2: Solar gains and main floor temperatures on January 24 (left) and July 2 (right)

Fig. 2 illustrates the cause for limited PCM effectiveness in winter and the ease of achieving benefits with PCMs in summer. Throughout the summer, PCM within the walls is used to store peak solar energy entering the space as the room temperature heats up. This effectively delays and reduces the operation of space cooling systems. However, in winter, the room air temperature setpoints and therefore space heating loads are greatest in the morning and evening during the occupancy hours. As such, the midday solar gains stored within the PCM can aid with the space heating energy required for the evening conditioning but have negligible effectiveness during morning heating. It is this discrepancy for heating and agreement for cooling seasons between the time conditioning systems are typically operational and the time of peak solar gains that leads to the overall effects on annual conditioning loads.

Fig. 3 shows a comparison of room air temperatures with and without 21ºC and 23ºC PCM in July in Ottawa, Canada, which further illustrates the benefits of PCM in decreasing the time during which the space cooling system operates. Fig. 3 illustrates the impact of PCM on a summer day compared to a house without PCM. The room air temperatures are more uniform with PCM included and due to the storage capacity of the PCMs, it took longer for the house with PCMs to reach the cooling setpoint temperature of 25ºC, thus leading the cooling equipment to operate for a shorter duration with PCM. The room air temperatures are not shown for a winter date such as January 24th, because there was insufficient solar energy added to the air to lead to a peak temperature above the setpoint of 16ºC or 19ºC. The constant room temperature regardless of PCM integration is an additional factor in leading the space heating loads to be less affected by PCM than space cooling loads.

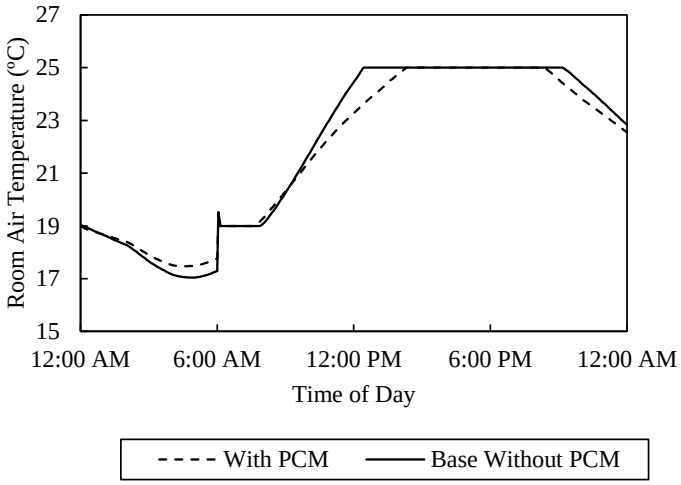

Fig. 3: Comparison of room air temperatures on July 2 in Ottawa with and without PCM

3.3. Partitioned House in Ottawa

The results shown in Fig. 1 through Fig. 3 are for an open concept house in Ottawa, Canada, while Fig. 4 illustrates the effects on annual conditioning loads of an east-west partition wall through the main floor, at various distances from the south wall. The base conditioning loads refer to those without PCM, while the 21ºC and 23ºC conditioning loads have both PCMs within the walls.

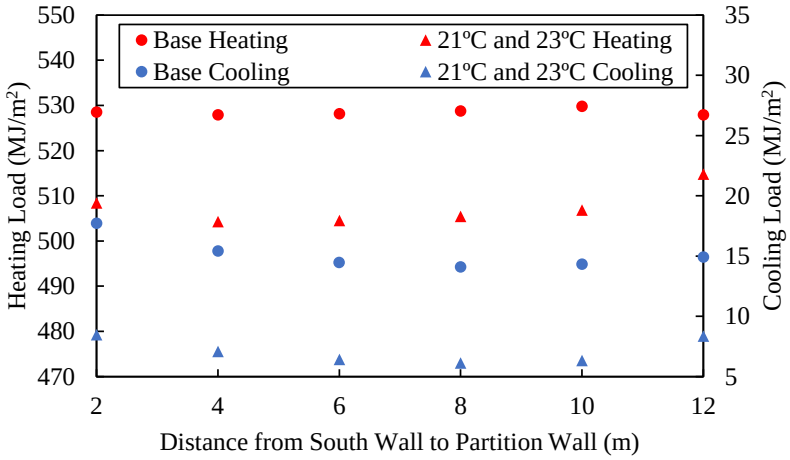

Fig. 4: Impact of dividing wall on annual conditioning loads in Ottawa

The house layout was found to have a small effect on the annual PCM performance, as shown in Fig. 4. When considering the energy savings between the base and PCM scenarios, it was found that implementing 21ºC and 23ºC PCM into all walls caused up to a 4.5% decrease in heating loads and a 56.5% decrease in cooling loads. Proportionally greater reductions were observed in cooling loads due to the relatively small base cooling values and due to the better alignment between solar gain storage and release for peak cooling than for times requiring heating.

It was found that partition wall layouts that split the main floor into areas that were close to equal in floor area (such as the 6 m partition distance) had slightly lower conditioning loads, particularly for cooling, in the base and PCM cases. This is caused because with a smaller front room (2 m), the front room is heated up and exposed to significantly more solar gains than the back room, so the PCM along the back walls is underutilized. In contrast, with larger front rooms (10 m), it takes a greater period of time to heat up the surfaces which reduces the time during which the PCM is within the temperature range for thermal storage. As such, the 6 m partition distance was found to balance the solar gains within the front room such that there was a sufficient portion of PCM available and able to reach temperatures that facilitated thermal storage of the PCMs throughout the greatest portion of the year. Due to this trend, a 6 m partition wall distance was

selected for the comparisons between Ottawa and Berlin.

3.4. Two Story House in Ottawa

A two-story house in Ottawa with the same floor area as the open concept and partitioned layouts was found to have a similar trend to that of the single-story options. The room air temperature for the main and second floors of a two-story house with and without PCM are shown in Fig. 5 for July 2.

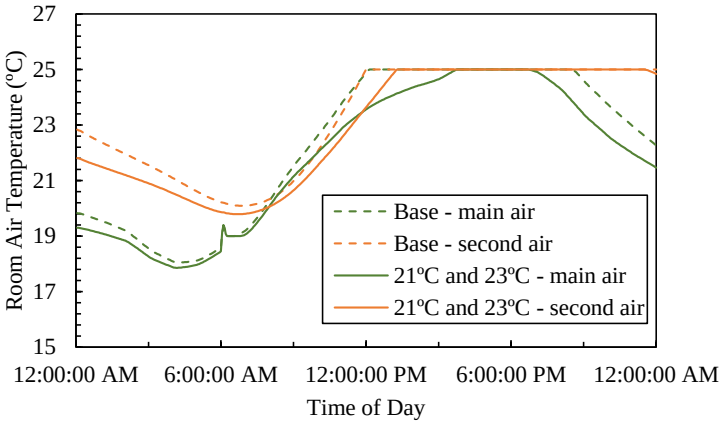

Fig. 5: Temperature profile of air with and without PCM in a two-story house

It can be seen from Fig. 5 that the PCM cases for both floors caused a more uniform temperature distribution throughout the space. The second-floor zone had less of an impact due to PCM than the first-floor zone due to there being no solar gains and less PCM into the second story. In the base cases without PCM, the living spaces were at the maximum temperature of 25ºC for up to 12 hours of the day on a hot summer day, while with PCM, the thermal storage capabilities prevented the air conditioning system from operating for as long of a duration. On a hot, sunny day in Ottawa like July 2, the thermal load within the air without PCM was so great that it led to the base case having higher temperatures than the PCM case even overnight while the PCM was slowly releasing the thermal load. This was an unusual instance, as PCM often causes greater overnight temperatures than cases without PCM due to this thermal load release.

In the two-story house of the same floor area, the heating and cooling loads were found to follow the same trends as the single-story alternatives, but with greater reductions of up to 4.7% and 48.6%, respectively. It was found that the 23ºC PCM minimized the space heating loads for the two-story case, due to the greater temperatures of the second story, compared to the bungalow layouts, which led to the 23ºC PCM storing more thermal energy than the other PCM cases.

3.5. Ottawa and Berlin Comparison

Fig. 6 and Fig. 7 show the heating and cooling load reductions, respectively, with one or two PCMs, in both Ottawa and Berlin. It can be seen that when a second PCM was added, there was a more significant benefit to space cooling than heating. This stems from the factors described from Fig. 2 and Fig. 3 in regards to the larger base cooling loads that lead to a proportionally greater offset and due to the ability of PCMs to reduce the duration of time the space is at peak cooling temperatures and limited ability of the PCMs to alter the space temperature during the heating season.

It was found that Berlin experienced reductions in heating loads of up to 6.5%, while Ottawa was limited to 4.7%; this is caused by the more northern latitude of Berlin, which has solar gains that are more directed towards the walls in the heating season to better facilitate thermal storage. In addition, the results illustrate that there are additional benefits of the PCM when there is a partition wall within the space, as opposed to an open concept layout, particularly in Ottawa. This is caused by the solar gains being more concentrated within the zone with a partition wall, thus leading to higher surface temperatures and increased latent thermal storage within the front zone of the main floor for any PCM melting temperature combination.

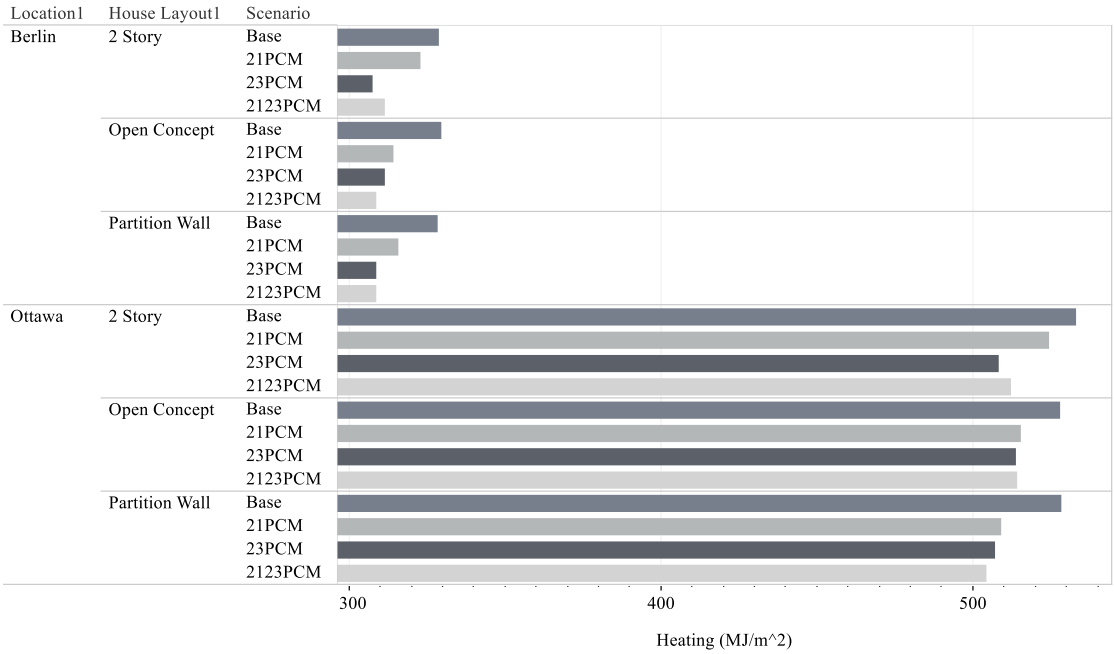

Fig. 6: Heating reductions with one or two PCMs

For both Berlin and Ottawa, the space heating load in the bungalow layouts was reduced most with two PCMs, while in the two-story layout the space heating load was reduced most with the 23ºC PCM. In addition, in all cases the 21ºC PCM alone was found to lead to the greatest heating loads because it requires cooling to 15ºC to fully solidify and utilize its full latent capacity, which does not occur frequently throughout the year. The results for cooling loads are shown in Fig. 7.

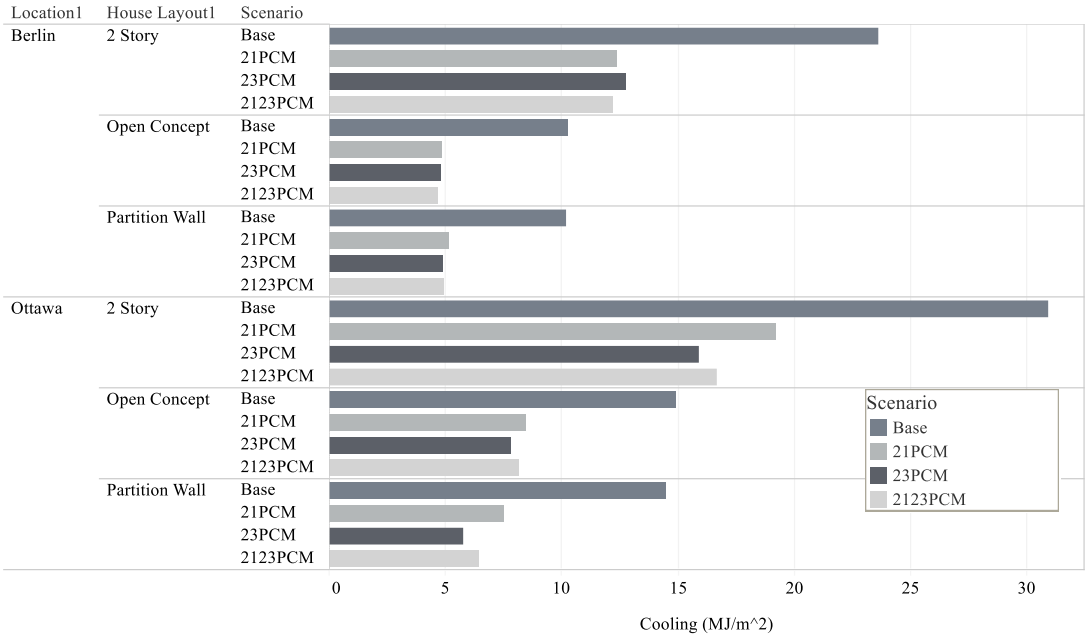

Fig. 7: Cooling reductions with one or two PCMs

Fig. 6 and Fig. 7 show that although there was found to be little difference between integrating one PCM or two for heating, the cooling load benefitted more significantly when only the PCM with melting temperature of 23ºC was included, particularly in Ottawa. However, in all cases, the cooling load was found to have little difference between the 23ºC melting temperature PCM and the use of two PCMs. It was found that although heating loads could be reduced most drastically with the two-story house layout, cooling loads were often

reduced most significantly with the partitioned bungalow layout due to the additional heat transfer area of the two-story house which resulted in greater space cooling loads that can be attributed to the second-floor zone.

4. Conclusions

In this study, three layouts of house were assessed in two locations (Canada and Germany) with PCM to determine the impacts of various assumptions associated with PCM system design. The objective of this was to determine the factors that lead to PCMs most reducing heating and cooling loads in locations with two distinct conditioning seasons. It was found that regardless of location, house layout, or PCM properties, the cooling loads could be reduced by over 60% in some cases, whereas the heating load could only be reduced by about 5%. Furthermore, utilizing two PCMs at melting temperatures of 21ºC and 23ºC was found to lead to comparable conditioning loads than the 23ºC melting temperature PCM alone, due to the large thermal storage temperature range of 17-23ºC that was utilized throughout both conditioning seasons with the 23ºC PCM. Heating loads were found to be reduced more substantially in Berlin than Ottawa due to its more northern location and thus more horizontal solar profile within the winter months that lead to increased thermal storage by the PCM. In terms of house layout, it was found that a two-story layout could decrease heating loads most significantly – up to 6.5% in Berlin and 4.7% in Ottawa, while the partitioned wall layout decreased cooling loads by 60.1% in Ottawa and 52.0% in Berlin.

4.1. Future Work

The future work of this study should include additional simulations to predict the performance of one or two PCMs in a wider range of climates to assess whether any locations would benefit more significantly from two PCMs compared to one. In addition, these future simulations can provide trends regarding the impacts of climate zones in general on PCM performance and implementation. A complete analysis of the emissions and embodied carbon, as well as the economic impacts of PCMs in various locations should be conducted to provide stakeholders with full knowledge of PCM effects prior to their widespread integration.

5. Acknowledgements

The authors wish to acknowledge the Natural Sciences and Engineering Research Council (NSERC) for supporting this research.

6. References

Al-Yasiri, Q., and Szabo, M. 2021. Performance Assessment of Phase Change Materials Integrated with Building Envelope for Heating Application in Cold Locations. European Journal of Energy Research, 1(1).

Alam, M., Jamil, H., Sanjayan, J., and Wilson, J. 2014. Energy saving potential of phase change materials in major Australian cities. Energy and Buildings, 78: 192–201. Elsevier Ltd. doi:10.1016/j.enbuild.2014.04.027.

Beradi, U., and Soudian, S. 2019. Experimental investigation of latent heat thermal energy storage using PCMs with different melting temperatures for building retrofit. Energy and Buildings, 185: 180–195.

Entrop, A.G., Brouwers, H.J.H., and Reinders, A.H.M.E. 2011. Experimental research on the use of micro-encapsulated Phase Change Materials to store solar energy in concrete floors and to save energy in Dutch houses | Elsevier Enhanced Reader. Solar Energy, 85: 1007–1020.

Gassar, A.A.A., and Yun, G.Y. 2017. Energy Saving Potential of PCMs in Buildings under Future Climate Conditions. Applied Sciences, 7(12): 1219. MDPI AG. doi:10.3390/app7121219.

Guarino, F., Athienitis, A., Cellura, M., and Bastien, D. 2017. PCM thermal storage design in buildings: Experimental studies and applications to solaria in cold climates. Applied Energy, 185: 95–106. doi:https://doi.org/10.1016/j.apenergy.2016.10.046.

Heim, D., and Clarke, J.A. 2004. Numerical modelling and thermal simulation of PCM-gypsum composites with ESP-r. Energy and Buildings, 36: 795–805.

Kheradmand, M., Azenha, M., de Aguiar, J.L.B., and Castro-Gomes, J. 2016. Experimental and numerical

studies of hybrid PCM embedded in plastering mortar for enhanced thermal behaviour of buildings. Energy, 94: 250–261. Elsevier Ltd. doi:10.1016/j.energy.2015.10.131.

Kosny, J., Shukla, N., and Fallahi, A. 2013. Cost Analysis of Simple Phase Change Material-Enhanced Building Envelopes in Southern U.S. Climates. Golden, CO.

Lakhdari, Y.A., Chikh, S., and Campo, A. 2020. Analysis of the thermal response of a dual phase change material embedded in a multi-layered building envelope. Applied Thermal Engineering, 179: 115502. Elsevier Ltd. doi:10.1016/j.applthermaleng.2020.115502.

Mathis, D., Blanchet, P., Lagière, P., and Landry, V. 2018. Performance of wood-based panels integrated with a bio-based phase change material: A full-scale experiment in a cold climate with timber-frame huts. Energies, 11(11): 1–15. doi:10.3390/en11113093.

Memarian, S., Kari, M., Fayaz, R., and Asadi, S. 2018. Single and combined phase change materials: Their effect on seasonal transition period. Energy & Buildings, 169: 453–472. doi:10.1016/j.enbuild.2018.03.085.

Mohseni, E., and Tang, W. 2020. Parametric analysis and optimisation of energy efficiency of a lightweight building integrated with different configurations and types of PCM. Renewable Energy, 168: 865–877. Elsevier BV. doi:10.1016/j.renene.2020.12.112.

Nikoofard, S., Ismet Ugursal, V., and Beausoleil-Morrison, I. 2015. Techno-economic assessment of the impact of phase change material thermal storage on the energy consumption and GHG emissions of the Canadian Housing Stock Article History. Building Simulation, 8: 225–238. doi:10.1007/s12273-014-0204-5.

NRCan. 2018. Comprehensive Energy Use Database. Available from http://oee.nrcan.gc.ca/corporate/statistics/neud/dpa/menus/trends/comprehensive_tables/list.cfm. [accessed 30 September 2019].

Placido, A.M. Di, and Pressnail, K.D. 2014. A Controlled Ventilation Strategy For Ontario Homes: A Comparative Analysis Of Energy-Use, Air Quality And Economics. *In* 14th Canadian Conference on Building Science and Technology.

US Department of Energy. 2021. EnergyPlus. Available from https://energyplus.net/. [accessed 23 March 2022].

Study of Thermal Degradation of Adipic Acid as PCM Under Stress Conditions: A Kinetic Analysis

Rocío Bayón[1], Redlich J. García[1], Laura Quant[1,2] and Esther Rojas[1]

[1] Thermal Energy Storage Unit, CIEMAT-PSA, Madrid (Spain)

[2] University of the Basque Country UPV/EHU, Bilbao (Spain)

Abstract

Adipic acid is a PCM with T_m= 152 ºC, which makes it very interesting for being used as latent storage medium for mid-temperature applications. Hence, thermal degradation analyses on this PCM are crucial for ensuring its long-term performance under operating conditions. For this purpose, both TG measurements and isothermal tests under stress conditions in an oven were carried and the experimental data were kinetically analyzed not only from the classical approach but also from the evaporation point of view. From the results of this analysis we concluded that adipic acid mainly undergoes evaporation as soon as it melts and this prevents this PCM for being used for latent storage in not sealed systems. Moreover, the strong color change from white to brown after isothermal test proved that it also undergoes other degradation mechanisms that could lead to changes in the thermophysical properties (T_m and ΔH_m). In a further step, the degradation products will be analyzed and additional isothermal test will be carried out in closed containers to avoid evaporation.

Keywords: PCM, Adipic acid, Degradation kinetics, Evaporation, TGA, Isothermal tests

1. Introduction

The storage of thermal energy is a key component in some domestic and industrial processes as well as in power generation systems. It ensures system reliability, power dispatchability and also economic profitability. The latent heat technology based on phase change materials (PCM) is a method of thermal energy storage (TES) that has gained renewed attention in recent years owing to its high thermal storage capacity, operational simplicity and transformative industrial potential. Phase change materials (PCM) with melting temperatures (T_m) above 100 ºC are of particular interest for solar thermal energy storage in the mid-temperature range. One of the most critical issues when choosing a PCM for a certain storage application is to be sure that it has a successful performance during its operation life-time. Usually melting/freezing cycles are carried out to assess the life-time performance, however, if a PCM undergoes some degradation after melting due to a chemical reaction or phase segregation, it will be hindered during the freezing period. This means that this kind of tests is not sufficient for validating a PCM. Another way to assess long-term performance of PCMs is to carry out kinetic studies of possible degradation processes (Bayón and Rojas, 2019). In principle, if a PCM undergoes degradation due to the occurrence of chemical reactions in liquid state, thermogravimetric (TG) measurements can be used for determining the kinetics of such reactions (Vyazovkin et al. 2011). However, care must be taken when the long-term behavior of a PCM is predicted only from the kinetic analys of TG measurements, because the results may not be realiable, specially if evaporation is one of the main degradation processes. On the other hand, from previous studies of lauric acid, which undergoes evaporation under stress thermal condidions (Bayón et al. 2020 and 2021), it was concluded that isothermal experiments with larger amounts of sample are necessary for obtaining degradation curves that are more representative of the degradation processes occurring under real operation conditions.

In this work, hexane dioic acid ($HOOC(CH_2)_4COOH$), also known as adipic acid, with a melting temperature of 152 ºC, was studied with the aim of being assessed as PCM for mid-temperature applications. Isothermal tests under stress conditions were carried out at various temperatures (160 ºC-240 ºC) and times (1h-6h) in open containers to evaluate the mass loss under these conditions. Alternatively, TG measurements were carried out under either N_2 or air atmosphere at various heating rates (β=2-20 ºC/min). Both kinds of experimental data were kinetically analyzed from the classical approach and also by considering evaporation as main degradation process. From the results of these studies, the long-term behavior of adipic acid in terms of evaporation has been predicted.

© 2022. The Authors. Published by International Solar Energy Society
Selection and/or peer review under responsibility of Scientific Committee
doi:10.18086/eurosun.2022.13.02 Available at http://proceedings.ises.org

1.1 Theoretical background

If a PCM undergoes degradation due to the occurrence of chemical reactions in liquid state, TG measurements can be used for determining the kinetics of such reactions (Vyazovkin et al. 2011). The starting point for the kinetic analysis of TG measurements is the equation that represents the reaction rate:

$$\frac{d\alpha}{dt} = Ae^{\left(\frac{-E}{RT}\right)}f(\alpha) \qquad \text{(eq. 1)}$$

where α is the degree of conversion at a certain time, calculated as $\alpha = (m_{ini} - \mathrm{m})/m_{ini}$; *A*, *E* and *R* are the frequency factor, the activation energy and the molar gas constant, all present in the Arrhenius law for the reaction rate constant and *f(α)* is a function whose form depends on the mathematical model describing the reaction mechanism.

In a dynamic TG measurement performed at constant heating rate $\beta = \frac{dT}{dt}$, eq. 1 becomes:

$$\frac{d\alpha}{dT} = \frac{Af(\alpha)e^{-E/RT}}{\beta} \qquad \text{(eq. 2)}$$

For the case of isothermal tests, the kinetic analysis is based on the fact that $k(T) = Ae^{(-E/RT)} = cte$, so that the general equation of the reaction rate becomes a linear expression (Vyazovkin & Wight, 1999):

$$g(\alpha) = \int_0^\alpha \frac{d\alpha}{f(\alpha)} = k(T)t \qquad \text{(eq. 3)}$$

Where α is the conversion calculated as and *g(α)* is a function associated to the reaction the mechanism through *f(α)*. Hence, by using the experimental values of *α*, *g(α)* function can be calculated assuming different reaction mechanism (Vyazovkin & Wight, 1999) and plotted vs. time in order to check which one leads to the best linear plot. Then the rate constant at a certain temperature is obtained from the corresponding slope. If this procedure is done for each isothermal test (i), the Arrhenius parameters, *A* and *E* can be determined from the linear plot:

$$\ln k(T_i) = \ln A - \frac{E}{RT_i} \qquad \text{(eq. 4)}$$

However, if evaporation is one of the main degradation processes, the kinetic analysis has to be done from a different approach. The general expression describing the free evaporation of a substance in vacuum is the Knudsen-Langmuir equation:

$$r = -\frac{dn}{Sdt} = \frac{\alpha_{vap}P_{eq}}{\sqrt{2\pi MRT}} \left[\frac{mol}{m^2 s}\right] \qquad \text{(eq. 5)}$$

Where *dn/Sdt* is the evaporation rate per unit area in mol/m^{2}s, being *S* the evaporating surface, P_{eq} is the equilibrium vapor pressure, *M* is the molecular weight of the evaporating substance, *R* is the gas constant, *T* is the temperature and α_{vap} is the vaporization constant whose value is 1 if the evaporation takes place in vacuum and condensation is neglected. However, this situation does not usually happen neither in TG measurements, where a gas carrier is used, nor in HDR oven tests, where the liquid evaporates from the sample surface due to a concentration gradient. Considering the specific experimental conditions of TG measurements, consisting in the diffusion of the evaporating liquid through a stagnant gaseous layer at atmospheric pressure in a cylindrical sample container, an alternative formulation of the evaporation rate has been proposed by some authors (Pieterse and Focke, 2003; Bassi, 2011).

$$r = -\frac{dn}{Sdt} = \frac{P_{eq}D}{zRT} \left[\frac{mol}{m^2 s}\right] \qquad \text{(eq. 6)}$$

As displayed in the scheme of Fig. 1, *z* is the distance between the top of the container (where the concentration of evaporating molecules is C=0) and the surface of the liquid (where $C=P_{eq}/RT$); and *D* is the diffusion coefficient of the substance in the stagnant inert gas (N_2 or air). This diffusion coefficient depends on the temperature and can be estimated by using different models based on functional group contributions (Poling et al. 2001). Although eq. 6 is normally used for evaluating vapor pressures from mass loss measured during TG analysis (Pieterse and Focke, 2003; Bassi, 2011), this equation could be used as well for evaluating the evaporation rate of a certain compound if vapor pressure is known, i. e. if the coefficients of Antoine equation are known.

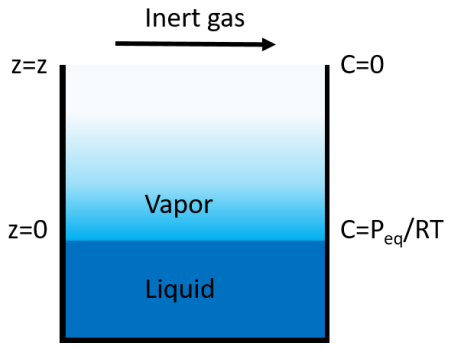

Fig. 1. Schematic of a TG measurement. The evaporating liquid diffuses from the surface through the gas region inside the pan and the purge gas swipes it as it emerges from top of the cup.

On the other hand, Vlasov (Vlasov, 2019) proposed another formulation of eq. 5 by applying the collision theory to the evaporation processes. The resulting equation for the evaporation rate is quite similar to eq. 5, but for the introduction of P as partial pressure near the liquid surface and the substitution of the vaporization constant, α_{vap}, by an exponential term depending on the activation energy of condensation, E_{con}.

$$r = -\frac{dn}{Sdt} = \frac{(P_{eq}-P)}{\sqrt{2\pi MRT}} e^{\frac{-E_{con}}{RT}} \quad \left[\frac{mol}{m^2 s}\right] \qquad \text{(eq. 7)}$$

As we can see, Eq. 7 does not include any geometric parameter associated to the experimental set-up apart from the sample surface. Also it does not consider an inert gas flowing so that evolved vapor molecules are not removed from the upper part of the container. However, it includes a classical kinetic term with an activation energy that meets the condition: $E_{con}=E_{ev}-\Delta H_{vap}$. In principle this equation cannot be applied to the case of TG experiments.

2. Experimental

Dynamic thermogravimetric (TG) analysis of adipic acid were performed in a Seiko TG-DTA 6300 apparatus and the measurements were carried out at heating rates, β, ranging from 2 ºC/min to 20 ºC/min under either N_2 or air atmosphere at 50 ml/min. Samples of 10-12 mg were contained in platinum crucibles of 4.5 mm diameter and 3 mm height. Isothermal tests were performed under air in the vertical oven (called HDR) displayed in Fig. 2, which has a cylindrical ceramic cavity where the sample can be allocated (left) and allows performing tests under controlled heating rate with stand-by periods at constant temperature. Its upper part can be covered with a double glass trap (Fig. 2. right), where most of the evolved gases can be condensed. The oven is installed inside an extraction hood for removing the non-condensed gases so that thermal degradation tests can be carried out in a secure way (Rathgeber et al., 2020).



Fig. 2: Pictures of HDR oven: experimental set-up for performing thermal degradation tests.

For isothermal tests, adipic acid samples of about 3,5 g were contained in open glass vials of 2 cm diameter and 5 cm height (see Fig. 2. left). The vial with the sample was located inside the ceramic cavity at room temperature and heated up to the test temperature. Tests were performed for periods of 1h to 6 h in the temperature range 160 ºC to 240 ºC and the heating rate to achieve the target temperature was 5 ºC/min. After each test, the oven was open and the sample was taken out and allow cool down at room temperature. Samples were weighed before and

after the tests in a scale with 0.1 mg accuracy and, in each case, a new vial was used so that the degraded sample could be stored for further characterization.

3. Results and discussion

3.1 Classical approach

Since the aim of this work is to assess the long-term performance of adipic acid working as PCM for latent heat storage, the evaluation of its thermal degradation kinetics is mandatory. Therefore, in a first approach, both TG measurements and isothermal tests in HDR oven were analyzed from the classical kinetics point of view. In this sense, TG measurements were analyzed by using Friedman method, which belongs to the so-called model-free isoconversional methods that allow the activation energy to be estimated as a function of α without choosing any reaction model. Friedman method is based in the following equation, which is derived from eq. 2 (Vyazovkin et al., 2011):

$$\ln\left[\beta\left(\frac{d\alpha}{dT}\right)_{\alpha}\right] = \ln[f(\alpha)A_{\alpha}] - \frac{E}{RT_{\alpha}} \qquad \text{(eq. 8)}$$

The basic assumption of isoconversional methods is that the reaction rate at constant extent of conversion, α, depends only on temperature so that constant activation energy values should be expected for the whole conversion range. Comparing with other isoconversional methods, Friedman's is one of the most accurate because it does not make any assumption or simplification beyond the one already stated.

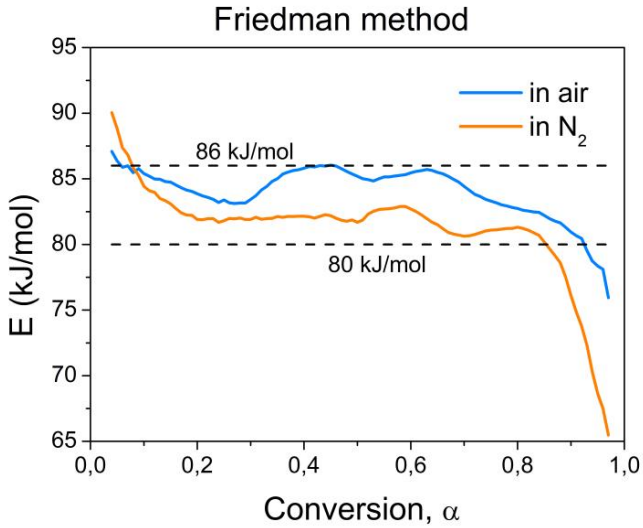

Fig. 3. Activation energy calculated by Friedman method for TG measurements of adipic acid carried out in N_2 and air.

As we can see, the values of activation energy, *E*, obtained for adipic acid samples are slightly below the value of vaporization enthalpy reported in de literature 89 ± 1 kJ/mol (Wright et al. 2004). Moreover, not much difference is observed between the values calculated from TG measurements under N_2 and air, although the energy values obtained in N_2 are lower. Isoconversional methods are not fully accurate, but still can be used for having a preliminary estimation of *E* (Budrugeac, 2018). However, the observed variation of E with α may be due to the occurrence of multi-step processes and their different relative contribution to the overall reaction rate.

For the samples tested under isothermal conditions in HDR oven, a mass decrease was observed in all cases and also an important amount of solid was deposited in the glass traps located at the top. In Fig. 4, the variation of conversion vs. time is displayed for the experiments performed at 4 different temperatures: 160 ºC, 180 ºC, 200 ºC and 220 ºC.

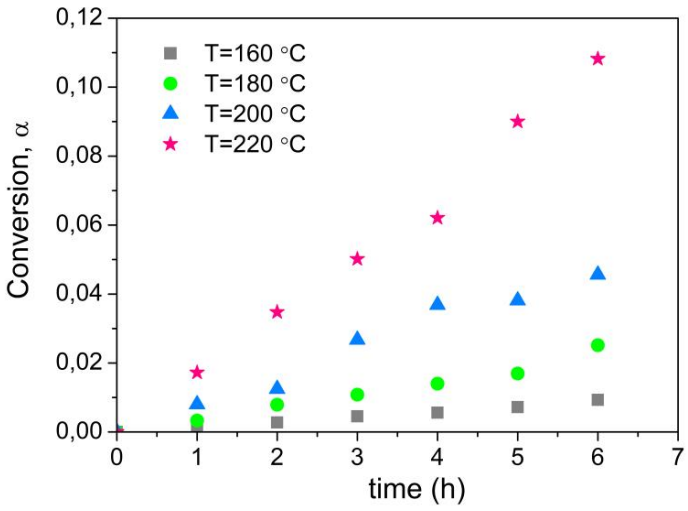

Fig. 4. Conversion vs. time for isothermal tests performed in HDR oven at different temperatures.

For evaluating the degradation of adipic acid, four different mechanisms were selected for applying eq. 3 (F0, F1, R2 and A2). Their corresponding *g(α)* expressions are recorded in Tab. 1. The mechanisms F0, F1 and R2 lead to quite good linear fits assuming that conversion is zero when reaction time is zero (see R^2 value recorded in Tab. 1). However, *g(α)* calculated for mechanism A2 did not show a linear behavior with time as evidenced by the low regression value obtained. In Tab. 1, the activation energies obtained from the linear plots of eq. 4 are recorded as well for reaction mechanism F0, F1 and R2. In all cases, a similar activation energy of about 72 kJ/mol is obtained. However, if we compare this activation energy with the ones obtained by applying Friedman's method to the TG measurements shown in Fig. 3, we can see that they are about 10-15 kJ/mol higher.

Tab. 1: Activation Energy obtained from isothermal tests assuming different reaction mechanism.

Mechanism	g(α)	R^2 for eq. 3	E (kJ/mol)	lnA (s-1)
F0	α	0.965	72,45	5,43
F1	$-ln(1-\alpha)$	0,965	73,63	5,76
R2	$1-(1-\alpha)^{1/2}$	0,965	73,03	4,90
A2	$[-ln(1-\alpha)]^{1/2}$	0,879	-	-

The difference between the activation energies calculated from the isothermal experiments, compared to the TG measurements, could be due to the fact that not a single mechanism is occurring during the thermal degradation of adipic acid. Therefore, a deconvolution of DTG curves to separate the possible mechanisms and evaluate them independently could be a next step. The similarity of the activation energies of adipic acid under air and nitrogen obtained by Friedman's isoconversional method is also noted, so it can be deduced that the ambient atmosphere does not have much influence on the degradation mechanisms of this fatty acid.

3.2 Evaporation approach

During isothermal tests it was observed that an important amount of adipic acid was evaporated and hence collected as a white powder in the glass traps placed at the top of the HDR oven. This means that evaporation is the predominant degradation process for the adipic acid in open systems so that the occurrence of this process must be taken into account when analyzing both TG measurements and isothermal tests in oven. In this sense, another approach was done for both kinds of experiments.

For the case of TG measurements, the eq. 6 proposed by Pieterse and Focke (Pieterse and Focke, 2003) and Bassi (Bassi, 2011) was applied for calculating de evaporation rate of this fatty acid. A more detailed study of how to analyze TG measurements when evaporation is one of the main degradation processes is presented at this

conference in another work (Quant et al. 2022). In the case of adipic acid evaporation, the parameters *S* and *z* were calculated from crucible dimensions (4.5 mm diameter and 3 mm height), *D* was calculated by using the method of Wilke and Lee (Poling et al., 2001) and P_{eq} was calculated from Antoine equation with the coefficients found in the literature (Stephenson and Malanowski, 1987). In Fig. 5 the resulting evaporation rate in mol/m^{2}s has been plotted together with the corresponding experimental curves for the TG measurements performed at different heating rates (β=2 ºC/min, 5 ºC/min, 10 ºC/min and 20 ºC/min). As we can see, the experimental curves fit quite well the theoretical curve predicted by eq. 6, although a slight difference in all the curves is observed, which could indicate that, apart from evaporation, and additional degradation process may be occurring.

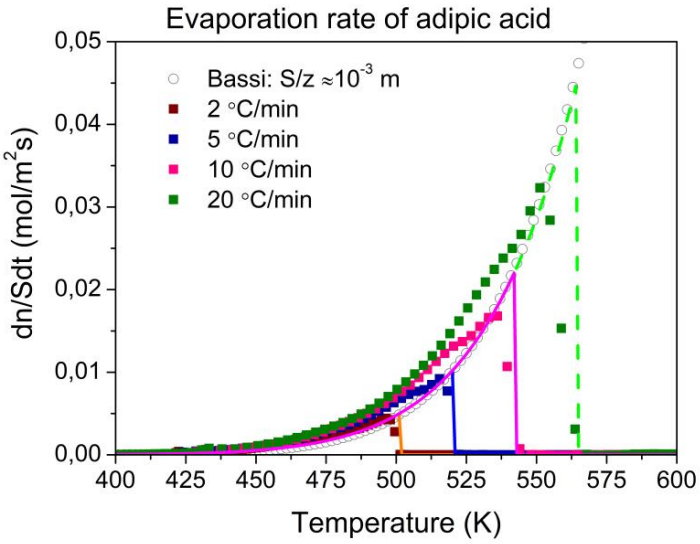

Fig. 5. Comparison of evaporation rate calculated from TG measurements at different heating rates with the predicted by eq. 6.

Alternatively, the conventional rate equation (eq. 1) can be adapted to the evaporation case by taking into account that it is a zero order process, so that $f(\alpha)=(1-\alpha)^0 = 1$. Therefore, eq. 1 expressed in mol/m^{2}s becomes:

$$-\frac{dn}{Sdt} = \frac{n_{ini}}{S} A e^{\left(\frac{-E}{RT}\right)} \qquad \text{(eq. 9)}$$

If eq. 9 is fitted to eq. 6, the resulting kinetic parameters for the case of adipic acid are: E= 81.82 kJ/mol and $n_{ini}A/S$=1.73 E6 mol/m^{2}s. It is interesting to note that the value obtained for the activation energy is in the range of the values calculated by Friedman method (see Fig. 3). However, in contrast to the classical approach, the pre-exponential factor in the evaporation approach not only depends on the initial amount of material, n_{ini}, but also on the sample surface, *S*.

From these results, it seems clear that adipic acid degradation must be approached from the evaporation point of view. In this sense, it must be taken into account that HDR tests are affected by the partial pressure of the vapor above the sample bottle, hence these measurements cannot be analyzed by eq. 6 because the experimental conditions do not meet the corresponding requirements (i. e. no purge gas removes the evaporated liquid from the sample top). Hence, for analyzing the isothermal tests in HDR oven, eq. 7 was used by assuming that temperature is constant. In such case eq. 7 becomes eq. 10 and is the evaporation rate, which is the term in brackets, is constant.

$$-\frac{dn}{S} = \left[\frac{(P_{eq}-P)}{\sqrt{2\pi MRT}} e^{\frac{-E_{con}}{RT}}\right] dt \qquad \text{(eq. 10)}$$

In Fig. 6, the amount of adipic acid lost in mol/m^2 has been plotted vs. time for each series of tests performed at the same temperature. The slope of each linear plot corresponds to the evaporation rate in mol/m^{2}s.

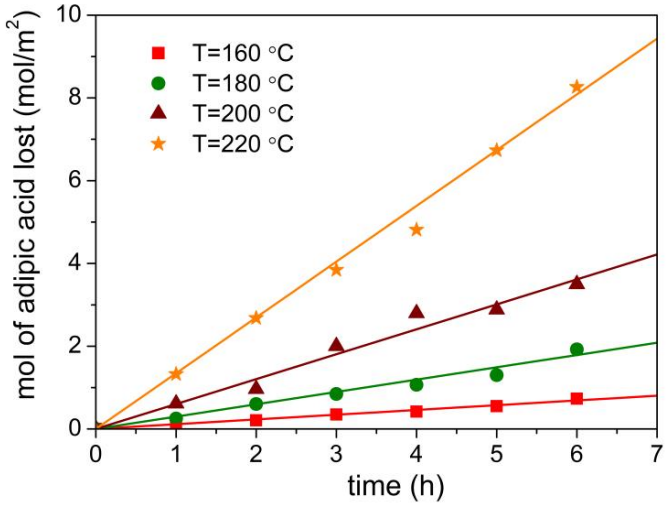

Fig. 6. Amount of adipic acid lost (in mol/m$_2$) vs. time for isothermal tests performed in HDR oven at different temperatures.

According to eq. 10, if the natural logarithm of evaporation rate is plotted vs. the inverse of its corresponding temperature, E_{con} could be obtained from the slope of the expected linear plot. However, it is very important to remark that the evaporation rate obtained for each temperature is expected to be affected by the partial presssure of adipic acid, *P*, which should depend on the temperature of the test. This means that, in principle, E_{con} cannot be obtained from the plot metioned above. In order to evaluate the effect of partial pressure when evaporation tests are carried out in HDR oven, water was evaporated at different temperaures because its E_{con} value is kown (32.3 kJ/mol) (Vlasov, 2019). For evaluating the effect of partial pressure in the HDR oven tests, eq. 6 was converted in eq. 11, the natural logarithm of evaporation rate for different partial pressures, *P*, was calculated and then plotted vs. the inverse temperature.

$$\ln r = \ln\left[\frac{(P_{eq}-P)}{\sqrt{2\pi MRT}}\right] - \frac{E_{con}}{RT} \qquad \text{(eq. 11)}$$

The resulting curves for the water are plotted in Fig. 7 (left) together with the logarithms of the evaporation rates obtained experimentally from HDR test. In this plot, the partial pressure values were selected so that evaporation rate curves could fit the experimental rate values (see graph legend) (Bayón et al. 2021). This graph also includes the evaporation rates reported by Borodacheva et al. (Borodacheva et al. 2011) who carried out experiments of steady-state water evaporation in an open system. As we can see, the rate values they obtained perfectly fit the evaporation rate curve of water when partial pressure is equal to zero. However, for the case of water evaporated in the HDR oven, partial pressures higher than zero had to be inclued in eq. 11 for the curves to fit the experimental rate values. As can be seen in the legend, the partial pressure of the vapor above the sample had to be increased with testing temperature and this decreased the evaporation rate.

A similar approach was done for analyzing the isothermal tests of adipic acid carried out in the HDR oven. In this case, since the activation energy of condensation that should be included in eq. 11 is not known, different E_{con} values were checked according to two criteria. If we assumed that the rate curve for *P*=0 crossed the evaporation rate obtained for the tests at 160 ºC, maximum E_{con} =40 kJ/mol had to be used. In contrast when the partial pressure, *P*, to be included in eq. 11 corresponded to an equilibrium temperature one degree below the test temperature, a minimum E_{con} =30 kJ/mol had to be selected. Taking into account this, E_{con} value for adipic acid could be estimated as 35 ± 5 kJ/mol. In Fig. 7 (right), the rate curves with E_{con}= 35 kJ/mol have been plotted together with the evaporation rates obtained experimentally from HDR tests. In the legend, the partial pressure of adipic acid used in the construction of each curve has been recorded as well together with its corresponding equilibrium temperature. Additonally, the evaporation rates obtained from TG measurements have been included for comparision. As we can see, the rates obtained from HDR tests are about one order of magnitude (ln10=2,3) lower than the rates obtained from TG measurementes. As discussed above, the evaporation in HDR oven is slowed down because the evaporated material is not removed from the sample surface so that the vapors justs

move upwards by diffusion and hence partial pressure is quite close to the equilibrium pressure. However it is interesting to note that evaparoation rates obtained from TG measurements are very close to the values predicted by eq. 11 when P=0 and hence there is no adipic acid on the liquid surface.

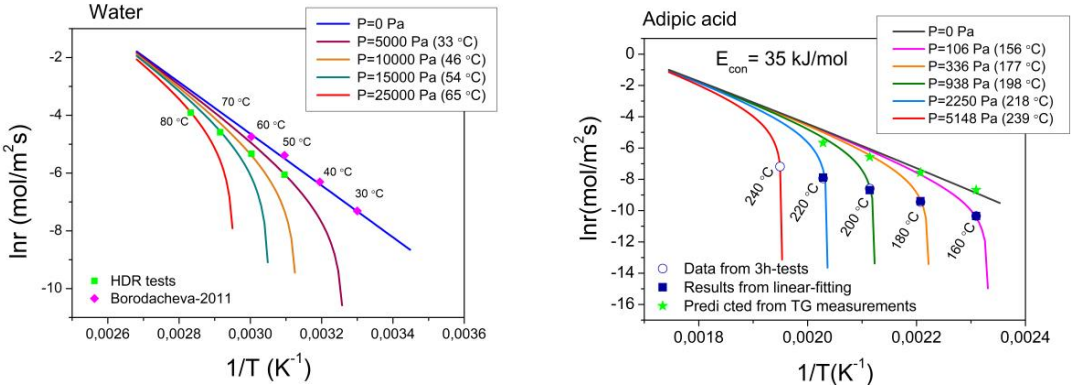

Fig. 7. Evaporation rates of water (left) and adipic acid (right) calculated with eq. 11 at different temperatures.

3.3 Prediction of evaporation under long-term working conditions

If we assume that the evaporation rate results obtained in previous section can be extrapolated to real working conditions, we could calculate the amount of adipic acid that would evaporate after a certain time if it is kept at constant temperature. Therefore for predicting the expected degradation of adipic acid due to the evaporation, the amount of this PCM lost over time at T_m+8 ºC (160 ºC), T_m+18 ºC (170 ºC) and T_m+23 ºC (175 ºC) was simulated with the evaporation rates calculated from both TG measurements and isothermal tests in the HDR oven. For the case of rates from TG measurements, a S/z ratio of 10^{-3} m was used while for the case of rates from HDR tests, they were calculated assuming the best situation in which partial pressure of adipic acid is the equilibrium pressure at 4 ºC below the constant operation temperature. It must be pointed out that this situation might not be very realistic because in real working conditions partial pressure can be lower than in HDR tests and hence evaporation rate would be higher. On the other hand, the situation described by TG measurements might not be realistic as well because this would imply that all adipic acid evaporated is immediately removed from the liquid surface. The resulting curves that predict the amount of adipic lost in kg by square meter of surface are plotted in Fig. 8. As expected, the mass loss predicted from TG measurements (Fig. 8. left) is much higher than the predicted from HDR tests (Fig. 8. right). However, even in the most favorable case in which evaporation rate is slowed down by the presence of adipic acid vapors on the liquid surface (Fig. 8. right), the amount of PCM lost after 1 year would be about 100 kg/m^2 even if temperature is kept only 8 ºC above T_m. The main issue is that adipic acid evaporates as soon as it melts, which prevents this PCM for being used for latent storage at least if the storage container is not sealed.

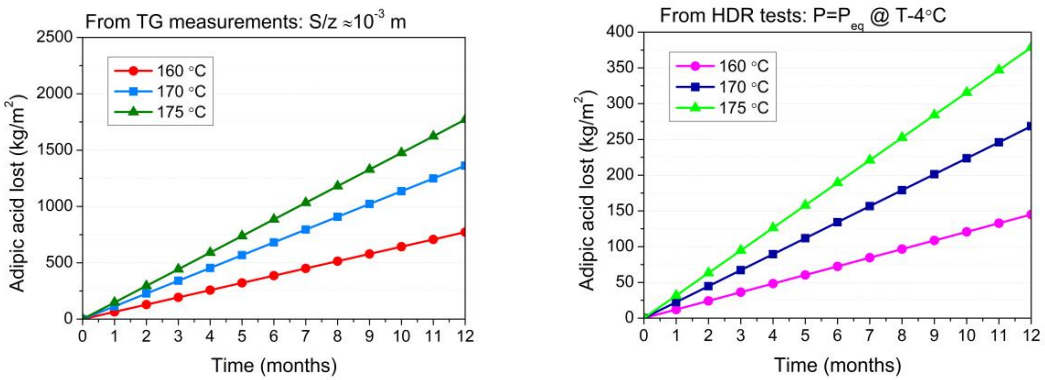

Fig. 8. Prediction of adipic acid mass loss over one year when kept melted at constant temperatures (T_m+8 ºC +18 ºC and +23 ºC), from the results of TG measurements (left) and HDR isothermal tests (right).

4. Conclusions and future work

In this work, the thermal degradation of adipic acid (T_m = 152 ºC) has been studied in order to assess its feasibility as PCM for latent storage in intermediate temperature ranges by predicting its long-term performance under operating conditions. For that purpose, TG measurements and isothermal tests under stress conditions in an open air oven have been carried out. In a first approach, both kinds of experimental data have been analyzed by applying the traditional kinetic approach and the approach assuming that evaporation is one of the degradation mechanisms. Although there are some differences in the kinetic results obtained by both approaches, we can conclude that adipic acid undergoes fast evaporation as soon as it melts, which prevents this PCM for being used for latent storage at least in not sealed (or open) systems. Apart from evaporation, a strong color change of adipic acid (from white to brown) after isothermal tests was observed. This proves that this PCM also undergoes other degradation mechanisms that that produce colored products, which could lead to changes in the thermophysical properties (T_m and ΔH_m). As future work, the formation of colored degradation products will be studied by Vis-UV spectroscopy and also by using other characterization techniques such as FTIR, DSC, chromatography, etc. Moreover, isothermal tests in closed containers will be performed as well to avoid evaporation and the possible effect of O_2 in adipic acid degradation.

Acknowledgments

This work has been supported by Comunidad de Madrid and European Structural Funds through ACES2030 Project (S2018/EM-4319) and by European Union's Horizon H2020 Research and Innovation Programme through SFERA III Project (GA Nº 823802) and StoRIES Project (GA Nº 101036910).

References

Bassi, M., 2011. Estimation of the vapor pressure of PFPEs by TGA. Thermochimica Acta 521(1-2) 197-201. https://doi.org/10.1016/j.tca.2011.04.024.

Borodacheva Y. V., Lotkhov, V. A., Dil'man, V. V., Kulov N. N. 2011. Kinetics of steady-state evaporation of single-component liquids into an inert gas. Theoretical foundations of chemical engineering 45 (6): 805-810. https://doi.org/10.1134/S0040579511060030.

Bayón, R., Rojas, E., 2019. Development of a new methodology for validating thermal storage media: Application to phase change materials. Int. J. Energy Res. 43, 6521-6541. https://doi.org/10.1002/er.4589.

Bayón R., Bonanos, A., Rojas. E. 2020. Assessing the long-term stability of fatty acids for latent heat storage by studying their thermal degradation kinetics. Proceedings of Eurosun 2020. Online conference. https://doi.org/10.18086/eurosun.2020.07.10.

Bayón R., Gismera, V., Rojas. E. 2021.Validation of lauric acid as PCM: study of thermal degradation under quasi-real working conditions. ENERSTOCK 2021. Online Conference. Oral presentation.

Budrugeac, P., 2018. A simple and precise differential incremental isoconversional method to kinetic analysis of heterogeneous processes under arbitrary temperature programs. Thermochimica Acta, 661, 116–123. https://doi.org/10.1016/j.tca.2013.05.020.

Pieterse, N.; Focke W. W. 2003. Diffusion-controlled evaporation through a stagnant gas: Estimating low vapour pressures from thermogravimetric data. Thermochimica Acta 406, 191-198. https://doi.org/10.1016/S0040-6031(03)00256-9.

Quant, L. Bayón, R., García R. J., Rojas, E. 2022. Kinetic analysis of TGA measurements when evaporation is a degradation process in PCM. Eurosun 2022. Kassel.

Rathgeber, C., Hiebler S., Bayón R., Cabeza L. F., Zsembinszki G., Englmair G., Dannemand M., Diarce G., Fellmann O., Ravotti R., Groulx D., Kheirabadi A. C., Gschwander S., Höhlein S., König-Haagen A., Beaupere N., Zalewski L. 2020. Experimental Devices to Investigate the Long-Term Stability of Phase Change Materials

under Application Conditions. Applied Sciences, 10, 7968. https://doi.org/10.3390/app10227968.

Poling, B. E. Prausnitz, J. M., O'Connell, J. P. 2001. The properties of gases and liquids, fith ed., McGraw-Hill, New York, Ch. 11. https://doi.org/10.1021/ja0048634

Shen, L., Alexander, K. S., 1999. A thermal analysis study of long chain fatty acids. Thermochimica Acta 340-341, 271-278. https://doi.org/10.1016/S0040-6031(99)00272-5.

Stephenson, R.M., Malanowski, S. 1987. Handbook for Physicochemical Properties of Organic Compounds, Elsevier Science, New York. https://doi.org/10.1007/978-94-009-3173-2_1

Vlasov, V. A. 2019. Modeling of evaporation and condensation processes: a chemical kinetics approach. Hear and Mass Transfer 55, 1661-1669. https://doi.org/10.1007/s00231-018-02549-y.

Vyazovkin, S., Wight, C. A., 1999. Model-free and model- fitting approaches to kinetic analysis of isothermal and nonisothermal data. 341, 53-68. https://doi.org/10.1016/S0040-6031(99)00253-1

Vyazovkin, S., Burnham, A. K., Criado, J. M., Pérez-Maqueda, L. A., Popescu, C., & Sbirrazzuoli, N., 2011. ICTAC Kinetics Committee recommendations for performing kinetic computations on thermal analysis data. Thermochimica Acta, 520(1–2), 1-19. https://doi.org/10.1016/j.tca.2011.03.034.

Wright, S.F., Dollimore, D., Dunn, J.G., Alexander. K., 2004. Determination of the vapor pressure curves of adipic acid and triethanolamine using thermogravimetric analysis. Thermochimica Acta 421, 25-30. https://doi.org/10.1016/j.tca.2004.02.021.

Comparative experiments on a novel $CaCl_2$-based composite material and zeolite 13X inside a sorption reactor for solar heat storage

Elise Bérut[1], Jonathan Outin[1], Michel Ondarts[1], Hugo Lange[1], Laurence Bois[2] and Nolwenn Le Pierrès[1]

[1] Université Savoie Mont-Blanc, CNRS, LOCIE UMR 5271, Le Bourget-du-Lac (France)

[2] Université Claude Bernard Lyon 1, CNRS, LMI UMR 5615, Villeurbanne (France)

Abstract

A novel sorbent material made of a silica matrix, polymer PEG-600 and 34% by weight of salt hydrate $CaCl_2$ was experimentally studied for thermochemical heat storage applications and compared to zeolite 13X, which is a commonly used material in this field. Four desorption / sorption cycles were carried out using 56 g of composite sorbent in a fixed bed reactor and a dry air flow rate of about 0.14 normal liter s^{-1}. The desorption temperature was set at 130 °C, while sorption was conducted with an air flow at 30 °C and 42% relative humidity. The resulting water sorption capacity is 0.37 g g^{-1} of dehydrated material, that is twice that obtained with zeolite 13X BFK in the same conditions. The energy density is also improved by 60% compared to zeolite: on average, its value was evaluated to be 782 kJ kg^{-1} of dehydrated material. Lastly, the sorption kinetics is much slower when using the salt composite. Saturation ($P_{v,out}/P_{v,in} = 0.95$) is reached after about 12 h, instead of 2 h 30 with zeolite.

Keywords: thermochemical storage, water sorption, composite, calcium chloride, silica

1. Introduction

Energy generation from renewable sources such as wind or solar radiation supports infrastructure resilience and reduces vulnerability to climate change (IPCC, 2022). Renewable energies are clean, abundant and decentralized, but they are also intermittent in nature, thus requiring energy storage systems. These systems allow for meeting variable energy demands despite the inability to produce renewable energy for 24 h a day. Heat storage technologies can also be used for waste heat recovery in many areas such as building, textile, automobile, health care, agriculture or food processing, thereby increasing energy efficiency on a large scale.

Since energy is mostly used for heating and cooling applications (Connolly *et al.*, 2014; European Commission, 2016), thermal energy storage has been extensively investigated. It includes sensible, latent and thermochemical heat storage. The latter is particularly attractive because heat is stored as chemical potential energy, which prevents heat loss during long-term storage. Besides, thermochemical energy storage (TCES) systems are able to achieve high energy densities (Desai *et al.*, 2021). However, they are still in the early stage of the development process. TCES systems are based on reversible sorption phenomena involving chemical or physical bonding: the phenomena for charging and discharging heat are endothermic and exothermic, respectively.

In the present experimental work, the TCES setup is at the laboratory scale and based on water vapor sorption, whose principle is presented in eq. 1 (Mette *et al.*, 2014):

$$A_{(s)} + n.H_2O_{(g)} \rightleftarrows A.n.H_2O_{(s)} + \Delta H_s \quad \text{(eq. 1)}$$

The TCES system is discharged by bringing the solid sorbant A in contact with water vapor, which bonds chemically or physically with the reactant. The solid product $A.n.H_2O$ is thus formed and the heat of sorption ΔH_s is released. During the charging process, also called desorption, the heat ΔH_s is supplied to the material, which is again dissociated into sorbent A and sorbate H_2O.

© 2022. The Authors. Published by International Solar Energy Society
Selection and/or peer review under responsibility of Scientific Committee
doi:10.18086/eurosun.2022.13.03 Available at http://proceedings.ises.org

Open TCES systems based on water vapor sorption can be coupled to solar thermal collectors such as flat plate or evacuated tube collectors, as depicted in Fig. 1. During sunny days, the sorbent is dehydrated using a dry air stream heated to more than 80 °C by the solar collectors. In this work, evacuated tube solar collectors are assumed to reach at least 130 °C during the charging phase. The sorbed water is extracted from the sorbent bed by the air stream, which becomes wetter and cooler and is eventually rejected outside. Since this process is endothermic, it allows heat storage. During cold periods, the stored heat can be released through hydration of the sorbent. To this end, a humid air stream is sent from the building into the sorbent bed. Part of the water vapor is then sorbed by the material. Since the sorption is exothermic, a dry and hot air stream exits the bed, which can be used for domestic space heating if its temperature is above 30 or 35 °C. This air stream cannot however be blown directly into the heated space because it has been in contact with the sorbent: a heat exchanger must be included (Fig. 1) to comply with safety requirements. The heat exchanger can also be used to reduce the overall energy consumption of the process (Tatsidjodoung *et al.*, 2016): during sunny days, it allows recovering the remaining heat of the air stream exiting the sorbent bed to pre-heat the ambient air entering the solar collectors. Lastly, during the coldest periods and depending on the size and performance of the sorbent bed, an auxiliary heater may be called for in order to meet the heating demand.

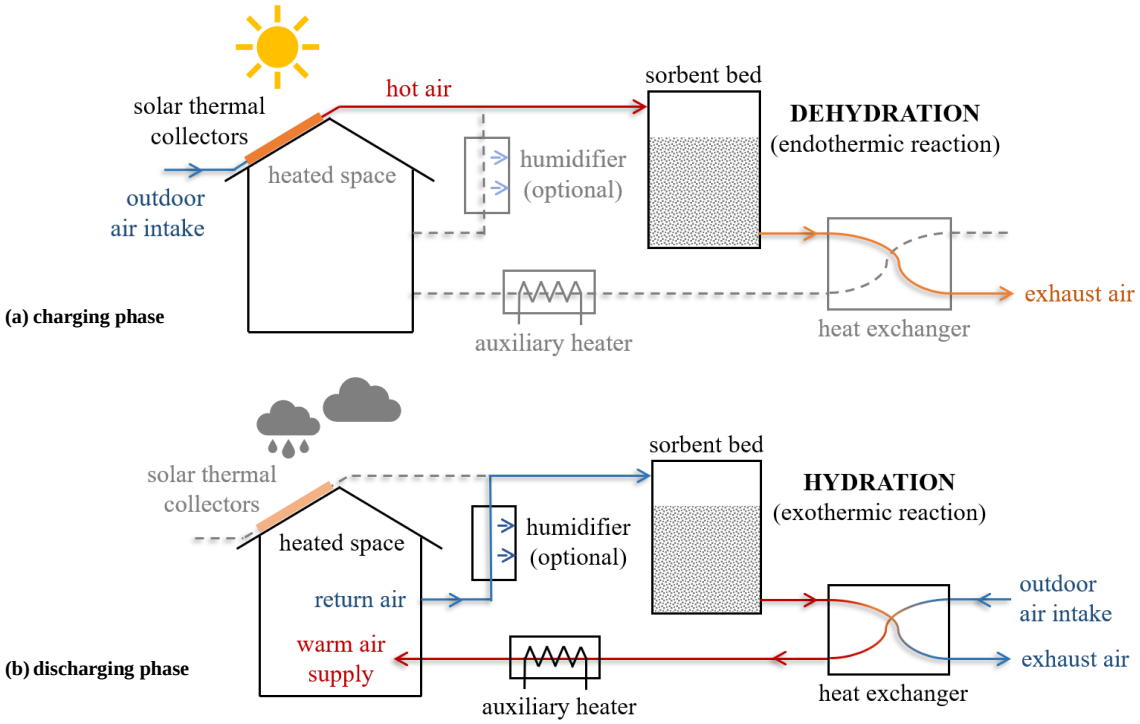

Fig. 1: Operating principle of an open TCES system based on water sorption coupled with solar thermal collectors

The viability of TCES systems depends on many parameters, not least the energy density of the storage material. Developing high energy density materials is essential for the systems to be compact and thus suitable for a wide range of applications, especially in the residential sector or vehicle industry. The most promising materials in this regard are salt hydrates, but their performance under actual operating conditions is unsatisfactory, mainly because of agglomeration, melting or deliquescence leading to poor heat and mass transfer (Zhao *et al.*, 2021). Consequently, composite materials are developed by impregnating salts into the pore structure of a host matrix, which exhibits a high specific surface area. The matrix promotes water-salt sorption interactions and is able to hold the salt and its solutions within its internal pore system (Lin *et al.*, 2021; Zhao *et al.*, 2021).

A novel composite material for TCES is studied in this paper. It is composed of a silica matrix, polymer PEG-600 and salt $CaCl_2$. This hydrophilic salt was chosen because it is able to react with water molecules at suitable temperature for the system (Fig. 1). Besides, composite materials containing calcium chloride exhibit the highest storage capacities and seem to be the most promising candidates among the different salt composites used for thermal storage applications (Jabbari-Hichri *et al.*, 2017; Lin *et al.*, 2021; Touloumet *et al.*, 2021; Xie *et al.*, 2019). The experimental storage performance of the composite material is compared with that obtained using zeolite 13X, which is a well-known sorbent material for this application.

2. Experimental heat storage setup

2.1. Description of the test facility

An open-cycle sorption storage system was designed (Fig. 2). It consists of a 46 mm inner diameter fixed bed reactor, a direct contact bubbling humidifier and a heating apparatus. The entering air flow rate is controlled by a mass flow controller. The uncertainty in this flow rate has been estimated to 0.004 normal liter s^{-1} over the range 0.03 to 0.30 normal liter s^{-1}. During the sorption phase, entering air is first saturated with water at a given temperature by flowing through the bubbler humidifier and then heated in order to reach the desired conditions (temperature and humidity) at the entrance of the reactor. The humidification temperature is controlled with a thermostatic bath. During charging (desorption), on the other hand, the humidifier is by-passed so that hot dry air enters the reactor.

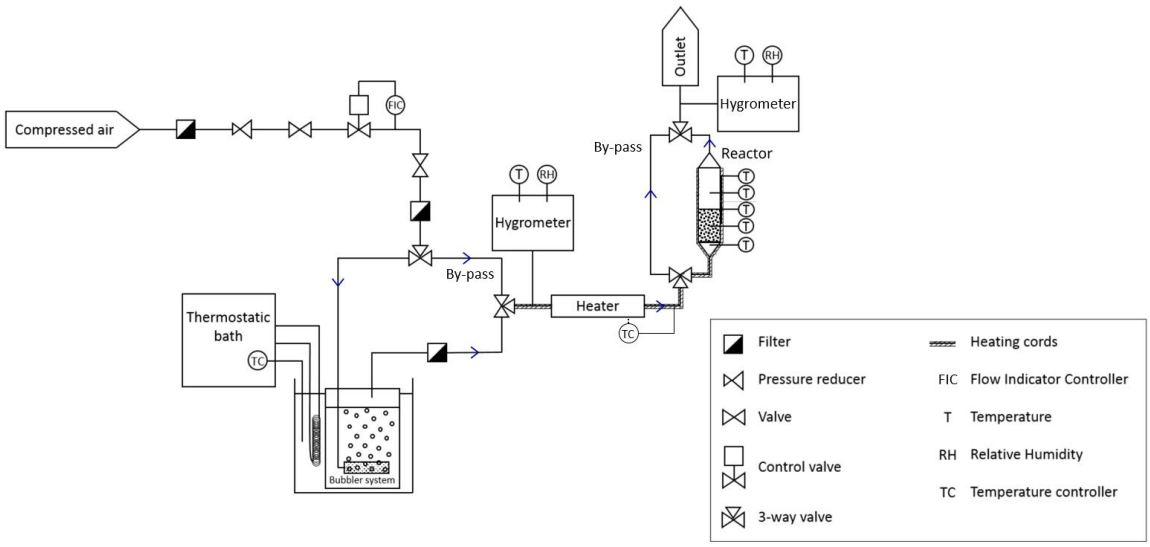

Fig. 2: Schematic of the experimental setup for the study of water sorption on a novel composite material

The air temperature and relative humidity at the inlet and outlet of the reactor are monitored using chilled mirror hygrometers (GE Sensing Optisonde D2). K-type thermocouples are placed inside the reactor, which is thermally insulated. Before testing, they have been calibrated over a 5 °C to 85 °C temperature range. The resulting uncertainty in temperature measurements is ± 0.5 °C. The location of the thermocouples is shown in Fig. 3. They are numbered from T_1 (bottom, reactor inlet) to T_5 (top, reactor outlet). Only one thermocouple is located inside the sorbent bed because of the limited amount of synthetized sorbent material. During experiments, measurements are recorded every ten seconds using LabVIEW acquisition software.

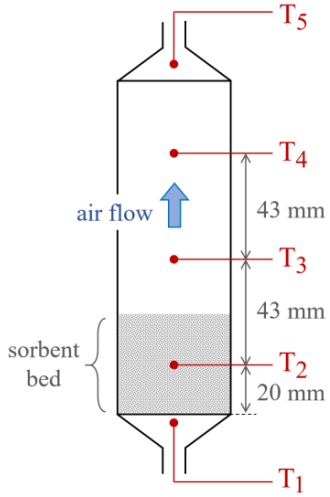

Fig. 3: Location of thermocouples T_1 to T_5 along the reactor

2.2. Testing procedure

Nominal experiments were conducted using 56 g of sorbent material and a dry air flow rate of about 0.14 normal liter s^{-1}, which leads to an acceptable pressure drop across the reactor. This flow rate leads to a bulk velocity of about 0.1 m s^{-1} through the sorbent bed, which falls within the usual range for sorption processes. The material, thereafter referred to as 'SC' for salt composite, was obtained by a sol-gel process. It contains 34% by weight of salt $CaCl_2$, as well as silica and polymer PEG-600. This salt content is close to that reported in previous studies about silica-$CaCl_2$ composites (Courbon *et al.*, 2017; Dawoud and Aristov, 2003; Jänchen *et al.*, 2004; Levitskij *et al.*, 1996; Touloumet *et al.*, 2021; Tso and Chao, 2012; Zheng *et al.*, 2014; Zhu *et al.*, 2006).

Prior to sorption, the sample is dried at 130 °C inside the reactor in order to remove residual moisture. Sorption is then performed with an air flow at 30 °C at the entrance of the reactor (temperature T_1) and 42% RH. These conditions are close to those found in residential buildings. To regenerate the sample, dry air at 130 °C is blown into the reactor during 4 h. This desorption temperature was set according to the outlet temperatures achievable by solar air collectors (Vengadesan and Senthil, 2020). Next, heating is switched off for the system to cool down. A new sorption cycle is then carried out and so on. Four successive desorption / sorption cycles were completed. A similar set of experiments was conducted using zeolite 13X BFK (Köstrolith® supplied by CWK, beads diameter from 1.2 to 2.0 mm). Three cycles were realized in this case in order to compare the results with those obtained with SC. The sorbent bed is slightly thinner when using zeolite instead of SC because it is more compact (bulk density increased by 13%). Still, the bed thickness is close to 40 mm in both cases.

2.3 Measurement data processing

The amount of water sorbed during each cycle is evaluated through a mass balance on the water vapor contained in the air flow. The mass balance is integrated over the duration of the sorption phase, yielding the following equation:

$$m_w = \int \dot{m}_w \, dt = \int \dot{m}_{da}(x_i - x_o)dt \approx \dot{m}_{da} \sum (x_i - x_o)\Delta t \qquad \text{(eq. 2)}$$

where $\dot{m}_w$ is the instantaneous mass flow rate of water sorbed by the material, $\dot{m}_{da}$ is the constant dry air flow rate going through the reactor, x_i and x_o are the specific humidities at the reactor inlet and outlet (in grams of water vapor per gram of dry air) and Δt is the time interval between two measurement readings.

Similarly, the sensible heat given to the air flow during the sorption phase is calculated as follows:

$$Q_{air} = \int \dot{Q}_{air} \, dt = \int \dot{m}_{da} \, c_{p,ha}(T_4 - T_1)dt \approx \dot{m}_{da} \sum c_{p,ha}(T_4 - T_1)\Delta t \qquad \text{(eq. 3)}$$

The heat capacity $c_{p,ha}$ of the *outlet* humid air is used in order to assess the potential for heat recovery by means of a heat exchanger placed after the reactor as closely as possible. In addition, the temperature T_4 is considered in the energy balance instead of T_5 to minimize the impact of thermal losses, and instead of T_3 for better temperature homogeneity over the channel cross-section.

The required properties of humid air (relative and specific humidity, specific heat capacity, water vapor partial pressure) are calculated using the CoolProp library (Bell *et al.*, 2014) from the dry bulb and dew point temperatures provided by each hygrometer.

Subsequently, the amount of sorbed water and the generated heat are expressed by mass or by volume of dehydrated material (at 130 °C for 4 h). The bulk density of dry SC was estimated to be 710 ± 70 kg m^{-3}, while that of zeolite is 800 ± 100 kg m^{-3}.

The heat loss from the reactor can be evaluated using the following relation:

$$Q_{loss} = U \int (\bar{T}_i - T_{amb})dt \approx U \sum (\bar{T}_i - T_{amb})\Delta t \qquad \text{(eq. 4)}$$

The overall heat transfer coefficient U between the ambient and the isolated reactor was determined experimentally in steady state using an inert material. It is about 0.0285 W K^{-1}. The heat loss also depends on the difference between $\bar{T}_i$, which is the mean temperature between T_1, T_2, T_3 and T_4, and the ambient temperature T_{amb} at each time step.

Finally, knowing the heat loss, the enthalpy of sorption of the material ΔH_s can be estimated under the tested conditions (humid air at 30 °C and 42% RH). Since the total energy stored in the reactor wall is negligible during

the sorption phase, it can be expressed as:

$$\Delta H_s = (Q_{air} + Q_{loss})/m_w \quad \text{(eq. 5)}$$

The enthalpy of sorption obtained in J g^{-1}_{H2O} can be compared to that measured by thermogravimetric analysis at the milligram scale.

2.4 Thermogravimetric analysis (TGA)

The enthalpy of sorption of the composite material was measured using a thermogravimetric analyzer coupled to a differential scanning calorimeter (Mettler Toledo, TGA/DSC 3+) and to a humidity generator (ProUmid MHG). The sample, which weights about 20 mg, is placed in an open alumina cell. It is first dehydrated under dry air flow at 30 °C for 24 h. Then, hydration is performed during 120 h under humid air flow at 30 °C and 42% RH, i.e., in the same conditions as those fixed at the reactor inlet during the sorption phase. The hydration step resulted in an exothermic peak on the heat flow curve. The integration of this signal enables the determination of the generated heat and, when expressed by mass of sorbed water, of the enthalpy of sorption. The relative error on the final value is about 5%.

3. Experimental heat storage results

3.1 Sorption kinetics

The breakthrough curves are presented in Fig. 4 for the four cycles carried out with SC. Such curves are used to characterize the sorption kinetics and to evaluate the sorption capacity of the tested material. Here, they are obtained from the ratio of the water outlet partial pressure $P_{v,out}$ to the water inlet partial pressure $P_{v,in}$.

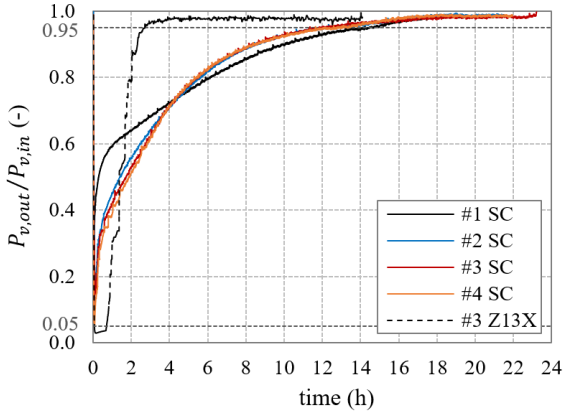

Fig. 4: Breakthrough curves during water sorption using SC and zeolite

The shape of the curve is significantly altered between the first cycle (black solid line) and second cycle (blue line). This is likely due to a change in the initial properties of the material. After that, curves #2 to #4 are overlapping, showing that the cycles are nearly identical and that SC properties are virtually stable. Fig. 4 also includes the breakthrough curve obtained with a similar mass of zeolite 13X (dashed line). Three cycles were performed in this case but, since all the curves overlapped, only that of the last cycle is presented to improve readability. Breakthrough takes place when the sorbate (water) starts to be detected at the outlet of the reactor. In this work, the breakthrough time has been taken when the vapor outlet partial pressure reaches 5% of the vapor inlet pressure ($P_{v,out}/P_{v,in} = 0.05$). Thus, breakthrough occurs after about 40 minutes with zeolite, while it is immediate for SC, which never fully sorbs the water vapor provided at the inlet for the considered bed thickness. Further, when using zeolite, the curve has a greater slope and saturation is reached much faster. Indeed, around 2 h 30 are required to reach saturation ($P_{v,out}/P_{v,in} = 0.95$) with zeolite, compared to 12 h for SC. The sorption kinetics of SC is thus much slower than that of zeolite. It may be limited by chemical kinetics, heat transfer or by water mass diffusion across the sorbent bed. The slow sorption kinetics of SC can be an advantage or a drawback depending on the considered application and the required power level.

The evolution of temperatures T_1 to T_5 during the sorption phase is shown in Fig. 5 for SC and zeolite. The temperature level is lower when using SC than zeolite. The maximum temperature is indeed around 54 °C in the

former case and 81 °C in the latter. This difference can be explained by the much slower sorption kinetics of SC. The temperatures return to their initial value (30 °C) after more than 10 h for SC versus 4 h for zeolite.

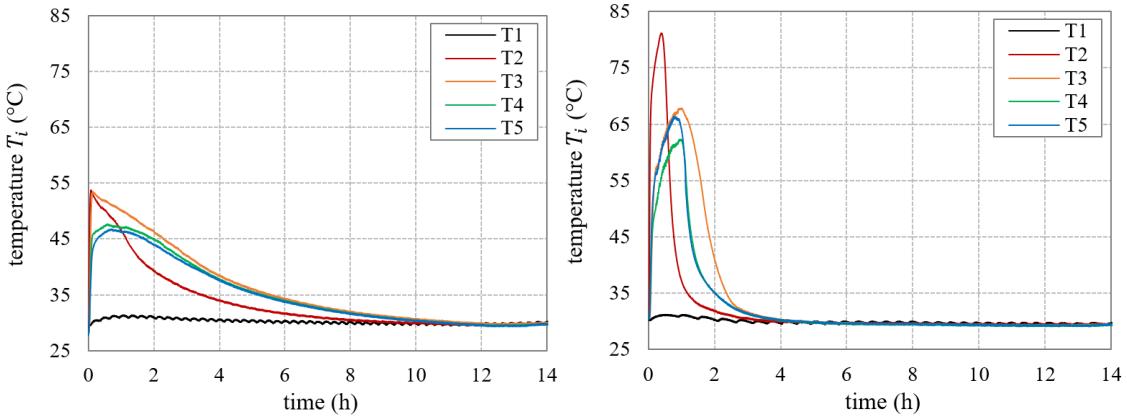

Fig. 5: Temperature curves over the sorption phase using SC (left, cycle #4) and zeolite (right, cycle #3)

3.2 Comparative performance analysis

The water sorption capacity of both sorbents (eq. 2) is given in Table 1, as well as the generated energy (eq. 3) and power during the sorption process for each cycle. The uncertainty in each value is indicated following a plus or minus sign. Uncertainties are evaluated using error propagation formulas and include the precision of the measuring instruments, the reproducibility of measurements and the uncertainties due to calibrations. Table 1 shows that the sorption capacity of SC is on average twice that of zeolite. As a result, the generated energy and the mass energy density increase by nearly 60% when SC is used instead of zeolite. The mass energy density amounts on average to 782 kJ kg^{-1} of dehydrated material for SC and to 493 kJ kg^{-1} for zeolite. The fact that the energy is not doubled can be partly explained by a weaker binding energy between water vapor molecules and SC sorbent than between water and zeolite (see part 3.4). The volumetric energy density increases slightly less than the mass energy density (+ 40%) because SC is less compact than zeolite. Finally, the maximum power is two times lower with SC, which is consistent with the temperature curves of Fig. 5.

Tab. 1: Comparison of water sorption capacity, generated energy and power (sensible heat) with SC and zeolite

	SC				Zeolite 13X BFK		
cycle	#1	#2	#3	#4	#1	#2	#3
quantity of sorbed water m_w (g)	20.3 ± 2.8	20.9 ± 2.9	21.3 ± 3.2	21.9 ± 3.1	10.7 ± 2.3	9.7 ± 2.2	11.6 ± 2.3
water sorption capacity (g_{H2O} g^{-1})	0.36 ± 0.06	0.37 ± 0.06	0.38 ± 0.07	0.39 ± 0.07	0.19 ± 0.05	0.17 ± 0.05	0.21 ± 0.05
generated energy Q_{air} (kJ)	37.4 ± 1.9	44.9 ± 2.3	48.1 ± 2.5	45.6 ± 2.3	26.3 ± 1.4	29.7 ± 1.6	27.1 ± 1.4
energy density (kJ kg^{-1})	665 ± 59	798 ± 70	856 ± 76	811 ± 71	468 ± 36	528 ± 41	482 ± 36
energy density (kWh m^{-3})	131 ± 18	157 ± 21	169 ± 23	160 ± 22	104 ± 16	117 ± 18	107 ± 16
maximum power $\dot{Q}_{air,max}$ (W)	1.7 ± 0.3	2.9 ± 0.3	3.1 ± 0.3	3.1 ± 0.3	5.6 ± 0.5	5.9 ± 0.6	5.8 ± 0.5

The energy densities estimated for zeolite are consistent with literature values. Jänchen *et al.* (2012) found a storage density of 600 kJ kg^{-1} for the binderless zeolite 13X they have synthetized and tested in an open storage apparatus (desorption at 200 °C, sorption at 23 °C and 35% RH). Bennici *et al.* (2020) studied the same zeolite that we used and give an energy density of about 850 kJ kg^{-1}. It was measured through TGA during hydration with an air flow at 30 °C and 60% RH. This high relative humidity partly explains the greater energy density found by the authors. The discrepancy is also due to the fact that the heat loss from the reactor was neglected in Table 1. As a result, the generated energies and powers are systematically underestimated in the present analysis. Two studies characterized the storage performance of zeolite 13X at a larger scale: Bales *et al.* (2008) obtained an energy density of 180 kWh m^{-3} and a maximum power of 800 W from a storage reactor containing 7 kg of zeolite, while Hauer (2007) found an energy density of 124 kWh m^{-3} and a maximum power of 130 kW for a scaled-up system containing 7 000 kg of zeolite.

To return to the composite material, the evolution of the results over the four cycles is worth examining. The quantity of water sorbed by SC is marginally altered from cycle #1 to cycle #4. The generated energy and power, however, increase significantly (+ 20% and + 70%) between the first and second cycles. Then, they are more stable, with a maximum variation of 7% between cycles. These results are consistent with the modification of the sorption kinetics observed in Fig. 4 between the first cycle and the next ones. According to Fig. 4, the quantity of water sorbed during the first four hours of cycle #1 is reduced compared to that sorbed at the beginning of the next cycles, which notably explains the variation of the maximum power shown in Table 1.

3.3 Hydration states of $CaCl_2$

Several salt hydrates have been identified and should theoretically appear successively during water sorption on calcium chloride at 30 °C: $CaCl_2{\cdot}H_2O$, $CaCl_2{\cdot}2H_2O$, $CaCl_2{\cdot}4H_2O$ and $CaCl_2{\cdot}6H_2O$ (Aristov, 2020). Then, above 1 gram of sorbed water per gram of salt, the latter dissolves and reaches the liquid state. In this study, the salt sorbs on average 1.10 g_{H2O} g^{-1} (or 6.8 mol_{H2O} mol^{-1} of $CaCl_2$), so part of it has likely turned to liquid inside the matrix pores. However, according to Aristov (2020), the properties of a confined salt differ from that of a bulk one. The transitions between hydration states may thus be modified depending on the composite structure.

Under the chosen experimental conditions, Table 1 shows that the quantity of water sorbed by SC is slightly increasing from one cycle to the next, and there is no performance degradation indicative of salt leakage. The host matrix thus managed to stabilize the hydrated calcium chloride. Still, special attention must be paid to salt leakage because $CaCl_2$ solutions are highly corrosive and the risk of leakage increases when operating at high humidities. A thorough characterization of the material is required to ensure its stability under a wide range of operating conditions.

3.4 Enthalpy of sorption

The enthalpy of sorption is the heat released by the sorption of a given amount of water. It characterizes the bonding strength between the water vapor molecules and the sorbent. It was measured both by TGA (see section 2.4) and at the reactor scale using eq. 5 (which includes the heat loss). The results obtained with SC are summarized in Table 2.

Tab. 2: Enthalpy of sorption of SC measured by TGA and estimated using eq. 5

cycle	#1	#2	#3	#4
ΔH_s measured by TGA (J g_{H2O}^{-1})	3275			
ΔH_s measured at the reactor scale (J g_{H2O}^{-1})	2450	2720	2830	2630
difference (%)	- 25	- 17	- 14	- 20

The uncertainty in the values from eq. 5 is significant (± 25%) because they depend on the heat loss, which is estimated. Besides, the mass of the sample analyzed by TGA amounts to a few tens of milligrams. Material inhomogeneities could therefore have a strong impact on the result. Despite these potential sources of error, the order of magnitude of the enthalpies are consistent between both methods, with a maximum deviation of 25%.

The enthalpy of sorption of the tested zeolite was evaluated by TGA to be 3450 J g_{H2O}^{-1} (Polimann, 2019). The analysis was however performed under conditions distinct from those of our experiments (25 °C, unspecified humidity). Still, the values calculated at the reactor scale from eq. 5 are comparable: on average, the enthalpy of sorption of zeolite is estimated to be 2980 J g_{H2O}^{-1} (- 14% compared to the TGA value).

Finally, the energy released during the sorption of a given mass of water is more important with zeolite than with SC: on average, the estimated enthalpy of sorption in J g_{H2O}^{-1} decreases by 11% with the latter. Yet, physical bonds are created in the first case (physisorption), while high-energy chemical bonds are supposed to form in the second case (chemisorption during hydration of $CaCl_2$). This apparent contradiction could be explained by the physisorption of part of the water on the silica matrix of the composite, thus decreasing the mean energy released. A control material containing only silica and PEG will be tested in the near future in order to quantify the actual benefit of adding calcium chloride. Regardless, the energy density of SC remains higher than that of zeolite due to its high sorption capacity.

4. Conclusion

Thermochemical heat storage is a promising technology to support the development of renewable energy on a large scale. The heat storage performance of a new composite material obtained by a sol-gel process has been characterized in an open-cycle sorption reactor, with moist air as the sorbate and heat transfer fluid. The salt composite (SC) contains 34% by weight of anhydrous calcium chloride ($CaCl_2$) dispersed in a matrix of silica and polymer PEG-600. Similar experiments were conducted using zeolite 13X BFK for comparison.

The average sorption capacity of SC is 0.37 grams of water per gram of dehydrated material, which is twice that of zeolite. The energy generated during the sorption of a given mass of water is however slightly increased when using zeolite. Indeed, the enthalpy of sorption measured by TGA (and consistent with that obtained at the reactor scale) is 3275 J g_{H2O}^{-1} for SC, compared to about 3450 J g_{H2O}^{-1} for zeolite. Thanks to its high sorption capacity, the energy density of SC is still increased by nearly 60% compared to that of zeolite (782 kJ kg^{-1} on average, versus 493 kJ kg^{-1} for zeolite).

The sorption kinetics is much slower when using SC than zeolite: around 12 h are required for SC to reach water vapor saturation ($P_{v,out}/P_{v,in} = 0.95$), compared to 2 h 30 with zeolite. Besides, breakthrough occurs immediately in the first case, and after 40 minutes in the second case. The slow sorption kinetics of SC leads to reduced temperatures and generated powers during the sorption phase. The maximum power is indeed two times smaller with SC than with zeolite. The temperatures are still around 50 °C, which is adequate for space heating applications.

The host matrix managed to stabilize the hydrated calcium chloride and to avoid leakage under the chosen experimental conditions. However, operating at higher humidities could promote deliquescence. A thorough characterization of the material is thus needed to ensure its stability under a wide range of operating conditions. The influence of the salt content on the risk of leakage and on the storage performance is also worth investigating.

Acknowledgments

This work was supported by the French National Research Agency (ANR) in the frame of the STOCK-CAR project, which is carried out in collaboration with IRCELYON (Institut de Recherche sur la Catalyse et l'Environnement de Lyon, UMR 5256), LMCPA (Laboratoire des Matériaux Céramiques et Procédés Associés, EA 2443) and LMI (Laboratoire des Multimatériaux et Interfaces, UMR 5615).

References

Aristov, Y.I., 2020. Nanocomposite sorbents for multiple applications. Jenny Stanford Publishing: Singapore, 446 p., ISBN 9789814267502.

Bales, C., Gantenbein, P., Jaenig, D., Kerskes, H., Summer, K., van Essen, M., Weber, R., 2008. Laboratory tests of chemical reactions and prototype sorption storage units. A report of IEA Solar Heating and Cooling programme, Task 32 – Report B4 of Subtask B.

Bell, I.H., Wronski, J., Quoilin, S., Lemort, V., 2014. Pure and pseudo-pure fluid thermophysical property evaluation and the open-source thermophysical property library CoolProp. Industrial & Engineering Chemistry Research, 53, 2498-2508. https://doi.org/10.1021/ie4033999

Bennici, S., Polimann, T., Ondarts, M., Gonze, E., Vaulot, C., Le Pierrès, N., 2020. Long-term impact of air pollutants on thermochemical heat storage materials. Renewable and Sustainable Energy Reviews, 117, 109473. https://doi.org/10.1016/j.rser.2019.109473

Connolly, D., Lund, H., Mathiesen, B.V., Werner, S., Möller, B., Persson, U., Boermans, T., Trier, D., Østergaard, P.A., Nielsen, S., 2014. Heat Roadmap Europe: combining district heating with heat savings to decarbonise the EU energy system. Energy Policy, 65, 475-489. https://doi.org/10.1016/j.enpol.2013.10.035

Courbon, E., D'Ans, P., Permyakova, A., Skrylnyk, O., Steunou, N., Degrez, M., Frère, M., 2017. Further improvement of the synthesis of silica gel and $CaCl_2$ composites: Enhancement of energy storage density and stability over cycles for solar heat storage coupled with space heating applications. Solar Energy, 157, 532-541. https://doi.org/10.1016/j.solener.2017.08.034

Dawoud, B., Aristov, Y., 2003. Experimental study on the kinetics of water vapor sorption on selective water sorbents, silica gel and alumina under typical operating conditions of sorption heat pumps. International Journal of Heat and Mass Transfer, 46, 273-281. https://doi.org/10.1016/S0017-9310(02)00288-0

Desai, F., Prasad, J.S., Muthukumar, P., Rahman, M.M., 2021. Thermochemical energy storage system for cooling and process heating applications: A review. Energy Conversion and Management, 229, 113617. https://doi.org/10.1016/j.enconman.2020.113617

European Commission, 2016. Communication from the Commission to the European Parliament, the Council, the European Economic and Social Committee and the Committee of the Regions - an EU Strategy on Heating and Cooling. Brussels, COM/2016/051 final. Available from < https://eur-lex.europa.eu/legal-content/EN/TXT/?uri=CELEX:52016DC0051> (accessed 27.04.2023).

Hauer, A., 2007. Adsorption systems for TES – Design and demonstration projects. Proceedings of the Thermal Energy Storage for Sustainable Energy Consumption Conference, Dordrecht, 409-427. https://doi.org/10.1007/978-1-4020-5290-3_25

IPCC, 2022. Climate change 2022: impacts, adaptation and vulnerability. Contribution of working group II to the sixth assessment report of the Intergovernmental Panel on Climate Change. *Cambridge University Press*, 3056 p., doi:10.1017/9781009325844.

Jabbari-Hichri, A., Bennici, S., Auroux, A., 2017. $CaCl_2$-containing composites as thermochemical heat storage materials. Solar Energy Materials and Solar Cells, 172, 177-185. https://doi.org/10.1016/j.solmat.2017.07.037

Jänchen, J., Ackermann, D., Stach, H., Brosicke, W., 2004. Studies of the water adsorption on zeolites and modified mesoporous materials for seasonal storage of solar heat. Solar Energy, 76, 339-344. https://doi.org/10.1016/j.solener.2003.07.036

Jänchen, J., Schumann, K., Thrun, E., Brandt, A., Unger, B., Hellwig, U., 2012. Preparation, hydrothermal stability and thermal adsorption storage properties of binderless zeolite beads. International Journal of Low-Carbon Technologies, 7, 275-279. https://doi.org/10.1093/ijlct/cts037

Levitskij, E.A., Aristov, Y.I., Tokarev, M.M., Parmon, V.N., 1996. "Chemical heat accumulators": a new approach to accumulating low potential heat. Solar Energy Materials and Solar Cells, 44, 219-235. https://doi.org/10.1016/0927-0248(96)00010-4

Lin, J., Zhao, Q., Huang, H., Mao, H., Liu, Y., Xiao, Y., 2021. Applications of low-temperature thermochemical energy storage systems for salt hydrates based on material classification: a review. Solar Energy, 214, 149-178. https://doi.org/10.1016/j.solener.2020.11.055

Mette, B., Kerskes, H., Drück, H., Müller-Steinhagen, H., 2014. Experimental and numerical investigations on the water vapor adsorption isotherms and kinetics of binderless zeolite 13X. International Journal of Heat and Mass Transfer, 71, 555–561. https://doi.org/10.1016/j.ijheatmasstransfer.2013.12.061

Polimann, T., 2019. Impact des polluants de l'air sur la durabilité de matériaux dédiés au stockage thermochimique de la chaleur solaire pour le bâtiment. *Ph.D. thesis*, Université Grenoble Alpes, France.

Tatsidjodoung, P., Le Pierrès, N., Heintz, J., Lagre, D., Luo, L., Durier, F., 2016. Experimental and numerical investigations of a zeolite 13X / water reactor for solar heat storage in buildings. Energy Conversion and Management, 108, 488-500. https://doi.org/10.1016/j.enconman.2015.11.011

Touloumet, Q., Silvester, L., Bois, L., Postole, G., Auroux, A, 2021. Water sorption and heat storage in $CaCl_2$ impregnated aluminium fumarate MOFs. Solar Energy Materials and Solar Cells, 231, 111332. https://doi.org/10.1016/j.solmat.2021.111332

Tso, C.Y., Chao, C.Y.H., 2012. Activated carbon, silica-gel and calcium chloride composite adsorbents for energy efficient solar adsorption cooling and dehumidification systems. International Journal of Refrigeration, 35, 1626-1638. https://doi.org/10.1016/j.ijrefrig.2012.05.007

Vengadesan, E., Senthil, R., 2020. A review on recent developments in thermal performance enhancement

methods of flat plate solar air collector. Renewable and Sustainable Energy Reviews, 134, 110315. https://doi.org/10.1016/j.rser.2020.110315

Xie, N., Niu, J., Wu, T., Gao, X., Fang, Y., Zhang, Z., 2019. Fabrication and characterization of $CaCl_2 \cdot 6H_2O$ composite phase change material in the presence of Cs_xWO_3 nanoparticles. Solar Energy Materials and Solar Cells, 200, 110034. https://doi.org/10.1016/j.solmat.2019.110034

Zhao, Q., Lin, J., Huang, H., Wu, Q., Shen, Y., Xiao, Y, 2021. Optimization of thermochemical energy storage systems based on hydrated salts: A review. Energy and Buildings, 244, 111035. https://doi.org/10.1016/j.enbuild.2021.111035

Zheng, S., Ge, T.S., Wang, R. Z., Hu, L.M., 2014. Performance study of composite silica gels with different pore sizes and different impregnating hygroscopic salts. Chemical Engineering Science, 120, 1-9. https://doi.org/10.1016/j.ces.2014.08.047

Zhu, D., Wu, H., Wang, S., 2006. Experimental study on composite silica gel supported $CaCl_2$ sorbent for low grade heat storage. International Journal of Thermal Sciences, 45, 804-813. https://doi.org/10.1016/j.ijthermalsci.2005.10.009

Nomenclature

c_p	specific heat capacity at constant pressure, J K^{-1} g_{da}^{-1}
ΔH_s	enthalpy (or heat) of sorption, J g_{H2O}^{-1}
m	mass, g
$\dot{m}$	mass flow rate, g s^{-1}
P_v	water vapor partial pressure, Pa
Q_{air}	sensible heat given to the air flow, J
$\dot{Q}_{air}$	heat transfer rate, W
Q_{loss}	heat loss, J
t	time, s
T_{amb}	ambient temperature, °C
T_i	i^{th} temperature measurement along the reactor, °C
$\bar{T}_i$	average of temperatures T_1 to T_4, °C
U	overall heat transfer coefficient between the ambient and the reactor, W K^{-1}
x	specific humidity, g_{H2O} g_{da}^{-1}

Subscripts

da	dry air
ha	humid air
i	reactor inlet
max	maximum
o	reactor outlet
w	sorbed water

Acronyms

PEG	polyethylene glycol
RH	relative humidity
SC	salt composite
TGA	thermogravimetric analysis

New Concept for High Temperature Thermal Energy Storage Using a Concrete Tank

Luisa F. Cabeza[1], David Vérez[1], Gabriel Zsembinszki[1], Emiliano Borri[1], Cristina Prieto[2]

[1] GREiA Research Group, University of Lleida, Lleida (Spain)

[2] University of Seville, Department of Energy Engineering, Seville (Spain)

Abstract

The use of concrete is showing great potential as thermal energy storage material for concentrating solar power plants (CSP) due to its versatility, relatively low cost, and the possibility to reach a high operating temperature, above 500ºC thus increasing the plant efficiency. However, actual configurations based on concrete show different drawbacks including difficulties during the manufacturing on-site, different thermal expansion coefficients between concrete and pipes, and poor thermal conductivity of concrete. In order to address those challenges, this study proposes a new TES concrete tank concept based on three main pillars: modularity, improved concrete formulation, and direct contact concept. A preliminary assessment of the thermal performances of the new concept was analyzed through simulations showing the temperature distribution of the modules.

Keywords: thermal energy storage; sensible TES; concrete; CSP; modular concept;

1. Introduction

Solar energy represents today the main renewable source to produce both thermal and electric power. One of the main large-scale technology to convert solar energy into electricity is represented by concentrating solar power (CSP) plants. According to REN21, in 2020 the total capacity installed worldwide amounts to 6.2 GWe (REN21, 2020). In order to deal with the intermittency of solar radiation at a given location, thermal energy storage (TES) is an essential component. Current CSP technologies mainly rely on the use of molten salts as storage medium. However, the main drawbacks of molten salts are corrosion issues and their limited operating temperature range (up to 565 ºC), which limits CSP in both global performance and cost. Amongst all storage medium alternatives, the use of concrete represents a viable option due to its versatility, relatively low cost, and the possibility to reach a high operating temperature above 565 ºC.

One of the first storage concepts using concrete was developed by DLR and tested at Plataforma Solar de Almeria. Regarding the storage material, blast furnace cement was used with iron oxides, flue ash, and auxiliary materials. The system used thermal oil as HTF flowing through an array of pipes (tube register) embedded in the storage medium (Laing et al., 2009a). Another concept, EnergyNest, developed and tested two modules of 500 kWth thermal energy storage capacity based on a modular design and concrete as a storage medium, named HEATCRETE vp1, able to resist temperatures up to 400 ºC (Hoivik et al., 2019a). The modules of the TES developed by EnergyNest consisted of cylindrically shaped thin-walled (0.4 mm) steel casing closed at one end and open at the other with integrated steel pipe heat exchangers.

Although concrete has a high potential for storage solution, there are still challenges related to this technology that needs to be addressed, which include its fabrication techniques, material formulation, and design, which limit the construction feasibility and thermal performance. In order to improve the currently available configurations, this study proposed a novel concept of thermal energy storage using concrete based on a modular concept, improved concrete formulation, and a direct contact design. Moreover, a preliminary assessment of the thermal performance of the new concept proposed in this study was analyzed using a 3D thermal analysis showing the temperature distribution throughout the modules.

© 2022. The Authors. Published by International Solar Energy Society
Selection and/or peer review under responsibility of Scientific Committee
doi:10.18086/eurosun.2022.13.04 Available at http://proceedings.ises.org

2. Challenges of concrete tank concepts

Today, concrete tanks concepts show different drawbacks that need to be overcome to ensure concrete TES deployment. Such drawbacks are:

(i) On-site construction

Laing et al. (2009a) pointed out that the first heating of the new concrete TES is crucial in the process. During this first heating, free water and a certain amount of chemically bound water evaporate, which could lead to excessive vapor pressure damaging the storage module. This pressure is higher the larger the TES module; also, in-situ production involves a higher water content in the concrete than production and curing in a controlled environment.

(ii) Different thermal expansion coefficients of steel and concrete

The difference between the thermal expansion coefficients of steel (heat transfer fluid pipes) and concrete can lead to cracks in the concrete, and erosion of the concrete by the friction of both materials, damaging the modules and causing a decrease of the contact surface between the storage material and the heat transfer fluid as the operating cycles of the system increase.

According to Laing et al. (2006), the thermal expansion in the axial direction of one of their concrete modules with a steel heat exchanger was 120 mm, therefore, the modules did expand by approximately 60 mm at the end. During cycling at operating temperatures, the temperature difference should only be about 40 K, so the movement would be less than 10 mm at each end. In this prototype, this was compensated using two metal sheets that acted as sliding planes.

Hoivik et al. (2019a) also mentioned the fact that different thermal expansion coefficients have to be taken into account, without giving further details, and investigated improvements to the materials to match their thermal expansion values. However, even if the concrete and metal pipes have similar thermal expansion coefficients, the thermal conductivity of the two materials is different, so during the cycle, the steel will reach temperature before the concrete, which will generate differential expansions.

(iii) Poor thermal conductivity of concrete

According to Asadi et al. (2018), concrete has a thermal conductivity between 0.4 W m^{-1} K^{-1} and 1.01 W m^{-1} K^{-1}. The addition of some components such as copper wires or phase change materials (PCM) may bring this thermal conductivity up to 3.84 W m^{-1} K^{-1}, but it can also decrease to 0.21 W m^{-1} K^{-1} .

Efforts to increase the thermal conductivity of concrete to be used in high temperature TES show that the use of calcium aluminate cement (CAC) brings higher thermal conductivity (up to 5 W m^{-1} K^{-1}) (Lucio-Martin et al., 2021), and the use of metal fibres shows an increase up to 2 W m^{-1} K^{-1} (Miliozzi et al., 2021). Finally, the literature shows that thermal cycling can lead to a decrease in thermal conductivity, usually attributed to an increase in open porosity (Boquera et al., 2021; Roig-Flores et al., 2021).

Therefore, it is possible to increase the thermal conductivity of concrete with improved formulations.

(iv) Thermal oil or molten salts with limited operating temperature range

Vignarooban et al. (2015) presented the thermophysical properties of commonly used heat transfer fluids (HTFs) in CSP plants. According to the data presented, the maximum temperature that the thermal oils (mineral or synthetic) can withstand is 450 ºC, therefore they cannot be used in CSP plants working at higher temperatures. Moreover, the other commercial HTF, molten salts, can theoretically withstand 600 ºC (Arias et al., 2022). Therefore, future CSP plants are considering the use of air as HTF (Bilal Awan et al., 2020).

(v) Migration of the HTF into the concrete

The use of thermal oils or molten salts as HTF when there is direct contact between the HTF and concrete would lead to migration of the HTF into the concrete, but also the contrary, contamination of the HTF by concrete components. The use of air as HTF avoids such migration and contamination, however, the low conductivity of the air presents new challenges to overcome.
In the design by Laing et al. (2008), the idea of using a tubeless design was investigated. The advantages of low

cost and direct heat transfer were identified as the main drivers to go in this direction. Nevertheless, according to the authors, the concrete did not allow for a high enough level of impermeability, even when restressed, causing leaks of the oil. Moreover, in this design, the pipe-storage unit junction became a technical challenge.

The challenges identified related to the use of concrete as high temperature storage medium can be summarized according to Fig. 1.

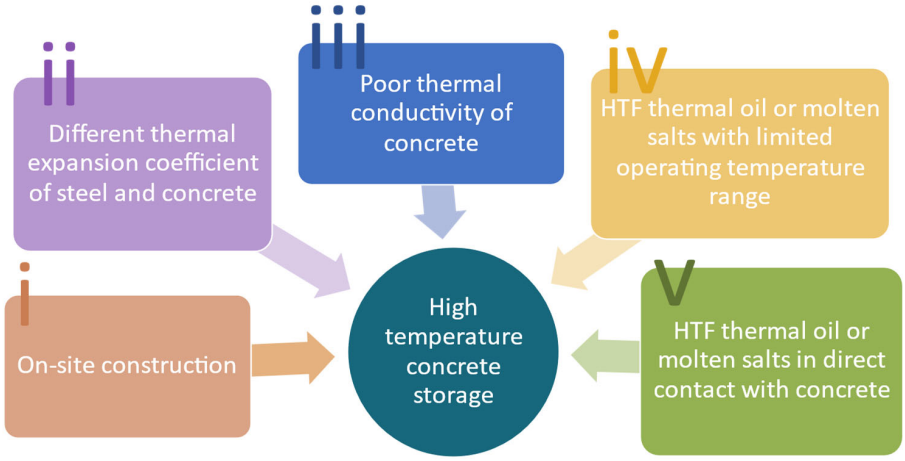

Fig. 1. Challenges of high temperature concrete

3. New concept proposal

To address the challenges presented in section 2, a new concrete TES design developed in Autodesk Fusion 360 (Autodek, 2022) is presented in this paper. The new concept is designed to work with air as HTF, and is based on hexagonal geometry concrete blocks of 460 mm diameter and 2000 mm height (Fig. 2) with a modular design with simple direct-fit male-female connections (Fig. 3). The blocks were designed to be stacked (Fig. 4a) and nested (Fig. 4b) to suit the thermal needs of the installation and the space available. To meet challenge (i), the design is based on a modular concept with blocks of relatively small dimensions that allow them to be manufactured in a controlled industrial environment and then transported to the installation site. In addition, to meet challenge (ii), the blocks are made exclusively of concrete, eliminating the need for metallic piping and thus the problems of thermal expansion differences between materials. Related to challenge (iii), a concrete mixture with improved thermal properties (Boquera et al., 2022) was implemented in the model, nevertheless, this challenge remains the subject of future work by optimizing the thermophysical properties of the simulated concrete with new materials that are being experimentally validated. Finally, the temperature limitation of molten salts and thermal oils, and their migration into the concrete due to the non-use of metallic pipes (challenges (iv) and (v)) are solved by using air as HTF.

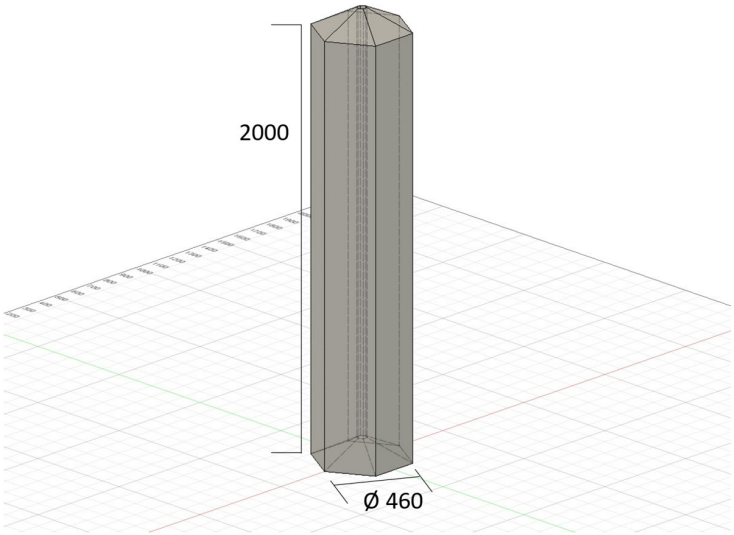

Fig. 2. Concept of concrete block and block dimensions [mm]

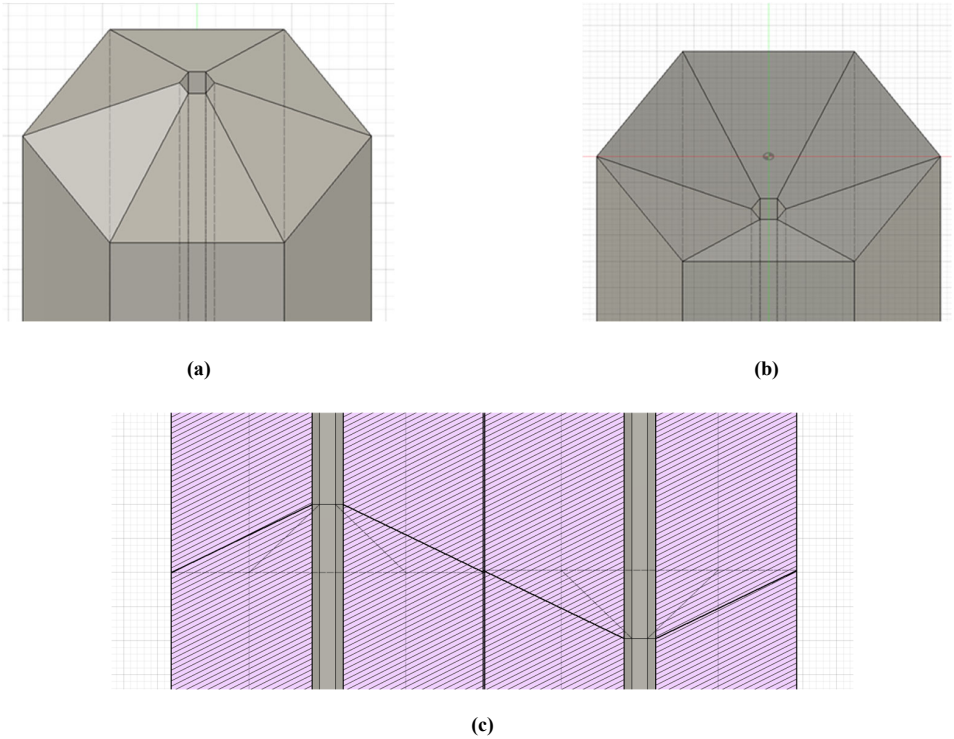

(a) **(b)**

(c)

Fig. 3. Concrete concept: (a) fitting connections, (b) stacked distribution example, and (c) connection points

In order to analyze the performance of the modular block design, a storage tank of 10 MWh (temperature of operation 265 ºC – 1000 ºC) was developed (Fig. 4a) and simulated for static thermal analysis to determine the fully charged steady-state temperature distribution and resultant heat flow. The tank consists of 57 concrete blocks distributed in three columns (Fig. 4a) of 19 blocks in a honeycomb distribution (Fig. 4b), two metallic collectors, and initially with a layer of 140 mm of calcium silicate board as insulation.

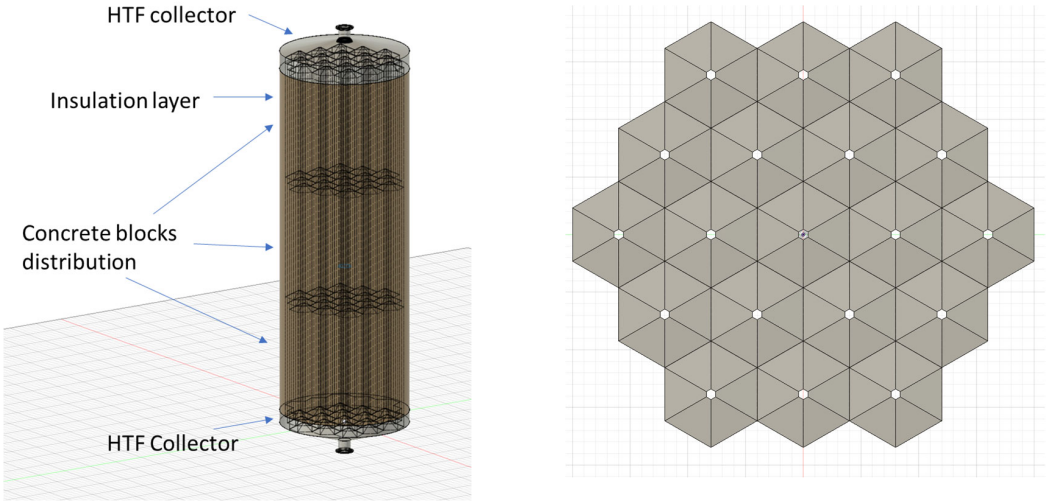

(a) (b)

Fig. 4. Concrete concept storage: (a) complete storage and (b) blocks distribution

The thermophysical properties of the concrete were extracted from Boquera et al. (2022) and shown in Tab.1. Moreover, Tab. 2 shows the insulation material properties used from the Autodesk database. In both cases, an isentropic model of the material with linear behavior was considered. Finally, the mesh dimensions were set to automatic with the parameters of Tab. 3.

Tab. 1. Thermophysical and optical properties of concrete implemented in the model

Property	Size
Thermal conductivity [W m^{-1} K^{-1}]	1.01
Density [kg m^{-3}]	2.7
Specific heat [kJ kg^{-1} K^{-1}]	1.2
Thermal expansion coefficient [µm m^{-1} K^{-1}]	1
Emissivity [-]	0.95
Transmissivity [-]	0

Tab. 2. Thermophysical and optical properties of the insulation material implemented in the model

Property	Size
Thermal conductivity [W m^{-1} K^{-1}]	0.002
Density [kg m^{-3}]	0.23
Specific heat [kJ kg^{-1} K^{-1}]	3.1
Thermal expansion coefficient [µm m^{-1} K^{-1}]	1
Emissivity [-]	0.2
Transmissivity [-]	0

Tab. 3. Simulation mesh parameter

Property	Size
Resolution factor	1
Edge growth rate	1.1
Minimum points on edge	2
Points on the longest edge	10
Surface limiting aspect ratio	20

The analysis was carried out by performing a full charge test of the tank at an initial temperature of 265 ºC simulating a real storage cycle and maintaining an applied temperature in the HTF of 1000 ºC until reaching a steady state. The results are shown in relation to the temperature distribution (Fig. 5a), heat flux (Fig. 5b), and thermal gradient (Fig. 5c). The analysis demonstrates that the honeycomb design manages to maintain a homogeneous distribution in the blocks without generating hot spots. However, due to the temperature difference between the concrete and the ambient temperature, the insulation becomes a critical factor in the design of the TES. For this purpose, the simulation was performed one more time, keeping the same conditions but increasing the thickness of the insulation layer of the tank from 140 mm to 280 mm (Fig. 6). Fig. 6 shows that the increase of the insulation reduces the temperature on the outer surface of the insulation by 30 ºC, therefore decreasing the thermal losses of the TES, and achieving a higher energy storage density.

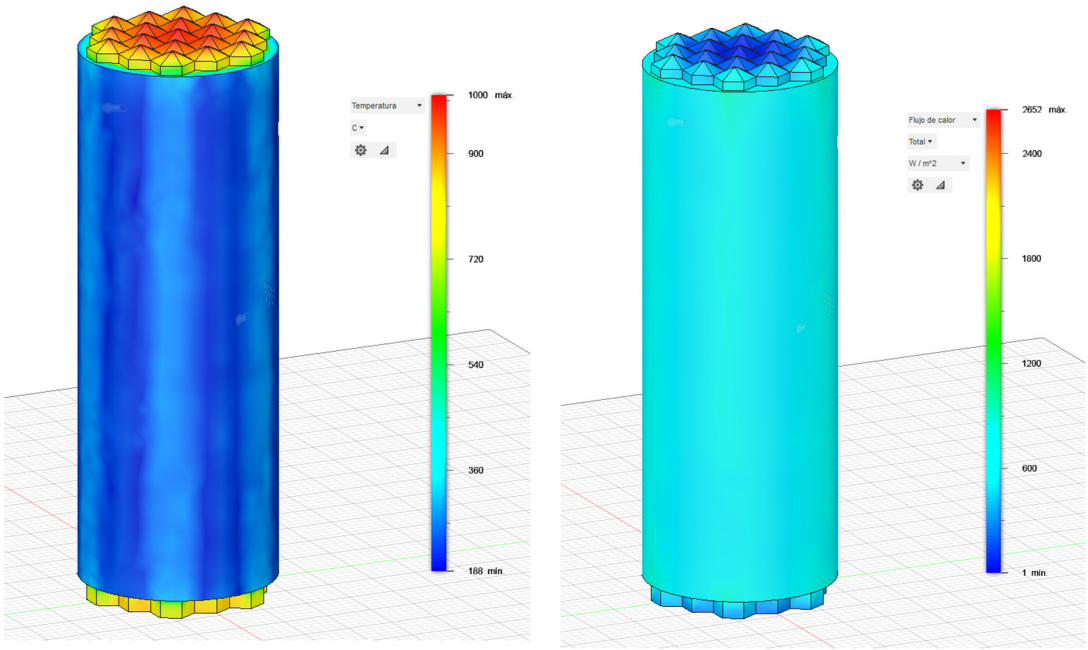

(a) **(b)**

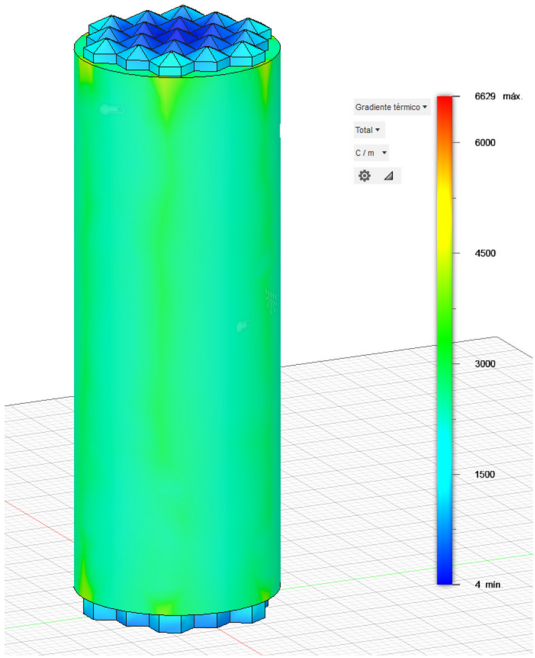

(c)

Fig. 5. Concrete concept storage steady-state thermal analysis: (a) temperature distribution (in ºC), (b) heat flux (in W m^{-2}), and (c) thermal gradient (in K m^{-1})

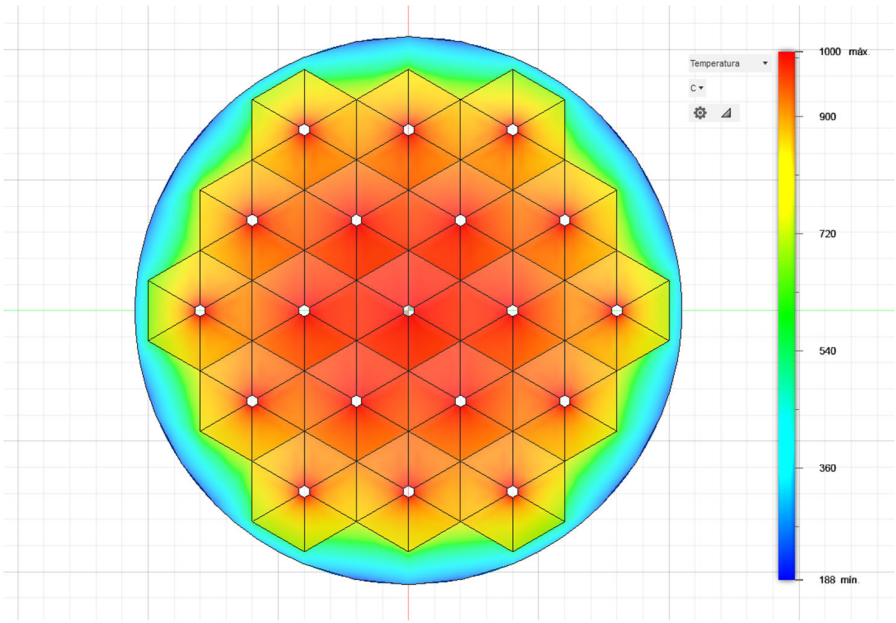

(a)

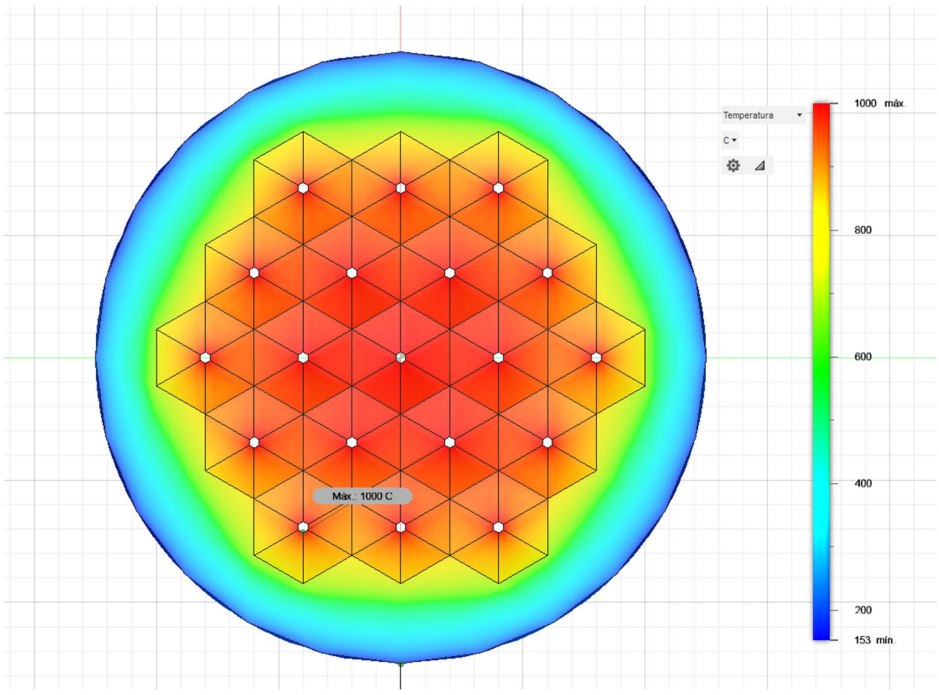

(b)

Fig. 6. Concrete concept storage steady-state thermal analysis: (a) analysis with 140 mm thick insulation and (b) analysis with 280 mm thick insulation

4. Conclusions

High temperature thermal energy storage has shown great potential to increase the penetration of renewable energies in the energy mix. The use of concrete represents a viable option due to its versatility, relatively low cost, and the possibility of reaching a high operating temperature above 565 °C. However, to become technologically and economically feasible, concrete storage systems must overcome a number of challenges.

This paper, through a comprehensive literature review, identified and analyzed the five key issues that current systems present. These are: (i) in-situ construction, (ii) different thermal expansion coefficient of steel and concrete, (iii) poor thermal conductivity of concrete, (iv) HTF thermal oil or molten salts with limited operating temperature range, and (v) migration of oil/salt into concrete in direct contact.

Considering the challenges identified, a first approach to a novel design of a high temperature thermal energy storage system with concrete was proposed and analyzed using thermal steady-state analysis techniques. The new design is composed of modular concrete blocks with direct-fit male-female connections and hexagonal design. These were designed to be stacked and interlocked in a honeycomb shape, thus enabling quick and easy customized sizing according to energy needs. The novel design proposed was able to overcome 4 of the 5 challenges identified. Only the low conductivity of the concrete remains to be further studied in future works. In addition, the plug and play design facilitates the construction of the modules, which can be manufactured under controlled conditions, guaranteeing the properties of the concrete.

Moreover, the streamlined design of the modules, the large abundance of material used, the potential low manufacturing cost once implemented on an industrial scale, as well as the results of the simulations present the proposed design as a highly competitive thermal energy storage solution. However, this new design also presents new challenges to be overcome such as the low specific heat capacity and convective heat transfer coefficient of the air used as heat transfer fluid, the tight junction between modules, and the debris of the concrete interacting with the HTF. Furthermore, the design of high temperature storage presents new challenges for adequate insulation. Therefore, material selection and optimal sizing of the insulation should be the subject of future studies.

Moreover, future work will address the following topics: analysis of the proposed design with other concrete

formulations or the addition of aggregates to increase the thermal conductivity of the storage material while maintaining the specific heat values; optimization of the design to improve the coefficient of internal convection to overcome the low conductivity of the air when it is used as HTF; the analysis of the connection between the modules and the heat supply/demand.

5. Acknowledgements

This work is part of PCI2020-120695-2 projects funded by Ministerio de Ciencia e Innovación - Agencia Estatal de Investigación (MCIN/AEI/10.13039/501100011033) and by the European Union "NextGenerationEU"/PRTR". This work was partially funded by the Ministerio de Ciencia, Innovación y Universidades de España (RTI2018-093849-B-C31 - MCIU/AEI/FEDER, UE) and by the Ministerio de Ciencia, Innovación y Universidades - Agencia Estatal de Investigación (AEI) (RED2018-102431-T- MCIU/AEI). The authors would like to thank the Catalan Government for the quality accreditation given to their research group GREiA (2017 SGR 1537). GREiA is a certified agent TECNIO in the category of technology developers from the Government of Catalonia. This work is partially supported by ICREA under the ICREA Academia programme.

6. References

Arias, I., Cardemil, J., Zarza, E., Valenzuela, L., Escobar, R., 2022. Latest developments, assessments and research trends for next generation of concentrated solar power plants using liquid heat transfer fluids. Renewable and Sustainable Energy Reviews. https://doi.org/10.1016/j.rser.2022.112844

Asadi, I., Shafigh, P., Abu Hassan, Z.F. bin, Mahyuddin, N.B., 2018. Thermal conductivity of concrete – A review. Journal of Building Engineering 20, 81–93. https://doi.org/10.1016/j.jobe.2018.07.002

Autodek, 2022. Autodesk Fusion 360 [WWW Document]. URL https://www.autodesk.es/products/fusion-360/overview (accessed 9.7.22).

Bilal Awan, A., Khan, M.N., Zubair, M., Bellos, E., 2020. Commercial parabolic trough CSP plants: Research trends and technological advancements. Solar Energy 211, 1422–1458. https://doi.org/10.1016/j.solener.2020.09.072

Boquera, L., Castro, J.R., Pisello, A.L., Fabiani, C., D'Alessandro, A., Ubertini, F., Cabeza, L.F., 2022. Thermo-mechanical stability of supplementary cementitious materials in cement paste to be incorporated in concrete as thermal energy storage material at high temperatures. J Energy Storage 54, 105370. https://doi.org/10.1016/j.est.2022.105370

Boquera, L., Castro, J.R., Pisello, A.L., Fabiani, C., D'Alessandro, A., Ubertini, F., Cabeza, L.F., 2021. Thermal and mechanical performance of cement paste under high temperature thermal cycles. Solar Energy Materials and Solar Cells 231, 111333. https://doi.org/10.1016/j.solmat.2021.111333

Hoivik, N., Greiner, C., Barragan, J., Iniesta, A.C., Skeie, G., Bergan, P., Blanco-Rodriguez, P., Calvet, N., 2019a. Long-term performance results of concrete-based modular thermal energy storage system. J Energy Storage 24, 100735.

Hoivik, N., Greiner, C., Barragan, J., Iniesta, A.C., Skeie, G., Bergan, P., Blanco-Rodriguez, P., Calvet, N., 2019b. Long-term performance results of concrete-based modular thermal energy storage system. J Energy Storage 24, 100735. https://doi.org/10.1016/j.est.2019.04.009

Laing, D., Lehmann, D., Fi, M., Bahl, C., 2009a. Test results of concrete thermal energy storage for parabolic trough power plants. Journal of Solar Energy Engineering, Transactions of the ASME 131, 0410071–0410076. https://doi.org/10.1115/1.3197844

Laing, D., Lehmann, D., Fi, M., Bahl, C., 2009b. Test results of concrete thermal energy storage for parabolic trough power plants. Journal of Solar Energy Engineering, Transactions of the ASME 131, 0410071–0410076. https://doi.org/10.1115/1.3197844

Laing, D., Steinmann, W.-D., Fiß, M., Tamme, R., Brand, T., Bahl, C., 2008. Solid Media Thermal Storage Development and Analysis of Modular Storage Operation Concepts for Parabolic Trough Power Plants. J Sol

Energy Eng 130. https://doi.org/10.1115/1.2804625

Laing, D., Steinmann, W.-D., Tamme, R., Richter, C., 2006. Solid media thermal storage for parabolic trough power plants. Solar Energy 80, 1283–1289. https://doi.org/10.1016/j.solener.2006.06.003

Lucio-Martin, T., Roig-Flores, M., Izquierdo, M., Alonso, M.C., 2021. Thermal conductivity of concrete at high temperatures for thermal energy storage applications: Experimental analysis. Solar Energy 214, 430–442. https://doi.org/10.1016/j.solener.2020.12.005

Miliozzi, A., Dominici, F., Candelori, M., Veca, E., Liberatore, R., Nicolini, D., Torre, L., 2021. Development and characterization of concrete/PCM/diatomite composites for thermal energy storage in CSP/CST Applications. Energies (Basel) 14, 4410. https://doi.org/10.3390/en14154410

REN21, 2020. Renewables 2020 Global Status Report, REN21 Secretariat.

Roig-Flores, M., Lucio-Martin, T., Alonso, M.C., Guerreiro, L., 2021. Evolution of thermo-mechanical properties of concrete with calcium aluminate cement and special aggregates for energy storage. Cem Concr Res 141, 106323. https://doi.org/10.1016/j.cemconres.2020.106323

Vignarooban, K., Xu, X., Arvay, A., Hsu, K., Kannan, A.M., 2015. Heat transfer fluids for concentrating solar power systems – A review. Appl Energy 146, 383–396. https://doi.org/10.1016/j.apenergy.2015.01.125

Load Management for Seasonal Heat Storage Applications based on Sorption Storage Technology

Nayrana Daborer-Prado[1], Bernhard Zettl[1], Issayan Gayaneh[1] and Lukas Gaisberger[1]

[1] University of Applied Sciences Upper Austria – Research group ASIC, Wels (Austria)

Abstract

Based on the current energetic scenario worldwide, it is possible to observe that the necessity of storing the large supply of solar energy available during summer and using it during winter, when the accessible quantity of energy is not so big, is greater than ever. Therefore, seasonal storage systems with both, high energy density and low thermal losses, are needed. Energy storage systems based on thermochemical materials like zeolite, such as the one described in this study, are the most adequate option to achieve this goal, due to their potential to fulfill both requirements earlier described. In the scope of this study a load management strategy was developed for a sorption storage system in which the material should be dried during summer and used during winter, working this way as a seasonal heat storage. The first results show the creation of the two storage containers, dryer and divider and how the weather data used can influence the system.

Keywords: Sorption, Storage, Thermochemical materials, Zeolite

1. Introduction

A broad deployment of energy storage technologies for an increased share of renewable energy is motivated by global climate action and the ambition of CO_2 reduction (Daborer-Prado, et al. 2020). Industrial waste heat, building integrated renewable energy generation, surplus heat but also electricity of power plants and grids which show fluctuation and volatile behavior, are reaching dimensions worth storing energy in larger quantities. Depending on the involved temperature levels the potential energy savings can be considerable, the highest being for the low temperatures ranging from 50 to 150°C.

Taking that into account, thermal energy storages (TES) are believed to be appropriate candidates to play an important role in the future thermal management system. They can be defined as the temporary storage of thermal energy at high or low temperatures for diverse periods of time, this way preventing the loss of thermal energy. TES systems have an important capacity of making the use of thermal equipment more effective and represent a relevant way of decreasing the mismatch between thermo-availability and demand, providing also an environmental and economic benefit by reducing the need for burning fuels (N. Daborer-Prado 2019).

The TES systems can be classified depending on the temperature range, primary heat source, storage material, storage duration and field of application. Regarding the physical storage principle, it can be categorized in the following forms (Haider und Werner 2013):

- Sensible heat storage
- Latent heat storage
- Thermochemical heat storage

Figure 1 presents the classification of thermal energy storage materials according to the state in which the TES reveal itself.

© 2022. The Authors. Published by International Solar Energy Society
Selection and/or peer review under responsibility of Scientific Committee
doi:10.18086/eurosun.2022.13.05 Available at http://proceedings.ises.org

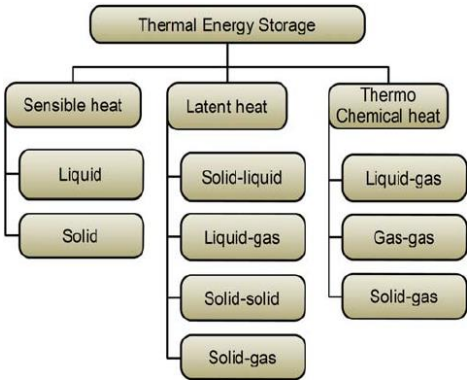

Figure 1: Classification of thermal energy storage technology based on the criterion of the state of the energy storage material. Source: *(Hauer, et al. 2020)*

The ability of thermochemical materials (TCM) to store energy long-term with practically no losses during the conservation phase makes them promising candidates for seasonal storage applications (Hauer, et al. 2020), (Issayan und Zettl 2021). High energy densities using the zeolite-water couple have been demonstrated for some applications, exceeding those of water storage by a factor of 2-3 (Issayan und Zettl 2022), (Issayan, Zettl und Somitsch 2021). Zeolites are crystalline aluminosilicates of alkali or alkali earth elements, such as sodium, potassium, and calcium. When dehydrated zeolite gets in contact with water vapor, the water molecules enter the internal crystal lattice and causes an adsorption reaction that leads to the release of heat. The reverse process happens when zeolite is heated to more than 100°C (desorption), when the water molecules are released from the sorption material. The adsorption/desorption process in zeolites can be repeated multiple times with practically no deterioration of the material (Socaciu 2012).

The physical principle of the sorption cycle is demonstrated in Figure 2: Gaseous water molecules can accumulate on the surface of the solid, releasing heat from binding and condensation (adsorption), when the temperature increases or the partial pressure decreases, the substances separate again (desorption).

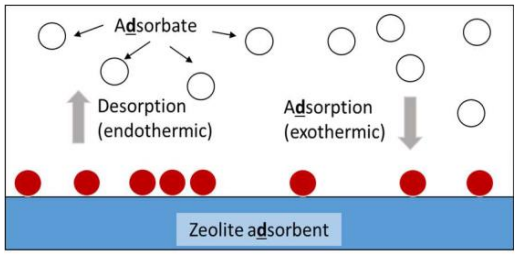

Figure 2: Adsorption principle - water vapor is attracted to the surface of another (solid) matter and heat is released. Meanwhile, the reversed process is the desorption

There are several process solutions for sorption technology, open and closed systems, as well as moving-bed and fixed-bed reactions, which have specific advantages (Hauer, 2020), (Krese, et al. 2018):

- Open: the reactor containing the sorbent material is at atmospheric pressure and throughout the charging process a dry air stream is conducted to it. One of its advantages is that it does not require the use of condensers, evaporators, or working fluid storage reservoirs, having this way a simpler and cheaper design when compared to closed systems.
- Closed: the reactor is under vacuum condition and requires one or more condensers and evaporators. The entire system is sealed from the surroundings and only water can flow through the conduct passage that connects the reactor to the evaporator/condenser. The reactor contains the reactive sorbent, and the condenser/evaporator is where the liquid water is collected.

The open moving bed reactions in particular offer the possibility of being able to freely dimension energy content and performance (B. Zettl 2020), (B. Zettl 2022). Air is used here as a moisture and heat carrier to dry the material in portions during the loading cycle. As this is a seasonal storage tank, the loading process is carried out in the summer during periods of high solar gains. However, storage loading requires a targeted strategy to take site-specific and environmental factors into account. Forecast models and learning algorithms are necessary for the energy management of the load. In contrast to large (fixed bed) storage vessels, the zeolite of a moved bed system

is heated up in small batches for shorter time periods for minimizing heat losses. The batch-wise treatment brings up the risk for under/over-dehydration of the batches that could sum up to a severe reduction of efficiency during the summer season. Several model predictive control schemes have been proposed to exploit the diversity of the available energy sources. (Darivianakis, et al. 2017) investigated a data driven stochastic optimization approach for the seasonal energy management. It uses available historical data to build bounds that present a high probability of holding an optimal charging trajectory of the seasonal storage and generates a piece-wise approximation of the value function of the energy stored in the seasonal storage at each time step. (Parisio, Vecchio und Vaccaro 2012), on the other hand, presented optimization approaches for the energy management in energy hubs.

In this study, a model of the charging management and optimization algorithms is presented in order to be able to achieve the goal of the most complete possible regeneration of the TCM at the end of the charging cycle, and to display the changes of the dehydration result due to deviations of weather profiles from the representative average.

2. Methods and methodology

2.1. Application principle

The thermochemical storage with zeolite consists of two containers for dry and moist material as well as a dryer and an adsorption reactor, which was previously described (Zettl, 2020). During the heating period, one container with dehydrated zeolite is emptied in portions to provide heat for heating and hot water and stored in the humid material container. In central European climate approx.100 portions of the storage material should be available for 100 heating days.

In summer, the storage material is regenerated by renewable energy that has a daily cycle. The material is removed from the container, then heated, and dehumidified in the dryer. The material is then stored in the second container or transported back to the wet container if it has not dried sufficiently. Depending on the drying result, there is an inhomogeneous material moisture content in the two containers, which, however, levels out again after several days of storage. This leveling process and the desorption processes in the dryer are to be simulated. Furthermore, a control strategy should be achieved in order to decide whether the material is transported back into the moist or into the dry container.

The daily cycle is assumed to consists of 10 consecutive steps with one hour duration each during the daytime, at night local moisture differences tend to equalize in the container. After every hour, one-tenth of the daily portion is transported to the dryer, where it is desorbed and then moved, based on the decision of the material switch to the target container. After approximately 150 days of sufficient regenerative energy, all 100 daily portions of the material have dried. A seasonal storage should complete its loading cycle by the end of summer therefore weather profiles from 1st of May until 30th of September are considered for simulation runs

For simulation purpose, the model of the container is to be divided into 1000 cells (batches of hourly treatment). All cells are arranged in serial (first in/first out), in a use case each cell would correspond to a material quantity of approx. 5-10 kg of zeolite. The material in each cell has a dimensionless homogeneous moisture content (0 to 1) in this study. The material temperature and thermal losses are ignored so far, the dehydration is simply related to the energy gain from the solar generator. Figure 3 is a graphical representation of how the system works.

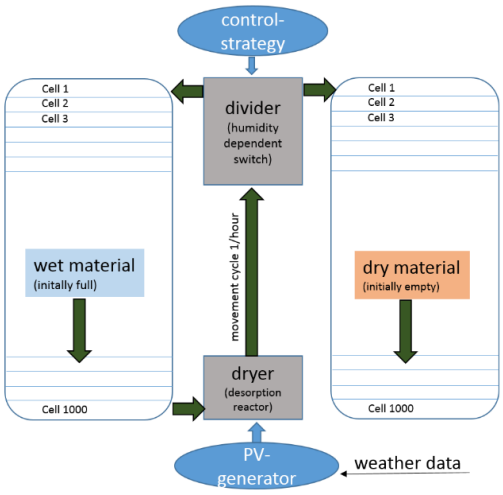

Figure 3: Principle of the material desorption cycle. Desorption is obtained by drying the TCM and transportation to one of the containers depending on the management strategy of the divider component

3. Results and discussion

3.1. Model implementation

The first step of this work was to create a mathematical model for the container. The moisture equalization process between the cells was represented as a conduction process, meaning that the higher the moisture difference between two neighboring cells, the more moisture is exchanged per unit of time, but no thermal process was considered.

In the simulation model, a characteristic constant that controls the conduction was chosen. This constant should work in a way that the leveling takes place up to a maximum difference of 1% (from one cell to its neighbors) within 24 or 48 hours. In practice, the greater the constant, the faster the process will take place. For clarity, Figure 4 and Figure 5 present the first results obtained by the creation of a mathematical model for the container and its behavior when an arbitrary change in humidity in certain cells takes place.

In both results, the first 10 cells had their humidity from 100% to 80% changed. Although the whole container presents 1000 cells, to better observe the outcomes, just the first 50 cells are shown in the graphs. The difference between the results lies in the humidity leveling factor used. In Figure 4, the factor was 0.1, and in Figure 5, it was 0.4. It is possible to observe that the higher the factor, the faster the humidity inside the container equalizes.

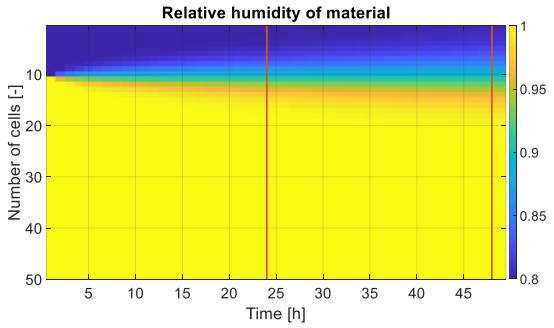

Figure 4: Relative Humidity in container with humidity leveling factor 0.2, leveling after 48 h

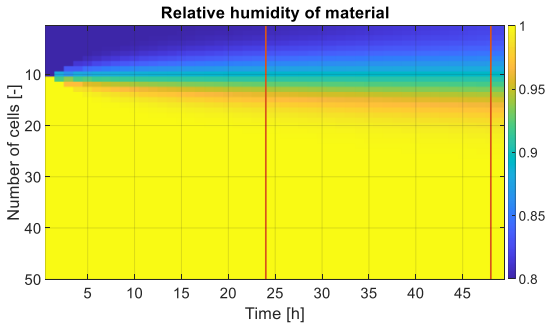

Figure 5: Relative Humidity in container with humidity leveling factor, leveling after 24h

As previously mentioned, the next step of the study was to add a second container to the model, as well as a material divider and a dryer. The second container was created based on the code of the first, with the difference that, the second container is initially empty and must be filled with dried material along the summer in a timeframe of 150 days. To avoid ambiguity, the first and second container will be named Drying and Store, respectively.

Dryer

The dehydration process is described in principle by a zeolite adsorption/desorption model already published. This model describes the increase or reduction of the material water content based on the applied process temperature and vapor pressure in the reactor (dryer). For simplification, the storage system including the dryer is operated on a dimensionless humidity factor (0 to 1) so far, and a nonlinear humidity reduction factor of the dryer (based on the input energy or solar irradiance).
For simulation a weather data was included in the model to simulate how the drying process will work based on the different solar irradiation values during the examined timeframe. Aiming to test the model with different types of data, three different files were extracted from the Carnot library (Juelich 2020):

- Weather of an average year
- Weather of an extreme summer
- Weather of an extreme cold summer

Depending on the solar irradiation input, the drying effect simulated in the dryer can be higher or lower. This effect is controlled by a lookup table created in the model. Essentially, the highest irradiance value will generate a drying effect of the material up to 80% The lowest irradiance measurement, usually zero, correspondingly represents a drying effect of zero as well. The irradiation values in between represent a drying effect ranging from 5% to 75% in a non-linear manner. During the night, the only process happening in the containers is the equalization of the moisture in the material stored.

Divider

Regarding the mathematical model of the divider, an operation principle was developed, in order to determine which action (transportation to one of the two containers) should take place after the material went through the dryer. During phase one (day 1 to 50) all material going through the drying process should be transported back to the Drying container in order to be dried once more, unless it has reached the “Low threshold”. In this case the material is then transported to the Store container. During the second phase (day 51 to 150), a variable threshold is set to define the minimum humidity in order to reach complete filling of the Store container. For that a “High threshold“ is set that represents the highest allowed humidity in the container for the “worst case” weather situation. Based on that, if the material’s humidity is higher than the threshold, it is transported back to the Drying container to be dried again and respectively, if the humidity is equal or lower the threshold, the material will be transported to the Store container The values for the "High threshold” and the “Low threshold” where obtained using the extreme (hot and cold) weather data set like explained in the next section.

3.2. Results

For the first results, the following input parameters were considered:

- Humidity leveling factor (hf): 0.4
- Divider threshold: 50%
- Number of cells in container: 1000
- Time: 150 days
- Average summer weather data

Figure 6 and Figure 7 present how the humidity inside of the containers change with time. The color bar on the right side displays the humidity of each cell, the dark blue cells have a material humidity between 0 and 30%, the light blue and green present a humidity between 40 and 60%, while the yellow cells have a humidity between 80 and 100%. It is possible to observe that in the drying container all the cells start the process with 100% humidity. As it was mentioned before, the material on the bottom of the container is removed to be dried and then it is placed back on the top of the container with a lower humidity, therefore as it can be seen, the humidity starts to change from the top to the bottom.

The equalizing process can also be noticed in Figure 6. Here the color of the cells goes from orange (80% humidity) back to yellow (100%) in the beginning of the drying season and then from green (60%) back to orange between days 60 and 100. Since no solar radiation is present during the night-time, the material stays in the Drying container and does not go through the dryer, therefore the humidity in the cells start to influence one another, meaning that the cells with less water content will absorb some from the cells with more water.

In Figure 7 it is possible to note that when the material is below the threshold humidity of 49% it is then transported to the Store container. By the end of the 150 days all material is transported to the Store container using the parameter defined above. Here, all the cells are represented in blue because of their similar humidity (around 40%-60%). Nevertheless, since each cell enter the container with a respective water content, the equalization process also takes place in this container.

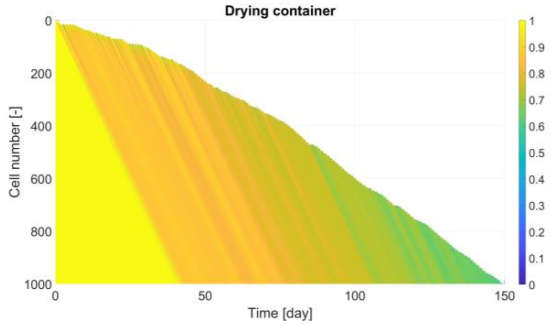

Figure 6: Humidity in the Drying container with 1000 cells and average weather

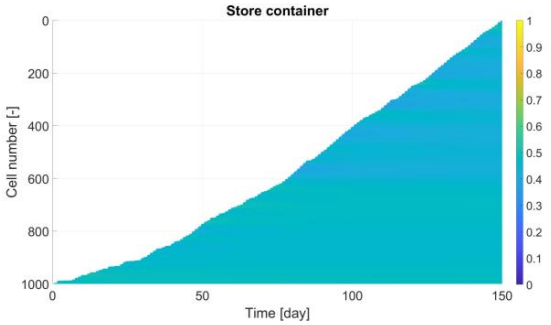

Figure 7: Humidity in the Store container with 1000 cells and average weather

Aiming to understand how the system behaves in different years, several varying weather data sets were used. In a real system, the solar generator and dryer operation hast to be sufficient to reach the storage requirements. In the simulation model that step corresponds to varying Heat transfer factors. In a given system, the threshold of humidity inside of the Store container can be raised or lowered, allowing different grades of humid material to be stored. Both operations can be implemented or just one of them, depending on the desired result.

Figure 8 and Figure 9 present the results using the following input parameters:

- Humidity leveling factor (hf): 0.4
- Divider threshold: 47%
- Number of cells in container: 1000
- Time: 150 days
- Extreme (warm) summer weather data

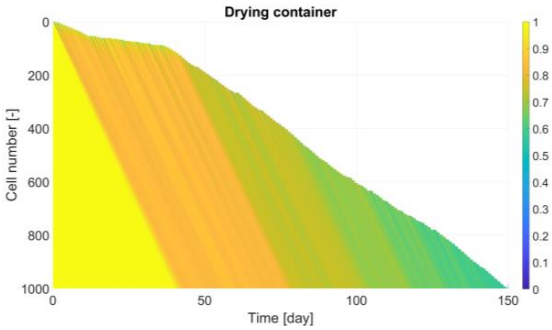

Figure 8: Humidity in the Drying container with 1000 cells and extreme summer weather

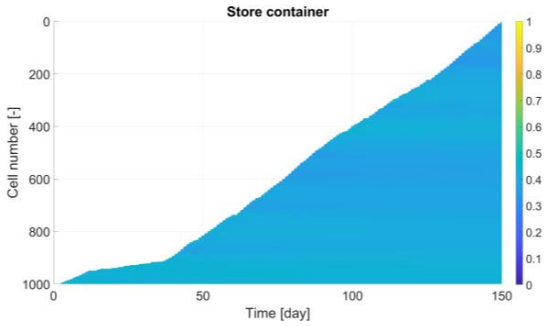

Figure 9: Humidity in the Store container with 1000 cells and extreme summer weather

Figure 8 presents similar behavior observed in Figure 6, but due to a weather data set that represents a hot summer, the divider threshold was set to 47%. Here the equalization also takes place during the night- time and it is also possible to observe the change in the colors of the cells from yellow (100% water content) till green (60%) by the

end of the season in the humid material container. The reason why the threshold of the divider is changed in this case is because the days of the extreme summer weather data present a higher irradiation value when compared to the average year weather data.

Figure 9 presents the humidity of the cells that were transported to the Store tank. It is possible to notice that in this case the material transported to the Store container presents darker shades of blue when compared to the material dried with an average year data. This means that during the year with a hot summer, the material will present lower water content as in a year with average irradiance values.

The following results were obtained by using a cool weather regime data. In this case the divider threshold had to be increased to 0.54 in order to have all the material in the Store tank by the end of the drying season. The following parameters were implemented:

- Humidity leveling factor (hf): 0.4
- Divider threshold: 54%
- Number of cells in container: 1000
- Time: 150 days
- Extreme cold weather data

As in the previous results, Figure 10 present how the cells behave inside of the Drying container before they reach the threshold and are moved to the Store container. In this case it is possible to notice that the orange area representing a humidity between 80 and 90% is larger in comparison with the other results. This means that due to the lower irradiance in this period, the material takes a longer time to be dried. Moreover, since the material that goes to the dryer returns to the Drying container with a water content minimally different from the one it had before the drying process, the equalization of the humidity needs a longer time to be observed.

In Figure 11 the equalization process can also be observed. It is possible to notice that the cells in the Dried container have a lighter shade of blue, which means that the water content lies in between 40 and 60%. In comparison, to the other results, in this case, the material presents the highest humidity by the end of the drying season.

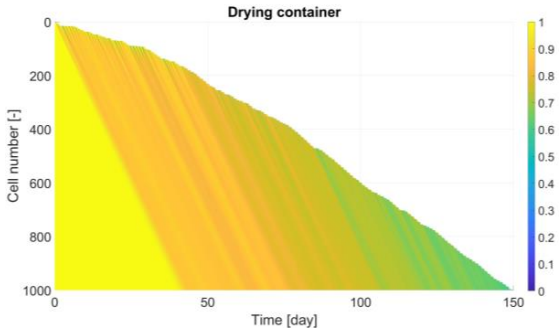

Figure 10: Humidity in the Drying container with 1000 cells and extreme cold weather

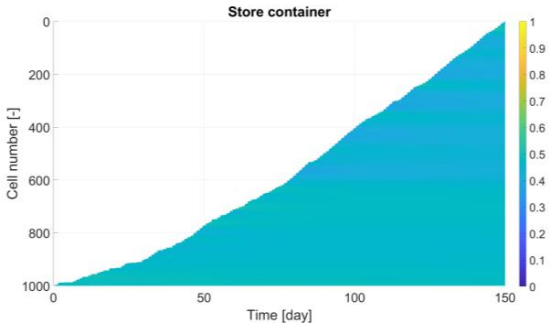

Figure 11: Humidity in the Store container with 1000 cells and extreme cold weather

3.3. Further work

Sorption model

As further steps of this work, an adsorption model will be implemented in the dryer to simulate how the zeolite will be dried based on the performance of a PV generator and the process parameters (temperature and ambient humidity) of a desorption reactor.

The numerical model to be used in this work represents an open sorption storage system with a fixed zeolite bed. An axial humid airflow drives the sorption process and allows direct charging/discharging of the sorption material. The model implementation was previously done in Simulink, an additional package of MATLAB by (Daborer-

Prado, et al. 2020). In order to perform the numerical simulations, the model is based on the following assumptions:

- The model assumes a one-dimensional approach, where no radial influence is considered
- A homogeneous model for storage material and air flow is used, i.e., it is assumed that the air leaves each store node with the node temperature TS(i), where (i) represents the node number
- The specific heat capacities of the solid and air are not function of the humidity or of the temperature in the system
- The sorption equilibrium is modelled by the Dubinin-Astakhov-approach and the reaction kinetics is described by a linear driving force ansatz.
- The specific heat capacity of the air is not a function of the humidity or of the temperature in the system; the specific heat capacity of the solid is only a function of humidity (water loading) but not of the temperature in the system.

Photovoltaic generator

The PV generator block to be used in combination with the sorption model of this project, calculates the DC output of a PV module in W based on the module characteristic parameters (Juelich 2020):

- Pmax: Peak power (Wp) of one module at Standard Test Conditions (STC) [W]
- Dirt and degradation effects
- ΔWp: Temperature coefficient of power drop of Pmax [1/K]

The following equation is used as base for the model calculation of power:

$$P = \frac{Solar\ radiation}{1000} * Incidence\ angle\ modifier * P_{max} * (1 - \left(T_{amb} + 40 * \frac{Solar\ Power}{1000}\right) - 25°C)$$

The incidence angle modifier is 1 for vertical direct solar radiation and the model follows the Fresnel law. The subsequent assumptions were made for the temperature model of the module:

- The module presents 25°C at STC
- 40 K temperature difference to ambient at full solar radiation (1000 W/m²)

Besides the characteristic parameters, the main inputs of the model are a weather data set and the position (azimuth and inclination) of the module.

4. Conclusions

As previously stated, in the past years, with the increase in use of renewable energy sources, the need for new methods of storage solutions is more important than ever. Special attention should be given to systems able to store the large supply of solar energy available during summer and applying it during winter, when the accessible quantity of energy is lower. In this study a seasonal storage system model was developed that should fulfill the aim of having a high energy density and low thermal losses.

In summary, this work presented the creation of two containers (Store and Drying) used to storage the dried and the humid material, respectively. A model for a dryer based on different types of weather data was presented, moreover, the operation principle for the divider was also developed. The results show how the weather data used can influence the system. By using the extreme weather data, the material in the Store container presents the lowest water content by the end of the drying season varying between 30 and 40%. On the other hand, with the extreme winter data, the material has the highest water content values (40-55%).

Further steps of this work are the inclusion of an adsorption model that takes into account the temperature of the ambient and inlet air as well as the material proprieties of the zeolite. Moreover, a PV generator will also be included in the next steps of this project. The generator will be used to power the adsorption system to be included in the dryer system.

5. Acknowledgments

This work is financed by research subsidies granted by the government of Upper Austria and the research project “SorSens- Development of a virtual sensor for State-of-charge determination of sorption heat storage” which is financially supported by the Austrian Climate and Energy Fund (KLIEN) and the Austrian Research Fund (FFG-grant number 881187).

6. References

Daborer-Prado, N., H. Kirchsteiger, B. Zettl, S. Asenbeck, and H. Kerskes. 2020. "Mathematical modeling of rotating sorption heat storages." Solar World Congress 2019 and IEA SHC International Conference on Solar Heating and Cooling. Santiago, Chile. doi:doi:10.18086/swc.2019.22.01.

Daborer-Prado, Nayrana. 2019. Modeling and Simulation of an Innovative Domestic Sorption Storage System. Wels: FH Oberösterreich.

Darivianakis, Georgios, Annika Eichler, Roy S. Smith, and John Lygeros. 2017. "A Data-Driven Stochastic Optimization Approach." IEEE CONTROL SYSTEMS LETTERS 394-399. doi:10.1109/LCSYS.2017.2714426.

Haider, Markus, and Andreas Werner. 2013. "An overview of state of the art and research in the fields of sensible, latent and thermo-chemical thermal energy storage." Elektrotech. Inftech 153-160. doi:https://doi.org/10.1007/s00502-013-0151-3.

Hauer, A., B. Fumey, S. Gschwander, D. Lager, A. Lázaro, C. Rathgeber, A. Ristić, W. van Helden, G. Issayan, and B., Zettl. 2020. Material and Component Development for Thermal Energy Storage. IEA EXES Annex 33- Final Report, p. 82-86, IEA SHC Task 58 / ECES Annex 33.

Issayan, G., and B. Zettl. 2021. "Processing Salt-Hydrates to Thermochemical Storage Composite Materials." 15th International Virtual Conference on Energy Storage ENERSTOCK. Book of Abstracts. p. 95 – 96.

Issayan, G., and B., Zettl. 2022. "Novel Thermogravimetric Characterization Method for Adsorption Cycles of TCM." 15th International Renewable Energy Storage Conference 2021 (IRES2021) AtlantisPress. doi:10.2991/ahe.k.220301.011.

Issayan, G., B. Zettl, and W. Somitsch. 2021. "Developing and Stabilizing Saltydrate Composites as Thermal Storage Materials." 14th International Renewable Energy Storage Conference 2020 (IRES2020). AtlantisPress. p.49-57. doi:10.2991/ahe.k.210202.008.

Juelich, Solar-Institute. 2020. "CARNOT Toolbox Ver. 7.0/2020 for Matlab/Simulink R2018a." Juelich, Solar-Institute.

Krese, Gorazd, Rok Kozelj, Vincenc Butala, and Uros Stritih. 2018. "Thermochemical seasonal solar energy storage for heating and cooling of buildings." Energy and Buildings 239-253. doi:10.1016/j.enbuild.2017.12.057.

Lago, Jesus & Sogancioglu, Ecem & Suryanarayana, Gowri & De Ridder, Fjo & De Schutter, Bart. 2019. "Building day-ahead bidding functions for seasonal storage systems: A reinforcement learning approach." IFAC Papers online 488-493. doi:https://doi.org/10.1016/j.ifacol.2019.08.258.

Parisio, Alessandra, Carmen Del Vecchio, and Alfredo Vaccaro. 2012. "A robust optimization approach to energy hub management." International Journal of Electrical Power & Energy Systems 98-104. doi:https://doi.org/10.1016/j.ijepes.2012.03.015.

Socaciu, L. 2012. "Thermal energy storage: an overview." Applied Math Mech 785-793.

Zettl, B. 2020. "Long-term thermochemical heat storage for low temperature applications." ISES Solar World Congress. p. 397-402. doi:10.18086/swc.2019.08.11.

Zettl, Bernhard. 2022. "State-of-Charge measurement techniques for PCM and TCM." Graz: IEA SHC T67/ ECES Annex 40, 2nd Expert Meeting.

Increasing Renewable Energy Integration Using Residential Thermal Energy Storage

Chris McNevin, Sébastien Brideau and Reda Djebbar

Natural Resources Canada, CanmetENERGY-Ottawa, Ottawa (Canada)

Abstract

A simulation study was conducted to assess the potential of increasing the integration of renewable energy such as wind or solar using thermal energy storage. Several electrically charged residential thermal energy storage technologies being introduced in the Canadian market were simulated in TRNSYS considering space and domestic water heating loads. This included several different configurations of innovative sensible storage, using ceramic bricks, and latent storage, using phase change material (PCM). Additionally, three examples of electric heating systems without storage were modeled. These were an air source heat pump (ASHP), a cold climate air source heat pump (CCASHP), and baseboard heaters. The systems were simulated with four different home archetypes, which are representative of common classifications of homes in Canada, using weather data for Halifax, Nova Scotia, Canada. The energy storage systems increased the renewable usage factor, quite significantly in most cases. It was found that in scenarios with high-performance homes and sensible storage systems, the storage heat losses could lead to the homes overheating. Annual peak time-of-use energy consumption was also able to be reduced, but the specific performance of the thermal storage system type and size of the building load influenced which system performed best.

Keywords: thermal energy storage, solar, wind, renewable integration

1. Introduction

Energy use in Canadian housing, buildings, and communities accounts for about a quarter of Canada's energy consumption (NRCan, 2019) and 17% of GHG emissions (ECCC, 2022). In Canada, residential space heating (SH) consumed 885 PJ of energy in 2016, 47% of which was supplied by natural gas (26% by electricity) (NRCan, 2016). Domestic hot water (DHW) represented an annual load of 284 PJ of which 68% was supplied by natural gas. There is a national effort in Canada occurring to decarbonize the nation's energy loads through clean electrification in order to reduce greenhouse gas emissions (ECCC, 2022). Shifting building space and DHW heating loads to electrically powered systems represents a major increase in electrical energy consumption and would require massive upgrades to the power grid (ICF, 2019). Shifting building heating to clean electricity will require increasing renewable energy production. The temporal and capacity mismatches between the renewable generation and new electrified loads will be an issue that must be overcome. A new system's ability to aid in the management and balancing of the electric grid's power generation and loads is also important to this end (ICF, 2019).

A technology that could aid the clean electrification of the housing sector is the use of residential thermal energy storage (RTES). RTES has the capacity to reduce peak loads on the grid as well as the ability to increase the use of intermittent renewable energy (Gils, 2015). Storing energy allows for the energy to be gained within the system during periods of low demand and/or high renewable generation (i.e., during summer or at night with off-peak electricity). The stored energy is then used to provide heat during times of high demands and on-peak electricity and/or low renewable energy production rather than the energy provided by the electrical grid. The use of thermal energy storage, along with heat pumps (HP) will be a very important component of electrifying heating loads and establishing a clean electricity grid with low GHG emissions (MacCraken, 2020)

This study uses TRNSYS (Version 18) simulations of a variety of integrated storage heat pump residential space heating and DHW electro-technologies to determine the potential impact of these technologies on peak power, total energy consumption, and on the ability to use increased amounts of renewable energy resources (i.e., wind and solar PV) on a selection of different home archetypes. This is a first step in an overall ongoing larger study to model the community-wide application of these technologies in a real community in Eastern Canada.

2. Background

Thermal energy storage has several applications, but a critical one is its use in the building sector to help with the

© 2022. The Authors. Published by International Solar Energy Society
Selection and/or peer review under responsibility of Scientific Committee
doi:10.18086/eurosun.2022.13.06 Available at http://proceedings.ises.org

use and management of renewable energy. A detailed study of all TES technologies and their performance is outside the scope of this study, but a basic background will be provided to provide context to the current study. A recent review of this topic (Sarbu and Sebarchievici, 2018) discussed many examples of different storage technologies to increase the usability of renewable energy and highlighted the types of TES (Fig. 1).

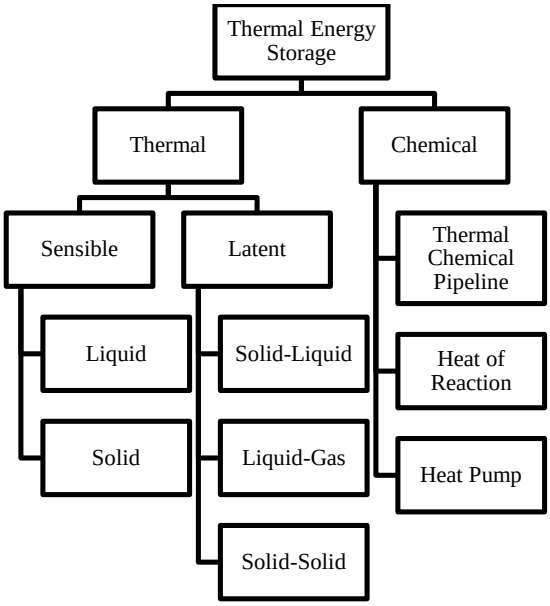

Fig. 1: Methods of thermal energy storage (Sarbu and Sebarchievici, 2018)

The use of thermal energy storage, via PCM storage, has been shown (Stropnik et al., 2019) to boost the performance of highly efficient homes and aid in the nearly net-zero energy operation as the loads in a building can be better distributed and controlled to match the timing of generation of on-site renewable energy. Onsite self-consumption of energy can be increased and stored when excess energy is available for later use. The PCM storage was also shown to help manage temperatures of heating systems to maintain them in temperature ranges which increased efficiency.

Studies have also focused on the ability of energy storage to increase the penetration of renewables and reduce renewable energy curtailments. The increase in self-consumption and peak shaving with battery storage was researched by Luthander et al. (2016) who found that storage capacity had a strong influence on the amount of energy curtailed. This is an interesting note as this study used electrical battery storage and did not electrify heating loads. As fossil-fuel powered heating loads electrify, this presents a large potential for increasing self-consumption, but also requires a larger storage capacity, something that is difficult with electrical battery storage due to the high costs associated with storing electricity electrically.

Thermal storage is a potential method to get around these issues. Hughes (2010) predicted that by using distributed sensible thermal energy storage units, 95% of heating loads in a 500-home reference community could be met with intermittent wind energy (from a 5.15 MW windfarm) in eastern Canada vs. 65% without energy storage and using electric baseboard heaters. In a different study, the combination of heat pumps and thermal energy storage was found to have benefits in reducing GHG emissions and operating costs, mitigating the impacts of variable renewable energy generation, and managing utility peak and base loads (Vorushylo et al., 2018).

Seasonal thermal energy storage in Germany was studied and results indicated that increasing storage to enable higher penetrations of renewable energy also increased lifetime costs (costs including fuel and energy costs, operation and maintenance, and investment costs). A target value of 60-80% renewable energy was recommended to have the best tradeoffs between costs, emissions, and performance (McKenna et al., 2019). Luo et al., (2021) studied a microgrid in China utilizing a CHP power plant, wind power generation, and the implementation of TES systems. The storage was found to reduce operating costs by increasing the amount of wind energy that was able to be utilized. In a study (Agbonaye et al., 2022) of the power grid in Northern Ireland, a region with significant renewable generation from wind power, curtailments were shown to be a significant cost and barrier to adding additional renewable generation. A solution was proposed using an optimized system of distributed thermal energy storage to absorb excess wind generation. The potential was found to reduce constraints by 78% and curtailments by 100%, but optimization found that to manage cost savings for subscribers (i.e., rate payers) a scheme that reduced constraints by 67% and curtailments by 74% was ideal.

These studies all featured similar approaches, but the exact values found for the benefits and performance of the various systems all varied. This highlights the need for location-based study for this application as each region has different renewable generation potential, climates, housing constructions, occupant behavior, operating costs, structures, and other location specific techno economic parameters to be considered.

3. Methodology

This study used the simulation software tool TRNSYS (Klein et al., 2017) to develop detailed models of each of the energy storage systems, as well as the multi-zone home and DHW heating loads and renewable energy generation with a five-minute time step. A Canadian Weather year for Energy Calculation (CWEC) weather file for Halifax, Nova Scotia was used to provide ambient temperature, wind speed, and solar radiation data to the simulation. The time-of-use (TOU) schedule and pricing central to the data analysis and control of the systems are those used by Nova Scotia Power (NSPower, 2021).

3.1 Base Electric Systems with No Storage

Three base case systems without storage were simulated in addition to the storage systems. These were homes heated with an air-source heat pump (ASHP), a cold-climate ASHP (CCASHP), and electric resistance baseboard heaters. The heat pump systems were connected to a central air system, while the baseboard systems featured heaters in each zone of the home.

3.2 Storage Systems

Two different thermal energy storage methods, ceramic brick sensible energy storage and phase change material (PCM) energy storage were studied in a variety of configurations. The operation, capacity, and performance of the ceramic brick sensible storage systems were based on systems that are commercially available (Tab. 1). The PCM storage systems were based on near commercialized systems in consultation with the manufacturer. The ceramic brick storage RTES technology being considered for this study is currently being demonstrated and tested in different electrical jurisdictions across Canada, while the PCM RTES technology considered will be field tested shortly for the first time in Halifax, Nova Scotia. There were several configurations of the ceramic brick system modelled. Two storage capacities of central forced air systems, 240 kWh or 33 kWh, and a zonally distributed baseboard system. The large ceramic brick system was based on the largest residential unit available. This was done to test the maximum potential of the technology in absorbing renewables and shifting loads. It could be difficult to install this in a typical house as the unit would require significant upgrades to a home's electrical systems, potentially including installing an additional 200 amp service to the home on top of existing electrical services. The zonal system features a baseboard-mounted storage system on each floor of the building (including the basement). The PCM RTES system is currently only available in one configuration and capacity (32 kWh), but it also has the additional function of pre-heating DHW. All storage systems modeled used electrical resistance elements to charge the storage.

Tab. 1: Specifications of storage systems.

System	Storage Capacity	Max. Storage Temperature	Storage Heater Capacity
Large Ceramic Brick	240 kWh	732 °C	38 kW
Small Ceramic Brick	33 kWh	732 °C	7.5 kW
Zonal Ceramic Brick	20 kWh	732 °C	7.5 kW
PCM	32 kWh	100 °C	5.4 kW

The ceramic brick TRNSYS storage models utilized a lumped capacitance methodology to predict the performance of the storage. This method was used as it was able to solve the performance calculations quickly and with good accuracy when validated against a more complicated finite difference mode. The PCM storage systems were TRNSYS modelled using a proprietary model based on the physical operation and thermodynamics of the PCM storage unit.

3.3 Storage Systems Control

The thermal storage systems featured auxiliary systems to provide an alternate source of heat. There were several different scenarios modelled to study the impact on the performance of the various thermal storage systems. Both the large and the small ceramic brick systems were each given three scenarios.

1. Electric Backup: The storage system was the primary source of heat. When there was a call for space

heating, heat was withdrawn from the storage until it was depleted or the call for heat ended. If the storage became depleted, a centralized electric resistance heater was activated to heat the homes.

2. ASHP Backup: The storage system was the primary source of heat. When there was a call for space heating, heat was withdrawn from the storage until it was depleted or the call for heat ended. If the storage became depleted, an ASHP was activated to heat the homes.
3. ASHP Primary: A smart controller was used to monitor the outdoor ambient temperature to determine the heat pump's expected COP and used the TOU electricity rates to determine if it was more economical for the residence to use low-cost, off-peak energy from storage, or to use the heat pump to provide heat. The ASHP would be used the majority of the time, and the storage would only be used when outdoor temperatures were low during on-peak rate periods.

The PCM storage system was not modelled with the electric backup option, as this is not available on the physical system the model was based on. The zonally distributed ceramic brick system was only modelled with the electric backup option as there is no available zonally distributed heat pump option for the physical unit the model was based on.

3.4 Home Space and DHW Loads

Four different building loads were investigated, each one representing an archetype found in Canada representing a range of construction dates and eras of building codes. Multi-zone TRNSYS home models were developed to characterize the yearly transient indoor temperature in the different main zones of the considered homes. Each archetype is described in Tab. 2 and the three-dimensional thermal model renderings are shown in Fig. 2. Cooling loads were not considered.

Tab. 2: Home archetype descriptions

Archetype	Living Space Floor Area	Type	Annual Heating Load
Pre-1980s (Fig. 2a)	91.2 m^2 (982 ft^2)	1-storey, detached	25762 kWh
1980-2000s (Fig. 2b)	146.2 m^2 (1574 ft^2)	2-storey, detached	24568 kWh
Post-2000s (Fig. 2c)	80.7 m^2 (869 ft^2)	1-storey, detached	15054 kWh
Net-Zero-Ready (Fig. 2d)	133.5 m^2 (1437 ft^2)	2-storey, mid-row, townhouse	2432 kWh

The homes were modelled with basements and full thermal interactions with the ground surrounding the basements. Each floor of the home (including the basement) was considered as a separate zone for the heating systems. The home's heating systems all used thermostats set to 21°C located on the first floor. The only exception was for the baseboard homes and the zonal ceramic brick homes, which had thermostats on the basement, first floor, and second floors (in archetypes with two stories). The central-air based systems each distributed air flows evenly between the basement, first floor, and second floors (in archetypes with two stories). The building models included unheated portions of the homes such as attics and garages, which were each modelled as zones separate from the living spaces.

Each system was assumed to have the same 170 L electric hot water tank and used the same morning-biased hot water draw profile with an average consumption volume (176 L/day) and an annual total energy draw of 4308 kWh (Edwards et al., 2015). Additionally, the systems using PCM storage were able to supply heat to the DHW as a preheat to water entering the DHW tank.

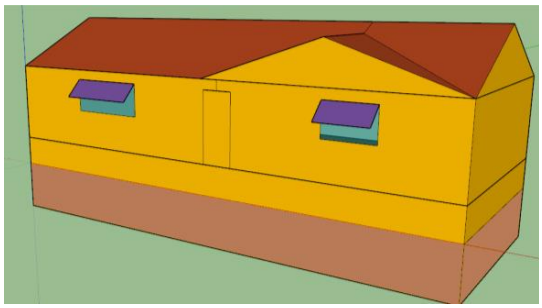

Fig. 2a: Pre-1980s home archetype

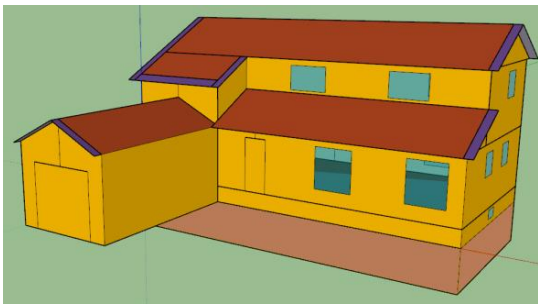

Fig. 2b: 1980-2000s home archetype

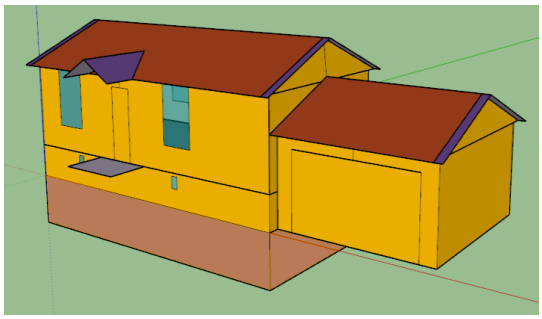

Fig. 2c: Post-2000s home archetype

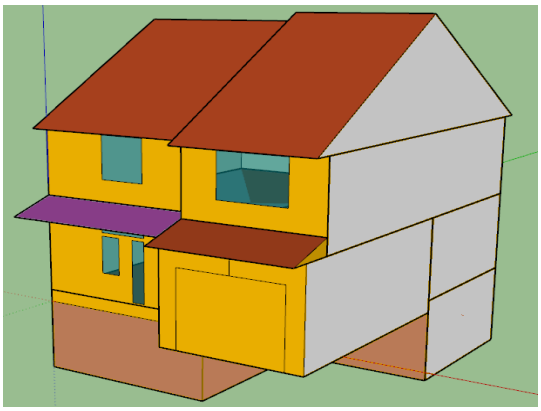

Fig. 2d: Net-zero-ready home archetype

3.5 Renewable Energy Generation

In order to determine the community-scale electrification implications of the considered RTES systems, a 3.3 MW wind turbine was simulated (Enercon GmbH, 2019), and a fraction of its output energy was made available to each of the modelled systems. Each simulated system was able to use up to 1/500th of the output power of the wind turbine (i.e., assuming the wind energy is evenly distributed in a community of roughly 500 homes). This creates a peak of 6.6 kW of available wind energy for one house.

Solar PV power was also modelled to give an identical peak capacity of 6.6 kW for the houses using the parameters from a typical PV panel (CanadianSolar, 2022). Due to the solar and wind conditions, the wind annual energy production was higher than the solar, but the peak power values of the systems were the same. This method of sizing both wind turbines and the solar PV array was used as a first step to assess the impacts of the different RTES technologies to be charged with coinciding onsite renewables and provide relief on peak loads and generation for the local utilities.

The renewable power generated at each time step was made available to the systems to be used to meet the heating loads. If there was excess renewable energy, the charge functions of the storage were activated. Typically, the storage systems can only charge during off-peak electricity TOU periods, but if renewable energy was available at any time, it could be used to charge the storage (until the storage was fully charged). This methodology was used to maximize the uptake of the renewable energy during times when otherwise the electricity grid would have to curtail the renewable power. The stored renewable energy could then be used to reduce peak loads during later time periods.

4. Results and Discussion

There are several key performance indicators (KPIs) that were considered in this study. They included: the amount of load shifting achieved (i.e., shifting from on-peak and mid-peak periods to off-peak); the renewable usage factor (defined as the annual renewable energy used by the space heating and DHW systems / the total available renewable energy); and total annual energy consumption. Other key simulation outputs were the indoor temperatures inside the various zones of the homes.

The example renewable usage factor results of the simulation for the pre-1980s home archetype, when considering

electro technologies with and without storage integrated systems, are shown in Fig. 3 for both wind and solar PV-generated renewable electricity.

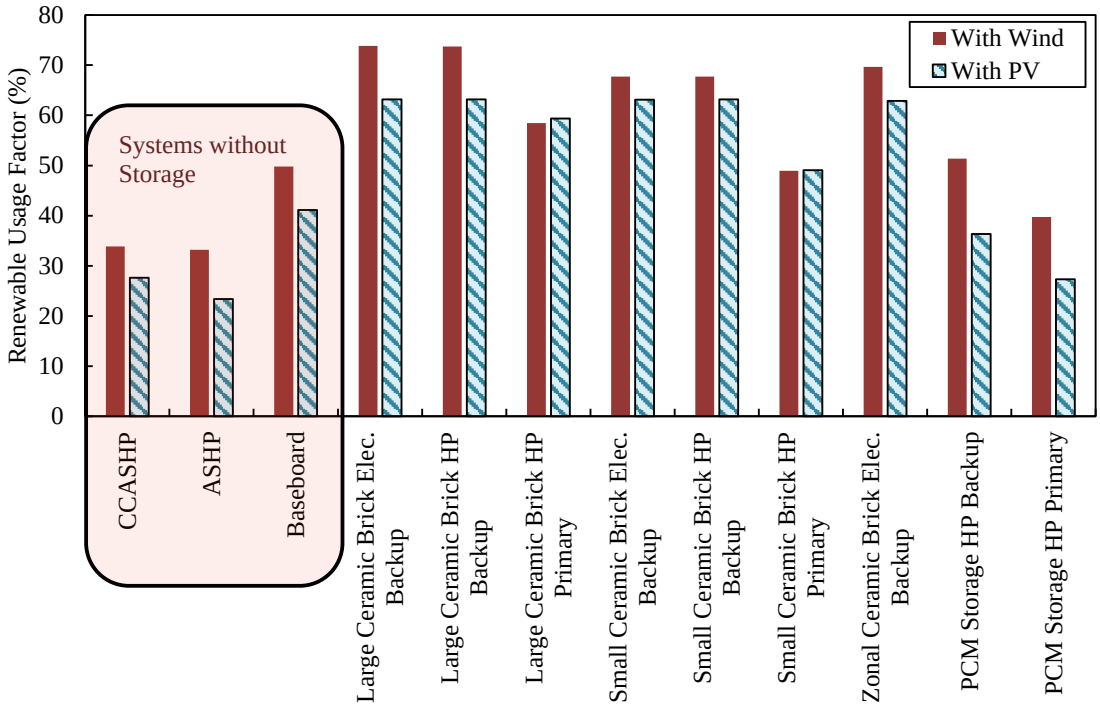

Fig. 3: Renewable usage factor for the various systems under study for a pre-1980s home archetype (The renewable usage factor is defined as the annual renewable energy used by the space heating and DHW systems / the total available renewable energy)

It was found that the use of the considered RTES technologies can increase the amount of renewable energy used. This is critical to the operators of the renewable energy plants as curtailments are a constant issue that limits the financial feasibility of the renewable energy generation stations. A method of storing unused renewable electricity which would otherwise be wasted or not generated through the deactivation of panels and turbines could reduce these curtailments. The differences in the temporal availability of the renewable resources between wind and solar played a key role in the higher renewable usage factor of wind over solar energy. Wind power is available day and night, and it is typically less variable than solar energy in the simulated eastern coast, ocean-adjacent climate. Solar energy is mostly available during periods when heating loads are smaller. Additionally, in the mornings, the storage systems are likely to be nearly fully charged, having access to off-peak electricity overnight, and they are less able to absorb the higher availability of solar energy at this time.

The larger ceramic brick storage systems were able to achieve the highest renewable usage factor, as they had excess storage capacity available to absorb additional renewable energy. They also had higher charging rates and were thus able to take on higher instantaneous power loads. When comparing the one PCM storage type of system, against the similar storage capacity of the small ceramic brick systems, the higher charge capacity of the sensible storage system was advantageous in being able to quickly absorb any renewable energy. The considered PCM system was designed to maintain low peaks to reduce the need for home upgrades and to slowly charge the storage overnight. The design goals were not to quickly charge, and thus in this particular comparison, they do not perform as well. The ceramic brick system's high charge rates require multiple circuits and potential upgrades to the homes due to the high current requirements.

The renewable energy usage factor is only part of the story of the energy storage systems, as different systems use greater annual amounts of energy (e.g., electric resistance heaters vs. heat pumps). This can inflate the renewable energy usage factor in ways that may not be desirable to other stakeholders. The total annual electricity consumption of the systems for the pre-1980s home archetype is shown in Tab. 3. Systems using heat pumps either as the sole heat source or as the primary heat source, with storage only being used when stored energy is cheaper than using peak energy with a heat pump, utilize less energy as expected. The PCM storage with the ASHP backup heat source used 26% more energy than the PCM storage with the ASHP acting as the primary heat source.

Tab 3: Annual total electricity consumption of the various space and DHW heating systems in a pre-1980s home archetype

CCASHP	17 MWh
Small Ceramic Brick HP Primary	20 MWh
PCM Storage HP Primary	20 MWh
ASHP	20 MWh
Large Ceramic Brick HP Primary	20 MWh
PCM Storage HP Backup	25 MWh
Small Ceramic Brick HP Backup	26 MWh
Zonal Ceramic Brick Elec. Backup	27 MWh
Small Ceramic Brick Elec. Backup	30 MWh
Baseboard	30 MWh
Large Ceramic Brick HP Backup	31 MWh
Large Ceramic Brick Elec. Backup	33 MWh

Another result from this study is shown in Fig. 3 and Fig. 4, which demonstrates the potential for shifting loads away from peak periods. Systems using HP back-ups are referenced back to a system using only a heat pump (Fig. 4a), and systems using electric resistance for backup are referenced to a system using electric baseboards (Fig. 4b).

Results indicate that the systems which used the HP as the primary heat source, and the storage only when most economical for the ratepayer had significantly less load shifting potential. The storage load shifting benefits are most apparent in systems that use the storage as much as possible, even though it may be more costly and consume more annual electricity. This is beneficial to the utilities/power generators, as the base loads are increased, and peak loads are decreased, which eases the difficult task of balancing the supply and demand requirements of electrical energy and increasing the use of base-load electricity production such as hydro or nuclear, vs carbon-emitting peaking power generators such as natural gas power plants. Other benefits are the balancing of peak loads, which reduces stress on the distribution grids and lowers the need for upgrading the grid as current non-electric building loads (e.g., propane, natural gas, or oil powered space heating systems) are electrified. This presents an interesting dilemma and a target area for future research. The community-wide implementation of such systems may provide enough benefit to the utility and grid that new pricing schemes can be used to not penalize the ratepayer for adding storage over using a heat pump alone.

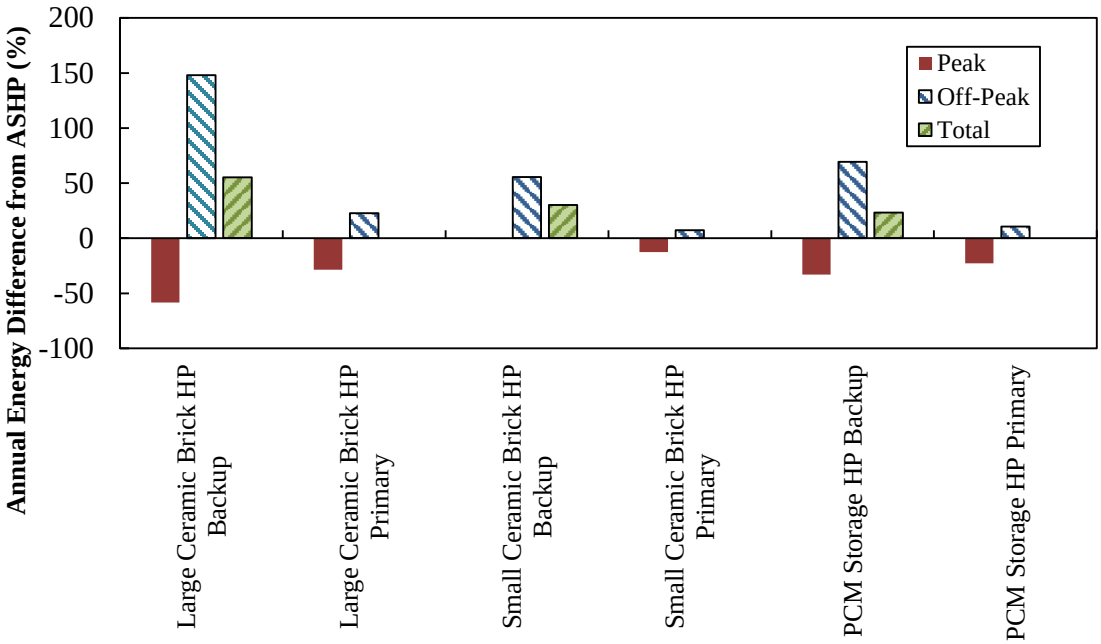

Fig. 4a: Difference between the total, peak, and off-peak ASHP annual system electricity consumption and the heat pump backup storage system's annual electric energy consumption

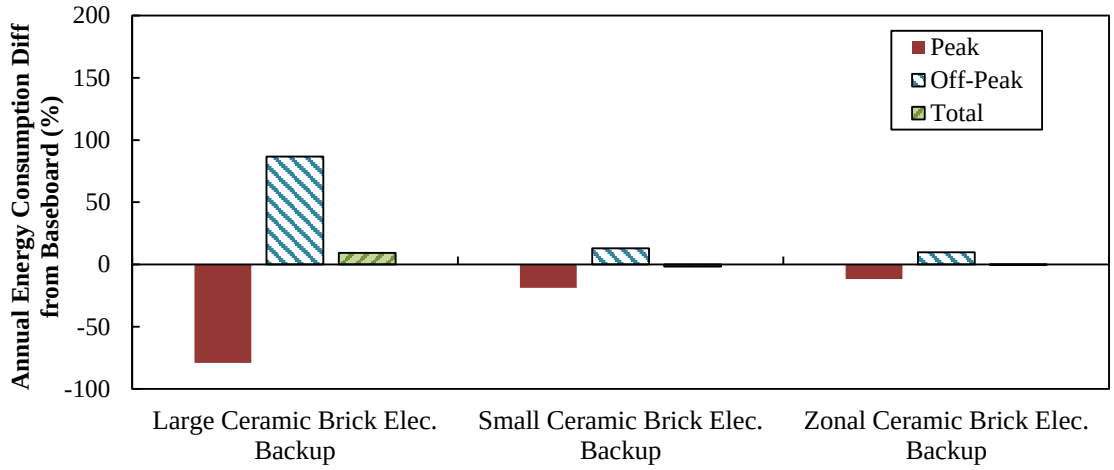

Fig. 4b: Difference between the total, peak, and off-peak baseboard annual system electricity consumption and the electric resistance backup storage system's annual electric energy consumption

When comparing the various system's load-shifting performances between the various considered four home archetypes, the results followed similar trends. An example of the results is shown in Fig. 5a where the large ceramic brick storage system with electric resistance backup is compared to the baseboard electric resistance heated system. The annual total heating loads of the pre-1980s and the 1980s-2000s home archetypes are quite similar (approximately 25 MWh vs 26 MWh respectively). The pre-1980s home archetype is a 91 m^2 single-story home with two occupants, while the 1980s-2000s archetype is a 146 m^2 two-story home with 4 occupants (282.5 kWh/m^2 vs. 168.0 kWh/m^2 respectively). The timing of the loads throughout the year was slightly different, with the pre-1980s home resulting in better load shifting potential. The post-2000s and the net-zero-ready home archetypes have smaller energy loads (19400 kWh and 6800 kWh respectively). The annual DHW loads (4600 kWh) play a much larger role in these loads as well, and thus the percentage capacity of peak load reductions was reduced as these are not impacted by the thermal storage systems in this case.

The same scenario, but with the PCM storage system (which has a smaller storage capacity, reduced heat losses, and can shift a small portion the of DHW loads energy to off-peak) is shown in Fig 5b. The peak load reduction and total energy consumption in the homes with lower demands was improved when compared to the ceramic storage in the same archetypes. Due to the lower overall thermal storage capacity of the considered PCM RTES system, the homes with larger loads had reduced load shifting (i.e., peak load reduction) potential.

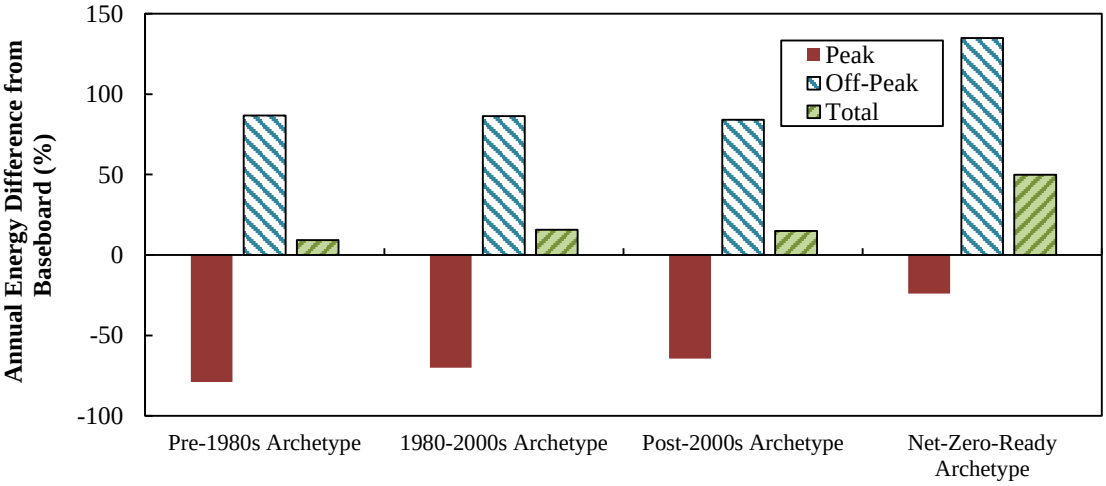

Fig. 5a: Large ceramic brick with electric backup load shifting performance in different house archetypes

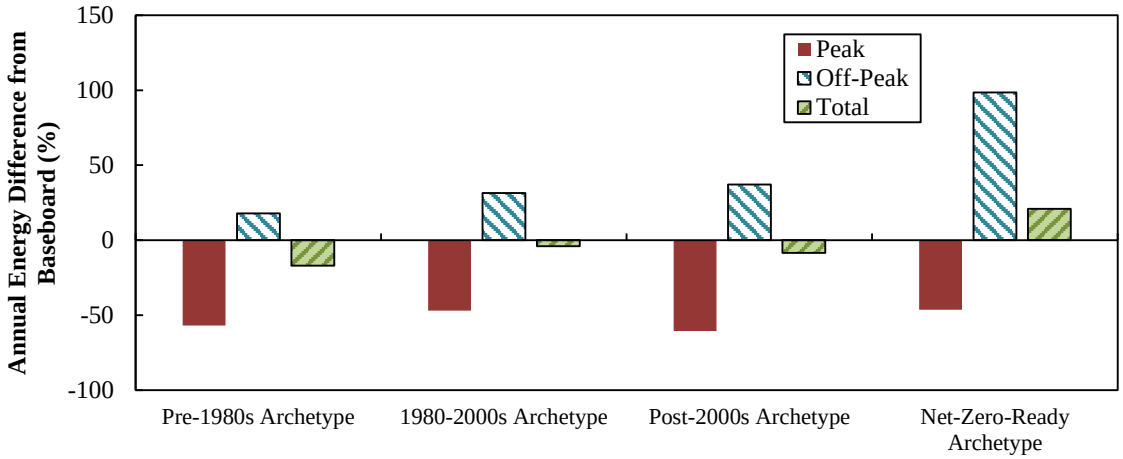

Fig. 5b: PCM storage load shifting performance in different house archetypes

For the case of the more efficient homes, results show that the energy storage was less beneficial. The total energy consumed percentage does increase more with these, as the additional energy requirements to heat the storage are larger when compared to the smaller base loads. Additionally, there is a greater ratio of heat loss from the storage to the space heating load. The heat losses from the storage tank were simulated as heat gains in the basement zones of the building models. This caused some of the home archetypes to overheat. This was especially apparent for the ceramic brick energy storage systems in the net-zero-ready home archetype (Tab. 4). The sensible storage operates at temperatures over 700°C and thus has significant heat losses. An outdoor air reset controller was simulated to reduce the storage set point temperature when the outdoor conditions were milder, but there was still significant overheating in some scenarios.

Tab. 4: Average winter temperature inside the two primary zones of the net-zero-ready home archetype

	First Floor	Basement
Baseboard	21.9 °C	18.3 °C
Large Ceramic Brick Elec. Backup	24.9 °C	28.0 °C
Small Ceramic Brick Elec. Backup	23.4 °C	24.0 °C
Zonal Ceramic Brick Elec. Backup	29.1 °C	26.4 °C
PCM Storage Elec. Backup	22.0 °C	19.4 °C

The DHW systems and resultant energy consumptions were modeled along with the space heating loads and the energy consumption was included in the total energy values discussed in this paper. The only storage systems that interfaced with the DHW system were the PCM storage units, as this was an extra feature of the systems on which the performance was based. The PCM system pre-heated any fresh mains water drawn into the house as makeup for hot water drawn inside the house. The water heaters and the PCM storage used electric resistance heating, thus, whether the water was heated by the DHW tank or the PCM storage, the energy consumption was the same. The PCM storage did not heat the water to the set point temperature of the DHW tank (55 °C), thus the thermostats in the DHW tank would still trigger the elements to heat the water, but the duration of the heating cycle was shorter. Overall, the impact of this on the total electricity consumption, and the load shifting of the energy demand was minimal. Further optimizations and methods to use the storage are required to improve the impact of this feature.

5. Conclusions

Several residential thermal energy storage systems being introduced into the Canadian market were simulated for use in Halifax, Nova Scotia, Canada. Four different home archetypes and several key performance indicators were studied and showed the potential benefits and drawbacks of the various systems. Additional renewable energy was able to be used and peak loads were shown to be reduced through the use of energy storage. The high heat losses of the ceramic brick storage systems were identified as a drawback in some cases as they could overheat homes when thermal energy storage systems with higher heat losses were used in a home with very small heating demands. In these cases, the PCM systems, with the reduced thermal losses and ability to load shift some energy from the DHW loads, were better suited and could increase the annual peak load energy consumption. The ceramic brick storage

systems were more appropriately used in homes with larger heating loads, as the increased storage capacity, and larger heater charge capacities were better utilized and able to shift more energy from peak periods and have a higher renewable energy utilization rate. The results of this study highlight how the specific nature of the loads including timing and scale of demand have a significant impact on the overall system performance, and thus the careful matching of the storage technology and the loads should be conducted, and a one size fits all application may cause over heating the basement issues that need to be addressed.

6. Acknowledgments

The authors would like to thank Lucio Mesquita (NRCan), Bilal El Zaylaa (Carleton University Co-op student), Jeff Thornton and David Bradly (TESS Inc.), Louis Desgrosseilliers (Neothermal Energy Storage Inc.), Al Takle (Steffes, LLC), and Ian Beausoleil-Morrison (Carleton University) for their contributions to many discussions on the topics studied in this paper and in the development of the TRNSYS models that were used for this study. Funding was provided by NRCan's Program of Energy Research and Development (PERD).

7. References

Agbonaye, O., Keatley, P., Huang, Y., Odiase, F.O. and Hewitt, N., 2022. Value of demand flexibility for managing wind energy constraint and curtailment. Renewable Energy, 190, pp.487-500.

CanadianSolar, 2022. HiKu7 Mono PERC CS7L-600.

ECCC, 2022. 2030 Emissions Reduction Plan: Canada's Next Steps for Clean Air and a Strong Economy. Environment and Climate Change Canada. Gatineau, Quebec.

Edwards, S., Beausoleil-Morrison, I., and Laperrière, A., 2015. Representative hot water draw profiles at high temporal resolution for simulating the performance of solar thermal systems. Solar Energy. 111, 43-52.

Enercon GmbH, 2019. EP-115 EP2 3.200.

Gils, H., C., 2015. Balancing of Intermittent Renewable Power Generation by Demand Response and Thermal Energy Storage. Ph.D. thesis. Institute of Energy Storage, University of Stuttgart.

Hughes, L., 2010. Meeting residential space heating demand with wind-generated electricity, Renewable Energy, 35 (8), 1765-1772. https://doi.org/10.1016/j.renene.2009.11.014.

ICF, 2019. Implications of Policy-Driven Electrification in Canada, Canadian Gas Association, Ottawa, Ontario.

Klein, S.A. et al., 2017. TRNSYS 18: A Transient System Simulation Program, Solar Energy Laboratory, University of Wisconsin, Madison, USA.

Luo, H., Ge, W., Sun, J., Jiang, Q., and Gong, Y., 2021. Using Thermal Energy Storage to Relieve Wind Generation Curtailment in an Island Microgrid. Energies, 14(10), p.2851.

Luthander, R., Widén, J., Munkhammar, J., Lingfors, D., 2016. Self-consumption enhancement and peak shaving of residential photovoltaics using storage and curtailment, Energy, 112, 221-231. https://doi.org/10.1016/j.energy.2016.06.039.

MacCraken, M., Electrification, Heat Pumps, and Thermal Energy Storage, ASHRAE Journal. July 2020, 32-39

McKenna, R., Fehrenbach, D., Merkel, E., 2019. The role of seasonal thermal energy storage in increasing renewable heating shares: A techno-economic analysis for a typical residential district, Energy and Buildings, 187, 38-49, https://doi.org/10.1016/j.enbuild.2019.01.044.

NRCan, 2016. Table 7: Space Heating Secondary Energy Use and GHG Emission by Energy Source, NRCan Energy Use Statistics Residential Sector, Natural Resources Canada, Ottawa, Ontario.

NRCan, 2019. Canada's Secondary Energy Use (Final Demand) by Sector, End Use, and Subsector, National Energy Use Database, Natural Resources Canada, Ottawa, Ontario.

NSPower, 2021. Time of Day Rates. Nova Scotia Power. Date Accessed: December 4, 2021. URL: https://www.nspower.ca/about-us/electricity/rates-tariffs/domestic-tod/time-of-day-rates.

Sarbu, I., Sebarchievici, C., 2018. A Comprehensive Review of Thermal Energy Storage. Sustainability 10, 191. https://doi.org/10.3390/su10010191.

Stropnik, R., Koželj, R., Zavrl, E., Stritih, U., 2019. Improved thermal energy storage for nearly zero energy buildings with PCM integration. Solar Energy, 190, 420-426. https://doi.org/10.1016/j.solener.2019.08.041.

Vorushylo, I., Keatley, P., Shah, N., Green, R., Hewitt, N., 2018. How heat pumps and thermal energy storage can be used to manage wind power: A study of Ireland. Energy, 157, 539-549. https://doi.org/10.1016/j.energy.2018.03.001.

Numerical Investigation of Energy Absorption in Dual Metal Hydride Bed based Thermo-Chemical Energy Storage System

Sumeet Kumar Dubey[1], K. Ravi Kumar[1], Vinay Tiwari[2] and Umish Srivastava[2]

[1] Department of Energy Science and Engineering, Indian Institute of Technology Delhi (India)

[2] Department of Solar Energy, Indian Oil Corporation (IOC) R&D Faridabad, Haryana (India)

Abstract

The analysis deals with the feasibility and performance study of a dual metal hydride bed system for thermal energy absorption at a higher temperature. An integrated dual bed system includes a metal hydride bed which acts as energy storage media operating at higher temperatures and another bed used as hydrogen storage media. $NaMgH_2F$ is used as high temperature metal hydride (HTMH), while Mg_2NiH_4 is used as low temperature metal hydride (LTMH). Study of the heat transfer phenomenon during thermal energy absorption in HTMH and hydrogen storage in low temperature metal hydride is performed. The variation of temperature, saturation fraction along with density variation of metal hydride bed is performed in this work.

Keywords: Concentrating solar power, High temperature thermal energy storage, Thermochemical energy storage, Dual metal hydride system.

1. Introduction

The decreasing reserves of fossil fuels and the effect on climate due to their combustion have forced masses to think about renewable energy sources. The high potential of solar energy to fulfill the energy demand with the objective of a clean and green environment makes solar energy favorable. Due to diurnal variation and the interrupted nature of solar energy, continuous power generation is one big challenge affecting the overall power generation capacity and unit cost of power generation. Integration of the energy storage system will help the power generation plant to operate for more hours, increasing the capacity of power generation and possibly bringing down the power generation cost.

Thermal energy storage (TES) systems are classified as sensible, latent, and thermochemical (Jain et al., 2021a). In a sensible storage system, the system stores energy by changing the temperature of the storage media, while the change of phase of storage media is responsible for thermal energy storage in the latent storage system. Thermochemical energy storage (TCES) systems store and release heat by carrying out endothermic and exothermic chemical reactions, respectively. The difference in thermal energy storage mechanisms can be understood clearly from figure 1.

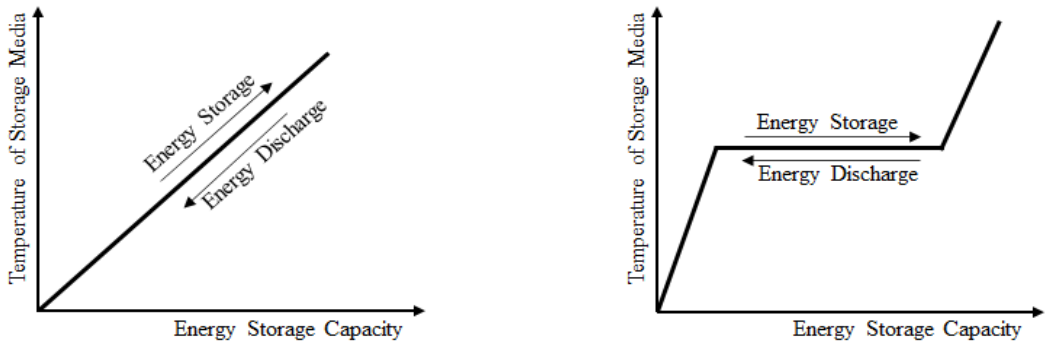

a) b)

© 2022. The Authors. Published by International Solar Energy Society
Selection and/or peer review under responsibility of Scientific Committee
doi:10.18086/eurosun.2022.13.07 Available at http://proceedings.ises.org

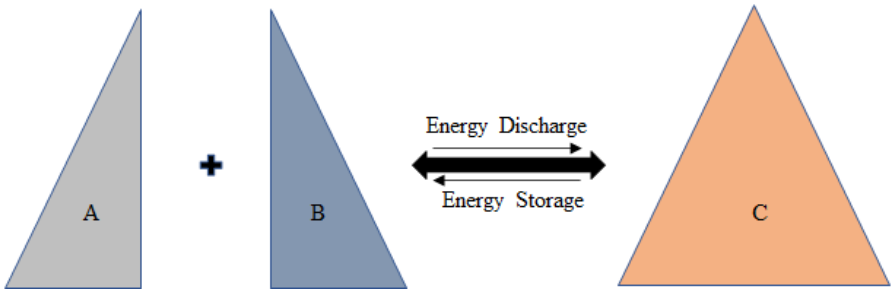

c)

Fig 1: Mechanism of thermal energy storage a) sensible, b) latent and c) thermochemical

Some metal alloys react with hydrogen and undergo an exothermic chemical reaction to form a metal hydride, which results in an energy discharge cycle, while during the endothermic chemical reaction, energy charging cycle takes place and metal hydride is dissociated into metal alloy and hydrogen.

Sensible energy storage technology is matured and commercially available for TES applications. The latest energy storage system has been studied, and several latent energy storage media are found appropriate for TES applications at higher temperature (Jain et al., 2021b; Ray et al., 2021). Several thermochemical energy storage systems have been reported suitable for high temperature TES applications (Chen et al., 2018; Choudhari et al., 2021; Liu et al., 2018; Møller et al., 2017; Pelay et al., 2017; Reilly and Wiswall, 1967; Sheppard et al., 2016b, 2016a; Sunku Prasad et al., 2019).

Metal hydride based TCES systems have been studied for TES applications. In earlier studies of metal hydride, Magnesium (Mg) alloys attracted researchers for thermal energy storage applications because of their higher thermal stability and reaction enthalpy. Mg based metal hydride was used for the application of steam generation application where the waste heat from the industries was stored in the Mg based hydride system and steam was produced by supplying thermal energy from Mg based hydride system. The system supplied heat at 370 ºC with a reported capacity of 9.08 kWh and 79.64% energy storage efficiency (Bogdanović et al., 1995). A small scale Mg hydride system used 19 gm of Mg hydride for analysis of energy absorption (Paskevicius et al., 2015). The study reported thermal energy storage at 420 ºC for 20 cycles with almost constant storage capacity. Due to the small capacity of the system, the heat losses were higher, but the author expected a reduction in heat losses with the increase in the capacity of the system. Nickel (Ni), cobalt (Co), and ferrous (Fe) were doped in Mg based hydride to study the variation in storage characteristics (Reiser et al., 2000a). With the addition of these elements, cyclic stability, reversibility, and operating temperature ranges of Mg hydride alloy have increased, while a slight reduction in thermal stability has been observed. Another study compared Ni doped Mg hydride with pure Mg hydride for hydrogen storage application, but the energy storage characteristics were also reported (Bogdanović et al., 1999). Authors reported improvement in cyclic stability, reversibility, and operating temperature range for Ni doped Mg hydride as compared to pure Mg hydride.

Numerical investigation of Magnesium Nickel (Mg-Ni) alloy aimed to study the outcome of variation in dimensional parameters of geometry on the charging and discharging characteristics (Dubey and Kumar, 2021a, 2021b). The study concludes that the reactor having lesser radial and higher longitudinal dimensions possesses better heat transfer and thus improves the charging and discharging characteristics. The energy storage capacity, discharge capacity, and storage efficiency for three cases of aspect ratio were evaluated in another analysis (Dubey and Kumar, 2022). The energy stored and released for the system was observed maximum for lower aspect ratio geometry, while the energy storage efficiency was maximum for higher aspect ratio geometry.

Several recent studies have been performed on dual metal hydride systems for thermal energy storage. Anna et al. performed the feasibility and performance study of two pairs of metal hydrides for TES applications. In one study, $NaMgH_2F$ acts as HTMH and $TiCr_{1.6}Mn_{0.2}$ acts as LTMH (D'Entremont et al., 2018). The energy storage system was found suitable, and the energy storage density was reported as 226 kWh/m^3. Next study used Mg_2FeH_6 as HTMH and Na_3AlH_6 as LTMH for a dual metal hydride system (D'Entremont. et al., 2017). The energy storage system was feasible and suitable for a temperature range of 450-500 ºC with an energy storage density of 132 kWh/m^3. This pair of metal hydrides (Mg_2FeH_6 and Na_3AlH_6) was also studied with fin arrangements for better heat transfer (Sofiene Mellouli et al., 2018). The system reported 96% energy storage efficiency with 90 kWh/m^3

energy storage density. Pair of Mg_2Ni alloy and $LaNi_5$ alloy was used in dual metal hydride based TES system. as HTMH and LTMH respectively was studied for TES applications (Malleswararao et al., 2020). The authors reported 89.4% energy efficiency with a energy storage density of 156 kWh/m^3. Some of the metal hydride systems for low temperature TES have been studied for their feasibility and performance (Choudhari and Sharma, 2020; Gambini et al., 2020; Malleswararao et al., 2022, 2021). Mg based alloys were studied and found suitable for TES applications for temperature range of 250 to 550 ºC (Bogdanović et al., 1999; Reiser et al., 2000b).

In this work, the dual metal hydride bed system with $NaMgH_2F$ as HTMH and Mg_2NiH_4 as LTMH is used for feasibility and performance analysis of the thermal energy absorption cycle. The geometric parameters such as the diameter to height ratio of metal hydride bed (Aspect Ratio) and the number of heat transfer tubes have been considered from the previously published work (Dubey and Kumar, 2022). The geometry section of the work discusses the details of the geometric parameter considered in the analysis. COMSOL Multiphysics 5.5 is used to perform the numerical analysis. The temperature, density, and heat transfer variations for the energy absorption cycle have been studied in this work.

2. Numerical Modelling

The study of TES in HTMH bed, which is coupled with LTMH bed is performed and discussed in this work. $NaMgH_2F$ is used as HTMH, which is used for TES, while Mg_2NiH_4 is used as LTMH, which stores hydrogen released from HTMH. 1 kg of HTMH is considered for the energy absorption analysis. The quantity of LTMH is calculated based on the quantity of hydrogen to handle. The geometry of the coupled metal hydride bed system is mentioned in figure 2

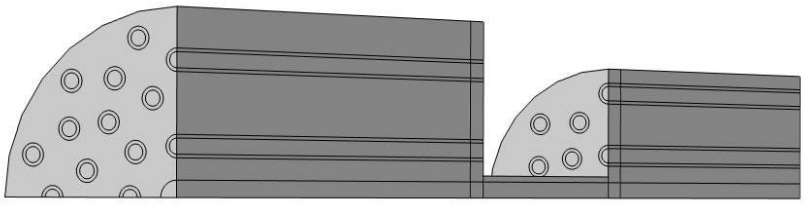

Fig 2: Coupled metal hydride bed geometry for numerical analysis

2.1. Governing Equations

The governing equations used in the numerical analysis includes mass, momentum, and energy balance equations. The energy balance equations used for different domains are represented notations in the subscript where MH bed, hydrogen gas, and heat transfer fluid are represented as “s”, “g”, and “l”, respectively. Equation (1) represents the mass balance equation for H_2 gas flowing in the porous bed, while equation (2) is the mass balance equation for the solid fraction of the porous domain. Equation (3) represents the volumetric rate of hydrogen mass desorbed. Equation (4) and (5) represents mass balance for hydrogen and HTF flow in tubes.

$$\varepsilon \frac{\partial \rho_g}{\partial t} + \nabla.\left(\rho_g u_g\right) = -S_m \quad \text{(eq. 1)}$$

$$(1-\varepsilon)\frac{\partial \rho_s}{\partial t} = S_m \quad \text{(eq. 2)}$$

$$S_m = C_a exp\left(\frac{-E_a}{RT}\right)\left(\frac{p-p_{eq}}{p_{eq}}\right) \quad \text{(eq. 3)}$$

$$\frac{\partial \rho_g}{\partial t} + \nabla.\left(\rho_g u_g\right) = 0 \quad \text{(eq. 4)}$$

$$\frac{\partial \rho_l}{\partial t} + \nabla.\left(\rho_l u_l\right) = 0 \quad \text{(eq. 5)}$$

Equation (6) represents the Brinkman equation used for the momentum balance of hydrogen flowing in the porous domain. Equation (7) and (8) represents the Navier Stokes equation used for the momentum balance of hydrogen and HTF flow in tubes.

$$\frac{\rho_g}{\varepsilon}\left(\frac{\partial u_g}{\partial t}+u_g.\frac{\nabla u_g}{\varepsilon}\right)=-\nabla p-\frac{\mu_g}{K}u_g-\frac{S_m}{\varepsilon^2}u_g+\nabla.\left[\frac{\mu_g}{\varepsilon}\left(\nabla u_g+\left(\nabla u_g\right)^T\right)-\frac{2\mu_g}{3\varepsilon}\left(\nabla.u_g\right)\right] \quad \text{(eq. 6)}$$

$$\left(\frac{\partial u_g}{\partial t}+u_g.\frac{\nabla u_g}{\varepsilon}\right)=-\nabla p+\nabla.\left[\mu_g\left(\nabla u_g+\left(\nabla u_g\right)^T\right)-\frac{2\mu_g}{3}\left(\nabla.u_g\right)\right] \quad \text{(eq. 7)}$$

$$\left(\frac{\partial u_l}{\partial t}+u_l.\frac{\nabla u_l}{\varepsilon}\right)=-\nabla p+\nabla.\left[\mu_l(\nabla u_l+(\nabla u_l)^T)-\frac{2\mu_l}{3}(\nabla.u_l)\right] \quad \text{(eq. 8)}$$

Equation (9), (13) and (14) are the energy balance equation for the porous domain, hydrogen gas and HTF flow in tubes respectively. Equation (10) and (11) expresses the relation to calculate effective thermal conductivity and effective heat capacity of metal hydride bed, which is calculated based on the average volume method. Equation (12) represents the energy source term, i.e., the volumetric energy absorption rate.

$$\left(\rho c_p\right)_{eff}\frac{\partial T}{\partial t}+\rho c_{pg}\left(u_g.\nabla T\right)=\nabla.\left(\sigma_{eff}\nabla T\right)+S_T \quad \text{(eq. 9)}$$

$$\sigma_{eff}=\varepsilon\sigma_g+(1-\varepsilon)\sigma_s \quad \text{(eq. 10)}$$

$$\left(\rho c_p\right)_{eff}=\varepsilon\left(\rho c_p\right)_g+(1-\varepsilon)\left(\rho c_p\right)_s \quad \text{(eq. 11)}$$

$$S_T=S_m(\Delta h) \quad \text{(eq. 12)}$$

$$\left(\rho_g c_{pg}\right)\left(\frac{\partial T}{\partial t}+u_g.\nabla T\right)=\nabla.\left(\sigma_g\nabla T\right) \quad \text{(eq. 13)}$$

$$\left(\rho_l c_{pl}\right)\left(\frac{\partial T}{\partial t}+u_l.\nabla T\right)=\nabla.(\sigma_l\nabla T) \quad \text{(eq. 14)}$$

The thermal and chemical properties of metal hydrides, hydrogen and heat transfer fluid are mentioned in table 1 and 2.

Table 1: Thermochemical properties of metal hydrides (D'Entremont et al., 2018; Nyamsi and Tolj, 2021; Sheppard et al., 2014)

Thermochemical Properties	**$NaMgH_2F$ (HTMH)**	**Mg_2NiH_4 (LTMH)**
Reaction rate constant (1/s)	1000000 (absorption)	175 (desorption)
Activation energy (J/mol)	102500 (absorption)	52200 (desorption)
Enthalpy of reaction (J/mol)	96800	64500
Entropy of reaction (J/mol K)	138	122.2
Specific heat capacity (J/kg K)	419	697
Gravimetric storage density (wt%)	2.5	3.6
Unsaturated density (kg/m3)	1390	3200
Saturated density (kg/m^3)	1424.75	3315.2
Thermal conductivity (W/m K)	0.5	0.2

Table 2: Geometric parameters and thermal properties of metal hydride, hydrogen, and heat transfer fluid

Thermal Properties	Value
Specific heat capacity of H_2 (J/kgK)	14539
Thermal conductivity of hydrogen (W/mK)	1
Porosity of metal hydride bed	0.5
Permeability of metal hydride bed (m^2)	10^{-8}

2.2. Assumptions

The following assumptions have been considered for the numerical analysis of energy absorption in the dual metal hydride bed system.

- Hydrogen gas is assumed as an ideal gas.
- Hydrogen gas and metal hydride bed are in thermal equilibrium.
- Metal hydride material is considered homogenous and isotropic.
- Heat transfer due to radiation is not considered inside the metal hydride bed.
- The thermal properties of metal hydride gas, hydrogen, and heat transfer fluid are considered constant.
- The outer surface of the metal hydride bed is assumed to be insulated; thus, the heat loss to the surrounding is neglected.

2.3. Geometric parameters

The dimension of the metal hydride bed is calculated based on the author's previous work (Dubey and Kumar, 2022). The geometry with an aspect ratio (ratio of diameter to height of metal hydride bed) of 0.5 has shown better heat transfer characteristics; therefore, both high and low temperature metal hydride beds are designed with an aspect ratio of 0.5. The number of heat transfer fluid tubes for both the metal hydride beds is calculated using the conclusion of the author's previous work. 1 kg of high temperature metal hydride powder is arranged in a cylindrical shape with a porosity of 0.5 and considering the aspect ratio of 0.5, the dimensions have been calculated. The low temperature metal hydride required to store the quantity of hydrogen released from high temperature metal hydride is calculated and with an aspect ratio and porosity of 0.5, the dimensions of low temperature metal hydride bed are calculated. The two metal hydride beds are connected with a tube length of 100 mm and inner and outer diameters of 9.5 and 13 mm, respectively.

Table 3: Geometric parameters of metal hydride bed

Parameter	$NaMgH_2F$ (HTMH)	Mg_2NiH_4 (LTMH)
Diameter of metal hydride bed (mm)	104	79
Height of metal hydride bed (mm)	208	158
Diameter of hydrogen supply tube (mm)	9.5	9.5
Inner diameter of heat transfer fluid tube (mm)	4.4	4.4
Outer diameter of heat transfer fluid tube (mm)	6.4	6.4
Number of heat transfer fluid tubes	44	24

2.4. Initial values and boundary conditions

Table 4: Initial values of different domains of the geometry

Initial Value	$NaMgH_2F$ (HTMH)	Mg_2NiH_4 (LTMH)
Initial temperature of metal hydride bed and HTF (K)	773	573
Initial pressure of metal hydride bed (bar)	4.64	3.18
Initial temperature of hydrogen in supply tube (K)	299	299
Initial pressure of hydrogen in supply tube (bar)	4.2	4.1
Initial pressure of heat transfer fluid (bar)	1	1
Initial density of metal hydride bed (kg/m^3)	1424.75	3200

3. Results and discussion

The results and discussion involve the analysis on the variation in temperature, density and energy absorption characteristics.

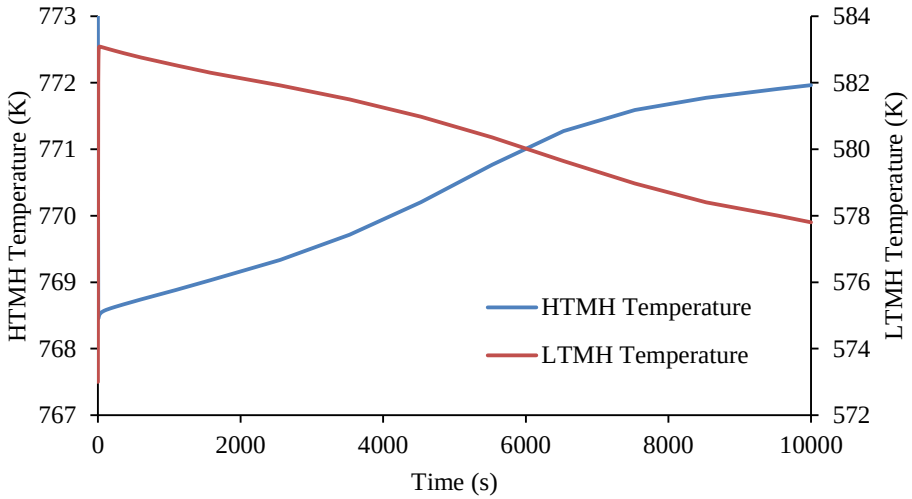

Fig. 3: Variation of average bed temperature of high and low temperature metal hydride bed with time

During energy absorption in high temperature metal hydride bed, the temperature of high temperature metal hydride bed decreases instantly because of localized energy absorption and activation energy required to initiate the endothermic chemical reaction. In low temperature metal hydride, the exothermic reaction occurs when hydrogen is absorbed, resulting in the instant increase in temperature of the metal hydride bed. After the instant variation in both beds, the average bed temperature slowly moves towards their respective steady state of the heat transfer fluid temperature, as shown in figure 3.

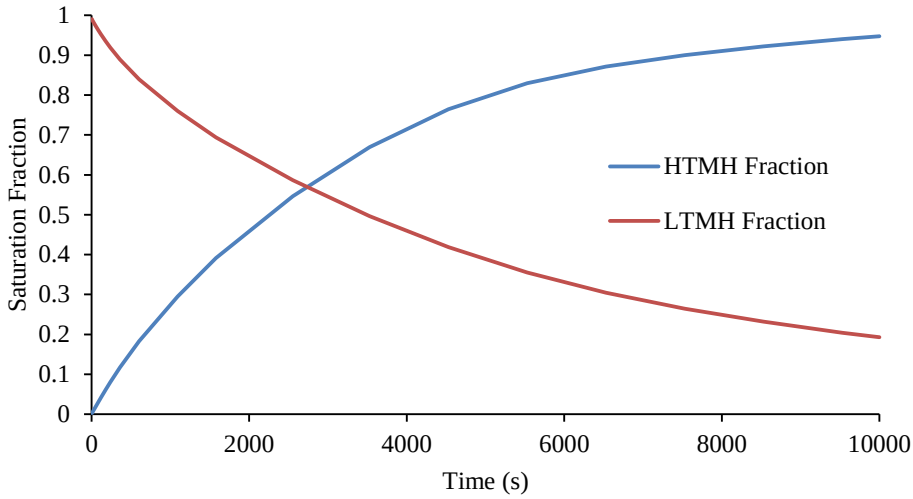

Fig. 4: Variation of saturation fraction HTMH and LTMH bed with time

The metal hydride saturation fraction has been studied for both metal hydride beds. Saturation fraction denotes the degree of energy stored in the metal hydride bed on a scale of 0 to1. 0 indicates the empty metal hydride bed, while 1 denotes the saturated metal hydride bed. The saturation fraction of the metal hydride beds are shown in figure 4.

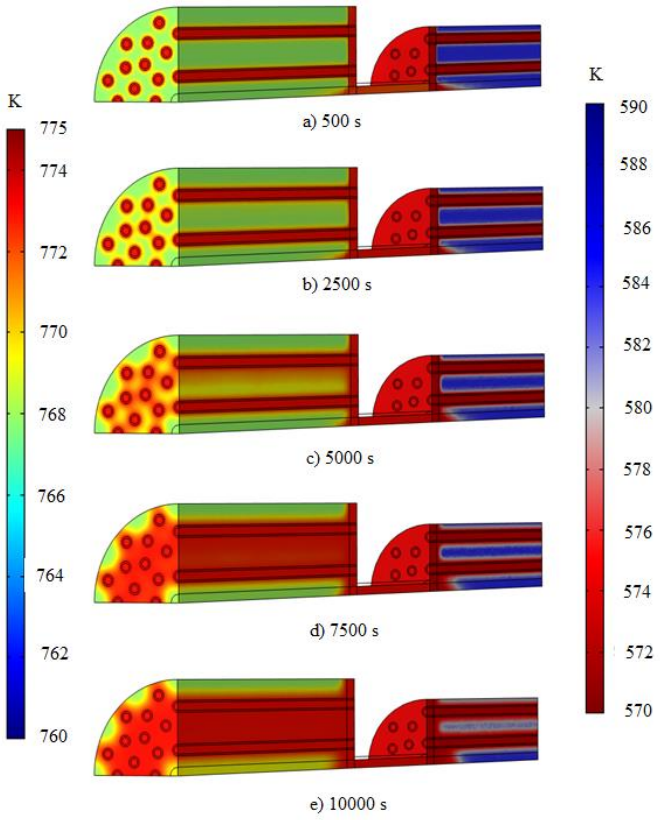

Fig. 5: Cross sectional temperature variation of geometry at different instants

The temperature and density contours of the dual metal hydride bed system at different instants are represented in figure 5 and 6, respectively. The temperature and density contours represent faster energy absorption during the initial stages, while the reaction kinetics is slower as the metal hydride beds achieve saturation.

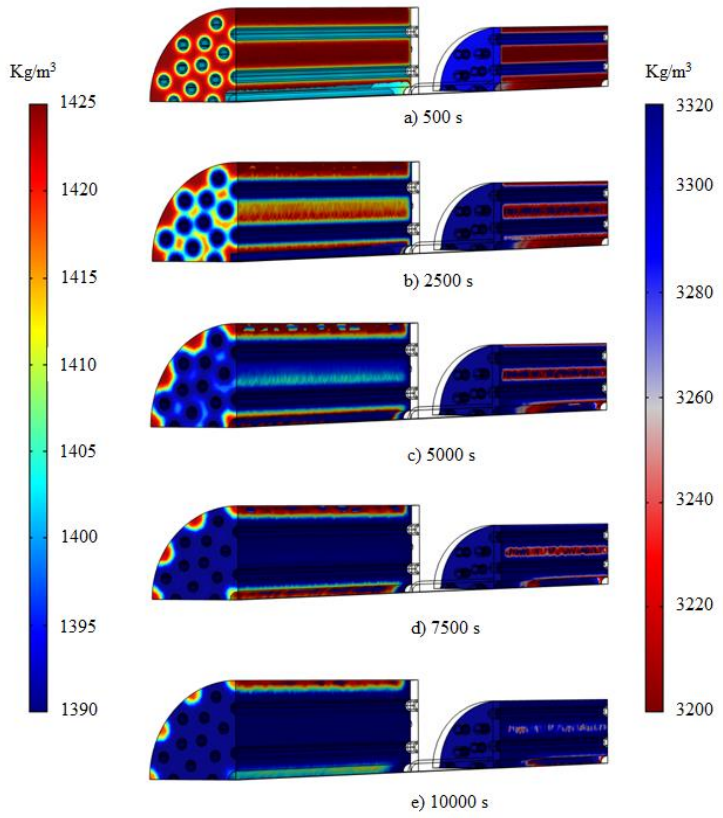

Fig. 6: Cross sectional density variation of geometry at different instants

The saturation fraction of high and low temperature metal hydride beds at different axial lengths has been studied and shown in figure 7. Three planes for both metal hydride beds at different axial lengths have been considered in the analysis. The plane closer to the connecting tube is represented as the top, while the one in the middle of the metal hydride bed is considered as middle and the third one at the opposite end is considered as the bottom,

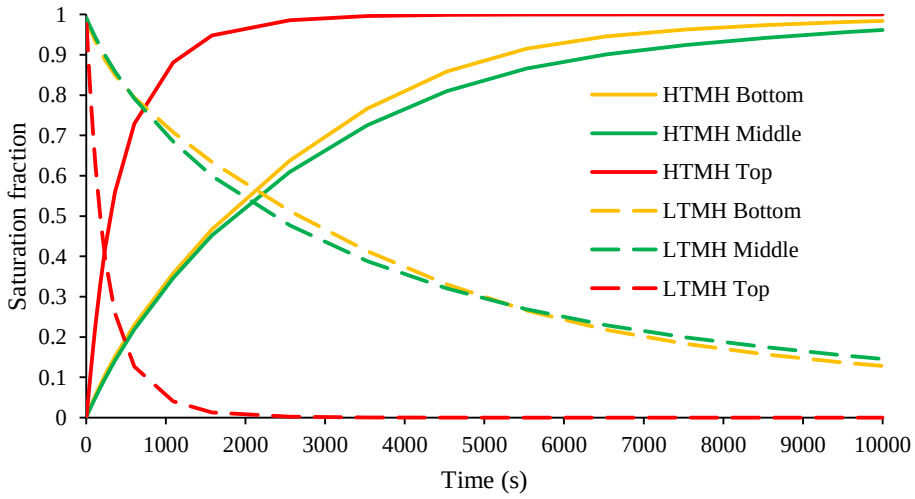

Fig. 7: Variation of saturation fraction of HTMH and LTMH bed at different axial lengths with time

The saturation fraction of the plane closer to the connecting tube is faster than the planes below it. The heat transfer fluid enters the tubes from the side of the plane at the top side and thus initially, the heat is transferred to the top plane and the plane at the top saturates in less time.

During the process of thermal energy absorption in high temperature metal hydride, a total of 256.79 kJ of thermal

energy was stored at an average bed temperature of 770 K. During the energy absorption in high temperature metal hydride, 6.93 g of hydrogen was liberated from high temperature metal hydride. The average temperature of low temperature metal hydride bed is observed as 580 K during the energy absorption process in high temperature metal hydride.

4. Conclusions

The $NaMgH_2F$ and Mg_2NiH_4 are used to study the feasibility and performance analysis of the energy absorption cycle. The two mentioned metal hydrides were found suitable for energy absorption at an average temperature of 770 K. The total thermal energy stored in the high temperature metal hydride bed is 256.79 kJ, for which 6.93 g of hydrogen was released from high temperature metal hydride. The variation of saturation fraction of the metal hydride bed with respect to time was analyzed. It is observed that the rate of energy storage in metal hydride bed is fast initially and further; the energy absorption rate decreases as the metal hydride bed moves toward saturation. The variation of saturation fraction with the axial length is also studied and the absorption rate is found to be faster for the section closer to the connecting tube.

5. Acknowledgments

The authors are thankful to Science and Engineering Research Board (SERB), Department of Science and Technology (DST), Government of India for awarding “Prime Minister Fellowship for Doctoral Research” to Mr. Sumeet Kumar Dubey in collaboration with Indian Oil Corporation Limited, Research and Development Centre and kind support from Confederation of Indian Industry (CII).

6. References

Bogdanović, B., Hofmann, H., Wessel, S., Schlichte, K., Reiser, A., Neuy, A., Spliethoff, B., 1999. Ni-doped versus undoped Mg–MgH2 materials for high temperature heat or hydrogen storage. Journal of Alloys and Compounds 292, 57–71. https://doi.org/10.1016/s0925-8388(99)00109-7

Bogdanović, B., Ritter, A., Spliethoff, B., Straßburger, K., 1995. A process steam generator based on the high temperature magnesium hydride/magnesium heat storage system. International Journal of Hydrogen Energy 20, 811–822. https://doi.org/10.1016/0360-3199(95)00012-3

Chen, X., Zhang, Z., Qi, C., Ling, X., Peng, H., 2018. State of the art on the high-temperature thermochemical energy storage systems. Energy Conversion and Management 177, 792–815. https://doi.org/10.1016/j.enconman.2018.10.011

Choudhari, M.S., Sharma, V.K., 2020. Thermodynamic simulation of hydrogen based thermochemical energy storage system. International Journal of Hydrogen Energy. https://doi.org/10.1016/j.ijhydene.2020.09.074

Choudhari, M.S., Sharma, V.K., Paswan, M., 2021. Metal hydrides for thermochemical energy storage applications. International Journal of Energy Research 1–28. https://doi.org/10.1007/978-3-319-68255-6_119

D’Entremont., A., Corgnale, C., Sulic, M., Hardy, B., Zidan, R., Motyka, T., 2017. Modeling of a thermal energy storage system based on coupled metal hydrides (magnesium iron – sodium alanate) for concentrating solar power plants. International Journal of Hydrogen Energy 42, 22518–22529. https://doi.org/10.1016/j.ijhydene.2017.04.231

D’Entremont, A., Corgnale, C., Hardy, B., Zidan, R., 2018. Simulation of high temperature thermal energy storage system based on coupled metal hydrides for solar driven steam power plants. International Journal of Hydrogen Energy 43, 817–830. https://doi.org/10.1016/j.ijhydene.2017.11.100

Dubey, S.K., Kumar, K.R., 2022. Charging and discharging analysis of thermal energy using magnesium nickel hydride based thermochemical energy storage system. Sustainable Energy Technologies and Assessments 52, 101994. https://doi.org/10.1016/j.seta.2022.101994

Dubey, S.K., Kumar, K.R., 2021a. Numerical Investigation of Thermal Energy Storage using Magnesium Nickel Hydride, in: 26th National and 4th International ISHMT-ASTFE Heat and Mass Transfer Conference. pp. 577–583. https://doi.org/10.1615/IHMTC-2021.870

Dubey, S.K., Kumar, K.R., 2021b. Numerical investigation of energy desorption from magnesium nickel hydride based thermal energy storage, in: 9th Eur. Conf. Ren. Energy Sys. Istanbul, Turkey, pp. 457–462.

Gambini, M., Stilo, T., Vellini, M., 2020. Selection of metal hydrides for a thermal energy storage device to support low-temperature concentrating solar power plants. International Journal of Hydrogen Energy 45, 28404–28425. https://doi.org/10.1016/j.ijhydene.2020.07.211

Jain, S., Dubey, S.K., Kumar, K.R., Rakshit, D., 2021a. Thermal Energy Storage for Solar Energy, in: Fundamentals and Innovations in Solar Energy. pp. 167–215. https://doi.org/10.1007/978-981-33-6456-1_9

Jain, S., Kumar, K.R., Rakshit, D., 2021b. Heat transfer augmentation in single and multiple (cascade) phase change materials based thermal energy storage : Research progress , challenges , and recommendations. Sustainable Energy Technologies and Assessments 48, 101633. https://doi.org/10.1016/j.seta.2021.101633

Liu, D., Xin-Feng, L., Bo, L., Si-quan, Z., Yan, X., 2018. Progress in thermochemical energy storage for concentrated solar power: A review. International Journal of Energy Research 42, 4546–4561. https://doi.org/10.1002/er.4183

Malleswararao, K., Aswin, N., Kumar, P., Dutta, P., Srinivasa Murthy, S., 2022. Experiments on a novel metal hydride cartridge for hydrogen storage and low temperature thermal storage. International Journal of Hydrogen Energy 1–12. https://doi.org/10.1016/j.ijhydene.2022.03.097

Malleswararao, K., Aswin, N., Murthy, S.S., Dutta, P., 2021. Studies on a dynamically coupled multifunctional metal hydride thermal battery. Journal of Alloys and Compounds 866, 158979. https://doi.org/10.1016/j.jallcom.2021.158979

Malleswararao, K., N, A., Srinivasa Murthy, S., Dutta, P., 2020. Performance prediction of a coupled metal hydride based thermal energy storage system. International Journal of Hydrogen Energy 45, 16239–16253. https://doi.org/10.1016/j.ijhydene.2020.03.251

Møller, K.T., Sheppard, D., Ravnsbæk, D.B., Buckley, C.E., Akiba, E., Li, H.W., Jensen, T.R., 2017. Complex metal hydrides for hydrogen, thermal and electrochemical energy storage. Energies 10. https://doi.org/10.3390/en10101645

Nyamsi, S.N., Tolj, I., 2021. The impact of active and passive thermal management on the energy storage efficiency of metal hydride pairs based heat storage. Energies 14. https://doi.org/10.3390/en14113006

Paskevicius, M., Sheppard, D.A., Williamson, K., Buckley, C.E., 2015. Metal hydride thermal heat storage prototype for concentrating solar thermal power. Energy 88, 469–477. https://doi.org/10.1016/j.energy.2015.05.068

Pelay, U., Luo, L., Fan, Y., Stitou, D., Rood, M., 2017. Thermal energy storage systems for concentrated solar power plants. Renewable and Sustainable Energy Reviews 79, 82–100. https://doi.org/10.1016/j.rser.2017.03.139

Ray, A.K., Rakshit, D., Ravikumar, K., 2021. High-temperature latent thermal storage system for solar power: Materials, concepts, and challenges. Cleaner Engineering and Technology 4, 100155. https://doi.org/10.1016/j.clet.2021.100155

Reilly, J.J., Wiswall, R.H., 1967. Reaction of Hydrogen with Alloys of Magnesium and Copper. Inorganic Chemistry 6, 2220–2223. https://doi.org/10.1021/ic50058a020

Reiser, A., Bogdanovic, B., Schlichte, K., 2000a. The application of Mg-based metal-hydrides as heat energy storage systems. International Journal of Hydrogen Energy 25, 425–430. https://doi.org/https://doi.org/10.1016/S0360-3199(99)00057-9.

Reiser, A., Bogdanovic, B., Schlichte, K., 2000b. The application of Mg-based metal-hydrides as heat energy storage systems. International Journal of Hydrogen Energy 25.

Sheppard, D.A., Corgnale, C., Hardy, B., Motyka, T., Zidan, R., Paskevicius, M., Buckley, C.E., 2014. Hydriding characteristics of NaMgH2F with preliminary technical and cost evaluation of magnesium-based metal hydride materials for concentrating solar power thermal storage. RSC Advances 4, 26552–26562. https://doi.org/10.1039/c4ra01682c

Sheppard, D.A., Humphries, T.D., Buckley, C.E., 2016a. Sodium-based hydrides for thermal energy applications. Applied Physics A: Materials Science and Processing 122, 1–13. https://doi.org/10.1007/s00339-016-9830-3

Sheppard, D.A., Paskevicius, M., Humphries, T.D., Felderhoff, M., Capurso, G., Bellosta von Colbe, J., Dornheim, M., Klassen, T., Ward, P.A., Teprovich, J.A., Corgnale, C., Zidan, R., Grant, D.M., Buckley, C.E., 2016b. Metal hydrides for concentrating solar thermal power energy storage. Applied Physics A: Materials Science and Processing 122, 1–15. https://doi.org/10.1007/s00339-016-9825-0

Sofiene Mellouli, Askri, F., Edacherian, A., Alqahtani, T., Algarni, S., Abdelmajid, J., Phelan, P., 2018. Performance analysis of a thermal energy storage based on paired metal hydrides for concentrating solar power plants. Applied Thermal Engineering 144, 1017–1029. https://doi.org/.1037//0033-2909.I26.1.78

Sunku Prasad, J., Muthukumar, P., Desai, F., Basu, D.N., Rahman, M.M., 2019. A critical review of high-temperature reversible thermochemical energy storage systems. Applied Energy 254, 113733. https://doi.org/10.1016/j.apenergy.2019.113733

Appendix: Units and Symbols

Table 1: Symbols for materials properties

Quantity	Symbol	Unit
Specific heat	c	J kg^{-1} K^{-1}
Rate constant	C	s^{-1}
Activation energy	E	J kg^{-1}
Thermal conductivity	σ	W m^{-1} K^{-1}
Permeability	K	m^2
Porosity	ε	
Viscosity	μ	kg m^{-1} s^{-1}
Reaction enthalpy	Δh	J mol^{-1}
Reaction entropy	Δs	J mol^{-1} K^{-1}
Heat transfer coefficient	h	W m^{-2} K^{-1}
Density	ρ	kg m^{-3}

Table 2: Symbols for miscellaneous quantities

Quantity	Symbol	Unit
Pressure	p	bar
Temperature	T	K
Velocity	u	m s^{-1}
Thermal conductivity	σ	W m^{-1} K^{-1}
Time	t	s

Table 3: Symbols for chemical compounds

Chemical element	Symbol
Magnesium	Mg
Nickel	Ni
Sodium	Na
Hydrogen	H
Fluorine	F
Lanthanum	La
Aluminium	Al
Iron (Ferrous)	Fe
Titanium	Ti
Chromium	Cr
Manganese	Mn
Cobalt	Co

Table 4: Subscripts

Description	Symbol
Metal hydride (solid)	s
Hydrogen (gas)	g
Heat transfer fluid	l
absorption	a
mass	m
Thermal energy	T

The Experimental Performance Characterisation of a Three Module Phase Change Energy Storage System for Domestic Heating Applications

Pawel D. Nycz, Mohamed Fadl and Philip C. Eames

CREST, Loughborough University, Loughborough (UK)

Abstract

The experimental thermal performance characterisation of a novel compact latent heat thermal energy storage unit comprised of three modules filled with a commercial phase change material (PCM) CrodaTherm™ 53, with a peak melting/crystallization temperature of 52 °C, was undertaken using a recently developed thermal storage module characterisation facility. For the intended space heating/hot water application a compact thermal energy storage system with at least 10kWh storage capacity was required, that could be charged using an air source heat pump and discharged to a low temperature hydronic heating system or to provide domestic hot water. Each of the three modules employed in the characterized thermal store are rectangular in cross section with a compact finned tube heat exchanger submerged into the PCM. The test facility allows the modules to be charged and discharged singly or concurrently in parallel or series with near constant heat exchange fluid inlet temperatures and volume flow rates. Experimentally measured store outlet temperatures, charge and discharge powers and cumulative heat charged and discharged to and from the store, are presented for the cases when charging and discharging the 3 modules comprising the store in both parallel and series flow modes. Fluid inlet temperatures of 70 °C were used for charging and 10 °C for discharging with four heat transfer fluid volume flow rates, 1.5, 3, 4.5 and 6 l/min.

Keywords: Phase change material, modular design, thermal energy storage, domestic heating applications

1. Introduction

Thermal energy storage (TES) is likely to play a significant role in the transition to low/zero carbon heating/cooling systems and in the electrification of heat in buildings because it can help to overcome the mismatch between energy production and demand. The mismatch to be addressed can be in temperature, time, location or power (Ibrahim et al. 2017, Eames et al. 2014). The large-scale application of heat pumps for domestic heat provision is planned in some countries with the intended phase out of domestic gas boilers, for example the UK plans to phase out installation of domestic gas boilers in new build dwellings by 2025 with the ambition to phase out gas boilers in all homes from 2035. Due to lack of diversity in space heating requirements which are strongly weather dependent, this is likely to lead to significantly increased loads on the low voltage electricity supply network and significant increases in peak winter electricity generating requirements. Another consequence of this is that there will probably be significant increases in electricity tariffs at these times. With an electricity generation mix that is increasingly renewables based, this will lead to greatly increased energy storage requirements. Using distributed thermal energy storage can allow heat generation and demand to be effectively decoupled, this will have the benefits of reducing peak electricity demands and grid loads and allow consumers to take advantage of any periods with low electricity tariffs to charge their thermal energy storage system. If the space required to install a thermal energy storage system is not an issue thermally stratified sensible water based heat storage can be employed, however, if space is at a premium a more compact store will be required due to space constraints and phase change material based stores may be an attractive option.

Phase change thermal energy storage systems have been proposed and trialled for both building heating and

© 2022. The Authors. Published by International Solar Energy Society
Selection and/or peer review under responsibility of Scientific Committee
doi:10.18086/eurosun.2022.13.08 Available at http://proceedings.ises.org

cooling applications. The range of phase change temperatures generally considered for building applications is 0-60 °C. Materials with phase change temperatures in this range include water/ice, a range of paraffin waxes, inorganic salt hydrates and bio based PCMs. Storage solutions developed have included micro encapsulated PCMS in for example wall boards, Tyagi et al. (2010), macro encapsulated PCMs in thermal stores with the heat transfer fluid flowing around them da Cunha and Eames (2017) and PCMs with embedded heat exchangers Fadl and Eames (2021) and Fadl et al. (2021).

An issue with PCM storage systems is that many PCMs when solid unfortunately have relatively low thermal conductivity, typically 0.2 to 0.6 $Wm^{-1}K^{-1}$, Agyenim et al. (2010). For heat storage applications when charging the store heat is transferred into the store raising the temperature of the solid PCM, causing it to melt adjacent to the heat exchange surface, when sufficient PCM melts natural convection is established enhancing heat transfer rates between the heat exchanger surfaces and solid PCM still to be melted. When discharging the store, PCM will solidify on the heat exchanger surfaces reducing the rate of heat transfer that occurs, this can lead to long discharge times and low power delivery rates. To address this important issue a number of different approaches have been proposed to increase heat transfer to and from the PCM, a review by Agyenim et al. (2010), provides an overview of some of the approaches adopted including the use of fins, embedded high thermal conductivity matrices, metal rings, carbon brushes, graphite flakes, micro and macro encapsulation. Using fins to improve heat transfer to the PCM is one of the key approaches identified with an increasing amount of research currently being performed. Amagour et al. (2021), performed a 3D CFD analysis of a compact finned tube heat exchanger to assess the effects of heat transfer fluid flow rate, heat transfer fluid inlet temperature and number of fins on charging and discharging performance. Fadl and Eames (2021) performed a detailed experimental investigation of the thermal performance of a PCM storage unit with a finned copper tube heat exchanger. Anish et al. (2021) performed simulations of an horizontal shell and tube PCM heat store with and without fins using a 2-d CFD model to assess changes in melting rates that could be achieved with different tube and fin arrangements.

2. Experimental program

2.1 PCM module and storage system design

The aim of the research undertaken was to develop a compact thermal energy storage system with at least a 10 kWh storage capacity that can be charged using an air source heat pump or electrical heating and discharged to a low temperature hydronic heating system or to provide domestic hot water.

The fabricated and characterised PCM system comprised of three identical modules. Each fabricated module shown in Fig. 1 was cuboid in shape and comprised of two containers with insulation inserted between the interior and exterior walls. To allow observation of the melting/solidification process during the charging and discharging process the containers were made so that the tops of the containers could be removed. The exterior dimensions of the inner containers made from 0.9 mm thick stainless steel 304 were 230 by 530 by 500 mm width, length, height). The interior dimensions of the outer container made from 1.2mm Aluminium were 310 by 610 by 580 mm (width, length, height). Foam board insulation of 30mm thickness was inserted at the sides and top and 40 mm at the base between the internal and external walls of the stores to reduce heat losses. A 72 pass compact copper tube and aluminium finned heat exchanger illustrated in Fig. 1 was used in each of the store modules. The exterior dimensions of the copper tubes were 12.7 mm and the aluminium fins were 0.2 mm thick, spaced 6.5 mm apart and extended continuously across the heat exchanger cross sectional area. The distance between centers of adjacent copper tubes was 35 mm. The heat transfer fluid flow arrangement through the heat exchanger leads to a vertical temperature gradient in the heat exchanger when charging and discharging. The surface area available for heat exchange per module was approximately 1.36 m^2 from the surface of the copper pipes, 8.89 m^2 from the aluminium fins, and 0.39 m^2 from the end plates providing a total heat transfer surface area of 10.64 m^2.

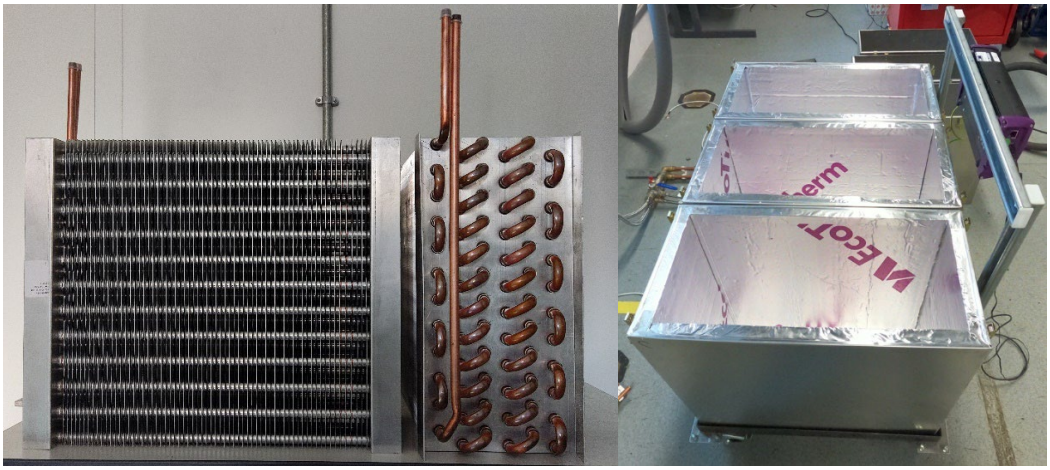

Fig. 1: Side and end view of the heat exchanger used in each of the PCM modules and the three exterior module containers with attached wall insulation.

The selection of the PCM CrodaTherm 53 that was used in these experiments was based on the delivery temperature available from a CO_2 air source heat pump, taken to be 70 °C, to charge the store, and the demand temperature, taken to be 40 to 45 °C, for low temperature hydronic heating systems, fan assisted radiators, underfloor heating or hot water for showers and baths. The key thermal properties of CrodaTherm 53 are presented in Tab. 1. From DSC and three-layer calorimetry it was found that the majority of the melting enthalpy is in the range from 51 to 54 °C with a peak at 52 °C, the majority of the crystallisation enthalpy is in the range 50 to 52 °C with the peak again at 52 °C.

Tab. 1: Thermal and physical properties of CrodaTherm™ 53 according to the manufacturer [Croda 2018].

Property	**Typical Value**
Peak melting/solidification temperature	52 °C
Latent heat, melting	226 kJ/kg
Bio-based content	100 %
Density at 22 ºC (solid)	904 kg/m^3
Density at 60 ºC (liquid)	829 kg/m^3
Specific heat capacity (solid)	1.9 kJ/(kg·K)
Specific heat capacity (liquid)	2.2 kJ/(kg·K)
Volume expansion 22ºC- 60 ºC	9.1%
Thermal conductivity (solid)	0.28 W/(m·K)
Thermal conductivity (liquid)	0.16 W/(m·K)

The weight of the PCM used in each module was 40 kg, assuming that the store is operated between 37 and 57 °C and that the phase change occurs over a 4 °C range based on Differential Scanning Calorimetry measurements, the heat that can be stored in the PCM using the data from table 1 is approximately 10,290 kJ or 2.85kWh (latent heat of 9,040kJ between 51 °C to 54 °C and sensible heat of 990kJ between 37 °C and 51 °C and 260kJ from 54 °C to 57 °C). Based on the mass of materials used in the interior container module construction and heat exchanger, the sensible heat capacity of these components over the 20 °C temperature range is approximately 210 kJ or 0.06 kWh, the heat capacity of the water heat transfer fluid over the same temperature range is 320kJ or 0.09kWh providing a total storage capacity of approximately 3 kWh per module. For the full range of temperatures used in the experimental program, assuming the store is operated from 10 °C to 70 °C, the energy storage

capacities in the range10 °C to 51 °C is 3,460kJ (0.96 kWh), from 51 °C to 54 °C is 9,080kJ (2.52kWh), and from 54 °C to 70 °C is 1,580kJ (0.44kWh) per module, or in total for each module 14,120 kJ (3.92kWh). For the full 3 module store this gives a heat storage capacity of 42,350 kJ or 11.76 kWh. From these figures it can be seen that the latent heat capacity makes up approximately 88% of the energy stored between 37 and 57 °C and for the larger temperature range, 10-70 °C, 64.3%. In addition, the mass of hot water in each module is approximately 3.7kg, the temperature of the store at the start of charging will be at 10 °C and at the end of charging 70 °C, which equates to an additional 980 kJ or 0.27 kWh increase in heat stored per module or 0.81 kWh for the 3 module store leading to a total heat storage capacity of 12.58 kWh.

2.2 PCM storage system testing

To charge and discharge PCM thermal energy storage systems a new experimental thermal store test facility was designed and developed that enables up to four PCM storage modules to be charged/discharged concurrently with well controlled heat transfer fluid volume flow rates and temperatures. The schematic in Fig. 2 shows the fluid flow circuits. A Huber Unistat 510W was used to cool the water flowing to the cooling loop storage tank and a Huber T320 was used to provide heat to the heating loop storage tank. Two and three way valves were used to select the fluid circuit flow paths and regulate the heat transfer fluid volume flows to each module. Flow meters were located on the pipe prior to the pipe connections used for attaching PCM modules for testing and in the main hot and cold fluid circulation loops.

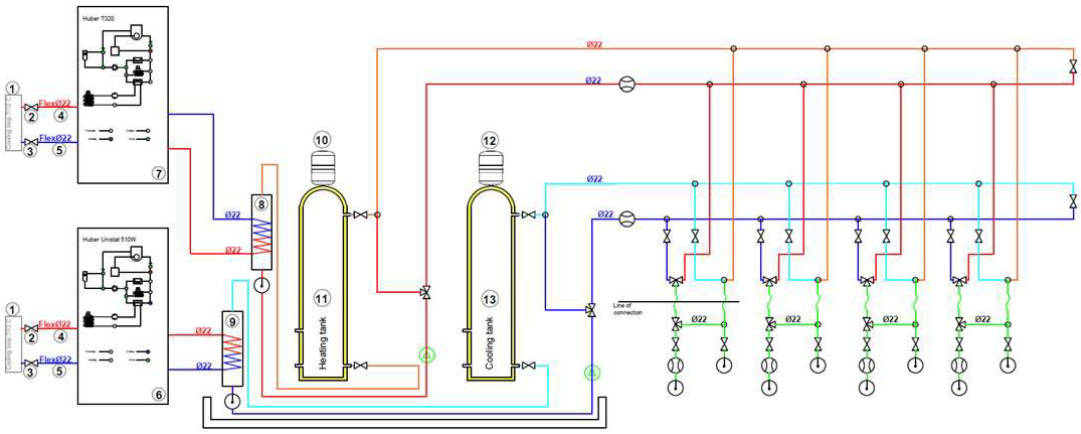

Fig. 2: A schematic diagram showing the fluid flow circuits and the key components in the developed thermal storage test loop.

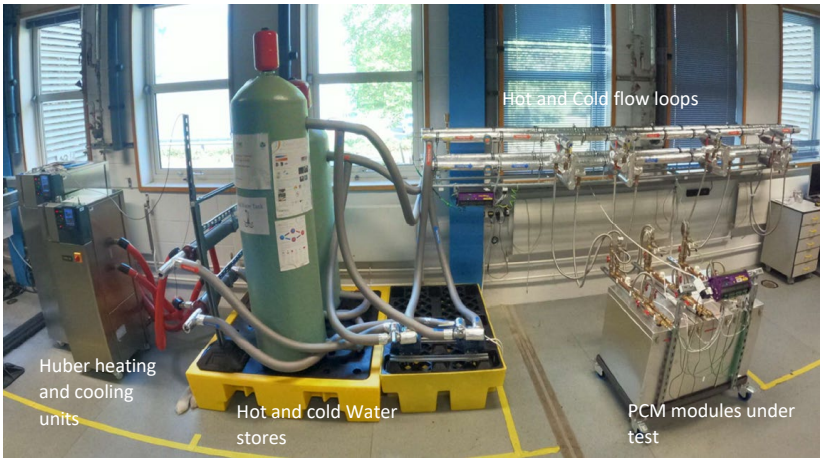

Fig. 3: An image of the developed laboratory PCM module test facility.

The developed laboratory test facility is shown in Fig. 3 with the 3 module PCM store connected prior to test.

2.3 The experimental test program

Two sets of experiments were performed, one with the PCM modules arranged in series and one with the modules arranged in parallel. The hot water charging temperature was set to 70 °C in all store charging experiments. The cold water inlet temperature for discharging was set to 10 °C in all store discharging experiments. For real charging conditions using a heat pump or electric heating constant heat input would be more realistic rather than a constant temperature input which is more likely if using a district heat supply to charge the storage system. The discharging temperature was selected to represent winter mains cold water temperatures. Fluid flow meters were used to measure flow volumes in the hot and cold flow loops and to each individual module. Temperatures were measured using T type thermocouples on the inlet and outlet pipes to each module and at a selection of locations within each PCM module monitored to enable the temperature distribution within the store to be determined. All temperature and flow measurements were taken on a 5 second basis for the full duration of each test and stored to a data logger. The heat transfer fluid flow volumes through each module used in the parallel module operation flow experiments were 0.5, 1, 1.5 and 2 l/min leading to combined flows of 1.5, 3, 4.5 and 6 l/s. For the experiments with the PCM modules arranged in series flow volumes of 1.5, 3, 4.5 and 6 l/s were used to enable direct comparison of performance characteristics. From the measurements of volume flow and inlet and outlet temperature the total heat delivered or extracted from the store and the instantaneous input/output power were determined

3. Experimental Results

3.1. PCM System Charging

With a set inlet temperature of 70 °C the measured store outlet temperatures for the four volume flow rates of 1.5, 3, 4.5 and 6 l/min for parallel and series flow operation are presented in Fig. 4.

It can be seen from Fig. 4 that for all volume flow rates the measured outlet temperatures increased more rapidly for the parallel flow arrangement than for the series flow arrangement. Higher heat transfer volume flow rates deliver greater amounts of heat and consequently lead to more rapid increases in temperatures with shorter periods of time required for each stage of charging. From Fig. 4 it can be seen that there are 4 distinct phases of charging. In the first phase of charging, (the area of the graph below line A) heat is transferred to the solid PCM from the hot inlet fluid, due to the low specific heat capacity of the solid PCM a rapid rise in PCM temperature results and the outlet fluid temperature rises rapidly. In the second phase of charging when the PCM commences melting, (the area of the graph between line A and line B) due to the high latent heat capacity the PCM temperatures increase slowly with a reduction in the rate of increase of the hot outlet fluid temperature. In the third phase after

the PCM melts (the area of the graph between line B and line C) heat is transferred to the liquid PCM, due to the low specific heat capacity of the liquid PCM the PCM temperature rises rapidly and the temperature of the outlet fluid again rises rapidly. In the fourth phase (the area of the graph above line C), the store outlet temperature approaches the heat transfer fluid inlet temperature, 70 °C, the rate of temperature increase in the PCM reduces due to the decreasing temperature difference between the hot heat transfer fluid and the PCM. Increased heat losses from the store will also occur due to the greater temperature difference between the store and the ambient environment.

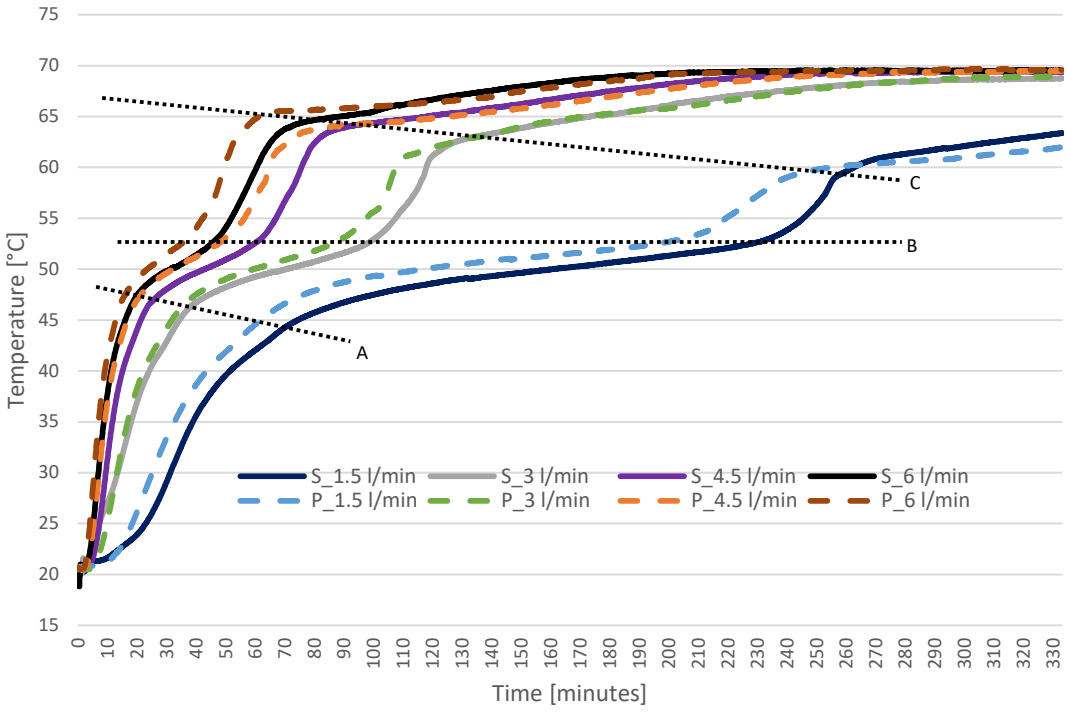

Fig. 4: The heat transfer fluid outlet temperatures from the PCM stores during charging for series (S) and parallel (P) flow arrangements with heat transfer fluid inlet temperature of 70 °C.

Using the measured inlet and outlet heat transfer fluid temperatures and the measured volume flow rates of heat transfer fluid through the PCM modules the rates of heat input to the store were calculated for both parallel and series flow arrangements for the fluid flow rates of 1.5, 3, 4.5 and 6 l/min and are presented in Fig. 6. Slight variations in the measured flow rates with time resulted in the noise that can be seen in the heat input values presented in Fig. 6. It can be seen that the heat input rates for parallel and series flow arrangements generally follow similar profiles, however the series flow arrangement maintains higher rates of heat input during phase change for slightly longer than the parallel flow arrangement. At the start of the charging process due to the large temperature difference between the hot heat transfer fluid and the store high heat input rates result, 21.5 kW for 6l/min, 15.5 kW for 4.5 l/min, 10 kW for 3 l/min and 5 kW for 1.5 l/min, a near linear relationship of peak heat input rates with flow volume. As the temperature of the PCM in the store increases the rate of heat input decreases. When PCM phase change commences the rate of decrease in heat input reduces with a period of more stable heat input. For the different flow rates 6, 4.5, 3 and 1.5 l/min the average values of heat input during phase change are 8, 6.25, 4.5 and 2kW for approximate durations of 25, 35, 70 and 170 minutes corresponding to heat inputs of 3.3kWh, 3.6kWh, 5.3 kWh and 5.7kWh clearly showing that the effects of phase change on outlet fluid temperatures are more significant for lower heat transfer fluid volume flow rates After the phase change period the rate of heat input decreases approaching zero for all but the 1.5 l/min flow by the end of the experiment at 330

minutes.

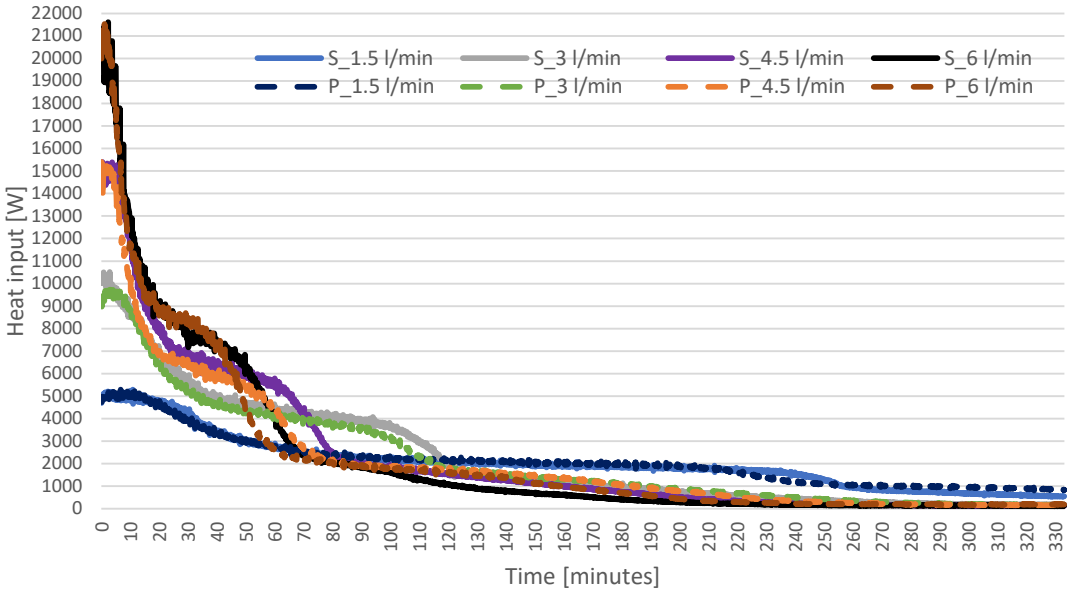

Fig. 5: The calculated rate of heat input to the 3 module PCM store for series (S) and parallel (P) flow arrangements

Using the instantaneous calculated values of heat input for each experimental test the cumulative heat input to the store during the charging period was calculated and is presented in Fig. 6. It can be seen from Fig. 6 that the series flow arrangement achieves more rapid charging for a given heat transfer fluid volume flow rate and that the rate of charging increases with increasing heat transfer fluid flow volume. For all tests the cumulative heat input to the store increases rapidly until approximately 2 kWh of heat is stored indicated by line A on Fig. 6, after this the rate of increase remains constant at a lower level until approximately 8.5kWh is stored indicated by line B, following this the rate of cumulative heat input again decreases reducing towards zero when approaching the maximum store storage capacity of 12.58 kWh.

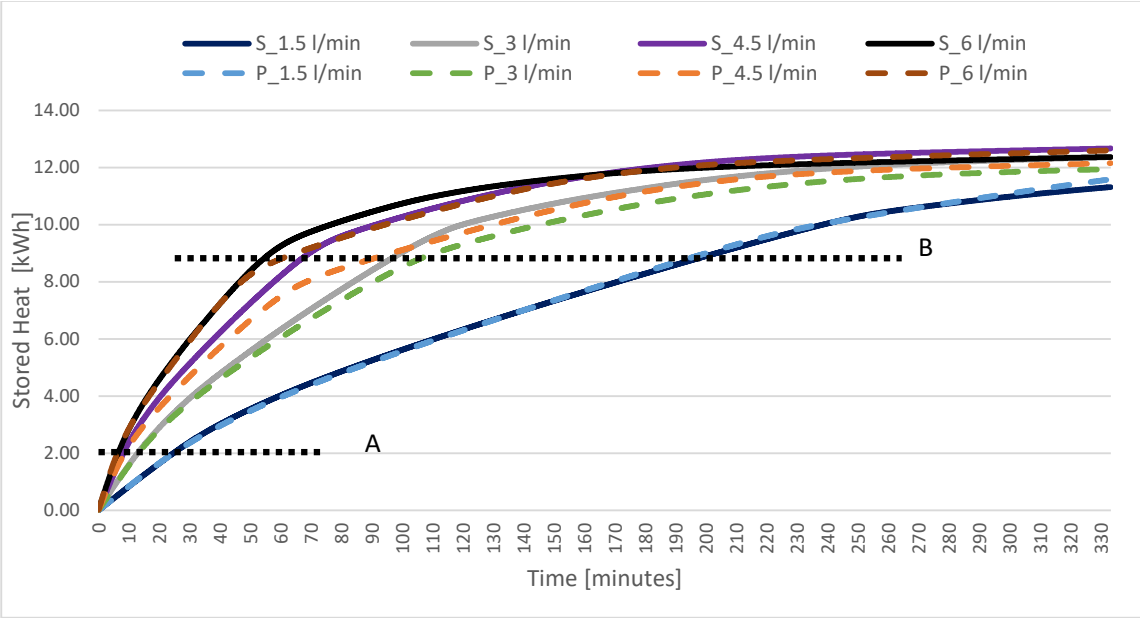

Fig. 6: The calculated cumulative heat charged to the 3 module PCM store for series (S) and parallel (P) flow arrangements

3.2. PCM System Discharging

With a set inlet temperature of 10 °C the measured outlet temperatures for the four volume flow rates 1.5, 3, 4.5 and 6 l/min for parallel and series flow operation are presented in Fig. 7. It can be seen from Fig. 7 that initially the outlet temperatures decrease rapidly at a near constant rate until phase change starts to occur indicated by line A. In the initial phase of discharging, duration decreasing with higher volume flow rate, heat is transferred from the liquid PCM to the cold inlet fluid leading to a rapid decrease in PCM temperature due to the low specific heat capacity of the liquid PCM and the outlet fluid temperature decreases rapidly to approximately 51 °C. Between line A and line B, corresponding to phase change of the PCM, the rate of decrease in outlet temperature initially reduces, followed by a period of constant outlet temperature and then starts to reduce again. The period of constant output temperature is dependent on the heat transfer fluid volume flow rate, being longer for lower volume flow rates. The constant outlet temperature is approximately 51 °C corresponding well to the temperature of the peak crystallization enthalpy of the PCM, 52 °C. For all volume flow rates the period for which a constant outlet temperature is maintained is greater for the series flow arrangement. After the PCM solidifies indicated by B on the Fig. 7 heat is transferred to the now solid PCM and the temperature of the outlet fluid again decreases rapidly to line C after which it then slowly decreases approaching the inlet fluid temperature.

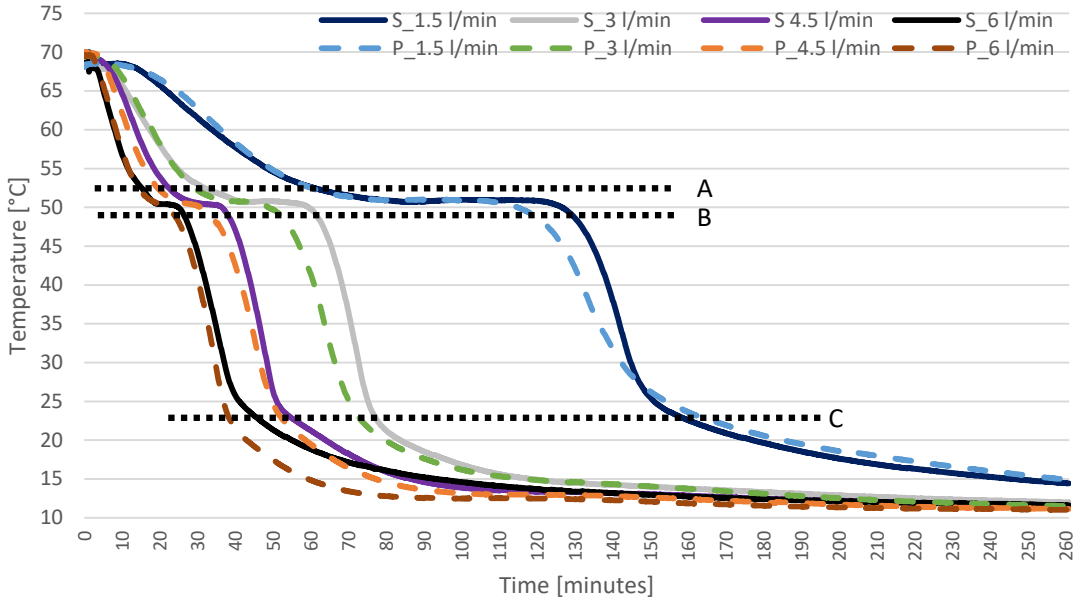

Fig. 7: The measured store outlet temperature during discharging from the PCM stores for series (S) and parallel (P) flow arrangements with heat transfer fluid inlet temperature of 10 °C.

Using the measured inlet and outlet temperatures and the measured volume flow rates of heat transfer fluid through the PCM modules the rate of heat transfer from the store was calculated for both parallel and series flow arrangements for the fluid flow rates of 1.5, 3, 4.5 and 6 l/min and is presented in Fig. 8. Slight variations in measured flow rate resulted in the noise in heat output values presented in Fig. 8. It can be seen that the heat output rates for parallel and series flow arrangements generally follow similar profiles, however the series flow arrangement maintains a constant power output during phase change for slightly longer than the parallel flow arrangement. At the start of the discharging process due to the large temperature difference between the cold heat transfer fluid and the store, high heat output rates result, over 24 kW for 6l/min, 18 kW for 4.5 l/min, 12 kW for 3 l/min and 5.5 to 6 kW for 1.5 l/min, a near linear relationship of heat output with flow volume. As the temperature of the liquid PCM in the store decreases the rate of heat output decreases. When the PCM phase change commences the rate of decrease in heat output reduces with a period of more stable heat output achieved. For the

different flow rates 6, 4.5, 3 and 1.5 l/min the average values of heat output during phase change are 15, 10.5, 8 and 4kW for approximate durations of 10, 20, 40 and 80 minutes corresponding to 2.5, 3.5, 5.3 and 5.3 kWh. After the phase change period the rate of heat output decreases slowly approaching zero.

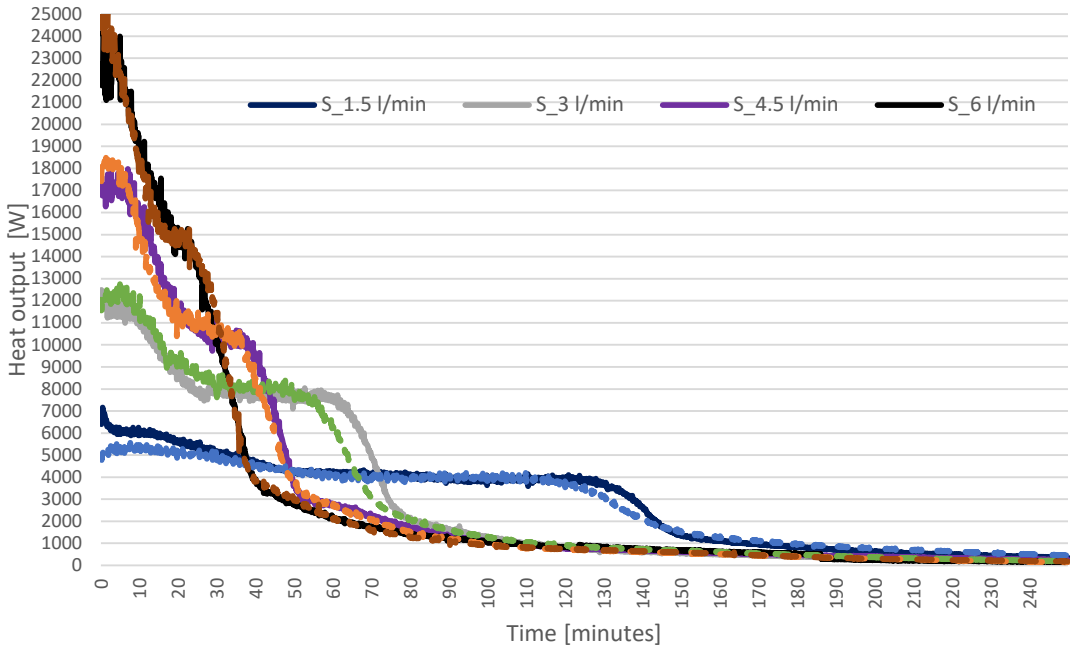

Fig. 8 The calculated heat output during store discharging from the PCM stores for series (S) and parallel (P) flow arrangements with heat transfer fluid inlet temperature of 10 °C.

Fig. 9 presents the calculated cumulative heat discharged from the PCM store. It can be seen that the heat discharged for parallel and series flow arrangements is similar for all volume flow rates. Prior to phase change commencing when sensible heat is being discharged from the liquid PCM the gradient of the lines gradually decreases corresponding to the reduction in temperature difference between the PCM and the cold heat transfer fluid. After this during phase change, below line A, the gradients of the lines are approximately constant corresponding to a steady temperature difference between the heat transfer fluid and the PCM. For the flow volumes of 1.5 and 3 l/min the slightly longer discharge at constant power can be seen for the series flow arrangement compared to the parallel flow arrangement. For the flow rates of 4.5 and 6 l/min the difference in the rate and amount of heat discharged is very small. Above line A the temperature difference between the solid PCM and the heat transfer fluid decreases with a consequent reduction in heat delivered.

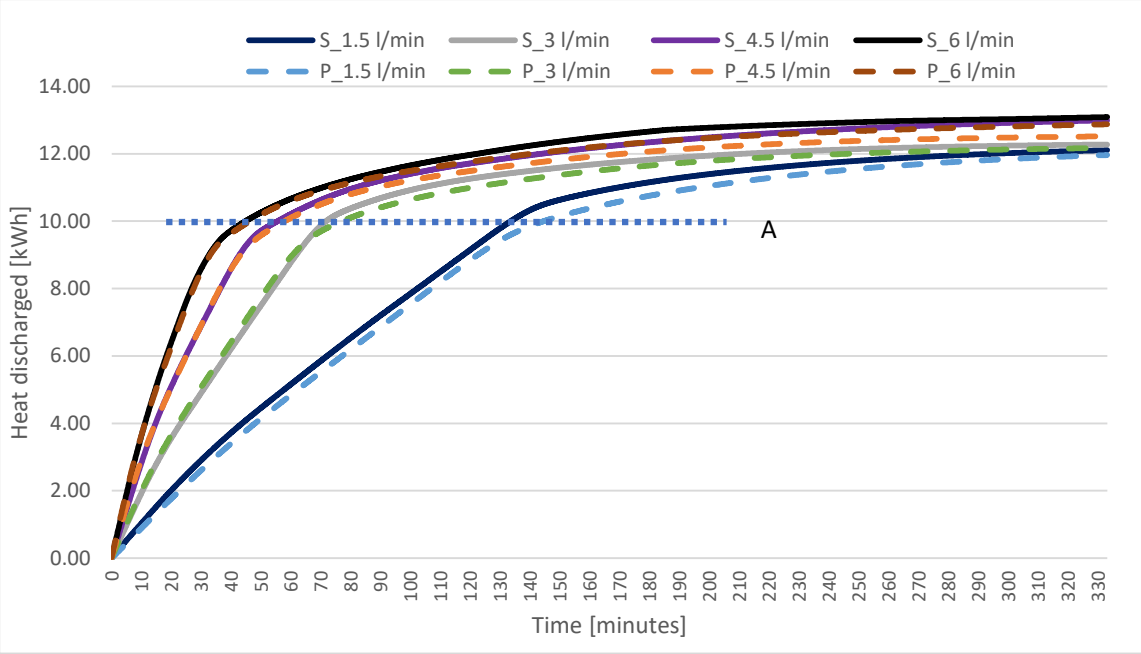

Fig. 9: The calculated cumulative heat delivered from the PCM store for series (S) and parallel (P) flow arrangements

Using figure 7 to determine the time for which outlet temperatures of over 50 °C can be delivered and figure 9 to determine the cumulative amount of heat delivered the volume of water that could be delivered at these temperatures after mixing with cold water can be determined. For example for series flow through the store with a flow of 6 l/min the duration of time for which the outlet temperature is above 50 °C is approximately 30 minutes with approximately 9.5 kWh of heat delivered, assuming that the hot water is mixed with cold water at 10 °C, 233 l can be delivered at 45 °C, sufficient to run approximately three baths.

The rate of heat output from the 3 module PCM stores achieved for flows of 1.5 l/min and 3 l/min were greater than 4 kW for 130 min and greater than 8kW for 60 min with the outlet temperatures above 51 °C. This would make the store feasible for use with a heat pump in a well insulated dwelling with a low temperature hydronic heating system, fan assisted radiators or underfloor heating. If the space heat load being met was 4kW the store if fully charged would allow the heat pump to be turned off for 2 hours at times of peak grid electrical load allowing high tariff periods to be avoided.

4. Conclusions

A 3 module PCM store was designed, fabricated and characterized for both parallel and series flow through the modules. When charged to 70 °C and discharged with heat transfer fluid flow volumes of 1.5, 3, 4.5 and 6 l/min and an inlet temperature of 10 °C heat transfer fluid outlet temperatures were maintained above 50 °C for series flow for periods of approximately 135, 65, 45 and 30min, slightly less for parallel flow. The heat delivery rate from the stores with flow rates of 1.5, 3, 5.5 and 6 l/min was greater than 4kW, 8kW, 10.5kW and 15kW for similar amounts of time. For a well insulated dwelling with a space heat load of 4kW using an heat pump to provide heating the fully charged store could provide sufficient heat for 2 hours at times of peak grid electrical load allowing high tariff periods to be avoided. If used to provide domestic hot water at temperatures of 45 °C for bathing, the hot water delivered from the store at temperatures above 50 °C when mixed with cold water would be able to run three 80 l baths at just under 45 °C. The modular approach allows additional modules to be added to increase the storage capacity. The option of parallel or series operation allows all modules or individual modules to be charged/discharged providing greater flexibility in operation.

5. Acknowledgments

The authors gratefully acknowledge the Engineering and Physical Sciences Research Council (EPSRC) for funding this research through grant EP/V012053/1, The Active Building Centre Research Programme (ABC RP) and EP/R045496/1 Low Temperature Heat Recovery and Distribution Network Technologies (LoT-NET).

6. References

Agyenim, F., Hewitt, N., Eames, P. and Smyth, M., 2010. A review of materials, heat transfer and phase change problem formulation for latent heat thermal energy storage systems (LHTESS). *Renewable and sustainable energy reviews*, *14*(2), pp.615-628. https://doi.org/10.1016/j.rser.2009.10.015

Amagour, M.E.H., Bennajah, M. and Rachek, A., 2021. Numerical investigation and experimental validation of the thermal performance enhancement of a compact finned-tube heat exchanger for efficient latent heat thermal energy storage. *Journal of Cleaner Production*, *280*, p.124238. https://doi.org/10.1016/j.jclepro.2020.124238

Anish, R., Joybari, M.M., Seddegh, S., Mariappan, V., Haghighat, F. and Yuan, Y., 2021. Sensitivity analysis of design parameters for erythritol melting in a horizontal shell and multi-finned tube system: Numerical investigation. *Renewable Energy*, *163*, pp.423-436. https://doi.org/10.1016/j.renene.2020.08.153

Croda. CrodaTherm 53, Croda Phase Change Materials 2018. https://www.crodatherm.

da Cunha, J.P. and Eames, P., 2017. Phase Change Materials to Meet Domestic Hot Water Demand in the UK-A Numerical Study. *Journal of Fluid Flow, Heat and Mass Transfer (JFFHMT)*, *4*(1), pp.11-18. DOI: 10.11159/jffhmt.2017.002

Eames P.C., Loveday D., Haines V., Romanos P. 2014, The Future Role of Thermal Energy Storage in the UK Energy System: An assessment of the Technical Feasibility and Factors Influencing Adoption. Res Rep (UKERC London)

Fadl, M. and Eames, P.C., 2021. Thermal performance evaluation of a latent heat thermal energy storage unit with an embedded multi-tube finned copper heat exchanger. *Experimental Heat Transfer*, pp.1-20. DOI: 10.1080/08916152.2021.1984342

Fadl, M., Mahon, D. and Eames, P.C., 2021. Thermal performance analysis of compact thermal energy storage unit-An experimental study. *International Journal of Heat and Mass Transfer*, *173*, p.121262. https://doi.org/10.1016/j.ijheatmasstransfer.2021.121262

Ibrahim N.I., Al-Sulaiman F.A., Rahman S., Yilbas B.S., Sahin A.Z., 2017. Heat transfer enhancement of phase change materials for thermal energy storage applications: A critical review. Renew Sustain Energy Rev 74, 26–50. https://doi.org/10.1016/j.rser.2017.01.169

Tyagi, V.V., Kaushik, S.C., Tyagi, S.K. and Akiyama, T., 2011. Development of phase change materials based microencapsulated technology for buildings: a review. *Renewable and sustainable energy reviews*, *15*(2), pp.1373-1391. https://doi.org/10.1016/j.rser.2010.10.006

Analysis of a latent heat storage unit using a pillow plate heat exchanger during real operations in a zero-emission building

Jorge Salgado-Beceiro[1], Olav Galteland[1] and Alexis Sevault[1]

[1] SINTEF Energy Research, Trondheim (Norway)

Abstract

The zero-emission building (ZEB) Laboratory (Trondheim, Norway) has an innovative latent heat storage (LHS) unit. It consists of 24 parallel pillow plates and 3 tons of phase change material (PCM) CT37 (biowax – transition temperature 37 ˚C). There are two different operation modes to charge and two to discharge the LHS system depending on the heat demand, electricity costs, and forecast prediction, as it can be combined with photovoltaic panels installed on the building. After several months of utilization with a time-based control strategy, results on the temperature of the LHS unit versus the heat output and heat storage capacity over four consecutive weeks in winter 2021-2022 have been analysed. The results here presented shown a good reversibility in the partial charge/discharge processes (~120 kWh) during real operations of the building. We also report the contribution of the LHS unit to stabilise the room temperature of the building and to its heat demand. The long-term heat loss (1.29%) was also calculated, confirming the previously predicted value. The results obtained in this work are of high interest to improve the system design and the development of a predictive control strategy for the energy management of the whole building.

Keywords: Latent heat storage, phase change materials, PCM, building, peak shaving, pillow plate

1. Introduction

In 2021, the zero emission building (ZEB) Laboratory (www.zeblab.no; Time et al., 2019), owned by SINTEF and NTNU, was commissioned in Trondheim (Norway) as an office building and living laboratory (see Fig. 1). This building and all its systems (construction phase, regular operations, and materials) were and are being made towards having the corresponding CO_2-emissions fully offset within the 60 first years of operations of the building. One of the technologies that were implemented and demonstrated to reach this goal is a latent heat storage (LHS) unit (see Fig. 2) using a phase change material (PCM) for the central heating system of the building (Nocente et al., 2021; Sevault et al., 2022, 2020, 2019; Sevault and Næss, 2020).



Fig. 1: Zero-emission building (ZEB) Laboratory. Photo: Nicola Lolli / SINTEF

The LHS unit is integrated together with a heat pump providing hot water to preheat domestic hot water and feed radiators and heat ventilation air for space heating (Sevault et al., 2019; Sevault and Næss, 2020). The local district heating is also connected to the heating system. The LHS unit was built to store the excess heat during low-heat demand and release it during high demand. This experimental unit was custom-designed and demonstrated by the integration path offering the most flexibility in the heating system.

© 2022. The Authors. Published by International Solar Energy Society
Selection and/or peer review under responsibility of Scientific Committee
doi:10.18086/eurosun.2022.13.09 Available at http://proceedings.ises.org



Fig. 2: 200-kWh PCM heat storage unit installed at the ZEB Lab. Photo: Alexis Sevault / SINTEF

The main objective of this study is to analyze the thermal performance of the LHS unit during real operations of the central heating system of the ZEB laboratory for several days.

The design and integration of the LHS unit have been previously described by Sevault and Næss, 2020. The building heating system has two main hydronic heat sources: an air-to-water heat pump and the return loop of the local district heating network (see Fig. 3) providing heat at around 40-47 °C.

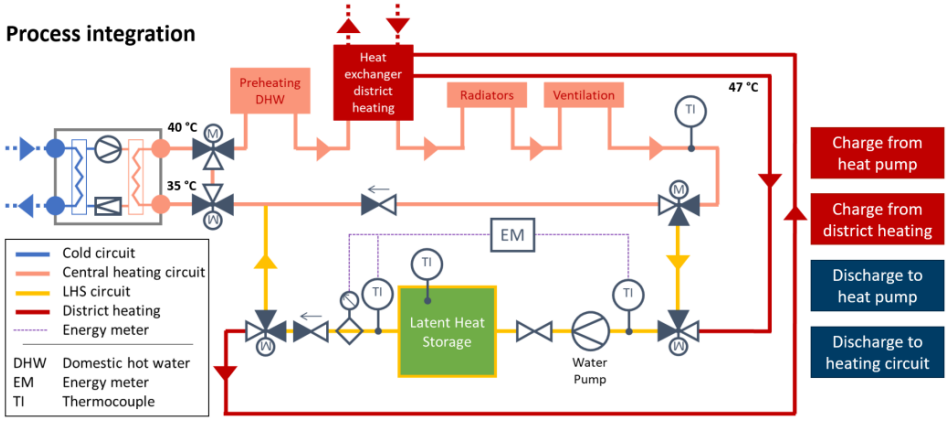

Fig. 3: Simplified process diagram of the central heating system focusing on the integration of the LHS unit, with four different operation modus. Only the instrumentation for control of the LHS unit is shown.

There are 4 different operation modes depending on the charge or discharge of the LHS unit: discharge to heat pump; charge from heat pump; discharge to the building heating system; or charge from the district heating. The system is currently following a time-based routine to establish a performance benchmark. However, a model predictive control strategy using combined economic and environmental objectives is in development and to be tested in the coming months.

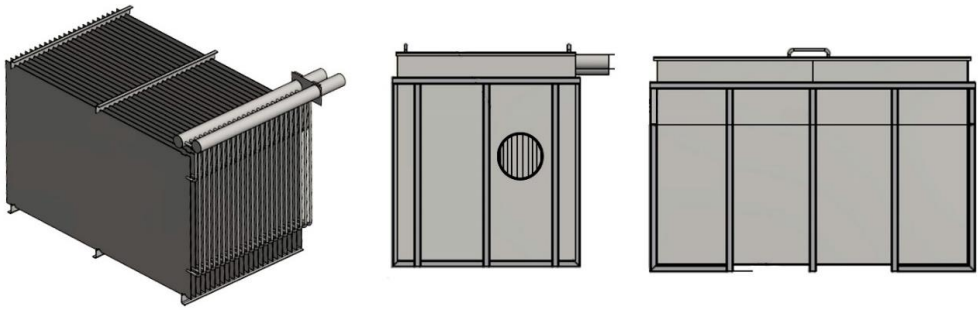

Fig. 4: Geometry of the LHS unit without container, left. The middle and right figures are lateral and front views, respectively.

The integrated LHS unit results from a design investigation (Sevault et al., 2019; Sevault and Næss, 2020) and is based on a pillow plate heat exchanger design (Mastani Joybari et al., 2022; Selvnes et al., 2019; Vocciante and Kenig, 2021) with 24 laser-welded stainless-steel pillow plates, mounted vertically in parallel. Water circulates in each of them following a 2-pass pattern. The LHS unit is filled with 3 tons of PCM CT37 (Crodatherm™ biowax – transition temperature 37 ˚C) to occupy the volume between the pillow plates. The specifications of the LHS unit and the PCM are described in Tab. 1. The geometry of the unit, with a pillow plate heat exchanger design, is shown in Fig. 4 (Sevault et al., 2022).

Tab. 1. Specifications of the LHS unit and the PCM CT37 (Sevault et al., 2022)

Dimensions of LHS unit (height * width * length) [m]	1.5 * 1.4 * 2.25
Measured PCM melting temperature range [°C]	35 – 39 (heat flow peak at 36.5)
Measured PCM solidification temperature range [°C]	32.5 – 35.5 (heat flow peak at 34.5)
Measured PCM latent heat of fusion [kJ/kg]	198.6
Measured PCM latent heat of crystallisation [kJ/kg]	196.4
PCM density [kg/m3]	957 (at 32 °C), 819 (at 75 °C)
PCM thermal conductivity [W/(m.K)]	0.24
PCM specific heat capacity [kJ/(kg.K)]	2.3 (solid), 1.4 (liquid)
PCM degradation temperature [°C]	90
Total theoretical thermal storage capacity [from 30 to 40 °C] [kWh]	194
The ratio of latent heat to total heat storage capacity	87 %

The performance of the LHS unit with a full charge and discharge was analyzed previously (Sevault et al., 2022). In that study, it was reported a maximum operating heat storage capacity of ca. 200 kWh. However, that study was run out of the time-based routine, so that the subsequent building conditions (very low or high temperature) could not affect the comfort of the users of the building. For a more realistic analysis of the performance of the LHS, it is necessary to carry out longer-term studies during the daily routine of the building, considering factors such as the energy demand of the building or the heat loss of the system, which were not included in the previous work. This complementary data, in addition to electricity cost and weather forecast (it is worth mentioning that the building has also photovoltaic panels) will help to develop the predictive control strategy for the energy system of the building (Drgoňa et al., 2020; Gholamibozanjani et al., 2018), so the LHS can operate with the most efficient modus depending on the conditions.

2. Monitoring system

For the analysis of the temperature distribution in the LHS system, 30 thermocouples were placed in different strategic locations. The thermocouples were distributed in 3 sets: PCM volume, along the pillow plates, and in the outer walls of the PCM-heat-exchanger tank. In addition to the thermocouples, energy meters were located outside the LHS unit to measure the process water mass flow rate and the inlet and outlet temperatures.

The analysis of the data collected in a full charge and discharge led to conclude different facts about the performance of the unit: there is a preferential water-course path inside the heat exchanger plates; and large free convection effects during charge were observed (Sevault et al., 2022). These phenomena did not significantly affect the performance of the LHS unit, but it must be noted that the mentioned analysis was run with a high temperature difference between the charge and the discharge. In the present work, we will focus on 4 weeks of performance of the unit during winter, pausing the activity during weekends. Also, the collected data will be compared to the calculated energy demand of the building and the external temperature.

3. Results and discussion

As the local thermal performance of the LHS system in its different parts was already studied, for this work we will show only the average temperature collected by the thermocouples along the heat exchanger plates over 4 weeks. Fig. 5 shows the calculated mean of the temperature from the sensors located in the pillow plates. We will consider this average as the temperature that the LHS can reach with the heating/cooling water that flows inside the pillow plates. The temperature range where the solidification and melting of the PCM take place is shaded in yellow and corresponds to 35-39 ˚C according to differential scanning calorimetry measurements from the previous work.

Observing Fig. 5, the temperature reached by the LHS unit is usually around the phase transition region. However, there are cycles where the maximum and minimum temperatures for charging and discharging (respectively) do not

reach much above or below the limits of the phase transition. This could mean that the LHS-unit is not fully charged or discharged, so it is necessary to look at the data collected by the energy meters for further analysis.

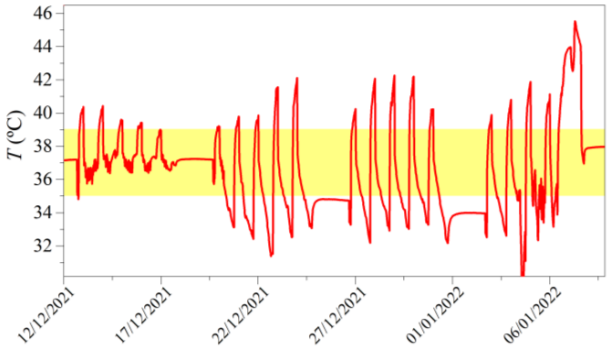

Fig. 5: Average temperature of the pillow plate thermocouples as a function of time. Yellow zone: phase change region (according to our own DSC measurements).

The process water mass flow rate, as well as its inlet and outlet temperatures, were measured using the energy meters located outside the LHS unit. Fig. 6 (left) shows the heat flow to the LHS unit. It can be observed that the heat flow is not constant during every charge and discharge. In the same way, the maximum charging and discharging temperatures are not constant either. This irregular heat flow is related to both varying inlet water temperature and the PCM along the pillow plates heating up or cooling down during discharge/charge processes and, thus, changing phase. The latter phenomenon significantly affects both the local thermal conductivity in the PCM and reduces the temperature difference between PCM along the pillow plate and water flow temperature, thus reducing the heat flow.

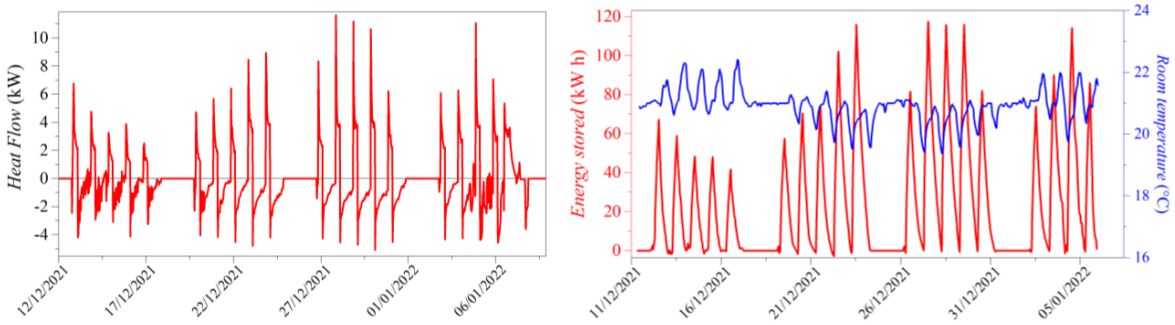

Fig. 6: (Left) Heat flow (power) measured by energy meters outside of the LHS unit, as a function of time for the LHS unit. Positive values indicate charging, while negative values indicate discharging. (Right) Red: Energy stored as a function of time calculated as the integral of the heat flow; The zero in the y-axis corresponds to the lowest recorded energy level in the LHS unit during the given period. Blue: average room temperature inside the building.

It can be observed that the maximum/minimum heat flow is reached when the temperature in the heat exchangers is considerably above or below the phase transition limits (35-39 ˚C). By integrating the energy flow as a function of time, the thermal energy storage capacity is obtained, and so is the energy level of the LHS unit (see Fig. 6, right). For the period studied in this work, the maximum energy stored was ca. 120 kWh. It takes around 6 hours to reach this level of charge in these operating conditions, but the charging time depends mostly on inlet water temperature, whose difference with the PCM average temperature was mostly under 5 K here. The discharging time for 120 kWh was around 18 hours in the given conditions. It must be noted that the LHS unit can be charged and discharged up to 200 kWh at maximum capacity, as was confirmed in our previous work.

By comparing the energy stored and released to the room temperature in the building, it can be observed that the processes of charge and discharge contribute to the regulation of the room temperature of the building (21±1 ˚C).

The total heat demand of the central heating system is the sum of heat produced by the heat pumps, heat extracted from district heating, heat discharged from LHS, minus the heat used charge the LHS. The calculated average daily heat demand is 22.2 kWh, while the peak heat demand was 104.8 kWh.

One important result from the partial charge and discharge tests shown here is that the energy level always comes down to zero between partial cycles. Since it was calculated form the energy meters outside the LHS unit, this means that it was possible to extract as much energy from the LHS unit as it was previously stored, despite the charge cycles not being completed. This shows reversibility in the partial charging/discharging processes, which ensures a close to 100 % round-trip thermal efficiency.

The average heat loss of the LHS unit has been calculated to be (107.8±0.2) W, which is an average heat loss of 1.29% over 24 hours. This has been calculated by linear regression of the heat flow into the unit over the period from January to June 2022. Due to the heat loss over time, more heat is supplied than what is discharged from the unit. This is in reasonable agreement with previous results (Sevault et al., 2022), which predicted the heat loss to be 1% over 24 hours based on the amount of insulation material on the unit. Note that the heat loss from the LHS-unit occurs inside the temperature-regulated building in this case, which is thus not a real energy loss for the building.

4. Conclusions

The zero-emission building (ZEB) Laboratory is an office building and living laboratory using an energy system with a latent heat storage (LHS) unit, which can be charged from heat pumps or district heating, and can be discharged to the central heating system. The performance of the LHS unit has been investigated in a period of four weeks during winter 2021-2022.

By analyzing the effect of the inlet and outlet temperatures to the LHS unit, it was observed that the unit is not always fully charged and often follow partial charge/discharge cycles. However, when the LHS-unit is partially charged, it releases almost the same energy in the discharge. The obtained heat loss over time is in agreement with the theoretically calculated in our previous work, which confirms the methodology for its prediction. Even though the maximum capacity of the LHS unit is 200 kWh from previous full charge tests, in this work we report a maximum storage capacity of 120 kWh (partial charge) under real operations in the building during 4 weeks. The maximum energy stored was linked to the actual heating demand of the building during the time period, when 200 kWh daily heat storage was not needed. Even though the LHS unit contributes to stabilise the room temperature of the building, the control system of the LHS unit is not optimal. The water inlet temperatures to the LHS unit should have a better prediction, so the system could decide under which modus it is operating in case a larger temperature difference for its charge or discharge is required. The heat demand of the building must also be included in the input data for the predictive control strategy to finely adjust the heat to be delivered by the LHS unit. Having now confirmed that the LHS unit operates efficiently in partial charges and discharges operations, the predictive system will confidently take into account partial charge/discharge as an extra degree of freedom of operations. These results will contribute to the design of the predictive control strategy to reach a higher efficiency of the whole heat management of the building.

5. References

Time, B., Nocente, A., Mathisen, H.M., Førland-Larsen, A., Myhr, A.R., Jacobsen, T., Gustavsen, A., 2019. ZEB Laboratory - Research Possibilities. SINTEF Notes 33, Trondheim.

Nocente, A., Time, B., Mathisen, H.M., Kvande, T., Gustavsen, A., 2021. The ZEB Laboratory: the development of a research tool for future climate adapted zero emission buildings. J. Phys.: Conf. Ser. 2069, 012109. http://dx.doi.org/10.1088/1742-6596/2069/1/012109

Sevault, A., Salgado-Beceiro, J., Pires Bjørgen, K.O., 2022. 200-kWh latent heat storage unit using a pillow-plate heat exchanger: demonstration in an office building. *15th IIR-Gustav Lorentzen Conference on Natural Refrigerants*, Trondheim, 13-15 June.

Sevault, A., Vullum-Bruer, F., Tranås, O.L., 2020. Active PCM-Based Thermal Energy Storage in Buildings, in: Reference Module in Earth Systems and Environmental Sciences. Elsevier, pp. 453-469. http://dx.doi.org/10.1016/B978-0-12-819723-3.00008-1

Sevault, A., Bøhmer, F., Næss, E., Wang, L., 2019. Latent heat storage for centralized heating system in a ZEB living laboratory: integration and design. *IOP Conference Series: Earth and Environmental Science*, Trondheim, 6-7 November.

Sevault, A., Næss, E., 2020. Active latent heat storage using biowax in a central heating system of a ZEB living lab. *14th IIR-Gustav Lorentzen Conference on Natural Refrigerants (GL2020)*. Kyoto, 7-9 December.

Mastani Joybari, M., Selvnes, H., Sevault, A., Hafner, A., 2022. Potentials and challenges for pillow-plate heat exchangers: State-of-the-art review. Applied Thermal Engineering 214, 118739. http://dx.doi.org/10.1016/j.applthermaleng.2022.118739

Selvnes, H., Hafner, A., Kauko, H., 2019. Design of a cold thermal energy storage unit for industrial applications using CO2 as refrigerant. *25th IIR International Congress of Refrigeration Proceedings*, Montreal, 24-30 August.

Vocciante, M., Kenig, E.Y., 2021. Pillow-Plate Heat Exchangers: an Overview on Advances, Limitations and Prospects. Chemical Engineering Transactions 88, 865–870. https://doi.org/10.3303/CET2188144

Sevault, A., Salgado-Beceiro, J., Pires Bjørgen, K.O., 2022. 200-kWh latent heat storage unit using a pillow-plate heat exchanger: demonstration in an office building. *15th IIR-Gustav Lorentzen Conference on Natural Refrigerants*, Trondheim, 13-15 June.

Drgoňa, J., Arroyo, J., Cupeiro Figueroa, I., Blum, D., Arendt, K., Kim, D., Ollé, E.P., Oravec, J., Wetter, M., Vrabie, D.L., Helsen, L., 2020. All you need to know about model predictive control for buildings. Annual Reviews in Control 50, 190–232. https://doi.org/10.1016/j.arcontrol.2020.09.001

Gholamibozanjani, G., Tarragona, J., Gracia, A. de, Fernández, C., Cabeza, L.F., Farid, M.M., 2018. Model predictive control strategy applied to different types of building for space heating. Applied Energy 231, 959–971. https://doi.org/10.1016/j.apenergy.2018.09.181

Numerical Investigation of Thermal Stratification and Numerical Diffusion in a Large-scale Water Pits Heat Storage

Meng Gao, Jianhua Fan and Simon Furbo

Department of Civil and Mechanical Engineering, Technical University of Denmark, Kgs. Lyngby, Denmark

Abstract

Large scale water pit heat storage (PTES) is a key component to increase the efficiency of solar thermal utilization. Based on the 1535-1301 model, this paper presents a two-dimensional simulation of the annual thermal performance of PTES using TRNSYS. This model encrypts the soil grid according to the water pit layers to improve the accuracy of heat loss calculation. The accuracy of the model is verified by comparing it with measured data from a solar plant in Dronninglund, Denmark. The results show that the average difference between the model and the measured data is approximately 2.5%. In addition, the temperature prediction error and numerical diffusion of each layer become smaller as the nodes number increases. The stratification coefficient averages about 200 for summer charging and decrease to 100 for winter discharging, Mix number is 0.7 at charge and 0.35 at minimum, indicating that stratification is more pronounced in summer and mixing is higher in winter. The parametric coupling study found that the nodes number and the time step are more accurate when they are negatively correlated, i.e., fewer nodes are paired with longer time steps. Adiabatic admixture decreases the Mix number prediction accuracy but increases the stratification coefficient one.

Keywords: Water pit heat storage, Numerical investigation, Thermal stratification, large-scale, numerical diffusion

1. Introduction

Reducing the utilization of fossil resources and carbon emission is very important for sustainable development around the world. Renewable energy, such as solar energy, is one of the main ways to solve this problem. As known to all, thermal storage technology is a key measure to solve the problem of low density, discontinuous fluctuation and unreliability of renewable energy, which can realize effective regulation of heat. Especially, seasonal thermal storage is significant in the large-scale district application of renewable energy (Vega, 2010).

Different STES technologies and applications have been extensively studied. The STES are normally categorized into four types: tank thermal energy storage (TTES), pit thermal energy storage (PTES), borehole thermal energy storage (BTES), and aquifer thermal energy storage (ATES) (Bauer, 2010). The best solution should be determined based on technical-economic assessment considering storage capacity, efficiency, requirements on regional conditions, building cost, etc. Originated from landfill technology, PTES has the advantages of high heat capacity, low construction investment, good corrosion protection and effective heat exchange. In recent years, many attempts of larger PTES have been carried out in Europe. More than 10 large-scale PTESs have been put into operation in Denmark (Bott, 2019).

Denmark is currently the leading country in the application of PTES. The first large PTES with a volume of 500 m^3 was built at the Technical University of Denmark and was investigated intensively (Heller, 1997). In the last decade, 75% of PTES construction projects have been built in Denmark (Bratseth, 2021). The integration of PTES on such a large scale is difficult to plan and implement because technical and economic differences pose different challenges for each country (Dahash, 2019). The commercialization of PTES is expected to accelerate in the coming years. However, large-scale PTES testing is difficult due to high experimental costs. Therefore, modeling and design optimization of PTES play a key role in ensuring feasibility.

TRNSYS performs well as a software for system simulation in modeling thermal storage of different types. However, the existing literature studies focus more on the system simulation including the selection and operation strategies of thermal storage. Few studies on thermal storage and especially PTES models have been especially validated by measurements. The current TRNSYS models are simplified to a vertical one-dimensional model of the water pit to reduce computational resources (Pan, 2022). The reason is that PTES shows a significant thermal stratification along

© 2022. The Authors. Published by International Solar Energy Society
Selection and/or peer review under responsibility of Scientific Committee
doi:10.18086/eurosun.2022.13.10 Available at http://proceedings.ises.org

the depth, while the horizontal temperature gradient is not prominent enough to be negligible. However, this simplification leads to some additional problems, i.e., numerical diffusion due to grid size and time step, and inverse mixing due to temperature differences in water delivery (Xiang, 2022). If these problems are not solved will result in large deviations in the calculation results and affect the accuracy of models.

In this paper, a model of PTES (Type 1535-1301) from TRNSYS containing 1D water pit and 2D soil is used as a research object. The measured data of 60,000 m^3 of PTES in Dronninglund, Denmark, in 2017 are utilized as input parameters and validation data. The stratification coefficient and Mix number are taken as an indicator to evaluate the stratification effect during the energy charging and discharging period. The coupling effects of layer number, time step and mixing revisions on the computational accuracy are investigated. The quantitative equation of the deviation value versus the simulation parameters is obtained by comparing the measured data. Thus, the discrete differences due to the simplification of the computational domain are corrected.

2. Methodology

2.1. The structure and principle of PTES

The geometry of the PTES at the Dronninglund SDH plant is an inverted truncated pyramid with a slope angle of 26.6°, as shown in Fig. 1. The lengths of the top and bottom edges are 90 m and 26 m, respectively. Three diffusers are installed at the top, middle and bottom of the water pit, switching as inlet or outlet according to the system's operating strategy. Disc-shaped stratifiers located above and below the diffusers greatly reduce turbulent mixing and maintain stable thermal stratification. During rainy days, nights or when heat demand is high, hot water is delivered from the top and cold water is fed to the bottom. At this time, the internal energy of PTES is reduced in what is called the discharge period. In sunny days, hot water is imported at the top and cold water is exported from the bottom. The increase of PTES energy at this moment is called the charge period.

Since the PTES is buried monolithically with only a 2.5 mm HDPE liner and a 2 mm geotextile layer on its sides and bottom, there is no additional insulation. Because the surrounding soil serves both as insulation and as a medium for thermal energy storage. Covering the top of the water pit storage with insulation is an effective way to reduce heat loss. In addition, multiple sets of drainage pipes are installed between the insulation and the waterproofing layer to prevent rainwater infiltration.

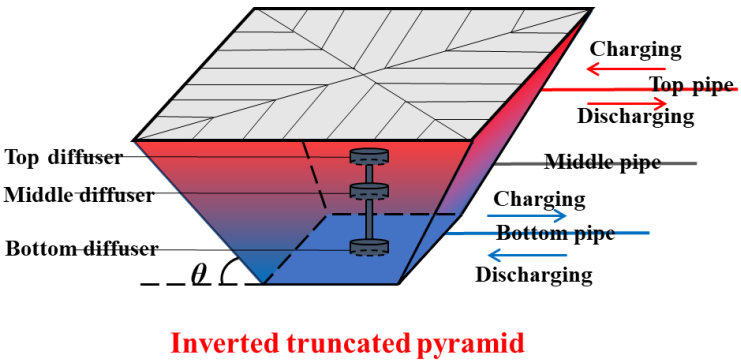

Fig. 1: The structure of water pit heat storage

2.2. The grid scheme of PTES

A PTES model written in FORTRAN is developed on TRNSYS, named type 1535-1301. The type 1535 is a one-dimensional water pit model including the heat exchanger in the interior. Because PTES has a significant temperature gradient only in the depth direction. The type 1301 is a two-dimensional surrounding soil model including the insulation layer above. The soil temperature varies only in one horizontal direction. The geometry of both types is simplified to central-symmetric inverted cylindrical coordinates with only radius-direction and axial-direction. Fig. 2 shows the mesh of the simplified PTES model. Encryption above and below the baseline of the puddle meshing interface. This gridding allows for more accurate heat transfer simulations at temperature stratification intersections. In addition, the grid near the PTES is refined, while the grid near the bottom soil boundary is coarsened.

In addition, some assumptions are made for the heat transfer calculations. Only half of the water pit is modeled with the left boundary as the axis. The convective coefficient between the water pit and the wall is set to a constant value. Only the thermal conductivity is available in the soil fraction due to the neglect of the effect of moisture and

groundwater flow.

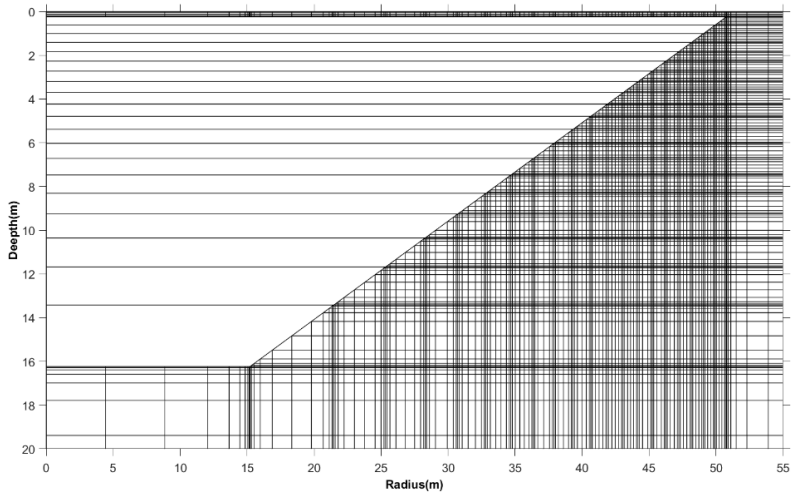

Fig. 2: The Mesh of Type 1535-1301 model

2.3. Mathematical description

The water pit node energy is a one-dimensional thermal conductivity calculation (Song, 2003). The explicit central differential form of the one-dimensional thermal conductivity equation is shown in Eq. (1), where the left part of the equation is the instantaneous energy change of the node, and the right part of the equation is the imported energy:

$$V_j C_p \rho_w \frac{\partial T_j}{\partial \tau} = \left[\frac{\lambda_w (r_j - r_{j+1})^2}{(z_{j+1} - z_j)} + m_j C_p + m_{mix,j} C_p\right](T_{j+1} - T_j) + \left(\frac{1}{h_w} + \frac{\delta_{\mathrm{HDPE}}}{\lambda_{\mathrm{HDPE}}} + \frac{\delta_{\mathrm{geo}}}{\lambda_{\mathrm{geo}}}\right)^{-1} A_{side,j}(T_{side,j} - T_j) + V_{in}\rho_w C_p (T_{in} - T_j) + Q_j \quad \text{(eq. 1)}$$

where Q_j denotes the additional energy input or output. At water pit of j = 1 and j = n (top and bottom nodes, respectively), Q_j satisfies the following formula:

$$Q_j = \begin{cases} U_{top} A_1 (T_{top} - T_1), & j = 1 \\ U_{bot} A_n (T_{bot} - T_n), & j = n \end{cases} \quad \text{(eq. 2)}$$

The soil and insulation are two-dimensional grids and therefore follow a two-dimensional heat transfer calculation as shown in Eq. (3). The partial differential equation uses the central difference method with *i,k* representing the radial and vertical nodes.:

$$V_{i,k} c\rho \frac{\partial T_{i,k}}{\partial \tau} = \frac{2 \cdot \lambda_s \cdot A_{i,k+1}}{z_{k+1} - z_k}(T_{i,k+1} - T_{i,k}) + \frac{2 \cdot \lambda_s \cdot A_{i,k-1}}{z_k - z_{k-1}}(T_{i,k-1} - T_{i,k}) + \frac{(z_{k+1} - z_k) \cdot \lambda_s}{2 \ln\left(\frac{r_{i+1}}{r_i}\right)}(T_{i+1,k} - T_{i,k}) + \frac{(z_k - z_{k-1}) \cdot \lambda_s}{2 \ln\left(\frac{r_i}{r_{i-1}}\right)}(T_{i-1,k} - T_{i,k}) + Q_{i,k} \quad \text{(eq. 3)}$$

where $Q_{i,k}$ denotes the boundary heat exchange and satisfies the following formula:

$$Q_{i,k} = \begin{cases} h_{am} A_{i,1}(T_{am} - T_{i,1}), & k = 1 \\ \frac{(z_k - z_{k-1}) \cdot \lambda_s}{\ln\left(\frac{r_{far}}{r_R}\right)} A_{R,k}(T_{far} - T_{R,k}), & i = R, k = (1, Z) \\ \frac{2 \cdot \lambda_s \cdot A_{i,k}}{z_Z - z_{Z-1}} A_{i,NZ}(T_{deep} - T_{i,NZ}), & i = (1, R), k = Z \\ U_{bot} A_{i,Nz}(T_{bot} - T_{i,Nz}), & i = (1, Nr), k = Nz \\ U_{side} A_{i,k}(T_{side,i,k} - T_{i,k}), & i = (Nr, NR), k = (NZ, Nz) \end{cases} \quad \text{(eq. 4)}$$

The average water pit temperature is obtained by volume averaging of all node temperatures, as shown in Eq. (5):

$$\bar{T} = \frac{\sum_{j=1}^{N} T_j V_j}{V_t} \quad \text{(eq. 5)}$$

2.4. Thermal stratification evaluations

Thermal stratification plays a crucial role in assessing the thermal performance of PTES. The optimal thermal stratification is the ideal plug flow, where the tank is divided into a high-temperature upper layer and a low-

temperature lower layer. The ideal thermal stratification allows for the lowest PTES mixing losses and the most stable heat extraction. The higher temperature difference between the top and bottom, the more efficient water-water heat pump as an auxiliary energy source. Furthermore, the lower return water temperature, the heat exchanger efficiency and collector efficiency will be increased. Consequently, even active cooling of the return water is required to obtain better stratification (Pinel, 2011). Mixing number and stratification coefficient are widely used to characterize the thermal stratification in heat storage.

The Eq. (6)-(9) calculate the mixing number by comparing the energy moments (Davidson, 1994), where M_c represents the energy moments obtained from experiments and simulations. When calculating the energy moment M_{mix} of the hybrid accumulator, the temperature of all layers is the same (Haller, 2009). The energy moment for complete stratification is represented by M_{str}, as shown in Eq. (8). Where the high and low temperature zone temperatures T_{hot} and T_{cold} are expressed as the highest and lowest inlet temperatures during the test, respectively:

$$M_c = \sum_{j=1}^{N} H_j \, \rho_w V_j C_p \cdot T_j \qquad \text{(eq. 6)}$$

$$M_{mix} = \sum_{j=1}^{N} H_j \, \rho_w V_j C_p \cdot \frac{Q_{sto}}{\rho_w \cdot C_p \cdot V_t} \qquad \text{(eq. 7)}$$

$$M_{str} = \sum_{j=1}^{N_{thermo}} \rho_w \, C_p V_j H_j \cdot T_{hot} + \sum_{j=N_{thermo}}^{N} \rho_w \, C_p V_j H_j \cdot T_{cold} \qquad \text{(eq. 8)}$$

$$MIX = \frac{(M_{str} - M_c)}{(M_{str} - M_{mix})} \qquad \text{(eq. 9)}$$

In addition, the stratification coefficient of equation (10) can also evaluate the thermal stratification effect. The stratification coefficient is more focused on the temperature level than the energy moment (Fernandez, 2007).

$$ST = \frac{\sum_j^N m_j (T_j - \bar{T})^2}{m_t} \qquad \text{(eq. 10)}$$

2.5. Model accuracy analysis

Model 1535-1301 is a pure thermal conductivity model, so discrete uncertainties can be ignored. The simplification of this model may lead to the following inaccurate results. The inlet and outlet values are considered as source terms of the equation and do not consider the thermal processes of the pipe. Changes in water content do not affect the thermal properties of the soil and may lead to an underestimation of heat losses. Constant convection coefficients lead to reduced accuracy in periods of high temperature fluctuations.

By comparing the calculated and measured parameters, the root mean square deviation (RMSD) was used, as shown in eq. (11).

$$RMSD = \sqrt{\frac{1}{N} \sum_{i=1}^{N} \left(P_{sim,i} - P_{mea,i} \right)^2} \qquad \text{(eq. 11)}$$

where, N presents the number of values in whole simulation period. $P_{sim,i}$ and $P_{mea,i}$ are respectively the calculated and the measured parameters every 10 mins.

The coefficient of determination R^2 is used to measure the accuracy of the model. This coefficient is a quantitative measure of the degree of variance in the data. Thus, it is possible to see how much of the variance in the data is captured (or predicted) by the modelled data. Where y denotes experimental data and f represents simulated data in equation (12).

$$R^2 = 1 - \frac{\sum_i (y_i - f_i)^2}{\sum_i (y_i - \bar{y})^2} \qquad \text{(eq. 12)}$$

2.6. Numerical diffusion

While Type1535-1301 greatly reduces the computational effort, the numerical diffusion caused by the simplification may affect the thermal stratification in the water puddle. As shown in Fig. 3, assume that each node in the water zone contains 2 kg of water with a stratification temperature difference of 10 °C. 1 kg/s of hot water enters the puddle from the top. Assuming no conduction and mixing between the nodes, the fluid in the first node will average 70°C over a time step of 2 seconds, while the other nodes will not be affected because there is no conduction or mixing between the nodes. However, the temperature of both the first and second nodes will be affected after 2 seconds at a time step of 1 second. The spurious diffusion of heat is caused by the simplified method of discretizing the geometry into a finite number of nodes; therefore, this is called numerical diffusion.

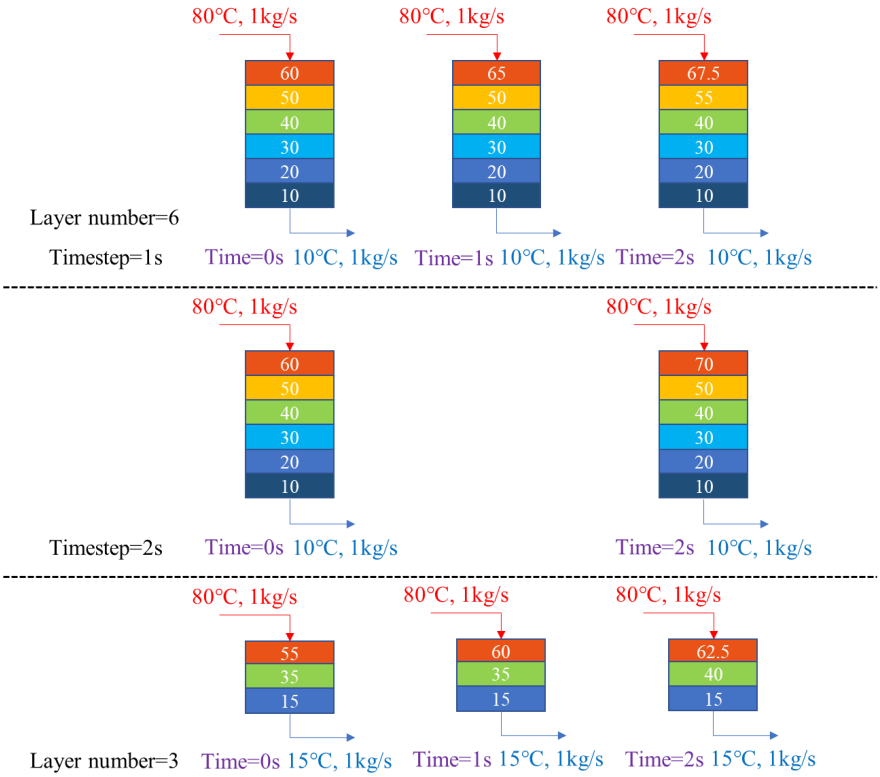

Fig. 3: Numerical diffusion in the simulation

It is possible to increase the number of nodes to try to improve the accuracy of the discretization, but this will lead to many computational nodes and longer computational times. And it may numerically extend the effect of node mixing, which in turn is detrimental to the accuracy. The second approach is to set a mixing factor in the model which can determine the volume to be mixed between the nodes. In order to explore the coupling effects of these parameters, the corresponding working conditions settings are given in Table 1.

Tab. 1: Parameter simulation working condition selection

Mixing factor (kg/h)	Timestep (mins)	Nodes number
adiabatic	0.5	15
0	1	20
1000	2	32
10000	5	50
	10	75
	30	100
	60	

3. Results and discussions

3.1. The influence of nodes number on thermal stratification

The nodes number (*N*) represent the number of one-dimensional meshes in the PTES, which can be used to study the relationship between meshes and calculation accuracy. Its physical expression can be seen in Fig. 2, which is represented by a symbol (*j*). The selection of nodes number and correlation diffuser location is provided in Table 2.

Table. 2: Storage discretization and diffuser's location

Nodes number *N*	Volume per node (m^3)	Top diffuser location	Middle diffuser location	Bottom diffuser location

15	4000	Node 1	Node 8	Node 15
20	3000	Node 2	Node 11	Node 20
32	1875	Node 3	Node 17	Node 32
50	1200	Node 4	Node 27	Node 50
75	800	Node 5	Node 40	Node 75
100	600	Node 7	Node 53	Node 100

For the evaluation of thermal stratification, Mix number and stratification coefficients draw different conclusions. Overall in terms of Fig. 4, both indicators reflect that more nodes result in better-calculated stratification. However, this is caused by large nodes ignoring mixing, which is invalid. Mix number agrees better with less than 20 nodes before July, deviates at least with 50 nodes from July to September, is closer to the results with 32 nodes from September to November, and is optimal again with less than 20 nodes after November. The reason for this strange result is the actual mixing at different periods. Although the TRNSYS model cannot calculate the mixing, the larger volume of individual nodes at low node numbers approximates the multilayer mixing. The individual nodes are smaller when the node number is high, thus effectively reducing the numerical diffusion but calculating the mixing worse. New methods are needed to solve this problem, such as setting the mixing coefficient or variable grid treatment. The accuracy of the stratification coefficient is positively correlated with node number because energy moments are not calculated in this formula. The stratification calculation is considered more reasonable as long as the temperature RMS sum is closer to the actual measurement. The Mix number is more realistic if the energy calculation accuracy is taken as a reference. The stratification coefficient is better if the temperature calculation precision serves as the basis.

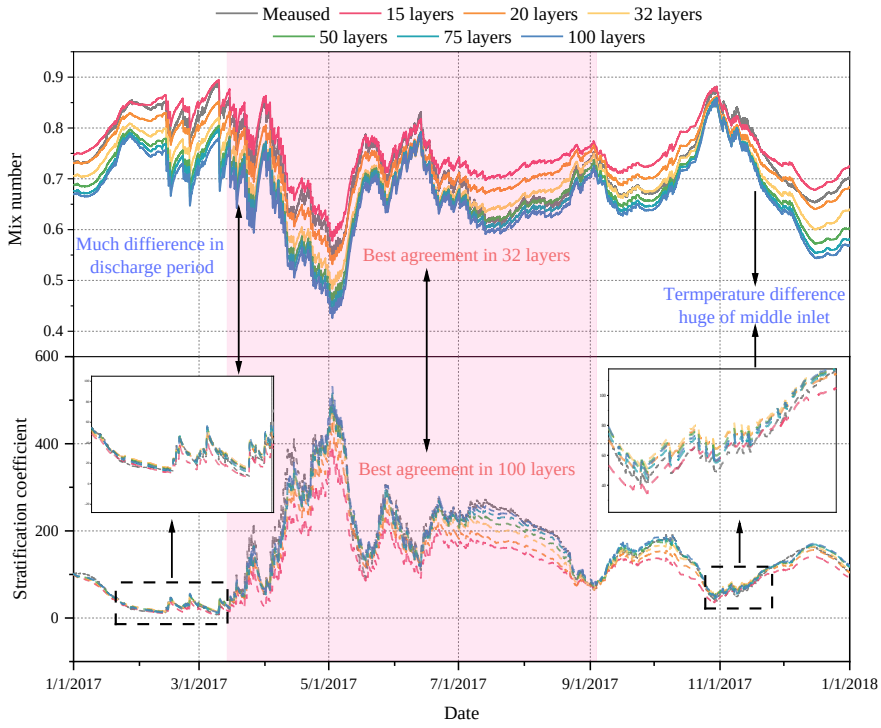

Fig. 4: Mix number and stratification coefficient changes with nodes number

3.2. The influence of timestep on thermal stratification

Fig. 5 reflects the effect of different time steps on the stratification calculation. The differences in Mix number and stratification coefficient are very small for time steps below 10mins, indicating that decreasing the time step does not significantly increase the computational accuracy. Therefore, it is undesirable to increase the calculation time by several times to increase the accuracy by less than 0.1%. And when the time step is larger than 30mins, the Mix number has a significantly larger deviation during the energy release. This indicates that too large a time step reduces the computation time at the expense of computational accuracy. Therefore, the time step selection should not be too large either, or 10mins seems to be the optimal choice at 50 node count. The influence law of stratification coefficient and Mix number is basically the same, only the difference will be smaller. It indicates that the temperature dispersion is not as sensitive to the change of time step compared to the energy dispersion.

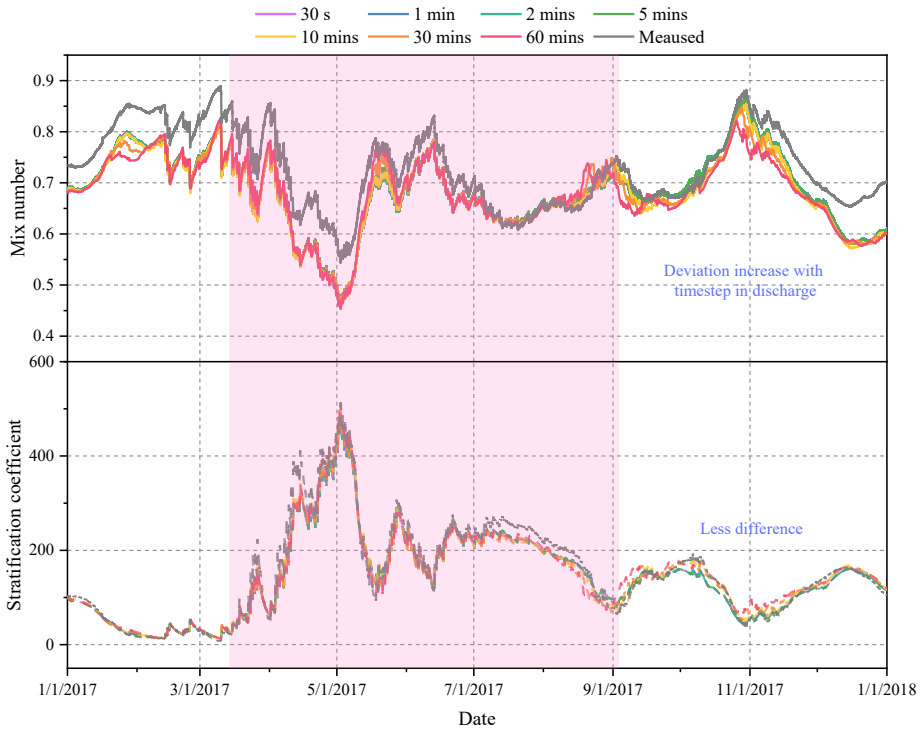

Fig. 5: Mix number and stratification coefficient changes with timestep

3.3. The influence of Mixing factor on thermal stratification

The treatment of mixing in this model is limited to the energy equation because the momentum equation is neglected. mixing within the PTES is caused by temperature differences and flow rates. Although the heat is eliminated by the assumption of thermal driving force, but it is not consistent with reality. Therefore, the concept of the mixing parameter mmix was introduced to correct this partial deviation. Fig. 6 gives a comparison of four forms of mixing with the actual measurements. 0 kg/h means no mixing, 1000 kg/h means small mixing, 10000 kg/h means large mixing, and finally adiabatic mixing represents node temperature reversal when j+1 node temperature is higher than j node temperature. The results show a significant difference between adiabatic mixing and the remaining parameters, especially between April and July during the charging phase. The accuracy of the adiabatic mixing calculation is slightly smaller for all the rest of the time, with the maximum Mix number difference reaching 0.1, implying that 10% of the volume is miscalculated. The exact opposite is true for the stratification factor calculations. The adiabatic blending improves the accuracy of the temperature discretization calculation. Overall, it is demonstrated that adiabatic blending overestimates the degree of dispersion within PTES, which is consistent with the temperature dispersion requirement but not with the energy moment variation.

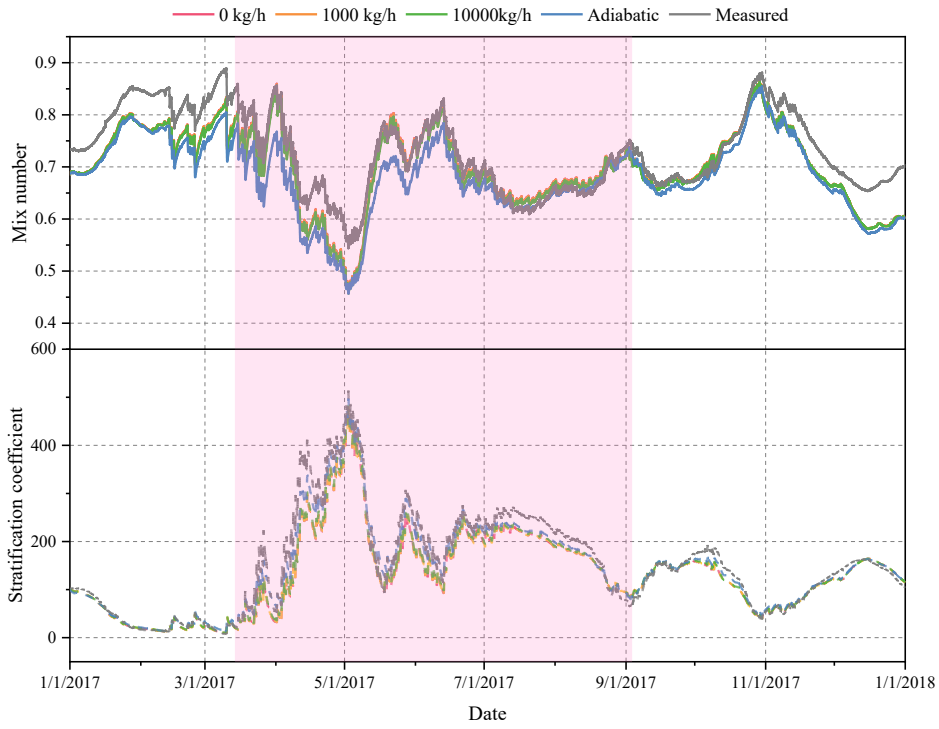

Fig. 6: Mix number and stratification coefficient changes with Mixing factor

3.4. Coupling effect of time step and nodes number on calculation accuracy

In the explicit finite difference calculation, the grid size corresponds to a minimum time step as shown in Eq. 13. However, this equation does not specify when the time step is large enough to meet the accuracy requirements with minimal computational resources. This is obviously a serious departure from reality, probably because this formula is only applicable to the refinement of small mesh sizes. Therefore, the mesh size is less meaningful for large size coarse simulations. In this paper, the number of stratifications is used instead of specific dimensions because it is dimensionless. The coupling effect of the number of layers and the time step on the computational accuracy is investigated.

$$min\left\{\frac{1}{\rho c V_k}\sum_j \frac{1}{R t_{kj}}\right\}\Delta\tau \leq 1 \qquad \text{(eq. 13)}$$

The Mix number represents the dispersion of the energy moment inside the PTES and the stratification coefficient represents the dispersion of the temperature inside the PTES. Therefore, only the deviation of the results of these two metrics from the actual measurement needs to be explored to cover all possible maximum deviations. The RMSD and R^2 are used to denote the root mean square error and the degree of variation of the stratification number, respectively. Figure 7(a) reflects the accuracy of Mix number calculation, and the results show that 15 nodes work best, with the highest accuracy at 1 min and 60 mins, and the accuracy decreases at 5mins. Conversely, the larger the number of nodes and time step, the worse the accuracy. In particular, at 100 nodes, the coefficient of variation is below 0.1 indicating that less than 10% of the parameters are fully captured and most of the results are not credible. The best matching scheme is 15 nodes with 60mins, 32 nodes with 10mins, 50 nodes with 5mins, and 100 nodes with 1min.

Figure 7(b) reflects the calculation accuracy of the stratification coefficients, and the results show that 100 nodes work best, and the smaller the time step the higher the accuracy. Conversely, the smaller the number of nodes, the worse the accuracy. The coefficient of variation is greater than 0.9 when the number of nodes is greater than 32, indicating that the calculation at this point can capture the experimental results well and with high confidence. 15 nodes have the lowest accuracy for the temperature discretization. The optimal time steps corresponding to each discrete node are 15 nodes with 60mins, 32 nodes with 60mins, 50 nodes with 10mins, and 100 nodes with 1mins.

In summary, it can be concluded that if we pursue computational speed, coarse grid with large time step unexpectedly can achieve good prediction results. This can significantly reduce the computational resource requirements and is suitable for long-term simulations of complex systems at the engineering level. If the highest accuracy is pursued, 32 nodes with 5mins can satisfy the maximum demand of Mix number and stratification factor. However, for the

number of temperature prediction nodes is still the more the better, then a new method is needed to correct the deviation of energy dispersion.

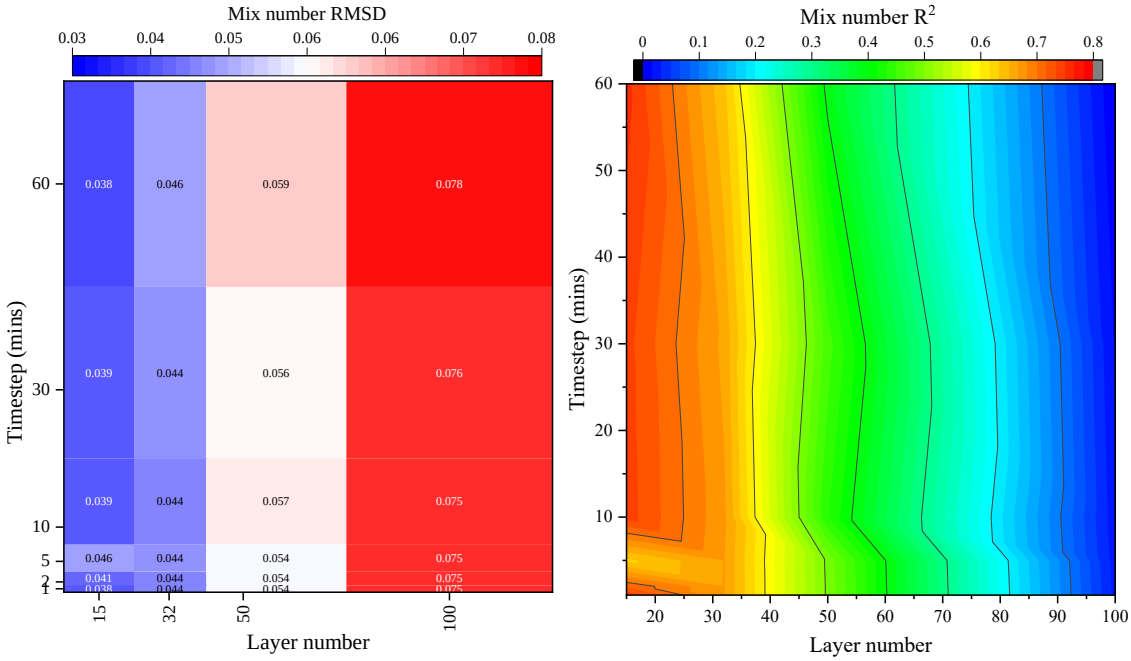

Fig. 7(a): The coupling effect of time step and nodes number on the Mix number calculation accuracy

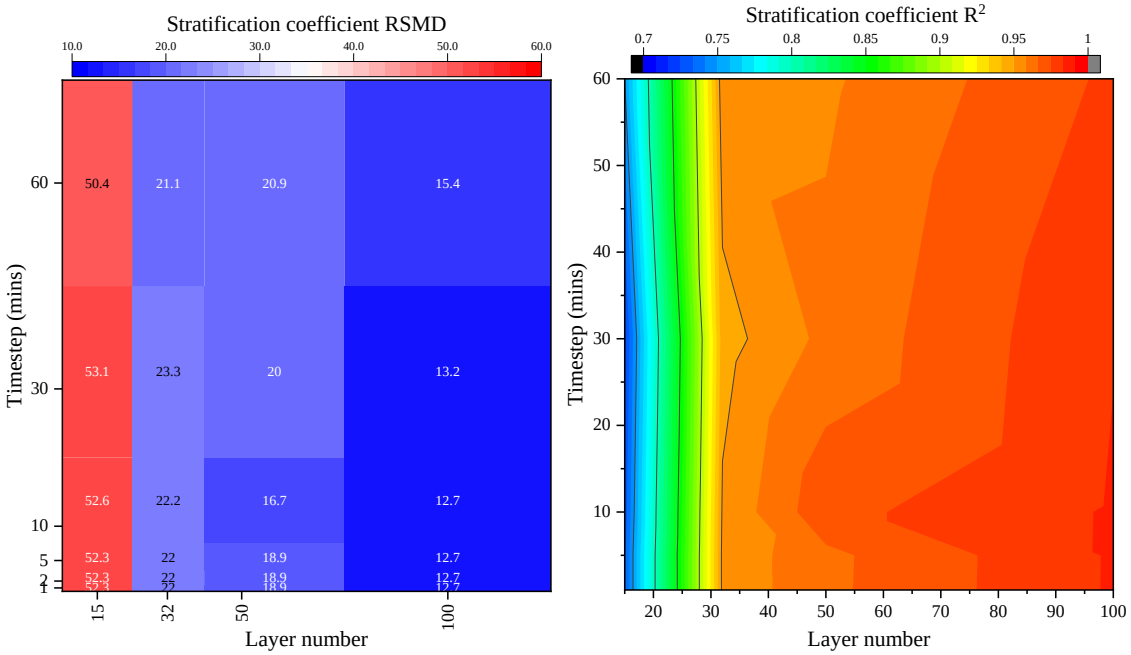

Fig. 7(b): The coupling effect of time step and nodes number on the stratification coefficient calculation accuracy

4. Conclusions

This paper presents a simulation study of large-scale puddle heat storage by Trnsys and compares it with measured data from a solar district heating plant. The analysis focuses on the computational accuracy of the model for thermal stratification. In addition, the combined effects of the number of nodes, time step and mixing factor on the numerical diffusion are discussed. The following conclusions are obtained.

(1) The number of nodes has the greatest effect on the deviation of the thermal stratification calculation results, with fewer nodes predicting best for energy dispersion and more nodes predicting best for temperature dispersion.

(2) Adiabatic blending and the rest of the mixing coefficients are significantly different, adiabatic blending for energy dispersion prediction is poor, but the prediction of temperature dispersion is better. When the difference between the

results of large blending and no blending is not significant, this indicates that there is not much time for heat transfer by inverse temperature blending.
(3) A small number of nodes is suitable for a long time step and a large number of nodes is suitable for a short time step. 15 nodes with 60mins are most suitable for Mix number prediction and 100 nodes with 1min is most suitable for stratification coefficient prediction.
The accuracy of the calculation of Mix number and stratification coefficients tends to be opposite for different parameters. Therefore, the thermal stratification results of coarse and fine meshes can be considered together when judging the model accuracy or pre-simulation.

5. References

Vega Novo, A., Rodríguez Bayón, J., Castro Fresno, D., & Rodríguez Hernández, J., 2010. Review of seasonal heat storage in large basins: water tanks and gravel-water pits. *Appl. Energy*, vol. 87, no. 2, pp. 390–397, doi: 10.1016/j.apenergy.2009.06.033.

Bauer, D., Marx, R., Nußbicker-Lux, J., Ochs, F., Heidemann, W., & Müller-Steinhagen, H., 2010. German central solar heating plants with seasonal heat storage. *Sol. Energy*, vol. 84, no. 4, pp. 612–623, doi: 10.1016/j.solener.2009.05.013.

Bott, C., Dressel, I., & Bayer, P., 2019. State-of-technology review of water-based closed seasonal thermal energy storage systems. *Renew. Sustain. Energy Rev.*, vol. 113, doi: 10.1016/j.rser.2019.06.048.

Heller, A., 1997. Floating lid constructions for pit water storage. A survey.

Egging-Bratseth, R., Kauko, H., Knudsen, B. R., Bakke, S. A., Ettayebi, A., & Haufe, I. R., 2021. Seasonal storage and demand side management in district heating systems with demand uncertainty. *Appl. Energy*, vol. 285, doi: 10.1016/j.apenergy.2020.116392.

Dahash, A., Ochs, F., Janetti, M. B., & Streicher, W., 2019. Advances in seasonal thermal energy storage for solar district heating applications: A critical review on large-scale hot-water tank and pit thermal energy storage systems. *Appl. Energy*, vol. 239, pp. 296–315, doi: 10.1016/j.apenergy.2019.01.189.

Pan, X., Xiang, Y., Gao, M., Fan, J., Furbo, S., Wang, D., & Xu, C., 2022. Long-term thermal performance analysis of a large-scale water pit thermal energy storage. *J. Energy Storage*, vol. 52, p. 105001, doi: 10.1016/J.EST.2022.105001.

Xiang, Y., Gao, M., Furbo, S., Wang, D., Tian, Z., & Fan, J., 2022. Heat transfer of a large-scale water pit heat storage under transient operations. *J. Energy Storage*, vol. 55, p. 105455, doi: 10.1016/J.EST.2022.105455.

Song, M., & Kovacevic, R., 2003. Numerical and experimental study of the heat transfer process in friction stir welding. *Proc. Inst. Mech. Eng. Part B J. Eng. Manuf.*, vol. 217, no. 1, doi: 10.1243/095440503762502297.

Pinel, P., Cruickshank, C. A., Beausoleil-Morrison, I., & Wills, A., 2011. A review of available methods for seasonal storage of solar thermal energy in residential applications. *Renewable and Sustainable Energy Reviews*, vol. 15, no. 7, doi: 10.1016/j.rser.2011.04.013.

Davidson, J. H., Adams, D. A., & Miller, J. A., 1994. A coefficient to characterize mixing in solar water storage tanks. *J. Sol. Energy Eng. Trans. ASME*, vol. 116, no. 2, doi: 10.1115/1.2930504.

Haller, M. Y., Cruickshank, C. A., Streicher, W., Harrison, S. J., Andersen, E., & Furbo, S., 2009. Methods to determine stratification efficiency of thermal energy storage processes–review and theoretical comparison. *Sol. Energy*, vol. 83, no. 10, doi: 10.1016/j.solener.2009.06.019.

Fernandez-Seara, J., Uhı, F. J., & Sieres, J., 2007. Experimental analysis of a domestic electric hot water storage tank. Part II: dynamic mode of operation. *Appl. Therm. Eng.*, vol. 27, no. 1, doi: 10.1016/j.applthermaleng.2006.05.004.

Appendix

Nomenclature

U	Heat transfer coefficient, W/(m^2·K)	h	Natural convection coefficient, W/(m^2·K)
A	Area, m^2	H	Height, m
g	Gravity, m/s^2	T	Temperature, K
D	Diameter, m	V	Volume, m^3
C_p	Specific heat of water, J/(kg·K)	c	Specific heat of soil, J/(kg·K)
r	Distance in radial direction, m	m	Mass quality of each tank node, kg
Q	Energy, J	z	Distance in vertical direction, m
M	Energy Moment, J·m	n	1-D simulation PTES nodes
ST	Stratification number	MIX	Mix number

Subscripts

mea	Measurement	sim	Simulation
w	Water	HDPE	HDPE-liner
geo	Geotextile	side	Side of the storage
bot	Bottom of the storage	top	Top of the storage
j	Elements in 1D region	i,k	Elements in 2D region
loss	Heat loss	in	Inlet
s	Soil	ins	Insulation
ch	Charging	dis	Discharging
mix	Mixing	t	Total
thermo	Thermocline	str	Stratification
cold	Inlet water in minimum temperature	hot	Inlet water in maximum temperature
far	Far-field of soil	c	current
deep	Deep of soil		

Greek

ρ	Density, kg/m^3	λ	Thermal conductivity, W/(m·K)
Δ	Difference	τ	Time, s
θ	Slope angle, °		

Sorption Test Bench for Zeolite and Salt-Composite Based Thermochemical Storage

Gayaneh Issayan[1] and Bernhard Zettl[1]

[1] University of Applied Sciences Upper Austria, Wels (Austria)

Abstract

The advancements in thermochemical storage technologies benefit strongly from a holistic research approach ranging from material and component development to demonstration applications. This work presents a sorption test bench developed and constructed to evaluate thermochemical materials, such as zeolites and salt-hydrate composites, in 0.01-1.0 kg batches and under fully controlled conditions. The test bench is utilized for thermogravimetric state of charge (SOC) determination of open sorption prototypes. Further, the influence of salt-hydrate mixtures on the sorption behavior of salt-composites were studied. The results on outlet storage temperatures for zeolite and salt-composite beds are presented in this work.

Keywords: thermochemical storage, sorption test bench, salt-hydrate composites, zeolites, SOC, thermogravimetry

1. Introduction

The urgency of a global shift to renewable energies and CO_2 reduction motivates energy storage and efficiency research efforts. Thermal energy storages (TES) impact multiple sectors of the renewable energy transition, such as sector coupling, improving grid resilience, and industrial processing. Thermochemical storages are based on the ability of thermochemical materials (TCM) to store energy without noticeable losses during the conservation phase through sorption processes or chemical reactions. Thermochemical storages can act as long-term storage to overcome the seasonal solar mismatch and regenerate waste heat. Although TCMs, such as zeolites, silica gels, metal-organic frameworks (MOFs), etc., are accounted for high theoretical energy densities and sufficient temperature rise on the material level, the demonstration applications have not redeemed themselves financially or energetically (Zettl, 2019). Low-cost salt-hydrates and various composites based on salt in matrix design have also been investigated to show disadvantages, such as poor stability towards cycling, insufficient temperature increase, low deliquescence, etc. (Lin et al., 2021, Scapino, 2017). As previously reported, salt-hydrate and natural zeolite composites have been developed in form of shape stable granules and pellets (Issayan et al., 2021). Consequently, a designated thermogravimetric setup was constructed suitable for the characterization of the latter composites in larger batches (10-50g) in both closed and open system settings (Issayan, Zettl, 2022a). The focus of current TCM studies is the influence of salt-hydrate mixtures on sorption behavior and cycling stability of composites (Katyal, 2020, Xueling et al., 2021). The preliminary results on chloride salts of magnesium, lithium, and calcium from latter thermogravimetric setup were reported (Issayan, Zettl, 2022b). The promising samples were then selected to be further investigated in larger batches.

In this work, a lab-scale (kilogram range), multi-mode (fluidized and fixed bed) open sorption test bench was developed to conduct a thermogravimetric state-of-charge determination of salt-containing composite storage materials. The results from a fixed bed storage simulation model were utilized to validate the results from the test bench for the common 13X BF (binder-free) zeolite bed, which will then act as a benchmark for further analysis of the composite material performance. This work presents the preliminary results of thermogravimetric investigations of various salt-hydrate containing TCMs in two different reactor constellations.

2. Methods and materials

2.1 Experimental setup

The realization of the open sorption systems differs mainly in implementation of the reactor bed design. Three

© 2022. The Authors. Published by International Solar Energy Society
Selection and/or peer review under responsibility of Scientific Committee
doi:10.18086/eurosun.2022.13.11 Available at http://proceedings.ises.org

main reactor beds are shown in Fig. 1. The open sorption setup was developed to conduct thermogravimetric analysis of thermochemical storage materials, mainly zeolites in fixed bed reactors. For salt-containing composites the setup was upgraded to also enable experiments in fluidized bed settings. The adsorption of water molecules in porous zeolites is limited by the pore volume and subsequently shows a natural saturation behavior when the pores fill up. In contrast to zeolites, the water molecules are incorporated into the crystal structure of the salts. If more water molecules are available, the salts "overhydrate" until a gel-like or dissolved layer forms, which prevents further absorption. For this reason, in fixed bed reactors a reaction front is formed, and the overhydrated layers prevent the optimal mass flow through the bed. Hence, fluidized bed measurements with smaller amounts of material and higher mass flows were also implemented.

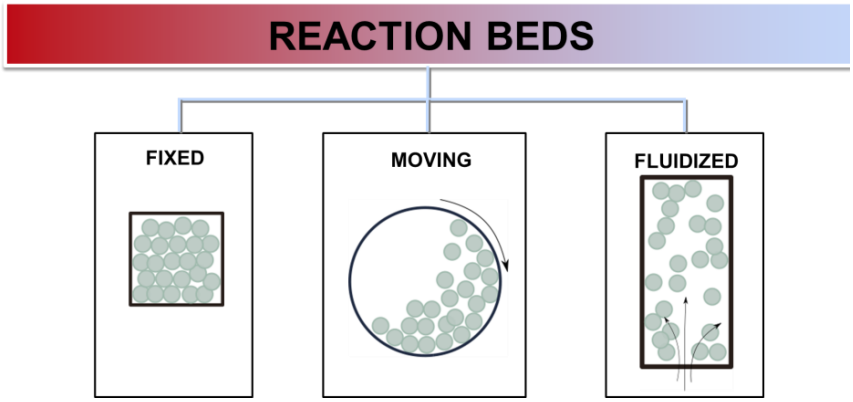

Fig. 1: Three main types of sorption reactor beds utilized in thermal storage applications.

A schematic sketch of the setup is presented in Fig. 2 and consists of analytical mass balance, heating element, fogger with the corresponding tank, and centrifugal blower. The fogger unit enables the generation of airflow with controlled humidity from ambient up to 90% relative humidity (RH). The heater itself can reach up to 300°C resulting in input air mass up to 250°C at the bed. The material is placed in a cylindrical glass container on the balance, where the temperature, humidity, and mass flow of the output air can be monitored. The containers vary in size, housing from 0.01 kg up to 1.0 kg material and can be equipped with further temperature sensors to record the temperatures in various positions of the bed. The three input parameters, temperature, humidity, and mass flow, are controlled individually, allowing for fixed-point measurements and programmed ramps and routines for cycling.

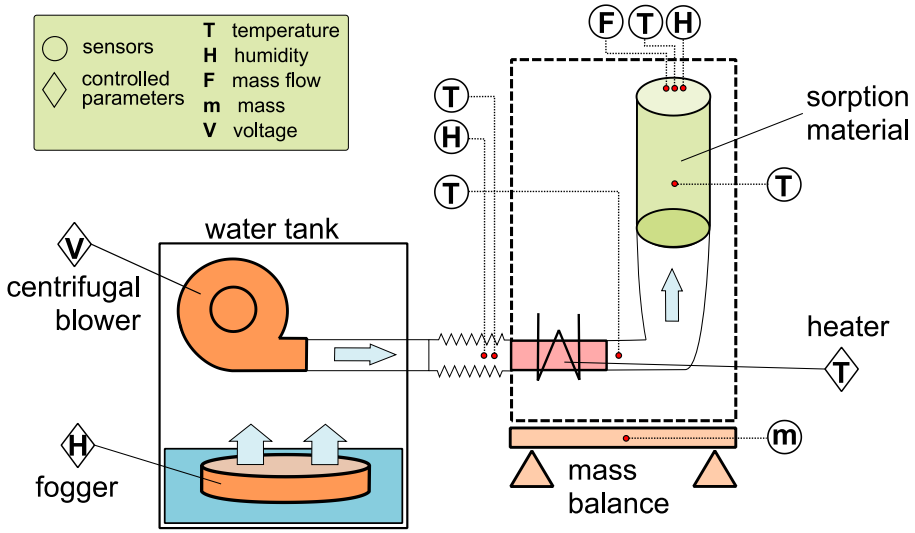

Fig. 2: Schematic representation of the sorption test bench including sensors and controlled parameters.

2.2 Materials

The reference synthetic zeolite 13X binder-free was purchased from CWK (Chemiewerk Bad Kösteritz) in two granule sizes and used with two different regeneration temperatures (see Tab. 1). As the study of salt-hydrate

mixtures was the focus of this work, salt-in-matrix composition was used to prepare simple composites and ease the handling of the samples during the experiments. Therefore, natural zeolite, clinoptilolite, was used as the porous matrix and was impregnated with magnesium, lithium and calcium chloride ($MgCl_2$, LiCl, $CaCl_2$). The salt-hydrates were purchased in anhydrous state with high purity. Saturated solutions of the mixtures of different salt fractions were prepared and impregnated in clinoptilolite, which was sieved in fine (40 µm – 1 mm) and coarse (1mm – 3 mm) granularity. The accumulated salt on the outer grain-surface of the dried samples were then washed out with water, which otherwise caused premature overhydration of the samples. Lastly, the samples were dried at 110°C. The sample names and detailed compositions of prepared samples are summarized in following Tab. 1.

Tab. 1 Prepared samples and their composition

Name	Composition	Desorption temperature
13XBF-small 13XBF-large	1.5 – 2.5 mm granules -> cycled 2.5 – 5.0 mm granules -> new purchase	200°C 250°C
CaLi-15 CaLi-20	fine clino + 15wt.% -> $CaCl_2$:LiCl – 50:50 fine clino + 20wt.% -> $CaCl_2$:LiCl – 50:50	110°C
MgLi-55f MgLi-82 MgLi-28 MgLi-55c	fine clino + 15wt.% -> $MgCl_2$:LiCl – 50:50 fine clino + 15wt.% -> $MgCl_2$:LiCl – 80:20 fine clino + 15wt.% -> $MgCl_2$:LiCl – 20:80 coarse clino + 15wt.% -> $MgCl_2$:LiCl – 50:50	110°C

3. Results and discussion

3.1 Reference zeolite

As previously mentioned, a numerical model of fixed bed open sorption system based on linear driving force model was used to validate the results from the test bench (Daborer-Prado et al., 2022). The simulation was conducted with material data of well-studied and demonstrated 13XBF zeolites. The model implementation was done in MATLAB®/Simulink. The results obtained from the simulation model were compared to the measurement results and validated the utilized methods.

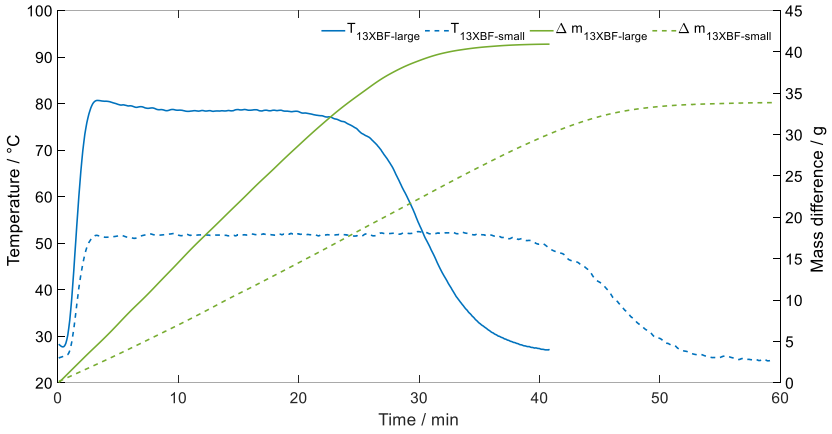

Fig. 3: Two measurements of zeolite 13XBF of different granule diameters and regeneration temperatures.

Two exemplary zeolite measurements are presented in this work. The experiments were conducted by varying the inlet mass flow and relative humidity of the air and recording the temperature and mass change of the sorption bed during adsorption. The material used for the experiments weighed 150 g. The experimental temperature outputs (blue lines) and mass change results (green lines) for an inlet air with 70% RH at 25°C and mass flow values of 4 kg/h are presented in Fig. 3. The solid lines represent larger granules, which allow better mass flow

through the sorption bed and were regenerated at 250°C. The dashed lines correspond to smaller granules, which have been cycled multiple times in experimental settings and regenerated at 200°C. The temperature levels achieved by the larger granules are distinctly higher, than those coming from the smaller ones. However, the high temperature plateau does only last about 30 minutes. Possible degradations in the pore structure of the smaller and often cycled granules could be the reason for the moderate to low temperature levels, which then last for 45 – 50 min. The green lines, which correspond to the mass gained by the material at the given conditions show saturation behavior appropriate to the temperature output. The 13XBF-small sample adsorbs 22.6 wt.% and 13XBF-large adsorbs 27.3 wt.%. According to product data sheets (water vapor - isotherms) both samples exhibit a maximum water saturation of over 30 wt.%. Apart from discrepancies attributed to heat losses, material qualities and measurement artifacts, the experimental results gained from the test bench agreed well with the previous measurements.

3.2 Salt-composites in fluidized bed

The test bench was mainly utilized to evaluate the temperature response of salt-containing composites in comparable settings. Due to $CaCl_2$ low deliquescence humidity, the salt is able to absorb water vapor in ambient conditions and tends to overhydration (Rammelberg et al., 2012). The sorption capacity and stability of $CaCl_2$ was shown to strongly benefit from addition of LiCl (Issayan, Zettl, 2022a). The latter pair was selected for the first fluidized bed measurements. One of the pressing issues regarding the impregnation was the salt content, as clinoptilolite has shown limited sorption capacity of around 5 – 10wt.%. Therefore, the air flow deploying 60% RH at 25°C was set in such way, that 50g of material was fluidized. The temperature profiles were obtained from samples with varying salt content CaLi-15 and CaLi-20 and are presented in Fig. 4. The sample with higher salt content did not show benefits regarding the temperature output, as well as the CaLi-15 sample, which was tested using more humid air flow (65%RH). Best results were obtained by using low humidity mass flow. Summarizing, the measurements on $CaCl_2$-LiCl mixtures were not satisfactory, as the temperature levels sank rapidly and overhydration of the samples could be observed.

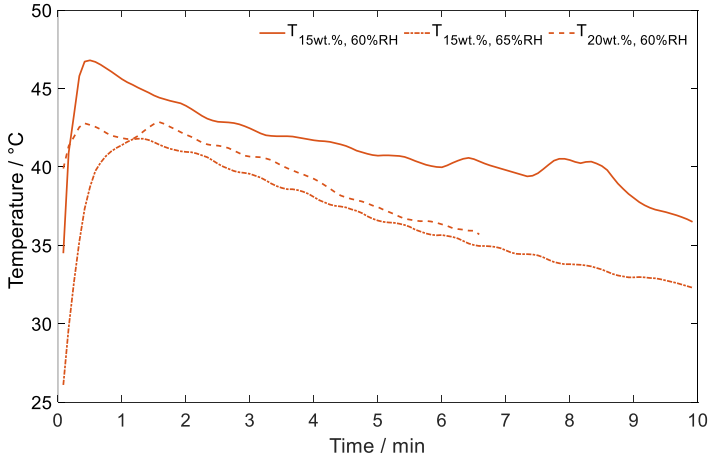

Fig. 4: CaLi-15 sample with 15wt.% salt content tested in fluidized bed with 60 and 65% RH (solid and dash-dotted lines) and compared to the sample with 20wt.% salt CaLi-20.

One of the well-studied salt-hydrates in thermochemical storage material context is $MgCl_2$ (Rammelberg et al., 2012). The MgLi-55f samples weighing 75 g were also tested using two humidity levels in fluidized bed setting and the results are depicted in Fig. 5. The highest temperature from the salt-composites is achieved at the beginning, after a steep rise, followed by a steady decrease. The higher the relative humidity of the air flow, the faster the material reaction and the higher the temperature response of the bed. The consequence of higher humidity is the faster decrease of the temperature. The temperature output was comparable to those of $CaCl_2$-LiCl mixtures. However, the sample was stable and did not show signs of overhydration, which will be further discussed in scope of fixed bed measurements. Beside the temperature, the mass increase is also presented as the green lines and shows a steady increase appropriate to the temperature response. The overall mass gains of 8 wt.% and 9.3 wt.% can almost entirely be attributed to salt-hydrates (< 15 wt.%).

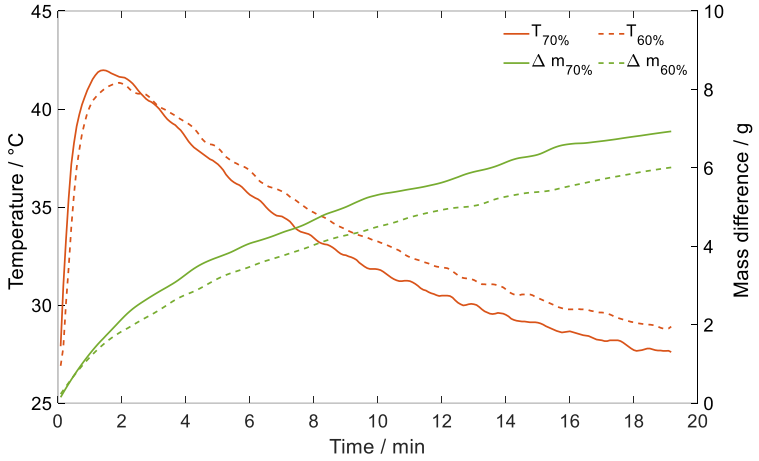

Fig. 5: MgLi-55f in fluidized bed setting and varying humidity.

3.3 Salt-composites in fixed bed

Fixed bed measurements were performed by using the same input parameters as for the zeolite measurements: 4 kg/h air flow with 70% RH at 25°C. In all measurements material bed weighted 150 g.

The results of fixed bed measurements of composites with varying granule sizes are presented in Fig. 6. The mass flow through the coarse composite bed caused the rapid temperature response slightly below 60°C, which drastically fell after the first 2 – 3 minutes. As the coarse samples have lower surface to volume ratio, it was not possible for the salts to penetrate the deeper pores. Therefore, the salt accumulations near the surface quickly overhydrated during the measurements. In comparison, the composites with fine granularity deploy the first high temperature level after around 5 min and hold temperatures above 55°C for further 20 minutes.

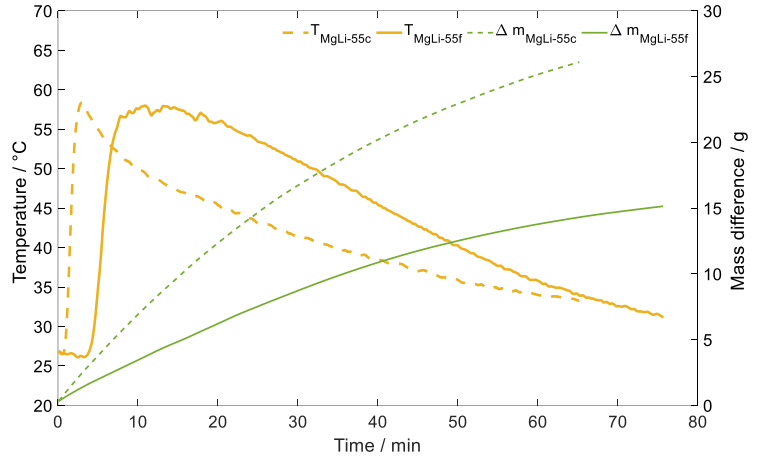

Fig. 6: Comparison of coarse and fine granular composites with $MgCl_2$-LiCl impregnation.

Adsorption data of $MgCl_2$-LiCl samples impregnated in microporous vermiculite were reported and have shown interesting trends (Issayan, Zettl, 2022b). Hence the motivation to investigate some of well-performing samples in the test bench. The adsorption data presented in Fig. 7 was collected in a closed vacuum chamber reported in (Issayan, Zettl, 2022b), where the samples were exposed to low partial pressures (10 mbar). The sorbent temperature inside the vacuum chamber and the normalized loading related to the initial mass of the sample are displayed on the left and right y-axes, respectively. The solid lines represent the sample with 50/50 weight ratio of $MgCl_2$-LiCl-mixture (~MgLi-55). The dashed lines correspond to 20/80 (~MgLi-28) and the dah-dotted lines to $MgCl_2$-LiCl-mixture (~MgLi-82). Clinoptilolite composites with the mentioned mixture ratio were prepared and measured in the test bench to study and compare the behavior of salt-mixtures in low-content composites and open and fixed bed storage setting versus those measured in closed vacuum chamber shown in Fig. 7. The results

of three $MgCl_2$-LiCl-mixtures are presented in Fig. 8. The line styles and sample names of the samples with the same ratio are kept similar to those in Fig. 7.

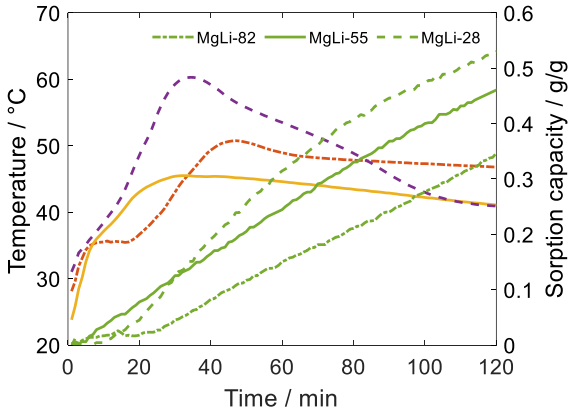

Fig. 7: Adsorption behavior of the $MgCl_2$-LiCl samples in vacuum chamber (Issayan, Zettl, 2022b).

After the first 30 minutes, MgLi-28 sample in Fig. 7 (vacuum chamber) reaches the highest temperature, which was attributed to the LiCl, as it performs the best in closed systems. MgLi-55 sample shows the lowest temperature increase. MgLi-82 sample has shown the moderate temperature increase. However, the temperature levels held for the longest duration. The adsorption process was decelerated for MgLi-82 sample. In fixed bed setting in Fig. 8, the latter mixture (red dashed line) achieved and held temperatures around 50°C in the first hour. The temperature output from MgLi-28 was the lowest yet held the longest. In both cases strong overhydration of the samples could be observed, which should be addressed in composite development phase of the future work. Hence, the only sample, which achieved temperatures over 50°C and showed stable behavior in fixed bed setting was the MgLi-55f sample. The temperature levels were held significantly shorter in comparison with those from other $MgCl_2$-LiCl ratios. The highest mass gain was registered for MgLi-28. The sorption capacities of all the samples in the vacuum chamber (Fig. 7) after eight hours are in the same order of magnitude: MgLi-55 ~0.9 g/g, MgLi-82 ~ 0.85 g/g and MgLi-28 ~ 1.0 g/g. Therefore, we can conclude that salt-hydrates absorb/adsorb roughly their initial mass. The samples in Fig. 8 show an increase in mass around 10 – 16 wt.%, which also corresponds to the salt-content impregnated in clinoptilolite.

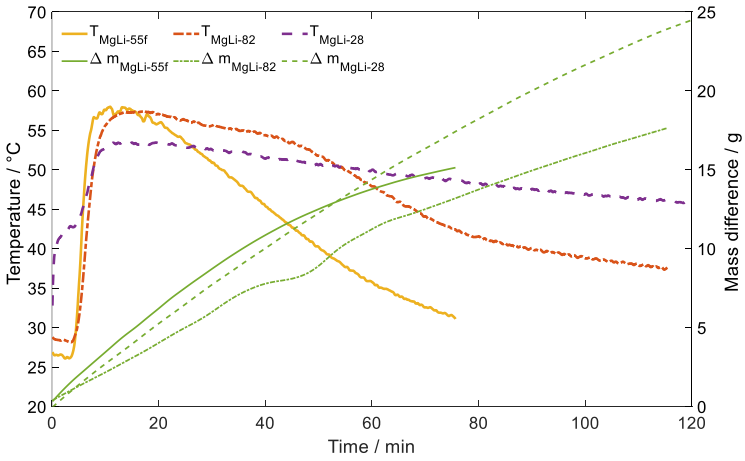

Fig. 8: Comparison of samples with different $MgCl_2$ to LiCl ratios.

4. Conclusion and outlook

The results from the test bench point out interesting characteristics of salt-composites and motivate further work in this field. The fluidized bed concept was implemented, which enabled the investigation of humidity sensitive samples. Steps will be taken to improve the setup and continuously increase the batch size of the material. Despite

the challenges with overhydration and poor mass flow through dense beds, fixed bed measurements delivered interesting and motivating insights. Considering the small amount of salt-hydrate in the composites and the low regeneration/desorption temperatures compared to the zeolites, all three samples from the $MgCl_2$-LiCl series showed promising temperature outputs. The samples MgLi-82 and MgLi-28 should be further stabilized regarding overhydration. Only the 50/50 mixture of $MgCl_2$-LiCl (sample MgLi-55f) was stable and did not overhydrate during the measurements.

Further goals are to develop stabilized composites using binders and fibers. The investigation of further salt-hydrate mixtures is also an ongoing work. The test bench was found to be appropriate for measurements on salt-containing materials and will be equipped to perform calorimetric measurements.

5. Acknowledgments

The funding for project TCMix is provided by the government of Upper Austria in the frame of the "Dissertationsprogramm der FH OOE" and is greatly acknowledged by the authors. Project Resinet is funded by EU- European Regional Development Fund (ERDF) and Federal Province of Upper Austria Investments in Growth and Jobs (IGJ). Read more about IGJ/ERDF on www.efre.gv.at

6. References

Daborer-Prado, N., Issayan, G., Zettl, B., 2022. Experimental validation of a solid sorption mathematical model. In Conference of Environmental and Climate Technologies (Connect 2022). Riga, Latvia. Environmental and Climate Technologies 26, no 1, pp 377-391. 10.2478/rtuect-2022-0029

Issayan, G., Zettl, B., Somitsch, W., 2021. Developing and stabilizing salt-hydrate composites as thermal storage materials. In 14th International Renewable Energy Storage Conference 2020 (IRES 2020). Atlantis Press. p. 49-57. 10.2991/ahe.k.210202.008

Issayan, G., Zettl, B., 2022a. Novel thermogravimetric characterization method for adsorption cycles of TCM. In 15th International Renewable Energy Storage Conference 2021 (IRES 2021). Atlantis Press. p. 108-117. 10.2991/ahe.k.220301.011

Issayan, G., Zettl, B., 2022b. Investigation of salt-mixtures for thermochemical material development. In 2nd International Sustainable Energy Conference (ISEC 2022), Graz, Austria. 10.32638/isec2022

Katyal, S., 2020. Experimental assessment of mixed salt hydrates for thermochemical storage. Master thesis, University of Eindhoven. Available at: https://pure.tue.nl/ws/portalfiles/portal/165891380/1282018_Master_Thesis_Report_Katyal.pdf (Accessed: 12 September 2022).

Lin, J., Zhao, Q., Huang, H., Mao, H., Liu, Y., Xiao, Y., 2021. Applications of low-temperature thermochemical energy storage systems for salt hydrates based on material classification: A Review. Solar Energy 214, p. 149-178. 10.1016/j.solener.2020.11.055

Rammelberg, H. U., Schmidt, T. and Ruck, W., 2012. Hydration and dehydration of salt hydrates and hydroxides for thermal energy storage – kinetics and energy release. Energy. Proced. 30, p. 362-369. 10.1016/j.egypro.2012.11.043

Scapino, L., Zondag, H. A., Van Bael, J., Diriken, J., Rindt, C. C., 2017. Sorption heat storage for long-term low-temperature applications: A review on the advancements at material and prototype scale. Appl. Energy. 190, 920-948. 10.1016/j.apenergy.2016.12.148

Xueling, Z., Feifei, W., Qi, Z., Xudong, L., Yanling, W., Yeqiang, Z., Chuanxiao, C., Tingxiang, J., 2021. Heat storage performance analysis of ZMS-Porous media/CaCl2/MgSO4 composite thermochemical heat storage materials. Solar Energy Materials and Solar Cells, 230, 111246. 10.1016/j.solmat.2021.111246

Zettl, B., 2019. Long-term thermochemical heat storage for low-temperature applications. Proceedings of Solar World Congress SWC, 4.-7.11 2019, Santiago, CHILE. 10.18086/swc.2019.08.11

Performance Investigation on Cascade Latent Heat Storage for Various Geometric Orientations

Shubham Jain[1], K. Ravi Kumar[1], Dibakar Rakshit[1], B. Premachandran[2], K. S. Reddy[3]

[1]Department of Energy Science and Engineering, Indian Institute of Technology Delhi, (India)

[2]Department of Mechanical Engineering, Indian Institute of Technology Delhi, (India)

[3]Department of Mechanical Engineering, Indian Institute of Technology Madras, (India)

Abstract

Storing solar thermal energy in the form of the latent heat of the phase change materials (PCMs) is a widely adopted method to assist energy applications in a sustainable manner. The cascading of the PCMs in a latent heat storage unit improves the uniformity of the heat transfer process. In this investigation, all the configurations of the storage (two single PCM-based storage having $NaNO_3$ and $NaNO_2$ as the PCMs and the 2-stage multi-PCM storage having both the PCMs) are designed to store the 1 MJ of latent thermal energy. The present study highlights that a 35.23% and 10.52% enhanced charging rate can be achieved in the 2-stage cascade latent heat storage (CLHS) than the single PCM-based storages, i.e., $NaNO_3$ and $NaNO_2$. Furthermore, the present study is extended to underline the effect of the geometric orientation of the CLHS over the melting behavior of the CLHS. The melt cycle time of the horizontal CLHS was found to be 39.04%, 15.78%, and 5.9% less than the corresponding charging time of the 1-stage $NaNO_3$ storage, 1-stage $NaNO_2$ storage, and 2-stage vertical CLHS, respectively. Although the horizontal orientation of the storage can enhance the melting rate in the PCMs of the CLHS, it is more suited for the part load charging conditions.

Keywords: Solar Thermal Energy Systems, Latent Heat Storage, Phase Change Materials, Computational Fluid Dynamics, Cascade Thermal Energy Storage.

1. Introduction

For sustainable development, a reduction in the dependency on fossil fuels is necessary. The inclination of the present generation toward renewable energy is the way to opt for eco-friendly solutions for the current energy demands. Solar energy is one of the widely opted energy resources to replace conventional energy resources. The unavailability of the Sun during the night and variable solar radiation intensity are the major shortcomings of the utilization of solar energy for various energy applications. Dedicated thermal energy storage can solve these problems. There are three ways to store the thermal energy of the Sun, i.e., in the form of the increased temperature of the medium (sensible thermal energy storage (STES)), in the form of phase transition enthalpy (latent thermal energy storage (LTES)) and in the form of the enthalpy of the chemical reactions (thermochemical energy storage (TCES)). In terms of maturity, STES is the most widely used storage solution for solar thermal applications. The problem of the low energy density of the STES can be solved using TCES, but the cost and the complications involved in the storage process restricts their commercial implementations. In terms of the high energy density, easy availability, easy operational cycle, and low cost, LTES (stores energy in the phase change materials (PCMs)) is one of the preferred storage solutions in solar thermal applications. The low thermal conductivity of the PCMs and non-uniform melting/solidification of the large volume LTES are the shortcomings on which researchers are working (Ray et al., 2021). The incorporation of conductive materials and structures such as metallic nanoparticles, metallic porous structures in the PCMs, and the use of extended surfaces are methods to solve the problem of low thermal conductivity of the PCMs, while the cascading of the PCMs in the single LTES can improve the process uniformity during the storing/retrieving cycle of the storage (Jain et al., 2021). Tiary et al. (Tiari et al., 2021) have investigated the effect of using the annular fins and reported a significant improvement in the charging process on increasing the fin length. The 30.3% and 28.2% reduction in the charge and discharge time, respectively, were reported by Wu et al. in the nano-enhanced paraffin (Wu et al., 2010). Efforts are made to enhance the performance of the LTES using heat pipes also. Another feasible technique of heat transfer augmentation is the utilization of porous metallic structures in the storage medium. Sardari et al. (Sardari et al.,

© 2022. The Authors. Published by International Solar Energy Society
Selection and/or peer review under responsibility of Scientific Committee
doi:10.18086/eurosun.2022.13.12 Available at http://proceedings.ises.org

2019) have reported an 85% reduction in the charge cycle time of the storage by using porous copper foam.

The cascading of the storage materials (PCMs) in the LTES unit can improve the process uniformity in the heat transfer between HTF and PCM, which results in the enhanced charging/discharging rate of the storage. Adine et al. (Adine and El Qarnia, 2009) have evaluated the performance of a 2-stage CLHS having organic PCMs. In this study, 2-stage CLHS was found to be more effective. Piero et al. (Peiró et al., 2015) have reported a 19.36% improvement in the effectiveness of the CLHS than the 1-stage. Researchers have analysed the CLHS with the hybrid enhancement of heat transfer also. In such a study, Shabgard et al. (Shabgard et al., 2012) highlighted the improved performance of the CLHS using heat pipes.

A few studies can be found that highlight the effect of the orientation on the performance of the single PCM storage. The effect of the orientation on the charging performance of the CLHS has not been investigated thoroughly. Here in the present study, efforts are made to underline the effect of the no. of stages on the charge cycle behavior of the CLHS as well as the effect of the geometric orientation of the CLHS on the energy storage process of the CLHS. The change in the energy transfer rate of the storage medium in one stage may affect the melting rate of the PCM in another stage. The present work will highlight the charging behavior of the CLHS for various geometric orientations, such as vertical and horizontal.

2. Numerical Modelling and Governing Equations

2.1. Description of the Model

In the present work, shell and tube-type LTES units having single and multiple PCMs on the shell sides are investigated. The study is further extended to highlight the charging performance of the storage for two different orientations, i.e., vertical and horizontal. The hot HTF flows through the concentric inner tube to transfer the thermal energy to the PCMs (Figure: 1). The storage configurations are designed to store 1 MJ of latent thermal energy (calculated based on average energy density). The storage consists of stainless steel (SS316) shell (outer diameter of 73 mm and thickness of 2.11 mm) and an inner concentric tube made of copper (outer diameter of 22.22 mm and thickness of 1.65 mm). The PCMs are kept shell side while the HTF flows through the inner copper tube. The total length of the storage is chosen as 888 mm, and the shell compartments are divided into equal lengths for storing multiple PCMs, as shown in Figure: 1. Here, attempts are made to develop a low-cost shell and tube-based CLHS to support the energy demand of the medium temperature applications. Therefore, $NaNO_3$ and $NaNO_2$ having melting temperatures of 579 K and 555 K, respectively, are utilized as the PCMs. Thermal oils are one of the widely used heat transfer fluids (HTF) for low to medium-temperature applications. Therefore, Therminol 66 is utilized here as the working HTF. The properties of the PCMs and HTF used in the study are given in Table: 1. Initially, the thermal performance of the two single PCM-based storage having $NaNO_3$ and $NaNO_2$ as the PCMs is compared with the thermal performance of the 2-stage CLHS having both the PCMs in the single unit for the charging cycle. Moreover, the performance of the cascade storage is further evaluated for the two different orientations such as vertical and horizontal.

2.2. Assumptions

The following assumptions are incorporated into the present model:

- All the phases of utilized materials are considered homogeneous and isotropic.
- The melted PCM is assumed to behave as a Newtonian fluid.
- The radiation heat transfer, volume variation during phase change, and viscous energy dissipation are neglected here.
- The Boussinesq assumption is used to model the natural convection in the PCMs.
- The insulated boundary condition is provided on the outer exposed wall of each configuration of the storage.

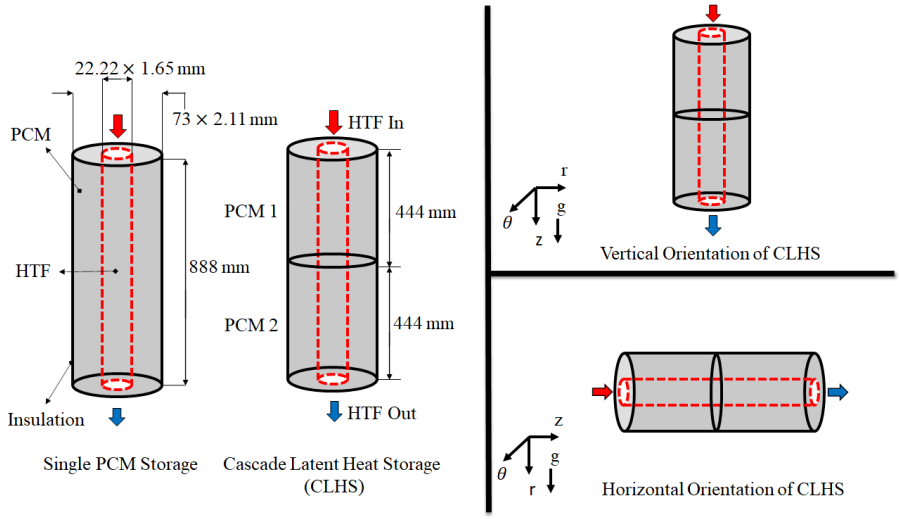

Fig. 1: Schematic of the storage configurations investigated in the present study

Tab. 1: Thermo-physical properties of PCMs and HTF used in the study (Alekseeva et al., 2019; Janz et al., 1979; Marušić and Lončar, 2020; Tiari et al., 2015)

Properties	**$NaNO_3$**	**$NaNO_2$**	**HTF**
Melting Temperature (K)	579	555	-
Phase Transition Enthalpy (kJ/kg)	176	180.12	-
Expansion Coefficient (1/K)	0.0004	0.00028	-
Specific Heat Capacity (kJ/kg K)	1.60 (s), 1.655 (l)	1.733 (s), 2.553 (l)	2.73
Thermal Conductivity (W/m-K)	0.8 (s), 0.68 (l)	0.765 (s), 0.665 (l)	0.0893
Density (kg/m^3)	1908	1812	775
Dynamic Viscosity $\times 10^{-4}$ (Pa-s)	26.9	26.66	3.36

2.3. Governing Equations

The phase transition process of the storage is modeled here using the 'Enthalpy Porosity Method' (Brent et al., 1988). The governing equations involved in the method are given below:

HTF:

Mass conservation equation:

$$\frac{\partial \rho_f}{\partial t} + \nabla \cdot \left(\rho_f \vec{V}\right) = 0 \qquad \text{(eq. 1)}$$

Momentum conservation equation:

$$\rho_f \left(\frac{D\vec{V}}{Dt}\right) = -\nabla \mathrm{p} - \frac{2}{3}\nabla\left(\mu_f \nabla \cdot \vec{V}\right) + \nabla \cdot \left[\mu_f\left(\nabla\vec{V} + \left(\nabla\vec{V}\right)^T\right)\right] \qquad \text{(eq. 2)}$$

Energy conservation equation:

$$\rho_f c_{p_f} \left(\frac{DT}{Dt}\right) = \nabla \cdot (\mathrm{k}_f \nabla \mathrm{T}) \qquad \text{(eq. 3)}$$

PCM:

Mass conservation equation:

$$\frac{\partial \rho}{\partial t} + \nabla \cdot \left(\rho \vec{V}\right) = 0 \quad \text{(eq. 4)}$$

Momentum conservation equation:

$$\frac{\partial \rho \vec{V}}{\partial t} + \nabla \cdot \left(\rho \vec{V} \vec{V}\right) = -\nabla p + \vec{g} \beta_t \rho_{ref} \left(T - T_{ref}\right) + \nabla \cdot \left(\mu \nabla \vec{V}\right) + \vec{S}_M \quad \text{(eq. 5)}$$

Here,

$$\vec{S}_M = -\frac{(1-\beta)^2}{\beta^3 + \varepsilon} A_{Mushy} \vec{V} \quad \text{(eq. 6)}$$

Here, A_{Mushy} is taken as 10^5 (Fadl and Eames, 2019). The body force term is included as $g \beta_t \rho_{ref} \left(T - T_{ref}\right)$ using Boussinesq approximation.

Energy conservation equation:

$$\frac{\partial (\rho H_t)}{\partial t} + \nabla \cdot \left(\rho \vec{V} H_t\right) = \nabla \cdot (k \nabla T) \quad \text{(eq. 7)}$$

The total enthalpy is further expressed as:

$$H_t = h_s + h_l \quad \text{(eq. 8)}$$

Here,

$$h_s = h_{ref} + \int_T^{T_m} C_p \partial T \quad \text{(eq. 9)}$$

$$h_l = \beta L \quad \text{(eq. 10)}$$

Melt fraction (β):

$$\beta = \begin{cases} \frac{T - T_{Solidus}}{T_{Liquidus} - T_{Solidus}}; & \text{when } T_{Solidus} < T < T_{Liquidus} \\ 0; & \text{when } T \leq T_{Solidus} \\ 1; & \text{when } T \geq T_{Liquidus} \end{cases} \quad \text{(eq. 11)}$$

2.4. Initial and Boundary Conditions

The initial domain temperature and the inlet HTF temperature are taken as 519K and 615 K, respectively. The HTF velocity considered in the analysis is 0.04 m/s. Furthermore, the following boundary and initial conditions are used in the modeling of the process:

HTF:

At $t = 0: \vec{v} = 0, T = T_{initial}$ (eq. 12)

At $r = r_i: \vec{v} = 0, T_{itf^+} = T_{itf^-}$ (eq. 13)

At $z = 0: u = u_{in},\ T = T_{in}$ (eq. 14)

At $z = l_{st}: p = p_0$ (eq. 15)

PCM:

At $t = 0: \vec{v} = 0, T = T_{initial}$ (eq. 16)

At $r = r_o: \vec{v} = 0,\ T_{itf^+} = T_{itf^-}$ (eq. 17)

At $r = R_i: \vec{v} = 0,\ \frac{\partial T}{\partial r} = 0$ (eq. 18)

At $z = 0: \vec{v} = 0,\ \frac{\partial T}{\partial z} = 0$ (eq. 19)

At $z = l_{st}$: $\vec{v} = 0,\ \frac{\partial T}{\partial z} = 0$ (eq. 20)

At $z = \frac{l_{st}}{2}$: $\vec{v} = 0,\ \frac{\partial T}{\partial z} = 0$ (for two-stage cascade storage) (eq. 21)

2.5. Validation of Numerical Model and Solution Procedure

The grid independence study and the time step independence study have highlighted that the 697500 elements and the time step size of 0.1s are appropriate for the numerical model (Figure: 2). The developed model is validated by using the results of the experimental study performed by Hosseini et al. (Hosseini et al., 2012). (Figure: 3). A maximum deviation of 2.5 K and 4.1 K in average and local temperature of the PCM is reported here (Hosseini et al., 2012).

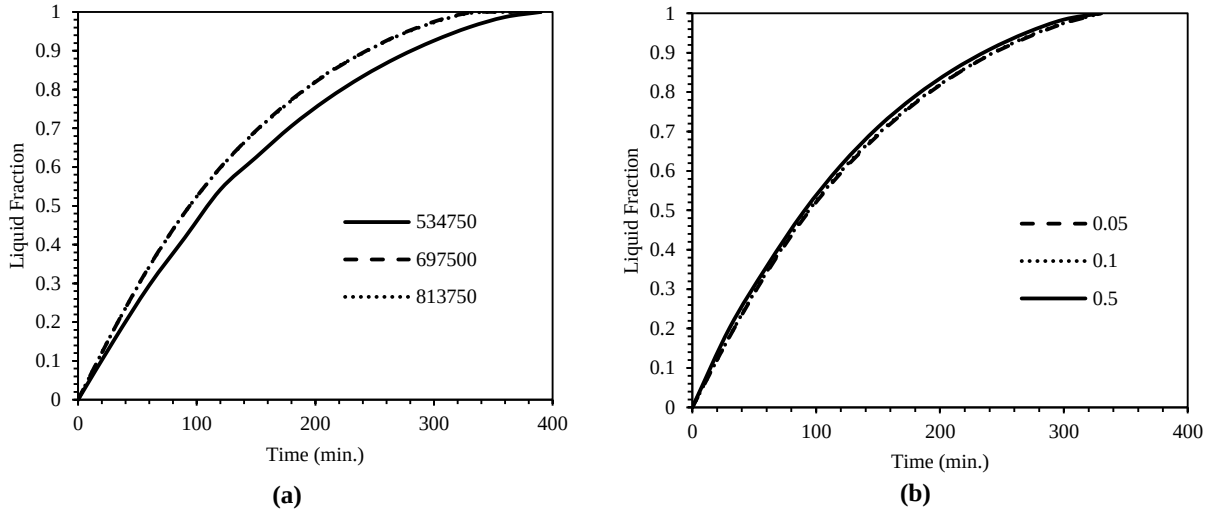

Fig. 2: (a) Grid independence study (b) Time step independence study

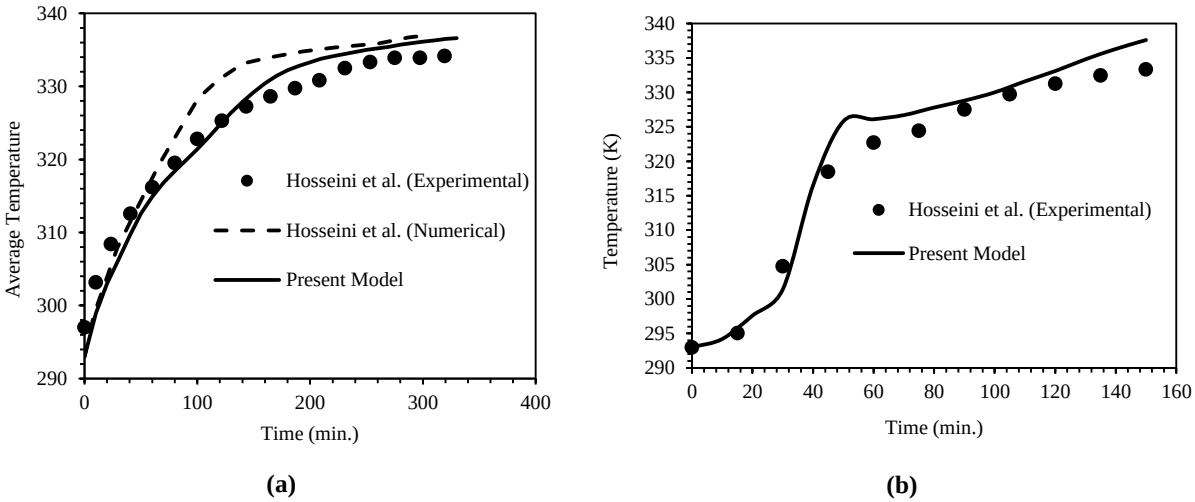

Fig. 3: Model validation (Hosseini et al., 2012) (a) Average temperature of the phase change material, (b) Local temperature in the phase change material

3D models are prepared for each configuration of the storage , and unsteady state simulations are performed using ANSYS Fluent 2020 R1 (ANSYS Inc (Release-15.0), 2015), where a pressure-based solver and SIMPLE algorithm are implemented (Mekrisuh et al., 2020). Here QUICK scheme is used for discretization, and pressure staggering option (PRESTO) is also incorporated (Mekrisuh et al., 2020). A convergence criterion of 10^{-3} is assigned for both mass and momentum equations, and on the other hand, a convergence criterion of 10^{-6} is assigned for the energy equation in the present numerical model.

3. Results and Discussion

In the present study, a comparative charge cycle performance evaluation is done between two single PCM-based vertical LTES having $NaNO_3$ and $NaNO_2$ as the PCMs and the two-stage vertical CLHS having both the PCMs together in a single storage unit. Moreover, the current study is extended further to highlight the effect of the geometric orientation (vertical and horizontal) of the storage on the melting cycle of the storage. All the storage configurations are designed to store the 1 MJ of latent thermal energy. The findings of the current study are as follows:

3.1. Comparative Assessment of Single and Multiple PCM-based Storage

Initially, a comparative analysis is done to highlight the effect of the cascading of the PCMs in a vertical LTES unit. In this context, the melting process in single-stage $NaNO_3$, $NaNO_2$, and two-stage $NaNO_3$/ $NaNO_2$ vertical storages is investigated. The HTF enters from the top of the storage and transfers heat to the surrounding PCM shell. The melting process is initiated almost at the same time (after 30 minutes) in $NaNO_3$ and $NaNO_3$/ $NaNO_2$ storage, while $NaNO_2$ shows an early initiation (after 20 minutes) of the melting process (Figure: 4 (a)). Owing to the significant temperature differential between the HTF and the phase transition temperature of the $NaNO_2$, a fast-charging rate can be seen at the initial stage of the melting. As the HTF passes through the inner HTF tube in the storage, the temperature of the HTF decreases, which further reduces the established energy transfer rate from HTF to the storage medium (PCM). The arrangement of the two different PCMs in the HTF movement direction having PCM of higher phase transition temperature in the primary stage maintains a better rate of heat transfer between HTF and PCM, which improves the charging process. Here $NaNO_3$, $NaNO_2$, and $NaNO_3$/ $NaNO_2$ configurations of the storage complete the melting after 525 minutes, 380 minutes, and 340 minutes, respectively of the charging process. The time of the complete charging of the 2-stage CLHS is found to be 35.23% and 10.52% less as compared to the $NaNO_3$ and $NaNO_2$ storage. Both the stages of the CLHS complete the melting after a nearly equal time period (stage 1 in 340 minutes, while stage 2 in 330 minutes), which is the best way to utilize the CLHS technology. Figure: 4(b) represents the variation of the average temperature of the PCMs in each configuration of the storage. The three different stages (sensible heating of solid PCM, phase transition, and the sensible heating of the liquid PCM) of the charging cycle of the LTES can be seen in the figure. $NaNO_3$ has a higher melting temperature as compared to $NaNO_2$; therefore, a long sensible heating phase can be seen in figure: 4(b). After the initiation of the melting, a slight increment in PCM temperature can be seen until the completion of the charging cycle. After that, it achieves a temperature equal to the inlet temperature of the HTF to complete the charging cycle. All the other PCMs follow the same trend to complete the charging cycle.

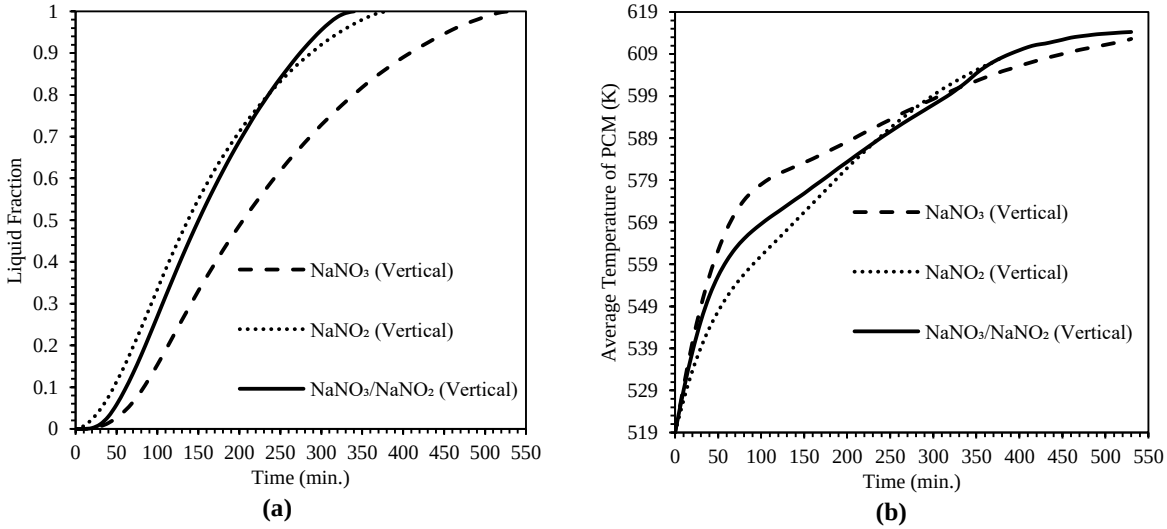

Fig. 4: (a) Variation of the liquid faction of the PCMs in the vertical storage configurations (b) Variation of the average temperature of the PCMs in the vertical storage configurations

A clear depiction of the melting front movement can be seen in Figures: 5 and 6. Figure: 5 represents the movement of the melt front on the central axial plane in the storage, while Figure: 6 represents the movement of the melt front on the two radial planes at an axial location of 222 mm (top) and 666 mm (bottom) from the inlet. In the vertical storage configurations, the HTF enters from the top of the storage and transfers energy to the PCM

through the adjacent copper wall; as the PCM starts melting, buoyancy-driven natural convection sets up in the PCM domain. Due to the low density of the liquid PCM, it tries to pile up at the top portion of the storage. The accumulation of the PCM at the top portion of the vertical storage enhances the energy transfer in that region. Therefore, a faster rate of energy transfer can be depicted in figure: 6 as compared to the bottom portion of the storage.

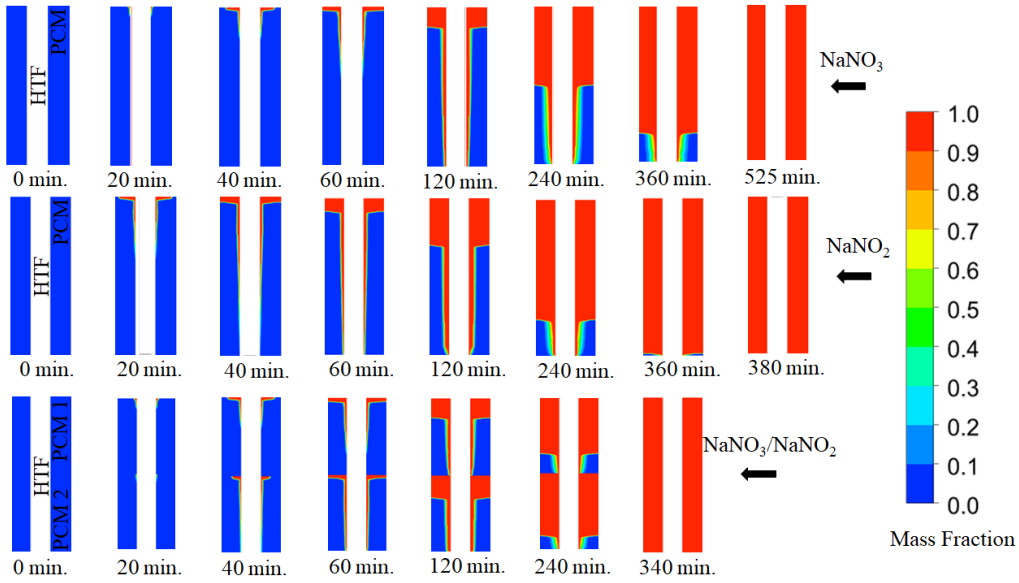

Fig. 5: Liquid faction contours in the vertical storage configurations (at a central axial plane)

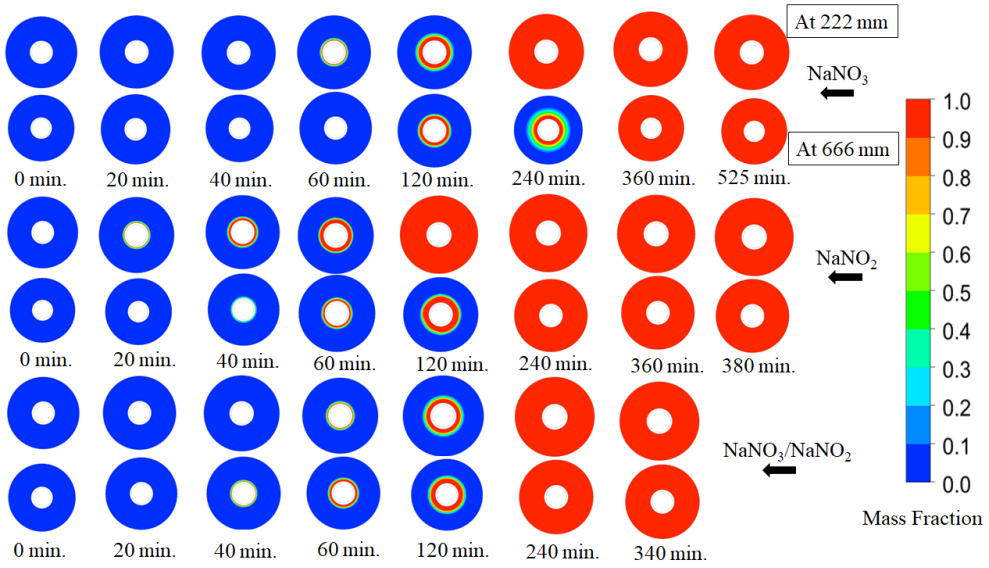

Fig. 6: Liquid faction contours in the vertical storage configurations (at the radial plane located at an axial distance of 222 mm (top) and 666 mm (bottom) from the inlet)

Figure: 7 represents the temperature contours on the axial plane in storage . It can be inferred from the figure that stage 2 has lower temperature distribution as compared to stage 1 of the CLHS because it reaches the melting state earlier than stage 1, as explained above. The significant movement of the melted PCM at the top region of the storage augments the rate of melting, which results in the high temperature of the PCM in that region.

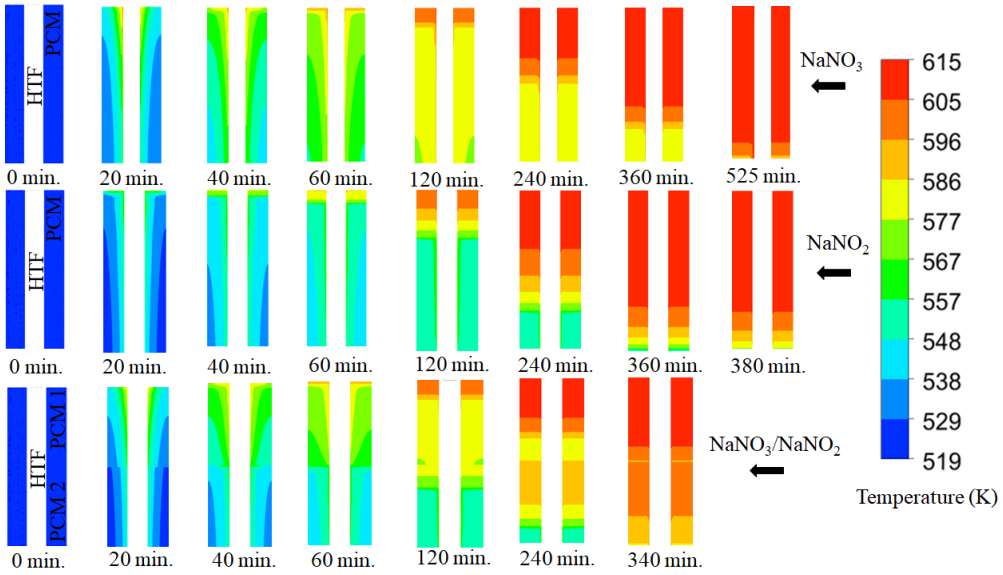

Fig. 7: Temperature contours in the vertical storage configurations (at a central axial plane)

3.2. Comparative Assessment of Cascade Latent Heat Storage for Various Geometric Orientations

The present study is further extended to investigate the effects of the various orientations of the CLHS on the charging process. In this context, the 2-stage CLHS is investigated for the vertical and horizontal orientations. The variation of the average melt fraction in the CLHS and the variation of the average melt fraction in the individual stage of the CLHS can be seen in Figure: 8. During the sensible heating of the solid PCMs, the conduction heat transfer will be dominant, due to which both the storages behave the same.

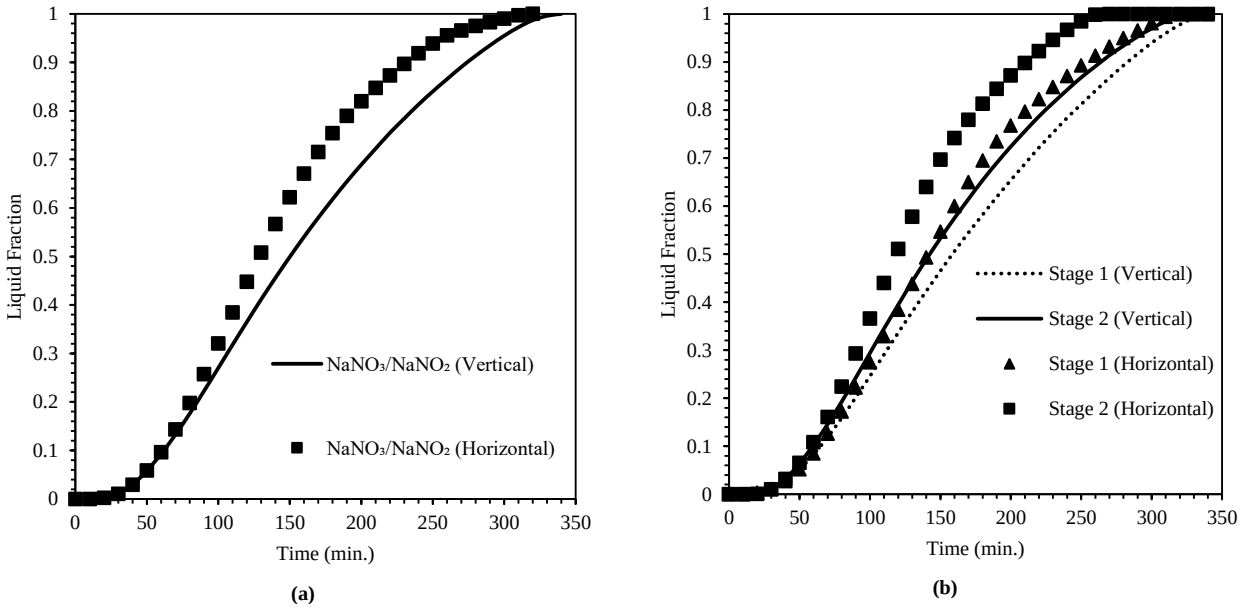

Fig. 8: Variation of the liquid faction of the PCMs in the vertical and horizontal CLHS (a) Average liquid fraction in CLHS (b) average liquid fraction in individual stages of CLHS

It can be depicted from the figure that initially, both vertical and horizontal CLHS shows the same rate of melting because of weak natural convection due to the less mass of the melted PCMs in each stage. After 70 minutes of the charging operation, a difference in the rate of melting can be seen in both configurations. As explained in the earlier section that due to the low density of the melted PCM, a natural convection current sets up in the domain which tries to move the liquid PCM in the opposite direction of the gravity (buoyancy-driven motion).

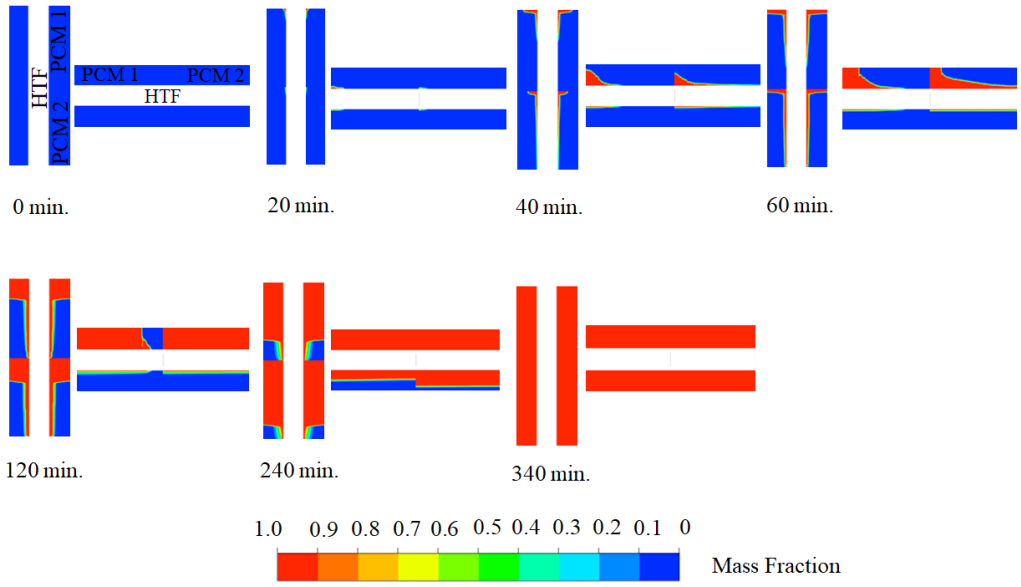

Fig. 9: Liquid faction contours in the vertical (left) and horizontal (right) CLHS (at a central axial plane)

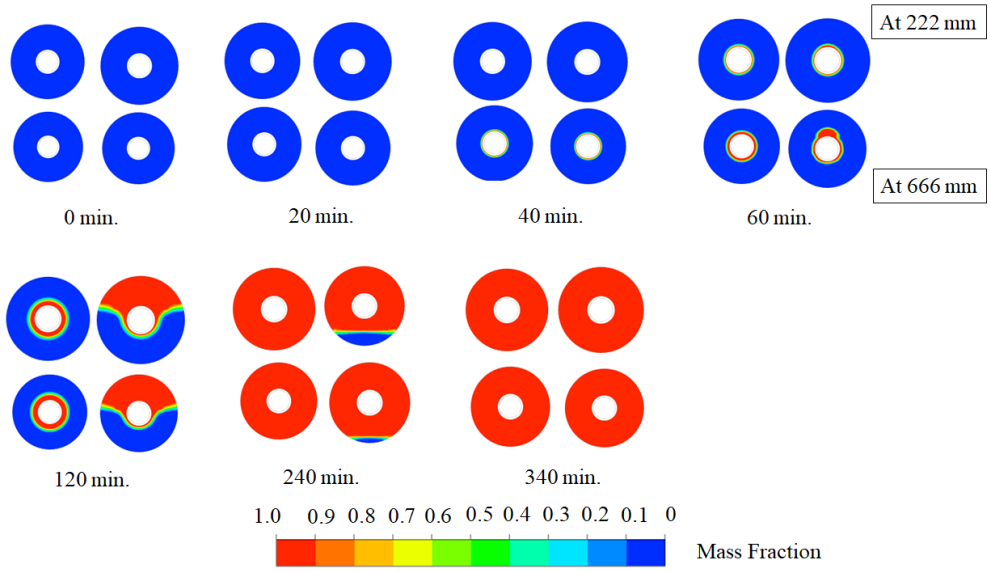

Fig. 10: Liquid faction contours in the vertical (left) and horizontal (right) CLHS (at the radial plane located at an axial distance of 222 mm (top) and 666 mm (bottom) from the inlet)

The gravitational force acts toward the HTF flow direction (z-direction) in the vertical orientation, while it acts in the radial direction (r direction) in the horizontal orientation. So, in the vertical orientation, the melted PCM tries to pile up in the top portion of the storage and improve the rate of heat transfer in that portion, which ultimately slows down the phase transition in the bottom portion of the storage (Figure: 9, 10). Conversely, in the horizontal orientation, the PCM tries to move in the radial direction (perpendicular to the HTF flow direction) and improves the heat transfer along the entire length of the storage (Figure: 9, 10). Therefore, a better charging rate can be seen in the horizontal CLHS as compared to the vertical CLHS.

An important observation can be made from the Figure: 9, and 10, that in horizontal CLHS, after the completion of the melting in the upper half domain of the CLHS, the rate of the heat transfer remains slow during the melting of the lower half domain of the CLHS due to accumulation of the melted PCM opposite to the direction of the gravity. Therefore, a slow rate of melting can be seen after the 50% charging of the storage. Therefore, it can be inferred that horizontal orientation is more suited for the part load operation of the CLHS. The charging period of the horizontal CLHS was found to be 39.04%, 15.78%, and 5.9% less than the charging period of the 1-stage $NaNO_3$ storage, 1-stage $NaNO_2$ storage, and 2-stage vertical CLHS, respectively (Figure: 11 (a)). In vertical CLHS, stage 2 (after 320 minutes of the charging operation) completes the melting 20 minutes earlier than stage

1(after 340 minutes of the charging operation) because of the high-temperature difference between the HTF (heat carrier fluid) and the melting temperature of the PCM in stage 2. However, in the horizontal CLHS, stage 2 (after 270 minutes of the charging operation) completes the melting 50 minutes earlier than stage 1(after 320 minutes of the charging operation). Therefore, it can be inferred that the orientation of the LTES affects the comparative melting behavior of the individual stage and increase the time range of the operation of the CLHS (Figure: 8(b)). Another essential parameter to judge the performance of the LTES is the total latent thermal energy stored during the complete charging process. Figure: 11 (b) represents the latent heat stored in the various configurations of the storage. All the configurations of the storage are designed to store 1 MJ of latent heat. It is inferred from the figure that after the 320 minutes of the charging process, 1-stage $NaNO_3$, 1-stage $NaNO_2$, and 2-stage vertical CLHS store 78%, 93%, and 98%, respectively, of the target latent thermal energy, while horizontal 2-stage CLHS is the only storage configuration which stores the 100% of the targeted energy.

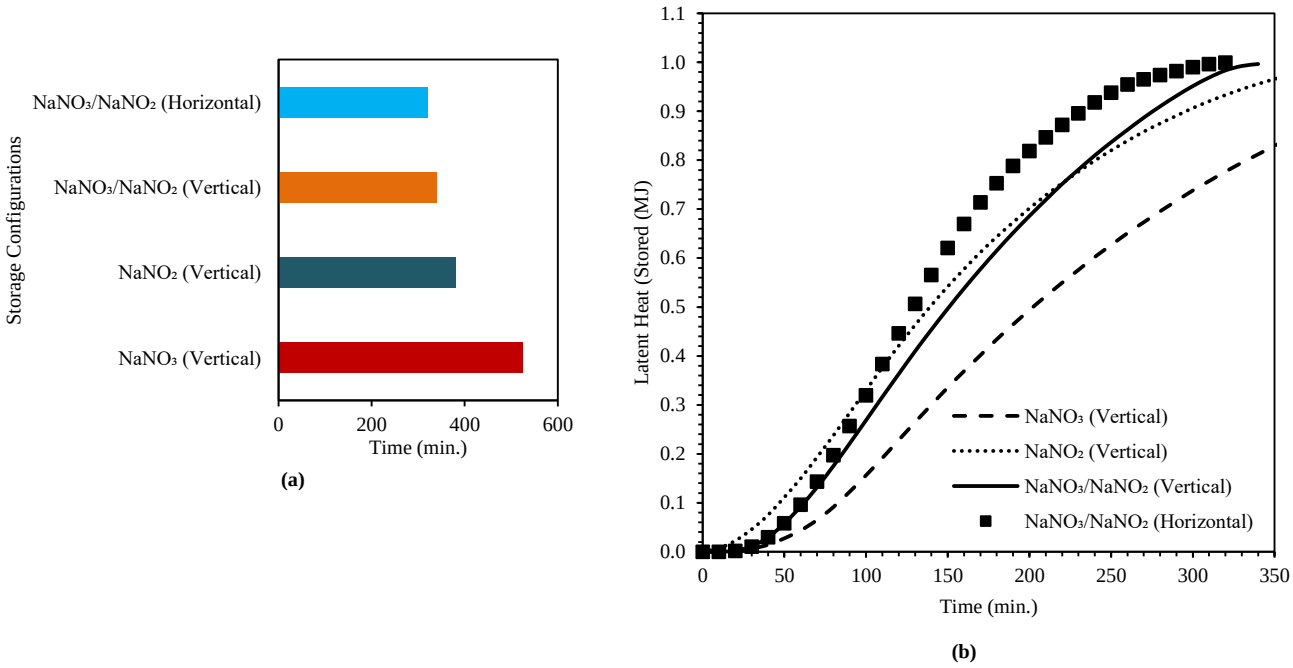

Fig. 11: (a) Total melting time of the storage configurations investigated in the present study (b) Latent thermal energy stored in the storage configurations investigated in the present study

4. Conclusion

In this investigation, a comparative thermal performance evaluation of the single PCM-based latent heat storage having $NaNO_3$ and $NaNO_2$ as the PCMs and the 2-stage cascade latent heat storage having both the PCMs is done. It is concluded that a 35.23% and 10.52% faster-charging rate than single PCM-based counterparts, i.e., $NaNO_3$ storage and $NaNO_2$ storage, respectively, can be obtained using 2-stage CLHS. The movement and accumulation of the liquid PCM at the top portion of the vertical storage slow down the melting in the other lower part of the storage. The use of any heat transfer enhancement method for the lower portion of the storage can boost the melting rate of the entire storage. Moreover, the present study also concludes that the charge cycle performance of the vertical CLHS can be reduced further by changing the orientation of the CLHS to horizontal. The charge cycle time of the horizontal CLHS was found to be 39.04%, 15.78%, and 5.9% less than the charge cycle time of the 1-stage $NaNO_3$ storage, 1-stage $NaNO_2$ storage, and 2-stage vertical CLHS, respectively. It also concluded that after the 320 minutes of the charging process, 1-stage $NaNO_3$, 1-stage $NaNO_2$, and 2-stage vertical CLHS store 78%, 93%, and 98%, respectively, of the target latent thermal energy, while horizontal 2-stage CLHS is the only storage configuration which stores the 100% of the targeted energy. The present study can further be extended for the discharging cycle to highlight the cyclic behavior of the multiple PCM-based storage.

Acknowledgments

The financial support for this research work is provided by the Department of Science and Technology (DST), Government of India, New Delhi, through the research project (Project Number: DST/TMD/CERI/RES/2020/14(G)).

References

Adine, H.A., El Qarnia, H., 2009. Numerical analysis of the thermal behaviour of a shell-and-tube heat storage unit using phase change materials. Appl. Math. Model. 33, 2132–2144. https://doi.org/10.1016/j.apm.2008.05.016

Alekseeva, O.A., Naberezhnov, A.A., Chernyshov, D.Y., Fokin, A.V., Sysoeva, A.A., Rysiakiewicz-Pasek, E., 2019. Thermal expansion coefficients of NaNO2 embedded into the nanoporous glasses. Nanosyst. Physics, Chem. Math. 10, 158–163. https://doi.org/10.17586/2220-8054-2019-10-2-158-163

ANSYS Inc (Release-15.0), 2015. ANSYS Fluent Theory Guide. ANSYS Inc., USA 15317, 1–759.

Brent, A.D., Voller, V.R., Reid, K.J., 1988. Enthalpy-porosity technique for modeling convection-diffusion phase change: Application to the melting of a pure metal. Numer. Heat Transf. 13, 297–318. https://doi.org/10.1080/10407788808913615

Fadl, M., Eames, P.C., 2019. Numerical investigation of the influence of mushy zone parameter Amush on heat transfer characteristics in vertically and horizontally oriented thermal energy storage systems. Appl. Therm. Eng. 151, 90–99. https://doi.org/10.1016/j.applthermaleng.2019.01.102

Hosseini, M.J., Ranjbar, A.A., Sedighi, K., Rahimi, M., 2012. A combined experimental and computational study on the melting behavior of a medium temperature phase change storage material inside shell and tube heat exchanger. Int. Commun. Heat Mass Transf. 39, 1416–1424. https://doi.org/10.1016/j.icheatmasstransfer.2012.07.028

Jain, S., Kumar, K.R., Rakshit, D., 2021. Heat transfer augmentation in single and multiple (cascade) phase change materials based thermal energy storage: Research progress, challenges, and recommendations. Sustain. Energy Technol. Assessments 48, 101633. https://doi.org/10.1016/j.seta.2021.101633

Janz, G.J., Allen, C.B., Bansal, N.P., Murphy, R.M., Tomkins, R.P.T., 1979. Physical Properties Data Compilations Relevant To Energy Storage - 2. Molten Salts: Data on Single and Multi-Component Salt Systems., National Bureau of Standards, National Standard Reference Data Series.

Marušić, A., Lončar, D., 2020. Experimental validation of high-temperature latent heat storage model using melting front propagation data. Appl. Therm. Eng. 164. https://doi.org/10.1016/j.applthermaleng.2019.114520

Mekrisuh, K. u., Singh, D., Udayraj, 2020. Performance analysis of a vertically oriented concentric-tube PCM based thermal energy storage system: Parametric study and correlation development. Renew. Energy 149, 902–916. https://doi.org/10.1016/j.renene.2019.10.074

Peiró, G., Gasia, J., Miró, L., Cabeza, L.F., 2015. Experimental evaluation at pilot plant scale of multiple PCMs (cascaded) vs. single PCM configuration for thermal energy storage. Renew. Energy 83, 729–736. https://doi.org/10.1016/j.renene.2015.05.029

Ray, A.K., Rakshit, D., Ravi Kumar, K., Gurgenci, H., 2021. Silicon as high-temperature phase change medium for latent heat storage: A thermo-hydraulic study. Sustain. Energy Technol. Assessments 46, 101249. https://doi.org/10.1016/j.seta.2021.101249

Sardari, P.T., Mohammed, H.I., Giddings, D., walker, G.S., Gillott, M., Grant, D., 2019. Numerical study of a multiple-segment metal foam-PCM latent heat storage unit: Effect of porosity, pore density and location of heat source. Energy 189, 116108. https://doi.org/10.1016/j.energy.2019.116108

Shabgard, H., Robak, C.W., Bergman, T.L., Faghri, A., 2012. Heat transfer and exergy analysis of cascaded latent heat storage with gravity-assisted heat pipes for concentrating solar power applications. Sol. Energy 86, 816–830. https://doi.org/10.1016/j.solener.2011.12.008

Tiari, S., Hockins, A., Mahdavi, M., 2021. Numerical study of a latent heat thermal energy storage system

enhanced by varying fin configurations. Case Stud. Therm. Eng. 25, 100999. https://doi.org/10.1016/j.csite.2021.100999

Tiari, S., Qiu, S., Mahdavi, M., 2015. Numerical study of finned heat pipe-assisted thermal energy storage system with high temperature phase change material. Energy Convers. Manag. 89, 833–842. https://doi.org/10.1016/j.enconman.2014.10.053

Wu, S., Zhu, D., Zhang, X., Huang, J., 2010. Preparation and melting/freezing characteristics of Cu/paraffin nanofluid as phase-change material (PCM). Energy and Fuels 24, 1894–1898. https://doi.org/10.1021/ef9013967

Abbreviations and Nomenclature

Table 1: Recommended symbols for materials properties

Quantity	Symbol	Unit
c_p	Specific heat	kJ kg^{-1} K^{-1}
$\vec{g}$	Gravitational acceleration	m sec^{-2}
H_t	Total enthalpy	kJ kg^{-1}
h_l	Enthalpy of phase change	kJ kg^{-1}
h_s	Specific sensible enthalpy	kJ kg^{-1}
k	Thermal conductivity	W/m^{-1} K^{-1}
L	Latent heat of PCM	kJ kg^{-1}
l	Length of the storage	m
m	Mass	kg
p	Pressure	Pa
r	Radial distance	m
R	Shell radius	m
T	Temperature	K
t	Time	s
$\vec{v}$	Velocity	m/s
z	Axial distance	m
Greek Symbols		
μ	Dynamic viscosity	Pa-s
ρ	Density	kg m^{-3}
θ	Angular distance	degrees
β	Melt fraction	-
β_t	Volumetric expansion coefficient	K^{-1}

Table 2: Recommended subscripts

Quantity	Symbol
Ambient	amb
Fluid (HTF)	f
Interface	itf
Inner	i
Melting	m
outer	o
Reference	ref
Storage	st

EuroSun 2022

CHARACTERIZATION OF ENHANCED BIOBASED PHASE CHANGE MATERIAL WITH GRAPHENE NANOPLATELETS – EARLY RESULTS

Elisangela J. D'Oliveira[1], Sol Carolina Costa Pereira[1], Dominic Groulx[2], Ulugbek Azimov[1]

[1]Department of Mechanical Engineering at Northumbria University at Newcastle

[2]Department of Mechanical Engineering at Dalhousie University

Abstract

Energy consumption is expected to continue rising, and in conjunction with greater environmental concern, it has boosted the development of renewable and sustainable energy sources, including storage media materials for thermal energy storage (TES) systems. Biobased Phase Change Materials (PCMs) are materials derived from renewable and environmentally friendly resources, such as palm oil, and are a great solution as they have similar properties to paraffin-based PCMs. Therefore, in view of designing a nano-enhanced PCMs (NePCMs) based on a commercial plant-based PCM, CrodaTherm60, was selected due to its high latent heat capacity as well as its medium melting point, 60 °C, making it suitable for solar domestic hot water systems (SDWHs). Whilst the selected PCM has desirable properties, it still possesses the most common limitations, such as its low thermal conductivity; thus, NePCMs were prepared and characterized using carbon-based nanoparticles, and graphene nanoplatelets (GNPs).

Keywords: Heat storage, biobased PCM, Thermal properties, Graphene nanoplatelets (GNP), Thermal conductivity.

1. Introduction

Thermal energy storage (TES) systems facilitate the energy balance between energy demand and supply, by storing the renewable energy when its available and release it when demand becomes higher. Energy demands for the residential sector vary seasonally; thus, incorporating a TES is essential for increasing renewable energy utilization. Currently, paraffin-based are the most studied type of organic PCMs for Latent Heat Thermal Energy Storage (LHTES) applications due to their favourable characteristics (Shi et al., 2013), which includes their high latent heat storage capacity and small temperature variation during the phase change process. However, these materials are not obtained from renewable sources, and their carbon footprint impact is often overlooked. Thereby, biobased PCMs are a promising alternative as they could have similar properties as paraffin waxes; thusly, over the recent years the research on this type of PCMs have grown exponentially (Wuliu et al., 2021, Liu et al., 2020, Hu et al., 2021).

Okogeri and Stathopoulos (2021) reviewed the research status of biobased PCMs with a focus on their promising perspectives as well as limitations and drawbacks; they also discussed the possibility of using waste materials such as waste cooking oil as potential alternatives to edible oil-based PCMs. Although biobased PCMs have many desirable properties, they still possess similar drawbacks as paraffin-based PCMs, such as

© 2022. The Authors. Published by International Solar Energy Society
Selection and/or peer review under responsibility of Scientific Committee
doi:10.18086/eurosun.2022.13.13 Available at http://proceedings.ises.org

low thermal conductivities. Thus, methods to improve the thermal conductivity of PCMs are widely investigated, and one of the methods often implemented is the incorporation of high conductive nanoparticles. Different nanoparticles have been studied to improve the thermal conductivity of the PCMs by different researchers (Jeong et al., 2013, Yu et al., 2014, D'oliveira et al., 2022), including nanoparticles based on carbon (Jeong et al., 2013, Yu et al., 2014), metal (Zhang et al., 2021, Cui et al., 2016), and metal oxides (Wang et al., 2012, Manoj Kumar et al., 2020).

Among carbon-based particles, graphene provides excellent properties for enhancing the heat transfer processes in the PCMs, such as high thermal conductivity, 5300 W/m.K (Sang et al., 2019), high aspect ratio and relatively low densities. Prado and Lugo (2020) developed and compared NePCMs based on PureTemp 8 as the PCM, provided by Entropy Solutions, with dispersions of GNPs (11-15 nm thickness) and MgO (35 nm diameter) nanoparticles purchased from IoLiTec; acetic acid, provided by Sigma-Aldrich, was used as a surfactant to improve the stability of the dispersions. Their results showed that more significant thermal conductivity improvements were obtained using GNPs as the conductive filler instead of MgO. Amin (2017) prepared and investigated NePCMs based on Beeswax as PCM and GNPs as nanoparticles, with a particle size of 2 nm. Including 0.3 wt% of GNPs into the PCM increased the thermal conductivity of the composite to 2.8 W/m.K, 11 times higher than the pure beeswax (0.25 W/m.K). Besides that, the inclusion of GNPs not only had a positive effect on the thermal conductivity of the Beeswax but also enhanced the latent heat of the material. Shi et al. (2013) prepared and investigated the thermal conductivity enhancement of paraffin, with a melting temperature of 61.6°C, with loadings of exfoliated graphite nanoplatelets (xGnP) and graphene. From the results obtained by the authors, the thermal conductivity enhancement with graphene was much smaller than expected, and they suggested that the reason was the interfacial thermal resistance because of the inefficient coupling of acoustic waves through the weak van der Waals interaction.

Although many studies were conducted with similar carbon-based nanoparticles, there are significant discrepancies, making the selection of the appropriate nanomaterial for a specific PCM unclear. To the best of authors' knowledge, regarding the preparation and characterization of NePCMs based on CrodaTherm60 as the PCM, no studies were found in the literature; however, researchers have investigated the thermal performance of latent heat thermal energy storage (LHTES) filled with CrodaTherm60 in systems such as multi-tube finned copper heat exchanger (Fadl and Eames, 2021). In the current study, NePCMs based on the commercially available PCM, CrodaTherm60, were incorporated with 2, 4 and 6 wt.% of GNPs through the magnetic stirring and ultrasonication synthesis process. Moreover, to study the effects of the different mass fractions of GNPs on the thermal performance of the CrodaTherm60, the main thermophysical properties, phase change temperatures, latent heat, densities, and thermal conductivity were studied experimentally.

2. Methodology

2.1 Materials

CrodaTherm60 a bio-organic PCM (derived from plant-based feedstock), with a melting temperature of 60 °C supplied by CRODA Energy Technologies was used as the PCM in this study. The thermal properties of the commercially available biobased PCM are shown in Tab. 1, To increase the thermal conductivity of the PCM, graphene nanoplatelets, with a thickness of 2 nm and specific surface area of 750 m^2/g, supplied from IoLiTec were used as the high conductive particles.

Tab. 1: Thermal properties of the commercially available CrodaTherm60

Density [kg/m^3]	Melting Temp. [°C]	Latent heat [kJ/kg]	Thermal conductivity [W/m.K]	Specific heat [kJ/kg. K]
922	60	217	0.29	2.3

2.2 Preparation of NEPCMs

The NePCMs were prepared following the magnetic stirring and ultrasonication process, which offers better incorporation of GNPs nanoparticles into the base of the CrodaTherm60 (Yu et al., 2014, Putra et al., 2017). First, 50 grams of CrodaTherm60 were melted in a water bath at a constant temperature of 80 °C. Afterwards, GNPs nanoparticles were incorporated into the melted PCM and mixed for 30 min with a magnetic stirring at 800 r/min and 80 °C. Having completed the first step of the synthesis process, the melted NePCMs were ultrasonicated in an ultrasonic bath for 30 min at the same temperature to break down the GNPs aggregation and to improve the dispersion of the nanoparticles into the base PCM. The synthesis process implemented in this study is illustrated in Fig. 1.

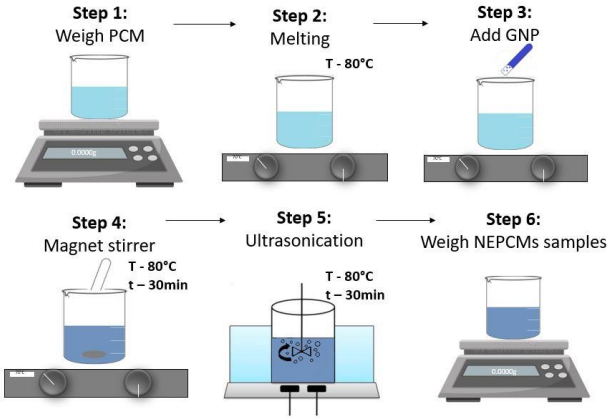

Fig. 1: Procedure of the NEPCMs sample preparation

2.3 Characterization techniques

The morphology and microstructure of the thermal enhanced CrodaTherm60 were observed using scanning electron microscopy (SEM, TESCAN MIRA3) at room temperature. The NePCMs samples were coated with a platinum coating, 5 nm in thickness, to increase the electrical conductivity of the samples. The SEM images were taken at an accelerating voltage of 5kV and the same view field.

Thermal properties of the PCM and NePCM, such as melting and crystallization temperature, latent heat and specific heat capacity, were measured using the Differential Scanning Calorimetry (DSC, 131 SETARAM). The DSC measurements were performed at two heating and cooling rates, 2 K/min and 10 K/min, in a temperature range of 15 to 90 °C for heating and 90 to 15°C for cooling, under a constant stream of argon gas atmosphere and nitrogen to better control heating and cooling rates. Three samples of 7-9 mg of each NePCMs were prepared using a balance with a precision of 0.1 mg.

The thermal conductivity of PCMs and NePCMs were measured by a thermal conductivity instrument (Linseis THB 100), with a measurement accuracy of 5 %. The samples prepared were 50mm x 25 mm with an average thickness of 5mm. The hot point sensor was placed between two samples, and a weight of about 2 kg was used to improve the contact with the sensor. The sensor was calibrated using polymethyl methacrylate (PMMA) with thermal conductivity of 0.194 W/m.K for a single-point calibration. The thermal conductivity was measured at room temperature, solid phase. Several measurements were taken for each sample, and the position of the sensor was changed each time, and the reported values were the mean. The uncertainty for the thermal conductivity reported was estimated to be less than 5 %.

The density of the solid samples was measured using the Arquimedes principles. The method is described in the BS EN ISO 1183-1 standard. The liquid used was ethanol at a temperature of 20 °C. The uncertainty for the density reported was estimated to be less than 1 %.

3. Results and Discussion

3.1 Morphology and microstructure of the NePCMs

The NePCMs samples prepared with 2, 4 and 6 wt.% mass fractions of Graphene nanoplatelets are shown in Fig. 2. The SEM images of the prepared NePCMs presented in Fig. 3, show that the GNPs are well dispersed. However, there is a significant agglomeration shown by the SEM images; with 2 wt.% of GNPs in the based PCM the clustering size was in the microscale and not nanoscale. It is observed that the agglomeration of the nanoparticles increases with the mass concentration of nanoparticles. As seen in Fig. 3 (b) and (c) the GNPs are separated into layers which could limit the formation of an effective heat conduction network.

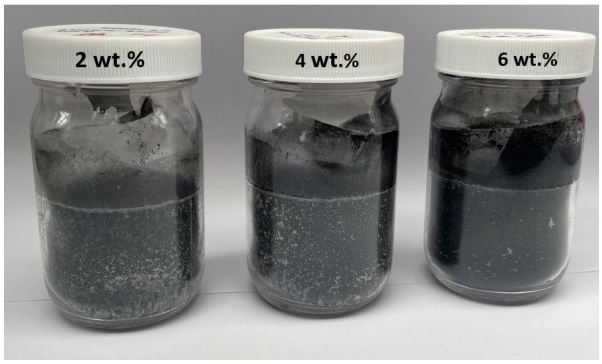

Fig. 2: NePCMs with mass fractions of 2, 4 and 6 wt.% GNPs

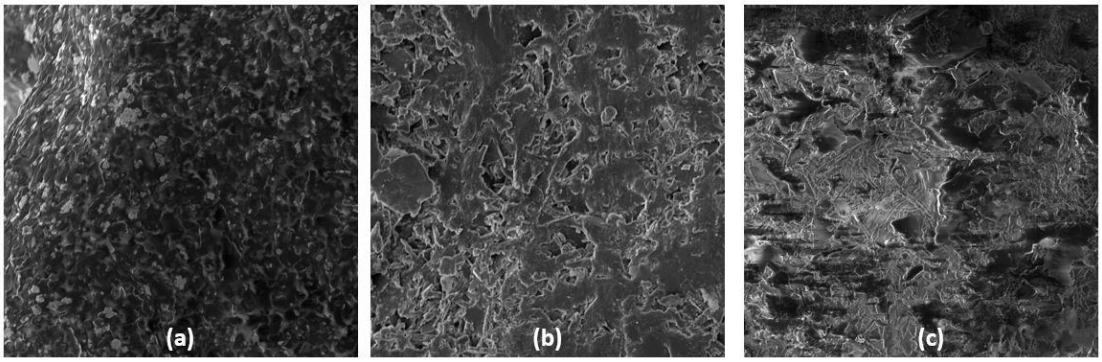

Fig. 3: SEM images of NePCMs with (a) 2 wt.%, (b) 4 wt.% and (c) 6 wt.% with a view field of 100 µm at a 5.0 kV

3.2 Thermal properties of the CrodaTherm60 and CrodaTherm60 NePCMs

The following thermal properties of the pure and enhanced phase change materials were investigated, including the onset temperature and latent heat capacity of melting and solidification processes obtained by the DSC equipment. The first cycle, at 10 K/min, was discarded to eliminate the thermal history of the sample before the measurements were taken; the consecutive cycles were effectively used to avoid discrepancies and outliers. The measurements for the latent heat capacity (ΔH) were taken at 10 K/min, as at this scanning rate the error is minimized, while at 2 K/min, the phase change transition (onset) value tends to be more accurate; thus, testing the samples at both heating rates allowed more accurate identification of the latter thermal properties stated (Müller et al., 2020). The detailed data obtained by the DSC measurements and the estimated latent heat capacity are shown in Tab. 2. It is expected that the addition of GNPs into the CrodaTherm60, will reduce the latent heat capacity of the NePCMs as the content of the base PCM is reduced. Theoretically, the reduction in the latent heat capacity of the NePCMs is directly proportional to the increase in the mass fraction of the additive content and can be calculated with the following equation (Feng et al., 2022, Yuan et al., 2016a):

$$\Delta H_{NePCM} = \varphi \Delta H_{PCM}$$

Where ΔH_{NePCM} is the latent heat of NePCMs, φ is the percentage of PCM and ΔH_{PCM} is the latent heat capacity of the PCM.

Tab. 2: Heat storage properties of CrodaTherm60 and thermal enhanced CrodaTherm60

Material	Wt.%	T_m [°C]	ΔH_m [kJ/kg]	Reduction in ΔH_m [%[	Theoretical ΔH_m [kJ/kg]	T_s [°C]	ΔH_s [kJ/kg]
CrodaTherm 60/ 2nm GNP	0	57.2±0.2	201.7±15.8	-	-	58.1±0.1	209.0±19.9
	2	57.5±0.3	183.6±6.7	-8.98%	197.7	58.3±0.1	186.9±9.1
	4	57.7±0.8	174.8±7.2	-13.34%	193.7	58.4±0.1	180.9±3.3
	6	57.3±0.1	178.5±10.4	-11.51%	189.6	58.4±0.1	183.6±8.8

The melting and solidification curves from the DSC measurements of CrodaTherm60 and the NePCMs with the different mass fractions of GNPs are shown in Fig. 4 (a). The DSC curves of the three NePCMs are similarly shaped to the pure CrodaTherm60, with an observably endothermic peak in the melting process and an exothermic peak in the solidification process. The latent heat capacity for melting and solidification is obtained by integrating the total area under the peaks for the solid-liquid transition curves of the NePCMs. The measured melting temperature of CrodaTherm60 is 57.2 °C, thus, the material is suitable to be used in domestic space and water heating systems. The melting and solidification latent heat are measured as 201.7 and 209.0 kJ/kg, respectively. The supplier, Croda Technologies, provides information about the melting temperature and latent heat (Tab. 1Tab.1) which can be compared to the measured values. In average, the deviaton from the supplier stated values for melting temperature is 4.7 %, however, for latent heat is 7.3 %.

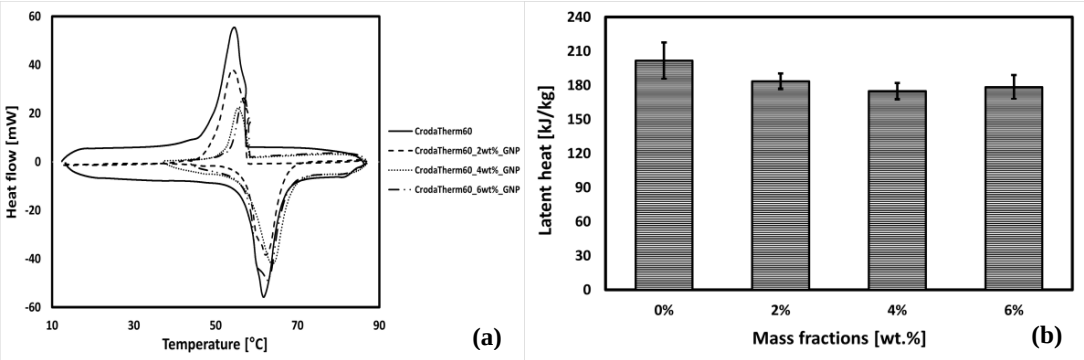

Fig. 4. (a) DSC curves of CrodaTherm60 and NePCMs and (b) difference in Latent heat capacity

The changes in the latent heat capacity with the increase in loadings of GNPs into the base PCM can be observed in Fig. 4 (b). As seen on Tab. 2 the latent heat increased with 6 wt.% when comparing with the NePCM with 4 wt.%, this could be explained due to the uncertainty of the measurements related to the precision of the balance used to weight the reference samples as well as the DSC equipment accuracy. Issues were also found when performing the DSC measurements, as there was leakage on the crucible pans from the samples, resulting in mass changes during the experiments.

3.3 Effects of the mass fraction on the densities

The density of CrodaTherm60 and NePCMs, with loadings of GNPs, at a solid state were experimentally measured and are show in Tab.3.

Tab. 3: Variation on the Density of the NePCMs with the incorporation of 2 nm GNPs

Material	Wt.%	Density (solid) [kg/m^3]	Standard deviation [kg/m^3]	Increase in density [%]
CrodaTherm60	0	937	±8.5	-
CrodaTherm60 + GNPs	2	949	±4.1	1.2
	4	974	±7.6	4.0
	6	996	±2.9	6.3

The effects of the GNPs mass fractions on the PCM density are illustrated in Fig. 5. The measured solid density of the CrodaTherm60 is 937 kg/m^3 which is 1.6% higher than the density reported by the suppliers, 922 kg/m^3. There is a strong linear correlation with a factor of 0.98, which indicates that the increase in the density of the NePCMs is directly proportional to the mass fraction of GNPs.

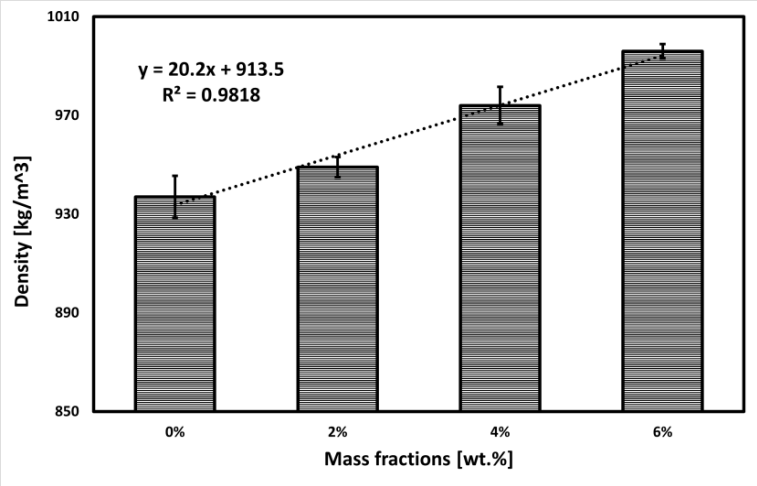

Fig. 5: Effects on the density with the increase of mass fractions wt.% of GNPs

3.4 Thermal conductivity

One of the performance indicators of the storage media material is the rate at which the energy can be stored and released, and it is highly dependent on the thermal conductivity of the material. Tab. 4 summarises the variation of the solid thermal conductivity of the CrodaTherm60 and NePCMs with different mass fractions, 2-4 wt.%, and the enhancement rates. The solid thermal conductivity measurements were taken at approximately 25 °C and for each sample, the tests were repeated 3 times and the value of each data is represented as mean ± standard deviation.

Tab. 4: Measured thermal conductivity in solid state at ambient temperature of CrodaTherm 60 with the incorporation of 2 nm GNPs

Material	Wt.%	Thermal conductivity [W/m.K]	Thermal conductivity enhancement [%]	Standard deviation [W/m.K]
CrodaTherm60	0	0.206	-	±0.021
CrodaTherm60 + GNPs	2	0.224	8.8	±0.007
	4	0.228	10.6	±0.011
	6	0.230	11.5	0.007

It can be seen from Fig. 6, that the thermal conductivity of the NePCMs increases along with the increase of GNPs contents. The thermal conductivity of the CrodaTherm60 was measured to be 0.206 W/m.K and the standard deviation in the measurement of thermal conductivity was up to 0.021 W/m.K. Although there was an increase in the thermal conductivity of the NePCMs, the thermal conductivity enhancement was lower than expected, despite the excellent thermal conductivity of the GNPs.

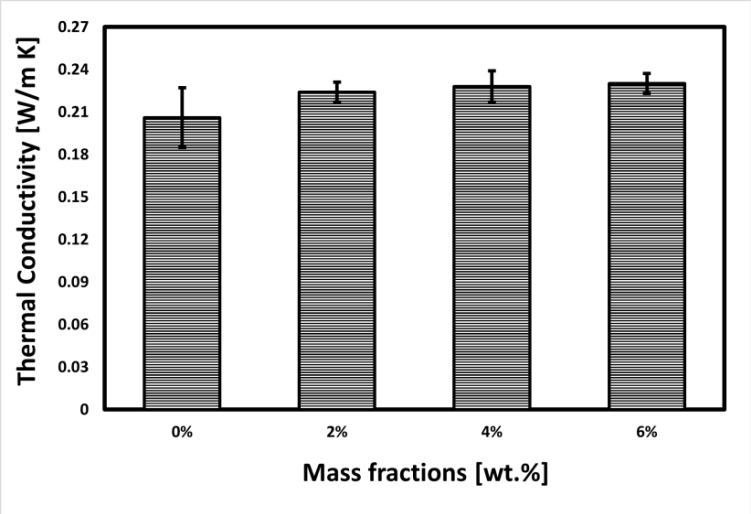

Fig. 6: Measured thermal conductivity of the solid NePCMs as a function of the loading of graphene nanoplatelets

Tab. 5 shows the results in the thermal conductivity enhancement in recent studies that have used carbon-based nanoparticles, mostly GNPs with similar geometries to the nanoparticles used in this study. There are significant discrepancies in the results reported in this study compared with previously published studies. The discrepancies could be attributed to numerous factors, some related to the differences in the nanocomposites, such as the size, thickness, specific surface area, and agglomeration of the nanoparticles and others related to the nonreported uncertainties in the measurements. The result reported in this study are preliminary; however, it is evident that the impact of carbon nanoparticles in the thermal conductivity should be further investigated.

Tab. 5: A summary of recent studies that used carbon-based nanomaterials as a conductive filler

Base PCM		**Nanoparticles**		**NePCMs**			**Ref.**
PCM/ T_m [°C]	**k [W/m.K]**	**Type**	**Size**	**[wt.%]**	**k [W/m.K]**	**$K_{enhancement}$ [%]**	
Paraffin [29-36°C]	0.20	GNPs	-	1	0.23	16 %	(Abdelrazik et al., 2020)
				5	0.24	20 %	
				10	0.26	28 %	
				20	0.30	47 %	
Palmitic-Stearic acid [54°C]	0.26	GNPs	Thickness: 4-20 nm Layers: <20 Size: 5-10µm	1	0.34	30 %	(Yuan et al., 2016b)
				2	0.44	65 %	
				4	0.62	134 %	
				8	0.98	273 %	
Myristic acid [54.4°C]	0.22	GNPs	Diameter: 5-10 µm Thickness: 3-10nm	1	0.45	104 %	(He et al., 2019)
				2	0.50	127 %	
				3	0.60	176 %	
n-nonacosane [61.6°C]	0.2	xGnP	-	2	0.75	25 %	(Shi et al., 2013)
				5	1.75	100 %	
				10	2.75	150 %	

A graphical comparison of the variation of the thermal conductivity of different carbon-based NePCMs as well as the current NePCMs prepared in this study is shown in Fig. 7. Yuan et al. (2016) investigated the thermal performance of palmitic-stearic acid with GNPs. The NePCMs were prepared using a similar synthesis process as the preparation process used in this study; however, the time taken for the magnetic stirring as well as the ultrasonication, were of 1 h each which was 30 min higher than the time taken for the preparation of the NePCMs in this study. This could have resulted in a better dispersion of the GNPs into the palmitic-stearic acid, resulting in less agglomeration. He et al. (2019) prepared and characterized myristic acid with different carbon nanoparticles including GNPs. The level of enhancement in the thermal conductivity with the increase of GNPs slowed down with the increase in the concentration of the nanoparticles.

The lower increase in the thermal conductivity of the NePCMs prepared in this study could be due to the agglomeration and sedimentation phenomena, and according to Xuan et al. (2003) the aggregation of the nanoparticles can have a negative impact on the thermal conductivity enhancement since Brownian motion will be slower. Although, the specific surface area of the nanomaterial play an important role in the shape stabilization of the PCMs, it can also accelerate the nanomaterial aggregation, which tends to weaken the thermal conductivity enhancement effect. The specific surface area of the GNPs used in this study is 750 m^2/g, thus, the low increase in the thermal conductivity could have been attributed to this phenomenon. Therefore, methods should be taken to avoid the aggregating issues that can be caused by the agglomeration and sedimentation issues.

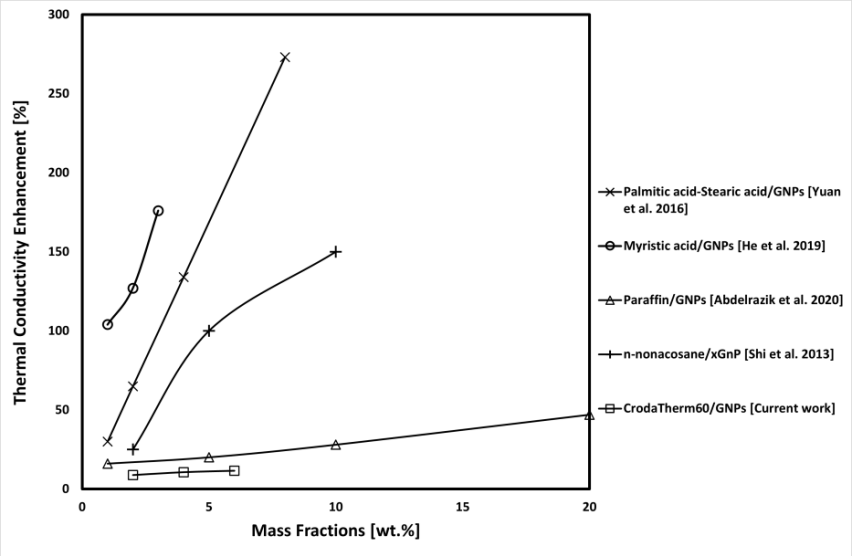

Fig. 7: Comparison of thermal conductivity enhancements of NePCMs vs additive mass fractions (wt.%) using carbon based nanomaterials

4. Conclusion

In this paper, the effects of adding graphene nanoplatelets in the main properties, phase change temperatures, latent heat capacities, density, and thermal conductivities of the CrodaTherm60 were investigated. The latent heat capacity of the NePCMs significantly decreased with the addition of GNPs into the CrodaTherm60 and the content of nanoparticles. The measured melting temperature of 57.2 °C and high latent heat capacity of 201.7 kJ/kg make this material suitable for space and domestic water heating applications. Due to weigh loss reported from the samples analysed through the DSC characterization, more samples using different crucibles are going to be prepared and analysed to reduce the error and uncertainties from the measurements taken. The GNPs were very ineffective in boosting the thermal conductivity of the CrodaTherm60 despite its high thermal conductivity. This can be associated to the high specific surface area of the GNPs which can be prone for agglomeration and sedimentation issues, seen from the SEM images taken from the NePCMs samples. Therefore, further efforts will be required to address the agglomeration issues, which might include increasing the time for ultrasonication during the preparation process to break the GNPs clusters as well as using nucleating agents to improve the dispersion of the nanoparticles into the PCM.

5. Credit author statement

Elisangela Jesus D'Oliveira: Conceptualization, Methodology, Data acquisition, Writing – original draft. **Sol Carolina Costa Pereira:** Supervision, Data acquisition, Methodology, Writing -review & editing**.** **Ulugbek Azimov:** Review & Editing. **Dominic Groulx:** Review & Editing.

6. Acknowledgements

This work was funded by EPSRC Centre for Doctoral Training in Renewable Energy Northeast Universities (ReNU), Project Reference EP/S023826/1. The authors would like to thank the in-kind contribution from Linseis Messgeraete GmbHand SemiMetrics Ltd

7. References

Abdelrazik, A., Al-Sulaiman, F. & Saidur, R. 2020. Numerical investigation of the effects of the nano-enhanced phase change materials on the thermal and electrical performance of hybrid PV/thermal systems. *Energy Conversion and Management,* 205**,** 112449.

Amin, M., Putra, N., Kosasih, E. A., Prawiro, E., Luanto, R. A. & Mahlia, T. 2017. Thermal properties of beeswax/graphene phase change material as energy storage for building applications. *Applied Thermal Engineering,* 112**,** 273-280.

Cui, W., Yuan, Y., Sun, L., Cao, X. & Yang, X. 2016. Experimental studies on the supercooling and melting/freezing characteristics of nano-copper/sodium acetate trihydrate composite phase change materials. *Renewable Energy,* 99**,** 1029-1037.

D'oliveira, E. J., Pereira, S. C. C., Groulx, D. & Azimov, U. 2022. Thermophysical properties of Nano-enhanced phase change materials for domestic heating applications. *Journal of Energy Storage,* 46**,** 103794.

Fadl, M. & Eames, P. C. 2021. Thermal performance evaluation of a latent heat thermal energy storage unit with an embedded multi-tube finned copper heat exchanger. *Experimental Heat Transfer***,** 1-20.

Feng, L., Wu, J., Sun, W. & Cai, W. 2022. Effects of Pore Structure and Pore Size of Expanded Graphite on the Properties of Paraffin Wax/Expanded Graphite Composite Phase Change Materials. *Energies,* 15**,** 4201.

He, M., Yang, L., Lin, W., Chen, J., Mao, X. & Ma, Z. 2019. Preparation, thermal characterization and examination of phase change materials (PCMs) enhanced by carbon-based nanoparticles for solar thermal energy storage. *Journal of Energy Storage,* 25**,** 100874.

Hu, X., Huang, H., Hu, Y., Lu, X. & Qin, Y. 2021. Novel bio-based composite phase change materials with reduced graphene oxide-functionalized spent coffee grounds for efficient solar-to-thermal energy storage. *Solar Energy Materials and Solar Cells,* 219**,** 110790.

Jeong, S.-G., Chung, O., Yu, S., Kim, S. & Kim, S. 2013. Improvement of the thermal properties of Bio-based PCM using exfoliated graphite nanoplatelets. *Solar Energy Materials and Solar Cells,* 117**,** 87-92.

Liu, L., Fan, X., Zhang, Y., Zhang, S., Wang, W., Jin, X. & Tang, B. 2020. Novel bio-based phase change materials with high enthalpy for thermal energy storage. *Applied energy,* 268**,** 114979.

Manoj Kumar, P., Mylsamy, K. & Saravanakumar, P. 2020. Experimental investigations on thermal properties of nano-SiO2/paraffin phase change material (PCM) for solar thermal energy storage applications. *Energy Sources, Part A: Recovery, Utilization, and Environmental Effects,* 42**,** 2420-2433.

Müller, L., Rubio-Pérez, G., Bach, A., Muñoz-Rujas, N., Aguilar, F. & Worlitschek, J. 2020. Consistent DSC and TGA Methodology as Basis for the Measurement and Comparison of Thermo-Physical Properties of Phase Change Materials. *Materials,* 13**,** 4486.

Okogeri, O. & Stathopoulos, V. N. 2021. What about greener phase change materials? A review on biobased phase change materials for thermal energy storage applications. *International Journal of Thermofluids***,** 100081.

Prado, J. I. & Lugo, L. 2020. Enhancing the thermal performance of a stearate phase change material with graphene nanoplatelets and MgO nanoparticles. *ACS applied materials & interfaces,* 12**,** 39108-39117.

Putra, N., Amin, M., Kosasih, E. A., Luanto, R. A. & Abdullah, N. A. 2017. Characterization of the thermal stability of RT 22 HC/graphene using a thermal cycle method based on thermoelectric methods. *Applied Thermal Engineering,* 124**,** 62-70.

Sang, M., Shin, J., Kim, K. & Yu, K. J. 2019. Electronic and thermal properties of graphene and recent advances in graphene based electronics applications. *Nanomaterials,* 9**,** 374.

Shi, J.-N., Ger, M.-D., Liu, Y.-M., Fan, Y.-C., Wen, N.-T., Lin, C.-K. & Pu, N.-W. 2013. Improving the thermal conductivity and shape-stabilization of phase change materials using nanographite additives. *Carbon,* 51**,** 365-372.

Wang, C., Feng, L., Li, W., Zheng, J., Tian, W. & Li, X. 2012. Shape-stabilized phase change materials based on polyethylene glycol/porous carbon composite: the influence of the pore structure of the carbon materials. *Solar Energy Materials and Solar Cells,* 105**,** 21-26.

Wuliu, Y., Liu, J., Zhang, L., Wang, S., Liu, Y., Feng, J. & Liu, X. 2021. Design of bio-based organic phase change materials containing a "safety valve". *Green Chemistry,* 23**,** 8643-8656.

Xuan, Y., Li, Q. & Hu, W. 2003. Aggregation structure and thermal conductivity of nanofluids. *AIChE Journal,* 49**,** 1038-1043.

Yu, S., Jeong, S.-G., Chung, O. & Kim, S. 2014. Bio-based PCM/carbon nanomaterials composites with enhanced thermal conductivity. *Solar Energy Materials and Solar Cells,* 120**,** 549-554.

Yuan, Y., Li, T., Zhang, N., Cao, X. & Yang, X. 2016a. Investigation on thermal properties of capric–palmitic–stearic acid/activated carbon composite phase change materials for high-temperature cooling application. *Journal of Thermal Analysis and Calorimetry,* 124**,** 881-888.

Yuan, Y., Zhang, N., Li, T., Cao, X. & Long, W. 2016b. Thermal performance enhancement of palmitic-stearic acid by adding graphene nanoplatelets and expanded graphite for thermal energy storage: A comparative study. *Energy,* 97**,** 488-497.

Zhang, Z., Duan, Z., Chen, D., Xie, Y., Cao, X. & Wang, J. 2021. Sodium acetate trihydrate-based composite phase change material with enhanced thermal performance for energy storage. *Journal of Energy Storage,* 34**,** 102186.

Loading Slim Hot Water Tanks With and Without Swirl Generation - First Results

Felix Oestreich[1], Thorsten Urbaneck[1]

[1] Chemnitz University of Technology, Professorship Applied Thermodynamics, Chemnitz (Germany)

Abstract

Hot water storage tanks (pressure vessels) enable the storing of pressurized water in the temperature range 95…200 °C. These storage tanks are often used in solar heat supply systems, in combined heat and power plants, in district heating networks and in industrial heat supply networks. During loading, flow effects occur in slim storage tanks, which are detrimental to the development of thermal stratification. This work compares the thermal stratification development for loading with conventional radial diffusers with a new diffuser design that generates swirl flow. Numerical flow simulation (CFD) studies show the behaviour in the diffuser and in the storage. The effects on thermal stratification are analysed and evaluated with known key figures.

Keywords: thermal energy storage, tank, pressure vessel, hot water, heat supply, stratification, charging device, diffuser, optimization, swirl, simulation

1. Introduction

To achieve the goals of the Paris climate agreement, the reduction of greenhouse gas emissions in the area of energy supply is essential (BMUV, 2022). The supply of space heating and tap water as well as the provision of process heat (56 % of final energy consumption in Germany, as of 2020) cause a large part of these emissions (AG Energiebilanzen, 2022). Therefore, the development of renewable energy supply is necessary for a climate-neutral or emission-free heat supply. Medium-temperature solar thermal energy can make a significant contribution in the area of district heating supply. This is confirmed, for example, by the studies of *Stahlhut* et al. (Stahlhut, 2022a, 2022b). The provision of heat by collector fields is predominantly time-delayed to the heat demand. Thermal energy storage systems can store surplus heat and supply it to the heating network or consumers with a time delay. In this way, the storage units enable a temporal decoupling. In district heating supply, hot water storage tanks fulfill this function.

Available storage tank designs are shown in Fig. 1 (Urbaneck, 2020). For the temperature range 95...140 °C, flat-bottom tanks are suitable as two-zone storage tanks (a4) as well as slim pressure vessels (b1) and compact pressure vessels (b2). This work deals with slim pressure vessels (b1). Fig. 2 shows such an installation with slim tanks. The operating pressure of 10 to 20 bar enables the storage of liquid water from 95 to approx. 200 °C. This means that these storage tanks are also suitable for industrial heat supply. Fig. 3 shows the specific storage investment costs for all storage types from Fig. 1. Consequently, storage design (b1) is particularly advantageous for high temperature differences (> 75 K) and medium storage capacities up to 400 MWh compared with other storage designs (Urbaneck, 2020).

Due to production in the factory, typical storage volumes are between 180 and 200 m³ per storage tank (Fig. 2). The schematic structure of a series connection of storage tanks (b1) is shown in Fig. 4. Larger storage volumes can be realized via series and parallel connection (Fig. 2). The storage are operated according to the displacement principle. The pressure is maintained outside the storage so that the storage are completely filled with water.

The operation of such storage facilities is complex and depends on many influencing factors. One essential aspect is the thermal stratification. The stratification characterizes the vertical temperature distribution and provides information about mixing processes in the storage tank. A high quality of thermal stratification indicates low internal storage losses. Internal storage losses are the temperature reduction of the storage water by mixing or heat conduction as well as further heat transfer processes in the storage. These losses can be described by the increase of entropy or the decrease of exergy. A significant influence on the stratification quality has the operating parameters (e.g. density difference, volume flow rate) during the loading process and the design (geometry, shape) of the loading system. The aim of this work is to improve the thermal stratification during the loading process of slim hot water storage tanks. The investigations are carried out with numerical flow simulation (CFD). The flow processes or heat transfer in the loading system and in the storage room were modeled. External losses (e.g. heat transfer processes in the storage tank wall) are not subject of this investigation.

© 2022. The Authors. Published by International Solar Energy Society
Selection and/or peer review under responsibility of Scientific Committee
doi:10.18086/eurosun.2022.13.14 Available at http://proceedings.ises.org

In order to achieve an improvement of the thermal stratification, different diffuser designs are investigated. A conventional radial diffuser is used for loading (Fig. 5 a)). This diffuser allows radial velocity decay and theoretically uniform inflow (equal distribution of direction and velocity at the diffuser outlet) of the loading fluid into the storage. Fig. 5 b) shows this behaviour in a very simplified way. In principle, this behavior is favorable for building up the thermal stratification.

Studies by (Brähmer, 2012) and (Lohse, 2012) show that, due to the relatively small storage radius, undesirable flow effects occur (e.g. formation of a wall jet and a large-scale mixing zone in the upper storage area), which lead to a poor starting position with regard to the stratification structure. To overcome this flow problem, (Platzer, 2017) proposes swirl loading. For swirl generation, guide elements are installed in the diffuser (Fig. 5 c)). These internal elements are characterized by the entrance α, the exit angle or swirl angle β and the number of internal elements z (Fig. 5 d)). The rotation is intended to reduce the momentum of the jet in the upper storage region. This fundamentally changes the flow behaviour (Fig. 5 e)), novel loading with swirl generation). First empirical investigations showed the advantageousness (Winkler, 2017). Subsequent experimental work did not provide clear results (Kroll 2020a, 2020b). Therefore, it must be fundamentally clarified whether loading with swirl has a positive influence on the quality of thermal stratification. For further optimization of the loading, a better understanding of the flow processes during loading with swirl generation is urgently needed as a next step.

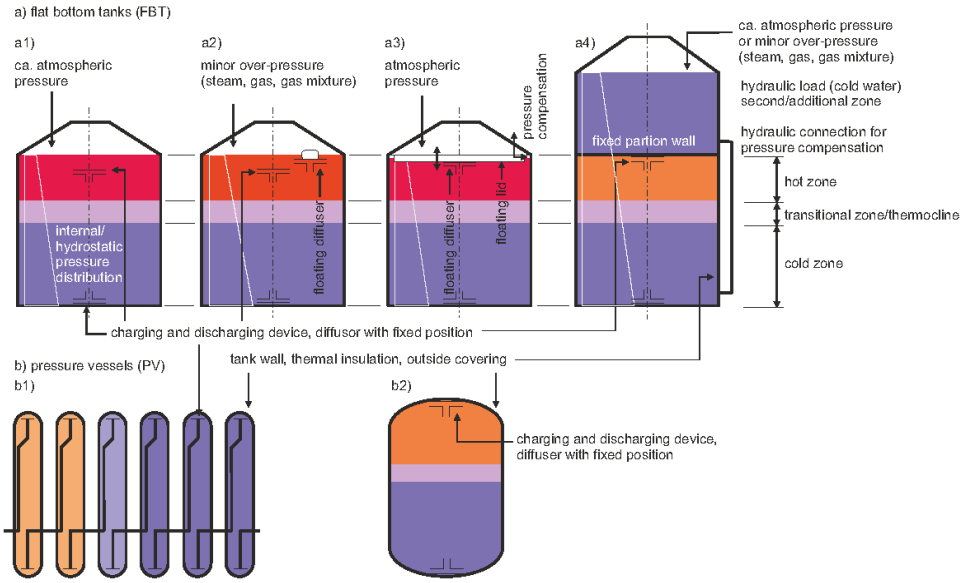

Fig. 1: Systematization of known tank storage constructions (Urbaneck 2020)



Fig. 2: Slim hot water storage tanks, four times nine storage tanks in series, Chemnitz (Germany) district heating supply, operator eins/inetz

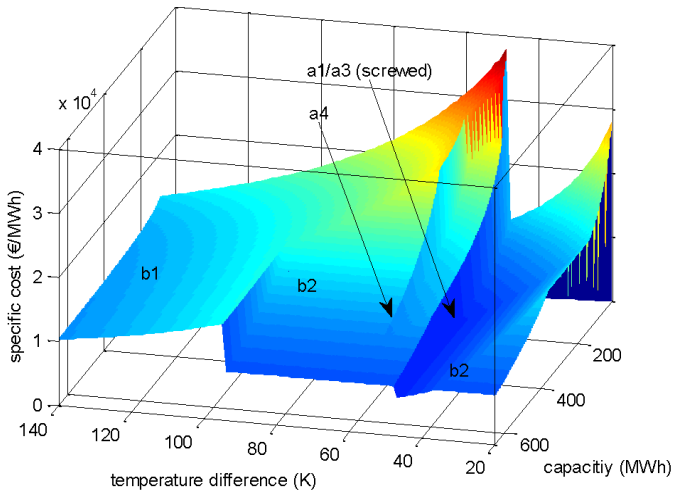

Fig. 3: Specific costs depending on storage capacity and temperature difference, cost calculation 2018 (Urbaneck 2020)

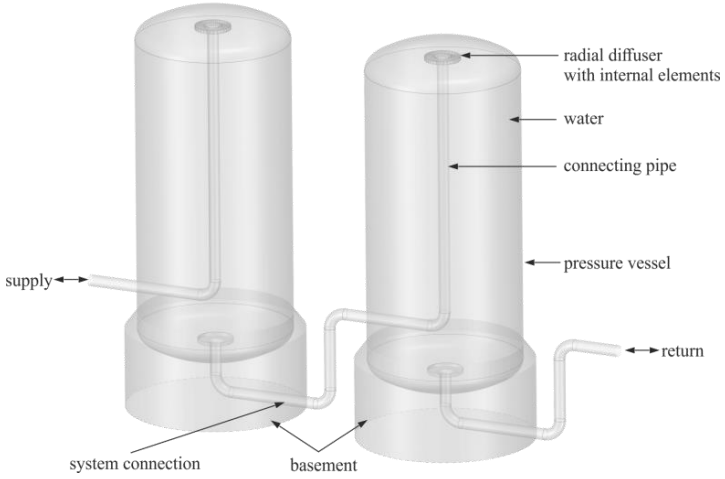

Fig. 4: Schematic structure of the storage type b1 (representation with low storage height) in a series connection, without thermal insulation, covering and auxiliary equipment

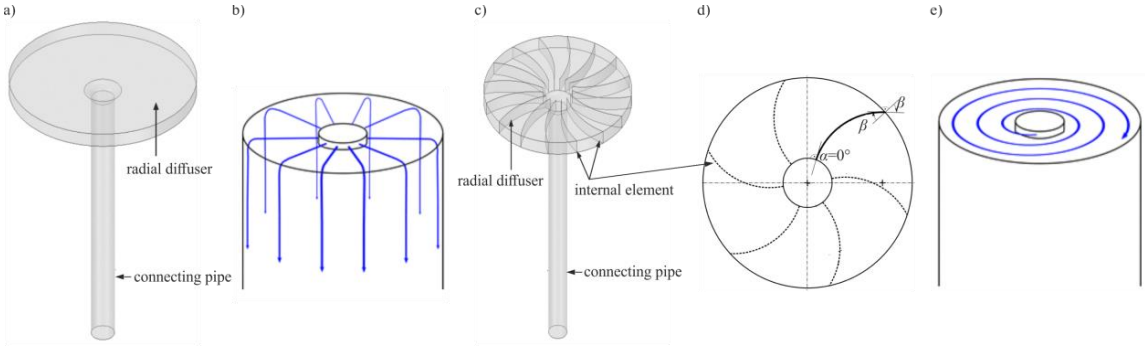

Fig. 5: a) radial diffuser, b) simplified representation of radial charging c) radial diffuser with internal elements, d) design sketch with selected parameters, e) simplified representation of charging with swirl generation (Winkler 2017)

2. Simulation

The Ansys CFD software is used to simulate the flow and heat transfer (Ansys, 2019). The simulation models for the diffuser and the storage are shown in Fig. 6. This division of the region and the use of sections reduces the computational effort. This means, there is no complete modelling of the storage space.

The geometric quantities are summarized in Tab. 1. These investigations refer to a simplified storage geometry

(cylinder) without dished bottom. The storage model considers the upper storage area with 30 % of the real storage height h_{St}. This is sufficient for the simulation of the loading behaviour (Urbaneck, 2019).

This paper presents two modeling variants. In variant *a*, only the storage model (Fig. 6 b)) is used. At the inlet the velocity components (Fig. 6 b)) are defined for the conventional diffuser (Fig. 5 a) and the diffuser with swirl generation (Fig. 5c)). Then there is an ideal uniform distribution of the velocity field. This means, the flow in the connecting pipe and diffuser is not considered.

In variant *b*, the diffuser model (Fig. 6 a)) should generate realistic inlet boundary conditions for the storage model (Fig. 6 b)). Therefore, the simulation is performed in two steps. First, the diffuser model is simulated. The results include the temperature and velocity field at the diffuser outlet. This is imposed as inlet boundary condition (inlet) on the storage model. In this investigation, the diffuser with swirl has a number of internal elements of 128 and 32, respectively, and a swirl angle of 50° and 10°, respectively. Then the section angle is 2.8° or 11.25°. The variants are then called *RD IE 128 50°* or *RD IE 32 10°*. The preliminary investigations in (Winkler, 2017) showed that these variants have advantages over the conventional diffuser (designation *RD*).

The simulations represent an ideal loading (e.g. constant temperature, constant volume flow). The storage geometry and the boundary conditions for the loading remain constant for all variants. The simulated loading time is 250 s. Then the thermal stratification is formed. The time step size is 0.1 s. For turbulence modeling, the $k-\omega$ −SST model with consideration of buoyancy is applied. Work by (Findeisen, 2016) shows the suitability of this turbulence model. The determination of the temperature- and pressure-dependent material values is done with the industrial formulation IAPWS-IF97 (Wagner and Kretzschmar, 2008). At time t = 0 s, the quiescent storage fluid (water) has a constant temperature. The evaluation refer to the end of the simulation at time t = 250 s. The horizontal evaluation planes (Fig. 6 a), yellow plane) are located at h_D= (0.025, 0.050, 0.075) m. The vertical evaluation line (Fig. 6 a), black plane) runs in the middle of the section.

Tab. 1: Geometrical sizes of the storage and the radial diffuser

quantity	value	quantity	value
h_{St} [m]	10.00	r_{CP} [m]	0.16
r_{St} [m]	2.00	h_{CP} [m]	1.50
r_D [m]	0.50	z [-]	32 / 128
h_D [m]	0.10	β [°]	10 / 50

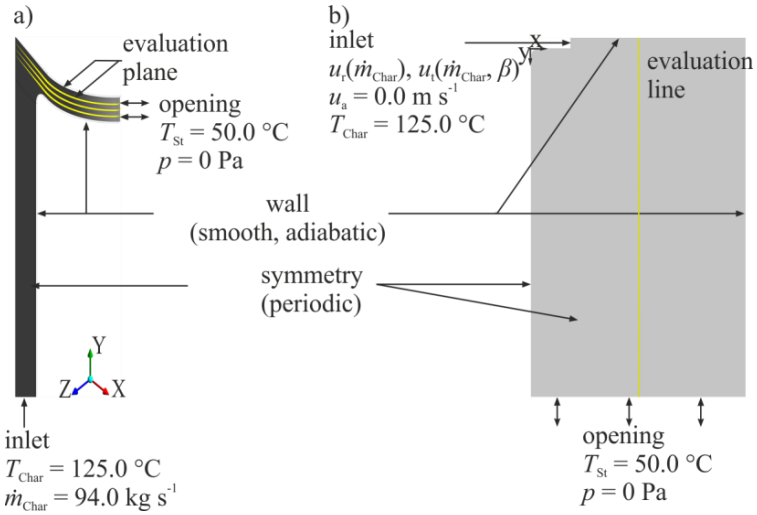

Fig. 6: Schematic representation of a) the diffuser model (curved section) and b) the storage model (normal circular section) with boundary condition for the numerical flow simulation (CFD)

3. Evaluation of the Thermocline

For the evaluation of the thermal stratification, three zones are defined in the first step (Fig. 7): the hot zone, the thermocline and the cold zone. The spatial distribution of these zones cannot be precisely determined due to the sliding vertical temperature distribution. Therefore, in the literature one can find different rules for the determination. In this work the following evaluation criteria are used: the average height of the thermocline $h_{\mathrm{tc,m}}$, the maximum temperature gradient $(\mathrm{grad}T_{St})_{\mathrm{max}}$, the average temperature in the warm zone T_{hZ}. The parallel use of different evaluation criteria allows a better analysis, because each criterion has advantages and disadvantages.

The 90/10% criterion is used to determine the average height of the thermocline $h_{\mathrm{tc,m}}$ (Fig. 7). The highest temperature $T_{\mathrm{St,max}}$ = 125 °C corresponds to the temperature of the loading fluid. The limit temperature for the hot zone is set at $T_{\mathrm{St,90\%}}$ = 117.5 °C (eq. 1). A set temperature for the supply of a network $T_{\mathrm{Su,S}}$ is often defined, e.g. for the flow of a heat distribution network. This target flow temperature defines the minimum permissible temperature for network operation. This means that the storage tank can only be discharged as long as this criterion is met. Thus, the set flow temperature limits the discharge. In this work, the following condition shall apply: $T_{\mathrm{St,90\%}} = T_{\mathrm{Su,S}}$. Beneath $T_{\mathrm{St,10\%}}$= 57.5 °C (eq. 2) is the cold zone. The lowest temperature $T_{\mathrm{St,min}}$ = 50 °C corresponds to the temperature of the storage fluid at the beginning of loading. Between both zones lies the thermocline. A reduction of the thermocline proves the advantage of a loading technique or a certain variant, which corresponds to the general aim of this work.

In Fig. 7, the zones are described with a horizontal line, which corresponds to a constant horizontal temperature. During loading, the flow processes in reality and in the simulation cause wavy boundaries between the zones. Therefore, the surfaces with temperatures $T_{\mathrm{St,90\%}}$ and $T_{\mathrm{St,10\%}}$ are spatially determined with a relatively new evaluation method. In *Ansys CFD Post*, the so-called *isosurfaces* are applied. Then the height of the thermocline can be calculated in every point (Findeisen 2016).

$$T_{\mathrm{St,90\%}} = T_{\mathrm{St,min}} + 0{,}9 \cdot (T_{\mathrm{St,max}} - T_{\mathrm{St,min}}) \qquad \text{(eq. 1)}$$

$$T_{\mathrm{St,10\%}} = T_{\mathrm{St,min}} + 0{,}1 \cdot (T_{\mathrm{St,max}} - T_{\mathrm{St,min}}) \qquad \text{(eq. 2)}$$

The vertical temperature gradient $\mathrm{grad}T_{\mathrm{St}}$ (Fig. 7) is determined with (eq. 3). Then there must be no horizontal temperature differences, which is true for the end of loading. Here the maximum value $(\mathrm{grad}T_{\mathrm{St}})_{\mathrm{max}}$ is of interest. The maximum temperature gradient is in the thermocline. If the maximum temperature gradient increases, the average height of the thermocline $h_{\mathrm{tc,m}}$, decreases, which has already been described as a target or evaluation criterion (Urbaneck 2009). In Fig. 6 b) the vertical evaluation line is shown, which is located in the centre at $r_{\mathrm{St}}/2$. The application of (eq. 3) is done by evaluating the temperature differences ΔT between the cells, which have a distance of Δy (eq. 4). The maximum value is then searched in the evaluation.

$$\mathrm{grad}T_{\mathrm{St}} = \frac{\partial T_{St}}{\partial h_{St}} \qquad \text{(eq. 3)}$$

$$\mathrm{grad}T_{\mathrm{St}} \cong \frac{\Delta T_{St}}{\Delta y} \qquad \text{(eq. 4)}$$

The average temperature of the hot zone $T_{\mathrm{hZ,m}}$ is the third evaluation criterion related to the hot zone. In *Ansys CFX Post*, the *isovolume* of the hot zone is evaluated. Here the following condition is valid: $T_{\mathrm{St}} > T_{\mathrm{St,90\%}}$.

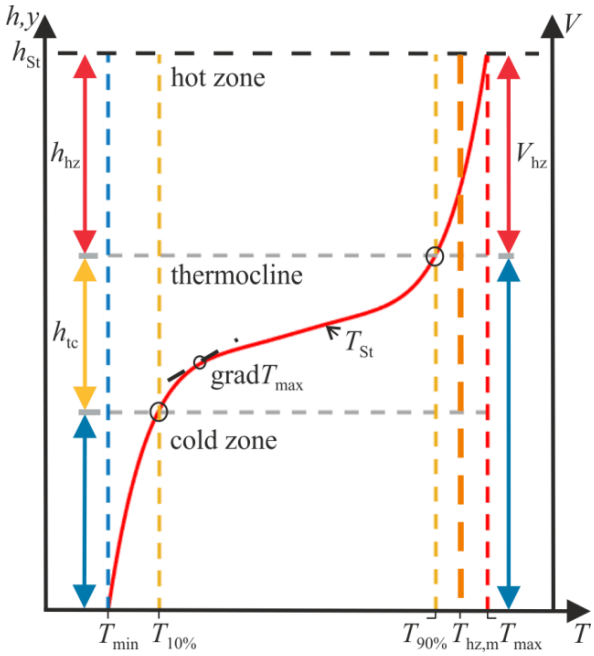

Fig. 7: Schematic representation of the vertical temperature distribution in a displacement storage and important parameters, in accordance with (Urbaneck, 2009)

4. Results

Diffuser model

The calculation of the flow in the connecting pipe and in the diffuser is intended to represent the realistic outflow behaviour into the storage tank. Here, only one sector of the storage space was modelled (Fig. 6). This procedure assumes a uniformly distributed outflow over the entire radius (direction, velocity, mass or mass flow). In reality or in a full three-dimensional simulation, a uniform distribution over the radius probably does not exist. This is shown, for example, by simulative and experimental work by (Findeisen, 2018). Thus, the results presented here involve ideal assumptions.

The flow effects in the diffuser are complex and cause a three-dimensional velocity distribution. To analyse the processes, first a perpendicular or curved section plane is placed in the section (Fig. 6 a)). This is followed by an observation of the velocity in the guide channel (room between two internal elements) perpendicular to the main flow direction.

The velocity profile in the diffuser (vertical section plane in Fig. 6 a)) for the *RD b*, *RD IE 128 50° b* and *RD IE 32 10° b* variants is provided in Fig. 8. The vectors show the main flow direction. This view is in the Z^+ axis in the middle of the section. In the transition area from the connecting pipe into the radial diffuser, the flow accelerates (red area), meets the upper diffuser wall and follows the curved guide channel (Fig. 8). A recirculation area (flow against the main flow direction in the guide channel) is formed in the lower diffuser area. This causes mixing effects at the diffuser outlet, especially at the beginning of the loading process. This is disadvantageous, but cannot be completely ruled out with the measures described here.

This is followed by an examination of the processes in the guide channel. Because the guide channel is curved, *Görtler* vortices are formed in addition to the effects shown above in Fig. 9 (Görtler 1940, Saric 1994). When a certain velocity is exceeded, boundary layer effects occur. Pressure gradients form between the flow close to the wall (outside of the guide channel) and the flow far from the wall in the guide channel. This results in a flow away from the wall (secondary flow) into the inner channel area with lower pressures. This flow behaviour with counter-rotating vortices is shown in Fig. 9 b). The vortices cover large parts of the guide channel and are transported out of the guide channel with the main flow direction. So-called longitudinal vortices are formed. This flow behaviour is confirmed by Fig. 10.

The following tendencies and theories can be read from the diagrams:

- A higher swirl angle β increases the formation of the counter-rotating vortices (Fig. 10 b)).
- A lower number of guiding channels results in a larger recirculation area (Fig. 10 c)).
- Both of the above effects favour the formation of *Görtler* vortices.

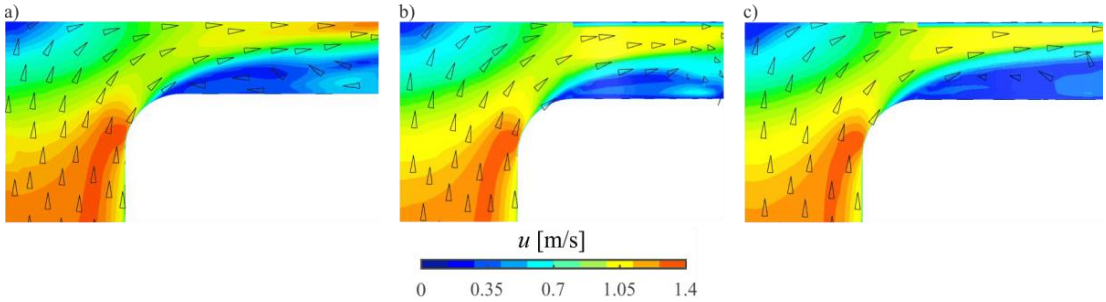

Fig. 8: Velocity with direction vectors in the centre of the section for a) *RD b*, b) *RD IE 128 50° b*, c) *RD IE 32 10° b*

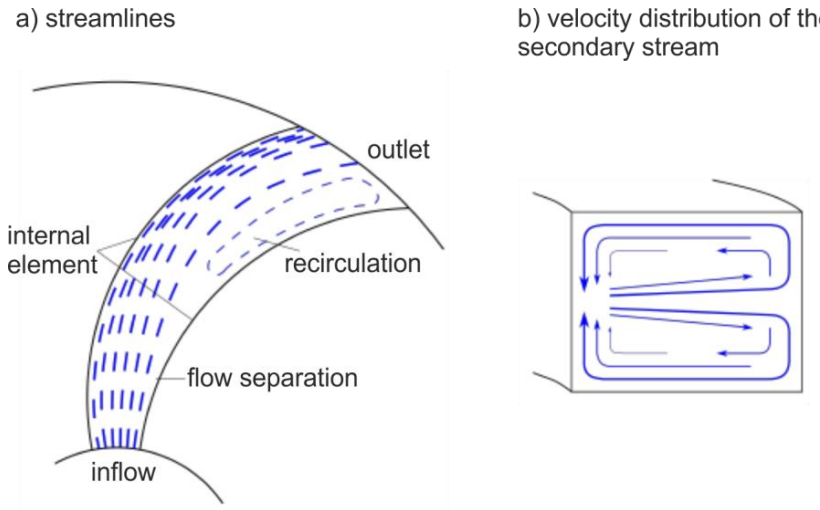

Fig. 9: a) schematic representation of the flow through the curved guiding channel (horizontal section) with the main flow direction and b) velocity arrows of the secondary flow across the flow cross-section (vertical section) in a guiding channel

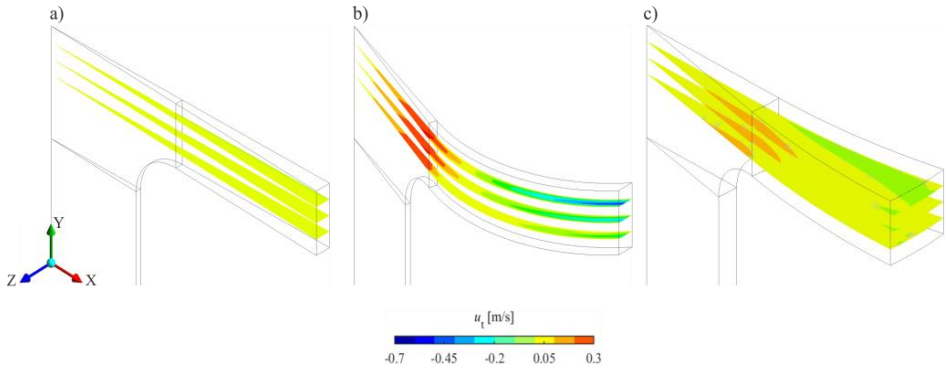

Fig. 10: Tangential velocity component (contour) for a) *RD b*, b) *RD IE 128 50° b*, c) *RD IE 32 10° b*

Fig. 11 a) shows the average velocity amounts and the velocity distributions over the diffuser outlet and the outlet at the guide channel. The *RD IE 128 50° b* variant has the lowest velocity differences. This "nose-shaped" velocity distribution (reversed here) with a velocity maximum near the diffuser wall flowed against by the pipe is often encountered and does not represent a problem in principle with density flows in flat-bottom tanks. The *RD b* variant has larger velocity differences compared to the variant and *RD IE 32 10° b* and *RD IE 128 50° b*. Significantly higher velocities occur in the upper range.

The conventional radial diffuser *RD b* has a horizontally layered distribution of velocities (Fig. 11 b)). The radial diffusers with swirl generation (*RD IE 128 50° b, RD IE 32 10° b*) show clearly different velocities in the

horizontal (Fig. 11 c) and d)), which can be explained by the additional effect of the *Görtler* vortices. A backflow may occur. This cannot be read from the magnitude of the velocity ($u = \sqrt{{u_a}^2 + {u_r}^2 + {u_t}^2}$) in Fig. 11 a)).

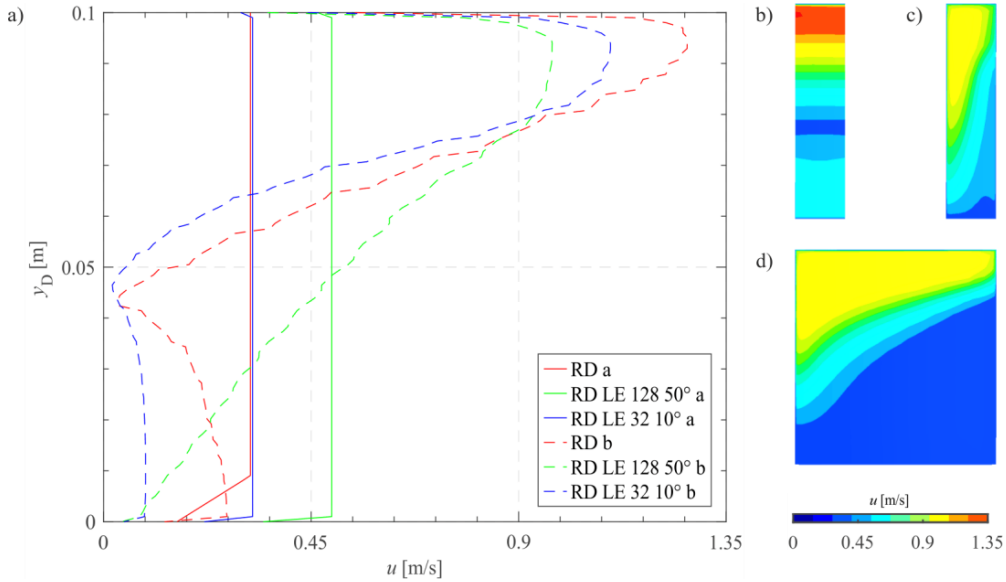

Fig. 11: a) magnitude of velocity and velocities over diffuser height at diffuser outlet and velocity distributions over outlet surfaces for b) RD b, c) RD IE 128 50° b, d) RD IE 32 10° b

Storage model

The effect of the inlet flow at the conventional radial diffuser (variant *RD b*) for different times is shown Fig. 12 a). The flow from the diffuser has the highest velocity. Consequently, a high momentum hits the storage wall. A typical wall jet is formed, which penetrates deep into the storage and causes mixing processes. When the temperature and density differences decrease due to advanced loading (t = 250 s), the penetration depth of the wall jet increases. The *RD IE 32 10° b* variant does not differ significantly from the *RD b* variant. The low swirl angle leads to a marginal weakening of the wall jet. The storage fluid in the upper storage area is moved slightly. For this reason, this variant is not shown.

The flow with swirl for different times and the variant *RD IE 128 50° b* is shown in Fig. 12 b). The inlet flow with swirl differs fundamentally from the previously described flow behavior. The flow enters the storage with a deflection angle and generates a rotation of the storage fluid in the upper storage area. This reduces the momentum impinging on the storage wall. The wall jet or its penetration depth decreases (Fig. 12 b), t = 50 s). With increasing loading time, the rotation of the storage fluid increases (Fig. 12 b), t = 150 s). At the end of loading, the storage fluid of the hot zone is in motion (Fig. 12 b), t = 250 s).

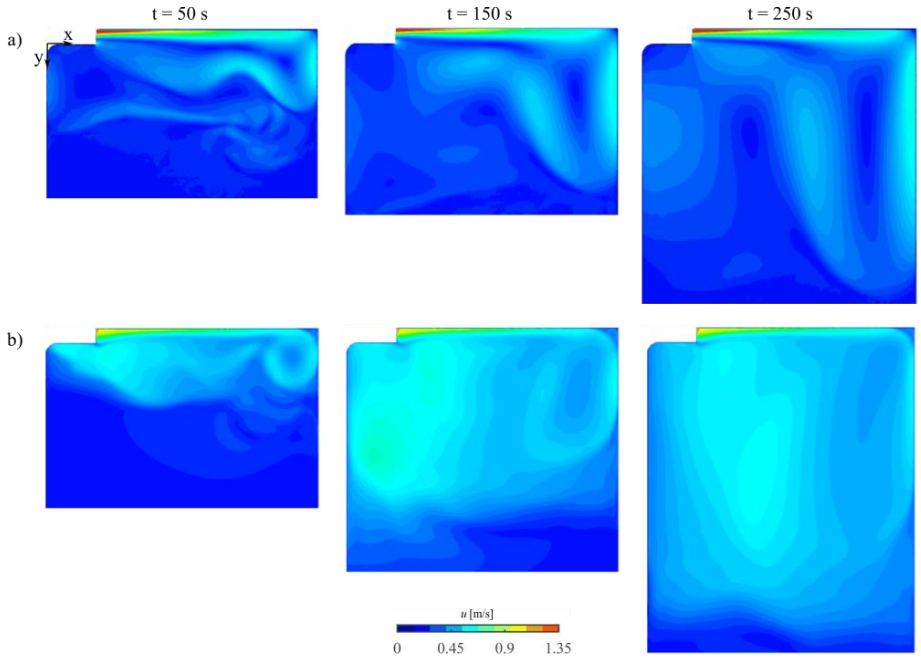

Fig. 12: Velocity fields in storage region for different times and for the variants a) *RD b*, b) *RD IE 128 50° b*

Fig. 13 presents the development of the average height of the thermocline. The *RD a*, *RD IE 128 50°* a and *RD IE 32 10° a* variants consistently deliver better results than the *RD* b, *RD IE 128 50° b* and *RD IE 32 10° b* variants. This can be explained by the uniform distribution of the inlet flow (direction, velocity). This confirms the approach with the reduction of inlet velocities. However, the technical implementation is difficult, as this investigation shows.

The relatively strong increase in variant *RD b* is due to the flow (e.g. effect of the wall jet) or the stratification structure and the evaluation with *isosurfaces*. The lower gradients for the variants *RD IE 128 50° b* and *RD IE 32 10° b* also confirm the reduction of the space in which mixing effects take place.

The above statements on the quality of the thermal stratification are also supported by the key figures in Tab. 2. supplemented by the vertical temperature distributions. Assuming that all variants *b* were modelled more realistically, variant *RD IE 128 50° b* achieves the best stratification quality. The variant provides by far the best results in the evaluation with the height of the thermocline $h_{\mathrm{tc,m}}$ and the maximum temperature gradient $(\mathrm{grad}T_{\mathrm{St}})_{\mathrm{max}}$. The average temperature in the hot zone does not differ so much from the other variant *RD IE 32 10° b* with swirl loading.

Tab. 2: Evaluation of the quality of the thermal stratification with key figures

key figures \ **variant**	***RD a***	***RD IE 128 50° a***	***RD IE 32 10° a***	***RD b***	***RD IE 128 50° b***	***RD IE 32 10° b***
average height of thermocline $h_{\mathrm{tc,m}}$ [m]	0.21	0.31	0.26	0.51	0.36	0.48
max. temperature gradient $(\mathrm{grad}T_{\mathrm{St}})_{\mathrm{max}}$ [K m^{-1}]	281.4	222.0	273.3	175.7	225.3	147.4
average temperature in the hot zone T_{hz} [°C]	123.85	123.35	124.05	121.65	122.95	122.55

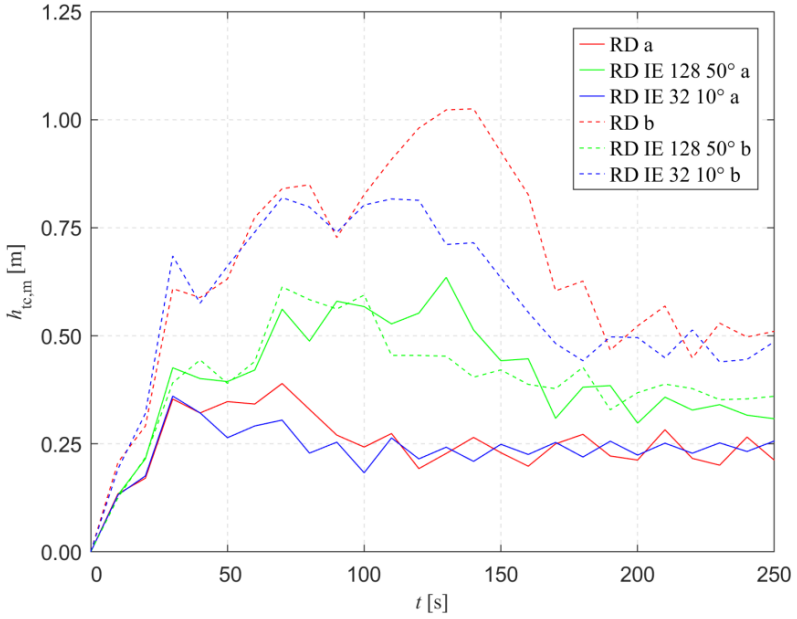

Fig. 13: Development of the average height of the thermocline

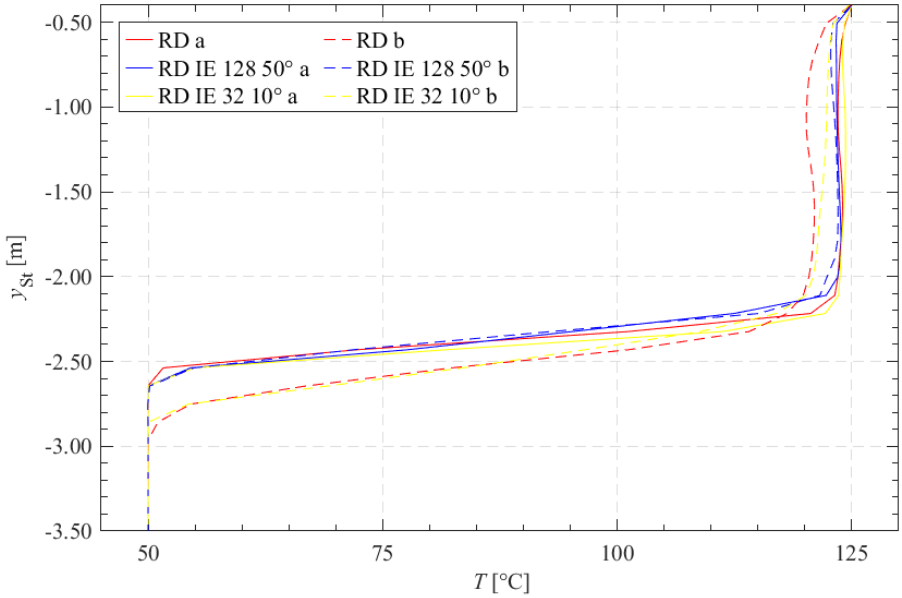

Fig. 14: Vertical temperature curves at $r_{St}/2$ (Fig. 6 b)) for all variants

5. Conclusion and Outlook

More efficient storage solutions are urgently needed to further integrate renewable energy sources and increase system efficiency in heat supply. Hot water storage tanks with a slim design can play a key role (Fig. 1, storage tank type b1)). Here, the internal losses must be minimized or the stratification behaviour improved. An essential prerequisite for this is a sufficiently precise understanding of flow and heat transfer processes during loading. The present work is intended to contribute to closing these knowledge gaps.

Three different diffuser designs (one conventional diffuser and two diffusers with swirl generation) are compared in this work for the improvement of stratification operation. A model for the diffuser with piping and a model for the storage are used in this work. An ideal and a realistic inlet flow with and without swirl generation are compared. The ideal inlet flows show the theoretical potential of perfect velocity decay. Furthermore, new flow effects in slim hot water stores were identified. In the radial diffuser with swirl generation, recirculation flows and so-called *Görtler* vortices are formed due to the wall effects of the curved guide channels. This fundamentally

changes the inlet flow into the storage compared to the conventional radial diffuser. The rotating and specially distributed inlet flow causes the upper storage volume to rotate, the momentum of the wall jet is weakened, and large-scale mixing effects in the upper storage area are reduced. With increasing loading time, the rotation of the storage mass increases. The studies show the advantages of swirl loading over loading with conventional diffusers in slim storage. Future studies aim to improve the understanding of the cause-effect mechanism of swirl loading. This will result in design recommendations of radial diffusers with swirl for different geometries and load cases.

6. Acknowledgement

This article is based on the cooperative project Innovative Loading Systems for Slim Hot Water Storage Tanks (InnoBeS). The Federal Ministry funds the joint project for Economic Affairs and Climate Action through the German Federation of Industrial Research Associations (AiF) as part of the Central Innovation Program for SMEs (ZIM) based on a resolution of the German Bundestag (ZF4746701ST9, ZF4147603ST9). Special thanks go to Dr. Ralf Hartmann of the AiF. The project is carried out in cooperation with the company Harald Liebers Behälterbau GmbH. Many thanks for the constructive cooperation.

7. References

ANSYS, Inc., 2019. ANSYS CFX 2019 R2. Canonsburg (USA).

AG Energiebilanzen e.V.: Anwendungsbilanzen zur Energiebilanz Deutschland, 2020. URL: ag-energiebilanzen.de, accessed on 23.07.2022.

Brämer, C., Urbaneck, T., Lohse, R., 2012. Influence of Geometry and Operation Parameters on Thermal Stratification. EuroHeat&Power, English Edition VWEW Energieverlag, Volume 9, Edition 4, pp. 30-36, ISSN 1613-0200.

Bundesministerium für Umwelt, Naturschutz, nukleare Sicherheit und Verbraucherschutz, 2022. Ziele des Übereinkommens von Paris. URL: www.bmuv.de, accessed on 23.07.2022

Findeisen, F., Urbaneck, T., Platzer, B., 2016. Radiale Diffusoren in Warmwasserspeichern – Funktionale Optimierung mittels CFD; Teil 1 Grundlagen und Modellierung, 2016. HLH Lüftung/Klima Heizung/Sanitär Gebäudetechnik. Volume 76, Edition 10, pp. S. 20-28, ISSN 1436-5103.

Findeisen, F., 2018. Radiale Diffusoren in Warmwasserspeichern – Einfluss der Beladergeometrie auf Strömungsverhalten und Schichtungsqualität. PhD Thesis, TU Chemnitz, ISBN 978-3-9811424-7-1.

Görtler, H., 1940. Über den Einfluss der Wandkrümmung auf die Entstehung der Turbulenz. Zeitschrift für Angewandte Mathematik und Mechanik, Volume 20, Edition 3.

Kroll, U., Mücke, J., Urbaneck, T., Platzer, B., 2020a. Radiale Diffusoren mit Drallerzeugung für schlanke Speicher - Teil 1: Grundlagen und Aufbau des Versuchsstands. HLH Lüftung/Klima Heizung/Sanitär Gebäudetechnik VDI Fachmedien, Volume 71, Edition 5-6, pp. 43-47, ISSN 1436-5103.

Kroll, U., Mücke, J., Urbaneck, T., Platzer, B., 2020b. Radiale Diffusoren mit Drallerzeugung für schlanke Speicher - Teil 2: Vorstellung und Auswertung der experimentellen Ergebnisse. HLH Lüftung/Klima Heizung/Sanitär Gebäudetechnik VDI Fachmedien, Volume 71, Edition 5-6, pp. 56-61, ISSN 1436-5103.

Lohse, R., Urbaneck, T., Brämer, C., Platzer, B., 2012. Effects during loading of hot water storages with a high aspect ratio. EuroHeat&Power, English Edition VWEW Energieverlag, Volume 9, Edition 3, pp. 42-47, ISSN 1613-0200.

Platzer, B., Findeisen, F., Urbaneck, U., Winkler, T., 2017. Verfahren und Vorrichtung zum Be- und/oder Entladen eines thermischen Energiespeichers, 2017. Patent Registration, 2017120716373300DE, Received on: 07.12.2017.

Saric W. S., 1994. Görtler Vortices. Annual Review of Fluid Mechanics, Volume 26:1, pp. 379- 409.

Stahlhut, M., Ackermann, C., Urbaneck, T. , 2022a. Exemplarische Untersuchung verschiedener Kollektoren zur Einbindung in Fernwärmenetze. EuroHeat&Power, VDE Verlag, Volume 51, Edition 01-02, pp. 40-48, ISSN 0949-166X.

Stahlhut, M., Ackermann, C., Urbaneck, T., 2022b. Exemplarische Untersuchung verschiedener Kollektoren zur Einbindung in Fernwärmenetze – Teil 2. EuroHeat&Power. VDE Verlag, Volume 51, Edition 03, pp. 44- 53.

ISSN 0949-166X.

Urbaneck, T., Möller, H., Kressner, T., Platzer, B., 2009. Kaltwasserspeicher mit radialen Diffusoren. Teil 2a: Schichtungsaufbau im Nahfeld - Grundlagen, Physik, Simulation. HLH Lüftung/Klima Heizung/Sanitär Gebäudetechnik, Volume 60, Edition 6, pp. 32-36. ISSN 1436-5103.

Urbaneck, T., Held, A., Platzer, B., 2011. Kaltwasserspeicher mit Rohrdiffusoren – Teil 3b: Einfluss der Betriebs- und Geometrieparameter. HLH Lüftung/Klima Heizung/Sanitär Gebäudetechnik, Volume 62, Edition 4, pp. 31-37. ISSN 1436-5103.

Urbaneck, T., 2012. Kältespeicher: Grundlagen, Technik, Anwendung. Oldenbourg Verlag, ISBN 3486719882.

Urbaneck, T., Oppelt, T., Fischer, J., Sehwöster, E., Bank, E. F., 2019. Große Druckbehälter als thermische Energiespeicher, Teil 2: Umsetzungsbeispiel. EuroHeat&Power, VWEW Energieverlag, Volume 48, Edition 01-02, pp. 32-42. ISSN 0949-166X.

Urbaneck, T., 2020. Water Tank Stores for Medium/Large Applications. Reference Module in Earth Systems and Environmental Sciences, Elsevier, ISBN 9780124095489.

Wagner, W., Kretzschmar, H., 2008. International steam tables: Properties of water and steam based on the industrial formulation IAPWS-IF97. Springer-Verlag Berlin Heidelberg. ISBN 978-3-540-74234-0, DOI https://doi.org/10.1007/978-3-540-74234-0.

Winkler, T., 2017. Radiale Diffusoren mit Drall – Grundlegende Untersuchungen für schlanke Speicher mit Drall. Bachelor Thesis, TU Chemnitz.

8. List of Symbols

Quantity	Symbol	Unit
average height of thermocline	$h_{\mathrm{tc,m}}$	m
entry angle	α	°
height	h	m
mass flow rate	$\dot{m}$	kg s^{-1}
number of internal elements	z	-
pressure	p	Pa
radius	r	m
swirl angle	β	°
temperature	T	°C
temperature gradient	grad$T$	K m^{-1}
time	t	s
velocity	u	m s^{-1}
vertical coordinate	y	m
volume	V	m³

Shortcut	Meaning
a	axial
c	critical
CFD	Computational Fluid Dynamics
Char	charging
CP	connecting pipe
D	Diffuser
hz	hot Zone
IAPWS-IF97	The International Association for the Properties of Water and Steam - Industrial Formulation 1997
IE	internal element
max	maximal
min	minimal
r	radial
rel	relative
RD	radial diffuser
RD IE	radial diffuser with internal elements
S	Set
St	Storage
Su	Supply
t	tangential
32 / 128	number of internal elements
10° / 50°	angle of swirl

Experimental Investigation of a Falling Film Horizontal Tube Bundle Absorber for Thermal Absorption Storage with H_2O/LiBr

Dieter Pressl[1], Eberhard Laevemann[1]

[1] Bavarian Center for Applied Energy Research (ZAE Bayern), Garching (Germany)

Abstract

Compared to state-of-the-art sensible and latent heat storage techniques, thermal absorption storage systems can theoretically achieve a significantly higher energy storage density, which increases with the concentration difference between diluted and concentrated sorbent solution. In the absorption process, the concentration difference can be increased by reducing the sorbent volume flow at the absorber. From first principles, this causes a reduction of the absorbed water vapor and therefore also of the heat removed from the absorber. Furthermore, a low sorbent volume flow can reduce the wetting of the absorber surface, which leads to a further reduction of the absorbed water vapor. Therefore, in the scope of developing a novel absorption cold storage process with H_2O/LiBr, we experimentally investigated the impact of reducing the salt solution volume flow on the mass and heat exchange on a falling film horizontal tube bundle absorber. In the experiments, we stepwise reduced the specific salt solution volume flow distributed over the absorber from 100 l/(h·m) to 20 l/(h·m) and determined the mass and heat transferred. We thereby experimentally quantified the dependence of the specific salt solution volume flow on the concentration difference and the area-specific heat flow for the tested absorber. The results indicate that reducing the specific salt solution volume flow is an effective way to significantly raise the concentration difference on a falling film horizontal tube bundle absorber. Hence, this absorber type seems to be suitable for thermal absorption storage systems with H_2O/LiBr.

Keywords: thermal absorption storage, absorption cold storage, absorber, H_2O/LiBr

1. Introduction

In recent years, there has been an increasing interest in thermal absorption storage systems particularly due to their potentially high energy storage densities and low energy losses during the actual storage period. Mainly, the research activities focused either on the seasonal storage of solar heat or on the flexibilization of solar driven absorption chillers, see e.g. Ibrahim et al., 2018; N'Tsoukpoe et al., 2009 and Wang et al., 2013. Another promising application scenario in the future could also be the recovery of waste heat, e.g. from industrial processes as described by Miro et al., 2016.

In principle, the energy storage density of thermal absorption storage systems increases with the concentration difference between diluted and concentrated sorbent solution realized in the absorption process. The technical implementation of the absorption process, however, is quite complex since it consists of a combined heat and mass transfer. In the past decade, there have been various studies on both the absorption process and the absorber design of thermal absorption storage systems. Overall, from these studies can be drawn that it is crucial to choose an absorber type appropriate for the sorbent used. Otherwise, the absorber suffers from an insufficient wetting resulting in low concentration differences associated with low area-specific heat flows, see e.g. Daguenet-Frick et al., 2017 and Le Pierres et al., 2017. This also applies for the working pair H_2O/LiBr. For example, N'Tsoukpoe et al. (2013) experimentally investigated a vertical falling film tube bundle absorber to be used in a seasonal solar driven absorption heat storage with H_2O/LiBr. They reported concentration differences of only 0.6-1.8 % and that no heat was transferred between salt solution and external heat transfer fluid. They concluded that the investigated absorber design is inappropriate for thermal absorption storage. A further investigation of the absorption tests by means of a numerical model indicated that the poor performance of the absorber was caused by insufficient wetting of the exchange surface (Huaylla et al., 2018).

© 2022. The Authors. Published by International Solar Energy Society
Selection and/or peer review under responsibility of Scientific Committee
doi:10.18086/eurosun.2022.13.15 Available at http://proceedings.ises.org

Although H_2O/LiBr is a promising working pair for thermal absorption storage, so far, no proper absorber design is known in the literature which meets the requirements of low specific salt solution volume flows typically applied in thermal absorption storage processes. Therefore, the aim of this study was to experimentally analyze whether falling film horizontal tube bundle heat and mass exchangers, typically used in conventional absorption chillers, principally are a suitable absorber type for H_2O/LiBr in thermal absorption storage applications. For this purpose, we experimentally investigated the effect of reducing the specific salt solution volume flow from 100 l/(h·m) to 20 l/(h·m) on both the concentration difference and the area-specific heat flow for a falling film horizontal tube bundle absorber in a 10-kW experimental plant.

2. Methods

2.1 Experimental plant

For the experiments of this study, we used a 10-kW-experimental plant of a thermal absorption storage. It is depicted in Fig. 1. The plant consists of three main components: one storage tank each for aqueous LiBr-solution and water, and a reactor. The solution storage tank is a vertically installed cylindrical vessel containing around 500 l of aqueous LiBr-solution. It includes various internal components, e.g. a stratification unit to prevent mixing of diluted and concentrated salt solution in the storage tank and a floating device to extract diluted salt solution from the uppermost layer in the solution storage tank. The water storage tank is horizontally installed and has a volume of 250 l. The reactor contains two heat exchangers separated by a radiation shield. When the plant is operated in absorption mode, they work as evaporator and absorber. In desorption mode, they are used as condenser and desorber. The experimental plant was fitted with extensive measuring equipment in order to ensure its functionality and to measure the absorption process properly.

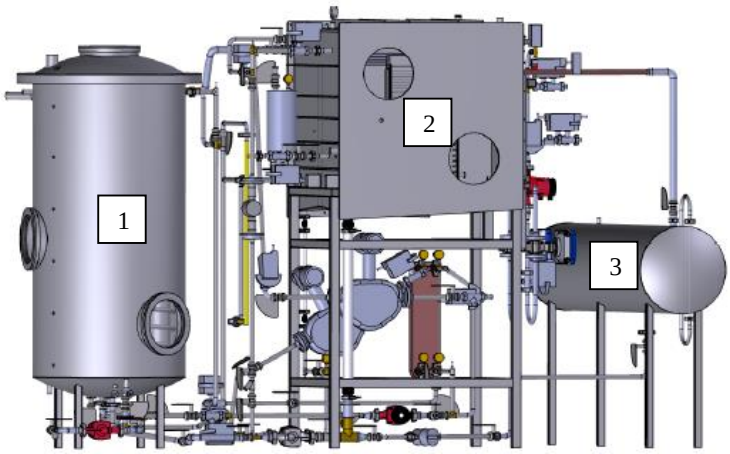

Fig. 1: Experimental plant of the thermal absorption storage with the main components: solution storage tank (1), reactor (2) and water storage tank (3)

2.2 Investigated absorber

The experimentally investigated absorber can be seen in Fig. 2. In general, the absorber is a conventional falling film horizontal tube bundle heat and mass exchanger similar to those used in commercial absorption chillers. It is built of stainless-steel tubes with an outer diameter of 18 mm and a wall thickness of 1 mm. It consists of 3 rows and 20 passes and its total exchange surface amounts to 1.5 m^2, see also Tab. 1.

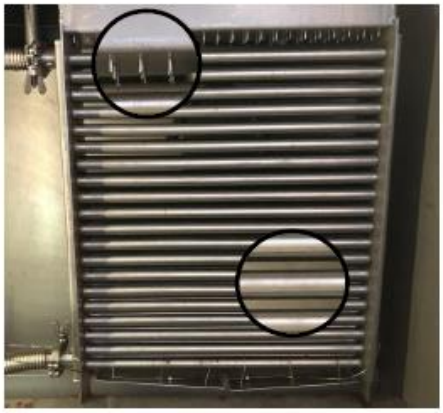

Fig. 2: Experimentally investigated falling film horizontal tube bundle absorber with an exchange surface of 1.5 m²

Tab. 1: Main data of the experimentally investigated absorber

	Unit	Value
Surface	m^2	1,5
Tube outer diameter	mm	18,0
Tube inner diameter	mm	16,0
Number of rows	-	3
Number of passes	-	20

2.3 Design of experiments

In the experiments, the specific salt solution volume flow γ given on the absorber was varied between 20 l/(h·m) and 100 l/(h·m) in steps of 20 l/(h·m). A value of 100 l/(h·m) is typically applied in conventional single-stage absorption chillers with H_2O/LiBr. In general, the specific salt solution volume flow is defined as

$$\gamma = \frac{\dot{m}_{S,in}}{\rho_{S,in} \cdot L},$$

with the mass flow $\dot{m}_{S,in}$ and the density $\rho_{S,in}$ of the salt solution distributed over the absorber and the total length L of the first row of tubes of the absorber. For each set point of γ, we determined both the concentration difference Δw_S and the area-specific heat flow $\dot{q}$ achieved in the absorption process. The temperature of the salt solution at the reactor inlet $T_{S,in}$ and the inlet salt mass fraction $w_{S,in}$ of the concentrated salt solution entering the reactor were kept constant in all experiments, see also Tab. 2. The temperature $T_{S,in}$ corresponded to the equilibrium temperature regarding its salt mass fraction $w_{S,in}$ at the reactor inlet and the water vapor pressure in the reactor resulting from the dewpoint T_p of the absorbed water vapor. This prevented the salt solution from absorbing or desorbing water before getting in contact with the exchange surface, which would cause an overestimation or underestimation of the mass transfer on the absorber. Additionally, we adjusted the inlet temperature of the external heat transfer fluid flowing inside the tubes of the absorber in order to achieve a temperature of 35 °C of the salt solution at the end of the absorption process. Thereby, the equilibrium salt mass fraction of the salt solution at the end of the absorption process was equal for all specific salt solution volume flows γ applied in the experiments. The volume flow rate of the external heat transfer fluid flowing through the absorber amounted to 0.42 l/s in all experiments.

Tab. 2: Setpoints of the internal process parameters in the experiments

Parameter	Unit	Value
Specific salt solution volume flow γ	l/(h·m)	20, 40, 60, 80, 100
Salt mass fraction of salt solution at reactor inlet $w_{S,in}$	%	60
Temperature of salt solution at reactor inlet $T_{S,in}$	°C	50
Temperature of salt solution at reactor outlet $T_{S,out}$	°C	35
Dewpoint of the absorbed water vapor T_p	°C	10
Volume flow rate of the external heat transfer fluid	l/s	0.42

3. Results and discussion

The experimental results are depicted in Fig. 3. As can be seen from the two graphs, there is a significant dependence of both the concentration difference Δw_S and the area-specific heat flow $\dot{q}$ on the specific salt solution volume flow γ. Reducing the salt solution volume flow γ results in an increase of the concentration difference Δw_S, while the area-specific heat flow $\dot{q}$ is reduced. For example, reducing the specific salt solution volume flow from 100 l/(h·m) to 60 l/(h·m) leads to an increase of the concentration difference from 3.9 % to 6.1 % and a decrease of the area-specific heat flow from 8.7 kW/m^2 to 8.0 kW/m^2. This is to say, a reduction of γ from 100 l/(h·m) to 60 l/(h·m) results in an increase of the concentration difference by 56 %, while the area-specific heat flow only decreases by 8 %.

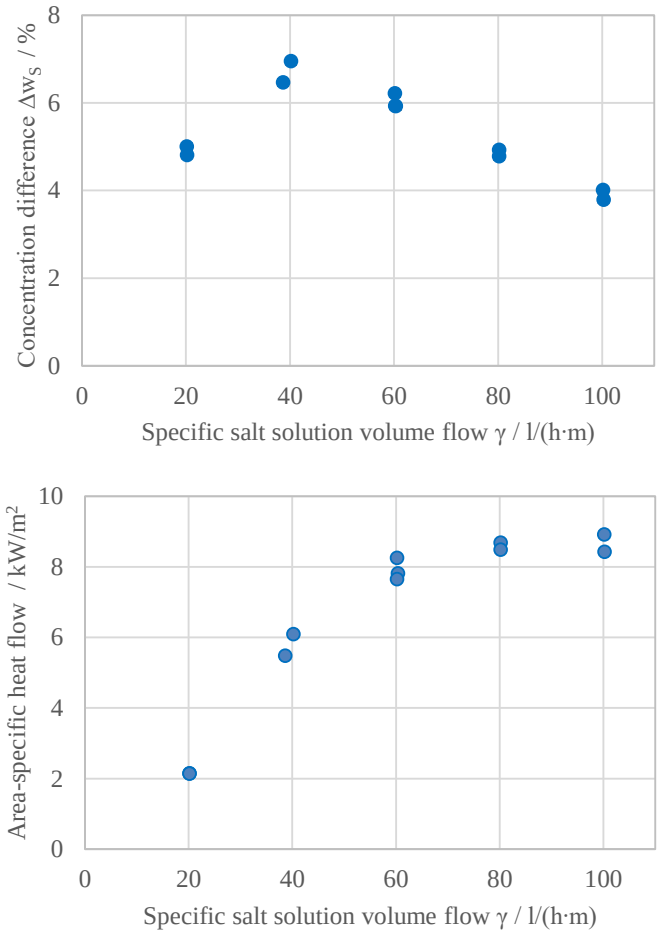

Fig. 3: Concentration difference Δw_S and area-specific heat flow $\dot{q}$ as function of the specific salt solution volume flow γ

A significant decrease in area-specific heat flow $\dot{q}$ is seen when γ is reduced to 40 l/(h·m): in this case, $\dot{q}$ only amounts to 5.8 kW/m^2. Due to this significant loss in area-specific heat flow, a reduction of the specific salt solution volume flow to values $\gamma \leq 40$ l/(h·m) seems not to be reasonable for thermal absorption storage systems. It is also apparent from the graphs that the investigated absorber is limited towards low specific salt solution volume flows: the concentration difference steeply decreases when γ is reduced from 40 l/(h·m) to 20 l/(h·m). This was mainly caused by the distribution unit of the absorber. At γ = 20 l/(h·m), the salt solution only leaked from the left part of the distribution unit, which meant that a considerable part of the exchange surface could not be wetted. This can be seen in Fig. 4. As a result, both the concentration difference and the area-specific heat flow decreased steeply. Hence, the distribution unit of the tested absorber is not suitable for specific salt solution volume flows $\gamma \leq 40$ l/(h·m).



Fig. 4: Insufficient wetting of the exchange surface of the tested absorber in the experiments with a specific salt solution volume flow of γ = 20 l/(h·m)

In conclusion, the results suggest that horizontal tube bundle heat exchangers principally are an appropriate absorber type for thermal absorption storage systems with the working pair H_2O/LiBr. However, an even distribution of the LiBr-solution on the exchange surface is of main importance. For the absorber tested, a specific salt solution volume flow in the range of 60 l/(h·m) seems to be a good compromise between achievable concentration difference and loss in area-specific heat flow.

4. Conclusions

This study set out to evaluate whether falling film horizontal tube bundle heat and mass exchangers are a suitable absorber type for thermal absorption storage systems with H_2O/LiBr. We therefore experimentally investigated the effect of reducing the specific salt solution volume flow on the concentration difference and the area-specific heat flow at the absorber. Thereby, we found that reducing the specific salt solution volume flow is an effective method to significantly increase the concentration difference in the absorption process. The decrease of the area-specific heat flow is comparatively low for specific salt solution volume flows in the range of 60 l/(h·m). In conclusion, the experimental results indicate that horizontal tube bundle heat and mass exchangers principally are a suitable absorber type for thermal absorption storages based on H_2O/LiBr.

5. Acknowledgments

This study is part of the project MAKSOR^E and was supported by the German Federal Ministry of Education and Research under the project code 03SF0441D. The responsibility for the content of this publication is with the authors.

6. References

Daguenet-Frick, X., Gantenbein, P., Müller, J., Fumey, B., Weber, R., 2017. Seasonal thermochemical energy storage: Comparison of the experimental results with the modelling of the falling film tube bundle heat and mass

exchanger unit. Renewable Energy 110, 162-173. https://doi.org/10.1016/j.renene.2016.10.005.

Huaylla, F., Stutz, B., Le Pierres, N., 2018. Numerical and experimental analysis of falling-film exchangers used in a LiBr-H_2O interseasonal heat storage system. Heat Transfer Engineering 40, 879-895. https://doi.org/10.1080/01457632.2018.1446850.

Ibrahim, N.I., Al-Sulaiman, F.A., Nasir Ani, F., 2018. Solar absorption systems with integrated absorption energy storage – A review. Renewable and Sustainable Energy Reviews 82, 1602-1610. https://doi.org/10.1016/j.rser.2017.07.005.

Le Pierres, N., Huaylla, F., Stutz, B., Perraud, J., 2017. Long-term solar heat storage process by absorption with the KCOOH/H_2O couple: Experimental investigation. Energy 141, 1313-1323. https://doi.org/10.1016/j.energy.2017.10.111.

Miro, L., Gasia, J., Cabeza, F., 2016. Thermal energy storage (TES) for industrial waste heat (IWH) recovery: A review. Applied Energy 179, 284-301. https://doi.org/10.1016/j.apenergy.2016.06.147.

N'Tsoukpoe, K.E., Liu, H., Le Pierrès, N., Luo, L., 2009. A review on long-term sorption solar energy storage. Renewable and Sustainable Energy Reviews 13, 2385-2396. https://doi.org/10.1016/j.rser.2009.05.008.

N'Tsoukpoe, K.E., Le Pierres, N., Luo, L., 2013. Experimentation of a LiBr-H_2O absorption process for long-term solar thermal storage: Prototype design and first results. Energy 53, 179-198. https://doi.org/10.1016/j.energy.2013.02.023.

Yu, N., Wang, R.Z., Wang, L.W., 2013. Sorption thermal storage for solar energy. Progress in Energy and Combustion Science 39, 489-514. https://doi.org/10.1016/j.pecs.2013.05.004.

Kinetic Analysis Of TGA Measurements When Evaporation Is A Degradation Process In PCM

Laura Quant[1,2], Rocío Bayón[2], Redlich J. García[2], Gonzalo Diarce[1], Ana García-Romero[1] and Esther Rojas[2]

[1]Enedi Research Group, University of the Basque Country UPV/EHU (Spain)

[2]Thermal Energy Storage Unit, CIEMAT-PSA, Madrid (Spain)

Abstract

Phase change materials degradation kinetics determination is very important in order to assure their use in the long term. Thermo-gravimetric analysis is generally used for determining PCM degradation kinetics. However, the general approach used do not take into account parameters such as the potential evaporation of the PCM, mass and container geometry on the measurements due to the oven's particular operating conditions. The present work aims to develop a methodology that includes these parameters to obtain reliable PCM lifetime predictions.

Keywords: PCM Phase Change Materials, Degradation Kinetics, Thermo-Gravimetric Analysis

1. Introduction

Thermal energy storage (TES) has become increasingly important in engineering applications that involve intermittent energy sources, such as most renewable energy sources. Latent heat thermal energy storage (LHTES) relies on the use of Phase Change Materials (PCMs) to store thermal energy through the latent heat required for the melting/solidification process. It is necessary to take into account some characteristics that a PCM must meet in order to be considered competitive and suitable for its function, such as high thermal storage capacity, adequacy to application phase change temperature, low price, low toxicity, etc. The selected materials should however also fulfill another important requirement, which is the thermal stability upon operating time and cycling (Mehling and Cabeza 2007).

Therefore, the importance of developing methodologies that allow determining the PCMs lifespan is crucial in PCM selection for a determined application. One of the aspects involved in the stability of the PCM is the thermal degradation under working conditions (Quant et al. 2021). The thermal degradation implies the transformation of the original material into other compounds due to the exposure over time to the operation temperatures and, potentially, gaseous environment. This transformation is undesired as it may change in some extent the ability of the PCM to store and release energy, i.e the purpose of PCMs.

If a certain material (for example a PCM) undergoes mass loss due to gaseous evolution, the reaction kinetics can be determined by using Thermo-Gravimetric Analysis, TGA, which consists in monitoring the mass loss of a sample when it is heated at determined constant rate under a gas flow. The kinetics of the degradation reactions can be obtained by analyzing TGA data using different methods (Vyazovkin et al. 2011). The rate of PCM disappearance can be expressed as a function of its residual fraction:

$$r = \frac{d\alpha}{dt} = k(T) \cdot f(\alpha) = A.e^{-\frac{E}{R.T}} \cdot f(\alpha)\ [s^{-1}] \qquad \text{(eq. 1)}$$

Where α is the degree of conversion or the fraction decomposed at time t, calculated as $\alpha = (m_{ini} - \mathrm{m})/m_{ini}$, k is the rate constant usually given by the Arrhenius law and depends on the temperature, *f(α)* is a function whose mathematical expression depends on the reaction mechanism.

Besides, estimations sometimes do not correspond to degradation occurring under real operation conditions. They

© 2022. The Authors. Published by International Solar Energy Society
Selection and/or peer review under responsibility of Scientific Committee
doi:10.18086/eurosun.2022.13.16 Available at http://proceedings.ises.org

usually overestimate the degradation process. In previous works Bayón et al. (2020; 2021) studied the degradation kinetics of lauric acid as PCM by analyzing TGA measurements. However, results showed that the lifetime estimations obtained from TGA data analysis and isothermal tests in oven (i. e. experimental conditions being similar to operation conditions) did not match. In their study they concluded that evaporation was one of the degradation processes taking place, thus TGA measurements did not only report mass loss due to degradation processes. In the consulted PCM characterization literature, mass loss in TGA measurements is exclusively accounted to occur due to the thermal decomposition reactions: however, a different data treatment should be accounted when evaporation process is known to occur additionally to potential thermal degradation.

The general expression describing the free evaporation of a substance is the Knudsen-Langmuir equation. This equation describes the evaporation in vacuum. Nevertheless, the condition for a Kdnusen flow (low evaporation rates in high vacuum) is not satisfied in standard TGA equipments (Bassi 2011). Considering the specific experimental conditions of TG measurements, consisting in the diffusion of the evaporating liquid through a stagnant gaseous layer at atmospheric pressure in a cylindrical sample container, an alternative formulation (equation 2) of the evaporation rate has been proposed by Pieterse and Focke (2003). Equation 2 includes the influence of the experimental geometry, the temperature and pressure (the substance partial pressure is assumed to be 0 due to the gas flow). Several authors (Barontini and Cozzani 2007; Bassi 2011; Beverley, Clint, and Fletcher 1999; Pieterse and Focke 2003) have studied evaporation and developed expressions that describe the phenomenon using a TGA equipment with similar expressions.

Although equation 2 has been previously used for evaluating vapor pressures from mass loss measured during TGA analysis, this work proposes using it as well for evaluating the evaporation rate of a certain compound if vapor pressure is known (can be determined if Antoine equation coefficients are known).

$$r = -\frac{dn}{Sdt} = \frac{P_{eq}D}{zRT} \quad \left[\frac{mol}{m^2 s}\right] \qquad \text{(eq. 2)}$$

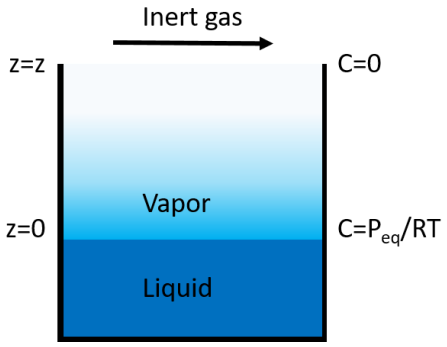

Fig. 1 Scheme of the TGA measurement spatial arrangement

As displayed in the scheme of Figure 1Fig. 1, z is de distance between the top of the container (where the concentration of evaporating molecules C=0) and the surface of the liquid (where $C=P_{eq}/RT$) and D is the diffusion coefficient of the substance in the stagnant inert gas (N_2 or air).

This diffusion coefficient depends on the temperature and can be estimated by using different models and group contributions (Poling et al., 2001). Taking into account a binary mixture of A and B, where A correspond to the PCM and B correspond to the gaseous environment, several proposed methods for estimating D_{AB} in low-pressure binary gas systems with empirical constants based on experimental data. These include Wilke and Lee (equation 3) and Fuller, et al. (equation 4) methods.

$$D_{AB\,Wilke-Lee} = \frac{\left[3{,}03-\left(\frac{0{,}98}{M_{AB}{}^{1/2}}\right)\right]10^{-3}T^{3/2}}{PM_{AB}{}^{1/2}\sigma_{AB}{}^{1/2}\Omega_D} \qquad \text{(eq. 3)}$$

$$D_{AB\,Fuller} = \frac{0{,}00143T^{1,75}}{PM_{AB}{}^{1/2}\left[\Sigma_A{}^{1/3}+\Sigma_B{}^{1/3}\right]^2} \qquad \text{(eq. 4)}$$

Where:

D_{AB} = binary diffusion coefficient [cm^2/s]
T = temperature [K]
M_A, M_B = molecular weights of A and B [g/mol]
$M_{AB} = 2\left[\frac{1}{M_A} + \frac{1}{M_B}\right]^{-1}$
P = pressure [bar]
σ_{AB} = characteristic length [Å]
Ω_D = collision diffusion integral [dimensionless]
Σ_A, Σ_B = diffusion volumes summation

The σ, Ω_D, and Σ parameters can be obtained from (Poling et al. 2001).

Finally, the objective of this research work is to develop a methodology for kinetic analysis of TGA measurements when evaporation is one of the processes occurring, by including the expressions developed by Pieterse and Focke to the traditional reaction kinetics approach. For this purpose, water was used as reference material in the first instance (no chemical reactions occurrence in the experimental conditions). A similar study was performed using fatty acids: lauric, adipic and myristic acids as PCMs to determine their evaporation rates and potential thermal degradation kinetics.

2. Experimental

A series of dynamic experiments were performed by means of TGA technique. Two apparatus were used to perform the TG measurements and are described in Table 1. Open alumina crucibles were used as samples containers. Dry nitrogen (99.999% pure) was used as purge gas at 50 ml/min. The materials used and experimental conditions are described in Table 2.

Tab 1. TGA apparatus used in the experimental

	Crucible dimensions	
Equipment	**Diameter (mm)**	**Height (mm)**
Mettler-Toledo TGA/DSC1	4.8	4
Seiko TG-DTA 6300	5	2.25

Tab 2. Materials used and experimental conditions

Material	Heating rates [K/min]	Sample mass [mg]	TG apparatus
Distilled water	2, 5, 10, 15, 20	35	Mettler-Toledo
Lauric acid	2, 5, 10, 20	≈10	Mettler-Toledo, Seiko
Adipic acid	2, 5, 10, 20	≈10	Seiko
Myristic acid	2, 5, 10, 20	≈10	Seiko

3. Results and discussion

3.1 Evaporation rate determination

- Methodology set-up using water as reference material

Water was used as reference material taking into account that in the applied experimental conditions evaporation occurs, but no other chemical reactions are present. Evaporation rate was calculated by using the formulation

proposed by Pieterse and Focke (equation 2) for measurements performed in TGA equipment. Since diffusion coefficients could not be determined for the PCMs under study using theoretical formulations due to the lack of availability of molecular data, two empirical methods were used: Wilke and Lee (equation 3), and Fuller et al. (equation 4). The determined diffusion coefficients using both methods were very similar for water (Figure 2.a).

In order to validate the Antoine parameters taken from the literature (NIST Research Library Publications 2022), the experimental rate was introduced in equation 2 to obtain equilibrium pressure, which was compared with the equilibrium pressure calculated from those parameters. For that purpose, the evaporation rate was calculated from TG measurements which were done under the experimental conditions described in Tab 1 and Table 2 in terms of crucible dimensions and initial sample mass.

Finally, the pressure values obtained from the experimental measurements were similar to the literature values, which validates the use of Pieterse and Focke method. Figure 2.b shows the general evaporation rate curve of water versus temperature obtained using equation 2 and the experimental values for the heating rates studied. It is clearly seen that the calculated general evaporation rate matches the experimental rate curves for each heating rate studied.

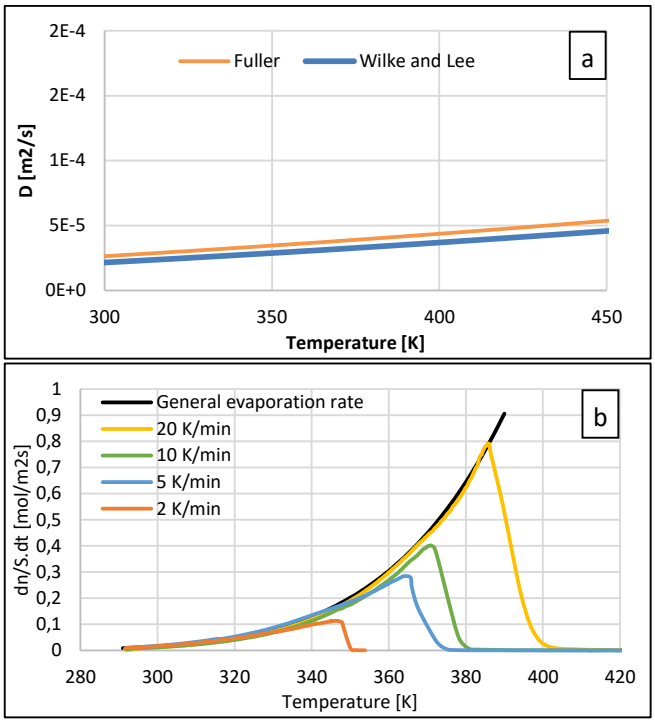

Fig. 2 a: Diffusion coefficient of water determined using Fuller and Wilke and Lee empirical methods. b: Evaporation rate of water per surface: general evaporation rate (determined using eq 2. and Wilke and Lee diffusion coefficient) and experimental curves for the tested heating rates

- Evaporation rate of fatty acids: lauric, adipic and myristic acid.

Lauric, adipic and myristic acid were submitted to TGA tests using the heating rates described in Table 2. In order to satisfy equation 2 Antoine parameters (Matricarde Falleiro et al. 2012) were used to determine the equilibrium pressures and the diffusion coefficients were determined using both Fuller and Wilke and Lee methods. As for the case of water both methods lead to similar values for these coefficients. The evaporation rates of the PCMs obtained using Wilke and Lee method are shown in Figure 3.

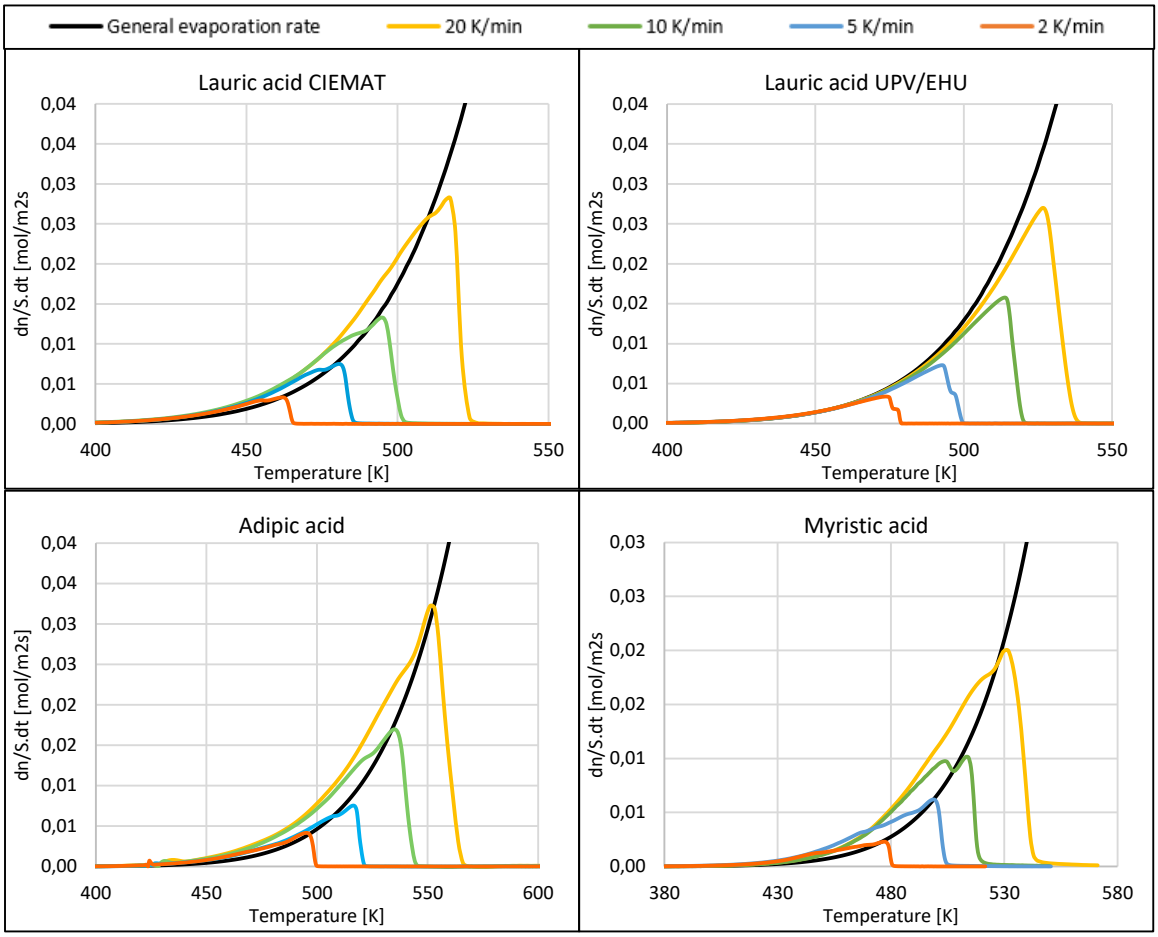

Fig. 3 Evaporation rate of lauric, adipic and myristic acids per surface: general evaporation rate (determined using eq 2. and Wilke and Lee diffusion coefficient) and experimental curves for the tested heating rates

3.2 Estimation of Arrhenius parameters

Once the evaporation rates per surface unity $\frac{dn}{Sdt}$ of the PCMs were obtained, they were fitted to the conventional rate equation (equation 1) adapted to the evaporation case by taking into account that it is a zero order process, so that $f(\alpha)=(1-\alpha)^0 = 1$. Therefore the energy of vaporization E_{vap} and the frequency factor $A_{n,S}$ was determined from equation 5 and the resulting values are shown in Table 3.

$$\frac{dn}{Sdt} = \frac{P_{eq}D}{zRT} \approx A_{n,S}e^{-E/RT}\ [\frac{mol}{m^2 s}] \qquad \text{(eq. 5)}$$

Tab 3. Estimation of E and A by fitting an F0 reaction mechanism ($f(\alpha)$=1) to the evaporation rates.

Material	Water	Lauric acid UPV/EHU	Lauric acid CIEMAT	Adipic acid	Myristic acid
E_{vap} [kJ/mol]	43.29	78.38	78.45	81.82	85.94
ΔH_{vap} [kJ/mol] NIST	40.6	81.3	81.3	92	88.9
$A_{n,S}$ [mol/m2s]	0.52 106	2.03 106	2.8 106	1.72 106	6.18 106

The activation energy of vaporization Evap of water obtained from the analysis of TGA measurements is 43.29

kJ/mol, which is very similar to the vaporization enthalpy ΔHvap= 40.6 kJ/mol. The value expected would be Evap = ΔHvap + Econ = 72.8 kJ/mol. On the other hand, the obtained Evap values for lauric, adipic and myristic acids were also very similar to ΔHvap reported in the literature (NIST Research Library Publications 2022) and shown in Table 3. This phenomenon has already been pointed out by Arias et al. (2009), who claim that the activation energy of vaporization is similar to the vaporization enthalpy in the case of caprylic acid. Besides, a plausible explanation is that the activation energy of vaporization decreases when low partial pressures are applied so that only the vaporization enthalpy is observed. This effect should be further studied and confirmed in the future.

Besides, lauric acid was measured in two different TGA equipments with different geometries available at CIEMAT and UPV/EHU. Differences in the experimental curves and in the determined general evaporation rate can be seen in Figure 3. It is believed that specific testing conditions have great influence on the mass variation at high temperature. Table 3 shows that the E_{vap} values obtained from both curves of lauric acid are very similar, however the An,S show greater variation due to the influence of the different experimental arrangements. It points out that the processes taking place are extremely sensitive to experimental conditions. It is important to point out that An,S is a function of the initial mass/moles and the particular geometry of the TGA equipment and should not be used straightforward for real condition rate estimations (Bayón et al. 2020).

3.3 Determination of potential chemical reactions: deconvolution of dTG curve

When evaporation and other chemical reaction are expected to takle place, each process will produce its own effect in the TG curve. Hence, if they are simultaneous processes, the TG curve will contain the addition of the individual contributions c_i, so that, $\sum_{i=1}^{n} \boldsymbol{c_i} = \mathbf{1}$. The resulting dTG curve would be expressed as:

$$\frac{d\alpha}{dT} = \frac{d\alpha_1}{dT} + \frac{d\alpha_2}{dT} + \cdots + \frac{d\alpha_n}{dT} = \frac{c_1}{\beta} A_1 e^{\left(\frac{-E_1}{RT}\right)} f_1(\alpha) + \frac{c_2}{\beta} A_2 e^{\left(\frac{-E_2}{RT}\right)} f_2(\alpha) + \cdots + \frac{c_n}{\beta} A_n e^{\left(\frac{-E_n}{RT}\right)} f_n(\alpha) \quad \text{(eq. 6)}$$

In such a case, experimental dTG curves should be deconvoluted in various peaks that would correspond to single step processes. Fraser-Suzuki FS functions (Cheng et al. 2015) are commonly used deconvoluting $\frac{d\alpha}{dT}$ vs. T curves into various peaks. The mathematical expression of the FS function is:

$$\frac{d\alpha}{dT} = h\, exp\left\{-\frac{ln2}{s^2}\left[\ln\left(1 + 2s\frac{T-p}{w}\right)\right]^2\right\} \quad \text{(eq. 7)}$$

The four parameters of the function are:

h: amplitude (height)
s: asymmetry factor
p: position
w: half height width

Some issues have to be taken into account when using this function for deconvoluting dTG curves. On the one hand, the FS curves used in the deconvolution should meet the requirement of the integral equal to 1 (=have a normalized area). Also, it is important to take into account that prior to any deconvolution it is worth having an estimation of values displayed by the FS parameters in relation to the different reaction mechanisms. This issues are will be analyzed and discussed in an out coming work.

If it is assumed that two processes occur in the TG measurement and one of them is evaporation, the curve of the unknown process can be determined taking into account the experimental curve and the evaporation curve determined above. As example, Figure 4 shows, the deconvolution for myristic acid tested at 5 K/min. The evaporation curve was built following the evaporation curve previously determined and a contribution of 55% and a F0 mechanism, and the curve potentially corresponding to other reactions was built to correspond to the 45% and an A3 (Avrami-Erofeev, n=3 (Vyazovkin et al. 2011)) mechanism. The addition of both curves render a curve very similar to the experimental curve. Once all experimental curves corresponding to several heating rates are deconvoluted, Kissinger method (Kissinger 1957) could be used to determine the kinetic triplet for the unkown reactions.

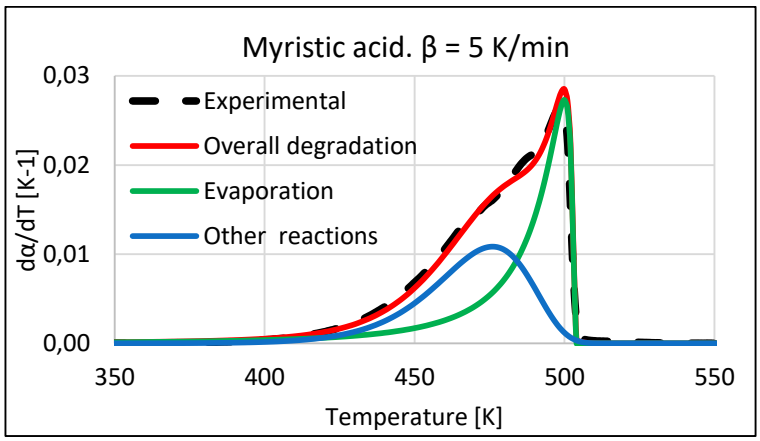

Fig. 4 Deconvolution of dα/dT curve of myristic acid at 5 K/min by means of Fraser-Suzuki functions

4. Conclusions

When used as PCM in latent storage systems, fatty acids are expected to suffer evaporation as one of their main degradation process under service conditions. Besides the potential evaporation, chemical degradation may also occur when heated above their melting temperature. TGA technique can evaluate both phenomena, however the resulting TG and dTG curves may be an addition of two or more process contributions: one potentially corresponding to evaporation and the others associated to chemical reactions taking place at high temperatures. Pieterse and Focke approach may serve as a tool to determine the evaporation rate and evaporation characteristics in the TGA specific conditions. With a known evaporation rate, deconvolution of dTG curves can be carried out by means of Fraser-Suzuki functions to determine the potential chemical reaction contribution to the TGA curve. The results of the present work point out that PCM degradation processes are extremely sensitive to experimental conditions: partial pressure, initial mass/moles and the particular geometry of the TGA equipment. Future work should include the extrapolation of the obtained kinetics to real operation condition kinetics.

5. Acknowledgments

This work has been supported by Comunidad de Madrid and European Structural Funds through ACES2030 Project (S2018/EM-4319) and by European Union's Horizon H2020 Research and Innovation Programme through SFERA III Project (GA Nº 823802) and StoRIES Project (GA Nº 101036910). The main author wants to thank the financial support of Margarita Salas post-doctoral research program from UPV/EHU 2021-2023 call (financed by the European Union - Next generation EU) and the Consolidated ENEDI Research Group (IT1730-22).

6. References

Arias, S., M. M. Prieto, B. Ramajo, A. Espina, and J. R. García. 2009. Model-Free Kinetics Applied to the Vaporization of Caprylic Acid. Journal of Thermal Analysis and Calorimetry 98(2):457–62. doi: 10.1007/s10973-009-0301-3.

Barontini, F. and Cozzani, V., 2007. Assessment of systematic errors in measurement of vapor pressures by thermogravimetric analysis. Thermochimica Acta 460(1–2):15–21. doi: 10.1016/j.tca.2007.05.005.

Bassi, M., 2011. Estimation of the vapor pressure of PFPEs by TGA. Thermochimica Acta 521:197–201. doi: doi:10.1016/j.tca.2011.04.024.

Bayón, R., Bonanos, A., Rojas, E., 2020. Assessing the long-term stability of fatty acids for latent heat storage by studying their thermal degradation kinetics. *EuroSun 2020: 13th International Conference on Solar Energy for Buildings and Industry*, Online, 1-3 September.

Bayón, R., Gismera, V., Rojas, E., 2021. Validation of lauric acid as PCM: Study of thermal degradation under quasi-real working conditions. *Enerstok 2021: 15th International Conference on Energy Storage*. Online, 9-11 June.

Beverley, K. J., Clint, J. H., Fletcher, P. D. I., 1999. Evaporation rates of pure liquids measured using a gravimetric technique. Phys. Chem. Chem. Phys., vol 1, 149-153.

Cheng, Z., Wu, W., Ji, P., Zhou, X., Liu, R., Cai, J., 2015. Applicability of Fraser-Suzuki function in kinetic analysis of DAEM processes and lignocellulosic biomass pyrolysis processes. Journal of Thermal Analysis and Calorimetry 119(2):1429–38. doi: 10.1007/s10973-014-4215-3.

Kissinger, H. E., 1957. Reaction kinetics in Differential Thermal Analyisis. Anal. Chem. 29:1702–6.

Matricarde Falleiro, R., Akisawa Silva, L., Meirelles, A., Krähenbühl, M., 2012. Vapor pressure data for fatty acids obtained using an adaptation of the DSC technique. Thermochimica Acta 547:6–12. doi: 10.1016/j.tca.2012.07.034.

Mehling, H., and Cabeza, L., 2007. Phase change materials and their basic properties. Thermal energy storage sustainability and energy consumption. doi: http://dx.doi.org/10. 1007/978-1-4020-5290-3_17.

Pieterse, N., and Focke, W., 2003. Diffusion-controlled evaporation through a stagnant gas: estimating low vapour pressures from the thermogravimetric data. Thermochimica Acta 406:191–98. doi: doi:10.1016/S0040-6031(03)00256-9.

Poling, B., Prausnitz, J., O'connell, J., 2001. Chapter 11. Diffusion Coefficients, in: The Properties of Gases and Liquids, Fifth Edition, McGraw-Hill.

Quant, L., Diarce, G., Bouzas, L., Bedecarrats, J.P., García-Romero, A., 2021. Long-term assessment of the thermal stability of sodium nitrate-urea eutectic phase change material. Solar energy materials and solar cells 230(111261).

NIST Research Library Publications. 2022. NIST Chemistry WebBook. Https://Webbook.Nist.Gov/Chemistry/.

Vyazovkin, S., Burnham, A., Criado, J.M., Pérez-Maqueda, L.A., Popescu, C., Sbirrazzuoli, N., 2011. ICTAC Kinetics committee recommendations for performing kinetic computations on thermal analysis data. Thermochimica Acta 520:1–19. doi: 10.1016/j.tca.2011.03.034.

Thermal Performance of Eccentric High-Temperature Latent Heat Storage System: Passive Heat Transfer Enhancement Strategy

Alok K. Ray[1], Dibakar Rakshit[2*], K. Ravi Kumar[2], Hal Gurgenci[3]

1- University of Queensland and IIT Delhi Academy of Research,Indian Institute of Technology, Delhi (India)

2-Department of Energy Science and Engineering, Indian Institute of Technology, Delhi (India)

3-School of Mechanical and Mining Engineering,University of Queensland (Australia)

Abstract

The present study demonstrates the combined influence of orientation of latent heat storage (LHS) domain and radial eccentricity of the heat transfer fluid (HTF) tube on the charging characteristics of high-temperature LHS system with help of a comprehensive numerical investigation. Charging duration of concentric horizontal configuration (e_x= e_y= 0, θ = 0°) is found to be 19.94 % lower than the vertical domain (e_x= e_y = 0, θ = 90°). Thereafter, three vertical radial eccentricity of HTF tube is considered for the domain θ = 0°. The spatio-temporal distribution of melting fraction and temperature during phase change are observed for both concentric and eccentric LHS domain. Degree of eccentricity in horizontal direction (e_x = 5 mm and 10 mm) does not produce significant variation as compared to concentric (e_x = e_y = 0) configuration. However, charging duration for the LHS domain having vertical eccentricity (e_y = -5 mm, θ = 0°) is observed to be 11.7 % lower than concentric domain.Furthermore, the charging duration for e_y = -10 mm is 17.64 % and 33.33% lower than θ = 0° and θ = 90° respectively.

Keywords: High-temperature, PCM, LHS, HTF, Eccentricity, Orientation

1. Introduction

Solar energy is one of the most abundant sustainable energy resources available to be harnessed. Solar thermal and Solar photovoltaic are the two technologies to convert solar energy to electrical energy. However, the spatial and temporal variability is a major bottleneck against wide-scale utilization of solar technology. Efficient storage solutions are paramount to address the intermittency problem and can result in higher dispatchability of solar power (Zablocki,2019). LHS technology involves three distinct stages as presented in Figure *1*. Utilizing high-temperature PCMs for LHS systems can provide numerous benefits such as high thermal stability, high storage density, and high exergetic efficiency (Robinson,2017). Hence, high-temperature LHS coupled to a high-temperature heat engine can be considered as a potential alternative for storing solar energy during the daylight hours and releasing the accumulated energy during periods without sunlight (Ray, 2021).

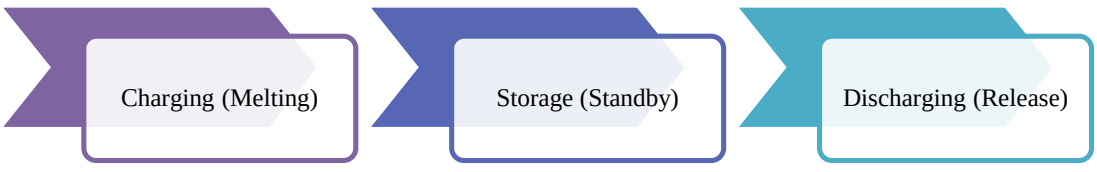

Figure 1:Three different stages of latent heat storage system

The major challenge for latent heat storage systems is that low thermal conductivity of the PCMs results in a low energy accumulation/release rate (Nazir, 2019). There are different heat transfer enhancement strategies to address this challenge (Jegadheeswaran, 2009). Active strategy involves use of metal based matrix and foams, nanoparticles, fins, cascaded arrangement, and encapsulation. However, adding fins, metal matrix and foams reduces the volume of PCM results loss in storage/release capacity (Al-Maghalseh, 2018). Passive enhancement includes change in place of HTF tube and variation in the orientation of the LHS prototype.

© 2022. The Authors. Published by International Solar Energy Society
Selection and/or peer review under responsibility of Scientific Committee
doi:10.18086/eurosun.2022.13.17 Available at http://proceedings.ises.org

The use of passive techniques results in an unchanged storage capacity as the PCM mass remains unaltered (Cao ,2018; Sarı, 2001).

For horizontal shell and tube energy storage unit, Yazici et al.,2014 (Yazici,2014) experimentally studied the effect of vertical relocation of the inner tube on the solidification behavior of paraffin wax. Among all eccentric cases, the results revealed that the concentric tube case had the least solidification time. Pahamli et al.,2016 (Pahamli, 2016) numerically studied the effect of varying each of the eccentricity of a circular inner tube and HTF specifications on the melting behavior of a PCM in shell and tube heat exchanger unit. It was concluded that increasing the inner tube eccentricity caused a reduction in the melting time. Alnakeeb et al.,2021 (Alnakeeb, 2021) studied the effect of eccentricity on the inner tube at different aspect ratios on the melting characteristics of the PCM storage unit. However, the cumulative impact of orientataion and radial eccentricity on thermal characteristics still requires extensive investigation.

The inference from the preceding literature survey is that there is a paucity of research on passive heat transfer augmentation techniques for high-temperature PCM. Hence, the present study numerically investigates the combined effect of the passive heat transfer augmentation techniques on thermal chacteristics of HT-LHS system. The orientation of the domain and radial eccentricity of HTF tube are simultaneously changed to observe the cumulative effect.

2. Problem statement and numerical formulation

2.1. Physical and computational domain

The physical domain of the system comprises of two tubes with HTF running through the inner tube and PCM present in the annulus.The schematic illustration of the computational domain and dimensions of the cross-section of the LHS systems are presented in *Figure 32 (a)*. The inner copper tube has an outer diameter of 26.7 mm and the outer steel shell has an inner diameter of 84.68 mm. The HTF (Therminol VP 1) flows through the copper tube and the annulus contains high-temperature PCM (Binary mixture of $NaNO_3$ and KNO_3). The hot HTF and the cold HTF enters the tube during charging and discharging, respectively. The conjugate heat transfer between PCM and HTF is through combined convection and conduction during charging and discharging. The heat transfer from fluid to outer tube wall is forced convection and melting of PCM generates free convection. Although the specific dimension of the LHS system is selected in this study, the outcomes are applicable for different dimensions and configurations since the thermohydraulic process involving conjugate heat transfer and phase change is similar in concentric tube LHS systems. Two orientations of the domain i.e. horizontal ($\theta = 0^o$) and vertical ($\theta = 90^o$) are considerd to observe the effect of orientation on the heat transfer characteristics. *Figure 3* illustrates the cross section of LHS system for four different radial eccentricity for $\theta = 0^o$ domain. Vertical eccentricity is provided in positive and negative direction ($\theta = 0^o$, $e_x = 0, e_y = c$). The temperature dependent thermophysical properties of the PCM and HTF are presented in Table 1 and Table 2 respectively.

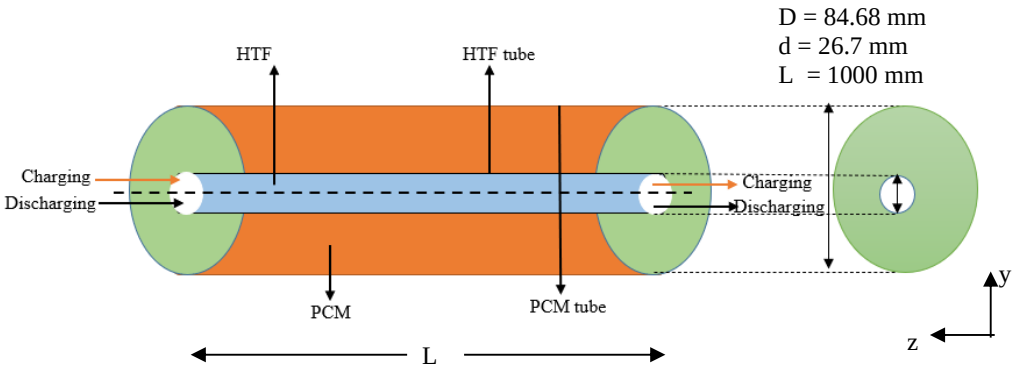

(a)

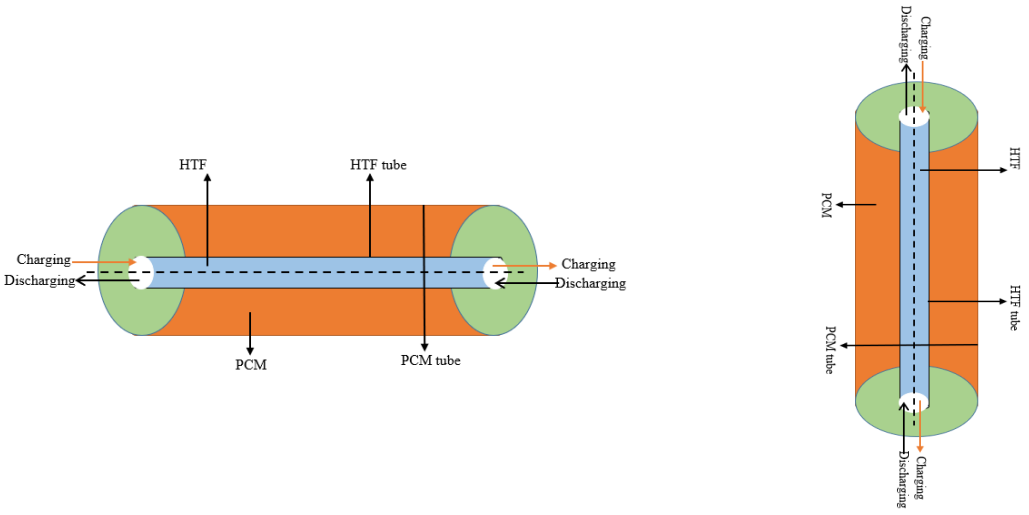

(b) (c)

Figure 2: (a) Dimensions of the physical domain of the concentric LHS system , (b) Horizontal orientation of the LHS domain,and (C) Vertical orientation of LHS domain

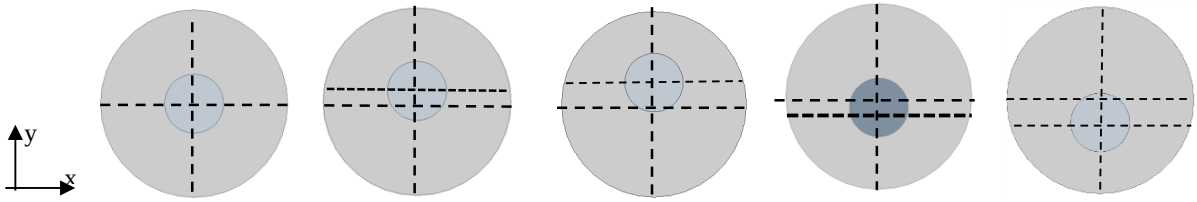

Figure 3: Cross-section of computational domain. (a) Concentric tube ($e_x = e_y = 0$),(b) $e_x = 0$,$e_y = 5$ mm ,(c) $e_y = 0$, $e_y = 10$ mm and (d) $e_x = 0$, $e_y = -5$ mm and (e) $e_x = 0$ mm, $e_y = -10$ mm .

Where e = eccentricity of HTF tube = Distance between center of outer and inner tube

Table 1: Thermophysical properties of PCM

Temperature (K)	Density (kg/m^3)	Specific heat (J/kgK)	Thermal conductivity (W/mK)$\times 10^{-3}$	Viscosity (Pa.s))$\times 10^{-3}$
500	1945	1486	486.5	5.5
550	1913	1495	496.1	3.839
600	1882	1503	505.8	2.707
650	1850	1512	515.6	1.992
700	1818	1520	525.4	1.583

Table 2: Thermophysical properties of HTF

Temperature (^oC)	Density (kg/m^3)	Specific heat (J/kgK)	Thermal conductivity (W/mK)	Viscosity (Pa.s)	Vapor pressure (kPa)
200	913	2048	0.114	0.000395	24
220	895	2101	0.111	0.000345	42
240	877	2154	0.107	0.000305	68
260	857	2207	0.104	0.000272	108
280	838	2260	0.100	0.000244	163
300	817	2314	0.096	0.000221	239

2.2. Numerical formulation

Enthalpy-Porosity technique is employed to investigate the solid-liquid phase change using Ansys Fluent®. The governing equations are formulated while taking the following assumptions into consideration:

- Molted PCM is assumed to be Newtonian and incompressible fluid
- Change in volume during melting is not considered

- Uniform thermophysical properties are considered for both solid and liquid phases
- Tube wall thermal resistance is neglected

The energy conservation equation is formulated as.

$$\frac{\partial(\rho H)}{\partial t} + \nabla.(\rho v H) = \nabla.(k\nabla T) + S_d \quad \text{(eq. 1)}$$

$$H = h_s + \beta\, \Delta H_{fusion} \quad \text{(eq.2)}$$

$$h_s = h_r + \int_{T_r}^{T} c_p dT \quad \text{(eq.3)}$$

Where H is total enthalpy, h_s is sensible enthalpy, δ is melting fraction, S_d is energy dissipation, h_r is sensible enthalpy at reference temperature and ΔH_{fusion} is the latent heat of fusion.

$$\beta\,(T) = \text{liquid fraction} = \begin{cases} 0 & T < T_{solid} \\ \frac{T - T_{solid}}{T_{liquid} - T_{solid}} & T_{solid} \le T \le T_{liquid} \\ 1 & T > T_{liquid} \end{cases} \quad \text{(eq. 4)}$$

Replacing δ in Equation (4), the energy equation can be expressed as:

$$\frac{\partial(\rho h_s)}{\partial t} + \nabla.(\rho v h_s) = \nabla.(k\nabla T) - \frac{\partial(\rho\beta \Delta \mathrm{Hfusion})}{\partial t} - \nabla.(\rho v \beta \Delta \mathrm{Hfusion}) + S_d \quad \text{(eq. 5)}$$

Where T = Local temperature

T_{solid} = Solidus temperature of PCM (K)

T_{liquid} = Liquidus temperature of PCM (K)

A value of δ = 0 corresponds to solid phase and δ = 1 defines liquid phase. Value of 0<δ <1 represents a mushy zone (pseudo porous zone) consisting of both solid and liquid phases.

The momentum equation to include natural convection can be expressed as:

$$\frac{\partial \rho v}{\partial t} + \nabla.(\rho v v) = -\nabla p + \nabla.(\mu \nabla v) + \rho g + M v \quad \text{(eq.6)}$$

$$M(\beta) = \frac{(1-\beta)^2}{\beta^3 + \epsilon} A \quad \text{(eq. 7)}$$

Where M = porosity function and A = Mushy zone constant which reflects the morphology of mushy zone. ϵ is a constant having a small value (0.001). M helps the momentum equation to approximate the Carman-Kozney equations for flow in porous media. 'A' measures the amplitude of velocity damping. The disparity in simulation could be caused by extremely high values of A. 'A' is 10^5 in the present study.

Boussinesq approximation assumes the constant fluid density in all terms of Eqn (6) except the buoyancy force which would generate convection in molten PCM. This body force is modeled using ρ_r and T_r. Hence, the momentum equation can be expressed as:

$$\frac{\partial \rho_r v}{\partial t} + \nabla.(\rho_r v v) = -\nabla p + \nabla.(\mu \nabla v) + (\rho - \rho_r) g + \frac{(1-\beta)^2}{\beta^3 + \epsilon} A v \quad \text{(eq. 8)}$$

$$(\rho - \rho_r) g = -\rho_r k_T (T - T_r) \quad \text{(eq.9)}$$

k_T is the coefficient of thermal expansion of molten PCM and ρ_r, T_r are reference density and temperature respectively.

The continuity equation can be expressed as:

$$\frac{\partial \rho}{\partial t} + \nabla.(\rho \vec{U}) = 0 \quad \text{(eq.10)}$$

As the flow is considered incompressible, the continuity equation can be expressed as

$$\nabla.\vec{U} = 0.$$

The transient simulation with the pressure staggering option (PRESTO) scheme is used for the pressure correction equation, and a SIMPLE algorithm is used for pressure–velocity coupling (Mat et al. 2013). A second order upwind scheme was used to solve the momentum and energy equations. First order implicit scheme is used to discretize the transient term.

2.3 Initial and boundary conditions

At t=0 the PCM is assumed to be at 488 K. HTF is introduced into the tube at temperature and mass flow rate of 525 K and 0.5 kg/s, respectively. Heat transfer from HTF to PCM during charging is simulated using coupled boundary conditions at the inner tube wall. The exterior wall of the shell is assumed to be entirely insulated. Outflow condition is employed at the exit of heat transfer fluid tube.

Mathematically, the mass and energy conservation for this specific problem can be expressed as:

$$\dot{m}_{in} - \dot{m}_{out} = 0 \quad \text{(eq. 11)}$$

$$\dot{E}_{in} - \dot{E}_{out} = \dot{E}_{transfer} \quad \text{(eq. 12)}$$

Where $'\dot{m}_{in}'$ is mass flow of HTF at inlet, $'\dot{m}_{out}'$ is mass flow of HTF at outlet.

3. Results and discussion

3.1 Model verification and validation

The numerical results are verified for grid and time independence before proceeding with the simulation.3D domain is considered for horizontal domain and 2D axisymmetric domain is considered for LHS system with vertical orientation. Figure 4 (a) performs grid independence for three different number of elements with time step of 0.01 s. The results did not alter extensively with an increase in elements from 2,04,918 to 2,44,900. Therefore, the model with 2,04,918 elements with time step 0.025 s is considered to achieve the predetermined convergence level.

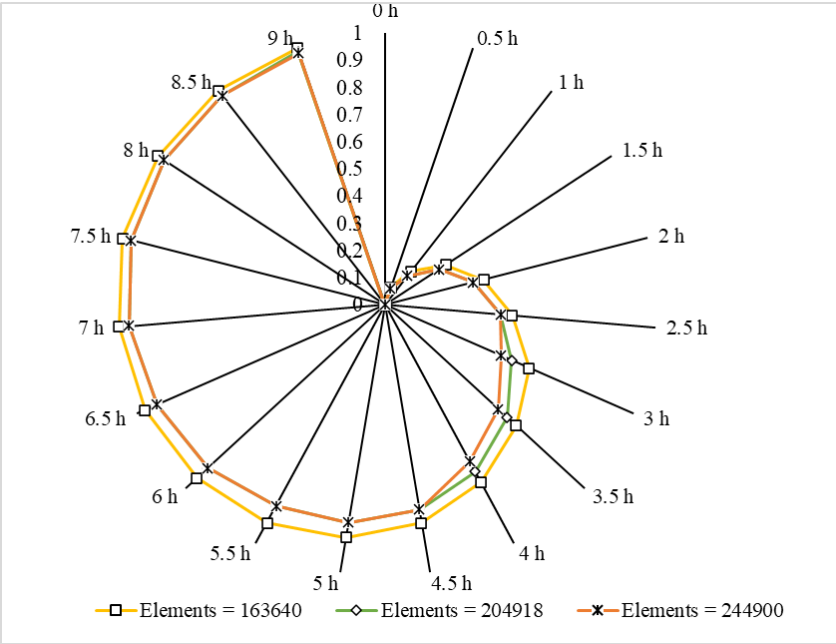

Figure 4: Grid independence test

The numerical model is verified by comparing predictions with previous experimental results from Hosseini et al. (Hosseini, Rahimi, and Bahrampoury 2014) and numerical results from Seddegh et al. (Seddegh, Wang, and Henderson 2016). Figure 5 compares the volumetric average temperature of the PCM domain during charging with the experimental and numerical findings during the charging process. The geometric and operating parameters are kept constant as previus literature to validate the methodology. The volume flow rate of 1 lpm, and inlet temperature of 343 K are considered for the test. The results from the simulation using present numerical technique reflect good agreement with previous results.

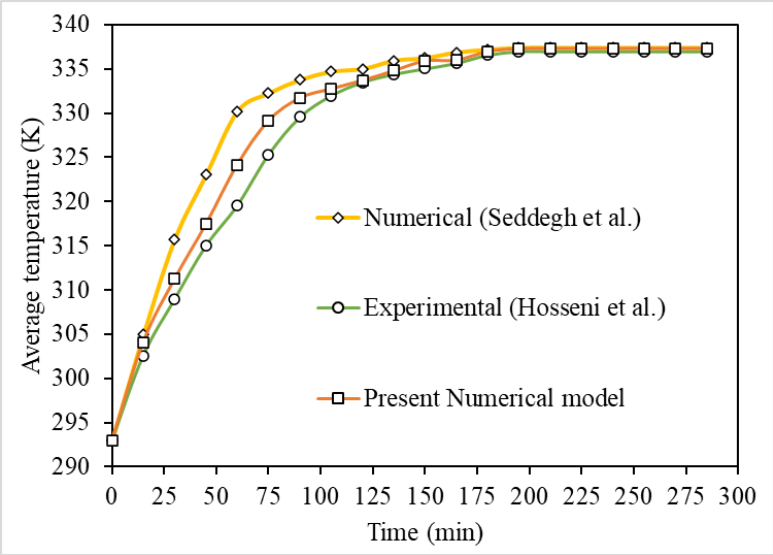

Figure 5: Validation of the present model with experimental and numerical model

3.2 Charging performance comparison between horizontal and vertical domain

Figures 6 (a) and 6 (b) display the liquid fraction and temperature variations respectively for concentric horizontal configuration as shown in Figure 2 (b). At the beginning of charging the solid phase change material in contact with the tube surface absorbs heat from hot heat transfer fluid and subsequently reaches the melting temperature. As a result, the recirculation zone is created in molten PCM, which generates an intense convection current. This intense movement between molten PCM and interface between liquid and solid PCM intensifies the melting. The melted PCM rises to top of the shell side, while solid PCM precipitates because of buoyancy. In the end, the melted PCM filled the upper half of the LHS system as depicted in Figure 6(a).

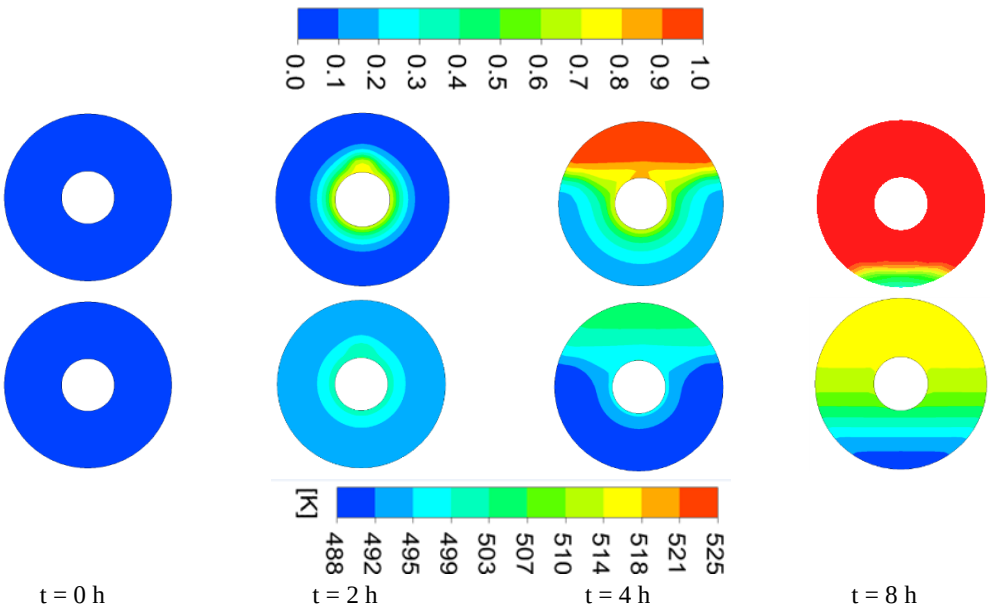

Figure 6: Liquid fraction and temperature contour distribution for horizzontal domain. Upper row: Liquid fraction,and lower row: Temperature

Figures 7 (a) and 7(b) illustrate the contours of liquid fraction and temperature respectively for vertical concentric system present in Figure 2 (c). Likewise horizontal domain, the solid PCM near the heat transfer tube absorbs heat from hot heat transfer fluid. When a layer of melted PCM is formed adjacent to the tube

surface, the melted PCM rises along the outer surface of the tube due to buoyancy. This motion creates a convective current in melted PCM between HTF tube and melted PCM and as well as between the liquid and solid interface. In contrast to horizontal system, the convective current persists and is effective during entire charging process for vertical LHS system. As a result, the vertical LHS system maintains nearly a constant charging rate. Figure 7 (b) displays practically lack of temperature stratification in the melted PCM.

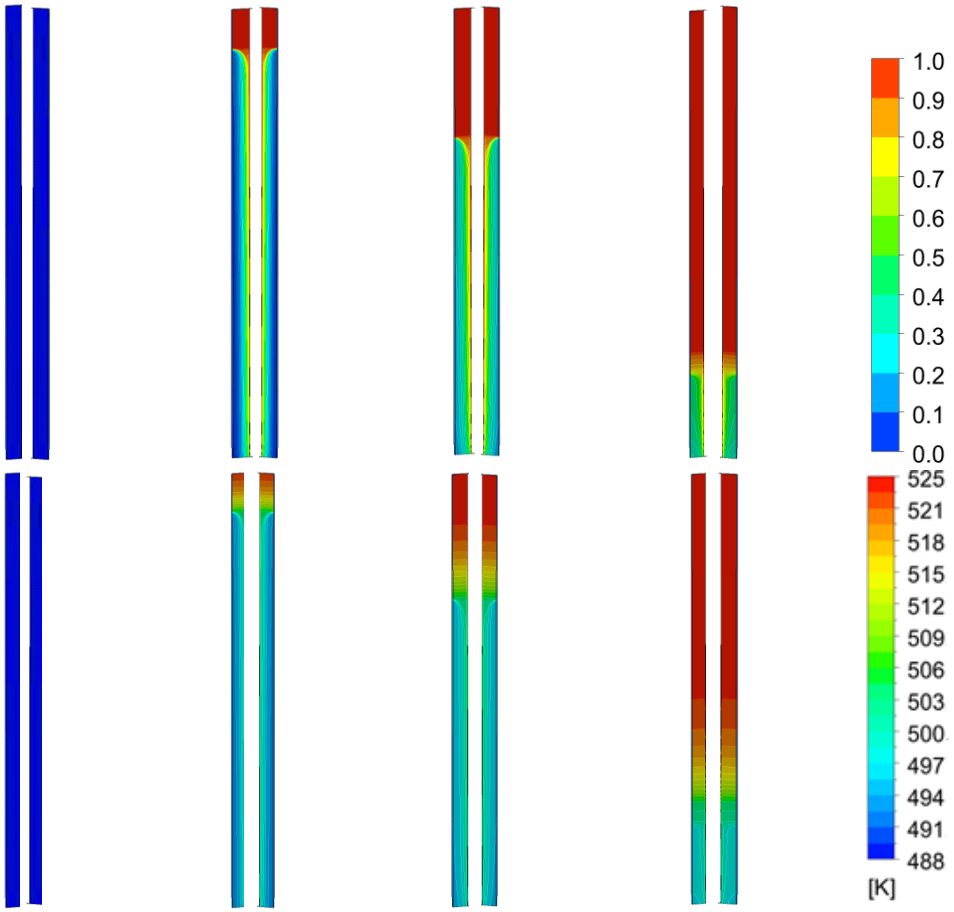

Figure 7: Liquid fraction and temperature contour for vertical domain. Upper: Liquid fraction , and Lower: Temperature

3.3 Combined influence of orientation and eccentricity on charging performance

Figure 8 compares the effect of horizontal and vertical orientation ($\theta = 0^o$ and $\theta = 90^o$) on the charging characteristics for latent heat storage. In the beginning, the rate of melting remains almost the same for both configurations. This can be attributed to the presence of only conduction at the start of the charging process which is independent of θ. A high melting rate during charging refers to the transition in thermal state of PCM from solid to the melted. When melting begins, the recirculation propagates in axial and radial directions in melted medium of the LHS system. For $\theta = 0^o$, the radial component helps to the increase in melting rate, and the axial component facilitates the melting along the length of the horizontal system. On the other hand, the same convective motion persists during the entire charging process in the vertical LHS domain.

Charging duration for LHS should be as small as possible for improved performance. From Figure 8, it is evident that the horizontal domain has superior performance compared to vertical domain. Hence, the horizontal configuration is subjected to change in eccentricity of the HTF tube to evaluate the combined effect.

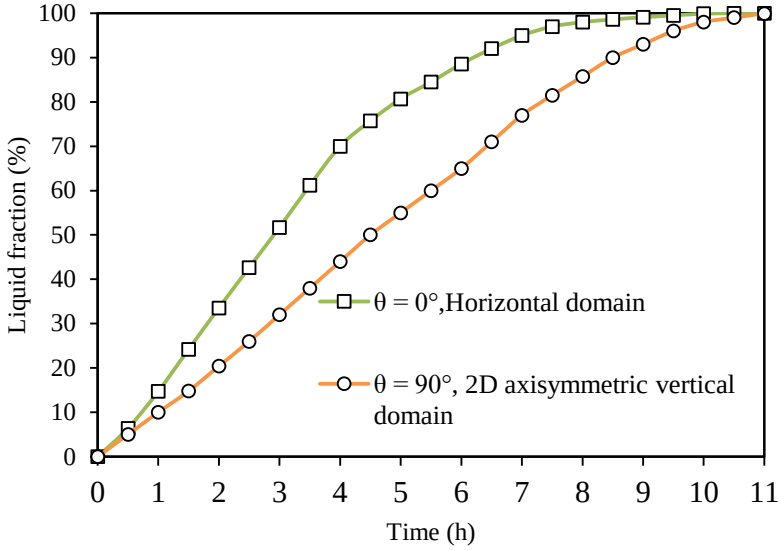

Figure 8: Temporal variation of liquid fraction for θ = 0° and θ = 90°

The degree of eccentricity is varied in both horizontal (e_x = c, $e_{y=0}$) and vertical direction (e_y = c, $e_{x=0}$). Figure 9 represents the liquid fraction and temperature contour for different degree of eccentricity for horizontal domain (**θ = 0°**). At the beginning, there are no difference in charging rate of eccentric tube as compared to concentric tube as visible from Figure 10 which is due to pure conduction heat transfer from inner tube wall to solid PCM. Gradually, temperature of PCM layer adjacent to the inner tube increases first and PCM starts to melt after temperature reaches the melting point. The molten PCM adjacent to lower part of the inner tube moves to upper side of inner tube due to buoyancy. This generates natural convection current in molten PCM which continues to dominate in eccentric system. When the eccentricity of inner tube descends downwards from the coaxial center with the outer tube, the area available for natural convection increases enhancing the melting rate. This can be attributed to the correlation between convective heat transfer with the effective surface area available for natural convection ($\dot{Q} \propto A_{eff}$). The eccentric geometry with e = -20 mm presented the shortest melting time due to enhanced convective heat transfer coefficient. On the contrary, the horizontal eccentricity does not affect the charging rate as buoyancy has no effect on horizontal direction. Table 3 summarizes the percentage of increase or decrease in charging duration corresponding to different configuration of LHS system.

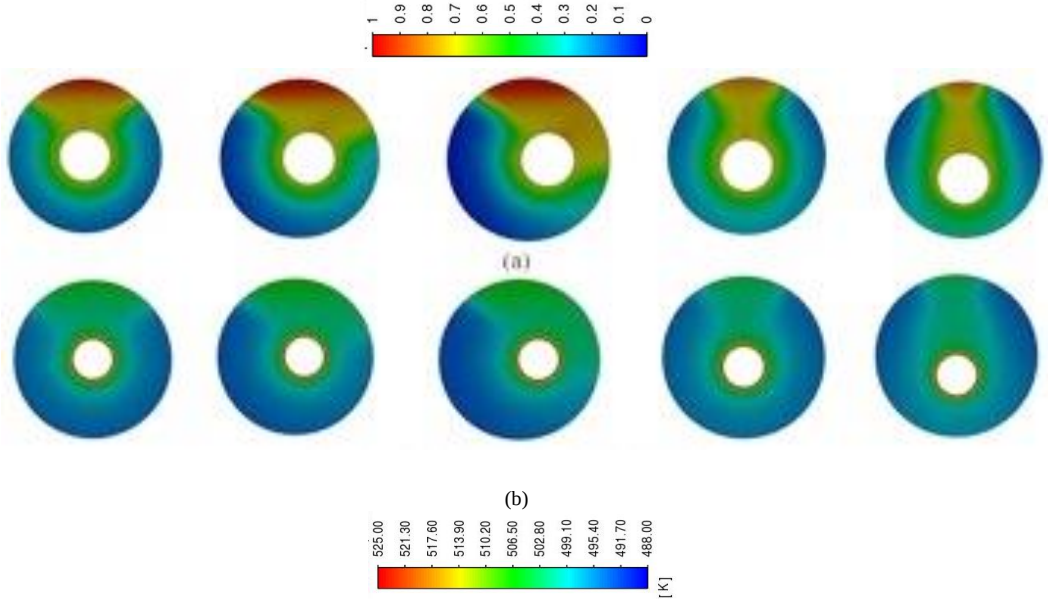

Figure 9: Liquid fraction and temperature distribution after 3 h of charging at z = 0.5 m cross section. (a) Liquid fraction and (b)Temperature

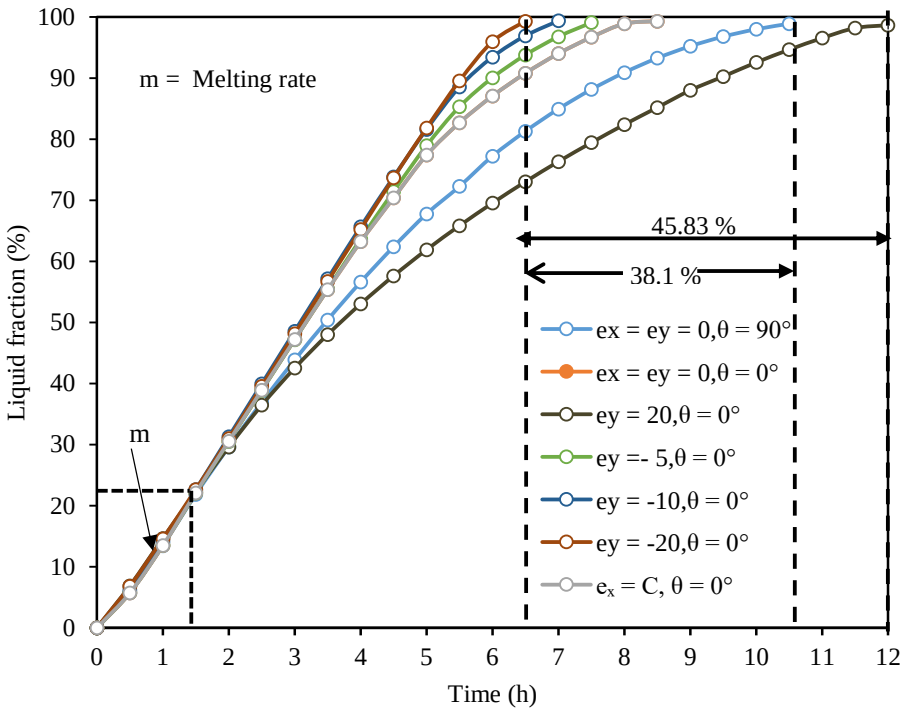

Figure 10: Combined effect of orientation and radial eccentricity on charging performance (e is in mm)

Table 3: Quantitaive illustration of combined effect of passive enehancement techniques

Configuration	Orientation, eccentricity (mm)	Charging duration (hrs)	Change wrt concentric vertical domain (%)
Concentric vertical Vertical	θ = 90°,e = 0	10.5	Reference
Change in orientation	θ = 0°, e = 0	8.5	19.04 ↓
Cumulative impact of orientation and eccentricity (-ve y direction)	θ = 0°, e_y = - 20	6.5	38.09 ↓
Cumulative impact of orientation and eccentricity (+ve y direction)	θ = 0°, e_y = 20	12	14.28 ↑
Cumulative impact of orientation and eccentricity (x direction)	θ = 0°, e_x = C	8.5	19.04 ↓

3.4 Effect of inlet temperatures and flow rates of HTF

From the previous section, horizontal eccentric domain having larger downward eccentricity is observed to have the best charging performance. Hence, a parametric analysis is carried out to evaluate the effect of the inlet temperatures and flow rates of HTF on the charging characteristics of the eccentric domain of θ=0° having downward vertical eccentricity. Three different temperatures at a constant HTF flow rate of 0.5 lpm and three different HTF inlet flow rates at a constant inlet temperature of 525 K are considered.

Figure 11 compares the liquid fraction and temperature of the PCM at different inlet temperatures during charging process. The temperature and liquid fraction are defined as average over the volume of the domain. The melting fraction and temperature menifests energy storage capacity of the LHS system at each instant during charging. The total charging duration is found to decrease with increase in inlet temperature. The reduction is explained by the intensified buoyancy and convective heat transfer in the PCM resulting from the high temperature gradient in the vicinity of the HTF tube. This results in increase in rate of energy transfer to the PCM. Figure 11 also reflects that the total melting time is reduced by 21.56 % and 44.53 % in the horizontal eccentric system as the HTF temperature is increased from 515 K to 520 K and then 530 K. The average temperature of PCM is increased by 1.1 % and 5% respectively as the HTF temperature is increased from 515 K to 520 K and then 530 K.

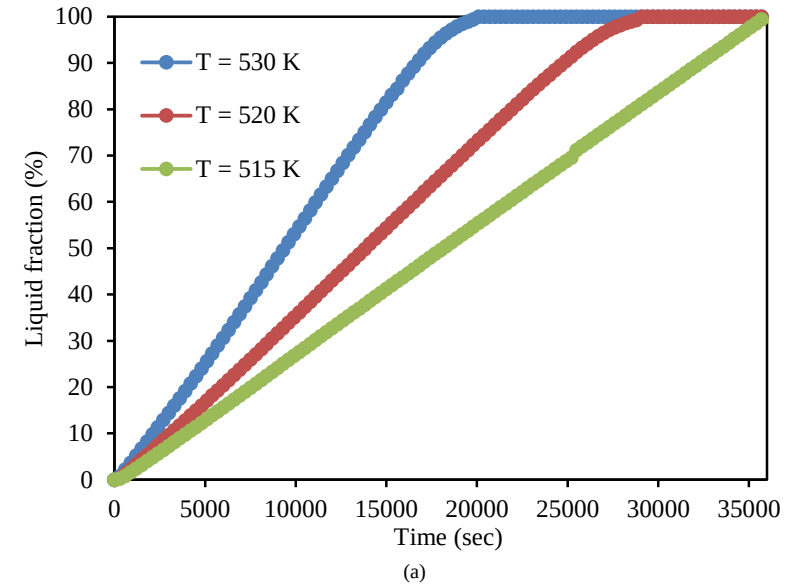

(a)

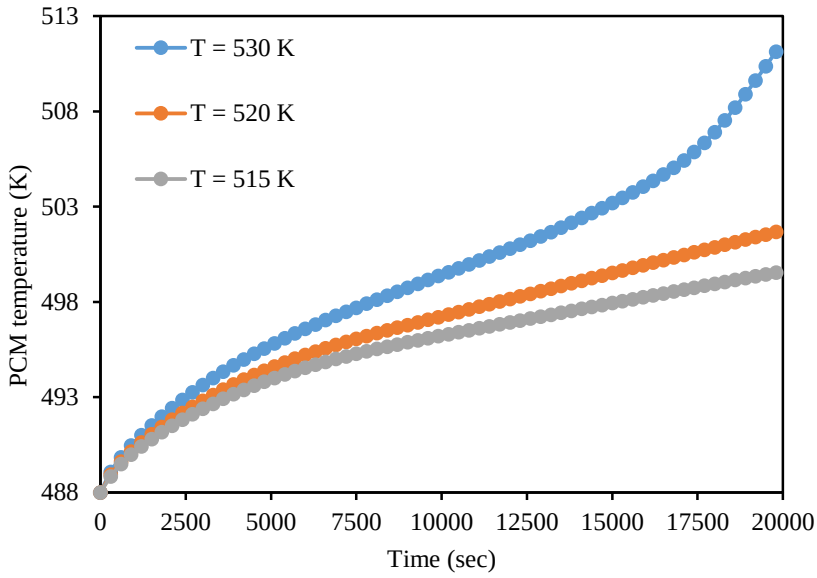

(b)

Figure 11: Thermal performance outputs in horizontal eccentric domain during the charging process. (a) PCM liquid fraction, and (b) PCM temperature

Figure 12 compares the liquid fraction of PCM under different Reynold's number during charging process. The increase of flow rate does not show significant changes in the total melting time during the charging process. This behaviour can be explained by the conjugate heat transfer mechanism from HTF to PCM. Heat transfer between the hot HTF and inner tube surface is by forced convection which has much higher heat transfer coefficient in comparison to natural convection in the liquid PCM. Change in flow rate of HTF affects the forced convection in HTF tube. However, the natural convection dominated heat transfer in the liquid PCM is not significantly affected by flow rate. Therefore, increasing the HTF flow rate has minimal effect on the thermal performance of any orientation.

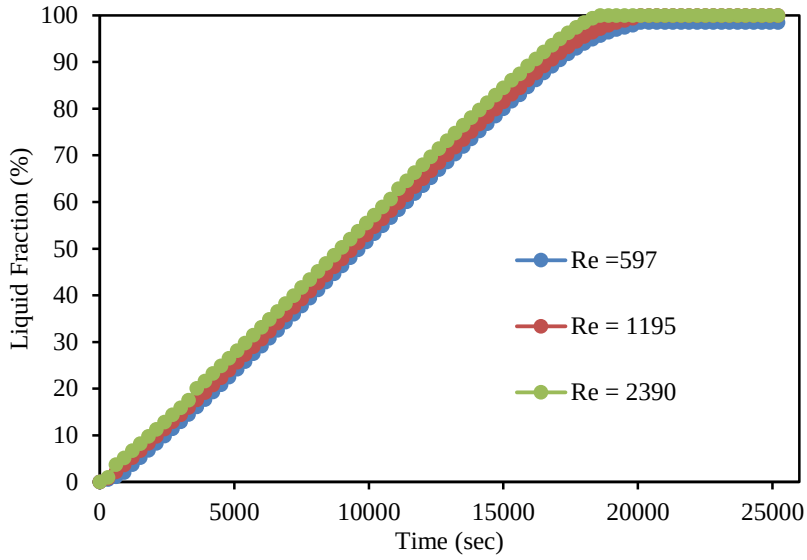

(a)

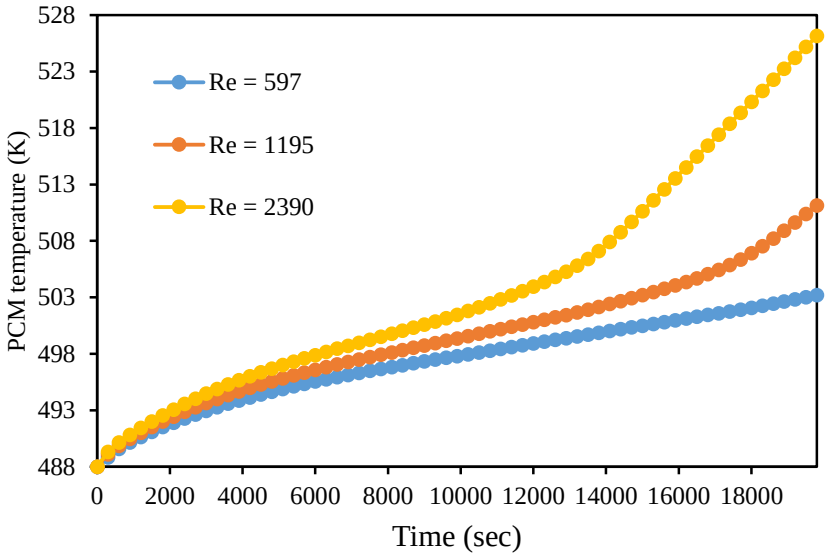

(b)

Figure 12: Thermal performance outputs in horizontal eccentric domain during the charging process. (a) PCM liquid fraction, and (b) PCM temperature

4. Conclusions:

The low heat transfer rate in LHS because of low thermal conductivity of inorganic PCM is the major technological bottleneck in designing HT-LHS systems. There are active and passive heat transfer enhancement methods to improve the heat transfer performance. Passive techniques such as variation in orientation of LHS domain and eccentricity of HTF tube can improve the thermal performance of HT-LHS system. Though individual effect of passive heat transfer enhancement techniques is relatively small compared to active heat transfer enhancement techniques, the combined effect is observed to be significantly large .

Changing the orientation from θ = 90° to θ = 0° with no eccentricity results in a 19 % increase in charging rate. Moreover, when both orientation and eccentricity are changed together, the charging rate increases by 38 % from θ = 90°,e = 0 mm to θ = 0°,e = -20 mm . However, if the eccentricity is upward at 20 mm for θ = 0°, the charging rate reduces by 41.12 % than θ = 0° without eccentricity. The increase in charging (melting) rate with vertical downward eccentricity is atrributed to larger available surface area for natural convection. The substantial increase in rate of charging would help to devise the HT-LHS system with horizontal

orientation and vertical downward ecentricity. The charging duration of eccentric domain with vertical downward eccentricity substantially decreases with increase in inlet temperature of hot HTF. However, the inlet flow rate has minimal impact on charging duration. The future study will consider the effect of combined strategies on discharging performance of HT-LHS system and will explore the intensity of turbulence on hear transfer characteristics.

Acknowledgment: Authors would like to thank UQIDAR to fund this collaberative research work

References

Al-Maghalseh, Maher and Khamid Mahkamov,2018.Methods of Heat Transfer Intensification in PCM Thermal Storage Systems: Review Paper. *Renewable and Sustainable Energy Reviews*, 92,pp.62–94. *https://doi.org/10.1016/j.rser.2018.04.064*.

Alnakeeb, Mohamed A., Mohamed A. Abdel Salam, and Mohamed A. Hassab,2021.Eccentricity Optimization of an Inner Flat-Tube Double-Pipe Latent-Heat Thermal Energy Storage Unit. *Case Studies in Thermal Engineering*, 25,pp.100969. *https://doi.org/10.1016/j.csite.2021.100969*.

Cao, Xiaoling, Yanping Yuan, Bo Xiang, and Fariborz Highlight, 2018.Effect of Natural Convection on Melting Performance of Eccentric Horizontal Shell and Tube Latent Heat Storage Unit. *Sustainable Cities and Society*, 38,pp.571–81. *https://doi.org/10.1016/j.scs.2018.01.025*

Hosseini, M. J., M. Rahimi, and R. Bahrampoury,2014.Experimental and Computational Evolution of a Shell and Tube Heat Exchanger as a PCM Thermal Storage System. *International Communications in Heat and Mass Transfer*, 50,pp.128–36. *http://dx.doi.org/10.1016/j.icheatmasstransfer.2013.11.008*

Jegadheeswaran, S. and Sanjay D. Pohekar, 2009.Performance Enhancement in Latent Heat Thermal Storage System: A Review. *Renewable and Sustainable Energy Reviews*, 13(9),pp.2225–44. *http://doi.org/10.1016/j.rser.2009.06.024*

Mat, Sohif, Abduljalil A. Al-Abidi, K. Sopian, M. Y. Sulaiman, and Abdulrahman Th Mohammad,2013. Enhance Heat Transfer for PCM Melting in Triplex Tube with Internal-External Fins. *Energy Conversion and Management*, 74,pp.223–36. *http://dx.doi.org/10.1016/j.enconman.2013.05.003*

Nazir, Hassan, Mariah Batool, Francisco J. Bolivar Osorio, Marllory Isaza-Ruiz, Xinhai Xu, K. Vignarooban, Patrick Phelan, Inamuddin, and Arunachala M. Kannan, 2019. Recent Developments in Phase Change Materials for Energy Storage Applications: A Review. *International Journal of Heat and Mass Transfer*, 129,pp.491–523. *https://doi.org/10.1016/j.ijheatmasstransfer.2018.09.126*

Pahamli, Younes, Mohammad J. Hosseini, Ali A. Ranjbar, and Rasool Bahrampoury,2016. Analysis of the Effect of Eccentricity and Operational Parameters in PCM-Filled Single-Pass Shell and Tube Heat Exchangers. *Renewable Energy*, 97,pp.344–57. *http://dx.doi.org/10.1016/j.renene.2016.05.090*

Ray, Alok K., Dibakar Rakshit, and K. Ravikumar, 2021. High-Temperature Latent Thermal Storage System for Solar Power: Materials, Concepts, and Challenges. *Cleaner Engineering and Technology*, 4,pp.100155. *https://doi.org/10.1016/j.clet.2021.100155*

Robinson, Adam, 2017. Ultra-High Temperature Thermal Energy Storage. Part 1: Concepts.*Journal of Energy Storage*, 13,pp.277–86. *http://dx.doi.org/10.1016/j.est.2017.07.020*

Sarı, Ahmet and Kamil Kaygusuz, 2001.Thermal Performance of Myristic Acid as a Phase Change Material for Energy Storage Application. *Renewable Energy*, 24(2),pp.303–17.

Seddegh, Saeid, Xiaolin Wang, and Alan D. Henderson,2016. A Comparative Study of Thermal Behaviour of a Horizontal and Vertical Shell-and-Tube Energy Storage Using Phase Change Materials. *Applied Thermal Engineering*, 93,pp.348–58. *http://dx.doi.org/10.1016/j.applthermaleng.2015.09.107*

Yazici, Mustafa Yusuf, Mete Avci, Orhan Aydin, and Mithat Akgun. 2014. On the Effect of Eccentricity of a Horizontal Tube-in-Shell Storage Unit on Solidification of a PCM. *Applied Thermal Engineering*, 64(1–2),pp.1–9. *http://dx.doi.org/10.1016/j.applthermaleng.2013.12.005*

Zablocki, Alexandra. 2019. “Energy Storage: Fact Sheet (2019).” *Eesi* 2040(February):1–8.

Development of an Open System for Evaluating Material Charging Characteristics from Industrial Waste Heat

Jack Reynolds[1], Jonathon Elvins[1] Eifion Jewell[1] and Justin Searle[1]

1 Swansea University, Swansea (United Kingdom)

Abstract

The current research tackles the energy trilemma, capture, storage, and re-use of industrial waste heat (IWH) by presenting the development of a laboratory-scale charge analyser for thermal storage (CATS) utilizing thermochemical materials (TCMs). The purpose of the study is to evaluate a material's charge performance relative to the reactor's capabilities. The temperature, flow rate, and material quantity are altered to generate an operational window. The reactor has been designed to work as an open system, whereby the IWH stream will pass directly through any TCMs under consideration. For this study, silica gel was chosen as the material for commissioning the reactor as it is well understood from a mass loss perspective and its relative ease of material preparation. The reactor can produce temperatures between 50-650°C and flows in the region of 200-900 l/min. During experimentation we can record the mass change (resolution 0.01g) up to a maximum of 10.2kg, temperature changes up to a maximum of 1100°C, and flows (between 0.2-25m/s).

Keywords: Industrial Waste Heat, Silica Gel, Thermochemical Materials

1. Introduction

With the exhaustion of our world's main fossil-based energy resources and the continued worsening of our environmental conditions in the past decades, it is vital we look to change the way we generate, use, and store our energy. For most of the industrial sector, heat energy is used in some way or another for manufacturing of the desired products. The heat energy is subsequently discharged from the process through thermal carriers such as gases or liquids and vented to atmosphere or discharged into local bodies of water. U.S. department of energy reported that between 20 to 50% of industrial energy input is lost as industrial waste heat (IWH) (BCS INC, 2008). Depending upon the process, IWH can be discharged over a large temperature range, however the majority of heat sources are below 200°C except for the Iron and Steel sector where the range is 200-1000°C (Papapetrou et al, 2018). This is highlighted in Figure 1. The inherent problem with utilising IWH can be its economics of recovery, discontinuous nature and the distance mismatch between the source and the end use. The solution to both these problems is effective heat storage.

Thermal energy storage (TES) is considered among passive IWH recovery technologies and could potentially fill the gap between energy supply and demand. Application of TES for IWH recovery could reduce investment cost, improve the capacity factor and reduce start-up and partial load losses in industries (Miró et al, 2016; Brueckner et al, 2014)

TES can be classified as sensible heat storage (SHS), latent heat storage (LHS) and thermochemical heat storage (TCS). SHS in comparison with other technologies is a simple, low-cost, and mature technology however is associated with inferior energy density and considerable storage volumes (Sunku Prasad et al, 2019). LHS offers greater energy density in comparison over the same temperature gradient, however LHS has some characteristic drawbacks such as corrosion and leakage. Both SHS and LHS are not suitable for long term application as heavy insulation is required to minimize typical energy leakage. (Wu et al, 2019; Fumey et al, 2019). TCS can store the energy at wide range of temperatures based on chemical bonds of suitable materials with minimum energy loss for long term application and higher associated energy storage density (Lin et al., 2021).

Sorption heat storage has been utilized for both mobile THS, transporting IWH to an off-site heat demand, and for inter-seasonal heat storage at the demand location (Krönauer et al., 2015; Sutton et al., 2018). For the lower end of IWH (<200°C) various salt hydrates could be suitable such as $CaCl_2$, $LiNO_3$ and $SrBr_2$ (Sutton et al.,

© 2022. The Authors. Published by International Solar Energy Society
Selection and/or peer review under responsibility of Scientific Committee
doi:10.18086/eurosun.2022.13.18 Available at http://proceedings.ises.org

2018; Salviati et al., 2019). For the higher end of IWH, there are far less options in terms of materials and research is scarce in comparison. Two stand out materials that have been studied are $Mg(OH)_2$ (Zamengo et al, 2015) and $Ca(OH)_2$ (Funayama et al, 2019) which are suitable for temperatures above 350°C and 550°C respectively.

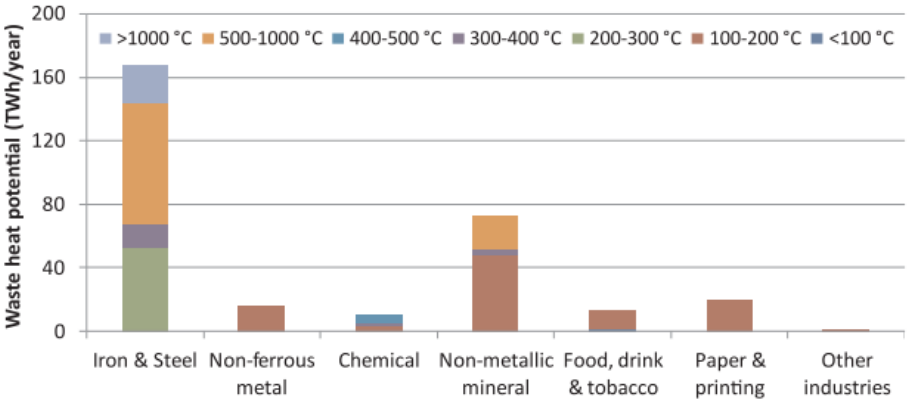

Fig. 1: Waste heat potential per industrial sector and temperature level for EU industry in 2015 (Papapetrou et al, 2018)

The aim of this work is to design and commission a reactor to assess the charging performance of various materials within the range of the reactor's capabilities of representing IWH. This will allow for decisions to be made on which material is best suited to a particular IWH stream. Here we will alter temperature, flow, and material quantity to produce an operational window. The reactor has been designed to work as an open system, whereby the IWH stream will pass directly through any TCMs in a fixed bed. The storage of the material in the reactor has been designed so it can be easily removed for transport. For this study, silica gel was chosen as the material for commissioning the reactor as it is well understood from a mass loss perspective and its relative ease of material preparation.

2. Design and Build of the Reactor

The performance of any materials selected for use in storage of IWH need to be assessed in a lab-scale reactor. To do this, the charging performance of a material should be assessed in terms of its resident time to become fully dehydrated at a given temperature and flow. In this work, the design and optimization of a charge analyser for thermal storage (CATS) capable of mimicking the flow of industrial waste heat on a lab-scale over a broad range of temperatures and flows in the low-medium temperature range is shown.

2.1. Reactor Requirements

Incorporating as many measurements as possible into a RIG is essential to giving a more accurate judgement and a better understanding of what is transpiring. To validate the discharge performance of the TCM, there are a couple of parameters to suggest the resident time required. These are as follows:

- Change in Mass
- Change in Temperature

For the replication of the IWH, a heat source is required that can provide the range of temperatures covered in the low-medium range (100-700°C) with the ability to easily control and monitor the temperature and the flow rate. An open structure with the ability to contain TCMs is needed with following necessities:

- Allow incorporation of sensors
- Ability to withstand heat
- Limit the amount of heat lost to the environment
- Allow flow of IWH through material
- Easy to remove and add materials

2.1.1 Mass Measurements

Accurately measuring mass of TCMs is the most accurate way of judging what state the salt is in. If a known quantity of salt is contained within a matrix, any additional weight gained can be attributed to absorbed water. By applying heat, this water can be removed and by weighing in stages it is possible to observe progress along a charging profile. However, this is not ideal in any situation for two reasons. First it is not possible to monitor the mass over time for a complete cycle with live results, and secondly, the act of removing the salt from the heat in normal conditions will affect the actual water content. To avoid this, we need to have mass measurements while heat the is being applied. The solution to this is to measure the whole RIG in which the SIM is contained. An example of this is shown in the work by Zamengo et al. (2015) where the packed bed reactor is sat on an electronic balance. To achieve this the electronic balance needs to have a high maximum load to allow for the weight of the RIG, while also have a high accuracy to account for the low mass changes occurring during the reaction. On top of this a data logging function is required so the mass can be monitored throughout experimentation.

2.1.2 Temperature Measurements

Temperature measurements need to be taken in the RIG for three reasons. The first is to monitor the temperatures coming from the IWH heat source are as expected. Secondly, we need to understand how much heat energy is being lost from the point of heat source to the location of our storage materials. Lastly, the temperature changes that may occur before and after the thermochemical materials (TCMs) need to be monitored which may give an indication of how far along the charge cycle progression is. The heat energy from the IWH stream should in theory be absorbed by the TCMs, breaking the bonds between the water molecules and the material in question. This should result in the temperature of the air stream being reduced at the outlet compared to the inlet. This continues until the salt reaches its anhydrous state or reaches a stable salt hydrate at a given temperature. At this point there should be a limited difference between the inlet and outlet, giving us an indication that the charge cycle is complete. The requirements of the thermocouples (TCs) are as follows. They need to be able to withstand the maximum temperature that may be subjected to the materials in the RIG. They will also need datalogging capabilities so the temperatures can be monitored throughout the charging profile.

2.1.3 IWH Source

The heat source itself needs to cover the range of temperatures most associated with IWH sources (Low/Medium Temperatures). This needs to be accurately controlled while also considering the flow of air. Safety of the device is the biggest concern, and there cannot be any risk of overheating, damage, or cause any harm in the close vicinity.

2.1.4 Apparatus to Hold TCMs

The materials utilised in the apparatus to hold the SIM and any other components involved in the RIG need to handle the temperatures that are capable from the chosen waste heat source replica. There needs flexibility of within the piping to allow separation of the RIG from the heat source to prevent impacting upon the mass measurements. The RIG should be insulated where possible to limit the amount of heat lost the environment. The RIG should include an easy to remove compartment for the materials so that they can be transferred to an alternative discharge unit. There needs to be small access points incorporated for any sensors that will be fitted into the RIG.

2.2. Reactor Design

Following all the design requirements mentioned above, the finalised reactor design is shown in Figure 2. The heat source is a Leister Hotwind System hot air blower. This is commonly utilised in continuous drying,

shrinking, and coating processes. The continuous nature makes it ideal for use as our IWH source, aswell as having control over temperature and flow between 50-650°C and 200-900 l/min respectively. To have even more control over temperature, the Leister CSS is incorporated and programmed to control the temperature from an external TC. This allows the required temperature to be set in the inlet of the RIG as opposed to within the air blower. The Hotwind System is also fitted with an alarm contact and combined with a fabricated alarm we can prepare for any situation where the air blower might be overheated. The entire system is then fixed to an adjustable platform to allow for any change in height while also preventing movement during experimentation.

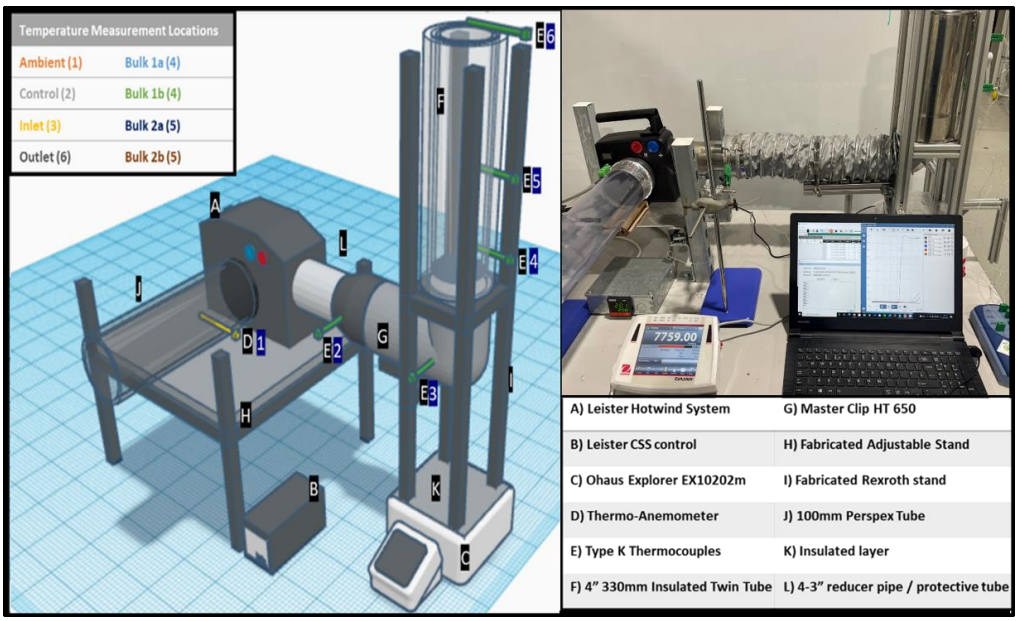

Fig. 2: 3D model of the lab-scale CATS highlighting all key components and locations (Left). Experimental set up (Right).

The main element of the RIG is the insulated twin tube with measurement adapters fitted in the side. The length of the tube is 330mm and the inner diameter (ID) is 100mm. The outer diameter is 150mm with 25mm of insulation held between the two stainless-steel tubes. Within this there is a removable stainless-steel tube with a perforated based capable of holding the testing TCM. The diameter of this tube is 94mm. This tube has holes present in the side that line up with the measurement adapters for incorporated sensors. The twin tube is then enclosed within a fabricated rexroth stand to allow for the elevation needed to fix the flexi tube underneath. This tubing is made from a flexible two-ply spiral hose made of heat-resistant fabric and steel spiral which is resistant up to temperature of 650°C. This has ID of 105mm and strapped to the inner twin tube by a SS jubilee clip. The flexibility of this piping allows for change in mass measurements during experimentation. To form a seal between the rig and the Hotwind, the tubing is strapped to a 4-3-inch reducer tube which has been welded to the protective tubing attachment of the Hotwind. The reducer tube has been fitted with holes for the control TC.

With a sufficient seal between the heat source and the RIG, the flow rate can be monitored prior to the hotwind to avoid the need of heat resistant flow sensors. To do this a 100mm Perspex tube has been fixed to the filter attachment of the hotwind. With a known diameter of the pipe and the flow speed, the flow rate through the RIG can be calculated. The air speed is monitored using a hot wire CFM thermo anemometer and datalogger. This system is capable of measuring air velocity between 0.2-25 m/s using a simple probe that can be inserted into the stream. As well as air velocity, the probe can measure temperatures up to 50°C. As this probe is located prior to the heat source, we can use this to simultaneously record the ambient temperature during the reaction. The rexroth is placed on top of a Ohaus Explorer EX10202m scale capable of measuring masses up to 10.2kg with a readability of 0.01g. The Ohaus scale connects with the Ohaus SPDC Data Collection software to send mass recording at desired intervals during the charge cycle. The scale itself is only operational to temperatures of 40°C. To prevent any heat transfer between the RIG and scale, a thin insulating layer is placed between the scale and the rexroth stand.

Type K TCs with 310 stainless steel sheath and a maximum operating temperature of 1100°C are used for temperature measurements through the RIG. The first two TCs are placed in the reducer tube just prior to Hotwind nozzle. One of these feeds straight to the CSS temperature control and the other to the data logger. At the end of the flexi pipe, just before reactor, a TC is placed and selected as the inlet temperature. In both measurement adapters, two TCs are placed with the aim of one being at the pipe centre and second close to the pipe walls. These are our bulk temperature recordings. The last TC is placed above the exit stream of the RIG and is the outlet temperature recording. All these TCs are connected to a Pico logger TC-08 which transfers the live temperature recording to the Pico data collecting software.

The CATS offers an ability to screen materials for use in THS. With this set-up an estimate a recharge efficiency is possible and any alterations to conditions and system design to best match the material under consideration can be done. Once operational windows are found, IWH sources can be targeted for capture within that range.

3. Material Preparation

Silica gel was chosen as the material for commissioning the CATS system as it is well understood from a mass loss perspective and the relative ease of material preparation. To add moisture evenly to the silcia gel, a Memmert constant climate chamber HPP110eco is used. Inital static vapor sorption (SVS) tests were first carried out at three different RH% values all at 25°C (Figure 3). 3 petri dishes, each containing 10g of Silica gel were located in a sealed chamber with controlled local relative humidity and left for 168 hours to assess the maximum water uptake. The maximum values were generally achieved within the first 24-48 hours showing no further uptake over the remaining test duration. The results show different maximum moisture uptake for different conditions and as such it is key to keep synthesis conditions the same if consistent discharged material is to me made. As the investigation will focus upon fully hydrated silica gel, 25°C and 75% RH are the conditions choosen for material synthesis.

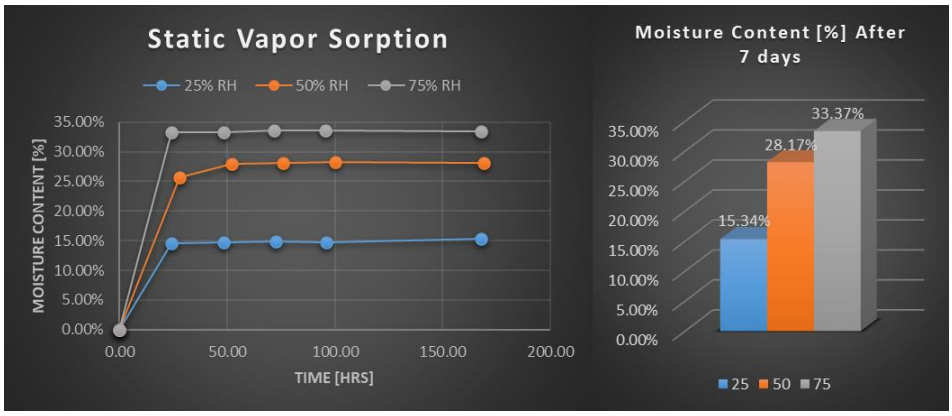

Fig. 3: Static vapor sorption (SVS) of 10g of Silica gel at 25°C at 25%, 50%, and 75% relative humidity (Left). Moisture content after 7 days (Right).

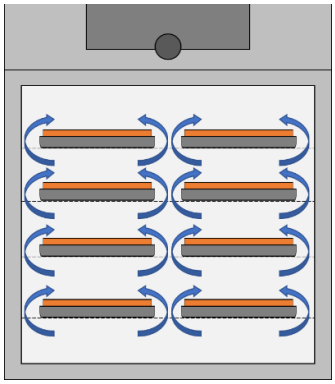

Fig. 4: Loading of Silica Gel in the Memmert constant climate chamber HPP110eco for large scale material preparation.

For bulk hydration, 300-400g of dry silica gel is loaded onto trays (32 x 23 cm) allowing for a thin layer of material to improve water uptake. Eight trays are then loaded into the climate chamber allowing for adequate air flow (Figure 4). At initial loading, the RH% of the oven drops due to rapid water uptake. Over the next 48 hours, this value equilibriates towards the set value. Once this is achieved it is possible to spot test the material and assess the moisture content. To do this a Ohaus MB120 moisture analyser is used. 5g of silica gel is subject to 200°C static drying with switch off criteria set to 1mg change over 120 seconds. If the moisture content is >33%, hydration is considered complete and materials are stored for use in the CATS.

4. Reactor Operation and Data

Example data received from the CATS is shown in Figure 5. The key indicators for duration of reaction come from the mass and temperature data. There is a steady loss of mass over time that flattens out when the charge reaction is deemed complete. This generally coincides with the outlet temperature that plateaus around its maximum observed value. The average flow data is used to show if there is any sudden change in the fixed bed during reaction and this, combined with the total reaction time proposed by the mass and temperature value, can give an estimate of the total energy used during the charge reaction. Any alteration to the IWH conditions, reactor design, and quantities of material used will change the energy required to charge the material set. With this data an operational window for silica gel to be used as an industrial waste heat storage material is defined

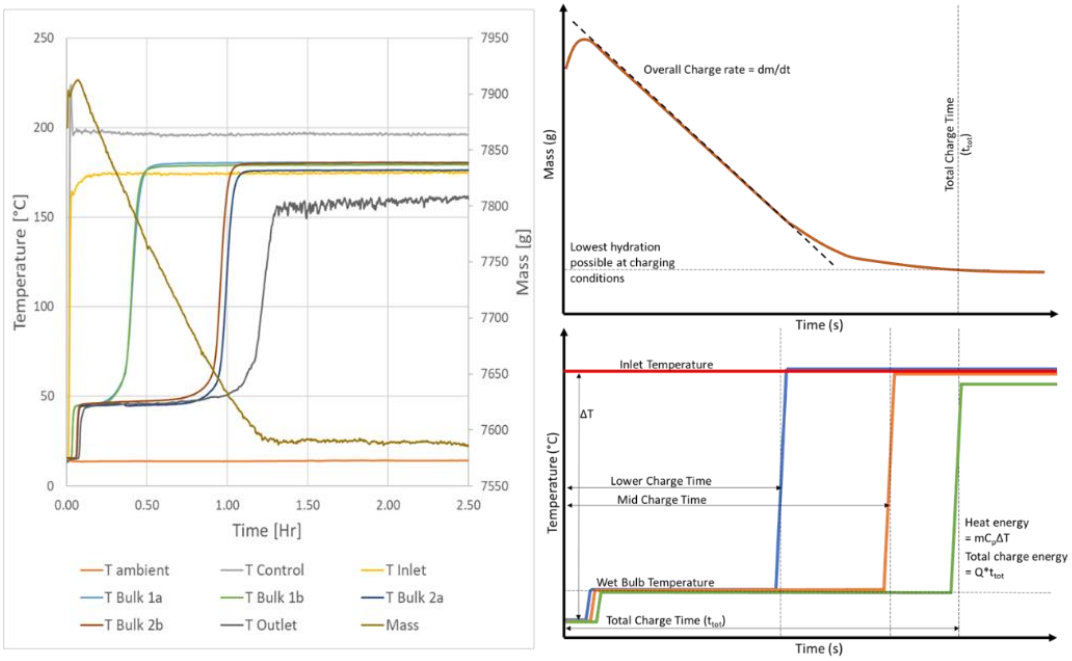

Fig. 5: Example data received from the CATS for silica gel at 200C set temperature and flow 7 set fan speed (Left). Data to be collected from the CATS (Right).

4.1. Air Speed to Mass Flow

As mentioned above a single point of measurement will be used to record air speed during experimentation, however the flow of air in a circular duct is not evenly spread across the plane of the duct. This is because of the friction that occurs at the duct walls that ultimately reduces the flow compared to the centre, creating the parabolic profile shown in Figure 6. Any obstruction such as fans, corners, duct fittings, tees, and coils all create turbulence in the duct, further changing the velocity over the cross section. To reduce the amount of turbulence, readings should be taken 7 duct diameters downstream and 1 and ½ upstream of any flow disturbance. For a round duct, the equal-area method should be used, whereby the air speed is taken at the centre of equal concentric areas and averaged. Figure 6. shows this where by two entry points, perpendicular

to each other, allow reading points to be taken vertically and horizontally through the centreline. An alternative method of obtaining the average flow is to take a measurement at the centre and multiple this by 0.9 (TSI Airflow, 2014). This can achieve an accuracy of +/- 5%. As the Thermo-Anemometer will remain central in the duct during experimentation, a comparison on the data received from the central data point and the traverse method is required to decide a multiplication factor the CATS system going forward.

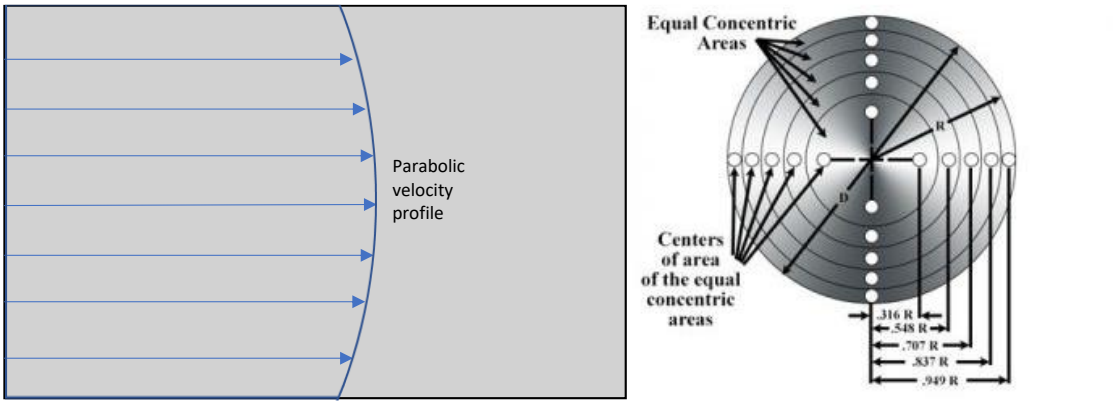

Fig. 6: Graph showing Actual Flow Rate vs Flow Setting varying Position, Temperature & Material.

Tab. 1: Results from air flow approximation experiment comparing central measurement point and traverse method at room temperature for flow setting 4 and 7.

Flow Setting 4		Flow Setting 7	
Method	**Air Speed [m/s]**	**Method**	**Air Speed [m/s]**
20 Point Traverse Method	1.40	20 Point Traverse Method	1.76
0.9 x Central Method	1.37	0.9 x Central Method	1.77
% Difference	1.68%	% Difference	0.69%

For each air speed measurement, the sensor was set in place and 30 data points were taken over 5 minutes (10s increments). The average of these values was then calculated as an input into table 1. The Traverse method was conducted over two different operational flow rates. For both sets of experiments the 0.9x Central Method was well within the quoted 5% difference of the 20 Point Traverse Method. This validates that a single point of flow measurement is sufficient to record during each experiment and a simple multiplication factor of 0.9 can be used to correct this.

To calculate the air mass flow (μ_{av}) the following equation can be used:

$$\mu_{av} = \nu \times CSA \times \rho_{air} \times 3240 \qquad \text{(eq. 1)}$$

- ν – Average Air Speed [*m/s*]
- CSA – Cross-sectional Area [m^2]
- ρ_{air} – Air Density [kg/m^3]
- 3240 – Multiplication factor for speed variation over a circular duct and to convert from units of seconds to hours.

4.2. Mass Measurement

To validate the scale's ability to record a mass change while connected to the flexi pipe, an experiment is set up to record the mass value of known weights. Four weights were chosen for this spread over a typical range expected from TCM mass losses. These are 74.80g, 118.9g, 125.27g & 191.32g. Each weight was placed on the scale 3 times at two different locations (Top and Base) and an average of the values calculated. The results from this are shown in Table 2. For all the results, the mass recorded was within 1% difference to the actual value. There is no significant trend suggesting this % difference changes when the mass of the object is changing. However, there is a difference in values from the mass measured at the base of reactor as opposed to the top of the reactor. All values at the base show a decrease in mass from the actual value, whereas all value at the top show an increase in mass from the actual value. This is considered to be an effect of the position of the weight in respect to the flexi pipe connection.

Tab. 2: Results from Scale Sensitivity Measurements

Mass at Base			Mass at Top		
Standard Mass	**Mass [g]**	**Av % Difference**	**Standard Mass**	**Mass [g]**	**Av % Difference**
1	74.8	0.77	1	74.8	-0.61
2	118.8	0.75	2	118.8	-0.57
3	125.3	0.77	3	125.3	-0.69
4	191.3	0.59	4	191.3	-0.33

The mass measurement is the first indicator of charge completion that results in a value of resident time (t_{rM}) used for total charge energy. Figure 5 shows that the mass linearly decreases for most of the charge duration before plateauing at its final 'dry' state. To obtain a residence time from this data, the gradient change during the reaction must be calculated. Using a selected 'end gradient' criteria, an exact time when the mass has levelled out to an appropriate state can be collected.

4.3. Temperature Measurement

The temperature is monitored at the system inlet to initially understand the heat loss in the distance between the Hotwind and the reactor. With knowledge of this we can then adjust the Hotwind temperature to get a desired temperature going through the material. This temperature reading subsequently allows comparison to all the other locations (Bulk1, Bulk 2, Outlet), assisting in defining charge completion at each point. Finally, the inlet is used to calculate the energy of the flow from the difference in temperature to ambient (25°C).

The loss of temperature in the flexi pipe between the heat source (Hotwind) and the reactor was investigated. The reactor was filled with a consistent amount of dry silica gel (1050g) and the Hotwind set at various flow settings and temperatures. The chosen flow settings were 4, 7, and 10. The chosen temperatures were 100°C, 200°C, and 300°C. For each experimental condition, the system was allowed to equilibrate for 10 minutes. 30 data points were subsequently recorded over 5 minutes and average values were calculated for the control and inlet TCs. The difference between these values is then labelled ΔT. The results are shown in Figure 7. Increasing the flow rate slightly decreases the loss of heat energy, however the largest losses occur through increases to the temperature. Generally, increasing the set temperature by 100°C increases the ΔT by around 20°C. Following this trend, selecting the Hotwinds maximum temperatures (650°C) and a maximum flow setting, temperature losses around 120°C would be expected, resulting in a maximum inlet temperature of around 530°C and flow speeds around 0.77 m/s. This is important to know when choosing TCMs with high charge temperatures for future experiments.

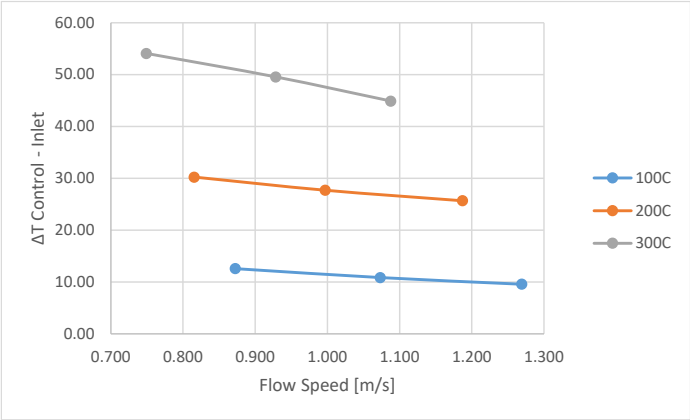

Fig. 7: Temperature lost between the Hotwind and the reactor (ΔT) at varying temperatures and flow rates.

The outlet TC is the second indicator of charge completion that results in a value of resident time (τ_{rT}) used for total charge energy. From Figure 5 it can be seen that the outlet TC values are the last to increase to values close to inlet temperature before equilibrating. However, unlike the mass data, the outlet temperature data has many points where the temperature has plateaued (ambient temperature, wet bulb temperature & final temperature). To work around this the 'end point' criteria is set to the last time gradient plateaus.

4.4. Energy Calculation.

Data collected from the CATS can now allow a calculation of charge energy for a material under the given drying conditions. Equation 2 highlights this:

$$Charge\ Energy\ (kJ) = \mu_{av} \times Cp \times \Delta T \times \tau_r \qquad \text{(eq. 2)}$$

- μ_{av} – Average Air Mass Flow [*kg/s*]
- Cp – Heat Capacity of Air [*kJ/KgK*]
- ΔT – Temperature Difference between Inlet and RT (25°C) [*K*]
- τ_r – Resident Time (Either based on Mass or Outlet Temperature) [*s*]

5. Results and Discussion

To assess the charge performance of silica gel, 1400g of discharged material was subject to three different temperatures (100°C, 200°C and 300°C) and various flow rates. The data received from Figure 7 was used to predict the temperature set at the Hotwind control TC to gain the desired inlet temperatures. For each temperature, 3 flow rates were chosen according to flow setting (Flow 4, Flow 7, and Flow 10) and 3 flow rates were chosen matching air mass flow values (20kg/hr, 25kg/hr, and 30kg/hr). This resulted in a total of 18 experiments shown in Figure 8.

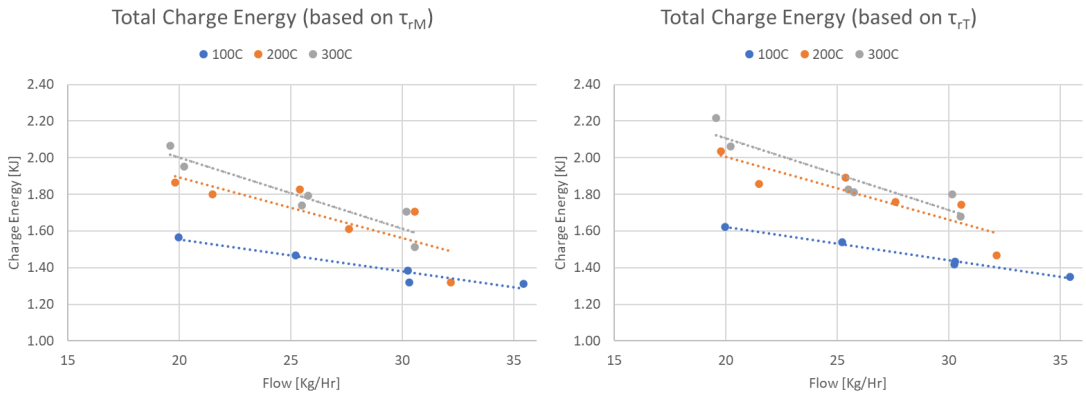

Fig. 8: Total energy to charge 1400g of fully discharged silica gel. Total charge energy based of τ_{rM} (Left). Total charge energy based of τ_{rT} (Right).

As mentioned above, there are two indicators of residence time (τ_r) which are mass and outlet temperature. The charge energy has therefore been calculated according to both values and presented on separate plots (Figure 8). Both sets of data show the same trends however the mass data generally gives slightly less energy values. This slight difference in τ_r values is due to fact that the mass data plateaus just before the outlet. Whereas the outlet temperature is a good indication of a complete reaction time, the mass data seems to slightly underestimate this. The rate of mass change towards the ends slows down before plateauing and exact final values is harder to identify. For this reason, outlet temperature can be considered a better indicator. Results show that an increase in flow rate and decrease in temperature leads to a reduced total charge energy and therefore a more efficient charge. The higher flow rates will allow easier removal of water vapor and the lower temperatures could suggest less heat energy is lost to the surroundings. If the reactor was better insulated this might improve the charge efficiency at elevated temperatures. This work suggests that if we have a waste heat source whereby we will capture that energy with silica gel, increasing the flow rate of that waste heat stream is more beneficial than maintaining higher temperatures. Additional fans or air supply could be considered for this.

The effect of material quantity on charge energy was assessed. Based on the previous study, the temperature was set at 100°C and three flow rates were selected (20kg/hr, 25kg/hr, and 30kg/hr). For each condition 6 mass values were chosen totaling 18 experiments shown in Figure 9.

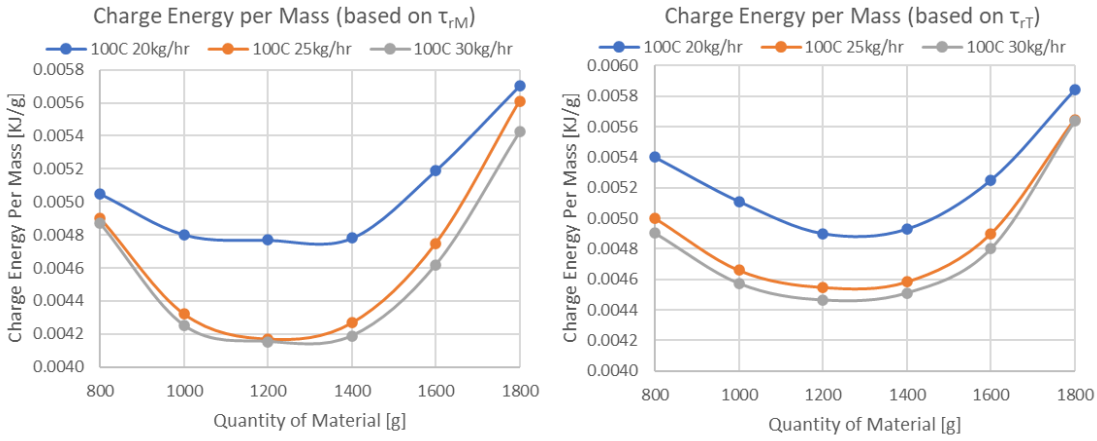

Fig. 9: Charge energy per mass for fully discharged silica gel. Charge energy based of τ_{rM} (Left). Charge energy based of τ_{rT} (Right).

Following the previous experiments, results are again presented on sperate plots whereby the charge energy per mass (kJ/g) was calculated based on τ_{rM} and τ_{rT}. As previously seen, the results based on mass data show slightly lower energy values. Whereas the trends observed are similar, the mass data is less consistent. The

data for outlet temperature is consistent between experiments (RT → Inlet Temp), whereas the mass change data varies due to there being varying mass changes. The mass gradient changes are less significant for the lower material quantities which might suggest the inaccuracy of this indicator at lower levels. However, the results show in both cases that there is an optimum material quantity around 1200g. Reduced efficiency before this value will be due to the energy lost in heating the reactor outweighing the energy used to charge to material. Reduced efficiency beyond this value would be due to reduced kinetics further up the reactor as more energy is being lost to the environment prior to the point. Figure 3 explains this by showing the reduced bulk 2 temperatures in comparison to bulk 1 (after a section is considered charged) that is further along the reactor. Again, better insulation could alleviate this problem allowing for better efficiency for higher material quantities. For a real-case heat capture solution, reactor material should be kept to a minimum and should be insulated as much as possible. To predict the best material quantity for any real-case, computational modelling should be done alongside this work where up-scaling can be easily considered.

6. Conclusion

The CATS has been developed and successfully demonstrated using silica gel as the commissioning material. It is predicted that maximum inlet temperatures of 530°C can be achieved using the Hotwind air flow system. Two indicators of residence time (mass and outlet temperature) have been used to calculate the total charge energy. Of the two, the outlet temperature data shows more consistent values and results that are a more accurate representation of a fully charged state. Total charge energy of silica gel has shown to decrease with higher flow rates and lower temperatures. In this case, 100°C was the lowest temperature applied. However, if silica gel is to be considered as a TCM, more work should be carried out at temperatures <100°C. The effect of material quantity on charge energy shows that there is an optimum quantity for silica gel in the reactor. The decrease in efficiency above 1200g is down to radiative heat loss increasing further up the reactor. Improvements in insulation properties should be considered to maintain efficiency at higher quantities. To predict the optimum quantity in real-case scenarios, future work on computational modelling will assist the transition from lab-scale to a full-scale demonstration. The CATS can now screen materials for their charge performance and make decisions on what material is best for real-case scenarios.

A synthesis protocol has also been developed for the consistent hydration of silica gel to hydration levels in the range of 33%, equivalent of a fully hydrated state. With use of the climate control oven, other materials that are capable of discharge within humid conditions (e.g. salt hydrates) could be successfully synthesized and analyzed for their charge performance in the CATS. Estimations of maximum inlet temperature indicate the possibility to study materials of higher charge temperature such magnesium hydroxide and calcium hydroxide.

7. References

BCS INC, 2008. Waste Heat Recovery: Technology & Opportunities in U.S. Industry. U.S. Department of Energy, Industrial Technologies.

Brueckner, S., Miró, L., Cabeza, L,F,. Pehnt, M., Laevemann, E., 2014. Methods to estimate the industrial waste heat potential of regions - A categorization and literature review. Renewable and Sustainable Energy Reviews. Elsevier. 38, 164–171. https://doi.org/10.1016/j.rser.2014.04.078.

Funayama, S., Takasu, H., Zamengo, M., Kariya, J., Kim, S., Kato, Y., 2019. Performance of thermochemical energy storage of a packed bed of calcium hydroxide pellet
s. Energy Storage. 1, e40. https://doi.org/10.1002/est2.40.

Fumey, B., Weber, R., and Baldini, L., 2019. Sorption based long-term thermal energy storage – Process classification and analysis of performance limitations: A review. Renewable and Sustainable Energy Reviews. Elsevier Ltd. 111, 57–74. https://doi.org/10.1016/j.rser.2019.05.006.

Krönauer, A., Lävemann, E., Brückner, S., Hauer, A., 2015. Mobile Sorption Heat Storage in Industrial Waste Heat Recovery. Energy Procedia. 73, 272-280. https://doi.org/10.1016/j.egypro.2015.07.688.

Lin, J., Zhao, Q., Huang, H., Mao, H., Liu, Y., Xiao, Y., 2021. Applications of low-temperature thermochemical energy storage systems for salt hydrates based on material classification: A review. Solar Energy. Elsevier Ltd. 214, 149–178. https://doi.org/10.1016/j.solener.2020.11.055.

Miró, L., Gasia, J., Cabeza, L.F., 2016). Thermal energy storage (TES) for industrial waste heat (IWH) recovery: A review. Applied Energy. 179, 284–301. https://doi.org/10.1016/j.apenergy.2016.06.147.

Papapetrou, M., Kosmadakis, G., Cipollina, A., La Commare, U., Micale, G, 2018. Industrial waste heat: Estimation of the technically available resource in the EU per industrial sector, temperature level and country. Appl. Therm. Eng. 138, 207-216. https://doi.org/10.1016/j.applthermaleng.2018.04.043.

Salviati, S., Carosio, F., Saracco, G., 2019. Hydrated salt/graphite/polyelectrolyte organic-inorganic hybrids for efficient thermochemical storage. Nanomaterials. 9, 420. https://doi.org/10.3390/nano9030420.

Sunku Prasad, J., Muthukumar, P., Densai, F., Basu, D,N., Rahman, M.M., 2019. A critical review of high-temperature reversible thermochemical energy storage systems. Applied Energy. Elsevier. 254, 113733. https://doi.org/10.1016/j.apenergy.2019.113733.

Sutton, R., Jewell, E., Elvins, J., Searle, J., Jones, P., 2018. Characterising the discharge cycle of CaCl2 and LiNO3 hydrated salts within a vermiculite composite scaffold for thermochemical storage. Energy Build. 162, 109-120. https://doi.org/10.1016/j.enbuild.2017.11.068.

TSI Airflow, 2014. Traversing a Duct to Determine Average Air Velocity or Volume. https://tsi.com/getmedia/1a11d344-0a58-4ca6-94fe-65721825686b/AF-106%20Traversing%20a%20Duct?ext=.pdf. Accessed July 2022.

Zamengo, M., Ryu, J., Kato, Y., 2015. Thermochemical performance of magnesium hydroxidee expanded graphite pellets for chemical heat pump. Energy Procedia. 71, 293-305. https://doi.org/10.1016/j.applthermaleng.2013.12.036.

Wu, H., Salles, F., and Zajac, J., (2019). A critical review of solid materials for low-temperature thermochemical storage of solar energy based on solid-vapour adsorption in view of space heating uses. Molecules. 24, 5. https://doi.org/10.3390/molecules24050945.

A Novel Alginate and Expanded Graphite Based Composite for use in Solar and Waste Heat Storage

Jack Reynolds[1], Rhodri Williams[1], Jonathon Elvins[1] Eifion Jewell[1], Justin Searle[1] and Xinyuan Ke[2]

1 Swansea University, Swansea (United Kingdom)

2 University of Bath, Bath (United Kingdom)

Abstract

Thermochemical heat storage composites based on hydrated salts enclosed within an expanded graphite/alginate polymer matrix are presented. The simple synthesis method offers flexibility in the size and shape of the composite material to best suit the application, with the option of easily being scaled up. The incorporated calcium chloride can release and store heat through the reversible hydration and dehydration reaction. The Dehydration of the reacting salt is appropriate for sources of heat ranging from transpired conventional solar collectors (<70°C) up to low grade waste heat sources (<150°). Salt loading values up to 84% have been achieved while maintaining visible porosity. The charge reaction is studied via static heat, while the discharge reaction is studied by passing a flow of humid air through the materials. Both reactions are compared to previously studied Vermiculite/$CaCl_2$. Further to this bulk density, surface area, and water vapor sorption are considered.

Keywords: Thermochemical Heat Storage, Expanded Graphite, Alginate, Calcium Chloride

1. Introduction

With the exhaustion of our world's main fossil-based energy resources and the continued worsening of our environmental conditions in the past decades, it is vital we look to change the way we generate, use, and store our energy. In 2017, almost half the energy consumed (760 TWh) in the UK was required for heating purposes, of which 57% was needed for domestic space heating (Ofgem, 2016). For the heating of the UK's 29 million homes and non-residential buildings, only 4.5% of the energy was from a low carbon source, which needs to increase drastically if the UK is to meet its 2050 net carbon zero target (Ofgem, 2020; Climate Change Act 2008). Two low carbon sources associated with an abundance of heat energy are solar heat and industrial waste heat (IWH), however both come with inherent problems. Solar heat has a timing mismatch between when heat is abundant and when heat is required (diurnally and seasonally), whereas IWH heat can be discontinuous and has a distance mismatch between the source and the necessity. The solution to both these problems is effective heat storage.

Thermochemical heat storage (THS) provides a convenient way to overcome these mismatch issues by storing heat energy in a reversible endothermic reaction. The benefits of THS over sensible heat storage (SHS) and latent heat storage (LHS) is its superior theoretical energy density and its ability to store heat energy indefinitely, which the two latter options cannot (Jarimi et al, 2019). Sorption heat storage has been utilized for both mobile THS, transporting IWH to an off-site heat demand, and for inter-seasonal heat storage at the demand location (Krönauer et al, 2015; Krese et al, 2018). The most popular sorption TCS materials in literature are 'Salt in Matrix' or SIM (Casey et al, 2015; Mohapatra and Nandanavanam, 2022; Brancato et al, 2021). Here, the enthalpy of the reversible hydration reaction of the salt is used to store energy within a physical scaffolding. The matrix provides a large surface (to aid the sorption kinetics) and high porosity while also acting as a protective structure to mitigate the problems of deliquescence and salt leakage (Sutton et al, 2018). Examples of typical materials used for this are vermiculite (Brancato et al, 2021), silica gel (Courbon et al, 2017), activated alumina (Zhang et al, 2018), activated carbon (Casey et al, 2015) and expanded graphite (Salviati et al, 2019). The latter is used for its low price and density, high surface area and associated higher thermal conductivity compared to other options. While the results are promising, expectations for the resulting composites in terms of energy density and cycle stability are rarely met due to lower bulk densities, agglomeration, and salt leakage (Clark et al, 2020). Recently, hybrid salt/expanded graphite have been prepared in a pellet form with additions of an organic polyelectrolyte (Salviati et al, 2019) and ethyl cellulose (Gaeini

© 2022. The Authors. Published by International Solar Energy Society
Selection and/or peer review under responsibility of Scientific Committee
doi:10.18086/eurosun.2022.13.19 Available at http://proceedings.ises.org

et al, 2018) to mitigate some of these problems. Both studies showed improvements in cycle stability in the presence of these additives due to the reduced leakage of salt and even a positive contribution to reaction kinetics. However, utilizing expanded graphite in pellet form would decrease its internal porosity thus preventing sufficient passage of air through the composite like vermiculite. A freeze-drying technique has been employed to create a porous structure to contain the salt hydrate, strontium bromide, using expanded graphite and nanocellulose (Salviati et al, 2020). Hydration kinetics were shown to improve by 54% compared to the stand-alone salt hydrate which was accredited to its highly porous structure. More recently there has been some work involving the use of sodium alginic acid as a host matrix due to its excellent features of microscopic shaping (Kallenberger and Fröba, 2018; Kallenberger et al, 2018). In the presence of a divalent cation such as Ca^{2+} or Sr^{2+}, two Na^{+} cations already present are displaced and crosslinking in the polymer occurs (gelation). The divalent cations coordinate to oxygen atoms from different polymer chains resulting in the formation of a stable hydrogel. With this process it is possible to make controllable shapes such as spherical beads. High loading of thermochemically active salts within the matrix has been achieved with storage densities upwards of 417 kWh/m^3 (Kallenberger et al, 2018). This alginate derived matrix is a passive host and does not comprise of any micro or mesoporosity unlike more the commonly utilized matrices.

Here, we present a novel approach to combine expanded graphite, for its high surface area and thermal conductivity, with alginate-based polymers for their ease of microscopic shaping, to achieve a highly porous and stable network to hold thermochemically active salts. To best of our knowledge this is the first time that these two materials have been successfully combined and used as a matrix for thermochemical heat storage applications. $CaCl_2$ has been chosen as the incorporated salt due to its ability to act as both the 'gelation salt' and the thermally active material, while also showing superior storage capabilities compared to other salt options. It also benefits from being low cost, appropriate for low and higher temperature charging, and readily reacts with moisture to release energy (Gaeini et al, 2018; Walsh et al, 2020).

2. Materials and Methods

2.1. Materials

Calcium chloride was purchased from Sigma-Aldrich® in its dehydrated form and the saturated solution was made at room temperature. Sodium alginate in powder form was purchased from Sigma-Aldrich®. Expandable graphite grade BLG300L-LT, with an expansion start temperature of 140-160°C was purchased from RMC Reason GmbH (Bad Säckingen, Germany). To obtain expanded graphite (EG), flake samples were heated at >200°C for 1h. Expanded natural graphite (mEG) in milled form, with 25m^2/g surface area (as reported in the material data sheet) was purchased from Imerys Graphite & Carbon (Bironico, Switzerland), commercial grade TIMREX® C-THERM012.

2.2. Composite Synthesis

Two different synthesis routes are depicted in Fig. 1. Alginate solution is formed using a ratio of 1g of alginate to 50ml of water. This is stirred at 80°C until fully dissolved. The graphite is then added to solution at varied ratios. Method 1 requires dropwise addition of the Alginate/EG solution into a saturated calcium chloride solution to allow cross-linkage between Ca^{2+} ions and the alginate polymer. This mixture is stirred until all solution is transferred. Once complete the formed beads are left in solution for >24h before being filtered and dried at 120°C for a further 24h. Method 2 allows more control over the size of the beads by transferring Alginate/EG solution to a mould of a specific size. This is the kept at -20°C for >2h to allow adequate solidification of the beads. These are then transferred to the saturated calcium chloride solution for cross-linking and impregnation over a 24h period. Once complete these are filtered and dried at 120°C. The 3-4mm and 6mm diameter beads produced via method 1 and method 2 respectively are shown in Fig. 2.

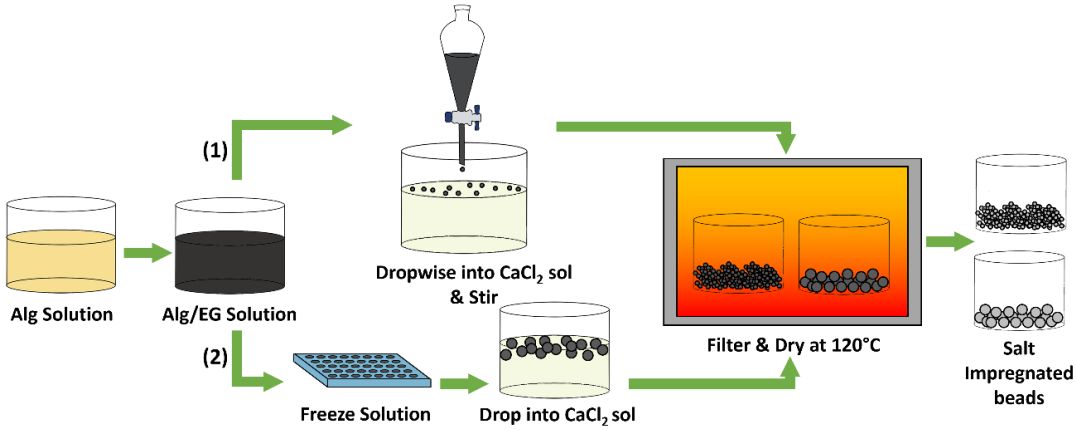

Fig. 1: Schematic illustration of fabrication of $CaCl_2$ impregnated Alg/EG beads 1) Dropwise method. 2) Freeze method

The choice of expanded graphite (mEG or EG) used in SIM synthesis results in completely different bead structure. This is highlighted in the SEM images shown in Fig. 3. The mEG beads show a large quantity of small pores on the surface, whereas the EG beads show much larger features. These consist of a few large surface pores, mostly filled with the impregnated salt. Surface porosity can have a large effect on reaction kinetics and cyclic stability. This is based on the ease of the reacting air reaching the salt and the ability of the salt to leak from the matrix. The size of the bead is dictated by the method of synthesis. Method 1 form beads in the range of -4mm, whereas for Method 2 the synthesized beads are greater than 6mm. The size of the formed beads effects the packing density, bulk density, and flow of reacting air. Smaller beads will increase the bulk density in a packed bead however will restrict the flow of air through the material. Salt loading can be controlled by the concentration of $CaCl_2$ in the gelation bath. All these parameters ultimately control the performance of the SIM during the charge and discharge cycles and the optimum synthesis parameters are to be found.

Tab. 1: Summary of Synthesized Composites

Sample	Method	Size	Expanded Graphite	EG:Alg
mEG-D	Drop Cast	3-4mm	C-Therm012	3:1
mEG-M	Mould	6mm	C-Therm012	6:1
EG-M	Mould	6mm	BLG300-LT	6:1
V-$CaCl_2$	Incipient Wetness	2-7mm	-	-



Fig. 2: Optical Images of synthesized beads. A) mEG-M. B) EG-M. C) mEG-D.

3. Characterization

The composite beads internal morphology was examined with a Zeiss Evo LS25 scanning electron microscope (SEM) with a 15kV accelerating voltage. The salt loading of the composites was determined from the analysis of chloride ion concentration by titration (Mohr's Method). The composite is washed in DI water for >1hour dissolving all the $CaCl_2$ that is present. This solution is then titrated against silver nitrate solution in the presence of a potassium chromate indicator. The bulk density of the sample was calculated from their mass reading (measured on a Ohaus Scout STX223 with a readability of 0.001g) in a known volume of a cylindrical container. The volume of the container is calculated from the filled mass of water ($1g=1cm^3$). The Micrometrics Tristar II 3020 is used to calculate the surface area of the of the porous structures by combining N_2 physisorption and BET analysis. Samples were dried prior to analysis using a micrometric VapPrep 061, which allowed samples to be degassed with nitrogen at 120°C for >12h. The charge performance was investigated using a Ohaus MB120 moisture analyser using a static drying profile. Prior to experiments, samples were subject to 30°C and 20%RH for >168h to achieve a uniform hexahydrate state. 5g of each sample were then subject to three different drying temperatures (120°C, 150°C & 200°C). To measure the discharge performance of the composites, a custom-built assembly is used (Fig.3). Prior to testing, materials are dried at 120°C for >24h to ensure the anhydrous state is achieved. Moist air is produced via a Cellkraft P-50 relative humidity generator. The flow of air is then fed into a reactor with a fixed volume of material. Temperature uplift and bulk temperature is calculated through a series of three thermocouples. Mass recordings are taken using three load cells situated at the base of the reactor. The water sorption kinetics of the composite beads were assessed via dynamic (water) vapor sorption (DVS) within the relative humidity range of 0 %–95 % at 25 °C, using the DVS Advantage instrument (Surface Measurement Systems). One bead was used for each test and the sample was stabilized at 0% RH before starting the water adsorption isotherm. For Static Vapor Sorption (SVS) tests, materials are dried at 120°C for >24h to ensure the anhydrous state is achieved. To add moisture evenly to the materails, a Memmert constant climate chamber HPP110eco is used. 3 petri dishes, each containing 10g of material, were subject to the three choosen relative humidity conditions (25%, 50% and 75% RH at 25°C) and left for 168 hours to assess the maximum water uptake. Mass recordings were taken every 24 hours.

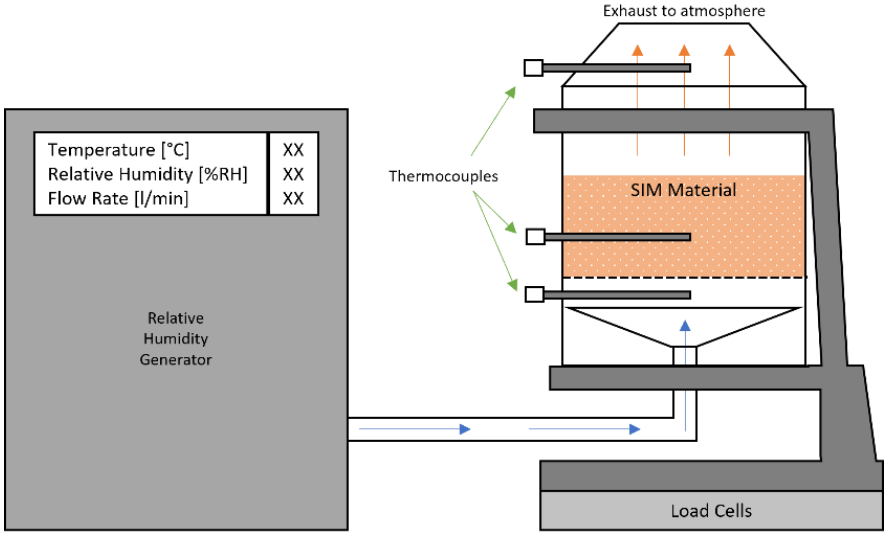

Fig. 3: Schematic of the experimental apparatus developed to investigate the discharge performance of typical thermochemical materials.

4. Results & Discussion

4.1. Morphological Analysis

The morphology of the bead composites was investigated by means of SEM. Fig. 4 reports the representative micrographs highlighting the surface and internal structures. The samples prepared with mEG clearly show the formation of beads with smaller pores and a large network of graphite scaffolding. Fig. 4d-f highlights a clear difference in the structure of $CaCl_2$ crystals inside the beads. The mEG samples form very small $CaCl_2$ crystals,

whereas the much larger structures present in EG seem to be completely covered in uniform layers. The presence of smaller crystals structures is advantageous as it enhances the contact area between a carrier gas and the salt. On the contrary, the smaller network of pores could cause restrictions from removing/adding moisture in the beads, leading to lower reaction kinetics.

As stated in previous work done by Sutton, N_2 physisorption can be considered in-accurate for the analysis of macro-porous material, however it is still suitable for the comparison between microporous materials. The surface area results are shown in Table 2. All graphite/alginate-based composites show a larger surface area than the previously studied V-$CaCl_2$. This indicates that these types of materials all form smaller crystal structures in their highly porous scaffolding, The two mEG samples have greatest surface area, which would be attributed to high surface area of the mEG giving a larger space for the salt to crystalize. Of these two samples the moulded beads show a higher surface area. This could be because of the larger mEG:Alginate ratio allowing more space for the salt to crystalise on the graphite surface. Alternatively, this could also be attributed to the freezing nature incorporated into the mould method. The freezing of solution may allow more time for the scaffolding to solidify before the melting, maintaining a larger network of pores.

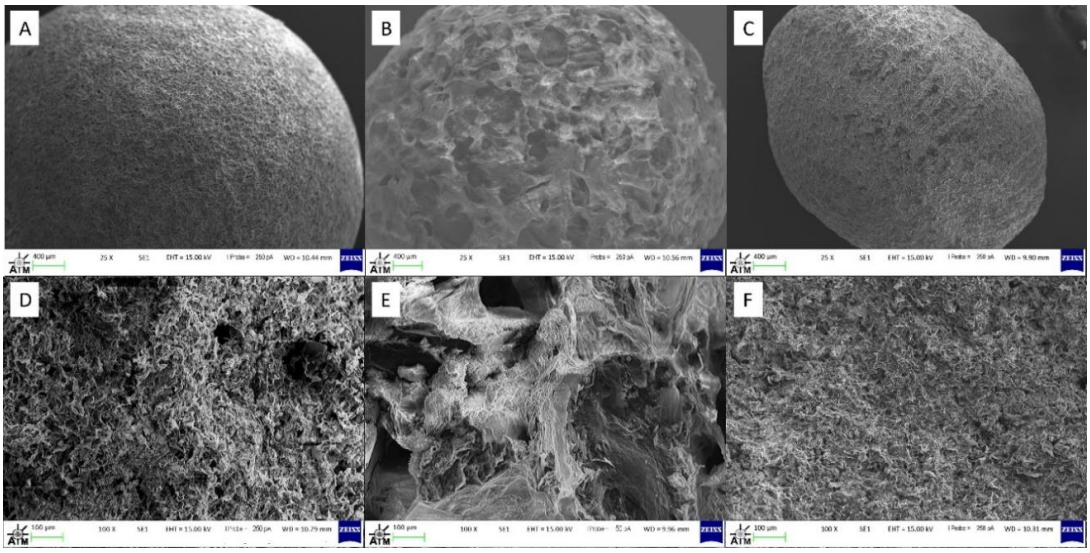

Fig. 4: SEM images showing the surface and internal structures of mEG-M (A,D), EG-M (B,E) and mEG-D (C,F) beads. A-C show surface structure. D-F show the bead cross-section.

Results from the Bulk density tests are shown in Table 2. Here we can see that the graphite alginate beads have a higher bulk density that previously studied V-$CaCl_2$. The highest of the three samples is the mEG-D beads which is expected due to the reduced diameter of the beads allowing the beads to fill more of the void fraction available in a given space. This could be beneficial to obtain more salt per unit of volume, however the resulting restriction of the carrier gas may have a negative impact on material performance. Of the two the mould samples, the mEG samples have a larger bulk density probably due to the higher surface area allowing more salt to be incorporated. This indicates a larger of amount of 'Matrix' material present per unit of volume.

4.2. Salt Characterization

Results from the Mohr's titration (Table 2) indicate the salt loading values for the expanded graphite materials are all higher than the V-$CaCl_2$ samples when salt content is based on the anhydrous state. Even with the addition of graphite, the composites can still achieve the high levels of salt loading which were observed with a pure alginate matrix (Kallenberger et al, 2018). Combining the Salt wt% and the bulk density values, we can estimate the salt volumetric density. From previous work on $CaCl_2$, we know the value of density (1830kg/m^3) and theoretical storage density (1.47 GJ/m^3) for the anhydrous state (Barreneche et al, 2015). Combining these values with the salt volumetric density value of our materials we can estimate the maximum theoretical storage density. The results show that mEG-D and mEG-M have around 3.5 and 2.5 more energy storage capabilities than V-$CaCl_2$.

Tab. 2: Physical characteristics of the Synthesized Materials.

Sample	Salt Loading [%]	Bulk Density [g/cm^3]	Salt Volumetric Density [g/cm^3]	Theoretical Storage Density [MJ/m^3]	Surface Area [m^2/g]
mEG-D	78	0.777	0.606	486.8	4.02
mEG-M	84	0.547	0.459	368.7	4.49
EG-M	72	0.365	0.263	211.3	2.80
V-$CaCl_2$	66	0.263	0.174	139.7	1.59

4.3. Water Sorption

A DVS isotherm conducted on the mEG-M and EG-M samples is shown in Fig. 5. Both samples start to take up water from around 30-35%RH then following a similar trend up to the same mass gain of 120wt% at 90%RH. This is characteristic of CaCl2 reaching its maximum hydrated state and slightly beyond. As the RH approaches 95% the materials begin to act differently. The EG-M sample rapidly increases to a 160wt% gain, whereas mEG-M sample flattens off. This suggests that the larger pores in the EG sample allow deliquescence to take place throughout the samples, whereas deliquescence occurring in the smaller pores at the surface of mEG may restrict this phenomenon throughout. As for the desorption cycle, the EG sample begins to lose water at 60% RH whereas the mEG sample doesn't begin to lose water until below 15% RH. The significant desorption hysteresis observed from both samples suggest the presence of ink-bottle type pore structure (Morishige and Tateishi, 2003) in consistent with the results shown in the SEM images and surface topography images. This also suggests that the water is easier desorbed from the material with the largest pores. In the mEG sample, the small pores may become blocked from salt block-ages close to the edge of the beads.

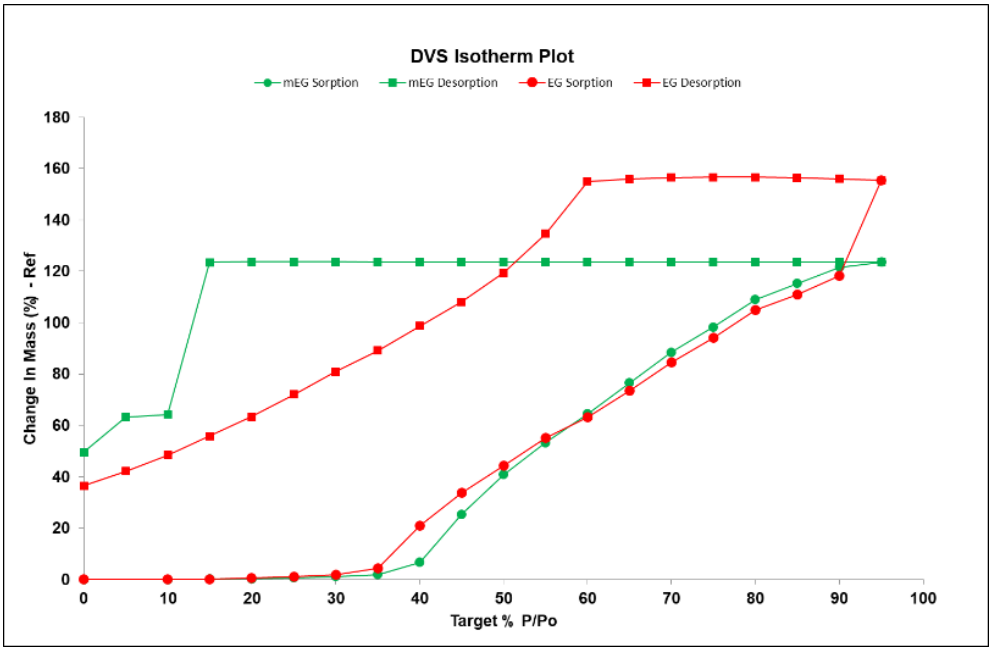

Fig. 5: DVS Isotherm of samples mEG-M and EG-M.

The raw SVS results and water uptake per unit volume data is shown in Fig. 6. The relative humidity values chosen were 25%, 50% and 75%. All conditions were conducted at 25°C. Interrogating the raw data, all four

materials take up moisture at a very similar rate over 24hrs. This is because unreacted salt is more easily accessible during this time frame, being close or directly on the surface of the aggregates. Beyond 24hrs, either the quantity of salt available or the kinetics of moisture transfer through the aggregates differentiates their uptake. For the lower RH%, the vermiculite and mEG-D samples show superior water uptake. This is because more of the salt is considered surface salt in vermiculite and the bead diameter is much smaller for mEG-D, reducing the distance for moisture transport. The shape of mEG-M and EG-M curves at this RH and the known salt wt% values suggest water uptake is not complete after 7 days for these samples. For the 50% and 75% conditions, the quantity of salt dominates the performance of the materials after 24 hrs. This is because the kinetics of moisture transport are much higher under these conditions. In both cases the quantity of moisture uptake aligns with the salt wt% of the materials. When looking at moisture uptake per unit volume, by considering the bulk density, we can see that all EG/Alg materials take up more water than V-CaCl2 on both the 24hr and 7-day period (Fig. 7). Interestingly, the mEG-M performs better than the mEG-D even though the latter has a higher salt volumetric density. This suggests that more salt is accessible in the moulded sample due to a higher surface area or larger network of internal pores.

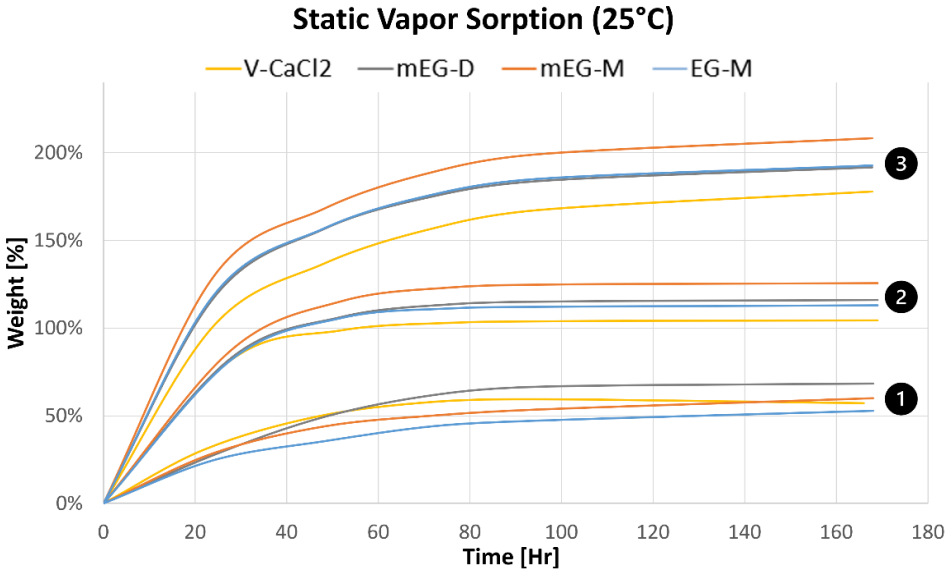

Fig. 6: SVS Analysis of all four samples at 25% (1), 50% (2) & 75% (3) RH.

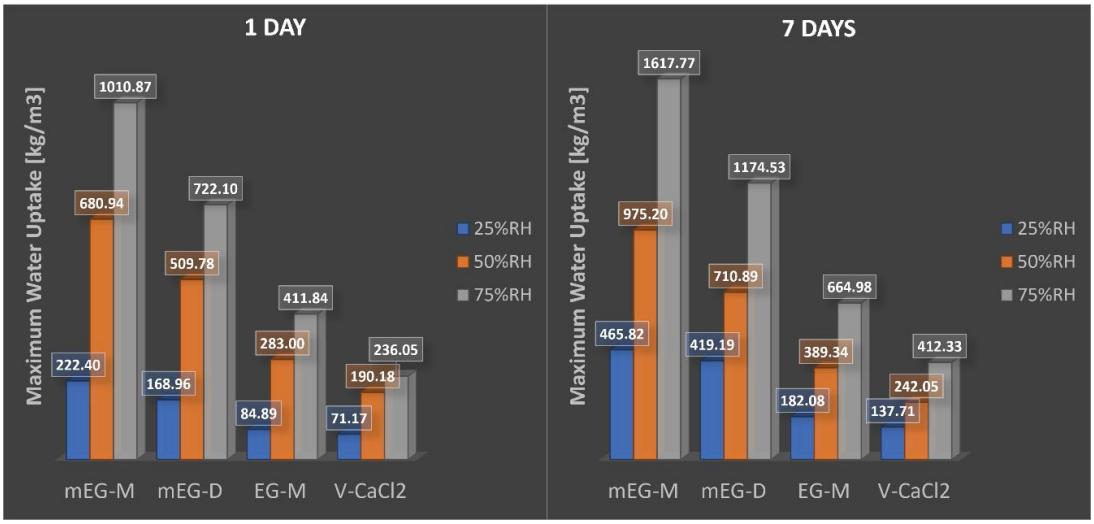

Fig. 7: Water uptake per volume of material over 1 day and 7 days.

4.4. Thermal Properties

To evaluate the thermal response of all the materials, each was placed inside the vertical cylindrical reactor with the air entering at the base (Fig.3). For each experiment, the reactor was loaded with 200cm^3 of material. To create a flow of air with consistent and controllable parameters, a Cellkraft P-50 relative humidity generator is used. The chosen conditions for the experiments were 60%RH, 20 l/min, 25°C for a duration of 3 hours. Fig. 8 shows the response of the materials to the given conditions. All four materials successfully release the chemically stored heat energy when subjected to moisture in the air flow.

Although the initial temperature spike varies slightly between samples, all the material act very similar. This is because there is only a certain amount of moisture being delivered in the flow of air. The mass data shows that all four materials take up moisture at the same rate owing to the equivalent amount of $CaCl_2$ being accessible for absorption over the 3-hour cycle. Knowing that, the energy output is expected to be similar. The initial spike in temperature for V-$CaCl_2$ would be characteristic of more salt available on the surface of material. As for the mEG-M sample, it is believed that there is good air flow through the packed bed because of the uniform spherical shape. This postulated the lower peak in mEG-D, as the smaller beads lead to tighter packing restricting air flow.

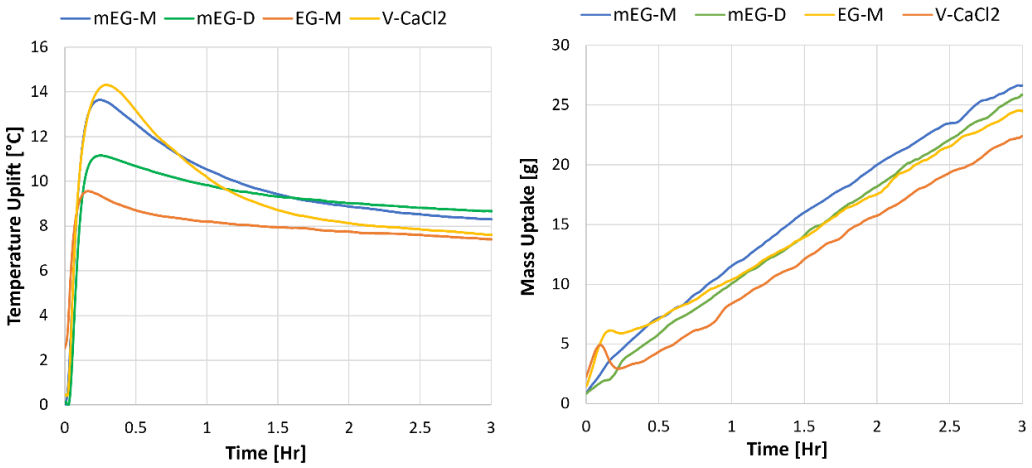

Fig. 8: Discharge results for each material. Temperature uplift from inlet to outlet (Left). Moisture uptake (Right).

Tab. 3: Estimation of reaction progression of each material based on the mass of CaCl2 and water uptake.

Sample	Volume of Material [cm^3]	Mass of $CaCl_2$ [g]	Hexahydrate Mass Uptake [g]	Reaction %
mEG-D	200	121.2	118.0	21
mEG-M	200	91.8	89.4	28
EG-M	200	52.6	51.2	49
V-$CaCl_2$	200	34.8	33.9	74

Thermal transfer will preferentially heat the localized walls of the reactor as opposed to quick initial heat release. The EG-M sample having the lowest peak maximum temperature is a consequence of lower salt, lower surface area, and harder to reach internal salt. All four materials gradually begin to reduce to a lower/ plateaued temperature uplift over time. This is expected because the energy associated with transitions from anhydrous to the dihydrate state is higher than the dihydrate/tetrahydrate to hexahydrate state. Over time, less anhydrous $CaCl_2$ is available and so less heat will be evolved. On top of this the kinetics of moisture uptake will reduce as the moisture will now have to travel to harder to reach places in the aggregates. Lowering the kinetics will directly affect the temperature uplift. Even considering this the EG/Alg materials still maintain

a good uplift after three hours with no direct sign of decreasing. To understand the reaction progression, we can take the moisture uptake value and compare this to the theoretical mass uptake to achieve a uniform hexahydrate state. Table 3 highlights the amount of $CaCl_2$ available for each experiment and the amount of water needed to reach the maximum hydrated state. To calculate to reaction %, a presumption that all materials have absorbed 25g of water is used. The results show that all EG/Alg materials have far more energy to release than V-$CaCl_2$. On this calculation it can be estimated that $CaCl_2$ has around 1hour left before reaction completion is achieved. As for mEG-D, mEG-M and EG-M, we can estimate they have around 12hrs, 9hrs and 3hrs left respectively.

Dehydration studies under static temperature conditions at 120°C, 150°C and 200°C are shown in Fig. 9. Mass data is logged until a variation of less than +/- 1mg change is observed for 120 seconds. In all three cases V-$CaCl_2$ has a higher rate of dehydration which is characteristic of the salt being spread over a much larger volume. Of the three expanded graphite materials, mEG-M shows the slowest rate. This is due to the larger spherical shape (larger distance for moisture transport) than mEG-D, and smaller structural porosity than EG-M. This agrees with the results shown from the desorption curves of the DVS analysis.

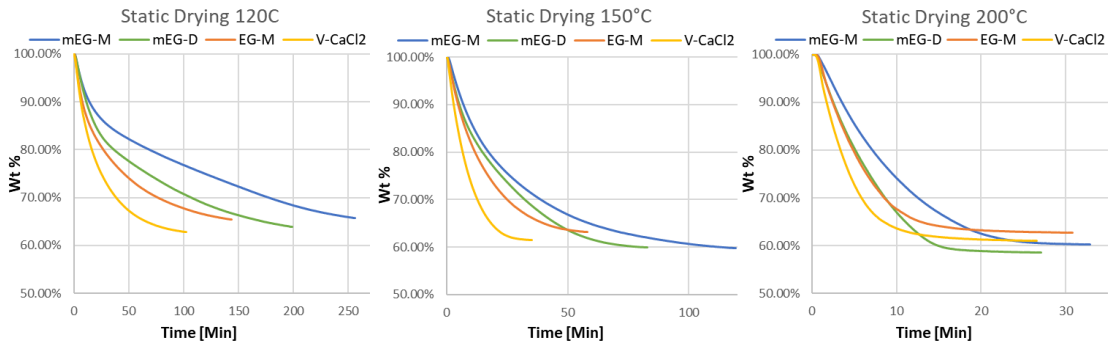

Fig. 9: Static Drying of 5g of material in the Ohaus MB120.

5. Conclusion

The successful synthesis of various EG/Alg based composites containing calcium chloride are presented. The synthesis method allows easy flexibility in size, shape, and material quantity to best suite the application at hand. Here we have used the Mould method to synthesis repeatable spherical beads of 6mm or the Drop-cast method to make beads between 3-4mm. Both methods offer a higher salt wt% than previously studied V-$CaCl_2$, achieving a maximum of 84% in the mEG-M sample. The spherical shape allows for good packing density achieving high salt volumetric densities. This is key when these materials are to be considered for transportation and storage at a domestic scale. The spherical nature also allows for good air flow through the packed bed during discharge reactions. Whereas V-$CaCl_2$ tends to create a very moist bottom layer in a packed bed, the larger beads (mEG-M and EG-M) create a more homogenous uptake of water. The output of heat energy is very promising achieving results like that of V-$CaCl_2$ while having a far superior amount of un-released energy at the point where V-$CaCl_2$ is considered exhausted. As for the dehydration process V-$CaCl_2$ performs better at small scale (5g) which is a comparison in terms of mass. To further assess the charge performance materials should be analyzed at a larger scale in volumetric terms. The superior air flow and salt volumetric densities should lead to better charge efficiency in the beads. At a larger scale, charge reactions might only be possible using a heat exchanger where heat transport will be key. For this, thermal conductivity studies should be conducted on materials. The benefit of using EG/Alg materials is that size and shape can be altered to improve these results.

Both synthesis methods can be easily upscaled to commercial use due to the simple and scalable synthesis routes. As well as this only cheap, abundant, and non-toxic materials are utilised. To further this work towards a point of real heat storage, larger scale tests should be conducted whereby sufficient cyclability should be significant goal. A common problem with salt hydrates is their ability to deliquesce. If this could be prevented or contained, material stability over time could be improved.

6. References

Barreneche, C., Fernández, A.I., Cabeza, L.F., Cuypers, R., 2015. Thermophysical characterization and thermal cycling stability of two TCM: CaCl2 and zeolite. Applied Energy. 137, 726–730. doi: 10.1016/j.apenergy.2014.09.025.

Brancato, V., Gordeeva, G,L., Capri, A., Grekova, A,D., Frazzica, A., 2021. Experimental comparison of innovative composite sorbents for space heating and domestic hot water storage. Crystals, 11, 5. doi: 10.3390/cryst11050476.

Casey, S. P., Aydin, D., Riffat, S., Elvins, J., 2015. Salt impregnated desiccant matrices for "open" thermochemical energy storage - Hygrothermal cyclic behaviour and energetic analysis by physical experimentation. Energy and Buildings. Elsevier B.V. 92, 128–139. doi: 10.1016/j.enbuild.2015.01.048.

Clark, R., Mehrabadi, A. and Farid, M. (2020). State of the art on salt hydrate thermochemical energy storage systems for use in building applications. Journal of Energy Storage. Elsevier. 27, 101145. doi: 10.1016/j.est.2019.101145.

Climate Change Act 2008 (no date) c. 27. Statute Law Database. https://www.legislation.gov.uk/ukpga/2008/27/section/1. Accessed July 2022.

Courbon, E., D'Ans, P., Permyakova, A., Skrylnyk, O., Steunou, N., Degrez, M., Frère, M., 2017. A new composite sorbent based on SrBr2 and silica gel for solar energy storage application with high energy storage density and stability. Appl. Energy. 190, 1184–1194. doi: 10.1016/j.apenergy.2017.01.041.

Gaeini, M., Rouws, A.l., Salari, J.W.O., Zondag, H.A., Rindt, C.C.M., 2018. Characterization of microencapsulated and impregnated porous host materials based on calcium chloride for thermochemical energy storage. Applied Energy. 212, 1165-1177. doi: 10.1016/j.apenergy.2017.12.131.

Jarimi, H., Aydin D., Yanan, Z., Ozankaya, G., Chen, X., Riffat, S., 2019. Review on the recent progress of thermochemical materials and processes for solar thermal energy storage and industrial waste heat recovery. International Journal of Low-Carbon Technologies. Oxford University Press. 44–69. doi: 10.1093/ijlct/cty052.

Kallenberger, P. A., Fröba, M., 2018. Water harvesting from air with a hygroscopic salt in a hydrogel–derived matrix. Communications Chemistry. Springer US. 1(1), 6–11. doi: 10.1038/s42004-018-0028-9.

Kallenberger, P.A., Posern, K., Linnow, K., Brieler, F.J., Steiger, M., Fröba, M., 2018. Alginate-Derived Salt/Polymer Composites for Thermochemical Heat Storage. Adv. Sustain. Syst. 2, 1700160. doi: 10.1002/adsu.201700160.

Krese, G., Koželj, R., Butala, V., Stritih, U., 2018. Thermochemical seasonal solar energy storage for heating and cooling of buildings. Energy and Buildings. 164, 239-253. doi: 10.1016/j.enbuild.2017.12.057.

Krönauer, A., Lävemann, E., Brückner, S., Hauer, A., 2015. Mobile sorption heat storage in industrial waste heat recovery. Energy Procedia, 2015. 73, 272-280. doi: 10.1016/j.egypro.2015.07.688.

Mohapatra, D., Nandanavanam, J., 2002. Salt in matrix for thermochemical energy storage - A review. Materials Today: Proceedings. Elsevier Ltd. doi: 10.1016/j.matpr.2022.05.453.

Morishige, K., Tateishi, N., 2003. Adsorption hysteresis in ink-bottle pore. The Journal of Chemical Physics. 119, 2301. doi: 10.1063/1.1585014.

Ofgem (2016). The Decarbonisation of Heat. Ofgem's Future Insights Series. https://www.ofgem.gov.uk/system/files/docs/2016/11/ofgem_future_insights_programme_-_the_decarbonisation_of_heat.pdf. Accessed July 2022.

Ofgem (2020). Ofgem Decarbonisation Action Plan. Ofgem. https://www.ofgem.gov.uk/system/files/docs/2020/02/ofg1190_decarbonisation_action_plan_revised.pdf. Accessed July 2022.

Salviati, S., Carosia, F., Saracco, G., Fina, A., 2019. Hydrated Salt/Graphite/Polyelectrolyte Organic-Inorganic Hybrids for Efficient Thermochemical Storage. Nanomaterials. 9(3), 420. doi: 10.3390/nano9030420.

Salviati, S., Carosia, F., Cantamessa, F., Medina, L., Berglund, L.A., Saracco, G., Fina, A., 2020. Ice-templated nanocellulose porous structure enhances thermochemical storage kinetics in hydrated salt/graphite composites. Renewable Energy. Elsevier Ltd. 160, 698–706. doi: 10.1016/j.renene.2020.07.036.

Sutton, R., Jewell, J., Searle, J., Elvins, J., 2018. Discharge performance of blended salt in matrix materials for low enthalpy thermochemical storage. Applied Thermal Engineering. Elsevier. 145, 483–493. doi: 10.1016/j.applthermaleng.2018.09.052.

Walsh, S., Reynolds, J., Abbas, B., Woods, R., Searle, J., Jewell, E., Elvins, J., 2020. Assessing the dynamic performance of thermochemical storage materials. Energies. 13(9). doi: 10.3390/en13092202.

Zhang, Y.N., Wang, R.Z., Li, T.X., 2018. Thermochemical characterizations of high-stable activated alumina/LiCl composites with multistage sorption process for thermal storage. Energy. 156, 240-249. doi: 10.1016/j.energy.2018.05.047.

Thermal energy storage capacity on mineral Zeolite

Oscar Seco Calvo[1], Helena López Moreno[1], Maria Nuria Sánchez Egido, Silvia Soutullo Castro[1], Rafael Olmedo[1] and José Antonio Ferrer Tevar[1]

[1] Energy Department, Energy Efficiency in Buildings Unit, CIEMAT, Madrid (Spain)

Abstract

This study analyses zeolite adsorption- systems based on the recovery of the residual heat generated in different urban processes. The quality and thermal storage capacity of natural zeolites has been experimentally evaluated focusing on the discharge process. This material is characterized by high porosity and cation exchange capacity, selective absorption and reversible hydration. Numerical models of natural zeolites define the geometry, boundary conditions and inlet variables. A specific prototype of zeolite reactor has been designed based on these numerical results. Different lab- experiments have been carried out, to evaluate natural zeolites performance under different conditions of drying (muffle, stove and desiccator) and operation. The sample is encapsulated in a cell and located in the middle position of a tube of about two meters length and outside air is blown through it. The empirical results show that the use of natural zeolites up to 8 cm size provides an increase in the temperature of the reactor due to heat conduction.

Keywords: Heat transfer, Building envelope, Thermal comfort, buildings, gaseous emissions, Physical-chemical characterization, Thermal, CAM

1. Introduction

Climate change mitigation needs to consider the design of sustainable urban areas, reducing the pollutant emissions and increasing the quality of life and the well-being of citizens (IPCC, 2022). To achieve these goals integrative energy systems should be implemented (UNEP 2015), connecting energy-efficient and energy-flexible buildings with global energy infrastructures, high renewable generation, low carbon emission systems and flexible management of the district's energy flows. Thus, European strategies are focused on the development of Positive Energy Districts and Neighborhoods, which aim to optimize the energy consumption through the active management and balance of demands, shaving peaks or/and shifting loads in mixed-use buildings and fostering sustainable energy sources (SET-Plan Working Group, 2018). In this framework, the storage systems act as energy buffers between energy demand and supply side, providing flexibility to the global energy system and increasing the resilience to the effects of climate change.

Storage systems are capable of effectively regulating energy from different urban sources (renewable energy, electricity grid, residual flows), through the modulation of its intensity in temporal and spatial terms. These elements store electrical and thermal energy according to the characteristics of the generation and consumption profiles (Kousksou et al., 2014), providing flexibility that allows urban flows to operate robustly and effectively. These solutions are especially valuable for covering peak energy demands or outages, which are becoming more frequent because of the extreme weather and disaster events as well as the energy market instability and uncertainties (Huang et al., 2021; De et al., 2020).

Even it is shown that thermal energy store it is cheaper than electrical storage (Hennessy et al. 2019), these systems must be deeply analyzed optimizing their dimensions, materials and operation, and taking advantage of the energy market prices to reduce end users costs (Telaretti et al., 2016).

Thermal storage systems play an important role balancing energy urban fluxes. These systems can be classified based on the state of the stored energy: sensible, latent and thermochemical (Guelpa and Vittorio, 2019). Currently, the use of thermochemical systems in cities are very innovative thanks to the high energy stored and low heat losses produced, nevertheless these technologies are mainly on the laboratory scale. The operating

© 2022. The Authors. Published by International Solar Energy Society
Selection and/or peer review under responsibility of Scientific Committee
doi:10.18086/eurosun.2022.13.20 Available at http://proceedings.ises.org

principle of these systems takes advantage of chemical transformations produced when absorbing heat to excite a reaction. Stored heat can be recovered by reversing the reaction, sometimes adding a catalyst (Kousksou et al., 2014).

There are many classifications for the thermochemical storage systems, but one of the most usual is based on the creation of new materials when a gas binds to the surface of a solid. Two typologies are identified: chemical reversible reactions / absorptions processes and adsorption processes (Guelpa and Vittorio, 2019). Adsorption processes highlight by the creation of different types of materials such as zeolites, aluminophosphates composites and metal-organic frameworks (Henninger et al., 2017). The performance of these materials will regulate the applicability, efficiency and profitability of these adsorption processes. The use zeolites as storage systems has a great potential due to their catalytic properties, the permeability as well as the adsorption properties thanks to its microporous structure (Feng et al., 2021). Currently it is easy to find natural zeolite on the marketplace because is a product that comes directly from the stone quarry and it is very common for building and construction uses. Therefore, its use as a thermal storage element has great economic and energy potential.

Previous studies reveal the high cationic exchange potential of zeolites (Seco et al. 2021). However, in order to deeply know the zeolites´ potential as an innovative thermal use storage, tailored experimental campaigns are needed. Thus, this study addresses a key issue in the development of sustainable cities quantifying the thermal storage capacity of thermochemical storage systems. Several configurations of natural zeolites have been evaluated with the aim of reducing the existing uncertainties in their operation. With this aim, numerical simulation models and laboratory experiments have been developed to quantify the thermal capacity of the studied zeolites.

To this end, it is defined the following specific objectives: a) Design of a Zeolite prototype reactor based on Computational Fluid Dynamic (CFD) simulation models. b) Based on previous input and output values, execution of the physical reactor at lab conditions showing first empirical results of the zeolite thermal storage behaviour. Therefore, Section 2 and Section 3 show the method applied along the experimental camping and the study case, while Section 4 presents the simulated and empirical results. Finally, section 5 describes main conclusions of the work.

2. Methodology

To quantify the performance of some material as thermochemical storage systems, a step-by-step methodology has been developed, whose main phases are:

- *Selection of the studied samples: natural zeolites.*
- *Development of the initial Computational Fluid Dynamic Models to provide first results that allow defining the pre-design of the experiments with the proposed zeolites.*
- *Definition of the Zeolite Reactor built in the laboratory.*
- *Laboratory experiments necessary to quantify the thermal performance of the studied zeolite.*

The application of these phases produces the experimental characterization of the thermal properties of natural zeolites, allowing the development of a more detailed CFD model that, once validated, will enable the study of different conditions and modes of operation. Furthermore, the systematization in the application of these phases will allow characterizing the thermal performance of other types of materials such as synthetic zeolites, giving rise to new reactors and new simulation models.

3. Case Study

The methodology developed in this paper includes the CFD simulation to define a pre-design of the prototype, the construction of a reactor prototype and the execution of batteries of experiments, to quantify the thermal performance of natural zeolites. The study considers the quantification of their cationic exchanges in thermal storage analysis including different sieves at lab conditions.

3.1. Selection of materials

In this study, natural zeolites have been selected to be tested as thermal storage material in buildings (see Figure 1). The use of this type of zeolites in sectors such as agriculture or industry has been known for years, but these stones also have high potential as thermal storage materials for the use in buildings thanks to their catalytic and adsorption properties as well as their permeability (Feng et al., 2021). However, this last application is still in the research and development phase, and it is necessary to numerically quantify the thermal behavior of some of its properties under the operating conditions required in the thermal conditioning of buildings.

Natural Zeolite selected is a natural rock with high porosity and cation exchange capacity, selective absorption and reversible hydration. For this study, the application of zeolites cationic exchanges in thermal storage has been assessed including different sieves. The cationic exchange produced by the selected zeolites is characterized by two phases:

- *Charge.*
- *Discharge.*

The dry phase, named activated (charge phase), is the one used to extract the energy in heat form (Xu et al., 2019). For charging, high temperature heat is supplied to the adsorber desorbing all adsorbed water. To discharge the storage, outside air is blown through the zeolite and vapour molecules are adsorbed releasing the heat of adsorption at a high temperature level.



Fig. 1: Natural zeolite sample: a) laboratory prototype and b) material sample

This microporous material of volcanic origin presents a regular crystalline structure with unique characteristics. All types of zeolite have a very similar structure, as well as their physical and chemical properties. Table 1 shows the main properties provided by natural zeolites. Zeolites have specific densities in the range 1900-2800 Kg/m^3 and hardness between 3-6 on the Mohs scale. Its structure is based on a set of cuboctahedrons each made up of 24 tetrahedrons. Zeolites have an unusual cage-like, three-dimensional crystal structure and extraordinary ion-exchange capacity, both on the surface and within the mineral. This phenomenon is due to their size and the freedom of movement of the water molecules they contain.

Its ordered structure presents a large number of channels and cavities with molecular diameters between 2.6 Å and 7.4 Å. This property is called micro-porosity because the dimensions are slightly larger than those of water molecules. The pores are the same, and therefore so are their size, shape and volume, giving zeolites the property

of molecular sieve with the capacity to retain cations and absorb water.

Tab. 1: Characteristics of the 4-8cm rock mineral Zeolite

Property	Units	Value
Density	Kg/m^3	1900-2800
Porosity	--	0.4
Thermal conductivity	W/m·K	2.0
Specific heat capacity at constant pressure	J/kg·K	910-1180
Dynamic viscosity	Pa·s	50

3.2. Development of Computational Fluid Dynamic Models

Once the material is selected, 4-5 cm natural zeolite rocks, advanced fluid mechanics tools are used to support the design of the key laboratory experimental equipment: a Zeolite reactor. The characteristics of the selected natural zeolites are considered in order to ensure a sufficient ventilation flow providing proper conditions to enhance the cation exchange processes associated with thermal storage in the material.

The numerical study has been focused on the discharging processes of these zeolites adsorbents. The developed numerical model simulates the ventilation airflow through the material, the natural zeolites, placed in the reactor vessel. This was done using the commercial computational fluid dynamics (CFD) code called FLUENT. The characterization of the airflow is relevant because it affects the thermal storage capacity of the natural zeolites in the reactor.

The analysis of the fluid-dynamic problem has been done solving the Navier- Stokes equations with the finite volumes method. To this end, a three-dimensional CFD model has been developed. The geometry of the reactor model has been defined to facilitate the experimentation to be carried out in the laboratory, considering the physical properties of the natural zeolites.

The resulting geometry of the Thermal Energy storage prototype is simple. It basically consists of a hollow cylindrical pipe with a cylindrical reservoir in the central inner part of the pipe. Zeolite sieves are introduced into the storage cylinder. Outside air is blown through the pipe along its length but the presence of the zeolite produces a fluid volume blockage inside the tube that is not physically represented in the geometry design. Then, the flow through the packed beds have been simulated by using a porous media model.

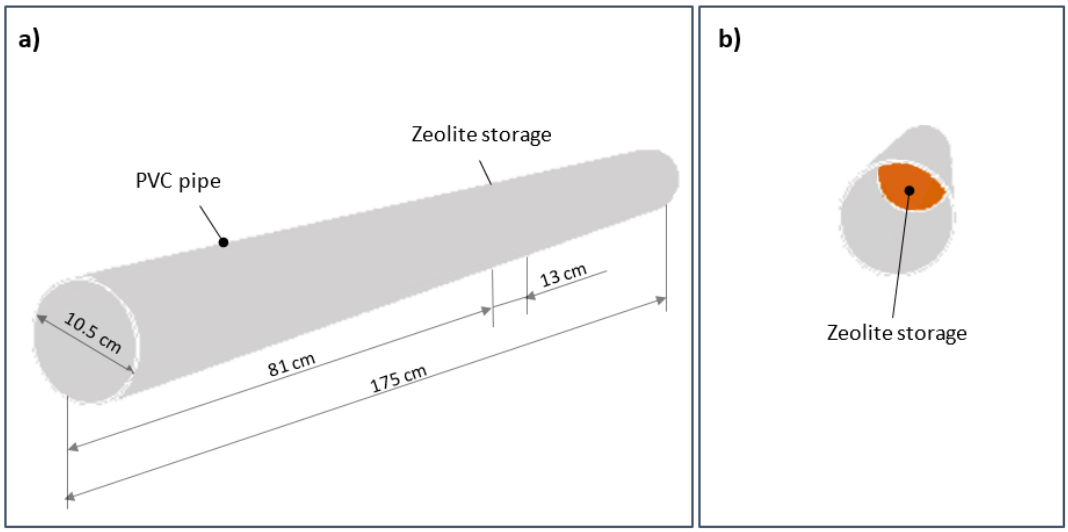

Fig. 2: Geometry of the natural zeolite reactor model: (a) Main dimensions, (b) zeolite storage chamber view

As shown in Figure 2, the geometrical model is a hollow cylindrical PVC pipe with an outside diameter of 11.0cm, an inside diameter of 10.5cm and a length of 175cm. A 13cm length storage cylinder is placed in the centre of the pipe. The reservoir is filled with 4-5 cm natural zeolite rocks.

The specific cells zone of the domain corresponding to the sample storage chamber is defined as "porous" and the flow resistance is determined in this volume by adding a momentum sink in the governing momentum equations composed of a viscous loss term and an inertial loss term. This momentum sink contributes to the pressure gradient in the porous media creating a pressure drop. This pressure loss in the flow is determined by using the superficial velocity porous formulation. The superficial velocity inside the storage cylinder is calculated based on the volumetric flow rate inside it and it is assumed that Zeolite reservoir is homogeneous and isotropic with reference to porosity. Then the resistance coefficients in all directions are the same. For deriving the appropriate coefficients, the semi-empirical correlation of the Ergun equation is applied and viscous (Eq. 1) and inertial loss (Eq. 2) constants are calculated. Turbulence is computed in the porous region just as in the bulk fluid flow.

$$\frac{1}{\alpha} = \frac{150}{{D_p}^2}\frac{(1-\epsilon)^2}{\epsilon^3} \qquad \text{(eq. 1)}$$

$$C_2 = \frac{3.5}{D_p}\frac{(1-\epsilon)}{\epsilon^3} \qquad \text{(eq. 2)}$$

Where Dp is the mean particle diameter and ϵ is the void fraction.

It is important to highlight that a proper definition of the boundary conditions in the simulation model leads to the best possible solution of equations system characterizing the behaviour of the zeolite reactor. The physical geometry and the expected pattern of the flow field solution has mirror symmetry so symmetry boundaries are applied in order to reduce the extent of the computational model. In this case the domain is reduced to a quarter pipe and two symmetry planes are defined (Figure 3). The exterior border, flow output, has a constant pressure and temperature condition equal to the atmospheric and ambient values. The velocity inlet conditions at the entrance of the fluid are fixed by the experimental conditions.

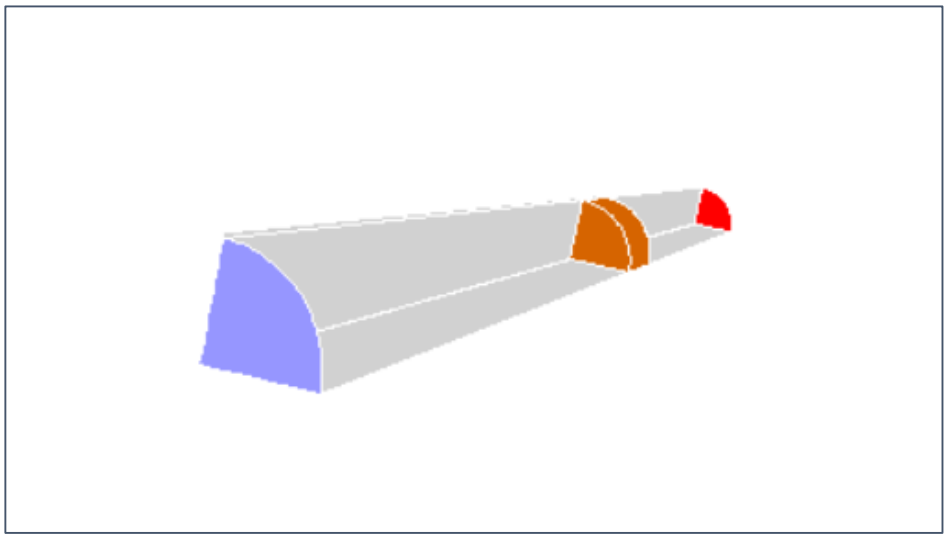

Fig. 3: Boundary conditions schema of the zeolite reactors

As regards the mesh, same type has been used in the domain: the unstructured one. The mesh has been refined in some parts of the geometry, such as the zones near the PVC pipe as shown in Figure 4. This increase in the cells density allows simulating accurately the airflow in the boundary layer close to the walls of the tube. A sensibility analysis of the mesh has been performed resulting in an optimized mesh with a total number of 0.4 million cells.

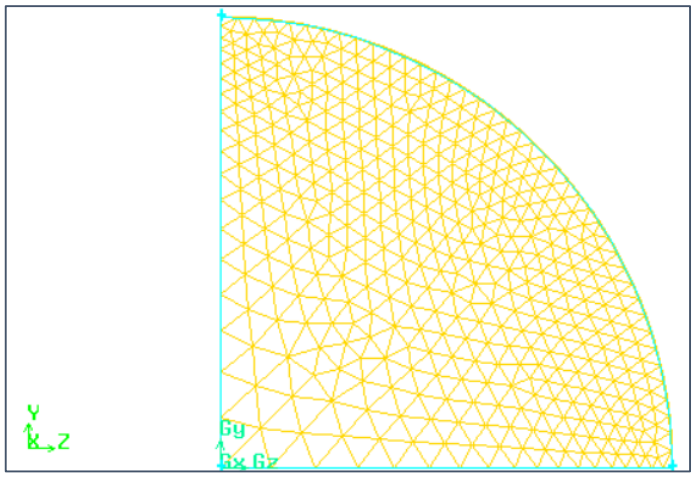

Fig. 4: Detail of the mesh in the inner volume of the tube

With respect to the solution methodology, the turbulence effects, as the ventilation flow inside the pipe is characterized by its turbulent regime, the k-ε RNG 3D RANS model of two equations has been tested and compared.

The porous zone is assessed by applying the Relative Velocity Resistance Formulation. A cylindrical coordinate system is used to define the loss coefficients. Porous model constants ie. viscous and inertial resistance coefficients, the Direction Vectors and the porosity, are calculated for the natural zeolite case of study. Viscous resistance coefficients (Direction X, Y, Z): $2.4*10^6$, Inertial Resistance coefficients (Direction X, Y, Z): $2.7*10^3$, and Direction Vectors (X,Y,Z): (1,0,0) and (0,1,0) are specified. Porosity of the porous medium is defined as the volume fraction of air within the zeolite region.

The turbulence equations have been solved using a second order discretization scheme, and the momentum equations with a second order - pressure staggered one. The pressure-velocity coupling employs the SIMPLE algorithm. And regarding the convergence criterion, a sufficient number of iterations has been computed to ensure all the residuals were lower than 10^{-5}.

3.3. Definition of the Zeolite Reactor

To check the thermal storage capacity of different types of zeolites, different reactor prototypes are needed. Given that natural zeolites have been selected in this study and based on the results obtained with the initial CDF models, a new Zeolite Reactor is designed and constructed in the laboratory scale at the CIEMAT facilities in Madrid (Spain). This reactor will allow testing the thermal storage capacity of the proposed natural zeolites under controlled laboratory conditions.

The final design of this reactor includes three sections (Figure 5):

- *Hollow cylindrical pipe with a bazooka at the beginning.*
- *Sample storage chamber.*
- *Hollow cylindrical pipe.*

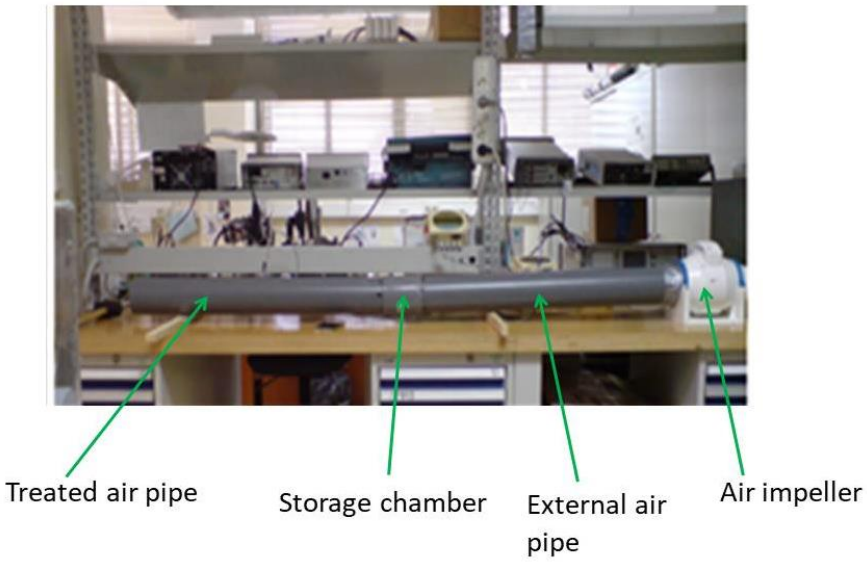

Fig. 5: Prototype built Natural zeolite reactor on the laboratory prototype

The hollow cylindrical pipe is made of PVC and has a global length of 175 cm divided in two sections: before and after the storage chamber. The pipe has an outside diameter of 11 cm and inside diameter of 10.5 cm. The storage chamber is a 13 cm long cylinder located in the center of the pipe. The interior of this chamber is used as a tank that is filled with 4-5 cm natural zeolite rocks. The air impeller located at the beginning of the tube allows controlled the entry of airflow into the reactor (see Figure 6). To regulate the flow of air circulating through the tube, a ventilation system is defined based on the diameter of the reactor.

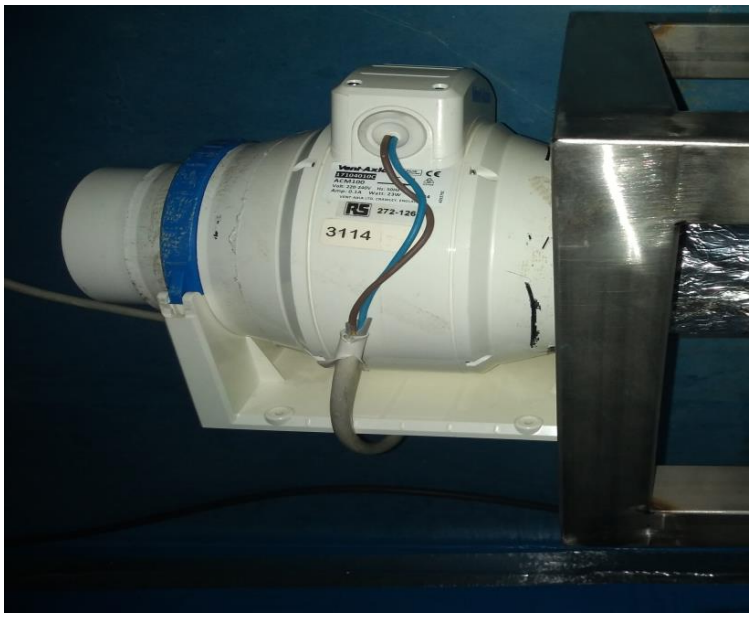

Fig. 6: Detail of the industrial air impeller located at the beginning of the tube

To characterize the thermal performance of natural zeolites under different ambient conditions of outside temperature, pressure and humidity rates, it is necessary to install anemometers and temperature sensors, both at the inlet and outlet of the tube. This arrangement will allow the evolution of the air flow inside the tube to be quantified, measuring temperature and air speed values in both positions. With this aim, Kimo transmitters have been installed to measure air velocity and airflows, as well as multi-variable measurement Kester and Fluke IR thermometers have been used to monitor temperature and air velocities. In addition, a thermographic camera ThermaCAM has been used to control the temporal evolution inside the tube and take pictures of the inside of the tube. These records will allow detailed CFD models to be better adjusted to real conditions. Table 2 shows the

main characteristics of the measuring instruments used in this reactor:

Tab. 2: Characteristics of the measuring instruments used in the new Zeolite reactor constructed

Equipment	Variables	Accuracy
"ThermaCAM SC660 Wes (TC)"	Temperature and photos	±1°C or ±1% of reading for limited temperature range; ±2°C or ±2% of reading with Thermal sensitivity NETD <30 mK @ +30°C
Kimo instrument CTV 200	Air velocity and airflows	Accuracy air velocity from 0 to 3 m/s : ±3% of reading ±0,03 m/s; Accuracy temperature ±0,5% of reading ±0,3°C
Kestrel 3000 Environmental meter and Fluke IR thermometer	Temperature and velocity	±3% of reading or ±0.1 m/s / ±1ºC

3.4. Laboratory experiments

Before running the experiments with natural zeolites in the new reactor, it is necessary to prepare these materials to operate in good conditions. The laboratory process to prepare the material has been done in four steps:

- *Sample heating* and *dehydration*
- *Storage in a desiccator*
- *Encapsulation*
- *Sample hydration*

The first step consists on using the powerful laboratory muffle furnaces to dehydrate the sample (see Figure 7). This process has been carried out with muffle furnaces available for temperatures up to 500°C in a small cell. The second step involves placing the sample in an oven at 110°C for one day in order to heat the material. Based on the numerical results obtained in the simulations, the natural zeolite cell reactor requires an internal capacity to storage 1 kg. The third step is to store the heated sample in a vacuum desiccator for further analysis. The most important consideration in this process is the absence of air or moisture in the room. At this time, the sample is ready for thermal heat capacity assessments in the reactor prototype. Finally to test the thermal performance of these natural zeolites in the reactor, it is necessary to encapsulate the prepared material in a cell located in the middle position of the tube. In this way, the samples are ready to be hydrated in the development of the experiment.



Fig. 7: Laboratory muffle furnace to dehydrate the Natural zeolite sample

Once both the samples and the measurement equipment have been prepared, the experimental batteries are carried out in the Zeolite Reactor. These campaigns allow different experimental conditions to be tested by controlling, in real time, the variables of ambient temperature and air humidity. This is achieved by regulating the entry of airflow through the first section of the reactor. The thermographic camera has been used to regulate the boundary

conditions and the thermal evolution of the ambient variables.

4. Results

The adsorption process has been modeled considering a hollow cylindrical tube, a cylindrical storage chamber located in the centre of the pipe, natural zeolites as storage elements and an air impeller that defines the boundary conditions of the study volume. The initial characteristics of this geometrical model are defined in table 3.

Tab. 3: Geometric and initial conditions defined for the natural zeolite reactor

Element	Characteristics and values
Cylindrical pipe	Outside diameter of 11 cm, inside diameter of 10.5cm and total length of 175cm
Air impeller	Inlet air velocity of 2 m/s
Storage cylinder	Length of 13cm and porosity value of 0.4
Reservoir	Filled with 4-5 cm natural zeolite rocks

Computational fluid dynamics simulations have been executed with Fluent in order to characterize the thermal performance of natural zeolites inside the pipe. Three-dimensional velocity (m/s) is obtained and showed in pipe section (Figure 8). With these conditions, the fluid flow is accelerated at the exit of the pipe up to a value of 2.5m/s. The velocity profile shows a maximum value at the center of the pipe.

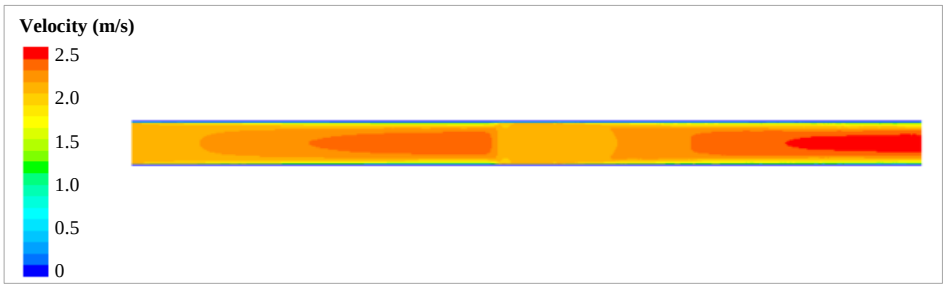

Fig. 8: Numerical results: air velocity inside the Zeolite reactor

To characterize the cationic capacity of the zeolite reactor, the thermographic camera TC has been used during the first experiments (Figure 9). These photos reveal high cationic exchange capacity for all types of zeolites (Seco et al., 2020)., where drying and cooling conditions in the absence of humidity have been seen to influence results in a high extent, as well as the adequate design of the reactor, to provide effective air friction with the zeolite sample.

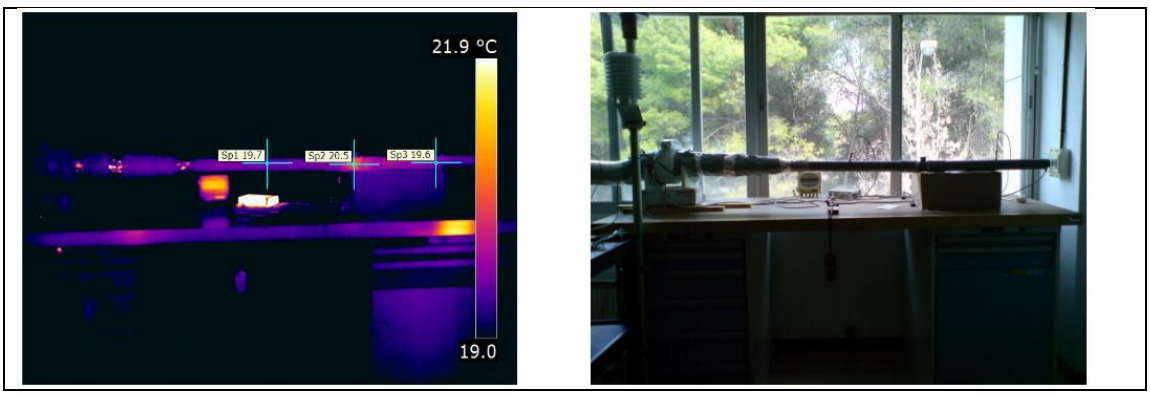

Fig. 9: Thermography done to characterize the cationic exchange of natural zeolites during the experiments

Under the internal storage capacity of 1 kg no thermal storage is achieved because outside air has almost the same temperature than the incoming ambient air. Process to dry the material uses laboratory muffle furnaces with temperatures up to 1.000°C in small cell. After different tests to check the necessary strength to apply in any zeolites tested, it has been observed that in any case with 1 kg of sample, 60 minutes at 465°C is enough energy to dehydrate completely the zeolite. At this moment, the sample is ready for thermal heat capacity analysis in the reactor prototype.

Figure 10 represent the evolution between incoming ambient air (blue lines) and the outlet air (green lines) once it passed through zeolite chamber. Two variables are represented: temperature (left side) and air velocity (right side) along the time. The outlet temperature presents higher value than ambient air, assuring the thermal store capacity of the zeolites.

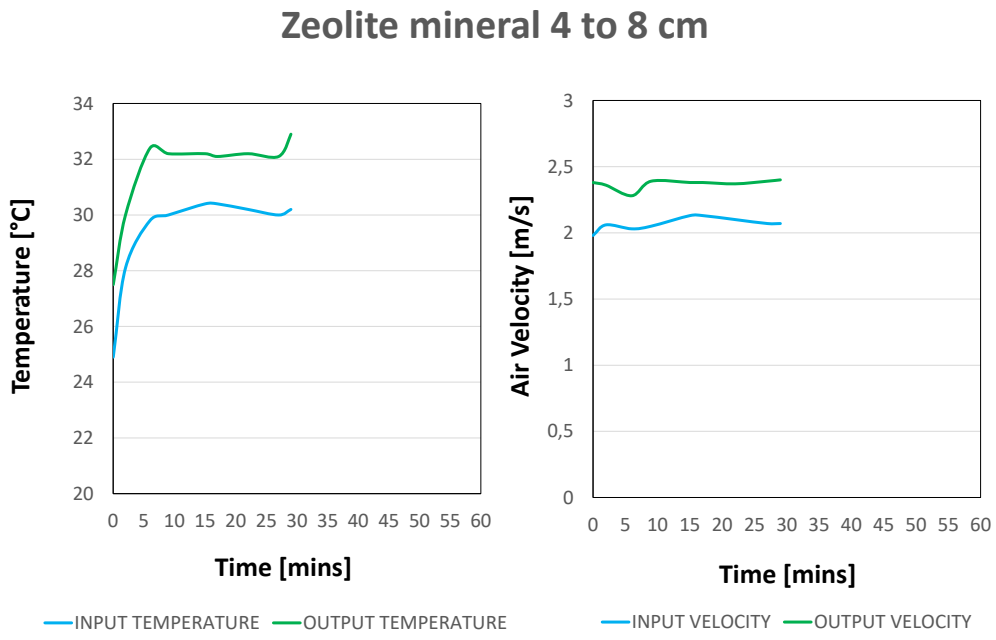

Fig. 10: Experimental results obtained using mineral zeolites: a) air temperature and b) velocity inside the Zeolite reactor

5. Conclusions

Thermal storage systems allow matching district energy consumption with energy generation depending on the urban requirements. There are several types of thermal storage available, but one of the most promising technologies uses natural zeolites. These storage systems take advantage of chemical processes by absorbing heat to excite a reaction and recovering heat reversing the reaction. These processes have been assessed through the use of fluid dynamic simulation models, which results made it possible to define and build a laboratory-scale zeolite reactor. The numerical results identify the main characteristics that are experimentally implemented in the zeolite reactor for the analysis under laboratory conditions. The experimental results indicate that the mineral zeolite does not obtain a regular cooling process throughout the study time. This fact highlights the importance of knowing how the zeolite gives the energy, since their characteristics define the type of storage application that can be applied.

Zeolite storage shows a very potential technology thanks to high energy storage and low heat losses. Nevertheless, it needs further development on a laboratory scale to be able to analyze different compositions, configurations and structures. With this aim, new models and new experimental developments will be made where different samples (synthetic zeolites) will be included for the new prototypes.

6. Acknowledgments

This research was funded by this project which has received funding from the European Union's Horizon Europe research and innovation programme under the grant agreement No. 101056862.

7. References

De, W., Shaohua, L., Guiliang, C., Lei, L.,2020. Cost-Earning Analysis of Regenerative Electric Heating Customer's Participation in Market Transaction By Load Aggregator Agent. 2020 IEEE 3rd Student Conference on Electrical Machines and Systems (SCEMS), Jinan, 4-6 December, pp. 543-549, https://doi.org/10.1109/SCEMS48876.2020.9352319.

Feng, C., Jiaqiang, E., Han, W., Deng, Y., Zhang, B., Zhao, X., Han, D., 2021. Key technology and application analysis of zeolite adsorption for energy storage and heat-mass transfer process: A review. Renew. Sust. Energ. Rev. 144, 110954. https://doi.org/10.1016/j.rser.2021.110954.

Guelpa, E., Vittorio, V., 2019. Thermal energy storage in district heating and cooling systems: A review. Appl. Energy 252, 113474. https://doi.org/10.1016/j.apenergy.2019.113474.

Huang, W., Zhang, X., Li, K., Zhang, N., Strbac, G., Kang, C., 2021. Resilience Oriented Planning of Urban Multi-Energy Systems With Generalized Energy Storage Sources. IEEE Trans. Power Syst. 37 (4), 2906–2918. https://doi.org/10.1109/TPWRS.2021.3123074.

Henninger, S.K., Ernst, S.J., Gordeeva, L., Bendix, P., Grekova, A.D., Bonaccorsi, L., Aristov, Y., Jaenchen, J., 2017. New materials for adsorption heat transformation and storage. Renew. Energy 110, 59-68. https://doi.org/10.1016/j.renene.2016.08.041

IPCC, 2022. Climate Change 2022: Impacts, Adaptation, and Vulnerability. Contribution of Working Group II to the Sixth Assessment Report of the Intergovernmental Panel on Climate Change [H.-O. Pörtner, D.C. Roberts, M. Tignor, E.S. Poloczanska, K. Mintenb

Kousksou, T., Bruel, P., Jamil, A., El Rhafiki, T., Zeraouli, Y., 2016. Energy storage: Applications and challenges. Sol. Energy Mater. Sol. Cells 120, 59-80. https://doi.org/10.1016/j.solmat.2013.08.015

SET-Plan Working Group, 2018. "Europe to Become a Global Role Model in Integrated, Innovative Solutions for the Planning, Deployment, and Replication of Positive Energy Districts." SET-Plan Action No 3.2 Implementation Plan, no. June: 1–72. https://setis.ec.europa.eu/implementing-actions/set-plan-documents_en.

Seco, O., López, H., Olmedo, R., Ferrer, J.A., 2020. Thermal Energy storage capacity on different types of zeolites. In Proceedings 13th International Conference on Solar Energy for Buildings and Industry. EuroSun2020. ISES. International Solar Energy, Kasse, 25-29 September.

Telaretti, E., Graditi, G., Ippolito, M.G., Zizzo, G., 2016. Economic feasibility of stationary electrochemical storages for electric bill management applications: the Italian scenario. Energy Policy 94, 126-137. https://doi.org/10.1016/j.enpol.2016.04.002.

UNITED NATIONS ENVIRONMENT PROGRAMME (UNEP), 2016. District energy in cities:: Unlocking the potential of energy efficiency and renewable energy. Editorial; United Nations. ISBN-10: 9211587328

Xu, S.Z., Wang, R.Z., Wang, L. W., Zhu, J., 2019. Performance characterizations and thermodynamic analysis of magnesium sulfate-impregnated zeolite 13X and activated alumina composite sorbents for thermal energy storage. Energy, 167, 889-901. https://doi.org/10.1016/j.energy.2018.10.200.

Effect of Design Characteristics on Pit Thermal Energy Storage Performance

Ioannis Sifnaios[1,2], Adam R. Jensen[1], Simon Furbo[1] and Jianhua Fan[1]

[1] DTU Civil and Mechanical Engineering, Technical University of Denmark, Kgs. Lyngby (Denmark)

[2] Sino-Danish College (SDC), University of Chinese Academy of Sciences, Beijing (China)

Abstract

Pit thermal energy storage (PTES) systems have been developed as a low-cost, water-based storage technology for district heating networks. While annual efficiencies greater than 90% have been realized, many existing storages have suffered from high heat losses and poor stratification. Thus, research is still necessary for identifying and optimizing the parameters that affect the operation and performance of PTES. This study investigated the effect of design characteristics and ambient temperature on PTES heat loss and efficiency. More specifically, the influence of aspect ratio and slope of the storage sides were investigated for three locations (Denmark, Finland, and Greece) using the software ANSYS Fluent. It was found that the slope of the PTES sides had a larger impact on the storage efficiency than the aspect ratio. The investigated PTES with steeper side-wall slopes had a 12% higher efficiency than one with a gradual slope, while the PTES with a rectangular shape had a 3% lower efficiency than a square one. Regarding different locations, a PTES in Greece would have 5% higher efficiency than one in Finland due to higher ambient temperatures that reduce heat losses.

Keywords: Heat storage, design optimization, heat loss, heat transfer, PTES

1. Introduction

Many different heat sources can be utilized in the district heating (DH) networks, such as waste incineration, biomass, wind, solar, geothermal energy, natural gas, oil, coal, and surplus heat from industry (Danish District Heating Association, 2021). In Denmark, where DH covers 64% of the country's residential heat demand, there is an effort to increase the share of renewables in the DH sector in order to be carbon neutral by 2050 (Ministry of Foreign Affairs of Denmark, 2020). To achieve this, energy storage has to be utilized due to the intermittent nature of renewable energy sources like solar and wind. For example, typical DH networks can achieve a solar fraction of 20%, whereas DH networks with seasonal energy storage systems can achieve solar fractions higher than 40% (Sveinbjörnsson et al., 2017).

One of the most promising storage technologies in the district heating sector is pit thermal energy storage (PTES), which is a low-cost technology that utilizes water as the storage medium. Several PTES systems have been demonstrated in Denmark and connected to large-scale solar collector fields (Soerensen and From, 2011). The current state-of-the-art PTES has an efficiency greater than 90% (Winterscheid and Schmidt, 2017), demonstrating that PTES can be a cost-effective heat storage technology with a large potential.

At the time of writing, there are five storages in operation in Denmark, namely in Dronninglund (60,000 m^3) (Schmidt and Sørensen, 2018), Marstal (75,000 m^3) (Jensen, 2014) , Vojens (200,000 m^3) (Rambøll, 2015), Toftlund (70,000 m^3) (Rambøll, 2016), and Gram (122,000 m^3) (PlanEnergi, 2015). Additionally, there is one PTES under construction in Høje Taastrup (70,000 m^3) (Aalborg CSP, 2020) and one in the planning stage in Odense (1,000,000 m^3). Outside of Denmark there is only one operational PTES, which is in Lagkazi, Tibet (15,000 m^3) (Aalborg CSP, 2019).

All the existing PTES systems were constructed after 2012, and the technology has mainly been developed by making minor changes to existing designs based on previous practical experience. For this reason, research is necessary on topics of major importance to their operation and performance, e.g., their design.

This paper investigated the effect of two key design characteristics of PTES; the slope of the storage sides and the

© 2022. The Authors. Published by International Solar Energy Society
Selection and/or peer review under responsibility of Scientific Committee
doi:10.18086/eurosun.2022.13.21 Available at http://proceedings.ises.org

aspect ratio (AR). Steeper side walls reduce the surface area of a storage, thus reducing heat losses. Similarly, an aspect ratio equal to one is desired from a heat loss perspective as it reduces the surface area of the storage. The effect of these parameters on heat loss and energy efficiency was investigated using a numerical simulation model in the software ANSYS Fluent. Last, the effect of ambient temperature on heat loss and efficiency was investigated using the same method.

2. Methods

The heat loss from a PTES can be divided into heat loss from the water through the insulated lid and the uninsulated side walls. The heat loss through the lid can be estimated as one-dimensional with high accuracy if the insulation properties are known. However, the heat loss to the soil is complex as it has to be modeled in 3D, and the soil's thermal capacity must be considered.

In order to investigate the effect of the design characteristics on the PTES performance, a model of the soil domain around the PTES was developed in ANSYS Fluent. Fluent is a computational fluid dynamics (CFD) software that uses the Green-Gauss Finite Volume Method (FVM) to discretize the conservation form of the partial differential equations.

The heat loss from the water to the soil was simulated by applying the water temperature (varying with height) to the soil boundary. This simplification is valid under the assumption that the convection coefficient between the water-soil interface is negligible relative to the conduction in the soil. By not including the PTES water in the model, only heat conduction in the soil had to be simulated instead of a fluid dynamics study; thus, the computation time was dramatically reduced.

2.1 Simulated PTES designs

The annual heat loss to the ground was calculated for five different storage configurations. The geometry of the reference case was modeled after the PTES in Marstal, and the water-soil interface was simulated using 16 vertical layers, each having a height of 1 m and a constant temperature for each time step.

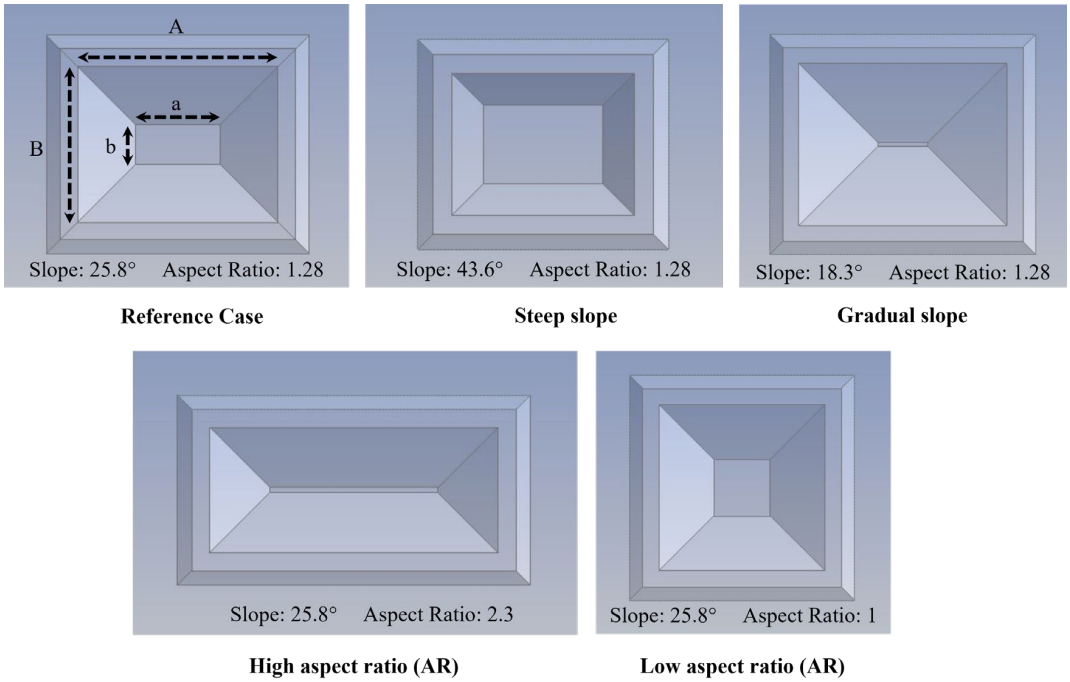

Fig. 1: Investigated PTES configurations.

The slope of the storage sides and the storage aspect ratio (AR) were investigated. The aspect ratio is the ratio of the long edge of the storage relative to the short edge, i.e., a square storage has an aspect ratio of 1, and a rectangular storage has an aspect ratio greater than 1. The five storage configurations are illustrated in Fig. 1, and their key characteristics are listed in Tab. 1. All the investigated storage configurations had the same storage volume, height, number of vertical layers, and volume per layer across PTES. Consequently, the area of the lid, side walls, and bottom walls varied greatly for the different designs. Also, it should be noted that the layers in each storage had different

heights for them to have the same water volume.

Tab. 1: Dimensions of the investigated scenarios.

Parameter	Reference case	Different slope tilt		Different aspect ratio		Units
		Steep slope	Gradual slope	High AR	Low AR	
Side slope	25.8	43.6	18.3	25.8	25.8	°
Lid aspect ratio	1.28	1.28	1.28	2.3	1	-
Bottom side length (a)	47.6	63.4	30.3	92	34.1	m
Bottom side width (b)	22.6	42	2	3.2	34.1	m
Top side length (A)	113.1	97	127.9	157.2	99.3	m
Top side width (B)	88.1	75.6	99.6	68.4	99.3	m
Sides and bottom area	11,022	9,110	13,396	11,971	10,886	m^2
Lid area	9,972	7,331	12,732	10,745	9,868	m^2
Storage height			16			m
Storage volume			76,929			m^3

From Tab. 1, it can be observed that the different slope tilts have a larger effect on the surface area of the storage. For example, the Steep slope case has 22% less surface area overall than the reference case, whereas the Gradual slope case has a 24% larger surface area compared to the reference case. On the other hand, the High AR case has an overall 8% larger area than the reference case, and the Low AR case has only a 1% smaller surface area than the reference case. These differences in the surface area are expected to impact the heat losses and efficiency of the PTES significantly.

2.2 Thermal properties of the ground and lid

It must be noted that the selected ground thermal properties are not necessarily exact for the PTES in Marstal. Instead, the selected values are indicative of the general soil conditions in eastern and central Denmark, which have moraine landforms with loamy soils rich in silt, clay, and sand (Adhikari et al., 2014). Typical values for moraine soil were taken from (Ditlefsen et al., 2012):

- Density: 2200 kg m^{-3}
- Specific heat: 1700 J kg^{-1} K^{-1}
- Thermal conductivity: 2 W m^{-1} K^{-1}

These values were used for the entire soil domain, which was initialized having a uniform temperature of 8 °C. The bottom of the soil domain (50 m below the bottom of the PTES) was simulated to have a fixed boundary temperature of 8 °C. The side walls of the soil domain were modeled using adiabatic boundary conditions. The top of the soil domain (which was in contact with the ambient air) was simulated to have a forced convection coefficient of 30 W m^{-2} K^{-1}, indicative of an average airflow velocity of 5 m/s according to Laloui and Rotta Loria (2020).

Regarding the lid, the thermal properties used in the calculations were chosen based on values of the original Nomalén (NMC Termonova, 2011) lid, which was initially installed in Marstal and Dronninglund. For calculating the heat loss through the lid, the following equation was used:

$$E_{lid\ loss} = A_{lid} \cdot k_{lid} \cdot h_{lid} \cdot (T_{top\ layer} - T_{amb}) \qquad \text{(eq. 1)}$$

where A_{lid} is the surface area of the lid, k_{lid} is the effective thermal conductivity of the lid structure (0.06 W m^{-1} K^{-1}), h_{lid} is the thickness of the lid (0.24 m), $T_{top\ layer}$ is the temperature of the storage's top layer, and T_{amb} is the ambient air temperature.

2.3 PTES and ambient temperature

The water temperatures from the Marstal PTES were used to simulate a seasonal heat storage operation from January 2013 to December 2015. The reference case (located in Denmark) was used for comparison, and with the same water-temperature profile, the storage was simulated for two additional locations, namely Finland and Greece. Regarding the ambient temperatures, Typical Meteorological Year (TMY) temperatures were used for Copenhagen (Denmark), Helsinki (Finland), and Athens (Greece). The data used in the simulations are presented in Fig. 2.

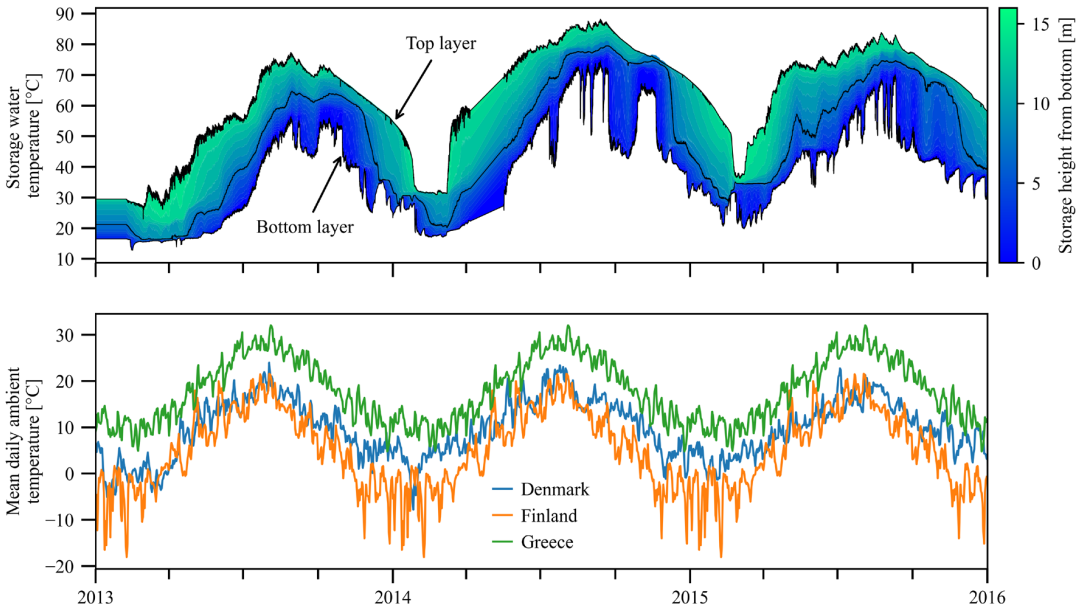

Fig. 2: PTES and ambient temperatures used in the simulations.

2.4 Efficiency calculation

The energy balance of a thermal storage system can be expressed as follows:

$$E_{out} = E_{in} - E_{loss} - \Delta E \qquad \text{(eq. 2)}$$

where E_{out} is the energy discharged from the storage, E_{in} is the charged energy, and E_{loss} is the energy lost due to heat losses. ΔE is the internal energy change of the storage, i.e., the difference between the internal energy at the start and end of the period of consideration.

Since all simulated PTES have the same volume and temperature per storage layer, they all have the same internal energy change. Assuming that they all have the same charged energy (E_{in}) and that the heat loss is calculated by the heat transfer CFD simulation, the discharged energy (E_{out}) can be calculated using Equation 2. Then the PTES energy efficiency can be calculated using Equation 3, as explained in (Sifnaios et al., 2022).

$$\eta_E = \frac{E_{out}}{E_{in} - \Delta E} = \frac{E_{out}}{E_{out} + E_{loss}} \qquad \text{(eq. 3)}$$

3. Results

So far, in all the constructed PTES, only the lid area has been insulated, whereas the sides and bottom have had no insulation. This decision was made for two main reasons:

1. It was difficult and expensive to find an insulation material that could withstand the weight of the water without collapsing.
2. It was not considered important due to most heat loss occurring through the lid's surface.

This last statement can be observed in Fig. 3, where the annual heat loss for the investigated PTES is presented. After three years of operation, for all cases, approximately 55% of the heat loss comes from the lid, while 42% from the sides and 3% from the bottom. However, it must be noted that the heat loss from the sides and bottom of the PTES decreases with time as the ground temperature stabilizes and that three years of operation are insufficient for a seasonal storage to stabilize the ground temperature.

In Fig. 3, it can be observed that the storage sides' slope considerably impacts the annual heat loss toward the ground. The main reason is that a steeper slope leads to a smaller surface area, thus leading to lower heat losses. The Steep slope case had 21% lower total heat loss overall and 16% lower heat loss toward the ground compared to the reference case. On the other hand, in the Gradual slope case, where the slope of the sides was less steep than in the reference case, the total heat loss was 22% higher, and the heat loss toward the ground was 17% higher. The Gradual slope case had lower bottom heat losses than the Steep slope case, but overall, the Steep slope had 35% lower heat losses.

Comparing the cases with the same slope (i.e., High AR and Low AR cases), it was found that a square PTES shape (aspect ratio=1) can decrease the lid heat loss by 9% and the loss toward the ground by also 9%.

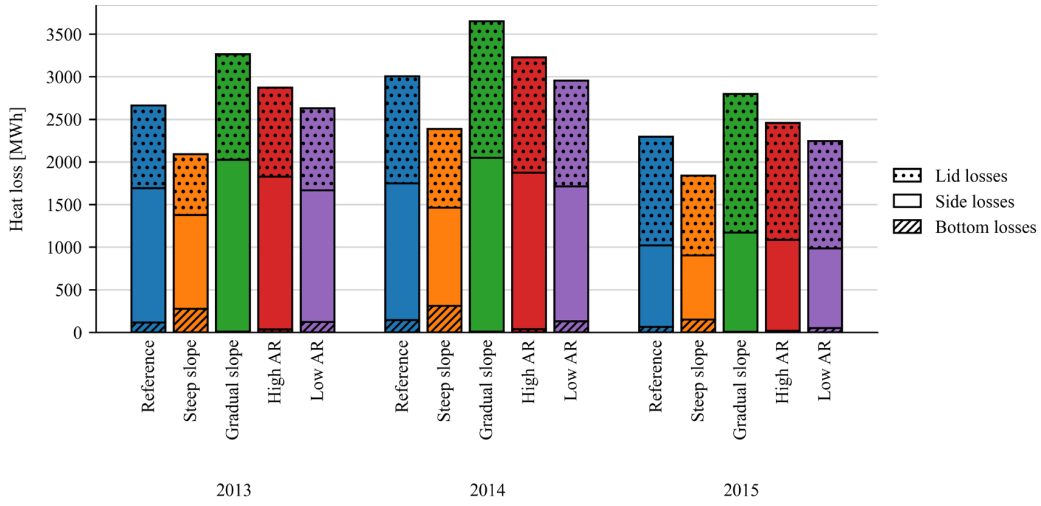

Fig. 3: Annual heat loss for the investigated PTES configurations.

The heat loss values for the last year of the simulation (2015) are reported in Tab. 2. The reason for showing only the values for 2015 is that, since there was preheating of the ground during the previous two years, the values for 2015 are considered more representative of the long-term operation of the PTES. The PTES energy efficiency was also calculated for 2015 for the different PTES configurations. It may be observed that the Steep slope had 6% higher efficiency than the reference case, while there was a 12% difference between the Steep and Gradual slope cases. Last, the square-shaped PTES of the Low AR case had 3% higher efficiency than the rectangular one of the High AR case. Although it is evident that the PTES design has a big impact on its performance, it has to be noted that, in many cases, its aspect ratio is dictated by the shape of the available plot of land. In addition, the side-wall slope is dictated by ground stability and, thus, the soil properties.

Tab. 2: Heat loss and efficiency for 2015 for the investigated PTES configurations.

Case	Bottom heat loss [MWh]	Side heat loss [MWh]	Lid heat loss [MWh]	Efficiency [%]
Reference case	63	957	1274	72
Steep slope	150	751	936	78
Gradual slope	4	1167	1626	66
High AR	17	1068	1373	70
Low AR	50	933	1261	73

The annual PTES heat loss for the different simulated countries is presented in Fig. 4. As expected, the storage in Finland had the highest heat loss as Finland had the lowest ambient temperature of the investigated countries. On the contrary, the lowest heat loss occurred in Greece, which had the highest ambient temperature. The PTES in Finland had, on average, 5% higher total heat losses compared to Denmark, while the one in Greece had 8% lower.

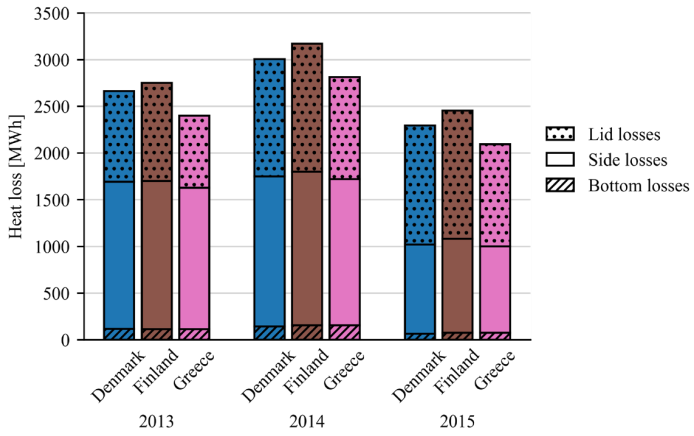

Fig. 4: Annual heat losses for Denmark, Finland, and Greece.

Table 3 presents the heat losses and efficiency for 2015 for the reference case for the three locations. The results show that the bottom heat loss is primarily affected by the storage temperature since all locations had the same bottom heat loss each year. The side heat losses were also comparable for the three locations, having a variation of approximately 9%. In contrast, the variation was much larger for the lid heat losses, namely 22%. Thus, the different ambient temperatures primarily affect the heat loss from the lid and, to a lesser extent, the heat loss from the sides. Last, a 5% variation in efficiency was calculated for the same storage water temperatures.

Tab. 3: Heat losses and efficiency for 2015 for Denmark, Finland, and Greece.

Country	Bottom heat loss [MWh]	Side heat loss [MWh]	Lid heat loss [MWh]	Efficiency [%]
Denmark	63	957	1274	72
Finland	63	1007	1373	70
Greece	63	923	1095	75

4. Conclusions

This study investigated the effect of two key design characteristics of pit thermal energy storage systems (the slope of the storage sides and the aspect ratio) and the effect of ambient temperature on storage heat loss and efficiency. A numerical simulation model was created in ANSYS Fluent that considered the soil domain around the PTES for investigating the heat loss from the water to the soil. Temperature data from the Marstal PTES were used to simulate the water domain from 2013 to 2015, and the design of the Marstal storage was used as the reference case. It was found that, due to a smaller surface area, a PTES with a steeper side slope had 21% lower total heat loss and 16% lower heat loss toward the ground compared to the reference one. Additionally, the square PTES design (aspect ratio=1) was shown to have a 9% lower total heat loss than the rectangular one. Furthermore, the slope of the PTES sides had a larger impact on the storage's efficiency than the aspect ratio; the variation in efficiency due to different side slopes was 12%, while the efficiency only varied by 3% due to different aspect ratios. Regarding different locations, a PTES in Greece was found to have 5% higher efficiency than one in Finland due to the higher ambient temperature that decreases the lid and side heat losses. Last, the heat losses through the bottom of a PTES were primarily affected by the storage temperature and not the ambient temperature since all simulated locations had the same bottom heat loss for each year.

5. Acknowledgments

This study was funded by the Danish Energy Agency through EUDP grant no. 64018-0134 and by the Sino-Danish Center for Education and Research (SDC) Ph.D. program.

6. References

Aalborg CSP, 2020. Aalborg CSP receives order for lid solution for Integrated Pit Thermal Energy Storage (PTES) System [WWW Document]. URL https://web.archive.org/web/20210417200554/https://www.aalborgcsp.cn/index.php?id=321&tx_news_pi1%5Bnews%5D=775&tx_news_pi1%5Bcontroller%5D=News&tx_news_pi1%5Baction%5D=detail&cHash=6

d7aff98a878e1d08d5ecd7f38e4fdbb (accessed 5.4.22).

Aalborg CSP, 2019. 15,000 M3 PTES for district heating, Tibet [WWW Document]. URL https://web.archive.org/web/20210418202632/https://www.aalborgcsp.com/projects/15000-m3-ptes-for-district-heating-tibet/ (accessed 5.4.22).

Adhikari, K., Minasny, B., Greve, M.B., Greve, M.H., 2014. Constructing a soil class map of Denmark based on the FAO legend using digital techniques. Geoderma 214–215, 101–113. https://doi.org/10.1016/j.geoderma.2013.09.023

Danish District Heating Association, 2021. Facts about district heating in Denmark [WWW Document]. URL https://web.archive.org/web/20220331213035/https://www.danskfjernvarme.dk/sitetools/english/about-us (accessed 5.4.22).

Ditlefsen, C., Vangkilde-Pedersen, T., Højberg, A.L., 2012. Geologi og jordvarmeboringer. Oversigt over geologiske forhold af betydning ved etablering af jordvarmeboringer i Danmark [WWW Document]. Natl. Geol. Undersøgelser Danmark og Grønl. URL https://geoenergi.org/xpdf/jordvarme-og-geologi-d3_2.pdf (accessed 9.5.22).

Jensen, M.V., 2014. Seasonal pit heat storages - Guidelines for materials & construction IEA-SHC Tech Sheet 45.B.3.2.

Laloui, L., Rotta Loria, A.F., 2020. Heat and mass transfers in the context of energy geostructures, Analysis and Design of Energy Geostructures. https://doi.org/10.1016/b978-0-12-816223-1.00003-5

Ministry of Foreign Affairs of Denmark, 2020. Global Climate Action Strategy [WWW Document]. URL https://web.archive.org/web/20220331213212/https://um.dk/en/foreign-policy/new-climate-action-strategy (accessed 5.4.22).

NMC Termonova, 2011. Nomalen 28N [WWW Document]. URL https://web.archive.org/web/20220426161150/https://azupcs365certviewer.azurewebsites.net/api/GetSDB?env=se&articleNr=550984 (accessed 4.20.22).

PlanEnergi, 2015. Long term storage and solar district heating [WWW Document]. URL https://web.archive.org/web/20220306155726/https://planenergi.dk/wp-content/uploads/2017/06/sol_til_fjernvarme_brochure_endelig.pdf (accessed 5.4.22).

Rambøll, 2016. Damvarmelagre [WWW Document]. URL https://web.archive.org/web/20220504080511/https://dk.ramboll.com/-/media/3fc11649e25942c195fa90e63ea41e11.pdf (accessed 5.4.22).

Rambøll, 2015. South-Jutland stores the sun's heat in the world's largest pit heat storage [WWW Document]. URL https://web.archive.org/web/20210827074933/https://ramboll.com/projects/re/south-jutland-stores-the-suns-heat-in-the-worlds-largest-pit-heat-storage?utm_source=alias&utm_campaign=sun-storage (accessed 5.4.22).

Schmidt, T., Sørensen, P.A., 2018. Monitoring Results from Large Scale Heat storages for District Heating in Denmark.

Sifnaios, I., Jensen, A.R., Furbo, S., Fan, J., 2022. Performance comparison of two water pit thermal energy storage (PTES) systems using energy, exergy, and stratification indicators. J. Energy Storage 52, 104947. https://doi.org/10.1016/j.est.2022.104947

Soerensen, P.A., From, N., 2011. High solar fraction with pit heat storages, in: 30th ISES Biennial Solar World Congress 2011, SWC 2011. pp. 3020–3030. https://doi.org/10.18086/swc.2011.21.07

Sveinbjörnsson, D., Laurberg Jensen, L., Trier, D., Ben Hassine, I., Jobard, X., 2017. Large Storage Systems for DHC Networks.

Winterscheid, C., Schmidt, T., 2017. Dronninglund District Heating Monitoring Data Evaluation for the Years 2015-2017.

Parametric Study of Structured Thermocline Storage Systems

Jordi Vera[1], Oriol Sanmartí[1], Santiago Torras[1], Carlos D. Perez-Segarra[1]

[1] Heat and Mass Transfer Technological Center, Technical University of Catalonia. Carrer de Colom 11, 08222 Terrassa (Barcelona), Spain.

Abstract

A thermal accumulator system for concentrated solar power is modeled to perform a parametric study. The thermal accumulation system is a type of structured thermocline where there is a solid filler material with some channels where the heat transfer fluid (HTF) circulates. The energy is accumulated in both the HFT (a molten salt) and the solid (a ceramic material). The model considers a simplified 3D domain for the solid, considering a single channel and taking advantage of the symmetries of the problem. For the fluid, a 1D step-by-step discretization is used, and the solid and fluid are coupled using a conjugate heat transfer (CHT) approach. The studied parameters are geometrical parameters (tank diameter, tank height, channel diameter, distance between channels, and channels arrangement) and operational parameters (charge and discharge cycles criteria, mass flow rates).

Keywords: Concentrated Solar Power, Thermal Energy Storage, Thermocline, CFD

1. Introduction

Solar towers are a type of solar renewable energy that consists of redirecting the direct solar energy from a set of mirrors, heliostats, to a small region, the receiver. These elements make up the solar field. The receiver has a circulating heat transfer fluid (HTF), generally a molten salt, that transports some of the thermal energy to a power block to generate vapor. The remaining thermal energy is stored in a thermal energy storage (TES) tank. The energy from this storage tank is used to power the turbine when needed (e.g., at night).

The traditional thermal storage consists of a two-tank system (Pelay et. al., 2017), where the high-temperature molten salt is stored in one tank, and the low-temperature molten salt is stored in the other one. An alternative storage system is using a single thermocline tank. Thermocline systems work with a porous filler material where the fluid can freely move, and the energy is stored on the solid filler material and the fluid. More information on these types of systems can be seen in (Galione et. al., 2015) and (Gonzalez et. al., 2016). A variant of this type of system is to consider that the filler material is arranged in a structured pattern, where the solid is a continuous material with some channels or tubes where the HTF can circulate. In this work, the structured variant will be studied.

2. Case geometry and operation conditions

A schematic representation of the studied storage tank is shown in Figure 1. It consists of a solid material called the bed, which has some drilled or manufactured channels inside. A molten salt flows inside the channels. To give an idea of the orders of magnitude of the studied case, the diameter of the tank is at the order of $D_{tank} \sim 45\ m$, its height is at the order of $H \sim 13\ m$, and the channels have a diameter of approximately 1 cm. In this particular case, the number of channels in the tank is greater than 4 million.

These channels/holes can be arranged in different geometrical patterns. One parameter that can be modified is the diameter of the channels, another parameter is the distance between channels, and finally how these channels are arranged. In the studied case, two channel arrangement are considered, one where all the tubes are in line (square arrangement) and another one where the tubes are staggered (triangular arrangement, as seen in Figure 1).

In addition to the HTF inside the channels, the tank has also bottom and top buffer zones with the HTF. The bottom part of the tank has molten salt at a low temperature ($T_d \sim 300\ ºC$) while the top of the tank has hot molten salt at a high temperature ($T_c \sim 565\ ºC$). The physical and thermal properties of the molten salt are taken from (Bonk et. al., 2018) and are temperature dependent. Therefore, this has to be considered in the analysis. The studied molten salt can have up to 10% variation in density due to temperature changes, so for a fixed mass, the volume will change. This change of volume occurs at the top buffer zone, where its free surface can move up and down to compensate for these changes in density.

© 2022. The Authors. Published by International Solar Energy Society
Selection and/or peer review under responsibility of Scientific Committee
doi:10.18086/eurosun.2022.13.22 Available at http://proceedings.ises.org

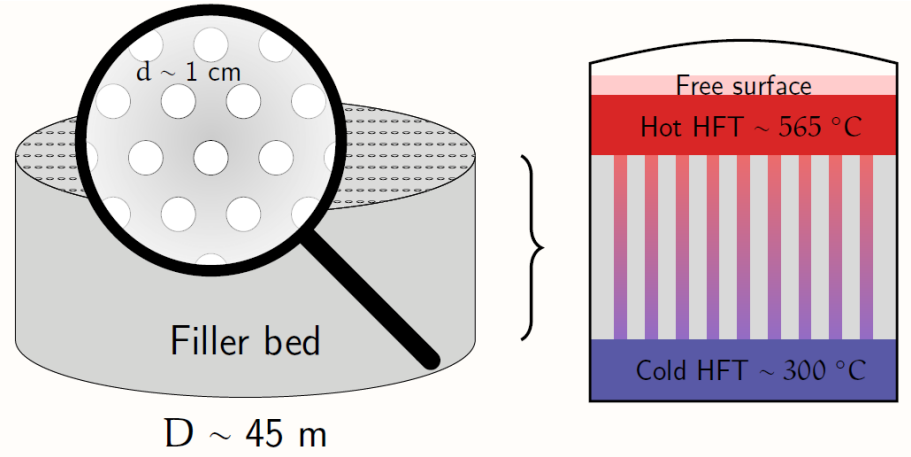

Fig. 1: Geometry of the filler bed (left) and the overall tank (right).

The working regime of the tank consists of two operational modes, one of charging (Figure 2, left) and the other of discharging (Figure 2, right). In the charging operation regime, the energy from the solar field heats the fluid (molten salt) that circulates downwards the storage tank, increasing the temperature of the solid filler material. In the discharging process, the molten salt circulates upwards and the energy stored is delivered to the fluid that goes to the power block to generate vapor.

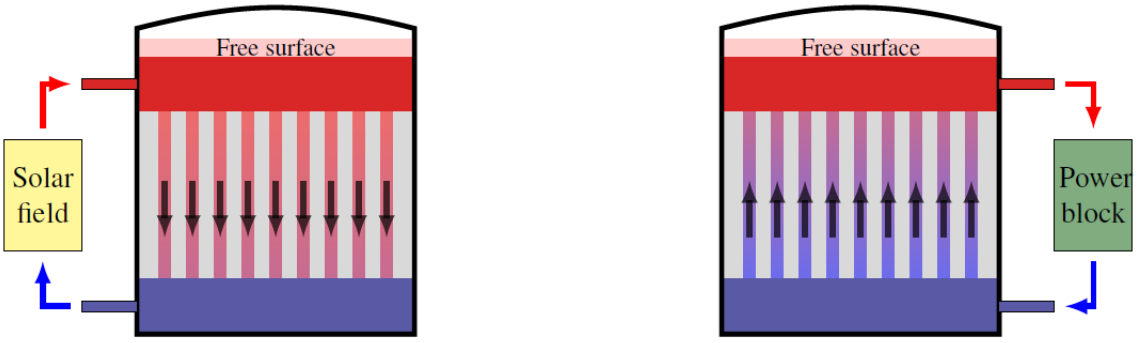

Fig. 2: Operation regimes of the tank. Charging process (left) and discharging process (right). Source: (Vera et. al., 2022).

In the case of our study, the behavior of the system over different cycles is evaluated, with particular emphasis on the case where it has reached a stationary cycling condition (once there is no significant difference between consecutive charging and discharging cycles). A cycle (shown in Figure 3) starts with the charging process. The solar field provides heated HTF from the top, and this HTF circulates from top to bottom heating the solid bed. Once the bottom buffer zone of the tank reaches a certain cutoff temperature increment $\Delta T_{co}^{(c)}$, the HTF stops circulating and the tank enters an idle mode over some prescribed time $t_{id}^{(cd)}$ (in the evaluated cases of this work this idle time is zero for both charging and discharging modes). After this idle period, the tank starts the discharging mode. The "cold" HTF circulates from bottom to top, and it gets heated with the energy from the solid bed of the tank. The HTF at high temperature of the top is then used to supply the power block. The process continues until the top buffer zone reaches a temperature drop greater than the cutoff temperature $\Delta T_{co}^{(d)}$, then the mass flow stops, the tank enters some idle cycle for some time $t_{id}^{(dc)}$ and then the charging process starts again and the cycle is repeated. In the simulation, several cycles are simulated until a cycling steady condition is reached.

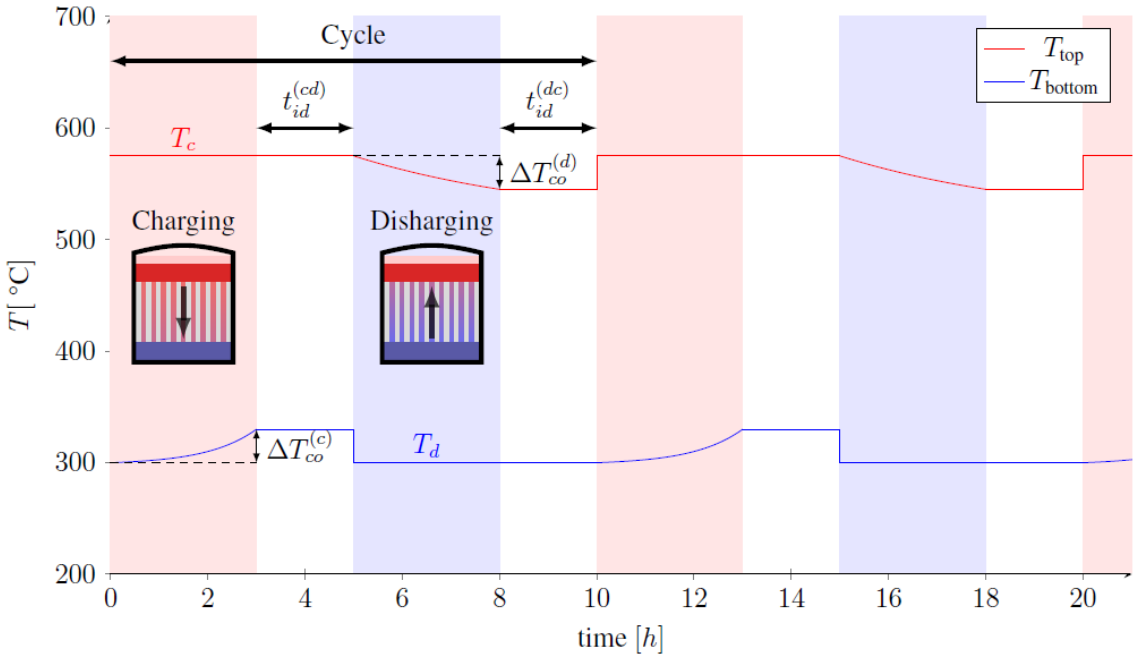

Fig, 3: Charging and discharging cycles for the thermocline. Source: (Vera et. al., 2022).

3. Methodology

The study of heat transfer is done using a conjugate heat transfer (CHT) approach. Assuming uniform flow distribution and negligible heat losses to the ambient, a basic cell of the domain is fully modeled. The selected region of the solid and fluid is shown in Figure 4. The computational domain is then chosen considering the planes of symmetry, and assuming that the inner tubes behave equally due to this symmetry.

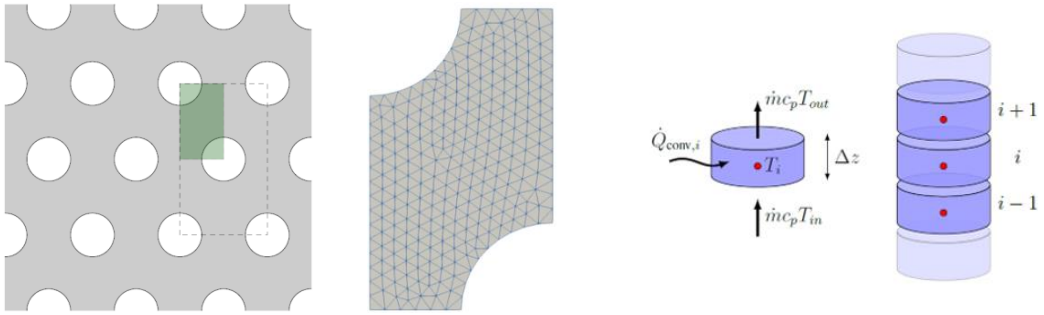

Fig. 4: Domain and meshing of the solid (left) and fluid (right).

The solid is discretized with a 3D extruded mesh. The conduction heat transfer equation (eq. 1) is solved by employing a finite volume approach, considering adiabatic boundary conditions for the walls at the symmetry planes, and a coupled convection boundary condition for the tube walls in contact with the fluid.

$$\rho_s c_{ps} \frac{\partial T}{\partial t} = \nabla \cdot (k_s \nabla \mathrm{T}) \qquad \text{(eq. 1)}$$

In the periodic faces, an adiabatic boundary condition $\dot{q} = 0$ is imposed.

The fluid is discretized using a 1D mesh. The continuity (eq. 2) and energy (eq. 3) equations are numerically solved with the Finite Volume Method (FVM).

$$\frac{\partial \rho_f}{\partial t} + \nabla \cdot \boldsymbol{v} = 0 \qquad \text{(eq. 2)}$$

$$\rho_f c_{pf} \left(\frac{\partial T}{\partial t} + \boldsymbol{v} \cdot \nabla T \right) = \nabla \cdot \left(k_f \nabla \mathrm{T} \right) \qquad \text{(eq. 3)}$$

For the continuity equation, the mass that enters and exits the domain are equal and imposed as boundary

conditions, and the height of the buffer zone at the top is calculated at each time iteration.

For the energy equation, the temperature is imposed at the top (for the charge cycle) or bottom (for the discharge cycle). For the charge cycle, the temperature is imposed at the top with T_c, while for the discharge cycle the temperature is imposed at the bottom with T_d.

The momentum equation is also solved to evaluate the pressure losses over the tubes, however, given the low speed and Reynolds number of the HTF inside the channels (order of magnitude of $v \sim 2$ mm/s and $Re \sim 18$), the pressure losses were shown to be mainly due to the change of potential energy of the HTF from bottom to top ($\rho g \Delta h$), while the other terms were negligible.

The time scale of the case is in the order of hours or even days, so a large timestep is needed to compute the case with affordable computational resources. Therefore, the solid and the fluid are discretized using an implicit approach to allow large timesteps. The CHT coupling between the solid and the fluid is done using a semi-implicit approach. More information on the model is shown in (Vera et. al., 2022)

A reference case with fixed parameters is defined (see Table 1). Then a parameter is chosen and this parameter is changed keeping the other parameters equal to the reference case. The studied parameters can be either geometrical changes (channel diameter, distance between channels, channel arrangement, tank diameter/height) or operational changes (mass flow rate, cutoff temperature).

Regarding the channel's geometry and arrangement, the influence of changing the diameter d, the distance between tubes L_{tp}, and their arrangement (either an inline arrangement or a staggered one) are studied. Figure 5 shows a schematic of the variation of the geometry of the channel.

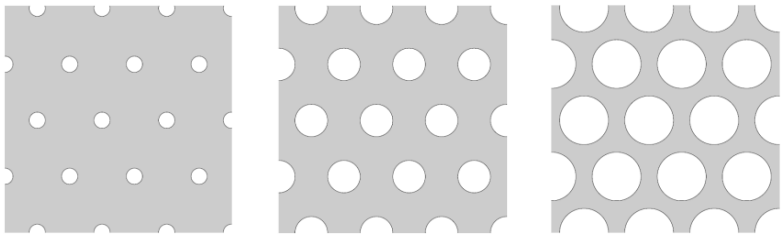

a) Channel diameters of 5mm, 10mm, and 15mm (from left to right).

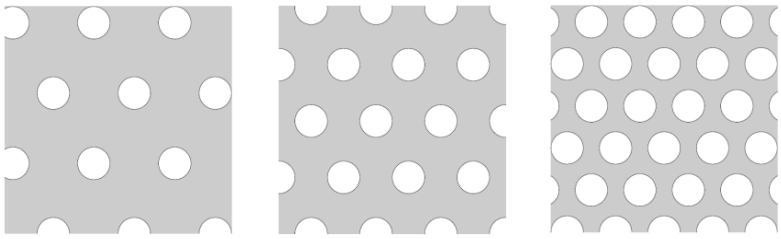

b) Distance between channels of 25mm, 20mm, and 15mm (from left to right).

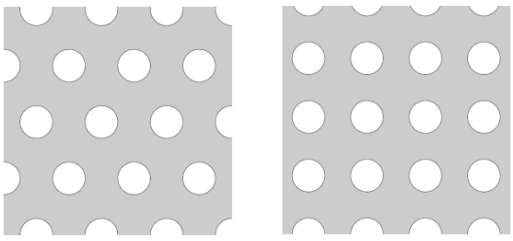

c) Channel arrangement, triangular 30° (left) and square 90° (right).

Fig. 5: Changes in the distribution and geometry of the channels .

The influence of the overall geometry of the tank is also studied. Figure 6 shows the variations in the tank

dimensions. The objective is to change the dimensions maintaining the bed volume constant, meaning that a change in the diameter will result in a change in the bed height. Given that the change in diameter influences the quantity of molten salt at the buffer zones (bottom and top), two ramifications of the cases are considered; maintain the top and bottom height, meaning that the volume of molten salt will change (see left Figure 6) or maintain the volume of molten salt and change the height (see right of Figure 6).

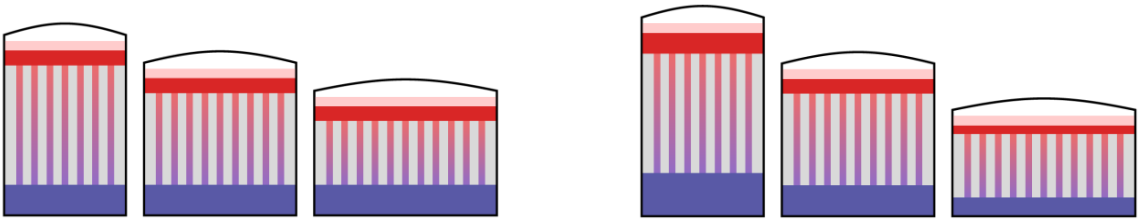

Fig. 6: Changes in the diameter and height of the tanks keeping the buffer zones height constant (left) and keeping the buffer zone volume constant (right).

The operational parameters that are studied are the cutoff temperature and the charge/discharge mass flow rate. The larger the cutoff temperature variation, the longer the duration of the cycle, so more energy is accumulated. For the mass flow, it would be expected that a high mass flow (maintaining the same geometry) increments the velocity of the molten salt, reducing the time cycle.

A summary table of all the cases and changed parameters are shown in Table 1.

Tab. 1: Summary of the values used for the parametric study (reference case in bold)

Parameter	Value	
Tank Diameter | Bed height (D_{tank} | h_{bed}) with constant bed volume and constant buffer zones height	39.40 m | 15.0 m **45.00 m | 11.5 m** 48.25 m | 10.0 m 53.95 m | 8.0 m	
Tank Diameter | Bed height (D_{tank} | h_{bed}) with constant bed volume and constant buffer zones volume, variable (h_{top} | h_{bottom})	39.40 m | 15.0 m **45.00 m | 11.5 m** 48.25 m | 10.0 m 53.95 m | 8.0 m	1.30 m | 0.65 m **1.00 m | 0.50 m** 0.87 m | 0.43 m 0.70 m | 0.35 m
Tube diameter d	5 mm **10 mm** 15 mm	
Distance between tubes L_{tp}	15 mm **20 mm** 25 mm	
Hole arrangement (constant d and void fraction)	**30º (Triangular)** 90º (Square)	
Cutoff temperature ΔT_{co}	**15 ºC** 30 ºC 45ºC	
Charge/Discharge mass flow ($\dot{m}_{charge}$ | $\dot{m}_{discharge}$) (Constant geometry)	744 kg/s | 307 kg/s **1488 kg/s | 615 kg/s** 2976 kg/s | 1230 kg/s	

4. Reference case results

For the reference case, the accumulated energy is 1311 MWh, with a charge cycle of 2.1 h of duration, and a discharge cycle of 5.1 h. It should be noted that the accumulation capacity of the thermocline storage tank is not the same at the first cycle as once it has performed multiple cycles. This behavior is shown in Figure 7. The thermocline solid bed starts all at 300 ºC and has greater accumulation capacity, and with each cycle, it loses some storage capacity until a steady state of accumulation capacity is reached.

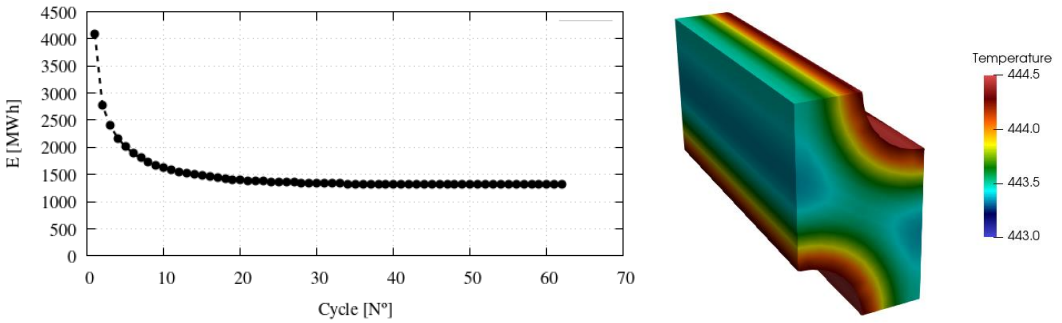

Fig. 7: Evolution of overall accumulated energy as a function of the cycle (left) and detailed temperature distribution on a region of the solid (right).

The solid bed can be studied in detail with the presented model. Figure 7 shows the instantaneous temperature distribution of the solid at some height of the channel in the cycle of charging. It can be seen that the difference between the hottest and coldest part of the solid in that section is less than 2 ºC. The solid accounts for 77% of the energy accumulation while the molten salt accounts for the remaining 23%.

The temperature distribution of the fluid over time can also be studied with the presented model. Figure 8 shows the temperature distribution of the HTF on different time instants for the charge and discharge cycles. The profiles are quite similar despite having different durations due to the difference in mass flow rates for the charge and discharge.

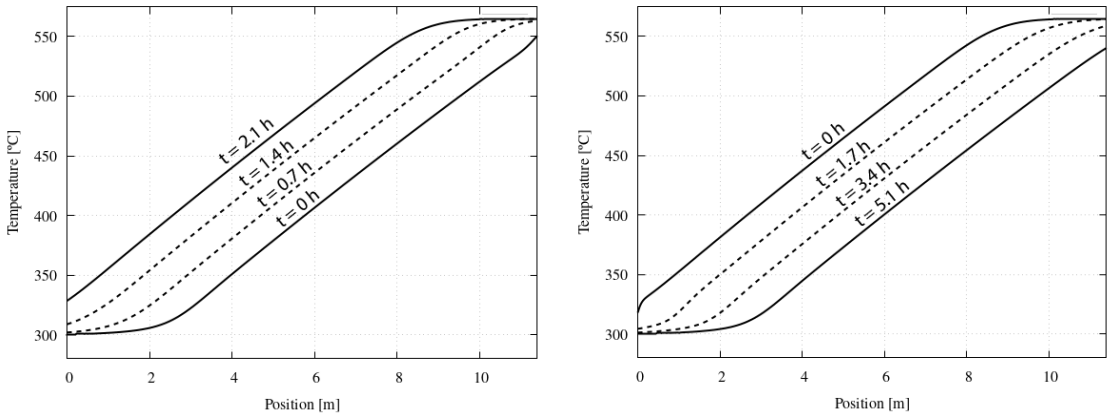

Fig. 8: Axial temperature distribution of the HTF for charging (left) and discharging (right) cycles over time.

For a fixed time instant, the HTF temperature could be approximated to a linear profile. In order to understand the duration of a cycle and the strong influence of the different parameters, let's introduce a simplified case. A perfect temperature linear profile is assumed, where the mass flow transport of the HTF is much greater than its heat convective losses. Another assumption is that there is no top or bottom buffer zone, so the cutoff criteria will be evaluated when the HTF is exiting the channels. The fluid temperature profile in this case would be similar to the one shown in Figure 9.

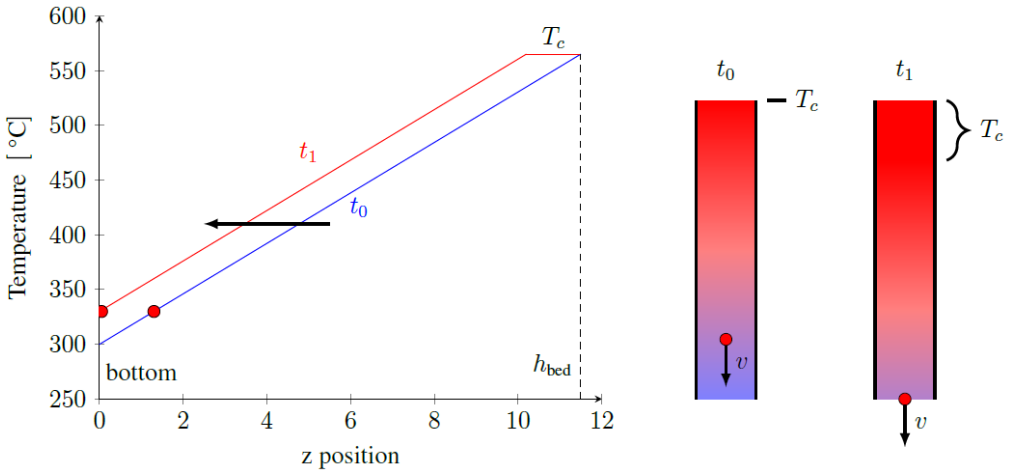

Fig. 9: Evolution of a linear fluid temperature profile over time.

The linear temperature distribution makes a translation over time. The temperature at the top has a fixed value (so a constant temperature is transported in this case). It can be seen that the velocity at which the plotted line moves is the speed of the fluid in the tubes. There is a strong dependence on the velocity of the HTF and the duration of the cycle, which affects the accumulation of energy. Furthermore, the power of the cycle seems to significantly change only with the mass flow rate.

If the buffer zone is neglected, the mean power of a cycle can be calculated with eq.4.

$$\bar{P} = \frac{\int_0^{t_{cycle}} \dot{m} c_p (T_{in} - T_{out}(t))\, dt}{\int_0^{t_{cycle}} dt} \qquad \text{(eq. 4)}$$

Considering a linear profile behavior for $T_{out}(t)$, eq. 5 expression is obtained.

$$\bar{P} = \dot{m} c_p \left((T_c - T_d) - \frac{\Delta T_{co}}{2} \right) \qquad \text{(eq. 5)}$$

Although in reality the temperature profile is not exactly linear and the results might change a bit, this gives an idea of the parameters that have more influence over the charge and discharge power, which are the temperature differences, the mass flow rate, and the cutoff temperature (although this last one has less influence).

The implication of this is that given a fixed mass flow rate, the accumulated energy will be almost proportional to the duration of the cycle. The duration is determined by how fast the outlet reaches an increment or decrease of the cutoff temperature. The worst-case scenario would be if the heat transfer from the fluid to the solid was very poor, so the fluid would not be able to transfer energy and the duration of the cycle would decrease, storing less energy. The ideal scenario would be that the heat transfer is very efficient, meaning that the fluid takes longer to reach the cutoff temperature because the heat gets dissipated to the solid, so the cycle is longer and the heat accumulated is increased. The two fluid temperature profiles of these hypothetical cases are shown in Figure 10.

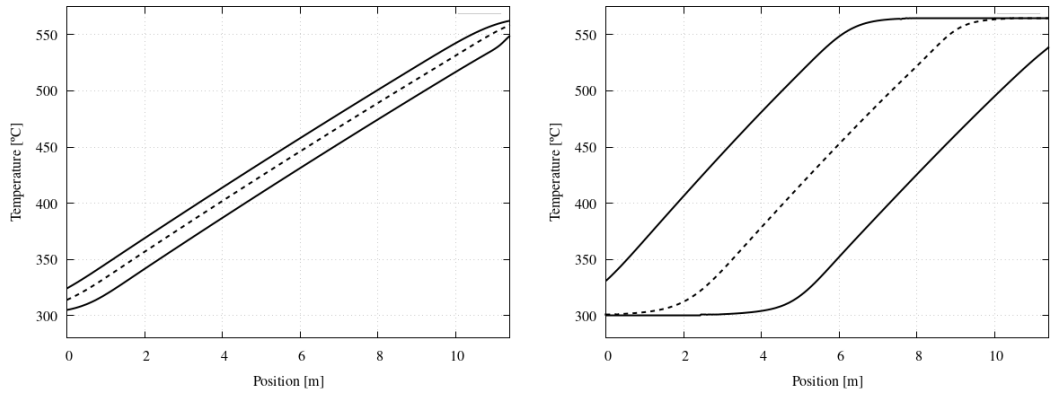

Fig. 10: Comparison of a case with low heat transfer to the solid (left) to one with high heat transfer (right).

5. Parametric results

The results of the parametric cases are shown in Table 2. The shown data correspond to a steady cycling condition, t_c and t_d are the duration of the charge and discharge cycle respectively, E_{acc} is the accumulated (or discharged) energy over a charge (or discharge) cycle, and P_c and P_d are the charge and discharge power.

Tab. 2: Results for the parametric study

#	Case	$t_c\ [h]$	$t_d\ [h]$	$E_{acc}\ [MWh]$	$P_c\ [MW]$	$P_d\ [MW]$
1	Reference case	2.1	5.1	1311	621	257
2	D=53.95m | h_{bed}=8m (const. h_{top} and h_{bot})	2.3	5.5	1411	619	256
3	D=48.25m | h_{bed}=10m (const. h_{top} and h_{bot})	2.2	5.3	1349	619	256
4	D=39.40m | h_{bed}=15m (const. h_{top} and h_{bot})	2.0	4.9	1248	621	257
2b	D=53.95m | h_{bed}=8m (const. V_{top} and V_{bot})	2.0	4.8	1222	618	256
3b	D=48.25m | h_{bed}=10m (const. V_{top} and V_{bot})	2.1	5.0	1279	619	256
4b	D=39.40 m | h_{bed}=15m (const. V_{top} and V_{bot})	2.2	5.3	1362	620	256
5	Tube diameter $d = 5mm$	1.3	3.1	786	614	254
6	Tube diameter $d = 15mm$	3.2	7.6	1960	622	258
7	Distance between tubes $L_{tp} = 15mm$	3.2	7.8	2005	623	258
8	Distance between tubes $L_{tp} = 25mm$	1.3	3.2	804	614	255
9	Square hole arrangement 90º	2.0	4.9	1264	620	256
10	Cutoff temperature $\Delta T_{co} = 30\ ºC$	4.0	9.7	2479	619	256
11	Cutoff temperature $\Delta T_{co} = 45\ ºC$	5.2	12.5	3187	616	255
12	Charge | discharge mass flow $\dot{m}_c = 744\ kg/s \mid \dot{m}_d = 307\ kg/s$	6.1	14.8	1903	312	128
13	Charge | discharge mass flow $\dot{m}_c = 2976\ kg/s \mid \dot{m}_d = 1230\ kg/s$	0.7	1.6	830	1230	509

For cases with the same mass flow rate, the charging/discharging power does not variate significantly. The accumulation of energy is defined by the duration of the cycle, which is determined by the temperature of the HTF at the outlet of the tube and the prescribed cut-off temperature.

It can also be observed that the influence of the geometrical parameters on the results is mainly due to the change in velocity. When the tube diameter increases and the mass flow is kept constant, the velocity of the fluid decreases. This means that the fluid takes longer to transport the temperature profile (while also it has more time to exchange energy with the solid), then, the cutoff temperature takes a longer time to be reached, increasing the duration of the cycle. The same effect is observed when the distance between tubes is reduced, meaning that the number of channels in the tank is greater, so the velocity decreases.

In the case of the tank diameter, if both buffer zones' heights are maintained constant, and the tank diameter increases, then the velocity will decrease and the duration of the cycle will be longer. However, if the volume of the buffer zones is kept constant, the height of these zones will change. For larger diameters, they will have less thermal inertia (than their constant height counterpart) decreasing the duration of the cycle, while for smaller diameters they will have more inertia, hence increasing the duration of the cycle.

The dependency of the accumulated energy on the velocity through a channel for the studied cases is shown in

Figure 11. In this plot, the cases for the different cutoff temperatures were neglected.

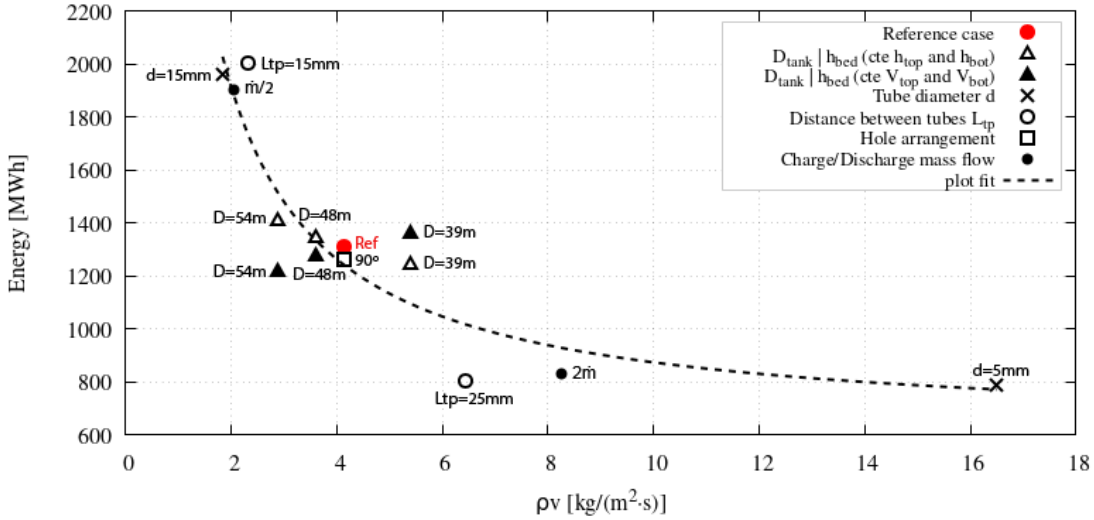

Fig. 11: Plot of the influence of velocity for the studied parametric cases (cases with different cutoff temperatures not included).

The accumulated energy trend can be modeled with an offset of some function of type $E \propto (\rho v)^{-1}$ (dashed line), although the fit is not entirely accurate for some cases, for example $L_{tp} = 25\ mm$.

6. Conclusions

A model was used to evaluate the performance of a structured type of thermocline storage tank for the accumulation of thermal energy in CSP plants. The model considers a coupled region of the fluid molten salt (1D discretization) and solid bed material (3D discretization). First, a case for a reference tank geometry was evaluated. It is observed that the capacity of thermal storage at the first cycles was greater and that is progressively reduced until it reaches the cycling periodic conditions of 1311 MWh with a charge cycle duration of 2,1h and a discharge cycle of 5,1h. Most of the energy (77%) is stored in the solid material. After that, the influence of several geometrical and operational parameters was studied. It is observed that the main difference between case results was due to the difference in fluid velocity, where this velocity is conditioned by the mass flow rate and the geometry of the tank or channels. For small velocities, the cycle is longer and the energy accumulated is greater, while for large velocities, the opposite is obtained.

Changing the diameter and height of the tank had some influence on the overall accumulation of energy, however, this influence was weak when compared to other parameters. The change in diameter and distance between tubes had a strong influence on the accumulated energy and cycle duration. If the void fraction (relation between the local volume occupied by the fluid and the total volume) increases, the energy accumulated is higher. However, more HTF is needed. In the case of the comparison of the arrangement of channels, the staggered (triangular) arrangement performed a bit better than the inline (square) arrangement, but with small differences. The increase of the buffer zone volume increases the duration of the cycles, as the HTF takes longer to reach the cutoff temperature. Also, if the cutoff temperature is increased, the system can accumulate more heat and the cycles are longer. Finally, charging and discharging power showed to be almost proportional to the mass flow rate. However, the duration of the cycles was also dependent on this mass flow rate. Even if the case of double mass flow rate had more charge/discharge power, the cycle was shorter and ended with less overall accumulated energy.

7. Acknowledgments

Newcline project is supported under the umbrella of CSP-ERA.NET 1st Cofund Joint Call and by the following National Agencies: AEI (Spain), CDTI (Spain), Jülich (Germany), SFOE (Switzerland). CSP-ERA.NET is supported by the European Commission within the EU Framework Programme for Research and Innovation HORIZON 2020 (Cofund ERA-NET Action, N° 838311).

8. References

Bonk, A., Sau, S., Uranga, N., Hernaiz, M., & Bauer, T., 2018. Advanced heat transfer fluids for direct molten salt line-focusing CSP plants. Progress in Energy and Combustion Science, 67, 69-87.

Galione, P. A., Pérez-Segarra, C. D., Rodríguez, I., Oliva, A., & Rigola, J., 2015. Multi-layered solid-PCM thermocline thermal storage concept for CSP plants. Numerical analysis and perspectives. Applied energy, 142, 337-351.

González, I., Pérez-Segarra, C. D., Lehmkuhl, O., Torras, S., & Oliva, A., 2016. Thermo-mechanical parametric analysis of packed-bed thermocline energy storage tanks. Applied energy, 179, 1106-1122.

Pelay, U., Luo, L., Fan, Y., Stitou, D., & Rood, M., 2017. Thermal energy storage systems for concentrated solar power plants. Renewable and Sustainable Energy Reviews, 79, 82-100.

J. Vera, G. Colomer, O. Sanmartí and C. D. Perez-Segarra, 2022. Modelization of a molten salt thermal energy storage for concentrated solar power. In 8th European Congress on Computational Methods in Applied Sciences and Engineering ECCOMAS 2022

Numerical Investigation and Performance Evaluation of Food Grain Drying Unit Integrated with the Thermal Energy Storage System

Ashutosh Verma[1], Rajeev Kukreja[1], Srinivas Tangellapalli[1],Dharam Buddhi[2]

[1]Dr. B. R. Ambedkar National Institute of Technology Jalandhar, Punjab (India)
[2]Uttranchal University Dehradun, Uttarakhand (India)

Abstract

In this work, the numerical study of a 10kW thermal energy storage (TES) system is conducted in order to facilitate the solar drying unit and to evaluate its potential. A drying chamber, a solar air collector, and a thermal energy storage system utilizing Phase Change Material (PCM) as a storage medium built up the investigated solar drying unit (SDU). The numerical model of the thermal energy storage system integrated with the drying unit is used to evaluate the potential of the solar dryer. The medium-range commercial-grade PCM X-180 is used for thermal energy storage purposes. The effect of various parameters on thermal energy storage (TES) and drying performance at various mass flow rates is evaluated. The results of this analysis show that the proposed design of SDU is worthy and promising since it utilizes renewable energy and reports savings between 30 to 70 % in operating cost for varying TES capacities and unit configuration.

Keywords*: Thermal energy storage, phase change material, solar drying unit, renewable energy*

1. Introduction

The drying process of agricultural commodities is essential for their preservation. Especially the drying process of pulses and grains requires a flow of hot air inside the dryer within the temperature range of 70-75ºC. To ensure the quality of the product while storage it is required to reduce the moisture content below 15ºC. A survey has been conducted for the collection of data from various food processing industries and the essential input and operational parameters of conventional grain/pulses dryer are used in this work. The conventional dryers used in process industries operate on electricity, fossil fuels, or biomass which in turn produces toxic gasses. Many of the researchers conducted an experimental study on the solar air dryer integrated with thermal energy storage (TES) for improving its efficiency, cost-effectiveness, and reducing carbon emission. Saeed Mehrana et.al [1] conducted an experimental study on a fluidized-bed dryer assisted with a solar water heater and solar powdered infrared lamp. The gas water heater used in the absence of solar energy produces a uniform drying temperature of 35 ºC and 45 ºC. The maximum energy required for the drying of rice paddy grains is 1.163kWh at the air velocity of 9m/s and drying temperature of 55ºC and 0.314kWh and air velocity of 7m/s and drying temperature of 45 ºC. The limitations with such types of dryers are less energy storage capacity due to sensible heat storage and reduced drying operation time in the absence of sunlight. However, the use of sensible storage maintains the moderate drying temperature which is the essential requirement for a quality outcome. Halil [2] conducted an experiment on the solar dryer equipped with packed bed TES used for the drying of 5 mm thick orange slices, reduces the moisture content from 93.5% to 10.28%. The exergy assessment reports the improvement of thermal efficiency of dryer, in case of using TES from 58.7% to 68.4% by the author. The average value of useful energy consumed during two set of experiments are 89.8MJ and 88.1 MJ respectively. The unavailability of solar energy in night and variation in solar radiations in day time promotes the use of TES to maintain the thermal stability and improve the drying performance and dryer efficiency. The Bilal et.al [3] conduct the numerical investigation on hybrid electric-solar dryer for food integrated with TES. These studies mostly involve the use of phase change material (PCM) suitable for sensible heat storage and low temperature latent heat storage materials with low melting point. The use of medium high temperature PCM in TES technology is the gap in literature. The present work is the theoretical model and its numerical simulation for the use of medium range PCMs in solar energy storage technologies used for drying grains/pulses.

© 2022. The Authors. Published by International Solar Energy Society
Selection and/or peer review under responsibility of Scientific Committee
doi:10.18086/eurosun.2022.13.23 Available at http://proceedings.ises.org

2. Material and method

The thermal performance and drying quality of the theoretically designed solar-drying unit (SDU) integrated with thermal energy storage (TES) have been examined in this study. Fig. 1 shows the schematic layout of the SDU and its main components (Solar collector, solar receiver, solar thermal energy storage, and air-drying chamber integrated with radiator type heat exchanger).

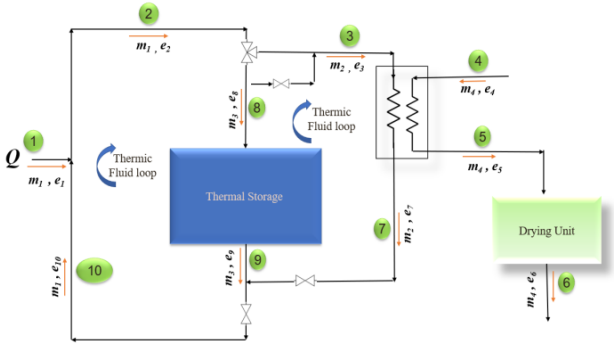

Fig. 1: Schematic layout of the solar drying unit

The solar radiation collected at the collector of 16m^2 of Scheffler dish is focused on the receiver, and transferred to the HTF passes through it. Operational parameters of the experimental investigation conducted by Dnyaneshwar Malwad [4] with the improved design of convex receiver with 68.4% of energy efficiency have been used under this study. Considering the solar radiation collected from three scheffler dishes this study is being carried out further for charging TES and drying pluses/grains. Thermophysical properties of heat transfer fluid (HTF) Thermenol 66 [5] and commercial grade PCM X-180 is used for this study, reported in table 1. The system is designed to operate in the dual-mode, wherein daytime direct drying allows the SDU to operate independently, while the TES supplies the essential energy during sunset (night). The pulses dryer facilitated with the radiator allows exchanging heat from the HTF to air, the working fluid in the pulse's dryer. The air coming from the outside passes through the radiator heat exchanger, where it heats up and then leads the drying unit to dry pulses. The thermic fluid pump of 0.75 kW and 0.5 kW air blower of calculated capacity are utilized to circulate HTF in closed-loop and air inside solar dryer, respectively. The thermophysical properties of commercial grade PCM X180 of company EPL ltd are used for this study[6] reported in Tab. 1.

Tab. 1: Thermophysical properties of PCM and encapsulation material

Material	Density (kg/m^3)	K (W/m-K)	Temperature (°C)		Latent heat (kJ/kg)	Specific heat (kJ/kg-K)
PCM X180	1330	0.36	Solid	179	280	1.4
			Liquid	180		
Aluminum	2719	202.4	--		--	8.71

3. System Design

3.1 Thermal Energy Storage (TES)

The availability of thermal energy storage of parabolic solar concentrators is the most distinctive, cost-effective, and resilient in the area of solar grain drying. The effective usage of a PCM depends on designing a device that offers adequate encapsulation for the PCM and a container for the heat transfer fluid (HTF). The geometric design of the storage system is critical for improving heat transfer rates and, as a result, for the improvement of latent heat thermal energy storage (LHTES) technology. A typical PCM-based TES device generally consists of components that can only work when incorporated into a system. Cascade arrangement of plates inside TES tanks for storing solar thermal energy utilizing PCM are technically and economically more advantageous[7]. Fig. 2 shows the configuration of plates inside the TES tank. Two distinct TES modules, one with fins and the other without fins, are used to examine the performance of the solar drying unit.

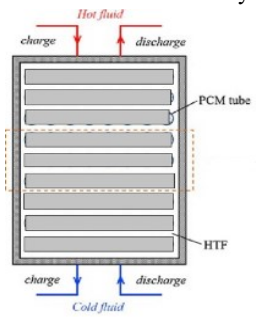

Fig. 2: Plates arrangements inside thermal energy storage (TES) tank

The hydrodynamic study is performed to determine, the gap of 2mm allow to flow HTF, between two slabs of thickness 50 mm. The one-dimensional heat flow model is derived to calculate the optimum heat transfer area and, subsequently, the fins required for the heat transfer.

3.2 Design of drying unit

The operational parameters of a continuous batch dryer of a capacity 20kg/batch are used to investigate the drying performance. The radiator-type heat exchanger of 4 kW, 0.45 effectiveness, and 6.3 m^2 of calculated area for exchanging heat from HTF to air is used[8]. The air blower of 0.75 kW forced the air at 0.21kg/s and temperature 75°C inside the dryer, reducing the moisture content from 14 to 4% in 45 minutes. The energy required for drying can be calculated using eq. 1, where M is the mass of feed, C_p is the specific heat in kJ/kg-K, MR is moisture ratio, and λ is latent heat in kJ/kg.

$$E_d = Mc_p(T_f - T_i) + MR.\lambda \qquad \text{(eq. 1)}$$

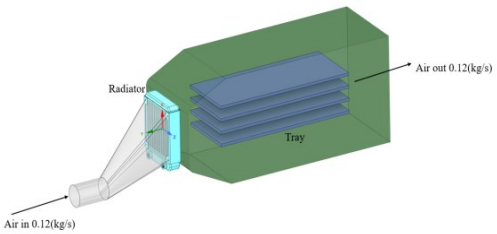

Fig. 3: Isometric view of the drying unit

4. Numerical approach

A 2D CFD dynamic model for the TES module with fin is developed using ANSYS® Fluent shown in Fig. 4. The CFD model is used to investigate the impacts of various HTF flow rates on the melting and solidification processes

of the TES and drying performance of the system. The UDF is interrupt to define HTF and PCM properties and standard k-ε turbulence model with standard wall function is selected. For the coupling of pressure and velocity, the Semi-Implicit Method for Pressure Linked Equations (SIMPLE) is used. The momentum and energy equations of the model are discretized using a second-order upwind method. The pressure staggering option (PRESTO) scheme used for the pressure correction equation. For pressure, density, body forces, momentum, liquid fraction, and energy, the relaxation factors are 0.3, 1.0, 1.0, 0.7, 0.9, and 1.0, respectively. To confirm convergence at each time step, the residual requirements are set to 10^6 for the continuity and momentum equations, and 10^9 for the energy equation.

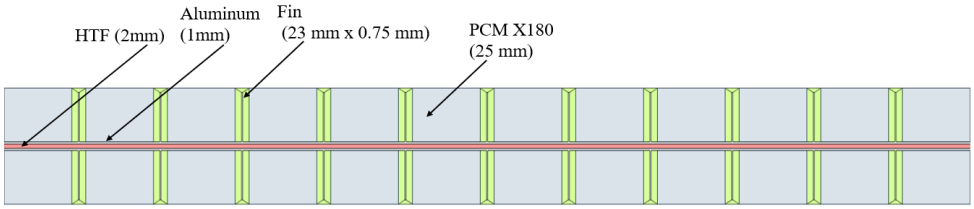

Fig. 4: 2D model for the numerical study

4.1 Governing Equation

To conduct the computation of three physical processes has been considered i.e.

I. Fluid flow modeling.
II. Conductive heat transfer.
III. Convective heat transfer.

4.2 Fluid flow modeling

The continuity equation along with Navier–Stokes equation need to be solved concurrently to mathematically model the dynamic behavior of the HTF flowing inside channel. The continuity equation is written as eq. 2:

$$\frac{\partial \rho_f}{\partial t} + \vec{\nabla} \cdot \left(\rho_f \vec{v} \right) = 0 \qquad \text{(eq. 2)}$$

Where v is the velocity and ρ_f is the density of the HTF. The N-S equation in cartesian coordinates, which accounts for momentum conservation, is given as eq. 3.

$$\rho_f \frac{D\rho_f}{Dt} = -\vec{\nabla} P + \mu \nabla^2 \vec{v} = 0 \qquad \text{(eq. 3)}$$

Where, P is the dynamic pressure term of the fluid field and μ is the dynamic viscosity of the HTF.

4.3 Conductive heat transfer: solid region

Conduction heat transfers from the HTF channel side walls to PCM must be solved using heat conduction eq. 4.

$$\rho_s C_{ps} \frac{\partial T}{\partial t} = k_s \nabla^2 T \qquad \text{(eq. 4)}$$

4.4 Convective heat transfer: solid to fluid region

Convective heat transfer from the HTF to the channel wall must be obtained solving energy equation using the velocities obtained from the answers of eq. 5. The following is the energy equation for the convective heat transfer process:

$$\rho_f C_{pf} \frac{DT}{Dt} = k_s \nabla^2 T \qquad \text{(eq. 5)}$$

Where C_{pf} is the HTF specific heat, k_s is the thermal conductivity of solid, and T is the temperature. DT/D is the material derivative term in Eq(5). governs the transient response during heat transfer process.

5. Model validation and numerical simulation

Larrinaga et.al. [7] provides a detailed description of the TES design employed in this investigation. The TES module, Case A is validated using same design parameters, material properties, boundary conditions and solver parameters used in authors experimental study. The energy accumulated and released in TES during charging and discharging process is validated with the experimental data reported in their study. The solution domain after validation is further scaled to increase the energy storage capacity for case A and in case B, fins are added to acquire the calculated heat transfer area. The time for discharging and charging of TES module for case A and case B is also calculated analytically using Eq. 8 which proves the validation of CFD results. Fig. 5 shows the energy accumulated and discharge from TES for the parameter used in Larrinaga et.al. [7] study.

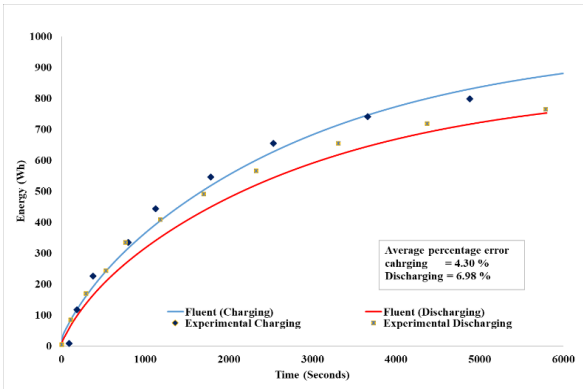

Fig. 5: Energy stored and released for the temperature range (60 - 65°C)

6. Grid independence test

A hybrid mesh is used for the discretization of the domain with an average aspect ratio of 1.1 and skewness of order 10^{-3}. Discharge of TES is computed for four different mesh for the same parameters to determine the optimal size of the element, as shown in Fig.6.

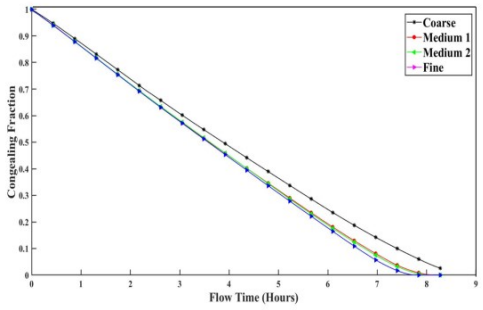

Fig. 6: Solidification Vs. Flow time at mass flow rate 0.11 kg/s

To save the computation time, medium 1 mesh is selected with 234521 elements from Tab. 2. For the optimal mesh size, the influence of the time step was investigated using three different values of 1, 0.1, and 0.5 seconds. The average

PCM liquid fraction changed very slightly when the time step was reduced from 0.5 to 1 second; consequently, the time step of 1 s was considered.

Tab. 2: Mesh details

Mesh Type	No of Elements	No of Nodes
Coarse Mesh	42000	43529
Medium Mesh 1	103500	105797
Medium Mesh 2	216000	219073
Fine Mesh	288000	291097

7. Results and discussion

For the both charging and discharging process the analysis of temperature distribution throughout domain, TES thermal efficiency, energy storage rate and the dryer performance is investigated and reported under this study. The drying quality from SDU integrated with TES is analyzed by comparing the performance assessment parameters for different mass flow rates. Fig. 7 shows the charging and discharging profile of TES system at different mass flow rate. Fig. 8 shows, the temperature contour and the high-temperature HFT near the tube wall in contact with the PCM resulting the phase transition and development of interface separating solid and liquid region separated by mushy zone. The interface propagates in the direction of negative temperature gradient resulting to the generation of wavefront of larger width near the inlet and subsequently shorter away from inlet. Due to addition of fins and large heat transfer area the charging and subsequent discharging is faster as compared to normal case.

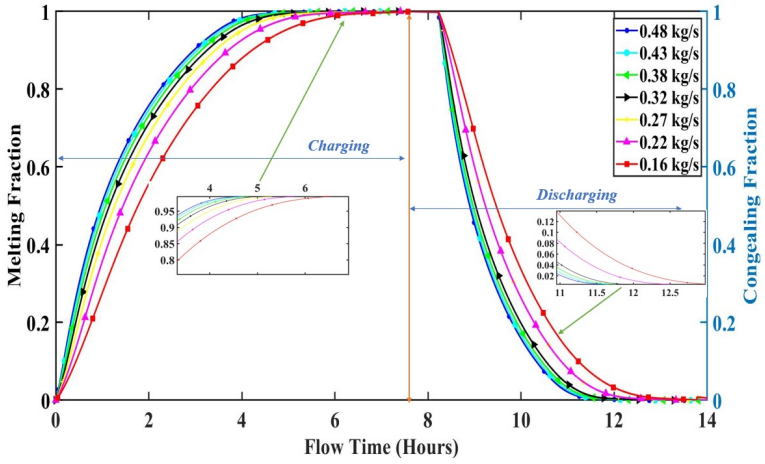

Fig. 7: Melting and solidification profile for Case A

The rate index and the efficiency index are the two most important metrics for evaluating the TES system's performance. Any TES system's efficiency must be calculated using the energy storage rate and discharge rate. The rate of energy storage in TES is computed using equation 4 and shown in figures 8 and the energy discharge and supplied to the dryer can be observed in figure 9. Assuming that the system is started at 150°C, and that the HTF enters the TES unit at 200°C, the higher initial energy transfer rate in figures 8 and figure 9 is due to the large temperature differential which is later steady.

As observed from the Fig 9 and 10, the energy difference gradually decreases and approaches to steady value, due to latent heat absorption of PCM and average temperature of the PCM reaches to its, melting point.

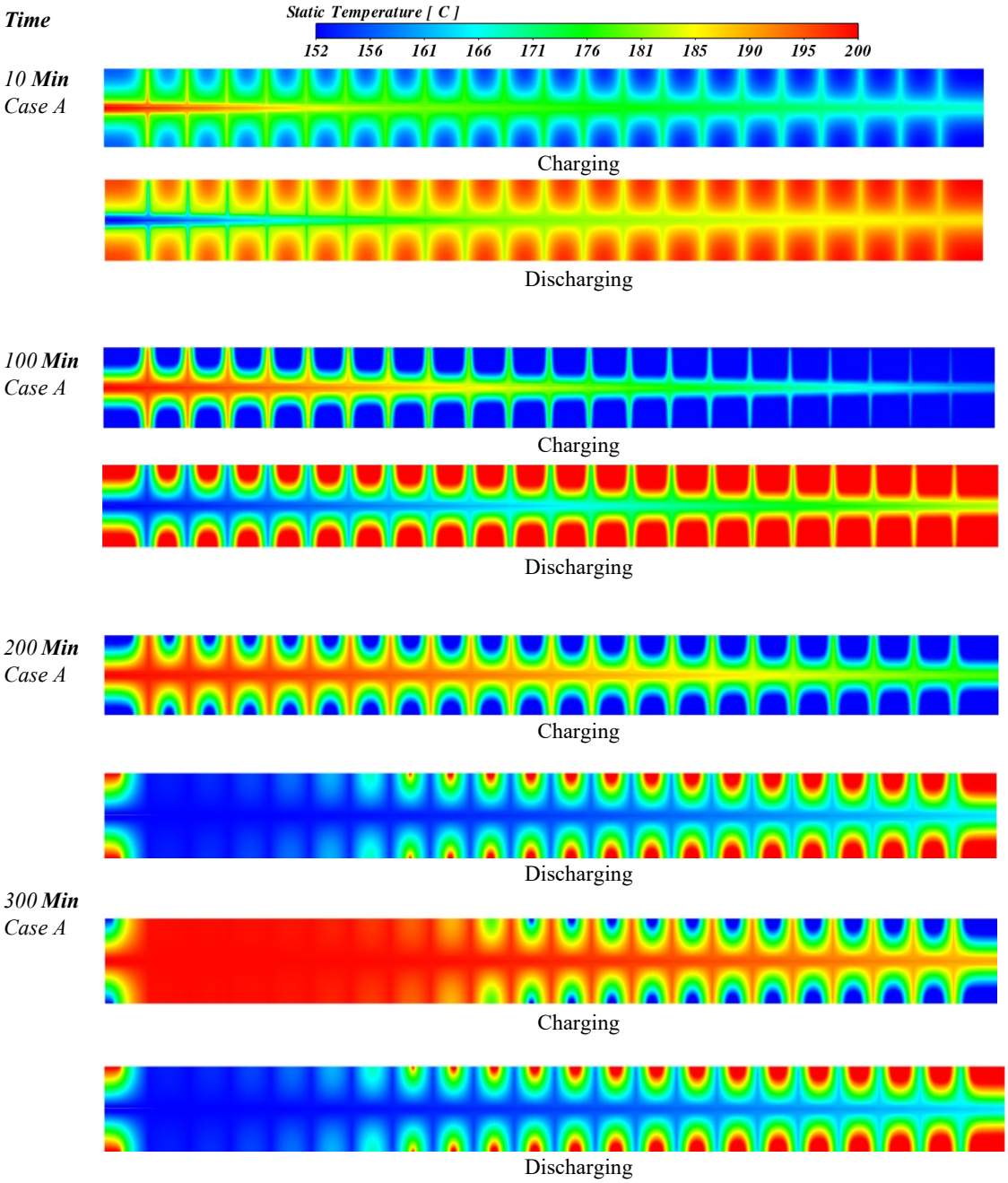

Fig. 8: Temperature contour in case of charging and discharging

It is clear from the observation that latent heat, which is directly related to the liquid volume fraction, dominates the heat storage and release processes due to presence of fin. The results of Fig. 8 shows temperature contour of the TES module with fin have a substantial impact on charging and discharging.

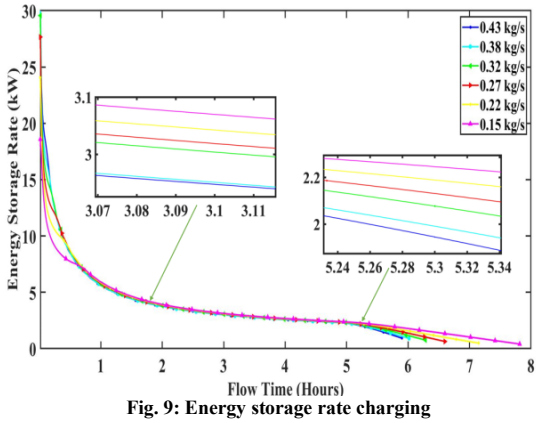

Fig. 9: Energy storage rate charging

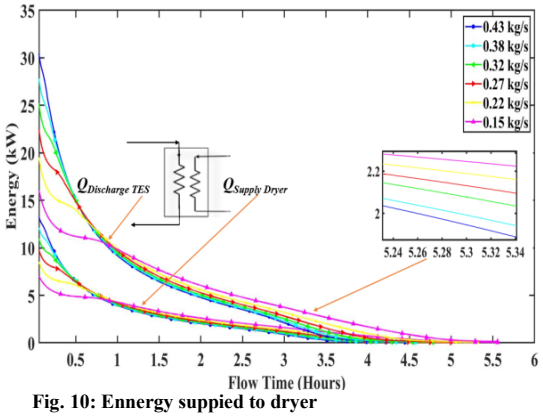

Fig. 10: Ennergy suppied to dryer

The following eq .6 is used to determine the time-averaged Nusselt number.

$$Nu = \frac{1}{\tau}\int_0^{\tau} Nu(\tau)d\tau = \frac{1}{\tau}\int_0^{\tau} \frac{qD_c d\tau}{(T_w - T_m)k_l} \qquad \text{(eq. 6)}$$

The creation of a thin liquid PCM layer near the outside wall of the heat transfer tube causes the Nusselt number to be higher at the beginning of the charging process. The Nusselt number then drops significantly once the heat resistance increases resulting to the growth of the liquid PCM layer. It's also worth noting that around t=0.4, for both the cases the Nusselt number steadily increases, showing that natural convection dominates heat transfer due to the creation of liquid PCM. The Nusselt number begins to rapidly decrease after around t= 0.8, until the charging process is completed. Because most solid PCM is entirely melted to the liquid, the heat transfer method is dominated by conduction, lowering the temperature field variation of the liquid PCM in the TES unit.

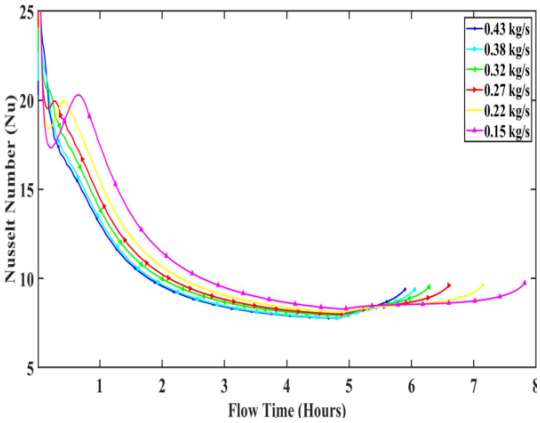

Fig. 11: Nusselt Number Charging

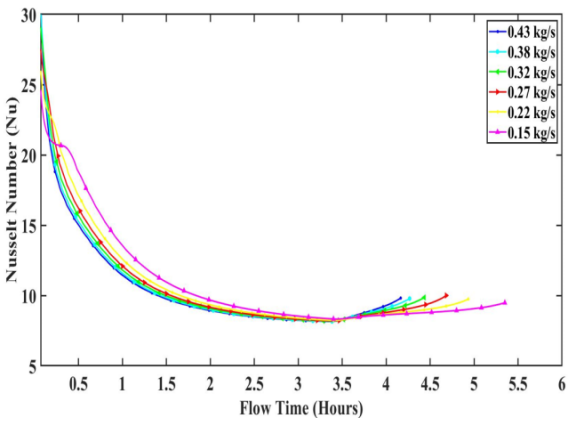

Fig. 12: Nusselt Number Discharging

The average value of Nusselt number observed over the total time duration during discharging is lower than the charging as reported in Fig. 11. The elevation in the Nusselt number curve for different mass flow rate in Fig. 11 and Fig. 12 for charging and discharging respectively is limited due to conduction is dominating and the length of heat transfer process is also greater. The typical charging and discharging inlet temperatures indicate the temperature range in which the TES system will operate. According to the experimental studies[9] conducted earlier the temperature range play a significant role in the thermodynamics and heat transport mechanisms. Fig. 13, shows the temperature profile during charging and discharging for both the case. After gaining sensible heat response of the system is more

stable in comparison during both charging and discharging, due to high uniformity index. However, the rating index and efficiency index is higher.

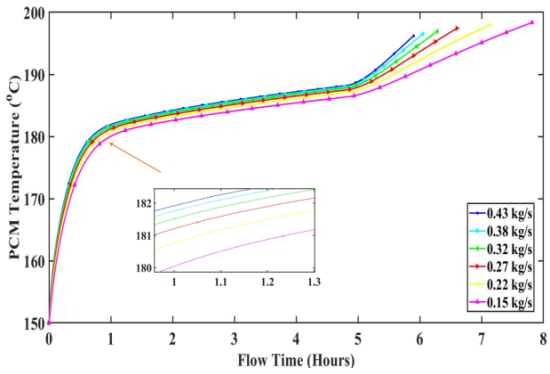

Fig. 13(a): PCM Temperature charging

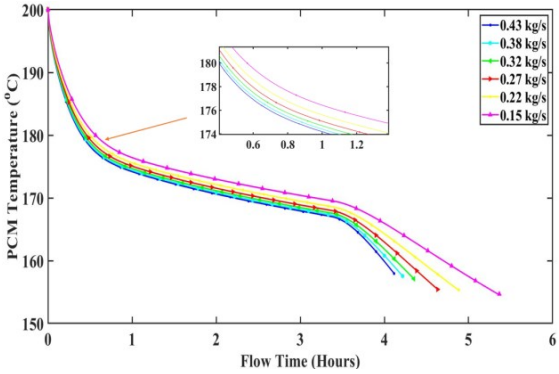

Fig. 13(b): PCM Temperature discharging

Fig. 13: Temperature profile for case A and case B

8. Conclusions

The SDU design integrated with TES for direct drying during sunshine hours and drying in off sunshine hour is proposed in this work. The performance of TES design, is numerically investigated for the different values of mass flow rate. At the lowest value of mass flow rate 0.15 kg/s the SDU performance is comparatively better. The gradient of energy supplied to the drier is less steep provides less variation in supplied energy, as observed from Fig. 9, and the time period of discharge is also increased. During discharge, the high mass flow rates reduce the unit's operational time and dried product quantity due to a sharp increase/decrease in a temperature gradient. The conventional dryer used at a commercial scale consumes either electric energy or energy released from burning fossil fuel or mass to heat air, utilized for drying. The proposed SDU unit for drying 20 kg/batch is worthy of replacing conventional dryers and utilizing renewable energy to reduce carbon and toxic gas emissions.

9. Acknowledgment

This work is conducted under Indo-Australian joint project entitled “Thermal Energy Storage for Food/Grain Drying with CST/RE to Lower Pollution” funded by DST, India

10. References

[1] Mehran S, Nikian M, Ghazi M, Zareiforoush H, Bagheri I., 2019. Experimental investigation and energy analysis of a solar-assisted fluidized-bed dryer including solar water heater and solar-powered infrared lamp for paddy grains drying. Sol Energy, 190, 167–84.

[2] Atalay H. Performance analysis of a solar dryer integrated with the packed bed thermal energy storage (TES) system. Energy 2019., 172, 1037–52.

[3] Lamrani B, Draoui A. Modelling and simulation of a hybrid solar-electrical dryer of wood integrated with latent heat thermal energy storage system. Therm Sci Eng Prog 2020, 18:100545.

[4] Malwad D, Tungikar V. Experimental performance analysis of an improved receiver for Scheffler solar concentrator., 2020. SN Appl Sci, 2.

[5] Therminol 66 Heat Transfer Fluid n.d. https://www.therminol.com/product/71093438.

[6] Crespo A, Barreneche C, Ibarra M, Platzer W. Latent thermal energy storage for solar process heat applications at medium-high temperatures – A review., 2019. Sol Energy, 192, 3–34..

[7] Larrinaga P, Diarce G, Campos-Celador Á, García-Romero A. Parametric characterization of a full-scale plate-based latent heat thermal energy storage system., 2020. Appl Therm Eng;178, 115441.

[8] Ng EY, Johnson PW, Watkins S. An analytical study on heat transfer performance of radiators with non-uniform airflow distribution 2005., 219, 1451–67.

[9] Al-Abidi AA, Mat S, Sopian K, Sulaiman MY, Mohammad AT. Internal and external fin heat transfer enhancement technique for latent heat thermal energy storage in triplex tube heat exchangers. 2013. Appl Therm Eng, 53, 147–56.

Development of a Virtual Sensor for State-of-Charge Evaluation of TCM-Energy Storage

Bernhard Zettl[1], Harald Kirchsteiger[1], Gayaneh Issayan[1], Waldemar Wagner[2], and Alois Resch[1]

[1] University of Applied Sciences Upper Austria (Austria)

[2] AEE- Institute for Sustainable Technologies (Austria)

Abstract

Sorption storage tanks for long-term heat storage have complex operating behavior that makes it difficult to determine the storage tank's state of charge. The approach of a virtual sensor is presented, which processes different measurement data and simulation data together in stages and thus helps to provide the process control with reliable and fail-safe data about the operating state of the memory.

Keywords: sorption storage, state of charge, zeolite, thermochemical energy storage, capacitive sensor

1. Introduction

Thermal energy storages (TES) are believed to be appropriate candidates to play an important role in the future thermal management system. Broad deployment of energy storage technologies for an increased share of renewable energy is motivated by global climate action and the ambition of CO2 reduction.

The ability of thermochemical materials (TCM) to store energy long-term with practically no losses during the conservation phase makes them promising candidates for seasonal storage applications. High energy densities using the zeolite-water couple have been demonstrated for some applications, exceeding those of water storage by a factor of 2-3 (Hauer, 2020) (Zettl, 2020). There are several process solutions for sorption technology, open and closed systems, as well as moving-bed and fixed-bed reactions, which have specific advantages.

For all types of energy storage, the current state of charge (SOC) is an important parameter for operation and control. In contrast to sensible heat storage, the state of charge of thermochemical storage cannot be determined via the current discharge temperature. Rather, the current moisture content of the material and the moisture distribution over the entire storage system is a representative value for the state of charge. Since the material moisture balance is much more difficult to measure with “inline” methods (without taking probes) than the temperature, various physical measurement methods were tested in a preliminary project. One of the best ways is to utilize the dielectric conductivity, or permittivity, which correlates with the moisture content of the material. It can be detected, for example, by utilizing microwaves or by determining electrical capacitance (Zettl, 2022). However, the moisture measurement methods react sensitively to density fluctuations and temperature differences in the material, therefore comprehensive error correction and the combination of different measurement methods can improve accuracy here. For this purpose, a virtual sensor is being developed that eliminates various factors that interfere with the measurement and significantly increases the measurement quality.

2. Methodology

2.1 Sensor architecture

There are currently no sensors available for directly measuring the state of charge of sorption materials storage systems. An indirect method relying on electrical capacitance measurement was shown to be feasible in a laboratory environment (Kirchsteiger and Kefer, 2020). However, the method suffers from calibration requirements which potentially restrict practical applications: Material density fluctuations in moving bed applications and temperature influences the signals widely. SOC determination can be significantly enhanced by combining hardware sensors with appropriate mathematical models for so-called virtual sensors.

© 2022. The Authors. Published by International Solar Energy Society
Selection and/or peer review under responsibility of Scientific Committee
doi:10.18086/eurosun.2022.13.24 Available at http://proceedings.ises.org

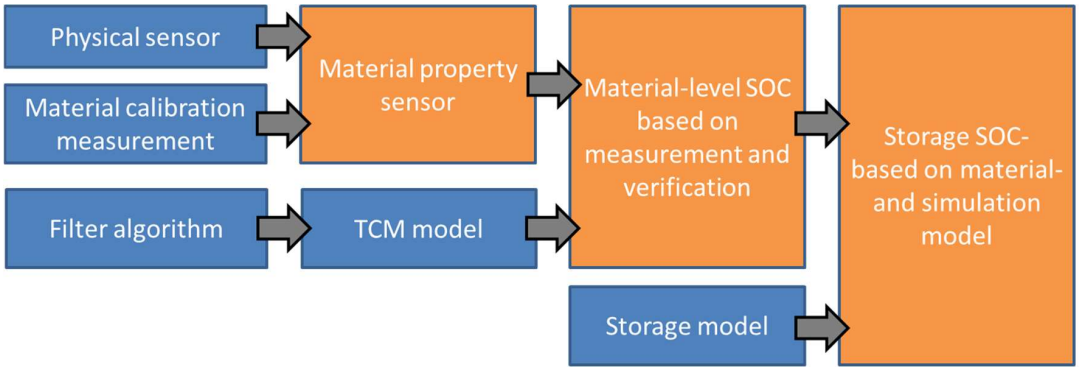

Fig. 1: Principle of the operating levels of the virtual sensor

From a systems-theory point of view, the SOC of the sorption storage is an internal state which is not accessible for direct measurement (orange elements in Fig.1). There is the possibility to estimate this internal state using sophisticated software tools such as dynamic state observers. A particular type of observer, known as Kalman-filter, is implemented to take advantage of a combined model-based and real-time measurement strategy. Appropriately tuned, the filter assures a balanced SOC estimate which is not directly affected by short-time measurement errors (for example: temporary drops in a temperature measurement) since they are not plausible compared to the implemented model. At the same time, inevitable systematic model deviations are compensated with the aid of real-time measurements.

2.2 Adsorption model

The material adsorption model used in this work represents a sorption storage system of a zeolite bed. An axial humid airflow or vapor diffusion drives the sorption process and allows direct charging/discharging of the sorption material. The model implementation is done in Simulink, an additional package of MATLAB. To perform the numerical simulations, the model is based on the following assumptions (Daborer-Prado, et al., 2019):

- a one-dimensional approach is assumed, where no radial influence is considered
- a lumped element storage model is used for material and airflow, it is assumed that the air leaves each store node with the node temperature
- the sorption equilibrium is modelled by the Dubinin-Astakhov-approach and the reaction kinetics is described by a linear driving force approach
- the specific heat capacity of the air is not a function of the humidity or the temperature in the system; the specific heat capacity of the solid is only a function of humidity (water loading) but not of the temperature in the system.

2.3 System simulation

The system simulation is based on the specific procedural features of the open and closed sorption systems, which differ in their boundary conditions. The principle of operation of typical reactor elements is shown in Fig. 2. These elements can be enlarged and combined into a more complex system to represent the storage system. Specific operating situations such as partial loading, diffusion, external losses, and internal leveling processes within the system and material changes (degradation) must be represented separately from the typical cells.

The SOC determination on the three levels, material properties, local SOC, and system SOC is intended to largely rule out errors:

- The material calibration procedure determines the relationship between the physical sensor signal and material properties
- The filter algorithm and the adsorption model verify the material property changes based on the process parameters and determine the (local) material loading,
- The storage simulation model considers the process technology and operational management of the entire

system (the sum of all cells and boundary conditions)

Using this step-by-step approach and with the help of an experimental setup and measured data for training and demonstrating the virtual sensor operation, a sophisticated approach to SOC determination for thermochemical storage is developed and a reliable metric for process control is developed.

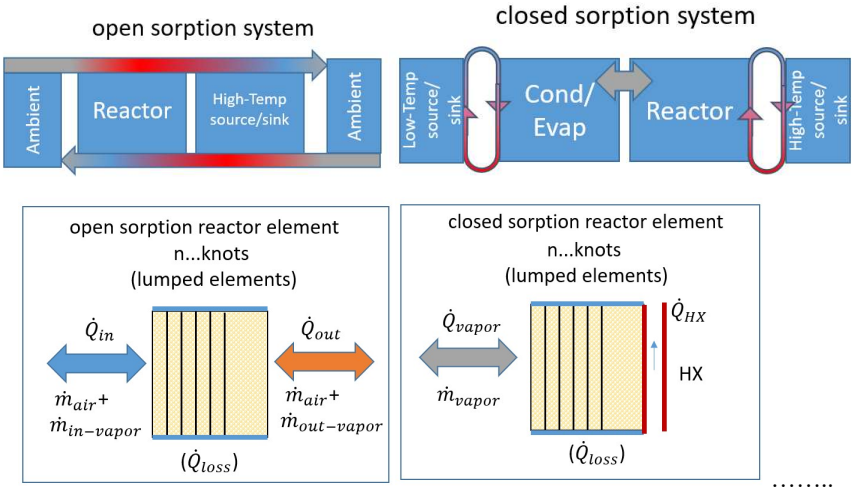

Fig. 2: Operating principle of the closed and open sorption TES (above) and the boundary conditions of two typical reactor elements

3. Experimental Results

3.1. Open Sorption Reactor

In an open moving bed reactor, a capacitive sensor is used between which electrodes the material is allowed to move freely (Fig. 3). Depending on the moisture content of the material, the electrical permittivity changes and with it the effective capacitance value of the capacitor.

To record the signal, the capacitor is integrated into a parallel resonant circuit and the resonant frequency of the resonant circuit is reacting on the moisture content of the material. The resonant frequency is therefore used as a relatively sensitive but stable indicator of the material moisture. The resonant frequency of the oscillating circuit is around 196 kHz, the capacitance of the unfilled capacitor 8.8 pF. A turntable with a diameter of 100 cm and a material volume of 15 litres simulates the moving bed of a storage system. The rotating speed of the disk is about 5 revolutions per minute.

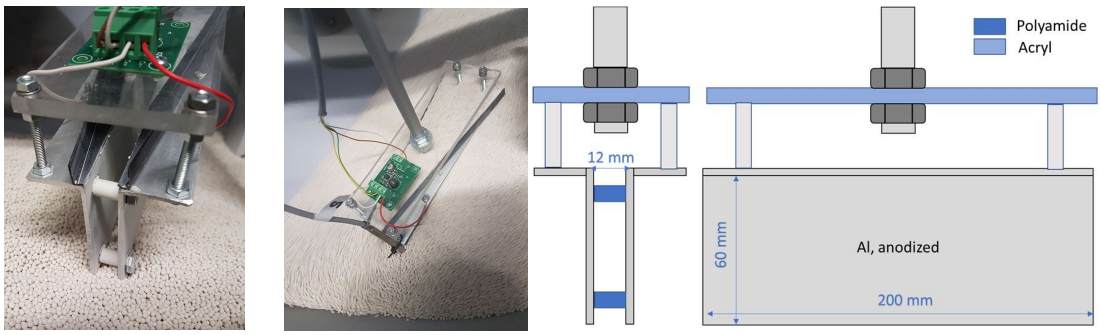

Fig. 3: Parallel plate capacitor placed in a moving bed of zeolite granules of 1.5-2.5mm diameter.

The dehydrated zeolite (12h @ 250°C) is filled into the turntable and ventilated with moist air from an ultrasonic fogger. Samples are taken at periodic intervals and the material moisture is measured using the reference measurement (2 hours in a drying furnace @ 350°C). The measurement ends when no further moisture increase is recognized in the zeolite bed. The material moisture content achieved in the experiment is approx. 5-10% lower compared to the manufacturer's data sheet.
The measurement result for two types of zeolite in four different varieties is shown in the figures below.

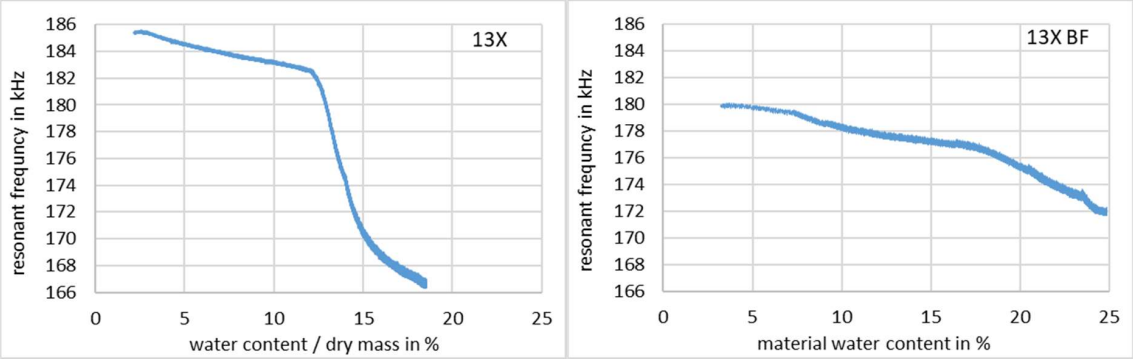

Fig. 4: Measured resonant frequency during the adsorption experiment at low temperature (25-40°C) in zeolite 13X (left) and 13X binder free (right), both 1.5-2.5 mm granules.

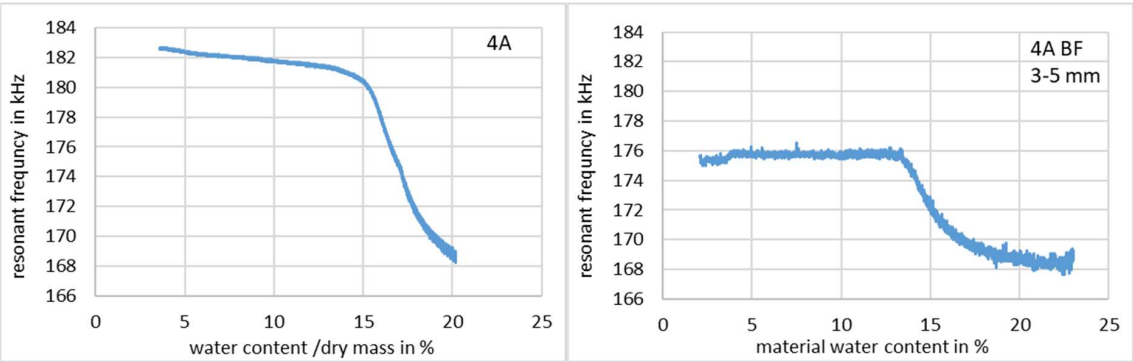

Fig. 5: Measured resonant frequency during the adsorption experiment at low temperature (25-40°C) in zeolite 4A 1.5-2.5 mm granules (left) and 4A binder free, 3-5 mm granules (right).

The results of the experiments show a clear influence of the material humidity on the resonant frequency. In general, the higher the humidity the lower the resonant frequency, but influence is non-linear: rate of frequency drop at the beginning of the experiment (dry material) is lower, for more humid material frequency drop is higher. For 4A-BF, no frequency change until approx. 13 wt.% of water was detected.

The temperature also plays a certain role, in general, higher temperatures tend to lower the resonant frequency. For adsorption reactions in the range of 30-50°C, the temperature plays no important role for zeolite 13X since the humidity influence is dominant. For other zeolites such as 4A-BF further calibration measurements should lead to a kind of temperature correction term for the resonant frequency. For high temperature desorption application (150-250°C) of the suggested measurement principle, separate calibration measurement would be necessary.

As mentioned earlier the resonant frequency relies on the active capacity in the electronic oscillator, while the capacity value itself consist of the addition of several parts: the electronic capacity inside the electronic circuit (C_p), the capacity of the sensor cable (C_C), and the sensor itself including the material (C_s). The built-in components of the oscillator are: C_p=470 pF and L=1.4 mH, the oscillator-print itself (without external components) exhibit an resonance frequency of 196.11 kHz.

$$f_r = \frac{1}{2\pi\sqrt{LC}} \quad \ldots . resonant\ frequnecy \qquad \text{(eq. 1)}$$

$$C = C_p + C_c + C_s \ldots . capacity \qquad \text{(eq. 2)}$$

$$C_s = \varepsilon \frac{A}{d}, \quad \varepsilon = \varepsilon_r \varepsilon_0, \quad \varepsilon_0 = 8{,}845\ 10^{-12} As/Vm \qquad \text{(eq. 3)}$$

A certain drop of the resonant frequency indicates an increase of the sensor capacity C_s, according to eq.1 and 2 due to an increase of relative permittivity ε_r according to eq.3. After connecting sensor and cable to the oscillator resonance frequency decreases by 3.3 kHz, which corresponds to an additional capacity C_c+C_s= 16.5 pF while C_s= 8,9 pF (according to eq.3). By measuring the further frequency decrease after inserting into the zeolite bed the permittivity of the material while humidified can be calculated.

$$\varepsilon_r = \frac{1}{\varepsilon_0}\frac{d}{A}\left(\frac{1}{L}\left(\frac{1}{2\pi f_r}\right)^2 - C_p - C_c\right) \qquad \text{(eq. 4)}$$

Calculating the relative permittivity out of the recorded frequencies leads to the results shown in Fig.6. The permittivity of the dry zeolite is in the range of ε_r =5….10, while in the hydrated material ε_r rises to 15…20. For comparison, dielectric properties of various minerals can be found in the literature. The values for sand or clay with a material moisture content between 0…..20% are comparable, with measured values of ε_r in the range of 5 to 20.

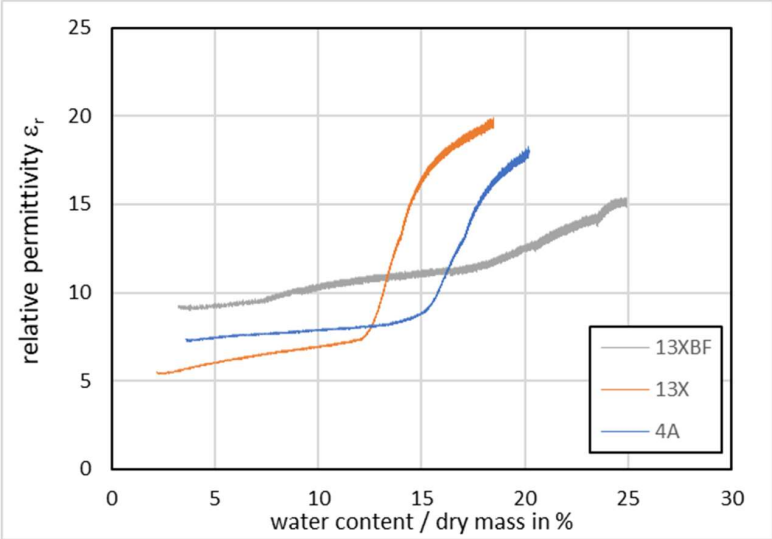

Fig. 6: Calculated relative permittivity of different zeolites

In literature the development of the dielectric constant is explained with the help of a multiphase model. In porous minerals and soils, water fraction below the point WP (Fig. 7) are addressed as “bound water”, above the porosity point P as “free water” and between as “mixed state”, producing a multi-phase signal (Park, C.-H., et.al., 2017). The so-called wilting point WP refers to a certain water fraction in a hydroscopic porous material, below which water is bound by adsorption (e.g., in clay and soil, plants are not able to benefit from it). In adsorption process engineering, the multiphase model refers to the formation of layers of adsorbate in the pores of the adsorbent: the first layer is bound more strongly than the second and subsequent ones, which form capillary condensation.

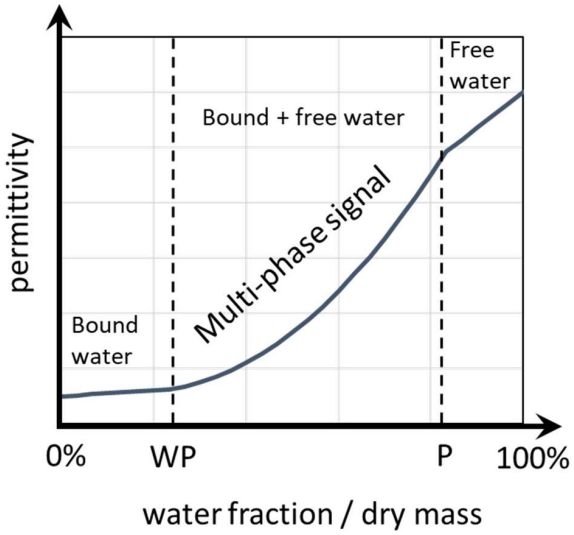

Fig. 7: Multiphase model of dielectric constant (permittivity) of humid minerals, redrawn from (Park, C.-H., et.al., 2017)

3.1. Closed Sorption Reactor

For the application in a closed sorption vessel, there are several challenges for the sensor technology, such as vacuum resistance, resistance to high temperatures (up to 200°C) during desorption, the influence of the measurement signal by the fixed-bed heat exchanger and by the locally different reaction states in the storage tank.

As shown in Fig. 8, a sector cylinder condenser was developed, which contains in the inside the same sorption material as the rest of the storage tank. The water uptake of the internal sorption material inside the enclosure

influences the capacitor and the measurement, therefore. Due to the large dimension of closed sorption vessels several regions are covered by linked sectors of the cylindrical capacitor.Fig. Fig. 9 shows a picture of several coupled sectors, so that several areas in the fixed-bed storage tank can be measured simultaneously with one sensor installation.

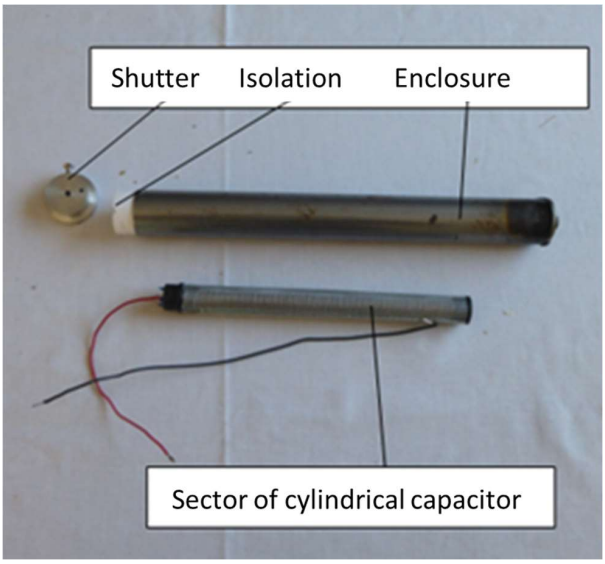

Fig. 8: Setup of the cylinder condenser



Fig. 9: Coupling of several sector cylinder condensers

Fig. 10 shows the characteristic frequency curves of the zeolite 13X BF as a function of the temperature and the degree of humidity in a fixed bet reactor. They act as the basis for programming a microprocessor when the measured frequencies and temperatures are interpreted as the degree of humidity in the measured sector.

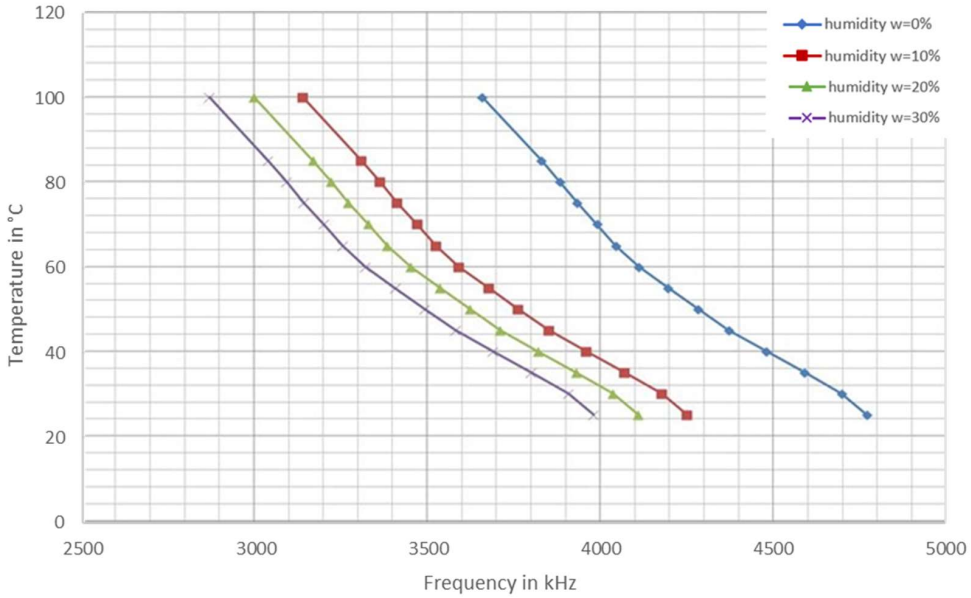

Fig. 10: Characteristic frequencies of zeolite 13X BF as a function of the temperature and the degree of humidity

The measurement results obtained by using an oscillator in the 2.5-5.0 GHz frequency range clearly show the combined humidity and temperature influence and are usable for calibration of the data controller, therefore.

4. Filter Development

4.1. General Function of Kalman Filter

A Kalman Filter is a virtual dynamical system (a computer algorithm) which is generating an estimate $\hat{x}$ of the current state x of a real dynamical system based on the history of input (u) and output (y) measurement data from the real system and a mathematical model of the system (Grewal and Andrews 2001). There are numerous applications of Kalman filters as real-time estimators, for example SOC and state of health estimation in battery cells, estimation of position and orientation of moving objects such as quadcopters for example, based on easily available accelerometer measurements. In general, it enables to estimate an internal quantity of a process which is otherwise not accessible through direct measurement, hence the alias "virtual sensor". Since the filter works with real-time measurement data, its results are affected by the corresponding measurement noise. However, under certain statistical assumptions (Simon 2006) it can be guaranteed that the Kalman Filter is a mathematically optimal estimator for linear systems in the sense that the covariance of the state estimation error is minimized.

4.2. Adsorption Model Adaption

The concept of the Kalman Filter is applied to the problem of determining the current state of charge of a sorption storage system. Here, we are considering a fixed-bed sorption storage using zeolite as sorption material as it was presented and mathematically modelled in Daborer-Prado, N., et.al. (2020). This model forms the basis for the model development required for the Kalman Filter. We are considering the 1-node model (the entire longitudinal direction of the storage is considered as one element with one lumped parameter for the water load) which uses as internal states to describe the dynamics

$$x = [x_s \quad x_G \quad T_s \quad T_{brd}]^T \qquad \text{(eq. 5)}$$

where x_s is the water load of the sorptive material, x_G is the water load of the gas flowing through the storage, T_s is the temperature of the sorptive material, and T_{brd} is the temperature on the storage exterior. The model inputs are

$$u = [m_G^{IN} \quad x_G^{IN} \quad T_G^{IN}]^T \qquad \text{(eq. 6)}$$

where m_G^{IN} is the mass flow of the gas through the storage, x_G^{IN} is the absolute humidity of the gas flow with respect to dry air, and T_G^{IN} is the temperature of the inflow gas. For details of the model development, we refer to the paper Daborer-Prado, N., et.al. (2020). The mathematical model to be used in the design phase of the Kalman Filter differs from the described simulation model. One central difference is the way how the water load x_G is treated: in the simulation model a spatial differential equation describes its behaviour with respect to the longitudinal direction, while temporal differential equations describe the outcome of the outflow water load x_G^{OUT} at the point where gas leaves the storage, depending on the other state variables x. A standard Kalman Filter requires a system of ordinary differential equations, therefore model adaptations were made in the following way.

A data-driven state space model of second order was developed which approximatively provides the quantity x_G^{OUT} as output and uses the quantities (x_s, T_S) as input. To estimate this model, data sequences at various stationary choices of the inputs u were generated using the simulation model. The estimated model obtained fit-values (a measure of the coincidence of model output and data sequences) of more than 90% on all datasets. This model contains two new state variables x_1 and x_2. The overall mathematical model for the Kalman Filter combines those two states with the ones from the simulation model described above to the augmented state vector

$$x_{KF} = [x_s \quad x_1 \quad x_2 \quad T_S \quad T_{brd}]^T \qquad \text{(eq. 7)}$$

Further assumptions were made in the development process of the Kalman Filter

- The input x_G^{IN} was assumed to be constant throughout an experiment
- The input T_G^{IN} was assumed to be constant throughout an experiment
- The states T_S and T_{brd} are assumed to be accessible through measurement on the device

Altogether, the mathematical model can be described in the general form of a continuous time nonlinear state-space model with the state x_{KF} and the input m_G^{IN}:

$$\dot{x}_{KF} = f(x_{KF}, m_G^{IN}) \quad \text{(eq. 8)}$$

As a next step, the model needs to be transferred into discrete-time. For this purpose, a simple Euler approximation with a sample time ΔT is utilized and given in the general formulation:

$$x_{k+1} = x_k + \Delta T\, f(x_k, u_k) \quad \text{(eq. 9)}$$

Note that this model is non-linear since the dynamics of the original simulation model are also nonlinear. Therefore, a standard linear Kalman Filter is not applicable and the extension of an extended Kalman Filter (EKF), see e.g. (Grewal and Andrews 2001) capable of dealing with nonlinearities could be used instead. A natural approach would also be to linearize the model around one stationary operating point and assume "small" deviations from this point during operation. There is, however, no stationary operating point in the considered application since the load x_s will continue to rise (in adsorption mode) even if all the input quantities are fixed to constant values inside the operating conditions. Therefore, an EKF was developed and implemented in the MATLAB® /Simulink™ environment using the built-in EKF functionality. The general overview of the system can be seen in Figure 11.

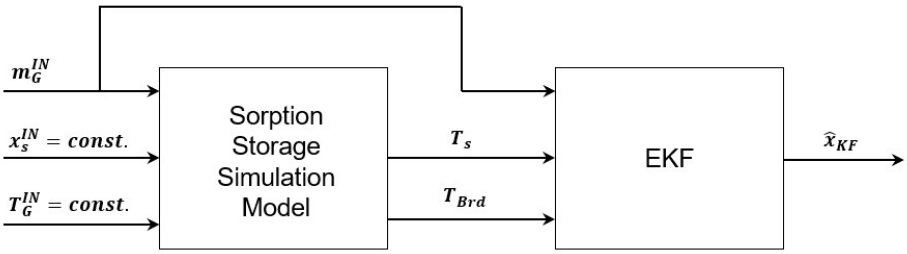

Fig. 11: Overview of the MATLAB® /Simulink™ simulation model

To demonstrate the quality of the state estimation, a simulation where the input was chosen to $m_G^{IN} = 300$ kg/h and the sorption material had an initial humidity of $x_s(t = 0) = 0.1$ was performed. The results are graphically shown in Figure 12, where the blue lines represent the quantities derived from the simulation model and the red lines are the state estimates from the EKF. Since the initialization of the EKF does not match precisely the initial conditions of the simulation model (which is a realistic assumption), there are minor deviations between the two lines in the beginning of the experiment. This is an expected behaviour of virtually any Kalman Filter application unless initial states are perfectly known. As the experiment continues, the lines begin to coincide, especially the two temperatures shown in the bottom two panels. This is because those temperatures are directly measured and the tuning of the EKF was done in such a way that the errors introduced in those measurements are assumed to be small in comparison to the errors introduced in the modelling of the states x_S and x_G. In other words, the measurement covariance was chosen much smaller than the covariance of the additive process noise affecting the model states. With respect to the actual variable of interest, the water load x_S, shown in the top panel, the EKF can reproduce its trajectory in a sufficient way and only introduces a minor offset.

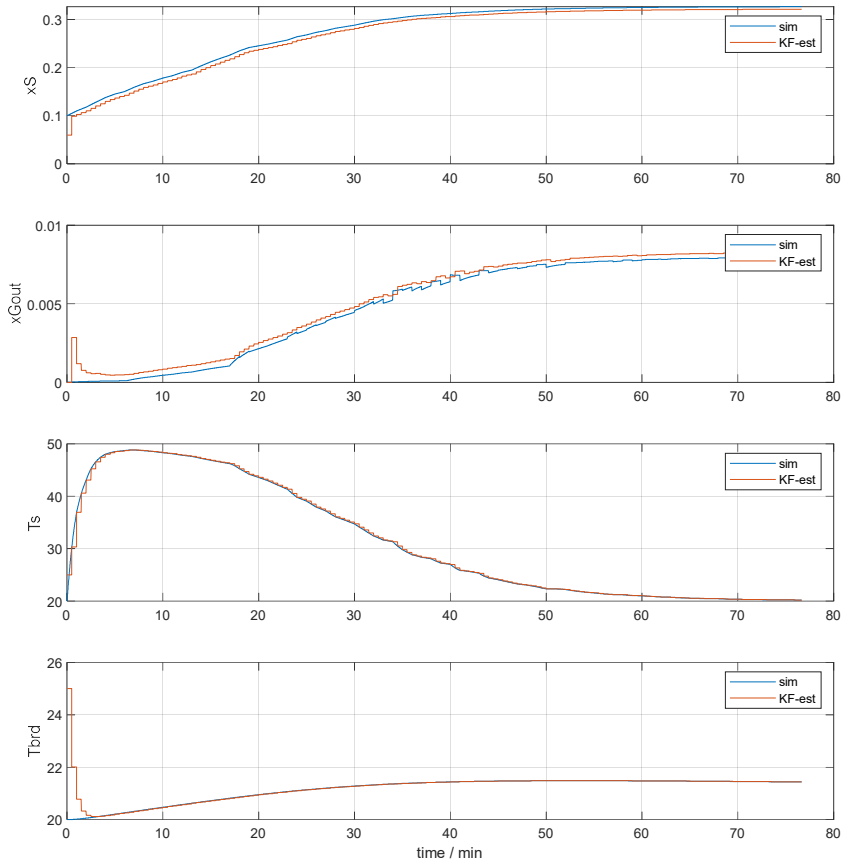

Fig. 12: Comparison of the EKF-estimated states with the simulation model

5. Summary

In order to develop a new State-of-Charge (SOC) sensor, the concept of a virtual sensor concept was applied, combining physical measurements, adsorption model, and system simulation.

- Calibration data is used to exhibit the material relative permittivity dependence to the material humidity.
- In the 200 kHz frequency range, material water content is the dominant factor that influences the relative permittivity of 13X-BF zeolite, other materials like zeolite 4A show little changes likewise.
- In the 2 MHz frequency range, a pronounced influence of both, temperature and humidity was measured.
- The Kalman-filter is suitable to repress sensor failures by estimating the material characteristics based on a modified adsorption model. The model allows the fast in-line prediction of the future material humidity load based on the current state, sensor signals and the modified adsorption model.
- A system simulation will be used to integrate the virtual sensor into a SOC determination of the entire storage system.

6. Acknowledgments

The work was carried out in the project “SorSens”, financially supported by the Austrian Climate and Energy Fund (KLIEN) and the Austrian Research Fund (FFG-grant number 881187). Ext. Projektnummer: WI-2020-701794/12-Cz and the project RESINET, funded in the framework if IWB Investitionen in Wachstum und Beschäftigung 2014 – 2020, Upper Austria. Furthermore, the work was supported by the research project “Heat Highway” (reference number 880797, funding program “Vorzeigeregion Energie”), co-financed by the “Klima- und Energiefonds” and the government of Upper Austria.

7. References

Daborer-Prado, N., Kirchsteiger, H., Zettl, B., Asenbeck, S., Kerskes, H., 2020. Mathematical modeling of rotating sorption heat storages. Proceedings of the ISES Solar World Congress 2019 and IEA SHC International Conference on Solar Heating and Cooling for Buildings and Industry 2019. DOI: http://dx.doi.org/10.18086/swc.2019.22.01

Grewal, M.S., Andrews, A.P., 2001. Kalman Filtering: Theory and Practice, 2nd edition, John Wiley & Sons, 2001. DOI: http://dx.doi.org/10.1002/9780470377819

Hauer, A., Fumey, B., Gschwander, S., Lager, D., Lázaro, A., Rathgeber, C., Ristić, A., van Helden, W., Issayan, G. Zettl, B., 2020. Material and Component Development for Thermal Energy Storage. IEA SHC Task 58 / ECES Annex 33 IEA ECES Annex 33 - Final Report, p. 82 – 86.

Issayan, G., Zettl, B., 2021. Processing Salt-Hydrates to Thermochemical Storage Composite Materials. 15th International Virtual Conference on Energy Storage ENERSTOCK, Book of Abstracts. p. 95 – 96

Issayan, G., Zettl, B., Somitsch, W., 2021. Developing and Stabilizing Salthydrate Composites as Thermal Storage Materials. 14th International Renewable Energy Storage Conference 2020 (IRES2020) AtlantisPress, p.49-57. DOI: http://dx.doi.org/10.2991/ahe.k.210202.008

Issayan, G., Zettl, B., 2022. Novel Thermogravimetric Characterization Method for Adsorption Cycles of TCM. 15th International Renewable Energy Storage Conference 2021 (IRES2021) AtlantisPress, p.108-117. DOI: http://dx.doi.org/10.2991/ahe.k.220301.011

Kirchsteiger, H. and Kefer, P. “A Novel State of Charge Sensor Concept for Thermochemical Heat Storage.” 13th international conference on solar energy for buildings and industry (EUROSUN 2020), Athens, Greece, 2020. DOI: http://dx.doi.org/10.18086/eurosun.2020.07.09

Jin, X., Yang, W., Gao, X., Li, Z., 2020. Analysis and Modeling of the Complex Dielectric Constant of Bound Water with Application in Soil Microwave Remote Sensing, Remote Sens. 12 (2020), pp 3544, DOI: http://dx.doi.org/10.3390/rs12213544

Park, C.-H., Behrendt, A., LeDrew, E., Wulfmeyer, V., 2017. New Approach for Calculating the Effective Dielectric Constant of the Moist Soil for Microwaves, Remote Sens. 9 (2017) pp 732. DOI: http://dx.doi.org/10.3390/rs9070732

Simon, D. 2006. Optimal State Estimation: Kalman, H∞, and nonlinear Approaches. John Wiley & Sons, 2006. DOI: http://dx.doi.org/10.1002/0470045345

Zettl, B., 2020. Long-term thermochemical heat storage for low temperature applications. Proceedings of the ISES Solar World Congress 2019, p. 397-402. DOI: http://dx.doi.org/10.18086/swc.2019.08.11

Zettl, B., 2022. State-of-Charge measurement techniques for PCM and TCM IEA SHC T67/ ECES Annex 40, 2nd Expert Meeting Graz, 2-4 April 2022. DOI: http://dx.doi.org/10.1016/j.egypro.2016.06.205

O. Testing, Certification and Monitoring

Accelerated ageing test bench for advanced ceramic slabs under extreme and controlled CST conditions

Inmaculada Cañadas[1], Jesús Fernandez-Reche[2], José Rodríguez[2], Jesús Ballestrín[2], Ángel Morales[3], Gemma San Vicente[3], José Galindo[2], Víctor Candelario[4]

[1] CIEMAT-PSA. Materials for Concentrating Solar Thermal Technologies Unit, Tabernas, Almería (Spain)

[2] CIEMAT-PSA. Point Focus Solar Thermal Technologies Unit, Tabernas, Almería (Spain)

[3] CIEMAT-PSA. Materials for Concentrating Solar Thermal Technologies Unit, Madrid (Spain)

[4] LiqTech Ceramics A/S, Ballerup, (Denmark)

Abstract

The behavior of ceramic materials exposed to high solar energy fluxes is of great interest for the study of the durability of materials, especially in Concentrated Solar Thermal (CST)technologies. A new accelerated ageing test bench has been developed at the SF40 Solar Furnace for the evaluation of advanced ceramic materials in operation solar conditions.

The description of this device, as well as the keys to its operation and testing of ceramic components under controlled and extreme CST conditions is shown in the present work.

Keywords: Accelerated solar ageing, durability, CST, solar furnace, focal point receivers, advanced ceramics

1. Introduction

The study of accelerated solar ageing of advanced ceramic materials that can be used as solar receivers in CST facilities is of great relevance for an industry that is set to replace fossil fuels in the global energy landscape.

Volumetric receiver technology has been developed since the early 1990s in various research and development projects (Avila, 2011). Due to their characteristics, ceramic materials are very attractive for use as volumetric absorbers in point focus solar thermal technologies. For the development of a new system and methodology to reproduce real test conditions, it is necessary to reproduce the same ageing mechanisms in accelerated ageing testing as in real CST conditions.

The use of point focus CST technologies is recommended in order to obtain the highest solar fluxes, being the solar furnaces and parabolic dishes the most suitable facilities to control the solar parameter in a small-scale solar test. Some previous test methods for solar furnaces are included in Table 1.

In recent years, different methods and test benches have been developed at Plataforma Solar de Almería for the accelerated ageing of metallic and ceramic materials, as well as reflectors, in solar furnaces. Thus, in projects such as Sfera III project, a test bench has been developed for tubular metal alloy receivers; in Raiselife project, a test bench for secondary reflectors in central receiver facilities, and in Nextower project, two test benches for the study and ageing of materials for volumetric absorbers, one of which is described in this work.

Among the ceramic materials, porous SiC is therefore a promising material to be used, which allows testing and evaluating ceramic samples under high solar energy fluxes, but the confidence in the reliability of innovative materials and components could still be checked and improved. Thus, in order to check its durability under extreme solar conditions, flat advanced slab based on SiC has been produced and a new accelerated ageing test bench (AATB) for advanced ceramic slabs subjected to high solar energy flux densities has been developed within the European NEXTOWER research project.

© 2022. The Authors. Published by International Solar Energy Society
Selection and/or peer review under responsibility of Scientific Committee
doi:10.18086/eurosun.2022.14.01 Available at http://proceedings.ises.org

Tab. 1: Different test methods for materials or components tested in solar furnaces (Cañadas, 2021).

Material or component tested	Project/ Receiver	Facility	Conditions	Variables measured	Reference
SIRCON Foam absorber made of SIRCON (Si_3N_4)	PLVCR-5	Solar furnace of Sandia (SNLA)	T average outlet air: 625°C T max outlet air: up to 1000°C Power: 5 kW P: 10 barFlux max.: 2 MW/m^2	Testing in solar conditions	(Pritzkow, W. 1991)
INCONEL with Pyromak 2500 layer	PROMES-CNRS	PROMES-CNRS SAAF	Samples: 1 mm Inconel (after spray-gun application of paint coating). Mean irradiance: 104 kW/m^2 - 173kW/m^2, 346 kW/m^2 Period: 10s,30s, Exposure time: 1000 s, 3000 s	Normal solar absorptance, thermal effusivity Thermal conductivity, thermal contact resistance between coating and substrate.	(Boubault A., et al. 2014)
Ceramic foams (SiC and ZrB_2) as high temperature volumetric solar absorber	OPTISOL project, SFERA project, and STAGE-STE	CNRS–PROMES 6 kW solar furnace. Kaleidoscope solar flux homogenizer	T_{out}: 833 to -998°C Mass flow rate: 1 g/s. α-SiC, Si-SiC, SiC, SiC + Al_2O_3, SiC + SiO2 + Al_2O_3, ZrB_2. SiC range of porosity (72–92%)	Calorimetry and fluxmetry	(Mey-Cloutier, S. et al. 2016)
Mullite	STAGE-STE. SFERA II H2CORK project	PSA-SF40	Tmax: average value of 1180 ± 35°C T differences ranging: - 200°C (700–900°C); - 400°C (700–1100°C) - 600°C (700–1300°C)	Mechanical properties: Typical strength, strain, microscopic techniques (SEM and optical microscopy).	(Oliveira, F.A.C., et al. 2019)

2. Materials and Methods

2.1. Materials

Among the most suitable ceramic materials as absorbers in point focus solar systems, porous SiC is one of the best candidates due to its thermal, optical and mechanical properties, as well as its chemical stability.

Porous SiC slabs, of 50x50x5 mm^3 have been produced by extrusion and partially sintered by LiqTech Ceramics using two granulometry of SiC powders and fired under argon atmosphere, at temperatures between 2100 and 2300ºC for 1.5 h, in a graphite furnace.

In order to demonstrate their durability, it is necessary to test these materials under real concentrated solar extreme and controlled thermal conditions, up to their working temperature. In this work, maximum temperatures of 800 to 1100ºC are studied and some of their optical properties.

2.2. Emittance test bench

Previously to accelerated ageing tests campaigns, the emittance at high temperature has been be estimated using a new method developed by CIEMAT. An adiabatic test bench has been developed, where the slabs are embedded in an alumina block (200×200mm^2, 100mm height) to achieve stationarity in thermodynamic variables. A group of first class type K thermocouples, 1.5mm diameter × 500mm long metallic sheath, allow measuring temperatures of alumina block and sample with an accuracy of σI =±0.004 T (375 °C≤T≤1000 °C). (Ballestrín et al., 2019), working under similar solar conditions than using the AATB at SF40. This procedure was based in Ballestrín et al. (2016)

2.3. Accelerated ageing test bench

Based on solar central receivers (SCR) technology, a new Accelerated Ageing Test Bench (AATB) has been designed and developed to be installed and tested at PSA-SF40 Solar Furnace for the evaluation of individual receiver ceramic components.

The test bench includes a support able to hold the samples. A porous support made of a material compatible with the SiC slabs has been chosen, as it allows a more homogeneous forced cooling of the slabs than if they were deposited on a continuous support.

Thus, the AATB consists of a 120x120x90 mm^3 SiC honeycomb module, inserted in a 130x130x93 mm^3 steel box, opened at its front side (Cañadas et al., 2021), developed to be tested at PSA-CIEMAT SF40 Solar Furnace (Rodriguez et al., 2016). As the durability tests of ceramic specimens are conducted in air, under solar central receiver conditions, the samples are directly exposed to concentrated solar radiation.

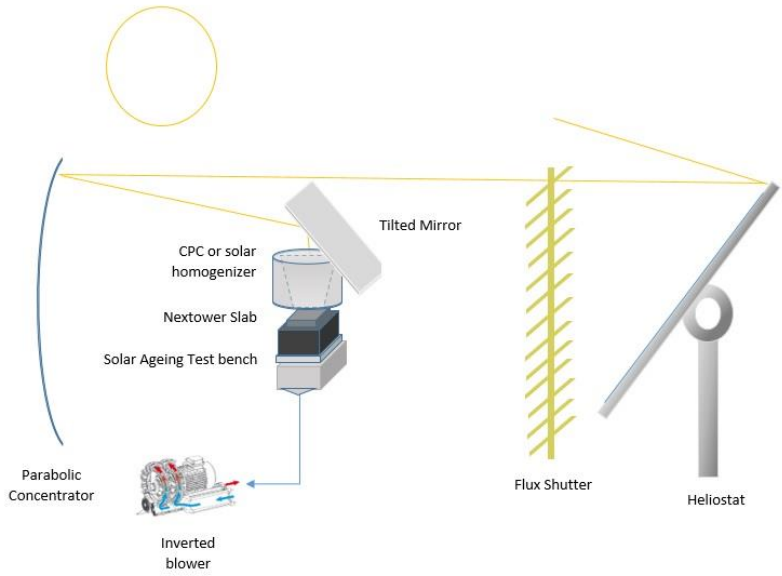

Fig. 1. Schematic draw of solar ageing test bench at PSA SF40 (CWA 17726, Cañadas et al. 2021).

A blind solar IR camera (Ballestrin, 2009) and a solar pyrometer (Ballestrin, 2010) are located in front of the samples in order to estimate the surface temperature, taking into account the emittance of the slabs at high temperature. Slabs are in contact with the front side of the honeycomb support. A solar homogenizer is placed in front of the samples to improve the solar flux on the ceramic samples (fig. 1). A flux shutter controls the power supply to the samples, and a double forced cooling system is implemented to complete the AATB and cool down the ceramic titles quickly. The forced cooling down system includes:

- A fast shutter closes instantaneously the flux on the samples (fig. 2).

- An inverted air blower, connected to the back side of the steel box, sucking the air and forcing to cool down the samples.

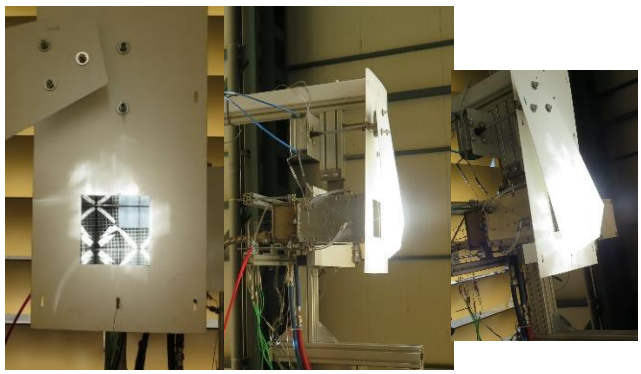

Fig. 2. a) Samples placed in solar focus with flux homogenizer, b) Fast shutter open, c) fast shutter closing under high solar flux conditions.

As the maximum temperature is reached, the cooling system starts, the forced cooling system is turned on to cool down the ceramic samples, and the flux shutter starts to closed. Depending of the desired cooling conditions, fast shutter is closed automatically, or depending of the thermal gradient, for controlling conditions. Please include acknowledgments here, before the references.

3. Accelerated solar ageing tests

The solar testing of advanced ceramics materials in the AATB, under high solar flux density (Figure 3), and correct operation and control of different SF40 parameters, allows to aged materials under extreme conditions as well as controlled CST conditions.

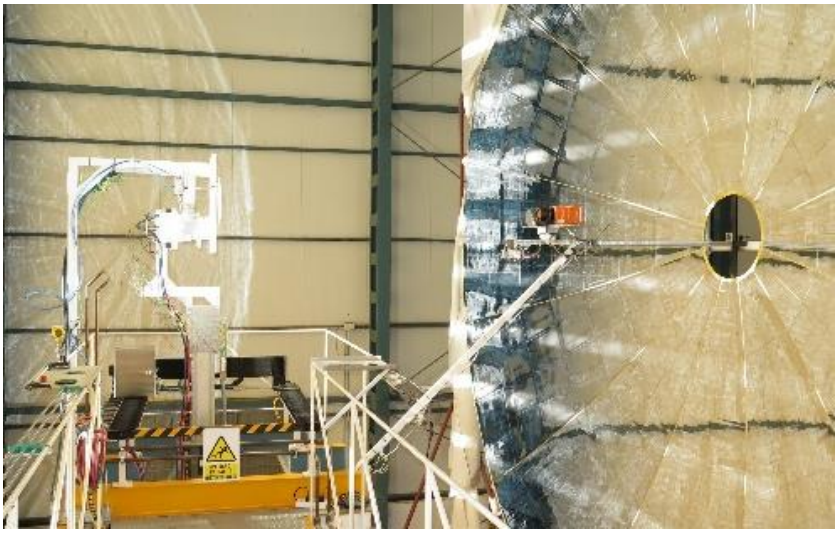

Figure 3. Accelerated ageing tests bench in solar operation at SF40.

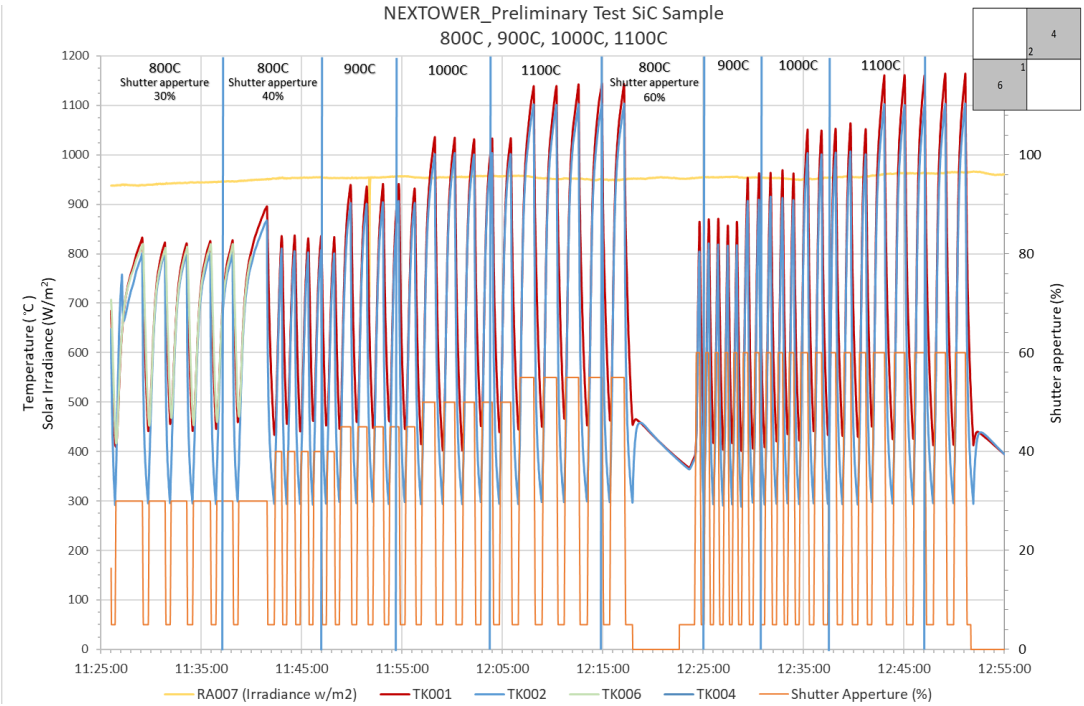

Figure 4. Preliminary test at temperatures up to 1150ºC

A preliminary test campaign was carried out to validate the test bench, and the behaviour of the materials under the solar accelerated ageing cycles (Figure 4). It shows a wide range of temperatures can be reached in accelerated conditions, controlling the maximum temperature and heating and cooling rates. Several K thermocouples

measure the temperature on the back side of the samples. A solarblind IR camera and a solar pyrometer show the temperature of the exposed surface.

Two groups of ceramic slabs were tested at PSA-SF during the initial period. Group 1 was tested in the initial configuration, as a vertical solar test bench (fig. 5.a). As far as some samples cracked due to the fixing system, the slabs were changed to the horizontal plane (fig. 5.b), in order not to limit no one of their freedom grade. So Group 2 slabs were aged using an optimized horizontal solar test bench.

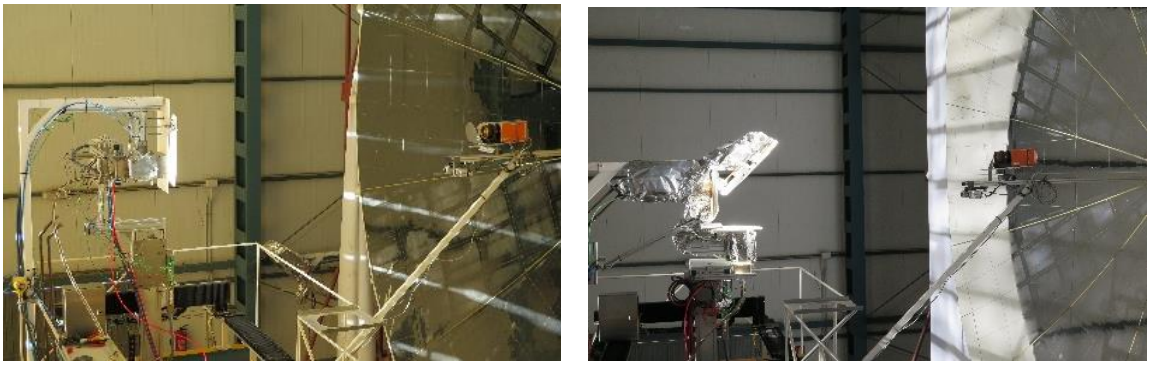

Figure 5. Comparative between a) vertical and b) horizontal plane test benches

Accelerated ageing tests are carried out by high frequency solar cycling on the ceramic tittles, as is showed in figure 6.

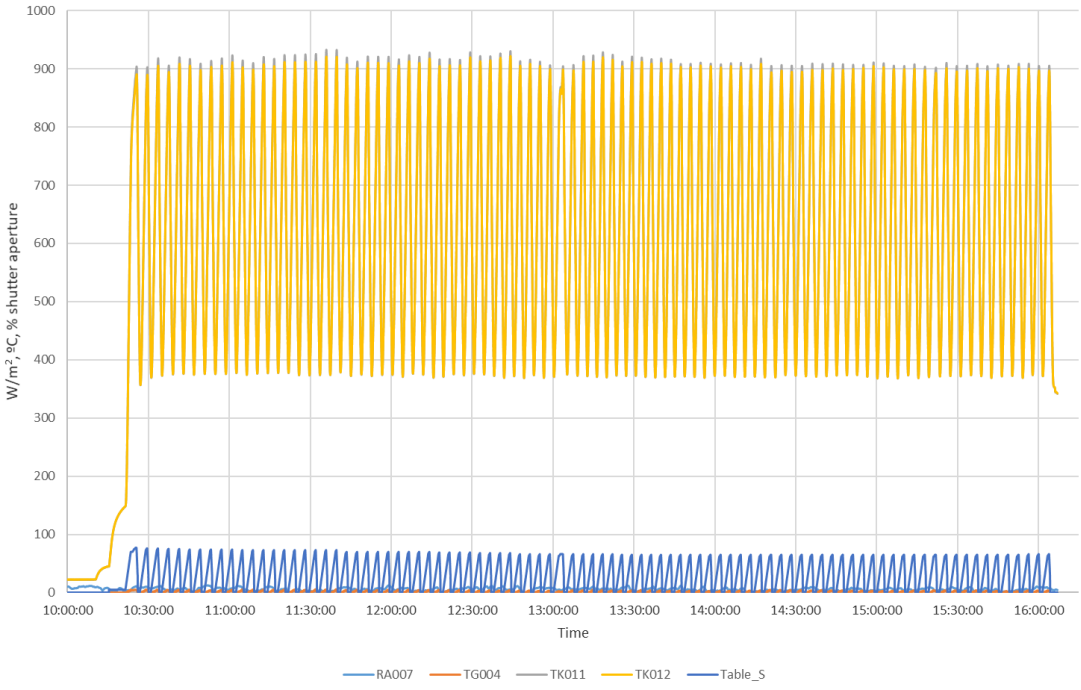

Fig. 6. Accelerated solar ageing test up to 900ºC

The solar testing of advanced ceramics materials in the AATB at SF40 Solar Furnace, under high solar flux density, controlling different operational parameters, allows to aged materials under extreme as well as controlled CST conditions. An experimental method to estimate the thermal gradient across the samples has been defined for the AATB under concentrated solar radiation. It includes two thermocouples, introduced in blind holes drilled in the samples, at different depths, in order to obtaining real thermal gradients across the sample. It is necessary to control the thermal gradient so as not to exceed the maximum allowed as it contributes to crack the slabs.

Cycles frequencies between 30 seconds per cycle up to more than 5 minutes per cycle have been studied in different groups of SiC samples. The control of heating and cooling rates and the inner thermal gradients is

necessary in order to avoid the cracking of the slabs. For these porous SiC slabs, maximum thermal gradients around 70ºC/cm are allowed in order to aged them in safe conditions.

4. Results

Different accelerated ageing campaigns, from 500 up to 10,000 solar cycles was carried out at SF40 in order to achieve up to 25 years of ageing in ceramic samples using accelerated ageing under real conditions of concentrated solar radiation.

Preliminary optical analysis shows the oxidation of the ceramics materials after the solar ageing testing. The hemispherical absorptance was measured by a Perkin Elmer Lambda spectrophotometer located at the Advanced Optical Coatings Laboratory – OCTLAB at room temperature. Emittance was estimated up to 1200ºC. Figure 7 compares the optical analysis of new samples with samples aged for 10,000 solar cycles. As figure 7 shows, the emittance has increased after the solar ageing tests, for all the samples and all the temperatures.

Fig 8 shows the preliminary absorbance αAM1.5D results of three different slabs at room temperature. This preliminary values shows absorbance increases after the solar ageing tests, for all the samples compositions, being the samples 1,3 and 5 the exposed side, and 2, 4, 6, the back side. The absorptance, as well as the maximum temperature, is higher in the exposed side, due to inner thermal gradients reached in the SiC slabs during the accelerated solar ageing test.

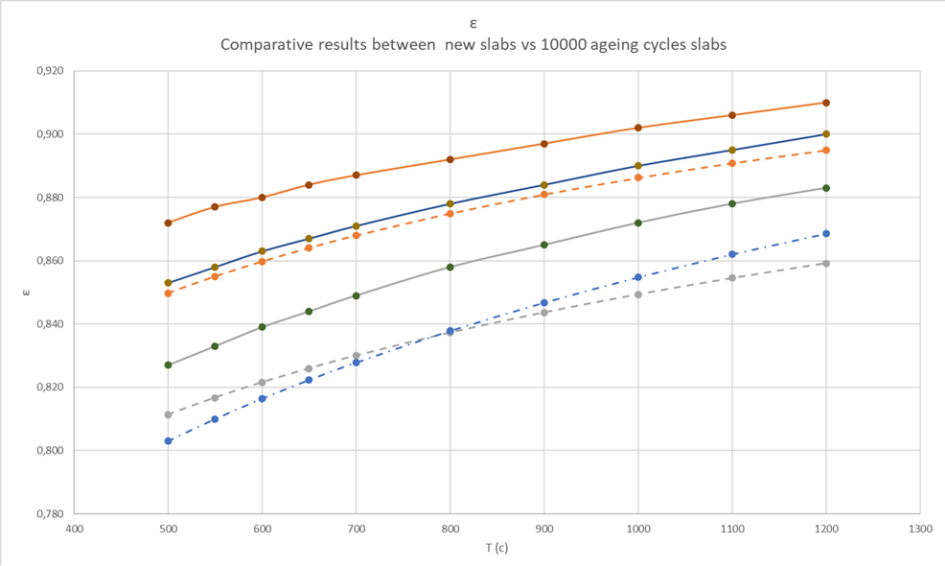

Fig 7. Comparative emittance results between different advanced slabs before solar ageing test, and after 10.000 ageing cycle. Discontinuous line (different composition new slabs); continuous line (aged slabs)

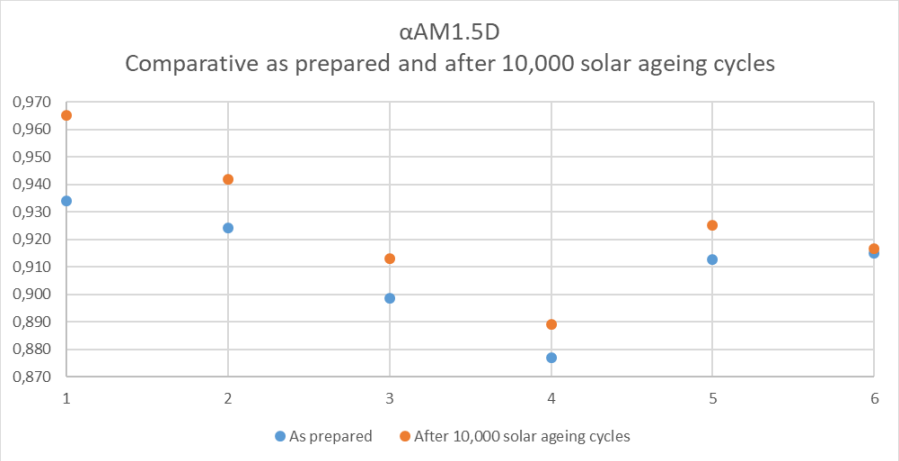

Fig. 8. αAM1.5D comparative as prepared (blue) and after 10,000 solar ageing cycles (orange)

5. Conclusions

Different ageing test campaigns have been developed during using the new AAATB, designed for the evaluation of individual plain receiver ceramic components. Experimental methods to measure the thermal gradient inside the samples and in the cups are carried out been developed, and control parameters have been improved in order to minimized the thermal gradient in slabs. Preliminary results show the emissivity increases at high temperatures. Some additional thermal and mechanical properties are described in Cañadas et al. 2021.

The results of their development and applications have been included as part of a CEN Workshop Agreement, CWA 17726 on "High temperature accelerated ageing of advanced ceramic specimens for solar receivers and other applications under concentrated solar radiation ", and their application continues in different projects such as CERAMITEC and HIDROFERR projects.

6. Acknowledgments

This study was carried out under the European NEXTOWER Project (grant n° 721045) funded by the European Commission. H2020. NMBP-17-2016 - Advanced materials solutions and architectures for high efficiency solar energy harvesting. IA - Innovation action.

7. References

Avila-Marin, A.L., 2011. Volumetric receivers in Solar Thermal Power Plants with Central Receiver System technology: A review. Solar Energy, 85, 891–910.

Ballestrín, J., Lopez, M, Rodríguez, J., Cañadas, I., Marzo, A., 2009. A solar-blind IR camera prototype. *Proceedings of 15th SolarPACES International Symposium on Concentrated Solar Power and Chemical Energy Technologies (SolarPACES2009)*. September 15-18. Berlin (Germany). ISBN 978-3-00-028755-8

Ballestrín, J., Marzo, A., Cañadas, I., Rodríguez, J., 2010. Testing a solar-blind pyrometer. Metrologia, 47 (6), pp. 646-651. DOI. 10.1088/0026-1394/47/6/003

J. Ballestrín, J. Rodríguez, M. E. Carra, I. Cañadas, M. I. Roldán, F. J. Barbero, A. Marzo. 2016. Pyrometric method for measuring emittances at high temperatures. AIP Conference Proceedings 1734, 130003; https://doi.org/10.1063/1.4949213

Ballestrín, J., Cañadas, I., Rodríguez, J., Galindo, J., Marzo, A., Carra, E., Fernández-Reche, J., Casanova, M. 2019. Emittance of materials at high temperatures for solar receivers. Infrared Physics and Technology 102, 103052. https://doi.org/10.1016/j.infrared.2019.103052

Boubault A., Claudet B., Faugeroux O., Olalde G., 2014. Aging of solar absorber materials under highly concentrated solar fluxes. Solar Energy. Materials & Solar Cells; 123:211-219.

Cañadas, I. et all. Characterization of Solar-Aged Porous Silicon Carbide for Concentrated Solar Power Receivers. Materials 2021, 14, 4627. https://doi.org/10.3390/ma14164627

CWA 17726 “High temperature accelerated ageing of advanced ceramic specimens for solar receivers and other applications under concentrated solar radiation”. https://www.cencenelec.eu/media/CEN-CENELEC/CWAs/RI/cwa17726_2021.pdf (last access December 10th 2021) https://tienda.aenor.com/norma-cen-cwa-17726-2021-74091 (last access September 5th 2022)

Koehl, M. Durability of solar energy materials, 2001. Renewable Energy 24, 597–607. https://doi.org/10.1016/S0960-1481(01) 00046-5

Mey-Cloutier, S.; Caliot , C.; Kribus , A.; Gray , Y. ; Flamant G. 2016. Experimental study of ceramic foams used as high temperature volumetric solar absorber. Solar Energy 136, 226–235

Oliveira, F.A.C., Fernandes, J.C., Galindo, J., Rodríguez, J., Cañadas, I., Rosa, L.G. 2019. Thermal resistance of solar volumetric absorbers made of mullite, brown alumina and ceria foams under concentrated solar radiation. Solar Energy Materials and Solar Cells 194:121–129. DOI: 10.1016/j.solmat.2019.02.008

Rodríguez; Cañadas, I; and Zarza, E., 2016. "New PSA high concentration solar furnace SF40", AIP Conference Proceedings 1734, 070028. https://doi.org/10.1063/1.4949175

Pritzkow, W. 1991, Pressure loaded volumetric ceramic receiver. Solar Energy Materials Volume 24, Issues 1–4, 2 December, Pages 498-507 https://doi.org/10.1016/0165-1633(91)90086-Z

NEXTOWER Project. https://www.h2020-nextower.eu (last access September 5th 2022).

RAISELIFE https://cordis.europa.eu/project/id/686008 ; http://193.146.147.223/ (last access September 5th 2022).

SFERA III https://sfera3.sollab.eu (last access September 5th 2022).

Accelerated Aging Test and Service Life Time Estimation for Solar Collectors

Stephan Fischer[1], Jens Ullmann[2] and Karl-Anders Weiß[2]

[1] Institute for Building Energetic, Thermotechnology and Energy Storage (IGTE)/University Stuttgart, Stuttgart (Germany)

[2] Fraunhofer Institute for Solar Energy Systems (ISE)/ Fraunhofer-Gesellschaft, Freiburg (Germany)

Abstract

Based the loads and degradation observed on flat plate collectors exposed in the period from 2012 to 2020 at different locations (Kochi (India), Negev (Israel), Gran Canaria (Spain), Beijing (China), Zugspitze (Germany), Freiburg (Germany) and Stuttgart (Germany)) accelerated aging tests were developed and carried out on identical solar collectors to simulate the degradation that occurred at the exposure sites and thus estimate the service life of the solar collectors.

After and during the multi-year exposure of 7 to 8 years, the performance of the solar collectors was tested according to ISO 9806 to determine the performance degradation caused by the loads. Based on these measurements and the loads measured at the exposure sites, a model for service life estimation of flat-plate collectors was developed.

Keywords: Accelerated aging test, service life prediction, solar thermal collector

1. Introduction

In the SpeedColl (www.speedcoll.de) and SpeedColl2 (www.speedcoll2.de) projects, a consortium consisting of Fraunhofer ISE, the Institute for Building Energy, Thermotechnology and Energy Storage at the University of Stuttgart (IGTE) and representatives from industry investigated the loads and developed tests to simulate the loads for solar thermal collectors and their components. For this purpose, first test specimens were exposed outdoors for a long time at various locations (Kochi (India), Negev (Israel), Gran Canaria (Spain), Beijing (China), Zugspitze (Germany), Freiburg (Germany) and Stuttgart (Germany)). Next accelerated ageing tests were developed and carried out in the laboratory on solar collectors of identical construction to simulate the degradation that occurred at the exposure sites and thus estimate the service life of the solar collectors. Figure 1 shows an overview of the different test locations.

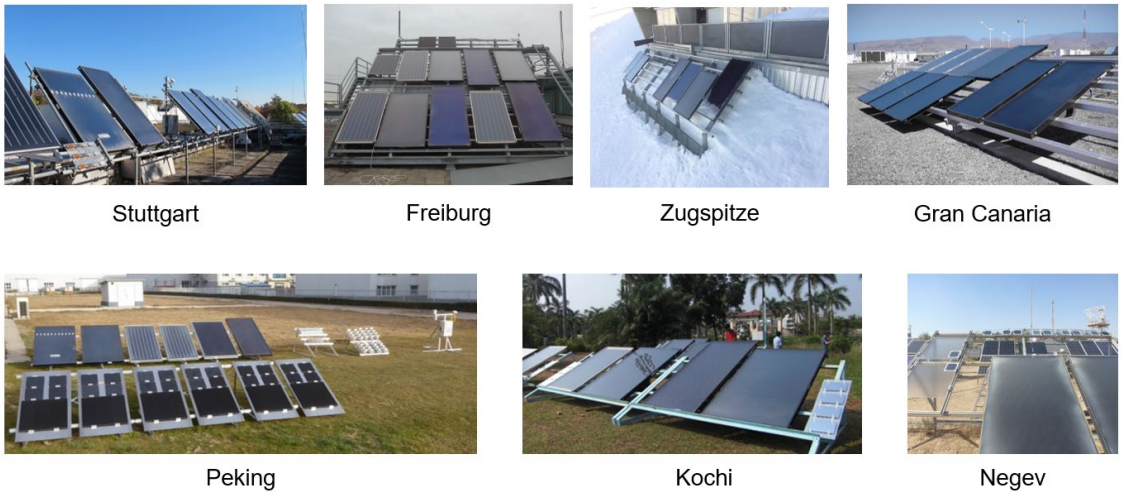

Fig. 1: Overview of the different exposure sites

The paper presents the performance degradation and degradation phenomena of the investigated collectors at the different locations. Furthermore, the revisions of the accelerated aging test procedures already defined in the

© 2022. The Authors. Published by International Solar Energy Society
Selection and/or peer review under responsibility of Scientific Committee
doi:10.18086/eurosun.2022.14.02 Available at http://proceedings.ises.org

SpeedColl project (Fischer, 2017) and their effect on the thermal performance of the solar collectors are presented and the service life of the solar collectors is estimated with the help of the results.

2. Performance degradation and degradation phenomena

All investigations and results presented in the following refer to the collectors of the 3 collector manufacturers involved in the project described in Table 1. These were exposed uncooled at the different locations for a period of 7 to 8 years.

Tab. 1: Brief description of the collector types investigated in the project

Collector	Description
Type I	Aluminium absorber, selective coating by means of Physical Vapour Deposition (PVD), copper absorber tubes, ultrasonically welded, aluminium casing, "floating" bearing of the glass cover with EPDM seal, solar glass, thermal insulation made of mineral wool (glass wool) on the rear wall and the side frame profiles.
Type II	Aluminium absorber, selective PVD coating, copper absorber tubes, laser-welded, aluminium casing, silicone bonding of frame and glass, solar glass, thermal insulation made of mineral wool (rock wool) on the rear wall.
Type III	Aluminium absorber, selective PVD coating, copper absorber tubes, laser-welded, aluminium casing and rear wall made of sheet steel, silicone bonding of frame and glass, solar glass with anti-reflective coating, thermal insulation made of melamine resin on rear wall and frame

After several years of exposure, the collectors were subjected to a performance test according to ISO 9806 and then opened. The main findings for the different collectors are summarised in Table 2.

Tab. 2: Damage of the different collectors

Collector	Damage
Type I	- Location-dependent dust and sand deposits on the absorber - Heavy corrosion on the collector frame and the absorber piping at the Gran Canaria site
Type II	- Location-dependent dust and sand deposits on the absorber - Heavy corrosion on the collector frame and the absorber at the Gran Canaria site - Contact glass absorber in the edge area - Fogging on the inside of the glass - Welding on collector pipes loosened
Type III	- Location-dependent dust and sand deposits on the absorber - Abrasion marks on absorber - Fogging on the inside of the glass - Welding on collector pipes loosened

Figure 2 to Figure 4 show examples of the performance curves and the difference to the new condition of the 3 collectors after 1 year, 3 years and 7.5 years of uncooled exposure at the Stuttgart site.

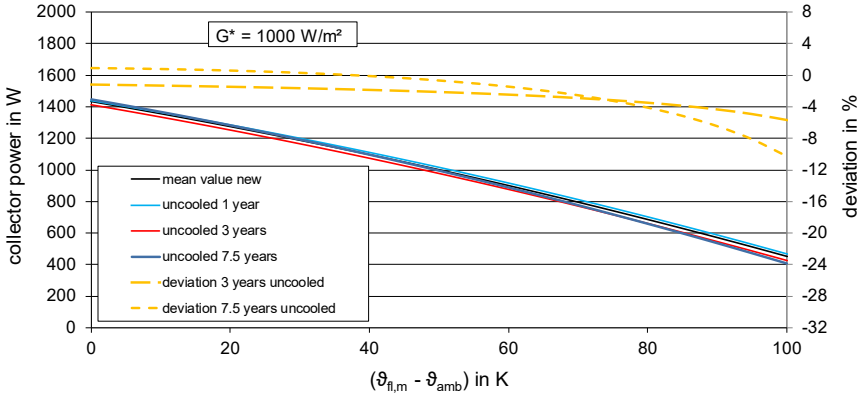

Fig. 1: Comparison of the power curves of collector type I in new condition after 1 year, 3 years, and 7.5 years of uncooled exposure at the Stuttgart site.

Collector type I shows a small performance degradation in the range of measurement uncertainty after 1 year, 3 years and 7.5 years of uncooled exposure at the Stuttgart site (see Figure 2).

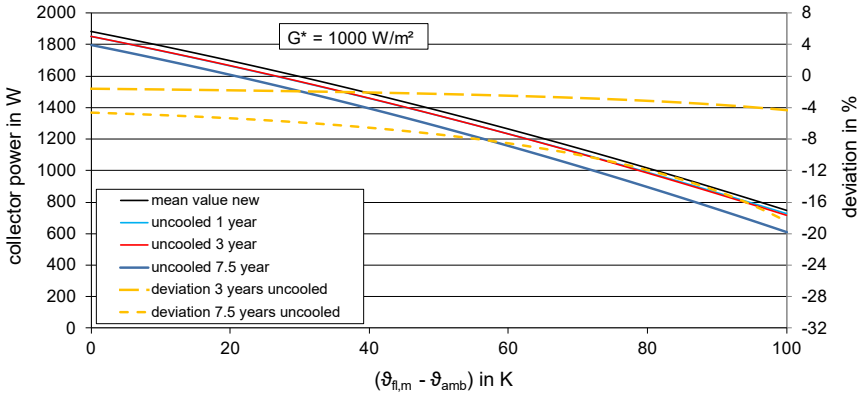

Fig. 3: Comparison of the power curves of collector type II in new condition after 1 year, 3 years, and 7.5 years of uncooled exposure at the Stuttgart site.

Collector type II shows a slight performance degradation within the measurement accuracy after 1 and 3 years of uncooled exposure at the Stuttgart site and a significant performance degradation after 7.5 years of uncooled exposure at the Stuttgart site (see Figure 3).

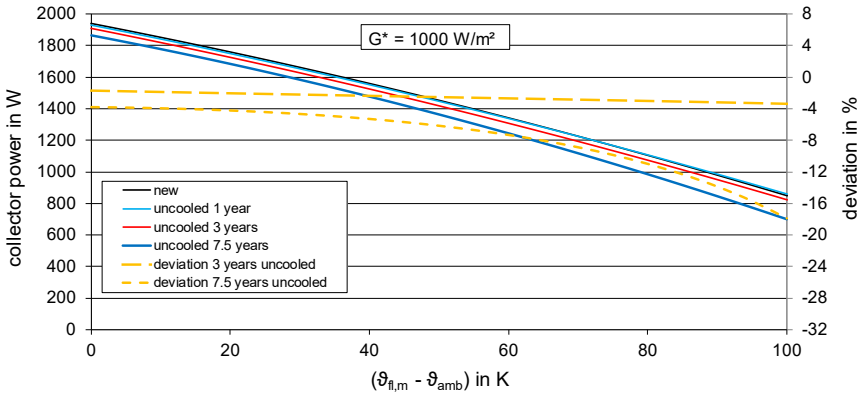

Fig. 4: Comparison of the power curves of collector type III in new condition after 1 year, 3 years, and 7.5 years of uncooled exposure at the Stuttgart site.

Collector type III shows no performance degradation after 1 year of uncooled exposure at the Stuttgart site, a slight one after 3 years (within the measurement accuracy) and a moderate one after 7.5 years (see Figure 4).

The power curves as shown above are suitable for an initial assessment of the performance degradation, but not for its quantification. A suitable measure for quantification is the change in energy savings in reference systems. To determine the influence of the collector performance degradation on the energy savings in a solar thermal system, system simulations were carried out with the simulation software TRNSYS using the reference system for domestic hot water heating (Bachmann et. al., 2018a) and reference combi system (Bachmann et. al., 2018b) defined in the IEA SHC TASK 54. The energy savings Q_{sav} achieved with the degraded collectors after the respective exposure in the corresponding system were determined.

Table 3 shows the ratio of the energy savings after exposure to the energy savings in new condition for the collectors in the combined system.

Tab. 1: Energy saving after exposure related to energy saving in new condition

	Typ I	**Typ II**	**Typ III**
Collector new	100.0 %	100%	100%
1 year uncooled (Stuttgart)	102.7 %	97.4 %	99.9 %
3 years uncooled (Stuttgart)	97.5 %	97.7 %	97.6 %
7.5 years uncooled (Stuttgart)	97.9 %	92.2 %	93.8 %

3 years cooled (Stuttgart)	100.5 %	98.1 %	98.9 %
7.5 years cooled (Stuttgart)	99.4 %	96.1 %	96.9 %
6.4 years (1.2 years cooled + 5.2 years uncooled) (Stuttgart)	102.7 %	-	92.0 %
5.4 years (1.2 years cooled + 4.2 years uncooled) (Stuttgart)	-	90.1 %	-
7.3 years uncooled (Freiburg)	93.0 %	89.4 %	90.8 %
3 years uncooled (Zugspitze)	94.7 %	93.7 %	97.8 %
8.1 years uncooled (Zugspitze)	94.1 %	83.9 %	-
2.5 years uncooled (Gran Canaria)	98.8 %	94.2 %	97.9 %
8.3 years uncooled (Gran Canaria)	-	84.8 %	95.1 %
3 years uncooled (Negev)	95.9 %	91.6 %	97.5 %
8.1 years uncooled (Negev)	-	85.7 %	90.2 %
2.5 years uncooled (Kochi)	100.1%	94.8 %	94.0 %
7.3 years uncooled (Kochi)	89.9 %	87.8 %	89.8 %

The results after 7.3 years of exposure in Kochi are not used in the rest of the paper due to the flooding that occurred at the Kochi site and the associated damage to the collectors.

The collector type I shows a low performance degradation at all locations. The maximum difference to the new condition is -7% of the energy saving. Values above 100% result from the measurement uncertainty in the measurement of the thermal performance. The collector type II shows a maximum difference in energy savings of -16 % at the Zugspitze site compared to the new condition. A moderate performance degradation of a maximum of -10 % of the energy saving compared to the new condition at the Negev site can be observed for collector type III. An overview of the damage patterns and their assessment based on exemplary measurements of the optical properties of the absorber layers from the collectors opened after exposure and the measurement of the thermal conductivity from the opened collectors are summarised in Table 4.

Tab. 4: Overview of the damage patterns of the different collectors

Damage	Type I	Type II	Type III
Dust and sand deposition on Absorber	yes	yes	yes
Salt deposition on absorber	yes	yes	yes
degradation optical properties of absorber	small	small	small
Welt seam detachment	No	small	small
Absorber deformation with contact to glass cover	No	small	small
Increase in thermal conductivity of insulation material	No	small	No
Fogging on glass cover	No	all over	partly
Loss of anti-reflective coating glass cover	not existent	not existent	not investigated

The assessment of the damage patterns listed in Table 4 leads to the following results:

1. Dust and salt deposits are present in all collector types and are more or less pronounced depending on the location and type. These lead to a performance degradation of 0 to approx. 2% related to the maximum collector performance.
2. The degradation of the optical properties of the absorber coating was determined by Fraunhofer ISE. It can be assumed that this can lead to a performance degradation of 0 to approx. 2% in relation to the maximum collector power. The performance degradation here depends, among other things, on the absorber temperature during exposure.
3. Weld seam detachment only occurs at collector type II and type III. However, the effect on the performance degradation is far below 1% in relation to the maximum collector performance.
4. Absorber deformation with contact to the glass cover in stagnation only occurs with collector type II and type III. However, the effect on the performance degradation is far below 1% in relation to the maximum collector performance.
5. An increase in the thermal conductivity of the thermal insulation can only be observed with collector type II (see IGTE measurements). However, the effect on the performance degradation is far less than 1% in relation to the power curve.

6. Fogging on the inside of the glass cover occurs over the entire surface of collector type II and over a large area of collector type III. The effect on the performance degradation is estimated at 2 to 4 % in relation to the maximum collector performance.
7. In case of collector type III, there may also be a loss or partial loss of the AR coating in addition to the reduction in transmission caused by the fogging, which would lead to a further reduction in transmission.

3. Accelerated aging tests

In the SpeedColl2 project, the accelerated aging tests developed in the previous SpeedColl project were revised and supplemented by the staff of IGTE and Fraunhofer ISE and the industrial partners. At the end of the project, the following service life tests were available, which are briefly explained below:

1. UV test
2. Internal thermal cycling test
3. External thermal cycling test
4. High temperature test
5. Condensation test
6. Salt spray test

3.1. UV test

The collector is placed in a climate chamber with a tilt angle of at least 60° and parallel to the light source. The light source is switched on and the climate chamber is set to 15 % ±5 % relative humidity. The temperature in the climatic chamber is then adjusted so that the surface temperature of the collector frame at the top of the collector reaches 80 °C ± 2 °C in an area that is not directly irradiated. When this temperature is reached, the test begins. During the test, ambient temperature, frame temperature and UV irradiance (280 nm - 400 nm) are measured and recorded. The test is finished when a UV irradiation of 280 kWh/m² (corresponding to approx. 5 years of exposure in Freiburg) is reached.

3.2. Internal thermal cycling test

During the internal thermal cycling test, the absorber of the collectors is subjected to thermal cycles of ± 75 K. During heating, the collector is operated with an inlet temperature of 95 °C until an outlet temperature of 90 °C is reached. During subsequent cooling, the collector is operated with an inlet temperature of 10 °C until an outlet temperature of 15 °C is reached. A total of 2000 cycles is carried out. This corresponds to the load that can be expected in real time operation within 25 years in a combi system. In addition, 4 thermal shocks are carried out according to ISO 9806. The number of 4 thermal shocks was determined on the basis of the assumption that this operating case can occur during the service life of a solar collector 1 time during commissioning and 1 time during each of the three service intervals during the service life, even though this should not occur if the collector is filled properly.

3.3 External thermal cycling test

The collector is placed in the climate chamber at ambient conditions (room temperature and appropriate relative humidity). The air in the climate chamber is cooled to a temperature that results in a temperature at the surface of the frame at the top of the collector of -40 °C ± 2 °C and kept at this temperature for 1 h. The climatic chamber is then adjusted to a temperature that results in a temperature on the surface of the frame at the top of the collector of +90 °C ± 2 °C and held for 1 h, see Figure 5. Throughout the test, the temperature and relative humidity inside the climatic chamber and the frame temperature at the top of the collector are measured and recorded. The test is completed when a total of 200 temperature cycles have been completed.

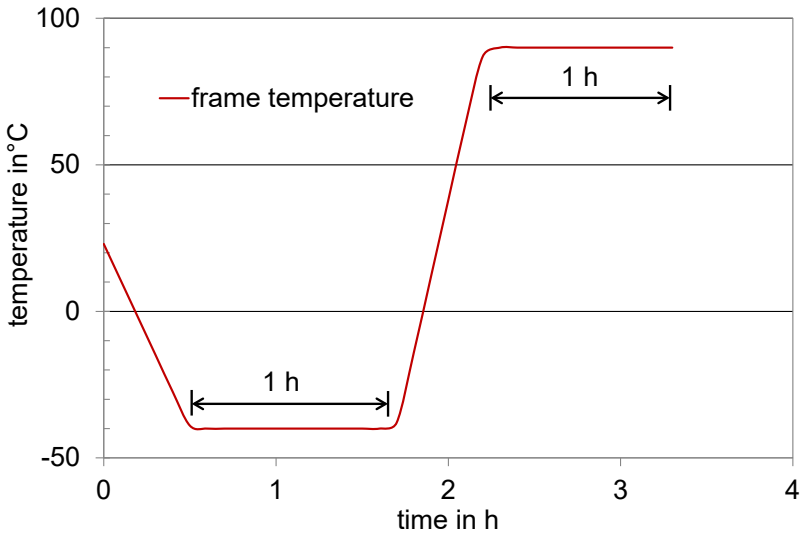

Fig. 5: Schematic test cycle of temperature cycle test

3.4 High temperature test

In the high-temperature test, the collector is exposed, unfilled and uncooled, to an irradiance of G = 1100 W/m^2 and an ambient temperature ϑ_{amb} = 40 °C for 8 hours. Alternatively, this operating condition can be achieved with a heat carrier flowing through the collector at the temperature resulting in the absorber temperature reached under the above mentioned operating conditions. After that the collector is exposed to an ambient temperature of 25 °C for 4 h without irradiation. The entire test consists of 15 cycles as described above. If necessary, the number of cycles can be increased.

3.5 Condensation test

The formation of condensation on the inside of the glass cover is a realistic scenario due to the cooling of the glass cover from the outside, e.g. by snow or radiation cooling. Condensation can be particularly harmful for solar glasses, especially for those with coatings (e.g. AR coating), and can lead to degradation. Furthermore, this test is intended to investigate whether the condensate drips onto the absorber and thus damages the selective layer of the absorber.

The collector to be tested is installed in a climate chamber at an angle of 30° to the horizontal. A condensate trap with thermal insulation above it is placed and fixed on the lower half of the collector.

During the test, the absorber of the collector is heated with an inlet temperature of 100°C. At the same time the climate chamber is operated at a temperature of 80°C and a relative humidity of 80%. In this way, the highest possible water loading of the air is generated for the greatest possible amount of condensate produced. Due to the difference between absorber and ambient temperature, a convection flow is forced inside the collector even without hemispherical irradiance. This ensures that there is an air exchange between the collector and the environment and that the humid air flows into the collector.

The condensate trap cools the transparent cover of the collector with a temperature of 50°C. Thus, a large amount of water in the air inside the collector will condense on the inside of the transparent cover.

3.6 Salt spry test

The salt spray test was developed on the basis of the main factors influencing the severity of the corrosive effect (presence of an oxygen-containing salt solution on the test specimen, temperature of the test specimen, temperature of the environment, relative humidity of the environment), following DIN EN 60068-2-52, severity level 3. The test procedure according to this standard is divided into three alternating phases: Salt spray phase, moisture phase and drying phase, which better reflects reality compared to continuous salt spray tests. In continuous salt spray tests, for example, a solid, constantly growing salt crust can form on the collector, which inhibits the oxygen supply to the collector and thus corrosion. The combination with humidity and drying phases

both prevents the formation of a constantly growing salt crust on the collector and supports the formation of an electrolyte (salt solution containing oxygen) on the collector. The test conditions according to DIN EN 60068-2-52 are shown in Table 5.

Tab. 5: Test conditions according to DIN EN 60068-2-52

	Salt spray phase	Moisture phase	Drying phase
Ambient temperature	(35 ± 2) °C	(40 ± 2) °C	(23 ± 2) °C
Relative humidity	ca. 100 %	93 (+ 2 - 3) %	50 (± 5) %

Furthermore, the following specifications were made:

- The salt content during the salt spray phase is fixed at 3 (± 0.5) % (reduction by 2 % compared to DIN EN 60068-2-52).
- The pH value of the brine should be between 6.5 and 7.2 at 20 °C (analogous to DIN EN 60068-2-52)
- The precipitation during the salt spray cycle on 80 cm² should be 1-2 ml/h (analogue DIN EN 60068-2-52)

With the boundary conditions mentioned, the test cycle was determined as follows:

1. humidity phase (5 h), collector flow at 60 °C, test room temperature (40 ± 2) °C
2. salt spray (2 h), 60 °C flow through the collector, test room temperature (35 ± 2) °C
3. humidity phase (10 h), collector not flowed through, test room temperature (40 ± 2) °C
4. salt spray (2 h), collector not flowed through, test room temperature (35 ± 2) °C
5. humidity phase (5 h), collector not flowed through, test room temperature (40 ± 2) °C
6. drying phase 24 h, 60 °C flow through collector, test room temperature (23 ± 2) °C

The flow through the collector at 60 °C stimulates the exchange of air between the test chamber and the inside of the collector. This supports the entry of salt into the collector. The collectors are to be tilted 30° to the horizontal during the test.

The corrosion test chamber of the ITGE does not have a climate control system that allows the regulation of the relative humidity during the humidity and drying phases as well as the temperature regulation during the drying phase. The relative humidity is 100 % during the entire humidity phase. During the drying phase, ambient air is fed into the test chamber by a fan. Since the corrosion chamber at IGTE is located in the basement, a relatively constant ambient climate is ensured throughout the year, so that reproducible test conditions can still be expected. Figure 6 shows an example of the course of the relative humidity and the temperature inside the test chamber of the corrosion test chamber (test room temperature) during a test cycle in the corrosion test chamber.

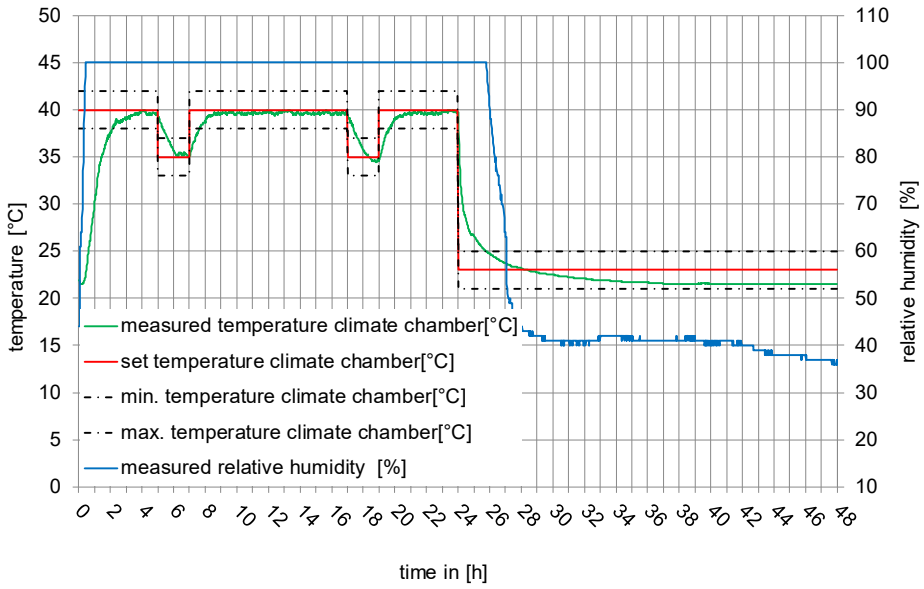

Fig 2: Test room conditions during a 48-hour test cycle in the corrosion test chamber

4. Thermal performance degradation after accelerated aging tests

Four of the accelerated aging tests described in section 3 were carried out on the collector type I, type II and type III in the following order:

- 1. UV test
- 2. internal temperature cycling
- 3. external temperature cycling
- 4. high temperature test

The results are shown in Figure 7 to Figure 9 in the form of power curves before and after the accelerated aging tests. After the accelerated aging tests, collector type I shows a very low performance degradation in the range of the measurement uncertainty (see Figure 7), collector type II a moderate one (see Figure 8) and collector type III a low performance degradation which, as with type I, is still in the range of the measurement uncertainty (see. Figure 9). Even though the performance degradation after the exemplary implementation is not as great as after the 7.5-year exposure, the collectors behave in a similar way to each other. This means that the developed accelerated aging tests are suitable for estimating the service life.

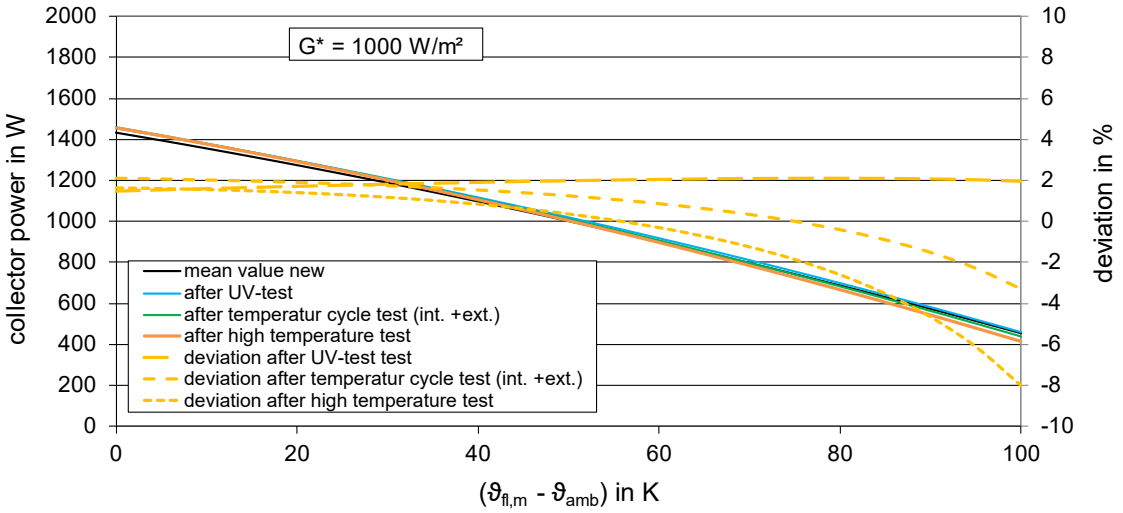

Fig 7: Comparison of the performance curves of collector type I in new condition, after the UV test, the internal and external thermal cycling test and the high-temperature test

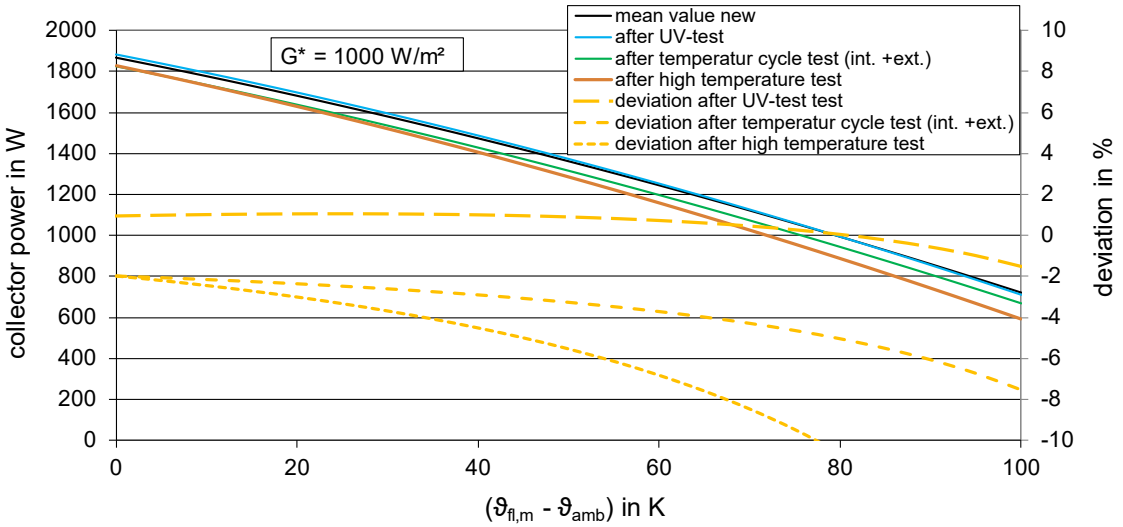

Fig 8: Comparison of the performance curves of collector type II in new condition, after the UV test, the internal and external thermal cycling test and the high-temperature test

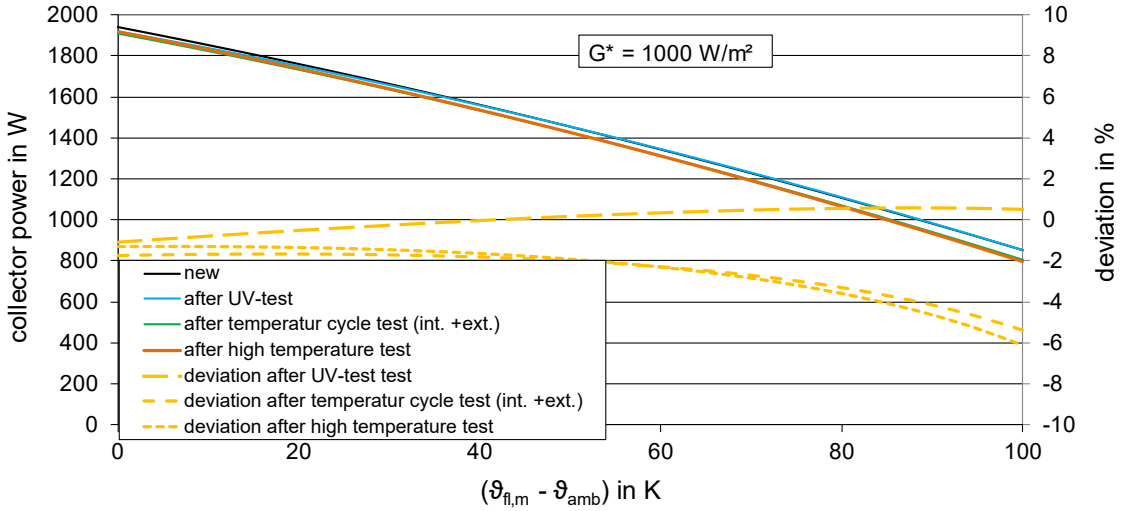

Fig 9: Comparison of the performance curves of collector type III in new condition, after the UV test, the internal and external thermal cycling test and the high-temperature test

Here, too, a system simulation was carried out for the reference combi system to quantify the change in energy savings. Table 6 shows the ratio of the energy savings after exposure to the energy savings in the new state for the collectors in the combined system.

Tab. 6: Energy savings after the exemplary service life tests in relation to the energy savings in new condition

	Type I	Type II	Type III
Collector new	100.0 %	100%	100%
After UV test	101.9 %	102.1 %	101.5 %
After internal temperature cycle test	99.9 %	98.3 %	101.0 %
After external temperature cycle test	99.8 %	97.6 %	98.5 %
After high temperature test	98.9 %	94.0 %	98.1 %

Both in the power curves shown and in the energy savings shown in the table above, a similar picture as after exposure to the extreme locations can be observed, albeit less pronounced.

The results presented in the following section give an indication of how many years of exposure and operation can be mapped with the accelerated aging tests carried out here.

5. Modelling of yield degradation and service life estimation

The load collectives and the absorber temperatures measured during exposure as well as the resulting reduction in energy savings in a typical combined system (see Table 3) were used to model the yield degradation.

The following influencing variables were determined to be significant for the performance degradation:

7. 1. the exposure duration t_{expo}
8. 2. the exposure time at an absorber temperature of 160 °C < $t_{160\text{-}200}$ < 200 °C
9. 3. the exposure duration at an absorber temperature of 200 °C > $t_{>200}$
10. 4. the exposure duration under salt load t_{Salt}
11. 5. the exposure duration under sand and/or dust load t_{Sand}

The degradation in the thermal performance was modelled as followed:

$$Q_{sav,t_{expo}=0} - Q_{sav,t_{expo}} = at_{expo} + bt_{160-200} + ct_{>200} + dt_{salz} + et_{sand} \quad \text{(eq. 1)}$$

For the Sede Boqer (Negev) site

$$t_{expo} = t_{sand} \quad \text{(eq. 2)}$$

was chosen and for the Gran Canaria site

$$t_{expo} = t_{salt} = t_{sand} \quad \text{(eq. 3)}$$

was chosen.

The model applies to "clean" collectors, i.e. any soiling of the transparent cover is not taken into account. Table 7 shows the model parameters determined for collector type I, type II and type III according to equation (1).

Tab. 7: Parameters for modelling yield degradation

Parameter	Type I	Type II	Type III
a [1/h]	2.02E-05	6.00E-05	4.21E-05
b [1/h]	2.45E-03	2.42E-03	7.62E-04
c [1/h]	1.68E-03	1.42E-02	2.64E-03
d [1/h]	0	1.62E-04	0
e [1/h]	0	1.29E-05	0

No significant dependence on the salt and sand load could be identified for the type I and type III collectors. The reason for this is the relatively tight housing of collector type III. The salt and sand load of the entering ambient air is largely separated in the lateral edge insulation of the collector, so that only small amounts reach the absorber. For the collector type I the amount of data was not sufficient to determine any significance, as the collector from Sede Boqer was already brought back for investigation purposes after the end of the previous project and the thermal performance of the collector from Gran Canaria could not be carried out due to a leak in the absorber.

Figure 10 shows an example of the agreement between the measured and the model-calculated reduction in energy savings in the reference combined system for the measured values and the values calculated for collector type II using the parameters shown in Table 7. The accuracy of the model here, as well as for collectors type I and type III, is ±2% points.

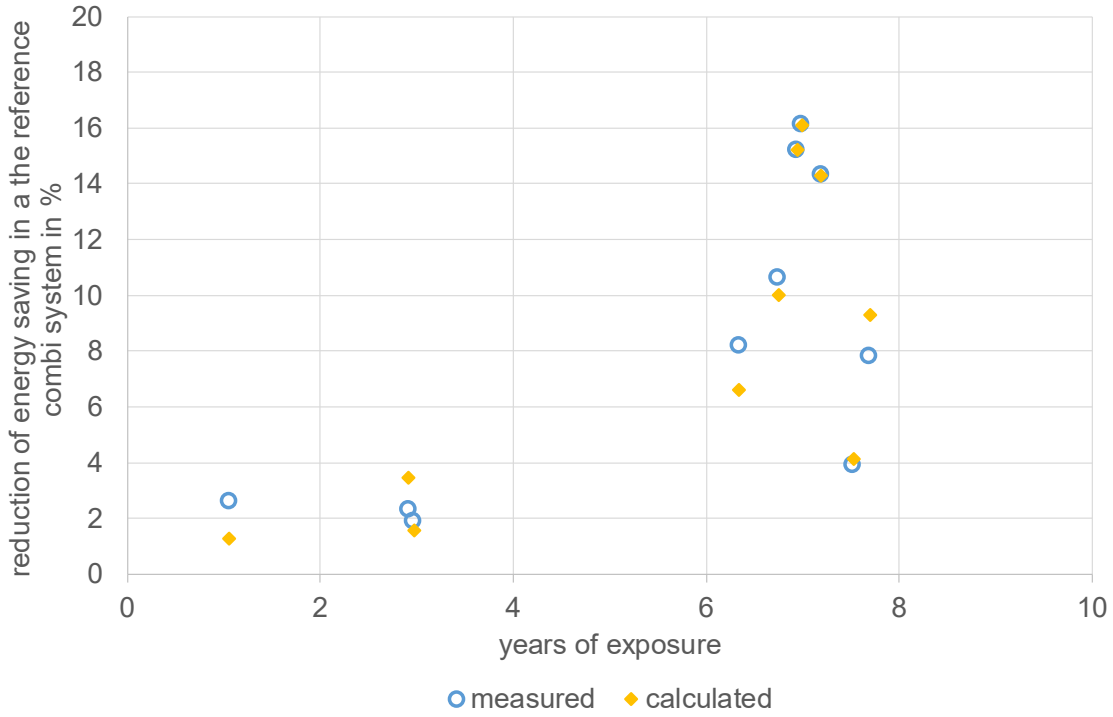

Fig. 3: Measured and calculated reduction in energy savings in the reference combi system for collector type II

Figure 11 shows the annual energy savings in relation to the energy savings in new condition in a typical combi system at the Würzburg site for an operating period of 30 years.

With the help of the yield degradation model, the service life can now be estimated depending on the user requirements. If, for example, a yield degradation of up to 20 % is accepted, this results in a service life of approx. 30 years for collector type II, and even significantly longer for type I and type III. However, if the yield

degradation is only allowed to be 10 %, the service life for collector type II is 15 years, for collector type III 23 years and for collector type I still more than 30 years.

If the model according to equation (eq. 1) is applied to the results in Table 6, it results that the proposed test cycle corresponds to an exposure time of 4 years in Stuttgart or 9 years of operation in a typical combi system at the Würzburg site. With this knowledge, the length or number of repetitions of the proposed accelerated aging tests can be adapted to the requirements of the collector manufacturers.

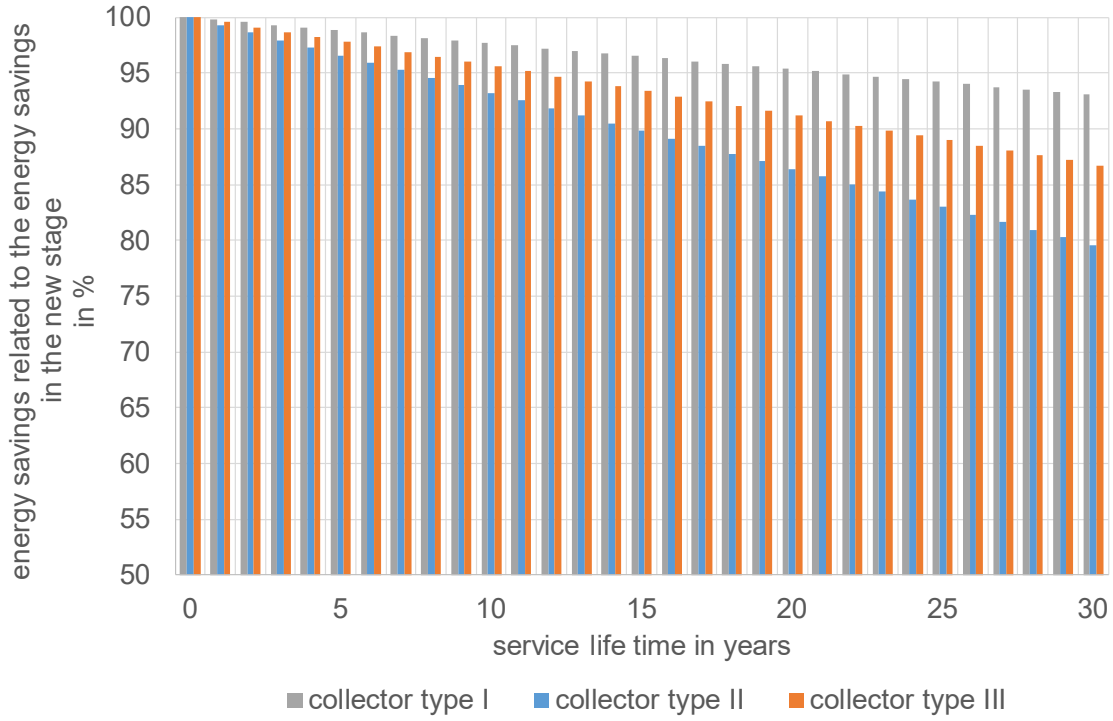

Fig 4: Annual energy savings related to the energy savings in new condition in a typical combined plant at the Würzburg site

6. Summary and outlook

In the SpeedColl and SpeedColl2 projects, a consortium consisting of the Institute of Building Energetics, Thermotechnology and Energy Storage at the University of Stuttgart (IGTE), Fraunhofer ISE and representatives from solar thermal industry examined the loads on solar thermal collectors in the period from 2011 to 2020. For this purpose, test specimens were exposed outdoors at various locations (Kochi (India), Sede Boker (Israel), Gran Canaria (Spain), Beijing (China), Zugspitze (Germany), Freiburg (Germany) and Stuttgart (Germany)). Based on the loads and degradation observed at the exposure sites, accelerated aging tests were developed and carried out on identical solar collectors to simulate the degradation that occurred at the exposure sites and thus estimate the service life of the solar collectors. After and during the multi-year exposure of 7 to 8 years, the solar collectors were subjected to a performance test according to ISO 9806 to determine the performance degradation caused by the loads. Based on these measurements and the loads measured at the exposure sites, a model for service life estimation of flat-plate collectors was developed.

The SpeedColl and SpeedColl2 projects have shown on the one hand that the collectors of German manufacturers are of high quality, but on the other hand they have also revealed weaknesses in individual designs. With the developed accelerated aging tests and the service life estimation, useful tools were created for the solar thermal industry to examine and estimate the quality and service life of their products and new developments. The developed accelerated aging tests can be incorporated into European or international standardisation if required.

7. Acknowledgments

The research project "Development of accelerated ageing test procedures for solar thermal collectors and their components", acronym "SpeedColl2", was funded by the Federal Ministry for Economic Affairs and Energy via the Project Management Organisation Jülich (PTJ) based on a resolution of the German Bundestag under the funding code 0325865A and B, as well as supported financially and in terms of content by the participating industry partners. The authors would like to thank all partners and colleagues involved for their excellent support, cooperation and commitment to the projects and take responsibility for the content of this paper

8. References

Bachmann, S., Fischer, S. et al. (2018a) Info Sheet A08: Reference System, Germany Solar Domestic Hot Water System for Single-Family House http://task54.iea-shc.org/Data/Sites/1/publications/A08-Info-Sheet--Ref-SF-SDHW-System--Germany.pdf

Bachmann, S., Fischer, S. et al. (2018b) Info Sheet A08: Reference System, Germany Solar Domestic Hot Water System for Single-Family House https://task54.iea-shc.org/Data/Sites/1/publications/A09-Info-Sheet--Ref-SF-Solar-Combisystem--Germany.pdf

Fischer, S., (2017), Test Procedure for Accelerating Aging of Solar Thermal Collectors, ISES Solar World Congress & SHC Conference, Abu Dhabi, 29.10. – 02.11.2017, ISBN 978-3-981 465 9-7-6

DHW Tanks – 40 % Savings by Better Stratification

Robert Haberl, Michel Y. Haller

SPF Institute for Solar Technology, Eastern Switzerland University of Applied Sciences (OST), Rapperswil (Switzerland)

Abstract

Thermal stratification of hot water storage is known to have a positive impact on the efficiency of systems for heat supply. An existing method for determining the thermal stratification of combi-storage tanks, based on the second law of thermodynamics, i.e. on the entropy balance of the storage system, was adapted for measuring domestic hot water storage tanks. The updated method uses tapping profiles from EN 16147 to test the stratification efficiency of different sized storage tanks, matching the size of the collector array to the tapping profiles when using solar thermal systems. The resulting test procedure was applied to several tanks and the results were evaluated. It is shown that the efficiency of the storage tanks and their influence on the operation mode of the charging varies considerably. A very well stratified storage tank concept not only achieved higher comfort and created better hygienic conditions, but in combination with a heat pump saved up to 40 % electrical energy compared to another storage tank. These results underline the need for an evaluation of the stratification efficiency of domestic hot water storage tanks, which can be done with the method presented here.

Keywords: Domestic Hot Water, Stratification efficiency, Measurement, Hardware-in-the-Loop, Dynamic operation, Entropy production, Exergetic efficiency

1. Introduction

Stratified water storage tanks are used for storing heat as hot water. When this kind of storage is used in combination with a heat pump, the temperature stratification of the storage is a decisive factor for the overall efficiency and thus for the consumed end energy of the system (Haller et al., 2019).

The temperature stratification of the water storage tanks is automatically established due to gravity and the temperature-dependent density of the water. However, this natural process is counteracted by processes, which can essentially be attributed to three causes:

- Heat conduction and diffusion in the water and in the storage tank internals.
- Plume entrainment caused by buoyant fluid movements.
- Mixing of the inlet jet due to kinetic energy and turbulence during direct storage charging.

Since mixing of fluids with different temperatures (de-stratification) and heat exchanging processes of any kind - and thus all of the effects described above - always result in entropy production (exergy loss), stratification indices can be determined based on the measurement and calculation of entropy and exergy balances.

(Haller et al., 2018) introduced a test method for the evaluation of stratification efficiency of combined storage tanks that store heat for domestic hot water and for space heating in one thermally stratified water storage tank. This method for the determination of stratification efficiency as a key performance indicator is based on the second law of thermodynamics, i.e. on the entropy balance of the storage system. The corresponding laboratory test is based on a 24 hour cycle where realistic and dynamic charging and discharging is applied according to boundary conditions of real weather data of a day in the year. The particular day of the year was chosen because of its representativeness for the effect of stratification on the system performance, such that the annual performance can be derived directly from the performance shown in the 24 h test cycle. The test method was developed in a research project funded by the Swiss Federal Office of Energy entitled "StorEx" (Haller et al., 2015).

© 2022. The Authors. Published by International Solar Energy Society
Selection and/or peer review under responsibility of Scientific Committee
doi:10.18086/eurosun.2022.14.03 Available at http://proceedings.ises.org

The results showed that the new KPI correlates well with the electricity demand of a heat pump that is charging the storage. While the stratification efficiency was the decisive factor for the energetic performance of the system, i.e. for the electric energy consumption of the heat pump, the determined heat losses of the storage system showed no correlation with the overall energetic performance of the system. However, no information has been available so far for similar kinds of tests for pure DHW storage tanks. Therefore, in this contribution, the existing method is extended to the evaluation of storage tanks for domestic hot water (without space heating), and results are presented for four DHW storage systems.

2. Test Method

2.1 Procedure

The general procedure for measuring the stratification efficiency of combistores is as follows:

- The storage tank is installed on the test bench, including the necessary hydraulics for charging and discharging.
- The test bench simulates and emulates a complete building during the 24-h test cycle, the heat demand of which must be covered. Based on the (real) temperatures measured in the storage tank and the specified test cycle, charging and discharging are started and controlled.
- Based on the measurements, the entropy balance of the storage system is determined.
- The stratification efficiency is determined based on a comparison of the measured entropy production of the storage system with the hypothetical entropy production of a completely mixed reference system.

This general procedure was adopted unchanged for DHW storage tanks. Of course, the emulation of space heating is in this case omitted. Furthermore, a new irradiance profile for the solar thermal collectors was defined and simplifications were made in the emulation of the auxiliary heating.

2.2 Test setup and boundary conditions

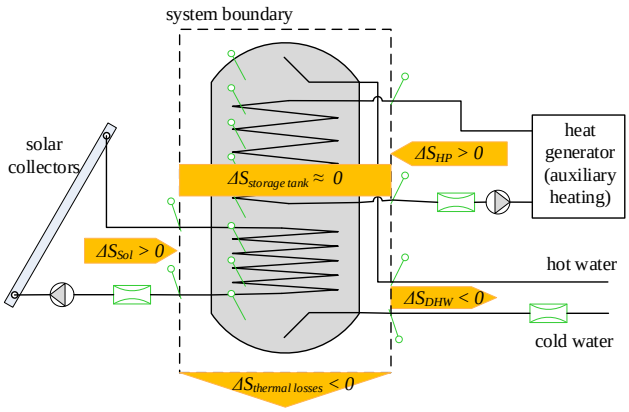

Fig. 1: System boundary for the measurement of stratification efficiency of DHW storage tanks, including the necessary measurement equipment and the entropy terms, which are to be determined from the measured data.

System boundaries

DHW storage systems usually involve heat exchangers for the transfer of heat to the fresh water. These heat exchangers may influence stratification and the heat transfer process as such is a source of entropy generation. Entropy may also be produced in external valves of the overall hydraulics where hot and cold fluids are mixed. That's why a complete storage system is evaluated instead of the bare storage tank.

Fig. 1 shows the system boundaries, using the example of a storage tank with two internal heat exchangers: one each for heat input from solar thermal and from a heat pump.

The parts outside the system boundaries, i.e. the collectors, the heat pump or other heat generators as well as a tapping profile, are simulated and emulated by the test bench.

DHW tapping profile

In the standard EN 16147: 2017 (European Committee for Standardization (CEN), 2017) 24-h load profiles are defined for the DHW demand. The energetic target value of the profiles varies from 0.345 kWh up to 93.52 kWh for one day, the highest target flow rate of a single tapping varies from 2 l/min up to 96 l/min.

The profiles contain the time for the taps, the target flow rate, the usable water temperature and the maximum temperature (minimum water temperature to be reached during a draw-off), whereby the usable temperature lies

in the range between 10 °C and 40 °C and the maximum temperature of 55 °C is only defined on a few taps per day. The set point of the incoming cold water is defined as 10 °C.

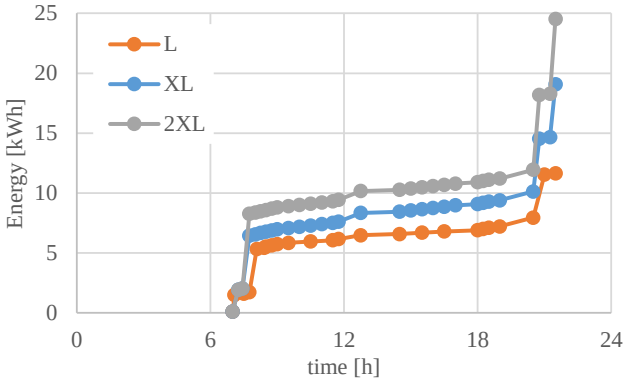

Fig. 2: Cumulated energy from the tapping profiles L, XL and 2XL.

For the measurement of stratification efficiency of DHW tanks, one of the profiles can be selected (depending on the volume/output capacity of the tested tank), with profile L with 11,655 kWh per day as the standard profile. During the measurement, according to the time and the selected tapping profile, the cold water is conditioned to a temperature of 10 °C at the required mass flow. From the difference with the outgoing hot water, the heat output is calculated, which is accumulated to the tapped energy from the moment the usable water temperature is reached. Tapping is stopped when the energy set point is reached.

Heat generator

In contrast to the predefined tapping profile, charging must be flexible. Two different heat sources can be used to charge the tested storage tank: Solar thermal collectors and a heat pump, respectively an auxiliary heater.

Tab. 1: Collector field characteristics.

η_0	a_1 [$Wm^{-1}K^{-1}$]	a_2 [$Wm^{-2}K^{-2}$]	$c_{eff,spec}$ [$Jm^{-2}K^{-1}$]
0.8	3.5	0.015	7000

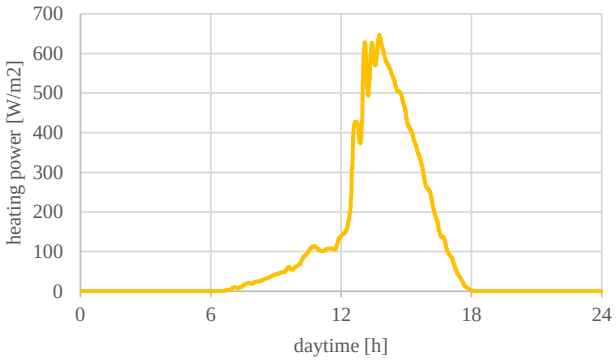

Fig. 3: Generated heat production per m² collector field before subtraction of thermal losses on the test day.

Tab. 2: Aperture area of the emulated collector array for measurement with different DHW tap profiles.

tapping profile [-]	Aperture area [m^2]
L	5.0
XL	8.2
2XL	10.5

For the simulation and emulation of the solar yield, the standard performance data for a flat plate collector from the IEA SHC Task 32 (Heimrath and Haller, 2007) are used, which were already applied in the StorEx project. The performance characteristics can be seen in Tab. 1. A south orientation with 45° inclination is assumed.

The irradiance on the collector field ($I = I_b + I_d$) was converted to heat produced within the collector ($\dot{Q}_{rad}$) before subtraction of heat losses according to (Eq. 1). The resulting profile for heat generated within the collector according to the irradiance and the incident angle modifiers is presented in Fig. 3.

In the simulation model used for the emulation of the solar yield, only the combination of the operating temperature and the power loss to the environment must then be calculated. The difference between the collector temperature and the storage temperature is used as a criterion for operating the collector circuit pump. The size of the collector array depends on the selected DHW tap profile of the test. Tab. 2 shows the aperture area for the different tapping profiles.

$$\dot{Q}_{rad} = A_{sol} \cdot (\eta_0 \cdot K_b \cdot I_b + \eta_0 \cdot K_d \cdot I_d) \quad \textbf{(Eq. 1)}$$

The simulation and emulation of an auxiliary heater is done with reference to a heat pump, meaning with a rather small temperature difference of 5 K. As a simplification, this temperature difference is assumed to be constant over the whole outlet-temperature range, which is limited to maximum 60 °C. The heat pump was chosen as the reference heat generator because, on the one hand, it reacts most sensitively to poor storage stratification and, on the other hand, it poses great challenges to the storage system due to the usually high mass flows at a small delta-T. Moreover, within the framework of Switzerland's energy strategy, heat pumps are considered to play a far more important role in water heating than combustion heat generators.

The temperature positions in the storage tank and on/off hysteresis for the pump are chosen by the manufacturer or commissioner of the storage system.

2.3 Evaluation of test results

Measured values and data acquisition

Temperatures and volume flow rates are determined at the boundary between the tested storage tank and the test rig. The positions are marked in green in Fig. 1. In addition, the temperature of the storage tank is measured with eight contact sensors placed equidistant on the storage wall.

At the limiting boundaries, the following quantities have to be determined based on appropriate measurement devices:

$$\dot{Q} = \dot{m} \cdot [h(\vartheta_{in}) - h(\vartheta_{out})] \quad \textbf{(Eq. 2)}$$

$$Q = \sum_i \dot{Q}_i \cdot \Delta t \quad \textbf{(Eq. 3)}$$

$$\dot{S} = \dot{m} \cdot [s(\vartheta_{in}) - s(\vartheta_{out})] \quad \textbf{(Eq. 4)}$$

$$\Delta S = \sum_i \dot{S}_i \cdot \Delta t \quad \textbf{(Eq. 5)}$$

Entropy balance

With positive values for heat input into the system and negative values representing heat outputs (or heat losses), the entropy balance, meaning the irreversible entropy production inside the storage system, can be calculated as:

$$\Delta S_{irr,exp} = -\left(\Delta S_{aux} + \Delta S_{sol} + \Delta S_{DHW} + \Delta S_{loss} + \Delta S_{storage\ change}\right) \quad \textbf{(Eq. 6)}$$

With the measurements and calculations described above at the measuring points at the system boundaries, the following terms can be determined: ΔS_{aux}, ΔS_{sol} and ΔS_{DHW}.

To calculate the entropy change due to the storage losses as well as the storage change, the losses themselves and also the storage temperature must be known. However, this temperature is neither constant over time nor over position. Therefore, the mean value over the height of the storage tank at the beginning and end of the 24-h test sequence $\vartheta_{TES,start}$ and $\vartheta_{TES,end}$ is calculated by means of the contact sensors on the storage tank, as well as the mean value over time $\overline{T_{TES,24h}}$. The calculation of the entropy is then done as:

$$\Delta S_{loss} = \frac{Q_{loss}}{\overline{T_{TES,24h}} + 273.15K} \quad \textbf{(Eq. 7)}$$

$$\Delta S_{storage\ change} = m_{TES} \cdot \left[s\left(\vartheta_{TES,end}\right) - s\left(\vartheta_{TES,start}\right)\right] \quad \textbf{(Eq. 8)}$$

Stratification efficiency

From the entropy production measured during the test cycle, the stratification efficiency is determined as a dimensionless quantity. For this purpose, the measured entropy production is set in relation to the entropy production of a completely mixed storage tank:

$$\zeta_{str} = 1 - \frac{\Delta S_{irr,ms}}{\Delta S_{irr,mix}} \quad \textbf{(Eq. 9)}$$

The entropy production of the completely mixed system depends on assumptions, such as the supply temperature

of the heat generator and also on the choice of the tapping profile used. Effectively, the entropy balance is simply the difference between charging and discharging:

$$\Delta S_{irr,mix} = \Delta S_{WW} - S_{60°C} \quad \textbf{(Eq. 10)}$$

For the charging of the completely mixed storage tank, it is assumed that the heat supply always corresponds to the highest temperature required to reach the set temperature of the storage tank, for which 60 °C is used in this case based on the specifications of SIA 385/1:2020. The amount of heat to be supplied corresponds to the load, i.e. the heat demand for hot water. In reality, the thermal losses of the storage tank must also be covered. However, since the entropy losses associated with heat losses are subtracted from the entropy production of the measured system, this entropy change is not shown in the reference system either. Thus applies:

$$S_{60°C} = Q_{DHW}/(273.15K + 60K)$$

The dissipated entropy production via the DHW tapping is calculated with the specific entropy $s(\vartheta)$ between the entering cold water and the required DHW temperature of 50 °C:

$$\Delta S_{WW} = \sum_i m_{WW,i} \cdot [s(T_{KW}) - s(T_{WW})] \quad \textbf{(Eq. 11)}$$

For the test method, tapping profiles from the EN 16147:2017 are used. The entropy production from charging and discharging as well as the balance or the resulting entropy production of the fully mixed storage tank is shown for different tapping profiles in Fig. 4 (left). In the same graphic is also the entropy production of some measured examples shown.

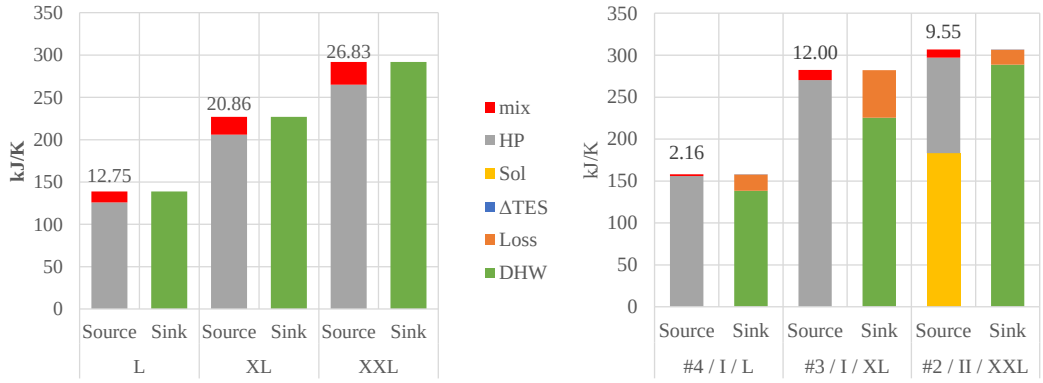

Fig. 4: Reference entropy input and output (left) for different tap profiles and measured examples (right).

Additional indicators

A temperature weighted by power was determined from the temperatures for charging and discharging the storage tanks. The flow temperature of the solar thermal collectors is determined according to (Eq. 12. The determination of the temperatures for the auxiliary heater as well as for the DHW supply is done similarly.

$$\overline{T_{HP,flow}} = \frac{\Sigma(T_{sol,flow,i} \cdot \dot{Q}_{sol,i})}{\Sigma Q_{sol,i}} \quad \textbf{(Eq. 12)}$$

3. Test Results

3.1 Tested tanks

The test method was applied to four different storage tanks with different concepts and sizes for a variety of boundary conditions such as different mass flow rates on the heat generator. Fig. 5 gives an overview on the schemes and the integration of the tested storage systems.

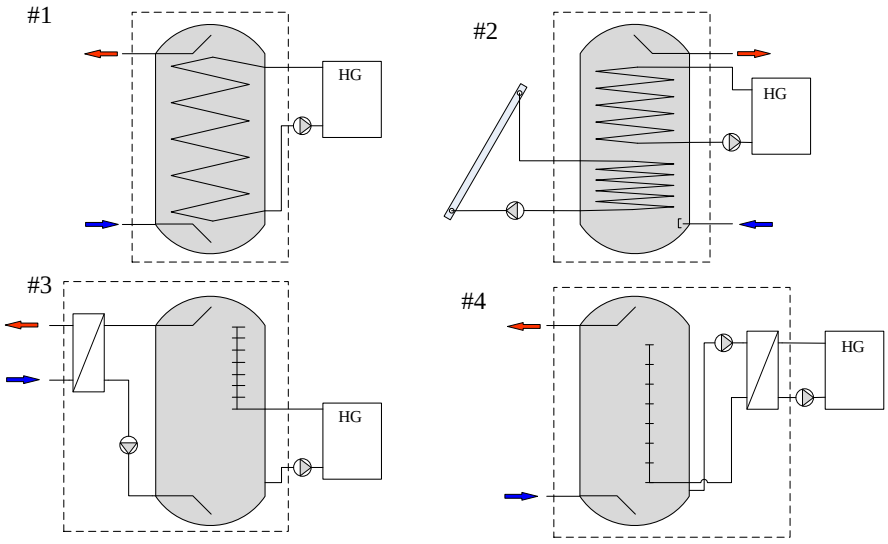

Fig. 5: Schemes and the integration of the tested systems.

Tab. 3: Description of the tested systems and the basic conditions of the measurements.

Tank		#1				#2		#3	#4	
Volume	[l]	200				780		1000	200	
Heat exchangers	DHW	-				-		ext HX	IHX	
	aux	IHX				IHX		-	ext HX	
	sol	-				IHX		-	-	
Test		I	II	III	IV	I	II	I	I	II
Profile		L	L	L	L	XL	XXL	XL	L	L
Solar		No	No	No	No	Yes	Yes	No	No	No
P_{aux}	[kW]	10	10	6	6	10	10	15	6	10
TW[(A)]	[-]	Yes	No	Yes	No	Yes	No	Yes	No	No

[(A)] Time Window for the DHW heating by the aux. heater.

3.2 Temperature curves

Fig. 6 shows the daily trend of a measurement with tank #1. The 200 l tank was charged with a 10 kW heat generator via an internal heat exchanger (IHX). One can see that the temperature on top of the tank drops significantly during the charging process. That's why the required DHW temperature of 50 °C could not be delivered while a charging process is ongoing.

Fig. 7 shows the course of a measurement of the bivalent storage tank #2. The heat of the collectors and the additional heating was brought into the storage via IHX in each case. At the DHW charges by the additional heating at 6:00 o'clock and at 16:00 o'clock it can be seen that only the upper part of the storage tank is heated up. At the top sensor there is no drop in temperature (a positive finding). The solar heat is brought to the lower part of the storage tank. The heat output of the collectors on the test day is not sufficient to charge the storage tank to the temperature of 50°C required for DHW heating.

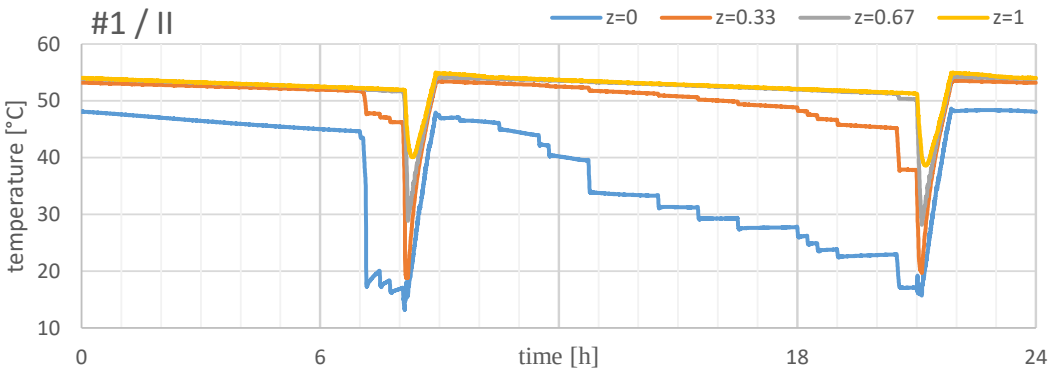

Fig. 6: Course of a measurement of a 200 l tank with IHX.

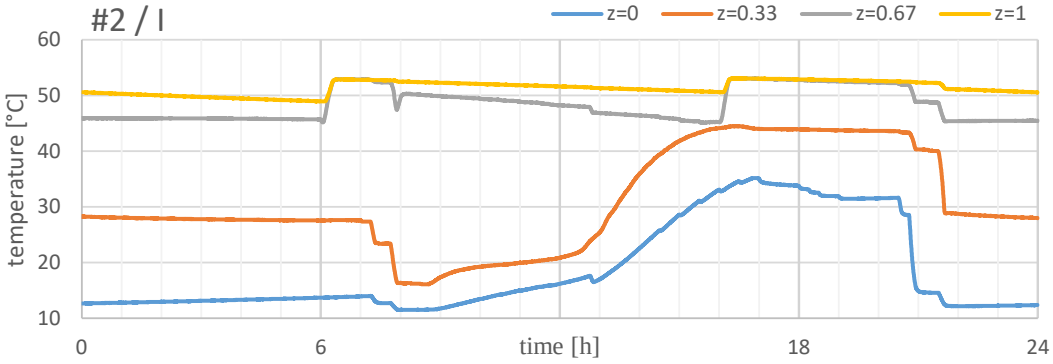

Fig. 7: Course of a measurement of a 780 l bivalent storage tank with two IHX.

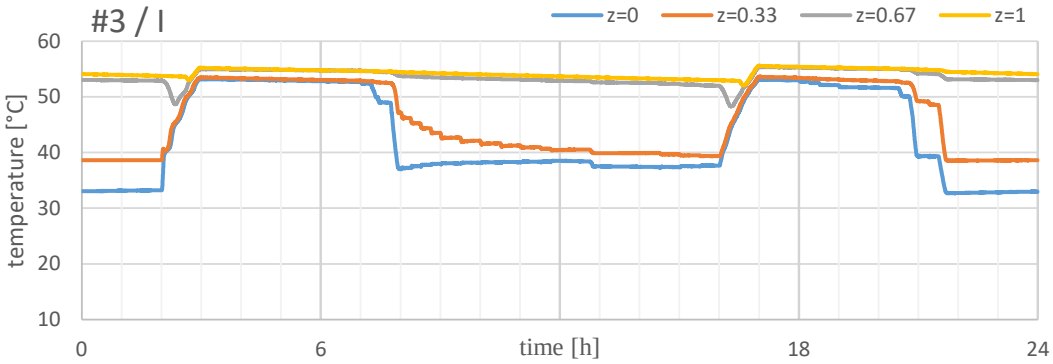

Fig. 8: Course of the measurement of a 1000 l storage tank with external HX for DHW.

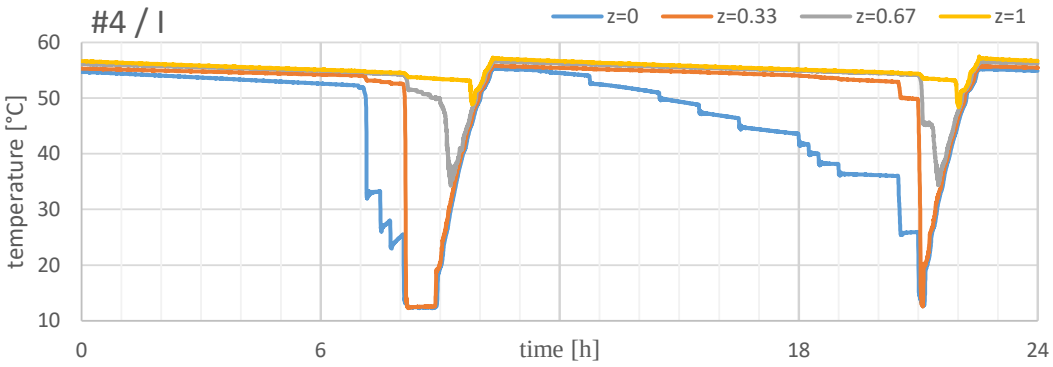

Fig. 9: Course of the measurement of a 200 l DHW tank with external HX for charging via an aux. heater.

Fig. 8 shows the course of a measurement with the 1000 l storage tank #3 that was combined with an external HX for DHW preparation. In opposite to the other measurements, it can be seen that the temperature in the lower part of the storage tank never drops below 30 °C. This has an unfavorable influence on the overall system performance. On a positive note, there is a barely perceptible drop in temperature in the top of the storage tank during charging.

Fig. 9 shows the course of a measurement with the 200 l tank #4 which is combined with an external HX for charging. Here you can see that the recharge is very late. Half of the storage volume is at just about 10°C when a recharge was triggered. During the recharge, the temperature at the top does not drop below 50°C. This means that the required comfort can be guaranteed at all times, despite the rather small storage volume.

The energy-temperature diagram of a typical charging processes for each of the tested tanks can be seen in Fig. 10. For this purpose, the energy from the aux. heating to the storage tank was sorted according to the flow temperature. In addition, the values were normalized for better comparison (in the figure on the right).

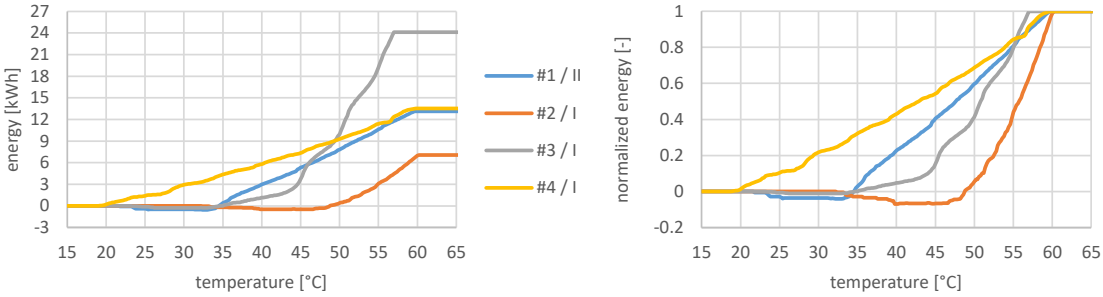

Fig. 10: Energy temperature diagram of the charging process via the aux. heating of one measurement each of the tested tanks. On the left: energy; on the right: normalized values.

The comparison of the charging of storage #1 and #4 at identical load clearly shows that the heat delivery with external HX and vertical stratifier in the storage was consistently at lower temperature level. For tank #1 with IHX, even a negative power of charging can be seen at the beginning of the loading (20 – 35 °C on the x-axis), which occurs due to the mixing processes in the storage. Also for the storage #3 that covers the energy demand for the XL-tap profile shows quite high flow temperatures. Approx. 60% of the energy was provided at over 50°C. The measurement of storage #2 shown was also carried out with the XL-tap profile. Here, however, only a part of the heat was supplied via the aux. heater, because low temperature heat was provided by solar thermal emulation. Hence, the part that was supplied by the aux. heater was in the range between 50°C and 60°C.

3.3 Energy, entropy and exergy

An example for a measured energy balance of a system over the 24-h test cycle is shown in Fig. 11 on the left. The main heat sources are the solar collectors and the auxiliary heater. The change in the net energy content of the storage over the test period is very small. The dominant heat sink is of course the DHW consumption, losses are minor in terms of the total energy turnover. Effects of mixing do not affect the thermal energy balance.

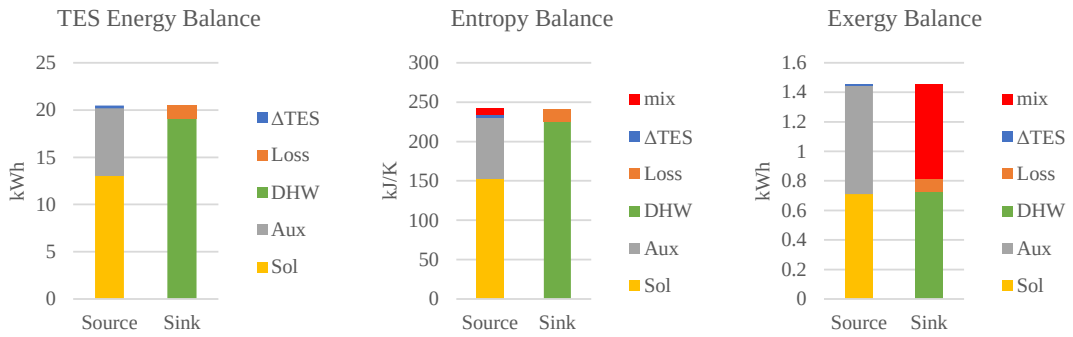

Fig. 11: Energy, Entropy and Exergy balance of the test #2 / I.

The entropy balance shown in the middle part of the same figure. It has a similar distribution, but now the entropy production is visible as a source term. Compared to the total entropy turnover, this value is quite small.

The total entropy production $\Delta S_{irr,exp}$ was 7.86 kJ/K. The entropy production of the reference system $\Delta S_{irr,mix}$ with the same DHW tapping profile is 20.86 kJ/K. The stratification efficiency of the shown example is: $\zeta_{str} = 1 - \frac{7.86 \frac{kJ}{K}}{20.86 \frac{kJ}{K}} = 0.623$ (62.3%). In the exergy balance that is shown on the right side of the figure, exegetic losses due to mixing are visible on the right side since they are exergy sinks. Quite notably, those internal exergetic losses (reference temperature = 20 °C) are high in comparison with the exergy turnover and by far higher than exergy losses caused by heat losses from the system.

3.4 Stratification efficiency

Fig. 12 shows a summary of the main results of the tested storages.

Storage #1 achieved stratification efficiencies between 52 % and 59 %. The fact that the internal heat exchanger reached almost to the top of the volume of the tank proved to be problematic. It leads to a significant mixing and temperature decrease at the top of the tank at the beginning of charging. As a result, the required DHW setpoint temperature of 50 °C cannot be guaranteed continuously.

Storage tank #2 achieved a stratification efficiency of 62 % in the test with the tapping profile XL. The charging by solar heat via a heat exchanger in the lower part of the storage tank raises the temperature in the storage tank volume, but without guaranteeing the required setpoint temperature for DHW heating. Therefore, the HP has to load the upper part at a high temperature level, reaching the maximum flow temperature of the aux heater.

Storage #3 achieves a stratification efficiency of only 45%. The reason for the low stratification efficiency is assumed to be, on the one hand, high return temperatures of the external HX used for short DHW taps and, on the other hand, circulation effects via the external hydraulics. The losses of the storage tank were with 5 kWh/d or 7.2 W/K more than twice as high as for the other storage tanks with losses in the range of 2.1 to 3.2 W/K.

Storage tank #4 showed very good stratification behavior upon charging by an external heat exchanger in combination with a vertical stratification device in the storage tank. Despite the small volume of 200 l, a consistently very high DHW temperature was ensured with simultaneous low average temperature of the charging. The stratification efficiency in the test with 6 kW and 10 kW HP was 83 % and 85 %, respectively, and thus far exceeded the results of all other tested tank configurations.

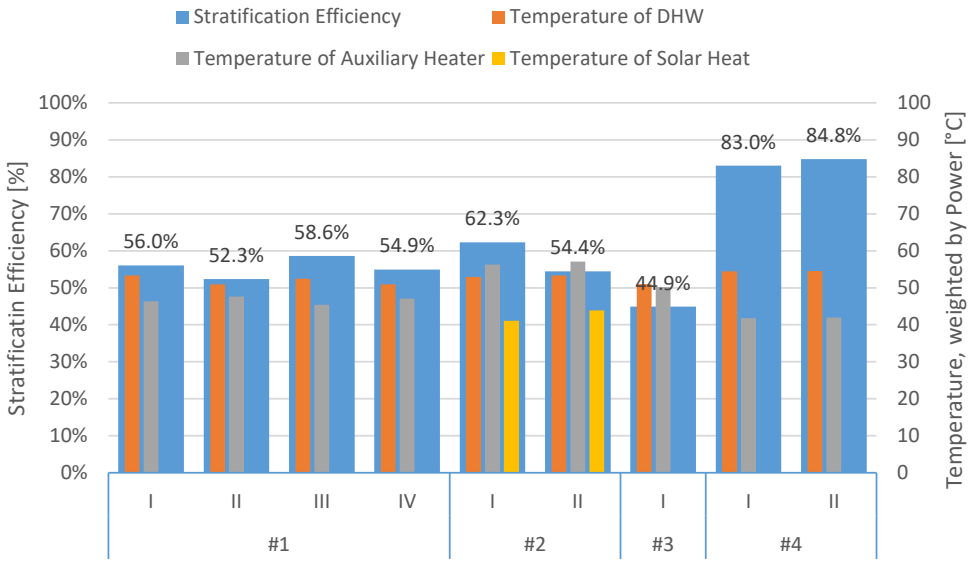

Fig. 12: Results of four different storage tanks with different concepts and sizes for a variety of boundary conditions.

4. Discussion

Based on the average flow temperature of the emulated HP from the individual measurements, weighted by power, an average COP of the heat pump for charging the storage tanks was calculated. Fig. 13 shows the COP of the assumed air-water heat pump as a function of flow temperature for an air inlet temperature of 12.9 °C (mean outdoor temperature of the test sequence). The triangles in the diagram represent the mean flow temperatures of the tested storage systems and their corresponding COPs illustrating the quite significant differences in performance that can be expected from the different storage tank configurations.

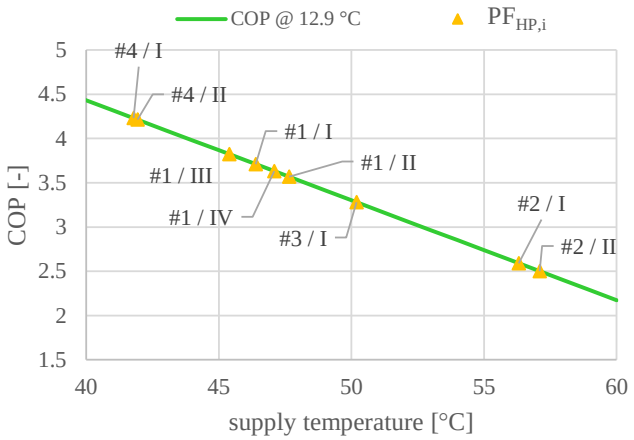

Fig. 13: COP as a function of the flow temperature for different ambient temperatures.

Based on the determined coefficients of performance, a demand for electrical energy for the HP was estimated for each case. The resulting values are presented in Tab. 4 and Fig. 14. With an identical DHW profile, the measurements at storage #1 show a 15% higher electricity demand than the measurements at storage #4, bearing in mind that the delivered DHW temperature of the more efficient storage #4 was up to 3.5 K higher than in storage #1, which in some DHW taps could not reach the required flow temperature of 50 °C. Overall, it is quite remarkable that storage tank #4 delivers the highest hot water temperatures overall, even though the lowest temperatures were measured for the storage tank charging. The system performance factor of 3.7 is also the highest of all the storage tanks, with exception of the solar thermal assisted system. The differences in the system performance factors suggest that the electrical savings of this storage tank compared to storage tank 1 (same tap profile) is 15%, and compared to a storage tank configuration like #3 (that could have profited from a larger tap profile) is as high as 42%, while providing greater comfort.

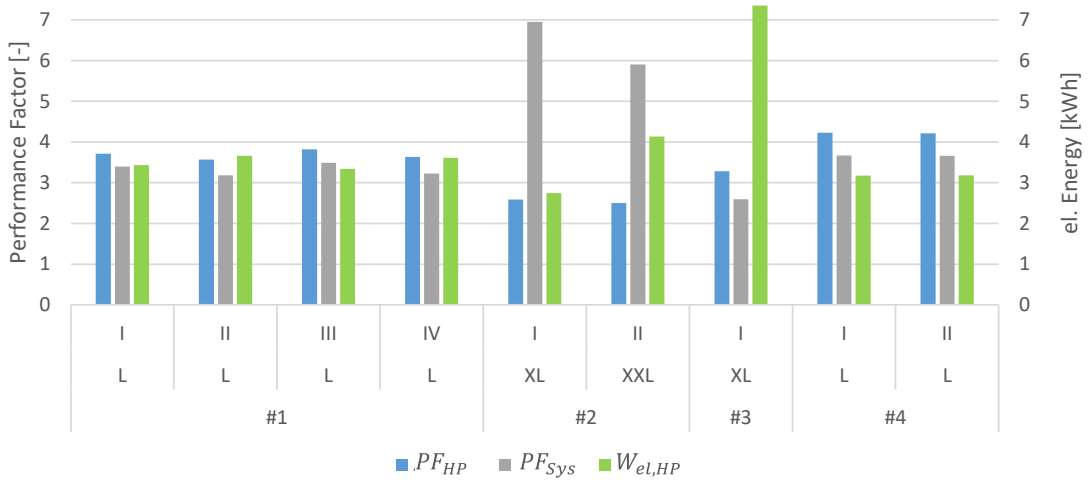

Fig. 14: Estimation of performance factors and el. energy demand.

The estimated electrical energy demand of the HP and the actually delivered DHW were used to determine the coefficient of performance of the storage system. This value, unlike the performance factor of the HP itself, is naturally by far highest for the system with solar thermal assistance. Among the storage systems without solar thermal, the range of results goes from 2.6 (storage system #3) up to 3.7 (storage system #4).

Tab. 4: Estimation of performance factors and electricity demand.

Tank		**#1**				**#2**		**#3**	**#4**	
Test		I	II	III	IV	I	II	I	I	II
ζ_{str}	**[%]**	**56.0**	**52.3**	**58.6**	**54.9**	**62.3**	**54.4**	**44.9**	**83.0**	**84.8**
$\overline{T_{aux,flow}}$	[°C]	46.4	47.6	45.4	47.1	56.3	57.1	50.2	**41.8**	**41.9**
$\overline{T_{DHW}}$	[°C]	53.3	50.9	52.5	51.0	52.9	53.4	51.0	**54.5**	**54.6**
PF_{HP}	[-]	3.7	3.6	3.8	3.6	2.6	2.5	3.3	4.2	4.2
$W_{el,HP}$	[kWh]	3.4	3.7	3.3	3.6	2.7	4.1	7.4	3.2	3.2
Q_{DHW}	[kWh]	11.7	11.7	11.7	11.7	19.1	24.4	19.1	11.7	11.7
PF_{Sys}	**[-]**	**3.4**	**3.2**	**3.5**	**3.2**	**7.0**	**5.9**	**2.6**	**3.7**	**3.7**

5. Conclusions

The method for measuring the stratification efficiency of combi-storage tanks was adapted and simplified for the measurement of hot water tanks with and without solar thermal.

The test method was applied to four different storage tanks with different concepts and sizes. The results of the measurements show clear differences between the individual models and thus reveal weak points in the storage tank configurations that would otherwise remain undetected. The differences between the storages were significantly higher than anticipated by the project team.

Based on the results, it can be assumed that a storage concept with a very good stratification efficiency (for example, storage #4) not only ensures greater comfort and safety (less water in a critical temperature range thanks to better stratification), but also leads to significant savings in final energy at the same time. In combination with a heat pump, this saving can be up to 40% of electrical energy.

The measurements carried out prove the applicability of the method on the basis of a wide range of storage concepts and storage sizes. The assessment of the tested storages on the basis of stratification efficiency is consistent with the simulated electrical (final) energy demand for loading the storage by a heat pump.

Thus, the method for determining stratification efficiency via entropy production can also be applied to hot water storage tanks in the future.

6. Acknowledgement

The authors would like to thank the Swiss Federal Office of Energy for supporting the project "DHWStrat" under contract number SI/500315-03 as well as the partners from industry for the provision of the material.

7. References

European Committee for Standardization (CEN), 2017. EN 16147:2017: Heat pumps with electrically driven compressors - Testing, performance rating and requirements for marking of domestic hot water units.

Haller, M.Y., Haberl, R., Persdorf, P., Reber, A., 2018. Stratification Efficiency of Thermal Energy Storage Systems – A new KPI based on Dynamic Hardware in the Loop Testing - Part I: Test Procedure. Energy Procedia, 12th International Conference on the Storage of Renewable Energies (IRES2018) 155, 188–208. https://doi.org/10.1016/j.egypro.2018.11.056

Haller, M.Y., Haberl, R., Persdorf, P., Reber, A., 2015. StorEx – Theoretische und experimentelle Untersuchungen zur Schichtungseffizienz von Wärmespeichern (Schlussbericht), Im Auftrag des Bundesamt für Energie BFE. SPF Institut für Solartechnik, Rapperswil.

Haller, M.Y., Haberl, R., Reber, A., 2019. Stratification efficiency of thermal energy storage systems – A new KPI based on dynamic hardware in the loop testing - Part II: Test results. Energy and Buildings 202, Article 109366. https://doi.org/10.1016/j.enbuild.2019.109366

Heimrath, R., Haller, M.Y., 2007. Project Report A2 of Subtask A: The Reference Heating System, the Template Solar System - A Report of IEA SHC Task 32: Advanced Storage Concepts for Solar and Low Energy Buildings.

Operational analysis of 5 PVT heat pump systems based on field measurement data

Sebastian Helmling[1], Robert Langner[2] and Konstantin Geimer[2]

[1] Fraunhofer Institute for Solar Energy Systems, Freiburg i. Br (Germany)

Abstract

On December 1, 2019, the integraTE joint project of the three research institutes Fraunhofer ISE, the Institute for Building Energetics, Thermotechnology and Energy Storage of the University of Stuttgart and the Institute for Solar Energy Research Hameln started. The aim of the project is to achieve an increased market penetration with technically as well as economically attractive systems for thermal and electrical energy supply by means of PVT collectors and heat pumps in the building sector. Within the framework of the project, demonstration plants in single family buildings are examined metrologically.

This conference paper presents the results of the metrological investigation of 5 demonstration plants over the period from June 2021 to July 2022.

Keywords: WISC PVT-collector, heat pump, ground source, single family building, monitoring

1. Introduction

T Since the start of the project a comprehensive measurement recording has been started for 5 demonstration systems in single family buildings. The plants are very heterogeneous in their characteristics. While all systems work in single-family homes, different collector technologies are used. Three buildings were renovated (RE), two are new buildings (NB) With two systems, the PVT collector is the only source of heat for heat pump. In the other three plants, a geothermal source comes along additionally. The following Tab 1 lists the characteristics of the examined plants.

Tab 1: characteristics of the demonstration plants,

plant nr.	type	heated area in m^2	final energy demand in kWh/m^2*a	PVT type	collector-surface in m^2	th. power PVT in kW	el. Power PVT/PV in kWh_p	battery - storage kWh	additional heat source	heating capacity HP (B0/W35) in kW	COP (B0/W35)	second heat producer
1	RE	411	80	PVT (WISC)	88	46.3	23.7	20.0	-	13	5	condens-ing gas
2	RE	246	100	Integrated in roof insulation	55	15.6	4.5	no	borehole 390 m	20	4.4	electric
3	RE	340	100	PVT (WISC)	30.6	19.2	14.4	no	borehole 170 m	16	4.6	electric
4	NB	190	40	PVT (WISC) with air HEX	15.8	10.7	12.3	7	-	4.7	4.3	electric
5	NB	310	50	PVT (WISC)	56.1	38.4	7.2	11.4	earth heat collector 25 m	12	4.8	electric

The plants are equipped with heat meters and electricity meters to measure all relevant energy flows as well as

© 2022. The Authors. Published by International Solar Energy Society
Selection and/or peer review under responsibility of Scientific Committee
doi:10.18086/eurosun.2022.14.04 Available at http://proceedings.ises.org

temperatures around heat pump, PVT collector and ground source. Ambient conditions such as temperature, humidity and global irradiation are measured additionally.

The systems are first evaluated regarding the efficiency of the heat pump heating system. For this purpose, the system performance factor SPF defined in the following is used.

2. Key performance indicators

In the following the balance boundary and the system seasonal performance factor is being defined. Subsequently the KPIs of the five plants are discussed.

Definition of the balance boundary and the system seasonal performance factor

The plants are evaluated on the basis of the system performance factor SPF_bST (seasonal performance factor before storage).

$$\text{SPF_bST} = \frac{\int (\dot{Q}_{HP} + \dot{Q}_{backup} + \dot{Q}_{PVT,parallel})\, dt}{\int (\dot{E}_{comp} + \dot{E}_{Heizstab} + \dot{E}_{Pumpen,prim})\, dt} \qquad \text{eq. 1}$$

with:

$\dot{Q}_{HP}$:	amount of heat delivered by the HP for space heating and domestic hot water [kWh].
$\dot{Q}_{backup}$:	amount of heat emitted by the heating rod[kWh]
$\dot{Q}_{PVT,parallel}$	amount of heat supplied to and removed from the storage tank by the PVT collector [kWh].
$\dot{E}_{comp}$	electrical energy consumed by the HP (compressor) [kWh].
$\dot{E}_{backup}$:	electrical energy consumed by the heating rod [kWh].
$\dot{E}_{Pumpen,prim}$	electrical energy consumed by heat source pump(s) [kWh].

System seasonal performance factor and temperatures of heat source and heat sink

The following Figure 1 shows the seasonal performance factor of the five examined plants sorted in descending order.

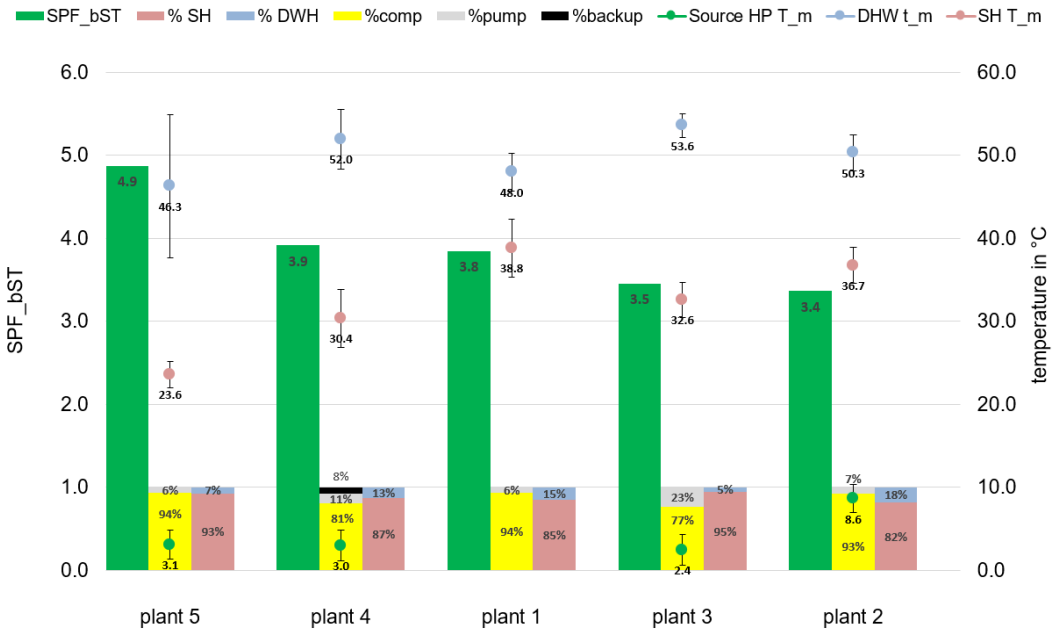

Figure 1: SPF_bST from June 2021 to July 2022

The SPF_bST is indicated as a green column. It reaches from 4.9 at plant 5 to 3.4 at plant 5 for the period under consideration. Next to the green column there is a stacked column. This column shows the share of the electrical energy demand of the compressor, the primary pump(s), and the backup heater in relation to the total electric energy consumption of the heat pump. The energy demand of the controller and the secondary pumps are not considered in this investigation.

At plant 5 the share of the compressor is at 94 %, while the brine pump consumes 6 % of the electrical energy. At plant 4 the compressors energy demand is at 81 % and the brine pump at 11 %. Plant 4 is the only plant where the electrical backup heater was in operation. The share of the electrical energy demand is at 8 % during the considered period.

At plant 1 and plant 5 the distribution of 94 % (93 %) and 6 % (7 %) corresponds to the usual values for those plants. At plant 3 there is a high share of the brine pump with 23 %. At this plant in summertime the PVT collector is used to recharge the borehole. For this reason, there is a high energy demand for the brine pump without the compressor being in operation.

The next stacked column shows the share of thermal energy provided by the heat pump for domestic hot water in blue and the share of energy provided for space heating in red. At plant 5 and plant 3 the share of domestic hot water is with 7 % (5 %) very low for a single-family house. At plant 4, plant 1 and plant 5 the share of domestic hot water ranges between 13 % and 18 %.

Figure 1 furthermore shows the energetically weighted temperatures of the heat source, domestic hot water production and space heating. The graph shows the middle temperature of the respective circuit. It is calculated by the arithmetic mean temperature between supply and return line. At plant 5, plant 4 and plant 3 the middle temperature of the heat source circuit of the heat pump is at 3.1 °C, 3.0 °C and 2.4 °C with a spread of 3 K. At plant 5 the temperature is at 8.6 °C with a spread of 4.4 K. Due to a failure on the heat meter the temperatures at plant 1 could not be measured.

The middle temperature of the domestic hot water production of the heat pump ranges between 46.3 °C with high

spread of 17 K and 53.6 °C with a spread of 2.8 K.

The middle temperature of the HP while in space heating mode ranges from 23.6 °C with a spread of 3.2 K at plant 5 and 38.8 °C with a spread of 7 K at plant 1.

The SPF_bSt of the plants is strongly influenced by the temperatures of the heat sink and heat source. Plant 5 has a temperature of the heat source of 3.1 K. The middle temperature of the space heating is at very low 23.6 °C. Furthermore, most of the heat (93 %) has been provided in the space heating mode. Plant 1 runs on a high temperature in the heating mode but has still a SPF_bST of 3.8. At this plant a large amount of heat in the heating mode is produced in summertime for heating the indoor swimming pool which is in the building. Thus, it is to be expected that the heat source temperature was very high at this time.

The SPF of plant 3 is negatively influenced by the high energy demand of the brine pump in summertime. On the other hand, recharging the borehole in summertime results in a better performance of the PV in summertime and a higher temperature of the borehole and consequently of the heat pumps heat source in wintertime.

Heat source PVT and borehole

The following Figure 2 shows once more the SPF_bST as a green column. The next stacked column shows the distribution of the heat pumps source energy. This energy is provided by either the PVT collector indicated in orange or by the borehole which is indicated in brown.

The middle temperature of PVT circuit is indicated in orange. The middle temperature of the borehole is indicated in brown, and the middle temperature of the heat pumps source circuit is indicated as a green dot.

At plant 5 60 % of the energy which is provided as a heat source for the heat pump is delivered by the PVT collectors at a middle temperature of 5.4 °C with a spread of 4.8 K. 40 % of the source energy is provided by the ground collector at a middle temperature of 1.7 °C with a spread of 3.2 K. This results in an average middle Temperature of the heat source of 3.1 °C for this plant.

At plant 4 the PVT collector is the only heat source for the heat pump. The middle temperature is at 3.0 °C with a spread of 3.6 K.

Due to a failure on the heat meter the temperatures at plant 1 could not be measured.

At plant 3, 43 % of the heat pumps source energy is directly provided by the PVT collector at a temperature of 4.4 °C. The borehole provides 57 % of the energy. The middle temperature of the borehole is 0.9 °C with a spread of 1.8 °C. At this plant the PVT collectors are used to recharge the borehole in summertime. When this energy is considered, 71 % of the heat pumps source energy has been delivered by the PVT collector. On a yearly basis the PVT collector was delivering a middle temperature of 13.9 °C with a spread of 5.6 K.

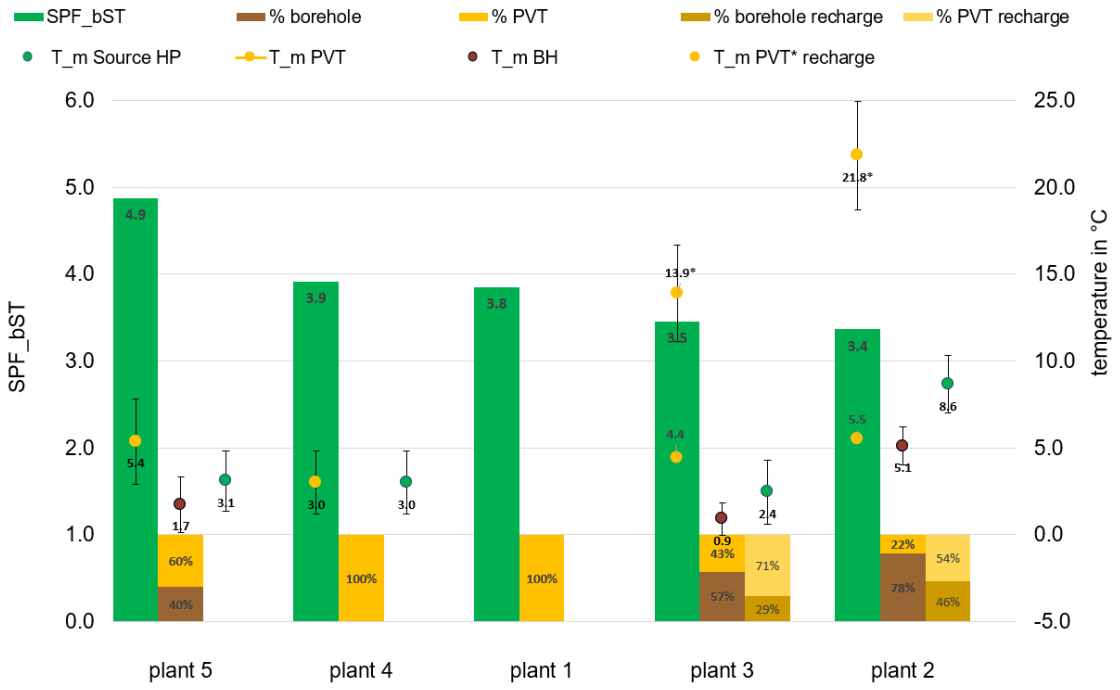

Figure 2: temperatures and energy share of PVT and ground source

At plant 2 22 % of the heat pumps source energy is directly provided by the PVT collector at a temperature of 4.4 °C. The borehole provides 57 % of the energy. The middle temperature of the borehole is 0.9 °C with a spread of 1.8 °C. At this plant the PVT collectors are used to recharge the borehole in summertime. When this energy is considered 54 % of the heat pumps source energy has been delivered by the PVT collector. On a yearly basis the PVT collector was delivering a middle temperature of 21.9 °C with a spread of 6.2 K.

Thermal Energy and temperatures provided by the PVT collector

In the following the thermal energy delivered by the collector is shown exemplarily for plant 4 and plant 3 on a monthly basis. Plant 4 uses WISC collectors with fins to optimize the heat exchange with the ambient air. This plant has no additional heat source for the heat pump. Plant 3 uses standard WISC PVT collectors in combination with a borehole of 170 m depth.

The following Figure 3 shows the amount of energy which is provided by the PVT for every month indicated as an orange column. The energy provided by the PVT collector reaches from 121 kWh in July to 1441 kWh in January. Since the PVT collector is the only heat source for the heat pump, the energy provided to the heat pump shows a direct dependence to the heating demand for domestic hot water and space heating.

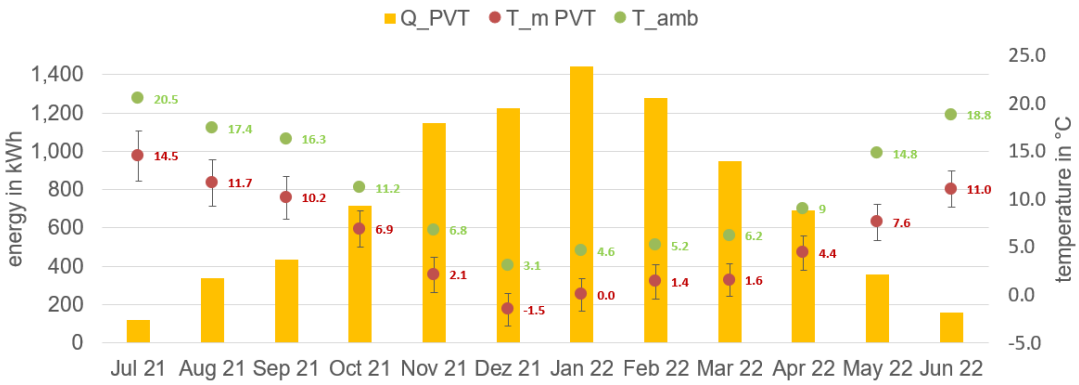

Figure 3; monthly energy and temperatures plant 4

The middle temperature of the PVT circuit is shown as a red dot. The middle temperature reaches from 14.5 °C with a spread of 5.2 K in July to – 1.5 °C with a spread of 3.4 K in December. The average monthly ambient temperature is shown as a green dot and reaches from 20.5 °C in July to 3.1 °C in January. The spread between middle temperature of the PVT circuit and average ambient temperature is at 6 K in July 21. Towards wintertime the spread decreases to its minimum value of 3.8 K in February. Towards summertime it increases again to 7.8 K. In summertime the spread between ambient temperature and middle temperature of the PVT collector is higher. This is caused by the ambient temperature and the solar irradiation at time of the day when the heat pump is in operation.

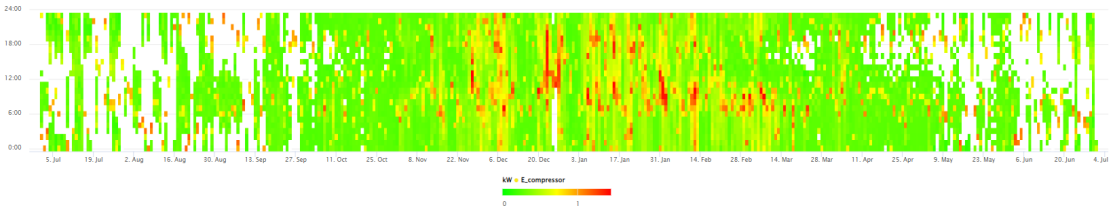

Figure 4: power consumtion of the compressor, plant 4

Figure 4 shows the power consumption of the heat pumps compressor during the year on a minutely basis. In summertime the heat pump is mostly in operation in the morning. At this time the ambient temperature and the solar irradiation is lower than at noon or afternoon. In wintertime the heat pump runs almost all day long. Additionally the phases with the highest energy demand are later during the day. As a result, the collector benefits more from solar radiation and from higher temperatures during the day in wintertime.

The following Figure 5 shows the amount of energy which is provided by the PVT for every month indicated for plant 3. The energy provided by the PVT collector reaches from 2722 kWh in July to 143 kWh in January. The PVT collector is used in summertime to recharge the borehole, which leads to the monthly energy distribution shown in the plot below.

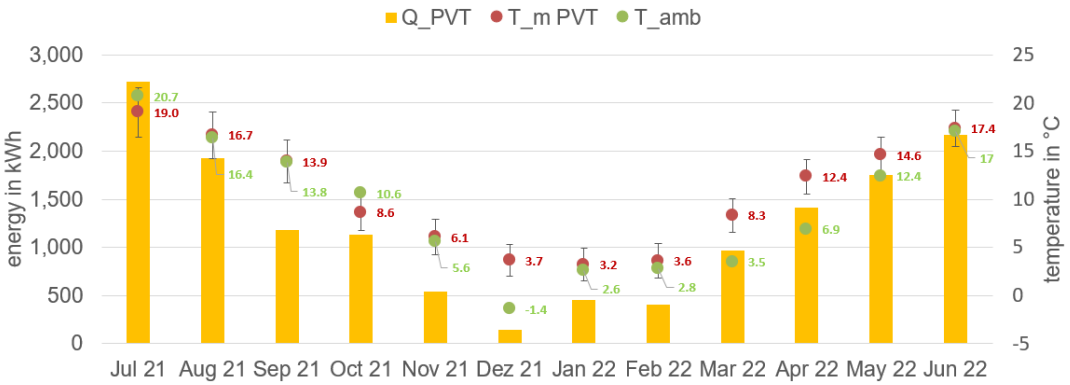

Figure 5: monthly energy and temperatures Plant 3

The middle temperature of the PVT reaches from 19.0 °C with a spread of 7.2 K in July to 3.7 °C with a spread of 1.4 K. The average monthly ambient temperature is shown as a green dot and reaches from 20.7 °C in July to -1.4 °C in January. The spread between middle temperature of the PVT circuit and average ambient temperature does not follow a trend.

The following Figure 6 shows the thermal power provided by the PVT circuit during the year on a minutely basis.

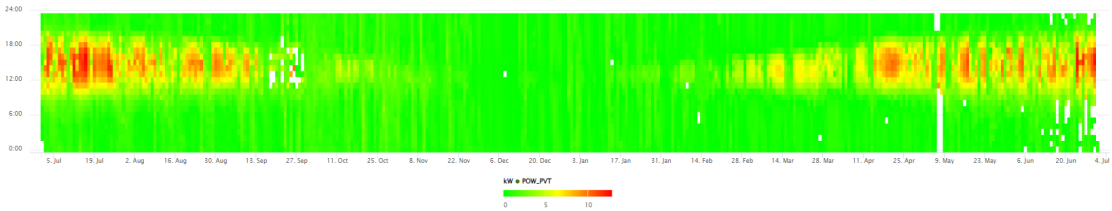

Figure 6: thermal power PVT circuit, plant 3

The PVT circuit was in operation at almost every minute of the year. In summer the thermal power reaches its maximum at 12.7 kW in June. In the winter months the maximum power is at 1.5 kW at daytime an 0.1 kW in the night.

3. Electrical energy demand and production of the plants

The following Figure 7 shows the amount of electrical energy which has been provided by the PV indicated as an orange column. This includes the PVT collectors as well as the additional PV collectors some plants have besides the PVT collectors. The energy consumption of the heat pumps compressor is given in yellow, brine pump(s) in grey and electrical backup heater in black. The green column shows the amount of energy which has been used in the heat pump system for compressor, brine pump(s) and backup heater and which was provided by the PV and the battery. This energy has been calculated on a minutely basis. Furthermore, in addition, the assumption is made that the electricity from PV and battery is provided exclusively to the heating system and is not consumed in the household.

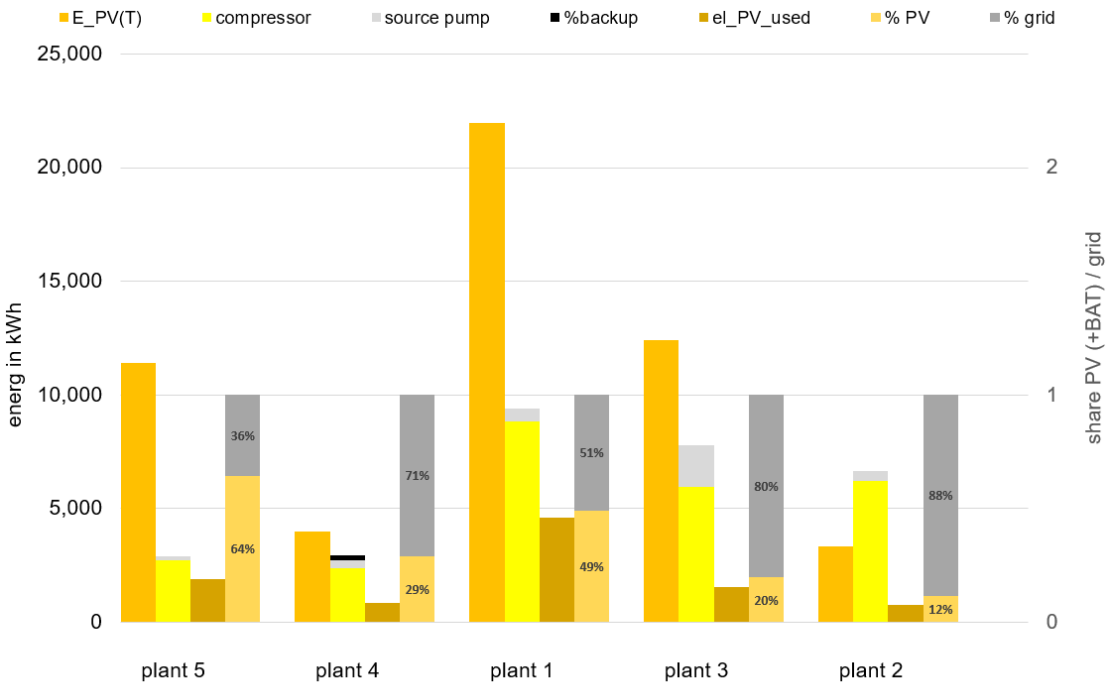

Figure 7: electrical energy PV(T) and heat pump

At plant 5 the PV provides 11400 kWh. The heat pump consumes 2913 kWh. 1876 kWh of the energy provided by the PV has been used in the heating system. That means that 64 % of the heat pumps energy demand has been covered by the PV and battery system. 36 % of the electrical energy was provided by the grid.

At plant 4 the PV provides 3981 kWh. The heat pump consumes 2944 kWh. 1876 kWh of the energy provided by the PV has been used in the heating system. That means that 29 % of the heat pumps energy demand has been covered by the PV and battery system. 71 % of the electrical energy was provided by the grid.

At plant 1 the PV provides 21980 kWh. The heat pump consumes 9401 kWh. 4623 kWh of the energy provided by the PV has been used in the heating system. That means that 51 % of the heat pumps energy demand has been covered by the PV and battery system. 49 % of the electrical energy was provided by the grid.

At plant 3 the PV provides 12408 kWh. The heat pump consumes 7789 kWh. 1533 kWh of the energy provided by the PV has been used in the heating system. That means that 80 % of the heat pumps energy demand has been covered by the PV and battery system. 20 % of the electrical energy was provided by the grid.

At plant 2 the PV provides 3323 kWh. The heat pump consumes 6666 kWh. 777 kWh of the energy provided by the PV has been used in the heating system. That means that 88 % of the heat pumps energy demand has been covered by the PV and battery system. 12 % of the electrical energy was provided by the grid.

In the following the coverage of the heat pumps energy demand by the PV and and the pv + the battery storage has been investigated on a monthly base. The following Figure 8 shows these values for plant 1. This plant is equipped with a battery with a capacity of 20 kWh.

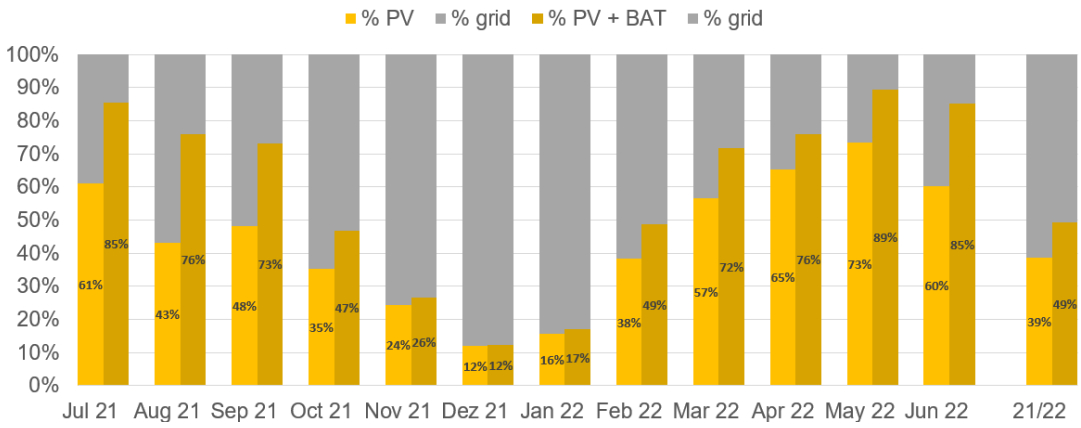

Figure 8: monthly coverage pv (+ bat) electricity, plant 1

In the summer months the heat pumps electricity demand can be covered up to 73 % by the PV. With the help of the battery this value can be raised to 89 %. In the winter months when the electricity demand of the heat pump system is high and the solar irradiation low, the coverage decreases to 12 %. During this time the self-sufficiency level of the system cannot be increased by the battery. During the entire period under consideration from July 21 to June 22, the PV coverage is 39 %. With the help of the battery, it can be raised up to 49 %. It has to be stated that this plant has a high thermal energy demand in summertime which is caused by an indoor swimming pool. This raises the PV coverage in the summer months in comparison to a normal single-family house.

The following Figure 9 shows the coverage of the heat pumps energy demand by the PV and and the pv + the battery storage at plant 4. This plant is equipped with a battery with a capacity of 7 kWh. It was not possible to measure the PV and the battery separately. For that reason, the following plot considers the electrical energy which has been delivered by the PV and the battery.

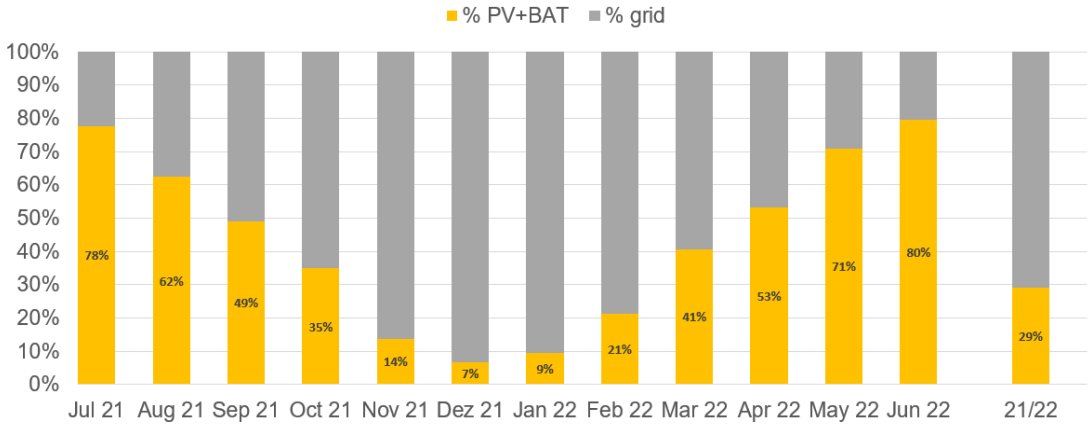

Figure 9: monthly coverage pv (+ bat) electricity, plant 4

In the summer months the heat pumps electricity demand can be covered up to 80 % by the PV and the battery. In the winter months when the electricity demand of the heat pump system is high and the solar irradiation low, the coverage decreases to 7 %. During the entire period under consideration from July 21 to June 22, the PV+BAT coverage is at 29 %.

4. Summary

PVT collectors are suitable as a heat source for building heating systems with heat pumps. The SPF of the five plants range between 3.4 and 4.9. As usual for heat pumps the SPF depends mostly on the heat sink temperatures. systems with a low heating circuit temperature and a low quantity of produced drinking hot water yield the highest SPF. When normal WISC collectors are used, the plant should either be equipped with an additional ground

source. In those cases, the PVT collectors can be used both to recharge the ground source during summertime and to increase the temperature of the heat source for the heat pump. As an alternative to that a condensing gas boiler can support the system in the winter months. WISC PVT collectors with an optimized ambient air heat exchanger can work as a single heat source for the heat pump system. The plant which has been the system convinces with a reasonable use of the heating rod in wintertime.

During the period under consideration of one year, the plants can cover between 12 % and 64 % of the electrical energy demand for the heating system by pv electricity. However, values above 20 % could only be achieved with the help of a battery.

The study also showed that there is potential for optimization in all plants. For example, all plants are heat-controlled. Shifting the operating times of the heat pump when solar radiation is at its highest could probably improve the performance of the systems even further. This will be a focus in the further course of the project.

Finally, I would like to thank the german federal ministry of economy and climate protection, the ptj, the Project Management Juelich and the industry and research partners whose work and financial support made this project possible.

Novel Hardware-in-the-loop Approach for Thermal Systems

Uygur Tepe[1], David Klump[2], Tobias Reum[2] and Tobias Schrag[2]

[1] University of Windsor, Windsor (Canada)

[2] Institute of New Energy Systems, Technische Hochschule Ingolstadt, Ingolstadt (Germany)

Abstract

Hardware-in-the-Loop is a method that allows real-time testing of complex systems. A physical system can be analyzed using a programmable logic controller and simulation-based periphery. In this paper, a Hardware-in-the-Loop system using a LabVIEW-controlled thermal test bench as well as a MATLAB simulation is presented. The LabVIEW program is able to take over the communication with the physical system and the simulation. The discrete time steps between each simulation call and test bench control are to be minimized to allow a near-continuous operation and control of the physical system. A heat pump-based domestic heating system was tested to analyze this approach. The test bench controls the volume flows and temperatures according to the current demand for space heating and domestic hot water from the simulation. By applying this software-based approach, no external programmable logic controllers are necessary for the realistic testing of thermal systems and, therefore, extend the applicability of the Hardware-in-the-Loop testing approach.

Keywords: Hardware-in-the-loop, software-based approach, thermal test bench, heat pump system

1. Introduction

Determining the realistic outcome of a specified hardware design or application can be complex and difficult without proper testing. The Hardware-in-the-Loop (HiL) approach utilizes real-time signals from a controller to communicate with a physical sub-system as if it is in a real system. Through the use of HiL, comprehensive, reliable, and scalable tests of a hardware component of sub-system are possible without the need of using a fully assembled system. HiL is used in a multitude of engineering applications (Nabi et al., 2004; Snider et al., 2022). One example is the investigation of domestic heating systems (Stutterecker et al., 2015).

In (El-Baz et al., 2018), a HiL system is being used to investigate a heating system consisting of a heat pump, thermal storage and a building. While the heat pump and storage are within a thermal test bench, the behavior of the building is being calculated within a simulation model. The communication between simulation model and testbench is implemented using an external programmable logic controller (PLC). Also, in (Nürenberg et al., 2017) thermal test bench setup is introduced, which is able to determine the performance of heat pump systems using HiL. The heat pump is installed within a thermal test bench, while the building is being simulated. As in a previous investigation, the communication is established using a PLC to combine the two worlds.

A PLC offers the possibility to physically separate the machine where the simulation is performed and where the communication is realized. This can be beneficial while dealing with complex simulations which are time consuming and therefore need to be run on a high-performance machine to calculate the system behavior in real-time. Since the simulation complexity can be reduced for some investigations, the physical separation of machine and simulation running device is not needed, therefore use of a PLC can be avoided by running communication and simulation on the same machine. By that, complexity and effort to setup a HiL-based investigation can be reduced. Also, laboratories or users that do not possess an external PLC can use the HiL approach presented for their experiments.

In this paper, a HiL approach that does not require a PLC is introduced by combining a LabVIEW controller with a MATLAB Simulink simulation. LabVIEW is a graphical programming environment for testing and measuring (National Instruments, n.d.) for different engineering applications. MATLAB Simulink is a

© 2022. The Authors. Published by International Solar Energy Society
Selection and/or peer review under responsibility of Scientific Committee
doi:10.18086/eurosun.2022.14.05 Available at http://proceedings.ises.org

graphical environment used to design and simulate systems (MathWorks, n.d.). By combining the LABVIEW controller directly with a MATLAB simulation, the PLC unit can be avoided implicitly. A disadvantage of this approach is that the communication between the hardware and software is not continuous anymore but communicates discreetly in certain time steps. Minimizing the time steps between each model execution can reduce the difference between the usual continuous HiL approach with an external PLC and the introduced discrete HiL approach. Furthermore, this disadvantage can be negligible for rather inert systems such as domestic heating systems. The introduced HiL approach was implemented and tested at the thermal testbench of the Institute for New Energy Systems (InES) at Technische Hochschule Ingolstadt (THI). A heat pump (HP)-based domestic heating system was investigated. Thus, a first the proof-of-concept of the novel HiL approach without a PLC is provided in this paper.

2. Setup of the exemplary system

2.1. System overview and communication structure

A simplified setup was used to show the functionality of the novel HiL approach. For that, the example of a ground source HP is used for either space heating (SH) or charging a domestic hot water (DHW) storage. Within this experiment the switching of the HP operation mode between SH and DHW will be investigated. Fig. 1 illustrates the setup of the HiL system.

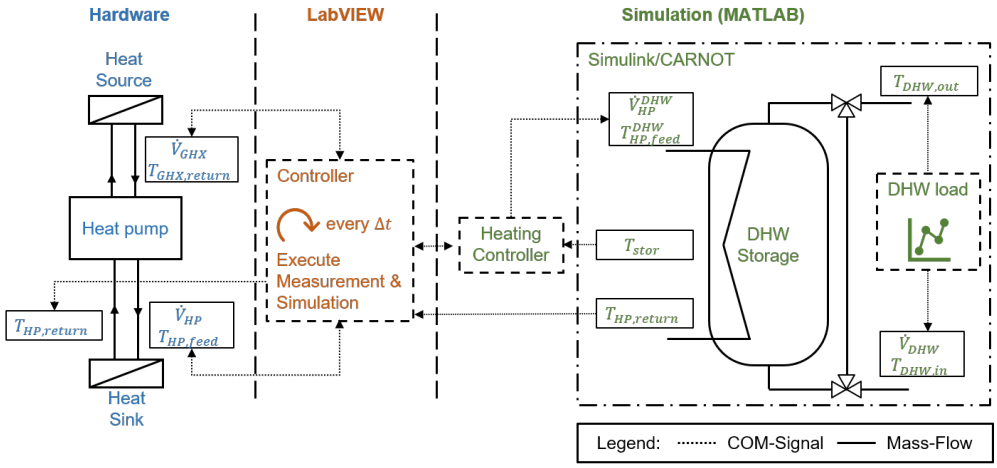

Fig. 1: Schematic drawing of the exemplarily investigated Hardware-in-the-Loop system

On the left side in blue the installation of the HP within the thermal test bench is shown. The test bench provides multiple hydraulic cycles acting as heat source or heat sink. The HP is connected with both a heat source and a heat sink via isolated pipes. The insulated pipes connecting the heat pump to the thermal test bench led to small delays in the control loop. This can be detected in the measurement results and influences the speed of the PID controller. The overall methodology is not impacted. Each hydraulic cycle includes pumps and valves to control its return temperature and volume flow. The heat source acts as a ground source heat exchanger (GHX) which is kept at a constant operation point during the investigation. It contains brine, a water-glycol mixture, to prevent freezing at realistic ground source heat exchanger temperatures. The heat sink is filled with water as it would be in a real domestic heating system. The operation mode of the heat sink is switched between the DHW and the SH mode. When in SH-mode, the heat sink operation is kept at constant values. When in DHW-mode the setpoints are received from a simulation model. This is implemented by specifying the setpoints for inlet and outlet temperatures $T_{HP,return}$, $T_{HP,feed}$ and the volume-flow $\dot{V}_{HP}$.

The control of the test bench components and the communication between hardware and simulation model is implemented in LabVIEW. The control of the test bench is implemented using PID controllers. By that, a setpoint can be specified inside the LabVIEW program and the operation point of pumps and valves are set to reach the setpoints. The control loop is executed at a fixed time-step Δt. As mentioned, the setpoints are calculated inside a simulation when the HP is in DHW-mode. For that, the measured values $\dot{V}_{HP}$ and $T_{HP,feed}$ are used to initialize the simulation model of the DHW storage. After initialization, the simulation model is

executed and simulated for the same Δt at which the control loop is iterated. As long as the calculation time of the simulation is smaller than Δt, the setpoints for the test bench are updated in real time. As already mentioned in the beginning, this is a limit of this approach which needs to be investigated in further experiments.

On the right side of the figure in green, the components inside the simulation model are shown. In the given case, the heating controller which determines the HP's operation mode is implemented within the MATLAB environment. This could also be done within LabVIEW. The behaviour of the DHW storage is modelled in the MATLAB Simulink environment using the CARNOT Toolbox (Solar-Institut Juelich, 2022). Whenever the HP charges the DHW storage, the heating controller sets the volume flow to the corresponding value $\dot{V}_{HP}^{DHW}$ and initializes the simulation together with $T_{HP,feed}^{DHW}$ from the test bench. Within the simulation the return temperature $T_{HP,return}^{DHW}$ after one time step Δt is calculated and fed back to the controller in LabVIEW. An exemplary DHW load profile is used to simulate the discharging of the DHW storage by setting the values for the tapping $\dot{V}_{DHW}, T_{FW}$, and T_{DHW} within the simulation model.

2.2. Heating controller

As described, the heating controller switches the operation mode of the investigated HP by changing the setpoints of the heat sink of the test bench. Therefore, the volume flow and the return temperature need to be determined for both charge and discharge modes. The heating controller reads the storage temperature at 50% height (T_{stor} in Fig.1). Depending on the value of T_{stor}, it changes the operation mode. When the temperature T_{stor} drops below a lower limit $T_{lim,low}$, the HP's operation is changed to DHW-mode. DHW preparation is commonly prioritized over SH operation (EVERGREEN ENERGY LTD., n.d.). The latter is a slow process due to the thermal inertia of heating systems. It remains in the DHW-mode until the storage temperature reaches an upper limit of $T_{lim,high}$. In every other case the HP is in SH-mode. Following this logic, the volume flow of the heat sink can be determined by the following equation:

$$\dot{V}_{HP} = \begin{cases} \dot{V}_{HP}^{DHW} & if\ T_{stor} \leq T_{lim,low}\ or\ (\dot{V}_{HP} = 500\ and\ T_{stor} \leq T_{lim,high}) \\ \dot{V}_{HP}^{SH} & otherwise \end{cases} \quad \text{(eq. 1)}$$

The return temperature is determined in the same way, while the setpoint during SH-mode is constant and during DHW-mode is being calculated within the simulation model and updated at each iteration.

2.3. Used system parameters

For the given investigation several parameters were specified to simulate a realistic scenario. Table 1 provides the system and simulation parameters.

Tab. 1: Specified Parameters within the investigation

Description	Value	Units
Inverter frequency level	75	%
Setpoint volume flow of heat source	$\dot{V}_{GHX} = 1250$	l/min
Setpoint temperature of heat source	$T_{GHX,return} = 10$	°C
Setpoint volume flow of heat sink	$\dot{V}_{HP}^{DHW} = 600$ $\dot{V}_{HP}^{SH} = 900$	l/min
Setpoint temperature of heat sink	$T_{HP,return}^{DHW} = f(sim)$ $T_{HP,return}^{SH} = 30$	l/min
Initial storage temperatures	$40 - 45$	°C
Volume of DHW storage	200	liter
Lower limit storage temperature	$T_{lim,low} = 40$	°C
Upper limit storage temperature	$T_{lim,high} = 45$	°C
Time step	$\Delta t = 2$	s

The HP used works as an inverter-driven brine source HP. The inverter frequency is set to 75 % relative speed for the duration of the experiment. Volume flow and return temperature of the heat source are kept constant at 1250 l/min and 10 °C respectively. Volume flow as well as return temperature of the heat sink vary according to the state changing between SH and DHW mode. The lower limit for the heating mode was set to 40 °C while the upper limit was set to 45 °C. The simulation model of the DHW storage is a 1D-model using 10 layers. The storage layers are initialized at a temperature between 40 to 45 °C. This represents a nearly fully charged DHW storage at the beginning of the investigation. The volume of the DHW storage has been set to a typical volume of a single-family house of 200 liters. With a time-step Δt of 2s, the simulation was consistently completed before the next iteration of the LabVIEW program took place.

3. Results

In this paper, the DHW mass flow, storage temperatures, and the temperatures of feed and return flow are analyzed in order to determine if the heat storage controller and model properly is communicating with the thermal test bench. This communication is essential to evaluate if using LabVIEW and MATLAB can be used together in a HiL setup for thermal systems. The LabVIEW testbench runs the thermal HP in a general day to day setting with the DHW storage being utilized throughout the day for various tasks such as showering, washing hands, dishes, or doing laundry. Whenever the DHW storage is used, the mass flow increases and tapping occurs until the task is completed. The task depends on the value of the DHW mass flow with more intense tasks requiring a larger mass flow (for example, filling a bathtub).

For this investigation the time period from 07:00 a.m. until 09:00 a.m. was chosen, when several and different quantities of DHW are tapped. In Fig. 2 the DHW mass flow, storage temperature and feed and return flow temperatures of the heat sink are displayed.

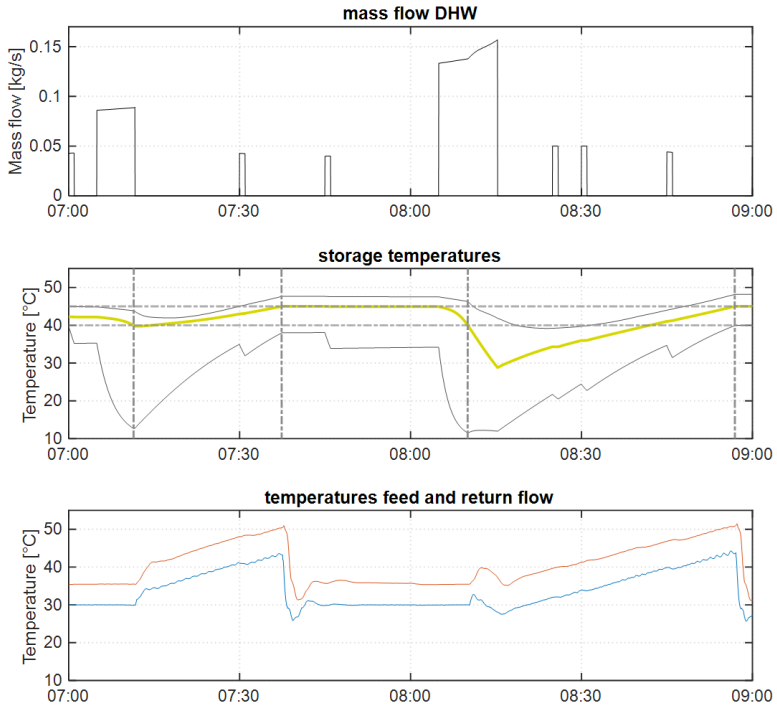

Fig. 2: DHW massflow, storage temperature, and heat sink's feed and return flow during the investigated time period from 07:00 a.m. until 09:00 a.m.

The x-axis represents the actual time within the day that the HP was running within the thermal system, starting at 07:00 and ending at 09:00. The first plot of DHW mass flow depicts this when the DHW storage is being utilized for various tasks within the two-hour run time of the HiL system. Below the simulated storage temperatures at top, middle and bottom are plotted. The green line refers to the temperature in the middle at 50 % storage height, which the heating controller uses as input to determine whether the HP is in DHW or SH mode. The horizontal dotted grey lines represent the limits of the heating controller as mentioned above. The

vertical dotted lines indicate the switching points when the HP switches its operation mode. The bottom plot displays the feed and return temperatures of the heat sink which were measured at the test bench.

At the beginning of the measurement a small tapping occurs. Due to the small quantity, this tapping lowers only the lower storage temperatures and doesn't lead to a switch of the HP's operation mode. Therefore, the HP stays in SH-mode which can be seen in the lower graph, where the feed and return temperature are stable at 35 °C and 30 °C respectively. During the first large tapping cycle occurring around 07:05, the water in the DHW storage decreases, and as expected the temperature of the storage levels decrease. Once the storage temperature at 50 % height reaches the lower threshold temperature, the HP goes into DHW mode. When in DHW mode the thermal test bench quickly increases the temperature of the return flow by about 5 °C, then increasing continuously. This is a result from the heat storage simulation and lets the HP feed temperature increase accordingly. At around 07:30 a small tapping occurs which slows down the charging process of the storage. It leads to a reduction in the lower storage temperatures and therefore, to a lower return flow temperature. At around 07:40 the storage is recharged again and the storage temperature at 50 % height reaches the upper threshold. As a consequence, the HP switches back to SH mode. This switch can be again identified also in the lower graph, where the feed and return temperatures switch back to their initial constant values at the beginning of the measurement. When switching back, the temperatures of feed and return flow take about 5 minutes until the values become stable again. The delay is caused by the parametrization of the PID-controllers for the volume and temperature control of the heat sink. This can be improved in the future by redefine the PID parameters and therefore improve the response of the test bench. Conclusively, this delay is not a consequence of the described HiL approach.

From 7:40 until 08:05 only a small tapping occurs, which lowers again only the lower storage temperatures. The next tapping occurs at around 08:05 and is the largest quantity during the whole investigation. During this tapping cycle, the temperature of the DHW storage levels decrease at a faster rate due to the higher DHW mass flow. This leads again to the HP going into DHW-mode at 08:12 before the tapping is completed as can be seen from the third vertical dash-dotted line. Although the HP is in charge mode, the storage temperatures continue to decrease as the HP power is not large enough. However, when the tapping stops at 08:15, the storage is being charged until the upper threshold storage temperature is reached as expected at the fourth vertical line.

During the phase from 08:10 until 8:15, when the storage is charging while tapping occurs, the storage temperatures continue to decrease. This can be seen more detailed in Fig. 3. There, the feed and return flow temperatures and the thermal storage temperatures are displayed during the second large tapping cycle.

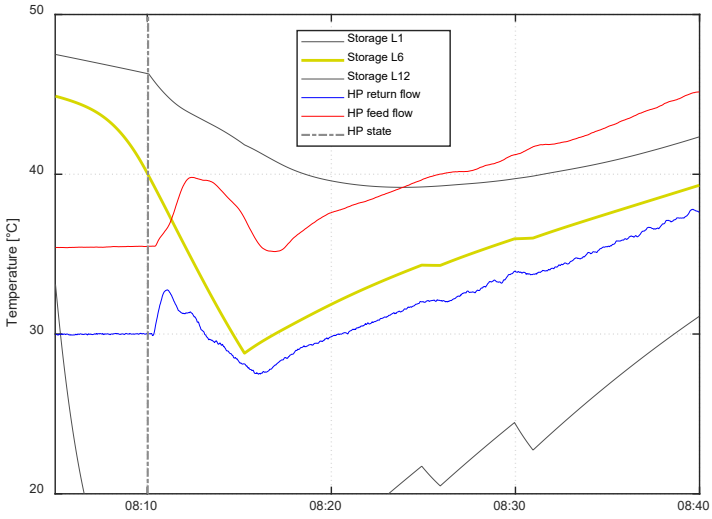

Fig. 3: Feed and Return flow output temperature with storage temperatures during the third switching point

The storage temperature at the top (upper grey line) is still decreasing until it crosses the HP's feed flow (red line) at around 08:24. The reason behind that is the mentioned temperature difference between feed and return flow which is for the investigated HP constantly around 7 °C. Since the return flow (blue line) at the end of

the tapping cycle is around 29 °C the feed flow temperature is at around 36 °C. Due to this fact, the feed flow temperature is lower than the storage temperature at the top from 08:10 until 08:24. This effect cools down the upper storage temperatures additionally to the DHW tapping. The main reason for this effect is the positioning of the heat exchanger inside the thermal storage and may not be the case in well-designed heating systems. Nevertheless, the fact that the results are can be reasonably explained conclude that the novel HiL approach is working as expected and can be used for further investigations.

4. Conclusion

This paper demonstrated a HiL system operating without a PLC by using LabVIEW as the communication interface between the thermal testbench and simulation system. To demonstrate the functionality of this approach, a physical HP and a simulated DHW storage were utilized. With this HiL approach, the heating controller reacted properly to the inputs and switched in and out of the DHW charging mode according to the simulated storage temperatures. Likewise, the test bench reacted to the simulation outputs and varied the return temperature and volume flow into the heat pump to demonstrate the different operation modes of SH and DHW preparation. The results matched the expectations.

Several interesting observations could be made during this switching process. During the second larger tapping, the response of the heat pump of not being able to cover the DHW tapping power can be seen. Even though the HP is charging already, the temperature levels still decrease until the tapping ends and the HP charges the DHW storage. This is commonly seen in heating systems, where the HP power usually does not cover the maximum DHW tapping power, but the DHW storage acts as a buffer tank in between. The control delay within the first few minutes is most likely an issue with the PID controller of the test bench. The effects of small DHW tapping cycles being low on the overall storage temperature level and only affecting the lowest layers is a realistic observation.

The investigated HiL approach can allow further studies on both the heat pump behavior as well as the heating controller. The studies range from varying the heat exchanger position within the DHW storage tank over the adjustment of the limit storage temperatures as well as a more detailed look into the heat pump reacting to different operation modes. However, the outcome was only evaluated qualitatively. Even though the results matched the expectations of such a heating system, the approach should still be validated with a physical heating system in the future. Furthermore, the limits of the approach need to be investigated more detailed. One limit could be the restrictions in simulation complexity in comparison to the available computational resources. Using a software-based system with LabVIEW and MATLAB promises to become an alternative to conventional PLC-based HiL operation. In the future, a software-based system can be tested on less inert systems.

5. References

El-Baz, W., Mayerhofer, L., Tzscheutschler, P. and Wagner, U., 2018. Hardware in the Loop Real-Time Simulation for Heating Systems: Model Validation and Dynamics Analysis. Energies 11, no. 11: 3159. https://doi.org/10.3390/en11113159

EVERGREEN ENERGY LTD., n.d., https://www.evergreenenergy.co.uk/. [Online] Available at: https://www.evergreenenergy.co.uk/heat-pumps/using-a-heat-pump-for-hot-water/ [Accessed 9 September 2022].

MathWorks (ed), n.d. *MATLAB Simulink* [Online]. Available at https://de.mathworks.com/products/simulink.html (Accessed 4 August 2022).

Nabi, S., Balike, M., Allen, J., and Rzemien, K., 2004. An Overview of Hardware-In-the-Loop Testing Systems at Visteon. SAE Technical Paper, 2004-01-1240. https://doi.org/10.4271/2004-01-1240

National Instruments (ed), n.d. *LabVIEW* [Online]. Available at https://www.ni.com/en-us/shop/LabVIEW.html (Accessed 5 September 2022).

Nürenberg, M., Mehrfeld, P., Huchtemann, K. and Müller, D., 2017. Hardware-in-the-Loop test bench setup and its application to determine seasonal performance of heat pump systems. 12th IEA Heat Pump Conference 2017, Rotterdam, 15-18 May.

Snider, E. J., Berard, D., Vega, S. J., Ross, E., Knowlton, Z. J., Avital, G. and Boice, E. N., 2022. Hardware-in-Loop Comparison of Physiological Closed-Loop Controllers for the Autonomous Management of Hypotension. Bioengineering 9, no. 9: 420. https://doi.org/10.3390/bioengineering9090420

Solar-Institut Juelich, 2022. *CARNOT Toolbox: for Matlab/Simulink (*7.3) [Computer program]. Available at https://www.fh-aachen.de/forschung/solar-institut-juelich/carnot.

Stutterecker, W., Schoberer, T. and Steindl, G., 2015. Development of a Hardware-in-the-Loop Test Method for Heat Pumps and Chillers. REHVA Annual Conference: *Advanced HVAC and Natural Gas Technologies*, Riga, 8-9 May. https://doi.org/10.7250/rehvaconf.2015.017

Flow rate estimation in glandless circulator pumps - influence of temperature and water-glycol heat-transfer fluids

Christian Sauer[1], Christoph Schmelzer[1], Matthias Georgii[1], Janybek Orozaliev[1], and Klaus Vajen[1]

[1] University of Kassel, Institute of Thermal Engineering, Department of Solar and Systems Engineering, Kassel (Germany)

Abstract

In this paper, the operation principle, uncertainty factors and the influence of water-glycol heat-transfer fluids at different temperature on a function that estimates the volumetric flow rate in a glandless circulator pump are investigated. The influences are examined theoretically and experimentally using a common circulator pump. Modern electronically controlled variable speed pumps determine the pump speed and power consumption. Combined with predefined characteristic maps, the pump electronics can act as a soft sensor and estimate the operating point and therefore the volumetric flow rate of the pump. To exchange this information with other systems, the LIN circulator profile, a standardized digital interface can be used. The flow rate estimation is based on characteristic maps that represent the real pump performance as accurately as possible. The extent to which deviations affect the flow rate estimation depends on the operating point of the pump. Especially at low speeds and steep head loss system curves, even small deviations lead to large uncertainties. In many thermal plants, e.g. solar thermal systems, water-glycol heat-transfer fluids are used. Here, the fluid properties deviate from clear water, which leads to a changing performance of the pump. Also, the fluid properties are highly temperature-dependent. This causes a strong effect on the flow rate estimation and leads to a wide possible error margin which is shown experimentally.

Keywords: flow rate estimation, soft sensor, circulator pump

1. Introduction

Quantifying volumetric flow rates plays an important role in the control, optimization, monitoring, and fault detection of HVAC systems. For this purpose, a wide range of sensors is available on the market. However, these sensors entail additional investment, installation, and maintenance costs. Especially in smaller systems, e.g. smaller solar thermals systems, they are a significant cost factor. But even in larger systems often not all volumetric flow rates are measured due to costs considerations.

Circulation pumps in these HVAC systems are a major energy consumer. In the European Union they were responsible for an electricity consumption of 50 TWh in 2005. To reduce this enormous demand for electricity, the EU member states decided to gradually introduce strict energy efficiency standards for circulators in Regulation (EC) 641/2009 as part of the Ecodesign Directives (ErP). Since 2013, only pumps that meet these efficiency requirements may be newly installed. Since 2020, the regulations have also applied to the replacement of existing pumps. The regulation has resulted in a technological shift, as the requirements can de facto only be met by speed-controlled circulator pumps with electronically commutated permanent magnet motors (ECM) (UBA, 2009).

One of the main efficiency advantages is based on an electronically controlled frequency converter, with which the motor speed can be reduced in part-load operation, thus lowering the power consumption of the pump. The pump electronics permanently record important operating data of the electric motor such as speed and power consumption. Based on this data and information on the pump characteristics, it is possible to estimate the flow rate delivered by the pump. Various manufacturers now offer pumps with this type of flow rate estimation. The flow rate and other values determined by the pump can, on the one hand, be used for control concepts implemented in the pump electronics. On the other hand, it can be used via communication interfaces, for instance with the new standardized Lin-Bus protocol, to exchange the acquired data with other systems. However, there is hardly any publicly available information on the quality of such a flow rate estimation or the impact of pumping media conditions that are often occurring in heating systems, such as varying temperature and propylene-glycol based heat-transfer fluids.

© 2022. The Authors. Published by International Solar Energy Society
Selection and/or peer review under responsibility of Scientific Committee
doi:10.18086/eurosun.2022.14.06 Available at http://proceedings.ises.org

2. Operating principle and relevant research

The performance characteristics of pumps can be described in the form of characteristic curves as a function of the flow rate Q. In the scope of this work the relevant parameters are the dynamic total delivery head H, the pump efficiency η and the power consumption P. The dynamic total delivery head H is a unit of energy that is often used in the in the context of pump performance. It is a measure of the specific work transferred by a pump to a fluid equivalent to the vertical rise and friction losses that occur in the system. The non-SI conform unit is meter liquid column.

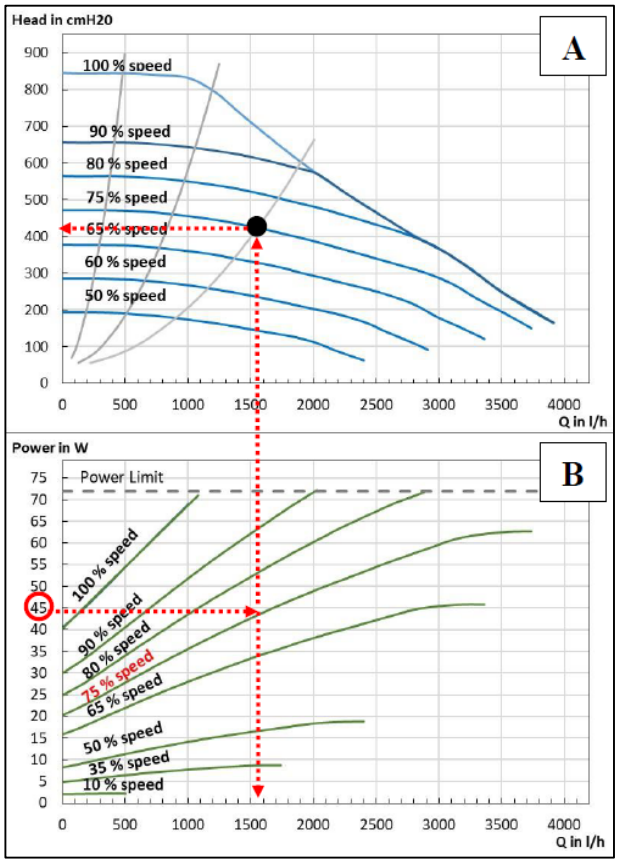

Fig. 1 A: H,Q-characteristic-curves for different pump speed levels (blue) and plant curves (grey)
B: P,Q-characteristic-curves for different pump speed levels(green). Relation between operating point, power, flow rate and speed marked red.

The head characteristic curve (H,Q-characteristic curve) describes the delivery head a pump can achieve at a specific flow rate. In Figure 1-A the exemplary characteristic of a circulator pump can be seen. The decreasing head with increasing flow rate is typical for the characteristic curve of a centrifugal pump.

The operating point is set where the head of the pump and the head-loss of the system are equal, seen as the point of intersection of the system head curve (grey) and the head characteristic curve of the pump (blue). System characteristics with high losses are called steep and the ones with low losses are called flat, according to the slope of the system head curves in the H,Q-diagram.

Various losses in the pump (fluid friction, gap flows, bearing losses, etc.) result in the mechanical energy of the pump impeller not being fully transferred to the pumped medium in the system. The efficiency of the pump describes the ratio of the mechanical power applied to the pump shaft and the hydraulic power transferred to the fluid.

The shaft power of the pump results from the required hydraulic power at the operating point and the efficiency of the pump at the operating point. The relationship of pumped flow rate and shaft power of the pump is given by the P,Q-characteristic-curve (Fig. 1-B).

For variable speed pumps these characteristic curves are not static. The head characteristic curve, the efficiency and power-flow rate relation are changing with variable speed.

This leads to a three-dimensional power-flowrate-speed-map (P,Q-characteristic-map). The power-flow curves at constant speed (P,Q-curves) are projections of this map. So, if power, speed, and the pump characteristics are known, the flow rate and head of the pump can be assigned unambiguously for most operating points.

3. Overview of relevant research

Based on this basic operating principle, various research works are dealing with the estimation of flow rate in centrifugal pumps.

Hammo and Viholainen (2005) test a method patented by ABB for a pump frequency inverter. Using laws of similarity, P,Q-characteristic curves for other speeds are calculated from a single P,Q-curve. For a centrifugal pump with 25 kW power, an estimation error between 0-28 % of the nominal flow rate is achieved.

Ahonen et al (2011) present a hybrid method. If the system curve is known, the flow rate is estimated, depending on the operating point, using the P,Q method or by estimating the delivery heads and then determining the flow rate from the intersection with the known system curve. The method was verified experimentally on one 11 kW centrifugal pump and shows lower estimation errors than the sole P,Q method.

Bakman and Vodovozov (2013) investigate the dynamic behavior of pressure and flow estimation for use in the control of centrifugal pumps.
Pöyhönen et al. (2019) show an approach that does not require pump curves given by the manufacturer or extensive measurements. With the help of four parameters: power, flow, head and speed at the nominal point and universal, dimensionless characteristics for centrifugal pumps, pump-specific characteristics are generated. Using the P,Q method, the volume flow rates are estimated from these. Applied to four pumps between 2.7 kW and 45 kW, the error is 7-15 % of the nominal flow rate.

All the considered publications deal with high power glanded pumps with a dedicated pump, motor, and inverter assemblies in cold water operation.
For the application of flow rate estimation for highly integrated glandless pumps with low power ratings (<2500 W), as often applied in small and medium sized HVAC applications, hardly any information can be found. However, various manufacturers now also implement a flow rate estimation feature in such small pumps.

4. Pump communication interface

Should the volume flow estimation be used as a soft sensor solution, a communication interface is needed to exchange data with other systems.
The Local Interconnect Network is as communication standard originally developed in the automobile industry for applications that are not time or safety critical such as the networking of seat and window controls. It is a widely used and cost-optimized digital communication standard that offers a relatively simple communication protocol and hardware requirements that are inexpensive to implement while maintaining a high reliability.
The LIN-BUS is a bidirectional, serial one-wire transmission interface. A LIN cluster is set up in a master-slave configuration. The master task makes a specific request to a LIN-slave in the form of a frame header. The associated LIN slave recognizes the header and responds with the requested information, the frame response. Header and response together form a LIN frame. The response can contain up to eight bytes of information. To detect transmission errors and to check the integrity of the data, a checksum is appended (Christmann, 2007).
In order to make the advantages of the Lin bus available for HVAC applications, a group of manufacturers has joined efforts to define a general LIN circulator profile (LCP) in VDMA Standard 24226. In the future, other plant-integrated components, such as burner fans, are also to be connected via the LIN bus (VDMA, 2020). The LCP uniformly defines an extensive number of instructions that can be sent to the pump and current operating and diagnostic data that can be retrieved from the pump. Table 3.1 shows a selection of available information.

Tab. 1: Selection of data points defined in the LIN circulator profile

Commands to the Pump	Pump operating data	Diagnostic data
• Set point • Control method (speed, head, flowrate) • Switch on/off • Additional manufacturer-specific data	• Operating status • Speed • Power output • Estimated flow rate • Estimated head • Fluid temperature (if available)	• Cumulative operating time, • Number of start-ups, • Min/max flow rate,

5. Influences on the uncertainty of the flow rate estimation

The shape of the characteristic pump map and the operating point of the pump are fundamental for the general uncertainty of the flow rate estimation. The general shape of the characteristic pump map is depending on the hydraulic design of the pump. The operating point and therefore the flowrate and head of the pump depends on the pump speed and the system head curve (cf. Fig 1 A).
The ratio of power and volume flow at a constant pump speed is described by P;Q-curves, the gradients of these P,Q-curves vary with the pump speed (cf. Fig 1 B). Here, P;Q-curves at lower speed levels have a decreases gradient, at 10 % pump speed the gradient is almost zero. It can also be seen that the gradient of a P,Q curve decreases at very high flow rates and finally also approaches zero. At this operation points a small uncertainty in power detection or a small deviation of the pump characteristics map have a very high influence on the estimated flow rate.
Fig. 5 shows the magnitude of this effect on uncertainty of the derived flow rate depending on the operating point in the H,Q-map of the investigated pump. An uncertainty in detecting the pump's power of +-0.72 W (+- 1% of the maximum pump power) is assumed. The flow rate is derived by two-dimensional linear interpolating from the existing characteristic map of pump. The uncertainty range of the derived flow rate relative to the real flow rate is shown in a colour map. For very low flow and head and also for very high flow rates no flowrate can be derived. The smallest uncertainty reached for flowrates between 1200 l/h and 3000 l/h and a delivery head between 300 cm and 859 cm, corresponding to relatively flat system head curves and moderate to high pump speeds.

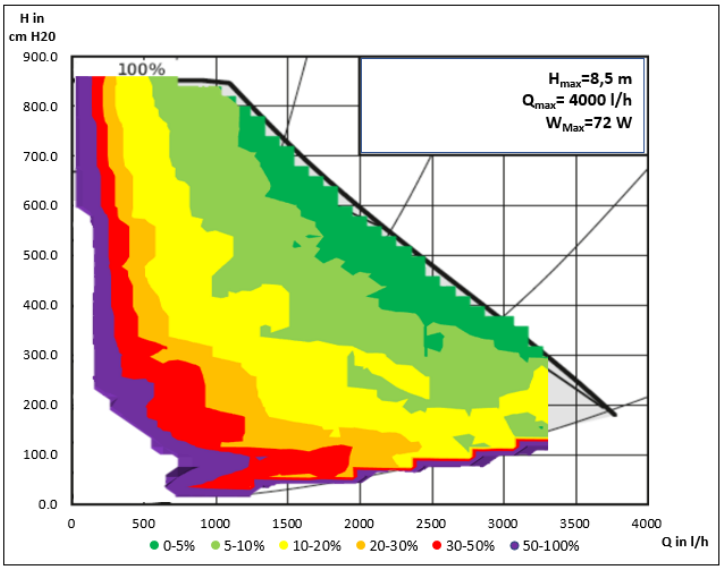

Fig. 2: Uncertainty of volume flow based on an induced power determination error of +-0.72 W

Also, the pump characteristic maps are typically created for standardized fluid conditions, (normally water at 20 °C). Fluid properties that deviate from these conditions can significantly influence the pump characteristics and therefore the accuracy of the flow rate estimation. The most important fluid characteristics in HVAC systems are the viscosity and the density of the fluid. Both properties have a significant temperature dependence. A higher fluid density causes an approximately direct proportional increase in power requirement. The influence of the viscosity is more complex. With increasing viscosity, the various friction losses in the guide vanes and especially the disc friction loss between fluid and pump impeller increases. This leads to a decreased overall pump efficiency and therefore an increased P,Q-ratio. The impact of decreased pump efficiency is also dependent on the speed, and to a lesser extent on the flow rate, and therefore on the operating point of the pump. The head characteristic curve is also influenced by the viscosity. Here, with increasing viscosity, the hydraulic performance of the pump changes, which leads to a reduction in the head characteristic curve. However, for the viscosity of water glycol-mixtures at typical operation temperature ($\nu<10$ mm²/s), this effect is very small and can usually be neglected (Gülich, 2014). Fig. 3 shows the effects of increased density and viscosity on the pump characteristics schematically.

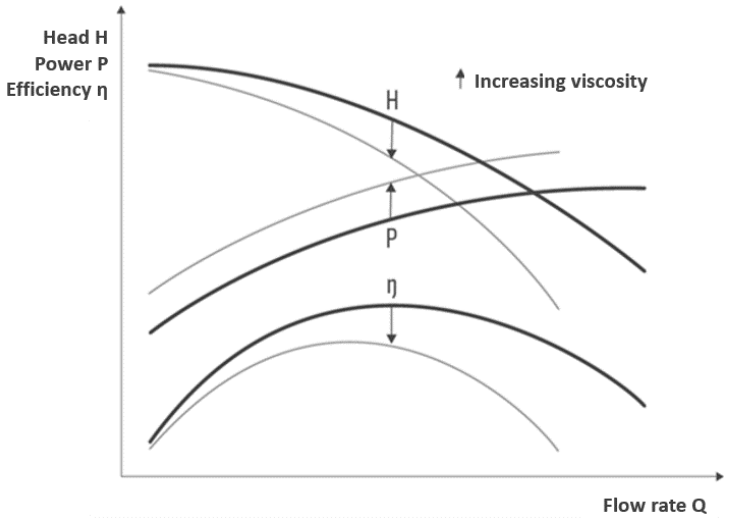

Fig. 3: Schematic representation of the viscosity influence on head, power and efficiency curves based on (EDUR, 2018).

6. Experimental investigation of the flow rate estimation

The tests are carried out on a closed loop test rig, see Fig. 4. With the aid of a restrictor valve, the pressure loss coefficient and thus the system characteristic can be adjusted. To compensate for the dissipating pump energy and guarantee a constant fluid temperature, excess heat can be removed with a heat exchanger. With a controlled flow heater, the fluid can be also heated up to 85 °C. A small storage tank reduces thermal and hydraulic oscillations in the system. The pressure difference between the suction and discharge side of the pump is measured by a differential pressure sensor. As a reference value for the flow rate estimation, the flow rate is measured by a calibrated electromagnetic flowmeter.

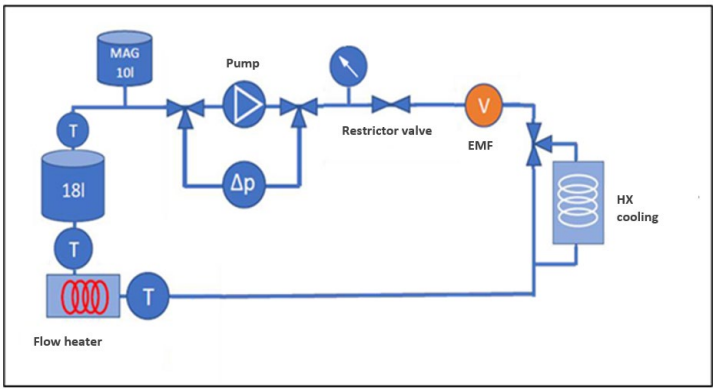

Fig. 4: Layout of the flow rate test rig

For control and communication with the pump, a LIN cluster is set up, consisting of only two nodes. An ATmega2560 microprocessor acts as master. All frame responses defined in the LCP can be retrieved from the pump and corresponding control signals, in this case the speed input, can be sent to the pump. The speed is defined according to LCP as integer per mil value of the maximum speed.

The flowrate estimation is examined systematically at different operating points of the pump.
The operating point and thus the real flow rate of the pump is determined by the system characteristic curve and the speed of the pump. The loss coefficient of the system curve can be adjusted via the regulator valve. The pump speed is given as the setpoint value. At each constant system characteristic curve 15 operating points are considered by varying the pump speed. The 15 speed levels are evenly distributed between 4800 rpm (100%) and the minimum

speed 499 rpm (10.3%). For each operating point the flow rate estimated by the pump Q_{pump} is compared with the flow rate measured by electromagnetic flowmeter Q_{meas} under steady state conditions. To evaluate the accuracy the relative estimation error f_Q is used (eq. 1) is used

$$f_Q = \frac{Q_{pump} - Q_{meas}}{Q_{meas}} * 100\% \qquad \text{(eq. 1)}$$

The approach with constant system curve and variable pump speed reflects the operating conditions as they are found, for example, in a solar circuit with variable flow rate (matched flow system).
In order to reproduce typical fluid conditions in such thermal plants, in addition to cold water, the operation with a 42%-propylene-glycol antifreeze mixture at temperatures between 20°C and 80°C was investigated.

7. Estimation uncertainty in operation with cold water

To examine the accuracy of the volume flow estimation in operation with clean water at 20°C water, Fig. 5 shows the relative estimation errors f_Q for three different system curves (A B C). The error for the 15 operating points is plotted versus the flow rate under constant system curve conditions.
For better comparability of different system curves, the flow rate at operating point is shown as fraction of the maximum flow rate Q_{max} that can be achieved with maximum pump speed for the respective system curve. With a constant system characteristic curve, the volume flow increases in direct proportion with the pump speed. This means that 50 % of the maximum flow rate of the system characteristic curve is also achieved at approximately 50 % of the maximum pump speed.
In Fig. 5 A (Top) the estimation error for a system characteristic curve with a maximum flow rate Q_{max} = 1250 l/h and a maximum head loss of H_{max} = 8.7 m at maximum pump speed can be seen. In part B (bottom left) the error for a much steeper curve with Q_{max} = 500 l/h and a head loss of H_{max} = 8.9 m is shown. A relatively flat system characteristic curve with an almost completely open restrictor valve, Q_{max} = 2000 l/h and H_{max} = 6.6 m is shown in part C (bottom right).

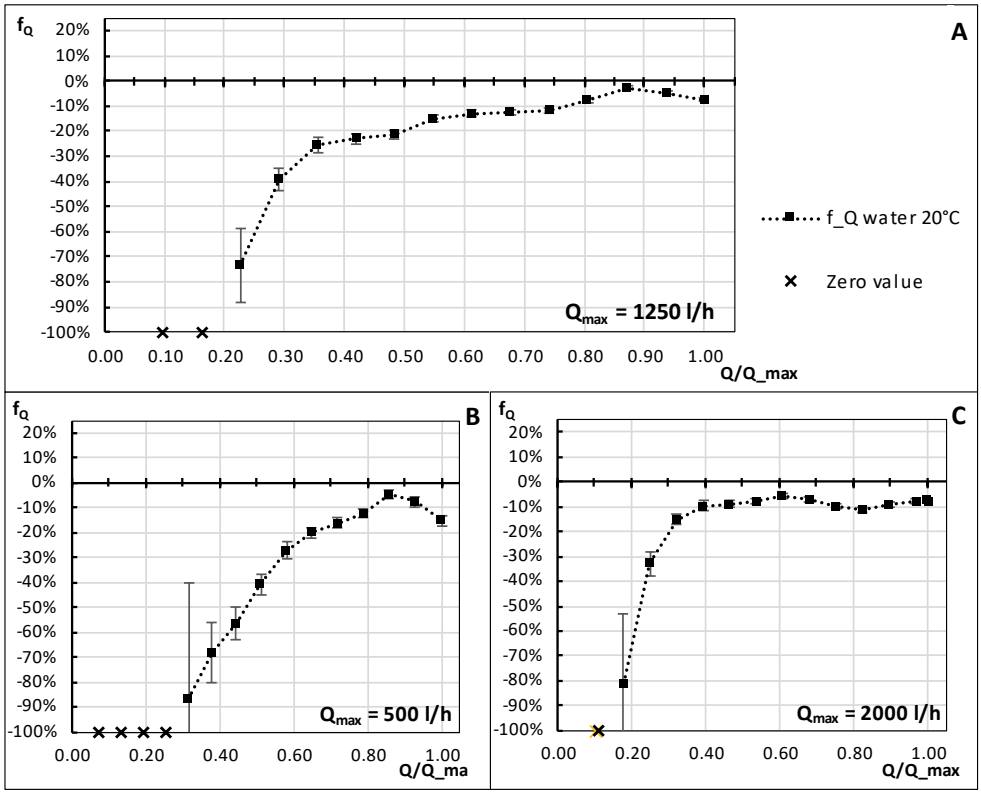

Fig. 5: Relative error of flow rate estimation over real dimensionless flow rate for different system characteristics with 500 l/h (B), 1250 l/h (A) and 2000 l/h (C) maximum flow rate

The flow rate in this operating condition is underestimated for all three system curves, i.e., it has a negative measurement error. With increasing flow rate (increasing pump speed), the relative measurement error tends to decrease. The error bars show the relative standard deviation of the estimated flow rate value received from the pump. Here for smaller volume flows/speeds, the flow rate value received from the pump fluctuates considerably.
For even lower speed points the pump only returns a zero value for the flow rate, the real flow rate is here outside the detection limit and the error is consequently -100 %. This is marked with a cross in the diagram.
Looking at a moderate system head curve (Fig. 5-A), the operating point at which a flow rate value is returned by the pump is at a relative volume flow of 23 % or 280 l/h. However, only a flow rate of 75 l/h is detected here and thus the flow rate is underestimated by 73 %. The smallest estimation error (-2.7 %) is reached at a relative volume flow of 87 %.
For the steep system characteristic curve with a maximum flow rate of 500 l/h in Fig. 5 B (bottom left), the lower detection limit shifts to higher relative flow rates. Also, the decrease of the measurement error with increasing flow rate is much less pronounced compared with the flatter system curves. An estimation error of less than 20 % can only be achieved at relative flowrates of 60% and more.
For very flat system curves as in Fig. 5 C (bottom right), the measurement error for small relative flows/speeds is also very large, but this quickly decreases with increasing flow and reaches a plateau with an estimation error ≤ 10 % at about 50 %of pump speed.

In order to further investigate the consistent underestimation of the volume flow, it useful to plot the measurement data as P,Q-characteristic curve (cf. Section 1 – Operating Principle).
Fig. 6 therefore shows the P,Q-curves based on real measured flow rate (black) and the P,Q-curve that results from the estimated flow rate (orange) of the pump. In this representation, the pumps speed levels are constant in P,Q-curves. It can be seen that all real performance P,Q-curves in comparison to the estimation P,Q-curves are shifted to the right, to a higher volume flow. That means, for a specific power determined by the pump, a larger volume flow than defined in the characteristic map that used for the estimation is delivered. The volume flow is consequently underestimated by the pump.

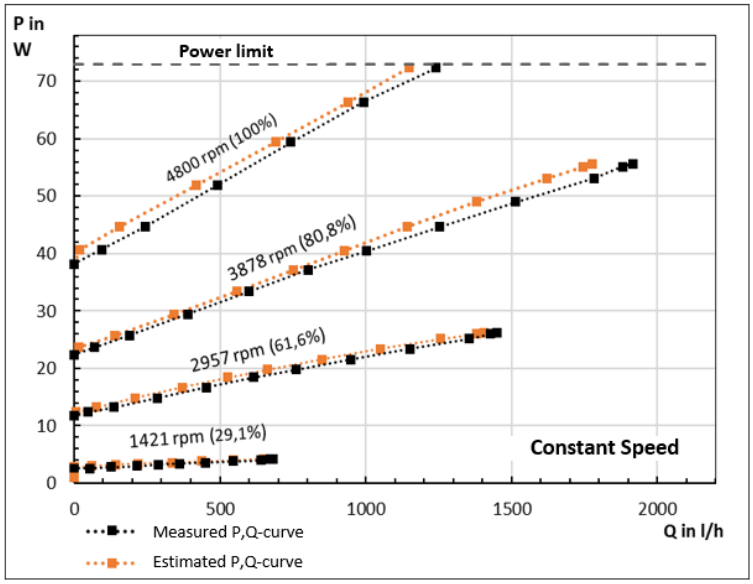

Fig. 6: P,Q-characteristic curve at constant speed levels for measured flow rate and pump estimated flow rate

It is shown that the error of the volumetric flow estimation varies very strongly with the operation point of the pump. For the regarded pump a reasonable quantification is only possible if the system characteristics are not too steep, and the pump speeds are relatively high.
These results are in line with the theoretical considerations in section 4. As the pump speed decreases, the uncertainty of the flow rate estimation increases. This effect is also much more noticeable with steep system curves and therefore lower flow rates. However, the root cause of the consistent estimation error is a significant deviation between the characteristic pump map that is used for the flow rate estimation and the real performance of the pump.
There are several possible reasons for the deviation between the real and the stored pump map. One potential cause are production-related variations of the pump performance.

Also, different design decisions can influence the estimation pump map. For example, the manufacturer may prioritize reliable detection of a required minimum flow rate over the lowest possible estimation error. This 'flow switch' function could be, for example used for fault and functions checks in a thermal system where otherwise there is no information on the flow rate at all.

8. Estimation uncertainty in operation with water-glycol heat-transfer fluids

The flow rate estimation in operation with a 42%-propylene-glycol water mixture is examined at temperatures of 20°C, 50°C and 80°C. Figure Fig. 7 shows the relative estimation errors f_Q for the three different system curves (A B C). For the glycol-mixture at 20°C (blue), the volume flow rate is significantly overestimated. This is true for all investigated system head curves and for most relative flow rates. For steep system curves (Fig. 7-B), the flow rate is overestimated by up to 65%. Only at very low pump speed the flow rate is underestimated here as well.

Compared to water, the lower detection limit shifts clearly to smaller flow rates. It is also noteworthy that a flow rate is indicated for the glycol-mixture at 20°C even with the restrictor valve fully closed. In contrast, in operation with water these zero flow rates can be detected reliably. At 50°C, the relative measurement error becomes smaller than in operation with cold water. Especially with large flow rates and flatter system-curves, the estimated flow rate value gets very small. (Fig. 7 C). But in contrast to the operation with pure water, the volume flow rate is both underestimated and overestimated here, depending on the speed and system characteristic curve. An interpretation as a guaranteed minimum flow is not possible.

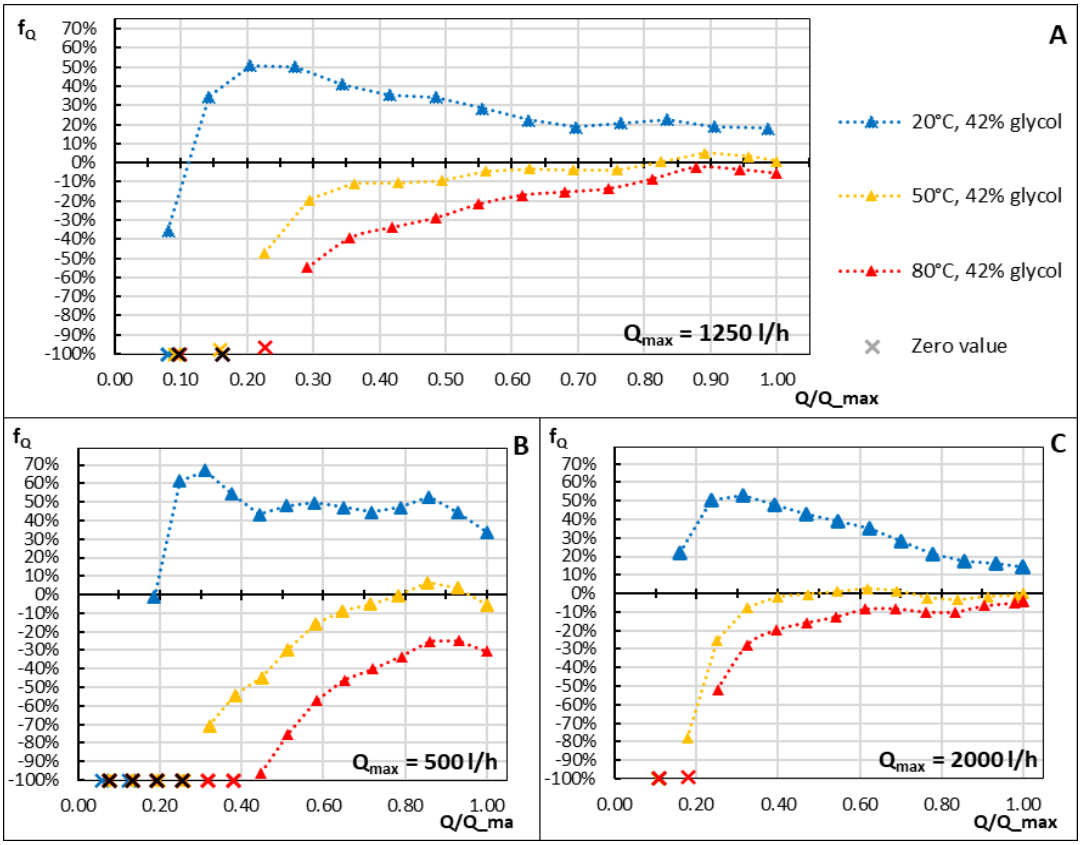

Fig. 7: Relative error of flow rate estimation over real dimensionless flow rate for different system characteristics with 500 l/h (B), 1250 l/h (A) and 2000 l/h (C) maximum flow rate in operation with 42%-glycol-water mixture at 20 °C (blue) 50 °C (yellow) and 80 °C (red)

In operation with glycol mixture at 80 °C (red) the flow rate is underestimated strongly at low speeds, the error decreases with increasing flow for all system curves. For steep system curves (Fig. 7 B) the estimation error is still at least 25% even at high speeds.

Comparing the estimation error in operation at 20°C (blue) and 80°C (red), the range between the error declines with increasing speed and flow rate. But even with the flattest considered system characteristic (Fig. 7 C), the temperature

induced error range is still at least 18% percentage point. In the worst case, steep system characteristic and low speed, the error range is over 165%.

In order to further investigate the large temperature-dependent variations in the flow rate estimation, the efficiency of the pump in the different operating conditions is considered in more detail. Figure 5.10 therefore shows the efficiency for constant speed levels for water at 20 °C and the antifreeze-mixture with 42 % glycol content at 20 °C The efficiency of the pump can be determined from the ratio of the hydraulic power measured on the test rig and the power consumption of the pump. Since this efficiency is determined based on the electric power consumption detected by the pump electronics, it includes both the efficiency of the electric motor and the hydraulic efficiency of the pump, losses in the power electronics are not included. For a better visualization a characteristic curve is interpolated between the measuring points. It can be seen that the pump efficiency with the cold glycol-mixture is indeed significantly lower than with water. The effect is also depending on the speed of the pump. At lower speed levels the relative decrease in efficiency, and therefore the negative influence on the P;Q-Characteristic curve is higher.

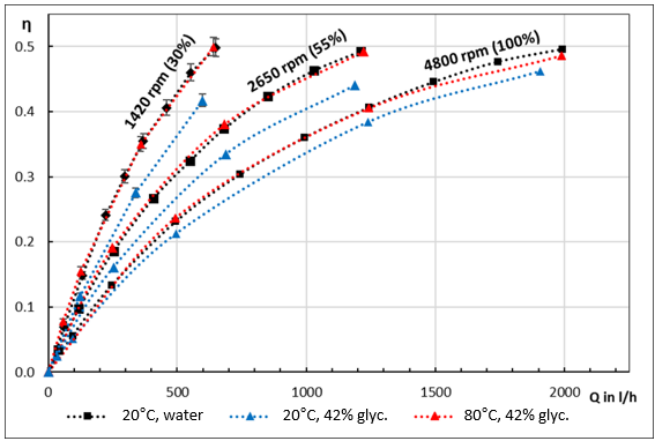

Fig. 1: Efficiency curves of the pump for water and a water-glyocle mixture at 20°C for different constant pump speeds.

The strong deviations can be explained based on the fluid properties of the 42%-glycol-mixture. The glycol-mixture at 20°C has a slightly higher density ρ=1039 kg/m^3 and much higher viscosity ν=5,12 mm^2/s than cold water (ρ=998 kg/m^3 ν=1,004 mm^2/s). Also, the fluid properties of glycol are highly temperature-dependent (e.g., at 80°C the viscosity decreases significantly to ν=1,1 mm^2/s). As described in section 4, a higher viscosity has a strong influence on pump efficiency and therefore on the P,Q-characteristic curve.

9. Summary and conclusion

Both the theoretical and the experimental investigation have shown that the flow rate estimation requires characteristic pump maps that match real pump performance as closely as possible. Even small deviations can lead to large estimation errors, especially at low speeds and for steep system curves.
For the investigated pump a reasonable estimation of the flow rate is only possible for some areas of the operational spectrum. In most operational conditions, the flow rate estimation could at least be used as a ‘flow switch’ to detect if a minimum required flow rate exist. But especially with glycol-mixtures, this is not possible in every operating point. Overall, the composition and the temperature of the pumped medium can have a strong influence on the efficiency of the pump and therefore on the flow rate estimation, while the intensity of the impact can differ depending on the operational point. For a reasonable quantification of glycol-water mixtures at varying temperatures, corrective measures must be taken. This could be done, for example, by a subsequent correction of the estimated flow rate via specific correction schemes that are provided by the pump manufacturer or with fluid property-based adjustments of the characteristic pump map.

10. Acknowledgement

We would like to thank Mr. Lars Diekkämper and Wilo SE for providing the investigated pump and comprehensive advice.

11. References

Ahonen, Tero; Tamminen, Jussi; Ahola, Jero; 2011: Laboratory evaluation of the VSD-based hybrid estimation method for the pump operational state. Power Electronics and Applications (EPE 2011), proceedings of the 2011-14th European Conference. Aug. 30 2011-Sept. 1 2011. https://link.springer.com/content/pdf/10.1007/s12053-018-9751-4.pdf., last checked 10.08.2021

Bakman, Ilja; Vodovozov, Valery, 2013: Sensorless pressure control of centrifugal pumps. In: International Conference on Compatibility and Power Electronics (CPE), 2013. 5 - 7 June 2013, Ljubljana, Slovenia., IEEE Industrial Electronics Society, Piscataway, NJ: IEEE, S. 304–309.

Christmann, Ernst, 2007: Datenkommunikation im Automobil Teil 3: Kostengünstiger Datenaustausch mit LIN. Hg. v. Vector Informatik GmbH. Stuttgart. https://vectoracademy.com/portal/medien/vector_elearning/PTR/SerielleBussysteme_Teil3_ElektronikAutomotive_200702_PressArticle_DE.pdf., last checked 10.08.2021

EDUR, 2018: EDUR Pumpenhandbuch. 3. Auflage. 3. Auflage, revidierte Ausgabe. EDUR Pumpenfabrik Kiel: https://www.edur.com/servicebereich/pumpenhandbuch, last checked 10.08.2021

Gülich, Johann Friedrich, 2014: Kreiselpumpen. Handbuch für Entwicklung, Anlagenplanung und Betrieb. 4., aktualisierte und erw. Aufl. Berlin: Springer-Vieweg.

Hammo, Simo; Viholainen, Juha, 2005: Testing the accuracy of pump flow calculation without metering. In: World Pumps 2005 (471), S. 36–39. DOI: 10.1016/S0262-1762(05)70846-4.

Pöyhönen, Santeri; Ahonen, Tero; Ahola, Jero; Punnonen, Pekka; Hammo, Simo; Nygren, Lauri; 2019: Specific speed-based pump flow rate estimator for large-scale and long-term energy efficiency auditing. In: Energy Efficiency 12 (5), S. 1279–1291. DOI: 10.1007/s12053-018-9751-4.

Umweltbundesamt 2009: Die EG-Verordnung für die umweltgerechte Gestaltung von Umwälzpumpen. Umweltbundesamt und Bundesanstalt für Materialforschung und -prüfung, Hg. v. Umweltbundesamt. Dessau-Roßlau. https://www.umweltbundesamt.de/sites/default/files/medien/publikation/long/3794.pdf, last checked 10.08.2021

VDMA 24226, 2020, LIN Profile for integrated Circulators, Beuth Verlag GmbH, 10772 Berlin https://www.beuth.de/de/technische-regel/vdma-24226/317935415, last checked 10.08.2021

Fault detection for solar thermal systems: Evaluation and improvement of existing algorithms

Christoph Schmelzer[1], Matthias Georgii[1], Christian Sauer[1], Janybek Orozaliev[1], and Klaus Vajen[1]

1 University of Kassel, Institute of Thermal Engineering, Department of Solar and Systems Engineering, Kassel (Germany)

Abstract

This paper evaluates fault detection algorithms for solar thermal systems, with regard to the most important faults in solar thermal systems. The relevant algorithms from literature are described and sorted according to their respective detection approach. The algorithms are then evaluated with measurement data from 10 solar thermal systems of different sizes (collector area between 3 m² and 2500 m²). The performance evaluation of the algorithms shows that most false alarm messages are generated due to transient system behaviour, which was not taken into account in the development or description of said algorithms. Main problems are caused by short operating phases, switching of the solar pump(s) in rapid succession, start phases of the solar thermal system, and delayed reactions of temperatures or sensors.

Keywords: Fault detection, solar heating, monitoring, function control, FDD

1. Introduction

Algorithm based fault detection and diagnosis (FDD) for solar thermal systems (STS) has been subject of research since the 1990s. Important foundations were laid by (Altgeld and Mahler, 1999), where they defined FDD algorithms for small solar thermal systems without heat meters (FUKS project). The algorithm-based approach was improved, refined, and adapted for different sized systems (Gerardts et al., 2011; Ohnewein et al., 2016) and led to the German VDI 2169 "Functional checking and yield rating of solar thermal systems" (VDI 2169, 2012). Even more algorithms or adaptations of already existing ones have been published in various papers and reports on research projects (Bartenstein, 2015; Brandstetter, 2007; Duff and Millard, 1980; Fink et al., 2010; Stryi-Hipp et al., 2007; Sun et al., 1999; Thür et al., 2011; Wiese, 2006). Despite the fact that these algorithms are publicly available and that the majority of solar controllers advertise an automatic function control, no system or approach is currently widely used.

2. Important faults in STS and existing algorithms

To show the reliability of solar thermal systems and to determine the most common faults or defects, several studies and projects have been conducted in the past. Often, the planning, installation, and operation of several STS was monitored to identify common mistakes and potential for optimisation for the whole life cycle.

In the projects "Solarthermie2000(+)" (Croy et al., 2011), OPTISOL (Fink et al., 2006), and COMBISOL (Thür et al., 2011) a large number of solar thermal systems were monitored. The studies focussed on assessing the performance of solar thermal systems, and to identify common faults and dysfunctions throughout planning, installation, and operation. For additional studies with the same or similar objectives, see (Breidler and Thür, 2010), (Fink et al., 2010), (Schenk et al., 2010). While the observations vary slightly between different publications, there is a common baseline regarding the reliability of STS. In every study a significant proportion of the investigated STS required repairs or at least optimisation. Since most of these dysfunctions were found by manually analysing system data and on-site evaluation of the systems, this process was very time consuming, requires expert knowledge, and therefore expensive. The following algorithm development aims at an automatic detection of the most important faults based on measurement data. With this, faults and system failure could be detected early and at low additional costs.

Based on the literature review and in discussion with several manufacturers of solar-assisted heating systems, the following list of important faults in STS was defined.

- Defective pumps (no volume flow)

© 2022. The Authors. Published by International Solar Energy Society
Selection and/or peer review under responsibility of Scientific Committee
doi:10.18086/eurosun.2022.14.07 Available at http://proceedings.ises.org

- Pumps too small (low volume flow)
- Undissolved air in solar circuit (unstable volume flow, uneven flow distribution)
- Soiling in heat exchangers and pipes, clogged filters (low volume flow)
- Collector temperature sensor at wrong position or does not measure fluid temperature
- Heat exchanger (HX) too small (or soiled) - UA value

Regarding these faults, several existing algorithms can be found. For better clarity and easier implementation, the algorithms can be sorted by fault groups (faults with similar or the same symptoms), see table 1.

Table 1: Fault groups and existing algorithms, sources: "FUKS" (Altgeld and Mahler, 1999), "VDI" (VDI 2169, 2012), "UNIKS" (Wiese, 2006), "PARA" (Bartenstein, 2015), "QSOL" (Brandstetter, 2007)

Group nr.	Faults	Algorithms
1	Defective pump(s) Blockage Undissolved air	[FUKS_FLOW] [FUKS_NOHEAT] [VDI_PUMP] [UNIKS_FLOWSENS] [PARA_PUMP] [QSOL_FAILURE_a/b]
2	Pumps too small [or wrong pump stage]	[FUKS_FLOW] [UNIKS_FLOWSENS]
3	(Undissolved) Air [unstable volume flow]	[VDI_UNEVEN_FLOWDIST] [UNIKS_UNSTABLE_FLOW] [QSOL_AIR] [FUKS_FLOW] [UNIKS_FLOWSENS]
4	T_{coll} wrong position or bad thermal contact	[UNIKS_TCOL_a/b]
5	HX too small (UA)	[VDI_HX] [UNIKS_HX]

Table 2 shortly presents the existing literature algorithms (concerning the prioritised faults). The respective main approaches are described and information on thresholds – if present in the literature source – are provided.

Table 2: Investigated algorithms and respective detection approaches

Algorithm	Source	Approach, Notes
FUKS_FLOW	(Altgeld and Mahler, 1999)	Check for high temperature differences between collector and storage; Threshold specified: $\Delta T_{nominal} + 15\ K$
VDI_PUMP	(VDI 2169, 2012)	Check volume flow rate during pump operation
VDI_UNEVEN_FLOW	(VDI 2169, 2012)	Compare outlet temperatures of parallel collector modules or fields; Deviations of less than 10 % are acceptable; fields must be of the same size
VDI_HX	(VDI 2169, 2012)	Check if secondary flow temperature is lower than primary return temp (in operation)
UNIKS_FLOWSENS	(Wiese, 2006)	Check flow sensor reading if temperature difference at HX indicates system operation
UNIKS_UNSTABLE_FLOW	(Wiese, 2006)	Check for decreased and/or unstable volume flow rate (and increased stagnation)
UNIKS_TCOL_a	(Wiese, 2006)	Check for increased switching operations of the pump

UNIKS_TCOL_b	(Wiese, 2006)	Check if flow temperature exceeds collector temperature after the pump starts
UNIKS_HX	(Wiese, 2006)	Calculate UA value; Proposes method to compare measured UA values to nominal data sheet values.
PARA_PUMP	(Bartenstein, 2015)	Check if collector or flow temperature stay constant after the pump was turned on
QSOL_FAIL_a	(Brandstetter, 2007)	Check if collector temperature is significantly higher than storage temperature while storage is not fully charged.
QSOL_FAIL_b	(Brandstetter, 2007)	Check for operation by temperature difference between collector and flow temperature, system should be in operation, if collector exceeds storage temperature by 10 K
QSOL_AIR	(Brandstetter, 2007)	Check for temperature spikes in the solar thermal system; Already checked with QSOL_FAIL_a

3. Evaluation of fault detection algorithms and common problems

To evaluate the existing algorithms, they are implemented in python and tested on measurement data of 10 STS with collector areas reaching from 3 m² to 2500 m² (data of 3 additional STS can only be used for very few algorithms due to the respective system design or sensor equipment). At least one year of measurement data is available for each system. For most of the systems, there is no additional information if there were faults, stagnation or stand still periods or repair works. On this basis, "false negative" alarms cannot be checked, but "false positive" alarm reports can be identified manually.

The overall main problem of almost all described literature algorithms lies in operating states of the STS that were not expected or disregarded in the development phase. Since most algorithms were not at all or scarcely tested on measurement data, many false symptoms are generated.

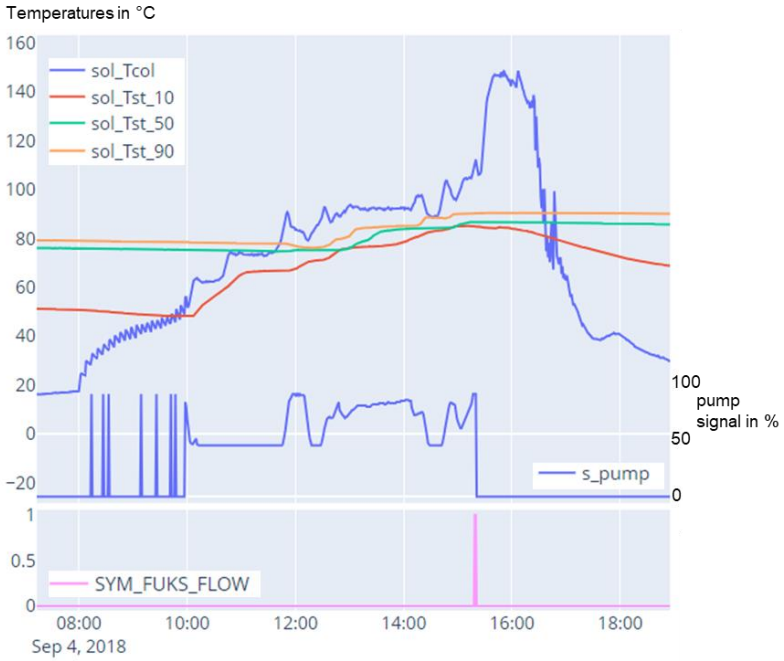

Figure 1: FUKS_FLOW algorithm applied to a small STS.

Figure 1 shows the application of the algorithm FUKS_FLOW for a small STS. The upper graph illustrates system temperatures (left y-axis) and the pump signal (right y-axis). Below this, the algorithm's output is

shown (0 – nothing detected; 1 – alarm message / symptom). It can be seen that the STS can increase the lower storage temperature "sol_Tst_10" from approx. 50 °C to 80 °C. Then probably a maximum temperature is reached, and a stagnation phase begins. In the transition between operation and stagnation, a few time steps of already very high temperatures can be observed while the pump is still running. This triggers the algorithm, without a real dysfunction being present.

Stagnation phases can generally be a problem for simple FDD algorithms since high collector temperatures usually signify a sufficient irradiation. If the storage temperatures are not checked for a maximum threshold, false alarm messages can be created easily. Of course, this problem is obvious for experts or operators and would be dismissed immediately in manual analysis, but for automated FDD algorithms every operating state or boundary condition must be considered explicitly.

Other problems arise if the pump is switched on and off in rapid succession. At the beginning of a day with sufficient irradiation to charge the storage, the collector field heats up gradually until the collector temperature exceeds the storage lower temperature by a defined threshold. Then, the pump is switched on and cold fluid from the pipes and/or storage is transported to the collector, usually causing a steep temperature decrease at the sensor. Depending on the collector area, irradiation intensity, and cold storage temperature, this can lead to several successive switching operations of the pump. Another scenario with rapid switching operations usually occurs at the end of operation phases on days with high irradiations. If the storage is charged to its maximum temperature, the pump is switched off. The storage temperature then decreases due to heat losses or energy demand, so that the STS is switched on again. Again, depending on the boundary conditions, this can lead to rapid successive switching operations. To a certain extent, both described scenarios are considered as normal system operation and do not justify alarm messages.

Figure 2 (left and right) shows the algorithms FUKS_NOHEAT and PARA_PUMP applied to small STS. Again, the upper graphs illustrate system temperatures (left y-axis) and volume flows or pump signals (right y-axis), the lower graphs depict the outputs of the respective algorithms. FUKS_NOHEAT (left) checks if the flow temperature is higher than the lower storage temperature at least once per operation phase. Since the operation phases are short in the beginning and even the lower storage temperature is > 40..50 °C, the flow temperature stays below the storage temperature for a few short operation periods, thus causing (unwanted) alarm messages. After this, the STS passes over to normal operation. The algorithm PARA_PUMP works differently: Here, the collector temperature is analysed after the pump starts – if it stays constant (in the limits of defined thresholds) a dysfunction is assumed. Figure 2 (right) shows the algorithm's performance. As the storage temperature draws near to its allowed maximum, the pump is switched on and off in rapid succession, while the collector and flow temperatures do not change much. Thus, a false alarm message is generated.

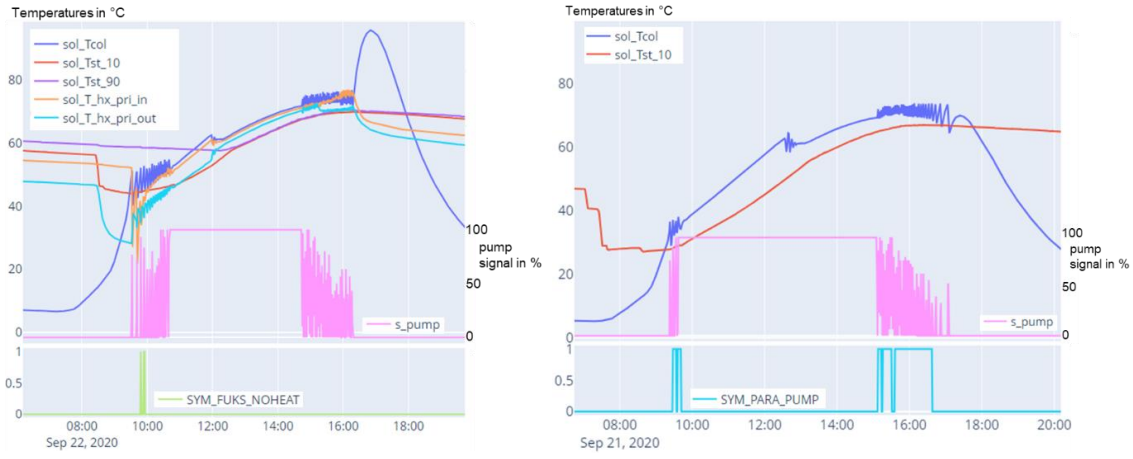

Figure 2: FUKS_NOHEAT (left) and PARA_PUMP (right) algorithms applied to small STS.

Figure 3 and figure 4 illustrate another main problem arising from unexpected operating states, or system behaviour during the algorithm development. Here, the delayed reaction of temperatures and temperature sensors are decisive. Figure 3 shows the application of the algorithms VDI_PUMP, VDI_HX, and UNIKS_TCOL_b. VDI_PUMP (left) checks the volume flow if the pump is turned on. It can be seen that the

flow sensor occasionally reacts slightly delayed. This causes an alarm message because for one or a few time steps no volume flow is detected despite a present pump signal. VDI_HX (right) checks if the flow temperature on secondary side is higher than the return temperature on the primary side of an external heat exchanger. For short operation periods, the temperature sensors at the heat exchanger may not measure the actual temperatures, because the heat supplied by the collector did not "arrive" at the HX. In these cases, alarm messages are created based on the fluid temperature in the pipes, which is not the original intention and only by chance indicates a real dysfunction.

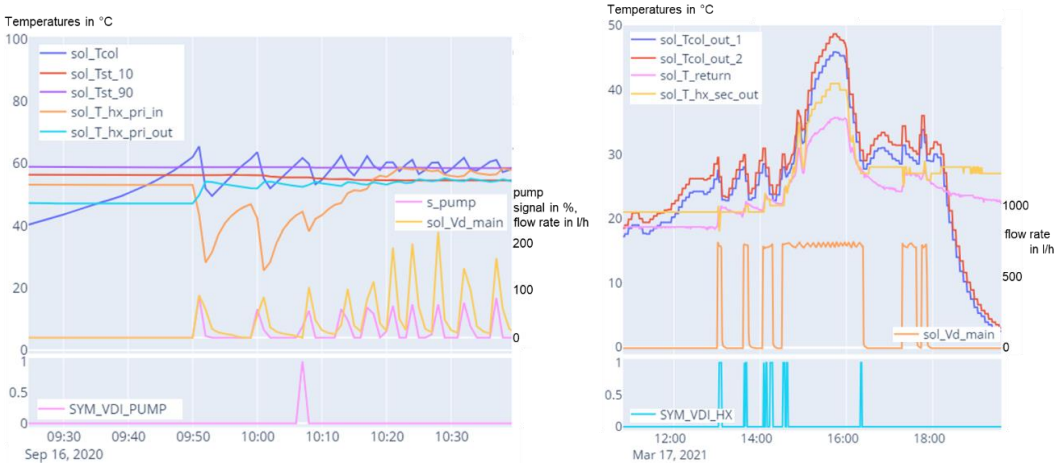

Figure 3: VDI_PUMP (left) and VDI_HX (right) algorithms applied to STS.

The performance of the algorithm UNIKS_TCOL_b is illustrated in figure 4. The algorithm compares temperatures as well, checking if the flow temperature is higher than the collector temperature after the pump starts. Here, a combination of circumstances causes false alarm messages: On the one hand, the system temperatures are rather high, starting with > 40 °C in the whole storage. This leads to high return temperatures in the primary and secondary solar circuit throughout the whole day. Moreover, the irradiation does not suffice for very high collector temperatures, only surpassing the storage temperature (plus hysteresis) slightly. Consequently, the pump is switched on/off often with only a few longer operation periods for the day. This causes several cases, where the current flow temperature is (slightly) higher than the current collector temperature.

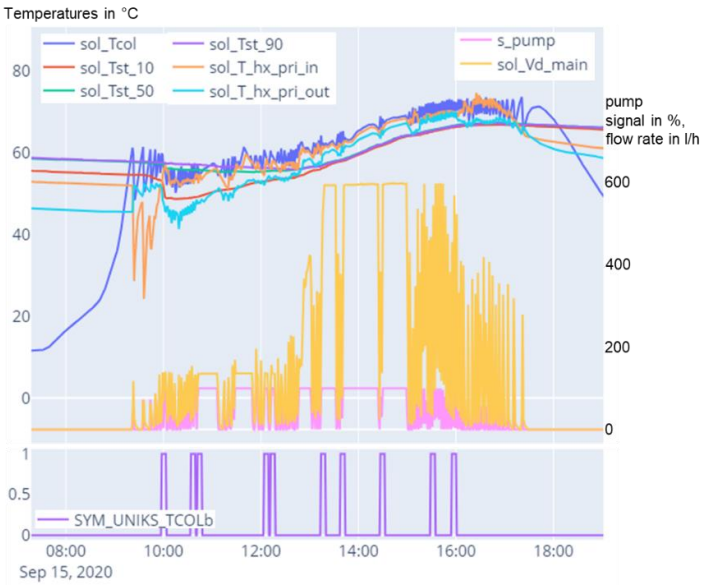

Figure 4: UNIKS_TCOL_b algorithm applied to a small STS.

Moreover, almost all existing algorithms share one central problem: the approaches for detecting faulty system behaviour are missing flexibility regarding the available sensor data. Even for the evaluation on real measurement data at hand, several algorithms had to be adjusted to work with a more flexible data base. STS are planned and built individually, especially including the measurement equipment. Except the collector and storage temperature sensor, almost no common sensor equipment can be assumed. And even this minimal equipment can cause ambiguity if two collector sensors are installed, e.g. for parallel fields. To compensate this individuality, algorithms must be developed, coded, and tested accordingly.

On the other hand, selected algorithms work well without the need for extensive adjustments:

UNIKS_FLOWSENS reliably detects if the flow sensor reading does not indicate an apparent system operation. In our available measurement data, no or few false alarms could be seen. However, for several plants the algorithm detects that the flow temperature does not decrease or reach the ambient temperature after an operation cycle. This could be an indicator for convection current.

UNIKS_TCOL_a checks the cumulated switching operations of the solar pump against a defined threshold. Since this approach does not rely on non-transient system states or explicitly involves temperatures or other measurements, it is quite robust. The informative value of the algorithm only depends on choosing the right threshold for each plant.

QSOL_FAIL_b like FUKS_FLOW checks the operational temperature difference between collector and storage. The plant's operation is assumed if the difference between collector and flow temperature undercuts a threshold. This approach (for detecting operation) is beneficial because transient start phases or very short operation phases are note used for the analysis. Thus, less false alarm messages are generated.

UNIKS_HX algorithm basically calculates the UA value of a heat exchanger. As described in (Wiese, 2006), system operation has to be stationary for an analysis of the UA value. Additionally, the UA value depends on the boundary conditions, e.g. flows and temperatures on primary and secondary side. Thus, the calculated UA value cannot usually be compared to the datasheet value (if available), but a reference value must be calculated according to the actual conditions. This drastically complicates the application of the algorithm. Moreover, not only the temperatures (flow and return) but also the flow rates must be measured on primary and secondary side for the algorithm to be applicable.

4. General recommendations and improvements for FDD algorithms

As shown, most literature algorithms tend to generate false alarm messages for non-stationary or transient operating states. These occur at the beginning (and end) of longer operating states, and especially if the pump is switched on/off in rapid succession. This can either be caused by hardly sufficient collector temperatures (or irradiation) or because of maximum temperature limits or hysteresis settings. False alarms because of delayed sensor readings or delayed temperature increases are covered by this as well. The easiest way to address this is to cut off start phases and only use operating phases with a minimum duration for the system analysis.

Figure 5 (right) shows the exemplary improvement of the algorithm PARA_PUMP. Here, the algorithm has been adjusted to only analyse the temperature at the start of operation phases that exceed a minimum duration of 10 minutes. Thus, short phases are filtered out. The improvement becomes clear in comparison to the original performance, see figure 5 (left). All false alarm messages from the afternoon are now prevented. For the beginning of the long operation period still an alarm message is generated. Here, the temperature change at the start of the phase simply does not exceed the expected 5 K.

Another general remark has to be made regarding the flexibility of FDD algorithms. The algorithms described above are inflexible regarding different sensor configurations. Thus, if a flow or temperature sensor is not available, the respective algorithm cannot be applied. To address this problem, "parallel" detection paths can be designed. For instance, the (theoretical) operation of the STS can be detected using the pump signals, a flow meter or temperature differences between flow and return or between collector and flow temperatures.

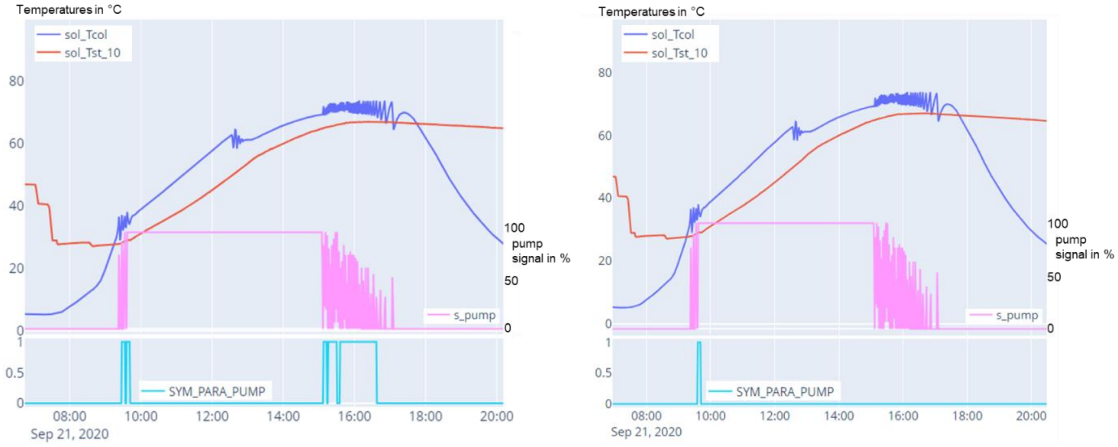

Figure 5: Performance of original (left) and improved algorithm (right) PARA_PUMP: the adjusted algorithm only analyses phases longer than specific duration (here 10 minutes)

5. Conclusion and outlook

As discussed in the performance evaluation, many of the algorithms show problems with transient system behaviour, which causes false alarm messages. Mostly, these problems occur because the respective system states were not considered in the development or description of the literature algorithms, and because the algorithms were not tested on real measurement data. Main problems are due to short operating phases, switching of the solar pump(s) in rapid succession, start phases of the solar thermal system, and delayed reactions of temperatures or sensors.

In the future work, flexible and robust FDD algorithms will be developed and tested on the available measurement data. The algorithms will build on the lessons learned from the described literature algorithms and will focus especially on the applicability for different sensor configurations. Moreover, the measurement data will be used to extract default values for thresholds to reduce false positive alarm messages.

6. Acknowledgement

We would like to thank our industry partners Enertracting, RESOL, SOLVIS, and Viessmann for the provision of measurement data to develop and test FDD algorithms.

7. References

Altgeld, H., Mahler, M., 1999. Funktionskontrollen bei kleinen thermischen Solaranlagen ohne Wärmemengenmessung. Saarbrücken.

Bartenstein, B., 2015. Gesicherte Solarerträge: Moderne Funktionskontrolle im Solarregler. FEE Heizungsjournal-Spec. 88–91.

Brandstetter, F., 2007. Qualitätssicherung solarthermischer Großanlagen: Qualitätssteigerung und Qualitätssicherung großer thermischer Solaranlagen in gebäudeübergreifenden Mikronetzen und im großvolumigen Geschoßwohnbau (Final Report), Energiesysteme der Zukunft. Wien.

Breidler, J., Thür, A., 2010. Umfangreiche Evaluierung und Monitoring von solaren Kombianlagen im Einfamilienhausbereich. Presented at the 20. Symposium Thermische Solarenergie, Bad Staffelstein.

Croy, R., Mies, M., Rehrmann, U., Wirth, H.P., 2011. Solarthermie-2000, Teilprogramm 2 und Solarthermie2000plus. Wissenschaftlich-technische Programmbegleitung und Messprogramm (Phase 4).

Duff, W.S., Millard, R.A., 1980. Procedures for on-line detection of sensor and operating faults in solar energy systems, in: Proc. Annu. Meet. - Am. Sect. Int. Sol. Energy Soc.; (United States). Research Org.: Colorado State Univ., Fort Collins.

Fink, C., Breidler, J., Ederer, D., Kapferer, R., Burtscher, H., Reiter, A., 2010. Funktionalitäts- und Qualitätsanalyse bei 120 Solarsystemen im Geschosswohnbau und in gewerblichen Anwendungen. Presented at the 20. Symposium Thermische Solarenergie, Bad Staffelstein.

Fink, C., Riva, R., Pertl, M., Wagner, W., 2006. OPTISOL - Messtechnisch begleitete Demonstrationsprojekte für optimierte und standardisierte Solarsysteme im Mehrfamilienwohnbau (Final Report). Gleisdorf.

Gerardts, B., Dröscher, A., Schgaguler, K., Putz, S., Ohnewein, P., Feichtner, F., Meißner, E., Luidolt, P., Köstinger, A., Heimrath, R., Holter, C., Streicher, W., 2011. IP-Solar: Development and Validation of a Web-Based Monitoring and Diagnostic Tool for Solar Thermal Systems. Presented at the Solar World Congress, International Solar Energy Society, pp. 1–9. https://doi.org/10.18086/swc.2011.28.11

Ohnewein, P., Tschopp, D., Schrammel, H., Gerardts, B., Poier, H., Krammer, S., Köstinger, A., Weinhappl, A., 2016. METHODIQA: Methodik-Entwicklung zur Qualitätssicherung für Erneuerbare Wärme Systeme durch intelligentes Betriebsmonitoring (Endbericht). AEE - Institut für Nachhaltige Technologien (AEE INTEC), Gleisdorf.

Schenk, E., Bollin, E., Huber, K., Jödicke, D., 2010. Funktionskontrolle solarthermischer Großanlagen auf Basis von Langzeitmonitoring durch die Hochschule Offenburg. Presented at the 20. Symposium Thermische Solarenergie, Bad Staffelstein.

Stryi-Hipp, G., Schnauss, M., Moch, F., 2007. GroSol: Studie zu großen Solarwärmeanlagen [WWW Document]. URL https://docplayer.org/23199660-Grosol-studie-zu-grossen-solarwaermeanlagen.html (accessed 2.4.22).

Sun, C.K., Chan, C.W., Tontiwachwuthikul, P., 1999. Intelligent diagnostic system for a solar heating system. Expert Syst. Appl. 16, 157–171. https://doi.org/10.1016/S0957-4174(98)00068-2

Thür, A., Kuhness, G., Breidler, J., 2011. CombiSol Solar-Kombianlagen für Einfamilienhäuser Stand der Technik und Optimierungspotenziale (No. 29/2011), Berichte aus Energie- und Umweltforschung. Gleisdorf.

VDI 2169, 2012. VDI 2169 - Functional checking and yield rating of solar thermal systems.

Verein Deutscher Ingenieure e.V., VDI-Fachbereich Technische Gebäudeausrüstung, 2012. VDI 2169 - Functional checking and yield rating of solar thermal systems.

Wiese, F., 2006. Langzeitüberwachung großer solarintegrierter Wärmeversorgungsanlagen. Universität Kassel, Kassel.

Cost-Effective Energy Balancing of Thermal Systems Based on Temperature Measurements Only

Manuel Joschka Seiz[1], Xiaoyong Lang[1], Harald Drück[1,2] and Dominik Bestenlehner[1,2]

[1] Solar- and Heat Technology Stuttgart (SWT), Stuttgart (Germany)

[2] University of Stuttgart, Institute for Building Energetics, Thermotechnology and Energy Storage (IGTE), Stuttgart (Germany)

Abstract

Usually, thermal systems, especially small solar thermal systems, are not energetically balanced for financial reasons. To overcome this problem, low cost but accurate measuring equipment is required. This paper describes a method to determine the volume flow rate in a pipe and hence the thermal energy transfer through a hydraulic circuit, with the exclusive use of low-cost temperature sensors. Evaluations based on experimentally measured data show, that the method is able to calculate a volume flow rate in a range of 130 and 910 l/h with a deviation of less than ±10% compared to values measured by conventional flow meters or heat meters respectively. The calculated volume flow rate is subsequently used to perform an energy balancing of a thermal system. Hereby the heat input and output of the hydraulic circuits into and out of the central hot water store is considered to perform this energy balancing. The accuracy of the calculation of the heat quantities varies depending on the type of circuit, e.g. if it is a circuit for space heating or domestic hot water preparation. However, the results on a monthly basis consistently show a deviation of less than ±10.8% compared to the results of conventional heat meters.

Keywords: Energy Balancing, Volume Flow Determination, Cost Efficiency, Thermal Systems, Temperature Profiles, Heat Meter

1. Introduction

Currently, the energy balancing of thermal systems, e.g. solar thermal systems, is based on the measurement of the temperatures in the hot and in the cold side, as well as the volume flow rate of the heat transfer fluid in the circuit under consideration. With these quantities, the heat input e.g. of a solar circuit into a hot water store can be determined by integrating the thermal power over time. The heat meters required for this lead often to considerable costs, which represent a significant share of the total investment, especially for small solar thermal systems. For this reason, the energy balancing of such small systems is often omitted, which makes a reliable surveillance of the system impossible. The aim of the project TeBwA (Temperaturbasierte energetische Bilanzierung wärmetechnischer Anlagen / Temperature-based Energy Balancing of Thermal Systems), which is funded by the German Federal Ministry for Economic Affairs and Climate Action, is to develop a technology that allows for energy balancing at significantly lower costs than energy balancing based on conventional heat meters.

Fig. 1 exemplary illustrates the setup for an energy balancing of a solar thermal domestic hot water system using three conventional heat meters that measure the volume flow rate and the temperatures in the hot and in the cold side of each hydraulic circuit attached to the central hot water store.

© 2022. The Authors. Published by International Solar Energy Society
Selection and/or peer review under responsibility of Scientific Committee
doi:10.18086/eurosun.2022.14.08 Available at http://proceedings.ises.org

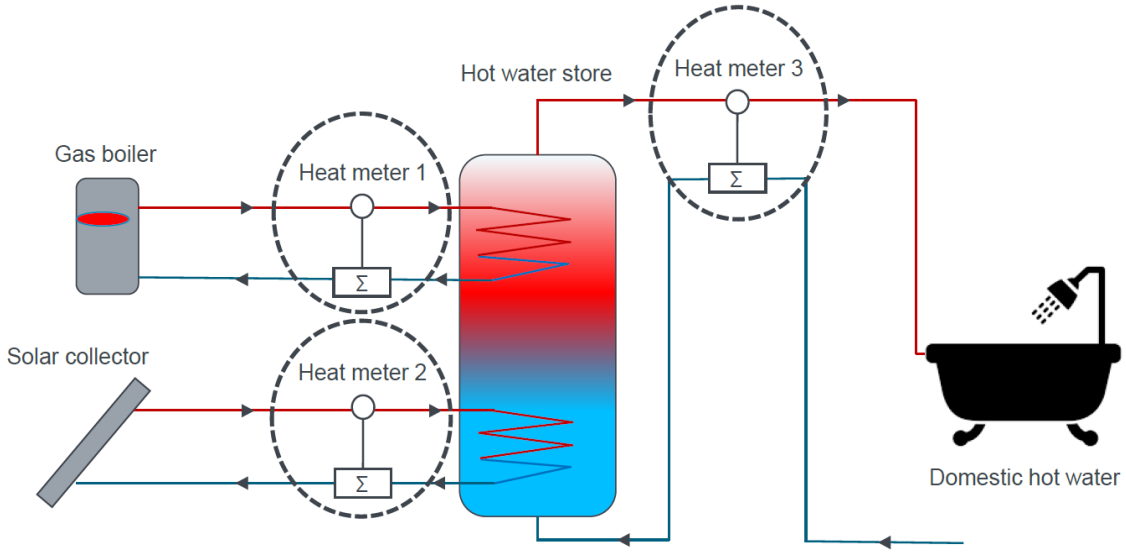

Fig. 1: Solar thermal domestic hot water system with a central hot water store and three attached hydraulic circuits equipped with three conventional heat meters that are required for energy balancing

The newly developed TeBwA method is based on the calculation of the volume flow rate derived from the temporal propagation of a temperature gradient in the fluid. To identify the propagation of a temperature gradient, the temperature of the heat transfer fluid in the pipe must be measured at two points. The initial work based on this approach is described by Frank (2000). To calculate the heat flux, a third temperature sensor is required in the second pipe, which is located on the other side of the hydraulic circuit under consideration. Fig. 2 shows the principle positioning of the three required temperature sensors for the developed TeBwA method.

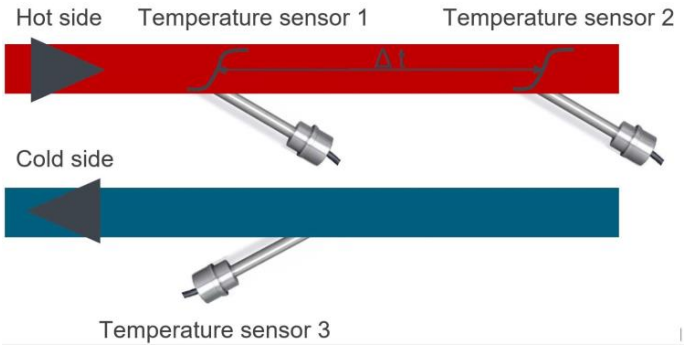

Fig. 2: Principal temperature sensors positioning in the hot side and in the cold side of a single hydraulic circuit

As Fig. 2 shows, in total only three low-cost temperature sensors and no flow meter are required for each hydraulic circuit. This makes the determination and recording of thermal energy much more favorable from a financial point of view.

The TeBwA project and the method developed in the project were already described by Nedumparambil (2021) and Seiz (2021). In the publications mentioned, the basic principle of the developed method is explained. In addition, the approaches followed at that time for calculating the volume flow rate within a pipe are explained and initial calculation results based on synthetically and experimentally generated measurement values are presented. In this context it is shown that, when using the TeBwA method, the volume flow rate within a pipe can principally be calculated with a deviation of less than ±10% compared to the value measured by means of a conventional flow meter being part of a heat meter.

The article at hand presents the current status and latest results of the development of the TeBwA method. Among others, it describes the approach chosen for calculating the volume flow rate within a pipe and the accuracy that can be achieved at different temperature levels and at different volume flow rates within the pipe. In addition, the present article reports about the results of the energy balancing of four field test systems, which are equipped with measurement technology. The energy balancing was carried out both, on the basis of the TeBwA method and by means of conventional heat meters. On this basis the accuracy with which an energy balancing of thermal systems can be carried out using the TeBwA method is presented. Hereby four different types of hydraulic circuits of the field test systems are considered. Finally, the article gives an overview of the plans regarding the further development of the TeBwA method and the market implementation strategy of the resulting product.

2. Basic principle of the method

2.1 Principle of temperature-based volume flow determination

As stated above, the newly developed TeBwA method allows for the calculation of the volume flow rate within a pipe based on temperature measurements at two points inside the pipe. The two temporal temperature profiles created on basis of the values supplied by the two temperature sensors are compared with each other in order to calculate the time which the flow requires to cover the distance between the two temperature sensors. Once this time is determined, the corresponding volume flow rate can be calculated if the distance between the temperature sensors and the pipe cross-section are known. A prerequisite for the successful implementation of this method is the presence of sufficiently high temperature dynamics. Fig. 3 shows exemplary temporal temperature profiles generated on basis of temperature values of the two temperature sensors of the measurement track of a test rig. For a detailed description of the test rig see Seiz (2021).

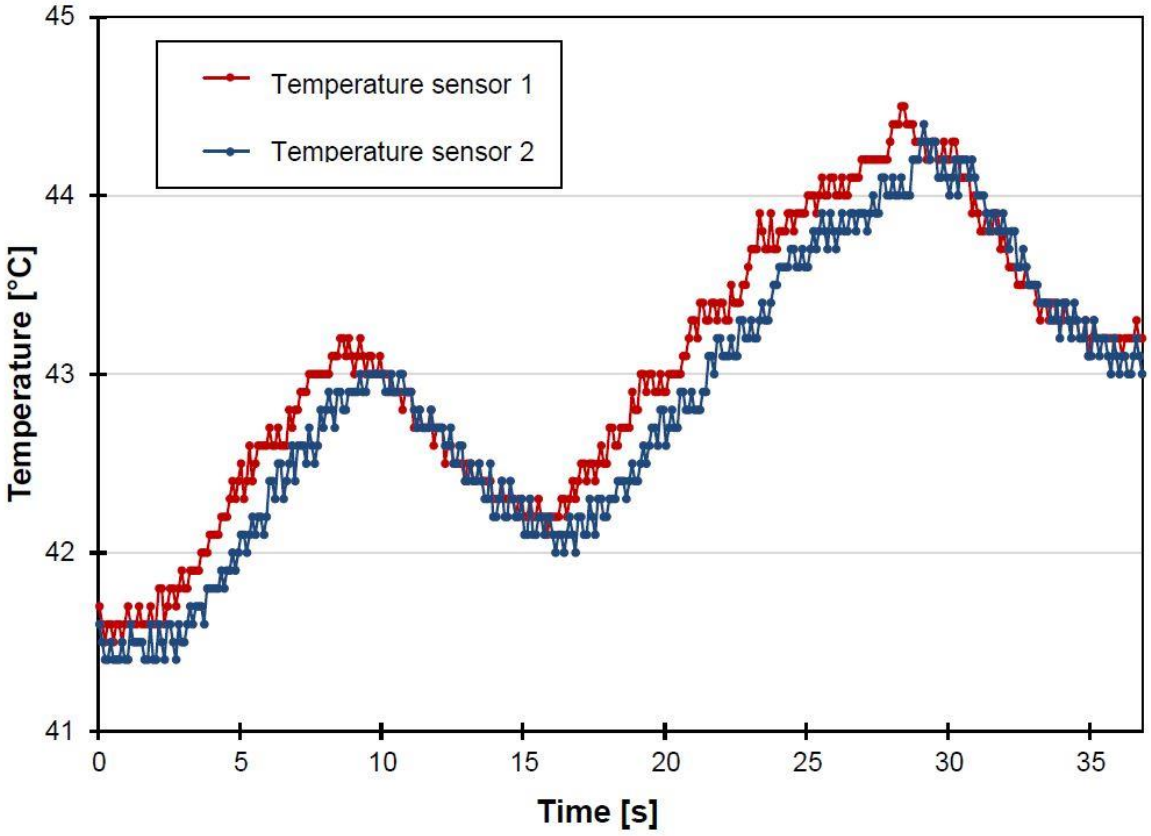

Fig. 3: Measurement values of two temperature sensors in the measurement track of a test rig - temporal temperature profiles

As Fig. 3 shows, the temperature profile of temperature sensor 1 can be approximately transformed into the temperature profile of temperature sensor 2 by a horizontal shift. This shift along the time axis corresponds to the time interval required by the flow to cover the distance between the two temperature sensors.

For a detailed description of the basic principle of the developed method see Seiz (2021) and Nedumparambil (2021). Both publications describe different approaches and each presents initial results for calculating the volume flow rate in a pipe on the basis of temperature measurements. Seiz (2022) describes further developed approaches and results for the calculation of the volume flow rate.

2.2 Principle of temperature-based energy balancing

In the following, starting from the temperature-based volume flow determination, this chapter explains how an energy balancing of a thermal system can be carried out. For a more detailed description of this procedure and for a detailed description of the technical components used in the four field test systems equipped with measurement technology, see Seiz (2021).

In order to carry out an energy balancing of a thermal system, first the volume flow rates in the hydraulic circuits connected to the central hot water store of the system must be determined. This is done on the basis of the temperature-based volume flow determination described in section 2.1. In order to be able to perform this successfully, measurement tracks (see Fig. 4) are installed in the hot side of each of the hydraulic circuits attached to the central hot water store. Two temperature sensors are located in each of the measurement tracks. The temperatures recorded by these sensors are primarily used to calculate the respective volume flow rate. In addition, an electrical heating element with a thermal output of 1.6 kW is installed in each measurement track. At times, when the temperature dynamics of a hydraulic circuit concerned are too low for a temperature-based volume flow determination, sufficient temperature dynamics can be ensured by activating the electrical heating element. For the actual energy balancing, the temperatures in the hot side and in the cold side of each hydraulic circuit must also be measured. The temperature sensors, which are required for the calculation of the volume flow rate, also serve this energy balancing, as one of the two measured values is included in the energy balancing as temperature value of the hot side of the respective hydraulic circuit. To enable energy balancing, a temperature sensor is also installed in the cold side of each hydraulic circuit in order to record the temperatures occurring there. In addition, for a complete energy balancing of the entire system, the temperatures inside the hot water store must also be determined. For this purpose, temperature sensors are installed on the outside of the metal wall of the hot water store, beneath the thermal insulation. In addition to the described technical components, which are required for the temperature-based energy balancing, conventional heat meters are installed in each hydraulic circuit. The values provided by these conventional heat meters were used to carry out a second energy balancing of the entire system. The result of this second energy balancing serves as a reference value for the energy balancing based on the newly developed TeBwA method. Fig. 4 shows one of the measurement tracks described, which, together with temperature sensors and an electrical heating element, is installed in one of the hydraulic circuits of a field test system. The actual measurement track is located between the two temperature sensors. Arrows in Fig. 4 mark the flow direction.

In order to keep the occurring heat losses as low as possible, the measurement tracks were well thermally insulated, following the creation of the photograph.



Fig. 4: Measurement track (a) with temperature sensors (b) and electrical heating element (c); Note: Shown without thermal insulation for better clarity

3. Temperature-based volume flow calculation

During the development of the method, the authors were investigating various approaches for determining the similarity of the compared temperature profiles and respectively the transit time of the fluid with regard to their suitability for calculating the volume flow rate within a pipe. Seiz (2021) gives a detailed description of these approaches.

The verification of the suitability of the different approaches was based on the accuracy with which the occurring volume flow rates could be calculated under different conditions. For this purpose, the authors used synthetically generated data, i.e. calculated with the simulation program TRNSYS, and experimentally measured data, produced with the test rig, that was set up for this purpose. In one of the approaches investigated in this context, cosine similarity is used as a similarity indicator. This approach achieved the best results over a large number of calculations performed. The cosine similarity κ is calculated according to eq. 1:

$$\kappa = 1 - \frac{a \bullet b}{||a||\ ||b||} = 1 - \frac{\sum_{i=1}^{n} a_i\, b_i}{\sqrt{\sum_{i=1}^{n}(a_i)^2} \bullet \sqrt{\sum_{i=1}^{n}(b_i)^2}} \qquad \text{(eq. 1)}$$

With:

a vector a, segment with values of temperature sensor 1 [-]
b vector b, segment with values of temperature sensor 2 [-]
n dimension of vectors, number of temperature values per segment [-]

After the crucial choice of an appropriate similarity indicator and the development of the evaluation algorithms based on this approach, the authors focused on the procedure for shifting the segments of the temperature values of temperature sensor 1 and temperature sensor 2 to be compared with each other (see Fig. 5). This shifting process also has a major influence on the achievable accuracy of the calculation of a present volume flow rate. Therefore, a suitable procedure for the shifting process was developed. Chapter 3.1. contains detailed explanation on the procedure of this shifting process.

Subsequently, chapter 3.2 presents result of the evaluation of experimentally generated data. In the evaluations carried out, the cosine similarity as a similarity indicator was combined with the developed procedure for the shifting of the temperature segments.

3.1 Shifting of the temperature segments

The first logical step in the newly developed algorithm is the calculation-based estimation of the time, required by the flow to cover the distance between the two temperature sensors. This is based on empirical values for the occurring volume flows, the measured distance between the two temperature sensors and the pipe cross-section. Then, the algorithm selects a segment of the temperature values from temperature sensor 1 that lies in the time range in which the volume flow rate should be calculated. After this the algorithm determines the segment of temperature values of temperature sensor 2 whose temperature values were measured at the same times as those of the segment previously selected for temperature sensor 1. Subsequently the algorithm calculates the similarity of the two segments according to eq. 1. After that, the actual shifting of the segments takes place. Hereby, the algorithm shifts the segment of temperature sensor 1 by one index position against the time axis and at the same time the segment of temperature sensor 2 by one index position along the time axis. At the same time the algorithm shortens the temperature segment of temperature sensor 1 by the last included temperature value and the temperature segment of temperature sensor 2 by the first included temperature value. Afterwards the algorithm again determines the similarity of the resulting segments of temperature sensor 1 and temperature sensor 2, followed by a new shift and shortening. Fig. 5 schematically shows the described shifting process.

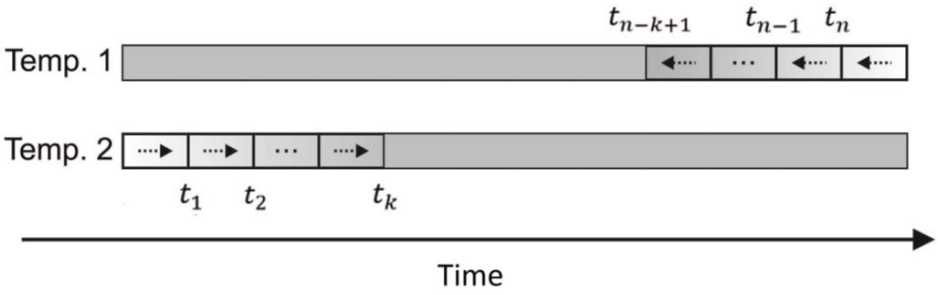

Fig. 5: Schematic illustration of the shifting process

The shifting of the two segments continues until the initially estimated maximum time required for the flow to cover the distance between the two temperature sensors is reached. In Fig. 5, the length of the gray horizontal bars, denoted by the letter n, represents the original length of the segments of temperature sensor 1 and of temperature sensor 2. The designation t_k stands for the assumed maximum time required by the flow to cover the distance between the two temperature sensors in the measurement track. In this context, the index k stands for the corresponding number of shifting steps. When using the cosine similarity as a method for determining the runtime or the similarity of two segments, a minimum of the similarity indicator Kappa (see eq. 1) stands for a maximum similarity between the two temperature segments compared with each other. Fig. 6 shows the resulting values for the similarity indicator Kappa for a comparison of two temperature segments.

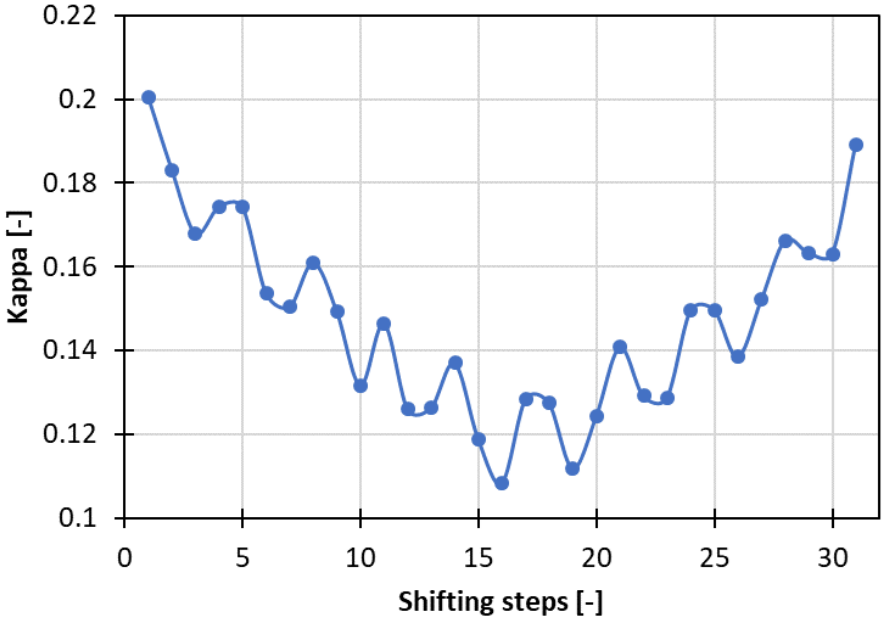

Fig. 6: Similarity indicator Kappa between two temperature segments at stepwise shifting

Fig. 6 shows a minimum of the similarity indicator Kappa at shifting step 16. Based on the number of shifting steps, the time required for the flow to cover the distance between the two temperature sensors can be derived. Afterwards the calculation of the magnitude of the volume flow rate can be executed.

3.2 Achievable accuracy - experimentally generated data

To investigate the suitability of the combination of the developed shifting process and the cosine similarity based approach, the authors generated data sets with different boundary conditions using the test rig developed in the project. In data set 1 medium-sized volume flow rates are considered. In data set 2, discussed further below, relatively large volume flow rates are considered and in data set 3, discussed even further below, relatively small volume flow rates are considered.

Fig 7 shows measured and calculated values of data set 1. The temperature profile shown in Fig. 7 was created by simultaneously using two electrical heating elements installed in the test rig. The temperature range considered extends from 40 to 80 °C and thus essentially corresponds to the temperature range that can also be expected in the regular operation of solar thermal systems. Hereby the primary electrical heating element, with an electrical power of 2 kW, was permanently activated in order to generate the basically increasing temperature profile and to cover an as large as possible temperature range. In addition, the secondary electrical heating element, with an electrical power of 1.6 kW, was periodically activated for 4.5 seconds and deactivated for 6.0 seconds, which resulted in the temperature fluctuations that can be seen in Fig. 7. Unfortunately, the activation of the secondary electrical heating element lead to a temporary drop of the supply voltage of the pump, which is installed in the test rig in order to create the fluid flow. This drop of the supply voltage of the pump resulted in the fluctuations in the measured volume flow rate that can be recognized in Fig. 7.

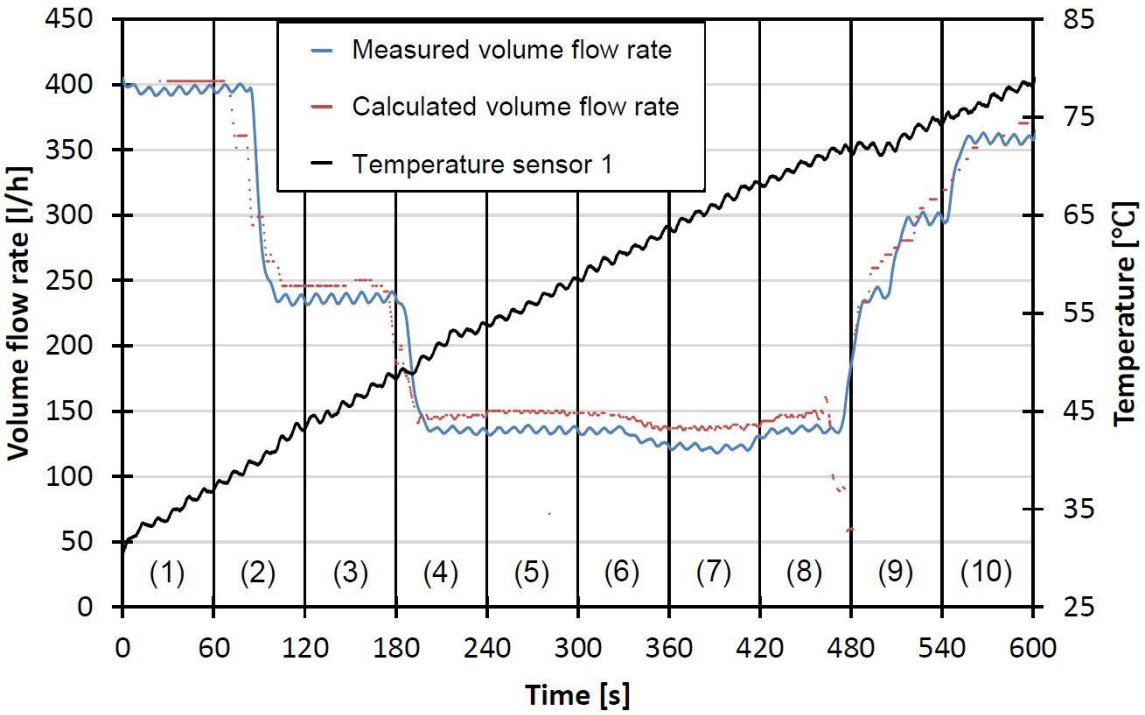

Fig. 7: Measured and calculated volume flow rate within sections (1) to (10) from data set 1

Fig. 7 shows the temperature of the volume flow entering the measurement track at temperature sensor 1 for data set 1. Fig. 7 does not show the temperature of the volume flow at temperature sensor 2, because this temperature is almost identical to the temperature at temperature sensor 1. Fig. 7 also shows the volume flow rate that was calculated using the newly developed method and the volume flow rate measured using an electromagnetic flow meter. The measured volume flow rate lay in a range between 130 and 400 l/h. Tab. 1 lists the calculated volume flow rate and the measured volume flow rate based on minutely average values for data set 1 as well as the deviation between the two values.

Tab. 1: Calculated and measured volume flow rate as well as deviation between both with the use of minutely average values - for data set 1

Section of data set 1 (According to Fig. 7)	**Calculated volume flow rate [l/h]**	**Measured volume flow rate [l/h]**	**Deviation [%]**
1	393.44	396.24	-0.71
2	252.11	250.44	0.67
3	210.36	213.53	-1.49
4	147.62	135.16	9.22
5	147.92	135.31	9.32
6	139.13	126.55	9.94
7	140.63	127.21	10.55
8	175.93	176.89	-0.54
9	305.05	308.29	-1.05
10	358.91	371.49	-3.39

Tab. 1 shows that the deviation between the calculated and measured volume flow rate is within ±10%, except for section 7. The evaluation of data set 1 could therefore demonstrate the suitability of the developed method for the calculation of volume flow rates in the afore mentioned volume flow range on the basis of experimentally generated measurement values. The developed algorithm removed individual outliers in the calculation of the volume flow rate. The identification of these outliers is based on the degree of similarity between the two temperature segments of temperature sensor 1 and temperature sensor 2 which are compared with each other; see Fig. 6. If the distance between the time indices of the two smallest values of Kappa was less than 5 time steps or 0.5 seconds respectively, the algorithm used the mean value of the two time indices to calculate the corresponding volume flow rate. Otherwise,

the algorithm considered the value as an outlier and excluded the value in question from the calculation process. After the removal of the outliers, calculated values for the volume flow rate remained available for approx. 47% of the operating time.

In order to test the suitability of the method also in a higher range of the volume flow rate, the volume flow rate was increased for the creation of data set 2 to a range between 400 and 910 l/h. The temperature ranged from approximately 54 to 64 °C. Due to limited available space this paper does not show the temperature and volume flow curves for data set 2. Tab. 2 lists the calculated volume flow rate and the measured volume flow rate based on minutely average values for data set 2 as well as the deviation between the two values.

Tab. 2: Calculated and measured volume flow rate as well as deviation between both with the use of minutely average values - for data set 2

Section of data set 2	Calculated volume flow rate [l/h]	Measured volume flow rate [l/h]	Deviation [%]
1	455.45	426.44	6.80
2	488.30	436.85	11.78
3	524.20	500.52	4.73
4	538.51	515.07	4.55
5	570.10	544.09	4.78
6	616.43	595.06	3.59
7	627.52	667.38	-5.97
8	683.59	698.23	-2.10
9	717.45	736.38	-2.57
10	750.87	761.48	-1.39
11	830.55	807.26	2.88
12	958.01	912.54	4.98

Tab. 2 shows that for data set 2, with the exception of section 2, the deviation between the calculated and the measured volume flow rate is within ±7%. The evaluation of data set 2 could therefore also demonstrate the suitability of the developed method for the calculation of large volume flow rates on the basis of experimentally generated measurement values.

When calculating small volume flow rates, a lower limit value must be defined. Otherwise the segment lengths of the temperature values of temperature sensor 1 and temperature sensor 2, which have to be compared with each other, would become very large. This would result in an unacceptable computational effort for the calculation of the volume flow rate. For the evaluation of data set 3, the lower limit value of the volume flow rate was set to 58 l/h based on experimental investigations. When data set 3 was created, the measured volume flow rate was between 35 and 65 l/h. The temperature ranged from approximately 58 to 74 °C. Due to limited available space this paper also does not show the temperature and volume flow curves for data set 3. Tab. 3 lists the calculated volume flow rate and the measured volume flow rate based on minutely average values for data set 3 and the deviation between the two values.

Tab. 3: Calculated and measured volume flow rate as well as deviation between both with the use of minutely average values - for data set 3

Section of data set 3	Calculated volume flow rate [l/h]	Measured volume flow rate [l/h]	Deviation [%]
1	61.29	50.37	21.67
2	58.96	46.54	26.69
3	60.63	46.17	31.33
4	70.08	62.66	11.83
5	72.49	63.32	14.49
6	102.94	49.86	106.47
7	58.30	35.21	65.55
8	58.25	36.89	57.91

Tab. 3 shows that the values of the calculated volume flow rate in parts deviate significantly from the values of the measured volume flow rate. These partly large deviations are the result of the necessarily determined lower limit value. The lower limit value of 58 l/h had the effect, that the algorithm could not determine volume flow rates with less than 58 l/h. Since there are also individual measured volume flow rates in data set 3 that are lower than the limit value mentioned, the calculated volume flow rate was overestimated. Therefore Tab. 3 shows significant relative deviations between the measured volume flow rate and the calculated volume flow rate in most of the sections of data set 3. However, while the relative deviations are high when comparing the minutely average values, the absolute deviations are small in most cases. Setting the lower limit to a lower value does increase the accuracy with which small volume flow rates can be calculated. But unfortunately this has the consequence that the accuracy with which medium and large volume flow rates can be calculated decreases. In addition, a decrease in the lower limit value is accompanied by an exponential increase in computational effort.

The authors assume, that the effect of this high relative but low absolute deviations in the calculation of volume flow rates in the low volume flow range is not significant when performing an energy balancing of a thermal system. To verify this assumption, the authors are currently carrying out corresponding investigations. It seems unambiguous, that the successful performance of an accurate energy balancing of a thermal system depends on a precise calculation of occurring volume flow rates in the medium and in the high volume flow range. The evaluations of data set 1 and of data set 2 proofed the suitability of the newly developed method for calculating volume flow rates in these volume flow ranges on the basis of experimentally generated data. Nevertheless, the evaluation algorithms developed so far are currently being improved in order to increase the accuracy with which small volume flow rates can be calculated. In addition, a modified measurement track is currently being developed and tested, that is expected to lead, in combination with an adapted calculation procedure, to more accurate results, especially for small volume flow rates.

4. Temperature-based energy balancing

This chapter reports about the achievable accuracy when using the TeBwA method to perform a temperature-based energy balancing of thermal systems. Hereby the thermal energy was considered, that was transferred within one month in four different types of hydraulic circuits of thermal systems. In order to receive the measurement values required to perform the necessary calculations, four field test systems were equipped with the necessary measurement technology; see section 2.2.

The four types of hydraulic circuits considered are the following:

- solar circuit,
- boiler circuit,
- heating circuit,
- domestic hot water circuit.

For the evaluation, the monthly transferred thermal energy determined using the TeBwA method was compared with the corresponding values measured by conventional heat meters as reference values.

Fig. 8 exemplary shows the accumulated thermal energy transferred within the month of June 2022 from the solar circuit of a solar thermal domestic hot water system to the central hot water store. These curves of accumulated transferred thermal energy are based on the one hand on the recorded values of a conventional heat meter and on the other hand on the values calculated on the basis of the TeBwA method.

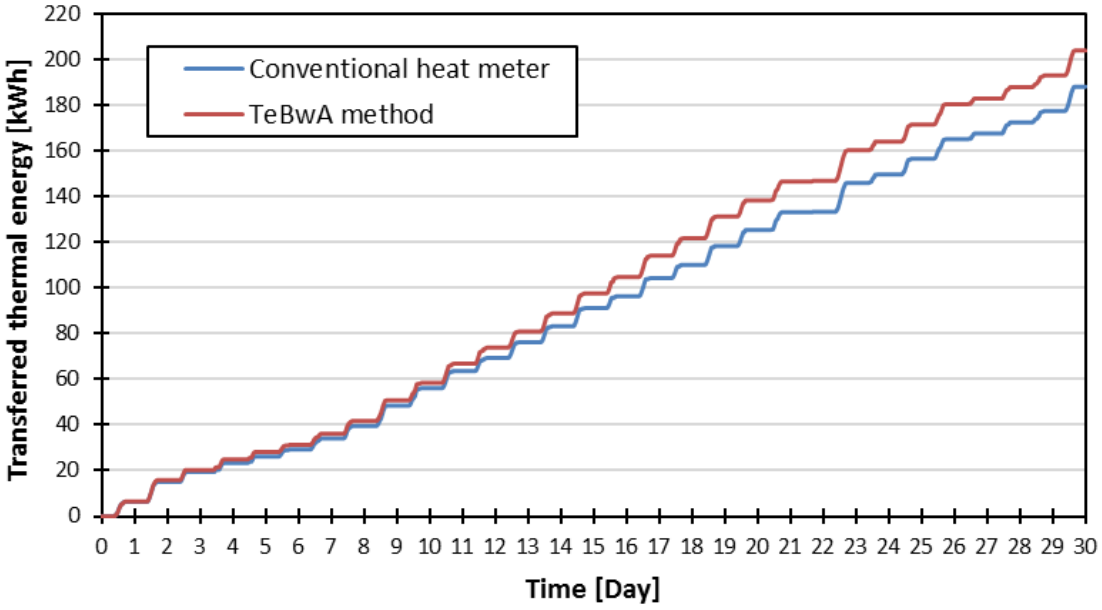

Fig. 8: Accumulated transferred thermal energy of the solar circuit of a solar thermal domestic hot water system in the month of June 2022

As Fig. 8 indicates, the thermal energy transferred, calculated on basis of the TeBwA method, amounts to approx. 204 kWh. The corresponding value determined with a conventional heat meter is approx. 188 kWh. Thus, there is a relative deviation of about +8.4%. The overestimation of the transferred thermal energy in solar circuits mainly occurs during periods of solar thermal stagnation. In periods of solar thermal stagnation, no volume flow exists in the solar circuit while the temperatures of the heat transfer fluid continuously rise up to certain, relatively high temperatures. The evaluation algorithms currently in use sometimes incorrectly detect the presence of a volume flow in the solar circuit during stagnation conditions. This incorrect detection of a volume flow, when actually there is none, can lead to the described overestimation of the transferred thermal energy. This effect occurred in the second half of June 2022. As can be seen in Fig. 8, this led to an increase in the daily deviations between the values determined using the TeBwA method and those based on a conventional heat meter. The algorithms used at present are currently under improvement, to address the stagnation problem described.

Due to limited available space, curves of the accumulated thermal energy transferred within one month for the other three types of hydraulic circuits are not shown. Tab. 4 lists the monthly transferred thermal energy for each of the hydraulic circuits based on the calculations performed by conventional heat meters and by the TeBwA method, as well as the relative deviation between both.

Tab. 4: Conventional and temperature-based energy balancing (TeBwA method) as well as deviation between both for the month of October 2021 for various solar thermal systems investigated

Field test system with corresponding hydraulic circuit		Conventional energy balancing by means of a heat meter [kWh]	Temperature-based energy balancing with TeBwA-method [kWh]	Deviation [%]
System 1*	Solar circuit	0.0	0.1	-
	Boiler circuit	467.0	503.5	+7.82
	Heating circuit	1,398.0	1,304.0	-6.72
System 2	Solar circuit	114.0	121.6	+6.70
	Boiler circuit	97.0	105.9	+9.18
	Domestic hot water circuit	57.0	60.5	+6.19

System 3**	Solar circuit	173.0	177.0	+2.36
	Boiler circuit	2,337.0	2,500.9	+7.01
	Heating circuit	2,024.0	2,015.0	-0.44
System 4***	Boiler circuit	872.0	943.5	+8.20
	Domestic hot water circuit	654.0	621.7	-4.94

* The solar circuit of field test system 1 was out of service in October 2021 due to technical problems with the controller.

** For field test system 3, a temporary problem occurred in October 2021 with the programs used for data acquisition. Therefore, only 25 days are included for the values shown in Tab. 4

*** Field test system 4 experienced temporary problems with the temperature sensors used in the boiler circuit in October 2021. In addition, modification work was carried out on the boiler. Therefore, for the boiler circuit only 23 days could be considered for the values presented in Tab. 4. For the domestic hot water circuit of field test system 4 only 28 days could be considered in Tab. 4 due to technical problems. As the solar collectors are damaged, the solar circuit of field test systems 4 is currently not in operation.

Since the solar yield in the month of October 2021 was relatively low due to a small number of sunny days, Tab. 5 shows supplementary results of the solar circuits of the field test systems for the month of June 2022.

Tab. 5 Conventional and temperature-based energy balancing (TeBwA method) as well as deviation between both for the month of June 2022 for various solar thermal systems investigated

Field test system with corresponding hydraulic circuit		**Conventional energy balancing by means of a heat meter [kWh]**	**Temperature-based energy balancing with TeBwA-method [kWh]**	**Deviation [%]**
System 1	Solar circuit	376.4	349.3	-7.20
System 2	Solar circuit	188.1	203.9	+8.41
System 3*	Solar circuit	582.3	519.5	-10.78
System 4**	Solar circuit	-	-	-

* For field test system 3, the measurement track of the solar circuit was temporarily removed to be modified. Therefore, only 26 days are included for the values given in Tab. 5.

** As the solar collectors are damaged, the solar circuit of field test system 4 is currently not in operation.

Tab. 4 and Tab. 5 show, that the monthly transferred thermal energy in the different types of hydraulic circuits can be calculated with high precision when using the newly developed TeBwA method for the temperature-based energy balancing of thermal systems. The calculation results deviate within a range of ±10.8% compared to the results of conventional heat meters. A precise energy balancing of thermal systems, using only low-cost temperature sensors, is therefore principally possible. It should be noted however, that the use of the electrical heating elements installed in the hydraulic circuits was deliberately omitted. This was done in order to determine the performance of the TeBwA method under regular operation of the systems and to avoid additional consumption of electricity. If the electrical heating elements were used, the achievable precision would even be higher.

When assessing the results presented in Tab. 4 and Tab. 5, it should also be taken into account that the comparison is based on monthly values. The deviations occurring for individual days are sometimes significantly greater than ±10%. Future work will therefore, among others, focus on further improving the temperature-based energy balancing algorithms developed so far.

5. Further Action

The next steps with regard to the further development of the TeBwA method for the temperature-based energy balancing of thermal systems are mentioned in the following.

The evaluation algorithms to reliably detect the presence of an occurring volume flow within a pipe and the evaluation algorithms to subsequently calculate the volume flow rate with high precision will be improved to further increase the accuracy of the TeBwA method.

Investigations will be performed how to increase the accuracy with which small volume flow rates can be calculated by using three, instead of two temperature sensors in a measurement track. By an appropriate placement of the three temperature sensors in the measurement track, two partial sections with different lengths can be realized. This allows a flexible reaction to volume flow changes in the hydraulic circuit under consideration.

Also, investigations will be performed regarding a targeted increase in the temperature dynamics of the pipe flows under consideration. This should enable more precise temperature-based volume flow calculation even if the temperature dynamics during regular operation of the hydraulic circuit are temporarily insufficient. Therefore, the use of electrical heating elements installed in the measurement tracks will be investigated. One important challenge here lies in the development of an activation strategy that leads only to a minimal additional use of electrical energy.

Additionally, it will be examined to what extent the temporal resolution with which the temperatures in the measurement track are recorded can be reduced, without leading to a significant influence on the calculated volume flow rates. This approach is intended to reduce the demands on the measurement technology used. This would allow for the use of cheaper components and thus reduce the overall costs of the TeBwA method.

Another aspect that is being investigated lies in a general abandonment of the measurement tracks currently in use. As an alternative the required temperature sensors are inserted at a defined distance apart from each other directly into the water-bearing pipes. The sections between the temperature sensors act as quasi measurement tracks. The abandonment of the presently used measurement tracks would result in a further reduction in costs and also the intervention in the hydraulic circuits of the thermal systems would be reduced.

In the medium term, the authors are intending to commercialize the newly developed TeBwA method for the temperature-based energy balancing of thermal systems. For this purpose, a partner from industry is sought at present. In cooperation with this partner, the future design of the technical components will be developed.

6. Acknowledgments

The activities described in this publication are being supported by the German Federal Ministry for Economic Affairs and Climate Action (BMWK) under the grand number 03ETW010 (research project TeBwA: Temperaturbasierte energetische Bilanzierung wärmetechnischer Anlagen / Temperature-based Energy Balancing of Thermal Systems). The authors gratefully acknowledge this support and carry the full responsibility for the content of this publication.

7. References

Frank, E., 2000. Untersuchungen zur Bestimmung von Kollektorkreis-Volumenströmen durch Auswertung von Temperaturflanken. State examination thesis, Philipps-Universität Marburg.

Nedumparambil, A.; Seiz, M.; Drück, H.; Bestenlehner, D., 2021. Temperature based determination of volume flow rates in pipes as a low-cost option for energy measurements of solar thermal systems, in: Proceedings of the Solar World Congress, 25.-29.10.2021, online, International Solar Energy Society, Freiburg, ISBN 978-3-9820408-7-5, pp. 608-619, viewed 12 September, 2022, http://proceedings.ises.org/swc2021/swc2021-proceedings.pdf.

Seiz, M.; Lang, X., Drück, H., Bestenlehner, D., 2022. Kostengünstige energetische Bilanzierung wärmetechnischer Anlagen durch eine temperaturbasierte Volumenstrombestimmung, in: Proceedings of the Symposium Solarthermie und innovative Wärmesysteme, 03.-05.05.2022, Bad Staffelstein, Conexio GmbH, Pforzheim, ISBN 978-3-948176-17-4, pp. 211-230, viewed 12 August, 2022, https://www.solarthermie-symposium.de/konferenz/tagungsunterlagen.

Seiz, M.; Nedumparambil, A.; Drück, H.; Bestenlehner, D., 2021. Kostengünstige Volumenstrombestimmung von Rohrströmungen mittels Temperaturmessungen, in: Proceedings of the Symposium Solarthermie und innovative Wärmesysteme, 27.-30.04.2021, online, Conexio GmbH, Pforzheim, ISBN 978-3-948176-13-6, pp. 352-368, viewed 12 August, 2022, https://www.solarthermie-symposium.de/konferenz/tagungsunterlagen.

P. Solar Resources and Energy Meteorology

Assessment of Downward Longwave Radiation Models in Clear-Sky Desert Conditions

Dunia Bachour[1], Daniel Perez-Astudillo[1], Hissa Al-Hajri[1] and Antonio Sanfilippo[1]

[1] Qatar Environment and Energy Research Institute, Hamad Bin Khalifa University, Qatar Foundation, Doha (Qatar)

Abstract

The longwave downward radiation (LDR), emitted by the atmosphere and clouds, is a crucial parameter for the determination of the radiative energy budget on the earth's surface. The direct measurement of LDR is very sensitive and requires specialized and expensive sensors, and is commonly not available at most meteorological monitoring sites, and considerable efforts have been made to determine LDR from the available atmospheric parameters of a particular site. This work presents an analysis of the longwave downward atmospheric radiation in a region of desert conditions. The performance of several downward longwave radiation models has been evaluated during clear-sky conditions, determining the more adapted empirical relation for the observed local conditions. For validation, ground measurements of LDR and atmospheric parameters were used at two different sites covering a period of several years. The statistical analysis using the original empirical coefficients of the models evaluated here shows under or over-estimation of the measured data. A local calibration was performed, retrieving the local coefficients over a period of one year, showing a decreased errors and a better statistical analysis for estimating clear-sky LDR under the local conditions of Qatar.

Keywords: longwave downward radiation, clear-sky, desert conditions, radiation budget

1. Introduction

The atmospheric longwave downward radiation (LDR) is an important parameter for the determination of the radiation budget at the earth's surface. It depends mainly on the vertical distribution of air temperature, water vapor, and the presence of aerosols and clouds in the atmospheric column within the first few kilometers above the ground.

Equation 1 shows the calculation of the net radiation budget Rn in W/m^2, including the absorption and reflection of the incoming shortwave solar radiation, as well as the longwave upward and downward radiation.

$$R_n = (1 - \alpha) * G + LDR - LUR \quad \text{(eq.1)}$$

where G is the global horizontal radiation received on the earth surface, α is the ground albedo and LUR is the longwave upper radiation emitted from the earth's surface towards the atmosphere.

Direct on-site measurements are usually the most accurate method used to obtain the long-wave downward radiation component of the atmosphere. When not available, several models exist in the literature for the estimation of the long wave downward radiation, generally based on the Stefan–Boltzmann law, and depending on the atmosphere's emissivity and the fourth power of the absolute temperature. The most accurate models are generally the numerical radiation transfer models used with the correct atmospheric input information; however, the correct input parameters are not usually available and these models are in general complex and time consuming. More simple models exist, based on empirical correlations between LDR and readily available meteorological observations, such as sunshine duration, air temperature and vapor pressure. These models are mostly developed under clear sky conditions, wherein the emissivity depends largely on the air temperature and water vapor pressure, and they are more adapted to the site where they were developed and locally calibrated.

In the present study, we evaluate 9 clear-sky models proposed in the literature to calculate the emissivity and consequently LDR, and compare it with LDR measured at ground level at two different sites in Qatar. The objective is to determine the more suitable emissivity model to the atmospheric conditions observed here, and to perform local calibration to develop local models.

© 2022. The Authors. Published by International Solar Energy Society
Selection and/or peer review under responsibility of Scientific Committee
doi:10.18086/eurosun.2022.15.01 Available at http://proceedings.ises.org

2. Methodology

In clear-sky conditions, LDR estimation follows the equation

$$LDR = \varepsilon * \sigma * T_a^4 \quad \text{(eq.2)}$$

where ε is the effective clear-sky emissivity of the atmosphere, σ is the Stefan Boltzmann constant and T_a is the integrated temperature over the atmospheric column above the ground that emits longwave radiation.

T_a is typically estimated from ground-based meteorological observations, and is considered here as the ambient air temperature in Kelvin.

ε is calculated with empirical equations: some of these equations consider the temperature alone such as in equations 3 (Swinbank, 1963) and 6 (Idso and Jackson, 1963), some consider the water vapor pressure e_a alone such as in equation 4 (Brunt, 1932), and some consider both T_a and e_a such as in equations 5 (Brutsaert, 1975), 7 (Idso, 1981), 8 (Sugita and Brutsaert, 1993), 9 (Duarte et al., 2006), 10 (Kruk et al., 2010), and 11 (Prata, 1996).

$$\varepsilon = 9{,}365 * 10^{-6} * {T_a}^2 \quad \text{(eq.3)}$$

$$\varepsilon = 0.52 + 0.065 * {e_a}^{1/2} \quad \text{(eq.4)}$$

$$\varepsilon = 1.24 * \frac{{e_a}^{1/7}}{T_a} \quad \text{(eq.5)}$$

$$\varepsilon = 1 - 0.261 * \exp(-0.00077 * (T_a - 273.13)^2)) \quad \text{(eq.6)}$$

$$\varepsilon = 0.7 + 5.95 * 10^{-5} * e_a * \exp(\frac{1500}{T_a}) \quad \text{(eq.7)}$$

$$\varepsilon = 0.714 * \frac{e_a^{0.0687}}{T_a} \quad \text{(eq.8)}$$

$$\varepsilon = 0.625 * \frac{e_a^{0.131}}{T_a} \quad \text{(eq.9)}$$

$$\varepsilon = 0.576 * \frac{e_a^{0.202}}{T_a} \quad \text{(eq.10)}$$

$$\varepsilon = 1 - ((1+\omega) * Exp\,(-(1.2 + 3*\omega)^{0.5})),\ \omega = 0.465 * (\frac{e_a}{T_a}) \quad \text{(eq.11)}$$

In order to determine the water vapor pressure e_a, we use the definition of the relative humidity RH and the water vapor saturation pressure calculation, following the equations by Wagne and Pruß (2002):

$$RH = \frac{e_a}{e_{as}} * 100\% \quad \text{(eq.12)}$$

$$\vartheta = 1 - \frac{T_a}{T_c} \quad \text{(eq.13)}$$

$$\ln\left(\frac{e_{as}}{e_c}\right) = \frac{T_c}{T_a} * (C_1\vartheta + C_2\vartheta^{1.5} + C_3\vartheta^3 + C_4\vartheta^{3.5} + C_5\vartheta^4 + C_6\vartheta^{7.5}) \quad \text{(eq.14)}$$

Where e_{as} is the water vapor saturation pressure, T_c and P_c are respectively the water vapor critical temperature (647.096 K) and critical pressure (220 640 hPa), and C_i are empirical coefficients.

In order to determine the clear sky conditions, we calculate a clear-sky ratio K_c as follows:

$$K_c = \frac{G}{Gc} \quad \text{(eq.15)}$$

Where G is the measured global horizontal irradiance and Gc is the clear-sky global horizontal irradiance calculated using the ESRA clear-sky model (Rigollier et al., 2000). The clear-sky conditions are those for which the clear-sky ratio is greater than 0.85.

In this study, we use the cited equations proposed in the literature to calculate the emissivity in clear-sky conditions, and then insert it into equation 2 to estimate LDR and compare it with LDR measured at ground level. All LDR and solar data are aggregated into 10-min averages in order to match the temporal resolution of the meteorological data.

3. Experimental setup

For the ground measurements of LDR two different pyrgeometers were used, a CGR4 and an MS-202, each installed at a different site (different location and conditions), with the sites located 85 km apart. The CGR4 pyrgeometer from Kipp and Zonen (highlighted with a red circle on the top right of figure 1), is part of a complete solar monitoring station installed at the rooftop of the research building of the Qatar Environment and Energy Research Institute in Doha, indicated here as site 1, measuring all the broadband solar radiation components, namely beam or direct normal (Gb), global horizontal (G) and diffuse horizontal (Gd) irradiances. The CGR4 is mounted on a sun tracker, and has a shading mechanism to prevent direct exposure to solar radiation. It also has a ventilation unit to help stabilize the dome temperature and reduce dust accumulation on the dome. An automatic weather station (AWS) is installed nearby on the same rooftop, measuring the meteorological parameters (temperature, relative humidity, pressure, and wind speed and wind direction), at 3m height from the rooftop surface. It is to be noted that the whole experimental setup described here for site 1 has been slightly relocated to another location within the same vicinity, therefore we differentiate in the data analysis between the period 2014-2017, and the period 2020-2021.

The MS-202 is installed as a standalone sensor on a horizontal platform (figure 1, bottom right) at a remote site in the desert, called here site 2. A high-quality solar monitoring station is also installed on-site, measuring G, Gb, and Gd. Few kilometers apart, an AWS is installed by the Qatar Meteorological Department and measures the meteorological components, at 10 m height from the ground. The analysed period for site 2 is for years 2020 and 2021.

Cleaning of the sensor domes and checking of the alignment of the radiation sensors are done regularly (twice a week). The solar and LDR data are collected as one-minute averages, and quality checks were applied to filter out low quality data, based on physically possible limits. The meteorological data are collected as 10-minute averages.

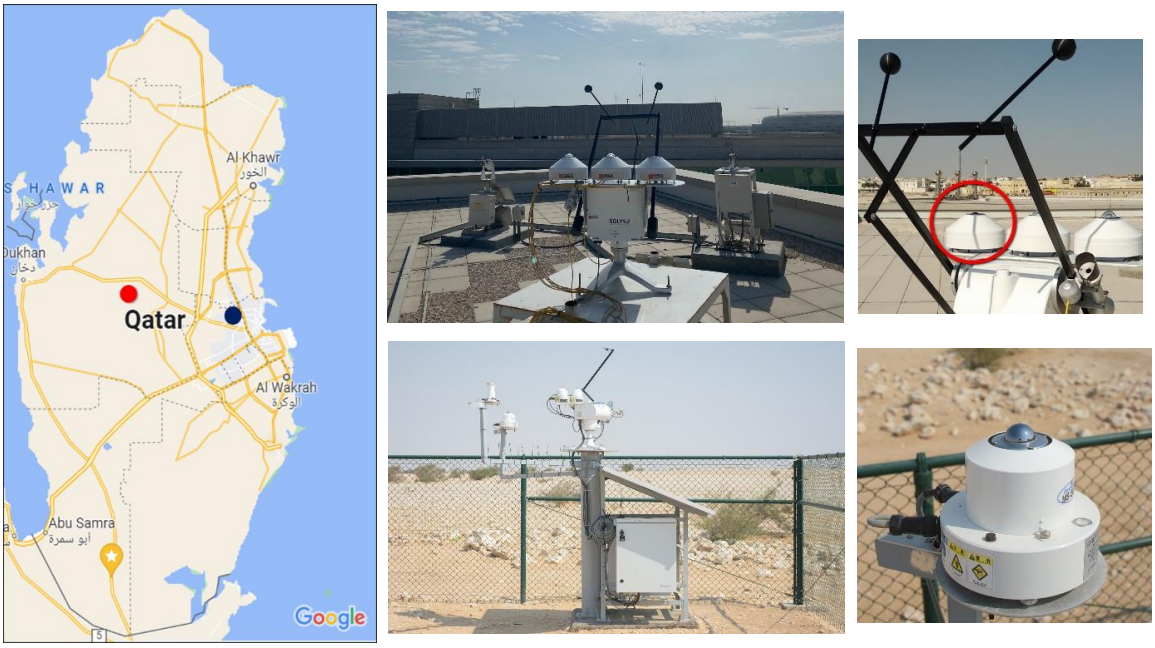

Fig. 1: Two experimental sites and two types of equipment: Kipp and Zonen station (top), EKO station (bottom).

4. Analysis and Results

For the comparison between the estimated and measured LDR, we represent the data in two-dimensional scatter plots. Figure 2 shows the scatter plot of the modeled and measured LDR at site 1 (left) and site 2 (right), using equations 4 and 3 respectively to determine the clear-sky emissivity for year 2020. The one-to-one line is indicated in red. As discussed above, the clear sky conditions are determined using the ESRA model to determine the clear-sky index. Only data with positive radiation values and solar zenith angle less than 90 degrees, and clear sky ratio higher than 0.85 are considered. The performance of the emissivity models described in equations 3 to 11 is evaluated in terms of the mean bias error (Bias) and the root mean square error (RMSE). The difference and its square between the estimated and measured LDR data at the same time stamps is calculated for a one-year period. These differences and their squares are summarized to determine the corresponding bias and root mean square error, and then expressed in relative values (rBias, rRMSE) with respect to the mean values calculated from the ground measurements. Tables

1 and 2 show the statistical parameters of the comparison between measured and estimated LDR, reporting the number of data points, the relative bias and the relative RMSE. The correlation factors were also calculated and found to be greater than 0.9 for all the comparisons considered here.

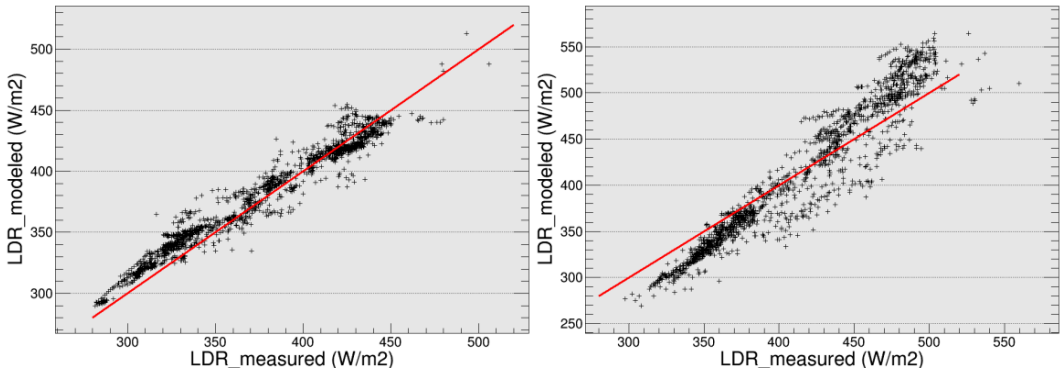

Fig. 2: Comparison between estimated and measured LDR for clear-sky conditions in year 2020. Site 1 (left). Site 2 (right).

Tab. 1: Statistical parameters for the validation of several models for estimating LDR. Site 1 (2014-2017). The lowest values are highlighted in red.

SITE 1								
Year	**2014**		**2015**		**2016**		**2017**	
Npoints	**1113**		**871**		**1862**		**1052**	
Error(%)	rBias	rRMSE	rBias	rRMSE	rBias	rRMSE	rBias	rRMSE
Eq 3	-8.17	9.06	-8.65	9.57	-9.02	9.9	-9.13	9.62
Eq 4	9.93	13.09	7.64	11.28	8.15	11.23	10.34	13.88
Eq 5	10.65	13.68	8.33	11.87	8.87	11.84	11.021	14.44
Eq 6	-3.92	5.7	-4.36	6.29	-4.72	6.38	-4.87	5.84
Eq 7	0.49	3.78	0.46	3.7	-0.52	3.99	-0.79	2.94
Eq 11	-14.14	14.77	-14.41	15.12	-15.21	15.68	-14.46	14.88

Tab. 2: Statistical parameters for the validation of several models for estimating LDR. Site 1 (2020-2021). The lowest values are highlighted in red.

SITE 1				
Year	**2020**		**2021**	
Npoints	**1721**		**1376**	
Error(%)	rBias	rRMSE	rBias	rRMSE
Eq 3	-7.04	7.88	-4.72	6.18
Eq 4	14.67	17.736	15.3	18.12
Eq 5	15.27	18.19	15.99	18.69
Eq 6	-2.90	4.87	-0.49	4.37
Eq 7	1.24	3.24	3.7	5.04
Eq 11	-12.58	13.11	-11.29	12.25

Tab. 3: Statistical parameters for the validation of several models for estimating LDR. Site 2 (2020-2021). The lowest values are highlighted in red.

SITE 2				
Year	**2020**		**2021**	
Npoints	**1613**		**1640**	
Error(%)	**rBias**	**rRMSE**	**rBias**	**rRMSE**
Eq 3	-15.87	16.57	-17.69	18.49
Eq 4	-0.96	6.59	0.13	6.22
Eq 5	-0.34	6.53	0.746	6.16

Eq 6	-11.96	12.89	-14.18	15.28
Eq 7	-8.71	9.96	-10.68	11.74
Eq 11	-23.15	23.69	-23.77	24.22

From the statistical parameters presented in tables 1,2, and 3, the performance of the different models evaluated here is consistent between the studied years of one site, however they are not the same if we compare the two sites between them. In site 1, the lowest errors are observed while using the emissivity modeled in equation 7 for all the studied years except for year 2021, while modeling the emissivity using equation 4 and 5 shows the lowest errors for site 2. The observed difference in the calculated errors of the two sites may be due to the fact that the meteorological parameters used in the emissivity model are firstly measured at two different heights between the two sites (at 3m in site 1 and 10 m in site 2), and secondly the AWS in site 2 is a few kilometers away from the main site, which may have introduced some local bias in the comparison between the estimated and measured LDR. Hereafter, we use the data of site 1 to determine the local calcibration for the LDR estimation.

The performance of the models in equations 8 to 10 were also evaluated, however their results are not displayed here since they show high errors. These models have a relation between the emissivity and the ratio e_a/T_a that is similar to the equation determined by Brutsaert in equation 5, but with different coefficients depending on the location where they were derived.

$$\boldsymbol{\varepsilon = C_1 * (\frac{e_a}{T_a})^{C_2}} \qquad \text{(eq 16)}$$

In order to determine the coefficients for the local conditions found in Qatar, we studied in figure 3 the relation between measured LDR and the ratio e_a/T_a, using clear-sky LDR data of year 2015 in site 1. The function found to better fit both was determined, and the two coefficients C_1 and C_2 are obtained from the fit and are shown in the statistics box of figure 3 as p0 and p1, respectively.

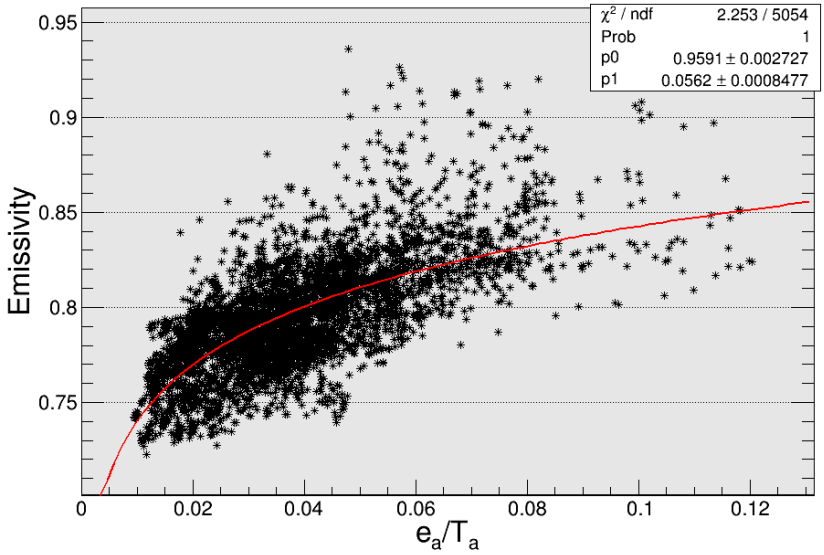

Fig. 3: Correlation between measured LDR and the ratio ea/Ta, using clear-sky LDR data of year 2015 in site 1.

The same local calibration was performed for equation 7 (the best performing model at site 1), using clear-sky LDR data of year 2015 in site 1. In order to determine the coefficients for the local conditions found in Qatar, we determined the function that better fit the data using equation 14; the two coefficients C_3 and C_4 are obtained from the fit and are shown in the statistics box of figure 4 as p0 and p1, respectively.

$$\boldsymbol{\varepsilon = C_3 + C_4 * e_a * \exp(\frac{1500}{T_a})} \qquad \text{(eq 17)}$$

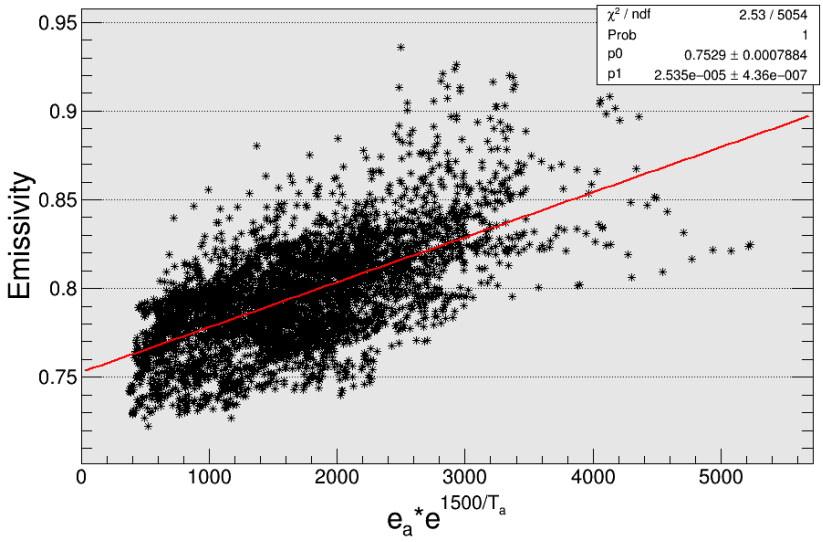

Fig. 4: Correlation between measured LDR and the ratio ea* exp(1500/Ta) using clear-sky LDR data of year 2015 in site 1.

In order to evaluate the performance of the two local models, we used a different dataset than the one used to develop the models. LDR is calculated using equations 15 and 16 and compared with ground measured LDR.

$$\boldsymbol{\varepsilon = 0.959 * (\frac{e_a}{T_a})^{0.0562}} \quad \text{(eq 18)}$$

$$\boldsymbol{\varepsilon = 0.753 + 2.535 * 10^{-5} * e_a * \exp(\frac{1500}{T_a})} \quad \text{(eq 19)}$$

The statistical parameters are displayed in table 4 and show a slight decrease in the error compared to the best performing model for site 1.

Tab. 4: Statistical parameters for the validation of several models for estimating LDR.

Year	2014		2016		2017	
Npoints	**1113**		**1862**		**1052**	
Error(%)	rBias	rRMSE	rBias	rRMSE	rBias	rRMSE
Eq 18	1.03	3.16	-0.06	2.69	0.44	2.44
Eq 19	1.32	3.43	0.16	2.87	0.57	2.54

5. Conclusions

In this contribution, the performance of several models estimating the longwave downward radiation is evaluated against ground measurements in two different locations in Qatar, for 5 years in site 1 and 2 years in site 2. The relative Bias and relative RMSE of the assessment are reported separately for each year. The results show that the models considering both the temperature and water vapour pressure perform better than the models using independently in their empirical relation either the temperature or the water vapor pressure. A local calibration was also performed and local empirical coefficients were determined. The results of the new determined models estimating LDR showed a good performance when validated with 3 years of ground measurements, separately, achieving errors lower than 3.5% with 10-minute resolution data. It is recommended to use these new empirical relations when determining clear-sky LDR in similar atmospheric conditions. A potential continuation of this work will include the validation and calibration of the LDR model under all-sky conditions.

6. References

Brunt, D. 1932. Notes on radiation in the atmosphere. Q. J. R. Meteorol. Soc., 58, 389–420. Doi:10.1002/qj.49705824704

Brutsaert, W. 1975. On a derivable formula for long-wave radiation from clear skies. Water Resour. Res., 11, 742–744. Doi:10.1029/wr011i005p00742

Duarte, H.F., Dias, N.L., Maggiotoo, S.R. 2006. Assessing daytime downward longwave radiation estimates for clear

and cloudy skies in Southern Brazil. Agricultural and Forest Meteorology, 139, 171–181. DOI:10.1016/j.agrformet.2006.06.008

Idso, S.B., Jackson, R. D. 1969. Thermal Radiation From the Atmosphere. J Geophys Res, 74, 5397–5403. DOI:10.1029/JC074i023p05397

Idso, S.B. 1981. A set of equations for full spectrum and 8- to 14-µm and 10.5- to 12.5-µm thermal radiation from cloudless skies. Water Resour. Res. 17, 295–304. DOI:10.1029/WR017i002p00295

Kruk, N.S., Vendrame, I.F., Rocha, H.R., Chou, S.C., Cabral, O. 2010. Downward longwave radiation estimates for clear and all-sky conditions in the Sertãozinho region of São Paulo, Brazil. Theoretical and Applied Climatology, 99, 115–123, 2010. DOI: 10.1007/s00704-009-0128-7

Prata, A.J.A. 1996. A new long-wave formula for estimating downward clear-sky radiation at the surface. Quarterly Journal of the Royal Meteorological Society, 122, 1127–1151. DOI:10.1002/qj.49712253306

Rigollier, C., Bauer, O., Wald, L. 2000. On the clear sky model of the ESRA - European Solar Radiation Atlas with respect to the Heliosat method. Solar Energy, 68 (1), 33-48. DOI:10.1016/S0038-092X(99)00055-9

Sugita, M., Brutsaert, W.H. 1993. Cloud effect in the estimation of instantaneous downward longwave radiation. Water Resources Research, 29, 599–605. DOI:10.1029/92WR02352

Swinbank, W.C. 1963. Long-wave radiation from clear skies. Q. J. R. Meteorol. Soc., 89, 339–348. DOI:10.1002/qj.49708938105

Wagner, W., Pruß. A. 2002. The IAPWS Formulation 1995 for the Thermodynamic Properties of Ordinary Water Substance for General and Scientific Use. Journal of Physical and Chemical Reference Data, 31 (2), 387-535. DOI:10.1063/1.1461829

A new framework to evaluate the adequation between the solar potential and energy demand of an urban-rural territory in a mountainous area

Apolline Ferry[1], Martin Thebault[1], Lamia Berrah[2], Antonio Gómez[3], Norberto Fueyo[3] and Christophe Ménézo[1]

1 LOCIE, Université Savoie Mont Blanc, CNRS UMR5271, F- 73376 Le Bourget du Lac, France

2 University Savoie Mont Blanc, LISTIC, F- 74944 Annecy-le-Vieux, France

3 Fluid Dynamics Technology Group, I3A, University of Zaragoza, Zaragoza, Spain

Abstract

The development of renewable energy is urgent given the current climate change and Europe energy supply contexts. Among the renewable sources, solar energy is promising and solar technologies spread quickly in the last years. The local production matching with the local energy demand is possible with these technologies and needs to be promoted in the next years to limit the loss induced by the transportation and storage of energy. However, solar potential (irradiation received on a surface) as well as demand are complex to model with accuracy, as many phenomena impact it (shading…). This study proposes a methodology to map solar potential in a rural area, considering several aspects such as the local climate, topography and global climate change. A first overview of the workflow developed is presented, combining several software in order to study the solar potential and its influence on the energy mix at the scale of a village located in a rural area. In particular, the focus is made on mountainous regions which are isolated areas with strong environmental constraints. This work will present a short state of the art, a first overview of the workflow developed which presents the tools that will be used to investigate the solar potential and the territory that will be studied.

Keywords: solar potential, renewable energy, energy mix, rural territory, energy modelling, software

1. Introduction

The world is currently facing an increase in global energy demand, partly caused by population growth. This leads to negative impacts on the environment through air and water pollution, gas emissions (with CO_2 emissions that are expected to rise). Therefore, there is a need to act to limit CO_2 emissions associated with energy consumption and production. Targets have been set by many states in this sense and achieve carbon neutrality by 2050. The overall population increase is mainly related to an increase of the population in urban areas, which results in the energy demand being located in cities, in addition to the fact that buildings consume a large proportion of the energy (75% of the energy demand in 2050).

In order to reduce global energy demand and achieve the carbon neutrality goal, one possibility is to decarbonize energy production through the development of renewable energies and the increase of sustainable energy sources sharing in the energy mix. However, these renewable energies face many challenges, which are intermittency, difficulty of forecasting and variability in time and space, which could induce a mismatch between demand and production, which will lead to the need to resort to fossil fuels/national grid or storage solutions.

To limit storage solutions as well as the injection of renewable energies into the grid (which creates an adverse impact on it), local consumption of energy in micro-grids or self-consumption of the energy produced should be considered. Thus, the spatial dispersion of renewable energies can be an advantage as it can allow them to be exploited locally, thus limiting the losses that can be induced during their transportation and distribution (reduction of the electricity sent to the national grid). Among the renewable energies, solar energy has many advantages: 1) it has a strong potential, 2) is a mature and competitive technology and 3) allows buildings (which are the first source of energy consumption) to contribute to the production of renewable energy, thanks in particular to the unused space on the roof (and possibly also on façades). However, solar energy cannot cover alone the needs of the whole territory (for

© 2022. The Authors. Published by International Solar Energy Society
Selection and/or peer review under responsibility of Scientific Committee
doi:10.18086/eurosun.2022.15.02 Available at http://proceedings.ises.org

example at night or on cloudy days). It is therefore important to study the complementarity of solar energy with other energies such as wind or hydropower to meet the need at every moment and thus limit storage and the use of the grid.

Despite the fact that energy is mainly consumed in cities, rural mountainous areas are the best locations for energy harvesting, as it offers large space and resources (like biomass from agriculture and livestock). These territories are isolated with less developed electricity networks, thus need autonomy and energy security but have quite strong environmental constraints (temperature, reflection, masks due to relief).

It could thus be interesting to study the possibility for these territories to be electrically or energetically self-sufficient, given their high potential and low energy intensity (compared to cities), with a view to limit energy transportation. Thus, we need to be able to estimate solar energy accurately in time and space, for each building and considering particular challenge of rural area as local climate, topography and also climate change.

This paper presents the whole framework (workflow, data, case studies) that will be employed to deal with all the above problems. The paper will be structured as followed: the section 2 will present an overview of the literature that helps us to define the methodology, the section 3 will present preliminary results that justify the study that will be conducted, the section 4 will present the framework of our work (including the methodology and the case studies that will be used thereafter).

2. State of the art

In order to determine the adequation between the demand and the production at the scale of a mountainous territory, it is necessary to determine solar potential for this place. The estimation of the solar potential has been widely discussed in the literature. However, the main works focus on estimating the solar potential at an urban scale (Barrag et al., 2019; Brito et al., 2012; Lobaccaro et al., 2019; Redweik et al., 2013). There are also many works relating to the estimation of solar potential at large scale: solar potential have been evaluated for Spain in (Izquierdo et al., 2008) through the use of statistical sampling, for Mexico in (Rosas-Flores et al., 2019) by estimating the number of panels possible to be installed by household with the methodology of peak sun hour, in Switzerland (Assouline et al., 2017, 2018) with machine learning approach or also in large region (Bergamasco & Asinari, 2011; Kodysh et al., 2013).

However, only few studies investigate solar potential in rural areas. For instance, in (Notzon et al., 2021), the study concerns buildings located in the Alps, researching for the self-consumption suitability of solar panels while considering the presence of snow and particular demand. Finally, two publications concern small villages in Switzerland. (Mavromatidis et al., 2015) study the village of Zernez, calculate the solar potential while considering the surrounding topography, use Swiss norms to define typical electrical profile in order to model the demand, and use the concept of Energy Hub which allows them to be linked to grid modelling and storage. The location of the photovoltaic systems to be installed is then optimized to limit costs while maximising the share of renewable energy. Similarly, (Mohajeri et al., 2019) study the village of Hemberg, develop a new workflow combining several modelling tools (ArcGIS, QGIS, CitySim, Homer, Meteonorm), which allow them to evaluate different strategies for sustainable development of the village. Indeed, it models heating and cooling demand, solar and wind potential considering future typical weather files and evaluate the influence of retrofitting and expansion of the village. Thus, it can be seen that there is a lack of study concerning rural and mountainous territories that must be filled.

The estimation of solar potential is a harsh task that needs to be handled with the numerical tools appropriate in term of both spatial and temporal scales. Several software could be used to study solar potential but Grasshopper environment with Ladybug plugin has been often used recently (with Honeybee for energy demand simulation) (Evola et al., 2020; Freitas et al., 2020; Hoseinzadeh et al., 2021; Notzon et al., 2021; Xu et al., 2021). In particular, the workflow developed by (Naboni et al., 2019) has drawn our attention: the workflow developed uses the software Rhinoceros and the Grasshopper environment and combines several plugins (Ladybug, Honeybee, Dragonfly, Butterfly) which allows to take many aspects into account (solar potential, energy demand, urban microclimate, climate change, fluid dynamic). Grasshopper is a python-based plugin, which allows to conduct parametric studies and can also be found in CitySim software (Peronato et al., 2017). These works have allowed us to define the numerical tools that will be used in the workflow.

Modelling building energy demand has been also widely discussed in the literature and lots of different methodologies could be employed, which depend mainly on the data availability and the objectives of the modelling. Building energy modelling could be classified into top-down (aggregated data (socio-econometric and technological indicators and building energy use)) and bottom-up approaches (disaggregated data)(Hu et al., 2021; Torabi Moghadam et al., 2017). Bottom-up approaches can also be classified into sub-categories : physics-based model

(analytical model, implemented in energy building modelling software), data-driven model (based on machine learning algorithms) and hybrid model (Wong et al., 2021). However, all these different methodologies are applied to case studies where lots of data are available (like energy consumptions per building, wall materials, year of construction). Top-down models could be the most suitable in our study, as it uses statistics and can deal with the lack of data.

After having estimated the solar potential and the energy demand, it is important to analyze this solar potential to encourage the deployment of solar systems. As the transportation of electricity induces energy losses, it is important to see if the energy produced could be used at local scale. Therefore, recent studies are focusing on the study of the matching of demand and production. It can be done at building scale for Net Zero Energy Buildings (Lund et al., 2011), including wind energy or storage (Cao et al., 2013). It can also be done at a larger scale, using TABULA and ISTAT database in order to model the energy demand and then finding the best locations for solar panels (Groppi et al., 2018), considering the evolution of the demand with prospective scenario (Groppi et al., 2018) or at a national scale (Al-Ghussain et al., 2021). Some studies also employed indicators as for example self-consumption rate (share of the electricity generated by the PV system that is consumed by the buildings where the panels are located), the self-sufficiency rate defines as the percentage of electricity demand that could be supplied by the PV systems or ramp rates (sudden variations of power due to the infection of electricity on the grid) to optimize the part of solar potential that will be transformed in electricity through PV panels (Freitas et al., 2018; Thebault and Gaillard, 2021).

3. Preliminary results

The first study carried out consisted in showing the interest of studying mountainous territories. For this, data collected in a previous study were used. The available data concern the territory of the Greater Geneva (Thebault et al., 2022). It contains the annual electrical consumption, the ground surface, the maximum installable solar panels surface, the electrical energy potentially producible in one year, the maximum peak power installable and the self-consumable energy per building. For each building in the Greater Geneva area, the altitude has been found by using a Digital Elevation Model DEM) in QGIS software. The DEM used was made under the framework of the Copernicus program and available for the European continent. As the goal is to study the influence of altitude, data concerning Geneva were removed by keeping only data were the altitude is above 470 m (the maximum altitude of Geneva is 463 m).

Two indicators were defined for this study:

- Annual PV system energy potential production (kWh/m²/y) divided by annual electric consumption (kWh/m²/y). It is an indicator providing some insight on the self-sufficiency potential, which allows to see if a building could, theoretically (on a yearly basis), produce enough electricity to match its consumption. Of course, without any electrical storage solution, this indicator is not an actual self-sufficiency indicator.
- Annual PV system energy potential production (kWh/m²/y) divided by ground surface (m²). It allows to assess the usable roof surface compared to the building footprint.

These two indicators have been plotted against altitude (Fig. 1 and 2). It appears that as altitude increases, the energy situation is different from that in the plain which requires a specific attention. On Fig. 1, it seems that the ratio between the energy that can be produced by solar systems and the energy consumed per building is getting higher when the altitude increases. Thus, the match between consumption and production is increasing with the altitude on an annual basis. It can be explained by the fact that when the altitude increases, the territory become more rural. There are more houses with garden than apartment blocks. Buildings are therefore less impacted by overshadowing and self-shadowing effect. It can also be assumed that, with increasing altitude, there is less impact of far shadow caused by mountains (mask effect). However, attention should be paid because only the electric consumption is available. It could be possible that the share of housing in mountainous areas where heating is provided by biomass, gas or oil boilers is greater than in urban areas.

Similarly, on the Fig. 2, it appears that the ratio between the energy that can be produced by PV systems and the ground surface is increasing with altitude. Thus, the energy that can be produced by one building should be more important if this building is located in a mountainous area rather than in the plain. It could also be explained by shadowing effect of neighboring buildings and mask effect. It could also be explained by the fact that apartment blocks have a smaller share of roof surface compared to houses (and in addition, these roofs are also used for facilities, like HVAC equipment (heating, ventilation and air-conditioning)). Thus the electricity produced by solar systems is reduced due to the smallest surface of panels.

The majority of the housing stock that will be present in 2050 is already built. The main actions to be implemented to control the consumption of buildings are the renovation of these buildings and installation of solar systems to increase the production of renewable energy (and reach the carbon neutrality). It is therefore important to study the buildings already present on the territory.

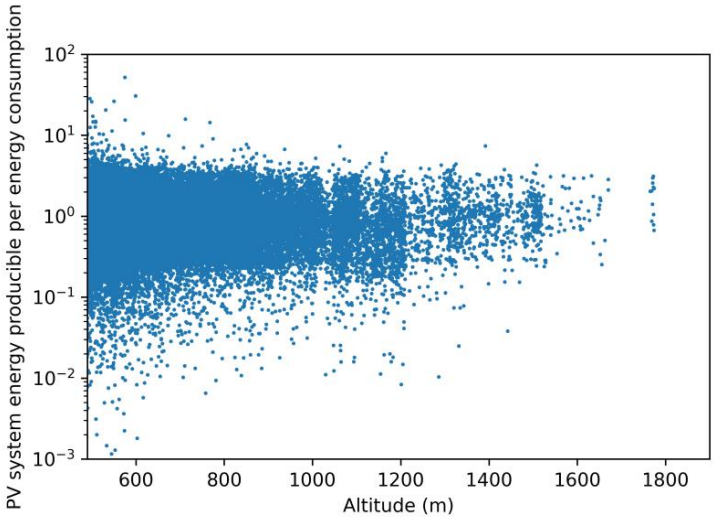

Fig. 1: Energy producible by solar systems divided by energy consumption according to altitude, per building (of the greater Geneva area)

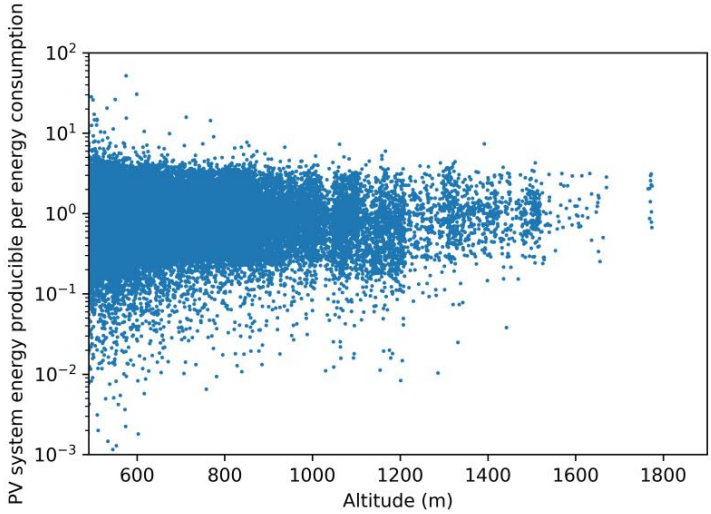

Fig. 2: Energy producible by solar systems divided by ground surface according to altitude, per building (of the greater Geneva area)

4. Framework

4.1 Methodology

After having investigated the actual literature background about solar modelling and renewable energy matching with demand in rural area and see that mountainous buildings present a good potential to harness solar energy, we present a working environment combining several software/plugins in order to study the solar potential (Fig.3). One possible combination could be the use of Rhinoceros for the 3D modelling of the study case and the use of the Grasshopper environment to compute parametric study. In Grasshopper, the plugins employed would be Ladybug for the estimation of the PV generation potential, Honeybee to simulate the energy demand, Dragonfly and Butterfly to consider the climatic specificities of the studied region (UWG, fluid dynamics, heat island effect). Meteonorm and QGIS/ArcGIS will also be used respectively to obtain climate data and mapping building in an appropriate model for solar analysis.

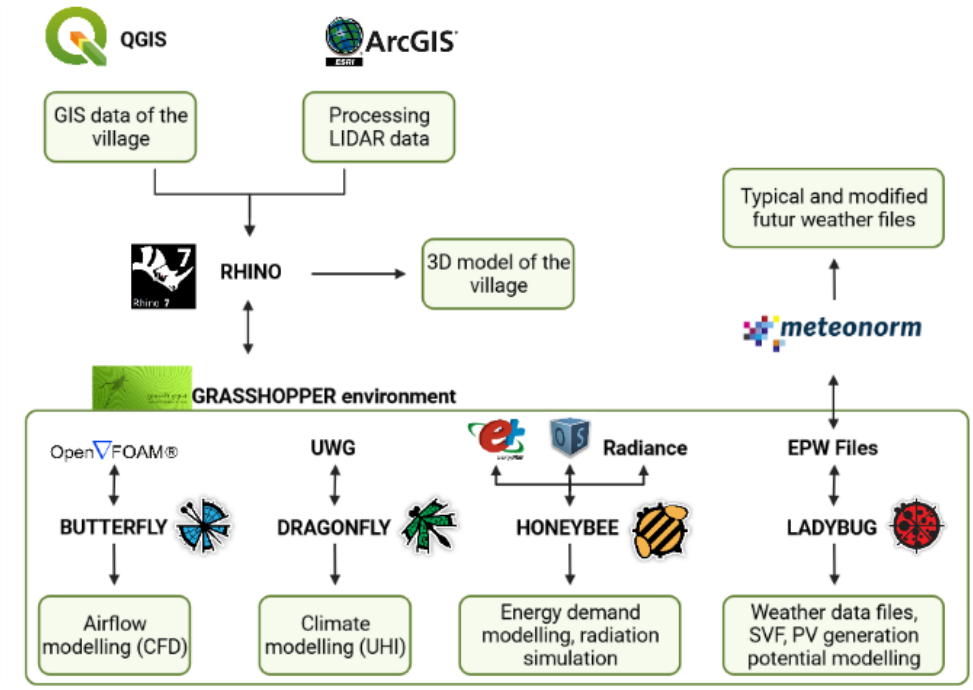

Fig. 3: Proposed workflow that will be implemented in the study

Before selecting the appropriate workflow to conduct our study using a multi-scale approach, several tools will be compared that are available for solar potential modelling including ArcGis using the Solar Analyst or CitySim software (which also offer the possibility of parametric modelling with a Python plugin and Grasshopper plugin).

Our approach, presented in the workflow in Fig. 3, is intended to be multi-scale, focusing at the same time on production and consumption at individual house level but also at the scale of the municipality. Indeed, the individual level is important to be precise in the modelling of solar potential and energy building consumption and the larger scale will allow to see if aggregation of the demand and the production could improve the matching between demand and supply. The selected software are relevant to answer this question as Rhinoceros coupled with Grasshopper plugins (Ladybug and Honeybee) could be used to study the scale of the neighborhood, like houses in the center of the selected rural village, and ArcGIS and Solar Analyst module could be used at a larger scale like the whole area.

The study of the solar potential will be focused on urban/rural territory, and more particularly on the specificities of a mountainous area. There will be a need to consider the topography (mask effect of the surrounding mountain), the local climate (specific climatic data of the area, effect of the wind in a valley) and the presence of snow in the winter season. The influence of climate change on the solar potential will also be investigated through the use of future weather files (considering exceptional event like heat waves). As it will be explained in the next section, it is particularly challenging to model rural territories because very few data are available compared to cities.

The objective is to consider the solar potential in the energy mix at the scale of a village and its influence on the share of renewable energies in the electricity mix. Thus, the goal will be also to model the energy demand-considering the influence of local climate on the demand. Several methods will be experimented to model the demand: using historical data of the studied area, using typical electric profiles depending on the type of building and number of inhabitants or using simulation tools (like CitySim or Honeybee plugin of Rhinoceros) (or using statistical methods). For the first two methods, the modelling should predict future consumption profile according to climate evolution.

Finally, the self-consumption and self-sufficiency at the scale of the village will be studied. The maximization of the self-consumption (maximization of the dynamic response of production to demand), limitation of storage options and minimization of the grid interactions could be possible through the optimization of the location of photovoltaic installations. The potential of other renewable energies, as for example wind energy with CFD studies, could be potentially investigated.

4.2 Case studies

The small town of Le Grand Bornand (Fig. 4 (a)) has been selected as a case study because this city, located in the French Alps (Fig. 4 (b)), is part of the project "Grand [La]Bo", in progress between the University of Savoie Mont Blanc and the territory of Le Grand Bornand and its actors. This project aims at investigating the impact of the town on its surrounding, on three themes: agriculture, tourism, and local community life (which includes energy, waste, air and water quality). The project wishes to carry out a transdisciplinary territorial diagnosis with the aim of having a sustainable trajectory (development of soft tourism for example), while keeping a sustainable economic model for the station and raising the awareness of political actors on these issues. The village faces particular stakes, as it wants to keep the image of a traditional mountainous village but become an attractive place for tourism with its ski station during winter (and summer).

However, very few data are available for this area. Actually, as the energy consumption is localized mainly in the city, rural areas are not much under studies, and the only data available is the village cadaster. Thus, it is not possible to have access to building geometry data, to population distribution, or even to building's height or year of construction, which are the data used by most of the methodology to estimate solar potential and building consumption. Currently, the National Institute of Geographic and Forest Information (IGN) is conducting a campaign to acquire high-density LiDAR data over the entire French metropolitan territory in order to offer the finest 3D description ever established on the scale of the entire country. The campaign has started this year and the first LiDAR tiles are publicly available. However, the selected area has not been yet recorded. In France, access to data is not easy also because of the privacy legislation, especially for residential building consumptions, that are measured but not publicly available. Concerning meteorological data, the weather stations are often located close to big cities, at airport for example. As urban weather generators are employed to correct these measures and make them correspond to the reality, the suitability of using these measures for rural areas must be verified. The lack of data is a real problem in our case study, it will be explained below how to deal with this issue.

For these reasons, as a first step an initial study will be carried out on a village of mid-mountains areas close to Le-Grand-Bornand but located in conurbation of the Greater Geneva where much more data are available. This first study will allow to become familiar with the tools that will be employed and understand the various problems that could be encountered during the use. The first step of the work will be to study the influence of the mountainous location, mainly through the topography and the temperature, compared to plain location. A particular attention will be put on the meteorological data.

In the long run, the goal will be to compare the results obtained with those of another small city in the Pyrenees in the Spanish part, as the topography would be similar. It would allow to see the impact of the climate and local specificities, like urban morphologies or building typologies. However, the methodology employed to study the area could change if the availability, the format, or spatial or temporal accuracy of data are different.

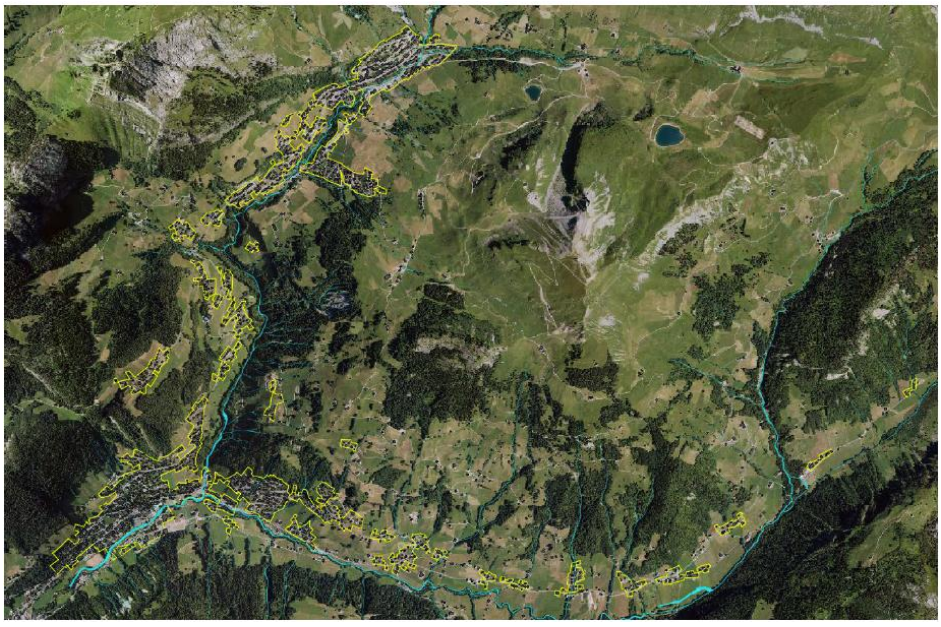

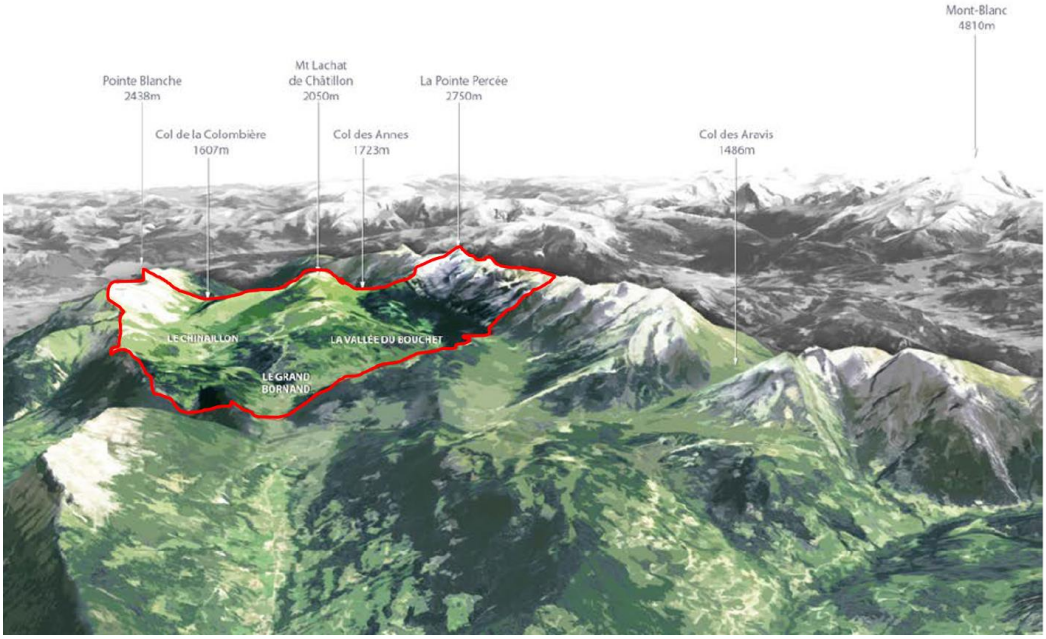

Fig. 4: Urban envelope of the village (a) and aerial view of the municipal territory (b) of Le Grand-Bornand (P.L.U. Le Grand Bornand)

5. Conclusion

In the present paper, it has been shown that there is a lack of studies concerning the modelling of solar energy and building energy consumption in mountainous territories. Moreover, it has been shown that the buildings in these areas present specific energetic situation. As these territories are isolated, it is relevant to study them and see if they could be self-sufficient (to avoid the transportation of energy). A workflow has been presented, which combines several numerical tools in order to study the solar potential in a mountainous area and the methodology that will be conducted. The territories that will be investigated are presented.

6. Acknowledgments

Our acknowledgments to European university UNITA for supporting this research. The project has also been supported by the Grand [La]Bo project, the Graduate school Solar Academy (ref. ANR-18-EURE-0016 – Solar Academy), and the CITEE French-swiss Chair.

7. References

Al-Ghussain, L., Abubaker, A. M., & Darwish Ahmad, A. (2021). Superposition of Renewable-Energy Supply from Multiple Sites Maximizes Demand-Matching: Towards 100% Renewable Grids in 2050. Applied Energy, 284(December 2020), 116402. https://doi.org/10.1016/j.apenergy.2020.116402

Assouline, D., Mohajeri, N., & Scartezzini, J. L. (2017). Quantifying rooftop photovoltaic solar energy potential: A machine learning approach. Solar Energy, 141, 278–296. https://doi.org/10.1016/j.solener.2016.11.045

Assouline, D., Mohajeri, N., & Scartezzini, J. L. (2018). Large-scale rooftop solar photovoltaic technical potential estimation using Random Forests. Applied Energy, 217(February), 189–211. https://doi.org/10.1016/j.apenergy.2018.02.118

Barrag, E. A., Zambrano-asanza, S., Zalamea-le, E. F., & Parra-gonz, A. (2019). Urban photovoltaic potential estimation based on architectural conditions , production-demand matching , storage and the incorporation of new eco-ef fi cient loads. 142, 224–238. https://doi.org/10.1016/j.renene.2019.03.105

Bergamasco, L., & Asinari, P. (2011). Scalable methodology for the photovoltaic solar energy potential assessment based on available roof surface area: Application to Piedmont Region (Italy). Solar Energy, 85(5), 1041–1055. https://doi.org/10.1016/j.solener.2011.02.022

Brito, M. C., Gomes, N., Santos, T., & Tenedório, J. A. (2012). Photovoltaic potential in a Lisbon suburb using LiDAR data. Solar Energy, 86(1), 283–288. https://doi.org/10.1016/j.solener.2011.09.031

Cao, S., Hasan, A., & Sirén, K. (2013). Analysis and solution for renewable energy load matching for a single-family house. Energy and Buildings, 65, 398–411. https://doi.org/10.1016/j.enbuild.2013.06.013

Evola, G., Costanzo, V., Magrì, C., Margani, G., Marletta, L., & Naboni, E. (2020). Energy & Buildings A novel comprehensive workflow for modelling outdoor thermal comfort and energy demand in urban canyons : Results and critical issues. Energy & Buildings, 216, 109946. https://doi.org/10.1016/j.enbuild.2020.109946

Freitas, J. de S., Cronemberger, J., Soares, R. M., & Amorim, C. N. D. (2020). Modeling and assessing BIPV envelopes using parametric Rhinoceros plugins Grasshopper and Ladybug. Renewable Energy, 160, 1468–1479. https://doi.org/10.1016/j.renene.2020.05.137

Groppi, D., de Santoli, L., Cumo, F., & Astiaso Garcia, D. (2018). A GIS-based model to assess buildings energy consumption and usable solar energy potential in urban areas. Sustainable Cities and Society, 40, 546–558. https://doi.org/10.1016/j.scs.2018.05.005

Hoseinzadeh, P., Khalaji, M., Heidari, S., Khalatbari, M., Saidur, R., Haghighat, K., & Sangin, H. (2021). Energy & Buildings Energy performance of building integrated photovoltaic high-rise building : Case study , Tehran , Iran. Energy & Buildings, 235, 110707. https://doi.org/10.1016/j.enbuild.2020.110707

Izquierdo, S., Rodrigues, M., & Fueyo, N. (2008). A method for estimating the geographical distribution of the available roof surface area for large-scale photovoltaic energy-potential evaluations. Solar Energy, 82(10), 929–939. https://doi.org/10.1016/j.solener.2008.03.007

Kodysh, J. B., Omitaomu, O. A., Bhaduri, B. L., & Neish, B. S. (2013). Methodology for estimating solar potential on multiple building rooftops for photovoltaic systems. Sustainable Cities and Society, 8, 31–41. https://doi.org/10.1016/j.scs.2013.01.002

Lobaccaro, G., Croce, S., Lindkvist, C., Munari Probst, M. C., Scognamiglio, A., Dahlberg, J., Lundgren, M., & Wall, M. (2019). A cross-country perspective on solar energy in urban planning: Lessons learned from international case studies. Renewable and Sustainable Energy Reviews, 108, 209–237. https://doi.org/10.1016/j.rser.2019.03.041

Lund, H., Marszal, A., & Heiselberg, P. (2011). Zero energy buildings and mismatch compensation factors. Energy and Buildings, 43(7), 1646–1654. https://doi.org/10.1016/j.enbuild.2011.03.006

Mavromatidis, G., Orehounig, K., & Carmeliet, J. (2015). Evaluation of photovoltaic integration potential in a village. Solar Energy, 121, 152–168. https://doi.org/10.1016/j.solener.2015.03.044

Mohajeri, N., Perera, A. T. D., Coccolo, S., Mosca, L., Le Guen, M., & Scartezzini, J. L. (2019). Integrating urban form and distributed energy systems: Assessment of sustainable development scenarios for a Swiss village to 2050. Renewable Energy, 143, 810–826. https://doi.org/10.1016/j.renene.2019.05.033

Naboni, E., Natanian, J., Brizzi, G., Florio, P., Chokhachian, A., Galanos, T., & Rastogi, P. (2019). A digital workflow to quantify regenerative urban design in the context of a changing climate. Renewable and Sustainable Energy Reviews, 113(June). https://doi.org/10.1016/j.rser.2019.109255

Notzon, D., Florio, P., & Schüler, A. (2021). Solar energy potential at the Great St Bernard Pass. Journal of Physics: Conference Series, 2042(1). https://doi.org/10.1088/1742-6596/2042/1/012104

Peronato, G., Kämpf, J. H., Rey, E., & Andersen, M. (2017). Integrating urban energy simulation in a parametric environment: A Grasshopper interface for CitySim. Proceedings of 33rd PLEA International Conference: Design to Thrive, PLEA 2017, 2(2009), 2124–2131.

Redweik, P., Catita, C., & Brito, M. (2013). Solar energy potential on roofs and facades in an urban landscape. Solar Energy, 97, 332–341. https://doi.org/10.1016/j.solener.2013.08.036

Rosas-Flores, J. A., Zenón-Olvera, E., & Gálvez, D. M. (2019). Potential energy saving in urban and rural households of Mexico with solar photovoltaic systems using geographical information system. Renewable and Sustainable Energy Reviews, 116. https://doi.org/10.1016/j.rser.2019.109412

Xu, S., Jiang, H., Xiong, F., Zhang, C., Xie, M., & Li, Z. (2021). Evaluation for block-scale solar energy potential of industrial block and optimization of application strategies : A case study of Wuhan , China. Sustainable Cities and Society, 72(March), 103000. https://doi.org/10.1016/j.scs.2021.103000

A Comparative Study on One-month Solar Radiation Datasets for Photovoltaic Energy Analysis in Trondheim

Mattia Manni[1], Alessandro Nocente[2], Kristian Stenerud Skeie[2], Martin Bellmann[2] and Gabriele Lobaccaro[1]

[1] Department of Civil and Environmental Engineering, Norwegian University of Science and Technology (NTNU), Trondheim (Norway)

[2] SINTEF AS, Trondheim (Norway)

Abstract

This study presents a comparative study on one-month solar radiation datasets for solar energy analysis in Trondheim. Such datasets differ among the sources (i.e., satellite observations, reanalysis, weather stations), the radiative parameters (i.e., global horizontal irradiance, diffuse horizontal irradiance, and direct normal irradiance), and the time resolutions (i.e., one-minute, one-hour). The plane of array irradiance amounts impinging on a photovoltaic panel are determined through the decomposition and transposition models implemented in the pvlib-python tool or measured with a pyranometer oriented as the photovoltaic panels. Then, the photovoltaic energy production is quantified and validated against experimental data and the accuracy of the estimation is evaluated with the Mean Biased Error (MBE) and the Root Mean Squared Error (RMSE). Data about photovoltaic energy generation are collected from the Zero Emission Building (ZEB) Test Cell Laboratory, in Trondheim (Norway). The main research goal is to determine which dataset can better estimate photovoltaic energy production in the chosen location. Datasets providing direct measures of the plane of array irradiance or direct normal and diffuse horizontal irradiance amounts allow to reduce the length of the model chain. In particular, the dataset with the hourly plane of array irradiance observations from the ZEB Test Cell Laboratory permits quantifying the hourly energy generation from photovoltaics with the highest accuracy (MBE is 3.97 Wh, RMSE is 45.60 Wh). The results demonstrated how the datasets based on observations are more accurate than the datasets based on satellite imaging or numerical reanalysis.

Keywords: Photovoltaic, Solar energy, Simulations, Monitoring, High latitudes.

1. Introduction

In the era of the energy transition towards a low-carbon society, it is necessary, among the others, to boost the exploitation of renewable energy sources (RES), to improve the energy efficiency of building stock towards energy positive districts, and to promote sustainable development actions (e.g., decarbonisation, greenification). In that regard, the deployment of RES and high energy efficiency measures can potentially contribute to 90% of the required greenhouse gas emissions (GHG) reductions (International Renewable Energy Agency, 2022).

The solar and wind energy represent the main drivers of the low-carbon energy transition. In particular, the solar photovoltaic (PV) showed the highest growth rate (average annual increase of 36% in the past 30 years) among the RES (International Energy Agency, 2021a). PV is expected to account for 13% of the power production by 2030 compared with the current 1.7% (International Renewable Energy Agency, 2022), and to cover up to 33% of the total global energy needs by 2050 (International Energy Agency, 2021b).

Within this framework, new opportunities for solar energy production are actively investigated in Norway to counterbalance the growing energy demand which is currently satisfied by hydropower and wind power. In Norway, the solar energy showed the greatest growth throughout the last five years and the installed solar power has increased from 3 MW (2015) to 140 MW (2020) (Fig. 1) (Energy Facts Norway, 2021). The misconception that the level of irradiation is much lower in the Nordics than in the Continental Europe partially contributed to such a delay in the exploitation of solar energy (Formolli et al., 2021). However, there are some advantages in installing PV systems at high latitudes like the high efficiency due to the low temperatures and the significant

© 2022. The Authors. Published by International Solar Energy Society
Selection and/or peer review under responsibility of Scientific Committee
doi:10.18086/eurosun.2022.15.03 Available at http://proceedings.ises.org

amount of solar energy which is reflected by the snow covering the ground (Dubey et al., 2013).

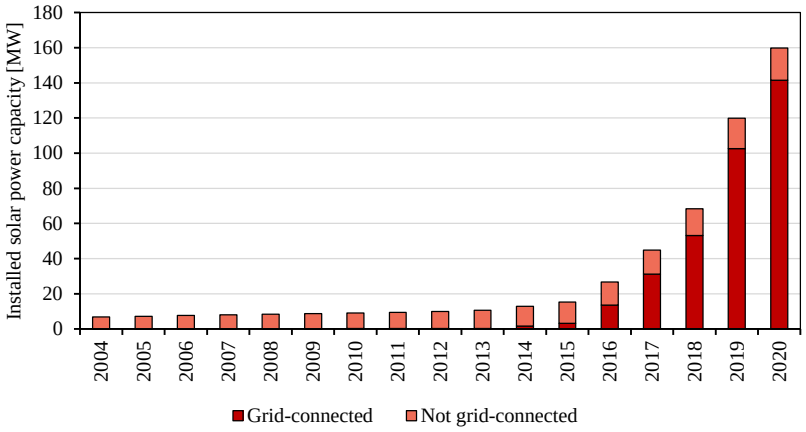

Fig 1: Development in installed capacity for solar power in Norway (Energy Facts Norway, 2021).

To boost more the solar energy penetration in Norway, it is necessary to design highly effective PV and to implement a model chain to accurately simulate their energy generation. Although the high number of overcast days (particularly in the wintertime) makes difficult to estimate the global irradiation impinging on PV, recent advancements in solar irradiance model chain enables more precise calculations methods (Yang, 2022). Decomposition models exploiting one-minute radiation datasets have been implemented to evaluate instantaneous effects such as the cloud and albedo enhancement, while some hourly transposition models appear to be equally applicable to one-minute data (Gueymard, 2017).

The present study focuses on the investigation of the influence of different solar radiation datasets on PV energy simulation. One-month solar radiation datasets for Trondheim location are retrieved from various sources (i.e., satellite observations, weather station) and then used as input parameters in the pvlib-python package (Holmgren et al., 2018) to estimate the plane of array irradiance (POA). The comparative analysis of the results against experimental data permits to preliminary identify the most adequate datasets to be used in PV energy analysis. In this context, this study is part of a wider research which aims at developing a model chain for prediction of energy generation from PV to be applied to high latitudes.

The paper is structured as follows: the section of materials and methods (section 2) defines the workflow, the exploited datasets, the tools, the accuracy indicators, and the case study; the section of results and discussion (section 3) provides an overview of the outcomes, discuss the PV analysis capability of the datasets, and outlines the study limitations. The study concludes with a summary of the most relevant findings and the implications for future advancements in model chain development and application at high latitudes (section 4).

2. Materials and methods

2.1. Workflow

The workflow is structured in four steps: (i) decomposition modelling, (ii) transposition modelling, (iii) PV energy assessment, and (iv) experimental validation (Fig. 2). In the first step, the global horizontal irradiation (GHI) is input to quantify the diffuse horizontal irradiation (DHI) and the direct normal irradiation (DNI) as outputs. The DNI and the DHI are considered as inputs in the second step. In the second step, the DHI and DNI are transposed from the horizontal plane to a tilted surface, and the POA is calculated. The tilted surface is defined according to the geometry properties of the PV panel (i.e., tilt angle, azimuth angle). Then, the amounts of POA are used to estimate PV energy generation. Finally, the modelled PV energy generation is validated against experimental data from the Zero Emission Building (ZEB) Test Cell Laboratory located at the Norwegian University of Science and Technology (NTNU) Gløshaugen Campus in Trondheim, Norway (Latitude 63.4305° N).

The model chain described in the workflow is flexible and its length (i.e., the number of steps) can change depending on the input. For example, if a dataset providing the DNI and DHI values is selected, the step about decomposition modelling is skipped, and the model chain is shortened. Thus, the full-length model chain starts

from step one and it includes decomposition, transposition, and energy modelling, while the shortest possible model chain has POA as input and it starts from step three.

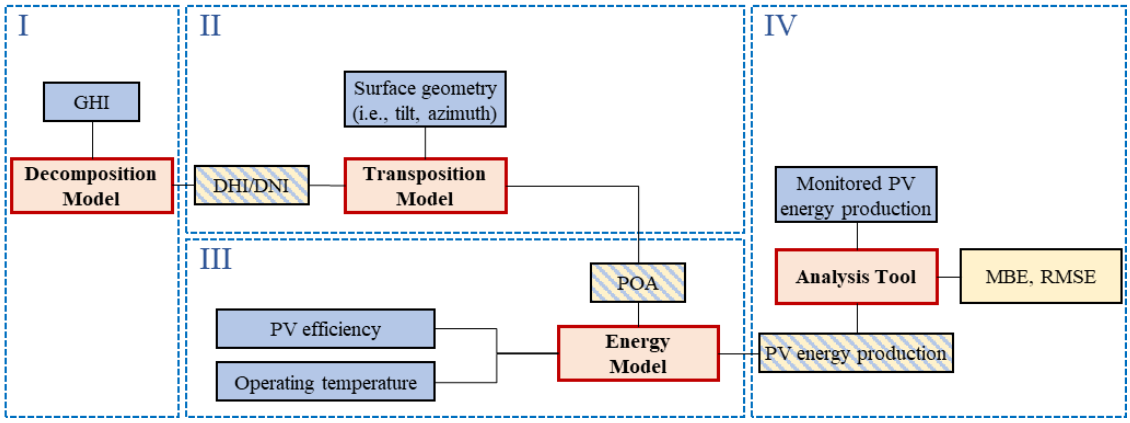

Fig. 2: Overview of the workflow followed in this study. The workflow is structured in four steps: (i) decomposition modelling, (ii) transposition modelling, (iii) PV energy assessment, and (iv) experimental validation.

2.2. Datasets

Weather datasets used in this work refer to Trondheim. The climate of Trondheim is classified as continental subartic climate (Dfc) in Köppen Geiger classification (Fig. 3) and it is moderately continental, with cold winters and mild summers. The analyses are carried out for the month of October 2021. The selected one-month datasets are characterized by a time resolution ranging from one minute to one hour depending on the source.

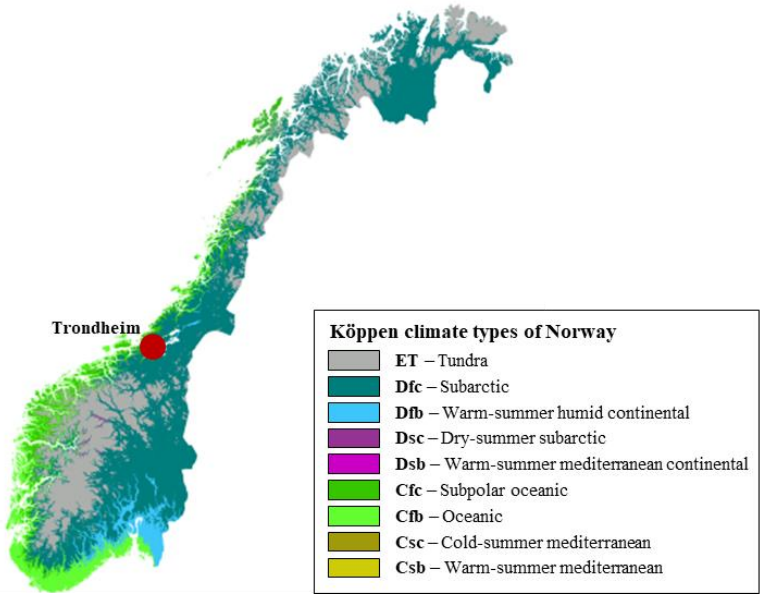

Fig. 3: The Köppen climate classification. Modified from "Köppen climate types of Norway" by Adam Peterson.

An overview of the used datasets and their principal properties (i.e., data type, time resolution, spatial resolution, parameters) is presented in Tab. 1. The month of October has been selected to assess the viability of the datasets to estimate the PV generation outputs during days characterized by overcast sky conditions. Before calculating the accuracy indicators (see sub-section 2.4), the datasets are resampled hourly, daily, and monthly.

Among the datasets provided by the European Centre for Medium-Range Weather Forecasts (ECMWF), the 5th generation of numerical reanalysis (ERA5-Land) is selected. ERA5-Land consists of a version of ERA5 which is specifically developed for land applications. According to the different field of applications, the spatial resolution of ERA5-Land (9 km) is greater than the one of ERA5 (around 30 km). Data cover a time horizon ranging from January 1950 to present, and concern the main variables related to temperature, lakes, snow, soil water, radiation and heat, evaporation, wind, pressure, and precipitation. The variables retrieved from the Copernicus Climate

Data Store for the time domain of this work (October 2021) are the surface solar radiation downwards (corresponding to the global horizontal irradiation), both the temperature and the dewpoint temperature at two meters from the ground, and the surface pressure. In particular, the accumulated radiation values of ERA5-Land are transformed to hourly values by subtracting the previous values within each forecast horizon.

Tab. 1: Characteristics of the datasets used in this study.

Data source	Data type	Timestep	Spatial resolution	Parameters
ERA5-land	Reanalysis	1 hour	9 km	GHI
CAMS	Satellite data	1 minute	3-5 km	DHI, DNI, GHI
Sentralbygg	Monitored data	1 minute	point	DHI, DNI, GHI
Test Cell Lab	Monitored data	5 minutes	point	GHI
Test Cell Lab	Monitored data	1 hour	point	GTI
Test Cell Lab	Monitored data	1 hour	point	PV energy generation

The Copernicus Atmosphere Monitoring Service (CAMS) Solar Radiation service combines output from the CAMS global forecast system on aerosol and ozone with detailed cloud information directly from geostationary satellites. The CAMS Solar Radiation service provides, among the others, historical values (2004 to present) of GHI, DHI, and DNI (both overcast and clear sky conditions) with a time resolution of 1 minute. Such irradiance parameters were retrieved for October 2021.

Alongside reanalysis and satellite observation, the amounts of solar irradiance are also measured through sensors installed in various facilities at the NTNU Gløshaugen campus. In particular, the hourly values of GHI and POA are collected through two pyranometers installed on the rooftop of the Test Cell Lab, while the DHI and the DNI are measured through a sun tracker located at the top of the tower of the Sentralbygg. The sun tracker follows the sun path over the horizon to orient the pyrheliometer in the same direction of the sunrays as well as to keep in the shadow the pyranometer which measures the DHI. The system is completed by an unshaded pyranometer which monitors the GHI. Different time resolutions are associated to these datasets, ranging from 1 minute (DNI and DHI) to 1 hour (POA). The GHI values are recorded every 5 minutes.

Finally, the energy generation from the PV panels installed on the rooftop of the Test Cell Lab is monitored with a time resolution of 1 hour. This timeseries is compared to the simulated ones which result from the different solar irradiance datasets.

2.3. Tools

The PV energy generation output is calculated using the pvlib-python package, an open-source and community-supported tool that simulates the performance of PV systems. The tool allows managing the whole model chain from the irradiance decomposition to the transposition process, and to the PV energy simulation. In particular, pvlib-python includes methods like the Perez model that are well established for hourly irradiance decomposition methods, and some one-minute decomposition methods (Yang, 2022). These models differ for the accuracy and for the predictors which are needed to estimate the diffuse fraction. In this study, the Engerer4 model is exploited to decompose the GHI into DNI and DHI. The model has been implemented by Bright and Engerer (Bright and Engerer, 2019) who updated the Engerer2 model by recalculating the parameters with datasets from 75 different stations worldwide.

Regarding the transposition models, the Perez anisotropic model is used since is the one exploited almost universally in building performance simulation, although other options are available in the pvlib-python package (e.g., the isotropic model (Loutzenhiser et al., 2007), the Hay-Davies model (Hay, 1993), and the Reindl model (Reindl et al., 1990)). The Perez model splits the diffuse irradiance into different components (i.e., isotropic, circumsolar, horizontal brightening band) and then estimate the amount of irradiance achieving the PV modules. The solar position (i.e., solar azimuth, solar zenith, apparent solar time) is one of the Perez model's input parameters, and it is estimated with the ephemeris function from the pvlib-python package.

Finally, the POA is used to estimate the energy amount generated by the PV panels. The energy generated by PV

modules is calculated with a simple equation from the EN 15316- 4-3:2017 standard:

$$E_{el,out} = \frac{E_{sol,pv} \cdot P_{pk} \cdot f_{perf}}{I_{ref}}$$

where $E_{sol,pv}$ is the solar irradiation impinging on the system expressed in Wh/m^2, P_{pk} is the system peak power in kW at reference conditions (I_{ref}= 1 kW/m^2).

The system performance factor, f_{perf}, accounts for losses due to soiling (φ_{soil}) and temperature (φ_{temp}), as well as to the specific array's configuration (φ_{array}) and the inverter's efficiency (η_{inv}). It is calculated according to the Norwegian technical guideline SN-NSPEK 3031:

$$f_{perf} = IAM \cdot \left(1 - \frac{\varphi_{soil}}{100}\right) \cdot \left(1 - \frac{\varphi_{temp}}{100}\right) \cdot \left(1 - \frac{\varphi_{array}}{100}\right) \cdot \frac{\eta_{inv}}{100}$$

where IAM is the Incident Angle Modifier. The η_{inv} equals 96%, while the IAM, is defined based on the empirical values proposed in the standard for the Trondheim location and the selected months. In particular, the IAM is 0.96, the φ_{soil} ranges between 2% and 5%, and the φ_{array} is 5.5%. Finally, the φ_{temp} depends on the cell's temperature (T_{cell}), and it is estimated as:

$$\varphi_{temp} = \alpha_{temp} \cdot (T_{cell} - 25°C)$$

where α_{temp} is a temperature coefficient and equals 0.40% per Celsius degree.

2.4. Accuracy indicators for PV output timeseries and data quality filter

To compare the capability of the different solar radiation datasets to estimate PV energy generation with overcast sky conditions, the Mean Bias Error (MBE) and the Root Mean Square Error (RMSE) are used. The two coefficients are defined as it follows:

$$MBE = \frac{1}{N} \cdot \sum_{i=1}^{N} (\bar{x}_i - x_i)$$

$$RMSE = \sqrt{\frac{1}{N} \cdot \sum_{i=1}^{N} (\bar{x}_i - x_i)^2}$$

where the $\bar{x}_i$ and the x_i are the simulated and the measured photovoltaic energy generation amounts, respectively.

A data quality filter (DQF) is applied to the measurements by excluding periods where the solar elevation is lower than 5 degrees. In fact, when solar elevation is lower than 5 degrees, the incidence angle of the solar beams on the sensor is very high, and thus, it can result in less accurate measurements. Evaluation metrics are calculated before and after the DQF is applied.

2.5. Case study

The ZEB Test Cell Laboratory (Fig. 4) consists of a large- and full-scale test cell building facility used, among the others, for outdoor natural climate testing of building materials, components, building management strategies and structure elements. This research facility is equipped with three different PV panels which are integrated in the rooftop. The three PV panels are made, respectively, of monocrystalline, polycrystalline, and amorphous solar cells and their energy production is monitored with a one-hour time resolution. Data from the polycristalline silicon (poly-Si) modules are used in the experimental validation of the model chain implemented in this study. The polycrystalline silicon modules are the 260PE series from REC. Each module is 1.65 m^2 and has 60 cells and 3 bypass diodes. The rated power is 260 W_p per module and the rated efficiency is 15.8%. Four modules, with a total power of 1040 W_p, are installed on the roof with a tilt and an azimuth angles of 40° abd 180°, respectively. The three solar panels are connected to a micro-converter/inverter system from SolarEdge enabling each module to always operate at the best possible conditions. The benefit of the micro-converter system is to prevent the whole string output to be reduced if a single module is shaded.



Fig. 4: Test Cell Lab facility at NTNU Gløshaugen campus. Pictures from: www.sintef.no.

3. Results and discussion

3.1. PV simulation over different time resolutions

Outcomes from the model chain described in section 2 are reported in the scatter plots in the Fig. 5 and Fig. 6. In particular, the observed PV outputs are showed against the modelled PV outputs which derives from:

- POA measured in the Test Cell Lab (gti_tc),
- DNI and DHI monitored in the Sentralbygg (dni/dhi_sb),
- GHI recorded in the Test Cell Lab (ghi_tc),
- DNI and DHI retrieved from CAMS (dni/dhi_cams),
- GHI calculated by ERA5-Land (ghi_era).

It is worth to highlight that the whole dataset is considered in the graphs in Fig. 5, while only the values satisfying the DQF requirements are considered in the graphs in Fig. 6. Hence, the length of the datasets is reduced from 300 to 224 datapoints.

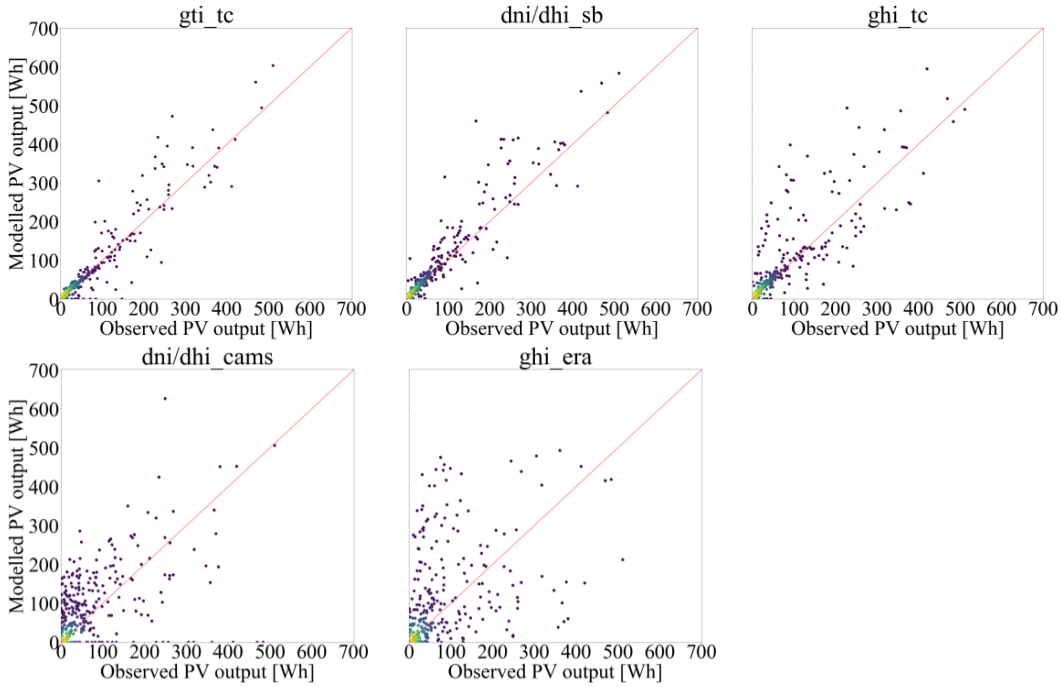

Fig. 5: Hourly observed PV energy production and modelled PV energy production during October 2021, before data quality filter. The yellow color indicates a high datapoint density, while the blue color represents a low datapoint density.

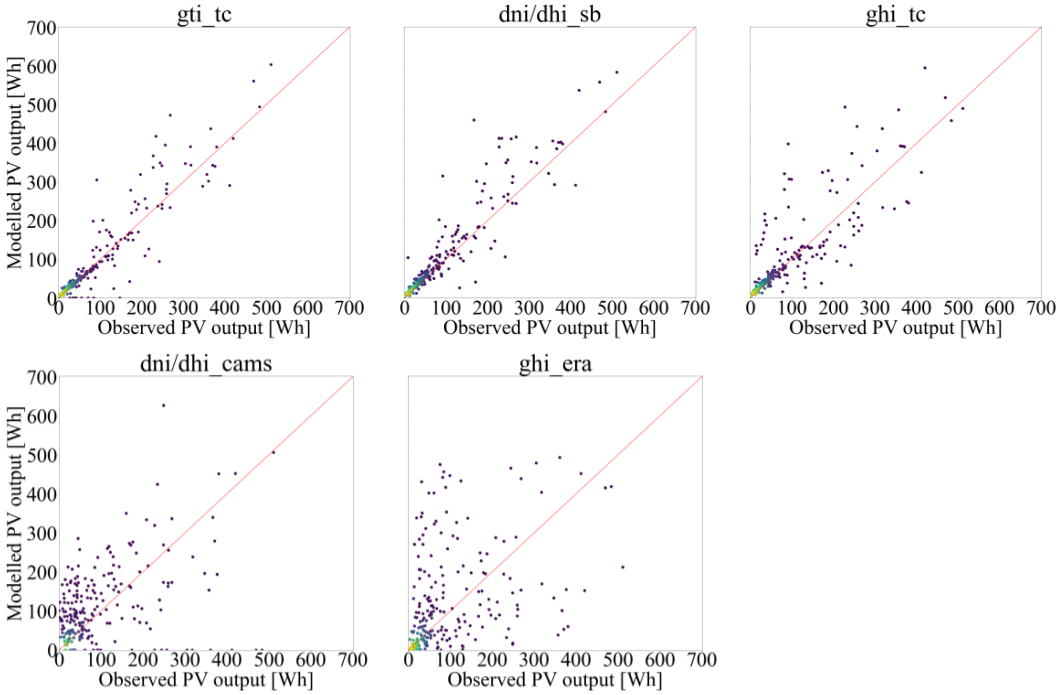

Fig. 6: Hourly observed PV energy production and modelled PV energy production during October 2021, after data quality filter. The yellow color indicates a high datapoint density, while the blue color represents a low datapoint density.

The plot of the results enables some preliminary considerations. Firstly, the monitored POA, DHI, and DNI values can estimate the energy generated by PV better than the others. Secondly, datasets from satellite observations are good as the datasets from Era5-Land reanalysis in PV simulation.

The accuracy indicators calculated for the five datasets confirmed such observations (Tab. 2). Before the DQF is applied, the model chain exploiting data of POA from the Test Cell Lab shows an MBE of 1.70 Wh and a RMSE of 25.50 Wh. These are the accuracy indicators corresponding to the best performance, while the worst results are obtained when satellite observations (MBE is 15.97 Wh, RMSE is 55.09 Wh) and numerical reanalysis are used (MBE is 11.95 Wh, RMSE is 83.50 Wh).

Tab. 2: Accuracy indicators calculated for the hourly datasets exploited in this study.

	gti_tc	**dni/dhi_sb**	**ghi_tc**	**dni/dhi_cams**	**ghi_era**
MBE [Wh]	1.70	5.70	6.26	15.97	11.95
RMSE [Wh]	25.50	28.96	42.10	55.09	83.50
MBE (DQF) [Wh]	3.97	16.61	12.87	37.48	23.71
RMSE (DQF) [Wh]	45.60	51.02	67.34	91.21	139.28

The application of the DQF leads to a general worsening of the PV simulation capability of the datasets. Although with a different magnitude, all the indicators are increased. In particular, the MBE calculated for the gti_tc is increased up to 3.97 Wh, while the RMSE is 45.60 Wh. The highest drop in the estimation performance is observed for dni/dhi_cams whose accuracy indicators are more than doubled (MBE is 37.48 Wh, RMSE is 91.21 Wh). Alongside these, the DNI and DHI values measured in the Sentralbygg (MBE is 16.61 Wh, RMSE is 51.02 Wh) calculated the PV energy generation better than the GHI values monitored in the Test Cell Lab (MBE is 12.87 Wh, RMSE is 67.34 Wh).

When it comes to the daily PV energy generation, the comparison between the measured values and the model outputs are reported in Fig. 7 and Fig. 8. It is worth to highlight that in this case the DQF causes the reduction of the observed amounts (i.e., amount of energy generated by the PV panel) and not the number of observations (i.e.,

number of recorded elements). As observed in the plots depicting the hourly values (see Fig. 5 and Fig. 6), the measured quantities better approximate the PV energy production.

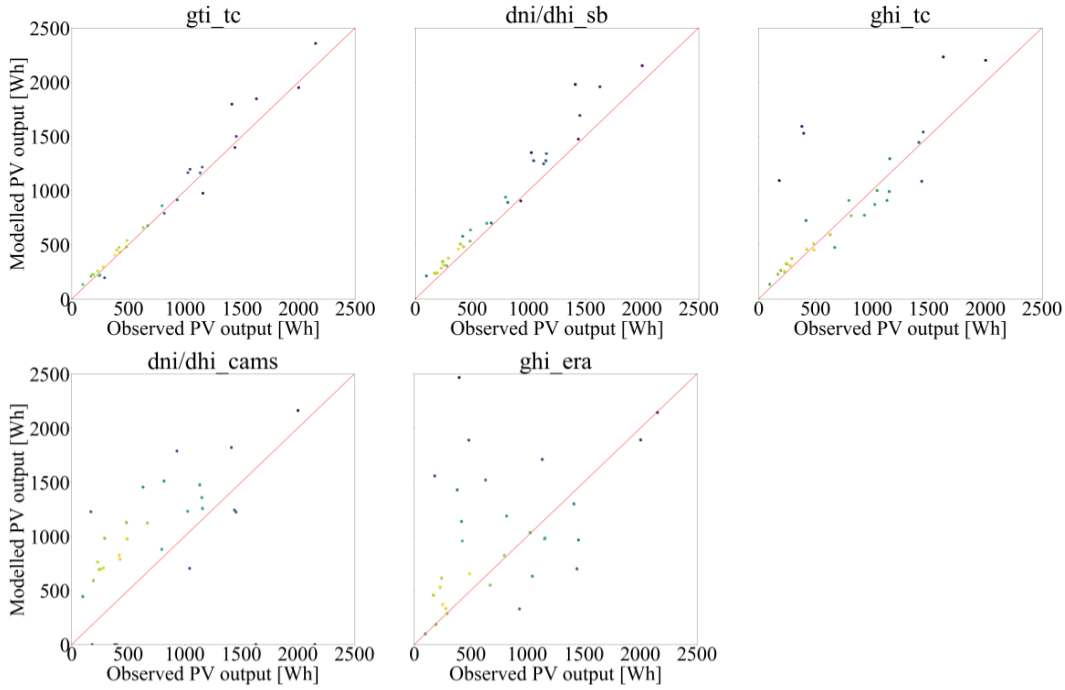

Fig. 7: Daily observed photovoltaic energy production and modelled photovoltaic energy production during October 2021, before the application of the data quality filter. The yellow color indicates a high datapoint density, while the blue color represents a low datapoint density.

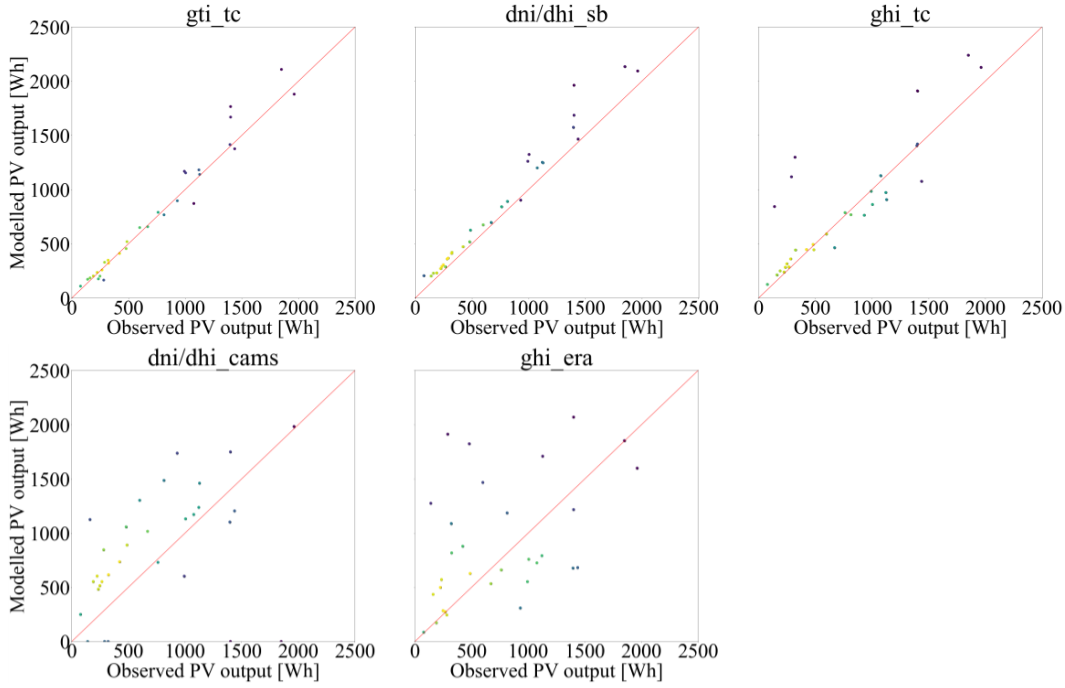

Fig. 8: Daily observed photovoltaic energy production and modelled photovoltaic energy production during October 2021, after the application of the data quality filter. The yellow color indicates a high datapoint density, while the blue color represents a low datapoint density.

The solar radiation datasets with POA amounts from the Test Cell Lab is the one with the lowest accuracy indicators (Tab. 3). In particular, the MBE of the gti_tc ranges from 40.77 Wh (before DQF) to 28.70 Wh (after DQF), while the RMSE is 107.58 Wh (before DQF) and 115.63 Wh (after DQF). Again, the worst performance

is observed for datasets derived from satellite observations and numerical analysis.

Tab. 3: Accuracy indicators calculated for the daily datasets exploited in this study.

	gti_tc	dni/dhi_sb	ghi_tc	dni/dhi_cams	ghi_era
MBE [Wh]	40.77	136.38	147.05	165.95	268.69
RMSE [Wh]	107.58	182.50	396.89	673.84	669.93
MBE (DQF) [Wh]	28.70	120.02	93.00	111.55	164.49
RMSE (DQF) [Wh]	115.63	166.29	306.37	577.11	592.72

Regarding the PV simulation over the whole month, the residues between the modelled and the monitored PV energy production values are presented (Table 4). Residues are expressed as a percentage, and they are defined as the difference between the model output and the observed value. The energy from the PV panel equals 23,954 Wh before the application of the DQF and 20,160 Wh after the DQF. The comparation of the residues confirm the gti_tc as the best dataset to estimate PV energy generation, while the ghi_tc turns out to be worse than datasets from satellite observations if DQF is not applied.

Tab. 4: Residues calculated between the observed and calculated monthly photovoltaic energy generation.

	gti_tc	dni/dhi_sb	ghi_tc	dni/dhi_cams	ghi_era
Before DQF [Wh]	5.01%	15.01%	16.18%	33.98%	26.36%
After DQF [Wh]	3.78%	14.08%	11.27%	28.52%	18.67%

3.2. Discussion

High-resolution datasets based on satellite imaging methods (i.e., CAMS) are found to be more accurate than one-hour datasets based on numerical weather prediction and assimilation methods (i.e., ERA5-Land global reanalysis) in Trondheim. A similar result was observed by Kenny and Fiedler (Kenny and Fiedler, 2022) in 30 locations in Germany. However, diffuse, and direct irradiance values which are measured by weather stations are generally preferable to those derived from satellite observations due to the lower error associated to the monitoring equipment, even if the two components are rarely measured (Manni et al., 2023). In fact, pyranometers measuring GHI are commonly used in solar monitoring campaign due to their lower investment costs if compared to the sun tracker equipment.

Based on the preliminary outcomes from this work, the length of the model chain determines the accuracy of the modelled PV energy generation more than the time resolution of the datasets. When variables measured by weather stations are considered, the one-hour POA dataset outperforms the one-minute dataset with monitored DNI and DHI values; it performs better than the GHI dataset having a time resolution of five minutes.

Finally, the following recommendations are carried out from this study:

- When available, solar radiation data from weather stations should be prioritized despite of their time resolution.
- DHI and DNI values from monitoring campaign or satellite imaging methods should be used instead of GHI datasets to reduce the length of the model chain.
- Measuring POA is also a valid option since it combines the short model chain to the low costs of the monitoring sensor (i.e., pyranometer).

3.3. Limitations of the study

In this section, the limitations of the study are outlined and commented. Firstly, the selected time interval is only one-month so the results are affected by the specific weather conditions and by the specific selected period of the year. In fact, datasets that perform badly in the overcast conditions in October 2021 (i.e., the analysis period)

might perform better during those months which show prevalently clear sky conditions (i.e., July, August). However, this study allows carrying out some preliminary considerations about the accuracy of the investigated model chains.

Secondly, October 2021 was mostly characterized by overcast sky conditions in Trondheim that affect the validity of the results. However, most of the numerical model and datasets are able to model PV energy generation during clear sky days, while simulating overcast sky conditions is more challenging.

Thirdly, the use of a single decomposition and transposition model can limit the reliability of the results. In fact, the use of a more effective combination of decomposition and transposition models could led to lower accuracy indicators for those datasets containing data about GHI or DNI and DHI. On the contrary the use of a different energy model for the simulation of the PV system would have had a less remarkable impact on the results since it is applied to all the datasets. Despite of that, the use of decomposition and transposition models and the longer model chain imply a low accuracy of the results.

4. Conclusive remarks

A comparative analysis of different solar radiation datasets and their capability of simulating PV is carried out. One-month solar radiation datasets from satellite observations, numerical reanalysis and weather stations are used as input parameters in the model chain combining the Engerer4 decomposition model and the Perez transposition model with the energy model described in sub-section 2.3. Outputs are compared against experimental data collected from the PV panel installed on the roof of the Test Cell Lab. The achievements from this study contribute to determine suitable irradiance dataset to be exploited in the model chain for the prediction of mono-facial PV energy generation at high latitudes as Trondheim.

The main findings are summarized in the following bullets:

- The POA data collected every hour in Test Cell Lab permit to estimate the hourly PV energy generation with the highest accuracy after the application of the data quality control filter (MBE is 2.65 Wh, RMSE is 39.78 Wh).
- Accuracy indicators calculated for the datasets based on observations are lower than the ones calculated for datasets based on satellite imaging or numerical reanalysis.
- Daily and monthly aggregation of the hourly datasets confirmed the POA data to better simulate the daily and monthly energy produced by the investigated PV panel.

Further insights into the model chain and solar radiation datasets are necessary. This includes:

- Assessing the capability of solar radiation datasets to estimate PV production over a wider time horizon such as one or more years instead of a single month.
- Performing a sensitivity analysis on different combinations of decomposition and transposition models to identify the most effective model chain at high latitude locations.
- Reiterate the comparative analysis for different PV panel technologies such as bi-facial PV systems which require a more accurate evaluation of the diffuse fraction.
- Validating the implemented model chain with experimental data from different high-latitude locations and different PV systems.

5. Acknowledgments

The authors acknowledge the financial support from the Norwegian Research Council (research project FRIPRO-FRINATEK no. 324243 HELIOS).

6. References

Bright, J.M., Engerer, N.A., 2019. Engerer2: Global re-parameterisation, update, and validation of an irradiance separation model at different temporal resolutions. J. Renew. Sustain. Energy 11, 33701.

https://doi.org/10.1063/1.5097014

Dubey, S., Sarvaiya, J.N., Seshadri, B., 2013. Temperature dependent photovoltaic (PV) efficiency and its effect on PV production in the world - A review, in: Energy Procedia. Elsevier, pp. 311–321. https://doi.org/10.1016/j.egypro.2013.05.072

Energy Facts Norway, 2021. Electricity Production [WWW Document]. URL https://energifaktanorge.no/en/norsk-energiforsyning/kraftproduksjon/ (accessed 3.27.22).

Formolli, M., Lobaccaro, G., Kanters, J., 2021. Solar energy in the Nordic built environment: challenges, opportunities and barriers. Energies 14. https://doi.org/10.3390/en14248410

Gueymard, C.A., 2017. Cloud and albedo enhancement impacts on solar irradiance using high-frequency measurements from thermopile and photodiode radiometers. Part 2: Performance of separation and transposition models for global tilted irradiance. Sol. Energy 153, 766–779. https://doi.org/10.1016/J.SOLENER.2017.04.068

Hay, J.E., 1993. Calculating solar radiation for inclined surfaces: Practical approaches. Renew. Energy 3, 373–380. https://doi.org/10.1016/0960-1481(93)90104-O

Holmgren, W.F., Hansen, C.W., Mikofski, M.A., 2018. PVlib Python: a Python package for modeling solar energy systems. J. Open Source Softw. 3, 884. https://doi.org/10.21105/joss.00884

International Energy Agency, 2021a. Renewables Information: Overview [WWW Document]. URL https://www.iea.org/reports/renewables-information-overview (accessed 8.2.22).

International Energy Agency, 2021b. Net Zero by 2050 [WWW Document]. URL https://www.iea.org/reports/net-zero-by-2050 (accessed 8.2.22).

International Renewable Energy Agency, 2022. World Energy Transition - Outlook 2022: 1.5°C Pathway. Abu Dhabi.

Kenny, D., Fiedler, S., 2022. Which gridded irradiance data is best for modelling photovoltaic power production in Germany? Sol. Energy 232, 444–458. https://doi.org/10.1016/J.SOLENER.2021.12.044

Loutzenhiser, P.G., Manz, H., Felsmann, C., Strachan, P.A., Frank, T., Maxwell, G.M., 2007. Empirical validation of models to compute solar irradiance on inclined surfaces for building energy simulation. Sol. Energy 81, 254–267. https://doi.org/10.1016/j.solener.2006.03.009

Manni, M., Nocente, A., Bellmann, M., Lobaccaro, G., 2023. Multi-Stage Validation of a Solar Irradiance Model Chain: An Application at High Latitudes. Sustainability 15. https://doi.org/10.3390/su15042938

Reindl, D.T., Beckman, W.A., Duffie, J.A., 1990. Diffuse fraction correlations. Sol. Energy 45, 1–7. https://doi.org/10.1016/0038-092X(90)90060-P

Yang, D., 2022. Estimating 1-min beam and diffuse irradiance from the global irradiance: A review and an extensive worldwide comparison of latest separation models at 126 stations. Renew. Sustain. Energy Rev. 159, 112195. https://doi.org/10.1016/J.RSER.2022.112195

Nomenclature

Acronyms

RES	Renewable Energy Sources
GHG	Greenhouse Gas
PV	Photovoltaic
NTNU	Norwegian University of Science and Technology
ECMWF	European Centre for Medium-Range Weather Forecasts

ERA5-Land	ECMWF 5th generation reanalysis for land application
CAMS	Copernicus Atmosphere Monitoring Service
DQF	Data Quality Filter

Variables

GHI	Global Horizontal Irradiance [Wh]
DHI	Direct Horizontal Irradiance [Wh]
DNI	Direct Normal Irradiance [Wh]
POA	Plane of Array Irradiance [Wh]
MBE	Mean Bias Error [Wh]
RMSE	Root Mean Square Error [Wh]
E	Energy [Wh]
f_{perf}	Temperature-dependent losses for semi-integrated panels and other configurations
P	Power [kW]
I_{ref}	Reference conditions for the investigated PV panel [kW/m^2]
N	Number of elements in the series
$\bar{x}_i$	i-th calculated values
x_i	i-th observations

Subscripts

el	Electricity
out	Output
sol	Solar
pv	Photovoltaic
pk	Peak

Quality Assurance Procedure for Solar Radiation at Minute Resolution

Diego Miranda[1], Leonardo Petribú[2], Janis Galdino[2], João Victor Furtado[2], Lucas Barboza[2], Olga Vilela[2], Alexandre Costa[2], Emerson Gomes[2], Alex Pereira[3], Eduardo Jatobá[3], Alcides Codeceira Neto[3] and José Bione Filho[3]

[1] Former affiliation: Center for Renewable Energy of the Federal University of Pernambuco (CER-UFPE), Recife (Brazil), now at German Aerospace Center (DLR), Institute of Networked Energy Systems, Oldenburg (Germany)

[2] Center for Renewable Energy of the Federal University of Pernambuco (CER-UFPE), Recife (Brazil)

[3] Companhia Hidro Elétrica do São Francisco (CHESF), Recife (Brazil)

Abstract

This article proposes a quality assurance (QA) procedure for evaluating measurements of global horizontal, diffuse horizontal and direct normal irradiances. The QA is divided into physical, comparative and refining tests, including Baseline Surface Radiation Network (BSRN) recommended quality tests. The comparative tests (tracker off and coherence tests) evaluate the connection among the three main radiation components. The coherence test as proposed by BSRN is complemented with a comparison between the measured radiation series with a validated clear sky model to define which of the three radiation components is presenting problems. Three stations in Pernambuco, Brazil and one in Gobabeb, Namib have been qualified using the proposed QA, with two of these stations belonging to BSRN (Petrolina and Gobabeb). The results show that the direct normal irradiance series can present considerable outliers due to soiling in pyrheliometers. For solar stations without periodic maintenance, the series of direct normal radiation measured by pyrheliometers can have more soiling problems than other radiation components measured by pyranometers.

Keywords: quality assurance, soiling in pyrheliometer

1. Introduction

Measuring solar radiation with accuracy is vital to analyse radiation models (for example, separation models, transposition models and power photovoltaic output models), apply site adaptation techniques, evaluate the accuracy of solar maps, and many other applications in solar energy. Thus, quality assurance (QA) of solar radiation data is an important tool to increase the reliability of the measured data. Many other works present QA solar radiation data procedures using different tests and techniques (NREL, 1993; Long and Dutton, 2002; Urraca et al., 2017; Perez-Astudillo et al., 2018). This work presents an approach for solar radiation quality assurance based on the Baseline Surface Radiation Network (BSRN) recommended quality tests. The quality assurance procedure focuses on the coherence test with a clear sky model validation and the tracker off test to increase the comparative tests analysis of the three radiation components.

2. Methodology

The QA for solar radiation evaluates time series of global horizontal (G), diffuse horizontal (G_d), and direct normal (G_b) irradiances in W/m², divided into three sets of tests: physical tests, comparative tests, and refining tests, as shown in Fig. 1 and Tab. 1 (Petribú et al., 2017). The global checks identify inconsistencies in the record of timestamps by the datalogger. First, the chronological record of date and hour is checked, ordering eventual timestamps and their respective measurements. Identical registered timestamps are checked as well. The gaps between consecutive records are filled with 'Not a Number' (NaN). This work uses six quality indicators, called flags, to classify the data. If one data is classified as 'good' (flag 1), it means the data was approved in all quality

© 2022. The Authors. Published by International Solar Energy Society
Selection and/or peer review under responsibility of Scientific Committee
doi:10.18086/eurosun.2022.15.04 Available at http://proceedings.ises.org

tests of the procedure. One data is classified as 'suspicious' (flag 2) when the test is not conclusive if the data was a rare occurrence or anomalous data. If one data is classified as 'anomalous' (flag 3) in one test, it will not be checked on the subsequent tests, being classified as 'previously anomalous' (flag 4). Finally, flag 5 is for non-tested data, and flag 6 is for unavailable data (NaN values). The tests are applied in the numerical sequence as shown in Tab. 1. The physical tests use equations based on solar geometry to evaluate the quality of irradiance data. The first test proposes limits to the measured irradiances, while the third test proposes limits to the clearness index ($G/G_{eff,h}$ for k_t), diffuse ratio (G_d/G for k_d), and normal transmittance (G_b/G_{eff} for k_n), called here k's limits, with the threshold values adapted from Raichijk (2012). G_{eff} is the extraterrestrial radiation with a mean value of 1361.1 W/m², according to Gueymard et al. (2018), varying throughout the year due to the sun-earth distance. $G_{eff,h}$ is the extraterrestrial radiation in a horizontal plane which is obtained multiplying G_{eff} by the cosine of solar zenith angle (Θ_z). The second test indicates that the procedure does not test the data above 7º of solar elevation (α), adapted from Maxwell (1973). The fourth test (Long and Dutton, 2002) defines lower and upper limits for irradiance measurements, while the fifth test is based on Rigollier et al. (2000) clear sky model using a link turbidity factor equal to 2.5, according to Ruiz-Arias et al. (2010). The comparative tests include the 'tracker off' to evaluate the solar tracker's operation, and the coherence test (BSRN), to judge the coherence among the three radiation components. It is important to note that the coherence test is analysed on clear days with a clear sky model validated by the QA procedure – here, the McClear model (Lefèvre et al., 2019) was chosen. Then, if the clear sky model reproduces the behavior of the global horizontal irradiance and direct normal irradiance on clear days, this model can be used to decide which of the three components is with measurement problems. Finally, the refining tests aim to evaluate abrupt solar radiation variations between consecutive data on minute resolution (step test) and the repetition of the same value of radiation consecutively in large windows (persistence test), as proposed by Sönmez (2013). In Tab. 1, data is classified as anomalous (flag 3) when the conditions are not satisfied for tests 1, 3, 4i and 8; suspicious (flag 2) when the conditions are not satisfied for tests 4ii and 5; and anomalous (flag 3) when the conditions are satisfied for the tracker off and persistence tests.

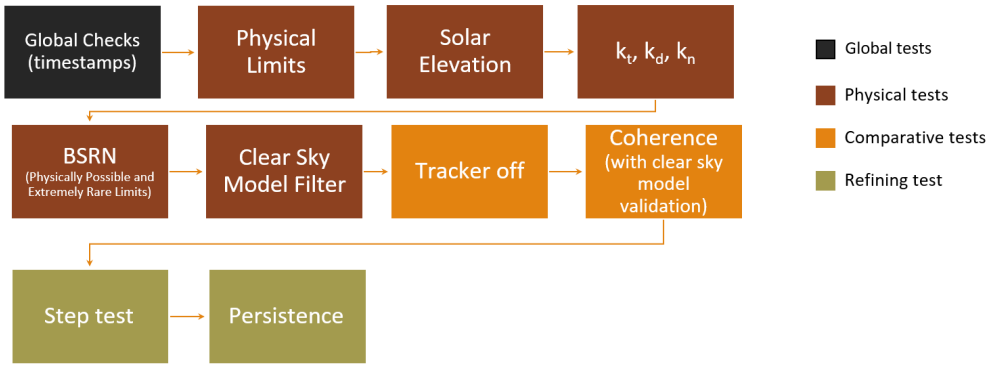

Fig. 1: Methodology of QA procedure.

Tab. 1: Tests proposed by the Quality Assurance procedure.

Physical Tests	
1 – Limits Test	$-5 < G, G_b$ and $G_d < 2000$ for irradiances in W/m²
2 – Solar Elevation	$\alpha < 7^o$ (non-tested data – flag 5); where α is the solar elevation (in degrees)
3 – k's Limits	$0 < k_t \leq 1.3; 0 < k_d \leq 1.1; 0 \leq k_n \leq 1.1$
4 – Extremely rare limits (i) and physically possible limits (ii) (BSRN)	i) Anomalous data: $-4 \leq G \leq G_{eff} 1.5 \cdot cos(\Theta_z)^{1,2} + 100; -4 \leq G_b \leq G_{eff}; -4 \leq G_d \leq G_{eff}\ 0.95 \cdot cos(\Theta_z)^{1,2} + 50$ for irradiances in W/m²
	ii) Suspicious data: $-2 \leq G \leq G_{eff} 1.2 \cdot cos(\Theta_z)^{1,2} + 50; -2 \leq G_b \leq G_{eff} 0.95 \cdot cos(\Theta_z)^{0,2} + 10; -2 \leq G_d \leq G_{eff} 0.75 \cdot cos(\Theta_z)^{1,2} + 30$ for irradiances in W/m²
5 – Clear Sky Filter Test	$G < 2{,}1 \cdot G_{csRig}; G_b < 2{,}1 \cdot G_{b,csRig}; G_d > 0{,}8 \cdot G_{d,csRig}$, where $G_{csRig}, G_{b,csRig}$ and $G_{d,csRig}$ are the Rigollier clear sky model for G, G_b and G_d

Comparative Tests	
6 – Tracker Off Test (anomalous data if the conditions are satisfied)	i) Daily Basis: $K_d > 0.75$ & $K_c > 0.7$ & $G_{b,daily} < 25\ W/m^2; K_c = \frac{G_{daily}}{G_{daily,McClear}}$ where K_d and K_c are the daily diffuse fraction and daily clear sky index, respectively; $G_{b,daily}$ and G_{daily} are the daily values for G_b and G; and $G_{dailyMcClear}$ is the daily G clear sky irradiance for McClear model.
	ii) Minutely Basis: $k_d > 0.75$ & $k_c > 0.85$ & $G_b < 5\ W/m^2$ & $\theta_z < 75°;\ k_c = \frac{G}{G_{cs,McClear}}$ where $G_{cs,McClear}$ is the McClear clear sky model for G (minute resolution).
7 – Coherence Test (BSRN). The results of this test should be compared with a validated clear sky model.	i) $\left\|\frac{G_d+G_b cos(\Theta_Z)-G}{G}\right\| \leq 0{,}08\ if\ \Theta_Z < 75°$ and $G_d + G_b\ cos\ (\Theta_Z) > 50\ W/m^2$ ii) $\left\|\frac{G_d+G_b cos(\Theta_Z)-G}{G}\right\| \leq 0{,}15\ if\ 75° < \Theta_Z < 90°$ and $G_d + G_b\ cos\ (\Theta_Z) > 50\ W/m^2$ iii) $k_d < 1{,}05\ for\ \Theta_Z < 75°\ and\ \mathrm{G} > 50\ W/m^2$ iv) $k_d < 1{,}1\ for\ 75° < \Theta_Z < 90°\ and\ G > 50\ W/m^2$
Refining Tests	
8 – Step test	$(\mathrm{G}, G_b, G_d)_t - (\mathrm{G}, G_b, G_d)_{t-1} \leq 1100\ W/m^2$ where t is the current timestamp and $t-1$ the previous (minute resolution)
9 – Persistence test	i) G data with successive repetitions ≥ 20 min are considered anomalous ii) G_b non-zero data with successive repetitions ≥ 30 min are considered anomalous

The BSRN coherence test does not identify which of the three radiation components presents problems when the first two equations (Tests 7i and 7ii) detect a considerable difference between the sum $G_d + G_b cos(\Theta_Z)$ and G. To determine which component is not measuring well, we proposed a three-step procedure for running the coherence test, as presented in Fig. 2. First, the procedure identifies clear sky days on the radiation time series using the G measurements and the McClear model for global irradiance (G_{cs}). The metrics clear sky ratio (K_c) and variability index (VI) are calculated on a daily resolution from the data in minute resolution, as proposed by Stein et al. (2012) with adaptations. These metrics aim to identify clear sky days in the conditions specified on the first diagram block ($K_c > 0.8$ and VI lower than the fifth percentile of VI), because clear sky days have high K_c and low VI. The VI metric quantifies how much solar radiation varied in a specific time window. It is the ratio between the sum of lengths (or line segments) of G and the sum of lengths of G_{cs}. In Eq. 1, it was used n = 1440 to obtain the VI values on a daily resolution from the data in minute resolution. Clear sky and overcast days have low values of VI, while days with variable radiation have high values of VI. In the first step of the proposed method, it is necessary to choose a well-adjusted global horizontal irradiance clear sky model.

$$VI = \frac{\sum_{i=2}^{n}\sqrt{(G_i - G_{i-1})^2 + 1}}{\sum_{i=2}^{n}\sqrt{(G_{cs,i} - G_{cs,i-1})^2 + 1}} \quad \text{(eq.1)}$$

After selecting the clear sky days, the clear sky model must be validated for the coherence test. The validation is made by statistically comparing the measurements of the previously selected clear sky days and the clear sky model. First, in step 2, the days containing data detected by the first equation (Test 7i) of the coherence test are dropped. Then, only the data without incoherence among the radiation components remain in the dataset. G and G_b are validated according to the statistics presented in the two last diagrams of step 2. The clear sky model can be used in the coherence test only if both G_{cs} and $G_{b,cs}$ (McClear model for G_b) are validated. The $G_{d,cs}$ (McClear model for G_d) was not validated because the diffuse measurement in clear sky conditions varies depending on the location, making it challenging to define an excellent statistical range for its validation.

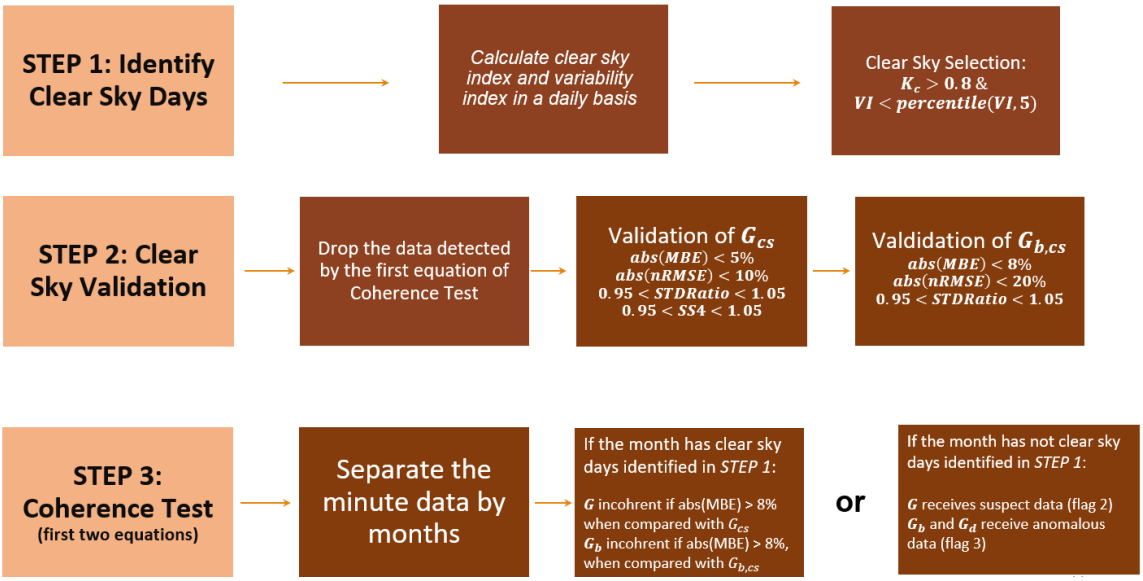

Fig. 2: Methodology of coherence test with clear sky validation.

The statistics used are the normalized mean bias error (nMBE), the normalized root mean square error (nRMSE), the Pearson correlation (*Corr*), the ratio between the standard deviation of the model and the standard deviation of the observation (STDRatio) and the skill score of Taylor (SS4). Eqs. 2 to 4 show the formulas for these statistics, where x_{mod} is the modeled time series, x_{obs} is the observed time series and $\bar{x}_{obs}$ is the mean of the observed time series.

$$nMBE = \frac{1}{N\,\bar{x}_{obs}} \sum_{i=1}^{N} (x_{mod}^{i} - x_{obs}^{i}) \quad \text{(eq. 2)}$$

$$nRMSE = \frac{1}{\bar{x}_{obs}} \sqrt{\frac{1}{N} \sum_{i=1}^{N} (x_{mod}^{i} - x_{obs}^{i})^2} \quad \text{(eq. 3)}$$

$$SS4 = \frac{(1+Corr)^4}{4\left(STDRatio + \frac{1}{STDRatio}\right)^2} \quad \text{(eq. 4)}$$

Finally, step 3 applies the first two equations of the coherence test (Tests 7i and 7ii). It consists of applying the first two equations presented in Table 1 for the coherence test monthly. Then, the minute measurements of G, G_b and G_d are analysed month by month. For each month, the script searches if clear sky days from the previously selected clear sky days (step 1) exists in the month in question. If there were one or more clear sky days on this particular month, a comparison is made between the clear sky measurements and the clear sky model on these specific days for G and G_b. The idea here is to analyse if the coherence issue lies in components G or G_b, instead of flagging all components detected by Tests 7i and 7ii. The absolute value of nMBE statistic was chosen to compare the clear sky model and measurements on clear sky days because the bias shows if a model is overestimating or underestimating the observations on the mean. The threshold values adopted were a mean bias error of 8% for the absolute difference $G - G_{cs}$ and $G_b - G_{b,cs}$. The value of 8% was chosen after a sensitive analysis of the ground measurements data employed. For example, if the absolute value of nMBE is higher than 8% for the difference $G_b - G_{b,cs}$, all G_b detected by the first two equations of the coherence test (Tab. 1 – Tests 7i and 7ii) for that month are considered incoherent. The evaluation of each month follows the cases shown in Tab. 2. In the cases where no clear sky days from the previous selection are present in a particular month, the detected data by Tests 7i and 7ii might attribute suspicious data for G (flag 2) and anomalous data for G_b and G_d (flag 3). For example, in the third row of Tab. 2, if the G_b data detected on clear sky days were considered incoherent (which was decided based on the difference $G_b - G_{b,cs}$ higher than 8% of nMBE on the selected clear

sky days) and the G data were coherent for the particular month, then the G_b component is causing the differences detected by Tests 7i and 7ii on that month and receives flag 3, while G receives good data and G_d suspicious data. Finally, the last two equations of coherence tests (Tab. 1 – Tests 7iii and 7iv) always attribute anomalous data for G and G_d, independent of the clear sky validation.

Tab. 2: Analysis of G and G_b on clear sky days of a particular month.

If on the clear sky days of a particular month...	Then, the detected data by the first two equations of the coherence test (Tab. 1, Tests 7i and 7ii) for that month will be flagged as		
	G	G_b	G_d
G_b is **coherent** and G is **coherent**	Suspicious data (flag 2)	Anomalous data (flag 3)	Anomalous data (flag 3)
G_b is **coherent** and G is incoherent	Anomalous data (flag 3)	Good data (flag 1)	Suspicious data (flag 2)
G_b is incoherent and G is **coherent**	Good data (flag 1)	Anomalous data (flag 3)	Suspicious data (flag 2)
G_b is incoherent and G is incoherent	Anomalous data (flag 3)	Anomalous data (flag 3)	Anomalous data (flag 3)

The tracker off test aims to find issues in the operation of the solar tracker. In the QA procedure, this test is applied in two steps: a daily analysis to find days whose tracker did not work all day and an analysis on minute resolution to find the moments when the tracker is not working for part of the day. To perform the daily analysis, the daily mean of G, G_b, G_d and G_{cs} are extracted, accepting an amount until 25% of missing data (NaN values) to calculate the mean of the variables considering only sunshine time. If there are more than 25% of NaN values on a particular day during sunshine, this particular day receives NaN instead of the daily mean. After having the four variables daily, the tracker off condition on a daily basis is applied (Tab. 1 – Test 6i). With this simple test, we can detect days when the tracker did not work all day. Otherwise, in the second step, the conditions presented in Tab. 1 (Test 6ii) are used to detect moments when the tracker did not work for part of the day, as proposed by Long and Shi (2006), with some adaptations.

Besides the objective tests presented in this QA procedure, it is worth to be noted that the quality assurance of measuring data should always be complemented with a rigorous analysis of the results and time series plots. In some cases, the tests cannot detect all kinds of anomalies, and an analysis by an expert could be fundamental to complement the objective procedure. Therefore, the QA procedure's results are manually analysed to complement the flagged process of possible anomalous data that were not detected by the objective QA procedure.

3. Datasets and results

Three meteorological stations located in the state of Pernambuco (CRESP Petrolina, SONDA Petrolina and Araripina), Brazil, and one located in the Gobabeb Namib Research Institute, Namib, were analysed in this study. Their stations' coordinates and solar sensors are presented in Tab. 3. All ground measurements data are in minutely resolution. Tab. 4 shows the final results of the QA procedure for all stations. The tracker off and the coherence tests were the tests that mostly identified anomalous data. Then, the results of these two tests are presented in major details in this section. The results of the three steps of the coherence test will be presented for CRESP Petrolina station to illustrate the methodology described for the coherence test. First, in step 1, 45 clear sky days were selected from CRESP Petrolina station. In step 2, 11 days were dropped from the selected clear days because they had measurement problems detected by the first equation of coherence test (Tab. 1 – Test 7i). Fig. 3 shows the 34 remained clear sky days used to validate the clear sky model for G_{cs} and $G_{b,cs}$. The statistical comparison results are shown in Tab. 5 for all stations. All the statistics are inside the ranges proposed on the diagram methodology for stations CRESP Petrolina, Araripina and SONDA Petrolina, so the clear sky models G_{cs} and $G_{b,cs}$ could be used to analyse the results of the first two equations of the coherence test. For Gobabeb station, $G_{b,cs}$ was not validated on the site because the STDRatio exceeds the proposed range. Then, the first two equations of the coherence test will attribute suspicious data for G and anomalous data for G_b and G_d for the detected data of Gobabeb station.

Tab. 3: Meteorological stations used for applying the QA procedure.

Station	Location and country	Coordinates	Elevation (m)	Solar variables and sensors
CRESP	Petrolina, Brazil	-9.1069, -40.4414	376	G (EKO MS-80A), G_b (EKO MS-57) and G_d (EKO MS-80A)
SONDA Petrolina (BSRN - PTR)	Petrolina, Brazil	-9.0689, -40.3197	387	G (Kipp&Zonen CMP22), G_b (Kipp&Zonen CHP1) and G_d (Kipp&Zonen CMP22)
Araripina	Araripina, Brazil	-7.5742, -40.5144	633	G (Kipp&Zonen CMP3), G_b (Kipp&Zonen CHP1) and G_d (Kipp&Zonen CMP3)
Namib (BSRN - GOB)	Gobabeb, Namib	-23.5614, 15.04198	407	G (Kipp&Zonen CMP22), G_b (Kipp&Zonen CHP1) and G_d (Kipp&Zonen CMP22)

Tab. 4: Results of QA procedure for all stations analysed.

Quality Flag	1 - Good data	2 - Suspicious data	**3 - Anomalous data**	5 - Non-tested data	6 - Data not available
G Araripina	42.54%	2.10%	**2.13%**	48.33%	4.90%
G_d Araripina	35.42%	5.85%	**5.66%**	48.10%	4.97%
G_b Araripina	33.20%	0.00%	**12.21%**	49.65%	4.94%
G SONDA Petrolina	34.42%	1.29%	**0.54%**	42.42%	21.33%
G_d SONDA Petrolina	30.76%	1.08%	**4.72%**	42.09%	21.35%
G_b SONDA Petrolina	30.43%	0,00%	**6.39%**	41.82%	21.36%
$G1$ CRESP Petrolina	38.81%	0.14%	**0.01%**	46.24%	14.80%
$G2$ CRESP Petrolina	38.88%	0.08%	**0.00%**	46.24%	14.80%
G_d CRESP Petrolina	37.81%	0.97%	**0.18%**	46.24%	14.80%
G_b CRESP Petrolina	37.72%	0.00%	**1.30%**	46.19%	14.79%
G Namíbia	44.60%	0.03%	**0.01%**	53.70%	1.66%
G_d Namíbia	44.50%	0.08%	**0.05%**	53.70%	1.67%
G_b Namíbia	44.52%	0.00%	**0.05%**	53.69%	1.74%

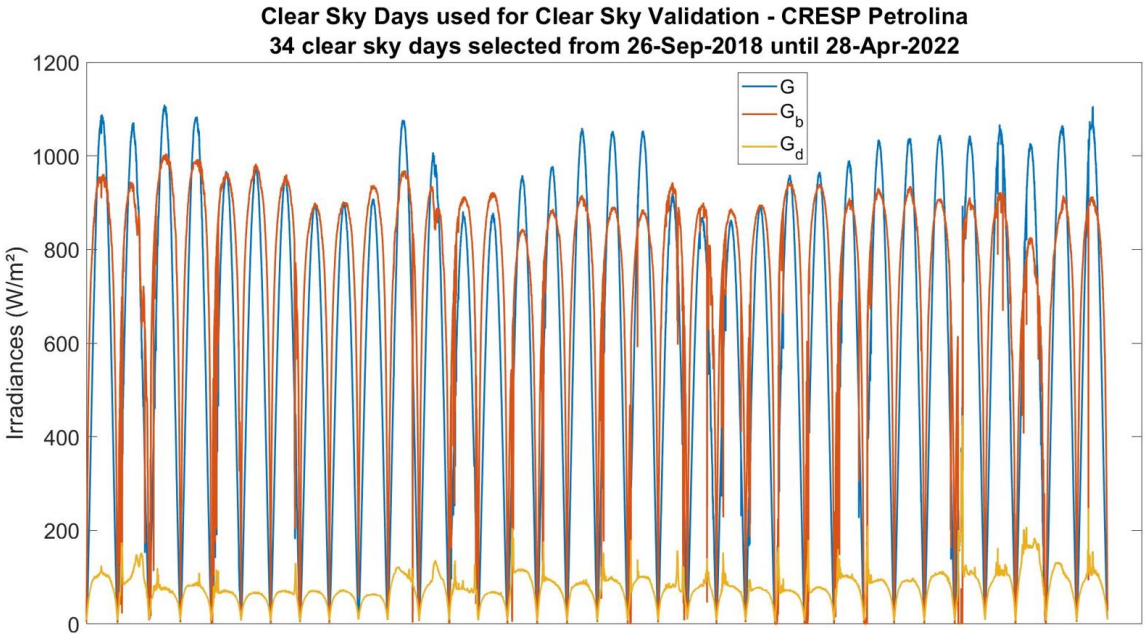

Fig. 3: Clear sky days used for the clear sky validation in CRESP Petrolina station.

Tab. 5: Results of clear sky validation.

CRESP Petrolina Station							
Clear Sky Model	BIAS (W/m²)	MBE (%)	STDRatio	RMSE (W/m²)	nRMSE (%)	Corr (.)	SS4 (.)
G_{cs} (McClear)	-13,37	-2,25%	1,00	32,35	5,45%	1,00	0,99
$G_{b,cs}$ (McClear)	-53,53	-7,33%	0,97	106,12	14,53%	0,93	0,86
SONDA Petrolina Station							
G_{cs} (McClear)	-21,38	-3,62%	1,03	40,94	6,93%	0,99	0,99
$G_{b,cs}$ (McClear)	-40,21	-5,68%	0,96	131,17	18,52%	0,87	0,77
Araripina Station							
G_{cs} (McClear)	-12,02	-1,92%	1,01	26,98	4,31%	1,00	0,99
$G_{b,cs}$ (McClear)	-50,59	-6,65%	0,99	85,29	11,22%	0,96	0,92
Gobabeb Station							
G_{cs} (McClear)	-9,99	-1,99%	1,03	16,33	3,26%	1,00	1,00
$G_{b,cs}$ (McClear)	33,28	4,39%	1,06	63,13	8,33%	0,98	0,95

Finally, in the third step, the 45 days detected in step 1 are separated according to the months where they occur. If the particular month has no clear days selected by step 1, the data detected by the first two equations receives flag 2 for G and flag 3 for G_b and G_d. Otherwhise, when the particular month has clear sky days detected by step 1, the nMBE is checked to decide if the G or G_b measurements are coherent or not, as shown in Fig. 4. The idea is to compare the clear sky model with the measurements only on clear sky days. As the clear sky model was validated in step 2, the model is a reference for what the observations should measure. Then, if the absolute value of nMBE is higher than 8% when comparing the measurements with the clear sky model, it means the measures are incoherent. If the measures are incoherent on the clear sky days, it is considered incoherent on all data detected by the two equations of coherence test for that particular month (Tests 7i and 7ii). For example, in September 2019, just one clear sky day was identified. On this clear sky day, there is a difference of 26% in the nMBE comparing the G_b and $G_{b,cs}$, and a difference of 3% comparing G and G_{cs}. Then, the measurements of G are coherent and the measurements of G_b are incoherent on this particular clear sky day. The data detected by the first two equations of coherence test (Tab. 2 – Tests 7i and 7ii) will receive anomalous data for G_b, good data for G and suspicious data for G_d on September 2019. Fig. 5 shows the clear sky day of September 2019 and the next day, which was a day with high solar radiation variability. It can be noted that G_b is below the clear sky model for direct normal radiation on September 1st, while both global radiation measurements (G_1 and G_2) match with the clear sky model for G and the diffuse horizontal irradiance also corresponds with the clear sky model for G_d on mean, with some difference on the morning. However, the direct normal irradiance presents a nMBE of 26% when compared with the clear sky model for G_b, as it is possible to see in Fig. 4 for September 2019. Then, the component with measurement problems is the direct normal irradiance, causing the difference between the global horizontal measurements (G_1 and G_2) and the sum $G_d + G_b cos(\Theta_Z)$, marked with black points in the plot. The major outliers found by the coherence test in CRESP Petrolina and Araripina stations are related to pyrheliometer underestimates, probably due to soiling. A possible explanation for the pyrheliometer underestimating is that the cylindric geometry of the pyrheliometer with the flat glass in front of the sensor and the surrounding rain screen can contribute to a greater soiling accumulation than in the pyranometer sensor, whose glass is semi-spherical (Geuder and Quaschning, 2006). Furthermore, dust affects the narrow pyrheliometer field of view more than on the pyranometer with its all-sky view. Fig. 6 shows the soiling problem on two stations: CRESP Petrolina and Araripina. The soiling layer stays on the pyrheliometer flat glass and works as a filter from the sunlight photons of direct normal irradiance causing the difference detected by the coherence test with clear sky validation.

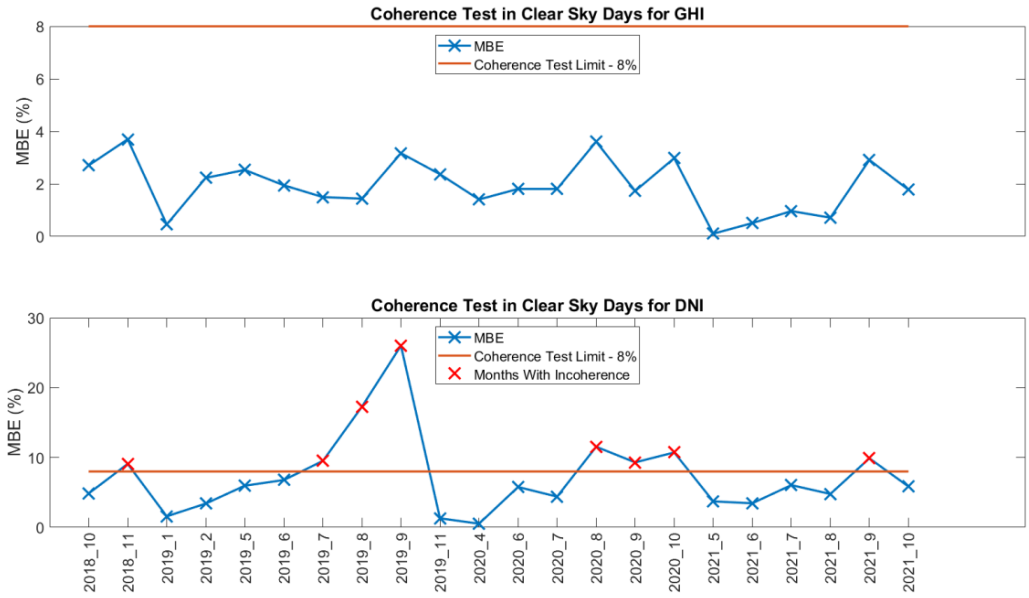

Fig. 4: Monthly analysis to check coherence of clear sky days occurring in each month.

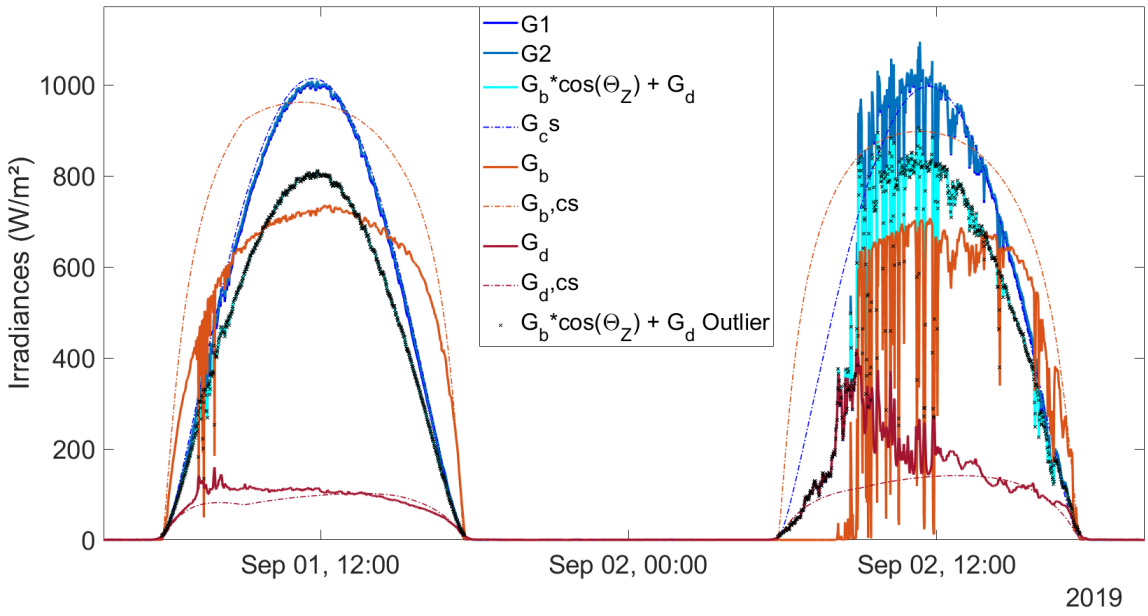

Fig. 5: Results of coherence test in September 2019 for CRESP Station.

The tracker off test presents interesting results for the daily test. For Araripina station, Fig. 7 shows the moments when the tracker did not work. The red points indicate days when the tracker did not work during all-day hours (Tab. 1 – Test 6i) while the black points indicate specific moments of days when the tracker was off (Tab. 1 – Test 6ii). In the detailed plot, two days were detected by the daily test. On 05 and 07 of July, the tracker was off because G_d is similar to G, and G_b is close to zero. It should be noted that the daily test did not detect any problem on July 6th, a day where the tracker was off too. Then, the QA procedure results analysis needs to be complemented to manually put some flags, such as the anomalous flag data in the morning of July 6th for G_d and G_b.

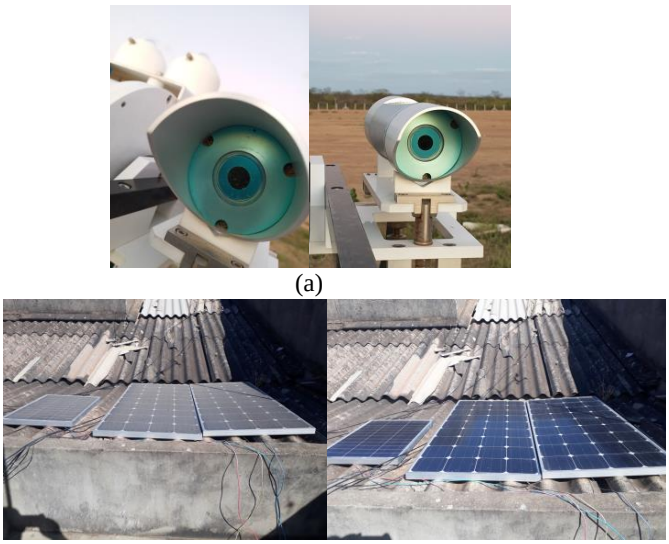

(a)

(b)

Fig. 6: a) Pyrheliometer of CRESP Station before cleaning (left) and after cleaning maintenance (right); b) Soiling on the modules that power the meteorological station of Araripina station before (left) and after (right) cleaning.

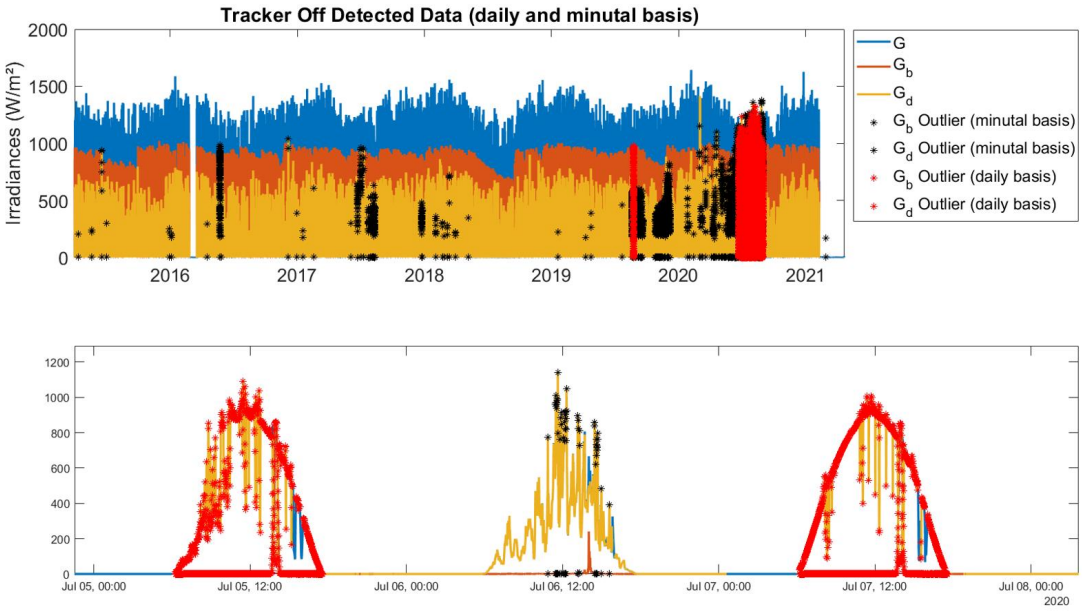

Fig. 7: Results of tracker off test for Araripina station.

In particular, the tracker off test could be helpful to compare the measurements of G and G_d pyranometers, because when the tracker is off, G and G_d should be equal. For example, Fig. 8 shows one tracker off day for SONDA Petrolina station and another for Araripina station, both clear days. The G and G_d pyranometers present close measurements for Araripina station, while in SONDA Petrolina station, G is measuring below G_d and G_{cs}. One linear regression was fitted in SONDA Petrolina, using exclusively the days identified by tracker off test on daily basis. The target of linear regression was G_d, while G was the variable regressor. After this correction, the G and G_d measurements of SONDA Petrolina station match in tracker off days, as shown by the third plot in Fig. 8. This correction is important because the clear sky model for global horizontal irradiance would not have been validated for SONDA Petrolina without the correction of G. The need for a correction was identified by analysing the results of tracker off test on a daily basis (Tab. 1 – Test 6i). Then, for SONDA Petrolina station, first the QA Procedure applies this correction in G component and, after, starts all the data qualification procedures. The performed correction for SONDA Petrolina station is shown in Fig. 9. In the set of days when the tracker was off, it is possible to observe that the diffuse pyranometer (current measuring global irradiance because the tracker is off) presents

higher measurements than the global pyranometer (left plot of Fig. 9). Therefore, a correction using linear regression is applied to the global pyranometer to fit the two global measurements in a line x = y trend, as shown by the right plot of Fig. 9.

Finally, Fig. 10 presents the scatterings k_d x k_t and k_n x k_t to all stations. These scatterings are helpful tools to identify if the QA procedure is filtering the data well. If some points are outliers in these scatterings, measuring problems remain on the dataset. If this occurs, an analysis of the outliers in these scatterings is recommended to complement the QA procedure.

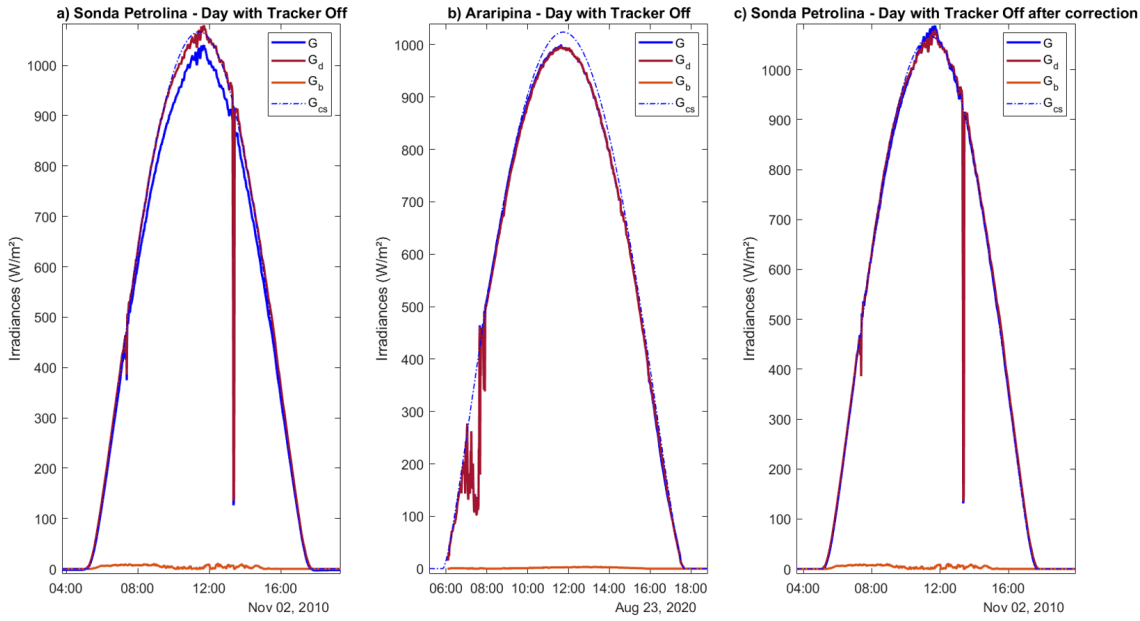

Fig. 8: Comparing the results of tracker off on daily basis for Araripina and SONDA Petrolina stations.

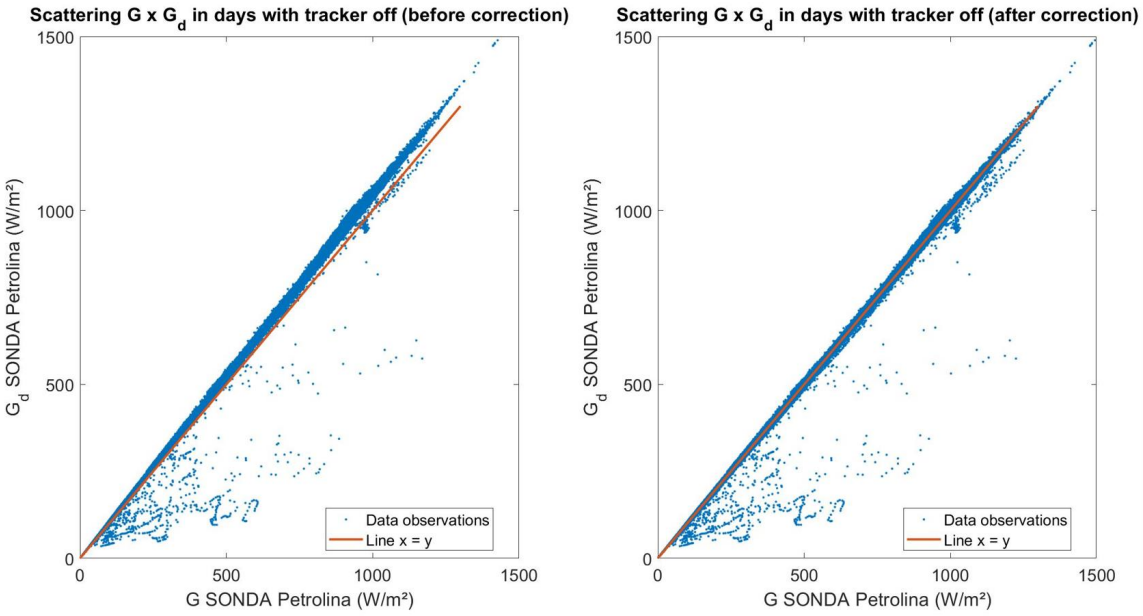

Fig. 9: Scattering G_d *x* G before (a) and after (b) G correction in SONDA Petrolina station.

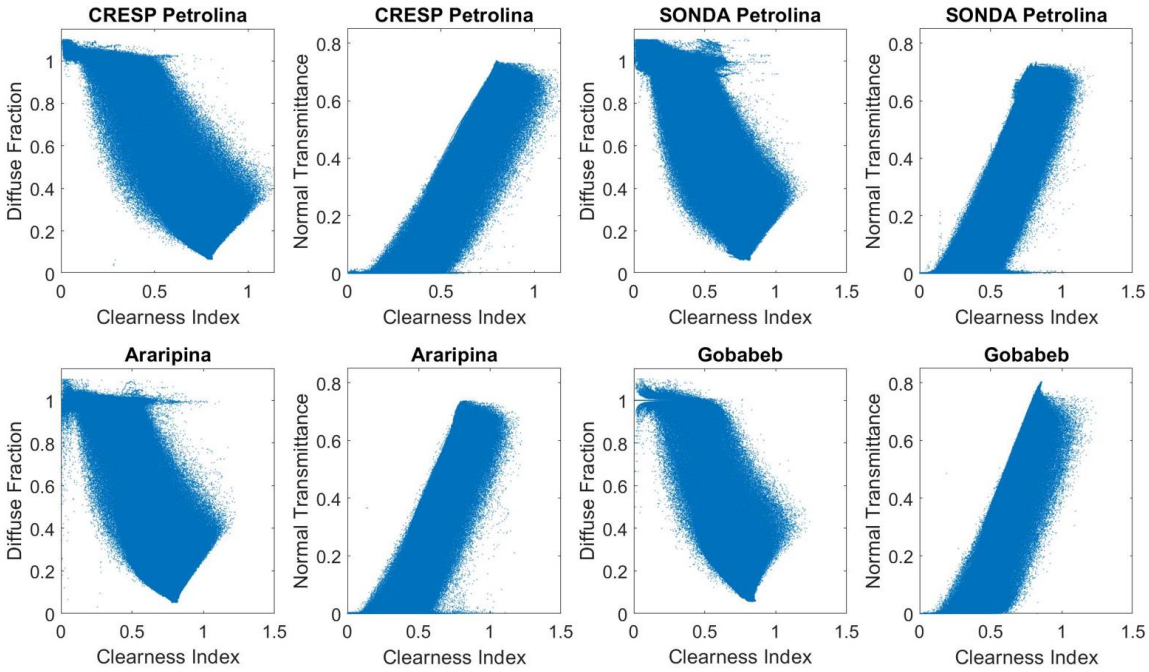

Fig. 10: Scattering k_d x k_t and k_n x k_t for all stations.

4. Conclusion

Quality assurance of the measured data is essential to increase its reliability to apply them in radiation models (separation models, transposition models and photovoltaic power output models) or to evaluate the solar irradiance for a site. The proposed QA procedure applied to the meteorological stations allowed the detection of anomalous data on the irradiances time series. The use of the coherence test with a clear sky validation to define which of the three radiation components are presenting problems detected by the first two equations of the coherence test and the tracker off methodology split into two different tests, one on daily basis and another using minutely measurements, are the two main innovations of the proposed QA procedure.

It was identified that the anomalous data detected by the coherence test in stations CRESP Petrolina and Araripina happened due to problems in the direct normal irradiance component, which presents lower amplitudes than expected. This issue with G_b was attributed to soiling on the pyrheliometers, which was validated empirically according to the maintenance of the stations. Another comparative test, an envelope test, is under development to complement the quality assurance methodology. The envelope test highlights a trend in the k_d x k_t and k_n x k_t scatterings, seeking to draw envelope curves for the upper and lower limits of these scatterings, similar to what was proposed by Yunnes et al. (2005).

5. Acknowledgments

The authors thank the financial support from the National Agency of Electric Energy (ANEEL) and Companhia Hidro Elétrica do São Francisco (Eletrobras CHESF) under the ANEEL R&D Program (CVI 23076.009704/2020-56). Likewise, the authors acknowledge the support of the World Radiation Monitoring Center - Baseline Surface Radiation Network (WRMC – BSRN), Instituto Federal de Pernambuco (IFPE) and Instituto Nacional de Pesquisas Espaciais (INPE) for providing part of the data used in this work and the Coordination for the Improvement of Higher Education Personnel (CAPES) in the scope of the graduate program of the UFPE members.

6. References

Geuder, N., Quaschning, V., 2006. Soiling of irradiation sensors and methods for soiling correction. Solar Energy, v. 80, p. 1402-1409, doi: https://doi.org/10.1016/j.solener.2006.06.001.

Gueymard, C. A., 2018. A reevaluation of the solar constant based on a 42-year total solar irradiance time series and a reconciliation of spaceborne observations. Solar Energy, v. 168, p. 2-9, doi: https://doi.org/10.1016/j.solener.2018.04.001.

Lefèvre, M., Oumbe, A., Blanc, P., Espinar, B., Gschwind, B., Qu, Z., Wald, L., Schroedter-Homscheidt, M., Hoyer-Klick, C., Arola, A., Benedetti, A., Kaiser, J. W., Morcrette, E.J.J., 2013. McClear: A New Model Estimating Downwelling Solar Radiation at Ground Level in Clear-Sky Conditions. Atmospheric Measurement Techniques, 6(9):2403–18, doi: https://doi.org/10.5194/amt-6-2403-2013.

Long, C.N., Dutton, E.G., 2002. BSRN Global Network recommended QC tests, V2.0.

Long, C. N. e Shi, Y., 2006. The QCRad value added product: Surface radiation measurement quality control testing, including climatology configurable limits. Atmospheric Radiation Measurement Program Technical Report, https://doi.org/10.2172/1019540.

Maxwell, E., Wilcox, S. e Rymes, M., 1993. Users manual for SERI QC software, assessing the quality of solar radiation data. Solar Energy Research Institute, Golden, CO.NREL, 1993. User's Manual for SERI_QC Software - Assessing the Quality of Solar Radiation Data.

Perez-Astudillo, D., Bachour, D., & Martin-Pomares, L., 2018. Improved quality control protocols on solar radiation measurements. Solar Energy, v. 169, p. 425–433, doi: https://doi.org/10.1016/j.solener.2018.05.028.

Petribú, L. B., Sabino, E., Barros, H., Costa, A., Barbosa, E., Vilela, O.C., 2017. Procedimento objetivo para a garantia de qualidade de dados de radiação solar. Avances en Energías Renovables y Medio Ambiente, vol. 21, p. 67-78.

Raichijk, C., 2012. Control de calidad de mediciones de radiación solar. Presentado en XXXV Reunión de Trabajo de la Asociación Argentina de Energías Renovables y Ambiente (ASADES), Rosario, Argentina.

Rigollier, C., Bauer, O., Wald, L., 2000. On the clear sky model of the ESRA - European Solar Radiation Atlas with respect to the Heliosat method. Solar Energy 68 (1), 33-48. , doi:10.1016/S0038- 092X(99)00055-9.

Ruiz-Arias, J., Alsamamra, H., Tovar-Pescador, J. e Pozo-Vázquez, D., 2010. Proposal of a regressive model for the hourly diffuse solar radiation under all sky conditions. Energy Conversion and Management 51(5): 881-893.

Stein, J. S.; Hansen, C. W.; Reno, M. J., 2012. The Variability Index: A New and Novel Metric for Quantifying Irradiance and Pv Output Variability. World Renewable Energy Forum, WREF 2012, Including World Renewable Energy Congress XII and Colorado Renewable Energy Society (CRES) Annual Conferen 4(May): 2764–70.

Sönmez, I., 2013. Quality control tests for western Turkey Mesonet. Meteorological Applications 20: 330-337.

Urraca, R., Gracia-Amillo, A. M, Huld, T., Martinez-de-Pison, F. J., Trentmann, J., Lindfors, A. V., Riihelä, A., Sanz-Garcia, A., 2017. Quality control of global solar radiation data with satellite-based products. Solar Energy, vol. 158, 49-62, https://doi.org/10.1016/j.solener.2017.09.032.

Younes, S., Claywell, R. e Muneer, T., 2005. Quality control of solar radiation data: present status and proposed new approaches. Energy 30(9): 1533-1549

Mapping radiative cooling potential predictions for Africa

Jesús Monterrubio[1], Roger Vilà[1], Albert Castell[1], Lídia Rincón[1] and Ingrid Martorell[1*]

[1]Sustainable Energy, Machinery and Buildings (SEMB) Research Group, INSPIRES Research Centre, Universitat de Lleida,
Pere de Cabrera s/n, 25001 Lleida, Spain
*Corresponding author: ingrid.martorell@udl.cat

Abstract

Radiative cooling (RC) is a passive cooling technology which enables to cool down surfaces by rejecting radiation to outer space. The potential of this phenomenon depends on environmental factors. Africa is a continent with most of its land within the tropics, so cooling needs are in general high along the year and radiative cooling can play an important role for covering them in a renewable way. A powerful spatial interpolation method, known as Kriging, has been used to estimate values at unknown points of Africa and thus create continuous maps of radiative cooling potential (q_c). Additional maps have been created, showing the dry bulb temperature and the relative humidity over Africa. Results showed mean annual values of cooling potential of 77.64 W/m^2 and peak values of 135.80 W/m^2 in the desert. Observing the resulting maps, the higher the temperature and the lower the relative humidity, the higher the cooling potential.

Keywords: Radiative cooling, renewable cooling potential, mapping, spatial interpolation, Kriging, Africa

1. Introduction

Radiative cooling (RC) phenomenon takes advantage of the high transparency of the atmosphere in the infrared longwave spectral band, from 8 to 13 μm (known as atmospheric window), to reject radiation, allowing to obtain temperatures below ambient (Li et al., 2019) in a renewable way. According to Bijarniya et al. (2020), environmental factors like ambient temperature, cloud cover, moisture, wind velocity and pollution affect RC performances.

Africa is a continent with most of its land within the tropics, so cooling needs are in general high along the year and radiative cooling can play an important role for covering them in a renewable way. In fact, a recent report by the International Energy Agency (Birol et al., 2018) predicts that the refrigeration demand will triple worldwide by 2050 if no action is taken. On the other hand, the physicist Aaswath Raman predicted that the cooling demand will have a sixfold increase by 2050 because of the increase in use of the Asiatic and African countries (Raman, 2018). Aili et al. (2021) mapped the annual all-day mean RC power of all the world and found a high cooling power in Africa, especially in the northern countries.

The Radiative Collector and Emitter (RCE) is a device which combines radiative cooling with solar heating (SH) in a single device using an adaptive cover. The concept was theoretically presented by Vall et al. (2018). The RCE provides hot water during the day (SH) and cold water during the night (RC). As for the cooling mode of the RCE it is required to know the nighttime RC power potential, this work focuses on developing the map of Africa with this information.

During the night, when solar radiation is null, considering an emittance of ideal surfaces (ε_s) equal to one and assuming the surface temperature equal to the ambient, RC is maximized and can be determined using eq. 1 and eq. 2 (Vilà et al., 2020). The first term in eq. 1 refers to radiative heat exchanges, the second term is the infrared energy rejected by the surface and by the sky (q_{sky}), while last terms refer to convective and conductive heat transfer, respectively.

$$q_c(T_a) = \sigma T_a^4 - q_{sky} - q_{conv} - q_{cond} \qquad [Wm^{-2}] \qquad \text{(eq. 1)}$$

© 2022. The Authors. Published by International Solar Energy Society
Selection and/or peer review under responsibility of Scientific Committee
doi:10.18086/eurosun.2022.15.05 Available at http://proceedings.ises.org

$$q_c(T_a) = \sigma T_a^4\left(1 - \varepsilon_{sky}\right) - q_{conv} - q_{cond} \quad [Wm^{-2}] \qquad \text{(eq. 2)}$$

where σ is the Stefan-Boltzmann constant $[W/m^2K]$, T_a is the ambient temperature $[K]$ and ε_{sky} is the sky emissivity $[-]$.

According to Chang and Zhang (2019), if the radiative surface is designed to work at a surface temperature equal to the ambient (T_a), convective and conductive heat exchanges can be neglected, as shown in eq. 3.

$$q_c(T_a) = \sigma T_a^4\left(1 - \varepsilon_{sky}\right) \quad [Wm^{-2}] \qquad \text{(eq. 3)}$$

Higher T_a implies high cooling potential at low relative humidity (RH) and low cooling potential at high RH (Dong et al., 2019). This study not only presents maps for radiative cooling (RC) potential, but also for temperature (T_a) and relative humidity (RH) of Africa, and determines the influence of these weather parameters in cooling potential.

2. Data acquisition and methodology

Meteonorm database (Remund et al., 2019) was used to download the information from weather stations in Africa, corresponding to the radiation period from 1991 to 2010 and the temperature period from 2000 to 2009.

A total amount of 615 weather files were downloaded from Meteonorm, but some of them implied a worse performance of the interpolation. After analyzing the effect of some weather stations on the metrics of the prediction model, the observations of Tamanrasset (south of Algeria), Saint Helena Island (south of the Atlantic Ocean) and Pozo Izquierdo (south of Las Palmas de Gran Canaria) were neglected, as shown in Fig. 1.

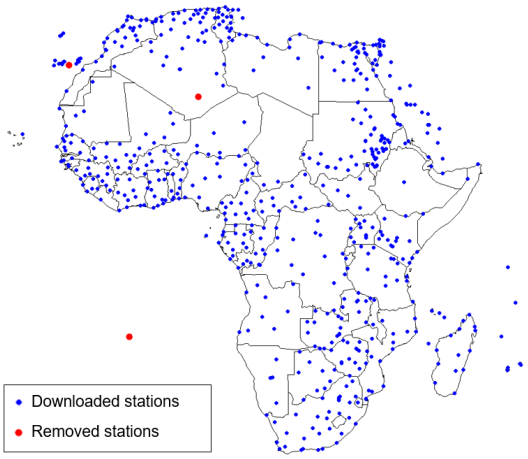

Fig. 1: Weather stations downloaded (blue) and removed (red)

RStudio was then used to clean and format the downloaded data, from which mean annual values at each location were calculated. Radiative cooling was determined using eq. 4. A mesh of 500,000 points was created to apply the spatial interpolation technique all over the continent. Although Northern Africa is the region where less stations are available, the selected interpolation method enables to have and accurate idea of RC potential on these countries.

$$q_c(T_a) = \sigma T_a^4 - q_{sky} \quad [Wm^{-2}] \qquad \text{(eq. 4)}$$

The infrared energy radiation emitted by the sky (q_{sky}) was obtained directly from the Meteonorm database, which calculates this parameter using the Aubinet model (Aubinet, 1994).

Kriging interpolation enabled to determine radiative cooling, dry bulb temperature and relative humidity at each point of the previously created grid of Africa. It is a geostatistical interpolation technique to estimate values and determine the uncertainty of each interpolated result (standard deviation). Weights are not only based on the distance (the points near to the point of study have a higher influence on the prediction), but also ensure an unbiased model and a minimum variance (Vilà et al., 2020). A variogram is used to determine the

weights of each point of the estimation and a mathematical model which best fits the variogram is found in order to minimize the error.

Data from the 612 files were divided into two subsets: 80% of the locations were used in the Kriging method, and the remaining 20% were used to evaluate the interpolation performance. 123 predicted values (x_{pred_i}) were compared with the observed ones (x_{obs_i}). The metrics of the prediction models examined were: the coefficient of determination (R^2, eq. 5) and the root mean squared error ($RMSE$, eq. 6).

$$R^2 = \frac{\sum_{i=1}^{N}\left(x_{pred_i} - x_{obs_i}\right)^2}{\sum_{i=1}^{N}\left(x_{obs_i} - \mu_i\right)^2} \quad \text{(eq. 5)}$$

$$RMSE = \sqrt{\frac{\sum_{i=1}^{N}\left(x_{pred_i} - x_{obs_i}\right)^2}{N}} \quad \text{(eq. 6)}$$

where μ_i is the arithmetic mean of the observed values (x_{obs_i}). R^2 is dimensionless, while $RMSE$ has the same units as the variable interpolated (cooling power, temperature and relative humidity).

3. Results and discussion

Annual values of average cooling power potential after interpolating are shown in Fig. 2. The highest RC potential is found in the Sahara Desert, especially in Algeria, Niger, north of Mali and Sudan; although with a lower capacity, South Africa also stands out.

A mean nighttime RC power potential of 77.64 Wm^{-2} is observed, which is higher than the average studied in United States (48.30 Wm^{-2}) (Li et al., 2019), Europe (47.30 Wm^{-2}) (Vilà et al., 2021) and Northwest China (Chinese region with the highest potential on average, 60.10 Wm^{-2}) (Chen et al., 2021).

Tropical region is remarkable for a low RC power potential with high temperature (above the average, Tab. 1) and very high relative humidity (around maximum values).

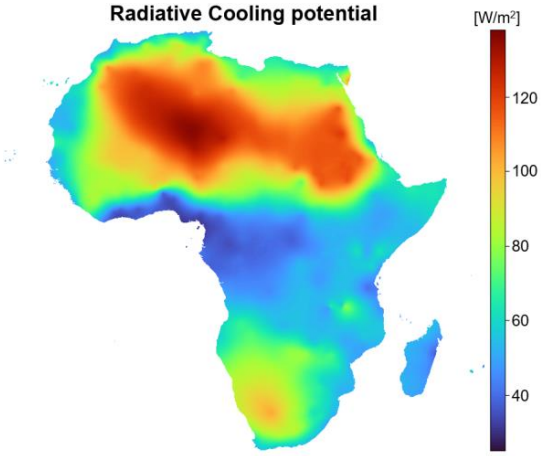

Fig. 2: Annual nighttime RC potential map of Africa

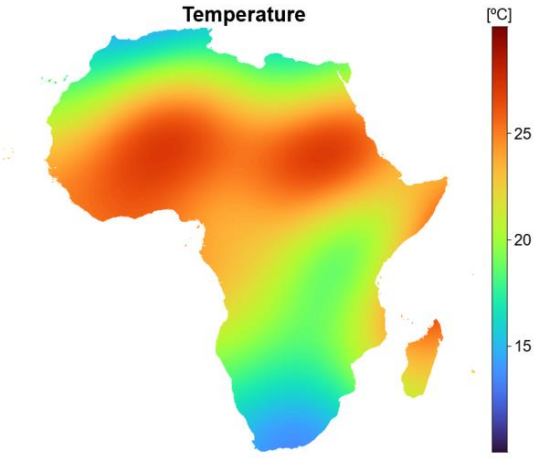

Fig. 3: Annual nighttime temperature map of Africa

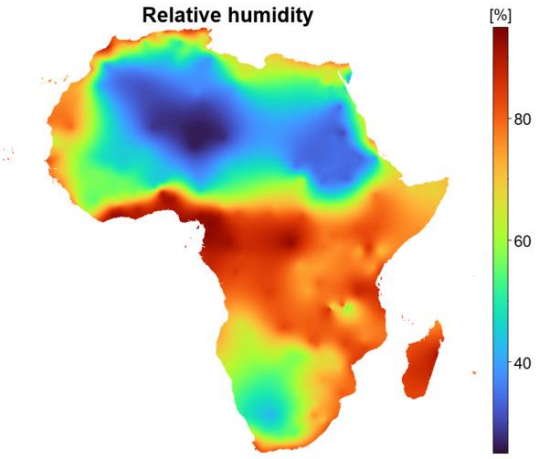

Fig. 4: Annual nighttime relative humidity map of Africa

The lowest RC potential is observed along the coastal zone from Nigeria to Gabon, with relative high T_a (Fig. 3) and extremely high RH (Fig. 4), confirming what demonstrated Dong et al. (2019).

It should be noted that the north of Africa is in the northern hemisphere, while the south of Africa is in the southern hemisphere. Both hemispheres have opposite seasons. The southern hemisphere is warmer in winter than the northern and cooler in summer (van Loon, 1991). On the other hand, countries like Gabon, Congo or Uganda, cross the equator and their climate conditions are stable through all the year. As the maps presented include mean annual results, these seasonal differences are not noticeable and do not affect the aim of this work: to estimate the average annual cooling power.

The best climate conditions in Africa for radiative cooling are: high temperature and low relative humidity, that is to say, the weather of the Sahara. Although there are some countries with low RH, specifically on the north, the tropical ones are very humid, which leads to mean values of RH above 60% (Tab. 1).

Tab. 1: Range and mean annual values of q_c, T_a and RH in Africa

	Minimum	Maximum	Mean
Radiative Cooling (q_c) [Wm^{-2}]	31.35	135.80	77.64
Temperature (T_a) [ºC]	13.63	27.96	21.95
Relative humidity (RH) [-]	25.98	93.29	60.93

Fig. 5, Fig. 6 and Fig. 7 show a clear comparison between predicted and observed data. A perfect interpolation would include all the points over the red straight line with a slope equal to 1. Analyzing the results, the average radiative cooling potential, temperature and relative humidity differences are 3.31 Wm^{-2}, 1.49 ºC and 2.68 %, respectively. As an overall, there are no big differences between the downloaded and the interpolated data, so results present a high coincidence.

On the other hand, the standard deviation maps (Fig. 8, Fig. 9 and Fig. 10) show that the points near the weather stations have less error (blue points), as expected. Maximum deviation points are located in regions with less climatic data available, like the Sahara Desert, Somalia and Namibia.

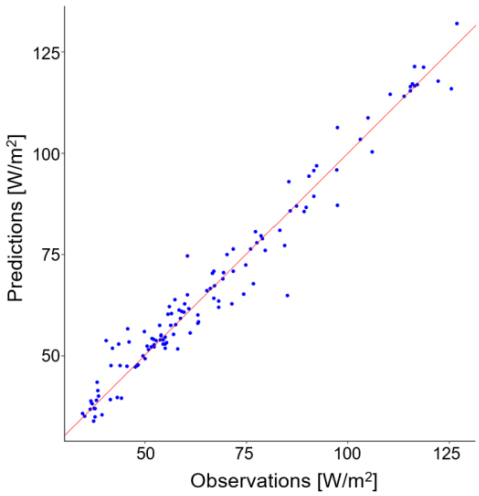

Fig. 5: Comparison between the predicted and the observed radiative cooling potential

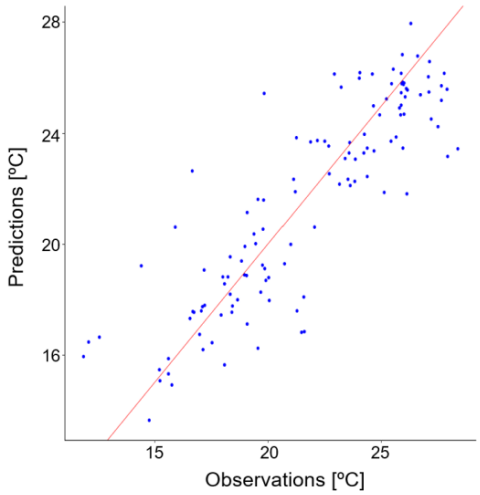

Fig. 6: Comparison between the predicted and the observed temperature

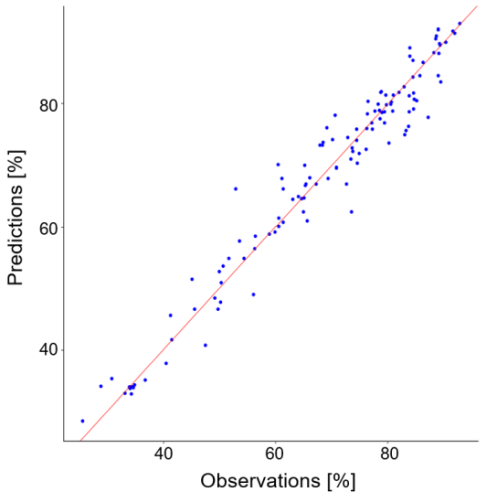

Fig. 7: Comparison between the predicted and the observed relative humidity

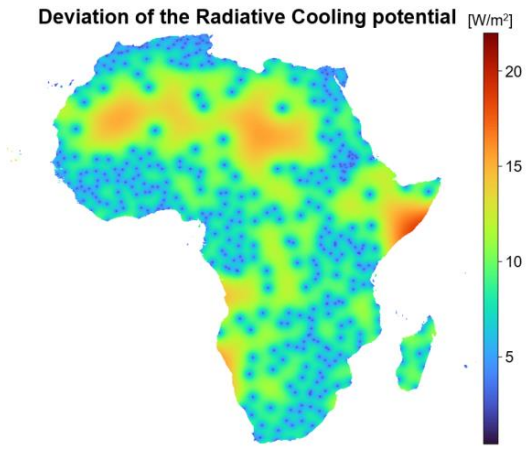

Fig. 8: Standard deviation of the nighttime radiative cooling potential of Africa

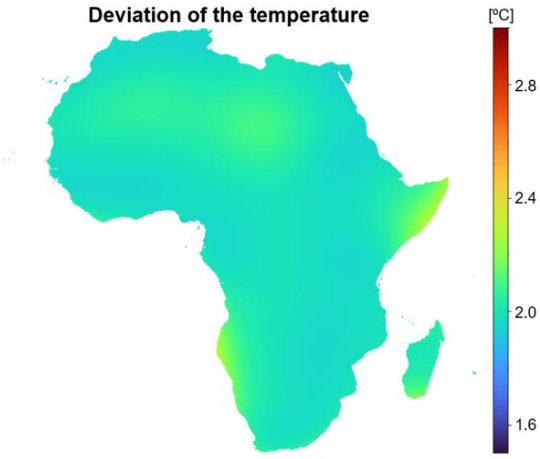

Fig. 9: Standard deviation of the nighttime temperature of Africa

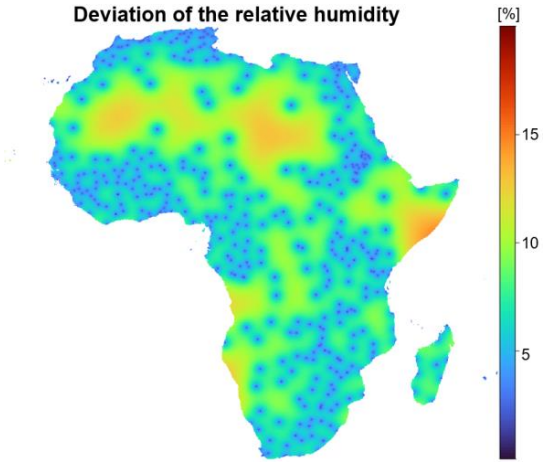

Fig. 10: Standard deviation of the nighttime relative humidity of Africa

q_c and RH show good accuracy (low RMSE values) and explain more than 95% of the variance (Tab. 2). Performance measures for the temperature show worse assessments metrics, but they are acceptable considering that the study by Li et al. (2016) (climatology field) endorse the results with a lower coefficient of determination.

Tab. 2: Measures of the prediction performance for each of the parameters calculated

	Radiative Cooling (q_c)	**Temperature (T_a)**	**Relative humidity (RH)**
R^2	0.96	0.75	0.95
RMSE	4.72 Wm^{-2}	2.01 ºC	3.75 %

4. Conclusions

In this work RC power potential has been mapped for Africa, showing an outstanding performance compared with United States, Europe and China, especially all over the Sahara Desert, where mean annual values above 100 Wm^{-2} are found, with peaks of 135.80 Wm^{-2}. Actually, the cooling potential of Africa is 64.14% higher than Europe, 60.75% higher than United States and 29.18% higher than Northwest China.

Vilà et al. (2021) found that the areas of Europe with the greatest RC power potential were the regions of southern Europe, so it makes sense that the north of Africa is characterized by the highest cooling power of this continent.

Temperature and relative humidity are climatic parameters which strongly affect RC and required conditions in Africa for 110 Wm^{-2} or more are: RH below 43% and T_a above 17ºC. Moreover, it has been corroborated what demonstrated Dong et al. (2019): high temperatures and low relative humidity are required to achieve high cooling power.

The spatial interpolation has correctly predicted nighttime RC power potential in Africa. Small differences between the predicted and the observed parameters are found and adequate metrics of R^2 and RMSE are obtained.

Future work could focus on the obtention of seasonal instead of annual values. This way, the effect of each hemisphere would be analyzed on the cooling power.

5. Acknowledgments

The authors would like to thank Generalitat de Catalunya for the project grant given to their research group (2017 SGR 659). The work was partially funded by the Spanish government under grant agreement RTI2018-097669-A-I00 (Ministerio de Ciencia, Innovación y Universidades). Jesús Monterrubio would like to thank Ministerio de Educación y Formación Profesional of the Spanish government for his fellowship of collaboration in University Departments.

6. References

Aili, A., Yin, X., Yang, R., 2021. Global Radiative Sky Cooling Potential Adjusted for Population Density and Cooling Demand. Atmosphere 12, 1379. https://doi.org/10.3390/atmos12111379

Aubinet, M., 1994. Longwave sky radiation parametrizations. Solar Energy 53, 147–154. https://doi.org/10.1016/0038-092X(94)90475-8

Bijarniya, J.P., Sarkar, J., Maiti, P., 2020. Review on passive daytime radiative cooling: Fundamentals, recent researches, challenges and opportunities. Renewable and Sustainable Energy Reviews 133, 110263. https://doi.org/10.1016/j.rser.2020.110263

Birol et al., 2018. The Future of Cooling. International Energy Agency.

Chang, K., Zhang, Q., 2019. Modeling of downward longwave radiation and radiative cooling potential in China. Journal of Renewable and Sustainable Energy 11, 066501. https://doi.org/10.1063/1.5117319

Chen, J., Lu, L., Gong, Q., 2021. A new study on passive radiative sky cooling resource maps of China. Energy Conversion and Management 237, 114132. https://doi.org/10.1016/j.enconman.2021.114132

Dong, M., Chen, N., Zhao, X., Fan, S., Chen, Z., 2019. Nighttime radiative cooling in hot and humid climates. Opt. Express 27, 31587. https://doi.org/10.1364/OE.27.031587

Li, M., Peterson, H., Coimbra, C., 2019. Radiative cooling resource maps for the contiguous United States. Journal of Renewable and Sustainable Energy 11, 036501. https://doi.org/10.1063/1.5094510

Li, Z., Wang, K., Zhou, C., Wang, L., 2016. Modelling the true monthly mean temperature from continuous measurements over global land. International Journal of Climatology 36, 2103–2110. https://doi.org/10.1002/joc.4445

Raman, A., 2018. How we can turn the cold of outer space into a renewable resource.

Remund, J., Müller, S., Kunz, S., Huguenin-Landl, B., Studer, C., Cattin, R., 2019. Meteonorm. Meteotest, Switzerland.

Vall, S., Castell, A., Medrano, M., 2018. Energy Savings Potential of a Novel Radiative Cooling and Solar Thermal Collection Concept in Buildings for Various World Climates. Energy Technology 6, 2200–2209. https://doi.org/10.1002/ente.201800164

van Loon, H., 1991. A review of the surface climate of the Southern Hemisphere and some comparisons with the Northern Hemisphere. Journal of Marine Systems 2, 171–194. https://doi.org/10.1016/0924-7963(91)90023-N

Vilà, R., Medrano, M., Castell, A., 2021. Mapping Nighttime and All-Day Radiative Cooling Potential in Europe and the Influence of Solar Reflectivity. Atmosphere 12, 1119. https://doi.org/10.3390/atmos12091119

Vilà, R., Rincón, L., Medrano, M., Castell, A., 2020. Radiative Cooling Potential Maps for Spain, in: Proceedings of the ISES EuroSun 2020 Conference – 13th International Conference on Solar Energy for Buildings and Industry. Presented at the EuroSun 2020, International Solar Energy Society, Online, pp. 1–9. https://doi.org/10.18086/eurosun.2020.09.01

Management and Operation of Qatar's Solar Radiation Monitoring Network

Daniel Perez-Astudillo[1], Dunia Bachour[1], Antonio Sanfilippo[1] and Hissa Al-Hajri[1]

[1] Qatar Environment and Energy Research Institute, Hamad Bin Khalifa University, Qatar Foundation, Doha (Qatar)

Abstract

Solar resource assessment in Qatar by the Qatar Environment and Energy Research Institute (QEERI) started in late 2012 with the deployment of a complete monitoring station in Doha to measure direct, global, diffuse and longwave (infrared) irradiances. In May 2019, another monitoring station was installed at the site of Qatar's first solar PV plant, and in collaboration with the Qatar Meteorological Department (QMD) a network of 13 high-precision monitoring stations was fully deployed later that year. Thus, QEERI's 15 stations across the country measure direct, global and diffuse radiations with one-minute resolution at all sites, in addition to the meteorological parameters measured by QMD, and some extra measurements (ultraviolet and infrared radiation) at two of the sites. This paper presents a description of the solar stations deployed in Qatar, with the related operation and management processes, covering from data collection to transmission and quality assurance, with an initial overview of the collected data.

Keywords: solar radiation, monitoring network, irradiance measurements, data quality

1. Introduction

At a latitude between 24 and 26 degrees north in the Middle East, Qatar is located in the Sun Belt region of the world, which promises a favourable potential for solar energy production; however, being a desert country with frequent sandstorm events, the local atmospheric conditions have important effects on the quality of available solar resources. Qatar has defined goals for the inclusion of renewable energy sources in its 2030 National Vision, primarily solar energy, with photovoltaic (PV) being the main technology, and Qatar's first large-scale PV plant is already operating since October 2022. Therefore, detailed studies of the solar resources are fundamental in order to not only properly assess Qatar's solar potential, but to support the deployment of solar power technologies both at large and small (including residential) scales.

QEERI, the Qatar Environment and Energy Research Institute, deployed its first complete high-precision solar radiation monitoring station in Education City, Doha, in November 2012 (Perez-Astudillo and Bachour, 2014), while a large network of stations across the country was being designed and developed, and QMD, the Qatar Meteorology Department, had been measuring global horizontal radiation (G) for some years already at several stations across Qatar (Bachour and Perez-Astudillo, 2014a and 2014b). In May 2019, QEERI installed a monitoring station at Al Kharsaah, the site where Qatar's first solar PV plant would be built (construction started near the end of 2020), and in the second half of 2019 QEERI deployed a network of 13 additional stations sharing several sites with QMD. In line with QEERI's vision of supporting the development of clean, renewable energy in Qatar, this network provides critical data for solar energy projects, both small- and large-scale, with some of the initial data already having been used for the planning development of the Al Kharsaah plant, with more projects currently in development.

The following sections describe the distribution of the monitoring stations and an overview of the managing process, from maintenance to data collection, retrieval and quality checking for monitoring the operation, and finally some initial views of data collected from the first years of operation.

2. Stations

© 2022. The Authors. Published by International Solar Energy Society
Selection and/or peer review under responsibility of Scientific Committee
doi:10.18086/eurosun.2022.15.06 Available at http://proceedings.ises.org

Figure 1 illustrates the locations of the 15 stations (see also Table 1). The top right-side graph in the figure presents the distances between all possible pairs of stations, while the bottom right-side graph shows the distances to the nearest neighbour. The longest distances are in the north-south direction, given the country's geography; note also that Qatar's geography is mostly flat, and the station elevations range between sea level and around 50 m above sea level. This dense monitoring network provides an excellent spatial coverage of the country, with a compact distribution of gap distances (bottom right of Fig.1) between 10 and 35 km.

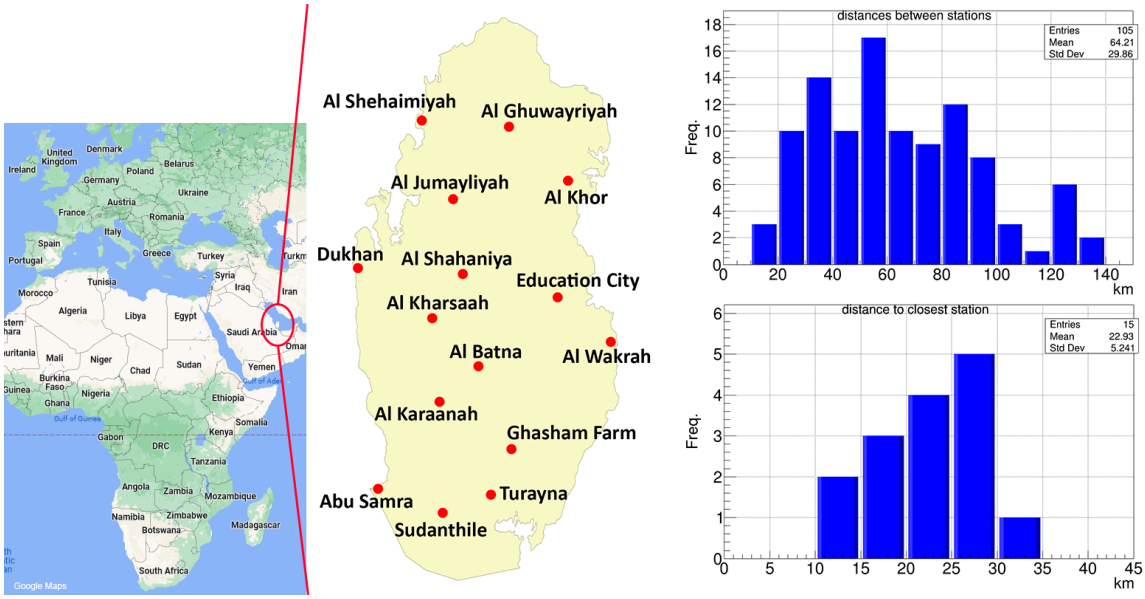

Figure 1: Locations of QEERI's solar radiation monitoring stations in Qatar, and the distributions of distances between them, and of distance to the nearest neighbouring station.

Tab. 1: Locations of the 15 solar radiations monitoring stations.

Site	Lat (deg. N)	Lon (deg. E)	Site	Lat (deg. N)	Lon (deg. E)
Abu Samra	24.75	50.82	Al Shahaniya	25.39	51.11
Al Batna	25.10	51.17	Al Shehaimiyah	25.86	50.96
Al Ghasham	24.85	51.27	Al Wakrah	25.19	51.62
Al Ghuwayriyah	25.84	51.27	Dukhan	25.41	50.76
Al Jumayliyah	25.61	51.08	Education City	25.32	51.42
Al Karaanah	25.01	51.04	Sudanthile	24.63	51.06
Al Kharsaah	25.22	51.00	Turayna	24.74	51.21
Al Khor	25.66	51.46			

At all 15 stations, the three so-called components of broadband solar radiation are measured, namely beam or direct normal (Gb), global horizontal (G) and diffuse horizontal (Gd) irradiances. All stations use ISO 9060:2018 Class A (https://www.iso.org/standard/67464.html) thermopile sensors (two pyranometers and one pyrheliometer) for each component, mounted on a sun tracker with sun sensor and shading ball or disk, and all are powered by solar panels with battery storage, except for the Education City station, which is located at the rooftop of QEERI's building.

Solar radiation measurements are sampled at 1 Hz and saved as one-minute averages in W/m^2 by their on-site data

loggers. The stations were deployed, and are managed, in three groups, hereby called “Education City”, “Al Kharsaah”, and “network of 13”. The process of data retrieval is automated for each of these groups as follows:

- Education City (red in Figure 2). The station is on the rooftop of the QEERI building in Doha, and the data logger is connected via a serial cable to a laboratory workstation, with automated data download every 30 minutes.
- Al Kharsaah (green in Figure 2). The logger uses a GSM modem and SIM card to connect to the internet, and a workstation in QEERI’s premises pulls the data every 30 minutes.
- Network of 13 (blue in Figure 2). The loggers also use a GSM modem and SIM card to connect to the internet. In an initial configuration, the loggers sent the data as email attachments to an email account, from which the data were pulled to a local server in QEERI, and then inserted into a database. Recently this has been changed to using a cloud server between loggers and local server, replacing the email method. As Ammonit data loggers are used in this network, the AmmonitOR cloud service (https://www.ammonit.com/en/products/online-services/product-details/ammonit-online-report-ammonitor/) is used, which allows for an easy user-friendly logger configuration, and provides an API for automated data downloads.

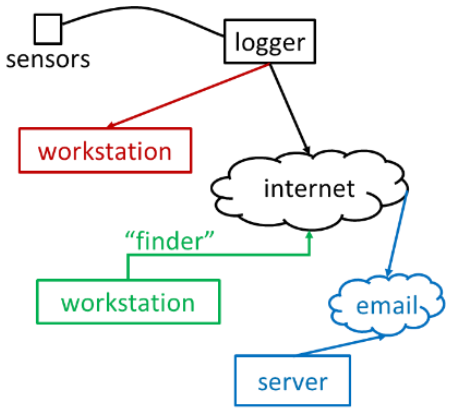

Figure 2: Representation of the data retrieval methods used.

Thus, in the 14 remote (outside Education City) stations, the data logger’s connection to the internet is currently done via Qatar’s mobile telephone providers. This means that data retrieval relies on the availability of the mobile service connection at the scheduled transmission times. Given that most stations are not located inside or next to cities or villages, and in spite of the good mobile coverage across Qatar, the loggers often lose connection and are unable to transmit data with the scheduled frequency. In their current setup, the loggers in the network of 13 stations can display the current strength of the mobile signal as a percentage from 0 to 100%, so a record has been kept of these values since 2020, sampled at each maintenance visit, i.e. twice per week (maintenance is described in the next section). Figure 3 shows the signal strengths observed at each visit and their averages per year for the 13 sites for 2020 and 2021, and from January to May 2022. As a whole, the all-site, all-time average is 69%, with the highest averages in Al Karaanah (100%) and Abu Samra (96%), and the lowest values in Al Shehaimiya (51%), Al Batna (53%) and Al Shahaniya (55%). Note, however, that these values are on-site samples taken by the maintenance team twice a week at best, and high values here do not necessarily imply that good connections are available all the time; due to the ‘manual’ and sporadic nature of the signal observations (which were not coincident with the time of scheduled data transmission) and to high variability of the signal strength (the value frequently had large oscillations during the few seconds in which the technicians made the observations), total uptime was not recorded, and a lower limit on the signal strength needed for successful transmission was not determined (except, naturally, that a signal of 0% results in no connection). Nevertheless, these values provided a general view of the communications conditions and highlighted a need for improvement; indeed, one possible cause of signal losses is that the modems used are 3G-capable only, and Qatar’s operators have moved to 4G and recently to 5G, so 3G coverage is less reliable.

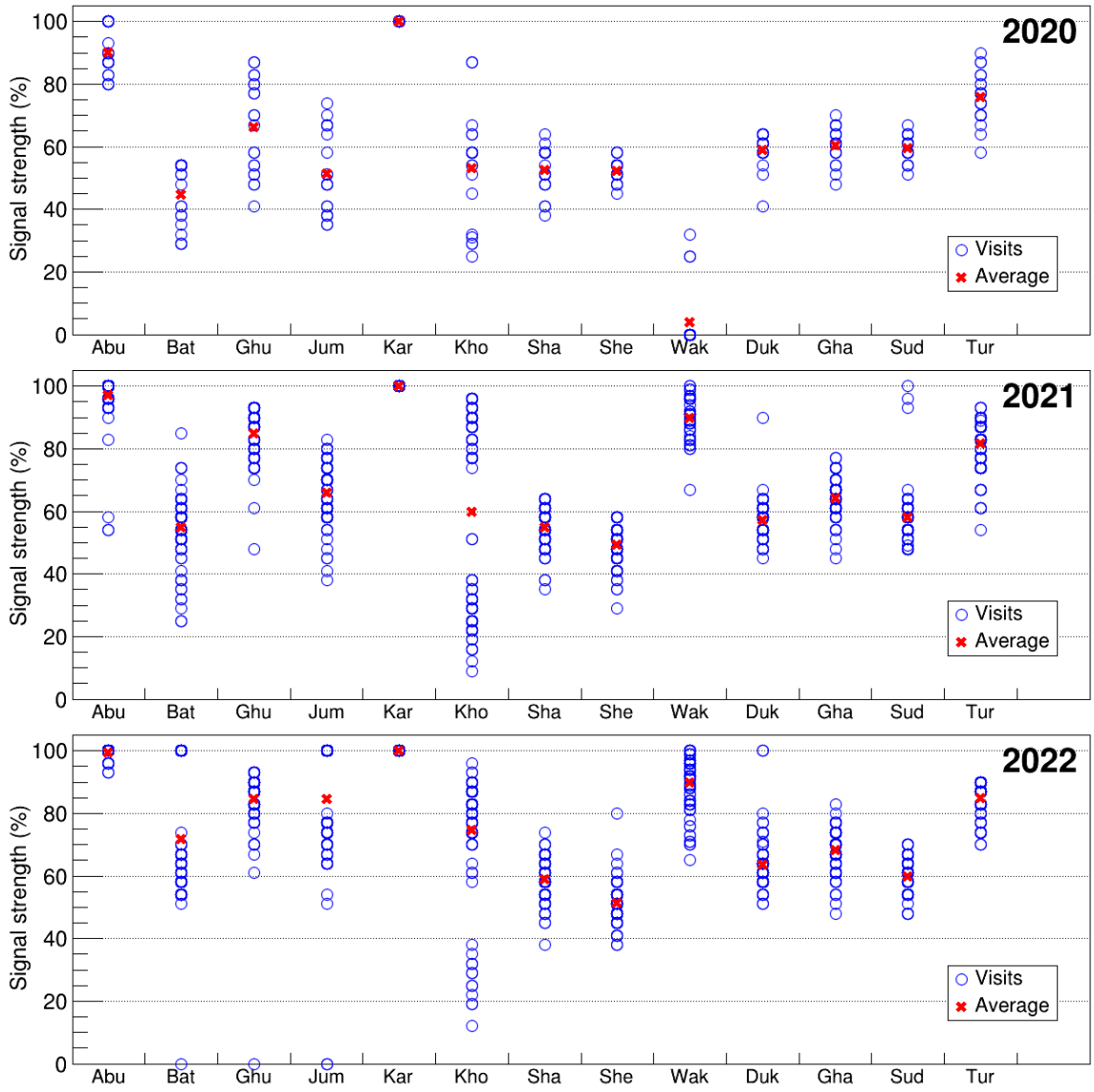

Figure 3: Mobile connection strength observed at each visit (blue circles) and their annual averages (red cross) at the 13 sites, Jan/2020 to May/2022.

3. Operations, data

3.1. Maintenance

A high-precision station, like the ones used here, requires itself close monitoring and frequent preventive maintenance in order to reduce risks and durations of malfunctions and low-quality measurements. Considering distances and nearby locations between the different stations, the schedule of the maintenance for the stations was designed in a way to cover all the 15 sites in three days, resulting in two site visits per week for all sites. Given the desert environment for these stations, the most important activities are the cleaning of sensor domes, windows, bodies (including tracker, cabinets and PV panels, etc.), but also include checks on alignment, levelling, shading and general site conditions.

In the period from 1/Jan/2020 to 31/May/2022, on average the stations were visited for maintenance once every 3.6 days. This average, however, excludes the values from two sites, namely Education City and Abu Samra, during 2020, when due to Covid-19 lock-downs access to these sites was restricted for some periods. Figure 4 shows the annual averages of days between visits for the 15 sites.

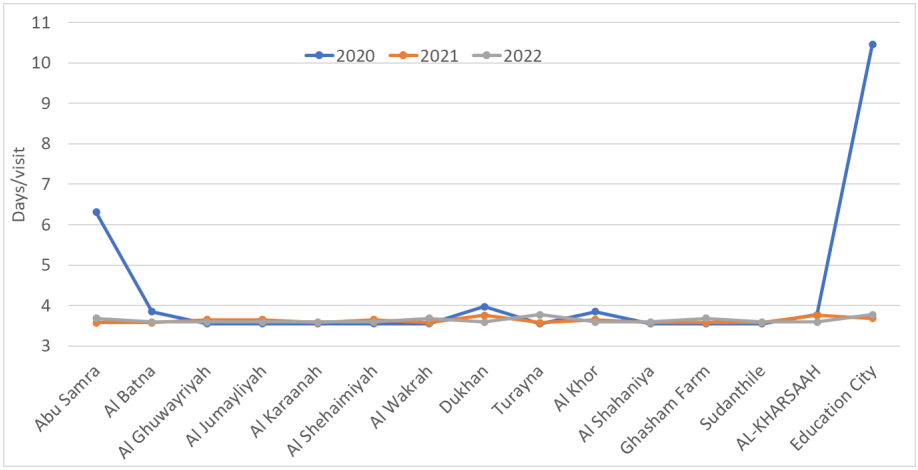

Figure 4: Annual averages of number of days between maintenance visits for all sites, Jan/2020 to May/2022.

Some of the most frequent corrections made by the technicians during these visits include the levelling of pyranometers. Also, at some sites the loggers occasionally report that the modem is unavailable, or that the signal strength is 0%; in these cases, a reboot of the modem generally corrects the issue with the signal strength restored to the usual value at the site. Other issues observed have been faster corrosion on cabinets at the coastal sites and, in a few pyranometers, an expansion and then disappearance of the bubble level, possibly due to an imperfect sealing of the bubble compartment and loss of liquid due to evaporation.

3.2. Data Monitoring

From here on, the rest of this work relates only to the data collected by the network of 13 stations, which, as explained in section 2, is managed as a group, and provides the largest amount of solar resource data. Data collected from the network of 13 stations is monitored in real time using a data display system based on the open-source web application Grafana (https://grafana.com), through which the measured data points are shown on maps, tables, or on graphs spanning a given time interval. This display system is designed for real-time monitoring of the general operation and of the data collection.

To complement this display system, a reporting tool was developed in-house that automatically runs every morning to analyse the data (from each of the 13 sites separately) of the previous day, doing quality checks and generating a report in PDF format and mailed to the person in charge. These reports (to be described in a separate paper) consist of one page per site showing different key details like the number of collected minutes and some results of the quality checks, with graphs that help identify some common problems. The quality checks done in this automatic tool include: maximum physically possible limits, consistency between Gb, G and Gd (i.e. G = Gb*cos(SunZenithAngle) + Gd) and ratio Gd/G as per the BSRN recommendations, and two custom checks on the clearness index Kt and diffuse fraction Kd:

$$Kt = G / ETh \qquad \text{(eq. 1)}$$

$$Kd = Gd / G \qquad \text{(eq. 2)}$$

where ETh is the (calculated) top-of-the-atmosphere solar radiation projected on a horizontal surface at the corresponding time. The quality tests are described and discussed in (Perez-Astudillo et al., 2018) and correspond to numbers 3-5, 7-10, 14 and 15 in Table 1 of that work.

3.3. Spatial coverage and variations

As discussed in section 2, QEERI's dense network of stations provides a thorough spatial coverage of the country. For an assessment of the spatial variation of solar resources in Qatar, the difference in measured irradiances can be studied between all possible pairs of stations as a function of distance, as depicted in Figure 5, which shows the relative values (in %) of the mean bias difference (rMBD), mean absolute difference (rMAD) and root-mean-squared difference (rRMSD) as function of distance between each pair of stations, obtained from the 1-minute measurements of Gb (left side), G (centre) and Gd (right side). As the order of stations in each pair was basically random, the sign of MBD does not provide meaningful information. The increase of differences with distance is

clear on MAD and RMSD, especially for the direct and diffuse irradiances, being more sensitive than the global irradiance to local atmospheric variations (clouds and aerosols). This shows that in spite of Qatar's small size and flat geography, solar resources do indeed have measurable variations across the country, mainly due to varying aerosol loads in the atmosphere between coastal and inland locations.

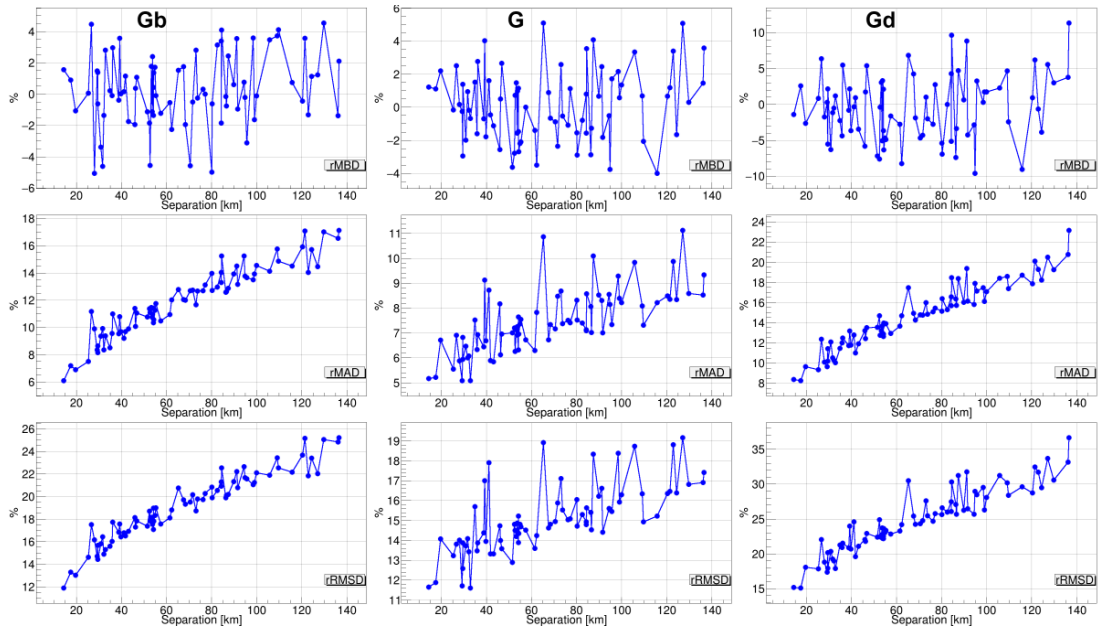

Figure 5: Relative differences (mean bias difference, mean absolute difference, root mean square difference) in measured Gb (left), G (centre) and Gd (right) at 1-min level, between all pairs of stations as function of distance, for the network of 13, Jan/2020 to May/2022.

As another indicator of spatial variability, the anomalies of daily irradiation in daily kWh/m^2 among sites are shown in Figure 6, for all days from 1/Jan/2020 to 31/May/2022. The anomalies here are calculated as the difference between the daily irradiation value from each station on a given day and the average of the daily values from all stations on that day. The empty bins correspond to days when a daily value could not be obtained for a given station due to a large number of missing data, where missing means either not collected or quality-rejected. As per the procedure established for these stations, a minimum of 85% of the daytime (from sunrise to sunset) 1-minute entries must pass the quality checks in order to allow for the calculation of a daily average; otherwise, the daily average is reported as missing. For sub-daily periods (e.g. 5-min, 10-min, 15-min, hourly), the criterion is that at least 50% of the minutes within that period must pass the quality checks. Therefore, a missing daily value does not necessarily mean that sub-daily averages are also missing. On the other hand, monthly and annual averages are obtained from the daily averages.

Overall, the largest variations are seen in direct irradiation, with not only the highest maximum and minimum, +3.10 and -3.15 kWh/m^2, respectively, but also more frequent larger anomalies throughout. For global irradiation, the maximum and minimum anomalies were +1.85 and -2.66 kWh/m^2, and for diffuse irradiation the values were +1.39 and -1.56 kWh/m^2. For context, the full-station, full-period average, maximum, and minimum of daily Gb were 5.70, 9.56, and 0.06 kWh/m^2 per day, respectively; for G, these values were 6.11, 8.58 and 1.27.

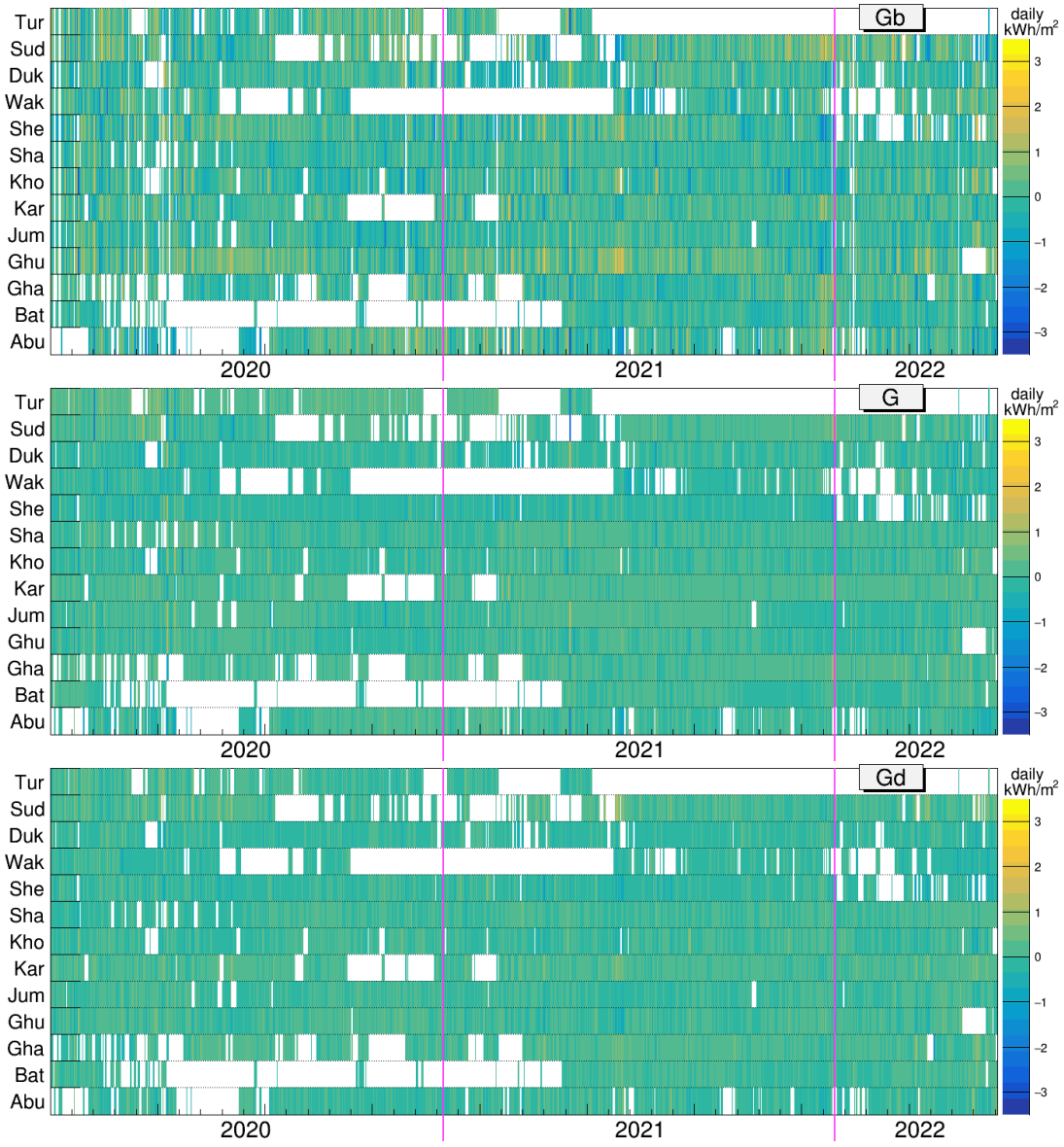

Figure 6: Daily irradiation anomalies, Jan/2020 to May/2022.

3.4. Longer-term view

To gain a better insight on the solar climate, it is important to look at data of as many years as possible; ideally at least one solar cycle. With the first 2.5 years of operation of the network of 13 stations, an initial view can be obtained. Figure 7 shows the monthly averages of the daily direct and global irradiations (values are daily kWh/m^2 during the month), as well as the monthly averages of daily clearness index Kt and diffuse fraction Kd (Kt and Kd are calculated first for each day from the daily values of G, Gd and ETh, and then averaged through the month).

Figure 8 shows the full-period (Jan/2020 to May/2022) averages of Kt and Kd. It can be seen that although Qatar has a relatively high clearness index (all-around average of 0.66), denoting usually low cloudiness, Kd is also high (all-around average of 0.38), denoting high levels of light diffusion that are unfavourable for concentrating solar technologies, for example.

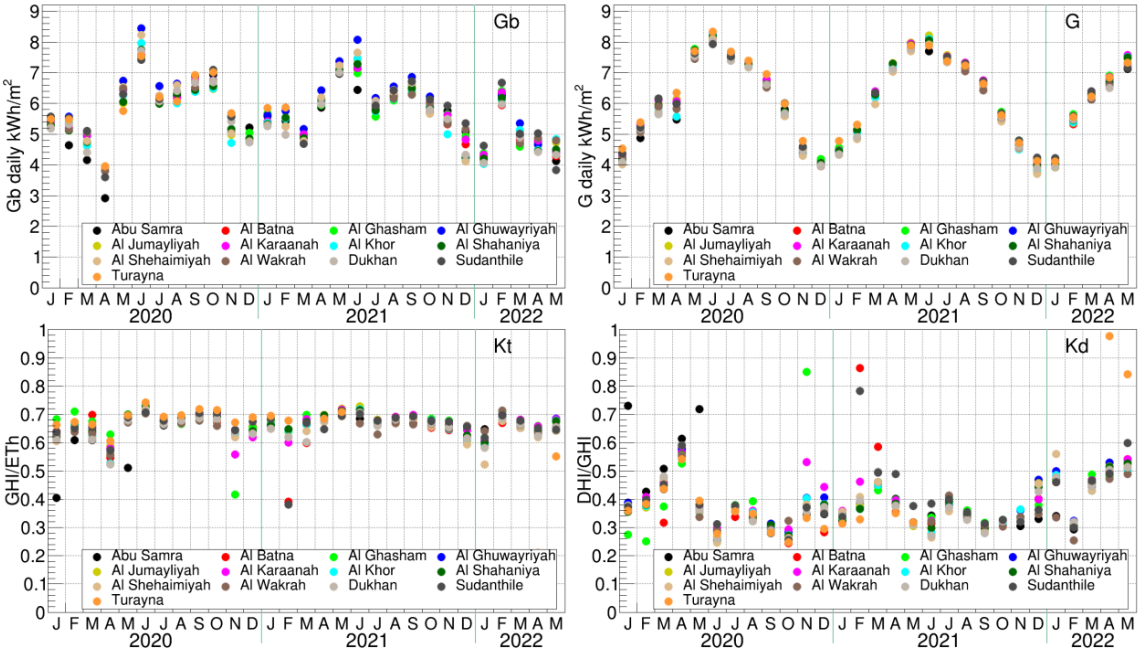

Figure 7: Monthly averages of Gb, G, Kt and Kd, Jan/2020 to May/2022, for each site.

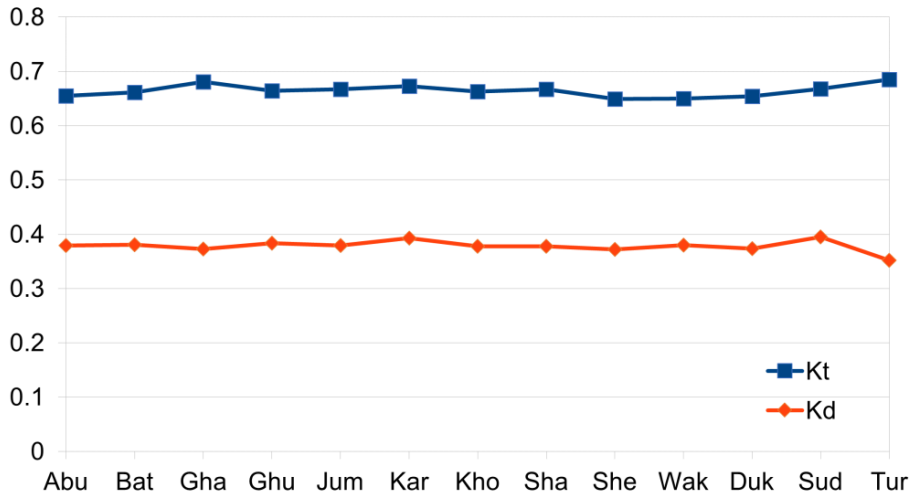

Figure 8: Full-period (Jan/2020 to May/2022) averages of Kt and Kd for each site.

4. Conclusions

QEERI currently operates 15 solar monitoring stations across Qatar, measuring direct, global and diffuse irradiances with high-precision pyranometers and pyrheliometers mounted on sun trackers. The generated one-minute data support the country's goals of sustainable and renewable energy production, with Qatar's first large-scale solar PV plant soon to start operations. This work provides a description of the continuous activities needed for maintaining and monitoring the operation of the stations, data retrieval and initial assessment of the quality of the generated data, with a first look at some results from the data collected during the first 2.5 years of country-wide monitoring. Although Qatar has a small size and mostly flat terrain, variations in solar resources, although not large, are observable. The stations provide a thorough coverage of the country, but the harsh weather conditions and difficult off-road access to some of the sites create challenges that have to be addressed or mitigated.

5. Acknowledgments

The authors thank the Qatar Meteorology Department for their support providing space in several of their weather monitoring sites to accommodate QEERI's monitoring stations.

6. References

Perez-Astudillo, D., Bachour, D. 2014. DNI, GHI and DHI Ground Measurements in Doha, Qatar. Energy Procedia 49, 2398-2404. DOI:10.1016/j.egypro.2014.03.254

Bachour, D., Perez-Astudillo, D. 2014a. Ground-measurement GHI Map for Qatar. Energy Procedia 49, 2297-2302. DOI:10.1016/j.egypro.2014.03.243

Bachour, D., Perez-Astudillo, D. 2014b. Ground measurements of Global Horizontal Irradiation in Doha, Qatar. Renewable Energy 71, 32-36. DOI:10.1016/j.renene.2014.05.005

Perez-Astudillo, D., Bachour, D., and Martin-Pomares, L. 2018. Improved Quality Control Protocols on Solar Radiation Measurements. Solar Energy 169, 425-433 DOI:10.1016/j.solener.2018.05.028

Study on Analysis of Solar Panel Efficiency in Vietnam- A Power Comparison before and post cleaning

Surender Rangaraju[1], Shakthi Bharath K[2], Amiya Bhaumik[3], Phu Le Vo[4] and Khuong Vinh Nguyen[5] ,

[1,3] Department of Business and Accountancy, Lincoln University College, Malaysia.

[1] Faculty of Business Administration, Van Lang University, Ho Chi Minh City, Vietnam.

[2] Department of Instrumentation and Control Engineering, PSG College of Technology - India

[4] Faculty of Environment and Natural Resources, Ho Chi Minh City University of Technology – Vietnam.

[4] Vietnam National University Ho Chi Minh City, Ho Chi Minh City, Vietnam

[5]School of Science, Engineering & Technology, RMIT University, Ho Chi Minh city, Vietnam

[5]Faculty of Electrical Engineering and Computer Science VSB - Technical University of Ostrava, Czech Republic

Abstract

Vietnam is developing as a solar energy powerhouse, ranking eighth in the world in terms of installed solar capacity. With a long coastline and continuous high solar irradiation levels, the country makes a strong push toward renewable energy to meet its rising demands for energy to drive economic growth. The effectiveness of solar panels installed in Vietnam are decreased due to mass accretion of dust, dirt spots, muddy build-ups and bird's droppings etc. Maintaining high-capacity panels would be a problematic if it is not consistently cleaned. In the PV sector, O&M aids in the effective cleaning process and ensures solar cell sustainability. Systematic polishing of solar panels leads to increase in the output power generation and tends to maintain a consistent performance in solar cells, allowing the country to meet its energy needs.

Keywords: Solar Panel maintenance, Solar efficiency analysis, O&M, PV cell sustainability

1. Introduction

Solar energy is expected to contribute for 0.5 percent of total energy output in 2020, 1.6 percent in 2025, and 3.3 percent in 2050, according to the Vietnam Renewable Energy Development Project to 2030 with a view to 2050. As a consequence, by 2050, total solar power output will have increased from a negligible level today to 12,000 MW. Massive financial investment in solar energy capacity is necessary to attain this goal. The continuous maximum effective energy absorbed from the sun particularly the solar panel, as the principal component in the supply system decreases installation and production costs while also making peak electrical power needs easier to meet (Duong Vu, 2021).

The experts have researched that the life expectancy of solar panels is 30 years (Surender Rangaraju O. I., 2021). The accumulation of dust has an impact on the net output power and reduces solar panel system performance dramatically. As a result, physical impurities such as dust, debris, dirty rain, bird droppings, and other potentially harmful elements must be kept away from the solar panels. The duration of the PV is determined by the scratching action on its surface (Energy & Natural Resources, 2017).

To clean solar panels, regular maintenance and monitoring activity is important; otherwise, the output efficiency would be dramatically reduced. Regular maintenance and the utilization of resources entail a significant expense, but conventional O&M services have guaranteed the yield of solar panels for a while. Yield for current and forthcoming new solar projects in Vietnam, an periodic O&M services will be the best alternative. As a consequence, cleaning PVs in line incessantly will make huge difference in output energy efficiency (Surender Rangaraju O. I., 2021).

© 2022. The Authors. Published by International Solar Energy Society
Selection and/or peer review under responsibility of Scientific Committee
doi:10.18086/eurosun.2022.15.07 Available at http://proceedings.ises.org

2. Literature survey

For the solar system to perform at its best, it must be clean. A crucial part of solar panel maintenance is routine cleaning. The amount of electricity delivered from a solar PV array varies daily, monthly, seasonally, and annually depending on the amount of dust that has accumulated on the solar panels. (Peng, 2023)

The quantity of irradiance that reaches the solar cells has a major impact on how much power a photovoltaic module can produce. The optimum yield or ideal output of a solar module depends on a variety of factors. However, one of the contributing factors that has a direct impact on photovoltaic performance is the environment. The performance of such systems may be compromised by environmental and natural variables such the accumulation of soil, salt, bird droppings, snow, etc. on the PV module surfaces. (Mohammad Reza Maghami, 2016)

It is becoming more crucial than ever to manage PV sites optimally and analyze their predicted performance. The summertime, when there is the most solar resource, is when soiling can have the biggest impact on efficiency. Sea salt, pollen, and other particulates from anthropogenic and natural causes like building, agriculture, and air pollution build up on the panels until they are washed off or cleared by rain. (Felipe A. Mejia, 2013)

The two main environmentally degrading variables that affect solar panels are high ambient temperatures and high levels of air dust. All solar plants across the world experience a significant reduction in energy generation due to the degradation of solar collector performance brought on by soiling. Transmission loss is brought on by the deposition of soil and other particles on solar collectors, or soiling. Due to the absorption and scattering losses of the incident light, the so-called "soiling" effect, which refers to particulate contamination of the optical surfaces, has been observed to significantly worsen energy yield. (Arash Sayyah, 2014)

Solar cleaning is a requirement in most solar manufacturers' warranties. The solar panel could not be covered by the warranty if it sustains damage and becomes inoperable. This is true if we are unable to show the manufacturers that the PV panels have been maintained properly. According to research, cleaned solar panels can operate up to 10% more efficiently than those that aren't constantly cleaned. The effectiveness of solar panels must therefore be maintained through routine cleaning. (Conserve Energy Future, n.d.)

Solar panels will need more regular and comprehensive maintenance if they are located in dust-prone places, such as close to busy roads and agricultural areas. Solar production may suffer if dust isn't removed from panels set in these locations. According to research, dust on PV panels reduces solar effectiveness by about 40%' in dust-prone areas. (Energy Matters, 2022)

The longevity of a solar panel system may be increased with regular cleaning. Solar panels that are dirty and aren't maintained and cleaned on a regular basis might not even survive as long. Solar panels are an expensive investment and ought to be handled accordingly. They can become soiled and damaged if they are not frequently cleaned, especially if material like bird droppings is left on them for an extended period of time. Maintaining PV panels and keeping them clean will not only help them produce the most electricity possible but will also ensure that they are not deteriorating more quickly than they should. In the end, routine cleaning makes sure you get the best potential return on your investment. (Karlsson, 2021)

Trina Solar, one of the top solar panel manufacturers in the world, includes the following in a maintenance and care manual... "A solar module's ability to produce energy is directly related to the amount of light that strikes it. Because a module with shaded cells will produce less energy, maintaining the module's cleanliness is crucial. (Solar Panel Cleaning LTD, n.d.)

What maintenance is necessary for my solar panels, advises Panasonic, a renowned global firm and producer of solar photovoltaics? Your solar panels should be cleaned of dust and debris twice a year. The following are some of Panasonic's limited warranty exclusions: "Inadequate maintenance" and "damage or corrosion brought on by environmental pollution like soot and mold." (Solar Panel Cleaning LTD, n.d.)

Canadian Solar, one of the top producers of solar pv modules, advises cleaning the panels if a lot of debris accumulates on them. They also suggest that the optimum water has a PH that is close to neutral and has a low mineral concentration.

First Solar states that "In locations with heavy soiling, properly timed module cleaning can improve energy yields." They also claim that "RO water provides the best results." (Solar Panel Cleaning LTD, n.d.)

According to 8.33 Solar, a company that has been providing services to the European solar sector since 2006, "Over time, dirt and dust can build up on the module's glass surface, decreasing its power production. To guarantee maximum power generation, Solar 8.33 advises routine cleaning of PV modules. (Solar Panel Cleaning LTD, n.d.)

Currently, it is estimated that cleaning solar panels uses roughly 10 billion gallons of water annually, which is enough to supply drinking water for up to 2 million people. Waterless cleaning methods require a lot of labor and can leave surfaces scratched permanently, which lowers their effectiveness. Now, a team of MIT researchers has developed a method of mechanically cleaning solar panels or the mirrors of solar thermal plants in a waterless, no-contact technique that might greatly minimize the dust issue. (Chandler, 2022)

At Google's 1.6 MW solar farm in Mountain View, California, a ground-breaking experiment was carried out, and it was discovered that cleaning solar panels was "the number one way to maximize the energy they produce." 15-month-old solar panels that had been operating for cleaning nearly increased their electrical production. (Singh, n.d.)

The solar panels shouldn't be trodden on while being cleaned. Water and other substances that may penetrate the panels through tiny holes might seriously damage the facility. In order to improve energy efficiency and assure sustainability in power plants, robot cleaning produces expert solutions. (Robsys, n.d.)

Solar panel cleaning robots are a solution that makes it possible to produce renewable energy more effectively without using any more precious natural resources. (Leichman, 2022)

The extent to which automation and robot module cleaning are being used by owners and operators of large-scale PV projects has been revealed through a first-of-its-kind survey. The use of robotics in solar operations and maintenance (O&M) is growing, and there is growing awareness of their advantages in terms of increased power production, maximized return on investment, and improved efficiency. This is the clear trend, which is reflected in the geographical expansion of solar and the growth of projects. Its capacity to effectively clean thousands of modules is one of the most important factors to take into account when selecting a robotic cleaning solution. Cleaning modules by hand is no longer feasible due to the hundreds or even thousands of megawatts of solar site capacity, both physically and monetarily. (PV MAGAZINE, 2022)

Solar panels' ability to convert sunlight into electricity is reduced when they are dirty. Solar panels perform worse when covered in dust and dirt. This causes a significant loss in both money and renewable energy. A fully automated solar panel cleaning service employs drones to install cleaning robots on solar panels. The panels can be made more effective, resulting in more green energy production and increased financial gain. (Neira, 2022)

3. Research Problem

Sao Mai PV1, one of the large scale solar project in Vietnam with the area of 275 hectares Which produces about 210MW of peak capacity. It is researched that there is a huge power production loss recent days. The assumptions are accumulation of dust and poor solar panel maintenance will be the reason for the losses occurred. So, research is carried out whether the augmentation of dust particles and dirt spots really a problem for shrinkage of average output efficiency.

4. Methodology and Tools

The experimental study on power comparison before and after cleaning is done. At First, readings are taken 7 times according to the company standards from 8:55 AM to 3.00 PM. All strings are connected to the string monitoring box and the readings are derived from the process display. For the research, a total of six sets of uncleaned solar strings (i.e. 1 to 6) and two sets of cleaned strings (i.e. 7 and 8) taken into account. A Continues cleaning of strings 7 and 8 immediately after every reading is done. It is observed that there is a tremendous difference in the output efficiency from the cleaned strings compared to the uncleaned strings. The research methodology concludes poor panel maintenance and accretion of dust caused a recurring loss.

We used a SCADA system (Supervisory Control and Data Acquisition), an efficient asset management system that use state of technology to efficiently and proactively manage huge solar farms to collect the readings. With the integration of CMS (Central Management System) asset managers and O&M provider can Optimize and control energy assets and maintain a productive environment. This study utilized the SCADA system deployed

by Inaccess company to monitor and control the solar panels deployed at Sao mai solar farm- Vietnam.

5. Efficiency Analysis in a Solar Farm

The energy from the solar panel is crucial. Maintaining the efficiency of the solar panel is necessary. The analysis was done at Sao Mai group solar farm in Vietnam. The study gone through the farm and analyzed certain factors that the panels are cleaned 100 days in a year and the efficiency is exceptionally high from cleaned string of panels when compared to uncleaned one.



Fig 1 : Sao Mai PV1 solar farm at vietnam

6. Cleaning Analysis

Traditional cleaning of solar panels at Vietnam requires manpower, water, water truck, cleaning liquid and cleaning equipment's. The total installed strings of panels are 17,967. For one string of panel, it consists of nearly 60 - 90 panels wired together. The cleaning and maintenance of the panels is done at frequency of twice a year.



Fig.2 : Traditional cleaning of panels

Generally, for cleaning a string a panel at least 9-10 individuals involved and a total of 200 individuals are employed for the entire cleaning process and the green vegetation grown also provide a disturbance for cleaning the panels and additional 20 employees are employed for clearing the ground.

7. Efficiency Analysis Before and After cleaning

The efficiency of the panel has produced a low output from string 1 to 6 and 7,8 in Fig 3.Since the string reading are taken at low irradiance level at 8:55 AM.The results shows that there is a slight increase in the average power comparing the values 6503.9 W and 6588.4 W.

uncleaned string -1,2,3,4,5,6				
Cleaned string - 7,8				
	Before Cleaning			
Time	**8:55 AM**			
String	**current I(A)**	**Voltage (V)**	**Power(W)**	**Average value(W)**
1	5	1267	6335	6503.9
2	5	1267	6335	
3	4.9	1267	6208.3	
4	5.2	1267	6588.4	
5	5.3	1267	6715.1	
6	5.4	1267	6841.8	
7	5.3	1267	6715.1	6588.4
8	5.1	1267	6461.7	
	performance before Cleaning			1%

Fig.3: Performance of the strings before cleaning

The readings taken at 10:30 AM, the average power value gets gained comparing values 3402.8 W and 3801 W . Thus after the cleaning procedures gets over we can see the average power value gets a drastic increases when compare to uncleaned strings at rate of 12 percent.

Time	**10:30 AM**			
String	**Current DC I(A)**	**Voltage DC (V)**	**Power DC (W)**	**Average value (W)**
1	3.2	1086	3475.2	3402.8
2	3	1086	3258	
3	3.1	1086	3366.6	
4	3.2	1086	3475.2	
5	3.1	1086	3366.6	
6	3.2	1086	3475.2	
7	3.5	1086	3801	3801.0
8	3.5	1086	3801	
	Performance after Cleaning			12%

Fig. 4: Performance of the cleaned strings at 10:30 AM

The readings taken at 11:30 AM, the average power value gets surged comparing values 11022.9 W and 12706.2 W at rate of 15 percent.

Time	11:30 AM			
String	Current DC I(A)	Voltage DC(V)	Power DC(W)	Average Value (W)
1	9.3	1086	10099.8	11022.9
2	9.6	1086	10425.6	
3	9.7	1086	10534.2	
4	10.8	1086	11728.8	
5	10.9	1086	11837.4	
6	10.6	1086	11511.6	
7	11.8	1086	12814.8	12706.2
8	11.6	1086	12597.6	
	Performance after Cleaning			15%

Fig. 5: Performance of the cleaned strings at 11:30 AM

The readings taken at 12:15 PM, the average power value gets stepped-up comparing values 15973.3 W and 18267.8 W at rate of 14 percent.

Time	12:15 PM			
String	Current DC I(A)	Voltage DC(V)	Power DC(W)	Average Value (W)
1	14.6	1059	15461.4	15973.3
2	14.6	1059	15461.4	
3	14.9	1059	15779.1	
4	15.2	1059	16096.8	
5	15.5	1059	16414.5	
6	15.7	1059	16626.3	
7	17.3	1059	18320.7	18267.8
8	17.2	1059	18214.8	
	Performance after Cleaning			14%

Fig. 6: Performance of the cleaned strings at 12:15 PM

The readings taken at 2:00 PM, the average power value gets boosted comparing values 13707.9 W and 15055.6 W at rate of 10 percent.

Time	2:00 PM			
String	Current DC I(A)	Voltage DC(V)	Power DC(W)	Average Value (W)
1	12.7	1064	13512.8	13707.9
2	12.8	1064	13619.2	
3	12.8	1064	13619.2	
4	12.9	1064	13725.6	
5	13	1064	13832	
6	13.1	1064	13938.4	
7	14.2	1064	15108.8	15055.6
8	14.1	1064	15002.4	
	Performance after Cleaning			10%

Fig. 7: Performance of the cleaned strings at 2:00 PM

The readings taken at 2:30 PM, the average power value gets incremented comparing values 6480 W and 7614 W at rate of 18 percent.

Time	2:30 PM			
String	Current DC I(A)	Voltage DC(V)	Power DC(W)	Average Value (W)
1	5.8	1080	6264	6480.0
2	5.8	1080	6264	
3	6	1080	6480	
4	6	1080	6480	
5	6.1	1080	6588	
6	6.3	1080	6804	
7	7	1080	7560	7614.0
8	7.1	1080	7668	
	Performance after Cleaning			18%

Fig. 8: Performance of the cleaned strings at 2:30 PM

The readings taken at 3:00 PM, the average power value gets hiked comparing values 3730.1 W and 4519.2 W at rate of 21 percent. The average power value is calculated in watts tends to be increase in efficiency of the string and total average power of cleaned strings surged at the rate 15 percent.

Time	3:00 PM			
String	Current DC I(A)	Voltage DC(V)	Power DC(W)	Average Value (W)
1	3.5	1076	3766	3730.1
2	3.3	1076	3550.8	
3	3.3	1076	3550.8	
4	3.5	1076	3766	
5	3.6	1076	3873.6	
6	3.6	1076	3873.6	
7	4.2	1076	4519.2	4519.2
8	4.2	1076	4519.2	
	Performance after Cleaning			21%
Average performance increase after Cleaning				15%

Fig. 9 : Total average performance of cleaned Strings

Consequently, the strings will always provide superior efficiency when the strings are scrubbed in a frequent manner.

8. Findings

The study was carried out on cleaned and uncleaned solar strings. It is found that dust spots and muddy build-ups drastically decrease output power value .The Test carried out cleaning 2 strings out of 8 strings on a regular basis. . From the study, the results showed an absolute contrast between the efficiency of the panels If the strings are not cleaned or maintained appropriately it will not only rupture the panel but also cause monumental damage to energy production.

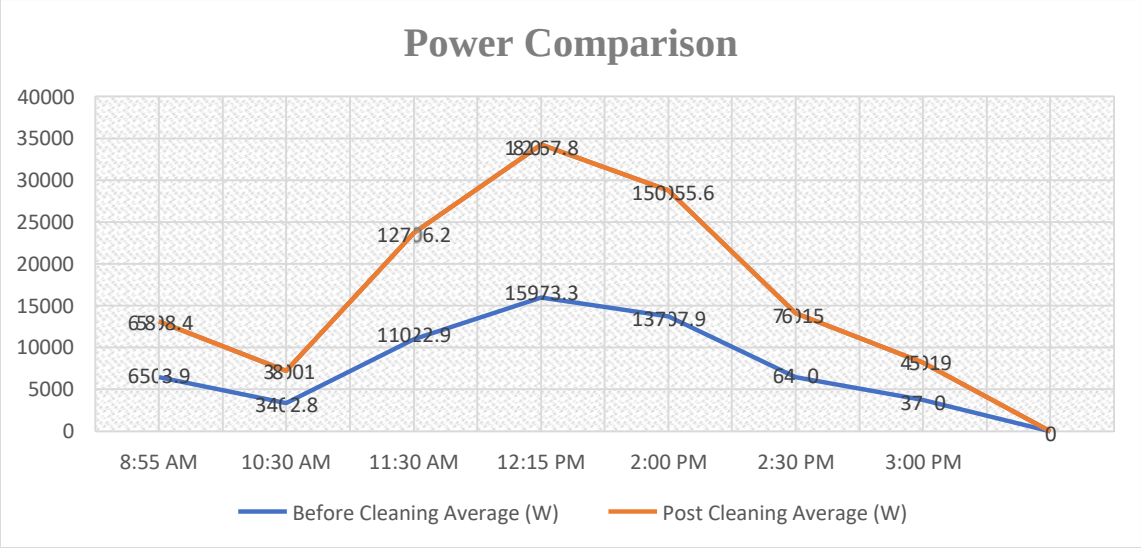

Fig. 10: Power Comparison Chart

9. Conclusion

Based on the study we emphasize that regular O&M services are extremely crucial in power generation that uses renewable energy sources, particularly solar energy. Even though, the maintenance includes labor expenses and other costs. Consistent washing is efficient in solar panel O&M which ensure panel free from dust and wrecks. More importantly in this efficiency analysis, the result from the solar farm shows tremendous surge of energy after cleaning compared to prior to cleaning of strings. As different methods of dusting are implemented to regulate strings tenability. The periodic serviceability on panels is indispensable in case of cell efficiency and durability.

10. Acknowledgments

I would like to thank the following people who have helped me undertake this analysis. Mr. Truong Vinh Thanh, Vice General Director- Sao Mai group, for his unconditional support, encouragement, and guidance. I also would like to thank Mr. Duy, Vice General Director and Mr. Nguyen Phung Quan, Manager – Sao Mai group for providing valuable insight on the solar plant installation and maintenance procedure. Without their support and guidance this analysis wouldn't be possible.

11. References

Arash Sayyah, M. N. (2014). Energy yield loss caused by dust deposition on photovoltaic panels. *Solar Energy*, 576-604. doi:https://doi.org/10.1016/j.solener.2014.05.030

Chandler, D. L. (2022, March 15). *solar-panels-waterless-clean*. Retrieved from www.weforum.org: https://www.weforum.org/agenda/2022/03/solar-panels-waterless-clean/?DAG=3&gclid=EAIaIQobChMIsZ6u4JXU_gIVl4WWCh1dUQ9WEAMYASAAEgJ_wvD_BwE

Conserve Energy Future. (n.d.). *how-clean-solar-panels*. Retrieved from conserve-energy-future.com: https://www.conserve-energy-future.com/how-clean-solar-panels.php

Duong Vu, A. A. (2021). Solution for robot cleaning the photovoltaic panels in Vietnam. *The 6th International Conference on Engineering Mechanics and Automation (ICEMA 6).*

Energy & Natural Resources. (2017). *Solar Panel Positioning Robots Market - Global Industry Analysis, Size,*

Share, Growth, Trends, and Forecast 2017 – 2025. Retrieved from transparencymarketresearch: https://www.transparencymarketresearch.com

Energy Matters. (2022, August 15). *solar-panels-cleaning*. Retrieved from www.energymatters.com.au: https://www.energymatters.com.au/renewable-news/solar-panels-cleaning/

Felipe A. Mejia, J. K. (2013). Soiling losses for solar photovoltaic systems in California. *Solar Energy*, 357-363. doi:https://doi.org/10.1016/j.solener.2013.06.028

Karlsson, D. (2021, September 2). *the-many-benefits-of-solar-panel-cleaning*. Retrieved from bigskyenergy.com.au: https://bigskyenergy.com.au/the-many-benefits-of-solar-panel-cleaning/

Leichman, A. K. (2022, 9 20). *robots that clean solar panels without water*. Retrieved from israel21c.org: https://www.israel21c.org/robots-that-clean-solar-panels-without-water/

Mohammad Reza Maghami, H. H. (2016). Power loss due to soiling on solar panel: A review. *Renewable and Sustainable Energy Reviews, 59*, 1307-1316. doi:https://doi.org/10.1016/j.rser.2016.01.044.

Neira, J. (2022, 03 07). *HELIOS robot cleans solar panels to make them more efficient*. Retrieved from www.designboom.com: https://www.designboom.com/technology/helios-art-robotics-solar-panel-cleaning-robot-03-07-2022/

Peng, V. (2023, January 3). *solar-panel-cleaning*. Retrieved from wattlogic.com: https://wattlogic.com/blog/solar-panel-cleaning/

PV MAGAZINE. (2022, 11 2). *Rise of the robot (cleaners)*. Retrieved from www.pv-magazine.com/: https://www.pv-magazine.com/2022/11/05/weekend-read-rise-of-the-robot-cleaners-2/

Robsys. (n.d.). *why should i clean my solar panels with cleaning robots*. Retrieved from https://rob-sys.com/: https://rob-sys.com/en/why-should-i-clean-my-solar-panels-with-cleaning-robots/

Singh, S. (n.d.). *Solar Panel Cleaning Guidelines*. Retrieved from https://www.yellowhaze.in/: https://www.yellowhaze.in/solar-panel-cleaning-guidelines/

Solar Panel Cleaning LTD. (n.d.). *why-clean-solar-panels*. Retrieved from solarpanelcleaningltd.co.uk: https://www.solarpanelcleaningltd.co.uk/why-clean-solar-panels/

Surender Rangaraju, O. I. (2021). Guaranteed O&M for Solar Plants in Vietnam. *International Journal of Engineering and Applied Sciences (IJEAS)*, 24-27.

Surender Rangaraju, O. I. (2021). Solar Panels Life After Death – An Overview on Solar Panel Recycling Methods and Imminent Business Opportunities. *International Journal of Multidisciplinary Research and Publications*, 1-5.

FIRM PV POWER SWITZERLAND

Jan Remund[1], Marc Perez[2] and Richard Perez[3]

[1] Meteotest AG, Bern, Switzerland

[2] Clean Power Research, Napa CA, USA

[3] Atmospheric Sciences Research Center, SUNY, Albany, NY, USA

Abstract

We investigate weather photovoltaic power generation can effectively and economically contribute to a massively renewable energy (RE) power generation future for Switzerland. Taking advantage of the country's flexible hydropower resources, we calculate the optimum PV/battery configurations that can meet the country's growing electrical demand firmly 24x365 at the least possible cost while entirely phasing out nuclear power generation. We explore several ultra-high RE "net zero" scenarios where PV and hydro would meet the bulk of the country's demand. Depending on future battery storage and cost predictions for PV and batteries, and a small contribution from in-country or imported dispatchable resources, we show that power production costs on the Swiss grid would range from 6 to 9 EUR cents per kWh. While this is well in line with historic market prices, it is much lower than the current ones on the regional TSOs

Keywords: storage, implicit storage, firm power generation, photovoltaics, grid integration, high penetration renewables

1. Methodology

24/365 firm power availability is a prerequisite for intermittent solar and wind resources if they are to evolve from their current position at the margin of a core of dispatchable generation to a grid-dominant position.

It is now well understood that the least expensive way to transform intermittent renewables into firm power generators entails: (1) applying implicit storage – i.e., overbuilding and dynamically curtailing the resources (Perez et al., 2021, O'Shaughnessy et al, 2021, Tong et al., 2021) to keep real energy storage requirements at economically reasonable levels – and (2) optimally combining renewable resources that may have different daily and seasonal availabilities (Perez, 2020).

The Clean Power Research CPT model (Perez et al., 2021) we apply in the present investigation was designed to derive the least cost combination of intermittent renewables (PV, wind) and storage – real and implicit – for any location/region. The model also accounts for region or policy-specific operational contexts, such as any allowance for dispatchable supply-side generation (e.g., thermal generation from natural gas or e-fuels), the availability of other renewables (e.g., hydro), or the application of demand-side load management strategies.

Inputs to the model include the Capital Expenses (CapEx) and Operating Expenses (OpEx) of all considered generation, storage, and load management resources as well as multi-year hourly site/time-specific time series of renewable electrical production and demand. The main output of the model is the levelized production Cost Of firm Electricity (LCOE) of the optimized resources' blend. The model also produces the optimal amounts of real and implicit storage required to achieve this optimum LCOE.

Results of previous investigations in the continental US (CONUS) and tropical island power grids indicate that a 95% optimized wind/solar blend and an allowance for 5% supply-side flexibility via natural gas could yield firm 24/365 LCOEs below 4 cents per kWh by 2040, with PV/wind overbuild of the order of 50% [Perez, 2020, Perez et al. 2020, Tapaches et al. 2020].

© 2022. The Authors. Published by International Solar Energy Society
Selection and/or peer review under responsibility of Scientific Committee
doi:10.18086/eurosun.2022.15.08 Available at http://proceedings.ises.org

2. The case of Switzerland

The situation in Switzerland is markedly different from our previous USA and tropical island case studies. It is characterized by both unique assets and unique challenges.

- Assets: Switzerland possesses a large existing hydro and hydro storage resource, including run-of-river hydropower and two types of storage systems: pumped hydro, and seasonal lakes, fed mainly by snow melt and holding large quantities of water released on demand. The storage systems are currently applied to maximize market economics (e.g., arbitrage in neighboring European markets). The specs of the hydropower assets are reported in Table 1 along with the other energy generating resources currently available in the country.
- Challenges: (1) it is environmentally difficult to deploy new wind, so large-scale natural wind-solar complementarities cannot be fully tapped. (2) The solar resource is highly seasonal with very low wintertime (Nov – mid Feb) solar production when electrical demand peaks.

Tab. 1: Current (2018-2020 average) power generation resources in Switzerland

	Installed capacity	Annual energy yield
Nuclear	3 GW	24.2 TWh
Run-of-river hydro	4.2 GW	17.6 TWh
One-way hydro buffer	8.2 GW	18 TWh*
Pumped hydro	2.9 GW	4.2Twh^
PV	2.4 GW	2.2 TWh
Wind	0.1 GW	0.1 TWh
Non-renewable thermal generation	0.42 GW	1.17 TWh
Renewable thermal generation	O.55 GW	1.84 TWh
Imports	7 GW	10.77 TWh
Exports	10 GW	-10 TWh

** the full-to-empty buffer system has a capacity of 10Wh.. Total output includes river-flow*
^ pumped hydro output -- net production in zero.

The annual (2018) dispatching of these resources is illustrated in Figure 1. 30-day running means have been plotted to remove short-term fluctuations and improve visualization. The top edge of the graph represents demand on the Swiss grid. Note that the Swiss current production is insufficient in winter and early spring, requiring imports from the rest of Europe. However, production exceeds demand in summer and is exported, mainly to the summer-peaking Italian grid.

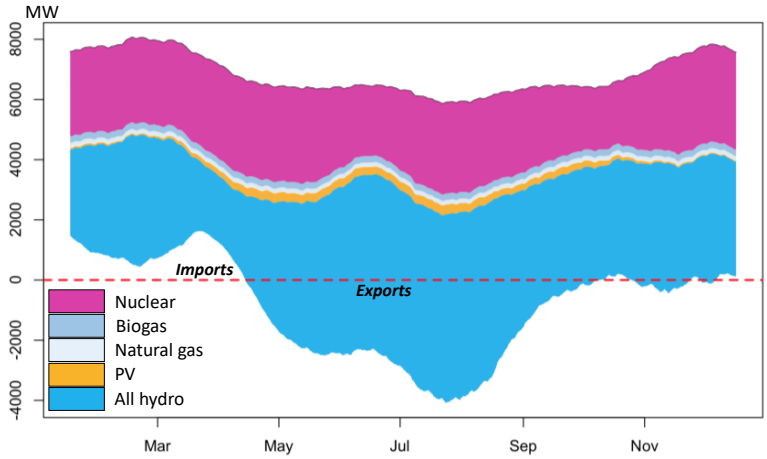

Fig. 1: Annual dispatch of Swiss-based of supply-side resources for the year 2020. The top line of the stacked graph represents the Swiss grid load [ENTSO-E, 2022]

3. Case study

We explore six scenarios at the 2050 horizon where the PV resource will be the central part of a high renewable energy (RE) firm power delivery system for the Swiss power grid. All scenarios include a phasing out nuclear power generation. All scenarios are based on the Energy perspectives 2050+ (SFOE, 2021). This matches net zero (carbon neutral) conditions, needed to fulfil the Paris climate agreement.

- •Scenario #1 –This scenario retains the current small contributions from thermal energy production and adds 2.1 GW of wind power generation amounting to a total wind energy production of 4.3 TWh/year. Pumped hydro capacity is increased from 2.9 to 5.7 GW with a commensurate increase in energy storage reserve. Seasonal hydro storage capacity is increased from 8.2 to 9 GW, with a 2 TWh increase in full-to-empty long term energy reserve.
- Scenario #2 – 10% imports, no restrictions. This scenario also retains the small current contributions from thermal production but adds only 1.0 GW of wind (2.15 TWh/yr). It allows for net imports from the European grid to total 8.25 TWh/yr. Pumped hydro capacity is only increased to 4.4 GW, while the buffer hydro storage capacity is increased to 8.5 GW with a full-to-empty energy reserve increase of 1 TWh.
- Scenario #3 – No imports, natural gas. This scenario is identical to scenario #2 but replaces the 8.25 TWh of imports with new thermal generation from natural gas (2.8 GW new capacity; prices including CO2 certificates). Net-zero import/export are limited to 3 GW with 10 TWh exchanged annually each way.
- Scenario #4 – No imports, e-fuels. This scenario is identical to scenario # 3, but replaces natural gas by e-fuels, produced either domestically or abroad. Note that this scenario is 100% renewable.
- Scenario #5 – Imports and e-fuels. This scenario retains the level of net imports from scenario # 2 and includes roughly half of the e-fuel thermal generation from scenario #4 (1.7 GW, 4.97 TWh/yr).
- Scenario #6 – Imports, e-fuels, and agri-PV. This scenario is identical to scenario #5, but with a slightly lower capital cost for new PV resulting from extensive agri-PV deployments (see below).

For all scenarios, the considered 2050 Swiss electrical demand is assumed to be 30% higher than current (from transportation/building electrification) and nuclear generation is eliminated. The new load demand profile is extrapolated upward from current load (+30% for all hours). The energy demand balance not met by hydro, or the wind/thermal/import resources identified above is met by new firm PV generation. Figure 2 summarizes the contribution all supply-side energy sources in each scenario compared to current. It clearly illustrates the central role to be played by new firm PV generation, ranging from 35% of total generation in scenarios #4 and 5 to 46% in scenario #1.

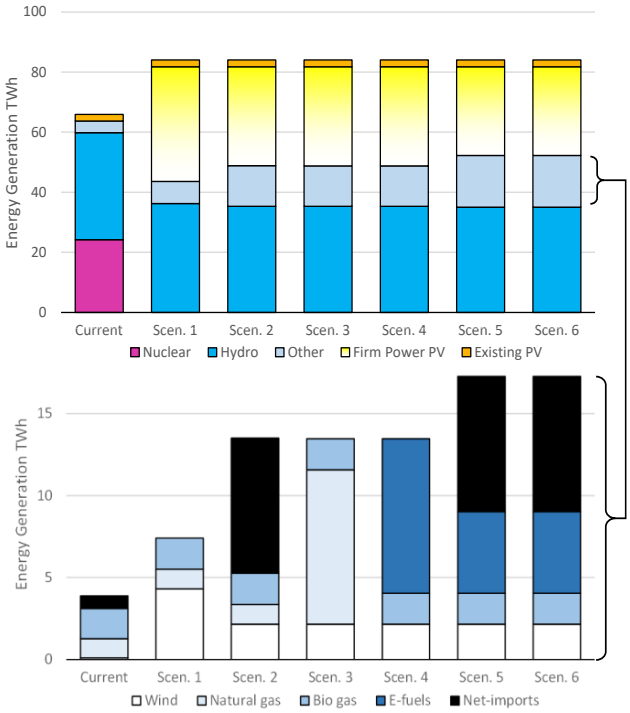

Fig. 2: Supply-side electrical energy resources for all scenarios compared to current. The bottom part of the figure provides details for the source labeled as 'other' in the top part. Note that scenario #4 is the only scenario that does not include non-renewable (nat. gas) or possibly non-renewable (imports) resources.

For each scenario, we investigate two sets of assumptions regarding (1) Switzerland interconnectivity with the larger European grid, and (2) the cost of new PV and electrochemical storage (battery) technologies.

For interconnectivity, we look at two configurations:

1. net-zero imports where the Swiss grid would continue to operate interconnected with the larger European grid and,
2. an extreme limit case where the grid would operate in full autonomy.

In the net-zero case, supply-side flexibility is provided by allowing 10 TWh/yr to be both exported from and imported onto the Swiss grid with a maximum capacity of 3 GW (note that this is above and beyond the supply-side-only imports identified in scenarios #2, 5, & 6) In the autonomous case, Switzerland would operate independently from the larger European grid to the exception of one-way imports considered in scenarios #2, 5 and 6. We note that this autonomous configuration is unlikely given the country's natural interconnectedness, but this limit case is nevertheless informative in quantifying extreme resiliency conditions.

Regarding technology, we consider two assumptions for PV and electrochemical storage CapEx at the 2050 horizon based conservative or optimistic predictions from the NREL technology roadmap[1].

1. The conservative assumption sets turnkey PV at $860/kW and electrochemical storage at $330/kWh.
2. The optimistic assumption prices these technologies at $390/kW and $45/kWh, respectively.

The first assumption reflects a conservative approach for small scale systems (e.g., user-sited) likely to be prevalent in the Swiss PV/storage build-up, while the second reflects utility-size systems that may also be [partially] considered. In both cases we use $4/kW/yr for PV OpEx, and 0.25%/yr for battery OpEx. Note that for scenario #6, we apply a smaller CapEx for the Swiss assumption – $786/kW – that is reflective of the larger

[1] https://atb.nrel.gov/

proportion of agri-PV deployment assumed in this scenario.

All supply-side resources to the exception of new PV are considered as either dispatchable or must-run. Their financial impact is captured through their electrical generation costs identified in Table 2, i.e., we assume that these market-based prices embody both their CapEx and Opex.

Tab. 2: Assumed 2050 power generation cost of supply-side and storage resources on the Swiss grid

		Generation cost (¢/kWh)	Notes
Dispatchable Resources	Hydro storage	7/6.5	*7 ¢/kWh for Scenario #1 only*
	Pumped Hydro	6/5.8	*6 ¢/kWh for Scenarios #1-4 --discharge cost*
	Thernal Natural gas	11.1/14.1	*14.1 ¢/kWh for Sceario #3 (E-certification fee)*
	Thermal Bio gas	11.1	
	Thermal e-fuels	19.7/17.9	*17.9 ¢/kWh for Scenario #4 only*
	Imports	6	
	Exports	-5	
Must-run Resources	Run-of-River hydro	5	
	Existing Wind	15	
	New Wind	12/11	*12 ¢/kWh for Scenario #1 only*
	Existing PV	6.9	

We apply the Clean Power Transformation model to determine the optimum PV and battery resources needed to meet demand firmly at the least possible cost while dispatchable resources are optimally deployed toward this minimum cost/firm power generation objective. The results of this optimization include the required quantities of new battery storage, new PV, curtailed PV output (implicit storage), the electricity generation cost of the optimum supply-side/storage blend that will supply Swiss demand 24x365.

Figure 3 show the order of dispatch in the model not including import and export.

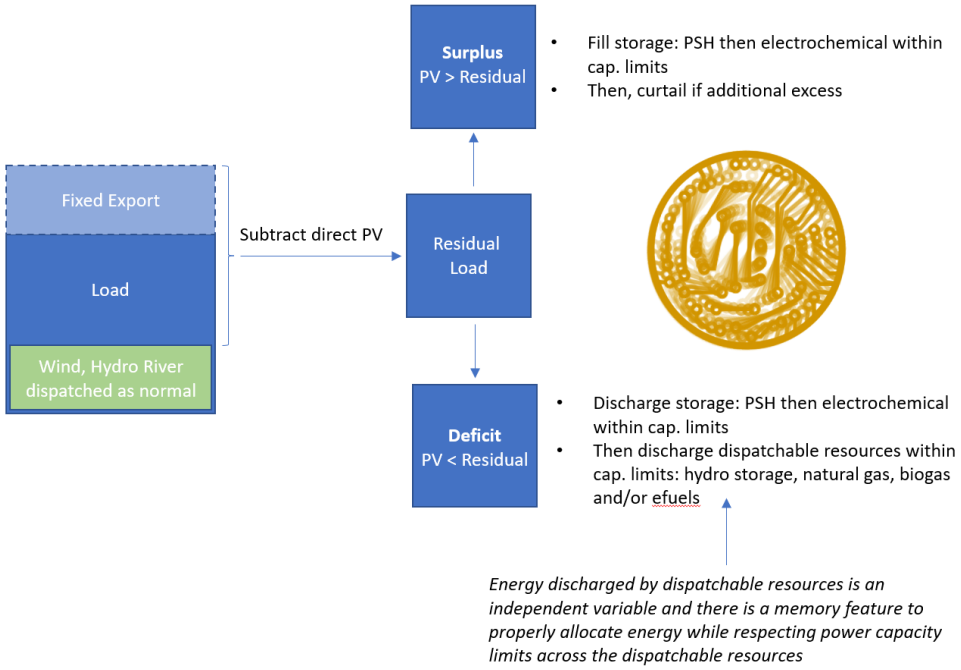

Fig. 3: Dispatch model applied in the Clean Power Transformation (CPT) model. PSH stands for pumped hydro storage.

We apply three years' worth (2018-2020) of experimental data consisting of hourly electrical demand, and measured hourly production of nuclear, PV, wind, and hydropower resources. Future new hourly PV generation is extrapolated from current measured production, prorating to new capacity.

We use a conservative approach as we do not include any climate change effects:

1. Climate change will enhance the run of hydro production in winter and lower it in summer (a switch of about 0.6 TWh until 2050).
2. Climate change will lower the duration of winter. Therefore, the need for seasonal storage is lowered.
3. Climate change will lower the heating needs – and enhances the cooling loads (which will be much lower than the heating loads in 2050). Both would be positive for integration of PV.

All three effects will lower the seasonal unbalance.

4. Results

In Figure 4, we report the new PV capacity, curtailed PV output (implicit storage), and battery storage required in each scenario to firmly meet demand on the Swiss power grid.

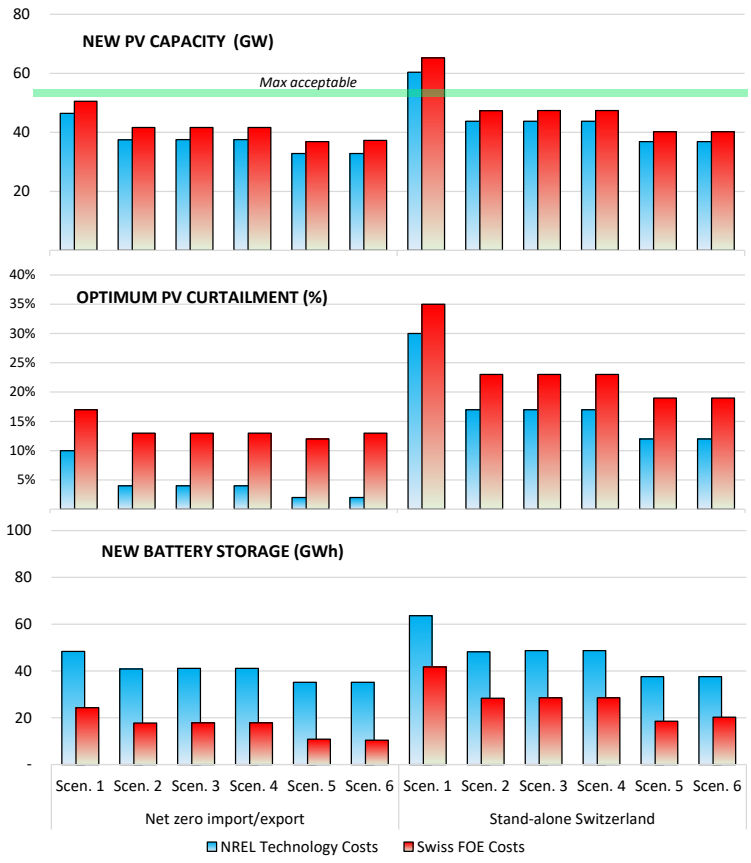

Fig. 4: New PV capacity, proactive curtailment, and battery storage required to meet the new Swiss demand 24x365 in each of the six scenarios, and each technology cost and grid interconnectivity assumption.

New PV capacities (Figure 4, top) range from 32.9 GW (scenario #5 & #6 with net-zero interconnectivity and optimistic technology costs) to 65.2 GW (scenario #1 stand-alone grid and conservative costs). Applying optimistic cost assumptions reduces new PV requirements by about 9% overall compared to conservative costs. Operating the Swiss grid stand-alone would require 17% more PV to be built than allowing net-zero interconnectivity. We plotted a “max acceptable” line indicating the maximum amount of new PV that could be reasonably deployed in the country. This amount is the result of a comprehensive analysis from Remund et al. (Remund et al., 2019) that considered all deployable in-country options (including roof space, exclusion zones,

farmland, etc.) given current PV efficiencies. Importantly, all but one scenario (#1 autonomous grid) fall under this upper limit.

PV output curtailment (Figure 4, middle) ranges from 2 % (scenario #5 & #6 with net-zero interconnectivity and optimistic tech costs) to 35% (scenario #1 autonomous grid and conservative costs). Technology cost assumptions have a strong influence on required curtailment. Applying optimistic cost reduces the need for curtailment by an average of 41%. Stand-alone grid operation, without net-zero flexibility would increase operational curtailment by 130%.

New battery storage requirements (Figure 4, bottom) range from 10.5 GWh (scenario #6 conservative cost assumptions) to 64 GWh (scenario #1 with stand-alone grid and optimistic tech costs). Applying optimistic cost assumptions leads to two times more battery storage overall. This significant difference is because future utility-scale NREL battery cost predictions are very low compared to the conservative small-scale estimates (8 times less) while the difference for PV between the two estimates amounts only to a factor of two. Interestingly, autonomous operation of the Swiss grid would only require 32% more battery storage than net-zero interconnected operation. In all cases, required battery storage is low, amounting to 0.3 hours of full PV capacity in the case of conservative cost assumptions, and ~1.2 hours in the case of optimistic cost assumptions. The bottom line is that no new long-term storage beyond the small addition to the existing buffer hydro system (+10% for scenarios #2-6, +20% for scenario #1), as is often assumed when envisaging ultra-high PV or wind penetration. This observation corroborates results obtained in the USA (Perez, 2020).

Figure 5 reports the blended all-resources power generation LCOEs on the Swiss power grid.

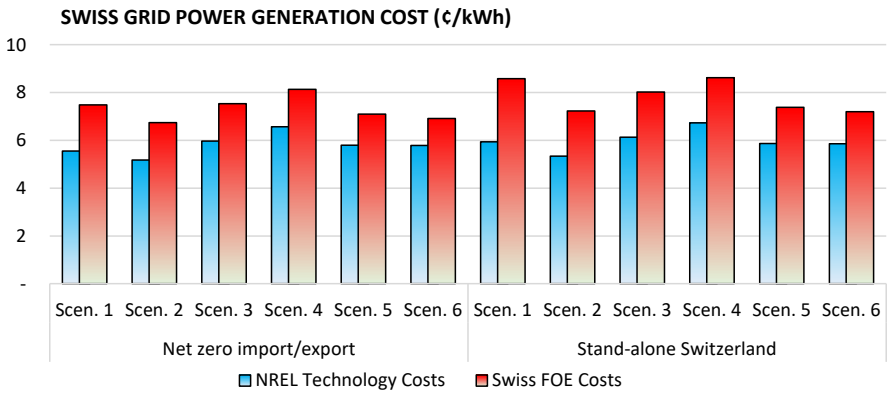

Fig. 5: Electric power generation cost on the Swiss grid in each of the six scenarios, and each technology cost and grid autonomy case.

Electricity production costs range from 5.2 ¢/kWh (scenario #2, net-zero interconnectivity, optimistic technology costs) to 8.9 ¢/kWh (scenario #1 autonomous grid operation and conservative, small-scale tech costs). Applying optimistic utility scale storage/PV cost assumptions reduces generation costs by an average of 22%. Importantly, as unlikely as this configuration may be, stand-alone grid operation would only increase these costs by an average of 5.5% i.e., not constituting a showstopper.

The new annual dispatch of all resources is illustrated in Figure 6 for the 100% RE (e-fuel) scenario #4. The top graph illustrates the net-zero import/export grid configuration, while the bottom graph illustrates the autonomous grid configuration. As in Figure 1, 30-day running mean have been plotted to remove short-term fluctuations and improve visualization.

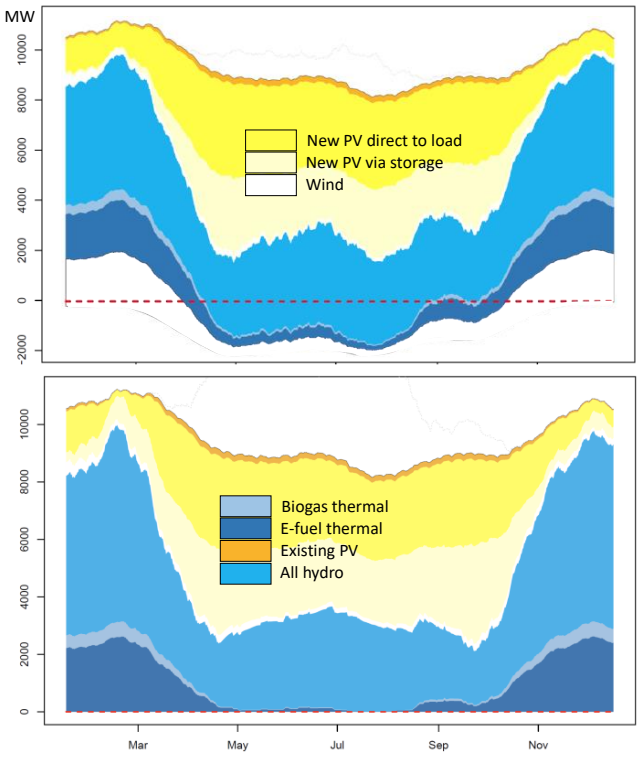

Fig.6: Annual dispatch of supply-side resources for the year 2020 illustrated for the 100% renewable scenario with e-fuels (#4). The top graph represents the net-zero interconnected configuration where winter imports are energetically matched to summer export amounting to net-zero. The bottom graph corresponds to the extreme stand-alone grid configuration.

Figure 7 shows the share of energy production in scenario #6.

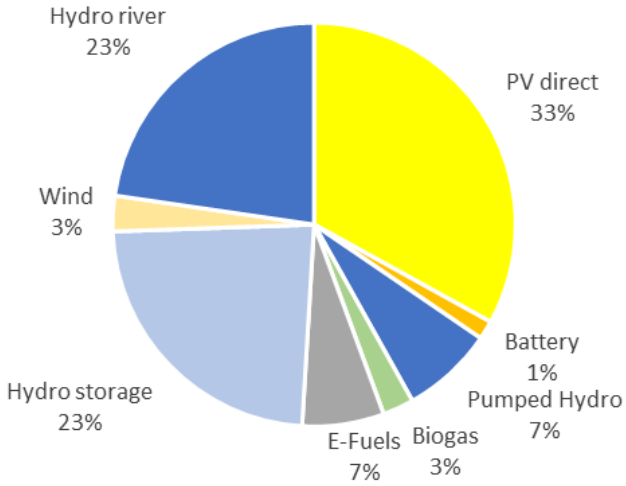

Fig. 7: Share of energy production types for scenario #6 for 2050.

Implicit storage impact: Figure 6 illustrates the importance of overbuilding and operationally curtailing the PV resource on the bottom line: production costs would be an average of 63% higher across all scenarios for the net-zero interconnected configuration, and 450% higher in the autonomous grid configuration. The main factor for this cost difference is the amount of new battery storage required that would respectively be 1300% and 7500% higher without PV oversize/curtailment.

Sensitivity analysis: The three years, analyzed independently, lead to very comparable firm power production cost results overall as seen in in Figure 8 for the 100% renewable scenario #4.

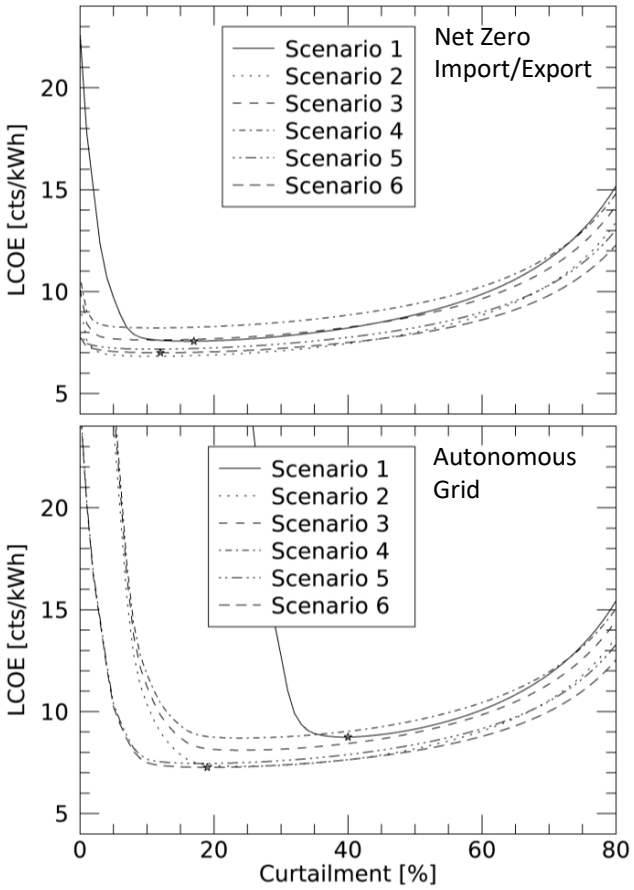

Figure 8: Electricity production cost on the Swiss power grid as a function of PV output curtailment for all scenarios. The top graph corresponds to the interconnected grid configuration with net-zero import/exports with the larger European grid. The bottom graph represents autonomous grid configuration.

5. Discussion

Our investigation shows that high-RE solutions for Switzerland, with PV playing a central role as a complementary resource to the Country's hydropower system, are both physically and economically reasonable, despite the minor role wind power can play, and the mediocre PV resource in winter months.

It is important to state that operational costs in all considered scenarios are reasonable compared to current wholesale market prices in Switzerland (these have been well above 20 ¢/kWh the last couple of months (Fraunhofer ISE and TNC, 2022). The present ultra-high RE costs are even reasonable when compared to earlier pre-crisis TSO wholesale prices (4-6 ¢/kWh) noting that these earlier TSO prices do not fully factor-in environmental or strategic externalities which, as we see today with international tensions, can be consequential.

Another particularly important observation is the result obtained for the 100% RE scenario (#4). Not only are operational generation costs reasonable (6½/-8½ ¢/kWh depending on technology and autonomy assumptions), but they show the supply-side flexibility catalyst role that e-fuels can play, even as expensive as they are expected to be at 18-20 ¢/kWh.

Finally, we stress the importance of implicit storage (i.e., optimally overbuilding the PV resources). Not implementing this deployment strategy would result in higher prices on the network. It is therefore important to operationalize optimal overbuilding and curtailment early-on, by e.g., implementing appropriate regulations that

would lead to firm power monetization, instead of current run-of-the-whether PV production.

Several studies in Switzerland pointed out lately that the energy transition is not easy to implement and that there are conflicting goals. The paper of Weiss et al. (2021) about the "Energy Trilemma" showed that sustainability (CO_2 emissions), affordability (consumers' costs) and security of supply are competing objectives. Similar to this study, Thaler and Hofmann (2022) discussed the impossible energy trinity: energy security, sustainability and sovereignty.

In the paper about "Future Swiss Energy Economy" (Züttel et al., 2022) three approaches for the complete substitution of fossil fuels with renewable energy from photovoltaics were considered: a purely electric system with battery storage, hydrogen, and synthetic hydrocarbons. This study noted that either huge areas for PV or huge hydrogen storage or hydro power systems would be needed inducing high costs and sustainability problems. Conflicting goals clearly exist: integration in Europe, biodiversity, climate change and affordability of energy are competing challenges to a certain level. However, Züttel et al. modelled unrealistic extreme scenarios with 100% renewable energies (no imports also not for e-fuels) and no efficiency gains – which in reality exists based alone on electrification for heating and mobility and reduces the respective energy need by a factor of 2–3). In our study based on Energy Perspectives 2050+, a part of the energy is imported (28%) – PTL and e-fuels – and air transports aren't included – to deliver those in Switzerland would indeed be difficult.

Additionally, all three referenced papers did not include curtailment of PV. With curtailment, a mostly isolated (with high security of supply) as well as e-fuels based scenarios (with low CO_2) lead to low costs of energy. As the modelling shows, no optimum scenario for all objectives exists. Nevertheless, scenarios like #2a (import of 8 TWh of electricity) and #4a (import of e-fuels, but not electricity) would enhance electricity costs only marginally by 0.5 cts/kWh (to 8–8.5 cts/kWh) – costs affordable for the Swiss customers.

The effects of higher levels of energy security (and less integration in the EU) and climate protection is levelled out by higher PV installations and higher curtailments. The energy trilemma exists, but is solvable to a big extent by overbuilding PV which can be induced by suitable regulations and incentives.

6. Acknowledgement

This work has been funded by the Swiss Federal Office of Energy (contract number SI/502264-01). The collaboration of the work on Firm PV Power is organized in the framework of IEA PVPS Task 16.

7. References

European Network Transmission System Operator, ENTSO-E (2022): https://transparency.entsoe.eu/ , last accessed: 09.09.2022

Fraunhofer ISE and TNC, (2022): Swiss Energy Charts. https://energy-charts.info/charts/price_spot_market/chart.htm?l=en&c=CH&interval=year&year=2022&legendItems=0000100000, last accessed: 09.09.2022

O'Shaughnessy, Eric, Jesse Cruce, and Kaifeng Xu. 2021. Solar PV Curtailment in Changing Grid and Technological Contexts: Preprint. Golden, CO: National Renewable Energy Laboratory. NREL/CP-6A20-74176. https://www.nrel.gov/docs/fy21osti/74176.pdf.

Perez, M., R. Perez, K. Rabago & M. Putnam, (2019): Overbuilding & curtailment: The cost-effective enablers of firm PV generation. Solar Energy 180, 412-422

Perez M., (2020): Pathways to 100% Renewables across the MISO Region. http://mnsolarpathways.org/ , last accessed: 09.09.2022

Perez, M. R. Perez & T. Hoff, (2021): IMPLICIT STORAGE – Optimally Achieving Lowest-Cost 100% Renewable Power generation. Solar World Congress. International Energy Society.

Tong, D., Farnham, D.J., Duan, L. et al. Geophysical constraints on the reliability of solar and wind power worldwide. Nat Commun 12, 6146 (2021). https://doi.org/10.1038/s41467-021-26355-z

Perez R., M. Perez, J. Schlemmer, J. Dise, T. E. Hoff, A. Swierc, P. Keelin, M. Pierro & C. Cornaro, (2020): From Firm Solar Power Forecasts to Firm Solar Power Generation an Effective Path to Ultra-High Renewable Penetration a New York Case Study. Energies 2020, 13, 4489.

Remund, J., Albrecht, S. & Stickelberger, D. Das Schweizer PV-Potenzial basierend auf jedem Gebäude. in Photovoltaik Symposium Bad Staffelstein (2019).

Swiss Federal Office of Energy (SFOE), 2021: Swiss Energy Perspectives 2050+. https://www.bfe.admin.ch/bfe/en/home/policy/energy-perspectives-2050-plus.html, last accessed: 09.09.2022

Tapaches, E., M. Perez, R. Perez, T. Chamarande, P. Lauret & M. David, (2020) : Synthese du Rapport Technique du Projet PEPS Reunion. ADEME, France. https://librairie.ademe.fr/energies-renouvelables-reseaux-et-stockage/53-projet-peps-reunion.html , last accessed: 09.09.2022

Thaler P. & Hofmann B., 2022: The impossible energy trinity: Energy security, sustainability, and sovereignty in cross-border electricity systems. Polit. Geogr. 94, 102579.

Weiss O., Pareschi G., Georges G. & Boulouchos K., 2021: The Swiss energy transition: Policies to address the Energy Trilemma. Energy Policy 148, 111926.

Züttel A. et al., 2022: Future Swiss Energy Economy, 2022: The Challenge of Storing Renewable Energy. Front. Energy Res. 9, 1–17.

Dual Axis Optimization of Solar Photovoltaic at Various Sites in Pakistan

Zia ul Rehman Tahir, Ahmad Nadeem, Hassan Raza, Muhammad Irfan, Ahmad Hassan, Sabtain Abbas, Muhammad Atif, Najam ud Din, Muhammad Saad, Muhammad Abdullah, Sajeer Ahmad, Muhammad Asim,

Department of Mechanical Engineering, University of Engineering and Technology Lahore, Pakistan

Abstract

This study aims to estimate solar irradiance of dual axis solar photovoltaic (PV) based on measured solar radiation data for nine stations in different climatic conditions. Six different sky models (isotropic and anisotropic) were compared to estimate the diffused component of the solar radiation incident on the PV surface. The optimum tilt and azimuthal angles were evaluated for one year using measured data. Solar radiation components (beam, diffused and reflected) were estimated by varying the tilt angle from 0° to 90°. The solar radiation on a tilted surface depends on the clearness index (K_T) with a correlation coefficient of 0.913. The total radiation on tilted surfaces is 1.2 and 1.3 times global horizontal irradiance (H_g) for Lahore and Khuzdar respectively. The annual mean irradiance on tilted surface for daily (annual) optimum tilt angle is 326.1 W/m^2 (190.0 W/m^2) and 209.5 W/m^2 (288.9 W/m^2) for respective sites. The mean monthly total radiation for these models shows an almost 6 to 11 % increase with monthly optimum tilt angle compared to latitude tilt angle for both sites. The maximum (minimum) azimuth angle is noted for June (December), which varies from -113.8° to 113.8° (-58.3° to 56.9°). The maximum mean monthly total irradiance for the optimum dual axis system is 630.9 W/m^2 (Lahore), 709.0 W/m^2 (Karachi) in April while 907.2 W/m^2 (Khuzdar) in February, and 884.0 W/m^2 (Quetta) in November. The comparison between the mean monthly total irradiance obtained using optimum tilt angle and dual axis tracking of PV collector shows an increase of about 7 to 26 % for both sites.

Keywords: Dual Axis Tracking, Optimal Azimuth Angle, Optimal Tilt Angle, Isotropic models, Anisotropic models

1. Introduction

The increasing energy demand and fossil fuel depletion have led to an increased demand for the rapid development of alternative energy resources. Fossil fuels are the primary source of energy generation and it generates energy up to 85 % for domestic and commercial use all around the globe (Bauen, 2006). Fossil fuel emissions (SO_x, NO_x, carbon monoxide and Hydrocarbons) are the major cause of ozone depletion and subsequent increases in global warming and air pollution. Different alternative energy resources are being utilized for power generation. Renewable energy resources (solar, wind, hydroelectric, geothermal, etc.) are the fastest growing energy alternatives due to their environment-friendly nature (Converse, 2006; Ellabban et al., 2014; Panwar et al., 2011). Solar energy is one of the best alternative resource for energy generation due to its huge potential and easy deployment on both smaller and larger scales (Li et al., 2015; Sefa et al., 2009).

Solar energy is being utilized to generate power using solar conversion devices such as photovoltaics (PVs) and Concentrated Solar Power (CSP). The output power generated by the solar conversion device is quantified by the radiation collected (Yao et al., 2014). The lower efficiency of these devices urges the implementation of some optimal way to enhance the power output by increasing the amount of incident radiations on the PV surface. The solar radiation incident over the surface can be improved by tracking the solar PV with sun orientation, which will eventually enhance the performance of the solar collectors. The output power of solar PVs can be enhanced by optimizing the azimuthal and tilt angle based on orientation of sun (Chang, 2010; Kaddoura et al., 2016).

The tilt angle optimization involves the conversion of global and diffuse horizontal solar radiation data into the tilted surface data (Demain et al., 2013). The total solar radiation (H_T) composed of beam radiations (H_B) (incident directly over the surface without any hindrance due to aerosol or cloud), reflected (H_R) radiations (incident after reflected from different surfaces) and diffused (H_D) radiations (scattered radiations due to aerosol or clouds radiations) (Drummond, 1956; Suckling and Hay, 1977). The tilted beam irradiance was estimated using the ratio of beam radiation for tilted to the horizontal PV surface (Huld et al., 2012). It is difficult to evaluate the diffused component of radiation as it depends upon various factors such as humidity, sky condition, clearness index (K_T), and turbidity. The researchers have suggested different techniques to estimate diffuse components of the radiations using maximum influencing factor (Duffie et al., 1994).

© 2022. The Authors. Published by International Solar Energy Society
Selection and/or peer review under responsibility of Scientific Committee
doi:10.18086/eurosun.2022.15.09 Available at http://proceedings.ises.org

Isotropic models are the simplified methodology for estimating diffused radiation by assuming the uniform scattering of radiation over the sky dome, while anisotropic models are the detailed insights considering both isotropic and anisotropic parts of the diffused radiations. Different isotropic and anisotropic models have been presented for estimating the diffused radiation component on a tilted surface. The formulation is based on the clearance index (K_T), solar hour, and relative humidity (R_h). Reindl et al. (Reindl et al., 1990) proposed their model based on the isotropic and anisotropic parts of diffused radiation and selected four significant factors from a set of 28 significant factors. Noorian et al. (Noorian et al., 2008) proposed the comparison of the performance of twelve different isotropic and anisotropic models at Karaj (35°55′N; 50°56′E) Iran to evaluate diffused radiation on the tilted surface for south and west-facing irradiance. The beam and ground reflected radiation estimation remain the same for all the isotropic and anisotropic models, whereas the diffused component is estimated using different techniques.

The azimuthal angle (γ) can be optimized by regulating different factors such as declination angle (δ), solar zenith angle (θ_z), solar inclination angle (α_s), and incident angle (θ_i) based on earth orientation. The surface is tracked with the sun radiation throughout the day from sunrise at a solar zenith angle (θ_z) of -85° to sunset, where it is 85° based on radiation, that is collected for 10 minutes from Jan 01 to Dec 31, 2016.

Sidek et al. (Sidek et al., 2017) proposed a self-positioning solar tracker with a precision control system for elevation and azimuthal angle. The result reveals a 12.8% and 26.9% increase in power than fixed-tilted collectors for heavy and clear overcast conditions. Abdallah, S. and Nijmeh, S. (Abdallah et al., 2004) conducted an experimental study based on the electromechanical dual-axis solar tracking system, controlled by a programmable logic controller (PLC) and investigated the effect of dual-axis on the output performance. The study reveals the increase of 41.34% collected energy as compared to a fixed PV system tilted at 32°. An experimental study was conducted to investigate the electrical power generation and the current-voltage characteristics for different types of a solar tracking system such as dual-axis, one axis east-west, one axis north-south and one axis vertical using flat-plate photovoltaic. The result illustrates the increase in volt-current characteristic and it was found that the recorded power gain for two axes was 43.87% with 37.53% for east-west, 34.43% for vertical and 15.69% for north-south tracking than a fixed PV system, the motor and control system energy consumption was less than 2% of the total collected energy (Abdullah and Management, 2004).

2. Methodology

The total solar radiation incident over the earth surface was classified into three components i.e., Direct or Beam radiation (H_B), diffused Radiation (H_D), and ground Reflected (H_R), as expressed by Eq. (1). Beam radiation incident directly over the solar PV surface without any deviation. The ground reflected are the beam incident over the surface after reflecting from the atmosphere due to phenomena of surface albedo as given by Eq. (2), while the diffused radiations are the scattered radiation incident over the PV surface because of the suspended particle and cloud in the atmosphere.

$$H_T = H_B + H_D + H_R \tag{1}$$

$$H_T = \left(H_g - H_d\right) \times R_b + H_D + 0.2H_g \times (1 + \cos\beta) \tag{2}$$

R_b represents the ratio of average daily beam radiations on tilted to the horizontal surface can be defined in terms of sunrise hour angle on horizontal (ω_s) and tilted (ω'_s) surface, latitude (ϕ) of the location in the northern hemisphere sloped towards equator, tilt angle (β) and declination angle (δ). The reflected radiation on an inclined surface (H_R) was expressed in terms of global horizontal radiation (H_g) and surface albedo (ρ). Generally, a standard fixed value used for surface albedo is 0.2, however, the surface albedo varies with time, and the hourly data is utilized for the surface albedo acquired from MERRA-2. The estimation for the daily average albedo calculated by the available ground albedo data was further used to calculate the average daily reflected radiation incident over the solar surface. R_d is a variable factor that can be estimated by sky models. Six sky models are selected to estimate the R_d. H_D is calculated from H_d and R_d using Eq. (3).

$$H_D = H_d R_d \tag{3}$$

Isotropic sky models are based on the assumption that the scattering of solar radiation is constant over the sky dome. The selected isotropic models include Liu and Jordan Model (LJ) (Liu and Jordan, 1961), Badescu Model (Ba) (Badescu, 2002), and Koronakis Model (Kr) (Koronakis, 1986).

The Liu and Jordan model is the base of multiple isotropic sky models, which best estimate the diffused radiation in cloudy sky. His proposed equation to estimate R_d mentioned as Eq. (4) relates the cloudiness index, extra-terrestrial and total solar radiation striking on the surface. Koronakis is an advanced form of Liu and Jordan model. It was proposed in 1986 to estimate the diffused radiation in Northern Hemisphere more accurately as given by Eq. (5). Liu and Jordan model defines the zenith angle on the basis of 2D theory, while Badescu model contradicts and defines the zenith and azimuthal angle based on the 3D model as shown by Eq. (6).

$$R_d = \frac{1}{2}(1 + \cos\beta) \tag{4}$$

$$R_d = \frac{1}{3}(2 + \cos\beta) \tag{5}$$

$$R_d = \frac{1}{4}(3 + \cos(2\beta)) \tag{6}$$

Anisotropic models are the advanced method to investigate diffused radiation. They estimate the anisotropic and isotropic diffused radiation around the sun and the rest of the sky. The anisotropic models include Hay Model (Ha) (Hay, 1979), Perez Model (Pr) (Perez et al., 1990), Ma Iqbal Modified Model (IM), and Gueymard Model (Gu) (Gueymard, 1987).

Hay model neglected the horizontal brightening factor and assumes isotropic and circumsolar are the only two components of diffused radiation. The proposed relation to estimating the R_d is given in Eq. (7). While MA Iqbal proposed a model assuming that diffused radiation consists of radiation emitted by the circumsolar region and the rest of the sky. MA Iqbal modified model is modified form of MA Iqbal model which is proposed by the Perez. He suggested to replace the clearance index factor K_t to modified clearance index factor K_t', which is given in Eq. (8). Gueymard proposed to calculate the radiance of a partly cloudy sky as a weighted sum of the clear and overcast sky radiance as given by Eq. (9)

$$R_d = \left(\frac{H_b}{H_o}\right) R_b + \left(1 - \frac{H_b}{H_o}\right)\left(\frac{1 + \cos\beta}{2}\right) \tag{7}$$

$$K'_T = \frac{K_T}{1.031 \exp\left(\frac{-1.4}{0.9 + \frac{9.4}{M}}\right) + 0.1} \tag{8}$$

$$R_d = (1 - N_g) R_{d0} + N_g R_{d1} \tag{9}$$

The above-listed models are utilized to estimate the diffused radiation. The monthly mean and daily mean solar irradiance for Lahore and Khuzdar is estimated on optimum and latitude fixed tilt angles.

3. Result and Discussion

The maximum solar insolation was calculated using six best performing models that includes three isotropic models (Liu-Jordan Model (LJ), Koronakis Model (Kr), Badescu Model (Ba), and three anisotropic models (Hay Model (Ha), MA Iqbal Modified (IM) and Gueymard Model (Gu)) respectively. The Gueymard model gives the best estimation of diffused radiation. The mean annual irradiance on an inclined plane for daily optimum angle and annual optimum tilt angle for Lahore with the lowest sky K_T is 209.525 W/m^2 and 190.036 W/m^2 respectively, and for Khuzdar it is 326.054 W/m^2 and 288.88 W/m^2 with highest K_T. The total annual mean irradiance on a tilted surface increases up to 16.67% compared to global horizontal irradiance (H_g) using the Gueymard diffuse model for Lahore. The same analysis revealed 30% enhancement in total annual mean irradiance on a tilted surface as compared to H_g on a fixed horizontal surface for Khuzdar.

The incident radiations at Khuzdar are high due to greater K_T. Further analysis showed that increase in total irradiance on the tilted surface relative to the H_g was strongly dependent upon the K_T. The correlation coefficient was calculated and comes out to be 0.913, which shows that the greater value of mean annual sky clearness index will increase total irradiance on the tilted surface compared to H_g for that specific station. Also, the Gueymard model best estimates total irradiance on the tilted surface among all isotropic and anisotropic diffuse models. The ratio of total radiations falling on the tilted surface is nearly 1.2 and 1.3 times of H_g for Lahore and Khuzdar respectively. A comparison among isotropic models and anisotropic models for monthly mean daily irradiance showed that anisotropic models estimate the high value of total solar irradiance on tilted surface. Among anisotropic models Gueymard model best estimates the total irradiance on a tilted surface with maximum solar

radiations during the summer month. Fig. 5 shows that the monthly mean daily irradiance in any month corresponding to daily optimum tilt angle is higher than one estimated against latitude tilt.

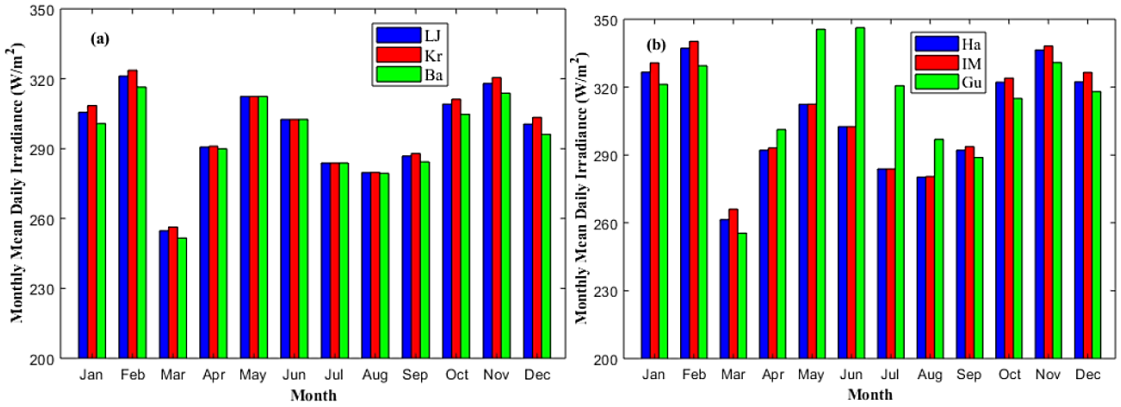

Fig. 1: Comparison of Monthly Mean Daily Irradiance (a) Isotropic and (b) Anisotropic Sky Diffuse Models for Daily Optimum

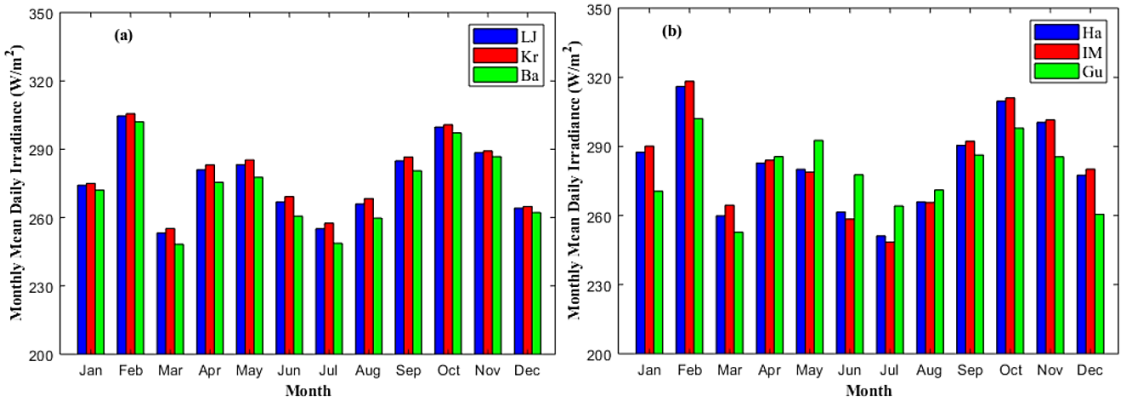

Fig. 2: Comparison of Monthly Mean Daily Irradiance (a) Isotropic and (b) Anisotropic Sky Diffuse Models for Latitude Fixed Tilt Angles for Khuzdar

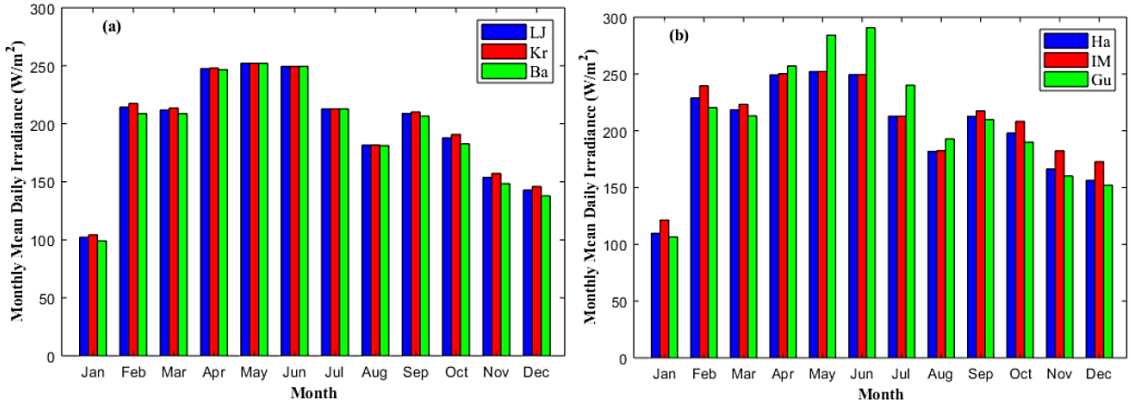

Fig. 3: Comparison of Monthly Mean Daily Irradiance (a) Isotropic and (b) Anisotropic Sky Diffuse Models for Daily Optimum Tilt Angles for Lahore

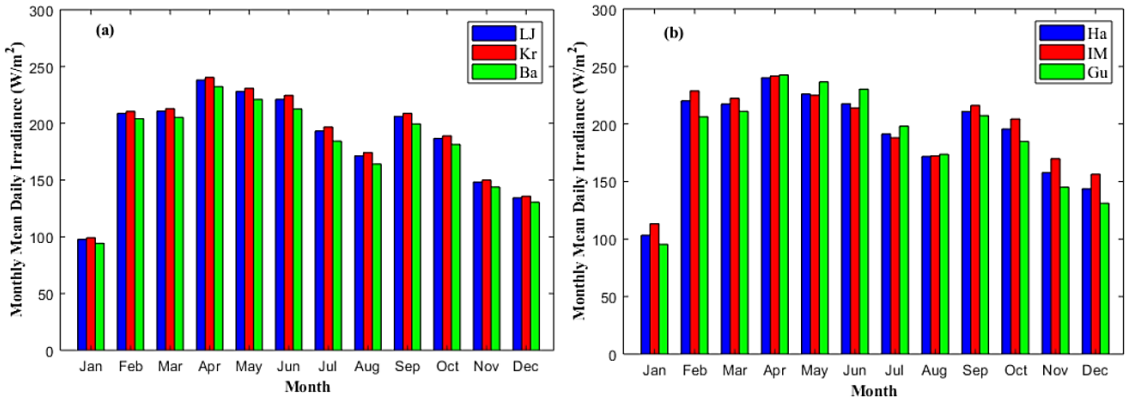

Fig. 4: Comparison of Monthly Mean Daily Irradiance (a) Isotropic and (b) Anisotropic Sky Diffuse Models for Latitude Fixed Tilt Angles for Lahore

The angle at which the H_T reaches its maximum value refers to an optimal tilt angle. The optimum tilt angle for each month was different for each model. Monthly optimum tilt angles were computed for Khuzdar by using maximum monthly mean daily irradiance, varying from 0° in June to 68° in July. The maximum tilt angle value for every station was observed in December, and its minimum was in June. The radiations on the tilted surface differed based on the sky condition and sky clearance index. The maximum radiations for Khuzdar were observed to be 326.5028 W/m^2 in December. The yearly average of the daily optimum tilt angle is observed to be the site latitude. The minimum radiation for Lahore station comes out to be 249.5495 W/m^2 for the corresponding minimum optimum tilt angle. The yearly optimum tilt angle is 27.14° and 28.58° for Lahore and Khuzdar respectively, having latitudes of 31.6° and 27.8°.

A comparison of monthly mean daily irradiance for the combination of six selected models for the monthly and latitude-based optimum tilt angle for Lahore is illustrated in Fig. 3 and Fig. 4 and it shows that for daily optimum tilt angle, the Gueymard model gives the maximum mean annual solar radiation of 209 W/m^2 incident on an inclined solar PV collector. Fig. 5 depicts the percentage enhancement of total irradiance incident on a tilted surface between monthly optimum and latitude tilt for Lahore and Khuzdar. The result shows the minimum enhancement in total Irradiance for Lahore is 5 % to 10 %, while for Khuzdar, it is 6 % to 11%. This information is used to compute the optimum tilt angle for selected stations against each diffused sky model.

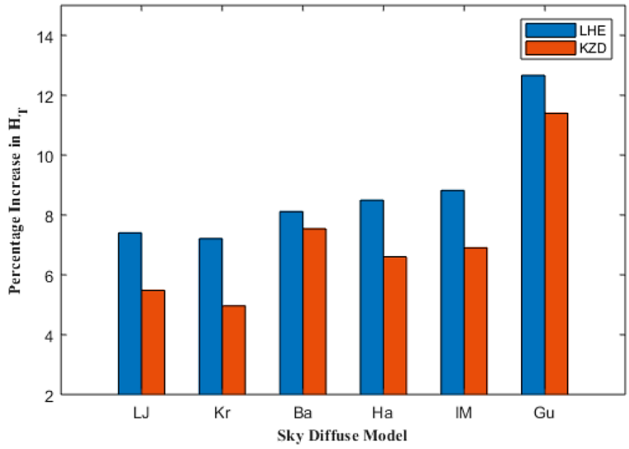

Fig. 5: Percentage Increase in H_T for Monthly Optimum Tilt as Compared to The Latitude Tilt

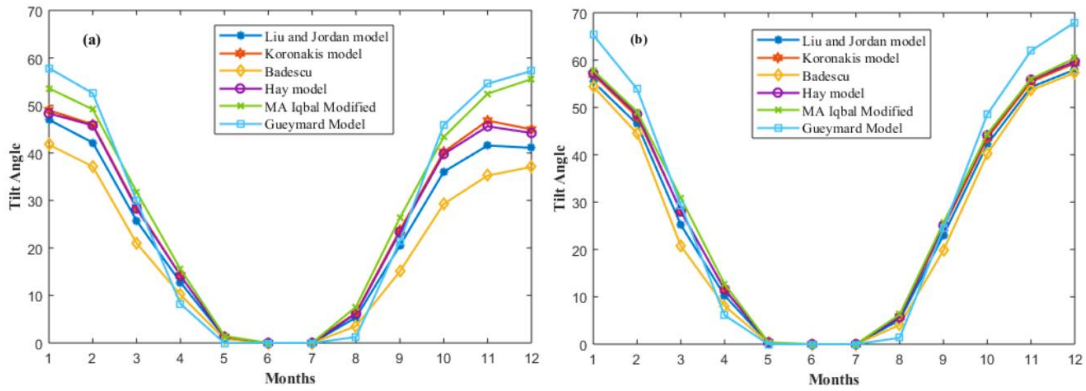

Fig. 6: Comparison of Monthly Optimum Tilt Angle for Isotropic and Anisotropic Sky Diffuse Models for (a) Lahore and (b) Khuzdar

The monthly optimum tilt angle against the isotropic and anisotropic models for the selected station were compared. Fig. 6 depicts the results for Lahore having a minimum K_T value of 0.49 and Khuzdar with a maximum K_T value of 0.68. The analysis shows that the optimum tilt angle for any specific month is different for every station as it depends on the latitude and declination angle of that site. The optimum tilt angle decreases from December solastic to June solastic as the declination angle increases and the radiation angle becomes steeper. From June onwards, the increase in declination angle causes an increase in the tilt angle as the radiation incident with a shallow angle on the earth's surface. The monthly averaged daily optimum tilt angle is 55.6° in December that decreases to 0° in June/July during which the declination angle varies from +23.17° to +21.37°. The total irradiance incident on the tilted surface is enhanced by the monthly adjustment of solar PV to an optimum tilt compared to annual tilt adjustment.

These models are compared in terms of maximum total solar irradiance (H_T) for the eight sites, as shown in Fig. 7 (a). The Gu-model best estimates the diffused radiations. The annual mean irradiance on tilted surface for daily (annual) optimum tilt angle is 326.05 W/m^2 (190.03 W/m^2) and 209.52 W/m^2 (288.88 W/m^2) for Lahore and Khuzdar respectively. The total irradiance on a tilted surface increases up to 16.67 % (Lahore), and 30 % (Khuzdar) compared to global horizontal irradiance (H_g) on a fixed horizontal surface using the Gueymard (Gu) diffuse model.

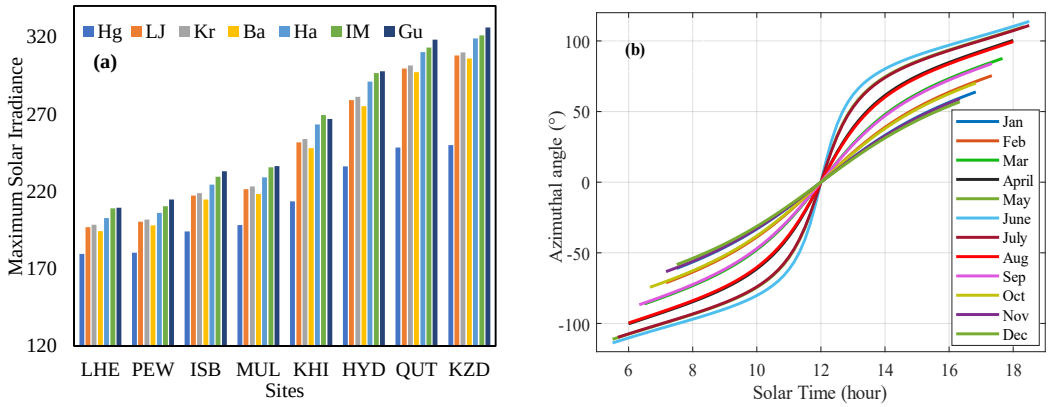

Fig. 7: Variations of (a) maximum solar irradiance for all sites and (b) Azimuthal angle for Lahore for 21st day of each month for a year (2016)

The solar irradiance on a tilted surface depends on the clearness index (K_T) with a correlation coefficient of 0.913, this shows that maximum H_T can be obtained using a flat plate collector at an optimum tilt angle. The solar PV collector tracking is from east to west facing south direction and azimuthal angle is zero at solar noon. The azimuthal angle varies from -113.81° to 113.81° throughout the day with a maximum range of variation in June as shown in Fig. 7 (b). The range of the solar PV tracking system decreases in winter season, with lowest range of -58.32° to 56.89° in December.

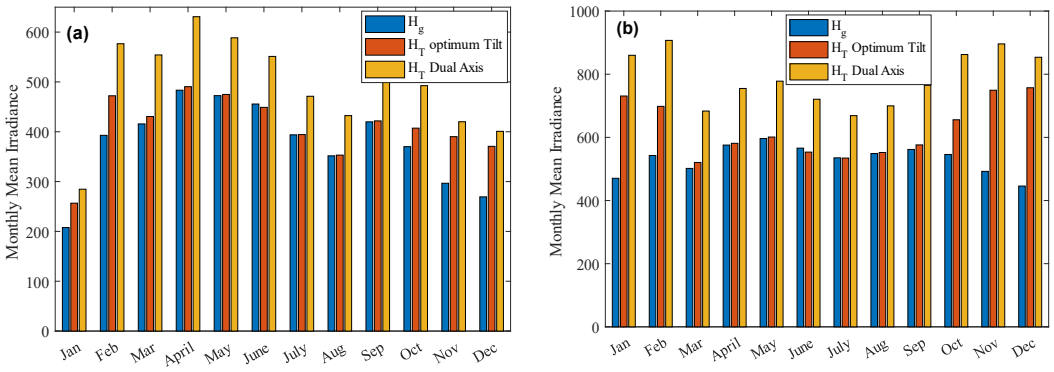

Fig. 8: Comparison of mean monthly total irradiance for optimum tilt and dual axis with Global Horizontal Irradiance (H_g) for a) Lahore b) Khuzdar

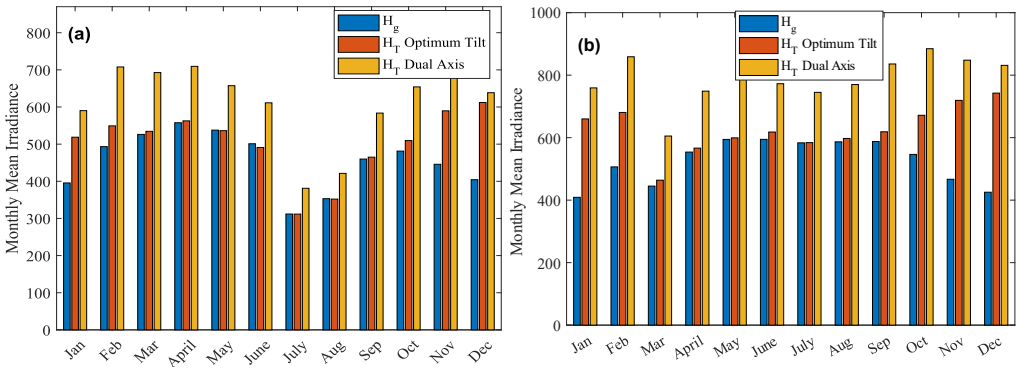

Fig. 9: Comparison of mean monthly total irradiance for optimum tilt and dual axis with Global Horizontal Irradiance (H_g) for a) Karachi b) Quetta

The maximum mean monthly total irradiance for the optimum dual axis system is 630.89 W/m^2 (Lahore) in April and 907.19 W/m^2 (Khuzdar) in February as shown in Fig. 8. The maximum mean monthly H_T for the tilted surface is increased up to 22.30 % and 24.67 % using dual axis tracking of collector for Lahore and Khuzdar respectively. Fig. 9 shows the result for monthly mean irradiance for Karachi and Quetta, the maximum irradiance for Karachi is 709W/m^2 and for Quetta is 884W/m^2 in April and November respectively, and shows the enhancement up to 22.82% and 25.96% for respective Sites while comparing with the single axis (Tilt) tracking.

4. Conclusion

This study was conducted to estimate the total irradiance on a fixed flat, single axis tracked and dual axis tracked surfaces. The irradiance on the fixed flat surface is total horizontal irradiance H_g. The mean radiation falling on a PV surface for annual and daily optimum tilt angle was calculated using six different isotropic and anisotropic sky models. The comparison shows that the Gueymard model gives the maximum mean yearly solar radiation incident on an inclined PV collector. Four different cities of Pakistan (Lahore, Khuzdar, Karachi and Quetta) were discussed in this study. A non-uniform variation in optimum tilt angle is observed; it remains nearly zero in spring and summer while increasing to 75° for autumn and winter. The total irradiance on a tilted surface increases more than 16 % and 30 % compared to Hg.

The optimum dual axis tracking was performed by adjusting the PV collector position with the orientation of sun from sunrises to sunset. The maximum solar were irradiance of Khuzdar is 907.19 W/m^2 which is maximum compared to the other sities, because of its high clearance index value of 0.69. An increase of 7 to 26 % was observed in mean monthly total irradiance using the optimum dual axis tracking compared with optimum tilt angle of PV collector.

5. References

Abdallah, S., Nijmeh, S.J.E.c., management, 2004. Two axes sun tracking system with PLC control. 45(11-12), 1931-1939.

Abdullah, S.J.E.C., Management, 2004. The effect of using sun tracking systems on the voltage-current characteristics and power generation of flat plate photovoltaic. 1, 1671-1679.
Badescu, V., 2002. 3D isotropic approximation for solar diffuse irradiance on tilted surfaces. REnewable Energy 26(2), 221-233.
Bauen, A.J.J.o.P.S., 2006. Future energy sources and systems—Acting on climate change and energy security. 157(2), 893-901.
Chang, Y.-P., 2010. Optimal the tilt angles for photovoltaic modules in Taiwan. International Journal of Electrical Power Energy Systems 32(9), 956-964.
Converse, A.O., 2006. The impact of large-scale energy storage requirements on the choice between electricity and hydrogen as the major energy carrier in a non-fossil renewables-only scenario. Energy Policy 34(18), 3374-3376.
Demain, C., Journée, M., Bertrand, C., 2013. Evaluation of different models to estimate the global solar radiation on inclined surfaces. REnewable Energy 50, 710-721.
Drummond, A.J.A.F.M., Geophysik Und Bioklimatologie, Serie B, 1956. On the measurement of sky radiation. 7(3), 413-436.
Duffie, J.A., Beckman, W.A., Worek, W., 1994. Solar engineering of thermal processes.
Ellabban, O., Abu-Rub, H., Blaabjerg, F., 2014. Renewable energy resources: Current status, future prospects and their enabling technology. Renewable sustainable energy reviews 39, 748-764.
Gueymard, C., 1987. An anisotropic solar irradiance model for tilted surfaces and its comparison with selected engineering algorithms. Solar Energy 38(5), 367-386.
Hay, J.E., 1979. Study of shortwave radiation on non-horizontal surfaces. Report No. 79-12.
Huld, T., Müller, R., Gambardella, A., 2012. A new solar radiation database for estimating PV performance in Europe and Africa. Solar Energy 86(6), 1803-1815.
Kaddoura, T.O., Ramli, M.A., Al-Turki, Y.A., 2016. On the estimation of the optimum tilt angle of PV panel in Saudi Arabia. Renewable Sustainable Energy Reviews 65, 626-634.
Koronakis, P.S., 1986. On the choice of the angle of tilt for south facing solar collectors in the Athens basin area. Solar Energy 36(3), 217-225.
Li, D.H.W., Lou, S.W., Lam, J.C., 2015. An Analysis of Global, Direct and Diffuse Solar Radiation. Energy Procedia 75, 388-393.
Liu, B., Jordan, 1961. Daily insolation on surfaces tilted towards equator. ASRAE J. 10.
Noorian, A.M., Moradi, I., Kamali, G.A., 2008. Evaluation of 12 models to estimate hourly diffuse irradiation on inclined surfaces. Renewable Energy 33(6), 1406-1412.
Panwar, N., Kaushik, S., Kothari, S., 2011. Role of renewable energy sources in environmental protection: A review. Renewable sustainable energy reviews 15(3), 1513-1524.
Perez, R., Ineichen, P., Seals, R., Michalsky, J., Stewart, R., 1990. Modeling daylight availability and irradiance components from direct and global irradiance. Solar Energy 44(5), 271-289.
Reindl, D., Beckman, W., Duffie, J., 1990. Evaluation of hourly tilted surface radiation models. Solar energy 45(1), 9-17.
Sefa, I., Demirtas, M., Çolak, I., 2009. Application of one-axis sun tracking system. Energy conversion Management 50(11), 2709-2718.
Sidek, M., Azis, N., Hasan, W., Ab Kadir, M., Shafie, S., Radzi, M., 2017. Automated positioning dual-axis solar tracking system with precision elevation and azimuth angle control. Energy 124, 160-170.
Suckling, P.W., Hay, J.E., 1977. A cloud layer-sunshine model for estimating direct, diffuse and total solar radiation. Atmosphere 15(4), 194-207.
Yao, Y., Hu, Y., Gao, S., Yang, G., Du, J., 2014. A multipurpose dual-axis solar tracker with two tracking strategies. Renewable Energy 72, 88-98.

Gap Filling in Solar Radiation Data using Artificial Neural Network for Nine Stations in Pakistan

Zia ul Rehman Tahir, Usama Zafar, Zahoor Akbar, Rahim Usman, Ibtasam Nawaz, Ali Hadi, Agha Haider Raza, Ahmad Hassan, Sabtain Abbas, Muhammad Taimoor Adil, Muhammad Abdullah, Sajeer Ahmad, Muhammad Asim

Department of Mechanical Engineering, University of Engineering and Technology Lahore, Pakistan

Abstract

This study presents an approach to fill gaps in ground measured solar radiation data using artificial neural network (ANN). The high quality global horizontal irradiance (*GHI*) measured data without gaps for nine stations in different climatic conditions was used. Six parameters were used as input and GHI as output to ANN. A parametric study was performed to find optimum number of neurons in the hidden layer. Two years GHI data (six days for every week with seventh day as gap) was used to train networks for nine stations. GHI data of seventh day of each week was predicted using trained networks. The predicted data of seventh day of each week was evaluated against actual measured data using statistical parameters (Mean Bias Error (rMBE), relative Mean Absolute Error (rMAE), relative Root Mean Square Error (rRMSE) and correlation coefficient (*R-value*)). The predicted data show good agreement with actual data with R-value ranging from 0.966 to 0.933. The approach proposed in this study can be used to fill gaps in measured data of solar radiation with acceptable accuracy.

Keywords: Solar Radiation, Global Horizontal Irradiance, Data gap filling, Artificial Neural Networks

1. Introduction

Global energy demand is rising steadily, therefore, it is important to use those resources that can produce sufficient energy. Energy extraction from fossil fuels (oil, natural gas, and coal) falls under conventional energy resources. These energy resources have been used for many years due to their ability to produce massive amount of energy. Fossil fuels are depleting and when burnt in large quantities, they emit solid residue and gases that are harmful for the ecosystem. These disadvantages demand an alternative resource that could serve the desired purpose. Now a days, renewable energy resources (wind power, solar power, biogas, biomass, hydropower and tidal energy) are getting popular due to their less adverse effects on the environment and their capability to produce enough energy as per the increasing needs. International Energy Agency has stated that renewable energy resources will make up 66% of the overall global energy supply by the year 2050 (Güney, 2019). Excessive use of fossil fuels for extracting energy leads to gradually increasing CO_2 emissions. Renewable energy resources are more environmentally friendly as compared to non-renewable energy sources because of their less CO_2 emissions which are the biggest pollutant (Gielen et al., 2019).

The initial power generated from wind energy is less expensive, but the maintenance cost of wind turbines is much more than that of solar panels. There are few feasible sites available for setting up wind plants as compared to solar plants. Hydropower plants require massive capital for the construction of dams. Solar energy production has no harmful effect on the environment and solar plants can be installed at any location due to easy availability of solar energy. Selection of site, yearly power output, and temporal performance are crucial factors for any solar project installation. These factors are directly linked with solar resource assessment of site. Solar resource assessment can be done by using ground measured data, satellite data, and reanalysis data (Amjad et al., 2021; Asim et al., 2021). Global solar radiation measurements are less common especially in developing countries because of high cost of installation and maintenance of measuring instruments. The pyranometer and pyrheliometer are the instruments that are commonly used for solar data measurement. (Ağbulut et al., 2021).

Ground measured data can have data gaps due to malfunctioning of instruments and discarded data due to quality issues. Satellite data is not easily available on a global scale and reanalysis data has quality issues due to assimilation methods. Hence, filling data gaps is extremely important for solar resource assessment (Asim et al., 2021; Denhard et al., 2022; Kumar and Ravindra, 2020).

© 2022. The Authors. Published by International Solar Energy Society
Selection and/or peer review under responsibility of Scientific Committee
doi:10.18086/eurosun.2022.15.10 Available at http://proceedings.ises.org

Several techniques have been developed to estimate global solar irradiance for effective solar resource assessment. Empirical and machine learning models are the most used approaches for estimation of global solar radiation. Empirical models (Sunshine-based, Temperature-based, Cloud-based and Hybrid) estimate global solar radiation by developing a linear or non-linear relationship between the meteorological parameters and global solar radiation. Sunshine-based models are extensively used to predict global solar radiation. Machine learning models are used for complex non-linear cases and hence, these models are more accurate (Fan et al., 2019). In recent decades, artificial intelligence has taken over all conventional methods in almost every engineering domain. Studies have proved that these machine learning methods give more accurate results for the prediction of solar irradiance than the empirical models (Ağbulut et al., 2021).

Several empirical and machine learning models were used in previous literature. The estimation accuracy depends on combination of meteorological parameters and training algorithm. Karakoti et al. (Karakoti et al., 2012) and Fend L et al. (Feng et al., 2018) used clearness index, relative humidity, sunshine duration ratio, and temperature as meteorological parameters to forecast daily and monthly diffused horizontal irradiance (DNI). Zhou et al. (Zhou et al., 2021) developed a novel multi-task learning and Gaussian process regression model to forecast global and diffused solar radiation for several locations in China. The same model was able to predict daily and monthly mean solar radiation simultaneously. Yadav et al. (Yadav and Chandel, 2014) analyzed solar radiation prediction models and concluded that ANN methods can give accurate results as compared to conventional methods. Quej et al. (Quej et al., 2017) used three machine-learning algorithms namely support vector machine, artificial neural network, and adaptive neuro-fuzzy inference system for the daily prediction of solar radiation at six stations in Mexico. Mehdizadeh et al. (Mehdizadeh et al., 2016) used artificial neural networks, adaptive neuro-fuzzy inference systems, and gene expression programming as their training models to predicted daily solar radiation in Kamren, Iran, and concluded that ANN gave the optimum results. In another study, Tyvimos et al. (Tymvios et al., 2005) compared two different models namely Angstrom and Artificial neural network for the prediction of global solar radiation. Authors concluded that ANN turned out to be the best model for it. Marzouq et al. (Marzouq et al., 2019) used ANN, k-NN, and some other empirical models to forecast daily global solar radiation. They concluded that k-NN gave the best results. Quej et al. (Quej et al., 2017) compared three different machine learning techniques (Adaptive Neuro-fuzzy, Support Vector Machine and Artificial Neural Network) to predict daily solar irradiance in a warm semi-humid conditions. Rasheed et al. (Al-Naimi et al., 2014) predicted the average daily global solar radiation of Baghdad using a model based on artificial neural network. Yildirim et al. (Yıldırım et al., 2018) used artificial neural network with regression analysis to estimate monthly global solar irradiance. The analysis was performed for four stations in Turkey and several meteorological parameters were selected for training the algorithm.

This study aims to fill gaps in solar radiation data using artificial neural network technique. The data used was measured by Energy Sector Management Assistance Program (ESMAP) at nine different stations (Lahore, Quetta, Khuzdar, Islamabad, Karachi, Hyderabad, Multan, Peshawar, and Bahawalpur) of Pakistan. Non-linear regressive models were developed with different combinations of input parameters. The evaluation was based on statistical parameters. Statistical insignificant parameters were excluded and a final model was developed for solar data gap filling.

2. Methodology

Gap filling of ground measured solar data was performed using machine learning approach for nine stations in Pakistan (Bahawalpur, Hyderabad, Islamabad, Karachi, Khuzdar, Lahore, Multan, Peshawar, and Quetta). Initially, ANN was used for 9 input parameters including Solar Zenith Angle (SZA), Extraterrestrial Solar Irradiance (G_{toa}), Clear Sky Irradiance (G_{cls}), Clear Sky Irradiance from McClear (G_{mcc}), Relative Humidity (RH), Temperature (T), Periodicity Factor (PF), Wind Speed (WS) and Pressure (P). These parameters were selected from literature based on their performance (Wang et al., 2012). 28 non-linear regression models with different combinations of these parameters were developed. Coefficient of correlation (R), Mean Biased Error (MBE), Mean Absolute Error (MAE), Root Mean Square Error (RMSE), Relative Standard Error (RSE), p-value, t-statistical value, normalized Akaike Information Criterion (AIC), Corrected Akaike Information Criterion (AICc) and Bayesian (Schwarz) Information Criterion (BIC) were utilized to assess the accuracy of the models.

Category I was comprised of models M01 to M08 in which SZA and G_{toa} are fixed based on previous studies (Stökler et al., 2016). Category II was comprised of models M09 to M14 in which RH was added at third place in accordance with its observed statistical significance. Category III was comprised of models M15 to M19 in which G_{mcc} was added at fourth place based on its observed statistical significance. Category IV was comprised of models M20 to M23 in which G_{cls} was added at fifth place based on its observed statistical significance. Category V was comprised of models M24 to M26 in which PF was added at sixth place based on its observed statistical significance. Category VI was comprised of models M27 and M28 in which T was added at seventh place based on its observed statistical significance. The models with lower values of errors and higher R-value were selected for further analysis. The details of combinations for these models are as follows;

Category I:

M01: $G_{mq} = b_1 + b_2\,SZA + b_3\,G_{toa}$

M02: $G_{mq} = b_1 + b_2\,SZA + b_3\,G_{toa} + b_4\,PF$

M03: $G_{mq} = b_1 + b_2\,SZA + b_3\,G_{toa} + b_4\,T$

M04: $G_{mq} = b_1 + b_2\,SZA + b_3\,G_{toa} + b_4\,RH$

M05: $G_{mq} = b_1 + b_2\,SZA + b_3\,G_{toa} + b_4\,P$

M06: $G_{mq} = b_1 + b_2\,SZA + b_3\,G_{toa} + b_4\,WS$

M07: $G_{mq} = b_1 + b_2\,SZA + b_3\,G_{toa} + b_4\,G_{cls}$

M08: $G_{mq} = b_1 + b_2\,SZA + b_3\,G_{toa} + b_4\,G_{mcc}$

Category II:

M09: $G_{mq} = b_1 + b_2\,SZA + b_3\,G_{toa} + b_4\,RH + b_5\,PF$

M10: $G_{mq} = b_1 + b_2\,SZA + b_3\,G_{toa} + b_4\,RH + b_5\,T$

M11: $G_{mq} = b_1 + b_2\,SZA + b_3\,G_{toa} + b_4\,RH + b_5\,P$

M12: $G_{mq} = b_1 + b_2\,SZA + b_3\,G_{toa} + b_4\,RH + b_5\,WS$

M13: $G_{mq} = b_1 + b_2\,SZA + b_3\,G_{toa} + b_4\,RH + b_5\,G_{cls}$

M14: $G_{mq} = b_1 + b_2\,SZA + b_3\,G_{toa} + b_4\,RH + b_5\,G_{mcc}$

Category III:

M15: $G_{mq} = b_1 + b_2\,SZA + b_3\,G_{toa} + b_4\,RH + b_5\,G_{mcc} + b_6\,PF$

M16: $G_{mq} = b_1 + b_2\,SZA + b_3\,G_{toa} + b_4\,RH + b_5\,G_{mcc} + b_6\,T$

M17: $G_{mq} = b_1 + b_2\,SZA + b_3\,G_{toa} + b_4\,RH + b_5\,G_{mcc} + b_6\,P$

M18: $G_{mq} = b_1 + b_2\,SZA + b_3\,G_{toa} + b_4\,RH + b_5\,G_{mcc} + b_6\,WS$

M19: $G_{mq} = b_1 + b_2\,SZA + b_3\,G_{toa} + b_4\,RH + b_5\,G_{mcc} + b_6\,G_{cls}$

Category IV:

M20: $G_{mq} = b_1 + b_2\,SZA + b_3\,G_{toa} + b_4\,RH + b_5\,G_{mcc} + b_6\,G_{cls} + b_7\,PF$

M21: $G_{mq} = b_1 + b_2\,SZA + b_3\,G_{toa} + b_4\,RH + b_5\,G_{mcc} + b_6\,G_{cls} + b_7\,T$

M22: $G_{mq} = b_1 + b_2\,SZA + b_3\,G_{toa} + b_4\,RH + b_5\,G_{mcc} + b_6\,G_{cls} + b_7\,P$

M23: $G_{mq} = b_1 + b_2\,SZA + b_3\,G_{toa} + b_4\,RH + b_5\,G_{mcc} + b_6\,G_{cls} + b_7\,WS$

Category V:

M24: $G_{mq} = b_1 + b_2\,SZA + b_3\,G_{toa} + b_4\,RH + b_5\,G_{mcc} + b_6\,G_{cls} + b_7\,PF + b_8\,T$

M25: $G_{mq} = b_1 + b_2\,SZA + b_3\,G_{toa} + b_4\,RH + b_5\,G_{mcc} + b_6\,G_{cls} + b_7\,PF + b_8\,P$

M26: $G_{mq} = b_1 + b_2\,SZA + b_3\,G_{toa} + b_4\,RH + b_5\,G_{mcc} + b_6\,G_{cls} + b_7\,PF + b_8\,WS$

Category VI:

M27: $G_{mq} = b_1 + b_2\,SZA + b_3\,G_{toa} + b_4\,RH + b_5\,G_{mcc} + b_6\,G_{cls} + b_7\,PF + b_8\,T + b_9\,P$

M28: $G_{mq} = b_1 + b_2\,SZA + b_3\,G_{toa} + b_4\,RH + b_5\,G_{mcc} + b_6\,G_{cls} + b_7\,PF + b_8\,T + b_9\,WS$

t-stat and p-value were evaluated to determine the statistical significance of input parameters in each model. t-stat was performed to indicate whether the result is meaningful or not. p-value is a probability that helps to find a correlation between observed values of a sample and population data. t-stat value greater than $|\pm 1.96|$ and p-value less than 0.05 was considered significant for the result.

2.1 Selection of Input Parameters

The input parameters were selected from literature and then shortlisted based on statistical significance. The accuracy of ANN results depends on selection of input parameters, training algorithm and number of neurons. The base model was initially made using two input parameters (SZA and G_{toa}) which were considered to be of primary importance. Different metrological parameters (T, RH, WS, P, PF, G_{cls}, G_{mcc}, Day and Hour) were added to build Subsequent models. Parameters were evaluated and shortlisted based on statistical significance using different statistical parameters such as t-stat, p value, R-value, and AIC, AICc and BIC errors. Only those parameters were selected that have t-stat > $|\pm 1.96|$ and p-value < 0.05 (Mandal, 2017). The selected input parameters based on statistical analysis were day, hour, SZA, G_{toa}, RH, T, G_{mcc}, and G_{cls}. After evaluating the input parameters, optimum number of neurons were estimated. The statistical parameters were used to evaluate the results obtained from ANN.

2.2 Evaluation of Models

The performance of the proposed models was assessed using statistical analysis. The statistical parameters reported in literature are MAPE, MBE, MABE, RMSE, t-stat and R-value. MAPE is commonly used for regression problems and model evaluation. It gives the mean value of relative error between the measured and estimated value as represented by eq. (1). The results will be better when the numerical model gives less errors. The MBE is based on the bias of a model, positive MBE represents overestimation whereas negative MBE represents underestimation by the model. The mathematical expression for MBE is shown by eq. (2). The positive and negative values of observation may cancel each other while calculating MBE, therefore MABE parameter represented by eq. (3). is used. RMSE gives the actual deviation between measured and estimated data. The smaller value of RMSE gives better estimation. The mathematical expression of RMSE is shown by eq. (4). The positive correlation coefficient determines the quality of results and ranges from zero to one, R-value closer to one show good result. t-stat expression is demonstrated by eq. (5). Generally, smaller value of t-stat is considered good for validation of empirical models. The models with high R-value and low errors were considered as best models among all.

$$MBE = \frac{1}{n}\sum_{i=1}^{n}(GHI_{ei} - GHI_{mi}) \quad \text{(eq.1)}$$

$$MABE = \frac{1}{n}\sum_{i=1}^{n}|GHI_{ei} - GHI_{mi}| \quad \text{(eq. 2)}$$

$$MSE = \frac{1}{n}\sum_{i=1}^{n}(GHI_{ei} - GHI_{mi})^2 \quad \text{(eq. 3)}$$

$$RMSE = \sqrt{\frac{1}{n}\sum_{i=1}^{n}(GHI_{ei} - GHI_{mi})^2} \quad \text{(eq. 4)}$$

$$t\text{-stat} = \sqrt{\frac{(n-1)(MBE)^2}{(RMSE)^2 - (MBE)^2}} \quad \text{(eq. 5)}$$

The analysis was performed using modern ANN technique of machine learning using MATLAB computation tool. Gaps were created in the high-quality data measured by ESMAP of the World Bank. The estimated solar data was then compared to the available ground measured solar data.

3. Results and Discussion

3.1 Effect of input parameters on ANN

The non-linear regression model with the highest accuracy was identified on basis of statistical parameters. 28 different models were analyzed using different combinations of nine input parameters. The best four models selected after statistical analysis of nine input parameters for forecasting purpose are as follows:

NM01: $G_{mq} = b_1 + b_2\ SZA + b_3\ G_{toa} + b_4\ RH + b_5\ G_{mcc} + b_6\ G_{cls} + b_7\ T$

NM02: $G_{mq} = b_1 + b_2\ SZA + b_3\ G_{toa} + b_4\ RH + b_5\ G_{mcc} + b_6\ G_{cls} + b_7\ T + b_8\ P$

NM03: $G_{mq} = b_1 + b_2\ SZA + b_3\ G_{toa} + b_4\ RH + b_5\ G_{mcc} + b_6\ G_{cls} + b_7\ T + b_8\ WS$

NM04: $G_{mq} = b_1 + b_2\ SZA + b_3\ G_{toa} + b_4\ RH + b_5\ G_{mcc} + b_6\ G_{cls} + b_7\ T + b_8\ PF$

The R-value, rRMSE, and rMAE for testing and training four models for nine stations are presented in Fig. 1(a, b, and c) respectively. The findings of this study demonstrate that three parameters (WS, P, and PF) out of the nine were relatively less significant. SZA, G_{toa}, RH, G_{mcc}, G_{cls} and T were included in all four new models based on their statistical significance. Further analysis was made by adding P (NM02), WS (NM03) and PF (NM04).

The addition of these parameters has negligible effect on *R*-value, rRMSE, and rMAE of 0.1, 1.0, and 1.5 respectively, therefore, these parameters were not included in the final model. Hence, NM01 with eight metrological parameters (day, hour, SZA, G_{toa}, RH, G_{mcc}, G_{cls} and T) was used for further analysis of solar data gap filling. The SZA and G_{toa} are considered as the prime parameters for the most accurate non-linear regression model evaluated in this study. The remaining four parameters were added in decreasing order of statistical significance in model NM01. It can be observed that Karachi gives the best result for model NM01 with R-value more than 0.97, rRMSE less than 13.6 and rMAE less than 8.8. The least accurate result was observed for Lahore with R-value more than 0.93%, rRMSE less than 24.5, and rMAE less than 15.9.

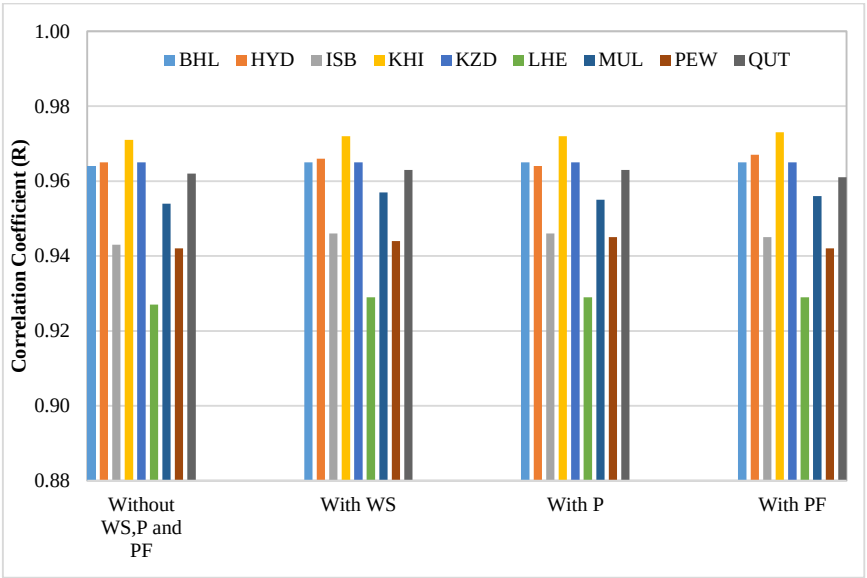

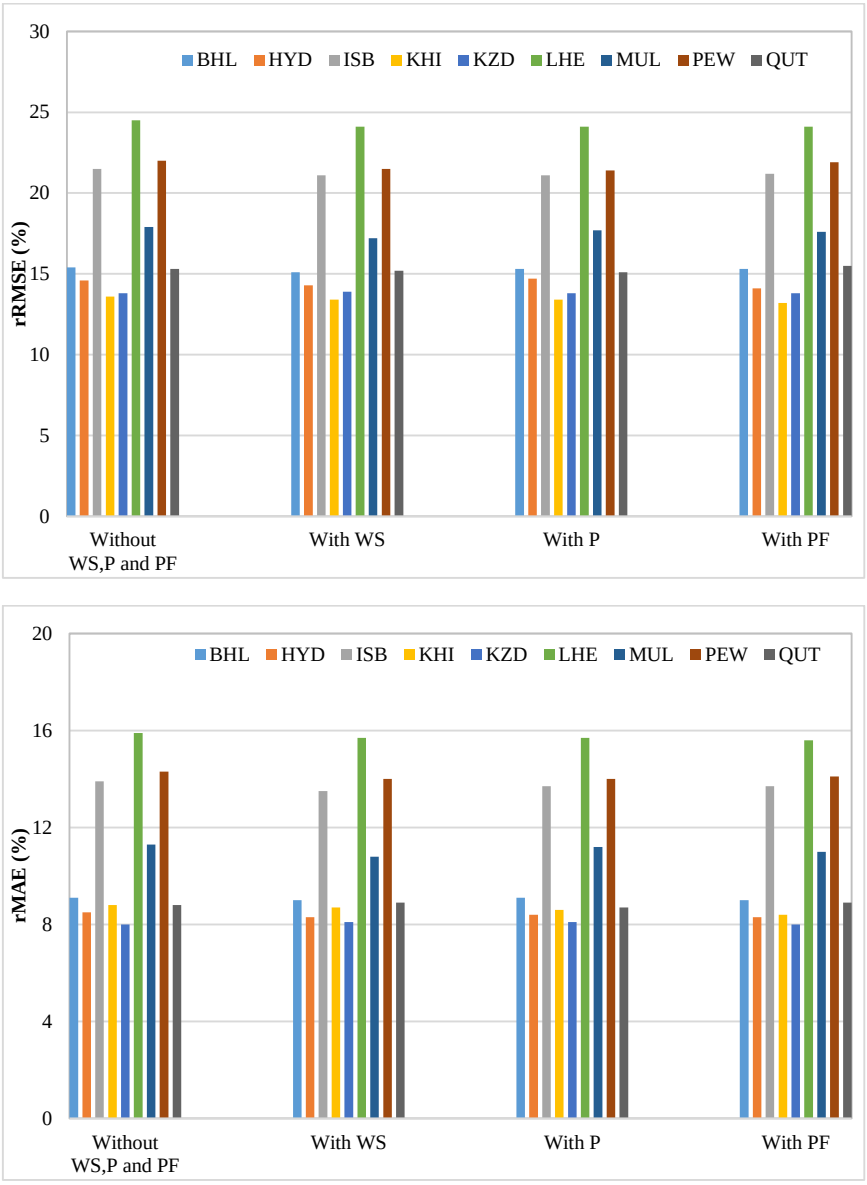

Figure 1: Input parameters (WS, P and PF) versus (a) R (b) rRMSE (c) rMAE for nine stations

3.2 Optimum Number of Neurons

The R-value, rRMSE, and rMAE values for testing and training of the selected model combined are presented in Fig. 2 (a and b) respectively with an increasing number of neurons. rRMSE and rMAE decrease whereas R-values increase with the increasing number of neurons up to five neurons and then became constant. The trend of these curves indicated that the overall performance of the model was converging from five to ten neurons, therefore, ten neurons were selected for further analysis.

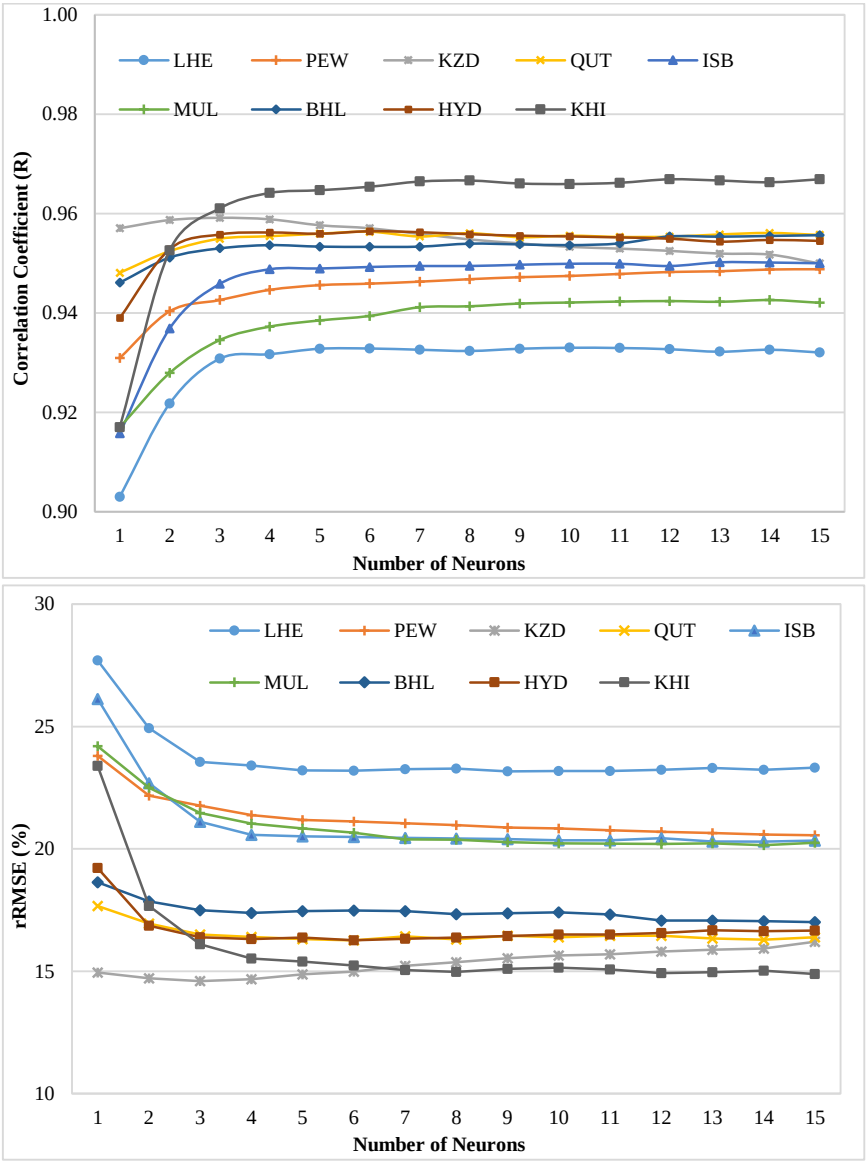

Fig. 2: Effect of neuron numbers on (a) R-value and (b) rRMSE for nine stations

3.3 GHI gap filling with selected model

The proposed model was used with ten neurons to fill the gaps created in measured solar data at nine stations. The predicted GHI values were compared with actual data available for the nine stations. The quality of predicted values in terms of R-value, rMAE, and rRMSE are shown in Fig. 3. Karachi gave the minimum rRMSE of 15.0 and a maximum R-value of 0.967, whereas, Lahore gave a maximum rRMSE of 23.1 and a minimum R-value of 0.933. Lahore also has the highest rMAE (14.8 %) while Khuzdar has the lowest (8.4 %). The low accuracy of *GHI* predictions in Lahore is due to high-grade air pollution and smog in its atmosphere but the correlation is considered significant.

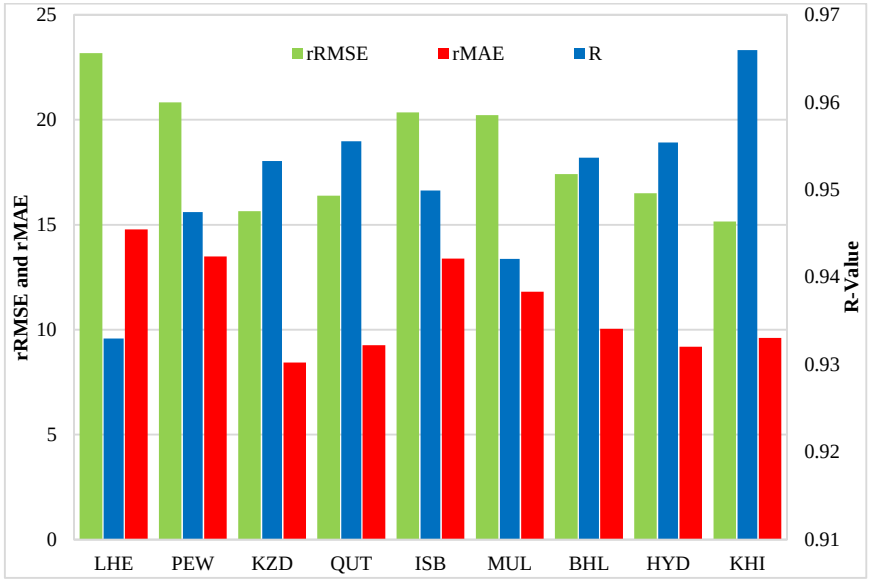

Fig. 3: rRMSE, rMAE and R values for nine stations

4. Conclusion

The self-created gaps in measured solar data were filled using artificial neural networks and predicted results were compared with the available actual data. rRMSE, rMAE, and R-values were evaluated for the prediction of H_g. The SZA, G_{toa}, RH, G_{mcc}, G_{cls} and T are significant training parameters for the nine test stations of Pakistan based on statistical analysis. Training of the ANN model gives best results at a specific number of neurons in the hidden layer. The results for optimum number of neurons in hidden layer converged around ten. Comparative analysis is performed to find the city with best prediction results. The comparison indicated that predicted data were most consistent with measured data for Karachi and least consistent for Lahore. There may be several reasons for the least accurate prediction of results for Lahore. One of them is air pollution. rRMSE for all nine stations was less than 23 % and regression was more than 0.93. The power produced using solar panels may easily be predicted once the data quality is assessed.

5. References

Ağbulut, Ü., Gürel, A.E., Biçen, Y., 2021. Prediction of daily global solar radiation using different machine learning algorithms: Evaluation and comparison. Renewable and Sustainable Energy Reviews 135, 110114.

Al-Naimi, R.H., Al-Salihi, A.M., Bakr, D.I., 2014. Neural network based global solar radiation estimation using limited meteorological data for Baghdad, Iraq. International journal of Energy and Environment 5(1), 79-85.

Amjad, M., Asim, M., Azhar, M., Farooq, M., Ali, M.J., Ahmad, S.U., Amjad, G.M., Hussain, A., 2021. Improving the accuracy of solar radiation estimation from reanalysis datasets using surface measurements. Sustainable Energy Technologies and Assessments 47, 101485.

Asim, M., Azhar, M., Moeenuddin, G., Farooq, M., 2021. Correcting solar radiation from reanalysis and analysis datasets with systematic and seasonal variations. Case Studies in Thermal Engineering 25, 100933.

Denhard, A., Bandyopadhyay, S., Habte, A., Sengupta, M., 2022. A Comparison of Time-Series Gap-Filling Methods to Impute Solar Radiation Data. National Renewable Energy Lab.(NREL), Golden, CO (United States).

Fan, J., Wu, L., Zhang, F., Cai, H., Zeng, W., Wang, X., Zou, H., 2019. Empirical and machine learning models for predicting daily global solar radiation from sunshine duration: A review and case study in China. Renewable and Sustainable Energy Reviews 100, 186-212.

Feng, L., Lin, A., Wang, L., Qin, W., Gong, W., 2018. Evaluation of sunshine-based models for predicting diffuse solar radiation in China. Renewable and Sustainable Energy Reviews 94, 168-182.

Gielen, D., Boshell, F., Saygin, D., Bazilian, M.D., Wagner, N., Gorini, R., 2019. The role of renewable energy in the global energy transformation. Energy Strategy Reviews 24, 38-50.

Güney, T., 2019. Renewable energy, non-renewable energy and sustainable development. International Journal of Sustainable Development & World Ecology 26(5), 389-397.

Karakoti, I., Das, P.K., Singh, S., 2012. Predicting monthly mean daily diffuse radiation for India. Applied Energy 91(1), 412-425.
Kumar, D., Ravindra, B., 2020. Gap-Filling Techniques for Solar Radiation Data and Their Role in Solar Resource Assessment, Advances in Energy Research, Vol. 1. Springer, pp. 555-564.
Mandal, P., 2017. Artificial neural network prediction of buckling load of thin cylindrical shells under axial compression. Engineering Structures 152, 843-855.
Marzouq, M., Bounoua, Z., El Fadili, H., Mechaqrane, A., Zenkouar, K., Lakhliai, Z., 2019. New daily global solar irradiation estimation model based on automatic selection of input parameters using evolutionary artificial neural networks. Journal of Cleaner Production 209, 1105-1118.
Mehdizadeh, S., Behmanesh, J., Khalili, K., 2016. Comparison of artificial intelligence methods and empirical equations to estimate daily solar radiation. Journal of Atmospheric and Solar-Terrestrial Physics 146, 215-227.
Quej, V.H., Almorox, J., Arnaldo, J.A., Saito, L., 2017. ANFIS, SVM and ANN soft-computing techniques to estimate daily global solar radiation in a warm sub-humid environment. Journal of Atmospheric and Solar-Terrestrial Physics 155, 62-70.
Stökler, S., Schillings, C., Kraas, B., 2016. Solar resource assessment study for Pakistan. Renewable and Sustainable Energy Reviews 58, 1184-1188.
Tymvios, F., Jacovides, C., Michaelides, S., Scouteli, C., 2005. Comparative study of Ångström's and artificial neural networks' methodologies in estimating global solar radiation. Solar energy 78(6), 752-762.
Wang, F., Mi, Z., Su, S., Zhao, H., 2012. Short-term solar irradiance forecasting model based on artificial neural network using statistical feature parameters. Energies 5(5), 1355-1370.
Yadav, A.K., Chandel, S., 2014. Solar radiation prediction using Artificial Neural Network techniques: A review. Renewable and sustainable energy reviews 33, 772-781.
Yıldırım, H.B., Çelik, Ö., Teke, A., Barutçu, B., 2018. Estimating daily Global solar radiation with graphical user interface in Eastern Mediterranean region of Turkey. Renewable and Sustainable Energy Reviews 82, 1528-1537.
Zhou, Y., Liu, Y., Wang, D., De, G., Li, Y., Liu, X., Wang, Y., 2021. A novel combined multi-task learning and Gaussian process regression model for the prediction of multi-timescale and multi-component of solar radiation. Journal of Cleaner Production 284, 124710.

A Comparison of Eight Transposition Models Applied for Different Orientations Under Different Albedo Scenarios

João Victor F. F. de Medeiros[1], Lucas Barboza[1], Janis Galdino[1], Diego Miranda[1], Olga Vilela[1], Emerson Gomes[1], Alex Pereira[2], Eduardo Jatoba[2], Alcides Neto[2], José Bione de Melo Filho[2]

[1] Center of Renewable Energy/Federal University of Pernambuco (CER-UFPE), Recife (Brazil)

[2] Hydroelectric Company of São Francisco (CHESF), Recife (Brazil)

Abstract

The simulation of photovoltaic and thermal systems requires accurate knowledge of the solar radiation incident on the plane of photovoltaic modules or thermal collectors. When irradiance in the tilted plane is not measured, transposition models are used to transpose the measurements from the horizontal plane to the plane of the array. In this work, eight models have been evaluated for four different orientations for a low-latitude city at a minute resolution, providing a better description of the radiation behavior. Three scenarios of albedo have been assessed for all orientations. A statistical comparison has been performed using normalized mean bias error, normalized root mean square error, the coefficient of determination, and a skill score (SS4) for the total solar radiation on a tilted plane. The Hay and Davies, Reindl, Muneer and Perez models presented the best results for Petrolina, Brazil (latitude 9.11ºS), where the sophisticated model of Perez presented the lowest values of nRMSE and highest values of R^2 and SS4 for all orientations. The detailed albedo analysis of the Petrolina soil indicated an average albedo of 27.72%, with higher data concentration between 25.52% and 27.80%. It was also observed that simulations conducted with albedo varying as a function of solar zenith angle or albedo considered constant, but based on local measurements, led to more accurate results than simulations conducted with constant albedo and indicated as default by commercial software for the soil in the region.

Keywords: Transposition models; Diffuse irradiance modeling; Inclined surfaces; Ground reflectance; semi-arid.

1. Introduction

The simulation of photovoltaic (PV) and thermal systems requires accurate knowledge of the solar radiation incident on the plane of PV modules or thermal collectors. Generally, the photovoltaic or thermal arrays are not installed horizontally, thus requiring transposition models. These models compute the global irradiance in the tilted plane as the sum of the direct, diffuse, and reflected irradiance from the ground (albedo). A simple geometric transformation is applied to the direct component. The reflected irradiance is estimated similarly, adding the influence of the ground type. The main difference between the transposition models is the approach to transposing the diffuse component, where two main groups are highlighted: 1) isotropic models, which consider only isotropic radiation; 2) anisotropic models, which add circumsolar and/or horizon brightness component into the analysis (García et al., 2021).

As the estimation models are strongly affected by the location's latitude due to site-specific characteristics and the stochastic nature of solar radiation, it is imperative to find the most accurate model for each site (Maleki et al., 2017). It is essential to evaluate the transposition models for different albedo scenarios, bearing in mind the advancing market for bifacial modules, and to evaluate those models for higher temporal resolution since data recording has been moved from hourly to a sub-hourly resolution to provide more information in the simulations (Gueymard and Ruiz-Arias, 2016). Moreover, the growth of solar energy has led to a massive increase in photovoltaic systems with different inclinations and orientations typically following the building construction aspects, notably BIPV (Building Integrated Photovoltaics) (Assoa et al., 2020).

In this context, the present work aims to investigate the performance of 8 widely used models to estimate total solar radiation on tilted surfaces with 1-minute measurements at Petrolina (Brazil) for four different orientations, north-, south-, east- and west-facing surfaces tilted at 45º. All models were evaluated in three different scenarios, with constant albedo and equal to 20%, average albedo measured at Petrolina and albedo varying as a function of the solar zenith angle. In addition, a detailed analysis of the local surface albedo was performed. The proposed study is performed within the framework of the R&D project "*Solar Platform of Petrolina - Development, Research and Innovation in Advanced Technologies*" (CHESF-ANEEL).

© 2022. The Authors. Published by International Solar Energy Society
Selection and/or peer review under responsibility of Scientific Committee
doi:10.18086/eurosun.2022.15.11 Available at http://proceedings.ises.org

2. Transposition Models

The global tilted irradiance (GTI) can be estimated by the sum of the direct and diffuse irradiance incident on the inclined plane plus the irradiance reflected by the ground seen by the photovoltaic (PV) array. The GTI is thus calculated by the expression:

$$GTI = DNI * \cos(AI) + DHI * SVF + RHI * GVF \quad \text{(eq. 1)}$$

The direct irradiance incident on the tilted plane can be obtained from a simple geometric transformation, where the direct normal irradiance (DNI) component is multiplied by the cosine of the angle of incidence (AI). The diffuse portion is obtained by the product of diffuse horizontal irradiance (DHI) and the sky view factor (SVF). The irradiance reflected by the ground that is seen by PV array can be obtained by the reflected horizontal irradiance (RHI) multiplied by the ground view factor (GVF). The RHI is the product of global horizontal irradiance (GHI) and the ground reflectance (ρ_g), also called albedo (see equation 2).

$$\rho_g = RHI/GHI \quad \text{(eq. 2)}$$

Ground reflectance (albedo) is known to vary with several factors, such as the nature of the ground surface, solar zenith angle, specularity, cloud cover, presence or absence of snow, and other factors (Thevenard et al., 2006). Dirmhirn and Eaton (1975) showed that water and snow reflection can be forward-augmented or backward-augmented. Since the evaluated ground is predominantly composed of sandy soil, the albedo analysis will be based on the isotropic reflection of radiation.

Among the three components in the calculation of GTI, diffuse irradiance is the most difficult to compute because it strongly depends on the cloudiness and clearness conditions of the atmosphere (Duffie and Beckman, 2013). Several authors have studied this component from different approaches, from isotropic models that consider only the isotropic diffuse (Badescu, 2002; Koronakis, 1986; Liu and Jordan, 1961), to more complex and elaborated models that treat the circumsolar diffuse and/or the horizon brightness in more detail, called anisotropic models (Hay and Davies, 1980; Klucher, 1979; Perez et al., 1990; Reindl et al., 1990). All these models evaluate the sky view factor (SVF) between the collecting surface and the visible part of the sky.

The isotropic model proposed by Liu and Jordan (1961) [LJ] considers an isotropic distribution of diffuse radiation, with the diffuse irradiance incident on the sloping surface being given by DHI corrected by a sky view factor, represented by $(1 + \cos \beta)/2$. In Koronakis (1986) [Ko], a correction in Liu and Jordan's geometric factor is proposed, being corrected to $(2 + \cos \beta)/3$. In Badescu (2002), a 3D approach is performed and compared to the isotropic model of Liu and Jordan (1961), showing that Badescu's model estimation with SVF of $(3 + \cos 2\beta)/4$ was slightly more accurate for surfaces with a low slope for a high latitude location. Table 1 presents all isotropic models considered in this study.

Tab. 1: Sky view factor of all isotropic models for comparative analysis.

Model	Code	Equation of sky view factor (SVF)
Liu e Jordan (1961)	LJ	$SVF_{LJ} = \frac{1 + \cos \beta}{2}$ (eq.3)
Koronakis (1986)	Ko	$SVF_{Ko} = \frac{2 + \cos \beta}{3}$ (eq.4)
Badescu (2002)	Ba	$SVF_{Ba} = \frac{3 + \cos(2\beta)}{4}$ (eq.5)

The model proposed by Hay and Davies (1980) considers isotropic diffuse radiation, and also the circumsolar radiation, which results from the scattering of solar radiation concentrated in the solar disk. In this model, the anisotropy index of Hay and Davies (F_{HD}) is used. In 1977, Temps and Coulson (1977) applied a correction factor for the isotropic diffuse in order to consider the brightness of the horizon. Based on this authors, Klucher (1979) modified this correction factor with a modulating function to describe an all-sky model. Similarly, Reindl et al. (1990) modified the model of Hay and Davies (1980), proposing the addition of the horizon brightening term. This model is commonly referred as HDKR in the literature (Duffie and Beckman, 2013) due to the contribution of the 3 papers in the development of this model, in this work Reindl et al. (1990), or HDKR, will be referred as Re.

Another anisotropic model widely used and studied in the literature is the Perez et al. (1990) model, where the isotropic, circumsolar and horizontal diffuse radiation are analyzed more in detail. In this model coefficients representing solid angles of the circumsolar region are used (coefficients a_1 and a_2). In addition, empirical functions of sky brightness describing circumsolar radiation (F_1) and horizon brightness (F_2) are used considering air mass (m), normal incident extraterrestrial radiation (DNI_{ext}) and zenith angle (θ_z).

In the same year as Perez's model, Muneer (1990) proposes a model that discerns between overcast and non-overcast sky conditions, equation 11 presented in Table 2, relates the diffuse from an inclined surface to DHI, where for a tilted surface on a cloudy day, F_{HD} becomes zero and the term T becomes a ratio between the irradiance of a tilted surface and the diffuse horizontal irradiance. T corresponds to a function of the radiation distribution (b) and the surface slope (β) for a given location, so the parameters of equation 13 are adjusted as a function of the location evaluated. Table 2 presents the sky view factors for all anisotropic models evaluated in this work.

Tab. 2: Anisotropic models selected for comparative analysis.

Model	Code	Equation of sky view factor (SVF)
Klucher (1979)	Klu	$SVF_{Klu} = \left(\frac{1+\cos\beta}{2}\right)\left(1+F\sin^3\left(\frac{\beta}{2}\right)\right) * [1+F\cos^2 AI \sin^3(90-\alpha)]$ (eq.6) *where F is the modulating function of Klucher*: $F = 1-\left(\frac{DHI}{GHI}\right)^2$ (eq.7)
Hay and Davies (1980)	HD	$SVF_{HD} = \left[(1-F_{HD})\left(\frac{1+\cos\beta}{2}\right)+F_{HD}R_b\right]$ (eq.8) *where F_{HD} is the anisotropy index of HD and R_b is the geometric factor*: $F_{HD} = \frac{DNI}{DNI_{ext}}$ (eq. 9) $R_b = \frac{\cos AI}{\cos(\theta_z)}$ (eq. 10)
Muneer (1990)	Mu	$SVF_{Mu} = T(1-F_{HD})+F_{HD}R_b$ (eq.11) *where*: $T = \cos^2\frac{\beta}{2}+\frac{2b}{\pi(3+2b)}\left[sin\beta-\beta\cos\beta-\pi\sin^2\frac{\beta}{2}\right]$ (eq.12) *for the globe*: $\frac{2b}{\pi(3+2b)} = 0.04-0.82F_{HD}-2.026{F_{HD}}^2$ (eq.13)
Reindl *et al.* (1990)	Re	$SVF_{Re} = \left[(1-F_{HD})\left(\frac{1+\cos\beta}{2}\right)*\left(1+f\sin^3\left(\frac{\beta}{2}\right)\right)+F_{HD}R_b\right]$ (eq.14) *where f is the modulation factor of Reindl*: $f = \sqrt{\frac{DNI\cos\theta_z}{\mathrm{GHI}}}$ (eq.15)
Perez *et al.* (1990)	Pe	$SVF_{Pe} = \left[\left(\frac{1+\cos\beta}{2}\right)(1-F_1)+F_1\frac{a_1}{a_2}+F_2\sin\beta\right]$ (eq.16) *where*: $a_1 = \max(0,\cos AI)\,;\, a_2 = \max(\cos 85\,,\cos\theta_z)$ (eq.17) $F_1 = \max\left\{0,\left[\mathrm{F}_{11}+F_{12}\Delta+F_{13}\theta_z\left(\frac{\pi}{180}\right)\right]\right\};F_2 = \left[\mathrm{F}_{12}+F_{22}\Delta+F_{23}\theta_z\left(\frac{\pi}{180}\right)\right]$ (eq.18) $\Delta = m\frac{DHI}{DNI_{ext}}\;;m = \frac{1}{\cos\theta_z}$ (eq.19) *Where the coefficients contained in the equations of F_1 and F_2 are obtained based on the discrete categories of sky brightness (ε), with κ equal to 1.041 and θ_z in radians.* $\varepsilon = \frac{\frac{DHI+DNI}{DHI}+\kappa\theta_z^3}{1+\kappa\theta_z^3}$ (eq.20)

3. Experimental setup

The solarimetric station was installed in Petrolina, Brazil (latitude 9.11ºS, 40.44W) with four LI-COR Li-200R photovoltaic solarimeters disposed at 45º to the North, South, East, and West orientations. Two photovoltaic solarimeters were also arranged to measure the global horizontal irradiance (GHI) and the reflected horizontal irradiance (see Figure 1) to measure the ground albedo. All sensors were previously and periodically calibrated with a Kipp & Zonen CMP22 secondary standard pyranometer. According to Köppen classification, the climate in Petrolina is considered semi-arid (BSh).



Fig. 1: Solarimetric station installed at Petrolina, Brazil.

Based on GHI, DNI and DHI data measured with EKO class A pyranometers (model MS-80) and pyrheliometer (model MS-57), eight transposition models were evaluated using 1-min data measured between December 04, 2021, to April 29, 2022. A quality control procedure was applied to the measured radiation data to identify and remove outliers. The methodology applied is described in Petribú et al. (2017), and this data quality procedure consists of applying objective and automatic tests that can be divided into two large groups: global tests, which identify anomalies in the timestamps of the analyzed series, assessing the quality of the time series as a whole, and local tests, which are specific for each analyzed variable and take into account the physical nature of the variables studied. Following this methodology, the measurements corresponding to solar elevations below 7º were discarded.

The models were assessed for three scenarios: (i) one with albedo considered constant and equal to 20%, which is the default value adopted in commercial software for the local soil, (ii) albedo constant and equal to the average value of the ground reflectance, and the third scenario, (iii) evaluating the transposition models with albedo (ρ_g) varying as a function of solar zenith angle (θ_z). The evaluation was performed at the minute resolution using three isotropic models, Liu and Jordan (LJ), Koronakis (Ko) and Badescu (Ba), and five anisotropic models, Klucher (Klu), Hay and Davies (HD), Reindl (Re), Muneer (Mu) and Perez (Pe).

The accuracy of the estimates for the global tilted irradiance is assessed using the usual error metrics, the normalized mean bias error (nMBE), the normalized root mean square error (nRMSE) and the coefficient of determination (R^2) defined in equations 21 to 23.

$$nMBE = \frac{1}{N\,\bar{x}_{meas}} \sum_{i=1}^{N} (x_{sim}^{i} - x_{meas}^{i}) \qquad \text{(eq. 21)}$$

$$nRMSE = \frac{1}{\bar{x}_{meas}} \sqrt{\frac{1}{N} \sum_{i=1}^{N} (x_{sim}^{i} - x_{meas}^{i})^2} \quad \text{(eq. 22)}$$

$$R^2 = 1 - \frac{\sum_{i=1}^{N} (x_{sim}^{i} - x_{meas}^{i})^2}{\sum_{i=1}^{N} (x_{sim}^{i} - \bar{x}_{meas}^{i})^2} \quad \text{(eq. 23)}$$

where N is the number of observations data, x_{meas}^{i}, $\bar{x}_{meas}$, and x_{sim}^{i} correspond, respectively, to the measured irradiance at moment *i*, the average value of the observations (measured) and the simulated irradiance obtained by the models at instant *i*.

The nMBE indicates how much the model underestimates or overestimates the results with respect to real measured data. When nMBE is negative, the model underestimates the measured values. nRMSE indicates the dispersion of the data. A model with a low nRMSE compared to the others, indicates that this model best fits the observational data. The R^2 quantifies the variance between the observational data and the estimated data; the closer it is to 1, the better the observed data is replicated by the model.

In addition, a skill score (SS4) which indicates the overall performance of a model, was selected to rank all models. This statistical presented in equation 24 considers correlation (R) and the standard deviation of a model (std_{mod}) normalized by the *std* of the observation (std_{obs}) (Taylor, 2001). Similar to the coefficient of determination, SS4 is a statistic that ranks the model from zero to one, being from worst to best quality, respectively.

$$SS4 = \frac{(1+R)^4}{4\left(\frac{std_{mod}}{std_{obs}} + \frac{1}{std_{mod}/std_{obs}}\right)^2} \quad \text{(eq. 24)}$$

4. Results and discussion

Since the comparative analysis of the transposition models in this work deals with the albedo for three different scenarios, the albedo is initially evaluated in order to calculate the average albedo of the ground (for scenario ii), and to evaluate the variation of the surface reflectance as a function of solar position, described by the zenith angle, scenario (iii). Scenario (i) assumes an albedo equal to 20%.

4.1. Albedo Evaluation

The early and late hours of the day, in other words, times when the Sun has low elevation and thus high zenith angle, tend to have higher albedos values than those observed at midday, this variation is explained in Marion (2020) due to the distribution of the solar spectrum shifting to longer wavelengths for these times. In addition, the albedo may increase due to the angle of incidence of the radiation on the surface being increased (Marion, 2020). The observed variation of the Petrolina ground reflectance is presented in Fig. 2. Note that the soil is predominantly sandy as observed in Fig. 1.

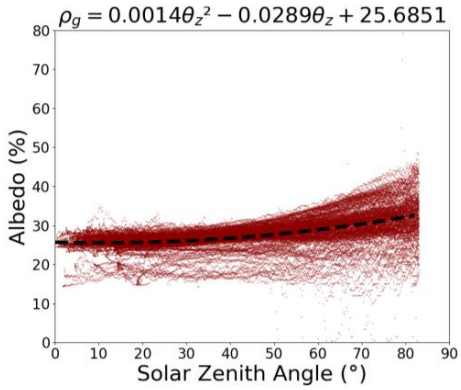

Fig. 2: Albedo as a function of solar zenith angle.

This upward profile is observed in other works, which relate both variables, in linear form (Lave et al., 2015), or from polynomial equations (Wang et al., 2005). Other works also relate albedo and solar elevation, applying exponential functions (Liu et al., 2008; Demain et al., 2013). From the data measured in Petrolina, a semi-arid region, albedo varies according to equation 25.

$$\rho_g = 0.0014\theta_z^2 - 0.0289\theta_z + 25.6851 \quad \text{(eq. 25)}$$

The highest concentration of albedo data is observed in the region above 25% (Fig. 3a). When evaluating the histogram (Fig. 3b) it is observed that this concentration of points is given for values between 25.52% and 27.80%, with the average albedo for the entire time series being 27.72%.

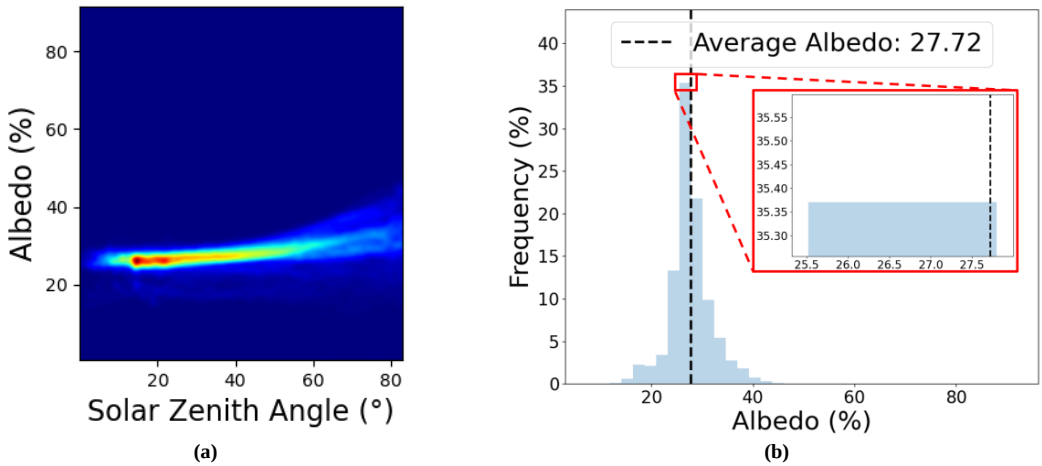

Fig. 3: Distribution of albedo data observed by a) colormap and b) histogram.

4.2. Transposition Models

A comparative analysis between the transposition models was performed for the three scenarios. The value of 20% was considered for the first scenario because it is usually applied as a default value in commercial software. For this scenario, the results indicate better performance of Perez model, with lower nRMSE and higher R^2 and SS4 for all orientations evaluated, similar to Yang (2016) and García et al. (2021). The north and south orientations evaluated presented lower nRMSE than the solarimeters facing east and west. Despite the higher values of nRMSE for the east and west orientations, it is observed the same description of the models, where the Hay and Davies (HD), Reindl (Re), Muneer (Mu) and Perez (Pe) models were predominantly performant, with an emphasis on Perez's model. Tab. 3, 4 and 5 present the statistical metrics for the three scenarios adopted, i, ii and iii respectively. The four best models have been highlighted in **bold** for each of the statistics, and the best model for each metric has been **underlined**.

Tab. 3: Statistics of all 8 models for scenario i) albedo constant and equal to 20%.

	North				South				East				West			
Model	**nMBE (%)**	**nRMSE (%)**	**R^2 (-)**	**SS4 (-)**	**nMBE (%)**	**nRMSE (%)**	**R^2 (-)**	**SS4 (-)**	**nMBE (%)**	**nRMSE (%)**	**R^2 (-)**	**SS4 (-)**	**nMBE (%)**	**nRMSE (%)**	**R^2 (-)**	**SS4 (-)**
Ba	-5,81	17,01	0,953	0,948	-7,44	16,09	0,956	0,952	-7,23	20,00	0,948	0,940	-11,52	22,34	0,954	0,931
HD	**-1,93**	**15,25**	**0,956**	**0,954**	-2,85	**13,07**	**0,964**	**0,962**	-3,73	**16,54**	**0,958**	**0,958**	-7,05	**16,98**	**0,964**	**0,958**
Klu	3,41	15,93	0,953	0,953	**1,58**	13,37	0,960	0,961	3,36	16,64	0,957	0,957	**-2,31**	17,07	0,958	0,949
Kor	3,71	16,91	0,947	0,947	**1,49**	14,03	0,956	0,956	**2,05**	18,91	0,944	0,941	**-3,64**	20,03	0,945	0,928
LJ	**0,66**	16,14	0,950	0,948	**-1,37**	13,90	0,957	0,956	**-0,92**	18,60	0,946	0,942	**-6,17**	20,35	0,949	0,930
Mu	**1,27**	**15,08**	**0,957**	**0,957**	**0,16**	**12,94**	**0,963**	**0,963**	**-0,67**	**16,46**	**0,959**	**0,958**	**-4,42**	**15,57**	**0,964**	**0,962**
Pe	-2,20	**14,19**	**0,962**	**0,961**	-2,25	**12,56**	**0,966**	**0,966**	**-1,54**	**14,21**	**0,968**	**0,968**	-6,72	**15,25**	**0,972**	**0,967**
Re	**-1,10**	**15,23**	**0,956**	**0,954**	-2,06	**12,92**	**0,964**	**0,963**	-2,93	**16,44**	**0,958**	**0,958**	-6,37	**16,69**	**0,964**	**0,958**

Tab. 4: Statistics of all 8 models for scenario ii) albedo constant and equal to 27.72%.

	North				South				East				West			
Model	**nMBE (%)**	**nRMSE (%)**	**R² (-)**	**SS4 (-)**	**nMBE (%)**	**nRMSE (%)**	**R² (-)**	**SS4 (-)**	**nMBE (%)**	**nRMSE (%)**	**R² (-)**	**SS4 (-)**	**nMBE (%)**	**nRMSE (%)**	**R² (-)**	**SS4 (-)**
Ba	-4,35	16,40	0,953	0,950	-6,07	15,36	0,956	0,954	-5,80	19,48	0,947	0,941	-10,31	21,58	0,953	0,933
HD	**-0,47**	**14,92**	**0,957**	**0,956**	**-1,48**	**12,65**	**0,965**	**0,964**	-2,30	**16,18**	**0,959**	**0,959**	-5,84	**16,30**	**0,964**	**0,959**
Klu	4,87	16,36	0,953	0,953	2,96	13,68	0,961	0,961	4,79	17,12	0,957	0,956	**-1,10**	16,89	0,957	0,949
Kor	5,18	17,28	0,947	0,947	2,87	14,25	0,956	0,956	3,48	19,20	0,943	0,941	**-2,43**	19,77	0,944	0,929
LJ	**2,13**	16,20	0,950	0,949	**0,01**	13,79	0,957	0,957	**0,50**	18,63	0,945	0,942	**-4,96**	19,92	0,948	0,931
Mu	2,74	**15,30**	**0,957**	**0,957**	1,53	**13,09**	**0,963**	**0,963**	**0,76**	**16,59**	**0,959**	**0,958**	**-3,21**	**15,20**	0,964	**0,962**
Pe	**-0,74**	**13,93**	**0,963**	**0,962**	**-0,88**	**12,33**	**0,966**	**0,966**	**-0,11**	**14,09**	**0,968**	**0,968**	-5,51	**14,58**	**0,972**	**0,968**
Re	**0,37**	**15,01**	**0,956**	**0,956**	**-0,69**	**12,60**	**0,964**	**0,964**	**-1,51**	**16,18**	**0,959**	**0,959**	-5,15	**16,07**	**0,964**	**0,959**

Tab. 5: Statistics of all 8 models for scenario iii) albedo as a function of θ_z.

	North				South				East				West			
Model	**nMBE (%)**	**nRMSE (%)**	**R² (-)**	**SS4 (-)**	**nMBE (%)**	**nRMSE (%)**	**R² (-)**	**SS4 (-)**	**nMBE (%)**	**nRMSE (%)**	**R² (-)**	**SS4 (-)**	**nMBE (%)**	**nRMSE (%)**	**R² (-)**	**SS4 (-)**
Ba	-4,53	16,49	0,953	0,949	-6,24	15,46	0,956	0,953	-5,99	19,52	0,948	0,941	-10,47	21,68	0,953	0,932
HD	**-0,66**	**14,96**	**0,957**	**0,956**	-1,65	**12,70**	**0,965**	**0,964**	-2,49	**16,18**	**0,959**	**0,959**	-5,99	**16,38**	**0,964**	**0,959**
Klu	4,68	16,27	0,953	0,953	2,78	13,60	0,961	0,961	4,60	17,01	0,957	0,957	**-1,25**	16,91	0,957	0,949
Kor	4,99	17,19	0,948	0,947	2,69	14,17	0,956	0,956	3,30	19,10	0,944	0,941	**-2,58**	19,77	0,945	0,929
LJ	**1,94**	16,17	0,950	0,949	**-0,17**	13,77	0,957	0,957	**0,32**	18,57	0,946	0,942	-5,11	19,95	0,948	0,931
Mu	2,55	**15,23**	**0,957**	**0,957**	**1,36**	**13,03**	**0,963**	**0,963**	**0,57**	**16,50**	**0,959**	**0,958**	**-3,36**	**15,23**	0,964	**0,962**
Pe	**-0,92**	**13,96**	**0,962**	**0,962**	**-1,05**	**12,35**	**0,966**	**0,966**	**-0,29**	**14,08**	**0,968**	**0,968**	-5,66	**14,68**	**0,972**	**0,968**
Re	**0,18**	**15,02**	**0,957**	**0,955**	**-0,87**	**12,63**	**0,964**	**0,964**	**-1,69**	**16,16**	**0,959**	**0,959**	**-5,31**	**16,15**	**0,964**	**0,959**

Similar to García et al. (2021), anisotropic models (HD, Klu, Mu, Pe and Re) presented better results than isotropic models (LJ, Ko and Ba) by better fitting the experimental data. It was also observed that simulations conducted with albedo varying as a function of solar zenith angle or albedo considered constant, but based on local measurements, led to more accurate results than simulations conducted with constant default albedo equal to 20%. This fact is valid for the models that underestimated the observational data, Badescu (2002), Hay and Davies (1980), Perez et al. (1990) and Reindl et al. (1990). These models presented negative nMBE for scenario i (albedo = 20%), as presented in Table 2. When the albedo adjustment was performed (scenarios ii and iii), considering the locally measured data (average albedo) and the variable albedo, a reduction in bias was observed for these models, as well as an improvement in the nRMSE. As an example, it can be seen the reduction in nRMSE for the Perez model with North orientation, the nRMSE is 14.19% with constant albedo (0.20), while the simulation with variable albedo resulted in the reduction of this statistical metric (13.96%).

Moreover, from Tab. 4 and Tab. 5, it can be seen that the input in the estimation of the global tilted irradiance with the local average albedo does not substantially impact R^2 and SS4 when compared to the simulations that consider the variable albedo. However, it tends to have better bias and better dispersion of the estimated data, thus leading to slightly better performance. In Nygren and Sundström (2021), photovoltaic systems with bifacial modules were evaluated for three albedo conditions, hourly variable albedo, fixed albedo and satellite-derived albedo. It was observed that for the modules' front face, the albedo type variation does not have a high impact. However, for the rear side, the simulations performed with variable albedo presented higher accuracy when compared to fixed albedo and satellite-derived albedo.

With the aim of facilitating the comparative analysis of the models, the Taylor diagram (Taylor, 2001) was adopted as a tool to evaluate the models against the measured results. Fig. 4 to Fig. 7 presents the diagrams for each orientation (north, south, east and west). Graphical statistical analysis is a valuable tool, where correlation, standard deviation, RMSE and SS4 are presented. The magenta color indicates the observed series and the dots indicate each model. The model that is closest to the magenta dot, indicated at the bottom of the graph, tends to describe the observational series best. Thus, models that are closer to the pink line and closer to the bottom of the frame highlighted in the figures, tend to have a better description of the observed data.

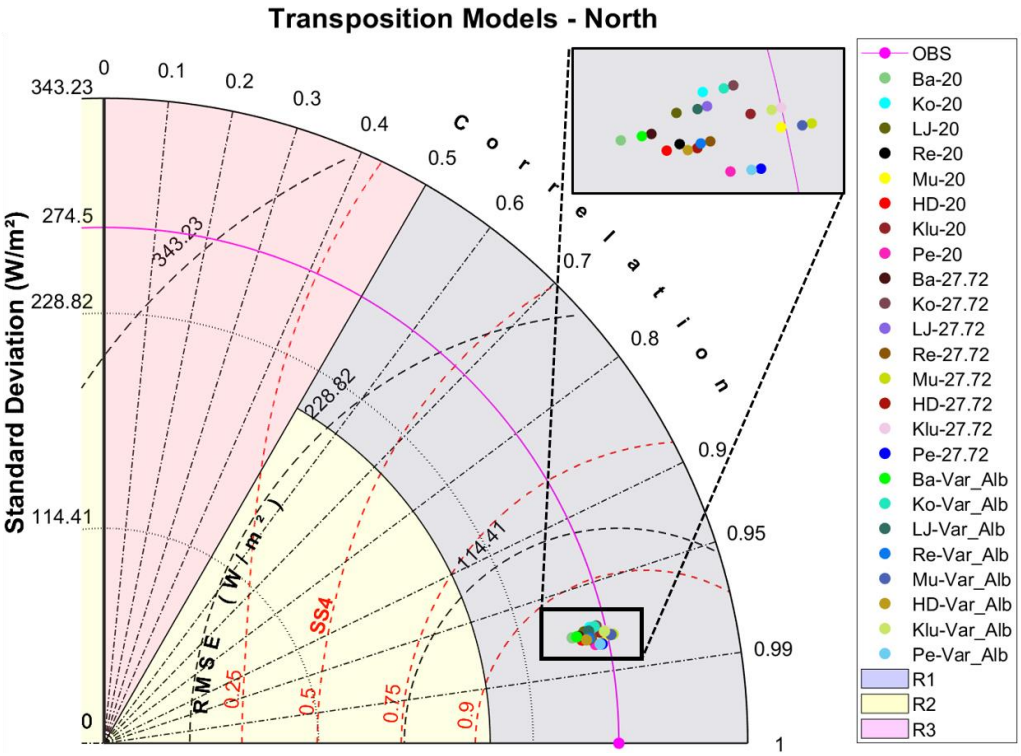

Fig. 4: Taylor diagram of all transposition models for North orientation (45º).

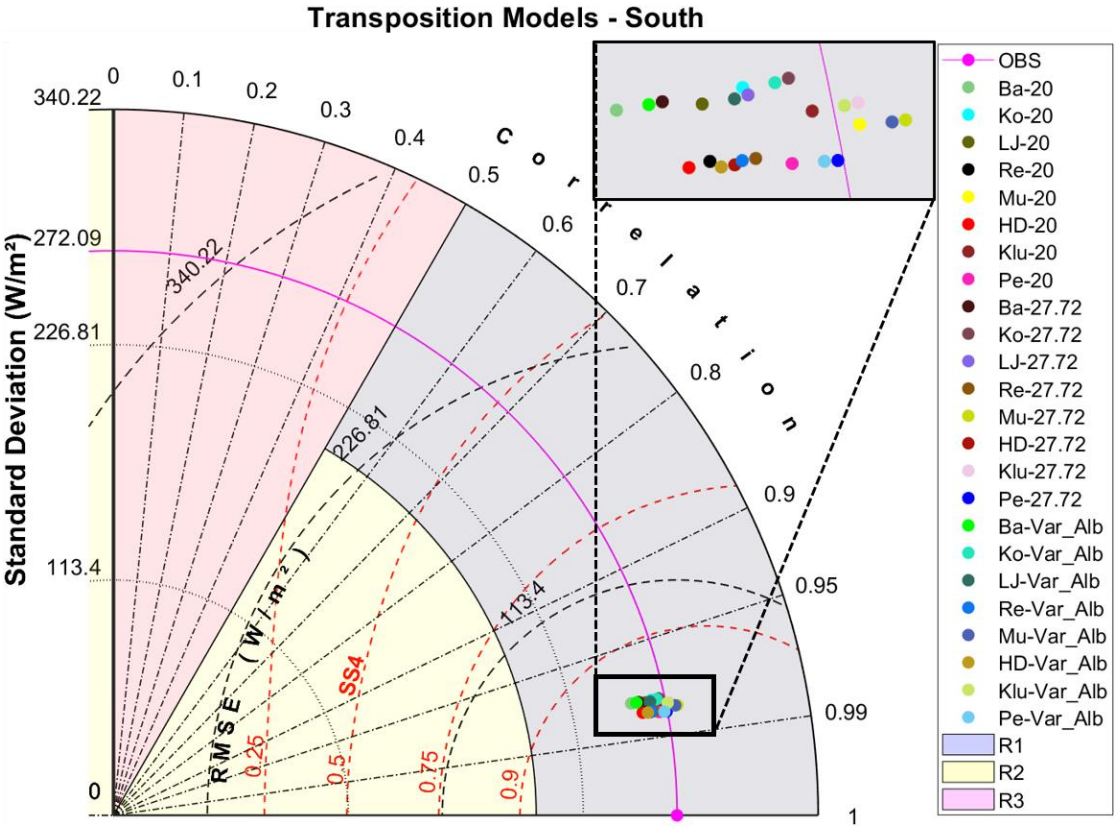

Fig. 5: Taylor diagram of all transposition models for South orientation (45º).

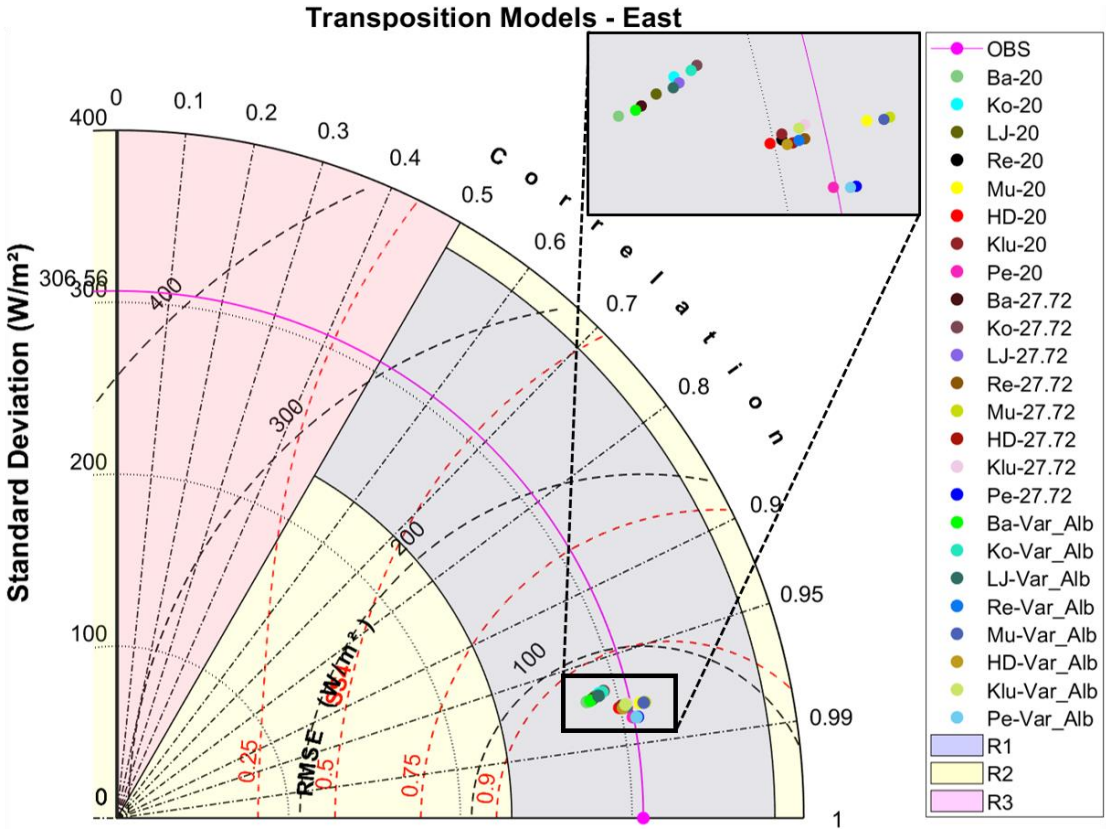

Fig. 6: Taylor diagram of all transposition models for East orientation (45°).

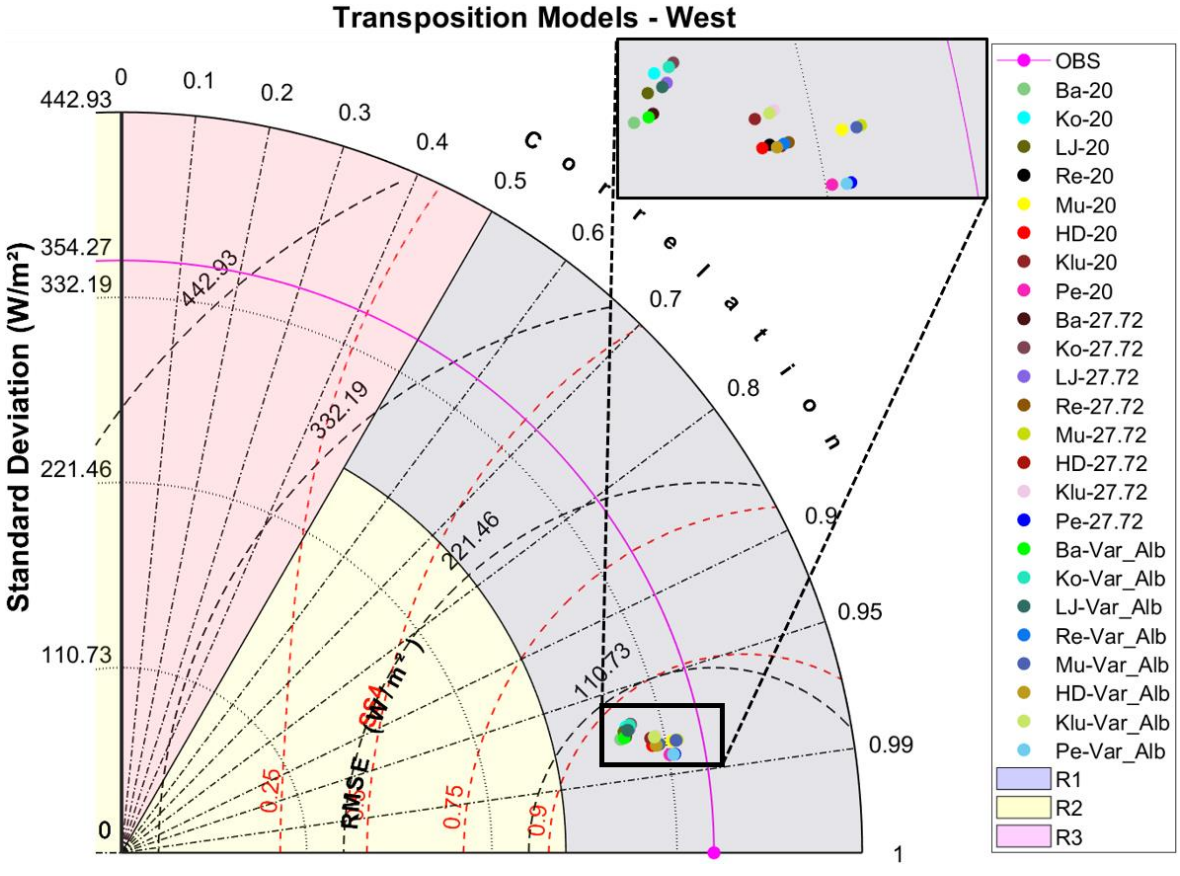

Fig. 7: Taylor diagram of all transposition models for West orientation (45°).

It can be observed from the graphs shown in Fig. 4 to 7 that the models do not present high differences between themselves. This fact may be linked to the climatic conditions of Petrolina because the DNI component has a high impact on GTI calculation. The modelling of the diffuse component does not have a powerful impact. However, although the differences are slight, it is observed that the Perez model tends to be closer to the magenta colour point (observation - OBS), presenting the best RMSE and SS4, thus demonstrating to be the best model for the location. The variation of the albedo scenarios, from constant albedo and equal to 20% for the two other scenarios, results in a slight difference between them. However, it improves the model performance from the Taylor skill score and the relationship between the standard deviations of the model with the observation for the North, South and West orientations.

It is worth noting that the present work evaluated the transposition models with measured DNI, DHI and GHI data as inputs. Applying GHI separation models at 1-min resolution may lead to even more variation in GTI calculations since DHI and DNI modelling can generate higher errors if the model employed does not fit the evaluated location (de Medeiros et al., 2022; Yang, 2022).

5. Conclusion

The present work investigated the performance of 8 models commonly used in the literature to estimate the radiation incident on tilted photovoltaic modules at Petrolina, Northeast region of Brazil. The results indicate that Hay and Davies, Reindl, Muneer, and Perez models presented the best performances, especially the Perez model that presented the best nRMSE and SS4 results for all orientations and scenarios evaluated.

Three albedo scenarios were considered to estimate the GTI irradiance, where it was observed that despite slight differences, the simulations conducted with the average albedo of the site resulted in greater accuracy. Furthermore, from the detailed analysis of the ground reflectance of Petrolina, an average albedo value corresponding to 27.72% was observed for the sandy soil type of Petrolina, with a higher concentration of data between 25.52% and 27.80% albedo values.

The graphical analysis of the Taylor diagram allowed a better visualization that the Perez model tends to be more in agreement with the observation, being able to describe the irradiance in the inclined plane better.

As future prospects, it is desired to evaluate the variable albedo for different sky conditions, assigning equations for cloudy sky, clear sky or partly cloudy sky, thus seeking to achieve more accurate simulations. Furthermore, it is intended to extend the analyses performed here, having as input data the results obtained by GHI separation models, to assess how the combination of separation + transposition models impacts the estimation of GTI irradiance.

6. Acknowledgments

The authors thank the financial support from the National Agency of Electric Energy (ANEEL) and Hydroelectric Company of São Francisco (CHESF) under the ANEEL R&D Program (CVI 23076.009704/2020-56). Likewise, the authors acknowledge the financial support provided by the Human Resources Training Program of the Brazilian National Agency for Petroleum, Natural Gas and Biofuels – PRH-ANP/FINEP, via PRH 48.1/UFPE (ANP Process number Nº48610.201019/2019-38), and to the Coordination for the Improvement of Higher Education Personnel (CAPES) in the scope of the graduate program of the UFPE members.

7. References

Assoa, Y.B., de Medeiros, J.V.F.F., Thony, P., 2020. Impact of Configurations on the Performance Prediction of Building Integrated Photovoltaic Modules. In EU PVSEC 2020, 37th European Photovoltaic Solar Energy Conference and Exhibition, pp. 1937-1940. https://doi.org/10.4229/EUPVSEC20202020-6CV.2.23.

Badescu, V., 2002. 3D isotropic approximation for solar diffuse irradiance on tilted surfaces. Renewable energy, 26(2), 221-233. https://doi.org/10.1016/S0960-1481(01)00123-9.

Demain, C., Journée, M. and Bertrand, C., 2013. Evaluation of different models to estimate the global solar radiation on inclined surfaces. Renewable energy, 50, pp.710-721. https://doi.org/10.1016/j.renene.2012.07.031.

de Medeiros, J.V.F.F., de Miranda, D.R., Gomes, E.T.A., Vilela, O.C., Pereira, A.C., Jatoba, E.B., de Melo Filho, J.B., 2022. Avaliação de modelos utilizados na estimativa da radiação difusa na resolução dos minutos para uma cidade de baixa latitude. In Congresso Brasileiro de Energia Solar-CBENS (pp. 1-10).

Dirmhirn, I., Eaton, F. D., 1975. Some characteristics of the albedo of snow. Journal of Applied Meteorology and Climatology, 14(3), 375-379. https://doi.org/10.1175/1520-0450(1975)014<0375:SCOTAO>2.0.CO;2.

Duffie, J. A., Beckman, W. A., 2013. Solar engineering of thermal processes, fourth ed. John Wiley & Sons.

García I., de Blas M., Hernández B., Sáenz C., Torres J.L., 2021. Diffuse irradiance on tilted planes in urban environments: Evaluation of models modified with sky and circumsolar view factors. Renewable Energy. 180, 1194-1209. https://doi.org/10.1016/j.renene.2021.08.042.

Gueymard, C.A., Ruiz-Arias, J.A., 2016. Extensive worldwide validation and climate sensitivity analysis of direct irradiance predictions from 1-min global irradiance. Solar Energy, 128, 1–30. https://doi.org/10.1016/j.solener.2015.10.010.

Hay, J. E., Davies, J. A., 1980. Calculation of the Solar Radiation Incident on an Inclined Surface. In: Proceedings of the First Canadian Solar Radiation Data Workshop. Ministry of Supply and Services, Toronto, Canada, 59.

Koronakis, P. S., 1986. On the choice of the angle of tilt for south facing solar collectors in the Athens basin area. Solar Energy, 36(3), 217-225. https://doi.org/10.1016/0038-092X(86)90137-4.

Klucher, T. M., 1979. Evaluation of models to predict insolation on tilted surfaces. Solar energy, 23(2), 111-114. https://doi.org/10.1016/0038-092X(79)90110-5.

Lave, M., Hayes, W., Pohl, A., & Hansen, C. W., 2015. Evaluation of global horizontal irradiance to plane-of-array irradiance models at locations across the United States. IEEE journal of Photovoltaics, 5(2), 597-606. https://doi.org/10.1109/JPHOTOV.2015.2392938.

Liu, B., Jordan, R., 1961. Daily insolation on surfaces tilted towards equator. ASHRAE J., 10.

Liu, H., Wang, B., Fu, C., 2008. Relationships between surface albedo, soil thermal parameters and soil moisture in the semi-arid area of Tongyu, northeastern China. Advances in Atmospheric Sciences, 25(5), 757-764. https://doi.org/10.1007/s00376-008-0757-2.

Maleki, S.A.M., Hizam, H., Gomes, C., 2017. Estimation of hourly, daily and monthly global solar radiation on inclined surfaces: Models re-visited. Energies, 10, 134. https://doi.org/10.3390/en10010134.

Marion, B., 2020. Albedo data sets for bifacial PV systems. In 2020 47th IEEE Photovoltaic Specialists Conference (PVSC) (pp. 0485-0489). IEEE. https://doi.org/10.1109/PVSC45281.2020.9300470.

Muneer, T., 1990. Solar radiation model for Europe. Building services engineering research and technology, 11(4), 153-163. https://doi.org/10.1177/014362449001100405.

Nygren, A., Sundström, E., 2021. Modelling bifacial photovoltaic systems: Evaluating the albedo impact on bifacial PV systems based on case studies in Denver, USA and Västerås, Sweden.

Perez, R., Ineichen, P., Seals, R., Michalsky, J., Stewart, R., 1990. Modeling daylight availability and irradiance components from direct and global irradiance. Solar energy, 44(5), 271-289. https://doi.org/10.1016/0038-092X(90)90055-H.

Reindl, D. T.; Beckman, W. A.; Duffie, J. A.. 1990. Evaluation of Hourly Tilted Surface Radiation Models. Solar Energy, 45(1), 9–17. https://doi.org/10.1016/0038-092X(90)90061-G.

Taylor, K.E., 2001. Summarizing multiple aspects of model performance in a single diagram. Journal of Geophysical Research: Atmospheres, 106, 7183-7192. https://doi.org/10.1029/2000JD900719.

Temps, R. C., Coulson, K. L., 1977. Solar radiation incident upon slopes of different orientations. Solar energy, 19(2), 179-184. https://doi.org/10.1016/0038-092X(77)90056-1.

Thevenard, D., Haddad, K., 2006. Ground reflectivity in the context of building energy simulation. Energy and buildings, 38(8), 972-980. https://doi.org/10.1016/j.enbuild.2005.11.007.

Yang, D., 2016. Solar radiation on inclined surfaces: Corrections and benchmarks. Solar Energy. 136. https://doi.org/10.1016/j.solener.2016.06.062.

Yang, D., 2022. Estimating 1-min beam and diffuse irradiance from the global irradiance: A review and an extensive worldwide comparison of latest separation models at 126 stations. Renewable and Sustainable Energy Reviews, 159, 112195. https://doi.org/10.1016/j.rser.2022.112195.

Wang, Z., Barlage, M., Zeng, X., Dickinson, R. E., Schaaf, C. B., 2005. The solar zenith angle dependence of desert albedo. Geophysical Research Letters, 32(5). https://doi.org/10.1029/2004GL021835.

Q. System Modelling, Artificial Intelligence, Digitalization

Implementation of Adapted Black Box Models for the Performance Characterization of Commercial Sorption Chillers

Amín Altamirano[1*], Charles Maragna[2] and Brice Tremeac[1]

[1] Laboratoire du froid et des systèmes énergétiques et thermiques (Lafset), Conservatoire national des arts et métiers, Paris (France)

[2] Bureau de Recherches Géologiques et Minière (BRGM), Orléans (France)

Abstract

Thermally-driven sorption chillers represent an excellent alternative to make use of low-temperature renewable energy sources such as solar or geothermal energy in the range of 60-120°C. In these cases, three commercially available geometries emerge: two closed sorption systems (single-stage absorption and adsorption chillers) and an open sorption system (Dissociative Evaporative Cooling system, DEC). Due to the complexity of these systems, their modeling (which is fundamental for viability studies) remains a complicated task. In this regard, black box models represent a simple alternative to simulate their performance. Two specially adapted methods have been used in the literature for the most common system (the absorption chiller): the adapted characteristic equation (CE) and the Carnot function model (CFM). The present work studies the implementation of these methods with different commercial sorption chillers and discusses their advantages and their limits regarding each technology. The feasibility of the implementation of the CFM and the adapted CE method with adsorption chillers and DEC systems is demonstrated. Despite its natural advantages, the CFM presented the highest deviations (especially with $\dot{Q}_e$ and $\dot{Q}_g$), the reason behind this might be that the COP_{carnot} is a physical parameter that cannot be fitted (as in the case of the $\Delta\Delta t'$ of the adapted CE method).

Keywords: sorption chiller, absorption chiller, adsorption chiller, DEC, black box, characteristic equation, Carnot function

1. Introduction

Given the current increase in the global energy demand related to cooling in the building sector, especially in tropical climates (IEA, 2018), the use of chillers that make use of renewable energy is becoming a necessity more than an option (Altamirano et al., 2019a). In this regard, thermally-driven sorption chillers represent an excellent alternative since these systems can make use of a renewable heat source (such as solar energy) to operate. These systems can be divided into two categories: closed cycle (in which the refrigerant fluid is not in direct contact with the air to be cooled, i.e., absorption and adsorption systems) and open cycle (in which the refrigerant fluid is in direct contact with the cooled air, i.e., Dissociative Evaporative Cooling systems). In terms of market penetration, among the thermally-driven systems, absorption chillers have the largest market share (82-84%), followed by adsorption (9-11%) and DEC systems (7%), respectively (Almasri et al., 2022).

The modeling of sorption systems is of fundamental importance for the evaluation of their performance, and in particular when they are coupled to other systems with variable requirements and availabilities (e.g., buildings, storage systems, and ambient source) (Altamirano et al., 2019b). Depending on the degree of physical insight on the machine, the different models can be divided into three categories: white box (physical), when it contains a complete insight into the physical phenomena in the system; gray box (semi-empirical), when there is some degree of physical insight, and black box, when no physical insight is required and the model is based on a dataset of experimental results In cases in which the potential of sorption chillers is to be estimated, no need for understanding the physical phenomena inside the machine is required and therefore, black box models are seem like the most suitable tool for these machines' modeling given their simplicity, accuracy, and ease of

© 2022. The Authors. Published by International Solar Energy Society
Selection and/or peer review under responsibility of Scientific Committee
doi:10.18086/eurosun.2022.16.01 Available at http://proceedings.ises.org

implementation with different dynamic thermal simulation programs such as TRNSYS.

Among the black box model possibilities, there are two options that might be especially useful in the modeling of sorption systems: the adapted characteristic equation (CE) method and the Carnot function model (CFM). Indeed, these modeling methods use parameters function of the thermal sources' temperatures (commonly used by researchers and manufacturers for their characterization) to situate the different machine operating regimes. These modeling methods, however, have only been studied in the context of absorption chillers (Altamirano et al., 2021). Nevertheless, the characterization of the other sorption chillers' options is also required to compare the different available solutions.

The present work consists of the modeling of commercial thermally driven sorption chillers (a single-stage absorption chiller, a single-stage adsorption chiller, and a DEC system) through the adapted CE and CFM methods. The study is divided into three parts. In the first part, a theoretical description of the studied systems, their operating conditions, and the performance evaluation parameters is presented. The following section describes the black box modeling methods used. Finally, the modeling results and the prediction accuracy of the different models on the selected systems are presented and discussed.

2. Operating conditions and performance evaluation parameters

Sorption systems make use of a physical or chemical affinity between two substances to generate cooling thanks to a heat source. One of these substances plays the role of the refrigerant, whereas the other one, with lower volatility, plays the role of the sorbent. The most general case (the case of closed systems) is represented by a theoretical machine with three heat sources at different temperature levels (Figure 1). In such a case, there is a component commonly named as desorber or generator, that receives heat ($\dot{Q}_g$) from a high-temperature source (T_g). There are also components, called condenser and ad/absorber, that reject heat ($\dot{Q}_{int}$) to a source that is at an intermediate temperature level (T_{int}). Finally, there is a component (an evaporator) that extracts heat ($\dot{Q}_e$) from a low temperature source (T_e). Different geometrical configurations are available for commercial closed-cycle sorption systems. However, the single-effect configuration is the most adapted for low-temperature renewable energy sources such as solar or geothermal energy in the range of 60-120°C (obtained through flat plate and evacuated tube collectors) (Alahmer and Ajib, 2020). In the case of open-cycle sorption systems, the most commonly manufactured system is based on the Pennington cycle (also known as ventilation cycle) (La et al., 2010), which is also adapted to similar driving temperature levels (Almasri et al., 2022). Taking this into consideration, three sorption chillers with a similar nominal capacity were selected: a 35-kW single-effect commercial absorption chiller (Yazaki Energy Systems Inc., 2018), a 30-kW single-effect commercial adsorption chiller (InvenSor GmbH, 2015), and a 20-kW DEC experimental system (Pons and Kodama, 1999) with similar nominal conditions than commercial systems (Robatherm GmbH, 2014).

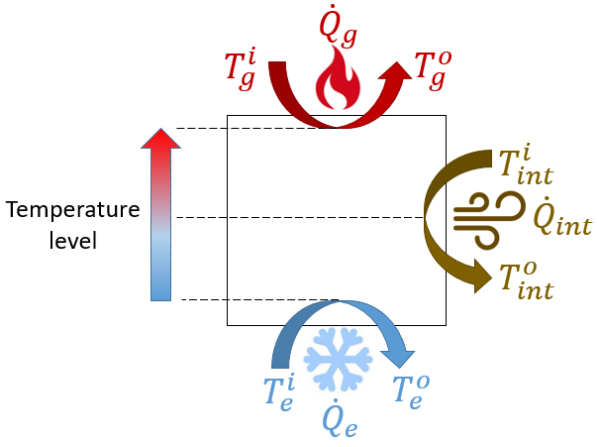

Fig. 1: Illustrative diagram of a sorption machine with three heat sources at different temperature levels.

The nominal and part-load operation range conditions of the selected systems are presented in Table 1. The data of the commercial systems (absorption and adsorption chiller) were extracted from the commercial catalogues (InvenSor GmbH, 2015; Yazaki Energy Systems Inc., 2018), whereas the data of the DEC system were obtained

from (Pons and Kodama, 1999). After the discretization and extraction of these data, the total number of operating conditions are 358, 28, and 9 for the absorption chiller, adsorption chiller, and DEC system, respectively.

Tab. 1: Operation range conditions of the studied systems (nominal conditions in parentheses) (InvenSor GmbH, 2015; Pons and Kodama, 1999; Yazaki Energy Systems Inc., 2018)

Variable	35-kW H_2O-LiBr Absorption Chiller	30-kW H_2O-Zeolite Adsorption Chiller	20-kW H_2O-Silica Gel DEC System
T_e^o $[°C]$	5 – 12 (7)	10 – 17.4 (14)	– (14)
$\dot{Q}_e$ $[kW]$	2.9 – 60.7 (35.2)	4.5 – 33.9 (29.5)	16 – 22.9 (20.2)
T_{int}^i $[°C]$	24 – 32 (31)	22 – 37 (27)	– (31)
$\dot{Q}_{int}$ $[kW]$	13.7 – 148.3 (85.4)	15.4 – 93.7 (78.5)	16 – 23 (20.2)
T_g^i $[°C]$	75 – 95 (88)	45 – 95 (85)	62 – 100.8 (80.4)
$\dot{Q}_g$ $[kW]$	10.9 – 87.7 (50.2)	10.2 – 59.8 (49)	30.9 – 63.1 (37.9)
COP_{th} $[-]$	0.26 – 0.8 (0.7)	0.39 – 0.68 (0.6)	0.36 – 0.54 (0.53)
COP_{carnot} $[-]$	1.24 – 4.58 (1.84)	1.22 – 6.77 (3.58)	1.56 – 3.15 (2.36)

The performance of sorption chillers depends on a large series of parameters that can be internal (the working fluid, the exchanger technology, or the control system) or external (the climatic conditions or the thermodynamic state of the heat transfer fluid) (Pons et al., 2012). Whereas the performance of mechanical compression machines is measured by the so-called electrical coefficient of performance (COP) (the cooling capacity divided by the electrical input to the compressor, defined by equation 1, in the case of sorption machines, because the driving source is heat, a thermal COP is often used, defined by equation 2. Moreover, some authors consider a global COP (equation 3), in which the heat source and the electrical supply (e.g., in the case of using pumps) are taken into account as energy sources.

$$COP_{el} = \frac{\dot{Q}_e}{\dot{W}_{el}} \quad \text{(eq. 1)}$$

$$COP_{th} = \frac{\dot{Q}_e}{\dot{Q}_g} \quad \text{(eq. 2)}$$

$$COP_{gl} = \frac{\dot{Q}_e}{\dot{Q}_g + \dot{W}_{el}} \quad \text{(eq. 3)}$$

Another important parameter in the study of thermodynamic systems is the Carnot COP (equation 4), which represents the COP of an ideal cycle, and which is a function of the temperatures of the sources at the three levels in the case of closed-cycle sorption machines. The COP_{carnot}, therefore, implies a reversible process with infinite (isothermal) energy sources, which for the heat transfer fluids corresponds to the temperatures at the generator inlet (T_g^i), at the ad/absorber and condenser inlet ($T_a^i = T_c^i = T_{int}^i$), and at the evaporator outlet (T_e^o). This definition is particularly suitable since manufacturers of closed-cycle sorption machines use the same temperatures to characterize their systems. DEC machines, unlike closed-cycle systems, do not have an intermediate temperature source and a cold temperature source in the strict sense. Pons and Kodama (1999) propose to use the ambient temperature as the intermediate temperature source and the conditioned air temperature as the low-temperature source for the calculation of the Carnot COP.

$$COP_{carnot} = \left(\frac{T_g^i - T_{int}^i}{T_g^i}\right)\left(\frac{T_e^o}{T_{int}^i - T_e^o}\right) \quad \text{(eq. 4)}$$

3. Adapted black box modeling methods

3.1. Adapted characteristic equation method

The adapted CE method (Kühn and Ziegler, 2005) is based on a multiple linear regression to obtain an arbitrary parameter, called the adapted characteristic temperature difference ($\Delta\Delta t'$, equation 5), which is a function of the external source temperatures (at the evaporator, generator, and heat sink) linearly correlated with the cooling power (equation 6). A second fitting is then employed to correlate the $\Delta\Delta t'$ to the thermal power of the generator (equation 7). The authors of the original method propose the use of the external arithmetic mean temperatures of the heat sources, however, an alternative is the use of the generator inlet temperature (T_g^i), heat sink inlet temperature (T_{int}^i), and evaporator outlet temperature (T_e^o), since these variables are commonly used to characterize the part-load behavior of sorption chillers (experimental prototypes and commercial machines).

$$\Delta\Delta t' = T_g^i - a \cdot T_{int}^i + e \cdot T_e^o \quad \text{(eq. 5)}$$

$$\dot{Q}_e^{ce\prime} = s' \cdot \Delta\Delta t' + r = s' \cdot T_g^i - s' \cdot a \cdot T_{int}^i + s' \cdot e \cdot T_e^o + r \quad \text{(eq. 6)}$$

$$\dot{Q}_g^{ce\prime} = b \cdot \Delta\Delta t' + c \quad \text{(eq. 7)}$$

3.2. Carnot function model

The Carnot function model (Boudéhenn et al., 2014), on the other hand, characterizes the thermal COP and cooling capacity of the system in terms of its Carnot COP (equation 8) through fitted parameters $\omega_1, \omega_2, \tau_1, \tau_2$, and F_0.

$$F^{cfm} = \omega_1 \cdot e^{(-COP_{carnot}/\tau_1)} + \omega_2 \cdot e^{(-COP_{carnot}/\tau_2)} + F_0 \quad \text{(eq. 8)}$$

4. Results and discussion

The present section shows the results of the implementation of the two black box modeling methods presented in section 3 to the three selected sorption chillers. The least squares method along with the generalized reduced gradient (GRG) nonlinear method were used to fit the parameters of the equations presented in section 3 to the data of the different machines. The fitted parameters of the adapted CE method are presented in Table 2, whereas those of the CFM are presented in Table 3.

Tab. 2: Fitted parameters of the adapted CE method

	35-kW H_2O-LiBr Absorption Chiller	**30-kW H_2O-Zeolite Adsorption Chiller**	**H_2O-Silica Gel DEC System**
s'	1.46	0.61	0.16
a	2.13	2.24	4.73
e	0.41	1.42	2.95
r	-2.79	0.55	23.78
b	1.96	0.96	0.70
c	-0.79	3.78	60.35

As previously mentioned, the main advantage of the adapted CE method and the CMF with sorption chillers is that they have a specific parameter that represents the operating regime of the machine. In other words, they correlate either the $\Delta\Delta t'$ (equation 5) or the COP_{carnot} (equation 4) to the cooling power that the machine can deliver under certain conditions of specific source temperatures (T_e, T_{int}, and T_g) and at the same time, they give information about the thermal performance related to those operating conditions. In the case of the adapted CE method, the influence of the external temperatures on the operating regime is represented by the factors 1, a, and e in equation 5 for T_g^i, T_{int}^i, and T_e^o, respectively. Table 1 shows that for the three selected systems, T_{int}^i has the highest influence, followed by T_e^o, with exception of the absorption chiller, for which T_e^o seems to have the lowest influence on the operating regime. The COP_{carnot}, being a physical parameter, cannot be adjusted to better divide

the effects of the external temperatures. However, from its definition (equation 4), T_{int}^{i} has a strong influence on the system's operating regime, especially at low values of T_{int}^{i}.

Tab. 3: Fitted parameters of the CFM

	35-kW H2O-LiBr Absorption Chiller		30-kW H2O-Zeolite Adsorption Chiller		H2O-Silica Gel DEC System	
	$\dot{Q}_e^{cfm}$	COP_{th}^{cfm}	$\dot{Q}_e^{cfm}$	COP_{th}^{cfm}	$\dot{Q}_e^{cfm}$	COP_{th}^{cfm}
ω_1	-75.07	-2.69	-173.59	-1.46	-49.52	-2.84
ω_2	-90.11	-4.46*10^{12}	-38.39	-4.48*10^{12}	-29.64	-4.52*10^{12}
τ_1	1.18	0.38	65.82	0.64	0.60	0.10
τ_2	1.18	0.04	1.18	0.021	0.64	0.03
F_0	61.43	0.71	187.60	0.62	22.56	0.45

The modeling results of the implementation of the (a) CFM and the (b) adapted CE method to the absorption chiller are presented in Figure 2. Figure 2a shows that even in the COP_{th} prediction of the CFM seems to be good, the cooling load does not follow the same evolution as the proposed function. This happens especially for chilled water temperatures that are either very low or very high. On the other hand, even though the adapted CE method seems to properly predict the behavior of the cooling and heat source loads, there are some regimes at elevated values of $\Delta\Delta t'$ that do not correspond to the proposed function. Again, these conditions correspond to low evaporator temperatures, for which the performance of the chiller decreases drastically.

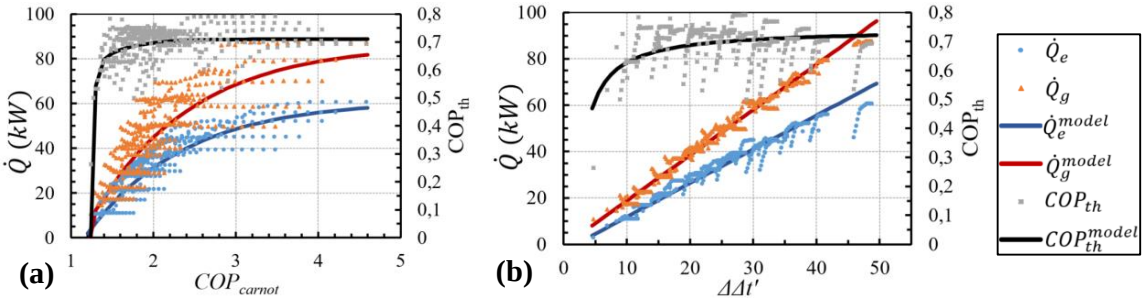

Fig. 2: Results of the implementation of the (a) CFM and the (b) adapted CE method with the absorption chiller

Figure 3 presents the comparison of the numerical results with the catalog data of the absorption chiller. $\dot{Q}_e^{cfm}$ has a coefficient of determination (R^2, useful to quantify the quality of the prediction of the model) of 0.8188, an average error of 17%, and 34.64% of the cooling loads that are predicted within an error of 10% or less (Figure 3a). Regarding $\dot{Q}_g^{cfm}$ (directly calculated having COP_{th}^{cfm} and $\dot{Q}_e^{cfm}$), it has a coefficient of determination of 0.7038, an average error of 19.22%, and 28.49% of the heat source loads that are predicted within an error of 10% or less (Figure 3b). Finally, regarding COP_{th}^{cfm}, it has a coefficient of determination of 0.2918, an average error of 6.12%, and 85.20% of the thermal COPs that are predicted within an error of 10% or less (Figure 3c).

$\dot{Q}_e^{ce\prime}$ has a coefficient of determination of 0.9485, an average error of 7.35%, and 70.95% of the cooling loads that are predicted within an error of 10% or less (Figure 3a). Regarding $\dot{Q}_g^{ce\prime}$, it has a coefficient of determination of 0.9767, an average error of 5.42%, and 88.27% of the heat source loads that are predicted within an error of 10% or less (Figure 3b). Finally, regarding $COP_{th}^{ce\prime}$ (directly calculated having $\dot{Q}_e^{ce\prime}$ and $\dot{Q}_g^{ce\prime}$), it has a coefficient of determination of 0.0861, an average error of 7.03%, and 78.21% of the thermal COPs that are predicted within an error of 10% or less (Figure 3c).

Figure 3a shows that the CFM has the largest prediction errors on the cooling load, especially at low operating regimes. It would seem from this figure that the COP_{carnot} has indeed some correlation with the cooling load. However, this correlation might not be good enough to be used in a performances prediction model. On the other

hand, the adapted CE method shows a good accuracy at low operating regimes and higher errors at high cooling loads, indicating that the hypothesis of a linear correlation of $\Delta\Delta t'$ with the cooling load might not be valid at these conditions. Similar results are observed for the comparison of the heat source load (Figure 3b). The adapted CE method, however, possesses low deviations in the whole range of operating conditions. The thermal COP is commonly overestimated by the models (Figure 3c). This might be due to missing data of the system operating at low performances (especially at heat source temperatures lower than 75°C). For a big part of the operating conditions, the machine operates with a COP_{th} close to the nominal one (0.7). Indeed, 70% of the operating conditions present a thermal COP between 0.65 and 0.75.

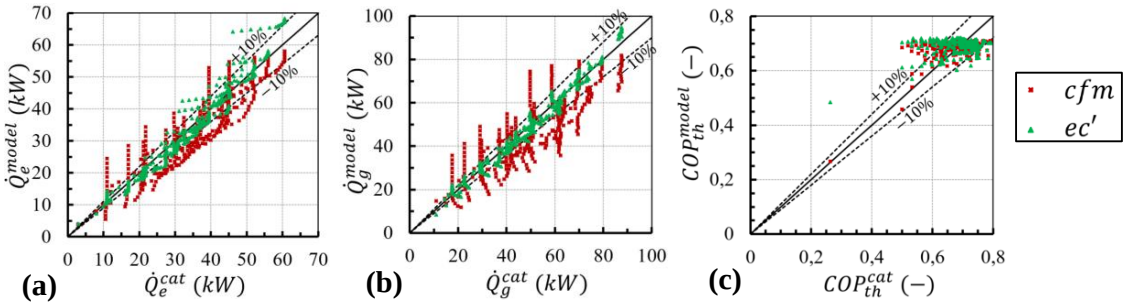

Fig. 3: Comparison between numerical and catalog results for the absorption chiller

The modeling results of the implementation of the (a) CFM and the (b) adapted CE method to the adsorption chiller are presented in Figure 4. To the best of our knowledge, this is the first time that these methods are applied to an adsorption chiller, and the results seem coherent and similar to those obtained with the absorption chiller.

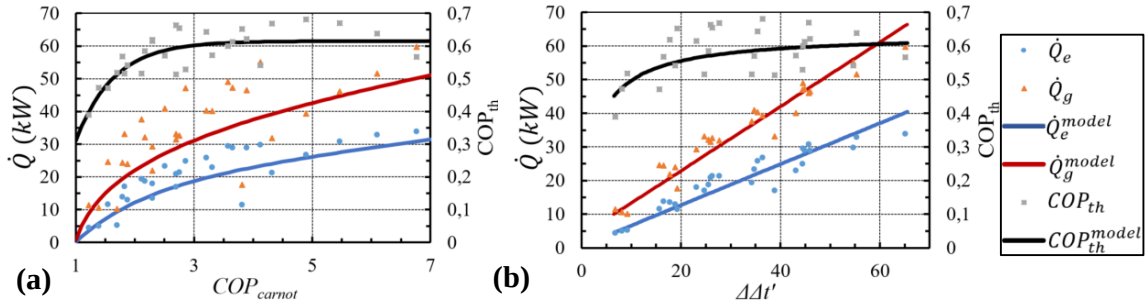

Fig. 4: Results of the implementation of the (a) CFM and the (b) adapted CE method with the adsorption chiller

Figure 5 presents the comparison of the numerical results with the catalog data of the adsorption chiller. $\dot{Q}_e^{cfm}$ has a coefficient of determination of 0.7590, an average error of 24.41%, and 14.29% of the cooling loads that are predicted within an error of 10% or less (Figure 5a). Regarding $\dot{Q}_g^{cfm}$, it has a coefficient of determination of 0.6207, an average error of 26.16%, and 14.28% of the heat source loads that are predicted within an error of 10% or less (Figure 5b). Finally, regarding COP_{th}^{cfm}, it has a coefficient of determination of 0.6379, an average error of 6.16%, and 85.71% of the thermal COPs that are predicted within an error of 10% or less (Figure 5c).

$\dot{Q}_e^{ce\prime}$ has a coefficient of determination of 0.8830, an average error of 13.44%, and 39.29% of the cooling loads that are predicted within an error of 10% or less (Figure 5a). Regarding $\dot{Q}_g^{ce\prime}$, it has a coefficient of determination of 0.94, an average error of 10.25%, and 57.14% of the heat source loads that are predicted within an error of 10% or less (Figure 5b). Finally, regarding $COP_{th}^{ce\prime}$, it has a coefficient of determination of 0.3365, an average error of 8.28%, and 50% of the thermal COPs that are predicted within an error of 10% or less (Figure 5c).

Similar to the case of the absorption chiller, the CFM presents the largest prediction errors on the cooling and heat source loads (Figures 5a and b). However, it has a higher precision on the thermal COP prediction (Figure 5c). For this machine, 42.86% of the operating conditions present a thermal COP between 0.55 and 0.65 (close to the nominal COP_{th} of 0.6). More information on the behavior of the machine at low operating performances is necessary for more accurate models.

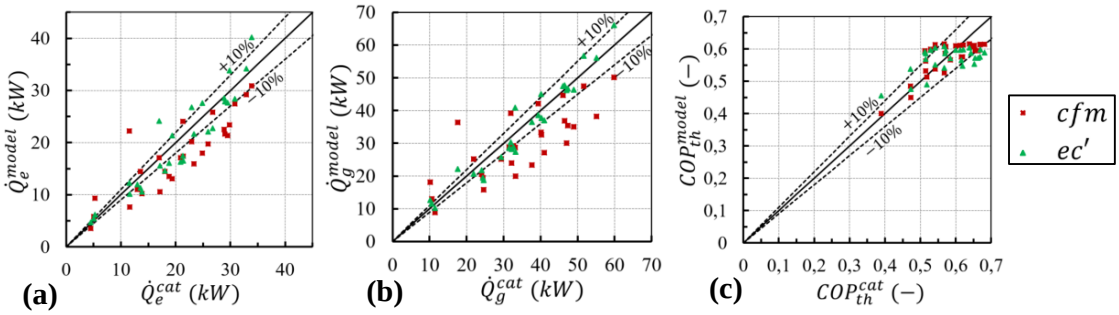

Fig. 5: Comparison between numerical and catalog results for the adsorption chiller

The modeling results of the implementation of the (a) CFM and the (b) adapted CE method to the DEC system are presented in Figure 6. To the best of our knowledge, this is the first time that these methods are applied to a DEC system and, from these figures, it seems that the CFM (Figure 6a) is well adapted to predict the cooling load of this system, however, this is not the case for the thermal COP, for which the model seems to have important deviations. One has to consider, however, that only 9 experimental conditions are available and therefore, the model prediction accuracy is highly dependent on the choice of said conditions. The adapted CE method seems to accurately predict the behavior of the DEC system (Figure 6b).

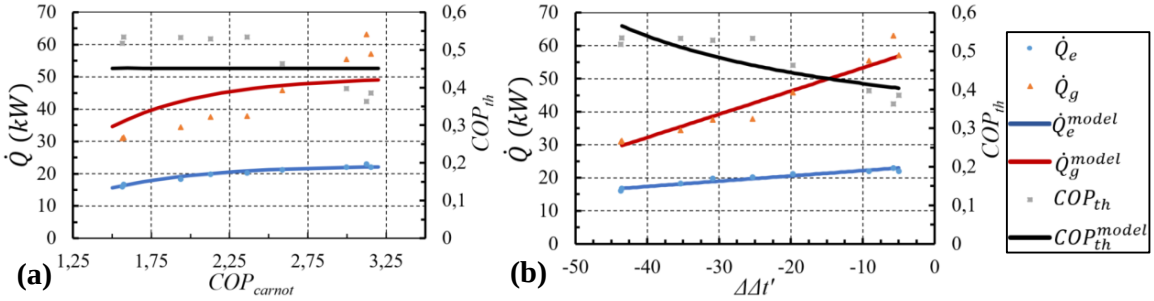

Fig. 6: Results of the implementation of the (a) CFM and the (b) adapted CE method with the DEC system

Figure 7 presents the comparison of the numerical results with the experimental data of the DEC system. $\dot{Q}_e^{cfm}$ has a coefficient of determination of 0.9602, an average error of 1.90%, and 100% of the cooling loads that are predicted within an error of 10% or less (Figure 7a). Regarding $\dot{Q}_g^{cfm}$, it has a coefficient of determination of 0.7136, an average error of 16.49%, and 11.11% of the heat source loads that are predicted within an error of 10% or less (Figure 7b). Finally, regarding COP_{th}^{cfm}, it has a coefficient of determination of 0.1760, an average error of 14.58%, and 11.1% of the thermal COPs that are predicted within an error of 10% or less (Figure 5c).

$\dot{Q}_e^{ce\prime}$ has a coefficient of determination of 0.9351, an average error of 2.49%, and 100% of the cooling loads that are predicted within an error of 10% or less (Figure 7a). Regarding $\dot{Q}_g^{ce\prime}$, it has a coefficient of determination of 0.9423, an average error of 4.80%, and 77.78% of the heat source loads that are predicted within an error of 10% or less (Figure 7b). Finally, regarding $COP_{th}^{ce\prime}$, it has a coefficient of determination of 0.6852, an average error of 7.24%, and 77.78% of the thermal COPs that are predicted within an error of 10% or less (Figure 7c).

Based on these results, it seems that the CFM and the adapted CE method might be adapted to predict the performances and cooling loads of DEC systems. However, this should be confirmed with experimental tests on systems in a larger operating conditions range and with more experimental points.

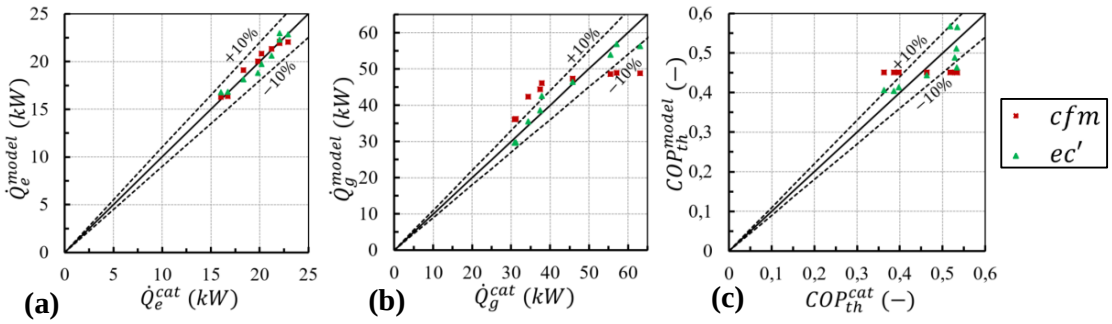

Fig. 7: Comparison between numerical and experimental results for the DEC system

5. Conclusions and perspectives

The present work demonstrated the feasibility of the implementation of the CFM and the adapted CE method (which had until now been exclusively used with absorption chillers) with adsorption chillers and DEC systems. These black box models, that use the external source temperatures as parameters to graphically situate the machine operating conditions, offer the advantages of ease of implementation with dynamic thermal simulation programs such as TRNSYS and a visual representation of the systems' operating regime either through the $\Delta\Delta t'$ or the COP_{carnot}. The main advantage of the COP_{carnot} as a tool to represent the systems' operating conditions is that it is a universal parameter with a physical sense and therefore, a comparison of machines of different nature or geometries in the same domain (COP_{carnot}) is possible. This parameter, however, cannot be fitted for better model prediction accuracy, such as in the case of the $\Delta\Delta t'$ of the adapted CE method, and this might be one of the main reasons why the CFM presented the highest deviations (especially with $\dot{Q}_e$ and $\dot{Q}_g$), limiting its utility for applications in system performance monitoring. A more detailed study is required to highlight the reasons behind these deviations since they might be related to the performances of the individual components (heat and mass exchangers) in the system or to the physical limitations of the theoretical cycle. This might help develop improved black box modeling methods with better accuracy.

6. Acknowledgments

The authors would like to thank the TEC project, funded by Europe's Interreg Caraïbes program, for its support to this research.

7. References

Alahmer, A., Ajib, S., 2020. Solar cooling technologies: State of art and perspectives. Energy Convers. Manag. 214, 112896. https://doi.org/10.1016/J.ENCONMAN.2020.112896

Almasri, R.A., Abu-Hamdeh, N.H., Esmaeil, K.K., Suyambazhahan, S., 2022. Thermal solar sorption cooling systems - A review of principle, technology, and applications. Alexandria Eng. J. 61, 367–402. https://doi.org/10.1016/J.AEJ.2021.06.005

Altamirano, A., Le Pierrès, N., Stutz, B., 2019a. Review of small-capacity single-stage continuous absorption systems operating on binary working fluids for cooling: Theoretical, experimental and commercial cycles. Int. J. Refrig. 106, 350–373. https://doi.org/10.1016/j.ijrefrig.2019.06.033

Altamirano, A., Le Pierrès, N., Stutz, B., Coronas, A., 2021. Performance characterization methods for absorption chillers applied to an NH_3-$LiNO_3$ single-stage prototype. Appl. Therm. Eng. 185, 116435. https://doi.org/10.1016/j.applthermaleng.2020.116435

Altamirano, A., Stutz, B., Le Pierrès, N., Domain, F., 2019b. H2O-LiBr Single-Stage Solar Absorption Air Conditioner with an Innovative Bi-Adiabatic Configuration: Dynamic Model, Nominal Conditions and Typical Day Operation, in: Solar World Congress. Santiago, Chili. https://doi.org/10.18086/swc.2019.55.01

Boudéhenn, F., Bonnot, S., Demasles, H., Lazrak, A., 2014. Comparison of different modeling methods for a single effect water-lithium bromide absorption chiller, in: International Conference on Solar Energy and Buildings, September 16-19. Aix-les-Bains, France. https://doi.org/10.18086/eurosun.2014.07.04

IEA, 2018. World energy outlook. Paris, France.

InvenSor GmbH, 2015. InvenSor LTC 30 e plus technical specifications.

Kühn, A., Ziegler, F., 2005. Operational results of a 10kW absorption chiller and adaptation of the characteristic equation., in: First International Conference on Solar Air Conditioning, October 6-7. Bad-Staffelstein, Germany.

La, D., Dai, Y.J., Li, Y., Wang, R.Z., Ge, T.S., 2010. Technical development of rotary desiccant dehumidification and air conditioning: A review. Renew. Sustain. Energy Rev. 14, 130–147. https://doi.org/10.1016/J.RSER.2009.07.016

Pons, M., Anies, G., Boudehenn, F., Bourdoukan, P., Castaing-lasvignottes, J., Evola, G., Le Denn, A., Le Pierrès, N., Marc, O., Mazet, N., Stitou, D., Lucas, F., 2012. Performance comparison of six solar-powered air-conditioners operated in five places. Energy 46, 471–483. https://doi.org/10.1016/j.energy.2012.08.002

Pons, M., Kodama, A., 1999. Second law analysis of the open cycles for solid desiccant air conditioners, in: Proceeding of ISHPC. Munich, Germany, pp. 389–394.

Robatherm GmbH, 2014. Sorption-Supported Air-Conditioning.

Yazaki Energy Systems Inc., 2018. Yazaki WFC-SC10 Series chiller instalation instructions.

Appendix: Nomenclature

Nomenclature		**Subscripts and superscripts**	
a	characteristic parameter (-)	*0*	Carnot function model y-intercept
b	characteristic parameter (-)	*a*	absorber
c	characteristic parameter (-)	*c*	condenser
CE	characteristic equation	*ec'*	adapted characteristic equation variable
CFM	Carnot function model	*cfm*	Carnot function model variable
COP	coefficient of performance (-)	*e*	evaporator
e	characteristic parameter (-)	*el*	electric
F	Carnot function model parameter (-)	*exp*	experimental
$\dot{Q}$	heat transfer rate (kW)	*g*	generator
r	characteristic parameter (-)	*gl*	global
s'	characteristic parameter (-)	*i*	inlet
T	external temperature (°C)	*int*	intermediate temperature source
$\dot{W}$	power (kW)	*nom*	nominal
		o	outlet
Greek letters		*th*	thermal
α	characteristic parameter (-)		
Δ	differential quantity		
$\Delta\Delta t'$	adapted characteristic temperature difference (K)		
τ	Carnot function model parameter (-)		
ω	Carnot function model parameter (-)		

Detection of Tracker Failures for a 2-Axis Photovoltaic System

Lucas E. A. Barboza[1], Olga de Castro Vilela[1], Gustavo de Novaes Pires[2], Emerson Torres Aguiar Gomes[1], Diego Rodrigues de Miranda[1], João V. F. F. de Medeiros[1] and Leonardo José de Petribú Brennand[1]

[1] Center of Renewable Energy, Federal University of Pernambuco, Recife (Brazil)

[2] Federal Institute of Pernambuco, Recife (Brazil)

Abstract

Solar trackers have been widely used in photovoltaic plants due to the increase in their capacity factor. However, the operation of tracker systems still has challenges, mainly related to failures during operation. The mechanical failures on trackers significantly impact the PV generation and, consequently, have a non-negligible impact on the economic return. The data on trackers' failures in operation situations is rare. The present paper will use a statistical method for daily failure detection from the relation between PV power output and plane-of-array (POA) irradiances. This methodology extracts features from data curves and classifies the days according to them. The accuracy obtained showed that new methods, such as those presented in this paper, may perform better in identifying tracking system failures.

Keywords: sun trackers, anomalies, detection, features, plane-of-array, fault, output power, irradiance

1. Introduction

Solar trackers have been widely used in photovoltaic (PV) plants due to the increase in their capacity factor. Despite this, the presence of trackers introduces uncertainties in the PV plant's performance because the tracking system is a piece of moving equipment. Then, the mechanical failures on trackers have a significant impact on the PV generation and, consequently, a non-negligible impact on the economic return of the plant. Therefore, studying trackers' failures during the operation is crucial. Nevertheless, the data on trackers' failures in operation situations is rare, and the literature on this subject use accelerated tests or others laboratories procedures to understand the phenomenon (Elerath, 2011; Elerath et al., 2011). In this sense, this study aims to develop a methodology for detecting days that the tracking system is stuck in a fixed position in a PV plant, in other words, days that it is not tracking the sun. Based on the Ruth and Muller (2018) publication, the present paper will use a statistical method for failure detection from the relation between the daily time series of the PV output power and plane-of-array (POA) irradiances for a given day.

2. Methods and Materials

Bazovsky (2004) defines failures as an intended period when a device or system does not adequately perform its purpose under operating conditions. From this definition, the main objective of a solar tracker is to increase power production by tracking the sun throughout the day. Thus, even if the tracking system can get stuck all day, if this does not significatively affect the energy production (as is best seen in subsection 3.3), it cannot be considered a failure. Thus, the criterion for determining failures in a tracker is the energy production associated with the photovoltaic system. Moreover, concerning the length of the time considered, it is intuitive to realize that slight deviations in the sun's tracking throughout the day do not generate significant losses in power production. In this sense, it is appropriate to consider the day as the scale of the time considered for the failure analysis. Therefore, this work will focus on daily failures.

The main idea of daily tacker failure detection is based on the relation between the time series of PV output power

© 2022. The Authors. Published by International Solar Energy Society
Selection and/or peer review under responsibility of Scientific Committee
doi:10.18086/eurosun.2022.16.02 Available at http://proceedings.ises.org

and plane-of-array (POA) irradiance (Ruth and Muller, 2018). As shown in Fig. 1, when the tracker functions as expected, the power curve has a shape similar to the POA curve for a system tracking the sun. On the other hand, when the tracker is stuck, the power curve is similar to the POA curve for a fixed collector (Fig. 2).

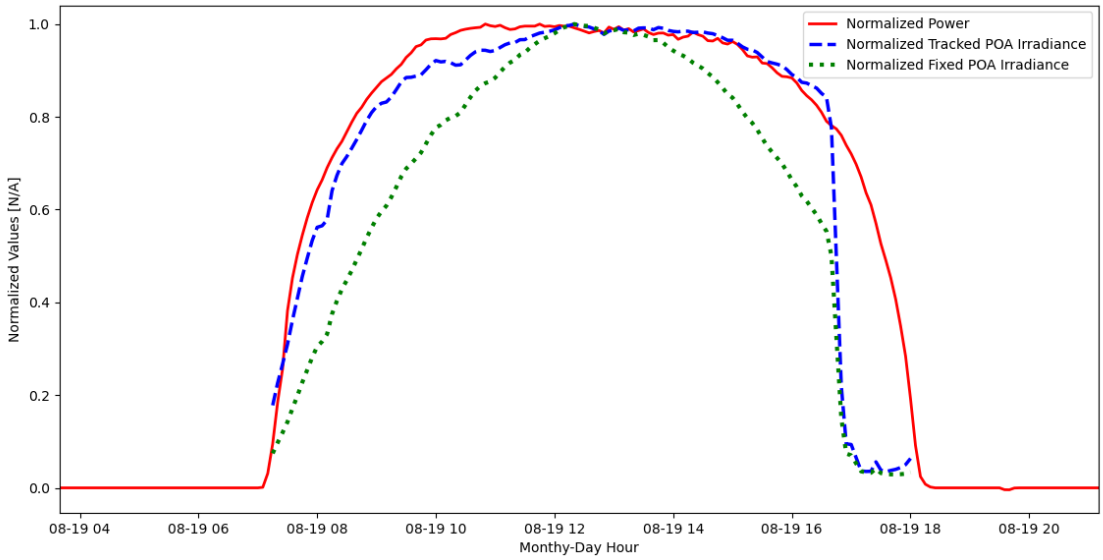

Fig. 1: Daily time series of PV output power and POA irradiances for a solar PV system with a dual-axis tracker, at site 2 in Desert Knowledge Australia Solar Centre, in Alice Springs, Central Australia, on August 19th, 2012. The solid red line represents the measured power; the dashed blue line is the dual-axis POA; the green dotted line the fixed-tilt POA. Note that when the tracker is working, the power curve is similar to the POA curve for a tracking collector.

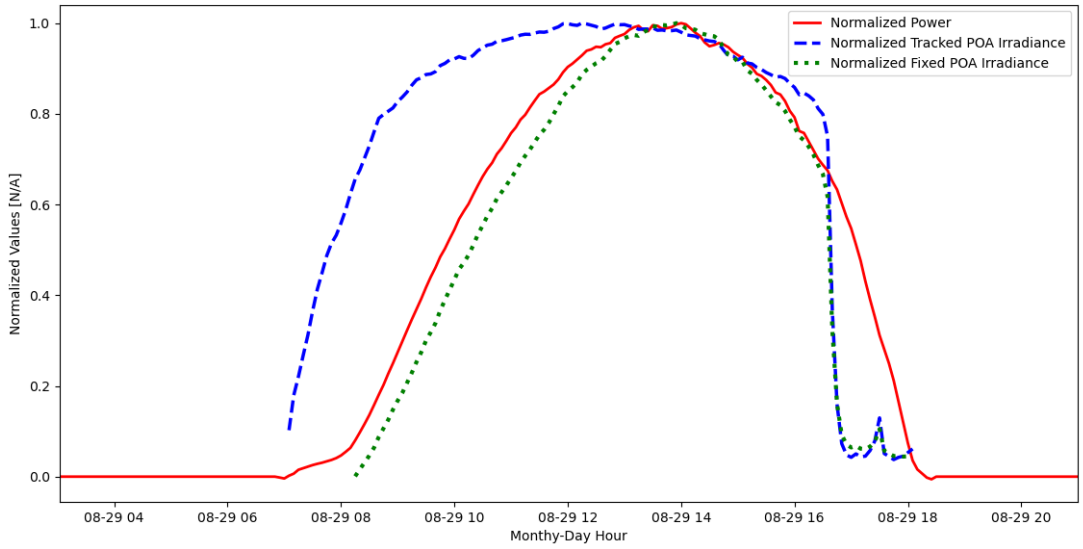

Fig. 2: Daily time series of PV output power and POA irradiances for a solar PV system with a dual-axis tracker, at site 2 in Desert Knowledge Australia Solar Centre, in Alice Springs, Central Australia, on August 29th, 2012. The solid red line represents the measured power; the dashed blue line is the dual-axis POA; the green dotted line the fixed-tilt POA. Note that when the tracker was stuck, the power curve was similar to the POA curve for a fixed collector.

3.1. Methodology

Plane-of-array (POA) irradiance is the total irradiance arriving at the collector plane (a tilted PV panel, for instance). This collector can be in a fixed position or moving from a tracking system. Usually, we obtain POA irradiance from local measurements of global (G), beam (G_b), and diffuse (G_d) irradiances in the horizontal plane. Eq. 1 shows the relation between G, G_b, and G_d, involving the azimuth angle θ_Z. If one of these horizontal irradiances isn't available, we can determine the missing irradiance from the other two. The eq. 2 shows how to calculate POA from G, G_b, and G_d, where β is the collector tilt angle, and 0.2 is the albedo (fraction of irradiance reflected by the ground). The angle θ is the incidence angle between the sun rays and the collector normal line. θ has a different expression for collectors fixed installed and for collectors with solar trackers. Tab. 1 presents the incidence and collector tilt angles for fixed and dual-axis systems (Rabl, 1985). It is necessary local latitude Φ, declination δ, and hour ω angles of the sun, azimuth γ and inclination β angles of the collector for eq.2. The expressions of these angles and their references can be found in Rabl (1985).

$$G = G_b \cos\theta_Z + G_d \qquad \text{(eq. 1)}$$

$$POA = G_b \times \cos\theta + {}^1\!/_2 \times G_d \times (1 + \cos\beta) + {}^1\!/_2 \times 0.2 \times G(1 - \cos\beta) \qquad \text{(eq. 2)}$$

Tab. 1: Cosine of incidence angle value for a tilted fixed collector, and a collector with dual axis tracker

	Tilted Fixed Collector	**Collector with dual axis tracker**
Cosine of incidence angle θ	$\cos\delta\cos\Phi\cos\beta\cos\omega$ $+\ \sin\delta\sin\Phi\cos\beta$ $+\cos\delta\sin\gamma\sin\beta\sin\omega$ $+\cos\delta\cos\gamma\sin\Phi\sin\beta\ \cos\omega$ $-\sin\delta\cos\Phi\sin\beta\cos\gamma$	1
Collector tilt angle β	Collector fixed tilt angle	Zenith angle θ_Z

Source: Rabl (1985).

In this context, the present methodology extracts three features from POA and output power curves aiming to identify daily tracker failures. First of all, the curves are normalized by their maximum values of the day. This normalization allows comparing two variables with different units: irradiance and power. The first feature is the Pearson correlation between the output power and the tracked collector POA irradiance, which reveals if the tracker is working as expected for a given day. The next step is comparing the output power with a fixed collector POA irradiance. For this comparison, the methodology sets a range of possible tracker stuck positions, calculates the Pearson correlation between the correspondent POA irradiance and power curves, and chooses the position with the most significant value. This procedure is necessary because there is no information about the precise stuck position. The third feature is also related to a fault in the tracking system. It involves the error curve, i.e., the curve resulting from the element-wise difference between the normalized series of output power and tracked POA irradiance. The error curve has a characteristic shape for stuck tracker days, as shown in Fig. 3. So, the feature extracted is the Pearson correlation between the real error curve (using real output power time series) and the theoretical error curve. This theoretical curve uses the modelled power instead of the actual power output. In this step, the stuck position is found for the second feature and is used to calculate the theoretical power from eq. 3 (Abd El-Aal et al., 2006; Navarte and Lorenzo, 2008). The nominal generator power P_{NOM}, the efficiency η, the power temperature loss coefficient β, and the coefficient K are constants in eq.3; and ambient temperature T_{AMB}, and POA irradiance are inputs of the model. The PV module datasheet informs the β value, and 0.03 is a good

approximation for K (Fuentes et al., 2007). The trust region reflective non-linear least squares method calculates the coefficient value η that best fits the data (Li, 1993).

$$P = \eta\, P_{NOM} \frac{POA}{1000}\{1 - \beta[(T_A + K \times POA) - 25]\} \qquad \text{(eq. 3)}$$

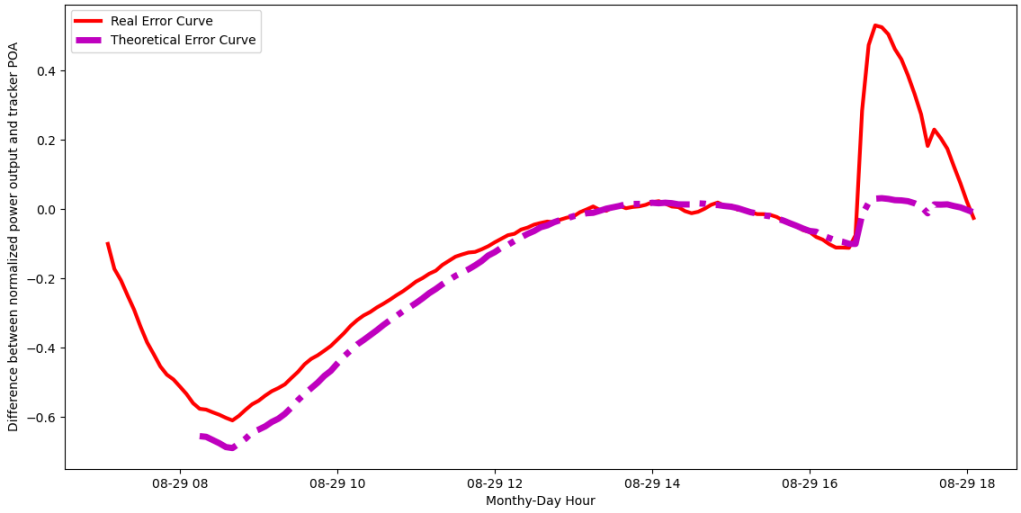

Fig. 3: Error Curves for a solar PV system with a dual-axis tracker failure at site 2 in Desert Knowledge Australia Solar Centre, in Alice Springs, Central Australia, on August 29th, 2012. These curves result from the element-wise difference between normalized series of power and normalized tracked POA. The solid red line represents the error curve obtained using the actual power output; the dashed magenta line is obtained using modelled output power.

The features used in the model are functioning correlation, fixed correlation, and error curve correlation. So, the method selects the days from the dataset and calculates these three features for each day. An interval value must be determined for a feature to classify a day as tracker functioning or tracker stuck. Since all features are Pearson correlations, we assume an interval that ends at one and begins at one minus 15% of the standard deviation of the corresponding feature series. So, the classification of days inside these ranges are tracker functioning, or tracker stuck: in the functioning correlation method, set as functioned; in the fixed or error curve correlations methods, selected as failed.

3.2. Observational Data

The sample data analysed in this work is from a 26.5kW photovoltaic system (Fig. 4) at the Desert Knowledge Australia Solar Centre (DKASC-2), site 2 in Alice Springs, Central Australia, at a longitude of 133.87°W and latitude of 23.76°S (DKA, n.d.). Between August 24th, 2010 to December 1st, 2012, a dual-axis tracker was working at the site. The lifetime of the tracking device totals 830 days. In addition, there are also some records of the maintenance staff during this period. The DKASC-2 data contain G, G_d and active power output, with a timestep of 5 minutes. The coefficients η, β and K from eq. 3 for DKASC-2 are in Tab. 2.

Tab. 2: The coefficients η, β and K from eq. 3 for DKASC-2.

η	β	K
0.75	$0.0045\ °C^{-1}$	$0.03\ °C\ W^{-1}m^2$



Fig. 4: The dual-axis tracker 26.5kW photovoltaic system of site 2 of the Desert Knowledge Australia Solar Centre (DKASC-2), in Alice Springs, Central Australia, working between August 24th,2010 to December 1st, 2012. Source: DKA.

3.3. Visual Inspection

The 830 days of the dual-axis tracker lifetime have visually been analyzed to identify failures aiming to validate the methodology explained in subsection 3.2. The days have been classified into function, failures, undetermined and missing. Curves like the left in Fig.1 are classified as 'function'; curves like the right in Fig.1 as 'failure'. The days when the maintenance staff identifies periods in which the tracker is stuck are set as failure days too. For instance, the tracker was stuck in a fixed position from March 22th, 2012, to May 30th, 2012, due to a porous clamp housing (DKA, n.d.). 'Missing' are days when power or irradiances daily series have less than half the expected sample data. Finally, as shown in Fig. 5, 'undetermined' are days when it is impossible to know whether the tracker is working. On the undetermined days, whether the tracker is working does not affect the daily power generation because many other problems could occur; then, it cannot be classified as 'failure'. On the other hand, it is impossible to ensure that the tracking system functioned as expected. In other words, in the absence of maintenance notes, on undetermined days (usually cloudy days), the tracker is in a simultaneous functionally and failure state due to visual inspection method limitation, and, it is not possible to ensure 'function' or 'failure' class to that day.

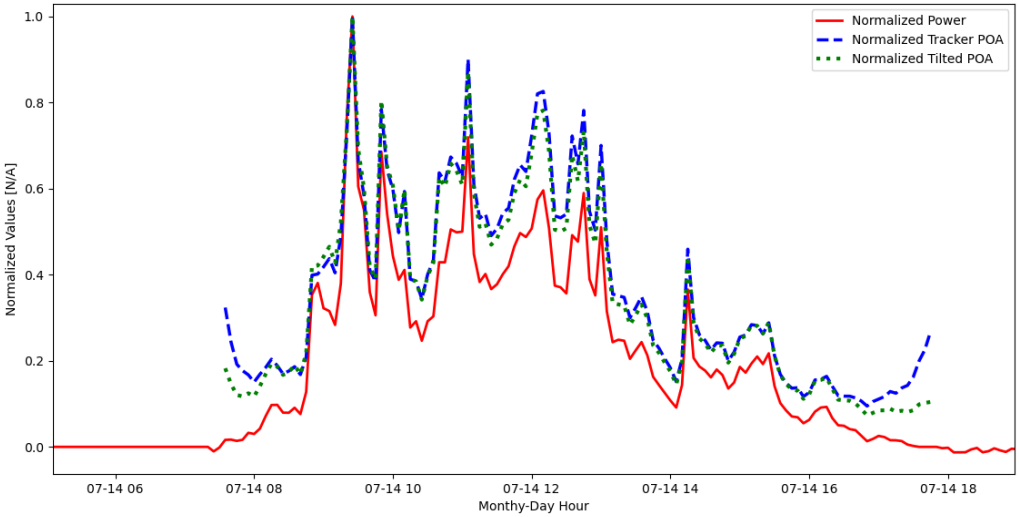

Fig. 5: Daily time series of PV output power and POA irradiances for DKASC-2 on July 12th, 2011. The solid red line represents the measured power; the dashed blue line is the dual-axis POA; the green dotted line the fixed-tilt POA. These days are classified as undetermined because visual inspection cannot determine the failure.

3.4. Model Performance Metrics

In the model performance analysis, the undetermined and missing days will be excluded from the control dataset because they do not assure if the tracker is functional or not, as explained in subsection 3.3. The present work uses confusion matrix and accuracy as model performance metrics (Costa et al., 2007). These metrics use the numbers of true and false positives (TP and TF, respectively) and true and false negatives (TN and FN, respectively). In this sense, the positive in the methodology using functioning correlation is identified as functional tracker days, while the method using fixed or error curve correlations is to identify tracker failure days. Tab. 3 shows the principle of a confusion matrix, and eq. 4 presents the formula for accuracy.

Tab. 3: Confusion Matrix.

	Predicted Class	
True Class	Positive	Negative
Positive	True positive (TP)	False negative (FN)
Negative	False positive (FP)	True negative (TN)

$$A_{CC} = \frac{TP+TN}{TP+FP+FN+TN} \qquad \text{(eq. 4)}$$

3. Results and Discussion

Tab. 4 shows the accuracies for each method. Remember that the missing and undetermined days are excluded from the control dataset for the accuracy calculation. The error curve correlation presents the best result in predicting the target, followed by fixed correlation and functioning correlation. In this sense, the methods that directly use the correlation between power and POA curves have the worst performances, while the process that uses an intermediate step (the error curve) has the best accuracy. This procedure differs from what Ruth and Muller (2018) found in their work. In Ruth and Muller's work, they used functioning and fixed correlations and achieved good results. Perhaps, this difference is because the present work uses sample data of a dual-axis tracker, not a single-axis. Then, the result suggests that using other features and methods can increase the models' performance.

Tab. 4: Confusion Matrix for DKASC-2 Error Curve Correlation series. Undetermined and missing days have been excluded from the control dataset.

Method	Accuracy
Functioning Correlation	0.49
Fixed Correlation	0.80
Error Curve Correlation	0.90

Fig. 6, Fig. 7 and Fig. 8 show the functional, fixed, and error curve correlations series, the classification obtained by visual inspection in each one, and their respective classification thresholds. Note that there is a kind of information complementarity, i.e., when a day is not set as a 'failure' day in the methods of error curve or fixed, it is because it is supposed to be classified as a 'function' day. Tab. 5, Tab. 6 and Tab. 7 present the confusion matrices.

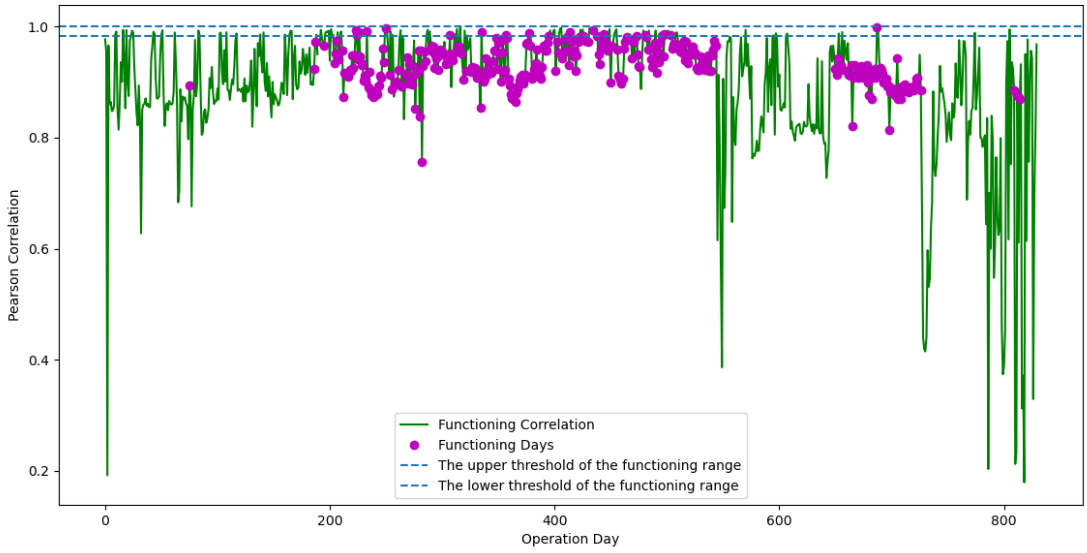

Fig. 6: Functional Correlation series for DKASC-2. The solid green line represents the correlation values; the magenta dots are the functional days identified in the visual inspection; the blue dashed lines represent the lower and upper range limits of detection of functioning days.

Tab. 5: Confusion Matrix for DKASC-2 Functional Correlation series. Undetermined and missing days have been excluded from the control dataset.

	Predicted Class	
True Class	Positive	Negative
Positive	17	324
Negative	0	294

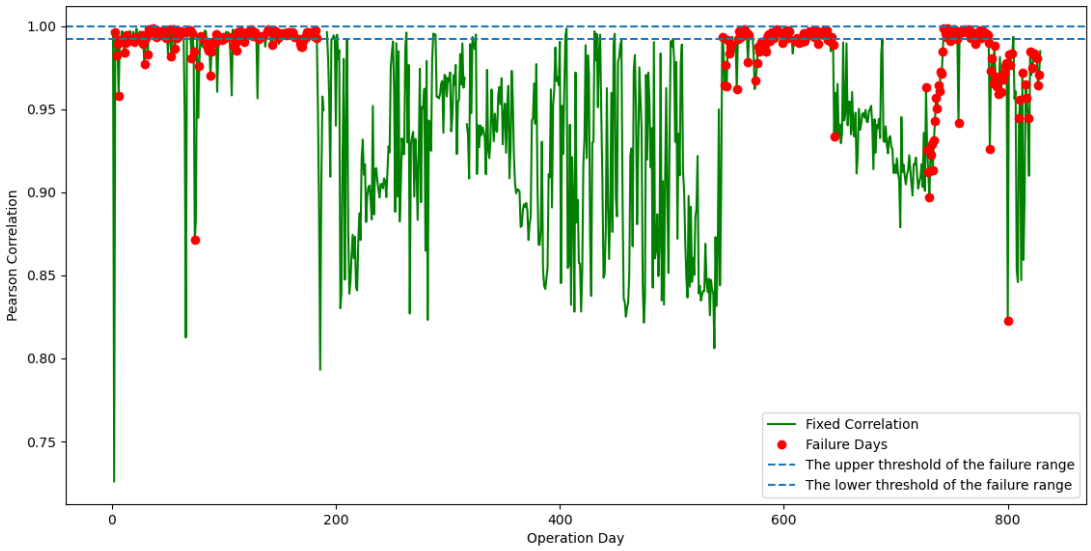

Fig. 7: Fixed Correlation series for DKASC-2. The solid green line represents the correlation values; the red dots are the failure days identified in the visual inspection; the blue dashed lines represent the lower and upper range limits of detection of failure days.

Tab. 6: Confusion Matrix for DKASC-2 Fixed Correlation series. Undetermined and missing days have been excluded from the control dataset.

	Predicted Class	
True Class	Positive	Negative
Positive	167	127
Negative	0	341

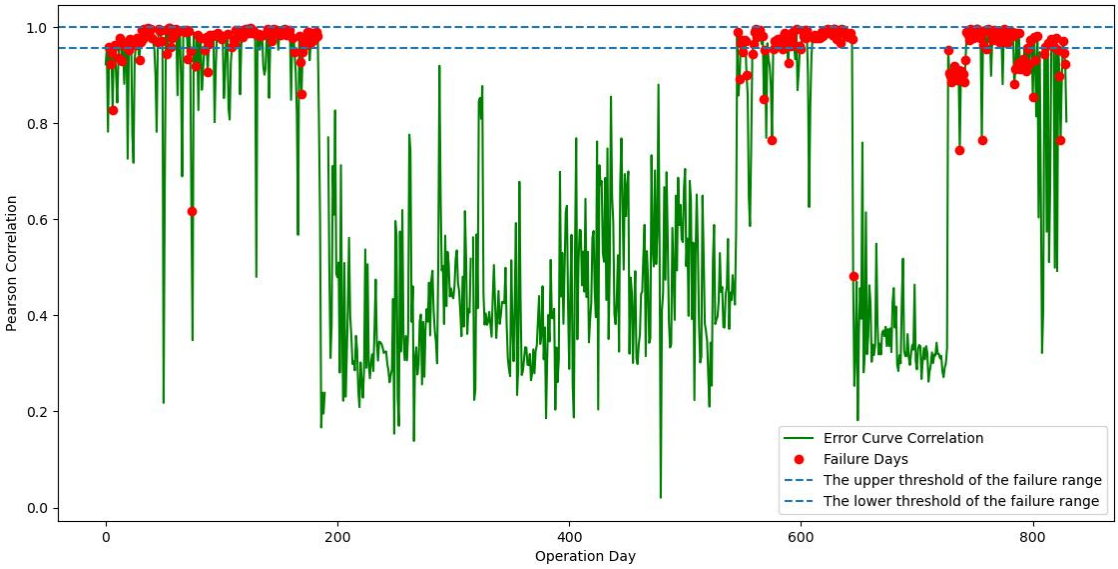

Fig. 8: Error Curve Correlation series for DKASC-2. The solid green line represents the correlation values; the red dots are the failure days identified in the visual inspection; the blue dashed lines represent the lower and upper range limits of detection of failure days.

Tab. 7: Confusion Matrix for DKASC-2 Error Curve Correlation series. Undetermined and missing days have been excluded from the control dataset.

	Predicted Class	
True Class	Positive	Negative
Positive	228	66
Negative	0	341

4. Conclusions

The work extracts features for each day of data from DKASC-2. The objective was to identify daily failures and regular working days by three features: functioning correlation, fixed correlation and error curve correlation. Different from Ruth and Muller (2018) paper, the results show that the error curve had the best accuracy, which indicates that developing more methods could increase detection performance. Furthermore, the three methods have a kind of complementarity of information that needs further studies.

5. Acknowledgments

The authors are grateful to the Desert Knowledge Australia Centre (e.g. Alice Springs) for the data provided, to the Brazilian Higher Education Personnel Improvement Coordination - CAPES and to the Postgraduate Program in Energy and Nuclear Technologies - PROTEN of Federal University of Pernambuco, Brazil. Finally, we also thank the Center of Renewable Energy (CER) team at the Federal University of Pernambuco.

6. References

Abd El-Aal, A. E. M. M., Schmid, J., Bard, J., & Caselitz, P. (2006). Modeling and optimizing the size of the

power conditioning unit for photovoltaic systems. Journal of Solar Energy Engineering, 128(1), 40-44.

Bazovsky, Igor. Reliability theory and practice. Courier Corporation, 2004.

Costa, E., Lorena, A., Carvalho, A. C. P. L. F., Freitas, A. 2007, July. A review of performance evaluation measures for hierarchical classifiers. In Evaluation methods for machine learning II: Papers from the AAAI-2007 workshop. pp. 1-6.

DKA, n.d. Desert Knowledge Australia Centre. Download Data. [WWW Document]. URL http://dkasolarcentre.com.au/download?location=alice-springs (accessed 11.16.21).

Elerath, J.G., 2011. Reliability assessment of high-concentration photovoltaic trackers, in: Proceedings - Annual Reliability and Maintainability Symposium. pp. 1–6. https://doi.org/10.1109/RAMS.2011.5754525

Elerath, J.G., Spencer, M., Horne, S., 2011. Demonstrating reliability in HCPV systems, in: 37th IEEE Photovoltaic Specialists Conference. IEEE, pp. 3547–3552. https://doi.org/10.1109/PVSC.2011.6185910

Fuentes, M., Nofuentes, G., Aguilera, J., Talavera, D. L., & Castro, M. (2007). Application and validation of algebraic methods to predict the behaviour of crystalline silicon PV modules in Mediterranean climates. Solar Energy, 81(11), 1396-1408.

Li, Yuying. 1993. Centering, trust region, reflective techniques for nonlinear minimization subject to bounds. Cornell University. https://hdl.handle.net/1813/6159

Narvarte, L., Lorenzo, E. (2008). Tracking and ground cover ratio. Progress in photovoltaics: research and applications, 16(8), 703-714.

Rabl, A., Oxford, N.Y., 1985. Active Solar Collectors and Their Applications, 1st ed. Oxford University Press, Inc, New York.

Ruth, D., Muller, M., 2018. A methodology to analyze photovoltaic tracker uptime. Progress in Photovoltaics: Research and Applications 26, 491–501. https://doi.org/10.1002/pip.3002

Data-Driven Approach Utilising Random Forest Regression for PV Performance Monitoring

Alexander David[1], Sabine Sint[1] and Thomas Bednar[1]

[1] Research Unit of Building Physics, TU Wien, Vienna (Austria)

Abstract

The performance monitoring of PV plants is essential to ensure their correct operation, detect faults, and maximise their output. To be able to decide whether a plant is operating within normal parameters, a reference is needed, which indicates the PV performance that the plant should have under certain weather conditions. Weather data and historical monitoring data from times when the PV plant was operating correctly can be used to train machine learning models, which can provide the reference PV performance. In this research, a random forest regression machine learning algorithm is used to train models which predict the electrical power that is measured by 19 PV inverters and the PV main electricity meter. Several random forest models utilising different parts of the available weather data were trained. Their prediction performance was evaluated for five different time resolutions and three different PV module orientations. The results indicate that random forest regression is a suitable tool to predict the performance of PV plants.

Keywords: photovoltaic, performance monitoring, performance prediction, machine learning, random forest regression

1. Introduction

There are several methods and tools to calculate the performance of PV plants (Tozzi and Ho Jo, 2017; Umar et al., 2018). The science behind PV technology and its relation to weather data, geometrical parameters (e.g., orientation), and the surroundings (e.g., shading) is well-known (Mayer and Gróf, 2021). Even though a PV plant might have been planned in detail in a sophisticated PV simulation tool, usually, the PV plant owner does not have access to detailed planning information. It is common that the owner only receives a report indicating the expected PV performance for a year with average weather conditions. Such reports might be useful to evaluate whether the magnitude of the monthly PV production is in the correct range or not, but they are useless for monitoring the correct plant operation on an hour-to-hour or at least day-to-day basis. For monitoring a correct plant operation or its health status, there are various methods and algorithms (Pillai and Rajasekar, 2018), some even facilitating machine learning algorithms (Chen et al., 2018; Yao et al., 2021).

One relatively simple yet powerful machine learning algorithm is “random forest”. It can be used for classification and regression (Breiman, 2001). While it can excel at predicting data within the range of the data they were trained with, it fails when tasked to extrapolate beyond its trained scope (Breiman, 2001; Hastie et al., 2017). Extrapolation should generally not be required to predict the nominal PV electricity production at a given location as long as the training data includes weather that can typically be expected during a year. Thus, random forest models could be useful for fulfilling this prediction task.

In this paper, we evaluate the prediction performance a random forest regressor machine learning algorithm can achieve when predicting PV electricity generation at particular weather conditions. Instead of calculating the reference PV performance out of detailed plant configuration information, it is derived from historical data from when the plant was operating correctly. Thus, the PV plant owner does not need a detailed model of the system and simulation tool to simulate it but only sufficient monitoring data of the plant and weather data.

The data source used in this research is from the energy monitoring system of TU Wien’s (Plus-)Plus-Energy Office High-Rise Building. It is a highly energy-efficient building developed according to a net-zero energy concept. Within this concept, the primary energy source is a PV plant, which is integrated into the building’s

© 2022. The Authors. Published by International Solar Energy Society
Selection and/or peer review under responsibility of Scientific Committee
doi:10.18086/eurosun.2022.16.03 Available at http://proceedings.ises.org

façade and mounted on its roof (Schöberl et al., 2014).

Fig. 1 shows the basic configuration of the building's PV plant. This graph summarises the information presented in (David et al., 2023). It illustrates the different PV sub-surfaces A_i connected to one inverter I_j and their PV module type. The stated surface sizes are the sum of the aperture sizes of the modules, and the stated power values are the sum of the modules' maximum power values at standard test conditions. The plant consists of four different parts: (i) southwest roof, (ii) southwest façade, (iii) southeast PV insulating glass, and (iv) southeast façade. Each illustrated combined surface is connected to one inverter – the only exception is inverter I_1, which is connected to the southwest-oriented surface A_0 and the southeast-oriented surface A_1. As indicated by Fig. 1, the plant's PV modules have one of these three orientations: (i) towards the southwest with a 15° inclination, (ii) towards the southwest with a 90° inclination, and (iii) towards the southeast with a 90° inclination.

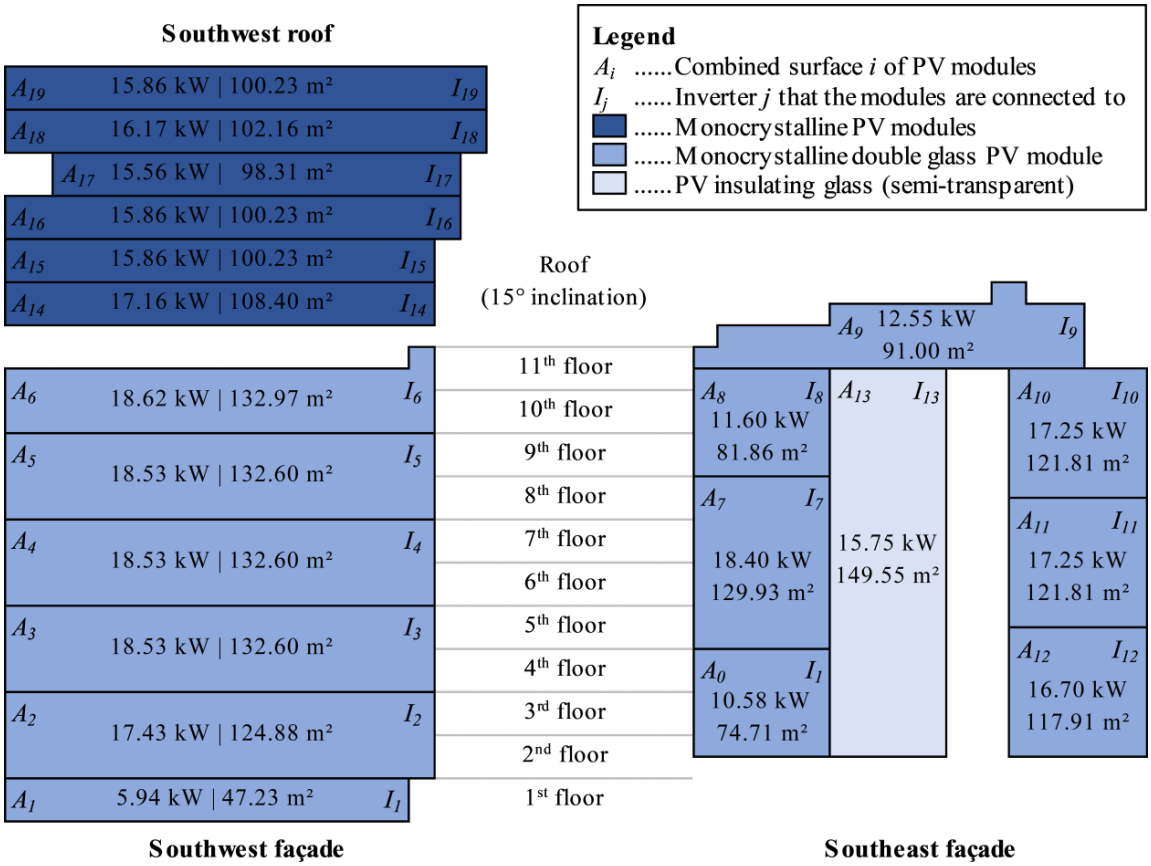

Fig. 1: Overview of the (Plus-)Plus-Energy Office High-Rise Building's PV plant at TU Wien

2. Method

This research aims to evaluate whether random forest regression is a suitable tool to predict the nominal performance of PV plants under certain weather conditions. For this purpose, historical weather data and PV monitoring data is needed from times when the PV plant operated as intended. This data must be split into a training and a test dataset – the training dataset for the training of the random forest models and the test dataset to evaluate their performance. This section shows how the monitoring data from the (Plus-)Plus-Energy Office High-Rise Building was processed and used to train and evaluate random forest models.

The (Plus-)Plus-Energy Office High-Rise Building is equipped with an extensive building energy monitoring system, which logs data from energy meters (electricity and thermal energy for heating and cooling), operational data (sensor data, setpoints and control signals), and weather data (external air temperature, global radiation, wind speed, …) in a 5-minute interval. One of the systems' electricity meters is the PV main meter, which meters the electricity production of the entire PV plant fed into the building's low-voltage main distribution. The electricity production of each of the 19 inverters is metered separately by integrated electricity meters. As every single meter from the 19 integrated ones and the PV main meter can be seen as the meter of a separate PV plant, they are treated

as such – each meter is used to train and evaluate a separate random forest model.

Since the integrated meters were initially not part of the building energy monitoring system, the data processed in this research is from when they were connected to the system, i.e., after January 2017. The monitoring data from the following two years was used for the training and the performance evaluation of the random forest models:

- Year 1: 04.02.2017 00:00 – 04.02.2018 00:00
- Year 2: 04.02.2018 00:00 – 04.02.2019 00:00

As the data from year 1 has several gaps with sizes ranging from a few days up to almost two weeks, and as year 2 is practically without gaps, year 2 was chosen as the training dataset and year 1 as the test dataset. All of the following processing steps described in this section were applied to both datasets.

Since inverters I_3 and I_{14} had some failures during year 2, and as the goal of this method is to train random forests to predict the nominal PV performance that the inverters should have, their data was excluded from this research. The PV main meter is also affected by the failures of those two inverters, but as they are only parts of the entire plant, their impact was expected to be less significant.

For each meter, the time series of the load profile of the PV electricity generation is derived by calculating the first-order difference quotient of the time series of the respective meter's counter. The random forest models were trained to predict these load profiles as the target variables.

Since the models are intended to predict PV electricity generation under given weather conditions, the time series of some of the measured weather parameters are the predictor variables (short: predictors). Tab. 1 illustrates the weather parameters that were used in the training of the random forest models.

Tab. 1: Parameters provided by the (Plus-)Plus-Energy Office High-Rise Building's weather station that are used as predictors in the random forest models

Measurement	Unit	Letter in the name of a random forest model if the model utilises this measurement for its predictions
(Global horizontal) irradiance	W/m²	i
(Air) temperature	°C	t
Relative humidity (of the air)	%	h
Illuminance on the north vertical surface	lx	n
Illuminance on the east vertical surface	lx	e
Illuminance on the south vertical surface	lx	s
Illuminance on the west vertical surface	lx	w

Besides the weather parameters presented in Tab. 1, some further predictors were calculated out of time stamp information – Tab. 2 shows two time indicators that were used as predictors:

- The indicator "Sinus of the year" encodes the time of the year in the form of a sinus curve, which is fitted to the times when the solstices and equinoxes occur during a year. At the time of the summer solstice, this indicator is 1; at the time of the winter solstice, it is -1; and at the time of the equinoxes, it is 0.
- The indicator "Sinus of the day" encodes the time of the day in the form of a sinus curve, which is fitted to the times when noon and midnight occur during a day. At noon, this indicator is 1; at midnight, it is -1; and at 6 AM and 6 PM, it is 0.

Tab. 2: Time indicators calculated out of time stamp information that are used as predictors in the random forest models

Time indicator	Unit	Letter in the name of a random forest model if the model utilises this indicator for its predictions
Sinus of the year	-	y
Sinus of the day	-	d

One crucial part of developing machine learning models is the model selection. The goal is to train models that can accurately predict the target variables. To do that, they have to grasp the underlying connections between the predictors and the target variables based on the provided training datasets. When providing machine learning

algorithms with too many predictors, there is the danger of overfitting the models to the respective training dataset. To find out which predictors are useful for predicting the target variables and avoid overfitting, several models utilising different combinations of predictors must be trained. Their prediction performance is then evaluated by providing them with the test dataset. The decision of which model is best for the task at hand is then made based on the evaluation results (Hastie et al., 2017).

All the predictors in Tab. 1 and Tab. 2 have been assigned a single unique letter. In this paper, the designation of the developed random forest models is a combination of the letters of the predictors that each respective model utilises. For instance, if the model designation is "nesw", the model uses all four illuminance measurements from the weather data, and if the model designation is "ithydnesw", the model utilises all of the predictors presented in Tab. 1 and Tab. 2. The following eight model configurations were investigated in this research: ithyd, ithydnesw, itydnesw, itynesw, itnesw, inesw, tnesw, and nesw.

All of the models are set up as random forest regressors "sklearn.ensemble.RandomForestRegressor" from the Python package "scikit-learn 0.22.1" (Pedregosa et al. 2011) in the standard configuration with 100 estimator trees. As randomness is one of the key aspects of random forests, the models were repeatedly trained with the training dataset (100 repetitions). Their prediction performance at each repetition was evaluated with the test dataset. For each of the eight researched model configurations and each of the eighteen load profiles (PV main meter and all inverter meters except I_3 and I_{14}), a random forest regressor was set up by providing it with the respective load profile from the training dataset as target and the corresponding utilised predictors.

The prediction performances of all models were evaluated by providing the models with the predictors from the test dataset in order for them to predict the respective load profile. Each predicted load profile was then compared with the actual load profile in the test dataset. This was done by calculating the R^2 score and the deviation of the cumulated predicted load profile from the cumulated actual load (short: deviation).

With n as the number of values in the time series of the load profile, $\hat{y}_i$ as the ith value of the predicted load profile, y_i as the ith value of the actual load profile, and $\bar{y}$ as the mean of the actual load profile, the R^2 score is calculated as shown in eq. 1, and the deviation is calculated as shown in eq. 2:

$$R^2(y,\hat{y}) = 1 - \frac{\sum_{i=1}^{n}(y_i-\hat{y}_i)^2}{\sum_{i=1}^{n}(y_i-\bar{y})^2} \qquad \text{(eq. 1)}$$

$$deviation(y,\hat{y}) = \frac{(\sum_{i=1}^{n}\hat{y}_i)-(\sum_{i=1}^{n}y_i)}{\sum_{i=1}^{n}y_i} \qquad \text{(eq. 2)}$$

While the R^2 score indicates of how well the course of the predicted load profile matches the course of the actual load profile, the deviation indicates the overall error that can be expected when predicting a whole year.

All of the steps described in this section were repeated for five different time resolutions: 5 min, 10 min, 15 min, 30 min, and 60 min. To accomplish this, the original energy monitoring data with a time resolution of 5 min was simply resampled to the other four time resolutions by utilising the method "pandas.DataFrame.resample" from the Python package "pandas 1.0.1" (McKinney, 2010) and calling its function "mean()".

As calculating PV electricity generation out of weather data is a problem with geometric transformations and strong linear dependencies, multiple linear regression should also be able to predict the eighteen load profiles accurately. Thus, a multiple linear regressor model utilizing the same predictors was also set up and examined for each of the eight investigated random forest model configurations. Due to the nature of multiple linear regression, their predicted PV electricity generation could be negative. To counteract this effect, negative values were always set to zero. The designation of the multiple linear regression models is identical to that of the random forest models but extended by the prefix "LR-".

3. Results

Even though in this research, the training and evaluation of regressor models were always conducted with the same training dataset and test dataset, the results from all repetitions, all time resolutions, and all model configurations are too numerous to be presented in detail. Thus, the results had to be condensed by grouping and averaging. To avoid that averaging of the achieved deviations cancels out the signs of the deviations, their average

is computed out of the absolute deviations.

Tab. 3 gives an overview of the average prediction performance (R^2 score and absolute deviation) that the eight different random forest model configurations achieved after being provided with data from the five different time resolutions. As the prediction results of the different load profiles of the inverters were quite similar if the orientation of their PV modules was the same, the results were grouped and averaged according to the PV module orientation. Since inverter I_1 is connected to PV modules with different orientations and as the PV main meter measures the sum of the load profiles of all inverters, they are displayed separately.

Tab. 3: Average prediction performance that the random forest models achieved at 100 repetitions

Time resolution	Random forest model	R^2 score					Absolute deviation				
		Mean of			Inverter I_1	PV main meter (sum of all inverters)	Mean of			Inverter I_1	PV main meter (sum of all inverters)
		South-west roof inverters	South-west façade inverters	South-east façade inverters			South-west roof inverters	South-west façade inverters	South-east façade inverters		
05 min	ithyd	0.910	0.684	0.699	0.832	0.923	1.12%	6.96%	0.99%	0.06%	0.17%
	ithydnesw	0.934	0.908	0.935	0.927	0.944	1.58%	0.37%	2.07%	2.18%	2.24%
	itydnesw	0.933	0.908	0.934	0.926	0.944	2.38%	0.78%	2.40%	2.85%	2.59%
	itynesw	0.932	0.907	0.932	0.923	0.943	2.46%	0.79%	2.65%	3.19%	2.85%
	itnesw	0.926	0.905	0.932	0.918	0.941	2.65%	0.61%	2.44%	2.96%	2.57%
	inesw	0.923	0.904	0.932	0.921	0.940	4.17%	0.57%	2.71%	2.37%	3.11%
	tnesw	0.921	0.899	0.929	0.914	0.938	2.22%	1.46%	2.45%	3.09%	2.62%
	nesw	0.916	0.897	0.928	0.914	0.936	3.53%	1.35%	2.67%	2.35%	3.05%
10 min	ithyd	0.943	0.754	0.788	0.882	0.957	0.33%	5.53%	0.75%	0.83%	0.76%
	ithydnesw	0.957	0.935	0.956	0.950	0.968	1.23%	0.54%	1.59%	1.69%	1.83%
	itydnesw	0.956	0.935	0.955	0.949	0.967	1.83%	0.39%	1.80%	2.15%	2.05%
	itynesw	0.955	0.934	0.954	0.948	0.967	1.89%	0.38%	1.95%	2.27%	2.15%
	itnesw	0.953	0.933	0.954	0.945	0.967	1.97%	0.37%	1.79%	2.04%	1.92%
	inesw	0.949	0.932	0.953	0.946	0.965	4.01%	0.34%	2.24%	1.86%	2.71%
	tnesw	0.950	0.931	0.953	0.943	0.966	1.16%	0.35%	1.72%	1.89%	1.71%
	nesw	0.947	0.930	0.952	0.943	0.964	2.92%	0.64%	2.10%	1.57%	2.45%
15 min	ithyd	0.958	0.792	0.827	0.909	0.969	0.19%	4.97%	0.75%	1.18%	1.22%
	ithydnesw	0.969	0.953	0.970	0.965	0.977	1.31%	0.50%	1.08%	1.45%	1.90%
	itydnesw	0.969	0.952	0.969	0.964	0.977	1.75%	0.31%	1.21%	1.84%	1.97%
	itynesw	0.969	0.952	0.969	0.963	0.976	1.75%	0.29%	1.27%	1.88%	1.97%
	itnesw	0.967	0.951	0.968	0.961	0.976	1.78%	0.34%	1.25%	1.89%	1.81%
	inesw	0.965	0.950	0.966	0.961	0.975	3.82%	0.38%	2.03%	1.97%	2.61%
	tnesw	0.965	0.950	0.968	0.960	0.977	0.49%	0.31%	1.18%	1.61%	1.53%
	nesw	0.964	0.949	0.966	0.960	0.975	2.42%	0.60%	1.91%	1.58%	2.26%
30 min	ithyd	0.978	0.854	0.891	0.945	0.982	0.56%	4.71%	0.65%	1.55%	1.55%
	ithydnesw	0.986	0.976	0.984	0.981	0.987	1.20%	0.68%	1.11%	1.21%	1.87%
	itydnesw	0.986	0.976	0.984	0.981	0.987	1.40%	0.56%	1.15%	1.38%	1.89%
	itynesw	0.986	0.976	0.984	0.981	0.987	1.35%	0.53%	1.20%	1.38%	1.88%
	itnesw	0.985	0.974	0.983	0.980	0.987	1.41%	0.47%	1.13%	1.47%	1.64%
	inesw	0.981	0.973	0.981	0.978	0.986	3.89%	0.29%	2.09%	1.78%	2.40%
	tnesw	0.984	0.974	0.983	0.978	0.988	0.06%	0.48%	1.07%	1.26%	1.29%
	nesw	0.982	0.973	0.980	0.976	0.986	2.29%	0.38%	2.00%	1.51%	2.01%
60 min	ithyd	0.987	0.891	0.932	0.969	0.987	0.94%	4.15%	0.70%	1.15%	1.66%
	ithydnesw	0.992	0.985	0.990	0.987	0.991	1.37%	0.57%	1.09%	1.34%	1.86%
	itydnesw	0.992	0.985	0.990	0.988	0.992	1.48%	0.49%	1.03%	1.42%	1.82%
	itynesw	0.992	0.985	0.990	0.988	0.992	1.47%	0.48%	1.05%	1.42%	1.81%
	itnesw	0.992	0.984	0.989	0.987	0.992	1.41%	0.29%	1.01%	1.52%	1.69%
	inesw	0.988	0.982	0.987	0.985	0.990	3.64%	0.59%	1.93%	1.87%	2.40%
	tnesw	0.991	0.983	0.989	0.986	0.992	0.06%	0.34%	0.95%	1.23%	1.43%
	nesw	0.988	0.982	0.987	0.985	0.990	2.05%	0.64%	1.86%	1.45%	2.13%

As seen in Tab. 3, the average prediction performance is generally relatively high. Almost all models achieve on average R^2 scores around or above 0.9 and absolute deviations well below 3%. It can be observed that with lower time resolutions (larger time intervals), the prediction performance increases: At a time resolution of 60 min, the R^2 score almost always reaches values around 0.99, and the majority of absolute deviations stays below 1.5%. The load profiles of the southwest roof inverters and the PV main meter generally achieved the best prediction performance – even in the case of the model "ithyd", which has the poorest overall performance. The results indicate that the reason for it being the poorest is the absence of the illuminance values in the model's predictor variables.

The order of the random forest models in Tab. 3 is the order in which the model configurations were executed. While the model "ithyd" utilises the weather parameters usually found in weather data and the time indicators that can easily be calculated, the model "ithydnesw" is the same but extended by information about the illuminance on the vertical surfaces of the four cardinal directions. As these illuminance measurements are usually not part of the data provided by weather stations, the initial intention of this work was to develop random forest models without them. But as the prediction performance increased significantly when utilising the illuminance measurements, they were kept as predictors for all following models.

Since "ithydnesw" is the largest model configuration, utilising all predictors, it was assumed that it might be overfitted to the training dataset. To find out whether this is true and to detect another model configuration with a better prediction performance, the model was scaled down by leaving out some of the predictors. Although there are slight variations in the prediction performance, the following smaller models generally performed slightly worse than the full model "ithyndesw" – but their performance was still the same magnitude. This observation is also valid for the smallest model configuration "nesw", which exclusively uses the illuminance measurements as predictors. Since none of the models performs better than "ithydnesw", and its prediction performance is generally quite high, it appears that the model is not overfitted.

All models that utilise the illuminance measurements can generally be recommended for predicting load profiles – they achieve high performances over all of the investigated PV module orientations. As the high performances are achieved even though there are no direct illuminance measurements of the southeast and the southwest orientation, it is assumed that the load profiles of PV modules with orientations in the four cardinal directions north, east, south, and west will also be predicted accurately by those models.

The results indicate that the random forest model "ithyd" only achieves good prediction results if the load profile correlates with the global horizontal irradiance. In this research setting, this is only the case for the load profiles from the southwest roof inverters and the PV main meter.

Even though the load profile of the PV main meter is impacted by the failures of the inverters I_3 and I_{14}, all random forest regressors still achieved a remarkably high R^2 score and relatively low absolute deviation. This indicates that their impact on the load profile of the PV main meter is indeed not too significant. Nevertheless, it is assumed that the random forest models would have performed even better if there were no inverter failures.

Tab. 4 gives an overview of the prediction performance that multiple linear regression models achieve when provided with the same data as the random forest models. Even though all of the eight model configurations were evaluated in this research, only the three most distinctive cases are displayed in Tab. 4: a model utilizing all data except the illuminance (ithyd), the full model (ithydnesw), and a model using only the illuminance (nesw). All other models that are not explicitly displayed showed results that lay between the results of "ithydnesw" and "nesw". Generally, the results exhibited a pattern similar to the results of the random forests: "ithyd" is the model with the worst and "ithydnesw" is the model with the best prediction performance.

When comparing the results of the multiple linear regression models (Tab. 4) with the results of the corresponding random forest models (Tab. 3), it becomes obvious that the prediction performance of the random forests exceeded the prediction performance of the multiple linear regressions: The R^2 score was generally always higher and, in most cases, the absolute deviation was smaller. That seems to be because none of the provided predictors directly correlates with PV electricity generation. We expect the multiple linear regression models to achieve much better prediction performances when the irradiation or illuminance for the exact surface orientation of the PV modules is provided as a predictor.

Tab. 4: Prediction performance that the multiple linear regression models achieved

Time resolution	Multiple linear regression model	R^2 score					Absolute deviation				
		Mean of			Inverter I_1	PV main meter (sum of all inverters)	Mean of			Inverter I_1	PV main meter (sum of all inverters)
		South-west roof inverters	South-west façade inverters	South-east façade inverters			South-west roof inverters	South-west façade inverters	South-east façade inverters		
5 min	LR-ithyd	0.884	0.546	0.510	0.750	0.865	1.73%	19.22%	5.15%	4.73%	3.17%
	LR-ithydnesw	0.898	0.825	0.872	0.855	0.907	0.44%	14.52%	3.37%	3.06%	2.43%
	LR-nesw	0.882	0.768	0.823	0.850	0.888	1.76%	7.10%	2.27%	0.54%	1.22%
10 min	LR-ithyd	0.921	0.566	0.532	0.786	0.899	0.72%	18.73%	5.06%	4.21%	2.46%
	LR-ithydnesw	0.938	0.870	0.908	0.895	0.947	0.95%	13.43%	2.54%	1.76%	1.28%
	LR-nesw	0.929	0.816	0.859	0.891	0.932	2.05%	7.00%	2.75%	1.04%	1.54%
15 min	LR-ithyd	0.938	0.576	0.543	0.802	0.910	0.32%	18.53%	5.09%	4.19%	2.26%
	LR-ithydnesw	0.957	0.894	0.925	0.913	0.960	1.58%	13.01%	2.21%	1.37%	0.91%
	LR-nesw	0.951	0.841	0.876	0.909	0.946	2.18%	7.11%	2.97%	1.11%	1.66%
30 min	LR-ithyd	0.956	0.590	0.556	0.821	0.922	0.29%	18.36%	5.10%	4.18%	2.11%
	LR-ithydnesw	0.976	0.921	0.945	0.934	0.973	2.09%	12.77%	1.96%	1.12%	0.63%
	LR-nesw	0.972	0.866	0.894	0.930	0.960	2.19%	7.18%	3.25%	0.96%	1.78%
60 min	LR-ithyd	0.962	0.600	0.563	0.833	0.927	0.40%	18.22%	5.12%	4.23%	2.02%
	LR-ithydnesw	0.983	0.934	0.955	0.946	0.979	2.35%	12.73%	1.91%	1.11%	0.53%
	LR-nesw	0.980	0.878	0.902	0.941	0.965	1.94%	7.14%	3.45%	0.89%	1.83%

These results indicate that when only data from surfaces with a different orientation than the PV modules is available as predictors, the random forest regressors significantly outperform the multiple linear regression.

A detailed inspection of the prediction results of single repetitions of the random forest models shows that the average prediction performances presented in Tab. 3 correctly depict the performances to be expected in the different cases. Fig. 2 and Fig. 3 show the performance of three selected random forest models during one of the repetitions for a time resolution of 5 min. The prediction performance of the best multiple linear regression model (LR-ithydnesw) is also displayed in both figures. Since no averaging is involved, the deviation in Fig. 3 is presented as it is – i.e., it is not the absolute deviation as in Tab. 3 and Tab. 4.

When comparing the results presented in Fig. 2 and Fig. 3 with those in Tab. 3, it becomes obvious that the averaged results are very close to the results of one specific case. Thus, they are a reasonable way to represent the performance expected from the random forest regressors in the different cases.

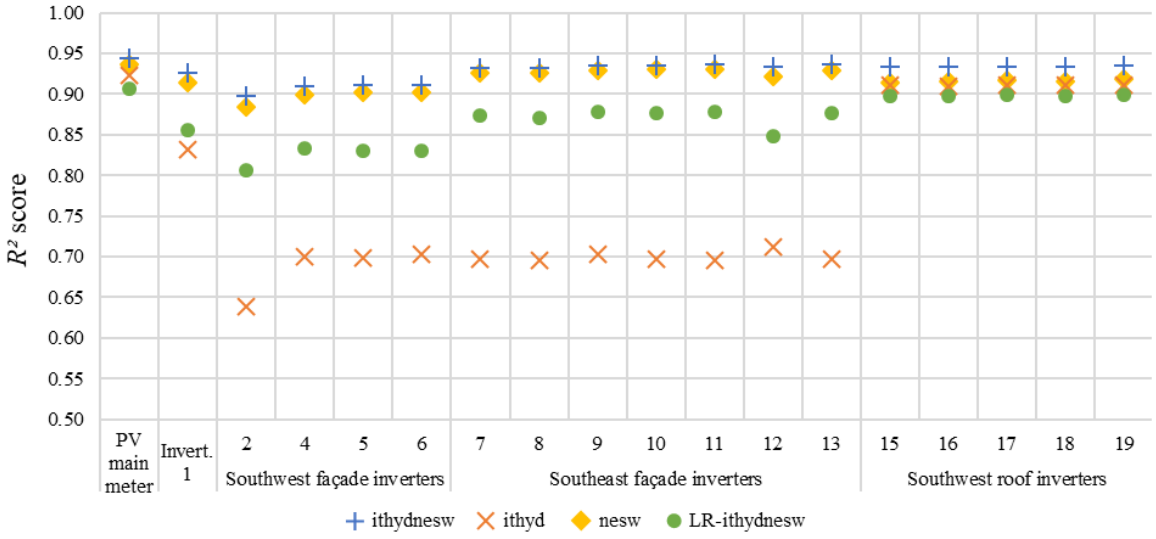

Fig. 2: Prediction performance (R^2 score) that was achieved by three selected random forest models in the case of a 5 min time resolution during one of the repetitions and prediction performance achieved by the best multiple linear regression model

Alike in Tab. 3, the performance of the models “ithydnesw” and “nesw” is remarkably high in Fig. 2: Regardless of the PV module orientation, the R^2 score lies between 0.9 and 0.95 for almost every load profile, and the absolute deviations are below 3% in most of the cases. Contrary to that, the model “ithyd” only performs well in the cases of the PV main meter and the southwest roof inverters. In the case of the façade inverters, its performance is significantly worse.

The best multiple linear regression model, “LR-ithydnesw”, never outperforms the random forest models “ithydnesw” and “nesw”. Except for the southwest roof inverters, this is also the case for the random forest model “ithyd”.

The depiction of the real deviation in Fig. 3 instead of the absolute deviation allows for additional observations: While the models “ithydnesw” and “nesw” generally underestimate the PV electricity production, the model “ithyd” generally overestimates it. As an underestimation could be explained due to the fact that the training dataset is from the year after the year that was used for the test dataset – the difference could (at least partially) be explained by the degradation of the PV modules. Further, in the case of the PV main meter, the difference most certainly is also caused by the failures of inverters I_3 and I_{14} during 2018.

At the moment, there is no obvious, plausible explanation for the overestimation of the PV electricity production by “ithyd” – maybe it is simply an expression of its poor prediction performance in some cases.

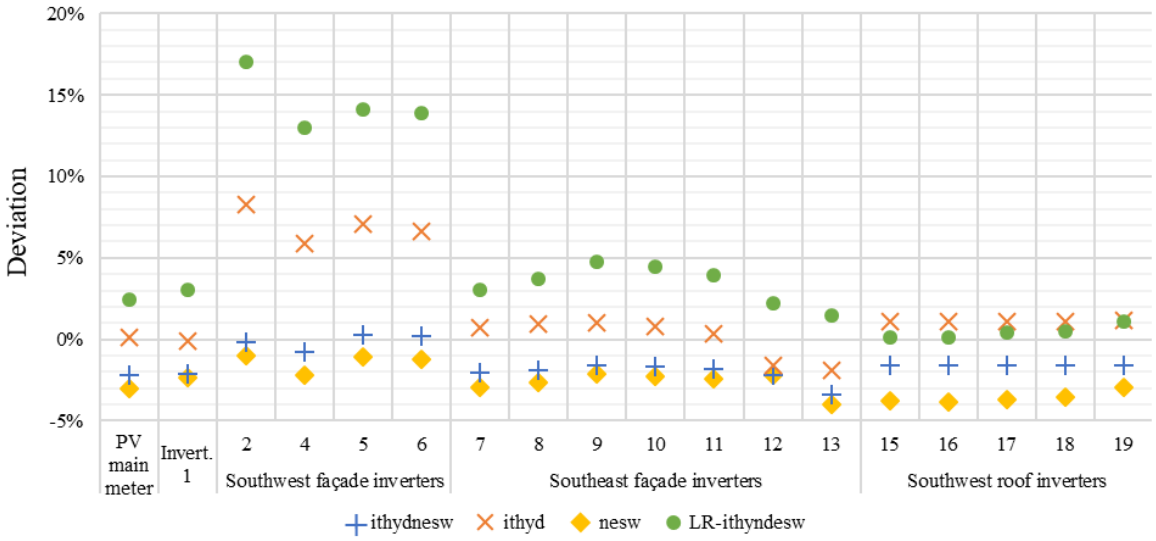

Fig. 3: Prediction performance (deviation of cumulated predicted load profile from the cumulated actual load profile) that was achieved by three selected random forest models in the case of a 5 min time resolution during one of the repetitions and prediction performance achieved by the best multiple linear regression model

All the results presented in Tab. 3, Tab. 4, Fig. 2, and Fig. 3 focussed on the performance indicators R^2 score and deviation of the cumulated predicted load profile from the cumulated actual load profile. To illustrate the underlying data and show which prediction accuracy can be expected during a day, Fig. 4 and Fig. 5 show comparisons of the time series of the predicted and actual load profiles. The presented time series are from the timespan 04.02.2017 00:00 - 09.02.2017 00:00, which is the very beginning of the test dataset. Again, the random forest models “ithydnesw”, “ithyd”, and “nesw” and the best multiple linear regression model “LR-ithydnesw” are shown in both depictions. The shown load profiles are only the profiles of inverter 7, one of the southeast façade inverters. This inverter was chosen on purpose, as in the case of the façade inverters, the model “ithyd” achieved a relatively poor prediction performance while the other models achieved a relatively high prediction performance. While Fig. 4 illustrates the case of a 5 min time resolution, Fig. 5 presents the case of a 60 min time resolution.

As seen in Fig. 4, the models “ithydnesw” and “nesw” could accurately predict the course of the actual load profile in the case of a 5 min time resolution. The predictions replicated the course of the PV electricity generation during a cloudy day (detail 1), its relatively smooth course during a sunny day (detail 2), and its more complex course on a sunny day with some clouds (detail 3).

These two random forest regressor models could accurately replicate the skewness of the daily course (caused by the southeast orientation of the inverter's PV modules) is remarkable – especially when considering the fact that none of the predictors directly correlates with the direct irradiation on a southeast-oriented surface. The random forest regressors appear to be able to infer the information needed to replicate such skewness from the predictors – assumedly by the irradiance measurements on the south vertical surface and the east vertical surface.

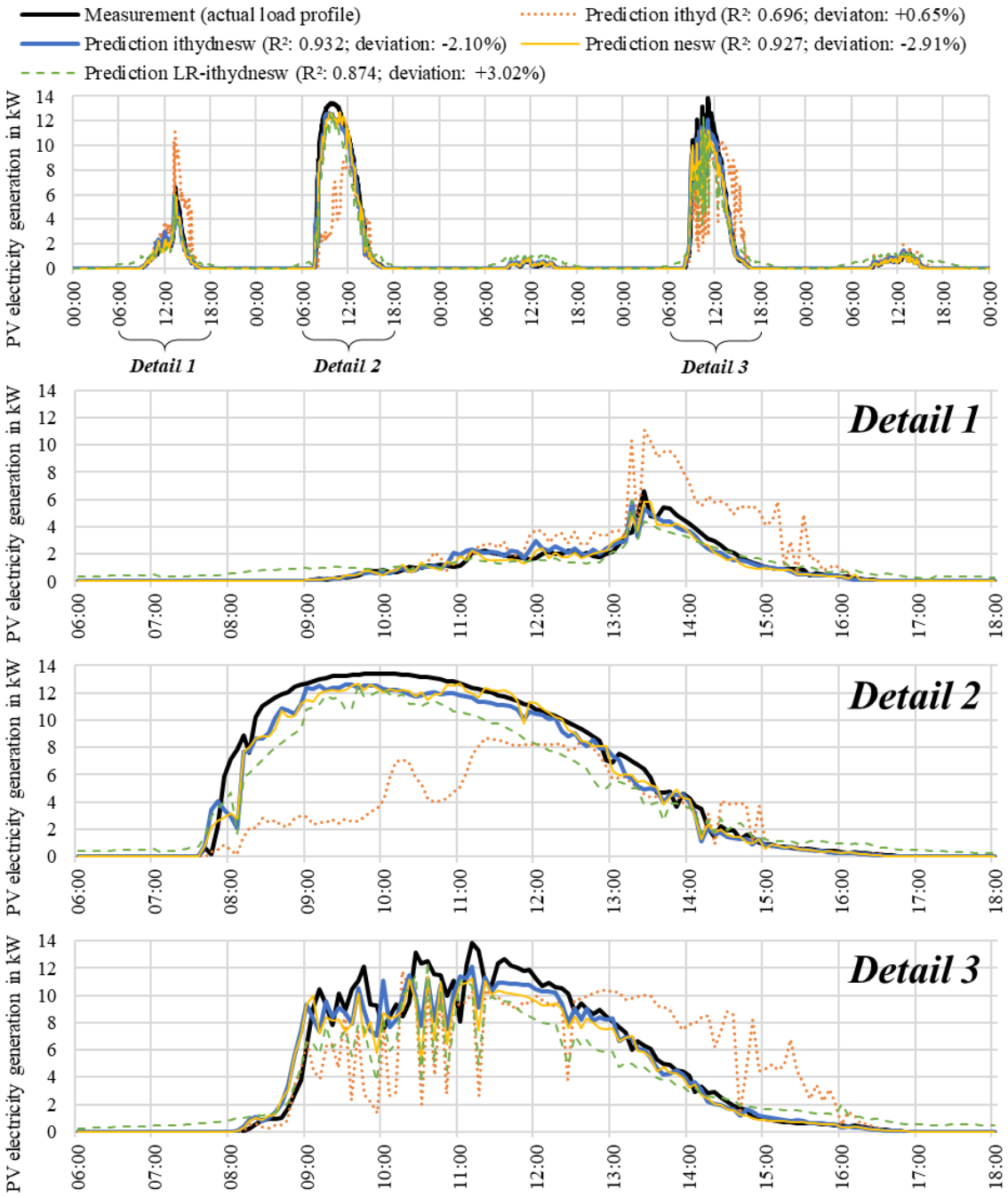

Fig. 4: Comparison of the measured PV electricity generation of inverter 7 (southeast façade inverter) and the predictions from three selected random forest models and the best multiple linear regression model in the case of a 5 min time resolution (shown R^2 scores and deviations are the values of the predictions of a whole year)

On the other hand, model "ithyd" predicted a load profile that is far off the real course of the actual load profile. The reason for that and the general poor prediction performance of "ithyd" seems to be that the information hidden in the "ithyd" training data is insufficient for the random forest model to correctly grasp the underlying connections between the predictors and the load profiles. It appears that the random forest regressors are simply

not able to reproduce the necessary geometric transformations out of weather data which only includes irradiation/irradiance values for one single surface orientation.

The load profile predicted by the multiple linear regression model "LR-ithydnesw" is also off the real course. It is generally too low during the day and too high during the night. Nonetheless, the prediction fits the actual load profile better than the prediction of "ithyd".

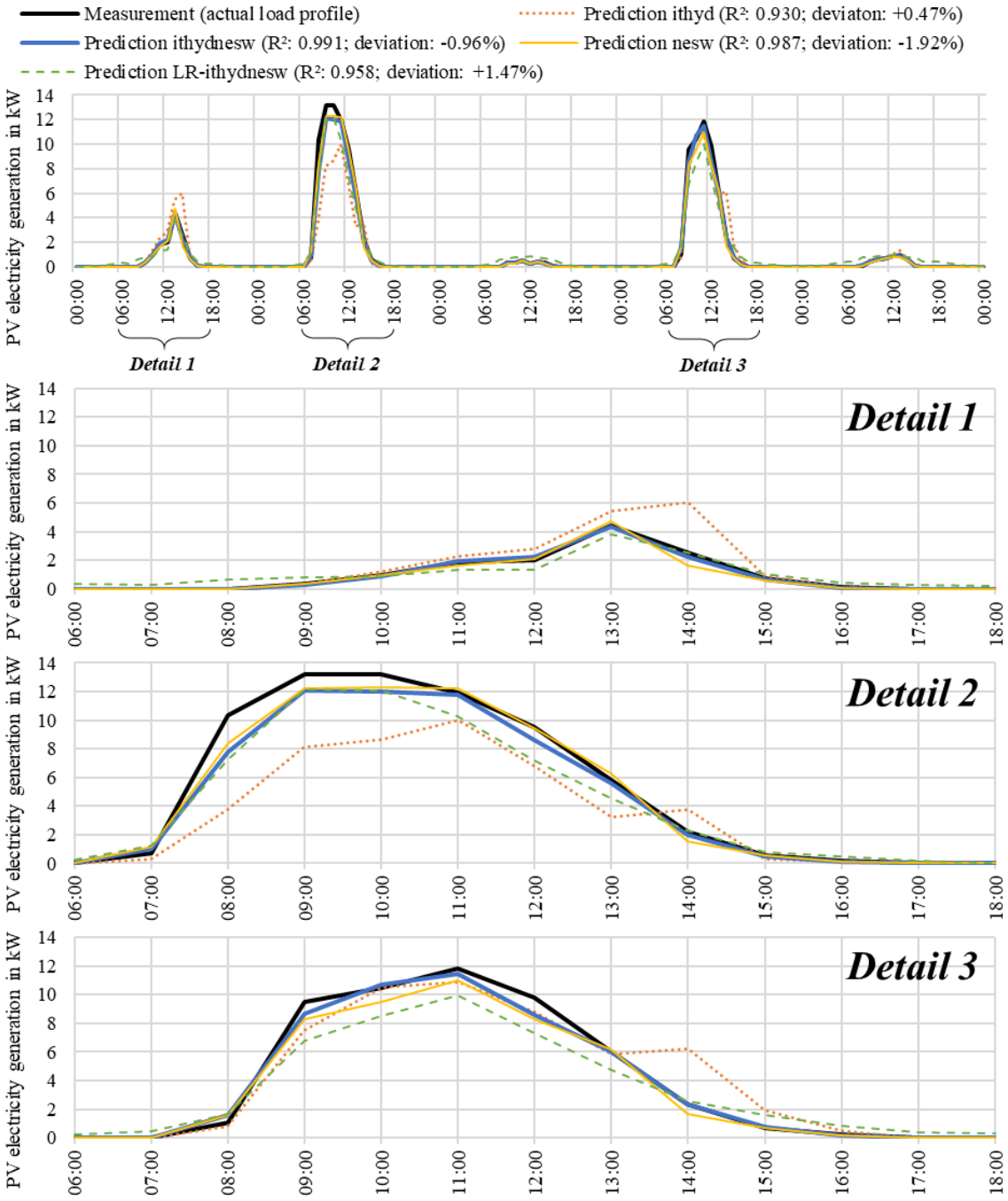

Fig. 5: Comparison of the measured PV electricity generation of inverter 7 (southeast façade inverter) and the predictions from three selected random forest models in the case of a 60 min time resolution (shown R^2 scores and deviations are the values of the predictions of a whole year)

For the case of a 60 min time resolution, see Fig. 5, the prediction performance of "ithyd" improved. Its prediction is much closer to the actual load profile, but it is still significantly worse than the predictions of the other three models. A direct comparison of Fig. 4 and Fig. 5 also explains the better R^2 score with decreasing time resolution: The load profile at a 60 min time resolution has a much smoother course than the one with a 5 min time resolution.

4. Conclusion

Given that the right weather data is available to be used as predictor variables, random forest regression is a suitable tool to accurately predict PV electricity generation. With increasing time resolution, the prediction performance generally gets slightly worse. The random forest regressors achieved remarkably high R^2 scores at a time resolution of 60 min. Thus, if the goal is to ensure the correct operation of the PV plant, predicting and comparing the PV electricity generation in a time resolution of 60 min can be recommended.

The best prediction performance can be expected from the full model ("ithydnesw"), which utilises all available weather information (horizontal global irradiance, air temperature, relative air humidity, and illuminance on the vertical surfaces of the four cardinal directions) and time indicators (yearly sinus function fitted to the solstices and equinoxes, daily sinus function fitted to noon and midnight). The model without the information about the illuminances ("ithyd") should only be used to predict PV electricity generation of plants where the load profile correlates with the global horizontal irradiance – this model cannot be recommended to predict load profiles of façade integrated PV modules.

The weather data used as predictors should include the illuminance measurements on the vertical surfaces of the four cardinal directions, north, east, south, and west, to achieve good prediction performances for all PV module orientations. In the case of the weather station used in this work, these parameters were not directly measured but instead calculated internally in the station itself. Since most weather stations do not provide illuminance on vertical surfaces, it is strongly recommended to calculate it using available weather data to use it as input for random forest regressors.

It is expected that if the illuminance is also calculated for all of the PV module orientations of a PV plant, multiple linear regression could also be generally recommended to predict PV load profiles. The downside is that at least the PV module orientations must be known, and the illuminance must be calculated specifically for each orientation.

The random forest regressors only need measurement data and the illuminance on the vertical surfaces of the four cardinal directions to achieve good prediction performances. The advantage is that the random forest regressors do not need specific knowledge about the PV module orientation predestines them for a large-scale application. They could be used in online monitoring systems provided by PV inverter manufacturers.

For such an application, the location of the PV plant must be known, and the weather data for this specific location must be obtained. The illuminance on the vertical surfaces of the four cardinal directions must be calculated from the weather data, and the sinus of the day and sinus of the year must be calculated from the time stamp information. After the monitoring data of the PV plant encompasses at least a whole year without uninterrupted operation, the full random forest regressor model ("ithydnesw") can be trained and then used to provide the reference for PV performance monitoring. To account for the degradation of the PV modules, the reference profile should be scaled down accordingly.

5. Acknowledgement

The authors acknowledge the BMVIT (Federal Ministry of Transport, Innovation and Technology), Kommunalkredit Public Consulting GmbH and MA20 (Vienna's municipal department for "Energy Planning") for funding this project. The authors also acknowledge all project partners, the TU Wien, the consortium of the Architects Hiesmayr-Gallister-Kratochwil, and the Bundesimmobiliengesellschaft as the building owner and operator.

6. References

Breiman, L., 2001. Random Forests. Machine Learning 45.1, 5-32.

Chen, Z., Han, F., Wu, L., Yu, J., Cheng, S., Lin, P., Chen, H., 2018. Random forest based intelligent fault diagnosis for PV arrays using array voltage and string currents. Energy Conversion and Management 178, 250–264.

David, A., Sint, S., Bednar, T., 2023. Comparison of the Simulated and Measured Performance of the PV Plant

of Austria's Largest (Plus-)Plus-Energy Office Building. *EuroSun 2022: ISES and IEA SHC International Conference on Solar Energy for Buildings and Industry*, Kassel, 25-29 September.

Hastie, T., Tibshirani, R., Friedman, J., 2017. The Elements of Statistical Learning. Data Mining, Inference, and Prediction. Second Edition, Springer.

Mayer, M. J., Gróf, G., 2021. Extensive comparison of physical models for photovoltaic power forecasting. Applied Energy 283, 116239. https://doi.org/10.1016/j.apenergy.2020.116239

McKinney, W., 2010. Data Structures for Statistical Computing in Python. *Proc. 9th Python Sci. Conf.* https://doi.org/10.25080/majora-92bf1922-00a

Pedregosa, F., Varoquaux, G., Gramfort, A., Michel, V., Thirion, B., Grisel, O., Blondel, M., Prettenhofer, P., Weiss, R., Dubourg, V., Vanderplas, J., Passos, A., Cournapeau, D., Brucher, M., Perrot, M., Duchesnay, É., 2011. Scikit-learn: Machine learning in Python, J. Mach. Learn. Res. 2825–2830.

Pillai, D. S., Rajasekar, N., 2018. A comprehensive review on protection challenges and fault diagnosis in PV systems. Renewable and Sustainable Energy Reviews 91, 18-40. https://doi.org/10.1016/j.rser.2018.03.082

Schöberl, H., Hofer, R., Leeb, M., Bednar, T., 2014. Berichte aus Energie- und Umweltforschung, Schriftenreihe 47/2014: Österreichs größtes Plus-Energie-Bürogebäude am Standort Getreidemarkt der TU Wien. Vienna: Bundesministerium für Verkehr, Innovation und Technologie.

Tozzi Jr., P., Ho Jo, J., 2017. A comparative analysis of renewable energy simulation tools: Performance simulation model vs. system optimization. Renewable and Sustainable Energy Reviews 80, 390-398. https://doi.org/10.1016/j.rser.2017.05.153

Umar, N., Bora, B., Banerjee, C., Panwar1, B. S., 2018. Comparison of different PV power simulation softwares: case study on performance analysis of 1 MW grid-connected PV solar power plant. IJESI 7. 7, 11-24.

Yao, S., Kang, Q., Zhou, M., Abusorrah, A., Al-Turki, Y., 2021. Intelligent and Data-Driven Fault Detection of Photovoltaic Plants. Processes 9. 1711, 1-21. https://doi.org/10.3390/pr9101711

Digital Representation of Heating Systems for Fault Detection Purposes

Matthias Georgii[1], Christoph Schmelzer[1], Christian Sauer[1], Janybek Orozaliev[1], and Klaus Vajen[1]

[1] University of Kassel, Institute of Thermal Engineering, Kassel (Germany)

Abstract

A concept for a graph based digital representation of heating systems is presented. It explicitly defines various relations between the components and data points. Thus, it allows a semantic description of the heating system and available data points which can be used for automated fault detection. Implementation of analysis algorithms can get complex considering the multitudes of options regarding different system configurations and measurement equipment. The semantic description enables a computer to make automatic conclusions, and thus can reduce this effort. Simultaneously, the concept also may reduce the effort to find and apply analysis algorithms for a specific system, since it allows for automated comparison between needed and available components along with their relations.

Keywords: function control, fault detection and diagnosis, FDD, Digital Twin

1. Introduction

Heating systems are getting more complex to achieve high efficiencies and high fractions of renewable energy. At the same time, they are often individually planned and assembled at each site, with individual parameterization of controller settings. This may lead to faults in planning, installation, and operation phases. Automated fault detection and diagnosis (FDD) can help to ensure the intended behaviour and efficiency of the system. While currently many sensor and signal data can be logged, the automated analysis of the data is less common. Often, data is just visualized and interpreted by an expert. This might have two causes.

Firstly, there is little or no information about validated detection algorithms publicly available. For instance, VDI 2169 (VDI, 2012) mainly describes rather rough concepts of detection ways than directly applicable algorithms. However, when implemented in the simple form, they will rise lots of false alarms, making them practically unusable.

Secondly, it is challenging to automatically select applicable detection algorithms and link available data to their inputs. These tasks of selecting and linking require meta information, which often is not stored at all, or just in an inconsistent, heterogenous way, which impedes easy access by machines (see fig. 1). In single monitoring projects, an expert uses his meta information knowledge to select the algorithms that should be executed, and to manually assign suitable data to their inputs. This approach would lead to high effort for greater numbers of monitored systems. For an automated analysis of many different systems, each heating system has to be represented digitally in a way that allows the automatic application of detection algorithms. One possibility is to use predefined blocks of components, as done in the Methodiqa project (Ohnewein et al., 2016). This works well when small parts like components or a group of nearby components are considered, and a limited number of detection paths. However, the block representation approach might get complex, if interactions of larger parts of the system or the whole system are to be considered, and more different sets of available data points and correspondingly different ways of deriving information have to be checked.

We therefore suggest a graph representation which explicitly states relations between the components or subsystems of the system and offers more flexibility.

© 2022. The Authors. Published by International Solar Energy Society
Selection and/or peer review under responsibility of Scientific Committee
doi:10.18086/eurosun.2022.16.04 Available at http://proceedings.ises.org

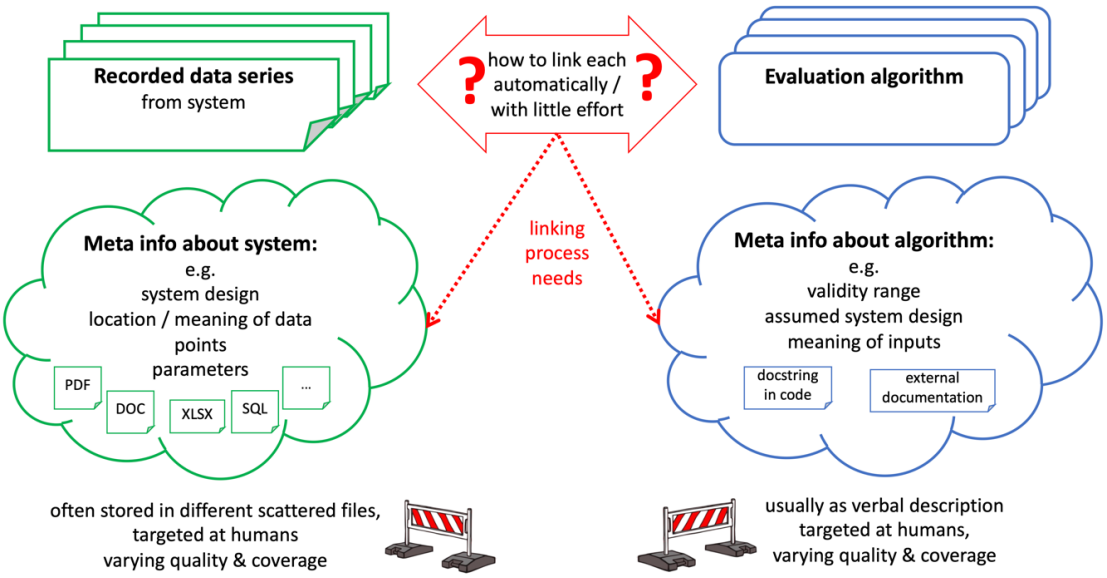

Fig. 1: Selecting applicable evaluation algorithms and linking them to recorded data requires meta information which often is not available in a consistent, machine-readable manner.

2. Graph representation

Depending on the intention, different views on a heating system are important.

- Geometry and Topology: distances and dimensions of subsystems and components, or their spatial adjacency or inclusion, e.g. lengths of pipes
- Function: what is the function of which subsystem, functional grouping of subsystems, what are intended interactions, e.g. supply pipe delivering heat from boiler to storage
- Control: which interactions between subsystems are actively controlled by which controller, and which of their signals are used for which control task, e.g. storage bottom temperature used as input for operating the solar circuit via a temperature hysteresis control
- Recorded data structure: identification, availability, and logical grouping of data points, in order to find the meaning of each time series of data
- Abstraction level of system components: for instance, an air-to-water heat pump might also be regarded as a general heat pump or heat generator or energy converter

Thus, those aspects should preferably be included in the graph representation. For FDD, geometry is the least important aspect and only needed in some specific evaluations, which is why it is omitted here. The function of a subsystems can also be considered in many respects. Since the purpose of a heating system is to generate heat and provide it to different consumers, it is useful to describe the function with respect to both the energy flow and the fluid flow that may transport the energy.

2.1. Energy flow graph

The energy flow graph describes the energy flows from heat generators to heat consumers. It already contains the basic structure and main components of a heating system. An energy flow graph that just contains heat generators, storages and sinks is illustrated in fig. 2. However, since a component, e.g. a storage, can have several ports at which energy is transferred, those ports have to be included as nodes as well in order to have nodes that uniquely identify a specific energy flow. An example of such an extended energy flow diagram is shown in fig. 3. It additionally contains the solar heat exchanger (which does not alter the energy flow in first approximation) and "logical" components ("XORDistributor", "Adder") that explicitly distribute or merge energy flows, ensuring that

there is only one incoming and one outgoing edge at each port node. This prevents ambiguities how to interpret several incoming/outgoing edges at a node. Of course, each component still needs an individual node representing the component, in order to describe, to which component an energy port belongs. The component node has the type of the component. Such a component node also indicates that energy flow (and/or state variables of associated medium flow) is significantly altered by conversion, merging, distributing, etc. For instance, a SolarThermalCollectorField node will convert irradiance into thermal energy of a heat medium, which are two different types of energy. Furthermore, such a conversion is known to have significant losses that cannot be ignored. Likewise, a distribution node indicates that energy flow of an incoming edge in general does not equal the energy flow of an outgoing node. Moreover, the temperatures of the incoming energy flows will be mixed, thus potentially being changed significantly. A heat exchanger node might not alter the magnitude of an energy flow significantly, but primary and secondary temperatures will differ. The magnitude of the energy flow and state variables of the assoiciated fluid flow may be propagated along an energy flow path, but propagation is never allowed across component nodes. The propagated value may be used as estimator for the case of ideal energy transfer, i.e. neglecting heat losses of the pipes. With this propagation mechanism, algorithms can increase the chance of the availability of needed data if propagated values are allowed. Please note that pipes were not included explicitly as component nodes here. For the case of long pipes whose heat losses and temperature drops are never to be ignored, their explicit inclusion as a component node indicates that no forwarding of energy flow and state variables must be made.

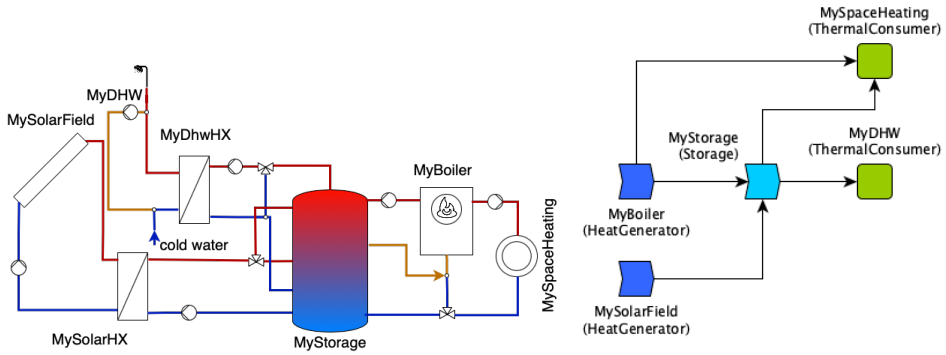

Fig. 2: A (too) simple energy flow graph (right) of a solar thermal combi system (left). Different node colors and shapes indicate different types of nodes. It carries too little information about system structure and allows for ambiguities.

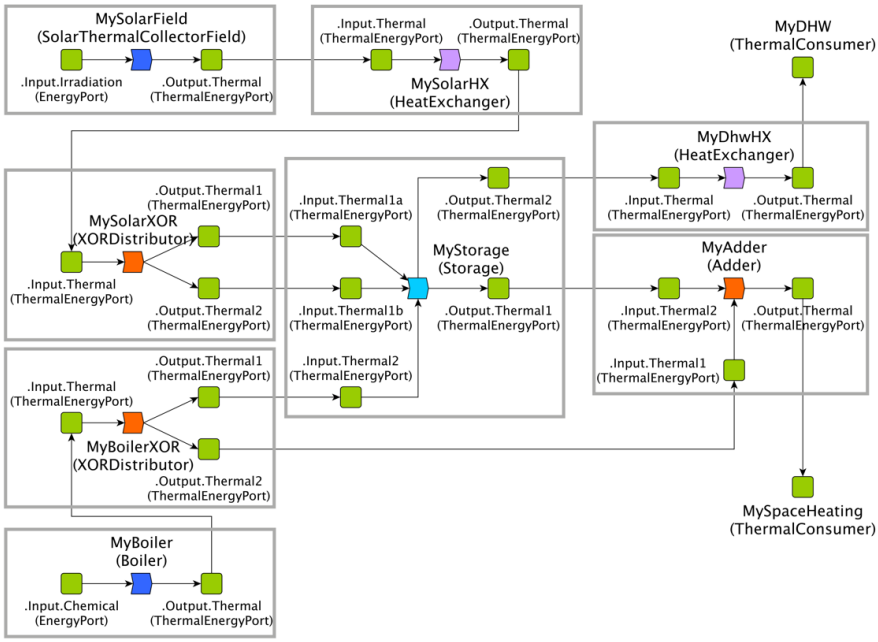

Fig. 3: Extended version of the energy flow graph in fig. 2, with port nodes and additional components. Energy demand for circulation is here included in MyDHW.

The energy flow graph can be created easily by hand with help of predefined subgraphs for the respective components. Only the links between the ports, i.e. the edges between gray boxes in fig. 3., have to be added. The creation and linking process might be automated to a higher degree if existing data about components and piping can be imported from BIM (Building Information Modeling) data in future.

While the energy flow graph is still simple, it already carries much information about the system. Thus, it can be used to describe a system on a basic level.

2.2. Medium flow graph

However, if details of medium flows get important, e.g. in order to trace return flows, a medium flow graph has to be specified. The medium flow graph describes possible flows of different media, e.g. the flow of water in a circuit. To make nodes in a medium flow graph identifiable, further relations and nodes are needed. This is explained for an external heat exchanger subgraph, shown in fig. 4. In order to relate a node to a component, a specific "belongsTo" relation is needed. Contrary to the energy flow graph in fig. 3, the fluid flow cannot be simply directed to a "HX" component node. Otherwise, this would have to be done for both primary and secondary fluid flows. This would effectively connect both fluid circuits to a single connected circuit. Additionally, a relation stating whether a node is on the primary or secondary side is needed. For further refinement, edges in the fluid flow are differentiated into "fluidTransfer" edges (dark blue in fig. 4) and "fluidProcess" edges (light blue in fig. 4). This differentiation adopts the role of the component nodes in the energy flow graph fig. 3. Along "fluidTransfer" edges, state variables may be propagated (as estimators for the case of ideal transfer), while propagation along "fluidProcess" edges is not allowed. In the latter kind of edges, it is indicated that state variables of the fluid change significantly. Thus, nodes at the beginning of a fluidProcess edge represent the state before a significant process (e.g. temperature rise of the fluid), and nodes at the target of fluidProcess edges the state after the process, accordingly.

To unify the graph structures, also the energy flow graph fig. 2 can be modified to contain "energyTransfer" and "energyProcess" edges, such that the permission for value propagation is likewise indicated by the type of the edge and not via the existence of a component node within the energy flow. The component node then is not located within the energy flow, but attached to energyNodes via a "belongsTo" relation.

Similar subgraphs like fig. 3 can be defined for other components like boilers, heat pumps, distributors, etc.

These can be used to quickly create graphs of a system. Thus, only "fluidTransfer" edges between FluidNodes of those subgraphs would have to be added.

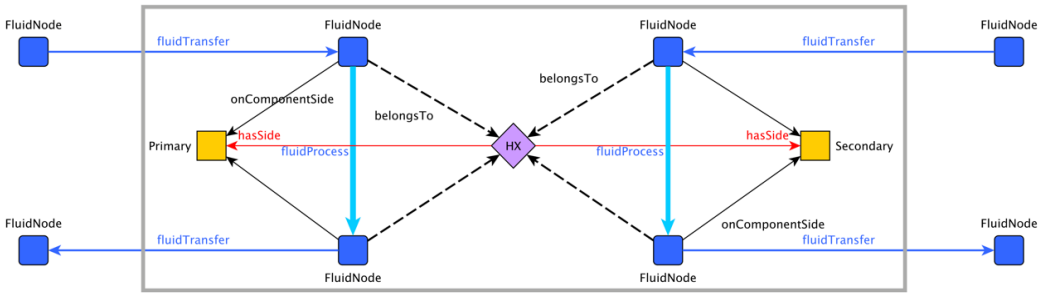

Fig. 4: Subgraph for a heat exchanger. Several nodes and relations are needed to identify nodes in a fluid/medium flow graph.

2.3. Data point identification

The graphs fig. 3 and fig. 4 still miss a connection to available data points, i.e. to actual data of recorded time series of measurement values or logged signals, e.g. the outlet temperature of the heat exchanger at secondary side. Moreover, data points can refer to parameters like storage volume, collector size, etc. In order to assign data points to a fluid, energy or component node, corresponding relations to data point nodes can be defined (compare fig. 5). To simplify data point identification, relative standard data point names can be linked to the data point nodes. For instance, each FluidNode can have data points with associated standard names like "Temperature" or

"VolumetricFlowRate", and each EnergyNode or ComponentNode likewise, allowing to also define standard component parameters. Each standard data point node can then be linked to another "providing" data point node that represents an existing data point that actually can provide data (time series of recorded values or parameter values). It is linked to the system specific unique identifier of that data point. The separation allows to link several standard name data point nodes to a single providing data point, and to explicitly differentiate between a defined and an actually available data point. Furthermore, it is possible to link standard data points to equivalence groups which can store which data points are considered equivalent, independently of the existence of a providing data point. The equivalence groups can be used to later automatically link all contained data points to a providing data point when it is added to the graph.

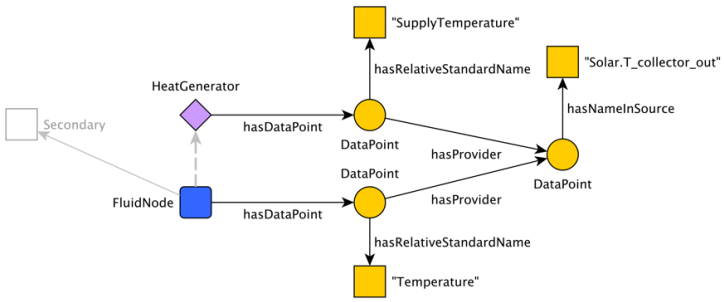

Fig. 5: Data point linking to a node. Actual data can be linked to different nodes with different standard data point names. The gray relations additionally indicate the relation of the "HeatGenerator" and the "FluidNode".

2.4. Component Abstraction levels

From perspective of algorithm authors, it is very useful to request existence of components at different abstraction levels. As described above, it might be sufficient to request a component to be a heat generator, or it might be necessary to require a more specific component like condensing gas boiler because the algorithm uses assumptions or characteristics that are only valid for the more specific component type. For instance, to calculate any coverage ratios, one needs to adress the considered (specific) heat generator as well as "all other heat generators" or "heat consumers" independent of their specific type. By integrating such class hierarchy relations of components into the graph, it is possible to adapt the abstraction level of each (component) node in the request. An example is shown in fig. 6. The graph structure also allows to define several class hierarchies (with other abstraction class nodes) in parallel and thus does not enforce to use a particular taxonomy.

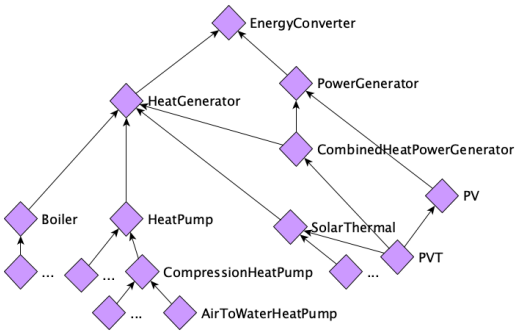

Fig. 6: Exemplary abstraction classes graph. Edges represent the relation "is subclass of" or equivalently "is specialization of".

3. Algorithm selection and linking

If a system is described via a graph with the relations shown in section 2, algorithms can formulate their expected components and relations by defining a requested subgraph structure (see fig. 7). Technically, this can be achieved by storing the system graph as set of RDF (**R**esource **D**escription **F**ramework) triplets, and defining SPARQL (**S**PARQL **P**rotocol **A**nd **R**DF **Q**uery **L**anguage) queries for each algorithm. SPARQL and RDF are standards

defined by the World Wide Web Consortium W3C. It might be necessary to not only check for existence of some relations, but also to check for non-existence of other similar relations (maybe of same type). This is also a reason why in the energy flow graph, explicit “Adder” and “Distributor” nodes are included. In this way, the request can allow or disallow further energy flows (besides the energy flow of interest) to arrive at a component port by simply adding or omitting a corresponding “Adder” node to the request. Without such a node, the number of incoming edges at a port node would have to be checked by different means, complicating the formulation of the algorithm’s requirements.

Furthermore, algorithms might be designed to not execute on each match separately but use a collection of matches as input for a single algorithm instance. For instance, an algorithm might want to cumulate the energies of all heat consumers, needing a collection of all heat consumers as input for a single algorithm instance. Thus, several modes for the process of converting matches to assignments of algorithms (=algorithm instances) must be provided.

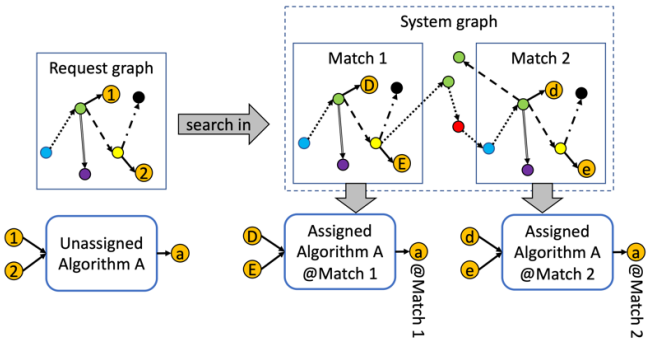

Fig. 7: Illustration for matching an algorithm’s request graph to the system graph. Different node colors and edge styles represent different node types and relations.

4. Conclusion and Outlook

A concept for the description of heating systems as graph for automated FDD has been presented. Advantages of a graph description are:

- Decoupled from specific usage or software solution
- Extensible by different stakeholders, no need to model whole system at once
- Quick compilation from predefined subgraphs
- Easy individual modification and addition of relations
- Standardized file formats for data exchange
- Standardized query language for data retrieval, allowing complex relation patterns to be queried

Further details of the graph description and its usage for fault detection in heating systems will be shown in future work.

5. References

Ohnewein, P., Tschopp, D., Schrammel, H., Gerardts, B., Poier, H., Krammer, S., Köstinger, A., Weinhappl, A., 2016. METHODIQA: Methodik-Entwicklung zur Qualitätssicherung für Erneuerbare Wärme Systeme durch intelligentes Betriebsmonitoring (Endbericht). AEE - Institut für Nachhaltige Technologien (AEE INTEC), Gleisdorf.

VDI Verein Deutscher Ingenieure e.V., 2012. VDI 2169 - Functional checking and yield rating of solar thermal systems. Beuth Verlag GmbH, Berlin.

A TRNSYS type for the simulation of temperature limiting heat pipe collectors

Julian Jensen, Bert Schiebler and Federico Giovannetti

Institute for Solar Energy Research (ISFH), Emmerthal (Germany)

Abstract

A number of commercially available simulation programs are already able to represent a temperature limitation in solar thermal collectors with a two-part collector efficiency curve. The use of this procedure for the simulation of temperature limiting heat pipe collectors would lead to deviations in its thermal behavior. This work presents a TRNSYS type which is able to represent the temperature limitation of heat pipes in solar thermal collectors correctly. For this purpose, we modified the TRNSYS type 832 regarding the correct temperature limitation behavior. For validation we use measurement data of four demonstration systems with temperature limitation in real operation. The range of consideration includes both flat-plate collectors and evacuated tube collectors with different system dimensions. The comparison shows only minor deviations between simulation and measurement of less than 5 % regarding the solar yield of the collector. Furthermore, the TRNSYS type is used in system simulations and compared to a reference direct-flow collector without temperature limitation, to identify the energetic impact of the temperature limitation onto the solar system performance. By using a direct-flow flat-plate collector, the saved auxiliary energy (f_{save}) increases by +15 %, which has to be considered under the design-related higher aperture area of + 9 %. The use of a direct-flow evacuated tube collector leads to an increased f_{save} of 1.1 %. Additionally, we have investigated the use of both TRNSYS collector types in the IEA SHC Task32 buildings, and reported similar results. The stagnation temperatures > 130 °C were reduced by 600 h and the maximum temperature was reduced by 115 K.

Keywords: solar thermal collector; temperature limitation; heat pipe; system simulation; TRNSYS

1. Introduction

Solar thermal systems are already well-established on the market as efficient renewable heat sources. In 2021, the worldwide installed capacity amounted to 746 million m² with a capacity of 522 GW_{th} (Weiss and Spörk-Dür 2022). High costs and high complexity, however, are major barriers to their dissemination and avoid the development of their large potential. New technical solutions are needed to improve their cost-effectiveness and general acceptance. Novel solar thermal collectors with heat pipes are a promising approach for this purpose. A suitable design provides for a high efficiency in the operating range as well as for the reduction of thermal stress in stagnation state. By using the dry-out effect of heat pipes, the maximum solar circuit temperature can be limited to 125 °C. Preventing overheating in the stagnation state enables cost-effective system configurations with polymeric pipes, smaller designed expansion vessels and cost-optimized solar stations. Furthermore, an easier installation process and low-maintenance operation can lead to a significantly higher profitability of such systems.

In normal operation mode, the incident solar radiation is converted into heat at the collector and then stored in the thermal storage tank. However, if there is no possibility to transfer the heat away from the collector (e.g. if the thermal storage is fully charged) and the solar availability is still high, the state of stagnation occurs. Thus, the solar pump stops its operation and the collector overheats up to its maximum (stagnation) temperature, when the thermal equilibrium is reached. In a usual solar thermal system, this process causes high temperatures and leads to the evaporation of the heat transfer fluid inside the solar circuit. In turn, this leads to high system pressure and to high temperatures in the whole solar system, which can cause significant damage to temperature sensitive components. Conversely, this means that the avoidance of high temperatures during stagnation can increase the lifetime of most system parts and decrease the overall costs due to a simplification in the system design and installation.

The avoidance of critical temperatures during stagnation can be easily accomplished by a collector coverage with an opaque material, however, this must be done by hand and is not beneficial to an efficient system operation. Many other methods have been developed in the past (Harrison and Cruickshank 2012; Frank et al. 2015; Kizildag et al. 2022; Müller et al. 2019) but most of them are not intrinsically safe.

A solution to this problem is the use of heat pipes. These are well-established on the solar thermal market and have been used in evacuated tube collectors for a long time. With the use of special designed heat pipes, the maximum

© 2022. The Authors. Published by International Solar Energy Society
Selection and/or peer review under responsibility of Scientific Committee
doi:10.18086/eurosun.2022.16.05 Available at http://proceedings.ises.org

temperature at the collector can be limited to such an extent that evaporation of the heat transfer fluid can be prevented. This approach has successfully been proved for evacuated tube collectors (Schiebler et al. 2018) as well as for flat-plate collectors (Schiebler et al. 2019).

2. TRNSYS type validation

So far, only one simulation program is known to be able to represent a temperature limitation in solar thermal collectors with the use of a two-part collector efficiency curve (T*SOL (Valentin Software 2022)). Even if this is the right procedure for some temperature limiting techniques (for example thermochromic collectors (Müller et al. 2019)) it does not fit for the heat pipe temperature limitation process and would lead to major deviations in the simulation, since the process is a function of both temperature and irradiance (cf. Fig. 1). For a defined stagnation temperature, the slope of the limitation curve is less steep at high irradiation than at low irradiation, which means, that the performance of the heat pipe collector is stronger affected (limited) at high then at low irradiation.

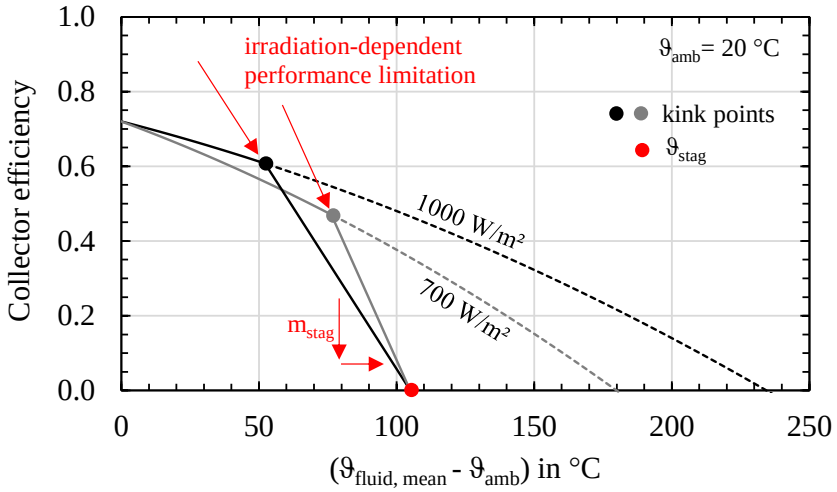

Fig. 1: Collector performance for a standard collector (---) in comparison with a temperature limiting heat pipe collector (-) with variation of the solar irradiance

To be able to correctly simulate temperature limiting heat pipe collectors, we have adapted the TRNSYS type 832 (Haller 2014), which is able to simulate flat-plate collectors (FPC) as well as evacuated tube collectors (ETC). For this purpose, we have implemented the two parameters ϑ_{Stag} and m_{Stag}, which describes the maximum occurring temperature in the stagnation state and the slope of the heat pipe shut-off function. Both parameters can be identified by means of collector performance measurement, as described in (Schiebler et al. 2018). Since m_{stag} is determined in a power-related measurement, but Fig. 1 shows the efficiency, different slopes result for m_{stag}. The temperature limitation is achieved by limiting the collector efficiency, starting at the so-called kink point. The position of the kink point is dependent on the current irradiation, due to the already mentioned different collector efficiency curves at different irradiation. In order to verify the functionality of this TRNSYS type, the measurement data of real demonstration systems (which are show in Tab. 1 and are also presented in (Schiebler et al. 2022)) were available.

Tab. 1: Overview of the demonstration plants FPC 1-2 and ETC 1-3 with the individual collector area A_{col} (gross area) and heat tank volume V_{tank}

FPC1	FPC2	ETC1	ETC2	ETC3
At institute	external	external	external	external
				

Type: DHW A_{col}: 5 m² V_{tank}: 0.3 m³	Type: Combi A_{col}:20 m² V_{tank}:1 m³	Type: DHW A_{col}:8 m² V_{tank}:0.3 m³	Type: Combi A_{col}:17 m² V_{tank}: 0.15+1 m³	Type: Combi A_{col}: 11 m² V_{tank}: 1 m³+2 m³
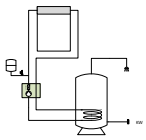	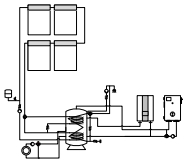	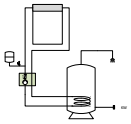	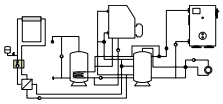	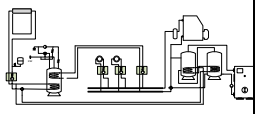

These systems have been monitored for more than one year regarding the system performance as well as the temperature distribution in the solar circuit. Fig. 2 shows the comparison between the measurements and the TRNSYS simulations for a chosen day of the FPC2 system by the use of the collector performance. To provide better visibility, the data are presented as a moving average of 2 min. For the sake of comparison, the original TRNSYS type 832 without temperature limitation is also shown. As simulation inputs, we use the measured weather data (irradiation, ambient temperature) as well as the measured collector input temperature.

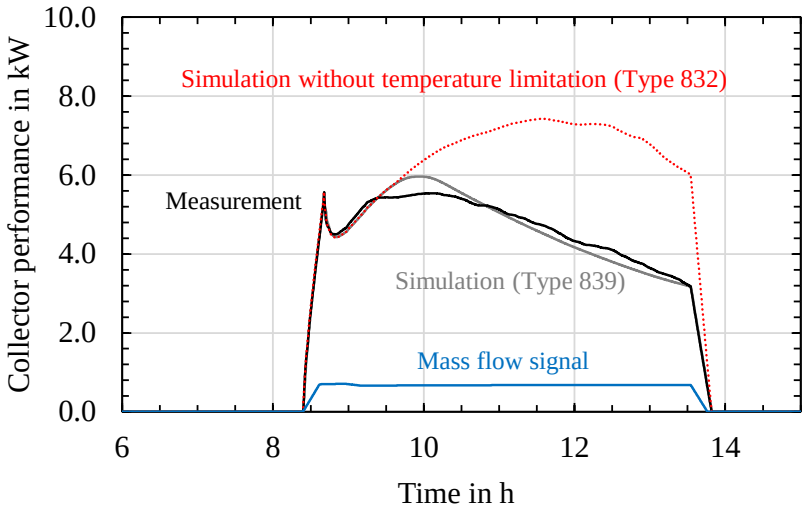

Fig. 2: Moving average (2 min) of the measured collector performance for the FPC2 with heat pipe temperature limitation and comparison of the TRNSYS type 839 with temperature limitation and the TRNSYS type 832 without temperature limitation

The graph shows, that the temperature limitation takes place at around 9:30 am for the measured collector. The simulated start of the temperature limitation is around 10 am. This difference in time occurs due to the ideally simulated collector behavior, which assumes an ideal transition from the working section to the temperature limiting section, which does not correspond to the real operation of a HP collector.

The transition (kink point) from the working section to the temperature limiting section has a huge impact onto the collector simulation, especially if the collector is often operated near to the kink point, as shown in Fig. 3 for the FPC1 system. Here, the simulation exceeds the measured performance due to uncertainties in modeling the limitation process of the heat pipes. The deviations in collector operation should not be neglected at this point and are caused by uncertainties in the measurement system.

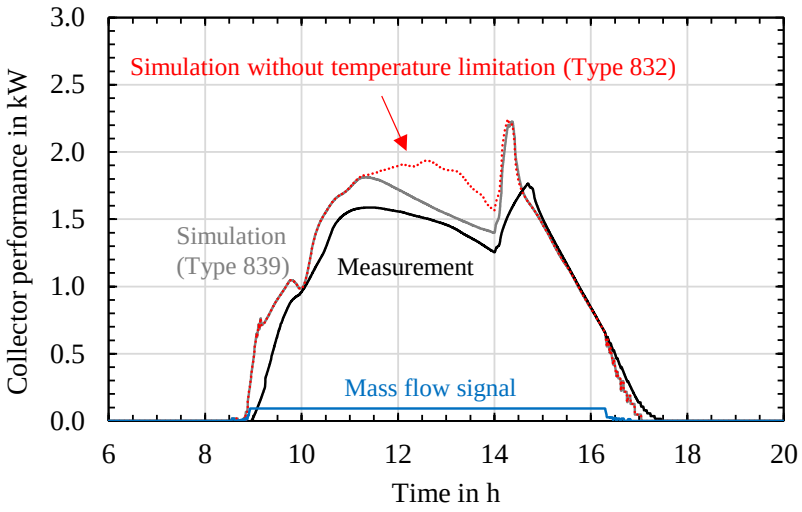

Fig. 3: Moving average (2 min) of the measured collector performance with heat pipe temperature limitation for the FPC1 operated near to the kink point and comparison of the TRNSYS type 839 with temperature limitation and the TRNSYS type 832 without temperature limitation

Furthermore, even small deviations in the heat pipe design and its overall heat transfer coefficient in the collector can lead to a large deviation in the collector behavior, especially in the temperature limiting section. Fig. 4 shows this correlation using the example of an evacuated tube collector.

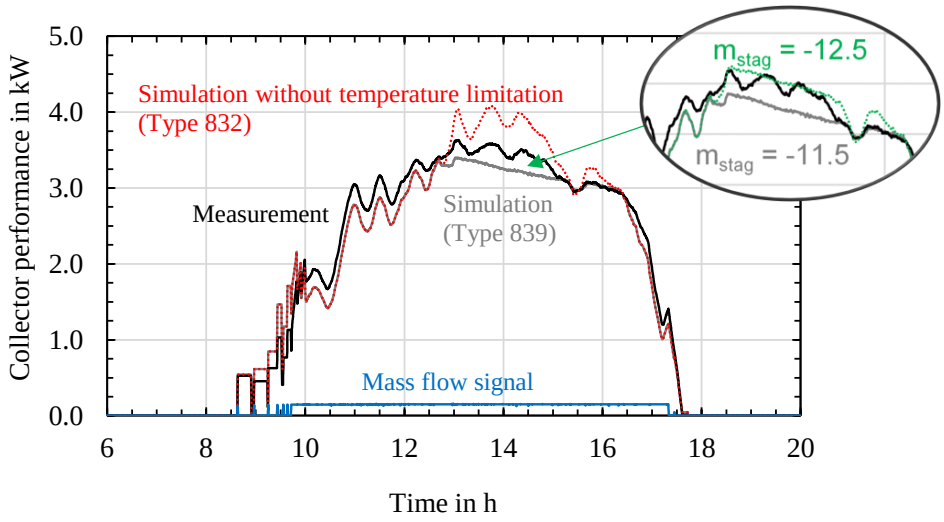

Fig. 4: Moving average (2 min) of the measured and simulated collector performance for ETC3 with heat pipe temperature limitation in comparison with the same collector without temperature limitation (chart) as well as the simulation with a varied parameter of mStag (top right corner)

The deviation can be caused by either a differing heat pipe design, which will cause slightly differing collector parameters, or by the uncertainties of the monitoring system. As shown in the top right corner of the graph, a slightly different value of the parameter m_{Stag} fits the measurement curve in a better way.

In conclusion, the use of the new temperature limiting heat pipe collector TRNSYS type can significantly reduce the deviations between simulation and measurement as it would be the case with the use of the TRNSYS collector type 832. The collector fields of all monitored external systems were also simulated for a period of one month, to investigate the difference between measurement and the simulation with the new TRNSYS type 839. June 2021 was chosen as test period, as it has sufficiently high solar radiation values. Fig. 5 shows the results of the determined solar yields in the observation period. The results are mostly within a satisfactory range of deviation and are in the range of the measurement accuracy of ± 7 % for all plants. The exception to this is the system ETC3, where the radiation measurement (pyranometer) was affected by the shadowing of a near building, which was not considered in the simulation. The FPC1 plant is a laboratory plant at the institute and was operated in the context of dynamic system tests (DST). A comparison of the system yields between the DST approach and TRNSYS is not further discussed here. Furthermore, the simulation results for the TRNSYS type 832 (without heat pipe limitation) are

shown. While the ETC systems experience almost no difference to the TRNSYS type 839 simulation, the result for the FPC system softens a significant increase in solar yield. This can be explained by the fact, that the ETC systems are rarely operated at higher temperatures where the heat pipe limitation takes place. The influence of the annual system yield is discussed later with Fig. 8.

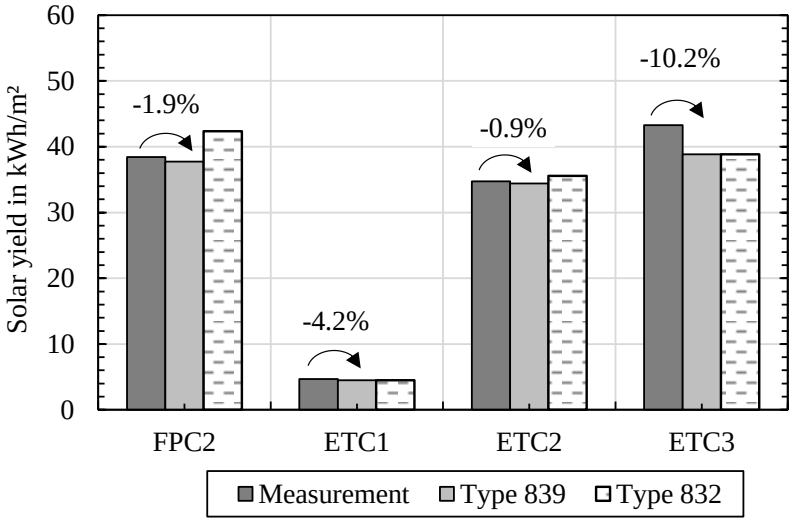

Fig. 5: Evaluation of the thermal gains from the solar thermal collectors in the monitored demonstration systems based on a one-month period (June 2021)

3. System simulations

3.1 Simulation of the monitored demonstration systems

After the experimental validation of the TRNSYS collector type, the monitored systems (solar and heating circuit) were implemented in TRNSYS. For the simulations, we used site-specific Meteonorm 8 weather data (Remund et al.) as well as the system-specific energy demand. The parameterization of the individual components is based on real system parameters. In the case of unknown parameters, standard system assumptions are used. An important parameter for the simulations carried out is the controller of the solar circuit pump, which limits the maximum collector temperature. In a conventional solar thermal system, this value is set to about 125 °C. In the HP system we choose 95 °C which would cause high stagnation times in a normal system. By using temperature-limiting heat pipe collectors and thus preventing steam formation, the operation of the solar circuit pump can be limited to 95 °C without any negative consequences. This allows the use of more cost-effective components and materials, such as polymeric-based piping (Schiebler et al. 2022).

The energetic evaluation of the systems is based on the f_{save} value (Streicher 2003), which expresses the savings in conventional auxiliary energy by the use of a solar thermal system (equation 1). In this equation, $Q_{aux,\ without\ ST}$ is the needed energy from the auxiliary heating device if no solar thermal collector is used. In contrast, Q_{aux} indicates the needed energy from the auxiliary heating device with the use of a solar thermal collector.

$$f_{save} = \frac{Q_{aux,without\ ST} - Q_{aux}}{Q_{aux,without\ ST}} \qquad \text{(eq. 1)}$$

The performance of the solar thermal system can be further evaluated via the solar fraction *sf* (equation 2) by using the solar thermal collector's energy gain Q_{Sol}.

$$sf = \frac{Q_{Sol}}{Q_{Sol} + Q_{aux}} \qquad \text{(eq. 2)}$$

Tab. 2 shows the results of the energetic evaluation of the demonstration plants for the measurement and the simulation. It should be noted that the f_{save} value requires the knowledge of $Q_{aux,\ without\ ST}$ which can only be measured for the system ETC1.

The measured data are affected by a measurement accuracy of approx. 7 %. Furthermore, the simulation is based on

average weather data. Both of these issues can cause discrepancies in the simulations. Even if the simulated values (e.g. for Q_{Sol}) are modeled with deviations in comparison with the measured values, the ratios of energy gain and energy demand are appropriate, so that the energetic key figures show only slight deviations from the measured values. It should be noted, that the ETC1 and ETC3 systems are not conventional installations (over- or undersized solar field), which explains the unusual results.

Tab. 2: Comparison between measured and simulated energetic key figures of the monitored systems over a one-year period

			FPC2	ETC1	ETC2	ETC3
Evaluation period			28.07.20 – 27.07.21	05.11.20 – 04.11.21	09.06.20 – 19.05.21	20.05.20 – 19.05.21
Q_{sol}	Measurement	kWh	5258±368	868±61	4451±312	2900±203
	Simulation	kWh	4864	974	4078	2669
f_{save}	Measurement	%	*	82±6	*	*
	Simulation	%	28	80	24	6
sf	Measurement	%	44±3	93±7	25±2	5±0.4
	Simulation	%	37	93	25	5

In the next step, the temperature limiting HP collector was changed with a direct-flow reference collector without temperature limitation. The used collector parameters for the simulations are shown in the appendix (Tab. 3). While the collector parameters for the heat pipe collector are based on a performance measurement carried out in the institute's solar simulator, the reference collector is based on data from a corresponding Solar Keymark certificate (Solar Keymark 2019, 2021). Fig. 6 shows the area specific solar yield for all the investigated systems, both for the use of a HP collector and for the direct-flow collector.

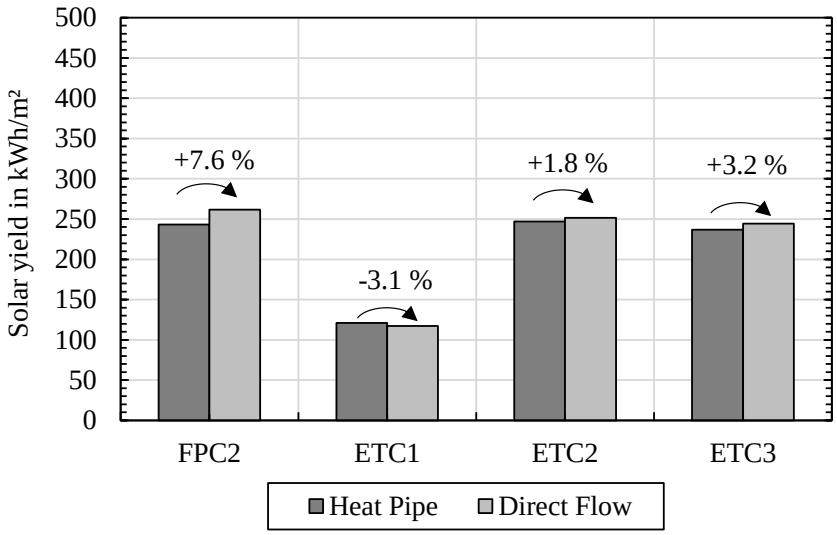

Fig. 6: Area specific solar yield for the investigated systems for both the heat pipe and the direct-flow collector

As expected, the direct-flow collector achieves an additional solar yield for most of the systems. ETC1 has a highly oversized collector area to gain high stagnation times in the system. Due to that, the HP collector can even gain a higher solar yield, caused by the better performance directly after a stagnation event. In general, it can be concluded, that the influence of the HP ETC onto the solar yield is lower than it is for the FPC. This is caused by the approximately 9 % smaller aperture area of the HP FPC in comparison with the HP direct-flow collector. Furthermore, the lower aperture area has a higher influence onto the saved auxiliary energy (f_{save}), as can be seen in Fig. 7. While the increase in the f_{save} - value remains about the same for the ETC, it increases significantly to 14 %

for the FPC. This correlation was also confirmed by parallel DST measurements at the institute's demonstration system FPC1 (Schiebler et al. 2022).

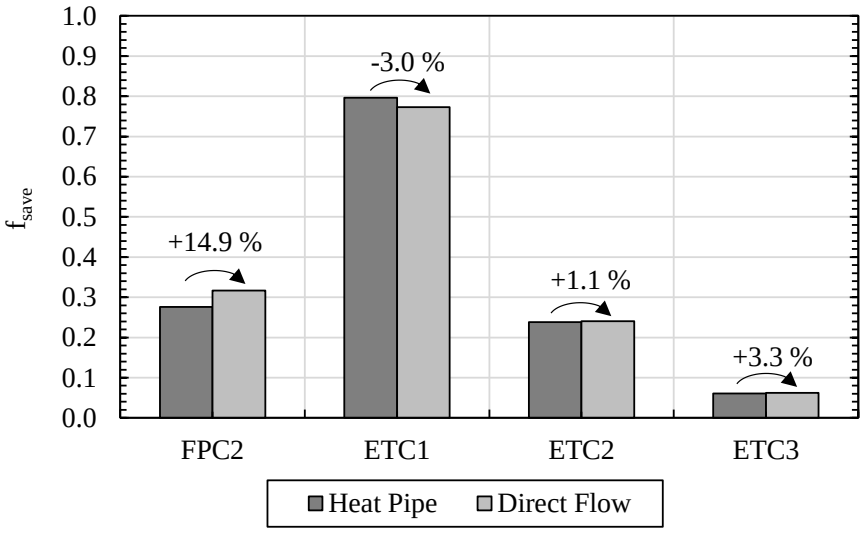

Fig. 7: Saved auxiliary energy due to the use of both the heat pipe collector and the direct-flow collector

In order to evaluate the results regarding the influence of the heat pipe limitation, we varied the maximum collector temperature ϑ_{Stag} (cf. Fig. 1) for all systems. Fig. 8 shows the simulated f_{save} value for each of the monitored systems in comparison with a heat pipe collector without temperature limitation (equivaltent to TRNSYS type 832). As it can be seen, the influence of the limitation process can be neglected for maximum temperatures of $\vartheta_{stag} > 120$ °C, which is the case for the ETC heat pipe collector in the demonstration systems. For $\vartheta_{stag} < 120$ °C, the heat pipe limitation starts to affect the f_{save} value, but in a small manner. It should be stated out, that the simulation of maximum temperatures of less than 100 °C is a pure hypothetical study, as the heat pipe process would not be functional in this way in real operation.

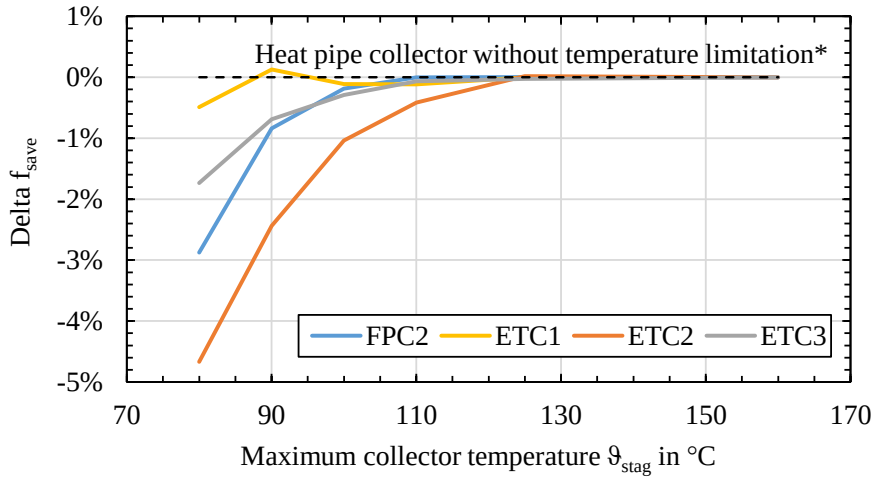

Fig. 8: Change of f_{save} due to the variation of the maximum collector temperature in comparison with a heat pipe collector without temperature limitation (*equivalent to TRNSYS type 832)

In summary, the given results indicate, that the solar yield of the simulated systems is not significantly affected by the heat pipe limitation and thus TRNSYS type 832 could also be used for its simulation without making any major errors. However, this statement must always be considered in the context of differing system configurations, which has a huge influence of the occurring collector temperatures and thus onto the influence of the heat pipe limitation. To correctly simulate the temperature limiting heat pipe collector, TRNSYS type 839 is needed.

3.2 Simulation of Task 32 building

In addition to the real demonstration systems, the corresponding collectors were simulated for two buildings of the IEA SHC Task 32 (Heimrath and Haller 2007) to achieve a better comparability by using a representative building with a customary solar system. The buildings represent a single-family house with a space heating demand of 45 kWh m^{-2} a^{-1} (SFH45) and 100 kWh m^{-2} a^{-1} (SFH100) at the Zürich site. These systems are simulated with both FPC and ETC, each in the HP and reference configuration (parameters are shown in Tab. 3 in the appendix). They consist mainly of 20 m² collector gross area and a 900 l thermal storage tank with a gas boiler as auxiliary heating.

Fig. 9 shows the distribution of the occurring collector temperatures for a one-year based simulation with the SFH45 building for an ETC on the Würzburg site. As it can be seen, the reference collector is exposed to temperatures above 130 °C, which accumulates for around 400 h per year with a maximum temperature of slightly above 240 °C. In contrast, the stagnation temperatures of the HP collector are switched to the 120 – 130 °C interval, since its maximum temperature is 125 °C. This equals a reduction of the maximum occurring temperature of 115 K. If this simulation is performed with TRNSYS type 832 (as discussed before), the frequency for temperatures above 130 °C would accumulate for around 600 h (which is higher than the frequency of the reference collector, since the controller shut-off is 95 °C for the HP collector). For the SFH100 building and other locations, the collector temperature distribution shows a similar pattern but with differing frequencies.

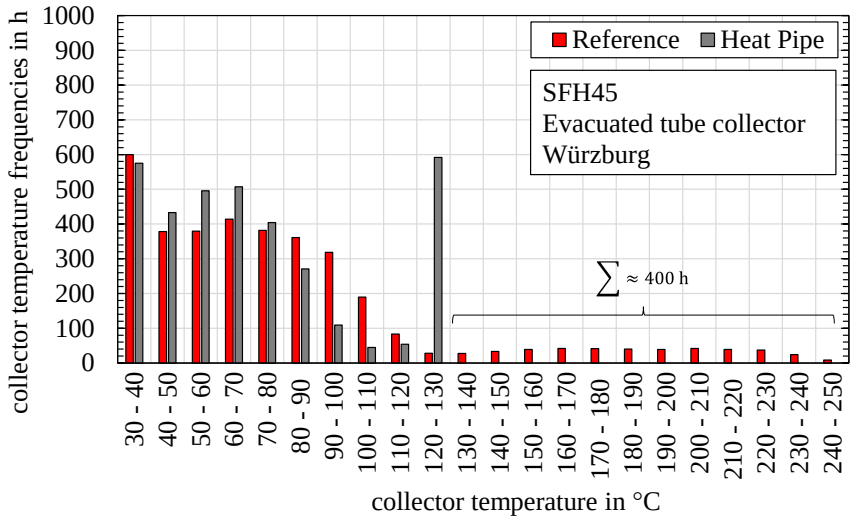

Fig. 9: Overall collector temperature frequencies for a simulation of the SFH45 building with 20 m² ETC collector gross area on the Würzburg site

Furthermore, we have compared the reference collector with the HP collector regarding the f_{save} value to evaluate the energetic impact of the temperature limitation. As it is shown inFig. 10, by using the flat-plate reference collector, the f_{save} value increases by 9.6 % for the SFH100 building at the Würzburg site. This result correlates very well with the 9% higher aperture area of the reference collector. For the SFH45 building, the increase is only 6.8 %, because stagnation and standstill effects of the collector occur more frequently, due to the lower space heating demand.

By using the evacuated tube reference collector, the increase in the f_{save} value is even lower (3.9 %), since higher collector temperatures are reached faster and thus the influence of stagnation and standstill effects is also larger.

In principle, an analogous behavior can be observed for the Athens site, but at a lower level of increase.

In general, the simulation of the Task32 buildings show similar results to our monitored demonstration systems (ETC less influence than FPC), but can extend this investigation to include other location. Especially for a location with high solar incidence (e.g. Athen), the energetic impact of the HP collector is small while at the same time, a temperature limitation is accomplished that can fully prevent stagnation.

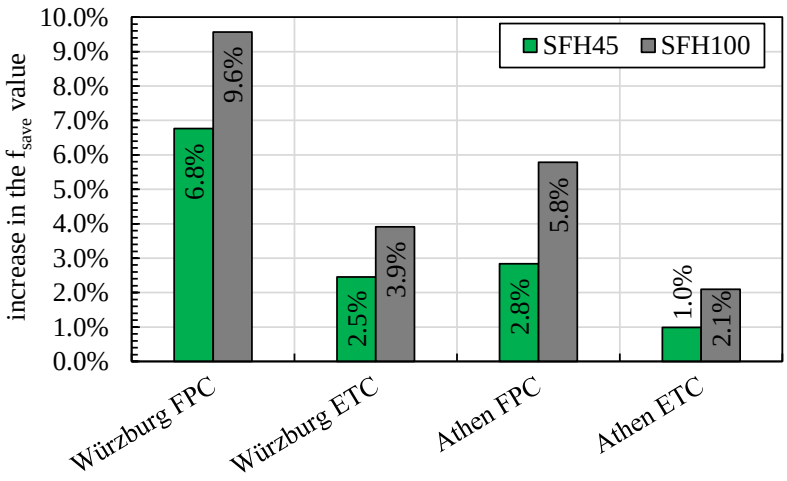

Fig. 10: Increase in the f_{save} value by replacing the temperature limiting HP collector with the direct-flow reference collector without temperature limitation

4. Conclusion

We simulated four solar thermal demonstration plants with temperature limiting heat pipe collectors (HP) in the TRNSYS simulation environment. For this purpose, the existing TRNSYS type 832 was adapted regarding the heat pipe based temperature limitation and validated on the basis of measurement data from the demonstration plants. Measured boundary conditions (radiation, inlet temperature, mass flow and other environmental conditions) were read into the model and the simulated collector performance was compared with the measured one. The heat pipe limitation is well reproduced, only in the kink point region there are small deviations, which are caused by the ideal model description and small uncertainties in the HP collector design. For an evaluation period of one month (June 2021), the deviation does not exceed 5 %.

After the model validation, we performed annual simulations with synthetic weather data and energy consumptions in TRNSYS. The aim of this simulation was to analyze the behavior of the systems when using different collectors (temperature-limited heat pipe collectors as well as direct-flow reference collectors). We evaluated the quality of the simulation based on the comparison between simulation and measurement. The resulting deviations increase with the complexity of the overall system, but are within a satisfactory range, considering the occurring measurement accuracy.

Based on these models, different parameter variations were performed and energetically evaluated. The replacement of the temperature-limiting heat pipe collector with a direct-flow reference collector was presented. For the two system configurations we report different results. In the flat-plate collector system presented, the use of the reference collector leads to an increase in conventional energy savings (f_{save}) of about 15 %. The reason for this, however, is not the shut-off behavior of the heat pipe, but rather its smaller aperture area of approx. 9 % due to the design, as well as the higher heat resistances in connection with the use of heat pipes. For the evacuated tube collector system, the f_{save} value increases by only 1.1 % when a direct-flow reference collector is used.

The simulations were also performed with the TRNSYS collector type 832 with the same collector parameters but without the heat pipe temperature limitation. The influence onto the solar yield is neglectable small (for the investigated systems) but high stagnation loads are simulated. Thus, TRNSYS type 832 could also be used for the simulation of the investigated systems without making any major errors regarding the solar yield but to correctly simulate the temperature limiting heat pipe effect, TRNSYS type 839 is needed.

Finally, two representative single-family buildings (SFH45 and SFH100), which were defined in the IEA Task 32, were simulated with both of the collectors. These simulations report similar results to those obtained during the simulation of the demonstration systems and confirm the essential statements of our experimental investigations, especially with regard to the differences between HP collector and reference collector as well as the influence of the shut-off temperature on the annual yield. We showed, that for the Würzburg site a significant reduction of the stagnation load of 400 h can be achieved by using the HP collector. Thereby the maximum temperature was reduced by 115 K from 240 °C to 125 °C.

5. Acknowledgments

The project “Development and demonstration of innovative, stagnation safe solar thermal systems with heat-pipe collectors” (reference number 03ETW005A-C) on which underlying this publication is based, was funded by the state of Lower Saxony and the German Federal Ministry of Economy and Climate Action, following a decision of the German Parliament. The investigations were carried out in cooperation with the companies KBB Kollektorbau GmbH and AKOTEC Produktionsgesellschaft mbH.

The authors are grateful for this support. The responsibility for the content of this publication lies with the authors.

Literature Cited

Frank, E., Mauthner, F., Fischer, S., 2015. Overheating prevention and stagnation handling in solar process heat applications. IEA SHC Task 49.

Haller, M., 2014. TRNSYS Type 832 v5.10 „Dynamic Collector Model by Bengt Perers“ Updated Input-Output Reference. Rapperswil, Switzerland.

Harrison, S., Cruickshank, C. A., 2012. A review of strategies for the control of high temperature stagnation in solar collectors and systems. Energy Procedia 30, 793-804.

Heimrath, R., Haller, M., 2007. The Reference Heating System, the Template Solar System of Task 32.

Kizildag, D., Castro, J., Kessentini, H., Schillaci, E., Rigola, J., 2022. First test field performance of highly efficient flat plate solar collectors with transparent insulation and low-cost overheating protection. Solar Energy 236, 239-248.

Müller, S., Giovannetti, F., Reineke-Koch, R., Kastner, O., Hafner, B., 2019. Simulation study on the efficiency of thermochromic absorber coatings for solar thermal flat-plate collectors. Solar Energy 188, 865-874.

Remund, J., Müller, S., Schmutz, M., Graf, P. Meteonorm Version 8. EUPVSEC 2020 online conference 07. - 11. September 2020.

Schiebler, B., Jack, S., Dieckmann, H., Giovannetti, F., 2018. Experimental and theoretical investigations on temperature limitation in solar thermal collectors with heat pipes: Effect of superheating on the maximum temperature. Solar Energy 171, 271-278.

Schiebler, B., Köhler, J., Wagner, L., Jensen, J., Giovannetti, F., 2022. Heat Pipe Collectors with Overheating Prevention in a Cost-Optimized System Concept: Monitoring of System Performance and Stagnation Loads under Real Conditions. EuroSun Conference, Kassel, Germany, 25-29 September (in press).

Schiebler, B., Weiland, F., Giovannetti, F., Kastner, O., Jack, S., 2019. Improved Flat Plate Collector with Heat Pipes for Overheating Prevention in Solar Thermal Systems. ISES Solar World Congress 2019/IEA SHC International Conference on Solar Heating and Cooling for Buildings and Industry 2019, Santiago, Chile, 3- 8 November.

Solar Keymark, 2019. Flat Plate collector KBB K420-DH: License number 011 - 7S323 F.

Solar Keymark, 2021. Evacuated Tube Collector ELCO Auron DF: Licence number 011-7S2979 R.

Streicher, W., 2003. Report on Solar Combisystems Modelled in Task 26 (System Description, Modelling, Sensitivity, optimisation): A technical report of Subtask C.

Valentin Software, 2022. T*SOL - The design and simulation software for solar thermal systems. Accessed Jul 26, 2022. https://valentin-software.com/en/products/tsol/.

Weiss, W., Spörk-Dür, M., 2022. Solar Heat Worldwide: Global Market Development Global Market Development and Trends 2021 Detailed Market Figures 2020. Gleisdorf, Austria.

Appendix

Tab. 3: Used collector parameters for the temperature limiting HP collector and the reference collector without temperature limitation for both the FPC and the ETC

		Flat-Plate (FPC)		Evacuated tube (ETC)	
Parameter	**Unit**	**Heat Pipe (HP)**	**Reference (Ref)**	**Heat Pipe (HP)**	**Reference (Ref)**
-	-	Measurement	011-7S323F	Measurement	011-7S2979 R
η_0	-	0.748	0.856	0.72	0.772
K_{diff}	-	0.870	0.870	0.920	0.88
a_1	W m^{-2} K^{-1}	3.940	3.710	1.9	1.403
a_2	W m^{-2} K^{-2}	0.0136	0.016	0.005	0.011
U_{int}	W m^{-2} K^{-1}	21	67	16	127
c_{abs}	J m^{-2} K^{-1}	4900	3179	1590	932
c_{fluid}	J m^{-2} K^{-1}	1350	2657	3160	5397
m_{Stag}	W m^{-2} K^{-1}	-13.0	-	-11.5	
T_{max}	°C	110 / 125 / 160	210	110/ 125 / 160	280
$A_{aperture}$	m²	2.12	2.3	1.01	1.01
A_{gross}	m²	2.51	2.51	1.61	1.61

Tab. 4: Used symbols and their quantities

Quantity	Symbol	Unit	Quantity	Symbol	Unit
area	A	m^2	auxiliary energy needed without the use of a solar thermal collector	$Q_{aux,without\ ST}$	kWh
linear heat loss coefficient	a_1	W m^{-2} K^{-1}	solar thermal yield	Q_{sol}	kWh
quadratic heat loss coefficient	a_2	W m^{-2} K^{-2}	specific solar thermal yield	q_{sol}	kWh m^{-2}
collector specific heat capacity without fluid	c_{abs}	J m^{-2} K^{-1}	solar fraction	sf	%
collector fluid specific heat capacity	c_{fluid}	J m^{-2} K^{-1}	internal heat transfer coefficient	U_{int}	W m^{-2} K^{-1}
solar irradiation	E	kW h m^{-2}	Volume	V	m³
saved auxiliary energy by the use of a solar thermal system	f_{save}	%	inclination angle (0° = horizontal)	α	°
incidence angle modifier for diffuse radiation	K_{diff}	-	zero-loss coefficient	η_0	-
slope of heat pipe power shut-off	m_{stag}	W m^{-2} K^{-1}	temperature	ϑ	°C
auxiliary energy needed in a solar thermal system	Q_{aux}	kWh			

Data-Based Modeling of High-Resolution Household Load Profiles

Harald Kirchsteiger and Lukas Gaisberger

ASIC Energy Research, University of Applied Sciences Upper Austria, Wels, Austria

Abstract

A novel method to generate synthetic household load profiles with a sample time of 5 minutes is presented. The method is entirely based on a dataset of measured electricity consumption over 5 consecutive years of 115 dwellings and does not require any other type of information such as household appliances in use or surveys on inhabitants' daily activities. It is shown that the collection of all synthesized signals resembles a typical seasonal variation as observed in the measurement data. At the same time, the individual load signals differ significantly from each other and therefore enable a realistic dispersion of a residential area. None of the synthesized signals is present as such in the measurement data, but all of them lie within the variability observed. A variety of different load signals of variable length can be generated which makes the method particularly interesting for large scale simulations of energy systems including large residential areas.

Keywords: load profile generator, synthetic load profile, smart grid, grid simulation

1. Introduction

Model-based development methods are state of the art in many engineering disciplines, especially also in power- and solar energy systems. Detailed mathematical models of various components in modern renewable energy systems enable sophisticated planning, design, and operation of future multi-energy grids (Martínez Ceseña et al. 2020). The significance of simulation results not only depends on the accuracy of the models, but also to a large extent on the numerical data used to feed the simulation. In this paper, the focus is on power- and energy flow simulation models for medium- to large geographic regions involving many individual consumers.

One particular requirement in such a situation is to feed the simulation with realistic electricity consumption data of individual households. For some cases, aggregating the load of a region to a single load profile (Meier et al. 1999) is a reasonable choice, for example when the interest lies in the characteristics of the transmission system. In other cases, load profiles of individual facilities have to be considered, for example when analyzing the load flow at lower grid voltage levels such as the 400V lines in Europe. This is getting even more important against the background of increasing shares of distributed solar generators at individual households, associated electricity storage devices and new consumer loads such as electric vehicles since the load variability increases (Schinke and Hirsch 2019).

Although the availability of measured individual household load profiles has kept increasing over the years, there is a need for synthetic load profile generators, which are able to reproduce realistic, original load traces in large numbers. Furthermore, a strong requirement is also the temporal resolution of the data. Only fast enough sampling rates enable the accurate consideration of energy management systems (Kirchsteiger and Steinmaurer 2020). In this paper, an algorithm to generate synthetic load profiles with a 5-minute sample time will be presented.

The problem of synthetic load data generation was considered in the literature before. Richardson et al. (2010) describe an algorithm to generate active and reactive electrical load data with a 1-minute sample time. The method relies on modeling the activities of occupants which are linked to specific appliances. Those activities, for example cooking or ironing, were gathered as part of a survey, where participants were asked what they do for how long on a typical weekend-day and weekday. This type of information is frequently called time use data (TUD). The model was validated using measurement data from 22 dwellings.

In Baetens et al. (2012) a statistical model based on similar principles as in Richardson et al. (2010) was extended with thermal demands. The combined load model was used to represent 33 dwellings in the IEEE 34 radial distribution node test feeder, designed specifically to represent residential areas.

© 2022. The Authors. Published by International Solar Energy Society
Selection and/or peer review under responsibility of Scientific Committee
doi:10.18086/eurosun.2022.16.06 Available at http://proceedings.ises.org

In Good et al. (2015), a demand-driven load model for both electrical and thermal demands is constructed with the aim to correctly represent the diversity observed in real dwellings and the coincidence observed within groups of buildings at the same time. Also in this work, the modeling of the electrical load relies in parts on the work of Richardson et al. (2010). For the thermal loads, the electrical analogy of R-C type of networks is used.

In Yamaguchi et al. (2019) various known approaches from literature for load generation were reviewed, re-implemented and compared against each other. A categorization of algorithms is provided, including the category of "empirical data-based time-dependent switch-on probability models". Three other categories identified all rely on TUD.

Lombardi et al. (2019) propose a TUD based method specifically to generate load profiles of remote areas. The model is available as open-source program coded in Python.

Pflugradt and Muntwyler (2017) describe an approach to load modeling which depends on first modeling the individual psychological desires of inhabitants, for example hunger, sleepiness, entertainment. This in turn relates to activities which the persons consider to fulfill their desires, such as eat, cook a meal, sleep, take a nap, or watch TV. The method does not rely on data and follows a truly bottom-up approach. The model is made freely available by the authors.

In Paatero and Lund (2006) datasets from 702 dwellings over 1 year and 1082 dwellings over 143 days were utilized to construct new profiles on an hourly basis. The synthesized data embeds a seasonal, hourly and social variability factor which are all derived from the datasets.

Gruber et al. (2014) calculate load profiles based on a wide range of individual household appliances and utilizing a probabilistic approach. Each appliance is assigned a specific load pattern, the synthesized data has a sample time of 15 minutes.

To conclude on the literature research, most load data models follow a so-called bottom-up approach where modeling starts by defining the individual appliances in the houses and daily patterns of the inhabitants. Those choices are typically supported by large-scale public surveys where persons are asked to note which appliance they are using at which time of the day. Overall, a rather large amount of additional information is required to parameterize the models. Moreover, the surveys typically only reflect a fragment of the whole variety in usage of home appliances. Only few methods such as Paatero and Lund (2006) are known where bottom-up models are also making use of measurement data (household load data timeseries), which decreases the amount of additional information required.

The contribution and novelty of the present paper is as follows. We are presenting a novel method to synthesize individual household electrical load data with a sample time of 5 minutes, which is a finer resolution than known methods from the literature, and a requirement for accurate optimization-based load management algorithms. The proposed method works without the use of any other additional information except a collection of historic load data profiles. Specifically, no information on household appliances and inhabitants' behavior is required. The individual profiles generated have a variation as observed in the training dataset. When large amounts of synthesized profiles are combined, the sum resembles the typical seasonal variability observed in real data. A variety of dwelling types in the training dataset, for example with and without photovoltaic system, battery storage, heat pump heating, ensures a realistic dispersion of synthesized data.

2. Problem Formulation

The problem considered is to develop an algorithm, which allows to construct new, original electrical load profiles with a high sample time. The new profiles should be different than all profiles in the training dataset, but at the same time, their combination has to agree with the combined training dataset. The problem is separated into two subproblems: (1) Data analysis: Find and extract the relevant statistical properties from the training dataset. In this step, the total daily energy (TDE) consumed is considered, which is known to exhibit a seasonal variation that has to be captured by the algorithm. (2) Data synthesis: use the discovered statistical properties to synthesize new data of household load consumption TDE. As part of this step, the new TDE profiles have to be merged with high resolution data to obtain the required 5 minute sample time signals.

3. Measurement Data

The data used in the present paper has been collected over five years by owners of photovoltaic systems with battery storage in the region of Upper Austria in the course of the accompanying research of a funding programme. The measurement data was received from the hybrid inverters which, in order to control the battery power in accordance with the consumption, are always equipped with an energy meter. This metering device is installed directly next to the meter of the power supply company such that both measure precisely the same values. Most inverters provide the power values in mean values with a temporal resolution of 5 minutes, however up to 15 minutes resolution was accepted. The various power measurement channels are shown in Fig. 1, though only P_L has been used in this analysis. The size of the households differed between two-person households to farmhouses where three generations are living, however single-family homes presented the largest proportion. The age and number of residents was diverse as well. The range varied from singles and young couples over families with 3 generations to older couples. In total, 191 houses monitored over 5 years resulted in 348.766 available days of load traces for analysis.

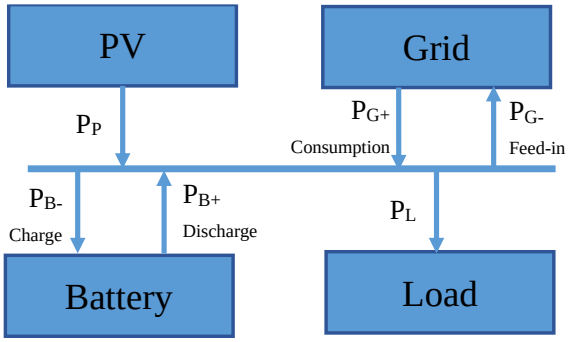

Fig. 1: Measurement data configuration

During this extensive period of measurement some issues regarding data quality arose. Aside from simply missing values, false values represented a major concern. Fortunately, most of the false values could be traced back to miscalculations in the raw data obtained from some inverters. These errors appear only in a limited time range. Datasets with more than 20 % of missing or false data have been removed from the evaluations, resulting in a dataset containing 115 households for further analysis as described below.

4. Methods

In this section the analysis of the total daily energy (TDE) profiles to derive at the characteristic values required for synthesis of new TDE profiles is described. The new TDE profiles are then used to construct high resolution load profiles.

4.1 Analysis of TDE profiles

From the dataset as described in chapter 3, $n_h = 115$ power consumption traces with a sample time of $\Delta T = 5$ minutes are available which will be denoted with $P(h,k)$ with the discrete time index $k = n\,\Delta T, n \in \mathbb{N}$ and h denoting the household index, $h = \{1,2,\ldots n_h\}$. From this, the TDE is derived for every household by simply summing up $P(h,k)$ for single days. The TDE is denoted as $E_{TD}(h,d)$ where d is again a discrete time index and represents the day of the year, $d = 1,2,n_d$. (For simplicity of exposition we are assuming only years with 365 days, i.e., without leap days.) The TDE signals are then normalized by subtracting the mean and dividing by the standard deviation to arrive at zero mean, unit variance signals denoted with $E_{TDN}(h,d)$. From those normalized signals, a seasonal variability signal s_V is derived by taking the mean value across all years and households, and applying a moving average filter of window length 40. This length was empirically found to result in a good trade-off between sufficient data smoothing and preserving the main characteristics in the data. The seasonal variability s_V is shown graphically in Fig. 2: the bold line represents the filtered signal while the thinner line is the mean value without any filtering.

The main algorithm for TDE characterization performs the following operations for every household h separately:

- Compute the individual deviation from a household from the seasonal variability, $e_1 = s_V - E_{TDN}$, and take the average $\bar{e}_1$ with respect to all available years of data.
- Remove the outliers from $\bar{e}_1$, based on the 25th (q_{25}) and 75th (q_{75}) quantile. A datapoint is classified as outlier if it is larger than $q_{75} + 1.5(q_{75} - q_{25})$ or smaller than $q_{25} - 1.5(q_{75} - q_{25})$. The signal without outliers is called $\bar{e}_{1OR}$.
- Filter the signal $\bar{e}_{1OR}$with a moving average filter of window length 14 to obtain $\bar{e}_{1ORF}$.
- Compute the second level deviation from the typical household seasonal deviation, $e_2 = \bar{e}_{1ORF} - \bar{e}_{1OR}$
- Fit a normal distribution $\mathcal{N}(\mu, \sigma)$ to the signal e_2 to obtain the two characteristic parameters μ (expectation) and σ (standard variation).

The moving average filter length was again found empirically to provide a reasonable data smoothing. Note that by performing the computations for all households, n_h different values $\mu(h)$ and $\sigma(h)$ are obtained. In a final step, two Burr distributions are fitted to those data. The probability density function (PDF) of the Burr distribution is given by (eq. 1) and depends on the three characteristic parameters α, c, κ.

$$f_B(x) = \frac{\frac{\kappa\, c}{\alpha}\left(\frac{x}{\alpha}\right)^{c-1}}{\left(1+\left(\frac{x}{\alpha}\right)^{c}\right)^{\kappa+1}} \qquad \text{(eq. 1)}$$

As a result of the TDE profile analysis, two sets of those characteristic values were obtained, for the distribution $f_B(\mu)$ of $\mu(h)$ and $f_B(\sigma)$ of $\sigma(h)$. The main reason for choosing a Burr distribution was that it provides the closest fit to the data among all the tested PDFs available (The Mathworks Inc., 2021), see also Fig. 6.

4.2 Synthesis of new TDE profiles

The algorithm for synthesis of a new TDE profile follows the steps listed below

- Draw a pair of random values (μ^*, σ^*) from the distribution $f_B(\mu)$ and from $f_B(\sigma)$
- Construct a normal distribution $\mathcal{N}(\mu^*, \sigma^*)$ and draw a random sequence r of length 365 from it. This sequence is a substitute for e_2 with embedded statistical properties of the training dataset.
- Synthesize a new TDE sequence $E^S_{TDN} = s_V - \bar{e}_{1ORF}(h^*) - r$ by choosing a deviation $\bar{e}_{1ORF}$ from a specific (random) household $h = h^*$ as seed.
- Undo the normalization by multiplying with a standard deviation within the limits as observed in $E_{TD}(h^*, d)$ and adding a mean value within the limits as observed in $E_{TD}(h^*, d)$ to obtain the sequence E^S_{TD}.

When this algorithm is used multiple times, an entirely new dataset of individual TDE sequences is constructed, from which in turn a seasonal variability can be computed in the same was as described above for the initial measurement dataset. The seasonal variability of such a new dataset is shown in Fig. 2 where again the bold red line is the result of a moving average filter applied to the thin red line.

4.3 Synthesis of new high resolution load profiles

A synthesized TDE signal E^S_{TD} from the algorithm in section 4.2 describes the total daily energy consumption for a (virtually constructed) household, from which power signals with a sample time ΔT will be constructed next. To do so, for every single day $d = d^*$ in the sequence E^S_{TD}, a day $d = d'$ with a similar TDE is looked up in the original load dataset $E(h^*, d)$. The variable h^* denotes the seed as used in the algorithm in section 4.2. The check for similarity is done by searching for similar TDE values within a ± 5 % interval and randomly choosing one of the candidates within this interval. In case the similarity search is not successful, the closest match is chosen and the data scaled to obtain the desired TDE. Then, the consumption profile of that day d' is used as power consumption on the day d^* in the new sequence.

5. Results and Discussion

As described in the Methods section, a seasonal variability s_V is computed for the original measurement dataset and for a newly generated synthetic dataset. The two profiles are compared against each other in Fig. 2 where the bold lines are filtered versions of the tinner lines. The results shown in the figure were constructed with $n_h = 115$ households for both datasets. In general, a very good agreement between the two profiles is observed indicating that the synthesized load profiles resemble the statistical properties of the measurement dataset. It is of interest to note that the signals are slightly higher at the end of December compared to the beginning of January which reflects the general trend of increased electricity consumption of the society as a whole.

As far as the individual TDE profiles are concerned, Fig. 3 shows two examples of E_{TD} for two different houses ($h = 1$ for the top and $h = 35$ for the bottom panel) from the measurement dataset on the left. On the right side, two synthetic profiles E_{TD}^{S} based on the very same houses are shown. That is, in the 3rd step of the synthesis algorithm stated above, h^* is 1 in the top panel and 35 in the bottom panel. Even if both signals (top left and top right) are based on the same sequence $\bar{e}_{1ORF}(1)$ they are significantly different from each other as can be seen in the figure. The same statement can be made for the bottom two sub-figures based on $\bar{e}_{1ORF}(35)$ and in fact for all $n_h = 115$ dwellings considered.

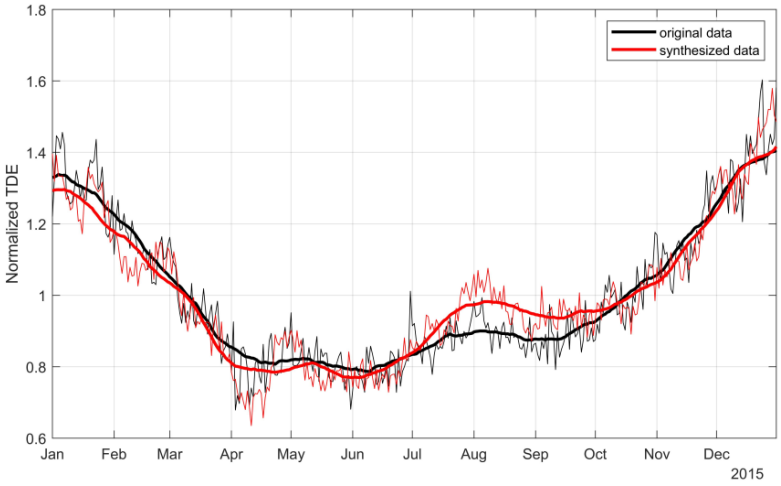

Fig. 2: Seasonal variability of the total daily energy for the measured data (black) and synthesized data (red)

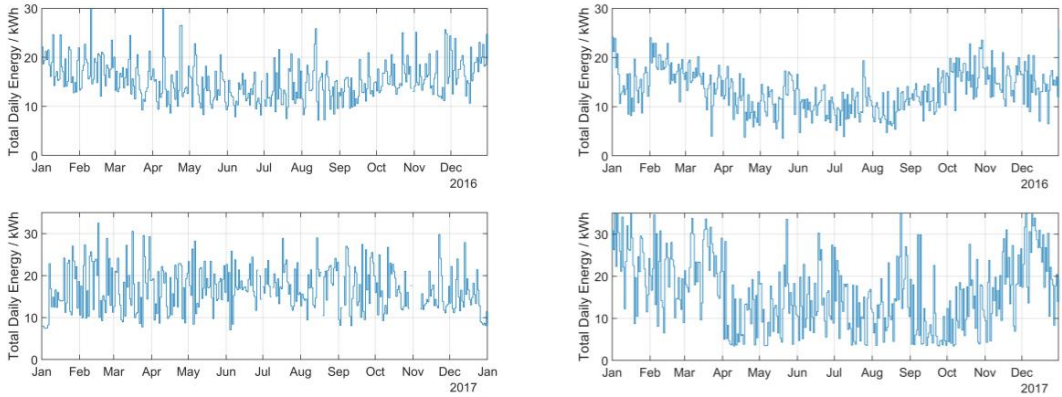

Fig. 3: TDE profiles of two dwellings (measured, left) and synthetic profiles (right)

In Fig. 4, two high resolution electrical load profiles are shown over a timespan of one year. While the top panel displays measured data, the bottom panel shows the result when applying the synthesis strategy described in section 4.3. Again, both signals rely on the same seed $\bar{e}_{1ORF}(h)$. A closer look at the signals, focusing on the

month March in Fig. 5, reveals that the synthesized signal at the bottom follows a similar and realistic pattern of nighttime consumption and daytime peaks as the measured data.

To motivate the computations done in steps 3 and 4 of the analysis algorithm stated in section 4.1, consider first the graph shown in Fig. 6 on the left which displays the autocorrelation function of the second level deviations e_2 for the first 20 households. The general shape is close to a white noise random signal with a significant peak only at zero lag. This indicates that there is no more information to be extracted from the data and a probability density function can be fitted as done in step 5 of the algorithm. A detailed look at the autocorrelation functions reveals peaks at lags of 7, 14, and 21 which is in correspondence with the well-known fact of a weekly dependence of the load profiles. Those peaks are, however, below a threshold level of 0.2. The right graphic in Fig. 6 shows the histograms of the parameters μ and σ estimated in the final step of the analysis algorithm. The red lines are showing the PDF of the Burr distribution fitted to the histograms. The PDF $f_B(\mu)$ is given by the parameters $\alpha = 0.5, c = 280,\ \kappa = 1.36$ and the PDF $f_B(\sigma)$ by $\alpha = 0.33, c = 12.9,\ \kappa = 0.48$.

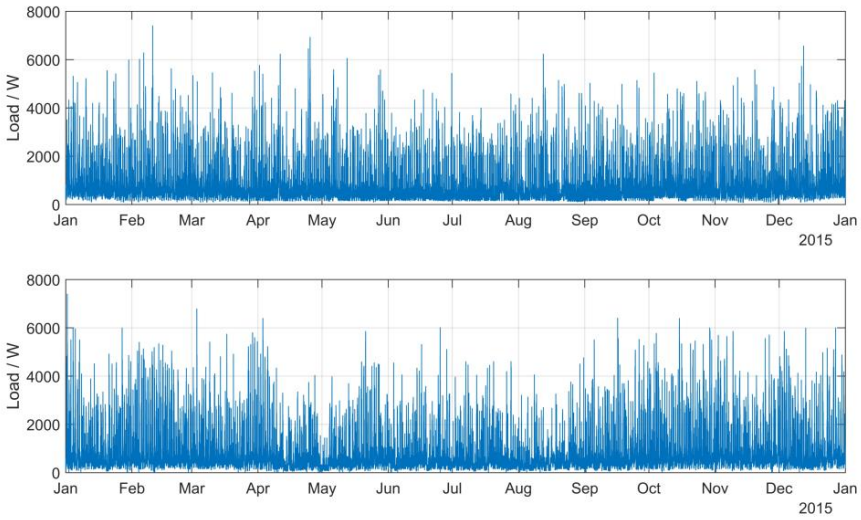

Fig. 4: Power signals $P(h = 1, k)$ (measured, top) and synthesized power signal (bottom)

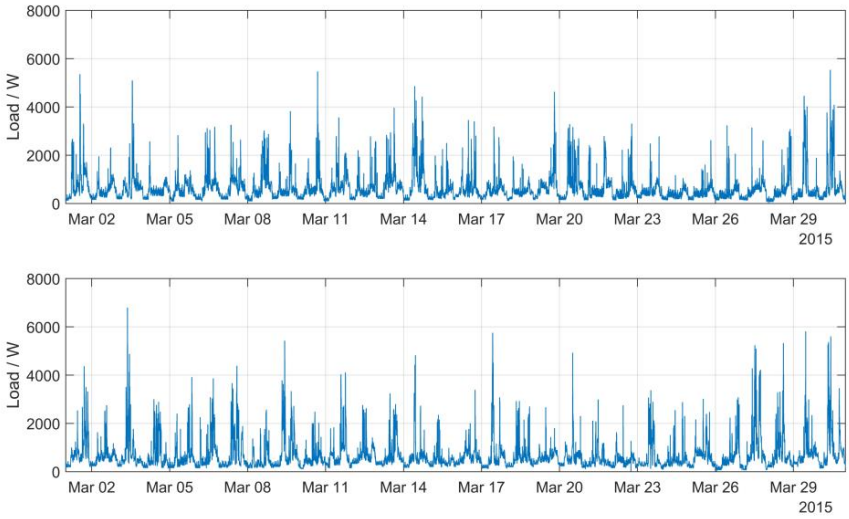

Fig. 5: Detail of Fig. 4 focusing on March: measurement (top), synthesized data (bottom)

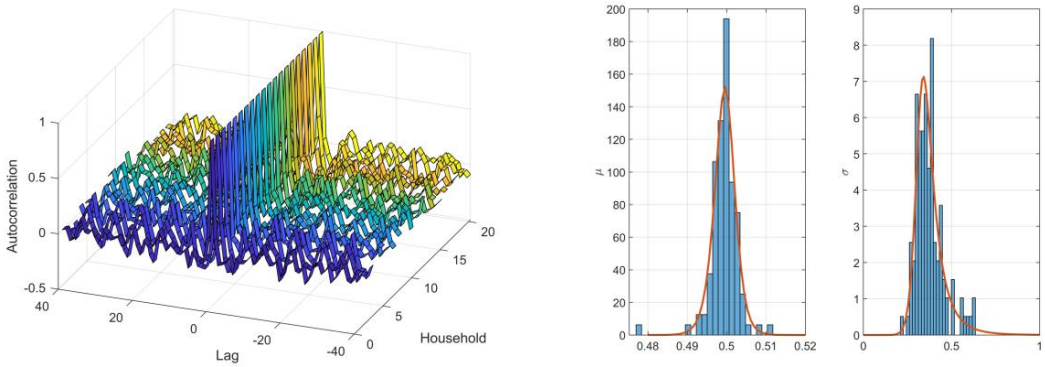

Fig. 6: Second level deviations e_2 (left) and fitted Burr distributions on $\mu(h)$ and $\sigma(h)$ (right)

6. Conclusion

A method to generate synthetic load profiles with a sample time of 5 minutes was presented. The method relies on a measurement dataset of 115 households over 5 years. It was shown that the synthesized datafiles as a whole possess a comparable seasonal variability as the original data while the individual traces are sufficiently diverse. Also on a smaller timescale, the synthesized data has similar patterns as the measurement data, for example day-night consumption changes.

The proposed method for generation of load profiles is well suited for defining individual load profiles of large residential areas in large-scale energy system simulation models. It is also well suited to generate load profiles over an extended time horizon of multiple years since the statistically learned seasonal variation inherently grows over time reflecting the general rise in energy consumption.

The generated load data are, however, not particularly suited for training load prediction algorithms. This is because as stated in section 4.3, on a short timeframe, the new and the original signal are identical, although it is a-priori unknown at which point in time this will be the case. A prediction algorithm could learn the patterns of this short timeframes in the data and correctly forecast them when they are recognized. Such a prediction would be impossible in a real-time environment using measurement data.

7. Acknowledgments

This project is financed by research subsidies granted by the government of Upper Austria. This project is funded by EU-European Regional Development Fund (ERDF) and Federal Province of Upper Austria Investments in Growth and Jobs (IGJ) under the research grant number WI-2020-701794/12-Cz. The work was also supported by the government of Upper Austria in the project Methodenentwicklung zur Energieflussoptimierung (Development of Methods for Optimization of Energy Flows)". Research Grant Wi-2017-450841/17.

8. References

Baetens, R., De Coninck, R., Van Roy, J., Verbruggen, B., Driesen, J., Helsen, L., Saelens, D., 2012. Assessing electrical bottlenecks at feeder level for residential net zero-energy buildings by integrated system simulation. Applied Energy. Vol. 96, pp. 193-210. https://doi.org/10.1016/j.apenergy.2011.12.098

Good, N., Zhang, L., Navarro-Espinosa, A., Mancarella, P., 2015. High Resolution Modelling of Multi-Energy Domestic Demand Profiles. Applied Energy. Vol. 137, pp. 193-210. https://doi.org/10.1016/j.apenergy.2014.10.028

Gruber J.K., Jahromizadeh, S., Prodanović, M., Rakočević, V., 2014. Application-oriented modelling of domestic energy demand. Electrical Power and Energy Systems. Vol. 61, pp. 656-664. https://doi.org/10.1016/j.ijepes.2014.04.008

Kirchsteiger H., Steinmaurer G., 2020. Optimal Energy Management of Residential Solar PV with Battery

Storage: Effects of Fast Load and Generation Transients. *7th International Conference on Control, Decision and Information Technologies*, Prague, 29 June – 02 July. https://doi.org/10.1109/CoDIT49905.2020.9263853

Lombardi, F., Balderrama, S., Quoilin, S., Colombo, E., 2019. Generating High-Resolution Multi-Energy Load Profiles for Remote Areas with an Open-Source Stochastic Model. Energy. Vol. 177, pp. 433-444. https://doi.org/10.1016/j.energy.2019.04.097

The Mathworks Inc., Statistics and Machine Learning Toolbox, Natick, Massachusetts, United States, 2021. Available at: https://mathworks.com/products/statistics.html

Martínez Ceseña, E.A., Loukarakis, E., Good, N., Mancarella, P., 2020. Integrated Electricity-Heat-Gas Systems: Techno-Economic Modeling, Optimization, and Application to Multienergy Districts. Proceedings of the IEEE. Vol. 108, no.9, pp.1392-1410. https://doi.org/10.1109/JPROC.2020.2989382

Meier, H., Fünfgeld, C., Adam, T., Schieferdecker, B., 1999. Repräsentative VDEW-Lastprofile. VDEW Materialien M-32/99.

Paatero, J.V., Lund P.D., 2006. A model for generating household electricity load profiles. International Journal of Energy Research. Vol. 30, no. 5, pp. 273-290. https://doi.org/10.1002/er.1136

Pflugradt, N., Muntwyler, U., 2017. Synthesizing residential load profiles using behavior simulation. Energy Procedia. Vol. 122, pp. 655-660. https://doi.org/10.1016/j.egypro.2017.07.365

Richardson, I., Thomson, M., Infield, D., Clifford, C., 2010. Domestic electricity use: A high-resolution energy demand model. Energy and Buildings. Vol. 42, no. 10, pp. 1878-1887. https://doi.org/10.1016/j.enbuild.2010.05.023

Schinke A., Hirsch H., 2019. Impact of Electric Vehicle Charging and Photovoltaic Generation on Distribution System Voltage Volatility. *2019 IEEE Power & Energy Society General Meeting*, Atlanta, 04-08 Aug. https://doi.org/10.1109/PESGM40551.2019.8973901

Yamaguchi, Y., Yilmaz, S., Prakash, N., Firth, S.K., Shimoda, Y., 2019. A cross analysis of existing methods for modelling household appliance use. Journal of Building Performance Simulation. Vol. 12, no. 2, pp. 160-179. https://doi.org/10.1080/19401493.2018.1497087

Building Information Modeling for solar energy systems

Wael Mandow[1], Fabian Edenhofner[2], Theresa Maier[3] and Federico Giovannetti[1]

[1]Institute for Solar Energy Research in Hamelin (ISFH), Hameln (Germany)

[2]ICoM, RWTH Aachen University, Aachen (Germany)

[3]Albert.ing GmbH, Frankfurt am Main (Germany)

Abstract

Building Information Modeling (BIM) is a promising method for energy analysis applications. Early and integral planning of a building's energy system with the BIM method results in many advantages with regard to the use of renewable energy sources such as solar energy because of available rich 3D building model. However, there are many limitations in using BIM for energy analysis. Almost all known stand-alone simulation programs are not compatible with the established BIM-based data formats. In addition, the available BIM-based object models of solar energy components like photovoltaic (PV) and solar thermal (ST) are neither standardly nor completely parameterized. For photovoltaic thermal systems (PVT), they make no contribution at all. Furthermore, the BIM method has so far mainly been used for the planning process. This paper presents two approaches for the use of the BIM method for the simulation and monitoring of PVT-systems. First of all, a parameterization for a PVT-system was developed based on several existing standards and approaches. In order to transfer the necessary parameters from the BIM-model to the simulation program TRNSYS automatically, a python intermediate tool was developed and validated. In order to use the BIM method in the operation phase for monitoring a facade integrated PVT-system, a BIM-model of an existing real laboratory with its PVT-facade was developed. It was further used to set up a mockup digital twin for monitoring in a Common Data Environment (CDE). This enables the display of thermal as well as electrical yield and the comparison with the simulation data, facilitating the identification of possible malfunctions and ensuring efficient system operation.

Keywords: BIM, IFC, PV thermal, TRNSYS, Digitalization, Monitoring

1. Introduction

Building Information Modeling (BIM) has become established as one of the generic terms for digitization in the value chain of designing, building and operating structures. With the BIM method, all lifecycle-relevant information of a building can be recorded, managed and exchanged in a centralized, model-based, digital and consistent manner for optimal transparent communication between the participants (architects, planners, assemblers, operators, etc.) involved in the various construction project phases (see Fig 1).

All building-related data can be stored in a Common Data Environment (CDE) and are thus accessible to all project participants at any time. Computer-based filtering and evaluation combined with the aspect of visualization helps in focusing and guiding.

Since BIM tends to be used in the planning phase nowadays, there is further potential to explore its application during the operation phase. Especially in the field of solar energy, the application of the BIM method is currently still a research topic. With reference to the operation phase this method is very promising.

With BIM for example an early integral design of the building with its energy supply system is possible in the planning phase. The information-rich 3D modeling of a building and its surroundings (shading) is also beneficial in terms of solar energy yield prediction. Thus, renewable energy and solar energy in particular can be better and thus more often taken into consideration in building design. Some companies like BIMobject (BIMobject 2021) or Bimetica (Bimetica 2021), the National BIM Library (NBS 2021) as well as some component manufacturers already provide BIM objects (3D model objects) with extensive parameters including aesthetic properties for their products, such as PV modules and ST collectors.

© 2022. The Authors. Published by International Solar Energy Society
Selection and/or peer review under responsibility of Scientific Committee
doi:10.18086/eurosun.2022.16.07 Available at http://proceedings.ises.org



Fig 1: Building Information Modeling (BIM), the networking of processes and of project participants

In addition, useful manufacturer information such as warranty information and maintenance instructions can be integrated into the BIM objects and thus increase the attractiveness of the products and contribute to their better operation. As part of a BIM-based monitoring approach for the operation of solar technologies, actual measured data can be compared with set data. The set data may result somewhat from the design or manufacturer specifications. If there is an unexpected deviation, the simulation data will be used for comparison. In the event of a deviation which is higher than a predefined limit in monitoring data, the malfunction (for example a defective module or collector) can be identified at an early stage and, if necessary, a repair or replacement can be undertaken. In the event of a repair or a replacement the BIM-model will be updated to display the actual as-is state.

In the event of the dismantling of a solar system, the creation of cost and time schedules can be facilitated analogously to the installation thanks to the BIM-based approach. Necessary information on the recyclability of the dismantled components can be stored in the BIM-model of the construction project. Basically, all lifecycle-relevant information of a construction project can be stored in a BIM-model.

For the data exchange of BIM-models a variety of possibilities exists. Most prominent are the Industry Foundation Classes (IFC), which allow an open data exchange. IFC is a vendor-neutral open source data format established worldwide as an ISO standard, which fundamentally enables collaboration in BIM projects between several participants and thus between different software. This data schema has been developed by buildingSMART (buildingSMART 2021), the international competence network for the digital design, construction and operation of buildings. The main task of this non-profit organization is the further development and standardization of open information exchange in BIM projects and the definition and standardization of corresponding work processes. The current IFC Version is IFC 4 and was published under ISO 16739-1:2018. Even though IFC 4 is more extensive, the older IFC Version 2x3 is still heavily used in the construction industry. IFC enables the object-oriented description of a construction project. A single IFC object contains diverse information about the attributes, properties, geometry, relationships and interactions. Fig 2 shows the BIM-model of the real laboratory Danish Pavilion in the (BIMPV 2023) Project. Furthermore, the basic hierarchy in a building project in the IFC standard and a schematic representation of a PVT as an IFC object instance of the "IfcSolarDevice" class (IfcSolarDevice 2019) is shown together with an excerpt of possible information.

Another possibility for the exchange of BIM-Models is the open source data format gbXML, which was developed by Green Building specifically for simulation or analysis tools (Green Building). Green Building is a non-profit organization, which contributes to support architects, engineers and energy modelers in designing energy efficient buildings.

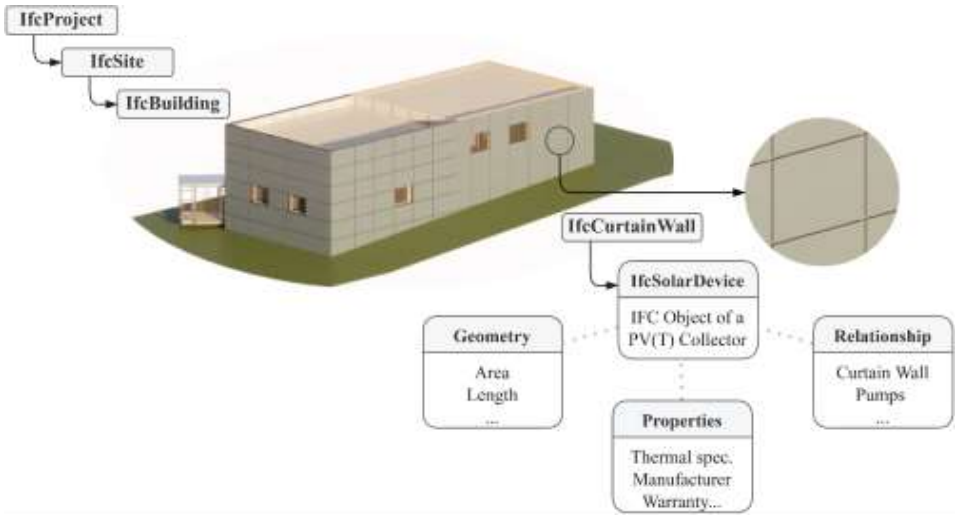

Fig 2: IFC model of the Danish Pavilion laboratory in Hanover in the BIMPV project with a schematic representation of an IFC object of a PVT collector

Designing an energy system for a building is costly and is usually postponed until the last phase of building design. The application of the BIM method supports the design of energy supply systems because the necessary data can be provided in a digital format in an early project stage. However, there are several challenges in this regard that still need to be addressed:

- The BIM objects generally available do not contain all the required data for energy simulations, especially for HVAC components properties such as thermophysical material properties (Cormier et al. 2011). Therefore, data extension via external files is required.
- Most available and usable standalone energy simulation software e.g. Polysun, TRNSYS, Matlab, Dymola, EnergyPlus and SIM VICUS are compatible neither with IFC nor with gbXML. Therefore, an (intermediate) tool must be used to connect a BIM model such as SketchUp (Soft 2021), OpenStudio, eveBIM (eveBIM 2021), etc.
- Data exchange through available intermediate tools (interfaces) is limited, e.g. for HVAC components and for thermal zone mapping (Cormier et al. 2011).
- New approaches and appropriate BIM-based object models are needed for innovative components, e.g., building-integrated (BI) solar technologies (PV, ST, and PVT).

In this study, a parametrization for an uncovered PVT was developed based on standards. Then the proposed IFC object model was built with the developed parametrization with FreeCAD. To transfer the necessary parameters from the BIM-model (IFC object model) into TRNSYS automatically, a python intermediate tool was developed and validated. To use the BIM method in the operation phase for monitoring a facade-integrated PVT, a BIM-model of a Danish Pavilion in Hanover was developed in the BIM authoring software Revit.

This paper is organized as follows: Section 2 gives a short review of the BIM data formats IFC and gbXML as well as the compatibility between the BIM-based data format and the building energy performance simulation software. Section 3 proposes a new parameterization for a PVT-IFC object model. Furthermore, a newly developed python intermediate tool is outlined between IFC and the simulation program TRNSYS. Moreover, a new case study is described using the BIM method in the operation stage of a PVT-facade. Resulting conclusions are drawn in the final section.

2. State of the art

In this section, the current status of the IFC and gbXML data exchange formats and the compatibility as well as the developed intermediate tools between the data exchange formats and energy simulation programs are presented. The Chapter concludes by presenting approaches for representing solar thermal collectors in BIM-based data formats.

2.1 BIM data formats IFC and gbXML

IFC and gbXML are open data schemas for describing building information models. Both are used internationally, but only the IFC format is defined as standard. While gbXML is mainly used for energy simulation, IFC is suitable for application over the life cycle of a construction project.
IFC is fundamentally more comprehensive and generically structured than gbXML (Maile et al. 2020). Regarding the use for energy simulation, a large number of properties (especially material properties or building object properties) are already defined in the IFC format (Hilaire et al. 2015). However, to date, the IFC schema does not support the mapping of all HVAC components, which is a major limitation for its use in energy simulation (El Asmi et al. 2015). It does not focus only on the energy domain in the main specification and does not directly define information exchange requirements specific to different project phases and between different actors and software applications (Maile et al. 2020). The latter weakness was recognized by buildingSMART, who developed the Model View Definitions (MVD) for this purpose (Maile et al. 2020). A MVD allows certain filter presets for IFC export of specific data from a BIM-model. The gbXML, on the other hand, is less complex and focuses on the characteristics of the building objects related to energy simulations. It allows easy inclusion of additional information for energy analysis and is fundamentally supported by many BIM, energy, and web-based tools (Maile et al. 2020). However, gbXML uses centerline theory when calculating building volume instead of using true 3D placement of space boundaries as is the case for IFC (Maile et al. 2020). This leads to errors in the volume calculation of a thermal zone or building. BuildingSMART and Green Building provide numerous IFC as well as gbXML classes (object models). For the representation of solar thermal collectors or PV modules there is an old class "IfcEnergyConversionDevice" in IFC 2x3 and a new class "IfcSolarDevice" in the IFC4 format (IfcSolarDevice 2019). In contrast, gbXML does not have a class for solar thermal collectors or PV modules.

2.2 BIM data formats and simulation programs

The buildingSMART website provides a list of all IFC-compatible software available on the market for a variety of architectural, engineering, and construction software. There are only two building energy performance simulation tools (BEPS) in the list: IDA ICE (version 4), developed by the Swedish company Equa Simulation, and RIUSKA (version 4.4.7), developed by the Finnish company Granlund Oy. These are IFC-compatible simulation software that support the automated import of building object geometries.

The basic model of a BIM-model is made in so-called BIM authoring software. Common commercial products are for example Autodesk Revit, ArchiCAD or SketchUp. For the direct modification and 3D visualization of an IFC object model, there are also a number of free open source software, e.g. the usBIMviewer+ software (ACCA 2021) from the Italian company ACCA Software and the 3D modeling software FreeCAD (FreeCAD 2022).

Tab. 1 shows the compatibility between IFC and gbXML data exchange formats with the most commonly used BEPS. Two main criteria are considered in the table:

- The possibility of reading/importing the IFC and gbXML data format.

- The possibility of storing/exporting the simulation results (outputs) in BIM format.

Furthermore, the possible need is specified for an additional intermediate tool for data transfer. The data read or stored back from IFC or gbXML files are geometry and specific HVAC data.

The French research center CSTB has recently developed the eveBIM (eveBIM 2021) tool. eveBIM can visualize and edit IFC files. CSTB has also developed an intermediate tool (plug-in) for eveBIM to connect it with the BEPS, TRNSYS and EnergyPlus. This intermediate tool allows both building geometric (thermal zones) and HVAC data to be transferred from a BIM model (IFC object model) to TRNSYS as well as EnergyPlus. However, this intermediate tool is currently no longer supported.

Moreover, there are many approaches in which the geometry was transferred from a BIM-model into TRNSYS using different intermediate tools such as SketchUp and IFC4javatoolbox, from the JAVA tool developer APSTEX (Apstex 2021). Additional tools as intermediate tools such as ArchiCAD were used between IFC files (geometry and HVAC data) and gbXML files (geometry data only) and EnergyPlus. The commercial and widely used energy performance simulation program Polysun has a BIM plug-in for importing an input file (importing load profiles in Excel format) from a data base connected to a CDE. However, Polysun is not compatible with either IFC or gbXML and, to date, does not have any intermediate tools (Vela Solaris 2021). An intermediate tool based on the Python library IfcOpenShell (Krijnen 2022) was developed for Modelica to transfer geometry and HVAC data from an IFC file. The open-source simulation program SIM VICUS, developed by the Institute of Building Climatology at the Technical University of Dresden, has an IFC plugin in the development phase. However, this is only used to transfer geometry data.

Tab. 1: Compatibility between BEPS and BIM data exchange formats IFC and gbXML

	TRNSYS	IDA ICE	EnergyPlus	Modelica	PolySun	SIM Vicus
Import IFC	Intermediate tool* Geometry & HVAC	Geometry	Intermediate tool* Geometry & HVAC	Intermediate tool *** Geometry & HVAC	-	Geometry (Development stage)
Import gbXML	-	-	Intermediate tool ** Geometry	-	-	-
Export IFC	-	Geometry	-	-	-	-
Export gbXML	-	-	-	-	-	-

*eveBIM **ArchiCAD ***Python tool

So far, only IDA ICE can store the simulation results back in an IFC file (e.g. for an optimization). For the gbXML format there is an intermediate tool just for EnergyPlus. However, a storage of the simulation results in gbXML format is not possible to date.

A review of the literature shows, that BIM-based design, installation, and operation of HVAC components can save time and money, however still have many limitations. Some of the existing limitations are summarized here:

- Some HVAC components, such as PV modules or ST collectors, do not have specific classes in the IFC2x3 or gbXML schema (Hilaire et al. 2015; Green Building). Certainly, there is an IFC object for PV as well as ST in IFC4.
- The available IFC as well as gbXML objects lack some required parameters and the description of the thermal zones of a building is not always possible (Andriamamonjy et al. 2018; Hilaire et al. 2015).
- Loss of information when exporting data via IFC format (Andriamamonjy et al. 2018).
- In multidisciplinary fields, as in the case of solar building envelopes, a clear definition of information categories (e.g., development stage or Level of Development (LOD)) should be adapted and standardized in the main phases of the process (BIPVBOOST 2019).
- The data transfer between BIM and BEPS is still limited especially for HVAC components.

2.3 BIM Method in PV and ST

The design and virtual optimization of technical components in BIM-based planning enables efficient and error-free actual construction and operation.

Few studies have been published on BIM-based energy simulation for technical systems and specifically for PV and ST. Different approaches on BIM-based solar collector (ST) models can be found in the literature.

The tool developed by Castro and Alvarado (2017) allows the integration of solar thermal systems by determining the thermal yield according to the roof pitch and orientation in the design phase of buildings. No information was given about the validation of the planning process. Robert et al. (2014) developed an interface between BIM, eveBIM and TRNSYS software and EnergyPlus. The approach developed could be used in BIM-based energy simulation for planning. In order to validate the approach developed, a building with a solar thermal system was represented as a BIM model and a derived IFC file was used as the input basis for the simulation.

Almost all recent studies were conceived for using the BIM method for the planning of the PV or ST.

3. BIM use cases: simulation and monitoring of PVT-systems

In the last two chapters different examples for the use of BIM-models for photovoltaic and solar thermal system simulations will be presented. The upcoming chapters introduce a BIM-based approach for the simulation and

monitoring of BIPV- and BIPVT-systems. The approach is currently under development as part of the BIMPV collaborative project. The BIMPV project tackles the lack of acceptance of BIPV(T)-systems through a lifecycle oriented use of BIM methods. For this purpose, a variety of BIM use cases have been developed. In this paper are illustrated excerpts from the BIM uses developed of "yield simulation "and "yield monitoring ".

As already stated in chapter 1 a BIM-based approach for the yield simulation of PV(T)-systems offers a range of advantages. In the BIM use example of „yield simulation "the digital representation of a BIPV(T)-system forms the base for a BIM-based yield simulation. The digital portrayal of the BIPV(T)-system, its surroundings and the given location through georeferencing of the BIM-model supply essential geometric information. Furthermore, deposited semantic information e.g. the module's efficiency can easily be retrieved and used for the simulation.

The „yield monitoring "use case is situated in the operation lifecycle phase of a BIPV(T)-system. By combining the BIM-model with live monitoring data, a digital twin of the system is created. For the display of the digital twin a suitable CDE is recommended. As part of the BIMPV project a CDE is developed with further capabilities for coping with the necessities of digital twins of BIPV(T)-systems.

For the adequate application of the BIM use cases presented, the BIM-models (PVT BIM-model) need to be parameterized with corresponding semantic information. In addition, an intermediate tool is needed to transfer the necessary information from the BIM-model (IFC object model) into TRNSYS and to transfer the simulation results into the BIM-model. In the next chapters a proposed approach for the necessary parameterization use cases and a prototypical tool developed for the realization of the BIM use cases is introduced. Finally, the potentials of a CDE as a monitoring platform are presented. For this purpose, a mockup digital twin was created on the CDE.

3.1 Own parameterization of PVT

In this paper, a parameterization for an uncovered PVT BIM-model is proposed based on VDI 3805 sheet 19 (VDI 3805), IEA SHC Task 60 (Kramer 2020), buildingSMART and BIPVBOOST (BIPVBOOST 2019). First, a BIM-model of a ST collector was obtained from the website (BIMobject 2021) as an IFC file and extended with semantic information using the software FreeCAD.

The guideline VDI 3805 specifies the general product data and the associated data structure for HVAC products. Sheet 19 contains a parameterization for the digital product data exchange for thermal solar collectors. Based on previous work, the parameterization of a PVT can be subdivided into the following property sets: Generic, Manufacturer, Warranty, Safety, Certificate, Environmental data, Optical specifications, Installation, Location, Geometry, Mechanical, Material, Thermal specifications, Electrical specifications and Economic data.

Regarding the Generic data, it contains information such as the area of application and the ID of the module as well as the ID of the string. Information about the manufacturer such as name, address and article number is included in the Manufacturer data. Information about the warranty like start as well as end date and content is included in the Warranty. Some information about safety like fire reaction class is included in Safety. Important information about certification like the institute that performed the test and the test flag is to be found under Certificate. Parameterization related to the environment like total primary energy consumption per unit as well as hazardous waste are considered in the Environmental data. The Optical specifications include parameters like the solar absorptance and solar refraction. Under the Installation category, a lot of parameters such as position (e.g. vertical), the type of installation (e.g. in-roof), collector orientation as well as inclination and the number of collectors are considered. Regarding the location of the project, there is information such as the coordinates as well as the height and the local hemispherical solar radiation (for the planning) aggregated in the Location category. The area of the collector, the length, width, thickness and other parameters like the volume are considered in the Geometry data. As Mechanical specifications, the total mass, the pressure of the heat transfer medium, among other things, are considered. Under the Material there is the possibility to add the material data such as the name as well as properties for each component layer like insulation or glass. The Thermal specifications contain the usual performance parameters such as conversion factor and heat transfer coefficient, the temperature- and wind-dependent heat transfer coefficient, the effective heat capacity and the minimum as well as the nominal volume flow. The Thermal specifications were taken from the VDI 3805 as well as from task 60 (under the steady-state test method for unglazed liquid heating collectors). Electrical parameterization such as maximum power voltage as well as current and the module efficiency is included in the electrical specifications. The electrical specifications were taken from project (BIPVBOOST 2019) as well as from IEA SHC task 60 (effective solar cell model). Parameters like economic efficiency (costs per m^2) are considered in the Economic data group.

3.2 Development of a Python intermediate tool between IFC format and TRNSYS

Common design software in the construction world already has interfaces for BIM-related data exchange formats (e.g. IFC and BCF). On the other hand, building energy performance simulation programs (BEPS), such as TRNSYS, EnergyPlus, Polysun and Modelica, have compatibility issues with BIM-based models as a starting point (see Tab. 1). For this, interfaces and reliable connection methods between energy simulation software and BIM-models have to be developed and validated.

For data transfer between the BIM-model (IFC) and TRNSYS Robert et al. (2014) developed an approach for an interface between TRNSYS as well as EnergyPlus and the BIM software eveBIM. Using eveBIM, the IFC file was visualized and processed. This approach was validated with a use case that included the building geometry (building envelope) and a solar domestic hot water system (HVAC). With reference to the use case described, this approach showed a good correspodence between the values simulated in TRNSYS as standalone software and the use of the coupling results (IFC file - eveBIM - TRNSYS). However, this approach requires a large effort to implement the system. In other studies, an Input Data File (IDF) containing building specifications is created with various software such as SketchUp and passed to TRNSYS like Cormier et al. (2011).

The interface between eveBIM and TRNSYS is no longer supported. The approach with IDF generation is just for building geometries and not for HVAC components. Furthermore, due to data loss and errors in generating the IDF file, a second tool was needed. In addition, some missing objects were added manually. The required parameters of the HVAC components were also added manually.

Based on the literature research conducted and on the analysis of the existing deficits, a Python-based intermediate tool for the integration of an IFC object model into TRNSYS has been developed within the scope of this study. For this reason, the free open-source Python library IfcOpenShell (Krijnen 2022) for reading and editing IFC files was used.

The intermediate tool developed is used to obtain the relevant parameters of an IFC object file of PVT modules, to analyze them, to check whether all the parameters required for TRNSYS simulation are available or not, to filter them and to transfer them to TRNSYS (see Fig 3). The TRNSYS PV-thermal model (type 203), developed by the Institute for Solar Energy Research in Hamelin (ISFH), is a model for uncovered liquid cooled PVT that is based on the combination of the parameters resulting from standard thermal and electrical performance measurement data (Stegmann et al.).

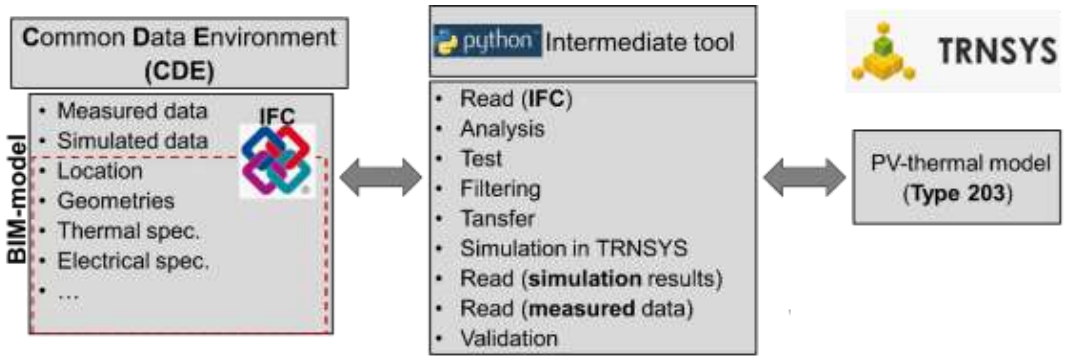

Fig 3: Schematic representation of the IFC-based Python interface between a CDE and TRNSYS

After that the tool generates a backup copy from the TRNSYS deck file and searches for the parameters required for TRNSYS simulation. It then extracts then the necessary parameters from the imported IFC file. In the next step, the parameters are transferred to TRNSYS and the simulation can be started. Once the simulation is finished, the selected results are visualized in the intermediate tool. At this step it is possible to perform a parameter variation. The intermediate tool is not only intended for the planning but also for the operation phase. For this purpose, the data measured e.g. thermal as well as electrical energy (see Fig 3) as well as the IFC file stored in a data base linked with the CDE can be read from the intermediate tool. The intermediate tool runs the simulation in TRNSYS and then imports the simulation results, compares them with the measurement results and then sends them to the data base

linked with the CDE. The simulation as well as the measurement results can be uploaded and visualized on the CDE with predefined time resolution. The intermediate tool is validated with measurement data. Moreover, the usage of the BIM method allows PVT plants to be optimized, flexibly monitored or maintained as needed. To date, the connection between the intermediate tool and the data base linked with the CDE has not yet been automated.

So far, the interface can only read an IFC file from a single ST collector, PV or PVT module and transfer it to TRNSYS. As a next step, the interface will be developed in order to read an IFC file from a collector array, recognize the system configuration (number of strings, number of collectors in a string, etc.), perform the required calculation of specific parameters (e.g. area of string) and finally transfer the parameters to TRNSYS.

3.3 CDE as a central base for yield monitoring and other use cases

A CDE serves as a central communication and collaboration platform as well as a single source of truth in any BIM-project. The main functions of a CDE cover aspects such as information exchange, collaboration, visualization, and quality-assurance. BIM-models, documents and collaboration-notes are exchanged over the CDE, whereby it provides the opportunity of exchanging various open data formats such as IFC and BCF to ensure successful project processing regardless of the software products used by the participants.

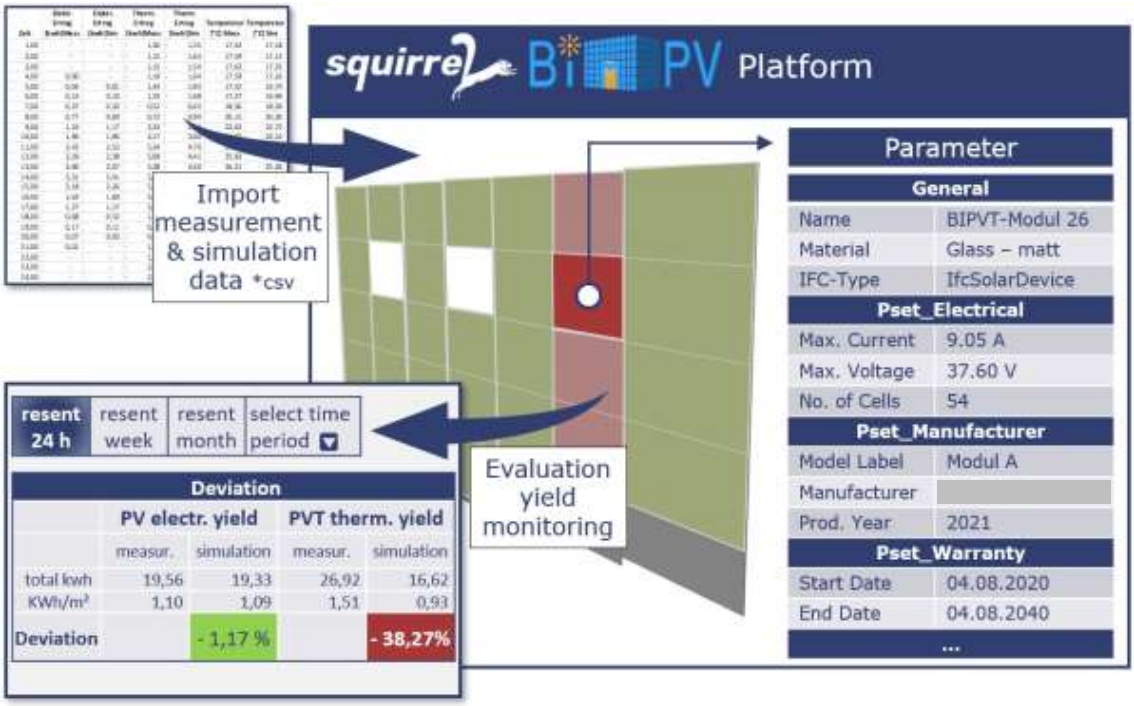

Fig 4: BIM-based monitoring concept of a PVT-facade

The browser-based CDE enables users to visualize the monitoring data retrieved in real time (dynamically). In addition, deviations from the presumed yield can be identified and the deficiency of certain modules can automatically be diagnosed. In the event of a real malfunction the deficient modules can easily be tracked and visualized through the 3D representation of the BIPV(T)-system.

The possibilities of using a CDE as a platform in projects including PV(T) and its monitoring are various. As shown in Fig 4 a CDE (in this case Squirrel) displays and links the objects and their properties to an IFC-model. For the monitoring the assumed yield, a CDE mockup was built, that allows the import of PVT simulation and measurement data. This platform highlights deviations in actual yields from forecast values that exceed a predefined tolerance level. All objects with strong deviations are colored red to enable a clear evaluability and thus a practicable operation of the PVT-system can be guaranteed. Further BIM-model-based use cases can be performed in similar ways. The CDE offers added value in the ability to connect data of various types and sources as well as provide and connect them in a handy way for evaluation and further use for any stakeholders.

4. Summary and outlook

Building Information Modeling is a very promising method for energy analysis applications. It improves the collaboration and data exchange between the stakeholders involved in the whole construction process. It can be used for the design, manufacture, installation, operation and dismantling phases. In energy analysis, BIM methods can reduce errors caused by data loss, manual data transfer or model duplication, and in this way save time and costs.

With the help of the BIM method, the specific planning of a building's energy system can be carried out more efficiently thanks to a larger amount of available information, which reduces the need for assumptions. Early and integral planning results in many advantages with regard to the use of renewable energy sources such as solar energy.

However, there are many limitations in using the BIM method for energy analysis. Almost all known stand-alone simulation programs such as TRNSYS or EnergyPlus are not compatible with the established BIM-based data formats, IFC and gbXML. In addition, the available IFC object model of the solar energy components like PV or ST are neither standardly nor completely parameterized. Furthermore, the use of the BIM method is so far limited to the planning process so far because of its complexity.

In this study a parametrization for an uncovered PVT was developed based on standards such as VDI 3805, IEA SHC task 60 and buildingSMART. Then the proposed IFC object model was built with the parameterization developed with FreeCAD. In order to transfer the necessary parameters from the BIM-model (IFC object model) into TRNSYS automatically, a python intermediate tool was developed and validated. This tool can start the simulation, visualize the simulation results, compare them with the measurement data exported and send them to the CDE.

In order to use the BIM method in the operation phase for monitoring a facade-integrated PVT, a BIM-model of a Danish Pavilion in Hanover was developed in the BIM authoring software Revit. The BIM-model was further used to create a mockup digital twin for monitoring the PVT-facade in the CDE. The CDE permits the display of the measured thermal as well as electrical yield of the PVT. Moreover, the measured data is compared with the simulation data and the deviation is used for monitoring of the PVT-facade. If the deviation between the measured and simulated data is higher than allowed, then the affected PVT-string is marked in red. In this event, the person responsible will be asked to check the strings.

As a further development of the intermediate tool, parameters of entire PVT fields should be transferred from an IFC file to TRNSYS. In this way, a solar plant can be monitored during the operating phase and adjusted or optimized if necessary. If, based on simulation results or from the comparison between measurement and simulation results, the need to change the IFC file on the CDE (areas, performance parameters, etc.) arises, this change can be made with the interface developed.

5. Acknowledgements

The collaborative "Retrospective BIM approach for life cycle optimized integration of BIPV systems in the building envelope" project (BIMPV, FKZ 03EN1010B), on which this publication is based, is funded by the German Federal Ministry of Economics and Climate Protection and the State of Lower Saxony. The authors gratefully acknowledge their support. Responsibility for the content of this publication lies solely with the authors.

6. References

ACCA ,2021. IFC Viewer | usBIM.viewer+. online available at https://www.accasoftware.com/en/ifc-viewer, last updated on 29.10.2021, last checked on 29.10.2021.

Andriamamonjy, A.,Saelens, D.,Klein, R. ,2018. An automated IFC-based workflow for building energy performance simulation with Modelica. In: *Automation in Construction* 91, S. 166–181. DOI: 10.1016/j.autcon.2018.03.019.

Apstex ,2021. apstex IFC Framework. online available at https://www.apstex.com/, last updated on 07.12.2021, last checked on 07.12.2021.

Bimetica ,2021. online available at https://bimetica.com/resultado-busqueda.php?lang=de, last updated on 02.12.2021, last checked on 02.12.2021.

BIMobject ,2021. Free download! | BIMobject®. online available at https://www.bimobject.com/de, last updated on 02.12.2021, last checked on 02.12.2021.

BIMPV ,2023. Joint project: BIMPV – Retrospective BIM approach for life-cycle oriented integration of BIPV systems in the facade | isfh.de. online available at https://isfh.de/bimpv-en/?lang=en, last updated on 14.05.2023, last checked on 14.05.2023.

BIPVBOOST ,2019. Information modelling/management for BIPV cost reduction. Digital adoption plan and guideline for a data-driven BIPV process and optimization strategies 2019.

buildingSMART ,2021. The International Home of BIM. online available at https://www.buildingsmart.org/, last updated on 04.11.2021, last checked on 09.11.2021.

Castro, A. B.,Alvarado, R. G. ,2017. BIM-Integration of solar thermal systems in early housing design. In: *rdlc* 16 (2), S. 323–338. DOI: 10.7764/RDLC.16.2.323.

Cormier, A.,Robert, S.,Roger, P.,Stephan, L.,Wurtz, E. ,2011. Towards a BIM-based service oriented platform : application to building energy.

El Asmi, E.,Robert, S.,Haas, B.,Zreik, K. ,2015. A standardized approach to BIM and energy simulation connection.

eveBIM ,2021. online available at https://www.evebim.fr/, last updated on 07.12.2021, last checked on 07.12.2021.

FreeCAD ,2022. Your own 3D parametric modeler. online available at https://www.freecadweb.org/, last checked on 11.01.2022.

Green Building. GreenBuildingXML_Ver6.01. online available at https://www.gbxml.org/schema_doc/6.01/GreenBuildingXML_Ver6.01.html#Link120, last checked on 01.11.2021.

Hilaire, B.,Burrows, S.,Bizzarri, G.,Ambrogi, O.,Pols, J.-P.,Häfele, K.-H.,Mazza, D. ,2015. D3.3 Review and benchmarking of energy simulation tools corresponding to the typology models of energy-efficient healthcare districts.

IfcSolarDevice ,2019. online available at https://standards.buildingsmart.org/IFC/RELEASE/IFC4/ADD2_TC1/HTML/schema/ifcelectricaldomain/lexical/ifcsolardevice.htm, last updated on 11.12.2019, last checked on 26.11.2021.

Kramer, K. ,2020. Status Quo of PVT Characterization (IEA SHC).

Krijnen, T. ,2022. IfcOpenShell. online available at http://ifcopenshell.org/, last updated on 10.01.2022, last checked on 10.01.2022.

Maile, T.,O'Donnell, J.,van Dessel, M. ,2020. BIM to Building Energy Performance Simulation: An Evaluation of Current Industry Transfer Processes. In: Vincenzo Corrado, Enrico Fabrizio, Andrea Gasparella und Francesco Patuzzi (Hg.): Proceedings of Building Simulation 2019: 16th Conference of IBPSA. Building Simulation 2019. Rome, Italy, 02.09.2019 - 04.09.2019: IBPSA (Building Simulation Conference proceedings), S. 92–99.

NBS ,2021. National BIM Library. online available at https://www.nationalbimlibrary.com/en/what-is-nbs-national-bim-library/, last updated on 02.12.2021, last checked on 02.12.2021.

Robert, S.,Mazza, D.,Hilaire, B.,Sette, P.,Vinot, B. ,2014. An approach to enhancing the connection between BIM models and building energy simulation – HVAC systems in the loop. In: Ardeshir Mahdavi, Bob Martens und Raimar Scherer (Hg.): eWork and eBusiness in Architecture, Engineering and Construction: CRC Press, S. 149–154.

Soft, S. ,2021. Simlab 3 D-Plugins - SketchUp-Export für 3 ds max. online available at https://www.simlab-soft.com/3d-plugins/SketchUp-from-3DS-main.aspx?locale=de, last updated on 08.04.2021, last checked on 08.12.2021.

Stegmann, M.,Bertram, E.,Rockendorf, G.,Janßen, S. Model of an Unglazed Photovoltaic Thermal Collector Based on Standard Test Procedures. In: 2011 – Proceedings of the ISES Solar, S. 1–9.

VDI 3805. Product data exchange in Building Services Solar collectors 2006 (Part 19).

Vela Solaris ,2021. Polysun BIM ein neues Tool, das den Weg in die Zukunft weist. online available at https://www.youtube.com/watch?v=8yz04YOG5Nc, last updated on 26.10.2021, last checked on 26.10.2021.

Efficiency Evaluation and Comparisons of Solar Cell Technologies Based on Measurements from the Arabian Peninsula

Yannis Pantazis[1], Evangelia Kalligiannaki[1], Yiannis Kamarianakis[1], Konstantinos Kotsovos[2], Issam Gereige[2], Marwan Abdullah[2], Aqil Jamal[2], Athanasios Tzavaras[3], Theodoros Katsaounis[*1, 4]

[1]Institute of Applied and Computational Mathematics, FORTH, Heraklion (Greece)
[2]Renewable Energy, Carbon Management Division, ARAMCO, Dhahran (Saudi Arabia)
[3]Computer, Electrical and Math. Science & Engineering, KAUST, Thuwal (Saudi Arabia)
[4]Dept. of Mathematics & Applied Mathematics, University of Crete, Heraklion (Greece)

Abstract

In this work, we model the power output (a.k.a., energy yield output) of three photovoltaic (PV) cell technologies using statistical learning tools and compare their performance efficiency under real-field conditions. We introduce and train regression models to elucidate the relationship between irradiance and energy yield output. The training is performed on historical records obtained from an adverse-for-solar-panels location and a long period of time. We use standard and robust estimation approaches to compute the model's parameters. We explored various families of predictive models and found that the best-performing model includes an intraday variability factor. We then applied residual error analysis and related the models' coefficient with the efficiency of the solar cells. Our analysis showed that the efficiency decreases over time, and each PV technology has a different rate of deterioration. Moreover, we observe seasonal fluctuations in the efficiency of each PV technology which we have quantified. The decrease in efficiency during the summer months can reach up to 40% relative to the efficiency during the winter months.

Keywords: predictive modeling, performance evaluation, solar cell technologies comparison

1. Introduction

The great majority of Saudi Arabia's landscape is located inside the sun belt resulting in a significant opportunity for renewable energy from solar panels (Almasoud and Gandayh 2015). However, the development of solar plants is quite limited, with the contribution to the national energy mix being about 0.5% for 2020. Given the high potential and the future need for renewable energy, this study aims to highlight the performance differences between various PV cell technologies and elucidate their behavior over a long period of time in the distinct weather conditions of Saudi Arabia. More specifically, the location of the PV solar cells for which historical observations are collected is the New Energy Oasis (NEO) test field near the Red Sea coast (22.30 N, 39.10 E), KAUST, Thuwal, Saudi Arabia. This work presents the statistical analysis and performance evaluation of three photovoltaic (PV) cell technologies under real operating conditions and a five-year period of observations. The location (KAUST, Thuwal) is a challenging place for solar panels because they often operate at temperatures far beyond the Standard Test Conditions (STC) and well above the range observed in most common PV installation locations worldwide (Katsaounis et al. 2019). The historical data consists of irradiance and energy yield (EY) observations which are recorded every 10 minutes. The following three technologies are tested: Aluminum Back Surface Field (AlBSF), Hetero Junction (HJT), and Back Contact (BC). Data cleaning and manual outlier removal have been applied to eliminate any kind of statistical artifact.

The purpose of this paper is threefold: (a) to estimate the efficiency of a PV cell (e.g., reveal the performance over time), (b) to perform statistical comparisons between solar cell technologies, and (c) to quantify the deterioration of the solar cell performance over the years. Towards this purpose, we employ tools from regression analysis and machine learning. A single-parameter baseline regression model was used to linearly relate the EY output with the irradiance. Due to strong seasonal variability, the relationship between irradiance and EY is not stationary; therefore, the parameter estimation is performed on a monthly basis leading to a time-varying

© 2022. The Authors. Published by International Solar Energy Society
Selection and/or peer review under responsibility of Scientific Committee
doi:10.18086/eurosun.2022.16.08 Available at http://proceedings.ises.org

coefficient. The obtained time-varying coefficient (i.e., the slope) serves as an estimate for the time-varying efficiency of a PV solar cell. The residual error analysis for the linear irradiance model revealed a systematic intraday variability of the EY output, which has also been quantified, and the best predictive model is determined using a k-fold cross-validation scheme. The observed temporal variation can also be attributed to the heat since the temperature in the afternoon (when the sun falls from its azimuth) is higher than in the morning (when the sun rises towards its azimuth).

Furthermore, we employed two approaches for cell technology comparisons. The first approach is non-parametric and depends only on the EY output. In this direct approach, we compute the average relative EY output difference between the technologies using only the measurements with common timestamps. The second approach utilizes the baseline model between EY and irradiance, and it is parametric. We compute the slope difference only for the common months since the non-stationarity of the efficiency could affect the comparison results. Indeed, an important advantage of having a parametric model with time-varying coefficients is that we can quantify both the deterioration of performance over time and the variations due to seasonal factors. The EY differences between cell technologies were small but distinctive. The highest, on average, power output was achieved by the BC technology. Indicatively, BC was, on average, 5.5-5.8% more efficient than AlBSF and 2.1-3.1% more efficient than HJT. Interestingly, on an annual comparison, there are years that the ranking is different. The deterioration over time is also evident; we estimated a 6-8% annual drop in power output efficiency depending on the cell technology. Data also revealed that the most dramatic performance difference was observed during seasonal alteration. The relative efficiency drop in summer relative to winter is occasionally more than 40%, eliminating the gains from summer's increased irradiance. Therefore, informed decision-making for PV installation projects should take into special account the temperature coefficient of the PV cells, while mitigation measures such as cooling may be worth considering and be financially viable.

2. Approach and Methodology

The available historical data consist of irradiance and EY observations from three cell technologies (AlBSF, HJT & BC) for the 2015-2019 calendar years. There are irradiance records for 60 months, and EY records for 33 months (AlBSF), 48 months (HJT), and 53 (BC). We initially performed an exploratory data analysis and visualization. We identified a tiny percent of the records which did not follow the overall sample distributions. Both irradiance and EY measurements had few problematic values, which we considered outliers, and thus all the necessary data cleaning and preprocessing steps were applied.

2.1. Predictive modeling and parameter estimation

A strong correlation between the irradiance and the EY is present in the data. Indeed, their association, as quantified by Pearson and Spearman correlation coefficients for each architecture, is above 0.9 (see Tab. 1). Recall that the Pearson correlation coefficient measures the linear correlation between the two variables while the Spearman correlation coefficient, which is a non-parametric measure of ranking, assesses how well the two variables can be described using a monotonic function. The fact that both correlation measures take similar values implies that the relationship between irradiance and EY is predominantly linear.

Tab. 1: Correlation coefficient for each of the three cell technologies using all available measurements.

	AlBSF	**HJT**	**BC**
Pearson	0.929	0.917	0.930
Spearman	0.927	0.920	0.928

Therefore, our baseline model is a single-parameter linear regression model. Letting x_i and y_i denote the *i*-th irradiance and EY output measurement, respectively, we model their association by

$$y_i = c_1 x_i + z_i \qquad \text{(eq. 1)}$$

where c_1 is the unknown coefficient while z_i corresponds to the residual error. We will also refer to c_1 as the slope, and it provides an estimate for the efficiency of the PV solar cell.

Our preliminary analysis also showed that the relationship between irradiance and energy yield is not stationary over the five-year period. Indeed, it is well documented that there are both long-term but also seasonal changes in the efficiency of a solar cell over time (Patel 2006, Dubey et al. 2013). Therefore, it is not optimal to compare the architectures on the coarse annual resolution; a more refined temporal resolution is required. Motivated by these observations, we estimate the linear irradiance predictive model month by month. Thus, we slice the data on a monthly basis and compute the slope using two standard estimation methods: Ordinary Least Squares (OLS) and Robust Least Squares (RLS) with Huber weights (Huber and Ronchetti 2009). We employ RLS because it is expected to be less sensitive to outlier values.
Additionally, we observed an almost-periodic intraday variability for the residual error of the linear model. This intraday variability is partially attributed to temperature differences between the morning and afternoon hours. We incorporate this behavior into the model with the addition of a periodic term with a period equal to one day. One day period corresponds to $T = 78$ data points; one data point for each ten-minute interval. Therefore, the new model is defined as

$$y_i = c_0 + c_1 x_i + \sum_{k=1}^{K} a_k cos\left(\frac{2\pi k t_i}{T}\right) + b_k sin\left(\frac{2\pi k t_i}{T}\right) \quad \text{(eq. 2)}$$

where $t_i \in \{1, \ldots, T\}$ corresponds to the time variable while K is the number of sinusoidal components to be determined. We also include the intercept parameter c_0.

2.2. Comparison metrics

We deploy two approaches for comparing the three solar cell technologies. The first approach is a straightforward calculation of the EY difference between two technologies measured at the same time points. This "synchronous" comparison is required because the variability in the EY values stemming from weather or maintenance factors or simply the existence of missing data could affect the statistics of the quantity of interest. Moreover, we further reduce the noise in the data by excluding measurements with EY values below 10 Wm^{-2}. The second approach is a parametric one, which is defined via the linear irradiance model (see eq. 1), motivated by the fact that the estimated correlation coefficient between irradiance and EY is above 92%, even when all records are considered. The linear irradiance model has only one parameter, the slope, and it is directly interpretable as the efficiency of the solar cell. We then compare the estimated slopes and utilize statistical testing to assess the significance of the differences.

3. Results and Discussion

Results on predictive modeling and residual error analysis, as well as the comparative results on the studied solar cell technologies, will be presented.

3.1. Quantify predictive performance and perform model selection

We determine the optimal number of sinusoids K of (eq. 2) using a standard cross-validation scheme. Tab. 2 reports the root mean square error (RMSE) for a series of predictive models determined by the number of sinusoids, K. The estimation method is OLS. In the table, we highlight in bold the best-performing model for each year and each architecture according to the RMSE and the minimum number of parameters in the case of ties. Based on the table, the best model has intercept and $K = 2$. Except for the months of 2015, where the mean RMSE is around 30 W/m^2 for all architectures, the mean RMSE is around 10 W/m^2 for all the remaining years. Moreover, it is worth noting that the intercept reduces the mean RMSE for 2015, but it does not improve the predictive performance in any of the other years.

Tab. 2: RMSE (in W/m^2) estimated on the test set of a 10-fold cross-validation and averaged over the months of each available year.

	Year	K = 0		K = 1		K = 2		K = 3		K = 4	
Intercept		Yes	No	Yes	No	Yes	No	Yes	No	Yes	No
AIBSF	2015	30.0±2.2	27.8±2.2	28.30±2.8	20.4±2.7	27.8±2.7	**19.2±2.2**	27.4±2.5	19.2±2.3	26.9±2.9	19.2±2.5
	2016	10.7±1.5	10.7±1.3	8.9 ± 1.7	8.9 ± 1.6	8.5 ± 1.5	**8.4 ± 1.8**	8.4 ± 1.6	8.5 ± 1.4	8.4 ± 1.6	8.4 ± 1.5

	2017	11.7±2.6	11.7±2.4	10.7 ± 2.6	10.7±3.2	10.4±2.6	10.4±2.5	10.4±2.8	**10.2±2.8**	10.4±2.9	10.4±2.8
	2018	9.8 ± 1.3	9.7 ± 1.3	8.4 ± 1.4	8.3 ± 1.6	**8.1 ± 1.6**	8.1 ± 1.5	8.1 ± 1.4	8.1 ± 1.4	8.1 ± 1.5	8.1 ± 1.6
	2019	9.6 ± 2.0	9.5 ± 1.8	8.4 ± 2.0	8.4 ± 2.1	**7.9 ± 2.5**	8.0 ± 1.9	7.9 ± 2.7	8.0 ± 2.2	7.9 ± 2.4	8.0 ± 2.2
HJT	2015	30.0±2.9	27.9±2.6	28.2 ± 2.6	19.7±2.4	27.8±2.7	**18.7±2.5**	27.6±2.6	18.7±2.4	27.0±2.3	18.7±2.1
	2016	11.4±2.0	11.3±1.9	9.4 ± 2.2	9.3 ± 2.3	9.0 ± 2.4	9.0 ± 2.5	9.0 ± 2.4	**8.9 ± 2.5**	9.0 ± 2.3	9.0 ± 2.4
	2017	10.7±3.4	10.7±3.0	9.3 ± 3.4	9.4 ± 3.2	9.2 ± 3.5	**9.1 ± 3.7**	9.4 ± 3.3	9.3 ± 3.3	9.4 ± 3.2	9.4 ± 4.1
	2018	13.9±1.6	13.8±1.9	13.7 ± 1.4	**13.5±1.6**	13.6±2.0	13.5±1.8	13.6±2.0	13.5±1.4	13.6±1.9	13.5±1.7
	2019	14.3±2.1	14.0±2.1	12.5 ± 2.5	11.3±1.8	12.4±2.2	**11.1±2.1**	12.3±2.1	11.1±2.2	12.2±2.1	11.1±2.3
BC	2015	29.8±2.5	27.2±2.3	27.9 ± 2.9	19.4±2.4	27.4±2.7	**18.2±2.4**	27.1±2.2	18.2±2.5	26.6±2.3	18.2±2.4
	2016	11.2±1.5	10.9±1.5	9.1 ± 1.7	9.1 ± 1.5	8.4 ± 1.8	8.4 ± 1.7	8.5 ± 1.6	8.4 ± 1.7	8.4 ± 1.8	8.4 ± 1.5
	2017	11.2±1.9	11.2±1.6	9.6 ± 1.9	9.6 ± 1.8	9.3 ± 1.9	**9.2 ± 1.9**	9.2 ± 2.0	9.2 ± 1.8	9.3 ± 1.8	9.2 ± 1.9
	2018	12.7±2.0	12.7±2.1	12.2 ± 2.3	12.2±2.4	12.1±2.3	12.1±2.2	12.1±2.2	12.1±2.5	12.2±2.0	12.2±2.0
	2019	11.3±1.8	11.2±1.9	9.7 ± 2.0	9.7 ± 1.9	9.6 ± 2.1	9.6 ± 2.0	9.6 ± 2.1	9.6 ± 2.0	9.6 ± 2.0	9.6 ± 2.0

Fig. 1 shows the residual error in terms of RMSE for the single parameter regression model (eq. 1), (slope only), and the regression model (eq. 2), the best model, according to Tab. 2 on a monthly basis.

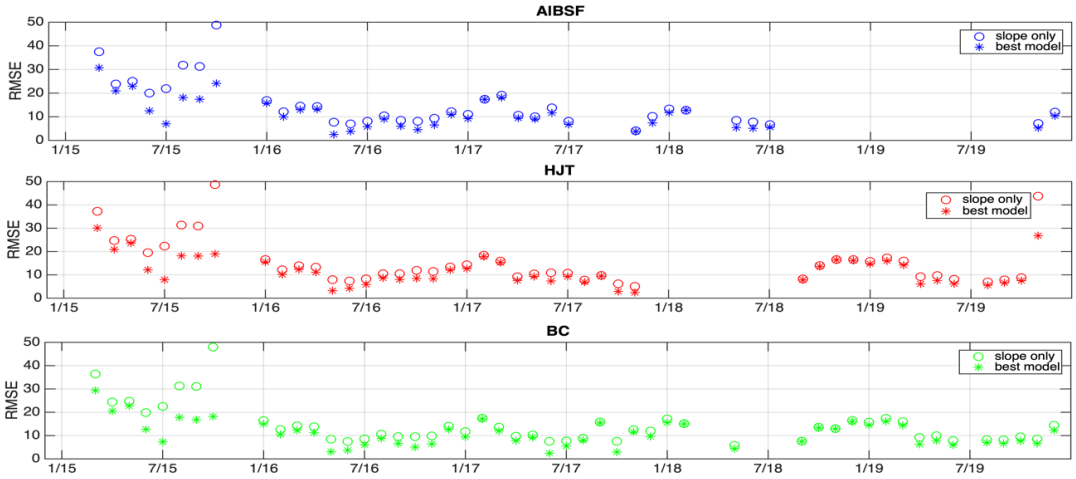

Fig. 1: RMSE for the baseline model (just one parameter, the slope) and for the best model (*K=2* with intercept). The best model which quantifies the intraday oscillations has 6 parameters in total.

3.2. Residual error analysis

Next, we study the residual error statistics and quantify the differences between the models and the estimation approaches. More specifically, we plot in Fig. 2 the residual error for three selected months for AlBSF technology as a function of the irradiance (left column of panels) and its histogram (right column of panels). The first observation is that the residual error is quite different depending on the studied month. The months of 2015 contain large residual error values, both positive and negative, for the baseline model (blue dots). On the other

hand, the best model (red dots) has only large negative residual error values. Given that OLS has zero mean residual error, the large negative residual error values imply a positive bias evident in Fig. 2 (upper panels). Using RLS, this positive bias is alleviated, as we observe in Fig. 3 (upper panels).

The months of 2016 contain intraday variability (blue dots in mid panel) which results in a bimodal distribution for the residual error of the baseline model. In contrast, the residual error's distribution of the best model is almost a normal distribution with zero mean implying that the best model predicts almost perfectly the energy yield output from the irradiance and the time variable. The modeling of the intraday variability resulted in improved predictive performance for the remaining years, however, the performance improvement is smaller as it is also evident from Fig. 3 (lower panels). Using RLS instead of OLS had a minimal effect on the residual error from 2016 and onward. We note that the same conclusions hold for the other two architectures.

As a final remark, the statistical modeling of the intraday variability does not affect the prediction of the total energy power produced during the course of the day. Thus, the baseline model will be as accurate as the best model for the coarse daily energy yield power output. However, modeling of the intraday variability is necessary when the hourly energy yield output is asked. Given that several power energy markets (e.g., various European countries) provide prices on an hourly basis, the bias due to intraday variability needs to be removed.

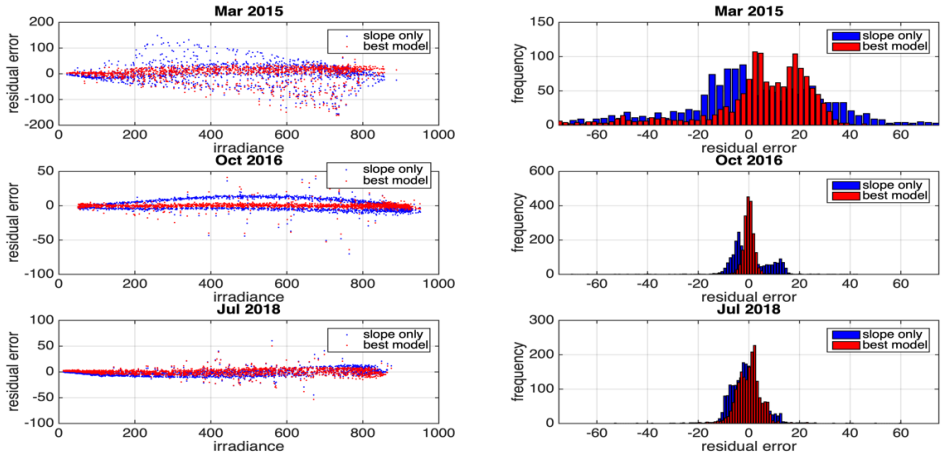

Fig. 2: Left column: the residual error as a function of the irradiance for three indicative months. OLS is the estimation method and measurements come from the AlBSF technology. Right column: the respective histograms for the residual error.

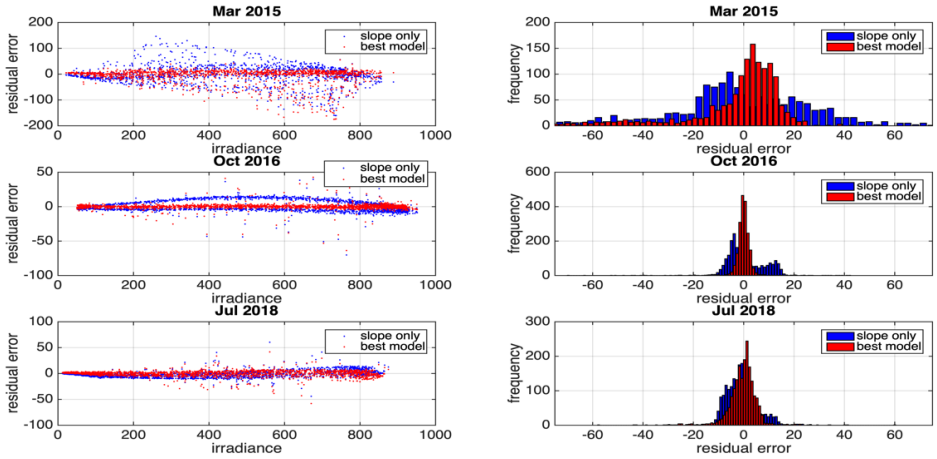

Fig. 3: Same as Fig. 2 using RLS with Huber weights as the estimation method.

3.3. Efficiency estimation

Next, we study the efficiency of each technology. The efficiency is defined as the percentage of irradiance that becomes energy power from the PV solar cell. Thus, the coefficient of the baseline model is a direct estimate of the efficiency. Fig. 4 depicts the estimated slope for every available month and for the three studied technologies

using both OLS (circles) and RLS (stars). The differences are small and statistically insignificant (p-value between 0.4 and 0.6) therefore both can be used as reliable estimates for the efficiency factor.

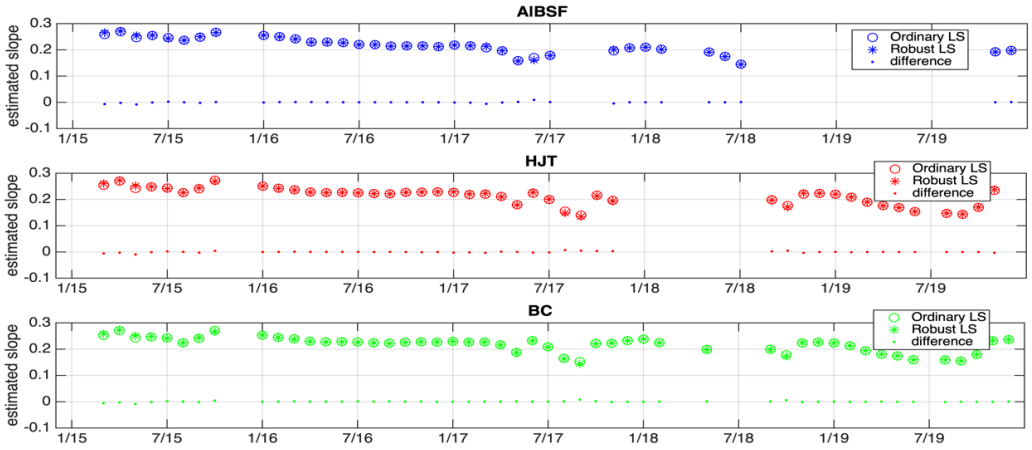

Fig. 4: Estimated slopes per month for the three technologies. The comparison between OLS and RLS reveals that there is no statistically significant difference in the estimation of the slope parameter.

Interestingly, the slope comparison between the baseline model and the best model (Fig. 5) showed that for 2015 the best model is significantly different than the baseline model. An ablation analysis revealed that the intercept is the parameter that makes the slope estimates so different between the two models. Therefore, in the subsequent section, the indirect (i.e., parametric) comparisons between the three architectures will be performed using the baseline model with the slope being estimated with OLS.

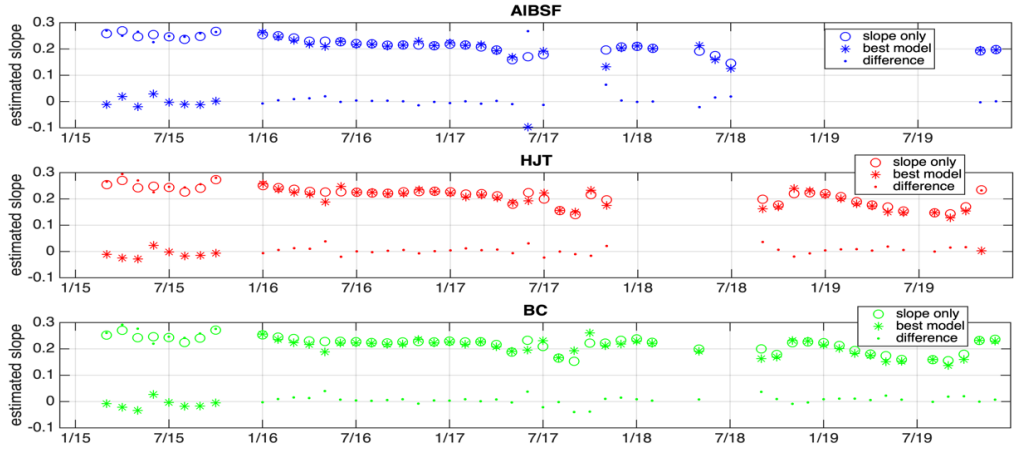

Fig. 5: Estimated slopes per month for the three technologies. The comparison is between the baseline model and the best model. A significant difference in the estimation of the slope is evident for 2015 implying that the best model's slope loses its physical interpretation.

3.4. Solar cell technologies comparisons

The upper plot of Fig. 6 shows the estimated slopes for the three cell technologies. The time-varying behavior of the slope, hence, of the solar cell efficiency, is evident. The seasonal variations of the estimated slope are rather striking (see also the lower plot of Fig. 6). The difference in the performance, as quantified by the slope difference, can be as large as 50%. We anticipate that those seasonal variations mainly stem from the differences in the air surface temperature (Patel 2006, Dubey et. al. 2013). Moreover, there is an annual deterioration of performance in all cell technologies (see thick dashed lines in Fig. 6). Using a linear regression model with two parameters (decay and intercept) and OLS we quantified the rate of deterioration for each technology. For BC, the average rate of deterioration was 5.8%, for HJT the rate was 6.9% while for AlBSF the average rate of deterioration was 7.5%.

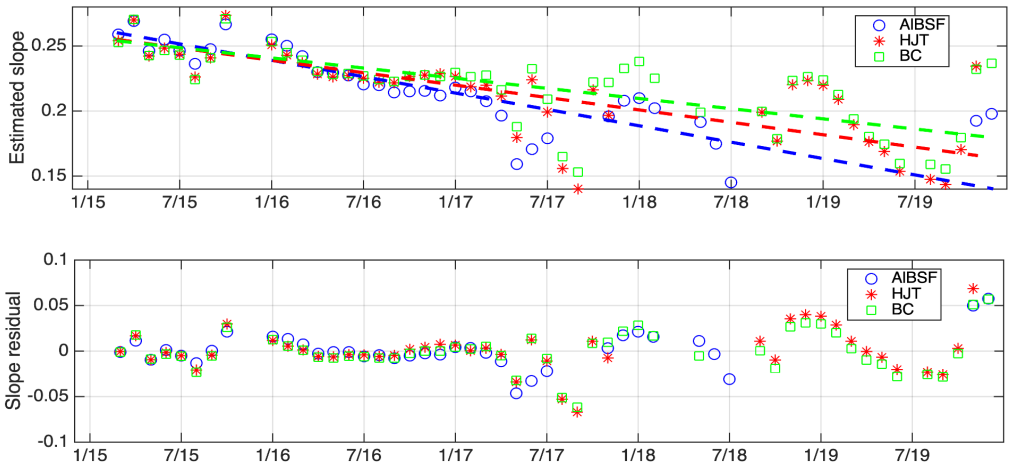

Fig. 6: Upper plot: Estimated slope on a monthly basis for the three cell technologies. The slope is a direct estimator of cell efficiency. Thick dashed lines correspond to the linear trend of the slopes for each cell type and reveal the drop of efficiency over time. Lower plot: The residual error of the slope after removing the linear trend. A seasonal variability is evident.

Tab. 3 reports the relative performance gain (or loss) between the three solar cell technology pairs averaged per each year and the total average. The relative performance results for both non-parametric (NP) and parametric (P) approaches are given. We stress once again that for a fair comparison the differences are evaluated at points for which data for both technologies are available.

Clearly, both approaches report qualitatively similar results. However, the parametric indirect approach is more conservative relative to the direct non-parametric approach. One possible explanation for this difference is that the parametric approach puts more weight on measurements with high irradiance value while the non-parametric approach treats all measurements equally. Given that more power output is produced when irradiance is higher, it is expected that the parametric approach provides more consistent comparisons. Overall, and despite being indecisive for 2015, it is evident for the subsequent calendar years that BC technology outperforms the other two.

Tab. 3: Relative performance difference between the three cell technologies. Positive values imply that the first cell technology is better. NP refers to the non-parametric approach while P to the parametric one.

	2015		**2016**		**2017**		**2018**		**2019**		**Average**		**Annual Average**	
	NP	**P**	**NP**	**P**	**NP**	**P**	**NP**	**P**	**NP**	**P**	**NP**	**P**	**NP**	**P**
BC vs AlBSF	0.5	-1.8	4.4	1.9	1 5.6	12.8	13.2	9.0	18.8	18.3	5.8	5.5	10.5	8.0
BC vs HJT	1.5	-0.4	2.4	0.6	5.4	4.8	3.0	1.0	4.8	3.5	3.1	2.1	3.4	1.9
HTJ vs AlBSF	-1.0	-1.4	2.1	1.3	12.4	8.6	-	-	-	-	2.5	3.2	4.5	2.8

4. Conclusions

In this study, we estimated and then analyzed the efficiency of three solar cell technologies over a five-year span from observations collected at KAUST, Thuwal, Saudi Arabia. The weather conditions of this particular location and specifically the high temperature have a quite adverse effect on solar panels operation. We first observed that efficiency varies over time; therefore, we estimated it on a monthly basis with regression. Our analysis of the time-varying efficiency revealed that solar cell performance deteriorates over the years with a rate between 5% and 8% per year. The observed annual deterioration rate is sizably higher than the rate provided by the manufacturers of the PV cell technologies. The time-varying efficiency also revealed that large performance differences during seasonal alteration are evident, which may reach up to more than 40% in some years (efficiency in winter is higher than in summer). Finally, we performed statistical comparisons between the three solar cell

technologies. Our analysis showed that newer technologies (i.e., BC and HJT) are more efficient than older technologies (i.e., AlBSF) mainly due to a lower deterioration rate over time.

5. Acknowledgments

The authors acknowledge the support of KAUST and Saudi Aramco R&D Center - Carbon Management Division for their financial support in developing this work. This work was partially supported by grant *#OSR–2020-4433.02* from KAUST and Saudi Aramco.

6. References

Almasoud, A.H, Gandayh, H.M, 2015, Future of solar energy in Saudi Arabia, J of King Saud University - Engineering Sciences 27, 153-157

Dubey, S., Sarvaiya, J.N, Seshadri, B., 2013, Temperature Dependent Photovoltaic (PV) Efficiency and Its Effect on PV Production in the World – A Review, Energy Procedia 33, 311-321

Huber, P.J, Ronchetti, E., 2009, Robust Statistics; 2nd Ed., John Wiley & Sons New Jersey, USA

Katsaounis, T., Kotsovos, K., Gereige, I., Basaheeh, A., Abdullah, M., Khayat, A.,Tzavaras, A. E. (2019). Performance assessment of bifacial c-Si PV modules through device simulations and outdoor measurements. Renewable Energy, 143, 1285–1298. doi:10.1016/j.renene.2019.05.057

Patel, M.R., 2006, Wind and Solar Power Systems, 2nd Ed., CRC Press, Florida, USA

KNN-based ensembles for day-ahead solar power output forecasting

Yiannis Kamarianakis[1], Yannis Pantazis[1], Evangelia Kalligiannaki[1], Theodoros D. Katsaounis[2], Konstantinos Kotsovos[3], Issam Gereige[3], Marwan Abdullah[3], Aqil Jamal[3] and Athanasios Tzavaras[4]

[1] Data Science Group, Institute of Applied and Computational Mathematics, Foundation for Research and Technology-Hellas, Heraklion Crete (Greece)

[2] Dept. of Mathematics and Applied Mathematics, University of Crete, Heraklion (Greece)

[3] Saudi Aramco R&D Center, King Abdullah University of Science and Technology (KAUST), Thuwal (Saudi Arabia)

[4] Computer, Electrical and Mathematical Sciences and Engineering Division, King Abdullah University of Science and Technology (KAUST), Thuwal (Saudi Arabia)

Abstract

This manuscript evaluates a recently proposed times series KKN (KNN_{TS}) methodology, in terms of its accuracy in day-ahead forecasting of PV power outputs. Specifically, KNN_{TS} is evaluated against three widely applied benchmarks: seasonal ARIMA, spline-based daily profiles (SDP) and the persistence model (PRS). Two different solar cell architectures are examined under real operating conditions: Aluminum Back Surface Field (Al-BSF) and Back Contact (BC). Our analyses suggest that KNN_{TS} does not dominate the alternative, benchmark specifications. However, linear combinations of KNN_{TS} with SDP, may produce significantly improved forecasts. The outcomes of the model-building procedure are incorporated in a light online forecasting system for solar panels located in KAUST, Thuwal, Saudi Arabia.

Keywords: solar power output forecasting, time series KNN, ensemble modeling, shrinkage methods

1. Introduction

Accurate forecasts of photovoltaic (PV) outputs are essential to Distribution System Operators and Transportation System Operators (Antonanzas et al., 2017) for efficient solar energy trading and management of electricity grids (EPIA, 2012). The main aim of this work is to develop specifications for day-ahead forecasting of PV energy outputs, which are solely based on historical information and combine satisfactory levels of forecasting accuracy with low computational and monetary costs. To this purpose, we evaluate a recently proposed, computationally-light time series KNN-regression scheme (KNN_{TS}) (Martinez et al., 2019a), using observed energy yields (EY) from 2 panel technologies: Aluminum Back Surface Field (Al-BSF) and Back Contact (BC).

KNN_{TS} is straightforward to implement online as it is based solely on historical data and does not require next-day meteorological predictions as input. Of course, advanced predictive models (e.g. penalized regressions, random forests, neural networks; Nespoli et al., 2019) that use meteorological information should dominate such relatively simple schemes by a significant margin, to justify their substantially increased cost (both computational and in terms of the price to acquire continuously updated meteorological forecasts). Online forecasting systems for PV and wind-farm energy outputs are expected to employ such benchmark specifications while in "safe-mode" operation, when for instance, access to day-ahead meteorological forecasts has been interrupted.

In what follows, KNN_{TS} is evaluated against three frequently adopted benchmark specifications: seasonal ARIMA, spline-based daily profiles (SDP) and the persistence model (PRS). Evaluation is based primarily on

© 2022. The Authors. Published by International Solar Energy Society
Selection and/or peer review under responsibility of Scientific Committee
doi:10.18086/eurosun.2022.16.09 Available at http://proceedings.ises.org

conventional RMSE; in addition, the relative accuracy metric proposed by Tofallis (2015) is monitored.

2. Methodology

The adopted KNN_{TS} methodology proposed recently by Martinez et al., (2019a), is implemented in `R` via the `tsfknn` package (Martinez et al., 2019b). Given a recently observed daily profile of PV outputs, conventional KNN identifies *k* profiles that are closest based on a chosen distance metric and reports the average of *k*, neighbor-specific subsequent values. The number of nearest neighbors is a decision variable that should be tuned. On the other hand, in KNN_{TS}, Martinez et al., (2019a) propose an ensemble scheme that instead of choosing *k*, averages forecasts corresponding to *k*=3,5,7. This scheme provided very satisfactory levels of accuracy in our preliminary analyses; hence all results depicted in the next sections are based on forecast combinations for *k*=3, 5, 7. In the application, a sensitivity analysis similar to the one presented in Martinez et al., (2019a) is performed, to evaluate alternative combination schemes (mean, median, weighted mean). Additional tuning decisions should be performed regarding a) the distance metric used to identify nearest neighbors (e.g. the widely adopted Euclidean, versus Manhattan distance; b) the multi-step ahead forecasting strategy and c) the time lags used as input variables. The first two choices are investigated in the application whereas for the third, we follow the recommendation in Martinez et al., (2019a) for periodic time series and set the number of time lags equal to the number of time-periods per day.

In contrast with KNN_{TS}, SDP reports daily profiles that utilize all measurements observed during a pre-specified time interval. Cowpertwait and Metcalfe (2009) present parametric specifications for SDP, based on a) dummy variables (SDP_a), or b) sine and cosine functions (SDP_b). Our preliminary experiments revealed that a non-parametric procedure based on regression splines can be more accurate relative to SDP_a and substantially faster to compute, relative to SDP_b without compromising forecasting performance. The procedure implemented herein, fitted piece-wise cubic polynomials with 15 knots (knots are breakpoints in the third derivative; the number of knots was chosen by performing a cross-validation experiment) arranged at equally-spaced time instants. The function `bs` in the `R` package `splines` is used to construct B-spline basis expansions. Daily profiles are then derived using conventional least squares estimation, which is compatible with the primary adopted accuracy criterion (RMSE). It is worth stressing that a simplified SDP-variant of the procedure applied here, typically computes static, month-specific daily profiles. This results in a straightforward online implementation which does not require computations on a daily basis; instead, reported forecasts are retrieved from a small database. On the contrary, here SDP is updated on a daily basis in terms of training data. Furthermore, the number of training weeks is a tuning parameter.

The persistence model (PRS) is a typical benchmark in PV-output forecasting experiments. PRS implies that current conditions remain unaltered and that a future daily profile will be very close to the one most recently observed. Hence observations that correspond to the most recent, fully observed day, are used to forecast an unknown daily profile. ARIMA models constitute a second widely adopted benchmark specification. In fact, PV-outputs behave similar to the classic textbook example of periodic time series with a trend [e.g. the airline series used in Brockwell and Davis (2009)]. In the example application ARIMA model building is performed with the `auto.arima` function, which is available in the `forecast` package. A-priori, PV-outputs are expected to behave as non-stationary processes, as daily periodicities are coupled with a decreasing trend, due to declining PV efficiencies. Non-stationarity is accounted for, by treating the number of training weeks for KNN_{TS}, ARIMA and SDP, as a tuning parameter. This ensures that the computational scheme in the online implementation is computationally light, with low requirements in terms of training data.

The prioritized accuracy metric in the example application, is RMSE, which is compatible with conventional least squares estimates. An alternative, widely used accuracy metric is the mean absolute percentage error (MAPE). Tofallis (2015) showed that MAPE systematically favors specifications that produce low forecasts. Specifically, MAPE regression can be viewed as a weighted median regression with the observed measurements taking the role of weights (Tofallis, 2015); hence the lowest measurements are more influential and the predictive specification is pulled towards them. To overcome the shortcomings of MAPE, Tofallis (2015) proposed an alternative relative error metric, namely *LnQ*, which, is formulated as follows:

$$LnQ = \frac{1}{N}\sum_{t=1}^{N}\left[ln\left(\frac{\hat{Y}(t)}{Y(t)}\right)\right]^2 \qquad \text{(eq. 1)}$$

with $Y(t)$ denoting observed and $\hat{Y}(t)$ forecasted values.

3. Data

EY measurements (W/m^2) are collected at KAUST, Thuwal, Saudi Arabia: a challenging location for solar panels, which often need to operate in the presence of dust and/or at temperatures far beyond the Standard Test Conditions (STC). The analysed data are recorded every 10 minutes, from 8AM to 5PM (as reported EY is negligible before 8AM and later than 5PM), for 364 consecutive days (52 weeks) in 2016, with starting (ending) date, 01 January 2016 (29 December 2016). Data cleaning (removal of extremely high, clearly erroneous measurements) has been applied to eliminate statistical artefacts. However, Fig. 1A suggests that some outliers still remain. In addition to outlying measurements the observed power output series contain gaps, which hamper application of the forecasting techniques that follow, especially TSKNN and ARIMA.

Specifically, missing values constitute 5.9% (6.9%) of the Al-BSF (BC) measurements. Typically sequences of missing values are short as in the vast majority of examined days the percentage of missing values is clearly below 10% (Fig.2). A simple linear interpolation scheme would have been sufficient in the presence of occasional short gaps. However, given a) the relatively large proportions of missing values occasionally observed [47 (52) days with missing percentage larger than 10% for Al-BSF (BC)] and b) available historical data included measurements of solar irradiance (W/m^2), an irradiance-based imputation scheme, which reveals intriguing characteristics of the two panel types, is adopted herein.

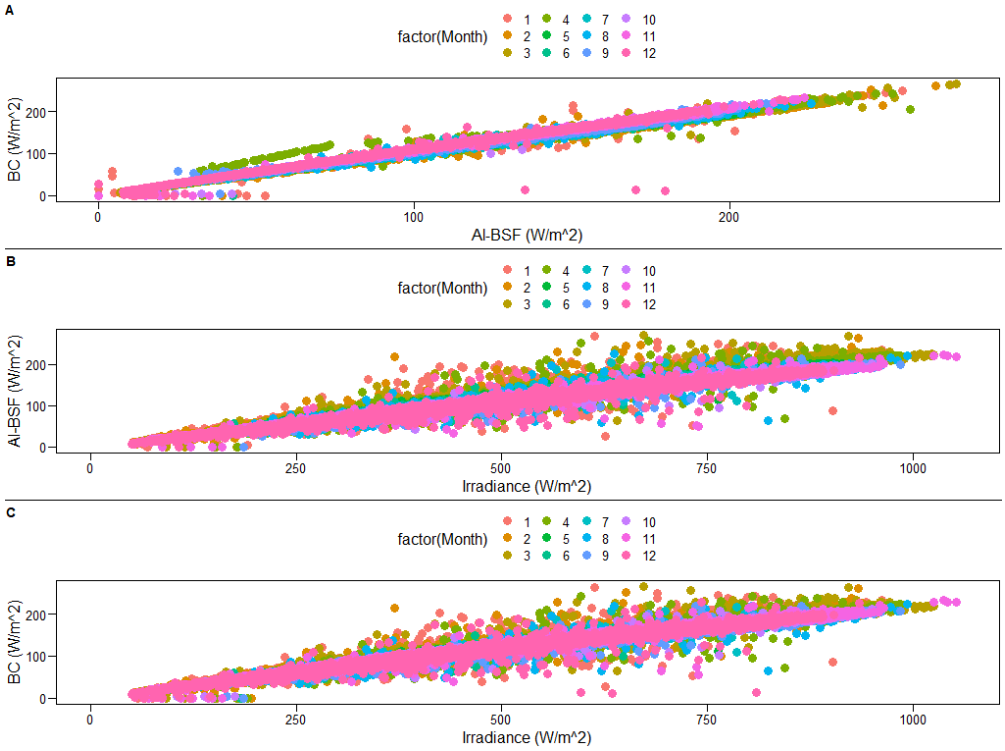

Fig. 1: Scatterplots for the associations between (A) Al-BSF versus BC energy outputs; (B) Al-BSF energy outputs versus irradiance; (C) BC energy outputs versus irradiance.

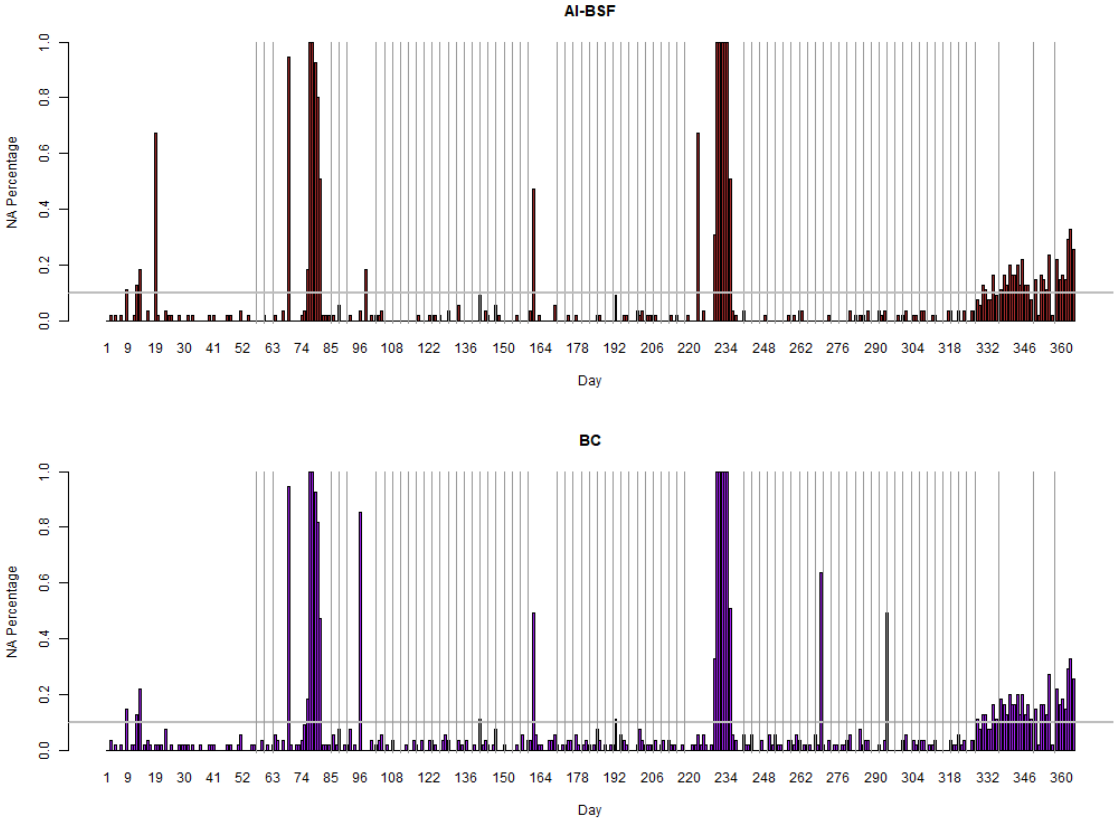

Fig. 2: Daily percentages of missing values for the two solar panel technologies. A horizontal line designates the 10% threshold, whereas vertical lines depict the days that comprise the first testing dataset.

A naïve imputation scheme would assume fixed performance rates for the two PV-technologies during the whole study period:

$$\tilde{Y}_i(t) = c_i X(t) \qquad \text{(eq. 2)}$$

with $X(t)$ denoting observed irradiance at time t, c_1, c_2 designating Al-BSF and BC efficiencies and $\tilde{Y}_1(t), \tilde{Y}_2(t)$, imputed Al-BSF and BC power outputs, respectively. The overly parsimonious approximation in (2) should achieve subpar levels of accuracy (Fig. 1), given the expected decreasing trend for PV efficiencies. A more flexible scheme, which allows for monthly-varying efficiencies is formulated as:

$$\tilde{Y}_i(t) = c_i^m X(t) \qquad \text{(eq. 3)}$$

with $m = 1, \ldots, 12$ denoting a monthly index. Fig. 3, presents outlier-robust, least absolute deviation (LAD, a.k.a. median regression) estimates of monthly efficiencies, which indeed decrease with time. Interestingly, although Al-BSF appears to perform slightly better than BC in the first six months, BC clearly outperforms Al-BSF during the last six months of the study period.

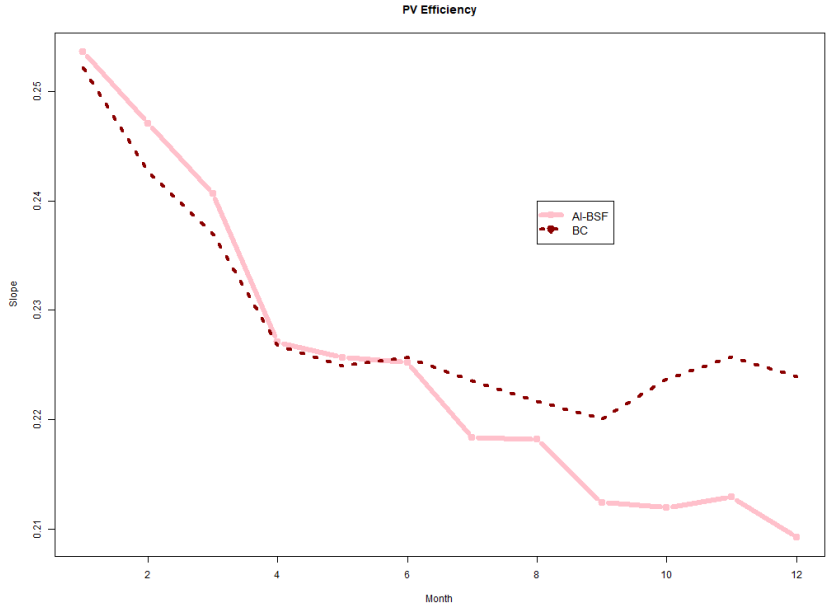

Fig. 3: LAD estimates for monthly efficiency rates corresponding to the specification shown in (3).

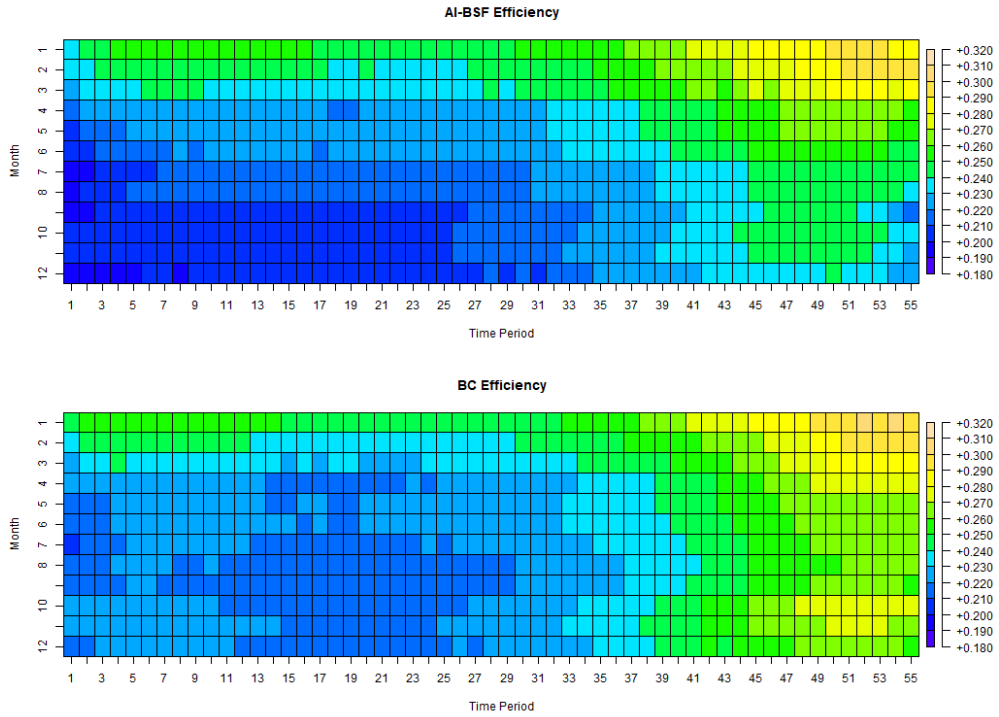

Fig. 4: LAD estimates of month-specific, daily efficiency rate profiles, captured by the slopes in (4). Row numbers correspond to months whereas columns represent time periods within a day: $t_d = 1$ ($t_d = 55$) denotes 8AM (5PM).

The adopted imputation scheme extends the model shown in (3) by allowing for month-specific, daily efficiency-rate profiles:

$$\tilde{Y}_i(t) = c_i^{m,t_d} X(t) \qquad \text{(eq. 4)}$$

with $t_d = 1, \ldots, 55$ designating 10-minute intervals [$t_d = 1$ ($t_d = 55$) corresponds to 8AM (5PM)]. Essentially the above specification takes (indirectly) into account dependence of PV efficiencies on operating temperatures (Skoplaki and Palyvos, 2009). Figures 4 and 5 depict curvilinear, increasing daily profiles, which are derived with outlier robust, median regression (Koenker, 2005). During the first months of the study period, differences in PV efficiencies are mainly observed when the levels of irradiance are low (around 8AM and 5PM). These differences increase with time; as shown in Fig. 5, BC achieves superior efficiency rates relative to Al-BSF towards the end of the study period, during the whole day.

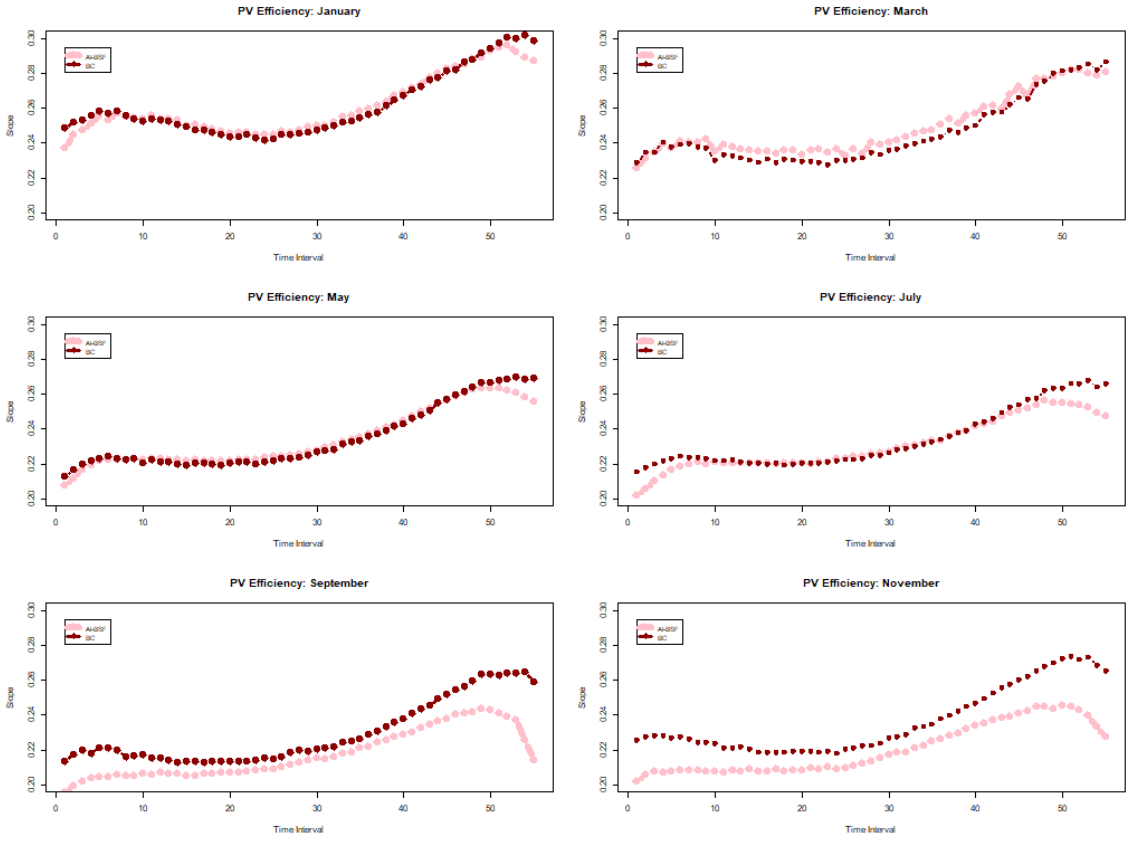

Fig. 5: LAD estimates of month-specific, daily profiles for the PV efficiency rates in (4).

As noted by a reviewer, Figures 4 and 5 indicate higher panel efficiencies in the afternoon, which is not in accordance with what one would expect, based for instance in Skoplaki and Palyvos (2009). Typically, cell temperature is lower in the morning and lower in the afternoon; on the other hand, an evaluation of the dataset analyzed in Katsaounis et al., (2019), which relates strongly to the data analyzed here, suggests that both air and cell temperatures drop substantially in the afternoon (< 30 °C) to reach similar magnitudes. Furthermore, Skoplaki and Palyvos (2009) assume that the open circuit voltage, one of the critical factors that influence electrical efficiency of a PV cell/module, decreases with temperature. Such a decreasing association is not clearly manifested in the dataset analyzed in Katsaounis et al., (2019).

Robust imputation is prioritized here, that is why alternative imputation procedures are evaluated via mean absolute error (MAE). Fig. 6 displays results of a leave-2-week-out cross-validation experiment, which evaluates imputation accuracy achieved from specifications (2), (3) and (4). In this experiment, measurements are divided in 16 consecutive 2-week periods. Each period is used as a testing subset, with the remaining

periods utilized as training data. Fig. 6 clearly demonstrates the superiority of the daily profiles in (4): the average MAE achieved from (4) across all periods is close to 5 W/m^2, whereas for the parsimonious scheme in (3) it is close to 10 W/m^2 for both technologies. Median regression estimates performed better than conventional least squares in terms of average MAE; that is why the adopted imputation scheme utilized (4) with coefficients estimated via LAD. Fig.7 presents observed and imputed data for the performance profiles that constitute the last week of the study period.

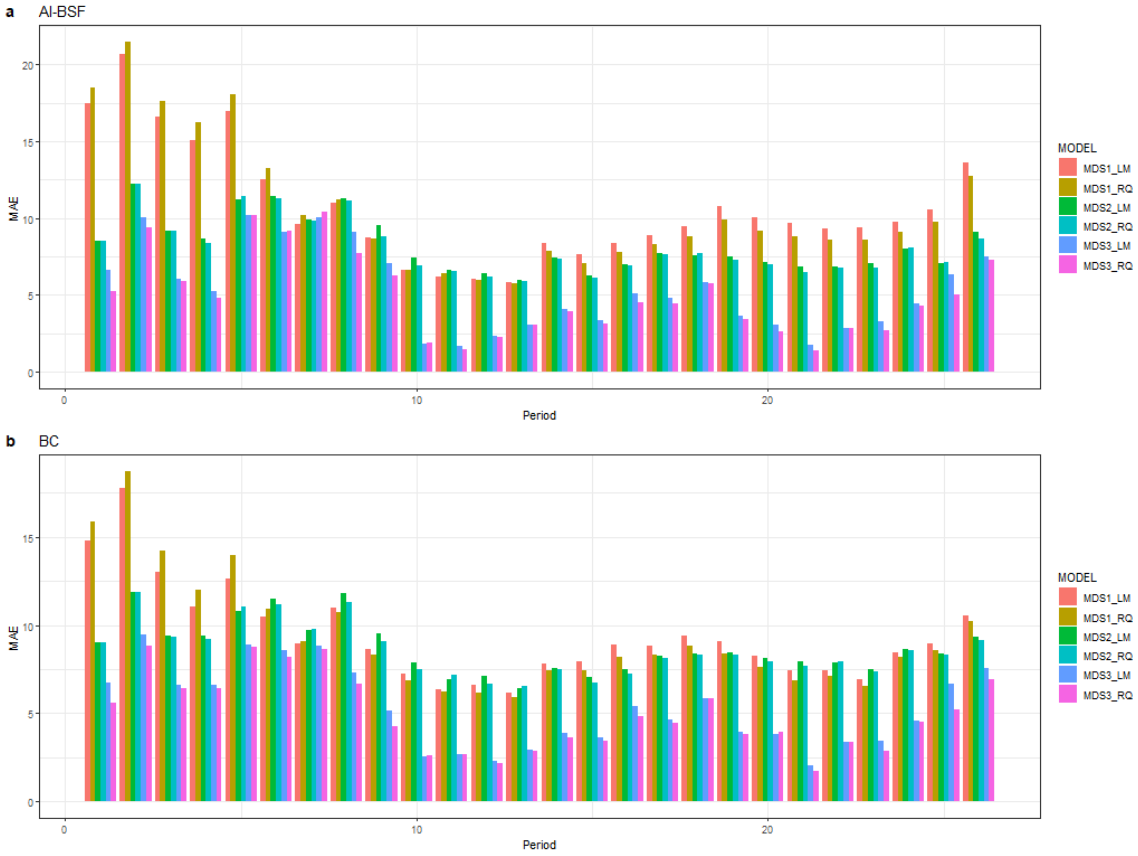

Fig. 6: MAE of alternative imputation schemes for Al-BSF (a) and BC (b). LM denotes conventional least-squares whereas RQ corresponds to outlier-robust median regression estimates (LAD). MDS1 represents the static model in eq. (2), MDS2 stands for the specification shown in eq. (3) and MDS3 is the adopted imputation scheme shown in (4).

4. Forecasting Experiment

This section presents a forecasting experiment which mimics real world, online implementation of the examined specifications. Specifically, the experiment comprises D = 76 testing days: sometime during each testing day d = 1,…,D (in reality around noon), a forecast is computed for the PV outputs of the next day. Days with significant percentages of missing data are not included in the testing set (Fig. 2). Training data consist of days before d and forecasts correspond to the day d+1. Computational times were less than 5 seconds for both SDP and KNN$_{TS}$, even when the number of training weeks, $N_W = 8$. ARIMA model building is substantially slower, with computational times close to 5 minutes on average, when $N_W = 8$.

Results of the experiment are depicted in Figures 8, 9 and Table 1. Interestingly, focusing on RMSE, SDP outperforms both KNN$_{TS}$ and ARIMA; in accordance with prior expectations, PRS is the worst performing method by a significant margin. Regarding KNN$_{TS}$ the optimal combination function used to aggregate the targets associated with the nearest neighbors is the median, by a small margin relative to the mean. ARIMA (KNN$_{TS}$) performance is optimal when the training data comprise 3 (8) weeks for both PV technologies. On

the other hand, SDP achieves minimum RMSE with 5 (3) training weeks for BC (Al-BSF). It should be stressed however that RMSE performances by SDP are very close when the number of training weeks, $N_W > 1$. $N_W = 3$ can be viewed as a choice that results in satisfactory performance for all examined models, while resulting in computationally fast implementations.

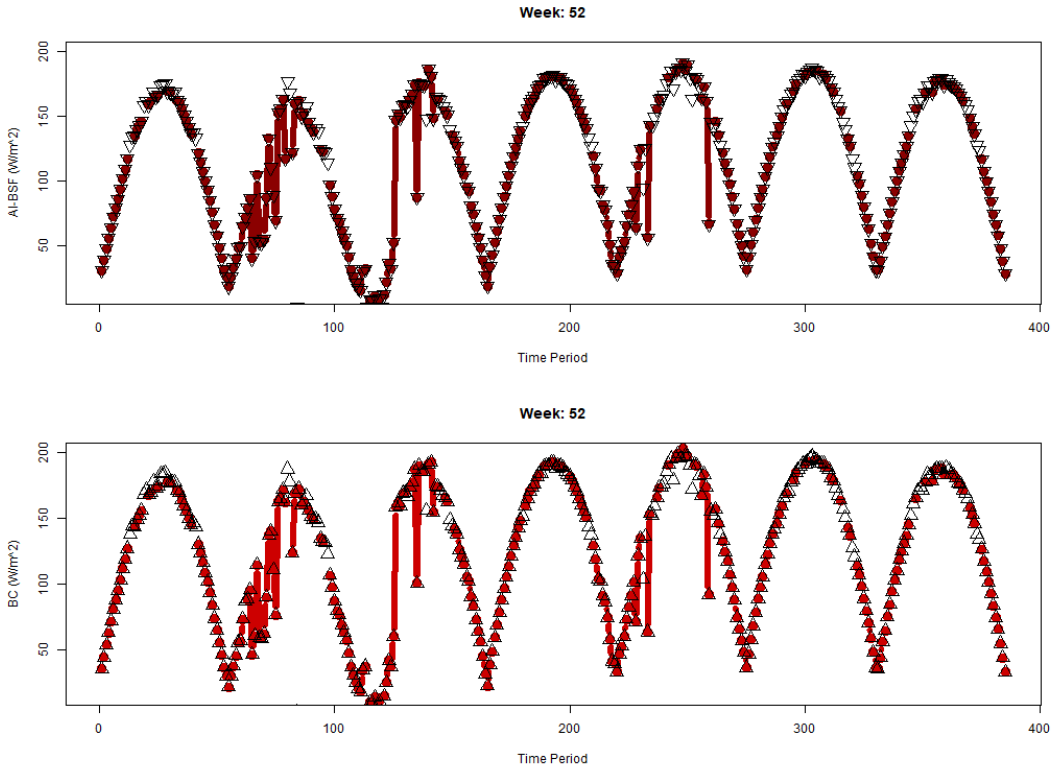

Fig. 7: Observed (imputed) measurements for the last week of the study period are shown as colored (empty) triangles: Al-BSF (top), BC (bottom).

The above evaluation is not insensitive to the chosen accuracy metric. A practitioner that focuses on relative accuracy and adopts LnQ to compare models, would not discard PRS, which despite its simplicity achieves levels of accuracy very close to ARIMA and SDP. Interestingly, KNN_{TS} is by far the worst performing methodology in terms of LnQ. The optimal combination function used to aggregate the targets associated with the nearest neighbors is again the median. SDP appears to dominate in terms of LnQ as it did for RMSE. It is worth emphasizing though, that its performance degrades significantly when $N_W \neq 2$ and that SDP is far from the best performing method when N_W is chosen with a priority on RMSE performance. Fig. 10 shows that forecasts from different methodologies are very strongly correlated. Hence the expected gains from a forecast combination scheme are not dramatic in this application.

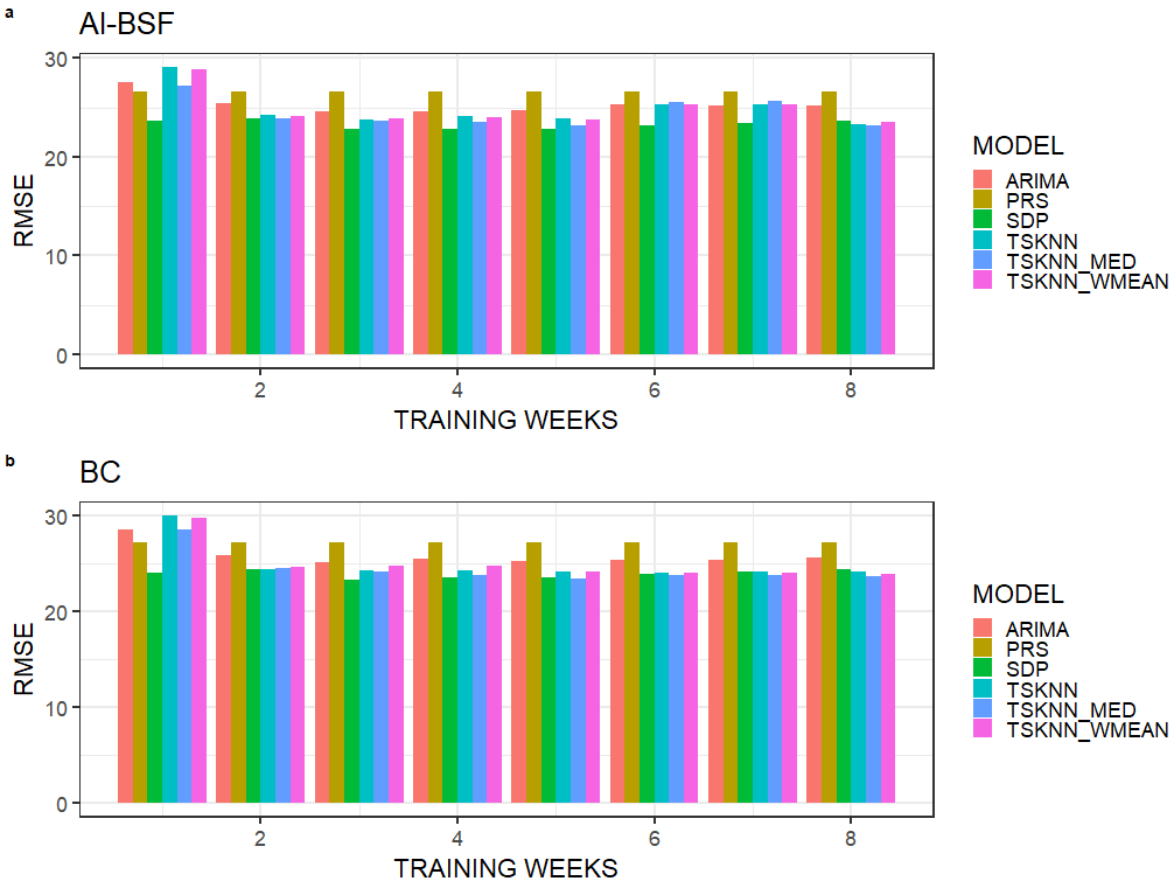

Fig. 8: RMSE performance of the persistence model, versus ARIMA, SDP, and 3 KNN_{TS} variants, with increasing training data. In TSKNN the combination function used to aggregate the targets associated with the nearest neighbors is the mean, in TSKNN_MED it is the median whereas in TS_WMEAN a weighted average is computed, with distance-based weights.

Tab. 1: RMSE and LnQ performance of the persistence model, versus ARIMA, SDP and KNN_{TS}. Reported accuracies depend on the number of training weeks N_W, which is shown in parentheses.

PV Type	Model	RMSE	LnQ
Al-BSF	PRS	26.619	42.462
Al-BSF	SDP	**22.809 (5)**	**41.441 (2)**
Al-BSF	ARIMA	24.582 (3)	43.601 (4)
Al-BSF	KNN_{TS}	23.120 (8)	56.394 (8)
BC	PRS	27.125	43.447
BC	SDP	**23.314 (3)**	**42.072 (2)**
BC	ARIMA	25.072 (3)	42.620 (3)
BC	KNN_{TS}	23.624 (8)	56.395 (8)

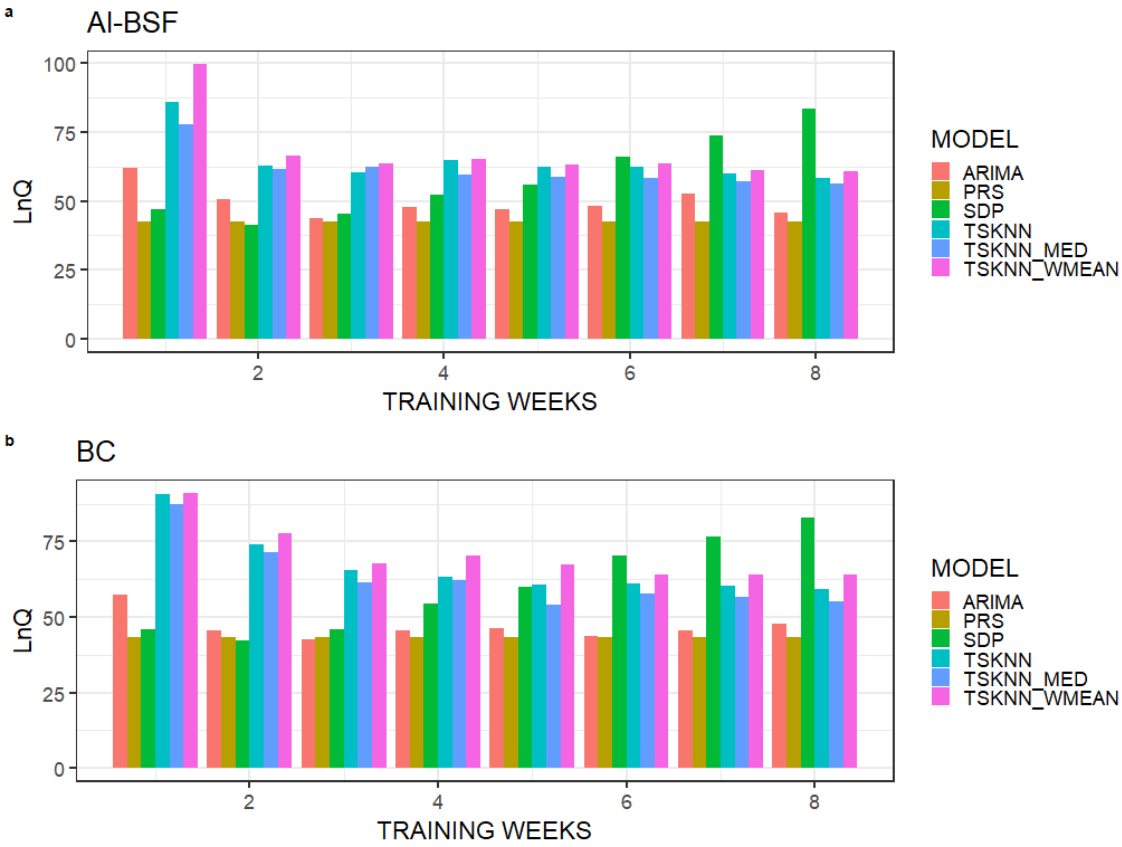

Fig. 9: LnQ performance of the persistence model, versus ARIMA, SDP, and 3 KNN_{TS} variants, with increasing training data. In TSKNN the combination function used to aggregate the targets associated with the nearest neighbors is the mean, in TSKNN_MED it is the median whereas in TS_WMEAN a weighted average (with distance-based weights) is computed.

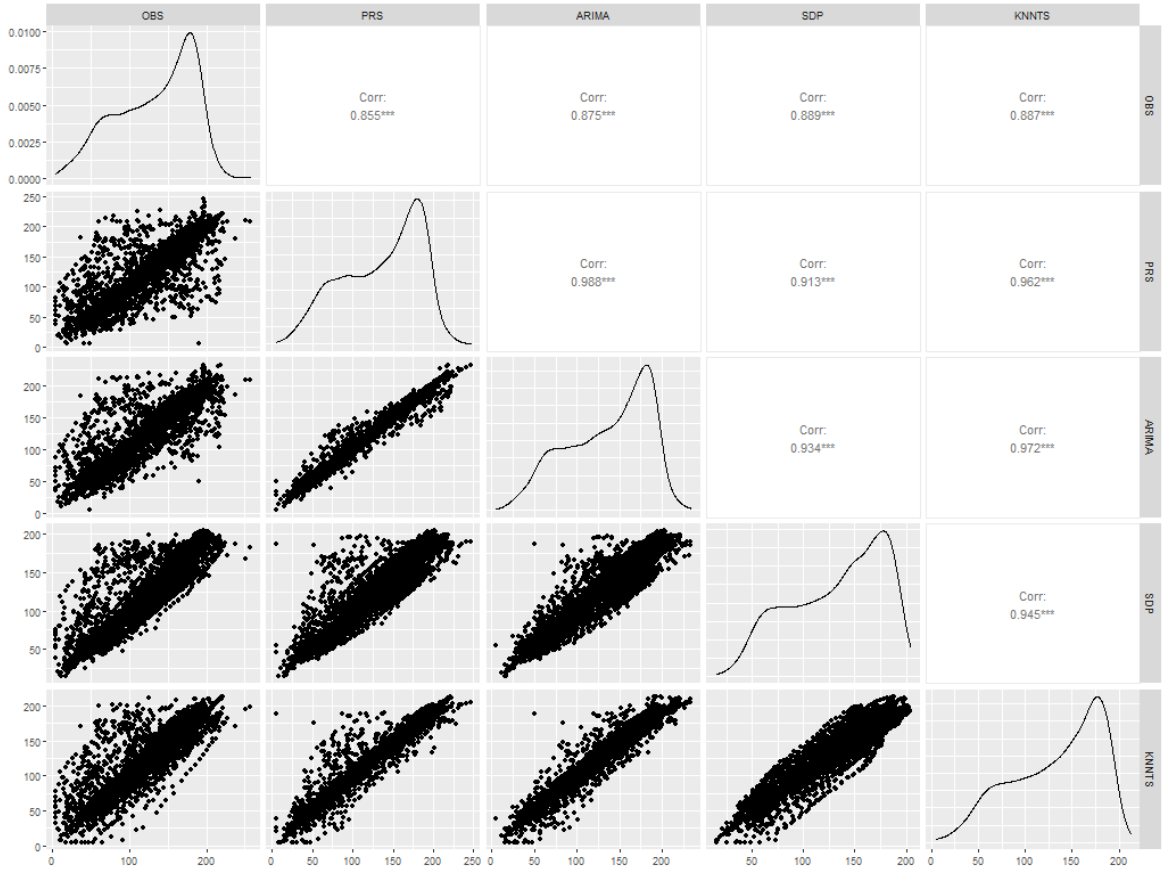

Fig. 10: Scatterplots and Pearson's bivariate correlation metrics for Al-BSF. Stars designate strong evidence against the null hypothesis that assumes zero correlation. Observed values (OBS), PRS, ARIMA with N_W=3, TSKNN with N_W=8 and SDP with NW=5 forecasts, are shown.

5. Concluding Remarks

This work evaluated a recently proposed time series KNN procedure against spline-based daily profiles, seasonal ARIMA and the persistence model, for day-ahead forecasting of PV outputs. Two types of solar panels are examined: Al-BSF and BC. Contrary to what one may expect, an extensive forecasting experiment revealed that KNN-based ensembles are not superior relative to the examined alternatives when performance is evaluated in terms of the widely adopted RMSE criterion. In fact, if one adopts a relative error metric, KNN_{TS} is by far the worst performing method. Despite the poor performance on the example application KNN_{TS} forecasts are expected to perform well when environmental conditions are highly variable, with regime-specific variability. The specifications examined here can be combined to result in a forecast combination scheme that is expected to perform as well as the best performing method. Such ensembles can be easily incorporated in a light (in terms of computations and data requirements) forecasting system. Construction of such ensembles via weighted combination schemes, is a research topic that we plan to examine next.

6. Acknowledgments

The authors acknowledge the support of KAUST and Saudi Aramco R&D Center - Carbon Management Division for their financial support in developing this work. This work was partially supported by grant #OSR–2020-4433.02 from KAUST and Saudi Aramco.

7. References

Antonanzas, J., Pozo-Vázquez, D., Fernandez-Jimenez, L.A., Martinez-de-Pison, F.J., 2017. The value of day-ahead forecasting for photovoltaics in the Spanish electricity market. Solar Energy 158, 140-146. https://doi.org/10.1016/j.solener.2017.09.043.

Brockwell, P.J., Davis, R.A., 1991. Time Series: theory and methods (2nd edition). Springer science & business media. http://dx.doi.org/10.1007/978-1-4419-0320-4

Cowpertwait, PSP, Metcalfe, A.V., 2009. Introductory Time Series with R, Springer. https://doi.org/10.1007/978-0-387-88698-5

EPIA, 2012. Available online: http://pvtrin.eu/assets/media/PDF/Publications/other_publications/263.pdf

Katsaounis, Th., Kotsovos, K, Gereige, I., Basaheeh, M., Abdullah, A., Khayat, A., Al-Habshi, E., Al-Saggaf, A., Tzavaras, A.E., 2019, Performance assessment of bifacial c-Si PV modules through device simulations and outdoor measurements, Renewable Energy, 143, 1285-1298. https://doi.org/10.1016/j.renene.2019.05.057

Koenker, R., 2005. Quantile Regression, Cambridge University Press. http://dx.doi.org/10.1017/CBO9780511754098

Martínez, F., Frías, M.P., Pérez, M.D., Rivera, A.J, 2019a. A methodology for applying k-nearest neighbor to time series forecasting. Artif Intell Rev 52, 2019-2037. http://dx.doi.org/10.1007/s10462-017-9593-z

Martínez, F., Frías, M.P., Charte, F., Rivera, A.J, 2019b. Time series forecasting with knn in R: the tsfknn package. R Journal, 11, 229. http://dx.doi.org/10.32614/RJ-2019-004

Nespoli A, Ogliari E, Leva S, Massi Pavan A, Mellit A, Lughi V, Dolara A., 2019. Day-Ahead Photovoltaic Forecasting: A Comparison of the Most Effective Techniques. Energies 12(9):1621. http://dx.doi.org/10.3390/en12091621

Skoplaki, E., Palyvos, J.A., 2009. On the temperature dependence of photovoltaic module electrical performance: A review of efficiency/power correlations. Solar Energy 83, 614-624. http://dx.doi.org/10.1016/j.solener.2008.10.008

Tofallis, C., 2015. A better measure of relative prediction accuracy for model selection and model estimation. Journal of the Operational Research Society, 66, 1352-1362. http://dx.doi.org/10.1057/jors.2014.103

DHgeN: Automated Generation of District Heating Network Layouts for feasibility studies

Giuseppe Peronato[1] and Jérôme H. Kämpf[1]

[1] Idiap Research Institute, Martigny (Switzerland)

Abstract

District Heating Networks (DHNs) are part of the solutions towards a low-carbon energy transition for space heating, making an efficient use of renewable or waste energy sources. In early-stage planning, their potential is often evaluated at the demand side, using large-scale building energy models. However, from the financial and energy efficiency standpoints, the actual potential is also depending on the development of the physical pipework connecting the supply heating station with the consumer substations. To this end, this work proposes a framework for the automated generation of a plausible network layout by solving a minimum spanning tree problem connecting the different stations and assigning a sizing peak power to each network element. Although fully adapted to data available in other contexts, we show here an application using Swiss open geodata, which allows for a quick analysis for any location in Switzerland with a few user inputs. The application in Broc (CH) shows a good match with the operating DHN in terms of piping linear length.

Keywords: district heating networks, Python module

1. Introduction

District Heating Networks (DHNs) are energy systems distributing heat generated in a central location to multiple building consumers using an insulated pipework. By the efficient use of local waste and renewable energy resources, also within cogeneration plants, district heating systems provide a viable solution to decarbonized heat supply to buildings.

Due to the long-term investment (Colmenar-Santos et al., 2017, chap. 3), DHNs require careful planning. Typical regional-scale potential assessments or early-stage viability studies (Bush and Bale, 2019; Gils et al., 2013) are commonly conducted by estimating heat density in a given region and hence selecting locations achieving a minimum threshold for DHN viability. Other studies focused on the potential allocation of demand and supply, in terms for example of excess industrial heat (Chambers et al., 2020) or geothermal energy (Li et al., 2022). However, the viability of a network is also depending on the necessary pipework to connect all consumer substations to the heating station(s) (Best et al., 2020).

Conceived as a flexible Python-based toolkit, DHgeN provides easy access to existing and new algorithms to generate a plausible network path and model the peak power of the network nodes and edges. Unlike existing optimization solutions (Best et al., 2020), it focuses on straightforward application of existing graph theory models from available geodata. Similarly to the work of Chambers (2020), it features a method for generating a network topology from open geodata, while focusing on the pipeline layout and with the goal of wrapping different models in a ready-to-use open-source Python module.

© 2022. The Authors. Published by International Solar Energy Society
Selection and/or peer review under responsibility of Scientific Committee
doi:10.18086/eurosun.2022.16.10 Available at http://proceedings.ises.org

2. Methodology

The module consists of a simple building peak power demand adapted to the Swiss context (§2.1) as well as an implementations of algorithms for generating the layout (§2.2), in particular for solving the minimum spanning tree (Steiner tree) and minimum cost flow (Simplex model) problems. Thanks to the presence of open data in Switzerland, the generation can be done with only a few user inputs while using some basic assumptions.

2.1 Model of the peak power demand

The peak power demand P [W] of buildings is modeled as follows:

$$\mathrm{P} = A \cdot \Delta T \cdot U \qquad \text{(eq. 1)}$$

where ΔT is the difference between the indoor T_{int} and outdoor temperature T_{out} [K], U is the standard envelope U-value (W/m^{2}K), and A is the building envelope area [m^2] calculated assuming a squared footprint and a 3-m floor height using the following equation:

$$\mathrm{A} = 4\sqrt{area_{footprint}} \cdot 3\, n_{floors} + 2\, area_{footprint} \qquad \text{(eq. 2)}$$

In Switzerland, the $area_{footprint}$ and n_{floors}, the period of construction and geographic coordinates of each building can be automatically retrieved from the Swiss Federal Register of Buildings and Dwellings (RegBL) available through an open API (see Tab. 1). The envelope U-value is set using the calibrated wall U-value for typical Swiss buildings for different periods (Perez, 2014, p. 177) and Swiss Society of Engineers and Architects (SIA) Norm 380/1:2009 for the most recent values. The T_{int} and T_{out} can be set by the user, for example using standard values from the SIA. Depending on the building use, a power density of 1 to 3 W/m^2 $_{\text{floor area}}$ is also considered, while internal loads, solar gains and window losses are neglected here.

Results are bounded to recommended power-to-floor-area densities for non-labeled buildings (SuisseEnergie, 2016), i.e., a minimum of 25 MW/m^2$_{\text{floor area}}$ (i.e., for recent buildings) and a maximum of 80 MW/m^2$_{\text{floor area}}$ (i.e., for poorly insulated commercial buildings), in order to avoid outliers due to possibly incorrect input data.

2.2 Model of the network layout and power distribution

The process of generating the network is illustrated in Fig. 2. The Python implementation is largely based on NetworkX (Hagberg et al., 2008, 2019) and GeoPandas (Jordahl et al., 2020) modules. An initial graph *G* is modeled as a regularly spaced grid, where the width and length of the cell nodes (by default 25 m) and rotation (by default 0°) can be set by the user. It is also possible to generate a custom tessellation instead of the regularly-spaced grid, but its implementation, using at the moment only input points from the (sub)stations data and a Voronoi diagram, is still basic.

In addition to the input (sub)stations, other geodata can be included in the module. If footprint data is added, the graph edges intersecting with the building footprints are removed from the initial graph *G*. If road data is added, a graph *R* is created from the vector paths, which are densified to the same resolution as *G*. The two graphs are connected by creating new nodes at their geometrical intersection resulting in graph *G'*.

The network *G''* is then created by connecting all heating (sub)stations *s* to the closest edge *ab*. This is done, as illustrated in Fig. 1a, by adding a new node *x* and new edge *sx* perpendicular to *ab*, splitting *ab* into two new edges *ax* and *bx* and removing the original edge *ab*.

The minimum spanning tree connecting all consumer (sub)stations *s* in graph *G''* is computed solving a Steiner tree problem. This method is commonly used for optimizing electrical grids and has been already implemented in DHN layout optimization (Delmastro et al., 2016). In our implementation, *G''*

edges can be weighted by a parameter set by the user, where a value lower than 1 can be used to give a priority to a road (i.e., from original graph *R*) over other edges (e.g., from original graph *G*) which by default have a value of 1.

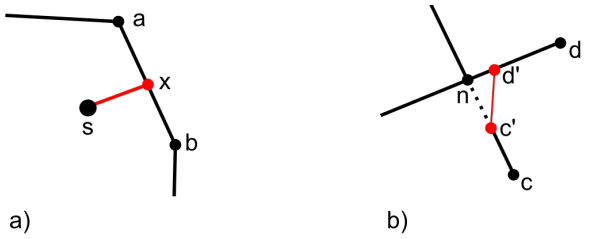

Fig. 1: Schematics of the main graph-processing algorithms: a) Connection of a substation *s* to the network b) Transformation of a 4-degree node *n* into two 3-degree (T-junction) nodes *n* and *d'*

In DHgeN, the user has the option to choose either Networkx's approximate Steiner tree model or a Steiner tree heuristics (Hušek et al., 2019). The latter model was developed in the framework of the PACE2018 Competition, where it obtained the 4th place in the track dedicated to heuristics with large tree width and high number of terminals (Bonnet and Sikora, 2019). It has been chosen for integration in DHgeN because of its complete documentation, easiness to compile, fitness to large graphs, and compatibility with the GPLv3 license.

In the final network, the degree of each graph node *n* is limited to a maximum value of 3, so as to accept only T-junctions. As illustrated in Fig. 1b), this is ensured by creating a new node *n'* translated over one of outgoing edges, e.g., *nd*. The *nd* edge is then replaced by two edges *nd'* and *d'd* and the original *nc* edge is replaced by the new edges *d'c'* and *c'c*.

The resulting non-directional graph is transformed into a directional graph originating from the heating station, whose spatial location can be set by the user, resulting in a typical branched DHN. Finally, the peak power of each edge of the network is computed using NetworkX simplex network model, using as demand the substations power (calculated in §2.1) and as weight the edges' priority (i.e, edge length multiplied by edge weight).

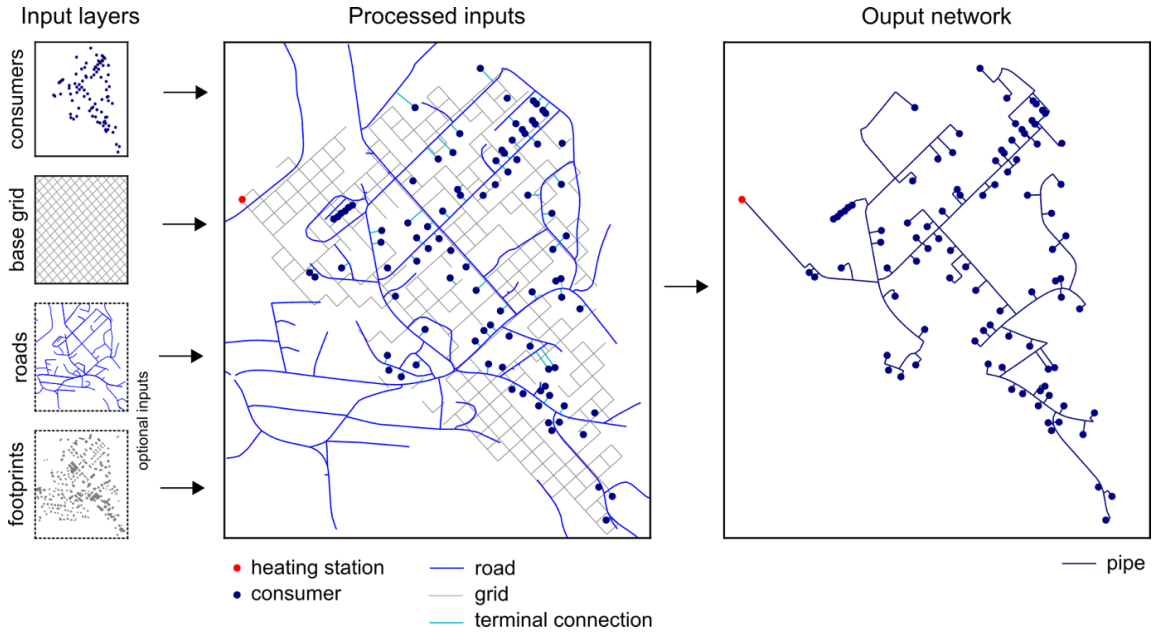

Fig. 2: Main datasets and processes involved to create the network layout.

3. Test-case application

We present here a test-case application in an area of the municipality of Broc (Switzerland) where a DHN is currently in operation. The online repository (see §4) contains also other examples of applications using either geodata from the GeoAdmin API available in Switzerland or a sample input file.

This section presents additional results comparing the modeled network in Broc with the data provided by the design engineering firm. The part using publicly-available data is reproducible using the scripts in the online repository

3.1 Presentation of the case study

In the data representing the status in 2019, the network in Broc is composed of 85 substations connected (or planned to be connected) to a heating station located at the north-west boundaries of the village. We delimit our analysis in the area bounded by this network, covering a surface of almost 500,000 m^2. It should be noted that not all buildings in the area are connected (or planned to be connected) to the DHN nor are listed in the Register of Buildings and Dwellings (RegBL) as such.

For the purposes of this study, we show the existing reference network R as well four modeled versions using as input layers:

1. The buildings classified in the RegBL as having access to the district heating network as of September 2022 (n=92) and connected by
    a. A grid-based graph;
    b. A grid-based graph including also the road network and excluding edges intersecting with the building footprints.
2. The substations coordinates as in the data available from the engineering company (n=85) connected through:
    a. A grid-based graph as in 1a;
    b. The same graph as in 2a, but including a road segment with its weight set to 10 to avoid crossing twice the railway lines. This variant is proposed to demonstrate how the user can add further constraints and is meant to have a layout that is more similar to R.

In all cases, a base graph formed by 25x25-m grid is used. This is rotated by 42°, so as to visually align with the main roads and produce more realistic results. In variants 1b and 2, the network also includes the road graph with a 0.5 weight.

For all variants, the peak power is modeled using data from the RegBL (see §2.1 and Tab. 1). In records with missing values default values of n_{floors} = 2 and U =1.35 W/m^2 K were used. It should be noted that these hypotheses are not necessary aligned with those used in the design of the network R.

Tab. 1: Extract of some records from a RegBL query run using the functions provided in DHgeN. The description of the fields and their keys can be found here: https://www.housing-stat.ch/fr/help/42.html (in German, French and Italian). The API documentation is available here: https://api3.geo.admin.ch

egid (unique identifier)	**geometry**	**gklas** (use)	**gastw** (n. of floors)	**gbaup** (construction period)	**garea** (footprint area in m^2)	**genh1** (heating source)
1509806	POINT (2573843.9 1161849.4)	1110	2	8016	97	7501
504110198	POINT (2574202.6 1161870)	1276	N/A	8011	140	N/A
1509810	POINT (2573952.2 1161852.4)	1122	7	8015	252	7530
1509812	POINT (2574008 1161873)	1122	4	8014	492	7580

3.2 Results

The resulting layout solutions and the reference network are compared in Tab. 2 and Fig. 3.

Since the number and location of the heating stations is slightly different for variants 1 compared to R, a fair comparison can be drawn only between variants 2a with R.

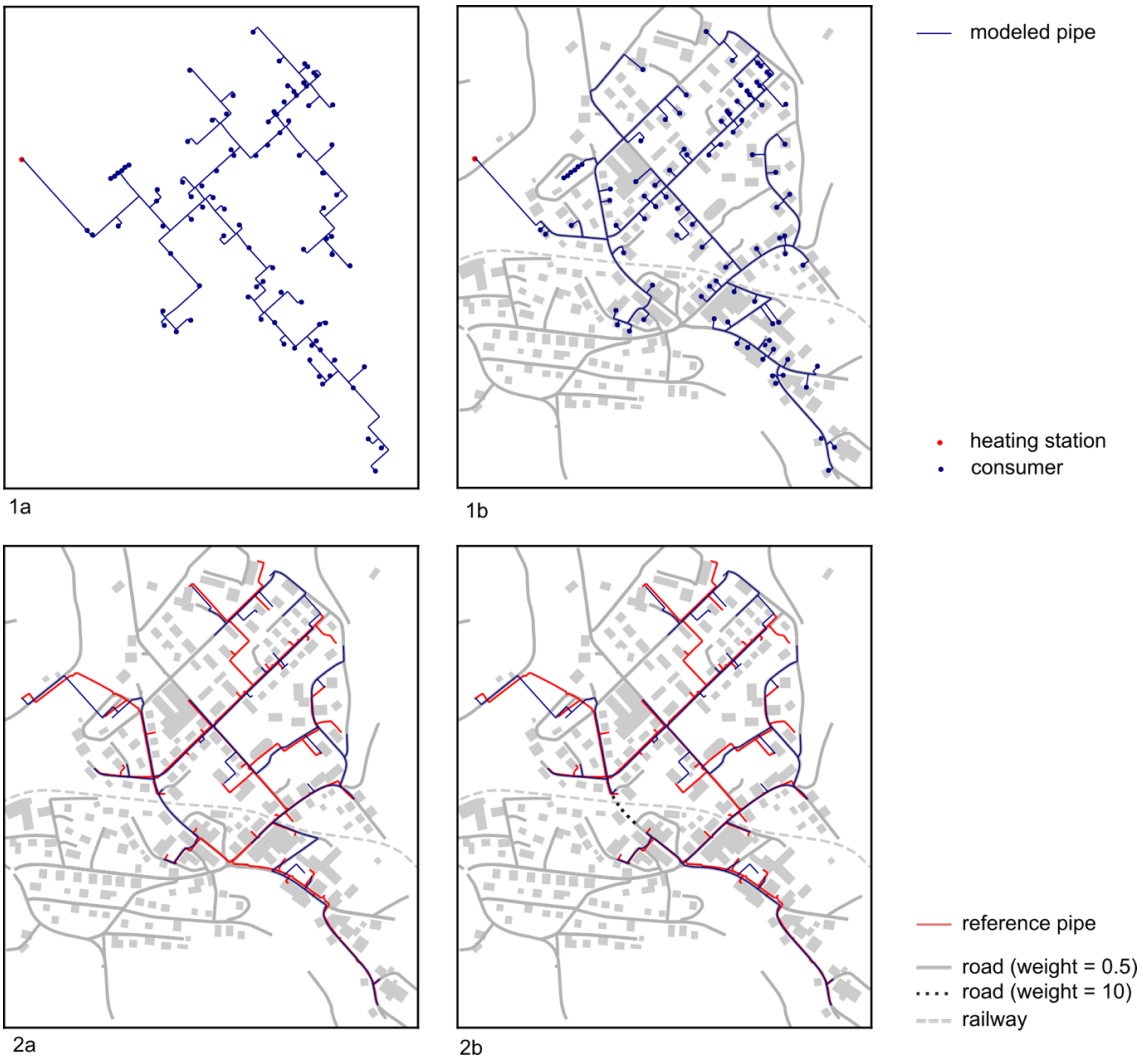

Fig. 3: Comparison of the paths generated by the algorithm. Layouts 2a and 2b are also compared to the actual path of the reference DHN: please note that the substations and their closest pipes are not shown here due to confidentiality. Layout 2b includes a custom weight = 10 for a road segment to avoid an additional crossing of the railway (drawn in the map, but not part of the inputs).

The length of the modeled networks present similar figures, while the cumulative power is underestimated compared to the reference. The length difference (+4%) between cases 2 and R seems negligible, both for expected power losses and costs due to longer piping. The modeled layouts look plausible, while in some cases differ from the reference one, particularly in the north-east area where more road options are possible. In terms of peak power of the substations (-20% of the reference), the figure can be considered a good estimate, before a safety margin at the heat exchanger level is added, as it was likely the case for the reference.

Variant 1a presents the shortest path, while, unsurprisingly, it is largely unfeasible because of the absence of constraints. Nonetheless, it could be still used as a design-support tool to select the best paths in a given area, especially when vector roads data and or building footprints are not available. In variants 1b, 2a and 2b, similar characteristics can be seen. In general, it can be noted that in some large lots,

longer paths are needed to connect to the substation consumers. These include some unrealistic U and T-shaped paths (see Fig. 3, variant 1b), which are due to the underlying grid.

In both variants 1b and 2b, in order to supply some consumers south of the railway lines, the algorithm selects a road crossing the railway line. It is interesting to note how this crossing was instead avoided in the actual design path, probably for construction complexity and costs. In this sense, setting a custom weight as in variant 2b helps avoid this crossing. In general, if some roads are to be avoided or preferred for specific reasons, setting custom weights would help further customize the layout.

Based on the peak power of the consumer substations, DHgeN also attributes the power of each pipe segment as well an estimated nominal diameter (DN). Fig. 4 shows the peak power for both consumers and pipes for variant 1b. We argue that these values can be used as a first estimate to pre-size the pipework and anticipate hence the main construction works.

Tab. 1: Comparison of some relevant figures of the actual and modeled networks.

	Reference network	**Modeled networks**			
Variants	R	1a	1b	2a	2b
Data source	Private database	Public API (RegBL)	Public API (RegBL)	Private database	Private database
Additional data from public APIs		-	Footprints and roads	Footprints and roads	Footprints and roads (with custom weight)
Length of supply pipework	3861 m	3598 m (-7%)	4371 m (+13%)	3999 m (+4%)	4005 m (+4%)
Number of pipes	563	303	553	542	546
Cumulative peak power of the substations	3.06 MW	2.63 MW (-14 %)		2.43 MW (-20%)	
Number of substations	85	92		85	

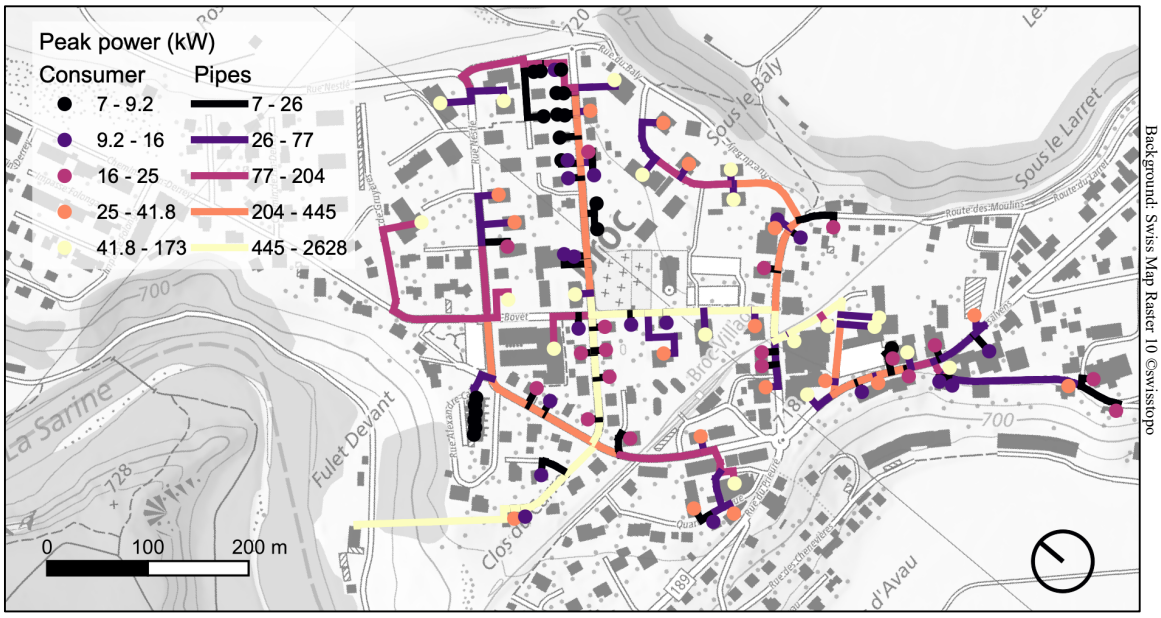

Fig. 4: Generated layout and power flow for variant 1b.

4. Software development and release

DHgeN is developed in Python using open-source libraries and is distributed under the GPLv3 license. It can be installed using pip. A Docker file is provided to allow for reproducibility and unit testing.

The source code is available at the following Git repository: https://www.github.com/idiap/dhgen. Any contribution is welcome using issues and merge requests.

5. Conclusion

This paper has given an overview of the DHgeN Python module at its current development stage (September 2022). DHgeN is released as open-source software under the GPLv3 license.

By using this tool, the user can test different planning scenarios, notably for choosing the optimal location of the heating station, minimizing the length of the pipework and/or the DN of the pipes.

The output of the models was compared to the layout of an existing DHN showing fairly realistic modeled layouts, only slightly longer than the reference one (+4%), i.e., a network partially planned and partially in operation designed by a local engineering firm. Based on these results, we argue that the proposed module can be used as a design-support tool to draft a DHN layout in the context of feasibility studies. The proposed layout can be then adjusted, also by setting custom parameters in the tool itself, to reach a further design phase.

Expected on-going and future development will be conducted along the following paths:

- Integration of further goals/constraints, also using an iterative approach. This, for example, would allow for the integration of further constraints (e.g., avoiding intersections) in the terminal connection from the main pipe network to the consumer substation;
- Improvement of the load model and interface to other tools for hydraulic/thermal simulation (CitySim, pyDHN);
- Integrating further geodata in the algorithm (fiber optics networks, railway lines, rivers);
- Creation of a user interface, either as web-application or as QGIS plugin.

6. Acknowledgments

This work has been conducted in the framework of the Eguzki research project, funded by the Swiss Federal Office of Energy (SFOE) under contract SI/502111-01, OIKEN SA, ALTIS Groupe SA, SATOM SA and RWB Valais SA.

The data of the Broc DHN was kindly provided by RWB Fribourg SA as a courtesy of the operator EBL Fernwärme AG. Further information on the DHN can be found in the municipality website (in French): https://www.broc.ch/environnement-et-energie/chauffage-distance

Additional datasets were retrieved using the GeoAdmin API: the layers *ch.swisstopo.swisstlm3d-strassen* (roads) and *ch.swisstopo.vec25-gebaeude* (footprints) of the Swiss Federal Office of Topography (Swisstopo), the layer *ch.bfs.gebaeude_wohnungs_register* (Swiss Federal Register of Buildings and Dwellings - RegBL) of the Swiss Federal Office of Statistics (SFS), and the layer *ch.bav.schienennetz* (railway) from the Swiss Federal Office of Transport (FOT). Further documentation on GeoAdmin can be found at https://api3.geo.admin.ch as well as in the DHgeN repository https://www.github.com/idiap/dhgen.

The authors would like to thank Roberto Boghetti (Idiap Research Institute) and Giona Galizia (RWB) for their feedback during the development of this module.

7. References

Best, R.E., Rezazadeh Kalehbasti, P., Lepech, M.D., 2020. A novel approach to district heating and cooling network design based on life cycle cost optimization. Energy 194, 116837. https://doi.org/10.1016/j.energy.2019.116837

Bonnet, É., Sikora, F., 2019. The PACE 2018 Parameterized Algorithms and Computational Experiments Challenge: The Third Iteration. Presented at the 13th International Symposium on Parameterized and Exact Computation (IPEC 2018). https://doi.org/10.4230/LIPICS.IPEC.2018.26

Bush, R.E., Bale, C.S.E., 2019. Energy planning tools for low carbon transitions: an example of a multicriteria spatial planning tool for district heating. J. Environ. Plan. Manag. 62, 2186–2209. https://doi.org/10.1080/09640568.2018.1536605

Chambers, J., 2020. Computationally scalable geospatial network and routing analysis through multi-level spatial clustering. MethodsX 7, 101072. https://doi.org/10.1016/j.mex.2020.101072

Chambers, J., Zuberi, S., Jibran, M., Narula, K., Patel, M.K., 2020. Spatiotemporal analysis of industrial excess heat supply for district heat networks in Switzerland. Energy 192, 116705. https://doi.org/10.1016/j.energy.2019.116705

Colmenar-Santos, A., Borge-Díez, D., Rosales-Asensio, E., 2017. District Heating and Cooling Networks in the European Union. Springer International Publishing, Cham. https://doi.org/10.1007/978-3-319-57952-8

Delmastro, C., Mutani, G., Schranz, L., 2016. The evaluation of buildings energy consumption and the optimization of district heating networks: a GIS-based model. Int. J. Energy Environ. Eng. 7, 343–351. https://doi.org/10.1007/s40095-015-0161-5

Gils, H.C., Cofala, J., Wagner, F., Schöpp, W., 2013. GIS-based assessment of the district heating potential in the USA. Energy 58, 318–329. https://doi.org/10.1016/j.energy.2013.06.028

Hagberg, A.A., Schult, D.A., Swart, P.J., 2019. networkx/networkx. NetworkX: Python software for complex networks.

Hagberg, A.A., Schult, D.A., Swart, P.J., 2008. Exploring Network Structure, Dynamics, and Function using NetworkX, in: Varoquaux, G., Vaught, T., Millman, J. (Eds.), Proceedings of the 7th Python in Science Conference. Pasadena, CA USA, pp. 11–15.

Hušek, R., Toufar, T., Knop, D., Masařík, T., Eiben, E., 2019. SteinerTreeHeuristics.

Jordahl, K., Bossche, J.V. den, Fleischmann, M., Wasserman, J., McBride, J., Gerard, J., Tratner, J., Perry, M., Badaracco, A.G., Farmer, C., Hjelle, G.A., Snow, A.D., Cochran, M., Gillies, S., Culbertson, L., Bartos, M., Eubank, N., maxalbert, Bilogur, A., Rey, S., Ren, C., Arribas-Bel, D., Wasser, L., Wolf, L.J., Journois, M., Wilson, J., Greenhall, A., Holdgraf, C., Filipe, Leblanc, F., 2020. geopandas/geopandas: v0.8.1. Zenodo. https://doi.org/10.5281/zenodo.3946761

Li, X., Walch, A., Yilmaz, S., Patel, M., Chambers, J., 2022. Optimal spatial resource allocation in networks: Application to district heating and cooling. Comput. Ind. Eng. 171, 108448. https://doi.org/10.1016/j.cie.2022.108448

Perez, D., 2014. A framework to model and simulate the disaggregated energy flows supplying buildings in urban areas (PhD thesis). Ecole polytechnique fédérale de Lausanne.

SuisseEnergie (Ed.), 2016. Détermination de la puissance du générateur de chaleur.

A Multistep Optimization Procedure for a Fair Sharing of Profits in Energy Communities

Gerald Steinmaurer[1]

1 FH OOE Forschungs & Entwicklungs GmbH, Wels (Austria)

Center of Excellence / Energy

Abstract

Renewable energy communities offer the possibility to share energy excess in your neighborhood. Especially for electrical energy exchange in the case of photovoltaic systems, this community is both a sustainable and also an economically interesting option.

The necessary task of distributing the energy flows in such communities will lead to different economic impacts on the participants. This work proposes a mathematical multi-step procedure to find a fair distribution of the gained cost savings in an energy community, depending on the contribution of every member of the community.

Keywords: Energy communities, optimization, photovoltaics, storage systems, optimal power flow, Multi-step

1. Introduction

In renewable energy communities, energy can be exchanged beyond household or company borders, and every participant of such a community is allowed to produce, sell, buy or store energy (EE-RL. 2018). This energy exchange is a very interesting option, especially for PV systems, because a typical design often results in electrical surpluses at noon.

Potential members of energy are in most cases interested in a sustainable but also in an economic operation of their energy supply. Several test cases (Steinmaurer, 2020) show, that not all members of energy communities benefit to the same extent from their participation in this community. This work aims to present a methodological development towards a fair distribution of profits in such electrical energy communities.

The paper is organized as follows: after a short introduction, a developed optimization method for PV- and battery systems in energy communities is presented. This method evaluates the contribution of every participant and uses this information in a multi-step procedure to distribute the economic advantages in energy communities.

2. Method

The presented method for finding a fair distribution of advantages in electrical energy communities is based on a previous publication (Steinmaurer, 2020). For easier understanding, the method used there is briefly listed here again. Every participant in a renewable energy community has properties, according to Fig. 1. The states $x_1 \dots x_8$ are power values of this player in the community and describe the energy flow situation. State x_5 refers to the state of charge of the storage unit. Arrows indicate possible energy flow directions, like load and PV production, costs for energy purchase (x_1) as well as remuneration for feed-in (x_2) are assumed to be known.

© 2022. The Authors. Published by International Solar Energy Society
Selection and/or peer review under responsibility of Scientific Committee
doi:10.18086/eurosun.2022.16.11 Available at http://proceedings.ises.org

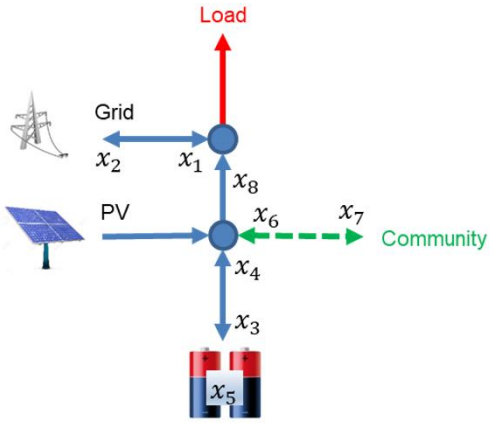

Fig. 1: Structure of energy flow optimization of one single participant in an energy community. States xi consider power flow at every time instant, from (Steinmaurer, 2020)

Every Energy community consists of *N* participants with properties of Fig. 1. Renewable energy will be exchanged via the public grid - but with different fees and costs (so the states x_6 and x_7 are necessary). Efficiencies for charging (x_3) and discharging (x_4) of the battery are also considered, the non-negative state x_8 avoids battery charging from the grid.

The overall energy flow coordination problem considering all time instants for every participating partner leads then to a linear programming procedure

$$\min_{\boldsymbol{x}} \boldsymbol{c}^T \boldsymbol{x} \qquad \text{(eq. 11)}$$

$$\boldsymbol{A}_{eq}\boldsymbol{x} = \boldsymbol{b}_{eq}$$

$$\boldsymbol{A}_{ineq}x \leq \boldsymbol{b}_{ineq}$$

$$\boldsymbol{x}_{lb} \leq \boldsymbol{x} \leq \boldsymbol{x}_{ub}$$

considering equality constraints $\boldsymbol{A}_{eq}\boldsymbol{x} = \boldsymbol{b}_{eq}$ ((eq. 1) to (eq. 4)) and inequality constraints for the states $\boldsymbol{x}_{lb} \leq \boldsymbol{x} \leq \boldsymbol{x}_{ub}$ (e.g. maximum and minimum power, storage limitations, …) and for additional limitations ($\boldsymbol{A}_{ineq}x \leq \boldsymbol{b}_{ineq}$). As mentioned, details can be found in (Steinmaurer, 2020).

This optimization procedure was used to find an optimal discrete time sequence of all states $\boldsymbol{x}$ from (eq. 1) for several test cases. The example in (Steinmaurer, 2020) with 4 participating partners shows that in some cases the optimal solution for the energy community (minimal summed up costs for all participants) can lead to disadvantages for some individual partners in the community, e.g. increased costs for partner P3 (-3.78€), while all other participants gain an advantage (see Tab.1)

The individual cost savings of each partner (with and without being part of the energy community) are listed in Tab. 1 in an absolute (S_i) and in a relative ($S_{i,r}$) representation

$$S_{i,r} = \frac{S_i}{F_i} 100\% \qquad \text{(eq. 2)}$$

Tab. 1: Resulting costs for each participant and the saving in comparison to the individual costs without being part of an energy community, adjusted from (Steinmaurer, 2020)

		P1	**P2**	**P3**	**P4**		**Sum**
Individual costs of partner *i* without energy community $\boldsymbol{F_i}$	€	103.95	34.15	14.72	118.50		$\sum_{i=1}^{4} F_i$ = 271.33

Savings of partner *i* through community $\boldsymbol{S_i}$	€	8.87	2.58	**-3.78**	27.31		$\sum_{i=1}^{4} S_i$ = 34.99
Relative cost savings $\boldsymbol{S_{i,r}}$	-	8.53%	7.56%	**-25,6%**	23,1%		$\frac{\sum_{i=1}^{4} S_i}{\sum_{i=1}^{4} F_i}$ 100% = 12.9%

Calculation of an Energy community contribution index

In (Steinmaurer, 2020) a first attempt to assess the importance of an individual participant was presented. This was done by eliminating single players from the energy community and observing the effects of cost savings on the community. This results in an assessment of the importance of participants to the economic viability of such energy communities (see Tab 2).).

In the next step, a community contribution index C_i of every participant $i = 1 \ldots N$ is defined

$$C_i = \frac{S_{C,i} - \sum_{i=1}^{N} S_i}{\sum_{i=1}^{N} S_i} \qquad \text{(eq. 3)}$$

where $S_{C,i}$ are the savings of the community without participant P_i , S_i are the savings of the individual participant *i* in a complete energy community with all participants (see tab. 1). This index is able to measure the importance of a single participant in a community.

Tab. 2: Assessment of the individual contribution to the energy community

	Community Savings $S_{c,i}$	**Community Contribution index** C_i
Community without **P1**	$S_{c,1}$ =19.04 €	0,458
Community without **P2**	$S_{c,2}$ =10.04 €	0,71
Community without **P3**	$S_{c,3}$ =29.79 €	0.148
Community without **P4**	$S_{c,4}$ =19.25 €	0,449
Community with **all participants**	$\sum_{i=1}^{4} S_i$ = 34.99€	

Fig. 2 shows a possible result of the contribution index as a function of the individual savings for all players in an energy community. Because the optimization procedure minimizes costs to the entire energy community, some participants may experience slightly higher costs after the optimization, although savings are made by the community itself. It is obvious, that such a situation - with some participants (indicated in red) have a disadvantage while others benefit - does not offer a perspective for long-term cooperation in this community.

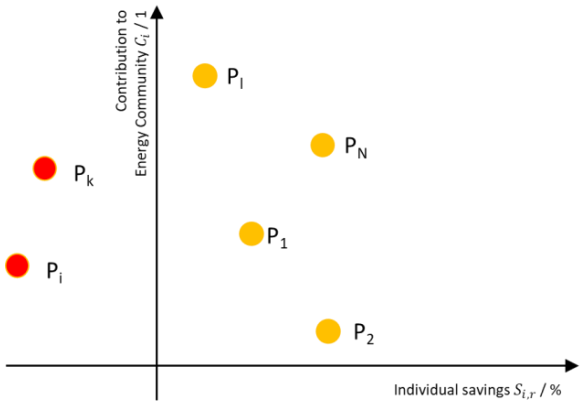

Fig. 2: Contribution index vs. individual savings in an energy community

There are two basic possibilities to avoid drawbacks for some participants:

- the community itself builds a mode for a financial balancing of these injustices after the energy exchange (cross-financing of the economic advantages) or
- a mathematical procedure to include the contribution index in the optimization task.

In this work, the second approach will be demonstrated.

Multistep-Procedure

The single-step procedure of (Steinmaurer, 2020) offers the drawbacks of non-consideration of negative savings of some participants, apart from that no information about the importance of a participant in an energy community is included in the optimization procedure.

The main concept of the proposed multistep procedure is

a) Compute the optimal solution (minimum costs) for the energy community

b) Compute the individual savings $S_{C,i}$ and the contribution index C_i of every participant

c) Define additional boundary conditions for minimum savings of every participant, depending on the parameters of b)

d) Solve the extended optimization task

e) If the solution of d) is feasible, then the requirements of c) are tightened and continue with c)

To realize a fair contribution of the economic advantages, the additional boundary conditions can be used to define the increasing minimum savings of every participant if the contribution index is increasing. This behavior can be realized with a simple linear function of minimum savings for all players. The minimum requirement and the starting point for further optimization for the energy community are, that no participant has higher costs for energy than without the community. To reward participants with higher contributions to the energy community, the minimum saving will be increased depending on the contribution. This will be done by restricting the solutions space of the optimization task linearly to Ci. As a result of that, the solutions must move to higher savings beyond the newly added minimum saving limit. The lower boundary condition for every participant is then calculated

$$S_{i,lb} = kC_i \qquad \text{(eq. 4)}$$

The slope k starts with $k = 0$ (left diagram of Fig. 3) and is increased until no solution to the optimizing task can be found. The last feasible solution is the result of this multistep procedure. (right diagram of Fig. 3, the

constraint of participant P_l is violated first while all other participants are still in the allowed Solution space).

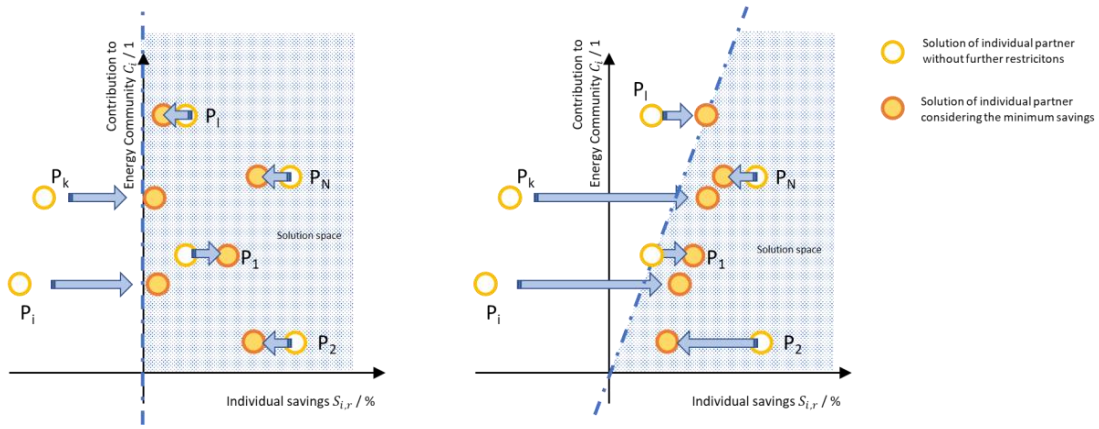

Fig. 3: Restriction of the solution space for the optimization procedure

3. Results

The multistep-procedure from chapter 2 is shown for the test cases with 4 participants of an energy community (from (Steinmaurer, 2020)). Starting with the initial optimization without restrictions on individual savings leads to a solution with an economic disadvantage for participant P3. Applying the presented multistep-procedure (starting with $k = 0$ leads then to the results of Tab. 3. The graphical representation can be seen in Fig. 4. Although all participants' solutions appear to lie on the optimal slope line, only P3 is exactly on this line, all other participants are inside the solution space.

Tab. 3: Results of the multistep-procedure

		P1	**P2**	**P3**	**P4**		**Sum**
Individual costs of partner *i* without energy community F_i	€	103.95	34.15	14.72	118.50		271.33
Community Contribution index C_i	1	0.458	0.71	0.148	0.449		
Savings of partner *i* through community S_i / $S_{i,r}$ without minimum savings	€ %	8.87 8.52	2.58 7.56	-3.78 -25.65	27.31 23.05		34.99 12.90
Savings of partner *i* through community S_i / $S_{i,r}$ with $k = 0$	€ %	8.87 8.52	2.58 7.56	0 0	22.03 18.6		33.49 12.34
Savings of partner *i* through community S_i / $S_{i,r}$ with max k	€ %	10.47 10.08	5.33 15.62	0.48 3.25	11.84 9.99		28.13 10.37

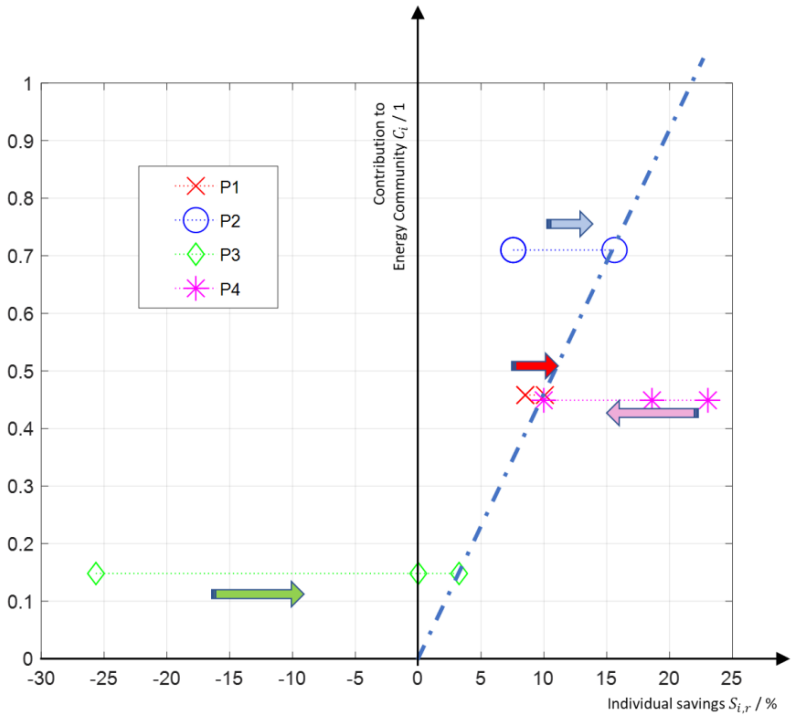

Fig. 4: Resulting individual savings of an energy community with 4 participants P1 … P4

4. Conclusions and Outlook

A renewable energy community is an ideal possibility to share excess energy with other participants and take economic advantage of this legal opportunity. The distribution of energy within this community can be seen as an optimization task, where the global costs of the community will be minimized. As demonstrated in an initial example, this minimization can lead to financial drawbacks for some community members. To avoid this injustice, a multistep-procedure was presented, where a community contribution index was used to determine a fair share of the community savings. This procedure can be used to define the economic advantages in energy communities of every participant in an understandable mathematical way.

5. Acknowledgments

This paper was elaborated in the framework of 2 research projects:

- The mathematical method development was funded by the government of Upper Austria, Project: “Methodenentwicklung für Energieflussoptimierung
- The research on use cases and the deviation to economic business models were granted in the project “Industrial Microgrids” (FFG number 868708), which was funded by the Austrian Climate and Energy Funds in the framework of “Vorzeigeregionen Energie – NEFI” and the government of Upper Austria.

6. References

EE-RL (2018): Directive (EU) 2018/2001 of the European Parliament and of the Council of 11 December 2018 on the promotion of the use of energy from renewable sources, Retrieved September 1, 2022 from *https://eur-lex.europa.eu/legal-content/EN/TXT/HTML/?uri=CELEX:32018L2001*

Steinmaurer, G. (2020). An Optimization Approach to Control the Energy Flows in Renewable Energy Communities. *EuroSun 2020, Athens, Greece*. doi: 10.18086/eurosun.2020.05.16

Applying Machine Learning Methods and Outlier Detection to Process and Analyse Incomplete Heat Meter Data

Ulrich Trabert, Felix Pag, Janybek Orozaliev, Klaus Vajen

University of Kassel, Institute of Thermal Engineering, Kassel (Germany)

Abstract

Digitalization plays an important role to achieve optimised operation of renewable-based energy supply systems coupling the sectors heat, electricity, and mobility. The benefit derived from optimization methods, however, also depends on the quality of the used data. Therefore, the present study analyses methods which can be applied for processing of low-quality heat meter data. Machine learning algorithms are used to fill the gaps of incomplete load and return temperature multi-year profiles retrieved from a dataset of five heat meters installed in a heating grid of an industrial consumer. On average, the coefficient of determination R^2 for the machine learning algorithm is 0.92. Additionally, two statistics-based filters, that are applied to detect outliers in continuous profiles, are compared. Those filters slightly improve the accuracy of the models and help to obtain more consistent profiles from the heat meter data. The completed datasets support enhanced data analysis, which lays the ground for redesigning fossil-fuelled and optimizing smart renewable energy systems.

Keywords: Digitalization, machine learning, outlier detection, heat meter data

1. Introduction

In the wake of digitalization, the amount of available datapoints from energy systems is strongly increasing. Analysis of that data gives detailed knowledge about the systems, which is useful for improving operational stability, energy efficiency and for remodelling of existing systems towards renewable energies.

While digitalization in the electricity sector is already well advanced, the heat sector lags behind as measuring heat flows requires more complex sensor technology with higher installation costs. In combination with historically lower costs for heat than for electricity, it is less attractive to monitor heat systems in detail. Therefore, accurate measured heat consumption data in a high temporal resolution (i.e. hourly) is usually rare. Additionally, the quality of the data depends on installation and signal transmission conditions. Adverse conditions may lead to effects like incomplete or irregular heat meter data, which is also true for the dataset used in this work.

2. Heat Meter Data Processing

The following chapters propose a procedure to improve low quality heat meter data. This includes the completion of fragmentary timeseries by predicting the missing data with a machine learning regression algorithm as well as two methods for statistical outlier detection. Furthermore, the impact of outlier detection on the accuracy of the models is analyzed.

2.1 Original dataset

The original dataset used in this study consists of three years of data which come from five heat meters measuring load, supply and return temperature in hourly resolution. They belong to a heating grid of an industrial complex with several buildings. The timeseries of the example dataset have gaps that, on average, account for 29 % of the time within the three-year period. These gaps are caused by an error-prone IT infrastructure, which is used to transfer the measured values of the heat meters and store them in a central database.

As an example, Fig. 1 shows the original heat load, supply and return temperature profiles for one heat meter for the year 2020. The heat load was normalized using its maximum value within the three-year period, as the actual values of the profile are irrelevant to the methods applied in this paper. The gaps are visible as zero values in the shown graphs. They mostly occur simultaneously in all three profiles but show no obvious patterns. The duration of missing periods varies from a few hours up to multiple weeks. All five heat meters have similar characteristics in terms of missing data, but the course of load and temperature profiles deviates according to the type of consumers. Both heat load and return temperature are strongly dependent on ambient temperature, because space heating accounts for the largest share in heat demand.

© 2022. The Authors. Published by International Solar Energy Society
Selection and/or peer review under responsibility of Scientific Committee
doi:10.18086/eurosun.2022.16.12 Available at http://proceedings.ises.org

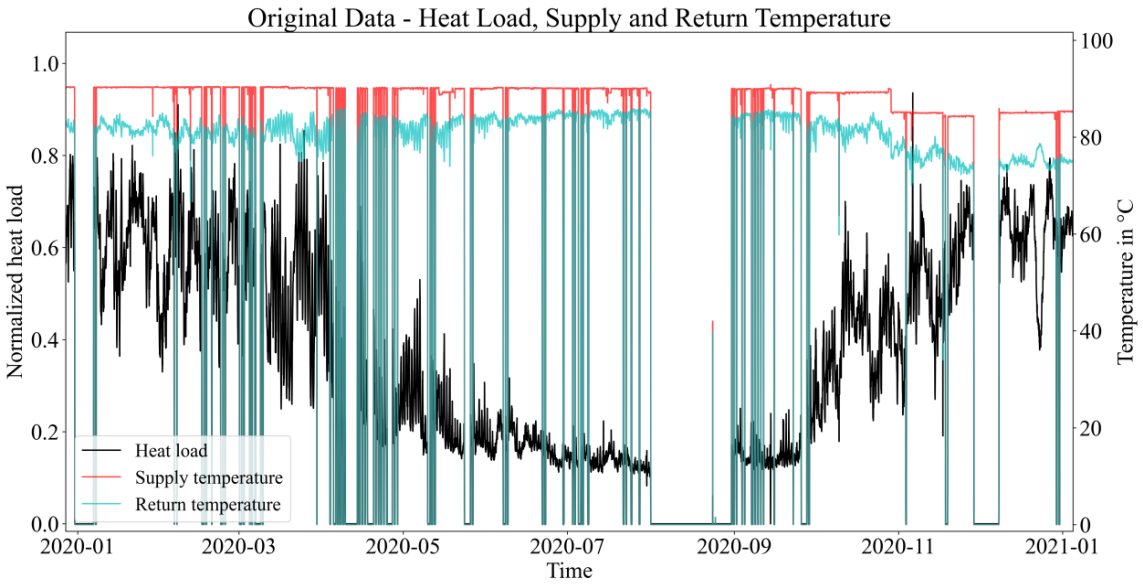

Fig. 1: Original data for a one-year period of one heat meter (heat load, supply and return temperature)

2.2 Completing missing heat meter data with machine learning models

Data analysis helps to understand and improve energy systems. However, continuous timeseries are required to prevent a bias from availability. In this work a machine learning algorithm is used to predict values for the gaps in the described profiles.

It has already been shown by Saloux and Candanedo (2018) and Bünning et al. (2020), that the use of machine learning algorithms can improve the accuracy of heat load forecasts. Filling gaps in historic load profiles is a rather similar use case and it is additionally applied to fill gaps in return temperature profiles here. The present work has been conducted using the scikit-learn machine learning library (version 0.24.0) in a python environment (Pedregosa et al., 2011). After comparing different available algorithms in scikit-learn, the Extreme Gradient Boosting (XGBoost) regression algorithm turned out to be the most suitable for filling gaps in measured data.

The general procedure for each timeseries is depicted in Fig. 2. In the first step, the input variables which are relevant for prediction of the desired outputs are chosen and included into the raw data. A preliminary visual analysis showed that ambient temperature, time, and solar radiation have a relevant influence on the load. In case of the return temperature, the supply temperature is an additional input variable. The raw data is pre-processed to ensure unbiased training of the machine learning algorithm. The timestamp is encoded (1, 0) into columns for each category (day of week, hour of day). Ambient and supply temperature show an almost normal distribution so that they are standardized, while solar radiation is normalized between 0 and 1.

Next, the gaps are identified by defining validity ranges that are applied to each profile individually. The validity ranges are:

- Heat load: $\dot{Q} > 0$
- Supply temperature: $T_{supply} = T_{supply,setpoint} \pm 2K$
- Return temperature: $T_{return} > 40\ °C$

The gaps are removed from the training dataset, which is fed into the machine learning algorithm (XGBoost) to build a black box model of the system. The trained model is then used to predict the missing values in the original data. Finally, the accuracy of the models is evaluated in order to determine their reliability. Common regression indicators are determined, including the coefficient of determination (R^2), the root mean squared error (RMSE) and the mean absolute percentage error (MAPE). They are calculated as the mean of five random data splits to ensure cross validation.

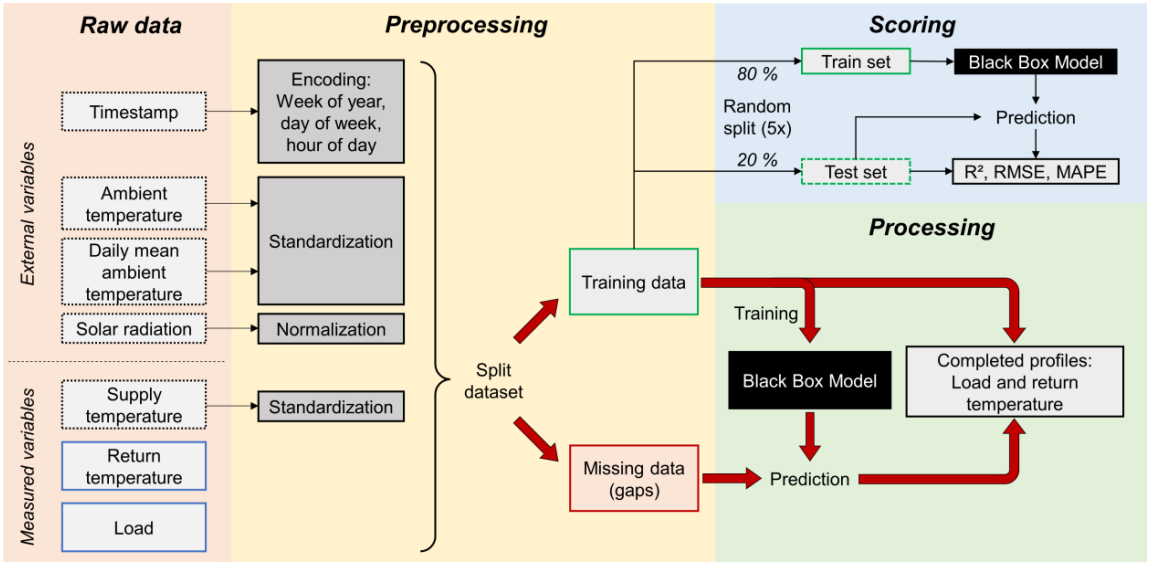

Fig. 2: Procedure diagram for completing missing data

2.3 Outlier detection through statistical deviations

Besides the obviously missing data points in a timeseries, there are also outliers where the values abnormally deviate from the course of a profile. Those can be caused for example by temporary external effects on the sensors or failures in data logging that last shorter than the actual temporal resolution of the timeseries. In this study two different methods based on statistics are developed and tested to detect outliers.

Z-filter

The Z-filter detects a value as an outlier, if it deviates from the mean of a floating period (i.e. one week) by a predefined number of standard deviations (see eq. 1). The period for the floating values (mean and standard deviation) is centred around each tested value. The period and the number of standard deviations (n_{std}) are free parameters adjustable to the relevant use case.

Z-criteria for outliers: $$\frac{|Y_i - \bar{Y}|}{\sigma} > n_{std} \qquad \text{(eq. 1)}$$

For this paper the parameters were chosen according to a visual analysis of the profile. Ideally the parameters are set by using a validation dataset, where the number of outliers is known. However, this was not available for this study.

Grubbs-filter

The Grubbs-filter uses the maximum normalized residual test (Grubbs-test) to detect outliers within a floating period (i.e. one week) centred around the tested value. An outlier is located by the maximum deviation of a value in terms of number of standard deviations from the mean within the given period (see eq. 2). This procedure is repeated until no outliers are detected at a significance level α.

Grubbs-criteria for outliers: $$G = \frac{max_{i=1,\dots,N}|Y_i - \bar{Y}|}{\sigma} \qquad \text{(eq. 2)}$$

The filter can be adjusted through the length of the floating period and the significance level. Grubbs-test only detects outliers by their value but does not consider the order of datapoints. However, the order is relevant when considering timeseries. Therefore, the Grubbs-test is applied to the second-degree gradient of a timeseries in this case. It can be used to locate outliers that deviate strongly from the course of a profile, because the first-degree gradient is low right before the outlier and high just after the outlier. Additionally, the timeseries of the second-degree gradient is approximately normally distributed, which is a prerequisite for using Grubbs-test. (Adikaram et al., 2015)

3. Results

The following sections show excerpts from the profiles to demonstrate the presented methods. The machine learning models are evaluated using R^2, RMSE and MAPE and the effects on the scores through the filters is shown. Additionally, the importance of the several input parameters is discussed.

3.1 Comparison of Grubbs-filter and Z-filter for Outlier Detection

The filters are applied after the gaps in the profiles are completed by the machine learning algorithm described in section 2.2. For the supply temperature profiles, the gaps are filled with the setpoint value, which is constant throughout the year and independent of ambient temperatures.

The floating period in both filters is set to one week (168 h) to account for the fact that the profiles are retrieved from an industrial consumer with characteristics related to the day of the week. The Z-filter is applied with n_{std} set to 2.5 and the Grubbs-filter with a significance level α at 0.05.

The supply temperature is only filtered with the Z-filter, as it works well to detect outliers in an almost constant profile. The values filtered in supply temperature profiles are replaced by the median of the two adjacent values.

The total number of detected outliers in the 15 profiles is documented in Tab. 1. It slightly differs between the five meters and between the three profile types (supply temperature, return temperature, heat load), but is mostly similar regarding the applied filters. The detected outliers amount to 0.6 % up to 1.8 % of the total dataset

Tab. 1: Comparison of the number of outliers detected by the two filtering methods in processed return temperature and heat load profiles

	Number of detected outliers				
Meter ID	**1**	**2**	**3**	**4**	**5**
Supply Temperature					
Z-filter	474	428	445	484	423
Return Temperature					
Z-filter	237	320	242	268	326
Grubbs-filter	226	298	257	149	308
Heat Load					
Z-filter	330	375	363	304	307
Grubbs-filter	385	353	332	280	304

Fig. 3 depicts an excerpt from the return temperature profile of meter 1 for May 2020 in hourly resolution. The graph shows that the Z-filter (black markers) only detects the outliers that deviate more than 2.5 standard deviations (green dashed line) from the mean value (grey dashed line) of the floating period, while the Grubbs-filter (red makers) also detects outliers that deviate from the course of the profile. This can also be observed in the excerpt of the heat load profile during the same period (Fig. 4).

On the one hand outliers are sometimes detected in both profiles (heat load and return temperature) at the same time, on the other hand some occurrences do not overlap. Some outliers are detected by both filters, others by only one of them. In order to confirm if the detected outliers are actually faulty meter data, a validation dataset is needed. As this was not available in this study, the accuracy of the filters cannot be evaluated quantitatively. Nevertheless, the most obvious outliers that can be detected visually, are mostly detected by the filters.

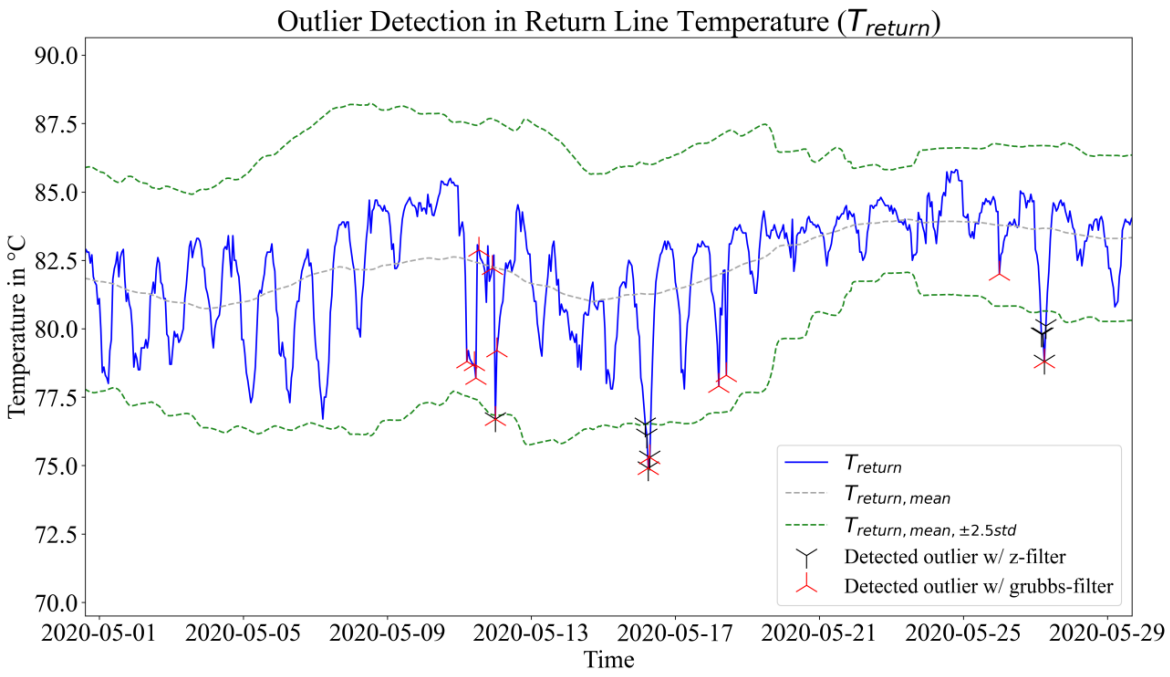

Fig. 3: Excerpt of a return temperature profile (meter 1, May 2020, hourly resolution) with Grubbs- and Z-filter applied

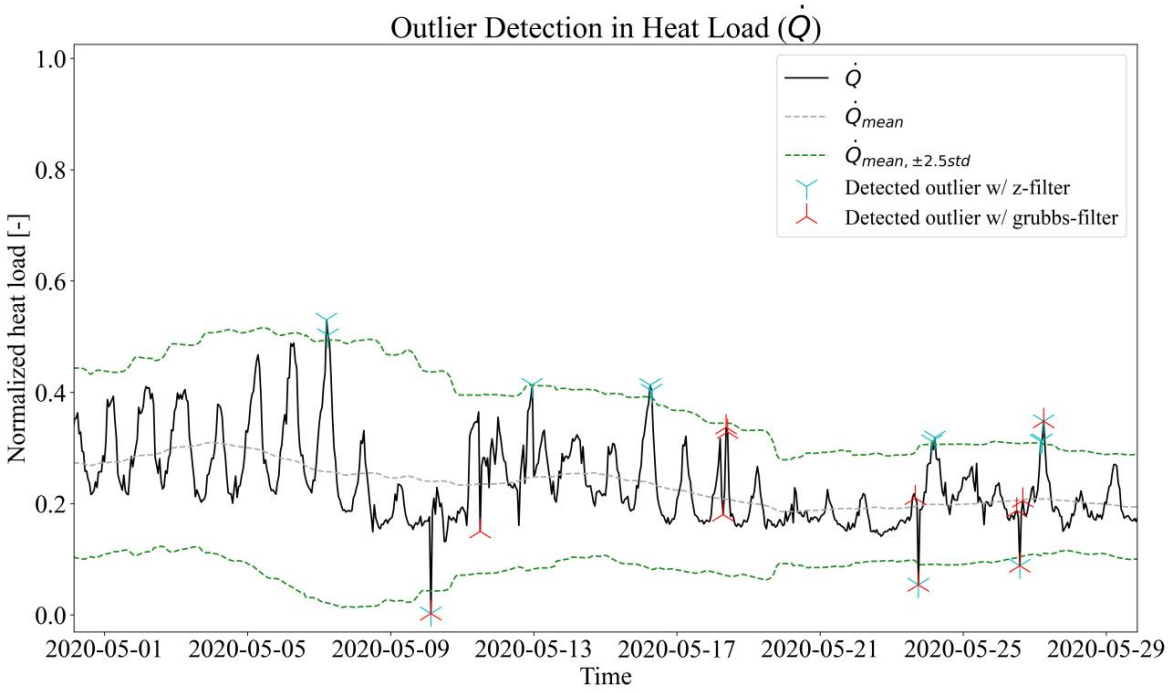

Fig. 4: Excerpt of a heat load profile (meter 1, May 2020, hourly resolution) with Grubbs- and Z-filter applied

3.2 Performance of the machine learning algorithm

The two following figures (Fig. 5 and Fig. 6) show the completed three-step processing of the profiles. The missing values in the original profiles (red and grey dashed lines) are visible as zero values and periods with constant supply temperature. In the first step, the missing values are replaced by predictions using the machine learning algorithm (cyan dashed lines). In the second step, the Grubbs-filter is applied (red markers). The figures show that detected outliers are frequently adjacent to missing periods. In the final profiles (solid lines), the detected outliers are removed from the training data of the machine learning algorithm and treated as missing values. Therefore, the course of the profiles created with the regression models in the third step slightly differs from those that in the first step.

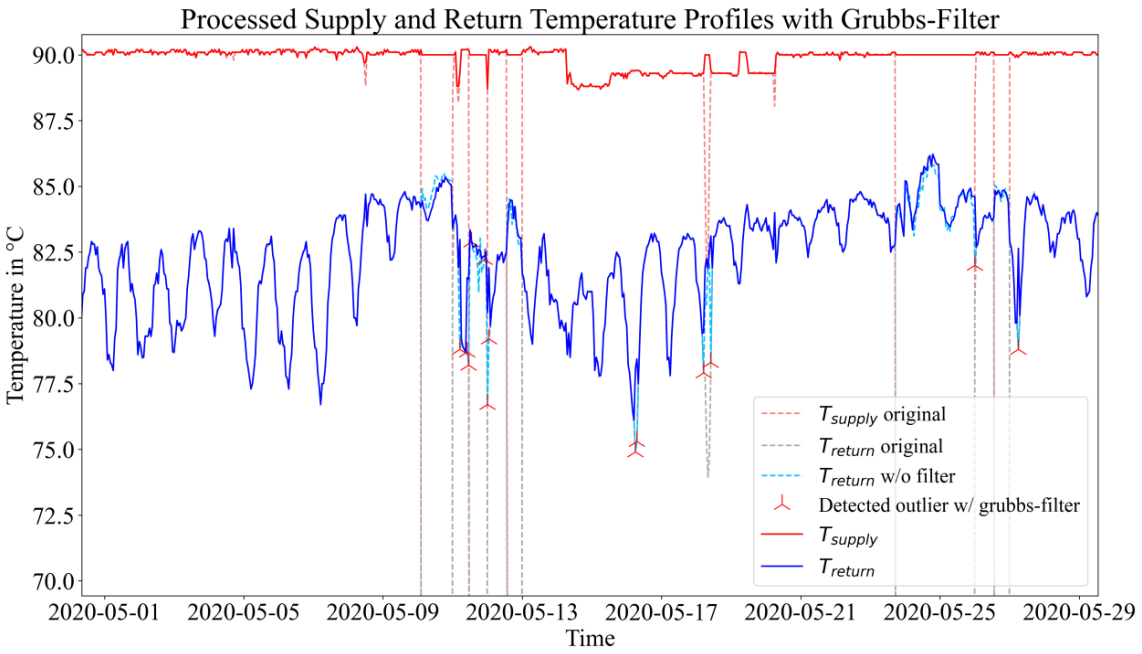

Fig. 5: Visualization of the three-step processing of supply and return temperature profiles – original (grey), processed profile with detected outliers (cyan), final processed profile (blue) (May 2020, hourly resolution)

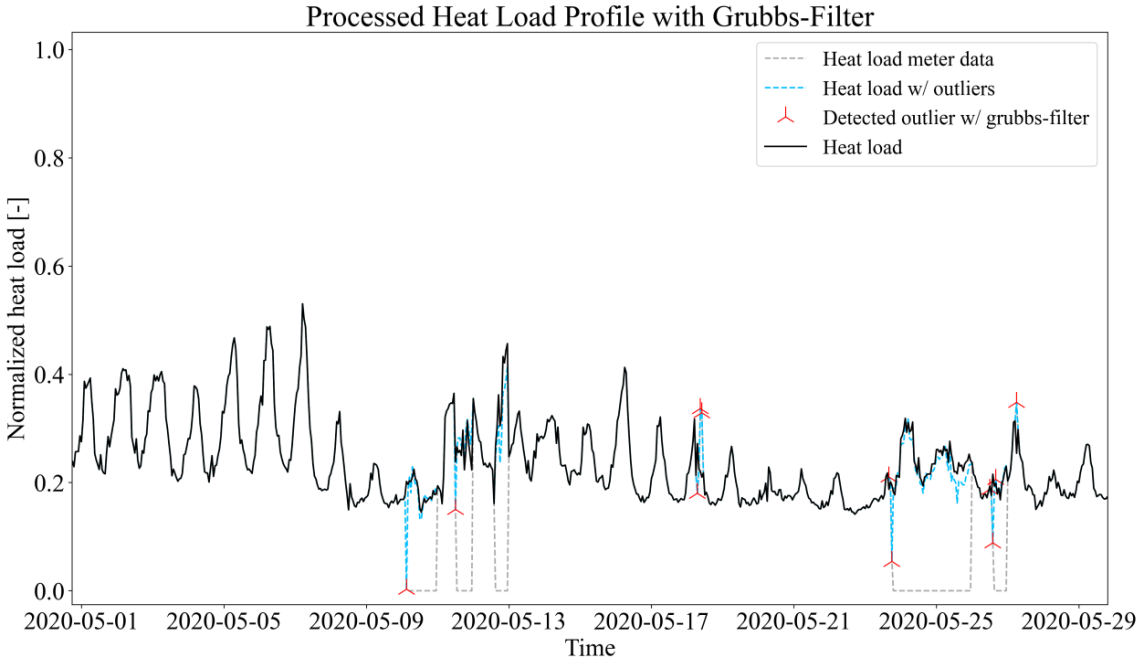

Fig. 6: Visualization of the three-step processing of supply and return temperature profiles – original (grey), processed profile with detected outliers (cyan), final processed profile(black) (May 2020, hourly resolution)

The accuracy of the presented machine learning algorithm is evaluated using the indicators R^2, RMSE and MAPE presented in Tab. 2 as the mean of the individual scores of the five meters for the base case (first step) and for either filter applied.

In general, the indicators confirm the visual impression from Fig. 5 and Fig. 6 that the models are able to predict realistic profiles for the missing values in the timeseries. The influence of the filters on the accuracy of the models is below 5 %. However, in all cases they improve the models by increasing R^2 but decreasing RMSE and MAPE. Since the number of detected outliers is relatively low (0.6 – 1.8%), the training data is only slightly altered by the filters compared to the base case. Therefore, impact of the filters on the overall performance of the algorithm is quite low. Additionally, there is no significant trend for favoring Grubbs- or Z-filter on the basis of the calculated indicators.

Tab. 2: Average performance of the machine learning algorithm as mean of the five meters and influence of the two filters

	Evaluation criterion								
	R^2			RMSE in K resp. kW			MAPE in %		
	w/o filter	*Grubbs*	*Z*	**w/o filter**	*Grubbs*	*Z*	**w/o filter**	*Grubbs*	*Z*
Return temperature	**0.917**	*0.921*	*0.922*	**0.94**	*0.91*	*0.92*	**5.41**	*5.23*	*5.23*
Heat load	**0.925**	*0.929*	*0.930*	**140.0**	*133.9*	*135.3*	**13.18**	*12.58*	*12.71*

In addition to the performance indicators, the processed profiles are evaluated in terms of annual mean supply and return temperature and total heat amount. Tab. 3 shows that the supply temperature in processed profiles barely deviates from the original data, while the return temperature is more than 1.8 % higher. Since the temperatures are volume flow weighted, no strong deviation is expected. However, the heat amount is more than 17 % higher than in the original data, where missing values occur in 29 % of the time. This is consistent with the visual impression that the gaps occur more frequently in summer when the heat load is below average.

Tab. 3: Average deviation of annual mean supply and return temperature and total heat amount of the five meters in processed profiles compared to original profiles

	Deviation		
Value	**w/o filter**	**Grubbs**	**Z**
Supply temperature	+0.27%	+0.27%	+0.27%
Return temperature	+1.84%	+1.87%	+1.81%
Heat amount	+17.34%	+17.66%	+17.45%

3.3 Importance of input parameters

Finally, the input parameters to the black box models, which are also called features in the machine learning domain, are analysed. The relative importance of the six features is retrieved from the machine learning algorithm in the scikit-learn library and is depicted in Fig. 7 for the several processed profiles of return temperature and heat load that are discussed in the previous section. It clearly shows that ambient temperature is the most influential input parameter with more than 35% and is followed by the hour of the day and the day of week. The supply temperature is only used as an input parameter to the return temperature models and has a medium relevance with about 15 %. There is no significant change in the feature importance when comparing the models with and without a filter.

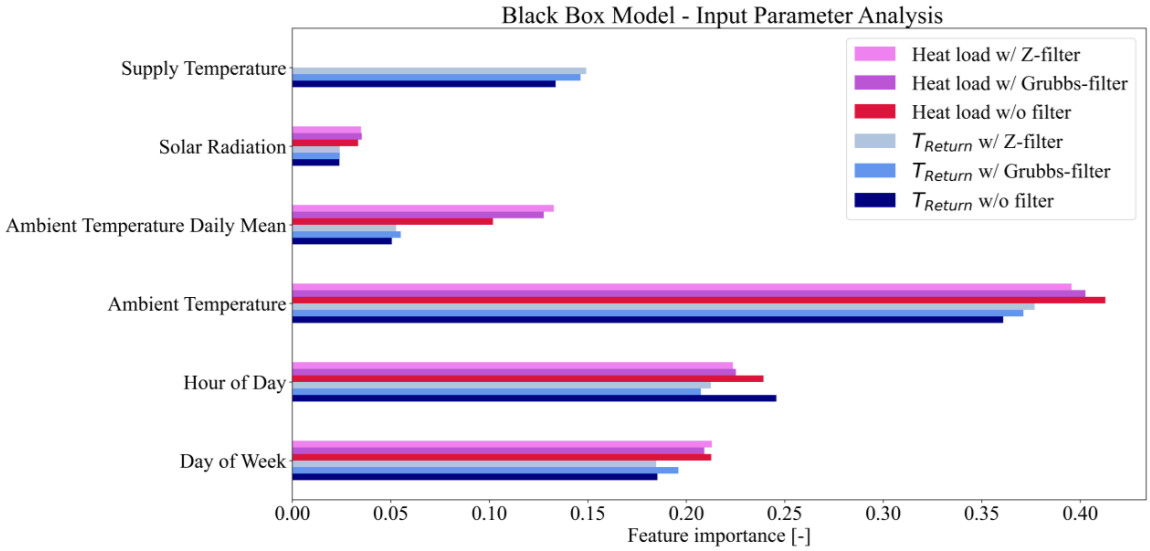

Fig. 7: Input parameter (feature) importance for return temperature and heat load prediction models with and without filters for outlier detection

4. Conclusion

The methods applied in this study enable to process faulty heat meter data and improve its consistency. Missing datapoints and detected outliers are replaced by using machine learning regression models. The performance of the models is evaluated with common indicators like R^2, RMSE and MAPE. A coefficient of determination R^2 of about 0.92 is achieved for both heat load and return temperature profiles. It should be noted that the indicators are calculated as mean values from five different meters to ease readability. However, the quality and availability of the training data of the profiles vary and strongly influence the accuracy of the individual models. It confirms the thesis that the better the data basis, the better the results of the model predictions.

The applied filters detect the most visually identifiable outliers, although some datapoints are detected which are difficult to distinguish from actual peaks. In a further step, it is therefore necessary to test the filters on data, where a corresponding validation dataset with known outliers exists. Nevertheless, the performance evaluation shows that the filters slightly improve the accuracy of the machine learning models.

The evaluation of the annual mean values points out that the processed profiles deviate from the original data, which is especially true for the heat amount with more than 17% deviation. This will likely cause errors when redesigning or continuously optimizing this energy system with the original profiles. After all, redesigning and optimizing are vital aspects for transforming the heat sector from conventional fossil-fuelled systems to smart energy-efficient systems based on renewable energies. Therefore, this work is aiming to contribute to a more efficient transformation process.

5. Acknowledgements

The project partners greatly acknowledge the financial support of the project by the Federal Ministry for Economic Affairs and Climate Action. (Funding Code: 03EN3023)

6. References

Adikaram, K.K.L.B., Hussein, M.A., Effenberger, M., Becker, T., 2015. Data Transformation Technique to Improve the Outlier Detection Power of Grubbs' Test for Data Expected to Follow Linear Relation. Journal of Applied Mathematics 2015, 1–9.

Bünning, F., Heer, P., Smith, R.S., Lygeros, J., 2020. Improved day ahead heating demand forecasting by online correction methods. Energy and Buildings 211, 109821.

Chen, T., Guestrin, C., 2016. XGBoost: A Scalable Tree Boosting System. KDD '16: Proceedings of the 22nd ACM SIGKDD International Conference on Knowledge Discovery and Data Mining 11 (34), 785–794.

Pedregosa, F., Varoquaux, G., Gramfort, A., Michel, V., Thirion, B., Grisel, O., Blondel, M., Müller, A., Nothman, J., Louppe, G., Prettenhofer, P., Weiss, R., Dubourg, V., Vanderplas, J., Passos, A., Cournapeau, D., Brucher, M., Perrot, M., Duchesnay, É., 2012. Scikit-learn: Machine Learning in Python. Journal of Machine Learning Research. 12, 2825–2830.

Saloux, E., Candanedo, J.A., 2018. Forecasting District Heating Demand using Machine Learning Algorithms. Energy Procedia. 149, 59–68.

Data Clustering and Genetic Algorithm for the Design Optimization of a Hybrid Concentrated Solar System for SHIP

Emilie Catel[1,2], Simon Kamerling[2,3] and Valery Vuillerme[2]

[1] Ecole Polytechnique (France)

[2] Université Grenoble Alpes, CEA, LITEN, INES (France)

[3] Université Savoie Mont-Blanc, USMB (France)

Abstract

Solar thermal systems for industrial process heat could greatly contribute to reduce global greenhouse gas emissions. Such installations should be cost-effective and energy-efficient, which is why this paper investigates a new algorithm for design optimization. Design optimization first requires to accurately simulate the system, which can be very time consuming when systems are as complex as solar thermal plants with thermal storage and variable load demands. Instead of simplifying models and losing in precision, it has been chosen here to use data clustering to reduce the computational time of simulations. A clustering algorithm of meteorological data originally developed for buildings heating is adapted for solar thermal energy production and the well-spread multi-objective genetic algorithm NSGA2 is performed to find the optimal sizing. The iterative use of both algorithms is investigated to gain in accuracy.

Keywords: SHIP, solar thermal energy, industrial heat, genetic algorithm, data clustering, design optimization, control strategy

1. Introduction

The industrial sector consumes approximately one third of global world-used energy, and is responsible for about 37% of greenhouse gases emissions. Almost three quarters of the industrial energy consumption is used for heat or cold production, most often produced with electricity or combustion of oil products as explain Kumar et al. (2019).

Tilahun et al. (2019) assert that installing solar thermal energy production technologies on industrial sites can significantly reduce greenhouse gas emissions and operating costs, while saving on electricity and fuel purchases. These systems consist of solar thermal collectors that heat a Heat Transfer Fluid (HTF), as well as a thermal storage system and an auxiliary heating that take over when solar energy is not sufficient to meet process heat requirements. Solar heat production in industrial processes is generally economically viable. However, it is necessary to optimize the systems design and control strategy in order to make investments even more attractive and reduce emissions as much as possible. Indeed, as pointed out by Thiel and Stark (2021), the solar thermal plant behaves as a complex system influenced and limited by the intermittency and low areal density of the available solar radiation as well as the variability of the temperature required for the processes. In this paper, the optimization design consists in the choice of the solar technology and the type of storage to be installed as well as their dimensioning: solar collectors area and tank volume, all to deliver maximal solar energy to the industrial process while minimizing the investment costs.

Design optimization algorithms require to run performance simulations on many different plant designs, which means that these simulations should be time constrained as explains Klemeš (2011). Physical models are used for simulating the energy production of solar thermal systems, and the more detailed models are the longer is the computational time of their simulations. A compromise between model accuracy and reasonable simulation time is often made, leading to a loss of quality of the simulation results. It is therefore interesting to look for new methods which allow time simulation reduction without degradation of model accuracy. One solution would be simulating the model on a few days instead of one full year, which implies choosing days that accurately represent the meteorological year, or replicate the annual performance profile of one important performance criterion: Sayegh (2020) shows that it can be done with clustering algorithms. Indeed, clustering algorithms are methods to find relevant groups in data and determine representative data points in each group, in order to use these particular points instead of the whole dataset and reduce the length of the simulations.

As building a solar thermal plant follows multiple objectives, such as minimizing gas emissions, maximizing the solar fraction, or minimizing the investment costs, it has been chosen to use a multi-objective algorithm for design

© 2022. The Authors. Published by International Solar Energy Society
Selection and/or peer review under responsibility of Scientific Committee
doi:10.18086/eurosun.2022.16.13 Available at http://proceedings.ises.org

optimization. The well-spread NSGA-II (Non Dominated Sorting Algorithm) developed by Deb et al. (2002) is used, and the simulations are run with the formerly defined short sequences of days instead of the whole year. A comparison with NSGA-II run on annual simulations is made to validate the model, and modifications of the algorithm were needed in order to meet the accuracy requirements.

2. The Typical Short Sequence Algorithm

One challenge of design optimization is to evaluate the objective function on different relevant weather data, to obtain optimized solutions that cover all possible climatic conditions of the site, while limiting data to restrain computational time simulations. Reducing data without losing accuracy is necessary in multiple scientific fields and many data grouping or clustering methods have been developed in the last decades to address the problem.

2.1. Data clustering

Data clustering is the art of finding groups in data (Kaufman and Rousseeuw, 2005). One of the most spread clustering algorithms used in literature is the k-means algorithm, which is implemented in Python in the Scikit-learn module detailed by Pedregosa et al. . It divides a set of data points into a predefined number k of disjoint clusters, each represented by one *centroid*, calculated as the mean of the samples in the cluster. This implies that the centroid is not necessarily a data point in the cluster, and it allows a faster computation. However, it can be better to select data points as representative instead of imaginary points, as in the k-medoids algorithm: the *medoid* chosen is the data point that has the least total distance to the other samples of its clusters. Fig. 1 presents the illustration of a partitioning around medoids methods with 20 data points and $k = 3$ clusters.

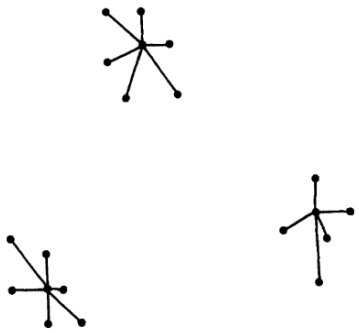

Fig. 1: Illustration of partitioning around medoids. Credit : Kaufman and Rousseeuw(2005).

Wallerand et al.(2018) used clustering methods in the design optimization of solar-assisted industrial processes. They chose the MATLAB k-medoids algorithm to obtain a reduced set of meteorological data that would be a subset of the original data. Tilahun et al. (2019) also use the MATLAB k-medoids algorithm for typical meteorological days selection, in order to optimize solar thermal energy systems design for industry. The k-medoids algorithm presents two disadvantages: it selects representative days directly on their meteorological parameters, and it is time consuming. A method that would select days according to their representativeness of the studied system performance instead of diverse meteorological parameters is more interesting, and was developed by Hasan Sayegh during his PhD: the *Typical Short Sequence* algorithm (*TypSS*).

2.2. Typical Short Sequence Algorithm

TypSS is a clustering algorithm developed by Sayegh (2020) which determines a series of typical days in order to obtain a short simulation sequence predicting the behaviour of a given system. It was developed to study buildings thermal performance, and was adapted in this paper for solar thermal industrial heat systems.
The mathematical and physical model used for simulating the systems performance is an intern tool developed by Kamerling et al. (2021) described in section 4.1.
The algorithm divides the year into distinct chronological periods iteratively and selects a representative day for each, trying to generate a reduced simulation sequence that replicates the annual sequence accurately. The code is divided into three main parts: the *initialization phase* where initial variables are calculated; the *period setting phase* where the year is iteratively divided into a predefined number of periods; and the *typical days' enhancement phase* where better representative days are searched for each period based on global performance values. During the period setting phase, at each step the performance of each period is evaluated by comparing the performance criterion value to the one of the annual simulation, and the worse performing period is divided into two halves. The global procedure of TypSS is presented in Fig. 2.

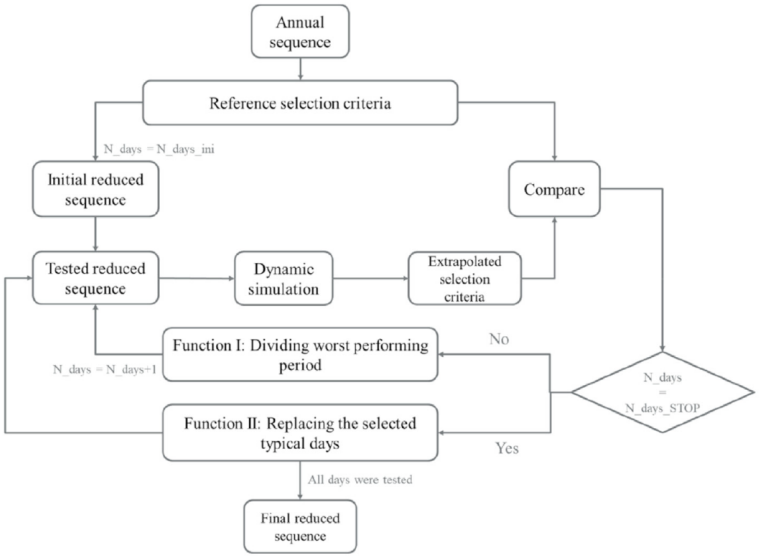

Fig. 2: Scheme of TypSS. Credit : Sayegh et al. (2022).

The parameters include all the data specified by the operator to the model and algorithm that are needed to operate. They are:

- The parametric configuration of an individual, e.g. the characteristics of the solar thermal plant tested common to all individuals and the decision variables specific to each one.
- *n_indv* the number of tested individuals.
- The weather data.
- *n_START* and *n_STOP* the lengths of the initial and final sequence.
- The chosen performance criterion;
- The days generation coefficient *coef_gen* corresponding to the percentage of days in each cluster tested by the algorithm to be the representative day.

3. Design Optimization

3.1 Optimization algorithms

According to Klemeš (2011) definition, an optimization problem consists of an objective function that corresponds to a performance criterion to be minimized or maximized (initial investment costs, fuel savings achievements...), given input parameters characterizing the model (e.g. in our case study the technologies used, typical meteorological data, thermal losses of the installations...), and decision variables whose optimal values have to be determined (e.g. total area of collectors, storage capacity...), as well as the equations modeling the underlying system.
There are a large number of optimization algorithms, which can be divided into two categories: algorithms based on the simulation and solving of a physical model, and those performing optimization via data such as machine learning. This paper investigated only the first category of algorithms, as the available data on the performance and costs of solar thermal power plants is largely insufficient to consider the second one.
Focusing on the design of a solar thermal power plant where the objective function is non-linear and highly unstable, Cabello et al. (2009) demonstrates that classical gradient-based optimization techniques such as MILP have less accurate results than the genetic algorithm he proposes.

3.2 Evolutionary algorithms

A genetic algorithm is inspired by natural evolution : Kalogirou (2004) explains that its principle rests on the evolution of a fixed-size population of solutions evolving in time, the fittest ones being selected for reproduction. It uses three principal operators: *selection*, *crossover* and *mutation*. Selection is performed thanks to a *fitness function* defined by the user for each problem: the solutions scoring best are given a higher probability of being chosen in the mating pool, where crossover happens to produce an *offspring*. Part of the new generation undergoes mutations to assure the exploration of diversified solutions. The initial population is generated randomly, and the algorithm stops when the maximal number of generations is reached or when some performance criteria are met. The *adjustable chromosomes* of the individuals are the variables that are modified during the algorithm, in this work they are: the number of loops of the solar installation and the number of storage hours.

3.3 Multi-objective optimization

In this paper, it has been chosen to optimize two objective functions : maximizing the annual solar fraction of the plant and minimizing its investment costs. A solution dominates another one if the first solution has at least one criterion strictly superior to the second solution, and no criteria strictly inferior. Mahmoudimehr and Sebghati (2019) defines an optimal or *non-dominated* solution as a solution for which there are no other possible solutions that dominate it : the solution then belongs to the Pareto front. In Fig. 3 below; the solutions A, B, C and D are not dominated by any solutions of the Solution domain, therefore they belong to the Pareto front.

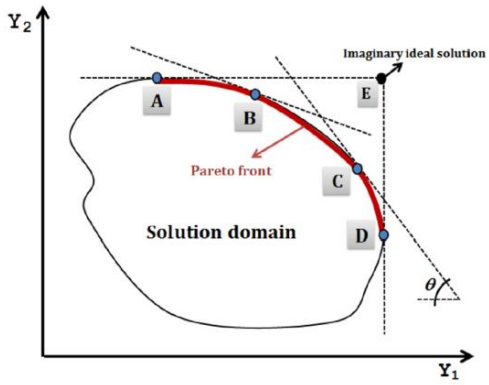

Fig. 3: Solution domain of a typical two-objective optimization problem. Credit : Mahmoudimehr and Sebghati (2019).

3.4 NSGA-II

NSGA-II is a well-spread multi-objective optimization algorithm proposed by Deb et al. (2002) that belongs to the genetic algorithms category. In this case, the fitness function is evaluated on individuals according to the two objective functions, and each solution is attributed to a Pareto Front (first front for Pareto optimal solutions, second front for the second best solutions that are only dominated by one solution and so on). They are then also sorted by their crowding distance, which is their Euclidean distance to the mean of their Pareto front. The algorithm selects for reproduction the solutions belonging to the firsts Pareto fronts and that have the highest crowding distance as can be seen in Fig. 4. This third parameter encourages the algorithm to select diversified solutions that allow better global exploration of the space solutions.

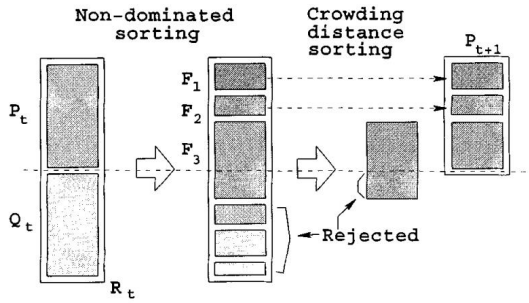

Fig. 4: NSGA-II sorting procedure. Credit : Deb et al. (2002).

Mahmoudimehr (2018) chose the NSGA-II algorithm for design optimization of a hybrid photovoltaic hydroelectric standalone energy system in Iran, with two objective functions being the investment cost and the loss of power supply probability. Silva et al. (2014) decided to apply another type of evolutionary algorithm : a memetic algorithm, which combines a genetic algorithm with a fast-local search algorithm. However, the algorithm is only single objective and three objective functions are successively studied, leading in very different optimal solutions.
In this paper, the NSGA-II algorithm is run in two different ways: the first one with evaluating the fitness functions on annual simulations for each individual, the second one with the evaluation performed on short sequences simulations, which reduces drastically the time computation. The algorithm is illustrated in Fig. 5.

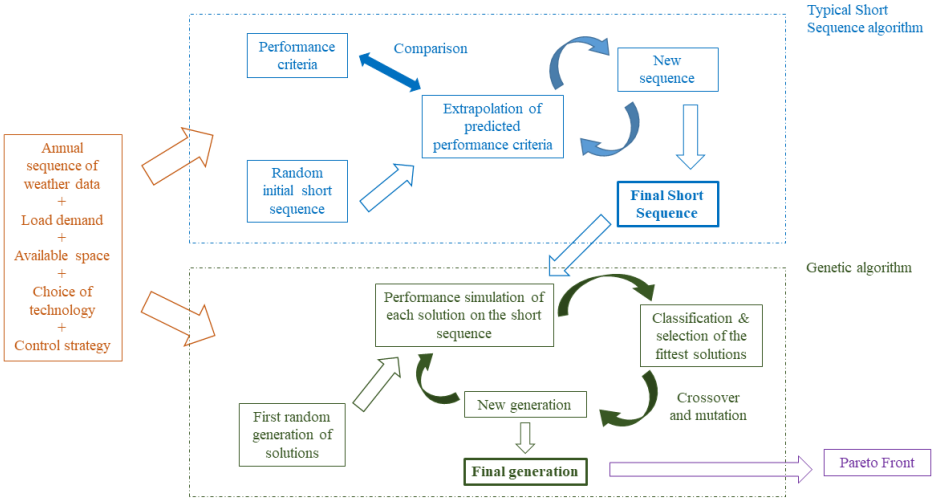

Fig. 5: NSGA-II combined with TypSS procedure.

3.5 OptiTypSS

As detailed in the PhD report of Sayegh (2020), running the NSGA-II algorithm with simulations applied on the predetermined short sequence does not give a good approximation of the Pareto Front. Indeed, the short sequence created by TypSS is designed to extrapolate the annual performance of specific individuals, chosen randomly at the start of the algorithm; therefore, it will not necessarily extrapolate well individuals near the Pareto Front. This problem was addressed by running iteratively the NSGA-II algorithm on a new short sequence determined by TypSS with added individuals chosen among the set of optimal solutions returned by the precedent iteration of NSGA-II, as shown in Fig. 6 below. Indeed, with this new approach, the second short sequence generated will have lower global accuracy but will be more precise for individuals around the first approximated Pareto front, which is supposed to be near the real Pareto front, and the second run of NSGA2 will therefore give a better approximated Pareto front, and so on.

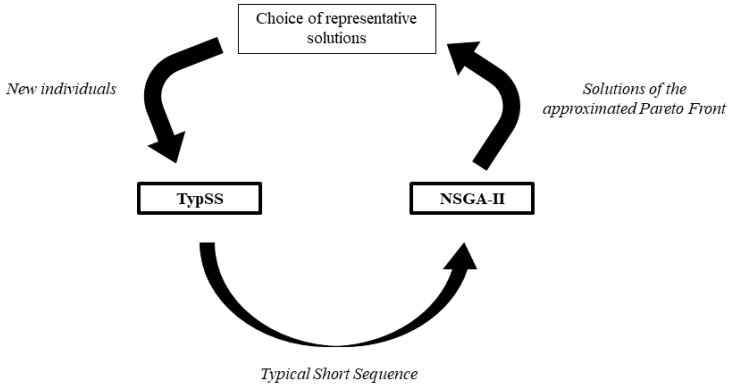

Fig. 6: OptiTypSS procedure.

4. Application to the Design Optimization of a Hybrid SHIP System

4.1 Hybrid SHIP System modeling

The Hybrid SHIP System chosen for the study is described by Kamerling et al. (2021) and illustrated in Fig. 7. It consists of a solar field, a two-tank storage and a boiler in series. Mass flow rate from the solar field ($\dot{m}_{SF}$) at the Solar Field's outlet temperature T_{SF} goes to the storage ($\dot{m}_{SF\rightarrow st}$) or to the boiler directly ($\dot{m}_{SF\rightarrow st}$). When needed, the Heat Transfer Fluid (HTF) comes from the hot tank ($\dot{m}_{st\rightarrow boiler}$) at the tank's temperature T_{st}. The storage state is characterized by the mass in the hot tank M_{st} and its temperature T_{st}, while the cold tank is not modeled. It is considered that the mass fluctuations in the hot tank are compensated by the cold tank. A third inlet coming from the

cold tank permits to bypass the solar field and storage ($\dot{m}_{aux}$). The three mass flow rates at the inlet of the boiler must be equal to the process's demand mass flow rate ($\dot{m}_{demand}$), when no energy comes from the hot tank and the solar field, the boiler heats up the total HTF's mass flow rate in order to reach the process's demand temperature.

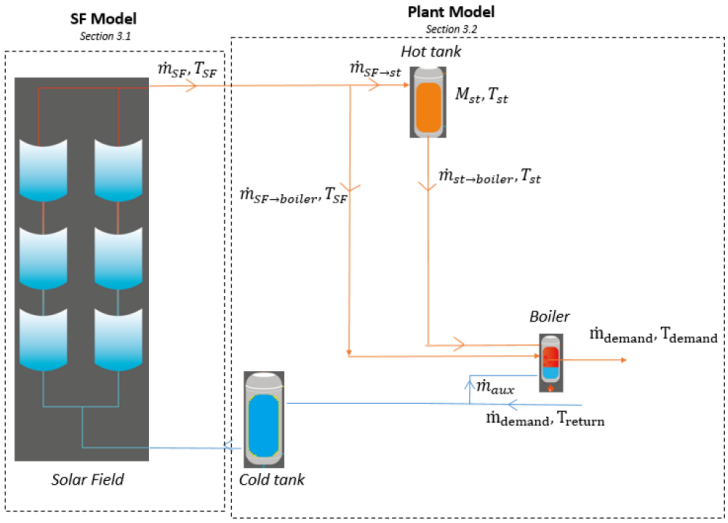

Fig. 7: Schematic of the Hybrid SHIP System of interest and control variables. Credit: Kamerling et al. (2021).

The solar field consists of a basic structure, called a *loop*, repeated a certain number of times in parallel. The loop contains low-cost parabolic trough collectors (PTC) in series with higher thermal efficiency Linear Fresnel Receivers (LFR). The two decision variables of the design optimization problem are the number of loops repeated (the number must be an integer) and the storage capacity in hours.
The algorithm *SwipeTools*, developed by S. Kamerling, calculates the solar production (i.e. heats and mass flow rates) during one year with hourly steps. It takes as input the process demand curve (hourly mass flow rates and return temperature), the meteorological data and the system design, and returns the detailed annual solar production. The main parameters taken into account in this paper are the hourly energy provided by the boiler during the full year and the annual solar fraction.

4.2. TypSS parametrization.

Several parameters were chosen based on the sensitivity analysis of the algorithm entry parameters carried out by Sayegh (2020), and are summarized in Tab. 1 below.

Tab. 1: Parametrization of TypSS.

Parameters	Values
n_indv	3
n_START	6
n_STOP	12
Performance criterion	Solar Fraction
Weather data	One typical year (Grenoble, FR)

Several number of final periods *n_STOP* were tested to find the best suited value for this case study, this parameter varying greatly between models. It has finally been chosen to determine short sequences of 12 typical days, the number realizing the best compromise between accuracy of the results and time convergence of the algorithm. Initially, the performance criterion used to compare annual and short sequence simulations was the annual solar fraction of the plant, this parameter being one of the two objective criteria in the optimization problem. However, it proved to induce a bias in the initial periods division: it led the algorithm to choose the smaller periods as the ones to be divided again. As can be seen in Fig. 8 below, it resulted in an inconsistent division of periods: five clusters contain more than 60 days while eight others contain less than 10 days, and more than half of the typical days are in July and August. This typical days repartition cannot approximate well one year of meteorological data, as it focuses on two particular months in summer, which are not representative of the variability of the resource during one year. The choice of an extensive criterion, the annual energy consumed by the boiler, instead of an intensive one solved the problem and resulted in a more coherent annual division with an even distribution of typical days during the year, as Fig. 9 shows.

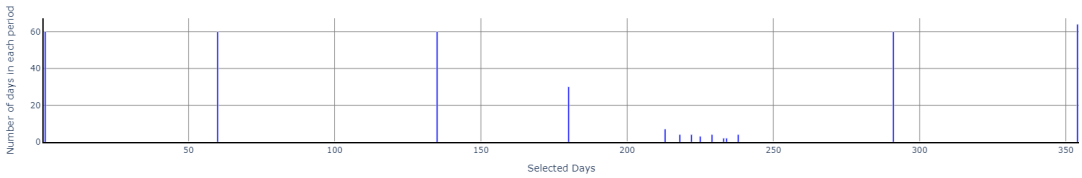

Fig. 8: Periods division and days selection for a short sequence of 14 typical days where the annual solar fraction is the performance criterion.

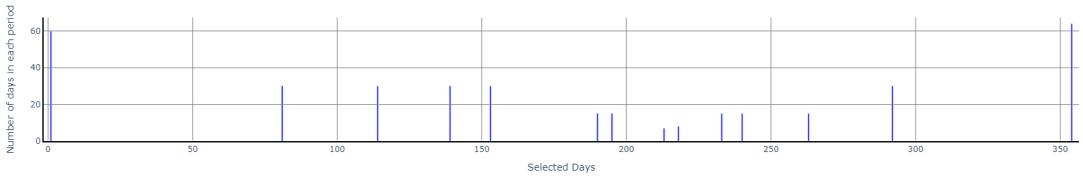

Fig. 9: Periods division and days selection for a short sequence of 14 typical days where the annual energy provided by the boiler is the performance criterion.

With these parametric configurations, the TypSS algorithm created typical short sequences that gave accurate approximation of the annual performance of the tested Hybrid SHIP System. One example of result obtain from the short sequence approximation is presented in Fig. 10. It corresponds to a plant with 88 loops and a storage capacity of 4.5 hours, belonging to the approximated Pareto front given by 3 iterations of OptiTypSS.

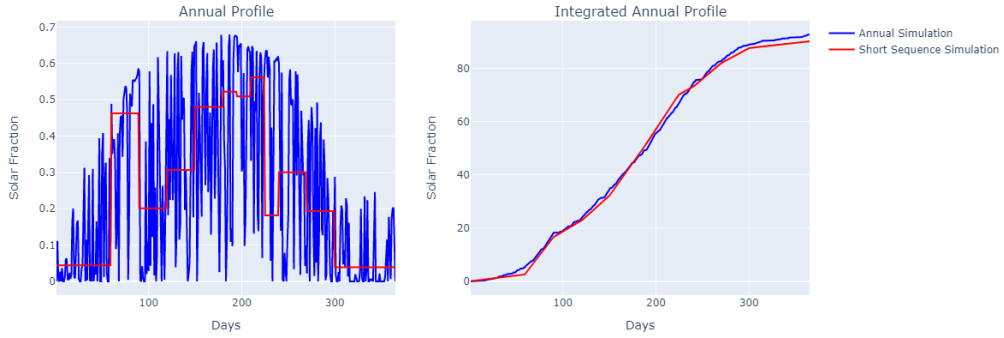

Fig. 10: Annual and integrated profiles of solar fraction with short sequence approximation

4.3. OptiTypSS Parametrization

The choice of parameters and limits for the decision variables are detailed in Tab. 2 below. The weather data was downloaded from the European Commission software PVGIS (PVGIS, 2019).

Tab. 2: Parametrization of OptiTypSS.

Decision variables	**Limits**
Number of loops (*integer*)	[|1,150|]
Storage capacity (h)	[0.5,10]
Parameters	**Values**
Population size	50
Number of parallel processes	20
Maximal number of identical generations	20
Weather data	One typical year (Grenoble, FR)

Fig. 11 presents the results of different design optimization tests with these parameters The tests were run on the same computer with 32 Go ram, with 20 sub-processes run in parallel. The NSGA-II algorithm was first run without use of short sequences: for each individual tested, the full annual system modeling was performed to calculate the annual solar fraction of the plant. It converged in 13h45 after 98 generations, and the Pareto front obtained is considered as the reference one - it is the blue curve in the figure below. After this, several iterations of OptiTypSS were tested to see the accuracy of the approximated Pareto front given. The first simulation corresponds to only one iteration of NSGA-II performed with the first typical sequence determined by TypSS on three random individuals. It is indeed further away from the reference curve than the others, with a quadratic error of 7% while the OptiTypSS algorithm performed with 2, 3 and 4 iterations reached a quadratic error of respectively 5.9%, 6% and 5%. The best approximation of the reference Pareto Front is therefore obtained by OptiTypSS with 4 iterations. However, as for certain optimization problems even 5% of quadratic error would be too much, another method for reducing time computation without losing in accuracy was investigated. An additional annual simulation was run with a different initial population : instead of generating random individuals, the initial population was taken as the resulting population of the first iteration of TypSS. The proximity of the initial population to the Pareto front led to a decrease in the number of generations needed for convergence : the algorithm stopped after 52 generations instead of 98, reducing the overall computation time of the algorithm by 6h while giving the same Pareto front. When accuracy is prior to time computation reduction, using one iteration of OptiTypSS before launching NSGA-II on annual simulations with its results as initial population still allows converging faster. A summary of time convergences and performances of the methods is provided in **Fig. *12***.

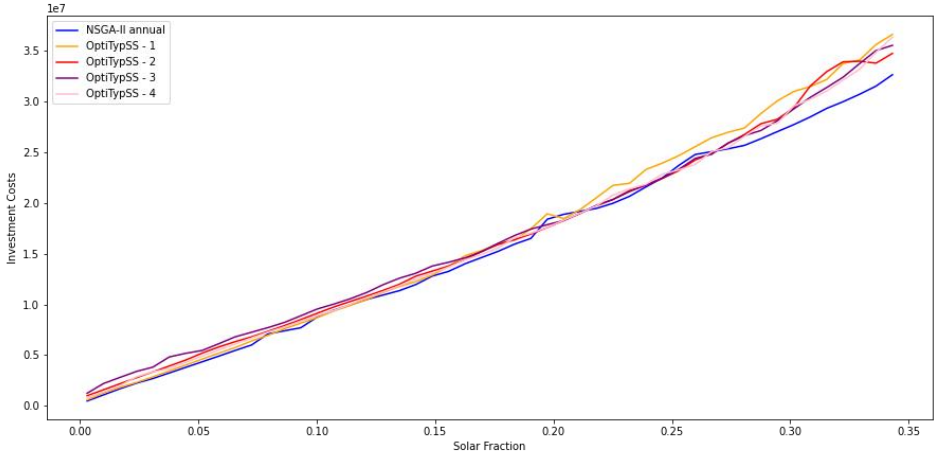

Fig. 11: Interpolations of the reference and the approximated Pareto fronts given by OptiTypSS

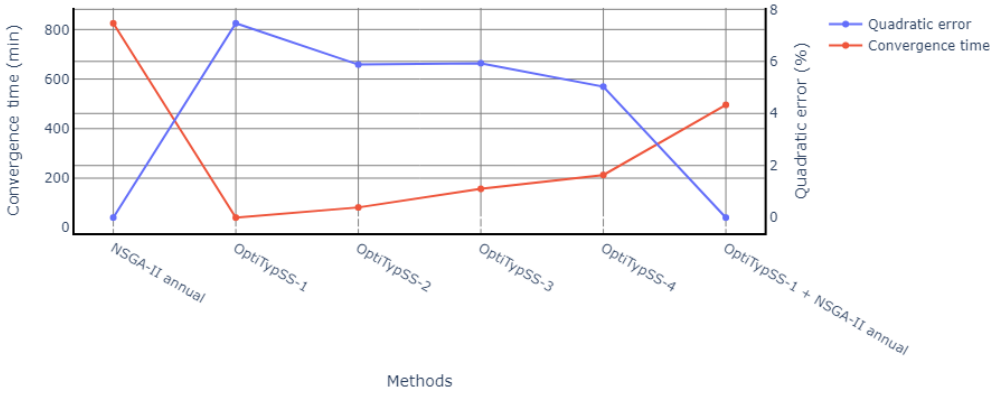

Fig. 12: Comparisons of the different algorithms performance.

4.4 Storage management and design in short sequences simulations

One important thing that was observed during the optimisation phase with OptiTypSS is that the approximated Pareto fronts were far more accurate in cases of lower investment costs than in cases of high investment costs, as shows Fig. 13. This means that for higher storage capacity and larger collectors area, the short sequences accuracy in simulation decreases. Indeed, looking at the design choices determined by the reference and OptiTypSS-4 simulations showed that for high investment costs (above 20 million euros), the storage capacity was underestimated by the optimization algorithm applied on short sequences, as presented in the Fig. 14.

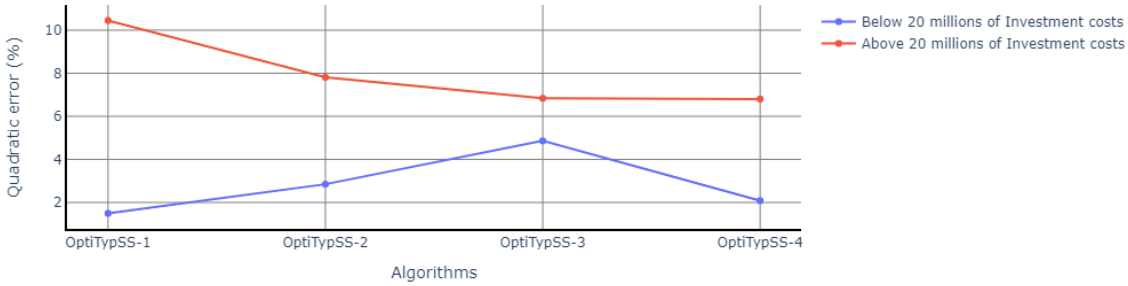

Fig. 13: Quadratic error of short sequences simulations for different ranges of investment costs.

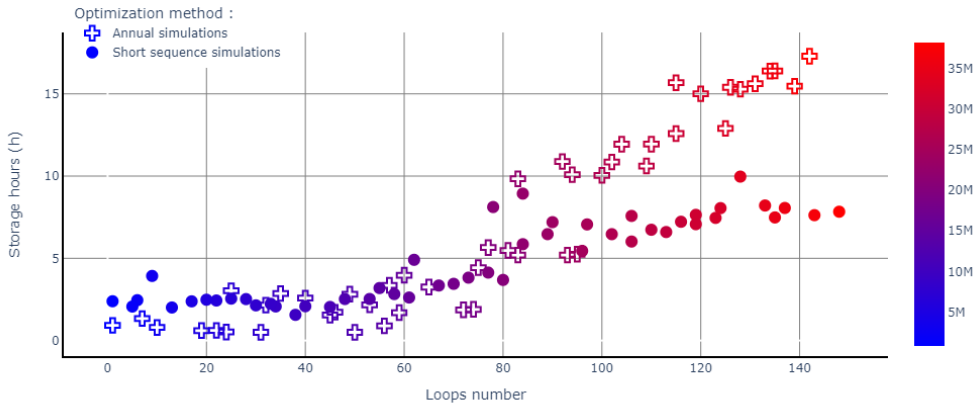

Fig. 14: Design choices difference with annual and short sequences simulations.

This outlined a bias in the short sequence algorithm : the storage management cannot be well simulated from one day to another, as the days tested consecutively do not belong to the same meteorological period. The structure of the Swipe Tools code first imposed that the storage had to be reinitialized at 0% at midnight between two days of the short sequence, which explains the limit of 8-10 hours storage recommendation in the optimization results: the code did not take into account higher capacities. A modification of the algorithm allowed to test simulations where the storage state of the precedent day of the short sequence was conserved for the beginning of the next days. Even if the days tested one after the other were not chronologically consecutive, it allowed the algorithm to take into account the possibility of using thermal energy stored even after midnight. This reduced the storage management difference

between reference and clustered simulations, as shows Fig. 15. Indeed, for the fourth iteration of OptiTypSS, the global quadratic error is equal to 3.5% against 5% previously, and the quadratic error for investment costs above 20 million euros fell from 6.8% to 4.6%. It is observed in Fig. 16 that OptiTypSS still underestimates the optimal storage capacity for large collectors area (high number of loops) but far less than previously, and there is no more a storage limit of 10 hours.

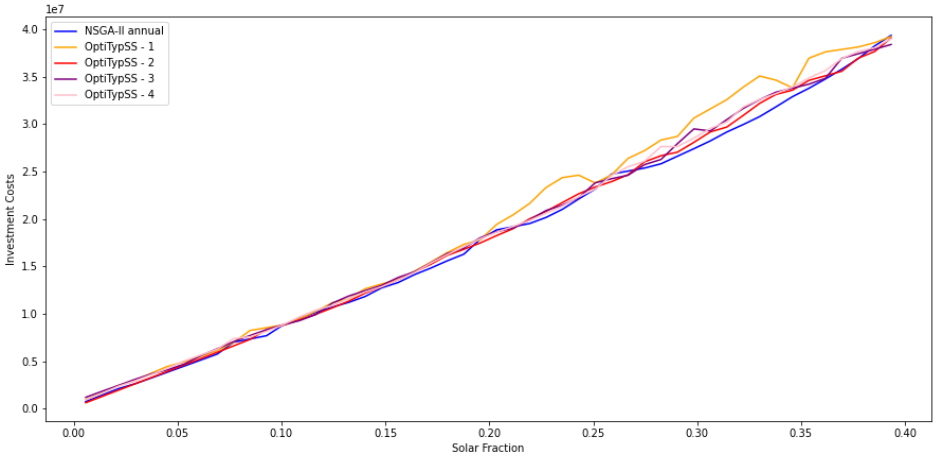

Fig. 15: Interpolations of the reference and approximated Pareto fronts given by OptiTypSS with storage state continuously modeled through the typical days.

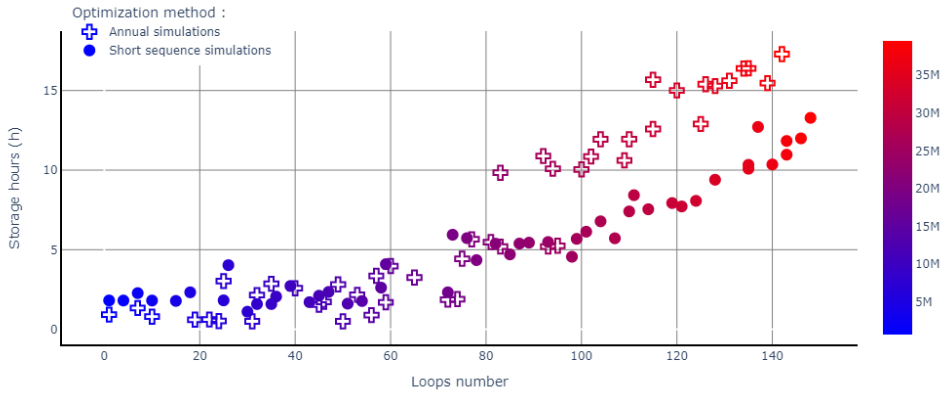

Fig. 16: Design choices comparison between annual NSGA-II and OptiTypSS with storage state continuously modeled through the typical days.

For specific plants with high storage capacity and with load demands that imply storing regularly energy through the night, the inaccuracy of storage state simulation with short sequence will have a significant impact on the quality of the results. In these cases, using the annual simulation with NSGA-II beginning with an initial population given by the first iteration of OptiTypSS could be a great compromise between time computation and results accuracy.
In the meantime, OptiTypSS is sufficiently accurate and can be used for design optimization for general types of plants. The great computation time reduction allows thinking of more complex optimization design problems, particularly by increasing the decision variables number. Indeed, more decision variables could be added such as the choice of the solar collectors technology, the design of the initial loop , or even the captors spacing and orientation.

5. Conclusion

This paper studies a new optimization method for design of solar thermal plants producing industrial heat. Instead of simplifying the model of the plant for an annual performance simulation, it investigates the use of meteorological data clustering with an intern algorithm selecting typical days in a year, named TypSS for Typical Short Sequence Algorithm. Originally developed by Sayegh (2020) for dynamic building performance simulations, it was adapted and validated in this paper for solar thermal plants‘ performance simulations. It determines the approximation of the annual solar fraction on hourly steps of a solar thermal plant with great accuracy, while reducing the computation time by 25 to 30 times depending on the short sequence length.

The NSGA-II (Non-dominated Sorted Genetic Algorithm II) well-spread optimization algorithm, presented by Deb et al. (2002), is used to obtain a Pareto front of optimal design solutions minimizing the initial investment costs while maximizing the predicted annual solar fraction. Applying this new method of performance calculation for solar plants with NSGA-II allows reducing greatly time calculation, even if it needs to regenerate more precise short sequences around the Pareto front space in order to gain in accuracy. However, one problem emerges for high storage capacities: the short sequences are not able to simulate accurately the storage state through one night, as two consecutive days of the typical sequence does not belong to the same meteorological period. It is therefore advised to use the annual simulations when the optimization design solutions looked for should make a significant use of night storage, while for plants with lower storage capacities OptiTypSS would be sufficient.

The algorithm developed allows obtaining faster many design optimization results for various problems: it can be very useful to test optimal design solutions variation with different initial parameters. Indeed, it was proved by Kamerling et al. (2021) that solar field output temperature optimization in control strategy could improve significantly the plant efficiency. It is planned to investigate whether taking into account the control strategy in design optimization would lead to greater results or if there is no need of making this choice before building the structure. This fast optimization tool will also permit running more complex design optimization problems with many more decision variables, which will be investigated in the future.

6. Acknowledgments

This work has received funding from the Ministère de l'Enseignement Supérieur, de la Recherche et de l'Innovation (MESRI), along with support from the European Union's Horizon 2020 re-search and innovation programme under grant agreement No 884213 (project FRIENDSHIP).

7. References

Cabello, J.M., Cejudo, J.M., Luque, M., Ruiz, F., Deb, K., Tewari, R., 2009. Optimization of the sizing of a solar thermal electricity plant: Mathematical programming versus genetic algorithms. In: 2009 IEEE Congress on Evolutionary Computation. Presented at the 2009 IEEE Congress on Evolutionary Computation (CEC), IEEE, Trondheim, Norway, pp. 1193–1200. DOI: 10.1109/CEC.2009.4983081

Deb, K., Pratap, A., Agarwal, S., Meyarivan, T., 2002. A fast and elitist multiobjective genetic algorithm: NSGA-II. IEEE Trans. Evol. Computat. 6, 182–197. DOI: 10.1109/4235.996017

Kalogirou, S.A., 2004. Optimization of solar systems using artificial neural-networks and genetic algorithms. Applied Energy 77, 383–405. DOI: 10.1016/S0306-2619(03)00153-3

Kamerling, S., Vuillerme, V., Rodat, S., 2021. Solar Field Output Temperature Optimization Using a MILP Algorithm and a 0D Model in the Case of a Hybrid Concentrated Solar Thermal Power Plant for SHIP Applications. Energies 14, 3731. DOI: 10.3390/en14133731

Kaufman, L., Rousseeuw, P.J., 2005. Finding groups in data: an introduction to cluster analysis, Wiley series in probability and mathematical statistics. Wiley, Hoboken, N.J. ISBN 0-47 1-73578-7

Klemeš, J.J. (Ed.), 2011. Sustainability in the process industry: integration and optimization, Green manufacturing & systems engineering. McGraw-Hill, New York. ISBN: 9780071605540

Kumar, L., Hasanuzzaman, M., Rahim, N.A., 2019. Global advancement of solar thermal energy technologies for industrial process heat and its future prospects: A review. Energy Conversion and Management 195, 885–908. DOI: 10.1016/j.enconman.2019.05.081

Mahmoudimehr, J., 2018. Optimal design of hybrid photovoltaic-hydroelectric standalone energy system for north and south of Iran. Renewable Energy 14. DOI: 10.1016/j.renene.2017.08.054

Mahmoudimehr, J., Sebghati, P., 2019. A novel multi-objective Dynamic Programming optimization method: Performance management of a solar thermal power plant as a case study. Energy 168, 796–814. DOI: 10.1016/j.energy.2018.11.079

Pedregosa, F., Varoquaux, G., Gramfort, A., Michel, V., Thirion, B., Grisel, O., Blondel, M., Prettenhofer, P., Weiss, R., Dubourg, V., Vanderplas, J., Passos, A., Cournapeau, D., n.d. Scikit-learn: Machine Learning in Python. MACHINE LEARNING IN PYTHON 6. https://hal.archives-ouvertes.fr/hal-00650905v2

PVGIS, 2019. EU SCIENCE HUB. Photovoltaic Geographical Information System [WWW Document]. URL https://ec.europa.eu/jrc/en/pvgis (accessed 6.16.21).

Sayegh, H., 2020. Holistic optimization of buildings based on the evaluation of annual performances from short simulation sequences 181. https://tel.archives-ouvertes.fr/tel-03219964v2

Sayegh, H., Leconte, A., Fraisse, G., Wurtz, E., Rouchier, S., 2022. Computational time reduction using detailed building models with Typical Short Sequences. Energy 244, 123109. DOI: 10.1016/j.energy.2022.123109

Silva, R., Berenguel, M., Pérez, M., Fernández-Garcia, A., 2014. Thermo-economic design optimization of parabolic trough solar plants for industrial process heat applications with memetic algorithms. Applied Energy 113, 603–614. DOI: 10.1016/j.apenergy.2013.08.017

Thiel, G.P., Stark, A.K., 2021. To decarbonize industry, we must decarbonize heat. Joule 5, 531–550. DOI: 10.1016/j.joule.2020.12.007

Tilahun, F.B., Bhandari, R., Mamo, M., 2019. Design optimization and control approach for a solar-augmented industrial heating. Energy 179, 186–198. DOI: 10.1016/j.energy.2019.04.142

Wallerand, A.S., Kermani, M., Voillat, R., Kantor, I., Maréchal, F., 2018. Optimal design of solar-assisted industrial processes considering heat pumping: Case study of a dairy. Renewable Energy 128, 565–585. DOI: 10.1016/j.renene.2017.07.027

Development of Models for Long-Term Simulations of District Heating Networks at High Temporal and Spatial Resolutions

Johannes Zipplies, Janybek Orozaliev, Klaus Vajen

University of Kassel, Institute for Thermal Engineering, Kassel (Germany)

Abstract

In innovative district heating systems with integration of distributed renewable heat sources, dynamic processes in the pipe network, such as flow reversals and zero flow periods due to decentral feed-in, and their effects on efficiency, service life and control strategies are getting more important. To investigate the effects of these processes, a dynamic thermo-hydraulic model for district heating networks using Modelica is developed. The new model builds upon available model libraries and adds improvements and design principles, that enable fast and accurate simulations. A general model design is proposed so that users can set-up correct district heating network models fast and easy. The new model is successfully validated against other software and measured data for representative load situations (high, medium, low load and a temperature step). On a regular computer, within six hours annual simulations of a district heating network with 85 consumer units can be run at a high temporal resolution of three minutes for all pipe segments including house lead-in pipes.

Keywords: district heating network, dynamic thermo-hydraulic simulation, Modelica, model design

1. Introduction

A vital element of the energy transition towards renewables is the integration of renewable heat sources into new and existing district heating networks (DHN). In many cases these renewable heat sources are distributed over the network, e.g., solar thermal units and waste heat sources. Their decentral feed-in results in an increase of dynamic processes in the DHN, such as flow reversals, compared to conventional DHNs with centralized heat supply units (Paulick et al., 2018).

This new situation creates a need for dynamic thermo-hydraulic models of DHNs, so that the effects on the network such as flow reversals, cold and hot plugs or temperature changes and their impacts on efficiency, service life as well as control strategies can be investigated. These models should enable dynamic simulations, that meet the following requirements:

- Long simulated times, up to one year, to examine the performance and relevant effects with seasonally variable heat sources and sinks
- High temporal resolutions, < 1 hour, to capture the fluctuating nature of renewable supply units
- High spatial resolutions, which means including all individual pipe segments, to capture the state of all parts of the DHN

In this contribution, the development and validation of such a model is described.

2. Model Development

To set up the dynamic model, the acausal, object-oriented modelling language Modelica (Modelica Association, 2013) and the simulation tool Dymola (Dassault Systèmes, 2019) are chosen, as this environment provides great capabilities to model thermo-fluid systems and a variety of high quality open-source model libraries such as the Modelica Standard Library (Modelica Association, 2019) and IBPSA library (IBPSA, 2018). Furthermore, the object-oriented approach of Modelica, including the usage of inheritance, enables a modular model design with good reusability and compatibility of the different component models. For the development of the component models, suitable base models from the Modelica Standard Library are used, wherever possible.

© 2022. The Authors. Published by International Solar Energy Society
Selection and/or peer review under responsibility of Scientific Committee
doi:10.18086/eurosun.2022.16.14 Available at http://proceedings.ises.org

2.1 Pipe model

The pipe model is based on a validated plug-flow model (van der Heijde et al., 2017) which calculates delay, heat-loss and the effect of the pipe wall heat capacity and is capable to handle flow reversals. The model efficiently handles varying inlet temperatures and flow reversals by using the Modelica spatialDistribution() operator (an inbuilt operator to implement plug-flow calculations) to calculate fluid and temperature propagation. The heat losses are modelled separately, using a Lagrangian approach, where the outlet temperature T_{out} of each fluid parcel is calculated from its dwell time in the pipe ($t_{\mathrm{out}} - t_{\mathrm{in}}$), its inlet temperature T_{in}, the temperature of the surroundings T_{b}, the thermal resistance between the fluid and the surroundings R and the heat capacity of the fluid C according to equation 1. This approach neglects changes of the temperature of the surroundings, axial diffusive heat transfer and effects of pressure loss, wall friction and dissipation, which are valid simplifications in most of the operational range of DHNs (van der Heijde et al. 2017).

$$T_{\mathrm{out}} = T_{\mathrm{b}} + (T_{\mathrm{in}} - T_{\mathrm{b}})\, exp\left(-\frac{t_{\mathrm{out}} - t_{\mathrm{in}}}{RC}\right) \qquad \text{(eq. 1)}$$

However, the original model produces hot plugs after zero flow periods as an artifact due to a simplification of the heat loss calculation: The pipe model contains a plug-flow model and a volume model in series (see Fig. 1). The original model allocates the heat loss only in the flow model and does not calculate heat losses for the volume model. This solution results in hot plugs of uncooled water, that get flushed through the network once the mass flow is reestablished after a zero flow period. A demonstration of this behavior is shown in Fig. 2 and Fig. 3. This is an unwanted artifact of the model and results in computational costs because the solver drastically reduces its timestep to accurately calculate the propagation of these hot plugs. To avoid this, heat losses for the volume model are included as well, while keeping the total heat loss of the pipe equal. The exact allocation of heat losses is undertaken by dividing the total heat conductivity according to the shares of heat capacity of water and pipe wall so that the volume model cools down simultaneously to the water in the plug-flow model. This improvement is important in case zero flow situations may occur often, for example in and close to feed-in points of solar thermal fields.

Another consequence of the original heat loss calculation is that the instantaneous heat loss of the pipe is not known, as just the heat loss of the fluid parcel leaving the pipe is calculated. While this is the same value at steady state conditions, in dynamic situations with varying mass flows or even zero flow periods the values may drastically differ (see Fig. 3, number 3). With the improved heat loss calculation above it is possible to estimate the instantaneous heat loss of the pipe from the temperature in its volume model. This new heat loss variable is added to the model, so that the instantaneous heat loss can be evaluated easily.

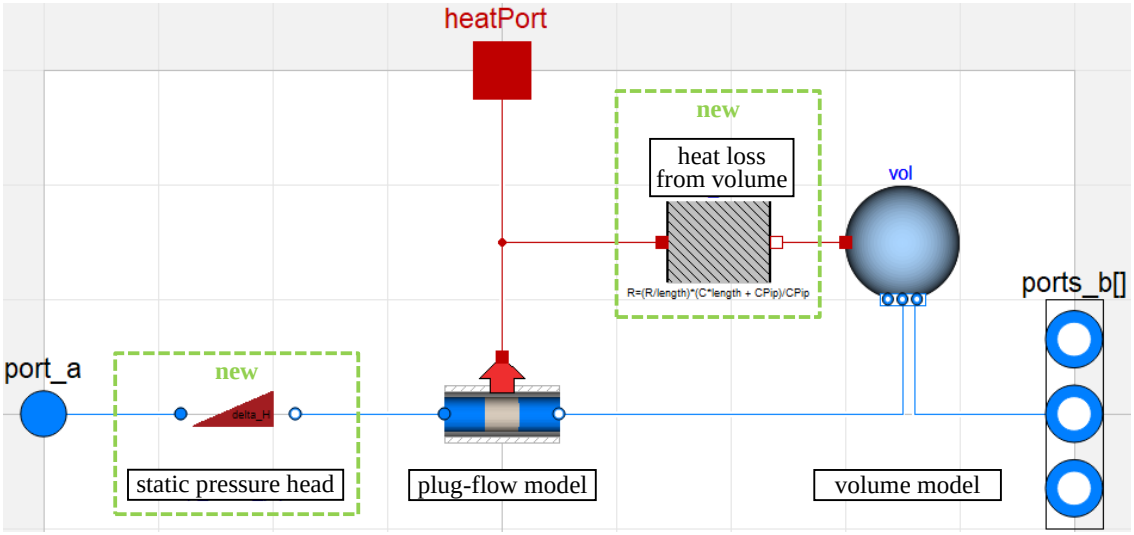

Fig. 1: Plug-flow pipe model consisting of a static pressure head model, a plug flow model, and a volume model with a heat loss component. Green boxes highlight improvements within this work compared to the original model (van der Heijde et al., 2017).

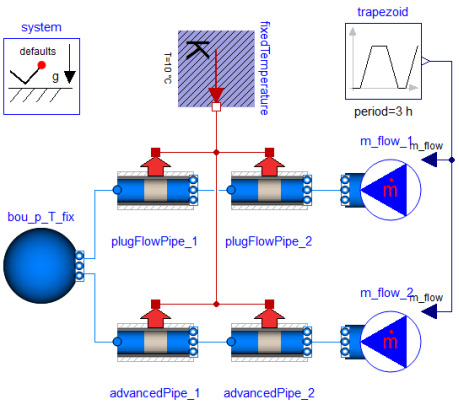

Fig. 2: Model to compare the original plug-flow pipe with the advanced version. Two serial pipes of each type experience a period of zero flow.

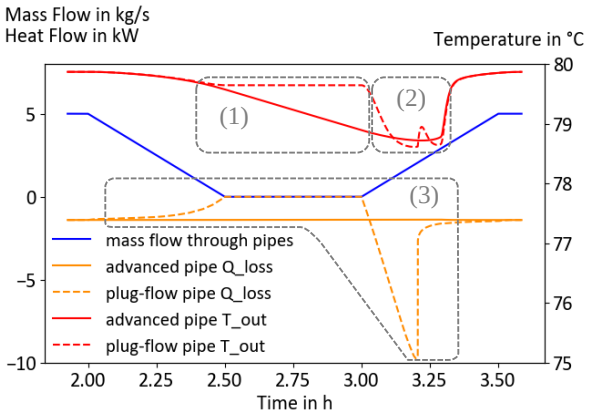

Fig. 3: Results that show the improvements of the advanced pipe model: realistic cooling during zero flow (1), no temperature peaks when pipes are flushed afterwards (2) and the heat loss variable that is independent from mass flow (3).

Furthermore, the calculation of the static pressure head was added and the detailed pressure calculation from the Modelica Standard Library (Modelica Association, 2019) was made available as an option in case it is needed instead of the simplified approximation that is already included. For a good usability, two pipe models are wrapped into a double pipe model representing supply and return line and an easy parametrization via pipe types is implemented. Multiple pipe models can be connected at network nodes through their vectorized ports, so that the pipe model instances can form any network layout.

2.2 Functional units

The functional units of the district heating network (supply units, loads and bypasses) are modelled as fluid boundary conditions (either pressure or flow boundary conditions at setpoint temperatures) without detailed modelling of the actual components, such as heat exchangers, pumps, or storages (see Fig. 4). The setpoints for pressures, mass flows and temperatures are calculated in control blocks from input data and relevant states in the network, such as the temperature at the outlet of the supply line pipe entering the respective functional unit. This reflects the underlying assumption, that all units follow their setpoints accurately enough, so that deviations from the setpoint can be neglected. Furthermore, in the functional units, there is no fluid model connection between supply and return line so that the fluid flow equations for supply and return line are decoupled, which reduces the computational effort.

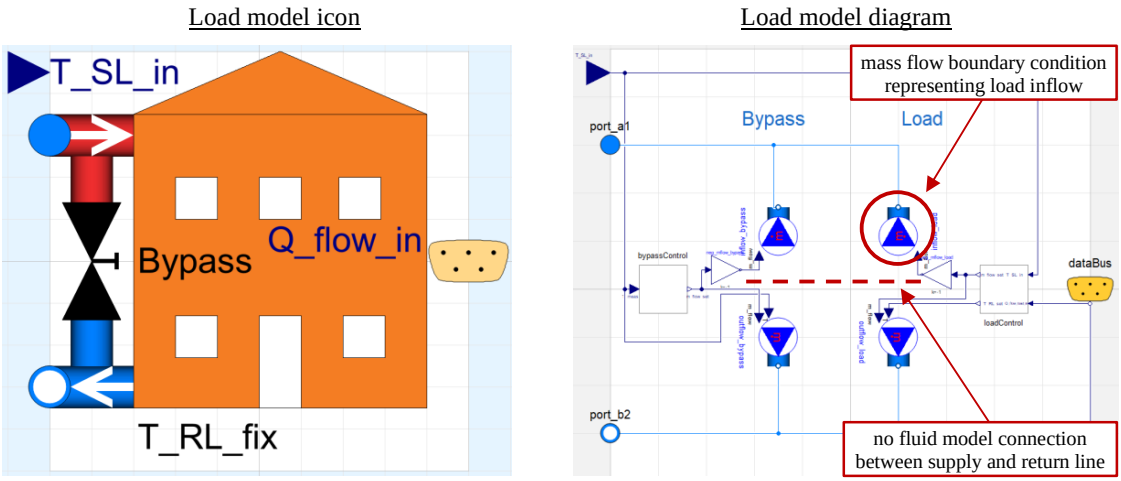

Fig. 4: The load model as an example for the model architecture of the functional units. The lefthand-side shows the model icon, which indicates the general model behavior and its connectors to other model instances, while the righthand side shows the model diagram with its inner structure. The inputs supply line temperature ("T_SL_in", top left) and load data ("dataBus" center right) are used to calculate the mass flows that occur. The fluid models are separated between supply and return line.

The mass flow calculations in the functional unit include time constants that restrict the dynamics of mass flow changes. This allows smooth simulations where the computation of highly dynamic effects (or artifacts) that are out of the relevant time scale are avoided.

2.3 General Model Design

The fluid in the network is modelled as constant property water, with the properties separately calculated for supply and return lines at the respective design temperatures. However, the models are still compatible to other variable property fluid models in case a user wishes to introduce them at the cost of higher computational effort.

The dynamic pressure effects in water occur on time scales below the focus of the model (< 1 s). Thus, the pressures in the network are calculated stationary assuming an incompressible medium and neglecting expansions of the hydraulic components. Therefore, the pressure control loop results in a large non-linear algebraic equation system, that must be solved iteratively for each timestep (so-called algebraic loop). This algebraic loop can be avoided by introducing a state variable within the loop (Jorissen et al., 2018). To do so, a PT1-block is included in the pressure control loop. Jorissen et al. point out, that this approach increases the computational effort for the integrator. However, in the use case of pressure control loops for large pipe networks in DHN, this additional effort is by far compensated by the advantage of avoiding the iterative solution of the non-linear algebraic system: For a case study of a radial DHN with about 400 pipe model instances, the introduction of the PT1-block reduces the CPU-time of a simulation by a factor >10.

The general model design includes a variety of further auxiliary models, that are bundled within a “DH environment” model, so that users can set-up a correct DHN model fast and easy. A diagram of a simple DHN model with all auxiliary models is shown in Fig. 5. The auxiliary models are:

- The system component builds upon the Modelica.Fluid.System model from the Modelica Standard Library (Modelica Association, 2019). It is used to set general parameters, that are important for the simulation. The original model is extended by parameters to set the time constant of the functional units, parameters to support the definition of nominal temperatures to be used in model instances wherever useful, parameters for pipe default settings and parameters for the network structure (e.g. number of network sections).
- Data input is managed via data readers (Modelica.Blocks.Sources.CombiTimeTable; Modelica Association, 2019) for temperature and load data. A data bus is used to automatically connect the numerous signals to the corresponding units. To ensure a correct signal propagation, the load units must be assigned with unique IDs and the input data table must be arranged accordingly.
- A heat loss connector is automatically connected to all pipe models on the one hand and the soil temperature signal on the other hand to ensure a correct heat loss calculation.
- The pressure control loop bundles and processes the pressure signals from the outlets of all pipes and the differential pressures at all loads so that the pressure setpoints can be followed using PI-controllers. The pressure control loop includes a PT1-block, to break the algebraic loop as described above.

Finally, the simulation timestep of the solver is limited to a maximum value to avoid propagating increasing numerical errors in series of pipe models that can be observed when the integrator timestep gets too large. These numerical errors especially occur within short pipe instances: Once the solver time step exceeds the dwell time within short pipe models (so that the plug-flow model is fully flushed within one time step), the temperature calculation becomes an error prone extrapolation. The numerical errors then propagate to the next pipe model, inducing sudden changes of temperature which then forces the solver to drastically reduce the simulation timestep until the temperature oscillation gets consumed by a load instance. The optimal value for the maximum simulation time step depends on the pipe lengths and the flow velocities (which themselves depend on load profiles, flow and return temperatures, and network design) within the network. Limiting the solver time step to a maximum value of 180 s has proven to be a decent choice for medium sized DHN with typical hourly load profiles for residential buildings.

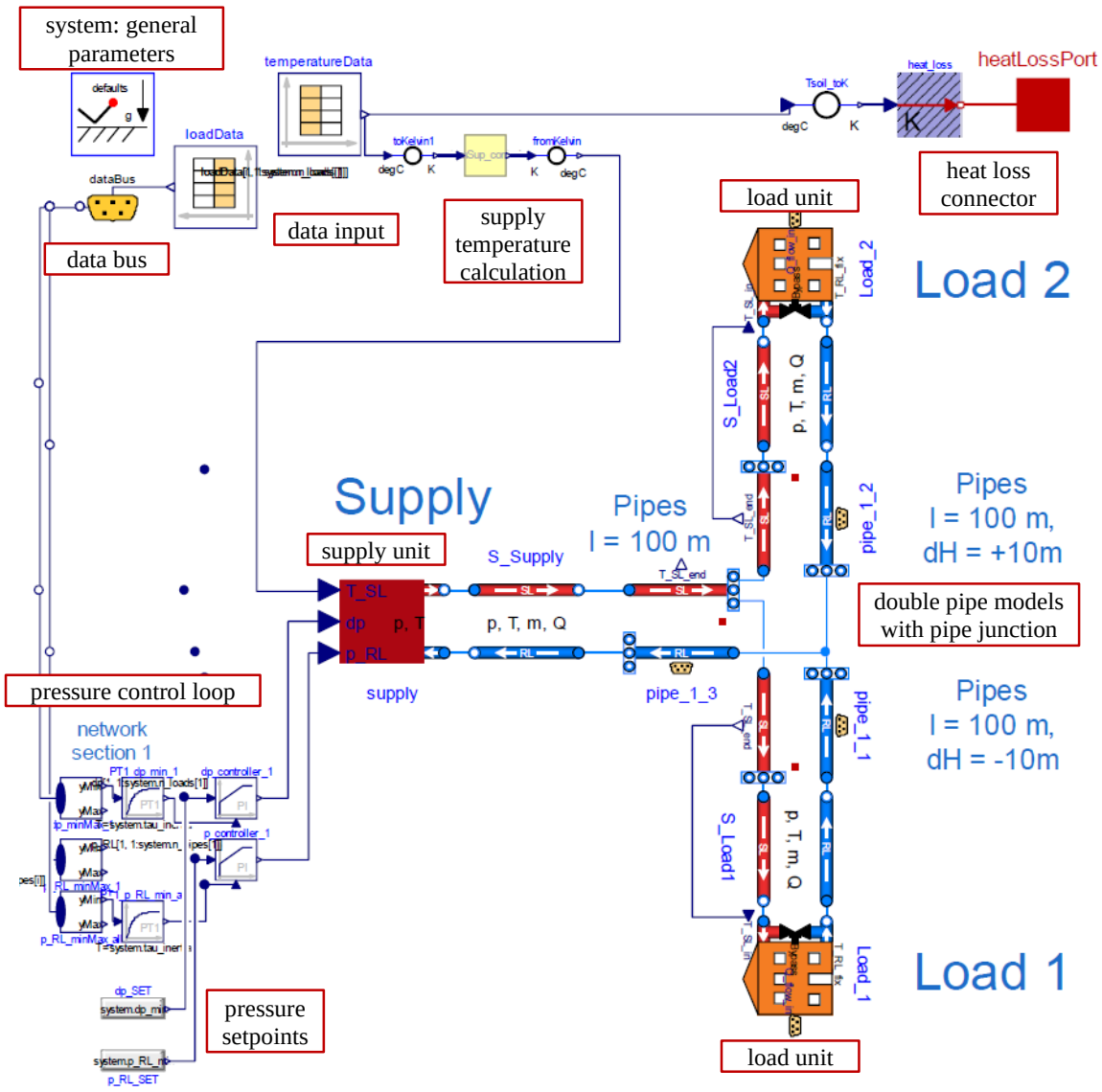

Fig. 5: Overview of the general model design showing a very simple DHN with one supply unit and two loads connected via pipe models with a pipe junction. The auxiliary models for general settings and parameters, data input and propagation, pressure control and heat loss calculation are arranged at the top and left side.

2.4 Development process and result

During the development process, the component's correct function and performance was permanently tested. Occurring issues were analyzed and solved, until through incremental improvements a proper performance of the full DHN model was reached. Finally, an annual simulation of a radial network with 85 loads at a high spatial resolution (no aggregation, including house lead-in pipes) can be run at a high temporal resolution (≤ 3 minutes) within six hours on a regular computer (Windows 10, 64 bit, CPU Intel i5-4300U @ 4x1.9 GHz, RAM 8 GB).

3. Model Validation

The first stage of the validation process was done by simulating a simple exemplary DHN in both, the commercial software STANET® (Ingenieurbüro Fischer-Uhrig, 2020) and using the new Modelica models. A variety of 100 randomly chosen static load situations was simulated. The results show, that for all important parameters (temperatures, differential pressures, heat losses and mass flows) the deviations are below 1 %. Thus, the new model proves highly accurate for stationary conditions.

The second stage of the validation process aims to validate the performance for dynamic situation. It is based on measured data (time resolution 15 min.) from a radial DHN with about 250 consumers. The accuracy of the measured data is limited, because at the consumer units, only momentary values are known, and these values are not exactly synchronous as they are transmitted via a serial bus system. Thus, the data was edited using the following procedure:

- Step 1, cross check of individual consumer data: At each consumer momentary mass flow, temperatures and heat meter values are known. Using the heat meter values, the mass flow data was upsampled to a 3-minute interval so that the mass flow timeseries is in line with the heat meter values. During this process, peaks were trimmed to a plausible duration and missing peaks were introduced.
- Step 2, using central measurement: At the central heat supply unit the total mean mass flow of the DHN is known accurately for each interval. However, the sum of all measured consumer mass flows is up to 10 % below this total mass flow. The reasons for this deviation may be inaccurate mass flow measurements and / or unmeasured mass flows in some parts of the network. As it was impossible to exactly identify the sources of deviation, the mass flow data at all consumers is increased by the deviation factor for each timestep.

This data editing procedure may in some cases confound the data due to incorrect adjustments. However, the raw data is inconsistent which would result in a failure of the validation process, while the edited data is a consistent, most applicable data set obtained by combining all available information. Yet, these limitations of the data quality restrict the achievable degree of agreement between measurements and simulation.

For the simulation, the edited timeseries of mass flow and return temperatures at the consumers and the supply temperature at the supply unit are used as an input. The simulation results are evaluated based on the resulting return temperatures and heat flows at the supply unit. The validation covers the full range of operating conditions throughout the year: periods of low, medium, and high load (each three days) and a period with a sudden rise of the supply temperature, as this is a highly dynamic situation in the measurement data. While these periods were simulated using the upsampled 3-minute timeseries and a maximum simulation timestep of 180 s, the evaluation of the agreement between simulation and data was done with 15-min mean values, as this is the data timestep at the central supply unit.

The results are shown in Fig. 6 to Fig. 9 for the different periods. Each figure shows the timeseries of heat flow, supply and return temperature at the supply unit from measurement and simulation (top-left) and scatter plots to compare measured and simulated values for mass flow (top-right), return temperature (bottom-left) and heat flow (bottom-right). The comparison of simulation and measurement shows:

- The general course of the timeseries is met very well by the simulation: Peaks and valleys of the heat load are simulated accurately, and subsequent changes of the return temperature agree very well in magnitude and shape. This indicates, that the edited measured timeseries form a consistent data set and that the model correctly captures the DHN's structure and physics.
- The relative mean deviations of mass and heat flow are small (< 2 %) for all load situations, apart from the low load period (see next bullet point).
- The deviations are highest for the low-load period: The simulation yields systematically larger return temperatures (+1.6 K) and thus lower heat powers (-11 %) than measured. A plausible explanation for this systematic deviation lies in the data quality and editing: During the low load period, the heat load is domestic hot water use. This leads to strongly varying return temperatures at the consumers: While actual tapping events or the charging of a discharged storage produce large heat flow peaks with low return temperatures, the compensation of heat losses from storages (if existing) and circulation pipes leads to small, constant heat flows with a high return temperature. These fluctuations of the return temperature are not sufficiently tracked by the measured data and cannot be reconstructed properly from the available data. The results indicate that the data editing procedure tends to overestimate the return temperature which leads to underestimated heat loads. Thus, the deviation is rather a consequence of data quality than of shortcomings of the simulation model.
- Finally, the temperature step situation (Fig. 9) deserves special attention: Here, first the supply

temperature slowly drops and then rises by 15 K within 30 minutes, which is a highly dynamic situation for a DHN. The results show that the simulation accurately reproduces the heat flow peak once the flow temperature rises and captures the course of the drop and subsequent delayed rise of the return temperature.

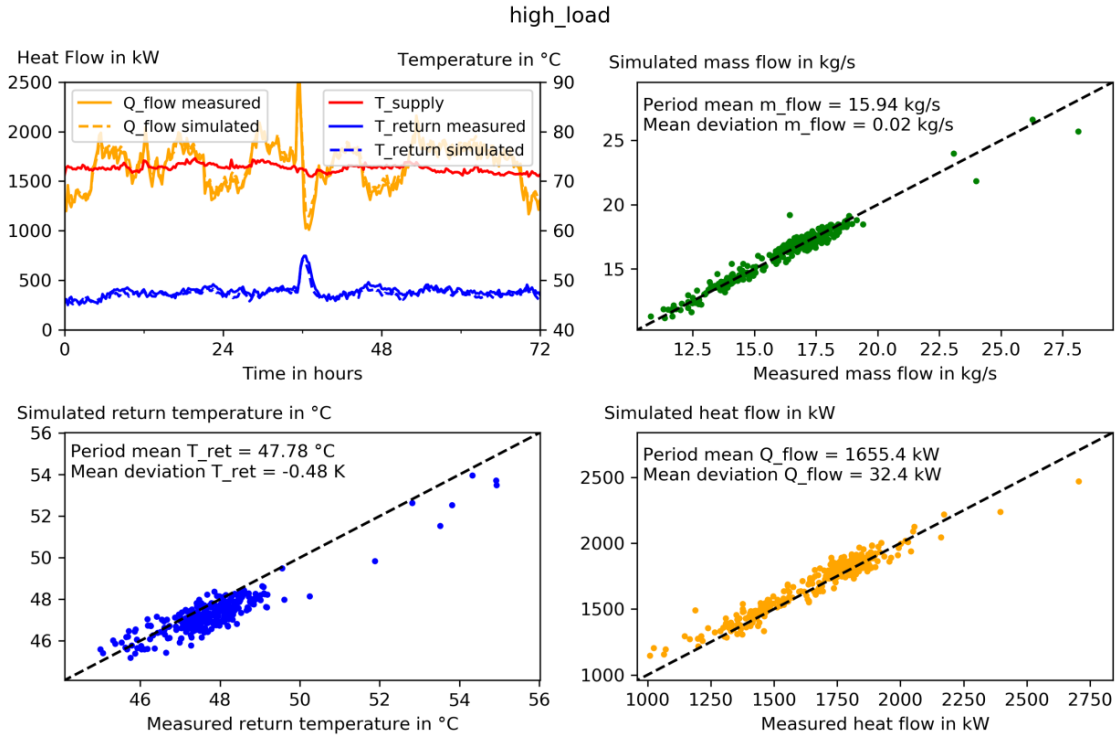

Fig. 6: Validation results for a high load period.

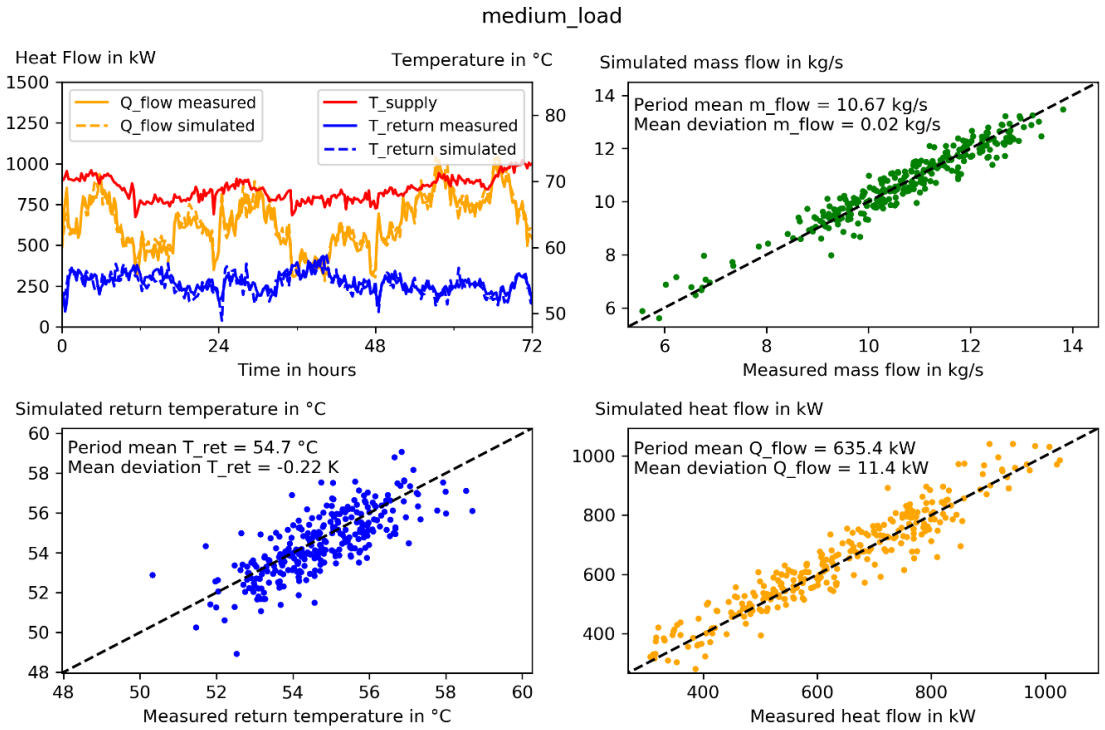

Fig. 7: Validation results for a medium load period.

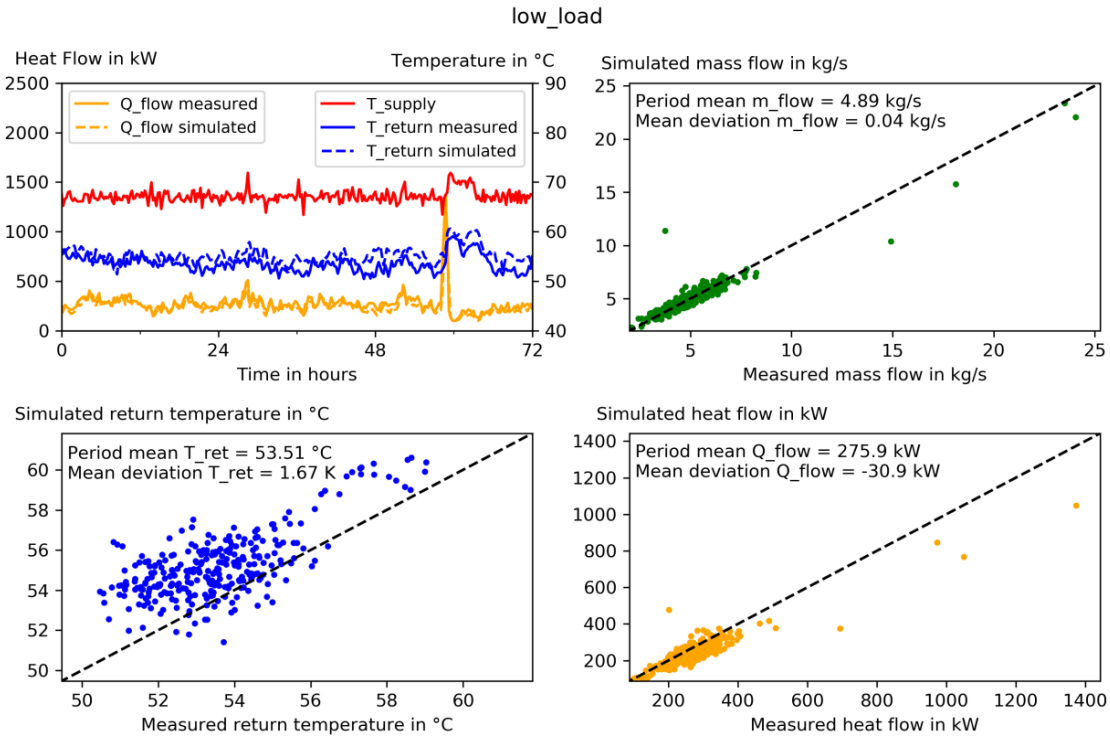

Fig. 8: Validation results for a low load period.

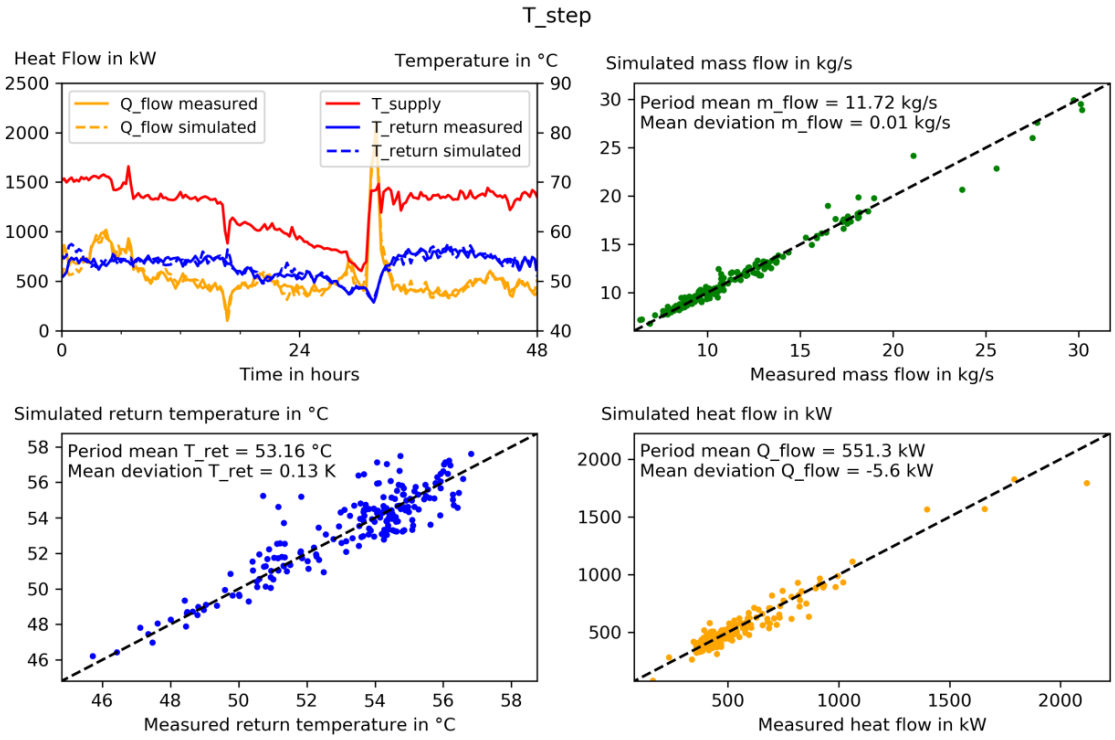

Fig. 9: Validation results for a period with a sudden flow temperature step.

In summary, the new model is successfully validated for static and dynamic situations comparing it to other simulation software and measured data from a real DHN.

4. Conclusion

A dynamic thermo-hydraulic model for the simulation of DHNs focusing on the dynamic processes within the pipe network (such as temperature wave formation and propagation) is successfully developed in the object-oriented modelling language Modelica. The model partly builds upon previously published open-source models with improvements concerning realistic behavior, usability of the models and computational performance. In particular, enhancements to the plug-flow pipe model by Jorissen et al., 2018 are proposed which yield realistic behavior and more stable simulations for situations with zero flow periods. Furthermore, design principles are proposed for the functional units, such as avoiding physical modelling of the inner hydraulic components and separation of fluid models for flow and return side to reduce the computational effort, and for the general model design with a set of auxiliary model components which facilitate the set-up of complete models of DHNs.

The model simulates a medium sized DHN (85 loads) at high temporal resolutions (3 min) for long simulated times (1 year) in about six hours on a regular computer. The new model is successfully validated for static states, compared to the commercial network simulation software STANET®. To also validate the model for dynamic conditions, measured data from a medium sized DHN for different load situations and a situation with a very sudden change of the flow temperature were processed and fed into the model. The simulation results show good agreement with the measured data. Thus, the newly developed model has proven its high performance and accuracy for dynamic simulations of DHNs.

5. Acknowledgments

This contribution is based upon the work conducted within the SINTEG project Csells funded by the German Federal Ministry for Economic Affairs and Energy (grant number 03SIN119).

6. References

Dassault Systèmes, 2019. Dymola. Dynamic Modeling Laboratory.

IBPSA, 2018. Modelica IBPSA Library. International Building Perfomance Simulation Association, https://github.com/ibpsa/modelica-ibpsa.

Ingenieurbüro Fischer-Uhrig, 2020. STANET 10.0. Netzberechnung.

Jorissen, F., Wetter, M., Helsen, L., 2018. Simplifications for hydronic system models in modelica. Journal of Building Performance Simulation 11 (6), 639–654.

Modelica Association, 2013. Modelica - A Unified Objet-Oriented Language for Systems Modeling. Language Specification. Version 3.2 Revision 2. https://modelica.org/documents/ModelicaSpec32Revision2.pdf. Accessed 13 December 2021.

Modelica Association, 2019. Modelica Standard Library. Modelica Association, Linköping.

Paulick, S., Schroth, C., Guddusch, S., Rühling, K., 2018. Resulting Effects On Decentralized Feed-In Into District Heating Networks – A Simulation Study. Energy Procedia 149, 49–58.

van der Heijde, B., Fuchs, M., Ribas Tugores, C., Schweiger, G., Sartor, K., Basciotti, D., Müller, D., Nytsch-Geusen, C., Wetter, M., Helsen, L., 2017. Dynamic equation-based thermo-hydraulic pipe model for district heating and cooling systems. Energy Conversion and Management 151, 158–169.

Optimal Control Based on Deep Learning Techniques for a Hybrid Solar-Biomass System for Residential Buildings

Gabriel Zsembinszki, Cèsar Fernández, Emiliano Borri, Luisa F. Cabeza

GREiA Research Group, University of Lleida, Lleida (Spain)

Abstract

The EU-funded H2020 project SolBio-Rev aims to develop an energy system based on the use of solar energy and biomass with the objective to increase the share of renewable energy needed to meet heating, cooling, domestic hot water, and electricity demand in buildings. In this study, deep reinforcement learning techniques were applied for a SolBio-Rev system designed for a residential building (multi-family house) located in a Mediterranean climate in order to define an optimal control policy able to minimize the operating cost during summer and winter. Results showed that the smart control is able to reduce the cost of operation during summer compared to a standard rule-based strategy. Nevertheless, in winter the operating cost results slightly higher suggesting a further optimization for future studies.

Keywords: Deep reinforcement learning, optimal control, smart control, modeling, residential buildings, hybrid energy systems, biomass

1. Introduction

The reduction of energy consumption in buildings and the production of energy through efficient systems based on renewables are fundamental actions to achieve a substantial reduction of gas emission to the atmosphere. Indeed, buildings are responsible for almost 40% of the overall energy consumption and gas emission into the atmosphere (IEA, 2019), therefore immediate actions are needed. Energy systems that can integrate more renewable sources can overcome the problem of their intermittency providing high flexibility and increasing the total share of renewables in buildings. In the framework of the EU-funded H2020 project SolBio-Rev, an energy system based on the use of solar energy and biomass is being developed to provide heating, cooling, domestic hot water, and electricity to different building typologies located in different climates. The novel system developed combines different technologies including a reversible organic Rankine cycle (ORC)/heat pump, solar collectors with thermoelectric generators, and a biomass boiler. The potential of this system to achieve a 100% share of renewable was studied in (Palomba et al., 2020) and (Palomba et al., 2021) in both residential and non-residential buildings located in different EU climates.

In order to achieve the maximum efficiency of energy systems, the implementation of an optimal control is essential. Different control strategies can be found to manage energy systems. One of the techniques which gained attention recently is Model Predictive Control (MPC). However, one of the main constraints of this technique is the need of specialized solvers to find optimal solutions, which are limited to certain type of non-linarites. Amongst other techniques, Deep Reinforcement Learning (DRL) was proved to be a successful technique for solving complex control problems that is gaining interest in the field of energy system. In literature, it is possible to find DRL architectures approximating MPC on complex systems, or DRL algorithms that successfully control an HVAC (heating, ventilation, and air conditioning) system for a given user comfort requirement (Wei et al., 2017). A DRL architecture was also implemented in a previous study by the authors (Zsembinszki et al., 2021) to deal with the complexity of an innovative hybrid energy storage system and to develop high-level control policies that minimize the operating cost of the system. In this study, the same DRL techniques were applied for a SolBio-Rev system designed for a residential building located in a Mediterranean climate in order to build an optimal control policy that can minimize the operating cost during summer and winter.

© 2022. The Authors. Published by International Solar Energy Society
Selection and/or peer review under responsibility of Scientific Committee
doi:10.18086/eurosun.2022.16.15 Available at http://proceedings.ises.org

2. Methodology

The SolBio-Rev system optimized for Mediterranean climate is shown in Fig. 1 and is composed of the following main components with the respective functions:

- Solar collectors with thermo-electric generators (TEGs) providing (1) heat to a short-term storage tank that is connected to a sorption chiller, a biomass boiler, and a domestic hot water (DHW) distribution system, and (2) electricity to auxiliary system components (i.e., pumps).
- Biomass boiler that supplies heat for DHW and space heating (SH) to the storage tank.
- Sorption chiller that works in cascade with a reversible heat pump during summer operation.
- Reversible heat pump to provide heating/cooling.
- Dry cooler that provides evaporation heat to the heat pump during winter operation and dumps condensation heat to the ambient during summer operation.
- Buffer tank to decouple the heat pump and the short-term storage tank from the heating/cooling distribution system.

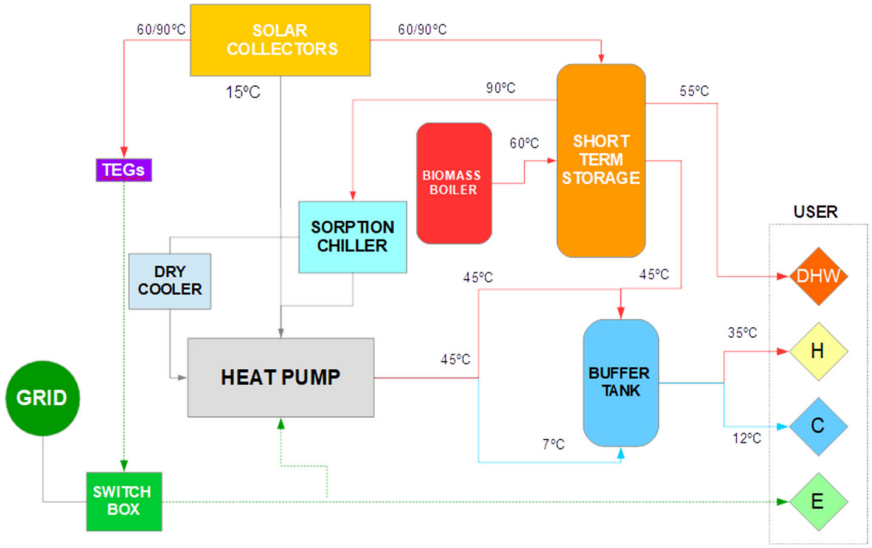

Fig. 1. System components for the SolBio-Rev designed for continental climate

The components were sized (Tab. 1) based on the energy demand obtained through simulations of a multi-family house located in Madrid. In this case, the multi-family house taken as a reference was the one from the EU project iNSPIRe (Dipasquale et al., 2014) with the U-values of a new/refurbished building according to the national building directive of Spain.

Tab. 1. Size of the SolBio-Rev system components

Component	Size
Sorption chiller	15 kW
Biomass boiler (without supplying heat to the ORC)	15 kW
Reversible heat pump	15 kW
Solar collectors with TEGs	50 m^2
Short-term storage tank	1500 litres
Buffer tank	800 litres

For each component, a detailed numerical model to be integrated in the DRL architecture was developed. In

particular, the solar collectors model is based on a commercial AkoTec OEM vario 3000-20 collector and the solar thermal power was calculated based on the global solar radiation and the overall efficiency of the solar collectors. The TEGs were modelled considering the total thermal resistance of the TEGs system and calculating the power output through a linear function related to the temperature difference between input and output. The heat pump and the sorption chiller were modelled using performance curves given as polynomial functions based on equations for the cooling power and coefficient of performance (COP) as a function of operating temperatures. The biomass boiler was considered to operate at constant power with a 98% of thermal efficiency. The two water storage tanks were model using energy balance equations between the inputs and outputs.

The system modelling considered two different time scale slots: a finer time slot (3 minutes), to numerically compute the SolBio-Rev system behavior for inner model operations and, a second, longer time slot (15 min was considered), to manage the high-level control system. Within the longer time slot, any action decided by the control system will not change until any of the subsystem limits is attained. The input and system variables considered as an input to the control includes the level of solar irradiance, the ambient temperature, the status of the different subsystems, and the energy demand profile for heating, cooling, and DHW. The set of actions that are taken by the control algorithm are based on the combination of operational modes of each subsystem/component shown in Tab. 2.

Tab. 2. Operational modes of the system components

Component	State no.	Description
Solar collectors + TEGs	0	Off
	1	Setpoint 60 ºC (SH+DHW production)
	2	Setpoint 90 ºC (sorption chiller-assisted operation of the heat pump for cooling)
	4	Feeding TEGs for electricity generation
	5	Setpoint 15 ºC (solar-assisted operation of the heat pump for heating)
Heat pump	0	Off
	1	On for space heating using dry cooler
	2	On for space heating using solar collectors
	3	On for cooling using dry cooler
	4	On for cooling using sorption chiller
Biomass boiler	0	Off
	1	On for short-term storage tank charging at 60 ºC
Buffer tank	0	Not charging
	1	Heat provided from the short-term storage tank
	2	Heat provided from the heat pump
	3	Cooling provided from the heat pump

The control policies of the smart control aimed at the minimization of the economic operational costs of the system (€) using a cumulative reward function calculated based on the costs associated to running the system in different operational modes. The objective function can be defined with the following equation:

$$Penalty\ (E_{dhw} - E_{dhw,supplied}) + \ Penalty\ (E_{sh} - E_{sh,supplied}) + \quad \text{(eq.1)}$$

$$+ Penalty\ (E_{cooling} - E_{cooling,supplied}) + \ E_{boiler} Cost_{pellets} + E_{grid} Cost_{grid}$$

where *Penalty* (€/kWh) is an economic penalization for not supplying the energy demand, E_{dhw} (kWh) is the DHW demand, $E_{dhw,supplied}$ (kWh) is the energy supplied for DHW by the SolBio-Rev system, E_{sh} (kWh) is the SH demand, $E_{sh,supplied}$ (kWh) is the energy supplied for SH by the SolBio-Rev system, $E_{cooling}$ (kWh) is the cooling demand, $E_{cooling,supplied}$ (kWh) is the energy supplied for cooling by the SolBio-Rev system,E_{boiler} (kWh) is the energy provided by the biomass boiler, $Cost_{pellets}$ (€/kWh) is the economic costs of the pellets, E_{grid}

(kWh) is the energy consumed from the grid, and $Cost_{grid}$ is the price of the electricity (€/kWh). A cost of 0.30 €/kg (0.72 €/kWh) was considered for the pellets, while a cost of 0.15 €/kWh and 0.30 €/kWh was considered for the grid electricity cost during off-peak and peak periods, respectively. The DRL algorithm was trained using the energy demand simulated for the reference multi-family house shown above using the weather data obtained from Meteonorm database for the location of Madrid available in TRNSYS (TRNSYS18, n.d.).

The smart controller algorithm based on DRL developed minimized the objective function defined as cumulative reward of the whole season, providing the optimal policy of actions. To evaluate the performance of the DRL control policy, a rule-based control (RBC) policy was first implemented for the different operational modes. To assess the RBC policies, exactly the same number of training and testing data and the same time-step for the control management were used. In particular, the data sets were created taking 150 days for winter and 80 days for summer. From each season set, days were shuffled and 10 days were taken for testing and 10 days for validation. The remaining days of each set were kept for training the algorithm. The results shown in the next section correspond to the validation set.

3. Results

The actions done by the RBC policy and the DRL algorithm during summer are shown in Fig. 2 and Fig. 3, respectively. The results show that, due to the constant need of cooling demand, the heat pump is operating most of the time in both cases. However, using an RBC policy, the heat pump is mostly running using the dry cooler, but it also runs in the mode using the sorption chiller. On the other hand, the smart control never uses the cascade mode with sorption chiller. Moreover, the RBC policy uses the TEGs to produce electricity more often than the DRL policy. Despite of this, in summer, the total cost using the smart control is very similar to the cost using the RBC policy (55 € vs. 57 €). In winter, when solar radiation is lower, the RBC (Fig. 4) shows a high use of the biomass boiler to satisfy both DHW and space heating, and, during periods of highest solar radiation, solar energy is used to run the TEGs. The heat pump in solar-assisted mode is never used. However, the smart control using DRL algorithm (Fig. 5) reduces the use of the biomass boiler by enhancing the use of the solar collectors. Moreover, the TEGs are almost always OFF. In this case, using the policy detailed by the smart algorithm, it is possible to reduce the operating cost in winter for 10 days of operation from 37 € to 24 €.

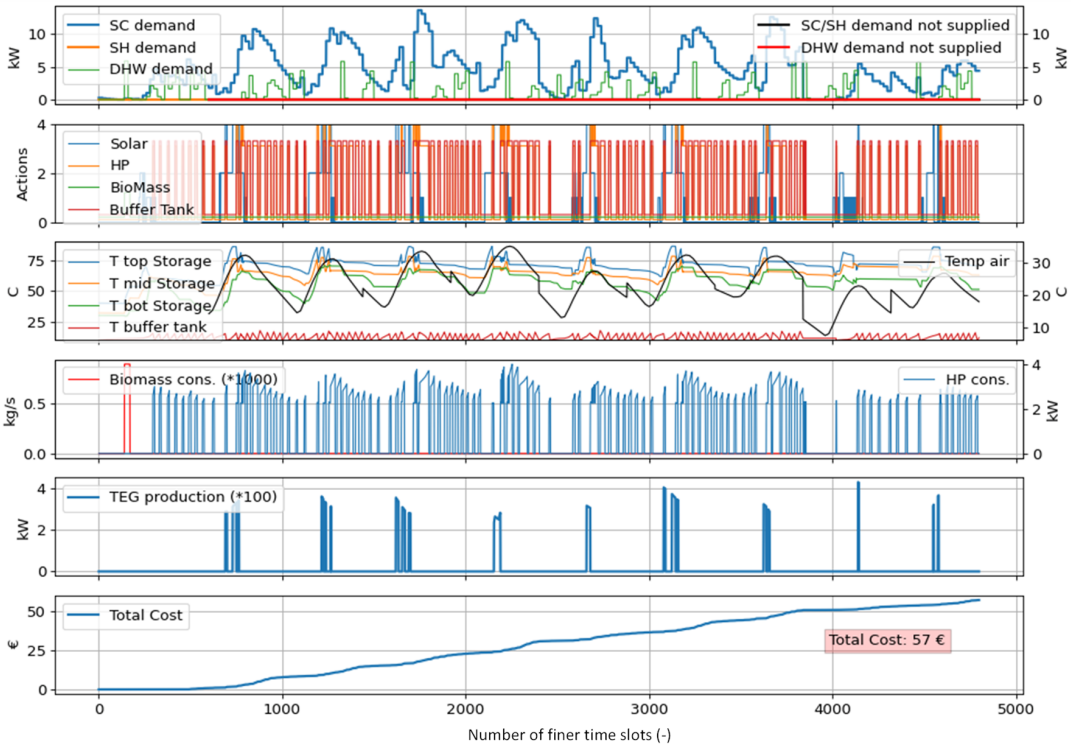

Fig. 2. RBC policy for summer season

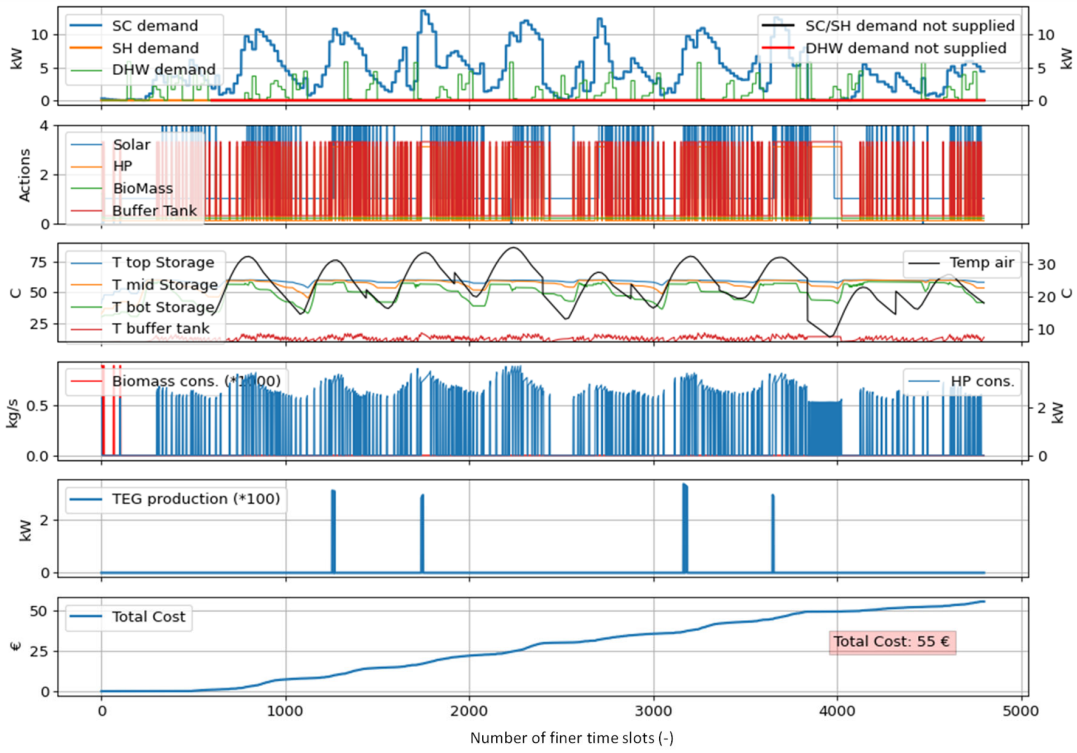

Fig. 3. Optimal control for summer season

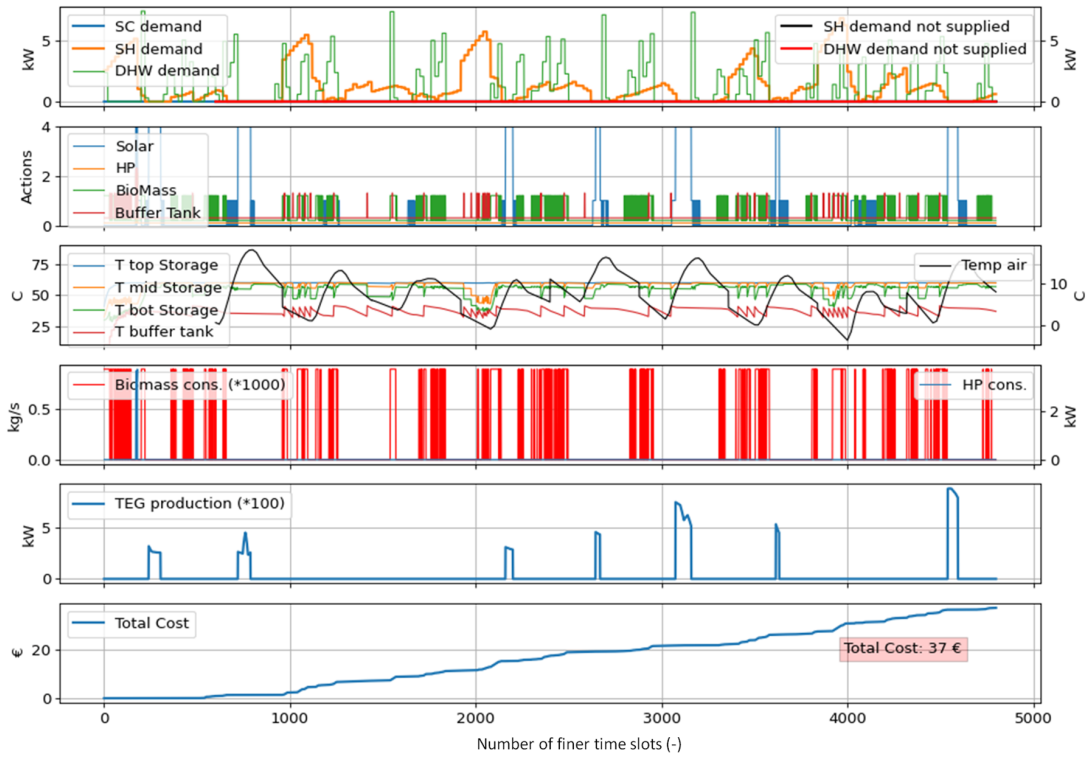

Fig. 4. RBC policy for winter season

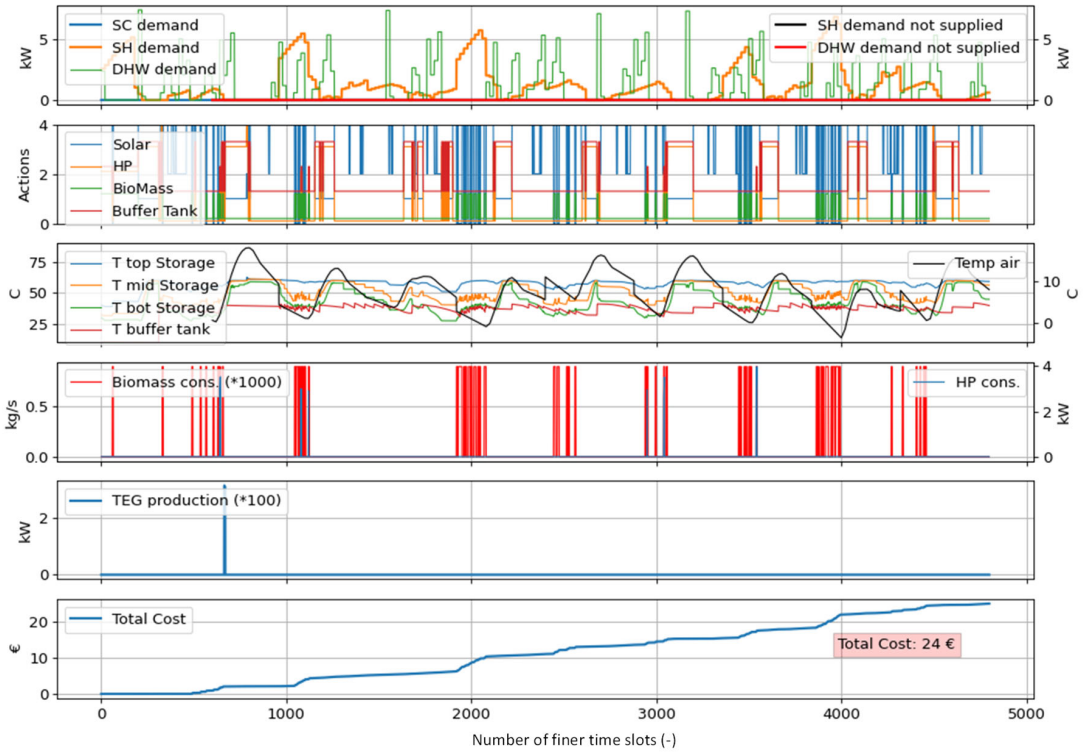

Fig. 5. Optimal control for winter season

4. Conclusions

In order to enhance flexibility of systems based on renewables sources, hybrid energy systems have a high potential to increase the total share of renewable energy used to satisfy the energy demand in buildings. The system developed within the SolBio-Rev project uses solar energy and biomass to provide heating, cooling, domestic hot water, and electricity for different building typologies in different climates. In this study, deep reinforcement learning (DRL) techniques were used to develop optimal control policies of the SolBio-Rev system to minimize the operating cost during all year. The SolBio-Rev system considered in this study was an optimized configuration for residential buildings located in Mediterranean climates. The smart control algorithm was trained using data of the energy demand of a multi-family house in Madrid obtained from simulations. In order to evaluate the goodness of the DRL control policy, a rule-based control policy was first implemented considering the different operational modes of the system components.

The results showed that the smart control is able to reduce the total cost in winter reducing the operation of the biomass boiler from 37 € to 24 € for 10 days of operation, due to a better operation of the solar collectors and a reduced use of the biomass boiler. However, in summer, the total cost using the smart control is very similar to the one achieved using the RBC policy. This can be explained by the low TEGs installed power and the fact that the reduction in the total energy consumption due to the coupling between the heat pump coupled and the sorption chiller is low. Further studies will aim to improve the DRL algorithm in order to define an optimal policy able to achieve higher savings in the energy cost in summer.

5. Acknowledgments

This project was funded by the European Union's Horizon 2020 Research and Innovation Programme under No. 814945 (SolBio-Rev). This work is partially supported by ICREA under the ICREA Academia programme. The authors would like to thank the Catalan Government for the quality accreditation given to their research group GREiA (2017 SGR 1537). GREiA is a certified agent TECNIO in the category of technology developers from the Government of Catalonia.

6. References

Dipasquale, C., Fedrizzi, R., Bellini, A., D'Antoni, M., Bales, C., Gustafsson, M., Ochs, F., Dermentzis, G., Birchall, S., 2014. D2. 1c Simulation Results of Reference Buildings. EC FP7 Proj. iNSPiRe, Grant Agreem.

IEA, 2019. Global Status Report for Buildings and Construction 2019. Paris.

Palomba, V., Borri, E., Charalampidis, A., Frazzica, A., Cabeza, L.F., Karellas, S., 2020. Implementation of a solar-biomass system for multi-family houses: Towards 100% renewable energy utilization. Renew. Energy 166, 190–209. https://doi.org/10.1016/j.renene.2020.11.126

Palomba, V., Borri, E., Charalampidis, A., Frazzica, A., Karellas, S., Cabeza, L.F., 2021. An Innovative Solar-Biomass Energy System to Increase the Share of Renewables in Office Buildings. Energies 14, 914. https://doi.org/10.3390/en14040914

TRNSYS18. Weather database: Meteonorm. Location: Nuremberg. Type of file: Typical Meteorological Year (TMY).

Wei, T., Wang, Y., Zhu, Q., 2017. Deep Reinforcement Learning for Building HVAC Control. Proc. - Des. Autom. Conf. Part 12828. https://doi.org/10.1145/3061639.3062224

Zsembinszki, G., Fernández, C., Vérez, D., Cabeza, L.F., 2021. Deep learning optimal control for a complex hybrid energy storage system. Buildings 11. https://doi.org/10.3390/buildings11050194

R. Sector Coupling and Grid Stabilization

Aluminium-Redox-Cycles for the Production of Heat and Electricity in Buildings based on Renewable Energy

Yvonne Isabell Baeuerle, Mihaela Dudita, Michel Y. Haller

Eastern Switzerland University of Applied Sciences (OST) Rapperswil, SPF Institute for Solar Technology

Abstract

Renewable metal fuels have great potential to act as a sector coupling seasonal energy storage. Renewable electricity can be generated in summer, transformed and stored in a metal fuel without losses as long as desired, and can provide decentralized heat and electricity at any time and any place. Aluminium as an energy carrier is of interest due to its high volumetric energy density (> 23 $MWh \cdot m^{-3}$). Therefore, the production of heat and hydrogen from seven different aluminium recycling streams was analyzed and a conversion efficiency of close to 100% was reached for all of them. However, some of the obtained solid reaction products showed metal impurities, which require a purification process in order to close the material cycle. The concept provides a seasonal energy storage solution with "storage" costs in the range of 90 Euro per MWh. Additionally, life-cycle greenhouse gas (GHG) emissions of all studied aluminium-redox-cycles were substantially lower when compared to natural gas mini CHP plants.

Keywords: Seasonal Energy Storage, Renewable Metal Fuel, Aluminium Energy Carrier, Aluminium Recycling, Sector Coupling

1. Introduction

The storage of large quantities of renewable energy over long periods (more than three months) is still an important unsolved issue of the energy transition. In Europe, energy security and resource dependency have gained new urgency, partly as a result of the geopolitical situation and associated reduction or shutdown of natural gas and oil imports from Russia. Energy prices have reached record levels across Europe and might rise further as the winter approaches. Today, renewable electricity and heat from solar energy can be produced at low-cost and can, in combination with a short-term storage, even fulfill daily demand profiles of households, in particular during the summer. Nevertheless, when people need to heat their buildings in winter, additional energy sources or a seasonal storage is required. In this regard, renewable metal fuels can offer a simple, safe, and efficient solution. If excess "summer" energy is converted into chemical energy carriers, which can be stored without losses over several months, it can easily fill this winter gap and reduce or eliminate the dependency on fossil fuels. Aluminium, in particular, is a very promising renewable metal fuel candidate (Trowel et al., 2020).

Based on a sector-coupled aluminium-redox-cycle concept (Figure 1), electricity from solar or other renewable sources can be used in a storage charging process to reduce aluminium oxide or aluminium hydroxide into elementary aluminium (Power-to-Al). This reduction process is carried out via the calcination and/or inert anode smelter process which emits only O_2 (CO_2-free Al smelter). In the storage discharging process, aluminium can be oxidized (Al-to-Energy) releasing hydrogen and heat, while again obtaining the by-product aluminium hydroxide at a reaction temperature below 280 °C or aluminium oxide at higher temperatures. The hydrogen can be electrochemically converted with a fuel cell system and the heat from both exothermal reactions (oxidation of aluminium as well as oxidation of hydrogen) can be used in buildings for the supply of domestic hot water and space heating. Therefore, aluminium acts as a seasonal renewable energy carrier with an energy recovery of more than 23 $MWh \cdot m^{-3}$ if it is stored as a solid block or, more realistically, 15 MWh m^{-3} as a bulk storage material (e.g. Al grit). This concept can cover a significant amount of heat and electricity in winter when implemented in decentralized combined heat and power generation (CHP) systems (Haller et al., 2021).

Dudita et al. (2019) investigated the aluminium-water oxidation reaction in alkaline solutions ($NaOH_{(aq)}$) with primary aluminium as a source material and showed that the reaction depends on various conditions. In particular, the particle size, shape, and quality of the aluminium can affect the reaction time and the precipitation of the by-product. However, from an economical point of view, potential low-cost aluminium recycling streams could be of interest. Therefore, different source material, including old scrap from post-consumer use, as well as new scrap

© 2022. The Authors. Published by International Solar Energy Society
Selection and/or peer review under responsibility of Scientific Committee
doi:10.18086/eurosun.2022.17.01 Available at http://proceedings.ises.org

from the manufacturing process of semi-fabricated and final products, were identified and tested. The goal was to answer questions concerning the suitability of secondary aluminium source material and their effect from an economic and environmental point of view.

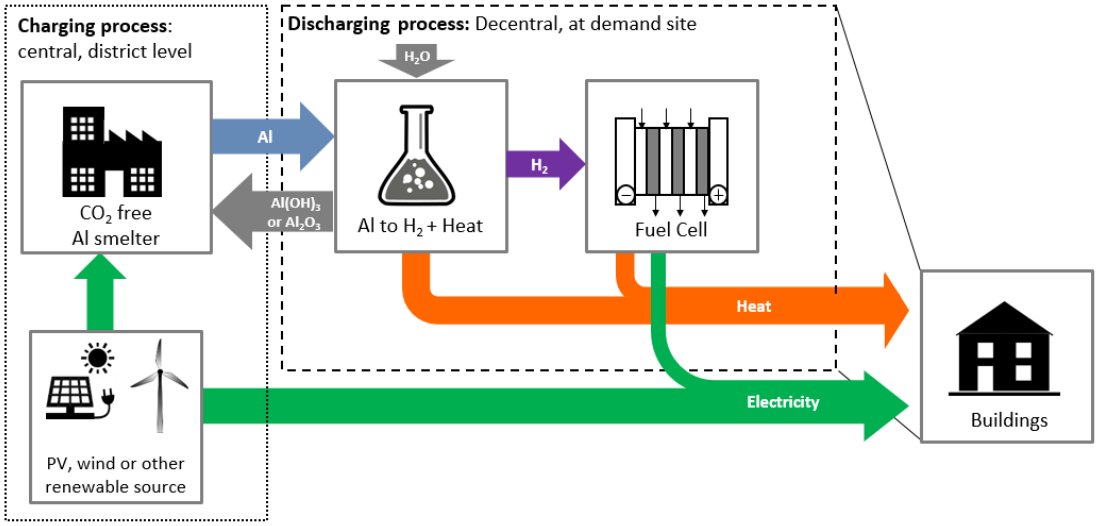

Figure 1: Overall sector coupling energy storage concept based on aluminium-redox-cycles, adapted from Haller et al (2019).

2. Procedure and methodology

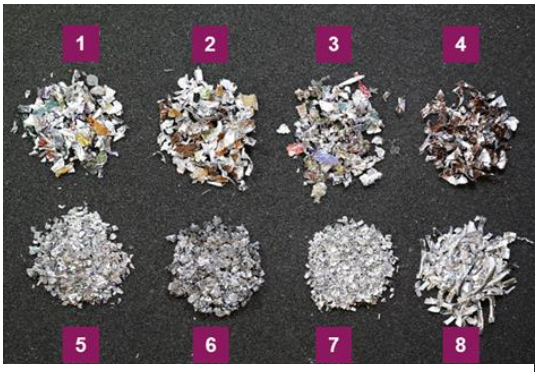

Figure 2: Visual aspect of the aluminium samples after cutting, shredding, cleaning, and drying.

To evaluate the suitability of secondary aluminium as a source material for the discharging process (oxidation reaction) and to assess the quality of the by-product and potential market applications, five aluminium materials from post-consumer use (sample 1 to 5 of Figure 2) and two new Al scrap samples from metal processing (sample 6 and 7) were selected. All samples contained various impurities, e.g. coffee residues, oil, surfactants, and other metals, and thus had to undergo a pre-treatment process before use. A pure aluminium reference (sample 8, class P1020) provided the baseline of the following chemical analysis.

2.1. Aluminium source material, pre-treatment and chemical analysis

Initially, a preparation process including cutting and shredding, cleaning and drying, as well as a thermal treatment for 30 minutes at a temperature of 550 °C, was implemented in order to remove unwanted non-metallic impurities as much as possible. In a next step, the prepared samples were chemically analyzed to obtain the elemental composition by Inductively Coupled Plasma - Optical Emission Spectrometry (ICP-OES).

To assess the completeness of the oxidation reaction, the efficiency and kinetics of each aluminium sample (prepared without thermal treatment) were studied at room temperature using a 6 M[1] $NaOH_{(aq)}$ solution as a reaction promoter. The maximum amount of hydrogen that can be produced from the aluminium sample was calculated according to eq. 1.

$$2\,Al + 6\,H_2O \rightarrow 2\,Al(OH)_3 + 3\,H_2 \qquad \text{(eq.1)}$$

Finally, aluminium hydroxide ($Al(OH)_3$) was obtained as a solid reaction product (from aluminium samples without thermal treatment) in a 6 M $NaOH_{(aq)}$ solution at a stable reaction temperature from 60 to 70 °C.

[1] The molarity (M) is defined as the number of moles of solute dissolved in one liter of solution.

The $Al(OH)_3$ was separated via vacuum filtration and washed until the pH of the filtrate decreased from 14 to 7. Before all samples were chemically analyzed via X-ray fluorescence (XRF) analysis, a thermal treatment for 1 hour at 1050 °C was implemented. In this case, the remaining dry mass can be associated with the presence of metal oxides.

2.2. Global Warming Potential (GWP)[2] and energy cost

The potential environmental advantages of the aluminium-redox-cycles were evaluated using the standardized procedures of LCA as per ISO 104040 (2006) and ISO 104044 (2006), which determine the environmental impact associated with the concept from resource extraction to end-of-life burdens. The functional unit was defined to present 1 MJ of energy produced. It is important to note that this functional unit contains a specific amount of heat and hydrogen or heat and electricity, depending on the system setup applied (without or with a fuel cell system). For this study, life-cycle GHG emissions and their associated impacts on climate change are used as the main indicators for the environmental performance of the aluminium-redox-cycles. All GHG emissions were assessed by the IPCC 2013 GWP 100a V1.03 method using the Ecoinvent database version 3.1. In addition to the background process of the PV electricity production from the Ecoinvent dataset, the updated life cycle inventory data set from Frischknecht et al. (2020) was also applied.

For the economic assessment, current world market prices or specific estimates from the industry were used. In general, two different cases can be distinguished for the use of recycling / scrap material for the aluminium-redox-cycles.

- Closed cycle: At the beginning, aluminium scrap is introduced into the Al-to-Energy cycle and the produced aluminium hydroxide is used for the production of new aluminium. In this case, the source material flow stays within the aluminium-redox-cycle after the first introduction. Thus, cost savings are only effective in the first year, since no (loss free cycle) or only little amounts of aluminium (to compensate material losses within the cycle) are introduced every year.
- Open cycle: Every year, aluminium scrap is introduced, and the resulting aluminium hydroxide is sold to be re-used in other processes, e.g., as a flame-retardant additive.

It should be noted that the closed cycle is dependent on the question whether the produced aluminium hydroxide or alumina is suitable for the inert anode smelter, and the open cycle is dependent on the question whether there will be any market and demand for the resulting by-product.

3. Results and Conclusion

3.1. Aluminium source material, pre-treatment, and chemical analysis

Results of the ICP-OES measurement identified iron as a metallic impurity in most samples. Sample 5 and 6 had a wide range of other impurities including Mg, Mn, Zn, Cu, Co, Cr, and Ni (Table 1).

Table 1: ICP-OES results indicating the aluminium content and the presence of metal impurities.

Sample	Al		Other metal impurities [mg/L]							
	mg/L	% [a)]	Mg	Fe	Cu	Co	Cr	Mn	Ni	Zn
1	4.0	93.3		0.03						
2	5.0	97.6		0.05						
3	4.9	97.1		0.04						
4	5.0	99.6		0.05						
5	4.7	88.6	0.07	0.21			0.04	0.03	0.02	
6	3.4	65.8	0.07	0.57	0.11	0.06	0.05	0.01	0.02	0.09
7	4.9	94.2	0.01	0.01						
8	5.3	99.7								

a) with respect to the mass of the (thermally treated) sample that was digested.

[2] The GWP is a measure of the emissions of greenhouse gases (GHG) such as CO_2, perfluorocarbon (PFC), and methane (CH_4), and is expressed as kilogram of CO_2 equivalent (CO_2eq).

Based on the analysis presented in Table 1, the aluminium content in the samples could be identified in the range of 63 to 93% (including weight losses from thermal treatment).

The analysis of the completeness of the reaction showed that some samples with metallic impurities (i.e., strong presence of elements other than aluminium) produced more hydrogen than could be expected from its aluminium content alone (Figure 3). The primary aluminium sample 8 (99.7% purity) produced 99 to 100% of the expected hydrogen. However, sample 6, which contained large fractions of iron and other elements, reached 142% of the theoretical value based on the aluminium content. Therefore, it is very likely that metals other than aluminium have reacted with water and produce hydrogen (Yavor Y. et al., 2015).

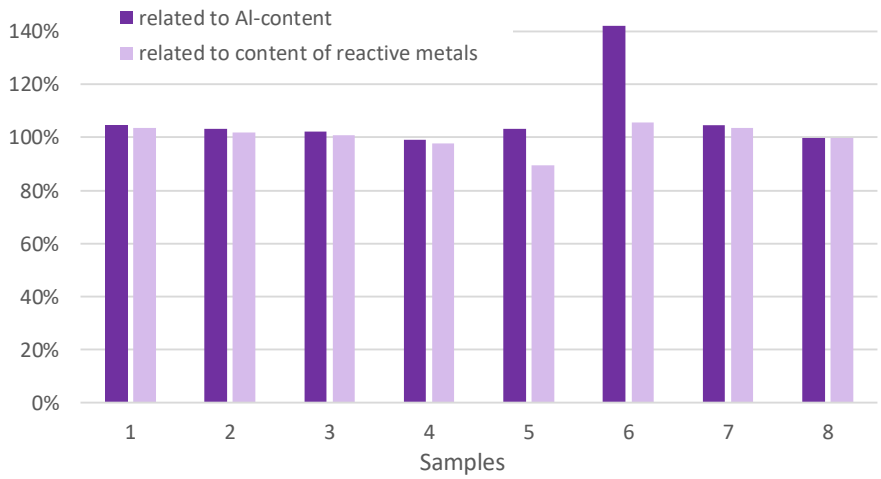

Figure 3: Completeness of the H_2 evolution reaction based on the max. theoretical H_2 production from Al content.

The XRF analysis of the aluminium hydroxide identified a considerable amount of sodium (Na_2O) in all samples with concentrations mostly below 2% (wt./wt. after subtraction of ignition losses (LOI)). This amount of sodium, present in the aluminium hydroxide after rinsing with water, indicates that about 6 to 10%[3] of the used NaOH for the reaction ends up in the aluminium hydroxide. Furthermore, most samples contained a considerable amount of iron, some magnesium, and, to a lesser extent, manganese, silicon, and zinc. These findings lead to the conclusion that for most samples (especially old scrap material) an additional treatment and purification step would be necessary in order to recycle them in a conventional aluminium smelter for a closed cycle application. Thus, it can be assumed that the market value of the obtained aluminium hydroxide is rather low. In case of an open cycle implementation, a market has to be identified or created. So far, there doesn't seem to exist an industrial process which would allow a direct application of the obtained alumina without further purification steps.

3.2. Global Warming Potential (GWP) and energy cost

Based on the LCA that used the avoided burden approach, it could be established that the selection of the source material (secondary vs. primary aluminium) had only a minor influence of 1 to 2% on the estimated total GHG emissions of the aluminium-redox-cycles. The same can be concluded for the sodium loss rate, which was varied from 3 to 10%. However, the GWP of the electricity (upstream supply chain) used in the aluminium inert electrode smelter process, as well as the renewable energy input to produce the required heat for the calcination process (forming alumina from aluminium hydroxide), had a significant influence, and accounted for more than 80% of the total estimated life cycle GHG emissions. It is important to point out that the results are based on the background Ecoinvent dataset version 3.1, "Electricity, production mix photovoltaic, at plant/CH", which corresponds to 21 g CO_2eq/MJ_e. The recently published new datasets from Frischknecht et al. 2020, on the other hand, assess GHG emissions of approx. 8.9 g CO_2eq/MJ_e (with a yield of 975 kWh/kW_p) for the electricity

[3] The percentage is referring to the amount of NaOH present in a 6 M NaOH solution that contains the stoichiometric amount of water needed for the reaction. As NaOH is not consumed by the reaction, no NaOH would have to be replaced in the ideal "loss-free" case. However, XRF data of the aluminium hydroxide produced indicated that about 6-10% of the NaOH ends up in the aluminium hydroxide sample even if this is rinsed to neutral pH after removal from the reaction vessel.

production from PV for an average Swiss PV module supplier mix from 2019. The main reason for the overestimation of the GWP in the Ecoinvent dataset is caused by outdated electricity mix data used in the production of the PV modules. Thus, the estimated total GWP for the aluminium-redox-cycles range from 48 g CO_2eq/MJ to less than 25 g CO_2eq/MJ of energy (hydrogen and heat) produced.

In order to compare the GWP of heat and electricity produced from the discharging process with an alternative mini CHP plant, a PEM fuel cell system was added to the system boundary with an electric efficiency of 50% (HHV), and 45% to heat efficiency. Providing heat and electricity from a natural gas micro-CHP unit (2 kW_e with a fuel to electric efficiency of 25% based on HHV and a total efficiency of 85%) is linked to a GWP of approx. 83 g CO2eq/MJ (Figure 4). In comparison, a reduction of GHG emissions of 33 to 64% per MJ can be achieved by the aluminium-redox-cycles. Furthermore, if a mix of electricity from hydropower (46% run-of-river and 53% from storage hydropower) would be used for the calcination and smelter process instead of PV electricity, an overall GHG emission reduction of over 80% is possible.

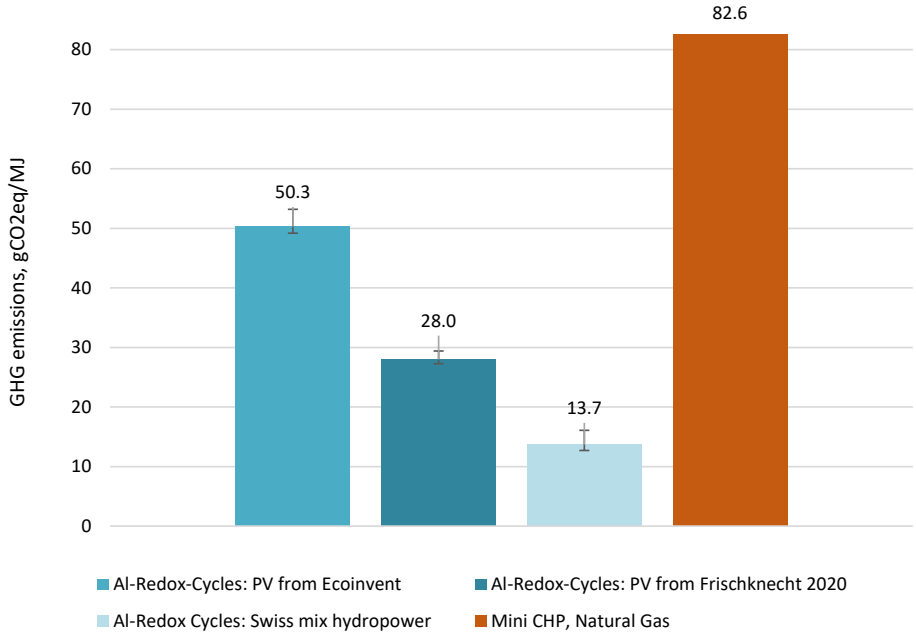

Figure 4: Average total life cycle GHG emission per 1 MJ of electricity and heat produced using primary and scrap aluminium as the source material (min. and max. values are indicated by the error bar). The results are based on PV electricity from Ecoinvent "photovoltaic, at plant/CH" (21 gCO_2eq/MJ_e), and values by Frischknecht et al. (2020) (8.9 gCO_2eq/MJ_e) as well the Ecoinvent Swiss mix of electricity production from hydropower (1.3 gCO_2eq/MJ_e). Size of mini-CHP plant: 2 kW_e.

The cost of primary aluminium and high quality (smelter grade) $Al(OH)_3$ (2'000 and 187 Euro per metric ton, respectively) were based on the past five years of market history. It was assumed that the low quality $Al(OH)_3$, containing many metal impurities, can be added into the Bayer process instead of Bauxite ore and thus giving a market price similar to the present market price for Bauxite ore (45 Euro·per metric ton). Therefore, depending on the value of the aluminium source material, the quality of the obtained $Al(OH)_3$, and the material flow scenario (open or closed cycle), a wide range of potential net material costs, i.e., cost of purchase minus revenue from the sale of $Al(OH)_3$, were estimated:

- High value scrap; High quality $Al(OH)_3$: **11** Euro/MWh (closed cycle) and **129** Euro/MWh (open cycle)
- Low value scrap; Low quality $Al(OH)_3$: **2** Euro/MWh (closed cycle) and **26** Euro/MWh (open cycle)
- Low value scrap; High quality $Al(OH)_3$: **0.4** Euro/MWh (closed cycle) and **-20** Euro/MWh (open cycle)

The results indicate that the net material cost per MWh of energy produced from aluminium ranges between - 20 and 130 Euro/MWh. However, these cost assumptions do not include any additional process steps for purification of material and thus do not present the full cost. Furthermore, for the closed cycle, the cost for the aluminium smelting would have to be added.

In general, aluminium “storage” costs in the range of 90 Euro/MWh can be expected for a Power-to-Al plant operating 2920 h per year. Not included in this storage cost are electricity input, transport of the material, and the conversion of aluminium back to energy in decentralized units (discharging process).

4. Acknowledgments

We like to thank the Swiss Federal office of Energy for supporting the project "AlEnCycles" under contract number SI/502127-01, and the industrial partners for their valid contribution: Nestlé Nespresso SA, Solenthaler Recycling AG, Aluminium Laufen AG, TRIMET Aluminium SE in Germany, Energie 360° AG and EWJR.

5. References

Dudita M., Farchado M., Englert A., Carbonell D., Haller M., 2019. Heat and power storage using aluminium for low and zero energy buildings. E3S Web Conf. 111, 04008. doi:10.1051/e3sconf/201911104008.

Frischknecht R., Stolz P., Krebs L., Wild-Scholten, M., Sinha P., 2020. Life Cycle Inventories and Life Cylce Assessment of Photovoltaic Systems. IEA PVPS Task12: PV Sustainability: ISBN 978-3-907281-14-7.

Haller MY, Amstad D, Dudita M, Englert A, Häberle A, 2021. Combined heat and power production based on renewable aluminium-water reaction. Renewable Energy: 174:879–93. doi:10.1016/j.renene.2021.04.104

Haller M, Dudita M, Amstad D, Carbonell Sanchez D, Häberle A, 2019. Seasonal Energy Storage in Aluminium for 100 Percent Solar Space Heat, DHW and Electricity. ISES Solar World Congress 2019, Santiago, Chile: 1312–20. doi:10.18086/swc.2019.24.04.

International Organization for Standardization, 2006. ISO 14040 Environmental management—Life cycle assessment—Principles and framework. Geneva, Switzerland.

International Organization for Standardization, 2006. ISO 14044 Environmental management—life cycle assessment—Requirements and guidelines. Geneva, Switzerland.

Trowell KA., Goroshin S., Frost DL., Bergthorson JM., 2020. Aluminum and its role as a recyclable, sustainable carrier of renewable energy. Applied Energy, 275: 115112. doi:10.1016/j.apenergy.2020.115112.

Yavor Y., Goroshin S., Bergthorson JM., 2015. Comparative reactivity of industrial metal powders with water for hydrogen production. International Journal of Hydrogen Energy, 40:1026-36. doi:10.1016/ j.ijhydene.2013.09.0

S. Renewable Energy Strategies, Scenarios, Financing and Policies

Impact of Incentives Towards Lowering the Levelized Cost of Electricity of Concentrating Solar Power Plants in India

Tarun Kumar Aseri[1,2], Chandan Sharma[2], Tara C. Kandpal[1]

[1] Department of Energy Science and Engineering, Indian Institute of Technology Delhi (India)

[2] Mechanical Engineering Department, Engineering College, Ajmer (India)

Abstract

The present study aims to assess the impact of various feasible incentives toward lowering the levelized cost of electricity (LCOE) of concentrating solar power (CSP) plants in India. For this purpose, two aspects (a) effect of increasing the extent of incentives on LCOE and (b) effect of different incentives for a given fixed government budgetary allocation for incentivization have been considered. 100 MW nominal capacity CSP plants with (i) wet-cooled parabolic trough solar collector and (ii) dry-cooled central tower receiver based CSP plants with the provision of 6.0 h and 12.0 h of thermal energy storage (TES) have been considered. From the results, it is observed that the provision of incentives in the early stage of useful life of the CSP plant leads to relatively higher reduction in LCOE. As the CSP plants with the provision of TES can deliver electricity during peak demand periods, the break-even value of time-of-delivery tariff for the electricity delivered by the CSP plants has also been estimated.

Keywords: CSP plant, financial incentives, levelized cost of electricity, thermal energy storage

1. Introduction

Among the two options for harnessing solar energy to produce electricity, the solar thermal route can facilitate relatively inexpensive thermal energy storage (TES) as compared to the storage options with photovoltaic (PV) route and helps in improving the dispatch ability of the electricity delivery due to variable and intermittent solar resource (REN21, 2021). However, presently the levelized cost of electricity (LCOE) for concentrating solar power (CSP) plants is much higher than that for PV power plants. Thus, several potential strategies are being explored to make them financially competitive as against other renewable and fossil fuel based electricity generation options (IRENA, 2022). The prominent strategies include (a) adoption of emerging CSP technologies (Aseri et al., 2020), (b) indigenization of components of CSP plants (ESMAP, 2013), (c) installation of large size plants to take benefit of economy of scale (Aseri et al., 2022), (d) improved financing structure (Mendelsohn et al., 2012) and (e) provision of incentive(s) (Kulichenko and Wirth, 2011). Amongst these measures, the appropriately designed financial/fiscal and regulatory incentives to stimulate the deployment of renewable energy based electricity generation (including CSP plants) is required. Several policy measures have been taken and/or incentives have been provided in the early stage of deployment of renewable energy based power generation options by many countries in the world (Atalay et al., 2017; DESIRE, 2020; Kulichenko and Wirth, 2011; MASEN, 2021). The primary aim of these policy measures is to provide either direct cash grant or tax rebate to project developer(s)/investor(s) for a specified period to make cash flow profitable and make the projects financially viable (Aseri et al., 2020b; Parrado et al., 2016; San Miguel and Corona, 2018).

In the first phase (1984-1990) of deployment of CSP plants in the Californian desert (USA), accelerated depreciation along with exemption from property tax was provided (SolarPACES, 2021). In the second phase (2007-2013), the deployment of CSP plants in Spain was stimulated with the provision of feed-in-tariff (FiT) with successful deployment of 49 CSP plants with total nominal capacity of 2.3 GW (Martín et al., 2015; Lilliestam et al., 2017). In the third phase, after the year 2013, incentives such as production and investment tax credits for equity investors and benefits of selling certified emission reduction units and/or renewable energy certificates have been provided (Abolhosseini and Heshmati, 2014; Madaeni et al., 2012; Malagueta et al., 2013; Sioshansi and Denholm, 2010) to promote the diffusion of CSP plants.

From the literature review, it was observed that specific studies pertaining to impact assessment of incentives for large scale dissemination of CSP plants has not been reported in Indian context. In order to design and implement appropriate incentivizing strategies for CSP based electricity generation in India, it would be highly insightful and useful to assess the impact of different potential incentives on the LCOE. In view of this, as a preliminary attempt (i) the effect of an increase in the extent of incentive on the LCOE has been studied and (ii) for a given fixed budget allocated by the government for incentivization, the maximum possible extent of each incentive and consequently its

© 2022. The Authors. Published by International Solar Energy Society
Selection and/or peer review under responsibility of Scientific Committee
doi:10.18086/eurosun.2022.18.01 Available at http://proceedings.ises.org

impact on the LCOE have been estimated. Since, unlike the case of PV and wind power plants, the CSP plants with TES can deliver electricity during peak demand periods, the break-even value of time-of-delivery tariffs for the electricity delivered have also been estimated.

2. Methodology

The location of Mandla, in the state of Madhya Pradesh was selected out of the potential locations identified in India for the deployment of CSP plants by Sharma et al. (2015) based on an annual threshold value of direct normal irradiance. 100 MW nominal capacity wet-cooled parabolic trough solar collector (PTSC) based and dry-cooled central tower receiver (CTR) based CSP plants with the provision of 6.0 and 12.0 hours of TES are considered for the analysis (Aseri et al., 2020a). A schematic of the methodology adopted in the study is presented in Fig. 1. The detailed procedure of the same is presented in the following paragraphs.

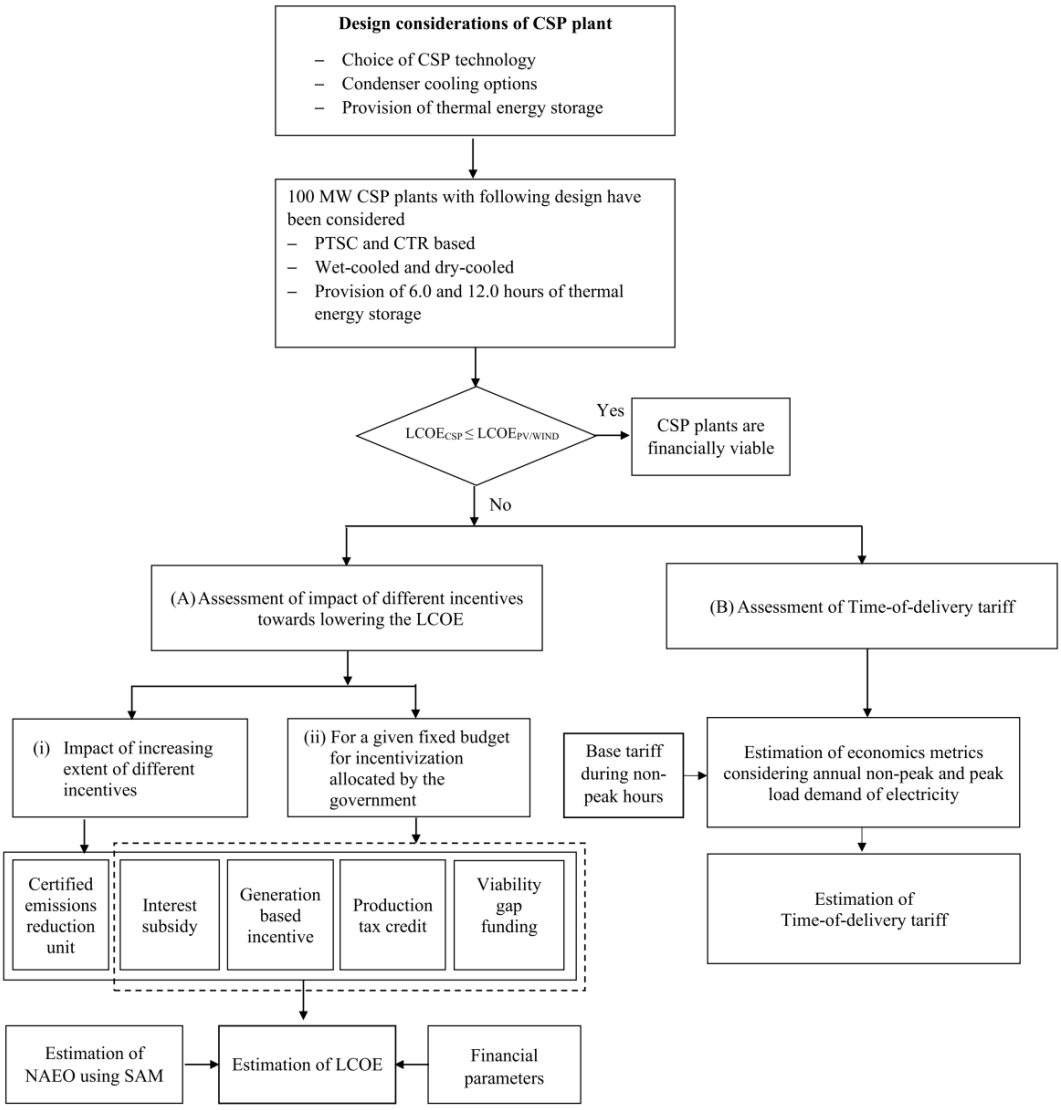

Fig. 1 Methodology for assessing impact of different incentives on LCOE and estimation of time-of-delivery tariff

Estimation of LCOE

The following expression is used to estimate the value of LCOE and the same allows to consider the time variation in the annual cost to be incurred in the project as well in the net annual electricity output delivered by the project.

$$LCOE\ (US\ \$/MWh) = \left(\frac{d(1+d)^n}{(1+d)^n - 1}\right) \times \sum_{i=1}^{n} \frac{AC_i \times (1+d)^{-i}}{NAEO_i \times 10^3} \quad \text{(Eq. 1)}$$

The annual cost (AC_i) of ith year comprises of annual cost of operation and maintenance of the plant, amount of interest on working capital, annual amount of return on equity and amount of annual loan repayment including the principal component and the interest on the loan. Moreover, monetary incentives available to the project have also been internalized as negative costs while estimating the annual cost. The effective annual cost (AC) for the plant is estimated as :

$$Effective\ annual\ cost = \begin{bmatrix} Cost\ of\ O\&M \\ including \\ escalation \end{bmatrix} + \begin{bmatrix} Interest\ on \\ working \\ capital \end{bmatrix} + \begin{bmatrix} Return\ on \\ equity \\ to\ investor \end{bmatrix} + \begin{bmatrix} Loan\ repayment \\ including \\ principal \\ and\ interest \end{bmatrix} - \begin{bmatrix} Applicable\ monetory\ benefits \\ due\ to\ incentive(s) \end{bmatrix} \quad \text{(Eq. 1)}$$

In the present study, the discount rate (d) has been estimated as the weighted average cost of capital (WACC) for the project using the following expression:

$$d = \text{WACC} = I_d F_d + R_e F_e \quad \text{(Eq.3)}$$

The net annual electricity output (NAEO) and other performance metrics for the CSP plants considered in the study, have been estimated using System Advisor Model (SAM, 2021). The hourly values of weather data for Mandla have been obtained from the National Solar Radiation Data Base, NREL, USA (NSRDB, 2018).

With the use of inventory of materials based approach proposed by authors (Aseri et al., 2020b), the capital costs of PTSC and CTR based CSP plants have been estimated. To decide the applicable values of financial parameters for the CSP plants, corresponding values as suggested by the CERC (Central Electricity Regulatory Commission, Government of India), have been considered (CERC, 2020) and the same are presented in Tab. 1. A spread sheet (Microsoft Excel) model has been developed to estimate the annualized cost, extent of incentive and subsequently their effect in reducing the LCOE. Assumptions made for assessing the efficacy of the incentives considered in the study are presented in Tab. 2.

Tab. 1. Values of financial parameters considered in the present analysis (CERC, 2020)

Financial parameter	Unit	Value
Share of debt: equity	fraction	0.7:0.3
Debt repayment (loan) term	Years	15
Annual rate of Interest rate on debt	fraction	0.0967
Annual rate of return on equity	fraction	0.14
Discount rate	fraction	0.1097
Annual rate of income tax	fraction	0.35
Amount of working capital	-	One-month O&M, 15% of O&M for spares, 2 months receivables
Annual rate of interest on working capital	fraction	0.1117
Annual rate of depreciation for loan term	fraction	0.0467
Annual rate of depreciation after loan term	fraction	0.02
Annual cost of operation and maintenance	US$/MW	31550
Annual rate of escalation in operation and maintenance cost	fraction	0.0572
Salvage value (as a fraction of the capital cost) at the end of useful life	fraction	0.10
Useful life of the plant	Years	30

Extent of incentives

While assessing the effect of increasing the extent of incentives on LCOE, the values for each incentive is selected based on literature and the same are presented in Tab. 3 (Aryani et al., 2020; Comello and Reichelstein, 2016; Ozcan, 2014; Thapar et al., 2016).

In order to assess the efficacy of incentives in lowering the LCOE, it is assumed that the government of India is willing to contribute financial support equivalent to a certain fraction of the capital cost for providing any of the four incentives indicated in Fig. 1. As an example, noting the fact that 30% investment tax credit was provided in the USA for rooftop PV plants (Comello and Reichelstein, 2016; DOE, 2021), the same value has been considered in

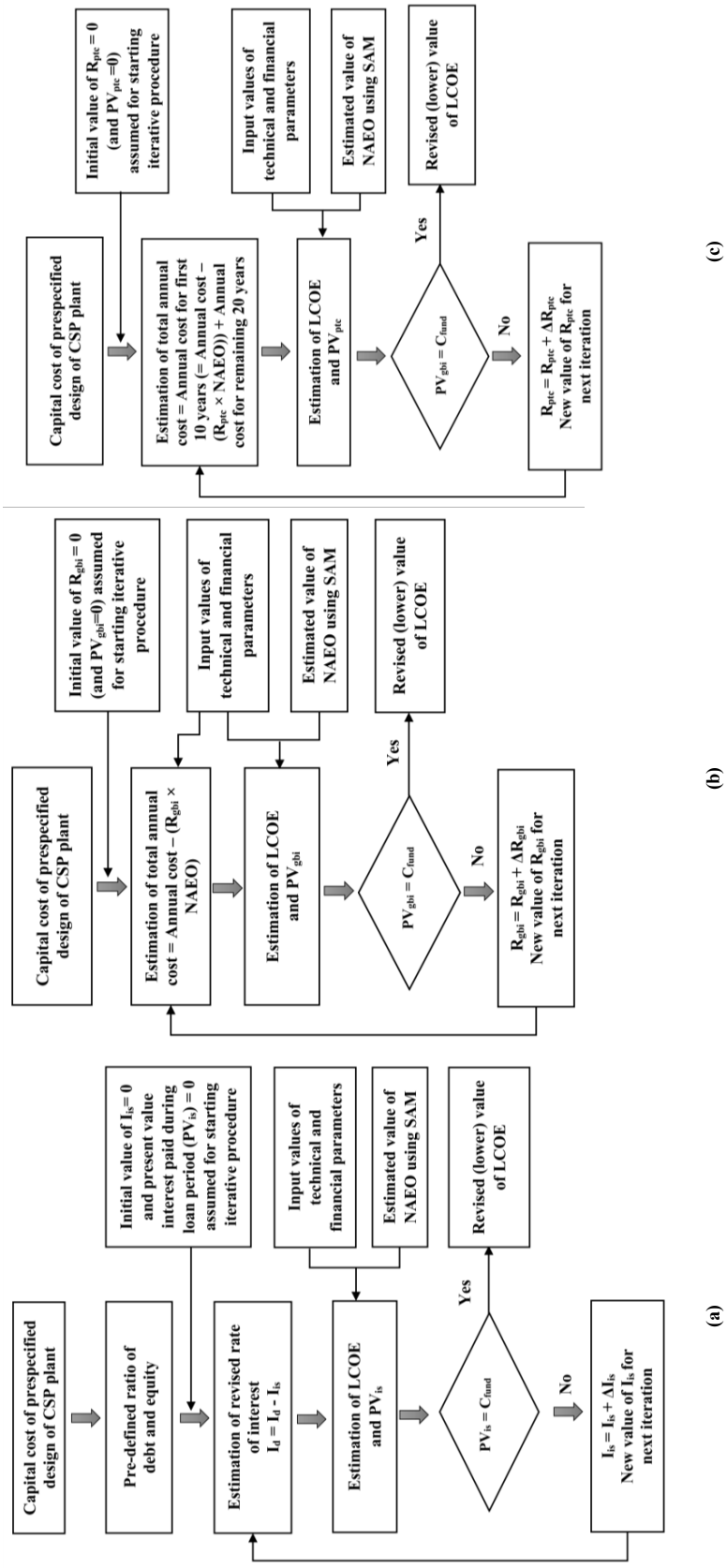

Fig. 2 Iterative procedure used to estimate the extent of (a) interest subsidy, (b) generation based incentive and (c) production tax credit

the present study to decide the amount of government funds that can be used for the incentivization of CSP plants in India through any of the incentives considered in the study. It is worth mentioning that to estimate the value of reduced LCOE due to the provision of the incentive considered, an iterative procedure has been used for the cases of interest subsidy, generation based incentive and production tax credit and the same is presented in Fig. 2.

Tab. 2. Assumptions made for studying the impact of incentives on the LCOE

Incentive	Assumption
Viability gap funding	Affects both the debt and equity components in 0.7:0.3 ratio
Interest subsidy	Affects only the loan repayment component
Generation based incentive	Provided for the entire useful life of the CSP plant
Production tax credit	Benefits of PTC shall be applicable for the first ten years of the useful life of the CSP plant
Certified emission reduction unit	– Benefits of CERU shall be applicable for the entire useful life of the CSP plant – The mean of the weighted average rate of CO_2-eq emissions of the past three years (2018-19, 2019-20 and 2020-21) in India for arriving at a value of 0.81 tCO_2/MWh for use in the study (CEA, 2022)

Tab. 3 Range of values of individual incentives considered in the study for assessing their effect on LCOE (Aryani et al., 2020; Comello and Reichelstein, 2016; Ozcan, 2014; Thapar et al., 2016)

Incentive	Unit	Value(s) considered in the analysis
Viability gap funding	% of capital cost	5, 10, 15, 20, 30, 35
Interest subsidy	%	1, 2, 3, 4, 5, 6, 7, 8
Generation based incentive	US$/MWh	5, 10, 15, 20, 25, 30, 40, 45
Production tax credit	US$/MWh	5, 10, 15, 20, 25, 30, 40, 45
Certified emission reduction unit	US$/$tCO_2$	10, 20, 30, 40, 50, 60, 70, 80, 90

Provision of time-of-delivery (ToD) tariff for CSP plants

The provision of TES in CSP plants can improve their dispatch ability and thus the plants can deliver electricity during the period of higher/peak demand besides enabling them to supply electricity during off-sunshine hours. Moreover, CSP plants with TES can supply electricity without introducing any grid stability issues. However, since the CSP plants with TES are relatively costlier than the plant without TES, a provision of time-of-delivery tariff for the electricity delivered by CSP plants at the time of higher demand of electricity may help to improve their financial attractiveness. In India, several electricity distribution utilities have adopted the ToD tariff in the form of surcharge/rebate on the base tariff for commercial users demanding load of more than 20kW and a summary of annual variation of tariff in states of India is presented in Fig. 3. The distribution utilities are applying surcharges during morning and evening peak demand periods and offering rebate during off-peak hours on the base tariff. In view of this, in the present study, it is assumed that during off-peak hours, the applicable tariff for electricity delivered by the CSP plants will be equal to average power purchase cost (APPC) of state electricity distribution utilities of Madhya Pradesh. The mean of APPC for last three financial years 2019-20 to 2020-22 has been estimated at US $50.9 per MWh (MPERC, 2022, 2021, 2020) and the same has been considered as a base tariff during off-peak hours (Tab. A.1 of Appendix A). The values of tariffs during the peak demand period, which would ensure the break-even condition for the CSP plants also have been estimated.

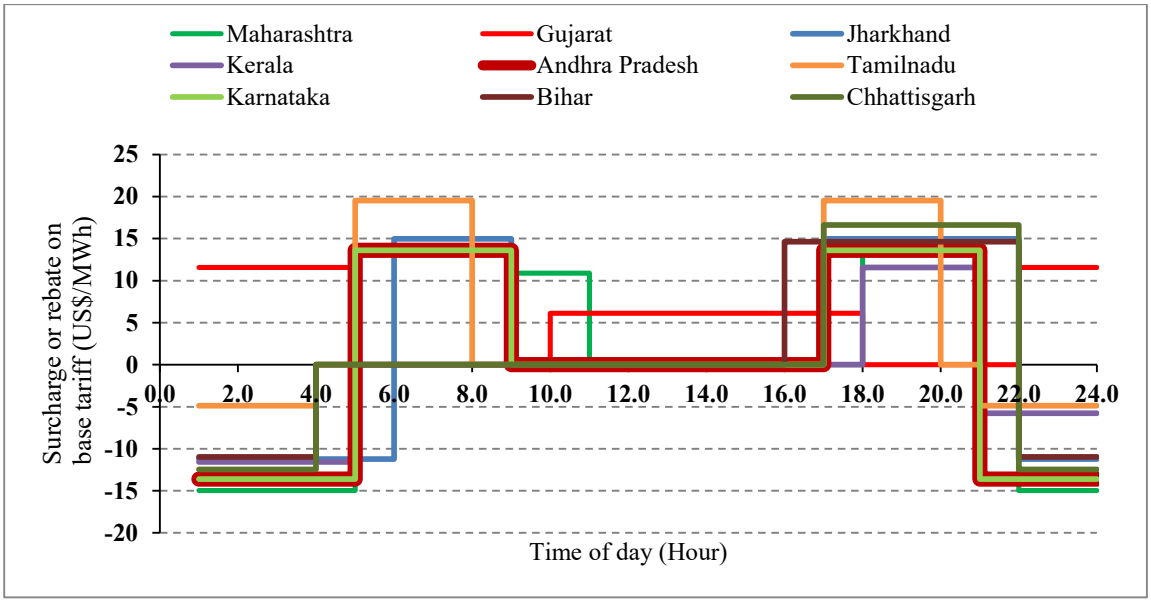

Fig. 3 Variation of surcharge/rebate in the electricity tariff imposed by different states regularities in India

3. Results and discussion

Using inventory of materials based approach, the capital costs of wet-cooled PTSC based CSP plants with 6.0 h and 12.0 h of TES are estimated at US $366.08 million and US $519.75 million respectively. The corresponding values for dry-cooled CTR based plants are estimated at US $346.96 million and US $486.03 million. As expected, with an increase in capacity of TES, the capital cost increases but due to higher incremental benefits than the incremental cost, the LCOE decreases that shows the presence of economy of scale with respect to the thermal energy storage capacity of the CSP plant. The effect of economy of scale is observed to be higher for CTR based plants as compared to PTSC based plants. Considering financial parameters (Tab. 1), the estimate of base LCOE for CTR based plant with 12.0 h of TES (US$100.5/MWh) is lower by 3.9% than that of plant with 6.0 h of TES (US $104.6/MWh). However, in PTSC based plants, the effect of economy of scale is observed to be only marginal as the values of base LCOE are very close and estimated at US$112.8/MWh and US$112.3/MWh for 6.0 h and 12.0 h of TES, respectively.

With the assumed range of different incentives, the values of LCOE and the cumulative present value of incentives provided each year have been estimated and are summarized in

for dry-cooled CTR based CSP plant with 6.0 hours of TES. Similar exercises have also been carried out for other CSP plants considered in the study. From the results obtained, it is observed that, as expected, with an increase in the extent of incentive, the LCOE decreases and the cumulative present value of amount required for incentivization increases. While comparing the amount of incentive required for the plants based on two different CSP technologies and two TES capacities, it may be observed that CTR based plants with 6.0 hours of TES requires least financial support.

As mentioned earlier, an attempt to assess the efficacy of individual incentives for a given fixed budget for incentivization allocated by the government has also been made and it is proposed that the Indian government shall contribute (C_{fund}) 30% of the capital cost of CSP plant. For this purpose, the capital costs of CTR based CSP plants have been considered as the same is lower than the capital cost of PTSC based CSP plants and the same are estimated US $104.1 million and US $145.8 million for CSP plants with 6.0 h and 12.0 h of TES, respectively. Using these values and following the iterative procedure, the maximum extent of each incentive and reduction in LCOE are estimated and the results are presented in Tab. 5. Fig. 4 represents the achieved percentage reduction in LCOE with the provision of incentives. From the results obtained, it can be observed that for a given fixed budget allocated by the government for incentivization in terms of viability gap funding, the LCOE can be reduced in the range of 26.4-28.2% from the base value of LCOE. The other incentives considered in the study such as interest subsidy (soft loan), generation based incentive and production tax credit are equally effective and can reduce the LCOE in the range of 25.8-27.5% from the based value of LCOE. Results also reveal that for a given fixed budget by the government, the LCOE of CTR based plants reduces by a somewhat greater extent as compared to the reduction likely to be achieved in the LCOE of PTSC based plants.

Tab. 4 Estimates of LCOE and cumulative present value of provision of incentives provided for dry-cooled CTR based CSP plant with 6.0 hours of TES

VGF (Fraction)	LCOE (US$/MWh)	Cumulative present value of provision of VGF (Million US$)	Interest subsidy (Fraction)	LCOE (US$/MWh)	Cumulative present value of provision of interest saved (Million US$)	Generation based incentive (US$/MWh)	LCOE (US$/MWh)	Cumulative present value of provision of GBI (Million US$)	Production tax credit (US$/MWh)	LCOE (US$/MWh)	Cumulative present value of provision of PTC (Million US$)	Certified emission reduction unit (US$/tCO$_2$)	LCOE (US$/MWh)	Cumulative present value of provision of CERU (Million US$)
0.00	104.6	0.0	0.00	104.6	0.0	0.0	104.6	0.0	0	104.6	0.0	0	104.6	0.0
0.05	99.8	17.3	0.01	101.5	11.5	5.0	99.6	18.4	5	101.3	12.4	10	96.5	29.8
0.10	95.0	34.7	0.02	98.4	23.0	10.0	94.6	36.8	10	97.9	24.9	20	88.4	59.6
0.15	90.1	52.0	0.03	95.3	34.5	15.0	89.6	55.2	15	94.5	37.3	30	80.3	89.4
0.20	85.3	69.4	0.04	92.1	46.0	20.0	84.6	73.6	20	91.1	49.8	40	72.2	119.2
0.25	80.6	86.7	0.05	89.0	57.6	25.0	79.6	92.0	25	87.7	62.2	50	64.1	149.0
0.30	75.7	104.1	0.06	85.9	69.1	30.0	74.6	110.4	30	84.3	74.7	60	56.0	178.8
0.35	70.9	121.4	0.07	82.7	80.6	35.0	69.6	128.8	35	81.0	87.1	70	47.9	208.6
			0.08	79.6	92.1	40.0	64.6	147.2	40	77.6	99.6	80	39.8	237.4
						45.0	59.6	165.6	45	74.2	112.0	90	31.7	268.2

Tab. 5 Effect of different incentives on LCOE (for the same budgetary allocation by the government for incentivization)

Modality		Unit	6.0 h TES		12.0 h TES	
			PTSC wet	CTR dry	PTSC wet	CTR dry
Capital cost of CSP plant		Million US$	366.08	346.96	519.75	486.03
NAEO		GWh	411.3	422.2	576.5	605.4
Capacity utilization factor		fraction	0.470	0.482	0.658	0.691
Annual water requirement		m^3	1301745	105690	1792380	151073
Base LCOE		US$/MWh	112.8	104.6	112.3	100.5
Proposed contribution from government		Million US$	104.1		145.8	
Viability gap funding	Feasible extent of VGF	%	28.4	30.0	28.1	30.0
	LCOE with VGF	US$/MWh	83.1	75.7	82.6	72.2
Interest subsidy	Allowable extent of interest subsidy	%	8.57	9.05	8.46	9.04
	Reduced interest rate	%	1.10	0.62	1.21	0.63
	LCOE with interest subsidy	US$/MWh	83.8	76.4	83.3	72.9
Generation based incentive	Allowable extent of GBI	US$/MWh	29.0	28.3	29.0	27.6
	LCOE with GBI	US$/MWh	83.8	76.3	83.3	72.9
Production tax credit	Extent of PTC	US$/MWh	42.9	41.8	42.9	40.8
	LCOE with PTC	US$/MWh	83.8	76.3	83.3	72.9

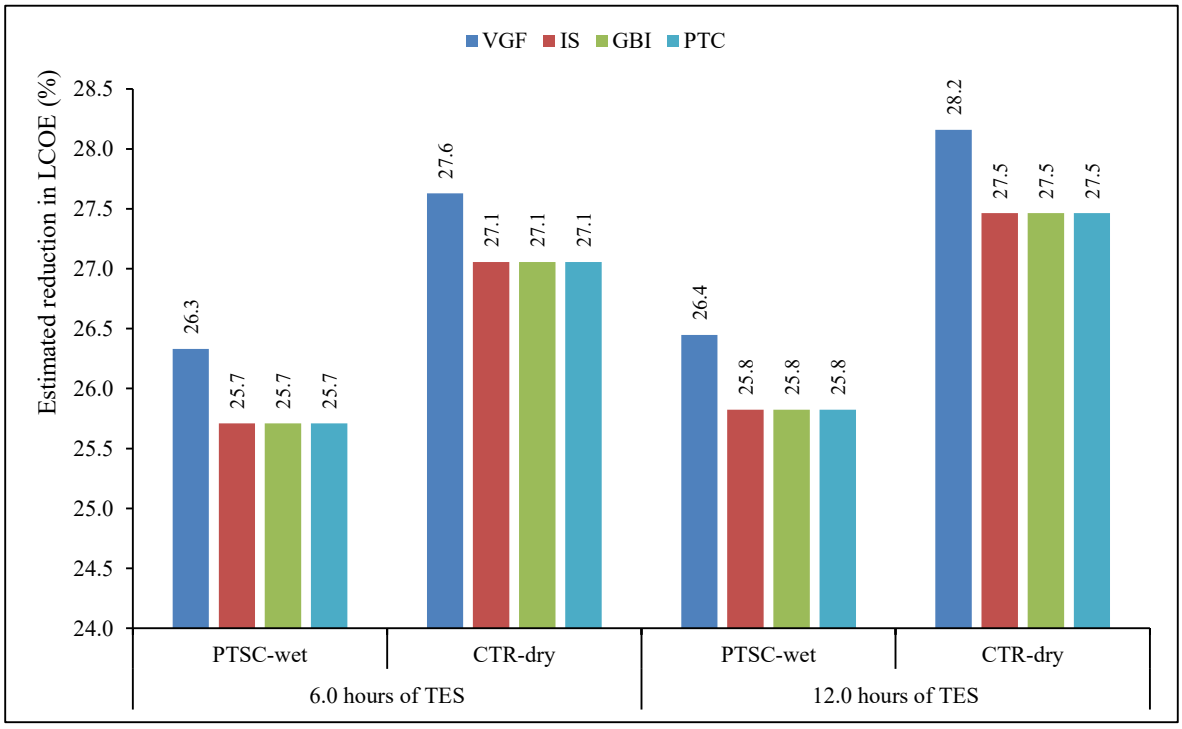

Fig. 4 Estimated reduction in LCOE for a given fixed budget for incentivization allocated by the government to CSP plants

As mentioned earlier, a preliminary attempt has also been made to estimate the break-even values of ToD tariffs for the electricity delivered by CSP plants with the provision of TES considering the base tariff at US $50.9/MWh during off-peak hours and the results of the same are presented in Tab. 6. The estimated values of ToD tariffs that would ensure a break-even condition for PTSC-wet and CTR-dry plants with 6.0 hours of TES are US $174.7/MWh and US $158.3/MWh respectively. For CSP plants with 12.0 hours of TES, the corresponding values of required ToD tariffs are estimated at US $143.0/MWh and US $125.3/MWh.

Tab. 6. Estimates of break-even values of electricity for PTSC and CTR based CSP plants during the peak demand

CSP plant	Hours of TES	Duration of non-peak demand of electricity in a day (Hours)	Duration of peak demand of electricity in a day (Hours)	Total duration of electricity delivered by the plant in a day (Hours)	Capital cost (Million US$)	NAEO (GWh)	LCOE (US$/ MWh)	ToD tariff (US $/MWh)
PTSC-wet	6.0	6.0	6.0	12.0	366.08	411.3	112.8	174.7
	12.0	6.0	12.0	18.0	219.75	576.5	112.3	143.0
CTR-dry	6.0	6.0	6.0	12.0	346.96	422.2	104.6	158.3
	12.0	6.0	12.0	18.0	486.03	605.4	100.5	125.3

4. Concluding remarks

The present study aims to identification of effectiveness of incentives for CSP plants in India to make them financially competitive. For this purpose, 100 MW CSP plants based on two CSP technologies (i.e., PTSC and CTR), two condenser cooling options (i.e., wet cooling in PTSC and dry cooling in CTR based plants) and two capacities of thermal energy storage (i.e., 6 hours and 12 hours) have been considered. The techno-economic performance has been undertaken for CSP plants at Mandla (Madhya Pradesh) using SAM and financial parameters expected to be applicable in Indian perspective.

As expected from the results obtained, it is observed that with an increase in the extent of an incentive, the LCOE decreases. The viability gap funding can reduce the LCOE by higher amount at lower cost to the government. Amongst the four plants, dry-cooled CTR based CSP plant with 6.0 hours of TES required the least amount of incentive.

While assessing the efficacy of incentives for a given fixed budget allocated by the government, it is noted that by providing viability gap funding the LCOE can be reduced in the range of 26.4-28.2% from the base value of LCOE. The other incentives considered in the study such as interest subsidy (soft loan), generation based incentive, and production tax credit are equally effective and can reduce the LCOE in the range of 25.8-27.5% from the based value of LCOE.

Considering base tariff (US$ 50.9/MWh) during non-peak demand of electricity, the time-of-delivery tariffs for CSP plants with 6.0 hours of TES are estimated at US $174.7/MWh and US $158.3/MWh for PTSC and CTR based plants respectively. The corresponding values for CSP plants with 12.0 hours of TES have been estimated at US $143.0/MWh and US $125.3/MWh.

Acknowledgments

The authors are thankful to the administration of Engineering College Ajmer, Rajasthan (India) and acknowledge the Department of Technical Education, Government of State of Rajasthan for providing permission to the first author (Tarun Kumar Aseri) to pursue doctoral research work at the Department of Energy Science and Engineering, Indian Institute of Technology Delhi.

References

Abolhosseini, S., Heshmati, A., 2014. The main support mechanisms to finance renewable energy development. Renew. Sustain. Energy Rev. 40, 876–885. https://doi.org/10.1016/j.rser.2014.08.013

Aryani, M., Ahmadian, M., Sheikh-El-Eslami, M.K., 2020. Designing a regulatory tool for coordinated investment in renewable and conventional generation capacities considering market equilibria. Appl. Energy 279, 115728. https://doi.org/10.1016/j.apenergy.2020.115728

Aseri, T.K., Sharma, C., Kandpal, T.C., 2022. A techno-economic appraisal of parabolic trough collector and central tower receiver based solar thermal power plants in India: Effect of nominal capacity and hours of thermal energy storage. J. Energy Storage 48, 103976. https://doi.org/10.1016/j.est.2022.103976

Aseri, T K, Sharma, C., Kandpal, T.C., 2020. Cost reduction potential in parabolic trough collector based CSP plants: A case study for India. Renew. Sustain. Energy Rev. 138, 110658. https://doi.org/10.1016/j.rser.2020.110658

Aseri, T.K., Sharma, C., Kandpal, T.C., 2020a. Estimating capital cost of parabolic trough collector based concentrating solar power plants for financial appraisal: Approaches and a case study for India. Renew. Energy 156, 1117–1131. https://doi.org/10.1016/j.renene.2020.04.138

Aseri, T.K., Sharma, C., Kandpal, T.C., 2020b. Assessment of water availability for wet cooling at potential locations for solar thermal power generation in India. Int. J. Ambient Energy 41, 1126–1141. https://doi.org/10.1080/01430750.2018.1507926

Atalay, Y., Kalfagianni, A., Pattberg, P., 2017. Renewable energy support mechanisms in the Gulf Cooperation Council states: Analyzing the feasibility of feed-in tariffs and auction mechanisms. Renew. Sustain. Energy Rev. 72, 723–733. https://doi.org/10.1016/j.rser.2017.01.103

CEA, 2022. CDM – CO2 Baseline Database Version 15.0, 16.0 and 17.0, Central Electricity Authority New Delhi. https://cea.nic.in/cdm-co2-baseline-database/?lang=en (accessed 9.1.22).

CERC, 2020. Determination of levellised generic tariff for FY 2020-21 under Regulation 8 of the Central Electricity Regulatory Commission (Terms and Conditions for Tariff determination from Renewable Energy Sources) Regulations, 2020,. Cent. Electr. Regul. Comm. http://www.cercind.gov.in/2020/orders/13-SM-2020.pdf (accessed 4.3.21).

Comello, S., Reichelstein, S., 2016. The U.S. investment tax credit for solar energy: Alternatives to the anticipated 2017 step-down. Renew. Sustain. Energy Rev. 55, 591–602. https://doi.org/10.1016/j.rser.2015.10.108

DESIRE, 2020. Database of State Incentives for Renewables and Efficiency, funded by U.S. Department of Energy and maintained by North Carolina State University. N.C. Clean Energy Technol. Cent. https://www.dsireusa.org/ (accessed 6.27.21).

DOE, 2021. Residential and Commercial ITC Factsheets. U.S. Dep. Energy. https://www.energy.gov/eere/solar/articles/residential-and-commercial-itc-factsheets (accessed 12.6.21).

ESMAP, 2013. Development of Local Supply Chain: The Missing Link for Concentrated Solar Power Projects in India, Energy Sector Management Assistance Program. Washington, USA.

FBIL, 2022. Foreign Exchange, Administering Independent Benchmarks. Financ. Benchmarks India Pvt. Ltd. https://www.fbil.org.in/ (accessed 9.2.22).

IRENA, 2022. Renewable power generation costs in 2021, International Renewable Energy Agency. Abu Dhabi.

Kulichenko, N., Wirth, J., 2011. Regulatory and Financial Incentives for Scaling Up Concentrating Solar Power in Developing Countries, The World Bank Group, Washington, DC. Discussion Paper No.24, June 2011.

Lilliestam, J., Labordena, M., Patt, A., Pfenninger, S., 2017. Empirically observed learning rates for concentrating solar power and their responses to regime change. Nat. Energy 2, 1–6. https://doi.org/10.1038/nenergy.2017.94

Madaeni, S.H., Sioshansi, R., Denholm, P., 2012. Estimating the capacity value of concentrating solar power plants: A case study of the southwestern United States. IEEE Trans. Power Syst. 27, 1205–1215. https://doi.org/10.1109/TPWRS.2011.2179071

Malagueta, D., Szklo, A., Borba, B.S.M.C., Soria, R., Aragão, R., Schaeffer, R., Dutra, R., 2013. Assessing incentive policies for integrating centralized solar power generation in the Brazilian electric power system. Energy Policy 59, 198–212. https://doi.org/10.1016/j.enpol.2013.03.029

Martín, H., De La Hoz, J., Velasco, G., Castilla, M., García De Vicuña, J.L., 2015. Promotion of concentrating solar thermal power (CSP) in Spain: Performance analysis of the period 1998-2013. Renew. Sustain. Energy Rev. 50, 1052–1068. https://doi.org/10.1016/j.rser.2015.05.062

MASEN, 2021. Morocco Solar Plan. Moroccan Agency for Solar Energyx. https://www.masen.ma/ (accessed 6.28.21).

Mendelsohn, M., Kreycik, C., Bird, L., Schwabe, P., Cory, K., 2012. The Impact of Financial Structure on the Cost of Solar Energy The Impact of Financial Structure on the Cost of Solar Energy. Technical Report: NREL/TP-6A20-53086. Natl. Renew. Energy Lab. USA 1–40.

MPERC, 2022. Aggregate Revenue Requirement and Retail Supply Tariff Order For FY 2021-22, Retail Supply Tariff Order FY 2021-22.

MPERC, 2021. Aggregate Revenue Requirement and Retail Supply Tariff Order For FY 2020-21, Retail Supply Tariff Order FY 2020-21.

MPERC, 2020. Aggregate Revenue Requirement and Retail Supply Tariff Order For FY 2019-20, Retail Supply Tariff Order FY 2019-20.

NSRDB, 2018. The National Solar Radiation Database (NSRDB). Natl. Renew. Energy Lab. USA.

https:/nsrdb.nrel.gov/ (accessed 4.3.18).

Ozcan, M., 2014. Assessment of renewable energy incentive system from investors' perspective. Renew. Energy 71, 425–432. https://doi.org/10.1016/j.renene.2014.05.053

Parrado, C., Marzo, A., Fuentealba, E., Fernández, A.G., 2016. 2050 LCOE improvement using new molten salts for thermal energy storage in CSP plants. Renew. Sustain. Energy Rev. 57, 505–514. https://doi.org/10.1016/j.rser.2015.12.148

SAM, 2021. System Advisor Model, Version 2021.12.02 Revision 1, SSC 238. National Renewable Energy Laboratory, Alliance for Sustainable Energy, LLC for Department of Energy, USA. https://sam.nrel.gov/ (accessed 3.3.22).

San Miguel, G., Corona, B., 2018. Economic viability of concentrated solar power under different regulatory frameworks in Spain. Renew. Sustain. Energy Rev. 91, 205–218. https://doi.org/10.1016/j.rser.2018.03.017

Sharma, C., Sharma, A.K., Mullick, S.C., Kandpal, T.C., 2015. Assessment of solar thermal power generation potential in India. Renew. Sustain. Energy Rev. 42, 902–912. https://doi.org/10.1016/j.rser.2014.10.059

Sioshansi, R., Denholm, P., 2010. The value of concentrating solar power and thermal energy storage. IEEE Trans. Sustain. Energy 1, 173–183. https://doi.org/10.1109/TSTE.2010.2052078

SolarPACES, 2021. Concentrating Solar Power Projects. Natl. Renew. Energy Lab. USA. https://solarpaces.nrel.gov/ (accessed 3.12.22).

Thapar, S., Sharma, S., Verma, A., 2016. Economic and environmental effectiveness of renewable energy policy instruments: Best practices from India. Renew. Sustain. Energy Rev. 66, 487–498. https://doi.org/10.1016/j.rser.2016.08.025

Appendix A

Nomenclature

Symbols

AC	Annual cost (Million US$)	NAEO	Net annual electricity output (GWh)
C_{fund}	Public/government fund (Million US$)	PV_{gbi}	Cumulative present value of annual cost of GBI (Million US$)
d	Discount rate (Fraction)		
F_d	Share of debt (Fraction)	PV_{is}	Cumulative present value of annual cost of interest paid on loan (Million US$)
F_e	Share of equity (Fraction)		
I_d	Interest rate on debt (Fraction)	PV_{ptc}	Cumulative present value of annual cost of PTC (Million US$)
I_{is}	Interest rate on loan (Fraction)		
n	Useful life of CSP plant (Years)	R_e	Rate of return on equity (Fraction)

Abbreviations

CERU	Certified emission reduction unit	PTSC	Parabolic trough solar collector
CSP	Concentrating solar power	PV	Photovoltaic
CTR	Central tower receiver	REC	Renewable energy certificate
FiT	Feed-in-Tariff	RPO	Renewable purchase obligation
GBI	Generation based incentives	SAM	System Advisor Model
IS	Interest subsidy	TES	Thermal energy storage
LCOE	Levelized cost of electricity	ToD	Time-of-delivery
O&M	Operation and maintenance	VGF	Viability gap funding
PTC	Production tax credit	WACC	Weighted average capital cost

Tab. A.1 Estimates of average unit cost of electricity for the state of Madhya Pradesh for the financial years 2019-20 to 2021-22 (MPERC, 2022, 2021, 2020)

Financial Year	Average power purchase cost (INR/kWh)	Conversion rate 1 US$ to INR#	Average power purchase cost (US$/kWh)
2019-20	3.99	70.88	56.3
2020-21	3.43	74.20	46.2
2021-22	3.74	74.51	50.2
	Mean of average power purchase cost (US$#/MWh) →		**50.9**

(FBIL, 2022)

Techno-Economics of Central Tower Receiver Power Plants in India: Effect of Heat Transfer Fluids/Thermal Storage Media

Tarun Kumar Aseri[1,2], Chandan Sharma[2], Tara C. Kandpal[1]

[1] Department of Energy Science and Engineering, Indian Institute of Technology, Delhi (India)

[2] Mechanical Engineering Department, Engineering College Ajmer (India)

Abstract

Results of a preliminary attempt to study the effect of different fluids as heat transfer fluid (HTF) as well as thermal energy storage (TES) medium on the techno-economics of a 100 MW nominal capacity CTR based plant with the provision of 12.0 hours of thermal energy storage are presented. For this purpose, solar salt, KCl-$MgCl_2$, NaCl-KCl-$MgCl_2$ and liquid sodium have been considered.

From the results obtained, it is observed that merely attaining higher temperatures for a heat transfer fluid or thermal storage media is not going to significantly affect the techno-economics of the CSP plant. The thermo-physical properties and cost of heat transfer/ thermal storage fluids have considerable effect on cost of thermal energy storage sub-system, parasitic requirements, as well as operational and maintenance requirements.

Keywords: CSP plant, techno-economics, heat transfer fluid, thermal energy storage, levelized cost of electricity

1. Introduction

Amongst the concentrating technologies for solar thermal power generation, parabolic trough solar collector (PTSC) and central tower receiver (CTR) have attained significant commercial maturity for large scale dissemination. CTR technology has been considered as a potential candidate for third generation CSP plants primarily due to achievable higher operating temperatures (>600˚C) resulting in higher power cycle efficiency (Neises and Turchi, 2019). It is also noted that the choice of material(s) for heat transfer fluid (HTF) and thermal energy storage (TES) medium is likely to affect the cycle efficiency, net annual electricity output, maintenance requirements and consequently cost of electricity delivery (Liu et al., 2016).

As shown in Fig. 1, the CSP plants typically consist of a solar energy collection system, a thermal energy storage/transfer system and a power generation system. In the case of a CTR based solar thermal power plant, the reflected solar radiation from the heliostat field gets absorbed at the receiver located at the top of the central tower to heat the heat transfer fluid. The hot fluid can be used directly to generate steam or can be stored in hot tanks (Palacios et al., 2020).

Presently, almost 75% of the total installed capacity (6.55GW) in the different parts of the world is based on PTSC while about 20% plants are based on CTR technology (SolarPACES, 2021). Several studies have been reported in the literature on the use of molten salt as heat transfer as well as thermal energy storage media in CTR based plants due to its favorable thermo-physical-economic properties (Aseri et al., 2021; Ortega et al., 2008; Parrado et al., 2016; Turchi and Heath, 2013). Since the installation of 11 MW nominal capacity commercial CTR based CSP plant (PS10) at Spain with one hour of thermal energy storage during 2005-2007, use of different thermal energy storage media has been considered. The operating restrictions associated with state-of-the-art solar salt, $NaNO_3$-KNO_3 has necessitated development of a new mixture of salts or consideration of alternative options such as direct steam generation and air heating. In view of this, González-Roubaud et al. (2017) have compared the performance of CTR based plants with direct steam generation and storage against the molten salt based TES system. The study observed that direct molten salt based TES delivers electricity at a lower cost due to less number of components involved. Analyzing the effect of nitrate, chloride, fluoride, carbonate based salts as heat transfer fluids on techno-economics for CTR based plants in China, the authors suggested that the integration of nitrate ($NaNO_3$-KNO_3) mixed solar salt based TES system can generate electricity at a lower cost than the other salts (Zhuang et al., 2019). In view of continued interest in solar thermal power generation in India, a preliminary attempt has been made in the present study to analyze the effect of different HTF/TES media based on binary or ternary mixtures of nitrate salts, chloride salts, and liquid metals on the techno-economics of CTR based CSP plants in India.

© 2022. The Authors. Published by International Solar Energy Society
Selection and/or peer review under responsibility of Scientific Committee
doi:10.18086/eurosun.2022.18.02 Available at http://proceedings.ises.org

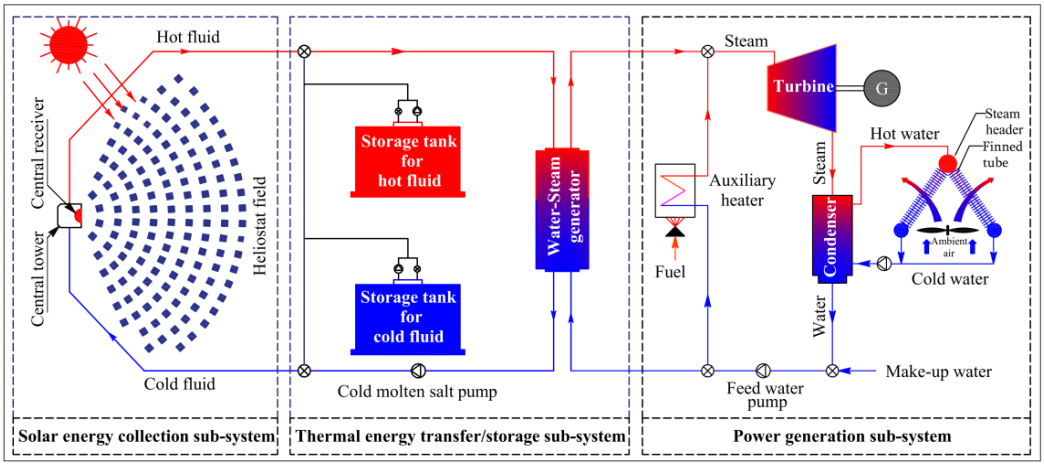

Fig. 1 Schematic of a dry-cooled CTR based CSP plant with two-tank direct thermal energy storage

2. Methodology

The outline of the methodology adopted to assess the techno-economic performance is presented in Figure 2 and the same is briefly described in the following paragraphs.

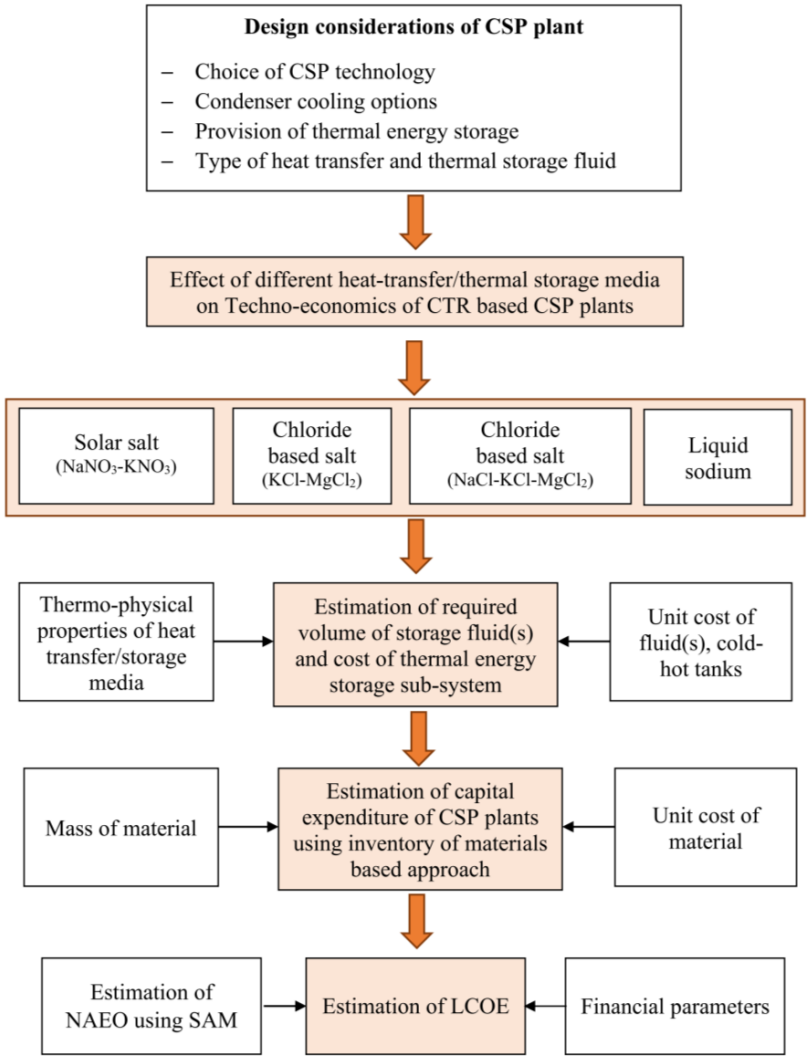

Fig. 2 A schematic representation of methodology adopted to assess the effect of HTF/TES medium on techno-economic performance of CTR based CSP Plant

Considering a threshold annual value (2000 kWh/m^2) of direct normal irradiance (DNI) at wastelands, Sharma et al. (2015) have identified 95 locations with potential for deployment of CSP plants in India, excluding potential wastelands suitable for solar PV and onshore wind power plants. Further, out of these locations, Aseri et al., (2020a) have found that at 67 potential locations (with high annual DNI), the wet cooled condenser technology is not feasible due to the unavailability of adequate amount of water for condenser cooling. Considering this, the district of Jaisalmer in the state of Rajasthan is selected as a potential location for deploying 100 MW nominal capacity dry-cooled CTR based CSP plant with a provision of 12.0 hours of direct thermal energy storage.

In the CTR based plants, the heat transfer fluid can also be stored directly in thermal energy storage system to operate the plant during off sunshine hours. Hence, in the present study, a single fluid is considered as heat transfer and storage fluid. In order to investigate the effect of the choice of heat transfer (as well as thermal storage) fluids on the techno-economics of CSP plants, four different fluids (i.e., a nitrate based salt, two chloride based salts and a liquid metal) have been considered. For these HTFs, the variation of thermo-physical properties with temperature is shown in Fig. 3. The thermo-physical properties along with unit cost (US$/kg) of various HTFs at 700°C temperature (500ºC for solar salt) are presented in Tab. 1.

With the use of hourly values of weather data (obtained from the National Solar Radiation Data Base, NREL, USA) and System Advisor Model (SAM), the technical performance parameters such as net annual electricity output (NAEO), capacity utilization factor, water requirements have been obtained (NSRDB, 2018; SAM, 2021). The design parameters and specifications used in the analysis pertaining to the heliostat field, receiver, tower, thermal energy storage and power block of CTR based CSP plants are presented in Tab. 2.

The increase in operating cycle temperature and change in heat transfer/thermal storage media affects the system design in terms of number of heliostats, height of central tower, size of central receiver, number of tanks and their sizes, etc. In the present study, these design parameters are estimated using SAM (2021) and the same are presented in Tab. 3.

In order to estimate the cost of thermal energy storage sub-system based on different fluids used as HTF and storage media the required volume of the thermal fluid (V_{tes}) to operate the power cycle for 12.0 hours at full load capacity is estimated from the following expression (SAM, 2021).

$$V_{tes}(m^3) = \frac{\frac{W_{gross}}{\eta_{pb}} H_{tes}}{\rho\, c_p\, \epsilon_{hex}\left[\left(T_{sf,out} - T_{hex,hot}\right) - \left(T_{sf,in} - T_{hex,cold}\right)\right]} \times (3.6 \times 10^6) \qquad \text{(Eq. 1)}$$

where W_{gross} represents the gross power output from the plant (MW), η_{pb} the efficiency of the power cycle, H_{tes} hours of thermal energy storage (hours), ρ the density of HTF (kg/m^3), Cp specific heat of salt (J/kg°C), ε_{hex} effectiveness of salt-to-steam generator, $T_{sf,in}$ and $T_{sf,out}$ inlet and outlet temperature at solar field (°C), and $T_{hex,hot}$ and $T_{hex,cold}$ hot and cold temperatures respectively at salt-to-steam generator (°C).

Following the inventory of materials approach developed and used by the authors (Aseri et al., 2020b), the capital expenditure (CAPEX) has been estimated for the CSP plant considered in the study with all fluids as HTF and TES media. The CAPEX estimated with solar salt as heat transfer and thermal energy storage fluid is considered as the base value of the CAPEX. It is worth mentioning that with a change in HTF, the required size of hot and cold tanks also changes due to change in thermo-physical properties of HTF, consequently affecting the CAPEX of CSP plants. The levelized cost of electricity (LCOE) which is essentially the breakeven value of the cost of electricity is estimated as

$$LCOE = \frac{\left(CAPEX \times \frac{d(1+d)^n}{(1+d)^n - 1}\right) + Annual\ operation\ and\ maintenance\ \ cost}{Net\ annual\ electricity\ output} \qquad \text{(Eq. 2)}$$

where *d* represents the discount rate (weighted average cost of capital) and *n* the useful life of the plant. In the present study, a discount rate of 10%, useful life of 30 years and annual operation and maintenance (O&M) cost of 2% of the CAPEX has been assumed.

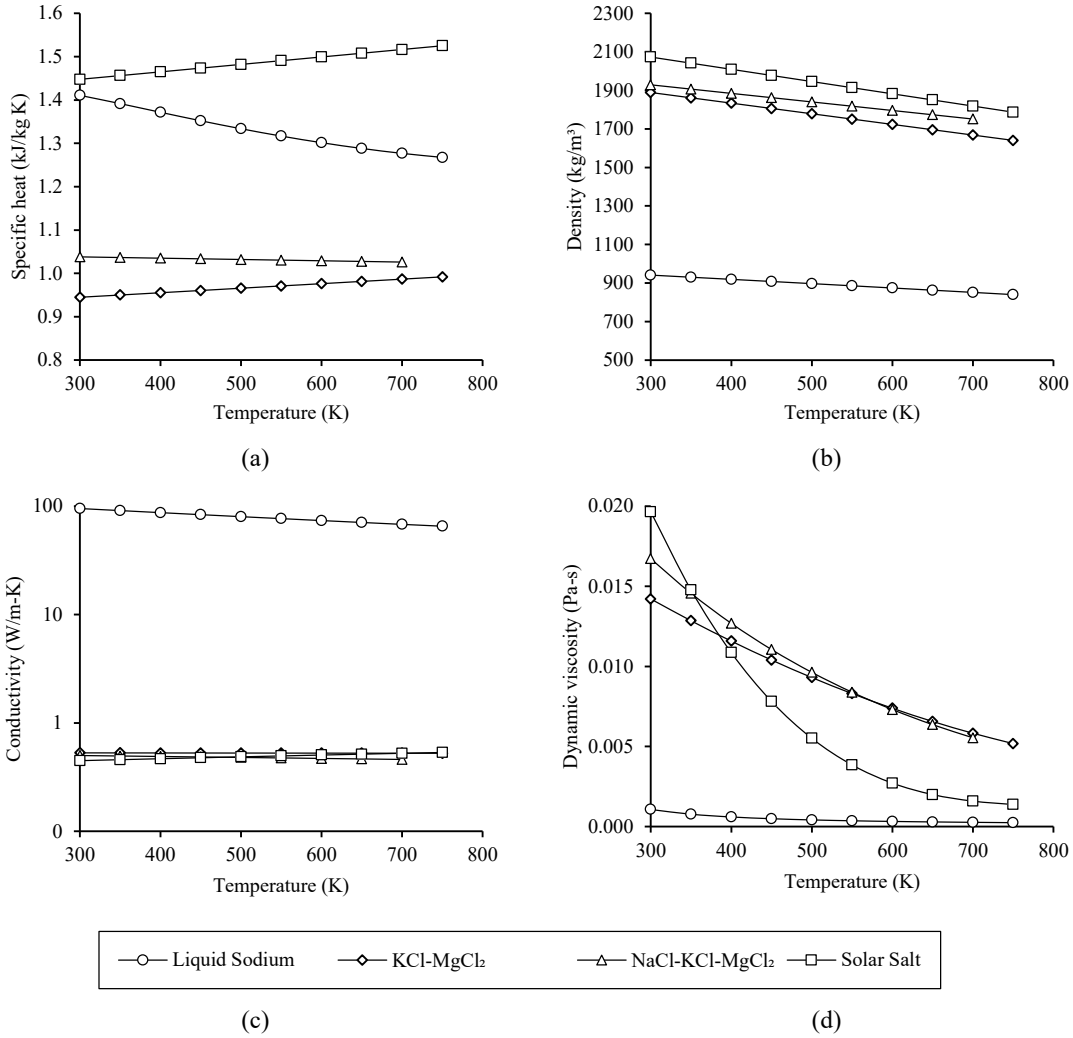

Fig. 3 Variation of thermo-physical properties of different heat transfer fluids with temperature

Tab. 1. Thermo-physical properties and unit cost of heat transfer cum thermal energy storage media (Manzolini et al., 2021)

Thermal fluid	Chemical and composition (fraction)	Melting temperature (°C)	Maximum operating temperature (°C)	Density (kg/m³)	Specific heat (J/kg-K)	Viscosity (Pa-s)	Thermal conductivity (W/m-K)	Cost (US$/kg)
Solar Salts	$NaNO_3$-KNO_3 (0.6-0.4)	223	600	1740	1538	0.0012	0.547	0.80
Chloride based salt	KCl-$MgCl_2$ (0.68-0.32)	445	>700	1556	1150	0.0015	0.4347	0.35
	$NaCl$-KCl-$MgCl_2$ (0.245-0.205-0.55)	383	>700	1631	1018	0.0021	0.4380	0.29
Liquid metal	Liquid Sodium (Na)	142	>800	787	1252	0.0002	55.31	2.0

Properties are estimated at a temperature of 700ºC except for solar salt (500ºC)

Tab. 2 Design parameters and specifications used in the analysis

Sub-System	Parameter	Unit	Value	Sub-System	Parameter	Unit	Value
Heliostat field	Solar collector used	-	Heliostat	Tower and Receiver	Receiver type	-	External
	Width of heliostat	m	12.2		Tube inner/outer diameter	m	0.0375/0.040
	Height of heliostat	m	12.2		Material of receiver tubes	-	SS AISI316
	No. of facets in a heliostat	-	16.0		Emittance of coating	-	0.88
	Aperture area of a heliostat	m^2	144.4		Absorptance of coating	-	0.94
	Heliostat reflectance	%	90.0		Design value of heat loss	kW_{th}/m^2	30.0
	Maximum heliostat distance to tower height ratio	-	9.5		Efficiency of HTF pump	-	0.85
					Design inlet temperature of HTF	°C	290
	Minimum heliostat distance to tower height ratio	-	0.75		Design outlet temperature of solar salt	°C	574
	Water requirement per wash	L/m^2	0.7		Design outlet temperature of KCl-$MgCl_2$	°C	610
	Washes per year	-	63.0				
Rankine cycle based power block	Turbine inlet temperature	°C	565, 600, 650		Design outlet temperature of NaCl-KCl-$MgCl_2$, liquid sodium	°C	670
	Gross to net conversion factor	-	0.9				
	Boiler operating pressure	bar	100	Thermal energy storage	Thermal energy storage media	-	Same as HTF
	Rated power block efficiency at 565°C	%	41.2				
	Rated power block efficiency at 600°C	%	42.7#		Height of storage tank	m	12.0
	Rated power block efficiency at 650°C	%	43.5#		Minimum design temperature of solar salt	°C	290
	Turbine over design operation	-	1.05		Minimum design temperature of KCl-$MgCl_2$	°C	260
	Blowdown fraction	%	2.0				
	Condenser cooling technology	-	Dry		Minimum design temperature of NaCl-KCl-$MgCl_2$	°C	430
	Condenser pressure	mm Hg	50.8				
	Annual decline in output	%	Nil		Minimum design temperature of liquid sodium	°C	280
	Availability of plant	%	96				

Efficiency is estimated considering isentropic expansion in the turbine and isentropic compression in the pump

Tab. 3 Design parameters considered for CSP plants based on different HTF cum TES medium (SAM, 2021)

Parameter	Unit	HTF / TES media used			
		Solar Salt	KCl-$MgCl_2$	NaCl- KCl-$MgCl_2$	Liquid Sodium
Thermal energy required from solar field	MW_{th}	755	728	715	715
Number of heliostats	-	16948	16334	16006	15991
Height of the central tower	m	254.53	247.95	247.36	247.8
Diameter of central receiver	m	23.30	23.07	23.60	23.05
Height of central receiver	m	25.47	24.56	24.29	24.40
Number of pairs of hot-cold tanks	-	6	7	10	10
Height of hot/cold tanks	m	12	12	12	12
Diameter of hot/cold tanks	m	17.3	18.2	18.3	18.0
Land area	km^2	14.9	14.5	14.2	14.1

3. Results and Discussion

Using the thermo-physical properties (Tab. 1) and Eq. (1), the required volume (or mass) of fluid used as HTF and TES medium and also the cost of 12.0 hours TES sub-system based on different heat transfer/storage fluids have been estimated and the same are presented in Tab. 4. The estimate for the cost of chloride salts based TES sub-system (US $26.4-35.9 million) is found close to that of the system based on nitrate salts (US $33.6 million) due to relatively small variation in thermo-physical properties. However, with the use of liquid sodium as HTF/storage medium the investment requirement is expected to increase by 94% in comparison to that for solar salt based TES sub-system. The lower density and higher cost (US $2.0/kg) of liquid sodium lead to higher cost of the TES sub-system.

Tab. 4 Estimates for the volume, mass and cost of 12.0 hours of TES sub-system based on different fluids

Storage fluid	Thermal energy in storage tanks (MWh_{th})	Volume of storage fluid (m^3)	Mass of storage fluid ($\times 10^6$ kg)	Unit cost of storage fluid (US$/kg)	Cost of storage fluid	Cost of hot-cold tanks	CAPEX of TES sub-system
					Million US$		
Solar Salt	3236.2	15530	27.02	0.8	21.6	12.0	33.6
KCl-$MgCl_2$	3119.6	20084	31.25	0.4	10.9	15.5	26.4
NaCl-KCl-$MgCl_2$	3065.1	28835	47.01	0.3	13.6	22.3	35.9
Liquid sodium	3065.1	27856	21.92	2.0	43.8	21.5	65.3

The CAPEX of 100 MW CTR based CSP plants with 12.0 hours of TES are estimated based on the inventory of materials based approach and detailed break-up of the same is presented in Tab. 5. From the estimates, it is observed that the CAPEX varies in the range of US$438.5 to US$490.9 million for 100 MW nominal capacity CSP plant considering nitrate, chlorides and liquid sodium as heat transfer fluids/storage media.

The parasitic power required by different components involved in HTF and TES sub-systems depends on the thermo-physical properties of HTF and TES medium used. The required annual parasitic power by different components/sub-systems of 100 MW CTR based CSP plants with 12.0 hours of TES is presented in Fig. 4. From the results it may be observed that highest parasitic power (33-66%) is required in the receiver and tower sub-system followed by condenser (10-22%). The annual parasitic requirement in receiver and tower sub-systems for plants based on solar salt, liquid sodium, KCl-$MgCl_2$ and NaCl-KCl-$MgCl_2$ has been estimated at 27.5 GWh, 42.0 GWh, 43.2 GWh and 100.2 GWh respectively. The increase in parasitic power in receiver and tower sub-system for NaCl- KCl-$MgCl_2$ based plant can be attributed to the fact that due to relatively lower heat capacity ($\rho \times C_p$), higher volume (28835 m^3) of salt is required to be pumped in different sub-systems.

Tab. 5 Estimates of capital expenditure for CTR based CSP plants with the provision of 12.0 hours of thermal energy storage with different HTF/TES media

System of CSP plant	Estimates of CAPEX (million US$) of CSP plant			
	Solar Salt	$KCl\text{-}MgCl_2$	$NaCl\text{-}KCl\text{-}MgCl_2$	Liquid Sodium
Direct cost				
Site improvement	67.1	65.1	56.2	58.6
Heliostat field	121.8	116.7	107.6	107.6
Tower/Receiver	18.4	17.6	16.3	16.3
Power block	31.7	31.1	30.1	30.1
Thermal energy storage	33.6	26.4	35.9	65.4
Sub-total	**272.5**	**256.9**	**246.1**	**278.0**
Contingency	19.1	18.0	17.2	19.5
Gross-total	**291.6**	**274.9**	**263.3**	**297.4**
Indirect cost				
Engineering, procurement & construction	29.2	27.5	26.3	29.7
Owner's cost	14.6	13.7	13.2	14.9
Soft cost	20.4	19.2	18.4	20.8
Land cost	74.8	72.6	62.7	65.4
Taxation	60.4	56.9	54.5	61.6
Sub-total	**199.3**	**190.0**	**175.1**	**192.4**
Total installation cost	**490.9**	**464.9**	**438.5**	**489.8**
Specific capital cost (US$/kW)	4909	4649	4385	4898

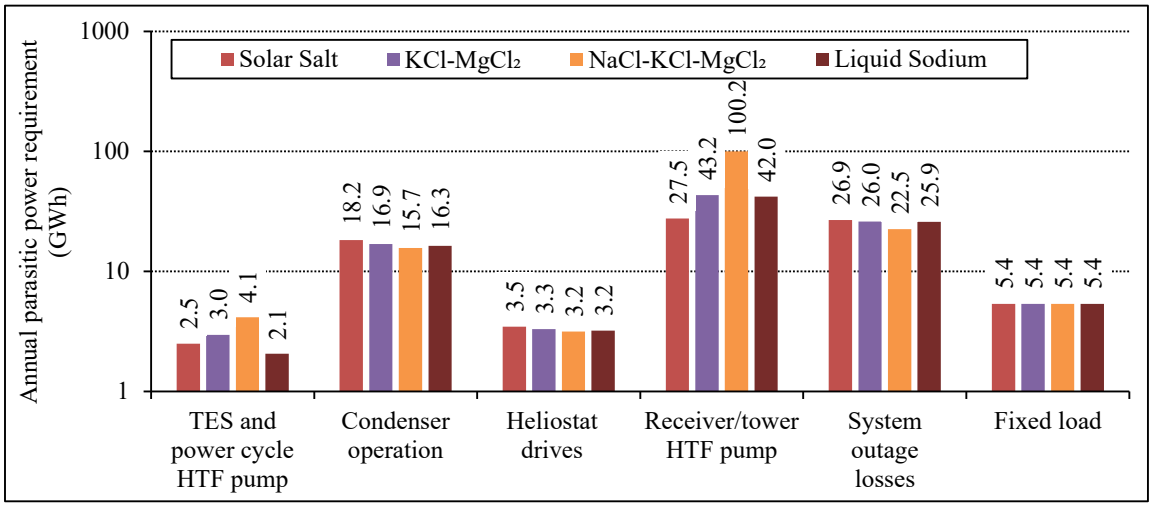

Fig. 4 Parasitic power requirement in different components of CTR based CSP plants

Fig. 5(a) shows net annual electricity output (NAEO) estimated for CSP plants based on different HTFs. From the results, it may be observed that CTR plant based on solar salt delivers highest NAEO (645.4 GWh) followed by plants with $KCl\text{-}MgCl_2$ (624.3 GWh), liquid sodium (621.4 GWh) and $NaCl\text{-}KCl\text{-}MgCl_2$ (539.5 GWh) as HTF /TES medium. A similar pattern is also observed in the estimates of capacity utilization of the CTR plants (Fig. 5(b)).

The estimated values of LCOE are presented in Fig. 6. As per the results obtained, the lowest LCOE can be achieved for $KCl\text{-}MgCl_2$ based plants (US $93.9/MWh), followed by plants using solar salt (US $95.9/MWh), liquid sodium (US $99.4/MWh) and $NaCl\text{-}KCl\text{-}MgCl_2$ (US $102.5/MWh) as HTF/TES media.

From the above mentioned results, it is worth mentioning that though the variation in LCOE for all the plants considered is not significant, the HTFs that has the highest achievable temperature shall definitely have an advantage for third generation CSP plants that are essentially based on supercritical CO_2 power cycle. The reason for the same is relatively lower volume of HTFs required and significantly lower cost of supercritical CO_2 power

block as compared to power block based on Rankine cycle. The metallurgical issues associated with chloride based salts leading to corrosive attacks give the liquid sodium based plant an edge over other HTF based plants (Ding and Bauer, 2021; Sarvghad et al., 2022).

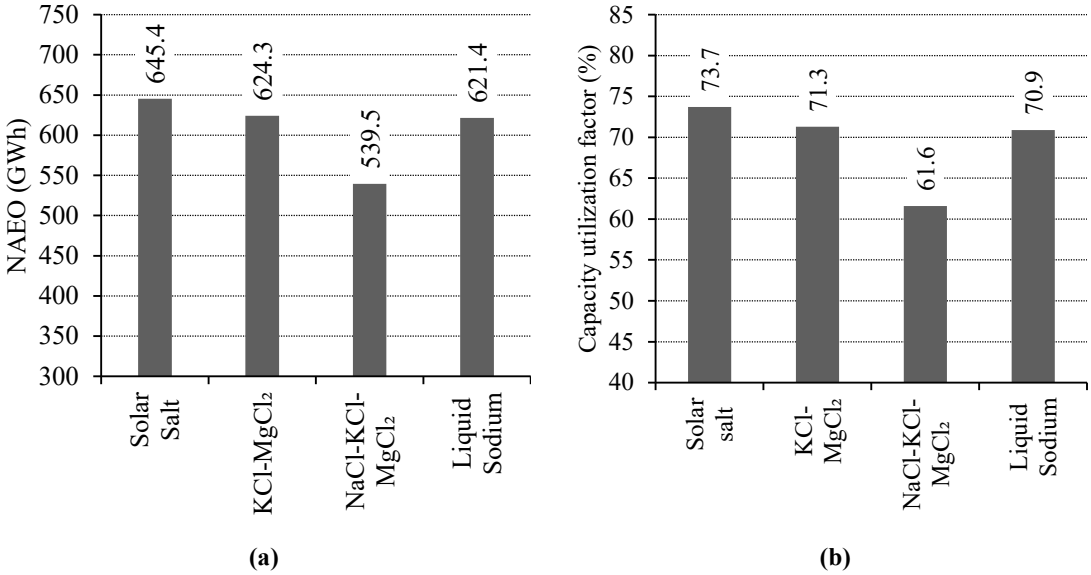

Fig. 5. Results of technical and economic performance (a) NAEO, (b) capacity utilization factor

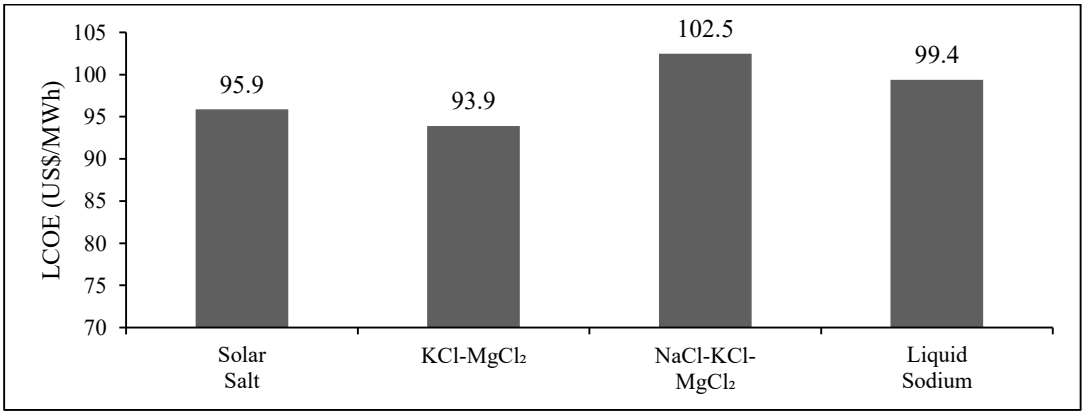

Fig. 6 Estimates of levelized cost of electricity for 100 MW CTR based plants with 12.0 h of TES

4. Concluding remarks

In the present study, an attempt has been made towards analyzing the effect of heat transfer fluid as well as thermal energy storage media on the techno-economics of a 100 MW dry-cooled CTR based CSP plant with the provision of 12.0 hours of thermal energy storage. Based on the availability of suitable wastelands and DNI, Jaisalmer (Rajasthan) in India has been selected as a potential site for deployment. In the present study, four different heat transfer fluids as well as thermal energy storage medium have been considered.

From the results obtained, it may be observed that the thermo-physical properties and cost of heat transfer (or thermal energy storage) fluids can affect techno-economic performance of CSP plants significantly. The parasitic requirement by the various components sub-systems depends on the HTF used thus affecting the net annual electricity output of the plants. Moreover, the cost and thermo-physical properties of the fluid used also affect the cost of thermal energy storage sub-systems and consequently the overall cost of the plant.

From the results of this preliminary study, it is observed that the value of LCOE is lowest with KCl-$MgCl_2$ (US$93.9/MWh) used as heat transfer and storage medium though the values of LCOE with other three HTF/storage media is marginally different - US$95.9/MWh for solar salt, US$99.4/MWh for liquid sodium, and US$102.5/MWh for NaCl-KCl-$MgCl_2$.

Acknowledgments

The authors are thankful to the administration of Engineering College Ajmer, Rajasthan (India) and acknowledge the Department of Technical Education, Government of Rajasthan for providing permission to the first author (Tarun Kumar Aseri) to pursue doctoral research work at the Department of Energy Science and Engineering, Indian Institute of Technology Delhi.

References

Aseri, T.K., Sharma, C., Kandpal, T.C., 2021. Estimation of Capital Costs and Techno-Economic Appraisal of Parabolic Trough Solar Collector and Solar Power Tower based CSP Plants in India for Different Condenser Cooling Options. Renew. Energy 178, 344–362. https://doi.org/10.1016/j.renene.2021.05.166

Aseri, T.K., Sharma, C., Kandpal, T.C., 2020a. Assessment of water availability for wet cooling at potential locations for solar thermal power generation in India. Int. J. Ambient Energy 41, 1126–1141. https://doi.org/10.1080/01430750.2018.1507926

Aseri, T.K., Sharma, C., Kandpal, T.C., 2020b. Estimating capital cost of parabolic trough collector based concentrating solar power plants for financial appraisal: Approaches and a case study for India. Renew. Energy 156, 1117–1131. https://doi.org/10.1016/j.renene.2020.04.138

Ding, W., Bauer, T., 2021. Progress in Research and Development of Molten Chloride Salt Technology for Next Generation Concentrated Solar Power Plants. Engineering 7, 334–347. https://doi.org/10.1016/j.eng.2020.06.027

González-Roubaud, E., Pérez-Osorio, D., Prieto, C., 2017. Review of commercial thermal energy storage in concentrated solar power plants: Steam vs. molten salts. Renew. Sustain. Energy Rev. 80, 133–148. https://doi.org/10.1016/j.rser.2017.05.084

Liu, M., Steven Tay, N.H., Bell, S., Belusko, M., Jacob, R., Will, G., Saman, W., Bruno, F., 2016. Review on concentrating solar power plants and new developments in high temperature thermal energy storage technologies. Renew. Sustain. Energy Rev. 53, 1411–1432. https://doi.org/10.1016/j.rser.2015.09.026

Manzolini, G., Lucca, G., Binotti, M., Lozza, G., 2021. A two-step procedure for the selection of innovative high temperature heat transfer fluids in solar tower power plants. Renew. Energy 177, 807–822. https://doi.org/10.1016/j.renene.2021.05.153

Neises, T., Turchi, C., 2019. Supercritical carbon dioxide power cycle design and configuration optimization to minimize levelized cost of energy of molten salt power towers operating at 650 °C. Sol. Energy 181, 27–36. https://doi.org/10.1016/j.solener.2019.01.078

NSRDB, 2018. The National Solar Radiation Database (NSRDB). Natl. Renew. Energy Lab. USA. https:/nsrdb.nrel.gov/ (accessed 4.3.18).

Ortega, J.I., Burgaleta, J.I., Téllez, F.M., 2008. Central Receiver System Solar Power Plant Using Molten Salt as Heat Transfer Fluid. J. Sol. Energy Eng. 130, 024501. https://doi.org/10.1115/1.2807210

Palacios, A., Barreneche, C., Navarro, M.E., Ding, Y., 2020. Thermal energy storage technologies for concentrated solar power – A review from a materials perspective. Renew. Energy 156, 1244–1265. https://doi.org/10.1016/j.renene.2019.10.127

Parrado, C., Marzo, A., Fuentealba, E., Fernández, A.G., 2016. 2050 LCOE improvement using new molten salts for thermal energy storage in CSP plants. Renew. Sustain. Energy Rev. 57, 505–514. https://doi.org/10.1016/j.rser.2015.12.148

SAM, 2021. System Advisor Model, Version 2021.12.02 Revision 1, SSC 238. National Renewable Energy Laboratory, Alliance for Sustainable Energy, LLC for Department of Energy, USA. https://sam.nrel.gov/ (accessed 3.3.22).

Sarvghad, M., Ong, T.C., Bell, S., Rumman, R., Delkasar, S., Woodcock, J.W., Will, G., Andersson, G., Lewis, D.A., Steinberg, A., 2022. On the compatibility of liquid sodium as heat transfer fluid for advanced concentrated solar thermal energy systems. Sol. Energy Mater. Sol. Cells 246, 111897. https://doi.org/10.1016/j.solmat.2022.111897

Sharma, C., Sharma, A.K., Mullick, S.C., Kandpal, T.C., 2015. Assessment of solar thermal power generation potential in India. Renew. Sustain. Energy Rev. 42, 902–912. https://doi.org/10.1016/j.rser.2014.10.059

SolarPACES, 2021. Concentrating Solar Power Projects. Natl. Renew. Energy Lab. USA. https://solarpaces.nrel.gov/ (accessed 3.12.22).

Turchi, C.S., Heath, G.A., 2013. Molten Salt Power Tower Cost Model for the System Advisor Model (SAM). Technical Report: NREL/TP-5500-57625, National Renewable Energy Laboratory, USA.

Zhuang, X., Xu, X., Liu, W., Xu, W., 2019. LCOE Analysis of Tower Concentrating Solar Power Plants Using Different Molten-Salts for Thermal Energy Storage in China. Energies 12, 1–17. https://doi.org/10.3390/en12071394

What can PV self-supply do for system integration?

Sarah Becker[1], Katja Metzler[2]

[1] Fraunhofer Institute for Energy System Technology and Energy Economics, Kassel (Germany)

[2] TU Braunschweig, Braunschweig (Germany)

Abstract

PV self-supply has been a key economic driver for increasing PV installations in Germany during the past years. The main economic advantage are the lower levelized costs of electricity from PV rooftop systems compared to grid electricity. Based on the European Renewable Energy Directive, self-supply systems benefit from wide exemptions from surcharges and network charges. PV self-supply systems are expected to require lower feed-in tariffs as well as to foster system integration by motivating households and industries to optimize consumption to match PV generation better in order to benefit from their own PV installations. We examine the effects of different shares of PV self-supply systems on electricity prices and the revenue situation of other market participants. We see small to moderate effects on electricity prices. While most other electricity generators are largely unaffected, peak units as well as battery storage systems face revenue reductions. Furthermore, we examine network charge exemptions and quantify effects on the network costs allocated to different consumer groups.

Keywords: PV self-supply, system integration, climate protection, cost allocation

1. Introduction

Today, PV self-supply systems form the largest part of current PV investments in Germany. Within the framework of the OwnPV-Outlook project, we aim to investigate and evaluate the development and integration of PV self-supply systems into the future energy system. We evaluate possible and probable designs of future frameworks for PV self-supply systems, considering economical, technical, behavioral and regulatory aspects. The aim is to narrow the wide range of potential developments by determining an energetically and economically efficient and thus sustainable integration of PV self-supply systems into the energy system. In particular, we target the evaluation regarding microeconomic, technical, and macroeconomic aspects. This paper investigates effects of different shares of PV self-supply in future scenarios while keeping total installed PV capacities constant. In this way, the effects of PV self-supply alone can be singled out.

2. Methods

A range of PV self-supply systems is modelled and integrated into the fundamental model SCOPE SD as described in (Böttger, Härtel 2021 and Härtel, Ghosh, 2020). Most investment decisions in SCOPE SD are made endogenously, based on minimal system cost subject to energy demand coverage and emission restrictions. In such a model setup, neither the investment decision for nor the dispatch of decentral self-supply systems by PV owners is captured since it only optimizes coverage of all demands at minimal total costs, neglecting the economic perspective of the individual owner of a PV self-supply system and not accounting for non-monetary motivations such as the wish to supply oneself or to contribute to climate protection measures. In order to evaluate the effects of PV self-supply systems on the total energy supply system, different shares of various PV self-supply systems are fixed exogenously instead and the rest of the system is optimized in order to see feedback effects.

After completion of the SCOPE SD model optimizations, resulting system costs are transferred into an evaluation of cost allocation in order to quantify redistribution effects.

The modelled PV self-supply systems include single-family as well as multi-family houses with and without electric vehicles. In the presence of electric vehicles, the charging time is assumed to be optimized for maximal share of own PV electricity, neglecting potential time-dependent grid electricity prices. For details on electric vehicle charging strategies, see von Bonin et al. (2022).

© 2022. The Authors. Published by International Solar Energy Society
Selection and/or peer review under responsibility of Scientific Committee
doi:10.18086/eurosun.2022.18.03 Available at http://proceedings.ises.org

2.1 The SCOPE SD model

The SCOPE SD model is a linear optimization model, taking into account the European energy supply. SCOPE SD is a loose acronym for "sector-coupled optimization model", run in the configuration "scenario development". It has a high temporal resolution of one hour, considers an entire consecutive year, and covers a broad range of technologies. An overview of the model is depicted in Fig. 1. The input data include investment as well as operation and maintenance costs, including fuel costs, technology potentials and restrictions, and technology-specific availability time series for a broad range of technological options, as well as comprehensive energy demand time series from different energy sectors. These data are combined into a linear optimization model with the objective to supply all demands at minimal costs, subject to emission targets or emission allowance prices. Demand flexibility is taken into account. It yields optimal investment decisions and dispatch time series of different technologies to cover the energy demands.

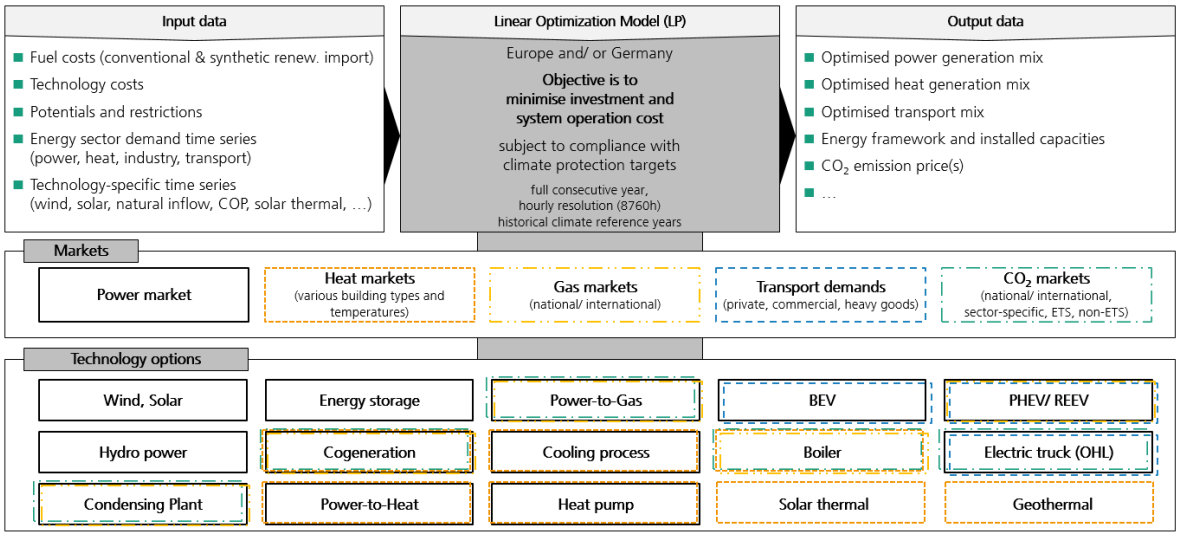

Fig. 1: Schematic overview of the SCOPE SD model components. Source: (Böttger, Härtel 2021).

Markets (energy demands and emission targets) are implemented as technology-coupling boundary conditions. For energy demands, that means that demand coverage is required with the option to use different technologies, such that the sum of all generation from different technologies meets the demands. For emissions, budget restrictions have to be observed and all emissions from different technologies are accounted for. Participation of a technology in a given market is indicated as a colored frame in Fig. 1.

2.2 Considered additional flexibility options

Additional flexibility options are considered only in the wholesale electricity market, not for system services. The extended usage of flexibility is incentivized by a reduction of electricity price components, which may be temporary and/or partial exemptions from all price components which are additional to procurement, trade, profit margin and emission allowances. These price components include taxes, charges and surcharges and are thus amenable to regulatory intervention. Modelled central technologies with additional flexibility potentials are electrolysis, synthetic methane production, central heat pumps (industrial or for district heating), direct electric heating, and central battery storage. To incentivize invest and operation of these flexible sector coupling technologies, they receive reductions in value-added tax, electricity tax and – if operated in a grid-friendly way – network charge exemptions. As usual, all central power plants participate in the electricity market and can thus also be considered as operating flexibly. The flexibility of wind and PV production of plants which receive a feed-in tariff is further increased by the option to shift remunerated generation to hours after the nominal end of their support scheme as opposed to producing as much as possible – even at negative prices – during their support period.

Decentral flexibility options modelled are charging of electric vehicles (EV), heat pump operation, PV self-supply systems with solar batteries, and air conditioning. Decentral technologies receive no exemptions from network charges, but investment and flexible operation are incentivized via electricity tax reductions and support for larger thermal storage capacities in heating and cooling technologies. Additionally, it is assumed that solar batteries can participate in the electricity market with charges and taxes only applied to storage losses.

2.3 Electricity demand, generation, and technological change

This paper considers the three scenario years 2030, 2040, and 2050. The assumed amounts of electricity generation from as well as consumption by different technologies are summarized in Fig. 2. The respective installed capacities for this base case scenario are depicted in Fig. 3, with details regarding total PV installations as well as PV self-supply systems in Fig. 4.

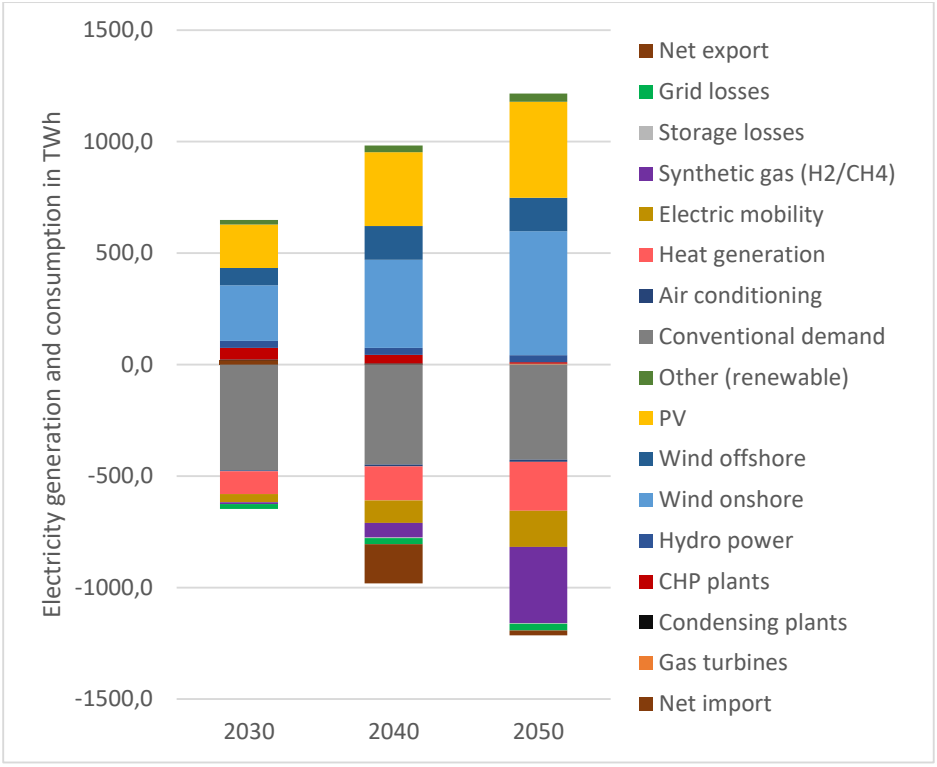

Fig. 2: Electricity generation and consumption for the three scenario years 2030, 2040, and 2050

Wind and PV installation increases are roughly in accordance with envisaged German government targets, with 205 GW total PV and 95 GW wind onshore capacity in 2030, rising to 450 GW PV and 200 GW Wind onshore in 2050. Wind offshore is installed up to “only” 40 GW. It is assumed that further offshore capacity is built – especially in later years –, but used exclusively for off-grid electrolysis. Another feature of the scenarios considered is the fast scale-up of synthetic gas production, yielding renewable hydrogen and methane.

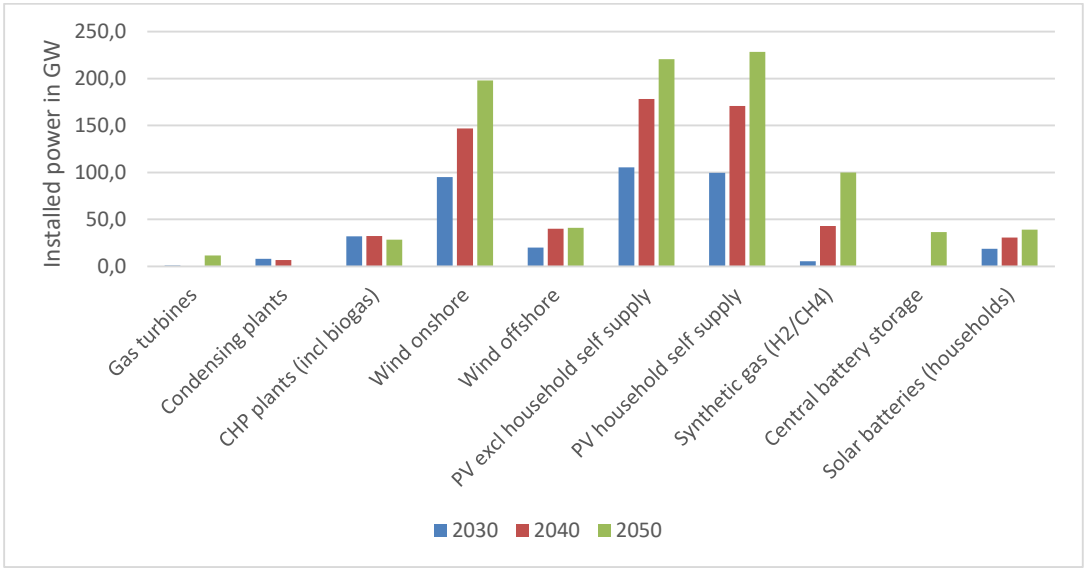

Fig. 3: Installed power capacities for the three scenario years 2030, 2040, and 2050

2.4 PV self-supply systems

In this work, PV self-supply systems for households usage are considered. Three different configurations are modelled: Single-family houses (SFH) with rooftop PV and solar batteries, SFH with rooftop PV, electric vehicles (EV) and solar batteries, and multi-family houses (MFH) with solar batteries and – on average – one EV per building. The solar batteries have a power capacity of 33% of the PV rooftop capacity for SFHs without EV, 20% for SFHs with EV, and 13% for MFHs with EV. The solar battery energy capacities range between 2.4 full load hours for MFH and 3.4 full load hours for SFH without EV (assuming charging/discharging with the batteries' full power capacity). EV charging strategies are described in detail in von Bonin et al. (2022). For the modelling under consideration in this paper, it is assumed that EVs are charged such that PV self-consumption is maximized. Further potential influences, such as spot-market dependent grid electricity prices or network load-dependent network charges are not taken into account.

In the base case scenario, it is assumed that these PV self-supply systems and other PV installations are roughly equal. As a sensitivity, the total installed PV capacity is kept constant, while the relative share of PV self-supply systems is varied between 75% and 125% of the base case scenario. These variants, together with the base case scenario, are illustrated in Fig. 4. The base case scenario is denoted as 100%, referring to a PV self-supply capacity of 100% of the base case. For the 75% scenario, PV self-supply is reduced to 75% of the 100% scenario, and for the 125% scenario, PV self-supply is increased to 125% of the 100% scenario, with changes in other PV installations compensating the change in total PV installations. It is apparent that for the 125% scenario in 2050, the PV self-supply capacity is in fact not increased to 125% of the base case. This is because the number of PV self-supply installations is capped by the number of respective buildings in Germany and it would be impossible to increase their number further. As a replacement, the non-self-supply PV installations are kept at their values of the base case scenario for this particular year.

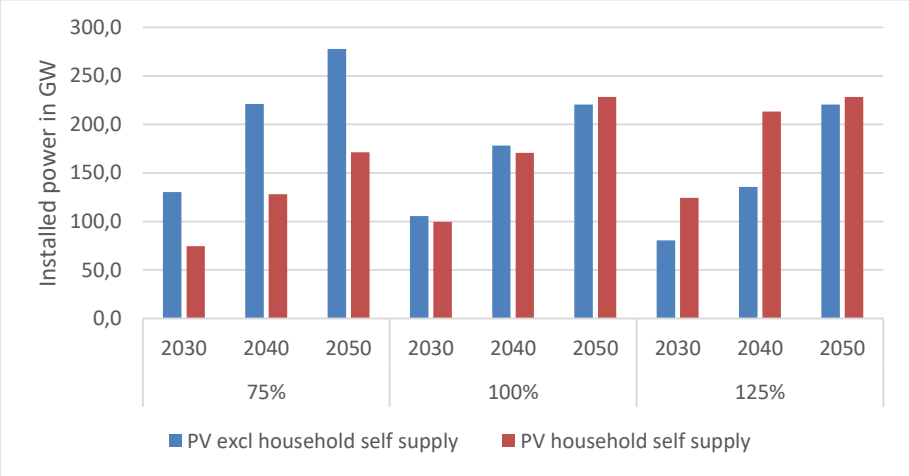

Fig. 4: Installed PV power capacities for the three scenario years 2030, 2040, and 2050, for the sensitivities of different shares of household PV self-supply

3. Results

3.1 Electricity prices and time series

Fig. 5 shows the average electricity prices and volatilities (standard deviations) for the base case 100% scenario as well as for the 75% and the 125% scenarios described in section 2.4.

There are no large deviations visible, but two trends can be observed:

- More PV self-supply → higher average wholesale market price
- More PV self-supply → lower volatility

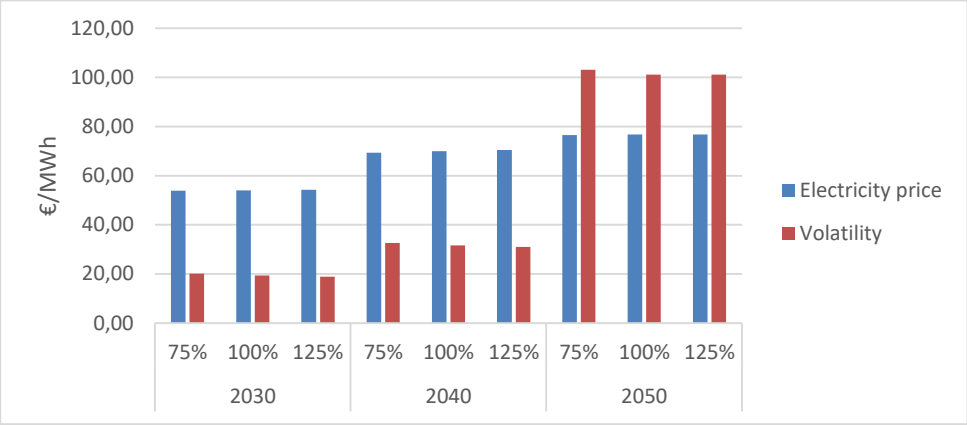

Fig. 5: Average electricity prices and price volatilities for the considered scenarios

Exemplary price time series for the base case 100% scenario for all three scenario years (2030, 2040 and 2050) for winter (January), the spring and fall transition periods (September), and summer (July) are shown in Fig. 6, Fig. 7, and Fig. 8, respectively.

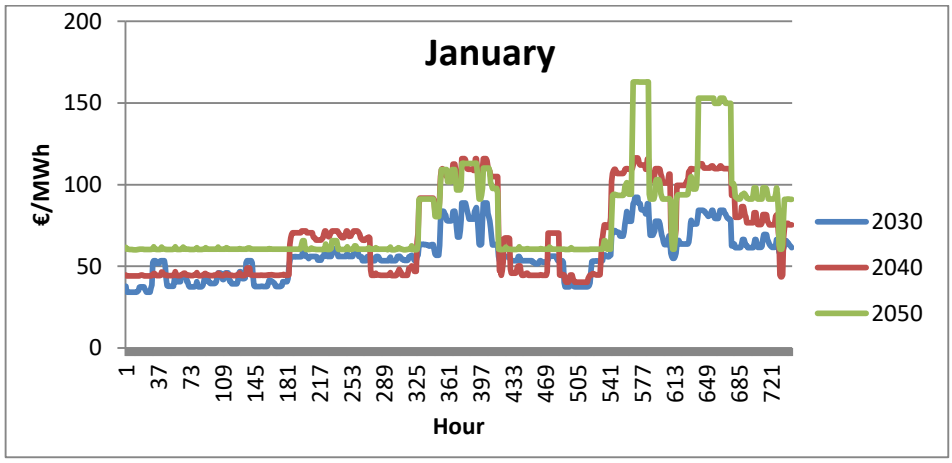

Fig. 6: Electricity prices for the different scenario years in January

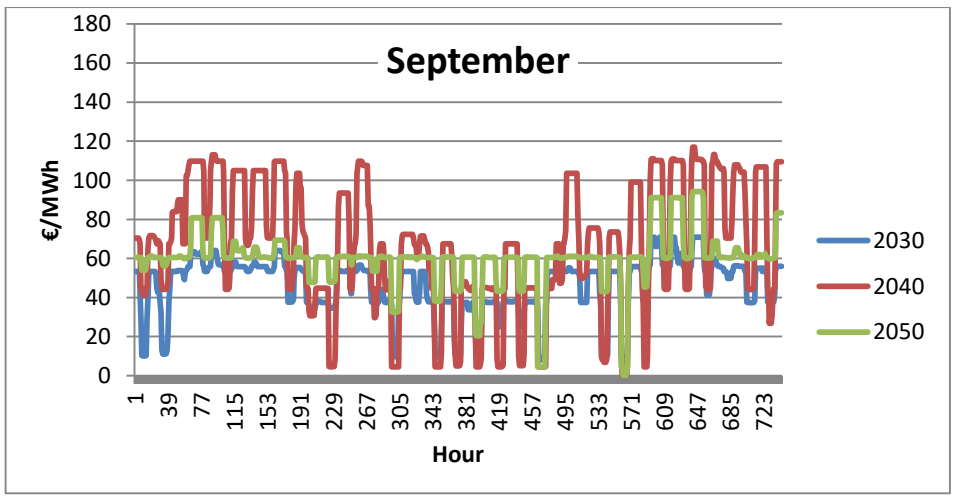

Fig. 7: Electricity prices for the different scenario years in September

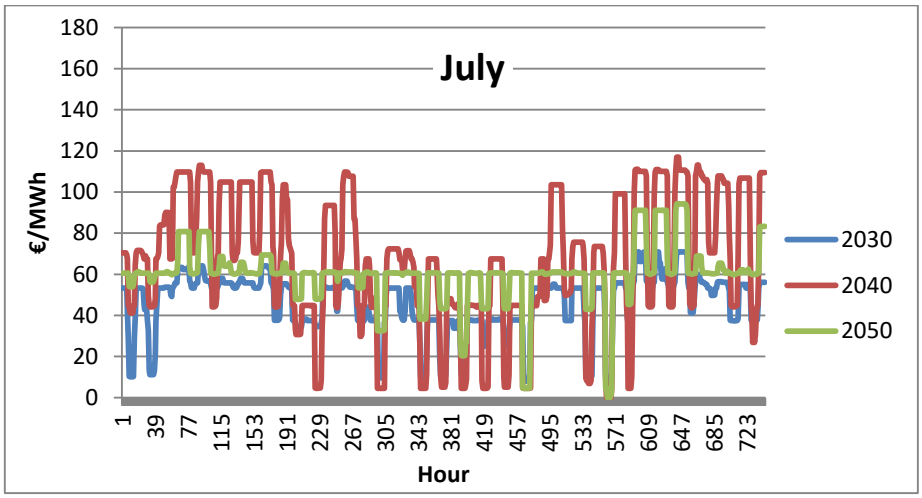

Fig. 8: Electricity prices for the different scenario years in July

Several general features can be observed in the price time series. First of all, the prices curves of different seasons show variations on different time scales. In winter, it is predominantly the scale of one to two weeks on which wind generation changes, which affects the electricity price. Transition periods and summer months are dominated by daily variations of PV production. When comparing the different scenario years, it is apparent that average prices and volatilities increase with time. Regarding the daily to weekly changes, the year 2040 plays a special role: Wind and PV generation has already been deployed to a large extent, whereas flexible consumption is lagging behind. This leads to particularly high amplitudes in daily price variations.

3.2 Revenue situation

What does a change in the PV self-supply share entail for the other participants of the electricity market? Fig. 9 shows the yearly average revenue from the wholesale electricity market for three selected technologies: The gas fired combined heat and power (CHP) plants, which serve heat generation as well as electricity generation, are not affected at all. Gas closed cycle (CCGT) plants likewise face very little change. Open-cycle gas turbines (OCGT), which operate only to serve rare peak demands, encounter larger changes. As a trend, their revenue decreases with increasing PV self-supply share. This is likely due to the added flexibility from solar batteries, making peak load plants less profitable.

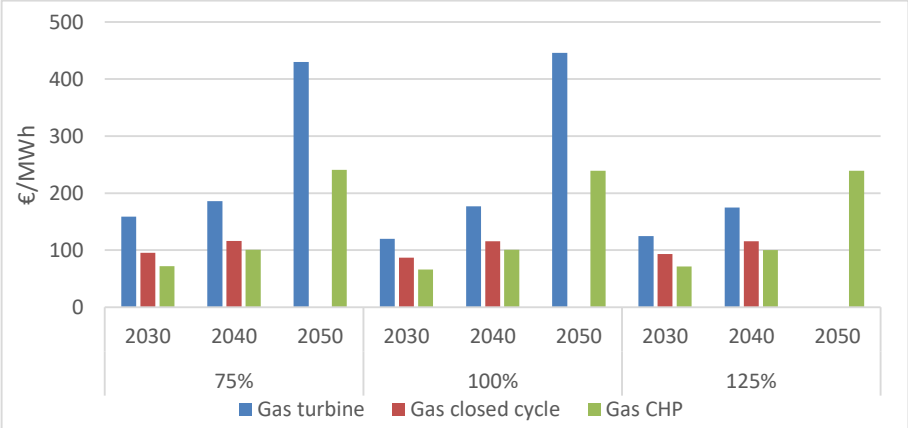

Fig. 9: Yearly average revenue of selected power plants

The revenue situation of the batteries, including the solar batteries, is shown in Fig. 10. Here, the trends are clearer: With solar batteries filling the niche of flexible storage, the average revenue per unit of stored energy goes down.

To sum up, the revenue situation of most electricity generation is largely unaffected by the share of PV self-supply systems in total installed PV capacity. For peak generators as well as batteries, the revenue decreases by small but noticeable amounts.

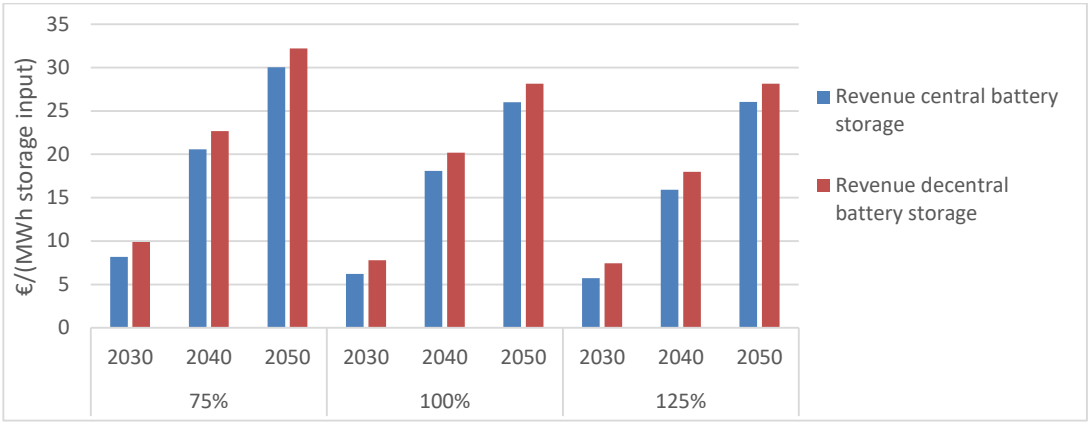

Fig. 10: Yearly average revenue of central and decentral battery storages. Due to storage losses, the input and output amount differ slightly. Here, € per MWh that is put into the storage is used

3.3 Allocation of network costs

As described in Section 2.2, the scenarios considered here come with extra amounts of flexibility, which are – among other measures – incentivized by network charge exemptions. In this section, the effects of these exemptions on other consumers are analyzed. To this end, two kinds of plots are used: The first compares total allocated network costs per consumer group, see Fig. 11 and Fig. 12. Network charge exemptions reallocate costs to non-privileged electricity consumers. In absolute terms, private households (household electricity, EV charging, heat pumps) make the largest contributions. The highest absolute network charge reductions are seen for energy intensive industries (mainly because they switch from fossil fuels to electric process heat) and synthetic hydrogen and methane production.

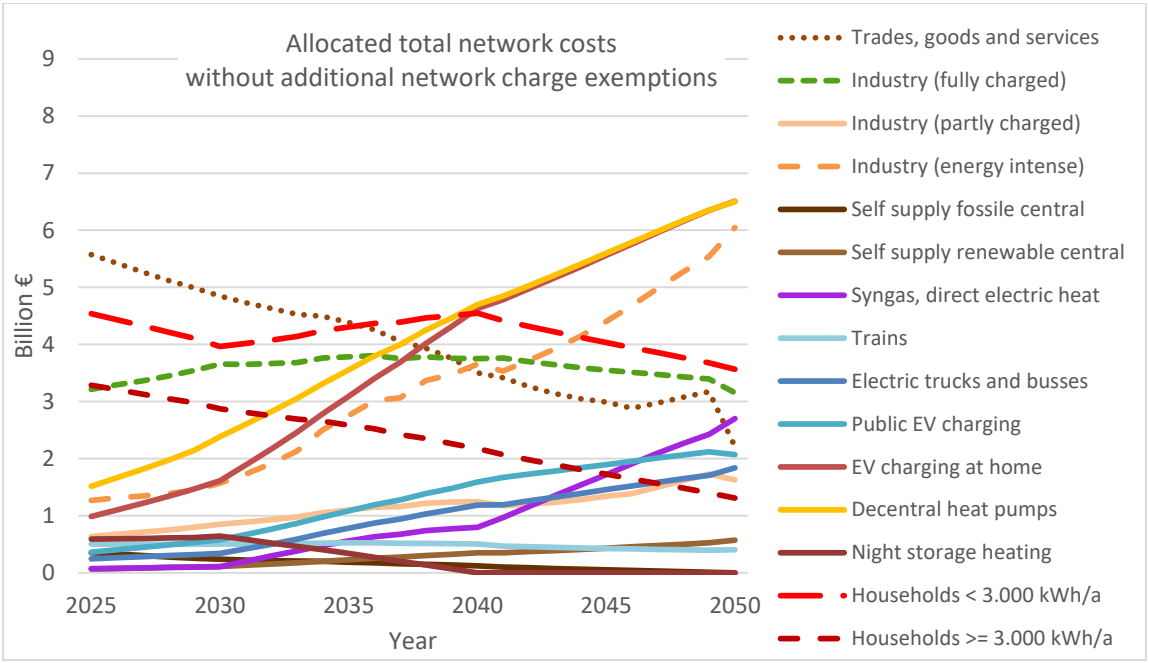

Fig. 11: Allocated total network costs without additional network charge exemptions, distributed across different types of consumption/consumer groups

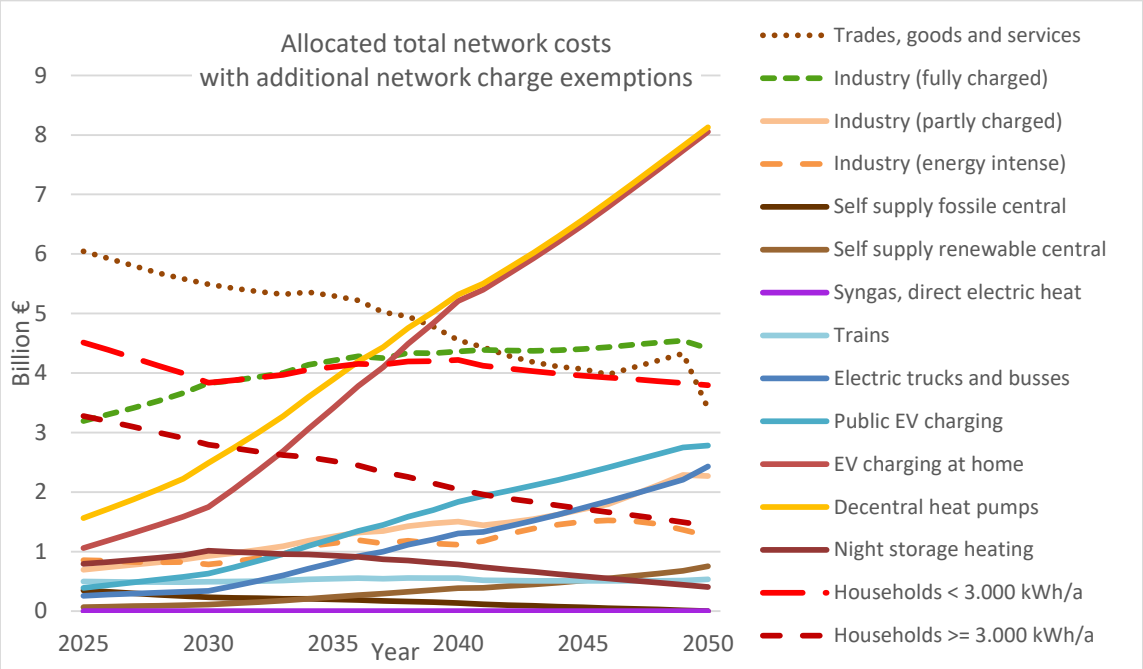

Fig. 12: Allocated total network costs with additional network charge exemptions, distributed across different types of consumption/consumer groups

Since the depiction of absolute costs does not take into account how much electricity is consumed by the various consumer groups, we use a second kind of plot, which shows the allocated grid costs relative to the total amount of energy consumed by the respective consumer groups. This is not to be confused with a volume-dependent network charge, as it includes all network costs allocated to a specific consumer group, regardless of how this contribution is made, which could be volume-specific tariffs, yearly payments, or peak load-dependent payments. According to our assumptions, the reduced network charge payments from exempt groups are uniformly distributed across all non-privileged consumers, such that the relative rise in network charges is the same for all non-privileged consumer groups.

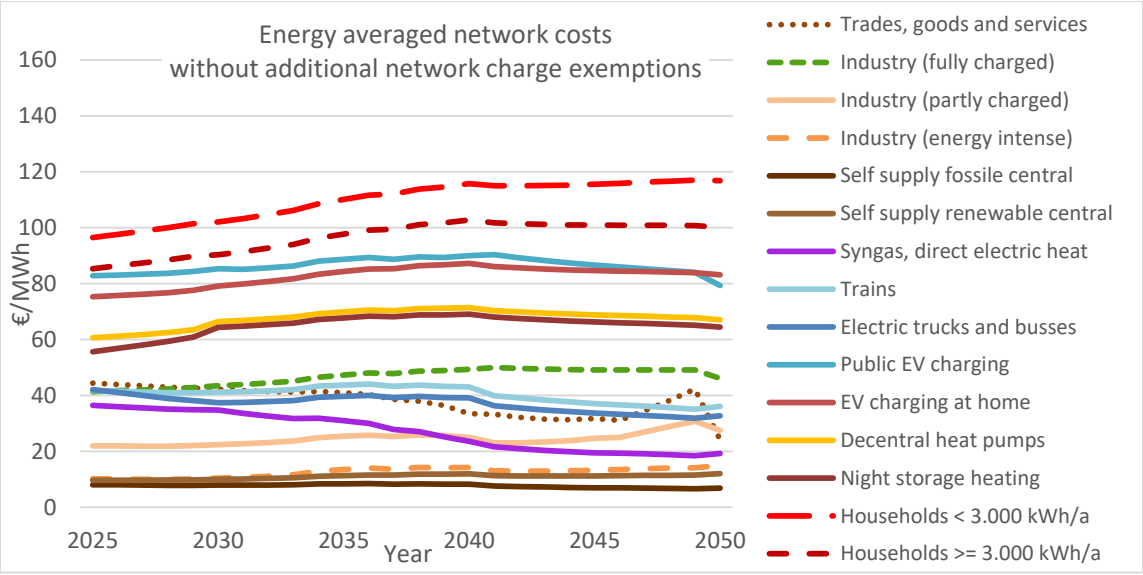

Fig. 13: Energy averaged network costs without additional network charge exemptions, distributed across different types of consumption/consumer groups

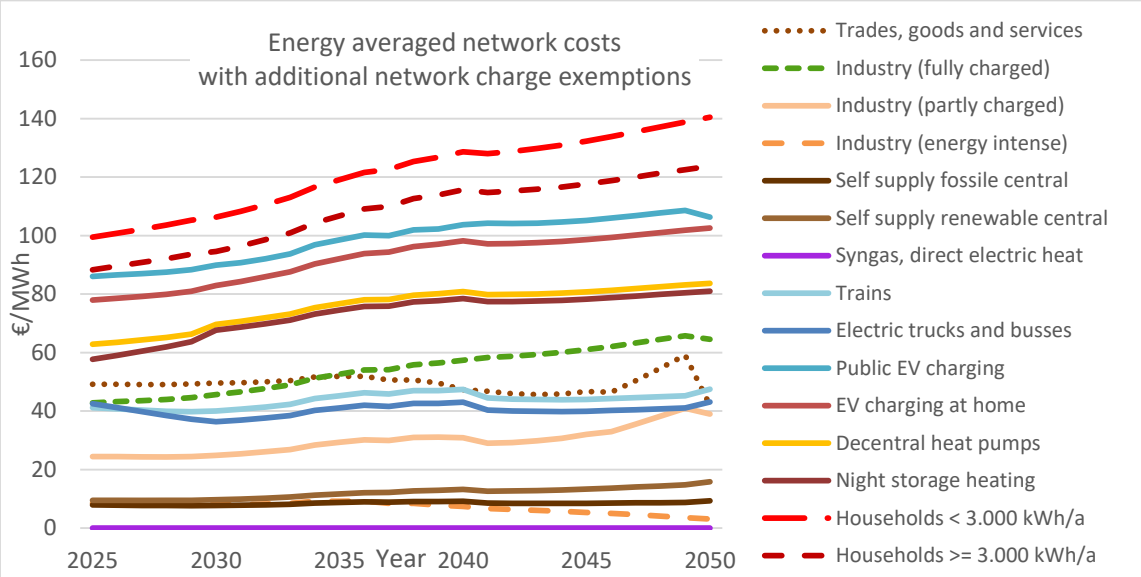

Fig. 14: Energy averaged network costs with additional network charge exemptions, distributed across different types of consumption/consumer groups

4. Conclusions and outlook

Electricity prices in wind and PV dominated power systems have seasonally different characteristics. In winter, weather fronts with a duration of one to two weeks determine wind generation, which in winter is the main source of power. Corresponding price fluctuations on this scale are clearly visible. In summer and to a smaller extent also in spring and fall, solar generation is prevalent and the daily PV generation pattern directly affects the electricity prices.

Electricity prices are relatively insensitive to different shares of PV self-supply systems among a constant amount of total installed PV electricity. As a tendency, the more PV self-supply systems there are, the less pronounced price extremes become. Average electricity prices tend to be marginally higher, and price volatility is slightly reduced. To sum up, PV self-supply systems have a tendency to improve PV system integration.

Higher shares of PV self-supply systems change the revenue situation of other market participants. For most market participants, the change is very slight, but for peak load units and battery storage, the change is more noticeable.

Network charge exemptions reallocate network costs to non-privileged electricity consumers. According to our assumptions, the reduced network charge payments from exempt groups are uniformly distributed across all non-privileged consumers, such that the relative rise in network charges is the same for all. In absolute terms, private households (household electricity, EV charging, heat pumps) make the largest contributions. The highest absolute network charge reductions are seen for energy intensive industries (who use power to heat applications) and synthetic gas production.

In this work, we restricted ourselves to the modelling of PV self-supply systems for the supply of private households. There are many more potential use cases, such as applications in industrial facilities or for trades, goods and services. In the latter two cases, the business cases are relatively straightforward, with one entity supplying itself. Additionally, more complex situations are conceivable, such as PV in combination with larger EV charging facilities or PV usage in city quarters for heat pumps, in order to supply several households with heat as well as electricity. These use cases will be addressed in future work.

5. Acknowledgments

The authors gratefully acknowledge financial support by the Federal Ministry of Economics and Climate Protection within the framework of the OwnPV-Outlook project (reference number 03EI1031A).

6. References

Böttger, D., Härtel, P., 2022. On Wholesale Electricity Prices and Market Values in a Carbon-Neutral Energy System. Energy Economics. 106, 105709. https://doi.org/10.1016/j.eneco.2021.105709

Böttger, D., Jentsch, M., Trost, T., Gerhardt, N., von Bonin, M. and Eschmann, J., 2018. Cost-Optimal Market Share of Electric Mobility Within the Energy System in a Decarbonisation Scenario. *Proceedings of the 15th International Conference on the European Energy Market (EEM)*. Lodz, 27-29 June. https://doi.org/10.1109/EEM.2018.8469846

Frischmuth, F., Härtel, P., 2022. Hydrogen sourcing strategies and cross-sectoral flexibility trade-offs in net-neutral energy scenarios for Europe. Energy. 238, Part B. 121598. https://doi.org/10.1016/j.energy.2021.121598

Härtel, P., Ghosh, D., 2020. Modelling heat pump systems in low-carbon energy systems with significant cross-sectoral integration. IEEE Transactions on Power Systems. https://doi.org/10.1109/TPWRS.2020.3023474

Härtel, P., Korpås, M., 2021. Demystifying market clearing and price setting effects in low-carbon energy systems. Energy Economics. 93. 105051. https://doi.org/10.1016/j.eneco.2020.105051

von Bonin, M., Dörre, E., Al-Khzouz, H., Braun, M., Zhou, X., 2022. Impact of Dynamic Electricity Tariff and Home PV System Incentives on Electric Vehicle Charging Behavior: Study on Potential Grid Implications and Economic Effects for Households. Energies. 15(3). 1079. https://doi.org/10.3390/en15031079

Electric Self-Production for LV Subscribers: Is It Better to Have Decentralized or Centralized PV Production?

Mariam Chouket[1], Essia Znouda[1] and Chiheb Bouden[1]

[1] National Engineering School of Tunis El Manar, Tunisia

Abstract

The Tunisian energy supply system is currently, being restructured to achieve 30% produced electricity from sustainable sources by the year 2030. The objective is to reach 3815 MW of renewable electrical power, with 1755 MW for wind power, 1510 MW for solar PV, 450 MW for CSP and 100 MW for biomass. Photovoltaic solar energy offers great national economic advantages. Grid-connected photovoltaic systems can be as decentralized or centralized production technology. Between decentralized and centralized PV production, the choice is a little difficult. In fact, with decentralized technology, the costs of transporting electricity and losses in transport circuits are eliminated. While for centralized production, the cost of installation is much lower due to the economy of scale. This study is solved using OSeMOSYS tool, which needs certain economic and technical data for each energy technology. Simulation results prove that centralized PV technology is more productive than decentralized one during certain years. Then, decentralized production begins to be more interesting where their cost would be equivalent to that of centralized PV. However, centralized PV technology can be more productive if there is an improvement in the quality of the transmission network.

Keywords: Photovoltaic Systems, decentralized, centralized, OSeMOSYS

1. Introduction

The Tunisian Solar Plan (TSP) is a national program aiming to reach the renewable energy development strategy targets (GIZ.de, 2022) (mrv.tn, 2022). The goal is to increase the total share of renewable energy in the electricity generation mix from 6% today to 30% by 2030, from wind power, solar PV, solar CSP and biomass and the rest of the electricity production coming from gas.

Photovoltaic solar energy offers an economically viable option to bridge the growing gap between supply and demand. According to the Global Atlas of the International Renewable Energy Agency (IRENA) (anme.tn, 2022), the annual production of electricity by solar photovoltaic systems in Tunisia can be between 1450 kWh / kWc in the northwest region and 1830 kWh / kWc in the far southeast.

Between decentralized and centralized PV production, the choice is a little difficult. In fact, with decentralized technology, the costs of transporting electricity and losses in transport circuits are eliminated. While for centralized production, the cost of installation is much lower due to the economy of scale. What are the production constraints that require each type of production for it to be promoted?

2. Methodology

This work consists of developing a comparative study between the two solar energy production technologies: centralized PV and decentralized PV in the Tunisian mix:

- Decentralized PV System: Any establishment, connected to the national electricity grid (STEG) can produce its own electricity from PV. This investment allows to consume the own electricity instantly, and thus save money on the next bills. Indeed, the surplus production is injected into the STEG network, which undertakes to subtract it from the consumption bill as part of a "net metering" billing contract.
- Centralized PV System: Thanks to the economies of scale afforded by a ground-based power plant, the cost is reduced compared to roof panels. Thus, photovoltaic solar power plants can be built on non-

© 2022. The Authors. Published by International Solar Energy Society
Selection and/or peer review under responsibility of Scientific Committee
doi:10.18086/eurosun.2022.18.04 Available at http://proceedings.ises.org

habitable areas, such as desert areas. This market can be attractive to households that are deprived of access to solar energy for several reasons, whether because they live in an apartment, their roof is not suitable or even for aesthetic reasons.

2.1. Introduction for the OSEMOSYS tool:

The Tunisian energy system is modeled using the Open Source Energy Modelling System (OSeMOSYS), which is a developed linear programming optimization model (Dhakouani, 2017) (Howells, 2011). Linear optimization (also known as LP linear programming) is a method of achieving the best result (such as the lowest cost) whose requirements are represented by linear relationships. In mathematical terms, OSeMOSYS is a framework for long-term modeling, linear and deterministic optimization.
OSeMOSYS calculates the energy mix that meets the demands for energy services each year and at each time step of the case studied, by minimizing the total discounted costs. It can cover all energy sectors or individually, including heat, electricity and transport, and has a user-defined spatial and temporal domain and scale. Energy demands can be met through a range of technologies schematized as a reference energy system (RES). Each technology present certain technical and economic characteristics and rely on a set of resources, defined by certain potentials and certain costs.
In addition, political scenarios may impose certain technical constraints, economic realities or environmental objectives.

2.2. Design of the reference energy system (RES):

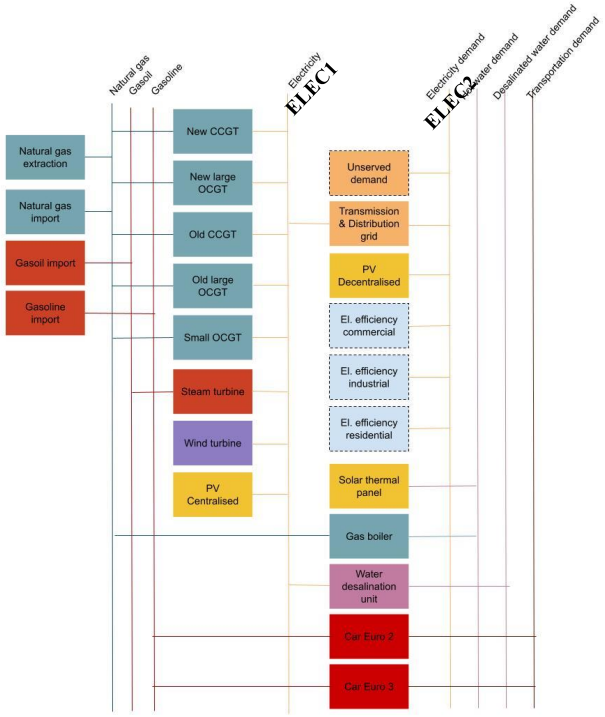

Fig. 1: The RES oft he Tunisian Energy Mix

The Reference Energy System (RES) is a simplified and aggregated graphical representation of the actual energy system to be analyzed.

The RES of the Tunisian energy mix is shown schematically in Fig1. Decentralized PV technology directly produces final electricity ELEC2, while centralized PV technology produces electricity for transmission ELEC1,

which is connected to the transmission and distribution technology to produce ELEC2.

2.3. OSeMOSYS Modeling and Data collection:

OSeMOSYS tool needs economic and technical data for each energy technology. The model adopted is originally developed by the GIZ called 'TENEM', on which modifications have been introduced according to the studied scenarios. The different data used for this modeling are collected from STEG, GIZ, ANME and the Ministry of Energy and Mines.

- Electricity demand: Fig 2 represent the electricity demand curve. The estimated electricity needs, are certainly multiplied by more than twice between 2020 and 2046.

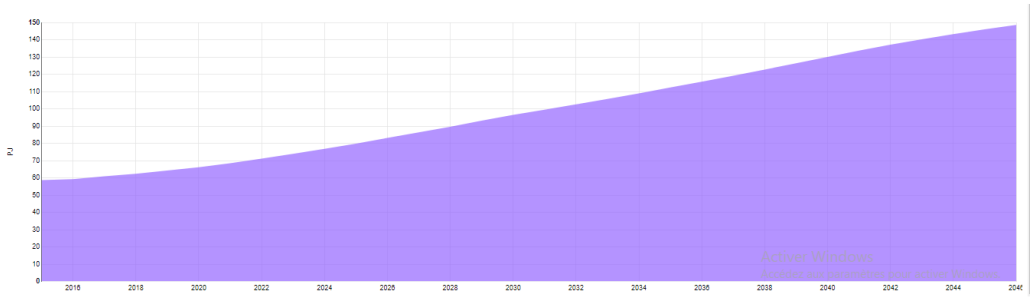

Fig.2: Estimated electricity demand in PJ

- Investment Costs: The investment costs of centralized and decentralized PV technologies, go through increasingly significant falls until the horizon of 2035 from which these costs stabilize at a fixed value. Due to the economy of scale, the investment cost of centralized technology is reduced compared to decentralized technology by 10%. The following graph summarizes the evolution of these costs over the years

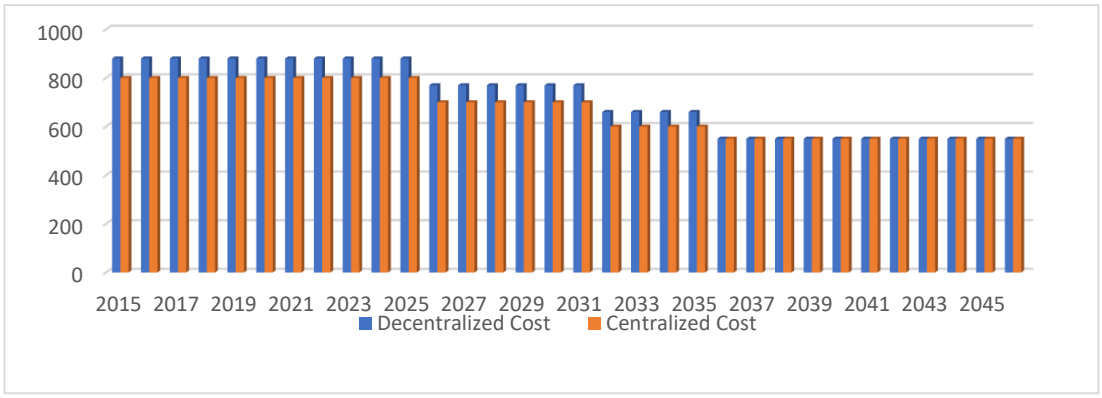

Fig. 3: Centralized and decentralized PV technology investment costs in $

- Capacity Factor: For each PV technologies: centralized and decentralized, capacity factors are given by the following table according to each time slice.

Tab. 1: Capacity Factor of PV technologies				
		Interme-diate	Summer	Winter
Workday	Day	0.4	0.51	0.29
	Night	0	0	0
weekend	Day	0.4	0.51	0.29
	Night	0	0	0

- Transmission losses: Between 2015 and 2046, transmission line losses decrease from 18% to 12% gradually.

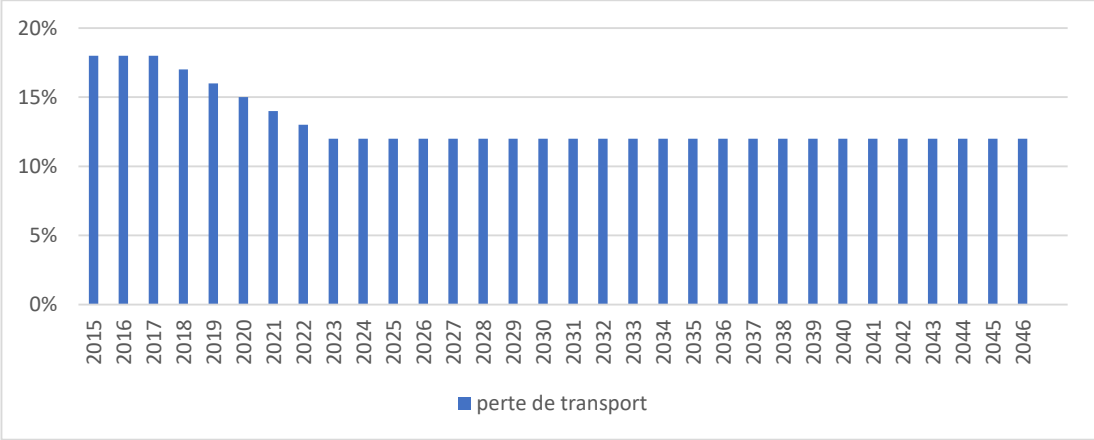

Fig. 4: Transmission line losses.

2.4. Scenarios

The model is tested under two different production scenarios:
Scenarios 1: Reference TENEM model: according to the original TENEM model, the centralized PV technology starts production in 2015 before the decentralized one. This model is tested respectively for:

- Limited solar energy production where annual installed capacity is restricted at most to 300MW.
- Unlimited solar energy production

Each case is studied with and without electricity transmission cost, and with a reduction in transmission losses.

Scenarios 2: Modified TENEM model: represents a case where decentralized and centralized technologies come into production at the same time, and with actualized installed capacity, according to recent statistics from STEG and ANME. In addition, this model is tested respectively for an annual production of limited and unlimited solar energy, taking into account the price of transport of electricity and by acting on transmission losses.

3. Results and discussion

To assess the benefit of integrating renewable energies into the Tunisian mix, the levelized cost of energy (LCOE) is calculated for three initial cases:

- Case1: Energy mix based on conventional energy only.
- Case2: Energy mix based on conventional energy and energy efficiency.
- Case3: Energy mix based on conventional energy, energy efficiency and renewable energy.

The general form of LCOE is written as follows:

$$LCOE = \frac{\sum_{t}^{n} \left(\frac{Operational\cos t}{(1+r)^t} + \frac{Invetment\cos t}{(1+r)^t} \right)}{\sum_{t}^{n} \frac{Productionannual}{(1+r)^t}}$$

Where:
n: years number of the energy project.
t: counter over the years.
r: attenuation rate;

$$r = \frac{i-\gamma}{1+\gamma}$$

i: interest rate = 6.25%.
γ: inflation rate = 5.3%

Tab. 2: Calculated LCOE

Case	1	2	3
LCOE (DT/KWh)	0.222	0.196	0.165

The results in Table 2 confirm that renewable energies as well as energy efficiency reduce the macroeconomic costs of energy production from 0.222DT / KWh to 0.165DT / KWh.

3.1. Scenarios 1: Reference TENEM Model:

According to the original TENEM model given by the GIZ, the centralized PV technology starts production in 2015 before the decentralized one. This model is tested respectively for:

- Limited solar energy production where annual installed capacity is restricted at most to 300MW, to achieve the TSP.
- Unlimited solar energy production

Each case is studied with and without electricity transmission cost, and with a reduction in transmission losses.

3.1.1: Limited Solar Energy Production:

- Case1: Without transmission cost:

Fig5.1 and Fig5.2 represents the evolution of the total capacity installed by restricted centralized and decentralized PV technologies without taking into account the transmission costs. The total installed capacity from centralized PV technology, is much larger than that from decentralized PV until 2041. Then, the profiles are reversed, and decentralized technology become dominant because its cost become more reducer over the years.

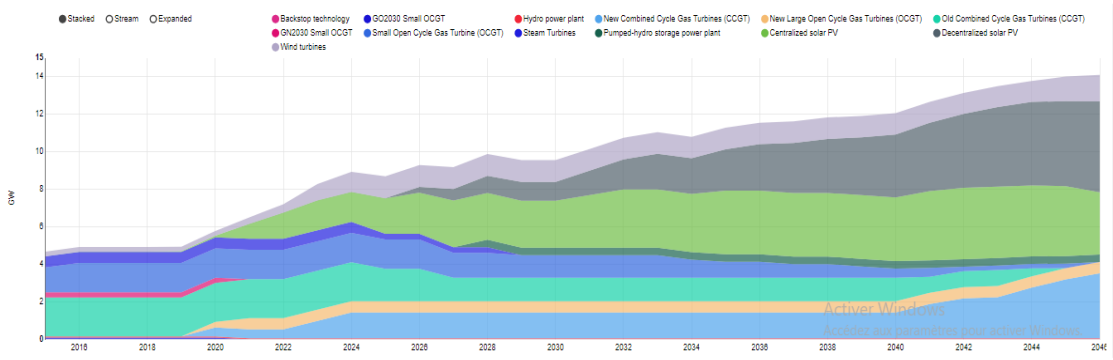

Fig. 5.1: Total installed capacity for all technologies without transmission cost

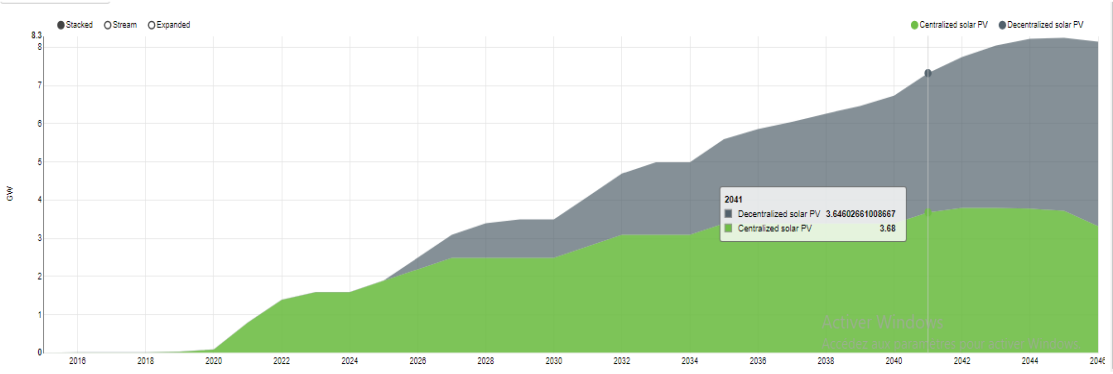

Fig. 5.2: Total installed capacity for centralized and decentralized PV technologies without transmission cost

- Case2: With transmission cost:

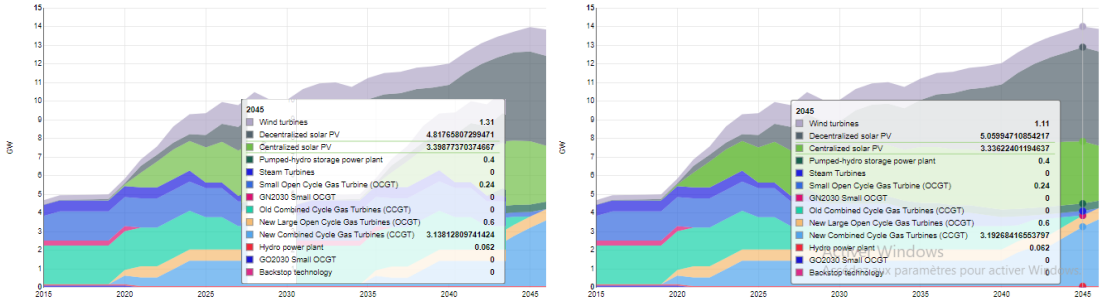

Fig. 6: Total installed capacity for centralized and decentralized PV technologies with transmission cost

The KWh transmission rate is set at 0.025DT. This tariff is introduced in the "variable cost" parameter of the transmission and distribution technology. As a result, the capacity produced by technologies that use transport has decreased such as centralized PV and wind turbines. As an example, in Fig6, the total power produced by centralized PV technology for the year 2045 drops almost by 60MW in return, the power produced by decentralized PV technology increases by 200MW.

Following these two previous cases, we can only deduce that decentralized PV technology have a tendency to be favored over centralized one, regardless of with or without transmission cost. So, if we want to increase the interest of centralized PV technology, all that remains is to reduce transmission losses.

- Case3: With transmission cost and reduced transmission losses:

Fig7, represents the total installed capacity, where the transmission cost is included and the transmission losses are reduced from 18% in Fig7.1 to 11% in Fig7.2.
Therefore, a simple improvement in the quality of the transmission network increases centralized PV production and decreases decentralized one.
This scenario recommends the Tunisian state to invest more in the quality of the STEG network and this can be achieved using the smart grid policy which help to reduce the economic losses of electricity transmission caused by fraudsters.

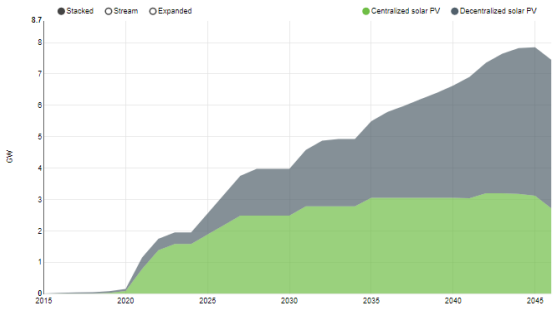

Fig. 7.1: Transmission losses 18%

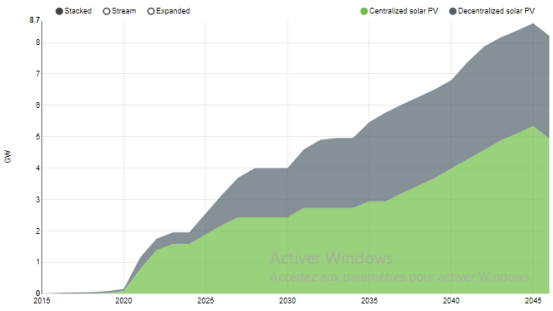

Fig. 7.2: Transmission losses 11%

3.1.2: Illimited solar production:

By eliminating the restriction on solar technologies, only the decentralized technology participates in the production, Fig8. This is convincing since this technology does not pass throw the technology of transport. So, whatever the case tested, without or with transport cost, decentralized PV technology is always favored. Centralized PV technology may be lucky if transmission losses are smaller.

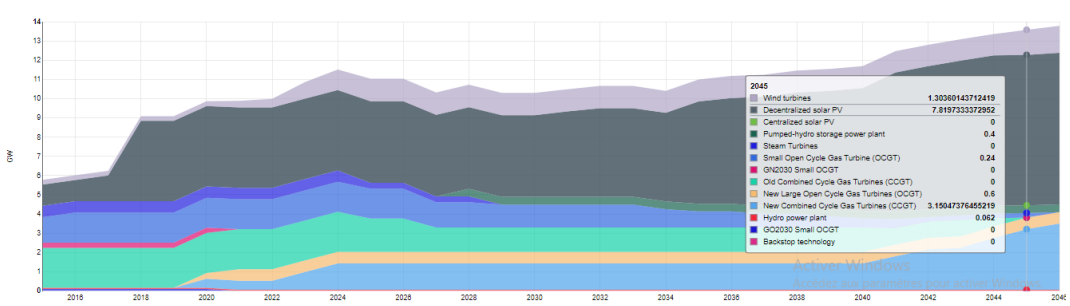

Fig. 8.1: Total installed capacity for all technologies, without restriction

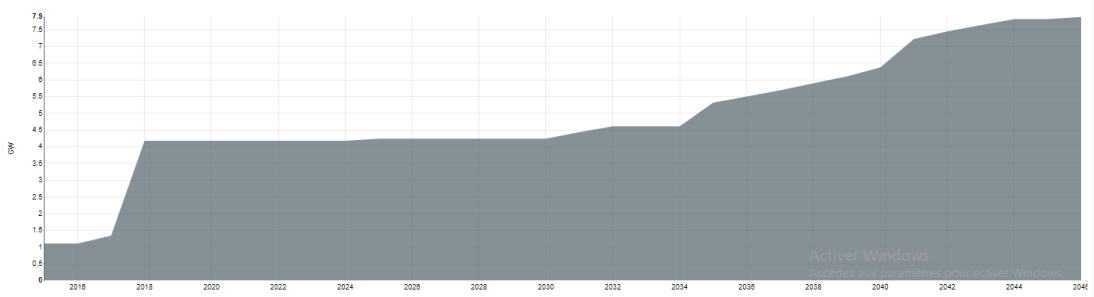

Fig. 8.2: Total installed capacity for centralized and decentralized technologies, without restriction

3.2. Scenarios 2: Modified TENEM model:

According to actualized data from STEG and ANME, decentralized PV technology starts production from 2015, with centralized technology, by introducing at least 10MW every year until now. This scenario is tested too, under 3 cases:

- Case1: Without transport cost:

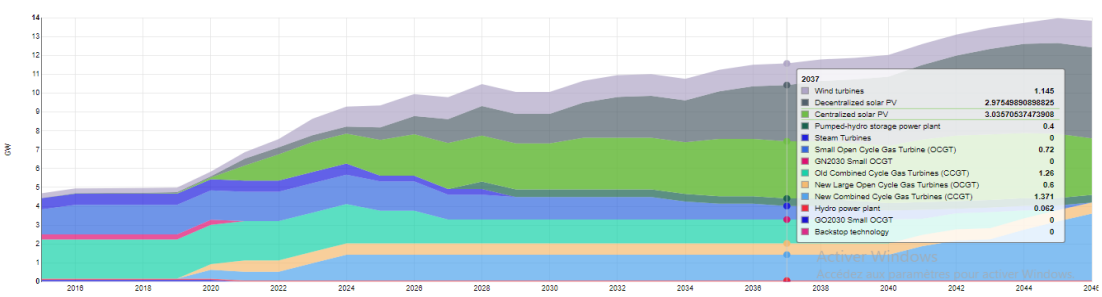

Fig. 9.1: Total installed capacity for all technologies without transmission cost

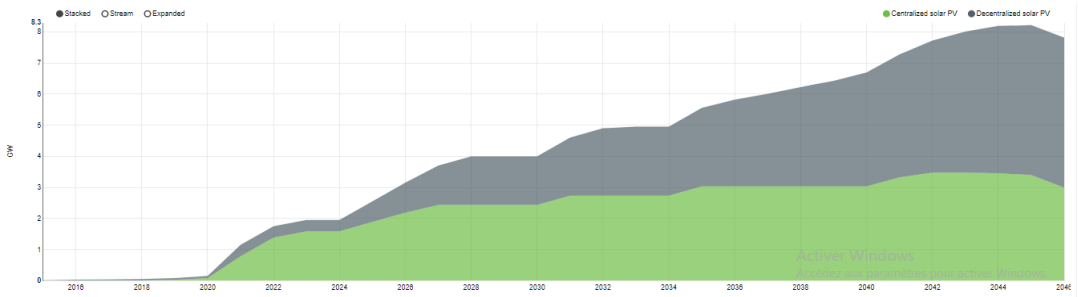

Fig. 9.2: Total installed capacity for centralized and decentralized PV technologies without transmission cost

Similar to the first scenarios, centralized technology is more productive but this time until it reaches 2037. Then, decentralized solar technology begins to be more favored because its cost become more reducer over the years.

- Case2: with transmission cost:

The addition of the transport cost, in Fig10, can only further decrease the chance of centralized PV technology production. Indeed, decentralized PV technology exceeds centralized PV technology in production from 2036.

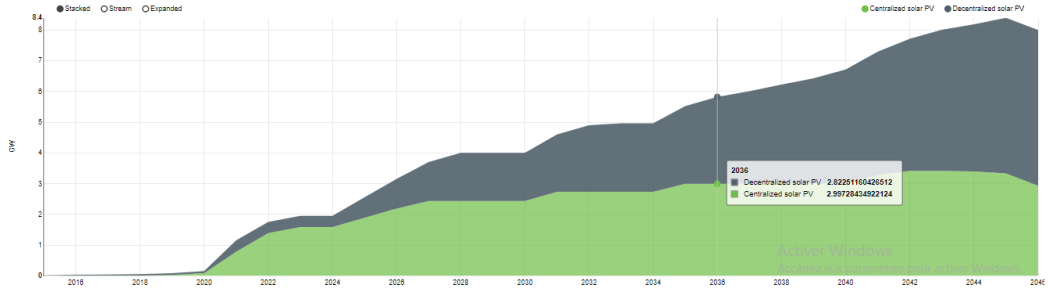

Fig. 10: Total installed capacity for centralized and decentralized PV technologies with transmission cost

Case3: With transmission cost and reduced transmission losses.

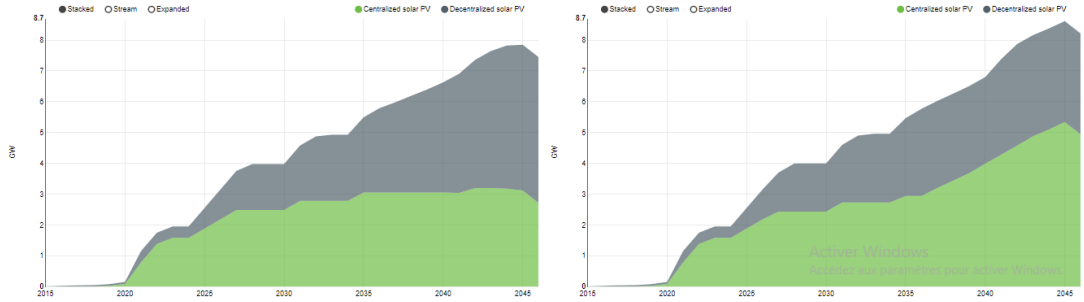

Fig. 11.1: Transmission losses 18%

Fig. 11.2: Transmission losses 11%

Fig11, represents the total installed capacity for the second scenario, where the transmission cost is included and the transmission losses are reduced from 18% to 11% .
Therefore, a simple improvement in the quality of the transmission network increases centralized PV production and decreases decentralized one.

3.3. Discussion:

To compare between those two scenarios, a calculation LCOE is developed in the following table:

Tab. 3: Calculated LCOE for different scenarios

	Limited solar generation + transmission losses 18%-12%		**Unlimited solar generation + transmission losses 18%-12%**	
	without transport cost	with transport cost	without transport cost	with transport cost
LCOE(DT/KWh): Scenarios 1	0.1654	0.1658	0.15158	0.15187
LCOE(DT/KWh): Scenarios 2	0.1635	0.1639	0.15158	0.15187

The lowest calculated LCOE (Levelized Cost of Electricity) values, presented in Tab. 3, are that relating to the unlimited solar production scenarios, which promotes the integration of renewable energy in the Tunisian mix. Respecting this optimistic scenario, the Tunisian state can increase the share of PV technologies in national energy production from 6% in 2022 to 37% in 2030 which exceeds the objective of the Tunisian solar plan.
Also, in terms of Greenhouse Gaz (GHG) emission, this scenario can contribute to reduce this emission from 6.35 Kton in 2022 to 3.054 Kton in 2030, that means a GHG emission reduction that can reach 48% between 2022 and 2030. These results, despite being optimistic, but they are a bit further from the new European Commission plans which aims to raise the greenhouse gas (GHG) emissions reduction target from 40% towards 55% by 2030 (Jager-Waldau, 2022).

4. Conclusion

Generally, because of its lower investment cost, the energy produced by centralized PV technology is more important than that produced by decentralized for the short run. Then, decentralized production begins to be more interesting where their cost would be equivalent to that of centralized PV, also by the transmission losses, which reduce the productivity of centralized PV technology. For another scenario, centralized PV technology can be favored if there is an improvement in the quality of the transmission network such that transmission losses are reduced to 11%. Adding up the cost of transport for all scenarios can only decrease centralized PV production and increase LCOE. The lowest calculated LCOE values are that relating to the unrestricted production scenario, which promotes the integration of renewable energy in the Tunisian mix and contribute to reduce the GHG emission.

5. References

anme.tn. (2022). Récupéré sur anme.tn: https://www.anme.tn/?q=fr/content/solaire-photovoltaique
Dhakouani, A. (2017). Long-term Optimisation Model of the Tunisian Power System. energy, 550-562.
GIZ.de. (2022). Récupéré sur GIZ.de: https://www.giz.de/en/worldwide/61321.html
Howells, M. (2011). OSeMOSYS: The Open Source Energy Modeling System an introduction to its ethos, structure and development. Energy Policy, 5850-5870.
Jager-Waldau, A. (2022). How photovoltaics can contribute to GHG emission reductions of 55% in the EU by 2030. Renewable and Sustainable Energy Reviews, 109836.
mrv.tn. (2022). Récupéré sur mrv.tn: http://www.mrv.tn/nama-du-plan-solaire-tunisien/

Definitions for Climate Neutrality and their Relevance for the Assessment of Solar Energy based Heating Systems

Harald Drück[1,2], Dominik Bestenlehner[1,2]

[1] University of Stuttgart
Institute for Building Energetics, Thermotechnology and Energy Storage (IGTE), Stuttgart (Germany)

[2] Solar- und Wärmetechnik Stuttgart / Solar and Heat Technology Stuttgart (SWT)
Research- and Testing Centre for Solar Thermal Systems (TZS), Stuttgart (Germany)

Abstract

This contribution presents three approaches for the definition of climate neutrality. These three approaches are based on different ways for balancing $CO_{2\,eq}$ emissions. Only with the third approach, called real climate neutrality, it will be possible to achieve climate neutrality on global level. The effort for achieving climate neutrality is varying significantly depending on the chosen approach. The calculation of climate neutrality is exemplarily performed according to the three approaches for a single-family house in Germany with different concepts for heat and power supply. The concept combining photovoltaic and solar thermal has by far the lowest $CO_{2\,eq}$ emissions and only moderate additional costs.

Keywords: Solar thermal, photovoltaic, CO_2 emissions, climate neutrality, heat pump

1. Introduction

The term "climate neutral" is today firmly established in our linguistic usage. However, what does climate neutral really mean?

In this contribution three approaches for achieving climate neutrality are described in detail and are additionally compared and assessed on the basis of ecological and economic aspects using as example different concepts for the heat and power supply of a single-family house in Germany.

In addition, it is shown that the use of solar thermal energy in combination with long-term energy storage is a key technology for achieving real climate neutrality.

2. Definitions of climate neutrality

A generally accepted definition of the term does not yet exist. In many publications and laws such as /1/, /2/ and /3/ "climate neutrality" is understood as net greenhouse gas neutrality, but without this being precisely defined. This leads to the fact that climate neutrality - depending on the individual motivation - is defined very differently. However, what all serious approaches have in common is, that they consider the emissions of climate-damaging gases such as carbon dioxide (CO_2), methane (CH_4) or nitrous oxide (N_2O). Since all gases have a different global warming potential (GWP), their individual GWP is related to the one of CO_2. The mass of greenhouse gases emitted during the production of a product, the provision of a service or the generation of a kilowatt-hour of electricity are therefore expressed in CO_2 equivalents, e.g. 400 g $CO_{2\,eq}$ per kilowatt-hour of electricity.

For a complete life cycle assessment of energy systems, the $CO_{2\,eq}$ emissions associated with their production, operation and maintenance, as well as disposal have to be taken into account.

The three most relevant approaches for defining "climate neutrality" are described and compared in the following. For reasons of simplicity and comprehensibility, only the $CO_{2\,eq}$ emissions resulting from the operation are considered here.

© 2022. The Authors. Published by International Solar Energy Society
Selection and/or peer review under responsibility of Scientific Committee
doi:10.18086/eurosun.2022.18.05 Available at http://proceedings.ises.org

2.1. Virtual climate neutrality

In this approach, the $CO_{2\ eq}$ emissions caused are compensated by certificates or other compensatory measures such as tree planting (see Fig. 1). There is no avoidance of additional $CO_{2\ eq}$ emissions and no $CO_{2\ eq}$ emissions are permanently extracted from the atmosphere. Objectively speaking, therefore, this approach does not contribute to climate protection.

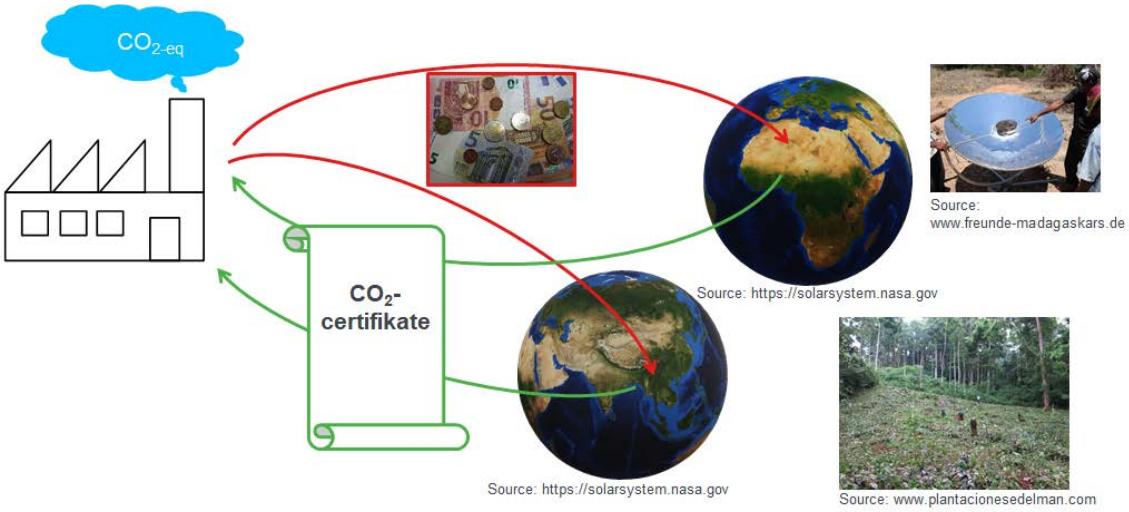

Fig. 1: Virtual climate neutrality

2.2. Balance sheet climate neutrality

Here, compensation for the $CO_{2\ eq}$ emissions caused also is carried out by a compensation that must take place within a certain period of time, usually one year.
If, for example, a building with a PV system draws electricity from the grid in the winter period and feeds electricity into the grid in the summer period, it is possible, depending on the amount of electricity and the size of the specific $CO_{2\ eq}$ emissions of the grid electricity and the PV electricity, that the building compensates for as many $CO_{2\ eq}$ emissions by feeding PV electricity into the grid as are associated with drawing electricity from the grid. Looking at a balance over the year, the $CO_{2\ eq}$ emissions related to the building are also zero or can even become negative. This means that a certain contribution to climate protection is made (see Fig. 2).

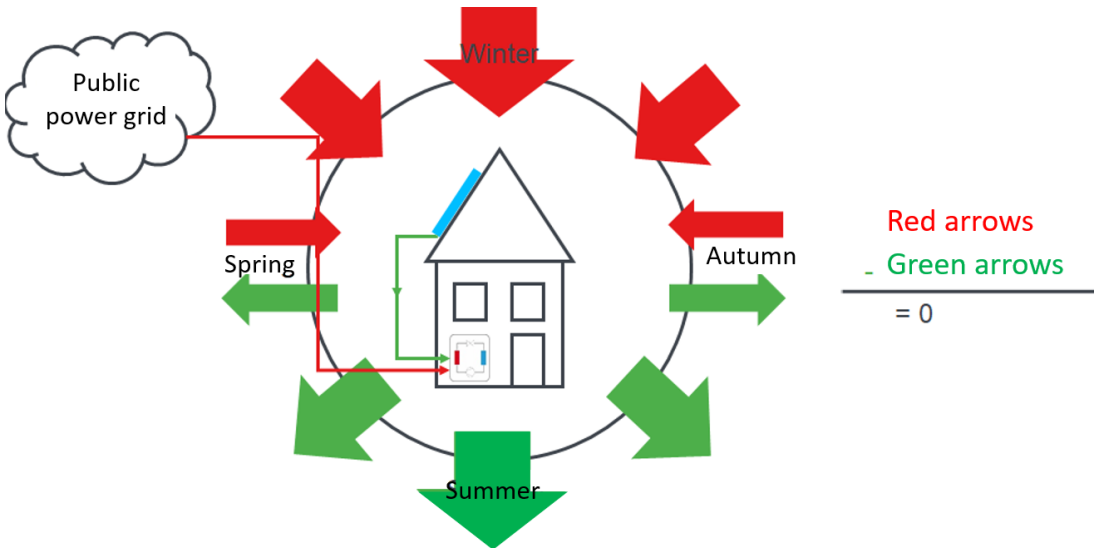

Fig. 2: Balance sheet climate neutrality

2.3. Real climate neutrality

In the case of real or genuine climate neutrality, the energy demand is continuously covered by the energy sources available locally, i.e. within the system boundary under consideration. For practical consideration, a balance period of 15 min has been established here, in which the energy balance must be balanced (see Fig. 3). If fluctuating energy sources, such as solar radiation energy, are used for energy generation, such a system can only be implemented in combination with energy storage devices.

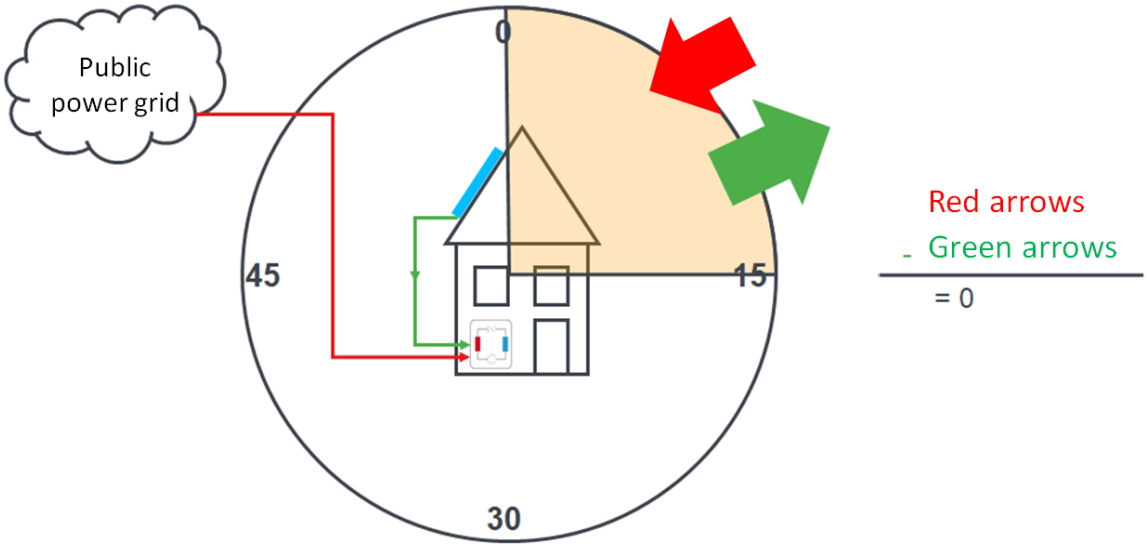

Fig. 3: Real climate neutrality

2.4. Discussion of the approaches

The first approach, referred to as "**virtual**", is characterized by the fact that it is currently very cost-effective. This is because a large number of climate-friendly measures are being carried out anyway, such as the reforestation of forests with a view to future timber harvesting or the generation of electricity from hydropower using existing hydropower plants. However, the virtual approach does neither make a substantial contribution to climate protection, nor can it be implemented globally on an unlimited scale, as there would then be a lack of corresponding compensation projects.

The **balance sheet** approach does not lead to actual climate neutrality either, as it also produces de facto substantial $CO_{2\,eq}$ emissions that contribute to global warming.

The approach referred to as "**real**" theoretically allows for achieving a true climate neutrality.

However, if solar radiation is used as the primary energy source, the realization of this approach is challenging, especially in our climate, from an economic and environmental point of view, since very large storage capacities are needed to fully cover the energy demand in winter. With regard to the heat supply of buildings, the seasonal storage of thermal energy can be reasonably implemented. However, seasonal storage of electrical energy is not practical with the technologies available today.

But complete real climate neutrality is not necessary either, since nature can compensate for a certain amount of anthropogenic, i.e. man-made, $CO_{2\,eq}$ emissions. This amount is about 2 tons of $CO_{2\,eq}$ per year and person. In Germany, however, we are still far away from this target, with 8 - 9 tons of $CO_{2\,eq}$ per person per year at present. As we do not only cause $CO_{2\,eq}$ emissions with our energy supply, but also through our nutrition and consumption, the $CO_{2\,eq}$ budget ultimately available for the energy supply of our residential buildings is less than one ton per year and person.

It is therefore obvious that for the energy supply of building, only concepts that focus very strongly towards real climate neutrality are viable in the long term. Such concepts can, for example, be based to a large extend on the usage of solar radiation for the energy supply of buildings. Since the development of systems and technologies for buildings predominately supplied with solar energy is of global interest, the IGTE of the University of Stuttgart (Germany) together with AEE INTEC from Gleisdorf (Austria) in the "Solar Heating and Cooling Programme"

(SHC) of the International Energy Agency (IEA) established the working group or Task 66 on the topic "Solar Energy Buildings - Integrated Solar Energy Supply Concepts for Climate Neutral Buildings and Neighborhoods for the City of the Future". Task 66 is led by Dr. Harald Drück from IGTE of the University of Stuttgart as Task Manager and has a duration from July 1st, 2021 to June 30th, 2024.
Further information: https://task66.iea-shc.org/

3. Comparison and assessment of the three approaches for climate neutrality

Using the example of a single-family house with different concepts for heat and power supply, this chapter compares and assesses the three approaches for defining climate neutrality under ecological and economic aspects.

3.1. The single-family house

It is assumed that the single-family house has a floor space of 145 m² and is located in the city of Würzburg, Germany The household electricity demand is 3,500 kWh/a and the heat demand is 11,000 kWh/a. This results from a heat demand of 9,000 kWh/a for space heating and 2,000 kWh/a for domestic hot water.

3.2. Total energy supply concepts

The following system concepts are considered for the total energy supply, i.e. the complete coverage of the heat and household electricity demand of the single-family house.

System "HP + Grid"
Provision of the entire heat demand for domestic hot water and space heating with an air-to-water heat pump with an annual performance factor of 4.0. The electricity required by the heat pump as well as the household electricity is completely drawn from the grid.

System "HP + PV"
Provision of the entire heat demand for domestic hot water and space heating with an air-to-water heat pump with an annual performance factor of 4.0.
In addition, the building has a PV system with an output of 9 kW_P. The electricity generated by the PV system is used primarily to the meet household electricity needs. If there is still a PV-electric power surplus, the heat pump is supplied with PV-electricity. Any other surpluses that may exist are fed into the power grid. This chosen prioritization for the use of the PV electricity is based on the fact that household electricity purchased from the grid at 0.35 €/kWh is more expensive than electricity to operate the heat pump at 0.25 €/kWh. The building has no electrical energy storage.
The difference between the total electricity demand for heat pump and household and the electricity supplied by the PV system is taken from the grid.

System "ST + Grid"
From a solar thermal system with 55 m² collector area and 4 m³ storage volume, 65 % of the heat demand for domestic hot water and space heating is covered. The remaining 35 % are provided by biomass combustion. The solar fraction of 65 % was chosen in particular because the planned amendment of the German Building Energy Act will stipulate that a minimum fraction of 65 % of the building's heat demand has to be covered by renewable energies /4/.
The electricity demand to cover the household electricity and the auxiliary electricity to operate the solar thermal system of 44 kWh/a is completely taken from the grid.

System "ST + PV"
The same combination of thermal solar system and biomass system is assumed as in the ST+grid variant.
In addition, the building is equipped with a PV system with a capacity of 3 kW_P to partially cover the household and auxiliary electricity demand. The building does not have an electrical energy storage system. The remaining electricity demand for household and auxiliary power is taken from the grid.

Additional assumptions

In addition to the systems as well as energy and financial parameters mentioned above, the following was assumed:

- Both the large PV system with 9 kW_P and the small one with 3 kW_P cover 30 % of the household and auxiliary power demand of the corresponding building simultaneously or at least in the time interval of 15 min used as a basis for the investigations carried out here.
- The share of self-used PV electricity for the operation of the heat pump is 30 %.
- The specific $CO_{2\,eq}$ emissions for electricity are 0.399 kg/kWh /5/.
- The same specific $CO_{2\,eq}$ emissions are applied for electricity taken from the grid and fed into the grid.
- No seasonal variance in specific $CO_{2\,eq}$ emissions.
- Specific $CO_{2\,eq}$ emissions for biomass are 0.029 kg/kWh /5/.
- Investment cost solar thermal system 31,500 € and useful lifetime 25 years.
- Investment costs for outdoor air heat pump 20,000 €, useful lifetime 15 years and annual performance factor 4.0.
- Investment costs for PV system 1,590 €/kW_P and useful lifetime 25 years.
- Feed-in tariff for partial self-consumption of PV electricity: 0.08 €/kWh
- Feed-in tariff in case of complete feed-in of the PV electricity: 0.12 €/kWh according to the plans in the "Easter Package" of the German government /6/
- Investment costs biomass heat source 7,000 € and useful lifetime 20 years
- specific costs biomass (fuel and maintenance): 0,09 €/kWh
- All costs and prices indicated are inclusive of value added tax of currently 19%.

3.3. Results - Power balances

Table 1 below shows the annual amounts of electricity used to meet the demand for household electricity (HH) and for the heat pump (HP) as well as auxiliary electricity, where needed.

Tab. 1: Annual electricity demand of the four overall energy supply concepts considered

	HP+Grid	**HP+PV**	**ST+Grid**	**ST+PV**
HH and auxiliary power	3,500 kWh/a	3,500 kWh/a	3,544 kWh/a	3,544 kWh/a
HP power	2,750 kWh/a	2,750 kWh/a	0 kWh/a	0 kWh/a
Total amount power	6,250 kWh/a	6,250 kWh/a	3,544 kWh/a	3,544 kWh/a
Electricity PV system	---	9,000 kWh/a	---	3,000 kWh/a
Power from grid at annual balance	6,250 kWh/a	0 kWh/a	3,544 kWh/a	544 kWh/a
Power fed into grid at annual balance	---	2,750 kWh/a	---	0 kWh/a
Power from grid at 15 min. balance	6,250 kWh/a	4,375 kWh/a	3,544 kWh/a	2,481 kWh/a
Power fed into grid at 15 min. balance	---	7,125 kWh/a	---	1,937 kWh/a

The household electricity amounts to 3,500 kWh/a for all variants considered, apart from the variants with solar thermal. Here, an additional electricity demand of 44 kWh/a was assumed as auxiliary energy for the operation of the solar circuit pump and the control system. For the variants with a heat pump to cover the heat demand, the assumed annual performance factor of 4.0 results in an electricity demand for the heat pump of 2,750 kWh/a. This means that the total electricity demand is 2,750 kWh/a. Thus, the total electricity demand for the variants with heat pump amounts to 6,250 kWh/a and for the variants with solar thermal to 3,544 kWh/a.

For the photovoltaic systems, a specific yield of 1,000 kWh/kWp is applied, resulting in a yield of 9,000 kWh/a for the variant with a PV system with 9 kWp and a yield of 3,000 kWh/a for the variant with the 3 kWp system.

Both variants without a PV system have to cover their entire electricity demand from the public grid, while with a balancing over one year the variants with a PV system do not need to draw any electricity from the grid (variant WP+PV), or significantly reduce the grid purchase to 544 kWh/a (variant ST+PV). However, if the balance is performed over a period of 15 min, the WP+PV variant draws 4,375 kWh/a and the ST+PV variant 2,481 kWh/a of electricity from the public grid. The reason why the electricity quantities taken from the grid are significantly larger for a balancing period of 15 min than for a balancing period of one year is the fact, that only at relatively few points in time there exists a simultaneous supply of electricity from the PV system and at least an equal demand for electricity for the heat pump or the household.

In principle the same relationships apply when PV electricity is fed into the public grid. When balancing over 15 min, variant WP+PV feeds in 7,125 kWh and variant ST+PV still 1,937 kWh/a.

3.4. Results - $CO_{2\,eq}$ balances

Using the three different approaches for defining climate neutrality described in Chapter 2 and the electricity quantities given in Table 1, the $CO_{2\,eq}$ emissions listed in Table 2 were calculated. For this purpose, it was assumed that each kilowatt-hour of electricity withdrawn from the grid causes $CO_{2\,eq}$ emissions of 399 g. Similarly, for each kilowatt-hour of electricity fed into the grid, avoided $CO_{2\,eq}$ emissions of 399 g were assumed.

For the virtual approach, it was assumed that, on the one hand, non-certified green electricity was purchased at an additional price of €0.01/kWh and, on the other hand, in the case of the variants with a PV system, the electricity generated was fed completely into the grid. The decisive factor for the assumption is the relatively high feed-in tariff of 0.12 €/kWh planned with the "Easter Package" /6/, which, however, only applies in the case of complete feed-in of the generated PV electricity, i.e. partial self-consumption is not permitted in this case.

Tab. 2: $CO_{2\,eq}$ emissions for the three approaches to defining climate neutrality

	HP + Grid	**HP + PV**	**ST + Grid**	**ST + PV**
Virtual	0 kg/a	-3,590 kg/a	110 kg/a	-1,086 kg/a
Balance sheet	2,493 kg/a	-1,097 kg/a	1,524 kg/a	327 kg/a
Real	2,493 kg/a	1,745 kg/a	1,524 kg/a	1,100 kg/a

In the figures shown in Table 2, positive values represent $CO_{2\,eq}$ emissions generated and thus de facto released into the atmosphere. Negative values are calculated for avoided $CO_{2\,eq}$ emissions, whereby it should be noted that the corresponding negative $CO_{2\,eq}$ emissions have of course not been or will not be extracted from the atmosphere.

It can be seen from Table 2 that the **virtual approach** arithmetically achieves the lowest $CO_{2\,eq}$ emissions or the highest credits. This is due to the fact that, on the one hand, the purchased electricity is green electricity and thus theoretically without $CO_{2\,eq}$ emissions, and, on the other hand, the generated PV electricity is completely fed into the grid and credited with 399 g $CO_{2\,eq}$/kWh.

In the **balance sheet approach**, the balance sheet is drawn up over a period of one year. Here, each kilowatt-hour of electricity purchased and fed into the grid is credited with the specific $CO_{2\,eq}$ emissions of 399 g/kWh. If the PV system generates more electricity over the year than is needed in the household and to operate the heat pump, this can even result in negative $CO_{2\,eq}$ emissions, as is the case here with -1,097 kg/a.

In the **real approach**, the electricity taken from the grid and fed in by the PV system is balanced over a time interval of 15 min. For the variants without a PV system, there are therefore no differences between the real and the balance sheet approach, since the calculation methodology for the purchase of grid electricity does not differ.

In the real approach, it is assumed that surplus PV electricity cannot be fed into the grid, or can only be fed into the grid to a negligible extent, since all other PV systems installed in the vicinity also feed into the grid at the same time. In this case, the electricity in the public grid is already completely "green" and no credits for avoided $CO_{2\,eq}$ emission can be credited. This assumption is especially justified if the corresponding technological approach, in this case PV+WP, is implemented on a large scale for the heat supply of a large number of buildings and a global climate neutrality is aimed at.

With the real approach for climate neutrality, there are significant differences in the variants with PV system compared to the virtual and balance sheet approach.

In particular, for the PV+WP concept, the transition from the balance sheet approach to the real definition of climate neutrality leads to an increase in $CO_{2\,eq}$ emissions of 2,842 kg/a, i.e., from -1,097 kg/a to 1,745 kg/a.

This effect is also observed for the PV+ST concept. However, it is much lower with an increase of the $CO_{2\,eq}$ emissions by 773 kg/a, i.e. from 327 kg/a to 1,100 kg/a.

With the real approach, the comparison between the two variants without PV system shows the great advantage of the solar thermal system with regard to $CO_{2\,eq}$ emissions, since these can be reduced by almost 40 % to 1,524 kg $CO_{2\,eq}$ emissions per year. However, the same also applies to the comparison of the variants with PV system. Here, the $CO_{2\,eq}$ emissions are significantly lower due to the coverage of the own electricity demand with the yields from the PV systems, whereby here, too, the variant with solar thermal has again 38 % lower $CO_{2\,eq}$ emissions than the variant without solar thermal.

3.5. Results - additional costs

This section lists the additional costs incurred for a "climate-neutral" overall energy supply for the single-family house under consideration. The "HP+grid" system was selected as the basis for this. In order to achieve virtual climate neutrality with this system, only the purchase of green electricity at an additional price of 0.01 €/kWh is required. The additional costs in this case are 6,250 kWh/a x 0.01 €/kWh = 62.50 €/a.

For the other overall energy supply concepts considered, the additional costs result primarily from the additional investment costs for the PV system or the higher costs for the large thermal solar system and the biomass system compared to a heat pump. Financial credits arise from feeding surplus PV electricity into the grid or, in the case of the virtual approach, from full feed-in of the generated PV electricity. Table 3 shows the additional costs incurred to achieve the respective $CO_{2\,eq}$ emissions.

Tab. 3: Additional costs for the four overall energy supply concepts depending on the approaches used to define climate neutrality

	HP+Grid	**HP+PV**	**ST+Grid**	**ST+PV**
Virtual	62.50 €/a	-302 €/a	659 €/a	537 €/a
Balance sheet	62.50 €/a	69 €/a	659 €/a	601 €/a
Real	62.50 €/a	294 €/a	659 €/a	601 €/a

When considering the overall energy supply concepts without PV system, it becomes clear that it is irrelevant for the calculation of additional costs which approach or definition of climate neutrality is used. It is therefore obvious to prefer the approach that arithmetically leads to the lowest $CO_{2\,eq}$ emissions, i.e. the virtual approach. However, the fact that this approach also contains a certain absurdity from an economic point of view is shown by the consideration of supply concepts with PV systems. Here, the virtual approach assumes full feed-in of the generated PV electricity in order to benefit from both, the high feed-in tariff of 0.12 €/kWh and to achieve low values for the $CO_{2\,eq}$ emissions. However, in return, all the electricity for the household and the heat pump must of course be purchased from the grid at a price of 0.25 €/kWh and 0.35 €/kWh, respectively.

Further, Table 3 shows that supply concepts with solar thermal are significantly more robust with respect to the choice of approach for defining climate neutrality. There are hardly any differences between the approaches in terms of additional costs. In contrast, the additional costs for the PV+WP concept change by a maximum of 596 €/a depending on the approach chosen to define climate neutrality, from -302 €/a for the virtual approach to 294 €/a for the real approach.

However, if only the additional costs of the real approaches are compared, the supply concept WP+grid with 62.50 €/a of additional costs shows that by the partial substitution of the grid electricity by a PV system in the concept WP+PV with only about 230 € additional annual costs (294 €/a- 62.50 €/a), the $CO_{2\,eq}$ emissions can be reduced from 2,493 kg/a to 1,745 kg/a by around 750 kg/a. If then the heat pump is replaced by a large solar thermal system in combination with a biomass heating to supply concept ST+PV, the additional costs amount to 601 €/a. This means that with another approx. 300 €/a of additional costs (601 €/a - 294 €/a) the $CO_{2\,eq}$ emissions can be reduced additionally by approx. 650 kg/a from 1,745 kg/a to 1,100 kg/a or another third.

Particularly noteworthy is the fact that when a supply concept based on solar thermal and biomass is supplemented with a small PV system, both the additional costs can be reduced by approx. 40 €/a and the $CO_{2\,eq}$ emissions can also be reduced by approx. 400 kg/a.

3.6. Discussion of the results

The studies that have been realized show that with a large solar thermal system for the heat supply and a moderately dimensioned PV system for partial coverage of the household electricity demand, by far the lowest $CO_{2\,eq}$. emissions are caused. This means that only with such energy supply concepts real climate neutrality can be achieved to a large extend. The resulting additional costs are moderate and amount to about 300 €/a compared to the PV+WP concept, and lead to an additional avoidance of about 650 kg $CO_{2\,eq}$ emissions per year.

The results shown here using the example of a single-family house can in principle also be transferred to multi-family houses as well as districts and complete cities. However, for the solar thermal heat supply of several buildings, solar local heating systems in combination with seasonal heat storage should be used instead of decentralized systems, as this technology is more efficient and cost-effective.

In order to effectively limit global warming and thus mitigate climate change, it is crucial to significantly reduce $CO_{2\,eq}$ emissions. Therefore, in the future, only technologies that enable real climate neutrality should be used. In the area of heat supply, these are primarily biomass and seasonal electricity or energy storage, e.g. using green hydrogen, in addition to solar thermal energy.

Biomass is cost-effective, but its potential is relatively limited and its use is associated with odor and particulate emissions. It should therefore preferably be used only on a small scale, e.g. as a supplementary heat source for thermal solar systems with high solar fractions.

Green hydrogen as seasonal energy storage medium or technology respectively, represents a technology that enables real climate neutrality in the area of heat supply in the same way as solar thermal in combination with seasonal heat storage - but with much higher costs and a significantly greater technological effort.

4. Summary

Using the example of the heat and power supply of a single-family house, it was shown for four different overall energy supply concepts that the specific definitions of climate neutrality are essential for the amount of $CO_{2\ eq}$ emissions calculated for an operation period of one year. But in fact, the actual $CO_{2\ eq}$ emissions are of course independent from the approach of defining climate neutrality and are only determined by the overall energy supply concept.

The approach chosen to define climate neutrality has a significant impact on the calculated $CO_{2\ eq}$ emissions, especially for the PV+WP concept. For concepts with large solar thermal systems to cover the heat demand, the influence of the chosen approach on the calculated $CO_{2\ eq}$ emissions is small.

The additional costs for achieving climate neutrality are primarily influenced by the definition of climate neutrality in the PV+WP concept. For the other overall energy supply concepts considered, the influence of the definition of climate neutrality on the additional costs is negligible.

Only on the basis of real climate neutrality (definition see Section 2.3) global climate neutrality is achievable. It is therefore important that this definition is used exclusively in the future.

This should also be in the interest of the solar thermal sector, as only by using the approach for real climate neutrality is it possible to make an objective ecological comparison of different overall energy supply concepts.

5. Acknowledgments

The leadership of the IEA SHC Task 66 "Solar Energy Buildings" by Dr. Harald Drück as well as the substantial work of the IGTE in Task 66 are funded in connection with the research project Sol4City "Development of integrated solar supply concepts for climate-neutral buildings of the 'City of the Future'" by the German Federal Ministry of Economics and Climate Protection (BMWK) via the Project Management Agency Jülich (PTJ) on the basis of a resolution of the German Bundestag under the funding code 03ETW019A.
The authors gratefully acknowledge the support and take the full responsibility for the content of this publication.

6. References

/1/ IPCC glossary: https://www.ipcc.ch/sr15/chapter/glossary

/2/ Bundes-Klimaschutzgesetz 2021:
https://www.bundesregierung.de/breg-de/themen/klimaschutz/klimaschutzgesetz-2021-1913672

/3/ Klimaschutzgesetz Baden-Württemberg 2021:
https://um.baden-wuerttemberg.de/de/klima/klimaschutz-in-baden-wuerttemberg/klimaschutzgesetz/

/4/ Koalitionsvertrag 2021 – Mehr Fortschritt wagen; Koalitionsvertrag zwischen SPD, Bündnis 90 / Die Grünen und FDP
https://www.bundesregierung.de/breg-de/service/gesetzesvorhaben/koalitionsvertrag-2021-1990800
Website accessed on 17.04.2022

/5/ ProBas – Prozessorientierte Basisdaten für Umweltmanagementsystem
https://www.probas.umweltbundesamt.de/php/index.php
Website accessed on 15.04.2022

/6/ Erste Details des EEG-„Osterpakets“ bekannt – Viele Verbesserung für Photovoltaik geplant
https://www.pv-magazine.de/2022/02/28/erste-details-des-eeg-osterpakets-bekannt-viele-verbesserung-fuer-photovoltaik-geplant/
Website accessed on 17.04.2022

Efficiency of Electricity Self-Production for Medium Voltage Subscribers in Tunisia

Khawla ELMalleh*, Mariam Chouket*, Essia Znouda*, Chiheb Bouden*

* University of Tunis El Manar, National Engineering School of Tunis, Tunisia.

Abstract

This paper discusses and studies the integration of photovoltaic plant connected to Medium Voltage (MV) network in the Tunisian energy mix and its competitiveness compared to other technologies, especially since the sale of MV electricity has grown to reach 34.17 % of all electricity sold by STEG (Société Tunisienne d'Electricité et de Gaz). It turned out to be a very competitive technology compared to mainly the centralized and decentralized photovoltaic plants with a Levelized Cost of Energy LCOE less than 0.160 TND/kWh.

Keywords: Tunisia Electricity Mix, Solar PV in medium voltage, OSeMOSYS.

1. Introduction

Energy transition in Tunisia is generally addressed as a technological and economic issue. Tunisian policy on energy is dominated by the national utility for electricity and gas named STEG. Since the independence, it has held a monopoly and enjoys forceful historical legitimacy for its achievements. Nevertheless, beginning the 2000s, national energy self-sufficiency was challenged (United Nations. 2017) so that the Tunisian government pushed for renewable energies. STEG was wary of these renewable technologies and has slowed its implementation. The Tunisian revolution has completely shaken the power's balance in the country, allowing for multi-level criticisms of STEG and for the making of new alliances for renewable energy projects. With the failed try of the Tunisian government to adapt regulatory and institutional frameworks to guarantee energy independence due to the continued uncertainty and oscillation of fossil fuels prices, the government was found under increasing pressure to create a long-term strategy towards energy self-sufficiency or in other words energy independence. Energy system models might be a tool for the decision makers in the country to draw an optimal long-term pathway for energy independence 5 (M. Howells et al. 2011), (OpenEnergy. July 2017), (OpenEnergy. October 2017) and (Energy Modelling. 2018). Which match the continuous increase in the demands, the availability of the Tunisian resources and the variability of prices.

In 2016, Tunisia adopted an energy strategy which aims to guarantee the security of supply of the country and ensure access to energy at an affordable price for the Tunisian economy. Tunisian energy policy aims to reduce primary energy consumption by 30% in 2030 (ANME. 2016) compared to the baseline scenario, while increasing the share of renewable energies in the Tunisian energy mix. So, in order not to miss the energy transition in Tunisia, we really have to think about some incentives that push MV subscribers to be self-producers, especially since the sale of MV electricity has grown to reach 6 956 GWh in 2019, which represents 34.17 % of all electricity sold by STEG as shown in figure 1.

© 2022. The Authors. Published by International Solar Energy Society
Selection and/or peer review under responsibility of Scientific Committee
doi:10.18086/eurosun.2022.18.06 Available at http://proceedings.ises.org



Fig. 1: Evolution of medium voltage electricity sales (STEG. 2015).

For the planning of national energy systems, different applications of energy systems modeling exist (Horizon. 2020). Decision makers are actually using some models to draw up long-term energy strategies like EnergyPLAN (D. Connolly et al. 2011), EU PRIMES (P. Capros *e*t al. 2016) and OSeMOSYS model. These applications share the characteristic of being bottom-up and optimization models. So that, they indicate the cost optimal pathways to decision makers to achieve given energy targets. Contrariwise, they differ by the type of modelling framework. While TIMES (R. Loulou. 2005) and PRIMES are partial equilibrium, MESSAGE (L. Schrattenholzer. 2016), and OSeMOSYS (Optimus community. 2017), (M. Welsch. 2015), (F. Gardumi. 2016) and (M. Welsch et al. 2012) are dynamic linear. And only OSeMOSYS is fully open source. The appropriate modelling framework is chosen based on the kind of insights the country model is intended to provide.

In order to help the decision makers with the elaboration of long-term strategies towards energy independence, we are going to study and discuss, in this paper, the integration of MV self-production in the Tunisian energy mix. So, we are going to identify whether this technology is a competitive one compared to mainly the centralized and decentralized photovoltaic installations or not.

2. Methodology

The modelling tool chosen for running this analysis is the Open-Source energy Modelling System – OSeMOSYS (M. Howells et al. 2011) and (F. Gardumi et al. 2021).

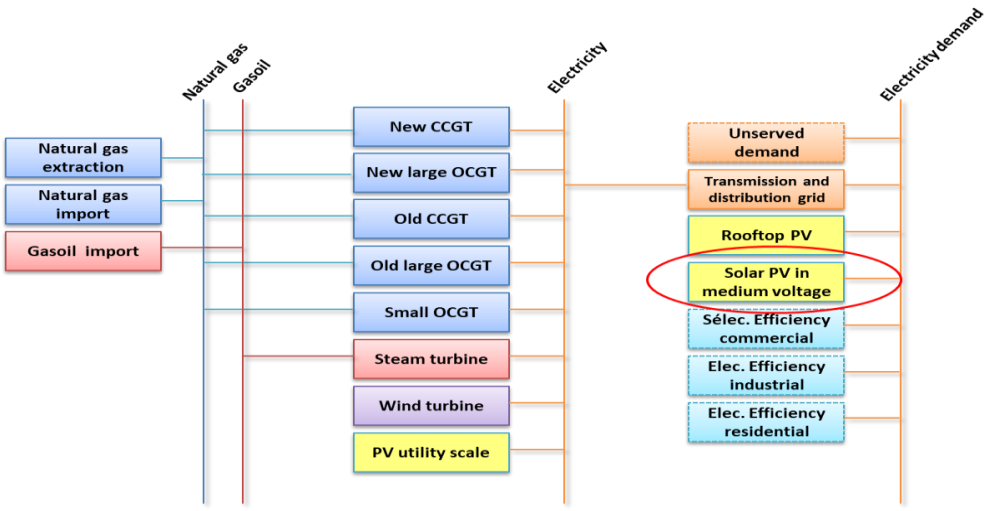

Fig. 2: Reference Energy System

The diagram represented in Figure 2 describes what in energy systems modelling is called a 'Reference Energy System' i.e. a simplified engineering scheme of the object of analysis. For the modelling, we started from a basic model called TENEM developed by the GIZ (The Deutsche Gesellschaft für Internationale Zusammenarbeit GmbH) and we added a new technology "Solar PV in medium voltage" to study its competitiveness compared to other technologies that generate electricity. The simulated model includes a number of supply chains connecting imported and domestic energy sources (both fossil and renewable) to the national electricity demand through aggregated conversion processes (e.g. extraction and import resources, conversion of primary sources to electricity, Transmission & Distribution network). As options for electricity supply from fossil fuels, all current gas power plants (open cycle gas turbines and both combined cycles) and the committed ones are represented separately. Energy efficiency options for the residential, commercial and industrial sectors are represented separately. They are considered as virtual technologies 'absorbing' part of the electricity demand. Each of the options is given specific user-defined techno-economic characteristics, used by the modelling tool to choose the future least-cost electricity supply mix. In this study we will focus on the efficiency of integrating the new technology "Solar PV in medium voltage" in the Tunisian energy mix.

3. Assumptions and Scenarios:

The sale of MV electricity is in the order of 6,956 GWh in 2019 (almost 25 PJ). To cover this demand, an installed capacity of 4.1 GWp is needed (given that each kWp produces 1700 kWh / year). Based on this data, we have identified 3 scenarios to consider:

- Scenario 1: slow progression in the power to be installed: that is to say, we will install each year a capacity equal to 0.041 GWp to achieve in 2045 a total capacity equal to 1.025 GWp allowing the satisfaction of 25% of electricity needs for MV subscribers in other words the satisfaction of 8.75% of electricity demand in Tunisia (since the MV electricity represents 35% of all electricity demand in Tunisia).
- Scenario 2: rapid increase in the capacity to be installed until reaching in 2045 the satisfaction of 50% of the electricity needs for MV subscribers. This represents 17.5% of electricity demand in Tunisia.
- Scenario 3: the max capacity investment parameter in OSeMOSYS software (expressed in GWp) is kept unlimited in order to see the economic efficiency of this new technology and its participation in the optimal energy mix in Tunisia.

For PV installations, we consider a new technology "Solar PV in medium voltage" which differs from the others by the cost of transport and the capital cost. In fact, for this technology we consider that the PV installations connected to the MV network are located near the consumption points so that the cost of transport is not considered like the case for the centralized installations. In addition, the capital cost considered is lower than the decentralized installations.

4. Results

It should be mentioned here that for all the scenarios, we kept the min capacity investment equal to zero. So, if the technology is not profitable and efficient, its participation in the Tunisian energy mix will be equal to zero.

Comparison of the first and second scenarios:

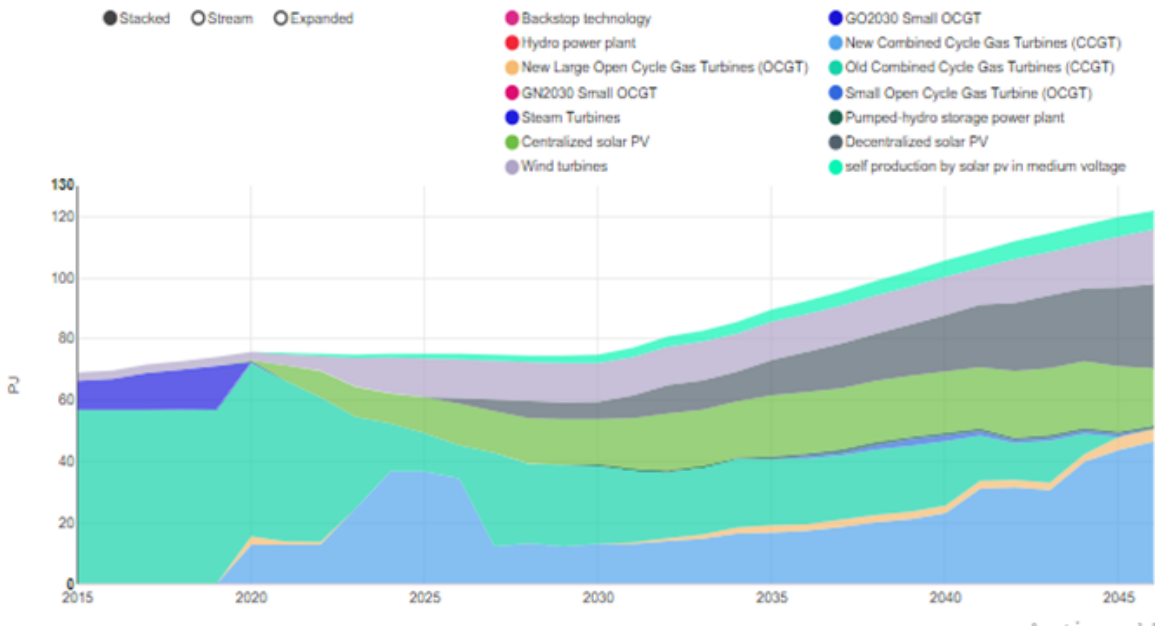

Fig. 3: Simulation of the first scenario of the Tunisian Electricity Mix (slow progression in the power to be installed)

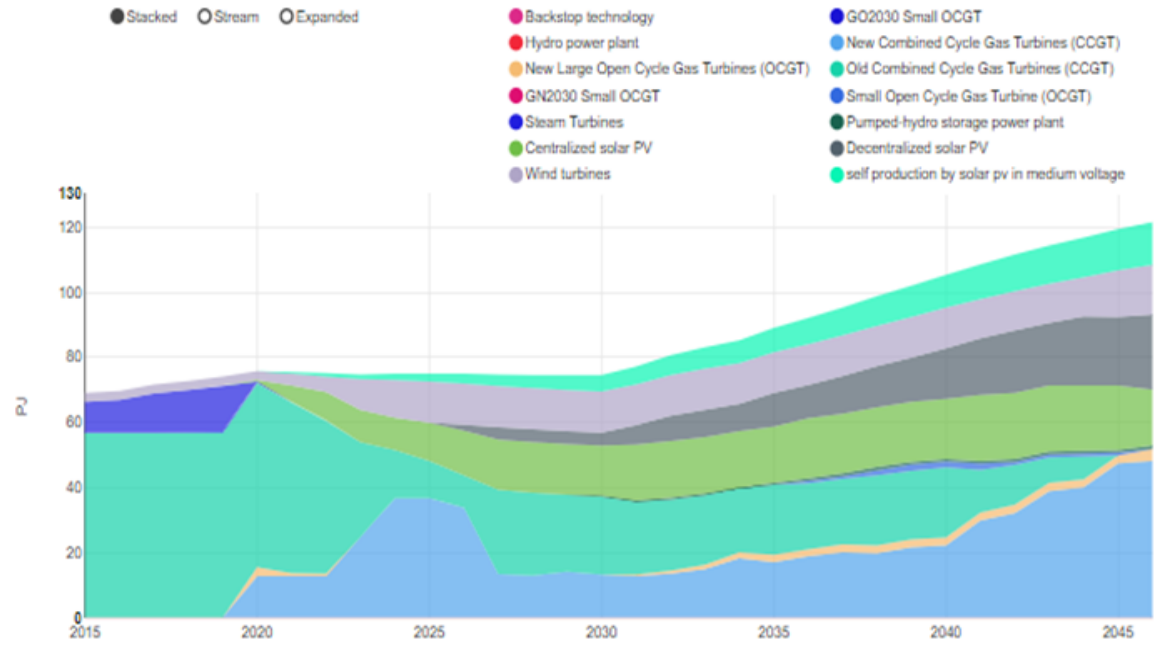

Fig. 4: Simulation of the second scenario of the Tunisian Electricity Mix (rapid increase in the capacity to be installed).

The simulation results show the significant participation of electricity produced from photovoltaic plants connected to the medium voltage grid in the totality of the final electricity produced despite the fact that the production of electricity from this technology has been limited for the first and second scenarios. In fact, for the first scenario, we fixed the max capacity investment for the new technology proposed so that we achieve, in 2045, 25% of the electricity demand for MV subscribers which is equivalent to 8.75% of the total final

electricity demand. Likewise, for the second scenario, we acted on the max capacity investment to achieve 50% of MV electricity needs in 2045.

Comparison of the second and third scenarios :

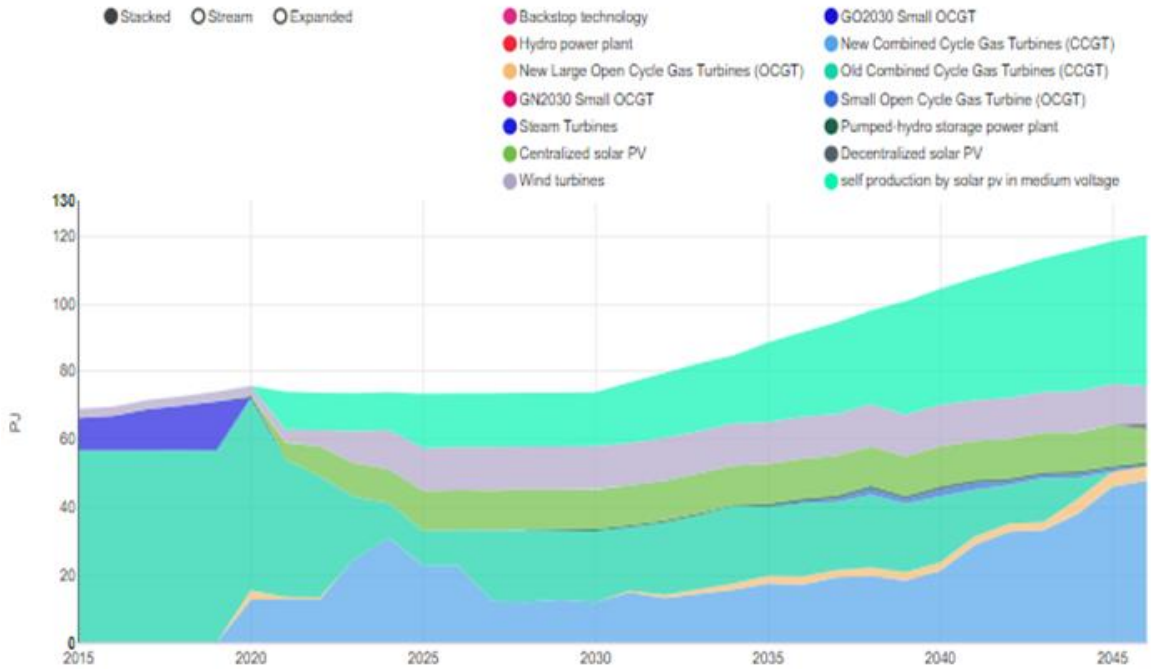

Fig. 5: Simulation of the third scenario of the Tunisian Electricity Mix (max capacity investment is kept illimited).

For the first and second scenarios, the max capacity investment was limited and in the simulation results we obtain every time the max of electricity production from the new proposed technology so we decided to maintain the max capacity investment for the third scenario unlimited to see what would be its participation in the Tunisian energy mix. The simulation results show that the new technology introduced is very competitive compared to other technologies especially compared to the decentralized solar PV technology which has practically disappeared and the centralized solar PV technology which has decreased in a very remarkable way. And this result is confirmed by the calculation of the LCOE. In fact, the LCOE for the first scenario is equal to 0.1618 TND/kWh versus 0.165 TND/ kWh for the basic scenario which did not include the new technology. The LCOE relative to the second scenario is equal to 0.1616 TND/kWh and the lowest value of LCOE is 0.1592 TND/kWh and it is relative to the third scenario.

Impact of the scenarios on LCOE:

In our study, the levelized cost of electricity and not energy was calculated by first taking the net present value of the total cost of the technologies. This number is then divided by the total electricity generation over its lifetime like it is shown in the equation.

$$\mathrm{LCOE} = \frac{\sum_t^n \left(\frac{operation\ cost}{(1+r)^t} + \frac{investment\ cost}{(1+r)^t}\right)}{\sum_t^n \frac{Production\ annual}{(1+r)^t}} \qquad (eq.\ 1)$$

Where n: number of years

t: counter

r: attenuation rate such as $r = \frac{i-\gamma}{1+\gamma}$=0.009

i: interest rate =6,25% .

γ: inflation rate =5.3% .

The calculation of the LCOEs of the different scenarios gave the following result:

Table 4: Impact of scenarios on LCOE

	Reference case: RES without the new technology	Scenario 1:	Scenario 2:	Scenario 3 :
LCOE (DT/kWh)	0,165	0,1618	0,1616	0,1592

Starting from the data obtained from the simulation results, LCOE was calculated for the reference case before adding the new technology and for each scenario after insertion the new technology. The results shown in Table 4 affirm that the more we invest in solar PV in medium voltage technology the more the cost of electricity decreases. This clearly shows the profitability of this technology.

Table 5: Gain in the subsidy on the cost of kWh

	Scenario 1:	Scenario 2:	Scenario 3 :
Gain of STEG in subsidy (in Million dinars)	173,9	347,8	1133,33

Assuming that the kWh is subsidized by 0.1 TND, we have therefore calculated the gain of STEG from this subsidy. And the result is shown in table 5.
For example, for the third scenario, we will have production by 2045 equal to 40.8 PJ = 11333.33 GWh. So, subsidy will be equal to 1133.33 million dinars in 2045.
Electricity consumption of MV subscribers represents 34% of total electricity. If they turn into self-producers 34% of the needs during peak hours will be met.

5. Conclusion

In this article, we studied the effect of the integration of photovoltaic systems connected to the medium voltage network in the Tunisian energy mix. It turned out to be a very competitive technology compared to other technologies especially since the lowest LCOE calculated is equal to 0.1592 TND/kWh and it is relative to the third scenario in which we did not limit the max capacity investment.So, in order not to miss the energy transition in Tunisia, we really have to think about some incentives that push MV subscribers to be self-producers.

Acknowledgements

This work has been produced in the scope of and has received funding through a project implemented by Deutsche Gesellschaft für Internationale Zusammenarbeit (GIZ) GmbH. Responsibility for the contents of this paper lies entirely with the authors and can in no way be taken to reflect the views of GIZ.

References

United Nations Statistical Commission, United Nations Sustainable DevelopmentKnowledge Platform, 2015. https://sustainabledevelopment.un.org/post2015/transforming our world , July 3, 2017.

M. Howells, H. Rogner, N. Strachan, C. Heaps, H. Huntigton, S. Kypreos, A. Hughes, S. Silveira, J. DeCarolis, M. Bazilian, A. Roehrl. OSeMOSYS: the open source energy modeling system: an introduction to its ethos, structure and development, Energy Pol. 39 (2011) 5850e5870 doi:0.1016/ j.enpol.2011.06.033.

Open Energy Modelling Initiative, OpenEnergy Platform, (n.d.). http://oep.iks.cs.ovgu.de , July 8, 2017.

Open Energy Modelling Initiative, Open Energy Modelling Initiative, (n.d.). https://wiki.openmod-initiative.org/wiki/Main_Page, October 2, 2017.

Horizon 2020 LCE21 Projects, Energy Modelling Platform for Europe, 2017. http://www.energymodellingplatform.eu, January 3, 2018.

ANME (Agence Nationale pour la Maîtrise de l'Energie), 2016. Plan Solaire Tunisien: Programmation, conditions et moyens de la mise en œuvre," Tunis, Study 2016.

STEG, 2015. Rapport Annuel, STEG, Tunis.

Horizon 2020 LCE21 Projects, Energy Modelling Platform for Europe, 2017. http://www.energymodellingplatform.eu/ (accessed January 3, 2018).

D. Connolly, H. Lund, B. V. Mathiesen, and M. Leahy, "The first step towards a 100% renewable energy-system for Ireland," *Appl. Energy*, vol. 88, no. 2, pp. 502–507, Feb. 2011.

P. Capros *et al.* EU Reference Scenario 2016-Energy, transport and GHG emissions Trends to 2050, 2016.

R. Loulou, U. Remme, A. Kanudia, A. Lehtila, G. Goldstein, Documentation for the TIMES Model Part I, 2005.

L. Schrattenholzer, The Energy Supply Model MESSAGE, Laxenburg, Austria, 1981. http://adsabs.harvard.edu/abs/1981STIN...8225632S, January 11, 2016.

Optimus community, OSeMOSYS GitHub, 2017. https://github.com/KTH-dESA/OSeMOSYS, October 3, 2017.

M. Welsch, M. Howells, M. Hesamzadeh, B. O Gallachoir, P. Deane, N. Strachan, M. Bazilian, D. Kammen, L. Jones, G. Strbac, H. Rogner, Supporting security and adequacy in future energy systems: the need to enhance long-term energy system models to better treat issues related to variability, Int. J. Energy Res. 39 (2015) 377e396, https://doi.org/10.1002/er.3250.

F. Gardumi, A Multi-dimensional Approach to the Modelling of Power Plant Flexibility, Politecnico di Milano, 2016.

M. Welsch, M. Howells, M. Bazilian, J. DeCarolis, S. Hermann, H. Rogner, Modelling elements of smart gridseenhancing the OSeMOSYS (open source energy modelling system) code, Energy 46 (2012) 337e350, https://doi.org/ 10.1016/j.energy.2012.08.017.

M. Howells et al., 2011. OSeMOSYS : the open source energy modelling system : an introduction to its ethos, structure and development,Energy Policy, vol. 39, no. 10, pp. 5850–5870.

F. Gardumi et al., 2021. A scenario analysis of potential long-term impacts of COVID-19 on the Tunisian electricity sector, Energy Strategy Reviews**, v**ol. 38, 100759.

Promotion of Solar Heat in Industrial Processes: Policy and Law Analysis Method Proposal with Focus on Turkiye and Germany

Yelda Erden Topal, Onur Cagdas Artantas[2] and Sevgi Deniz Akdemir[2]

[1] Middle East Technical University, Ankara (Turkiye)

[2] Hacettepe University, Ankara (Turkiye)

Abstract

In this research paper, we propose a method to examine the policy and legal framework for solar heat in industrial processes (SHIP) in Germany and Turkiye with a comparative analysis. To enable industry actors to make use of the large growth potential of SHIP with its numerous application areas, targeted policies and legislation are to be adopted. For this reason, this research paper aims to fill the respective gap in analyzing and designing renewable energy law and policy frameworks for SHIP. A comparative analysis explores potential approaches to promote SHIP in Turkiye and Germany. To this end, the paper proposes a step-by-step method to pursue research milestones of both academic and practical interest by examination and comparison of the current extent of deployment of SHIP technologies and the current status of SHIP policy and law frameworks in both countries. It is an attempt to develop a method to compare two different and complementary contexts with an analysis of law and policy frameworks. The method includes five steps of (1) Literature review- State-of-the-art (2) Stakeholder Mapping (3) Status of SHIP applications (4) Status of Policy & Law 5) Future of Policy & Law. This method mainly serves to impose policy proposals for SHIP applications in both countries.

Keywords: solar heat, renewable energy, law, policy, comparative study, method, industrial prosumer, border tax adjustments, Turkiye, Germany, , SHIP

1. Introduction

Solar thermal energy can meet a large amount of thermal demand in industrial processes in any given country and regardless of the geographical position, an analysis under the aegis of the International Renewable Energy Agency has found (IRENA 2015). Several industrial sectors (e.g. the textile, concrete, and food manufacturing industries) can benefit from this energy source given their demand for hot water and steam at temperatures of up to 400°C for processes such as curing, drying, dyeing, washing, boiling, pasteurization and sterilization. Solar Heat in Industrial Processes (hereinafter SHIP) systems may also contribute to a stable energy supply if the problem of volatility of solar energy is adequately dealt with. To this end, SHIP applications may also include heat storage units. For small and medium-sized enterprises, solar process heat may minimize the reliance on unpredictable fossil fuel prices. Despite the technological potential as well as the potential economic advantages of using solar heat in manufacturing, the current extent of deployment remains relatively low. This is for a number of reasons, among which the infant industry effect, inappropriate legislation, lack of awareness, and problems in the legitimation of the technology feature prominently.

As countries always seek to have clean energy solutions for industrial growth, the paper focuses on green energy production as a mechanism for generating income and improving industrial competitiveness. In order to improve green industrialization, "industrial prosumers" comes up, which is new for Turkiye. The United Nations Industrial Development Organization (UNIDO) defines "Industrial Promoter of Renewable Energy" as an industry that produces and uses renewable energy sources such as solar, wind, bioenergy and other renewable energy sources (UNIDO, 2015). Promoting industrial prosumers is essential worldwide, but it is crucial for countries with energy-intensive industries such as Turkiye and Germany. Over the last couple of years, the share of solar energy prosumer has increased rapidly in Germany. Despite the fact that Germany, which is one of the countries with the best technology position in the world, has a lower capacity in terms of solar energy potential compared to Turkiye, it has more than 40,000 MW of installed power (Keskin, 2019). In Germany, the rapid transformation of the energy sector has been boosted by the formation of hundreds of thousands of small "prosumers" within the stable, long-term policy structures.

© 2022. The Authors. Published by International Solar Energy Society
Selection and/or peer review under responsibility of Scientific Committee
doi:10.18086/eurosun.2022.18.07 Available at http://proceedings.ises.org

Turkiye has large domestic markets and strong industrial capacities for domestic solar thermal hot water technologies. The prosumer term can be a new pattern to provide a win-win approach for companies and governments to support the actions for climate change and sustainable growth by combining clean energy sources into their power supply as well as their heating and cooling needs. Solar thermal energy can meet a large amount of thermal demand in industrial processes in any given country regardless of geographical position. In developing economies, solar thermal energy can provide about half of this energy consumption theoretically by providing hot water and steam at temperatures of up to 400°C. In particular, agriculture, the textile, concrete and food manufacturing industries are important industrial sectors, solar thermal energy can supply hot air and hot water required for curing, drying, dyeing, washing, boiling, pasteurization and sterilization. The SHIP system may also include a heat storage unit that can be used to increase the time of day when the heat is supplied to substitute for fluctuations in the solar resource. For small and medium-sized industries, solar process heat may minimize the reliance on unpredictable fossil fuel prices. Despite the technological potential as well as the potential economic advantages of using solar heat in manufacturing, the current extent of deployment remains relatively low (ETSAP & IRENA, 2015).

Drawing on these many advantages, having great potential and considering the growing attractiveness of solar thermal technologies to industrial consumers, it is time for policymakers to begin to realize the significant potential that exists for industrial prosumers to contribute to the green and circular economy. The development of the right policy and regulatory frameworks for this to happen would be a fundamental step. Research and development must also be recognized as an industrial policy measure. German energy research is a strategic component in German energy policy and is crucial for the energy transition's long-term success. Additionally, German producers are global technology leaders in the field of renewable energy and energy efficiency. There is an opportunity to take lesson-learn and generate components of Turkiye's modern energy supply system (ETSAP & IRENA, 2015). That is why market creation and comparison have to go hand in hand in facilitating the development and implementation of these technologies with law and policy frameworks.

Among the industrial policy measure, research and development must also be recognized. German energy research is a strategic component in German energy policy and is crucial for the energy transition's long-term success. Additionally, German producers are global technology leaders in the field of renewable energy and energy efficiency. There is an opportunity to take lesson-learnt and generation of components of Turkiye's modern energy supply system. For the reasons mentioned above, this paper proposes a Policy and Law Analysis Method" with a focus on the promotion of solar heat in industrial processes with a comparative analysis of Turkiye and Germany.

2. Literature Review

As we look at the literature, we can see that the legal scholarly literature on the promotion of green energy is rich. Firstly, there are several editorial books which directly deal with the issue. Hancher, Hauteclocque, Salerno (2017), and more recently Hunter et. al (2020) offer a valuable introduction to the state aid and regulation for the green energy sector. German legal literature is promising as well. Pritzsche and Vacha (2017) and Steinbach (2017) both offer introductions to the field. On the Turkish side, Çakmak (2018) is the prominent book on green energy promotion. However, legal literature that directly deals with SHIP applications is non-existent. This paper is an attempt to compile the first pieces of legal literature to form a method proposal for policy and regulation analysis. As the method is developed and implemented in further studies, it adds value to the legal framework analysis in renewable energy and specifically in solar heat in industrial processes.

Beyond the doctrinal legal literature, there are policy-related sources from various governmental organizations, especially in Germany. German Federal Ministry for Economic Affairs and Energy (BMWi) regularly publishes reports on the development of the Energiewende process (BMWi, 2018 and BMWi, 2019). On the Turkish side, the strategy paper of the Energy and Natural Sources Ministry (ETKB, 2019) covers the energy transition policy between 2019-2023. The energy efficiency strategy paper (ETKB, 2012) for between 2012-2023 offers insights into the Turkish energy efficiency policies.

The research method of the paper includes desk research of documents (papers, report, legal document, policy proposals, related funding programme calls) to propose the method of law and policy analysis. This method is to design including document scanning (desk research) as well as collaborative meetings to interact, communicate and exchange knowledge and experience between researchers for proposing legal and political documents specific

to SHIP applications. It aims to take up prior research on innovation and law, power-to-x technologies/sector coupling, and the governance of renewable energy and energy innovations which so far has not specifically dealt

The comparative approach taken in this research and the selection of Turkiye and Germany as countries of reference are particularly well suited to contribute to the overarching research goal for a number of reasons. Most importantly, the research design fosters mutual learning. Learning from the individual experience of each country may facilitate the successful deployment of SHIP applications supported by appropriate policy measures, which in turn is pivotal to reducing fossil fuel reliance and related carbon emissions in both developed and emerging economies. The focus on Germany and Turkiye and the collaboration of researchers from both countries promise particularly fruitful insights. Regardless of the substantial differences in economic development terms, both countries offer significant potential for growth for renewable energy deployment. On the one hand, Turkiye's green energy sector has been rapidly developing in a "solar boom", and the country features strongly in research promoting energy from solar sources. Among other factors, this leads to a reduced cost of renewable energy sources in Turkiye compared to other (European) countries, and in particular Germany. Also, research from the Turkish institutions involved has shown great potential in expanding the utilization of PV and solar-thermal systems as energy sources. Germany, on the other hand, has been a frontrunner and role model in promoting renewable energy. Germany's approach to promoting renewable energy in the "Energiewende", a term coined already in the 1990s, has since gained significant momentum abroad. The experiences of both countries are thus complementary. Combining the perspective of both German and Turkish researchers in a comparative approach helps to make sure that the potential for creating synergies in knowledge is properly made use of when SHIP promotion policies are designed.

3. Method and Material

First of all, this paper put emphasis on researching the potential of promoting the deployment of SHIP applications through dedicated law and policy making. To date, the topic is widely under-researched, despite the clear potential of SHIP to contribute to a more stable, secure and sustainable supply of energy in order to partly cover the high industrial energy demand. The potential of SHIP has been highlighted mainly from a practical, technology-oriented perspective. With regard to reasons why the potential remains underexplored, the high costs of SHIP appliances and their maintenance compared to conventional energy sources are deemed to be the main limiting factor (see IRENA 2015 and cited literature). However, due to their limited scope, prior analyses on the subject do not altogether or at least not sufficiently explore how this hindrance can be overcome by means of policy measures. Hence, there is a fundamental gap in academic research from a policy-oriented perspective – including legal issues – that the paper seeks to fill through cooperative research.

The paper seeks to make a significant contribution to research in the European Research Area on a topical issue in line with current European policy and legal framework developments. In particular, the paper examines a technology that is able to build a bridge between high standards of environmental protection and climate action on the one hand and economic growth on the other. The focus on Turkiye, which is not only an important trade partner to Germany but also a rapidly emerging economy, is furthermore worthwhile considering the EU's aim for global leadership in tackling climate change by means of creating technological innovations and progress and exporting them worldwide. Due to its comparative and cooperative approach, the method to be developed aims to substantially strengthen the relations between these two countries at the institutional and implementation level.

4. Preliminary Analysis and Prospective Research

First, the paper aims to address a particular academic literature gap. The policy and law of SHIP are not appropriately dealt with to this date, the paper proposes a method that begins with prior research on innovation and law, power-to-x technologies/sector coupling, and the governance of renewable energy and energy innovations. Especially the interdisciplinary approach to SHIP including legal scholars is novel. Second, the paper produces a policy proposal method, contributing to both countries' policymaking processes.

Examining SHIP policy and law in Germany and Turkiye from a comparative perspective facilitates the transfer of knowledge and experience on the issue. The authors (two of whom are studying in renewable energy diffusion in Turkiye, and one of them is studying the same issues in a comparative perspective of Germany and Turkiye) pool their findings and compile texts together by scanning the legal framework documents in the original language.

Additionally, planned research visits form cornerstones of the research since they will further ensure knowledge transfer. The outcomes of the joint research (with the further works of one policy report and at least one scientific paper) will benefit stakeholders, policy-makers, and legislators in Turkiye and Germany. The policymakers will be able to refer to our policy report in developing new SHIP promotion strategies. On the other hand, the stakeholders will be able to refer to our policy report in their future projections and communications with the policymakers. Our scientific papers will serve as a starting point for social scientists who aim to work in the SHIP field specifically for Turkiye.

5. Conclusion: The Method Proposal

The paper is ongoing research and is first presented in Eurosun 2022. The research is being done by an interdisciplinary team and in close collaboration between Middle East Technical University (METU) and Hacettepe University (HU) from Turkiye. Dr Erden Topal (the corresponding author) has extensive experience in researching renewable energy policymaking. She has been closely collaborating with Professor Dr Derek K. Baker (METU and ODTU GUNAM – Center for Solar Energy Research and Applications) on several EU Projects and National Initiatives for Concentrated Solar Thermal Technology (CST) Development, Diffusion and Policy Making (ODAKTr). Prof. Baker specializes in CST technologies including SHIP applications and provides his technical expertise and experience in the field of solar energy technologies. MSc. S. Deniz Akdemir (Co-author and MSc Student of Professor Baker) is an environmental engineer on the Turkish side and completed her Master of Science Thesis about SHIP in Turkiye in 2020. Dr Onur Cagdas Artantaş (co-author) is completed his Ph.D. on Renewable Energy Law in Turkiye in comparison with Germany under the supervision of Prof. Fehling in Bucerius Law School/ Germany.

With this interdisciplinary team, we propose a method for designing proposals and possible implications of legal and policy frameworks. The case studies are to be Germany and Turkiye as a comparative case study exercise. This proposed method for the promotion of SHIP is a stepwise approach and made up off the steps of:

STEP 1: Literature Review- State of the Art (in SHIP Policy and Legal Frameworks)

The first step will be a thorough analysis of the existing literature regarding (i) the functioning and potential of SHIP technology more generally; (ii) the current status of deployment of SHIP in Germany and Turkiye; (iii) economics, policy, and law relevant to the promotion of SHIP in both countries. This measure will reveal the state-of-the-art in these three areas on which the method proposal and the analysis is accrued by using this method that is built on. The researchers will define the exact scope of the method based on the findings in this step. Here, the scope is the key target to reach to define the framework and borders of the research.

STEP 2: Stakeholder Mapping (in Germany and Turkiye's SHIP Landscapes)

The second step will involve examining the current situation and general conditions of energy, Concentrated Solar Technologies (CST) and the SHIP industry in Germany and Turkiye scanned in the first step of the method. In this step, the first finding of the H2020 Horizon STE Project - Implementation of the Initiative for Global Leadership in Solar Thermal Electricity (GA No: 838514) deliverable titled Integrated Country Report (submitted on July 30, 2022,:j and now is available after EU Approval) is benefitted. This report is a comprehensive document that includes both Turkiye's and Germany's (in addition to Spain, Italy, Portugal, France, Greece, Denmark, and Belgium) outlook in CST technologies countries The relevant stakeholders will be mapped out in each country according to their connections with each other. This includes industry actors as well as institutional or university actors, e.g. in the field of engineering. This "stakeholder map" helps to prepare the research and networking activities in further steps in this specific technology area of SHIP to further develop legal and policy frameworks.

STEP 3: Status of the SHIP Applications

The third step aims to deepen the overview of the current status of SHIP deployment in Germany and Turkiye gained through the former steps. To this end, further information will be collected from the regulators and industry stakeholders in each country. Here can be seen as field research conducted with a sample of stakeholders in each country determined in the second step. The aim is to compile a preliminary report, which will be used in later research phases with first-hand data of expert interviews in each country. The report will discuss the current technological level, the structure of the SHIP sector and of the relevant industry branches, financial endowment,

and the percentage of local equipment used in the SHIP applications from the perspective of key stakeholders in each country.

STEP 4: Status of SHIP Policy & Law

The fourth step contributes to one of the two focuses of the paper as the current status of the SHIP policy and law in Germany and Turkiye. The previously collected information (e.g., state-of-the-art, stakeholder map, the status of the SHIP applications) will be utilized here at a different level. All relevant policy documents and legislation will be examined in detail to assess their strengths and weaknesses in promoting SHIP mainly in Germany, and to take the lessons learnt from the German case to further develop the Turkish case in SHIP applications.

STEP 5: Future of SHIP Policy & Law (Proposals on Policy and Legal Frameworks)

This step contributes to the second of the two research aims. In this step, different scenarios of policy development will be examined against the background of stakeholder needs, the desire to further technological development and the emission reduction targets of the EU. This may include a "Business as Usual" (BaU) and a "Successful Promotion of SHIP" (SPoS) scenario. It will be presented how the SPoS diverges from the BaU route in terms of reduction of power consumption, emission mitigation and estimated added financial value. Policy proposals for the SPoS route will be made, including recommendations for amendments in legislation.

6. Acknowledgement

This paper's preparation and presentation are supported by the H2020 Horizon STE Project - Implementation of the Initiative for Global Leadership in Solar Thermal Electricity (GA No: 838514). The authors would like to acknowledge the support provided by H2020 Horizon STE Project. Moreover, in the follow-up stage, another project proposal is targeted and is being prepared mainly focusing on the development of this policy and law analysis method proposal and implementing it in Germany and Turkiye in the context of cooperation and collaboration in the SHIP area. This follow-up project proposal preparation is supported by H2020 SolarTwins Project – SolarTwinning the create solar Research twins (GA No: 856619). The authors would like to acknowledge the support provided by H2020 SolarTwins Project.

7. References

BMWi, Sechster Monitoring-Bericht zur Energiewende, 2018. https://www.bmwi.de/Redaktion/DE/Publikationen/Energie/sechster-monitoring-bericht-zur-energiewende.pdf?__blob=publicationFile&v=26, Last acess: May 13, 2023

BMWi, Second Progress Report on the Energy Transition, 2019, https://www.bmwi.de/Redaktion/EN/Publikationen/Energie/second-progress-report-energy-transition.pdf?__blob=publicationFile&v=3, Last acess: May 13, 2023

Çakmak, M.2018. İdare Hukuku Açısından Yenilenebilir Enerji (in Turkis), Seçkin Yayınları.

ETKB, 2019. 2019-2023 Strateji Planı, https://sp.enerji.gov.tr/ETKB_2019_2023_Stratejik_Plani.pdf, Last acess: May 13, 2023

ETKB, 2012. Enerji Verimliliği Strateji Belgesi 2012-2023 (in Turkish), https://www.resmigazete.gov.tr/eskiler/2012/02/20120225-7.htm, Last acess: May 13, 2023.

ETSAP & IRENA, 2015. Solar Heat Industrial Processes. The International Renewable Energy Agency.

Hancher, L., Hauteclocque, A.& Salerno, F. M. 2017, State Aid and the Energy Sector, Hart.

Hunter, T.; Herrera, I.; Crossley, P. and Alvarez, G., 2017. Routledge Handbook of Energy Law, Routledge.

IRENA (2015), Solar Heat for Industrial Processes- Technology Brief, https://t1p.de/irena-brief, Last acess: May 13, 2023

Keskin, T., 2019. Climate Change Training Module Series 6. Ankara: Ministry of Environment and Urbanization of Turkiye.

Pritzsche, K. U and V. Vacha,. 2017. Energierecht: Einführung und Grundlagen. C.H. Beck.

Steinbach, P., 2017. Das Ordnungsrecht der Wärmewende, Peter Lang Publishing,

UNIDO, 2015. Industrial Prosumers. Vienna: UNIDO.

Standardized Economic Evaluation Criteria of Solar Process Heat in Hybrid Systems – Results from IEA SHC Task 64 Subtask E

Jürgen Fluch[1], Felix Pag[2], Peter Nitz[3], Jana Fuchsberger[1]

[1] AEE INTEC, Gleisdorf (Austria)

[2] Universität Kassel, Kassel (Germany)

[3] Fraunhofer Institute for Solar Energy Systems ISE, Freiburg (Germany)

Abstract

Industry accounts for more than 30% of the total energy demand and faces significant challenges in achieving the set decarbonization goals. Therefore, it is crucial to provide end users with state-of-the-art technologies like solar process heat and optimized combinations with other technologies like excess heat recovery and heat pumps. A barrier, that hinders industrial end users from implementing available solutions, is the challenge of assessing developed concepts not only from technical perspectives but also applying economic parameters The objective of the Subtask E of the joint IEA SHC Task 64 / SolarPACES Task IV is to identify existing barriers, used assessment criteria of all relevant stakeholders and the definition of mandatory parameters, merging the perspectives of solar process heat with other technologies. To achieve this, a survey was performed to collect feedback from the stakeholders concerning technical and economic criteria. Analysis of the results reveals the relevance of various criteria with respect to different project phases. Different economic parameters and the CO_2 abatement costs turn out to be highly relevant throughout all project phases, while the relevance of investment and operating costs exhibits peaks in the detailed planning and operating/implementation project phase respectively.

Keywords: economic indicators, standardized evaluation criteria, SHIP, industrial energy systems

1. Introduction

The industrial sector accounts for about 30% of the total energy demand in the EU and OECD countries, of which about 60% is used to cover process heat demand (Eurostat, 2022, Werner, 2006, Eurostat, 2023). This corresponds to more than 1,900 TWh per year in the EU27 and is also valid for worldwide statistics on energy demand and consumption (IEA, 2021). If the sector is to be decarbonized sustainably, in addition to the buzzwords electrification and hydrogen with significant research demand, solutions are needed that are immediately available and do not shift the challenges to the generation of very large amounts of renewable electricity. Solar process heat is a proven technology, especially in the temperature range up to about 400°C, which is highly significant as already mentioned about 60% of industrial heat demand is in this temperature range (Werner, 2006). In order to achieve high coverage rates of renewable heat, the focus is increasingly shifting to the design and operation of hybrid systems in which solar process heat is combined with excess heat recovery, heat pumps and PV. This results in the challenge of already introducing uniform criteria for all technologies in the planning of these projects, which allow an objective technical and, above all, economic evaluation over the utilization period of all technologies (Braumann, 2020, AEE INTEC, 2016, Avila, 2015, Brunner, 2015). This is well reflected in the demand for tailor-made funding and financing instruments (Fluch, 2015, Giralda, 2016), also based on the outcome of performed energy audits and the development for decarbonization concepts (Kulterer, 2015a, 2015b) Within the framework of the joint IEA SHC Task 64 / SolarPACES Task IV, Subtask E (Guideline to Market) and Subtask A (Integrated Energy Systems) specifically address whether currently used typical evaluation parameters such as payback periods from the perspective of solar process heat will also be suitable in the future to support industrial companies and project developers in the implementation of such hybrid systems and how new approaches must be taken into account in the different project phases from the idea to implementation and operation. This is becoming more and more important as in the Energy Directive of the European Commission, the defined objectives are defined, including the demand for decarbonisation (European Commission, 2023).

© 2022. The Authors. Published by International Solar Energy Society
Selection and/or peer review under responsibility of Scientific Committee
doi:10.18086/eurosun.2022.18.08 Available at http://proceedings.ises.org

2. Methodology

Through Subtask E, relevant parameters for the assessment of renewable technologies were collected and categorized by involving all relevant stakeholders of solar process heat (technology suppliers, project developers, industrial companies, research and investors). Based on identified and evaluated available funding programmes on Solar heat for industrial processes (Nitz, 2021), performed within the Subtask E of the SHC Task, this demand is already highlighted. A total of 65 criteria were assigned to four categories (general project information as well as economic, technical and methodological parameters) and subsequently evaluated for different project phases from the idea to a feasibility study, rough and detailed planning, implementation/commissioning and operation. These results were finally transferred into a representative survey with the aim of ascertaining whether the importance or the necessary level of detail of the different parameters changes in these project phases.

The survey was done in a two-step approach. First the questions were shared within the participants of the IEA SHC Task 64 / SolarPACES Task IV group and afterwards spread, using the communication channels of the whole SHC Task as well the lead partner of the Subtask E. The survey was integrated in a web-based platform (SurveyMonkey) and included in total 26 questions, subdivided into the following sections:

- General questions on the background of the participants as company's main area of operation, industrial sector, size of the company, home country as well position, background and experience with renewable energy and solar heat specifically of the person filling in the survey
- Importance of different pre-defined economic (CAPEX and OPEX) parameter/KPIs in different project phases (pre-feasibility, detailed engineering, implementation/operation)
- Importance of ecologic and technical parameter in project phases
- Interest and if possible, share of personal contact data

The survey was done in two rounds including a reminder sent via email. Afterwards the feedback was evaluated by downloading the data and fed in tables and figures, as shown below.

3. Results

The survey included 51 participants at 18 different sites, see Figure 1, with no significant impact of survey participants' location on the results. It is important to understand, that the importance of investment (CAPEX) and operating (OPEX) costs varies over the 3 different phases of project development (pre-feasibility, detailed engineering, implementation/operating). The survey results demonstrate the need to consider new approaches to evaluation that go beyond simply looking at payback time. In Fig. 3, it can be seen that the payback period, the levelized cost of heat and the internal rate of return are of high importance in all project phases. The depreciation, P50/P90 value as well as the net present value are considered moderately important in the pre-feasibility phase but gain importance in the later project phases.



Fig. 1: Location of survey participants

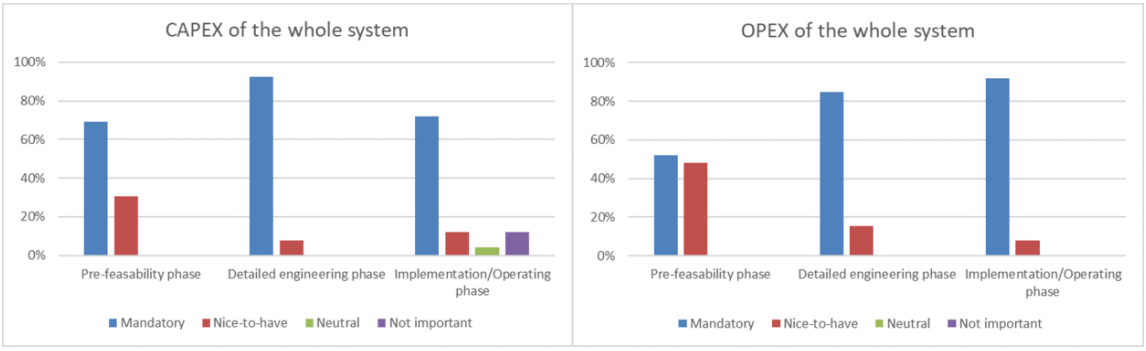

Fig. 2: Survey results regarding the criteria "OPEX of the whole system" (top) and "CAPEX of the whole system" (bottom) and their relevance in project phases: mandatory, nice-to-have, neutral, not important (n=51)

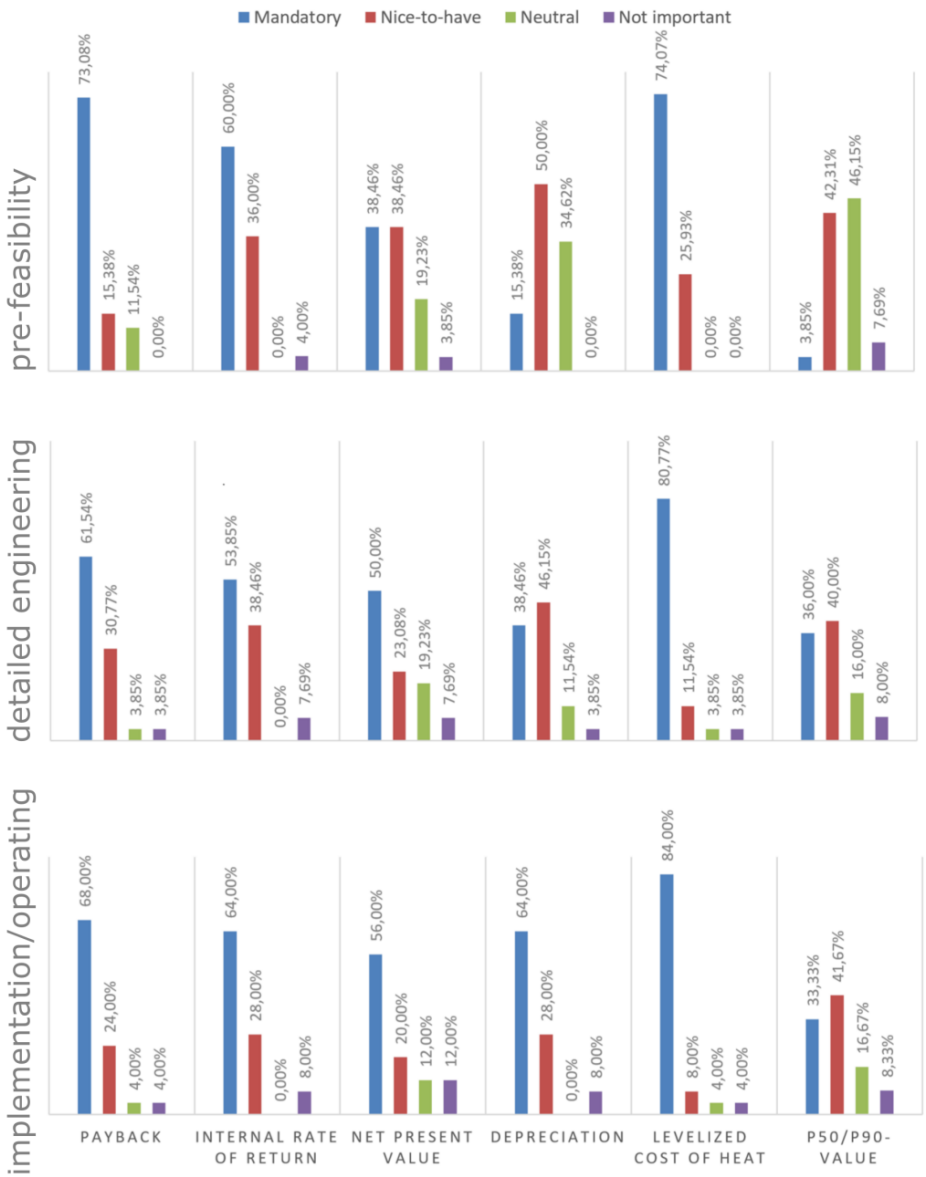

Fig. 3: The importance of the economic parameters in all three phases of a project

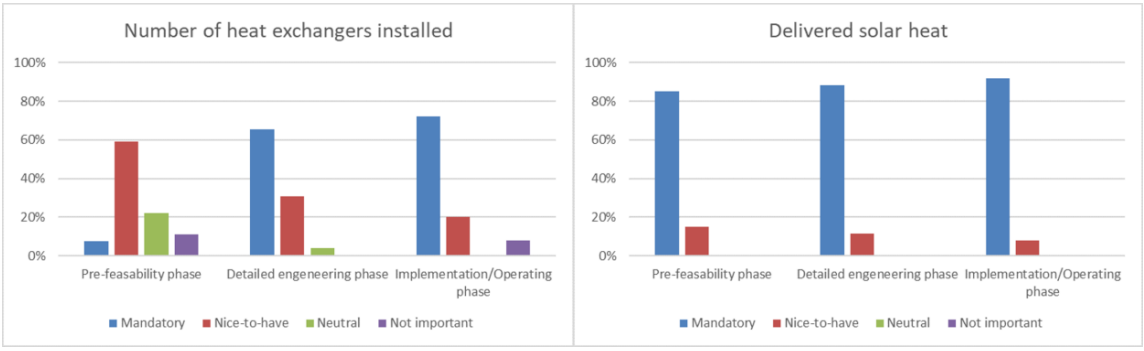

Fig. 4: Survey results regarding the technical criteria "number of heat exchangers installed" (left) and "delivered solar heat" their relevance in project phases: mandatory, nice-to-have, neutral, not important (n=51)

The OPEX (operating expenditures) of individual components and the entire system are considered moderately important in the pre-feasibility phase, with significant increases in importance in the later project phases, see Fig. 3. The CAPEX (capital expenditures) are generally of high interest, with the importance of CAPEX of all system components, as well as that of the entire system (see Fig. 2 and Fig. 3) and process integration, being highest in the detailed planning phase. The increase in the relevance of the OPEX parameters in the later project phases and the peak in the relevance of the CAPEX parameters in the detailed planning phase confirm our expectations and correspond to the general prioritization in the course of a project.

The analysis of the technical parameters shows that the relevance of the delivered solar heat, the storage size and the installed area is considered to be very high in all project phases. The number of installed heat exchangers is of lower importance, especially at the beginning of the design, but increases in the later project phases, see Fig. 4.

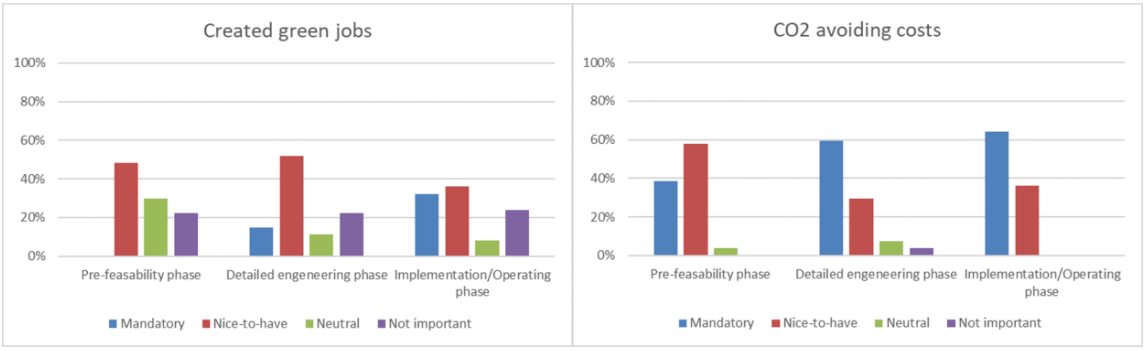

Fig. 5: Survey results regarding the green economy criteria "created green jobs" (left) and "CO_2 abatement costs" their relevance in project phases: mandatory, nice-to-have, neutral, not important (n=51)

As expected, CO_2 abatement costs are considered as relevant parameter in all phases. Surprisingly, the green jobs created (Green Jobs) are in contrast of relatively less interest and even in the implementation and operation phases the relevance of this parameter remains low, see Fig. 5.

4. Outlook

The overall goal of IEA SHC Task 64 / SolarPACES Task IV is to place solar process heat as an important component of future hybrid supply systems in the industrial sector. For this purpose, the results from Subtask E will be further processed and the most relevant evaluation criteria will be defined. Defining a standardized calculation method for the different parameters is the core task. This method is mainly based on results from previous projects and will enable comparison with aforementioned technologies like waste heat recovery, heat pump or PV. Additionally, the importance of different criteria regarding different project development phases is analyzed. Finally, these findings will be incorporated into the work of Subtask A on the design of integrated energy systems and thus contribute to sustainably strengthening the role of solar process heat.

In summary, the following key findings of the survey can be stated:

- **Economic parameters** such as heat production costs, payback time or internal rate of return are considered highly relevant in all project phases. Innovative approaches such as P50/P90 are of increasing interest to investors.
- **Operating costs** of individual components and of the whole system are considered moderately important in the first project phase of feasibility studies, increasing significantly in the later project phases.
- **Investment costs** are generally of high interest, with importance peaking in the detailed design phase.
- **CO_2 abatement costs** are considered an extremely relevant parameter in all phases, while the created **green jobs** are surprisingly of lesser interest.
- There is **no significant impact of the location of the survey participants** on the survey results.

The survey results confirm the need for new evaluation criteria for SHIP (technical, economic, environmental, non-energy benefits) while calling for a clear definition of these criteria for the entire sector. This will enable comparability of the technology with other renewable energy sources and strengthen the role and recognition of SHIP in future industrial energy systems. In addition, specific target groups require different criteria.

5. References

AEE INTEC, Fraunhofer ISE, reenag, eceee, Universidade de Évora, und ainia, „TrustEE - Report on current status of Process heat in Europe: sectors, processes, geographical distribution, system layouts and energy sources“, 2016. [Online]. Verfügbar unter: https://www.trust-ee.eu/files/otherfiles/0000/0008/TrustEE_D1_1.pdf

Avila C., et.al., 2015. Transnational Survey on Funding and Financing Instruments, Deliverable, IEE project GREENFOODS IEE/12/723.SI2.645697

Braumann W., et.al, 2020. TrustEE – Innovative market based Trust for Energy Efficiency investments in industry, publishable report, H2020 project GA number 696140 - TrustEE - H2020-EE-2014-2015/H2020-EE-2015-3-MarketUptake

Brunner C., et.al., 2015. GREENFOODS – Towards zero fossil CO2 emission in the European food and beverage industry, publishable report, IEE project GREENFOODS IEE/12/723.SI2.645697

European Commission, „Energy efficiency directive“. https://energy.ec.europa.eu/topics/energy-efficiency/energy-efficiency-targets-directive-and-rules/energy-efficiency-directive_en#the-2012-energy-efficiency-directive (zugegriffen 19. April 2023).

Eurostat, „Final energy consumption in industry - detailed statistics“, Nov. 2022. [Online]. Verfügbar unter: https://ec.europa.eu/eurostat/statistics-explained/index.php?title=Final_energy_consumption_in_industry_-_detailed_statistics

Eurostat, „Energy Efficiency statistics“. 2023.

Fluch J., et.al., 2015. Development of funding and financing instruments, Deliverable, IEE project GREENFOODS IEE/12/723.SI2.645697

Girlada R., et.al., 2016. Comprehensive analysis of funding mechanisms, Deliverable, H2020 project GA number 696140 - TrustEE - H2020-EE-2014-2015/H2020-EE-2015-3-MarketUptake

IEA, „World Energy Balances: Overview“, Paris, License: CC BY 4.0, 2021. [Online]. Verfügbar unter: https://www.iea.org/reports/world-energy-balances-overview

Kulterer K., et.al., 2015a. Best practice Guide financing instruments, Deliverable, IEE project GREENFOODS IEE/12/723.SI2.645697

Kulterer K., et.al., 2015b. Mapping of existing funding programmes and financing instruments, Deliverable, IEE project GREENFOODS IEE/12/723.SI2.645697

Nitz P., Fluch J., 2021. Collection of available solar process heat related national and transnational research and

funding programmes, report from SHC Task 64 / SolarPACES Task IV: Solar Heat and work performed in Subtask E: Guideline to market, Deliverable Report D.E1

Werner S., 2006. ECOHEATCOOL—Workpackage 1. The European Heat Market. Final Report IEE ALTENER Project, Brussels, Belgium, http://www.euroheat.org/Files/Filer/ecoheatcool/documents/Ecoheatcool_WP1_Web.pdf

Technical Feasibility Study of Micro-Grid Integration to Electrify Rural Settlements of Sub-Saharan Africa

Bertha Lwakatare[1], Kedar Mehta[1], Mathias Ehrenwirth[1], Wilfried Zörner[1], Christoph Trinkl[1], James Katende[2], Joseph Shigwedha[3] and Helvi Ileka[3]

[1] Institute of new Energy Systems, Technische Hochschule Ingolstadt, Ingolstadt (Germany)

[2] Namibia University of Science and Technology, Windhoek (Namibia)

[3] Namibia Energy Institute, Windhoek (Namibia)

Abstract

Two thirds of Sub-Saharan Africa's (SSA) population reside in rural communities. SSA is the least electrified region in the world with approximately half of its population lacking access to electricity which hinders its citizens' livelihood and economic engagement. Electrification efforts by member nations have and continue to be done according to the respective energy policies. While the national utility companies are at the forefront of this process, geographical, economic, and time factors constrain the achievement of targeted electricity access rates in allocated timelines. Alternative electrification approaches, therefore, need to be implemented. As a case study, this paper focuses on electrification by integrating existing micro-grids into mini-grids to electrify currently unelectrified business and household settlements of Uutsathima village in Namibia. This approach averts the hindering factors for grid extension whilst utilizing the abundant and untapped solar energy. Results of this study indicate that exiting micro-grids have substantially higher electricity production than the primary consumers' demand. This allows for connecting new consumers within the proximity of the grids provided prior analysis of their energy demand is done. Given that minimal infrastructure upgrade is done, for instance, Uutsathima's business centre can be electrified. For result replicability, the methodology of this paper serves as a guide to determining the best scenarios in other off-grid regions of SSA.

Keywords: Electricity, micro-grid, mini-grid, Namibia, off-grid regions, Sub-Saharan Africa, unelectrified settlements

1. Introduction

1.1 Background and context

Given the population share Sub-Saharan Africa (SSA) has in comparison to the global population, cross-cutting issues such as the United Nation's sustainable development goals (SDG) require emphasis to avoid imbalanced development against social welfare (IEA, 2022). Since 2016, in response to the SDG 7, member countries of SSA have continually dedicated efforts, policies, and regulations to increase both reliable electricity access and affordability to its citizens. Whilst focus was put on extending the radius of the national grid, infrastructural, economic constraints, and off-grid RE global initiatives discourage these efforts. At electrification rates of 25% and 71% for rural and urban areas respectively, alternative solutions are necessary to fasten the electrification efforts (Fritzsche et al., 2019). While only 2% of the total utilized primary energy in SSA is accounted by renewable energies (RE), the region exhibits high potential of solar, wind, hydro, biomass among other RE sources (International Renewable Energy Agency (IRENA), 2022).

Introduction and implementation of off-grid as well as hybrid solutions across the region continue to grow, even though varying between countries due to differences in policies and regulatory frameworks which determine the attraction of private and international RE investors. Solar mini-grids for example, range from 5 to 100 per country (Fritzsche et al., 2019). While the term mini-grid is used mainly to describe a standalone grid of a capacity up to 2 MW (Opfer et al., 2022), this study focuses on grids with smaller capacities as low as 2.88 kW, herein termed as micro-grids. Solar micro-grids have mainly been used to electrify single consumer groups in SSA but record a notable increase in overall national electrification as well as the quality of services of business and public institutions which indicates the potential in these alternative electrification approaches.

This study examines the potential of micro-grid integration as an engineering innovative solution in achieving universal electricity access in off-grid regions.

© 2022. The Authors. Published by International Solar Energy Society
Selection and/or peer review under responsibility of Scientific Committee
doi:10.18086/eurosun.2022.18.09 Available at http://proceedings.ises.org

1.2 Renewable energy strategies in SSA

Due to accelerated electrification rates and efforts of the international RE and off-grid projects, some of the rural off-grid settlements got equipped with solar-based electricity networks. A practical example is the initiative by the government of Namibia in 2016 to electrify its public institutions by use of solar micro-grids. While this proved to answer the electricity dilemma in public institutions, such installations often neglect the private sector. In the rare case that the private sector was addressed, these systems were often sized incorrectly due to inaccurate energy audit on electricity consumption and requirements of the settlements. Factors such as energy consumption, income scenario of the people and population growth have, in the past, been neglected or underestimated. Uutsathima village, located in the Omusati region in Namibia, home to about 444 people, residing in 81 households is used in this context. The village qualifies as a relevant and typical rural SSA settlement with low population density, low-income citizens, unelectrified settlements and yet within the reach of erected micro-grids.

Uutsathima's micro-grids were commissioned as complete systems of photovoltaic modules, batteries, and inverters. The capacities are shown in Tab.2. Because of the abundance of solar energy, the suitability of solar systems was identified by the Namibian Ministry of Mines and Energy as a solution for the remote off-grid settlements such as Uutsathima. An aerial photo (c.f. Fig.1) of Uutsathima's business centre shows how scattered Uutsathima's settlements are. This layout impacts electricity distribution systems.

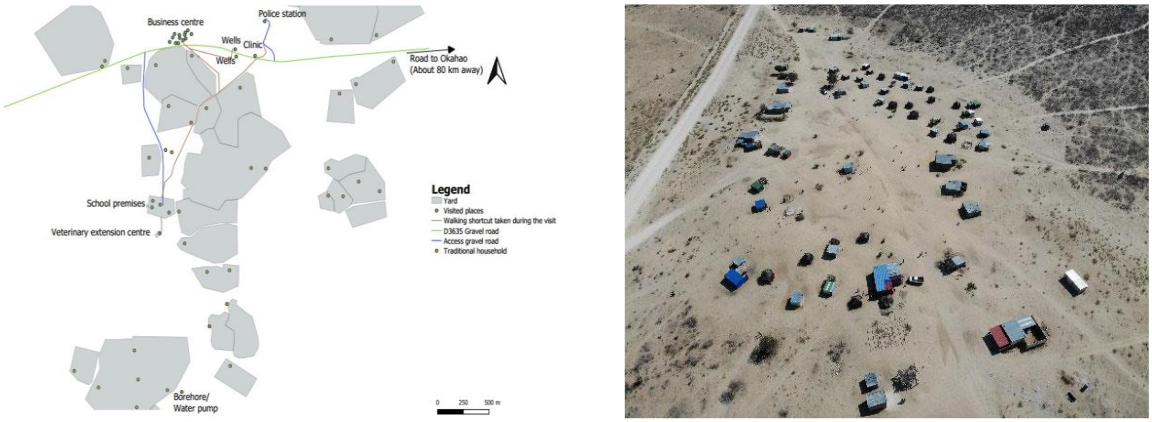

Fig. 1: GIS (Geographic information system) and aerial view of Uutsathima settlement (source: author)

Likewise, the households and business establishments in Uutsathima were neglected. Only the clinic, school, police station, and veterinary extension centre as shown in Fig.2, were recipients of solar off-grid solutions.



Fig. 2: Containerized and rooftop PV systems at the veterinary centre and school in Uutsathima (source: author)

This paper derives its motivation from two areas of focus namely research and implementation. Previous research work as well as existing electrification approaches have overlooked the potential of micro-grid integration which is described consequently.

1.3 Previous works

To date, SSA has adapted various electrification schemes as indicated in Fig.3. To eliminate dependence on the grid as well as non-fossil fuels, solutions ranging from imported solar appliances to mini-grid have been employed from small to large off-grid regions (Vanadzina et al., 2019).

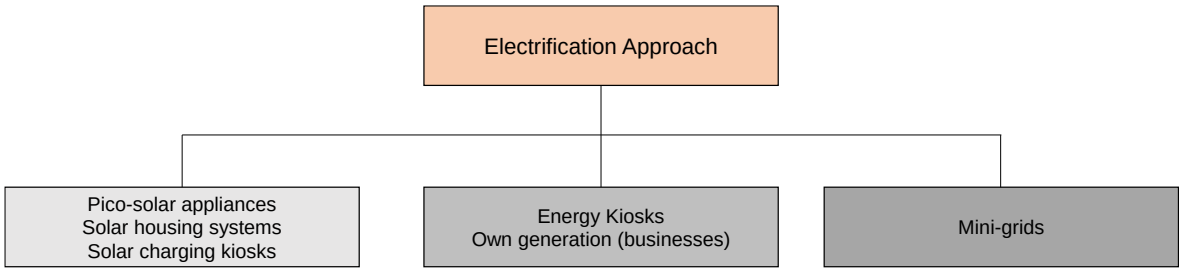

Fig. 3: Existing decentralized electrification solutions in rural SSA (own illustration based on the literature review)

Decentralized solutions have mainly taken two forms, one of which is much supported by international programs and the other relies on imported (mainly from China) and local sales of solar kits and lighting appliances to SSA off-grid regions (Jaglin, 2019). While these may serve as intermittent solutions, none of these thoroughly examine the potential of utilizing the existing infrastructure and grids to expand the radius of electricity access. A thorough search in publication and journal entries was carried out on the topic of micro-grid integration prior to this paper. The literature review results show that research has been devoted towards the role, potential and economic modality of micro-grid operation rather than the idea of integration.

1.4 Gap in the research and research motivation

This existing gap between rural and urban electrification rates as well as public, business and household electrification call for an electrification balance. The integration of the micro-grid is a suitable and simple approach for electrification. However, there is no scientific evidence available for electrification strategies through micro-grid integration for low-population rural settlements in SSA. In response, this paper focuses on the electrification approach by utilizing the already existing microgrids to electrify the previously neglected rural segments. The approach is not prone to barriers and constraints discussed in previous studies in that it uses a demand-side approach to study and analyze the actual electricity demand based on usage patterns as well as appliance ownership. This study also serves as a base for the depiction of future scenarios of micro-grid integration according to the segments making up a unit of settlement. In this case, categorization is given as public institutions, business settlements and households. Results and recommendations also allow for interpolation and translation into other SSA countries or villages depending on the status quo concerning Uutsathima.

2. Research Methodology

To meet the main objective, this paper identifies the implication of residents' actual electrical energy demand to the micro-grids' production. A scenario-based approach is used to generate a blue-print for the electrification approach. Prior to analyzing energy schemes, the selection of a sample rural settlement whose features reflect those of a typical SSA rural settlement was done. Population distribution, electrification situation, geographical behavior especially in effect to solar irradiance and PV potential as well as economic standings prop the selection of Uutsathima village. This paper goes further into segmenting the settlement types within the village based on their activities. Whilst income, number of inhabitants as well as seasonality are often crucial factors to consider in clustering, Lorenzoni et al (2020) report that in rural settings, human activities can be grouped into household needs, community service as well as business or income-generating activities on a small scale with minimal requirement of machinery such as refrigerators. That finding was considered when clustering Uutsathima, especially due to the dominance of pensioners and scholars in the population make-up. As can be seen in Fig.4, this paper follows a specific methodology in attaining the presented results.

Within Uutsathima, a thorough and engineered energy audit was done to understand the demand of the categorized settlements as well as the generation capacities of the existing roof top and containerized micro-grids. Considering that apart from public institutions, the village is mainly unelectrified, the on-site research stays, observations, measurements, and interviews were done to obtain custom data to analyze the actual village energy situation. Such on-site energy audit grants simplicity to generate synthetic load profiles (SLP) that display precise energy consumption values and patterns, due to the absence of electricity meters. Therefore, data collection of precise information on existing appliances per settlement type, their power rating, pattern of use as well as inhabitants' behavior was done. A bottom-up approach was used to generate the community load profile (c.f. Fig.5). The input data were simulated using a MATLAB (The Mathworks Inc., 2021) algorithm which looped every appliance to create independent SLP which were then aggregated to form a single settlement's SLP and then resulted in a single

Uutsathima village load profile as well as scenarios.

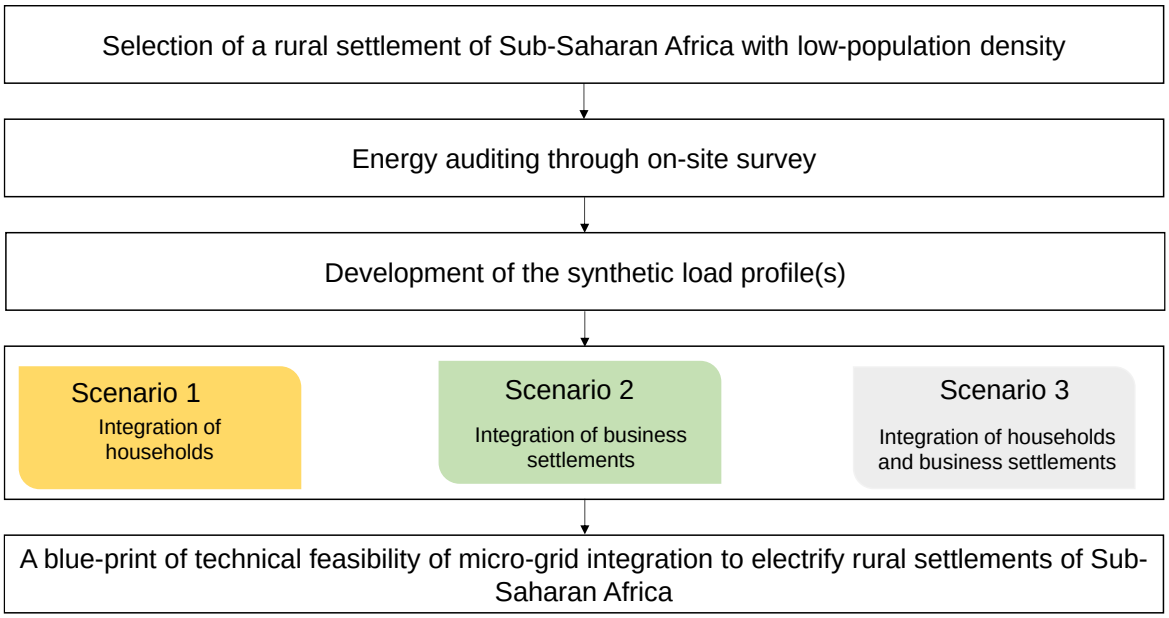

Fig. 4: General research methodology flowchart

An on-ground survey in 2019, identified households as the largest consumer group in Uutsathima and the business centre as a crucial economic zone such that both require electrification to increase safety and productivity. In the presented paper, therefore, three scenarios were considered for mini-grid integration; scenario-1: integration of households, scenario-2: integration of business community and scenario 3: integration of household and business community. The scenarios were also developed by consideration of the local circumstances such as population, income status and routine behavior of the residents.

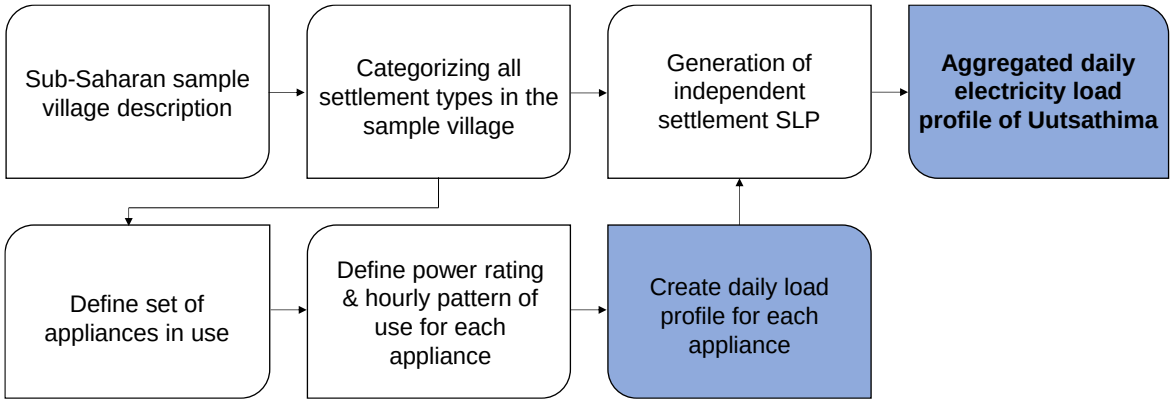

Fig. 5: Methodology for load profile generation

To determine the viability of the presented electrification approach per scenario, respective SLPs were fed into PVsyst (Webgenève, 2022) to size mini-grids whose capacity would meet the actual demand of the integrated consumers. The results from PVsyst (Webgenève, 2022) were then compared in terms of electricity generation as well as storage capacity to envision the feasibility of the existing capacity in meeting the demand and infrastructural requirement for generation, storage, and distribution of electricity.

3. Community Load Profile Development

To understand the electricity demand of the settlement types in Uutsathima as well as the village, this chapter outlines the generated daily average load profiles. The on-site energy audit identified the trend of activities coupled with electricity consumption hence obtaining corresponding peak power, average daily electricity demand and the consumption pattern.

3.1 Description of societal activities and composition

The generation of SLP is crucial for designing, planning, and forecasting electricity production and distribution networks (Chuan and Ukil, 2020). Considering Uutsathima's make-up of 81 households, keenness on the difficulty in forecasting of residential loads due to the variation in load profile resulting from dynamic fluctuations of home appliances is accounted. However, rural settlements often have an advantage of having fewer appliances and activities interlinked with electricity consumption (Flor et al., 2021). Therefore, uniform SLPs are assumed for households. The business centre is segmented into local alcohol vendors, herein termed 'Kapana shops', traditional shops, herein termed 'Kiosk', modern shops that offer cold beverages and phone charging services herein termed 'Shop' and a milling shop. The last cluster considered is the public institutions which encompass the school, clinic, veterinary centre, police station as well as the water pumping station.

3.2 Development of Synthetic Load Profiles (SLP)

The methodology used for development of SLPs (c.f. Fig.5) applies for all customer categories and scenarios. As an outcome, Fig.6 illustrates a daily aggregated SLP of the Uutsathima households upon applying the discussed methodology. It indicates low electrical activities in the households with peak demand at night and no demand at all during the day. A peak power of 6.399 kW at 08:00 PM can be seen. This can be explained by the appliance ownership of in rural regions of developing countries is limited to mainly lights, radios and phones as discussed by (Narayan et al., 2020). The pattern of use indicates the beginning and of the day for household inhabitants suggesting the demand in the mornings and evening when either they wake up or prepare for bed. The afternoon zero electricity demand is explained by the absence of inhabitants during farming or schooling hours. At these hours, cell phones are charged at the shop and radio usage is initiated in the evening for national news and recreation after the end of their outdoor socio-economic activities.

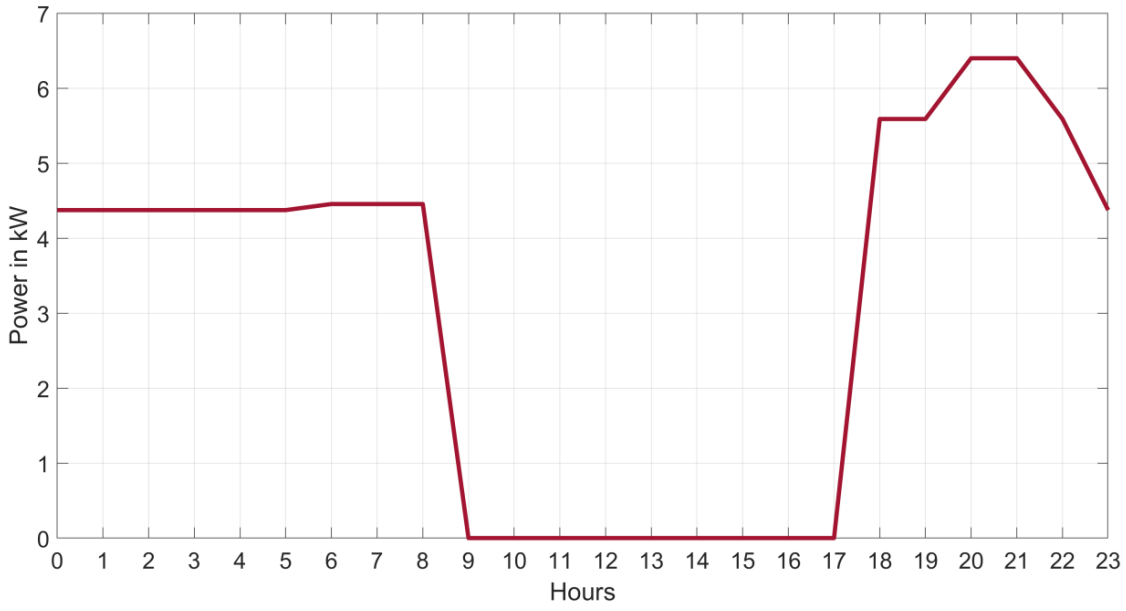

Fig. 6: Daily SLP for Uutsathima households

The business centre, likewise, exhibits an evening peak at 06:00 PM also accounting for the increased business engagement in the evening especially due to the dominance of Kapana shops and the highly rated milling shop in comparison to other electrical appliances. As illustrated in Fig.7, the Kapana shops and kiosks which are limited to lighting application have very low electricity demand in comparison to the shop and milling shop. This can also be seen in Tab.1 which breaks down the peak power and average daily energy consumption per business category. Contrary to the kiosk, the shop exhibits sharp peaks due to the availability of refrigerators and phone chargers. The behavior of power consumption of these activities overshadows the lighting demand. The milling shop whose machine is rated at 3.5 kW can be seen to dominate the electrical demand in the business centre.

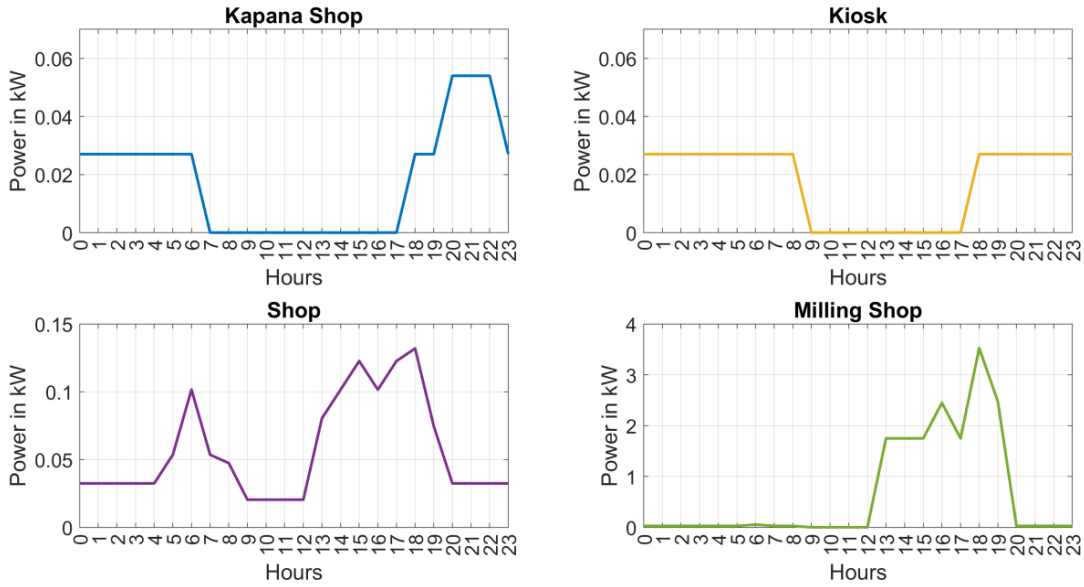

Fig. 7: Daily SLP for business settlements

Due to low income, residents have limited economic capability to mill their flour in large amounts and therefore the need for milling services close to mealtimes. Hence, the milling shop despite its regular opening hours, also exhibits a peak in the evening due to an increase in milling services demand.

Tab. 1 Peak power and daily energy consumption of business segments

Business Unit	Units	Peak Power (kW)	Average Energy (kWh/day)
Kapana shop	50	0.054	0.432
Kiosk	10	0.027	0.405
Shop	4	0.132	1.365
Milling shop	1	3.500	15.832
Business centre	1	5.675	46.942

The public institutions of Uutsathima which are also the primary and the connected consumers to the existing micro-grids exhibit different consumption patterns (c.f. Fig.8). The school in Uutsathima combines the administrative block and the teachers' as well as students' hostel.

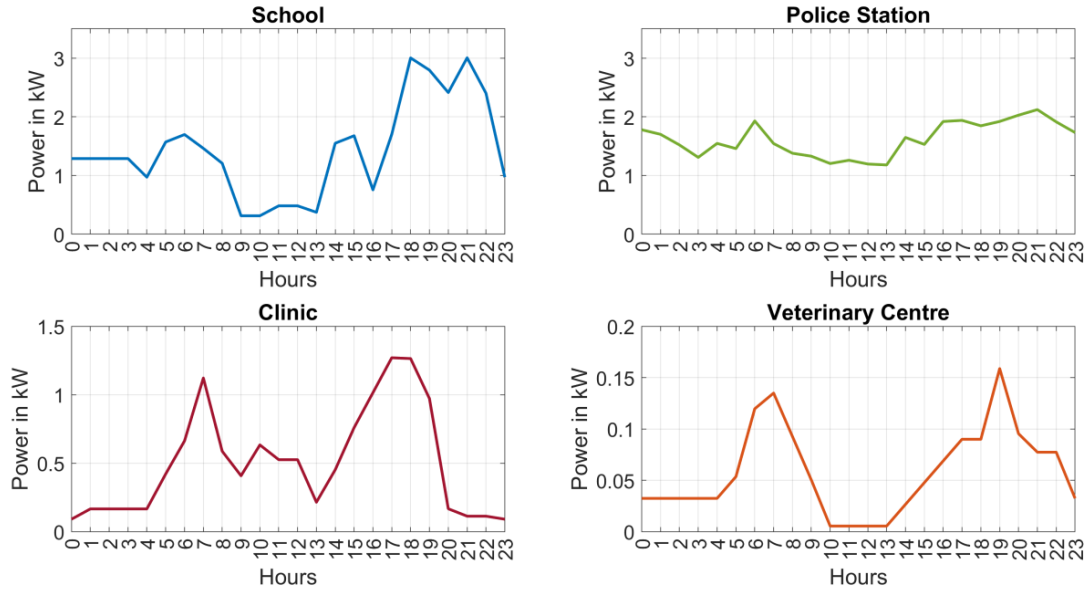

Fig. 8: Daily electrical load profile of Uutsathima's public institutions

The SLP follows the pattern such as that of a residential household due to higher demand in residences than in the school classrooms and offices. However, during the afternoon, power is consumed on printing and photocopying service which results into mid-day peaks. Due to the availability of always-on devices such wi-fi routers and monitors the school always has an electrical consumption. The clinic and veterinary centre were learnt to be equipped with refrigerators due to the demand in medicinal cold storage facilities. An addition of the workers' residence also explains the evening peaks. This research faced a challenge in accessing the police station and therefore the SLP was generated as a 20% factored-down annual SLP of the police station in Tsumkwe, which is a similar off-grid settlement in Namibia.

3.3 Aggregated load profile of Uutsathima village

Based on the generated clustered SLPs, an aggregated profile for the village was then generated to understand the typical consumption of a SSA off-grid rural village. The MATLAB (The Mathworks Inc., 2021) algorithm looped over every appliance and then every settlement to formulate the resulting Uutsathima SLP. The village exhibits a daily peak power and average energy consumption are 15.629 kW and 217.804 kWh/day, respectively.

Fig.9 shows a morning peak mainly due to household consumption and the Uutsathima village water pump turned on at 7:00 AM. Reduced activities at households, schools, and veterinary residences demonstrate a drop in consumption, leaving minor consumption and the water pump until the pump is switched off. In the evenings, the village exhibits higher demand due to increased residential activities, milling activities and liquor sales at the business centre.

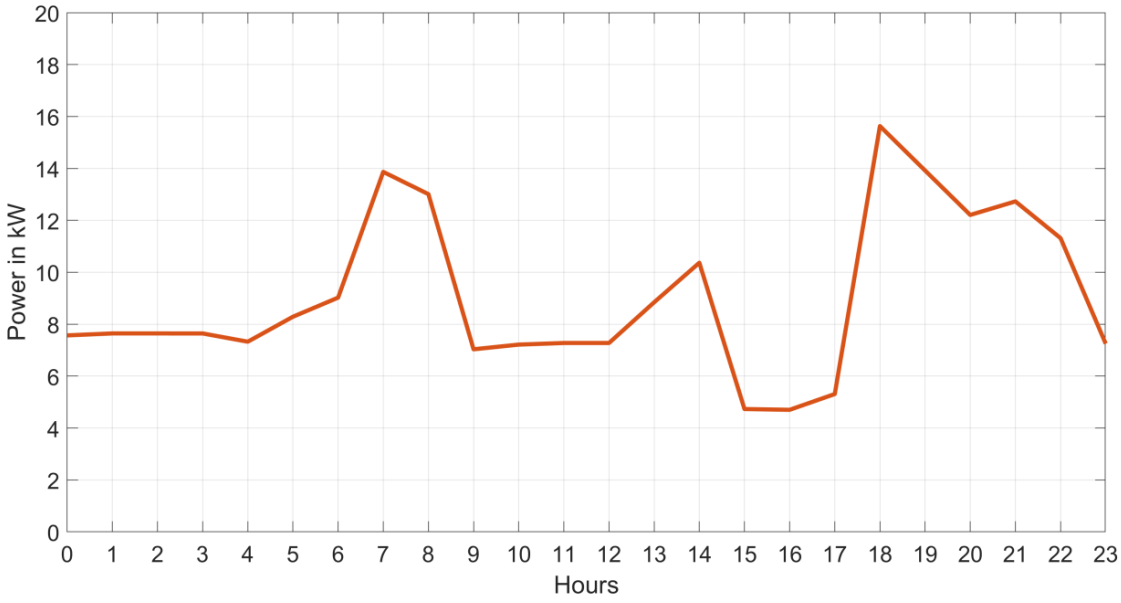

Fig. 9: Aggregated daily SLP of Uutsathima village

4. Energy Supply Scenario

Integration of micro-grids relies solely on the pre-existing capacity. In this chapter, the existing capacities which were obtained through the on-site survey are presented. Likewise, the generation of three scenarios by illustration of SLP is explained.

4.1 Existing micro-grid capacities

The energy supply is based on the existing micro-grids whose capacities (c.f. Tab.2) are, in this paper, analyzed on whether it is suitable to cover for the energy demand of the unelectrified categories. In the analysis of this paper, all capacities are considered regardless of their status of operation.

Tab. 2 Overview of the existing Uutsathima micro-grids

Micro- Grid	Component Capacities			Status
	PV Module (kWp)	Batteries (kWh)	Inverter (kW)	
Clinic	6.00	43.20	8	Operational
Veterinary centre	2.88	72.96	5	Not operational
School residences	2.88	109.44	3	Operational
School administration	2.88	109.44	5	Operational
Police station	8.00	87.36	5	Operational
Police water treatment	3.51	28.80	4	Operational

The answer to the research question, categorizing the demand side into different possible approaches, is done to identify the best applicable approach to utilize the total capacity of the existing micro-grids. The scenarios were distinguished and integrated into three scenarios.

Scenario 1: Integration of households

Scenario 2: Integration of business community

Scenario 3: Integration of household and business community (the whole village except the water pump)

4.2 Scenarios

Due to the pattern of consumption of the village as well as the high evening demand, the availability of enough storage capacity is crucial which relies on the generation time. However, due to the water pump's dominance in energy consumption at peak production hours, the pump was in neglected from all scenario generations. Fig.10 shows the consumption pattern of the water pump which in fact accounts for 19% of the daily villages' electrical energy consumption share. This paper recommends the use of a solar-powered borehole pump for water pumping purposes in such rural settlements.

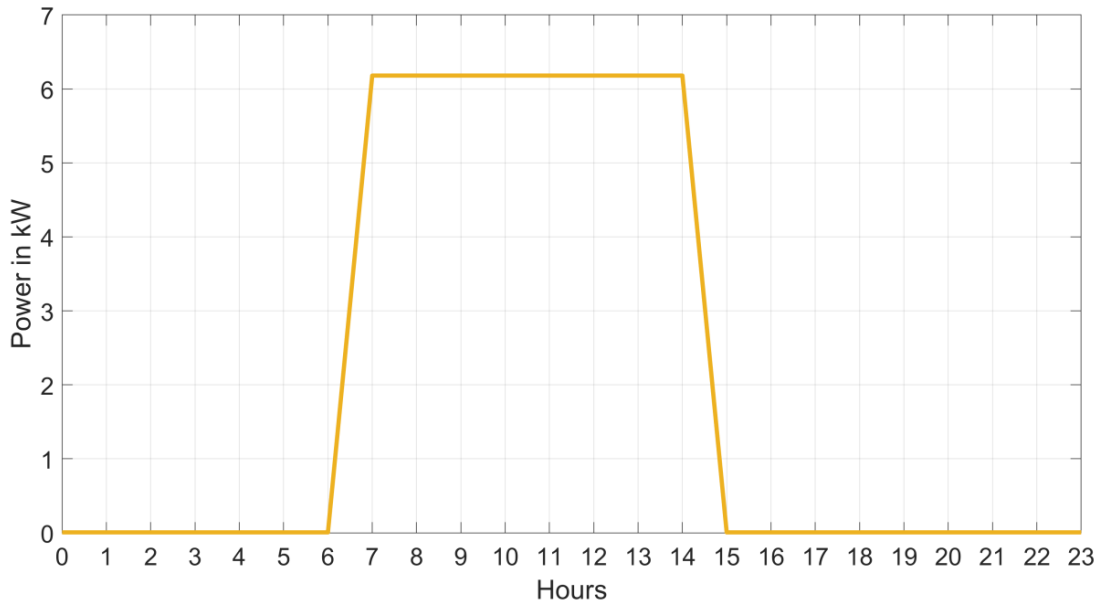

Fig. 10: Daily electricity load profile of the water pump

Since public institutions remain the primary consumers of the existing generated electrical power, all three scenarios integrate their demand. Fig.11 shows a comparison between the electricity demand of the generated scenarios. Scenario 1 exhibits a peak power of 12.62 kW, an average power of 5.58 kW and total average energy consumption

of 134 kWh/day. It can be noted that regardless of the inclusion of all public institutions in the load profile, the influence of households dictates the shape of the curve (c.f. Fig 11). While households exhibit no energy demand during the day, refrigerators and Wi-Fi routers from public institutions raise the energy demand during the day.

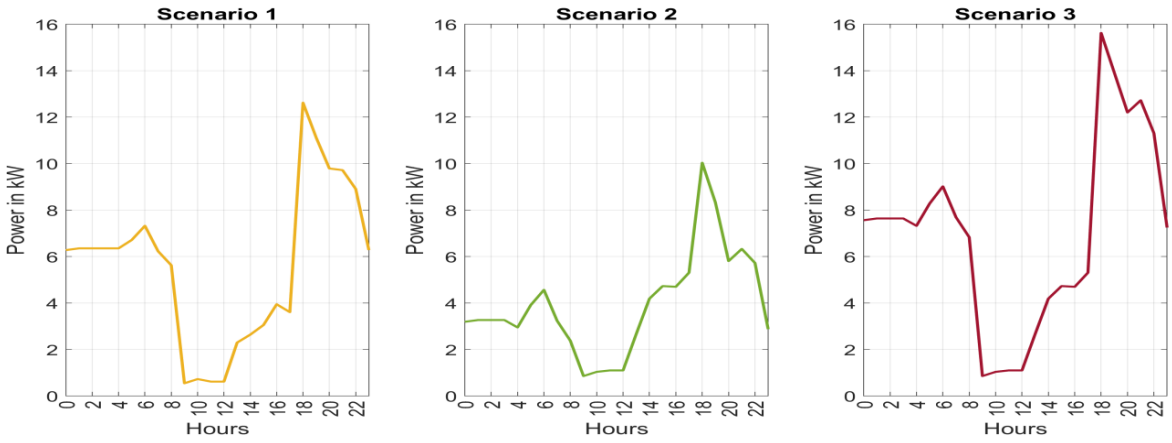

Fig. 11: Daily electricity load profile for generated scenarios

Scenario 2 exhibits the lowest energy demand due to small loads at the business centre. Peak power of 10.03 kW at 6:00 PM is mainly due to the business centre's milling machine, which is the highest-rated appliance in Uutsathima. Due to low demand at the business centre and the irregular consumption pattern, the load profiles take shape mainly of the public institutions except for the evening peak, which explains the high demand due to most business entities operating in evening hours.

Scenario 3 exhibits peak power of 15.62 kW at 7:00 PM, influenced by an increase in activity in households, business centre and all other residential settlements at the school, clinic, and veterinary centre's residents. It also has an average power consumption of 7.01 kW and daily energy consumption of 168 kWh/day. This scenario excludes the water pump and is therefore no summation or aggregation of scenario 1 and 2.

Tab.3 summarizes the peak power and daily energy demand per scenario.

Tab. 3 Peak power and daily energy consumption of scenarios

Scenario description	Peak power (kW)	Daily energy (kWh)
Integration of households	12.62	134
Integration of business community	10.03	95
Integration of household and business community	15.62	168

5. Results & Discussion

Using the simulation and energy audit methods discussed, this chapter presents the results from running PVsyst simulations to size a mini-grid for every scenario using elaborate illustrations and graphs. The PVsyst simulation also input meteo data on Uutsathima's temperature, diffuse and direct solar irradiation over the last decade to achieve custom reliable results.

5.1 Design of mini-grids for developed scenarios

For scenario 1 and assuming a uniform profile throughout the year, system components for storage and PV arrays were selected. Due to the absence of critical loads and low energy demand, one day of autonomy is considered for the battery bank. System design in PVsyst yields a mini-grid of 25.30 kWp and an annual energy production of 46.43 MWh/year. Scenarios 2 and 3 were simulated using the same approach. The mini-grid capacities obtained were 18.40 kWp with annual production of 33.69 MWh/year and 32.20 kWp with annual production of 58.02 MWh/year for scenarios 2 and 3 respectively. Scenario 3, unlike the previous two, has a collective summation of Uutsathima's power consumption. An increase in demand suggests that a larger capacity mini-grid would be required to meet the village's electricity demand. A summary of the three sized mini-grids is given in Tab.4. For feasibility of micro-grid integration, both the PV and battery storage capacities should sustain the energy demand of the expected consumers. In this case the comparison can be made against the sized mini-grids per scenario. Fig.12 shows the monthly mini-grid

energy production for every scenario.

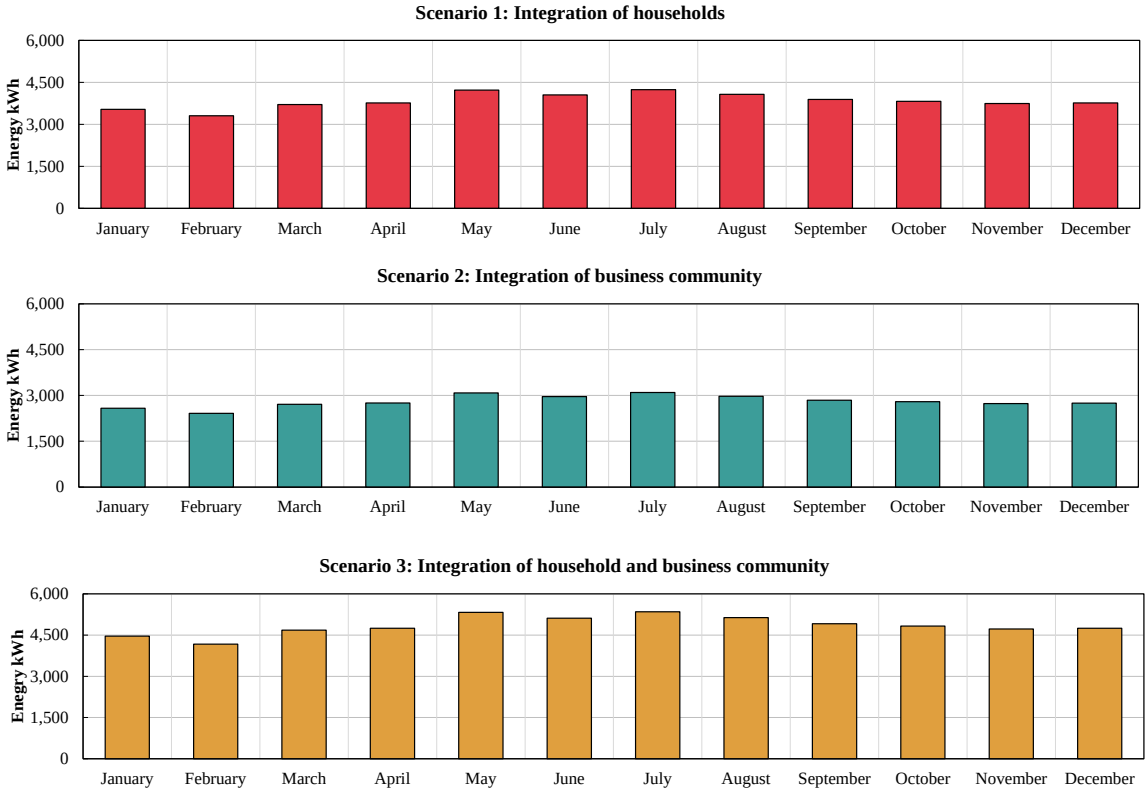

Fig. 12: Monthly PV mini-grid electricity generation for scenarios 1, 2 & 3

5.2 Result discussion

To establish the feasibility of micro-grid integration, this paper used a bottom-up approach to generate load profiles representing the actual demand of Uutsathima village. Categorizing its settlements helped link demand and supply sides by considering three different scenarios. Whilst the goal is to meet the village's demand by utilizing the existing capacity, the engineering approach used was to size a mini-grid for each scenario to determine the required capacity.

Tab. 4 Mini-grid results for the three case scenarios

Parameter	Value			Number of components		
Scenario	1	2	3	1	2	3
System capacity (kWp)	25.30	18.40	32.00	1	1	1
PV modules (Wp)	230.00			110	80	140
Batteries (V / kWh)	96 / 559.10	96/ 279.60	96/279.60	96	48	48
Performance ratio (%)	74.01	74.42	72.64	-		

The location and distance between existing micro-grids affect the infrastructure for transmission and distribution of electricity when integration is to be implemented. This means that an addition of transmission and distribution components would be required in the case of micro-grid integration so it can sustain the community's layout. However, based on these capacities, possible solutions and recommendations are reached.

5.3 How can the existing capacity cover Uutsathima's electricity demand?

This paper brings forward three possible solutions for micro-grid utilization to cover the electricity demand in Uutsathima. Tab.5 identifies which solutions may be implemented in the case of Uutsathima. However, infrastructural configuration is important to note. The orientation and sparse distribution of settlements in Uutsathima limits any possibility of physical integration between the village.

Tab. 5 Examination of micro-grid integration per case scenario

Grid	Nominal Capacity (kWp)	Battery Capacity (kWh)	Integration (technically feasible)
Existing micro-grids	26.15	451.20	Yes
Scenario 1	25.30	559.10	No
Scenario 2	18.40	279.60	Yes
Scenario 3	32.20	679.60	No

The comparison between the nominal capacities of the existing micro-grids and scenarios 1 & 2 shows a difference of 0.85 kWp and 7.75 kWp, respectively. This indicates that existing micro-grids generate excess unused energy that could potentially be made available to the household and business settlements. This study also established that if a mini-grid were to be sized for public institutions alone, a capacity of approximately 10 kWp could cover 100% of their electrical demand leaving an excess of 16.15 kWp of nominal capacity. Therefore, the first discovery in these results is that there is, in fact, a potential of using the existing capacity to extend electrification within Uutsathima. However, due to the dispersed orientation of the settlements some limitations arise. Thus, while arithmetically, there is a potential in utilizing the excess capacity, technically, this requires transmission and adjustment of system components. The business centre, for example, is close to the clinic and police station and further from the veterinary centre and school, while household settlements are sparsely distributed. The viability of micro-grid integration then depends on the relative location between them and the unelectrified settlements. If this approach is chosen, the replacement of system components such as the independent inverters with a single mini-grid inverter and placement of battery banks relative to the PV arrays and inverter should be done. Additionally, transmission cables should be run through the distances. To implement this approach, recommendations are to consider the costs for system adjustment, consumers' location relative to the existing grid, and susceptible system losses.

Alternatively, electrification of the business centre is a possible could be electrified by micro-grid integration. The capacity at the clinic and police is 17.51 kWp, and the collective demand for case scenario 2 is slightly higher. This indicates that the demand for the business centre can be supplied from the clinic and police station, given that the battery capacity is sized accordingly. While the load profile of the police station is relatively flat throughout the day, that of the business centre and the clinic has peaks in the evening, suggesting high demand during evening times. The feasibility of this solution depends highly on the battery capacity and, in the case of Uutsathima, the remaining lifetime of the batteries. Consideration in this scenario is given due to the business centre’s location being very near the two public institutions. Replacement of the inverters is again required due to the integration of the three independent grids at the clinic and police containerized grid and water treatment systems.

Arguably, the objective of this paper is to find a means to electrify the complete village of Uutsathima. Therefore, due to the technical complexity of micro-grid integration resulting from the population and settlement distribution as well as additional costs, a third solution is presented in this paper. It also identifies the difficulty of energy audit during load profiles and answers the question of why most mini-grids in rural unelectrified regions are either oversized or undersized. Availability of excess energy generated greater than the used energy or load energy demand indicates a lack of prior analysis of the consumers’ actual energy demand in Uutsathima.

While scenario 3 sizes a mini-grid to cover Uutsathima’s total energy demand inclusive of public institutions, the development of a new mini-grid for all the unelectrified settlements is another technically simplified solution. To avoid various decentralized generation and control systems, a single mini-grid with centralized inverter and storage units for the distribution of electricity into the village’s settlements is recommended. This also leaves provision for load evolution at the public institutions by using the available excess energy.

6. Conclusion

The distinction between rural and urban regions of SSA extends to the difficulty and ease of energy and specifically electricity accessibility. While urban areas are prone to easier electrification by grid extension, rural regions of SSA are hindered by low population densities, poor infrastructure, and low economic engagement, which altogether reduce the viability of grid extension. To avoid these economic and time constraints, alternative electrification schemes must be implemented to fasten electrification in rural regions. Many projects and research focus on

implementing new off-grid solutions, however, there lies a potential in assessing the feasibility of micro-grid integration, eliminating time factors and high investment costs. This paper used a rural low, population density, and low-income community in Namibia to analyze the energy status quo and draw scientific results and recommendations. The bottom-up approach using a MATLAB algorithm was used to generate independent settlement and aggregated load profiles. Three scenarios were considered by doing further PVsyst simulations to identify the most feasible solution. Findings of the analysis showed that while approximately 50% of the existing Uutsathima micro-grids generation capacity was not used, integration of existing micro-grids is highly dependent on the distribution and location of new consumers relative to the existing micro-grids. Replacement of many system components, expansion of the storage capacity, and establishing transmission lines pose additional costs that deem integration invalid when settlement density is too low. The results identified integrating Uutsathima's police station and clinic micro-grids and business centre load inclusion, as well as an erection of an independent mini-grid to electrify households as the most feasible solution. While this paper only examined the technical feasibility, further analysis needs to compare the economic benefit of integration by system component replacement and inquire about new inverters for micro-grid integration versus the erection of a new mini-grid.

7. Acknowledgments

This research was funded by the Federal Ministry of Education and Research (BMBF) of the Federal Republic of Germany within the CLIENT II funding programme "International Partnerships for Sustainable Innovations" under the project "PROCEED" (Project ID 03SF0570A-D). The authors highly acknowledge their support and contribution as well as the support from the Namibian Ministry of Mines and Energy, for their continued support in the PROCEED project under which this paper was written.

8. References

Chuan, L., Ukil, A., 2020. Modeling and Validation of Electrical Load Profiling in Residential Buildings in Singapore, 1. DOI: 10.1109/TPWRS.2014.2367509

Flor, M., Herraiz, S., Contreras, I., 2021. Definition of Residential Power Load Profiles Clusters Using Machine Learning and Spatial Analysis. Energies 14 (20), 6565. DOI: 10.3390/en14206565

Fritzsche, K., Shuttleworth, L., Brand, B., Blechinger, P., 2019. Exploring the Nexus of Mini-Grids and Digital Technologies. Potentials, challenges and options for sustainable energy access in Sub-Saharan Africa.

IEA, 2022. Africa Energy Outlook 2019 – Analysis - IEA. https://www.iea.org/reports/africa-energy-outlook-2019. Accessed 30 August 2022.

International Renewable Energy Agency (IRENA), 2022. Country Profiles: Namibia. https://www.irena.org/Statistics/View-Data-by-Topic/Renewable-Energy-Balances/Country-Profiles. Accessed 30 August 2022.

Jaglin, S., 2019. Off-grid Electricity in sub-Saharan Africa: from rural experiments to urban hybridisations.

Lorenzoni, L., Cherubini, P., Fioriti, D., Poli, D., Micangeli, A., Giglioli, R., 2020. Energy for Sustainable Development. Classification and Modeling of Load Profiles of Isolated Mini-grids in Developing Countries. Energy for Sustainable Development 59, 208–225. DOI: 10.1016/j.esd.2020.10.001

Narayan, N., Qin, Z., Popovic-Gerber, J., Diehl, J.-C., Bauer, P., Zeman, M., 2020. Stochastic load profile construction for the multi-tier framework for household electricity access using off-grid DC appliances. Energy Efficiency 13 (2), 197–215. DOI: 10.1007/s12053-018-9725-6

Opfer, K., Beaucamp, L., Njamnshi, A.B., 2022. A Factsheet for Civil Society. Renewable Energy for a Decentralised, People-Centred Energy Transition in Africa.

The Mathworks Inc., 2021. Self-Paced Online Courses - MATLAB & Simulink. MATLAB R2021b & Simulink. https://matlabacademy.mathworks.com/. Accessed 2 September 2022.

Vanadzina, E., Pinomaa, A., Honkapuro, S., Mendes, G., 2019. An innovative business model for rural sub-Saharan Africa electrification. Energy Procedia 159, 364–369. DOI: 10.1016/j.egypro.2019.01.001

Webgenève, 2022. PVSyst (Version 7.2) Photovoltaic Software. https://www.pvsyst.com/. Accessed 2 September 2022.

Mini-Grid or Grid Extension? The Strategies for Electrification Schemes Concerning Population Density in Sub-Saharan Africa

Kedar Mehta[1], Bertha Lwakatare[1], Mathias Ehrenwirth[1], Christoph Trinkl[1], Wilfried Zörner[1], James Katende[2], Joseph Shigwedha[3] and Helvi Ileka[3]

[1] Institute of new Energy Systems, Technische Hochschule Ingolstadt, Ingolstadt (Germany)

[2] Namibia University of Science and Technology, Windhoek (Namibia)

[3] Namibia Energy Institute, Windhoek (Namibia)

Abstract

Sub-Saharan Africa (SSA) is the second-largest continent in the world and homes an estimated quarter of the world's population. While the region has the fastest-growing population, it is dominated by scattered settlements between cities, towns, and villages. To date, SSA is the least electrified region in the world with lower electrification rates in its developed regions than in the least electrified regions in developed countries. This study uses Namibia, the least densely populated SSA country to assess the viability of mini-grids versus grid extension. Two main electrification options were considered within the presented work: grid extension and mini-grids. The study identified the key factors for fostering electrification in rural Namibia. The method applied in this paper follows various features starting from data collected from the field, literature review and geospatial approach to detailed analysis through techno-economic and social perspective. Summing up, the article presented the economic estimation for selected electrification options. Based on the analysis, the presented study attempted to provide a technical framework (based on the local boundary conditions). Even the LCOE is more subjective to various factors compared to grid-extension, it is recommended mini-grid for low-population off-grid. The derived result can serve as fundamental inputs for decision makers / policymakers to define the strategies for electrification schemes.

Keywords: electricity, grid extension, mini-grid, Namibia, population density, Sub-Saharan Africa

1. Introduction

1.1 Mapping out the scene

Access to electricity is considered one of the fundamental elements of human development (Sarkodie and Adams, 2020). In 2016, 1.1 billion people lacked access to electricity. At the end of 2021, the number of people without access to electricity dropped from 1.1 billion to almost 768 million. Around 60% of them live in sub-Saharan African (SSA) countries. Despite ongoing efforts of the electrification activities, ensuring access to affordable and reliable, sustainable, and modern energy for all (Sustainable Development Goal 7) is challenging. The current trajectory estimates that around 700 million people remain unelectrified until 2030, and the majority of them (600 million) will be from SSA (IEA, 2017; Falchetta et al., 2020). With a major electrical scarcity, it is difficult to foresee a developing modern economy or healthy and productive households. SSA holds the lowest energy access rates in the world. Around 13 countries in SSA have less than 25% electricity access rate. SSA's population is structured with approximately two-thirds of settlers in rural communities. However, it is the least electrified region in the world with about half of its population lacking access to not only electricity but also reliable electricity which both hinders the livelihood and productivity of the region. It is certain that grid extension cannot single-handedly thrust electrification rates and electrify the entire SSA. Electrification is even more crucial for low-population density countries in SSA. Because low population densities affect electrification schemes as there exist very long distances between regions and therefore pose infrastructural, time, economic, resource availability as well as technical awareness constraints (Trotter, 2016).

1.2 Introducing the special focus on Namibia

Namibia is a small country of about 2.5 million people. It lies along the coastline on the South Atlantic bordering South Africa, Botswana, Zambia, and Angola. The country identifies as the driest country in SSA with 70% of its population depending on natural resources for their livelihood (Schick and Pierre, 2021). Around 60% of Namibian electricity is imported from South Africa's Eskom and Southern African Power Pool (Marambire, 2020). Of the renewable primary energy resources, hydropower is highly exploited in Namibia. Due to climatic changes, hydrological regimes and capacity generation of the existing power plants are expected to reduce or vary (Ministry

© 2022. The Authors. Published by International Solar Energy Society
Selection and/or peer review under responsibility of Scientific Committee
doi:10.18086/eurosun.2022.18.10 Available at http://proceedings.ises.org

of Mines and Energy, 2020) especially with Southern African Power Pool (SAPP) failing to meet the demand of its primary customers in South Africa therefore reduction of imported electricity to Namibia. Namibia has electrification rates of 45% national wide and 19% for household settlements. At 3 people per km^2 with 79% of its population in rural settlements, grid extension is prone to the same constraints to reach its energy targets. Fig.1 represents the electrification timeline of Namibia put in place by the government to achieve universal electrification.

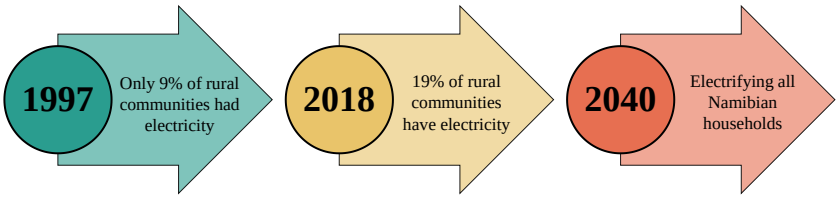

Fig. 1: Electrification timeline of Namibia (own illustration based on Buasai et al. (2019) and Ministry of Mines and Energy (2020))

Whilst the region is investing in formulating policies and regulations to increase its electricity access, often the remote and least developed areas are neglected. Namibian Ministry of Mines and Energy (MME) states within the rural electrification program that "*Rural electrification is part of the Government's economic development policy to expand the electricity supply infrastructure to rural areas to improve the socio-economic conditions of Namibian citizens and to create the necessary incentives for economic development in the targeted areas*" (Ministry of Mines and Energy, 2020). Recently, it was identified that the Ministry of Mines and Energy has a plan to electrify all Namibian households by the year 2040 (Pressreader, 2022). To achieve the target, Namibian energy policies approached several ways of electrification which are presented in Fig.2.

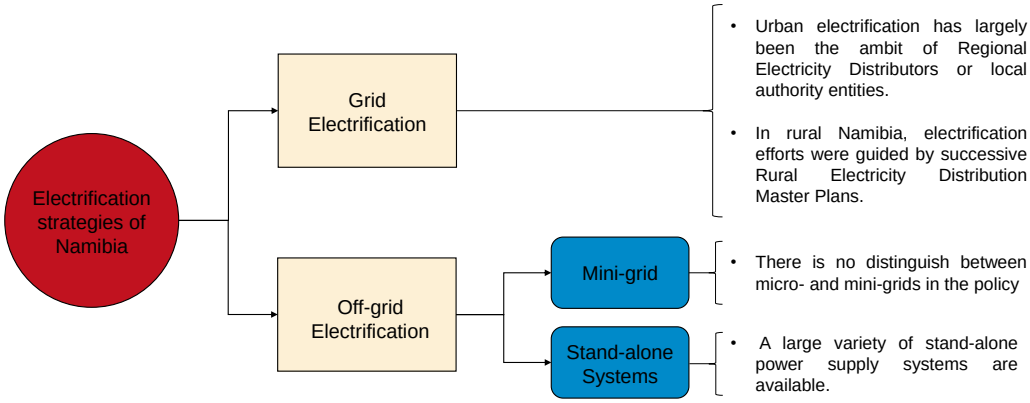

Fig. 2: Electrification strategies of Namibia (based on Ministry of Mines and Energy (2020))

1.3 Gap in the research and key objectives

To achieve the electrification target, naturally, rural settlements would probably be approached through either mini-grid technology or grid extensions under the scheme of "rural electrification program". Stand-alone systems are designed for primary energy needs (i.e., home lighting, mobile charging, radio etc.). However, stand-alone systems are of limited energy access in rural settlements which are formulated with some business establishments due to the requirement of higher energy amounts, the vast range of appliances as well the ability to easily expand and develop their energy demand (Scott-George et al., 2021). The recent theoretical development mentioned that there are two classic approaches available for rural electrification. One suitable way is to extend the grid to remote areas and electrify the isolated regions. Another one is the installation of a mini-grid system for remote settlements. However, selection of the suitable options from the above-mentioned solutions is one of the critical tasks for the policymakers. This is significantly applicable to countries with a low population density because the rural areas are situated far away from the major energy production centers and isolated geographically. This can be considered as one of the results of the low electrification rate (especially in the rural regions) in Namibia.

The lack of studies focusing on electrification policies that take into consideration population density and distribution limits the insight into answering the question of whether grid extension surpasses mini-grids as an electrification approach. In the case of Namibia, for instance, the government set out a strategy to adapt off-grid schemes only to public institutions. However, there is a gap in the research that outline the strategies for the electrification schemes at the household-level / settlement level. To address the research gap, the presented study is the first attempt to provide a framework for the electrification scheme in Namibia (a low population density country) and thoroughly

discusses the viability of the grid extension versus mini-grid on the country level. It brings forward results to this unaddressed comparative analysis with transferability to other SSA remote communities. Such study can serve as a fundamental base for decision makers / policymakers for adequate planning for the electrification strategies and targets.

2. Research Methodology

The method applied in this paper follows a multifaceted approach to achieve the key objective of the paper which is presented in Fig.3. The study starts with the problem statement by studying the energy situation in Namibia and the potential of rural electrification in the country. Based on that outlook, the presented article set a research question. To foster electrification, it is important to identify the key challenges / barriers to understanding the existing situation. Based on the expert opinion, geospatial data and literature review, the paper recognised the key electrification challenges for a typical rural settlement in Namibia. To actualise the technical framework, the article selected a typical rural settlement from SSA which holds a low population density and is situated far away from the national grid. For the presented study, Uutsathima was selected, and two main electrification options were considered: grid extension and mini-grids.

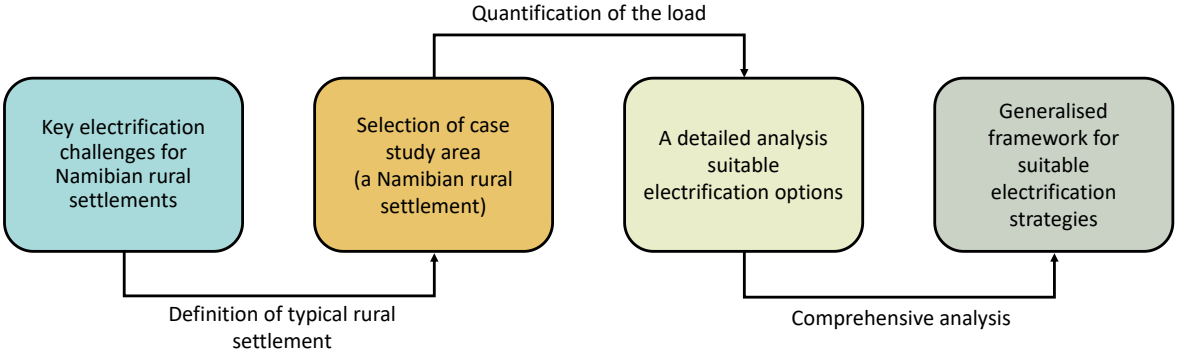

Fig. 3: Research methodology of the presented paper

The study brought out a comparative picture of suitable electrification options for rural Namibian settlement and provided a generalised framework on the country level (based on the on-site survey, technical analysis, literature survey and socio-economic indicators).

3. Derivation of key electrification challenges for rural settlements

Rural electrification in Namibia faced several challenges that deem typical electrification approaches impractical. This chapter intends to discuss the real challenges based on open-source geographic data, extensive literature, and field visits.

3.1 Population density

Population density gives an overview of how sparsely a country's population is distributed. In SSA, Namibia ranks last at three people per km^2. The population density affects infrastructure and economic efforts in grid expansion as it may deem it unaffordable and / or time-consuming. The distribution system network in low population density communities requires a vast distribution network coverage for the non-comparable amount of low energy consumption customers. This limits the value for electricity per square kilometer of coverage. Therefore, regardless of there being other alternatives such as generators and traditional exploitation of biomass energy, risks such as putting inhabitants' health at risk as well as limiting the economic activities carried out due to unreliable access still prevail. Especially with rising fuel costs, auxiliary solutions such as diesel gensets also do not put forth the best solution for rural inhabitants.

Gesto Energia (2018), identified that in Senegal the grid extension is recommendable in areas of higher population density as well as consumption. This is never the case for rural settlements, which explains the opaque grid extension efforts by various SSA member states' governments and ministries. Fig. 4 (b) illustrates the population density of Namibia. The interpretation of the map is that Namibia is substantially low populated with most regions appearing empty or unresized which may be interlinked with the dryness of the country. Apart from the northern region whose population is affected by the immigration of Angolans who fled their country in search of basic needs due to drought

in Angola (Nhongo, 2021), the remaining of the country especially the rural regions have very small population densities. Likewise, the youths and working class of Namibia tend to migrate into urban and semi-urban regions in search of energy ergonomic conditions. Namibia, therefore, serves the best for the evaluation of grid extension versus mini-grid implementation feasibility in concern of population density.

3.2 Limited availability of the transmission network

While rural regions, worldwide, are mainly defined by low population, low economic activity and recreational engagement, geographical outlook, among other factors, rural regions of SSA are predominantly interlinked with poor infrastructure and low to no electricity access. In SSA, less than 6 out of 10 households are connected to the main grid while less than 43% always enjoy a reliable supply of electricity without blackouts.

Rural residents have half the probability of that urban residents to have access to the main grid (Lee et al., 2022). To argue this fact, this paper presents a map (c.f. Fig 4 (c)) of Namibia which represents the transmission line of the national electricity grid. The map indicates that the grid is mainly concentrated in the central part of the country where the capital city, Windhoek lies. Contrary to that region, the northern, western, and southern parts are hardly within the reach of the grid. While this may again be interlinked with the absence of residence, arguably, this neglects most of Namibia's rural settlers whose geographical location denies them of their prerequisite need of access to clean and reliable electricity.

To define the non-electrified areas more specifically in-line with the availability of transmission network, Fig. 4 (d) represents the night light imagery applied which is defined by light emissions and the absence of the light emissions.

3.3 Low income

Residents of rural SSA communities are mainly associated with small-scale economic activities. In fact, the economic engagement in rural settlements is characterized by daily income-generating activities that can only sustain short-term needs rather than economic growth or savings. Rural regions mainly have a set of business establishments such as local kiosks selling basic household groceries, a few modern shops offering cellphone charging services and cold beverage, milling shops, and the most dominating are local alcohol shops for recreational purposes. In 2019, agriculture accounted for half the jobs in SSA and industries - mining industry - came at 13% in 2019 (United Nations Conference on Trade and Development (UNCTAD), 2021), however rural engagement in such activities remains very limited and if at all then food crop agriculture is predominant.

In Namibia, around 45% of the population live in multidimensional poverty / low-income. The low-income scenario is even more intense in rural Namibia (Namibia Statistics Agency, 2021). The lack of access to modern and reliable energy has contributed to the limitation of economic engagement of rural residents (Gesto Energia, 2018). Rural residents are linked with low income and are therefore unable to pay the electricity costs. Fig. 4 (e) illustrates the average household income in Namibia which indicates a higher generation in Windhoek (mainly in Khomas region) and a reduction of income as the map stretches towards the north and south of the country into rural regions.

3.4 High electricity costs

Despite the unavailability of the grid and high costs accompanied with grid extension, costs of electricity in rural SSA are often higher than the average earner can comfortably afford. Of the Southern-African Development Community (SADC), Namibia had the second highest electricity tariff of 0.167 € cents/kWh even though this was argued to be the most cost-reflective tariff in the region in 2018. Between 2017 and 2018, the tariff experienced a 6% increase for household consumers (Electricity Control Board (ECB), 2018). However, these reflective but expensive tariffs are also understood to grant and secure the viability and longevity of the energy solutions. On the 6th of May, 2022 the ECB in Namibia announced an increase for bulk electricity tariffs by 7.30%, and placed residential prepaid electricity at 0.087 €/kWh in the year 2022/23 (New Era, 2021).

The Ministry of Mines and Energy, in Namibia, reports that the existing tariff for rural low-income consumers is exclusive of capital and operation costs. This way the cost of electricity is reflective of the economic status of the consumers. However, the ministry identifies that capital and operational subsidies are crucial to compensate for the high supply costs which may be achieved through external funding to reduce or eliminate the risk of electrification failure in rural regions. The high electricity costs are, therefore, at present a burden for the government, operator, and consumer (Ministry of Mines and Energy, 2021).

(a) Administrative map
(Data: DIVA -GIS)



(b) Population density
(Data: United Nations OCHA)

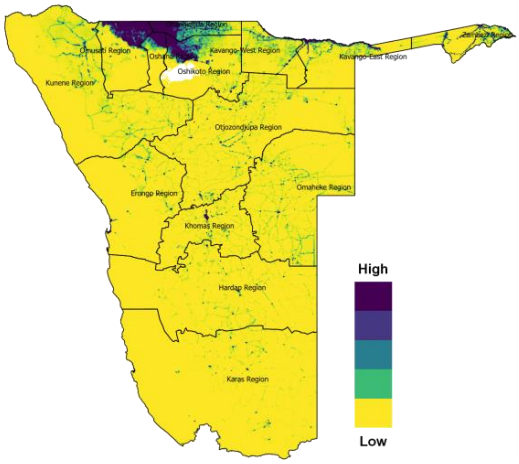

(c) Transmission network
(Data: NamPower)

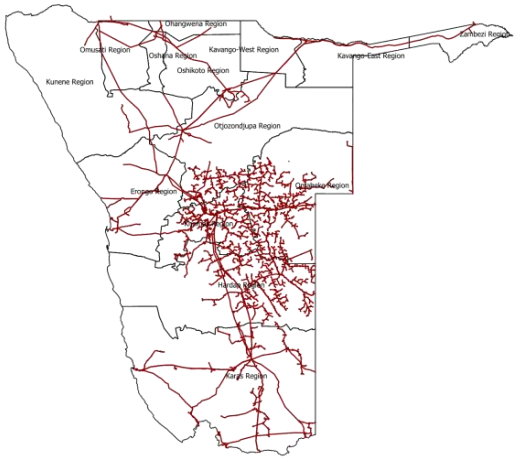

(d) Nightlight view
(Data: NASA Earth Observatory)

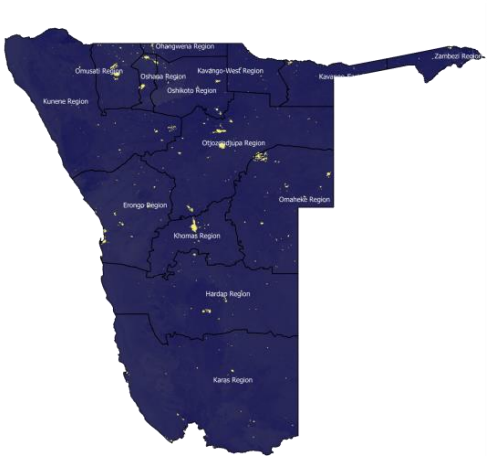

e) Household income

(Data: Buasai et al. (2019))

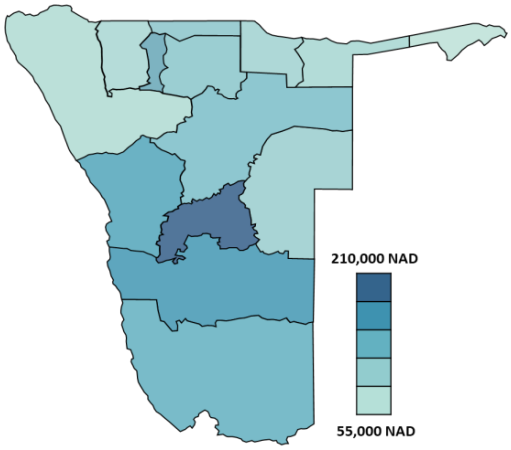

(f) Solar irradiation

(Data: The World Bank)

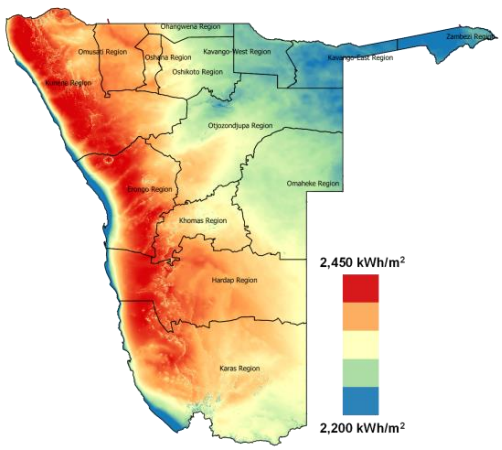

Fig. 4: The selective geographical datasets for Namibia (own illustration based on the GIS data mentioned respectively)

3.5 Less exploitation of solar energy for electrification

Namibia is one of the sunniest countries in the world, as shown in Fig. 4 (f), with solar irradiation ranging from 2,200 to 2,460 kWh/m2 annually. Despite this, over 60% of the country's energy is imported, and most rural areas are without electricity. Only three off-grid regions, Gobabeb, Tsumkwe, and Gam, have installed pilot mini-grids using solar energy. This indicates a lack of solar energy utilization for electrification. This paper focuses on solar energy as an alternative electricity source, particularly for mini-grids, in Namibia, which has a low population density and substantial potential in solar irradiation and photovoltaic technology.

4. Typical rural Namibian settlement - Uutsathima

A typical SSA rural settlement is characterized as a large constellation of very distributed settlements. Often the areas are with large open land or a small population density with minimal business engagement. While the areas belong to a governmental structure, seldom do they benefit from development and budgetary schemes as they are the least prioritized regions. Services such as education, health, electricity, clean water, and infrastructure such as roads are very limited in rural regions of SSA. The rural settlements in Namibia have identical structure to those in the SSA region and all over the country. This paper goes further to select a rural settlement in Namibia for precise and realistic findings. This chapter describes Uutsathima, a typical Namibian rural settlement and its electrical condition, consumption, and demand which is used to design and recommend electrification options for a low population density community.

4.1 General setup of Uutsathima

Uutsathima, Namibia is a rural village located in the north-eastern part of Namibia in the Omusati region at 18° 27´ 36´´ S, 14° 50´ 24´´ E. Fig. 5 shows its geographical information orientation. As of 2022, Uutsathima's households and business settlements are still mainly unelectrified, while a few businesses use diesel generators or solar panels for phone charging services. The households use either candles, paraffin, or solar-powered lanterns for lighting purposes while they all use wood stoves and charcoal for cooking.

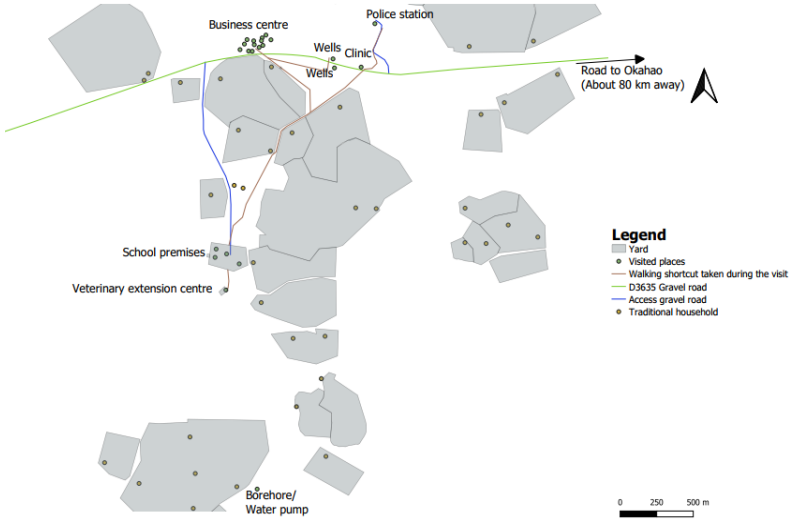

Fig. 5: Geographic information system (GIS) representation of Uutsathima village

The village is mainly sub-categorized into households, businesses, and public settlements. The business centre of Uutsathima is comprised of 50 local alcohol shops, 10 local shops, 4 modern shops as well as a milling shop. The public institutions include a police station, a school with teachers and students' residence, a clinic, and a veterinary centre. The village also has a water pumping station that uses a Lister-peter diesel powered surface pump to fill in the village water storage tanks. This paper recognizes the prerequisite lack of electricity access to the households and business settlements as a barrier to their general livelihood and herein utilizes the situation to analyse and answer the question of which option between grid extension or mini-grid implementation best fits the electricity access coverage when population density comes in question. To do that, the electrical consumption of Uutsathima is studied.

4.2 Load profile of Uutsathima village

Low-income resident dominated rural settlements of SSA are characterized by limited electrical demand and access as well as few electrical appliances based on the significance of demand. The Global LEAP, an international

association that promotes the world's best off-grid appliances, identifies lighting, mobile charging, radio, television, and music sound systems as the most electrical applications by order of significance (Narayan et al., 2020).

In Uutsathima, the same electrical demand and behaviour was observed through an on-site survey. A social and technical survey was done, to distinguish the customer clusters, the appliance ownership across the categorized clusters and their power rating, as well as the consumption behaviour -as influenced by related economic or domestic activities- on an hourly basis. This survey was done over a research stay which included interviewing, questionnaire filling as well as on-site survey and energy audit of available appliances across the electrified public institutions. Due to minor economic engagement and existence of only one business centre, all establishments including the public institutions were audited. As the households were completely unelectrified, random sample household respondents were interviewed. Data was therefore collected on existing appliances and projections for the appliance ownership in unelectrified consumer categories based on the respondents' information. The collected data was used to create load profiles for all distinct appliances and settlements using a MATLAB algorithm. Using the collected data, each appliance, its rated power, and the vector for the hourly usage is loaded into MATLAB and an independent appliance load profile is created. This MATLAB loop runs over all appliances in each settlement with the corresponding usage vector. Once the loop is completed over one consumer/ settlement, the aggregated load profile is computed for each settlement/ consumer. MATLAB then aggregates the individual settlement/ consumer load profiles into the Uutsathima village load profile presented in Fig.6.

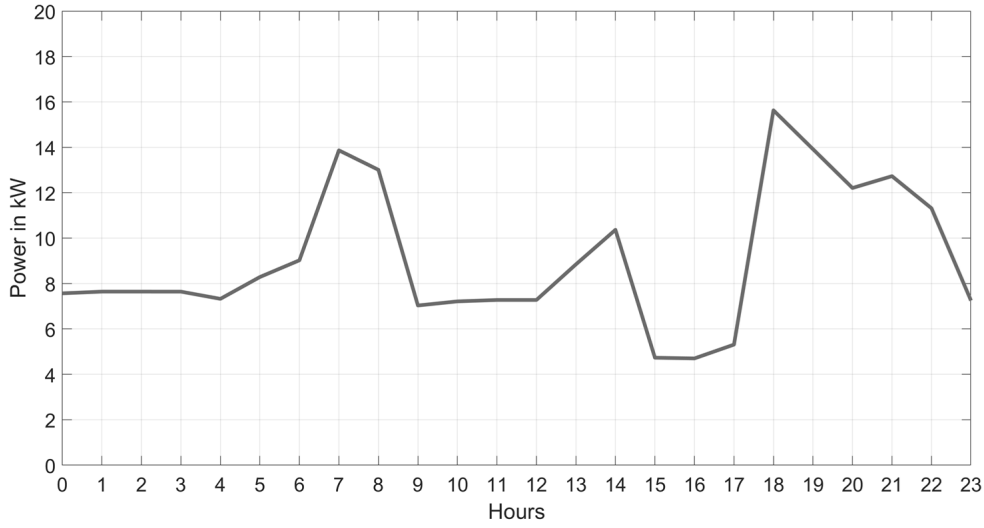

Fig. 6: Aggregated electrical load profile of Uutsathima village

The load profile of Uutsathima village represents the aggregated demand of all settlements within the village. Fig. 6 shows a morning peak mainly due to household consumption and the water pump turned on at 7:00 AM. Reduced activities at households, schools, and veterinary residences demonstrate a drop in consumption, leaving minor consumption and the water pump until the pump is switched off. In the evenings, the village exhibits higher demand due to increased residential activities, milling activities and alcohol sales at the business centre. The daily peak power and average energy consumption are 15.629 kW and 217.804 kWh/day, respectively.

The load profile depicts that the village has higher demand in the evenings than during the day which this study considers an indicator of the need for sufficient storage capacity. Therefore, since the consumption of energy is highest in the evening, that implies that during peak production hours, the charging of the batteries is crucial. To avoid extreme diesel consumption by running the diesel generator and/or evening and nighttime electricity black outs, this paper further suggests excluding the 6 kW water pump in the load profile. As is the pump is currently operated6 hours during peak production times (i.e., from 08:00 AM until 02:00 PM). This complements the storage capacity and assures reliable supply in peak hours. Since the water pump is currently diesel powered, the recommendation is to maintain it or replace it with a solar powered pump and operate it independent of the mini-grid serving other consumers. Fig. 6 shows the load profile of Uutsathima village with a decreased demand in the afternoon and is therefore used to examine the two electrification approaches.

5. Detection of potential electrification options

After quantifying the settlement electrical load, this chapter throws light on how to meet that load through suitable electrification. In that regard, two main electrification options were considered grid extensions and mini-grids. This chapter further presents a comprehensive analysis of both electrification options. Due to limited availability / unavailability of information on the economic dimensions, cost estimation was considered based on the literature review. However, the robust technical information provided in the presented article (i.e., load profile of a typical settlement, required size of mini-grid, the distance of the settlement from the available grid etc) will allow the scientific community to develop accurate economic analysis as a future scope.

- Mini-grid-based electrification:

  Based on the load profile generated for Uutsathima village, a mini-grid to meet the demand of the village was sized using PVsyst (Webgenève, 2022). The simulation results will allow understanding the size of the mini-grid for Uutsathima village. Based on the size, a rough estimation was made for LCOE for electrification through mini-grid.

- Grid-extension based electrification:

  For grid extension into Uutsathima, two key factors were considered. The closest grid point to Uustathima was found through consultation with the Namibian Energy Institute (NEI). Then, assuming a standard cost of grid extension per km, a rough capital investment for extension was attained.

5.1 Mini-grid for Uutsathima

The developed load profile became an input for the simulation through the PVsyst. Fig.7 represents the detailed technical results of the simulation results for electrification through mini-grid. The mini-grid annual energy production is 52 MWh/yr.

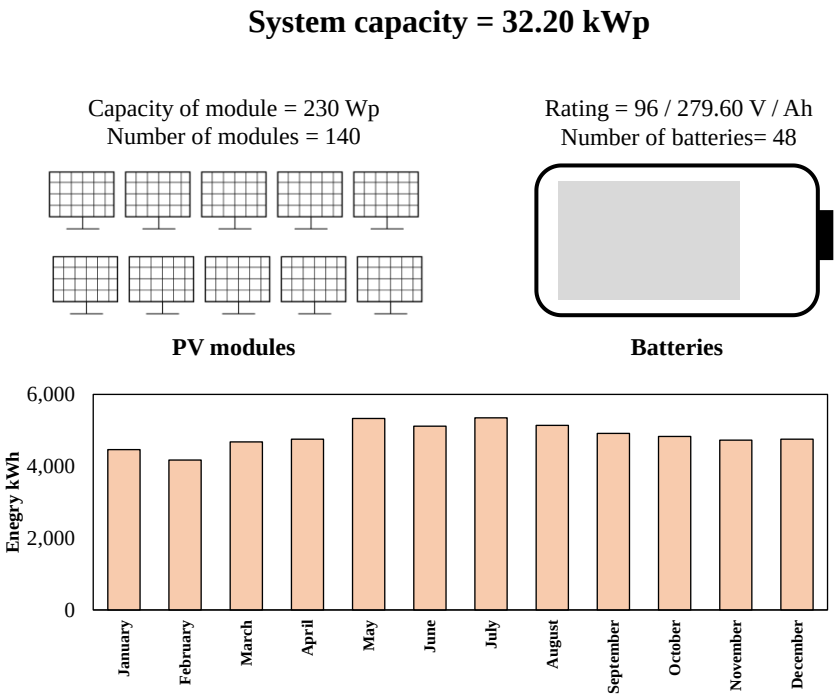

Fig. 7: Technical specification for the suggested mini-grid and monthly Uutsathima PV mini-grid electricity generation

By considering the abundant solar energy resources, the presented simulation study considered the solar PV-based mini-grid for electrification. However, as the presented article deals with the general blueprint and technical framework, Fig. 8 represents the LCOE of various mini-grid technology for the scientific community. One can study Come Zebra et al. (2021) for in-depth economic assessment of mini-grid for off-grid electrification in developing countries. By considering the enormous potential of solar energy as well as the robustness of the solar-based mini-grid, the presented article selects the solar PV-based mini-grid. In the case of Uutsathima as the system size for the mini-grid is 32.20 kWp, the estimated LCOE is 0.55 €/kWh based on the literature review.

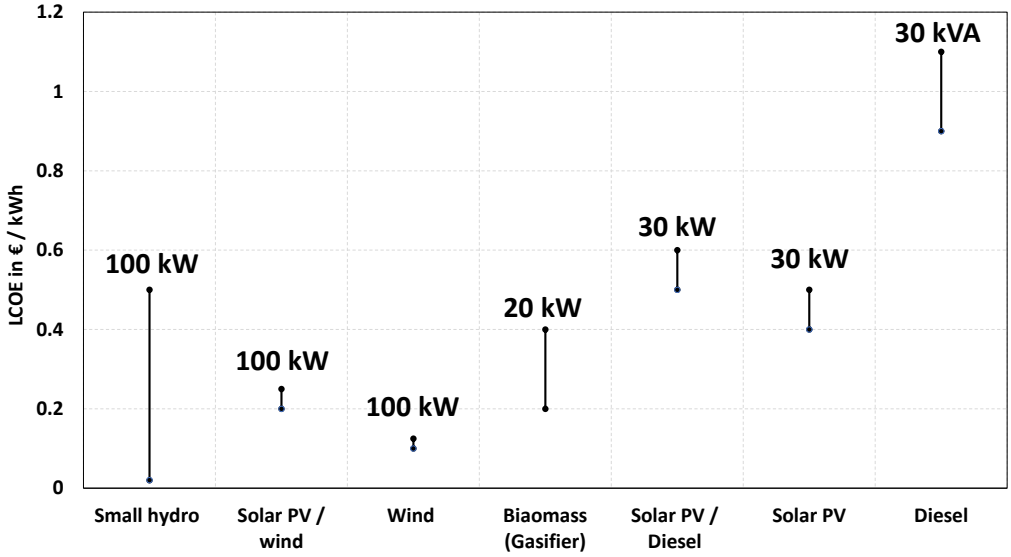

Fig. 8: LCOE (€/kWh) of mini-grid and hybrid mini-grid options at different scales based on Come Zebra et al. (2021)

5.2. Grid-extension for Uutsathima

The United Nations sustainable development goal 7 (SDG 7) motivated governments in SSA to formulate solutions in efforts to increase energy access. In the case of electrical energy, most governments enacted grid extension as a premium solution. However, connection costs remain high for an average-earning household. Economically advantaged households are twice likely to get connected to the grid in comparison to a poor household, the percentage probability is 83% to 43% (Lee et al., 2022). Whilst these connections imply only in the case that the grid is within proximity, the corresponding governments also face significant investment cost implications in grid extension.

In 2019, the cost of grid extension was reported by the World Bank to range up to 35,080 €/km (Sessa et al., 2021). Research showed that 87% of new connections are within 5 km of the existing distribution network and 77% within 2 km (Sanghvi, 2020). This implies that for villages, such as Uutsathima, whose closest grid distribution network is tens of kilometres away, the economic feasibility of grid extension is impractical especially with little to no budget allocation by the responsible ministries and governments. Okahao is the closest semi-urban town to Uutsathima. 20 km from the town is the nearest grid point to both Okahao and Uutsathima. An approximate of 60 km lies between the grid point and Uutsathima. At the rated cost of extension per km as per Sessa et al (2021), a grid extension investment of approximately 2.1 million euros would be required to Uutsathima. In instances that member countries of SSA have extended their grid into rural regions, electricity costs continue to surpass the economic capability of rural abilities to purchase despite their willingness to pay for electrical energy.

6. Outlook / Discussion

6.1 Recommended technical framework for electrification in Namibia

Previous research is available that used different methodologies / decisive matrices for electrification of the non-electrified regions. However, in particular, for Namibia, there is a lack of scientific knowledge available about decision-making. Hence, based on the literature review and discussion with the energy experts in the field, the presented technical framework attempt to quantify the derived key challenges and portrays the robust technical framework for electrification which can be considered as a novel contribution. The presented analysis will serve as the fundamental input for the policymakers / decision-makers to design the electrification plan for Namibia.

Naturally, high population density in the village / community is immediately interlinked with higher load density (i.e. kW demanded / km^2). Ochs and Gioutsos (2017) mentioned that "*Areas with higher load densities require less low-voltage line materials and labour for their installation, which reduces distribution costs and often swings the economic favourability towards mini-grids. Cost savings are found to diminish at around 400 people per square kilometre*". However, Namibia is already a low population density country and therefore it is difficult to transfer the results to Namibia. The author suggests that further research work needs to be carried out here to quantify the population density as a decision making for Namibia for available electrification options. It is recommended that the

living area / settlement near power transmission lines within the proximity of 5 to 25 km is cost-effective for electrification through grid extension (Szabó et al., 2011; Bertheau et al., 2017; Ochs and Gioutsos, 2017). Fig 4 (c) already presented the recent transmission network of Namibia. One can easily identify the unelectrified region through that and try to measure the distance from the nearest grid point. This approach will now give a better understanding that grid extension is a feasible option or not from the cost-effectiveness. Compared to solar home light systems, mini-grids are usually installed in the range of 10 kW to 10 MW and therefore provide large-scaled loads (Come Zebra et al., 2021). Naturally, the large cumulative load cut down the cost and makes the mini-grid generation economically viable. Based on the previous analysis, Fig. 9 presents a suitable electrification option selection for Namibia.

Considering that Namibia's tariffs exclude capital and operational costs for grid extension for rural unelectrified regions implies that from the implementation phase developing countries such as Namibia, function at an economic disadvantage. Unaffordability of electricity cannot be solved by incurring losses therefore, secure models should be adapted. The literature review showed that in most of the cases, LCOE of mini-grid is low compared to grid extension. However, the LCOE considers all-around investment and operations costs and if subsidization and cross-subsidies are adopted, this could see a decrease in price for rural consumers.

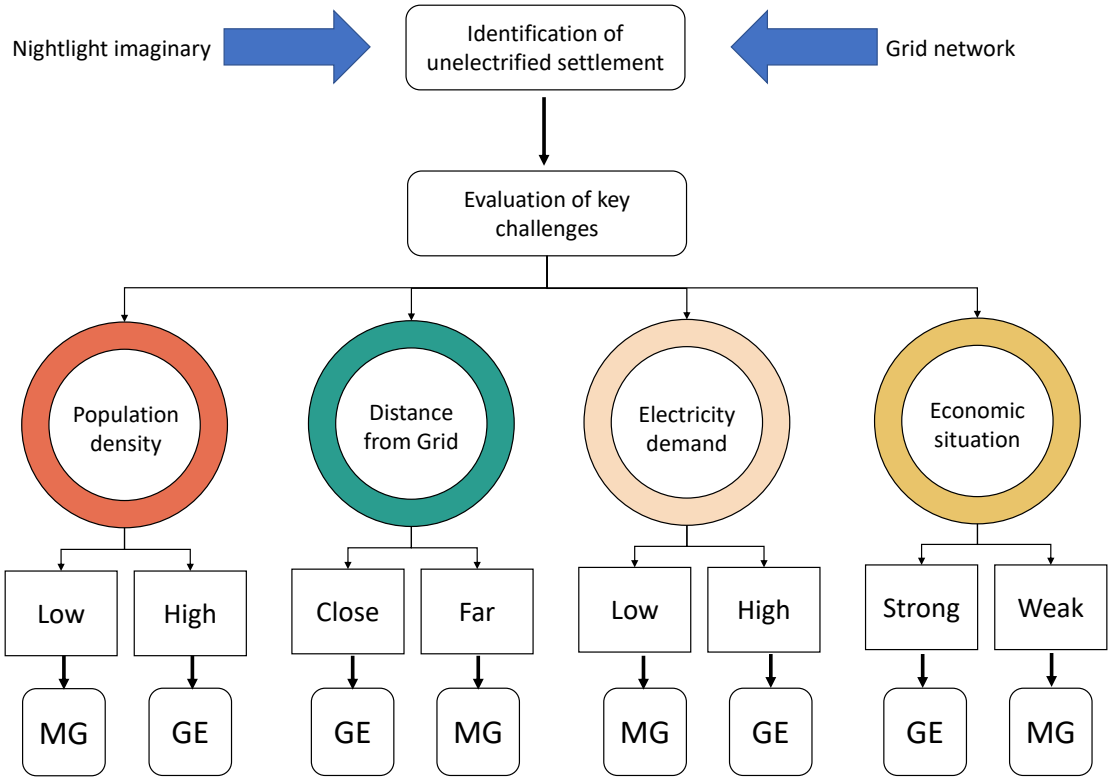

Fig. 9: A derived technical framework for deciding electrification schemes that can help to provide best-served electrification approach to electrify Namibia (MG = Mini-grid and GE = Grid extension)

6.2 Limitations of the study

The presented study provides a conceptual framework that was generalized and scaled up to the country level based on the on-grid and mini-grid assessment. Hence, the study will not only be limited to Uutsathima (settlement level) but, instead, the results were applied to Namibia (on the country level). However, the decision for suitable electrification can not only be made from the advantages and disadvantages of the technology. There is an immediate need to consider the key challenges / local factors which were derived in the presented article.

6.3 Comparative analysis of both electrification options in the context of SSA

This chapter provides a comparative overview of the pros and cons of both the selected electrification options in through the assessment in the local context. This overview will help an international reader to understand the individual electrification option closely.

Tab. 1: Comparative overview of mini-grid and grid-extension technology

	Advantages	Disadvantages
Mini-grid	• Utilization of local resources • Community based solution • Integration of productive use cases • Enables "link" to (national) power grid • Depending on location: Lower LCOE as compared to grid extension	• High investment costs / Investor required • Regular maintenance is mandatory • Limited correlation between demand / capacity • Requires battery storage and / or backup generator
Grid-extension	• Low maintenance costs • "Technology-agnostic" • Battery storage optional • A robust, reliable solution	• (Very) high investment costs • (Very) long implementation time • Not (necessarily) linked to the expansion of renewable energy

7. Conclusion

The presented research article tried to answer the research question "what is the suitable electrification strategy for rural Namibia?". Therefore, this study conclusively identifies the selection possibilities between mini-grids and grid extension for rural electrification in Namibia. The results were obtained by consideration of the vision, goals, and efforts of the Namibian electrification and energy policies. The research looked at how to bring electricity to rural areas in Namibia. The study found two options that could work: mini-grids and grid extension. The study compared the benefits and challenges of each option, which could save money and make electricity available faster. The standard option in developed countries is the grid connection for almost all households. This highly capital and rigorous electrification option may take a longer time for developing countries to achieve fast electrification. At the same time, mini-grid technology is a well-established (technically) option. However, it requires sufficient high local demand density. However, it does not disregard the role of grid extension and therefore identifies regions that are least scattered, further from existing transmission plants and with denser load to utilize grid extension. Consideration of population increase, as well as an increase in economic activities, may, in the future, increase the demand and therefore the inflexibility of mini-grid expansion can be limiting but policies such as integrating them into the grid once it arrives may be the ideal solution. The study recommends studying the demographic influence of areas as well as sizing off-grid networks as per demand to avoid surplus generation, losses, or high costs. Summing up, the presented article derived a general framework to demonstrate where which technology will be feasible based on the key criteria discussed in the article. Due to this demographic similarity in remote areas of SSA, the findings of this study can be transferred to any member country. One may further analyze the utilization of other standalone off-grid systems such as solar housing to classify which electrification scheme fits for further scattered and less dense settlements.

8. Acknowledgments

This research was funded by the Federal Ministry of Education and Research (BMBF) of the Federal Republic of Germany within the CLIENT II funding programme "International Partnerships for Sustainable Innovations" under the project "PROCEED" (Project ID 03SF0570A-D). The authors highly acknowledge their support and contribution as well as the support from the Namibian Ministry of Mines and Energy, for their continued support in the PROCEED project under which this paper was written.

9. References

Bertheau, P., Oyewo, A., Cader, C., Breyer, C., Blechinger, P., 2017. Visualizing National Electrification Scenarios for Sub-Saharan African Countries. Energies 10 (11), 1899.

Buasai, S., ElShahks, B., Kelsey, B., Whitehorn, L., 2019. Data Portal for Rural Electrification in Namibia, 2019.

Come Zebra, E.I., van der Windt, H.J., Nhumaio, G., Faaij, A.P., 2021. A review of hybrid renewable energy systems in mini-grids for off-grid electrification in developing countries. Renewable and Sustainable Energy Reviews 144, 111036.

Electricity Control Board (ECB), 2018. Electricity Supply Industry Statistical Bulletin Rural Electrification in Namibia 2018.

Falchetta, G., Pachauri, S., Byers, E., Danylo, O., Parkinson, S.C., 2020. Satellite Observations Reveal Inequalities in the Progress and Effectiveness of Recent Electrification in Sub-Saharan Africa. One Earth 2 (4), 364–379.

Gesto Energia, 2018. Senegal's SE4ALL Rural Electrification. Action agenda and investment prospectus.

IEA, 2017. Energy Access Outlook 2017.

Lee, H.E., Kim, W.Y., kang, H., Han, K., 2022. Still lacking reliable electricity from the grid, may Africans turn to other sources.

Marambire, A., 2020. Sustainable finance. An essential tool to enable access to affordable and clean energy in Namibia.

Ministry of Mines and Energy, 2020. Republic of Namibia - National Electrification Policy. First Draft. https://www.ecb.org.na/images/docs/Economic_Regulation/1st%20DRAFT%20-%20National%20Electrification%20Policy%20-%20Rev%202%20-%2020200916.pdf. Accessed 23 April 2022.

Ministry of Mines and Energy, 2021. National Electrification Policy. Final Draft.

Namibia Statistics Agency, 2021. Namibia Multidimensional Poverty Index (MPI) Report 2021, Windhoek, Namibia. https://ophi.org.uk/wp-content/uploads/Namibia_MPI_report_2021.pdf.

Narayan, N., Qin, Z., Popovic-Gerber, J., Diehl, J.-C., Bauer, P., Zeman, M., 2020. Stochastic load profile construction for the multi-tier framework for household electricity access using off-grid DC appliances. Energy Efficiency 13 (2), 197–215.

New Era, 2021. Electricity price to surge… NamPower granted 7.3% tariff increase. https://neweralive.na/posts/electricity-price-to-surge. Accessed 5 September 2022.

Nhongo, K., 2021. Namibia Under Pressure from Angolan Migrants Fleeing Drought. https://www.bloomberg.com/news/articles/2021-10-07/namibia-under-pressure-from-angolan-migrants-fleeing-drought. Accessed 6 September 2022.

Ochs, A., Gioutsos, D., 2017. Rural Electrification in Sierra Leone: The Role of Mini Grids vis-à-vis Stand-alone Home Systems and Grid Extension.

Pressreader, 2022. Tsumkwe West residents receive electricity, Namibia.

Sanghvi, A., 2020. National Electrification Strategy. Implementation Plan and Mechanisms for achieving Universal Electricity access (2020-2030). Terms of Reference.

Sarkodie, S.A., Adams, S., 2020. Electricity access, human development index, governance and income inequality in Sub-Saharan Africa. Energy Reports 6, 455–466.

Schick, A., Pierre, I., 2021. Namibian bush encroachment in context. An ecological perspective on current and future drylan greening.

Scott-George, A., Li, C., Tang, Y.K., Saha, S., Bin Ali, M.T., Marma, A., Pal, S., 2021. A review on the sustainability of solar home system for rural electrification. E3S Web Conf. 294, 2003.

Sessa, V., Bhandari, R., Ba, A., 2021. Rural Electrification Pathways: An Implementation of LEAP and GIS Tools in Mali. Energies 14 (11), 3338.

Szabó, S., Bódis, K., Huld, T., Moner-Girona, M., 2011. Energy solutions in rural Africa: mapping electrification costs of distributed solar and diesel generation versus grid extension. Environ. Res. Lett. 6 (3), 34002.

Trotter, P.A., 2016. Rural electrification, electrification inequality and democratic institutions in sub-Saharan Africa. Energy for Sustainable Development 34, 111–129.

United Nations Conference on Trade and Development (UNCTAD), 2021. Reaping the potential benefits of the African Continental Free Trade Area for inclusive growth.

Webgenève, 2022. PVsyst (Version 7.2) Photovoltaiv software. https://www.pvsyst.com/. Accessed 12 September 2022.

100% renewable energies at Majorcan Hotels

Andreu Moià-Pol[1], Víctor Martinez-Moll[1] and Vincent Canals[1]

[1] GREEN, Engineering and Construction Department, Universitat de les Illes Balears

Cra Valldemossa km 7,5. 07122, Palma (Spain)

Abstract

The Balearic Islands have to decarbonize by 2050 the Majorcan tourist sector, whose priority will be to change before 2030 the fossil gas and diesel consumption. This paper analyses how to perform the change of fossil fuels in hotels to renewable energy, with a special focus on how to convert all energy demand with renewable energies. The goal is to determine a new model of designing new energy systems, and coupling it as much as possible, to the Solar Energy production with the energy demand. The Hotels can guarantee good comfort with 100% of renewable energies, especially with solar thermal and photovoltaic systems combined with heat pumps and Hydrogens systems. The implementation of high solar fraction combined with other renewables energies will be considered. New design with advanced sustainable building technology could arrive to zero emissions buildings or positive energy.

Keywords: Decarbonization, hydrogen, solar energy, Heat Pumps, Hotels

1. Introduction

The Balearic Island's government wants to achieve zero emissions in the tourist sector by 2035, some Hotels being the first ones to make a step towards this energy transition next year. The effort to decarbonize the Islands will be reached on one hand in each building and on the other hand at electric and gas systems, with high renewable fraction. Renewables in Spain reach a share close to 47% of Electric production in 2021 and a production of 10% more than 2020. The gas sector is planning in the future to increase the fraction of biogas and H_2 input to the net, but some new designs and materials will be necessary for this implementation. Actually, there is an interesting project GREEN HYSLAND which will also deliver a roadmap towards 2050 that compiles a long-term vision for the development of a widespread H_2 economy in Mallorca and the Balearic Region, in line with the environmental objectives set for 2050. A fully functioning H_2 ecosystem in the island of Mallorca is intended to be deployed, turning the island into Europe's first H_2 hub in Southern Europe. This can be achieved by producing green hydrogen from solar energy and delivering it to the end users, such as the island's tourism, including gas grid injection for green heat and power local end-use. Indeed, hydrogen will help to increase the penetration of renewable energy in the Balearic energy system, demonstrating how the Tourist sector can move towards a full decarbonization of the economy.

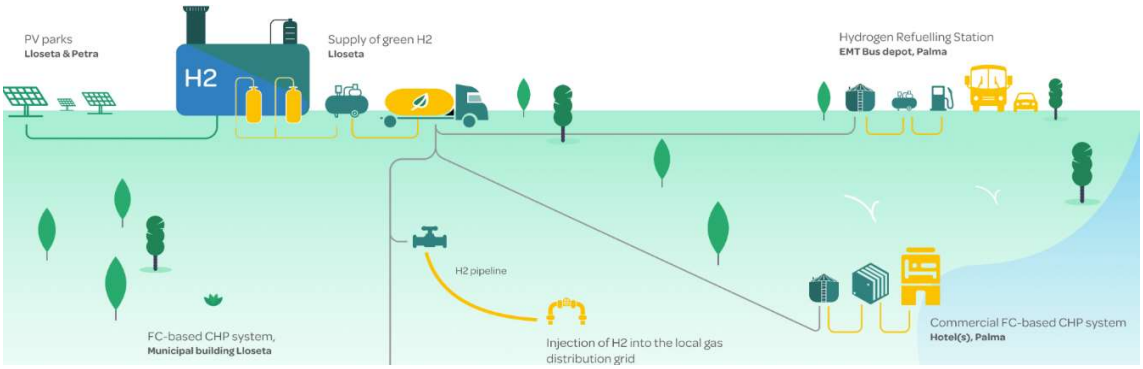

Fig. 1: Greenhysland scheme project. Source https://greenhysland.eu/

© 2022. The Authors. Published by International Solar Energy Society
Selection and/or peer review under responsibility of Scientific Committee
doi:10.18086/eurosun.2022.18.11 Available at http://proceedings.ises.org

2. Hotels with 100% of renewable energies

Currently in the Balearic Islands, where the largest Spanish hotel holdings are located, a great effort on key issues of sustainability and circular economy is being set up, such as waste disposal, energy generation, consumption of local products and welfare issues. In the first step of this strategic conversion, the Spanish hotel holding companies are putting in place systems of circular economy systems, the commitment to generate decent and sustainable jobs commented in the studies of Esther González Arnedo and others.

The annual average energy consumption in a Mediterranean Hotel is about 150 kWh/m^2, with a 50% of fossil fuels for thermal uses according to the studies of Moià-Pol et Alt., and another 30% for the rest of thermal uses with electricity (cooling, refrigeration,etc). The usual design for the thermal demand of a hotel is a boiler (diesel or gas) for Domestic Hot Water (DHW) and heating, gas for kitchen devices and a Heat Pump (HP) for cooling, a small refrigeration system for freezing rooms with electricity. The last years in order to increase the energy efficiency and reduce de fossil fuel consumption, hotels are changing the facilities design and are unifying the thermal systems - heating, cooling and hot water- in one by changing the conventional fossil fuel boiler for Biomass boiler combined with solar thermal systems or by using only electricity produced by photovoltaics.

PV and wind power combined with HP could provide for the majority of the demand of energy. Some thermal uses such as natural gas kitchen devices could be changed actually by electric or in the future with Hydrogen produced by renewable energy sources.

Wind power presents certain challenges in the building integration and most of the Biomass is produced in other areas and with external suppliers, and sometimes it results expensive to use and maintain. Mediterranean areas present a huge solar potential; thermal collectors can reach up 500-1000 kWh/m^2 year and PV 200-400 kWh/m^2 year. The renewable mix have to be chosen according to the technical complexity of the installation and the monthly energy profile. Hotels which are open all year round and need a bigger thermal fraction, they can use biomass whereas those which open only at summer could be designed only with solar energy and a properly storage system.

The new legislation of the Insular Consell of Mallorca (CIM) wants to reduce the energy consumption of the Hotels with the following rules:

- Energy label of A or B.

- Have a minimum of 50-70% of self-consumption produced by renewables energies.

- The 70% of the Domestic Hot Water has to be heated with Solar energy.

The methodology of this work has been to collect real data from 200 hotels and find the best real rehabilitation practices in approximately 20 hotels, renovated in the last 5 years, as well as data from manufacturers and installers in the Balearic Islands. The main consumptions and the analysed designs are commented below.

2.1. Domestic Hot Water

The new generation of Heat Pumps with new refrigerants (R290, R32, R744,..) can substitute completely the boiler for hot water; the condensation system can work more than 60ºC with high efficiency and the evaporation system can arrive to -10ºC with high efficiency, the main problem is economically being still expensive, due to an emerging technology with high pressure compressor. In order to reduce the initial, even conventional Heat Pumps or Simple effect absorption units could be used until 55ºC but they need to supply a fraction with other technologies for increase the temperature up to 60ºC, in order to reduce the bacteria in Hot Water (especially the Legionella), high solar fraction systems have been studied by Vassiliki Drosou et alt. some years ago in Mediterranean countries with solar thermal fraction up to 70%. Another option is to combine standard HP with small new HP with high temperature or Hydrogen or Joule effect, always combined with PV.

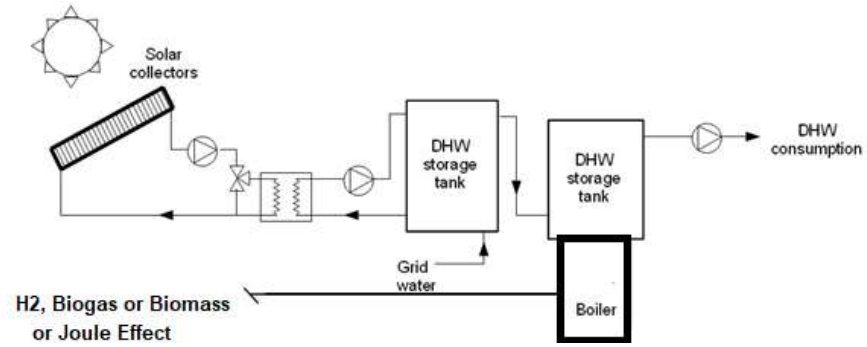

Fig. 2. Example of a system with Solar Thermal energy

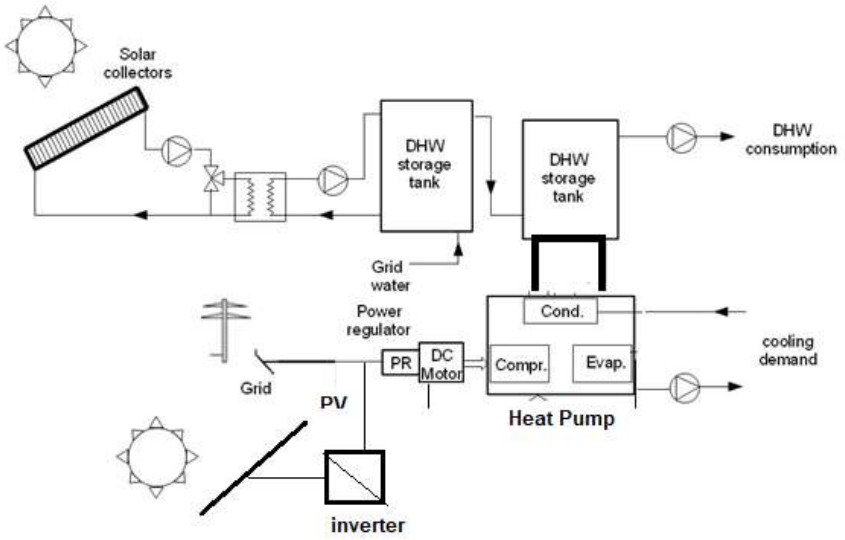

Fig. 3. Example of a system with Heat Pump, Solar Thermal and PV energy

There are a lot of combinations of these technologies, and each hotel, according to the surface t and he level of the maintenance staff could be different. Different combination from real cases has been studied by Moià-Pol et alt. with an estimation of energy cost and CO_2 emissions see at the table 1.

Tab. 1: Renewable mix for Hotels with different fraction for DHW

DHW Generation	ST	PV	HP_Low	HP_High	Joule	€/MWh	kg CO_2/m^2
Natural Gas/Diesel	0%	0%	0%	0%	0%	85	13,5
ST-Natural Gas	70%	0%	0%	0%	0%	40	4,1
ST-PV-Joule effect	70%	30%	0%	0%	30%	32	0
ST-PV-HP_low_Joule	70%	30%	25%	0%	5%	22	0
ST-PV-HP_low_high	70%	30%	25%	5%	0%	21	0
ST-PV-HP_High	70%	30%	30%	30%	0%	24	0
PV-Joule	0%	100%	0%	0%	100%	65	0
PV-HP_low_Joule	0%	100%	80%	80%	20%	34	0
ST-PV-HP_low_high	0%	100%	80%	20%	0%	28	0
PV-HP_high	0%	100%	100%	100%	0%	37	0

2.2. Heating and Cooling Systems.

The last years some hotels have changed completely the Heating and cooling systems, changing the diesel or gas boiler for heat pump, with 100% of electrict consumption (Power to Heat), combined with PV fraction, (figure 4), in mediterranean countries the standard heat pumps with air have a good efficiency all the year even at winter. The PV combined with cooling storage will reduce to zero the cooling and freezing consumption, and is a very easy technology. The other electric consumption will have to implement of smart strategies, but a small percentage will have to be stored in batteries or in other emerging technologies like Fuel Cell with Hidrogen and Hydrolysis, in order to arrive to a highest self-consumption system, avoiding as much as possible the injection of electricity to the grid.

As we have commented before, always the most efficient technology is solar thermal systems, with a higher efficiency and less surface than the PV systems, even if we combine them with high efficiency heat pumps.

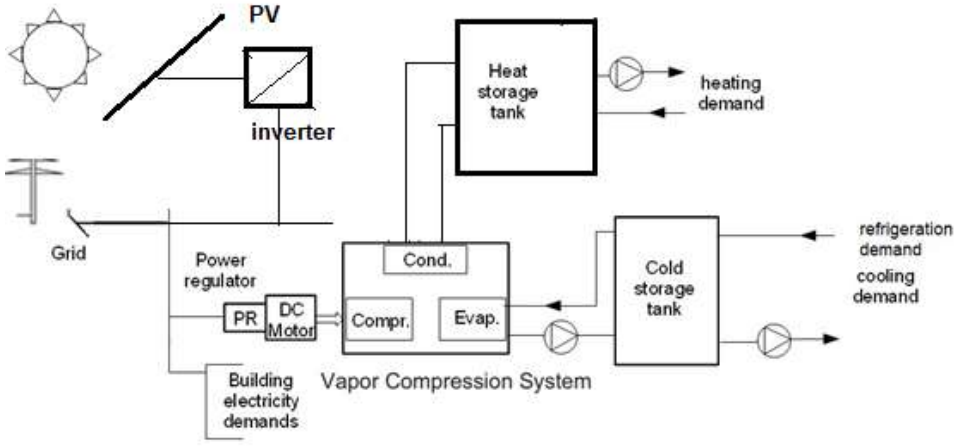

Fig. 4. Example of a Heating system with 100% electric system (Power to Heat)

The ideal system for high thermal loads could be 100% thermal system, with a large Solar thermal absortion refrigeration and a less investment and less generation cost almost 30%, but unforntunately few buildings have large solar systems in their designs.

However, in most of the hotels, specially the ones that open half year or have a high consumption only at summer, the compression systems with PV are better because they can do net metering or sell the overproduction of the PV, the ST will be intersting in areas with District Heating, but unfortunately in the Balearic Islands there isn't any touristic area with DH. In order to increase the self-consumption and a high thermal storage reducing the electric storage which is more expensive than the thermal, an Optimal system has been designed integrating all the thermal systems in one with heat and cold storage.

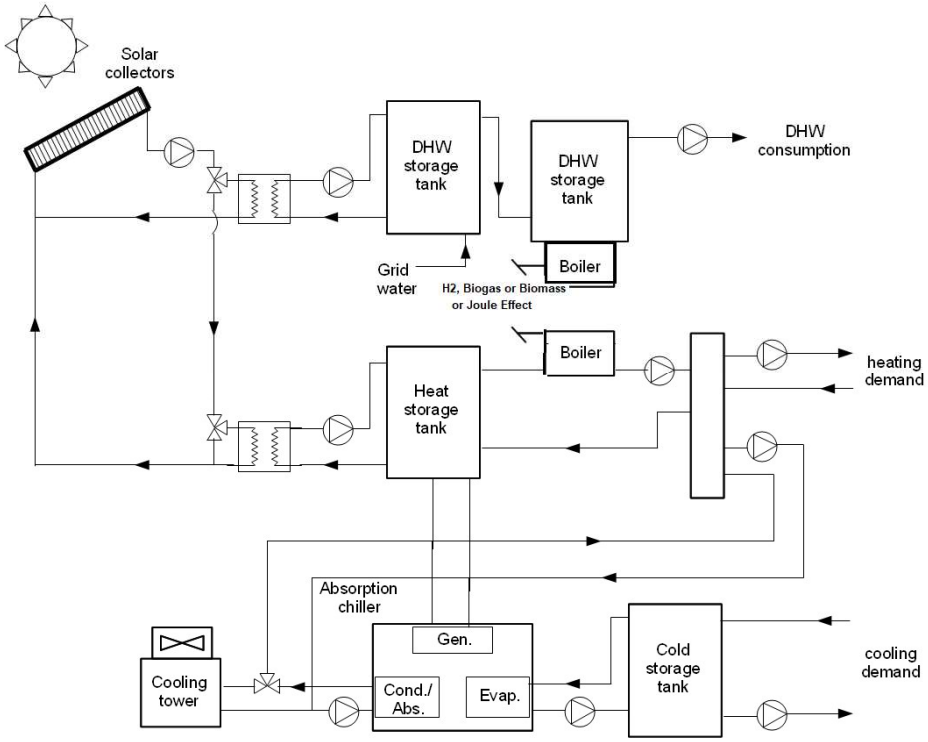

Fig. 5. Example of a Heating system with High fraction of Solar Thermal

2.3. Hotels with Combined Heat and Power.

The CHP systems have been installed in hotels the last 20 years, but they need a high thermal consumption and stable fossil fuel prices in order to be economically feasible. Due to the high variation of the fossil fuel prices, high cost maintenance and changes of grants in the electricity, a lot of these facilities have failed.

The renewable energy technologies could open a new market, being stable and more easy to maintain. Hotels with a high fraction of PV systems like the one proposed in the figure 4 could combine the thermal hotels proposed in the figure 5, using the hydrogen like a vector. At the heart of most Power-to-X concepts is the utilization of renewable excess electricity to produce hydrogen through the electrolysis of water. This hydrogen can be used directly as a final energy carrier. The fuel cell could help to provide 100% of the energy demand of a hotel, with higher efficiency than the Hydrogen produced in central plants, due to all the thermal exhaust of the hydrolyzer and the fuel cell could be used to supply the thermal necessities of the hotels and reduce the high energy consumption during the compression and the transport.

The big issue of Power-to-Hydrogen: converting electricity into hydrogen implies energy losses; Power-to-Hydrogen aims to achieve an emissions-free process by using renewable electricity in an electrolyzer to produce hydrogen from water. The main problem of the hydrogen produced with PV is the low efficiency of the whole process, less than 5%. However, using fuel cell in the main buildings could optimize the efficiency using the exhaust thermal from the fuel cell, recovering the heat and a total efficiency of nearly 10% could be reached by PV system. All the energy demand with a high efficiency could be provided with the help of the fuel cell, and that is the best storage for large periods. In the PV systems with Hydrogen we will need almost 4 times more surface than the Solar Thermal systems used directly for thermal uses, but as we have commented before, the storage and the management of the PV systems is easier, especially at Mediterranean tourist areas without District Heating systems. The gas sector could use in the future the existing pipeline as net metering systems for Hydrogen for Hotels like actually the Electric companies do. In this way will be easier to storage the excess of energy and avoid the collapse of the electrical systems, in a future scenario of 100% of renewable energies.

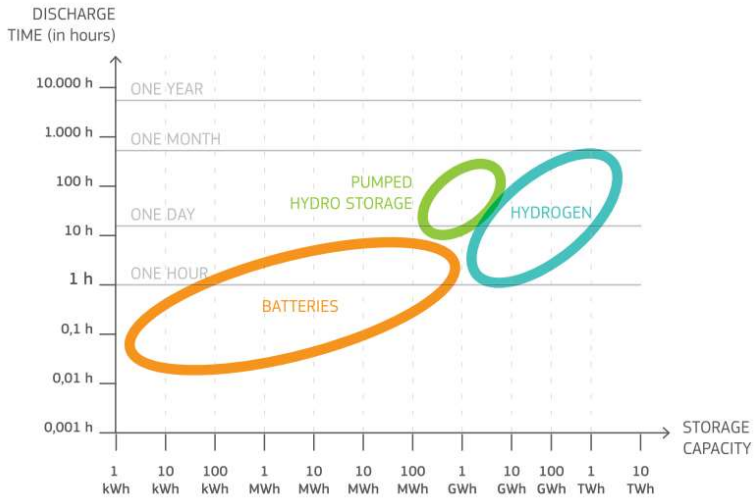

Fig. 6. Energy Storage. Source; Clean energy for EU islands, Technology solutions booklet

The suitability of storage technologies depends on the storage capacity required and the amount of time during which energy needs to be stored. The figure 6 shows only the three storage technologies that are included in the Clean energy for EU islands, Technology solutions booklet. The fuel cell has a great advantage that doesn't have mechanical parts and the maintenance is easier than the standard CHP systems.

The Hydrogen technologies will be studied with a deep analysis in the next years in the project Green hysland, where a Hotel with a commercial Fuel Cell of 50 kW as a demonstration site (as we can see at the figure 1 will be taken into consideration. The objective is to obtain the best solution in all the points of view; energetically, environmentally and economically, and find the optimal mix in each case.

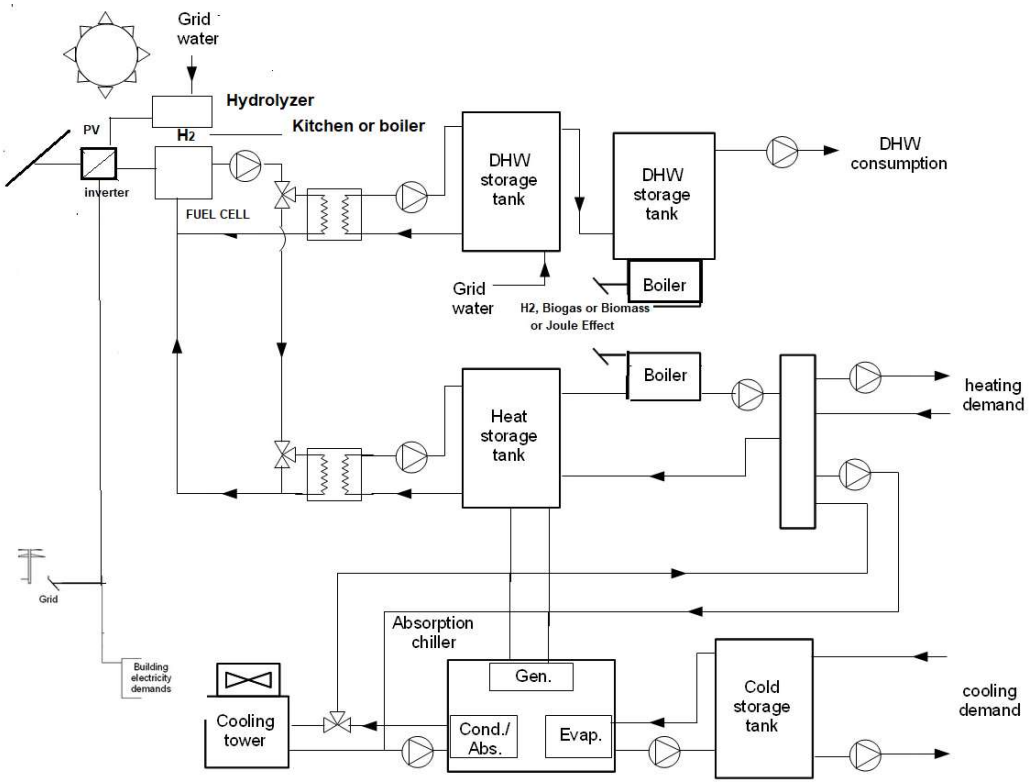

Fig. 7. Future Hydrogen Hotel

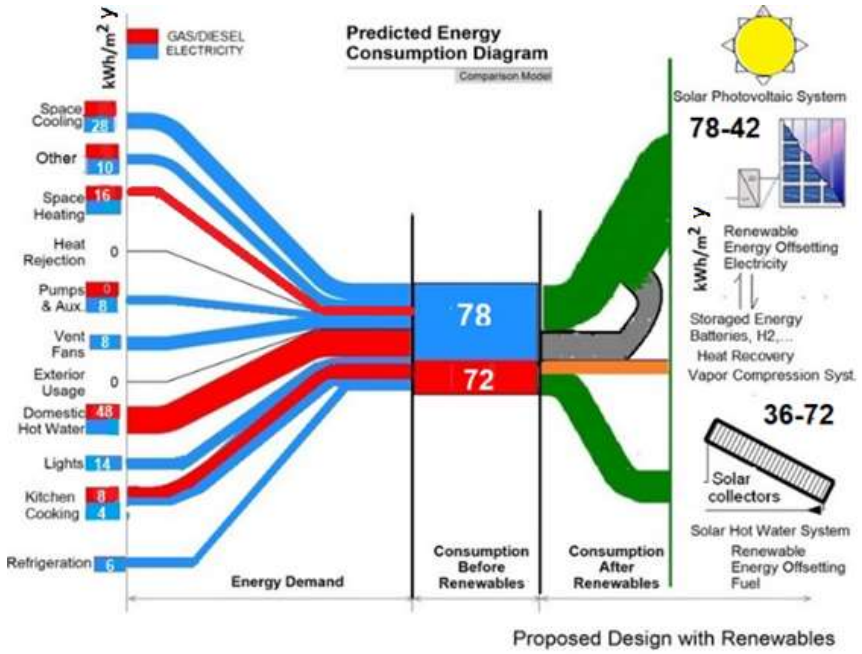

Fig. 8. Energy Sankey diagram in a average Hotel in kWh/m^2 year with 100% of solar energy

Actually in Majorca there are hotels which consume energy from 100% renewable sources (only with solar and biomass). The reduction of cost of some technologies (PV and Hydrogen technologies) could open other systems with 100% of solar energy. The hotels with only solar energy power will have to implement smart strategies, large thermal storage and small fraction with batteries or in other emerging technologies like Fuel Cell with Hydrogen(H_2) and Hydrolysis, in order to arrive to zero emissions systems, studied by Moià-Pol et alt. at 2020. Optimizing the energy mix of the hotels according to their demand and the

available surface will be best scenario, using biomass or solar thermal with photovoltaics and small percentage of hydrogen in order to arrive to 100% of renewable energies. See at the table 2 some scenarios with renewable energies.

Tab. 2: Renewable mix for Hotels with different fraction

	ST	PV	W	Biomass	H_2	€/m² year
Hotel Biomass	0%	0%	0%	100%	0%	11,4
Hotel B-PV-W	0%	32%	6%	62%	0%	9,8
Hotel ST-PV-B-W	46%	30%	6%	18%	0%	7,7
Hotel PV-ST-B-W	14%	62%	8%	16%	0%	5,6
Hotel PV-ST	32%	68%	0%	0%	0%	5,6
Hotel PV-ST-W	16%	76%	8%	0%	3%	4,4
Hotel PV-W	0%	83%	17%	0%	7%	5,5

Another possible option in the future for Hotels will be for example, -to wait until the Electricity and the Gas will be produced 100% with renewable energies and use the standard technologies, but for this scenario we will have to wait more than 20 years that maybe the climate change will be irreversible. The big energy consumers like the Hotels need to be more active in the effort of decarbonizing the Islands. In the following table you can see how a future scenario could be that with the total number of Hotels in Majorca we could cover all the energy demand with the consumption of renewable energies.

Tab. 3: New scenario of the Majorcan Hotels with 100% solar energy. Source; Ibestat.caib.es

Category	Number	Beds	Electric Consumption (MWh/year)	Thermal consumption (MWh/year)	Category	Energy kWh/ m² year	Min. PV kWp/hotel	ST m² /hotel
5*	52	10981	18843	15417	5*	377	1047	256
4*	350	106221	74497	49665	4*	237	564	138
3*	200	51340	14360	7731	3*	158	175	33
2*	35	4583	2280	977	2*	120	148	23
1*	14	1069	848	212	1*	65	64	49
TOTAL	**651**	**174194**	**110828**	**74003**	**Average**	**191**	**400**	**100**

3. Conclusions

Applying new systems and Solar Energy to the hotels can result in a large economic and energetic saving and a reduction in CO_2 emissions without a significant change in client comfort by the increase of RES, especially the ST and PV systems. By changing from fossil fuels to solar energy sources (photovoltaic and solar thermal), we can arrive at zero or even positive building energy. In the future the Hydrolyzer with fuel cell will be 0able to integrate traditional heating systems of the Hotels and one can create a highly efficient system by operating with solar energy sources, based on fuel cell, solar collectors and photovoltaic elements for zero energy Hotels with low electrical storage and reasonable thermal storage.

4. Acknowledgments

The autors would like to appreciate ABTECIR, Consell Insular de Mallorca and the european project greenhysland.eu/ grant Agreement No 101007201.

5. References

A Moià, B. Rosselló-Batle, Pujol R., V. Martínez. Net zero energy in hotels and touristic areas in the Balearic Islands. Eurosun 2010.

Andreu Moià-Pol, Miquel Alomar Barceló, Ramon Pujol Nadal, Víctor Martínez Moll. Domestic solar/heat pump heating systems with low and high efficiency collectors in Mediterranean areas. Proceedings of the Solar World Congress 2011, Kassel, Germany

Vassiliki N. Drosou.Panagiotis D. Tsekouras , Th.I. Oikonomou, Panos I. Kosmopoulos, Constantine S. Karytsas. The HIGH-COMBI project: High solar fraction heating and cooling systems with combination of innovative components and methods. Renewable and Sustainable Energy Reviews 29 (2014) 463–472

A. Moià-Pol, P. Rullan, B. Alorda. Intelligent Thermal Storage in the Balearic Islands Hotels. Workshop proceedings of Intelligent Environments and Buildings. IEB'20.(2020) Madrid, Spain 252-258

https://greenhysland.eu/ Grant Agreement No 101007201.

Clean energy for EU islands. Technology solutions booklet. EU publications. ISBN 978-92-76-41545-9

Statistic Department of Balearic Government https://ibestat.caib.es/

Esther González Arnedo, Jesús Alberto Valero-Matas and Antonio Sánchez-Bayón. Spanish Tourist Sector Sustainability: Recovery Plan, Green Jobs and Wellbeing Opportunity. Sustainability 2021, 13(20), 11447; https://doi.org/10.3390/su132011447

Renewable Energy Education: Gendered-Design and Innovation in the Context of Small Island Economy

M. K. Elahee, S. Poorun (Sheena), D. Juggurnath, A. Khoodaruth, R. Sultan[1]

[1] The University of Mauritius, Reduit (Mauritius)

Abstract

Small island states still rely significantly on imported fossil fuels in spite of their potential for renewable energy, particularly from the sun, wind, biomass and ocean energy. These islands are negligible contributors to global greenhouse gas emissions but they are the most vulnerable to climate change. This paper is based on research conducted in the Republic of Mauritius to evaluate the integration of gender issues in the design and innovation of renewable energy systems for local context, an important issue to be addressed towards renewable energy transition in small island economies. The focus is on the household sector where both gender-considerations and the scope for achieving Sustainable Development Goals through education are significant. A case-study based on the design of a small vertical-axis wind turbine for use in the household sector is looked into with an attempt to integrate gender considerations along with computational simulation conducted on a prototype typical of those implemented in hybrid renewable energy system combining photovoltaic and wind generation, with or without storage.

Keywords: Renewable Energy, Education, Gender, Small Islands, Design, Wind, Behavior, Mauritius

1. Introduction

Use of electricity, including the supply of renewable power, contributes to the Sustainable Development Goals (SDG), namely SDG 7 on Affordable and Clean Energy, SDG 5 on Gender Equality and SDG 13 on Climate Action. As per Fathallah and Pyakurel (2020), the literature reveals a gap in terms of rigorous empirical studies to better understand gendered impacts of energy, thus a need of identifying innovative methods of integrating renewable energy, in particular, in educational programmes such as those for engineering studies. Osunmuyiwa and Ahlborg (2020) discuss the knowledge gaps with reference to gender-sensitive designs towards promoting equal opportunity. They identify the overlapping areas covering electricity, entrepreneurship and gender and highlight the opportunities related to delocalized local energy systems with renewable energy implementation. In the context of small island economies which are most vulnerable to climate change and also are highly dependent on imported fossil fuels, the Republic of Mauritius being an example, consideration of gender issues in the design of sustainable energy systems is an area of explorative research that is of high relevance.

In 2019, in the 'Renewable Energy Roadmap 2030 for the Electricity Sector' developed by the Ministry of Energy and Public Utilities of the Republic of Mauritius, a pathway to achieve 35% of renewable energy in the electricity mix was set for 2025 (MEPU, 2019). In 2021, in the Government Budget Speech 2021-2022, this target has been upscaled to 60% of renewable energy by 2030 (MEPU, 2022). The current figure is 22% for the share of renewable energy in the electricity mix. The total installed capacity is about 700 MW and the annual consumption about 3000 GWh, with 78% being derived from imported coal and fuel oil (SM, 2022). Yet the potential of solar, wind, biomass and ocean energy is significant (MEPU, 2022).

The objective of this research is to determine how the integration of gender issues in the design and innovation of renewable energy systems can promote implementation of renewable energy. The scope relates to small islands, particularly the case of islands of Mauritius (about 2000 km^2) and Rodrigues (about 100 km^2), forming part of the Republic of Mauritius. The focus is on the household sector where the potential of sustainable energy promotion through education is targeted by means of behavioral change as well as renewable technology introduction.

2. Methodology

The energy sector has largely been dominated by men. The participation of women is key to ensure that everyone benefits from and is part of any energy transition. For a successful transition, a change is needed from the past with an inclusive approach. In Mauritius in 1990, women represented 30.4% of the labour force while in 2020, the figure has risen to 39% (SM, 2022); but currently there are no statistics specifically for the energy sector. At the same time, women continue their conventional role within the family as the average time spent on household work and care of family persons per day is 3.6 hours for females compared to 1.8 hours for male. Women-headed households are also significantly on the increase (SM, 2019).

According to IRENA (2019) report on Renewable Energy: A Gender Perspective, women have been usually

© 2022. The Authors. Published by International Solar Energy Society
Selection and/or peer review under responsibility of Scientific Committee
doi:10.18086/eurosun.2022.18.12 Available at http://proceedings.ises.org

underrepresented in the energy sector. Major designs of renewable energy systems, including wind turbines and solar panels, are generally assumed to be gender-neutral. But this assumption can be challenged as it is more likely that, in fact, gender issues were not even thought of in the design process. This represents a major barrier for women to enter and advance in the energy sector. In order to promote women as an active player in the energy sector, gender-based energy considerations are also important at micro level, for instance in households (Fathallah and Pyakurel, 2020). Information on behaviors, practices, priorities, and constraints in relation to energy must be systematically collected and analysed before integration in design or in policy-making (IRENA, 2019).

In the conclusions of a United Nations Development Programme report for Mauritius, (UNDP Mauritius, 2015) on Gender Assessment, it is stated that there is a need for gender-disaggregated data and indicators to establish a baseline in which to measure improvements and identify areas of focus. This holistic approach to consider the behavioral aspects of agents in relation to energy is the essence to guide the development of gender-based systems –the focus of the present study. Gender matters for the production of energy as well as for the management of renewable energy systems, but there is a lack of empirical studies on how it matters, what the consequences are and what the solutions are. This study focuses on defining tools to collect and analyze gender-disaggregated data in a specific context and investigate how people use, save and think about energy with an objective to identify gendered elements which will become the core components of the educational and innovation process to design renewable energy systems. A case-study for small-scale vertical-axis wind turbines for domestic use with particular reference to a small-island economy like the islands Mauritius and Rodrigues is considered.

Interlinked with the design aspect, this research thus also investigates gender-based energy practices and behaviors. Gender considerations have long been overlooked and omitted as a factor for energy production and consumption. Clancy & Roehr (2003) stated that there is a lack of sex-disaggregated data on domestic energy-related attitudes and practices. Gender-disaggregated data on how people interact with energy seems to be an important piece of the sustainable transitions puzzle. It is evident from available data that men and women have different consumption patterns (Räty & Carlsson-Kanyama, 2010). Dym et al. (2003) noted that technologies specifically employed by women have mostly been designed without considerations for women. This, in any case, does not mean that such technologies should exclusively be designed for women or by women. A proper design approach should consider several parameters, including gender, cultures, religions, disabilities and socio-economic standings, all throughout the design process. Several of these parameters are inter-related. Conceived as such, the design would meet the needs of a wider range of people but it is complex to seek all-around satisfaction. Gender differences, however, need to be considered and analyzed during the project cycle as a matter of ethical principle in view on ensuring inclusiveness and equity.

The first objective of this study, which was to understand gender-based energy behaviors, was accomplished by conducting a two-level survey. Level 1 survey was comparatively more general and was performed across the Republic of Mauritius and included the island of Rodrigues. Level 2 survey, on the other hand, was relatively more detailed and particularly focused on regions where a low response rate was recorded from Level 1 survey. The need for a bottom-up approach engaging the population, in particular household women, was largely satisfied by the conduct of these elaborate surveys in a two-tier approach.

In Mauritius, there is a single grid network provider and there are about 400,000 households connected to the grid. Using the sample size calculator and applying a confidence level of 95% and 5% margin errors, a sample size of 384 is identified for the survey. Questionnaires were designed to target households. Households with one specific gender was not a requirement as gender-disaggregation refers to data. The conventional definition of gender limited to two main genders was retained.

Before starting with the surveys, in-depth focus group discussions were held with representatives of women organizations, and stakeholders. The outcome was used to design the questionnaire with due recognition of the importance and role of women. Reference to the literature and use of proper research methodologies were also important to ensure relevance and statistical significance for the surveys.

The survey questions were devised with clear objectives in English and in Creole to ensure understanding. Creole is spoken widely as it is the national language in the Republic of Mauritius and is very much like French.

2.1 Level 1 survey – July 2021

Level 1 survey contained a total of 20 questions which were split as follows:

- Questions on respondent's demography including family income and level of education. - 9 questions

- Respondents 'Opinion on wind turbines for households'. They were required to advise how important aesthetics of the equipment was for them and did they consider it as a danger. - 7 questions
- Respondents 'Opinion on energy usage'. Last question invited respondents to write their views on the subject. – 4 questions

Survey questionnaires were issued online in view of the pandemic situation. After receiving 121 responses online over 2 weeks, incoming responses slowed down. This could be due to the social context related to the pandemic where such surveys are secondary concerns with several families struck by health, economic and social problems. Some 95 mail solicitations and reminders remained unanswered. Decision was taken to start distributing hard copies of the questionnaires as permitted during the less strict pandemic restrictions later introduced. 300 copies were made. The questionnaires were distributed randomly to people from all walks of life and different districts in Mauritius. The region, location and streets were used as the random component to choose the respondents. The randomness was later checked to tally with the requirements for statistical significance.

A total of 392 responses were secured, including the online ones. It has been assumed that online and direct responses are not any different.

2.2 Level 2 - longer questionnaires addressing specific issues – November 2021

Level 2 survey contained a total of 31 questions which were split as follows:

- Questions on respondent's demography including family income, level of education, electricity bill details and any renewable energy equipment currently in use in their house. - 11 questions
- Respondent's views on renewable energy in households. They were required to advise whether food cooked using solar cookers was of any interest and which equipment in their house they would like to power through renewable energy. - 3 questions
- Respondents views on 'Energy saving culture'. Responses to this section was an eye-opener as it showed a sharp contrast about energy saving attitudes when it concerns a person's home electricity bill as compared to indifference to energy wastage at their work place. – 3 questions
- Questions on daily activities involving electricity at home. The responses have shown that households remain a non-negligible energy consumer even during working hours. – 4 questions
- Opinions on wind turbines for households. – 3 questions
- Opinions on Energy Management. Respondents were required to advise what changes they were ready to make in their lives to reduce their energy consumption. – 4 questions
- Respondents were required to provide their vision of the future of energy. Majority of Respondents were favorable to the introduction of renewable energy in their households provided government subsidy is available. A general optimism for the future of renewable energy was noted but at the same time most respondents considered that the cost of electricity will continue to increase. – 3 questions

Level 2 survey favored regions from where a low response was noted under Level 1 survey. For example, more questionnaires were sent to Black-River region in the west of Mauritius. The reason for this is to ensure that the low response is better understood. In no way, other regions were left out in Level 2 or the statistical significance was compromised.

Level 1 and Level 2 survey received a total of 467 responses. Appendix 1 shows the response details per district over the map of the Island of Mauritius. The Statistics Mauritius, 2020, Digest of Demographic Statistics per district are compared against the survey statistics. In analyzing the data to ensure a suitable representation, the total number of respondents were also compared to actual number of households per district, urban and rural, and age group.

In the course of the surveys, with due respect to confidentiality and non-disclosure requirements, historical data was collected on actual practices, electricity bills and daily activities. It is good to note that the legislation in Mauritius does not allow the utility provider to share consumer information with third parties.

The data analysis concentrated in separating and comparing males and females using statistical methods, testing using a reasonable degree of significance (5%). Statistical analysis included regression (logistic regression) to fully model the behavior of respondents taking into account their characteristics.

3. Findings

Key findings from the survey are as follows:

a) Solar water heaters were the most common type of renewable energy used at household level. From the survey, 56% of respondents stated that they had solar water heaters at home. As per the last Household Budget Survey conducted in 2017 when the total number of households was 368,400, 31.9% of households were equipped with a solar water heater. Five years later, with the increase in the number of households by around 10% and a general increase in average household income, the corresponding figure for households equipped with solar water heaters is expected to have increased. However, this progression may have been negatively impacted by the 2020-2021 pandemic. Upcoming Household surveys by Statistics Mauritius could confirm the tendency.

From this survey, it was interesting to observe the percentages within the various income group respondents who owned solar water heaters (SWH):

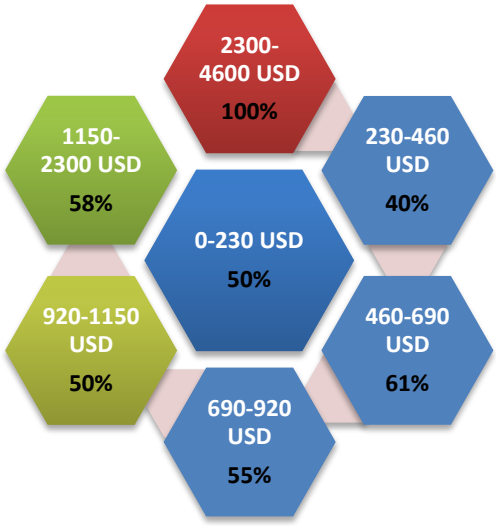

Figure 1 – % within the different income groups owning SWHs (1 MUR=0.023USD)

The percentages remain promising even within the low income groups (0-920USD), thus showing a good interest for solar water heater government subsidies offered for this income group.

59% of respondents who own solar water heaters are University educated.

b) Respondents showed interest in decreasing their electricity bills by introducing renewable energy in their homes. A strong interest of persons below 40 years of age was noted, equally shared by men and women. As to which appliance the respondents considered a priority in using renewable energy, 60% stated that it would be the refrigerator. 42% of respondents choosing refrigerators were women whilst 58% were men.

c) The responses received to the question "What is your opinion on renewable energy for households?" is evaluated below by comparing Mauritius/Rodrigues and women/men.

Mauritius Island

85% of respondents believe that with energy management measures, renewable energy can bring energy autonomy in households. 64% of the persons who hold this belief are below the age of 40. Within this age group, this optimism is held by 62% females and 38% males.

Analyzing further the 62% optimistic female respondents who are below the age of 40, it is noted that the majority (56%) are not married i.e. they are generally still living with their parents.

Looking at all age groups, 51% of the respondents who believe in Energy Management are university educated. Thus positive views about energy management is equally shared by university educated and non-university educated respondents.

From monthly family income perspective, the outcome is as follows:

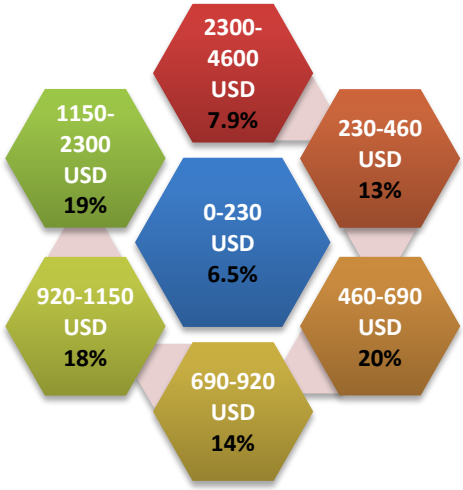

Figure 2 - family income vs. Energy Management

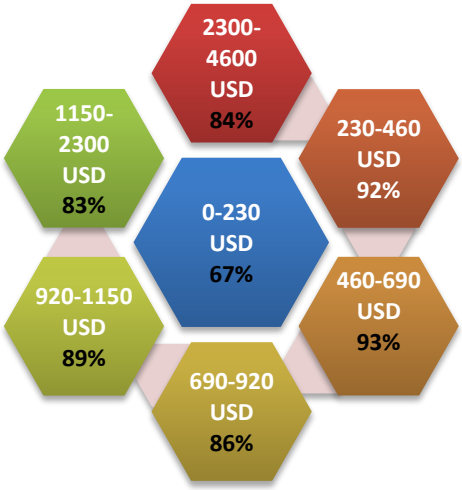

Figure 3 - % within the different income groups believing in EM

The highest optimism is noted within the 460-690 USD income group.

57% of those believing in Energy Management were women and 42% were men, i.e. women were found to be more optimistic than men.

Rodrigues Island

96% of respondents believe that '*With energy management measures, renewable energy could bring energy autonomy in households*'. 57.7% of those believing in the future of Energy Management were women and 42% were men, i.e. women were found to be more optimistic than men.

Thus, general optimism in this matter was more prevalent in Rodrigues (96%) than in Mauritius (85%).

d) Questions 13 and 14 of the questionnaire read as follows:

"13. Do you think these wind turbines could help generate electricity for households?
14. Do you think these wind turbines may pose problems or represent any danger in residential areas, such as on roof-tops?"

From responses received for questions 13 and 14 of the questionnaire, 85% of respondents believed that a vertical axis wind turbine could contribute to the electricity of households and more than 57% considered that wind turbines represented a danger on roof-tops. For those who were positive about having a wind turbine, this opinion was equally shared between males and females.

The findings from the present survey showed that the respondents aged between 41 to 60 years old were 11 times more optimist about such wind turbines than those aged beyond 61 years old. However, the latter age group might be under-represented in the survey. Age group might be a more relevant parameter to consider than gender.

A high share of respondents, 43%, gave importance to the noise level from wind turbines while 25% considered the appearance as important. Figure 4 illustrates the share and breakdown of respondents who were 'Neutral' as to the appearance and noise aspects of small-scale wind turbines. Thus noise was given slightly more importance than appearance.

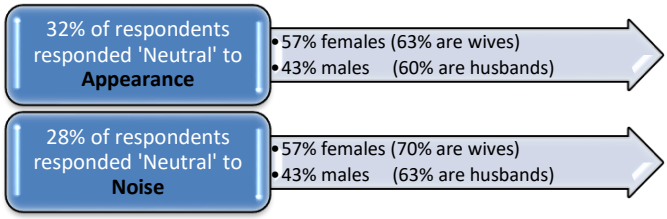

Fig. 4: Share and breakdown of respondents with neutral views on the appearance and noise level of wind turbines

e) The Level 2 questionnaire contained the following series of questions concerning a small vertical axis wind turbine for households. An image with indicative dimensions was provided, questions 22 to 24 of the survey.

Table 1 – Questions 22 to 24 - Wind turbine for households

Question 22 - Would you support wind turbine development for households as a source renewable energy?	
Question 23 - Do you consider your house a good place for installing a small wind turbine on the roof? A vertical axis wind turbine as in the picture below can operate and produce energy under low wind conditions.	
Question 24 - For a small vertical axis wind turbine as in the picture, would you prefer to have it on the roof of your house or on a separate structure? The dimensions are indicative only.	

Figure 5 demonstrates a breakdown of respondents who considered installing a small axis wind turbine at home.

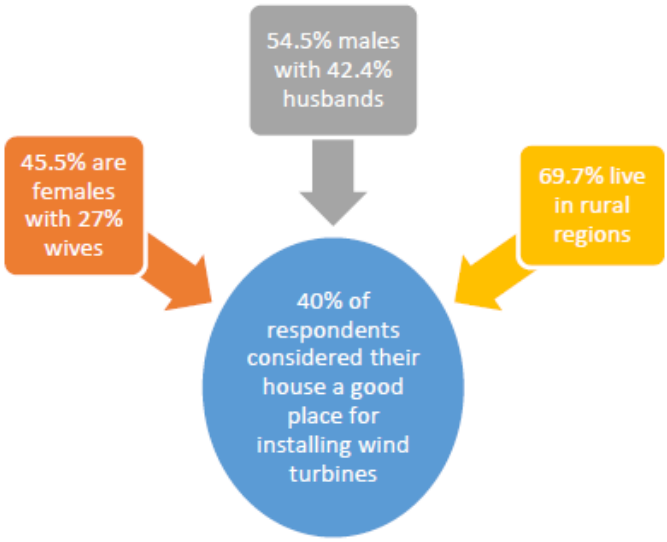

Fig.5: Breakdown of respondents considering installing small wind turbines at home-Question 23

As per Statistics Mauritius Census 2022, 94.8% of houses in Mauritius have a concrete roof. From the same census, it is reported that separate houses dominate. Separate buildings, that is buildings made up of only one housing unit, dominate among residential and partly residential buildings, and comprised around 77.8% of such buildings, compared to 76.7% in 2011. With that perspective, a separate question concerning preference for installation of small axis wind turbine was included.

Figure 6 demonstrates a breakdown of respondents who considered the possibilities proposed for installing the small axis wind turbines.

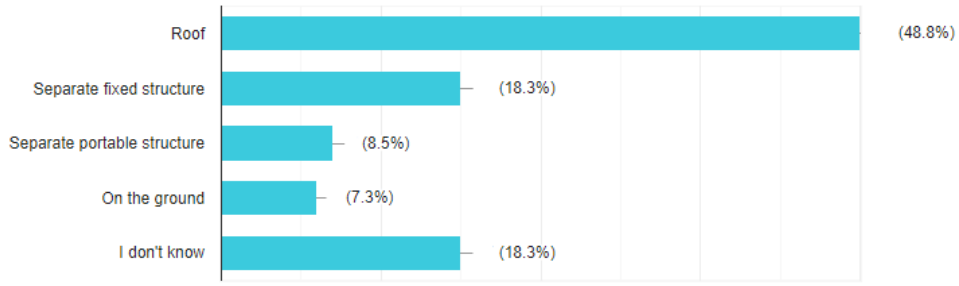

Fig.6: Breakdown of respondents considering installing small wind turbines at home-Question 24

Out of the 49% who opted for the roof, 58% are males and 43% are females. International Energy Agency & Council on Energy, Environment and Water (2019) stated that a lack of safety and security at rooftop solar project sites could discourage women from undertaking work in male-dominated positions. A safe access to the roof may contribute in reversing the above findings.

f) Two worldwide studies carried out by IRENA, International Renewable Energy Agency, were reviewed to identify relevant gender issues:

- IRENA (2019), Renewable Energy: A Gender Perspective. IRENA, Abu Dhabi.
- IRENA (2020), *Wind Energy: A Gender Perspective.* IRENA, Abu Dhabi.

Both studies, have one point in common. 'Perception of gender roles' and 'Cultural and social norms' have been reported by women around the world as an important barrier to the gender equality in the field of renewable energy. It is also stated that because of prevailing views of women's abilities, women continue to have a limited presence in these fields.

In this survey, in spite of 91% of female respondents agree that '*With energy management measures, Renewable energy can bring energy autonomy in households*', only 51% of women respondents were agreeable to cook rice, pulses and other food items using solar cookers.

g) Respondents were required to provide their opinion on the question of whether males or females are more sensitive to energy management in households. The response received are:

Table 2 – Which gender is most sensitive to energy saving?

Responses	Females are more sensitive	Males are more sensitive	Gender does not matter
Total	34.4%	18.1%	44.6%

The majority of respondents have stated that Gender does not matter. For the 55.4% respondents who have responded that gender matters, 79% of females are University educated as compared to only 33% of males who are university educated.

As per Davis (2022), women are more likely to perceive gender inequality than men. It would appear that education at school level in Mauritius is not contributing in bringing gender inequalities to the attention of female students. This may be the result of the fact that at school level, the majority of teachers are females, 79% at primary level and 63% at secondary level (Statistics in Mauritius, A Gender Approach 2018). However, at tertiary level, there are only 41% of female academic staffs (UNESCO Institute for Statistics, uis.unesco.org, Data as of September 2021, https://data.worldbank.org/indicator/SE.TER.TCHR.FE.ZS?locations=MU). This may explain the high contrast in gender inequality consciousness between University educated females and males.

Out of the 48.6% females who have responded that gender does not matter, 46% are wives. And out of the 51.4% males who have responded that gender does not matter, 57% are husbands.

Out of the 34.4% who chose females as being most sensitive to energy saving, only 23% are males. Similarly for the 18.1% who chose males as being most sensitive to energy saving, only 25.4% are females. The percentages choosing the opposite gender are almost same.

Generally studies have qualified females as being more sensitive to energy management in households. As per a research carried out by Isnin et al. (2018) for Institute of Electrical and Electronics Engineers, a strong relationship was established between females and intention for energy conservation behavior. It was concluded that policy makers and government may need to create energy efficiency programs which involve women due to their influence on their households' affair.

This survey is showing a more balanced outcome. Males and females are showing equal sensitivity to energy saving by stating as a majority that gender does not matter. It may be considered that qualifying females as being more sensitive to Energy Saving may be just a perception held by females and not shared by males.

h) The computational modelling of a small-scale vertical axis wind turbine (VAWT) for household use in the local environment in Mauritius was a case-study investigated, with possible hybrid use along with solar photovoltaics, with and without battery storage. The possible integration of gender issues in the design process was looked into. A literature review conducted by Al-Kayiem et al. (2016) described the relevant parameters that need to be considered while designing the Savonius wind turbine which is the preferred type for conditions identified in the local context. It suggested that a two-bladed VAWT performed better that a three-bladed one. The considered Savonius wind turbine had a turbine diameter of 400 mm, a blade diameter of 230 mm and a height of 400 mm (Aymane 2017, Utomo et al, 2018). A two-bladed S-shaped rotor with one stage was considered.

i) Figure 7 shows the variation of angular velocity with time to reach steady state for different wind speeds using Ansys Fluent software. It was therefore deduced that velocities of less than 2 m/s should be avoided to avoid long stabilisation time. The same result is confirmed in Figure 8 showing variation with tip speed ratio.

j) Wind speeds of 3 m/s, or better between 4 and 5 m/s, provide the required conditions for steady operation whilst ensuring efficiency, hence, better cost feasibility. The next plots refer to 5 m/s simulations.

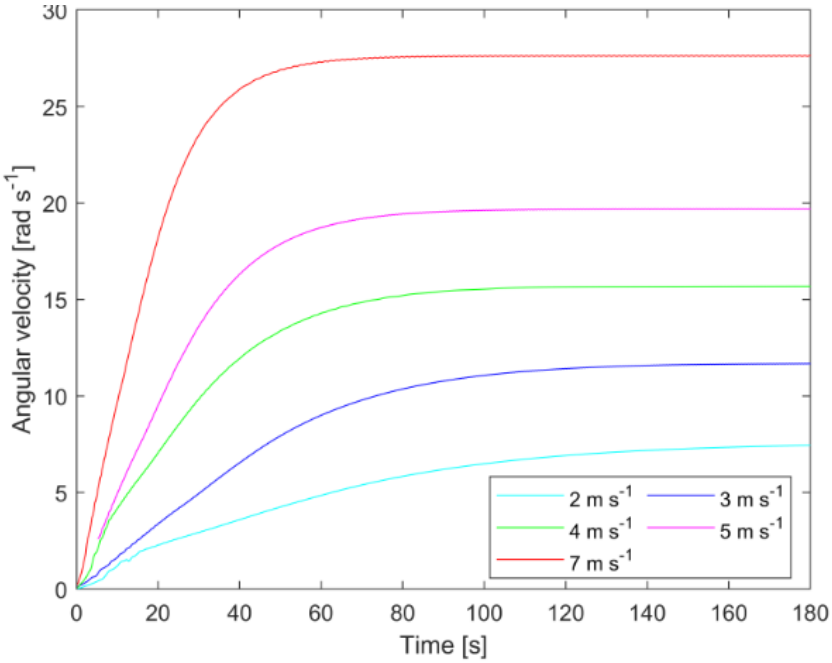

Figure 7. Variation of angular velocity with time for different wind speeds

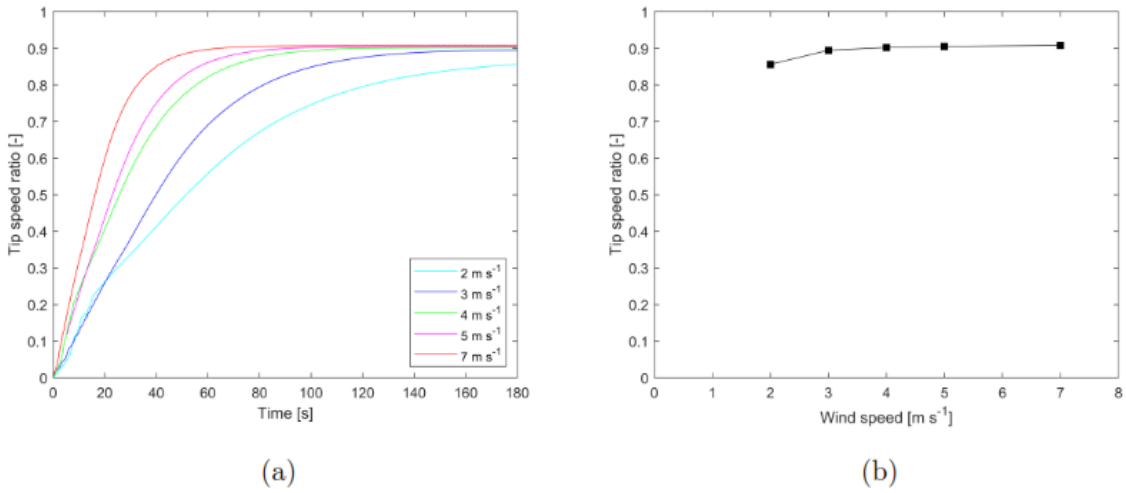

Figure 8. Variation of tip speed with (a) time and (b) wind speed for stable condition.

k) Figure 9 illustrates the turbulence kinetic energy contour plots for the investigated wind turbine at a wind field of 5 m/s at angular positions of (a) 0°, (b) 90°, (c) 225° and (d) 315°. It is evident that the downstream conditions are important to be considered in design. This will need to be further investigated to reconcile with other considerations like space availability, for example if hybrid solar-wind systems are to be implemented (with or without storage).

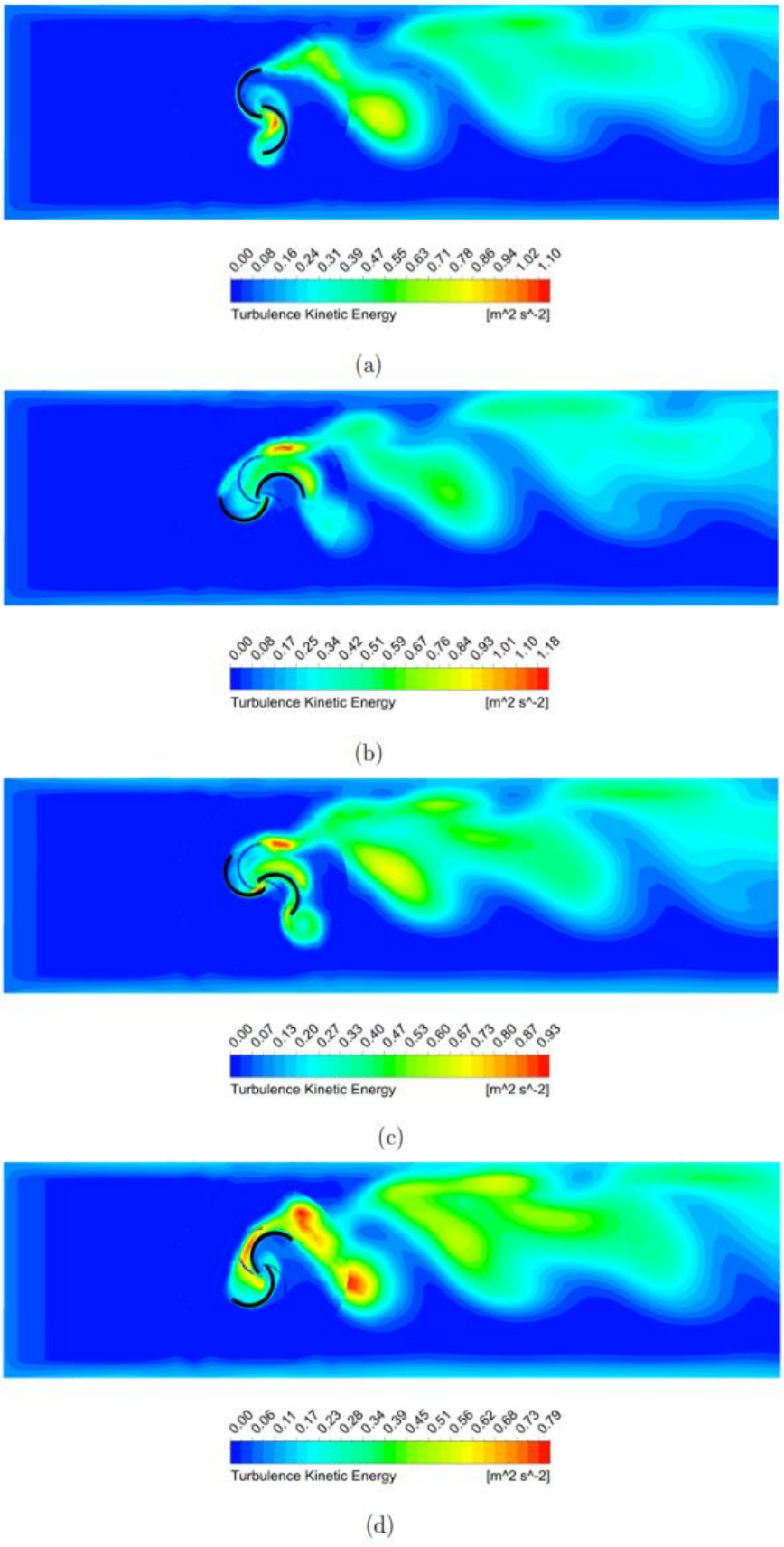

Figure 9. Turbulence kinetic energy contour at angular positions of

(a) 0°, (b) 90°, (c) 225° and (d) 315°.

4. Conclusions

The survey in Mauritius revealed that there is an interest at household level for powering specific household appliances, such as refrigerators, through a small-scale roof-top renewable energy system supported with or without battery. Along with existing deployment of solar water heaters which is progressing rapidly, small vertical axis wind turbines may also be introduced along with possibly solar photovoltaic panels.

The integration of gender considerations with respect to renewable energy systems, particular in the case-study for vertical axis wind turbine of Savonius type, rests upon the need to consider specific safety considerations related to women accessing the facilities. Gender considerations are hard to identify, particularly in relation to design with computational methods. For instance, the problem of noise is not more gender-sensitive for men than for women. Space considerations e.g whether on roof-top or on independent supporting structures, as well as the layout of different renewable and storage technologies are probably important to be addressed from a gender perspective. In comparison to men, women have shown a lower interest for the roof for the deployment of renewable energy systems at home, at least in the case of the survey conducted. The local context and building/housing structure combined with the personality traits of women are therefore two key drivers that designers must consider.

It is promising to note a strong engagement of middle income families.

5. Acknowledgements

The authors gratefully acknowledge the sponsorship of the International Development Research Centre of the Government of Canada under the Gendered-Design in STEAM programme run by Carleton University, Canada.

6. References

Al-Kayiem, H., Bhayo, B., & Assadi, M. (2016). Comparative critique on the design parameters and their effect on the performance of S-rotors. Renewable Energy, 99, 1306-1317.

Aymane, E. (2017). Savonius Vertical Wind Turbine: Design, Simulation, and Physical Testing. Ph.D Thesis, Al Akhawayn University, Morocco.

Clancy, J., & Roehr, U. (2003). Gender and energy: is there a Northern perspective?. *Energy for Sustainable Development, 7*(3), 44-49.

Dym, C., Wesner, J., & Winner, L. (2003). Social dimensions of engineering design: Observations from Mudd Design Workshop III. *Journal of Engineering Education, 92*(1), 105-107.

Davis, Nancy J., and Robert V. Robinson, (2022) "Men's and Women's Consciousness of Gender Inequality: Austria, West Germany, Great Britain, and the United States." American Sociological Review, vol. 56, no. 1, 1991, pp. 72–84. JSTOR, https://doi.org/10.2307/2095674 . Accessed 5 Jun. 2022

Fathallah, J., & Pyakurel, P. (2020). Addressing gender in energy studies. *Energy Research & Social Science, 65*, 101461.

International Energy Agency & Council on Energy, Environment and Water. (2019). *Women working in the rooftop solar sector.* Paris: International Energy Agency.

IRENA (2019), Renewable Energy: A Gender Perspective. IRENA, Abu Dhabi.

IRENA (2020), Wind Energy: A Gender Perspective. IRENA, Abu Dhabi.

Isnin, N. S., Z. Zakaria, Z. Mat Yasin, (2018), IEEE, "Analysis on Gender Differences in Energy Conservation Behaviour", Centre of Electrical Power Engineering Studies, Faculty of Electrical Engineering University Teknologi MARA, Shah Alam, Selangor, Malaysia

Ministry of Energy and Public Utilities (MEPU), Republic of Mauritius, *Long Term Energy Strategy and Action Plan*, 2019.

Ministry of Energy and Public Utilities (MEPU), Republic of Mauritius, *Renewable Energy Roadmap 2030 for the Electricity Sector*, 2022. Osunmuyiwa, O., & Ahlborg, H. (2019). Inclusiveness by design? Reviewing sustainable electricity access and entrepreneurship from a gender perspective. *Energy Research & Social Science, 53*, 145-158.

Räty, R., & Carlsson-Kanyama., A. (2010). Energy consumption by gender in some European countries. *Energy policy, 38*(1), 646-649.

Statistics Mauritius (SM), 2019. *Household Budget Survey 2017*, Mauritius: Statistics Mauritius.

Statistics Mauritius (SM), 2020. *Energy and water statistics - 2020,* Mauritius: Statistics Mauritius.

Statistics Mauritius, 2020, Digest of Demographic Statistics

Statistics Mauritius (SM), 2022. *Energy and water statistics - 2021,* Mauritius: Statistics Mauritius.

Statistics Mauritius Census 2022, Mauritius: Statistics Mauritius.

UNDP Mauritius. (2015), United Nations Development Programme, Mauritius, 2015, *Accelerating the transformational shift to a low-carbon economy in the Republic of Mauritius.*

Utomo, I., Tjahjana, D., & Hadi, S. (2018). Experimental studies of Savonius wind turbines with variations sizes and fin numbers towards performance. AIP Conference Proceedings, 1931, p. 030041

Appendix 1

Comparing Statistics Mauritius, 2020, Digest of Demographic Statistics per district
vs
Demographics of survey conducted

Legend – Demographic Statistics Mauritius 2020 / Survey Statistics

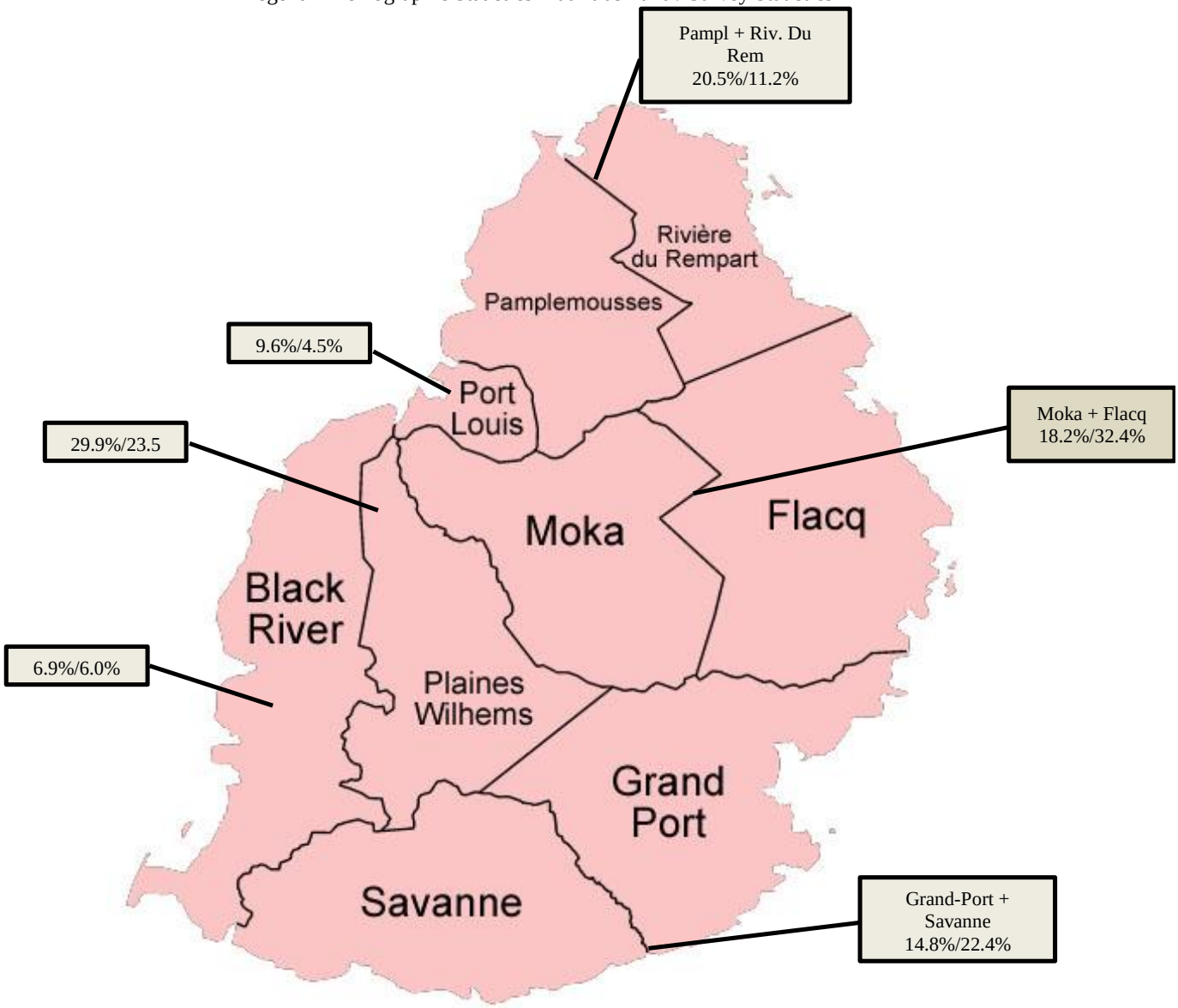

Data mapped on map of Mauritius

In the responses received, Pamplemousses/Riviere du Rempart and Port-Louis have been underrepresented while Moka/Flacq and Grand-Port/Savanne have been overrepresented.

T. Renewable Energy Education

Energy scenarios: Designing the renewable world of tomorrow together

Theresa Gothe[1], Anne Schierenbeck[2]

[1] University of Applied Sciences Osnabrück (Germany)

[2] University of Applied Sciences Osnabrück (Germany)

Abstract

If you are thinking in terms of the goal, you can take the right intermediate steps and avoid bad decisions. Studies show that a supply from 100 % renewable energies is achievable by 2045 in Germany. The coupling of sectors plays a prominent role in this, as does the short-term to seasonal storage of energy. The use of the 100prosim simulation tool in target group-oriented workshops can help people to understand the interrelationships between energy production and the use side more clearly. The energy system of the future is developed jointly in a participatory process using the scenario technique. This article gives an insight into the use of the tool combined with the workshop methodology and summarises the experiences of numerous workshops and practical applications with different stakeholders.

Keywords: scenario, 100 % renewable, coupling of sectors, simulation, workshops, future energy system

1. Introduction

The energy transition is complex and, in addition to technical adjustments and innovation, requires a social change process. The German climate protection plan stipulates that the implementation of the action plan and its further development should be linked to social discourse processes (Federal Ministry for the Environment, Nature Conservation and Nuclear Safety, 2016). Even if almost 90 % of Germans support the expansion of renewable energies (Agentur für Erneuerbare Energien, 2021), there is often resistance to the concrete implementation.

Studies from Prognos, Öko-Institut, Wuppertal-Institut on behalf of Agora Energiewende (2021), the German Energy Agency, dena (2021) and the Wuppertal Institute (2020) show that a complete decarbonisation of Germany is possible. In order to achieve an energy supply from 100 % renewable energies, their expansion is essential. In addition, energy storage, energy networks (for electricity and heat) and the infrastructure for hydrogen must be expanded (Bundesnetzagentur, 2019; Siemens, 2020). Energy savings through efficiency and sufficiency are inevitable. The expansion of renewables is associated, inter alia, with a high demand for land, which could result in competition for its use (Weyberg, 2021). The need for a renewable energy supply, therefore, poses particular challenges for regions with high energy requirements in relation to land area (Niepelt, 2021). There is not only competition for use, but also conflicts of interests and goals.

Participation and an open discourse are essential for the sustainable and effective implementation of the energy transition (Ried et al., 2017; Schreiber, 2012, Renn 2015, Ernst 2017, Fraune et al. 2019). Ried et al. (2017) state that the development of new structures in the energy supply represents a very complex challenge that requires a lot of specialized knowledge. There is a lack of this knowledge which must be compensated for, especially among municipal decision-makers (Rohe and Chlebna, 2021). Confidence in the procedures and competence of key actors in the energy transition on site, such as local administration and politics, is also closely linked to local acceptance (Hübner et al., 2020).

Transformation research shows that model-based energy scenarios can be combined with systematic elaborations of social and political contexts (Schmidt-Scheele et al., 2019). One method for involving experts and stakeholders is the scenario technique. This technique is particularly useful for looking at long-term future developments, since it does not make any statements about *one* future but considers several alternative possible futures (Wassermann and Niederberger, 2015). It is particularly suitable for the analysis of complex topics and their realistic development possibilities. This also applies when the aim is to understand the future together more effectively (Minx and Böhlke, 2006). The interactive methodology with due regard to the scenario technique (Meinert, 2004) provides room for different points of view and helps to create a future scenario that is considered jointly

© 2022. The Authors. Published by International Solar Energy Society
Selection and/or peer review under responsibility of Scientific Committee
doi:10.18086/eurosun.2022.19.01 Available at http://proceedings.ises.org

acceptable. This strength makes the tool interesting for a wide range of target groups. In this context it is very important to communicate about the assumptions made in the model and to make clear which input parameters on which base are used to make the model more valid and trustful.

The use of the 100prosim simulation tool in target group-oriented workshops is explained in this article. The scenario technique of so-called 'backcasting' is used in the application of the tool. What the future should look like in the best case – which means here a carbon neutral energy production based on renewables without any nuclear or fossil energy sources – and how this scenario can be achieved is determined in the backcasting process (Robinson, 1982). The aim of the workshops is to help people to understand the complexity of the energy transition and get to know the interrelationships between energy production and energy use.

Various workshops with different stakeholders were conducted and evaluated in the last three years. The research questions in this article are: In which areas of application was the 100prosim modelling tool used in connection with workshops and which results can be stated?

2. Tool and workshop methodology

The 100prosim is an open source Excel simulation tool. The software is offered and continuously developed by the registered association "Erneuerbare Energie-Szenarien e.V." (www.ernes.de). The 100prosim tool reflects the use of energy across all sectors and establishes expansion targets. All energy needs should be covered by renewable energies in a target year determined by climate protection requirements, such as 2040. The data basis of the tool is a report for the state government of Lower Saxony (Niedersächsisches Ministerium für Umwelt und Klimaschutz, 2015).

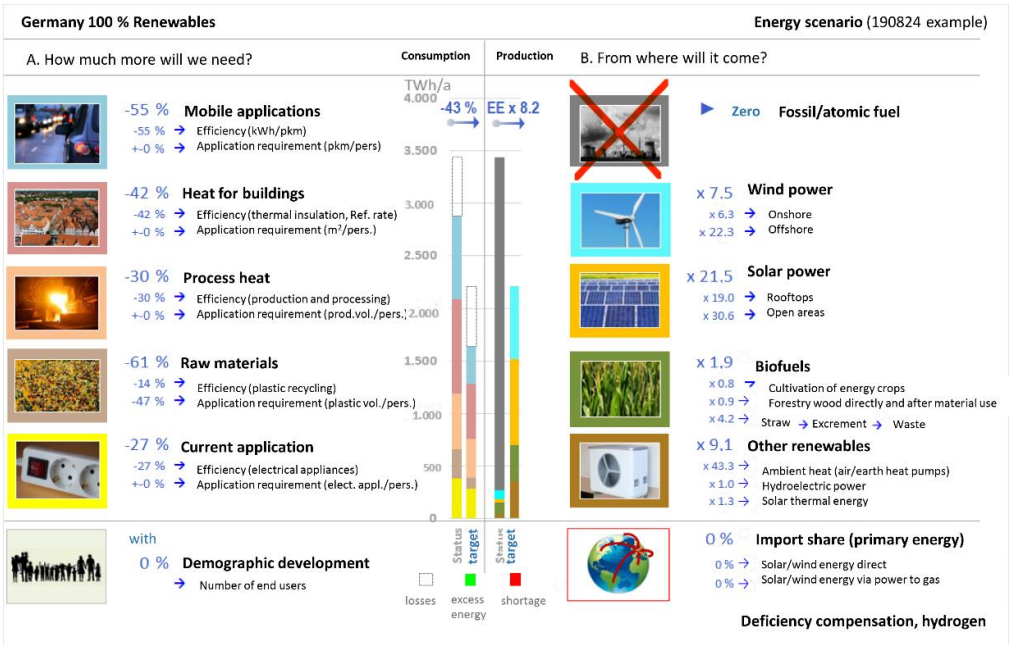

Fig 1: User interface 1 of the 100prosim modelling tool.

Energy consumption and production are illustrated graphically in the future scenario in comparison to the status, as shown in *Figure 1*. Among other things, energy losses, surpluses and deficits are visualised and the connections between the individual sectors and the consumption and production side are shown. The necessary generating and storing technologies, the extent of their use and the changed utilisation structures compared to today become clear. Sector coupling with electricity as a central element will also become tangible.

The energy consumption side includes the sectors of mobile applications, building heat, process heating and electricity applications. Hydrocarbon-based raw materials used in the industry are also included. These are synthesized from green hydrogen in the model. On the one hand, efficiency is taken into account, for example, through the technological potential in the area of drives and alternative fuels (Gmelin et al., 2008) and the technology used (Fraunhofer IWES/IBP, 2017). On the other hand, sufficiency plays an important role in the

model, for example, concerning the size of heated living area or the number of kilometres driven by cars or flown by planes.

Regarding the energy production side, the energy requirement in the target year will be covered completely without fossil fuels or nuclear energy sources. The energy production is based on wind and solar power and biofuels from energy crop production. Ambient heat is used to supply heating to buildings using heat pumps. Hydrocarbon-based raw materials and fuels are synthesized from hydrogen. The current figures for the installed capacity of the individual technologies are taken into account for the energy production through renewables (Fraunhofer-Institut, 2020; Marktstammdatenregister, 2020) as well as the potential and respective space requirements (Bundesverband Windenergie, 2011; Deutsche Windguard, 2017). The power efficiency levels and their developments of the specific technologies are also considered accordingly (FGW, 2015; Fraunhofer ISE, 2011). Different sectors or energy production sources can be adapted in the user interface 2 of the 100prosim modelling programme (shown in *Figure 2*). Influencing variables, such as the population, are included in the simulation to calculate the energy consumption and production. The tool also takes into account the detailed land use, for example, for grain (Regionalstatistik, 2020), grassland (Johann-Heinrich-von-Thünen Institut, 2012) and forest (Umweltbundesamt, 2014).

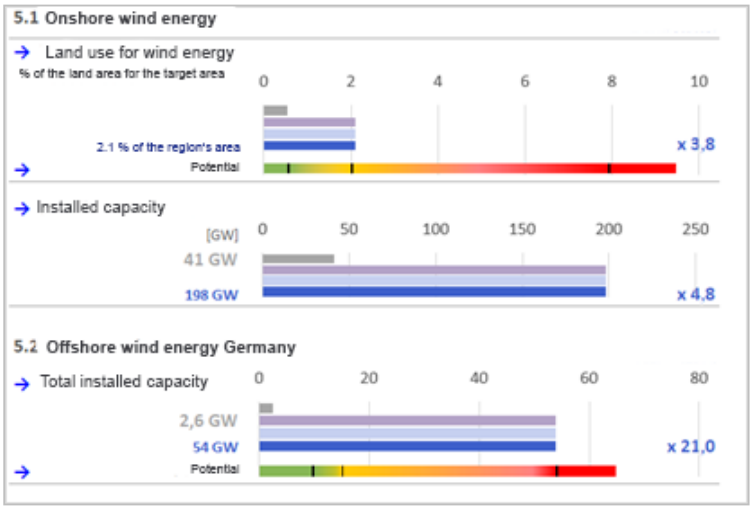

Fig 2: User interface 2. In this case, for wind energy. There is a more detailed visualisation for each sector and technology.

A scenario for energy supply in the future is jointly developed under guidance and moderation in the workshops. The workshop methodology is characterised by a co-operative and moderated way of working and aims to stimulate the discussion and increase the participants' knowledge in the area of energy transition. Most of the workshops were conducted during the COVID-19 pandemic and were carried out completely digitally. These workshops had a uniform structure, as shown in *Figure 3*. After a presentation about the climate crisis, CO_2-budget and –emissions in different sectors in Germany as well as the energy transition in general, the interactive part follows. Here, the participants use the digital voting platform Mentimeter to vote on various values in the areas of efficiency and sufficiency (e.g. the application of electric or hydrogen drives in the mobility sector or the expansion of wind power). These values are discussed and transferred directly into the scenario. The model of the future energy system makes simplifications in the area of grids and storage so that ad hoc changes in the workshops are visible directly.



Fig. 3: Scheme of workshop methodology

After working on the energy consumption side, the graphical user interface shows whether the assumptions made result in supply gaps and how large the shortfall is. The participants then look at the energy production side and can adjust the technologies installed based on the land available. In order to create a balance between consumption and production, the tool can carry out an automatic alignment based on either onshore wind turbines or open space

solar power systems. In the end of the workshop, a future scenario for energy supply is jointly discussed and developed.

The 100prosim tool – in combination with the workshop methodology described – was applied in various fields: Workshop concepts at secondary school to master's degree level have been developed and implemented in a project funded by the Lower Saxony Ministry of Science and Culture. Four different energy scenarios were developed by workshop participants and analysed in the context of this project. Twelve digital workshops with various stakeholders were conducted and evaluated in another project that ran from June 2020 until August 2021. The workshops were recorded in their entirety using the Zoom video conferencing software and transcribed anonymously for the qualitative evaluation of their communicative content. The transcription of the workshops is done with the software MAXQDA. The evaluation is based on the theory of qualitative content analysis by Kuckartz (2016).

3. Results

3.1 Substantially expand wind and solar power, reduce energy use

As described earlier, the simulation tool compares the energy consumption across all sectors with the energy production required to cover it. Various input values e.g. the area for wind energy or solar power plants can be varied in order to achieve full supply from renewables. The corresponding effects on other sectors are illustrated directly after each change, making the interrelationships in the energy system understandable.

As shown in *Figure 3*, the 100prosim tool demonstrates a comparison of energy consumption (left) and energy production (right) regarding scenario 4 from *Figure 4* and *5*. Values in blue next to the individual areas indicate the energy quantities required/produced in the target year 2040 compared to today. With a halving of demand compared to business as usual, 33 % of the total electricity demand would still have to be imported, with expansion rates of 11 GW per year for wind power and 15 GW per year for solar power. The building heating demand is almost completely covered by heat pumps and a renovation rate of over 4 % per year is assumed, which would reduce the building heating demand massively. The switch to electric vehicles in the mobility sector allows for large energy savings.

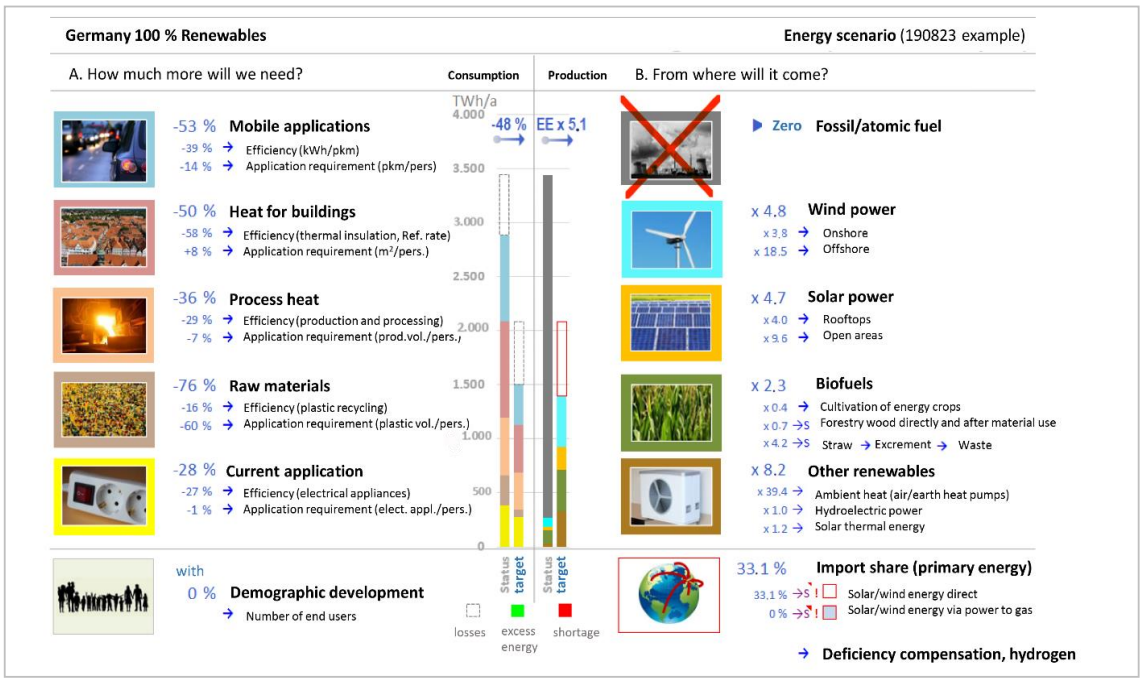

Fig. 3: Illustration of the overview page "Cockpit 1" from the100prosim modelling tool. Parameters adapted as in scenario 4.

In the workshops, participants can adjust the capacity of wind and solar power installed and see the impact of the change immediately. As shown in *Figure 3*, the scenarios have in common that wind and solar power will be the main pillars of the future energy supply. The installed capacity of wind power (onshore and offshore) ranges from

166 GW in scenario 4 to a maximum of 435 GW in scenario 2.

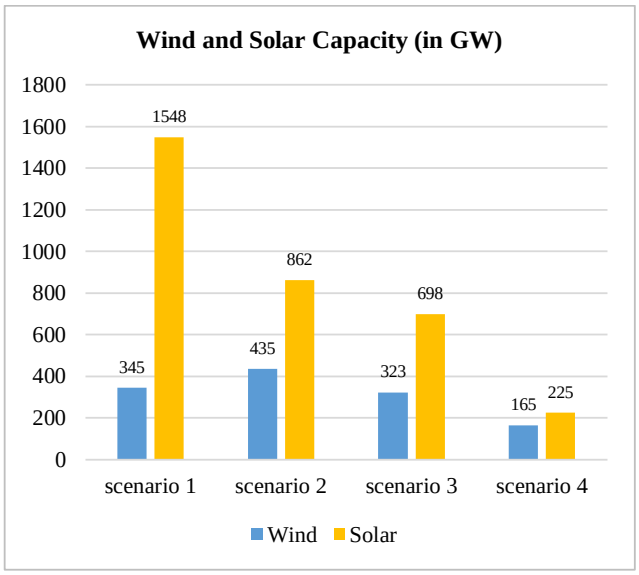

Fig. 4: Results of four different scenarios created in workshops with different target groups using 100prosim showing the installed capacity of wind power (onshore + offshore) and solar power (rooftop + open space). With the exception of scenario 4 (import of approx. 700 TWh/a), the primary energy demand indicated on the right is completely covered by renewable energies within its own area (reference Germany).

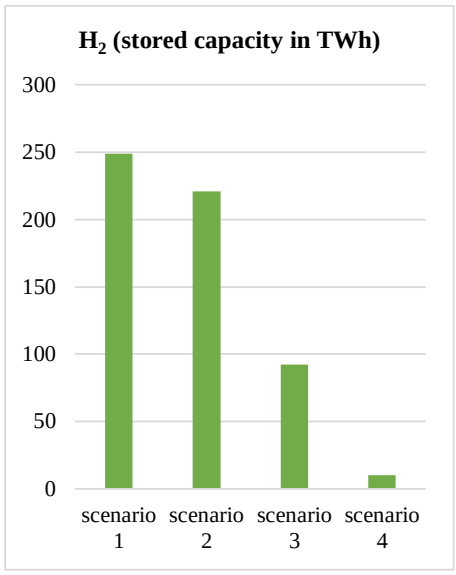

Fig. 5: Amount of green hydrogen storage (stored capacity in TWh) to compensate for power shortage phases.

The excess production of electricity on many days (especially in summer) is converted in 100prosim through electrolysers into hydrogen and is stored. In times of shortage, the hydrogen is converted back into electricity. Accordingly, both the electrolysis capacity necessary and the storage capabilities required emerge from the model. Green hydrogen, which is stored on a large scale underground in salt caverns, serves to compensate for periods of power shortage. This is also visualised in the tool, as shown in *Figure 6*. In order to minimise the storage capacities required, the generation of wind versus solar power should not be neglected.

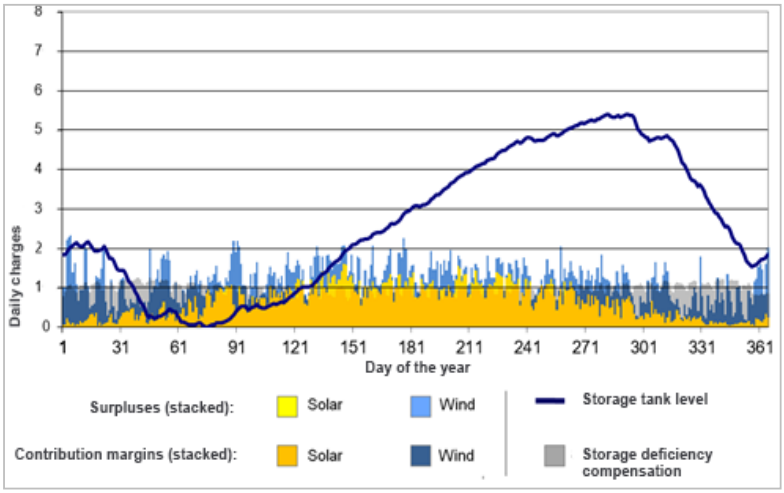

Fig. 6: Visualisation of annual electricity generation and consumption in 100prosim

A homogeneous, positive attitude regarding the assessment of solar installations on roofs was shown in the qualitative evaluation of all twelve workshops. The participants basically agree with the expansion of solar systems on roofs and still see a lot of potential here.

An ambivalent attitude towards the expansion of solar plants in open spaces can be observed in the workshops. The negative attitude in the workshops goes hand in hand with land consumption. In the context of careful and

efficient land use, agrivoltaic systems are mentioned as a sensible approach by stakeholders from the agricultural sector.

Regarding wind power, participants of the workshops assumed that the expansion of offshore wind farm areas will increase in the future. This rise is justified by various aspects: on the one hand, due to greater social acceptance and, on the other hand, due to the potential of such installations. Furthermore, the fact that no land area is taken up is mentioned. Heterogeneous opinions prevail regarding the expansion of onshore wind energy. Critical voices report individual experiences with the loudness of the turbines and the shadow cast. The sympathy towards onshore wind energy plants is reflected mainly in the fact that an expansion of wind energy is demanded and potential is seen in it, thus, the further promotion of the plants is advocated.

The participants generally express the opinion that existing renewable energy plants, such as wind power and biogas, should continue to be promoted. Distance regulations and restrictions for onshore wind energy plants, which make some plants impossible, are questioned and the lack of expansion in southern Germany is criticised. In addition, it is said that photovoltaic systems on roofs should be further expanded. Participants, therefore, actively propose solutions: exemplarily, tendering and approval procedures should be simplified, European Union-wide standards for expansion targets should be agreed upon and new technologies should be adequately promoted.

The analysis facilitates the definition of suitable measures to reach the target set. The challenges for society are manifold and the necessary number and capacity of generating, converting and transmitting plants is large, which is why workshop participants see the energy transition as a joint task.

3.2 Application in university teaching

The 100prosim simulation tool was used with students in the Bachelor's and Master's degree programmes.

The workshops in the Bachelor's programmes were conducted in a seminar room at the university. The model is shown to the participants via laptop and beamer and posters are used for the discussion. The students get together in groups of two and go from poster to poster. They discuss the respective topic, jointly determine the value for the parameter and mark it with a dot on the poster. A framework for the selection is given by specifying the scale in the presentation. This is justified in the tool by deposited studies. The students define their target values for different areas: increasing the energy efficiency in the areas of process heating, space heating and electricity use with a sticky dot per group.

The creation of the energy scenario is divided into two course sessions in the module "Introduction to Energy Economics" at the Master's level. The students have the task of creating their own individual scenario between the first and second session. In the second session, the individual scenarios are then combined into several group scenarios and, finally, a joint scenario is created in the plenary session.

Very ambitious expansion goals are set. By contrast, lifestyle restrictions are rarely targeted. However, the more wind and solar energy needed to meet the energy demand, the greater the electrolysis capacity for hydrogen and the corresponding storage volumes must be in these scenarios. An increased use of biogas can reduce the amount of hydrogen needed to compensate for the shortage.

The Bachelor students felt rather overwhelmed by the high complexity of the tool. According to them, they need more time in which to understand the tool more comprehensively. It becomes clear here that it is very important in the three-hour course session to explain the functioning of the tool well in advance and also during the application. The number and the changes between the applications PowerPoint for the presentation, Mentimeter for the queries and the different views of the simulation tool should be reduced to a minimum during an online seminar to allow the participants a better chance to understand.

The Master's students criticised the superficial application. They would have liked to discuss the results in more detail. It is also noted that the scenario includes unrealistic goals and, therefore, what is realistically feasible should be discussed. In addition, they students criticised that the model does not take into account some points, such as fuel cell mobility and free-field solar thermal energy.

The evaluation of both application shows the high value of the tool in terms of knowledge transfer for participants with little or no prior knowledge. The interactivity of the application was very positively received. The 100prosim tool in combination with the learning method applied increased the motivation for the subject and the satisfaction

with the course generally among the Bachelor students.

An important result is that working in small groups increases the activity and participation of all students. Discussions take place in which individual preferences and prior knowledge are exchanged. Additionally, the positive feedback is that the creation of energy scenarios helps students to gain an overview and understand interrelationships better. According to the students, it is also possible to understand the effects of changes in the system. The application helps them be able to assess expansion targets.

3.3 Use case policy advice

The ever higher targets for reducing greenhouse gas emissions at both a European and federal level require concrete action at the local level. The “planetary boundaries” in spatial planning and development have to be taken into account. One of them is the change of land use – for example, for fields, settlements or photovoltaic plants and bioenergy (Desing et al., 2019). Regional planning in Germany plays a crucial role in the planning and expansion of renewable energies on-site and the implementation of a federal energy policy (Wirth and Leibenath, 2017). The area of tension is between the economic incentives at the national level and the spatial planning options that are more local and regional (Klagge and Arbach, 2013). Land and use competition (e.g. in the designation of areas for wind energy plants or open-space photovoltaic plants) plays a decisive role in this context and poses challenges for regional planning.

The registered association “Erneuerbare Energie-Szenarien e.V.” carried out about 30 workshops directed at processes of regional development, organised by or with the participation of political bodies, local or state administrations and energy agencies. Five of these workshops in Lower Saxony, Germany, gave concrete impulses and suggestions for later spatial planning processes.

Different points of view could be introduced and tested immediately in workshops with experts from the field of political consultancy using 100prosim. The direct experience of the effects on the energy balance made it possible to develop a common view within a short period of time. The holistic view of the energy system makes it clear that the 100 % target places much higher demands on politics and society than is generally realised. In addition to the rate of expansion, this concerns, first and foremost, the idea of sufficiency, i.e. a reduction in energy consumption over and above increases in efficiency. Fields of action can be found, for example, in the size of living space or individual mobility.

4. Conclusion

The workshops have shown that the methodology is very well-suited to understand the energy system of the future and its challenges. The limited availability of land for energy production is made clear. The visualisation of the abstract topic through the graphics of the software also conveys to the participants, inter alia, the limits of energy-saving possibilities through efficiency and the important role of sufficiency in the context of the energy transition. Stakeholders expressed different opinions in the workshops, but these cannot be attributed to specific groups for the time being, but are spread across all workshops. Advocacy for or criticism of individual technologies are mostly justified by personal experience.

The use of the 100prosim simulation tool ensures that the future scenarios are created within the limits of what is technically possible on the space available. Source information is available for each parameter, therefore, this tool is highly trusted. In principle, the energy transition is often supported, but limits, obstacles and risks are also strongly emphasised in some cases. However, the tool cannot be understood and operated without guidance due to the complexity of the energy system. In addition, the database must be constantly updated due to technical innovations and the interrelationships of the dynamic energy sector.

The experience with the tool and the workshops shows that it is also possible to conduct the workshops both online and offline. The method has to be slightly adapted and materials or techniques prepared accordingly. But is has to be noted that to achieve a more effective discussion, it is better to conduct the workshops offline in a ‘real’ workshop setting.

The concepts developed for courses at a Bachelor’s and Master’s level are suitable for increasing the understanding of the energy system as a whole. By reflecting on and discussing different areas, it is also possible to experience that the energy transition is not a purely technical project, but must be accepted and implemented

politically and socially.

It also became apparent that there are still gaps in the knowledge in some areas. The discussions about hydrogen was one such example. Many people were not yet aware of hydrogen as a long-term energy source and its use in industrial processes. Many were also not aware of the increased energy input for the production of hydrogen. Additionally, people also need more information about the energy transition in the sectors of transport or heating. Neutral, independent and target group-specific information is urgently needed.

In order to get closer to the participants and their own possibilities for action, the authors suggest that future projects look at expansion targets and energy consumption at the district or municipal level. Accordingly, a new version of the tool is being developed and not only the energy transition in Germany or a federal state, such as Lower Saxony, can be discussed, but also on a smaller scale regional level. This avoids thinking of "the others" first when it comes to the necessary expansion or behavioural changes. What needs to be done in one's own municipality or district becomes more concrete.

5. References

Agentur für Erneuerbare Energien, 2021. Zustimmung für den Ausbau der Erneuerbaren Energien bleibt hoch. https://unendlich-viel-energie.de/themen/akzeptanz-erneuerbarer/akzeptanz-umfrage/zustimmung-fuer-den-ausbau-der-erneuerbaren-energien-bleibt-hoch (accessed 25 August 2022).

Bundesnetzagentur, 2019. Netzentwicklungsplan Strom 2030, 2nd draft, https://www.netzentwicklungsplan.de/de/netzentwicklungsplaene/netzentwicklungsplan-2030-2019 (accessed 1 July 2022).

Bundesverband Windenergie e.V. /Fraunhofer IWES, 2011. Potenzial der Windenergienutzung an Land. Long version. ISBN: 978 3 94257993.

Desing, H., Widmer, R., Beloin-Saint-Pierre, D., Hischier, R., Wäger, P., 2019. Powering a sustainable and circular economy, an engineering approach to estimating renewable energy potentials within earth system boundaries. Energies 12(24), 4723; https://doi.org/10.3390/en12244723.

Deutsche Energie-Agentur GmbH (Hrsg.) (dena, 2021). „dena-Leitstudie Aufbruch Klimaneutralität" www.dena.de/newsroom/publikationsdetailansicht/pub/abschlussbericht-dena-leitstudie-aufbruch-klimaneutralitaet/ (accessed 1 July 2022).

Deutsche Windguard, 2017. Status des Offshore Windenergie-Ausbaus in Deutschland; Varel, https://www.wind-energie.de/sites/default/files/attachments/page/offshore/20180117-factsheet-status-offshore-windenergieausbau-2017.pdf (accessed 1 July 2022).

Ernst, A., 2017. Beteiligungsprozesse im Zuge der Energiewende: Zwischen Anspruch und Wirklichkeit [Participation Processes within the German Energy Transition (Energiewende)]. ET. Energiewirtschaftliche Tagesfragen.

Federal Ministry for the Environment, Nature Conservation, Nuclear Safety and Consumer Protection, 2016. Klimaschutzplan 2050. Klimaschutzpolitische Grundsätze und Ziele der Bundesregierung. https://www.bmuv.de/fileadmin/Daten_BMU/Download_PDF/Klimaschutz/klimaschutzplan_2050_bf.pdf (accessed 25 August 2022).

Fraune C., Knodt M., Gölz S., Langer, K., 2019. Einleitung: Akzeptanz und politische Partizipation – Herausforderungen und Chancen für die Energiewende, in: Fraune, C., Knodt, M., Gölz, S., Langer, K. (Eds.), Akzeptanz und politische Partizipation in der Energietransformation. Springer VS, Wiesbaden, pp. 1-26.

Fördergesellschaft Windenergie und andere Erneuerbare Energien FGW e. V., 2015. Veröffentlichung der EEG-Referenzerträge. http://www.wind-fgw.de/eeg_referenzertrag.htm (accessed 1 May 2022).

Fraunhofer IWES/IBP, 2017. Wärmewende 2030. Schlüsseltechnologien zur Erreichung der mittel- und langfristigen Klimaschutzziele im Gebäudesektor. Studie im Auftrag von Agora Energiewende.

Fraunhofer-Institut für Solare Energiesysteme, 2020. Wege zu einem klimaneutralen Energiesystem, https://www.ise.fraunhofer.de/content/dam/ise/de/documents/publications/studies/Fraunhofer-ISE-Studie-Wege-

zu-einem-klimaneutralen-Energiesystem.pdf (accessed 1 May 2022).

Fraunhofer ISE, 2011. Wärmepumpen Effizienz - Messtechnische Untersuchung von Wärmepumpenanlagen zur Analyse und Bewertung der Effizienz im realen Betrieb. Kurzfassung. http://wp-effizienz.ise.fraunhofer.de/download/wp_effizienz_endbericht_kurzfassung.pdfrgieausbau-2017.pdf (accessed 1 May 2022).

Gmelin, T.C., Hütting, G., Lehmann, O., 2008. Zusammenfassende Darstellung der Effizienzpotenziale bei Flugzeugen unter besonderer Berücksichtigung der aktuellen Triebwerkstechnik sowie der absehbaren mittelfristigen Entwicklungen. Im Auftrag des Bundesministeriums für Umwelt, Naturschutz und Reaktorsicherheit. http://www.bmub.bund.de/fileadmin/Daten_BMU/Download_PDF/Verkehr/workshop_effizienz_flugverk_studie.pdf (accessed 1 May 2022).

Hübner, G., Pohl, J., Warode, J., Gotchev, B., Ohlhorst, D., Krug, M., Salecki, S., Peters, W., 2020. Akzeptanzfördernde Faktoren erneuerbarer Energien. Bundesamt für Naturschutz. 10.19217/skr551. https://www.bfn.de/sites/default/files/BfN/service/Dokumente/skripten/skript551.pdf (accessed 8 September 2022).

Johann-Heinrich-von-Thünen Institut, 2012. Thünen-Report 17 – Berechnung von gas- und partikelförmigen Emissionen aus der deutschen Landwirtschaft 1990 – 2012. http://www.ti.bund.de/media/publikationen/thuenen-report/Thuenen-Report_17.pdf (accessed 1 May 2022).

Klagge, B., Arbach, C., 2013. Governance-Prozesse für erneuerbare Energien Hannover. = Arbeitsberichte der ARL 5. URN: http://nbn-resolving.de/urn:nbn:de:0156-37935.

Kuckartz, U. 2016. Qualitative Inhaltsanalyse. Methoden, Praxis, Computerunterstützung, Beltz Verlagsgruppe, 69 469 Weinheim. ISBN: 9783779943860.

Marktstammdatenregister, 2022. https://www.marktstammdatenregister.de/MaStR (accessed 1 May 2022).

Meinert, S., 2004. Denken in Alternativen – Scenario-Workshops als didaktischer Ansatz in der Politischen Bildung, in: Gust, M., Seebacher, U.G. (Eds.), Innovative Workshop-Konzepte, Erfolgsrezepte für Unternehmer, Manager und Trainer. USP Publishing, pp. 239-255.

Minx, E. & Böhlke, E., 2006. Denken in alternativen Zukünften. 61. 14-22.

Niedersächsisches Ministerium für Umwelt und Klimaschutz, 2015. Stellungnahmen und Anmerkungen der Mitglieder des Runden Tisches zum Szenario 1 des Gutachtens Energieszenarien 2050. http://www.umwelt.niedersachsen.de/energie/rundertisch/dokumente/stellungnahmen135092.html (accessed 1 July 2022).

Niepelt, R., 2021. Woher kommt der grüne Wasserstoff? In: Themen 202. Mit Wasserstoff zur Klimaneutralität – von der Forschung in die Anwendung, Forschungsverbund Erneuerbare Energien (FVEE), Berlin, ISSN 0939-7582.

Prognos, Öko-Institut, Wuppertal-Institut, 2021. Klimaneutrales Deutschland 2045. Wie Deutschland seine Klimaziele schon vor 2050 erreichen kann. Zusammenfassung im Auftrag von Stiftung Klimaneutralität, Agora Energiewende und Agora Verkehrswende. Online: https://static.agora-energiewende.de/fileadmin/Projekte/2021/2021_04_KNDE45/A-EW_209_KNDE2045_Zusammenfassung_DE_WEB.pdf. (accessed 8 September 2022).

Regionalstatistik, 2020. Statische Ämter des Bundes und der Länder: Regionaldatenbank Deutschland, Online Angebot Genesis, https://www.regionalstatistik.de/genesis/online/logon (accessed 2 July 2022).

Renn, O., 2015. Akzeptanz und Energiewende: Bürgerbeteiligung als Voraussetzung für gelingende Transformationsprozesse. JCSW, 56, 133-154.

Ried, J., Braun, M., Dabrock, P., 2017. Energiewende: Alles eine Frage der Partizipation? Governance-Herausforderungen zwischen Zentralität und Dezentralität. ZFE. 41(3), 203-212.

Robinson, J.B., 1982. Energy backcasting. A proposed method of policy analysis, Energy Policy 10(4), 337-344.

ISSN 0301-4215, https://doi.org/10.1016/0301-4215(82)90048-9.

Rohe, S., Chlebna C., 2021. „Wir haben die Vorgaben seit Jahren erfüllt!“ – Regionale Entscheidungsträger und die Windenergie. Energiewirtsch. Tagesfr. 71(9).

Schmidt-Scheele R., Bauknecht, D., Poganietz W.-R., Seebach, D., Timpe, C., Weimer-Jehle, W., Weiss, A.,2019. Leitmotive und Storylines der Energiewende – Wie Stakeholder-Positionen systematisch in Transformationspfade integriert werden können, TATuP. TATuP. 28(3), 27-33.

Schreiber, M., 2012. Bewertungskriterien einer optimierten Energieversorgung regionaler Verbünde mit hohen Anteilen erneuerbarer Erzeugung. Z. Energiewirtsch. 36, 257-265. https://doi.org/10.1007/s12398-012-0090-4

Siemens, 2020. Whitepaper Wasserstoffinfrastruktur – tragende Säule der Energiewende. https://www.get-h2.de/wp-content/uploads/200915-whitepaper-h2-infrastruktur-DE.pdf (accessed 28 August 2022).

Wassermann, S., Niederberger, M., 2015. Methoden der Experten- und Stakeholdereinbindung in der sozialwissenschaftlichen Forschung. Springer Fachmedien, Wiesbaden.

Umweltbundesamt, 2014. Treibhausgasneutrales Deutschland im Jahr 2050. http://www.umweltbundesamt.de/publikationen/treibhausgasneutrales-deutschland-im-jahr-2050-0 (accessed 28 August 2022).

Weyberg, S., 2021. Fläche: Die Währung der Zukunft. Vortrag auf den Niedersächsischen Energietagen in Hannover am 203 November 2021. https://www.efzn.de/fileadmin/documents/Niedersaechsische_Energietage/Vortr%C3%A4ge/2021/NET2021_Weyberg.pdf (accessed 6 July 2022).

Wirth, P., Leibenath, M., 2017. The role of regional planning in dealing with wind power conflicts in Germany and prospects for spatial research. Spat Res. Plan. 75(4), 389-398. doi: 10.1007/s13147-016-0436-1.

Wuppertal Institut, 2020. CO_2-neutral bis 2035: Eckpunkte eines deutschen Beitrags zur Einhaltung der 1,5-°C-Grenze. Bericht. Wuppertal. https://epub.wupperinst.org/frontdoor/deliver/index/docId/7606/file/7606_CO2-neutral_2035.pdf (accessed 28 August 2022).

Master's Courses at Solar Energy Conferences

Klaus Vajen[1] and Yoann Louvet[1]

[1] University of Kassel, Institute of Thermal Engineering, Kassel (Germany)

Abstract

Bringing master's students closer to established scientists and scientific content was the main underlying idea for establishing a master's course in connection with international solar energy conferences in the early 2000s. Since then, the course has been held at eleven conferences and will takes place for the twelfth time at EuroSun 2022. The organisation of the course spreads over four to six months but the work of the students on the technical content is concentrated over two to three weeks, culminating in active participation in the conference for one week. In addition to participating in networking activities, students work in pair on an assigned topic, attend the conference sessions on their topic and present their findings on the last day of the course. The results of a retrospective evaluation survey conducted at the end of 2021 show that the course was overwhelmingly a positive experience for the 26 former students who responded and that, for most of them, it had a positive impact on their following studies and careers. Due to the universal character of conferences in the scientific world, the concept can be replicated, with a few basic requirements, for other regional or thematic target groups. By sharing practical advises and lessons learned from previous editions of the course, the authors aim to facilitate this process.

Keywords: solar education, master's course, survey

1. Introduction

Scientific conferences, especially international ones, offer established and young researchers, often doctoral students, the opportunity to exchange content, to identify research trends and to build and maintain networks. In principle, undergraduate and master's students can also participate in international conferences. This is often encouraged with discounted conference fees. Diverse studies in literature, mostly with undergraduate students, showed that the participation of students in conferences confirms or even reinforces their interest in research, both for their further studies and for their future professional life. These benefits have been found both for students who present their work at conferences (Mabrouk, 2009; Kneale et al., 2016) and also for those who attend only as audience members (Hall, 2015).

Involving students in scientific conferences is not a new idea. Specially dedicated Undergraduate Research Conferences exists in different research fields and are notably widespread in the Anglo-Saxon world (Kneale et al., 2016). Presenting results at "normal" conferences is also an option and the impact on undergraduate students was studied for instance by Mabrouk (2009) in the field of chemistry. Two years in a row, Mabrouk submitted a survey to undergraduate research students who presented their findings in a dedicated poster session at a national US American conference. Of the 81 students who responded to the survey, 94 % rated their experience with the conference as "life changing or positive". It also motivated them to continue their undergraduate research project (40 % very strongly).

Since 2000 an innovative approach, so far with no equivalent found in literature, has been developed. It is dedicated to graduate students studying a master's degree with knowledge in the field of solar energy, solar buildings and related topics. It consists in bringing international students together at an international conference related to solar energy in the framework of a master's course. In this contribution, the objectives as well as the detailed organisational aspects of the course are presented. Lessons learned along the years are shared to facilitate future reproductions of the concept. The results of a retrospective survey sent to former students are also presented.

© 2022. The Authors. Published by International Solar Energy Society
Selection and/or peer review under responsibility of Scientific Committee
doi:10.18086/eurosun.2022.19.02 Available at http://proceedings.ises.org

2. Starting point and objectives of the course

There are many barriers limiting the access of students to scientific conferences. In addition to financial restrictions, the main obstacles are uncertainties about entering a professional environment that is completely new to them. This takes away the opportunity to come into direct contact with established academics, which could be very helpful for writing master's theses and for a well-founded assessment of doctoral options. Also, students who leave the university directly after graduation would otherwise most likely never get an impression of a scientific conference.

Based on this situation, the master's course has been initiated in 2000 in connection with the EuroSun Conference and the Solar World Congress (SWC), two biennial conferences related to the field of solar energy and organised by the International Solar Energy Society (ISES) and a host institution. Since then, the course has been held at nine EuroSun conferences (2000, 2004, 2006, 2008, 2010, 2012, 2014, 2016 and 2018) and twice at the SWC (2011 and 2021). The course at the last SWC took place for the first time online, as the conference was held virtually due to the COVID-19 pandemic. The course will take place this year again at EuroSun 2022. Along the years with the experience gained and external constraints, some features of the course have evolved. Nevertheless, the main goals and features of the master's course remain the same since its introduction and consist in (a) proposing an organisationally and financially attractive opportunity for students to participate in an international conference, (b) creating an atmosphere in which students feel safe and confident at the conference, (c) fostering opportunities for international networking with other students and doctoral candidates, but especially with established scientists, and (d) providing cutting-edge scientific knowledge on the topics of the conference.

3. Organisation of the course

The course is mainly organised by one or two professors and their assistants, depending on the years. The first author of this paper who initiated the course usually pairs with a professor from the host institution of the conference. The professors and assistants, also named lecturers in the following, are in charge of the practical organisation of the course, the communication with the conference organisers and ISES as well as the supervision and evaluation of the students.

The course is open to a maximum of 20 international students. The course and conference language is English. Students meet in person at the location of the conference which lasts between three to four days and is organised every second year in a different country in Europe (EuroSun) or in the world (SWC). Even though the main, in-person, part of the course is concentrated over the week of the conference, which usually takes place in autumn, the preparation for the course stretches over four to six months. A detailed time schedule is shown in Fig. 1.

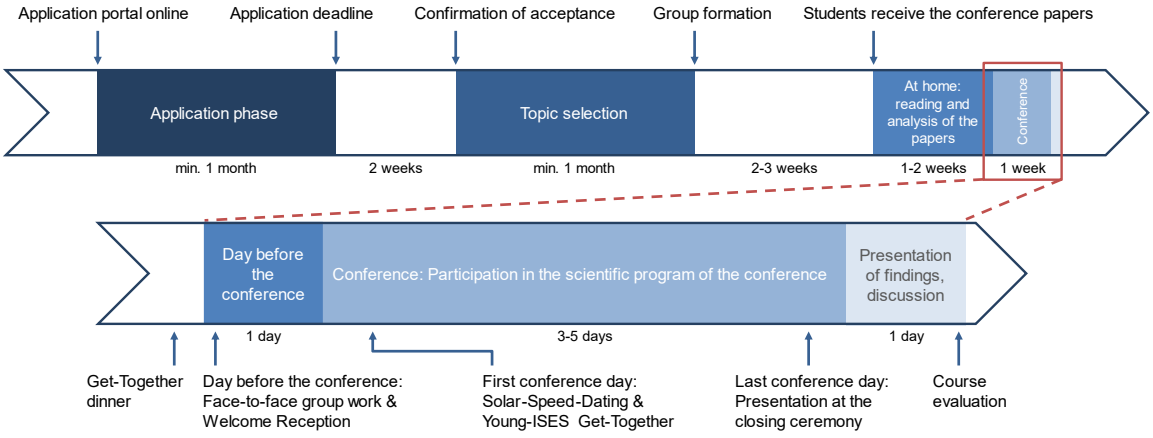

Fig. 1: Schematic timeline of the master's course

Application for the course is the first step and takes place online four to six months before the conference. The course is advertised worldwide through various networks, so that the composition of the group is very international. Students are offered a free access to the conference from the conference organisers but must pay for their own travel and (part of) accommodation costs. During the selection process, in addition to the educational background of the students, attention is paid to the greatest possible diversity in terms of fields of study, countries

of origin, languages and gender. After confirming their participation, the students choose each three to four topics of their choice from the 15 to 20 different themes of the conference. Topics could be, for example, “Solar heat for industrial processes”, “Innovative photovoltaic systems” or “Thermal Energy Storage”. On this basis, international pairs are formed, i.e. a maximum of 10 groups in total, each of which concentrates on one of the topics during the course.

One to two weeks before the conference, the students start working on the technical content. They receive the long version of the conference papers submitted by the conference participants and should read, analyse and discuss the contents with their respective partners. The goal is to come to the conference with already an in-depth knowledge of the conference contributions on the topic that was assigned to their group. This preparation makes it easier for them to follow the scientific discussions and interact with the authors during the conference. On the last day of the course, which takes place the day after the conference ended, the students present the content-related findings on their topic to the other students and the lecturers. In their group presentation, they give a brief overview of the current state of research on their topic. Then they present the two to three conference papers they consider most relevant and critically discuss their findings. Following each 20-minutes presentation, a discussion of about the same length ensues with the group of students and the lecturers. At the end of the presentation day, the course is evaluated in a joint discussion round.

4. Originality of the teaching concept

The teaching concept is unique – no equivalent is known to the authors or could be found in literature – and the objectives, listed above, are much broader than simply learning technical skills on a given topic.

As reported by Hall (2015) quoting a student, after an experiment bringing undergraduate students to a conference “the students felt a little uncertain about their presence as […] “the role of the student at the conference was not set out clearly””. The concept of the master’s course presented here tries to overcome this issue in creating an environment where the students feel at ease during the conference. This is achieved with the organization of several networking activities and involvement in the activities of the conference. On the evening before the welcome reception, students and lecturers meet for the first time personally at a joint dinner in a suitable location. The day before the start of the official technical content of the conference, a room with internet access is available to the student for joint content-related work. On the first day of the conference, a “solar-speed-dating” event as well as a young professional get-together event are organised by the ISES. The students of the master’s course are encouraged to participate in both events which are open to all students, PhD candidates and young professionals participating in the conference. During the “solar-speed-dating” small groups of four to six students and young professionals can exchange ideas with established experts on a previously selected topic. After 20 to 30 minutes, groups and topics change. This is repeated once or two times. Overall, these events are explicitly intended to help students of the course to get to know more conference participants in an informal way and specifically to reduce inhibitions about approaching established scientists. This all contributes to the fact that the students already know a relevant part of the participants at the conference and no longer feel isolated. Pictures illustrating shared moments during the course are presented in Fig. 2.



Fig. 2: Pictures of shared moments during the course: group photo at EuroSun 2006 in Glasgow, United Kingdom (left), students working in group on their presentations at EuroSun 2008 in Lisbon, Portugal (center) and get-together dinner at EuroSun 2014 in Aix-les-Bains, France (right).

Furthermore, when preparing for their final presentation, students are encouraged to talk to the authors to discuss the results and more practically to get their slides as material for the final presentation. Also, during the week of the conference, a daily time slot is arranged for the students to meet with the lecturers to ask organisational and

content-related questions, or questions regarding the conference in general. Last but not least the students are given the task of presenting their motivation, impressions and gained knowledge as well as a message to the solar community in five to ten minutes during the closing ceremony. They do not get real guidelines for this presentation, so the content varies in an original way from year to year. Pictures of presentations during the closing ceremony are shown in Fig. 3.



Fig. 3: Pictures of presentations of the master's course during the closing ceremony at EuroSun 2004 in Freiburg, Germany (left), EuroSun 2012 in Rijeka, Croatia (center) and EuroSun 2016 in Palma de Mallorca, Spain (right).

Emphasis is also placed on improving the presentation skills of the students. During the discussion round following each presentation on the last day of the course, students are asked to evaluate their own performance. Did everything go as planned? Were they too nervous? Did they always look at the audience as they had planned? In addition to the content of the presentation, the discussion provides suggestions for improving the presentation technique and the structure of the slides. Pictures taken during the last day of the course are shown in Fig. 4.



Fig. 4: Pictures of the last day of the course during the final presentations of the students at EuroSun 2010 in Graz, Austria (left), EuroSun 2012 in Rijeka, Croatia (center) and EuroSun 2018 in Rapperswil, Switzerland (right).

Overall, the students work intensively over a period of two to three weeks in an international environment that was previously unknown to them. They learn to manage their time very well. In addition to their topic, for which they have to prepare their final presentation, they naturally have the opportunity to participate in all the other sessions and events of the conference. With these different features of the course, the students learn (a) working in an international environment, for almost all of them in a foreign language, (b) cutting-edge knowledge of current developments in the field of solar energy, (c) time management under time pressure, (d) presentation techniques and self-criticism, (e) networking competences with international students, doctoral students, and experts. Moreover, their fear of contact with science in general and with established scientists in particular is reduced.

5. Retrospective evaluation of the course

To grasp the long-term impact of the course on the students, a short survey with 16 multiple choices questions and one final open question was sent at the end of 2021 to all participants of nine editions of the course between 2004 and 2018. The email addresses gathered along the years were used for this purpose and 155 people contacted. With 26 full questionnaires answered the response rate of 16.7 % is relatively low and is certainly mostly linked to the delay between the events and receipt of the survey. A first hurdle was the validity of the contact data as 26 % of the sent emails resulted in a "Delivery Status Notification (failure)".

In the following the main results of the survey are presented in Fig. 6 to Fig. 10. For each question, the number of respondents *n* is specified. The questions as they are formulated in the survey are given in the title of the figures. When assessing the results, it should be borne in mind that a long period of time had elapsed between the course

and the survey, more than 15 years for some of the respondents. The survey was anonymous, but the year the students participated in the course was asked. An overview is presented in Fig. 5. Interestingly students from all nine courses responded, except from EuroSun 2004 for which the share of invalid email addresses is especially high (64 %).

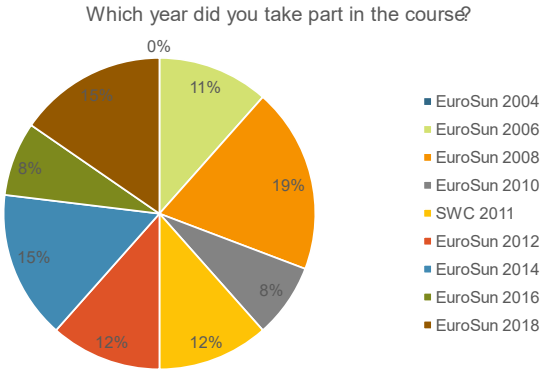

Fig. 5: Year of course participation of the respondents to the survey (n = 26).

A few general questions were asked first. For the large majority of the respondents (84 %) the course was their first participation at an International Conference (Fig. 6, left). Most of them (60 %) are not in contact anymore with other course participants (Fig. 6, right). For those who do (10 respondents), the number of former students they are still in contact with was asked in a text field and varies between one and three (2.3 in average). One answer is unprecise ("less than 10").

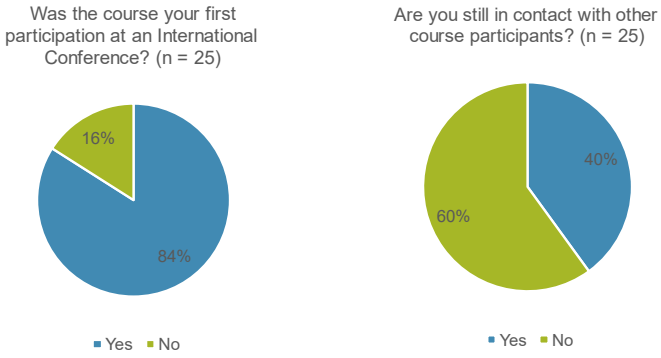

Fig. 6: Answers of the respondents to two general yes and no questions.

The large majority (88 %) of the respondents is still active in the renewable energy and/or the energy efficiency sector (Fig. 7, left). Further details about the current activity of the respondents who positively answered the question "Are you still active in the renewable energy and/or energy efficiency sector?" are shown in Fig. 7 (right). Several choices were possible to answer the question "Which of the following describe best your current activity?". The checkbox "Other" was accompanied with a text field for specifications. Overall, more than half of the respondents (52 %) are still involved with research, and seven of them (30 %) are connected to academia. Industry (35 %), consulting (30 %) and planning (17 %) are the other main fields the current activity of the respondents is related to.

After the general questions, more specific questions related to a retrospective evaluation of the courses were asked. The answers to a first set of questions are presented in Fig. 8. For each question the scale goes from 1 (fully applies) to 5 (does not apply), with the possibility not to answer. Overall, the course was a positive experience for the respondents, 73 % keeping positive memories of the course (fully applies) and 77 % would recommend other students to participate in a similar course (fully applies). For most of the respondents the experience gained during the course was significantly helpful for the rest of their studies (62 % in categories 1 and 2), as well as for their careers (62 % in categories 1 and 2), even though less significantly for the latter. The impact of the course on the career path is less marked, as it is significant (categories 1 and 2) in 30 % of cases. For 31 % of the respondents the course had a limited or no impact on their career path (categories 4 and 5).

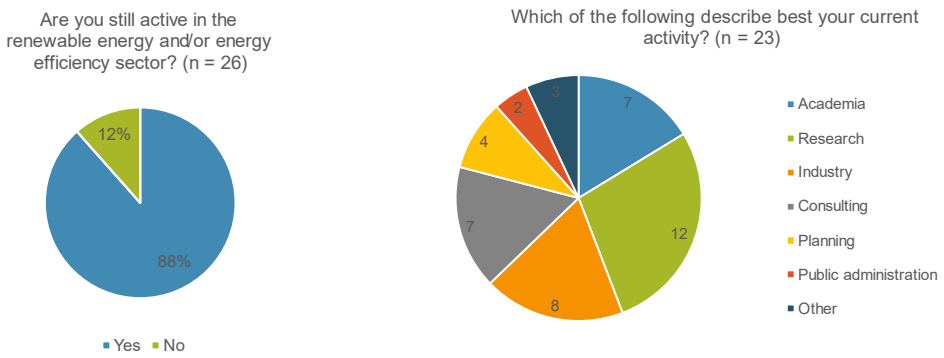

Fig. 7: Answers of the respondents to the questions related to their current activity. Multiple choices were possible for the question "Which of the following describe best your current activity?" (right) and only the answers of the respondents who answered yes to the question "Are you still active in the renewable energy and/or energy efficiency sector?" (left) are integrated.

The participants to the survey were also asked to evaluate the pedagogical content of the course on four different aspects from a scale from 1 (very good) to 5 (very poor), with the possibility not to answer (Fig. 9). Opportunities to improve or acquire knowledge and skills is rated very good in 54 % of the cases for the networking skills, 38 % for the presentation skills and 27 % for the language skills and the technical knowledge. It is rated good in 54 % of the cases for the technical knowledge, 50 % for the presentation and language skills and 23 % for the networking skills.

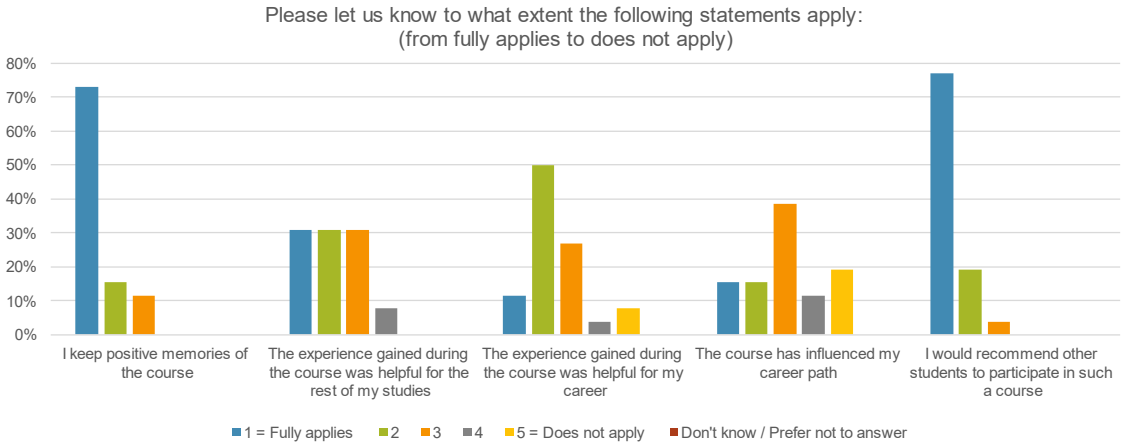

Fig. 8: Answers of the respondents to the questions related to the retrospective evaluation of the courses (n = 26).

Finally, an overall evaluation of the course was asked (Fig. 10) on a scale from 1 (very good) to 5 (very poor), with the possibility not to answer. 92 % of the respondents positively rate the course (categories 1 and 2), among which 42 %-point give a very good assessment.

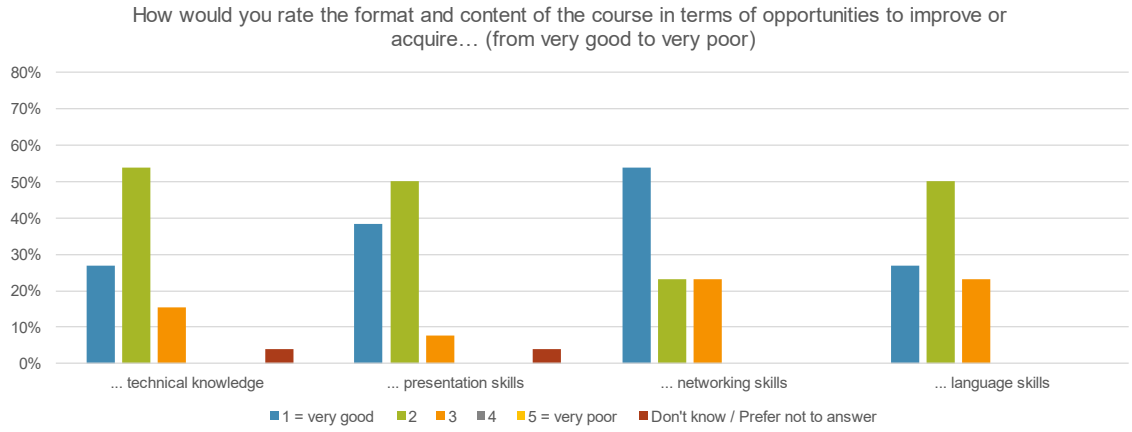

Fig. 9: Answers of the respondents regarding the pedagogical aspects of the course (n = 26).

Even though the low response rate to the survey leads to an imperfect representation of the opinion of the former students who participated in the course, the responses obtained are in line with the objectives of the course. For most of them the course was their first participation in an international conference. It is not a direct objective of the course but interestingly the majority of the respondents are still working in the research field or even in academia for almost a third of them, which is high considering that in 2019 in the EU27 2.8 million people were working as researcher, which represents 3.5 % of the population aged 15..64 with tertiary education (Eurostat, 2022a, 2022b; World Bank, 2019). The causal relationship between having participated in the course and a high inclination to work in the academic and research field cannot be inferred from the survey data. It can however be noticed that three (43 %) of the respondents still active in academia responded with fully applies to the statement "The course has influenced my career path". Two answers to the final open question "Would you like to add one or two sentences about you and the course?" from former students still active in the research field are even more explicit as one states that "[the course] has helped shape [her/his] career" and the second that "participat[ing] at an international scientific conference as a student encouraged [her/him] to pursue a career in research".

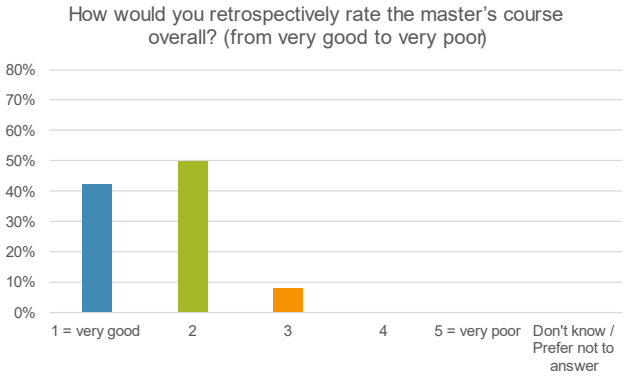

Fig. 10: Answers of the respondents to the overall evaluation of the course (n = 26).

Concerning the opportunity to learn new skills, networking is rated at the highest among the four assessed, which is not surprising giving the context of the course organised with various group activities at a scientific conference which is by essence centred around networking. This is also reflected in the fact that a non-negligible share of the respondents remains in contact with former course students. The method chosen to evaluate the presentation of the students in the last day of the course as detailed in section 4 also seems to be successful as the opportunity to learn presentation skills is rated at the second highest.

6. Practicalities and lessons learned

The format of the course can basically be multiplied and transferred almost at will, as regular international (European) conferences are also common in other academic disciplines. However, some basic requirements must be met. First, the conference organisers must be willing to provide access to a limited number of students at very attractive conditions, ideally free of charge. For the students to be able to work on the technical contents, the written conference papers must be available in full length (not only abstracts) at least a few days before the conference. The lecturers must also be prepared to bear the significant organisational burden of the course, although only a minority of the participants come from their own universities.

Over the years several organisational aspects have been improved. Especially in recent years, a significant number of students who had registered online for the course and were selected to participate have not kept their commitment, so that they needed to be replaced by students from the waiting list. This is an iterative and time-intensive process. In the worst cases students cancelled in the last days before the conference or (rarely) did not even show up, making it difficult to replace them. To reinforce commitment, it was decided in the last editions of the course to introduce a registration fee as a precondition for participation in the form of a compulsory registration as Young ISES Member. Registration costs of 22 € (half for students from low-income countries) are acceptable for students and act as a commitment check. Registration as Young ISES Member is an existing procedure that has been preferred to a direct fee transfer for instance which would require greater administrative efforts. During the month of topic selection (Fig. 1), students must confirm their participation by completing Young ISES Member registration. Students who did not complete their registration after a given deadline are replaced by others from

the waiting list until the group reaches 20 students or the waiting list is exhausted.

Shared accommodation was suggested by the students to encourage group dynamics, so where possible, rooms for the students are pre-booked in a youth hostel at the conference venue. In recent editions of the course, funds have been raised to subsidise (part of) the accommodation costs of students staying at the youth hostel. On the one hand, this reduces the financial burden on the students who have to finance their travel costs, and on the other hand, it prevents students from choosing alternative accommodation, in which case the creation of a group dynamic would be hindered.

All in all, participation in the course requires more financial and organisational efforts from the students than participation in regular courses at their own universities. These unavoidable barriers to participation act as "motivational check" so that the participants are often already highly motivated and committed students, eager to learn more about solar energy and renewable energy in general.

Besides the various financial incentives, the students receive at the end of the course a graded certificate of achievement from the home universities of the lecturers. The grade is awarded based on their final presentations and corresponds to an assumed workload of 90 hours or three ECTS credits. Thus, by having the certificate recognised at their home university, students can ensure that the work invested in the course also counts towards their studies. To date, there is no known case of a university in Europe not wanting to recognise this certificate of achievement in a relevant master's programme.

In terms of technical content, a wide choice of topics is available, but students are always assigned one of the three or four topics they have selected. Conference themes are thematically grouped together when necessary to form the list of topics proposed to the students of the course. This avoids having topics with an unequal number of scientific contributions.

7. Conclusions and outlook

In more than 20 years, eleven conferences and soon twelve, the innovative concept of the master's course presented in this contribution has proven successful. The course is now well established and is a standard feature of the EuroSun conferences. According to the informal feedback the authors have received, other conference participants are usually pleased to see young scientists participating enthusiastically and therefore happy to answer their questions. In addition, the course is often mentioned as one of the conference highlights in the speeches at the closing ceremony.

The answers to a retrospective evaluation survey sent to former students confirm that the vast majority of the 26 respondents had a positive experience of the course. Besides the opportunity to improve or acquire various skills and knowledge, it appears that the course had a substantial impact on their following studies and even on their careers. It is interesting to note that most of the survey respondents are still involved in research in their current activity.

With this contribution, the authors encourage others to replicate the concept, which should be possible in most academic fields with only a few basic requirements. The main hurdle is probably the time needed to organise the course. Over time the authors have developed and improved material such as an online registration form, a detailed timetable for the organisation of the course, answers to frequently asked questions or standard emails for communication which could be shared with interested parties on request.

8. Acknowledgments

The authors are thankful to the former students of the course for responding to the survey that was sent to them.

9. References

Eurostat, 2022a. Population by educational attainment level, sex and age (%) - main indicators [WWW Document]. Eurostat Data Browser. URL https://ec.europa.eu/eurostat/databrowser/view/EDAT_LFSE_03__custom_3212410/default/table?lang=en (accessed 8.17.22).

Eurostat, 2022b. R&D personnel by sector of performance, professional position and sex [WWW Document]. Eurostat Data Browser. URL https://ec.europa.eu/eurostat/databrowser/view/rd_p_persocc/default/table?lang=en (accessed 8.17.22).

Hall, N., 2015. Delineating the Learning Process in Generating a Research Culture among Undergraduate Social Work Students: A Case Study of Student Participation in an Academic Conference. Social Work Education 34, 829–845. https://doi.org/10.1080/02615479.2015.1072709

Kneale, P., Edwards-Jones, A., Walkington, H., Hill, J., 2016. Evaluating undergraduate research conferences as vehicles for novice researcher development. IJRD 7, 159–177. https://doi.org/10.1108/IJRD-10-2015-0026

Mabrouk, P.A., 2009. Survey Study Investigating the Significance of Conference Participation to Undergraduate Research Students. J. Chem. Educ. 86, 1335. https://doi.org/10.1021/ed086p1335

World Bank, 2019. Population ages 15-64, total - European Union [WWW Document]. The World Bank – Data. URL https://data.worldbank.org/indicator/SP.POP.1564.TO?locations=EU (accessed 8.17.22).

Solar Decathlon prototypes and their use as post-competition living labs in higher education

Torsten Masseck

[1] Universitat Politècnica de Catalunya (UPC) - BarcelonaTech, Sant Cugat del Vallès (Spain)

Abstract

Solar Decathlon (SD) competitions offer to participating universities a unique opportunity for introducing into higher education a learning by building approach, with students as important drivers of the whole process. Making Solar Decathlon projects available for an intense after-competition use in the field of teaching and research multiplies their impact in the field of research and education. Within Annex 74: Competitions and Living Labs of the International Energy Agency's (IEA) Energy in Buildings and Communities (EBC) program 22 living lab projects have been analysed, resulting in a detailed description of their contribution in the fields of new educational methodologies and educational materials, impact on higher education curricula and campus as well as the generation of educational networks. Challenges have been identified regarding organization and management, integration into the established academic settings, or sustainability of projects over time, which need to be addressed to integrate more widely living labs as educational tools in higher education.

Keywords: Solar Decathlon, living labs, higher education, solar houses, prototypes

1. Introduction

Solar Decathlon is an international student-centered competition that challenges the selected teams to design, build and operate highly efficient and innovative housing prototypes powered exclusively by solar energy. The positive impact of the event can be prolonged through a well planned and executed after-competition use of the prototype buildings. Tracking projects of earlier competitions shows that many of the projects lacked a solid after-competition use concept, and as a result or could not be reconstructed, or had only a limited lifespan due to a lack of financing, lack of options for a final location or a lack of use and management concept, among others. Making Solar Decathlon projects available for an intense after-competition use in the field of teaching and research multiplies their impact in the field of research and education, especially when used as educational living labs which showcase sustainability strategies for buildings in the field of efficiency, sufficiency and consistency to a broad public in and outside universities.

Living labs can be defined as interoperable collaboration environments supporting user-driven open innovation processes (European Commission 2009). Whereas innovation has been formally a task of individuals as entrepreneurs, a collaborative approach to innovation with multiple stakeholders seems to be a valid and useful option in a world of increasing complexity (Almirall 2009). Open Innovation is defined as an open process where multiple stakeholders collaborate in the process of jointly developing new products or services (Chesbrough 2006). Schuurman et al. (2013) differentiate living labs that support context research and co-creation from living labs focused on knowledge exchange, focused on exploration and not on co-creation. Nevertheless, a review on case studies of living labs shows a huge diversity of concepts and denominations, e.g. applied research centre, showcase home, research laboratory, demonstration building, experimental platform, community lab, prototype home, and observational research facility among others (Masseck 2016).

In the context of Solar Decathlon competitions and higher education, a living lab can be understood as a place where construction, monitoring and evaluation can happen at one place through a multi-stakeholder approach (students, researcher, companies, administration, general public), in a co-creation or open innovation process. This allows for user-centered research under real conditions of use (house occupancy experiments) with real-time

© 2022. The Authors. Published by International Solar Energy Society
Selection and/or peer review under responsibility of Scientific Committee
doi:10.18086/eurosun.2022.19.03 Available at http://proceedings.ises.org

feedback about performance data, user comfort, user-building interaction, energy management and energy efficiency among others (Masseck 2017). Therefor living labs deriving from the experimental housing prototypes of Solar Decathlon competitions can essentially support the holistic search for truly sustainable housing concepts.

In result, getting inspired by successful examples of post-competition living labs and learning about related challenges and obstacles is a useful contribution for future teams and their stakeholders. The presented research has been carried out in the framework of Annex 74: Competitions and Living Labs within the International Energy Agency's (IEA) Energy in Buildings and Communities (EBC) program.

2. Objectives

The purpose of this research is to make knowledge available about the after-competition use of Solar Decathlon projects as living labs to those with the intention to participate in a living lab competition and those who are on the way to set up their own living lab. The results should allow a compact overview for future organizers and teams about successfully implemented living labs. Main sources have been the in-depth analysis of former editions of the Solar Decathlon, mainly the European editions, but also case studies from the US and Africa, together with survey results and experts' interviews which summarize the stories and experiences behind the projects.

One principal idea of this focus report is to let the project leaders speak about their personal experience in the post-competition use phase of Solar Decathlon (SD) prototypes. These key players have been asked about which outcomes they can report, which successful actions could be implemented and what has been achieved during this important use phase of SD prototypes. On the other side survey and semi-structured interviews allowed gathering information about the challenges they have encountered, the learnings that could be achieved, and asked for recommendations to be given to future SD participants, teams and project leaders.

This research focuses specifically on living labs which are used for educational purposes in their after-competition use phase, as this allows a prolonged positive impact in the field of higher education, with the possibility to train and educate whole generations of future professionals in and around the prototypes.

3. Methodology

This research has been structured in two parts: Online research regarding the current location, use and ownership of former Solar Decathlon (SD) projects on one side, and a survey and interview-based research on specific projects based on direct communication with their current directors on the other. Projects from the original US competition since 2002, the Solar Decathlon Europe (SDE) competitions since 2010, and the first Solar Decathlon Africa competition (SDA 2019) have been taken into consideration. A total of 152 projects from US competitions since 2002 have been revised regarding their post-competition use as educational living labs. 25 projects have been selected in a first search for current operative living labs related to education. 15 projects have been further analysed and 11 resulted in educational living labs with a high interest for this research. On a European level, competition participants since 2010 have been listed and searched through the corresponding webpages, especially the www.building-competition.org website, supported by the Annex 74 work. 12 potential current operating educational living labs have been identified and after a deeper analysis, 9 have been selected as educational living labs with a high interest for this research. Regarding the Solar Decathlon Africa (SDA2019) competition 4 potential living lab projects have been identified and 2 projects could be further analysed and information about current activities has been facilitated for this research.

After the selection of potential interesting projects and based on the information encountered, a data sheet has been drafted based on previous research of the author (Masseck 2016) with a summarized description of each of the projects, pictures of its current state, contact details to owners or operators, as well as links to publications of current activities. In parallel an educational living lab survey has been designed with 4 blocks of questions. A first block focuses on concepts of each educational living lab, asking for the educational methodologies applied, educational materials generated, target groups who benefit from the project, its impact on higher education curricula and campus, and about new educational networks which could be generated. In a second block of questions project leaders have been asked for a critical view on their living lab project, focusing on the challenges and obstacles encountered in the 3 areas of concept and implementation, costs and maintenance, and operation and outcomes.

Based on the received survey answers, a semi-structured interview has been requested to the project leaders, and 7 interviews could be held, gathering valuable additional information about specific success stories as well as individual drawbacks of projects, which could not be collected through the standardized survey.

4. Results

4.1. The post-competition lifespan of Solar Decathlon prototypes

Project leaders have been asked to estimate the foreseen lifespan of their projects, and answers have been given between 3 years and "no end foreseen", but an average lifespan between all documented projects can be estimated in around 5-6 years, with the oldest ones operating over 14 years and the newest ones recently starting their post-competition use phase.

It is worth to mentions that lifespan is an important aspect for the payback of energy, effort, and money of a project after a Solar Decathlon participation, but the intensity of use must also be taken into consideration for evaluating the overall success of the after-competition use. Some prototypes show very low activity during a longer period after competitions, before being activated and used again. Others get immediately reconstructed and used for ongoing research or dissemination activities. This often depends on how the after-competition use phase has been planned beforehand and important aspects like final location, use rights, maintenance and management have been clarified and corresponding agreements have been closed among partners.

4.2. Educational methodologies and teaching formats applied

Due to the character of the Solar Decathlon competitions as a student-driven event, which allows in-depth learning by planning, building, and operating real prototype buildings, all projects are linking teaching, research and innovation during their development and execution.

In the after-competition use phase some projects seem to focus more on research activities, others foster specifically educational initiatives, and many of them maintain a mix of both. Regarding the specific use for education, online research and survey results allow the following description of the post-competition use of projects:

- Prototype exploration through students (materials, systems, concepts) (20 out of 22)
- Measurements and evaluation of the prototype in-situ (thermal comfort, system performance, bioclimatic solutions, comparison of measurements and simulation) (20 out of 22)
- Seminars/workshops inspired by the special place (18 out of 22)
- Co-creation initiatives for new projects, bringing together different stakeholders (students, researchers, companies, administration…) (10 out of 22)

4.3. Educational materials generated

A major outcome of Solar Decathlon projects are project documentations, monitoring results and results of testing of innovative materials, components and installations regarding their energetic, constructive and aesthetic performance. Beside these technical documents, many dissemination materials are generated like leaflets, video presentations and recorded guided visits, as well as open online courses (MOOCs), virtual or augmented reality presentations among others.

Online research and survey results allow the following description of generated educational materials:

- Documentation of the prototype used regularly as case study for teaching (16 out of 22)
- Articles published about the prototype (5 out of 22)
- MOOC course developed in or around the prototype building (2 out of 22)
- Augmented / virtual reality representations (3 out of 22)

4.4. Positive impact on higher education curricula and campus

Solar Decathlon projects do have a major impact on a faculty due to its duration from start to competition of around 2 years, the intensity of workload for students and teaching staff, as well as the high visibility of the project in and outside university.

Online research and survey results allow the following description of positive impact on higher education curricula and campus:

- Creation of new infrastructure (19 out of 22)
- Creation of new forms of teaching focused on real project and construction (12 out of 22)

Project leaders describe the impact on HE curricula as following:

- *As I have presented the projects in my lectures at the faculty, most students now know them. What works particularly well are three films we have made: two mini-documentaries and a mini-film. Students and people across the world love these and share them in social media.*
- *The main impact on our curriculum is an increased ratio of practical studies and experiments with a real building. The SD prototype is now used as a seminar room, in which we can descriptively discuss with the students about building energy efficiency, indoor climate and the usage of renewable energy for buildings.*
- *Our school is focus on acting on the reality. This kind of projects allows us to inspire to the students in order to go further than the typical classes.*
- *The project helped us to identify the strengths and weaknesses of the different courses of the faculty, highlighting the need for more in-depth interdisciplinary teaching. For this purpose, the teaching staff must be trained or have an interdisciplinary background. This is one of the best ways to give the different classes and respond to the questions and concerns of students.*
- *In general, the project has reinforced the idea of mixing students from different disciplines (architecture, civil engineering and environmental engineering) under a single course type workshop.*
- *There is more room now for collaboration between different disciplines and more collaboration with companies*
- *Our university is convinced of the educational value of teaching by project.*
- *The students and professor of the project continue to work together within the framework of an association they created and new research subjects related to the theme are launched: PVT, Phase change materials, ...*

4.5. New educational networks generated

A Solar Decathlon participation is for universities a major opportunity for building up networks of students, researchers, companies and institutions, which support the project during development and construction through contribution of material and know-how, participation in linked research projects or funding, among others. These networks across disciplines are useful for education, research and market-uptake objectives, according to the interest of each partner. Networks often persist in the post-competition phase and are valuable outcomes of the competition for universities on medium and long-term.

Online research and survey results allow the following description of positive outcomes regarding the generation of educational networks:

- Creation of student networks which persist in the post-competition phase and often result in a common professional project like a start-up or a cooperative (15 out of 22)
- Creation of research networks which allow generating research and innovation outcomes in and around the prototypes (6 out of 22)
- Creation of institutional networks which keep supporting the project in the post-competition phase, a new participation in a later competition or a similar project on local or regional level (7 out of 22)

In this context it is worth to mention the specific UPC experience during Solar Decathlon Europe Competitions since 2010. The UPC prototypes LOW3 (SDE 2010) (Figure 1), e(co) (SDE 2012) (Figure 2), Ressò (SDE 2014) (Figure 3), and TO (SDE 2019) (Figure 4), resulted in the generation of cooperatives of former team members, creating sustainability focused architecture practices, as well as prolonged collaboration as operators of the respective prototypes together with public administration and university as stakeholders.

LOW3 (SDE 2010) allowed to generate a first collaboration of second- and third-year students at the Vallès School of Architecture (ETSAV) of UPC. 2 years later these students formed a new competition team for SDE 2012, using LOW3 as on-campus infrastructure for their meetings and networking activities.

E(co) (SDE 2012) has been the core project that initiated the foundation of the Arqbag cooperative (www.arqbag.coop), which at the date of this report states of 7 founding members and 3 collaborators, developing sustainable architecture projects with a specific focus on the social innovations like neighborhood facilities and co-housing projects. Some Arqbag members are also part of the current teaching staff at ETSAV (UPC), and through this link transmit their knowledge, attitude and experience gained in the last years to following generations of students.

Ressò (SDE 2014) gave place to the association Accio-Ressò, constituted by former SDE students, which after the competition in 2014 directed the re-building and implementation process of Ressò as a neighborhood facility at Sant Muç (Rubí) in cooperation with the city council of Rubí. Ressò since then has served as a platform and space for multiple activities which contributed to improve the living quality of the neighborhood. It has served as a multifunctional space for educational activities regarding energy efficiency, it supported the implementation of energy efficiency projects in the neighborhood, and it hosted other activities like yoga classes or similar offers for a neighborhood which lacks this kind of offers. Administrative issues led to the temporary closure of the installation at the time of writing, but according to the drivers of the project, a re-activation is planned.

TO (SDE 2019) is the newest project at UPC and has been rebuilt at the UPC Campus South Diagonal in the beginning of 2020, with the aim to start activities as a Living Lab that allows guided visit and educational initiatives for UPC students and the general public. The project has received support for this post-competition use by the city council of Barcelona and the Barcelona Energy Agency. Due to the pandemic outbreak, specific activities could only start from early 2022 onward. Currently the house is occupied by students who live and evaluate the house under real conditions of use.

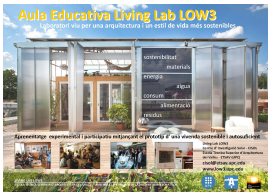

Fig. 1: LOW3 (SDE 2010) (Picture: Torsten Masseck)



Fig. 2: (e)co (SDE 2012) (Picture: Arqbag)



Fig. 3: RESSÒ (SDE 2014) (Picture: Torsten Masseck)



Fig. 4: TO (SDE 2019) (Picture: Torsten Masseck)

Learnings for a successful after-competition use of SD prototypes can be especially achieved through a critical review of processes, obstacles and success stories linked to specific projects. A critical analysis by project leaders themselves and specific recommendations out of their experiences made, are most valuable in this context.

4.6. Concepts and Implementation

The after-competition use of Solar Decathlon prototypes requires a concept for the implementation of prototypes, especially a place where to rebuild the house, with the possibility to stay for a certain period. Also, entities must be linked for this new phase of operation and exploitation through agreements and contracts.

Project leaders reported the following aspects and experiences through the survey and personal inter-views:

- *Getting it rebuilt after the competition has proved to be very hard compared to the speed of construction during the competition, because everyone was tired and busy again with other things, and the weather was bad during winter. It was a struggle. We have also had trouble getting things arranged regarding the hand-over.*
- *It is very hard to find a building site on the university campus where a SD prototype can stay for several years (this process had a duration of 3 years in our case)*
- *To re-build it again was an achievement itself. And we started pretty well with neighbors. But city hall did not allow them to self-manage the space.*
- *The main difficulty is the situation (the use of the land) and the creation of a convention with the owner of the land. In this case the convention defines that the cultural exploitation of the prototype is in the hand of one entity, and the maintenance (with associated costs) is of … the two institutions that use it as research infrastructure.*
- *It requires a different attitude from teachers*

- *Here are some obstacles and drawbacks when using our SD prototype post-competition as an educational living lab: the project is too far from our university, there is a lack of operating budget and also a lack of a regulatory framework for the operation of the project: after two years an agreement is still being prepared*

These quotations and the additional information given through interviews, as well as the knowledge about projects which suffered from the lack of adequate location for their after-competition use and therefore had to be dismantled, show that a clear planning for location and after competition use is essential.

4.7. Costs and Maintenance

Cost and Maintenance of prototypes in the post-competition use phase are critical aspects. After competition end resources are often limited, many teams even have accumulated debts during the whole process of development, construction and competition, and new funding is necessary to cover cost for reconstruction at a new location.

Project leaders reported the following aspects and experiences through the survey and personal interviews:

- *Arranging well that one party can do the maintenance, operation and eventual demolition was a struggle. The money has gone and parties taking over usually want to be paid for it, which in our case came down to dodgy arrangements for which the faculty eventually paid the bill. Better to have this arranged beforehand with people who are trustworthy.*
- *The SDE competition format doesn't really consider the necessary costs for the reconstruction in the post competition phase.*
- *The maintenance is a big issue because city hall does not want to spend money regularly. The re-assembly was relatively easy. The maintenance is much more complicated.*
- *Who takes care of it and who pays are the key questions. A usage convention has solved this.*
- *It is difficult to find a viable business model.*
- *Lack of operating and maintenance budget for the project.*

These testimonies focus on the importance to secure financial resources for re-construction forehand. Estimating the maintenance costs of the prototype in the post-competition phase and clarifying who will take them over and for how long are key questions to be approached as early as possible.

4.8. Operation and Outcomes

Operation in the post-competition phase might be critical. New agents might have taken over the responsibility of the project, or shared operation is agreed among several entities. Daily operation also requires personal and material resources as well as knowledge about the prototype itself. All this leads to critical situations of the operation and exploitation of prototypes which must be handled and solved.

Project leaders reported the following aspects and experiences through the survey and personal inter-views:

- *You definitely need partners in the administration of your institution which love the project.*
- *The operation was thanks to good will from the team members and illusion from neighbors.*
- *Ensuring that the prototype is operational for research purposes and that the sensor data is correctly uploaded to the database etc. is a special challenge. In general, the facility management of the prototype created for a temporary competition is not an easy task due to the "test" component of its creation.*
- *Finding a balance between the needs of education and the needs of companies.*
- *Lack of a regulatory framework for the operation of the project: after two years an agreement is still being prepared.*
- *Overall, it can be stated that the following aspects are most relevant: Plan operation beforehand and clarify administrative support as early as possible to avoid de-lays due to necessary negotiations and missing framework. Consider that technical challenges might appear, as prototypes are student built and might need improvement for long-term operation and monitoring.*

According to the testimonies it results key to plan operation beforehand and clarify administrative support as early as possible to avoid delays due to necessary negotiations and missing framework. Furthermore, it must be considered that technical challenges might appear, as prototypes are student built and might need improvement for long-term operation and monitoring.

4.9. Integration in academic curricula

Solar Decathlon prototypes in their post-competition use phase con be valuable objects and places for new teaching formats, interdisciplinary educational formats, and innovative experience-based learning initiatives. Nevertheless, existing higher education curricula are generally little flexible regarding innovations in form or content.

Based on the survey and personal interviews, project leaders described their experience regarding the integration of Solar Decathlon prototypes into the academic curricula as following:

- *The Idea is to integrate the prototype in some specific subjects, but COVID postponed all.*
- *I use the prototype examples in my lectures, and they are used for tours of new students coming in in August, but furthermore, there is no embedding in the curriculum. We do ask students to connect graduation projects to the prototypes, which has been done regularly.*
- *This worked very, very good in our case. No challenges.*
- *Not much. One studio was focus on this reassembly for a year and it helps to do the next SDE edition.*
- *The prototype has been very much exploited during its elaboration so at a curricular level the interest has decreased, but the willingness to make use of the prototype for a facility management via digital tools such as the BIM is now up to date.*
- *It takes time.*
- *The project is too far from our university.*

These testimonies allow drawing the conclusion that it is important to integrate new teaching based on living labs in academic curricula as early as possible, as little flexibility exists generally for adapting higher education curricula to new academic formats or contents. It is also mentioned that reconstruction of SD prototypes requires time and resources which might delay the readiness for post-competition uses, but also opens the possibility to consider reconstruction and operation itself as an academic activity to be embedded in HE curricula. Finally, digital tools (MOOCs, BIM) might open up possibilities for additional use in higher education curricula when academic interest in the SD prototype itself decreases over time due to loss of novelty.

5. Conclusions

The explanations given by project leaders about the post-competition phase and resulting initiatives and activities give testimony about the prolonged positive influence of Solar Decathlon prototypes, when implemented properly for a post-competition use as living labs.

It shows that the generation of networks among the huge diversity of participants is one of the most interesting outcomes which benefit all type of stakeholders of a project. Companies get into touch with potential future collaborators, Higher Education Institutions (HEI's) build up or improve their university-industry relationships and their collaboration with public institutions, students build up interdisciplinary networks that often allow generating a core group for a start-up initiative, or any other type of cooperative enterprise linked to the project, but also beyond. Educational networks based on a university project evolve many times towards professional relationships over time.

After describing the diverse impacts achieved, obstacles encountered, and conclusions drawn by the interviewed project leaders it can be stated that there also exists a certain pressure for teams to convert SD projects into high impact post-competition labs and only a view really succeed in achieving a high visibility and high impact through a holistic implementation and a strong concept.

Nevertheless, beyond the visible part of a post-competition use as living lab, almost all projects generate a huge number of distributed, small-scale benefits, which are difficult to detect and to document, but which exist, like new professional projects, e.g. cooperatives or students getting employed by companies which supported and collaborated in SD projects, or simply the human networks generated.

Solar Decathlon projects are generally milestones for faculty advisors which have a high component of stress, risk, but also rewards as researchers and lecturers. Struggle with after-competition use seems to be typical, with conflicts to solve regarding the available work force, because students are exhausted or leaving university, lack

of financial resources with many teams come back from the competition without resources left or even with some debts to deal with, and a lack of organizational support e.g., for finding appropriate location and operational support at university.

The analysis of 22 projects allowed a detailed description of their contribution in the field of new educational methodologies, educational materials, impact on HE curricula and campus as well as the generation of educational networks. Projects often generate participatory teaching and learning processes in interaction with many other relevant societal stakeholders. The analyzed living lab projects show the diversity of possible approaches and their potential to create impact, but also allow identifying a series of challenges of the concept regarding organization and management, integration into the established academic settings or sustainability of projects over time, which need to be addressed to integrate more widely living labs as educational tools in higher education.

6. Acknowledgments

This work is based on PhD research of the author at UPC and has been further developed within the framework of the IEA EBC Annex 74 “Living Labs and Competitions” with the kind support of many Annex 74 working group members and colleagues at UPC. The author is a Serra Hunter Fellow at the Valles School of Architecture (ETSAV) of UPC.

7. References

Almirall, E., 2009. Understanding Innovation as a Collaborative, Co-Evolutionary Process. Ramon Llull.

Chesbrough, H., 2006. Open Innovation: A New Paradigm for Understanding Industrial Innovation, in: Open Innovation: Researching a New Paradigm, 1–12. https://doi.org/citeulike-article-id:5207447.

European Commission, 2009. Living Labs for User-Driven Open Innovation - an Overview of the Living Labs Methodology, Activities and Achievements. Facilities. European Commision, Information Society and Media. https://doi.org/10.2759/34481.

Masseck, T., 2016. Teaching Sustainability - Living Labs in Architecture. Universitat Politècnica de Catalunya. http://hdl.handle.net/2117/96265.

Masseck, T., 2017. Living Labs in Architecture as Innovation Arenas within Higher Education Institutions. Energy Procedia, 115, 383–89. https://doi.org/10.1016/j.egypro.2017.05.035.

Schuurman, D., Mahr, D., De Marez, L., Ballon, P., 2013. A Fourfold Typology of Living Labs : An Empirical Investigation amongst the ENoLL Community. *ICE & IEEE-ITMC - Conference, Proceedings*, 11.

Development of a Small-Scale Plant for Electricity and Water Supply in Rural Regions of Côte d'Ivoire as Part of the First Ivorian Dual Study Program with Focus on Renewable Energies

Lukas Saars[1], Charlotte Newiadomsky[1], Ahoutou Paul Kouakou[2], N'guessan Raymond Kre[2] and Arne Graßmann[1]

[1] Hochschule Niederrhein, SWK E² - Institute for Energy Technology and Energy Management, Krefeld (Germany)

[2] Université NANGUI ABROGOUA, Unité de Formation et de Recherche Sciences Fondamentales Appliquées, Abidjan (Côte d'Ivoire)

Abstract

In many African countries, access to electricity and potable water is capable of development, especially in rural areas. Another issue is the lack of practical components in the education system which is one source of the high unemployability rate since it is more theoretically oriented. The project 'Industry Integrated Dual Engineering Studies in a North-South Collaboration (IIDES-NSC)' aims to address the issue of limited access to electricity and water in the West African state of Côte d'Ivoire. To reach these purposes, the first dual study program in Côte d'Ivoire is developed and introduced at the University NANGUI ABROGOUA. It combines theoretical, practice-oriented, and project teaching modules, which enable the students to work on a prototype for a self-sufficient electricity and water supply system to be installed in a model village. To acquire the competencies demanded by the industry, technical, economic, and social modules have been included in the development of the curriculum, together with relevant stakeholders from industry, public institutions, and universities. One of the four semesters of the study program will take place at the Hochschule Niederrhein in Germany, where the Ivorian students will develop and build one out of a total of two prototypes and simultaneously increase their intercultural skills. In the end, the study program can make an important contribution to combating the high unemployment rate among graduates and at the same time accelerate the expansion and security of renewable energies and water supply infrastructure in Côte d'Ivoire.

Keywords: Academic Education, Industry, Dual Study Program, Côte d'Ivoire, Electricity and Water Supply

1. Problem and Motivation

The access to electricity and water in rural areas in Côte d'Ivoire as well as in large parts of Africa is limited. According to Ivorian government sources, the national coverage rate of drinkable water and electricity was on average about 80% in 2020, whereas there are differences between rural and urban regions. The coverages are lower in rural areas that are situated far from the governmental infrastructures. Africa is a priority region in the World Energy Outlook 2019 to provide a robust, evidence-based platform for energy decision-makers (International Energy Agency, 2019). The 'Sustainable Africa Scenario' of the African Energy Outlook 2022 wants to achieve universal access to affordable electricity by 2030, although 43% of the total population in Africa lacks access to electricity at present (International Energy Agency, 2022). As the African population continues to grow, the absolute number of people without access to electricity and water continues to increase. The supply of electricity and clean water is closely intertwined and leads to direct interdependencies and impacts (Newiadomsky and Tietze, 2017).

The safely managed national coverage rate of drinkable water in Côte d'Ivoire in 2020 was 35.20% (14.58% in rural areas and 54.47% in urban areas) (WHO/UNICEF JMP, 2021). In addition, only 69.70% of the Ivorian population had access to electricity in 2020, (94.50% of the urban population and only 43.10% of the rural population) (The World Bank, 2022). The sometimes long and time-consuming supply chain for potable water, which is largely handled by adolescents, especially girls, severely limits the educational and training opportunities of those affected (Mitsubishi UFJ Research and Consulting Co., Ltd., 2013; Noubactep, 2016).

© 2022. The Authors. Published by International Solar Energy Society
Selection and/or peer review under responsibility of Scientific Committee
doi:10.18086/eurosun.2022.19.04 Available at http://proceedings.ises.org

The poor supply of electricity also hinders education, since there are often no possibilities for students to learn after sunset. It also affects economic power, so only a limited production of goods (e.g. with the help of electrical tools) is possible. Besides, increasing electricity demand is predicted in Côte d'Ivoire due to economic growth (International Energy Agency, 2019). The highest potential for electricity generation in Côte d'Ivoire lies in solar energy, which is why the Ministry of Energy plans to expand the installed capacity of photovoltaic plants by up to 424 MW by 2030 (Seier, 2016). The following figures show that the potential for electricity generation from photovoltaics in Côte d'Ivoire is very large. The figure on the left side (Fig. 1) shows the global horizontal irradiation and the one on the right side (Fig. 2) the photovoltaic power potential in Côte d'Ivoire.

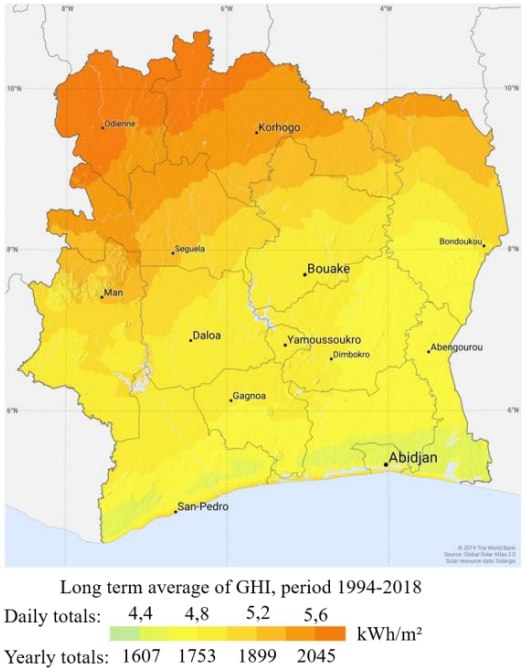

Fig. 1: Global Horizontal Irradiation in Côte d'Ivoire (Solargis, 2022a)

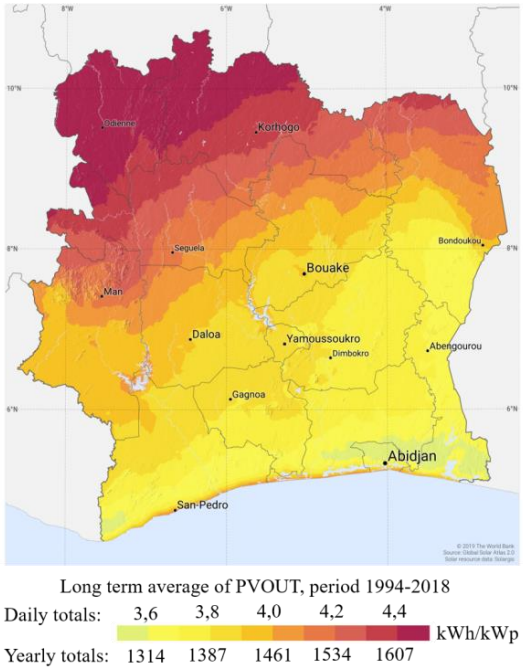

Fig. 2: Photovoltaic Power Potential in Côte d'Ivoire (Solargis, 2022b)

Despite the large photovoltaic power potential, the share of electricity production from renewable energies (excluding hydroelectric) in total electricity production in Côte d'Ivoire is still extremely low with only 1.2% in 2015 (The World Bank, 2022). The Ivorian government's expansion plans are essential to provide decentralized renewable energy to the growing population, especially in rural areas.

This conflict can be complemented by other areas, such as education. In most of the public universities in Côte d'Ivoire, learning is more theoretical than practical. Human resources managers at Ivorian companies often complain that university graduates' knowledge is based on a purely theoretical foundation and their practical experience is still lacking. Therefore, in industrial human resources management it is said that university graduates are not ready to enter the industry. In general, graduates have to start working as a trainee in industrial companies for around two years after graduation, to be considered as potential full employees. As a result, universities and companies in Côte d'Ivoire rarely work together or enter into long-term collaborations. According to Yapo (2018a), the recruitment rate of graduates in Côte d'Ivoire was only 14.43% in 2016, which means that almost 86% of these graduates were unemployed. At the same time, the average overqualification rate in Côte d'Ivoire is 29.69%, from which workers with secondary and higher general education are more affected (38.15% and 30.68%, respectively) and especially women are more exposed than men (30.97% versus 29.25%, respectively). As a result, graduates often start to work in sectors that do not require the special knowledge of their former studies, so a quick adaption to the field of work is necessary.

Introducing a dual study program, where theoretical and practical knowledge are gained simultaneously, is a big step forward to improving the economic power in Côte d'Ivoire and helps students to get in contact with

interested companies early, who might be willing to employ them after their graduation. The practical relevance is the biggest advantage of dual study programs. The main goal is to enable students to simultaneously gain theoretical knowledge as well as practical experience from working in a local company in the field of e.g. energy or water supply. Since students who study in dual programs already gain a lot of work experience during their studies, they are better prepared for professional life in terms of working experience. Currently, there are no dual study programs in Côte d'Ivoire, although they have great potential to strengthen cooperation between universities and companies and reduce unemployment rates among graduates. This and the fact that the Ivorian government has issued optimistic targets for the expansion of renewable energies lead to the development of the project idea and concept. The dual study program will contribute to the development of the Ivorian economy by improving electricity and water supply in rural areas, employability of graduates through practice-oriented higher education, cooperation with local institutions and companies as well as enabling the local population to solve electricity and water supply problems independently and sustainably.

2. Application-Oriented Study Program

This paper presents some solutions to tackle the beforementioned problems in Côte d'Ivoire by implementing a dual study program that combines practical and theoretical teaching modules with a focus on renewable energies (specifically solar energy) and water supply. The students will not only learn engineering-specific content but will simultaneously work on a prototype of a small-scale plant to supply electricity and water in a model village in a rural region. This can make an important contribution to combating the high unemployment rate among graduates and simultaneously accelerate the expansion of renewable energies and water supply infrastructure in Côte d'Ivoire.

The first group of students will develop and construct a small-scale electricity and water supply plant within the framework of practice-oriented teaching modules. One of the key objectives of the project is that the developed and implemented dual study program at the University of NANGUI ABROGOUA will remain after the end of the project so that a sustainable expansion of Ivorian academic education and acceleration of renewable energy development can be achieved. The following groups of students will then work on other projects accompanying their studies, which will meet the requirements of the industry. The basic structure of the Ivorian dual study program is shown in the following figure.

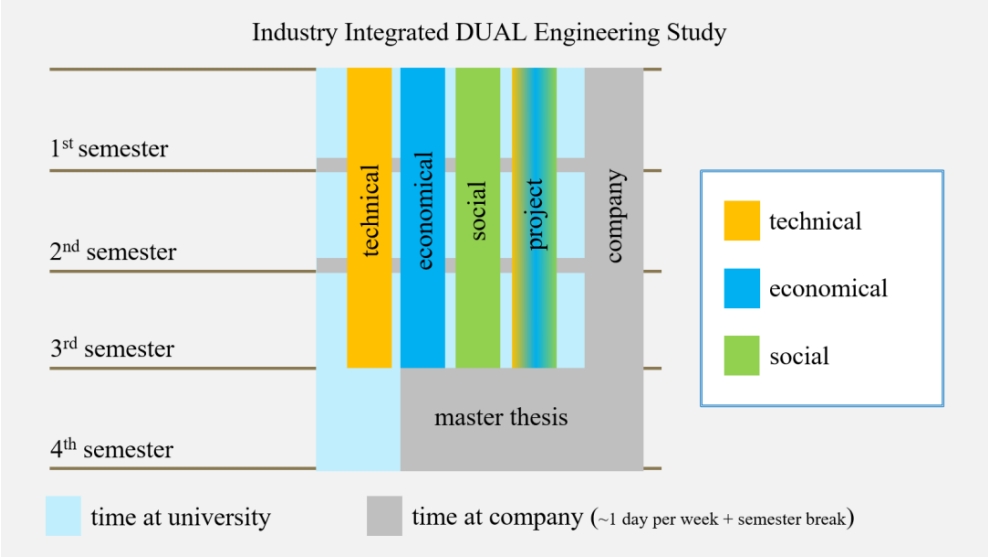

Fig. 3: Basic Structure of the Dual Study Program

As shown in Fig. 3, the Master's program that will take place at the University NANGUI ABROGOUA in Côte d'Ivoire is a four-semester continuing education program. It's composed of technical, economic, social, and project modules, partly to be conducted at the university and partly to be conducted at a company to have competitive training. One semester abroad at the Hochschule Niederrhein is firmly anchored in the curriculum (third semester of the study program). The study in Germany is to be structured with a duration of one semester

including the practical part.

The first two practice-oriented project modules of the study program are intended for concept development and detailed planning of a prototype by the Ivorian students. During the third semester, the students travel to the Hochschule Niederrhein in Krefeld (Germany) to build up and operate the first prototype. After finishing the semester abroad, the training material and facilities are to be transferred to the University NANGUI ABROGOUA in Côte d'Ivoire. Subsequently, students from the Hochschule Niederrhein from existing study programs fitting thematically into the topic of the study program in Côte d'Ivoire, will visit the University NANGUI ABROGOUA to work together with the Ivorian students on a second prototype. The mixed student group has to consider its experiences during the build-up of the first prototype as well as local sourcing for components and necessary work to be done.

In the dual study program, the Ivorian and German students will learn how business models are set up and what is important during development, using the prototype as an example. The best business model will be selected in the program of a competition, involving local financiers and industry partners. The first prototype is set up at the campus in Abidjan and put into operation. Afterwards, the procurement of local materials for the second prototype starts and the workspace is prepared.

Further German students (not necessarily from the mentioned group before) travel to Côte d'Ivoire during the fourth semester to write their thesis about the project from technical and economic perspectives. At the same time, the Ivorian students build and implement the second prototype on campus. After the successful installation and operation of the second prototype at the University NANGUI ABROGOUA, it is brought to the selected model village and put into operation. The last practice-oriented task during the study program is the evaluation of the operation experience and an improvement of the planning steps. The existing plans for the first two prototypes should be improved or enhanced in a way to create a basis for a small series. Furthermore, possible additional industry partners will be addressed to develop business models for a small series of the system.

3. System Design of a Small-Scale Plant for Electricity and Water Supply in Côte d'Ivoire

One possible design of a small-scale plant is shown as an Inventor drawing (cp. Fig. 4) and as a Piping and Instrumentation Diagram (P&ID) (cp. Fig. 5).

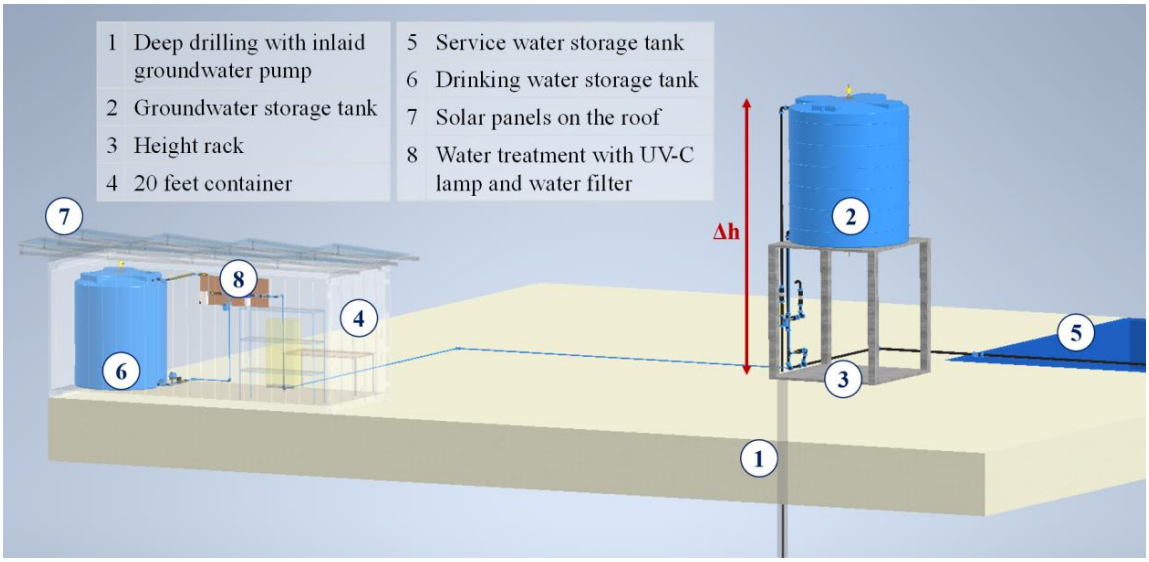

Fig. 4: Inventor drawing of the small-scale water supply powered by a solar energy plant

Fig. 4 shows the overall concept of the small-scale plant for electricity and water supply for rural areas. For water supply, groundwater will be pumped into a so-called groundwater storage tank installed at a certain height. From there, the groundwater is transported either to the water treatment station inside the 20-feet container to be chemically and bacteriologically treated or directly into a service water storage tank to be

distributed to the population. The needed electricity for the small-scale plant is provided by several solar panels, which are installed on racks on top of the container. Surplus electricity not used by the water treatment system will be used by the population for other needs. Further usage of surplus electricity still has to be designed according to the local needs of the model village.

The chosen model village is located near the city of Duékoué in western Côte d'Ivoire, 400 km from Abidjan. It is a village of cocoa tree farmers that is not connected to the public electrical and water grid. There are many other villages in the surrounding area, so the developed concept can serve as a flagship for other villages. For the design of the prototype, all basic conditions like the number of villagers, service and drinking water demand of the model village must be recorded and included as parameters in the calculations.

The students of the master's program at University NANGUI ABROGOUA will be enabled to create and communicate visualizations using internationally common tools. To be able to build a small-scale water and electricity plant, it is necessary to develop a P&ID diagram (cp. Fig. 5) in advance. Gaining the skill to do so will be part of the dual study program as the students will have to develop this diagram on their own within group work.

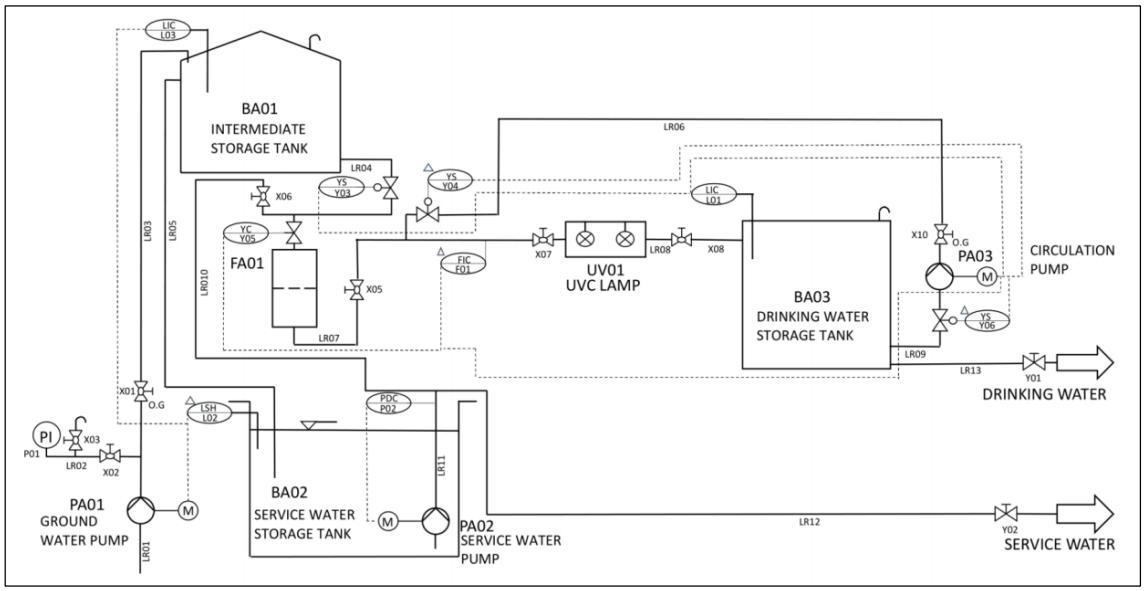

Fig. 5: P&ID diagram of the small-scale water supply and treatment plant

The purpose of P&ID diagrams is to show the plant's components and the associated connecting parts and measuring devices. It is possible to locally purchase each necessary part to build the plant in remote rural areas, which do not have a connection to the national electricity and water grid.

Fig. 5 shows the main parts of the plant, the groundwater pump PA01, the intermediate storage tank BA01, the service water storage tank BA02, the service water pump PA02, the UV-C lamp UV01, and the drinking water storage tank BA03, and the circulation pump PA03. The capacity of the storage tank must at least equal the daily drinking water demand of the model village, where the plant will be operated. From there, the groundwater is either pumped to the water treatment station inside the container or into the service water storage tank BA02, depending on the filling level of the drinking water storage tank BA03 and the overall demand for drinking water. The service water pump PA02 is switched on automatically with a differential pressure switch if water is withdrawn and the pressure in the connected pipelines drops. It is possible to use the service water in emergency operations for drinking water treatment, for example, in the event of a malfunction of the groundwater pump PA01. For this purpose, the service water is led to the drinking water treatment. A consistently high drinking water quality is guaranteed by the circulation of the drinking water through the UV lamp UV01. The circulation is carried out by the circulation pump PA03. Flow sensor F01 controls the circulation pump PA03 and guarantees that the maximum flow rate of the UV-C lamp UV01 is not exceeded even when the drinking water is circulated.

Particularly in the case of decentralized plants for electricity and water supply in rural regions, there are mostly

no specialized personnel and materials available on site. The system should therefore be as robust and simple as possible so that errors or malfunctions can be rectified by trained personnel on-site. For the developed concept and the associated business model to be successful on a large scale, the highest possible water quality must be achieved at a low cost. The system should therefore also be designed to be as inexpensive as possible. The plant design in Fig. 5 can be adapted and thus an alternative more robust version can be worked out. The P&ID diagram of a more robust version is shown in the following figure.

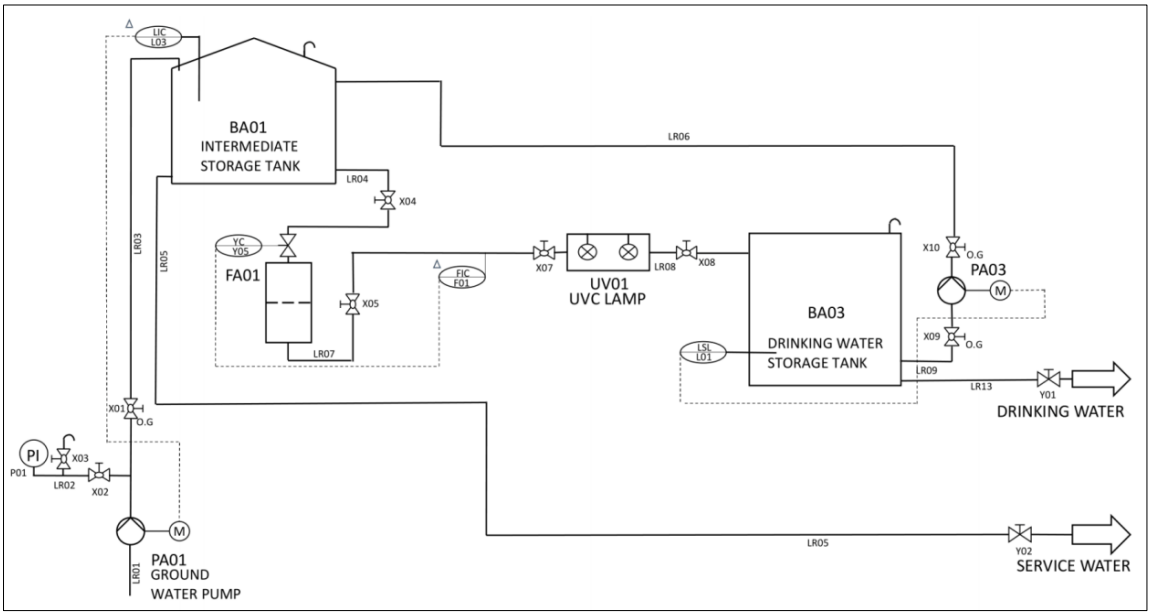

Fig. 6: P&ID diagram of the small-scale plant (optimized for robustness)

This version (Fig. 6) is designed for the case where the villagers have in-house storage tanks. Therefore, in this version there is no need for an automated circulation of drinking water by directing the circulation to the intermediate storage tank BA01 through the pipeline LR06. From the intermediate storage tank, the groundwater as well as the circulating water is directed gravimetrically through the treatment system to the drinking water storage tank BA03, as in the previous version. The flow is controlled manually by an operator via valve Y05 and local flow meter F01. The flow rate must be set by the operator at the maximum level of the intermediate storage tank to the permissible flow rate. Dry running of the circulation pump PA03 is prevented by the digital level sensor L01. The pump is automatically switched off whenever the level of the drinking water storage tank falls below it.

4. Conclusion and Perspectives

The project thus makes a significant contribution to achieving some of the 17 Sustainable Development Goals (SDGs) of the United Nations. The dual study program developed in the project is not only intended to combat unemployment of highly qualified personnel (SDG 8: Decent Work and Economic Growth) but also to improve unrestricted access to water and electricity for the Ivorian population in rural regions (SDG 6: Clean Water and Sanitation; SDG 7: Affordable and Clean Energy). With the implementation of the first dual study program in Côte d'Ivoire, the project contributes to the achievement of SDG 4 (Quality Education). An equal number of female and male students are selected to start the program in a gender-neutral way (SDG 5: Gender Equality). With the practice-oriented teaching content, the link between academic teaching and industry is established so that it is easier for engineers to enter the business world (SDG 9: Industry, Innovation, and Infrastructure).

The goal of the project is to introduce the dual study program by October 2022 and to install the small-scale plant in the model village by the end of 2024. In addition, the study program is to be maintained through long-term cooperation between the participating universities and the integration of new practice-oriented project modules so that the project can have a long-lasting impact.

5. Acknowledgments

The authors would like to thank the German Academic Exchange Service (DAAD) which finances the project IIDES-NSC (funding number 57571294) with funds from the German Federal Ministry of Economic Cooperation and Development (BMZ).

6. References

International Energy Agency, 2019. Africa Energy Outlook 2019: World Energy Outlook Special Edition. IEA, Paris. Accessed September 03, 2020. https://www.iea.org/reports/africa-energy-outlook-2019, published in November 2019. License: CC BY 4.0.

International Energy Agency, 2022. Africa Energy Outlook 2022 - English Version. World Energy Outlook Special Report. IEA, Paris. Accessed July 27, 2022. https://www.iea.org/reports/africa-energy-outlook-2022, published in June 2022. License: CC BY 4.0.

Mitsubishi UFJ Research and Consulting Co., Ltd., 2013. Country Gender Profile: Côte d'Ivoire. Japan International Cooperation Agency, Tokyo. Accessed September 04, 2020. https://www.jica.go.jp/english/our_work/thematic_issues/gender/background/c8h0vm0000anjqj6-att/cotedivoire_2013.pdf, published in March 2013.

Newiadomsky, C., Tietze, I., 2017. Beitrag Erneuerbarer Energien zur Verfügbarkeit von Elektrizität und Wasser in Afrika: Ansätze für eine nachhaltige Entwicklung?,. in: Filho, W.L. (ed), Innovation in der Nachhaltigkeitsforschung: Ein Beitrag zur Umsetzung der UNO Nachhaltigkeitsziele. Springer Spektrum, Berlin, pp. 39–59.

Noubactep, C. (ed.), 2016. Approvisionnement En Eau Potable En Afrique: Une Technologie Appropriée Pour Relever Le Défi. Afrika & Wissenschaft / Africa & Science / Afrique & Science, second. ed. Africa & Science, Frankfurt/Main.

Seier, S., 2016. Länderprofil Elfenbeinküste. Bundesministerium für Wirtschaft und Energie (BMWi) (Eds.), Berlin. Accessed April 14th, 2022. https://www.german-energy-solutions.de/GES/Redaktion/DE/Publikationen/Marktanalysen/Laenderprofile/elfenbeinkueste.pdf, published on August 30th, 2016.

Solargis, 2022a. Global Horizontal Irradiation (English Version). Accessed August 23, 2022. https://solargis.com/file?url=download/Cote%20d%20Ivoire/Cote-d-Ivoire_GHI_mid-size-map_156x209mm-300dpi_v20191015.png&bucket=globalsolaratlas.info

Solargis, 2022b. Photovoltaic Electricity Potential (English Version). Accessed August 23, 2022. https://solargis.com/file?url=download/Cote%20d%20Ivoire/Cote-d-Ivoire_PVOUT_mid-size-map_156x209mm-300dpi_v20191015.png&bucket=globalsolaratlas.info

The World Bank, 2022. World Bank Global Electrification Database from: Tracking SDG 7: The Energy Progress Report. Accessed on: April 8th, 2022. https://data.worldbank.org/indicator/EG.ELC.ACCS.ZS?locations=CI. License: CC BY 4.0.

WHO/UNICEF JMP, 2021. Estimates on the use of water, sanitation and hygiene in Côte d'Ivoire, in: Joint Monitoring Programme for Water Supply, Sanitation and Hygiene. Accessed on: April 8th, 2022. https://washdata.org/data/country/CIV/household/download, published in July 2021.

Yapo, A.R., 2018a. Les origines du problème de surqualification en Côte d'Ivoire, article in : The Conversation. Accessed on April 12th, 2022. https://theconversation.com/les-origines-du-probleme-de-surqualification-en-cote-divoire-99004, published on July 17th, 2018.

Yapo, A.R., 2018b. En Côte d'Ivoire, les travailleurs surqualifiés gagnent moins que les travailleurs qualifiés, article in : The Conversation. Accessed on April 12th, 2022. https://theconversation.com/en-cote-divoire-les-travailleurs-surqualifies-gagnent-moins-que-les-travailleurs-qualifies-101689, published on September 23rd, 2018.

The Life and Death of a Solar Energy Course – Lessons in Challenge Based Learning

Nelson Sommerfeldt

KTH Royal Institute of Technology, Stockholm (Sweden)

Abstract

This paper presents the experiences of developing and executing a graduate solar energy engineering course designed around challenge based learning (CBL). The course structure is presented and mapped to CBL principles, followed by an assessment of student outcomes and lessons learned by the instructors. The course has increased in popularity and feedback from students suggest the CBL format is a large reason. Graduated students also see the value of CBL in their careers, beyond traditional engineering training. The time needed by both students and instructors to execute a course is seen as a possible limitation and requires dedication to the approach. CBL is recommended for course instructors working with complex energy systems, particularly in prosumer situations, where relationships between technological, economic, and social aspects are present.

Keywords: Challenge driven education, solar energy systems, prosumers, simulation, multi-objective

1. Introduction

Interest and application of challenge based learning (CBL) in higher education has grown significantly over the past decade, and is commonly seen as an effective method for engineering students to expand their disciplinary knowledge into socio-economic spaces (Gallagher and Savage, 2020). While a commonly accepted definition is lacking, a proposal from Malmqvist et al. (2015) is oft cited:

Challenge-based learning takes places through the identification, analysis and design of a solution to a sociotechnical problem. The learning experience is typically multidisciplinary, involves different stakeholder perspectives, and aims to find a collaboratively developed solution, which is environmentally, socially and economically sustainable.

Likewise, Leijon et al. (2021) identify several keywords from the Apple computer company's definition (2008), where the term "challenge based education" was coined, which present many similar themes: multidisciplinary, teaching and learning, technology, real-world problems, collaborative, communities, ask, subject area knowledge, solve challenges, take action, and share.

The course "Solar energy systems for buildings and cities" was a graduate level course (year four of a five-year master's degree) at KTH Royal Institute of Technology designed primarily for students in the Sustainable Energy Engineering (SEE) program. It was developed in 2016 around the CBL model and given six times between 2017 and 2022. While many (if not most) courses in the program rely on project-based learning in groups, the CBL aspect of this course make it somewhat unique. Due to the restructuring of the master's program, many topic-specific courses have been absorbed into larger courses on integration, including this course. The experiences of developing and executing the course are presented here as a case study in CBL as applied to solar energy engineering and aim to act as a reference and inspiration for future course development.

2. Course Structure

The overall aim of the course is to give students a fundamental understanding of solar energy applications in the built environment and skills in designing solar energy systems. Since the students are mostly coming through the SEE program, it is expected that they have prior understanding of solar radiation, the basic function of solar thermal collectors, and the photovoltaic (PV) process, however it is not given as a strict prerequisite requirement. This course is therefore focused predominantly on systems design and the specific intended learning outcomes (ILO) are:

© 2022. The Authors. Published by International Solar Energy Society
Selection and/or peer review under responsibility of Scientific Committee
doi:10.18086/eurosun.2022.19.05 Available at http://proceedings.ises.org

- ILO1: Describe the principles of solar thermal and photovoltaic technologies for buildings, including; design, economics, and application
- ILO2: Analyze and communicate the techno-economic characteristics of solar energy systems for the built environment

ILO1 is examined using an individual home assignment consisting of short answer questions (100-200 words) where students demonstrate critical understanding of the material. ILO2 is examined using a group project (three students per group) with a final report (approximately 30 pages) and a final presentation (10 minutes). The course is worth 6 ECTS credits (1.5 to ILO1 and 4.5 to ILO2) and is given over nine weeks, meaning that each student is expected to spend, on average, 16 hours per week on the course. In total there are 14 hours of lecture (not including the two-hour introduction), eight hours of software demonstration, a two-hour seminar at the course midpoint and a two-hour final seminar. In this case, one "hour" consists of 45 minutes due to breaks within and between course events. There are also four occasions where the groups can register for a 30-minute consultation to get personalized assistance (analogous to office hours), and a study visit to the department's rooftop laboratory where they can see a multitude of solar technologies related to the instructors' research.

The course is designed around the CBL project with nearly all course activities work to support its completion. The lectures and software demos are heavily biased to the first three weeks of the course, whereas later weeks are open for project/assignment work. The first lecture (after the introduction) takes a high-level view of solar energy in buildings by introducing technical and economic key performance indicators (KPI). Since both solar thermal and PV systems will be analyzed, it is critical for students to think early on about what they hope to achieve in their design and how it relates to the goals of their client, the occupants, and society. Educational content is delivered in a 4+4 format, where a topic receives four hours of lecture and four hours of software demo in a single week. This approach helps reinforce concepts through repetition; the lectures present the theory which is then repeated and animated through the construction of a functioning model. The final four hours of lecture are dedicated to systems integration, which also has some repetition of previous concepts, and but is largely aimed at demonstrating more clearly the tradeoffs involved with various design choices.

The assignment follows a similar structure to the course content and is designed to test recall and explain core concepts. Since the assignment is given on the first day and is due (at latest) the same day as the project, the questions are also written in such a way that they can also help form critical connections for completing the project. For example, asking students to contrast and compare two relevant KPIs in the assignment can help them formulate their project analysis and avoid mistakes. Three weeks before the final seminar, there is an early deadline for the assignment that gives students the opportunity for bonus points. The points are the external motivation for students, however the educational motive for doing this is twofold; first it means students will focus on understanding concepts which will benefit their work in the project, and second it better distributes workloads, which inevitably piles up at the end the course (and all their other courses on top of it).

Due to the mixture of technical, economic, and social aspects, a single textbook could not be found to base the course on. Specific chapters from two books are instead referenced in the lectures and recommended for further reading; for solar thermal it is venerable Solar Engineering of Thermal Processes (Duffie and Beckman, 2013) and for PV it is Solar Energy Engineering (Kalogirou, 2009). These however only provide core concepts, and more nuance on market forces and policy are provided through the IEA's annual Solar Heat Worldwide (Weiss and Spörk-Dür, 2021) and Trends in Photovoltaic Applications (IEA, 2021). Finally, a number of scientific articles and reports are referenced in the lectures and provided as additional resources for voluntary reading beyond the core concepts.

There are two computer programs to execute the analysis – Polysun (Velasolaris, 2020) for solar thermal and System Advisor Model, or SAM (National Renewable Energy Laboratory, 2020) for PV. In the first few years, Polysun was used for both technologies, however row-to-row shading of the modules was also applied to the building, causing changes to heating loads and inconsistency in the analysis. SAM also has a superior parametric analysis feature, which makes completing the project easier. As an educational tool for building heating systems, Polysun has the advantage of combining an intuitive graphical interface with a low barrier to entry. Students are able to get working models quickly and can reference one of the many templates if needed. Even though the instructors are using TRNSYS in their research, the steep learning curve, difficulty in debugging models, and greater effort needed to export and post-process results make it challenging to use in a shorter course. Even in a five-month long solar energy course, students have asked for more time to learn TRNSYS or dedicated software training (Kummert, 2016). Polysun is also more commercially oriented, meaning it is more likely to be used in a professional environment, whereas TRNSYS tends to be used more often in academia.

3. Challenge Based Learning Project

The group project is presented to students as though they are energy consultants, and their client is a real estate developer that wants a solar energy design strategy for multi-family housing units across Europe. The building is standardized (i.e. identical in all locations) and as much roof area as possible is left open for solar energy capture. The firm is technology agnostic, therefore the students must deliver the "best" system that "optimizes" the technical and economic potential of the roof space.

Placing "best" and "optimize" in quotations is a key aspect of the description, as it represents the problem formulation portion of CBL. The students are forced to think about what "optimum" means, for the client (real estate company), the building's eventual owners/tenants, and for society (i.e. climate change or other environmental factors). They are given the freedom to define "optimum" for themselves (with motivation), necessitating their own selection of technical, economic, and environmental key performance indicators (KPI) and the methods of applying them.

3.1 The Target Building

All groups work with an identical building: a four story, multi-family house with 18 apartments and an air-to-water heat pump to supply domestic hot water and space heat, with the Polysun system diagram shown in Figure 1. Students can optionally use a system with both heating and cooling if they are in a cooling dominated climate. The building demand and mechanical system are pre-defined and provided in a Polysun file, meaning students are only asked to add solar energy supply to the system. The roof is flat with an area of 16 x 28 m available for collectors or modules, and the long side of the building is facing south. There is also an option to install building-integrated PV via translucent glass in the balconies on the southern facade, which are already planned to have traditional glass.

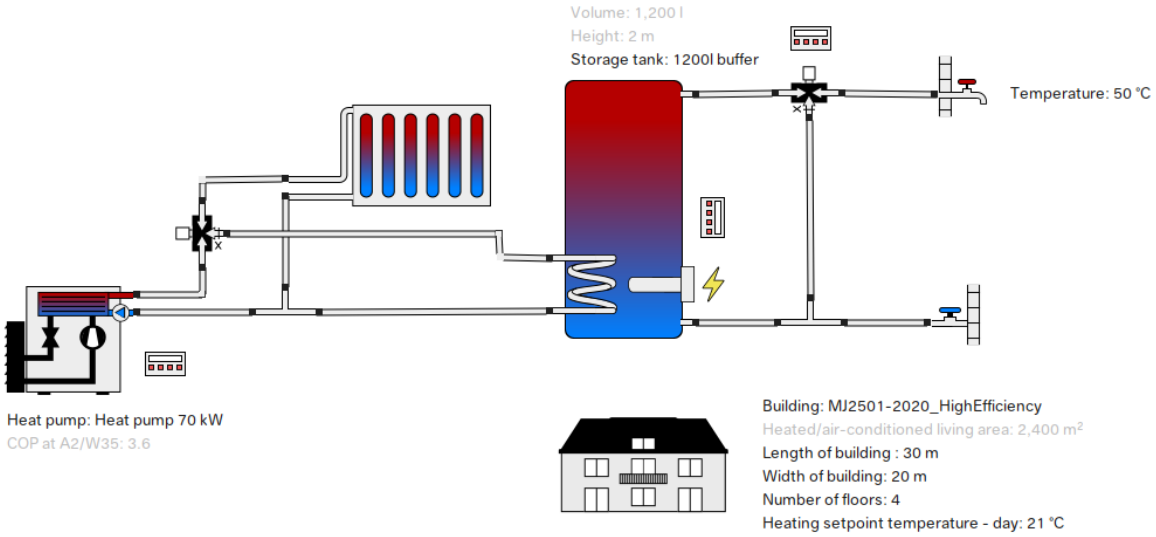

Fig. 1 - Baseline heating system provided with the target building

3.2 Locations

There are eight locations across Europe with each group assigned to one: Stockholm, Copenhagen, Paris, Munich, Milan, Barcelona, Thessaloniki, and Izmir (Turkey). The locations are specifically selected to represent a diverse range of climates and solar generation potential, as well as electricity prices and generation portfolios with varied greenhouse gas emissions, as shown in Table 1. For example, Copenhagen's greater need for heating (i.e. electricity demand) combined with high electricity prices can produce better economic outcomes than Izmir, even though Izmir has 70% more annual irradiation. Climate files using the same data but formatted for each program are provided, and aside from electricity prices, which are location specific, all other economic boundary conditions are standardized across all groups. This includes a selection of solar collectors, PV modules, and PVT collectors available in each program's library, a list of generic components (e.g. tanks, valves, inverters) with prices, and prices for installation.

Tab. 1 - Solar, electricity price, and greenhouse gas emissions of each location

Location	GHI	Avg. Temp.	Purchase	Sell	GHG
Units	*kWh/m²/yr*	*°C*	*€/kWh*	*€/kWh*	$g_{CO2\text{-}eg}/kWh$
Copenhagen, Denmark	982	8.3	0.241	0.046	386
Paris, France	1070	11.1	0.161	0.071	93
Munich, Germany	1124	8.0	0.259	0.072	574
Thessaloniki, Greece	1566	15.4	0.143	0.070	757
Milan, Italy	1292	11.8	0.189	0.073	448
Barcelona, Spain	1460	15.7	0.190	0.067	312
Stockholm, Sweden	923	6.5	0.155	0.054	25
Izmir, Turkey	1690	16.7	0.085	0.066	750

3.3 Analysis Approach

As mentioned above, the students are given the freedom to choose their own design goals and KPIs with which to measure those goals, and their analysis must motivate their "optimal" recommendation to the client. This is achieved through several rounds of semi-structured parametric analysis. Given the large number of variables, particularly within solar thermal systems, it is impractical to test every possible configuration parametrically in a single course. The analysis structure, shown in Table 2, gives students a process to follow and is also used in examination. For example, if a group is only interested in achieving an E-grade for the project, they only need to successfully complete the basic level analysis. Generic settings are provided at lower levels to make the analysis possible, which are then tested/replaced later on. For example, it is suggested to use a single inverter for each row of the PV system to make it easy to test all possible capacities and tilts in a single parametric analysis, however an inverter selected specifically for the final design must be made at the end of the analysis to receive the highest grade. The students are advised to study each technology independently using comparable KPIs. Once completed, they can decide if they wish to take one technology, mix the two, or use a PVT hybrid. Again, this decision should be made using their selected KPIs to demonstrate that their design is brings the solution closer to their stated goal(s).

Tab. 2 - Parameters tested at the three levels of analysis

Level	Thermal	Photovoltaic
Basic	Collector area Tilt angle Tank size	Capacity Tilt angle Azimuth
Intermediate	Tank connections Temp. sensor	Module type Building load
Advanced	Tank splitting Controller settings	Inverter selection Battery / BIPV

There is a small difference in the approach for thermal and photovoltaic systems. With solar thermal, the design specifications chosen at one level can be locked in when moving up to the next level. For example, once the collector area is chosen, it can remain at that size when altering control parameters. For PV, it is expected to repeat the full parametric analysis for capacity and tilt angle at the intermediate level. This is done for two reasons; first, the results can vary significantly, particularly with testing the different building load profiles for heating/cooling only or the full site load with apartments included. And second, SAM makes it relatively easy to accomplish this once the parametric study is established so the workload is not an excessive burden. A common challenge through the project is the balance of tasks and time, which is discussed further throughout the paper.

4. Student Outcomes

In the early years of the course, the delivered projects often lacked technically successful systems. Students were given free reign and encouraged to try nearly any design or technology they liked so long as it could be qualitatively motivated with thermodynamic theory. This limited their ability to complete a parametric analysis, or in the worst cases, get a successfully running simulation. Many were enticed by advanced concepts like borehole thermal storge, which is tantamount to attempt running before being able to crawl. This led to a standardized mechanical system

being provided (Figure 1) and adding more analysis structure (Table 2), providing the students with a clear(er) pathway through the design process. This was particularly helpful to students experiencing a CBL project without clearly pre-defined goals for the first time in their engineering education.

Most students tended to prioritize the needs of their client, the real estate developer, and make their aim economic maximization. The KPI of choice does vary between internal rate of return (IRR) and net present value (NPV), with most using NPV. This is likely due to one of the lectures demonstrating how optimizing NPV can lead to larger system designs, so it is seen as a middle way as compared to optimizing for IRR or maximizing solar fraction. In practice, students find multi-criteria optimization challenging and resort to an interactive approach of reevaluating their priorities once they've generated results. This often leads to somewhat subjective system designs that aim to balance solar fraction with economic benefits. The other most common design goal is to maximize solar productivity so long as NPV remains positive, however this is usually only used by one or two groups per year.

From a design standpoint, the analysis structure somewhat limited the types of solar thermal systems explored. Only once since the introduction of the standardized mechanical system did a group present a combi-system – the rest are all domestic hot water only. At no point are students told they cannot study combi-systems, some are even encouraged when their location and goals make it more suitable, but the short course period, a desire to complete all level of the analysis, and no higher grade for the extra work makes it easy to simply add solar thermal to the hot water tank and avoid the extra headaches of replumbing the heating circuit.

Conversely, the open nature of the CBL project leaves room for motivated and interested students to explore novel ideas and go beyond the standard analysis structure. One example, shown in Figure 2, is a case where students used the concept of a Pareto frontier, which was pulled in from a different course given in parallel, to display results and select a system balancing technical and economic factors. There have also been several groups who created their own multi-criteria index based on technical, economic, and environmental KPIs to remove seemingly arbitrary decisions when balancing non-comparable benefits. An important learning point with this approach is that the weighting of each KPI is also subjective, meaning the index does not escape the subjectivity of the decision, only hides it. In another case where the economic outcomes were not as positive, the students made a carbon pricing sensitivity analysis as part of a policy recommendation to encourage solar development in their region. The CBL structure helps to drive their own curiosity to do the extra work, even if it doesn't necessarily lead to additional grading points.

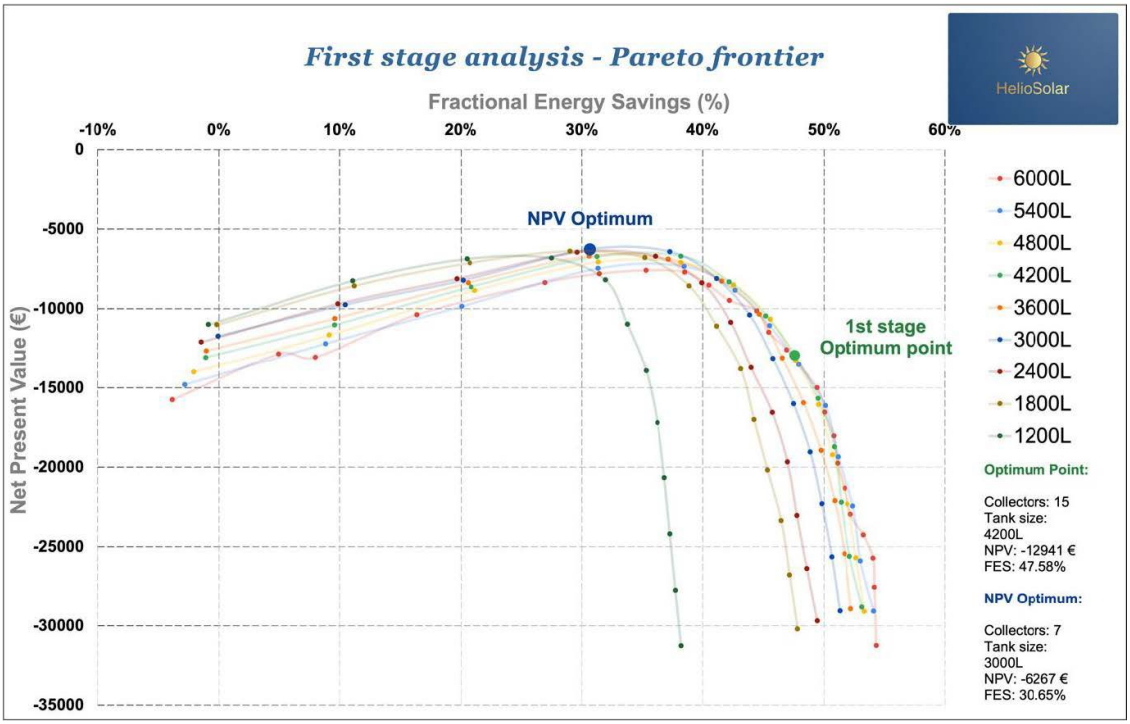

Fig. 2 - Example of a Pareto frontier used in the solar thermal analysis

A limitation of the CBL format as it is applied here is that comparison between projects is often difficult or impossible due to the differences in design objectives, KPIs, and quality of analysis. One aim of the project structure is that students should see how design outcomes vary with the influence of climate and energy prices, expanding the scope of the project to all of Europe. This does happen to a degree, however if a group uses their own novel KPI or makes

a mistake in its application, then direct comparisons are not possible. At one point it was considered to require a certain set of KPIs to be used and reported ahead of the final seminar, which would make it possible to present all the results together and strengthen this part of the learning. However, mistakes would still be present, limiting the effectiveness, and it would take away from the problem formulation. The need to define the problem/goal for themselves is what distinguishes the course from being challenge based versus project based, which was considered more valuable than a quantitative comparison of each location. A qualitative comparison is still made as part of the closing comments of the final seminar and is sufficient given the wide range of uncertainty present in the results.

5. Student Feedback and Lessons Learned

In all KTH courses, student feedback is primarily collected using standard surveys sent out once final grades have been delivered. There are several versions of the survey with different lengths, and for this course the full 22 question survey has always been used. Students respond anonymously and are asked to score their agreement with a given statement from on a seven-point Likert scale ranging from "Strongly Agree" to "Strongly Disagree." The wording is such that stronger agreement (i.e. higher scores) are considered positive, and the results are converted from a -3 to +3 rating in the survey to a 0 to 7 scale when reported to instructors. Students are also able to leave a general comment and specific comments for each question. In its six years, the course has garnered a strongly positive response with an overall score of 6.2. This is in part due to it being an elective (note the high score for Question 1 in Table 3), mandatory courses often get more criticism from those unhappy to be forced into it, but there are some common themes in the feedback related to CBL that support the high score.

Table 3 lists the most relevant questions to CBL and the general structure of the project. Question 3 on being able to learn by trying their own ideas, is one of the core principles of the project and has received a high score of 6.4. Many students stated that they had never had a project or course designed in this way and that they found it very interesting and valuable. There are however a small number of students who found the whole concept very confusing and lost a lot of time just trying to understand how to approach the project. This is reflected in Question 13 on expectations, which still had a high average of 6.1, but also has a high variance. Students also found the course challenging in a stimulating way (Question 4) which ties back to the extra work they are willing to do to explore their designs.

Tab. 3 - Sample of student survey questions with results from all six years (74 respondents out of 216 total)

Question	Minimum	Weighted Average	Maximum
1. I worked with interesting issues	6.3	6.7	6.9
3. I was able to learn by trying out my own ideas	5.8	6.4	6.8
4. The course was challenging in a stimulating way	5.8	6.2	6.6
5. I felt togetherness with others in the course	5.0	5.8	6.2
13. I understood what I was expected to learn to obtain a certain grade	5.0	6.1	6.9
21. I was able to learn by collaborating and discussing with others	5.8	6.2	6.7
22. I was able to get support if I needed it	6.4	6.6	6.8

A somewhat surprising result is the poor score on Questions 5 regarding interactions with fellow students. This is likely due to conflicts within project groups, which varies a lot year to year, and is a common limitation with group projects not unique to this course. It is also an issue of gender given that women have often (but not always) given a worse score for Question 5, in some years much worse. Question 21 has a much higher score and is likely based on the inter-group discussions that occur in the computer lab and in seminars. Comments on the mid-term seminar reveal that in the week leading up it is felt as a source of unnecessary stress given that the seminar is ungraded and comes relatively early in the design process. Students find it unusual to make a presentation where you might not even have results, just an assessment of the problem and their plan of attack to solve it. Afterwards, it is viewed as one of the most useful points in the project because they can see how others in the course are thinking about the problem and it can help them correct course or spark new ideas. Moving forward it is wise to take this positive collaboration found between groups and ensure that the same positivity is experienced within them.

What is abundantly clear from both the survey score of Question 22 and the student comments is that instructor support is critical in a CBL project like this. The relative openness of the task means students can get lost quickly, and if a mistake is found late in the course it can mean many hours of last-minute re-simulation. This makes frequent and useful feedback is critical. The mid-term seminar is already mentioned, where the instructor makes the majority

of questions/comments during discussion, but students are also able to submit a mid-term report for more detailed feedback. Then there are the weekly consultations, which over the years have been found to be best when 30 minutes long. Too short and the students run out of time and/or the sessions run behind, too long and a lot of the instructors' time is taken up.

The CBL approach means each student group is on their own journey, which does require more time and mental effort of the instructors. When course numbers are relatively low (20-30 students) it is manageable, however there have been years with 50 students (16 groups) where it becomes challenging, and a teaching assistant is necessary. The same issue extends to examination, which is done via a 30-to-40-page report and 10-minute presentation that involves careful reading to extract methods and meaning such that fair examination on disparate learning aspects can be made.

The overwhelming sentiment from students is that they wished they had more time. Not that the workload was too much, many state they spend the same or less amount of expected time on the course, but that they want more time to explore and contemplate. The short nine-week period means that they need to rush the analysis and make decisions sooner than they would like. The rushed schedule also leads to specialists forming within the group, where one or two take on solar thermal and the other(s) take PV, to make the project more efficient. With more time the students would have the ability to be more hands on with each technology if they wished.

In addition to formal course surveys, informal interviews are made with one or two students each year and has also extended to students who have graduated and working in solar developers or engineering consultancies in Europe and North America. The interviews with students directly following the course largely reinforces the insights gained during the survey, with a bit more detail and nuance that can be used to adjust the course. The feedback from those working with solar in the field is that the techno-economic analysis needed is surprisingly easy thanks to their education and that it is the non-energy related factors that provide the greatest challenges in their jobs. They say that the experience of working a CBL project (referring to the course, not CBL by name) helps them assess and solve challenges tangential to their core discipline.

6. Conclusions

This paper presents a case study of challenge based learning as applied in a graduate level solar energy engineering course. Over its six-year lifetime, the course grew to become one of the most popular electives in the department with one of the highest student evaluation scores. Many students specifically mention the project format, with its real-world framing and flexible approach, as a particularly positive experience. Graduates have stated that critical thinking induced by the CBL format is particularly valuable in their careers, where the hard problems are often unstructured. The relatively individualized experiences of each student (or student group) mean that executing the course requires dedication from the instructor(s) to give timely and useful feedback, as well as be available for individual consultations.

Actionable points of improvement from this case study are two-fold – to provide the maximum amount of time available for the course (i.e. a full semester) and to minimize the potential conflict within groups. The former is straight forward, the latter is more challenging. There will always be a distribution of priorities and motivation within students, so grouping them together, especially if they are unknown to each other prior to the course will always have the potential for conflict. There are potential solutions, such as shuffling groups during the course, but any solution needs to be considered withing the context of CBL such that the most valuable benefits are not lost.

The death of the course is a product of solar energy's success as a technology. Solar energy systems are now expected or even regulated on many new building developments around the world. Even prior to the 2022 energy crisis in Europe, the retrofit market was returning to prominence after a 10-year lull. Solar is now an integral part of building and urban energy systems and higher education programs/courses need to adapt (Witzig et al., 2016). The CBL format provides an excellent platform for students to learn about complex energy systems and their technical, economic, environmental, and social characteristics. CBL is recommended for course leaders hosting and developing sustainable energy courses/programs, particularly for prosumer energy systems.

7. Acknowledgements

I would like to thank the course examiner and my partner in building this course, Hatef Madani. Thank you also to Chris Bales and Bengt Perers, for providing excellent lectures on solar thermal systems during our early years, and to Viktoria Martin for providing lectures on solar energy storage.

8. References

Duffie, J.A., Beckman, W.A., 2013. Solar Engineering of Thermal Processes, Fourth. ed. John Wiley & Sons, Inc., Hoboken, NJ.

Gallagher, S.E., Savage, T., 2020. Challenge-based learning in higher education: an exploratory literature review. Teaching in Higher Education 0, 1–23. https://doi.org/10.1080/13562517.2020.1863354

IEA, 2021. Trends in Photovoltaic Applications (T1-41:2021). Paris.

Kalogirou, S., 2009. Solar Energy Engineering: Process and Systems, First. ed. Elsevier Inc., Oxford. https://doi.org/10.1016/B978-0-12-374501-9.00001-7

Kummert, M., 2016. Using TRNSYS in a Graduate Course on Solar Energy, in: Proceedings of the EuroSun 2016 Conference. International Solar Energy Society, Palma de Mallorca, Spain, pp. 1–12. https://doi.org/10.18086/eurosun.2016.10.01

Leijon, M., Gudmundsson, P., Staaf, P., Christersson, C., 2021. Challenge based learning in higher education– A systematic literature review. Innovations in Education and Teaching International 00, 1–10. https://doi.org/10.1080/14703297.2021.1892503

Malmqvist, J., Kohn Rådberg, K., Lundqvist, U., 2015. Challenge-Based learning experiences, in: Proceedings of the 11th International CDIO Conference. Chengdu, Sichuan, P.R. China.

National Renewable Energy Laboratory, 2020. System Advisor Model (2020.2.29).

Nichols, M.H., Cator, K., 2008. Challenge Based Learning White Paper. Cupertino, California.

Velasolaris, 2020. Polysun 11.2.

Weiss, W., Spörk-Dür, M., 2021. Solar Heat Worldwide. IEA Solar Heating and Cooling Programme.

Witzig, A., Wolf, A., Kunath, L., Alyaseen, A., Axthelm, R., 2016. Teaching Renewable Energy Systems by Use of Simulation Software: Experience At Universities of Applied Sciences, in In-Service Training, and from International Know-How Transfer, in: Proceedings of the EuroSun 2016 Conference. International Solar Energy Society, Palma de Mallorca, Spain. https://doi.org/10.18086/eurosun.2016.10.03

Renewable Energy and PtX-Technologies in Education

Birgit Steffenhagen[1], Johannes Gulden[1], Andreas Sklarow[1], Romy Sommer[1]

[1] Hochschule Stralsund, Stralsund (Deutschland)

Abstract

To achieve the global targets opposing climate change, it is necessary to reduce CO2 emissions from fossil sources to negligible levels until 2050 at the latest. Thus, the energy demand of the industry, for mobility and for power supply must be covered predominantly by inherently volatile renewable sources. To ensure sufficient grid stability, various storage and reconversion technologies are needed. Power-to-X (PtX) technologies will play a central role in this effort and become an essential basis of our energy supply. The first step of the process is power-to-hydrogen, for which electrolysers in the gigawatt (GW) range are currently being planned or have already been realized. Designed as highly dynamic loads, they take over essential functions for balancing smart grids and supplementing the secondary and minute reserve that can be represented by intelligent power converters and battery storage. Our university has been engaged in the development and operation of Power to Gas (PtG) for more than twenty-five years through various industrial research, regional development projects, as well as practical study programs. We combine laboratory training at industrial plants with various student projects, such as the ThaiGer-H2-Racing Team who built the currently most efficient hydrogen prototype with a consumption of only 8,04 grams of hydrogen per 100 km. The multiple use of these systems for research and educational purposes combined with the motivation and experience of the staff allow a very instructive, hands-on and cost-effective education in the field of PtX technologies and their contribution to grid stability.

Keywords: Education, renewable energy, PtX technologies, PtGas, Power-to-Hydrogen, energy storage, fuel cell applications, smart grids, ThaiGer - light weight race car

1. Introduction

In the future, we will be confronted with enormous challenges converting the generation of energy to rely on renewable sources, the supply of energy via smart grids, and new mobility concepts. The grid infrastructure, built over a period of more than a century to support conventional centralized power generation, must now meet the challenges created using renewable energy. With the help of modern IT applications as well as the integration of modern storage solutions and technologies for sector coupling, intelligent energy supply networks can be created that will secure transnational and local energy supply in the future. This demanding goal requires networking of the protagonists in industrial realization, research and education regarding the mandatory fundamental changes in society. These topics have to be reflected in a practical student education, so that the demand for specialists for these enormous challenges can be met. At the focus of all activities there is the vital question of how we can foster the students' intrinsic motivation to continue working in this innovative field and to develop a sustainable power supply and mobility solutions for various applications.

2. Ptx technologies and Sector coupling

On the one hand, future smart grids will have to automatically activate storage facilities or switch off suitable consumers in the rare case of a supply deficit of regenerative energy. On the other hand, when there is a surplus of renewable energy, the power grid will have to be managed in such a way that the energy requirements of the heating sector, mobility, and the demand for materials in industrial production can be met without carbon dioxide emissions and at minimum cost. This is referred to as sector coupling. Concerning energy consumption, efficient conversion technologies will be necessary in various areas such as the production of electricity, heat supply, mobility, and the chemical industry, as there is a need to decarbonize almost all processes which are still based on fossil raw materials. This requires suitable storage capacities in the form of hydrogen, methane, and liquids such as methanol or ethanol since gases and liquids can be stored easier than electricity. Highly efficient

© 2022. The Authors. Published by International Solar Energy Society
Selection and/or peer review under responsibility of Scientific Committee
doi:10.18086/eurosun.2022.19.06 Available at http://proceedings.ises.org

and cost-effective conversion processes are to be preferred to avoid a future surge of energy costs. In this respect, existing infrastructures must undergo testing for their use and energetic system short circuits must be avoided.

Therefore, power-to-heat (compare (1) in Fig. 1) with direct heat generation such as the electric heating of heat storages for district heating systems possibly advanced heat pumps with a coefficient of performance (COP) of up to 4 using heat from the environment or the direct power supply of electric railroads and the charging of battery vehicles often involves smaller conversion losses than PtG technology. However, PtG ((2) in Fig. 1) can solve the storage problem very advantageously with the first step (PtH = Power to Hydrogen) producing hydrogen using electrolysers as a storable energy rich gas. Hydrogen can be used in a variety of direct and highly efficient ways in fuel cell vehicles such as cars, trains, ships as well as for decentralized power supply. Power-to-power refers to short-term electrical battery storage for primary control of power grids in the hourly range but also in the minute range using intelligent power electronics. Since power-to-power in the long-term range is only possible with a maximum efficiency of 30%, this technology must be kept to a minimum by the intelligence of the grid control in smart grids [Gamallo, 2007]. Chemical long-term storage with hydrogen (PtH + HtP) or synthetic methane amend the technological spectrum. The use of bioenergy completes this overview. Bioenergy provides biofuels for mobility and biomethane for CHP plants. However, the economically exploitable potential of bioenergy in Germany is only about 25 % of the total energy demand. [FNR e.V.]

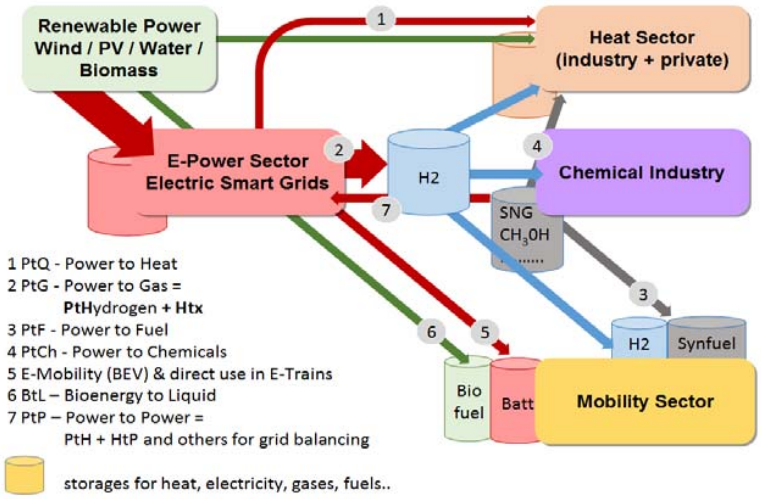

Figure 1: Ptx technologies for sector coupling and some storage options [Steffenhagen et al. 2018]

3. Local and international research projects and infrastructure of the Stralsund University of Applied Sciences

3.1. Research activities in the field of renewable energies and Ptx technologies

The educational opportunities of the Stralsund University of Applied Sciences have developed since 1994 in close connection with the establishment of the interdepartmental complex laboratory Alternative Energies. It constitutes the central scientific institution of the Stralsund University of Applied Sciences, the Institute for Renewable Energies (IRES) and the Institute for Environment e. V. The Institute for Regenerative Energy Systems (IRES) is focused on research in the fields of conversion, generation, storage and utilization of renewable energies and hydrogen as well as the automation of the associated systems. The question of how to utilize wind and solar power (solar thermal and photovoltaics) bioenergy as well as hydrogen including the associated manufacturing technologies, materials research and system integration, are the subject of applied research. Which is usually carried out in cooperation with companies and research institutes in the state. This particularly includes the work on PEM and SOFC fuel cell systems, e.g. for the maritime sector. The analysis and design of infrastructure scenarios regarding hydrogen/ methane storage and distribution have been and continue to be the basis of research work on hybrid power plants, modular energy container solutions, storage concepts and the grid integration of renewable energies.

Some of the latest research projects will be briefly explained below. The project MethaCycle for example

investigated the possibilities to produce methanol from renewable hydrogen and carbon dioxide. [Gulden et al. 2021] The methanol was supposed to be handled in a cycle so that the carbon dioxide could be used with hydrogen again.

In the project ELMAR the Institute for Renewable Energy Systems was looking at the different possibilities to use electric propulsion for maritime applications, specifically in the southern Baltic region, and the missing links in the supply chain of small and medium-sized local enterprises were analyzed. [Voss et al. 2020] HyStarter had the goal to create a network of the necessary key players regarding a hydrogen infrastructure in the region Stralsund/Rügen, which led to the funding of the HyExperts project, which now investigates the needed steps to implement the infrastructure in the region. Led by the INP in Greifswald the CAMPFIRE project explores the prospects of ammonia as a hydrogen storage medium. The contribution of the IRES is the analysis of the needed components for an ammonia-propelled ship. To generate these huge amounts of green hydrogen offshore wind farms are a viable option. In the project PowerH2 we investigate methods to transport the generated energy ashore from water. In this respect a hydrogen pipeline seems feasible. [Hayduk et al. 2022]

The focus of the research network "Netz-Stabil", consisting of research groups from the University of Rostock, Stralsund and Greifswald, was on solving problems related to energy transition as part of the excellence research program of the federal state of Mecklenburg-West Pomerania. One of the challenges was the volatility of renewable energy sources. These fluctuations cause instability in the electrical power grid and therefore threaten the balance between generated and consumed energy. Another problem is the increasing use of drives coupled with inverters. As a consequence, grid frequency and power consumption are decoupled which leads to a decreased self-regulating effect of the grid. In this context, the project group at Stralsund University of Applied Sciences conducted research on suitable storage technologies as well as storage management and built a hybrid energy storage system (HESS), including the necessary power electronics and control algorithms. [Bierhoff et al.] Combining lithium-ion batteries with double-layer capacitors, the focus of this storage system is on short-term volatility due to renewable energy sources in the range of milliseconds to hours. The HESS was combined with a test bed to simulate volatile energy sources such as wind and solar power plants. This then allowed studies to be conducted on the design of individual storage components and to find optimal operating strategies for real wind and solar farms. [Soliman, Bierhoff, 2022,a,b]. Figure 2 shows the basic setup of a possible application in which the HESS is combined with a wind turbine to compensate for power fluctuations. The prototype has a capacity of about 25 kWh and a peak power of about 150 kW.

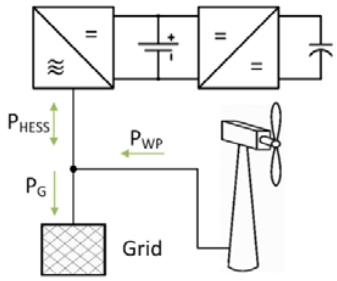

Fig. 2: Hybrid Energy Storage System [Steffenhagen et al. 2018]

The aforementioned topics of applied research are not only comprehensively conveyed in teaching, but they also pose challenging topics for student projects as well as bachelor's and master's theses as a prerequisite for a subsequent career. The equipment developed or acquired in these research projects serves as the basis for student laboratory practicals on state-of-the-art technology.

3.2. Modernization of the complex laboratory to the SMART-GRID-LAB

As early as 1993, the Integrated Energy System Laboratory (Complex Laboratory) was established as a multidisciplinary laboratory with state-of-the-art industrial equipment for the research area of renewable energies, it was continuously expanded and modernized to become a Smart Grid Laboratory last year. With its new switchgear, it enables the intelligent and open networking of energy generators, storage facilities and consumers, realistic upscaling in the simulation area as well as studies on sector coupling. The complex laboratory was constantly extended by new equipment. Starting in 1996, a wind-PV-hydrogen chain with grid-connected reconversion (the first plant worldwide with components from 10 - 100 kW) was installed. It served

as a research, experience and teaching platform for hybrid energy and storage solutions. Furthermore, it is used to operate our CHP in natural gas-hydrogen mixed gas operation in addition to testing and developing PEM and SOFC fuel cell systems including their components. The laboratory itself consists of the following individual systems(Fig. 3): A Stirling engine [50 kWth and 10 kWel], a catalytic hydrogen boiler [21 kW], a biomass boiler [50 kWth], an adsorption refrigeration system [10 kW] with a solar thermal system [40 kW], and fuel cell systems [20 W ... 2 kW]. Since 2020, a lithium-ion battery storage component [10 kWh] complements the whole system, which is important in terms of grid stability. Thus, the complex laboratory is equipped with sophisticated devices and systems from all areas of renewable energies and storage technologies.

The switchgear technology of the Complex Laboratory was put into operation in 1995 with the establishment of the laboratory. Although the system was repeatedly optimized and adapted to the requirements of laboratory operation and for teaching purposes, and the individual systems including the associated measurement and safety technology of the laboratory were adapted as well as expanded to the corresponding state of development, it no longer met the requirements of a future energy supply to intelligently link consumers and generators. Therefore, the idea was born to equip the IRES research and training laboratory, which consists of various renewable energy generator and storage technologies as well as different consumers, with SMART-GRID functionality. The SMART-GRID-LAB at Stralsund University of Applied Sciences could then be put into operation in 2021. The intelligent and open linking of generators, storage units and consumers now enables realistic upscaling in the simulation area. With the new switchgear technology, the interaction of renewable energy suppliers with storage facilities and energy consumers can now also be investigated during a comprehensive sector coupling. This makes it possible to accompany the introduction of regional smart-grid solutions directly and soundly by grid operators, but also to map research and training in the field of PtX technologies in a smart-grid environment. The University of Stralsund is furthermore planning to connect other specialist laboratories of the university in the energy and automation sector with the SMART-GRID-LAB to form a cross-functional platform, so that they can communicate and exchange data via the platform. The students are thereby able to directly access the Complex Laboratories plant technology via the communication interfaces. This includes the configuration of hybrid power supply solutions, their parameterization, experiment planning/ sequencing and the associated data evaluation.

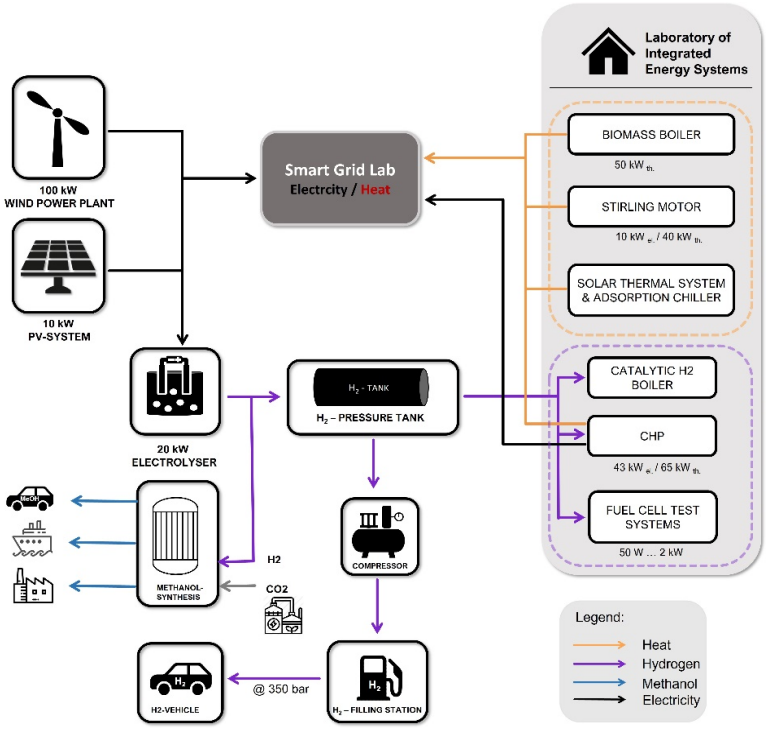

Figure 3: Structure of the IRES-Laboratory of Integrated Energy Systems (KAE) at Hochschule Stralsund

The authors plan to expand the SMART GRID LAB later to make data interfaces available to the cooperating energy suppliers and thus to significantly increase the consistency in the processing of highly particular tasks of

the industrial partners. An outstanding performance in controlling and logging the process is critical for the analysis of the interaction between individual system components and consumers within a SMART-GRID. The system offers update times of 1 µs per I/O module at local bus level. With the higher-level PROFINET bus system, the processes can be run and analyzed in real time. Modbus TCP and Modbus RTU are used to communicate with the devices and systems (see Fig. 4). Thus, the automation system of the research laboratory is state of the art. It now provides the basis for implementing the intended functionality of the SMART-GRID as a laboratory platform. The components interacting within the SMART-GRID-LAB network can be configured, adapted, controlled and evaluated with regard to their operating behavior by remote access via the network with the aid of the implemented control technology and the visualization system in accordance with the experimental tasks. New components can be added at any time due to the modular design.

The system configuration complies with the following specifications:

- Performance on local bus level with update times of 1 µs per I/O module (transmission of fast samples according to standard part IEC 61850-9-2)
- Real-time capability according to IEC 61850
- PROFINET at the programmable logic controller level according to IEC 61850
- Modbus TCP and Modbus RTU on the communication level between the devices and systems of the lab
- Use of industry standard components to ensure reliability considering the high loads which are to be expected, compatibility of individual components with each other.

With this new modular automation concept, extensive data acquisition is possible and thus constitutes the basis for innovative research and training.

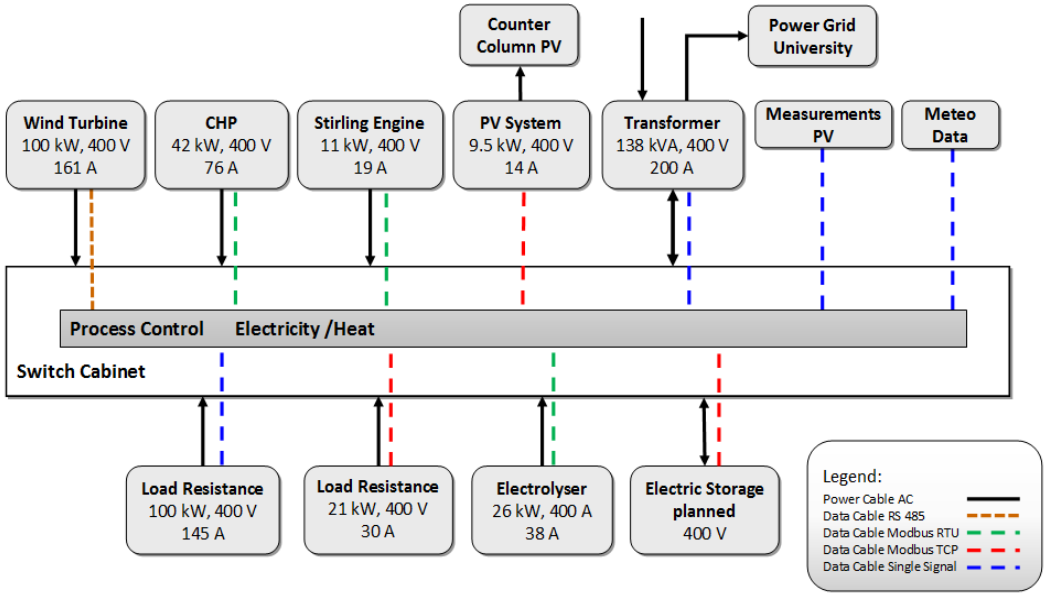

Figure 4: Overview Integrated Energy System Laboratory - Electricity [Steffenhagen et al. 2018]

4. Education in Renewable Energy, Ptx technologies and E-Mobility

4.1. Development and overview of various education programs

To meet the growing demand for specialized personnel, our university has a long tradition of research and education in renewable energy and hybrid energy systems management. Various educational formats have been developed. These include a German-language bachelor's program in renewable energy since 2009 and a German-language master's program in electrical engineering with a specialization in renewable energy since 2007, as well as an English-language master's program in renewable energy and E-Mobility since 2018. This master's program also promotes international cooperation with our partners in Europe, Thailand and South America. For shorter study visits of international students, we have a postgraduate program in renewable energy and hydrogen technology since 1997 (offered in English language, five months in winter semester) and a two-week international spring school in English for students from our partner countries.

A high level of practical relevance and the associated motivation of the students play a very important role in the training. By means of interdisciplinary student projects, such as the ThaiGer-H2 Racing Team, a practical education had to be ensured. The fact that said team is able to participate in international competitions achieving excellent results provides a boost to motivation. Since 2008, our team has been competing in the Shell Eco-Marathon. In the "Hydrogen Fuel Cell Prototype" category we obtained first place four times in a row between 2018 and 2022. The goal of this competition is to achieve minimal fuel consumption during a race lasting 39 minutes at a speed of approximately 25 km/h. Building and driving the race car encourages interdisciplinary teamwork and multicultural thinking. The race car project is also covered during spring school and team members work as tutors during lab experiments. In this way, both the spring school participants and the team members can gather experience and the students' motivation to deal with new technologies is promoted.

In order to raise pupils' interest in renewable energies and related technologies as well as new mobility concepts, we have long maintained close contacts with local schools. We started with a hydrogen truck model built by pupils and students. We also organize project days on a regular basis where pupils can access this new technology in practical experiments. Since 2017, a school team named "GreenDrive" has also been participating in the Shell Eco-Marathon with a battery-powered race car in the category "Prototype Battery Electric". In 2022 their efforts were rewarded with a fourth place in Nogaro (France). Another accomplishment of this engagement is that the first student members of this team have started their studies at our university.

4.2. Bachelor Programms

At the same time as the Complex Laboratory was being constructed and the research focus on renewable energies and hydrogen technology was being established, teaching concepts were being developed. Initially, modules from the field of renewable energies and hydrogen technologies were included in the diploma program and later in the bachelor's program in electrical engineering. In 2009, we started a standalone cross-faculty bachelor-study-program "renewable energies" with two specializations: electrical and thermal energy systems. It contains additional scientific and mechanical engineering fundamentals and offers more scope for regenerative energy converters and systems, energy storage, hydrogen technology and fuel cells as well as the associated plant engineering. Furthermore, energy efficiency issues are considered. The program has a duration of seven semesters and is graduated with a Bachelor of Science (B.Sc.) degree. It was successfully reaccredited in 2019 by the Accreditation Council until September 30, 2027. It is a practical degree program, which is accompanied by extensive laboratory training, student projects and a twelve-week practical phase in the seventh semester. This ensures optimal starting conditions in the industry. The curriculum is structured as follows:

1. **Natural science basics**
   mathematics I and II, physics, thermodynamics and fluid mechanics, modeling and simulation
2. **Technical basics**
   electrical engineering I, II and III, electronics, mechanics, construction and materials, PLC programming and actuator technology, measurement and sensor technology, control engineering, process engineering
3. **Specialization renewable energy**
   fundamentals of energy conversion, hydrogen technology, fundamentals of solar systems, energy efficiency, energy management (plant design, energy economics, energy storage), regenerative energy converters I (geothermal, wind, hydropower), regenerative energy systems.
4. **Interdisciplinary qualifications**
   scientific work, technical English, presentation and rhetoric, business administration, integrative elective module 1 out of 3 (project management, environmental management/environmental law, environmental engineering)
5. **Specialization**
   Electrical energy systems: electrical machines, power electronics, electrical power generation, electrical power supply, low voltage systems, high voltage systems, elective module.
   Thermal energy systems: electrical machines and power electronics, thermal energy systems I and II, regenerative energy converters II, fluid machinery, two elective modules.
6. **Finishing study work:** Project work, practical phase in a company, bachelor's thesis with colloquium

4.3. SpringSchool and Postgraduate Course in Renewable Energy

For study visits of international students, we established a one-semester postgraduate course in renewable energy and hydrogen technology as well as a two-week international SpringSchool in English. We started the SpringSchool as early as 1992. 30 years ago, the use of hydrogen as an energy storage medium in combination

with renewable energy sources was a rather fictional idea, still far away from functional applications. Therefore, we invited scientists from Sweden, Argentina, Poland, and Norway and some of their most enthusiastic students to come and collaborate with us. This scientific fiction has become a reality. Participants from various countries look forward a varied program with practice-related experiments and interesting excursions every year.

The Spring School was funded by the Erasmus Program of the European Union from 1992 to 2014 and received the European Award for SpringSchool in 2008. This placed us among the top ten ERASMUS intensive programs out of more than 200 in Europe, and at that time we were the only program dealing with renewable energy and hydrogen technology [Bauch 2011]. After that, we were able to secure financing from the university and continue this successful tradition. Participants only have to pay a small contribution for room and board. Over the years, we have adapted the content of the SpringSchool to the current state of knowledge and incorporated the work of researchers and lecturers from our partner universities. The current title, FUSES+ (FUture Sustainable Energy Supply) based on renewable energy and hydrogen technology, is a combination of an in-depth introduction to hydrogen, fuel cells and system automation, extended by current developments in renewable energy sources, power quality and electric mobility. In April 2022, the 29th SpringSchool was held with lecturers and students from Finland, Norway, Brazil, Lithuania, and Poland to share our knowledge with an international community.

As we aimed at deepening the cooperation with our international partners and enabling the students to prolong their stay at our university, e.g. within the European Erasmus exchange program or with the help of our partners from Thailand, we established an international Postgraduate Study Course in 1997. This one-semester intensive course between September and February is designed to deal with future issues of ecological relevance, which allows students from Spring School to come back to our university and deepen their knowledge. Initially, we were not yet able to offer a full master's program and thus this intensive course could help to meet the growing demand for engineers in the field of renewable energy. This program still exists today. It is suitable for final year students as well as PhD students of technical fields from Germany and abroad [Luschtinetz et al]. Since this study course promotes international cooperation students have arrived from the European Erasmus exchange program, from South America sponsored by the DAAD, and from partner universities with which the University of Stralsund made bilateral agreements. Moreover, even postgraduates and company workers attend this study course. Some participants then stayed for another semester and did research at our IRES institute or completed special trainee programs in their own countries up to the PhD degree. The course program is constantly adapted to current developments and currently includes the following topics: environmental energy management, hydrogen technology, fuel cells, hydrogen laboratory, bioenergy, wind power plants, solar energy (photovoltaics, solarthermal energy), power systems technology and electrical power quality, a Small Project and an Energy Excursion Program. An examination completes the course and students, if they pass, can obtain a maximum of 30 ECTS credits, which are then accepted at the home university.

4.4. Master’s Programmes

Motivated by the great interest of the students in the previous international programs, we established a new specialization in renewable energy in our German-language master's program in Electrical Engineering in 2007. Initially, we focused on the field of renewable energy and hydrogen technology and started with modules such as Solar Systems, Wind Power, Electrochemistry, Fuel Cell Systems, Hydrogen Technology, CHP Systems and Bioenergy, and renewable energy Systems. Later, modules were added from the field of drive technology and alternative emission-free drive concepts. Most of the modules include laboratory training or the students work on their own projects, so that the training is very practical. Although this requires a great deal of supervision, it helps to motivate students, promotes independent work as well as group work, and optimally prepares students for a later career in science and applying their knowledge.

The program is addressed to students with a bachelor's degree in electrical engineering or related courses of at least 180 ECTS. The duration of the program is three semesters and yields 90 ECTS credits. Students graduate with the academic degree of Master of Science (M.Sc.) which generally qualifies for admission to a doctoral program at a university. The lectures are delivered in German and English. The Master's program was successfully accredited by the Accreditation Council in 2022 until September 30, 2030. In the first semester, which is usually the summer semester, mainly basic knowledge on a theoretical level is taught. However, it also includes an elective module with a practical background in addition to an integrative elective module called "Project Management". The winter semester is used for specialization in areas such as hydrogen technology,

fuel cells, bioenergy, solar systems, wind turbines, electromobility, alternative non-fossil mobility, vehicle management systems, power electronics, special problems of drive technology, modern methods of control engineering and automation technology. The winter semester consists mainly of application-oriented elective modules where the lecture language is usually English. The winter semester is often used as a sandwich semester in Master's/PhD study programs by foreign students. Students can enroll in either the summer or winter semester. The study schedule starting in the summer semester can be seen in Figure 6. When enrolling in the winter semester, the first two semesters are reversed. Based on the postgraduate course "Renewable Energy and Hydrogen Technology" several f international cooperations with different countries like Thailand, Russia, Poland, Brazil, Norway and Finland have developed. Following that path, a desire to deepen the cooperation arose and to enable double degrees as well. To accomplish this, however, we needed not just a single semester in English, but an English-language master's program in renewable energy. In the development of this new English-language master's program, our many years of international experience with English-language events with our international partners on site, were eminently useful. Additionally, the master's program of "Electrical Engineering" with a focus on renewable energies as well as the postgraduate course "Renewable Energy and Hydrogen Technology" have been incorporated. In addition to modules dealing with the use of renewable energy sources and hydrogen technology such as solar radiation in PV and solar thermal systems, biomass, wind and hydropower as well as the use of hydrogen as a storage medium, we established a new focus on electro mobility, a highly innovative, fast-growing and future-oriented sector in Germany and abroad.

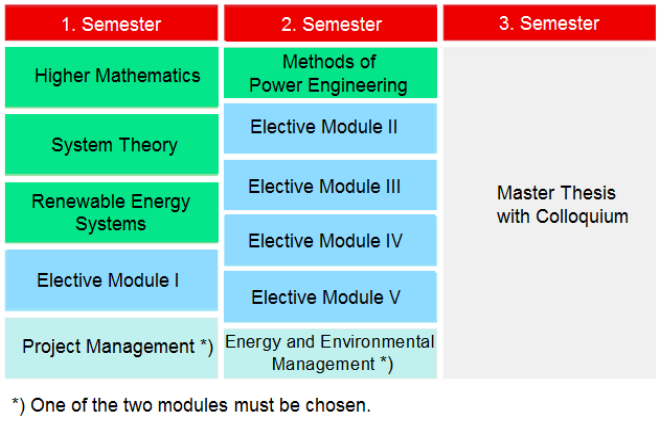

Figure 5: Curriculum Master Electrical Engineering, specialization renewable energy

The electrification of the automobile in combination with hydrogen as a storage medium can be an important step toward making mobility more environmentally friendly in the coming decades and maintaining the competitiveness of our automotive industry. The new study program, in which the first students enrolled in 2018, addresses these future topics and helps to meet the growing demand for engineers. There is no equivalent range of courses in northern Germany. The master's program "Renewable Energy and E-Mobility" is aimed at students with a bachelor's degree in electrical engineering, mechanical engineering or related courses or physics. It is offered in a three- and four-semester option, as foreign students often come to us with a bachelor's degree of 180 ECTS. The four-semester option includes either additional practical or study semesters. Enrollment for the previously mentioned course starts only in the summer semester, the course with a duration of three semesters can be begun in summer and winter semesters. In addition to compulsory modules based on mathematical-technical fundamentals as well as interdisciplinary qualifications, such as energy and environmental management or quality management in the automotive industry, application-specific knowledge is taught in both compulsory and elective modules in the two focus areas. The student can choose from elective modules in the areas of renewable energies or e-mobility as well as independent elective modules to also acquire inter-disciplinary or in-depth electrotechnical expertise. In the final semester, students work on their master's thesis.

Since the range of courses we offer is not limited to students with a degree in electrical engineering, we thought it is crucial to give students with a mechanical engineering degree, for example, the opportunity to acquire any specialist knowledge they might lack, especially in the field of electromobility. At first, we left it up to the students to compensate for any technical deficits through independent elective modules. However, the students did not make sufficient use of this option, which led to problems in the more advanced modules. For this reason,

we have adapted the modules in the first semester to match the underlying bachelor's degree. Thus, the module "Power Electronics" does not have to be taken by students who have already completed the module in the bachelor's degree. These students can then choose a different elective module. In addition, students who come to us with a bachelor's degree in mechanical engineering must take the module electrical energy transmission and conversion as a first elective module. This decision was made by the admissions committee. Since the level of proficiency and the knowledge imparted to foreign applicants vary significantly, we have introduced the following admission requirements step-by-step:

- **Bachelor's degree** in electrical engineering, power engineering, renewable energies, mechanical engineering, physics or related subjects
- **Proof of knowledge in the following fields** with a minimum of:
  - Measurement technology at least 4 SWS or 5 ECTS- Control engineering at least 4 SWH or 5 ECTS
  - Fundamentals of electrical engineering at least 4 SWH or 5 ECTS
  - Electrical machines at least 2 SWH or 3 ECTS
- **Proof of English language skills at B2 level**
- Grade point average of at least 1.8 in the first degree
  (With a grade point average of 1.9 to 2.3, a case-by-case assessment is made based on a letter of motivation and other documents)

The master's program is in very high demand. We have between 400 and 700 applicants for the four-semester version in the summer semester. This master's program enables us to deepen existing international collaborations and to find new cooperation partners, e.g. in Brazil. The curriculum of the master's program "Renewable Energy and E-Mobility" in the three-semester-option is structured as follows:

1. **Mathematical-scientific basics:** modelling of physical systems, system theory
2. **Specialized technical bases of renewable energy technology**:
   renewable energy systems, methods of power engineering, power electronics
3. **Application-oriented knowledge**: (elective modules, min. four modules must be chosen)
   current topics of renewable energy, solar systems, wind power plants, hydrogen technology, fuel cell systems, control of electrical drives, sustainable non-fossil mobility, advanced power electronics, project seminar e-mobility, vehicle management systems, vehicle simulation & test drive
4. **Interdisciplinary qualifications:** quality in automotive industry or energy and environmental management
5. **Master's thesis**

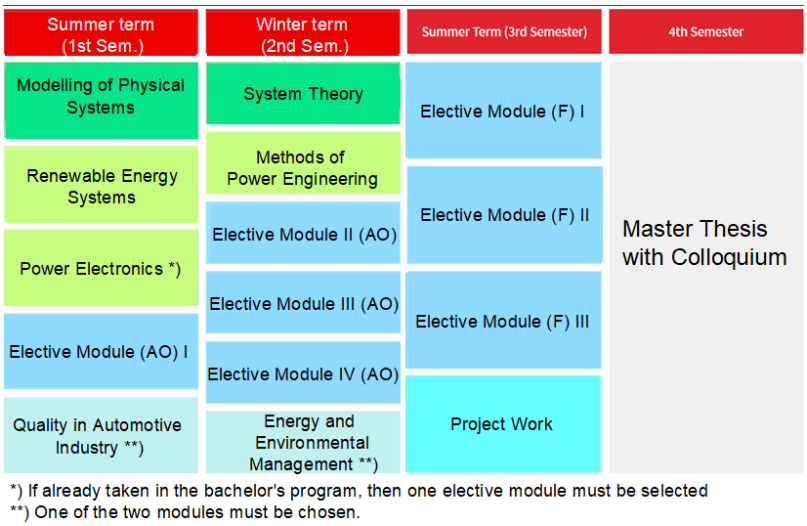

Figure 6: Curriculum Master Renewable Energy and E-Mobility, 4 semesters without internship semester

In the four-semester version, students can choose to complete an internship semester in the third semester or choose three independent elective modules and complete a project thesis.

The following modules are available as independent electives: selected topics of control engineering, electrical energy Conversion und Transmission, International Accounting, Human Resources Management, German as a

foreign language I and II (A1 or A2 level) and all application-oriented modules. The students are involved in various student projects such as the ThaiGer and also in current research projects, which enhances motivation and independent work. The practical semester, which is chosen by many students, makes the education particularly hands-on and the students are well-prepared for their careers to come in this field of future relevance.

5. Light weight race car projects

5.1. ThaiGer - a student project

The ThaiGer-H2-Racing Team is a student team at the Stralsund University of Applied Sciences, which has been developing and building hydrogen-powered prototype vehicles for over 14 years. With this international team our university managed to acquire a lot of experience motivating young students to develop and implement new technologies. This successful project started in 2008 with students from Thailand, Spain, Poland and Germany in Stralsund, hence the name ThaiGer (Thailand + Germany). Students from the international postgraduate course and later also from the Renewable Energy and E-Mobility (REEM) master's course have worked in this team and participated in competitions across Europe. The cross-faculty and interdisciplinary collaboration promotes the multicultural and interdisciplinary idea of the study program. Currently, the team includes about 30 students from the Stralsund University of Applied Sciences, coming from all faculties and different study programs. However, the students are united by one thing - the goal of building the most efficient hydrogen-powered vehicle for the Shell Eco-marathon in the "Hydrogen Fuel Cell Prototype“ category. Annually, the ThaiGer team competes in the largest efficiency competition, the Shell Eco-marathon Europe, and has won first place in the "Hydrogen Fuel Cell Prototype“ category in 2017, 2018, 2019 and 2022. All vehicles compete in their respective categories, on a racecourse of approximately 16 km to determine the most efficient vehicle. The course must be completed at an average speed of 25 km/h in a given time. The vehicle with the lowest fuel consumption wins the race.

Our team improved gradually each year and in 2016 took second place with the result of 2029 km with one litre of gasoline equivalent. In 2017, with the new very light ThaiGer VI race car (23 kg), the team improved again and took first place ahead of the team from Turin, which is sponsored by Ferrari. A significant weight reduction was achieved by a new monocoque frame made of carbon fibre and the power train was revised, too. In the first victory in 2017, hydrogen consumption was 17.8 litres, which corresponds to 880.5 km with one cubic meter of hydrogen or a range of over 2600 km with one litre of gasoline equivalent. The ThaiGer VI also competed in the following two years, 2018 and 2019, and again performed exceptionally well in 2019 with 1083 km/m^3 of hydrogen, comparable to a range of 3295 km with one litre of gasoline equivalent.

After the Corona break, the ThaiGer team returned to Nogaro (France) as defending champions in 2022. The goal of becoming European champion for the fourth time in a row was achieved with an excellent result. For the 2022 Shell Eco-marathon in Nogaro, the team developed a new vehicle the ThaiGer 7. The monocoque frame was made completely of carbon prepreg. Compared to its predecessor it was now 25 cm shorter, its weight was reduced, and the aerodynamic behaviour was improved. The new design of the ThaiGer 7 vehicle is striking, reflecting the function of the fuel cell. The front part of the vehicle features hydrogen and oxygen molecules, which are torn into individual atoms by the blue lightning bolts. After releasing energy, the atoms then connect to form water at the rear of the vehicle.

In addition, the fuel cell system was particularly optimized to achieve higher efficiency. The fuel cell itself is constructed from bipolar plates and membranes that were purchased externally. The end plates for the FC stack were developed by the team and are made of carbon. The fuel cell is the main energy supplier in the vehicle and is supported by a small supercap battery. Furthermore, the membrane pumps for the air supply were replaced by a self-developed, more efficient side channel blower. Moreover, a two-phase cooling system for the fuel cell was developed and manufactured as part of a bachelor’s thesis. In contrast to the old water cooling system, the new cooling system does not require a circulating pump, which has made it possible to reduce self-consumption and weight. The race car is propelled by a highly efficient permanent magnet axial BLDC motor (brushless DC motor) which was developed and manufactured as part of the team's project and a final thesis. The motor is integrated into the rear wheel, which is made of carbon. Due to the construction method and the renouncement of iron package, an efficiency of over 95% could be obtained.



Figure 7: ThaiGer-Team with ThaiGer 7 in 2022

A new pressure reducer (see fig. 8) was also designed for the race, which won the Technical Innovation Award. The Technical Innovation Award is presented as an off-track award alongside the main race. The device reduces the pressure of hydrogen from a gas cylinder with 200 bar to the 0.3 bar which constitutes the pressure required for the fuel cell. The two-stage pressure reducer is equipped with two pressure relief valves as well as a solenoid valve and pressure display. Weighing roughly 300 grams, the pressure reducer is much lighter and more compact than conventional fittings.



Figure 8: New pressure reducer (own development) of the ThaiGer 7

This development certainly contributed to the victory. But just as important in the end, however, was the team spirit and its close cooperation. With 1118 km/m³ of hydrogen, the ThaiGer-H2-Racing team won the European championship title for Stralsund and was far ahead of the second-place team, H2politO from Italy's Politecnico Di Torino, which achieved 899 km/m³ of hydrogen. The hydrogen category is considered the supreme discipline of the competition and requires a great deal of skill and know-how. Thus, out of the twelve teams that competed in this category, only five teams managed at least one valid scoring run.

5.2. GreenDrive

Collaboration with local schools has long been proven to motivate pupils to get involved in green technology and new mobility concepts, as well as to study at our university later on. For example, since 2016, students from the ThaiGer team have been supporting the "Greendrive" school team from the secondary school "Schulzentrum am Sund". Their goal was to compete in the Shell Eco-marathon with a battery electric vehicle in the "Prototype Battery Electric" category. The pupils who developed the car in collaboration with Stralsund University of Applied Sciences were delighted to come in fourth this year with a result of 682.9km/kWh.

The ten pupils normally come to the university once a week for two hours with a supervising teacher. Just before the Shell Eco-marathon, they were present more often, naturally, including Saturdays. The student team was founded in 2016 and first converted the old vehicle, the ThaiGer V, to an all-electric drive. Putting it into practice, the team participated in its first race at the Challenge Event in Le Mans, France in 2017. The Challenge Event is a small-scale Shell Eco-marathon for new teams and is also organized by Shell. The Greendrive team was able to qualify for the big Shell Eco-marathon the following year in 2018. The school team was able to repeat that success in 2019 and 2022. In 2022, the pupils competed with the same monocoque frame as the ThaiGer7 but with green flashes and wheels. The vehicle is powered by a small lithium polymer (LiPo) battery. The weight of the entire vehicle is 18 kg. This made it the lightest vehicle competing in the Shell Eco-marathon

by far. It is even 4 kg lighter than ThaiGer 7 because the fuel cell system, hydrogen bottle, supercap battery etc. were replaced by one small battery. Furthermore, the same wheel hub motor was used as in ThaiGer 7. The motor, which is already in its third generation, was largely manufactured by the pupils themselves as part of a MINT project. The precision of the manufacturing process was improved compared to the old motor, which made it possible to reduce the air gap between the magnets and the winding and increase efficiency. Compared to 2019 in London, the result was improved by 10 km/kWh on a much more challenging racetrack in Nogaro. A total of 25 teams registered in this category and 17 teams managed at least one scoring run. [Greendrive, 2022]

6. Summary

Various factors play a role in the education of students in the use of renewable energy sources, PtX technologies, smart grids, and electric mobility. On the one hand, this includes the acquisition of suitable teaching staff, sufficient laboratory equipment as well as practical research and cooperation with regional industry. Nonetheless, the interaction of all stakeholders involved to enhance the motivation of the students is an equally significant aspect. The education of students, research, industrial cooperation with regional partners and public commitment should be developed at the same time in a sustainable way, as all aspects involved mutually benefit each other. By using equipment created or acquired through research projects in teaching, from publicly funded research equipment to self-made prototypes and small test beds, costs can be minimized and additional experience can be gained for the next steps in the process of research. Students being responsible for their own projects as well as laboratory training on all available equipment embedded in all educational programs, enable practical training and promote student and lecturer motivation. Due to the early entry into PtH and PtP technology in research and teaching 30 years ago, the Stralsund University of Applied Sciences was able to provide many impulses for industrial use and the training of engineers in the field of PtX technologies.

7. References

Bauch, H.-F., Luschtinetz, T. et. al, 2011. FUSES – Future Sustainable European Energy Supply –19th International SpringSchool at FH Stralsund, 18. REGWA-Symp., Stralsund.

Bierhoff M., Soliman, R., J. R. Espinoza C., 2020. Analysis and Design of Grid-Tied Inverter With LCL Filter," in *IEEE Open Journal of Power Electronics*, vol. 1, pp. 161-169, doi: 10.1109/OJPEL.2020.2995105.

FNR e.V., 2022. https://bioenergie.fnr.de/bioenergie/biomasse/biomasse-potenziale, May 6, 2022

Gamallo, F., Lehmann, J., Luschtinetz, O. u. T., Miege, A., Sponholz, C., 2007. Hydrogen Production as a Suitable Alternative for Grid-balancing. Proc. 6th World Wind Energy Conference, Mar del Plata, Argentina.

Greendrive, 2022. http://www.schulzentrum-am-sund.de/nachrichtenleser/Greendrive-2022.html

Gulden, J., Sklarow, A., Sommer, R., Kirchner, J., Schweizer, C., 2021. Dynamic production of green methanol by controlling the CO2 flow; Hypothesis XVI 2021The project

Hayduk, M., Sommer, R., Gulden, J., 2022. Integrated planning tool for cost and 3D structural planning for offshore wind farms for the generation of H2; WHEC 2022

Luschtinetz, T., Bauch, H.-F., Krause, S., Lehmann, J., 2012. Sustainable, comprehensive and motivating education in the pioneering hydrogen technology,19 th World Hydrogen Energy Conference (WHEC), Toronto

Soliman, R., Bierhoff, M., 2022, a. Sizing and Operation of a Hybrid Energy Storage System to Compensate Forecast Errors of Wind Farms – An Approach, IEEE International Symposium on Industrial Electronics.

Soliman, R., Bierhoff, M., 2022, b. Simple Design Strategy and Comparison of Operation Strategies for a Hybrid Energy Storage System to Counteract Forecast Errors of Wind Power, submitted to IEEE Transactions on Sustainable Energy.

Steffenhagen, B., Gulden, J., Luschtinetz, T., Solimann, R., 2018. PtX technologies for smart grids. 4th ASEAN Smart Grid Congress.

Voss, L., Sommer, R., Gulden, J., 2020. ELMAR – Elektromobilität auf dem Wasser; RET.CON 2020 – 3. Regenerative Energietechnik

A

Abbas, S.
Dual Axis Optimization of Solar Photovoltaic at Various Sites in Pakistan **1649**
Gap Filling in Solar Radiation Data using Artificial Neural Network for Nine Stations... . . . . . **1657**

Abdullah, M.
Dual Axis Optimization of Solar Photovoltaic at Various Sites in Pakistan **1649**
Efficiency Evaluation and Comparisons of Solar Cell Technologies Based on Measurements... . . . . . **1747**
Gap Filling in Solar Radiation Data using Artificial Neural Network for Nine Stations... . . . . . **1657**
KNN-Based Ensembles for Day-Ahead Forecasting of Solar Power Outputs **1755**

Abido, M.
Non-Tracking Asymmetric Shadeless (NASH) Solar Collectors for Decarbonizing Industrial... . . . . . **372**

Adil, M.T.
Gap Filling in Solar Radiation Data using Artificial Neural Network for Nine Stations... . . . . . **1657**

Afshari, A.
Early-stage Feasibility Study of an Ambient-temperature District Thermal Network:... . . . . . **275**

Ahmad, S.
Dual Axis Optimization of Solar Photovoltaic at Various Sites in Pakistan **1649**
Gap Filling in Solar Radiation Data using Artificial Neural Network for Nine Stations... . . . . . **1657**

Ahmed, S.
Estimating Rooftops' Suitability for PVs Using Pleiades-1B Satellite Image for Charging... . . . . . **965**

Ahn, Y.
Energy Performance Investigation of PVT Assisted Heat Pump System for a Net Zero... . . . . . **642**

Ajona, J.I.
Energy Analysis Of A Solar-Driven Hybrid Air Conditioning System With An Absorption... . . . . . **566**

Akbar, Z.
Gap Filling in Solar Radiation Data using Artificial Neural Network for Nine Stations... . . . . . **1657**

Akdemir, S.D.
Promotion of Solar Heat in Industrial Processes: Policy and Law Analysis with Focus... . . . . . **1884**

AlHajri, H.
Assessment of Downward Longwave Radiation Models in Clear-Sky Desert Conditions **1574**

Al-Hajri, H.
Management and Operation of Qatar's Solar Radiation Monitoring Network **1620**

Alkishriwi, N.
Study and Simulation of Low Energy Solar Powered House in Libya **1**

Alonso Tristán, C.
Evaluation of Angular Distribution Models to Estimate Sky Diffuse Irradiance on Tilted... . . . . . **1019**

Altamirano, A.
Implementation of Adapted Black Box Models for the Performance Characterization of... . . . . . **1678**

Altan, H.
A Novel Statistical Method to Improve Energy Efficiency of Housing Stock in the Eastern... . . . . . **166**

Alvarado Alvarado, E.E.
An Energy Trading Model for a Lab-scale PV Microgrid in the Tunisian Context **11**

Amini Sedehi, A.
Investigation of Creep-Fatigue Lifetime in Solar Photovoltaic Module Interconnections **630**

Ammann, S.
100 % Solar Heating with Seasonal Thermal Storage, Solar Thermal Collectors, PV and... . . . . . **202**

Annamalai, M.
Experimental Studies on Solar Multi - Effect Desalination System **846**
Experiments On a Solar Vapour Absorption Refrigeration Cold Storage System **492**
Falling Film Measurements Using High Speed Camera and High Speed Infra-Red Camera **858**

Aparecida Oliveira de Sousa, J.
Metrics Behind the Implementation of Photovoltaic Solar Energy in Urban Area **20**

Arendt, M.
Measures for Energy Optimization for Resource-Saving Consumption Development on a... . . . . . **875**

Arpagaus, C.
Comparative Techno-Economic Analysis of High Temperature Heat Pump and Parabolic... . . . . . **456**

Artantas, O.C.
Promotion of Solar Heat in Industrial Processes: Policy and Law Analysis with Focus... . . . . . **1884**

Aseri, T.K.
Impact of Incentives Towards Lowering the Levelized Cost of Electricity of Concentrating... . . . . . **1827**
Techno-Economics of Central Tower Receiver Power Plants in India: Effect of Heat... . . . . . **1838**

Asim, M.
Dual Axis Optimization of Solar Photovoltaic at Various Sites in Pakistan **1649**
Gap Filling in Solar Radiation Data using Artificial Neural Network for Nine Stations... . . . . . **1657**

Aste, F.
Experimental Investigation on Solar-Driven GAX-based Absorption Heat pump for Domestic... . . . . . **811**

Atif, M.
Dual Axis Optimization of Solar Photovoltaic at Various Sites in Pakistan **1649**

Azimov, U.
Characterization of Enhanced Biobased Phase Change Material with Graphene Nanoplatelets **1374**

B

Baby, B.A.
Adapted Components and Show Cases on Solar Cooling Systems in Sunbelt Region Countries **504**

Bachmann, M.
A Holistic Energetic Transformation Concept for the Heating and Cooling Supply of... . . . . . **953**

Bachour, D.
Assessment of Downward Longwave Radiation Models in Clear-Sky Desert Conditions **1574**
Management and Operation of Qatar's Solar Radiation Monitoring Network **1620**

Baeuerle, Y.I.
Aluminium-Redox-Cycles for the Production of Heat and Electricity in Buildings based... . . . . . **1819**

Ballestrín, J.
Accelerated Ageing Test Bench for Advanced Ceramic Slabs under Extreme and Controlled... . . . . . **1495**

Bapat, S.L.
Effect of HTF Flow Direction on Thermal Performance in an Upward Facing Cavity Receiver **425**

Barboza, L.
A Comparison of Eight Transposition Models Applied for Different Orientations Under... . . . . . **1666**
Detection of Tracker Failures for a 2-Axis Photovoltaic System **1688**
Quality Assurance Procedure for Solar Radiation at Minute Resolution **1601**

Barthwal, M.
Spectral Beam Splitting in Compound Parabolic Collector Based Photovoltaic Thermal... . . . . . **1097**

Baylis, C.
Modelling Analysis of Phase Change Materials for Reducing Cold Climate Space Conditioning... . . . . . **1254**

Bayón, R.
Kinetic Analysis of TGA Measurements When Evaporation Is a Degradation Process in... . . . . . **1402**
Study of Thermal Degradation of Adipic Acid as PCM under Stress Conditions: A Kinetic... . . . . . **1265**

Beccali, M.
Adapted Components and Show Cases on Solar Cooling Systems in Sunbelt Region Countries **504**

Becker, S.
What Can PV Self-supply Do for System Integration? **1847**

Bednar, T.
Comparison of the Simulated and Measured Performance of the PV Plant of Austria's... . . . . . **894**
Data-Driven Approach Utilising Random Forest Regression for PV Performance Monitoring **1699**

Behrends, T.
Software-supported Investment Optimization for District Heating Supply Systems **282**

Belkhodja, I.S.
An Energy Trading Model for a Lab-scale PV Microgrid in the Tunisian Context **11**

Bellmann, M.
A Comparative Study on Solar Radiation Datasets for Photovoltaic Energy Prediction... . . . . . **1589**

Beltrán, F.
Empirical Validation of Low-Temperature PVT Collector for Heat Pump Integration **1109**

Bennacer, R.
Simplified Thermal Performance Model for the Design of a PVT Heat Exchanger Dedicated... . . . . . **618**

Bennani, A.A.
An Energy Trading Model for a Lab-scale PV Microgrid in the Tunisian Context **11**

Bergstraesser, W.
Identification of Waste Heat Potentials and Their Integration Into a District Heating... . . . . . **884**
Transformation of a University Campus: Comparison of Ranking Methods for Temperature... . . . . . **941**

Beringer, J.
Sustainable Housing Insulation for High-Altitude Kyrgyzstan: A Technical Guide **58**

Bernard, T.
Modular Refurbishment of Multi-Family Houses with PVT-PCM Heat Pump Systems and Self-Learning... . . . . **715**

Berrah, L.
A new Framework to Evaluate the Adequation between the Solar Potential and Energy... . . . . . **1581**

BERRAH, L.
Evaluation of Building Energy Performance: Comparison Before and After Envelope Retrofitting **133**
Metrics Behind the Implementation of Photovoltaic Solar Energy in Urban Area **20**

Bérut, E.
Comparative Experiments on a Novel CaCl2-Based Composite Material and Zeolite 13X... . . . . . **1275**

Best, I.
Impact of Domestic Hot Water Preparation Systems on District Heating Network Design... . . . . . **225**
Municipal Heat Planning to Exit from Coal, Oil and Natural Gas in a German Major... . . . . . **1078**

Bestenlehner, D.
Cost-Effective Energy Balancing of Thermal Systems Based on Temperature Measurements... . . . . . **1561**
Definitions for Climate Neutrality and their Relevance for the Assessment of Solar... . . . . . **1867**

Betzold, C.
Heat Pumps in Positive Energy Districts **1085**

Beuth, H.
The Potential of Combined PV and Air Source Heat Pump Systems in German Residential... . . . . . **738**

Bhaumik, A.
Study on Analysis of Solar Panel Efficiency in Vietnam a Power Comparison Before... . . . . . **1629**

Bhusal, Y.
Non-Tracking Asymmetric Shadeless (NASH) Solar Collectors for Decarbonizing Industrial... . . . . . **372**

Birchler, D.
Buried Twin Pipe Model Validation for System Simulations of Ice Storage Tanks in... . . . . . **1070**

Bläsi, B.
Angel-Dependent Features of MorphoColor TM Solar Collectors: Color Stability, IAM,... . . . . . **1195**

Bless, F.
Comparative Techno-Economic Analysis of High Temperature Heat Pump and Parabolic... . . . . . **456**

Bockelmann, F.
Heat Pumps in Positive Energy Districts **1085**
Sustainable and Efficient Energy Supply for the Development of Tourist Villages at... . . . . . **110**

Böckmann, O.
Optimal Conceptual Design of a Novel Façade-Integrated Adsorption Cooling System **595**

BODDAERT, S.
Failure Risk Analysis of Photovoltaic Systems Based on Literature Review **660**

Bogdanovics, R.
Supply Temperature Stabilization of Decentralized Solar Thermal Collectors for Integration... . . . . . **977**

Bohara, K.
100 % Solar Heating with Seasonal Thermal Storage, Solar Thermal Collectors, PV and... . . . . . **202**
Comparison of a Centralized with Decentralized Heat Pump Systems in a Multy Family... . . . . . **748**

Bois, L.
Comparative Experiments on a Novel CaCl2-Based Composite Material and Zeolite 13X... . . . . . **1275**

Bonomolo, M.
Adapted Components and Show Cases on Solar Cooling Systems in Sunbelt Region Countries ***504***

Borri, E.
New Concept for High Temperature Thermal Energy Storage Using a Concrete Tank ***1285***
Optimal Control Based on Deep Learning Techniques for a Hybrid Solar-Biomass System... . . . . . ***1811***

Boß, V.
About the Efficiency of District Heating with Flexible Heat and Temperature Distribution ***302***
Integration of Renewable Energies into Cityscape ***987***

Bosshard, I.
Renovation of a Multi-Family-House with External Wall Heating System ***121***

Bouden, C.
Efficiency of Electricity Self-Production for Medium Voltage Subscribers in Tunisia ***1876***
Electric Self-production for LV Subscribers: Is It Better to Have Decentralized or... . . . . . ***1857***

Braas, H.
Impact of Domestic Hot Water Preparation Systems on District Heating Network Design... . . . . . ***225***
Municipal Heat Planning to Exit from Coal, Oil and Natural Gas in a German Major... . . . . . ***1078***

Brauchli, L.
100 % Solar Heating with Seasonal Thermal Storage, Solar Thermal Collectors, PV and... . . . . . ***202***

Brdeau, S.
Increasing Renewable Energy Integration using Advanced Residential Thermal Energy... . . . . . ***1304***

Brennand, L.J.d.P.
Detection of Tracker Failures for a 2-Axis Photovoltaic System ***1688***

Brinkley, J.
Non-Tracking Asymmetric Shadeless (NASH) Solar Collectors for Decarbonizing Industrial... . . . . . ***372***

Brotas, L.
Photovoltaic Panels and Planning in the UK ***998***

Brottier, L.
Numerical Study of the Effect of Hybrid Solar Collectors on the Performances of the... . . . . . ***768***
Simplified Thermal Performance Model for the Design of a PVT Heat Exchanger Dedicated... . . . . . ***618***

Brunner, C.
Nexus Energy and Water: Integration Concepts for Solar Energy in Industrial Water... . . . . . ***869***

Buddhi, D.
Numerical Investigation and Performance Evaluation of Food Grain Drying Unit Integrated... . . . . . ***1474***

Bueno, B.
Angel-Dependent Features of MorphoColor TM Solar Collectors: Color Stability, IAM,... . . . . . ***1195***

Buitrago Otalora, A.C.
An Energy Trading Model for a Lab-scale PV Microgrid in the Tunisian Context ***11***

Büttner, C.
Solar-Thermal Activation of Rear-Ventilated Façades as a Source for Heat Pump Based... . . . . . ***727***

C

Cabeza, L.F.
New Concept for High Temperature Thermal Energy Storage Using a Concrete Tank **1285**
Optimal Control Based on Deep Learning Techniques for a Hybrid Solar-Biomass System... . . . . . **1811**

Calabrese, T.
Renovation of a Multi-Family-House with External Wall Heating System **121**

Cammi, A.
Numerical Investigation of the Performance of a Solar Air Heater Equipped with a... . . . . . **1138**

Canadas, I.
Accelerated Ageing Test Bench for Advanced Ceramic Slabs under Extreme and Controlled... . . . . . **1495**

Canals, V.
100% of Renewable Energies at Mallorca Hotels **1921**

Candelario, V.M.
Accelerated Ageing Test Bench for Advanced Ceramic Slabs under Extreme and Controlled... . . . . . **1495**

Canosci, E.
Hidden Colored Building Integrated Photovoltaics: Technology Overview and Design... . . . . . **88**

Carbonell, D.
Buried Twin Pipe Model Validation for System Simulations of Ice Storage Tanks in... . . . . . **1070**

Cardemil, J.M.
Hybrid Solar Thermal Field (FPC-PTC) Applied for Solar Heating and Cooling Process... . . . . . **576**

Castell, A.
Covering Energy Demands of Africa with Radiative Cooling and Solar Collection using... . . . . . **583**
Mapping Radiative Cooling Potential Predictions for Africa **1613**

Castro, J.
Experimental Testing of a Solar Thermal Collector with composited TIM of Plastic... . . . . . **1121**
Numerical modeling and simulation comparisons of a cost efficient novel CPVT Solar... . . . . . **1128**

Cazorla-Marín, A.
Modeling of a Solar Heat for Industrial Processes (SHIP) System using Fresnel Collectors **396**

Chhugani, B.
Decarbonizing Heating Supply Systems in Existing Single-family Houses Through PVT... . . . . . **606**
Numerical Study of the Effect of Hybrid Solar Collectors on the Performances of the... . . . . . **768**
Techno-Economical Assessment of a Solar Regenerated Borehole Heat Exchanger Field... . . . . . **360**

Choi, H.J.
Radiant Cooling System without Any Energy Input **213**

Chouket, M.
Efficiency of Electricity Self-Production for Medium Voltage Subscribers in Tunisia **1876**
Electric Self-production for LV Subscribers: Is It Better to Have Decentralized or... . . . . . **1857**

Christodoulaki, R.
The Application of Concentrating Solar Thermal Systems in Hospital Buildings **516**

Civioc, R.
Optimized Adsorption Heat Pump for Efficiency Increase of District Heating Networks **312**

Coca-Ortegón, A.
Energy Performance of Four Prototypes of PVT Collectors. A Comparative Study **690**

Comino, F.
Energy Analysis Of A Solar-Driven Hybrid Air Conditioning System With An Absorption... . . . . . **566**

Commandeur, L.
Parabolic Trough Collector (PTC) System for Combined Cooling and Heating Supply for... . . . . . **559**

Coronas, A.
Energy Analysis Of A Solar-Driven Hybrid Air Conditioning System With An Absorption... . . . . . **566**

Costa, A.
Quality Assurance Procedure for Solar Radiation at Minute Resolution **1601**

Costa Pereira, S.C.
Characterization of Enhanced Biobased Phase Change Material with Graphene Nanoplatelets **1374**

Cruickshank, C.A.
Modelling Analysis of Phase Change Materials for Reducing Cold Climate Space Conditioning... . . . . . **1254**

Curto, I.
ATLAS-FeliCity: Supporting Energy Retrofit of the Heritage Building Stock Through... . . . . . **178**

D

Daborer-Prado, N.
Development of a Virtual Sensor for State-of-Charge Evaluation of TCM-Energy Storage **1484**
Load Management for Seasonal Heat Storage Applications based on Sorption Storage... . . . . . **1295**

Dabrock, K.
The Potential of Combined PV and Air Source Heat Pump Systems in German Residential... . . . . . **738**

Daguenet, X.
Optimized Adsorption Heat Pump for Efficiency Increase of District Heating Networks **312**

Dahash, A.
Techno-Economic Comparison of Steam Generation Systems with Industrial Heat Pumps **384**

Dai, Y.
Comparative Analysis of the Performance of Four Different Photovoltaic-Thermal Modules **672**

David, A.
Comparison of the Simulated and Measured Performance of the PV Plant of Austria's... . . . . . **894**
Data-Driven Approach Utilising Random Forest Regression for PV Performance Monitoring **1699**

David Hernández, M.A.
Modeling of a Solar Heat for Industrial Processes (SHIP) System using Fresnel Collectors **396**

de Keizer, C.
Prefabricated Renewable Energy Facades for Cost-effective Buildings (PREFAB) **702**

Delachaux, V.
Simplified Thermal Performance Model for the Design of a PVT Heat Exchanger Dedicated... . . . . . **618**

Demasles, H.
Experimental Investigation on Solar-Driven GAX-based Absorption Heat pump for Domestic... . . . . . **811**

de Medeiros, J.
Detection of Tracker Failures for a 2-Axis Photovoltaic System **1688**
Quality Assurance Procedure for Solar Radiation at Minute Resolution **1601**

de Medeiros, J.V.F.F.
A Comparison of Eight Transposition Models Applied for Different Orientations Under... . . . . . **1666**

de Melo Filho, J.B.
A Comparison of Eight Transposition Models Applied for Different Orientations Under... . . . . . **1666**

Demonchy, G.
Performance Monitoring of an 800m2 Solar Thermal Plant with Evacuated Flat Plate... . . . . . **234**

Derai, A.
Evaluation of Building Energy Performance: Comparison Before and After Envelope Retrofitting **133**

Dermentzis, G.
Heat Pumps, Photovoltaics and Energy Storage in Buildings –Load Characteristics and... . . . . . **1058**
Modelling and Simulation of Booster Heat Pump for DHW Preparation in a Multi-Family... . . . . . **1046**
Towards Net-Zero Neighborhoods in Greece **1010**

Dhar, A.
A Performance Analysis of a Parabolic Trough Collector using Numerical Computation... . . . . . **1222**

Diarce, G.
Kinetic Analysis of TGA Measurements When Evaporation Is a Degradation Process in... . . . . . **1402**

Díez-Mediavilla, M.
Evaluation of Angular Distribution Models to Estimate Sky Diffuse Irradiance on Tilted... . . . . . **1019**

Dimoudi, A.
The Application of Concentrating Solar Thermal Systems in Hospital Buildings **516**

Djebbar, R.
Increasing Renewable Energy Integration using Advanced Residential Thermal Energy... . . . . . **1304**

Dongellini, M.
Annual Energy Performance of a Solar/Biomass HVAC System: Experimental Characterization... . . . . . **528**

Dörenkämper, M.
Prefabricated Renewable Energy Facades for Cost-effective Buildings (PREFAB) **702**

Dreier, A.
Sustainable and Efficient Energy Supply for the Development of Tourist Villages at... . . . . . **110**

Drosou, V.
The Application of Concentrating Solar Thermal Systems in Hospital Buildings **516**

Drück, H.
Definitions for Climate Neutrality and their Relevance for the Assessment of Solar... . . . . . **1867**
Development of a Combined Model Predictive and Adaptive Control Strategy for the... . . . . . **350**
Quasi-Dynamic Testing of Thermal Sun Air Collectors and Numerical Simulations of... . . . . . **263**

Drueck, H.
Cost-Effective Energy Balancing of Thermal Systems Based on Temperature Measurements... . . . . . **1561**

Dubey, S.K.
Numerical Investigation of Energy Absorption in Dual Metal Hydride Bed based Thermo-Chemical... . . . . . **1315**

Dudita Kauffeld, M.
Aluminium-Redox-Cycles for the Production of Heat and Electricity in Buildings based... **1819**

Durán-García, M.D.
Validation of an Alternative Methodology for Direct Steam Generation Modelling in... **1149**

Duret, A.
Operability of District Heating Plants Combining a Large-Scale Solar Thermal Field... **243**
Optimized Adsorption Heat Pump for Efficiency Increase of District Heating Networks **312**
Performance Monitoring of an 800m2 Solar Thermal Plant with Evacuated Flat Plate... **234**

Dusek, S.
Techno-Economic Comparison of Steam Generation Systems with Industrial Heat Pumps **384**

E

Eames, P.
Optimisation of a Theoretical 4th Generation District Heating Network located at... **290**
The Experimental Performance Characterisation of a Three Module Phase Change Energy... **1327**

Ebadi, H.
Numerical Investigation of the Performance of a Solar Air Heater Equipped with a... **1138**

Edenhofner, F.
Building Information Modeling for Solar Energy Systems **1737**

Ehrenwirth, M.
Agri Solar Thermal Systems: A Brief Study on the Energetic Potential of Bifacial... **1245**
Experimental Investigation of a Novel Hybrid Heat Pump **824**
Mini-Grid or Grid Extension? The Strategies for Electrification Schemes Concerning... **1909**
Sustainable Housing Insulation for High-Altitude Kyrgyzstan: A Technical Guide **58**
Technical Feasibility Study of Micro-Grid Integration to Electrify Rural Settlements... **1897**

Eicker, U.
Analysis of Constructive Modifications for Enhancing the Performance of Solar Collector/Regenerators... **540**
A New Method for Determining the Nusselt and Sherwood Numbers in Simultaneous Heat... **550**

Ekere, N.N.
Investigation of Creep-Fatigue Lifetime in Solar Photovoltaic Module Interconnections **630**

ELAHEE, M.K.
Renewable Energy Education: Gendered Design and Innovation in the Context of a Small... **1929**

Elayeb, M.
Study and Simulation of Low Energy Solar Powered House in Libya **1**

Elmalleh, K.
Efficiency of Electricity Self-Production for Medium Voltage Subscribers in Tunisia **1876**

El-Morsi, M.
Estimating Rooftops' Suitability for PVs Using Pleiades-1B Satellite Image for Charging... **965**

Elvins, J.
A Novel Alginate/Expanded Graphite based Composite for use in Solar and Waste Heat... **1434**
Development of an Open System for Evaluating Material Charging Characteristics from... **1422**

Erban, C.
Fire Protection Requirements and Solutions for the Implementation of BIPV on a High-Rise... **645**

Erden Topal, Y.
Promotion of Solar Heat in Industrial Processes: Policy and Law Analysis with Focus... . . . . . **1884**

Escobar, R.A.
Hybrid Solar Thermal Field (FPC-PTC) Applied for Solar Heating and Cooling Process... . . . . . **576**

Eslami Majd, A.
Investigation of Creep-Fatigue Lifetime in Solar Photovoltaic Module Interconnections **630**

Exner, D.
ATLAS-FeliCity: Supporting Energy Retrofit of the Heritage Building Stock Through... . . . . . **178**

F

Fadl, M.
The Experimental Performance Characterisation of a Three Module Phase Change Energy... . . . . . **1327**

Fan, J.
Effect of Design Characteristics on Pit Thermal Energy Storage (PTES) Performance **1457**

Febrer, R.
Experimental Testing of a Solar Thermal Collector with composited TIM of Plastic... . . . . . **1121**

Feike, F.
Direct Excess Heat Utilization from a High Performance Computer in an Existing Unrenovated... . . . . . **324**

Felsmann, C.
About the Efficiency of District Heating with Flexible Heat and Temperature Distribution **302**
Integration of Renewable Energies into Cityscape **987**
Measures for Energy Optimization for Resource-Saving Consumption Development on a... . . . . . **875**

Ferchichi, S.
An Energy Trading Model for a Lab-scale PV Microgrid in the Tunisian Context **11**

Fernández, C.
Optimal Control Based on Deep Learning Techniques for a Hybrid Solar-Biomass System... . . . . . **1811**

Fernández-Reche, J.
Accelerated Ageing Test Bench for Advanced Ceramic Slabs under Extreme and Controlled... . . . . . **1495**

Ferrer Tevar, J.A.
Thermal Energy Storage Capacity on Mineral Zeolite **1445**

Ferry, A.
A new Framework to Evaluate the Adequation between the Solar Potential and Energy... . . . . . **1581**

Fieback, T.
Monitoring Results of the Energy Consumption Behaviour of Two Highly Solar-Powered... . . . . . **82**

Filho, J.B.
Quality Assurance Procedure for Solar Radiation at Minute Resolution **1601**

Fischer, S.
Accelerated Aging Test and Service Life Time Estimation for Solar Collectors **1503**
Quasi-Dynamic Testing of Thermal Sun Air Collectors and Numerical Simulations of... . . . . . **263**

Fleig, D.
Energy Savings for Gas Preheating in the Gas Transport Sector with Air Dehumidification... . . . . . **479**

Fluch, J.
Standardized Economic Evaluation Criteria of Solar Process Heat in Hybrid Systems... . . . . . **1890**

Foss, S.E.
Comparative Analysis of the Performance of Four Different Photovoltaic-Thermal Modules **672**

Fox, S.
Identification of Temperature Reduction Potentials in Heating Circuits based on Measurements **906**

FRAISSE, G.
Failure Risk Analysis of Photovoltaic Systems Based on Literature Review **660**

Friebe, M.
A Holistic Energetic Transformation Concept for the Heating and Cooling Supply of... . . . . . **953**

Frühschütz, L.
Solar Decathlon - New Ways of Construction for Decarbonised Buildings **30**

Fuente, R.
A PVT Driven Direct Expansion Heat Pump Field Operation Results **683**

Fueyo, N.
A new Framework to Evaluate the Adequation between the Solar Potential and Energy... . . . . . **1581**

Funtan, P.
Fire Protection Requirements and Solutions for the Implementation of BIPV on a High-Rise... . . . . . **645**

Furbo, S.
Effect of Design Characteristics on Pit Thermal Energy Storage (PTES) Performance **1457**
Numerical Investigation of a Large-Scale Water Pit Heat Storage **1344**
Solar Energy Buildings with High Degree of Independence of Energy Supply from Grids **70**

G

Gäbler, A.
Monitoring Results of the Energy Consumption Behaviour of Two Highly Solar-Powered... . . . . . **82**

GAILLARD, L.
Failure Risk Analysis of Photovoltaic Systems Based on Literature Review **660**

Gaisberger, L.
Data-Based Modeling of High-Resolution Household Load Profiles **1728**
Load Management for Seasonal Heat Storage Applications based on Sorption Storage... . . . . . **1295**

Galdino, J.
A Comparison of Eight Transposition Models Applied for Different Orientations Under... . . . . . **1666**
Quality Assurance Procedure for Solar Radiation at Minute Resolution **1601**

Galindo, J.
Accelerated Ageing Test Bench for Advanced Ceramic Slabs under Extreme and Controlled... . . . . . **1495**

Galmarini, S.
Optimized Adsorption Heat Pump for Efficiency Increase of District Heating Networks **312**

Galteland, O.
Demonstration of a Latent Heat Storage Unit Using a Pillow-Plate Heat Exchanger in... . . . . . **1338**

Gambardella, A.
A Novel Method for Assessing the Techno-Economical Compatibility of Solar Thermal... . . . . . **408**

Gantenbein, P.
Optimized Adsorption Heat Pump for Efficiency Increase of District Heating Networks **312**

Gao, M.
Numerical Investigation of a Large-Scale Water Pit Heat Storage **1344**

García, I.
Evaluation of Angular Distribution Models to Estimate Sky Diffuse Irradiance on Tilted... . . . . . **1019**
Towards a More Sustainable Campus, Proposal of Improvement Through Renewable Energies... . . . . . **918**

García, R.
Kinetic Analysis of TGA Measurements When Evaporation Is a Degradation Process in... . . . . . **1402**

García, R.J.
Study of Thermal Degradation of Adipic Acid as PCM under Stress Conditions: A Kinetic... . . . . . **1265**

García-Fuente, M.
Towards a More Sustainable Campus, Proposal of Improvement Through Renewable Energies... . . . . . **918**

García-Rodríguez, A.
Towards a More Sustainable Campus, Proposal of Improvement Through Renewable Energies... . . . . . **918**

García-Rodríguez, S.
Towards a More Sustainable Campus, Proposal of Improvement Through Renewable Energies... . . . . . **918**

García-Romero, A.
Kinetic Analysis of TGA Measurements When Evaporation Is a Degradation Process in... . . . . . **1402**

Garrachón-Gómez, E.
Towards a More Sustainable Campus, Proposal of Improvement Through Renewable Energies... . . . . . **918**

Gayaneh, I.
Load Management for Seasonal Heat Storage Applications based on Sorption Storage... . . . . . **1295**

Gentile, N.
Evaluating the Potential of Annual Solar Heat Gains from Manually Operated Shading... . . . . . **49**

Georgii, M.
Digital Representation of Heating Systems for Fault Detection Purposes **1711**
Fault Detection for Solar Thermal Systems: Evaluation and Improvement of Existing... . . . . . **1553**
Flow Rate Estimation In Glandless Circulator Pumps - Influence Of Temperature And... . . . . . **1543**

Gerber, A.
Solar Decathlon - New Ways of Construction for Decarbonised Buildings **30**

Gereige, I.
Efficiency Evaluation and Comparisons of Solar Cell Technologies Based on Measurements... . . . . . **1747**
KNN-Based Ensembles for Day-Ahead Forecasting of Solar Power Outputs **1755**

Ghasemi, M.
Comparative Techno-Economic Analysis of High Temperature Heat Pump and Parabolic... . . . . . **456**

Gil, J.D.
Hybrid Solar Thermal Field (FPC-PTC) Applied for Solar Heating and Cooling Process... . . . . . **576**

Giovannetti, F.
A TRNSYS Type for the Simulation of Temperature Limiting Heat Pipe Collectors **1717**
Building Information Modeling for Solar Energy Systems **1737**
Collector Efficiency Curves considering an Adapted Calculation Approach for Convective... . . . . . **1170**
Decarbonizing Heating Supply Systems in Existing Single-family Houses Through PVT... . . . . . **606**

Gomes, E.
A Comparison of Eight Transposition Models Applied for Different Orientations Under... . . . . . **1666**
Quality Assurance Procedure for Solar Radiation at Minute Resolution **1601**

Gomes, E.T.A.
Detection of Tracker Failures for a 2-Axis Photovoltaic System **1688**

Gómez Castro, F.M.
Analysis of Constructive Modifications for Enhancing the Performance of Solar Collector/Regenerators... . . . **540**
A New Method for Determining the Nusselt and Sherwood Numbers in Simultaneous Heat... . . . . . **550**

Gómez Samper, A.
A new Framework to Evaluate the Adequation between the Solar Potential and Energy... . . . . . **1581**

Gonzalez-Mora, E.
Validation of an Alternative Methodology for Direct Steam Generation Modelling in... . . . . . **1149**

González-Peña, D.
Evaluation of Angular Distribution Models to Estimate Sky Diffuse Irradiance on Tilted... . . . . . **1019**
Towards a More Sustainable Campus, Proposal of Improvement Through Renewable Energies... . . . . . **918**

Gonzálvez Macia, J.
Modeling of a Solar Heat for Industrial Processes (SHIP) System using Fresnel Collectors **396**

Gothe, T.
Energy Scenarios: Designing the Renewable World of Tomorrow Together **1942**

Granados-López, D.
Evaluation of Angular Distribution Models to Estimate Sky Diffuse Irradiance on Tilted... . . . . . **1019**
Towards a More Sustainable Campus, Proposal of Improvement Through Renewable Energies... . . . . . **918**

Graßmann, A.
Development of a Small-Scale Plant for Electricity and Water Supply in Rural Regions... . . . . . **1970**

Greiner, A.
Optimal Conceptual Design of a Novel Façade-Integrated Adsorption Cooling System **595**

Gross, R.
SmartPrioGIS - A Concept for Recording, Holding and Evaluating Data as a Contribution... . . . . . **926**

Groulx, D.
Characterization of Enhanced Biobased Phase Change Material with Graphene Nanoplatelets **1374**

Guedea, I.
Energy Performance of Four Prototypes of PVT Collectors. A Comparative Study **690**

Gulden, J.
Renewable Energy and PtX-Technologies in Education **1985**

Gumhalter, M.
Participation Potential for Energy-Active Facades in Future Flexibility Markets **190**

Gurgenci, H.
Thermal Performance of Eccentric High-Temperature Latent Heat Storage System: Passive... . . . . . **1410**

H

Haas, F.
ATLAS-FeliCity: Supporting Energy Retrofit of the Heritage Building Stock Through... . . . . . **178**

Haase, M.
Comparison of Solar Planning Tools **1029**
Renovation Towards NZEB with PV **145**

Haberl, R.
Annual Energy Performance of a Solar/Biomass HVAC System: Experimental Characterization... . . . . . **528**
Comparison of a Centralized with Decentralized Heat Pump Systems in a Multy Family... . . . . . **748**
DHW Tanks - 40 % Savings by Better Stratification **1515**

Hadi, A.
Gap Filling in Solar Radiation Data using Artificial Neural Network for Nine Stations... . . . . . **1657**

Hafner, B.
Development of a Combined Model Predictive and Adaptive Control Strategy for the... . . . . . **350**
Quasi-Dynamic Testing of Thermal Sun Air Collectors and Numerical Simulations of... . . . . . **263**

Haller, M.
100 % Solar Heating with Seasonal Thermal Storage, Solar Thermal Collectors, PV and... . . . . . **202**
Aluminium-Redox-Cycles for the Production of Heat and Electricity in Buildings based... . . . . . **1819**
Renovation of a Multi-Family-House with External Wall Heating System **121**

Haller, M.Y.
Comparison of a Centralized with Decentralized Heat Pump Systems in a Multy Family... . . . . . **748**
DHW Tanks - 40 % Savings by Better Stratification **1515**
Increasing PV Self-Consumption with Heat Pumps – Sense or Non-Sense of additional... . . . . . **756**

Han, G.
Energy Performance Investigation of PVT Assisted Heat Pump System for a Net Zero... . . . . . **642**

Harrison, S.
Development and Indoor Testing of a High-Performance PV/thermal (PVT) Panel with... . . . . . **1215**

Hassan, A.
Dual Axis Optimization of Solar Photovoltaic at Various Sites in Pakistan **1649**
Gap Filling in Solar Radiation Data using Artificial Neural Network for Nine Stations... . . . . . **1657**

Heinz, A.
Increasing PV Self-Consumption with Heat Pumps – Sense or Non-Sense of additional... . . . . . **756**

Helminger, F.
Techno-Economic Comparison of Steam Generation Systems with Industrial Heat Pumps **384**

Helmling, S.
Operational Analysis of 5 PVT Heat Pump Systems Based on Field Measurement Data **1526**

Hendrix, A.
Evaluating the Potential of Annual Solar Heat Gains from Manually Operated Shading... . . . . . **49**

Höhn, O.
Angel-Dependent Features of MorphoColor TM Solar Collectors: Color Stability, IAM,... . . . . . **1195**

Holway, S.
Using Heat Maps to Assess the Energy Efficiency of Industrial Companies **420**

I

Ibañez, P.
A PVT Driven Direct Expansion Heat Pump Field Operation Results **683**

Ileka, H.
Mini-Grid or Grid Extension? The Strategies for Electrification Schemes Concerning... . . . . . **1909**
Technical Feasibility Study of Micro-Grid Integration to Electrify Rural Settlements... . . . . . **1897**

Indranil, R.
Development and Indoor Testing of a High-Performance PV/thermal (PVT) Panel with... . . . . . **1215**

Irfan, M.
Dual Axis Optimization of Solar Photovoltaic at Various Sites in Pakistan **1649**

Issayan, G.
Development of a Virtual Sensor for State-of-Charge Evaluation of TCM-Energy Storage **1484**
Sorption Test Bench for Zeolite and Salt-Composite Based Thermochemical Storage **1355**

J

Jaafar, M.A.
Numerical Study of the Effect of Hybrid Solar Collectors on the Performances of the... . . . . . **768**

Jain, S.
Performance Investigation on Cascade Latent Heat Storage for Various Geometric Orientations **1362**

Jamal, A.
Efficiency Evaluation and Comparisons of Solar Cell Technologies Based on Measurements... . . . . . **1747**

Janybek, O.
Impact of Domestic Hot Water Preparation Systems on District Heating Network Design... . . . . . **225**

Jaspers, K.
The Future of Solar Integration: Towards Efficiency in Solar Design through Aesthetics,... . . . . . **37**

Jatoba, E.
A Comparison of Eight Transposition Models Applied for Different Orientations Under... . . . . . **1666**

Jatobá, E.
Quality Assurance Procedure for Solar Radiation at Minute Resolution **1601**

Jensen, A.
Effect of Design Characteristics on Pit Thermal Energy Storage (PTES) Performance **1457**

Jensen, J.
A TRNSYS Type for the Simulation of Temperature Limiting Heat Pipe Collectors **1717**

Jesus D'Oliveira, E.
Characterization of Enhanced Biobased Phase Change Material with Graphene Nanoplatelets **1374**

Jewell, E.
A Novel Alginate/Expanded Graphite based Composite for use in Solar and Waste Heat... . . . . . **1434**
Development of an Open System for Evaluating Material Charging Characteristics from... . . . . . **1422**

Jobard, X.
Operability of District Heating Plants Combining a Large-Scale Solar Thermal Field... . . . . . **243**
Optimized Adsorption Heat Pump for Efficiency Increase of District Heating Networks **312**
Performance Monitoring of an 800m2 Solar Thermal Plant with Evacuated Flat Plate... . . . . . **234**

Johannes, Z.
Impact of Domestic Hot Water Preparation Systems on District Heating Network Design... **225**

Jordan, U.
Analysis of Constructive Modifications for Enhancing the Performance of Solar Collector/Regenerators... **540**
A New Method for Determining the Nusselt and Sherwood Numbers in Simultaneous Heat... **550**
Collector Efficiency Curves considering an Adapted Calculation Approach for Convective... **1170**
Energy Savings for Gas Preheating in the Gas Transport Sector with Air Dehumidification... **479**
Impact of Domestic Hot Water Preparation Systems on District Heating Network Design... **225**
Municipal Heat Planning to Exit from Coal, Oil and Natural Gas in a German Major... **1078**

Juggurnath, D.
Renewable Energy Education: Gendered Design and Innovation in the Context of a Small... **1929**

K

Kalligianaki, E.
Efficiency Evaluation and Comparisons of Solar Cell Technologies Based on Measurements... **1747**
KNN-Based Ensembles for Day-Ahead Forecasting of Solar Power Outputs **1755**

Kamarianakis, Y.
Efficiency Evaluation and Comparisons of Solar Cell Technologies Based on Measurements... **1747**
KNN-Based Ensembles for Day-Ahead Forecasting of Solar Power Outputs **1755**

Kamerling, S.
Data Clustering and Genetic Algorithm for the Design Optimization of a Hybrid Concentrated... **1790**

Kämpf, J.H.
DHgeN: Automated Generation of District Heating Network Layouts for Feasibility Studies **1767**

Kandpal, T.C.
Impact of Incentives Towards Lowering the Levelized Cost of Electricity of Concentrating... **1827**
Techno-Economics of Central Tower Receiver Power Plants in India: Effect of Heat... **1838**

Kannappan, T.
Experimental Studies on Solar Multi - Effect Desalination System **846**
Falling Film Measurements Using High Speed Camera and High Speed Infra-Red Camera **858**

Karellas, S.
Testing a Flexible Configuration of a Solar-Assisted Heat Pump with PVT Collectors... **777**

Katende, J.
Mini-Grid or Grid Extension? The Strategies for Electrification Schemes Concerning... **1909**
Technical Feasibility Study of Micro-Grid Integration to Electrify Rural Settlements... **1897**

Katsaounis, T.
Efficiency Evaluation and Comparisons of Solar Cell Technologies Based on Measurements... **1747**
KNN-Based Ensembles for Day-Ahead Forecasting of Solar Power Outputs **1755**

Kaunda, J.
Mini-Grid or Grid Extension? The Strategies for Electrification Schemes Concerning... **1909**
Technical Feasibility Study of Micro-Grid Integration to Electrify Rural Settlements... **1897**

Ke, X.
A Novel Alginate/Expanded Graphite based Composite for use in Solar and Waste Heat... **1434**

Kelch, J.
Solar District Heating versus Renovation of Buildings as Measures for Decarbonization... . . . . . ***254***

Ketelaars, E.W.
The Future of Solar Integration: Towards Efficiency in Solar Design through Aesthetics,... . . . . . ***37***

Khalifa, I.
An Energy Trading Model for a Lab-scale PV Microgrid in the Tunisian Context ***11***

Khjoa, A.
ATLAS-FeliCity: Supporting Energy Retrofit of the Heritage Building Stock Through... . . . . . ***178***

Khoodaruth, A.
Renewable Energy Education: Gendered Design and Innovation in the Context of a Small... . . . . . ***1929***

Kim, D.
Case Study of a Positive Energy Community for Renewable Energy Sharing ***1041***

Kim, H.
Case Study of a Positive Energy Community for Renewable Energy Sharing ***1041***

Kim, J.
Case Study of a Positive Energy Community for Renewable Energy Sharing ***1041***
Energy Performance Investigation of PVT Assisted Heat Pump System for a Net Zero... . . . . . ***642***

Kim, M.
Case Study of a Positive Energy Community for Renewable Energy Sharing ***1041***
Energy Performance Investigation of PVT Assisted Heat Pump System for a Net Zero... . . . . . ***642***

Kirchsteiger, H.
Data-Based Modeling of High-Resolution Household Load Profiles ***1728***
Development of a Virtual Sensor for State-of-Charge Evaluation of TCM-Energy Storage ***1484***

Kizildag, D.
Experimental Testing of a Solar Thermal Collector with composited TIM of Plastic... . . . . . ***1121***
Numerical modeling and simulation comparisons of a cost efficient novel CPVT Solar... . . . . . ***1128***

Klaus, V.
Impact of Domestic Hot Water Preparation Systems on District Heating Network Design... . . . . . ***225***

Klauß, S.
Derivation of Heating Load Profiles on the Basis of Demand-Consumption Analyses ***934***
SmartPrioGIS - A Concept for Recording, Holding and Evaluating Data as a Contribution... . . . . . ***926***

Klump, D.
Novel Hardware-in-the-Loop Approach for Thermal Systems ***1536***

Knissel, J.
Identification of Temperature Reduction Potentials in Heating Circuits based on Measurements ***906***
Transformation of a University Campus: Comparison of Ranking Methods for Temperature... . . . . . ***941***

Knosala, K.
The Potential of Combined PV and Air Source Heat Pump Systems in German Residential... . . . . . ***738***

König, K.
Scenario based Heating and Cooling Load Profiles in Piglet Production Systems ***436***

Kononenko, N.
A Holistic Energetic Transformation Concept for the Heating and Cooling Supply of... . . . . . ***953***

Kosmadakis, G.
Testing a Flexible Configuration of a Solar-Assisted Heat Pump with PVT Collectors... . . . . . ***777***

Kotegov, R.
Energy Analysis Of A Solar-Driven Hybrid Air Conditioning System With An Absorption... . . . . . ***566***

Kotsovos, K.
Efficiency Evaluation and Comparisons of Solar Cell Technologies Based on Measurements... . . . . . ***1747***
KNN-Based Ensembles for Day-Ahead Forecasting of Solar Power Outputs ***1755***

Kotzur, L.
The Potential of Combined PV and Air Source Heat Pump Systems in German Residential... . . . . . ***738***

Kouakou, A.P.
Development of a Small-Scale Plant for Electricity and Water Supply in Rural Regions... . . . . . ***1970***

Kracht, N.
Techno-Economical Assessment of a Solar Regenerated Borehole Heat Exchanger Field... . . . . . ***360***

Krause, M.
Derivation of Heating Load Profiles on the Basis of Demand-Consumption Analyses ***934***
Fire Protection Requirements and Solutions for the Implementation of BIPV on a High-Rise... . . . . . ***645***

Kre, N.R.
Development of a Small-Scale Plant for Electricity and Water Supply in Rural Regions... . . . . . ***1970***

Kremonke, A.
Measures for Energy Optimization for Resource-Saving Consumption Development on a... . . . . . ***875***

Kriegel, M.
A Holistic Energetic Transformation Concept for the Heating and Cooling Supply of... . . . . . ***953***

Kroyer, T.
Angel-Dependent Features of MorphoColor TM Solar Collectors: Color Stability, IAM,... . . . . . ***1195***

Kuhn, T.
Angel-Dependent Features of MorphoColor TM Solar Collectors: Color Stability, IAM,... . . . . . ***1195***

Kukreja, R.
Numerical Investigation and Performance Evaluation of Food Grain Drying Unit Integrated... . . . . . ***1474***

Kumar, A.
Building Energy Efficiency Enhancement through Load Reduction in Air Conditioning... . . . . . ***98***

KUMAR, K.R.
Thermal Performance of Eccentric High-Temperature Latent Heat Storage System: Passive... . . . . . ***1410***

Kumar, P.
A Performance Analysis of a Parabolic Trough Collector using Numerical Computation... . . . . . ***1222***

Kumar, S.
Effect of HTF Flow Direction on Thermal Performance in an Upward Facing Cavity Receiver ***425***

Kumar, S.R.
Evaluating the Potential of Annual Solar Heat Gains from Manually Operated Shading... . . . . . ***49***

KUMAR PATEL, M.
Metrics Behind the Implementation of Photovoltaic Solar Energy in Urban Area ***20***

Kusyy, O.
Solar District Heating versus Renovation of Buildings as Measures for Decarbonization... . . . . . ***254***

Kütt, M.L.
The Future of Solar Integration: Towards Efficiency in Solar Design through Aesthetics,... . . . . . **37**

L

Laevemann, E.
Experimental Investigation of a Falling Film Horizontal Tube Bundle Absorber for... . . . . . **1396**

Lämmle, M.
Performance of Heat Pump Systems with PVT Collectors with Optimized Finned Heat Exchangers... . . . . . **654**

Lang, X.
Cost-Effective Energy Balancing of Thermal Systems Based on Temperature Measurements... . . . . . **1561**

Lange, H.
Comparative Experiments on a Novel CaCl2-Based Composite Material and Zeolite 13X... . . . . . **1275**

Lara, Y.
Energy Performance of Four Prototypes of PVT Collectors. A Comparative Study **690**

Lázaro, A.
Analysis of Solar Thermal Polygeneration Systems for the Residential-Commercial Sector **97**

Lee, D.
Case Study of a Positive Energy Community for Renewable Energy Sharing **1041**

Leibbrandt, P.
Collector Efficiency Curves considering an Adapted Calculation Approach for Convective... . . . . . **1170**

Leibfried, U.
Modular Refurbishment of Multi-Family Houses with PVT-PCM Heat Pump Systems and Self-Learning... . . . . **715**

Le Pierrès, N.
Comparative Experiments on a Novel CaCl2-Based Composite Material and Zeolite 13X... . . . . . **1275**

Leu, F.
PV Driven Air Heat Pump Using Overheating Effects as Thermal Battery in Single Family... . . . . . **833**

Li, Z.
Comparative Analysis of the Performance of Four Different Photovoltaic-Thermal Modules **672**

Lichtensteiger, F.
100 % Solar Heating with Seasonal Thermal Storage, Solar Thermal Collectors, PV and... . . . . . **202**

Liu, W.
Experimental Investigation on A Novel Flat-Plate Water-Based Photovoltaic-Thermal... . . . . . **1176**

Lobaccaro, G.
A Comparative Study on Solar Radiation Datasets for Photovoltaic Energy Prediction... . . . . . **1589**

Lohse, L.
SmartPrioGIS - A Concept for Recording, Holding and Evaluating Data as a Contribution... . . . . . **926**

Lokurlu, A.
Parabolic Trough Collector (PTC) System for Combined Cooling and Heating Supply for... . . . . . **559**

López Moreno, H.
Thermal Energy Storage Capacity on Mineral Zeolite **1445**

Lott, S.
Quasi-Dynamic Testing of Thermal Sun Air Collectors and Numerical Simulations of... . . . . . **263**

Louvet, Y.
Energy Savings for Gas Preheating in the Gas Transport Sector with Air Dehumidification... . . . . . **479**
Master's Courses at Solar Energy Conferences **1952**

Lozano, M.A.
Analysis of Solar Thermal Polygeneration Systems for the Residential-Commercial Sector **97**

Luzi, G.
Hidden Colored Building Integrated Photovoltaics: Technology Overview and Design... . . . . . **88**

Lwakatare, B.
Mini-Grid or Grid Extension? The Strategies for Electrification Schemes Concerning... . . . . . **1909**
Technical Feasibility Study of Micro-Grid Integration to Electrify Rural Settlements... . . . . . **1897**

Lwiwa, C.
Interception on Solar Absorbers: Ray Tracing for Comparison between a Parabolic Reflector... . . . . . **1184**

Lygnerud, K.
Low Temperature District Heating as a Key Technology for a Successful Integration... . . . . . **330**

M

Maas, A.
Derivation of Heating Load Profiles on the Basis of Demand-Consumption Analyses **934**
SmartPrioGIS - A Concept for Recording, Holding and Evaluating Data as a Contribution... . . . . . **926**

Maccarini, A.
Early-stage Feasibility Study of an Ambient-temperature District Thermal Network:... . . . . . **275**

Madani, H.
Empirical Validation of Low-Temperature PVT Collector for Heat Pump Integration **1109**

Magni, M.
Heat Pumps, Photovoltaics and Energy Storage in Buildings –Load Characteristics and... . . . . . **1058**
Modelling and Simulation of Booster Heat Pump for DHW Preparation in a Multi-Family... . . . . . **1046**

Maier, T.
Building Information Modeling for Solar Energy Systems **1737**

Mandow, W.
Building Information Modeling for Solar Energy Systems **1737**

Manni, M.
A Comparative Study on Solar Radiation Datasets for Photovoltaic Energy Prediction... . . . . . **1589**

Maragna, C.
Implementation of Adapted Black Box Models for the Performance Characterization of... . . . . . **1678**

marcos del Cano, J.D.
Analysis of the Electrical Consumption of an Air-Cooled Single Effect Ammonia/Water... . . . . . **801**

Marcos del Cano, J.D.
Analysis of the Electrical Consumption of an Air-Cooled Single Effect Ammonia/Water... . . . . . **801**

Maret, P.
Comparative Analysis of the Performance of Four Different Photovoltaic-Thermal Modules **672**

Martín, A.J.
A PVT Driven Direct Expansion Heat Pump Field Operation Results **683**

Martinez-Moll, V.
100% of Renewable Energies at Mallorca Hotels **1921**

Martorell, I.
Mapping Radiative Cooling Potential Predictions for Africa **1613**

Masseck, T.
Solar Decathlon Prototypes and their Use as Post-Competition Living Labs in Higher... . . . . . **1961**

Mathieu, A.
Failure Risk Analysis of Photovoltaic Systems Based on Literature Review **660**

Maturi, L.
Hidden Colored Building Integrated Photovoltaics: Technology Overview and Design... . . . . . **88**

Matuska, T.
Modelling and Experimental Verification of an Unglazed Metal Facade Collector Model **1234**

McNevin, C.
Increasing Renewable Energy Integration using Advanced Residential Thermal Energy... . . . . . **1304**

Medrano, M.
Covering Energy Demands of Africa with Radiative Cooling and Solar Collection using... . . . . . **583**

Mehnert, S.
Angel-Dependent Features of MorphoColor TM Solar Collectors: Color Stability, IAM,... . . . . . **1195**

Mehta, K.
Mini-Grid or Grid Extension? The Strategies for Electrification Schemes Concerning... . . . . . **1909**
Sustainable Housing Insulation for High-Altitude Kyrgyzstan: A Technical Guide **58**
Technical Feasibility Study of Micro-Grid Integration to Electrify Rural Settlements... . . . . . **1897**

Meiers, J.
Hardware-in-the-Loop Integration of PVT Models using Internet of Things-enabled Communication **1204**

Meitz, S.
Nexus Energy and Water: Integration Concepts for Solar Energy in Industrial Water... . . . . . **869**

Ménézo, C.
A new Framework to Evaluate the Adequation between the Solar Potential and Energy... . . . . . **1581**

Meramveliotakis, G.
Testing a Flexible Configuration of a Solar-Assisted Heat Pump with PVT Collectors... . . . . . **777**

Mesquita, L.
Development and Indoor Testing of a High-Performance PV/thermal (PVT) Panel with... . . . . . **1215**

Metzler, K.
What Can PV Self-supply Do for System Integration? **1847**

Mhlanga, S.
Design of a Small-scale Maize Dryer **441**

Miranda, D.
A Comparison of Eight Transposition Models Applied for Different Orientations Under... . . . . . **1666**
Detection of Tracker Failures for a 2-Axis Photovoltaic System **1688**
Quality Assurance Procedure for Solar Radiation at Minute Resolution **1601**

Mlecnik, E.
Experiences from Local Authorities Stimulating the Adoption of Low-Carbon Technologies... . . . . . **156**

Moià-Pol, A.
100% of Renewable Energies at Mallorca Hotels **1921**

Monterrubio, J.
Covering Energy Demands of Africa with Radiative Cooling and Solar Collection using... . . . . . **583**
Mapping Radiative Cooling Potential Predictions for Africa **1613**

Morales, A.
Accelerated Ageing Test Bench for Advanced Ceramic Slabs under Extreme and Controlled... . . . . . **1495**

Morini, G.L.
Annual Energy Performance of a Solar/Biomass HVAC System: Experimental Characterization... . . . . . **528**

Müller, R.
Fire Protection Requirements and Solutions for the Implementation of BIPV on a High-Rise... . . . . . **645**

Munz, G.
Performance of Heat Pump Systems with PVT Collectors with Optimized Finned Heat Exchangers... . . . . . **654**

Mussard, M.
Comparative Analysis of the Performance of Four Different Photovoltaic-Thermal Modules **672**

Muusha, P.
Design of a Small-scale Maize Dryer **441**

N

Nadeem, A.
Dual Axis Optimization of Solar Photovoltaic at Various Sites in Pakistan **1649**

Naldi, C.
Annual Energy Performance of a Solar/Biomass HVAC System: Experimental Characterization... . . . . . **528**

Nawaz, I.
Gap Filling in Solar Radiation Data using Artificial Neural Network for Nine Stations... . . . . . **1657**

Nefodov, D.
Emission-Free Heat Supply of Residential Districts with Solar Thermal Energy and... . . . . . **789**

Neto, A.
A Comparison of Eight Transposition Models Applied for Different Orientations Under... . . . . . **1666**
Quality Assurance Procedure for Solar Radiation at Minute Resolution **1601**

Neugebauer, M.
Buried Twin Pipe Model Validation for System Simulations of Ice Storage Tanks in... . . . . . **1070**
Renovation of a Multi-Family-House with External Wall Heating System **121**

Neususess, H.
Transformation of a University Campus: Comparison of Ranking Methods for Temperature... . . . . . **941**

Newiadomsky, C.
Development of a Small-Scale Plant for Electricity and Water Supply in Rural Regions... . . . . . **1970**

Nielsen, E.
Solar Energy Buildings with High Degree of Independence of Energy Supply from Grids **70**

Nitz, P.
Standardized Economic Evaluation Criteria of Solar Process Heat in Hybrid Systems... . . . . . **1890**

Nocente, A.
A Comparative Study on Solar Radiation Datasets for Photovoltaic Energy Prediction... . . . . . **1589**

Novaes, G.
Detection of Tracker Failures for a 2-Axis Photovoltaic System **1688**

Nycz, P.
The Experimental Performance Characterisation of a Three Module Phase Change Energy... . . . . . **1327**

Nydal, O.
Interception on Solar Absorbers: Ray Tracing for Comparison between a Parabolic Reflector... . . . . . **1184**

O

Ochs, F.
Heat Pumps, Photovoltaics and Energy Storage in Buildings –Load Characteristics and... . . . . . **1058**
Heat Pumps in Positive Energy Districts **1085**
Modelling and Simulation of Booster Heat Pump for DHW Preparation in a Multi-Family... . . . . . **1046**

Oestreich, F.
Loading Slim Hot Water Tanks with and without Swirl Generation - First Results **1384**

Olmedo Mezcua, R.
Thermal Energy Storage Capacity on Mineral Zeolite **1445**

Omlin, L.
Annual Energy Performance of a Solar/Biomass HVAC System: Experimental Characterization... . . . . . **528**

Ondarts, M.
Comparative Experiments on a Novel CaCl2-Based Composite Material and Zeolite 13X... . . . . . **1275**

Oppelt, L.
Monitoring Results of the Energy Consumption Behaviour of Two Highly Solar-Powered... . . . . . **82**

Orozaliev, J.
Applying Machine Learning Methods and Outlier Detection to Process and Analyse Incomplete... . . . . . **1782**
Development of Models for Long-Term Simulations of District Heating Networks at High... . . . . . **1802**
Digital Representation of Heating Systems for Fault Detection Purposes **1711**
Fault Detection for Solar Thermal Systems: Evaluation and Improvement of Existing... . . . . . **1553**
Flow Rate Estimation In Glandless Circulator Pumps - Influence Of Temperature And... . . . . . **1543**
Identification of Waste Heat Potentials and Their Integration Into a District Heating... . . . . . **884**
Municipal Heat Planning to Exit from Coal, Oil and Natural Gas in a German Major... . . . . . **1078**
Solar District Heating versus Renovation of Buildings as Measures for Decarbonization... . . . . . **254**
Transformation of a University Campus: Comparison of Ranking Methods for Temperature... . . . . . **941**

Outin, J.
Comparative Experiments on a Novel CaCl2-Based Composite Material and Zeolite 13X... . . . . . **1275**

Ozarisoy, B.
A Novel Statistical Method to Improve Energy Efficiency of Housing Stock in the Eastern... . . . . . **166**

P

Pag, F.

Applying Machine Learning Methods and Outlier Detection to Process and Analyse Incomplete... **1782**
Energy Savings for Gas Preheating in the Gas Transport Sector with Air Dehumidification... **479**
How To Combine a Solar Heating Plant and a CHP most Efficiently for Industrial Applications? **450**
Scenario based Heating and Cooling Load Profiles in Piglet Production Systems **436**
Standardized Economic Evaluation Criteria of Solar Process Heat in Hybrid Systems... **1890**
Using Heat Maps to Assess the Energy Efficiency of Industrial Companies **420**

Palacios Lorenzo, M.

Analysis of the Electrical Consumption of an Air-Cooled Single Effect Ammonia/Water... **801**

Panitz, F.

Software-supported Investment Optimization for District Heating Supply Systems **282**

Pans Castillo, M.A.

Optimisation of a Theoretical 4th Generation District Heating Network located at... **290**

Pantazis, Y.

Efficiency Evaluation and Comparisons of Solar Cell Technologies Based on Measurements... **1747**
KNN-Based Ensembles for Day-Ahead Forecasting of Solar Power Outputs **1755**

Papadopoulos, A.

Towards Net-Zero Neighborhoods in Greece **1010**

Pärisch, P.

Decarbonizing Heating Supply Systems in Existing Single-family Houses Through PVT... **606**
Techno-Economical Assessment of a Solar Regenerated Borehole Heat Exchanger Field... **360**

Park, S.

Optimal Conceptual Design of a Novel Façade-Integrated Adsorption Cooling System **595**

Pauletta, S.

Performance Monitoring of an 800m2 Solar Thermal Plant with Evacuated Flat Plate... **234**

Paulick, S.

About the Efficiency of District Heating with Flexible Heat and Temperature Distribution **302**

Paya Herrero, J.

Modeling of a Solar Heat for Industrial Processes (SHIP) System using Fresnel Collectors **396**

Pelle, M.

Hidden Colored Building Integrated Photovoltaics: Technology Overview and Design... **88**

Pereda, A.

A PVT Driven Direct Expansion Heat Pump Field Operation Results **683**

Pereira, A.

A Comparison of Eight Transposition Models Applied for Different Orientations Under... **1666**
Quality Assurance Procedure for Solar Radiation at Minute Resolution **1601**

Perez, M.

24/365 Firm Solar Power Generation in Switzerland **1638**

Perez, R.

24/365 Firm Solar Power Generation in Switzerland **1638**

Perez-Astudillo, D.
Assessment of Downward Longwave Radiation Models in Clear-Sky Desert Conditions **1574**
Management and Operation of Qatar's Solar Radiation Monitoring Network **1620**

Pérez-Garcia, M.
Hybrid Solar Thermal Field (FPC-PTC) Applied for Solar Heating and Cooling Process... . . . . . **576**

Perez Segarra, C.D.
Parametric Study of Structured Thermocline Storage Systems **1464**

Peronato, G.
DHgeN: Automated Generation of District Heating Network Layouts for Feasibility Studies **1767**

Petribú, L.
Quality Assurance Procedure for Solar Radiation at Minute Resolution **1601**

Pflugradt, N.
The Potential of Combined PV and Air Source Heat Pump Systems in German Residential... . . . . . **738**

Phan, H.T.
Experimental Investigation on Solar-Driven GAX-based Absorption Heat pump for Domestic... . . . . . **811**

Philippen, D.
Renovation of a Multi-Family-House with External Wall Heating System **121**

Phu, V.L.
Study on Analysis of Solar Panel Efficiency in Vietnam a Power Comparison Before... . . . . . **1629**

Piccoli, E.
Optimized Adsorption Heat Pump for Efficiency Increase of District Heating Networks **312**

Pilou, M.
Testing a Flexible Configuration of a Solar-Assisted Heat Pump with PVT Collectors... . . . . . **777**

Pina, E.A.
Analysis of Solar Thermal Polygeneration Systems for the Residential-Commercial Sector **97**

Pino, A.
How To Combine a Solar Heating Plant and a CHP most Efficiently for Industrial Applications? **450**

PIOT, A.
Evaluation of Building Energy Performance: Comparison Before and After Envelope Retrofitting **133**

Polo López, C.S.
ATLAS-FeliCity: Supporting Energy Retrofit of the Heritage Building Stock Through... . . . . . **178**

POORUN, S.(.
Renewable Energy Education: Gendered Design and Innovation in the Context of a Small... . . . . . **1929**

Premachandran, B.
Performance Investigation on Cascade Latent Heat Storage for Various Geometric Orientations **1362**

Pressl, D.
Experimental Investigation of a Falling Film Horizontal Tube Bundle Absorber for... . . . . . **1396**

Prieto, C.
New Concept for High Temperature Thermal Energy Storage Using a Concrete Tank **1285**

Prieto, J.
Energy Analysis Of A Solar-Driven Hybrid Air Conditioning System With An Absorption... . . . . . **566**

Q

Quant, L.
Study of Thermal Degradation of Adipic Acid as PCM under Stress Conditions: A Kinetic... . . . . . **1265**

Quant Colón, L.
Kinetic Analysis of TGA Measurements When Evaporation Is a Degradation Process in... . . . . . **1402**

R

Rahmati Darvazi, A.
Investigation of Creep-Fatigue Lifetime in Solar Photovoltaic Module Interconnections **630**

Rakshit, D.
Building Energy Efficiency Enhancement through Load Reduction in Air Conditioning... . . . . . **98**
Performance Investigation on Cascade Latent Heat Storage for Various Geometric Orientations **1362**
Spectral Beam Splitting in Compound Parabolic Collector Based Photovoltaic Thermal... . . . . . **1097**
Thermal Performance of Eccentric High-Temperature Latent Heat Storage System: Passive... . . . . . **1410**

Ramesh, A.
Parabolic Trough Collector (PTC) System for Combined Cooling and Heating Supply for... . . . . . **559**

Ramschak, T.
Participation Potential for Energy-Active Facades in Future Flexibility Markets **190**

Rangaraju, S.
Study on Analysis of Solar Panel Efficiency in Vietnam a Power Comparison Before... . . . . . **1629**

Ray, A.K.
Thermal Performance of Eccentric High-Temperature Latent Heat Storage System: Passive... . . . . . **1410**

Raza, A.H.
Gap Filling in Solar Radiation Data using Artificial Neural Network for Nine Stations... . . . . . **1657**

Raza, H.
Dual Axis Optimization of Solar Photovoltaic at Various Sites in Pakistan **1649**

Reddy, K.S.
Performance Investigation on Cascade Latent Heat Storage for Various Geometric Orientations **1362**

Reiter, J.
Standardized Economic Evaluation Criteria of Solar Process Heat in Hybrid Systems... . . . . . **1890**

Remund, J.
24/365 Firm Solar Power Generation in Switzerland **1638**

Resch, A.
Development of a Virtual Sensor for State-of-Charge Evaluation of TCM-Energy Storage **1484**

Reum, T.
Experimental Investigation of a Novel Hybrid Heat Pump **824**
Novel Hardware-in-the-Loop Approach for Thermal Systems **1536**

Reynolds, J.
A Novel Alginate/Expanded Graphite based Composite for use in Solar and Waste Heat... . . . . . **1434**
Development of an Open System for Evaluating Material Charging Characteristics from... . . . . . **1422**

Richter, M.
Emission-Free Heat Supply of Residential Districts with Solar Thermal Energy and... . . . . . **789**

Riedl, J.
Techno-Economic Comparison of Steam Generation Systems with Industrial Heat Pumps **384**

Rigola, J.
Numerical modeling and simulation comparisons of a cost efficient novel CPVT Solar... . . . . . **1128**

Rincón, L.
Mapping Radiative Cooling Potential Predictions for Africa **1613**

Rodríguez, J.
Accelerated Ageing Test Bench for Advanced Ceramic Slabs under Extreme and Controlled... . . . . . **1495**

Roefs, L.H.H.M.
The Future of Solar Integration: Towards Efficiency in Solar Design through Aesthetics,... . . . . . **37**

Rojas, E.
Kinetic Analysis of TGA Measurements When Evaporation Is a Degradation Process in... . . . . . **1402**
Study of Thermal Degradation of Adipic Acid as PCM under Stress Conditions: A Kinetic... . . . . . **1265**

Roman, E.
A PVT Driven Direct Expansion Heat Pump Field Operation Results **683**

Rosales-Pérez, J.F.
Hybrid Solar Thermal Field (FPC-PTC) Applied for Solar Heating and Cooling Process... . . . . . **576**

Ruesch, F.
100 % Solar Heating with Seasonal Thermal Storage, Solar Thermal Collectors, PV and... . . . . . **202**
Buried Twin Pipe Model Validation for System Simulations of Ice Storage Tanks in... . . . . . **1070**

Rühling, K.
Integration of Renewable Energies into Cityscape **987**

Ruiz de Adana, M.
Energy Analysis Of A Solar-Driven Hybrid Air Conditioning System With An Absorption... . . . . . **566**

S

Saad, M.
Dual Axis Optimization of Solar Photovoltaic at Various Sites in Pakistan **1649**

Saars, L.
Development of a Small-Scale Plant for Electricity and Water Supply in Rural Regions... . . . . . **1970**

Saini, P.
A Novel Method for Assessing the Techno-Economical Compatibility of Solar Thermal... . . . . . **408**
A Performance Analysis of a Parabolic Trough Collector using Numerical Computation... . . . . . **1222**
Comparative Techno-Economic Analysis of High Temperature Heat Pump and Parabolic... . . . . . **456**

Salgado-Beceiro, J.
Demonstration of a Latent Heat Storage Unit Using a Pillow-Plate Heat Exchanger in... . . . . . **1338**

Sanchez Egido, M.N.
Thermal Energy Storage Capacity on Mineral Zeolite **1445**

sanfilippo, A.
Assessment of Downward Longwave Radiation Models in Clear-Sky Desert Conditions **1574**

Sanfilippo, A.
Management and Operation of Qatar's Solar Radiation Monitoring Network **1620**

Sanmarti, O.
Parametric Study of Structured Thermocline Storage Systems **1464**

Santos, D.
Numerical modeling and simulation comparisons of a cost efficient novel CPVT Solar... . . . . . **1128**

San Vicente, G.
Accelerated Ageing Test Bench for Advanced Ceramic Slabs under Extreme and Controlled... . . . . . **1495**

Sanz, A.
A PVT Driven Direct Expansion Heat Pump Field Operation Results **683**

Sauer, C.
Digital Representation of Heating Systems for Fault Detection Purposes **1711**
Fault Detection for Solar Thermal Systems: Evaluation and Improvement of Existing... . . . . . **1553**
Flow Rate Estimation In Glandless Circulator Pumps - Influence Of Temperature And... . . . . . **1543**

Sauerwein, D.
Direct Excess Heat Utilization from a High Performance Computer in an Existing Unrenovated... . . . . . **324**

Savoldi, L.
Numerical Investigation of the Performance of a Solar Air Heater Equipped with a... . . . . . **1138**

Schabbach, T.
Collector Efficiency Curves considering an Adapted Calculation Approach for Convective... . . . . . **1170**

Schäfer, M.
Optimal Conceptual Design of a Novel Façade-Integrated Adsorption Cooling System **595**

Schellhase, L.
Derivation of Heating Load Profiles on the Basis of Demand-Consumption Analyses **934**

Schett, B.
PV Driven Air Heat Pump Using Overheating Effects as Thermal Battery in Single Family... . . . . . **833**

Schiebler, B.
A TRNSYS Type for the Simulation of Temperature Limiting Heat Pipe Collectors **1717**

Schierenbeck, A.
Energy Scenarios: Designing the Renewable World of Tomorrow Together **1942**

Schlosser, F.
Modular Refurbishment of Multi-Family Houses with PVT-PCM Heat Pump Systems and Self-Learning... . . . . **715**

Schmelzer, C.
Digital Representation of Heating Systems for Fault Detection Purposes **1711**
Fault Detection for Solar Thermal Systems: Evaluation and Improvement of Existing... . . . . . **1553**
Flow Rate Estimation In Glandless Circulator Pumps - Influence Of Temperature And... . . . . . **1543**

Schmidt, D.
Low Temperature District Heating as a Key Technology for a Successful Integration... . . . . . **330**

Schrag, T.
Experimental Investigation of a Novel Hybrid Heat Pump **824**
Novel Hardware-in-the-Loop Approach for Thermal Systems **1536**

Schubert, M.
Buried Twin Pipe Model Validation for System Simulations of Ice Storage Tanks in... . . . . . **1070**

Schüler, M.
Identification of Temperature Reduction Potentials in Heating Circuits based on Measurements ***906***

Schumann, F.
A Holistic Energetic Transformation Concept for the Heating and Cooling Supply of... . . . . . ***953***

Searle, J.
A Novel Alginate/Expanded Graphite based Composite for use in Solar and Waste Heat... . . . . . ***1434***
Development of an Open System for Evaluating Material Charging Characteristics from... . . . . . ***1422***

Seco Calvo, O.
Thermal Energy Storage Capacity on Mineral Zeolite ***1445***

Seiz, M.J.
Cost-Effective Energy Balancing of Thermal Systems Based on Temperature Measurements... . . . . . ***1561***

Serag El Din, M.A.
Estimating Rooftops' Suitability for PVs Using Pleiades-1B Satellite Image for Charging... . . . . . ***965***

Serra, L.M.
Analysis of Solar Thermal Polygeneration Systems for the Residential-Commercial Sector ***97***

Sevault, A.
Demonstration of a Latent Heat Storage Unit Using a Pillow-Plate Heat Exchanger in... . . . . . ***1338***

Sharma, C.
Impact of Incentives Towards Lowering the Levelized Cost of Electricity of Concentrating... . . . . . ***1827***
Techno-Economics of Central Tower Receiver Power Plants in India: Effect of Heat... . . . . . ***1838***

Sharma, R.K.
Building Energy Efficiency Enhancement through Load Reduction in Air Conditioning... . . . . . ***98***

Shemelin, V.
Modelling and Experimental Verification of an Unglazed Metal Facade Collector Model ***1234***

Shen, W.
Comparative Analysis of the Performance of Four Different Photovoltaic-Thermal Modules ***672***

Sifnaios, I.
Effect of Design Characteristics on Pit Thermal Energy Storage (PTES) Performance ***1457***

Simón-Allué, R.
Energy Performance of Four Prototypes of PVT Collectors. A Comparative Study ***690***

Sint, S.
Comparison of the Simulated and Measured Performance of the PV Plant of Austria's... . . . . . ***894***
Data-Driven Approach Utilising Random Forest Regression for PV Performance Monitoring ***1699***

Skeie, K.S.
A Comparative Study on Solar Radiation Datasets for Photovoltaic Energy Prediction... . . . . . ***1589***

Sklarow, A.S.
Renewable Energy and PtX-Technologies in Education ***1985***

Solé, C.
Covering Energy Demands of Africa with Radiative Cooling and Solar Collection using... . . . . . ***583***

Sommer, R.
Renewable Energy and PtX-Technologies in Education ***1985***

Sommerfeldt, N.
Empirical Validation of Low-Temperature PVT Collector for Heat Pump Integration **1109**
The Life and Death of a Solar Energy Course - Lessons in Challenge Based Learning **1977**

Soutullo Castro, S.
Thermal Energy Storage Capacity on Mineral Zeolite **1445**

SRIVASTVA, U.
Numerical Investigation of Energy Absorption in Dual Metal Hydride Bed based Thermo-Chemical... . . . . . **1315**

Stahlhut, M.
Integration of Different Solar Collectors into District Heating Networks and Floor... . . . . . **340**

Stange, P.
Software-supported Investment Optimization for District Heating Supply Systems **282**

Stanica, D.
A Holistic Energetic Transformation Concept for the Heating and Cooling Supply of... . . . . . **953**

Steffenhagen, B.
Renewable Energy and PtX-Technologies in Education **1985**

Steinmaurer, G.
A Multistep Optimization Procedure for a Fair Sharing of Profits in Energy Communities **1775**

Stinson, B.
Development and Indoor Testing of a High-Performance PV/thermal (PVT) Panel with... . . . . . **1215**

Stolten, D.
The Potential of Combined PV and Air Source Heat Pump Systems in German Residential... . . . . . **738**

Storch, T.
Monitoring Results of the Energy Consumption Behaviour of Two Highly Solar-Powered... . . . . . **82**

Stricker, T.
Derivation of Heating Load Profiles on the Basis of Demand-Consumption Analyses **934**

Stürtz, S.
Modular Refurbishment of Multi-Family Houses with PVT-PCM Heat Pump Systems and Self-Learning... . . . . **715**

Sultan, R.
Renewable Energy Education: Gendered Design and Innovation in the Context of a Small... . . . . . **1929**

Summ, T.
Agri Solar Thermal Systems: A Brief Study on the Energetic Potential of Bifacial... . . . . . **1245**
Experimental Investigation of a Novel Hybrid Heat Pump **824**

T

Tadlimbekar, S.
Upgradation of Khoa Production Method in Manchar, India using Solar Thermal System **467**

Tahir, Z.u.R.
Dual Axis Optimization of Solar Photovoltaic at Various Sites in Pakistan **1649**
Gap Filling in Solar Radiation Data using Artificial Neural Network for Nine Stations... . . . . . **1657**

Taimoor, M.
An Energy Trading Model for a Lab-scale PV Microgrid in the Tunisian Context **11**

Tangellapalli, S.
Numerical Investigation and Performance Evaluation of Food Grain Drying Unit Integrated... . . . . . **1474**

Tchuenbou-Magaia, F.
Investigation of Creep-Fatigue Lifetime in Solar Photovoltaic Module Interconnections **630**

Thebault, M.
A new Framework to Evaluate the Adequation between the Solar Potential and Energy... . . . . . **1581**
Failure Risk Analysis of Photovoltaic Systems Based on Literature Review **660**

Thebault, S.
Failure Risk Analysis of Photovoltaic Systems Based on Literature Review **660**

Thür, A.
PV Driven Air Heat Pump Using Overheating Effects as Thermal Battery in Single Family... . . . . . **833**

TIWARI, V.
Numerical Investigation of Energy Absorption in Dual Metal Hydride Bed based Thermo-Chemical... . . . . . **1315**

Torio, H.
Upgradation of Khoa Production Method in Manchar, India using Solar Thermal System **467**

Torras, S.
Parametric Study of Structured Thermocline Storage Systems **1464**

Torres, J.L.
Evaluation of Angular Distribution Models to Estimate Sky Diffuse Irradiance on Tilted... . . . . . **1019**

Tosatto, A.
Heat Pumps, Photovoltaics and Energy Storage in Buildings –Load Characteristics and... . . . . . **1058**

Trabert, U.
Applying Machine Learning Methods and Outlier Detection to Process and Analyse Incomplete... . . . . . **1782**

Tremeac, B.
Implementation of Adapted Black Box Models for the Performance Characterization of... . . . . . **1678**

Trinkl, C.
Agri Solar Thermal Systems: A Brief Study on the Energetic Potential of Bifacial... . . . . . **1245**
Mini-Grid or Grid Extension? The Strategies for Electrification Schemes Concerning... . . . . . **1909**
Sustainable Housing Insulation for High-Altitude Kyrgyzstan: A Technical Guide **58**
Technical Feasibility Study of Micro-Grid Integration to Electrify Rural Settlements... . . . . . **1897**

Troi, A.
ATLAS-FeliCity: Supporting Energy Retrofit of the Heritage Building Stock Through... . . . . . **178**

Tzavaras, A.
Efficiency Evaluation and Comparisons of Solar Cell Technologies Based on Measurements... . . . . . **1747**
KNN-Based Ensembles for Day-Ahead Forecasting of Solar Power Outputs **1755**

U

ud Din, N.
Dual Axis Optimization of Solar Photovoltaic at Various Sites in Pakistan **1649**

Ullmann, J.
Accelerated Aging Test and Service Life Time Estimation for Solar Collectors **1503**
Development of a Combined Model Predictive and Adaptive Control Strategy for the... . . . . . **350**

Urbaneck, T.
Emission-Free Heat Supply of Residential Districts with Solar Thermal Energy and... **789**
Loading Slim Hot Water Tanks with and without Swirl Generation - First Results **1384**

Usman, R.
Gap Filling in Solar Radiation Data using Artificial Neural Network for Nine Stations... **1657**

V

Vachhani, A.
Identification of Waste Heat Potentials and Their Integration Into a District Heating... **884**

Vajen, K.
Applying Machine Learning Methods and Outlier Detection to Process and Analyse Incomplete... **1782**
Development of Models for Long-Term Simulations of District Heating Networks at High... **1802**
Digital Representation of Heating Systems for Fault Detection Purposes **1711**
Energy Savings for Gas Preheating in the Gas Transport Sector with Air Dehumidification... **479**
Fault Detection for Solar Thermal Systems: Evaluation and Improvement of Existing... **1553**
Flow Rate Estimation In Glandless Circulator Pumps - Influence Of Temperature And... **1543**
How To Combine a Solar Heating Plant and a CHP most Efficiently for Industrial Applications? **450**
Identification of Waste Heat Potentials and Their Integration Into a District Heating... **884**
Municipal Heat Planning to Exit from Coal, Oil and Natural Gas in a German Major... **1078**
Scenario based Heating and Cooling Load Profiles in Piglet Production Systems **436**
Solar District Heating versus Renovation of Buildings as Measures for Decarbonization... **254**
Transformation of a University Campus: Comparison of Ranking Methods for Temperature... **941**
Using Heat Maps to Assess the Energy Efficiency of Industrial Companies **420**

Varga, S.
Annual Energy Performance of a Solar/Biomass HVAC System: Experimental Characterization... **528**

Vasta, S.
Adapted Components and Show Cases on Solar Cooling Systems in Sunbelt Region Countries **504**

Vaupel, T.
Municipal Heat Planning to Exit from Coal, Oil and Natural Gas in a German Major... **1078**

Vavalos, P.
The Application of Concentrating Solar Thermal Systems in Hospital Buildings **516**

Venturi, E.
Heat Pumps, Photovoltaics and Energy Storage in Buildings –Load Characteristics and... **1058**
Modelling and Simulation of Booster Heat Pump for DHW Preparation in a Multi-Family... **1046**

Vera Fernandez, J.
Parametric Study of Structured Thermocline Storage Systems **1464**

Vérez, D.
New Concept for High Temperature Thermal Energy Storage Using a Concrete Tank **1285**

Verma, A.
Numerical Investigation and Performance Evaluation of Food Grain Drying Unit Integrated... **1474**

Vijayakumar, S.
Experiments On a Solar Vapour Absorption Refrigeration Cold Storage System **492**

Vilà, R.
Covering Energy Demands of Africa with Radiative Cooling and Solar Collection using... . . . . . **583**
Mapping Radiative Cooling Potential Predictions for Africa **1613**

Vilela, O.
A Comparison of Eight Transposition Models Applied for Different Orientations Under... . . . . . **1666**
Detection of Tracker Failures for a 2-Axis Photovoltaic System **1688**
Quality Assurance Procedure for Solar Radiation at Minute Resolution **1601**

Villa, S.
Prefabricated Renewable Energy Facades for Cost-effective Buildings (PREFAB) **702**

Villarruel-Jaramillo, A.
Hybrid Solar Thermal Field (FPC-PTC) Applied for Solar Heating and Cooling Process... . . . . . **576**

Villasmil, W.
100 % Solar Heating with Seasonal Thermal Storage, Solar Thermal Collectors, PV and... . . . . . **202**

Völker, L.
Energy Savings for Gas Preheating in the Gas Transport Sector with Air Dehumidification... . . . . . **479**

Vuillerme, V.
Data Clustering and Genetic Algorithm for the Design Optimization of a Hybrid Concentrated... . . . . . **1790**

W

Wagner, W.
Development of a Virtual Sensor for State-of-Charge Evaluation of TCM-Energy Storage **1484**

Wallner, S.
Modular Refurbishment of Multi-Family Houses with PVT-PCM Heat Pump Systems and Self-Learning... . . . . **715**

Weber, S.O.
Optimal Conceptual Design of a Novel Façade-Integrated Adsorption Cooling System **595**

Weena, B.
Impact of Domestic Hot Water Preparation Systems on District Heating Network Design... . . . . . **225**

Weiland, F.
Techno-Economical Assessment of a Solar Regenerated Borehole Heat Exchanger Field... . . . . . **360**

Weiss, k.
Accelerated Aging Test and Service Life Time Estimation for Solar Collectors **1503**

Weiss, W.
Adapted Components and Show Cases on Solar Cooling Systems in Sunbelt Region Countries **504**

Wemhoener, C.
Heat Pumps in Positive Energy Districts **1085**

Widyolar, B.
Non-Tracking Asymmetric Shadeless (NASH) Solar Collectors for Decarbonizing Industrial... . . . . . **372**

Williams, R.
A Novel Alginate/Expanded Graphite based Composite for use in Solar and Waste Heat... . . . . . **1434**

Wilson, H.
Angel-Dependent Features of MorphoColor TM Solar Collectors: Color Stability, IAM,... . . . . . **1195**

Winston, R.
Non-Tracking Asymmetric Shadeless (NASH) Solar Collectors for Decarbonizing Industrial... . . . . . **372**

WOLOSZYN, M.
Evaluation of Building Energy Performance: Comparison Before and After Envelope Retrofitting **133**

Worlitschek, J.
100 % Solar Heating with Seasonal Thermal Storage, Solar Thermal Collectors, PV and... . . . . . **202**

X

Xiao, S.
Emission-Free Heat Supply of Residential Districts with Solar Thermal Energy and... . . . . . **789**

Y

Yao, J.
Experimental Investigation on A Novel Flat-Plate Water-Based Photovoltaic-Thermal... . . . . . **1176**

Yoo, S.
Radiant Cooling System without Any Energy Input **213**

Z

Zafar, U.
Gap Filling in Solar Radiation Data using Artificial Neural Network for Nine Stations... . . . . . **1657**

Zajacs, A.
Supply Temperature Stabilization of Decentralized Solar Thermal Collectors for Integration... . . . . . **977**

Zehnder, M.
Comparison of a Centralized with Decentralized Heat Pump Systems in a Multy Family... . . . . . **748**

Zettl, B.
Development of a Virtual Sensor for State-of-Charge Evaluation of TCM-Energy Storage **1484**
Load Management for Seasonal Heat Storage Applications based on Sorption Storage... . . . . . **1295**
Sorption Test Bench for Zeolite and Salt-Composite Based Thermochemical Storage **1355**

Zhao, Y.
Comparative Analysis of the Performance of Four Different Photovoltaic-Thermal Modules **672**
Experimental Investigation on A Novel Flat-Plate Water-Based Photovoltaic-Thermal... . . . . . **1176**

Zheng, J.
Experimental Testing of a Solar Thermal Collector with composited TIM of Plastic... . . . . . **1121**

Zhu, J.
Comparative Analysis of the Performance of Four Different Photovoltaic-Thermal Modules **672**

Zipplies, J.
Development of Models for Long-Term Simulations of District Heating Networks at High... . . . . . **1802**
Solar District Heating versus Renovation of Buildings as Measures for Decarbonization... . . . . . **254**

Znouda, E.
Electric Self-production for LV Subscribers: Is It Better to Have Decentralized or... . . . . . **1857**

Znoudi, E.
Efficiency of Electricity Self-Production for Medium Voltage Subscribers in Tunisia **1876**

Zoras, S.
The Application of Concentrating Solar Thermal Systems in Hospital Buildings ***516***

Zörner, W.
Agri Solar Thermal Systems: A Brief Study on the Energetic Potential of Bifacial... . . . . . ***1245***
Mini-Grid or Grid Extension? The Strategies for Electrification Schemes Concerning... . . . . . ***1909***
Sustainable Housing Insulation for High-Altitude Kyrgyzstan: A Technical Guide ***58***
Technical Feasibility Study of Micro-Grid Integration to Electrify Rural Settlements... . . . . . ***1897***

Zsembinszki, G.
New Concept for High Temperature Thermal Energy Storage Using a Concrete Tank ***1285***
Optimal Control Based on Deep Learning Techniques for a Hybrid Solar-Biomass System... . . . . . ***1811***